

Nanotechnologies for the Life Sciences

Edited by Challa Kumar

WILEY-VCH

# Biofunctionalization of Nanomaterials



**NLS** 

## Contents

**Preface** XIII

**List of Contributors** XVII

<b>1</b>	<b>Biofunctionalization of Fluorescent Nanoparticles</b>	<b>1</b>
	<i>Michael J. Murcia and Christoph A. Naumann</i>	
1.1	Introduction	1
1.2	Fluorescent Nanoparticle Probes	2
1.2.1	Dye-doped Nanoparticles	3
1.2.2	Quantum Dots (QDs)	5
1.2.3	Metal Nanoparticles	7
1.2.4	Hybrid Architectures Involving Fluorescent Nanoprobes	9
1.2.4.1	Metal–Dye	9
1.2.4.2	Dye-doped Silica Shells	9
1.2.4.3	Quantum Dot-containing Microspheres	10
1.3	Bioconjugation of Fluorescent Nanoparticles	11
1.3.1	General Considerations	11
1.3.1.1	Overview	11
1.3.1.2	Common Coupling Reactions	13
1.3.2	Bioconjugation of Polymeric Nanoparticles	13
1.3.2.1	Noncovalent Approaches	13
1.3.2.2	Covalent Approaches	15
1.3.3	Bioconjugation of Quantum Dots	15
1.3.3.1	Noncovalent Approaches	16
1.3.3.2	Covalent Approaches	16
1.3.4	Bioconjugation of Metallic Nanoprobes	16
1.3.4.1	Noncovalent Approaches	17
1.3.4.2	Covalent Approaches	17
1.4	Design of Biocompatible Coatings	17
1.4.1	General Considerations	17
1.4.1.1	Overview	17
1.4.1.2	Colloidal Stability	18
1.4.1.3	Biocompatible Surfaces	19

1.4.1.4	Cytotoxicity	20
1.4.2	Nanoparticle-stabilizing Coatings	21
1.4.3	Low Cytotoxicity Coatings	23
1.5	Applications	23
1.5.1	Biosensing	24
1.5.1.1	Polymeric Sensors	25
1.5.1.2	Quantum Dot Sensors	25
1.5.1.3	Metallic Sensors	26
1.5.2	Fluorescent Nanoparticles as Labels in Biological Imaging	27
1.5.2.1	Dye-doped Nanoparticles	27
1.5.2.2	Quantum Dots	27
	References	29
<b>2</b>	<b>Biofunctionalization of Carbon Nanotubes</b>	<b>41</b>
	<i>Elena Bekyarova, Robert C. Haddon, and Vladimir Parpura</i>	
2.1	Introduction	41
2.2	Carbon Nanotubes – Types, Structures and Properties	42
2.3	Synthesis of Carbon Nanotubes	43
2.4	Approaches to Aqueous Solubilization of Carbon Nanotubes	47
2.4.1	Chemical Modifications	47
2.4.2	Use of Water-compatible Surfactants	47
2.4.3	Functionalization with Water-soluble Polymers	48
2.4.4	Interaction and Functionalization with Biological Molecules	49
2.4.4.1	Noncovalent Biofunctionalization	50
2.4.4.2	Covalent Biofunctionalization	52
2.5	Applications of Biofunctionalized Carbon Nanotubes	54
2.5.1	Assembly of Electronic Devices	54
2.5.2	Biosensing	58
2.5.3	Substrates for Neuronal Growth	63
2.6	Concluding Remarks	65
	Acknowledgments	65
	References	65
<b>3</b>	<b>Biofunctionalization of Magnetic Nanoparticles</b>	<b>72</b>
	<i>Yong Gao</i>	
3.1	Introduction	72
3.2	Functionalization of Magnetic Nanoparticles for <i>In Vitro</i> Protein/Cell Separation	74
3.3	Functionalization of Magnetic Nanoparticles for Biochemical/Chemical Synthesis of Therapeutic Drugs and Their Intermediates	80
3.4	Functionalization of Magnetic Nanoparticles for <i>In Vivo</i> Bio-imaging, Drug Targeting and Tumor Hyperthermia Treatments	82
3.4.1	MR Imaging	83
3.4.2	Targeted Drug Delivery	86
3.4.3	Magnetic Hyperthermia	87

3.5	Conclusions	88
	Acknowledgments	89
	References	89
<b>4</b>	<b>Biofunctionalization of Gold Nanoparticles</b>	<b>99</b>
	<i>Ming Zheng and Xueying Huang</i>	
4.1	Introduction	99
4.2	General Synthetic Routes	99
4.2.1	Direct Synthesis of Ligand-protected Au NPs	100
4.2.1.1	Strongly Ionic Ligand-protected Au NPs	102
4.2.1.2	Weakly Ionic Ligand-protected Au NPs	102
4.2.1.3	Au NPs Protected with Neutral Ligands	102
4.2.2	Ligand Exchange Reaction	103
4.3	Preparative-scale Synthesis and Solution-phase Characterization of DNA-directed Nanoparticle Assemblies	103
4.4	Bifunctional Proteins for Programmable Assembly of Nanoparticles	111
4.5	Strategies for Eliminating Nonspecific Interactions and Enabling Specific Binding with Biomolecules	113
4.6	Biological Applications	118
4.6.1	Nucleic Acids	118
4.6.2	Proteins	118
4.6.3	Cells and Virus	119
	Acknowledgments	120
	References	120
<b>5</b>	<b>Biofunctionalization of Phospholipid Polymer Nanoparticles</b>	<b>125</b>
	<i>Junji Watanabe, Jongwon Park, Tomomi Ito, Madoka Takai, and Kazuhiko Ishihara</i>	
5.1	Introduction	125
5.2	Nanofabrication for Biomedical Applications	126
5.2.1	Nano-scaled Processing	126
5.2.2	Key Materials for Nanofabrication	127
5.3	Design of Bioconjugate Nanoparticles	129
5.3.1	Bioconjugate Phospholipid Polymer	129
5.3.2	Solution Properties by Fluorescence Probe	129
5.3.3	Bioconjugate Nanoparticles	131
5.3.4	Surface Elemental Analysis by X-ray Photoelectron Spectroscopy	132
5.3.5	Surface $\zeta$ -Potential on Nanoparticles	132
5.3.6	Particle Size by Dynamic Light Scattering and Morphology by Scanning Electron Microscope	134
5.3.7	Determination of Active Ester Groups on Nanoparticles	135
5.4	Biofunction on Nanoparticles	137
5.4.1	Design of Sequential Enzymatic Reaction	137
5.4.2	Amplified Signal on Nanoparticles	138

5.5	Application for Molecular Diagnosis	139
5.5.1	Example of C-reactive Protein Detection Using Nanoparticles	139
5.5.2	High-performance Diagnosis in Serum	143
5.6	Conclusions	145
	Acknowledgments	145
	References	145
<b>6</b>	<b>Biofunctionalization of Metallic Nanoparticles and Microarrays for Biomolecular Detection</b>	<b>150</b>
	<i>Grit Festag, Uwe Klenz, Thomas Henkel, Andrea Csáki, and Wolfgang Fritzsche</i>	
6.1	Introduction	150
6.1.1	Applications	151
6.1.2	Array Fabrication	151
6.1.3	Detection Methods	153
6.1.3.1	Optical Absorbance	153
6.1.3.2	SPR Imaging	155
6.1.3.3	Raman Scattering	155
6.1.3.4	Electrical Detection	156
6.1.3.5	Electrochemical Detection	156
6.1.3.6	Gravimetric	158
6.2	Nanoparticles and their Biofunctionalization	158
6.2.1	Types of Nanoparticles used for Biomolecular Detection	159
6.2.1.1	Metal Nanoparticles	159
6.2.1.2	Core/Shell Particles	159
6.2.1.3	Magnetic Nanoparticles	160
6.2.1.4	Quantum Dots	160
6.2.2	Synthesis of Gold (Silver) Nanoparticles	161
6.2.3	Biofunctionalization	161
6.2.3.1	Modification of Gold Nanoparticles with Oligonucleotides/DNA	162
6.2.3.2	Modification of Gold Nanoparticles with Proteins	165
6.2.3.3	Biofunctionalization of other Metal Nanoparticles	167
6.2.4	Biological Applications of Gold Nanoparticles	167
6.3	Substrates and their Biofunctionalization	168
6.3.1	Molecular Thin Films	169
6.3.1.1	Self-assembly Monolayers	169
6.3.1.2	Optimization of Gold Nanoparticle-based Microarrays for DNA Detection	171
6.3.2	Nanoporous Gels	172
6.4	Outlook	175
	References	176
<b>7</b>	<b>Conjugation of Nanomaterials with Proteins</b>	<b>183</b>
	<i>Mohammed J. Meziani, Yi Lin, and Ya-Ping Sun</i>	
7.1	Introduction	183
7.2	Coupling of Inorganic Nanoparticles with Proteins	184

7.2.1	Chemical Functionalization Methods	184
7.2.2	Protein-assisted Assemblies of Inorganic Nanoparticles	188
7.2.2.1	Crosslinking Route through Protein Recognition	188
7.2.2.2	Template-directed Approach	191
7.2.3	Supercritical Fluid Methods	195
7.2.3.1	BSA-conjugated Silver Nanoparticles	196
7.2.3.2	BSA-conjugated Semiconductor Nanoparticles	197
7.2.3.3	Assembly and Disassembly of Nanoparticles through Protein Isomeric Conversion	202
7.3	Coupling of Carbon Nanotubes and Proteins	204
7.3.1	Non-specific Adsorption	206
7.3.2	Specific Conjugation and Biorecognition	211
7.4	Conclusions and Perspectives	221
	Acknowledgment	221
	References	222
<b>8</b>	<b>Stabilization and Functionalization of Metallic Nanoparticles: the Peptide Route</b>	<b>235</b>
	<i>Raphaël Lévy and R. Christopher Doty</i>	
8.1	Introduction	235
8.2	Metallic Nanoparticles – An Overview	236
8.2.1	Metallic Nanoparticles – Preparation	236
8.2.2	Metallic Nanoparticles – Optical Properties	238
8.2.3	Metallic Nanoparticles – Applications	242
8.3	Stabilization and Functionalization of Metallic Nanoparticles – The Peptide Route	248
8.3.1	Peptides, Proteins and Nanoscale Science	248
8.3.2	Peptide Toolbox for Bionanotechnology	249
8.3.3	Peptides as Capping Ligands	250
8.3.3.1	Interactions of Amino Acids with Noble Metals	250
8.3.3.2	Peptides as Reducing Agent and Template in Metallic Nanoparticle Synthesis	250
8.3.3.3	Rational Design of a Peptide Capping Ligands for Gold Nanoparticles: CALNN	251
8.3.3.4	Combinatorial Exploration of Peptides as Capping Ligands: the CALNN Family	252
8.3.3.5	Peptide-capped Silver Nanoparticles	252
8.3.3.6	Peptides as Capping Ligands for Fluorescent and Magnetic Nanoparticles	252
8.3.4	Peptide Extensions to Introduce Functionalities	253
8.3.4.1	Biotin and Strep-tag II	253
8.3.4.2	Peptide-DNA Hybrids	254
8.3.4.3	His-tag and Nickel Nitrilotriacetic Acid (Ni-NTA)	254
8.3.5	Chromatography of Peptide-capped Nanoparticles	255
8.3.5.1	Size-exclusion Chromatography	256

8.3.5.2	Affinity Chromatography	256
8.3.6	Recognition of Materials	256
8.3.7	Peptide-based Linkers	258
8.3.7.1	A Peptide-Peptide Linker Based on Leucine-zipper Sequences	259
8.3.7.2	A Peptide-DNA Linker Based on Metallopeptides	259
8.3.7.3	A Peptide-Texas Red Linker Obtained by Phage Display	259
8.3.8	Biologically Active Peptides	259
8.3.9	Self-assembling Peptides	260
8.3.9.1	Fibers and Nanotubes	260
8.3.9.2	Peptide-based Amphiphiles	262
8.4	Concluding Remarks	262
	References	263

## 9 Folate-linked Lipid-based Nanoparticles for Tumor-targeted Gene Therapy 270

*Yoshiyuki Hattori and Yoshie Maitani*

9.1	Introduction	270
9.2	Gene Delivery and Expression System	270
9.3	Nanoparticles for Gene Delivery System	271
9.4	Folate-linked Vectors	272
9.4.1	Folate Receptors	273
9.4.2	Folate Receptor-targeting Liposomes	273
9.5	Folate-linked Lipid-based Nanoparticles	277
9.5.1	Formulations	277
9.5.2	Nanoplex and Transfection Activity <i>In Vitro</i>	280
9.5.3	Selectivity of Folate-linked Nanoparticle	282
9.5.4	Transfection Activity <i>In Vivo</i>	285
9.6	Application of Suicide Gene Therapy	287
9.7	Conclusions	291
	List of Abbreviations	292
	References	293

## 10 Magnetic Core Conducting Polymer Shell Nanocomposites for DNA Attachment and Hybridization 299

*Jean-Paul Lellouche*

10.1	Introduction	299
10.2	Chemical Design of DPyr- and DCbz-containing Monomers: Introduction of Molecular Diversity	301
10.3	Synthetic Approaches for Mono- and Dicarboxylated DPyr-/DCbz-based Monomers	302
10.4	Oxidative Polymerization of DPyr-/DCbz-based Monomers around Magnetite Nanoparticles	305
10.4.1	General Considerations	305
10.4.2	Characterization of Magnetically Responsive PolyDPyr- and PolyDCbz-Magnetite Nanocomposites	307

10.5	Development of a DNA-based Biological System for Nanocomposite Parallel Screening	311
10.5.1	Covalent Attachment of an NH <sub>2</sub> -5'-modified 20-mer DNA Probe onto NCs towards DNA-Biofunctionalized NCs. Covalent Amide Bond Chemistry and Resulting NC-Supported DNA Hybridizations	313
10.5.2	Attachment of a Biotin-5'-modified 20-mer DNA Probe to DNA-biofunctionalized NCs. Quasi-covalent Linkage Using the Streptavidin–Biotin System and the Resulting NC-supported DNA Hybridizations	318
10.5.3	Storage: Medium-term Stability of Some PolyDPyr-/PolyDCbz-Magnetite NCs	320
10.6	Typical Experimental Procedures for NC Fabrication and NC-Supported DNA Hybridizations	320
10.6.1	Typical Optimized Procedures for NC Fabrication Including Magnetite Preparation	320
10.6.1.1	Magnetite Preparation Using the Oxidative Hydrolysis of Iron(II) Sulfate in an Alkaline KOH Medium	320
10.6.1.2	PolyDPyr-Magnetite Nanocomposites	322
10.6.1.3	PolyDCbz-Magnetite Nanocomposites	322
10.6.2	Covalent Attachment of an Aminated NH <sub>2</sub> -5'-modified DNA Probe. Hybridization Experiments onto PolyDPyr-/PolyDCbz-Magnetite NCs. Typical Experimental Procedures	323
10.6.2.1	Specific Reagents, Buffers and Washing/Assay Solutions	324
10.6.3	Quasi-covalent Attachment of a Biotin-5'-modified DNA Probe and DNA Hybridization Experiments onto Streptavidin-modified PolyDPyr-(5a)/PolyDCbz(5b)-magnetite NCs. Typical Experimental Procedures	324
10.7	Conclusions and Research Outlook	325
	Acknowledgments	325
	References	326
<b>11</b>	<b>Gelatin Nanoparticles and Their Biofunctionalization</b>	<b>330</b>
	<i>Sushma Kommareddy, Dinesh B. Shenoy, and Mansoor M. Amiji</i>	
11.1	Introduction	330
11.2	Gelatin and Gelatin Derivatives	331
11.2.1	Gelatin	331
11.2.2	Chemical Modification of Gelatin	332
11.2.2.1	PEGylation	333
11.2.2.2	Thiolation	335
11.2.2.3	Other Conjugates of Gelatin	335
11.3	Nanoparticulate Carriers of Gelatin and Gelatin Derivatives	337
11.3.1	Desolvation	337
11.3.1.1	Desolvation Using Ethanol	338
11.3.1.2	Two-step Desolvation	338
11.3.2	Coacervation	338



**XII** | *Contents*

11.3.3	Nano-encapsulation by Water-in-oil Emulsion Method	339
11.4	Characterization of Gelatin and Modified Gelatin Nanoparticles	340
11.5	Loading and Release of Payload from Gelatin Nanoparticles	342
11.6	Biocompatibility Studies	343
11.7	Applications of Gelatin and Modified Gelatin Nanoparticles	344
11.8	Conclusions	347
	References	348
	<b>Index</b>	<b>353</b>

## Preface

On behalf of a great team of nano researchers who have been part of this exciting project, I am pleased to introduce to the scientific community a comprehensive ten volume series on *Nanotechnologies for the Life Sciences (NtLS)*, which is going to be a knowledge base of encyclopedic proportions for applications of nanotechnologies in biology, biotechnology and medicine. This is a unique series of books on an important facet of nanotechnology being presented by the nanotechnologists for the nanotechnologists. What you have in your hand is the first volume, *Biofunctionalization of Nanomaterials*, in this exciting series.

The first volume has eleven chapters covering various aspects and techniques for functionalization of different nanomaterials with variety of biomolecules. The book begins with an exciting chapter by *Michael J. Murcia* and *Christoph A. Naumann* from the Indiana University-Purdue University, USA, which provides an overview of developments in *biofunctionalization and biocompatible coating of fluorescent nanoparticles*. There is an explosion of knowledge on carbon nanotubes, long, thin cylinders of carbon, discovered in 1991 by S. Iijima and the focus of their practical applications have been due to their unique physical properties such as optical, electrical, thermal, elastic behavior and so on. However, once it was demonstrated that it is possible to functionalize them with biomolecules, there has been a great interest amongst nanoresearchers to investigate their potential in life sciences. The University of California team of researchers from Riverside, USA, *Elena Bekyarova*, *Robert C. Haddon* and *Vladimir Parpura*, has done a remarkable job in capturing the up-to-date information in their chapter entitled *biofunctionalization of carbon nanotubes*. Metallic and metal oxide nanoparticles are well studied and their extraordinary physical and chemical properties make them useful in variety of applications. Not surprisingly, a great deal of research work was carried out to make them not only biocompatible, but also attach biological molecules in order to extend their applications into the life sciences. Four chapters have been dedicated to capture this information and the authors of these four chapters – 3, 4, 6 and 8 – have done a thorough job in comprehensively providing the information on biofunctionalization aspects of a wide variety of metallic/metal oxide nanoparticles. *Yong Guo* from the Southern Illinois University, Carbondale, USA, dealt with *biofunctionalization of magnetic nanoparticles*. *Ming Zheng* and *Xueying Huang* from DuPont Central Research and Development, USA, described some unique aspects

of *biofunctionalization of gold nanoparticles*. Grit Festag, Uwe Klenz, Thomas Henkel, Andrea Csllki and Wolfgang Fritzsche from the Institute for Physical High Technology, Jena, Germany, in a very unique fashion reviewed several approaches towards *biofunctionalization of metallic nanoparticles* for biosensing. In addition to the completely chemical based approach for biofunctionalization, Raphael Levy and Chris Doty from the University of Liverpool, UK, provided a state-of-the-art review on the use of biomolecules themselves for stabilization of metallic nanomaterials in the chapter entitled *stabilization and biofunctionalization of metallic nanoparticles: the peptide route*.

In addition to metallic nanoparticles, polymeric nanoparticles have been widely investigated for their applications in life sciences primarily in the area of drug delivery. It is again very important for the polymeric nanoparticles to be either biocompatible or biofunctionalized in order to be suitable for life science applications. *Biofunctionalization of phospholipid polymeric nanoparticles* by Junji Watanabe, Jongwon Park, Tornomi Ito, Madoku Takai, and Kazuhiko Ishihara from the University of Tokyo, Japan, provides information, based on their own research experience, on phospholipid polymeric nanoparticles and their biofunctionalization. The chapter *magnetic core conducting polymer shell nanocomposites for DNA attachment and hybridization* contributed by Jean-Paul Lellouche of Bar-Ilan University, Israel, presents an interesting perspective towards biofunctionalization of magnetic core polymer shell nanomaterials. The researchers from the Northeastern University, Boston, USA, – Sushama Kommareddy, Dinesh B. Shenoy and Mansoor M. Amiji – brought out comprehensive information on *gelatin nanoparticles and their biofunctionalization*.

Amongst all the biomolecules, proteins are unique and their conjugation to nanomaterials provides a very broad base for life science researchers. The research group from Clemson University, USA, led by Ya-Ping Sun with Mohammed J. Meziani and Yi Lin brought out an excellent in-depth analysis of various conjugation approaches to bind proteins to variety of nanomaterials in their chapter entitled *conjugation of nanomaterials with proteins*. In this chapter, they provide an overview of current and emerging approaches in the coupling of metal and semiconductor nanostructures with proteins and their assemblies into different architectures followed by approaches to conjugation of carbon nanotubes with proteins and the mechanistic issues involved with nanotube-protein interactions. The chapter entitled *folate-linked lipid based nanoparticles for tumor-targeted gene therapy* by Yoshiyuki Hattori and Yoshie Maitani, Institute of Medicinal Chemistry, Japan, contains a review of literature on folate-linked liposomes and nanoparticles, and show the effectiveness of folate-linked lipid-based nanoparticles as a vector for DNA transfection and for suicide gene therapy to treat human nasopharyngeal and prostate tumors.

I am very grateful to all the authors who have shared my enthusiasm and vision by contributing high quality manuscripts, on time, keeping in tune with the original design and theme of not only this particular volume but also the whole series. You will not be having this book in your hand but for their dedication, perseverance and sacrifice. I am thankful to my employer, the Center for Advanced Micro-

structures and Devices (CAMD), and especially to my superior, Prof. Josef Hormes, Director of CAMD, who has been supporting me in all my creative ventures. Without this backing it would be impossible to make this venture of such magnitude a reality. No words can express the understanding of my wife, Suma, in allowing me to make my office a second home and bearing with my spending innumerable number of hours in front of the computer at home. My little daughter, Saakshi, has been the source of joy and inspiration in bringing forth my intellectual creativity. My families, friends and mentors are integral part of my existence and continue to shape my life and I am indebted to them. While it would be impossible to thank everyone individually in this preface, I must make a special mention of the support from Wiley VCH publishers in general and the publishing editor, Dr. Martin Ottmar, in particular, who has been working closely with me to ensure this project becomes a reality. I am grateful for this support.

I also would like to take this opportunity to provide few glimpses of the rest of the nine volumes in this series. As I write this preface, I am pleased to let you know that the second and the third volumes are in press and will be published shortly after volume one. The second volume, *Biological and Pharmaceutical Nanomaterials*, provides information on variety of nanomaterials from natural sources and also those that are particularly relevant from pharmaceutical stand point of view. As life scientists learn about nanotechnologies, they also need to be familiarized with tools and techniques for characterization and the third volume, *Nanosystem Characterization Tools in the Life Sciences*, brings forth the required information. The rest of the volumes in this series deal in general with sensing, controlled release, devices, engineering, biomimetic approaches that are relevant to life sciences. These volumes are currently under preparation and I hope to present them to you as soon as possible.

As I stop for moment and ponder at the amount of information that the dedicated team of scientists have been compiling for this ten volume series, I can't help but become philosophical. Scientific endeavors by their very nature, while providing answers to several questions, create more and more questions. If one examines the growth of various scientific disciplines one would realize that while we made tremendous progress in scientific achievements, we continue to be puzzled by several unanswered questions in addition to several more new ones popping up every day. In the words of one philosopher, "the measure of our intellectual maturity is our capacity to feel less and less satisfied with our answers to better problems." One could say that the progress in science is directly proportional to the number of unsolved problems. It is pertinent to remember what Einstein said once, "We can't solve problems by using the same kind of thinking we used when we created them." What we need as scientists is lateral thinking. In order for developing lateral thinking one needs to comprehend the existing knowledge and develop the ability to connect seemingly unconnected points in the web of knowledge.

Nanoscience and nanotechnology is beginning to gain respectable place in this web of knowledge that we scientists have been creating. This new scientific discipline is being touted as the greatest revolution in the history of mankind and is

anticipated to positively affect every facet of our existence. It is anticipated to improve quality of our life in leaps and bounds. However, Nanotechnology's greatest gift to mankind, in my view, is its ability to promote lateral thinking amongst not only scientists but all those who are associated with this new approach to problem solving. This is what I would like to call "nano vision or nano thinking". It is the ability to think small while thinking big and to connect small and big at the same time." The followers of "nano thinking", so called "nano thinkers", are growing day by day and their presence is beginning to be felt strongly in the field of life sciences. It is my endeavor to be a catalyst in inculcating this new thinking by providing a multi-pronged base of knowledge in nanotechnologies for the life sciences. The ten volume series *NtLS* is anticipated to be the solid foundation for all those who are interested in applying "nano thinking" in life sciences. I am leaving the book in your hands and take your leave sharing a quotation from one of the greatest thinkers from the United States of America, Oliver Wendell Holmes, who said "Man's mind, once stretched by a new idea, never regains its original dimensions." It is my hope that this book series will help in stretching the limits of thinking in all those who come in contact with it.

Challa S. S. R. Kumar

# 1

## Biofunctionalization of Fluorescent Nanoparticles

*Michael J. Murcia and Christoph A. Naumann*

### 1.1 Introduction

The current revolution in life sciences is strongly linked to the availability of sophisticated new experimental tools that enable the manipulation of biomolecules and the study of biological processes at the molecular level using state-of-the-art imaging techniques, such as single molecule imaging. Optical microscopy is fundamental to furthering our understanding of the structural, organizational, and dynamic properties of biological systems because a wide variety of complementary, non-invasive optical techniques exemplified by wide-field microscopy techniques, such as brightfield, darkfield, phase contrast, and DIC exist. Among these optical detection techniques, fluorescence microscopy is particularly important because it facilitates highly sensitive and specific imaging experiments. In addition, more sophisticated imaging approaches such as confocal and near-field imaging provide the opportunity for 3D and sub-diffraction limit imaging, respectively.

Optical microscopy is now sensitive enough to track individual molecules if they are conjugated to appropriate imaging probes. Traditionally, such single molecule probes were  $\mu\text{m}$ -size colloidal particles and single fluorophores [1]. Colloidal probes such as gold or fluorescently labeled polystyrene beads are typically much larger (0.1–1  $\mu\text{m}$ ) than the biomolecule to be studied. However, fluorescent dyes, though smaller, show pronounced photo-instabilities, including blinking (due to fluorescence intensity fluctuations) and photobleaching, thus complicating single molecule tracking experiments and other fluorescence-based long-term studies. From the above description, further progress in the field of optical single molecule imaging obviously depends on the availability of appropriate labels that combine small size and high photostability with the ability to be used in multicolor studies. Fluorescent nanoparticles fulfill these important criteria. To be used in a biological environment, these nanoprobles need to be biofunctionalized appropriately, which remains a significant challenge.

The main focus of this chapter is to provide an overview of recent developments addressing the bioconjugation of fluorescent nanoparticles and their surface modification using biocompatible coatings. Section 1.2 summarizes the different types

of fluorescent nanoparticles, including dye-doped nanoparticles, quantum dots (QDs), metal nanoparticles, and  $\mu\text{m}$ -size hybrids comprising fluorescent nanoprobes. Section 1.3 describes recent developments concerning the conjugation of biomolecules to fluorescent nanoparticles, and compares the different conjugation approaches for nanoparticles consisting of polymeric, semiconductor, or metallic materials. An overview of published design architectures of biocompatible surface coatings as applied to fluorescent nanoparticles is given in Section 1.4. Finally, Section 1.5 lists representative examples of how biofunctionalized nanoprobes can be applied to problems in biosensing, as well as single cell and biological tissue imaging.

## 1.2

### Fluorescent Nanoparticle Probes

Gold nanoparticles that are surface-functionalized with proteins have been used in electron microscopy (EM) applications for quite some time [2]. A prominent example is the specific labeling of tissue by use of antibody-conjugated Au-nanoparticles (10–40 nm diameter) and their imaging by use of transmission electron microscopy (TEM). Such EM studies can achieve the detection of Au-probes with a resolution of less than 10 nm [3]. Though this demonstrates a great sensitivity, EM is limited by its inability to image living biological systems. Optical microscopy may overcome this limitation. For example, colloidal gold of 30–40 nm diameter has been used as an optical imaging label on multiple single molecule tracking experiments at the cellular level [1, and references therein]. Here, colloidal gold is used as a Rayleigh scatterer, for which the scattering  $\propto d^6$  ( $d$  = diameter), thus making tracking experiments with probe diameters of less than 30 nm extremely challenging or even impossible.

Fluorescent nanoparticles are highly attractive imaging probes because, in contrast to scattering probes, their detection is not limited by the Rayleigh scattering condition. As a consequence, fluorescent nanoprobes  $> 1$  nm can be detected if appropriate imaging setups are used. Importantly, at this size range, such nanoprobes do not exceed the size of individual proteins, thus addressing an important condition for high-quality imaging at the molecular level. In addition, single molecule detection is improved because the weak scattering of the probes lowers the optical background and thus enhances the imaging sensitivity. Figure 1.1 illustrates the size range of these probes in comparison with that of other nanoparticles. The most common types of fluorescent nanoparticles, dye-doped nanospheres and luminescent quantum dots (QDs), are described below in more detail, together with some recently introduced hybrid architectures of fluorescent nanoprobe-containing  $\mu\text{m}$ -size particles. Also included is an overview of optically active metal nanoparticles because these probes are highly relevant in single molecule spectroscopy.

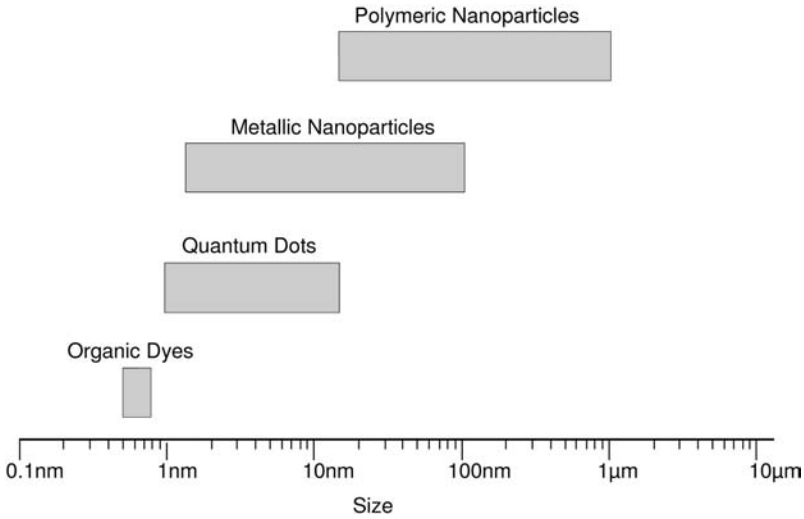


Fig. 1.1. Size ranges of commonly used fluorescent nanoprobes.

### 1.2.1

#### Dye-doped Nanoparticles

Dye-doped nanoparticles are polymer or silica-based particles containing organic or inorganic dyes [4, 5]. Dyes can be attached to the nanoparticle surface or can be embedded inside the particles either noncovalently or covalently. For imaging applications, dye-doped nanoparticles containing embedded dyes are particularly attractive because their photostability can be enhanced due to the better protection of the dyes from oxygen. For example, incorporation of pyrene dyes into polystyrene particles using a normal microemulsion approach led to a 40-fold increase in emission intensity with respect to the pure dye at the identical concentration [6]. Brightness of the fluorescence signal from such imaging probes can be controlled by the number of dye molecules per nanoparticle, with the maximum dye density limited only by self-quenching. Therefore, dye-doped nanoparticles can be quite photostable without showing fluorescence intensity fluctuations (blinking).

Typical polymer-based dye-doped nanoparticles are made of hydrophobic polymers. The hydrophobic dye molecules are kept within such nanoparticles through noncovalent hydrophobic interactions, thus preventing the gradual release and photooxidation of the dyes. Dye-doped polymeric nanoparticles have been applied down to a size of  $\sim 20$  nm [7]. Although they are reasonably photostable, the hydrophobic nature of these probes complicates imaging applications in aqueous environments, which are required for studies on biological systems. Common unwanted phenomena are clustering and non-specific binding. To overcome these problems, the hydrophobic core particles can be surface-functionalized with hydro-



philic coatings such as polymers like poly(ethylene glycol) (PEG), polysaccharides such as dextran, or proteins such as bovine serum albumin (BSA).

Dye-doped silica nanoparticles are attractive imaging probes because their hydrophilic nature reduces the problems of non-specific binding and clustering. Silica shows several additional properties beneficial for optical imaging applications in biological systems, including chemical inertness, transparency, and the ability to act as stabilizers in protecting the embedded dyes from the outside environment [4]. In addition, the surface hydroxyl groups can be chemically modified, allowing for the straightforward surface modification with amines, carboxyls, or thiols. In addition, pH changes do not lead to swelling and porosity changes, and silica particles are less prone to attack from microbes [8]. However, the incorporation of hydrophobic dyes into the hydrophilic silica matrix is challenging, requiring specific modifications of either the dye molecules or the silica. For example, dyes can be modified with a hydrophilic molecule such as dextran or a hydrophobic silica-precursor can be used during nanoparticle synthesis [9]. Dye-doped silica particles were first synthesized using the Stoeber method [10]. However, this method leads to polydispersity and average particle sizes of  $>100$  nm. More recently, these limitations have been overcome by use of a reverse microemulsion method that can create monodisperse dye-doped silica particles down to a size of 15 nm (Fig. 1.2) [11]. Notably, this elegant approach facilitates the size-tuning via adjustment of the microemulsion composition and does not require elevated temperatures and pressures [11, 12]. Silica also has been used to create hollow silica nanospheres filled with dye molecules [13].

Rare-earth-doped  $\text{LaPO}_4$  nanoparticles are another interesting class of nanoprobes that show promising properties for diagnostic and imaging applications [14]. These systems combine small size ( $<10$  nm), high chemical stability, very good quantum yield, and high photostability. Furthermore, they are expected to show low cytotoxicity. Recently, such rare-earth-doped  $\text{LaPO}_4$  nanoparticles were successfully surface-functionalized to allow their subsequent coupling to biomole-

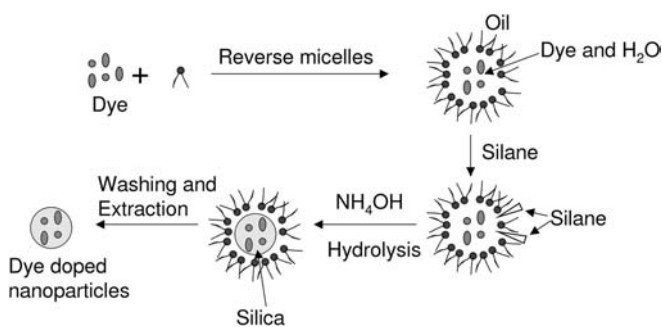


**Fig. 1.2.** Schematic of the reverse microemulsion method for the synthesis of dye-doped silica nanoparticles (adapted from Bagwe et al., 2004) [11]. In this method, nm-sized water droplets, which are stabilized by

surfactant molecules, are formed in a continuous oil phase, thus forming a thermodynamically stable oil–water–surfactant microemulsion.

cules [15]. The nanoparticle surface was first functionalized with aminohexanoic acid and then linked to avidin using EDC coupling.

### 1.2.2

#### Quantum Dots (QDs)

Nanocrystals based on semiconductor materials began attracting the interest of physicists three decades ago because of their interesting quantum properties. These properties are the result of size-dependent band gaps, which cause the color emitted by a semiconductor nanocrystal of a specific composition to be a function of its diameter. Physically, quantum properties (in this case a size-dependent fluorescence emission) are expected to occur if electron–hole pairs (excitons) are confined to dimensions that are smaller than the electron–hole distance (exciton diameter) [16–19]. As a result of this condition, the state of free charge carriers within a nanocrystal is quantized and the spacing of the discrete energy states (emission colors) is linked to the size of the nanoparticle. It is this quantum confinement effect that led to the term “quantum dot”.

Quantum dots can be based on metallic or semiconductor materials. Most widely used are CdSe and CdTe quantum dots because their quantum confinement region spans the entire optical spectrum. More recently, there has been growing interest in quantum dots with near-infrared emission properties, such as CdTe/CdSe, InAs, or PbS (which are of use in animal imaging studies) [20, and references therein]. In addition, several groups have studied silicon nanocrystals [21–23]. Quantum dots also show other fascinating optical properties, including broad absorption and narrow emission bands, which allows a single laser to excite dots of a wide size-range, with each dot emitting its own specific color. This is in contrast to organic-based fluorophores, which are characterized by narrow Stokes shifts (difference between maximum wavelengths of absorption and emission bands). To protect their surface from photobleaching, quantum dots can be passivated by use of a higher-bandgap semiconductor shell or an organic layer [24]. In fact, successfully passivated, quantum dots show dramatically enhanced photostability, enabling their long-term observation in optical experiments [25]. Furthermore, quantum dots can be brighter than their dye counterparts at an equivalent quantum yield [26] because of their notably higher extinction coefficients [20]. Given the above properties, quantum dots bring fascinating possibilities for single molecule cellular imaging studies because they combine small size, broad absorption, narrow size-tunable emission (covering the entire optical spectrum), and excellent photostability. These features outperform traditional fluorescent dyes in many respects.

The traditional approach to synthesizing quantum dots relies on heating specific organic solvents and injection of semiconductor precursors. In a typical preparation [27], Cd(CH<sub>3</sub>)<sub>2</sub> and elemental Se are combined with trioctylphosphine oxide (TOPO), which acts as a solvent and stabilizing agent. This mixture is subjected to high temperature (about 350 °C) for 24 hours at which time the mixture is cooled and Zn(CH<sub>3</sub>)<sub>2</sub> and S(SiMe<sub>3</sub>)<sub>2</sub> added to form a stabilizing ZnS shell. To cre-

ate nanocrystals of a narrow size distribution, an additional size-selective precipitation step needs to be included. Because dialkylmetal compounds are very sensitive to oxygen and water and become pyrophoric upon exposure to air, alternative approaches of quantum dot synthesis have been explored. Consequently, CdSe quantum dots can be formed using CdO, selenium, and hexylphosphonic acid or tetradecylphosphonic acid [28]. This synthesis reduces the reaction times to less than 30 min, but still uses temperatures upwards of 300 °C. In another example, our group has synthesized CdSe/ZnS quantum dots by use of sonochemistry [29]. This low-temperature approach not only produces spherical high-quality quantum dots with quantum yields of up to 70% and emission bands of less than 50 nm (FWHM), but also allows for straightforward control of the synthesis parameters. Figure 1.3 shows the photoluminescence spectra of CdSe core quantum dots and

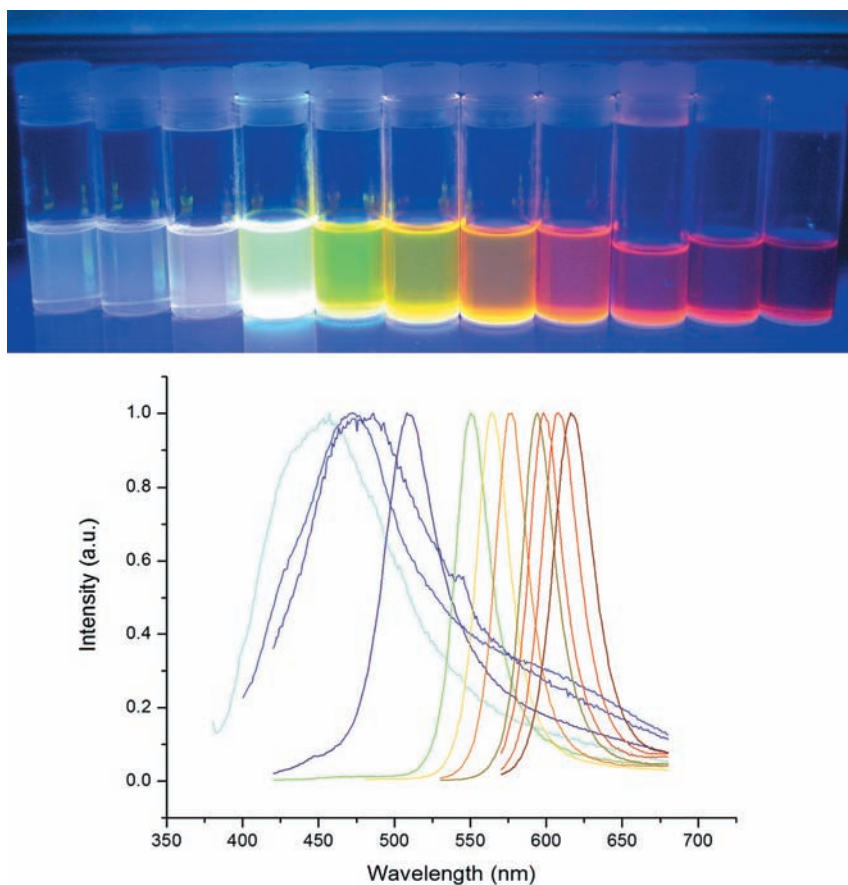


**Fig. 1.3.** Quantum dots show size-tunable emission properties. The samples represent different sizes of quantum dots, which produce different colors upon UV light. Within the quantum confinement region, an increase in particle sizes produces a redshift in the emission spectrum. Spectra and photograph were obtained from CdSe quantum dots synthesized sonochemically [29].

the colors of these samples upon UV illumination, which are representative of this procedure.

To be of use in biological imaging applications, quantum dots need to be water-soluble. Indeed, synthetic approaches for CdTe [30–32] and CdS [30, 33–38] have utilized aqueous solvent conditions. However, these nanocrystals usually lack the quantum yield and narrow size distribution observed for TOPO-synthesized quantum dots. TOPO-stabilized quantum dots, however, show hydrophobic surface properties. To disperse TOPO-stabilized quantum dots in aqueous solution, several surface modification strategies have been pursued (Fig. 1.4). A common approach is to synthesize quantum dots in TOPO and replace the hydrophobic TOPO layer with bifunctional molecules containing thiol and hydrophilic moieties separated by a molecular spacer (Fig. 1.4: approach I) [39, 40]. The thiol groups bind to the CdSe or ZnS surface, while the hydrophilic moieties radiate from the surface of the corresponding semiconductor. Unfortunately, thiols bind less strongly to ZnS than to Au, which leads to a dynamic equilibrium between bound and unbound thiols. This behavior reduces the long-term water solubility of ZnS-capped quantum dots. To shift the equilibrium towards bound moieties, monothiols have been replaced with molecules containing more than one thiol group (Fig. 1.4: approach II) [41–43]. Another stabilization concept is to enhance binding via surface cross-linking of bound molecules. On the basis of this concept, ZnS-shelled quantum dots have been made water-soluble by adding a silica shell to the nanoparticles by using alkoxysilanes during the polycondensation (Fig. 1.4: approach III) [44–48]. Two types of silanes have been used to stabilize quantum dots in aqueous solution. The first includes silanes whose surface functional groups are positively or negatively charged at neutral pH [48]. The second type includes silanes with poly(ethylene glycol) chains [48, 49]. TOPO-coatings also can be made water-soluble without their replacement by adding amphiphilic molecules such as lipopolymers or amphiphilic diblock copolymers, whose hydrophobic moiety stabilizes the TOPO-coating via hydrophobic forces and whose hydrophilic moiety is exposed to the solvent environment, guaranteeing water-solubility (Fig. 1.4: approach IV). The last approach has the advantage of not exposing the sensitive surface of the quantum dot during a surface exchange step.

### 1.2.3

#### **Metal Nanoparticles**

In contrast to noble metals in bulk, nanoparticulate forms of such materials result in interesting photochemical and electronic properties [50]. Three strategies have been pursued to study the photochemical activity of metal nanoparticles: (a) direct excitation of the metal nanoparticles; (b) indirect excitation of the metal nanoparticles via surface-conjugated dye molecules; and (c) photocatalytic processes in semiconductor–metal nanocomposites [50]. After excitation with UV or visible light, metal nanoparticles show several interesting phenomena, including photoluminescence [51–53], nonlinear optical phenomena [54, 55], and surface-enhanced

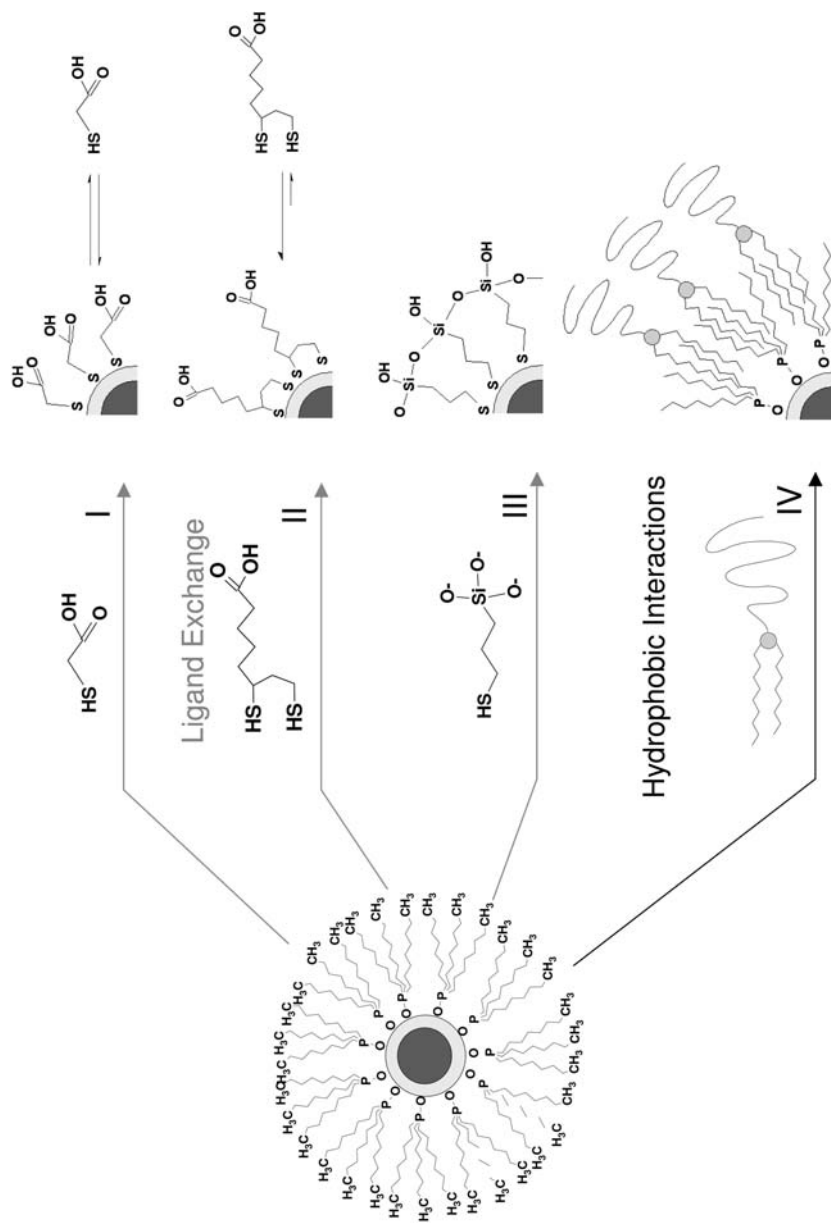


**Fig. 1.4.** Schematic representation of four common approaches to hydrophilic surface modification of TOPO-stabilized quantum dots. Approach I: TOPO replacement with a heterofunctional linker consisting of a thiol end group, a spacer, and a hydrophilic end group such as carboxylic acid. II: TOPO replacement with a linker consisting of two thiol groups on one end and a hydrophilic end group on the other end. Approach III: TOPO replacement with a silane forming a stable shell via crosslinking. Approach IV: Stabilization of TOPO layer using amphiphilic molecules such as PEG lipopolymers or amphiphilic diblock copolymers that are held on the surface by hydrophobic interaction with the octyl chains of TOPO.

Raman scattering (SERS) [56–61]. Due to the significant field enhancement, SERS can be used as an extremely sensitive analytical tool, thereby exceeding the sensitivity from luminescence-detecting techniques. For example, biomolecules can be detected with 1000-fold better sensitivity if they are bound to Au nanoparticles [62]. Silver nanoparticles also are useful in this respect. The main experimental challenge in SERS is to keep the surface roughness uniform and reproducible.

There are multiple strategies for synthesizing metal nanoparticles [50]. For example, they can be synthesized using a biphasic reduction approach [63–69]. In this procedure, a noble metal salt such as  $\text{HAuCl}_4$  is dissolved in water and phase-transfer extracted into an organic solvent followed by reduction with  $\text{NaBH}_4$ . Metal nanoparticles also have been synthesized using reverse micelle procedures where the size and size distribution of nanospheres can be controlled by the micelle composition [12, 70–73]. Gold nanoparticles are particularly attractive for studies in a biological environment because they show no surface oxidation and high biocompatibility without any surface modification. In addition, thiol chemistry can be applied to conjugate molecules to the gold surface.

#### 1.2.4

### Hybrid Architectures Involving Fluorescent Nanoprobes

#### 1.2.4.1 Metal–Dye

Another interesting application of metal nanoparticles is their use in combination with conjugated dye molecules (Fig. 1.5). Such hybrid systems are attractive because they can be studied by use of electron microscopy in addition to fluorescence-based techniques such as fluorescence microscopy and spectroscopy. Importantly, if conjugated to biomolecules, metal nanoparticle–dye hybrids can be used as very sensitive biomolecular imaging probes [74, 75]. Interestingly, dye molecules attached to metal nanoparticles can show enhanced emission. For example,  $\text{Py-CH}_2\text{NH}_2$  molecules bound to gold particles show pronounced emission that is much stronger than that for unbound  $\text{Py-CH}_2\text{NH}_2$  in THF [50]. The main disadvantage of this approach is that the surface-exposure of the dyes promotes their photooxidation.

#### 1.2.4.2 Dye-doped Silica Shells

To reduce photooxidation, dyes also can be embedded within the nanoparticle. As illustrated in Fig. 1.5(B), dyes can be incorporated into a nanoparticle-capping silica shell. For example, up to 12 alternating fluorescent and nonfluorescent silica shells have been added to silica core particles, where the shells were doped with six dyes of different emission wavelengths. Dyes of multiple colors have been incorporated previously in silica beads throughout the matrix of the particle [76], but not in an ordered fashion [77]. This multi-shell approach helps to reduce unwanted energy transfer. As a multiplexing probe, the system is not as simple to analyze as a quantum dot-based one. Re-absorption of the fluorescence emission,

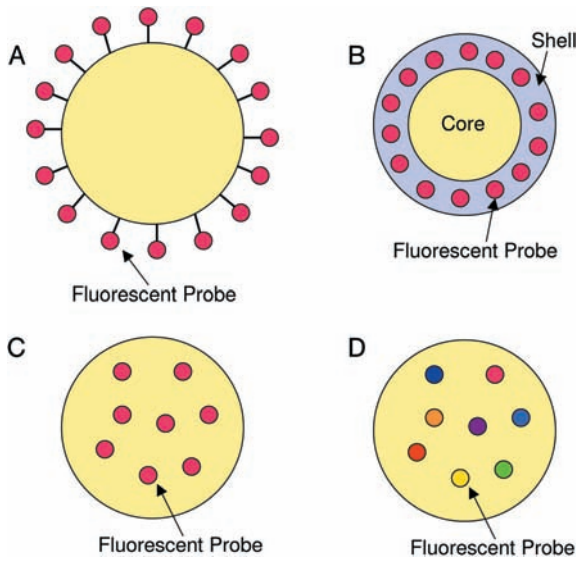


**Fig. 1.5.** Common hybrid architectures containing fluorescent nanoprobables include (A) dyes bound to a nanoparticle surface; (B) dyes incorporated into the silica shell of a nanoparticle; (C) fluorescent probes such as quantum dots or dyes incorporated into the core of microparticles; and (D) a multiplexing approach by embedding probes of different colors.

which is related to the identity of the fluorophore, alters the emission intensity. As a result, it is difficult to determine the possible number of spectral combinations in a designed system, and a flow cytometer must be used to identify the number of individual species in the mixture. This shelling approach has also been reported for single dye systems for enhanced fluorescence [10].

#### 1.2.4.3 Quantum Dot-containing Microspheres

An interesting hybrid architecture that has been developed recently is the quantum dot embedded microsphere. Unlike a dye embedded polymeric bead, the quantum dot microbeads utilize the narrow emission of quantum dots combined with their broad absorption characteristics to perform multicolor detection experiments with one excitation wavelength [78–81]. By incorporating up to six different colors of quantum dots and ten intensities of those colors, the quantum dot microbeads can, theoretically, optically “bar code” biomolecules with one million possible spectral signatures. Realistically, the number is likely to be substantially lower due to spectral overlap, fluorescence intensity variations, and signal-to-noise requirements. The multiplexing approach has been tried with organic dyes, but was limited to two colors due to spectral overlapping and the inability to excite more than two or three dyes with the same wavelength [82].

## 1.3 Bioconjugation of Fluorescent Nanoparticles

### 1.3.1 General Considerations

#### 1.3.1.1 Overview

To apply fluorescent nanoparticles to biosensing and biomedical imaging applications, it is crucial to develop strategies towards their biofunctionalization. These include the proper linkage of biomolecules to nanoparticles (bioconjugation) and the design of appropriate biocompatible coatings. This section outlines the different aspects of bioconjugation, and Section 1.4 provides a corresponding discussion of biocompatible coatings.

Bioconjugation can be described as any procedure that links a nanoparticle to a biomolecule under mild conditions [83]. As described above, the synthesis of nanoparticles often does not render them capable of attachment to biomolecules, because their surface-chemical properties are not appropriate. Therefore, nanoparticles frequently must undergo surface transformations to create the chemistry needed for coupling to biomolecules under mild (physiological) conditions. There are a few key requirements for successful bioconjugation reactions [4]. Crucially, the conjugation process must avoid compromising the activity of biomolecules. In addition, the bioconjugation ideally should not hinder the signal of the nanoparticle. Another requirement is the ability to control the number of linkage sites on the nanoparticle surface where biomolecules can bind. This requirement can be quite challenging. In addition, the biomolecule–nanoparticle coupling should be stable and, for crystalline particles, the surface should be covered to avoid free valence states. Finally, the thickness of any nanoparticle shell should remain as small as possible relative to the nanoparticle size.

Figure 1.6 illustrates several possible strategies to bioconjugate nanoparticles. Simple adsorption of biomolecules to the nanoparticle surface via noncovalent forces represents the least demanding approach (Fig. 1.6A). However, in this case, the activity of bound biomolecules may be compromised and the amount of bound biomolecules per nanoparticle is difficult to control. In addition, this bioconjugation approach does not target one protein preferentially. Another concept is based on the physisorption (noncovalent coupling) of biomolecules to molecules (e.g., other biomolecules) acting as mediators between biomolecule and nanoparticle surface (Fig. 1.6B). This design may be advantageous over the first one, because it may help biomolecules to bind in a proper orientation. Figure 1.6(C) is based on the chemical coupling between reactive groups of biomolecules (e.g., thiols and primary amines) and crosslinker molecules. These crosslinkers may bind to the nanoparticle surface via physisorption or chemisorption (covalent coupling). However, there are frequently multiple active sites on the target biomolecule to which the probe can bind, thus preventing controlled binding. Furthermore, uncontrolled



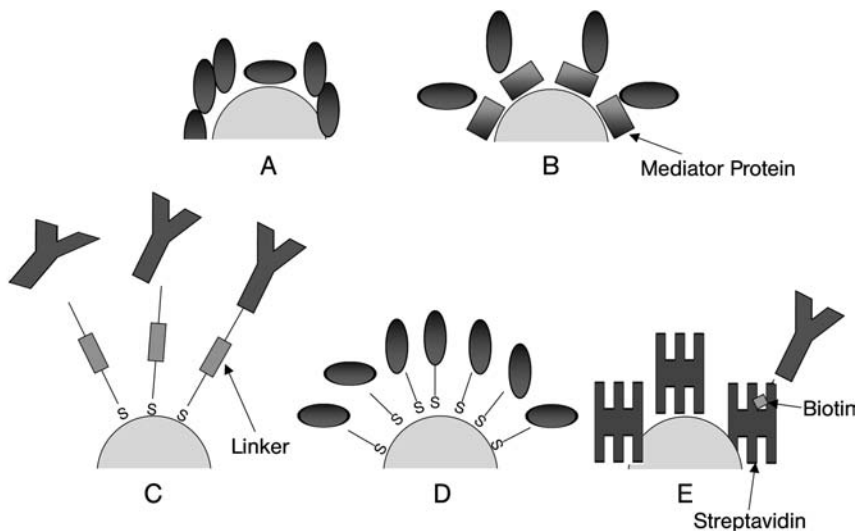


**Fig. 1.6.** Common strategies for the conjugation of biomolecules to nanoparticles include direct physisorption of biomolecules (A), assisted physisorption using pre-bound molecules (B), chemical linkage of biomolecules to crosslinkers either physisorbed or

chemisorbed on the nanoparticle surface (C), direct chemical coupling of biomolecules to nanoparticles (D), and the targeted binding of biotinylated biomolecules to streptavidin-coated nanoparticles via biotin–streptavidin coupling (E).

binding may interfere with the biologically active sites of biomolecules. To overcome this limitation, a ligand (typically an antibody) can be bound to the nanoparticle via the crosslinker. This ligand then facilitates coupling to the biomolecule of interest with high specificity. These crosslinker-based bioconjugation strategies are best executed if appropriate heterobifunctional crosslinkers are used. A large variety of such crosslinker molecules is now commercially available. Alternatively, homobifunctional crosslinkers can be used where one reactive end group is protected. Here, nanoparticle and biomolecule are coupled by binding of the partially protected linker to either nanoparticle or biomolecule and by deprotecting the linker prior to bioconjugation. Unprotected homobifunctional crosslinkers are always problematic because they can induce the clustering of nanoparticles. Figure 1.6(D) shows a facile approach for the chemical coupling of biomolecules to nanoparticles. This approach is particularly useful for attaching oligonucleotides to nanoparticles, e.g., via mercapto groups [84–86]. Still, control over the number of bound biomolecules per nanoparticle remains a challenging endeavor. To achieve such control, a separation step, such as nanoparticle separation using gel electrophoresis, must be added [87]. Another popular approach is to link biotinylated ligands or target biomolecules to streptavidin (or avidin)-functionalized nanoparticles with high specificity (Fig. 1.6E). In this case, the biotin-binding proteins, avidin or streptavidin, act as linker molecules [88, 89].

### 1.3.1.2 Common Coupling Reactions

The bioconjugation of nanoparticles is critically dependent on the availability of effective covalent coupling procedures. Figure 1.7 lists the most common coupling procedures. The reaction between primary amine and carboxylic acid groups is a very popular coupling procedure (Fig. 1.7A). In a first step, a carboxylic acid reacts with 1-ethyl-3-(3-dimethylaminopropyl)carbodiimide (EDAC) and *N*-hydroxysulfosuccinimide (NHS) to form an acyl amino ester that subsequently reacts with the primary amine to create a stable amide bond. This approach also is attractive because preparation of the ligands is less demanding. A widely used approach is based on the reaction between thiol and maleimide groups (Fig. 1.7B). This affords a stable thioether bond, typically with good yield at physiological pH. Most prominently, this reaction can be used to directly link maleimide-functionalized ligands to thio-groups of proteins. If no thiols are available, they can be created by using heterobifunctional crosslinkers with one thiol endgroup or by reducing disulfide bonds within the target protein. The coupling of two thiols to form a disulfide linkage is another straightforward reaction approach (Fig. 1.7C). Unfortunately, the resulting disulfide bond is relatively labile in biological fluids like serum. Another useful reaction scheme is based on the covalent linkage between aldehyde and hydrazide groups to form a hydrazide bond (Fig. 1.7D). Reactive aldehyde groups can be created by oxidation of carbohydrate groups. Obviously, mild oxidation conditions have to be used for the oxidation reaction on relatively unstable molecules like antibodies. Chemical reaction between two primary amines is another approach for bioconjugation applications (Fig. 1.7E). In this case, coupling can be achieved using homobifunctional crosslinkers such as glutaraldehyde [90, 91].

## 1.3.2

### Bioconjugation of Polymeric Nanoparticles

From a bioconjugation perspective, polymeric nanoparticles are attractive because they can be prepared with various different reactive groups on their surface. The obvious benefit is that a comparably broad spectrum of conjugation chemistry approaches can be used, including covalent and noncovalent ones (Fig. 1.6). These different bioconjugation strategies are reviewed below.

#### 1.3.2.1 Noncovalent Approaches

One of the most widely applied approaches in bioconjugating polymeric nanoparticles is simple physisorption of the biomolecules on the particle surface (Fig. 1.6A) [93–97]. Because biomolecule activity is compromised by uncontrolled adsorption, spacer molecules have been introduced (Fig. 1.6B). For example, nanoparticles first coated with Protein A (isolated from the cell wall of *Staphylococcus aureus*), which attaches specifically to the Fc fragment of the IgG antibody, have proper Fab orientation for antibody binding [97]. Unfortunately, such simple adsorption approaches are only of limited use when applied in serum. This is because serum proteins compete with antibodies for adsorption sites [93–95]. Furthermore, *in vivo* experiments have revealed that such simply designed nanoparticles tend to accumulate



in the liver and spleen. Using a similar design strategy, polystyrene nanoparticles have been functionalized with humanized mAb HuEP5C7.g2 [98]. These delivery systems target cells expressing E and P-selectin.

### 1.3.2.2 Covalent Approaches

Obviously, the activity of ligands bound to nanoparticles strongly depends on the stability of the ligand–nanoparticle linkage and the proper orientation of the ligand. To address these needs, ligands have been bound covalently to polymeric nanoparticles using several different conjugation approaches (Fig. 1.6E) [7, 99–102]. For example, an amide linkage strategy was pursued to bind lactose to the poly(vinylamine)-grafted nanoparticles [99]. Such lactose-functionalized carrier systems are useful because they specifically bind to lectin RCA<sub>120</sub>. The same amide-based linkage chemistry was used to bind proteins to dye encoded latex particles [7]. In another approach, transferrin was conjugated to PEG coated poly(cyanoacrylate) nanocrystals, with the transferrin bound to PEG via periodate oxidation [100]. A heterobifunctional linker was used to bind antibodies to BSA-containing nanoparticles [101, 102]. In this case, the crosslinker (glutaraldehyde) was bound to BSA to provide free aldehyde groups, which could then be linked to the primary amines of the antibodies. Another interesting strategy is based on formation of ligand-carrying nanoparticles via polymerization of monomers with bound ligands. Such a strategy has been applied to create nanoparticles with biotin groups, which then allowed for specific linkage to avidin [103, 104]. The grafting of carbohydrates to poly(L-lysine) was also reported [105]. This carrier can bind to carbohydrate-binding proteins on the surface of target cells.

### 1.3.3

#### Bioconjugation of Quantum Dots

Though quantum dots are very small, their surface area is large enough for linking to multiple biomolecules [106]. There are several ways to bind biomolecules to quantum dots. These involve either direct binding to the quantum dot surface or attachment via a stabilizing layer acting as a crosslinker between the ligand and reactive surface of the nanoparticle. In the first case, ligand binding can be achieved covalently or noncovalently. Direct covalent coupling is accomplished commonly by use of thiol coupling chemistry, although a silane-based coupling is needed if quantum dots carry a stabilizing silica shell. Noncovalent ligand-quantum dot coupling, however, is typically pursued using electrostatic or hydrophobic forces. On the basis of these general concepts, several bioconjugation strategies have been pursued. These are discussed below.

**Fig. 1.7.** Commonly used chemical reactions in the bioconjugation of fluorescent nanoparticles. Shown are the coupling chemistries between (A) carboxylic acid and primary amine, (B) thiol and maleimide

groups, (C) two thiols to form a disulfide bond, (D) hydrazide and aldehyde groups, and (E) two primary amines. (Adapted from Nobs et al., 2004 [92].)

### 1.3.3.1 Noncovalent Approaches

An electrostatic coupling approach has been applied to link negatively charged CdTe quantum dots and positively charged enzymes [107]. Electrostatic coupling also was pursued in several applications to bind positively charged protein domains (pentahistidine segment) to oppositely charged alkyl-COOH-capped quantum dots [31, 42, 88, 108–112]. An alternative electrostatic-based coupling strategy has been used to bind nanocrystals coated with trimethoxysilylpropyl-urea and acetate groups with high affinity in the cell nucleus [44]. Here the binding of the silanized nanocrystal surface is controlled with an anionic silane reagent. Negatively charged quantum dots have also been electrostatically bound to positively charged Maltose Binding Protein [113]. Quite often, adsorbed proteins show a stabilizing effect on the quantum dot surface, thereby improving the optical properties of the probes. For example, a two-fold increase in fluorescence was observed after adsorption of 10–15 Maltose-Binding Protein Pentahistidine (MBP-5HIS) to the quantum dot surface [114].

### 1.3.3.2 Covalent Approaches

A relatively straightforward covalent bioconjugation approach is based on the replacement of thiol acids present on the quantum dot surface with thiolated biomolecules. This strategy has been used to attach oligonucleotides, DNA [41, 84] and bovine serum albumin (BSA) [86] to quantum dots. Proteins also have been conjugated to quantum dots by reacting carboxylic acid groups on the nanoparticle surface with amine groups of the proteins [115]. A similar strategy was used to covalently attach IgG and streptavidin to quantum dots. The IgG system was applied as a cancer marker, whereas the streptavidin system was utilized for labeling actin, microtubules and the cell nucleus [116].

In another application, antibodies have been bound to quantum dots via sulfo-NHS crosslinking [117]. In a different approach, reactive biotin was covalently linked to either surface sulfhydryl or amine functionalities, thus allowing for the biotinylation of the quantum dot surface and the subsequent binding to streptavidin [44]. A biotin–streptavidin coupling approach was chosen, for example, to bind quantum dots to fibroblasts [44]. In this case, the nanocrystals were functionalized with biotinamidocaproic acid 3-sulfo-*N*-hydroxysuccinimide ester and then allowed to bind to fibroblasts previously incubated with phalloidin–biotin and streptavidin. A combination of covalent and noncovalent coupling strategies was pursued by conjugating quantum dots stabilized with amphiphilic PEG lipids to DNA. Here, the DNA coupling was achieved by replacing  $\frac{1}{2}$  of the PEG-PE phospholipids with amino PEG-PE. Thiol modified DNA was then covalently coupled to the amines on the surface of the quantum dot [118].

### 1.3.4

#### Bioconjugation of Metallic Nanoprobes

Most conjugation concepts described for the linkage of ligands to quantum dots can also be applied to metal nanoparticles, such as Au or Ag nanoprobes. Again,

surface modification is accomplished using thiol-coupling chemistry. The binding of biomolecules to these nanoparticles can be covalent or noncovalent. With respect to biofunctionalization, gold nanospheres are particularly attractive because gold shows excellent biocompatibility properties, and does not require additional surface chemical modification prior to bioconjugation. In addition, gold nanoparticles can be made with very narrow size distribution. This is advantageous if accurate control of the number of bound biomolecules per nanoparticle is required.

#### 1.3.4.1 Noncovalent Approaches

One option for bioconjugation is the direct attachment of a biomolecule to the metallic nanoparticle surface. Short peptide chains such as tiopronin [119] and the tripeptide glutathione [120] have been conjugated directly to a gold surface. Globular proteins have also been directly conjugated. Miziani et al. conjugated globular proteins directly to the surface of silver sulfide nanoparticles [121]. In another application, gold nanoparticles were coated with BSA via electrostatic interactions under mild conditions [122]. Due to the bioinertness of gold, biomolecules directly bound on the gold surface can retain their activity, as shown, for example, for redox enzymes [123] and cytochrome c [124]. Biotin–streptavidin coupling concepts have also been used. For example, disulfide-modified biotin was conjugated to gold nanoparticles and subsequently reacted with streptavidin [125].

#### 1.3.4.2 Covalent Approaches

Direct coupling of biomolecules to the surface of metal nanoparticles represents a very facile bioconjugation strategy. Among the different metals, this conjugation strategy is best suited for gold because of its excellent bioinertness. For example, thiol-modified DNA has been conjugated directly to gold particles [74, 126–128]. Direct thiol coupling was also pursued to conjugate SH modified PEG to gold-shelled silica nanoparticles [129]. Covalent bioconjugation to the nanoparticle can also be mediated by heterobifunctional crosslinker molecules. One example is the surface modification of iron oxide nanoparticles with a trifluoroethylester-terminal poly(ethylene glycol) (PEG) silane and the subsequent coupling of biomolecules via their terminal amine or carboxyl groups [130].

## 1.4

### Design of Biocompatible Coatings

#### 1.4.1

##### General Considerations

##### 1.4.1.1 Overview

Though multiple bioconjugation strategies have been worked out, the routine application of fluorescent nanoparticles in biomedical imaging remains challenging. This is largely because not only appropriate conjugation between biomolecules to nanoparticles is required but other important criteria concerning biocompatibility

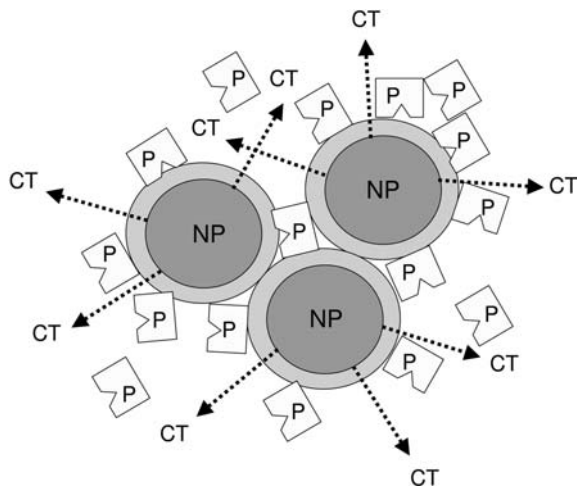


**Fig. 1.8.** Potential problems compromising the biocompatibility of fluorescent nanoparticles, including nanoparticle (NP) clustering, non-specific adsorption of proteins (P), and release of cytotoxic ions (CT).

have to be fulfilled. These criteria include (a) prevention of nanoparticle aggregation in a biological environment, (b) effective suppression of non-specific adsorption of biomolecules at the nanoparticle surface or their accumulation close to the surface, and (c) low cytotoxicity (Fig. 1.8). To address these criteria, nanoparticles need to be capped with protective coatings that show passivating surface properties. Notably, the first criterion, good colloidal stability, does not guarantee the biocompatibility of nanoparticles as, firstly, ions and proteins may be accumulated on or near the nanoparticle surface, thus varying the complex molecular composition nearby. Secondly, especially with heavy metal-containing quantum dots (e.g., CdSe, CdTe), individual nanoparticles may remain cytotoxic if the coating does not protect the biological environment from released heavy metals ions.

#### 1.4.1.2 Colloidal Stability

The dispersion stability of nanoparticles is well-described by the Derjaguin–Landau–Verwey–Overbeek (DLVO) theory, which predicts that such stability is determined by the balance between attractive van der Waals and repulsive electrostatic forces. As a result, nanoparticles are expected to remain stable (show no particle aggregation) if the strength of the repulsive electrostatic force exceeds that of the attractive van der Waals (vdW) force. In other words, nanoparticles show no aggregation if they contain a sufficient density of surface charges. Indeed, particles with charged surface properties do not aggregate in ion-free solutions. At the same time, this balance can clearly be shifted in favor of vdW forces if the charges on the particle surface are screened by counter ions in the solution. This is an important aspect to consider during chemical surface modification, because such

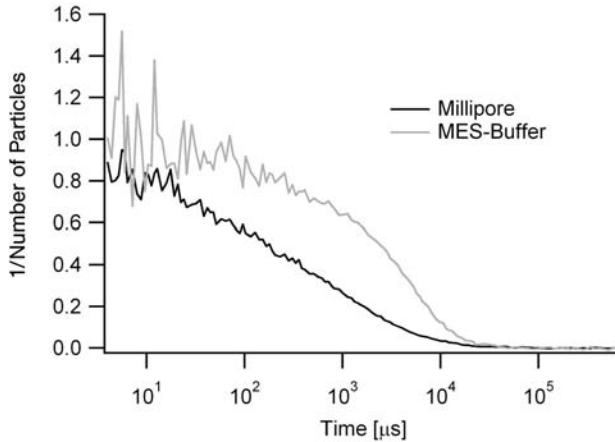


**Fig. 1.9.** Fluorescence correlation spectroscopy autocorrelation curves of ZnS-capped CdSe quantum dots surface-functionalized with carboxylic acid in Millipore water (dark curve) and 10 mM MES buffer (lighter curve). The notably higher diffusion time obtained for the buffer-based system indicates nanoparticle clustering.

modifications may result in surface charge neutralization, thereby compromising dispersion stability. More importantly, nanoparticles with charged surfaces tend to become unstable (show aggregation) in a biological environment. Figure 1.9 shows the loss of colloidal stability due to charge screening. Here comparative fluorescence correlation spectroscopy (FCS) autocorrelation curves from our laboratory are presented for CdSe/ZnS quantum dots with negatively charged carboxylic acid surface groups in Millipore water and in 10 mM MES buffer. As illustrated, the nanoparticles in MES buffer show notably higher diffusion times, indicating their increasing aggregation. If quantum dots are surface-functionalized with a layer of hydrophilic polymers such as poly(ethylene glycol) (PEG), colloidal stability can be achieved even in the presence of ions in solution. Such particle stabilization via polymer coatings is attributed to the flexibility of polymer chains and their repulsive “entropic spring” effect during particle–particle interaction. Currently, the concept of stabilization of nanoparticles due to the addition of polymeric coatings is widely accepted. Indeed, several experimental results seem to support the concept [131, 132]. Peptides adsorbed to the quantum dot surface can also have a similar stabilizing effect [133]. Conversely, it has been theoretically predicted that homopolymers, if end-grafted to nanoparticles in good solvents, may lead to nanoparticle attraction [134].

#### 1.4.1.3 Biocompatible Surfaces

To make fluorescent nanoparticles ‘bioinert’, their surfaces need to be designed so as to prevent the non-specific adsorption of all relevant molecules in the biological medium. It is challenging to improve the design of surface coatings to a level of sophistication that fulfills this requirement. Fortunately, promising strategies for



the creation of bioinert surfaces are known from biomaterials research in the biomedical engineering community. As a result, our understanding about the host response of living tissue with respect to biomaterials has improved significantly and numerous sophisticated biomaterials have been developed [135]. A key aspect for the creation of colloidal solids with sufficient stealth properties in a cellular environment is the understanding of protein adsorption. Like surfactants, proteins have a high tendency to adsorb at interfaces. Interactions between proteins and surfaces are primarily noncovalent and include electrostatic, hydrophobic, and hydrogen-bonding interactions [136]. The different interactions result from the “surface inhomogeneity” of proteins, which typically are characterized by surface patches that may be charged, neutral, hydrophilic, or hydrophobic in character [137]. Consequently, surface properties of biomaterials affect the mechanism, rate, and extent of protein adsorption. Protein adsorption can be suppressed most efficiently on biomaterials whose surfaces are neutral, hydrophilic, and highly dynamic [138]. A paradigm of a protein-resistant surface is a solid substrate surface-functionalized with grafted PEG chains [139]. This is so because PEG is electrically neutral, thus minimizing electrostatic interactions, and highly hydrophilic, thus minimizing hydrophobic interactions. As the PEG chains are highly dynamic in an aqueous environment, the formation of strong hydrogen-bonding between protein and polymer is effectively suppressed. Besides those enthalpic effects, the high dynamics of the PEG chains results in a high entropy, which is also unfavorable for protein adsorption. It has been generally assumed that the surface resistance of PEG functionalized substrates is a result of the steric repulsion grafted PEG chains show for adsorbing proteins [138, 140, 141]. However, this assumption is valid only if the grafted PEG chains are of very high molecular weight and show large enough grafting densities to form polymer brushes [142]. Interestingly, Prime and Whitesides found that protein adsorption is prevented effectively even if the PEG chains have only two ethylene oxide segments, thus indicating that surface coverage is the most important parameter to prevent protein adsorption [143, 144]. In the same context, Single-chain Mean Field Theory (SCMF) calculations and experimental studies showed that protein adsorption on hydrophobic surfaces is prevented because PEG chains bind to the hydrophobic substrate, thereby blocking possible protein binding sites [145]. A later SCMF study by Szleifer and co-workers found that polymers with a low substrate affinity are more effective for kinetic control, whereas those with a higher affinity lead to a lower equilibrium concentration of adsorbed proteins [146]. Obviously, protein adsorption on substrates surface grafted with synthetic polymers is dependent on both the steric hindrance effect of the grafted polymer layer and the affinity of the underlying substrate for proteins and other molecules.

#### 1.4.1.4 Cytotoxicity

Several potential processes lead to cytotoxicity. One source of nanoparticle-induced cytotoxicity, rather independent of particle composition, occurs if nanoparticles adsorb to cell surfaces [147, 148] or if they get ingested by cells [149, 150]. The cytotoxicity of CdSe/ZnS quantum dots is suggested to be due mostly to their inter-

action with cells [151]. Another source of nanoparticle-induced cytotoxicity occurs when the nanoparticle is composed of toxic materials that can be gradually released. A prominent example concerning fluorescent nanoparticles is the gradual release of heavy metal ions such as  $\text{Cd}^{2+}$  from CdSe or CdSe/ZnS quantum dots [152, 153]. Heavy metal ions are cytotoxic and often show several pathways of cytotoxicity. Indeed,  $\text{Cd}^{2+}$  may induce hepatotoxicity, immunotoxicity, and nephrotoxicity; apoptosis being a critical part of each toxicity type [154]. Studies concerning Cd-induced hepatotoxicity show, for example, the relevance of direct and indirect cytotoxic pathways [155]. The direct pathway is caused by  $\text{Cd}^{2+}$  binding to sulfhydryl groups on key mitochondrial molecules, thus damaging the mitochondria. The indirect pathway, though, is assumed to occur via activation of Kupffer cells. However, not all metals show such pronounced cytotoxicity. For example, gold nanoparticles have good biocompatibility properties [156]. From the above information, nanoparticles only show very low cytotoxicity if all potential sources of cytotoxicity are prevented efficiently.

#### 1.4.2

#### Nanoparticle-stabilizing Coatings

To enhance the biocompatibility of nanoparticles, one popular strategy has been to cap the nanoparticles with polymeric coatings of high biocompatibility. In particular, poly(ethylene glycol) (PEG) has been applied as a coating material because of its excellent biocompatibility properties. Originally studied on flat macroscopic surfaces for biomaterials applications, PEG coatings have been widely applied to sub-micron sized delivery systems and imaging probes [48, 49, 116, 118, 131, 157, 158]. Delivery systems coated with PEG have notably longer circulation times in the blood, thus exceeding traditional non-nanoparticle-based delivery methods for the prolonged delivery of drugs, diagnostics, genes, and vaccines [159–162]. Based on the success of PEG coatings in drug delivery systems, similar coating strategies have been applied to the design of biocompatible coatings of nm-size imaging probes in biological and biomedical imaging. A facile approach for adding a PEG layer to the quantum dot surface is via physisorption of amphiphilic molecules [116, 118]. Here one interesting strategy has been to use PEG-containing lipopolymers, which result in excellent colloidal stability in *Xenopus* embryo cells over several days [118]. In an alternative amphiphilic passivation approach, block copolymers have been utilized to enable colloidal stability of quantum dots [116, 163, 164].

Chemically coupled PEG coatings have even greater stability. Wuelfing et al. reported the surface functionalization of gold nanoparticles using  $\text{CH}_3\text{O-PEG-SH}$  [131]. Covalent PEG coatings were also used to increase the colloidal stability of CdSe [49], CdS, [158] and  $\text{SiO}_2$ -capped CdS [48] quantum dots. However, in these cases, the PEG coatings lack reactive surface groups, thus preventing the further immobilization of ligands on the PEG layer. To overcome this limitation, nanoparticles need to be surface-functionalized via mixtures of mono-functional PEGs and other linker molecules [48] or via heterobifunctional PEG-linkers. Heterobifunc-

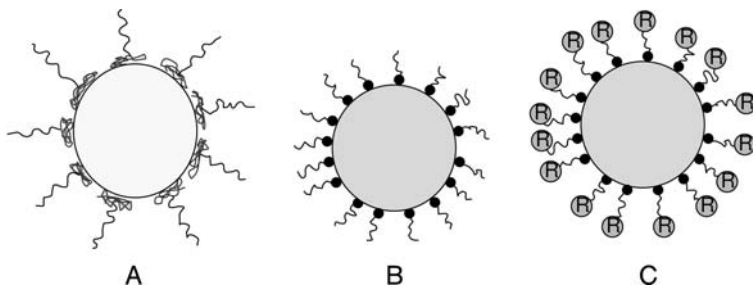


**Fig. 1.10.** Design of nanoparticles with stabilizing, biocompatible coatings, including (A) adsorption of amphiphilic molecules such as amphiphilic diblock copolymers; (B) chemical coupling of hydrophilic polymeric systems; and (C) linkage of spacer molecules with hydrophilic surface groups.

tional PEG-linkers can be synthesized via monoprotected symmetric PEG linkers, such as monoprotected diamines derived from tetraethylene glycol [165–167]. Another strategy for the synthesis of heterobifunctional PEG linkers is based on the ring-opening polymerization of ethylene oxide using a metal alkoxide initiator [168–171]. For example,  $\alpha$ -acetal-PEG-SH has been synthesized using this strategy [172]. Here the facile modification of the acetal group into a reactive aldehyde allowed the immobilization of ligand molecules on the surface of PEGylated gold particles [173]. Meanwhile, various heterobifunctional PEG linkers are also commercially available. Figure 1.10 shows the design of a biocompatible surface coating where a few linkers support the targeted immobilization of ligand molecules. Such a design can be accomplished by using a mixture of homofunctional and heterobifunctional PEGs. An excess of homofunctional PEG molecules, which have no reactive surface groups after surface coating, suppresses the non-specific binding of proteins, whereas the heterobifunctional linkers facilitate the targeted coupling to ligands. Notably, however, a PEG layer does not prevent cytotoxic side reactions due to the leaching of toxic heavy metal ions from quantum dots. In those cases, an additional protective layer preventing the egress of harmful ions is essential [153].

PEG-based coatings are not the only biocompatible polymeric coatings. For example, poly(acrylic acid) has been used to stabilize luminescent silicon nanoparticles [174]. Because this anionic polyelectrolyte has a high density of carboxylic acid moieties, the immobilization of amine-containing molecules is straightforward. A similar concept has been applied to conjugate CdS quantum dots with aminodextran [175]. Dendrimers have also been used as stabilizing coating material [176]. Quantum dots have been embedded into larger polymeric spheres via a facile procedure using block copolymers [163, 177], and CdSe-ZnS quantum dots have been incorporated into glyconanospheres via electrostatic coupling with carboxymethyl-dextran and polylysine [178]. Several other procedures have afforded gold glyconanospheres [173, 179, 180]. Quantum dots capped with specific peptide coatings have recently been shown to be quite promising biocompatible imaging

probes that can be designed for targeted labeling of biomolecules [20, and references therein].

### 1.4.3

#### Low Cytotoxicity Coatings

As stated before, successful application of fluorescent nanoparticles in a biological environment requires not only high dispersion stability and the suppression of non-specific biomolecule adsorption, but also should show low cytotoxicity. This topic is particularly important for applications involving quantum dots where toxic heavy metal ions can be released [152]. If properly passivated, quantum dots seem to show no significant cytotoxicity. For example, a study on *Xenopus* embryos did not reveal significant cytotoxicity after injection of  $2 \times 10^9$  and  $5 \times 10^9$  CdSe/ZnS quantum dots per cell [118].

Several strategies have been pursued to suppress this oxidation process. One approach is simply to passivate the quantum dot surface with binding ligands [181]. Importantly, such a passivation not only lowers the cytotoxicity of nano-probes, but also enhances their quantum yields. Quantum dots can be further passivated by adding a protecting semiconductor shell. Such coatings also significantly lower the cytotoxicity of CdSe quantum dots, but do not completely eliminate the problem [152]. Surface silanization is another promising approach to suppressing surface oxidation [44, 46, 182–184]. The stability of the coating is provided by crosslinks within the siloxane shell. Importantly, such shells are quite stable in a biological environment [46]. Furthermore, CdSe/ZnS quantum dots with a protective shell of crosslinked silica significantly reduce the release of  $\text{Cd}^{2+}$ , thus lowering the cytotoxicity of fluorescent nanoparticles [153]. Interestingly, the addition of a bovine serum albumin (BSA) layer further reduced the cytotoxicity of CdSe/ZnS quantum dots [152]. The BSA, added to the mercaptoacetic acid-functionalized quantum dot surface using EDC coupling, may act as a diffusion barrier for  $\text{O}_2$  molecules.

Based on the above discussion, the appropriate biofunctionalization of nanoparticles clearly must address the features of colloidal stability, bioinertness, specificity with respect to target biomolecules, and low cytotoxicity. Figure 1.11 shows a biofunctionalization architecture where these crucial features are considered in its design.

## 1.5

### Applications

Our growing ability to synthesize and surface-functionalize nanoparticles has provided new opportunities in bioanalytical and biological imaging applications. Metallic nanoparticles have been used primarily in bioanalytical projects. Nanoparticle-based imaging applications, however, rely more on dye-doped polymeric nanoparticles and quantum dots due to their excellent fluorescence proper-

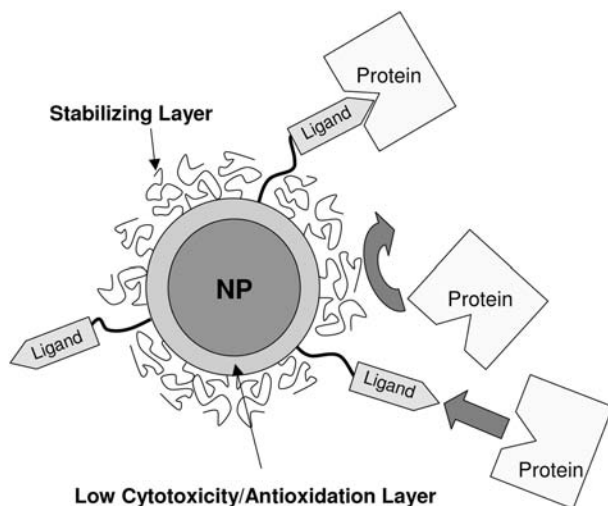


**Fig. 1.11.** Schematic of an appropriately biofunctionalized quantum dot. The inner coating protects from surface oxidation whereas the outer coating guarantees dispersion stability and biocompatibility. Immobilized ligands mediate the specific binding to biomolecules.

ties and photostability. While dye-doped systems have been used initially in such imaging applications, quantum dots have recently increasingly become the nanoparticle systems of choice. It is fair to say that further progress in bioanalytical and imaging applications is strongly linked to the availability of novel biofunctionalized nanoparticles of improved designs. Though developing rapidly, this highly interdisciplinary field is still in its infancy. The rapidly growing number of publications over the last decade reflect its relevance.

Though this chapter focuses primarily on the relevant *concepts* of biofunctionalization, this section describes recent *applications* using biofunctionalized fluorescent nanoparticles. We do not claim to review all published applications where such particles have been used because this is clearly beyond the scope of the chapter. Instead, the intent is to provide a representative overview of recent nanoparticle-related applications in the fields of diagnostics and live cell and *in vivo* imaging.

### 1.5.1

#### Biosensing

Fluorescent nanoparticles are highly promising probes for bioanalytical applications. In particular, their use in the field of biosensors is attractive because fluorescence-based techniques are extremely sensitive and nanoparticle probes show high photostability, thus allowing for long-term observations.

### 1.5.1.1 Polymeric Sensors

Bioanalytical applications based on polymeric nanoparticles are now well established. In one application, the combination of two silica precursors, tetraethyl-orthosilicate and phenyltriethoxysilane, was used to synthesize organic dye-doped silica nanoparticles. The nanoparticles were coated with avidin to determine biotinylated bovine serum albumin. In addition, a glutamate sensor was designed by immobilizing glutamate dehydrogenase on the nanoparticle surfaces [185]. In another application, a BODIPY-doped polymeric nanoparticle was designed for the detection of  $\text{Cu}^{2+}$ . Here the metal-chelating receptor, cyclam, was covalently bound to the surface of the nanoparticle. In the presence of  $\text{Cu}^{2+}$  the fluorescence emission of the BODIPY is quenched by the overlapping adsorption band of the metal-chelator complex [186]. Fluorescent polymeric nanoparticles have also been used for the intracellular monitoring of key biological components. Using three different nanoparticle fabrication technologies, sensors based on polyacrylamide, cross-linked decyl methacrylate, and silica-based sol-gel have been characterized in aqueous solution and intracellular surroundings. Each matrix can be combined with specific “free dyes”, ionophores, or enzymes to produce sensors selective for the biological component of interest. These nano-optodes are termed PEBBLEs (probes encapsulated by biol. localized embedding). Spherical sensors less than 600 nm in diam. (and reducible to below 100 nm) have been made from all three matrices. Acrylamide-based sensors have been used to monitor intracellular pH and calcium (with proven selectivity over  $\text{Mg}^{2+}$ ). Decyl methacrylate has been successfully applied to intracellular potassium monitoring with probes 1000× more selective for potassium than sodium. Such a sol-gel-based approach has also proven useful for monitoring intracellular oxygen at physiologically interesting concentrations. PEBBLEs, with a wide range of both simple and complex sensing schemes, provide a unique tool for minimally invasive intracellular monitoring, with many significant advantages over free dyes as well as over fiber-optic sensors [187–189].

### 1.5.1.2 Quantum Dot Sensors

The great potential of quantum dots for sensing applications has been demonstrated in several instances. In one application, quantum dots have been utilized as maltose sensors [114]. Here quantum dots were surface-functionalized with a maltose-binding protein (MBP) containing  $\beta$ -cyclodextrin-QSY-9 attached to the binding site to quench the quantum dot emission. The sensor concept is that maltose displaces the  $\beta$ -cyclodextrin-QSY-9, thus inducing quantum dot emission. Another reported quantum dot-based maltose sensor using MBP acts as a double FRET sensor [114]. Here the quantum dot emission excites Cy3 that is adsorbed on the surface of the MBP. The Cy3 emission then excites the  $\beta$ -cyclodextrin-Cy3.5 whose emission is observed. Once maltose is introduced to the sensor, the Cy3 emission is no longer quenched by the Cy3.5, because the  $\beta$ -cyclodextrin-Cy3.5 has been displaced by maltose [114].

Quantum dots also show great promise in immunoassays. For example, an immunoassay has been performed by binding an antibody covalently to a glass chip,

followed by binding of the antigen. The antigen was then detected with the addition of antibody labeled quantum dots, which bound selectively to the captured antigen [190]. In another application, Tran et al. prepared quantum dot conjugates with the immunoglobulin G (IgG) binding domain of streptococcal protein G (PG) appended with a basic leucine zipper attachment domain (PG-zb). They also demonstrated that the quantum dot/PG conjugates retain their ability to bind IgG antibodies, and that a specific antibody coupled to quantum dots via the PG functional domain efficiently binds its antigen. Preliminary results indicated that electrostatically self-assembled quantum dot/PG-zb/IgG bioconjugates can be used in fluoro-immunoassays [191]. Quantum dot–antibody conjugates were again successfully used in fluoro-immunoassays to detect both a protein toxin (staphylococcal enterotoxin B) and a small molecule (2,4,6-trinitrotoluene) [108]. Goldman et al. described a conjugation strategy employing an engineered molecular adaptor protein, attached to the quantum dots via electrostatic/hydrophobic self-assembly, to link quantum dots with antibodies. Quantum dots can also be used as sensors for sugars; a quantum dot FRET application using adsorbed MBP has been mentioned [114].

Powerful sensor concepts can also be designed using the multiplexing capability of quantum dots. This results from the broad excitation and narrow, size-dependent emission bands of quantum dots. This concept has been used, for example, to embed quantum dots of six different colors and ten intensities per color in nanoparticles composed of styrene, divinylbenzene, and acrylic acid. This combination can, theoretically, code one million nucleic acids or protein sequences [80]. In another application, a high-throughput assay has been developed for the parallel detection of antibodies using quantum dot microbeads. In this case, a custom designed microfluidic chip with multiple micro-wells was utilized for capturing of microbeads, antibody injection into each micro-well, QD injection, and fluorescence detection [192]. These beads could be identified with a standard flow cytometer at a rate of 1000 beads  $s^{-1}$  [193].

#### 1.5.1.3 Metallic Sensors

Gold nanoparticles (2.5 nm) have been used to recognize and detect specific DNA sequences and single-base mutations. Detection is based on fluorescently tagged, thiol modified oligonucleotides bound to the surface of the gold nanoparticle. Upon self-assembly, the fluorophores arch toward the gold surface, quenching the fluorescence. Upon binding the appropriate target sequence, the oligonucleotide undergoes a conformational change, moving it away from the gold nanoparticle surface, and restoring the fluorescence [194]. Another interesting approach to ultrasensitive detection of DNA hybridization is based on Au nanoparticle-amplified surface plasmon resonance (SPR). Interestingly, even without further optimization, the sensitivity of this technique begins to approach that of traditional fluorescence-based methods for DNA hybridization and oligonucleotide detection [62]. Gold nanoparticles have also been used in the detection of glucose and glucose oxidase. The growth of the Au nanoparticles requires  $H_2O_2$  and converts it into  $O_2$ . In the presence of glucose oxidase and glucose,  $O_2$  is converted into

H<sub>2</sub>O<sub>2</sub>, allowing the Au nanoparticles to grow, thus giving a shift in absorbance over time [195]. Finally, Ag has also been employed for surface plasmon-based nanosensors concerning the detection of Alzheimer's disease. Autopsied brain samples of humans with Alzheimer's disease show elevated levels of amyloid-derived diffusible ligands (ADDLs), which suggest that a definitive chemical diagnosis of Alzheimer's could be achieved with a sensitive method to detect ADDL or anti-ADDL antibodies. The  $\lambda_{\max}$  of silver nanoparticles conjugated with anti-ADDL was monitored before and after the incubation with ADDL. The resulting  $\Delta\lambda_{\max}$  indicated that it is possible to monitor the interaction between ADDL and anti-ADDL using Ag nanoparticles. While undergoing a promising initial trial, the practicality of the system as a sensor is limited because its specificity becomes low at nM concentrations of anti-ADDLs [196].

## 1.5.2

### Fluorescent Nanoparticles as Labels in Biological Imaging

#### 1.5.2.1 Dye-doped Nanoparticles

Though very small, fluorescent dyes are only of limited applicability in biological imaging because of their poor photostability and limited brightness. To improve the photostability, initially, dye-doped nanoparticles have been used as photostable imaging probes. For example, 20 nm dye-doped latex nanoparticles have been linked to DNA-binding proteins (restriction enzyme EcoR1) to probe specific sequences on stretched DNA [7]. In addition, ruthenium bipyridyl-doped silica nanoparticles can be used to stain and image leukemia cells [4]. More recently, Ru(bpy)-doped silica nanoparticles have been applied successfully in several fluorescent imaging applications, including immunocytochemistry, immunohistochemistry, and DNA and protein microarrays [197]. Here the nanoparticles were surface-functionalized with avidin, thus allowing straightforward coupling to biotinylated antibodies. In one case, avidin-capped, dye-doped silica nanoparticles were conjugated with biotinylated mouse anti-hIgM to stain human peripheral blood mononuclear cells. In another case, these photostable nanoprobe were coupled to biotinylated goat anti-ChAT antibodies to label choline acetyltransferase to image mouse brain tissue. Interestingly, these dye-doped silica nanoparticles are not outperformed by quantum dots with respect to photostability.

#### 1.5.2.2 Quantum Dots

Among the different types of fluorescent nanoparticles, quantum dots seem to show the greatest promise as labels in biological imaging applications. Since their introduction as labels in cellular imaging in 1998 [44, 115], multiple reports have shown the strengths of these nanoprobe for tagging and imaging applications in biological systems. This strength is based on the impressive photostability of quantum dots and on their broad excitation and narrow size-dependent emission properties. Most importantly, the high photostability guarantees the observation of biomolecules over longer time periods. Dubertret et al. have reported a very elegant example of such a long-term observation of biological processes [118]. Here, quan-



tum dots with biocompatible coatings were injected into *Xenopus* embryos and their movement into different cells during tadpole development was monitored over several days.

Quantum dot multi-color imaging in cells is another fascinating imaging approach. For example, quantum dots biofunctionalized with streptavidin and IgG have been used to label the breast cancer marker Her2 on fixed and live cancer cells, to tag actin and microtubules, and to stain nuclear antigens inside the nucleus [116]. Quantum dots have also been shown to be useful in studying ATP driven biological processes. The *in vitro* sliding of quantum dot labeled actin filaments was observed over periods of 10–12 s [198]. The chaperonin proteins GroEL (from *Escherichia coli*) and T.th ('T.th cpn', from *Thermus thermophilus* HB8) typically encapsulate denatured proteins within a cavity and release them in the presence of ATP. This encapsulation and release technique was used to give quantum dots high thermal and chemical stability in various aqueous mediums, while also allowing the controlled release of quantum dots [199].

Quantum dot labels are particularly advantageous over traditional organic dyes in single-molecule tracking applications because dye-based tracking experiments are limited by very short observation times [200, 201]. Quantum dot-based single molecule tracking in biological systems represents a fascinating emerging research area. The first results indicate great promise. Dahan et al. have successfully tracked individual quantum dot-tagged glycine receptors in the neuronal membrane of live cells and analyzed the diffusion properties [202]. Furthermore, this technique allowed them to observe the entry of individual glycine receptors into the synapse, which was confirmed by electron microscopy experiments. The ability to detect quantum dots not only optically but also by electron microscopy is clearly a very powerful feature. Another recent single-molecule application was related to the monitoring of quantum dot-labeled epidermal growth factor. In this case, a new transport process was discovered [203].

Fluorescent nanoparticles have also been applied in animal imaging experiments; again, quantum dots seem to show great promise. Proper biocompatible surface coating is essential for long-term stability of the probes in a biological environment [204]. In another application, quantum dots have been targeted *in vivo* via peptides immobilized on the quantum dot surface [205]. Here, several types of peptides were used to label different regions of the mice tissue. Thus, quantum dots with lung-targeting peptides were shown to accumulate in the lungs of mice whereas other peptides targeted quantum dots to blood or lymphatic vessels in tumors. Targeted quantum dot transport in live animals was recently reported in mice [164]. In this case, PEG-coated nanoprobe were used that carried conjugated antibodies directed against prostate-specific membrane antigens. A clear boost in animal imaging should be expected from the recent development of quantum dots with emission bands in the near-infrared (NIR) because this wavelength range offers an optical window for tissue imaging. Indeed, NIR quantum dots have been applied successfully to conduct imaging experiments on rat and porcine tissue [206, 207]. In one case, rat coronary vasculature was studied. In the other case, porcine sentinel lymph nodes were imaged. Interestingly, when injected interdermally

on the thigh of a 35 kg pig, doctors could visualize the nearby sentinel lymph nodes within 3–4 min and use the infrared signal as a guide during surgery. Despite the relatively low power NIR excitation used ( $5 \text{ mW cm}^{-2}$ ) the sentinel lymph nodes were observed as deep as 1 cm below the skin surface.

## References

- 1 SAXTON, M. J., JACOBSON, K., Single particle tracking: Applications to membrane dynamics. *Annu. Rev. Biophys. Biomol. Struct.* **1997**, *26*, 373–399.
- 2 KREUTER, J., in *Microcapsules and Nanoparticles in Medicine and Pharmacy* (Ed.: N. DOMBROW), CRC, Boca Raton, FL, **1992**.
- 3 NIEMEYER, C. M., Nanoparticles, proteins, nucleic acids: Biotechnology meets Materials Science. *Angew. Chem. Int. Ed.* **2001**, *40*, 4128–4158.
- 4 BAGWE, R. P., ZHAO, X., TAN, W., Bioconjugated luminescent nanoparticles for biological applications. *J. Dispers. Sci. Technol.* **2003**, *3*(4), 453–464.
- 5 SANTRA, S., WANG, K., TAPEC, R., TAN, W. H., Development of novel dye doped silica nanoparticles for biomarker applications. *J. Biomed. Opt.* **2001**, *6*, 160–166.
- 6 GAO, H., ZHAO, Y., FU, S., LI, B., LI, M., Preparation of novel polymeric fluorescent nanoparticles. *Colloid Polym. Sci.* **2002**, *280*, 653–660.
- 7 TAYLOR, J. R., FANG, M. M., NIE, S., Probing specific sequences on single DNA molecules with bioconjugated fluorescent nanoparticles. *Anal. Chem.* **2000**, *72*, 1979–1986.
- 8 JAIN, T. K., ROY, I., DE, T. K., MAITRA, A. N., Nanometer silica particles encapsulating active compounds: a novel ceramic drug carrier. *J. Am. Chem. Soc.* **1998**, *120*, 11092–11095.
- 9 ZHAO, X. J., TAPEC-DYTIOCO, R., WANG, K. M., TAN, W. H., Collection of trace amounts of DNA/mRNA molecules using genomic magnetic nanocaptors. *Anal. Chem.* **2003**, *75*, 3476–3483.
- 10 VAN BLAADEREN, A., VRJI, A., Synthesis and characterization of colloidal dispersions of fluorescent, monodisperse silica spheres. *Langmuir* **1992**, *8*, 2921–2931.
- 11 BAGWE, R. P., YANG, C., HILLARD, L. R., TAN, W., Optimization of dye-doped silica nanoparticles prepared using a reverse microemulsion method. *Langmuir* **2004**, *20*, 8336–8342.
- 12 BAGWE, R. P., KHILAR, K. C., Effects of intermicellar exchange rate on the formation of silver nanoparticles in reverse microemulsions of AOT. *Langmuir* **2000**, *16*, 906–910.
- 13 MAKAROVA, A. V., OSTAFIN, A. E., MIYOSHI, H., NORRIS, J. R., MEISEL, D., Adsorption and encapsulation of fluorescent probes in nanoparticles. *J. Phys. Chem. B* **1999**, *103*, 9080–9084.
- 14 MEYSSAMY, H., RIWOTZKI, R., KORNOWSKI, A., NAUSED, S., HAASE, M., Wet-chemical synthesis of doped colloidal nanomaterials: Particles and fibers of  $\text{LaPO}_4\text{:Eu}$ ,  $\text{LaPO}_4\text{:Ce}$ , and  $\text{LaPO}_4\text{:Ce,Tb}$ . *Adv. Mater.* **1999**, *11*, 840–844.
- 15 MEISER, F., CORTEZ, C., CARUSO, F., Biofunctionalization of fluorescent rare-earth-doped lanthanum phosphate colloidal nanoparticles. *Angew. Chem. Int. Ed.* **2004**, *43*, 5954–5957.
- 16 BRUS, L. E., A simple model for the ionization potential, electron affinity, and aqueous redox potentials of small semiconductor crystallites. *J. Chem. Phys.* **1983**, *79*, 5566–5571.
- 17 BRUS, L. E., Electron-electron and electron-hole interactions in small semiconductor crystallites: the size dependence of the lowest excited

- electronic state. *J. Chem. Phys.* **1983**, *80*, 4403–4409.
- 18 CHESTNOY, N., HARRIS, T. D., HULL, R., BRUS, L. E., Luminescence and photophysics of cadmium sulfide semiconductor clusters: the nature of the emitting electronic state. *J. Phys. Chem.* **1986**, *90*, 2555–2560.
- 19 BAWENDI, M. G., STEIGERWALD, M. W., BRUS, L. E., The quantum mechanics of larger semiconductor clusters (“quantum dots”). *Annu. Rev. Phys. Chem.* **1990**, *41*, 477–496.
- 20 MICHALET, X., PINAUD, F. F., BENTOLILA, L. A., TSAY, J. M., DOOSE, S., LI, J. J., SUNDARESAN, G., WU, A. M., GAMBHIR, S. S., WEISS, S., Quantum dots for live cells, in vivo imaging, and diagnostics. *Science* **2005**, *307*, 538–544.
- 21 WILSON, W. L., SZAJOWSKI, P. F., BRUS, L. E., Quantum confinement in size-selected surface-oxidized silicon nanocrystals. *Science* **1993**, *262*, 1242–1244.
- 22 BLEY, R. A., KAUZLARICH, S. M., A Low-temperature solution phase route for the synthesis of silicon nanoclusters. *J. Am. Chem. Soc.* **1996**, *118*, 12461–12462.
- 23 HOLMES, J. D., ZIEGLER, K. J., DOTY, R. C., PELL, L. E., JOHNSTON, K. P., KORGEL, B. A., Highly luminescent silicon nanocrystals with discrete optical transitions. *J. Am. Chem. Soc.* **2001**, *123*, 3743–3748.
- 24 HINES, M. A., GUYOT-SIONNEST, P., Synthesis and characterization of strongly luminescing ZnS-capped CdSe nanocrystals. *J. Phys. Chem.* **1996**, *100*, 468–471.
- 25 STSIAPURA, V., SUKHANOVA, A., ARTEMYEV, M., PLUOT, M., COHEN, J. H. M., BARANOV, A. V., OLEINIKOV, V., NABIEV, I., Functionalized nanocrystal-tagged fluorescent polymer beads: synthesis, physicochemical characterization, and immunolabeling application. *Anal. Biochem.* **2004**, *334*, 257–265.
- 26 REISS, P., BLEUSE, J., PRON, A., Highly luminescent CdSe/ZnSe core/shell nanocrystals of low size dispersion. *Nano Lett.* **2002**, *2*, 781–784.
- 27 PENG, X., WICKHAM, J., ALIVISATOS, A. P., Epitaxial growth of highly luminescent CdSe/CdS core/shell nanocrystals with photostability and electronic accessibility. *J. Am. Chem. Soc.* **1998**, *120*, 5343–5344.
- 28 PENG, Z. A., PENG, X., Kinetics of II–VI and III–V colloidal semiconductor nanocrystal growth: “Focusing” of size distributions. *J. Am. Chem. Soc.* **2001**, *123*, 183–184.
- 29 MURCIA, M. J., SHAW, D. L., WOODRUFF, H., NAUMANN, C. A., YOUNG, B. A., LONG, E. C., Facile sonochemical synthesis of highly-luminescent ZnS-shelled CdSe quantum dots. Submitted to *Chem. Mater.*
- 30 ROGACH, A. L., KATSIKAS, L., KORNOWSKI, A., SU, D., EYCHMUELLER, A., WELLER, H., BUNSENGES, B., Synthesis, morphology, and optical properties of thiol-stabilized CdTe nanoclusters in aqueous solution. *Berich. Bunsen Gesell.* **1997**, *101*(11), 1668–1670.
- 31 MAMEDOVA, N. N., KOTOV, N. A., ROGACH, A. L., STUDER, J., Albumin-CdTe nanoparticle bioconjugates: Preparation, structure, and interunit energy transfer with antenna effect. *Nano Lett.* **2001**, *1*, 281–286.
- 32 LAKOWICZ, J. R., GRZYCZYNSKI, I., GRZYCZYNSKI, Z., MURPHY, C. J., Luminescence spectral properties of CdS nanoparticles. *J. Phys. Chem. B* **1999**, *103*, 7613–7620.
- 33 TORIMOTO, T., YAMASHITA, M., KUWABATA, S., SAKATA, T., MORI, H., YONEYAMA, H., Fabrication of CdS nanoparticle chains along DNA double strands. *J. Phys. Chem. B* **1999**, *103*, 8799–8803.
- 34 LAKOWICZ, J. R., GRZYCZYNSKI, I., GRZYCZYNSKI, Z., NOWACZYK, K., MURPHY, C. J., Luminescence spectral properties of CdS nanoparticles. *Anal. Biochem.* **2000**, *280*, 128–136.
- 35 BIGHAM, S. R., COFFER, J. L., Thermochemical passivation of DNA-stabilized Q-cadmium sulfide nanoparticles. *J. Cluster Sci.* **2000**, *11*, 359–372.
- 36 LI, X., COFFER, J. L., Effect of pressure

- on the photoluminescence of polynucleotide-stabilized cadmium sulfide nanocrystals. *Chem. Mater.* **1999**, *11*, 2326–2330.
- 37 WILLNER, I., PATOLSKY, F., WASSERMAN, J., Photoelectrochemistry with controlled DNA-cross-linked CdS nanoparticle arrays. *Angew. Chem. Int. Ed.* **2001**, *40*, 1861–1864.
- 38 CHEN, H. M., HUANG, X. F., XU, L., XU, J., CHEN, K. J., FENG, D., Self-assembly and photoluminescence of CdS-mercaptoacetic clusters with internal structures. *Superlatt., Microstruct.* **2000**, *27*, 1–5.
- 39 PENG, X., SCHLAMP, M. C., KADAVANICH, A. V., ALIVISATOS, A. P., Epitaxial growth of highly luminescent CdSe/CdS core/shell nanocrystals with photostability and electronic accessibility. *J. Am. Chem. Soc.* **1997**, *119*, 7019–7029.
- 40 PASSOW, T., LEONARDI, K., HOMMEL, D., Optical and structural properties of CdSe/Zn(S)Se quantum dot stacks. *Phys. Stat. Sol. B* **2001**, *224*, 143–146.
- 41 PATHAK, S., CHOI, S. K., ARNHEIM, N., THOMPSON, M. E., Hydroxylated quantum dots as luminescent probes for in situ hybridization. *J. Am. Chem. Soc.* **2001**, *123*(17), 4103–4104.
- 42 MATTOUSSI, H., MAURO, J. M., GOLDMAN, E. R., ANDERSON, G. P., SUNDAR, V. C., MIKULEC, F. V., BAWENDI, M. G., Bioconjugation of highly luminescent colloidal CdSe-ZnS quantum dots with an engineered two-domain recombinant protein. *J. Am. Chem. Soc.* **2000**, *122*, 12142–12150.
- 43 MATTOUSSI, H., MAURO, J. M., GOLDMAN, E. R., GREEN, T. M., ANDERSON, G. P., SUNDAR, V. C., BAWENDI, M. G., Bioconjugation of highly luminescent colloidal CdSe-ZnS quantum dots with an engineered two-domain recombinant protein. *Phys. Stat. Sol. B* **2001**, *224*(1), 277–283.
- 44 BRUNCHEZ, M. J., MORONNE, M., GIN, P., WEISS, S., ALIVISATOS, A. P., Semiconductor nanocrystals as fluorescent labels. *Science* **1998**, *281*, 2013–2016.
- 45 LIZ-MARZÁN, L. M., GIERSIG, M., MULVANEY, P., Synthesis of nanosized gold-silica core-shell particles. *Langmuir* **1996**, *12*, 4329–4335.
- 46 GERION, D., PINAUD, F., WILLIAMS, S. C., PARAK, W. J., ZANCHET, D., WEISS, S., ALIVISATOS, A. P., Synthesis and properties of biocompatible water-soluble silica-coated CdSe/ZnS semiconductor quantum dots. *J. Phys. Chem. B* **2001**, *105*, 8861–8871.
- 47 SCHROEDTER, A., WELLER, H., Ligand design and bioconjugation of colloidal gold nanoparticles. *Angew. Chem. Int. Ed.* **2002**, *41*, 3218–3221.
- 48 PARAK, W. J., GERION, D., ZANCHET, D., WOERZ, A. S., PELLEGRINO, T., MICHEEL, C., WILLIAMS, S. C., SEITZ, M., BRUEHL, R. E., BRYANT, Z., BUSTAMANTE, C., BERTOZZI, C. R., ALIVISATOS, A. P., Conjugation of DNA to silanized colloidal semiconductor nanocrystalline quantum dots. *Chem. Mater.* **2002**, *14*, 2113–2119.
- 49 SKAFF, H., EMRICK, T., The use of 4-substituted pyridines to afford amphiphilic, pegylated cadmium selenide. *Chem. Commun.* **2003**, 52–53.
- 50 KAMAT, P. V., Photophysical, photochemical and photocatalytic aspects of metal nanoparticles. *J. Phys. Chem. B* **2002**, *106*, 7729–7744.
- 51 WILCOXON, J. P., MARTIN, J. E., PARSAPOUR, F., WIEDENMAN, B., KELLEY, D. F., Photoluminescence from nanosize gold clusters. *J. Chem. Phys.* **1998**, *108*(21), 9137–9143.
- 52 MOFFITT, M., VALI, H., EISENBERG, A., Spherical assemblies of semiconductor nanoparticles in water-soluble block copolymer aggregates. *Chem. Mater.* **1998**, *10*, 1021–1028.
- 53 HUANG, T., MURRAY, R. W., Visible Luminescence of water-soluble monolayer-protected gold clusters. *J. Phys. Chem. B* **2001**, *105*, 12498–12502.
- 54 SATO, T., ICHIKAWA, T., ITO, T., YONEZAWA, Y., KADONO, K., SAKAGUCHI, T., MIYA, M., Nonlinear optical properties of silver sols prepared by photoreduction method. *Chem. Phys. Lett.* **1995**, *242*, 310–314.

- 55 FRANÇOIS, L., MOSTAFAVI, M., BELLONI, J., DELOUIS, J. F., DELAIRE, J., FENEYROU, P., Optical limitation induced by gold clusters: 1. Size effect. *J. Phys. Chem. B* **2000**, *104*, 6133–6137.
- 56 KEATING, C. D., KOVALESKI, K. K., NATAN, M. J., Heightened electromagnetic fields between metal nanoparticles: Surface enhanced raman scattering from metal-cytochrome c-metal sandwiches. *J. Phys. Chem. B* **1998**, *102*, 9414–9425.
- 57 HULTEEN, J. C., TREICHEL, D. A., SMITH, M. T., DUVAL, M. L., JENSEN, T. R., VAN, R. P., Nanosphere lithography: Size-tunable silver nanoparticle and surface cluster arrays. *J. Phys. Chem. B* **1999**, *103*, 3854–3863.
- 58 MICHAELS, A. M., JIANG, J., BRUS, L., Ag nanocrystal junctions as the site for surface-enhanced Raman scattering of single rhodamine 6G molecules. *J. Phys. Chem. B* **2000**, *104*, 11965–11971.
- 59 OLDENBURG, S. J., WESTCOTT, S. L., AVERITT, R. D., HALAS, N. J., Surface enhanced Raman scattering in the near infrared using metal nanoshell substrates. *J. Chem. Phys.* **1999**, *111*, 4729–4735.
- 60 LEE, P. C., MEISEL, D., Adsorption and surface-enhanced Raman of dyes on silver and gold sols. *J. Phys. Chem.* **1982**, *86*(17), 3391–3395.
- 61 FREEMAN, R. G., HOMMER, M. B., GRABAR, K. C., JACKSON, M. A., NATAN, M. J., Ag-clad Au nanoparticles: Novel aggregation, optical, and surface-enhanced Raman scattering Properties. *J. Phys. Chem.* **1996**, *100*, 718–724.
- 62 HE, L., MUSICK, M. D., NICEWARNER, S. R., SALIAS, F. G., BENKOVIC, S. J., NATAN, N. J., KEATING, C. D., Colloidal Au-enhanced surface plasmon resonance for ultrasensitive detection of DNA hybridization. *J. Am. Chem. Soc.* **2000**, *122*, 9071–9077.
- 63 BRUST, M., WALKER, M., BETHELL, D., SCHIFFRIN, D. J., WHYMAN, R. J., Synthesis of thiol-derivatised gold nanoparticles in a two-phase liquid–liquid system. *J. Chem. Soc., Chem. Commun.* **1994**, *7*, 801–802.
- 64 BRUST, M., FINK, J., BETHELL, D., SCHIFFRIN, D. J., KIELY, C. J., Synthesis and reactions of functionalised gold nanoparticles. *J. Chem. Soc., Chem. Commun.* **1995**, *16*, 1655–1656.
- 65 KOLB, U., QUASIER, S. A., WINTER, M., REETZ, M. T., Investigation of tetra-alkylammonium bromide stabilized palladium/platinum bimetallic clusters using extended X-ray absorption fine structure. *Chem. Mater.* **1996**, *8*, 1889–1894.
- 66 FINK, J., KIELY, C., BETHELL, D., SCHIFFRIN, D. J., Self-organization of nanosized gold particles. *Chem. Mater.* **1998**, *10*, 922–926.
- 67 PEREZ, M., PRADEAU, J. P., ALBOUY, P. A., PEREZ-OMIL, J., Synthesis and characterization of functionalized platinum nanoparticles. *Chem. Mater.* **1999**, *11*, 3460–3463.
- 68 SUBRAMANIAN, V., WOLF, E., KAMAT, P. V., Semiconductor-metal composite nanostructures. To what extent do metal nanoparticles improve the photocatalytic activity of TiO<sub>2</sub> films. *J. Phys. Chem. B* **2001**, *105*, 11439–11446.
- 69 NIIDOME, Y., HORI, A., SATO, T., YAMADA, S., Enormous size growth of thiol-passivated gold nanoparticles induced by near-IR laser light. *Chem. Lett.* **2000**, 310–311.
- 70 BAGWE, R. P., MISHRA, B. K., KHILAR, K. C., Effect of chain length of oxyethylene group on particle size and absorption spectra of silver nanoparticles prepared in non-ionic water-in-oil microemulsions. *J. Disp. Sci. Technol.* **1999**, *20*(6), 1569–1579.
- 71 BAGWE, R. P., KHILAR, K. C., Effects of intermicellar exchange rate on the formation of silver nanoparticles in reverse microemulsions of AOT. *Langmuir* **1997**, *13*(24), 6432–6438.
- 72 SHAH, D. O., BAGWE, R. P., PARMAR, B. S., The effects of interfacial viscosity on the kinetics of formation of silver nanoparticles using water-in-oil microemulsions as nanoreactors. *Mater. Res. Soc. Symp. Proc.* **2002**, *704*, W10.1.1–W10.1.8.

- 73 SCHLUPEN, J., HAEGEL, F. H., KUHLMANN, J., GEISLER, H., SCHWUGER, M. J., Synthesis of nano-sized gold-silica core-shell particles. *Colloid Surf. A* **1999**, *156*, 335–347.
- 74 ELGHANIAN, R., STORHOFF, J. J., MUCIC, R. C., LETSINGER, R. L., MIRKIN, C. A., Selective colorimetric detection of polynucleotides based on the distance-dependent optical properties of gold nanoparticles. *Science* **1997**, *277*, 1078–1080.
- 75 HAINFELD, J. F., FURUYA, F. R., A 1.4 nm gold cluster covalently attached to antibodies improves immunolabeling. *J. Histochem. Cytochem.* **1992**, *40*, 177–184.
- 76 MATTHEWS, D. C., GRONDAHL, L., BATTERSBY, B. J., TRAU, M., Multi-fluorescent silica colloids for encoding large combinatorial libraries. *Aust. J. Chem.* **2001**, *54*(9 & 10), 649–656.
- 77 LAWRIE, G. A., BATTERSBY, B. J., TRAU, M., Synthesis of optically complex core-shell colloidal suspensions: Pathways to multiplexed biological screening. *Adv. Funct. Mater.* **2003**, *13*(11), 887–896.
- 78 GOLDMAN, E. R., CLAPP, A. R., ANDERSON, G. P., UYEDA, H. T., MAURO, J. M., MEDNITZ, I. L., MATOUSSI, H., Multiplexed toxin analysis using four colors of quantum dot fluororeagents. *Anal. Chem.* **2004**, *76*, 684–688.
- 79 ROSENTHAL, S. J., Bar-coding biomolecules with fluorescent nanocrystals. *Nat. Biotechnol.* **2001**, *19*(7), 621–622.
- 80 HAN, M., GAO, X., SU, J. Z., NIE, S., Quantum-dot-tagged microbeads for multiplexed optical coding of biomolecules. *Nat. Biotechnol.* **2001**, *19*(7), 631–635.
- 81 XU, H., SHA, M. Y., WONG, E. Y., UPHO, J., XU, Y., TREADWAY, J. A., TRUONG, A., O'BRIEN, E., ASQUITH, S., STUBBINS, M., SPURR, N. K., LAI, E. H., MAHONEY, W., Multiplexed SNP genotyping using the Qbead system: a quantum dot-encoded microsphere-based assay. *Nucleic Acids Res.* **2003**, *31*, e43/1–e43/10.
- 82 FULTON, R. J., MCDADE, R. L., SMITH, P. L., KIENKER, L. J., KETTMAN JR., L. R., Advanced multiplexed analysis with the FlowMetrix™ system. *Clin. Chem.* **1997**, *43*, 1749–1756.
- 83 VERONESE, F. M., MORPURGO, M., Bioconjugation in pharmaceutical chemistry. *Farmaco* **1999**, *54*(8), 497–516.
- 84 MITCHELL, G. P., MIRKIN, C. A., LETSINGER, R. L., Programmed assembly of DNA functionalized quantum dots. *J. Am. Chem. Soc.* **1999**, *121*(35), 8122–8123.
- 85 ZHANG, C. Y., MA, H., NIE, S. M., DING, Y., JIN, L., CHEN, D. Y., Quantum dot-labeled trichosanthin. *Analyst* **2000**, *125*, 1029–1031.
- 86 WILLARD, D. M., CARILLO, L. L., JUNG, J., ORDEN, A. V., CdSe-ZnS quantum dots as resonance energy transfer donors in a model protein-protein binding assay. *Nano Lett.* **2001**, *1*(9), 469–474.
- 87 PARAK, W. J., GERION, D., PELLEGRINO, T., ZANCHET, D., MICHEEL, C., WILLIAMS, S. C., BOUDREAU, R., LE GROS, M. A., LARABELL, C. A., ALIVISATOS, A. P., Biological applications of colloidal nanocrystals. *Nanotechnology* **2003**, *14*, R15–R27.
- 88 GOLDMAN, E. R., BALIGHAIAN, E. D., MATTOUSSI, H., KUNO, M. K., MAURO, J. M., TRAN, P. T., ANDERSON, G. P., Avidin: A natural bridge for quantum dot-antibody conjugates. *J. Am. Chem. Soc.* **2002**, *124*, 6378–6382.
- 89 BAEUMLE, M., STAMOU, D., SEGURA, J. M., HOVIUS, R., VOGEL, H., Vitro sliding of actin filaments labelled with single quantum dots. *Langmuir* **2004**, *314*(2), 529–534.
- 90 TORCHILIN, V. P., KHAW, B. A., SMIRNOV, V. N., HABER, E., Preservation of antimyosin antibody activity after covalent coupling to liposomes. *Biochem. Biophys. Res. Commun.* **1979**, *85*, 1114–1119.
- 91 MAGNANI, P., PAGANELLI, G., MODORATI, G., ZITO, F., SONGINI, C., SUDATI, F., KOCH, P., MAECKE, H. R., BRANCATO, R., SICCARDI, A. G., FAZIO, F., Quantitative comparison of direct antibody labeling and tumor

- pretargeting in uveal melanoma. *J. Nucl. Med.* **1996**, *37*, 967–971.
- 92 NOBS, L., BUCHEGGER, F., GURNY, R., ALLÉMANN, E., Current methods for attaching targeting ligands to liposomes and nanoparticles. *J. Pharm. Sci.* **2004**, *93*, 1980–1992.
- 93 ILLUM, L., JONES, P. D. E., KREUTER, J., BALDWIN, R. W., DAVIS, S. S., Adsorption of monoclonal antibodies to polyhexylcyanoacrylate nanoparticles and subsequent immunospecific binding to tumour cells in vitro. *Int. J. Pharm.* **1983**, *17*, 65–76.
- 94 ILLUM, L., JONES, P. D., BALDWIN, R. W., DAVIS, S. S., Tissue distribution of poly(hexyl 2-cyanoacrylate) nanoparticles coated with monoclonal antibodies in mice bearing human tumor xenografts. *J. Pharmacol. Exp. Ther.* **1984**, *230*, 733–736.
- 95 KUBIAK, C., MANIL, L., COUVREUR, P., Sorptive properties of antibodies onto cyanoacrylic nanoparticles. *Int. J. Pharm.* **1988**, *41*, 181–187.
- 96 MANIL, L., ROBLOT-TREUPEL, L., COUVREUR, P., Isobutyl cyanoacrylate nanoparticles as a solid phase for an efficient immunoradiometric assay. *Biomaterials* **1986**, *7*, 212–216.
- 97 COUVREUR, P., AUBRY, J., BREIMER, D. D., SPEISES, P., Monoclonal antibodies for the targeting of drugs: Application to nanoparticles. *Top. Pharmaceut. Sci.* **1983**, *305*–316.
- 98 BLACKWELL, J. E., DAGIA, N. M., DICKERSON, J. B., BERG, E. L., GOETZ, D. J., Ligand coated nanosphere adhesion to E- and P-selectin under static and flow conditions. *Ann. Biomed. Eng.* **2001**, *29*, 523–533.
- 99 SERIZAWA, T., UCHIDA, T., AKASHI, M., Synthesis of polystyrene nanospheres having lactose-conjugated hydrophilic polymers on their surfaces and carbohydrate recognition by proteins. *Biomater. Sci. Polym. Ed.* **1999**, *10*, 391–401.
- 100 LI, Y., OGRIS, M., WAGNER, E., PELISEK, J., RÜFFER, M., Nanoparticles bearing polyethylenglycol-coupled transferrin as gene carriers: preparation and in vitro evaluation. *Int. J. Pharm.* **2003**, *259*, 93–101.
- 101 AKASAKA, Y., UEDA, H., TAKAYAMA, K., MACHIDA, Y., NAGAI, T., Preparation and evaluation of bovine serum albumin nanospheres coated with monoclonal antibodies. *Drug Des. Disc.* **1988**, *3*, 85–97.
- 102 ROLLAND, A., BOUREL, D., GENETET, B., LE VERGE, R., Monoclonal antibodies covalently coupled to polymethacrylic nanoparticles: in vitro specific targeting to human T lymphocytes. *Int. J. Pharm.* **1987**, *39*, 173–180.
- 103 GAUTIER, S. N., GRUDZIELSKI, N., GOFFINET, G., DE HASSONVILLE, S. H., DELATTRE, L., JÉRÔME, R., Preparation of poly(D,L-lactide) nanoparticles assisted by amphiphilic poly(methyl methacrylate-co-methacrylic acid) copolymers. *J. Biomater. Sci. Polym.* **2001**, *12*, 429–450.
- 104 GREF, R., COUVREUR, P., BARRATT, G., MYSIAKINE, E., Surface-engineered nanoparticles for multiple ligand coupling. *Biomaterials* **2003**, *24*, 4529–4537.
- 105 MARUYAMA, A., ISHIHARA, T., KIM, J. S., KIM, S. W., AKAIKE, T., Nanoparticle DNA carrier with poly(L-lysine) grafted polysaccharide copolymer and poly(D,L-lactic acid). *Bioconj. Chem.* **1997**, *8*, 735–742.
- 106 CHAN, W. C. W., MAXWELL, D. J., GAO, X., BAILEY, R. E., HAN, M., NIE, S., Luminescent quantum dots for multiplexed biological detection and imaging. *Curr. Opin. Biotechnol.* **2002**, *13*(1), 40–46.
- 107 LIN, Z., CUI, S., ZHANG, H., CHEN, Q., YANG, B., SU, X., ZHANG, J., JIN, Q., Studies on quantum dots synthesized in aqueous solution for biological labeling via electrostatic interaction. *Anal. Biochem.* **2003**, *319*(2), 239–243.
- 108 GOLDMAN, E. R., et al., Conjugation of luminescent quantum dots with antibodies using an engineered adaptor protein to provide new reagents for fluoroimmunoassays. *Anal. Chem.* **2002**, *274*, 841–847.
- 109 MATTOUSSI, H., et al. in *Optical Biosensors: Present and Future* (Ed.: F. S. LIGLER, C. A. ROWE TAITT), Elsevier, The Netherlands, **2002**.

- 110 KAGAN, C. R., MURRAY, C. B., BAWENDI, M. G., Long-range resonance transfer of electronic excitations in close-packed CdSe quantum-dot solids. *Phys. Rev. B* **1996**, *54*, 8633–8643.
- 111 WANG, L. Y., KAN, X. W., ZHANG, M. C., ZHU, C. Q., WANG, L., Fluorescence for the determination of protein with functionalized nano-ZnS. *Analyst* **2002**, *127*, 1531–1534.
- 112 HANAKI, K., MOMO, A., OKU, T., KOMOTO, A., MAENOSONO, S., YAMAGUCHI, Y., YAMAMOTO, K., Semiconductor quantum dot/albumin complex is a long-life and highly photostable endosome marker. *Biochem. Biophys. Res. Commun.* **2003**, *302*, 496–501.
- 113 TRAN, P. T., GOLDMAN, E. R., ANDERSON, G. P., MAURO, J. M., MATTOUSSI, H., Use of luminescent CdSe-ZnS nanocrystal bioconjugates in quantum dot-based nanosensors. *Phys. Stat. Sol. B* **2002**, *229*(1), 427–432.
- 114 MEDINTZ, I. L., CLAPP, A. R., MATTOUSSI, H., GOLDMAN, E. R., FISHER, B., MAURO, J. M., Self-assembled nanoscale biosensors based on quantum dot FRET donors. *Nat. Mater.* **2003**, *2*(9), 630–638.
- 115 CHAN, W. C. W., NIE, S., Quantum dot bioconjugates for ultrasensitive nonisotopic detection. *Science* **1998**, *281*(5385), 2016–2018.
- 116 WU, X., LIU, J., LIU, H., HALEY, K. N., TREADWAY, J. A., LARSON, J. P., GE, N., PEALE, F., BRUCHEZ, M. P., Immuno-fluorescent labeling of cancer marker Her2 and other cellular targets with semiconductor quantum dots. *Nat. Biotechnol.* **2003**, *21*, 41–46.
- 117 WANG, S. P., MAMEDOVA, N., KOTOV, N. A., CHEN, W., STUDER, J., Antigen/antibody immunocomplex from CdTe nanoparticle bioconjugates. *Nano Lett.* **2002**, *2*, 817–822.
- 118 DUBERTRET, B., SKOURIDES, P., NORRIS, D. J., NOIREAUX, V., BRIVANLOU, A. H., In vivo imaging of quantum dots encapsuled in phospholipid micelles. *Science* **2002**, *298*, 1759–1762.
- 119 TEMPLETON, A. C., CHEN, S., GROSS, S. M., MURRAY, R. W., Water-soluble, isolable gold clusters protected by tiopronin and coenzyme A monolayers. *Langmuir* **1999**, *15*, 66–76.
- 120 SCHAAFF, T. G., KNIGHT, G., SHAFIGULLIN, M. N., BORKMAN, R. F., WHETTEN, R. L., Isolation and selected properties of a 10.4 kDa gold: Glutathione cluster compound. *J. Phys. Chem. B* **1998**, *102*, 10643–10646.
- 121 MIZIANI, M. J., SUN, Y. P., Protein-conjugated nanoparticles from rapid expansion of supercritical fluid solution into aqueous solution. *J. Am. Chem. Soc.* **2003**, *125*, 8015–8018.
- 122 BURT, J. L., GUTIERREZ-WING, C., MIKI-YOSHIDA, M., JOSE-YACAMAN, M., Noble-metal nanoparticles directly conjugated to globular proteins. *Langmuir* **2004**, *20*(26), 11778–11783.
- 123 CRUMBLISS, A. L., PERINE, S. C., STONEHUERNER, J., TUBERGEN, K. R., ZHAO, JUNGUO, HENKENS, R. W., O'DALY, J. P., Colloidal gold as an enzyme immobilization matrix for electrochemical biosensors. *Biotechnol. Bioeng.* **1992**, *40*, 483–490.
- 124 BROWN, K. R., FOX, A. P., NATAN, M. J., Morphology-dependent electrochemistry of cytochrome c at Au colloid-modified SnO<sub>2</sub> electrodes. *J. Am. Chem. Soc.* **1996**, *118*, 1154–1157.
- 125 SASTRY, M., LALA, N., PATIL, V., CHAVAN, S. P., CHITTIBOYINA, A. G., Optical absorption study of the biotin-avidin interaction on colloidal silver and gold particles. *Langmuir* **1998**, *14*(15), 4138–4142.
- 126 ALIVISATOS, A. P., JOHNSON, K. P., PENG, X., WILSON, T. E., LOWETH, C. J., BRUCHEZ JR., M. P., SCHULTZ, P. G., Organization of 'nanocrystal molecules' using DNA. *Nature* **1996**, *382*, 609–611.
- 127 MUCIC, R. C., STORHOFF, J. J., MIRKIN, C. A., LETSINGER, R. L., DNA-directed synthesis of binary nanoparticle network materials. *J. Am. Chem. Soc.* **1998**, *120*, 12674–12675.
- 128 ZANCHET, D., MICHEEL, C. M., PARAL, W. J., GERION, D., ALIVISATOS, A. P.,



- Electrophoretic isolation of discrete Au nanocrystal/DNA conjugates. *Nano Lett.* **2001**, *1*, 32–35.
- 129 HIRSCH, L. R., STAFFORD, R. J., BANKSON, J. A., SERSHEN, S. R., RIVERA, B., PRICE, R. E., HAZLE, J. D., HALAS, N. J., WEST, J. L., Nanoshell-mediated near-infrared thermal therapy of tumors under magnetic resonance guidance. *Proc. Natl. Acad. Sci. U.S.A.* **2003**, *100*(23), 13549–13554.
- 130 KOHLER, N., FRYXELL, G. E., ZHANG, M., A bifunctional poly(ethylene glycol) silane immobilized on metallic oxide-based nanoparticles for conjugation with cell targeting agents. *J. Am. Chem. Soc.* **2004**, *126*(23), 7206–7211.
- 131 WUELFING, W. P., GROSS, S. M., MILES, D. T., MURRAY, R. W., Nanometer gold clusters protected by surface-bound monolayers of thiolated poly(ethylene glycol) polymer electrolyte. *J. Am. Chem. Soc.* **1998**, *120*, 12696–12697.
- 132 QUARONI, L., CHUMANOV, G., Preparation of polymer-coated functionalized silver nanoparticles. *J. Am. Chem. Soc.* **1999**, *121*, 10642–10643.
- 133 PINAUD, F., KING, D., MOORE, H. P., WEISS, S., Bioactivation and cell targeting of semiconductor CdSe/ZnS nanocrystals with phytochelation-related peptides. *J. Am. Chem. Soc.* **2004**, *126*(19), 6115–6123.
- 134 ROAN, J. R., Attraction between nanoparticles by end-grafted homopolymers in good solvent. *Phys. Rev. Lett.* **2001**, *86*, 1027–1030.
- 135 OKANO, T., *Biorelated Polymers and Gels*, Academic Press, Boston, **1998**.
- 136 HORBETT, T. A., BRASH, T. J. L., *Proteins at Interfaces II.*, ACS Symposium Series 602, Washington, DC, **1995**.
- 137 ANDRADE, J. D., HLADY, V., WEI, A. P., Adsorption of complex proteins at interfaces. *Pure Appl. Chem.* **1992**, *64*, 1777–1781.
- 138 JEON, S. I., LEE, J. H., ANDRADE, J. D., DE GENNES, P. G., Protein-surface interactions in the presence of polyethylene oxide. I. Simplified theory. *J. Colloid Interface Sci.* **1991**, *142*, 149–158.
- 139 HARRIS, J. M., *Poly(ethylene glycol) Chemistry, Biotechnical and Biomedical Applications*, Plenum Press, New York, **1992**.
- 140 IKADA, Y., Blood-compatible polymers. *Adv. Polym. Sci.* **1984**, *57*, 104–140.
- 141 AMIJI, M., PARK, K., Surface modification of polymeric biomaterials with poly(ethylene oxide), albumin, and heparin for reduced thrombogenicity. *J. Biomater. Sci. Polym. Ed.* **1993**, *4*, 217–234.
- 142 SZLEIFER, I., Polymers and proteins: interactions at interfaces. *Curr. Opin. Solid State Mater. Sci.* **1997**, *2*, 337–344.
- 143 PRIME, K. L., WHITESIDES, G. M., Self-assembled organic monolayers: model systems for studying adsorption of proteins at surfaces. *Science* **1991**, *252*, 1164–1167.
- 144 OSTUNI, E., CHAPMAN, R. G., HOLMLIN, R. E., TAKAYAMA, S., WHITESIDES, G. M., A survey of structure-property relationships of surfaces that resist the adsorption of protein. *Langmuir* **2001**, *17*, 5605–5620.
- 145 MCPEARSON, T., KIDANE, A., SZLEIFER, I., PARK, K., Prevention of protein adsorption by tethered poly(ethylene oxide) layers: experiments and single-chain mean-field analysis. *Langmuir* **1998**, *14*, 176–186.
- 146 SATULOVSKY, J., CARIGANO, M. A., SZLEIFER, I., Kinetic and thermodynamic control of protein adsorption. *Proc. Natl. Acad. Sci. U.S.A.* **2000**, *10*, 9037–9041.
- 147 GHITESCU, L., FIXMAN, A., Surface charge distribution on the endothelial cell of liver sinusoids. *J. Cell Biol.* **1984**, *99*, 639–647.
- 148 JORDAN, A., SCHOLZ, R., WUST, P., SCHIRRA, H., SCHIESTEL, T., SCHMIDT, H., FELIX, R., Visualization and registration of three-dimensional E-field distributions in annual-phased-array applicators. *J. Magn. Magn. Mater.* **1999**, *194*, 185–196.
- 149 WILHELM, C., BILLOTEY, C., ROGER, J.,

- BITTOUN, J., PONS, J. N., BACRI, J. C., GAZEAU, F., Intracellular uptake of anionic superparamagnetic nanoparticles as a function of their surface coating. *Biomaterials* **2003**, *24*, 1001–1011.
- 150 KLOEPFER, J. A., MIELKE, R. E., WONG, M. S., NEALSON, K. H., STUCKY, G., NEDEAU, J. L., Quantum dots as strain- and metabolism-specific microbiological labels. *Appl. Environ. Microbiol.* **2003**, *69*, 4205–4213.
- 151 HOSHINO, A., FUJIOKA, K., OKU, T., SUGA, M., SASAKI, Y. F., OHTA, T., YASUHARA, M., SUZUKI, K., YAMAMOTO, K., Physicochemical properties and cellular toxicity of nanocrystal quantum dots depend on their surface modification. *Nano Lett.* **2004**, *4*, 2163–2169.
- 152 DERFUS, A. M., CHAN, W. C. W., BHATIA, S. N., Probing the cytotoxicity of semiconductor quantum dots. *Nano Lett.* **2004**, *4*, 11–18.
- 153 KIRCHNER, C., LIEDL, T., KUDERA, S., PELLEGRINO, T., JAVIER, A. M., GAUB, H. E., STOELZLE, S., FERTIG, N., PARAK, W. J., Cytotoxicity of colloidal CdSe and CdSe/ZnS nanoparticles. *Nano Lett.* **2005**, *5*(2), 331–338.
- 154 KONDOH, M., ARARAGI, S., SATO, K., HIGASHIMOTO, M., TAKIGUCHI, M., SATO, M., Cadmium induces apoptosis partly via caspase-9 activation in HL-60 cells. *Toxicology* **2002**, *170*, 111–117.
- 155 RIKANS, L. E., YAMANO, T., Mechanisms of cadmium-induced acute hepatotoxicity. *J. Biochem. Mol. Toxicol.* **2000**, *14*, 110–117.
- 156 HAYAT, M., *Colloidal Gold: Principles, Methods and Applications*, Academic, San Diego, **1989**.
- 157 OTSUKA, H., NAGASAKI, Y., KATAOKA, K., PEGylated nanoparticles for biological and pharmaceutical applications. *Adv. Drug Deliv.* **2003**, *55*, 403–419.
- 158 QI, L., COLFEN, H., ANTONIETTI, M., Synthesis and characterization of CdS nanoparticles stabilized by double-hydrophilic block copolymers. *Nano Lett.* **2001**, *1*, 61–65.
- 159 MUMPER, R. J., LEDEBUR, H. C., Dendritic cell delivery of plasmid DNA: applications for genetic vaccines. *Mol. Biotechnol.* **2001**, *19*, 79–95.
- 160 MACLAUGHLIN, F. C., MUMPER, R. J., WANG, J., TAGLIAFERRI, J. M., ROLAND, A. P., Nanotemplate engineering of cell specific nanoparticles. *J. Controlled Rel.* **1998**, *4*(56), 259–272.
- 161 KREUTER, J., Nanoparticles as adjuvants for vaccines. *Pharm. Biotechnol.* **1995**, *6*, 463–472.
- 162 DOUGLAS, S. J., DAVIS, S. S., ILLUM, L., Nanoparticles in drug delivery. *Crit. Rev. Ther. Drug Carrier Syst.* **1987**, *3*, 233–261.
- 163 WANG, C. W., MOFFITT, M. G., Surface-tunable photoluminescence from block copolymer-stabilized cadmium sulfide quantum dots. *Langmuir* **2004**, *20*(26), 11784–96.
- 164 GAO, X., CUI, Y., LEVENSON, R. M., CHUNG, L. W. K., NIE, S., In vivo cancer targeting and imaging with semiconductor quantum dots. *Nat. Biotechnol.* **2004**, *22*(8), 969–976.
- 165 BERTOZZI, C. R., BEDNARSKI, M. D., The synthesis of heterobifunctional linkers for the conjugation of ligands to molecular probes. *J. Org. Chem.* **1991**, *56*, 4326–4329.
- 166 COOK, R. M., ADAMS, J. H., HUDSON, D., The preparation and synthetic application of heterobifunctional biocompatible spacer arms. *Tetrahedron Lett.* **1994**, *35*, 6777–6780.
- 167 SCHWABACHER, A. W., LANE, J. W., SCHIESHER, M. W., LEIGH, K. M., JOHNSON, C. W., Desymmetrization reactions: Efficient preparation of unsymmetrically substituted linker molecules. *J. Org. Chem.* **1998**, *63*, 1727–1729.
- 168 NAGASAKI, Y., KUTSUNA, T., IIJIMA, M., KATO, M., KATAOKA, K., Formyl-ended heterobifunctional poly(ethylene oxide): synthesis of poly(ethylene oxide) with a formyl group at one end and a hydroxyl group at the other. *Bioconj. Chem.* **1995**, *6*, 231–233.
- 169 NAGASAKI, Y., IIJIMA, M., KATO, M., KATAOKA, K., Primary amino-terminal heterobifunctional poly(ethylene

- oxide). Facile synthesis of poly(ethylene oxide) with a primary amino group at one end and a hydroxyl group at the other. *Bioconj. Chem.* **1995**, *6*, 702–704.
- 170** NAGASAKI, Y., OGAWA, R., YAMAMOTO, S., KATO, M., KATAOKA, K., Synthesis of heterotelechelic poly(ethylene glycol) macromonomers. Preparation of poly(ethylene glycol) possessing a methacryloyl group at one end and a formyl group at the other end. *Macromolecules* **1997**, *30*, 6489–6493.
- 171** NAKAMURA, T., NAGASAKI, Y., KATAOKA, K., Synthesis of heterobifunctional poly(ethylene glycol) with a reducing monosaccharide residue at one end. *Bioconj. Chem.* **1998**, *9*, 300–303.
- 172** AKIYAMA, Y., OTSUKA, H., NAGASAKI, Y., KATAOKA, K., Selective synthesis of heterobifunctional poly(ethylene glycol) derivatives containing both mercapto and acetal terminals. *Bioconj. Chem.* **2000**, *11*, 947–950.
- 173** OTSUKA, H., AKIYAMA, Y., NAGASAKI, Y., KATAOKA, K., Quantitative and reversible lectin-induced association of gold nanoparticles modified with  $\alpha$ -lactosyl- $\omega$ -mercapto-poly(ethylene glycol). *J. Am. Chem. Soc.* **2001**, *123*, 8226–8230.
- 174** LI, Z. F., RUCKENSTEIN, E., Water-soluble poly(acrylic acid) grafted silicon nanoparticles and their use as fluorescent biological staining labels. *Nano Lett.* **2004**, *4*, 1463–1467.
- 175** SONDI, I., SHIMAN, O., KOESTER, S., MATIJEVIC, E., Preparation of aminodextran-CdS nanoparticle complexes and biologically active antibody-aminodextran-CdS nanoparticle conjugates. *Langmuir* **2000**, *16*, 3107–3118.
- 176** WANG, Y. A., LI, J. J., CHEN, H. Y., PENG, X. G., Stabilization of inorganic nanocrystals by organic dendrons. *J. Am. Chem. Soc.* **2002**, *124*, 2293–2298.
- 177** MOFFITT, M., VALI, H., EISENBERG, A., Spherical assemblies of semiconductor nanoparticles in water-soluble block copolymer aggregates. *Chem. Mater.* **1998**, *10*, 1021–1028.
- 178** CHEN, Y., JI, T., ROSENZWEIG, Z., Synthesis of glyconanospheres containing luminescent CdSe-ZnS quantum dots. *Nano Lett.* **2003**, *3*, 581–584.
- 179** DE LA FUENTE, J. M., BARRIENTOS, A. G., ROJAS, T. C., ROJO, J., CANADA, J., FERNÁNDEZ, A., PENADÉS, S., Gold glyconanoparticles as water-soluble polyvalent models to study carbohydrate interactions. *Angew. Chem. Int. Ed.* **2001**, *40*, 2258–2261.
- 180** ROJAS, T. C., DE LA FUENTE, J. M., BARRIENTOS, A. G., PENADÉS, S., Gold glyconanoparticles as binding blocks for nanomaterials design. *Adv. Mater.* **2002**, *14*, 585–588.
- 181** ALDANA, J., WANG, Y. A., PENG, X. G., Photochemical instability of CdSe nanocrystals coated by hydrophilic thiols. *J. Am. Chem. Soc.* **2001**, *123*, 8844–8850.
- 182** CORREA-DUARTE, M. A., GIERSIG, M., LIZ-MARZÁN, L. M., Stabilization of CdS semiconductor nanoparticles against photodegradation by a silica coating procedure. *Chem. Phys. Lett.* **1998**, *286*, 497–501.
- 183** MULVANEY, P., LIZ-MARZÁN, L. M., GIERSIG, M., UNG, T., Silica encapsulation of quantum dots and metal clusters. *J. Mater. Chem.* **2000**, *10*, 1259–1270.
- 184** ROGACH, A. L., NAGESHA, D., OSTRANDER, J. W., GIERSIG, M., KOTOV, N. A., “Raisin bun”-type composite spheres of silica and semiconductor nanocrystals. *Chem. Mater.* **2000**, *12*, 2676–2685.
- 185** TAPEC, R., ZHAO, X. J., TAN, W., Development of organic dye-doped silica nanoparticles for bioanalysis and biosensors. *J. Nanosci. Nanotech.* **2002**, *2*(3–4), 405–409.
- 186** MEALLET-RENAULT, R., PANSU, R., AMIGONI-GERBIER, S., LARPENT, C., Metal-chelating nanoparticles as selective fluorescent sensor for Cu<sup>2+</sup>. *Chem. Commun.* **2004**, (20), 2344–2345.
- 187** BRASUEL, M., KOPELMAN, R., AYLOTT, J. W., CLARK, H., XU, H., HOYER, M., MILLER, T. J., TJALKENS, R., PHILBERT, M. A., Production, characteristics and applications of fluorescent PEBBLE

- nanosensors: potassium, oxygen, calcium and pH imaging inside live cells. *Sensors Mater.* **2002**, *14*(6), 309–338.
- 188** PARK, E. J., BRASUEL, M., BEHREND, C., PHILBERT, M. A., KOPELMAN, R., Ratiometric optical PEBBLE nanosensors for real-time magnesium ion concentrations inside viable cells. *Anal. Chem.* **2003**, *75*(15), 3784–3791.
- 189** BUCK, S. M., XU, H., BRASUEL, M., PHILBERT, M. A., KOPELMAN, R., Nanoscale probes encapsulated by biologically localized embedding (PEBBLEs) for ion sensing and imaging in live cells. *Talanta* **2004**, *63*(1), 41–59.
- 190** SUN, B., XIE, W., YI, G., CHEN, D., ZHOU, Y., CHENG, J., Microminaturized immunoassays using quantum dots as fluorescent label by laser confocal scanning fluorescence detection. *J. Immunol. Methods* **2001**, *249*(1–2), 85–89.
- 191** TRAN, P. T., GOLDMAN, E. R., MATTOUSSI, H., ANDERSON, G. P., MAURO, J. M., Bioconjugates of luminescent CdSe-ZnS quantum dots with an engineered two-domain protein G for use in fluorimmunoassays. *Int. Soc. Opt. Eng.* **2001**, *4258*, 1–7.
- 192** YUN, K. S., LEE, D., KIM, M. S., KIM, H. S., LEE, G. M., YOON, E., High-throughput bio-molecule detection using microbead-based assay with quantum dot fluorescence in a microfluidic chip, in *Micro Total Analysis Systems 2004*, Vol. 2, (Ed.: Royal Society of Chemistry), Cambridge, UK, **2004**, pp. 222–224.
- 193** GAO, X., NIE, S., Quantum dot-encoded mesoporous beads with high brightness and uniformity: Rapid readout using flow cytometry. *Anal. Chem.* **2004**, *76*(8), 2406–2410.
- 194** MAXWELL, D. J., TAYLOR, J. R., NIE, S., Self-assembled nanoparticle probes for recognition and detection of biomolecules. *J. Am. Chem. Soc.* **2002**, *124*(32), 9606–9612.
- 195** ZAYATS, M., BARON, R., POPOV, I., WILLNER, I., Biocatalytic growth of Au nanoparticles: From mechanistic aspects to biosensors design. *Nano Lett.* **2005**, *5*(1), 21–25.
- 196** HAES, A. J., HALL, W. P., CHANG, L., KLEIN, W. L., VAN DUYN, R. P., A localized surface plasmon resonance biosensor: First steps toward an assay for Alzheimer's disease. *Nano Lett.* **2004**, *4*(6), 1029–1034.
- 197** LIAN, W., LITHERLAND, S. A., BADRANE, H., TAN, W., WU, D., BAKER, H. V., GULIG, P. A., LIM, D. V., JIN, S., Ultrasensitive detection of biomolecules with fluorescent dye-doped nanoparticles. *Anal. Biochem.* **2004**, *334*, 135–144.
- 198** MANSSON, A., SUNDBERG, M., BALAZ, M., BUNK, R., NICHOLLS, I. A., OMLING, P., TAGERUD, S., MONTELIUS, L., In vitro sliding of actin filaments labeled with single quantum dots. *Biochem. Biophys. Res. Commun.* **2004**, *314*(2), 529–534.
- 199** DAISUKE, I., KAZUSHI, K., YASUHIRO, I., NORIYUKI, I., MINA, O., MASAFUMI, Y., TAKUZO, A., Chaperonin-mediated stabilization and ATP-triggered release of semiconductor nanoparticles. *Nature* **2003**, *423*, 628–632.
- 200** SCHMIDT, T., SCHUETZ, G. J., BAUMGARTNER, W., GRUBER, H. J., SCHINDLER, H., Characterization of photophysics and mobility of single molecules in a fluid lipid membrane. *J. Phys. Chem.* **1995**, *99*, 17662–17668.
- 201** DEVERALL, M. A., GINDI, E., SINNER, E. K., RUEHE, J., SAXTON, M. J., NAUMANN, C. A., Membrane lateral mobility obstructed by polymer-tethered lipids studied at the single molecule level. *Biophys. J.* **2005**, *88*, 1875–1886.
- 202** DAHAN, M., LÉVI, S., LUCCARDINI, C., ROSTAING, P., RIVEAU, B., TRILLER, A., Diffusion dynamics of glycine receptors revealed by single-quantum dot tracking. *Science* **2003**, *302*, 442–445.
- 203** LIDKE, D. S., NAGY, P., HEINTZMANN, R., ARNDT-JOVIN, D. J., POST, J. N., GRECO, H. E., JARES-ERIJMAN, E. A., JOVIN, T. M., Quantum dot ligands provide new insights into erbB/HER receptor-mediated signal transduction. *Nat. Biotechnol.* **2004**, *22*, 198–203.
- 204** BALLOU, B., LAGERHOLM, B. C., ERNST,

- L. A., BRUNCHEZ, M. P., WAGGONER, A. S., Noninvasive imaging of quantum dots in mice. *Bioconj. Chem.* **2004**, *15*, 79–86.
- 205 ÅKERMAN, M. E., CHAN, W. C. W., LAAKONEN, P., BHATIA, S. N., RUOSLAHTI, E., Nanocrystal targeting in vivo. *Proc. Natl. Acad. Sci. U.S.A.* **2002**, *99*, 12617–12621.
- 206 KERSHAW, S. V., HARRISON, M., ROGACH, A. L., KORNOWSKI, A., Development of IR-emitting colloidal II–VI quantum-dot materials. *IEEE J. Sel. Top. Quantum Electron.* **2000**, *6*, 534–543.
- 207 KIM, S., LIM, Y. T., SOLTESZ, E. G., DE GRAND, A. M., LEE, J., NAKAYAMA, A., PARKER, J. A., MIHALJEVIC, T., LAURENCE, R. G., DOR, D. M., COHN, L. H., BAWENDI, M. G., FRANGIONI, J. V., Near-infrared fluorescent type II quantum dots for sentinel lymph node mapping. *Nat. Biotechnol.* **2004**, *22*, 93–97.

## 2

# Biofunctionalization of Carbon Nanotubes

*Elena Bekyarova, Robert C. Haddon, and Vladimir Parpura*

### 2.1

#### Introduction

The decade long history of carbon nanotubes (CNTs) has been largely devoted to investigation of their growth mechanism and physical and chemical properties. This has led to sustained progress in the synthesis of materials of higher purity, to chemically functionalized CNTs with specifically tailored properties, and to the development of technologies for the processing and assembly of CNTs into functional structures and devices. Recent research on the chemical interactions between biological molecules and CNTs has led to the assembly of functional hybrid (CNT-biomolecule) structures for nanoelectronics, scaffolds for cell and tissue growth, and high-performance biosensors. While much remains to be accomplished, this fascinating nanomaterial clearly offers great potential for the development of revolutionary hybrid structures and devices, and work in this field has propelled CNTs to a point that their entry into the realm of nanobiotechnology and nanomedicine is now a reality [1].

In this chapter, we overview the currently available methods for biofunctionalization of CNTs and some of their applications in biology and nanotechnology. We briefly discuss the structure, properties, and most common methods for synthesis of CNTs, focusing on current progress in patterned growth and purification of CNTs. We summarize the achievements in chemical modification of CNTs that are related to the solubilization of CNTs in water, since the dispersion and stabilization of CNTs in aqueous media is a key step in developing biological applications. We present various schemes for noncovalent and covalent modifications of CNTs with biological molecules. Additionally, we review the applicability of the modified CNTs in the assembly of electronic devices, for biosensing, and as scaffolds or substrates for neuronal growth.

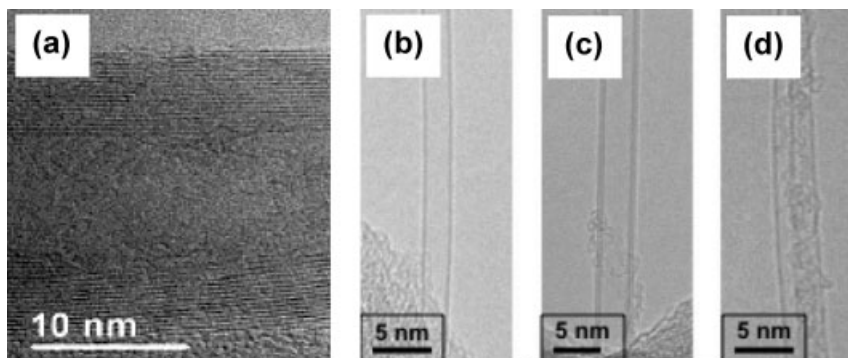


**Fig. 2.1.** Transmission electron microscopy images of (a) multi-walled carbon nanotubes, (b) single-walled carbon nanotubes, (c) double-walled carbon nanotubes, and (d) a bundle of single-walled carbon nanotubes. (TEM micrographs in (b)–(d) [112] are reproduced by permission of the American Chemical Society Publications.)

## 2.2

### Carbon Nanotubes – Types, Structures and Properties

CNTs can be classified according to the number of concentric graphene cylinders that constitute their structure (Fig. 2.1). Multi-walled CNTs (MWNTs) consist of several concentric graphene cylinders with their ends individually capped with hemispheres of fullerene molecules. Typically, their outer diameter ranges from 2 to 100 nm, while their inner diameter is about 1–3 nm. The MWNTs are from 1 to several hundred  $\mu\text{m}$  long. Double-walled CNTs (DWNs) are composed of two concentric graphene cylinders, and represent an intermediate structure between MWNTs and single-walled CNTs (SWNTs), the later consisting of a single graphene cylinder. Although the smallest SWNTs reported have a diameter of 0.4 nm [2, 3], which corresponds to a hemispherical fragment of the  $\text{C}_{20}$  dodecahedron, SWNTs are usually produced with a random distribution of diameters (0.7–2 nm) and exist in hexagonally close-packed bundles held together by van der Waals forces.

Based on their hexagonal lattice structure, SWNTs are classified as armchair, zigzag and chiral (Fig. 2.2). The wrapping angle of the graphene sheet determines the electronic properties of SWNTs [4–6]. All armchair nanotubes are conductive (metallic), while the zigzag and chiral nanotubes can be either metallic or semiconducting. Most currently available synthetic methods produce SWNTs with a random distribution of metallic and semiconducting nanotubes in a ratio of 1:2. Because CNTs are either metallic or semiconducting, they provide the necessary building blocks for molecular electronics. In addition, they are ballistic conductors with high effective mobility and can sustain very high current densities. A rope of SWNTs has a room temperature conductivity in the range  $10\,000\text{--}30\,000\text{ S cm}^{-1}$  [7]. These properties provide a unique opportunity to develop miniature advanced

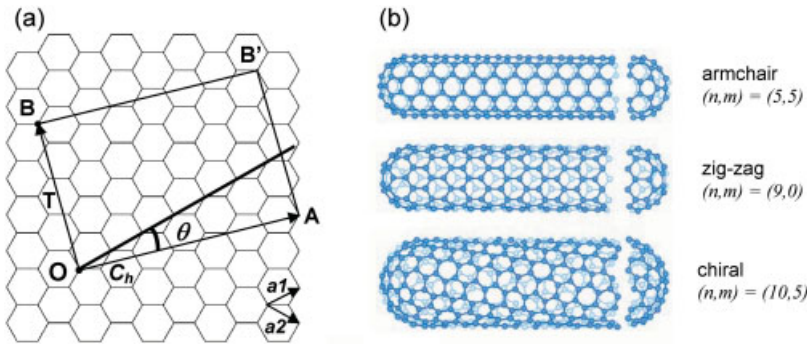


**Fig. 2.2.** (a) Two-dimensional graphene sheet. A carbon nanotube is formed by rolling up the graphene sheet and superimposing the two ends OA of the chiral vector ( $C_h$ ). The chiral vector is defined as  $C_h = na_1 + ma_2$ , where  $a_1$  and  $a_2$  are unit vectors in the two-dimensional hexagonal lattice, and  $n$  and  $m$  are integers. The pair of integers  $(n, m)$  and the chiral angle ( $\theta$  – the angle between  $C_h$  and  $a_1$ ) define the nanotube type: armchair ( $n = m$ ,  $\theta = 30^\circ$ ), zigzag ( $n$  or  $m = 0$ ,  $\theta = 0^\circ$ ) and chiral ( $\theta$  between  $0$  and  $30^\circ$ ). The diagram is constructed for a  $(5, 2)$  carbon nanotube.  $T$  is the basic translation vector for the tubule and the unit cell of this tubule is defined by  $OABB'$ . (b) Schematic models for the three types of SWNTs. (Courtesy of Riichiro Saito, Tohoku University, Japan.)

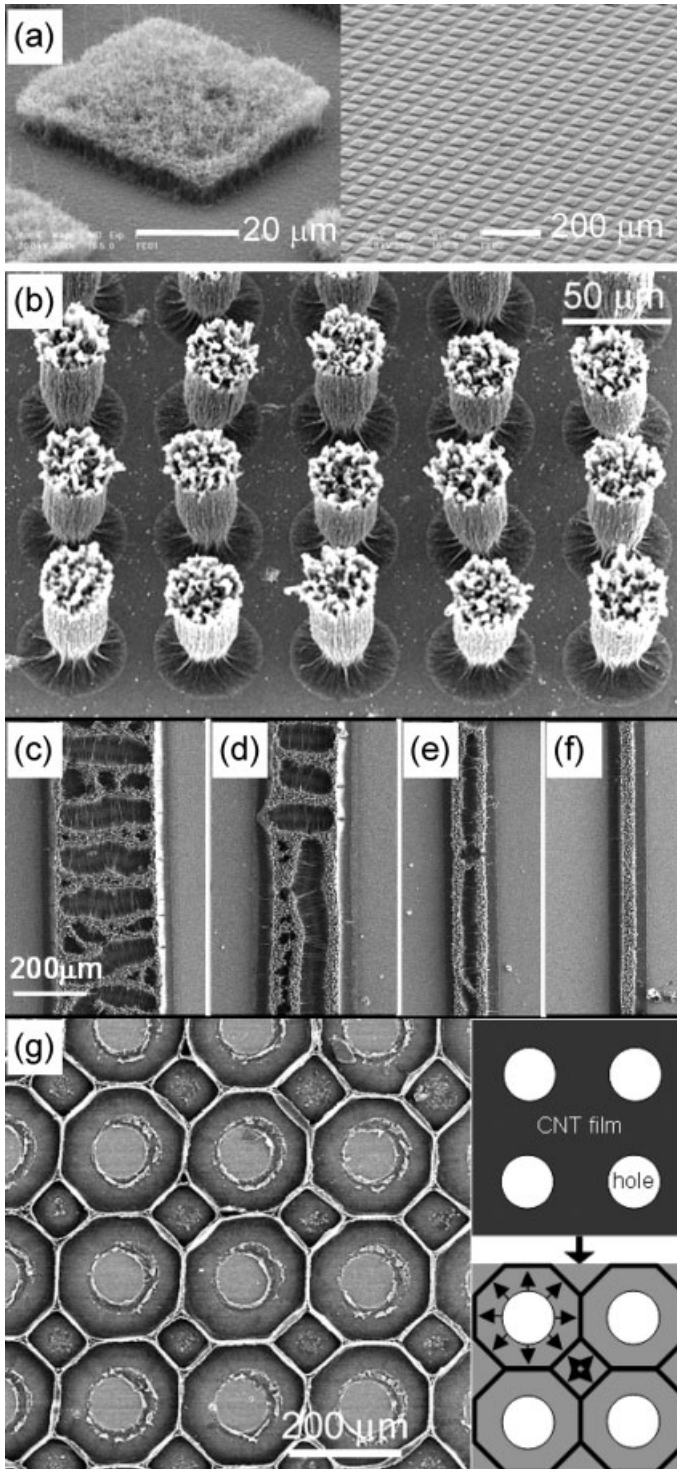
sensors [8] for rapid, label-free electronic detection of different biological materials (Section 2.5.2). With a Young's modulus of  $\sim 1$  TPa [9, 10], CNTs also have exceptional mechanical strength – a useful feature for tissue scaffolds and engineering.

### 2.3 Synthesis of Carbon Nanotubes

The most widely used techniques for synthesis of CNTs are electric arc discharge, laser ablation, chemical vapor deposition (CVD) and high-pressure carbon monoxide disproportionation (HiPco) [11]. The first two methods involve the vaporization of carbon in an inert atmosphere, whereas CVD and HiPco are based on catalytic decomposition of hydrocarbons. The synthesis of CNTs has advanced to the point that patterns of aligned MWNTs or SWNTs can be engineered. Such patterned growth is of interest in tissue engineering [12]. CNT-based scaffolds have some advantages over bio-degradable synthetic polymers currently used in tissue engineering as they possess the structural integrity and high mechanical stability to support developing tissue and to withstand *in vivo* forces [12].

SWNTs can be aligned by applying an electric field during CVD growth of the nanotubes [13–15], and vertically aligned arrays of MWNTs (Fig. 2.3) are routinely produced in standard CVD experiments [16–19]. Network architectures have been produced by the reassembly of dense CNT arrays using the capillary forces induced





by the evaporation of liquids from the CNT films or mats (Fig. 2.3) [12, 19]. In this process, the nanotubes collapse to cellular structures due to the induced surface tension; the resulting periodic architectures might find applications as scaffolds for tissue engineering. Indeed, similar structures composed of MWNTs (Fig. 2.4) have been used to support the cellular adhesion and growth of mouse fibroblasts [12].

While patterned films and mats that are attractive for cell growth, biosensors, and bioelectronics all require relatively small amounts of material, applications may be envisaged in which bulk quantities of CNTs are necessary. Although bulk production is a necessary step, the purity of the CNT material is an essential prerequisite for further progress. MWNTs of high purity can be readily synthesized. However, SWNTs typically contain a substantial fraction of carbonaceous impurities together with the metal that is used as a catalyst in the synthesis. Quality control in SWNT manufacturing is a major issue, and the absence of widely accepted and established methods for quality assessment has raised questions regarding the purity of commercially available CNT materials [20]. Certainly, high purity material is required if SWNTs are to play an important role in biotechnology. Although quality control is virtually nonexistent in the CNT industry, analytical tools for reliable evaluation of the quality of SWNT materials exist, and efforts to establish standards in the field may help to reform current CNT industrial practices. Solution phase near-infrared (NIR) spectroscopy [21–24], Raman spectroscopy [25, 26], thermogravimetric analysis [25, 27], and combinations of these analytical methods [28] have been used to evaluate SWNT purity. At this point, NIR spectroscopy has been established as the simplest, fastest, most efficient and unambiguous technique for the quantitative assessment of the carbonaceous purity of SWNTs [29], while thermogravimetric analysis can reliably estimate the metal content based on the residue remaining after pyrolysis of the carbon content of the sample.

The quality of CNTs can be improved by progress in the synthesis or purification techniques, and significant achievements in both areas have been reported. Recently, very high purity, metal-free SWNTs (carbonaceous purity of 99.98%) have been synthesized [30]. The purification processes are based on a combination of several steps, which usually include gas or vapor-phase oxidation, wet chemical oxidation, centrifugation, filtration or chromatography (see Refs. [31–35] and references therein).

←

**Fig. 2.3.** (a) Patterned MWNTs grown by CVD. (b)–(g) Patterned carbon nanotube films. (b) Wine glass-like structures obtained by the evaporation of liquids from cylindrical MWNT arrays. (c)–(f) Cellular structures of aligned MWNTs formed after immersion of the nanotube sample in acetone and drying under ambient conditions. (g) Carbon nanotube structure of a patterned MWNT array. The consolidation of the rims during the drying of the patterned CNT array affords a structure with mainly square and octagonal cells. The inset represents schematics of this process. Arrows indicate the direction of the CNT collapse due to surface tension [19]. (Reproduced by permission of the National Academy of Sciences U.S.A.)

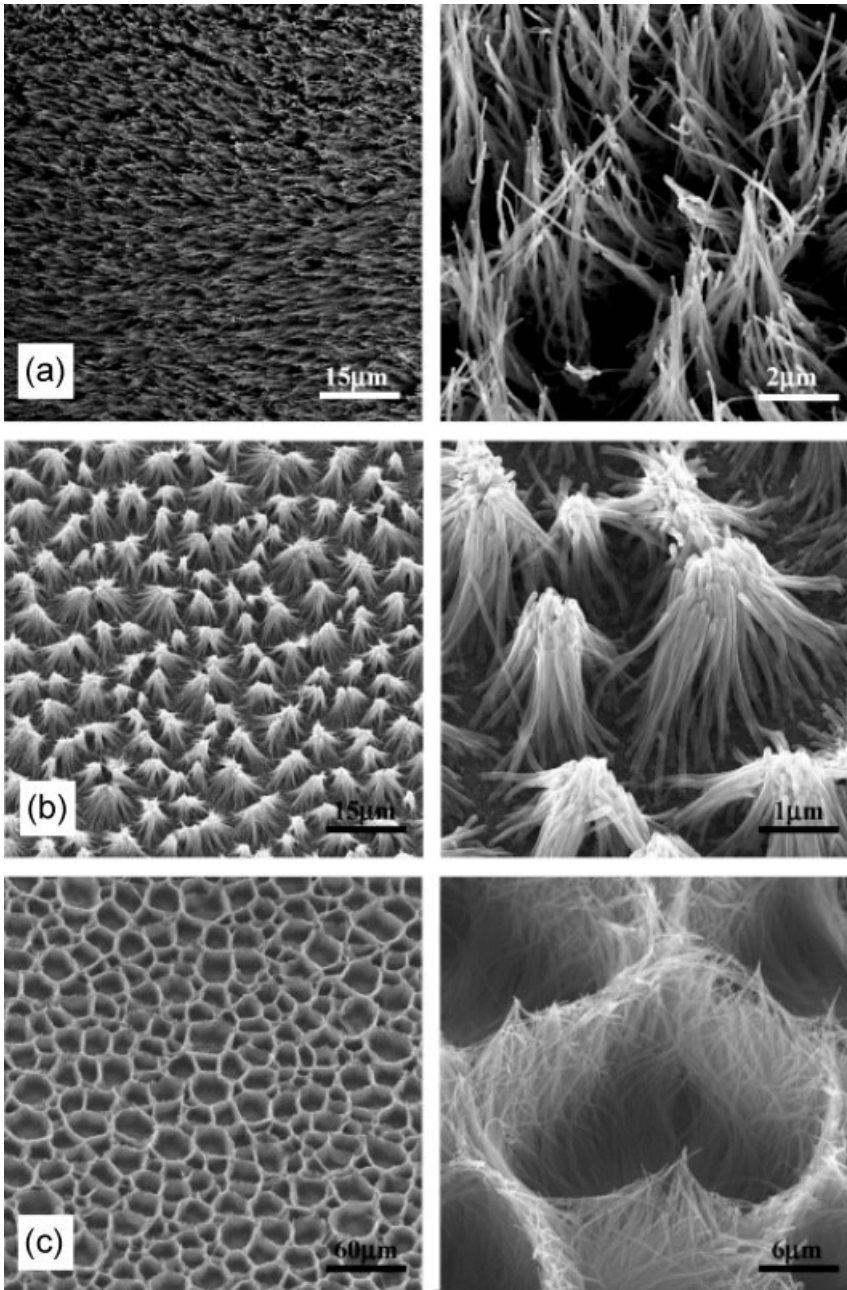


**Fig. 2.4.** SEM micrographs of MWNT structures used as scaffold for fibroblast growth. Left-hand column, low magnifications; right-hand column, high magnifications. (a)

Perpendicularly aligned CNTs. (b) Pyramid-like structures. (c) Network of crosslinked CNT walls forming cavities [12]. (Reproduced by permission of the American Chemical Society.)

## 2.4

### Approaches to Aqueous Solubilization of Carbon Nanotubes

#### 2.4.1

##### Chemical Modifications

As-prepared SWNTs self-assemble in hexagonally packed bundles, in which the nanotubes are held together by van der Waals forces. The strength of these attractive forces makes the exfoliation of individual CNTs from the bundle and their stabilization in solution difficult. An additional complication arises from the chemical inertness of the CNTs due to the absence of functional groups in their graphitic structure, making their dissolution in a solvent a complex issue. Consequently, chemical functionalization has been used as a valuable route to the solubilization and exfoliation of individual CNTs from the bundles.

One of the most widely used chemical approaches to introduce functionalities onto CNTs involves treatment with strong oxidizing agents such as nitric and sulfuric acids. These strong acids preferentially disrupt the aromatic ring structure at the caps of CNTs and lead to the introduction of carboxylic acid groups at the open ends [21, 31, 34, 36, 37]; this functionality can undergo further reactions to produce a large family of tailored materials. Numerous amidation and esterification reactions of oxidized SWNTs have been reported [36, 38]. Typically, carboxylic acid functionalized SWNTs (SWNT-COOH) are treated with thionyl chloride ( $\text{SOCl}_2$ ) to form the acyl chloride intermediate (SWNT-COCl) [31], which is then reacted with an amino derivative. This approach has been used to covalently attach octadecylamine to the open ends of the SWNTs, affording SWNT-CONH(CH<sub>2</sub>)<sub>17</sub>CH<sub>3</sub>, a form of the carbon nanotubes that proved to be soluble in various organic solvents (Fig. 2.5) [21]. This approach has proved to be applicable to various functionalities. However, the solubilization of CNTs in aqueous solutions – a prerequisite for use in many biological applications – is a more challenging task because of the hydrophobic nature of CNTs. Although stable aqueous solutions of SWNTs have been obtained by ultrasonication in a mixture of sulfuric acid and hydrogen peroxide [39], the more common methods of dispersing CNTs in aqueous solutions involve: (a) coating CNTs with surfactants, (b) functionalization of CNTs with water-soluble polymers, and (c) interaction of CNTs with biological molecules. These methods are detailed below.

#### 2.4.2

##### Use of Water-compatible Surfactants

Surfactant-induced dispersion of CNTs depends on the presence of hydrophilic and hydrophobic regions in the surfactant molecule. Adsorption of the surfactant on the side walls of the nanotubes occurs through the hydrophobic tail of the surfactant molecule, which can adopt a wide range of orientations with respect to the tube, leaving the hydrophilic moiety oriented towards the aqueous phase. This can induce stable dispersions of surfactant-coated SWNTs in water. SWNTs were

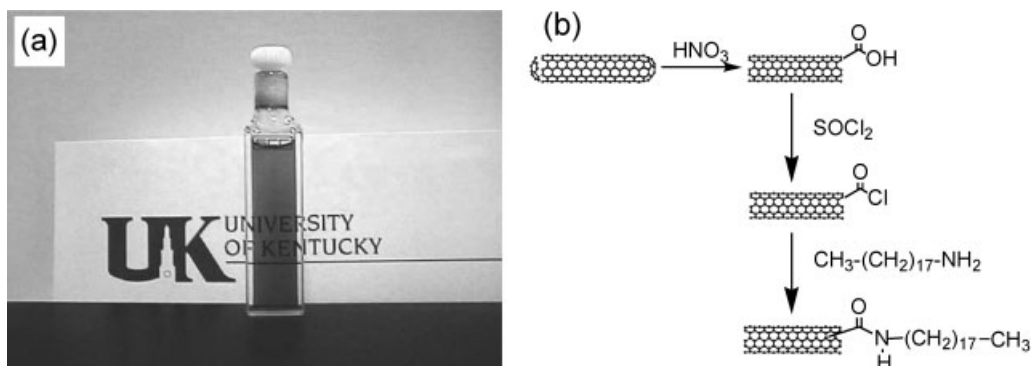


**Fig. 2.5.** (a) A solution of SWNTs chemically functionalized with octadecylamine [21] by the general functionalization scheme illustrated in (b).

successfully dispersed in water with various surfactants [40–42]. This surfactant detached tubes from the bundles during vigorous sonication and stabilized individual SWNTs in solution [41]. Since the individual nanotube encased in a close-packed SDS micelle had a lower specific gravity than SDS-coated bundles, centrifugation led to their separation. This made it possible to use spectroscopy to study individual SWNTs, which displayed a bright photoluminescence in the NIR [41]. Since then, surfactant-assisted dispersion of nanotubes has been widely used by several research groups for fundamental studies of the electronic properties of individual SWNTs, as these properties give rise to distinctive features in the optical spectra [43–47].

Various anionic, nonionic, and cationic surfactants have been studied for their ability to disperse SWNTs in water [46]. Typically, a solution of a specific surfactant concentration is mixed with the nanotubes using high shear homogenization, followed by ultrasonication, and ultracentrifugation.

Among ionic surfactants, sodium dodecylbenzene sulfonate (SDBS) and SDS are the most efficient dispersing agents. For nonionic systems, surfactants with higher molecular weight suspend higher amounts of SWNT material [46].

### 2.4.3

#### Functionalization with Water-soluble Polymers

The covalent attachment of water-soluble polymers is an efficient approach to the dispersion of CNTs in water. By applying the functionalization scheme of Fig. 2.5, poly-*m*-aminobenzene sulfonic acid (PABS) [48, 49] and polyethylene glycol (PEG) [49] have been covalently linked to SWNTs to form water-soluble nanotube-graft copolymers (Fig. 2.6) [48, 49]. Several other types of functionalized SWNTs bearing water-soluble moieties have been synthesized (Scheme 2.1), including the attachment of water-soluble linear polymers, such as monoamine-terminated polyethylene oxide (PEO) [50], diamine terminated polyethylene glycol (PEG<sub>1500N</sub>) [51],

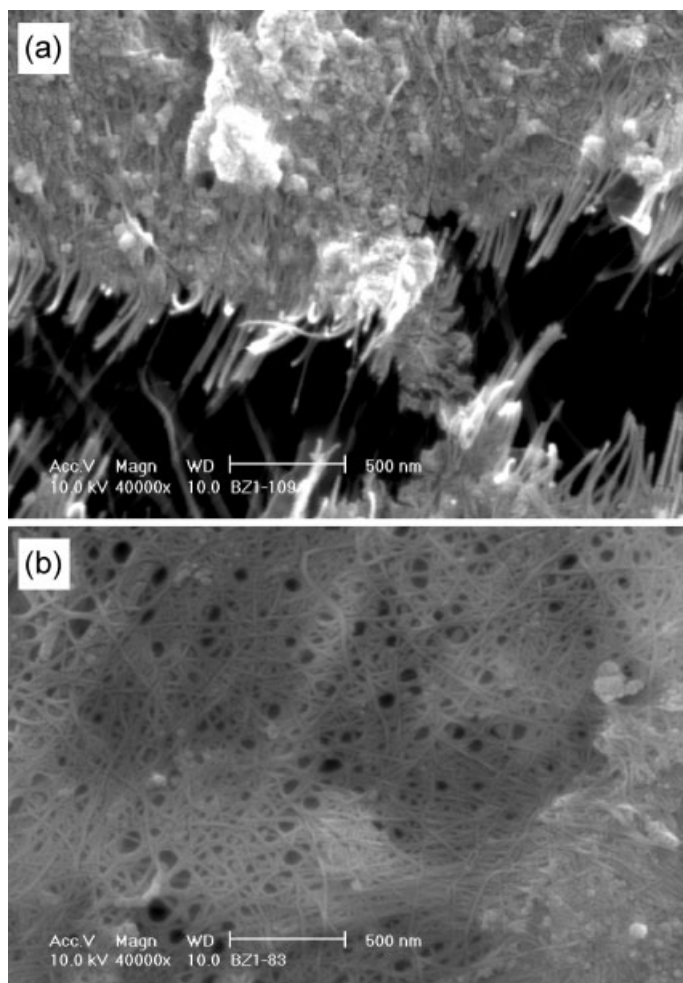


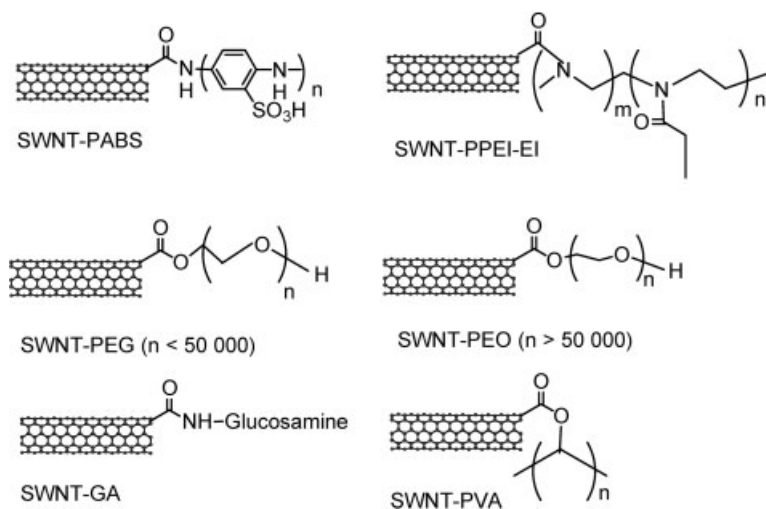
Fig. 2.6. SEM images of (a) SWNT-PABS and (b) SWNT-PEG [49].

poly(propionylethylenimine-*co*-ethylenimine) (PPEI-EI) [51], poly(vinyl alcohol) (PVA) [51], and glucosamine (GA) [52] to CNTs. Since these functionalized nanotubes have high solubility in water ( $8\text{--}89\text{ mg mL}^{-1}$ ) [51], this is clearly an efficient route for the aqueous dissolution of carbon nanotubes.

#### 2.4.4

#### Interaction and Functionalization with Biological Molecules

Interactions of CNTs with biological molecules, such as lipids, DNA and proteins, efficiently disperse the CNTs in water. Noncovalent modification is the preferred method if the electronic characteristics of the nanotubes need to be preserved. Co-



**Scheme 2.1.** Structures of SWNTs functionalized with polymers: PABS – poly(*m*-aminobenzenesulfonic acid), PEG – poly(ethylene glycol), GA – glucosamine, PPEI-EI – poly(propionylethylenimine-*co*-ethylenimine), PEO – poly(ethylene oxide) and PVA – poly(vinyl alcohol).

valent chemistry, which takes place via modifications of the CNT side walls, disturbs the extended  $\pi$ -network, leading to a localization of electrons at the defect sites that are generated at the point of attachment. However, covalent chemistry at the ends of the SWNTs retains the SWNT electronic properties and provides a robust linkage to the biological molecule, although with some variability in the endogenous properties and functions of these molecules.

#### 2.4.4.1 Noncovalent Biofunctionalization

Various lipids and proteins, including enzymes, peptides and nucleic acids, adsorb strongly to CNTs [53–59]. These interactions between CNTs and biological molecules provide a more efficient means to solubilize the nanotubes in water than the use of surfactants and polymers. In a similar manner to surfactants, amphiphilic biological molecules, which possess hydrophobic and hydrophilic moieties, solubilize CNTs in aqueous media. For example, MWNTs form stable dispersions in water upon interaction with specific lipid derivatives composed of a lipidic chain of 12 and 18 carbon atoms and a polar head group [56]. Single-chain lipidic reagents self-organize on the nanotube walls, forming supramolecular assemblies. Similar highly ordered heterogeneous structures have been found upon adsorption of other biological molecules. For example, HupR, a DNA binding protein from the nitrogen-regulatory protein subfamily, and streptavidin interacted strongly with MWNT to form highly ordered helical structures, but the exact solubility in water was not reported [53]. However, an efficient protocol for dispersion of CNTs

in water using a specifically designed amphiphilic  $\alpha$ -helical peptide, which functioned by wrapping individual CNTs, has been reported and this led to a stable dispersion of CNTs at a concentration of  $0.7 \text{ mg mL}^{-1}$  [60].

Single-stranded DNA (ssDNA) interacts strongly with CNTs to form stable CNT-DNA hybrids, which efficiently disperse CNTs in aqueous solution [57, 61]. A concentration of CNTs of  $0.2\text{--}0.4 \text{ mg mL}^{-1}$  was readily achieved upon dispersion with DNA, and it was possible to further concentrate the CNTs solution to  $4 \text{ mg mL}^{-1}$  [61]. It has been suggested that this highly efficient mechanism for dispersion of individual SWNTs in solution involves  $\pi$ -stacking interactions between the nanotube walls and the DNA bases, resulting in helical wrapping of the nanotubes. In addition, the hydrophilic interactions between the sugar-phosphate groups in the backbone of DNA and surrounding water molecules render the hybrid structure soluble in water. The phosphate groups on the SWNT-DNA hybrid provide a negative charge density on the surface of the CNT, enabling the debundling and dispersion of individual SWNTs [57, 61, 62]. The wrapping of the nanotubes with ssDNA was found to be sequence dependent, and the interaction between certain DNA sequences and individual SWNTs allowed ion-exchange chromatography separation based on the electronic characteristics of SWNTs. The separation procedure takes advantage of the different electrostatic charges on the hybrid macromolecules, which are composed of metallic and semiconducting SWNTs [57, 61]. Since the separation of metallic and semiconducting SWNTs is the most important obstacle to the application of carbon nanotubes in nanoelectronics, this DNA-assisted separation demonstrates the power of hybrid CNT-biological molecules for solving problems in nanotechnology.

A combination of surfactants and polymers has also been used for noncovalent attachment of proteins to CNTs, in which the successive adsorption of surfactants (Triton X-100 or Triton X-405) and biotin-functionalized polymer (PEG) provides an interface for binding with streptavidin [63].

Biomolecules can be attached to noncovalently functionalized CNTs. In this approach 1-pyrenebutanoic acid succinimidyl ester (1-PBA) is irreversibly adsorbed on the hydrophobic graphene surface of the CNTs via  $\pi$ -stacking interactions [64]. The protein is then covalently attached to the succinimidyl functionality of 1-PBA through a nucleophilic substitution reaction by an amine group of the protein (Fig. 2.7). This approach for immobilization of proteins onto CNTs has been utilized in development of biosensors based on glucose oxidase-functionalized SWNTs (Section 2.5.2) [55].

An important question that arises is whether the immobilized biological molecules retain their biological activity. Studies regarding this issue are limited. In one study on the structure and functions of proteins adsorbed on SWNTs, it was shown that the proteins undergo conformational changes upon interaction with the carbon walls [59]. The authors used enzymes as highly sensitive probes of the protein functions and found that, depending on the nature of the protein, SWNTs can differentially affect the biological activity of the adsorbed proteins; soybean peroxidase retained 30% of its native activity, while  $\alpha$ -chymotrypsin retained only 1% of its native activity, and was denatured when attached to SWNTs [59].



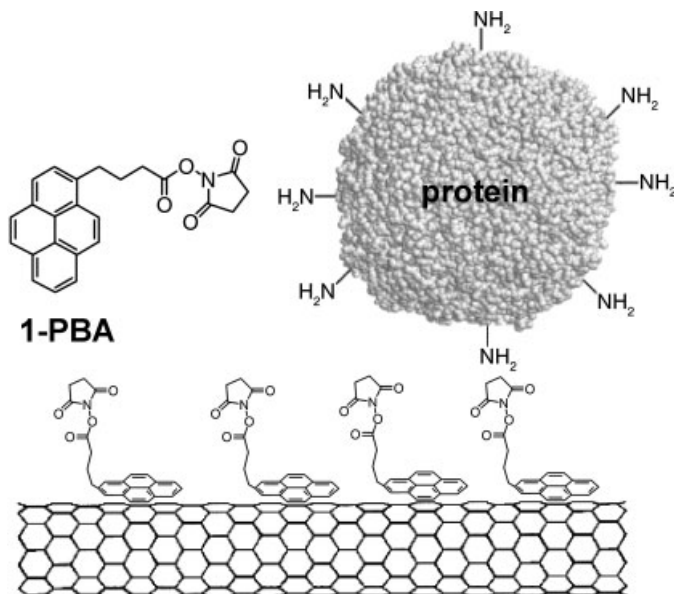
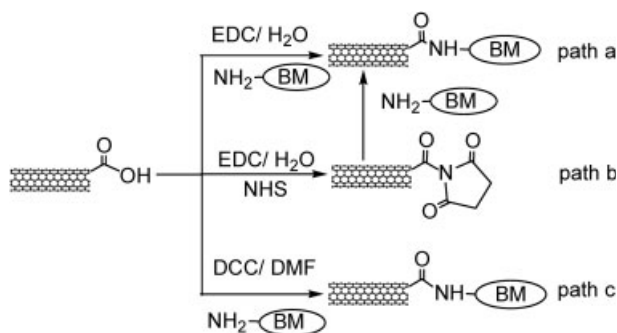


**Fig. 2.7.** 1-Pyrenebutanoic acid succinimidyl ester (1-PBA), adsorbed on the side-wall of a SWNT via  $\pi$ -stacking, has been used to immobilize protein due to interactions with the protein's amino groups. (Modified from Ref. [64].)

#### 2.4.4.2 Covalent Biofunctionalization

Carbodiimide chemistry can be readily applied to covalently link CNTs to various biological molecules. Carbodiimide activates the carboxylic acid groups, which are easily introduced into the CNTs by the oxidative treatments discussed earlier, and it facilitates their reaction with the amino groups present in the biological molecules. Carbodiimide coupling agents commonly utilized for these reactions are the water-soluble derivatives 1-ethyl-3-(3-dimethylaminopropyl)-*t*-carbodiimide (EDC) (Scheme 2.2, paths a, b) and *N,N'*-dicyclohexylcarbodiimide (DCC) (Scheme 2.2, path c), which are often used with dimethylformamide (DMF) as a solvent. *N*-Hydroxysuccinimide (NHS), which reacts with the carboxylic groups to form an active intermediate ester, is often used to assist amide bond formation in the presence of EDC (Scheme 2.2, path b). These general reactions have been utilized to functionalize CNTs with proteins [65] and amine-terminated DNA [66, 67].

Alternatively, CNTs can be chemically modified by introducing amine moieties [68], which can be further reacted with the biological molecules (Scheme 2.3). In the first step, the carboxylic acid groups of the SWNTs, introduced by oxidation with nitric acid, are reacted with thionyl chloride to form an acyl chloride intermediate, which is then crosslinked with ethylenediamine to produce amine-terminated SWNTs (SWNT-NH<sub>2</sub>). These SWNT-NH<sub>2</sub> have been used for covalent attachment of DNA [68]. This was achieved by introducing maleimide groups to SWNT-NH<sub>2</sub>

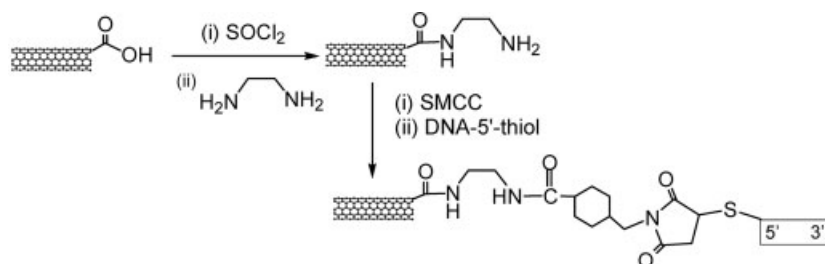


BM - biomolecule (protein,  $\text{NH}_2$ -terminated DNA)  
 EDC - 1-ethyl-3-(3-dimethylaminopropyl)-carbodiimide  
 NHS - N-hydroxysuccinimide  
 DCC - dicyclohexyl-carbodiimide  
 DMF - dimethylformamide

**Scheme 2.2.** Schematic illustration of carbodiimide procedures for covalent functionalization of SWNTs with biological molecules. (Modified from Ref. [1].)

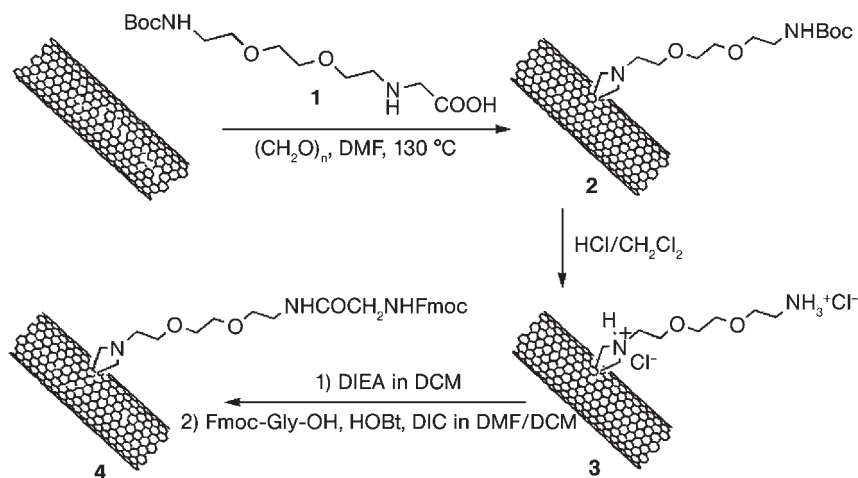
by crosslinking with succinimidyl 4-(*N*-maleimidomethyl)cyclohexane-1-carboxylate (SMCC) and further reacted with thiol-terminated DNA [68]. The resulting DNA-CNT hybridized selectively with complementary DNA sequences, while showing little interaction with non-complementary DNA sequences, indicating that the procedure preserves DNA specificity.

In addition to the chemistry that occurs at the oxidized open ends of CNTs, the side walls undergo 1,3-cycloaddition reactions (Scheme 2.4) [69, 70], and both SWNTs and MWNTs have been covalently linked to *N*-protected amino acids by this technique, which can be used to prepare water-soluble CNTs [70]. In such functionalization schemes the amino acid is condensed with paraformaldehyde in



SMCC - Succinimidyl 4-(*N*-maleimidomethyl) cyclohexane-1-carboxylate

**Scheme 2.3.** Schematic of the maleimide procedure for covalent functionalization of SWNTs with biological molecules.



**Scheme 2.4.** Covalent functionalization of carbon nanotubes with amino acids. Boc – butoxycarbonyl protecting group, DMF – dimethylformamide, DCM – dichloromethane, DIEA – diisopropylethylamine, DIC –

diisopropylcarbodiimide, HOBT – *N*-hydroxybenzotriazole, Fmoc – 9-fluorenylmethoxycarbonyl, Gly – glycolic acid [70]. (Reproduced by permission of the Royal Society of Chemistry.)

the presence of CNTs dispersed in DMF (Scheme 2.4; 1); the protecting group, *N*-tetrabutoxycarbonyl (Boc), in the derivative (Scheme 2.4; 2) is cleaved by reaction with HCl. The resulting amino acid functionalized CNTs (Scheme 2.4; 3) have a remarkable solubility in water ( $20\text{ mg mL}^{-1}$ ). Additionally, amino acid functionalized CNTs can be reacted easily with *N*-terminal protected amino acid (Fmoc-Gly-OH) via a coupling reaction activated with *N*-hydroxybenzotriazole (HOBT) and diisopropylcarbodiimide (DIC) (Scheme 2.4; 4).

## 2.5

### Applications of Biofunctionalized Carbon Nanotubes

#### 2.5.1

##### Assembly of Electronic Devices

Biofunctionalization of CNTs can potentially facilitate the use of these materials in functional structures and for the bottom-up design of nanodevices if it is possible to make use of the powerful self-assembly properties of natural substances. Because CNTs are promising building blocks for molecular electronics, the nanofabrication of electronic devices utilizing CNTs based on the self-assembly principles of biology has been attempted. For example, the bottom-up fabrication of field-effect transistors (FETs) based on individual SWNTs has been attempted by using DNA-mediated self-assembly and homologous genetic recombination [71]. A long

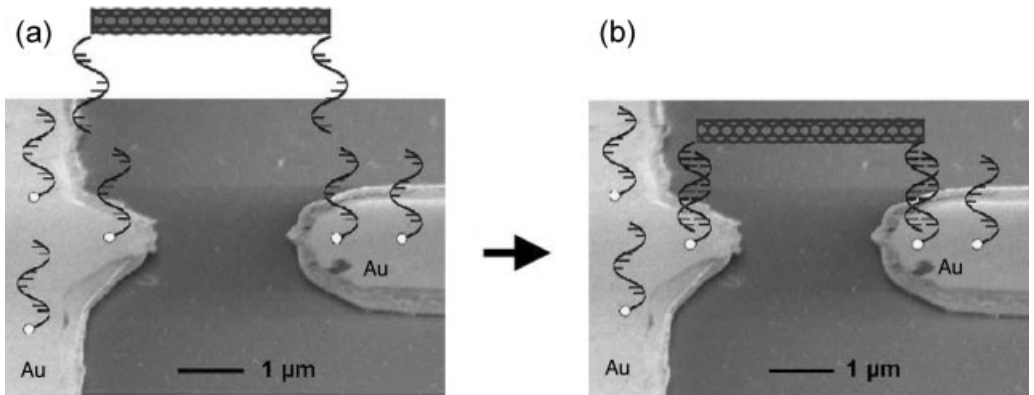
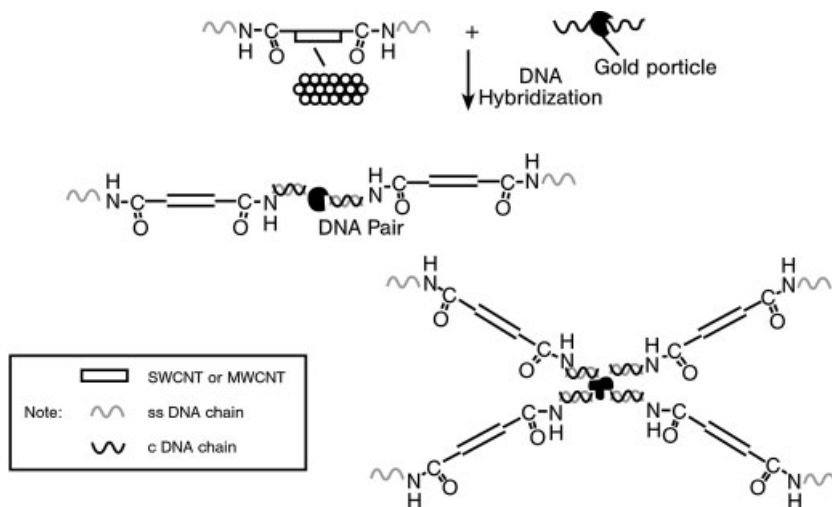


**Fig. 2.8.** DNA-templated deposition of SWNT between gold electrodes. (a) DNA-bearing gold electrodes immersed in a solution of oligonucleotide-functionalized SWNT. (b) Bridging the two electrodes with a SWNT by hybridization between the complementary strands [72]. (Reproduced by permission of Elsevier.)

DNA molecule was used as a scaffold onto which streptavidin-functionalized SWNTs were assembled, utilizing primary antibodies against RecA, a protein from *Escherichia coli*, and biotinylated secondary antibodies. This allowed a controlled localization of a semiconducting SWNT at a desired address on the DNA scaffold molecule. Electrical contact to the nanotubes may be obtained by metallization of the scaffold DNA molecule. Because the nanotubes are usually a mixture of metallic and semiconducting constituents, the fabrication of devices with reproducible characteristics represents a challenge, although the emerging methods for separating CNTs based on their electronic properties will assist this endeavor [57, 61]. However, the approach involves a complex multi-step process, and thus would lead to a low production yield of devices.

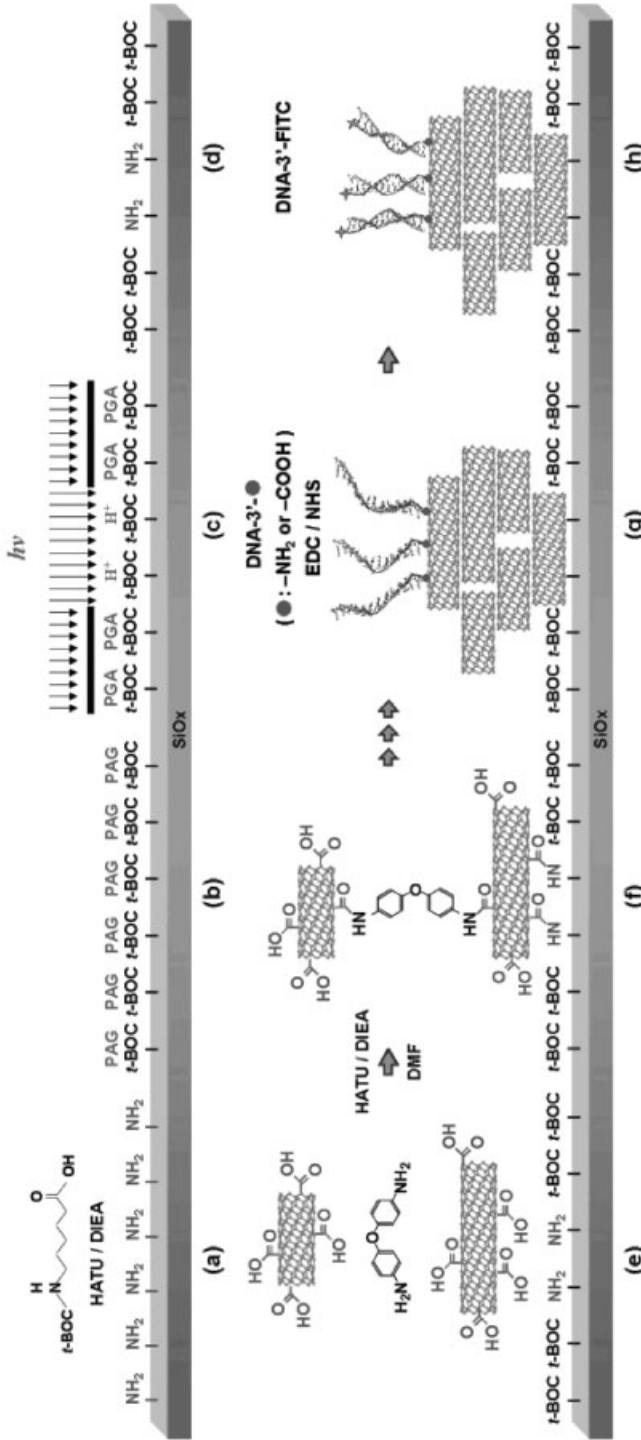
A suggested alternative approach for fabrication of an FET, with a reduced number of reaction steps, could enable the production of devices in high yield. This approach utilized the hybridization between short complementary DNA sequences located on metal contacts and SWNTs (Fig. 2.8) [72]. The thiol-terminated oligonucleotides were deposited on gold contacts, and the devices were immersed in a solution of SWNTs functionalized with complementary oligonucleotides. This allowed the hybridization of the complementary oligonucleotides, with one strand on the electrodes and the other attached to the SWNTs; the success of this operation led to the placement of individual SWNTs or small bundles between the electrodes, with efficient electrical contacts to the SWNTs at both electrodes in about 12% of the devices [72]. Those devices that exhibited efficient electrical contacts had stable electrical characteristics over hundreds of measurements. Indeed, this technique was also implemented to assemble SWNT-FET devices [73]. Although both approaches described above are far from a general technology, they highlight the potential use of biofunctionalized CNTs and self-assembly approach for bottom-up construction of CNT-based electronics.



**Scheme 2.5.** Schematic of procedures for DNA directed self-assembling of multiple carbon nanotubes and gold nanoparticles [75]. (Reproduced by permission of the American Chemical Society Publications.)

Controlled assembly of multifunctional SWNT structures is of interest for development of devices for biosensing. The functionalization of CNTs with biological molecules facilitates the formation of such functional structures and it also increases their versatility. Nanoparticle–CNT structures have been prepared using a DNA-directed self-assembly [74, 75]. In one approach DNA-graft gold nanoparticles have been attached to SWNTs grafted with complementary DNA chains, using the carboxylic group of the SWNT-COOH and amine-terminated DNA [75]. This approach has been used to assemble CNTs into various multicomponent structures, containing interconnected MWNTs and SWNTs, (Scheme 2.5) [75], and multifunctional structures could be obtained by varying the base sequence and the number of complementary DNA chains grafted to the gold nanoparticle.

Besides the assembly of functionalized CNTs (above), it is possible to functionalize pre-formed films of CNTs and prepare CNT film-based devices. Such preparations are readily achieved by spraying [8] or filtration [76, 77]. Additionally, the versatile chemistry at the open ends of the CNTs forming the film [36, 37] affords the opportunity to interconnect the nanotubes and to form patterned multi-layered SWNT films [78, 79]. Thus, carboxylic acid terminated CNTs have been interconnected using 4,4'-oxydianiline as a linker molecule [78]. The functionalized CNTs can be stacked on aminated glass substrates, which allows a diverse patterning of the CNT films and the introduction of various functional groups for further conjugation with biological molecules [78]. For example, DNA oligonucleotides have been attached, using carbodiimide chemistry (Scheme 2.2), to pre-patterned CNT multilayer films to give interfaces that exhibit a high sensitivity in subsequent hybridization (Scheme 2.6) [78]. Although their performance is inferior to individual



**Scheme 2.6.** Patterned SWNT multilayer films with selectively immobilized DNA molecules: (a) protection of the surface with *t*-Boc, (b) deposition of a layer of photoacid generator (PAG), (c) exposure to UV light using a photomask for patterning, (d) development process, (e) selective immobilization of the nanotubes onto the aminated regions of the substrate, (f) covalent functionalization of SWNT layers using a 4,4'-oxydianiline as a linker molecule and *O*-(7-azabenzotriazol-1-yl)-*N,N,N',N'*-tetramethyl uranium hexafluoro-

phosphate (HATU) as a condensation agent, (g) covalent immobilization of oligonucleotides onto the patterned SWNT multilayers, and (h) hybridization of the fluorescently (FITC)-labeled complementary oligonucleotide [78].  
 DIEA – diisopropylethylamine, DMF – dimethylformamide, *t*-Boc – *t*-butoxycarbonyl, EDC – 1-ethyl-3-(3-dimethylaminopropyl)-*t*-carbodiimide, NHS – *N*-hydroxysuccinimide. (Reproduced with permission from the American Chemical Society Publications.)

CNT devices, film-based devices made of CNTs provide convenient manufacture and have led to a powerful sensor platform [8]. Since this approach can lead to patterning at a specific location on a substrate, it could advance the development of sensors requiring site specificity.

SWNTs functionalized with poly-L-lysine (PLL) have been reported to assemble in functional structures, which have been used as a platform for electrodes with enhanced biosensing properties [80]. Assembly was achieved by reacting carboxylic acid bearing SWNTs with some of the amino groups of PLL (Scheme 2.7). The unreacted amino groups were available for subsequent attachment of the SWNT-PLL graft copolymer to the carboxylic acid bearing gold electrodes and also for conjugation to horseradish peroxidase. Attachment of this enzyme led to the construction of electrodes for amplified sensing of hydrogen peroxide [80]. Indeed, various enzymes could be attached using this method to the PLL-functionalized CNTs for the development of sensor devices. Because PLL is a permissive substrate for cellular adhesion and growth, this methodology could be exploited for development of composite substrates that would serve a dual role; they would support cellular growth and also serve as sensors.

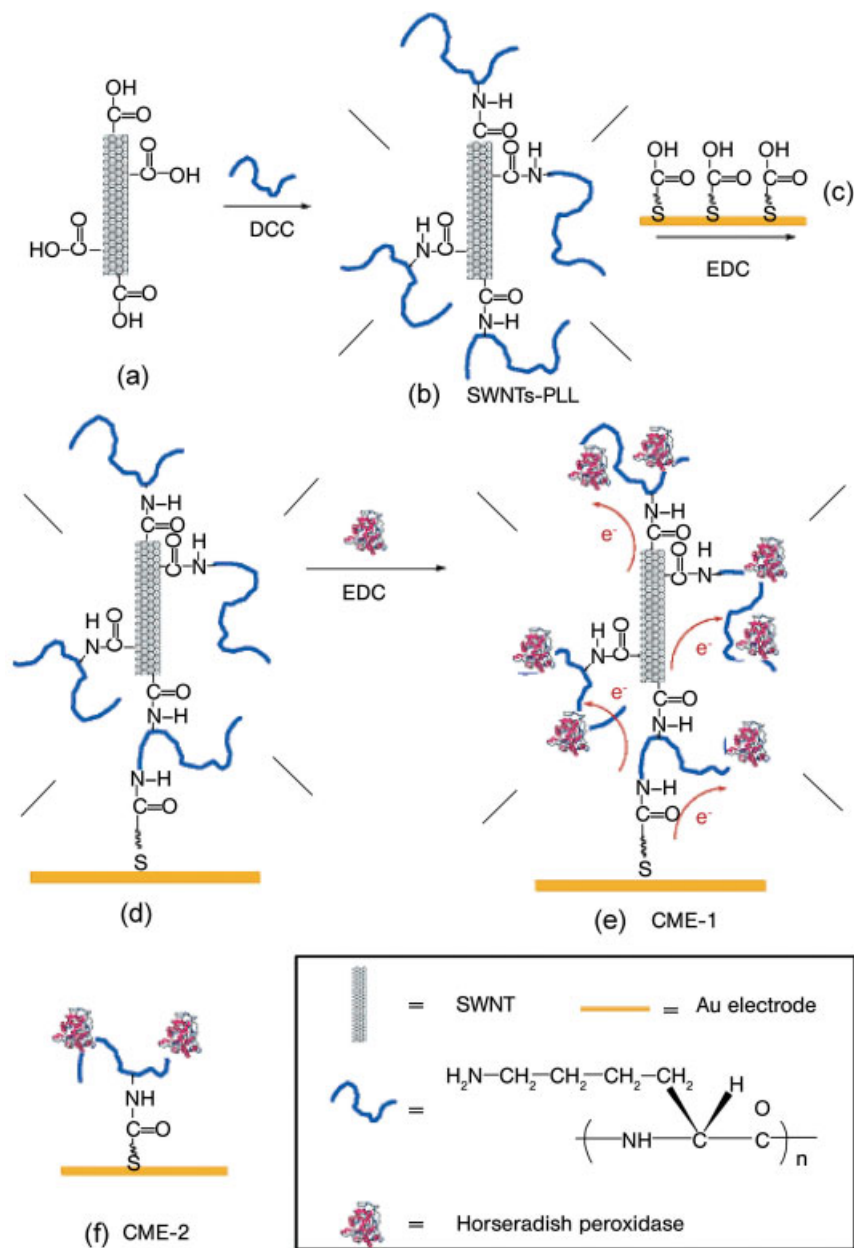
### 2.5.2

#### **Biosensing**

Among the potential usage of CNTs in biology and medicine, the development of advanced biosensor devices has emerged as the most promising short-term application. CNTs offer a unique combination of quasi-1D structure and excellent electronic properties, which can dramatically improve the miniaturization prospects for electronic biosensor devices. Additionally, CNTs offer new opportunities for rapid, sensitive and label-free detection of biological agents, with the selectivity of detection provided by biofunctionalization of the CNTs. Furthermore, the nanotubes can clearly serve both as the transducer and as the platform where the bio-recognition event occurs. Taken together, these prospects make CNTs one of the most promising materials for advanced biosensors.

Several groups have already demonstrated the use of SWNTs in biosensors [55, 81–92]. Research on CNT-based biosensors is currently focused on exploiting two major fundamental approaches: the development of CNT electrodes for the electrochemical detection of biological agents and fabrication of transistor devices for electronic detection of binding events.

Electronic detection of biological species is very attractive because it offers a fast and direct, label-free detection, while sampling data in real time. Additionally, it does not require preparation steps and multiple reagents, making the use of these sensors quite simple. Electronic detection is possible because a semiconducting SWNT exhibits a significant conductance change in response to interaction with gas molecules, which can change the electron density on the nanotube [93, 94]. Similar electronic changes in the behavior of SWNTs have been found upon interaction with small biological molecules and proteins [55, 89, 95, 96]. The *in situ* electronic detection of proteins using CNTs has proved to be very sensitive. Adsorp-



**Scheme 2.7.** Illustration of the assembling of SWNTs, poly-L-lysine (PLL), and horseradish peroxidase and the fabrication of chemically modified electrodes (CME) [80]. DCC – *N,N'*-

dicyclohexylcarbodiimide, EDC – 1-ethyl-3-(3-dimethylaminopropyl)-*t*-carbodiimide. (Reproduced with permission from the American Chemical Society Publications.)



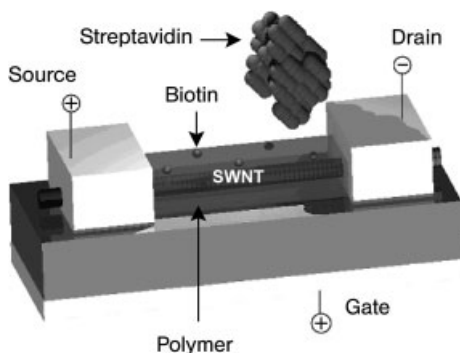


**Fig. 2.9.** Schematic of a nanotube field-effect transistor (FET). The nanotube (SWNT) is functionalized with biotin using a polymeric functional layer, which coats the nanotubes. (Modified from Ref. [89]; by permission of the American Chemical Society Publications.)

tion of cytochrome *c*, a redox catalyst in the respiratory chain of mitochondria, on an individual SWNT in a transistor configuration induced a sufficient decrease in the conductance of the device to allow the detection of a few tens of molecules [96].

An FET composed of an individual pristine SWNT (Fig. 2.9) has been shown to change its resistance upon exposure to proteins [89]. For example, adsorption of streptavidin on the SWNT shifted the transconductance towards negative gate voltages with little change in the current. Taking into account that the nanotubes before the adsorption exhibited p-type electronic behavior, presumably due to doping from environmental oxygen [94], these changes indicate an electron transfer from the streptavidin molecule to the nanotube. This hybrid, streptavidin-SWNT has been shown to be sensitive to the presence of biotin, which specifically binds to streptavidin, resulting in a decrease of the current. Because the interaction between streptavidin and SWNTs is non-specific it is necessary to impart selectivity to the device and to prevent non-specific interactions; this can be accomplished by coating the SWNTs with hydrophilic polymers, PEG and polyethyleneimine (PEI), containing biotin. The polymer coated/biotin functionalized SWNTs devices are very sensitive in the detection of streptavidin – down to as few as 10 protein molecules [89].

Although the mechanism of chemical sensing exhibited by SWNTs has not been unambiguously identified, as discussed above it seems probable that the resistance change in the devices originates from doping of the CNTs as a result of charge-transfer processes that are associated with interactions between the SWNTs and the analyte [8]. In some cases the conductance change originates from electronic effects occurring at the metal–nanotube contacts during adsorption [97].

In addition to direct sensing with SWNTs, biologically functionalized SWNTs also show promise as sensors. For example, glucose oxidase (GO) has been covalently attached to a semiconducting SWNT and used as the conducting channel in an FET [55]; the attached GO retained its enzymatic activity and imparted sensitiv-

ity to the nanotubes towards glucose. Importantly, the increase in conductance measured with such devices in the presence of glucose was rapid, which has implications for real time studies of enzymatic activity at molecular level. The GO-coated SWNT devices were very sensitive to pH, whereas the conductance of pristine SWNT was pH independent in the range 4–5.5; after modification of the nanotube with GO, a strong increase in conductance with decreasing pH was observed [55]. On changing the pH from 4 to 5.5, the effective gate voltage changed by 20 mV, which corresponded to a 30  $\mu\text{S}$  change in the conductance of the nanotube. These measurements show that it is possible to detect the doping induced by the binding of about 50 protein molecules to a  $\sim 600$  nm long semiconducting SWNT.

Several research groups have explored the electrochemical detection of biological molecules with electrodes consisting of CNTs in their pristine or modified forms; details of the achievements in electrochemical biosensing using CNTs have been outlined in a recent review [98]. Since their introduction into electrochemistry, CNT electrodes have demonstrated an enhanced sensitivity compared with conventional carbon electrodes. For example, detection of transmitter dopamine exhibited characteristic cyclic voltammograms at conventional electrodes such as glassy carbon and pyrolytic carbon fibers, as well as at CNT electrodes [81]. However, the conventional electrodes suffered from poor reversibility, while CNT electrodes exhibited excellent reversibility and were also very sensitive in the analysis of goat brain tissue. This illustrates the potential to use CNT electrodes for *in vivo* and *in vitro* neurotransmitter investigations involving dopamine, and possibly with other oxidizable transmitters. Similarly, the ultrasensitivity of CNT electrodes in electrochemical detection of proteins and DNA has been reported [91]. Covalent coupling of the alkaline phosphatase (ALP) enzyme to CNTs has led to the highest sensitivity (detection limit 1  $\text{pg L}^{-1}$ ) reported thus far for electrical detection of DNA. This CNT-ALP-linked assay can be modified for antigen detection by using specific antibody–antigen recognition, which could provide a fast, simple solution for molecular diagnosis in pathologies where molecular markers exist, such as DNA or protein.

Ultrasensitive DNA detection has been also achieved with a nanoelectrode array composed of aligned MWNTs embedded in silicon dioxide. The nanoelectrodes have been fabricated by a bottom-up approach, which resulted in precisely positioned and well-aligned MWNTs embedded in the silicon dioxide matrix. This configuration provided structural integrity to the electrodes and allowed the sensitivity of the array to be tailored by controlling the nanotube density [83]. The sensitivity was increased dramatically upon lowering the nanotube density in the array, allowing for the detection of less than a few attomoles of oligonucleotide.

A similar approach has been used to develop a MWNT-based nanoelectrode array for selective detection of glucose [85]. Nanotubes in the array were embedded in an epoxy matrix. The exposed nanotube tips were functionalized with glucose oxidase using carbodiimide chemistry. The devices showed a linear response to glucose up to a concentration of about 30 mM with the detection limit down to 0.08 mM, achieving a much wider range than necessary for sampling glucose in human blood and urine.

Alternative approaches for the development of glucose biosensors involve conducting polymer coated CNT arrays [86, 87]. In this approach GO was incorporated into a layer of conducting polymer, such as polypyrrole [87] or polyaniline [86], which coated aligned nanotubes. The amperometric response from these aligned nanotube–polymer nanowires was much higher than that of conventional electrodes using conducting polymers.

An additional advantage of CNT-based biosensors is the possibility of the favorable improvement of screen-printed graphite sensors by their modification with CNTs [92]. MWNTs have been used for modification of working graphite ink electrodes; the nanotubes were deposited on the graphite surface by evaporation of a solution of MWNTs in DMF, and the electrodes were further modified by adsorption of organophosphorus hydrolase, which allowed detection of the pesticide paraxon with greater sensitivity than for previous detection methods [92].

Atomic force microscopy (AFM) is a CNTs biosensing application that also impacts structural biology; due to their high aspect ratio, strength and chemical versatility, CNTs can be used to improve upon standard AFM tips in several ways. The most obvious is to enhance the image resolution as the tip size is significantly reduced when SWNTs are utilized. Standard commercial silicon-based tips have radial curvatures of about 5–10 nm, while SWNT AFM tips with a diameter in the range of 1–3 nm have already been fabricated [99, 100]. The improved resolution of the CNT tips has been demonstrated clearly in an AFM study of isolated proteins at room temperature in which a MWNT tip reproducibly resolved the distinct Y-shape of an isolated immunoglobulin G (IgG) [101], while previous images obtained with conventional tips yielded only a heart-shaped structure. Similarly, SWNT tips were used for high-resolution imaging of isolated DNA molecules [102]. This method has been implemented for determination of haplotypes on UGT1A7 [101], a gene suggested to be a cancer risk factor. Using SWNTs as a tip gives a resolution of approximately 10 bases, which enables direct reading of DNA sequences, and the utilization of SWNT tips in haplotyping clearly could be applied to the understanding and diagnosis of genetic diseases.

AFM probes with functionalized SWNTs as tips have been proposed as the ideal high-resolution probe for mapping chemical domains by using chemical force microscopy [103]. SWNT tips are extremely sensitive to surface polarity, pH and many other chemical characteristics of the sample, as demonstrated by tapping mode AFM studies using a tip of CNTs with terminal carboxylic groups [104], where it was possible to chemically map the patterned substrate containing areas of methyl and carboxylic groups (Fig. 2.10). The ability of AFM tips to detect biological molecules has also been demonstrated, and biotin-modified SWNT AFM tips have been used to study biotin interaction with streptavidin immobilized on a mica surface [104]. This method offers the opportunity to detect the spatio-temporal location of a specific molecule; in this approach the temporal resolution would be limited by the scanning speed and biosensor properties, while the spatial resolution would be limited by the diameter of the nanotube. For example, nanotubes capable of sensing glucose [105, 106] or neurotransmitters could be used to scan for the uptake and release of these compounds from specific cells under various stimuli.

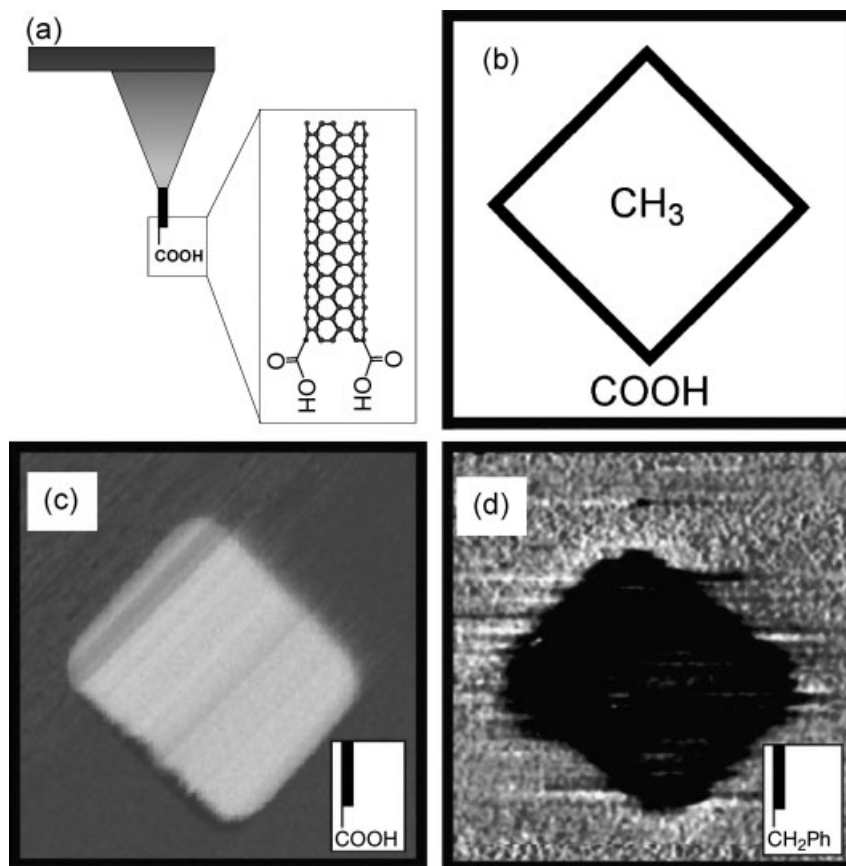


**Fig. 2.10.** (a) Schematic of a SWNT tip with attached carboxylic acid groups. (b)–(d) Chemical mapping with functionalized SWNT tip. (b) Schematic of a patterned substrate consisting of a self-assembled monolayer (SAM) region terminated with methyl groups and surrounded by carboxylic acid-terminated

SAM. (c) Tapping mode phase image of the patterned SAM in (b) imaged with a carboxylic acid-terminated SWNT tip, and (d) phase image of a similar substrate imaged with a C<sub>6</sub>H<sub>5</sub>-terminated SWNT tip. (Courtesy of Charles M. Lieber, Harvard University, USA.)

### 2.5.3

#### Substrates for Neuronal Growth

The first use of CNTs in contact with living cells made use of carbon nanotubes as a substrate for neuronal growth [107]. In this work, cultured hippocampal neurons were grown on MWNTs deposited on PEI-coated coverslips. Scanning electron microscopy was used to visualize the morphological parameters of neuronal growth. The neuronal bodies adhered to the surface of the MWNTs, showing outgrowth of neurites that elaborated into many small branches. The neurons remained alive on the MWNTs for at least 11 days.

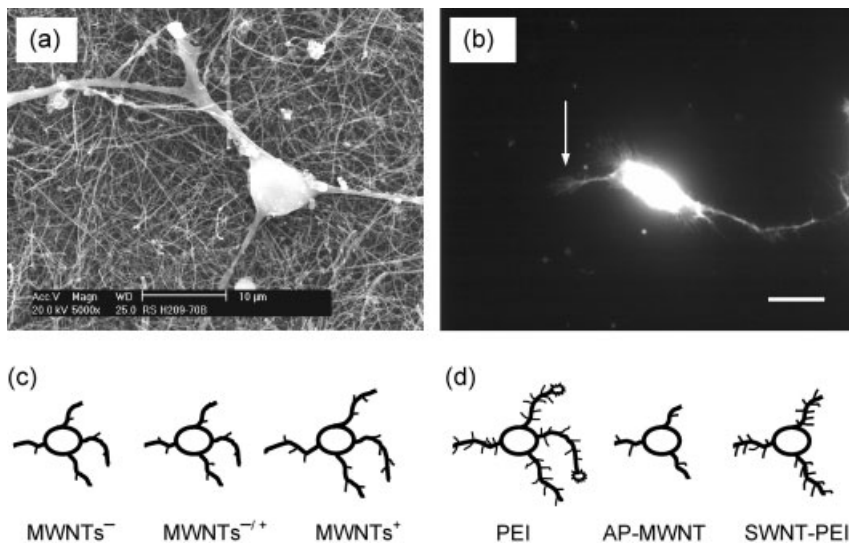


**Fig. 2.11.** (A) SEM image of a neuron grown on as-prepared MWNTs (AP-MWNTs). (b) Fluorescence image showing a live neuron on AP-MWNTs, which accumulated the vital stain, calcein. Arrow indicates a growth cone. Scale bar, 20  $\mu\text{m}$ . (c) Drawing summarizing the

effects of MWNT charges and (d) the effects of graft copolymer SWNT-PEI on growth cones, neurite outgrowth and branching. PEI, polyethyleneimine. (Modified from Refs. [108, 109].)

More recently, this work was extended by characterizing the morphological features of live neurons labeled with the fluorescent dye calcein, and visualized with a fluorescence microscope (Fig. 2.11) [108]. Neuronal growth was systematically controlled by modified MWNTs, prepared by covalently conjugating CNTs with functionalities designed to carry negative, neutral or positive charges at physiological extracellular pH. By using these CNTs as the scaffold for neuronal growth, it was found that the neurons grown on positively charged MWNTs showed more numerous growth cones, longer neurite outgrowth and more successful neurite branching than neurons grown on negatively charged CNTs (Fig. 2.11). Thus, by varying the electrostatic charge on the MWNTs it was possible to manipulate the growth pattern of the neurons. Similarly, neuronal growth was also modulated by using a SWNT-PEI graft copolymer as a scaffold or substrate for cultured neurons [109]. SWNT-PEI promoted neurite outgrowth and branching; neurons grown on SWNT-PEI showed more extensive neurite branching than neurons grown on as-prepared (AP-) MWNT, but having quantitatively similar neurite branching to those of neurons grown on PEI. The number of their growth cones was comparable to those on neurons grown on AP-MWNTs; the neurite lengths were intermediate and fell between those of neurons grown on AP-MWNTs and PEI (Fig. 2.11). Where PEI was combined with SWNTs, the positive charge on the PEI was reduced, perhaps by  $\sim 20\%$ , in proportion to the SWNT loading in the copolymer. The surface charge

reduction could be the basis for the effect of the copolymer on neuronal growth characteristics. Besides giving new information on the sensitivity of neuron growth parameters to substrate quality and charge, the data gathered may provide the basis for the development of materials where the ratio of SWNT/PEI in the copolymer could control neurite outgrowth and branching.

Taken together these studies demonstrate that CNTs can be used as a scaffold or substrate for neuronal growth and that modifications of CNTs, including graft copolymers with PEI, can be employed to modulate the arborization of neuronal processes and their outgrowth. This suggests that it may become possible to employ suitably functionalized CNTs as neural prostheses in neurite regeneration.

## 2.6

### Concluding Remarks

It is apparent from the body of work detailed in this chapter that there is already an impressive array of currently available methods for biofunctionalization of CNTs and of CNT applications in biology and nanotechnology. As a result of their unique properties and the sophistication of the chemistries available for their modification, CNTs have immense potential in biotechnology and biomedicine that are only now starting to be realized – although their toxicity remains a concern [110, 111]. Presently, CNTs are mainly under investigation in research laboratories, but if there is widespread commercialization of CNTs, the exposure of the general populace to this material must not occur without adequate testing. At this point there is no indication that CNTs will be any more hazardous than other forms of carbon, and their enormous potential in nanomedicine mandates the continued investigation of this unique nanomaterial from the biological standpoint.

### Acknowledgments

We thank Erik Malarkey for his comments on an earlier version of this manuscript. The authors' work is supported by the National Institute of Mental Health (MH 069791) and by DOD/DARPA/DMEA under Award No. DMEA90-02-2-0216. V.P. is an Institute for Complex Adaptive Matter Senior Fellow.

### References

- 1 BEKYAROVA, E., NI, Y., MALARKEY, E.B., MONTANA, V., MCWILLIAMS, J.L., HADDON, R.C., PARPURA, V., Applications of carbon nanotubes in biotechnology and biomedicine. *J. Biomed. Nanotechnol.* **2005**, *1*, 3–17.
- 2 QIN, L.-C., ZHAO, X., HIRAHARA, K., MIYAMOTO, Y., ANDO, Y., IIJIMA, S., The smallest carbon nanotube. *Nature* **2000**, *408*, 50.
- 3 WANG, N., TANG, Z.K., LI, G.D., CHEN, J.S., Single-walled 4 Å carbon

- nanotube arrays. *Nature* **2000**, *408*, 50–51.
- 4 MINTMIRE, J.W., DUNLAP, B.I., WHITE, C.T., Are fullerene tubules metallic? *Phys. Rev. Lett.* **1992**, *68*, 631–634.
  - 5 HAMADA, N., SAWADA, S.I., OSHIYAMA, A., New one-dimensional conductors: graphitic microtubules. *Phys. Rev. Lett.* **1992**, *68*, 1579–1581.
  - 6 SAITO, R., FUJITA, M., DRESSELHAUS, G., DRESSELHAUS, M.S., Electronic structure of chiral graphene tubules. *Appl. Phys. Lett.* **1992**, *60*, 2204–2206.
  - 7 FISCHER, J.E., DAI, H., THESS, A., LEE, R., HANJANI, N.M., DEHAAS, D.L., SMALLEY, R.E., Metallic resistivity in crystalline ropes of single-wall carbon nanotubes. *Phys. Rev. B* **1997**, *55*, R4921–R4924.
  - 8 BEKYAROVA, E., DAVIS, M., BURCH, T., ITKIS, M.E., ZHAO, B., SUNSHINE, S., HADDON, R.C., Chemically functionalized single-walled carbon nanotubes for ammonia sensors. *J. Phys. Chem. B* **2004**, *108*, 19717–19720.
  - 9 SALVETAT, J.P., BRIGGS, G.A.D., BONARD, J.M., BASCA, R.R., KULIK, A.J., STOCKLI, T., BURNHAM, N.A., FORRO, L., Elastic and shear moduli of single-walled carbon nanotube ropes. *Phys. Rev. Lett.* **1999**, *82*, 944–947.
  - 10 YU, M.F., FILES, B.S., AREPALLI, S., RUOFF, R.S., Tensile loading of ropes of single wall carbon nanotubes and their mechanical properties. *Phys. Rev. Lett.* **2000**, *84*, 5552–5555.
  - 11 JOURNET, C., BERNIER, P., Production of carbon nanotubes. *Appl. Phys. A* **1998**, *67*, 1–9.
  - 12 CORREA-DUARTE, M.A., WAGNER, N., ROJAS-CHAPANA, J., MORSCZECK, C., THIE, M., GIERSIG, M., Fabrication and biocompatibility of carbon nanotube-based 3D networks as scaffolds for cell seeding and growth. *Nano Lett.* **2004**, *4*, 2233–2236.
  - 13 ZHANG, Y., CHANG, A., CAO, J., WANG, Q., KIM, W., LI, Y., MORRIS, N., YENILMEZ, E., KONG, J., DAI, H., Electric-field-directed growth of aligned single-walled carbon nanotubes. *Appl. Phys. Lett.* **2001**, *79*, 3155–3157.
  - 14 JOSELEVICH, E., LIEBER, C.M., Vectorial growth of metallic and semiconducting single-wall carbon nanotubes. *Nano Lett.* **2002**, *2*, 1137–1141.
  - 15 YU, Z., LI, S., BURKE, P.J., Synthesis of aligned arrays of millimeter long, straight single-walled carbon nanotubes. *Chem. Mater.* **2004**, *16*, 3414–3416.
  - 16 DAI, H., Carbon nanotubes: synthesis, integration, and properties. *Acc. Chem. Res.* **2002**, *35*, 1035–1044.
  - 17 RAO, A.M., JACQUES, D., HADDON, R.C., ZHU, W., BOWER, C., JIN, S., In situ-grown carbon nanotube arrays with excellent field emission characteristics. *Appl. Phys. Lett.* **2000**, *76*, 3813–3815.
  - 18 GEOHEGAN, D.B., SCHITTENHELM, H., FAN, X., PENNYCOOK, S.J., PURETZKY, A.A., GUILLORN, M.A., BLUM, D.A., JOY, D.C., Condensed phase growth of single-wall carbon nanotubes from laser annealed nanoparticulates. *Appl. Phys. Lett.* **2001**, *78*, 3307–3309.
  - 19 CHAKRAPANI, N., WEI, B., CARRILLO, A., AJAYAN, P.M., KANE, R.S., Capillary-driven assembly of two-dimensional cellular carbon nanotube foams. *Proc. Nat. Acad. Sci. U.S.A.* **2004**, *101*, 4009–4012.
  - 20 GILES, J., Growing nanotech trade hit by questions over quality. *Nature* **2004**, *432*, 791.
  - 21 CHEN, J., HAMON, M.A., HU, H., CHEN, Y., RAO, A.M., EKLUND, P.C., HADDON, R.C., Solution properties of single-walled carbon nanotubes. *Science* **1998**, *282*, 95–98.
  - 22 ITKIS, M.E., NIYOGI, S., MENG, M., HAMON, M., HU, H., HADDON, R.C., Spectroscopic study of the Fermi level electronic structure of single walled carbon nanotubes. *Nano Lett.* **2002**, *2*, 155–159.
  - 23 ITKIS, M.E., PEREA, D., NIYOGI, S., RICKARD, S., HAMON, M., HU, H., ZHAO, B., HADDON, R.C., Purity evaluation of as-prepared single-walled carbon nanotube soot by use of solution phase near-IR spectroscopy. *Nano Lett.* **2003**, *3*, 309–314.
  - 24 NISHIDE, D., KATAURA, H., SUZUKI, S., TSUKAGOSHI, K., AOYAGI, Y., ACHIBA,

- Y., High-yield production of single-wall carbon nanotubes in nitrogen gas. *Chem. Phys. Lett.* **2003**, *372*, 45–50.
- 25 DILLON, A.C., GENNETT, T., PARILLA, P.A., ALLEMAN, J.L., JONES, K.M., HEBEN, M.J., Evaluating the purity of single-wall nanotube materials. *Mater. Res. Soc. Symp. Proc.* **2001**, *633*, A5.2.1–A5.2.6.
- 26 DRESSSELHAUS, M.S., DRESSSELHAUS, G., JORIO, A., SOUZA FILSHO, A.G., PIMENTA, M.A., SAITO, R., Single nanotube Raman spectroscopy. *Acc. Chem. Res.* **2002**, *35*, 1070–1078.
- 27 ZHANG, M., YUDASAKA, M., KOSHIO, A., IJIMA, S., Thermogravimetric analysis of single-wall carbon nanotubes ultrasonicated in monochlorobenzene. *Chem. Phys. Lett.* **2002**, *364*, 420–426.
- 28 AREPALI, S., NIKOLAEV, P., GORELIK, O.P., NADJIEV, V.G., HOLMES, W., FILES, B., YOWELL, L., Protocol for the characterization of single-wall carbon nanotube material quality. *Carbon* **2004**, *42*, 1783–1791.
- 29 ITKIS, M.E., PEREA, D., JUNG, R., NIYOGI, S., HADDON, R.C., Comparison of analytical techniques for purity evaluation of single-walled carbon nanotubes. *J. Am. Chem. Soc.* **2005**, *127*, 3439–3448.
- 30 HATA, K., FUBATA, D.N., MIZUNO, K., NAMAI, T., YUMURA, M., IJIMA, S., Water-assisted highly efficient synthesis of impurity-free single-walled carbon nanotubes. *Science* **2004**, *306*, 1362–1364.
- 31 LIU, J., RINZLER, A.G., DAI, H., HAFNER, J.H., BRADLEY, R.K., BOUL, P.J., LU, A., IVERSON, T., SHELIMOV, K., HUFFMAN, C.B., RODRIGUEZ-MACIAS, F., SHON, Y.-S., LEE, T.R., COLBERT, D.T., SMALLEY, R.E., Fullerene pipes. *Science* **1998**, *280*, 1253–1256.
- 32 CHIANG, I.W., BRINSON, B.E., SMALLEY, R.E., MARGRAVE, J.L., HAUGE, R.H., Purification and characterization of single-wall carbon nanotubes. *J. Phys. Chem. B* **2001**, *105*, 1157–1161.
- 33 NIYOGI, S., HU, H., HAMON, M.A., BHOWMIK, P., ZHAO, B., ROZENZHAK, S.M., CHEN, J., ITKIS, M.E., MEIER, M.S., HADDON, R.C., Chromatographic purification of soluble single-walled carbon nanotubes (s-SWNTs). *J. Am. Chem. Soc.* **2001**, *123*, 733–734.
- 34 HU, H., ZHAO, B., ITKIS, M.E., HADDON, R.C., Nitric acid purification of single-walled carbon nanotubes. *J. Phys. Chem. B* **2003**, *107*, 13838–13842.
- 35 HADDON, R.C., SIPPEL, J., RINZLER, A.G., PAPADIMITRAKOPOULOS, F., Purification and separation of carbon nanotubes. *MRS Bull.* **2004**, *29*, 252–259.
- 36 NIYOGI, S., HAMON, M.A., HU, H., ZHAO, B., BHOWMIK, P., SEN, R., ITKIS, M.E., HADDON, R.C., Chemistry of single-walled carbon nanotubes. *Acc. Chem. Res.* **2002**, *35*, 1105–1113.
- 37 ZHAO, B., HU, H., BEKYAROVA, E., ITKIS, M.E., NIYOGI, S., HADDON, R.C., Carbon nanotubes: Chemistry. *Encyclopedia. Nanosci. Nanotechnol.* **2004**, 493–506.
- 38 SUN, Y.P., FU, K., LIN, Y., HUANG, W., Functionalized carbon nanotubes: properties and applications. *Acc. Chem. Res.* **2002**, *35*, 1096–1104.
- 39 ZHAO, W., SONG, C., PEHRSSON, P.E., Water-soluble and optically pH-sensitive single-walled carbon nanotubes from surface modification. *J. Am. Chem. Soc.* **2002**, *124*, 12418–12419.
- 40 RINZLER, A.G., LIU, J., DAI, H., NIKOLAEV, P., HUFFMAN, C.B., RODRIGUEZ-MACIAS, F.J., BOUL, P.J., LU, A.H., HEYMAN, D., COLBERT, D.T., LEE, R.S., FISCHER, J.E., RAO, A.M., EKLUND, P.C., SMALLEY, R.E., Large-scale purification of single-wall carbon nanotubes: process, product and characterization. *Appl. Phys. A* **1998**, *67*, 29–37.
- 41 O'CONNELL, M.J., BACHILLO, S.M., HUFFMAN, C.B., MOORE, V.C., STRANO, M.S., HAROZ, E.H., RIALON, K.L., BOUL, P.J., NOON, W.H., KITTRELL, C., MA, J., HAUGE, R.H., WEISMAN, B.R., SMALLEY, R.E., Band gap fluorescence from individual single-walled carbon nanotubes. *Science* **2002**, *297*, 593–596.



- 42 O'CONNELL, M.J., BOUL, P., ERICSON, L.M., HUFFMAN, C., WANG, Y., HAROZ, E., KUPER, C., TOUR, J., AUSMAN, K.D., SMALLEY, R.E., Reversible water-solubilization of single-walled carbon nanotubes by polymer wrapping. *Chem. Phys. Lett.* **2001**, *342*, 265–271.
- 43 DYKE, C.A., TOUR, J.M., Unbundled and highly functionalized carbon nanotubes from aqueous reactions. *Nano Lett.* **2003**, *3*, 1215–1218.
- 44 HELLER, D.A., BARONE, P.W., SWANSON, J.P., MAYRHOFER, R.M., STRANO, M.S., Using Raman spectroscopy to elucidate the aggregation state of single-walled carbon nanotubes. *J. Phys. Chem. B* **2004**, *108*, 6905–6909.
- 45 ZHANG, X., LU, Z., WEN, M., LIANG, H., ZHANG, J., LIU, Z., Single-walled carbon nanotube-based coaxial nanowires: synthesis, characterization, and electrical properties. *J. Phys. Chem. B* **2005**, *109*, 1101–1107.
- 46 MOORE, V.C., STRANO, M.S., HAROZ, E.H., HAUGE, R.H., SMALLEY, R.E., SCHMIDT, J., TALMON, Y., Individually suspended single-walled carbon nanotubes in various surfactants. *Nano Lett.* **2003**, *3*, 1379–1382.
- 47 RIGGS, J.E., WALKER, D.B., CARROLL, D.L., SUN, Y.-P., Optical limiting properties of suspended and solubilized carbon nanotubes. *J. Phys. Chem. B* **2000**, *104*, 7071–7076.
- 48 ZHAO, B., HU, H., HADDON, R.C., Synthesis and properties of a water soluble single-walled carbon nanotube-poly (m-aminobenzene sulphonic acid) graft copolymer. *Adv. Funct. Mater.* **2004**, *14*, 71–76.
- 49 ZHAO, B., HU, H., YU, A., PEREA, D., HADDON, R.C., Synthesis and characterization of water soluble single-walled carbon nanotube graft copolymers. *J. Am. Chem. Soc.* **2005**, *127*, 8197–8203.
- 50 SANO, M., KAMINO, A., OKAMURA, J., SHINKAI, S., Self-organization of PEO-graft-single-walled carbon nanotubes in solutions and Langmuir-Blodgett films. *Langmuir* **2001**, *17*, 5125–5128.
- 51 FERNANDO, K.A.S., LIN, Y., SUN, Y.P., High aqueous solubility of functionalized single-walled carbon nanotubes. *Langmuir* **2004**, *20*, 4777–4778.
- 52 POMPEO, F., RESASCO, D.E., Water solubilization of single-walled carbon nanotubes by functionalization with glucosamine. *Nano Lett.* **2002**, *2*, 369–373.
- 53 BALAVOINE, F., SCHULTZ, P., RICHARD, C., MALLOUH, V., EBBESEN, T.W., MIOSKOWSKI, C., Helical crystallization of proteins on carbon nanotubes: A first step towards the development of new biosensors. *Angew. Chem. Int. Ed.* **1999**, *38*, 1912–1915.
- 54 ERLANGER, B.F., CHEN, B.X., ZHU, M., BRUS, L., Binding of an anti-fullerene IgG monoclonal antibody to single wall carbon nanotubes. *Nano Lett.* **2001**, *1*, 465–467.
- 55 BESTEMAN, K., LEE, J.-O., WIERTZ, F.G., HEERING, H.A., DEKKER, C., Enzyme-coated carbon nanotubes as single-molecule biosensors. *Nano Lett.* **2003**, *3*, 727–730.
- 56 RICHARD, C., BALAVOINE, F., SCHULTZ, P., EBBESEN, T.W., MIOSKOWSKI, C., Supramolecular self-assembly of lipid derivatives on carbon nanotubes. *Science* **2003**, *300*, 775–778.
- 57 ZHENG, M., JAGOTA, A., STRANO, M.S., SANTOS, A.P., BARONE, P., CHOU, S.G., DINER, B.A., DRESSELHAUS, M.S., MCLEAN, R.S., ONOA, G.B., SAMSONIDZE, G.G., SEMKE, E.D., USREY, M.L., WALLS, D.J., Structure-based carbon nanotube sorting by sequence-dependent DNA assembly. *Science* **2003**, *302*, 1545–1548.
- 58 ZORBAS, V., ORTIZ-ACEVEDO, A., DALTON, A.B., YOSHIDA, M.M., DIECKMANN, G.R., DRAPER, R.K., BAUGHMAN, R.H., JOSE-YACAMAN, M., MUSSELMAN, I.H., Preparation and characterization of individual peptide-wrapped single-walled carbon nanotubes. *J. Am. Chem. Soc.* **2004**, *126*, 7222–7227.
- 59 KARAJANAGI, S.S., VERTEGEL, A.A., KANE, R.S., DORDICK, J.S., Structure and function of enzymes adsorbed onto single-walled carbon nanotubes. *Langmuir* **2004**, *20*, 11594–11599.
- 60 DIECKMANN, G.R., DALTON, A.B.,

- JOHNSON, P.A., RAZAL, J., CHEN, J., GIORDANO, G.M., MUNOZ, E., MUSSELMAN, I.H., BAUGHMAN, R.H., DRAPER, R.K., Controlled assembly of carbon nanotubes by designed amphiphilic peptide helices. *J. Am. Chem. Soc.* **2003**, *125*, 1770–1777.
- 61 ZHENG, M., JAGOTA, A., SEMKE, E.D., DINER, B.A., MCLEAN, R.S., LUSTIG, S.R., RICHARDSON, R.E., TASSI, N.G., DNA-assisted dispersion and separation of carbon nanotubes. *Nature Mater.* **2003**, *2*, 338–342.
- 62 STRANO, M.S., ZHENG, M., JAGOTA, A., ONOA, G.B., HELLER, D.A., BARONE, P.W., USREY, M.L., Understanding the nature of the DNA-assisted separation of single-walled carbon nanotubes using fluorescence and Raman spectroscopy. *Nano Lett.* **2004**, *4*, 543–550.
- 63 SHIM, M., KAM, N.W.S., CHEN, R.J., LI, Y., DAI, H., Functionalization of carbon nanotubes for biocompatibility and biomolecular recognition. *Nano Lett.* **2002**, *2*, 285–288.
- 64 CHEN, R.J., ZHANG, Y., WANG, D., DAI, H., Noncovalent sidewall functionalization of single-walled carbon nanotubes for protein immobilization. *J. Am. Chem. Soc.* **2001**, *123*, 3838–3839.
- 65 HUANG, W., TAYLOR, S., FU, K., LIN, Y., ZHANG, D., HANKS, T.W., RAO, A.M., SUN, Y.-P., Attaching proteins to carbon nanotubes via diimide-activated amidation. *Nano Lett.* **2002**, *2*, 311–314.
- 66 DWYER, C., GUTHOLD, M., FALVO, M., WASHBURN, S., SUPERFINE, R., ERIE, D., DNA-functionalized single-walled carbon nanotubes. *Nanotechnology* **2002**, *13*, 601–604.
- 67 WILLIAMS, K.A., VEENHUIZEN, P.T.M., DE LA TORRE, B.G., ERITJA, R., DEKKER, C., Nanotechnology: Carbon nanotubes with DNA recognition. *Nature* **2002**, *420*, 761.
- 68 BAKER, S.E., CAI, W., LASSETER, T.L., WEIDKAMP, K.P., HAMERS, R.J., Covalently bonded adducts of deoxyribonucleic acid (DNA) oligonucleotides with single-wall carbon nanotubes: synthesis and hybridization. *Nano Lett.* **2002**, *2*, 1413–1417.
- 69 GEORGAKILAS, V., KORDATOS, K., PRATO, M., GULDI, D.M., HOLZINGER, M., HIRSCH, A., Organic functionalization of carbon nanotubes. *J. Am. Chem. Soc.* **2002**, *124*, 760–761.
- 70 GEORGAKILAS, V., TAGMATARCHIS, N., PANTAROTTO, D., BIANCO, A., BRIAND, J.P., PRATO, M., Amino acid functionalization of water soluble carbon nanotubes. *Chem. Commun.* **2002**, 3050–3051.
- 71 KEREN, K., BERMAN, R.S., BUCHSTAB, E., SIVAN, U., BRAUN, E., DNA-templated carbon nanotube field-effect transistor. *Science* **2003**, *302*, 1380–1382.
- 72 HAZANI, M., HENNRICH, F., KAPPES, M., NAAMAN, R., PELED, D., SIDOROV, V., SHVARTS, D., DNA-mediated self-assembly of carbon nanotube-based electronic devices. *Chem. Phys. Lett.* **2004**, *391*, 389–392.
- 73 HAZANI, M., SHVARTS, D., PELED, D., SIDOROV, V., NAAMAN, R., Self-assembled carbon-nanotube-based field-effect transistors. *J. Appl. Phys.* **2004**, *85*, 5025–5027.
- 74 MOGHADDAM, M.J., TAYLOR, S., GAO, M., HUANG, S., DAI, L., MCCALL, M.J., Highly efficient binding of DNA on the sidewalls and tips of carbon nanotubes using photochemistry. *Nano Lett.* **2004**, *4*, 89–93.
- 75 LI, S., HE, P., DONG, J., GUO, Z., DAI, H., DNA-directed self-assembling of carbon nanotubes. *J. Am. Chem. Soc.* **2005**, *127*, 14–15.
- 76 HU, L., HECHT, D.S., GRUNER, G., Percolation in transparent and conducting carbon nanotube networks. *Nano Lett.* **2004**, *4*, 2513–2517.
- 77 WU, Z., CHEN, Z., DU, X., LOGAN, J.M., SIPPEL, J., NIKOLOU, M., KAMARAS, K., REYNOLDS, J.R., TANNER, D.B., HEBARD, A.F., RINZLER, A.G., Transparent, conductive carbon nanotube films. *Science* **2004**, *305*, 1273–1276.
- 78 JUNG, D.-H., KIM, B.H., KO, Y.K., JUNG, M.S., JUNG, S., LEE, S.Y., JUNG, H.-T., Covalent attachment and

- hybridization of DNA oligonucleotides on patterned single-walled carbon nanotube films. *Langmuir* **2004**, *20*, 8886–8891.
- 79 JUNG, D.H., JUNG, M.S., KO, Y.K., SEO, S.J., JUNG, H.-T., Carbon nanotube conducting arrays by consecutive amidation reactions. *Chem. Commun.* **2004**, 526–527.
- 80 ZHANG, Y., LI, J., SHEN, Y., WANG, M., LI, J., Poly-L-lysine functionalization of single-walled carbon nanotubes. *J. Phys. Chem. B* **2004**, *108*, 15343–15346.
- 81 BRITTO, P.J., SANTHAMAN, S.K.V., AJAYAN, P.M., Carbon nanotube electrode for oxidation of dopamine. *Bioelectrochem. Bioenerg.* **1996**, *41*, 121–125.
- 82 GUISEPPi-ELIE, A., LEI, C., BAUGHMAN, R.H., Direct electron transfer of glucose oxidase on carbon nanotubes. *Nanotechnology* **2002**, *13*, 559–564.
- 83 LI, J., NG, H.T., CASSELL, A., FAN, W., CHEN, H., YE, Q., KOEHNE, J., HAN, J., MEYAPPAN, M., Carbon nanotube nanoelectrode array for ultrasensitive DNA detection. *Nano Lett.* **2003**, *3*, 597–602.
- 84 GOODING, J.J., WIBOWO, R., LIU, J., YANG, W., LOSIC, D., ORBONS, S., MEARNS, F.J., SHAPTER, J.G., HIBBERT, D.B., Protein electrochemistry using aligned carbon nanotube arrays. *J. Am. Chem. Soc.* **2003**, *125*, 9006–9007.
- 85 LIN, Y., LU, F., TU, Y., REN, Z., Glucose biosensors based on carbon nanotube nanoelectrode ensembles. *Nano Lett.* **2004**, *4*, 191–195.
- 86 SOUNDARRAJAN, P., PATIL, A., DAI, L., Surface modification of aligned carbon nanotube array for electrochemical sensing applications. *J. Vac. Sci. Technol. A* **2003**, *21*, 1198–1201.
- 87 GAO, M., DAI, L., WALLACE, G.G., Biosensors based on aligned carbon nanotubes coated with inherently conducting polymers. *Electroanalysis* **2003**, *15*, 1089–1094.
- 88 WANG, J., MUSAMEH, M., Carbon nanotube/Teflon composite electrochemical sensors and biosensors. *Anal. Chem.* **2003**, *75*, 2075–2079.
- 89 STAR, A., GABRIEL, J.-C.P., BRADLEY, K., GRUNER, G., Electronic detection of specific protein binding using nanotube FET devices. *Nano Lett.* **2003**, *3*, 459–463.
- 90 LUONG, J.H., HRAPOVIC, S., WANG, D., BENSEBAA, F., SIMARD, B., Solubilization of multiwall carbon nanotubes by 3-aminopropyltriethoxysilane towards the fabrication of electrochemical biosensors with promoted electron transfer. *Electroanalysis* **2004**, *16*, 132–139.
- 91 WANG, J., LIU, G., JAN, M.R., Ultrasensitive electrical biosensing of proteins and DNA: Carbon-nanotube derived amplification of the recognition and transduction events. *J. Am. Chem. Soc.* **2004**, *126*, 3010–3011.
- 92 TROJANOWICZ, M., MULCHANDANI, A., MASCINI, M., Carbon nanotubes-modified screen-printed electrodes for chemical sensors and biosensors. *Anal. Lett.* **2004**, *37*, 3185–3204.
- 93 KONG, J., FRANKLIN, N.R., ZHOU, C.W., CHAPLINE, M.G., PENG, S., CHO, K.J., DAI, H.J., Nanotube molecular wires as chemical sensors. *Science* **2000**, *287*, 622–625.
- 94 COLLINS, P.G., BRADLEY, K., ISHIGAMI, M., ZETTL, A., Extreme oxygen sensitivity of electronic properties of carbon nanotubes. *Science* **2000**, *287*, 1801–1804.
- 95 BRADLEY, K., BRIMAN, M., STAR, A., GRUNER, G., Charge transfer from adsorbed proteins. *Nano Lett.* **2003**, *4*, 253–256.
- 96 BOUSSAAD, S., TAO, N.J., ZHANG, R., HOPSON, T., NAGAHARA, L.A., In situ detection of cytochrome c adsorption with single walled carbon nanotube device. *Chem. Commun.* **2003**, 1502–1503.
- 97 CHEN, R.J., CHOI, H.C., BANGSARUNTIP, S., YENILMEZ, E., TANG, X., WANG, Q., CHANG, Y.-L., DAI, H., An investigation of the mechanism of electronic sensing of protein adsorption on carbon nanotube devices. *J. Am. Chem. Soc.* **2004**, *126*, 1563–1568.
- 98 ZHAO, O., GAN, Z., ZHUANG, Q., Electrochemical sensors based on

- carbon nanotubes. *Electroanalysis* **2002**, *14*, 1609–1613.
- 99 HAFNER, J.H., CHEUNG, C.L., LIEBER, C.M., Direct growth of single-walled carbon nanotube scanning probe microscopy tips. *J. Am. Chem. Soc.* **1999**, *121*, 9750–9751.
- 100 HAFNER, J.H., CHEUNG, C.-L., OOSTERKAMP, T.H., LIEBER, C.M., High-yield assembly of individual single-walled carbon nanotube tips for scanning probe microscopies. *J. Phys. Chem. B* **2000**, *105*, 743–746.
- 101 WOOLEY, A.T., CHEUNG, C.L., HAFNER, J.H., LIEBER, C.M., Structural biology with carbon nanotube AFM probes. *Chem. Biol.* **2000**, *7*, R193–R204.
- 102 CHEN, L., CHEUNG, C.L., ASHBY, P.D., LIEBER, C.M., Single-walled carbon nanotube AFM probes: Optical imaging resolution of nanoclusters and biomolecules in ambient and fluid environments. *Nano Lett.* **2004**, *4*, 1725–1731.
- 103 WONG, S.S., WOOLLEY, A.T., JOSELEVICH, E., CHEUNG, C.L., LIEBER, C.M., Covalently-functionalized single-walled carbon nanotube probe tips for chemical force microscopy. *J. Am. Chem. Soc.* **1998**, *120*, 8557–8558.
- 104 WONG, S.S., JOSELEVICH, E., WOOLEY, A.T., CHEUNG, C.L., LIEBER, C.M., Covalently functionalized nanotubes as nanometre-sized probes in chemistry and biology. *Nature* **1998**, *394*, 52–55.
- 105 WANG, S.G., ZHANG, Q., WANG, R., YOON, S.F., A novel multi-walled carbon nanotube based biosensor for glucose detection. *Biochem. Biophys. Res. Commun.* **2003**, *311*, 572–576.
- 106 TANG, H., CHEN, J., YAO, S., NIE, L., DENG, G., KUANG, Y., Amperometric glucose biosensor based on adsorption of glucose oxidase at platinum nanoparticle-modified carbon nanotube electrode. *Anal. Biochem.* **2004**, *331*, 89–97.
- 107 MATTSON, M.P., HADDON, R.C., RAO, A.M., Molecular functionalization of carbon nanotubes and use as substrates for neuronal growth. *J. Mol. Neurosci.* **2000**, *14*, 175–182.
- 108 HU, H., NI, Y., MONTANA, V., HADDON, R.C., PARPURA, V., Chemically functionalized carbon nanotubes as substrates for neuronal growth. *Nano Lett.* **2004**, *4*, 507–511.
- 109 HU, H., NI, Y., MANDAL, S.K., MONTANA, V., ZHAO, B., HADDON, R.C., PARPURA, V., Polyethyleneimine functionalized single-walled carbon nanotubes as substrates for neuronal growth. *J. Phys. Chem. B* **2005**, *109*, 4285–4289.
- 110 SERVICE, R.F., Nanotechnology. Sorting technique may boost nanotube research. *Science* **2003**, *300*, 2018.
- 111 SERVICE, R.F., Nanotoxicology. Nanotechnology grows up. *Science* **2004**, *304*, 1732–1734.
- 112 CHIKKANANAVAR, S.B., LUZZI, D.E., PAULSON, S., JOHNSON, A.T., JR., Synthesis of peapods using substrate-grown SWNTs and DWNTs: An enabling step toward peapod devices. *Nano Lett.* **2005**, *5*, 151–155.

### 3

## Biofunctionalization of Magnetic Nanoparticles

Yong Gao

### 3.1

#### Introduction

Advances in information storage technologies since the 1950s have led to tremendous progress in the preparation of magnetic particles of nanometer dimensions with defined properties [1, 2]. Since then, magnetic nanoparticles have found applications in biomedicine [3]. Magnetic particles with a grain size down to the nanometer scales have been used for *in vitro* cell/protein bio-separation, and chem-/bio-syntheses of pharmaceutical drug molecules. They have also been employed for *in vivo* magnetic drug targeting, magnetic resonance imaging (MRI) and magnetic hyperthermia tumor therapy [4–12]. More recently, due to rapid advances in nanotechnology, novel synthetic routes for fabricating magnetic nanoparticles with the ability to rigorously control the microstructures of magnetic nanoparticles, for example, coating, crystallinity and size uniformity, have been reported [13–38]. The development of these new types of magnetic nanomaterials has led to renewed research efforts on the functionalization of magnetic nanoparticles for their expanded biomedical applications.

*In vitro* and *in vivo* applications of magnetic nanoparticles in biomedicine are due to numerous beneficial factors associated with the unique nanometer-scale magnetic and physiological properties of magnetic nanospheres. Below a critical size, magnetic nanoparticles become single-domain and exhibit phenomena that differ from those of micrometer-sized counterparts, such as superparamagnetism, quantum tunneling of the magnetization, and unusually large coercivities, [1, 39–41]. Superparamagnetic iron oxide nanoparticles have been used as MRI contrast agents because of their very large magnetic moments – typically three orders of magnitude greater than those of other paramagnetic materials [4–6]. In addition to endowing them with unique magnetic properties, the small dimensions of magnetic nanoparticles, which range from several nanometers to hundreds of nanometers, typically smaller than those of proteins, cells and viruses, allow magnetic nanoparticles to have “close” contacts with a biological entity of interest. Thereby, magnetic nanoparticles can be utilized as a support for immobilization of bioactive molecules for bio-separation and bio-labeling applications since these nano-

particular supports present minimal steric hindrance to the surface-loaded proteins and cells. Magnetic nanoparticles also have advantages over their micrometer counterparts in *in vivo* bioapplications due to their small sizes. For example, *in vivo* applications of magnetic particles usually prefer a particle dimension below 20 nm for high tissue penetration [42]. The small sizes can also help magnetic nanoparticles evade hepatic clearance from the bloodstream by the mononuclear phagocyte system (MPS). This will increase the plasma half-life of nanoparticles and, thus, increase the probability of attaining the desired target inside the body with magnetic nanoclusters [43].

A core/shell structure is usually required in many biomedical applications of magnetic nanoparticles. Such nanoclusters have an inorganic core, e.g., iron oxide, surrounded by an outer layer of shell wall that consists of long-chain organic ligands or inorganic/organic polymers. For many biomedical applications, the inorganic cores need to be superparamagnetic. For instance, the Food and Drug Administration (FDA) approved iron oxide MRI contrast agents have a superparamagnetic nano-core coated with dextran polymers. Superparamagnetism is also preferred for bio-separation and bio-labeling applications of magnetic nanoparticles. This is because (1) superparamagnetic cores will respond to an external magnetic field, but retain no magnetic properties once the field is removed [7]. The lack of magnetic remanence will allow magnetic materials to be repeatedly dispersed and concentrated in solution without forming magnetized clusters; and (2) superparamagnetic materials have large magnetic moments, permitting the use of low-field magnets for efficiently concentrating nanoparticles. Recently, progress has been made on the synthesis of monodisperse and structurally well defined iron oxide and other types of magnetic nanoparticles [13–33]. These new materials can be employed for constructing the interior cores of the core/shell magnetic nanoparticles – potentially endowing them with improved magnetic properties. Hyeon has recently reviewed developments in the chemical synthesis of magnetic nanoparticles [44].

The shell wall of core/shell magnetic nanoparticles is of particular importance to the bioapplications, stability and magnetic properties of nanoparticulate complexes. Due to anisotropic dipolar attraction, nanoparticles tend to aggregate into large clusters that cause the loss of specific properties associated with single-domain nanostructures. Consequently, long-chain organic ligands or a layer of polymers are usually introduced to coat the inorganic cores to prevent core aggregations. In addition to improving the stability of nanoparticles, the shells also determine the solubility of nanocomplexes in aqueous buffer media and provide a platform for the functionalization of nanoclusters. Bio-active molecules, e.g., antibodies and proteins, can be immobilized onto the surface of shell walls and interact with a biological entity in surrounding solutions. However, as the size of nanoparticles decreases, the influence of surface interactions upon the magnetic properties of magnetic nanoparticles becomes more significant due to the increased volume fraction of surface atoms. The symmetry is reduced for the chemical surroundings of magnetic metal cations at the surface due to the incomplete coordination sphere. As a consequence, the magnetic properties of the nanoparticle surfaces

usually differ from those in the body of the nanoparticle, and surface effects could become increasingly important to the overall magnetic properties of magnetic nanoparticle as its size decreases [45–50].

The present chapter focuses on recent developments in the synthesis and biofunctionalization of core/shell magnetic nanoparticles as well as their applications in biological and medical sciences. Although widely used in bio-separation applications, micrometer-sized magnetic particles are outside the scope of this review. This chapter is divided into three sections: functionalization of magnetic nanoparticles for (a) *in vitro* protein/cell separation (Section 3.2); (b) *in vitro* biochemical/chemical synthesis of therapeutic drugs and their intermediates (Section 3.3); and (c) *in vivo* bio-imaging, drug targeting and tumor hyperthermia treatments (Section 3.4), which includes some recent work on molecular imaging and gene therapy using functionalized magnetic nanoparticles. Although most reported molecular imaging and gene therapy experiments were carried out under *in vitro* environments, the ultimate goal in these two areas is to develop novel techniques using magnetic nanoclusters for *in situ* cellular visualization and gene therapy in living animals. Therefore, functionalization of magnetic nanoparticles for cellular imaging and gene therapy is listed under the *in vivo* applications of magnetic nanoparticles.

## 3.2

### Functionalization of Magnetic Nanoparticles for *In Vitro* Protein/Cell Separation

The synthesis of core/shell magnetic nanoclusters and the attachment of bio-active ligands to the surface of the outer shells are key to bioapplications of magnetic nanoparticles. Several strategies have been developed recently for coating magnetic cores. The most common method is to use long-chain organic ligands to wrap up the inorganic cores. Hydrophobic interactions between ligands from neighboring nanoparticles will prevent adjacent inorganic cores agglomerating into a larger cluster. However, biological applications usually require magnetic nanoparticles to have good solubility in aqueous media. Hydrophobic long-chain alkanes will lower the solubility of magnetic nanoparticles in aqueous buffers. To solve this problem, our group has investigated the employment of charged bipyridinium carboxylic acids for coating iron oxide cores to make these nanoparticles water-soluble (Fig. 3.1) [51]. The positive charges on the surface of nanoparticles not only stabilize nanoparticles, by repelling neighboring clusters from forming aggregation, but also improve the solubility of nanoparticles in aqueous media. This is particularly important with biotin-functionalized maghemite nanoparticles since biotin is practically insoluble in distilled water. Both biotin and bipyridinium ligands were anchored to the surface of inorganic cores, having an average dimension of about 13 nm due to interactions between carboxyl groups and iron oxide. Such biotin-functionalized maghemite nanocomposites have been utilized for affinity isolation of fluorescein-labeled protein avidin.

A similar strategy using a bidentate enediol dopamine as a stable anchor of mag-

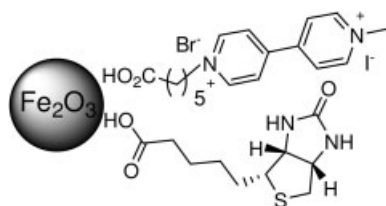


**Fig. 3.1.** Structure of magnetite nanoparticles coated with biotin and bipyridinium carboxylic acids. (Adapted from Fan et al. [51].)

netite nanoparticles for protein separation has been reported by Xu (Fig. 3.2A) [52]. Two types of superparamagnetic nanoparticles were synthesized and tested as supports for immobilization of nitrilotriacetic acid: one has a cobalt core with a  $\text{Fe}_2\text{O}_3$  shell, and the other has a  $\text{SmCo}_{5.2}$  core surrounded by an  $\text{Fe}_2\text{O}_3$  shell. Dopamine was anchored to magnetic nanoparticles via interactions between its bidentate enediol functional group and surface iron oxide. Nitrilotriacetic acid was linked to dopamine through a long tether. Upon chelation to  $\text{Ni}^{2+}$ , dopamine-functionalized magnetic nanoparticles separated histidine-tagged proteins from a cell lysate with high efficiency and capacity. Histidine-tagged proteins were segregated from the solution due to interactions between a histidine tag and  $\text{Ni}^{2+}$  complexed with nitrilotriacetic acid. The separation process was readily achieved by applying an external small magnet. A similar bidentate enediol functional group, C-undecylcalix[4]resorcinaren, has also been reported for coating cobalt magnetic nanoparticles that self-assemble into bracelet-like rings [53].

Interactions between a sulfur group and FePt have been utilized to immobilize nitrilotriacetic acid for the separation of histidine-tagged proteins from a cell lysate

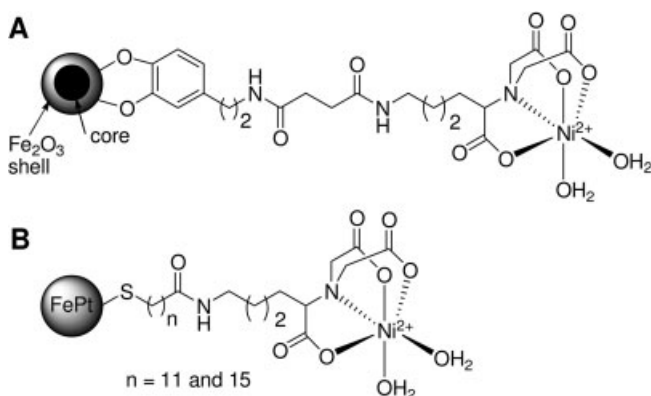


**Fig. 3.2.** Structures of magnetic nanocomposites using dopamine (A) and sulfur (B) to anchor nitrilotriacetic acid for separating histidine-tagged proteins. (Adapted from Xu [52, 54].)



(Fig. 3.2B) [54]. Many other functional groups, such as  $-OH$ ,  $-SH$  and  $-NH_2$ , have also been tested for their interactions with metals and metal oxides as capping agents of magnetic metal and metal oxide cores. For instance, the amino groups of vancomycin have been employed for immobilizing the antibiotic to the surface of FePt nanoparticles [55]. Such complexes could capture and detect vancomycin-resistant enterococci and other Gram-positive bacteria at concentrations of  $10^1$  cfu mL $^{-1}$  within an hour. Additional examples of using amino groups for the functionalization of magnetic nanoparticles have also been reported [56, 57]. A similar nanocomposite of IgG and magnetite has also been employed by Chen's group as an effective affinity probe to concentrate target bacteria selectively [58]. IgG was immobilized onto the surface of a magnetite core via an ester bond. Other than antibodies, DNA/RNA-functionalized magnetic nanoparticles have also been used for the isolation and extraction of DNA/RNA targets [59]. The surfaces of these nanoparticles were usually coated with molecular beacon DNA probes for specific recognition of DNA/RNA targets in solution.

The  $-OH$ ,  $-SH$  and  $-NH_2$  functional groups are usually introduced through a surface exchange reaction with pre-synthesized magnetic nanoparticles coated with a different functional group [31, 60, 61], or by co-precipitation of an aqueous solution of metal ion salts such as  $Fe^{2+}/Fe^{3+}$  in the presence of these organic capping groups [42]. For example, iron oxide nanoparticles coated with  $\alpha$ -cyclodextrin (CD) were obtained by a surface exchange reaction from iron oxide nanoparticles protected by oleate [62].  $\alpha$ -CD was added to the surface of nanoparticles by vigorously stirring, at room temperature, mixtures of hexane suspensions of iron oxide nanoparticles coated with oleate and an equal volume of  $\alpha$ -CD aqueous solution. Oleate-stabilized nanoparticles were transferred from organic into aqueous phase by surface modification using  $\alpha$ -CD. CD molecules have  $-OH$  groups that can bind to the surface of iron oxide cores.

An interesting way of capping magnetic iron oxide cores is to use phospholipids to form nanometer-sized magnetoliposomes. An example [63] of such phospholipid-coated magnetite nanoparticles, employing 1,2-myristoyl-*sn*-glycerol-3-phosphoglycerol, sodium salt and 1,2-dimyristoyl-*sn*-glycerol-3-phosphocholine, had an iron oxide core dimension of 8 nm and a phospholipids/surfactant shell of 4 nm. These particles were effective ion exchange media for the recovery and separation of proteins from protein mixtures. These nanocomposites demonstrated high adsorptive capacities of proteins and exhibited none of the diffusion resistances offered by conventional porous ion exchange media.

Due to strong interactions with metal oxide, organosilane groups have also been explored for anchoring bioactive molecules onto the surface of iron oxide nanocores. Zhang has reported a novel approach using bifunctional trifluoroethyl ester polyethylene glycol (PEG) silane for the functionalization of iron oxide nanoparticles (Fig. 3.3) [64]. Folate acid, a widely used targeting agent for cancer therapies [65], was attached to the outer terminus of the PEG chain to demonstrate the effectiveness of bio-active ligand immobilization by this strategy. Silylation of magnetite is key to the functionalization of magnetic nanoparticles in this route. Introduction of PEG molecules as a linker will potentially benefit *in vivo* applications of these

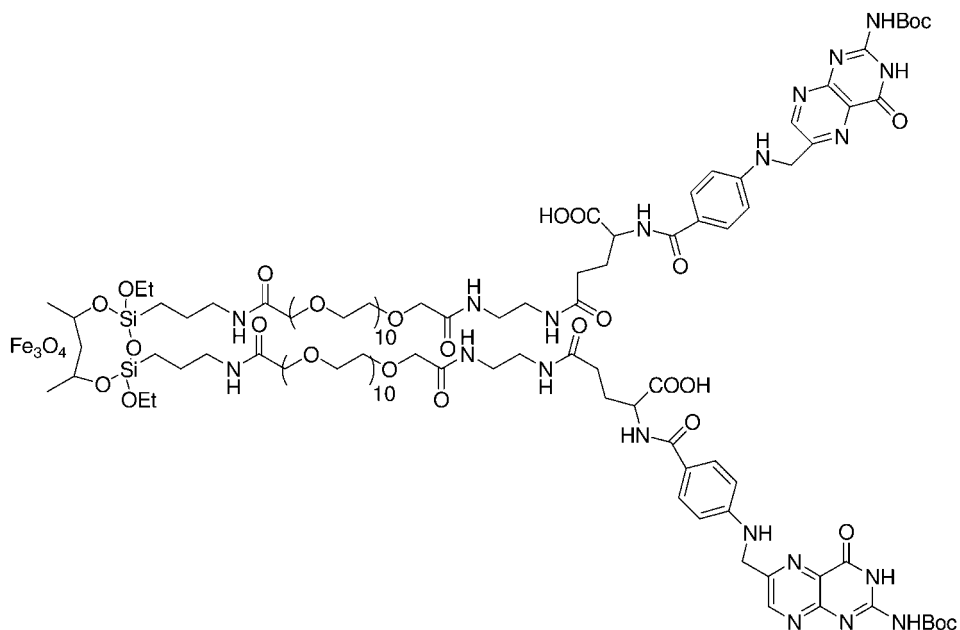


**Fig. 3.3.** Structure of magnetite nanoparticles coated with PEG and folic acid. (Adapted from Kohler et al. [64].)

nanoparticles since PEG molecules are nonimmunogenic, nonantigenic and protein resistant and can increase particulate circulation time in the blood. Willner has used the silylation of magnetic metal oxide surfaces for the immobilization of redox functions to magnetite particles. Such complexes were used in constructing a magneto-switchable bioelectrocatalysis sensor [66].

Sol-gel approaches have been examined for coating magnetic metal oxide cores to form a core/shell structure having an inorganic metal oxide core wrapped with a layer of silica [67–76]. Two different strategies have been investigated to generate silica coatings on the surface of iron oxide particles. The first method relies on the well-known Stöber process [77], in which silica is formed *in situ* through the hydrolysis and condensation of a sol-gel precursor. For example, Xia has reported the use of tetraethyl orthosilicate (TEOS) for coating mixed-crystalline iron oxide nanoparticles (water-soluble ferrofluid) [74]. Because the iron oxide surface has a strong affinity towards silica, no primer was required to promote the deposition and adhesion of silica, allowing magnetic nanoparticles directly coated with amorphous silica to be formed via the hydrolysis of TEOS. A second sol-gel approach is based on a microemulsion strategy, in which micelles or inverse micelles are used to confine and control the coating of silica on core nanoparticles. The microemulsion approach can control the thickness of the silica shell wall coating so that the stability and solubility of the formed magnetic nanoparticles in aqueous media can, presumably, be tuned for different bio-applications. An example is discussed

in Section 3.3 (Fig. 3.7 below) [75]. Core/shell magnetite/silica nanoparticles were synthesized by a microemulsion approach and functionalized with protein  $\beta$ -lactamase to promote hydrolysis.

Natural polymers and their derivatives have been widely utilized for coating magnetic metal and metal oxide nanocore surfaces. In particular, natural biopolymers such as dextrans, proteins/peptides and PEG are usually the materials of choice for the synthesis of core/shell magnetic nanoparticles designated for *in vivo* applications. This is because such natural polymers are inexpensive and are known to be nonimmunogenic and nonantigenic in the body. Natural polymers are usually anchored onto the surfaces of magnetic metal oxide cores through carboxylate groups on their side chains. Section 3.4 includes detailed discussions and examples of using these natural polymer-functionalized magnetic nanoparticles for *in vivo* applications.

Tremendous research efforts have focused on the employment of synthetic polymers for coating the surfaces of magnetic inorganic cores to generate core/shell magnetic nanoparticles. For example, layer-by-layer deposition of charged polymers onto the surfaces of magnetic inorganic cores in sequence has been reported [78]. Although progress has been made, the layer-by-layer assembly strategy has yet to become the method of choice for coating very small, sub-20 nm magnetic nanoparticle cores because of the curvature of nanoparticle surfaces and the mechanical strength of the polymeric chains. Unfortunately, magnetic nanoparticles with an overall dimension below 20 nm are usually preferred for some *in vivo* applications due to their high tissue penetration capability and long blood circulation time [42, 43]. Here we focus on two alternative strategies that can potentially be utilized and expanded for synthesizing magnetic nanoparticles of various sizes and shapes.

The first approach is to utilize surface-initiated polymerization to grow polymer chains on the surface of inorganic cores. Free radical initiators are first immobilized onto the surfaces of metal and metal oxide cores followed by polymer growth outwards to give rise to a radius structure. Among many polymerization routes, living free radical polymerization, especially atom transfer radical polymerization (ATRP), has become the method of choice for the surface-initiated polymerization synthesis of core/shell magnetic nanoparticles (Fig. 3.4) [79]. ATRP is a versatile technique that offers several advantages over other polymerization routes, including control over molecular weight and molecular weight distribution for the synthesis of well-defined and complex macromolecular architectures of magnetic nanoparticles [80]. For example, by manipulating reaction time and the concentration of polymerizable ligands in solution one can control the shell wall polymer molecular weight and, thus, the thickness of the polymeric shell wall of core/shell magnetic nanoparticles. ATRP also allows the polymers to be end-functionalized or block copolymerized upon the addition of other monomers. Not only does this feature offer tailorability of the polymer coating with various compositions and functionalities, but also provides the platform for functionalization of the polymeric shell wall with bio-active functional groups. As a consequence, extensive research has been carried out by many groups using ATRP for the synthesis of core/shell polymer magnetic nanoparticles [79, 81, 82]. Our group has examined

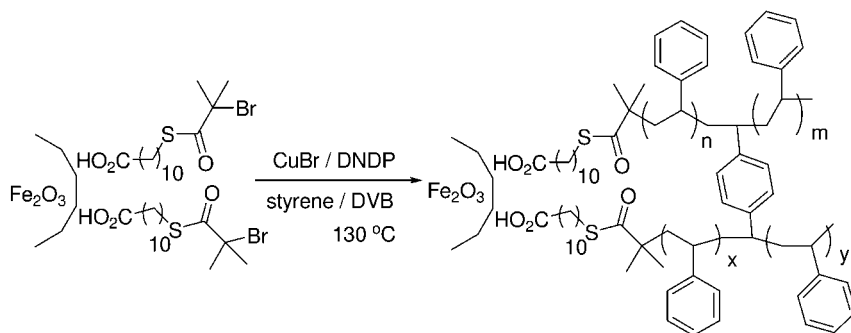


**Fig. 3.4.** Surface-initiated ATRP synthesis of polymeric core/shell nanoparticles using divinylbenzene (DVB) as a crosslinking agent. (Reproduced by permission of the American Chemical Society.)

recently an ATRP method for the preparation of core/shell maghemite/polystyrene nanocrystals (Fig. 3.4) [79]. Our inorganic cores have an average size of about 11 nm while the thickness of the crosslinked polystyrene shells were maintained to only about 4.7 nm (Fig. 3.5). However, further work is needed to adapt ATRP techniques for the synthesis of hydrophilic and water-soluble magnetic nanoparticles for biomedical applications. A recent paper from Armes [83] on the synthesis of hydrophilic polymer-grafted ultrafine inorganic oxide particles suggested that such water-soluble polymeric magnetic nanoparticles can potentially be achieved through a different ATRP method.

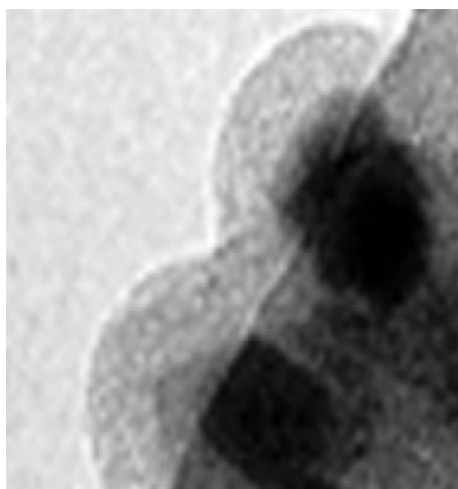


**Fig. 3.5.** TEM micrograph of 10% DVB-crosslinked  $\text{Fe}_2\text{O}_3$ /polystyrene core/shell nanoparticles on a lacey carbon film coated copper grid (300 mesh) consisting of woven-

mesh-like holes. The polystyrene shells are visible at the edge of a hole. Dark spots on the carbon film are  $\text{Fe}_2\text{O}_3$  cores. (Reproduced by permission of the American Chemical Society.)

A second, extensively researched, approach to synthesizing polymeric core/shell magnetic nanoparticles is to use pre-formed synthetic polymers as a matrix to confine and control the formation of magnetic cores. For example, core/shell magnetic nanoparticles have been produced by chemical co-precipitation of iron salts in an aqueous solution of the poly(ethylene oxide) (PEO)/poly(propylene oxide) (PPO)–poly(acrylic acid) (PAA) graft copolymers [84]. After magnetite nucleation begins, carboxylic acid groups on the PAA backbone bind to the particle surface, limiting the magnetic core growth. The bifunctional polymer shell is formed from the hydrophilic PEO and hydrophobic PPO side chains in the graft copolymer. These nanoparticles are stable and soluble in organic solutions. Similar magnetite nanoparticles coated with long poly(vinyl-*N*-alkylpyridinium) chains have also been synthesized by this strategy [85]. Alkylated polyethylenamines made these materials highly bactericidal toward both Gram-positive and Gram-negative pathogenic bacteria. Other types of polymers such as poly(vinylpyrrolidone) [86, 87], polylactide [88], poly(isopropylacrylamide) [89], polyacrylate [90], poly(methacrylate) [91], poly(vinyl alcohol) [92] and polysiloxane block copolymers [93] have also been reported as matrices for the synthesis of core/shell magnetic nanoparticles.

### 3.3

#### **Functionalization of Magnetic Nanoparticles for Biochemical/Chemical Synthesis of Therapeutic Drugs and Their Intermediates**

Catalysts are widely used in pharmaceutical and chemical industries in producing therapeutical drug molecules and their intermediates. Catalysts such as biocatalysts (enzymes) and metal catalysts (homogeneous and heterogeneous catalysts) can promote organic and biological reactions that are otherwise too slow for industrial standards. Recycling and reuse of industrial catalysts is particularly important for cutting industrial operation costs and minimizing environmental pollutions, especially when expensive and toxic heavy metals are used [94].

Recently, efforts have been directed towards the use of magnetic nanoparticles as supports for immobilization of biocatalysts [75, 95, 96]. Core/shell magnetic nanoparticles are usually covalently attached with biocatalyst enzymes on their shell surfaces. Due to the small sizes of particles, nanoparticle-immobilized proteins are usually soluble in aqueous buffers, which differs from other supports such as polystyrene beads, in which proteins are usually suspended in solution. The magnetic, usually superparamagnetic cores will allow these biofunctionalized particles to be magnetically concentrated with the assistance of an external magnetic field. This could allow immobilized enzymes to be used repeatedly or continuously in various reactors. Enzymes can be easily separated from soluble reaction products and unreacted substrates, thus simplifying work-up and preventing protein contamination of the final products. This will also simplify the control of microbial contamination in immobilized proteins.

*Candida rugosa* lipase (E.C.3.1.1.3) has been immobilized on maghemite nanoparticles with an average size of about  $20 \pm 10$  nm (Fig. 3.6) [95]. A carboxylate

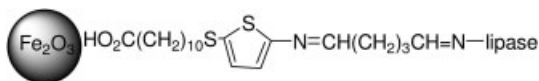


**Fig. 3.6.** Representative structure of magnetic nanoparticles immobilized with *Candida rugosa* lipase. (Adapted from Dayal [95].)

group was used to anchor a 2-thiophene thiolate linker and the enzyme was chemically bonded to the nanoparticle surface through a C=N bond using glutaraldehyde. The amount of immobilized enzyme was determined by standard BCA protein assays of the original lipase solution, the supernatants and washing solutions after immobilization, respectively. The presence of protein on the surface of nanoparticles was also confirmed by AFM measurements of a small amount of the enzyme-functionalized magnetic nanoparticles on a thin layer of glue deposited on a steel disk. Enzymatic activity of the immobilized lipase was determined by following the ester cleavage of *p*-nitrophenol butyrate aqueous solution with UV spectroscopy. The enzymatic activity for *Candida rugosa* lipase immobilized on maghemite nanoparticles was lower than that of the free enzymes, but the loss in activity on nanoparticles was significantly lower than that reported for enzyme immobilized on micrometer-sized polymeric beads using physisorption. The most significant advantage of the nanoparticle-immobilized enzyme is its long-term stability. The hybrid enzyme–nanoparticle composites showed only a ~2% decrease in activity over 14 days due to desorption or denaturation. This long-term stability illustrates the advantages of attaching enzymes chemically to the nanoparticles.

A similar investigation was also reported recently using magnetic nanoparticles for immobilization of  $\beta$ -lactamase I (Fig. 3.7) [75]. Here, a layer of silica coating was placed on the surface of an iron oxide core. TEM images determined the average size inorganic core to be about 9.1 nm, with a silica shell of about 3.5 nm.  $\beta$ -Lactamase I was immobilized onto the surface through glutaraldehyde and C=N bonds. An assay evaluation, using a UV spectrometer, of active  $\beta$ -lactamase I on nanoparticle composites was carried out at room temperature using phenoxymethylpenicillin as the substrate in a buffer. The nanoparticle-immobilized enzyme showed an activity of about 53.76% of that of the free enzyme in solution. However, a kinetic study has shown that the  $K_M$  of the immobilized enzyme matches well that of the parent free enzyme. This suggests that nanoparticle-immobilized enzymes do not suffer from the mass-transfer problems frequently encountered with insoluble supports used for immobilizing enzymes.

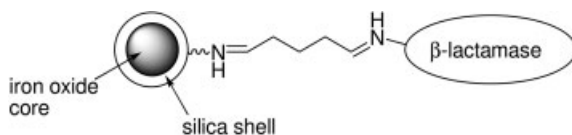


**Fig. 3.7.** Immobilization of enzyme  $\beta$ -lactamase I to core/shell iron oxide/silica nanoparticles. (Adapted from Gao [75].)

Other than biocatalysts, metal catalysts, especially homogeneous metal catalysts, have also been immobilized onto the surfaces of core/shell magnetic nanoparticles. Due to their small sizes, the solubility of magnetic nanoparticles in organic media can be tuned by controlling the structure of organic and polymer coatings of nanoparticles. Such soluble supports could be magnetically concentrated and isolated from reaction media by applying an external magnetic field. Magnetic nanoparticles are an ideal soluble support, providing a unique solution to the problem of recycling homogeneous catalysts in pharmaceutical and chemical industries. The reader is referred to two recent papers in this emerging field [97, 98].

### 3.4

#### **Functionalization of Magnetic Nanoparticles for *In Vivo* Bio-imaging, Drug Targeting and Tumor Hyperthermia Treatments**

Magnetic nanoparticles have been explored extensively as contrast agents for *in vivo* magnetic resonance imaging (MRI), magnetic guides for drug targeting and mediators for magnetic hyperthermia treatments of a large variety of diseases. With proper coatings, superparamagnetic nanoparticles can interact with an external magnetic field and deliver radiotherapeutic and chemotherapeutic agents to a target area – minimizing the cytotoxicity of tumor therapeutic agents to healthy body compartments. This is important in the treatment and diagnosis of certain types of cancers due to, for example, their lack of specific tumor markers and the presence of the blood–brain barrier (BBB). A further medical use of magnetic nanoparticles is to utilize superparamagnetic nanoclusters as MRI contrast agents for cancer diagnosis and detection. A third major *in vivo* application of magnetic nanoparticles is magnetic hyperthermia therapy. Magnetic nanoparticles can be made to resonantly respond to a time-varying magnetic field, with advantageous results related to the transfer of energy from the exciting field to the nanoparticles. This is utilized to make magnetic nanoparticles heat up, which leads to their use as hyperthermia mediators, delivering toxic amounts of thermal energy to targeted tumor cells.

Typical magnetic nanoparticles used in *in vivo* studies consist of a magnetic core surrounded by a biocompatible polymeric coating. Iron oxide particles such as magnetite or its oxidized form maghemite are by far the most commonly employed for *in vivo* applications. Highly magnetic materials such as cobalt and nickel are toxic and susceptible to oxidation and hence are often overlooked for *in vivo* biomedical applications. Iron oxide nanoparticles are physiologically well tolerated. For example, dextran-magnetite has no measurable toxicity index LD<sub>50</sub> [99–101]. This is partially because the body is designed to process excess iron. In the human body iron is stored primarily in the core of the iron storage protein ferritin. Iron contained in endosomes and lysosomes is metabolized into elemental iron and oxygen by hydrolytic enzymes, where the iron joins normal body stores [101]. Iron homeostasis is well controlled by adsorption, excretion and storage. As a consequence, iron from iron nanoparticles in the body can be processed and iron oxide

can be tolerated by the body. However, notably, iron has a rather limited bioavailability, and in some situations it can also be toxic to cells [102].

*In vivo* applications require that these magnetic nanoparticles have a long-circulating time in the body in order to reach the target sites [43] before being eliminated from the blood circulation through clearance by the mononuclear phagocyte system (MPS) [103]. The MPS, also known as the reticuloendothelial system, is defined as the cell family consisting of bone marrow progenitors, blood monocytes and tissue macrophages such as Kupffer cells in the liver. These macrophages are widely distributed and strategically placed in many tissues of the body to recognize and clear senescent cells, invading microorganisms and particles [104]. The first step of the clearance mechanism is the opsonization process. Opsonins, circulating plasma proteins, adsorb themselves spontaneously onto the surface of an invading entity. Particles of different surface characteristics, size and morphology attract different arrays of opsonins, which can interact with the specialized plasma membrane receptors on monocytes and macrophages [105]. Then, endocytosis/phagocytosis of the particles by the circulating monocytes or the fixed macrophages leads to the elimination of particles from circulation.

Previous studies of liposomes and polymeric nanoparticle systems have shown that, among many surface factors, the size, surface charge density and hydrophilicity/hydrophobicity have a profound effect on opsonization [43]. Therefore, significant efforts have been directed at exploring various biocompatible coating materials to increase plasma half-life as long as possible in order to increase the probability of reaching the desired targets in the body [106]. Neutral and hydrophilic natural and synthetic polymers have become the materials of choice. For example, dextrans have been frequently used for coating iron oxide nanocrystals [43]. Other biological macromolecules such as heparin and polysaccharides that complement regular proteins have also been investigated [107, 108]. Among synthetic polymers, poloxamers, poloxamines and their block-copolymers increase their circulation time [109, 110], and can potentially be utilized for coating iron oxide nanoparticle cores for this purpose. An alternative approach is to covalently anchor PEG macromolecules onto the nanoparticle surfaces. PEG is an effective polymer for suppressing the protein adsorption-opsonization process [65]. Immobilization of PEG to drug carrier surface is well known in liposome drug delivery where PEG macromolecules are conjugated to the surfaces of liposomes to improve their circulation lifetime, bioavailability and decrease their immunogenicity [111]. Recent successes using this PEG strategy in a quantum dots biodistribution study [112] has offered the possibility of extending this method to other nanomaterials, including iron oxide nanoparticles.

#### 3.4.1

##### MR Imaging

Superparamagnetic nanoparticles represent a class of MRI contrast agents that are usually referred to as  $T_2$  (transversal relaxation time) or  $T_2^*$  contrast agents [113] as opposed to  $T_1$  (longitudinal relaxation time) agents such as paramagnetic gado-



linium chelates [114]. MRI is based on the NMR (nuclear magnetic resonance) signal of protons from water in tissues and organs through the combined effects of a strong static magnetic field ( $B_0$ ) and a transverse radiofrequency field (rf field) [115]. After rf excitation, hydrogen nuclei attempt to return to their ground states through two independent relaxation processes: (1) longitudinal relaxation, which is also called  $T_1$ -recovery or “spin–lattice” relaxation; hydrogen atoms release the previously absorbed energy to the surrounding tissue (lattice) in their attempt to re-align with  $B_0$ . (2) Transverse relaxation, also called  $T_2$  decay or “spin–spin” relaxation, which is due to the exchange of energy between spinning hydrogens in tissues. MR images of biological tissues are constructed from relaxation data collected by a computer applying a two-dimensional Fourier transformation to give the amplitudes of NMR signals [116–118]. While, in many clinical situations, the intrinsic differences in relaxivity ( $1/T$ ) between tissues are small, exogenous contrast agents can be utilized to improve greatly the diagnostic value of MRI for a better delineation of tissues [100]. Gadolinium complexes are the most commonly used  $T_1$  contrast agents while superparamagnetic iron oxide nanoparticles are FDA-approved  $T_2$  agents.

Depending on their size, colloidal iron oxide nanoparticles of magnetite ( $\text{Fe}_3\text{O}_4$ ) to maghemite ( $\gamma\text{-Fe}_2\text{O}_3$ ) are often called SPIO (superparamagnetic iron oxide) with a particle size typically larger than 50 nm, and USPIO (ultra-small superparamagnetic nanoparticles), with a dimension  $< 50$  nm [6, 119]. Hydrophilic polymers such as heparin [107], dextran [120], chitosan [121], starch [122], DNA [123], and cyclodextrin [124] have been employed for coating the iron oxide cores. These water-soluble macromolecules are employed to stabilize nanoclusters by preventing aggregation of their inorganic cores and reduce opsonization process. However, the structure of surface coating materials greatly influences the magnetic properties of magnetic nanoparticles [45–50]. Adoption of different polymers for coating iron oxide cores could significantly alter MR relaxation properties of the overall nanoparticle contrast agents [124].

Due to their size, SPIOs usually can be cleared out of the blood circulation and accumulated in MPS organs very quickly, especially in liver and spleen [113, 125]. For example, about 80% of the injected SPIO doses were found in liver and 5–10% in the spleen with a plasma half-life of less than 10 min [4]. As a consequence, SPIOs can decrease the liver and spleen signals within several minutes after i.v. administration, and this type of agent is usually used for liver and spleen imaging [126–129]. USPIOs, however, are smaller than SPIOs. They usually have longer plasma life, higher than 2 hours, and therefore remain in the blood long enough to act as blood-pool agents for MR angiography [113]. Also because of their small sizes, USPIOs can leak into the interstitium, where they can be accumulated in the lymph nodes and thereby used for imaging lymphatic systems [130–135].

Progress has been made on the functionalization of core/shell magnetic nanoparticles for tissue/organ-specific *in vivo* imaging. Antibodies such as human polyclonal IgG and L6 antibodies have been physically adsorbed or covalently attached to iron oxide nanoparticles [136–138]. Investigations in rodents revealed that

antibodies led to a high concentration of magnetic nanoparticles at specific sites. Recently, Moore has reported using a peptide [139] for the functionalization of iron oxide nanoparticles for tissue-specific *in vivo* imaging. The synthetic peptide EPPT1(YCAREPPTRTFAYWG) – a short fragment of the CDR3 V<sub>h</sub> region of a monoclonal antibody ASM2 – was covalently linked to the surface of aminated crosslinked superparamagnetic iron oxide nanocomplexes (CLIO-NH<sub>2</sub>). CLIO-NH<sub>2</sub> consists of a core of superparamagnetic iron oxide and a crosslinked coating of dextran with amino groups [140, 141]. EPPT1 peptide has significant affinity towards under-glycosylated mucin-1 antigen (uMUC-1), which is overexpressed on many cancer cell lines. A Cy5.5 dye was also immobilized onto the surface of CLIO-NH<sub>2</sub> as a near-infrared fluorescence optical probe. *In vivo* MRI and near-infrared-imaging experiments on tumor-bearing mice showed specific accumulation of the probe in uMUC-1-positive tumors and no signal in control tumors. The high specific concentration of magnetic nanoparticles at the target sites was due to the presence of EPPT1 peptide on the surface of dextran–iron oxide nanoparticles. Similar experiments using folate-labeled magnetic nanoparticles for *in vivo* imaging of tumors with overexpressed folate receptors have also been reported recently [142].

Cellular imaging has long attracted a great deal of research interest [143]. Studies using unfunctionalized iron oxide nanoparticles for labeling various types of cell lines such as leukocytes, lymphocytes and monocytes for MR imaging of cells have been reported [124, 144–146]. If a cell can be sufficiently loaded with magnetic materials, then MRI can be adopted for use in cell tracking with a resolution of 20–25  $\mu\text{m}$  or higher, approaching the size of single cells [6]. However, cellular uptake of dextran-coated iron oxide nanoparticles was low. Improvements are still needed to increase the cellular uptake of magnetic nanoparticles. Recently, progress has been made towards this goal for high-efficiency internal labeling of large numbers of cells. Iron oxide nanoparticles with a HIV-1 tat peptide fragment attached at the outer surface of their dextran coating (CLIO-NH<sub>2</sub>) increase the cellular uptake of nanoparticles over 100-fold into lymphocytes when compared to untagged particles [147, 148]. HIV-1 tat peptide carries a transmembrane and a nuclear localization signal within its sequence and is, therefore, capable of translocating exogenous nanoparticles into cells [149]. Folic acid has also been immobilized onto iron oxide nanoparticles for targeting the folate receptor-bearing cells [150, 151]. Folate-mediation internalized folate-labeled nanoparticles and increased the cellular uptake of iron oxide nanoparticles that were used as contrast agents for cellular imaging. Iron oxide nanoparticles functionalized with the C<sub>2</sub> domain of synaptotagmin I [152] and dendrimers [153] have also been synthesized and utilized for MRI studies of cells. A further goal in this area is to exploit the use of MRI techniques to image transgene expression. Research in this area has focused on depicting the activity of endocytotic receptors for cellular uptake of functionalized iron oxide nanoparticles [154, 155]. A growing number of cell biologists, molecular biologists and experts in MRI are working together to develop techniques for the *in situ* visualization of gene expression in living animals [143].

## 3.4.2

**Targeted Drug Delivery**

Magnetic drug targeting has attracted a great deal of attention. This approach is an alternative to antibody-directed drug targeting, offering additional advantages for the treatment and diagnosis of certain types of cancers due to, for example, their lack of specific tumor markers and presence of the BBB [156]. *In vivo* experiments of magnetic drug targeting have usually been performed in rodents [157], but investigations using swine [158] and rabbits [159] have also been reported. Generally, iron oxide cores are coated with silica, and polymers such as PVA and dextran. The first clinical trials in humans with a magnetic drug targeting were reported by Lübke et al. [160, 161]. They used a ferrofluid (size about 100 nm) coated with starch polymers and anionic phosphate groups for loading the drug epirubicin. The shell phosphate group forms strong anionic interactions with the positively charged amino sugars of epirubicin. During infusion and for 45 min afterwards, a magnetic field was applied about less than 0.5 cm from the tumor site. It took about only 30 min in half of the patients before the ferrofluids could be successfully directed to the tumors. Similar investigations using liposomes containing magnetic nanoparticles and drugs have also been reported [162]. Magnetic drug targeting has been employed to deliver cytotoxic drugs to brain tumors, which are difficult to treat due to the BBB. Pulfer and Gallo demonstrated that particles as large as 1–2  $\mu\text{m}$  could be concentrated at the site of intracerebral rat glioma-2 tumors [156].

Despite early success, magnetic drug targeting still needs to be improved to make it more effective. Limitations [161] include (1) difficulties in scaling up from small rodent models to humans or large animals due to the requirement of much stronger external magnetic fields; (2) the possibility of embolization of the blood vessels in the target region due to accumulation of the magnetic carriers; and (3) difficulties in controlling the release of drug molecules from carriers and the molecular uptake of these therapeutic agents by tumor cells.

Some of the aforementioned limitations can be overcome if magnetic nanoparticle carriers are utilized for delivering radiotherapeutic agents for tumor radiotherapy. In contrast to chemotherapeutic drugs, radioisotopes can be delivered close to the tumor sites and exert their cytotoxicity over a defined, radioisotope-dependent distance – the chelated metals do not need to be released from the carriers so that they can bind to or enter the cells to be cytotoxic. The effectiveness of this technique has been confirmed by several investigations using yttrium-90 [163] and rhenium-188 [164] in both animal and cell culture studies.

Arbab et al. have recently demonstrated the possibility of using iron oxide nanoparticles for delivering mesenchymal stem cells (MSCs) to a targeted area in an animal model by applying an external magnet [165]. MSCs were labeled with iron oxide nanoparticles and the resulting magnetic cell complexes were intravenously injected into two groups of rats with or without a magnet placed over the livers. Experiments showed that the external magnets influenced the movement of labeled MSCs as higher iron concentration and increased labeled cell numbers

were detected in rat livers with external magnets. These results demonstrated that cells could be retained in the region of interest inside the body using magnetic forces, and magnetic drug targeting can be utilized for *in vivo* delivery of stem cells or genetically altered cells to the target sites.

A further area of interest in the use of targeted magnetic nanoparticles is in the field of gene therapy. One of the impediments to successful gene therapy is the inefficient delivery of genes because of low transfection efficiencies. This can be addressed by using a viral vector carrying the therapeutic gene loaded on magnetic carrier surface. An external magnetic field was applied to allow the viral vector a longer period of time in contact with the tissues, thereby increasing the efficiency of gene transfection and expression [166–168]. Research in this area has recently attracted a great deal of interest – a review article is listed here [169] for interested readers.

### 3.4.3

#### **Magnetic Hyperthermia**

Magnetic hyperthermia is a promising form of cancer therapy aside from the well-known methods of surgery, chemotherapy and radiotherapy [170, 171]. Magnetic nanoparticles are used as mediators for magnetic hyperthermia. In broad terms, magnetic hyperthermia involves dispersing magnetic particles through the targeted tissue, and then applying an AC magnetic field of sufficient strength and frequency to cause the particle to heat. This heat conducts into the immediately surrounding diseased tissue. Hyperthermia treatment of cancers is based on observations that some cancer cells are more sensitive to temperatures in excess of 41 °C than their normal healthy counterparts. Two kinds of heat treatment are currently distinguished: mild hyperthermia is performed between 41 and 46 °C to stimulate the immune response for non-specific immunotherapy of cancers, and thermoablation between 46 and 56 °C for thermal destruction of tumors by direct cell necrosis, coagulation or carbonization [170, 171].

Generally, two types of magnetic nanoparticles have been used for magnetic hyperthermia, via two different mechanisms: (a) heating of ferromagnetic nanoparticles when exposed to a time varying magnetic field, which is essentially due to hysteresis losses and Brownian relaxation losses of the particles; and (b) Brown and Néel heating mechanisms that contribute to the heating of superparamagnetic nanoparticles. The heating power of the particles is quantified as the specific absorption rate (SAR) and describes the energy amount converted into heat per time and mass. Superparamagnetic nanoparticles usually give higher SAR than ferromagnetic nanoparticles because the hysteresis loop of ferromagnetic nanoparticles can rarely be fully used because of physiological and technical restrictions on the external field amplitude [4]. Consequently, dispersions of superparamagnetic nanoparticles appear to be the most promising since they are used as ferrofluids. This technique is termed magnetic fluid hyperthermia (MFH) [170]. However, ferromagnetic nanoparticles remain potentially useful due to their Curie tempera-

ture – providing one of the more powerful methods for controlling the maximal temperature *in vivo*.

Maghemite nanoparticles encapsulated in polymer matrix beads have been tested successfully for the treatment of macroscopic liver tumors [172, 173], which were introduced through the arterial embolization method, taking advantage of the fact that liver tumors take their blood supply from the hepatic arterial system. Such beads appear to be safe and well-tolerated as there was no significant hepatic clearance 28 days after injection [174]. Under inductive applicator conditions of 53 kHz and  $30 \text{ kA}^{-1}$ , an intratumoral temperature of  $48 \text{ }^\circ\text{C}$  was reached after 5 min. Smaller magnetic nanoparticles have also been investigated for magnetic hyperthermia. Magnetite nanoparticles from ferrofluids coated with dextran can be taken up by carcinoma cells. However, cellular uptake of these dextran-iron oxide nanoparticles was low. To solve this problem, magnetic nanoparticles were coated with aminosilane groups; *in vitro* cellular uptake of such nanoparticles in glioblastoma cells was found to be  $1000\times$  higher than for their dextran-magnetite counterparts [175]. To further improve mediator uptake by cancer cells for better intracellular hyperthermia treatment efficacy, monoclonal IgG antibody was immobilized onto the surface of PEG-coated magnetite nanoparticles [176]. These particles exhibited an improved *in vitro* specificity for cancer cells and, thus, higher cellular uptake by tumor cells than non-functionalized PEG-magnetite nanoparticles. Similar investigations using various antibodies and their fragments for labeling magnetoliposomes have also been tested for improving the cellular uptake of magnetic liposomes during hyperthermia experiments [177–179]. *In vivo* experiments were performed by injecting these magnetic liposomes into the tumor-harboring mice. Most of the mediators accumulated in the tumor tissue while the rest were distributed in liver and spleen. After these mice were exposed to an AC magnetic field, the temperature of the tumor tissue increased and the growth of tumor usually ceased over a period of time [177–179]. However, few studies have been reported on the administration of mediators through i.v. injections. Functionalization of magnetic nanoparticles for *in vivo* hyperthermia is still in its early stages. Collaboration between materials scientists and hyperthermia experts is needed to further develop this promising therapy.

### 3.5

#### Conclusions

This chapter has summarized recent advances in the synthesis of functional biomolecule–magnetic nanoparticle hybrid systems. The uses of such biofunctionalized nanoparticles for *in vitro* protein/cell isolation and immobilization of biocatalysts for drug synthesis as well as *in vivo* applications such as drug targeting, MR imaging and hyperthermia therapies have been discussed. Nanometer-sized magnetic particles have many advantages over their micrometer counterparts in biomedical applications due to the unique physical, chemical and physiological properties associated with their small dimensions. A combination of the unusual

properties of nanomaterials and biomaterials provides a unique opportunity for physicists, chemists, biologists, material scientists and experts from many other fields to mold this new area of nanobiotechnology. Based on recent advances in the field, exciting new science and novel systems can be anticipated from such an interdisciplinary effort.

## Acknowledgments

Financial support from the SIU Materials Technology Center, American Cancer Society and the NSF through a career award to Y.G. is acknowledged.

## References

- CORNELL, R. M., SCHWERTMANN, U. *The Iron Oxides: Structure, Properties, Reactions, Occurrence and Uses*, VCH, New York, 1996.
- SCHMID, G. *Nanoparticles: From Theory to Applications*, Wiley-VCH, Weinheim, 2004.
- HÄFELI, U., SCHÜTT, W., TELLER, J., ZBOROWSKI, M. *Scientific and Clinical Applications of Magnetic Carriers*, Plenum, New York, 1996.
- MORNET, S., VASSEUR, S., GRASSET, F., DUGUET, E., Magnetic nanoparticle design for medical diagnosis and therapy. *J. Mater. Chem.* **2004**, *14*, 2161–2175.
- PANKHURST, Q. A., CONNOLLY, J., JONES, S. K., DOBSON, J., Applications of magnetic nanoparticles in biomedicine. *J. Phys. D: Appl. Phys.* **2003**, *36*, R167–R181.
- BERRY, C. C., CURTIS, A. S. G., Functionalisation of magnetic nanoparticles for applications in biomedicine. *J. Phys. D: Appl. Phys.* **2003**, *36*, R198–R206.
- BAUER, L. A., BIRENBAUM, N. S., MEYER, G. J., Biological applications of high aspect ratio nanoparticles. *J. Mater. Chem.* **2004**, *14*, 517–526.
- KATZ, E., WILLNER, I., Integrated nanoparticle-biomolecule hybrid systems: synthesis, properties and applications. *Angew. Chem. Int. Ed.* **2004**, *43*, 6042–6108.
- TARTAJ, P., MORALES, M. D. P., VEINTEMILLAS-VERDAGUER, S., GONZÁLEZ-CAPPEÑO, T., SERNA, C. J., The preparation of magnetic nanoparticles for applications in biomedicine. *J. Phys. D: Appl. Phys.* **2003**, *36*, R182–R197.
- NIEMEYER, C. M., Nanoparticles, proteins, and nucleic acids: biotechnology meets materials science. *Angew. Chem. Int. Ed.* **2001**, *40*, 4128–4158.
- LANDFESTER, K., PAMÍREZ, L. P., Encapsulated magnetic particles for biomedical applications. *J. Phys.: Condens. Matter.* **2003**, *15*, S1345–S1361.
- MATSUNAGA, T., OKAMURA, Y., TANAKA, T., Biotechnological applications of nano-scale engineered bacterial magnetic particles. *J. Mater. Chem.* **2004**, *14*, 2099–2115.
- PUNTES, A. F., KRISHNAN, K. M., ALIVISATOS, A. P., Colloidal nanocrystal shape and size control: the case of cobalt. *Science* **2001**, *291*, 2115–2117.
- SUN, S., MURRAY, C. B., WELLER, D., FOLKS, L., MOSER, A., Monodisperse FePt nanoparticles and ferromagnetic FePt nanocrystal superlattices. *Science* **2000**, *287*, 1989–1992.
- PARK, J., AN, K., HWANG, Y., PARK, J.-G., NOH, H.-J., KIM, J.-Y., PARK, J.-H., HWANG, N.-M., HYEON, T., Ultra-large-scale synthesis of mono-

- disperse nanocrystals. *Nat. Mater.* **2004**, *3*, 891–895.
- 16 REDL, F. X., CHO, K.-S., MURRAY, C. B., O'BRIEN, S., Three-dimensional binary superlattices of magnetic nanocrystals and semiconductor quantum dots. *Nature*, **2003**, *423*, 968–971.
- 17 SONG, Q., ZHANG, Z. J., Shape control and associated magnetic properties of spinel cobalt ferrite nanocrystals. *J. Am. Chem. Soc.* **2004**, *126*, 6164–6168.
- 18 NGO, A. T., PILENI, M. P., Nanoparticles of cobalt ferrite: influence of the applied field on the organization of the nanocrystals on a substrate and on their magnetic properties. *Adv. Mater.* **2000**, *12*, 276–279.
- 19 SHAFI, K. V. P., ULMAN, A., YAN, X., YANG, N.-L., ESTOURNES, C., WHITE, H., RAFAILOVICH, M., Sonochemical synthesis of functionalized amorphous iron oxide nanoparticles. *Langmuir*, **2001**, *17*, 5093–5097.
- 20 JANA, N. R., CHEN, Y., PENG, X., Size- and shape-controlled magnetic (Cr, Mn, Fe, Co, Ni) oxide nanocrystals via a simple and general approach. *Chem. Mater.* **2004**, *16*, 3931–3935.
- 21 LI, Z., CHEN, H., BAO, H., GAO, M., One-pot reaction to synthesize water-soluble magnetic nanocrystals. *Chem. Mater.* **2004**, *16*, 1391–1393.
- 22 SUN, S., ZENG, H., ROBINSON, D. B., RAOUX, S., RICE, P. M., WANG, S. X., LI, G., Monodisperse  $MFe_2O_4$  ( $M = Fe, Co, Mn$ ) nanoparticles. *J. Am. Chem. Soc.* **2004**, *126*, 273–279.
- 23 TARTAJ, P., SERNA, C. J., Synthesis of monodisperse superparamagnetic Fe/Silica nanospherical composites. *J. Am. Chem. Soc.* **2004**, *125*, 15754–15755.
- 24 TENG, X., YANG, H., Synthesis of face-centered tetragonal FePt nanoparticles and granular films from  $Pt@Fe_2O_3$  core-shell nanoparticles. *J. Am. Chem. Soc.* **2003**, *125*, 14559–14563.
- 25 JI, T., JIAN, W.-B., FANG, J., The first synthesis of  $Pb_{1-x}Mn_xSe$  nanocrystals. *J. Am. Chem. Soc.* **2003**, *125*, 8448–8449.
- 26 SHEVCHENKO, E. V., TALAPIN, D. V., SCHNABLEGGER, H., KORNOWSKI, A., FESTIN, Ö., SVEDLINDH, P., HAASE, M., WELLER, H., Study of nucleation and growth in the organometallic synthesis of magnetic alloy nanocrystals: the role of nucleation rate in size control of  $CoPt_3$  nanocrystals. *J. Am. Chem. Soc.* **2003**, *125*, 9090–9101.
- 27 LI, Q., LI, H., POL, V. G., BRUCKENTAL, I., KOLTYPIN, Y., CALDERON-MORENO, J., NOWIK, I., GEDANKEN, A., Sonochemical synthesis, structural and magnetic properties of air-stable Fe/Co alloy nanoparticles. *New. J. Chem.* **2003**, *27*, 1194–1199.
- 28 CARNES, C. L., KLABUNDE, K. J., Unique chemical reactivities of nanocrystalline metal oxides toward hydrogen sulfide. *Chem. Mater.* **2002**, *14*, 1806–1811.
- 29 FRIED T., SHEMER, G., MARKOVICH, G., Ordered two-dimensional arrays of ferrite nanoparticles. *Adv. Mater.* **2001**, *13*, 1158–1161.
- 30 BOURLINOS, A. B., SIMOPOULOS, A., PETRIDIS, D., Synthesis of capped ultrafine  $\gamma-Fe_2O_3$  particles from iron(III) hydroxide caprylate: a novel starting material for readily attainable organosols. *Chem. Mater.* **2002**, *14*, 899–903.
- 31 LU, J., FAN, J., XU, R., ROY, S., ALI, N., GAO, Y., Synthesis of alkyl sulfonate/alcohol-protected  $\gamma-Fe_2O_3$  nanocrystals with narrow size distributions. *J. Colloid Interface Sci.* **2003**, *258*, 427–431.
- 32 LYON, J. L., FLEMING, D. A., STONE, M. B., SCHIFFER, P., WILLIAMS, M. E., Synthesis of Fe oxide core/Au shell nanoparticles by iterative hydroxylamine seeding. *Nano Lett.* **2004**, *4*, 719–723.
- 33 VAUCHER, S., FIELDEN, J., LI, M., DUJARDIN, E., MANN, S., Molecule-based magnetic nanoparticles: synthesis of cobalt hexacyanoferrate, cobalt pentacyanonitrosylferrate, and chromium hexacyanochromate coordination polymers in water-in-oil microemulsions. *Nano Lett.* **2002**, *2*, 225–229.

- 34 MOONEY, K. E., NELSON, J. A., WAGNER, M. J., Superparamagnetic cobalt ferrite nanocrystals synthesized by alkalide reduction. *Chem. Mater.* **2004**, *16*, 3155–3161.
- 35 GU, H., ZHENG, R., ZHANG, X., XU, B., Facile one-pot synthesis of bifunctional heterodimers of quantum dot and magnetic nanoparticles. *J. Am. Chem. Soc.* **2004**, *126*, 5664–5665.
- 36 KANG, Y. S., RISBUD, S., RABOLT, J. F., STROEVE, P., Synthesis and characterization of nanometer-sized  $\text{Fe}_3\text{O}_4$  and  $\gamma\text{-Fe}_2\text{O}_3$  particles. *Chem. Mater.* **1996**, *8*, 2209–2211.
- 37 ELKINS, K. E., VEDANTAM, T. S., LIU, J. P., ZENG, H., SUN, S., DING, Y., WANG, Z. L., Ultrafine FePt nanoparticles prepared by the chemical reduction method. *Nano Lett.* **2003**, *3*, 1647–1649.
- 38 HOU, Y., KONDOH, H., KOGURE, T., OHTA, T., Preparation and characterization of monodisperse FePd nanoparticles. *Chem. Mater.* **2004**, *16*, 5149–5152.
- 39 MAJETICH, S. A., JIN, Y., Magnetization directions of individual nanoparticles. *Science* **1999**, *284*, 470–473.
- 40 GAMBARDILLA, P., RUSPONI, S., VERONESE, M., DHESI, S. S., GRAZIOLI, C., DALLMEYER, A., CABRIA, I., ZELLER, R., DEDERICHS, P. H., KERN, K., CARBONE, C., BRUNE, H., Giant magnetic anisotropy of single cobalt atoms and nanoparticles. *Science* **2003**, *300*, 1130–1133.
- 41 DORMANN, J. L., FIORANI, D. *Magnetic Properties of Fine Particles*, North-Holland, New York, 1991.
- 42 PORTET, D., DENIZOT, B., RUMP, E., LEJEUNE, J.-J., JALLET, P., Nonpolymeric coatings of iron oxide colloids for biological use as magnetic resonance imaging contrast agents. *J. Colloid Interface Sci.* **2001**, *238*, 37–42.
- 43 MOGHIMI, S. M., HUNTER, A. C., MURRAY, J. C., Long-circulating and target-specific nanoparticles: theory to practice. *Pharmacol. Rev.* **2001**, *2*, 283–318.
- 44 HYEON, T., Chemical synthesis of magnetic nanoparticles. *Chem. Commun.* **2003**, 927–934.
- 45 VESTAL, C. R., ZHANG, J., Effects of surface coordination chemistry on the magnetic properties of  $\text{MnFe}_2\text{O}_4$  spinel ferrite nanoparticles. *J. Am. Chem. Soc.* **2003**, *125*, 9828–9833.
- 46 MIKHAYLOVA, M., KIM, D. K., BOBRYsheva, N., OSOLOWSKY, M., SEMENOV, V., TSAKALAKOS, T., MUHAMMED, M., Superparamagnetism of magnetic nanoparticles: dependence on surface modification. *Langmuir* **2004**, *20*, 2472–2477.
- 47 GRADMANN, U., Surface magnetism. *J. Magn. Magn. Mater.* **1991**, *100*, 481–496.
- 48 TRONC, E., EZZIR, A., CHERKAoui, R., CHANEAC, C., NOGUES, M., KACHKACHI, H., FIORANI, D., TESTA, A. M., GRENECHE, J. M., JOLIVET, J. P., Surface-related properties of  $\gamma\text{-Fe}_2\text{O}_3$  nanoparticles. *J. Magn. Magn. Mater.* **2000**, *221*, 63–79.
- 49 GAZEau, F., BACRI, J. C., GENDRON, F., PERZYNSKI, R., RAIKHER, Y. L., STEPANOV, V. I., DUBOIS, E., Magnetic resonance of ferrite nanoparticles: evidence of surface effects. *J. Magn. Magn. Mater.* **1998**, *186*, 175–187.
- 50 KODAMA, R. H., BERKOWITZ, A. E., MCNIFF, E. J., JR., FONER, S., Surface spin disorder in ferrite nanoparticles. *J. Appl. Phys.* **1997**, *81*, 5552–5557.
- 51 FAN, J., LU, J., XU, R., JIANG, R., GAO, Y., Use of water-dispersible  $\text{Fe}_2\text{O}_3$  nanoparticles with narrow size distributions in isolating avidin. *J. Colloid Interface Sci.* **2003**, *266*, 215–218.
- 52 XU, C., XU, K., GU, H., ZHENG, R., LIU, H., ZHANG, X., GUO, Z., XU, B., Dopamine as a robust anchor to immobilize functional molecules on the iron oxide shell of magnetic nanoparticles. *J. Am. Chem. Soc.* **2004**, *126*, 9938–9939.
- 53 TRIPP, S. L., PUSZTAY, S. V., RIBBE, A. E., WEI, A., Self-assembly of cobalt nanoparticle rings. *J. Am. Chem. Soc.* **2002**, *124*, 7914–7915.
- 54 XU, C., XU, K., GU, H., ZHONG, X., GUO, Z., ZHENG, R., ZHANG, X., XU, B., Nitritoltriactic acid-modified



- magnetic nanoparticles as a general agent to bind histidine-tagged proteins. *J. Am. Chem. Soc.* **2004**, *126*, 3392–3393.
- 55 GU, H., HO, P.-L., TSANG, K. W. T., WANG, L., XU, B., Using biofunctional magnetic nanoparticles to capture vancomycin-resistant enterococci and other gram-positive bacteria at ultralow concentration. *J. Am. Chem. Soc.* **2003**, *125*, 15702–15703.
- 56 KUMAR, C. S. S. R., LEUSCHNER, C., DOOMES, E. E., HENRY, L., JUBAN, M., HORMES, J., Efficacy of lytic peptide-bound magnetite nanoparticles in destroying breast cancer cells. *J. Nanosci. Nanotech.* **2004**, *4*, 245–249.
- 57 CHEN, D. W., LIAO, M. H., Preparation and characterization of YADH-bound magnetic nanoparticles. *J. Mol. Catal. B: Enzym* **2002**, *16*, 283–291.
- 58 HO, K.-C., TSAI, P.-J., LIN, Y.-S., CHEN, Y.-C., Using biofunctionalized nanoparticles to probe pathogenic bacteria. *Anal. Chem.* **2004**, *76*, 7162–7168.
- 59 ZHAO, X., TAPEC-DYTIOCO, R., WANG, K., TAN, W., Collection of trace amounts of DNA/mRNA molecules using genomagnetic nanocaptors. *Anal. Chem.* **2003**, *75*, 3476–3483.
- 60 BOAL, A. K., DAS, K., GRAY, M., ROTELLO, V. M., Monolayer exchange chemistry of  $\gamma$ -Fe<sub>2</sub>O<sub>3</sub> nanoparticles. *Chem. Mater.* **2002**, *14*, 2628–2636.
- 61 BOURLINOS, A. B., BAKANDRITSOS, A., GEORGAKILAS, V., PETRIDIS, D., Surface modification of ultrafine magnetic iron oxide particles. *Chem. Mater.* **2002**, *14*, 3226–3228.
- 62 WANG, Y., WONG, J. F., TENG, X., LIN, X. Z., YANG, H., “Pulling” nanoparticles into water: phase transfer of oleic acid stabilized monodisperse nanoparticles into aqueous solutions of  $\alpha$ -cyclodextrin. *Nano Lett.* **2003**, *3*, 1555–1559.
- 63 BUCAK, S., JONES, D. A., LAIBINIS, P. E., HATTON, T. A., Protein separation using colloidal magnetic nanoparticles. *Biotechnol. Prog.* **2003**, *19*, 477–484.
- 64 KOHLER, N., FRYXELL, G. E., ZHANG, M., A bifunctional poly(ethylene glycol) silane immobilized on metallic oxide-based nanoparticles for conjugation with cell targeting agents. *J. Am. Chem. Soc.* **2004**, *126*, 7206–7211.
- 65 REDDY, J. A., LOW, P. S., Folate-mediated targeting of therapeutic and imaging agents to cancers. *Crit. Rev. Ther. Drug Carrier Syst.*, **1998**, *15*, 587–627.
- 66 HIRSCH, R., KATZ, E., WILLNER, I., Magneto-switchable bioelectrocatalysis. *J. Am. Chem. Soc.* **2000**, *122*, 12053–12054.
- 67 ENNAS, G., MUSINU, A., PICCALUGA, G., ZEDDA, D., GATTESCHI, D., SANGREGORIO, C., STANGER, J. L., CONCAS, G., SPANO, G., Characterization of iron oxide nanoparticles in an Fe<sub>2</sub>O<sub>3</sub>-SiO<sub>2</sub> composite prepared by a sol-gel method. *Chem. Mater.* **1998**, *10*, 495–502.
- 68 GRASSET, F., LABHSETWAR, N., LI, D., PARK, D. C., SAITO, N., HANEDA, H., CADOR, O., ROISNEL, T., MORNET, S., DUGUET, E., PORTIER, J., ETOURNEAU, J., Synthesis and magnetic characterization of zinc ferrite nanoparticles with different environments: powder, colloidal solution, and zinc ferrite-silica core-shell nanoparticles. *Langmuir* **2002**, *18*, 8209–8216.
- 69 VESTAL, C. R., ZHANG, Z. J., Synthesis and magnetic characterization of Mn and Co spinel ferrite-silica nanoparticles with tunable magnetic core. *Nano Lett.* **2003**, *3*, 1739–1743.
- 70 LU, H., YI, G., ZHAO, S., CHEN, D., GUO, L.-H., CHENG, J., Synthesis and characterization of multi-functional magnetic, up-conversion fluorescence and bio-affinity properties. *J. Mater. Chem.* **2004**, *14*, 1336–1341.
- 71 DEL MONTE, F., MORALES, M. P., LEVY, D., FERNANDEZ, A., OCAÑA, M., ROIG, A., MOLINS, E., O’GRADY, K., SERNA, C. J., Formation of  $\gamma$ -Fe<sub>2</sub>O<sub>3</sub> isolated nanoparticles in a silica matrix. *Langmuir* **1997**, *13*, 3627–3634.
- 72 HUTLOVA, A., NIZNANSKY, D., REHSPRINGER, J.-L., ESTOURNÉS, C., KURMOO, M., High coercive field for nanoparticles of CoFe<sub>2</sub>O<sub>4</sub> in

- amorphous silica sol-gel. *Adv. Mater.* **2003**, *15*, 1622–1625.
- 73** KOBAYASHI, Y., HORIE, M., KONNO, M., RODRÍGUEZ-GONZÁLEZ, B., LIZ-MARTZÁN, L. M., Preparation and properties of silica-coated cobalt nanoparticles. *J. Phys. Chem. B.* **2003**, *107*, 7420–7425.
- 74** LU, Y., YIN, Y., MAYERS, B. T., XIA, Y., Modifying the surface properties of superparamagnetic iron oxide nanoparticles through a sol-gel approach. *Nano Lett.* **2002**, *2*, 183–186.
- 75** GAO, X., YU, K. M. K., TAM, K. Y., TSANG, S. C., Colloidal stable silica encapsulated nano-magnetic composite as a novel bio-catalyst carrier. *Chem. Commun.* **2003**, 2998–2999.
- 76** ALIEV, F. G., CORREA-DUARTE, M. A., MAMEDOV, A., OSTRANDER, J. W., GIERSIG, M., LIZ-MARZÁN, L. M., KOTOV, N. A., Layer-by-layer assembly of core/shell magnetite nanoparticles: effect of silica coating on interparticle interactions and magnetic properties. *Adv. Mater.* **1999**, *11*, 1006–1010.
- 77** STÖBER, W., FINK, A., BOHN, E., Controlled growth of monodisperse silica spheres in the micron size range. *J. Colloid Interface Sci.* **1968**, *26*, 62–69.
- 78** CARUSO, F. in *Colloids and Colloid Assemblies*, CARUSO, F. (Ed.), Wiley-VCH: Weinheim, 2004, pp. 246–283.
- 79** LI, G., FAN, J., JIANG, R., GAO, Y., Cross-linking the linear polymeric chains in the ATRP synthesis of iron oxide/polystyrene core/shell nanoparticles. *Chem. Mater.* **2004**, *16*, 1835–1837.
- 80** MATYJASZEWSKI, K., XIA, J., Atom transfer radical polymerization. *Chem. Rev.* **2001**, *101*, 2921–2990.
- 81** VESTAL, C. R., ZHANG, Z. J., Atom transfer radical polymerization synthesis and magnetic characterization of MnFe<sub>2</sub>O<sub>4</sub>/polystyrene core/shell nanoparticles. *J. Am. Chem. Soc.* **2002**, *124*, 14312–14313.
- 82** WANG, Y., TENG, X., WANG, J.-S., YANG, H., Solvent-free atom transfer radical polymerization in the synthesis of Fe<sub>2</sub>O<sub>3</sub>@polystyrene core-shell nanoparticles. *Nano Lett.* **2003**, *3*, 789–793.
- 83** CHEN, X. Y., ARMES, S. P., GREAVES, S. J., WATTS, J. F., Synthesis of hydrophilic polymer-grafted ultrafine inorganic oxide particles in protic media at ambient temperature via atom transfer radical polymerization: use of an electrostatically adsorbed polyelectrolytic macroinitiator. *Langmuir* **2004**, *20*, 587–595.
- 84** MOESER, G. D., GREEN, W. H., LAIBINIS, P. E., LINSE, P., HATTON, T. A., Structure of polymer-stabilized magnetic fluids: small-angle neutron scattering and mean-field lattice modeling. *Langmuir* **2004**, *20*, 5223–5234.
- 85** JIN, J., QIU, S., LEWIS, K., KLIBANOV, A. M., Bactericidal properties of flat surfaces and nanoparticles derivatized with alkylated polyethylenimines. *Biotechnol. Prog.* **2002**, *18*, 1082–1086.
- 86** SUN, Y.-P., ROLLINS, H. W., GUDURU, R., Preparation of nickel, cobalt, and iron nanoparticles through the rapid expansion of supercritical fluid solutions (RESS) and chemical reduction. *Chem. Mater.* **1999**, *11*, 7–9.
- 87** SUN, S., ANDERS, S., HAMANN, H. F., THIELE, J.-U., BAGLIN, J. E. E., THOMSON, T., FULLERTON, E. E., MURRAY, C. B., TERRIS, B. D., Polymer mediated self-assembly of magnetic nanoparticles. *J. Am. Chem. Soc.* **2002**, *124*, 2884–2885.
- 88** GÓMEZ-LOPERA, S. A., PLAZA, R. C., DELGADO, A. V., Synthesis and characterization of spherical magnetite/biodegradable polymer composite particles. *J. Colloid Interface Sci.* **2001**, *240*, 40–47.
- 89** DENG, Y., YANG, W., WANG, C., FU, S., A novel approach for preparation of thermoresponsive polymer magnetic microspheres with core-shell structure. *Adv. Mater.* **2003**, *15*, 1729–1732.
- 90** LIAO, M.-H., CHEN, D.-H., Preparation and characterization of a novel magnetic nano-adsorbent. *J. Mater. Chem.* **2002**, *12*, 3654–3659.
- 91** YU, S., CHOW, G. M., Carboxyl group (–CO<sub>2</sub>H) functionalized ferromagnetic

- iron oxide nanoparticles for potential bio-applications. *J. Mater. Chem.* **2004**, *14*, 2781–2786.
- 92 TONG, X.-D., XUE, B., SUN, Y., A novel magnetic affinity support for protein adsorption and purification. *Biotechnol. Prog.* **2001**, *17*, 134–139.
- 93 RUTNAKORNPIITUK, M., THOMPSON, M. S., HARRIS, L. A., FARMER, K. E., ESKER, A. R., RIFFLE, J. S., CONNOLLY, J., ST. PIERRE, T. G., Formation of cobalt nanoparticle dispersions in the presence of polysiloxane block copolymers. *Polymer* **2002**, *43*, 2337–2348.
- 94 COLE-HAMILTON, D. J., Homogeneous catalysis-new approaches to catalyst separation, recovery, and recycling. *Science* **2003**, *299*, 1702–1706.
- 95 DAYAL, A., LOOS, K., NOTO, M., CHANG, S. W., SPAGNOLI, C., SHAFI, K. V. P. M., ULMAN, A., COWMAN, M., GROSS, R. A., Activity of *Candida rugosa* lipase immobilized on  $\gamma$ -Fe<sub>2</sub>O<sub>3</sub> magnetic nanoparticles. *J. Am. Chem. Soc.* **2003**, *125*, 1684–1685.
- 96 KONERACKA, M., KOPCANSKY, P., TIMKO, M., RAMCHAND, C. N., DE SEQUEIRA, A., TREVAN, M., Direct binding procedure of proteins and enzymes to fine magnetic particles. *J. Mol. Catal. B: Enzym.* **2002**, *18*, 13–18.
- 97 YOON, T.-J., LEE, W., OH, Y.-S., LEE, J.-K., Magnetic nanoparticles as a catalyst vehicle for simple and easy recycling. *New J. Chem.* **2003**, *27*, 227–229.
- 98 STEVENS, P. D., FAN, J., GARDIMALLA, H. M. R., YEN, M., GAO, Y., Superparamagnetic nanoparticle-supported catalysis of Suzuki cross-coupling reactions. *Org. Lett.* **2005**, *11*, 2085–2088.
- 99 BABINCOVA, M., SOURIVONG, P., LESZCZYNSKA, D., BABINEC, P., Blood-specific whole-body electromagnetic hyperthermia. *Med. Hypoth.* **2000**, *55*, 459–460.
- 100 MULLER, R. N., ROCH, A., COLET, J.-M., OUAKSSIM, A., GILLIS, P. in *The Chemistry of Contrast Agents in Medical Magnetic Resonance Imaging*, MERBACH, A. E., TÓTH, E. (Eds.), Wiley: Chichester, 2001, pp. 417–435.
- 101 PANTOPOULOS, K., Iron metabolism and the IRE/IRP regulatory system: an update. *Ann. N. Y. Acad. Sci.* **2004**, *1012*, 1–13.
- 102 DOBSON, J., Nanoscale biogenic iron oxides and neurodegenerative disease. *FEBS Lett.* **2001**, *496*, 1–5.
- 103 HUME, D. A., ROSS, I. L., HIMES, S. R., SASMONO, R. T., WELLS, C. A., RAVASI, T., The mononuclear phagocyte system revisited. *J. Leukocyte Biol.* **2002**, *72*, 621–627.
- 104 DAVIS, S. S., Biomedical applications of nanotechnology – implications for drug targeting and gene therapy. *Trends Biotechnol.* **1997**, *15*, 217–224.
- 105 MOGHIMI, S. M., PATEL, H. M., Serum-mediated recognition of liposomes by phagocytic cells of the reticuloendothelial system. The concept of tissue specificity. *Adv. Drug Delivery Rev.* **1998**, *32*, 45–60.
- 106 GAUR, U., SAHOO, S. K., DE, T. K., GHOSH, P. C., MAITRA, A., GHOSH, P. K., Biodistribution of fluoresceinated dextran using novel nanoparticles evading reticuloendothelial system. *Int. J. Pharm.* **2000**, *202*, 1–10.
- 107 ARBAB, A. S., YOCUM, G. T., KALISH, H., JORDAN, E. K., ANDERSON, S. A., KHAKOO, A. Y., READ, E. J., FRANK, J. A., Efficient magnetic cell labeling with protamine sulfate complexed to ferumoxides for cellular MRI. *Blood* **2004**, *104*, 1217–1223.
- 108 BERRY, C. C., CHARLES, S., WELLS, S., DALBY, M. J., CURTIS, A. S. G., The influence of transferrin stabilised magnetic nanoparticles on human dermal fibroblasts in culture. *Int. J. Pharm.* **2004**, *269*, 211–225.
- 109 MOGHIMI, S. M., HUNTER, A. C., Poloxamers and poloxamines in nanoparticle engineering and experimental medicine. *Trends Biotechnol.* **2000**, *18*, 412–420.
- 110 MOGHIMI, S. M., Prolonging the circulation time and modifying the body distribution of intravenously injected polystyrene nanospheres by prior intravenous administration of poloxamine-908. A ‘hepatic-blockade’ event or manipulation of nanoparticle surface in vivo? *Biochim. Biophys. Acta* **1997**, *1336*, 1–6.

- 111 MOLINEUX, G., PEGylation: engineering improved pharmaceuticals for enhanced therapy. *Cancer Treatment Rev.* **2002**, *28*, 13–16.
- 112 GAO, X., CUI, Y., LEVENSON, R. M., CHUNG, L. W. K., NIE, S., *In vivo* targeting and imaging with semiconductor quantum dots. *Nat. Biotechnol.* **2004**, *22*, 969–976.
- 113 BONNEMAIN, B., Superparamagnetic agents in magnetic resonance imaging. Physicochemical characteristics and clinical applications. A review. *J. Drug Targeting* **1998**, *6*, 167–174.
- 114 LAUFFER, R. B., Paramagnetic metal complexes as water proton relaxation agents for NMR imaging: theory and design. *Chem. Rev.* **1987**, *87*, 901–927.
- 115 BROWN, M. A., SEMELKA, R. C. *MRI: Basic Principles and Applications*, Wiley, New York, 2003.
- 116 BULTE, J. W. M., BROOKS, R. A., MOSKOWITZ, B. M., BRYANT, L. H., JR., FRANK, J. A., Relaxometry and magnetometry of the MR contrast agent MION-46L. *Magn. Reson. Med.* **1999**, *42*, 379–384.
- 117 GILLIS, P., KOENIG, S. H., Transverse relaxation of solvent protons induced by magnetized spheres: application to ferritin, erythrocytes, and magnetite. *Magn. Reson. Med.* **1987**, *5*, 323–345.
- 118 MULLER, R. N., GILLIS, P., MOINY, F., ROCH, A., Transverse relaxivity of particulate MRI contrast media: from theories to experiments. *Magn. Reson. Med.*, **1991**, *22*, 178–182.
- 119 BRIGGER, I., DUBERNET, C., COUVREUR, P., Nanoparticles in cancer therapy and diagnosis. *Adv. Drug Delivery Rev.* **2002**, *54*, 631–651.
- 120 MOLDAJ, R. S., MACKENZIE, D., Immunospecific ferromagnetic iron-dextran reagents for the labeling and magnetic separation of cells. *J. Immunol. Methods* **1982**, *52*, 353–367.
- 121 GRÜTTNER, C., TELLER, J., SCHÜTT, W., WESTPHAL, F., SCHÜMICHEN, C., PAULKE, B.-R. in *Scientific and Clinical Applications of Magnetic Carriers*, HÄFELI, U., SCHÜTT, W., TELLER, J., ZBOROWSKI, M. (Eds.), Plenum: New York, 1996, pp. 53–67.
- 122 KIM, D. K., MIKHAYLOVA, M., WANG, F. H., KEHR, J., BJELKE, B., ZHANG, Y., TSAKALAKOS, T., MUHAMMED, M., Starch-coated superparamagnetic nanoparticles as MR contrast agents. *Chem. Mater.* **2003**, *15*, 4343–4351.
- 123 BYRNE, S. J., CORR, S. A., GUN'KO, Y. K., KELLY, J. M., BROUGHAM, D. F., GHOSH, S., Magnetic nanoparticle assemblies on denatured DNA show unusual magnetic relaxivity and potential applications for MRI. *Chem. Commun.* **2004**, 2560–2561.
- 124 KALISH, H., ARBAB, A. S., MILLER, B. R., LEWIS, B. K., ZYWICKE, H. A., BULTE, J. W. M., BRYAN, L. H., JR., FRANK, J. A., Combination of transfection agents and magnetic resonance contrast agents for cellular imaging: relationship between relaxivities, electrostatic forces, and chemical composition. *Magn. Reson. Med.* **2003**, *50*, 275–282.
- 125 VAN BEERS, B. E., PRINGOT, J., GALLEZ, B., Iron oxides as contrast agents for MRI of the liver. *J. Radiol.* **1995**, *76*, 991–995.
- 126 KUBASKA, S., SAHANI, D. V., SAINI, S., HAHN, P. F., HALPERN, E., Dual contrast enhanced magnetic resonance imaging of the liver with superparamagnetic iron oxide followed by gadolinium for lesion detection and characterization. *Clin. Radiology* **2001**, *56*, 410–415.
- 127 HALAVAARA, J., TERVAHARTIALA, P., ISONIEMI, H., HOCKERSTEDT, K., Efficacy of sequential use of superparamagnetic iron oxide and gadolinium in liver MR imaging. *Acta Radiol.* **2002**, *43*, 180–185.
- 128 REIMER, P., BALZER, T., Ferucarbotran (Resovist): a new clinically approved RES-specific contrast agent for contrast-enhanced MRI of the liver: properties, clinical development, and applications. *Eur. Radiol.* **2003**, *13*, 1266–1276.
- 129 FAHLVIK, A. K., HOLTZ, E., KLAVENESS, J., Relaxation efficacy of paramagnetic and superparamagnetic microspheres in liver and spleen. *Magn. Reson. Imaging* **1990**, *8*, 363–369.
- 130 GELLISSEN, J., AXMANN, C., PRESCHER,

- A., BOHNDORF, K., LODEMANN, K.-P., Extra- and intracellular accumulation of ultrasmall superparamagnetic iron oxides (USPIO) in experimentally induced abscesses of the peripheral soft tissues and their effects on magnetic resonance imaging. *Magn. Reson. Imaging* **1999**, *17*, 557–567.
- 131 MUHLER, A., ZHANG, X., WANG, H., LAWACZECK, R., WEINMANN, H. J., Investigation of mechanisms influencing the accumulation of ultrasmall superparamagnetic iron oxide particles in lymph nodes. *Invest. Radiol.* **1995**, *30*, 98–103.
- 132 MOORE, A., MARECOS, E., BOGDANOV, A., JR., WEISSELEDER, R., Tumoral distribution of long-circulating dextran-coated iron oxide nanoparticles in a rodent model. *Radiology* **2000**, *214*, 568–574.
- 133 GUIMARAES, R., CLEMENT, O., BITTOUN, J., CARNOT, F., FRIJA, G., MR lymphography with superparamagnetic iron nanoparticles in rats: pathologic basis for contrast enhancement. *Am. J. Roentgenol.* **1994**, *162*, 201–207.
- 134 BELLIN, M. F., LEBLEU, L., MERIC, J. B., Evaluation of retroperitoneal and pelvic lymph node metastases with MRI and MR lymphangiography. *Abdom. Imaging* **2003**, *28*, 155–163.
- 135 RÉTY, F., CLÉMENT, O., SIAUVE, N., CUÉNOD, C.-A., CARNOT, F., SICH, M., BUISINE, A., FRIJA, G., MR lymphography using iron oxide nanoparticles in rats: pharmacokinetics in the lymphatic system after intravenous injection. *J. Magn. Reson. Imaging* **2000**, *12*, 734–739.
- 136 CERDAN, S., LOTSCHER, H. R., KUNNECKE, B., SEELIG, J., Monoclonal antibody-coated magnetite particles as contrast agents in magnetic resonance imaging of tumors. *Magn. Reson. Med.* **1989**, *12*, 151–163.
- 137 WEISSELEDER, R., LEE, A. S., FISCHMAN, A. J., REIMER, P., SHEN, T., WILKINSON, R., CALLAHAN, R. J., BRADY, T. J., Polyclonal human immunoglobulin G labeled with polymeric iron oxide: antibody MR imaging. *Radiology* **1991**, *181*, 245–249.
- 138 REMSEN, L. G., MCCORMICK, C. I., ROMAN-GOLDSTEIN, S., NILAVER, G., WEISSELEDER, R., BOGDANOV, A., HELLSTROM, I., KROLL, R. A., NEUWELT, E. A., MR of carcinoma-specific monoclonal antibody conjugated to monocrySTALLINE iron oxide nanoparticles: the potential for noninvasive diagnosis. *Am. J. Neuroradiol.* **1996**, *17*, 411–418.
- 139 MOORE, A., MEDAROVA, Z., POTTHAST, A., DAI, G., In vivo targeting of underglycosylated MUC-1 tumor antigen using a multimodal imaging probe. *Cancer Res.* **2004**, *64*, 1821–1827.
- 140 PALMACCI, S., JOSEPHSON, L., Synthesis of polysaccharide covered superparamagnetic oxide colloids. *U.S. Pat.* 5,262,176, 1993.
- 141 JOSEPHSON, L., TUNG, C.-H., MOORE, A., WEISSELEDER, R., High-efficiency intracellular magnetic labeling with novel superparamagnetic-Tat peptide conjugates. *Bioconjugate Chem.* **1999**, *10*, 186–191.
- 142 CHOI, H., CHOI, S. R., ZHOU, R., KUNG, H. F., CHEN, I.-W., Iron oxide nanoparticles as magnetic resonance contrast agent for tumor imaging via folate receptor-targeted delivery. *Acad. Radiol.* **2004**, *11*, 996–1004.
- 143 LOK, C., Picture perfect. *Nature* **2001**, *412*, 372–374.
- 144 SIPE, J. C., FILIPPI, M., MARTINO, G., FURLAN, R., ROCCA, M. A., ROVARIS, M., BERGAMI, A., ZYROFF, J., SCOTTI, G., COMI, G., Method for intracellular magnetic labeling of human mononuclear cells using approved iron contrast agents. *Magn. Reson. Imaging* **1999**, *17*, 1521–1523.
- 145 MOORE, A., MARECOS, E., BOGDANOV, A., JR., WEISSELEDER, R., Tumoral distribution of long-circulating dextran-coated iron oxide nanoparticles in a rodent model. *Radiology* **2000**, *214*, 568–574.
- 146 SCHULZE, E., FERRUCCI, J. T., JR., POSS, K., LAPOINTE, L., BOGDANOVA, A., WEISSELEDER, R., Cellular uptake and trafficking of a prototypical

- magnetic iron oxide label in vitro. *Invest. Radiol.* **1995**, *30*, 604–610.
- 147 ZHAO, M., KIRCHER, M. F., JOSEPHSON, L., WEISSELEDER, R., Differential conjugation of Tat peptide to superparamagnetic nanoparticles and its effects on cellular uptake. *Bioconjugate Chem.* **2002**, *13*, 840–844.
- 148 KOCH, A. M., REYNOLDS, F., KIRCHER, M. F., MERKLE, H. P., WEISSELEDER, R., JOSEPHSON, L., Uptake and metabolism of a dual fluorochrome Tat-nanoparticle in HeLa cells. *Bioconjugate Chem.* **2003**, *14*, 1115–1121.
- 149 FRANKEL, A. D., PABO, C. O., Cellular uptake of the tat protein from human immunodeficiency virus. *Cell* **1988**, *55*, 1189–1193.
- 150 ZHANG, Y., KOHLER, N., ZHANG, M., Surface modification of superparamagnetic magnetite nanoparticles and their intracellular uptake. *Biomaterials* **2002**, *23*, 1553–1561.
- 151 STELLA, B., ARPICCO, S., PERACCHIA, M. T., DESMAËLE, D., HOEBEKE, J., RENOIR, M., D'ANGELO, J., CATTEL, L., COUVREUR, P., Design of folic-acid nanoparticles for drug targeting. *J. Pharm. Sci.* **2000**, *11*, 1452–1464.
- 152 ZHAO, M., BEAUREGARD, D. A., LOIZOU, L., DAVLETOV, B., BRINDLE, K. M., Non-invasive detection of apoptosis using magnetic resonance imaging and a targeted contrast agent. *Nat. Med.* **2001**, *7*, 1241–1244.
- 153 BULTE, J. W., DOUGLAS, T., WITWER, B., ZHANG, S. C., STRABLE, E., LEWIS, B. K., ZYWICKE, H., MILLER, B., VAN GELDEREN, P., MOSKOWITZ, B. M., DUNCAN, I. D., FRANK, J. A., Magnetodendrimers allow endosomal magnetic labeling and in vivo tracking of stem cells. *Nat. Biotechnol.* **2001**, *19*, 1141–1147.
- 154 HOGEMANN, D., JOSEPHSON, L., WEISSELEDER, R., BASILION, J. P., Improvement of MRI probes to allow efficient detection of gene expression. *Bioconj. Chem.* **2000**, *11*, 941–946.
- 155 MOORE, A., JOSEPHSON, L., BHORADE, R. M., BASILION, J. P., WEISSELEDER, R., Human transferrin receptor gene as a marker gene for MR imaging. *Radiology* **2001**, *221*, 244–250.
- 156 PULFER, S. K., GALLO, J. M. in *Scientific and Clinical Applications of Magnetic Carriers*, HÄFELI, U., SCHÜTT, W., TELLER, J., ZBOROWSKI, M. (Eds.), Plenum: New York, 1996, pp. 445–455.
- 157 WIDDER, K. J., MORRIS, R. M., POORE, G. A., HOWARD, D. P., SENYEI, A. E., Selective targeting of magnetic albumin microspheres containing low-dose doxorubicin: total remission in Yoshida sarcoma-bearing rats. *Eur. J. Cancer Clin. Oncol.* **1983**, *19*, 135–139.
- 158 GOODWIN, S. C., BITTNER, C. A., PETERSON, C. L., WONG, G., Single-dose toxicity study of hepatic intra-arterial infusion of doxorubicin coupled to a novel magnetically targeted drug carrier. *Toxicol. Sci.* **2001**, *60*, 177–183.
- 159 ALEXIOU, C., ARNOLD, W., KLEIN, R. J., PARAK, F. G., HULIN, P., BERGEMANN, C., ERHARDT, W., WAGENPFEIL, S., LUBBE, A. S., Locoregional cancer treatment with magnetic drug targeting. *Cancer Res.* **2000**, *60*, 6641–6648.
- 160 LÜBBE, A. S., ALEXIOU, C., BERGEMANN, C., Clinical applications of magnetic drug targeting. *J. Surg. Res.* **2001**, *95*, 200–206.
- 161 LÜBBE, A. S., BERGEMANN, C. in *Scientific and Clinical Applications of Magnetic Carriers*, HÄFELI, U., SCHÜTT, W., TELLER, J., ZBOROWSKI, M. (Eds.), Plenum: New York, 1996, pp. 457–480.
- 162 MÜLLER-SCHULTE, D., FÜSSL, F., LUEKEN, H., DE CUYPER, M. in Ref. [161], pp. 517–526.
- 163 HÄFELI, U., PAUER, G. J., ROBERTS, W. K., HUMM, J. L., MACKLIS, R. M. in Ref. [161], pp. 501–516.
- 164 HÄFELI, U., PAUER, G., FAILING, S., TAPOLSKY, G., Radiolabeling of magnetic particles with rhenium-188 for cancer therapy. *J. Magn. Magn. Mater.* **2001**, *225*, 73–78.
- 165 ARBAB, A. S., JORDAN, E. K., WILSON, L. B., YOCUM, G. T., LEWIS, B. K., FRANK, J. A., *In vivo* trafficking and targeted delivery of magnetically

- labeled stem cells. *Human Gene Therapy* **2004**, *15*, 351–360.
- 166 BERGEMANN, C., MULLER-SCHULTE, D., OSTER, J., BRASSARD, L., LÜBBE, A. S., Magnetic ion-exchange nano- and microparticles for medical, biochemical and molecular biological applications. *J. Magn. Magn. Mater.* **1999**, *194*, 45–52.
- 167 HUGHES, C., GALEA-LAURI, J., FARZANEH, F., DARLING, D., Streptavidin paramagnetic particles provide a choice of three affinity-based capture and magnetic concentration strategies for retroviral vectors. *Mol. Therapy* **2001**, *3*, 623–630.
- 168 SCHERER, F., ANTON, M., SCHILLINGER, U., HENKE, J., BERGEMANN, C., KRUGER, A., GANSBACHER, B., PLANK, C., Magnetofection: enhancing and targeting gene delivery by magnetic force in vitro and in vivo. *Gene Therapy* **2002**, *9*, 102–109.
- 169 PLANK, C., SCHILLINGER, U., SCHERER, F., BERGEMANN, C., REMY, J.-S., KROETZ, F., ANTON, M., LAUSIER, J., ROSENECKER, J., The magnetofection method: Using magnetic force to enhance gene delivery. *Biol. Chem.* **2003**, *384*, 737–747.
- 170 JORDAN, A., SCHOLZ, R., WUST, P., FÄHLING, H., FELIX, R., Magnetic fluid hyperthermia (MFH): cancer treatment with AC magnetic field induced excitation of biocompatible superparamagnetic nanoparticles. *J. Magn. Magn. Mater.* **1999**, *210*, 413–419.
- 171 MOROZ, P., JONES, S. K., GRAY, B. N., Magnetically mediated hyperthermia: current status and future directions. *Int. J. Hyperthermia* **2002**, *18*, 267–284.
- 172 MOROZ, P., JONES, S. K., GRAY, B. N., Arterial embolization hyperthermia in porcine renal tissue. *J. Surg. Res.*, **2002**, *105*, 209–214.
- 173 MOROZ, P., JONES, S. K., GRAY, B. N., Tumor response to arterial embolization hyperthermia and direct injection hyperthermia in a rabbit liver tumor model. *J. Surg. Oncol.* **2002**, *80*, 149–156.
- 174 MOROZ, P., JONES, S. K., METCALF, C., GRAY, B. N., Hepatic clearance of arterially infused ferromagnetic particles. *Int. J. Hyperthermia* **2003**, *19*, 23–34.
- 175 JORDAN, A., SCHOLZ, R., WUST, P., SCHIRRA, H., SCHIESTEL, T., SCHMIDT, H., FELIX, R., Endocytosis of dextran and silica-coated magnetite nanoparticles and the effect of intracellular hyperthermia on human mammary carcinoma cells in vitro. *J. Magn. Magn. Mater.* **1999**, *194*, 185–196.
- 176 SUZUKI, M., SHINKAI, M., KAMIHIRA, M., KOBAYASHI, T., Preparation and characteristics of magnetite-labeled antibody with the use of poly(ethylene glycol) derivatives. *Biotechnol. Appl. Biochem.* **1995**, *21*, 335–345.
- 177 ITO, A., KUGA, Y., HONDA, H., KIKKAWA, H., HORIUCHI, A., WATANABE, Y., KOBAYASHI, T., Magnetite nanoparticle-loaded anti-HER2 immunoliposomes for combination of antibody therapy with hyperthermia. *Cancer Lett.* **2004**, *212*, 167–175.
- 178 LE, B., SHINKAI, M., KITADE, T., HONDA, H., YOSHIDA, J., WAKABAYASHI, T., KOBAYASHI, T., Preparation of tumor-specific magnetoliposomes and their application for hyperthermia. *J. Chem. Eng. Jpn.* **2001**, *34*, 66–72.
- 179 SHINKAI, M., LE, B., HONDA, H., YOSHIKAWA, K., SHIMIZU, K., SAGA, S., WAKABAYASHI, T., YOSHIDA, J., KOBAYASHI, T., Targeting hyperthermia for renal cell carcinoma using human MN antigen-specific magnetoliposomes. *Jpn. J. Cancer Res.* **2001**, *92*, 1138–1145.

## 4

# Biofunctionalization of Gold Nanoparticles

*Ming Zheng and Xueying Huang*

### 4.1

#### Introduction

Gold (Au) as a precious material was first extracted in the 5<sup>th</sup> millennium BC [1]. The “soluble” gold, which we now call colloid gold, was developed around the 5<sup>th</sup> or 4<sup>th</sup> century BC [1]. Even though several scientists studied the formation and synthesis of colloid Au, such as using phosphorous in CS<sub>2</sub> to reduce chloroaurate (AuCl<sub>4</sub><sup>-</sup>) [2], colloid Au did not gain wide attention or became a subject of broad interest in the scientific community until very recently, especially in the last decade. The interest in such tiny Au particles partially arises from the commercial and industrial needs for new, advanced materials. These particles are nanometer size materials with unique optic, electronic, and magnetic properties. Macromolecular biological molecules, also in the nanometer size range, possess functionalities that enable recognition and self-assembly. The integration of nanoparticles and biological molecules is very attractive and has gained tremendous attention from academics and industry, because such a combination could create new materials for electronics and optics, and lead to new applications in genomics, proteomics, and biomedical and bioanalytical areas [3–8]. To be integrated with biological molecules or be used in biological systems, Au nanoparticles (NPs) have to be soluble in aqueous solution. This chapter, therefore, is mainly focused on the synthesis of water-soluble Au NPs, their surface functionality and modification, and biological applications. Section 4.2 reviews two general synthetic routes for obtaining monolayer-protected Au nanoparticles. Examples of programmable assembly of these particles using biomolecules, i.e. DNA and proteins, are covered in Section 4.3. The problem of nonspecific binding between nanoparticles and biomolecules is discussed in Section 4.5. Finally, Section 4.6 reviews biological and biomedical applications of Au nanoparticles.

### 4.2

#### General Synthetic Routes

Generally, Au nanoparticles are synthesized by reduction of aurate salts, usually chloroaurate (AuCl<sub>4</sub><sup>-</sup>) with reducing agents, such as sodium borohydride (NaBH<sub>4</sub>),



thiocyanate, phosphorus, citrate, ascorbic acid, and even ethyl alcohol [9]. The synthesized Au NPs have particle sizes ranging from sub-nanometer, e.g. 0.8 to 80 nm with their color changing from yellow-orange to red-purple to blue-green. The size of Au NPs determines their unique optical and electronic properties. Au NPs synthesized by the reduction of aurate salts are composed of an internal core of pure Au that is surrounded by a surface layer of adsorbed  $\text{AuCl}_2^-$  ions [9]. These negatively charged surfaces prevent Au NPs aggregating. However, these Au NPs are very sensitive to their environmental factors such as pH, temperature, electrolytes, and solvent. For these Au NPs to be utilized, a key issue is their surface chemistry and functionalization that determine their stability, functionality and applications. To solve this issue, various ligand-protected Au NPs have been synthesized recently, mainly by direct synthesis and ligand exchange reaction.

#### 4.2.1

##### Direct Synthesis of Ligand-protected Au NPs

In the past three decades, two major classes of ligand-protected Au NPs have been developed. The first is phosphine-protected Au NPs, which were originally reported by McPartlin et al. in 1969 [10] and then modified by Cariati et al. in 1971 [11]. Synthesis was achieved through reduction by  $\text{NaBH}_4$  of either an aurate salt, such as  $\text{HAuCl}_4$  in the presence of triarylphosphine in a two-phase system of toluene and water, or  $\text{Au(L)X}$  (here L is triarylphosphine and X is an anion, such as  $\text{I}^-$ ,  $\text{SCN}^-$ , or  $\text{CN}^-$ ) in an organic solvent such as ethanol. As Au–P bonding is very weak the phosphine ligand could be easily replaced by other ligands. Apart from being used as the starting materials for other functionalized Au NPs, phosphine ligand-protected Au NPs have very limited use. The second class is thiol- or amine-ended ligand-protected Au NPs, first developed by Brust et al. in 1994 [12]. In their initial report, Brust et al. synthesized toluene-stable dodecanethiol-protected Au NP by using  $\text{NaBH}_4$  to reduce  $\text{HAuCl}_4$  in a two-phase system with tetraoctylammonium bromide as the phase-transfer, [Fig. 4.1(route a)]. Subsequently, they developed a one-phase synthesis by using methanol as the reaction solvent [13] [Fig. 4.1(route b)]. These Au NPs are mainly organic-soluble. Since

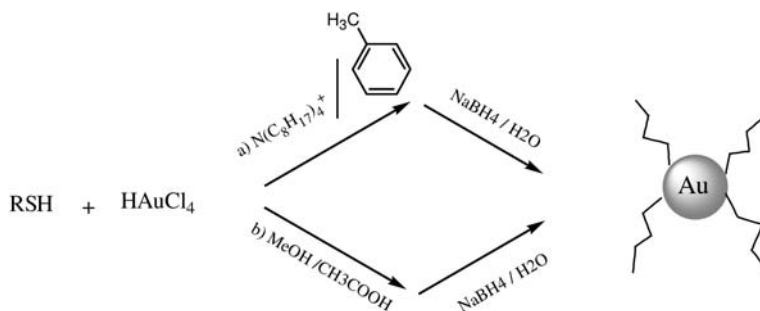


Fig. 4.1. Au NPs synthesized through a two-phase route (a) and a one-phase route (b).

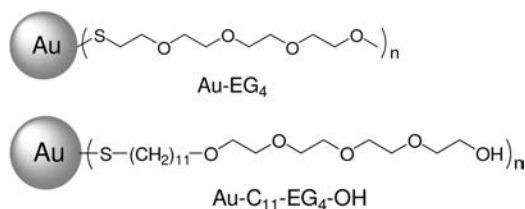
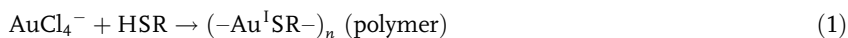


Fig. 4.2. Schematic structures of tetra(ethylene glycol) and thioalkylated oligo(ethylene glycol) protected Au NPs.

1998, this synthetic strategy has been extended, initially by Schaaff et al. [14] and Murray et al. [15] and then by many other researchers, to the synthesis of various water-soluble Au NPs. Compared with phosphine ligand-protected Au NPs, thio-protected Au NPs have a much more stable Au-S bond, giving the nanoparticles higher stability and wider utility.

A few authors have proposed a mechanism for the formation of the thiol monolayer on protected Au NP [12, 16, 17]. As shown in Eqs. (1) and (2), the electron-rich thiol group (HS-) in R-SH reacts with AuCl<sub>4</sub><sup>-</sup> to form a polymer intermediate. The polymer is then reduced by BH<sub>4</sub><sup>-</sup> to form the nanoparticle.



Although the synthetic methods developed by Brust et al. and Murray et al. provide guidelines for preparing ligand-protected Au NPs, the details for NP formation, such as solvent selection, control of nucleation and aggregation, are still not well understood. There is still an element of art in the synthesis of a new ligand-protected Au NP. Among various reaction conditions to be optimized, solvent selection for the synthesis is especially important. This is demonstrated by the synthesis of tetra(ethylene glycol) protected Au NP (Au-EG<sub>4</sub>) (Fig. 4.2). Foos et al. first reported the synthesis of short ethylene oxide chain protected gold nanoparticles by ligand exchange reaction [18]. The procedure involved synthesis of hexanethiol (C6) protected gold nanoparticles followed by two steps of replacing C6 with ethylene glycol thiol molecules. Direct synthesis of ethylene glycol protected nanoparticle was, unsuccessfully, also attempted by Foos et al. using published methods. Bartz et al. synthesized Au-EG<sub>4</sub> NP directly in aqueous phase with a very low molar ratio of reducing agent (NaBH<sub>4</sub>) and tetrachloroauric acid, resulting in partial reduction [19]. With increasing amount of NaBH<sub>4</sub>, the reaction increased aggregation. The yield was very low. We also synthesized Au-EG<sub>n</sub> (n = 2-4) using methanol as the solvent. The reagents HAuCl<sub>4</sub> and EG<sub>n</sub>-SH, for example, were dissolved in a mixture of methanol and acetic acid; a freshly prepared NaBH<sub>4</sub> solution in methanol was then added with rapid stirring. Au-EG<sub>4</sub> nanoparticles formed as soon as the NaBH<sub>4</sub> methanol solution was added. After purifying and drying, the nanoparticle is readily redissolved in water to form a clear red/purple solution. However, the yield is very low (>10%). No precipitation was ob-

served in the reaction mixture, meaning that the reduction reaction of  $\text{HAuCl}_4$  was not complete. The mechanism of partial reduction in methanol was not investigated. After many trials, we established a direct synthesis of ethylene glycol  $[\text{HS}-(\text{CH}_2\text{CH}_2\text{O})_n-\text{CH}_3, n = 2-4]$  protected gold nanoparticles in a mixed solvent of methanol and water by utilizing the  $\text{NaBH}_4$  reduction method, with much improved yield [20, 21]. The key for this synthesis is the control of water content in the reaction mixture. A water content of 9–18% (v/v) is the optimum for the formation of stable, water-soluble nanoparticles. Instead of  $\text{Au-EG}_4$ , Brust et al. successfully synthesized a thioalkylated oligo(ethylene glycol) ligand-protected Au NP by using a mixed solvent of 2-propanol and methanol (Fig. 4.2) [22].

Even though the solvent effect on the synthesis of water-soluble nanoparticles was not systematically investigated in our original work, the polarity and solubility of the ligand are relevant to solvent selection for the synthesis. The solubility of Au NPs is determined by the capping ligand. Capping ligands for preparing water-soluble Au NPs can be classified into three categories: cationic, anionic, and neutral based on the charge on the molecules. In view of synthetic conditions for preparing Au NPs, we divide the capping ligands into different categories: strongly ionic, weakly ionic, and neutral. Here we briefly review solvent selection in each category of Au NP synthesis. Such a review should be beneficial as a reference for synthesizing new ligand-protected Au NPs.

#### 4.2.1.1 Strongly Ionic Ligand-protected Au NPs

For strongly ionic ligands, including strong cationic and strong anionic, water as the single solvent is sufficient for synthesizing water-soluble nanoparticles. Examples include the synthesis of gold nanoparticles capped with coenzyme A [23], *N,N*-trimethyl(undecylmercapto)ammonium [24], 5-mercapto-2-benzimidazole sulfonic acid sodium salt [25], and the zwitterionic ligand cysteine [26].

#### 4.2.1.2 Weakly Ionic Ligand-protected Au NPs

For weakly ionic ligands, a mixture of water and a water-miscible organic solvent, such as methanol, is usually used for the synthesis. Examples include the synthesis of gold nanoparticles protected with tiopronin [14], glutathione (GSH) [15], and mercaptosuccinic acid [27, 28]. In the synthesis of tiopronin-protected gold nanoparticles, using water as the only solvent leads to a water-insoluble product [14]. For the synthesis of GSH protected gold nanoparticle, a 2:3 water-methanol medium is used to prevent uncontrolled reduction reaction [15]. Presumably, the ratio of water to organic solvent in the mixed solvent system is related to the structure and polarity of the ligand. When a weak anionic ligand is highly polar and water soluble, water as the sole solvent could be sufficient for the synthesis of NPs. Examples include synthesis of Au NPs protected with meso-2,3-dimercaptosuccinic acid [29], and L-cysteine [30].

#### 4.2.1.3 Au NPs Protected with Neutral Ligands

A mixed solvent of water and a water-miscible organic, such as methanol or ethanol, is usually a good start to synthesize neutral ligand protected Au NPs. Neutral

ligands for coating nanoparticles include ethylene glycol small molecules, as described above, and poly(ethylene glycol) (PEG) molecules. With increasing units of ethylene glycol from 2 to 4 to 70 [31], or aldehyde derivatized PEG ( $M_n = 3090$ ) [32], the solvent used in the synthesis of nanoparticles changes from a mixture of water and methanol to simply water. Sugar molecules and oligosaccharides are another important type of water-soluble ligand. Glyco-Au NPs have been synthesized in a mixed solvent of water and methanol [33–37]. Apparently, the solubility of the ligand molecules plays a major role in choosing the right solvent for the synthesis. Although the mechanistic reasons for this correlation are not clear, this summary should nevertheless provide a useful guidance for the synthesis of new types of water-soluble Au NPs.

#### 4.2.2

#### Ligand Exchange Reaction

Au-X ( $X = P, S, \text{ or } N$ ) is quite labile. This unique character can be utilized to synthesize versatile surface functionality. One of the earliest examples, demonstrated by Schmid et al., replaced the triarylphosphine ligand on Au NP with a sulfonated triarylphosphine ligand [38]. Murray et al. pioneered the thiol ligand exchange reaction [39], a general route for the preparation of ligand-protected Au NPs. Since then, ligand exchange or  $S_N2$  reactions have been widely used for preparing nanoparticles protected with either a homogeneous monolayer or a heterogeneous monolayer (also called mixed monolayer). Mixed monolayer protected Au NPs are especially important because they are used most in applications in electrochemistry [40, 41], conductivity [42, 43], fluorescence [44, 45], biological bindings [46, 47], and coatings [48]. Synthetically, the ligand replacement reaction has both advantages and disadvantages compared with direct synthesis. Versatility is its biggest advantage. By using ligand replacement reaction, various different mixed monolayer protected Au NPs can be synthesized that do not heavily depend on the nature of the ligands and the reaction conditions. However, the ligand replacement reaction certainly has several disadvantages. First, unlike direct synthesis, it is a multi-step process. Secondly, for the preparation of mixed monolayer protected Au NPs, it is difficult to control the number of ligands on a nanoparticle. The composition of the mixed monolayer is essential and directly responsible for the surface properties and interactions with the target molecules.

#### 4.3

#### Preparative-scale Synthesis and Solution-phase Characterization of DNA-directed Nanoparticle Assemblies

In the previous section, we reviewed synthetic strategies for preparing ligand-protected Au NPs. These materials serve as building blocks for the assembly of higher order nanoparticle structures that could be used for applications as well as for fundamental studies. One assembly strategy involves using DNA molecules.

DNA has the unique self-assembly capability, i.e. hybridization. In addition, DNA is very hydrophilic and negatively charged. Unless the nanoparticles are positively charged, there is not much nonspecific binding between DNA and nanoparticles. Those two unique features have allowed many successful routes for the controlled assembly of nanoparticles using DNA functionalized Au NPs. These include nanoparticle assemblies through either specific hybridization of a single strand DNA attached on the nanoparticle [49, 50] or by electrostatic interaction of positively charged nanoparticles with DNA molecules [51, 52]. In addition, Niemeyer et al. have prepared nanoscale networks and aggregates using biotinylated DNA and streptavidin [53, 54]. DNA functionalized nanoparticles have been used successfully for DNA detection and as biosensors [55, 56].

Bio-based assembly of nano-scale materials into higher order structures is an active area of research. Previous studies by Alivisatos et al. [50, 57] and Mirkin et al. [49, 58] have demonstrated the power of using DNA hybridization to assemble nanoparticles into higher order structures. Work from Alivisatos et al. in particular has demonstrated the possibility of using DNA-directed assembly to make small-scale finite nanoparticle complexes that resemble artificial molecules. These structures may serve as model systems for studying nano-scale phenomena, and have potential applications in nanoelectronic circuits, optoelectronics and biosensors. One critical issue that needs to be addressed is the scale of the synthesis of these nanoparticle-based artificial molecules. Also lacking is the direct solution characterization of such assemblies, so that structure–function relationships can be established for these artificial molecules. We describe here our methods for solving the scaling-up problem, and the solution characterization of some simple nanoparticle assemblies we have made.

For this study, we first developed ligand-protected Au NPs with high stability and relatively uniform-size distributions. Following known synthetic routes, we have made glutathione and tiopronin [*N*-(2-mercaptopropionyl)glycine] monolayer-protected Au NPs [14, 59]. However, these particles, as synthesized, still have a size distribution that is too broad for our subsequent assembly studies. We have, thus, developed a non-solvent precipitation method as a very efficient way to fractionate particles of different sizes to obtain highly monodispersed nanoparticles [60]. By adding increasing amounts of either methanol or ethanol, particles of larger to smaller sizes are precipitated out of solution. After centrifugation, particles of a particular size can be selected for further assembly. A typical example for fractionation of Au-Tp NPs is given here. Au-Tp NPs (0.3 g) were dissolved in 50 mL of a 100 mM sodium chloride solution. The first fraction of the nanoparticles was precipitated out by adding methanol to the nanoparticle solution to a final content of 10% by volume. Nanoparticles were collected by centrifugation at 4000 rpm for 1 min in a Sorvall® RT7 PLUS centrifuge (Kendro Laboratory Products, Newtown, CT). More methanol was then added to the supernatant to a final content of 20% by volume and the precipitated nanoparticles were collected as described above, as the second fraction, which was used for the following experiments.

To label nanoparticles with single-stranded DNA (ssDNA), we chose the ligand

**Tab. 4.1.** Stoichiometry for attaching ssDNA to Au NPs by using ligand replacement reaction (volume unit =  $\mu\text{L}$ ).

	<i>Rxn 1</i>	<i>Rxn 2</i>	<i>Rxn 3</i>	<i>Rxn 4</i>	<i>Rxn 5</i>	<i>Rxn 6</i>
Au-Tp (60 $\mu\text{M}$ )	3	3	3	3	3	3
SsDNA (40 $\mu\text{M}$ )	0	1	2	4	8	1.6 (400 $\mu\text{M}$ )
NaCl (1 M)	1.5	1.5	1.5	1.5	1.5	1.5
H <sub>2</sub> O	10.5	9.5	8.5	6.5	2.5	8.9
Total ( $\mu\text{L}$ )	15	15	15	15	15	15

replacement reaction described in Section 4.2. A typical example is as follows. Single-stranded DNA (ssDNA) oligo nucleotides were purchased from Integrated DNA Technologies, Inc. (Coralville, IA), with 5' C6 SH modification. Materials were used as-received without further treatment. For this example, a ssDNA with sequence AAA AAA GCG TGG GCG TGG GCG TGG GCG TGG GCG was used. The gold particles had a concentration of 60  $\mu\text{M}$  in H<sub>2</sub>O. To determine the optimal ratio of Au-Tp vs. ssDNA for labeling reaction, a titration experiment was set up by mixing appropriate amounts of Au-Tp, ssDNA, NaCl, and H<sub>2</sub>O (Table 4.1). Each reaction was carried out in a 1.5 mL volume test tube. The reaction mixture was incubated at 60 °C for 15 min and allowed to slowly cool to room temperature over 30 min. Products were analyzed by gel electrophoresis using a 4% agarose/Tris-Borate-EDTA (TBE) gel (BioWhittaker, Rockland, ME). The gel was immersed in 1X TBE running buffer (89 mM Tris, 89 mM boric acid, 2 mM EDTA, pH 8.3), and electrophoresis was carried out at a constant voltage of 90 V for 80 min in an Horizon 58 gel box (Life Technologies, Rockville, MD). The gel image (Fig. 4.3A) was recorded using a HP ScanJet 6300C scanner (Agilent Technologies, Wilmington, DE). Lanes 1–6 correspond to reactions 1–6, respectively, in Table 4.1.

This experiment showed that Au particles with different numbers of ssDNAs labels can be clearly resolved by a 4% agarose gel (Fig. 4.3A). As the ratio of ssDNA vs. Au-Tp increases, more ssDNAs can be found on a particle. Thus, the stoichiometry of ssDNA and Au-Tp can be used to control the average number of ssDNAs on the surface of Au particles.

Due to the narrow size distribution of our nanoparticles, we were able to use liquid chromatography to obtain Au particles with an exact number of ssDNAs attached. After the labeling reaction, we separated reaction mixture with a size exclusion gel filtration column. A typical example of the separation of Au NPs with different numbers of single-stranded DNAs is given here. Here, the labeling reaction was performed as follows: 400  $\mu\text{M}$  ssDNA (986-ZF) (8  $\mu\text{L}$ ) and 1 M NaCl (12  $\mu\text{L}$ ) were added to 100  $\mu\text{L}$  of Au-Tp (60  $\mu\text{M}$ ). The reaction mixture was incubated at 60 °C for 15 min and allowed to slowly cool to room temperature over 30 min. This mixture was then injected into a Superdex 200 gel filtration column (Amersham Biosciences, Piscataway, NJ) mounted on a BioCAD/SPRINT HPLC system (PerSeptive Biosystems, Framingham, MA), and eluted with 0.05 NaCl/0.15 M NaHPO<sub>4</sub> buffer (pH 7) at 0.5 mL min<sup>-1</sup>. The elution profile is shown in

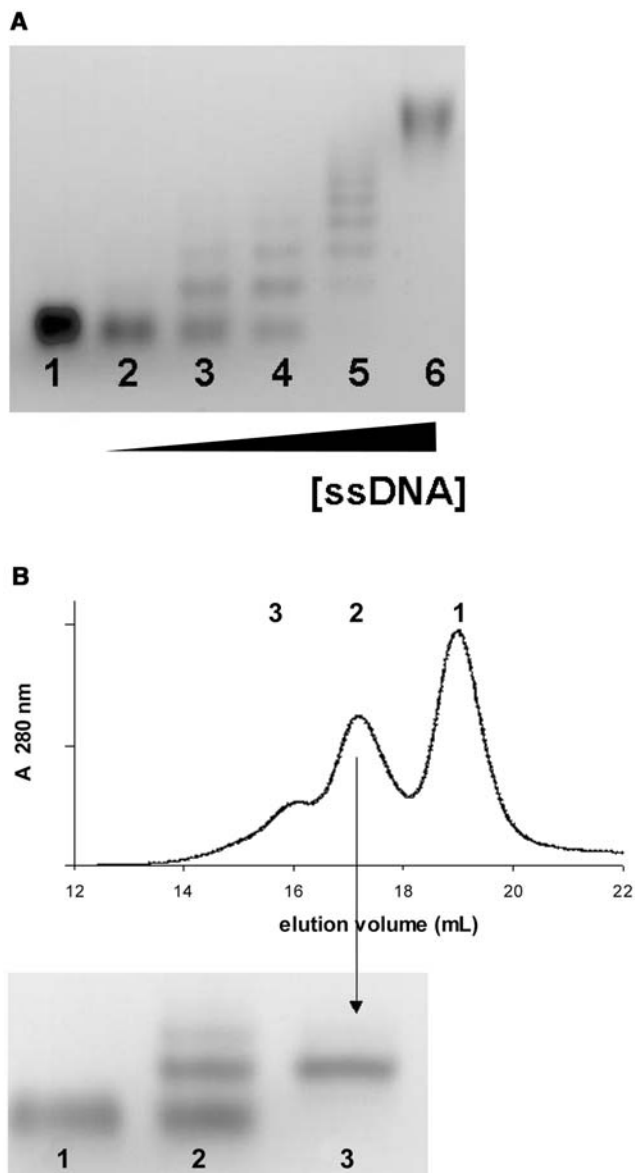


**Fig. 4.3.** (A) Gel electrophoresis (4% agarose gel) of gold nanoparticles reacted with increasing amounts of ssDNA molecules (Table 4.1). (B) Gel filtration separation and subsequent gel electrophoresis of gold nanoparticles labeled with different numbers of ssDNA molecules. A Superdex 200 gel filtration column (Amersham Biosciences, Piscataway, NJ) mounted on a BioCAD/SPRINT HPLC

system (PerSeptive Biosystems, Framingham, MA) was used. Elution was performed with 0.05 M NaCl/0.15 M NaHPO<sub>4</sub> buffer (pH 7) at 0.5 mL min<sup>-1</sup>. Peaks 1–3 correspond to nanoparticles labeled with 0, 1 and 2 ssDNA, respectively. The gel image compares Au-Tp (lane 1), Au-Tp/ssDNA reaction mix (lane 2), and the column fraction corresponding to peak 2 (lane 3).

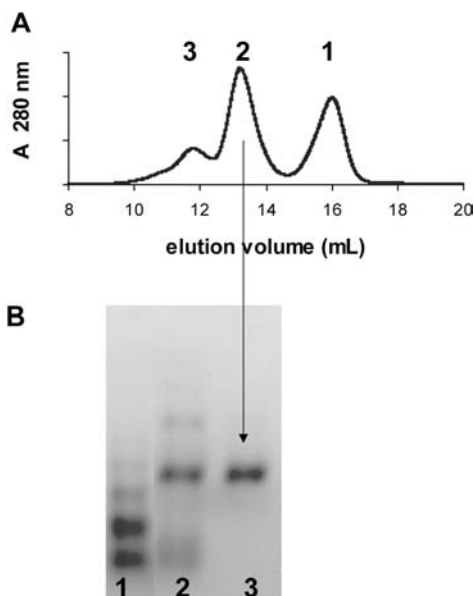


**Fig. 4.4.** (A) Gel filtration separation of a hybridization reaction of ssDNA-labeled gold particles, with conditions similar to those described in Fig. 4.3. (B) Gel electrophoresis of the separated fractions from (A).

Fig. 4.3(B). Peaks 1–3 correspond to nanoparticles labeled with 0–2 ssDNA, respectively. The gel image at the bottom of Fig. 4.3(B) compares Au-Tp (lane 1), Au-Tp/ssDNA reaction mix (lane 2), and the column fraction corresponding to peak 2 (lane 3). The gel mobility of the peak 2 fraction is consistent with the material being a one-particle/one-ssDNA species. By following the above procedure, we have labeled Au particles with two different ssDNA sequences that are complementary. The hybridization reaction was then carried out by mixing these two types of particles. The hybridization mixture was separated again by size exclusion gel filtration. A typical elution profile is shown in Fig. 4.4(A). In addition to the major product eluted in peak 2, side-products represented by peaks 1 and 3 are noticeable. These arise from impurities in the starting materials, which contain a small fraction of particles with 0, 2 and more ssDNA attached. Figure 4.4(B) shows a gel image, comparing the Au-Tp/ssDNA reaction mix (lane 1), the hybridization reaction mix (lane 2), and the column fraction corresponding to peak 2 in Fig. 4.4(A) (lane 3). The gel mobility of the peak 2 fraction is consistent with it being a dimer species. This material was analyzed by transmission electron microscopy (TEM) [Fig. 4.5(A)]. Quantitatively, over 90% of the purified species is dimeric Au NPs. Figure 4.5(B) provides an enlarged view of some dimer structures.

The synthetic procedure we have developed could be used to construct more complex structures. As a demonstration, we have synthesized a triatomic structure



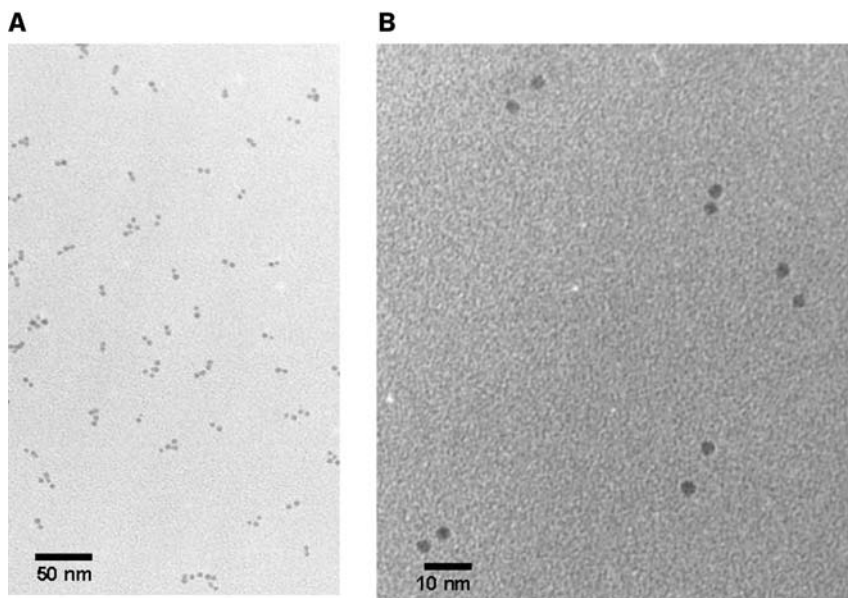
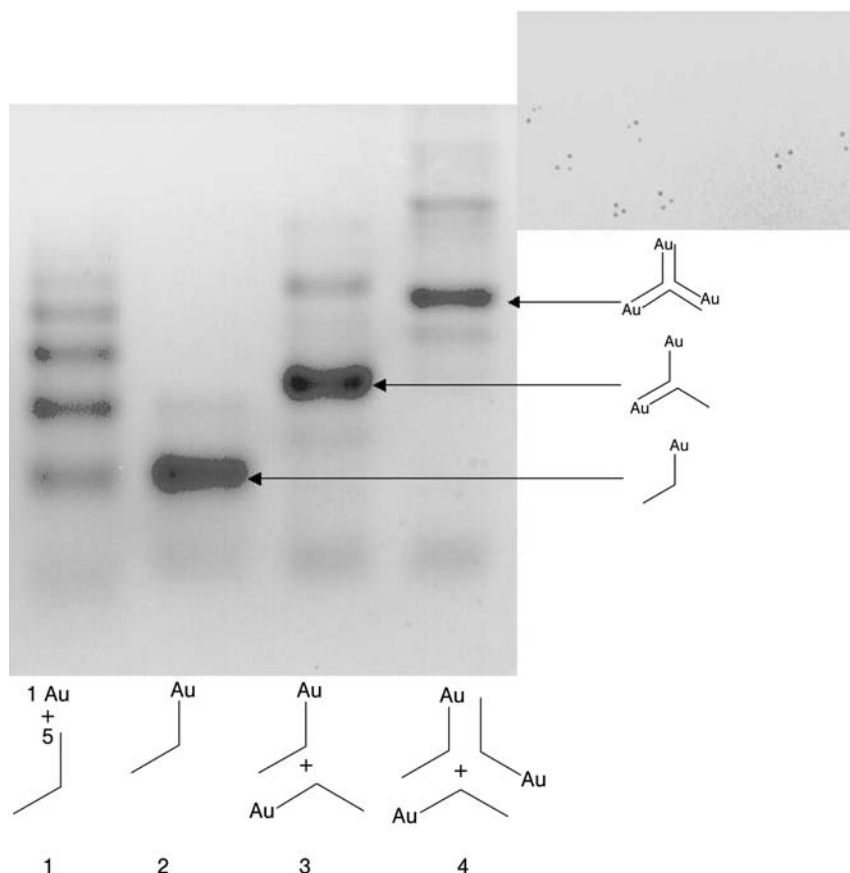


Fig. 4.5. TEM images of gold nanoparticle dimer structures prepared according to Fig. 4.4.

involving hybridization of three ssDNAs, each of which contain two segments that are complementary to part of the other two sequences (Fig. 4.6). Using the ligand exchange reaction and size exclusion separation techniques described above, we first obtained Au particles labeled with each of the three ssDNAs (lane 2 in Fig. 4.6). Hybridization between two types of Au particles labeled with two different ssDNA yielded a two-particle assembly (lane 3 of Fig. 4.6). The complete trimer structure (lane 4) was obtained by mixing the purified two-particle assembly with third-type ssDNA labeled Au particles. TEM images of the purified final hybridization mixture confirmed formation of the designed product.

Large-scale preparation has allowed us to measure directly solution structures of nanoparticle assemblies by small angle X-ray scattering (SAXS). Previous studies of nanoparticle assemblies have relied on TEM, which has the advantage of requiring small samples. However, TEM is performed under vacuum conditions and the projection nature of the TEM image prevents a direct measure of the geometric parameters of particle assemblies. Large-scale synthesis allows us for the first time to use solution methods to measure directly the geometry of nanoparticle assemblies we have made. SAXS spectroscopy proved to be ideal for our Au nanoparticle complexes, because of the large electron density on Au particles. We have measured two dimer structures of different bond lengths (Fig. 4.7). Dimer A was constructed with a 24 base pair long dsDNA with a C6 spacer on each side. Dimer B was similarly constructed with a 33 base pair long DNA. The measured Au–Au separation is 11.5 and 13.7 nm for dimers A and B, respectively. In both cases, the monomer diameter, as measured by the position of the first peak, is 3.6 nm. Assuming



**Fig. 4.6.** Gel electrophoresis and TEM image of gold particle trimer structures prepared by the DNA hybridization process. Lane 1 is from a DNA labeling reaction mixture. Lanes 2-4 are monomeric, dimeric and trimeric Au particle complexes, respectively.

the C6 spacer is 1 nm long and the diameter of Au particles is 3.6 nm, then from the measured length of either dimer one obtains  $0.246 \text{ nm bp}^{-1}$  (dimer A) or  $0.245 \text{ nm bp}^{-1}$  (dimer B). However, C6 might be flexible, and the estimated 1 nm might be a source of error. Thus, the base-separation parameter was also calculated by the length difference between the two dimers: the length difference of 2.2 nm between two dimers can be attributed to the 9 base pair difference. This gives  $0.244 \text{ nm bp}^{-1}$ , which is consistent with the previous estimation. Table 4.2 lists the derived structure parameters. To our surprise, the particle-particle separations in these dimer structures are consistent with the A- instead of the B-form DNA structure (the latter is expected under normal physiological conditions).

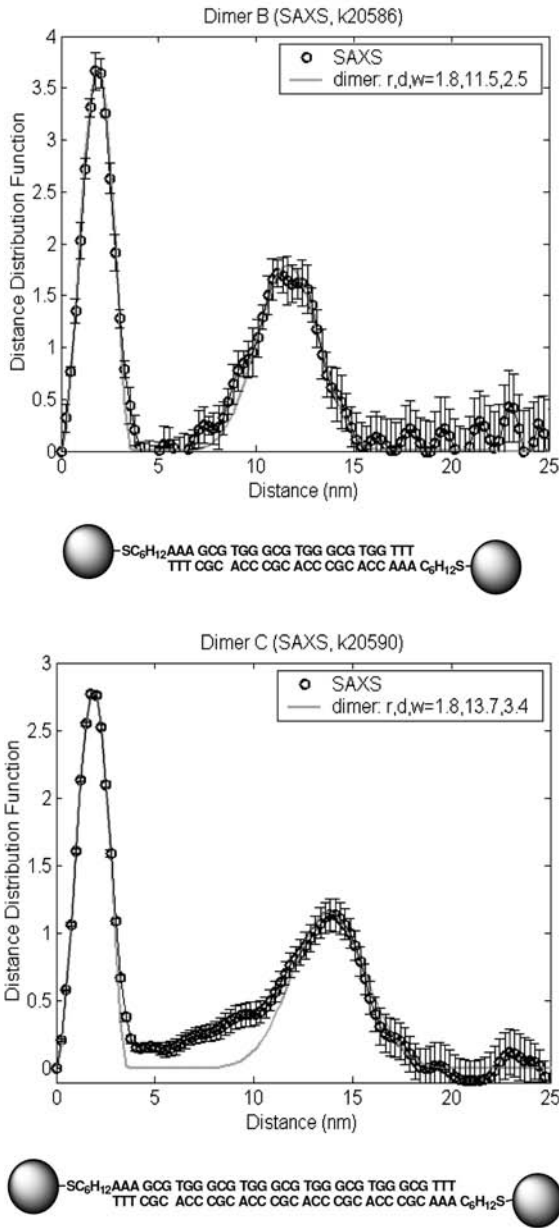


**Fig. 4.7.** SAXS measurements of two gold particle dimer structures linked with different lengths of DNA. In the two data plots, open circles are the experimental data, and the solid lines are simulations using the parameters shown.

Tab. 4.2. Geometrical parameters of two Au particle dimers obtained by SAXS measurement.

<i>Dimer</i>	<i>Number of base pairs</i>	<i>Expected Au–Au separation (assuming A-form DNA, 0.25 nm per bp) (nm)</i>	<i>Expected Au–Au separation (assuming B-form DNA, 0.34 nm per bp) (nm)</i>	<i>Measured Au–Au separation (nm)</i>
A	24	11.6	13.8	11.5
B	33	13.9	16.8	13.7

In summary, we have established a simple yet effective way to make large quantities of nanoparticle-based diatomic and triatomic artificial molecules. Monodispersed Au-Tp NPs are obtained through direct synthesis, followed by fractionation using an alcohol precipitation procedure. Au-Tp particles with one DNA oligonucleotide molecule per particle are obtained in large quantity by size exclusion chromatography. From these particles, simple diatomic and triatomic artificial molecules are self-assembled through DNA hybridization reactions. Relatively large quantities of pure diatomic and triatomic structure are obtained after fractionation and purification by size exclusion chromatography, allowing for the first time characterization of these structures in solution. SAXS data revealed that double-stranded DNA bridging two gold nanoparticles adopts, unexpectedly, the A-type conformation, illustrating the dramatic effect of environmental conditions on DNA structures.

#### 4.4

#### Bifunctional Proteins for Programmable Assembly of Nanoparticles

DNA hybridization is only one of many possible ways to assemble nanoparticles. We have explored the possibility of using DNA as a template to define spatial locations for the assembly of nanoparticles. As one such way of using DNA, we sought to create a protein that has bifunctionality: it would bind with high affinity and specificity to DNA as well as nanoparticles. Our approach is to create a fusion protein composed of a DNA binding domain and a nanoparticle binding domain (Fig. 4.8).

There are many proteins that recognize a specific sequence of DNA. Transcription factors involved in gene regulation possess such a property. We decided to use the class of DNA binding proteins called Zn fingers, owing to their high binding affinity and specificity, and because many such proteins are available. Comparison of the human genome sequence with a few other sequenced mammalian species showed that the Zn finger domain is the most frequently observed protein domain in mammalian cells [61, 62]. One can even evolve Zn finger proteins to bind DNA sequences of one's choice. A well-characterized Zn-finger protein Zif268 [63, 64] was chosen here for demonstration. For the nanoparticle binding domain, we chose well-characterized ligand binding protein domains to bind to

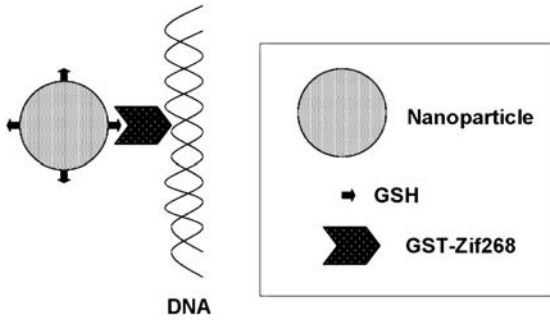


Fig. 4.8. Design of bifunctional proteins to assemble nanoparticles onto DNA.

nanoparticles that are surface coated with the cognate ligands. The GST (glutathione S-transferase)-GSH (glutathione) pair was chosen for demonstration (Fig. 4.8). We constructed the bifunctional protein following conventional molecular biology protocol, overexpressed it in *E. coli* cells, and purified the protein using GST affinity purification.

We performed a set of protein functional assays to demonstrate that, indeed, the designed protein has bifunctional binding capabilities. The Zif268 DNA binding site was defined by sequence 5'-GCGTGGGCG-3'. When the purified protein was incubated with a DNA construct that contains multiple Zif268 binding sites, we observed a clear band shift in a gel electrophoresis assay, indicating that the purified GST-Zif268 fusion protein binds to the target DNA sequence. Similarly, we showed that the protein binds to GSH-modified Au NPs (Fig. 4.9).

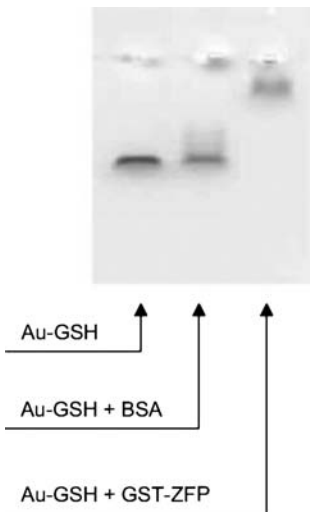
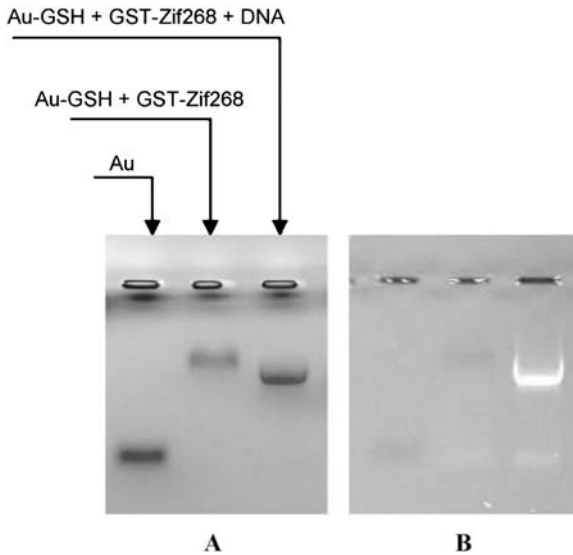


Fig. 4.9. Gel electrophoresis analysis of protein binding to Au-GSH particles.



**Fig. 4.10.** Gel electrophoresis analysis of GST-Zif268 and DNA binding to Au-GSH particles. (A) Is a direct gel image, whereas (B) is the gel image under UV illumination.

Evidence for the bifunctional binding activity was provided by an experiment shown in Fig. 4.10(A) and 10(B). This is a gel shift assay on the purified GST-Zif268 protein binding to both Au-GSH nanoparticles and DNA. Figure 4.10(A) is a direct gel image, whereas Fig. 4.10(B) is the gel image under UV illumination, indicating where the DNA band is located. As can be seen in Fig. 4.10, addition of a piece of DNA that contains protein recognition sequence caused the protein-particle complex to migrate at a different speed, and DNA co-migrated with Au particles. These results indicate that the bifunctional protein can indeed direct particles onto DNA. However, we also noticed a problem in this system that limits the efficiency of assembly by the bifunctional protein: the positively charged Zif268 has a tendency to nonspecifically bind to the negatively charged Au-GSH nanoparticles. Effectively, the Au-GSH particles compete with the DNA for the Zif268 binding site, and reduce the efficiency of the intended assembly. Such a problem triggered us to look into the general issue of nonspecific binding, which will be discussed in detail in the next section.

#### 4.5

#### Strategies for Eliminating Nonspecific Interactions and Enabling Specific Binding with Biomolecules

It is very attractive to integrate nanoparticles with biological molecules such as DNA, and proteins to create new materials for potential new applications in

electronics, optics, genomics, proteomics, and biomedical and bioanalytical areas. However, for proteins, nonspecific binding could be a serious issue. Proteins are much more complicated than DNA. They can be either hydrophobic or hydrophilic, with either positive or negative charge, making it extremely challenging to avoid nonspecific binding with nanoparticles. To fully utilize the potential of protein–nanoparticle hybrids, we synthesized ethylene glycol monolayer protected gold nanoparticles that are very stable in aqueous media and have complete resistance to nonspecific bindings with proteins, DNA and RNA [20]. However, these biologically inert nanoparticles do not provide functionality. To allow specific interactions or bindings with biological entities, a specific binding functionality has to be introduced onto the nanoparticles. For this purpose, we designed nanoparticles protected with a mixed monolayer of an ethylene glycol molecule and a ligand. The ethylene glycol short chains with well-defined lengths function as a shielding component to minimize nonspecific interaction between nanoparticles and biological molecules, whereas the ligand acts as a capture agent to engage biological molecules specifically. To demonstrate this method, we prepared a Au NP protected with a mixed monolayer of tri(ethylene glycol) and glutathione [ $\text{Au}-(\text{S}-\text{EG}_3)_n\text{GSH}$ ] by adding a reducing agent ( $\text{NaBH}_4$ ) to a mixture of  $\text{HAuCl}_4$ ,  $\text{EG}_3-\text{SH}$ ,  $\text{GSH}$ , methanol and acetic acid in a one-step direct synthesis (Fig. 4.11). We discovered

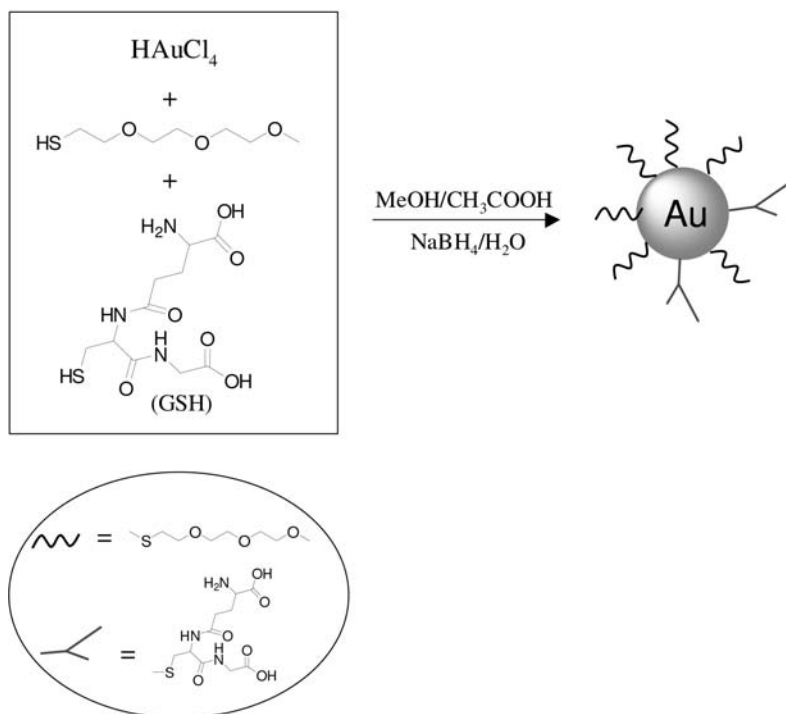


**Fig. 4.11.** Reaction scheme for making  $(\text{EG}_3-\text{S}-)/\text{GSH}$  mixed monolayer protected nanoparticles.

that in a one-step direct synthesis the water content in the reaction mixture was critical for synthesizing Au NPs in high yield. The optimum water concentration is 9–18%. This method also applies to the synthesis of other Au NPs protected with a mixed monolayer in which ethylene glycol is the major component. The synthesis utilized the optimum condition such that water for dissolving  $\text{NaBH}_4$  was added into the mixture of reagents to a final concentration of 12.5% (v/v). Under this condition, the reaction went well and no precipitation was seen. The yield was about 40%. The purified nanoparticles were very stable in pure water as well as concentrated electrolyte solutions, such as 1.0 M aqueous NaCl. These nanoparticles did not degrade after one-year storage in water.

In such a mixed monolayer protected Au NP system, GSH as a ligand molecule enables specific binding to a target. However, GSH might also contribute to the nonspecific binding. Thus, quantitative control of the ligand number or percentage is crucial to achieve specific interaction. The feeding ratio of  $\text{EG}_3\text{-SH}$  and GSH is easily controlled in the direct synthesis approach, but the essential information is the relative amount of  $\text{EG}_3\text{-S-}$  and GSH on the nanoparticle surface, which is directly responsible for the surface properties and interactions with the target molecules. To control the relative amount of the shielding component ( $\text{EG}_3\text{-S-}$ ) and the capture component (SGH), we envisage two approaches. The first is to study the relative reactivities of  $\text{EG}_3\text{-SH}$  and GSH by synthesizing a series of Au NPs with controlled feeding molar ratios of the shielding and capture components, followed analysis of the surface composition. The measured surface composition can be plotted against the feeding ratio to determine the relative reactivity of the shielding and capture components, which could be used to control the surface composition. For example, we have used  $^1\text{H}$  NMR spectroscopy as an analytical tool for measuring the surface composition of  $\text{EG}_3\text{-S-}$ /tiopronin on Au NPs and determined that the  $\text{EG}_3\text{-SH}$  is three times more reactive than tiopronin [59]. However, in many cases of mixed monolayer protected Au NPs, it is not easy to determine an accurate surface composition. In addition, NMR analysis is very tedious and needs sophisticated equipment.

For most applications, accurate understanding of the surface composition might not be necessary. The correlation of the feeding ratio of  $\text{EG}_3\text{-SH}$  and the ligand with the nanoparticle binding performance should be sufficient information to design the synthesis of nanoparticle with only specific interactions. Based on this consideration, we developed the second approach by using gel electrophoresis analysis to identify a critical feeding ratio for the nanoparticle to avoid nonspecific interactions and in the meantime to provide maximum binding to a specific target. We used  $\text{Au}(-\text{S}-\text{EG}_3)_n\text{GSH}$  as an example. With a constant ratio of  $\text{HAuCl}_4$  and capping agents ( $\text{EG}_3\text{-SH}$  and GSH) at 2.0, a series of nanoparticles were synthesized with the feeding ratio of  $[\text{EG}_3\text{-SH}]/[\text{GSH}]$  at 1, 4, 14, and 19, respectively.  $\text{Au}(-\text{S}-\text{EG}_3)_{4\text{fr}}\text{GSH}$  represents the nanoparticle synthesized when the feeding ratio of  $[\text{EG}_3\text{-SH}]/[\text{GSH}] = 4$ . The charge density of  $\text{Au}(-\text{S}-\text{EG}_3)_{n\text{fr}}\text{GSH}$  nanoparticles representing the surface density of GSH was characterized qualitatively with their migration speed in the gel electrophoresis [Fig. 4.12(a)]. Lane 1 is  $\text{Au}(-\text{S}-\text{EG}_3)_{1\text{fr}}\text{GSH}$  nanoparticles with an  $\text{EG}_3\text{-SH}/\text{GSH}$  feeding ratio of 1:1.



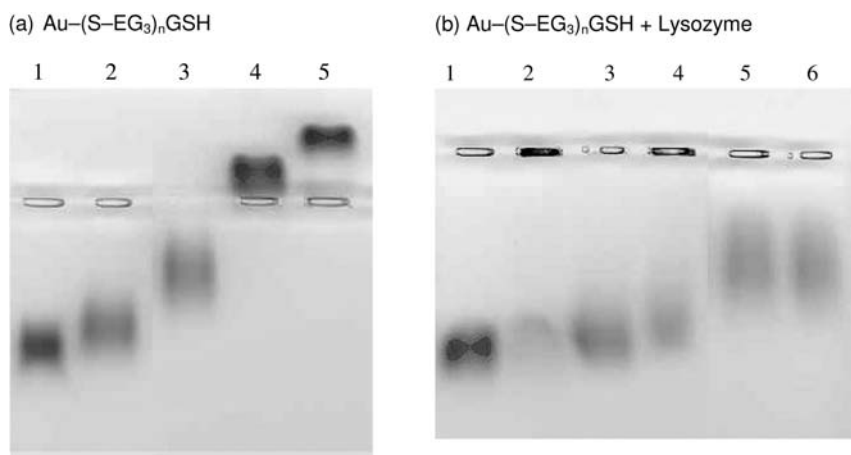


**Fig. 4.12.** (a) Gel electrophoresis image illustrating the migration of  $(EG_3-S-)/GSH$  mixed monolayer protected nanoparticles as a function of feeding ratio of  $[EG_3-S-]/[GSH]$ . A 4% agarose gel was used and run at 90 V for 40 min. Lanes 1–4 are  $Au(-S-EG_3)_{nfr}GSH$  with  $n = 1, 4, 14,$  and  $19,$  respectively. Lane 5 is the pure  $Au-S-EG_3$  nanoparticle. In all cases,  $10 \mu L$  of Au particles at concentration of  $50 \mu M$  were loaded onto the gel. (b) Gel electrophoresis image of the nanoparticles from Fig. 4.12(a) bonded with lysozyme. A 1% agarose gel was used and run at 90 V for 20

min. Lanes 1, 3 and 5 are  $Au(-S-EG_3)_{nfr}GSH$  with  $n = 1, 4,$  and  $14,$  respectively. Lanes 2, 4, and 6 are the mixture of lysozyme and  $Au(-S-EG_3)_{nfr}GSH$  with  $n = 1, 4,$  and  $14,$  respectively. Protein binding reactions were carried out by mixing  $7 \mu L$  of  $50 \mu M$  Au nanoparticles with  $7 \mu L$  of  $1 mg mL^{-1}$  lysozyme solution for 10 min incubation time at room temperature. (Reprinted with the permission from Ref. [59], M. Zheng, X. Huang, *J. Am. Chem. Soc.* **2004**, 126, 12047–12054. © 2004 American Chemical Society.)

Lanes 2–5 are the same amount of  $Au(-S-EG_3)_{nfr}GSH$  nanoparticles with  $n = 4, 14, 19,$  and pure  $Au-S-EG_3,$  respectively. The migration speed of  $Au(-S-EG_3)_{nfr}GSH$  nanoparticles decreased with decreasing percentage of GSH on the nanoparticle surface. In the mixed monolayer of  $(EG_3-S-)/GSH$  protected gold nanoparticles, the major contribution for nonspecific binding is from the electrostatic interaction introduced by GSH molecules. Therefore, a positively charged protein lysozyme is a very good indicator for testing the nonspecific binding. Binding results for  $Au(-S-EG_3)_nGSH$  nanoparticles are shown in Fig. 4.12(b). Lanes 1, 3, and 5 are  $Au(-S-EG_3)_{nfr}GSH$  nanoparticles with  $n = 1, 4,$  and  $14,$  respectively. Lanes 2, 4, and 6 are the same amount of  $Au(-S-EG_3)_{nfr}GSH$  nanoparticles with  $n = 1, 4,$  and  $14,$  respectively, mixed with lysozyme. When the molar feeding percentage of GSH is less than 20%,  $(EG_3-S-)/GSH$  mixed monolayer protected nanoparticles have negligible binding with lysozyme. In this example, the ratio of  $(EG_3-S-)/GSH$  on the nanoparticle surface was not measured and is unknown.

The GSH molecule on the  $Au(-S-EG_3)_nGSH$  particle is a natural substrate for the enzyme glutathione-S-transferase (GST). The GST–GSH binding pair thus provides an opportunity to demonstrate the specific binding between nanoparticles

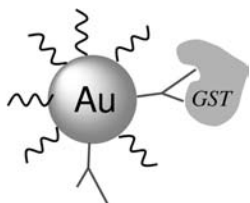


**Fig. 4.13.** Schematic of specific binding of GST protein to  $\text{Au}(-\text{S}-\text{EG}_3)_n\text{GSH}$  particles.

and proteins under more common biological conditions (Fig. 4.13). From the nonspecific binding tests for  $\text{Au}(-\text{S}-\text{EG}_3)_{n\text{fr}}\text{GSH}$  (Fig. 4.12) we saw negligible binding with lysozyme when the nanoparticle  $[\text{EG}_3-\text{SH}]/[\text{GSH}]$  feeding ratio is at 4. Nanoparticles with feeding ratios of 9 and 14 were chosen for specific interaction with GST protein. Figure 4.14 demonstrates that neither  $\text{Au}(-\text{S}-\text{EG}_3)_{9\text{fr}}\text{GSH}$  nor  $\text{Au}(-\text{S}-\text{EG}_3)_{14\text{fr}}\text{GSH}$  bound to lysozyme (lanes 2 and 5, respectively), while both particles migrated faster (lanes 3 and 6) after incubation with GST protein, indicating their specific interaction with GST. The faster migration of the  $\text{Au}(-\text{S}-\text{EG}_3)_{n\text{fr}}\text{GSH}/\text{GST}$  complex is, presumably, due to the negative charge of the GST protein (pI 6.2) in the pH 8 gel running buffer (TBE).

In summary, gel electrophoresis of the nanoparticles has been used to identify the optimum feeding ratio of a capture ligand and  $\text{EG}_3-\text{SH}$  at which the nanoparticle enables maximum specific binding with a biological target without the interference of nonspecific interactions. This approach could be easily applied to other nanoparticles protected with a mixed monolayer of an ethylene glycol molecule and a ligand.



**Fig. 4.14.** Gel electrophoresis image illustrating specific binding of  $\text{Au}(-\text{S}-\text{EG}_3)_{n\text{fr}}\text{GSH}$  ( $n = 9$  and  $14$ ) with GST protein. A 0.8% agarose gel was used and run at 90 V for 20 min. Gold particles were suspended in  $\text{H}_2\text{O}$  with a concentration of  $\sim 50 \mu\text{M}$ . Lane 1 is  $10 \mu\text{L}$  of  $\text{Au}(-\text{S}-\text{EG}_3)_{9\text{fr}}\text{GSH}$ ; lanes 2 and 3 are the same amount of Au

particles incubated with  $1 \mu\text{L}$  of lysozyme ( $10 \text{ mg mL}^{-1}$  in water) and  $5 \mu\text{L}$  of GST ( $0.5 \text{ mg mL}^{-1}$  in water), respectively. Lanes 4–6 are identical to lanes 1–3, except that  $\text{Au}(-\text{S}-\text{EG}_3)_{14\text{fr}}\text{GSH}$  was used. (Reprinted with the permission from Ref. [59], M. Zheng, X. Huang, *J. Am. Chem. Soc.* **2004**, 126, 12047–12054. © 2004 American Chemical Society.)

## 4.6

### Biological Applications

Water-soluble Au NPs have numerous applications in biology, medicine, catalysis, electronics, and optics. Here, we briefly review current efforts towards biological applications, which can be divided into subjects relating to nucleic acids, proteins, and cells and viruses.

#### 4.6.1

##### Nucleic Acids

Mirkin et al. first demonstrated the Au NP color change from red to blue when two complementary strands of DNA on two different Au NPs hybridize to form a NP aggregate [49]. Mirkin et al. further discovered that the Au NP aggregate could be converted back into individual Au NPs by heating the NP aggregate to dehybridize DNA, and that this was a reversible process in solution [65]. When a multilayer of Au NPs was formed on a glass substrate by hybridization of DNA attached on the NPs, a sharp response of plasma resonance intensity to temperature was observed [66]. Based on these fundamental discoveries, Reichert et al. developed a chip-based optical detection of DNA through hybridization of the surface-immobilized capture probe oligonucleotide and the target probe attached on Au NPs [67]. Storhoff et al. developed an easy “spot-and-read” colorimetric detection method for highly sensitive DNA detection [68]. Mirkin et al., furthermore, developed a multiplexed detection of DNA targets in a microchip format with the detection limit as low as 20 femtomolar [56]. Such a high detection sensitivity was achieved by applying a thin Ag coating to the surface of DNA hybridized Au NPs and then using surface-enhanced Raman spectroscopy (SERS) as the detection tool. By developing a magnetically-induced solid-state electrochemical detection method instead of SERS, Wang et al. achieved a DNA detection limit at the level of  $\sim 1.2$  fmol [69]. Another DNA detection method utilizes the ability of Au NP to quench fluorescence, which happens when a Au NP (2–3 nm) is in relatively close contact with a fluorophore (1–2 nm range), due to non-radioactive energy transfer from the excited fluorophore to Au NP [70]. This method employs a single stranded DNA with one end attached to an Au NP and the other end to a fluorophore to form a constrained loop DNA structure. When the DNA molecule on the Au NP hybridizes with a target ssDNA, the probe DNA loop on the Au NP opens and the fluorophore lights up. Based on this method, researchers have developed single-mismatch detection for oligonucleotides [70, 71]. Using DNA hybridization, Au NPs have also been assembled on the surface of carbon nanotubes [72].

#### 4.6.2

##### Proteins

Unlike DNA, which is very hydrophilic and negatively charged, proteins are much more complicated. They can be either hydrophobic or hydrophilic, with either pos-

itive or negative charge. In addition, nonspecific binding can be a serious issue. Unsurprisingly, therefore, applications of Au NPs with proteins have been far less developed than with DNA. However, several published papers deal with the interactions between nanoparticles and proteins, and applications in protein detection [73, 74], enzyme inhibition [75, 76], biosensor [77–79], nano-domain structure control [80, 81], and control of the nonspecific interaction of nanoparticles with proteins [59]. The interaction between Au NPs and proteins has been studied extensively. Examples include controlling the orientation of cytochrome *c* on Au NPs [82] and maintaining the enzymatic activity of fungal protease on Au NPs [83]. For protein detection, Thanh et al. [74] used antigen-coated Au NPs to detect antibodies by measuring the Au NP plasmon resonance shift induced by the aggregation of Au NPs. The detection limit could reach  $1 \mu\text{g mL}^{-1}$ . Mirkin et al. [77] used DNA hybridization to attach antigens to Au NPs and to then detect antibodies by a colorimetric scanner with a detection limit of  $\sim 20 \text{ nM}$ . This group also capped oligonucleotide-Raman dye conjugated molecules on Au NPs, attached antigens through hybridization, and then detected antibodies by using SERS [78]. Mirkin's methods are suited for the detection of multiple proteins. In a different approach, Willner et al. [79] developed an amplified optical detection of thrombin by using the binding between aptamer attached Au NPs and adsorbed thrombin on aptamer functionalized surface (detection limit at  $2 \text{ nM}$ ). In the area of enzyme inhibition, Rotello et al. have developed anionically functionalized, amphiphilic Au NPs to efficiently inhibit chymotrypsin through electrostatic interaction [75, 76]. They further demonstrated that Au NPs functionalized with alkanethiol-tetra(ethylene glycol) acetic acid bind to chymotrypsin, and the enzyme on the Au NP surface retains its activity and exhibits pronounced substrate chemoselectivity [84]. To build controlled Au NP structured materials, functionalized double stranded DNA has been used as a template to assemble protein attached Au NPs through the interaction between biotin bound on DNA and streptavidin on Au NP [80]. Enzymes, such as bacterial DNA methyltransferases could be used to manipulate the structure of DNA molecules linked with Au NPs, thus resulting in control of the distance between Au NPs [81]. In a biosensor application, Lu et al. demonstrated a colorimetric lead biosensor by using DNAzyme-directed assembly of Au NPs [85, 86]. The unique features of this method are its high speed ( $\sim 10 \text{ min}$ ) and high sensitivity ( $\sim 100 \text{ nM}$  for  $\text{Pb}^{+2}$ ).

#### 4.6.3

#### Cells and Virus

Functionalized Au NPs have many attractive properties. They are nanometer in size, and may have various functional ligands on the surface. These special properties provide them with many possible modes of interaction with biological cells, such as specific binding to the cell membrane and penetration through the membrane to interact with biological molecules inside a cell or virus. For example, carbohydrate-functionalized Au NPs have been developed to explore their multivalent interactions with cell membrane surfaces, such as lectins [87]. These studies

could have potential applications in lectin detection, control of cell fertilization, proliferation, viral infection, and inflammatory response. Dragnea et al. incorporated citrate-protected Au NPs inside brome mosaic virus and used them as a spectroscopic marker that could open up new opportunities for *in vivo* monitoring of viral capsid transitions [88].

## Acknowledgments

We thank Dr David Londono, for the SAXS measurements, and Ms Ellen D. Semke for her contribution in protein purification.

## References

- 1 M.-C. DANIEL, D. ASTRUC, Gold nanoparticles: assembly, supramolecular chemistry, quantum-size-related properties, and applications toward biology, catalysis, and nanotechnology. *Chem. Rev.* **2004**, *104*, 293–346.
- 2 M. G. WARNER, J. E. HUTCHISON in *Synthesis, Functionalization and Surface Treatment of Nanoparticles* (Ed. M.-I. BARATON), American Scientific Publishers: Stevenson Ranch, California, **2003**, Chapter 5, p. 67.
- 3 U. KREIBIG, M. VOLLMER, *Optical Properties of Metal Clusters*; Springer Series in Material Science, No. 25; Springer-Verlag: Berlin, **1995**, pp 187–201.
- 4 K. MOTESHAREI, D. C. MYLES, Molecular recognition in membrane mimics: A fluorescence probe. *J. Am. Chem. Soc.* **1994**, *116*, 7413–7414.
- 5 C. A. MIRKIN, T. A. TATON, Materials chemistry: Semiconductors meet biology. *Nature* **2000**, *405*, 626–627.
- 6 M. SASTRY, N. LALA, V. PATIL, S. P. CHAVAN, A. G. CHITTOBOYINA, Optical absorption study of the biotin-avidin interaction on colloidal silver and gold particles. *Langmuir* **1998**, *14*, 4138–4142.
- 7 D. FITZMAURICE, S. CONNOLLY, Programmed assembly of gold nanocrystals in aqueous solution. *Adv. Mater.* **1999**, *11*, 1202–1205.
- 8 S. MANN, W. SHENTON, M. LI, S. CONNOLLY, D. FITZMAURICE, Biologically programmed nanoparticle assembly. *Adv. Mater.* **2000**, *12*, 147–150.
- 9 D. A. HANDLEY in *Colloid Gold: Principles, Methods, and Applications*, (Ed. M. A. HAYAT), Academic Press, Inc.: San Diego, California, **1989**, Volume 1, Chapter 2.
- 10 M. G. WARNER, J. E. HUTCHISON in *Synthesis, Functionalization and Surface Treatment of Nanoparticles* (Ed. M.-I. BARATON), American Scientific Publishers, 2003, Chapter 5, p. 71.
- 11 F. CARIATI, L. NALDINI, Trianionoeptakis(triarylphosphine) undecagold cluster compounds. *Inorg. Chim. Acta* **1971**, *5*, 172.
- 12 M. BRUST, M. WALKER, D. BETHELL, D. J. SCHIFFRIN, R. WHYMAN, Synthesis of thiol-derivatised gold nanoparticles in a two-phase liquid–liquid system. *J. Chem. Soc., Chem. Commun.* **1994**, 801–802.
- 13 M. BRUST, J. FINK, D. BETHELL, D. J. SCHIFFRIN, C. J. KIELY, Synthesis and reactions of functionalised gold nanoparticles. *J. Chem. Soc., Chem. Commun.* **1995**, 1655–1656.
- 14 T. G. SCHAFF, G. K. KNIGHT, M. N. SHAFIGULLIN, R. F. BORKMAN, R. L. WHETTEN, Isolation and selected properties of a 10.4 kDa gold:glutathione cluster compound. *J. Phys. Chem. B* **1998**, *102*, 10643.
- 15 A. C. TEMPLETON, D. E. CLIFFEL, R. W. MURRAY, Redox and fluorophore

- functionalization of water-soluble, tiopronin-protected gold clusters. *J. Am. Chem. Soc.* **1999**, *121*, 7081.
- 16 T. G. SCHAAFF, M. N. SHAFIGULLIN, J. T. KHOURY, I. VEZMAR, R. L. WHETTEN, W. CULLEN, P. N. FIRST, C. GUTIERREZ-WING, J. ASCENSIO, M. JOSE-YACAMAN, Isolation of smaller nanocrystal Au molecules: robust quantum effects in optical spectra. *J. Phys. Chem. B* **1997**, *101*, 7885–7891.
- 17 A. C. TEMPLETON, W. P. WUELFING, R. W. MURRAY, Monolayer-protected cluster molecules. *Acc. Chem. Res.* **2000**, *33*, 27–36.
- 18 E. E. FOOS, A. W. SNOW, M. E. TWIGG, M. G. ANCONA, Thiol-terminated di-, tri-, and tetraethylene oxide functionalized gold nanoparticles: A water-soluble, charge-neutral cluster. *Chem. Mater.* **2002**, *14*, 2401.
- 19 M. BARTZ, J. KUTHER, G. NELLES, N. WEBER, R. SESHADRI, W. J. TREMEL, Monothiols derived from glycols as agents for stabilizing gold colloids in water: synthesis, self-assembly and use as crystallization templates. *J. Mater. Chem.* **1999**, *9*, 1121.
- 20 M. ZHENG, F. DAVIDSON, X. HUANG, Ethylene glycol monolayer protected nanoparticles for eliminating nonspecific binding with biological molecules. *J. Am. Chem. Soc.* **2003**, *125*, 7790–7791.
- 21 M. ZHENG, Z. LI, X. HUANG, Ethylene glycol monolayer protected nanoparticles: synthesis, characterization, and interactions with biological molecules. *Langmuir* **2004**, *20*, 4226–4235.
- 22 A. K. KANARAS, F. S. KAMOUNAH, K. SCHAUMBURG, C. J. KIELY, M. BRUST, Thioalkylated tetraethylene glycol: a new ligand for water soluble monolayer protected gold clusters. *Chem. Commun.* **2002**, 2294–2295.
- 23 A. C. TEMPLETON, S. CHEN, S. M. GROSS, R. M. MURRAY, Water-soluble, isolable gold clusters protected by tiopronin and coenzyme A monolayers. *Langmuir* **1999**, *15*, 66–76.
- 24 D. E. CLIFFEL, F. P. ZAMBORINI, S. M. GROSS, R. W. MURRAY, Mercaptoammonium-monolayer-protected, water-soluble gold, silver, and palladium clusters. *Langmuir* **2000**, *16*, 9699–9702.
- 25 X.-M. LI, V. PARASCHIV, J. HUSKENS, D. N. REINHOUDT, Sulfonic acid-functionalized gold nanoparticles: A colloid-bound catalyst for soft lithographic application on self-assembled monolayers. *J. Am. Chem. Soc.* **2003**, *125*, 4279–4284.
- 26 K. NAKA, H. ITOH, Y. TAMPO, Y. CHUJO, Effect of gold nanoparticles as a support for the oligomerization of L-cysteine in an aqueous solution. *Langmuir* **2003**, *19*, 5546–5549.
- 27 S. CHEN, K. KIMURA, Synthesis and characterization of carboxylate-modified gold nanoparticle powders dispersible in water. *Langmuir* **1999**, *15*, 1075–1082.
- 28 H. YAO, O. MOMOZAWA, T. HAMATANI, K. KIMURA, Stepwise size-selective extraction of carboxylate-modified gold nanoparticles from an aqueous suspension into toluene with tetraoctylammonium cations. *Chem. Mater.* **2001**, *13*, 4692–4697.
- 29 Y. NEGISHI, T. TSUKUDA, One-pot preparation of subnanometer-sized gold clusters via reduction and stabilization by *meso*-2,3-dimercaptosuccinic acid. *J. Am. Chem. Soc.* **2003**, *125*, 4046–4047.
- 30 K. NAKA, H. ITOH, Y. TAMPO, Y. CHUJO, Effect of gold nanoparticles as a support for the oligomerization of L-cysteine in an aqueous solution. *Langmuir* **2003**, *19*, 5546–5549.
- 31 W. P. WUELFING, S. M. GROSS, D. T. MILES, R. W. MURRAY, Nanometer gold clusters protected by surface-bound monolayers of thiolated poly(ethylene glycol) polymer electrolyte. *J. Am. Chem. Soc.* **1998**, *120*, 12696–12967.
- 32 H. OTSUKA, Y. AKIYAMA, Y. NAGASAKI, K. KATAOKA, Quantitative and reversible lectin-induced association of gold nanoparticles modified with  $\alpha$ -lactosyl- $\omega$ -mercapto-poly(ethylene glycol). *J. Am. Chem. Soc.* **2001**, *123*, 8226–8230.

- 33 J. M. DE LA FUENTE, A. G. BARRIENTOS, T. C. ROJAS, J. ROJO, J. CANADA, A. FERNANDEZ, S. PENADES, Gold glyconanoparticles as water-soluble polyvalent models to study carbohydrate interactions. *Angew. Chem. Int. Ed.* **2001**, *40*, 2257–2261.
- 34 A. G. BARRIENTOS, J. M. DE LA FUENTE, T. C. ROJAS, J. ROJO, A. FERNANDEZ, S. PENADES, Gold glyconanoparticles: synthetic polyvalent ligands mimicking glycocalyx-like surfaces as tools for glycobiological studies. *Chem. Eur. J.* **2003**, *9*, 1909–1921.
- 35 C.-C. LIN, Y.-C. YEH, C.-Y. YANG, C.-L. CHEN, G.-F. CHEN, C.-C. CHEN, Y.-C. WU, Selective binding of mannose-encapsulated gold nanoparticles to type 1 Pili in *Escherichia coli*. *J. Am. Chem. Soc.* **2002**, *124*, 3508–3509.
- 36 C.-C. LIN, Y.-C. YEH, C.-Y. YANG, C.-L. CHEN, G.-F. CHEN, C.-C. CHEN, Y.-C. WU, Quantitative analysis of multivalent interactions of carbohydrate-encapsulated gold nanoparticles with concanavalin A. *Chem. Commun.* **2003**, 2920–2921.
- 37 B. NOLTING, J.-J. YU, G.-Y. LIU, S.-J. CHO, S. KAUZLARICH, and J. GERVAY-HAGUE, Synthesis of gold glyconanoparticles and biological evaluation of recombinant Gp120 interactions. *Langmuir* **2003**, *19*, 6465–6473.
- 38 G. SCHMID, N. KELIN, I. KORSTE, U. KREIBIG, D. SCHOENAUER, Large transition metal clusters – VI. Ligand exchange reactions on  $\text{Au}_{55}(\text{PPh}_3)_{12}\text{Cl}_6$  – the formation of a water soluble  $\text{Au}_{55}$  cluster. *Polyhedron* **1988**, *7*, 605–608.
- 39 M. J. HOSTETLER, S. J. GREEN, J. J. STOKES, R. W. MURRAY, Monolayers in three dimensions: synthesis and electrochemistry of functionalized alkanethiolate-stabilized gold cluster compounds. *J. Am. Chem. Soc.* **1996**, *118*, 4212–4213.
- 40 D. T. MILES, R. W. MURRAY, Redox and double-layer charging of phenothiazine functionalized monolayer-protected clusters. *Anal. Chem.* **2001**, *73*, 921–929.
- 41 S. CHEN, Nanoparticle assemblies: “rectified” quantized charging in aqueous media. *J. Am. Chem. Soc.* **2000**, *122*, 7420–7421.
- 42 S. CHEN, R. PEI, Ion-induced rectification of nanoparticle quantized capacitance charging in aqueous solutions. *J. Am. Chem. Soc.* **2001**, *123*, 10607–10615.
- 43 F. P. ZAMBORINI, M. C. LEOPOLD, J. F. HICKS, P. J. KULESZA, M. A. MALIK, R. W. MURRAY, Electron hopping conductivity and vapor sensing properties of flexible network polymer films of metal nanoparticles. *J. Am. Chem. Soc.* **2002**, *124*, 8958–8964.
- 44 T. GU, T. YE, J. D. SIMON, J. K. WHITESSELL, M. A. FOX, Subpicosecond transient dynamics in gold nanoparticles encapsulated by a fluorophore-terminated monolayer. *J. Phys. Chem. B* **2003**, *107*, 1765–1771.
- 45 T. HUANG, R. W. MURRAY, Quenching of  $[\text{Ru}(\text{bpy})_3]^{2+}$  fluorescence by binding to Au nanoparticles. *Langmuir* **2002**, *18*, 7077–7081.
- 46 K. K. SANDHU, C. M. MCINTOSH, J. M. SIMARD, S. W. SMITH, V. M. ROTELLO, Gold nanoparticle-mediated transfection of mammalian cells. *Bioconj. Chem.* **2002**, *13*, 3–6.
- 47 G. WANG, J. ZHANG, R. W. MURRAY, DNA binding of an ethidium intercalator attached to a monolayer-protected gold cluster. *Anal. Chem.* **2002**, *74*, 4320–4327.
- 48 J. F. HICKS, Y. SEOK-SHON, R. W. MURRAY, Layer-by-layer growth of polymer/nanoparticle films containing monolayer-protected gold clusters. *Langmuir* **2002**, *18*, 2288–2294.
- 49 C. A. MIRKIN, R. L. LETSINGER, R. C. MUCIC, J. J. STORHOFF, *Nature* **1996**, *382*, 607–611.
- 50 A. P. ALIVISATOS, K. P. JOHNSON, X. PENG, T. E. WILSON, C. J. LOWETH, M. P. BRUCHEZ JR., P. G. SCHULTZ, Organization of ‘nanocrystal molecules’ using DNA. *Nature* **1996**, *382*, 609–611.
- 51 G. WANG, J. ZHANG, R. W. MURRAY, DNA binding of an ethidium intercalator attached to a monolayer-

- protected gold cluster. *Anal. Chem.* **2002**, *74*(17), 4320–4327.
- 52 M. SASTRY, M. RAO, K. N. GANESH, Electrostatic assembly of nanoparticles and biomacromolecules. *Acc. Chem. Res.* **2002**, *35*, 847–855.
- 53 C. M. NIEMEYER, W. BURGER, J. PEPLIES, Covalent DNA-streptavidin conjugates as building blocks for novel biometallic nanostructures. *Angew. Chem. Int. Ed.* **1998**, *37*, 2265–2268.
- 54 C. M. NIEMEYER, M. ADLER, S. GAO, L. CHI, Supramolecular nanocircles consisting of streptavidin and DNA. *Angew. Chem. Int. Ed.* **2000**, *39*, 3056–3059.
- 55 C. M. NIEMEYER, Bioorganic applications of semisynthetic DNA-protein conjugates. *Chem. Eur. J.* **2001**, *7*, 3189–3195.
- 56 Y. CAO, R. JIN, C. A. MIRKIN, Nanoparticles with Raman spectroscopic fingerprints for DNA and RNA detection. *Science* **2002**, *297*, 1536–1540.
- 57 C. J. LOWETH, W. B. CALDWELL, X. PENG, A. P. ALIVISATOS, P. G. SCHULTZ, DNA-based assembly of gold nanocrystals. *Angew. Chem., Int. Ed. Engl.* **1999**, *38*, 1808–1812.
- 58 J. NAM, S. PARK, C. A. MIRKIN, Bio-barcode based on oligonucleotide-modified nanoparticles. *J. Am. Chem. Soc.* **2002**, *124*, 3820–3821.
- 59 M. ZHENG, X. HUANG, Nanoparticles comprising a mixed monolayer for specific bindings with biomolecules. *J. Am. Chem. Soc.* **2004**, *126*, 12047–12054.
- 60 X. HUANG, M. ZHENG, *US Pat.* **2004**, 0115345 A1.
- 61 S. A. WOLFE, L. NEKLUDOVA, C. O. PABO, DNA Recognition by Cys<sub>2</sub>His<sub>2</sub> zinc finger proteins. *Annu. Rev. Biophys. Biomol. Struct.* **2000**, *29*, 183–212.
- 62 J. C. VENTER et al, The sequence of the human genome. *Science* **2001**, *291*, 1304–1351.
- 63 N. P. PAVLETICH, C. O. PABO, Zinc finger-DNA recognition: crystal structure of a Zif268-DNA complex at 2.8 Å. *Science* **1991**, *252*, 809–817.
- 64 J. S. KIM, C. O. PABO, Getting a handhold on DNA: design of poly-zinc finger proteins with femtomolar dissociation constants. *Proc. Natl. Acad. Sci. U.S.A.* **1998**, *95*, 2812–2817.
- 65 J. J. STORHOFF, A. A. LAZARIDES, R. C. MUCIC, C. A. MIRKIN, R. L. LETSINGER, G. C. SCHATZ, What controls the optical properties of DNA-linked gold nanoparticle assemblies. *J. Am. Chem. Soc.* **2000**, *122*, 4640–4650.
- 66 T. A. TATON, R. C. MUCIC, C. A. MIRKIN, R. L. LETSINGER, The DNA-mediated formation of supramolecular mono- and multilayered nanoparticle structures. *J. Am. Chem. Soc.* **2000**, *122*, 6305–6306.
- 67 J. REICHERT, A. CSAKI, J. M. KOHLER, W. FRITZSCHE, Chip-based optical detection of DNA hybridization by means of nanobead labeling. *Anal. Chem.* **2000**, *72*, 6025–6029.
- 68 J. J. STORHOFF, A. D. LUCAS, V. GARIMELLA, Y. P. BAO, U. R. MULLER, Homogeneous detection of unamplified genomic DNA sequences based on colorimetric scatter of gold nanoparticle probes. *Nature Biotechnol.* **2004**, *22*, 883–887.
- 69 J. WANG, D. XU, R. POLSKI, Magnetically-induced solid-state electrochemical detection of DNA hybridization. *J. Am. Chem. Soc.* **2002**, *124*, 4208–4209.
- 70 B. DUBERTRET, M. CALAME, A. J. LIBCHABER, Single-mismatch detection using gold-quenched fluorescent oligonucleotides. *Nat. Biotechnol.* **2001**, *19*, 365–370.
- 71 D. J. MAXWELL, J. R. TAYLOR, S. NIE, Self-assembled nanoparticle probes for recognition and detection of biomolecules. *J. Am. Chem. Soc.* **2002**, *124*, 9606–9612.
- 72 B. J. TAFT, A. D. LAZARECK, G. D. WITHEY, A. YIN, J. M. XU, S. O. KELLEY, Site-specific assembly of DNA and appended cargo on arrayed carbon nanotubes. *J. Am. Chem. Soc.* **2004**, *126*, 12750–12751.
- 73 W. SHENTON, S. A. DAVIS, S. MANN, Directed self-assembly of nanoparticles into macroscopic materials using antibody-antigen



- recognition. *Adv. Mater.* **1999**, *11*, 449–452.
- 74 N. T. K. THANH, Z. ROSENZWEIG, Development of an aggregation-based immunoassay for anti-protein A using gold nanoparticles. *Anal. Chem.* **2002**, *74*, 1624–1628.
- 75 N. O. FISCHER, C. M. MCINTOSH, J. M. SIMARD, V. M. ROTELLO, Inhibition of chymotrypsin through surface binding using nanoparticle-based receptors. *Proc. Natl. Acad. Sci. U.S.A.* **2002**, *99*, 5018–5023.
- 76 N. O. FISCHER, A. VERMA, C. M. GOODMAN, J. M. SIMARD, V. M. ROTELLO, Reversible “irreversible” inhibition of chymotrypsin using nanoparticle receptors. *J. Am. Chem. Soc.* **2003**, *125*(44), 13387–13391.
- 77 J.-M. NAM, S.-J. PARK, C. A. MIRKIN, Bio-barcodes based on oligonucleotide-modified nanoparticles. *J. Am. Chem. Soc.* **2002**, *124*, 3820–3821.
- 78 Y. C. CAO, R. JIN, J.-M. NAM, C. S. THAXTON, C. A. MIRKIN, Raman dye-labeled nanoparticle probes for proteins. *J. Am. Chem. Soc.* **2003**, *125*, 14676–14677.
- 79 V. PAVLOV, Y. XIAO, B. SHLYAHOVSKY, I. WILLNER, Aptamer-functionalized Au nanoparticles for the amplified optical detection of thrombin. *J. Am. Chem. Soc.* **2004**, *126*, 11768–11769.
- 80 H. LI, S. H. PARK, J. H. REIF, T. H. LABEAN, H. YAN, DNA-templated self-assembly of protein and nanoparticle linear arrays. *J. Am. Chem. Soc.* **2004**, *126*, 418–419.
- 81 C. S. YUN, G. A. KHTROV, D. E. VERGONA, N. O. REICH, G. F. STROUSE, Enzymatic manipulation of DNA-nanomaterial constructs. *J. Am. Chem. Soc.* **2002**, *124*, 7644–7645.
- 82 C. D. KEATING, K. M. KOVALESKI, M. J. NATAN, Protein:colloid conjugates for surface enhanced Raman scattering: stability and control of protein orientation. *J. Phys. Chem. B* **1998**, *102*, 9404–9413.
- 83 A. GOLE, C. DASH, C. SOMAN, S. R. SAINKAR, M. RAO, M. SASTRY, On the preparation, characterization, and enzymatic activity of fungal protease-gold colloid bioconjugates. *Bioconj. Chem.* **2001**, *12*, 684–690.
- 84 R. HONG, T. EMRICK, V. M. ROTELLO, Monolayer-controlled substrate selectivity using noncovalent enzyme-nanoparticle conjugates. *J. Am. Chem. Soc.* **2004**, *126*, 13572–13573.
- 85 J. LIU, Y. LU, A colorimetric lead biosensor using DNAzyme-directed assembly of gold nanoparticles. *J. Am. Chem. Soc.* **2003**, *125*, 6642–6643.
- 86 J. LIU, Y. LU, Accelerated color change of gold nanoparticles assembled by DNAzymes for simple and fast colorimetric Pb<sup>2+</sup> detection. *J. Am. Chem. Soc.* **2004**, *126*, 12298–12305.
- 87 D. C. HONE, A. H. HAINES, D. A. RUSSELL, Rapid, quantitative colorimetric detection of a lectin using mannose-stabilized gold nanoparticles. *Langmuir* **2003**, *19*, 7141–7144.
- 88 B. DRAGNEA, C. CHEN, E.-S. KWAK, B. STEIN, C. C. KAO, Gold nanoparticles as spectroscopic enhancers for in vitro studies on single viruses. *J. Am. Chem. Soc.* **2003**, *125*, 6374–6375.

## 5

# Biofunctionalization of Phospholipid Polymer Nanoparticles

*Junji Watanabe, Jongwon Park, Tomomi Ito, Madoka Takai, and Kazuhiko Ishihara*

### 5.1

#### Introduction

Recently, our interest in biomaterials has shifted to nanobiomaterials, which is integrated with nanofabrication. Nano-scaled fabrication is based on molecular assemblies such as micelles, self-assembled monolayers, and supramolecular compounds [1–8]. Also, many kinds of nano-scaled devices, such as bio-chips and nanoparticles, have been proposed and designed [9–17]. Nano-scaled chemistry and nanofabrication focus on chemical reactions and sensing. The most fascinating phenomena, chemical reactions, are created in a nano-scaled world, but are never carried out on an ordinary scale. In these nano-scaled devices, the bio-interface property is the dominant factor in providing excellent performance. To enhance biofunctionalization it is most important for the nano-scaled device to suppress non-specific protein adsorption since the surface is exposed to many biological components; blood, serum, and cells. Few researchers have understood the importance of materials in the design of biointerfaces and bioconjugations on the nanoscale [18–21]. This chapter summarizes newly engineered materials using bioinspired phospholipid polymer chemistry for biofunctionalization, with particular focus on phospholipid polymer nanoparticles for molecular diagnosis. Phospholipid polymers are available in numerous situations for specific biomaterials [22–25], and could function as a molecular machine [26–28]. Ishihara et al. proposed a fundamental concept for the synthesis of phospholipid polymers in the early 1990s [29, 30]. Now, we easily purchase many kinds of products containing phospholipid polymer – cosmetics, eye care products, textile goods, and fine chemicals for advanced bioreactions – which were designed through collaborations between Professor Ishihara and industrial companies. This is typical process and development – from laboratory materials to commercial products. The developed phospholipid polymer synthesis has been recognized world-wide, and much work has been reported subsequently (see Ref. [31] for an excellent review). Further research into nanofabrication may well provide us with a better “quality of life” –

perhaps especially when the design of biomaterials is based on phospholipid polymers.

## 5.2

### **Nanofabrication for Biomedical Applications**

Nanoparticles are a good substrate for bioconjugation. They have (a) a relatively high specific surface area, (b) good dispersivity in aqueous media, and (c) can be combined with nano-processed bio-chips. These characteristics can be used in a wide variety of applications, e.g. medical diagnosis, drug delivery carriers for targeting, micro-total analysis systems, and biosensors [32–35]. The most important factor in improving the nanoparticles is the enhancement of specificity to the target biomolecule such as antigen, substrate, and DNA (i.e. selectivity), and the suppression of non-specific interactions (sensitivity). Thus, bioinspired phospholipid polymers are key materials in the research on and development of nanoparticles.

#### 5.2.1

##### **Nano-scaled Processing**

Nanoparticles are a promising architecture for analyzing chemical species and providing a dynamic response. Many kinds of nanoparticles with unique structures have been prepared; Mori et al. have reported hybrid nanoparticles composed of a polymer shell with a silica core [36–38]. The polymer shell was carefully designed by the use of atom transfer radical polymerization, forming a hyperbranched structure. The nanoparticles showed reversible pH-induced complexations in a polyelectrolyte. Nanoparticles based on silica can be designed with unique structures, for easy dissolution by hydrogen fluoride. Kamata et al. have fabricated a core-shell spherical colloid with a hollow interior [39]. The hollow colloid provides a small container, in which a gold particle was trapped. The colloid particle, with its movable core, resembles a bell. The nanoparticles reported above could not be applied as advanced biomedical materials in their present form. However, suitable preparative techniques for biofunctionalization should soon be available.

Vertegel et al. have examined the size effect on the stabilization of immobilized enzyme by using silica nanoparticles (particle size 4–100 nm) [40]. Their report is impressive and important in terms of expressing biofunctions effectively. For enzyme immobilization, stronger protein–particle interactions exist on larger nanoparticles, resulting in multipoint immobilizations. The immobilized enzymes show less enzymatic activity. Akashi et al. have synthesized directly core-corona nanoparticles (one-pot preparation), which consist of a hydrophobic core and hydrophilic corona, by using water-soluble macromonomers [41, 42]. The key item is the water-soluble macromonomer; a typical example was reported using a methacrylate monomer containing a methoxy-terminated poly(ethylene glycol) side chain. The water-soluble segment was enriched spontaneously at the interface between the hydrophobic core and water, thus stabilizing the interfacial energy. The

preparative conditions are easily changeable to prepare many kinds of nanoparticles with core-corona morphology. Recently, lectin-conjugated nanoparticles have been prepared for the purpose of detecting the HIV virus [42]. From human serum, the virus is easily captured, and the nanoparticles formed in a precipitation. Caldwell et al. evaluated surface coverage by the immobilization of biomolecules; in particular, oligonucleotides were attached to polystyrene-based nanoparticles [43]. A number of the attached oligonucleotides were evaluated using the sedimentation field flow fractionation technique (a type of chromatography). This characterization technique is a powerful tool for estimating surface conditions: a number of functional groups, active linkage for bioconjugation, immobilized proteins, and binding target molecules in each step.

### 5.2.2

#### Key Materials for Nanofabrication

We have proposed recently the assembly of phospholipids polar group on nanoparticles. Nanoparticles are generally unstable as colloid particles in aqueous media. A hydrophilic moiety and ionic groups are incorporated onto the surface to prepare the interface. One unusual interface is the cell membrane, which is composed of phospholipid molecules, glycoproteins, and channel-forming proteins. It provides not only division between the cytoplasm and the outer environment but also allows communication via antenna molecules and channels. Ishihara et al. have designed and synthesized a novel functional monomer with a phospholipid polar group, 2-methacryloyloxyethyl phosphorylcholine (MPC, Fig. 5.1), in order to fabricate the cell membrane structure as a biointerface [29–31]. MPC (methacrylate derivative) easily polymerized with any kind of acrylate and methacrylate monomers by conventional radical, living radical, and atom transfer radical polymerizations [44–47]. Finely designed polymers with phospholipid polar groups were easily prepared by these polymerization techniques. The phospholipid polymer could form the cell membrane-like interface using coating, polymer blending, and polymer graft techniques [48–53]. A typical phospholipid polymer is copolymerized with *n*-butyl methacrylate (BMA); the phospholipid polymer-coated surface is illustrated in Fig. 5.2. The phospholipid polymer provided a very bio-inert interface; in particular, a non-specific interactive biointerface was obtained on diverse materials, and many biomedical devices have been developed using phospholipid polymer technology [22–25]. The stability of the phospholipid polymer-modified enzyme was also significantly prolonged in comparison with the native enzyme [26–28]. Furthermore,

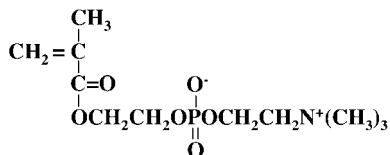


Fig. 5.1. Chemical structure of 2-methacryloyloxyethyl phosphorylcholine (MPC).

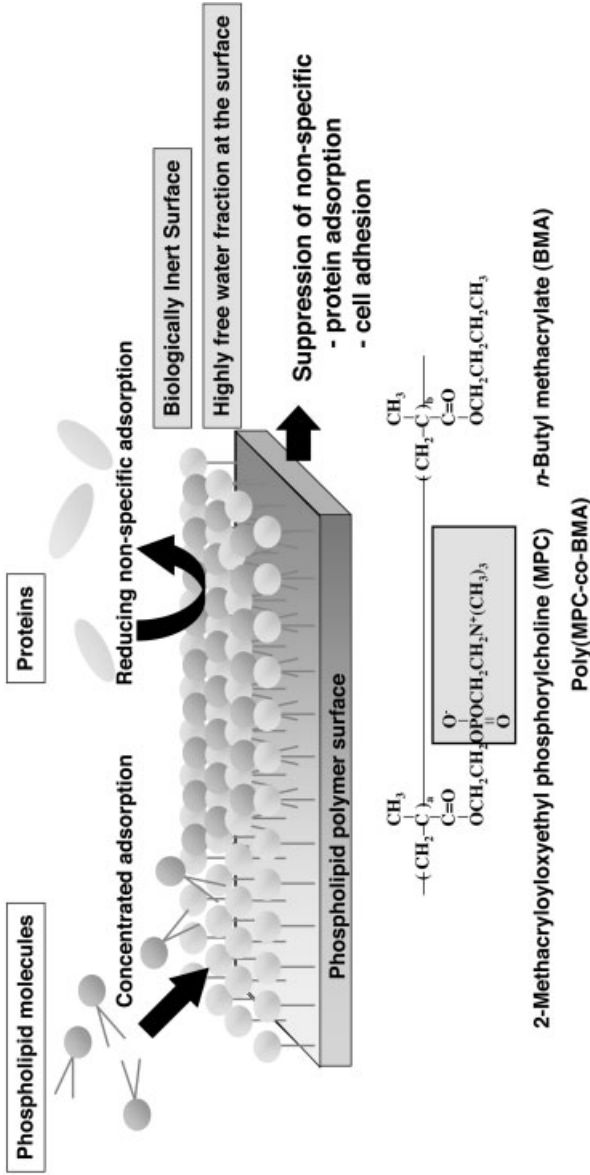


Fig. 5.2. Schematic illustration of bioinert properties on phospholipid polymer surfaces by poly(MPC-co-BMA).

the phospholipid polymer spontaneously formed nano-structured aggregations, indicating amphiphilic and surfactant-like properties [54]. Employment of a polymer-based biomimetic surface is a promising approach to prepare nano-scaled devices for biofunctionalization.

### 5.3

#### Design of Bioconjugate Nanoparticles

Bioconjugate nanoparticles have contributed to the development of advanced biomedical research. Nano-scaled materials are both available and very interesting. The most favorable characteristics of the nanoparticles are their ability to form fine, stable dispersions in aqueous media, the ease in which immobilized biomolecules can be located, and their relatively large surface area.

##### 5.3.1

#### Bioconjugate Phospholipid Polymer

The phospholipid polymer was designed for bioconjugation with biomolecules such as proteins, peptides, and DNA. We have synthesized a functional monomer – a *p*-nitrophenyloxycarbonyl poly(oxyethylene) methacrylate (MEONP) – having an active ester linkage for bioconjugation [55]. MPC, MEONP, *n*-butyl methacrylate (BMA) were copolymerized to prepare the bioconjugate phospholipid polymer (PMBN, Fig. 5.3) by a conventional radical polymerization technique with 2,2'-azobisisobutyronitrile as an initiator. This polymer serves two functions – suppression of non-specific adsorption from the human body and the connection of biomolecules via an active ester group. Table 5.1 shows typical synthetic results. Two kinds of the phospholipid polymers were prepared with regards to solubility in water. The MPC unit is highly hydrophilic, so the solubility was changeable by MPC unit composition. Below 30 mol% of MPC unit, the phospholipid polymer could not dissolve in water but did so in ethanol. The water-insoluble polymer provided a stable biointerface for capillary electrophoresis [56]. A bioconjugate phospholipid polymer having 40 mol% of MPC could easily dissolve in water; 2 mol% of active ester groups were incorporated.

##### 5.3.2

#### Solution Properties by Fluorescence Probe

The fluorescence probe sodium 1-anilinoanthracene-8-sulfonate (ANS) is used as an indicator for the estimation of polarity in hydrophobic environments, showing a maximum fluorescence at 515 nm ( $\lambda_{EM}$ ) in water and 475 nm ( $\lambda_{EM}$ ) in *n*-butyl alcohol [excitation at 370 nm ( $\lambda_{EX}$ )]. The maximum fluorescence wavelength depended on various environmental conditions. For example, it is possible to estimate micro-environment factors such as change in higher-ordered conformation in proteins. Generally, amphiphilic polymers spontaneously aggregate in an aqueous media.

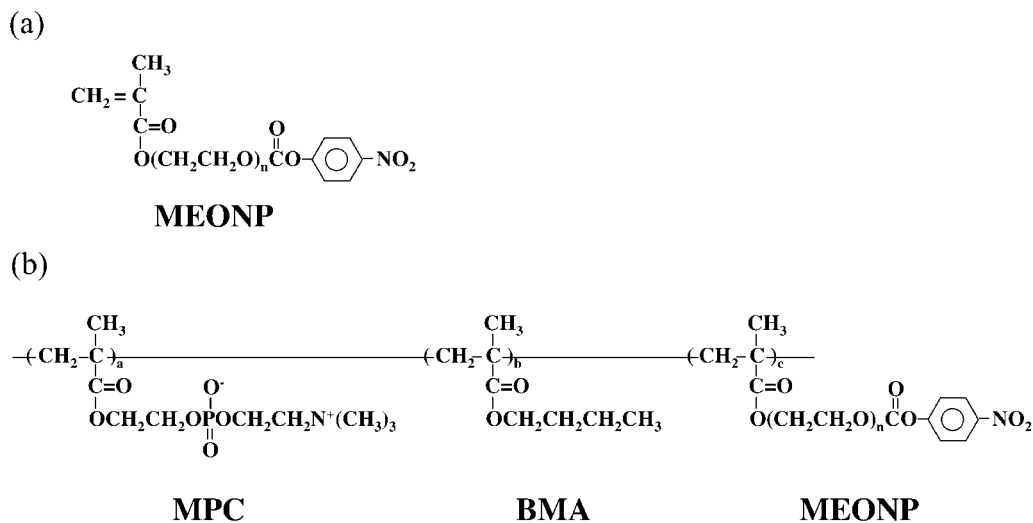


**Fig. 5.3.** Chemical structure of active ester monomer (MEONP) formed using *p*-nitrophenyl chloroformate (a) and the bioconjugate phospholipid polymer (PMBN) (b) derived from the copolymerization of MPC, BMA and MEONP. The average number of oxyethylene units was 4.5.

We evaluated the change in the maximum fluorescence wavelength by ANS. Figure 5.4 indicates that the maximum wavelength shifted upon increasing the polymer concentration. Above 0.1 mg mL<sup>-1</sup> of polymer, the wavelength was below 480 nm, indicating that the ANS molecule is trapped in lower polarity. The change in maximum wavelength showed that the phospholipid polymer spontaneously formed aggregates, indicating that it could form hydrophobic domains in a water

**Tab. 5.1.** Synthetic results of bioconjugate phospholipid polymers.

	Monomer unit composition (mol%)		Time (h)	Yield (%)	$M_w^{[b]}$	Solubility in water <sup>[c]</sup>
	In feed	In copolymer <sup>[a]</sup>				
	MPC/BMA/MEONP	MPC/BMA/MEONP				
PMBN30	30/65/5	27/61/12	6	–	$3.8 \times 10^4$	–
PMBN40	40/55/5	36/62/2	3	77	$6.2 \times 10^4$	++

[Monomer] = 1.0 mol L<sup>-1</sup>, [AIBN] = 10 mmol L<sup>-1</sup>

Reaction temperature 60 °C.

Precipitated by Diethyl ether/chloroform (8:2).

<sup>a</sup>Determined by <sup>1</sup>H NMR.

<sup>b</sup>Determined by GPC in water/methanol (3:7), PEO standard.

<sup>c</sup>Solubility described as soluble (++) and insoluble (–).

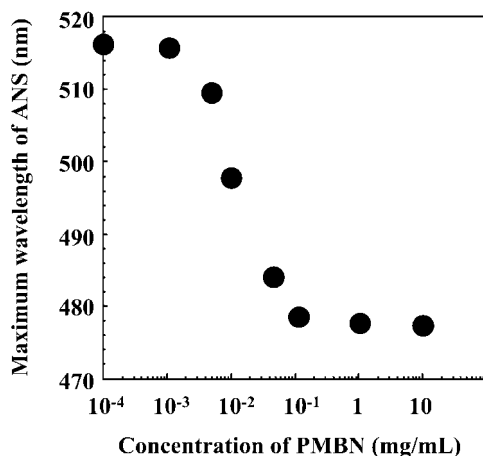


Fig. 5.4. Change in maximum fluorescence wavelength caused by phospholipid polymer aggregation ( $\lambda_{\text{EX}} = 370 \text{ nm}$ ).

environment. Therefore, phase-separated organic solvent containing polymer as core materials of the nanoparticles was stably dispersed in the phospholipid polymer aqueous solution as an emulsion, and the interface on the emulsion covered with the phospholipid polymer was then prepared. The ANS test confirmed that the phospholipid polymer aggregated in water above a concentration of  $0.1 \text{ mg mL}^{-1}$ , and could therefore be employed as an emulsifier and a surface modifier for nanoparticles.

### 5.3.3

#### Bioconjugate Nanoparticles

Bioconjugate nanoparticles have been prepared by solvent evaporation methods for the systematic design of core materials – polystyrene (PS) as a conventional polymer and poly(L-lactic acid) (PLA) as a biodegradable polymer. According to the molecular design of the bioconjugate phospholipid polymer, the hydrophobic chains, *n*-butyl groups, were considered to penetrate on the surface of nanoparticles. The phospholipid polar groups and active ester groups, which formed domains, were concentrated at the nanoparticle surface to stabilize the interface, and the *p*-nitrophenyl ester groups can freely conjugate with biomolecules (Fig. 5.5). In this section, we examine whether the characteristics of nanoparticles would alter by changing the core materials. As core polymer materials, PLA and PS were used to prepare PMBN/PLA or PMBN/PS nanoparticles by a solvent evaporation technique in aqueous medium [55, 57, 58]. In this process, the PMBN was utilized as an emulsifier, and the polymer concentration regulated the average diameter of the nanoparticles. The diameter decreased with increasing initial concentration of PMBN. Typical preparative concentrations of PMBN, PLA, and PS were 1.0, 10



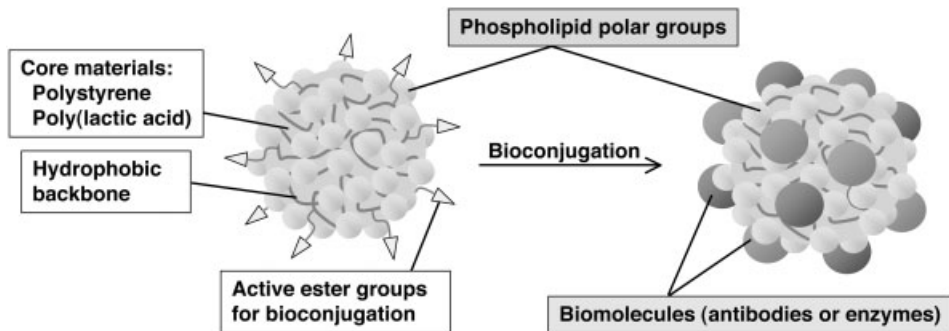


Fig. 5.5. Schematic illustration of bioconjugate phospholipid polymer nanoparticles.

and  $10 \text{ mg mL}^{-1}$ , respectively. The surface of the nanoparticles was characterized by X-ray photoelectron spectroscopy (XPS), surface  $\zeta$ -potential, dynamic light scattering (DLS), scanning electron microscopy (SEM), and determination of active ester groups.

#### 5.3.4

##### Surface Elemental Analysis by X-ray Photoelectron Spectroscopy

Surface analysis of the PMBN/PLA nanoparticles was carried out with XPS to estimate the phospholipid polar groups on the surface. Figure 5.6 shows the XPS spectra of  $\text{C}_{1s}$ ,  $\text{O}_{1s}$ ,  $\text{N}_{1s}$ , and  $\text{P}_{2p}$  on the surface of the PMBN nanoparticles. From the XPS analysis,  $\text{O}-\text{C}-\text{O}$  and  $\text{C}=\text{O}$  peaks from the phospholipid polymer were observed at 287.0 and 289.0 eV, respectively. Furthermore, a small broad peak attributed to an aromatic group based on the *p*-nitrophenyl ester group was also observed at 291.5 eV. Additionally,  $\text{N}_{1s}$  and  $\text{P}_{2p}$  peaks attributed to choline methyl (403.0 eV) and phosphate ester (134.0 eV) were observed. Moreover, the PMBN/PS nanoparticle was also characterized (Fig. 5.6). These results strongly indicated that the interface on the PMBN/PLA and PMBN/PS nanoparticles was covered with phospholipid polar groups and *p*-nitrophenyl ester groups.

#### 5.3.5

##### Surface $\zeta$ -Potential on Nanoparticles

As an alternative characterization, surface  $\zeta$ -potential was measured to estimate the coverage of the bioconjugate phospholipid polymer. The phospholipid polar group contains a quaternary choline methyl group (cation) and a phosphate ester group (anion). Their ions form an intramolecular ion pair; therefore, their charge is neutralized [59]. If the nanoparticles were covered with phospholipid polymers, the  $\zeta$ -potential on the surface would be roughly 0 mV. That is why the  $\zeta$ -potential was

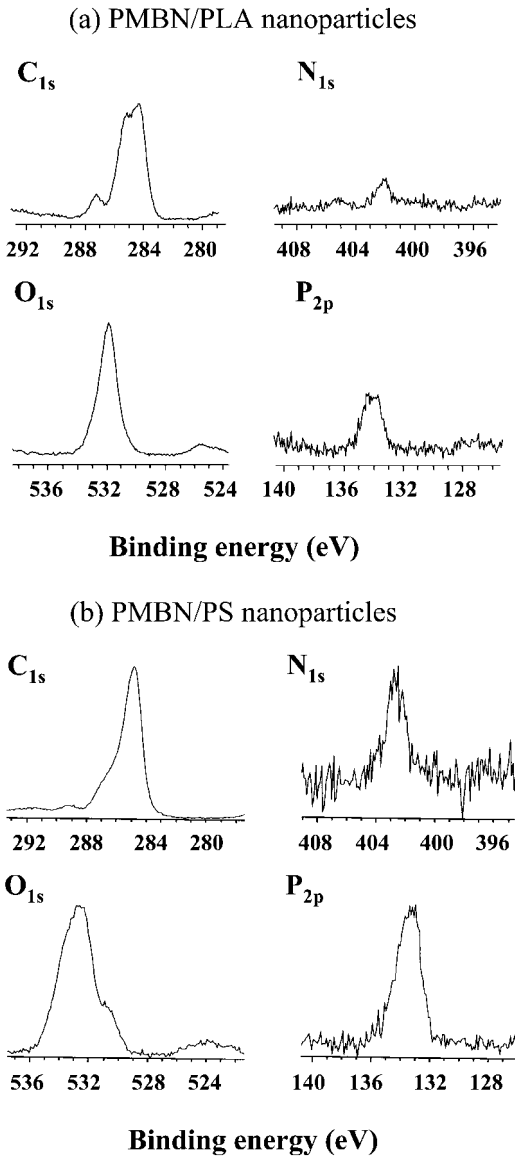


Fig. 5.6. X-ray photoelectron spectra of PMBN/PLA nanoparticles (a) and PMBN/PS nanoparticles (b).

measured for the phospholipid polymer coverage. The  $\zeta$ -potential of the PMBN/PLA and PMBN/PS nanoparticles were  $-2.1 \pm 3$  mV and  $-2.3 \pm 2$  mV, respectively. The obtained  $\zeta$ -potential is almost the same ratio and roughly 0 mV, as we expected. Farokhzad et al. reported a bioconjugate polymer nanoparticle composed

of aptamers for targeting drug delivery to prostate cancer cells. The polymer used was PLA-*block*-poly(ethylene glycol) (PEG) with a terminal carboxylic group (PLA-PEG-COOH) [60]. According to the report, the  $\zeta$ -potential of the PLA-PEG-COOH was  $-50 \pm 3$  mV, and of the PLA bare particle was  $-24 \pm 5$  mV. This indicates that the surface potential was significantly shifted to a more negative charge than the unmodified PLA nanoparticles, as a result of surface modification. Veronesi et al. reported that vanilloid (VR1) receptors on the cell membrane were activated by membrane depolarization, which is induced by charged polystyrene nanoparticles [61]. The acid-sensitive ionic channels could be activated by the electrostatic charge carried on chemically modified particles: neutral polystyrene nanoparticles (particle size: 750 nm), negative polystyrene nanoparticles (having carboxyl groups) (particle size: 860 nm), and positive polystyrene nanoparticles (having diamino groups) (particle size: 850 nm). The  $\zeta$ -potential of each nanoparticle was  $-55$  (neutral),  $-88$  (carboxyl), and  $-23$  (diamino) mV, respectively. From their reports, the nanoparticles showed a negative charge to maintain stability by electrostatic repulsion. For nanoparticles covered with the phospholipid polymer, the surface charge was nearly neutral, because it formed intramolecular ion pairs in phosphorylcholine groups. From the  $\zeta$ -potential results, the phosphorylcholine groups were assembled on the nanoparticles.

### 5.3.6

#### **Particle Size by Dynamic Light Scattering and Morphology by Scanning Electron Microscope**

The particle size and size distribution of phospholipid polymer nanoparticles have been determined by dynamic light scattering measurements (DLS). The concentration of PMBN/PLA and PMBN/PS nanoparticles was  $2.5 \text{ mg mL}^{-1}$ . The size distribution of the nanoparticles is shown in Fig. 5.7. The particle size of PMBN/PLA was  $270 \pm 100$  nm, and that of PMBN/PS was  $320 \pm 100$  nm. It is considered that these two particles have almost the same diameter with monodispersity. The miscibility between the phospholipid polymer and core polymer materials was slightly different; the PLA core is a little superior to the PS core material. Monodispersed nanoparticles were easily, and in large quantities, prepared by an emulsion technique.

The particle size of the phospholipid polymer nanoparticles was observed using a scanning electron microscope (SEM). Figure 5.7 shows SEM pictures of the nanoparticles. From this result, the size of the PMBN/PLA and PMBN/PS nanoparticle were seen to be approximately similar, showing good agreement with the DLS measurement. Particle morphology was quite good, with a spherical form. Generally, the nanoparticle was utilized up to  $100 \text{ } \mu\text{g mL}^{-1}$ . Bioreactions were carried out in a 96-well multiplate, providing a maximum volume of  $300 \text{ } \mu\text{L}$ . To prepare nanoparticles in large quantities (mg scale), several kinds of bioreaction and biofunctionalizations can be fully designed at a laboratory level. With our emulsion technique, preparative conditions can easily be scaled-up, and the nanoparticles can then be produced on an industrial scale.

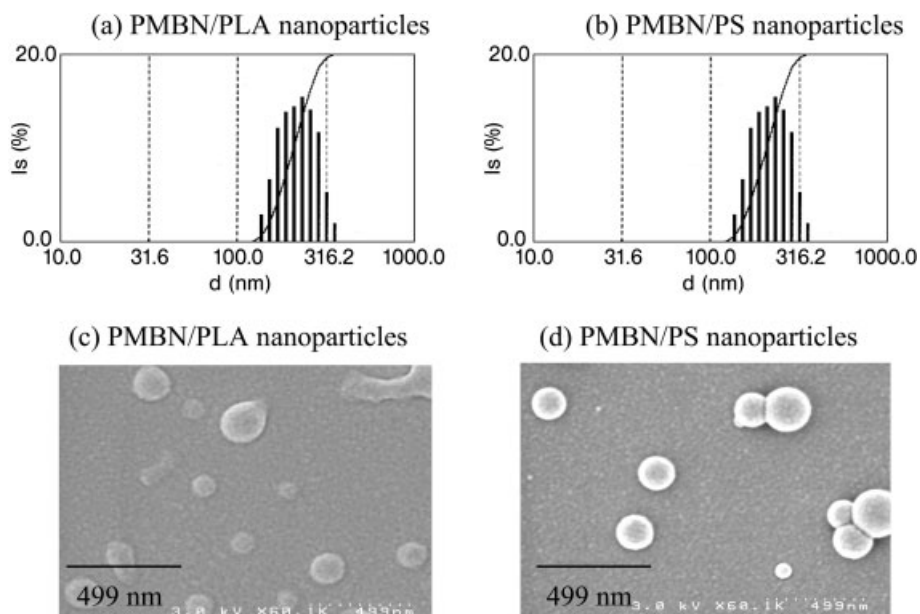


**Fig. 5.7.** Size distribution by dynamic light scattering of PMBN/PLA (a) and PMBN/PS (b) nanoparticles, and scanning electron microscope pictures of PMBN/PLA (c) and PMBN/PS (d) nanoparticles.

### 5.3.7

#### Determination of Active Ester Groups on Nanoparticles

Biomolecules can be quite easily immobilized on phospholipid polymer nanoparticles. A protein-bound amino group could, for example, couple to the ester groups on the polymer under physiological conditions, producing *p*-nitrophenol as a leaving group (Fig. 5.8). The bioconjugate reaction is accelerated under weak alkaline conditions. The conversion is easily estimated by the released *p*-nitrophenol. To quantify the active ester groups on the phospholipid polymer nanoparticles, NaOH aqueous solution ( $0.1 \text{ mol L}^{-1}$ ) was added to each suspension of PMBN/PLA and PMBN/PS for complete hydrolysis of the active ester groups. The released *p*-nitrophenol was detected by UV measurement at 400 nm. The molar extinction coefficient of the *p*-nitrophenol was calculated as  $\epsilon_{400} = 1.8 \times 10^4 \text{ L mol}^{-1} \text{ cm}^{-1}$ . Figure 5.9 shows the change in UV spectra of PMBN/PLA nanoparticles after and before hydrolysis. From this result, the active ester groups on the PMBN/PLA nanoparticles were estimated as  $1.0 \times 10^{-9} \text{ mol (mg-nanoparticle)}^{-1}$ . Thus, an active ester group exists on the PMBN/PLA nanoparticles, and the amount of such groups on PMBN/PS nanoparticles was roughly the same as on PMBN/PLA nanoparticles. The *p*-nitrophenyl ester groups, which could connect with the amino

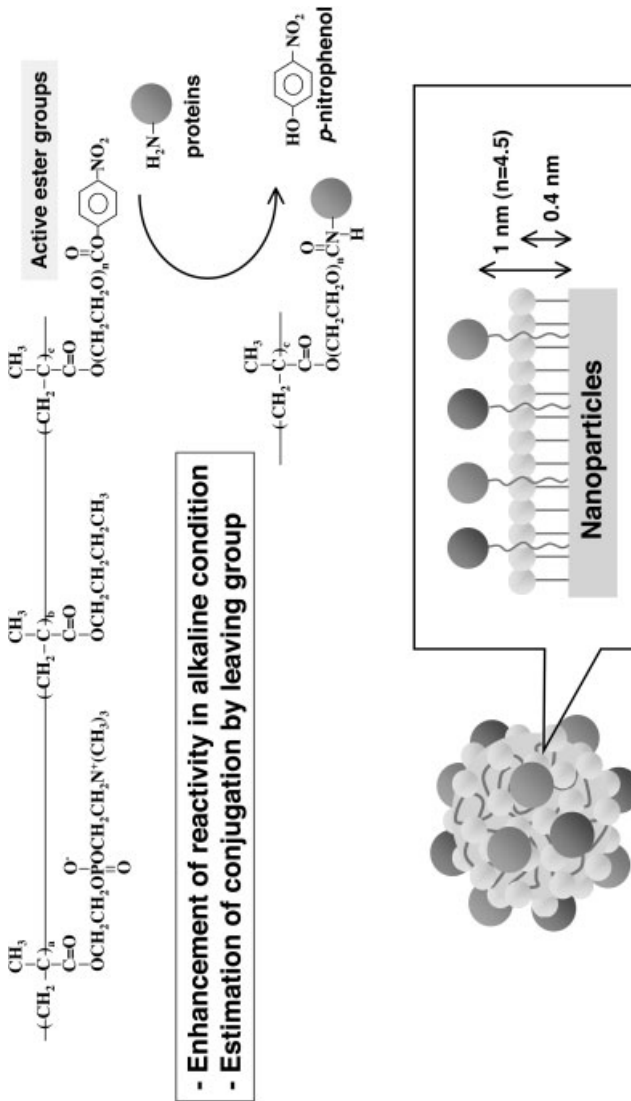
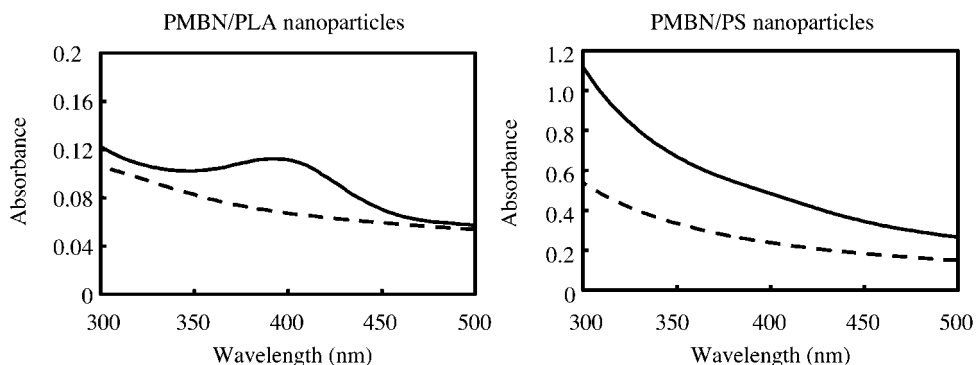


Fig. 5.8. Schematic illustration of bioconjugation on phospholipid polymer nanoparticles.



**Fig. 5.9.** UV spectra of *p*-nitrophenol (abs. 400 nm) before (dashed line) and after (solid line) hydrolysis of PMBN/PLA or PMBN/PS nanoparticles in 0.1 M NaOH aqueous solution.

groups on the proteins, were at the surface of the nanoparticles. Therefore, the interface of the PMBN/PLA and PMBN/PS nanoparticles was covered with active ester groups as well as phospholipid polar groups.

## 5.4

### Biofunction on Nanoparticles

One biofunctional enzyme reaction has been evaluated on phospholipid polymer nanoparticles. In addition, a sequential enzymatic reaction has also been designed. The most favorable characteristic is the local concentration of enzyme on the nanoparticles. An increase in this local concentration is effective for valuable and rare biomolecules.

#### 5.4.1

##### Design of Sequential Enzymatic Reaction

We have recently proposed a novel signal amplified diagnosis system using a sequential enzymatic reaction on nanoparticles. The nanoparticles are composed of a phospholipid polymer with active ester groups and polystyrene core. The amplified signal was evaluated by using choline oxidase and peroxidase, which were co-immobilized onto the nanoparticles. The choline oxidase reacts with choline chloride, producing hydrogen peroxide that is used as a substrate in the next enzymatic reaction by peroxidase. In this sequential reaction, the amount of tetramethylbenzidine is evaluated by change in absorbance, for the single enzymatic reaction (peroxidase) and/or sequential enzymatic reaction (choline oxidase and peroxidase) (see below for more details).

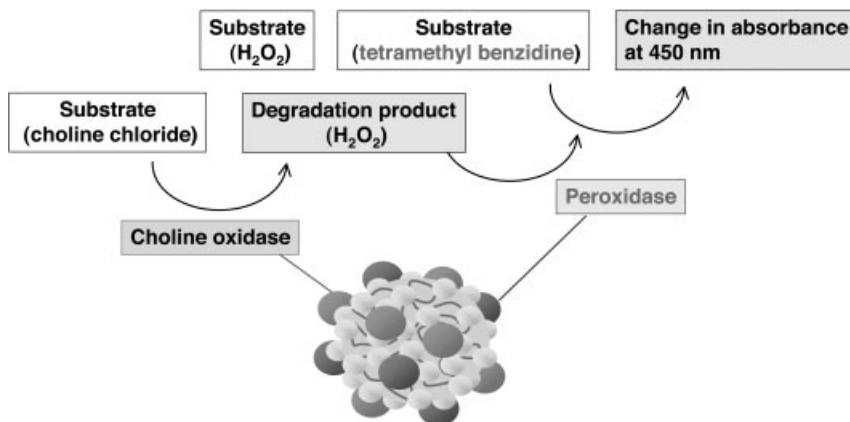


Fig. 5.10. Scheme of sequential enzymatic reactions via degradation product.

#### 5.4.2

#### Amplified Signal on Nanoparticles

The active ester group on the nanoparticles is labile to the primary amino group, affording a carbamate linkage for bioconjugation. We have already estimated the conversion of the active ester linkage; 40% of the active ester linkage was converted by a reaction with proteins [58]. Two kinds of enzymes, choline oxidase and peroxidase, were co-immobilized onto the surface, and the sequential enzymatic reaction was then evaluated. The combination of the enzymes displayed communication via the degradation product (hydrogen peroxide) (Fig. 5.10). As a substrate, choline chloride (Cho), tetramethylbenzidine (TMBZ), and hydrogen peroxide (H<sub>2</sub>O<sub>2</sub>) were used. The Cho was oxidized by the choline oxidase, and H<sub>2</sub>O<sub>2</sub> was newly produced as a degradation product. The produced H<sub>2</sub>O<sub>2</sub> was used for the next enzymatic reaction; the oxidation of TMBZ by peroxidase. The H<sub>2</sub>O<sub>2</sub>, which was originally added to the media, could also be used as substrate.

Two kinds of protocol regarding the enzymatic reaction were examined: (a) TMBZ and H<sub>2</sub>O<sub>2</sub> were added to the suspension and (b) Cho was added to the suspension with TMBZ and H<sub>2</sub>O<sub>2</sub> (TMBZ/Cho). With protocol (a), only the enzymatic activity of the peroxidase was evaluated. However, newly produced H<sub>2</sub>O<sub>2</sub> would enhance the sequential enzymatic reaction [protocol (b)]. The result of the enzymatic reaction was evaluated by the change in absorbance at 450 nm (Fig. 5.11). Enzymatic reaction on the nanoparticles was significantly greater than that of a simple enzyme solution, when TMBZ was added as the substrate. The total amount of enzymes in the enzyme solution was larger than that of the immobilized enzyme on the nanoparticles, because the concentration of the enzymes in the solution was the same as the feed concentration for the preparation of the enzyme-immobilized nanoparticles. Taking the total amount of the enzyme concentration into account, choline oxidase and peroxidase were considered to be locally concentrated on the particle surface in comparison with the solution.

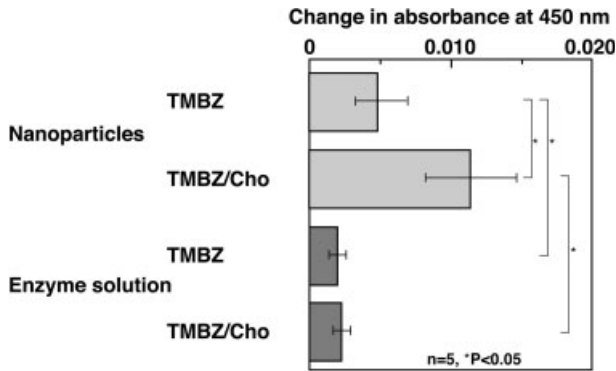


Fig. 5.11. Characterization of enzymatic reaction by changing substrate addition.

The sequential enzymatic reaction was also compared. The change in absorbance increased with addition of TMBZ/Cho, which was twice as large as that of the addition of only TMBZ. The increased enzymatic activity was considered to be based on choline oxidase, and the produced  $H_2O_2$  was effectively free to move to its binding site at the substrate. Initially, sufficient  $H_2O_2$  was added to the media to promote the enzymatic reaction; therefore, the increased enzymatic reaction was caused by  $H_2O_2$  newly produced by choline oxidase. With nanoparticles, the enzymes, choline oxidase and peroxidase, were closely immobilized onto the nanoparticles; therefore, the diffusion pathway of the produced  $H_2O_2$  was significantly shorter than that in solution. Thus, the produced  $H_2O_2$  was differed from the originally added  $H_2O_2$ , which needed a long pathway to react with the peroxidase. Conversely, no significant difference in the enzyme solution was observed between the single reaction (TMBZ) and the sequential reaction (TMBZ/Cho). This indicated that the reaction with peroxidase proceeded through a single reaction, even if Cho was added to the media.

## 5.5

### Application for Molecular Diagnosis

Recently, molecular diagnosis using bioconjugate nanoparticles has focused on the biomedical field. The obtained S/N ratio (signal/noise) generally decreased due to non-specific protein adsorption under physiological conditions. In this section we introduce a hyper-sensitive C-reactive protein detection system using the phospholipid polymer nanoparticles.

#### 5.5.1

##### Example of C-reactive Protein Detection Using Nanoparticles

The C-reactive protein (CRP) is synthesized by the liver in response to interleukin-6 and is well known as one of the classical acute-phase reactants and as a marker of



inflammation. For some time, the measurement of CRP concentration has been used as a clinical bio-marker for monitoring autoimmune diseases and infectious processes, such as rheumatoid arthritis. It has recently been suggested that a marker of inflammation, along with serum cholesterol, are critical components in the development and progression of atherosclerosis [62, 63]. However, the prospect of using CRP as a predictor of future vascular risks faced a large obstacle because existing conventional assay methods were neither sensitive enough to detect very low-levels of CRP in serum nor concerned about problems of non-specific protein adsorption and denaturation of conjugated biomolecules [64, 65]. Among conventional analytical methods, immunoassay, which uses the specific affinity of antigen-antibody, has been considered as a useful technique for clinical analyses and medical diagnostics [66]. Major progress in the use of immunoassay principles occurred with the development of several fundamental techniques [67]. Among several methods, immunoagglutination using colloidal particles has been widely used because of its rapid, simple, and inexpensive properties [68, 69]. There have been many innovations in diagnostics since microsphere agglutination was first used in medical diagnosis as agglutination-based tests in the late 1950s [70]. Although various types of colloidal particles (e.g., latex, gold, sol, and polymeric particles) have been introduced to immobilize the biorecognition element (e.g., antibody, DNA, etc.) for immunoagglutination, the latex particle, prepared by emulsion polymerizations, has been widely used in the diagnostics of various infections and to detect biomarkers or some chemical compounds in biological fluids [71]. However, several problems need to be addressed to produce a sensitive and reliable immunoassay. For example, for medical diagnostics such as CRP detection, latex particles suffered from non-specific binding, which originated from plasma proteins in serum, because of its highly hydrophobic surface. Also, the immobilized biomolecule became denatured and inactivated when it was physically adsorbed on the latex particle surface despite several advantages of immunoagglutination. These findings reduced the sensitivity, and thus the reliability, of the diagnostics. To address these challenges, we prepared novel nanoparticles as immunoagglutination substrates based on our phospholipid polymer that had already solved existing problems.

The nanoparticles were prepared by the solvent evaporation technique under the systematic design of PMBN/PLA. According to the molecular design of PMBN, the PMBN chains, particularly *n*-butyl group, were considered to miscibly interpenetrate on the surface of PLA particle. The MPC domains were arranged at the surface owing to hydrophilicity, and then the *p*-nitrophenyl ester groups, which can be conjugated with biomolecules, were also freely arranged toward the outside. Mono-dispersion of the PMBN/PLA ( $d = 205 \pm 43$  nm) measured by DLS was confirmed by field emission scanning electron microscopy (FE-SEM) [Fig. 5.12(a)]. Additionally, the  $\zeta$ -potential of PMBN/PLA ( $-5.6$  mV by electrophoresis light scattering measurement) indicated a slightly negatively charged surface. Biocomponents, including the plasma proteins, commonly have a slightly negative charge. Therefore, PMBN/PLA with a large negative  $\zeta$ -potential must suffer from non-specific protein binding when it is used as an immunosensing tool. MPC-PNP was ex-

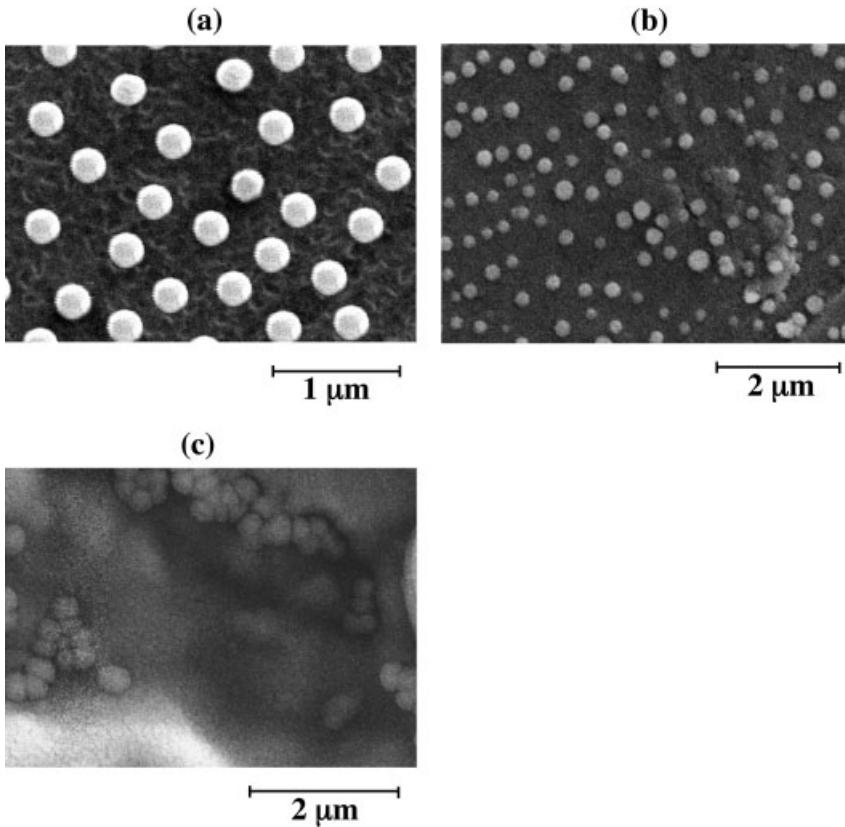


**Fig. 5.12.** SEM observations of anti-CRP antibody-immobilized PMBN/PLA nanoparticles: magnified view (a), normal view (b) and agglutination by antigen (c).

pected to show biocompatibility against non-specific binding of the plasma proteins with a slightly negatively charged surface, caused by arrangement of phosphorylcholine groups that were regarded as important to reduce protein adsorption, on PMBN/PLA.

PMBN/PLA can bind with biomolecules such as antibodies because it has *p*-nitrophenyl ester groups on its surface. Through a condensation reaction between amino groups of the antibody and *p*-nitrophenyl ester groups, the anti-CRP monoclonal antibody was immobilized on the MPC-PNP. For optimization, a fluorescent probe (Alexa Fluor 488, Molecular Probes, USA) labeled anti-CRP antibody was used to determine accurately the amount of antibody on PMBN/PLA. The immobilized amount of antibody was measured directly and calculated from the fluorescence intensity after immobilization. On the basis of experimental results,  $100 \mu\text{g mL}^{-1}$  of anti-CRP antibody was regarded as the optimal concentration for immobilization on PMBN/PLA. The remaining *p*-nitrophenyl ester groups

on the surface were thoroughly blocked by 20 mM glycine. The  $\zeta$ -potential of the PMBN/PLA ( $-25.3$  mV) was further decreased after antibody immobilization because the antibody has a negative charge.

After preparation of the anti-CRP antibody immobilized PMBN/PLA, it was applied to detect serum-free CRP by the immunoagglutination method. Figure 5.12 also indicates FE-SEM photographs of the immunoagglutination at an initial state (b) and after aggregation (c). The immunoagglutination of PMBN/PLA was clearly successfully achieved by specific antigen–antibody binding. Following the confirmation of immunoagglutination, the dependency for serum-free CRP concentration was investigated with the anti-CRP antibody immobilized PMBN/PLA and commercially available polystyrene nanoparticles. The increase in optical density was investigated to evaluate the degree of immunoagglutination when agglutination occurred among particles. To avoid interference of light absorbance into antibody molecules, the optical density was measured at 570 nm when immunoagglutination was thoroughly performed for 90 min at 37 °C.

Figure 5.13 shows the calibration curves for serum-free CRP by PMBN/PLA and polystyrene nanoparticles. For PMBN/PLA, the calibration curve clearly had a linear correlation for serum-free CRP concentrations (from 0.01 to 10 mg dL<sup>-1</sup>); polystyrene nanoparticles, however, had a limited linearity (from 0.1 to 10 mg dL<sup>-1</sup>). The difference between the two calibration curves might be related to the resistance of protein adsorption on the surface of particles. With polystyrene nanoparticles, it could be that antigen–antibody binding did not occur and, instead, non-specific adsorption of CRP took place that affected the detection results. Overall, for polystyrene nanoparticles it was difficult to detect CRP at low concentrations although non-specific adsorption could be ignored at high concentrations because of the high response from antigen–antibody binding. Conversely, low concentrations

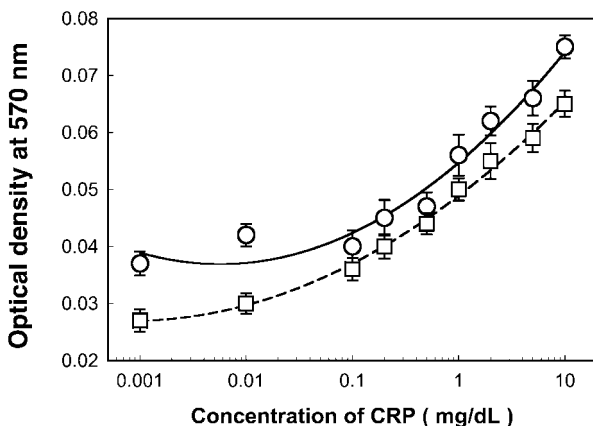
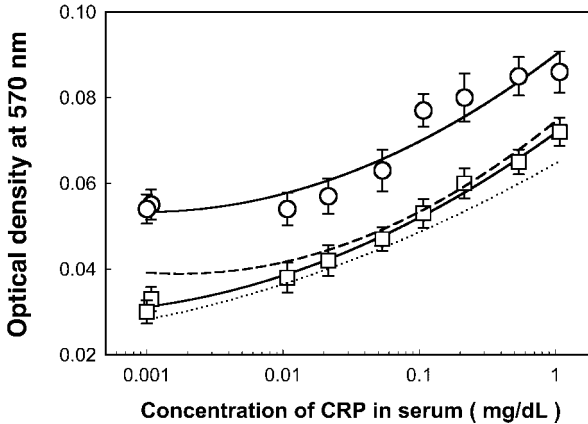


Fig. 5.13. Standard calibration curve for serum-free CRP obtained from the change in optical density at 570 nm when the immunoagglutination among anti-CRP antibody conjugated PMBN/PLA nanoparticles ( $\square$ ) and conventional polystyrene nanoparticles ( $\circ$ ) was completed following each serum-free CRP injected.



**Fig. 5.14.** Consideration of the regulating effect of non-specific binding from plasma proteins in human serum by comparing the calibration curves for serum-free CRP and CRP in serum; PMBN/PLA nanoparticles (□) and conventional polystyrene nanoparticles (○).

of CRP could be detected by PMBN/PLA because there were no problems with non-specific binding of CRP. From successfully obtained calibration curves, CRP detection was investigated with CRP in serum; the previous calibration curves in Fig. 5.13 were considered as standard calibration curves for CRP.

### 5.5.2

#### High-performance Diagnosis in Serum

Figure 5.14 indicates the change in optical density of serum-containing particles with CRP concentrations in serum. These were compared with standard calibration curves to consider non-specific binding from plasma proteins in serum. Adsorption of plasma proteins, such as BSA and  $\gamma$ -globulin, in serum on the particles might induce the agglutination of particles, and this non-specific agglutination would be a major problem for reliable CRP detection. As shown in Fig. 5.14, polystyrene nanoparticles gave a quite different standard curve because non-specific agglutination occurred, resulting in plasma protein adsorption. This phenomenon could also be explained by particle preparation parameters such as ionic strength and hydrophobicity. However, the calibration curve was almost identical when PMBN/PLA was used to detect the CRP in serum. Thus, non-specific binding of plasma proteins rarely occurred on the MPC-PNP, and highly sensitive and reliable CRP diagnostics could be obtained. Normally, the detection limit for CRP was below  $0.06 \text{ mg dL}^{-1}$  for medical diagnostics. Furthermore, with infants, much lower detection limits are required to detect CRP. The MPC-PNP fully satisfied the requirement for CRP detection.

To determine their thermal stability, anti-CRP antibody immobilized PMBN/PLA

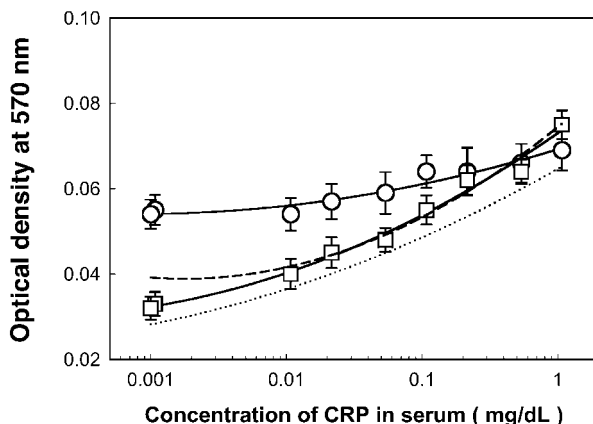


**Fig. 5.15.** Remaining immunologic activities of conjugated anti-CRP antibody on PMBN/PLA nanoparticles and conventional polystyrene NP; the calibration curves for serum-free CRP were obtained after 2 h storage 55 °C; PMBN/PLA nanoparticles (□) and conventional polystyrene nanoparticles (○).

and polystyrene nanoparticles were stored at 55 °C for 2 h, and were then used to detect serum-free CRP under the same conditions as for the determination of the standard calibration curves. Figure 5.15 shows the calibration curve for serum-free CRP obtained after this treatment. From the figure, the calibration curve of the PMBN/PLA was almost the same as the standard curve. However, the polystyrene nanoparticles gave a very different curve, indicating that anti-CRP antibody immobilized on polystyrene nanoparticles was denatured by the high temperature treatment and almost lost its selectivity for CRP. However, for PMBN/PLA, the immobilized antibody was clearly not influenced by the increase in temperature.

The resistance of protein adsorption and suppression of antibody denaturation on PMBN/PLA might be related to the hydration state of the phosphorylcholine groups. The following concept is generally accepted when considering protein adsorption on a polymer substrate [72]. Water molecules bind to the hydrophobic part of the polymer through van der Waals forces. These bound water molecules cause protein adsorption by hydrophobic interaction. When a protein molecule is adsorbed on a polymer surface, the water molecules between proteins and the polymer need to be replaced. This phenomenon induces a much stronger interaction with a change in the denaturation of the proteins. If the water at the surface is in a similar state to bulk water, the protein does not need to release bound water molecules even if the protein molecules are in contact with the surface. Under the hypothesis concerning the effect of water states, our group has previously analyzed the water state of hydrated MPC polymers, and recognized that the water state on the MPC polymer surface is naturally maintained [73, 74]. For PMBN/PLA, this hypothesis can also be used to explain several experimental results because its sur-

face was successfully covered with MPC units. Furthermore, as additional proof of the hypothesis, the colloidal stability of the PMBN/PLA was also explained. Generally, colloidal stability can be achieved in two ways: (a) the particles can be given an electric charge (either positive or negative) and if all have the same charge they will repel one another more or less strongly when they approach; (b) the particles can be coated with an adsorbed layer of some material (say a polymer), which itself prevents their close approach. Although the PMBN/PLA did not correspond to either situation it has good colloidal stability – as indicated in the FE-SEM picture for initial colloidal states [Fig. 5.12(a)]. On the basis of our hypothesis, it was strongly solvated with water molecules, and polar groups like bound water molecules resist coagulation among the PMBN/PLA nanoparticles.

## 5.6

### Conclusions

Nanofabrication is a promising technique that opens up a new scientific field, integrating biochemistry, bioscience, material science, polymer chemistry, and nano-scaled processing. Under the nano-scale environment, surface properties (biointerface) are dominant factors and, thereby, regulate biofunctions. In particular, non-specific protein adsorption is a typical phenomenon in nanofabrication. A series of phospholipid polymers are good candidates for nanofabrication involving biofunctionalization.

### Acknowledgments

Part of this study, which was carried out by the authors, was financially supported by the Industrial Technology Research Grant Program (03A23011a) from the New Energy and Industrial Technology Development Organization (NEDO) of Japan and the Scientific Research Fund (16650098) from the Japanese Society for the Promotion of Science.

### References

- 1 HARADA, A., KATAOKA, K., Chain length recognition: core-shell supramolecular assembly from oppositely charged block copolymers. *Science* **1999**, *283*, 65–67.
- 2 AKIYOSHI, K., KANG, E.-C., KURUMADA, S., SUNAMOTO, J., PRINCIPI, T., WINNIK, F. M., Controlled association of amphiphilic polymers in water; thermosensitive nanoparticles formed by self-assembly of hydrophobically modified pullulan and poly(N-isopropylacrylamides). *Macromolecules* **2000**, *33*, 3244–3249.
- 3 YATVIN, M. B., KREUTZ, W., HORWITZ, B. A., SHINITZKY, M., pH-Sensitive liposome: possible clinical implications. *Science* **1980**, *210*, 1253–1255.
- 4 ORBAN, J. M., FAUCHER, K. M., DLUHY, R. A., CHAIKOF, E. L., Cytomimetic biomaterials. 4. In-situ photopolymerization of phospholipids

- on an alkylated surface. *Macromolecules* **2000**, *33*, 4205–4212.
- 5 TEGOULIA, V. A., COOPER, S. L., Leukocyte adhesion on model surfaces under flow: effects of surface chemistry, protein adsorption, and shear rate. *J. Biomed. Mater. Res.* **2000**, *50*, 291–301.
  - 6 CHOI, H. S., OOYA, T., SASAKI, S., YUI, N., OHYA, Y., NAKAI, T., OUCHI, T., Preparation and characterization of polypseudorotaxanes based on biodegradable poly(L-lactide)/poly(ethylene glycol) triblock copolymers. *Macromolecules* **2003**, *36*, 9313–9318.
  - 7 YUI, N. (Ed.), *Supramolecular Design for Biological Applications*, CRC Press, Boca Raton, FL, **2000**.
  - 8 YUI, N., MRSNY, R. J., PARK, K., *Reflexive Polymers and Hydrogels: Understanding and Designing Fast Responsive Polymeric Systems*, CRC Press, Boca Raton, FL, **2004**.
  - 9 GOODRICH, T. T., LEE, H. J., CORN, R. M., Direct detection of genomic DNA by enzymatically amplified SPR imaging measurements of RNA microarrays. *J. Am. Chem. Soc.* **2004**, *126*, 4086–4087.
  - 10 LIU, R. H., YANG, J., LENIGK, R., BONANNO, J., GRODZINSKI, P., Self-contained, fully integrated biochip for sample preparation, polymerase chain reaction amplification, and DNA microarray detection. *Anal. Chem.* **2004**, *76*, 1824–1831.
  - 11 SONTOROU, C. G., NIKOLELIS, D. P., TARUS, B., DUMBRAVA, J., KRULL, U. J., DNA biosensor based on self-assembled bilayer lipid membranes for the detection of hydrazines. *Electroanalysis* **1998**, *10*, 691–694.
  - 12 OKI, A., ADACHI, S., TAKAMURA, Y., ISHIHARA, K., OGAWA, H., OGAWA, Y., ICHIKI, T., HORIIKE, Y., Electro-osmosis injection of blood serum into biocompatible microcapillary chip fabricated on quartz plate. *Electrophoresis* **2001**, *22*, 341–347.
  - 13 SHIMIZU, N., SUGIMOTO, K., TANG, J., NISHI, T., SATO, I., HIRAMOTO, M., AIZAWA, S., HATAKEYAMA, M., OHBA, R., HATORI, H., YOSHIKAWA, T., SUZUKI, F., OOMORI, A., TANAKA, H., KAWAGUCHI, H., WATANABE, H., HANDA, H., High-performance affinity beads for identifying drug receptors. *Nat. Biotechnol.* **2000**, *18*, 877–881.
  - 14 SERIZAWA, T., HAMADA, K.-I., AKASHI, M., Polymerization within a molecular-scale stereoregular template. *Nature* **2004**, *429*, 52–55.
  - 15 NAM, J.-M., THAXTON, C. S., MIRKIN, C. A., Nanoparticle-based bio-bar codes for the ultrasensitive detection of proteins. *Science* **2003**, *301*, 1884–1886.
  - 16 BOAL, A. K., ILHAN, F., DEROUCHÉY, J. E., THURN-ALBRECHT, T., RUSSELL, T. P., ROTELLO, V. M., Self-assembly of nanoparticles into structured spherical and network aggregates. *Nature* **2000**, *404*, 746–748.
  - 17 OLIVA, A. g., CRUZ, H. J., ROSA, C. C., Immunosensors for diagnostics. *Sensors Update* **2001**, *9*, 283–312.
  - 18 SIEGERS, C., BIESALSKI, M., HAAG, R., Self-assembled monolayers of dendritic polyglycerol derivatives on gold that resist the adsorption of proteins. *Chem. Eur. J.* **2004**, *10*, 2831–2838.
  - 19 SIGAL, G. B., MRKSICH, M., WHITESIDES, G. M., Effect of surface wettability on the adsorption of proteins and detergents. *J. Am. Chem. Soc.* **1998**, *120*, 3464–3473.
  - 20 JENKINS, S. H., HEINEMAN, W. R., HALSALL, H. B., Extending the detection limit of solid-phase electrochemical enzyme immunoassay to the attomole level. *Anal. Biochem.* **1988**, *168*, 292–297.
  - 21 ISHIHARA, K., Bioinspired phospholipid polymer biomaterials for making high performance artificial organs. *Sci. Technol. Adv. Mater.* **2000**, *1*, 131–138.
  - 22 MORO, T., TAKATORI, Y., ISHIHARA, K., KONNO, T., TAKIGAWA, Y., MATSUSHITA, T., CHUNG, U.-I., NAKAMURA, K., KAWAGUCHI, H., Surface grafting of artificial joints with a biocompatible polymer for preventing periprosthetic osteolysis. *Nat. Mater.* **2004**, *3*, 829–836.
  - 23 YONEYAMA, T., SUGIHARA, K.-I.,

- ISHIHARA, K., IWASAKI, Y., NAKABAYASHI, N., The vascular prosthesis without pseudointima prepared by antithrombogenic phospholipid polymer. *Biomaterials* **2002**, *23*, 1455–1459.
- 24 ISHIHARA, K., IWASAKI, Y., NOJIRI, C., Phospholipid polymer biomaterials for making ventricular assist devices. *J. Congestive Heart Failure Circulatory Support* **2001**, *1*, 265–270.
- 25 KONNO, T., WATANABE, J., ISHIHARA, K., Enhanced solubility of paclitaxel using water-soluble and biocompatible 2-methacryloyloxyethyl phosphorylcholine polymers. *J. Biomed. Mater. Res.* **2003**, *65A*, 210–215.
- 26 MIYAMOTO, D., WATANABE, J., ISHIHARA, K., Effect of water-soluble phospholipid polymers conjugated with papain on the enzymatic stability. *Biomaterials* **2004**, *25*, 71–76.
- 27 MIYAMOTO, D., WATANABE, J., ISHIHARA, K., Highly-stabilized papain conjugated with water-soluble phospholipid polymer chain having a reacting terminal group. *J. Appl. Polym. Sci.* **2004**, *91*, 827–832.
- 28 MIYAMOTO, D., WATANABE, J., ISHIHARA, K., Molecular design of reactive amphiphilic phospholipid polymer for bioconjugation with an enzyme. *J. Appl. Polym. Sci.* **2005**, *95*, 615–622.
- 29 ISHIHARA, K., UEDA, T., NAKABAYASHI, N., Preparation of phospholipid polymers and their properties as hydrogel membrane. *Polym. J.* **1990**, *23*, 355–360.
- 30 ISHIHARA, K., OSHIDA, H., ENDO, Y., UEDA, T., WATANABE, A., NAKABAYASHI, N., Hemocompatibility of human whole blood on polymers with a phospholipid polar group and its mechanism. *J. Biomed. Mater. Res.* **1992**, *26*, 1543–1552.
- 31 WATANABE, J., ISHIHARA, K., Biointerface, bioconjugation, and biomatrix based on bioinspired phospholipid polymers, in *Handbook of Nanostructured Biomaterials and Their Applications*, Ed. by H. S. NALWA, American Scientific Publishers, CA, **2005**, 129–165.
- 32 STIRIBA, S.-E., FREY, H., HAAG, R., Dendritic polymers in biomedical applications: from potential to clinical use in diagnostics and therapy. *Angew. Chem. Int. Ed.* **2002**, *41*, 1329–1334.
- 33 SATO, K., HOSOKAWA, K., MAEDA, M., Rapid aggregation of gold nanoparticles induced by non-cross-linking DNA hybridization. *J. Am. Chem. Soc.* **2003**, *125*, 8102–8103.
- 34 TABUCHI, M., UEDA, M., KAJI, N., YAMASAKI, Y., NAGASAKI, Y., YOSHIKAWA, K., KATAOKA, K., BABA, Y., Nano-spheres for DNA separation chips. *Nat. Biotechnol.* **2004**, *22*, 337–340.
- 35 MUCIC, R. C., STORHOFF, J. J., MIRKIN, C. A., LETSINGER, L., DNA-directed synthesis of binary nanoparticle network materials. *J. Am. Chem. Soc.* **1998**, *120*, 12674–12675.
- 36 MORI, H., SENG, D. C., ZHANG, M., MÜLLER, A. H. E., Hybrid nanoparticles with hyperbranched polymer shells via self-condensing atom transfer radical polymerization from silica surfaces. *Langmuir* **2002**, *18*, 3682–3693.
- 37 MORI, H., SENG, D. C., LECHNER, H., ZHANG, M., MÜLLER, A. H. E., Synthesis and characterization of branched polyelectrolytes. 1. Preparation of hyperbranched poly(acrylic acid) via self-condensing atom transfer radical copolymerization. *Macromolecules* **2002**, *35*, 9270–9281.
- 38 MORI, H., MÜLLER, A. H. E., KLEE, J. E., Intelligent colloidal hybrids via reversible pH-induced complexation of polyelectrolyte and silica nanoparticles. *J. Am. Chem. Soc.* **2003**, *125*, 3712–3713.
- 39 KAMATA, K., LU, Y., XIA, Y., Synthesis and characterization of monodispersed core-shell spherical colloids with movable cores. *J. Am. Chem. Soc.* **2003**, *125*, 2384–2385.
- 40 VERTEGEL, A. A., SIEGEL, R. W., DORDICK, J. S., Silica nanoparticle size influences the structure and enzymatic activity of adsorbed lysozyme. *Langmuir* **2004**, *20*, 6800–6807.
- 41 AKAGI, T., KAWAMURA, M., UENO, M.,



- HIRAIISHI, K., ADACHI, M., SERIZAWA, T., AKASHI, M., BABA, M., Immunization with inactivated HIV-1-capturing nanospheres induces a significant HIV-1-specific vaginal antibody response in mice. *J. Med. Virol.* **2003**, *69*, 163–172.
- 42 KANEKO, T., SHIMOMAI, S., MIYAZAKI, M., BABA, M., AKASHI, M., IgG responses to intranasal immunization with cholera toxin-immobilized polymeric nanospheres in mice. *J. Biomater. Sci. Polym. Edn.* **2004**, *15*, 661–669.
- 43 ANDERSSON, M., ELIHN, K., FROMELL, K., CALDWELL, K. D., Surface attachment of nanoparticles using oligonucleotides. *Colloids Surf. B: Biointerfaces* **2004**, *34*, 165–171.
- 44 INOUE, Y., WATANABE, J., TAKAI, M., ISHIIHARA, K., Surface characteristics of block-type copolymer composed of semi-fluorinated and phospholipid segments synthesized by living radical polymerization. *J. Biomater. Sci. Polym. Edn.* **2004**, *15*, 1153–1166.
- 45 INOUE, Y., WATANABE, J., ISHIIHARA, K., Dynamic motion of phosphorylcholine groups at the surface of poly(2-methacryloyloxyethyl phosphorylcholine-random-2,2,2-trifluoroethyl methacrylate). *J. Colloid Interface Sci.* **2004**, *274*, 465–471.
- 46 FENG, W., BRASH, J., ZHU, S., Atom-transfer radical grafting polymerization of 2-methacryloyloxyethyl phosphorylcholine from silicon wafer surfaces. *J. Polym. Sci. Part A: Polym. Chem.* **2004**, *42*, 2931–2942.
- 47 INOUE, Y., WATANABE, J., TAKAI, M., ISHIIHARA, K., Regulation of nano-surface properties by finely synthesized fluorinated phosphorylcholine polymers. *Trans. Mater. Res. Soc. Jpn.* **2004**, *29*, 181–184.
- 48 ISHIIHARA, K., ISHIKAWA, E., IWASAKI, Y., NAKABAYASHI, N., Inhibition of cell adhesion on the substrate by coating with 2-methacryloyloxyethyl phosphorylcholine polymers. *J. Biomater. Sci. Polym. Edn.* **1999**, *10*, 1047–1061.
- 49 ISHIIHARA, K., FUKUMOTO, K., IWASAKI, Y., NAKABAYASHI, N., Modification of polysulfone with phospholipid polymer for improvement of the blood compatibility. Part 1. Surface characterization. *Biomaterials* **1999**, *20*, 1545–1551.
- 50 OGAWA, R., IWASAKI, Y., ISHIIHARA, K., Thermal properties and processability of elastomeric polymer alloy composed of segmented polyurethane and phospholipid polymer. *J. Biomed. Mater. Res.* **2002**, *62*, 214–221.
- 51 YE, S. H., WATANABE, J., IWASAKI, Y., ISHIIHARA, K., Novel cellulose acetate membrane blended with phospholipid polymer for hemocompatible filtration system. *J. Membr. Sci.* **2002**, *210*, 411–421.
- 52 IWASAKI, Y., NAKABAYASHI, N., ISHIIHARA, K., Preservation of platelet function on 2-methacryloyloxyethyl phosphorylcholine graft polymer compared to various water-soluble graft polymers. *J. Biomed. Mater. Res.* **2001**, *57*, 74–79.
- 53 FURUZONO, T., ISHIIHARA, K., NAKABAYASHI, N., TAMADA, Y., Chemical modification of silk fibroin with 2-methacryloyloxyethyl phosphorylcholine I. Graft-polymerization onto fabric using ammonium persulfate and interaction between fabric and platelets. *J. Appl. Polym. Sci.* **1999**, *73*, 2541–2544.
- 54 ISHIIHARA, K., IWASAKI, Y., NAKABAYASHI, N., Polymeric lipid nanosphere constituted of poly(2-methacryloyloxyethyl phosphorylcholine-co-n-butyl methacrylate). *Polym. J.* **1999**, *31*, 1231–1236.
- 55 KONNO, T., WATANABE, J., ISHIIHARA, K., Conjugation of enzymes on polymer nanoparticles covered with phosphorylcholine groups. *Biomacromolecules* **2004**, *5*, 342–347.
- 56 TAKEI, K., KONNO, T., WATANABE, J., ISHIIHARA, K., Regulation of enzyme-substrate complexation by phospholipid polymer conjugates for cell engineering. *Biomacromolecules* **2004**, *5*, 858–862.
- 57 PARK, J.-W., KUROSAWA, S., WATANABE, J., ISHIIHARA, K., Evaluation of novel 2-methacryloyloxyethyl phosphorylcholine (MPC) polymeric nanoparticles for immunoassay of C-reactive

- protein detection. *Anal. Chem.* **2004**, *76*, 2649–2655.
- 58 WATANABE, J., ISHIHARA, K., Highly efficient sequential enzymatic reaction on bio-conjugate phospholipid polymer nanoparticles. *Kobunshi Ronbunshu* **2004**, *61*, 547–554.
- 59 KIRITOSHI, Y., ISHIHARA, K., Preparation of cross-linked poly(2-methacryloyloxyethyl phosphorylcholine) gel and its strange swelling behavior in water/ethanol mixture. *J. Biomater. Sci. Polym. Edn.* **2002**, *13*, 213–224.
- 60 FAROKHZAD, O. C., JON, S., KHADEMOSSEINI, A., TRAN, T.-N. T., LAVAN, D. A., LANGER, R., Nanoparticle-aptamer bioconjugates: a new approach for targeting prostate cancer cells. *Cancer Res.* **2004**, *64*, 7668–7672.
- 61 VERONESI, B., WEI, G., ZENG, J.-Q., OORTGIESEN, M., Electrostatic charge activates inflammatory vanilloid (VR1) receptors. *Neuro Toxicol.* **2003**, *24*, 463–473.
- 62 WHICHER, J., BIASUCCI, L., RIFAI, N., The acute phase response and atherosclerosis. *Clin. Chem. Lab. Med.* **1999**, *37*, 495–503.
- 63 PENTIKANEN, M. O., OORNI, K., ALAKORPELA, M., KOVANEN, P. T., Trigger of atherosclerosis and inflammation in the arterial intima. *J. Intern. Med.* **2000**, *247*, 359–370.
- 64 RIDKER, P. M., CUSHMAN, M., STAMPFER, M. J., TRACY, R. P., HENNEKENS, C. H., Plasma concentration of C-reactive protein and risk of developing peripheral vascular disease. *Circulation* **1998**, *97*, 425–428.
- 65 HAVERKATE, F., THOMPSON, S. G., PYKE, S. D. M., GALLIMORE, J. R., PEPYS, M. B., Production of C-reactive protein and risk of coronary events in stable and unstable angina. *Lancet* **1997**, *349*, 462–466.
- 66 DIAMANDIS, E. P., Analytical methodology for immunoassays and DNA hybridization assays-current status and selected systems. *Clin. Chim. Acta* **1990**, *194*, 19–50.
- 67 ACETI, A., PENNICA, A., TEGGI, A., GRILLI, A., CAFERRO, M., CELESTINO, D., LERI, O., SEBASTIANI, A., DE ROSA, F., The serological diagnosis of human hydatid disease by time-resolved fluoroimmunoassay. *J. Infect.* **1991**, *22*, 135–141.
- 68 MOLINA-BOLIVAR, J. A., GALISTEO-GONZALEZ, F., HIDALGO-ALVAREZ, R., Fractal aggregates induced by antigen-antibody interaction. *Langmuir* **2001**, *17*, 2514–2520.
- 69 VELEV, O. D., KALER, E. W., In situ assembly of colloidal particles into miniaturized biosensors. *Langmuir* **1999**, *15*, 3693–3698.
- 70 BUNDY, J., FENSELAU, C., Lectin-based affinity capture for MALDI-MS analysis of bacteria. *Anal. Chem.* **1999**, *71*, 1460–1463.
- 71 PEREZ-AMODIO, S., HOLOWNIA, P., DAVEY, C. L., PRICE, C. P. Effect of the ionic environment, charge, and particle surface chemistry for enhancing a latex homogeneous immunoassay of C-reactive protein. *Anal. Chem.* **2001**, *73*, 3417–3425.
- 72 LU, D. R., LEE, S. J., PARK, K., Calculation of solvation interaction energies for protein adsorption on polymer surfaces. *J. Biomater. Sci. Polym. Edn.* **1991**, *3*, 127–147.
- 73 KITANO, H., SUDO, K., ICHIKAWA, K., IDE, M., ISHIHARA, K., Raman spectroscopic study on the surface of water in aqueous polyelectrolyte solutions. *J. Phys. Chem. B* **2002**, *104*, 10425–10429.
- 74 KITANO, H., IMAI, M., MORI, T., IDE, G., YOKOYAMA, Y., ISHIHARA, K., Structure of water in the vicinity of phospholipid analogue copolymers as studied by vibrational spectroscopy. *Langmuir* **2003**, *19*, 10260–10266.

## 6 Bifunctionalization of Metallic Nanoparticles and Microarrays for Biomolecular Detection

*Grit Festag, Uwe Klenz, Thomas Henkel, Andrea Csáki, and  
Wolfgang Fritzsche*

### 6.1 Introduction

Characterization of molecular interactions represents a core technology for today's biomedical research. The specific binding of bioactive compounds to certain pathogens, the discovery of novel pathways in the cell, or the early detection of low numbers of disease-related molecules are examples of the wide application of biomolecular detection. With the ongoing elucidation of the molecular bases for life processes, a further demand for testing the presence and, eventually, the quantity of molecules of interest is expected. One interesting development is the field of point-of-care (POC) diagnostics that describes the application of biomolecular detection outside the dedicated laboratory and near the patient, such as in the medical practice. Other applications with similar technical requirements are, for example, the testing for toxic organisms in food processing factories or the detection of pathogens in air conditioning systems. This set of applications requires a highly robust technology, both regarding a minimized maintenance and stability against users not trained as laboratory personnel. It includes a signal that is easily transformed into results, without the need for user input or extended processing. The decentralized character of this approach asks for cost-efficiency of detection equipment that has to be provided in large quantity. The resulting need for miniaturization is matched by the general development towards minimal sample liquid volume. Although sample holders with several thousands of detection sites have been described already for gene expression chips, typical analytical questions for POC diagnostics will be limited to a handful of parallel tests. Moreover, the highly-developed fluorescence readers needed for the readout of expression chips are hardly suitable for POC applications due to their high costs and complicated detection setup.

What measurement principles are best suited for this novel field in bioanalytics? The demonstration of DNA-conjugated metal nanoparticles [1, 2] was the starting point for a novel family of detection techniques based on these particles. These particles allowed for various elegant detection schemes with sensitivities comparable or even better than for fluorescence-based assays. Surprisingly, the – in comparison

to fluorescent dyes – large mass of the particles does not interfere with the specificity of the binding of the conjugated molecules. In certain applications they even enhance the specificity compared with fluorescence assays [3].

This chapter describes the application of biofunctionalized nanoparticles for biomolecular detections. The first section describes application aspects, including typical assay formats, array fabrication, and the numerous detection schemes established. The most important types of nanoparticles (regarding their composition) are introduced in Section 6.2.1. The following section describes the synthesis of metal particles. Particle biofunctionalization represents the key step for an integration of the nanoparticles into biological assays. The various bioconjugation approaches regarding gold nanoparticles are introduced in Section 6.2.3.1 for DNA and Section 6.2.3.2 for proteins. Other metal nanoparticles follow in Section 6.2.3.3. Section 6.2.4 gives the outlook for further applications of bioconjugated particles.

Although biofunctionalized particles are important for assays, substrates modified with capture molecules are often required to realize chip-based detection with its potential for miniaturization as well as parallelization. Such substrates usually exhibit self-assembled monolayers to bind the capture molecules (Section 6.3.1.1). For a typical system, optimization, regarding blocking of undesired unspecific interactions, is required (Section 6.3.1.2). Beside molecular layers, nanoporous gels provide another interesting option for efficient binding of capture molecules (Section 6.3.2). This chapter concludes with an outlook (Section 6.4) that forecasts future developments.

### 6.1.1

#### **Applications**

Nanotechnologies extend the limits of molecular diagnostics to the nanoscale and offer a broad spectrum of potential applications in molecular diagnostics, as summarized by Jain [4]. Beside technologies such as nanowires or nanopores, we will focus on nanoparticle technologies using, especially, gold nanoparticles as labels for biomolecule probes.

A typical assay in biomolecular detection probes the presence of target molecules by using capture molecules that are complementary to the targets. These capture molecules bind the target, and this binding is detected using labels that are either attached to the targets (e.g. by PCR in the case of DNA or RNA) or added by another binding molecule in a kind of sandwich assay (Fig. 6.1). Capture probes attached to solid substrates are easily incubated and washed. Moreover, by using separate binding spots for various capture probes, the assay can be multiplexed with only minimal sample volume requirement.

### 6.1.2

#### **Array Fabrication**

The need for analytical methods that can deal with many probes, and, ideally, analyze all of them together, led to the development of so-called microarrays or bio-

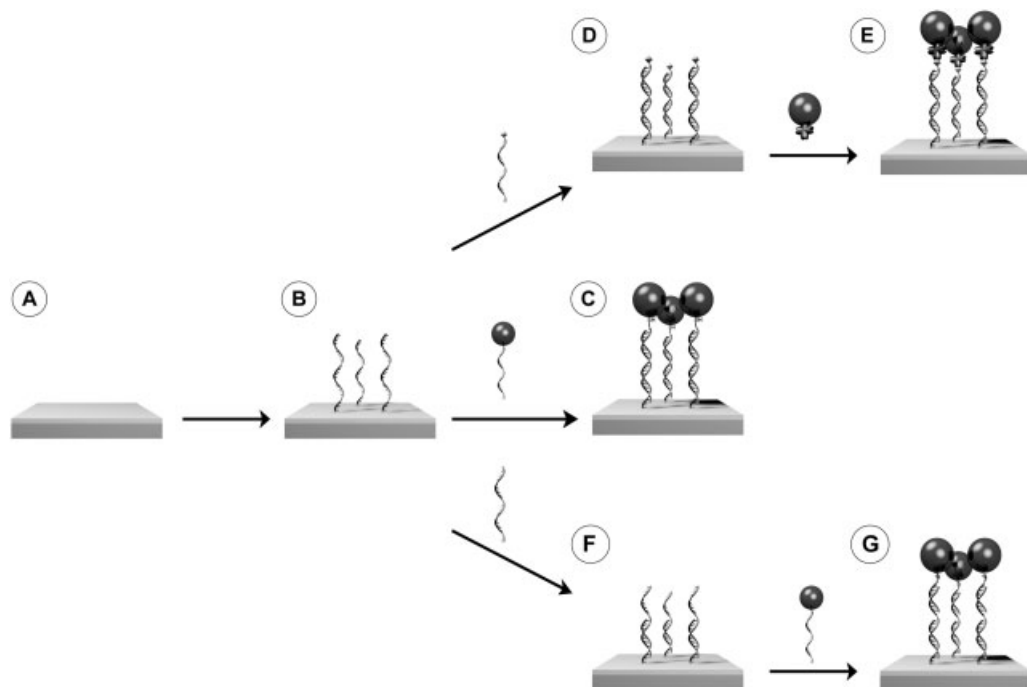


**Fig. 6.1.** Microarray-based, sequence-specific DNA detection with gold nanoparticle labels. (A) Solid substrate, functionalized for binding of capture probes. (B) Covalent attachment of capture-oligonucleotides. (C)–(E) For the direct detection scheme, the target probes have to be labeled prior to hybridization. (C) Hybridization of DNA target strands labeled with gold nanoparticles or (D) biotin molecules. (E) Labeling of the biotin-tagged targets with streptavidin-modified nanoparticles. (F) In the indirect approach (sandwich), the unlabeled target strands are hybridized to the capture strands first, (G) followed by an additional hybridization with labeled DNA probes.

chips, which enable massive parallel mining of biological data, multiplexing, and automation in a miniaturized format [5]. The particular strength of array analysis results from the highly redundant measurement of many parallel biomolecular hybridization or recognition events, which leads to an extraordinary level of assay validation [6, 7].

DNA microarrays can be fabricated by two strategies. In the first approach, the on-chip (*in situ*) synthesis of capture oligonucleotides at defined places provides high yields of capture probes that are consistent over the surface of the support. It permits combinatorial strategies for the fabrication of large oligonucleotide arrays. In the second strategy, an off-line approach in which pre-synthesized oligonucleotides have been deposited onto the substrate (*ex situ*), available in most biology laboratories, enables assessment of the capture probes before they are attached to the surface. Deposition is also the method of choice for long sequences as PCR products. When many arrays are needed with the same probes, deposition may be more economical than *in situ* synthesis.

### 6.1.3

#### Detection Methods

Different applications of metal nanoparticles for biomolecular detection are favored by their multi-purpose possibility of signal development.

The most common characterization techniques of metal nanoparticles are high-resolution transmission electron microscopy (HRTEM) as well as scanning tunneling microscopy (STM), atomic force microscopy (AFM), small-angle X-ray scattering, and X-ray diffraction [8]. For paralleled assays in microarray format, electrical/electrochemical and optical methods are preferred, such as optical absorbance as well as optical scattering, surface plasmon resonance (SPR) imaging, and surface-enhanced Raman spectroscopy (SERS).

##### 6.1.3.1 Optical Absorbance

Imaging the optical absorbance of surface-bound particles is probably the simplest method for analyzing nanoparticle-labeled DNA at surfaces. The extinction coefficient of metal nanoparticles can exceed those of organic dyes by many orders of magnitude, which has been explained by the collective resonance of conduction electrons in the metal (surface plasmon resonance, SPR, [9–11]). An important enabling step for DNA labeling by nanoparticles was the development of a method in 1996 that allowed the direct oligonucleotide modification of gold nanoparticles [1, 2]. This enabled a simple optical characterization by monitoring a color change during hybridization events of two complementary DNA–nanoparticle complexes in solution. Solutions of gold nanoparticle aggregates with interparticle distances larger than the average particle size appear red. But when biomolecular recognition events lead to significantly decreased interparticle spacings the solution turns blue, which is detectable in a spectral shift. The dependency on interparticle spacing was also used in colorimetric, heterogeneous biomolecule detection schemes on thin-layer chromatography plates [12]. By using solid supports the color differentiation was enhanced; this is attributable to increased aggregation of the pre-organized DNA-linked nanoparticles upon drying the solution on the support, which also prevented samples (heated above the DNA dissociation temperature) from re-hybridizing. Thus, a permanent record of the test could be obtained. Furthermore, gold nanoparticle-labeled probes exhibited characteristic, exceptionally sharp “melting transitions” compared with those of fluorophore-labeled targets, which allows the discrimination of even small DNA sequence defects. By aligning the oligonucleotides in a “tail-to-tail” [13] rather than “head-to-tail” fashion on the nanoparticles the sensitivity could be further improved, and it was even possible to distinguish target sequences with single nucleotide polymorphisms from the fully complementary target. The altered melting profiles yielded a selectivity that was over three times higher than that observed for fluorophore-labeled targets [3]. The absorbance signal of the surface-bound gold nanoparticles could be further amplified by autocatalytic deposition of silver metal [14]. Such silver enhancement leads to a growth of the gold nanoparticles (Fig. 6.2) and makes the nanoparticle-based assays readable by simple flatbed scanners. The sensitivity of this scanomet-

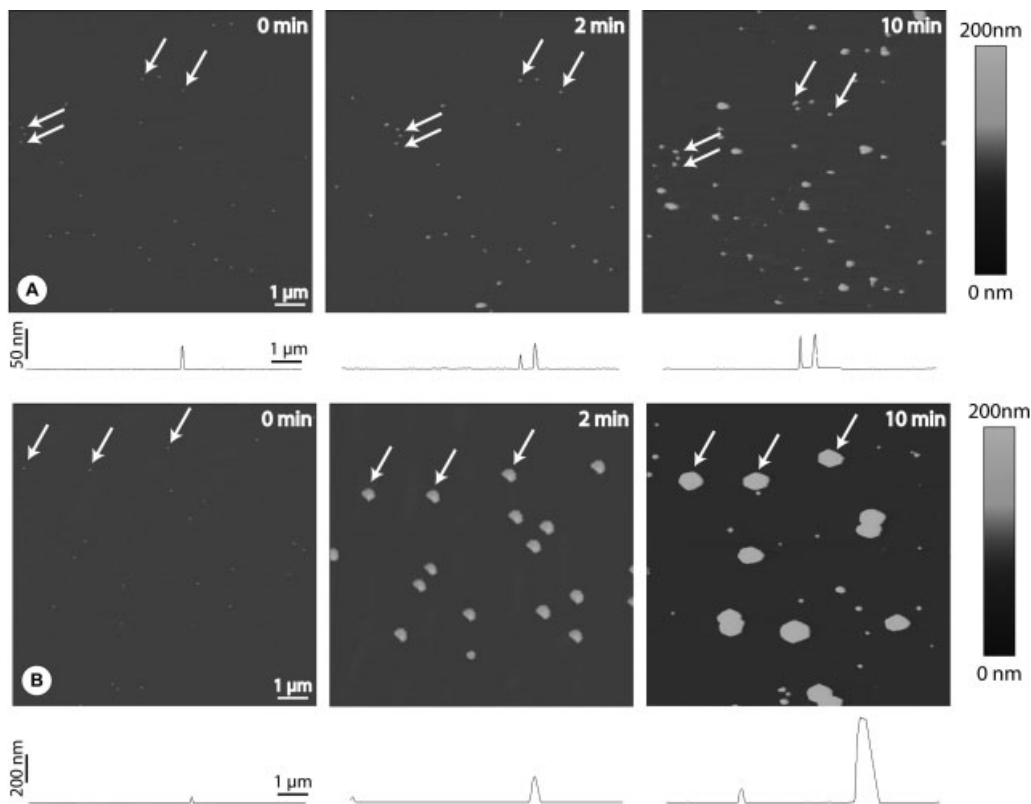


**Fig. 6.2.** Metal enhancement of gold nanoparticles by a stepwise electroless deposition of silver. Atomic force microscopy (AFM) images and their corresponding section analyses show the growth of single 30 nm-sized gold nanoparticles after 0, 2 and 10 min enhancement time, as examples. For orientation, selected particles are marked by

arrows through the experiments. (A) Slowly growing particles by a homemade silver acetate/hydroquinone silver enhancement solution (average height of 31, 38 and 48 nm, respectively). (B) Fast growing particles by means of a commercial silver enhancement kit (Silver Enhancement Solution™, British Biocell) (31, 130, and 442 nm, respectively).

ric array detection exceeds that of analogous fluorophore systems by two orders of magnitude (50 fM vs. 5 pM, respectively) [3].

Microstructured biochips were introduced in this field to monitor the binding of nanoparticle-labeled target DNA to arrayed capture DNA probes by both reflected and transmitted light [15]. Moreover, the authors found that the intensity of reflected light directly relates to the number of bound particles and to the concentration of hybridizable targets in solution.

Beside the large extinction coefficient there is a just as huge scattering coefficient that enables extremely sensitive imaging and quantification of nanoparticle-tagged biomolecules by scattered light. This was shown for selenium nanoparticle-antibody conjugates that – bound to biotinylated target DNA – could be imaged by

scattering light in an evanescent field [16]. The use of an internally reflecting waveguide allows for measurement of real-time binding or melting of a light-scattering label of a DNA array.

As well as for the optical absorbance, the spectrum and intensity strongly depends on the size, shape, and material composition of the nanoparticles. Thus, the use of different-sized gold nanoparticles as scattering labels results in different colors of scattered light, e.g. green-scattering 50 nm and orange-scattering 100 nm particles [17].

Li and Rothberg introduced a completely different approach by designing – in combination with gold nanoparticles – a novel fluorescent assay for DNA hybridization based on the electrostatic properties of DNA without the need for probe or surface modification [18]. The fluorescence of single-stranded dye-tagged DNA was efficiently quenched when the DNA probes had bound to gold nanoparticles, whereas double stranded DNA refused to adsorb to the particles (Section 6.2.3.1). Hence, these hybridization events could be measured indirectly as fluorescence signals.

#### 6.1.3.2 SPR Imaging

In the past decade, SPR methods have contributed significantly to the sensing and quantification of biomolecule interactions; four emerging application areas have been identified: food analysis, proteomics, immunogenicity, and drug discovery [19]. SPR biosensors enable the measurement of analyte binding to immobilized biomolecules without using labels. The first SPR biosensor, introduced by Biocore AB in 1990, can detect protein–protein interactions and, moreover, was combined with miniaturized flow systems for efficient sample delivery to the sensor surface. Since it was possible to reproducibly self-assemble gold nanoparticles from solution onto glass surfaces – functionalized with amine or thiol groups – new SPR biosensors were developed that enable label-free optical detection in a chip-based format [20]. In a typical SPR spectroscopy setup a laser beam is aimed at the back of a substrate. Although even subtle changes in the refractive index at the surface of the substrate result in changes of its resonant reflection angle, nanoparticles bound to the sensed analytes increase the shifts in deflection angles, leading to a considerably elevated detection sensitivity [21].

#### 6.1.3.3 Raman Scattering

The enhancement of optical signals by metal nanoparticles is also exploited at detection by Raman scattering [22, 23]. Especially, silver and gold nanoparticles are extremely effective at enhancing the scattering signal from adsorbed, Raman-active molecules. Thus, it was possible to detect different DNA target molecules by the use of DNA probes simultaneously labeled with both Raman-active ligands and nanoparticles by Raman spectroscopy [24]. The microarray format included capture DNA strands immobilized on a chip and, thereafter, incubated with target probes. Gold nanoparticles modified with Cy3-labeled, alkylthiol-capped oligonucleotides were used to monitor the presence of specific target DNA strands.



Initially, the nanoparticle probes were not visible to the naked eye, and no Raman signal was detectable. The authors assumed a lack of electromagnetic-field enhancement for the nanoparticles due to the large nanoparticle spacings compared with closely spaced gold nanoparticles that were shown to give a surface-enhanced Raman scattering (SERS) enhancement [25]. But, in contrast to the undeveloped particles, silver enhancement of the bound DNA-nanoparticle probes resulted in the growth of an Ag layer around each Cy3-labeled nanoparticle probe, thereby leading to large Raman scattering enhancements with an unoptimized detection limit of 20 fM target concentration.

#### 6.1.3.4 Electrical Detection

In addition to these versatile optical detection schemes metal nanoparticles offer the possibility for an electrical readout. Owing to their conductivity, it seems self-evident to use them as a conductive bridge between two electrical leads. This can be used in DNA detection schemes by immobilizing capture oligonucleotides in a gap between two electrodes and a subsequent labeling with gold nanoparticles. Möller et al. were able to hybridize complementary, gold-nanoparticle-tagged oligonucleotides to the surface-bound capture DNA between two microstructured electrodes [26]. An additional silver enhancement step makes the bound nanoparticles grow and come into contact, thereby bridging the gap. The resulting drop of resistance was measured by an integrated measurement system consisting of a 'DNA chip reader' with an embedded PC [27] (Fig. 6.3). The microstructured chip had 42 1  $\mu\text{m}$ -wide electrode gaps, each independently accessible and simultaneously read out. The system is transportable, autonomously working and therefore also suitable for readout outside the laboratory. It could detect 5  $\mu\text{M}$  of target DNA concentration. Park et al. have described a similar resistive system with which they could detect target DNA down to 500 fM as well as single-nucleotide polymorphisms with a selectivity of up to  $10^5:1$  without a thermal-stringency wash [28].

By depositing biofunctionalized nanoparticles on electrode arrays Campas et al. were recently able to measure the hybridization efficiency by amperometry [29]. They achieved significant differences in current density between complementary and mutated oligonucleotide sequences. Similarly, electrodeposition of enzyme-modified colloidal gold on electrodes provided a proof-of-principle concept for enzymatic multisensors.

#### 6.1.3.5 Electrochemical Detection

Other approaches used colloidal gold labels in novel, sensitive electrochemical sensors [30]. After oxidative gold metal dissolution under acidic conditions the resulting aqueous metal ions were detected by anodic stripping voltammetry (ASV). Dequaire et al. used disposable carbon-based electrodes and evaluated the method for a noncompetitive heterogeneous immunoassay of an immunoglobulin G with a detection limit of 3  $\mu\text{M}$  [30]. In addition, ASV has been assigned to an electrochemical DNA detection method [31]. The combination of sensitive gold(III) determination at screen-printed microband electrodes with the large number of gold(III) ions released from each gold particle allowed detection of as low as 5  $\mu\text{M}$  amplified

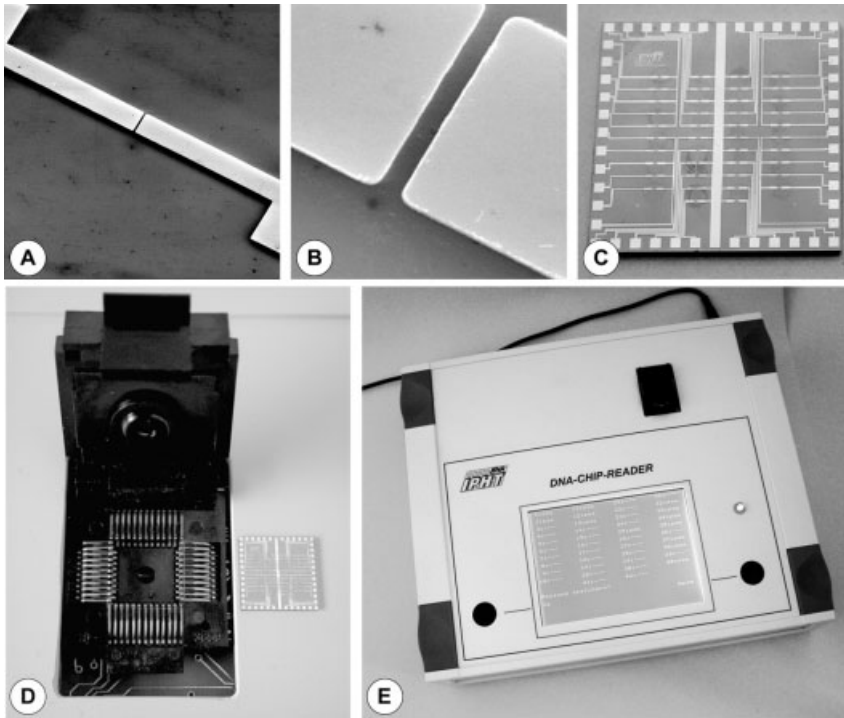


**Fig. 6.3.** Electrical detection of gold nanoparticle-labeled DNA. DNA strands ('captures') that bind the molecules of interest ('targets') are immobilized between microstructured electrode gaps on a chip. If any complementary target DNA is present, the target molecules, labeled with gold nanoparticles, will bind and form the starting point of subsequent metal enhancement steps. The resulting metal layer is detected by a

significant drop in electrical resistivity between the electrodes. (A) Gold electrodes 10  $\mu\text{m}$  wide were used to create gaps. (B) The zoom visualizes the details of one of the 1  $\mu\text{m}$  gaps on the silicon oxide substrate. (C) Overview showing the half-inch chip. (D) DNA chip socket of the paralleled readout system. (E) The portable DNA chip reader. (Modified after Ref. [27].)

DNA fragment. Both an advanced magnetic processing technique and a deposition of gold onto the immobilized gold labels increased the sensitivity of the system by forcing DNA duplex isolation and increasing the number of gold atoms for the oxidation, respectively [32]. The use of different nanoparticles (PbS, CdS, ZnS) with different redox potentials enabled Wang et al. to establish a multilabel system, where every nanoparticle species encodes a different DNA sequence and can be selectively identified by ASV [33]. Using voltammetry makes the integration of a higher number of probes on one substrate problematic. Although Ozsoz et al. did not address the question of microarray formats, their use of differential pulse voltammetry would be appropriate for direct simultaneous detection of many nanoparticle probes at arrayed microelectrodes [34].

#### 6.1.3.6 Gravimetric

Beside their advantageous optical and electrical properties, metal nanoparticles have a high specific mass that can be exploited in detection schemes based on gravimetric principles, as has been shown for both quartz-crystal-microbalances (QCMs) and oscillating microcantilevers. Extremely small mass changes at the oscillating surface cause characteristic changes in the frequency of nanomechanical resonator detectors.

Okahata et al. even reported binding kinetics of a protein to double stranded DNA immobilized on a QCM [35]. Metallic nanoparticles also enhance the sensitivity of gravimetric DNA sensors, up to a picomolar range, when using them as DNA labels [36]. A further increase, up to femtomolar sensitivities, was obtained either by hybridizing a second layer of nanoparticles to the first one [37] or by additional gold deposition on the nanoparticle labels [38].

Conversely, cantilever-based optical deflection assays were able to discriminate DNA single-nucleotide mismatches even without the need for external labeling. In these approaches the microcantilevers were functionalized with capture molecules. A subsequent biomolecule recognition reaction could be detected due to the induced deflection of the cantilever [39]. While hybridization of complementary target oligonucleotides resulted in net positive deflection, targets containing one or two internal mismatches caused net negative deflection. According to Thundat and colleagues, this cantilever approach can be adapted to high-throughput array formats providing distinct positive/negative signals for an easy interpretation of DNA hybridization. Moreover, Gimzewski and co-workers extended these oligonucleotide hybridization assays on individual cantilevers to cantilevers in an array [40]. The differential deflection of the cantilevers provided true molecular recognition signals despite the nonspecific responses of individual cantilevers. Beside the detection of oligonucleotide hybridization, the general applicability to biomolecular processes was demonstrated by monitoring molecular recognition between proteins as well.

## 6.2

### **Nanoparticles and their Biofunctionalization**

Colloidal nanoparticles differ from bulk material due to their large surface-to-volume ratio. Since inorganic nanoparticles show interesting – strongly size-dependent – optical, electrical, magnetic, and/or electrochemical properties, they offer many opportunities in biological applications. Some of these will be described subsequently. Reference [41] reviews the different physical characteristics of metal nanoparticles and their implementation in assays.

The intense optical absorption of metal colloids is due to the collective electronic (or plasmon) resonance and is defined by the nanoparticle material, size, and geometry. Consequently, not only the size but also their shape plays an important role.

## 6.2.1

### Types of Nanoparticles used for Biomolecular Detection

#### 6.2.1.1 Metal Nanoparticles

Metal nanoparticles are dispersions of a solid phase in a liquid phase, mostly as metal colloids with dimensions of nm to  $\mu\text{m}$  (Au [42], Ag [43], [44], Pt [45], Pa [46], Cu, Fe, and Hg [47]). The most important metal particles are gold and silver sols synthesized from metal salts. Gold particles are composed of a starting atom surrounded by a defined quantity of gold-atoms, magic numbers corresponding to the formula  $[10n^2 + 2]$  [8, 48], where  $n$  is the number of layers in the particle. The minimum size of these colloid particles is 13 atoms. Such particles are close to icosahedrons or dodecahedrons [49], approximating to spheres with increasing diameter.

#### 6.2.1.2 Core/Shell Particles

Metal core/shell nanoparticles also have interesting optical properties. Heterogenic bimetallic nanoparticles exhibit two plasmon resonances, appropriate to the electronic bands of the pure elements (of both the core and the shell metal phases) [49]. The optical properties of such nanoparticles are explained by the Mie theory for cladded particles [50, 51]. Compared with heterogeneous species, homogenous bimetallic nanoparticles, synthesized, for example, by alloying under laser irradiation, exhibit only one surface plasmon peak, which lies between the absorption bands of the pure metals [49]. Bimetallic (mostly heterogeneous) nanoparticles also play an important role in biomolecular detection when Raman-active ligands are used [24].

Furthermore, pure metal nanoparticles have some disadvantages concerning their chemical stability or when used in different solvents. To prevent particle coalescence, colloids can be coated with a dielectric shell, e.g. a silica shell. Liz-Marzán et al. have used silane coupling agents as surface primers to make the particle surface vitreophilic, followed by self-assembly of a hydrated silica monolayer [43]. Thus, the resulting silica surface enables the same bioconjugation strategies as for silica nanoparticles. This has been summarized recently by Drake et al. [52].

After surface modification the inert metal core/dielectric shell nanoparticles could be transferred into practically any solvent. The thickness of the optically transparent silica layer could be determined in a controlled way. Varying the silica shell thickness and the refractive index of the surrounding solvent allowed control over the dispersions' optical properties. For example, the intensity of the plasmon bands of such nanoparticles depends on the shell thickness. With increasing silica shell thickness, up to a defined size, the intensity of the plasmon band increased and, simultaneously, the absorption peak shifted to longer wavelengths (redshift) due to the increased local refractive index around the particles. However, above the defined layer thickness of 80 nm scattering becomes significant, resulting in a strong increase in absorbance at shorter wavelengths (blue-shift), which is similar to the properties of gold-free silica particles. The same results were caused by (bio-)polymeric adsorption onto the metal particle surface. The polymeric shell

also changed the geometric and dielectric parameters of the particles [53]. Moreover, the dependence of variations in extinction and light scattering spectra on the gold core diameter, the shell refractive index and thickness could adequately be described by the dipole approximation of the Mie theory.

Another type of nanoparticle composite consists of a metal shell encapsulating a dielectric core [54]. The optical properties of such monodisperse silica nanoparticles (so-called Stöber particles [55]) can be influenced by covering the particles with a thin, uniform metallic shell. Keeping the size of the dielectric core constant, the optical absorption shift is relatively sensitive to the shell thickness. Assuming a constant core/shell size ratio it depends on the absolute size whether the particles absorb or scatter light [56]. Implementation of such nanoshells in living tissue and application of near-infrared light can photothermally destroy the labeled cells [57].

#### 6.2.1.3 **Magnetic Nanoparticles**

Magnetic nanoparticles are mostly compounds with iron oxides ( $\text{Fe}_3\text{O}_4$ /magnetite and  $\gamma\text{-Fe}_2\text{O}_3$ /maghemite) and are, therefore, not pure metal particles. However, they are mentioned here because they are also powerful, versatile nanoscaled tools in biology and medicine. There are two types of magnetic particles: (1) so-called magnetic beads containing nm-sized iron oxide particles surrounded by a polymer-silica matrix and (2) pure metal oxide particles in the nm-range (real nanoparticles, strictly speaking). Suspensions of small ferrimagnetic single-domain iron oxide particles are called ferrofluids and can be used for medical applications if biocompatible. Functionalization of these magnetic beads or nanoparticles, respectively, enables the binding of protein or DNA and, therefore, their application in biomolecular detection and their potential use in medical diagnostics and therapies, e.g. in thermal tumor treatment (magnetic hyperthermia [58]) where only biocompatible magnetic nanoparticles are usable. For many diagnostic applications both magnetic beads and nanoparticles are usable. Thus, they are employed as contrast agents in magnetic resonance imaging (MRI) as well as in detecting biomolecular binding events by means of magnetic sensors. Magneto-resistive detection methods exploit the fact that an applied magnetic field, e.g. due to magnetic particles attached to the sensor, causes a shift in electric resistivity [59–62]. Additionally, the magnetic separation of biomolecules attached to magnetic beads is a standard laboratory method. Thus, Ho et al. employed antibody-presenting magnetic nanoparticles as effective affinity probes for selectively concentrating traces of target bacteria from sample solutions [63].

#### 6.2.1.4 **Quantum Dots**

Quantum dots are nanocrystals of cadmium chalcogenides (CdS, CdSe, CdTe), in the range of 200–10 000 atoms, that exhibit strongly size-dependent optical and electrical properties [64]. Irradiated with low-energy light of a broad, continuous excitation spectrum, semiconductor nanocrystals have a narrow, tunable emission spectrum, and, moreover, they are photochemically stable and therefore complementary, and in some cases perhaps even superior, to conventional fluorophores [65]. But, dependent on their size, the photoluminescence signal can consist of

the entire spectrum of visible light. This enables the excitation of different sizes of quantum dots at the same time and makes them suitable as luminescent probes for labeling of biological systems [4, 66, 67].

### 6.2.2

#### **Synthesis of Gold (Silver) Nanoparticles**

The method used most for the synthesis of gold (as well as other metal) nanoparticles is the reduction of metal salts by different reducing agents (organic acids [68], substituted ammonias [68, 69], formaldehyde [70], hydrogen peroxide, phosphorus [71], gases, protecting agents [72, 73], and electrical fields [74]. Gold colloids are mostly synthesized by the reduction of gold(III) salts, and, among these, the citrate reduction of  $\text{HAuCl}_4$  is the most common procedure [68], where sodium citrate acts both as a nucleating and reducing agent [47]. Initially, the citrate is oxidized to acetone dicarboxylic acid [49]. In the following step, gold ions become atoms by forming an intermediate complex and, thereafter, nucleation islands. The smallest island is composed of 13 gold atoms [75]. Further metal ions are reduced on the surface of such nucleation centers to give larger particles. The particle size (12–147 nm) is determined by the quantity of citrate ions [76]. The resulting polycrystalline, nearly spherical particles are polydispersed, showing a relatively uniform shape and homogeneous size distribution (standard deviations of 10–15%, depending on the particle diameter).

The stability of the citrate-reduced colloids is determined by the concentration of salt ions in the solution. A dielectric shell of charged ions keeps the particles apart, therefore stabilizing the solution against aggregation. Small changes in reaction conditions can make this shell partially unprotected, resulting in an irreversible coagulation of the colloid solution. By using different ligands during or after the synthesis the particles can be sterically stabilized (Section 6.2.3).

Another approach to synthesizing metal (gold) nanoparticles is the Brust–Schiffrin method, involving the phase transfer of a tetrachloroaurate complex from aqueous to organic solution, followed by reduction with sodium borohydride in the presence of a thiol-stabilizing ligand [72, 73, 77]. The resulting particles are smaller (1–3.5 nm) and more monodispersed than the citrate colloids.

Size control of gold nanoparticles by the use of different stabilizing agents depends on the ligand type and its properties [78]. For alkane thiol ligands the molar ratio of aurate to thiol influences the average particle size [79]. By using a multivalent alkane thiol stabilizer Yonezawa et al. obtained smaller, more monodisperse gold nanoparticles than with conventional monoalkanethiols, thereby enabling systematic size control with atomic precision [80].

### 6.2.3

#### **Biofunctionalization**

Colloidal metal particles can be modified either during or after particle synthesis. Similar to the formation of self-assembled monolayers (SAMs) on planar surfaces

(Section 6.3.1.1) the post-synthetic coupling of biomolecules to the particle surface occurs in various steps. First, the biomolecules bind through electrostatic interactions by displacing the surrounding citrate ions. Thereafter, a chemical bond between the ligand and the particle follows, e.g. a thiol-gold coupling.

#### 6.2.3.1 **Modification of Gold Nanoparticles with Oligonucleotides/DNA**

Oligonucleotides can be attached to metal nanoparticles in different ways. Since the resulting DNA-nanoparticle conjugates differ in oligonucleotide surface densities, the availability for hybridization to targets, and in the tendency to nonspecifically bind to surfaces, the attachment chemistry impacts significantly on their use in heterogeneous detection schemes [81]. Bioconjugate chemistry has been studied most intensively for gold nanoparticles. As they provide the simplest, most stable conjugation chemistry for oligonucleotides, we will focus on the biofunctionalization of colloidal gold (Fig. 6.4).

**Thiol, Di-, Trisulfide** Nuzzo et al. have shown that gold surfaces can be easily functionalized by free thiols and disulfides [82, 83]. Their adsorption studies of methanethiol and dimethyl disulfide showed a strong binding of both adsorbates to gold surfaces, with the bonding of disulfide being greatly favored, probably due to dissociation of the disulfide bond to give a stable surface thiolate. However, these oligonucleotide-gold conjugates lose activity as hybridization probes when soaked in solutions containing thiols, which displace the derivatized oligonucleotide from the gold surface. To overcome this drawback Letsinger et al. described a new steroid-cyclic disulfide anchoring group for binding oligonucleotides to gold surfaces [84]. The resulting nanoparticle conjugates kept their hybridization activity and were much more resistant to attack by a thiol than conventional gold conjugates that contain alkyl mono-thiol or acyclic disulfide linkers. The same authors subsequently reported that oligonucleotides connected to gold through three sulfur groups were even more stable than these dithiane conjugates, stabilizing gold particles even larger than 30 nm in diameter [85].

Gold nanoparticles are usually linked to oligonucleotides by a thiol at the 5' or 3' end of the oligonucleotide, leaving the nucleotides unobstructed for hybridization to their complements. However, dependent on oligonucleotide content, length, and coverage, DNA tends to adsorb nonspecifically to gold surfaces through the nucleotides, inhibiting hybridization [86, 87]. To prevent DNA surface adsorption, mixed monolayers of the thiol-derivatized probe and a spacer-thiol have been explored. On planar surfaces, mercaptohexanol (MCH) can orient the DNA perpendicularly and facilitate hybridization by displacing the non-covalent and nonspecific adsorption of thiolated DNA [88–90]. Park et al. considered MCH concentration and reaction time as a key to controlling the conformation changes of oligonucleotides attached to gold nanoparticles [91]. With increasing MCH concentration (1  $\mu\text{M}$ –1 mM) the electrophoresis mobility of the Au-DNA conjugates slightly decreased towards those of gold nanoparticles without DNA attached, but stabilized by BPS [bis(*p*-sulfonatophenyl)phenylphosphine dihydrate, dipotassium salt]. This result points to a stepwise loss of surface-bound oligonucleotides, which suggests that

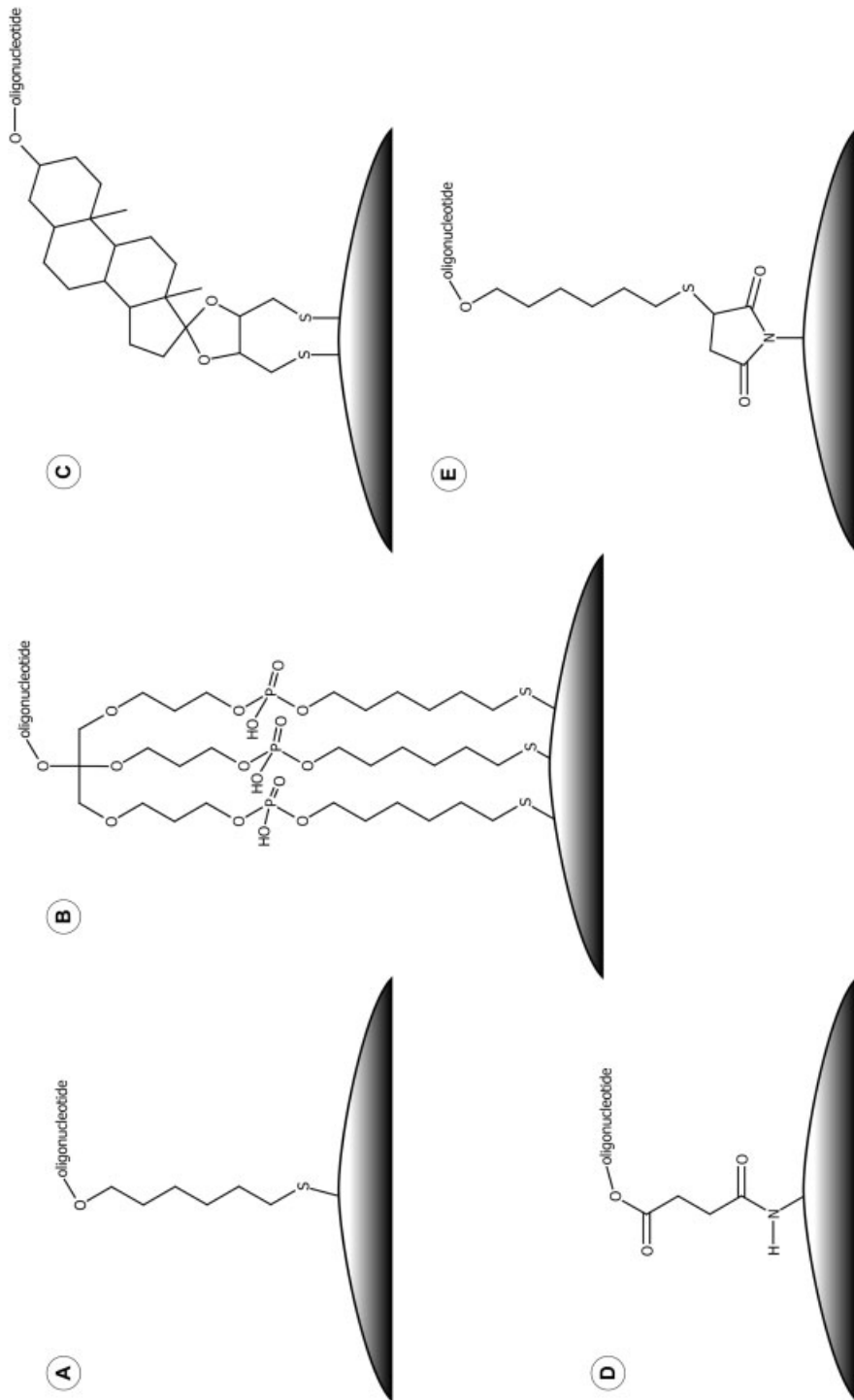


**Fig. 6.4.** Scheme of the covalent attachment of oligonucleotides to gold nanoparticles by different linker groups: (A) alkyl-thiol, (B) multiple-thiol anchor, (C) steroid disulfide, (D) amine/succinimide, and (E) maleimide.





**Fig. 6.5.** Formation of oligonucleotide layers on gold nanoparticle surfaces. The conformation depends on the DNA molecule density on the surface. (A) At very low surface coverage, no steric interactions occur between strands on the surface. (B) For higher molecule densities, collisions will occur between the ends of neighboring oligonucleotides, restricting the possible strand orientations and forcing the DNA strands to “stand up”. (C) As surface coverage increases, the oligonucleotides approach their theoretical limit of a densely packed monolayer of “standing up” DNA strands. (Modified after Ref. [92].)

reaction with concentrated MCH displaces the DNA molecules from the nanoparticle surface. Changes in effective size ( $D_{\text{eff}}$ ) of the Au-DNA conjugates were quantified by the Ferguson plot method. The obtained drop in  $D_{\text{eff}}$  confirmed the loss of surface-bound oligonucleotides with higher MCH concentrations ( $>0.1$  mM). However, MCH led to an increased hybridization capacity, presumably due to better availability of the oligonucleotides to base pairing. In addition, Rant et al. characterized the conformation of oligonucleotide layers on Au surfaces by fluorescence investigation [92] (Fig. 6.5).

Although thiols and mercaptoalkyl residues can be incorporated into DNA simply by adding the suitable phosphoramidite modifier through solid-phase DNA synthesis [93], thiol- or disulfide-modified DNA is commercially available.

**Other Coupling Strategies (Phosphine, Maleimide, Amine/Succinimide, Lysine)** In 1969, McPartlin et al. were the first to describe very small gold clusters that were passivated by organic groups (phosphines). This undecagold contains a gold core of 11 atoms, with the gold atoms on the surface attached covalently to phosphine groups [94]. By altering the organic groups the clusters were made water soluble [95] and derivatized to link to proteins [96–98]. Larger gold clusters were subsequently developed, showing better visibility at high magnification by transmission electron microscopy (TEM) and increased enhancement with silver [98]. These 1.4 nm-sized gold nanoparticles ( $\text{Au}_{55}$ ) are commercially available bearing a single activated functional group (Nanogold<sup>TM</sup>, Nanoprobes Inc.). They have been reacted with proteins or appropriately modified oligonucleotides to form 1:1 nanoparticle:biomolecule conjugates. Using a maleimide group or an *N*-hydroxysuccinimide, the gold clusters can react specifically with thiols or amino groups, respectively [100]. Thus,  $\text{Au}_{55}$  clusters passivated with a phosphine ligand shell, which is functionalized with a single reactive maleimide group, were used to prepare DNA–gold conjugates from disulfide-modified and thiolated oligonucleotides [101, 102].

As well as thiolated oligonucleotides, Ozsoz et al. used amino-modified oligonucleotide probes to covalently attach to gold nanoparticles bearing carboxy-groups [34]. After modifying the gold colloids with L-cysteine, standard activation methods

converted the carboxylic acids into succinimide esters, which allow the formation of a peptide bond with amino-modified DNA.

DNA–nanoparticle conjugates are also an interesting alternative “bottom-up” fabrication technology to produce nanowires using long DNA molecules as templates. Due to the relatively poor intrinsic electric conductivity of DNA, metallization is required and can be achieved by nanoparticles. An *ex situ* approach uses the electrostatic interaction between positively charged particles and the negatively charged DNA phosphate backbone to attach lysine-capped gold colloidal particles to DNA double-helices [103, 104]. However, Harnack et al. discovered that negatively charged tris(hydroxymethyl)phosphine (THP)-capped gold nanoparticles also bind densely to DNA [105]. Although the binding mechanisms of THP-gold nanoparticles to DNA, and the factors controlling the binding efficiency, were still unclear, the authors expected hydrogen-bonding interactions to be important since each THP ligand provides three hydroxyl groups that can serve as either OH donors or O acceptors. Cooperative, THP-gold conjugates preferably adsorb to hydrophilic areas such as DNA molecules.

Supporting these observations, but in contrast to conventional wisdom, Li and Rothberg also showed that single stranded DNA (ss-DNA) adsorbed on negatively charged gold nanoparticles whereas double stranded oligonucleotides (ds-DNA) did not [106]. They attributed these different electrostatic propensities to the flexible structure of ss-DNA. Single strands can uncoil sufficiently to expose their bases so that attractive Van der Waals forces cause sticking to the gold. However, the duplex structure of ds-DNA does not permit the uncoiling needed to expose the bases. Hence, repulsion between the negatively charged phosphate backbone and the adsorbed citrate ions dominates so that ds-DNA will not adsorb. Moreover, they demonstrated that the adsorption rate of ss-DNA to gold nanoparticles is length and temperature dependent [107] and, additionally, can effectively stabilize the gold colloid against salt-induced aggregation. Exploiting these observations, they designed a simple, fast colorimetric hybridization assay that does not require functionalization of the gold, the probe or the target DNA, but was able to easily detect single base mismatches.

### 6.2.3.2 Modification of Gold Nanoparticles with Proteins

Proteins bind to gold colloids for three main reasons: sulfur bonding (cysteine and methionine), charge (lysine), and hydrophobic attraction (tryptophan) (Fig. 6.6). Generally, this conjugation is irreversible, but long-term storage at high pH or in a buffer containing surfactant may cause some proteins to dissociate.

Initially, the coupling of gold nanoparticles to proteins was used to visualize cellular structures by electron microscopy because of the high electric densities [108], as shown for antibodies and lectin [109, 110]. More recently, Ho et al. reported a method for fabricating biofunctionalized nanoparticles by attaching human immunoglobulin (IgG) on their surfaces through either electrostatic or covalent binding [63]. By selective binding of these IgG-presenting gold nanoparticles to bacterial cell walls they were able to study the interactions between IgG and pathogens by transmission electron microscopy.

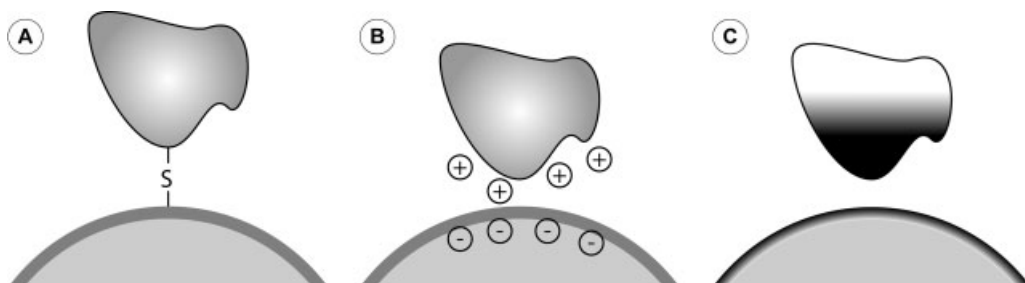


**Fig. 6.6.** Schematic summary of functionalization approaches of proteins to gold nanoparticles. Proteins bind to the particle surface by (A) sulfur bonding, (B)

charge interactions, and/or (C) hydrophobic attractions (white: hydrophilic, black: hydrophobic regions), dependent on the amino acids exposed to the particle surface.

The first nanoparticle labeling of genomic nucleic acids was applied using the biotin/streptavidin biorecognition reaction [111].

Studying the association of proteins onto gold particles at various protein concentrations yield typical saturation curves [14]. The number of bound molecules depends on the molar concentration of the protein free in solution, the number of possible adsorption sites and inversely correlates with the equilibrium constant for dissociation of protein from particles. The applicability of Scatchard analysis to the formation of protein–gold complexes indicates a finite number of adsorption sites, leading to saturation, which is best explained by assuming a monomolecular shell of protein around the particles.

In the past, colloidal gold–protein complexes were used extensively in immunocytochemistry as secondary reagents for the localization of antigens. Horisberger et al. examined the adsorption of protein A onto 11.2 nm-sized gold nanoparticles, regarding the process and extent of the adsorption, the optimal conditions of preparation, and the stability of such gold–protein complexes [112]. The adsorption isotherm was independent of pH at low protein coverage. However, in the presence of a large excess of protein A, the highest coverage was obtained at pH 5.1, the isoelectric point of the protein. Furthermore, the extent of protein association onto gold particles also varied with the different protein coverage and decreased with increasing coverage. The obtained complexes were stable under storage at low but not at high protein coverage (up to 12 and 26 molecules adsorbed per particle, respectively). Beside use in immunoassays by coupling antibodies to colloidal gold, the streptavidin–biotin system [113] offers further possible applications (for a review see Ref. [114]). The tetravalent protein streptavidin can bind the small biomolecule biotin with high sensitivity and affinity. Thus, streptavidin-functionalized nanoparticles can be coupled easily to other molecules modified by biotin. By attaching biotinylated oligonucleotides to streptavidin-functionalized particles, DNA–nanoparticle conjugates have been formed [115], enlarging the recognition capacity of streptavidin by a highly specific binding site for the complementary DNA sequence. This offers the opportunity to detect DNA–DNA hybridization events

by gold nanoparticles. Furthermore, Niemeyer and Ceyhan have described a DNA-directed functionalization of colloidal gold with protein [116]. Thereby, oligonucleotide-modified gold nanoparticles were coupled to complementary DNA–streptavidin conjugates, which also have been functionalized with biotinylated antibodies. The bioactivity of the resulting protein–gold conjugates was proved in an immunoassay.

Recently, Levy et al. have demonstrated a general approach to the synthesis of extremely stable gold nanoparticles using a pentapeptide ligand [117]. Based on protein folding considerations, the basic design principle aimed at a ligand that can readily attach to the surface of the gold particle and form a well-packed passivation layer with a hydrophilic terminus. The resulting pentapeptide thiol capping ligand was able to convert citrate-stabilized gold nanoparticles into stable, water-soluble nanoparticles with chemical properties comparable to those of proteins. The stability of different particle preparations conferred by ligands of various peptide sequences has been evaluated by exposing the particles to increasing salt concentrations until precipitation occurred. This stability depended on the ligand length, hydrophobicity, and charge.

In contrast to bioconjugation after nanoparticle synthesis, direct conjugation methods eliminate the need for intermediate stabilizing agents or dense passivation that minimizes the free surface area for interactions with the desired adsorbates and often tends to aggregation with even mild processing. Burt et al. were able to produce water-soluble gold nanoparticles less than 2 nm in diameter directly conjugated to bovine serum albumin (BSA) protein without application of high temperature or high pressure. They obtained a near-quantitative yield of well-dispersed, protein-conjugated gold nanoparticles that remain stable indefinitely in solution under ambient conditions [118].

#### 6.2.3.3 Biofunctionalization of other Metal Nanoparticles

Oligonucleotides have been less successfully attached to nanoparticles made from materials other than gold (such as Ag, Cu, Pd, Pt), probably because of the weaker bond energies between sulfur and the other metals. Thiols possibly bound to these surfaces are readily displaced by oxidants or other competing ligands (including the DNA bases). A thin gold shell grown around metal cores of different materials and shapes can improve biomolecule attachment, retaining the characteristics of the core material, as shown for core-shell Ag/Au nanoparticles by Mirkin's group [115].

#### 6.2.4

#### Biological Applications of Gold Nanoparticles

Due to their binding specificity as well as their large variety of functional groups, biomolecules (nucleic acids, proteins) are able to offer new opportunities for the functionalization of nanoparticles. Furthermore, efforts have been made to combine the intrinsic opportunities of proteins, e.g. optical, catalytic, mechanical or switchable properties, with the specific features of nanoparticles.

Gold nanoparticle-oligonucleotide-conjugates are of great interest since complementary DNA base pairing makes them specifically addressable. This can be used for biomolecular detection schemes as well as for organizing supramolecular nanostructures. It also offers versatile applications in the field of biosensors, disease diagnosis, gene expression, and molecular nanotechnology [8]. There are two pioneering strategies for the functionalization of gold nanoparticles with oligonucleotides. In 1996, Mirkin et al. used short DNA molecules as a linker between 13 nm-sized particles, resulting in macroscopic assemblies. The DNA attached to the gold nanoparticles remained accessible to hybridization with complementary DNA in a sequence-specific but reversible manner [1]. Conversely, DNA can be used as a template to bind small gold nanoparticles on a single oligonucleotide strand [2]. Furthermore, there are other strategies for forming supramolecular aggregates, e.g. semi-synthetic conjugates by self-assembly of nucleic acids, inorganic nanoparticles, and proteins such as streptavidin [119].

### 6.3

#### Substrates and their Biofunctionalization

Oligonucleotides and other biomolecules cannot be coupled directly to the surface silanol groups of silicon oxide or glass substrates. Therefore, the surface must be functionalized with a group that can be used either to initiate oligonucleotide synthesis or to which the pre-synthesized capture oligonucleotides can be attached. In principle, there are two means of obtaining substrates that can bind biomolecular capture probes: (1) nearly monomolecular thin films and (2) nanoporous gels (Fig. 6.7). The first method provides binding sites two-dimensionally, whereas the latter ones form 3D arrangements. The advantage of impermeable, monomolecular binding layers over nanoporous membranes/gels is that there is no need for diffusion into pores, i.e. capture and target molecules can access the probes immediately. This enhances the rate of capture probe immobilization as well as hybridization/binding rates, especially for extended molecules and/or labels that would be influenced by steric hindrance. However, 3D nanoporous gels yield a

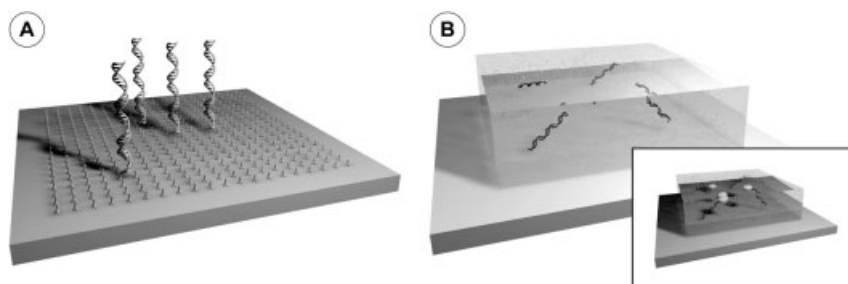


**Fig. 6.7.** Strategies of substrate biofunctionalization: (A) functional planar interfaces and (B) microscaled reaction volumes (nanoporous hydrogels). Inset: nanoparticle-labeled oligonucleotide strands immobilized in the gel.

largely enhanced surface area and, therefore, a higher capacity for binding of capture and target probes, leading to enhanced signal levels.

### 6.3.1

#### Molecular Thin Films

##### 6.3.1.1 Self-assembly Monolayers

Adsorption of organic thin-films enables the biofunctionalization of planar surfaces. Typical approaches are either Langmuir–Blodgett (LB) techniques or a spontaneous organization of molecules into stable, well-defined structures (self-assembly). Self-assembled monolayers (SAMs) are widely used, highly ordered monomolecular films that spontaneously form on surfaces by chemisorption. These 2D monolayers consist of oriented molecules containing a head group that is reactive towards the surface. The alkyl chain usually influences the physico-chemical properties and stabilizes the SAM by intermolecular interactions, whereas the tail groups define the binding properties of the layer to further possible ligands. Compared with the similar LB films, in SAMs the ligand covalently binds to the surface, resulting in a very strong bonding. Several systems give SAMs, e.g. organosulfur compounds on metal surfaces or carboxy groups on metal oxides [120, 121].

Exposure of gold surfaces to alkane-thiol solutions leads to the self-assembly of these molecules. The resulting organic ultrathin film can be monitored by surface plasmon resonance spectroscopy (SPRS). Peterlinz and Georgiadis introduced a novel two-color SPR method, with which they obtained both film thickness and film dielectric constant and studied the chain length- and concentration-dependent kinetics of film formation in different solvents. Self-assembly in ethanol consists of three distinct kinetics steps, whereas the formation in heptane can be described with a single-step Langmuir adsorption model [122]. In ethanol, the results were most consistent with a film formation mechanism involving adsorption of both chemisorbed and physisorbed molecules. Expanding their SPRS studies the authors examined the formation kinetics for a two-component monolayer film containing thiol-modified single strand DNA (ssDNA including a hexamethylene linker) as well as mercaptohexanol [123]. After adsorbing HS-C6-ssDNA, exposure to an aqueous solution of mercaptohexanol results in a very rapid mercaptohexanol adsorption followed by a slow desorption of HS-C6-ssDNA. The final coverage of thiol-tethered DNA with mercaptohexanol diluent was estimated as  $5.2 \times 10^{12}$  HS-C6-ssDNA  $\text{cm}^{-2}$ . This corresponds to coverage densities described elsewhere [124–126]. Coverage versus time data calculated from the two-color SPR best fitted those of a model that accounts for adsorption, desorption, and diffusion (ADD) of the adsorbate, although this model predicts a saturation coverage of  $1 \times 10^{14}$  molecules  $\text{cm}^{-2}$ . The adsorption and hybridization kinetics of surface-bound thiolated ssDNA hybridized to fully complementary ssDNA were remarkably similar for these two different interfacial binding processes. The occurrence of sequence-specific hybridization was confirmed by SPRS melting studies. The amount of surface-immobilized duplexes differed only slightly from that for the same du-

plexes in free solution. A hybridization coverage of about one-third of that for the adsorption accounts for a loss of some adsorbed HS-C<sub>6</sub>-ssDNA during rinsing and mercaptohexanol-mediated desorption as well as for the hybridization efficiency.

The effect of DNA length and the presence of a thiol anchoring group on the assembly of oligonucleotides at gold surfaces was investigated by Steel et al. [127]. The thiol-anchoring group strongly enhanced oligonucleotide immobilization. Adsorbed thiol-ssDNA oligonucleotides shorter than 24 bases tended to organize in an end-tethered configuration, for which the surface coverage is largely independent of oligonucleotide length. However, for strands longer than 24 bases, the surface coverage starts to decrease considerably with probe length, presumably corresponding to a less ordered arrangement of DNA chains. Furthermore, Shchepinov et al. investigated the influence of steric factors on the hybridization of nucleic acids to oligonucleotide arrays [128]. They used spacer molecules to reduce steric interference of the support on the hybridization behavior of immobilized oligonucleotides. The optimal spacer length was determined to be at least 40 atoms, resulting in up to a 150-fold increased hybridization yields. Beyond this, steric hindrance can also be a problem if the surface-bound oligonucleotides are too close to each other. The highest hybridization yields were given for surfaces containing about 50% of the maximum oligonucleotide concentration. A further important factor influencing the hybridization efficiency is the base composition of the reacting oligonucleotides, owing to the lower stability of A:T versus G:C pairs. Southern et al. described the mechanism of duplex formation as a process that starts with the formation of a transient nucleation complex from the interaction of very few base pairs [129]. Mismatches close to the centre of an oligonucleotide have a strongly destabilizing effect on the duplex, whereas mismatches at the end are less destabilizing and thus more difficult to discriminate.

However, organosilicon derivatives on silicon oxide and glass are the most important for biological applications – and therefore we will focus on these.

Since all the standard surface modifications require silanol groups, the absolute number and relative distribution of surface hydroxyl (silanol) groups is important [130]. By varying the concentration of silanol groups it is possible to substantially change the properties of such a surface. Zhuravlev has studied the surface concentration of hydroxyl groups (silanol number  $\alpha_{\text{OH}}$ ) for a large variety of amorphous silicas [131]. By using the deuterio-exchange method with mass spectrometric analysis he estimated a silanol number of about 5.0 OH groups per nm<sup>-2</sup> (corresponding to  $5 \times 10^{14}$  cm<sup>-2</sup>), independent of the origin and structural characteristics of the fully hydroxylated surfaces, and considered the value as a physicochemical constant. However, preliminary vacuum treatment within the range from 200 to 1100 °C significantly decreased the concentration of hydroxyl groups ( $\alpha_{\text{OH}} < 0.15$ ), pointing to strong dehydroxylation of the surface.

Furthermore, the coating morphology, including silane layer thickness, density, and the orientation of the surface molecules, strongly depends on the amount of water the solvent contains [130]. Once the surface offers functional groups for subsequent biomolecule coupling, there are different strategies for covalent attachment of DNA (or proteins) to glass surfaces to build microarrays, as described in Ref. [132]. To enable molecular interactions with other biomolecules (e.g. hybrid-

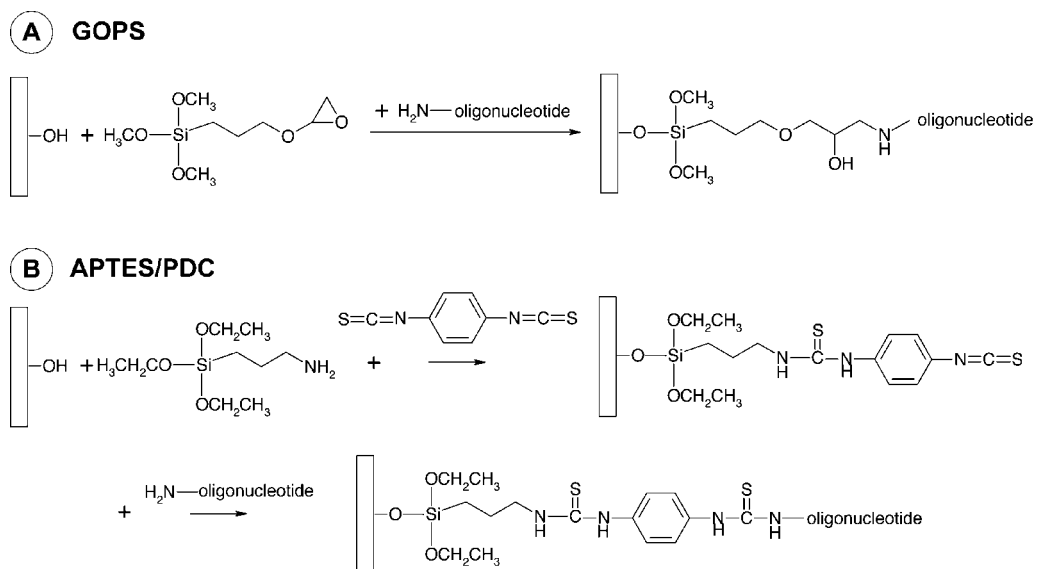


**Fig. 6.8.** Surface modification with silanes for DNA attachment. (A) Direct binding of amino-modified DNA by epoxy-groups of 3-glycidoxypropyltrimethoxysilane (GOPS). (B) Amino-attachment chemistry of 3-

aminopropyltriethoxysilane (APTES). The binding of amino-modified oligonucleotides works indirectly by the bifunctional crosslinker 1,4-phenylenediisothiocyanate (PDC) [135].

ization) the immobilized capture probes should be fixed at their extremities. Therefore amino- or carboxy-modified DNA molecules are normally used, requiring adequate functionalized substrate surfaces. Consolandi et al. have described two robust procedures for oligonucleotide microarray preparation, including glass functionalization with appropriate silanes (Fig. 6.8), a coating step using polymers, and a surface activation step to allow for the attachment of amino-modified oligonucleotides [133]. These chemical platforms showed an overall high loading capacity and availability to hybridization against targets, a good uniformity, resistance to consecutive probing/stripping cycles, and the possibility of performing enzymatic reactions.

Recently, Martin-Palma et al. have presented a novel biofunctionalization technique for the deposition of amine groups on different surfaces [134]. The proposed activation method induced amino-group fixation on the surface of materials ranging from semiconductors to metals and insulating materials. The reactivity of the functionalized surfaces could be determined by using a fluorescent reagent that specifically reacts with amine groups.

### 6.3.1.2 Optimization of Gold Nanoparticle-based Microarrays for DNA Detection

However, substrate modification with silanes (as a prerequisite for capture DNA binding) often leads to inhomogeneous surfaces and/or non-specific binding of the labeled DNA. For that reason, Fritzsche and co-workers examined different cleaning strategies as a prerequisite for substrate functionalization, characterizing



two different surface modification methods with silanes so as to provide functional groups for covalent attachment of amino-modified DNA [135]. To reduce non-specific binding of gold-tagged DNA molecules, different blocking strategies were examined, especially those for nanoparticle labeling. The two examined silanes differed in their DNA binding homogeneity, maximum signal intensities, and sensitivity. Non-specific gold binding could be blocked by treatment in 3% bovine serum albumin (BSA). Another approach to characterizing surface modification methods by silanes employed atomic force microscopy (AFM) [136]. After silanization of the silicon oxide substrate, parts of the surface were covered by an elastomeric mask and then treated with oxygen plasma, leading to damage of the silane layer. AFM characterization of the surface (Fig. 6.9) revealed a height difference of  $\sim 1.8$  nm, which can be attributed to the thickness of the silane layer.

### 6.3.2

#### Nanoporous Gels

As well as glass or silicon surfaces, organic polymers offer another interesting option for the immobilization of nanoparticles. A higher loading capacity can be obtained by using thick layers consisting of a 3D network.

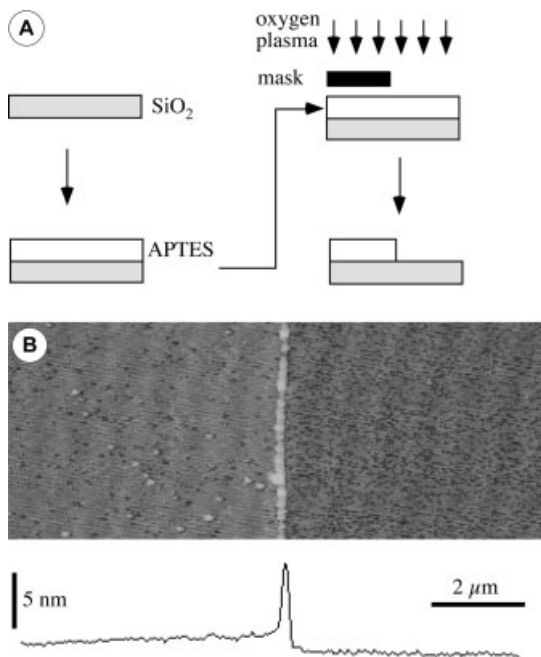


**Fig. 6.9.** DNA immobilization using APTES surfaces. A step in an APTES surface to measure the layer thickness was fabricated as follows: (A) parts of the silanized surface were covered by an elastomeric mask and thereby protected against damage by subsequent

oxygen plasma. (B) The resulting step of about 1.8 nm is visible in the scanning force micrograph and represents the height of the silane layer. (Modified after Ref. [136] with permission of Oxford University Press.)

Since the first introduction of solid-phase synthesis on an organic polymer support (2% crosslinked polystyrene [137]), new biomaterials with polyethylene backbone structures have been developed. These materials are characterized by improved hydrophilic/hydrophobic properties as well as a good biocompatibility. Another important feature of these polymers is the resistance to standard solvents and their good swelling properties [138].

In addition to other applications the polymers can be used as beads for combinatorial synthesis resins such as Tentagel™ [139, 140], polyethylene glycol–polystyrol (PEG-PS) [139] and polyethylene glycol–polyacrylamide copolymers (PEGA) [141]. Furthermore, polymers suitable for solid-phase synthesis have been micropatterned by spinning-on the pure monomers without functionalization, followed by light-induced polymerization [142]. More recently, Amirgoulova et al. described polymer coatings based on PEG for the study of immobilized biomolecules [143]. The crosslinked, star-polymer derived surfaces not only allowed reversible protein unfolding and refolding but also interacted negligibly with the immobilized proteins.

While preparing the polymer, bacteria cells [144] as well as proteins [145, 146] can be enclosed for different microfluidic reactors and for biochemical reactions, respectively. Although in these processes the enzymes and cells were non-covalently bound at the matrix of the polymer, they were restrained/prevented sterically from leaving the gel.

Bieber and co-workers were able to immobilize *Salmonella* antibodies in a 3D polymer network based on acrylamide derivatives and polyethylene linkers [147]. To extend this strategy the applied polyethylene glycol diacrylates and bisacrylated bis-diamino polyethylene glycols ( $M_r = 4000, 6000, \text{ and } 8000$ ) were functionalized by using hydroxy acrylate. Thus it was possible to bind biomolecules covalently instead of simply enclosing them in the polymer. Additionally, both the network structure (e.g. width of the meshes) and the functionality of the synthesized polymer could be adapted by an adjustable crosslinking reaction and the specific loading with functional groups, respectively. The resulting loading capacity of these spaces of biorecognition reactions were up to  $1000\times$  higher than those of plain 2D surfaces.

Before their immobilization by covalent binding in the nanoporous gel the biomolecules should be tested for their ability to penetrate coats of different hydrogels. A simple possibility is to use gel electrophoresis primarily employed for the separation and purification of DNA and proteins [148] (Fig. 6.10).

The investigated gels were loaded with a protein standard mixture and treated with sodium dodecyl sulfate (SDS), which binds to the amide groups in the protein. Thus, the protein becomes negatively charged, in dependency of the length of its amino acid chain. Application of an electric field forces the molecules through the gel with different electrophoretic mobility due to their different electric charge, which is proportional to the size of the molecule. Higher polymer concentrations and smaller monomers yield a 3D network with tighter meshes. Larger molecules are, therefore, unable to penetrate into the gel.

In addition to the immobilization of biomolecules on functionalized surfaces,  $10\ \mu\text{m}$ -thin coats of functionalized spots of polyethylene glycol-based polymers

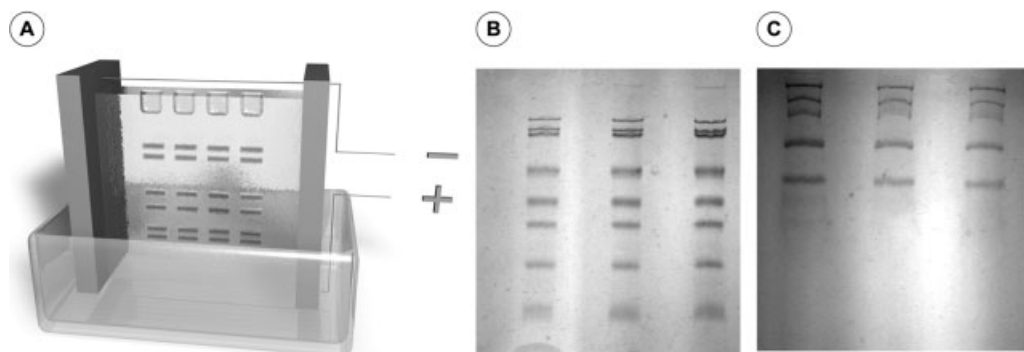


**Fig. 6.10.** (A) Electrophoresis is a rapid method for separating biomolecules according to their charge and molecular size/weight. When exposed to an electric field, biomolecules in the electrophoresis gel move towards one of the electrodes in a manner that depends on the molecule's charge and molecular size and on the size of the gel pores/meshes. Thereby, sodium dodecyl sulfate (SDS) gel electrophoresis is a rapid qualifying and quantifying method for proteins that can be separated only by their molecular weights. SDS binds to hydrophobic domains of proteins, masking their individual charge differences. SDS-protein complexes have a negative charge and can be size-separated since the resulting charge of the complex is proportional to the molecular weight of the protein. During separation, SDS-protein complexes are attracted to the anode and

separated by enforcement through the porous gel structure, which allows small proteins to move very fast, whereas larger molecules show a significant decelerated mobility. (B) This principle can be utilized to characterize the pore size of nanoporous gels. A mixture of proteins of known size and mass (116.0, 66.2, 45.0, 35.0, 25.0, 18.0, and 14.4 kDa) was driven by an applied electric field into two different gels. A standard 12% polyacryl amide gel (A) leads to certain mobility and a complete separation of the mixture. (C) Under similar conditions regarding voltage and time, a 12% poly (bisacryl polyethylenglycol<sub>4000</sub>) gel shows significantly different results: The proteins move much more slowly, and fewer bands are observed. This is because molecules above a certain threshold size become stuck in the gel, resulting in a band consisting of the remaining larger molecules.

(0.5–2 mm in diameter) have been prepared on glass substrates. These functionalized arrays are easy to use and suitable for commercial spotting systems. After activation of the glass supports and their modification with acrylsilane the monomer solution, containing a photo-initiator, was coated. To generate the spots ultraviolet radiation was applied through a mask, leading to polymerization at the exposed areas. At the non-exposed areas, unreacted monomer solution was rinsed off after polymerization had finished. Thereby, the loading of the hydrogel is influenced by the ratio of the different functional groups in the monomer solution. In subsequent steps the prepared hydroxy-functionalized spots were transformed into carboxylic acids and active esters, which can react with amino-modified, fluorescence-labeled DNA. Finally, the oligonucleotides are bound covalently at the polymer matrix and are then qualitatively and quantitatively detectable by the fluorescent group (Fig. 6.11).

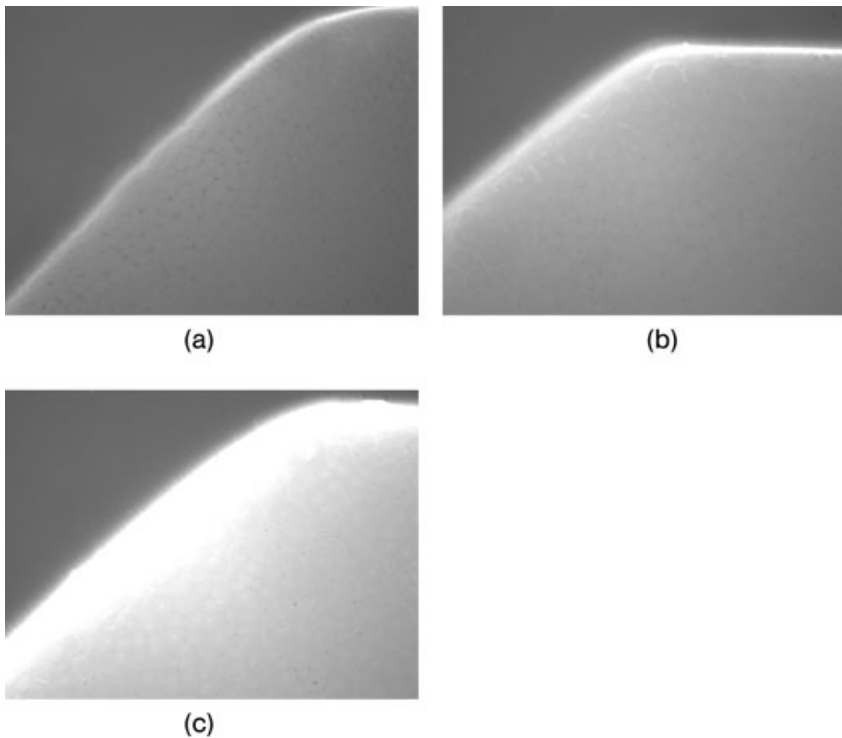


**Fig. 6.11.** Binding of fluorescence-labeled DNA molecules in a nanoporous hydrogel demonstrated by fluorescence microscopy. The gels were prepared with different hydroxy acrylate concentrations, (a) 0, (b) 1 and (c) 10 mM, leading to different concentrations

of hydroxy groups in the gel network and, therefore, different binding capacity of the biomolecule/DNA loading. The area-related loading capacity of these reaction spaces is up to 1000× higher than for plain 2D surfaces.

#### 6.4 Outlook

The detection and characterization of bioactive molecules represents a field of great importance for various aspects of our daily life, such as health management, food quality control, forensic, or environmental protection. Further development aims to increase the sensitivity and specificity of the assays; other important parameters are the robustness of the methods and their mobility to enable measurements outside dedicated laboratories and at the point of application. Thin molecular layers on solid substrates with nanometer dimensions are a key component of promising approaches in this field. Further developments aim for even simpler read-out schemes (as demonstrated by metal nanoparticle-based assays), label-free assays, and handheld instrumentation to realize visions such as point-of-care diagnostics.

## References

- 1 MIRKIN, C.A., et al., A DNA-based method for rationally assembling nanoparticles into macroscopic materials. *Nature*, **1996**, 382(6592), 607–9.
- 2 ALIVISATOS, A.P., et al., Organization of ‘nanocrystal molecules’ using DNA. *Nature*, **1996**, 382(6592), 609–11.
- 3 TATON, T.A., C.A. MIRKIN, R.L. LETSINGER, Scanometric DNA array detection with nanoparticle probes. *Science*, **2000**, 289, 1757–1760.
- 4 JAIN, K.K., Nanodiagnosics: application of nanotechnology in molecular diagnostics. *Expert Rev. Mol. Diagn.*, **2003**, 3(2), 153–161.
- 5 SOUTHERN, E.M., DNA chips: analysing sequence by hybridization to oligonucleotides on a large scale. *Trends Genet.*, **1996**, 12(3), 110–5.
- 6 SCHENA, M., et al., Microarrays: biotechnology’s discovery platform for functional genomics. *Trends Biotechnol.*, **1998**, 16(7), 301–6.
- 7 NIEMEYER, C.M. and D. BLOHM, DNA Microarrays. *Angew. Chem.*, **1999**, 111(19), 3039–3043.
- 8 DANIEL, M.C. and D. ASTRUC, Gold nanoparticles: assembly, supra-molecular chemistry, quantum-size-related properties, and applications toward biology, catalysis, and nanotechnology. *Chem. Rev.*, **2004**, 104(1), 293–346.
- 9 KREIBIG, U. and M. VOLLMER, *Optical Properties of Metal Clusters*, Series in Materials Science, Vol. 25, **1995**, Springer, Berlin.
- 10 YGUERABIDE, J. and E.E. YGUERABIDE, Light-scattering submicroscopic particles as highly fluorescent analogs and their use as tracer labels in clinical and biological applications. I. Theory. *Anal. Biochem.*, **1998**, 262(2), 137–156.
- 11 YGUERABIDE, J. and E.E. YGUERABIDE, Light-scattering submicroscopic particles as highly fluorescent analogs and their use as tracer labels in clinical and biological applications. II. Experimental characterization. *Anal. Biochem.*, **1998**, 262(2), 157–176.
- 12 ELGHANIAN, R., et al., Selective colorimetric detection of polynucleotides based on the distance-dependent optical properties of gold nanoparticles. *Science*, **1997**, 277(5329), 1078–81.
- 13 STORHOFF, J.J., et al., One pot colorimetric differentiation of polynucleotides with single base imperfections using gold nanoparticle probes. *J. Am. Chem. Soc.*, **1998**, 120, 1959–1964.
- 14 HACKER, G.W. in *Colloidal Gold: Principles, Methods, and Applications*, M.H. HAYAT, (Ed.), **1989**, Academic Press: New Jersey, p. 297–321.
- 15 REICHERT, J., et al., Chip-based optical detection of DNA hybridization by means of nanobead labeling. *Anal. Chem.*, **2000**, 72, 6025–6029.
- 16 STIMPSON, D.I., et al., Real-time detection of DNA hybridization and melting on oligonucleotide arrays by using optical wave guides. *Proc. Natl. Acad. Sci. U.S.A.*, **1995**, 92(14), 6379–83.
- 17 TATON, T.A., G. LU, C.A. MIRKIN, Two-color labeling of oligonucleotide arrays via size-selective scattering of nanoparticle probes. *J. Am. Chem. Soc.*, **2001**, 123, 5164–5165.
- 18 LI, H. and L.J. ROTHBERG, DNA sequence detection using selective fluorescence quenching of tagged oligonucleotide probes by gold nanoparticles. *Anal. Chem.*, **2004**, 76(18), 5414–7.
- 19 KARLSSON, R., SPR for molecular interaction analysis: a review of emerging application areas. *J. Mol. Recognit.*, **2004**, 17(3), 151–61.
- 20 NATH, N. and A. CHILKOTI, A colorimetric gold nanoparticle sensor to interrogate biomolecular interactions in real time on a surface. *Anal. Chem.*, **2002**, 74(3), 504–9.
- 21 LYON, L.A., M.D. MUSICK, M.J. NATAN, Colloidal Au-enhanced surface plasmon resonance immunosensing. *Anal. Chem.*, **1998**, 70(24), 5177–83.
- 22 CREIGHTON, J.A., Surface enhanced Raman scattering, in *Metal Colloids*,

- R.K. CHANG and T.E. FURTAK (Eds.), 1982, Plenum: New York. p. 315–338.
- 23 FREEMAN, R.G., et al., Self-assembled metal colloid monolayers: an approach to SERS substrates. *Science*, 1995, 267, 1629–1632.
- 24 CAO, Y.W., R. JIN, C.A. MIRKIN, Nanoparticles with Raman spectroscopic fingerprints for DNA and RNA detection. *Science*, 2002, 297, 1536–1540.
- 25 MUSICK, M.D.K., C.D. KEEFE, H. MELINDA, M.J. NATAN, Stepwise construction of conductive Au colloid multilayers from solution. *Chem. Mater.*, 1997, 9, 1499–1501.
- 26 MÖLLER, R., et al., Electrical classification of the concentration of bioconjugated metal colloids after surface adsorption and silver enhancement. *Langmuir*, 2001, 17, 5426–5430.
- 27 URBAN, M., R. MÖLLER, W. FRITZSCHE, A paralleled readout system for an electrical DNA-hybridization assay based on a microstructured electrode array. *Rev. Sci. Instrum.*, 2003, 74, 1077–1081.
- 28 PARK, S.J., T.A. TATON, C.A. MIRKIN, Array-based electrical detection of DNA with nanoparticle probes. *Science*, 2002, 295(5559), 1503–6.
- 29 CAMPAS, M. and K. IOANNIS, Strategy for the development of sensor platforms for multi-analysis. *Int. J. Environ. Anal. Chem.*, 2004, 84(11), 799–807.
- 30 DEQUAIRE, M., C. DEGRAND, B. LIMOGES, An electrochemical metalimmunoassay based on a colloidal gold label. *Anal. Chem.*, 2000, 72(22), 5521–8.
- 31 AUTHIER, L., C. GROSSIORD, P. BROSSIER, Gold nanoparticle-based quantitative electrochemical detection of amplified human cytomegalovirus DNA using disposable microband electrodes. *Anal. Chem.*, 2001, 73(18), 4450–6.
- 32 WANG, J., et al., Metal nanoparticle-based electrochemical stripping potentiometric detection of DNA hybridization. *Anal. Chem.*, 2001, 73(22), 5576–81.
- 33 WANG, J., G. LIU, A. MERKOCI, Electrochemical coding technology for simultaneous detection of multiple DNA targets. *J. Am. Chem. Soc.*, 2003, 125(11), 3214–5.
- 34 OZSOZ, M., et al., Electrochemical genosensor based on colloidal gold nanoparticles for the detection of Factor V Leiden mutation using disposable pencil graphite electrodes. *Anal. Chem.*, 2003, 75(9), 2181–7.
- 35 OKAHATA, Y., et al., Quantitative detection of binding of PCNA protein to DNA strands on a 27 MHz quartz-crystal microbalance. *Nucleic Acids Symp. Ser.*, 2000, (44), 243–4.
- 36 ZHOU, X.C., S.J. O'SHEA, S.F.Y. LI, Amplified microgravimetric gene sensor using Au nanoparticle modified oligonucleotides. *Chem. Commun.*, 2000, 953–954.
- 37 PATOLSKY, F., et al., Dendritic amplification of DNA analysis by oligonucleotide-functionalized Au-nanoparticles. *Chem. Commun.*, 2000, 1025–1026.
- 38 WEIZMANN, Y., F. PATOLSKY, I. WILLNER, Amplified detection of DNA and analysis of single-base mismatches by the catalyzed deposition of gold on Au-nanoparticles. *Analyst*, 2001, 126(9), 1502–4.
- 39 HANSEN, K.M., et al., Cantilever-based optical deflection assay for discrimination of DNA single-nucleotide mismatches. *Anal. Chem.*, 2001, 73(7), 1567–71.
- 40 FRITZ, J., et al., Translating biomolecular recognition into nanomechanics. *Science*, 2000, 288(5464), 316–8.
- 41 FRITZSCHE, W. and T.A. TATON, Metal nanoparticles as labels for heterogeneous, chip-based DNA detection. *Nanotechnology*, 2003, 14, R63–R73.
- 42 BRUST, M., et al., Synthesis and reactions of functionalized gold nanoparticles. *J. Chem. Soc., Chem. Commun.*, 1995, 1655–1656.
- 43 LIZ-MARZÁN, L.M., M. GIERSIG, P. MULVANEY, Synthesis of nanosized gold-silica core-shell particles. *Langmuir*, 1996, 12(18), 4329–4335.

- 44 LEE, P.C. and D. MEISEL, Adsorption and surface-enhanced Raman of dyes on silver and gold sols. *J. Phys. Chem.*, **1982**, *86*, 3391–3395.
- 45 TURKEVICH, J., R.S. MINER, L. BABENKOVA, Further studies on the synthesis of finely divided platinum. *J. Phys. Chem.*, **1986**, *90*(20), 4765–4767.
- 46 TURKEVICH, J. and G. KIM, Palladium: Preparation and catalytic properties of uniform size. *Science*, **1970**, *169*, 873–879.
- 47 KUYPER, A.C., The oxidation of citric acid. *J. Am. Chem. Soc.*, **1933**, *55*(4), 1722–1727.
- 48 WEITEN, R.L., et al., *Adv. Mater.*, **1996**, *8*, 428.
- 49 ABID, J.P., Laser induced synthesis and non linear optical properties of metal nanoparticles, in *Laboratoire d'Electrochimie*, **2003**, Ecole Polytechnique Federale de Lausanne: Lausanne.
- 50 MIE, G., Beiträge zur Optik trüber Medien speziell kolloidaler Metallösungen. *Ann. Physik*, **1908**, *25*, 377–445.
- 51 DEBYE, P., Der Lichtdruck auf Kugeln von beliebigem Material. *Ann. Phys.*, **1909**, *30*(57–136).
- 52 DRAKE, T.J., X.J. ZHAO, W. TAN, Bioconjugated silica nanoparticles for bioanalytical applications, in *Nanobiotechnology*, Wiley-VCH: Weinheim, **2004**, p. 444–457.
- 53 KHLEBTSOV, N.G., et al., Two-layer model of colloidal gold bioconjugates and its application to the optimization of nanosensors. *Colloid J.*, **2003**, *65*(4), 508–518.
- 54 WESTCOTT, S.L., et al., Formation and adsorption of clusters of gold nanoparticles onto functionalized silica nanoparticle surfaces. *Langmuir*, **1998**, *14*, 5396–5401.
- 55 STÖBER, W., A. FINK, E. BOHN, Controlled growth of monodisperse silica spheres in the micron size range. *J. Colloid Interface Sci.*, **1968**, *26*(1), 62–69.
- 56 HALAS, N., The optical properties of nanoshells. *Optics & Photonic News*, **2002**, 26–30.
- 57 HIRSCH, L.R., et al., Nanoshell-mediated near-infrared thermal therapy of tumors under magnetic resonance guidance. *Proc. Natl. Acad. Sci. U.S.A.*, **2003**, *100*(23), 13549–54.
- 58 HIERGEIST, R., et al., Application of magnetite ferrofluids for hyperthermia. *J. Magn. Magn. Mater.*, **1999**, *201*(1–3), 420–422.
- 59 BASELT, D.R., et al., A biosensor based on magnetoresistance technology. *Biosens. Bioelectron.*, **1998**, *13*(7–8), 731–9.
- 60 EDELSTEIN, R.L., et al., The BARC biosensor applied to the detection of biological warfare agents. *Biosens. Bioelectron.*, **2000**, *14*(10–11), 805–13.
- 61 GORSCHLUTER, A., et al., Electromagnetic base technology for extremely sensitive immunosensors and DNA-chips. *Biomed. Tech (Berl)*, **2002**, *47*(Suppl 1, Pt 1), 213–6.
- 62 SCHOTTER, J., et al., A biochip based on magnetoresistive sensors. *IEEE Trans. Magn.*, **2002**, *38*(5), 3365–3367.
- 63 HO, K.-C., et al., Using biofunctionalized nanoparticles to probe pathogenic bacteria. *Anal. Chem.*, **2004**, *76*(24), 7162–7168.
- 64 ALIVISATOS, A.P., Semiconductor clusters, nanocrystals, and quantum dots. *Science*, **1996**, *271*, 933–937.
- 65 BRUCHEZ, M., JR., et al., Semiconductor nanocrystals as fluorescent biological labels. *Science*, **1998**, *281*(5385), 2013–6.
- 66 WU, X., et al., Immunofluorescent labeling of cancer marker Her2 and other cellular targets with semiconductor quantum dots. *Nat. Biotechnol.*, **2003**, *21*(1), 41–6.
- 67 NIEMEYER, C.M., Functional hybrid devices of proteins and inorganic nanoparticles. *Angew. Chem. Int. Ed.*, **2003**, *42*(47), 5796–800.
- 68 TURKEVICH, J., P.L. STEVENSON, J. HILLER, Nucleation and growth process in the synthesis of colloidal gold. *Discuss. Faraday Soc.*, **1951**, *11*, 55–75.
- 69 GUTBIER, A., Beiträge zur Kenntnis anorganischer Kolloide. *Z. Anorg. Chem. (Now: Z. Anorg. Allgem. Chem.)*, **1902**, *32*(1), 347–356.
- 70 ZSIGMONDY, R.A., Zur erkenntnis des

- kolloide gold. *Z. Elektrochem.*, **1889**, *4*, 546.
- 71 ROTH, J., The preparation of protein A-gold complexes with 3 nm and 15 nm gold particles and their use in labelling multiple antigens on ultrathin sections. *Histochem. J.*, **1982**, *14*(5), 791–801.
- 72 SCHMID, G., et al., Au<sub>55</sub>[P(C<sub>6</sub>H<sub>5</sub>)<sub>3</sub>]<sub>12</sub>Cl<sub>6</sub> – Ein Goldcluster ungewöhnlicher Größe. *Chem. Ber.*, **1981**, *114*, 3634–3642.
- 73 BRUST, M., et al., Synthesis of thiol-derivatized gold nanoparticles in a two-phase liquid-liquid system. *J. Chem. Soc., Chem. Commun.*, **1994**, 801–802.
- 74 OSTWALD, W., *Practical Colloid Chemistry*, **1924**, New York: Dutton.
- 75 TÜRKEVICH, J., Colloidal gold part I: Historical and preparative aspects, morphology and structure. *Gold Bull.*, **1985**, *18*, 86–91.
- 76 FRENS, G., Controlled nucleation for the regulation of the particle size in monodisperse gold suspensions. *Nature*, **1973**, *241*, 20–22.
- 77 SCHMID, G. and A. LEHNERT, The complexation of gold colloids. *Angew. Chem., Int. Ed. Engl.*, **1989**, *28*(6), 780–781.
- 78 GIERSIG, M. and P. MULVANEY, Preparation of ordered colloid monolayers by electrophoretic deposition. *Langmuir*, **1993**, *9*(12), 3408–3413.
- 79 HOSTETLER, M.J., et al., Alkanethiolate gold cluster molecules with core diameters from 1.5 to 5.2 nm: Core and monolayer properties as a function of core size. *Langmuir*, **1998**, *14*(1), 17–30.
- 80 YONEZAWA, T., K. YASUI, and N. KMIZUKA, Controlled formation of smaller gold nanoparticles by the use of four-chained disulfide stabilizer. *Langmuir*, **2001**, *17*, 271–273.
- 81 NIEMEYER, C.M., Nanoparticles, proteins, and nucleic acids: biotechnology meets materials science. *Angew. Chem. Int. Ed.*, **2001**, *40*(22), 4128–4158.
- 82 NUZZO, R.G., B.R. ZEGARSKI, L.H. DUBOIS, Fundamental studies of the chemisorption of organosulfur compounds on gold(111). Implications for molecular self-assembly on gold surfaces. *J. Am. Chem. Soc.*, **1987**, *109*(3), 733–740.
- 83 NUZZO, R.G. and D.L. ALLARA, Adsorption of bifunctional organic disulfides on gold surfaces. *J. Am. Chem. Soc.*, **1983**, *105*, 4481–4483.
- 84 LETSINGER, R.L., et al., Use of a steroid cyclic disulfide anchor in constructing gold nanoparticle-oligonucleotide conjugates. *Bioconj. Chem.*, **2000**, *11*(2), 289–91.
- 85 LI, Z., et al., Multiple thiol-anchor capped DNA-gold nanoparticle conjugates. *Nucleic Acids Res.*, **2002**, *30*(7), 1558–62.
- 86 STORHOFF, J.J., et al., Sequence-dependent stability of DNA-modified gold nanoparticles. *Langmuir*, **2002**, *18*(17), 6666–6670.
- 87 PARAK, W.J., et al., Conformation of oligonucleotides attached to gold nanocrystals probed by gel electrophoresis. *Nano Lett.*, **2003**, *3*(1), 33–36.
- 88 HERNE, T.M. and M.J. TARLOV, Characterization of DNA probes immobilized on gold surfaces. *J. Am. Chem. Soc.*, **1997**, *119*, 8916–8920.
- 89 LEVICKY, R., et al., Using self-assembly to control the structure of DNA monolayers on gold: A neutron reflectivity study. *J. Am. Chem. Soc.*, **1998**, *120*, 9787–9792.
- 90 MBINDYO, J.K.N., et al., DNA-directed assembly of gold nanowires on complementary surfaces. *Adv. Mater.*, **2001**, *13*(4), 249–254.
- 91 PARK, S., K.A. BROWN, K. HAMAD-SCHIFFERLI, Changes in oligonucleotide conformation on nanoparticle surfaces by modification with mercaptohexanol. *Nano Lett.*, **2004**, *4*(10), 1925–1929.
- 92 RANT, U., et al., Structural properties of oligonucleotide monolayers on gold surfaces probed by fluorescence investigations. *Langmuir*, **2004**, *20*(23), 10086–92.
- 93 BEAUCAGE, S.L., Oligodeoxyribonucleotides synthesis. Phosphoramidite approach. *Methods Mol. Biol.*, **1993**, *20*, 33–61.



- 94 MCPARTLIN, M., R. MASON, L. MALATESTA, Novel cluster complexes of gold(0)-gold(I). *J. Chem. Soc., Chem. Commun.*, **1969**, 334.
- 95 BARTLETT, P.A., B. BAUER, S.J. SINGER, Synthesis of water-soluble undecagold cluster compounds of potential importance in electron microscopic and other studies of biological systems. *J. Am. Chem. Soc.*, **1978**, *100*(16), 5085–5089.
- 96 REARDON, J.E. and P.A. FREY, Synthesis of undecagold cluster molecules as biochemical labeling reagents. 1. Monoacyl and mono[N-(succinimidooxy)succinyl] undecagold clusters. *Biochemistry*, **1984**, *23*(17), 3849–56.
- 97 SAFER, D., L. BOLINGER, J.S. LEIGH, JR., Undecagold clusters for site-specific labeling of biological macromolecules: simplified preparation and model applications. *J. Inorg. Biochem.*, **1986**, *26*(2), 77–91.
- 98 HAINFELD, J.F., A small gold-conjugated antibody label: improved resolution for electron microscopy. *Science*, **1987**, *236*(4800), 450–3.
- 99 HAINFELD, J.F. and F.R. FURUYA, A 1.4-nm gold cluster covalently attached to antibodies improves immunolabeling. *J. Histochem. Cytochem.*, **1992**, *40*(2), 177–84.
- 100 HAINFELD, J.F. and R.D. POWELL, New frontiers in gold labeling. *J. Histochem. Cytochem.*, **2000**, *48*(4), 471–80.
- 101 DUBERTRET, B., M. CALAME, A.J. LIBCHABER, Single-mismatch detection using gold-quenched fluorescent oligonucleotides. *Nat. Biotechnol.*, **2001**, *19*(4), 365–70.
- 102 XIAO, S., et al., Selfassembly of metallic nanoparticle arrays by DNA scaffolding. *J. Nanoparticle Res.*, **2002**, *4*, 313–317.
- 103 KUMAR, A., et al., Linear superclusters of colloidal gold particles by electrostatic assembly on DNA templates. *Adv. Mater.*, **2001**, *13*(5), 341–344.
- 104 SASTRY, M., et al., DNA-mediated electrostatic assembly of gold nanoparticles into linear arrays by a simple drop-coating procedure. *Appl. Phys. Lett.*, **2001**, *78*(19), 2943–2945.
- 105 HARNACK, O., et al., Tris(hydroxymethyl)phosphine-capped gold particles templated by DNA as nanowire precursors. *Nano Lett.*, **2002**, *2*(9), 919–923.
- 106 LI, H. and L. ROTHBERG, Colorimetric detection of DNA sequences based on electrostatic interactions with unmodified gold nanoparticles. *Proc. Natl. Acad. Sci. U.S.A.*, **2004**, *101*(39), 14036–9.
- 107 LI, H., L.J. ROTHBERG, Label-free colorimetric detection of specific sequences in genomic DNA amplified by the polymerase chain reaction. *J. Am. Chem. Soc.*, **2004**, *126*(35), 10958–61.
- 108 PALADE, G.E., Transport in quanta across the endothelium of blood capillaries. *Anat. Rec.*, **1960**, *136*, 254.
- 109 FAULK, W.P. and G.M. TAYLOR, An immunocolloid method for the electron microscope. *Immunochemistry*, **1971**, *8*, 1081.
- 110 HORISBERGER, M., J. ROSSET, H. BAUER, Colloidal gold granules as markers for cell surface receptors in the scanning electron microscope. *Experientia*, **1975**, *31*, 1147.
- 111 HIRIYANNA, K., et al., Electron microscopic visualization of sites of nascent DNA synthesis by streptavidin-gold binding to biotinylated nucleotides incorporated in vivo. *J. Cell Biol.*, **1988**, *107*(1), 33–44.
- 112 HORISBERGER, M. and M.F. CLERC, Labelling of colloidal gold with protein A. A quantitative study. *Histochemistry*, **1985**, *82*(3), 219–23.
- 113 CHAIET, L. and F.J. WOLF, The properties of streptavidin, a biotin-binding protein produced by *Streptomyces*. *Arch. Biochem. Biophys.*, **1964**, *106*, 1–5.
- 114 DIAMANDIS, E.P. and T.K. CHRISTOPOULOS, The biotin-(strept)avidin system: principles and applications in biotechnology. *Clin. Chem.*, **1991**, *37*(5), 625–36.
- 115 CAO, Y., R. JIN, C.A. MIRKIN, DNA-modified core-shell Ag/Au nanoparticles. *J. Am. Chem. Soc.*, **2001**, *123*(32), 7961–2.
- 116 NIEMEYER, C.M. and B. CEYHAN,

- DNA-directed functionalization of colloidal gold with proteins. *Angew. Chem. Int. Ed.*, **2001**, 40(19), 3685–3688.
- 117 LEVY, R., et al., Rational and combinatorial design of peptide capping ligands for gold nanoparticles. *J. Am. Chem. Soc.*, **2004**, 126(32), 10076–84.
- 118 BURT, J.L., et al., Noble-metal nanoparticles directly conjugated to globular proteins. *Langmuir*, **2004**, 20(26), 11778–83.
- 119 NIEMEYER, C.M., Semi-synthetic DNA-protein conjugates: novel tools in analytics and nanobiotechnology. *Biochem. Soc. Trans.*, **2004**, 32(Pt 1), 51–3.
- 120 XIA, Y. and G.M. WHITESIDES, Soft lithography. *Angew. Chem. Int. Ed.*, **1998**, 37, 550–575.
- 121 ULMAN, A., Formation and structure of self-assembled monolayers. *Chem. Rev.*, **1996**, 96(4), 1533–1554.
- 122 PETERLINZ, K.A. and R.M. GEORGIADIS, In situ kinetics of self-assembly by surface plasmon resonance spectroscopy. *Langmuir*, **1996**, 12, 4731–4740.
- 123 GEORGIADIS, R.M., K.A. PETERLINZ, A.W. PETERSON, Quantitative measurements and modelling of kinetics in nucleic acid monolayer films using SPR spectroscopy. *J. Am. Chem. Soc.*, **2000**, 122(13), 3166–3173.
- 124 REICHERT, J., Herstellung und Charakterisierung lateraler mikrostrukturierter molekularer Monofilme auf Silicium- und Glaschips für die Anwendung in Biochips. **2003**, Friedrich Schiller Universität Jena: Jena.
- 125 STEEL, A.B., T.M. HERNE, M.J. TARLOV, Electrochemical quantitation of DNA immobilized on gold. *Anal. Chem.*, **1998**, 70(22), 4670–7.
- 126 O'DONNELL-MALONEY, M.J. and D.P. LITTLE, Microfabrication and array technologies for DNA sequencing and diagnostics. *Genet. Anal.*, **1996**, 13(6), 151–7.
- 127 STEEL, A.B., et al., Immobilization of nucleic acids at solid surfaces: effect of oligonucleotide length on layer assembly. *Biophys. J.*, **2000**, 79(2), 975–81.
- 128 SHCHEPINOV, M.S., S.C. CASE-GREEN, E.M. SOUTHERN, Steric factors influencing hybridisation of nucleic acids to oligonucleotide arrays. *Nucleic Acids Res.*, **1997**, 25(6), 1155–61.
- 129 SOUTHERN, E., K. MIR, M. SHCHEPINOV, Molecular interactions on microarrays. *Nat. Genet.*, **1999**, 21(1 Suppl), 5–9.
- 130 VAN DER VOORT, P. and E.F. VASANT, Silylation of the silica surface. A review. *J. Liq. Chromatogr. Relat. Technol.*, **1996**, 19(17&18), 2723–2752.
- 131 ZHURAVLEV, L.T., Concentration of hydroxyl groups on the surface of amorphous silicas. *Langmuir*, **1987**, 3, 316–318.
- 132 ZAMMATTEO, N., et al., Comparison between different strategies of covalent attachment of DNA to glass surfaces to build DNA microarrays. *Anal. Biochem.*, **2000**, 280(1), 143–50.
- 133 CONSOLANDI, C., et al., Two efficient polymeric chemical platforms for oligonucleotide microarray preparation. *Nucleosides Nucleotides Nucleic Acids*, **2002**, 21(8–9), 561–80.
- 134 MARTIN-PALMA, R.J., et al., Surface biofunctionalization of materials by amine groups. *J. Mater. Res.*, **2004**, 19(8), 2415–2420.
- 135 FESTAG, G., et al., Optimization of gold nanoparticle-based DNA detection for microarrays. *J. Fluoresc.*, **2005**, 15(2), 161–170.
- 136 MÖLLER, R., et al., DNA probes on chip surfaces studied by scanning force microscopy using specific binding of colloidal gold. *Nucleic Acids Res.*, **2000**, 28(20e91), 1–5.
- 137 MERRIFIELD, B., Solid phase synthesis. *J. Am. Chem. Soc.*, **1963**, 85(14), 2149–2154.
- 138 MELDAL, M., PEGA: A flow stable polyethylene glycol dimethyl acrylamide copolymer for solid phase synthesis. *Tetrahedron Lett.*, **1992**, 33(21), 3077–3080.
- 139 BAYER and RAPP, New polymer supports for solid-liquid-phase peptide synthesis in *Chemistry of Peptides and Proteins*. Vol. 3, **1986**,

- Walter de Gryter & Co., Berlin, pp. 3–8.
- 140 BARANY, G., et al., Biopolymer syntheses on novel polyethylene glycol-polystyrene (PEG-PS) graft supports. *Peptides: Chemistry and Biology*, J.A. Smith and J.E. Revier (Eds.), 1992, Escom: Leiden, 603–604.
- 141 RENIL, M., et al., PEGA support for combinatorial peptide synthesis and solid-phase enzymatic library assay. *J. Peptide Sci.*, 1998, 4, 195–210.
- 142 REVZIN, A., et al., Fabrication of poly(ethylene glycol) hydrogel microstructures using photolithography. *Langmuir*, 2001, 17, 5440–5447.
- 143 AMIRGOULOVA, E.V., et al., Biofunctionalized polymer surfaces exhibiting minimal interaction towards immobilized proteins. *ChemPhysChem*, 2004, 5(4), 552–5.
- 144 HEO, J., et al., A microfluidic bioreactor based on hydrogel-entrapped *E. coli*: Cell viability, lysis and intracellular enzyme reactions. *Anal. Chem.*, 2003, 75(1), 22–26.
- 145 ZHANG, W., G.H. SEONG, R.M. CROOKS, Hydrogel-based microreactors as a functional component of microfluidic systems. *Anal. Chem.*, 2002, 74(18), 4647–4652.
- 146 DEMERS, N., et al., Immobilization of native and poly(ethylene glycol)-treated ('PEGylated') bovine serum amine oxidase into biocompatible hydrogel. *Biotechnol. Appl. Biochem.*, 2001, 33, 201–207.
- 147 BIEBER, I., et al., Antibody arrays on micropatterned surfaces and in three-dimensional gel structures for detection of Salmonella isolates. *Biotest Bull.*, 2002, 6, 235–342.
- 148 LÄMMLI, U., Cleavage of structural proteins during assembly of the head of bacteriophage T4. *Nature*, 1970, 227, 680–685.

## 7

# Conjugation of Nanomaterials with Proteins

*Mohammed J. Meziani, Yi Lin, and Ya-Ping Sun*

### 7.1

#### Introduction

The coupling of biomolecular entities and materials at the nanoscale has the potential to revolutionize many fields of science and technology, potentially having a significant impact on current biomedical technologies, nanoelectronics, and related areas [1–9]. Because nanoparticles and biomolecules typically have the same nanometer length scale, they are natural companions in hybrid systems. The availability of various nanostructures, such as semiconductor and metal particles and carbon nanotubes, with controlled properties at the nanoscale makes them extremely attractive candidates for use in biotechnological systems. These nanostructures possess strongly size-dependent optical, electrical, magnetic, and electrochemical properties [1–9]. In addition, simple modifications of these nanostructures, e.g. to their surface layer for enhanced aqueous solubility, biocompatibility or biorecognition, make them better suited for integration.

In the early stages, nucleic acids were preferentially investigated in the functionalization of nanostructures because they are more readily available by synthetic chemical means and more adaptable than proteins [10, 11]. Recently, significant progress has been made in extending the adaptability of nanostructures with proteins [1, 2, 12–22]. Proteins are involved in almost all biological processes and are employed in a wide range of forms because of their excellent functional specificity. Protein-based nanostructures are expected to offer some additional advantages and play a key role in the development of multifunctional materials and devices for biotechnological applications [1, 2, 12–22]. For example, nanostructures provide numerous complementary systems with a wide range of free energies of association. Also, methods for working with these systems are known from standard procedures in biochemistry and molecular immunology. Indeed, protein recognition chemistry has been widely applied in diagnostic testing. Future investigations are predicted to focus on the generation of altered protein building blocks for the self-assembly of novel biological reaction compartments using today's powerful techniques of molecular biology. Mutagenesis and protein engineering will allow the design of recombinant proteins that have optimized recognition capabilities for

the assembly of distinctively shaped superstructures and have appropriate amino acid residues for the effective nucleation of organic and inorganic nanomaterials [1].

The conjugation of nanomaterials with proteins is a very broad field, especially in the light of recent advances in the development of various nanomaterials. In this chapter, we focus on nanomaterials based on nanoscale semiconductors and metals and on carbon nanotubes. Other significant classes of nanomaterials not covered here include polymeric nanoparticles and related nanostructures [23–27], fullerenes and derivatives [28–33] etc., which are by no means less important. Despite our interest in these other classes [34–39], it is probably better to cover them elsewhere. In the present chapter, we first provide an overview of current and emerging approaches in the coupling of metal and semiconductor nanostructures with proteins and their assemblies in different architectures. We then report recent achievements in the use of supercritical fluid processing technology as an alternative process. We also highlight recent successes in the conjugation of carbon nanotubes with proteins and the mechanistic issues involved with nanotube–protein interactions. Finally, we briefly summarize the challenges and perspectives in this interdisciplinary field.

## 7.2

### Coupling of Inorganic Nanoparticles with Proteins

#### 7.2.1

##### Chemical Functionalization Methods

Wet-chemical preparation of conjugated nanoparticles involves mixing a protein with modified nanoparticles in solution. The modification of nanoparticles prior to mixing is usually by chemical functionalization with a linker. Here, the linker serves three functions: (1) it converts the hydrophobic nanoparticles into hydrophilic species to enable them to be transferred into aqueous solution, (2) to stabilize the nanoparticles to avoid their uncontrolled particle growth or agglomeration and (3) it has to recognize the protein (Fig. 7.1). The linker has to be chosen carefully for every nanoparticle material. The functional coupling groups in proteins are either available in the native form or incorporated by chemical means or by genetic engineering.

Figure 7.1 shows examples of chemical interactions used for the coupling of nanoparticles with protein molecules. Coupling to the particle surface is frequently performed through citrate, thiol, and phosphane groups [1, 2]. With a labile capping layer, such as citrate, proteins can be linked directly with a metal particle by exchange reactions with stronger binding ligand. This method has been applied in the coating of colloidal gold with thiol-containing proteins, such as immunoglobulins (IgG) and serum albumins, which have cysteine residues that are accessible for heterogeneous interphase coupling [40, 41]. Gold and silver nanoparticles stabilized by citrate ligand have been functionalized with IgG molecules at a high pH,

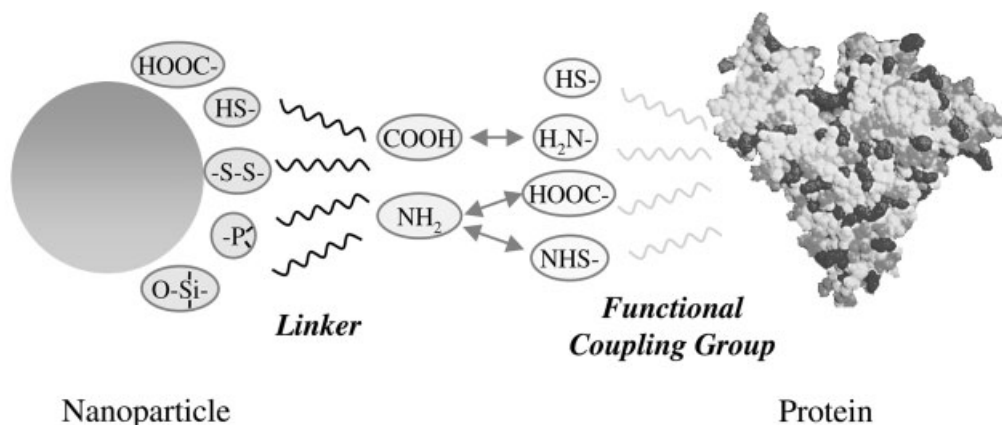


Fig. 7.1. Schematic representation of functional groups used to couple nanoparticles with protein species.

slightly above the isoelectric point of the citrate ligand [40]. Coupling was carried out by an effective binding between the negatively charged citrate groups of the colloids and the positively charged amino acid side chains of the protein. Other kinds of proteins were similarly coupled through electrostatic interactions [42–47], e.g., the directed adsorption of heme-containing redox enzymes at citrate-stabilized silver nanoparticles [42–44]. In a different approach, nanoparticles were also coupled to proteins by using linkers based on thiols or disulfides and phosphane ligands, which possess terminal carboxy, amino, and maleimide groups [48, 49]. Here the coupling is achieved by means of carbodiimide-mediated esterification and amidation or reaction with thiol groups. This strategy was routinely used for histological purposes by coupling proteins with well-defined 0.8 nm undecagold nanoclusters stabilized with arylphosphanes [48]. Cyclic disulfide linkers for coupling showed a better affinity to nanoparticles, and these conjugates are more stable towards ligand exchange than those prepared with a single thiol group or acyclic disulfide units. The high stability is probably a result of attaching the ligands to the nanoparticles through two sulfur atoms. These disulfide linkers have been used in generating gold nanoparticle–oligonucleotide conjugates as probes for recognizing specific sequences in DNA segments and as building blocks for assembling novel structures and materials [50].

The above-mentioned ligands have also been exploited to impart biocompatibility and bioactive functionalities to semiconductor nanoparticles through surface modification with biomolecules [10, 11, 16, 51–58]. There has been significant progress in the understanding of specificity and binding capabilities of proteins toward nanoscale semiconductor particles. [10, 11, 16, 51–64]. Globular protein bovine serum albumin (BSA) has been one of the widely used proteins. For example, BSA was used to form a bioconjugate with luminescent CdTe, CdS and CdSe nanoparticles, often referred to as quantum dots (QDs) [56, 61]. Such QDs are character-

ized by broad excitation and size-tunable photoluminescence spectra with narrow emission bandwidths that span the visible spectrum, allowing simultaneous excitation of several particle sizes at a single wavelength. They also have exceptional photochemical stability and relatively high quantum yields when used as luminescent probes in biological labeling [17–22]. Mamedova et al. [56] generated bioconjugates of BSA protein with cysteine-capped 2 nm-sized CdTe nanoparticles by using glutaric dialdehyde as a crosslinking agent. Such conjugation was reported to increase the luminescence intensities of the CdTe nanoparticles, which was attributed to the possible presence of resonance energy transfer from the tryptophan moieties in BSA to the CdTe nanoparticles. In a different study by Willard et al. [61] CdSe-ZnS core/shell particles of  $\sim 3$  nm were coated by chemisorption to biotinylated BSA, which was specifically attached to tetramethylrhodamine-labeled streptavidin (Sav-TMR) (Fig. 7.2). In this conjugate, the TMR fluorescence caused by fluorescence resonance energy transfer (FRET) from the QD donors to the TMR acceptors was enhanced. In separate work, the same CdSe-ZnS core/shell nanoparticles, stabilized by dihydrolipoic acid ligands, were also coated with a recombinant variant of maltose-binding protein (MBP) containing a pentahistidine segment at its C-terminus and a single Cy3 fluorophore covalently attached to a distinct cysteine residue [62]. The binding sites of the approximately 10 MBP molecules per QD were occupied by  $\beta$ -cyclodextrin-Cy3.5 ( $\beta$ -CD-Cy3.5) conjugates. Also within these defined conjugates, the protein-bound Cy3 served as a bridging acceptor/donor for energy transfer from the QD to the maltose-displaceable  $\beta$ -CD-Cy3.5.

In many other cases, however, a simple thiol bond to the particle surface was not sufficient to accomplish a permanent linkage. Instead, an equilibrium is established, with dynamic ligand exchange. To avoid this, a shell of silica is often grown on the particle by means of a sol-gel technique, and the linkage groups pointing outward are added as functionalized alkoxysilanes during the polycondensation process [17]. Recently, thiolated DNA has been linked to the surface of silanized CdSe/ZnS particles through a heterofunctional linker. On an ideally shaped surface, the number of linkage groups should be adjustable, and inert functional groups that determine the solubility and the surface potential of the particles should be added. The linkage groups of the ligands should adhere to the crystallite surface as much as possible, and the ligands should be covalently linked together to avoid exchange completely.

Two fascinating examples of coupling biomolecules with inorganic nanoparticles have been reported recently. One, by Ishii et al. [58], used a wrapping approach to encapsulate 2–4 nm-sized CdS particles within chaperonin proteins. The chaperonin proteins GroEL and *T.th* encapsulate denatured proteins inside a cylindrical cavity. After refolding, the encapsulated proteins are released by the action of ATP, which induces a conformational change in the chaperonin's cavity. These proteins are characterized by a cylindrical cavity with a diameter of 4.5 nm and a wall thickness of 4.6 nm. For complexation, a solution of 2–4 nm-sized CdS particles in dimethylformamide was mixed with an aqueous solution of the chaperonin proteins in Tris-HCl buffer. The characteristic photoluminescence of the CdS particles within the chaperonin-CdS nanoparticle complex lasted for an unusually

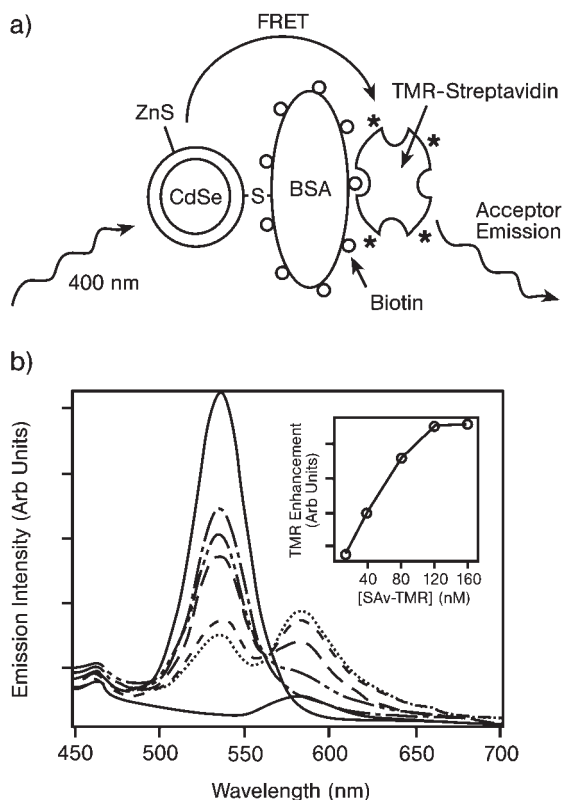


**Fig. 7.2.** (a) Scheme of a FRET system assembled by chemisorption of thiol-modified biotinylated BSA to CdSe (QD) and subsequent coupling of TMR-STV. (b) Fluorescence emission spectra from solutions containing  $\sim 15$  nM QD-bBSA and 0 (—), 16 (— — —), 40 (— — — —), 80 (— — — — —), 120 (— — — — — —), and 160 nM (— — — — — — — —)

SA/TMR. The lower solid curve is from a 160 nM SA/TMR control. An excitation wavelength of 400 nm was used for all samples. Inset: enhanced TMR fluorescence intensity at 585 nm from QD-bBSA/SA/TMR solutions as a function of SA/TMR concentration. (From Ref. [61].)

long time (more than 400 days) in the presence of GroEL complexes; in the absence of GroEL, photoluminescence disappeared within 2 hours. The second example, reported by Willner and et al. [64], consisted of nanowiring redox enzymes with gold nanoparticles to enhance the routing of electrons from the enzymes to electrodes. An “electrical nanoplug” was obtained by assembling an Au nanoparticles (1.4 nm)–glucose oxidase (GOx) conjugate at the macroscopic Au electrode. The bridge between the macroscopic electrode and the gold nanoparticles consisted of dithiol spacer units. Investigation of the catalytic properties of the assembly by cyclic voltammetry revealed that glucose oxidation occurred with a unimolecular electron-transfer seven times higher than the electron-transfer rate constant of native GOx with  $O_2$ .



While the use of surface-modified nanoparticles has been a typical route in preparing conjugates, the linker and chemical functionalization for the modification are added complications to an already sophisticated conjugate system. However, despite some obvious advantages, direct conjugation of biological species to inorganic nanoparticles has not been a common practice. This is probably a result of the generally incompatible experimental conditions required for biological species and for the formation and stabilization of nanoparticles. Some recent examples of direct coupling are highlighted below.

### 7.2.2

#### **Protein-assisted Assemblies of Inorganic Nanoparticles**

Self-assembly processes represent the state-of-the-art for organizing nanoscale objects into periodically ordered macroscopic materials. While this biomimetic process is not new, scientists have only recently begun to realize its potential for the artificial control of matter. This interesting class of nanomaterials provides exceptional potential for a wide variety of applications, including photonic and memory devices, two-dimensional (2D) arrays of magnetic nanoparticles [65–70]. Methods developed to produce these bulk-like hierarchical structures include biomimetic methods and amphiphile and colloidal templating, among others. In this section, we review only those approaches related to the use of proteins as crosslinkers, or as templates (assemblies and systems), in the organization and patterning of inorganic nanoparticles into two- and three-dimensional functional structures.

##### **7.2.2.1 Crosslinking Route through Protein Recognition**

Protein molecules can serve as crosslinkers because of their tremendous recognition capabilities. Their coupling to nanoparticles has generally been performed in three ways (Fig. 7.3): (a) nanoparticles are functionalized with individual recognition groups that are complementary; (b) particle-bound recognition groups are bridged through a bispecific linker molecule; and (c) a bispecific linker that directly recognizes the surfaces of the nanoparticles is used.

One protein system with highly specific recognition properties consists of antibodies and antigens, which are excellent candidate molecules for the programmed assembly of a wide range of nanoparticles in solution. Shenton et al. [40] first reported a strategy based on the surface attachment of either IgE or IgG antibodies followed by interparticle conjugation of gold and silver in the presence of bivalent antigens with appropriate double-headed functionalities (Fig. 7.3). The resulting structures were in the form of macroscopic filaments that consisted of a network of spatially separated Au and Ag nanoparticles. Similarly, streptavidin (STV)–biotin binding has been used to assemble nanocrystals in solution or onto a substrate. The STV–biotin interaction is considered the strongest ligand–receptor interaction currently known [12, 13]. Another great advantage of STV is its extreme chemical and thermal stability. Connolly and Fitzmaurice [13] used this approach to functionalize gold nanocrystals by chemisorption of a disulfide biotin analogue (DSBA), and then crosslinked by multi-site binding on subsequent addition of the

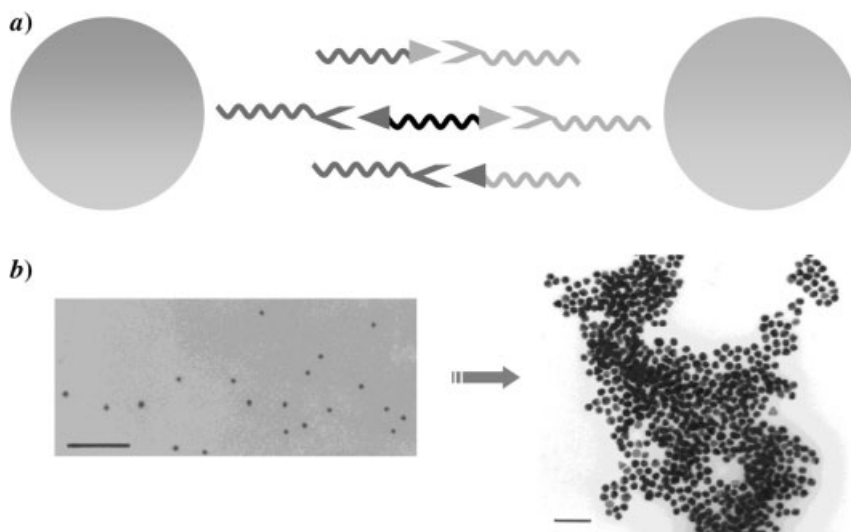
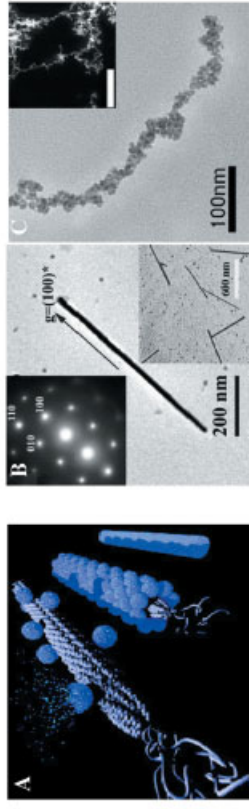
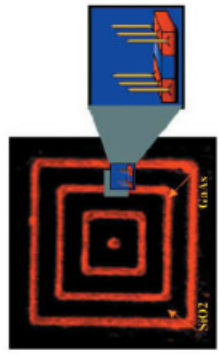
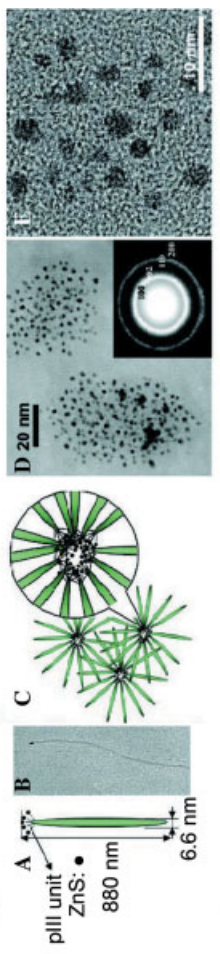
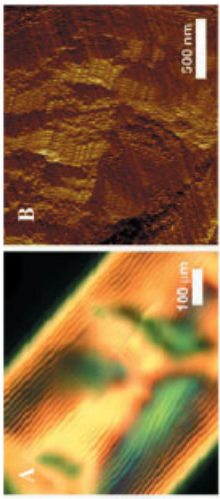
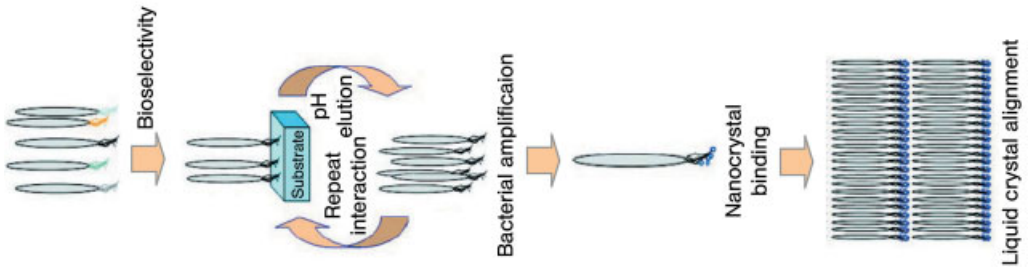


**Fig. 7.3.** (a) Scheme showing the approaches based on protein recognition systems for the assembly of nanoparticles in solution. (b) Example of TEM images showing colloidal Au/anti-dinitrophenyl DNP antibody conjugate before (left) and after (right) addition of DNP-DNP double-headed antigen. Scale bars 150 and 60 nm, respectively. (From Ref. [40].)

protein, streptavidin. The applicability of the STV–biotin system for generating supramolecular aggregates is also enhanced by the availability of various biotin analogues [71, 72] and recombinant STV mutants [73–77].

Today, with the power of biotechnological innovations, it is also possible to generate new proteins that can specifically recognize and grow inorganic “building blocks” (Fig. 7.4). This is a promising approach for selecting peptides that can recognize specific inorganic crystals and crystallographic orientations of nonbiological origin, including InP, GaAs, and Si [52], and can control II–VI (ZnS, CdS, CdSe, ZnSe, and PbS) semiconductor nanocrystal size, crystal structure, shape, and optical properties.

To identify the appropriate compatibilities and combinations of biological–inorganic materials, a combinatorial library of genetically engineered M13 bacteriophage was used to rapidly select peptides that could not only recognize but also control the growth of specific inorganic materials (Fig. 7.4). The phage display library is based on a combinatorial library of random peptides of a given length (e.g., 7 or 12 mers) that are fused to the pIII minor coat protein of the filamentous coliphage M13. Five copies of the fused random pIII coat protein are located on one end of the phage particle and account for 10–16 nm of the particle. Belcher and co-workers [52] used phage display to select peptide sequences with binding specificity for III–V semiconductor materials based on pIII minor coat protein expression. Brown [78] used repeating polypeptides displayed on the surface of the



bacterium *Escherichia coli* to bind selectively to metal particles. Selected viral-bound pIII peptides can also be used to nucleate II–VI materials for which they were selected [79]. Highly ordered composite material from genetically engineered M13 bacteriophage and ZnS nanocrystals has been generated by using a liquid crystal system (Fig. 7.4) [80–82]. The nucleating peptides have also been expressed in higher copy number along the protein VIII (pVIII) major protein coat of the virus, facilitating the organization of II–VI nanocrystals into highly ordered nanowires [83]. Recently, a virus-based scaffold produced through the self-assembly motifs employed by the M13 bacteriophage was used as a template for the synthesis of single-crystal ZnS, CdS, and freestanding chemically ordered CoPt and FePt nanowires, with the means of modifying substrate specificity through standard biological methods [84].

### 7.2.2.2 Template-directed Approach

An alternative approach to establish nanoparticle organization in supramolecular architectures involves the *in situ* formation of nanoparticles within preformed biological or biomimetic templates; in particular, those based on regular 2D lattices of bacterial cell surface proteins and hollow biomolecular compartments such as virus particles.

Crystalline bacterial cell surface layers (S-layers) are one of the most common outermost cell envelope components of a broad spectrum of bacteria and archaea. These S-layers are monomolecular arrays composed of a single protein or glycoprotein species and represent the simplest biological membranes developed during evolution. S-layer lattices exhibit either oblique, square or hexagonal lattice symmetry with unit cell dimensions in the range of 3–30 nm, and they are generally

---

**Fig. 7.4.** Left-hand side: scheme of the process used to generate nanocrystal alignment by the phage display method. Right-hand side: (a) Characterization of the liquid crystalline suspensions of A7 phage-ZnS nanocrystals (A7-ZnS) and cast film. (A) Characteristic fingerprint texture of the cholesteric phase of an A7-ZnS suspension ( $76 \text{ mg mL}^{-1}$ ). (B) AFM image of a cast film from an A7-ZnS suspension showing close-packed structures of the A7 phage particles. (b) (A) Scheme of the individual A7 phage and ZnS nanocrystals. (B) TEM image of an individual A7 phage and ZnS nanocrystals, stained with 2% uranyl acetate. (C) Schematic of the micelle-like structures, in which ZnS nanocrystal aggregates are surrounded by A7 phage. (D) The sample shows that 100 to 150 nanocrystals formed aggregates. (E) High-resolution TEM image of A7-ZnS suspension, showing lattice fringe images of wurtzite ZnS nanocrystals. (From Ref. [80].) (c) Phage recognition of semiconductor heterostructures; fluorescence images related to GaAs recognition by phage. (From Ref. [52].) (d) Visualization of the M13 bacteriophage and subsequent nanowire synthesis. (A) The nanowire synthesis scheme is visualized for the nucleation, ordering, and annealing of virus-particle assemblies. (B) Bright-field TEM image of an individual ZnS single-crystal nanowire formed after annealing. Inset, upper left: ED pattern along the [001] zone axis, showing a single-crystal wurtzite structure of the annealed ZnS nanowire. Inset, lower right: Low-magnification TEM image showing the monodisperse, isolated single-crystal nanowires. (C) TEM image of the unannealed CoPt nanoparticle-virus system. Inset: STEM image of the unannealed CoPt wires. (From Ref. [84].)

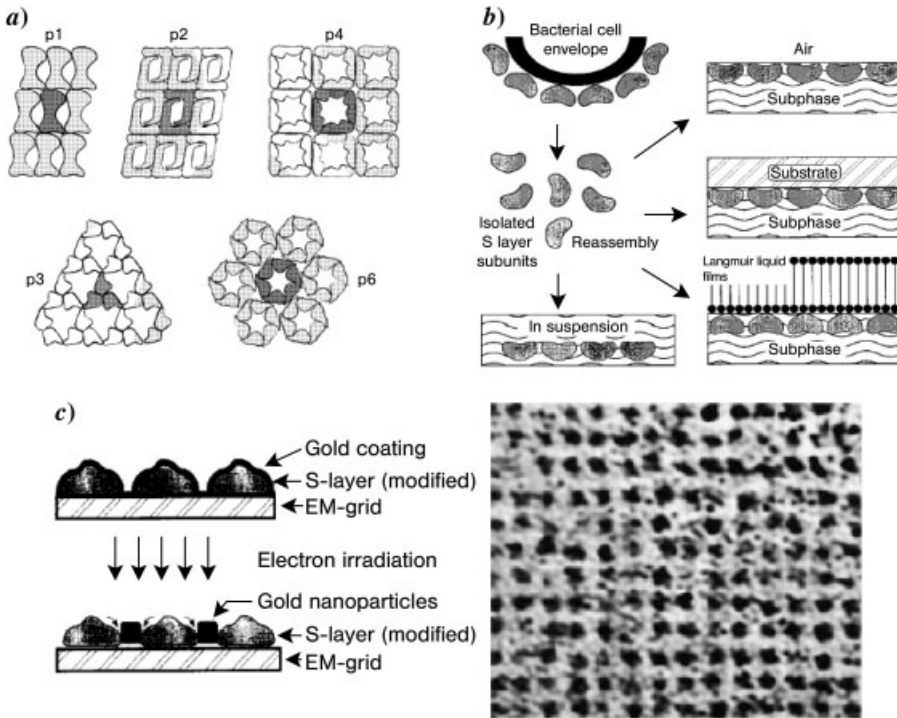


**Fig. 7.5.** (a) Different S-layer lattice types with oblique (p1, p2), square (p4), or hexagonal (p3, p6) symmetry. (b) Isolation of S-layer proteins from bacterial cells and their reassembly into crystalline arrays in suspension. (c) TEM image of gold nanoparticles prepared by using a square S-layer lattice. (From Ref. [85].)

5–10 nm thick and show pores of identical size (diameter, 2–8 nm) and morphology. The availability of these regular pores within the 2D protein crystal S-layers has allowed controlled nucleation of inorganic nanoparticles into ordered arrays (Fig. 7.5) [85].

Recently, it was demonstrated that S-layer proteins recrystallized on solid supports, or S-layer self-assembly products deposited on such supports, may be used to induce the formation of CdS particles [86] or gold nanoparticles [87, 88]. Inorganic superlattices of CdS with either oblique or square lattice symmetries were prepared by exposing self-assembled S-layer lattices to CdCl<sub>2</sub> solutions followed by slow reaction with H<sub>2</sub>S. Precipitation of the inorganic phase was confined to the pores of the S-layers, with the result that CdS superlattices with prescribed symmetries were prepared. In a similar procedure, a square superlattice of uniform 4 to 5 nm-size gold particles with a 12.8 nm repeat distance was generated [87]. In this procedure, a square S-layer lattice chemically modified with thiol groups was exposed to tetrachloroauric(III) acid and then electronically irradiated through TEM.

The shape of the gold particles resembled the morphology of the pore region of the square S-layer lattice. Electron-diffraction patterns revealed that the gold nanoparticles failed to form a perfect lattice. These experiments were repeated with a broad range of metal salts, such as  $\text{PdCl}_2$ ,  $\text{NiSO}_4$ ,  $\text{KPtCl}_6$ ,  $\text{Pb}(\text{NO}_3)_2$ , and  $\text{K}_3\text{Fe}(\text{CN})_6$  [89]. In general, the inner cavities of the protein layer serve as localized reservoirs of cations that are reduced *in situ* to metal clusters under the electron beam. These experiments clearly demonstrated that nanocrystal superlattices can be induced by S-layers as templates with a broad range of particle sizes (5–15 nm in diameter), interparticle spacings (up to 30 nm), and lattice symmetries (oblique, square or hexagonal).

Other processes dealing with the hollow protein compartments have also yielded fascinating results in the generation and assembly of nanoparticles (Fig. 7.6). For instance, the ferritin-like protein of the bacteria *Listeria innocua* [90] and the cowpea chlorotic mottle virus (CCMV) [91] furnished a suitable constrained reaction environment for the synthesis of monodisperse inorganic nanoparticles since they have hollow spherical supramolecular structures with internal cavity diameters of 5 and 18–24 nm, respectively. In both systems, the interior surfaces have regions of high charge density, which act as sites for synthetic mineral nucleation. Iron oxide particles of about 5 and 27 nm, respectively, were generated through incubation of these protein templates with iron(II) solutions at controlled pH and temperature followed by oxidation [90, 91]. The organization of these bioinorganic nanoparticles into network structures was also explored, e.g., through the coupling of biotin recognition groups to the ferritin and then conjugation in solution with streptavidin [14]. In other work, iron oxide nanoparticles of about 8 nm were also synthesized within the cavity of lumazine synthase protein [92].

Similarly, wild-type and recombinant tobacco mosaic virus (TMV) hollow cylinders have been used as templates to generate inorganic-organic nanotube composites by means of template mineralization [93–96]. The highly polar exterior surface of TMV has been used for surface mineralization of iron oxyhydroxides, CdS, PbS, and silica [95]. These materials form a thin coating over the virus nanorod, affording inorganic nanofibrils 20–30 nm in diameter and as long as 1  $\mu\text{m}$ . Dujardin et al. [96] recently used TMV as a template for the alignment and controlled deposition of Pt, Au, and Ag nanoparticles. By varying the deposition conditions, they demonstrated that one can either specifically decorate the external surface with metallic nanoparticles via the chemical reduction of  $[\text{PtCl}_6]_2^-$  or  $[\text{AuCl}_4]_2^-$  or obtain constrained growth of Ag nanoparticles within the 4 nm internal channel present in the virus through the photochemical reduction of Ag salts. In principle, as suggested by these investigators, 1D arrays of a wide range of quantum dots should become accessible by engineering and templated mineralization of the internal and external surfaces of TMV tubules. Microtubules prepared by polymerization of the protein tubulin have also been utilized as templates for the synthesis of inorganic nanomaterials [97].

The above examples demonstrate that sophisticated nanostructured architectures can be designed when protein molecules and nanoparticles are combined. Future

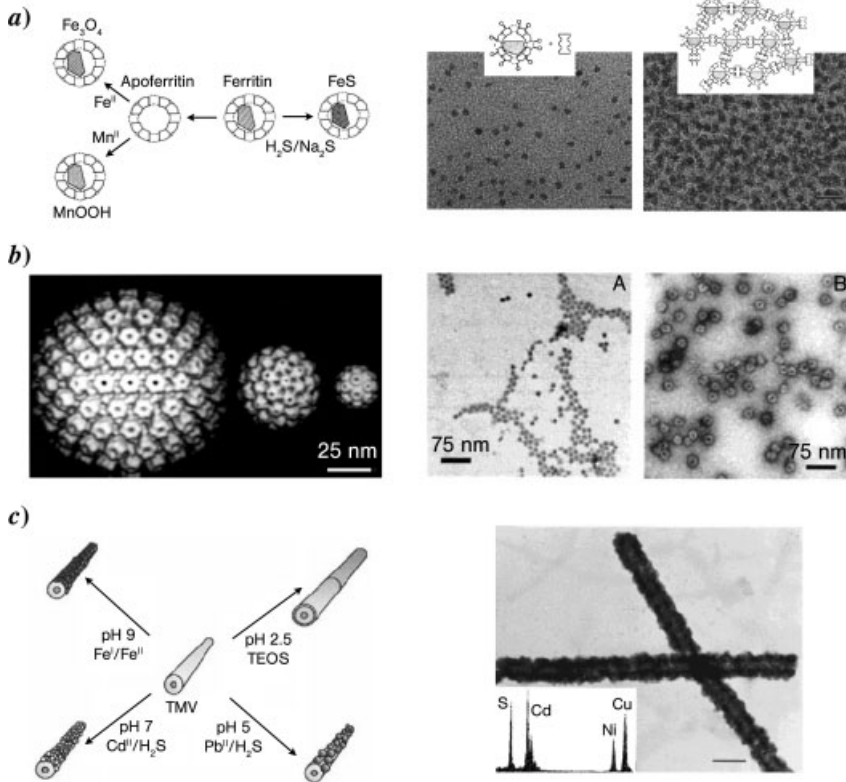


**Fig. 7.6.** (a) (left): Hollow protein cages used for the growth of inorganic nanoparticles; (right) schematic and TEM images showing biotin–streptavidin crosslinking of inorganic magnetic nanoparticles encapsulated within ferritin. (From Ref. [14].) (b) (left): Image reconstructions of spherical viruses with different diameters: equine herpes (100 nm), cauliflower mosaic (50 nm), and CCMV (26 nm). (right) TEM images of (A) assembled

CCMV virions mineralized with cores of  $(\text{NH}_4)_{10}\text{H}_2\text{W}_{12}\text{O}_{42}$  showing electron dense mineral particles and (B) negatively stained samples of mineralized CCMV, showing the presence of the protein coat surrounding each mineral particle. (From Ref. [54].) (c) (left): Synthesis of nanotube composites using TMV templates. (right) Example TEM image of CdS-mineralized TMV particles, scale bar 50 nm. (From Ref. [95].)

development in this field will benefit from the rapid advances being made in chemistry and protein technology. However, there is still a great demand for alternative methods to resolve typical problems that arise in the biofunctionalization of inorganic nanoparticles. In particular, harsh reaction conditions often lead to the degradation and inactivation of sensitive biological compounds, and to the formation of unstable bioconjugates because of ligand-exchange reactions that occur at the colloid surface. Among other limitations associated with these processes are excessive solvent use, disposal and trace residues, and multi-step operations.

## 7.2.3

**Supercritical Fluid Methods**

Supercritical fluid (SCF) technology in nanomaterial preparation and processing is one alternative method in the biofunctionalization of inorganic nanoparticles that shows great promise in addressing many of the challenges highlighted above. SCFs are solvents operating above their critical temperature and pressure. Among the most important properties of SCFs are their low and tunable densities, which can be easily varied from gas-like to liquid-like via a simple change in pressure at constant temperature. Numerous investigations have been conducted on SCFs [98–103]. Results have demonstrated their unique advantages as alternative media for both chemical reactions and materials processing. Example applications and related advantages are their use as environmentally benign solvents [98], the ability to selectively tune chemical reactions or processes [104–110], enhancement of reaction rates due to the low viscosities or high diffusivities in the fluids [109–110], the ability to solvate or precipitate solutes selectively [111], and the production of fine particles and fibers via rapidly expanding SCF solutions [112, 113].

Among the most widely investigated techniques for the processing of fine particles are SAS (Supercritical Anti-Solvent) [114–117] and RESS (Rapid Expansion of Supercritical Solutions) [118–123]. These techniques have comprehensively reviewed [102, 103]. Briefly, in RESS the solute is dissolved in a SCF, and then the solution is rapidly expanded through a small nozzle or orifice into a region of lower pressure [114, 118, 124, 125]. The rapid reduction in pressure (and thus, density) results in rapid precipitation of the solute. Experimentally, the supercritical solution can be generated either by heating and pressurizing a solution from room temperature or by continuously extracting the solute using an extraction column [125]. The RESS process is driven by a decrease in pressure, which can propagate at up to the speed of sound in the expansion nozzle. Because solubilities in SCFs can be up to a million times higher than those under ideal gas conditions, rapid expansion from supercritical pressure to ambient pressure results in extremely high supersaturation (and, consequently, homogeneous nucleation of the solute), leading to narrow size distributions in the products. Cosolvents, such as methanol or acetone, can be mixed with carbon dioxide (CO<sub>2</sub>) to increase the solvating power in RESS.

Because some compounds in commonly used SCFs have low solubility, the SAS process was developed. In SAS precipitation, one or more solutes immiscible with SCF are dissolved in a conventional solvent that is miscible with SCF. The solution is then “mixed” with the SCF to precipitate the solute particles. This can be achieved by introducing the SCF into a batch of solution in a chamber or by spraying solution through a nozzle into an SCF-filled chamber. A variation of this process is to mix solution and SCF continuously in a co-current or a counter-current fashion. Other minor variations of this mode of operation of antisolvent process are the bases for several techniques now in use, including Precipitation with Compressed Antisolvent (PCA), Solution Enhanced-dispersion by Supercritical fluids (SEDS), and Aerosol Supercritical Extraction System (ASES) [126–128]. All these



processes have been used to produce micron and submicron particles from various materials, including inorganics (metal, semiconductor), polymers, proteins, and other small organic molecules such as drugs [102, 103]. For example, several pharmaceutical compounds, such as lovastatin, stigmaterol, salicylic acid and theophylline, have been processed via RESS into micron- and sub-micron-sized particles [102]. Several reports have also considered using the RESS process for the direct formulation of drug:polymer systems by a co-precipitation strategy. The SAS process also produced micron-sized particles of proteins such as insulin, lysozyme and trypsin. Adding a polymer to the system as a carrier may furnish active protein-loaded microparticles.

Results from these experiments and others suggest that these processes generally produce micron- or submicron-sized particles [113, 129–132]. For nano-sized particles, Sun and co-workers [102, 103] made a simple but significant modification to the traditional RESS by using a liquid solvent or solution at the receiving end of the supercritical solution expansion, or the Rapid Expansion of a Supercritical Solution into a Liquid SOLvent (RESOLV). The RESOLV process produces exclusively nanoparticles from various materials [59, 60, 102, 103, 133–140]. For example, cadmium sulfide (CdS) nanoparticles of  $\sim 3$  nm in average diameter have been prepared using RESOLV by rapidly expanding a supercritical ammonia solution of  $\text{Cd}(\text{NO}_3)_2$  into a room-temperature aqueous or ethanol solution of  $\text{Na}_2\text{S}$  [133]. The nanoparticles so-produced could be prevented from aggregating by the presence of a polymeric or other protection agent in the receiving solution [133]. The same RESOLV process with a similar reaction scheme has been applied to the production of many other metal and semiconductor nanoparticles. These nanoparticles are all small, on average less than 10 nm in diameter, and are protected to form stable suspensions [59, 60, 102, 103, 133–138]. As recognized by Sun and co-workers [59, 60, 138], a unique feature of the RESOLV process for nanoparticle production is that it requires no nanoscale templating agents for nanoparticle formation because the templating effect is provided by the supercritical fluid rapid expansion process, thus offering a clean way to directly couple nanoparticles with biological species. For example, Sun and co-workers have demonstrated recently that the metal and semiconductor nanoparticles coated directly with natural protein species could be prepared in the RESOLV process [59, 60, 138]. Figure 7.7 shows a typical RESOLV apparatus for preparing protein-conjugated nanoparticles.

#### 7.2.3.1 BSA-conjugated Silver Nanoparticles

An example use of RESOLV in the direct conjugation of nanoparticles with proteins is the coupling of nanoscale Ag with bovine serum albumin (BSA) [138]. Typically, a methanol solution of  $\text{AgNO}_3$  was added to the syringe pump, followed by evaporation of the solvent methanol. The syringe pump was then filled with liquid ammonia. When pumped through the heating unit, the ammonia solution of  $\text{AgNO}_3$  was heated and equilibrated at  $160^\circ\text{C}$  before reaching the expansion nozzle. The supercritical solution was rapidly expanded via a  $50\ \mu\text{m}$  fused silica capillary nozzle into a room-temperature aqueous solution of  $\text{N}_2\text{H}_4$  or  $\text{NaBH}_4$ . The system pressure was kept constant during the rapid expansion. BSA protein was in

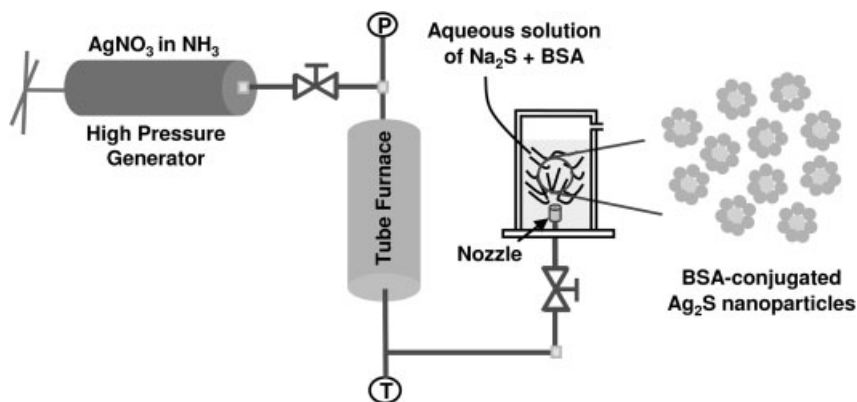


Fig. 7.7. Experimental setup for preparing protein-conjugated Ag<sub>2</sub>S nanoparticles via RESOLV [60].

the aqueous receiving solution for direct conjugation with the Ag nanoparticles as they form in the rapid expansion process.

The BSA-conjugated Ag nanoparticles form a stable aqueous suspension that resembles a homogeneous solution. As shown in Fig. 7.8(a), the surface plasmon absorption band ( $\sim 420$  nm) of the Ag nanoparticles broadens upon protein conjugation, reflecting changes in nanoparticle surface properties due to interactions with the protein species. X-Ray powder diffraction analyses of the solid-state samples (Fig. 7.8a) confirmed the expected presence of nanoscale Ag (fcc) particles. Figure 7.8(b) shows the low and high-resolution TEM images of BSA-protected Ag nanoparticles with hydrazine reductions. The average particle size and size distribution standard deviation are 43 and 10 nm, respectively. These nanoparticles appear to be polycrystalline with multiple misaligned lattice fringes, suggesting that the BSA-protected Ag nanoparticles are probably agglomerated smaller nanoparticles. Gel electrophoresis, used to analyze the conformation of BSA protein conjugated to Ag nanoparticles, showed two bands corresponding to BSA monomer and dimer that were much weaker in the nanoparticle sample than in the blank BSA sample; most of the nanoparticle sample becomes stationary, appearing at the gel onset. These low mobility species are probably BSA-protected Ag nanoparticles.

The assembly of smaller Ag nanoparticles produced initially in RESOLV with chemical reduction is likely driven by protein aggregation to form larger, but relatively well-organized, structures of Ag nanoparticles (Fig. 7.8c).

### 7.2.3.2 BSA-conjugated Semiconductor Nanoparticles

BSA-conjugated Ag<sub>2</sub>S and CdS nanoparticles have also been prepared via the RESOLV procedure [59, 60]. Similar experimental parameters were used to produce Ag<sub>2</sub>S and luminescent CdS nanoparticles. Here, a supercritical ammonia solution of AgNO<sub>3</sub> or Cd(NO<sub>3</sub>)<sub>2</sub> was used in the rapid expansion and a room-temperature aqueous solution of Na<sub>2</sub>S (10 mg mL<sup>-1</sup>) was at the receiving end. After rapid ex-

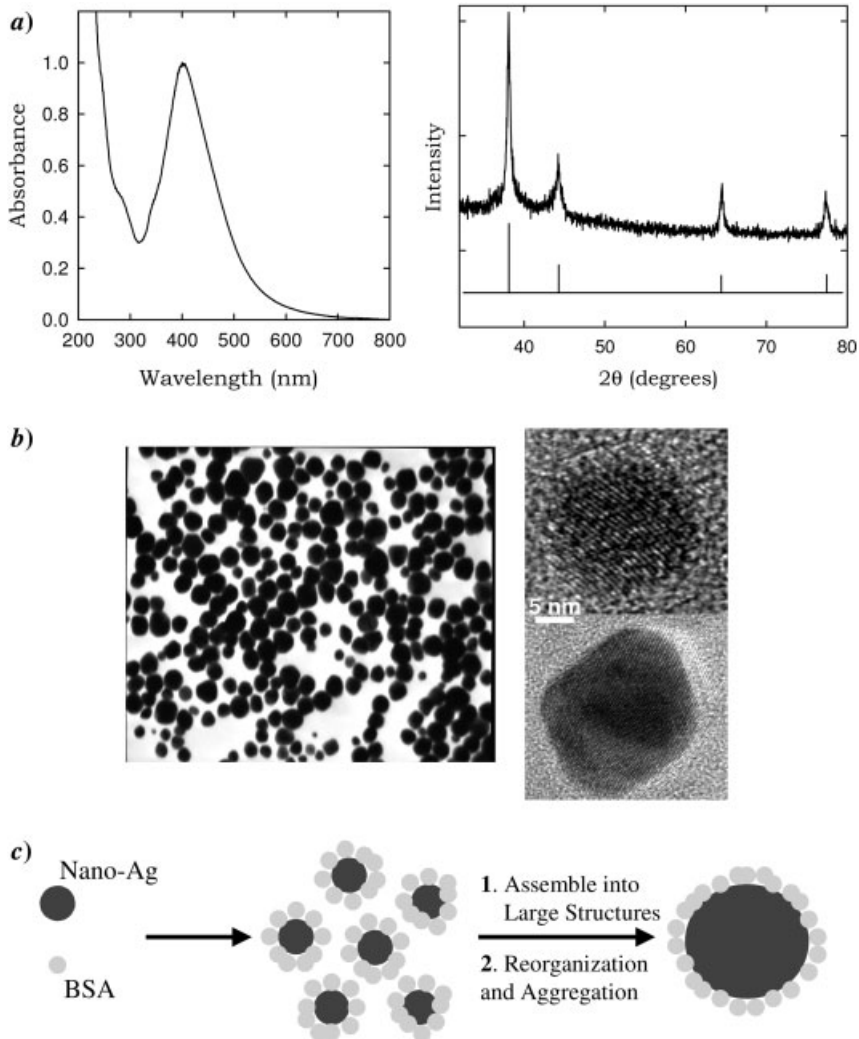


**Fig. 7.8.** (a) UV/Vis absorption spectrum (left) and X-ray powder diffraction pattern (right) of the BSA-conjugated Ag nanoparticles prepared via RESOLV. (b) TEM images of BSA-conjugated Ag nanoparticles. (c) Scheme illustrating the assembly of smaller protein-conjugated Ag nanoparticles into larger and organized structures, driven by protein aggregation. (From Ref. [138].)

pansion was complete, the ambient suspension of nanoparticles was transferred to membrane tubing with large pore sizes for dialysis to remove free BSA and other salts and reagents.

BSA-conjugated  $\text{Ag}_2\text{S}$  nanoparticles thus produced in RESOLV form a yellowish suspension without precipitation under ambient conditions. The UV/Vis absorption spectrum of the nanoparticle suspension is a structureless curve with gradu-

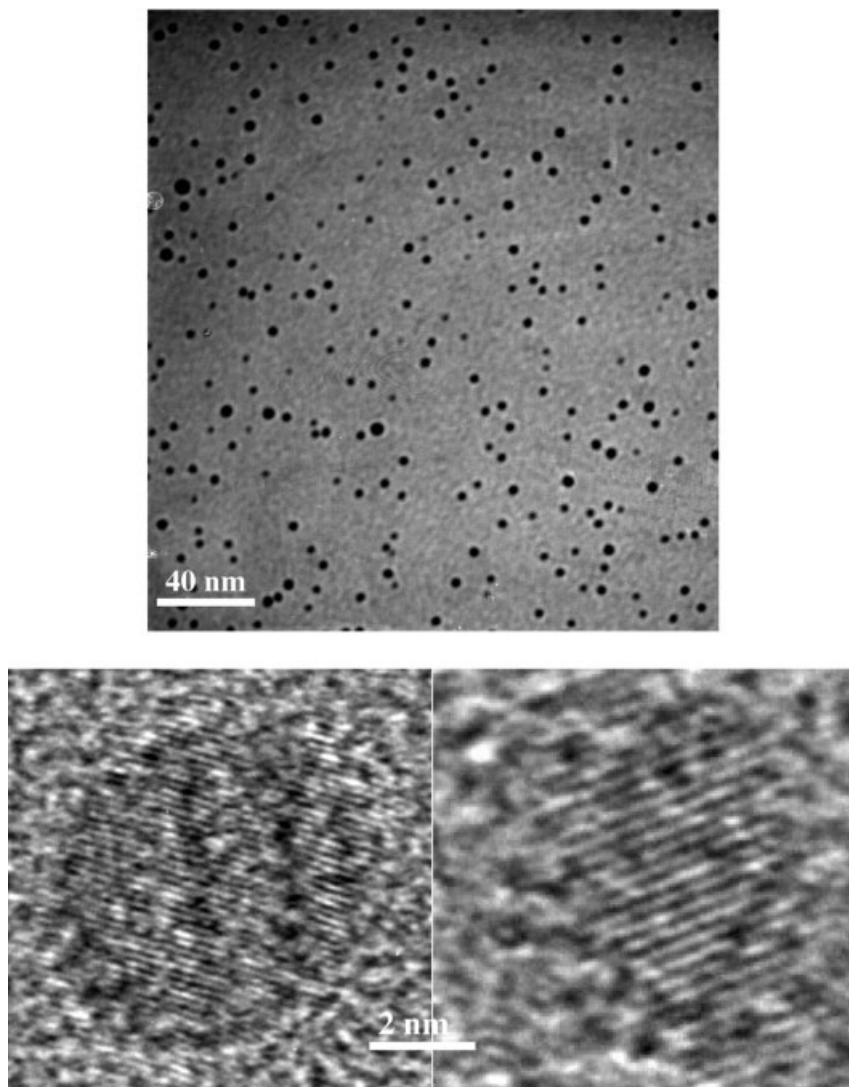


**Fig. 7.9.** TEM images of BSA-conjugated  $\text{Ag}_2\text{S}$  nanoparticles prepared via RESOLV and then dialysis. (From Ref. [60].)

ally increasing absorbance towards shorter wavelengths, indicating that these nanoparticles are quantum confined. According to TEM analyses (Fig. 7.9), the BSA-conjugated  $\text{Ag}_2\text{S}$  nanoparticles are well-dispersed, mostly single crystals, with an average particle size of 6.3 nm and a size distribution standard deviation of 1.6 nm.

Atomic force microscopy (AFM) results (Fig. 7.10) provide strong evidence for well-dispersed  $\text{Ag}_2\text{S}$  nanoparticles uniformly coated with BSA in a core/shell-like

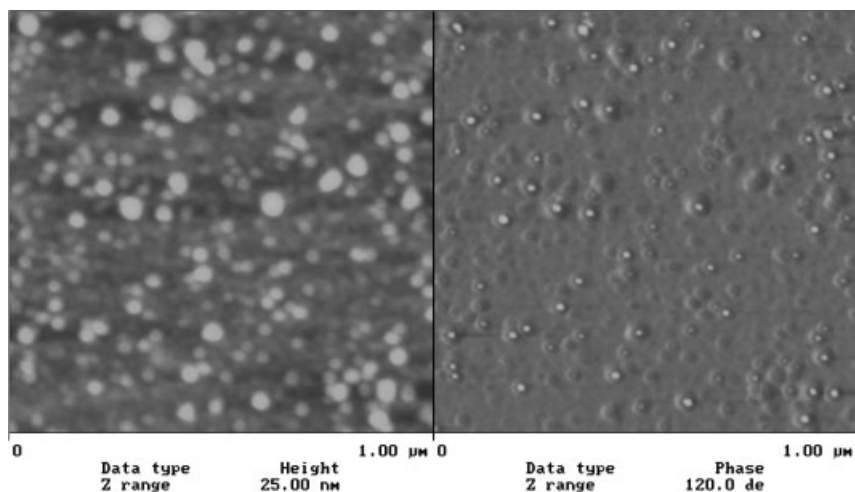


**Fig. 7.10.** Height (left) and phase (right) images from the AFM analysis of BSA-conjugated  $\text{Ag}_2\text{S}$  nanoparticles prepared via RESOLV and then dialysis. (From Ref. [60].)

arrangement, with overall circular features of 20–30 nm (the larger apparent particle size is due to the tip convolution effect [141]).

Similarly, a yellowish homogeneous suspension of BSA-conjugated CdS nanoparticles was obtained after dialysis. Apparently, interactions between BSA protein species and CdS nanoparticles are relatively strong to sustain the conjugation [59]. The UV/Vis absorption spectrum of the suspension exhibits a well-defined peak at 320 nm (Fig. 7.11a), indicating that the BSA-conjugated CdS nanoparticles are around 2–3 nm in diameter [142]. According to powder X-ray diffraction analysis, the nanoparticle sample is probably a mixture of cubic and hexagonal CdS. TEM results (Fig. 7.11b) show that the CdS nanoparticles are mostly single crystals with an average particle size of 2.9 nm and a size distribution standard deviation of 0.7 nm.

BSA protein species conjugated to the CdS nanoparticle surface have been visualized via AFM imaging (Fig. 7.12a). These images are dominated by circular features of around 20 nm in size, which are consistent with well-dispersed individual CdS nanoparticles that are each coated with BSA protein species in a core/shell-like arrangement [59]. The presence of BSA on the CdS nanoparticle surface is also made evident by the well-known affinity of the conjugate to the surface of nanoscale gold (Fig. 7.12b) [16, 143].

BSA-conjugated CdS nanoparticles produced via RESOLV have interesting luminescence properties (Fig. 7.13). The luminescence spectrum has a relatively narrow bandwidth close to the absorption onset with no surface defect emissions at long wavelengths. This is primarily the exciton emission associated with band-gap excitation [142]. The observed luminescence quantum yield is high, ~20% with

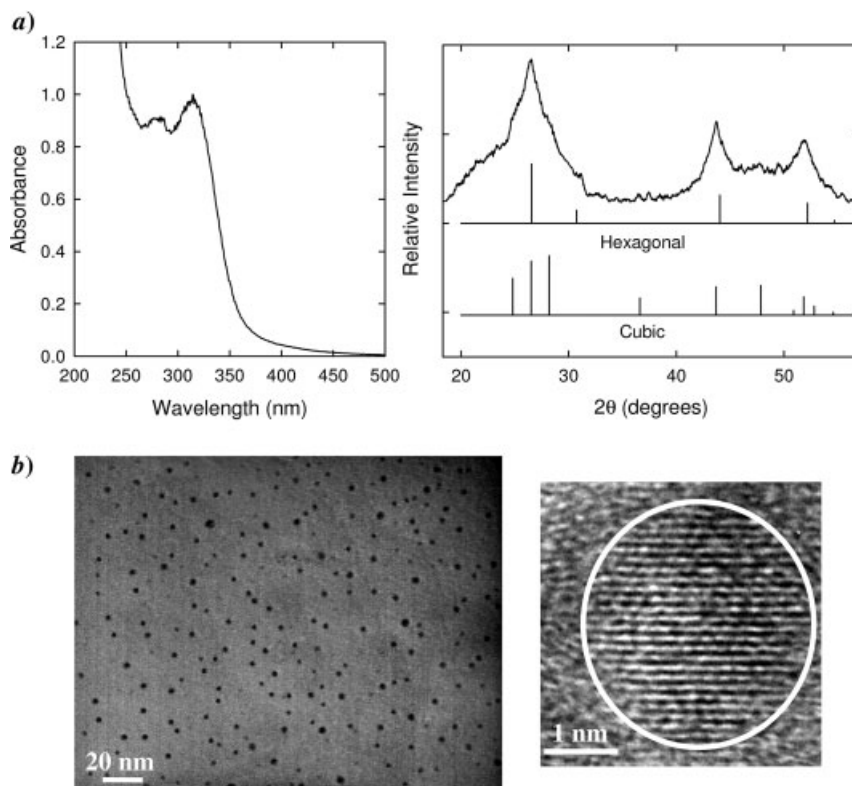


**Fig. 7.11.** (a) UV/Vis absorption spectrum (left) and X-ray powder diffraction pattern (right) of the BSA-conjugated CdS nanoparticles. (b) TEM images of the BSA-conjugated CdS nanoparticles. (From Ref. [59].)

reference to the fluorescence standard 9,10-diphenylanthracene, which is also consistent with substantial contributions from exciton emission [142]. The rapid expansion of supercritical ammonia solution may have a special passivation effect on the nanoparticle surface [133], suppressing the surface defect luminescence and enhancing the exciton emission from the CdS nanoparticle [133, 142, 144]. Conversely, the broad emission seen for CdS nanoparticles generated by other methods, such as those encapsulated in the micelles of sodium dioctyl sulfosuccinate (AOT) [145], is due primarily to energy trapping states associated with surface defects [142, 144, 145].

BSA protein species conjugated to the  $\text{Ag}_2\text{S}$  and CdS nanoparticles through the RESOLV process remain intact, according to the modified Lowry assay for total protein analysis [146–148]. BSA conjugation serves the dual purposes of stabilizing these nanoparticles to prevent agglomeration in aqueous suspension and introducing biocompatible functionalities into these nanoparticles for further biological interactions or couplings (e.g., antibody attachment).

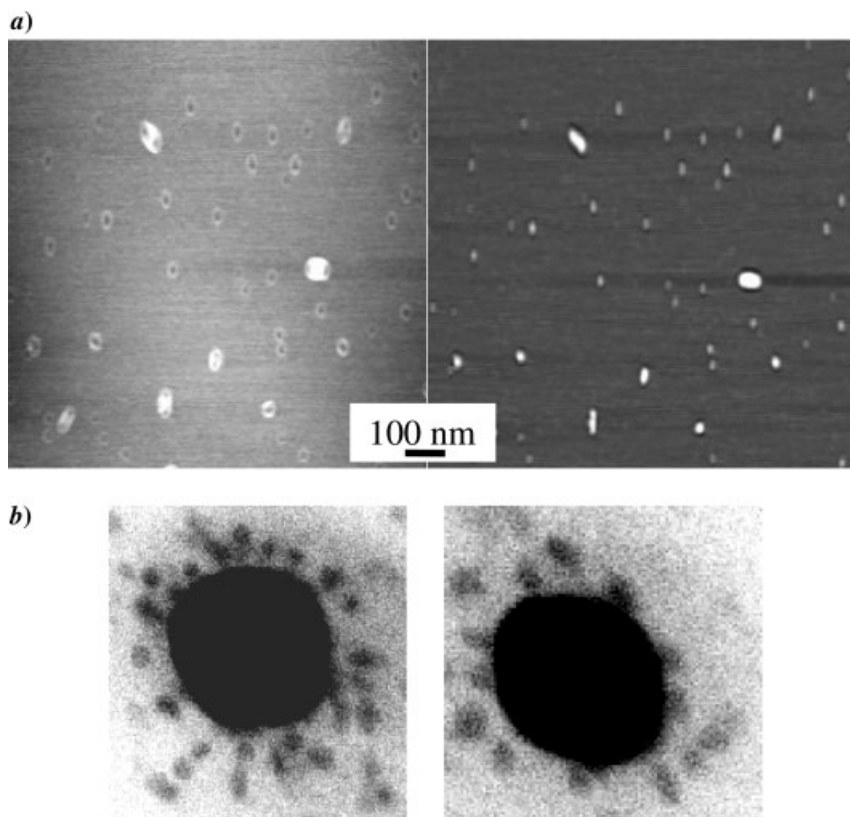


**Fig. 7.12.** (a) Height (left) and phase (right) images from the AFM analysis of BSA-conjugated CdS nanoparticles. (b) Scanning TEM (Z-contrast mode) image for the coating of colloidal gold by BSA-conjugated CdS nanoparticles. (From Ref. [59].)

Mechanistically, the relatively strong interactions between BSA and these semiconductor nanoparticles (strong enough to remain stable in dialysis) are worth noting. BSA protein contains 60 amino moieties in lysine residues, 26 arginine moieties in guanidino side chains, and also 17 disulfide bonds with one free thiol in cysteine residues [149]. These functionalities are probably responsible for the conjugation to these nanoparticles through thiolate linkages and/or weak covalent bonds with alkylamines [150–152].

### 7.2.3.3 Assembly and Disassembly of Nanoparticles through Protein Isomeric Conversion

Protein-conjugated semiconductor nanoparticles produced through the supercritical fluid processing method RESOLV can also be organized into supramolecular architectures by simply using isomeric conformations of proteins. For example,

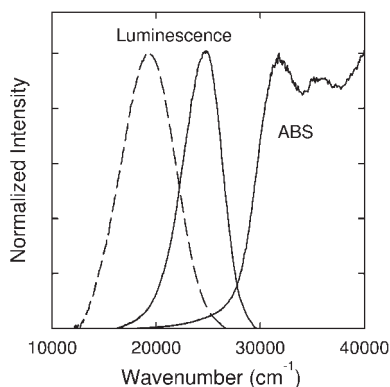


**Fig. 7.13.** Luminescence spectrum of BSA-conjugated CdS nanoparticles in a stable aqueous suspension (—) compared with that of the similarly sized CdS nanoparticles prepared and encapsulated in AOT micelles (---). (From Ref. [59].)

Meziani et al. [60] have demonstrated the possibility of assembling and disassembling BSA-conjugated  $\text{Ag}_2\text{S}$  and CdS nanoparticles by adjusting solution pH. Under high pH conditions ( $\text{pH} \sim 12$ ), BSA is expected to be in the aged form, in which the protein drastically expands and forms soluble aggregates through intermolecular disulfide exchanges [60]. Aggregation is reflected by the clustering of these nanoparticles, as observed in AFM images of the  $\text{Ag}_2\text{S}$  sample (Fig. 7.14). In these clusters, individual  $\text{Ag}_2\text{S}$  nanoparticles are still separated by protein species and protected from agglomeration into larger  $\text{Ag}_2\text{S}$  nanoparticles. At neutral

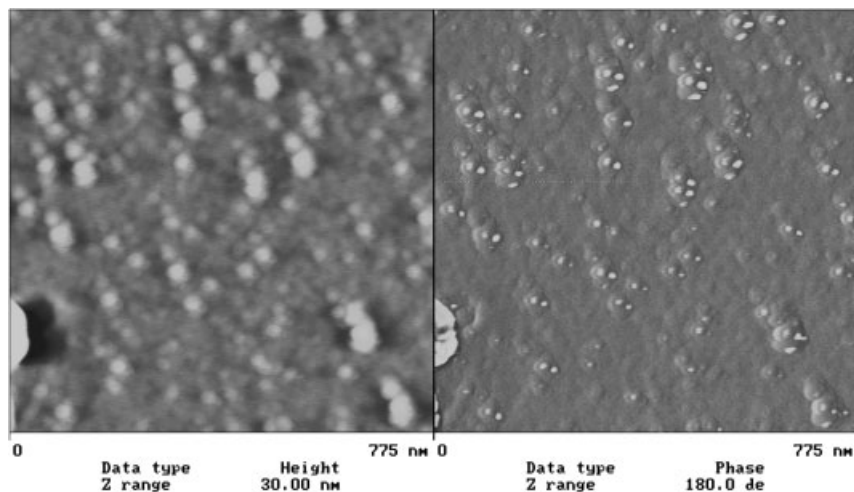


**Fig. 7.14.** AFM height (left) and phase (right) images of BSA-conjugated  $\text{Ag}_2\text{S}$  nanoparticles at high  $\text{pH} \sim 12$ . (From Ref. [60].)



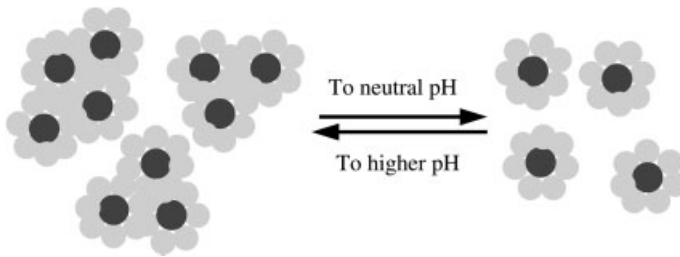


**Fig. 7.15.** Scheme illustrating the assembly and disassembly of BSA-conjugated semiconductor nanoparticles due to changes in BSA conformations at different solution pHs. (From Ref. [60].)

pH, the BSA protein coating the well-dispersed  $\text{Ag}_2\text{S}$  nanoparticles (Fig. 7.10) is predominantly in the native form. This pH-dependent assembly and disassembly of BSA-conjugated  $\text{Ag}_2\text{S}$  nanoparticles, driven by the isomeric conversion of the protein, is qualitatively reversible [60]. In the isomeric conversion, BSA protein is relatively unharmed at high pH and, for the most part, can return to its native configuration, thus making it possible to maintain the reversibility (Fig. 7.15).

In summary, the supercritical fluid processing method RESOLV can be used effectively as an alternative and unique way of producing clean, active protein-conjugated nanoparticles. Since the nanoparticle formation involves no templating agents in an aqueous environment, the method can enable direct conjugation of nanoparticles to proteins. These protein-conjugated nanoparticles are stable (without agglomeration and precipitation) in an aqueous suspension, and the protein species associated with the nanoparticles remain intact, and are amenable to further biofunctionalizations. The produced semiconductor nanoparticles, such as CdS, can have strongly luminescent features, which are particularly valuable in biosensor-related applications.

### 7.3

#### Coupling of Carbon Nanotubes and Proteins

Among various large-aspect-ratio nanomaterials, carbon nanotubes possess unique and rich physical and chemical properties because of the one-dimensional structural arrangement of a chemically versatile element [153–156]. Conceptually, carbon nanotubes may be formed by rolling graphene sheets into tubular structures – single-walled carbon nanotubes (SWNTs) from a single graphene layer and multiple-walled carbon nanotubes (MWNTs) from multiple layers [153]. The chiral vector for rolling-up ( $\mathbf{C}_h = n\mathbf{a}_1 + m\mathbf{a}_2$ ), often referred as the chiral index ( $n, m$ ), uniquely defines the diameter ( $d$ ) and the chiral angle ( $\theta$ ) of the SWNT (Fig.

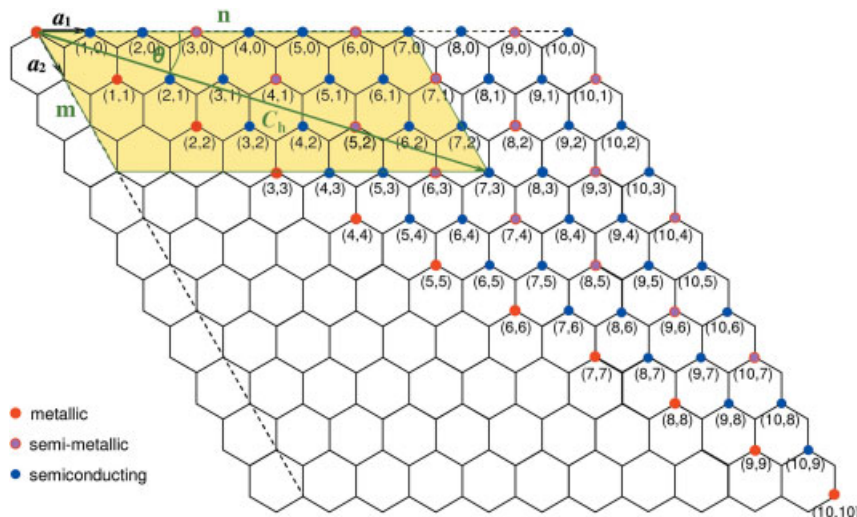


Fig. 7.16. Conceptual formation of carbon nanotubes by rolling up a graphene sheet.

7.16) [Eqs. (1) and (2), where  $a_{c-c}$  ( $\sim 0.142$  nm) is the nearest neighbor C–C distance].

$$d = \frac{\sqrt{3}a_{c-c}}{\pi} \sqrt{n^2 + nm + m^2} \quad (1)$$

$$\theta = \tan^{-1}[\sqrt{3}m/(2n + m)] \quad (2)$$

The chiral index also directly determines the electronic structure of the nanotube: metallic when  $(n - m)/3$  is integer (“semi-metallic” if  $n \neq m$ ) and otherwise semiconducting [154].

Biological applications of carbon nanotubes through their integration with bioactive molecules in particular have been investigated both in solution phase and in solid state [157–163]. For solution-phase applications, such as substance delivery [163–168], pathogen detection [169, 170], and other biomedical applications, the nanotubes should be dispersible or soluble in physiological environments. Thus, the aqueous solubilization of carbon nanotubes is essential [158, 159, 161–163], and has benefited enormously from recent developments in the chemical functionalization of nanotubes [171–175]. Examples of solid-state bioapplications of carbon nanotubes include scaffolds for cell growth [162, 176–178], biosensors and biocatalytic electrochemical devices [157, 160, 179], electromechanical devices [180], sharp scanning microscopy probes [181], etc.

Protein–carbon nanotube conjugates were among the earliest and most popular topics in multidisciplinary research efforts on the bioapplications of nanotubes. These conjugates may be formed either non-specifically or specifically (see below). Examples in various related applications are also reviewed below.

## 7.3.1

**Non-specific Adsorption**

Like other nanomaterials, carbon nanotubes have a high surface area, but with a surface of quantum-confined conjugated carbon networks. However, it was the nanometer-sized hollow interior of these tubular species that drew most initial attention, stimulating the imagination that they could be used as carriers to encapsulate and deliver bioactive species to selected targets [182–185]. As supportive evidence, some enzymes encapsulated in MWNTs seemed to retain their biocatalytic properties [183]. However, the encapsulate-and-deliver idea is still a matter of theory since there has been no report of the controlled release of these encapsulated species from nanotubes at any targeted site. Furthermore, problems with such encapsulation are far from resolved.

The early experiments on encapsulating proteins into nanotubes revealed that proteins were adsorbed on the MWNT exterior surface [185]. This phenomenon became widely known when Balavoine et al. [186] found that streptavidin and HupR readily adsorbed onto the MWNT surface, with the adsorbed proteins sometimes even forming helical array structures along the nanotube sidewall. Although the reproducibility for the ordered arrays was poor, these results suggested strongly that there are indeed competent noncovalent and non-specific interactions between carbon nanotubes and protein species.

Despite efforts to ensure the specific conjugation of carbon nanotubes and proteins (Section 7.3.2), several groups realized that non-specific interactions between these two entities are almost inevitable. Dai and co-workers [179, 187] reported that streptavidin, avidin, BSA,  $\alpha$ -glucosidase, and staphylococcal A are adsorbable to SWNTs. Similarly, Azamian et al. [188] found that proteins with different isoelectric points, such as cytochrome *c* ( $pI \sim 10.8$ ) and ferritin ( $pI \sim 4.6$ ), exhibit similar affinity toward SWNTs (Fig. 7.17).

Since ferritin contains an iron core, Lin et al. [189] used it as a model protein to study protein–nanotube interactions in aqueous media via TEM. It was qualitatively but unambiguously demonstrated that non-specific interactions between ferritin and SWNTs were so significant that the nanotubes were solubilized in water as a result. In agreement with reports by Azamian et al. [188], the ferritin–nanotube conjugation via such non-specific interactions was quite similar to that in the presence of special reagents for covalent coupling during reaction. Despite the visual similarity, the non-specific conjugates were much less stable than covalent ones (Section 7.3.2) [189].

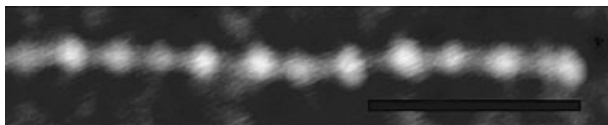


**Fig. 7.17.** AFM image of a cytochrome *c*–SWNT conjugate from non-specific adsorption. Scale bar = 90 nm. (From Ref. [188].)

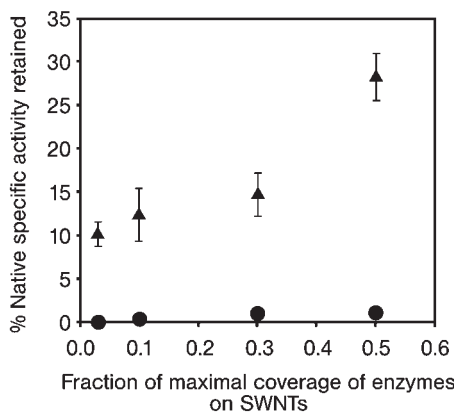


**Fig. 7.18.** Enzymatic activity retained as a function of surface coverage of enzymes on SWNTs: adsorbed SBP (▲) and adsorbed CT (●). Each point represents an average of a minimum of three separate experiments, with

some points showing errors smaller than the symbol. Specific activities above half-maximal coverage could not be obtained because of leaching of the adsorbed enzyme during activity measurement. (From Ref. [191].)

Rege et al. [190] reported enhanced retention of the enzymatic activity of  $\alpha$ -chymotrypsin (CT) embedded in polymer–SWNT composite films compared with those without nanotube fillers. They speculated that this could be a consequence of enzyme–nanotube hydrophobic interactions that slowed the leaching of enzymes from the films. However, other reported results contradict this conclusion. As recently reported by Karajanagi et al. [191], CT almost completely lost its enzymatic activity upon non-specific conjugation with SWNTs (Fig. 7.18), possibly due to its structure unfolding. These authors showed by AFM that the tertiary structures of CT molecules, upon adsorption onto SWNTs, changed significantly from those in solution phase. However, another enzyme, soybean peroxidase (SBP), retained its structure when adsorbed, which is consistent with the observed retention of a reasonable fraction of activity. Also consistent are quantitative FT-IR investigations, which demonstrated much more significant secondary structural changes of CT than SBP in both  $\alpha$ -helix and  $\beta$ -sheet contents upon the enzyme–nanotube conjugation [191].

Microscopy techniques are widely used to visualize both aqueous soluble protein–nanotube conjugates and those on substrates. For the latter, other instrumental techniques are also used to obtain additional information. For example, quartz crystal microbalance (QCM) has been used to trace the protein adsorption event on a SWNT film that was evenly formed on a gold-coated QCM quartz crystal substrate [179]. The signal change marked the adsorption events on the film and scaled with the concentration of the protein solution for adsorption. The results obtained for adsorptions of various proteins on SWNTs are in reasonable agreement with microscopy observations. However, protein adsorption on the substrates could interfere in such evaluations unless the substrates are fully covered by a monolayer of nanotubes.

Protein adsorption on carbon nanotubes can also be detected electrochemically. In particular, solid-state field-effect transistor (FET) devices from semiconducting SWNTs have been envisioned for use as biosensors [160, 179, 192]. In principle, some small perturbation on the electronic structure of the semiconducting SWNT from the adsorption of even a trace amount of guest molecules may induce a detectable electrical response in the device characteristics [192–195]. Metallic SWNTs, however, are much less sensitive to changes in chemical environments. For example, the adsorption of cytochrome *c* ( $pI \sim 10.8$ ) in a buffer solution onto a SWNT FET device was detected by measuring the device conductance change [196]. Consistent with microscopy results, the change in conductance was quantified to be from the adsorption of  $\sim 20$  protein molecules per  $\mu\text{m}$  length of a semiconducting SWNT under the given experimental conditions. In fact, the detection limit of such FET devices is of the order of 100 pM of cytochrome *c*.

A consistent observation by different groups is that the conductance of the nanotubes decreases upon protein adsorption, regardless of the charge of the proteins at physiological pH. This is obviously not solely due to the electrostatic gating effect from charge injection from protein molecules to the p-type semiconducting SWNT [179, 196, 197]. Besteman et al. [197] proposed that such a conductance decrease (as a function of the liquid-gate voltage) could originate from the nanotube capacitance change upon the adsorption event, during which ion proximity to the nanotube is limited. However, vigorous debates continue on whether the device response is from the non-specific adsorption of proteins on nanotubes at all [198]. It has been argued that the adsorption of proteins with rather small charge ( $pI \sim 5\text{--}7$ ) at the electrode–nanotube contacts contributes more to the detected conductance change than that along the nanotube sidewall [198]. Poly(ethylene glycol) (PEG) is a well-known protein-resistant material that is often used to protect surfaces from protein adsorption [199, 200]. By selectively applying a PEG layer onto the metal electrodes, these researchers showed that there was no detectable electronic response of the nanotube FET device to the adsorption events at protein concentrations of 100 nM [198] (Fig. 7.19). There was an exception, avidin, which is highly positively charged at neutral pH ( $pI \sim 10\text{--}11$ ). This protein was capable of inducing a response even when the electrodes were protected, although the signals were much weaker than those from non-protected devices. As expected, when the nanotube surface was also protected via protein-resistant species, no device response could be detected with any of the proteins investigated.

Whatever the sensing mechanism might be in the FET devices upon protein–nanotube conjugation, the evidence is already overwhelming for non-specific adsorption of proteins onto carbon nanotubes. The mechanism for such conjugation, however, is complicated and subject to further investigation. The nanotube surface has been widely considered as being hydrophobic [201]. Thus, it has been suggested intuitively that the hydrophobic interactions between nanotubes and certain protein structural units play a significant role in the observed adsorption. For example, Karajanagi et al. [191] attributed the differences in changes in the structures and enzymatic activities of two enzymes (SBP and CT, *vide supra*) upon their adsorption on SWNTs to hydrophobic interactions. For SBP, there is a hydrophobic

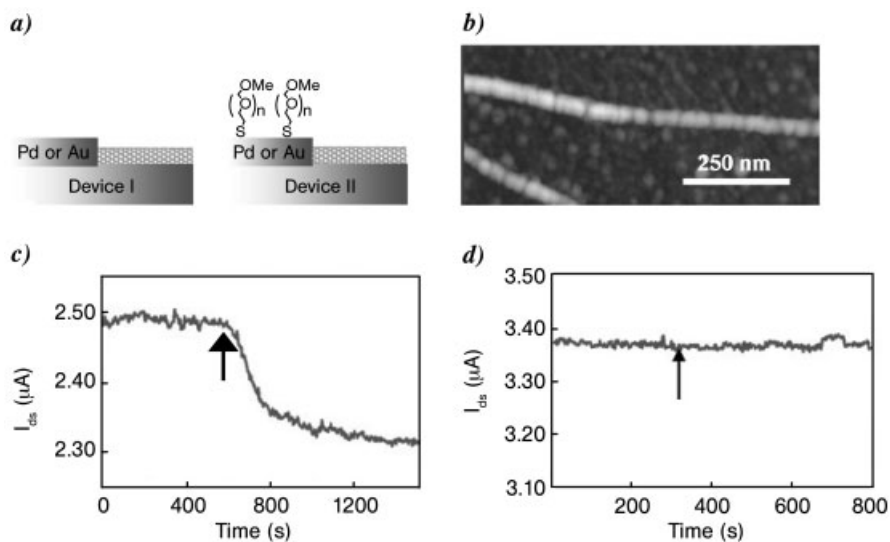


**Fig. 7.19.** (a) Configuration sketches of SWNT FET devices type I (unprotected Pd/Au electrodes) and type II (electrodes coated with a PEG self-assembled monolayer). (b) AFM image of a SWNT type II device after exposure to human chorionic gonadotropin (hCG). (c) Electrical data of type I device during exposure to hCG. (d) Electrical data of type II device during exposure to hCG. (From Ref. [198].)

“pocket” with 19 amino acid residues on the surface, distant from the enzymatic active sites in its tertiary structure, which may help the enzyme to retain a significant fraction of its activity. Conversely, CT does not contain a large hydrophobic cluster, which was speculated to be the cause for the loss of activity upon its adsorption onto SWNTs with significant secondary and tertiary structural changes [191]. Also consistent with the hydrophobic interaction scheme is the finding that the amphiphilicity of the large peptide species favors their binding with nanotubes in aqueous solution, similar to the surfactant effects [202]. Dieckmann and co-workers [203, 204] took advantage of a similar concept and designed an amphiphilic peptide with an  $\alpha$ -helix secondary structure for the noncovalent aqueous solubilization of SWNTs (Fig. 7.20). However, one example is clearly inconsistent with the hydrophobic scheme. Fibrinogen, a well-known soluble plasma glycoprotein that is affinitive to many hydrophobic surfaces, was found to be inert to SWNTs. This might be due to the protein’s large size (molecular weight  $\sim 340$  kDa) [187].

Among other possible mechanisms for non-specific protein–nanotube conjugation are electrostatic interactions and hydrogen bonding, especially when carbon nanotubes are pre-treated with oxidative acids. After such treatment, the nanotube surface usually becomes defective, with many oxygen-containing groups, such as carboxylic acids, hydroxyls, ketones, etc., at the defect sites [205–207]. These organic groups make electrostatic interactions and hydrogen bonding between nanotubes and certain surface residues of proteins quite plausible. Electrostatic interactions obviously do not dominate as several groups have shown that SWNTs are

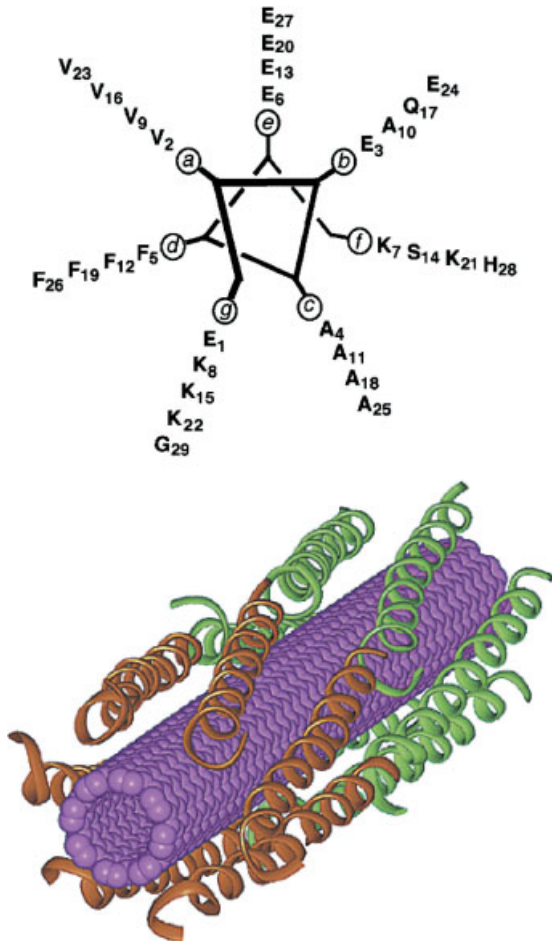


**Fig. 7.20.** Design of  $\alpha$ -helix peptide (top) and a model sketch of the peptide-SWNT conjugate by noncovalent interaction (bottom). (From Ref. [203].)

attractive to both positively and negatively charged protein species in aqueous solutions [188] and at device level [179, 198] at physiological pH.

The increasing evidence for amino-affinity of semiconducting SWNT surfaces [194, 208–210] might also help to explain the above phenomenon, since most proteins under consideration contain lysine and/or arginine units that provide primary amino groups. For example, previous studies show that there is  $\sim 0.04$  electron donation to a semiconducting SWNT per adsorbed amine [211]. From such a unit quantity of charge transfer, Bradley et al. [212] estimated that a significant portion of the threshold shift of the gate voltage in a nanotube FET device upon streptavidin adsorption is due to charge transfer from amino groups to the semi-

conducting SWNT. However, they also suspected that other residues, such as tryptophan and tyrosine, may play a secondary role in the charge transfer because they contain aromatic structures. Indeed, investigations conducted with a peptide library have found that the tryptophan residue, in particular, was affinitive towards the SWNT surface [202].

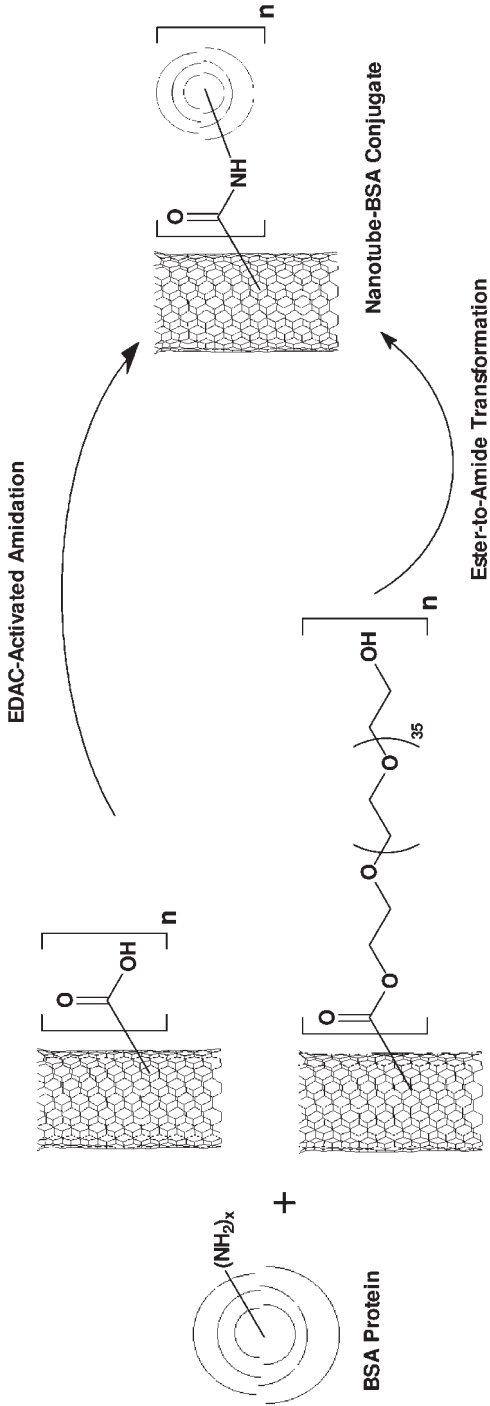
### 7.3.2

#### Specific Conjugation and Biorecognition

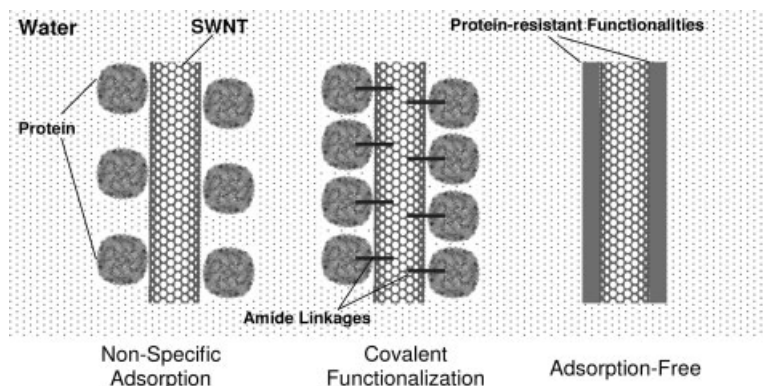
Specific conjugation of proteins and carbon nanotubes is opposite to non-specific conjugation. In the former, selected chemical reagents are used with known chemistry to link proteins to nanotubes in a more controllable fashion. Protein surface amino groups from residues, such as lysine, are widely involved in some of these specific conjugations. For example, nanotube-bound carboxylic acids, often generated from oxidative acid treatments, can be coupled with protein amines to form amide linkages (Scheme 7.1), which was extrapolated from chemistry developed previously for functionalizing carbon nanotubes with other polymeric and oligomeric molecules [171–175, 181, 213]. Various types of proteins, such as BSA, ferritin, and cytochrome *c*, have been conjugated to carbon nanotubes via this route [188, 189, 214, 215]. The reactions were often carried out in the presence of carbodiimide reagents, such as 1-ethyl-3-(3-dimethylaminopropyl)carbodiimide (EDAC), which are specific for the formation of amide linkages by converting carboxylic acids into more reactive intermediates toward coupling with amines. The carbodiimide-nanotube reaction has been referred to as the activation step and is sometimes assisted by sonication [213]. Many proteins also contain carboxylic acids, which may compete with those from nanotubes in the amidation reactions, resulting in possible protein self-aggregation. Thus, the activation step is better carried out in the absence of proteins so that excess carbodiimide molecules can be removed before the conjugation reaction. The addition of *N*-hydroxysuccinimide (NHS) after carbodiimide activation may further enhance the stability of the reactive intermediate, and thus be beneficial to the yields of the covalent protein–nanotube conjugates [215]. This and similar strategies have been used to functionalize carbon nanotubes with other biomolecules (such as nucleic acids and their analogs [216, 217]) under physiologically benign conditions.

Amide linkages between proteins and carbon nanotubes have also been reported to be formed in room-temperature ester-to-amide transformation reactions in aqueous solution (Scheme 7.1) – an even milder approach [218]. In the reaction, a water-soluble nanotube sample with ester-attached oligomeric PEG functionalities was placed in small-pore-size dialysis tubing with a protein (e.g. BSA). Although the PEG functionalities on the nanotubes might have resisted approaching proteins in aqueous solution, the final protein–nanotube conjugation obtained this way was in fact quite similar to that obtained by carbodiimide-activated coupling reactions [214]. The driving force for such a mild transformation, which overcomes the initial protein-resistivity of nanotube-bound PEG groups, likely comes from both the thermodynamic stability of the amide linkages (compared with ester





Scheme 7.1



Scheme 7.2

ones) and the *in situ* removal of relatively small PEG molecules via dialysis. In addition, hardly any NMR signals from PEG moieties could be detected from the conjugates after the reaction, indicating the effectiveness of the method.

Covalent functionalization seems to facilitate the aqueous solubilization of SWNTs, resulting in enhanced yields of solubilized nanotubes compared with non-specific interactions under similar conditions [189]. Aqueous-soluble covalent protein–nanotube conjugates are also much more stable than non-specific conjugates. For example, as discussed in Section 7.3.1, water-soluble covalent ferritin–SWNT conjugates are much more stable in solution when subjected to long-period standing or vigorous dialysis conditions than non-specific ones. After dialysis, although there seemed to be some protein loss in the covalent conjugates, the protein–nanotube association was still much more pronounced than that in non-specific conjugates similarly dialyzed [189]. Probably, the non-specific adsorption contributes significantly to the initial approaching of proteins toward nanotubes during covalent conjugation. The formation of amide linkages then “locks” the proteins on the nanotube surface defect sites where carbodiimide-activated intermediates are present (Scheme 7.2) [159, 189].

Covalent water-soluble protein–nanotube conjugates have found some applications in bacterial detection. Elkin et al. [169] adsorbed anti-*Escherichia coli* polyclonal antibodies onto BSA-functionalized SWNTs in physiological solutions. The nanotube-bound antibodies efficiently captured *E. coli* O157:H7 in solution, which was demonstrated by both SEM (Fig. 7.21) and confocal microscopy. Because of the high surface area and one-dimensional flexible structure of SWNTs, such multiplicity antibody displays might be of enhanced pathogen detection sensitivity and could also potentially be used for decontamination of bacterial cells in complex matrices.

Another form of interaction of carbon nanotubes with cells is the translocation of nanotubes through the cell membranes – internalization. In a recent example, SWNTs were functionalized with biotin using a similar carbodiimide coupling

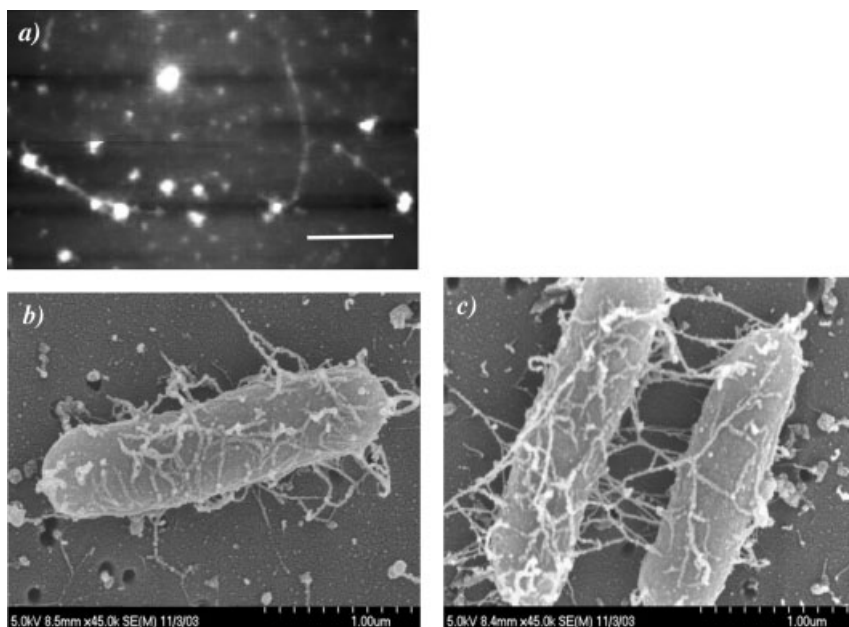


**Fig. 7.21.** (a) AFM image of a covalent BSA-SWNT conjugate sample. (b) and (c) SEM images showing the strong interactions of immuno-SWNTs (SWNT-BSA-antibody goat anti-*Escherichia coli* O157 conjugate) with pathogenic *E. coli* O157:H7 cells. (From Ref. [169].)

method, and then conjugated to streptavidin via selective biotin–streptavidin interactions [167]. While streptavidin proteins cannot enter cells by themselves, the water-soluble SWNT–biotin–streptavidin conjugates were able to internalize into many types of cells, such as human promyelocytic leukemia (HL60), Chinese hamster ovary, and 3T3 fibroblast cells (Fig. 7.22). Streptavidin alone did not show appreciable cytotoxicity to HL60 cells. However, the cytotoxicity of SWNT–biotin–streptavidin conjugates toward the same cell line was dose-dependent, which is consistent with protein internalization via nanotube carriers. SWNT–biotin–streptavidin internalization is probably accomplished through endocytosis, which could be blocked at 4 °C. Co-localization of SWNTs and endosomes formed during such endocytosis is direct evidence for internalization.

SWNTs functionalized by a peptide that mimics the function of  $G_s$  protein were able not only to penetrate human and murine fibroblast and keratinocytes cells membranes but also to translocate into the cell nucleus [161, 165]. The nanotube functionalization was covalent, but based on 1,3-dipolar addition of azomethine ylides onto the nanotube sidewalls [161, 164]. The functional group end-capped with amine was then modified with peptide sequences to obtain peptide–SWNT conjugates. Murine 3T3 fibroblast cells were still largely viable when the soluble

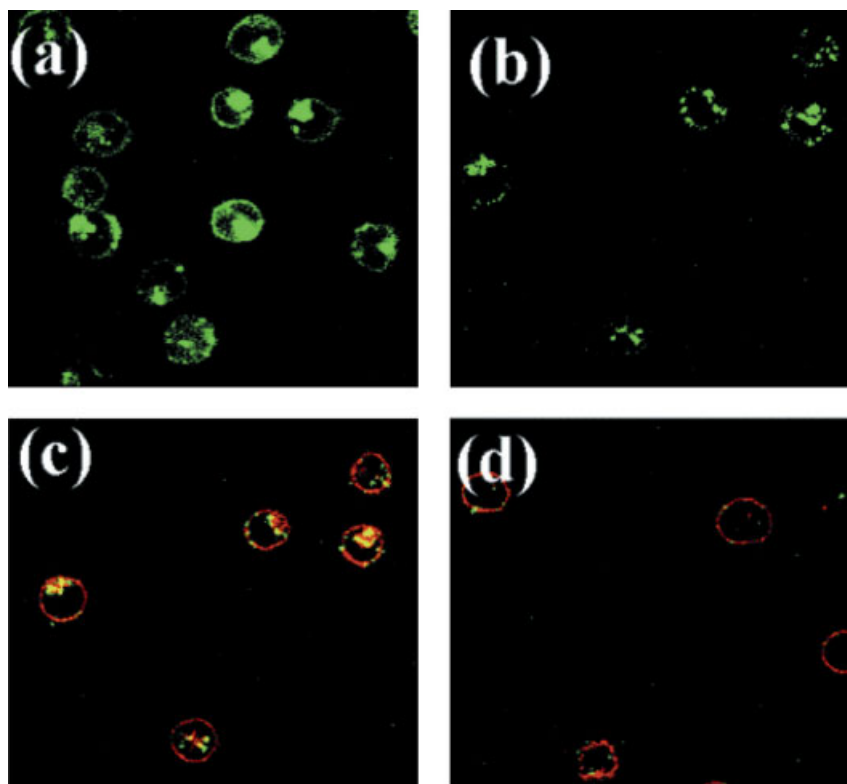


**Fig. 7.22.** Confocal images of HL60 cells after incubation in solutions of (a) a fluorescein-labeled SWNT sample; (b) a mixture of SWNT-biotin-fluoresceinated streptavidin conjugate (green) and the red endocytosis marker FM 4-64 at 37 °C (image showing fluorescence in the green region only); (c) same as (b) but with additional red fluorescence shown due to FM 4-64 stained endosomes; (d) same as (c) after incubation at 4 °C. (From Ref. [167].)

functionalized SWNT concentration was as high as 5  $\mu\text{M}$ , but the nanotube solution quickly became toxic to these cells upon increasing the concentration by only twice as much. The uptake mechanism, however, is not due to endocytosis, since the internalization is temperature independent (the same at both 4 and 37 °C) [165]. Nevertheless, there are several other reports on the cell internalization of both non-functionalized carbon nanotubes and those functionalized with other bioactive species (such as nucleic acids) [166, 219, 220]. These reports discuss the cytotoxicity of carbon nanotubes [219] and their potential in bioimaging (via nanotube near-IR fluorescence) [220] and drug, vaccine, and gene delivery systems [164–168].

In addition to direct covalent methods, specific protein–nanotube conjugation can also be achieved through the use of a bifunctional molecule, with one end attaching to the protein and the other end to the nanotube. Chen et al. [221] reported

the use of 1-pyrenebutanoic acid succinimidyl ester as a linker for indirect protein–SWNT conjugation. The pyrene moieties of the bifunctional molecules are proposed to interact noncovalently with the nanotube surface via “ $\pi$ – $\pi$ ” stacking, while the succinimides react with pendant amino groups on the protein to form amide linkages. This method was successfully applied to SWNTs at device level [197]. However, the necessity of using this linker molecule has never been seriously determined, especially considering the competitive non-specific interaction bindings from proteins themselves. In Chen et al.’s original control experiment [221], it was claimed that no binding was found between ferritin and SWNTs grown on a TEM grid without the presence of the linker molecule. This contradicts later observations by other workers, who consistently found that ferritins are actually very affinitive to SWNTs, even in aqueous solution [188, 189].

Although considered to be specific conjugation modes, neither direct covalent functionalization nor the usage of pyrene-succinimide bifunctional molecule could provide the selectivity for carbon nanotubes to bind one protein but repel another. One general prerequisite to obtaining such selectivity or biorecognition is efficient elimination of non-specific adsorption. Thus, the application of a protein-resistant layer (such as PEG) on the nanotubes prior to protein conjugation is essential. Shim et al. [187] first demonstrated such a possibility by adsorbing surfactant Triton X-100 and then PEG to SWNTs on silica surface. They proposed that the hydrophobic part of Triton molecule adsorbs onto SWNTs, while its hydrophilic tail facilitates subsequent adsorption of PEG, which alone hardly interacts with the nanotube surface. SWNT devices protected this way were resistant to streptavidin and other protein molecules. With biotin modification on adsorbed PEG, however, streptavidin efficiently coated the nanotube surface, which still repelled other proteins [187]. The well-known biotin–streptavidin interaction obviously accounts for such observed selectivity or biorecognition.

Although each Triton molecule contains an oligomeric ethylene glycol chain as its hydrophilic tail, a simple Triton coating is not sufficient to prevent non-specific adsorption of proteins on nanotubes [187]. Some other surfactants, such as Tween-20, which has dendritic PEG tails, protect the nanotubes much better, even without additional PEG adsorption. Such surfactant coating is quite useful for SWNTs on substrates in devices [179], but not so impressive in aqueous solutions [188]. In a report by Erlanger et al. [222], an anti-fullerene IgG monoclonal antibody was claimed to be specifically conjugated to SWNTs in the presence of Tween-20 in an aqueous environment. Although this antibody is known to be specific to fullerene C<sub>60</sub>, the observed binding might simply be another example of non-specific adsorption. Further evidence is definitely required to prove whether the anti-fullerene antibody is truly selective toward SWNTs.

Nevertheless, biorecognition sites can be created similarly at the PEG end of Tween-20 surfactant molecules. For example, with biotin attachment to the dendritic PEG tails of Tween-20 prior to its adsorption on SWNT FET devices, no protein except streptavidin could be conjugated [179]. In another report, PEG was co-adsorbed onto SWNT devices with another functional polymer, polyethylene

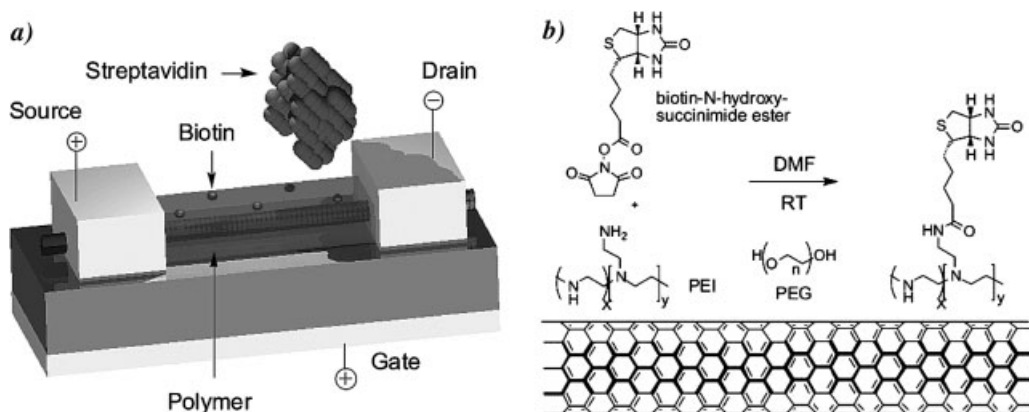


**Fig. 7.23.** (a) Schematic diagram illustrating a biotinylated SWNT-FET for streptavidin recognition. (b) Biotinylation of PEI on the nanotube surface, with co-adsorbed PEG. (From Ref. [223].)

imine (PEI), instead of surfactant molecules [223]. The pendant primary amine groups on PEI were available for subsequent biotin derivatization and, thus, streptavidin recognition (Fig. 7.23).

The protein-resistivity of PEG-coated SWNTs on substrates may be interfered with by the same PEG coating on substrates themselves [Fig. 7.24(a, b)]. The availability of highly water-soluble SWNTs with PEG functionalities [224, 225] provides an excellent opportunity to demonstrate unambiguously the protein-resistant function of the PEG layer on the nanotubes in aqueous solution. As Lin et al. [189] reported, PEG-functionalized SWNTs can totally repel ferritins in aqueous solution. As shown in the TEM image (Fig. 7.24c), ferritins surround the nanotubes, but obviously at a distance, which is due to the PEG functionalities. Other water-soluble SWNTs, such as those functionalized by poly(propionyl ethylenimine-co-ethylenimine) (PPEI-EI) [213, 226] or poly(vinyl alcohol) (PVA) [227], similarly repel proteins in aqueous solution [189]. The protein-resistance coupled with the water-solubility of these functionalized SWNTs could be important in their biomedical applications. Data from other PEG-containing materials suggest that such protein-resistant nanotubes may have reduced cytotoxicity and increased retention time in the circulatory system [228]. All of these hypotheses, however, remain to be verified.

In addition to the well-known biotin–streptavidin interaction, biorecognition may also be achieved through other biologically known supramolecular pairwise selective interactions, such as the antibody–antigen interaction, carbohydrate–lectin interaction, and others. For this purpose, the indirect but selective attachment of different types of proteins to carbon nanotubes can be achieved via initial nanotube functionalization with the corresponding counterpart species. For in-

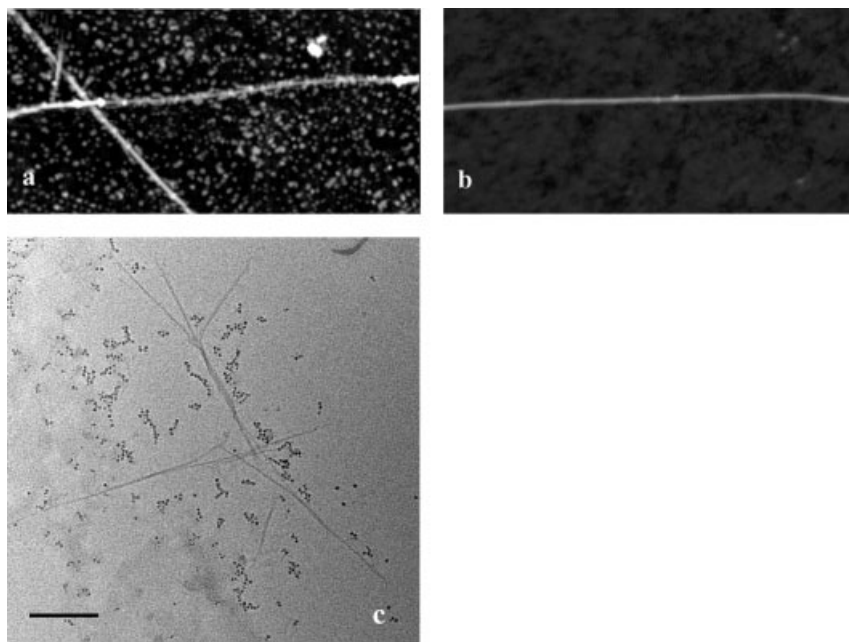


**Fig. 7.24.** (a) AFM image showing the non-specific binding of streptavidin on SWNTs as-grown on substrate. (b) AFM image showing that the non-specific binding was largely prevented by coating SWNTs with surfactant

Triton X-100 followed by PEG. (From Ref. [187].) (c) TEM image showing that the non-specific binding of ferritin species to water-soluble SWNTs was completely prevented by the covalent PEG functionalities on SWNTs.

stance, an antigen named U1A was attached to Tween-20 molecules and adsorbed onto a SWNT FET device, which was then only responsive to the U1A's antibody counterpart, 10E3 [179]. SWNTs were also co-functionalized in a carbodiimide-activated reaction with an antibody and an enzyme, alkaline phosphatase (ALP), with the latter serving as the electrochemical tag [229]. Such conjugates have been used in combination with immunological magnetic beads for ultrasensitive immunosensing or antigen detection. The antigen was attached in a sandwich-like configuration to nanotube-bound and magnetic-bead-bound antibodies. The captured antigens were then separated magnetically. The electrochemical detection signals were enhanced by comparing multiple copies of enzymatic species on the nanotube surface to single enzyme tags. DNA sensing was achieved via a similar strategy, with selectivity coming from the complementary DNA sequence hybridization instead of antibody–antigen interactions [229].

A natural  $\beta$ -1,3-glucan, schizophyllan (SPG), was found to be able to noncovalently wrap around and solubilize SWNTs in water [230]. Using SPG with lactoside appendages, the carbohydrate-functionalized SWNTs can be conjugated to *Ricinus communis* agglutinin, a lactoside-specific lectin that is inert to other carbohydrates

such as  $\alpha$ -mannose and some other monosaccharides. In another example taking advantage of carbohydrate–lectin specific interactions,  $\beta$ -D-galactose-functionalized SWNTs could be crosslinked by a galactoside-specific lectin from the peanut *Arachis hypogaea*, forming interconnected networks [231].

Very recently, noncovalent functionalization of SWNTs by a mucin-mimic with  $\alpha$ -N-acetylgalactosamine ( $\alpha$ -GalNAc) moieties has been reported [232]. These sugar moieties could be recognized by *Helix pomatia* agglutinin (HPA),  $\alpha$ -GalNAc's specific counterpart (Fig. 7.25). When HPA was plugged with free GalNAc, no binding occurred between the deactivated agglutinin and the  $\alpha$ -mucin mimic-SWNT conjugate. Specificity was further demonstrated by a noncovalent conjugate sample of SWNTs with a similar mucin mimic but bearing sugar moieties of  $\beta$ -configuration. Again, no binding was found between HPA and the  $\beta$ -mucin mimic-SWNT conjugate.

In a similar strategy, Gu et al. [170] reported recently multivalent carbohydrate display on SWNTs for the detection of *E. coli* O157:H7, which took advantage of the selective interactions of the nanotube-bound sugar moieties ( $\beta$ -D-galactose) with the periplasmic galactose-binding proteins on the pathogen surface. The pathogen cells could be agglutinated by the  $\beta$ -D-galactose-functionalized SWNTs, while inert to those functionalized by either  $\alpha$ -D-mannose or BSA protein [170].

Reconstitution of flavoenzymes was also used for enzyme–nanotube conjugation for the purpose of subsequent electronic sensing of a catalytic event via nanotube conductor arrays. As reported by Patolsky et al. [233], the glucose oxidase (GOx) cofactor, flavin adenine dinucleotide (FAD), was first functionalized covalently onto the SWNT array, which was formed by self-assembly on an Au substrate as the electrode. With the protection of SWNTs with PEG, apo-GOx proteins were then immobilized onto the SWNTs via apoenzyme-FAD reconstitution. The conversion of glucose into gluconic acid by the redox enzyme was found to be efficiently transferred to the Au electrode and was highly dependent upon the lengths of the nanotubes, which apparently serve as the pathway for electron transfer [233].

Since these supramolecular but selective interactions are well-known in biology, scientists in the bio-nano field are more inclined to use these interactions to conjugate proteins and nanomaterials, including carbon nanotubes, for biologically and biomedically significant purposes. Proteins conjugated this way probably retain their bioactive structures and functions. However, when proteins are conjugated to carbon nanotubes via other covalent or noncovalent pathways, their secondary and other advanced structures are largely unknown because of their close proximity to the nanotubes. This should be investigated, especially in the light of a recent valuable attempt by Karajanagi et al. [191] on the advanced structures of two enzymes (SBP vs. CT) upon adsorption on SWNTs. From that work, it seems that the secondary and tertiary structures of proteins could easily be affected when adsorbed onto carbon nanotubes. However, the structural and biofunctional alterations to each protein induced in the conjugation events will need to be carefully evaluated on a case-by-case basis before mechanistic details of the interactions



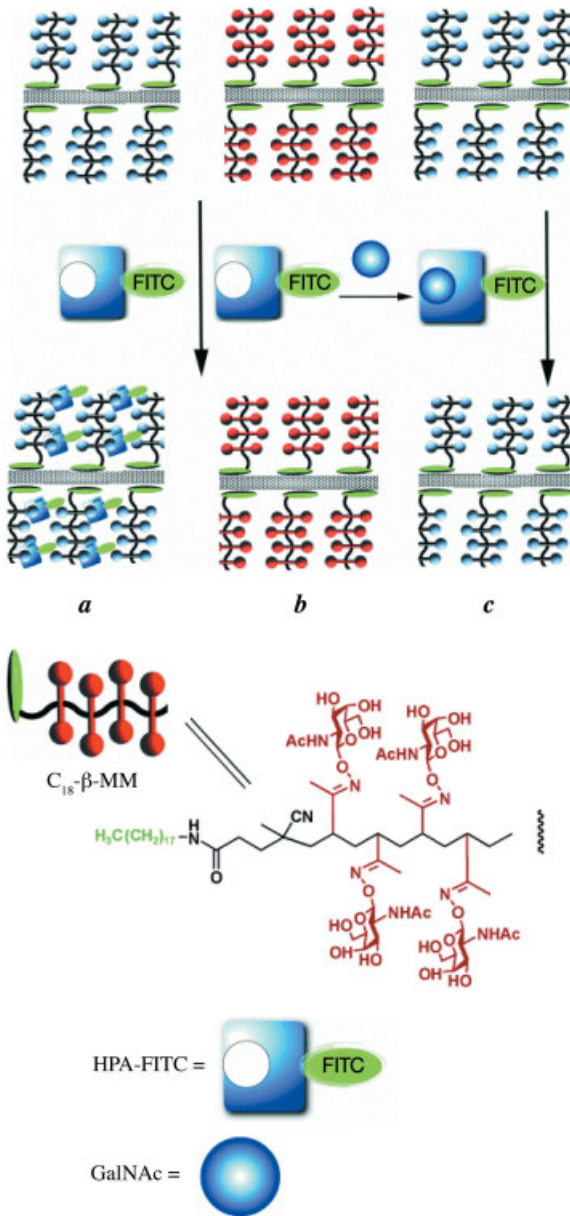


Fig. 7.25. Specific binding of HPA to  $\alpha$ -mucin mimic-coated nanotubes: (a) specific binding of HPA to the surface of  $\alpha$ -mucin mimic-SWNTs; (b) lack of binding of HPA to  $\beta$ -mucin mimic-SWNTs; and (c) inhibition of HPA binding by soluble GalNAc. (From Ref. [232].)

and any potential regulations for the changes in protein structures and biological functions are understood.

#### 7.4

#### Conclusions and Perspectives

As described in this chapter, exciting progress has been made over the past few years in the coupling and assembly of proteins and nanostructured materials (metal, semiconductor and nanotubes). A typical route for preparing these conjugates involves mixing proteins with chemically modified nanomaterials. Protein molecules can also act as crosslinkers or as templates to build nanometer-sized supramolecular structures by self-assembly. The field continues to grow and contribute to new interdisciplinary areas concerned with the synthesis, self-assembly, and processing of organized matter. Despite the progress made, this field is still in its infancy, with many challenges ahead. For example, there is still great demand for alternative and selective coupling methods that allow the preparation of stable, clean, and stoichiometrically well-defined bioconjugate nanomaterials. In this regard, an interesting recent development is the use of supercritical fluid processing, wherein a protein can be attached directly to inorganic nanoparticles in an effective and clean fashion. Other areas where there is much to be learnt are the surface interaction and the interface between nanomaterials and proteins and the control of shape and physico-chemical properties of proteins by means of genetic engineering and bioconjugate chemistry.

Among the enormous challenges are how to design well-ordered structures and how to adapt them efficiently in the macroscopic world. Here, the electrostatic and topographic properties of biological macromolecules, such as bacterial superstructures and hollow protein compartments, still must be understood. Research effort on the discovery, selection and development of peptides from combinatorial peptide and protein libraries will also benefit this field. It will allow the production of even more suitable biological structures, since they can provide recombinant protein units that have optimized recognition capabilities for inorganic materials and their assemblies in distinctively shaped superstructures.

Further future investigations should also address the issues of the applications of these bioconjugate materials. Interdisciplinary research in this field has great potential for discovering and producing advanced materials, which can then lead to novel devices for sensing, signal transduction, catalysis, and new biocompatible materials and interfaces desired for biomedical sciences and tissue engineering.

#### Acknowledgment

Financial support from NSF, NASA, Department of Energy, and the Center for Advanced Engineering Fibers and Films (NSF-ERC at Clemson University) is gratefully acknowledged.

## References

- 1 NIEMEYER, C. M., Nanoparticles, proteins, and nucleic acids: biotechnology meets materials science. *Angew. Chem. Int. Ed.* **2001**, *113* (22), 4128–4158; Functional hybrid devices of proteins and inorganic nanoparticles. *Angew. Chem. Int. Ed.* **2003**, *42* (47), 5796–5800.
- 2 KATZ, E., I. WILLNER, Integrated nanoparticle-biomolecule hybrid systems: synthesis, properties, and applications. *Angew. Chem. Int. Ed.* **2004**, *43* (45), 6042–6108.
- 3 KATZ, E., A. N. SHIPWAY, I. WILLNER, Biomaterial-nanoparticle hybrid systems: Synthesis, properties and applications, in *Nanoparticles – From Theory to Applications*, (Ed.: G. SCHMID), Wiley-VCH, Weinheim, 2003, 368–421.
- 4 PARAK, W. J., D. GERION, T. PELLEGRINO, D. ZANCHET, C. MICHEEL, S. C. WILLIAMS, R. BOUDREAU, M. A. LE GROS, C. A. LARABELL, A. P. ALIVISATOS, Biological applications of colloidal nanocrystals. *Nanotechnology* **2003**, *14* (7), R15–R27.
- 5 CSAKI, A., G. MAUBACH, D. BORN, J. REICHERT, W. FRITZSCHE, DNA-based molecular nanotechnology. *Single Mol.* **2002**, *3* (5–6), 275–280.
- 6 PENN, S. G., L. HEY, M. J. NATAN, Nanoparticles for bioanalysis. *Curr. Opin. Chem. Biol.* **2003**, *7* (5), 609–615.
- 7 WEST, J. L., N. J. HALAS, Engineered nanomaterials for biophotonics applications: improving sensing, imaging, and therapeutics. *Annu. Rev. Biomed. Eng.* **2003**, *5*, 285–292.
- 8 ALIVISATOS, A. P. The use of nanocrystals in biological detection. *Nat. Biotechnol.* **2004**, *22*, 47–52.
- 9 VERMA, A., V. M. ROTELLO. Surface recognition of biomacromolecules using nanoparticle receptors. *Chem. Commun.* **2005**, *3*, 303–312.
- 10 STORHOFF, J. J., C. A. MIRKIN, Programmed materials synthesis with DNA. *Chem. Rev.* **1999**, *99* (7), 1849–1862.
- 11 MIRKIN, C. A. Programming the assembly of two- and three-dimensional architectures with DNA and nanoscale inorganic building blocks. *Inorg. Chem.* **2000**, *39* (11), 2258–2272.
- 12 NIEMEYER, C. M., W. BÜRGER, J. PEPLIES, Covalent DNA – streptavidin conjugates as building blocks for novel biometallic nanostructures. *Angew. Chem. Int. Ed.* **1998**, *37* (16), 2265–2268.
- 13 CONNOLLY, S., D. FITZMAURICE, Programmed assembly of gold nanocrystals in aqueous solution. *Adv. Mater.* **1999**, *11* (14), 1202–1205.
- 14 LI, M., K. W. K. WONG, S. MANN, Organization of inorganic nanoparticles using biotin-streptavidin connectors. *Chem. Mater.* **1999**, *11* (1), 23–26.
- 15 NIEMEYER, C. M., B. CEYHAN, DNA-directed functionalization of colloidal gold with proteins. *Angew. Chem. Int. Ed.* **2001**, *40* (19), 3685–3688.
- 16 KREUTER, J. Nanoparticles – preparation and applications, in *Microcapsules and Nanoparticles in Medicine and Pharmacy*, (Ed.: M. DONBROW), CRC, Boca Raton, FL, **1992**, 125–148.
- 17 BRUCHEZ, JR., M., M. MORONNE, P. GIN, S. WEISS, A. P. ALIVISATOS, Semiconductor nanocrystals as fluorescent biological labels. *Science* **1998**, *281* (5385), 2013–2015.
- 18 CHAN, W. C. W., S. M. NIE, Quantum dot bioconjugates for ultrasensitive nonisotopic detection. *Science* **1998**, *281* (5385), 2016–2018.
- 19 MATTOUSSI, H., J. M. MAURO, E. R. GOLDMANN, G. P. ANDERSON, V. C. SUNDAR, F. V. MICULEC, M. G. BAWENDI, Self-assembly of CdSe-ZnS quantum dot bioconjugates using an engineered recombinant protein. *J. Am. Chem. Soc.* **2000**, *122* (49), 12142–12150.
- 20 WU, X. Y., H. J. LIU, J. Q. LIU, K. N. HALEY, J. A. TREADWAY, J. P. LARSON, N. F. GE, F. PEALE, M. P. BRUCHEZ, Immunofluorescent labeling of cancer marker Her2 and other cellular targets with semiconductor quantum dots. *Nat. Biotechnol.* **2003**, *21* (1), 41–46.

- 21 JAISWAL, J. K., H. MATTOUSSI, J. M. MAURO, S. M. SIMON, Long-term multiple color imaging of live cells using quantum dot bioconjugates. *Nat. Biotechnol.* **2003**, *21* (1), 47–51.
- 22 HAN, M. Y., X. H. GAO, J. Z. SU, S. M. NIE, Quantum-dot-tagged microbeads for multiplexed optical coding of biomolecules. *Nat. Biotechnol.* **2001**, *19* (7), 631–635.
- 23 KONNO, T., J. WATANABE, K. ISHIHARA, Conjugation of enzymes on polymer nanoparticles covered with phosphorylcholine groups. *Biomacromolecules* **2004**, *5* (2), 342–347.
- 24 QI, K., Q. MA, E. E. REMSEN, C. G. JR. CLARK, K. L. WOOLEY, Determination of the bioavailability of biotin conjugated onto shell cross-linked (SCK) nanoparticles. *J. Am. Chem. Soc.* **2004**, *126* (21), 6599–6607.
- 25 SOPPIMATH, K. S., T. M. AMINABHAVI, A. R. KULKARNI, W. E. RUDZINSKI, Biodegradable polymeric nanoparticles as drug delivery devices. *J. Controlled Release* **2001**, *70* (1–2), 1–20.
- 26 SAKUMA, S., M. HAYASHI, M. AKASHI, Design of nanoparticles composed of graft copolymers for oral peptide delivery. *Adv. Drug Deliv. Rev.* **2001**, *47* (1), 21–37.
- 27 TAKEUCHI, H., H. YAMAMOTO, Y. KAWASHIMA, Mucoadhesive nanoparticulate systems for peptide drug delivery. *Adv. Drug Deliv. Rev.* **2001**, *47* (1), 39–54.
- 28 NEDNOOR, P., M. CAPACCIO, V. G. GAVALAS, M. S. MEIER, J. E. ANTHONY, L. G. BACHAS, Hybrid nanoparticles based on organized protein immobilization on fullerenes. *Bioconj. Chem.* **2004**, *15* (1), 12–15.
- 29 HASOBE, T., P. V. KAMAT, V. TROIANI, N. SOLLADIE, T. K. AHN, S. K. KIM, D. KIM, A. KONGKANAND, S. KUWABATA, S. FUKUZUMI, Enhancement of light-energy conversion efficiency by multiporphyrin arrays of porphyrin-peptide oligomers with fullerene clusters. *J. Phys. Chem. B* **2005**, *109* (1), 19–23.
- 30 NAKAMURA, E., H. ISOBE, Functionalized fullerenes in water. The first 10 years of their chemistry, biology, and nanoscience. *Acc. Chem. Res.* **2003**, *36* (11), 807–815.
- 31 PANTAROTTO, D., A. BIANCO, F. PELLARINI, A. TOSSI, A. GIANGASPERO, I. ZELEZETSKY, J.-P. BRIAND, M. PRATO, Solid-phase synthesis of fullerene-peptides. *J. Am. Chem. Soc.* **2002**, *124* (42), 12543–12549.
- 32 MURAKAMI, H., R. MATSUMOTO, Y. OKUSA, T. SAGARA, M. FUJITSUKA, O. ITO, N. NAKASHIMA, Design, synthesis and photophysical properties of C-60-modified proteins. *J. Mater. Chem.* **2002**, *12* (7), 2026–2033.
- 33 BOSI, S., T. DAROS, G. SPALLUTO, M. PRATO, Fullerene derivatives: an attractive tool for biological applications. *Eur. J. Medic. Chem.* **2003**, *38* (11–12), 913–923.
- 34 FU, K. F., A. KITAYGORODSKIY, Y.-P. SUN, Fullerene-centered macromolecules as unimolecular micellar structures. *Chem. Mater.* **2000**, *12* (8), 2073–2075.
- 35 MARTIN, R. B., K. F. FU, H. P. LI, D. COLE, Y.-P. SUN, Interesting fluorescence properties of C-60-centered dendritic adduct with twelve symmetrically attached pyrenes. *Chem. Commun.* **2003**, *18*, 2368–2369.
- 36 SUN, Y.-P., G. E. LAWSON, W. J. HUANG, A. D. WRIGHT, D. K. MOTON, Preparation and characterization of highly water-soluble pendant fullerene polymers. *Macromolecules* **1999**, *32* (26), 8747–8752.
- 37 TAYLOR, S., L. QU, A. KITAYGORODSKIY, J. TESKE, R. A. LATOUR, Y.-P. SUN, Synthesis and characterization of peptide-functionalized polymeric nanoparticles. *Biomacromolecules* **2004**, *5* (1), 245–248.
- 38 QU, L., P. G. LUO, S. TAYLOR, Y. LIN, W. HUANG, N. ANYADIKE, T.-R. J. TZENG, F. STUTZENBERGER, R. A. LATOUR, Y.-P. SUN, Visualizing adhesion-induced agglutination of *Escherichia coli* with mannosylated nanoparticles. *J. Nanosci. Nanotechnol.* **2005**, *5* (2), 320–323.
- 39 QU, L., L. GU, H. LI, S. TAYLOR, T. ELKIN, P. G. LUO, T.-R. J. TZENG, X. JIANG, R. A. LATOUR, F. STUTZENBERGER, A. WILLIAMS, Y.-P. SUN,

- Galactosylated polymeric nanoparticles: Synthesis and adhesion interactions with *Escherichia coli*. *J. Biomed. Nanotechnol.* **2005**, *1* (1), 61–67(7).
- 40 SHENTON, W., S. A. DAVIES, S. MANN, Directed self-assembly of nanoparticles into macroscopic materials using antibody-antigen recognition. *Adv. Mater.* **1999**, *11* (6), 449–452.
- 41 HAYAT, M. A. *Colloidal Gold: Principles, Methods, and Applications*, Academic Press, New York, **1989**.
- 42 KEATING, C. D., K. M. KOVALESKI, M. J. NATAN, Protein: colloid conjugates for surface enhanced Raman scattering: Stability and control of protein orientation. *J. Phys. Chem. B* **1998**, *102* (47), 9404–9413.
- 43 BRODERICK, J. B., M. J. NATAN, T. V. OHALLORAN, R. P. VAN DUYN, Evidence for retention of biological-activity of a nonheme iron enzyme adsorbed on a silver colloid – a surface-enhanced resonance Raman-scattering study. *Biochemistry* **1993**, *32* (50), 13771–13776.
- 44 SCHULTZ, S., D. R. SMITH, J. J. MOCK, D. A. SCHULTZ, Single-target molecule detection with nonbleaching multi-color optical immunolabels. *Proc. Natl. Acad. Sci. U.S.A.* **2000**, *97* (3), 996–1001.
- 45 MACDONALD, I. D. G., W. E. SMITH, Orientation of cytochrome c adsorbed on a citrate-reduced silver colloid surface. *Langmuir* **1996**, *12* (3), 706–713.
- 46 ROSPENDOWSKI, B. N., K. KELLY, C. R. WOLF, W. E. SMITH, Surface-enhanced resonance Raman-scattering from cytochromes-P-450 adsorbed on citrate-reduced silver sols. *J. Am. Chem. Soc.* **1991**, *113* (4), 1217–1225.
- 47 BURT, J. L., C. GUTIERREZ-WING, M. MIKI-YOSHIDA, M. JOSE-YACAMAN, Noble-metal nanoparticles directly conjugated to globular proteins. *Langmuir* **2004**, *20* (26), 11778–11783.
- 48 SAFER, D., L. BOLINGER, J. S. LEIGH, Undecagold clusters for site-specific labeling of biological macromolecules – simplified preparation and model applications. *J. Inorg. Biochem.* **1986**, *26* (2), 77–91.
- 49 HAINFELD, J. F., F. R. FURUYA, A 1.4-nm gold cluster covalently attached to antibodies improves immunolabeling. *J. Histochem. Cytochem.* **1992**, *40* (2), 177–184.
- 50 LETSINGER, R. L., R. ELGHANIAN, G. VISWANADHAM, C. A. MIRKIN, Use of a steroid cyclic disulfide anchor in constructing gold nanoparticle-oligonucleotide conjugates. *Bioconj. Chem.* **2000**, *11* (2), 289–291.
- 51 DAMERON, C. T., R. N. REESE, R. K. MEHRA, A. R. KORTAN, P. J. CARROLL, M. L. STEIGERWALD, L. E. BRUS, D. R. WINGE, Biosynthesis of cadmium-sulfide quantum semiconductor crystallites. *Nature* **1989**, *338* (6216), 596–597.
- 52 WHALEY, S. R., D. S. ENGLISH, E. L. HU, P. F. BARBARA, A. M. BELCHER, Selection of peptides with semiconductor binding specificity for directed nanocrystal assembly. *Nature* **2000**, *405* (6787), 665–668.
- 53 HERMANSON, G. T. in *Bioconjugate Techniques*, Academic Press, New York, **1996**.
- 54 DOUGLAS, T., M. YOUNG, Host-guest encapsulation of materials by assembled virus protein cages. *Nature* **1998**, *393* (6681), 152–155.
- 55 GESTWICKI, J. E., L. E. STRONG, L. L. KIESSLING, Visualization of single multivalent receptor-ligand complexes by transmission electron microscopy. *Angew. Chem. Int. Ed.* **2000**, *39* (24), 4567–4570.
- 56 MAMEDOVA, N. N., N. A. KOTOV, A. L. ROGACH, J. STUDER, Albumin-CdTe nanoparticle bioconjugates: preparation, structure, and interunit energy transfer with antenna effect. *Nano Lett.* **2001**, *1* (6), 281–286.
- 57 WANG, S. P., N. N. MAMEDOVA, N. A. KOTOV, W. CHEN, J. STUDER, Antigen/antibody immunocomplex from CdTe nanoparticle bioconjugates. *Nano Lett.* **2002**, *2* (8), 817–822.
- 58 ISHII, D., K. KINBARA, Y. ISHIDA, N. ISHII, M. OKOCHI, M. YOHDA, T. AIDA, Chaperonin-mediated stabilization and ATP-triggered release of semiconductor nanoparticles. *Nature* **2003**, *423* (6940), 628–632.

- 59 MEZIANI, M. J., P. PATHAK, B. A. HARRUFF, R. HUREZEANU, Y.-P. SUN, Direct conjugation of semiconductor nanoparticles with proteins. *Langmuir* **2005**, *21* (5), 2008–2011.
- 60 MEZIANI, M. J., Y.-P. SUN, Protein-conjugated nanoparticles from rapid expansion of supercritical fluid solution into aqueous solution. *J. Am. Chem. Soc.* **2003**, *125* (26), 8015–8018.
- 61 WILLARD, D. M., L. L. CARILLO, J. JUNG, A. VAN ORDEN, CdSe-ZnS quantum dots as resonance energy transfer donors in a model protein-protein binding assay. *Nano Lett.* **2001**, *1* (9), 469–474.
- 62 MEDINTZ, I. L., A. R. CLAPP, H. MATTOUSSI, E. R. GOLDMAN, B. FISHER, J. M. MAURO, Self-assembled nanoscale biosensors based on quantum dot FRET donors. *Nat. Mater.* **2003**, *2* (9), 630–638.
- 63 MEDINTZ, I. L., J. H. KONNERT, A. R. CLAPP, I. STANISH, M. E. TWIGG, H. MATTOUSSI, J. M. MAURO, J. R. DESCHAMPS, A fluorescence resonance energy transfer-derived structure of a quantum dot-protein bioconjugate nanoassembly. *Proc. Nat. Acad. Sci. U.S.A.* **2004**, *101* (26), 9612–9617.
- 64 WILLNER, I., E. KATZ, Integration of layered redox proteins and conductive supports for bioelectronic applications. *Angew. Chem. Int. Ed.* **2000**, *39* (7), 1180–1218.
- 65 ZHONG, Z. Y., B. GATES, Y. N. XIA, D. QIN, Soft lithographic approach to the fabrication of highly ordered 2D arrays of magnetic nanoparticles on the surfaces of silicon substrates. *Langmuir* **2000**, *16* (26), 10369–10375.
- 66 ZAHN, M., Magnetic fluid and nanoparticle applications to nanotechnology. *J. Nanoparticle Res.* **2001**, *3* (1), 73–78.
- 67 SHI, J., S. GIDER, K. BABCOCK, D. D. AWSCHALOM, Magnetic clusters in molecular beams, metals, and semiconductors. *Science* **1996**, *271* (5251), 937–941.
- 68 LEBRETON, C., C. VIEU, A. PÉPIN, M. MEJIAS, F. CARCENAC, Y. JIN, and H. LAUNOIS, Coulomb blockade effect through a 2D ordered array of Pd islands obtained by colloidal deposition. *Microelectron. Eng.* **1998**, *42*, 507–510.
- 69 YOFFE, A. D. Semiconductor quantum dots and related systems: electronic, optical, luminescence and related properties of low dimensional systems. *Adv. Phys.* **2001**, *50* (1), 1–208.
- 70 KOUWENHOVEN, L. P., D. G. AUSTING, S. TARUCHA, Few-electron quantum dots. *Rep. Prog. Phys.* **2001**, *64* (6), 701–736.
- 71 SINHA, B. K., C. F. CHIGNELL, The synthesis and use of spin-labeled analogs of biotin in the study of avidin. *Methods Enzymol.* **1979**, *62*, 295–308.
- 72 PIRAN, U., W. J. RIORDAN, Dissociation rate-constant of the biotin-streptavidin complex. *J. Immunol. Methods* **1990**, *133* (1), 141–143.
- 73 SANO, T., M. W. PANDORI, X. M. CHEN, C. L. SMITH, C. R. CANTOR, Recombinant core streptavidins – a minimum-sized core streptavidin has enhanced structural stability and higher accessibility to biotinylated macromolecules. *J. Biol. Chem.* **1995**, *270* (47), 28204–28209.
- 74 SANO, T., C. R. CANTOR, Intersubunit contacts made by tryptophan-120 with biotin are essential for both strong biotin binding and biotin-induced tighter subunit association of streptavidin. *Proc. Natl. Acad. Sci. U.S.A.* **1995**, *92* (8), 3180–3184.
- 75 REZNIK, G. O., S. VAJDA, C. L. SMITH, C. R. CANTOR, T. SANO, Streptavidins with intersubunit crosslinks have enhanced stability. *Nat. Biotechnol.* **1996**, *14* (8), 1007–1011.
- 76 SCHMIDT, T. G. M., J. KOEPKE, R. FRANK, A. SKERRA, Molecular interaction between the Strep-tag affinity peptide and its cognate target, streptavidin. *J. Mol. Biol.* **1996**, *255* (5), 753–766.
- 77 SANO, T., S. VAJDA, C. R. CANTOR, Genetic engineering of streptavidin, a versatile affinity tag. *J. Chromatogr. B* **1998**, *715* (1), 85–91.
- 78 BROWN, S. Engineered iron oxide-

- adhesion mutants of the Escherichia coli phage-lambda receptor. *Proc. Natl. Acad. Sci. U.S.A.* **1992**, *89* (18), 8651–8655.
- 79** FLYNN, C. E., C. MAO, A. HAYHURST, J. L. WILLIAMS, G. GEORGIU, B. IVERSON, and A. M. BELCHER, Synthesis and organization of nanoscale II–VI semiconductor materials using evolved peptide specificity and viral capsid assembly. *J. Mater. Chem.* **2003**, *13* (10), 2414–2421.
- 80** LEE, S.-W., C. MAO, C. E. FLYNN, A. M. BELCHER, Ordering of quantum dots using genetically engineered viruses. *Science* **2002**, *296* (5569), 892–895.
- 81** LEE, S.-W., B. M. WOOD, A. M. BELCHER, Chiral smectic C structures of virus-based films. *Langmuir* **2003**, *19* (5), 1592–1598.
- 82** LEE, S.-W., S.-K. LEE, A. M. BELCHER, Virus-based alignment of inorganic, organic, and biological nanosized materials. *Adv. Mater.* **2003**, *15* (9), 689.
- 83** MAO, C. B., C. E. FLYNN, A. HAYHURST, R. Y. SWEENEY, J. QI, J. WILLIAMS, G. GEORGIU, B. IVERSON, and A. M. BELCHER, Viral assembly of oriented quantum dot nanowires. *Proc. Natl. Acad. Sci. U.S.A.* **2003**, *100* (12), 6946–6941.
- 84** MAO, C. B., D. J. SOLIS, B. D. REISS, S. T. KOTTMANN, R. Y. SWEENEY, A. HAYHURST, G. GEORGIU, B. IVERSON, and A. M. BELCHER, Virus-based toolkit for the directed synthesis of magnetic and semiconducting nanowires. *Science* **2004**, *303* (5655), 213–217.
- 85** SLEYTR, U. B., P. MESSNER, D. PUM, M. SARA, Crystalline bacterial cell surface layers (S layers): from supramolecular cell structure to biomimetics and nanotechnology. *Angew. Chem. Int. Ed.* **1999**, *38* (8), 1034–1054.
- 86** SHENTON, W., D. PUM, U. B. SLEYTR, S. MANN, Synthesis of cadmium sulphide superlattices using self-assembled bacterial S-layers. *Nature* **1997**, *389* (6651), 585–587.
- 87** DIELUWEIT, S., D. PUM, U. B. SLEYTR, Formation of a gold superlattice on an S-layer with square lattice symmetry. *Supramol. Sci.* **1998**, *5* (1–2), 15–19.
- 88** HALL, S. R., W. SHENTON, H. ENGELHARDT, S. MANN, Site-specific organization of gold nanoparticles by biomolecular templating. *Chem. Phys. Chem.* **2001**, *2* (3), 184–186.
- 89** MERTIG, M., R. KIRSCH, W. POMPE, H. ENGELHARDT, Fabrication of highly oriented nanocluster arrays by biomolecular templating. *Eur. Phys. J. D* **1999**, *9* (1–4), 45–48.
- 90** ALLEN, M., D. WILLITS, J. MOSOLF, M. YOUNG, T. DOUGLAS, Protein cage constrained synthesis of ferrimagnetic iron oxide nanoparticles. *Adv. Mater.* **2002**, *14* (21), 1562–1565.
- 91** DOUGLAS, T., E. STRABLE, D. WILLITS, A. AITOUCHEN, M. LIBERA, M. YOUNG, Protein engineering of a viral cage for constrained nanomaterials synthesis. *Adv. Mater.* **2002**, *14* (6), 415–418.
- 92** SHENTON, W., S. MANN, H. CÖLFEN, A. BACHER, M. FISCHER, Synthesis of nanophase iron oxide in lumazine synthase capsids. *Angew. Chem. Int. Ed.* **2001**, *40* (2), 442–444.
- 93** STRYER, L. *Biochemistry*, Freeman, New York, 1988.
- 94** STUBBS, G. in *The Viruses*. (Eds.: A. MC PHERSON, F. JURNAK), Wiley, New York, 1984, Vol. 1, 149–202.
- 95** SHENTON, W., T. DOUGLAS, M. YOUNG, G. STUBBS, S. MANN, Inorganic-organic nanotube composites from template mineralization of tobacco mosaic virus. *Adv. Mater.* **1999**, *11* (3), 253–256.
- 96** DUJARDIN, E., C. PEET, G. STUBBS, J. N. CULVER, S. MANN, Organization of metallic nanoparticles using tobacco mosaic virus templates. *Nano Lett.* **2003**, *3* (3), 413–417.
- 97** BOAL, A. K., T. J. HEADLEY, R. G. TISSOT, B. C. BUNKER, Microtubule templated synthesis of inorganic nanomaterials. Biomolecular materials and interfaces. *Mater. Res. Soc. Symp. Proc.* **2004**, *823*, 3–8.
- 98** SHAW, R. W., T. B. BRILL, A. A. CLIFFORD, C. A. ECKERT, E. U. FRANCK, Supercritical water – a

- medium for chemistry. *Chem. Eng. News* **1991**, 69 (51), 26–39.
- 99 SAVAGE, P. E., S. GOPALAN, T. I. MIZAN, C. J. MARTINO, E. E. BROCK, Reactions at supercritical conditions – applications and fundamentals. *AIChE J.* **1995**, 41 (7), 1723–1778.
- 100 CLIFFORD, T., K. BARTLE, Chemical reactions in supercritical fluids. *Chem. Ind.* **1996**, 12, 449–452.
- 101 BUNKER, C. E., H. W. ROLLINS, Y.-P. SUN, Fundamental properties of supercritical fluids, in *Supercritical Fluid Technology in Materials Science and Engineering: Synthesis, Properties, and Applications*. (Ed.: Y.-P. SUN), Marcel Dekker, New York, 2002, 1–57.
- 102 SUN, Y.-P., H. W. ROLLINS, B. JAYASUNDERA, M. J. MEZIANI, C. E. BUNKER, Preparation and processing of nanoscale materials by supercritical fluid technology, in *Supercritical Fluid Technology in Materials Science and Engineering: Synthesis, Properties, and Applications*. (Ed.: Y.-P. SUN), Marcel Dekker, New York, 2002, 491–576.
- 103 SUN, Y.-P., M. J. MEZIANI, P. PATHAK, L. W. QU, Polymeric nanoparticles from rapid expansion of supercritical fluid solution. *Chem. Eur. J.* **2005**, 11, 1366–1373.
- 104 ANDREW, D., B. T. DES ISLET, A. MARGARITIS, A. C. WEEDON, Photo-fries rearrangement of naphthyl acetate in supercritical carbon-dioxide – chemical evidence for solvent-solute clustering. *J. Am. Chem. Soc.* **1995**, 117 (22), 6132–6133.
- 105 HRNJEZ, B. J., A. J. MEHTA, M. A. FOX, K. P. JOHNSTON, Photodimerization of isophorone in supercritical trifluoromethane and carbon-dioxide. *J. Am. Chem. Soc.* **1989**, 111 (7), 2662–2666.
- 106 KIMURA, Y., Y. YOSHIMURA, M. NAKAHARA, Chemical-reaction in medium density fluid – solvent density effects on the dimerization equilibrium of 2-methyl-2-nitrosopropane in carbon-dioxide. *J. Chem. Phys.* **1989**, 90 (10), 5679–5686.
- 107 KIMURA, Y., Y. YOSHIMURA, Chemical-equilibrium in fluids from the gaseous to liquid states – solvent density dependence of the dimerization equilibrium of 2-methyl-2-nitrosopropane in carbon-dioxide, chlorotrifluoromethane, and trifluoromethane. *J. Chem. Phys.* **1992**, 96 (4), 3085–3091.
- 108 WEINSTEIN, R. D., A. R. RENSLO, R. L. DANHEISER, J. G. HARRIS, J. W. TESTER, Kinetic correlation of Diels-Alder reactions in supercritical carbon dioxide. *J. Phys. Chem.* **1996**, 100 (30), 12337–12341.
- 109 ISAACS, N. S., N. J. KEATING, The rates of a Diels-Alder reaction in liquid and supercritical carbon dioxide. *J. Chem. Soc., Chem. Comm.* **1992**, 876–877.
- 110 BUNKER, C. E., H. W. ROLLINS, J. R. GORD, Y.-P. SUN, Efficient photodimerization reaction of anthracene in supercritical carbon dioxide. *J. Org. Chem.* **1997**, 62 (21), 7324–7329.
- 111 KSIBI, H., P. SUBRA, Y. GARRABOS, Formation of fine powders of caffeine by RESS. *Adv. Powder Technol.* **1995**, 6 (1), 25–33.
- 112 SUBRA, P., P. TESTIN, Powders elaboration in supercritical media: comparison with conventional routes. *Powder Technol.* **1999**, 103 (1), 2–9.
- 113 WEBER, M., M. C. THIES, Understanding the RESS process, in *Supercritical Fluid Technology in Materials Science and Engineering: Synthesis, Properties, and Applications*. (Ed.: Y.-P. SUN), Marcel Dekker, New York, 2002, 387–437.
- 114 DEBENEDETTI, P. G., J. W. TOM, X. KWAIK, S. D. YEO, Rapid expansion of supercritical solutions (RESS) – fundamentals and applications. *Fluid Phase Equilib.* **1993**, 82, 311–321.
- 115 REVERCHON, E. Supercritical antisolvent precipitation of micro- and nano-particles. *J. Supercrit. Fluids* **1999**, 15 (1), 1–21.
- 116 DIXON, D. J., G. LUNABARCENAS, K. P. JOHNSTON, Microcellular microspheres and microballoons by precipitation with a vapor-liquid compressed fluid antisolvent. *Polymer* **1994**, 35 (18), 3998–4005.
- 117 DIXON, D. J., K. P. JOHNSTON, R. A. BODMEIER, Polymeric materials formed by precipitation with a



- compressed fluid antisolvent. *AIChE J.* **1993**, *39* (1), 127–139.
- 118 TOM, J. W., P. G. DEBENEDETTI, Particle formation with supercritical fluids – a review. *J. Aerosol Sci.* **1991**, *22* (5), 555–584.
- 119 KRUKONIS, V. J. Supercritical fluids nucleation of difficult-to-comminute solids. *Paper at Annual Meeting AIChE*, San Francisco, November 1984.
- 120 MATSON, D. W., J. L. FULTON, R. D. SMITH, Formation of fine particles in supercritical fluid micelle systems. *Mater. Lett.* **1987**, *6* (1–2), 31–33.
- 121 MATSON, D. W., R. C. PETERSEN, R. D. SMITH, Formation of silica powders from the rapid expansion of supercritical solutions. *Adv. Ceram. Mater.* **1986**, *1*, 242–246.
- 122 MATSON, D. W., J. L. FULTON, R. C. PETERSEN, R. C. SMITH, Rapid expansion of supercritical fluid solutions – solute formation of powders, thin-films, and fibers. *Ind. Eng. Chem. Res.* **1987**, *26* (11), 2298–2306.
- 123 MATSON, D. W., R. C. PETERSEN, R. C. SMITH, Production of powders and films by the rapid expansion of supercritical solutions. *J. Mater. Sci.* **1987**, *22* (6), 1919–1928.
- 124 ECKERT, C. A., B. L. KNUTSON, P. G. DEBENEDETTI, Supercritical fluids as solvents for chemical and materials processing. *Nature* **1996**, *383* (6598), 313–318.
- 125 MCHUGH, M. A., V. J. KRUKONIS, in *Supercritical Fluid Extraction: Principles and Practice*; 2 edn. Butterworth-Heinemann Series in Chemical Engineering, Butterworth-Heinemann, Stoneham, MA, 1994.
- 126 JUNG, J., M. PERRUT, Particle design using supercritical fluids: literature and patent survey. *J. Supercrit. Fluids* **2001**, *20* (3), 179–219.
- 127 YORK, P. Strategies for particle design using supercritical fluid technologies. *Pharm. Sci. Tech. Today* **1999**, *2* (11), 430–440.
- 128 STANTON, L. A., DEHGHANI, F., FOSTER, N. R. Improving drug delivery using polymers and supercritical fluid technology. *Aust. J. Chem.* **2002**, *55* (6–7), 443–447.
- 129 MOHAMED, R. S., D. S. HALVERSON, P. G. DEBENEDETTI, R. K. PRUD'HOMME, Solids formation after the expansion of supercritical mixtures, in *Supercritical Fluid Science and Technology*, (Eds.: K. P. JOHNSTON, J. M. L. PENNINGER), ACS symposium Series 406, Washington DC, 1989, 355–378.
- 130 DOMINGO, C., E. BERENDS, G. M. VAN ROSMALEN, Precipitation of ultrafine organic crystals from the rapid expansion of supercritical solutions over a capillary and a frit nozzle. *J. Supercrit. Fluids* **1997**, *10* (1), 39–55.
- 131 KRÖBER, H., U. TEIPEL, H. KRAUSE, Manufacture of submicron particles via expansion of supercritical fluids. *Chem. Eng. Technol.* **2000**, *23* (9), 763–765.
- 132 HELFGEN, B., M. TÜRK, K. SCHABER, Theoretical and experimental investigations of the micronization of organic solids by rapid expansion of supercritical solutions. *Powder Technol.* **2000**, *110* (1–2), 22–28.
- 133 SUN, Y.-P., H. W. ROLLINS, Preparation of polymer-protected semiconductor nanoparticles through the rapid expansion of supercritical fluid solution. *Chem. Phys. Lett.* **1998**, *288* (2–4), 585–588.
- 134 SUN, Y.-P., H. W. ROLLINS, R. GUDURU, Preparation of nickel, cobalt, and iron nanoparticles through the rapid expansion of supercritical fluid solution (RESS) and chemical reduction. *Chem. Mater.* **1999**, *11* (1), 7–9.
- 135 SUN, Y.-P., R. GUDURU, F. LIN, T. WHITESIDE, Preparation of nanoscale semiconductors through the rapid expansion of supercritical solution (RESS) into liquid solution. *Ind. Eng. Chem. Res.* **2000**, *39* (12), 4663–4669.
- 136 SUN, Y.-P., P. ATORNGITJAWAT, M. J. MEZIANI, Preparation of silver nanoparticles via rapid expansion of water in carbon dioxide microemulsion into reductant solution. *Langmuir* **2001**, *17* (19), 5707–5710.
- 137 MEZIANI, M. J., P. PATHAK, L. F. ALLARD, Y.-P. SUN, Nanoparticle formation in rapid expansion of water-

- in-carbon dioxide microemulsion into liquid solvent, in *Supercritical Carbon Dioxide Separations and Processes*, (Ed.: A. S. GOPALAN, C. M. WAI, H. K. JACOBS), ACS Symposium Series 860, Washington DC, 2003, 309–323.
- 138 MEZIANI, M. J., H. W. ROLLINS, L. F. ALLARD, Y.-P. SUN, Protein-protected nanoparticles from rapid expansion of supercritical solution into aqueous solution. *J. Phys. Chem. B* **2002**, *106* (43), 11178–11182.
- 139 MEZIANI, M. J., P. PATHAK, R. HUREZEANU, M. C. THIES, R. M. ENICK, Y.-P. SUN, Supercritical-fluid processing technique for nanoscale polymer particles. *Angew. Chem. Int. Ed.* **2004**, *43* (6), 704–707.
- 140 PATHAK, P., M. J. MEZIANI, T. DESAI, Y.-P. SUN, Nanosizing drug particles in supercritical fluid processing. *J. Am. Chem. Soc.* **2004**, *126* (35), 10842–10843.
- 141 WANER, M. J., M. GILCHRIST, M. SCHINDLER, M. DANTUS, Imaging the molecular dimensions and oligomerization of proteins at liquid/solid interfaces. *J. Phys. Chem. B* **1998**, *102* (9), 1649–1657.
- 142 WANG, Y. Photophysical and photochemical processes of semiconductor nanoclusters. *Adv. Photochem.* **1995**, *19*, 179.
- 143 QUARONI, L., G. CHUMANOV, Preparation of polymer-coated functionalized silver nanoparticles. *J. Am. Chem. Soc.* **1999**, *121* (45), 10642–10643.
- 144 WANG, Y., A. SUNA, J. MCHUGH, E. F. HILINSKI, P. A. LUCAS, R. D. JOHNSON, Optical transient bleaching of quantum-confined CdS clusters – the effects of surface-trapped electron-hole pairs. *J. Chem. Phys.* **1990**, *92* (11), 6927–6939.
- 145 HARRUFF, B. A., C. E. BUNKER, Spectral properties of AOT-protected CdS nanoparticles: quantum yield enhancement by photolysis. *Langmuir* **2003**, *19* (3), 893–897.
- 146 LOWRY, O. H., N. J. ROSENBROUGH, A. L. FARR, R. J. RANDALL, Protein measurement with the folin phenol reagent. *J. Biol. Chem.* **1951**, *193*, 265–275.
- 147 OHNISHI, S. T., J. K. BARR, A simplified method of quantitating proteins using the biuret and phenol reagents. *Anal. Biochem.* **1978**, *86* (1), 193–200.
- 148 PETERSON, G. L. Review of the Folin phenol protein quantitation method of Lowry, Rosebrough, Farr and Randall. *Anal. Biochem.* **1979**, *100* (2), 201–220.
- 149 FOSTER, J. F. in *Albumin Structure, Function and Uses*. (Eds.: V. M. ROSENER, M. ORATZ, M. A. ROTHSCHILD), Pergamon, Oxford, U.K., 1977, 53–84.
- 150 SASAKI, Y. C., K. YASUDA, Y. SUZUKI, T. ISHIBASHI, I. SATOH, Y. FUJIKI, S. ISHIWATA, Two-dimensional arrangement of a functional protein by cysteine-gold interaction: Enzyme activity and characterization of a protein monolayer on a gold substrate. *Biophys. J.* **1997**, *72* (4), 1842–1848.
- 151 BRELLE, M. C., J. Z. ZHANG, L. NGUYEN, R. K. MEHRA, Synthesis and ultrafast study of cysteine- and glutathione-capped Ag<sub>2</sub>S semiconductor colloidal nanoparticles. *J. Phys. Chem. A* **1999**, *103* (49), 10194–10201.
- 152 LEFF, D. V., L. BRANDT, J. R. HEATH, Synthesis and characterization of hydrophobic, organically-soluble gold nanocrystals functionalized with primary amines. *Langmuir* **1996**, *12* (20), 4723–4730.
- 153 DRESSSELHAUS, M. S., G. DRESSSELHAUS, P. C. EKLUND, *Science of Fullerenes and Carbon Nanotubes*, Academic Press, New York, 1996.
- 154 AJAYAN, P. M., Nanotubes from carbon. *Chem. Rev.* **1999**, *99* (7), 1787–1800.
- 155 Special issue on carbon nanotubes. *Acc. Chem. Res.* **2002**, *35* (12).
- 156 Special issue on advances in carbon nanotubes. *MRS Bull.* **2004**, *29* (4).
- 157 DAVIS, J. J., K. S. COLEMAN, B. R. AZAMIAN, C. B. BAGSHAW, M. L. H. GREEN, Chemical and biochemical sensing with modified single walled carbon nanotubes. *Chem. Eur. J.* **2003**, *9* (16), 3732–3739.
- 158 BIANCO, A., M. PRATO, Can carbon

- nanotubes be considered useful tools for biological applications? *Adv. Mater.* **2003**, *15* (20), 1765–1768.
- 159 LIN, Y., S. TAYLOR, H. LI, K. A. S. FERNANDO, L. QU, W. WANG, L. GU, B. ZHOU, Y.-P. SUN, Advances toward bioapplications of carbon nanotubes. *J. Mater. Chem.* **2004**, *14* (4), 527–541.
- 160 KATZ, E., I. WILLNER, Biomolecule-functionalized carbon nanotubes: Applications in nanobioelectronics. *ChemPhysChem* **2004**, *5* (8), 1084–1104.
- 161 BIANCO, A., K. KOSTARELOS, C. D. PARTIDOS, M. PRATO, Biomedical applications of functionalised carbon nanotubes. *Chem. Commun.* **2005**, (5), 571–577.
- 162 BEKYAROVA, E., Y. NI, E. B. MALARKEY, V. MONTANA, J. L. McWILLIAMS, R. C. HADDON, V. PARPURA, Applications of carbon nanotubes in biotechnology and biomedicine. *J. Biomed. Nanotech.* **2005**, *1* (1), 3–17.
- 163 PASTORIN, G., K. KOSTARELOS, M. PRATO, A. BIANCO, Functionalized carbon nanotubes: Toward the delivery of therapeutic molecules. *J. Biomed. Nanotech.* **2005**, *1* (2), in press.
- 164 PANTAROTTO, D., C. D. PARTIDOS, J. HOEBEKE, F. BROWN, E. KRAMER, J.-P. BRIAND, S. MULLER, M. PRATO, A. BIANCO, Immunization with peptide-functionalized carbon nanotubes enhances virus-specific neutralizing antibody responses. *Chem. Biol.* **2003**, *10* (10), 961–966.
- 165 PANTAROTTO, D., J.-P. BRIAND, M. PRATO, A. BIANCO, Translocation of bioactive peptides across cell membranes by carbon nanotubes. *Chem. Commun.* **2004**, (1), 16–17.
- 166 PANTAROTTO, D., R. SINGH, D. MCCARTHY, M. ERHARDT, J.-P. BRIAND, M. PRATO, K. KOSTARELOS, A. BIANCO, Functionalized carbon nanotubes for plasmid DNA gene delivery. *Angew. Chem. Int. Ed.* **2004**, *43* (39), 5242–5246.
- 167 KAM, N. W. S., T. C. JESSOP, P. A. WENDER, H. DAI, Nanotube molecular transporters: Internalization of carbon nanotube-protein conjugates into mammalian cells. *J. Am. Chem. Soc.* **2004**, *126* (22), 6850–6851.
- 168 LU, Q., J. M. MOORE, G. HUANG, A. S. MOUNT, A. M. RAO, L. L. LARCOM, P. C. KE, RNA polymer translocation with single-walled carbon nanotubes. *Nano Lett.* **2004**, *4* (12), 2473–2477.
- 169 ELKIN, T., X. JIANG, S. TAYLOR, Y. LIN, L. GU, H. YANG, J. BROWN, S. COLLINS, Y.-P. SUN, Immuno-carbon nanotubes and recognition of pathogens. *ChemBioChem* **2005**, *6* (4), 640–643.
- 170 GU, L., T. ELKIN, X. JIANG, H. LI, Y. LIN, L. QU, T.-R. J. TZENG, R. JOSEPH, Y.-P. SUN, Single-walled carbon nanotubes displaying multivalent ligands for capturing pathogens. *Chem. Commun.* **2005**, (7), 874–876.
- 171 CHEN, J., M. A. HAMON, H. HU, Y. CHEN, A. M. RAO, P. C. EKLUND, R. C. HADDON, Solution properties of single-walled carbon nanotubes. *Science* **1998**, *282* (5386), 95–98.
- 172 HIRSCH, A. Functionalization of single-walled carbon nanotubes. *Angew. Chem. Int. Ed.* **2002**, *41* (11), 1853–1859.
- 173 BAHR, J. L., J. M. TOUR, Covalent chemistry of single-walled carbon nanotubes. *J. Mater. Chem.* **2002**, *12* (7), 1952–1958.
- 174 NIYOGI, S., M. A. HAMON, H. HU, B. ZHAO, P. BHOWMIK, R. SEN, M. E. ITKIS, R. C. HADDON, Chemistry of single-walled carbon nanotubes. *Acc. Chem. Res.* **2002**, *35* (12), 1105–1113.
- 175 SUN, Y.-P., K. FU, Y. LIN, W. HUANG, Functionalized carbon nanotubes: Properties and applications. *Acc. Chem. Res.* **2002**, *35* (12), 1096–1104.
- 176 MATTSO, M. P., R. C. HADDON, A. M. RAO, Molecular functionalization of carbon nanotubes and use as substrates for neuronal growth. *J. Mol. Neurosci.* **2000**, *14* (3), 175–182.
- 177 HU, H., Y. NI, V. MONTANA, R. C. HADDON, V. PARPURA, Chemically functionalized carbon nanotubes as substrates for neuronal growth. *Nano Lett.* **2004**, *4* (3), 507–511.
- 178 CORREA-DUARTE, M. A., N. WAGNER, J. ROJAS-CHAPANA, C. MORSZCZEK, M. THIE, M. GIERSIG, Fabrication and

- biocompatibility of carbon nanotube-based 3D networks as scaffolds for cell seeding and growth. *Nano Lett.* **2004**, *4* (11), 2233–2236.
- 179 CHEN, R. J., S. BANGSARUNTIP, K. A. DROUVALAKIS, N. W. S. KAM, M. SHIM, Y. LI, W. KIM, P. J. UTZ, H. DAI, Noncovalent functionalization of carbon nanotubes for highly specific electronic biosensors. *Proc. Natl. Acad. Sci. U.S.A.* **2003**, *100* (9), 4984–4989.
- 180 BAUGHMAN, R. H., C. CUI, A. A. ZAKHIDOV, Z. IQBAL, J. N. BARISCI, G. M. SPINKS, G. G. WALLACE, A. MAZZOLDI, D. DE ROSSI, A. G. RINZLER, O. JASCHINSKI, S. ROTH, M. KERTESZ, Carbon nanotube actuators. *Science* **1999**, *284* (5418), 1340–1344.
- 181 WONG, S. S., E. JOSELEVICH, A. T. WOOLLEY, C. C. CHEUNG, C. M. LIEBER, Covalently functionalized nanotubes nanometre-sized probes in chemistry and biology. *Nature* **1998**, *394* (6688), 52–55.
- 182 TSANG, S. C., J. J. DAVIS, M. L. H. GREEN, H. A. O. HILL, Y. C. LEUNG, P. J. SADLER, Immobilization of small proteins in carbon nanotubes – High-resolution transmission electron-microscopy study and catalytic activity. *J. Chem. Soc., Chem. Commun.* **1995**, (17), 1803–1804.
- 183 DAVIS, J. J., M. L. H. GREEN, H. A. O. HILL, Y. C. LEUNG, P. J. SADLER, J. SLOAN, A. V. XAVIER, S. C. TSANG, The immobilisation of proteins in carbon nanotubes. *Inorg. Chim. Acta* **1997**, *272* (1–2), 261–266.
- 184 TSANG, S. C., Z. GUO, Y. K. CHEN, M. L. H. GREEN, H. A. O. HILL, T. W. HAMBLEY, P. J. SADLER, Immobilization of platinated and iodinated oligonucleotides on carbon nanotubes. *Angew. Chem. Int. Ed.* **1997**, *36* (20), 2198–2200.
- 185 GUO, Z., P. J. SADLER, S. C. TSANG, Immobilization and visualization of DNA and proteins on carbon nanotubes. *Adv. Mater.* **1998**, *10* (9), 701–703.
- 186 BALAVOINE, F., P. SCHULTZ, C. RICHARD, V. MALLOUH, T. W. EBBESEN, C. MIOSKOWSKI, Helical crystallization of proteins on carbon nanotubes: A first step towards the development of new biosensors. *Angew. Chem. Int. Ed.* **1999**, *38* (13/14), 1912–1915.
- 187 SHIM, M., N. W. S. KAM, R. J. CHEN, Y. LI, H. DAI, Functionalization of carbon nanotubes for biocompatibility and biomolecular recognition. *Nano Lett.* **2002**, *2* (4), 285–288.
- 188 AZAMIAN, B. R., J. J. DAVIS, K. S. COLEMAN, C. B. BAGSHAW, M. L. H. GREEN, Bioelectrochemical single-walled carbon nanotubes. *J. Am. Chem. Soc.* **2002**, *124* (43), 12664–12665.
- 189 LIN, Y., L. F. ALLARD, Y.-P. SUN, Protein-affinity of single-walled carbon nanotubes in water. *J. Phys. Chem. B* **2004**, *108* (12), 3760.
- 190 REGE, K., N. R. KARAVIKAR, D.-Y. KIM, L. S. SCHADLER, P. M. AJAYAN, J. S. DORDICK, Enzyme-polymer-single walled carbon nanotube composites as biocatalytic films. *Nano Lett.* **2003**, *3* (6), 829–832.
- 191 KARAJANAGI, S. S., A. A. VERTEGEL, R. S. KANE, J. S. DORDICK, Structure and function of enzymes adsorbed onto single-walled carbon nanotubes. *Langmuir* **2004**, *20* (26), 11594–11599.
- 192 DAI, H., Carbon nanotubes: Synthesis, integration, and properties. *Acc. Chem. Res.* **2002**, *35* (12), 1035–1044.
- 193 TANS, S. J., A. R. M. VERSCHUEREN, C. DEKKER, Room temperature transistor based on a single carbon nanotube. *Nature* **1998**, *393* (6680), 49–52.
- 194 KONG, J., N. R. FRANKLIN, C. ZHOU, M. G. CHAPLINE, S. PENG, K. CHO, H. DAI, Nanotube molecular wires as chemical sensors. *Science* **2000**, *287* (5453), 622–625.
- 195 AVOURIS, P. Carbon nanotube electronics and optoelectronics. *MRS Bull.* **2004**, *29* (6), 403–410.
- 196 BOUSSAAD, S., N. J. TAO, R. ZHANG, T. HOPSON, L. A. NAGAHARA, *In situ* detection of cytochrome c adsorption with single walled carbon nanotube device. *Chem. Commun.* **2003**, (13), 1502–1503.
- 197 BESTEMAN, K., J.-O. LEE, F. G. M. WIERTZ, H. A. HEERING, C. DEKKER,

- Enzyme-coated carbon nanotubes as single-molecule biosensors. *Nano Lett.* **2003**, 3 (6), 727–730.
- 198 CHEN, R. J., H. C. CHOI, S. BANG-SARUNTIP, E. YENILMEZ, X. TANG, Q. WANG, Y.-L. CHANG, H. DAI, An investigation of the mechanisms of electronic sensing of protein adsorption on carbon nanotube devices. *J. Am. Chem. Soc.* **2004**, 126 (5), 1563–1568.
- 199 SADANA, A. Protein adsorption and inactivation on surfaces – Influence of heterogeneities. *Chem. Rev.* **1992**, 92 (8), 1799–1818.
- 200 VERMETTE, P., L. MEAGHER, Interactions of phospholipid- and poly(ethylene glycol)-modified surfaces with biological systems: Relation to physico-chemical properties and mechanisms. *Colloids Surf. B* **2003**, 28 (2–3), 153–198.
- 201 O'CONNELL, M. J., S. M. BACHILO, C. B. HUFFMAN, V. C. MOORE, M. S. STRANO, E. H. HAROZ, K. L. RIALON, P. J. BOUL, W. H. NOON, C. KITTRELL, J. MA, R. H. HAUGE, R. B. WEISMAN, R. E. SMALLEY, Band gap fluorescence from individual single-walled carbon nanotubes. *Science* **2002**, 297 (5581), 593–596.
- 202 WANG, S., E. S. HUMPHREYS, S.-Y. CHUNG, D. F. DELDUCCO, S. R. LUSTIG, H. WANG, K. N. PARKER, N. W. RIZZO, S. SUBRAMONEY, Y.-M. CHIANG, A. JAGOTA, Peptides with selective affinity for carbon nanotubes. *Nat. Mater.* **2003**, 2 (3), 196–200.
- 203 DIECKMANN, G. R., A. B. DALTON, P. A. JOHNSON, J. RAZAL, J. CHEN, G. M. GIORDANO, E. MUNOZ, I. H. MUSSELMAN, R. H. BAUGHMAN, R. K. DRAPER, Controlled assembly of carbon nanotubes by designed amphiphilic peptide helices. *J. Am. Chem. Soc.* **2003**, 125 (7), 1770–1777.
- 204 ZORBAS, V., A. ORTIZ-ACEVEDO, A. B. DALTON, M. M. YOSHIDA, G. R. DIECKMANN, R. K. DRAPER, R. H. BAUGHMAN, M. JOSE-YACAMAN, I. H. MUSSELMAN, Preparation and characterization of individual peptide-wrapped single-walled carbon nanotubes. *J. Am. Chem. Soc.* **2004**, 126 (23), 7222–7227.
- 205 LIU, J., A. G. RINZLER, H. DAI, J. H. HAFNER, R. K. BRADLEY, P. J. BOUL, A. LU, T. IVERSON, K. SHELMOV, C. B. HUFFMAN, F. RODRIGUEZ-MACIAS, Y. S. SHON, T. R. LEE, D. T. COLBERT, R. E. SMALLEY, Fullerene pipes. *Science* **1998**, 280 (5367), 1253–1256.
- 206 HU, H., P. BHOWMIK, B. ZHAO, M. A. HAMON, M. E. ITKIS, R. C. HADDON, Determination of the acidic sites of purified single-walled carbon nanotubes by acid-base titration. *Chem. Phys. Lett.* **2001**, 345 (1–2), 25–28.
- 207 MAWHINNEY, D. B., V. NAUMENKO, A. KUZNETSOVA, J. T. YATES, J. LIU, R. E. SMALLEY, Surface defect site density on single walled carbon nanotubes by titration. *Chem. Phys. Lett.* **2000**, 324 (1–3), 213–216.
- 208 KONG, J., H. DAI, Full and modulated chemical gating of individual carbon nanotubes by organic amine compounds. *J. Phys. Chem. B* **2001**, 105 (15), 2890–2893.
- 209 BASIUK, E. V., V. A. BASIUK, J. G. BANUELOS, J. M. SANIGER-BLESA, V. A. POKROVSKIY, T. Y. GROMOVOY, A. V. MISCHANCHUK, B. G. MISCHANCHUK, Interaction of oxidized single-walled carbon nanotubes with vaporous aliphatic amines. *J. Phys. Chem. B* **2002**, 106 (7), 1588–1597.
- 210 CHATTOPADHYAY, D., I. GALESKA, F. PAPADIMITRAKOPOULOS, A route for bulk separation of semiconducting from metallic single-wall carbon nanotubes. *J. Am. Chem. Soc.* **2003**, 125 (11), 3370–3375.
- 211 BRADLEY, K., J.-C.-P. GABRIEL, M. BRIMAN, A. STAR, G. GRUNER, Charge transfer from ammonia physisorbed on nanotubes. *Phys. Rev. Lett.* **2003**, 91 (21), 218301.
- 212 BRADLEY, K., M. BRIMAN, A. STAR, G. GRUNER, Charge transfer from adsorbed proteins. *Nano Lett.* **2004**, 4 (2), 253–256.
- 213 HUANG, W., Y. LIN, S. TAYLOR, J. GAILLARD, A. M. RAO, Y.-P. SUN, Sonication-assisted functionalization and solubilization of carbon

- nanotubes. *Nano Lett.* **2002**, *2* (3), 231–234.
- 214 HUANG, W., S. TAYLOR, K. FU, Y. LIN, D. ZHANG, T. W. HANKS, A. M. RAO, Y.-P. SUN, Attaching proteins to carbon nanotubes via diimide-activated amidation. *Nano Lett.* **2002**, *2* (4), 311–314.
- 215 JIANG, K., L. S. SCHADLER, R. W. SIEGEL, X. ZHANG, H. ZHANG, M. TERRONES, Protein immobilization on carbon nanotubes via a two-step process of diimide-activated amidation. *J. Mater. Chem.* **2004**, *14* (1), 37–39.
- 216 DWYER, C., M. GUTHOLD, M. FALVO, S. WASHBURN, R. SUPERFINE, D. ERIE, DNA-functionalized single-walled carbon nanotubes. *Nanotechnology* **2002**, *13* (5), 601–604.
- 217 WILLIAMS, K. A., P. T. M. VEENHUIZEN, B. G. DE LA TORRE, R. ERITJA, C. DEKKER, Carbon nanotubes with DNA recognition. *Nature* **2002**, *420* (6917), 761.
- 218 FU, K., W. HUANG, Y. LIN, D. ZHANG, T. W. HANKS, A. M. RAO, Y.-P. SUN, Functionalization of carbon nanotubes with bovine serum albumin in homogeneous aqueous solution. *J. Nanosci. Nanotechnol.* **2002**, *2* (5), 457–461.
- 219 MONTEIRO-RIVIERE, N. A., R. J. NEMANICH, A. O. INMAN, Y. Y. WANG, J. E. RIVIERE, Multi-walled carbon nanotube interactions with human epidermal keratinocytes. *Toxicol. Lett.* **2005**, *155* (3), 377–384.
- 220 CHERUKURI, P., S. BACHILO, S. H. LITOVSKY, R. B. WEISMAN, Near-infrared fluorescence microscopy of single-walled carbon nanotubes in phagocytic cells. *J. Am. Chem. Soc.* **2004**, *126* (48), 15638–15639.
- 221 CHEN, R. J., Y. ZHANG, D. WANG, H. DAI, Noncovalent sidewall functionalization of single-walled carbon nanotubes for protein immobilization. *J. Am. Chem. Soc.* **2001**, *123* (16), 3838–3839.
- 222 ERLANGER, B. F., B.-X. CHEN, M. ZHU, L. BRUS, Binding of an anti-fullerene IgG monoclonal antibody to single wall carbon nanotubes. *Nano. Lett.* **2001**, *1* (9), 465–467.
- 223 STAR, A., J. C. P. GABRIEL, K. BRADLEY, G. GRUNER, Electronic detection of specific protein binding using nanotube FET device. *Nano Lett.* **2003**, *3* (4), 459–463.
- 224 HUANG, W., S. FERNANDO, L. F. ALLARD, Y.-P. SUN, Solubilization of single-walled carbon nanotubes with diamine-terminated oligomeric poly(ethylene glycol) in different functionalization reactions. *Nano Lett.* **2003**, *3* (4), 565–568.
- 225 FERNANDO, K. A. S., Y. LIN, Y.-P. SUN, High aqueous solubility of functionalized single-walled carbon nanotubes. *Langmuir* **2004**, *20* (11), 4777–4778.
- 226 LIN, Y., A. M. RAO, B. SADANADAN, E. A. KENIK, Y.-P. SUN, Functionalizing multiple-walled carbon nanotubes with aminopolymers. *J. Phys. Chem. B* **2002**, *106* (6), 1294–1298.
- 227 LIN, Y., B. ZHOU, K. A. S. FERNANDO, P. LIU, L. F. ALLARD, Y.-P. SUN, Polymeric carbon nanocomposites from carbon nanotubes functionalized with matrix polymer. *Macromolecules* **2003**, *36* (19), 7199–7204.
- 228 UHRICH, K. E., S. M. CANNIZZARO, R. S. LANGER, K. M. SHAKESHEFF, Polymeric systems for controlled drug release. *Chem. Rev.* **1999**, *99* (11), 3181–3198.
- 229 WANG, J., G. LIU, M. R. JAN, Ultrasensitive electrical biosensing of proteins and DNA: Carbon-nanotube derived amplification of the recognition and transduction events. *J. Am. Chem. Soc.* **2004**, *126* (10), 3010–3011.
- 230 HASEGAWA, T., T. FUJISAWA, M. NUMATA, M. UMEDA, T. MATSUMOTO, T. KIMURA, S. OKUMURA, K. SAKURAI, S. SHINKAI, Single-walled carbon nanotubes acquire a specific lectin-affinity through supramolecular wrapping with lactose-appended schizophyllan. *Chem. Commun.* **2004**, (19), 2150–2151.
- 231 MATSUURA, K., K. HAYASHI, N. KIMIZUKA, Lectin-mediated supramolecular junctions of galactose-derivatized single-walled carbon nanotubes. *Chem. Lett.* **2003**, *32* (3), 212–213.

**232** CHEN, X., G. S. LEE, A. ZETTL, C. R. BERTOZZI, Biomimetic engineering of carbon nanotubes by cell surface mucin mimics. *Angew. Chem. Int. Ed.* **2004**, *43* (45), 6112–6116.

**233** PATOLSKY, F., Y. WEIZMANN, I. WILLNER, Long range electrical contacting of redox enzymes by SWCNT connectors. *Angew. Chem. Int. Ed.* **2004**, *43* (16), 2113–2117.

## 8

# Stabilization and Functionalization of Metallic Nanoparticles: the Peptide Route

*Raphaël Lévy and R. Christopher Doty*

### 8.1

#### Introduction

Gold and silver nanoparticles have attracted a great deal of recent attention due to their potential use in a numerous applications such as biosensing, bottom-up assembly of nanodevices, and catalysis. The advantages of these particles include easy, non-toxic synthesis and chemical modification protocols, and outstanding optical properties that enable single-particle detection with no blinking or bleaching. Many of these applications depend crucially on the stabilization and functionalization of metal nanoparticles with adequate capping ligands.

This chapter begins with a discussion of aqueous synthesis protocols for different shapes and sizes of gold and silver nanoparticles, and various strategies to transfer nanoparticles synthesized in organic solvents into water. As the nanoparticle size increases, the dominant optical characteristic changes from fluorescence to absorbance to scattering. For each regime there is an optical technique capable of achieving single-particle detection. The role of Au nanoparticles in DNA sensing is discussed along with the use of DNA and proteins to assemble Au nanoparticles into discrete structures. Long-range ordering of Au nanoparticles on two-dimensional (2D) protein crystal templates is presented as an alternative assembly method. The chapter continues with a description of stabilization and functionalization of metallic nanoparticles using peptides. The concept of a peptide toolbox for bionanotechnology containing capping ligands, recognition and self-assembly motifs is introduced. The interaction of amino acids, peptides and proteins with gold and silver is briefly reviewed. Rational and combinatorial designs of peptides provide capping ligands to convert nanoparticles into protein-like materials. A major advantage of the peptide route is that stabilization and functionalization are achieved in a single step. A wide variety of functions can be easily transferred to the nanoparticles using peptides with extensions. Furthermore, their protein-like properties open up new possibilities to purify and handle nanoparticles and prepare conjugates with a defined number of recognition groups per particle. Finally, some remarkable properties of peptides that have not yet been used in the context of nanoparticles are presented.



## 8.2

### Metallic Nanoparticles – An Overview

#### 8.2.1

##### Metallic Nanoparticles – Preparation

While fluorescence from semiconductor nanocrystals ranging from the UV to the near-IR is best achieved with particles less than 10 nm in diameter, sizes easily obtained by syntheses in organic solvents, metal nanocrystals need to be greater than 30 or 40 nm in diameter to take advantage of their light-scattering properties. This is too large for synthesis in organic solvents, but an aqueous synthesis utilizing sodium citrate as both reducing agent and electrostatic stabilizer can produce Au nanocrystals between 10 and 150 nm in diameter [1]. For reproducible, quantitative results, nanocrystals need to be monodisperse in both size and shape. Unfortunately, the citrate-reduction synthesis gives highly polydisperse results for nanocrystals greater than ca. 30 nm in diameter. Recent work using 12 nm citrate-stabilized Au nanocrystals as seeds for the growth of larger nanocrystals has allowed the synthesis of monodisperse, spherical nanocrystals, with diameters between 30 and 110 nm, and monodisperse, ellipsoidal nanorods of similar size [2, 3] (Fig. 8.1A).

Gold nanoparticles in the shape of rods, rectangles, cubes, triangles, hexagons, and branched structures can be synthesized in very high yield by varying the ratios of an interdependent mixture of small Au nanoparticle seeds, cetyltrimethylammonium bromide (CTAB),  $\text{HAuCl}_4$ ,  $\text{AgNO}_3$ , and ascorbic acid [4–6] (Fig. 8.1B–D). For some shapes, especially rods, the presence of  $\text{Ag}^+$  was essential for their synthesis in high yield. The precise role of the Ag ions is unknown, but it is believed that an interaction with the Br ions of CTAB affects either the surface of the Au nanoparticle or the shape of the CTAB template.

Although tremendous advances have been made in the synthesis of large, water-soluble Au nanocrystals, the same cannot be said for Ag nanocrystals. Silver oxidizes much more readily than Au, and the larger van der Waal's attraction between Ag spheres compared with Au spheres reduces the effectiveness of electrostatic repulsion as a method of stabilization. Thus far, this problem has been solved by depositing Au around the Ag nanocrystal, much like the seeded growth syntheses mentioned above, to reduce oxidation of the Ag surface. In monolayer and bilayer quantities, this does not affect the absorption or light-scattering properties of the original Ag core [7].

Silver nanoparticles have also been synthesized as rods, wires, and triangular prisms – the first two shapes by a very similar procedure to that used to obtain Au nanorods [8]. Silver nanoparticle seeds (4 nm diameter) were added to a growth solution containing  $\text{AgNO}_3$ , CTAB, and ascorbic acid. The pH was then increased with NaOH to enable the ascorbic acid to reduce the Ag ions. The ratio of nanoparticle seeds to Ag ions and the pH are key factors in determining whether rods or wires are produced. Nanorods can be synthesized reproducibly with aspect ratios between 2.5 and 15 for widths of 10 to 15 nm. Nanowires of similar width and up

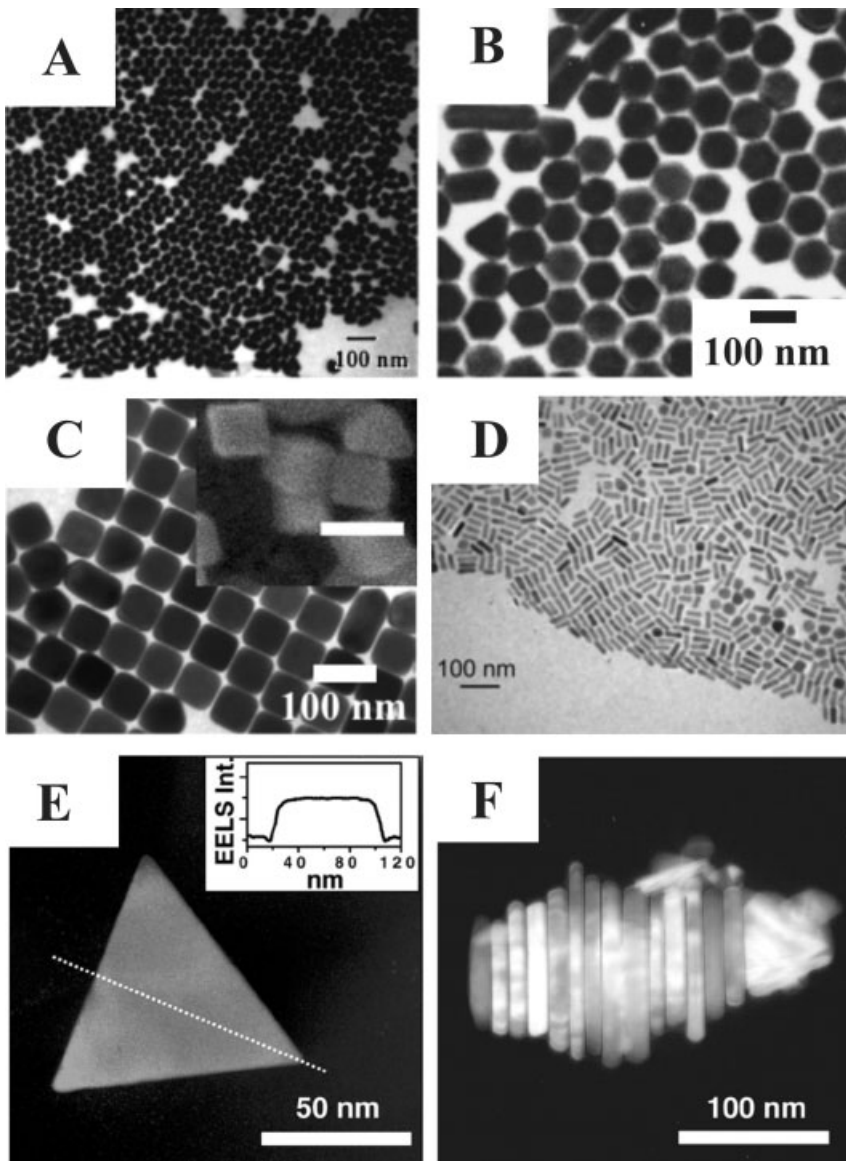


**Fig. 8.1.** Transmission electron microscope (TEM) images of (A) 37 nm Au spheres, (B) 70 nm Au hexagons, (C) 90 nm Au cubes, (D)  $50 \times 15$  nm Au rods, and (E) and (F) 100 nm Ag prisms. The inset to (C) is a scanning electron microscope image showing the three-dimensional nature of the Au cubes. Inset to (E) is an electron energy loss spectroscopy scan, showing that the Ag prisms are flat on top and not shaped like pyramids. This is also

displayed in (F), where several Ag prisms are stacked together. (A) reprinted with permission from [3]. Copyright (2001) by the American Chemical Society (ACS). (B) and (C) reprinted with permission from [6]. Copyright (2004) by the ACS. (D) reprinted with permission from [5]. Copyright (2004) by the ACS. (D) and (E) reprinted with permission from [9]. Copyright (2001) by the AAAS.

to 4 mm long have been produced. The many spherical Ag nanoparticles produced along with the nanorods and nanowires must be removed by centrifugation. Triangular prisms have been synthesized in very high yield by the photoinduced conversion of spherical Ag nanoparticles [9]. A solution containing 8 nm citrate-stabilized Ag nanoparticles and a particle stabilizing agent were irradiated with a 40 W fluorescent light for 3 days. The spherical nanoparticles were gradually converted into nanoprisms with an edge length of 100 nm [Fig. 8.1(E) and 8.1(F)].

In addition to synthesis in aqueous solutions, nanoparticles can be synthesized in organic solvents and transferred into the aqueous phase via ligand-exchange. Solubilization via ligand-exchange requires displacement of the hydrophobic molecule attached to the nanoparticle surface by a hydrophilic one, usually a carboxylic acid-terminated molecule [10, 11]. A particularly good example of this technique is the use of a thioalkylated monohydroxy tetraethylene glycol (PEG-OH) to transfer tetraoctylammonium bromide-stabilized Au nanoparticles from toluene to water [12]. These 5 to 8 nm particles displayed excellent stability between pH 0 and 14 and in 3.5 M NaCl. They also did not aggregate in the presence of proteins. The particles' extraordinary stability is due to the bifunctional nature of the PEG-OH capping ligand. The alkanethiol end forms a strong bond with the Au surface and a tight hydrophobic shell around the particle while the ethylene glycol end imparts water solubility and presents an uncharged surface to the aqueous environment. Gold nanoparticles have also been synthesized in the presence of PEG-OH [12]. These particles had diameters between 2 and 4 nm and displayed the same excellent stability as the larger nanoparticles produced by ligand-exchange. The efficiency of ligand exchange depends upon the relative bond strengths between the two molecules and the nanoparticle surface, and usually requires a large excess of the hydrophilic molecule in solution during the ligand exchange. Unfortunately, this requirement precludes direct attachment of some biological molecules that are not available, or are prohibitively expensive, in such large quantities, e.g. many peptides and proteins.

Another approach to making nanocrystals water-soluble is to encapsulate them in a layer of silica/siloxane via a surface silanization procedure [13, 14]. In subsequent crosslinking reactions, charged molecules can be incorporated into the shell to provide electrostatic stabilization to the water-soluble nanocrystals, or long-chained, hydrophilic molecules, such as polyethylene glycol, can be used to provide steric stabilization. The resulting silica shell has exposed amino, mercapto, and phosphate groups that can be used to further functionalize the nanocrystal surface. While the silica-encapsulated nanocrystals are very stable and do not aggregate in aqueous solution, gradual decomposition of the silica layer eventually leads to nanocrystal precipitation and limits the length of time they can be left in water.

### 8.2.2

#### **Metallic Nanoparticles – Optical Properties**

Almost every application of metallic nanoparticles takes advantage of their ability to strongly absorb and scatter light. This is because they possess a distinctive opti-

cal property known as surface plasmon resonance, which is effectively due to the collective oscillation of free electrons. For Ag and Au nanocrystals the wavelength at which this occurs is in the vicinity of 400 and 500 nm, respectively, and is a function of the nanocrystal size and composition, the molecules attached to the surface of the nanocrystal, and the surrounding medium. Many biological applications of metal nanocrystals will rely on their light scattering properties because scattered light can be detected thousands of times more sensitively than transmitted light [15, 16]. A solution of nanocrystals will scatter an incident beam of monochromatic light without changing its frequency, but when illuminated with an incident beam of white light, the wavelength at which the scattered light is a maximum is a function of particle size, shape, and composition (Fig. 8.2A and 8.2B). Through a combination of Ag and Au nanocrystals of different sizes, one can view scattered light of every color in the visible light spectrum (Fig. 8.2C). The particle size dependence of the wavelength of scattered light was predicted by Mie using classical electromagnetic theory [1, 17]. In the Rayleigh limit ( $R < \lambda/20$ , where  $R$  is the radius of the nanocrystal and  $\lambda$  is the wavelength of incident light) the wavelength of scattered light remains unchanged, while the intensity increases as  $R^6$ . For nanocrystals outside the Rayleigh limit, an increase in particle size broadens the scattering spectrum and shifts it to longer wavelengths. In general, the maximum intensity of light scattered from an Ag nanocrystal is at least  $10\times$  that of an Au nanocrystal of the same size, and the spectral shifts with regard to particle size are more pronounced. The scattering spectra are also affected by the refractive index of the medium containing the nanocrystals. Increasing the refractive index increases the intensity of scattered light and shifts it to longer wavelengths. The intensity of scattered light for Au nanocrystals is enhanced by an increase in the medium refractive index more so than Ag, but the spectra of Ag shift more than those of Au [15]. These effects are important experimentally, because raising the refractive index of the medium increases the signal-to-noise ratio of a particular measurement, by both increasing the scattering from the metal nanocrystals and decreasing the background scattering from dielectric materials. Light scattering from metal nanocrystals cannot be quenched, and the nanocrystals do not degrade under optical excitation like many molecular fluorophores, permitting time-dependent studies. In fact, the scattered light intensity of a 60 nm diameter Au nanocrystal is approximately equivalent to the fluorescent light intensity of 270 000 fluorescein molecules [15]. This allows the detection of a single particle using a simple optical microscope in dark-field mode. The main drawback of this detection strategy is the background scattering from the biological sample and from defects in microscope slides. This background cannot be removed by an emission filter in an experiment where the illumination and detection have to be at the same wavelength, but, as mentioned above, refractive index matching can be effective. To ensure that the detected light comes from a metallic particle, more sophisticated instrumentation is needed in which the scattered light is analyzed using a spectrometer coupled to the microscope or a tunable filter to recognize the characteristic scattering spectrum of the metallic nanoparticles.

While light absorption and scattering are practical detection methods for large

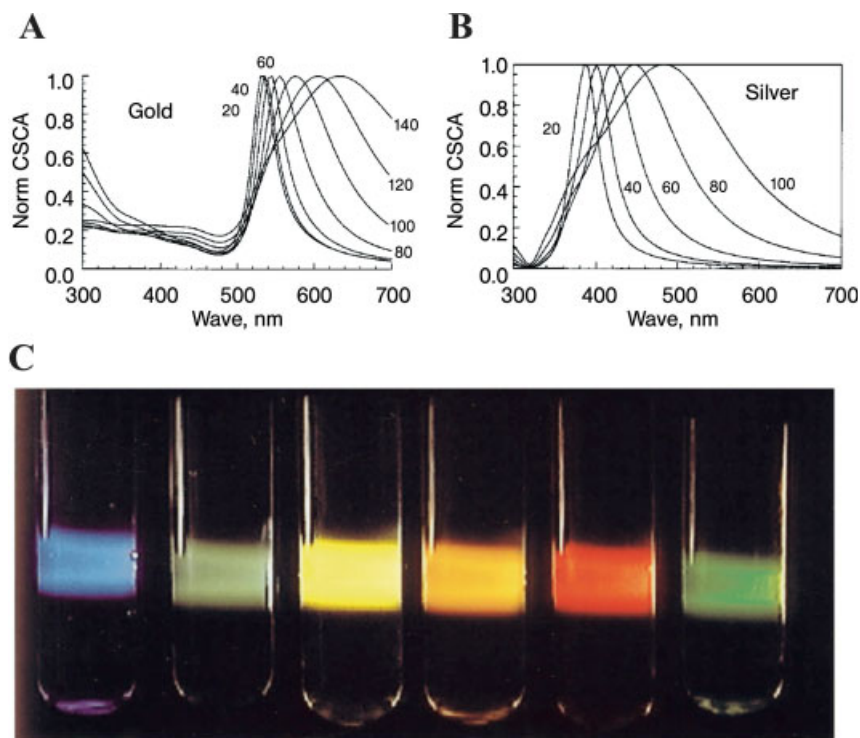


**Fig. 8.2.** Normalized scattering cross-sections as a function of wavelength for (A) gold and (B) silver nanoparticles of various sizes. (C) Light scattering from aqueous solutions of (from left to right) 40 nm Au nanoparticles; 40, 78, 118, and 140 nm Au nanoparticles; and fluorescein illuminated by a single beam of white light. (Reprinted with permission from [15]. Copyright (1998) by Academic Press.)

metal nanoparticles, small (diameter  $< 5$  nm) nanoparticles can be detected by light emission. Previous work has shown blue, red, and near-IR emission from water-soluble Au nanoparticles [18, 19]. The exact mechanism is unknown, but it is thought that relaxation of excited conduction electrons into sp- and d-band holes, intraband and interband, respectively, combined with surface effects from the ligand shell can explain the different light emission peaks. Although these nanoparticles show a million-fold enhancement in fluorescence quantum yield compared with bulk gold, the quantum yields ( $10^{-3}$ – $10^{-5}$ ) are still much lower than for organic fluorophores and semiconductor quantum dots. Recent work on nanodots, however, has further increased the quantum yield of Au one hundred-fold [20, 21]. An eight-atom cluster of Au stabilized by a poly(amidoamine) (PAMAM) dendrimer emits blue light ( $\lambda_{\text{max}} = 450$  nm) with a quantum yield of  $41 \pm 5\%$  [20]. Additional work on 5-, 13-, 23-, and 31-atom clusters extended the emission into the UV and the near-IR (Fig. 8.3), with a quantum yield of 70% for the five-atom, UV-emitting cluster [21]. The quantum yield decreases to 10% as the emission energy decreases from the UV to the near-IR, as a result of increased competition

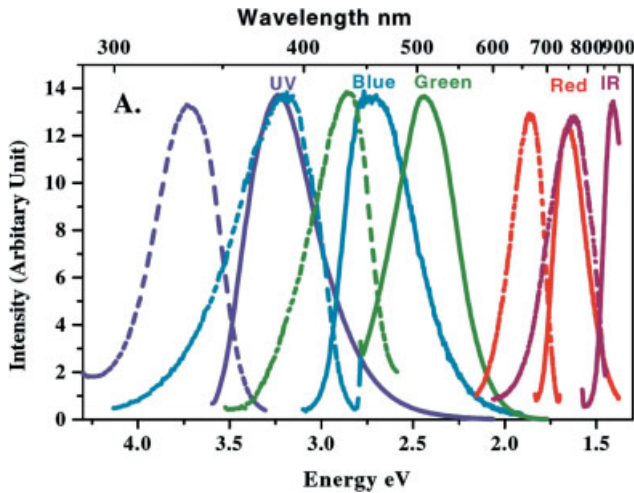


Fig. 8.3. Photoluminescence excitation (dashed lines) and emission (solid lines) spectra for Au nanodots with cluster sizes of 5, 8, 13, and 31 atoms. The emission spectra redshift as cluster size increases. (Reprinted with permission from [21]. Copyright (2004) by American Physical Society (APS).)

from nonradiative pathways. The emission energy scales with the number of atoms, as predicted by a jellium model, indicating that the fluorescence is “proto-plasmonic” and arises from intraband transitions of the free electrons. The clusters are stable over long periods in water, can be stored as dry powders, and, unlike semiconductor quantum dots, their synthesis is easy and non-toxic. Their discrete excitation spectra, however, excludes their use in the single-excitation, multiplexed bioassays for which semiconductor quantum dots show so much promise. However, it does allow them to function as energy transfer pairs and long lifetime fluorescent labels for *in vivo* imaging.

In addition to Au nanodots, Dickson and co-workers have also produced fluorescent Ag nanodots [22, 23]. Silver ions were photoreduced in the presence of PAMAM dendrimers to produce two- to eight-atom clusters [22]. Single nanodot fluorescence was detected at between 530 and 650 nm. Photoluminescence beyond 600 nm was also seen from Ag nanodots formed by the chemical reduction of Ag ions in the presence of oligonucleotides [23]. Mass spectral analysis showed that the cluster size was between one and four Ag atoms. Chemical shifts in the NMR spectra of the cytosine bases suggest that base-specific interactions may play an important role in nanodot formation and that oligonucleotides with specific sequences may be able to control cluster stoichiometry. Unlike the Au nanodots discussed above, the photoluminescence of different-sized Ag nanodots can be excited by a single source, making them available for applications that require a degree of multiplexing.

Particles that are too small to be detected by light scattering and too big to fluoresce with any efficiency can be detected using a recently developed photothermal

technique [24]. Called photothermal interference contrast, it relies on the increase in temperature around a metal nanoparticle when it absorbs laser light at the same frequency as its plasmon resonance. Changes in the temperature-dependent local index of refraction can be detected optically using a second laser beam. One benefit of this technique is that it does not detect non-absorbing scatterers. For instance, 10 and 80 nm Au particles were mixed with 300 nm latex spheres and spin-coated onto a substrate. As shown in Fig. 8.4(A), the 80 nm Au particles and 300 nm latex spheres were detected using differential interference contrast. Using the photothermal technique, only the 80 and 10 nm Au nanoparticles were detected (Fig. 8.4B and 8.4C). Nanoparticles as small as 2.5 nm have been optically detected using the photothermal detection system [24]. Another benefit of this technique is that organic and biological samples have a negligible photothermal background. This was shown in the visualization of individual 10 nm Au particles attached to membrane proteins of COS7 cells. By tilting the sample, 3D images of the Au nanoparticles were obtained [25]. Because absorption is used, there is no photobleaching, blinking, or saturation of the metal nanoparticles. One concern with this technique is that the temperature rise around the nanoparticles could interfere with the function of live biological samples. For a 10 nm particle, the temperature increase on the surface of the particle is estimated to be 15 K. This can be lowered by changing the laser power and the location of the laser beams in relation to the particles.

### 8.2.3

#### **Metallic Nanoparticles – Applications**

The uniformity of citrate-stabilized Au nanocrystals, the ease with which the citrate molecules can be displaced from the Au surface, and the unique optical properties of both individual and aggregated clusters of Au nanocrystals are all critical to successful utilization in biological applications. An area of early success was the attachment of thiol-terminated DNA oligonucleotides to Au nanocrystals, in which complementary strands of DNA were used to assemble both dimers and trimers and large, aggregated structures of nanocrystals [26, 27]. The nucleotide-induced aggregation caused a red to blue color change in the aqueous nanocrystal solution. This aggregation is reversible upon heating the solution above the melting temperature of the DNA [28]. In this way the absorbance of Au nanocrystals is used to detect DNA hybridization [29, 30]. A more solid-state approach to the detection of DNA hybridization is to immobilize a strand of DNA on a substrate and flow a solution of nanocrystals containing the complementary strand of DNA over the substrate [31, 32] (Fig. 8.5). The attachment of nanocrystals on the surface can be detected by light scattering. This technique offers greater sensitivity and can detect DNA in the femtomolar concentration range [31, 33].

Complementary strands of DNA can be attached to nanocrystals of different size, shape, and/or composition. In this way, large nanocrystals can be surrounded by small ones [34], metal nanocrystals can be surrounded by semiconductor ones [35], and vice-versa [36]. The challenge with this technique is to control the degree of nanocrystal ordering (Fig. 8.6). Ideally, one would form dimers, trimers, and

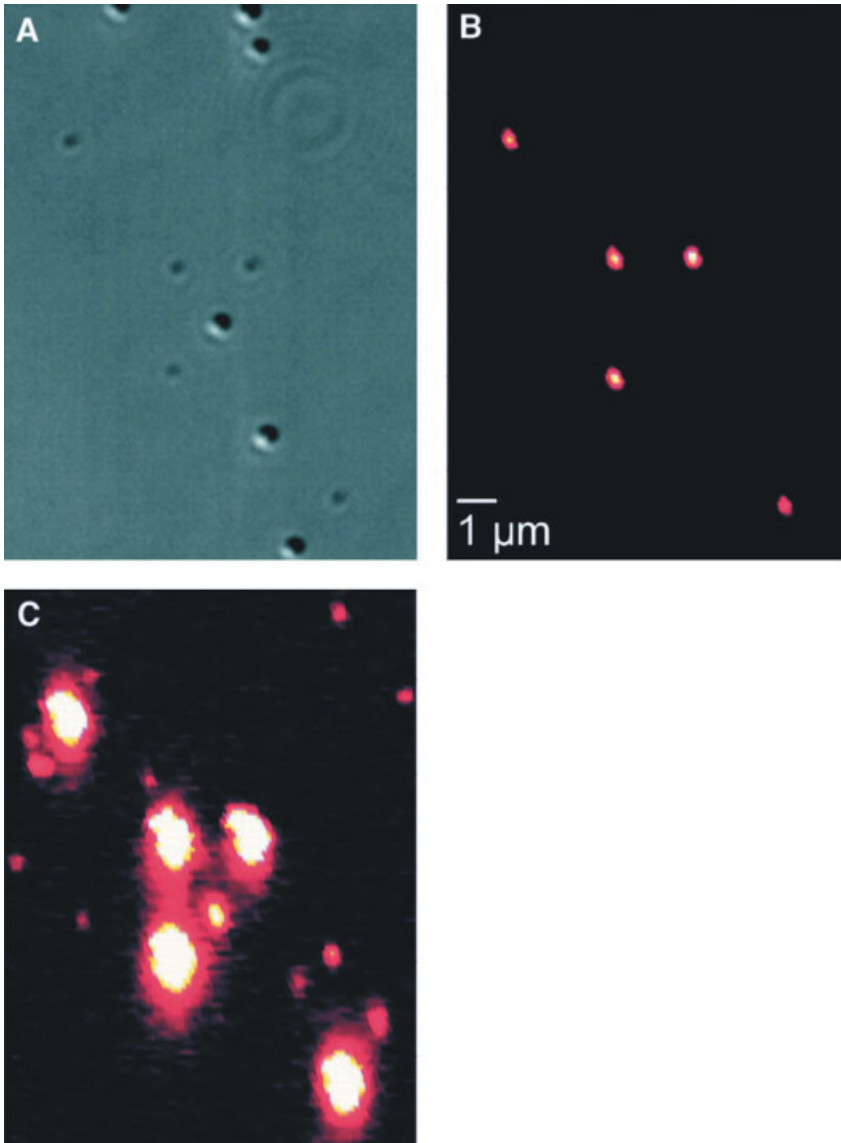


**Fig. 8.4.** (A) Differential interference contrast image of 10 and 80 nm Au particles with 300 nm latex particles. Only the 80 nm Au and 300 nm latex particles can be detected. (B) Photothermal image at low heating laser

power shows the 80 nm Au particles but not the 300 nm latex particles. (C) Increasing the laser power brings the 10 nm Au particles into view. (Reprinted with permission from [24]. Copyright (2002) by AAAS.)



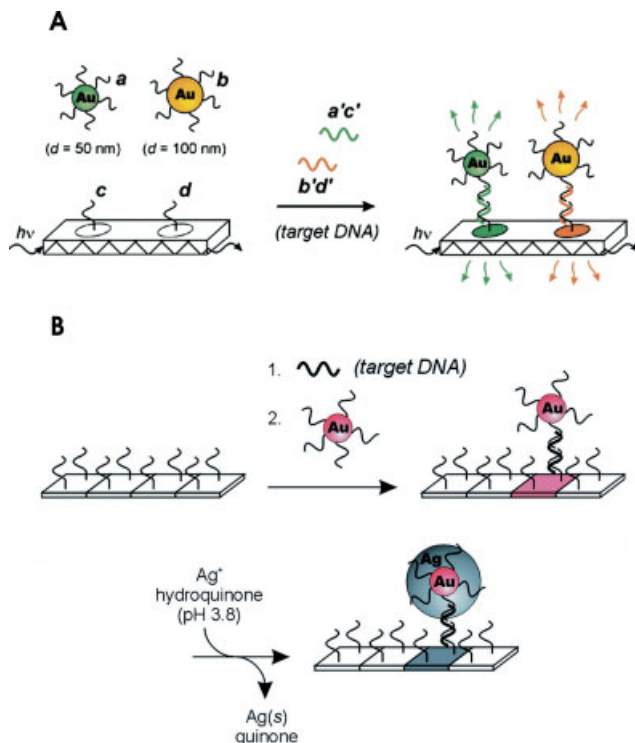


**Fig. 8.5.** Two different types of three component sandwich assays for oligonucleotide detection. (A) A two-color detection method taking advantage of the light scattering properties of different sized Au nanoparticles. (B) An extremely sensitive

detection method in which silver atoms are reduced onto 13 nm Au particles to amplify the signal for detection by a flatbed scanner. (A) reprinted with permission from [32]. Copyright (2001) by ACS. (B) reprinted with permission from [31]. Copyright (2000) by AAAS.

other well-defined structures, such as monolayers and multilayers [37]. However, this requires precise control of the number of DNA molecules attached to the nanocrystal surface, and it is not currently possible to generate a solution of nanocrystals with only, and exactly, one (or two, or three, etc.) DNA molecule per nanocrystal. In a given solution there is a statistical distribution of desired capping ligands per nanocrystal. The challenge then is to separate the nanocrystals with one oligonucleotide from those with two, three, four, etc., which at present has only been consistently achieved by gel electrophoresis [36, 38, 39]. To achieve maximum resolution the nanocrystals should be size-monodisperse and homogeneous in charge, and the DNA molecules should have a mobility similar to that of the nanocrystals so that the attachment of only one or two oligonucleotides has a significant effect on the overall mobility through the gel. Besides being time-consuming and relatively inefficient, the pore size of the gel presents a serious limitation to the size of nanocrystals that can be separated.

In addition to using nanoparticles to detect biological molecules, biological mol-

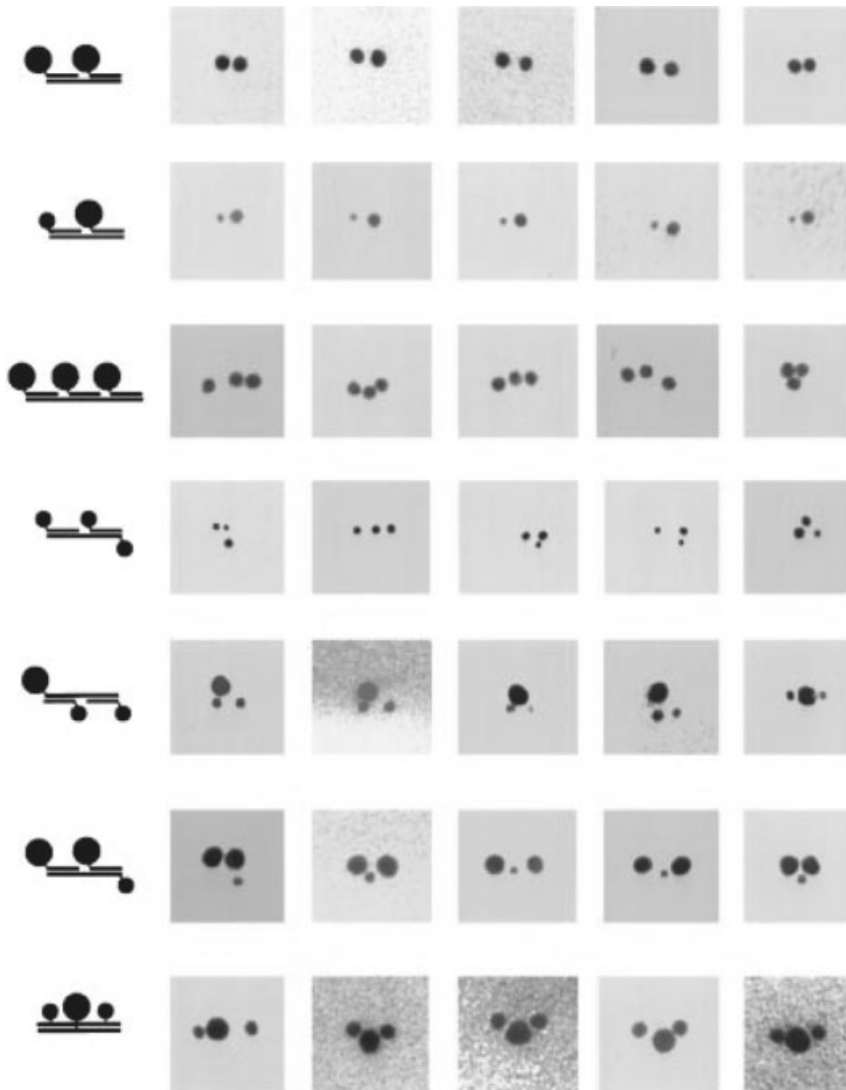


**Fig. 8.6.** TEM images of dimers and trimers of 5 and 10 nm Au nanoparticles linked by DNA. A schematic of the particular DNA-based assembly method is shown to the left of the TEM images. (Reprinted with permission from Ref. [37].)

ecules can be used to self-assemble nanoparticles into patterns that are not otherwise thermodynamically or kinetically favorable. As discussed in the previous section, DNA has been used to assemble dimers, trimers and much larger aggregated structures. Another potentially powerful, high-yield method for creating dimers, trimers, or chains of nanoparticles involves the use of solid-phase reactions on PS

Wang or HMPA-PEGA resins and Fmoc protecting groups [40]. This technique takes advantage of the low-density packing of functional groups, in this case lysine, on the resins. Thus, a 2.2 nm Au nanoparticle with a ligand shell consisting of equal parts octanethiolate and mercaptoundecanoic acid will react with only one lysine. Protection of the remaining carboxyl groups in the ligand shell with methylamine followed by cleavage of the resin bead leaves a single carboxylic acid on the nanoparticle available for further functionalization. Monofunctionalization was tested by dimerizing nanoparticles with ethylenediamine. The overall efficiency of this process is extremely low, however; only 3% and 15% of the nanoparticles remained after cleavage of the PS Wang and HMPA-PEGA resins, respectively. Of those remaining particles, around 60% formed dimers, with some forming higher-order clusters. To form chains of nanoparticles using this method, the efficiency needs to be much higher, but it is nonetheless a powerful method for monofunctionalizing nanoparticles.

A single biotinylated dextran molecule has been conjugated to 15 nm Au particles through careful consideration of the molecular weight of the aminodextran molecules and the surface area of the nanoparticles [41]. A 2000 kDa aminodextran was functionalized with pyridyldithio propionate to create the disulfide bonds, and biofunctionality was imparted by conjugation with biotin. The benefit of this technique is the stability imparted to the nanoparticle by coating it with one molecule capable of forming hundreds of thiol bonds rather than with hundreds of individual thiol-containing molecules. As proof of this the particles were run through a typical polymerase chain reaction protocol without loss of biological activity. This technique can be expanded beyond biotin to include haptens, antibodies, and oligonucleotides. The number and type of functional molecules per dextran can be altered as required for use in sensitive bioassays or programmed self-assembly.

In addition to the well-known biotin–streptavidin system, antibodies and antigens can be used to link nanoparticles together. Mann and co-workers have shown that Au nanoparticles stabilized by IgE and IgG antibodies assemble into 3D networks in the presence of bivalent antigens [42]. Macroscopic filaments with aspect ratios greater than 100 precipitated from solution when the conformational freedom of the bivalent hetero-antigen was increased by doubling the size of the spacer between its functional ends. They were also able to form bimetallic aggregates by mixing IgE-stabilized Au nanoparticles and IgG-stabilized Ag nanoparticles with a bivalent hetero-antigen. The feasibility of aggregation-based immunoassays has been demonstrated by Thanh and Rosenzweig [43]. At a comparable sensitivity to ELISA, the concentration of anti-protein A in serum samples was determined by following the aggregation of protein-A coated Au nanoparticles with a UV/Visible spectrophotometer.

Thus far, the aggregation-based techniques intended for the long-range assembly of ordered nanoparticle structures have resulted in large, disordered 3D clusters. A template-based method for precise positioning of nanoparticles using S-layer proteins is an interesting alternative [44, 45]. S-layer proteins are found on the surface of prokaryotic (e.g., bacteria) cells and can self-assemble into 2D structures on solid supports. Interestingly, for nanotechnology, the symmetry and lattice constants of

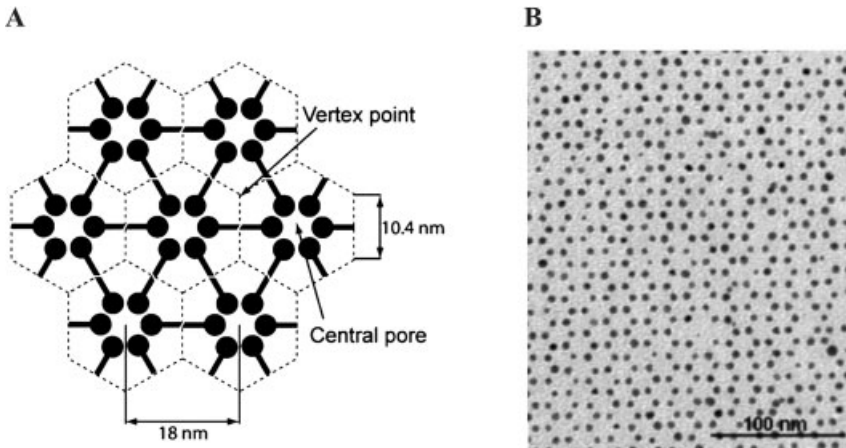


**Fig. 8.7.** (A) Schematic representation of the hexagonal ordering of S-layer proteins. Protein monomers arrange to form a central pore 2 nm in diameter and 18 nm apart. Vertex points are 10.4 nm apart. (B) TEM image of 5 nm citrate-stabilized Au nanoparticles on the

hexagonally packed S-layer. Addition of 25 mM NaCl resulted in the long-range ordering shown. The interparticle spacing is 10 nm. (Reprinted with permission from [45]. Copyright (2004) by ACS.)

the self-assembled structure can be tailored, and the protein units contain identical central pores with diameters that can range between 2 and 6 nm. An S-layer protein investigated recently for long-range ordering of nanoparticles has hexagonal symmetry, a central pore size of 2 nm, and a lattice constant of 18 nm (Fig. 8.7A). Mann and co-workers found that negatively charged citrate-stabilized Au nanoparticles with a diameter of 5 nm formed long-range, ordered assemblies with hexagonal symmetry and a center-to-center distance of 18 nm [44]. The same was true of a solution of 10 nm citrate-stabilized Au particles, except that the particles that bound to the S-layer template were 8.0 nm. They also found that the 5 nm particles bound preferentially to the 9.7 nm particles when a solution containing a mixture of the two was placed on the protein template. Particles larger than the lattice constant of the template only bound randomly to the structure, as did smaller Au nanoparticles with a positive surface charge. While Mann and co-workers were unable to determine if the nanoparticles were located in the central pore of the S-layer protein units, Bergkvist et al. showed that the nanoparticles were in fact located at the vertex point of three protein units [45]. The center-to-center distance of 18 nm was maintained by nanoparticle adsorption to every other vertex point. Adding 25 mM NaCl during nanoparticle adsorption resulted in the occupation of every vertex point and a center-to-center distance of 10 nm [Fig. 8.7(B)]. Nanoparticle adsorption to the protein template is a result of electrostatic interactions between the negatively charged Au nanoparticles and positively charged residues of the S-layer protein, while interparticle separation is controlled by electrostatic repulsions between Au nanoparticles.

Metal nanoparticles could also be used as scaffolds for the self-assembly of

enzymes and receptors. Still in its infancy, several proof of principle experiments have been published, mainly by the groups of Rotello and Scrimin [46]. The mobility of thiols on gold surfaces and the possibility to easily make mixed self-assembled monolayers presenting various chemical moieties are key ingredients in these studies. An early example demonstrated that flavin binding sites could be imprinted in a gold nanoparticle supported monolayer containing both hydrogen bonding and aromatic stacking elements [47]. More recently, dipeptide-functionalized nanoparticles with esterase-like activity have been prepared [48]. Confinement of the catalytic units in the monolayer drives a 300-fold enhancement of activity compared with the dispersed monomeric dipeptide, demonstrating the crucial role of cooperativity in these systems.

### 8.3

#### Stabilization and Functionalization of Metallic Nanoparticles – The Peptide Route

##### 8.3.1

##### Peptides, Proteins and Nanoscale Science

Peptides are short sequences of amino acids linked by peptide bonds. When a sequence is longer than 30  $\alpha$ -amino acids, the molecule is generally called a protein or a polypeptide if it is a synthetic polymer. Proteins are biopolymers composed of the 20 natural  $\alpha$ -amino acids. Essential components of life, they fulfill the roles of elastic material, enzymes, motors, signal transducers etc. Protein function arises from precisely defined folding of the polymer chain into a 3D structure. Whereas elaborate tasks are generally assumed by large proteins or complexes of proteins (3–100 nm), short sequences composed of less than ten  $\alpha$ -amino acids are used by living organisms as highly specific recognition sequences (e.g., cellular localization sequences, enzyme substrate and ligand–receptor recognition sequences).

Understanding the relationship between the amino acid sequence of a protein and its structure is a major and fundamental field of research known as the folding problem. It has wide implications for drug development and discovery. One of the tests of this understanding is the ability to design from first principles unnatural sequences that fold according to predictions. This has been successfully achieved at the level of secondary structures (e.g. helix and beta-sheet) [49–51], while the *de novo* design of catalytic proteins is an emerging field (e.g., Kaplan and colleagues have reported the design of an O<sub>2</sub>-dependent phenol oxidase whose structure, sequence, and activity have been designed from first principles [52]).

One of the challenges of nanotechnology is to create nanostructures capable of handling complex tasks. In the nanometer range, proteins are fairly clearly the most advanced devices known. Furthermore, molecular biology offers powerful tools to modify, adapt, purify and manipulate these natural devices. Therefore, two complementary approaches have been taken. The first seeks to modify existing proteins or viruses [53, 54] to solve technological problem on the nanoscale [55],

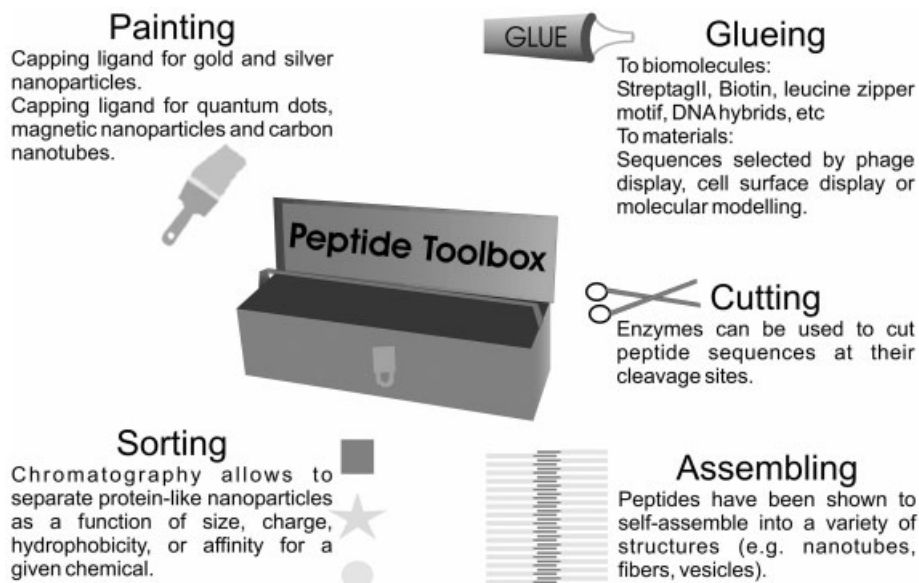


Fig. 8.8. Peptide toolbox for bionanotechnology.

whereas the second seeks to confer protein-like properties to artificial nanomaterials having useful physical properties (e.g., metallic nanoparticles, quantum dots and carbon nanotubes). In the following, we focus on protein-like metallic nanoparticles obtained using peptides as capping ligands.

### 8.3.2

#### Peptide Toolbox for Bionanotechnology

Peptides are a large family of commercially available molecules. The concept of a *peptide toolbox* is emerging from recent work. As illustrated in Fig. 8.8, this toolbox contains sequences that can achieve various tasks. Peptides can be used as a capping ligand to control the surface properties of nanomaterials. They offer various affinity pairs as well as binding motifs to synthetic materials. Enzymes can be used to cleave or modify peptide sequences at precisely defined sites. Most powerful biochemistry tools are intrinsically parts of the peptide toolbox and are readily available to handle and modify peptide-capped materials. This includes various chromatography techniques that allow nanomaterials to be separated on the basis of size, charge, hydrophobicity and affinity as well as various well-established bioconjugation reagents. Designed peptides can self-assemble into extended structures from micelles, fibers, and nanotubes to vesicles and hydrogels. The toolbox has only been superficially explored in the context of nanoparticles and their assemblies. Most importantly, peptide-capped nanoparticles may offer a path for

integrating various properties into well-defined complex materials. Examples will be given to show that peptide properties can be readily transferred to metallic nanoparticles by using peptides as capping ligands.

### 8.3.3

#### **Peptides as Capping Ligands**

##### **8.3.3.1 Interactions of Amino Acids with Noble Metals**

To our knowledge, no systematic study of amino acid interactions with gold is available. However, thiols and amine groups are known to interact strongly with gold. For example, alkanethiol, mercapto- and amino-dextrans have been used as capping ligands for gold nanoparticles [56, 57]. Therefore, as expected, cysteine (thiol on its side chain) and lysine (primary amine on its side chain) do bind to gold nanoparticles [58].

Sastry and co-workers have published several studies on amino acid interactions with metallic nanoparticles (Ref. [59] gives a more complete review). Cysteine, [60] lysine [61] and tryptophan [62] were used as a capping ligand for silver or gold nanoparticles. Lysine-capped nanoparticles disperse in acidic aqueous solution, while aggregation attributed to hydrogen bonding occurs at neutral and basic pH [61]. In addition, water-dispersible gold nanoparticles have been synthesized by the spontaneous reduction of aqueous chloroaurate ions by tryptophan [62]. The same group has used isothermal titration calorimetry to characterize the pH-dependant binding of lysine and aspartic acid to gold nanoparticles [63]. Xu and colleagues have shown that lysine-capped nanoparticles can be assembled into suprastructures through peptide bond formation in the presence of a condensation agent [EDC, ethyl-3-(dimethylaminopropyl)carbodiimide] [64]. Modulation of the lysine to gold ratio allows the assembly of linear chains of nanoparticles [65]. Aggregation of nanoparticles has been seen upon addition of thiol-containing amino acids and peptides [66, 67].

Lysine residues on proteins play an important role in their adsorption onto gold. Xie and colleagues have characterized in detail the use of peptide–bovine serum albumin (BSA) conjugates as capping ligand for gold nanoparticles (BSA contains 59 lysines, of which up to 35 are thought to reside on its surface) [68]. BSA can also be used during the synthesis of gold nanoparticles, resulting in water-soluble sub-2 nm particles [69].

##### **8.3.3.2 Peptides as Reducing Agent and Template in Metallic Nanoparticle Synthesis**

Peptides were first used in noble metal nanoparticle synthesis in the seminal work of Schaaff and colleagues in 1998, where the tripeptide glutathione GSH was used to obtain 1.5 nm gold clusters encapsulated in a peptide layer. Synthesis involved the decomposition of polymeric Au(I)SG compounds [70]. Inspired by biological mechanisms for the reduction and mineralization of noble metals, Slocik and colleagues have used a histidine-rich peptide to mediate the formation of various metal, metal oxide and metal sulfide clusters [71, 72]. They have also shown that, in some cases, antibodies can recognize the peptide sequence immobilized on the

particle surface. Djalali and colleagues reported that the same histidine-rich peptide immobilized on a heptane dicarboxylate nanowire template was able to control the nucleation and growth of monodisperse highly packed gold nanoclusters [73, 74]. This approach has been extended to the synthesis of continuous platinum nanowires using a slightly different peptide sequence [75]. Two-dimensional arrays of a self-assembled protein complex, chaperonin, have been used for the constrained synthesis of Ni-Pd and Co-Pd nanoparticles [76]. The sub-unit proteins were genetically engineered to expose a large number of histidines inside the solvent-accessible pore of the chaperonin and, hence, promote the binding of metal ions. Sequences selected by phage-display technology for their affinity to metallic surfaces have been used in silver and cobalt nanoparticle synthesis [77]. In an even more elaborate study, the same group has immobilized a silver-binding peptide in the inner cavity of the self-assembled cage protein ferritin [78]. Controlled growth of a silver nanocrystal within the cavity was observed in the presence of silver nitrate. This approach might be extended to other materials using other peptide templates.

### 8.3.3.3 Rational Design of a Peptide Capping Ligands for Gold Nanoparticles: CALNN

Based on protein folding considerations, we have recently designed a pentapeptide ligand, CALNN, that converts citrate-stabilized gold nanoparticles into extremely stable protein-like gold nanoparticles [79]. Soluble proteins are usually folded in such a way that their hydrophobic groups are located in the interior of the macromolecule, while charged and hydrophilic groups are exposed to water. The pentapeptide CALNN (Chart 8.1) was designed to mimic this architecture. The thiol group in the side chain of the N-terminal cysteine (C) can bind covalently to the gold surface. Alanine (A) and leucine (L) in positions 2 and 3 possess hydrophobic side chains and were chosen to promote the self-assembly of the peptide. Asparagine (N) in positions 4 and 5 is an uncharged, but hydrophilic amino acid due to the amide group on the side chain, and the C-terminal asparagine in position 5 bears a negative charge due to the terminal carboxylic group.

This design proved to be extremely successful at providing peptide-capped particles that are stable over a wide range of pH and ionic strength (up to 1 M NaCl for 13 nm gold nanoparticles at pH 7 and up to 4 M NaCl for 4 nm gold nanoparticles). Importantly, CALNN-capped nanoparticles can be manipulated like a robust protein, e.g., they can be freeze-dried and resuspended in water, purified by size-exclusion and ion-exchange chromatography.

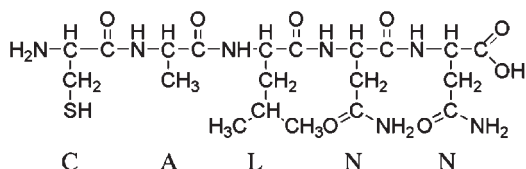


Chart 8.1. CALNN structure.



#### 8.3.3.4 Combinatorial Exploration of Peptides as Capping Ligands: the CALNN Family

CALNN is one of 3 200 000 possible sequences of five natural amino acids, and the remarkable stability that it imparts to gold nanoparticles encouraged us to further investigate its structural basis. Thus, exactly like mutagenesis is used to identify the active domain of proteins, we studied the effect of systematic variations of peptide sequence on stability to achieve a better understanding of peptide capping ligands [79]. The variation criteria were the peptide length, N-terminal amino acid (first amino acid), which when cysteine is likely to be the anchor, the peptide core (second and third amino acids), and the peptide carboxyl terminus (fourth and fifth amino acids). A subset of these peptides induced immediate aggregation of the nanoparticle solution. A common feature of peptides in this subset was the presence of two groups having a strong affinity for gold (cysteine, lysine and arginine) at the two ends of the sequence. A striking example is NNLAC, the reverse sequence from CALNN that has the N-terminus amino group at the distal end from the cysteine and induces immediate aggregation, whereas CALNN is an excellent capping ligand. This exemplifies how subtle changes in peptide sequences can have a dramatic effect on performance as capping ligand.

The effect of the remaining peptides on the electrolyte-induced aggregation of gold nanoparticles was then systematically studied. Quantitative analysis of the experimental data corroborates the initial design criteria, establishing the need for a cysteine as an anchor to the gold nanoparticle, a clear correlation between peptide length and stability, and the need for interaction between adjacent peptide chains through hydrophobic interactions or hydrogen bonding. The balance between peptide charge and cohesive interaction also plays a major role.

#### 8.3.3.5 Peptide-capped Silver Nanoparticles

Despite having superior light absorption and scattering properties, silver nanoparticles have not had the same impact as gold nanoparticles in applications that require work in aqueous environments. This is due primarily to a tendency to oxidize that leads to a complete loss of particle stability, most notably in acidic environments. Also, a higher van der Waals' interaction results in particle aggregation at lower ionic strengths than for Au nanoparticles – a problem for biological applications that take place in buffered saline solutions. All of these issues have been overcome through the use of the pentapeptide CALNN [80]. Addition of peptide to relatively unstable 15 nm citrate-stabilized Ag particles results in peptide-stabilized Ag nanoparticles that are stable between pH 4 and 12 and in 1 M solutions of NaCl. Peptide-stabilized Ag nanoparticles 8 nm in diameter can also be synthesized using a modified two-phase arrested precipitation method. These nanoparticles are also stable over a wide pH range (6–12) and in 1 M NaCl solutions.

#### 8.3.3.6 Peptides as Capping Ligands for Fluorescent and Magnetic Nanoparticles

Similar approaches have been used successfully for the stabilization and functionalization of other types of nanomaterials. Weiss' group has used synthetic phytochelatin-related peptides as an organic coat on the surface of colloidal CdSe/

ZnS semiconductor nanocrystals [81]. The peptides are designed to bind to the nanocrystals through a C-terminal adhesive domain composed of multiple repeats of cysteine pairs flanked by hydrophobic 3-cyclohexylalanines. This adhesive domain is followed by a flexible hydrophilic linker domain to which various bio-affinity tags can be attached, resulting in water-soluble, monodisperse peptide-coated nanoparticles with high colloidal stability and ensemble photophysical properties similar to those of the original, TOPO-coated nanocrystals. PEG-modified peptides were used to improve the accessibility of bio-affinity tags (e.g., biotin). In a recent review focused on quantum dots in biology, the same authors discuss the possibilities offered by a *peptide toolkit* to control surface and photophysical properties [82]. These include switching the emission by using a quencher linked to the nanocrystal through an enzyme-cleavable peptide sequence.

Belcher and colleagues have reported phage display-selected peptides as a template to grow FePt magnetic nanoparticles [83]. The particles obtained are ferromagnetic at room temperature, possessing coercivities up to 1000 Oe and may have some applications in high-density memory devices. Fernig and colleagues have reported the first synthesis of peptide-capped water-soluble cobalt nanoparticles [84]. The peptides facilitated the formation of nanoparticles and partly protected the nanoparticles from oxidation.

#### 8.3.4

#### Peptide Extensions to Introduce Functionalities

The introduction of specific recognition groups at the surface of gold nanoparticles is an important prerequisite for their use in bioanalytical assays. Peptides having extensions can be used to introduce functions on the nanoparticles surface. Using a peptide mixture containing a matrix peptide (e.g., CALNN) and one or more functional peptides (e.g., CALNN-XXX where XXX is or bears the functional group), particles having a wide range of functions can be prepared. In contrast to most previously reported approaches, the stabilization and the functionalization of particles in this system are independent, but, crucially, both are achieved preparatively in the same step. Therefore, the number of recognition functions present on each particle can be easily controlled and reduced to a single or very few moieties without compromising the stability of the particles [85]. Recently, particles presenting various chemical groups have been successfully prepared by this approach. These include peptide sequences consisting of natural amino acids as well as artificial amino acids and hybrid sequences consisting of amino acids and oligonucleotides.

##### 8.3.4.1 Biotin and Strep-tag II

Nanoparticles functionalized with biotin and with a peptide analogue of biotin (Strep-tag II: WSHHPQFEK) [86] have been obtained using a peptide mixture containing, on a molar basis, 90% CALNN and 10% CALNNGK(biotin)G or CALNNGGWSHHPQFEK [79]. The nanoparticles were purified from excess peptides by size-exclusion chromatography and immobilized on a nitrocellulose mem-

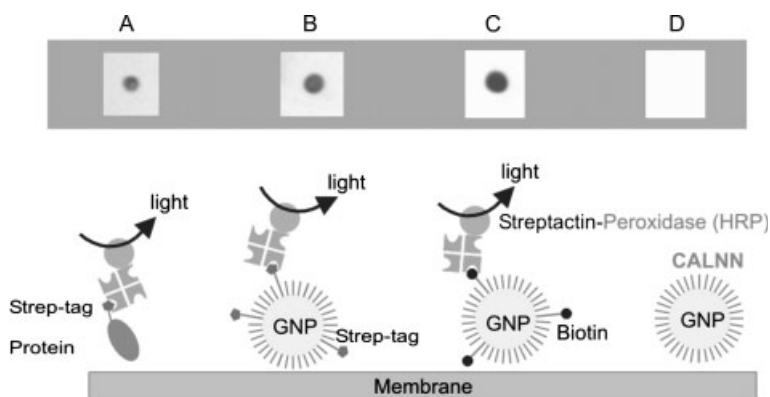


**Fig. 8.9.** Streptactin-peroxidase specific recognition of Strep-tag II and biotin on peptide-capped gold nanoparticles. (A) Engineered fibroblast growth factor receptor (FGFR) with a Strep-tag II sequence. (B)

CALNN-capped nanoparticles decorated with Strep-tag II. (C) CALNN-capped nanoparticles decorated with biotin. (D) CALNN-capped nanoparticles. (Reprinted with permission from [79]. Copyright (2004) by ACS.)

brane. Streptactin-peroxidase was then used to detect the presence of biotin and of its peptide analogue on the membrane (Fig. 8.9). The results demonstrate the presence of functional groups as well as the absence of non-specific binding to the CALNN-capped nanoparticles by streptactin-peroxidase.

#### 8.3.4.2 Peptide-DNA Hybrids

Gold nanoparticles stabilized by thiol-modified oligonucleotides have been used for the programmed self-assembly of nanostructures and for oligonucleotide detection. Wang and colleagues have shown that a peptide-DNA hybrid molecule, i.e., CALNN-DNA, provides a simple route to DNA functionalized particles. Moreover, the ratio of CALNN-DNA to CALNN in the preparation mixture directly controls the amount of DNA available on the nanoparticle surface. The particles retain the stability of the peptide-capped particles. Importantly, this work extends the peptide toolbox to DNA-based assays and DNA-based nanostructured materials. Thus, it is possible to prepare, in a one-pot synthesis, particles functionalized with DNA(s) and other recognition motifs (e.g., peptide recognition motif to inorganic materials). As proof of principle, particles bearing both DNA and biotin extensions have been prepared and detected in a microarray format (Fig. 8.10) [85].

#### 8.3.4.3 His-tag and Nickel Nitrilotriacetic Acid (Ni-NTA)

Immobilized metal affinity chromatography (IMAC) is extensively used in biological research to purify engineered proteins having a histidine tag (generally composed of six consecutive histidines) [87, 88]. Nitrilotriacetic acid immobilized on a gel chelates nickel ions that interact specifically with the histidine tag. The relevant proteins are then eluted from the column using a competitor (imidazole) or a pH

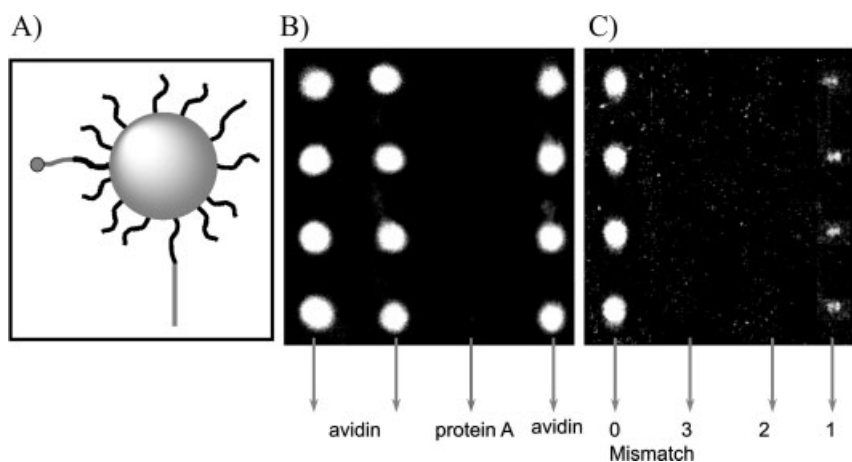


**Fig. 8.10.** Binding of bifunctional peptide-capped particles labeled both with biotin and DNA on microarrays. (A) Scheme of the bifunctional particles. (B) Dark field imaging of the protein microarray after binding of the particles and silver enhancing. (C) Dark field imaging of the DNA microarray after binding of the particles and silver enhancing. (Adapted from [85] with permission.)

change. A large variety of derived protocols based on this interaction have been developed, e.g., Ni-NTA magnetic beads and nanoparticles [89] for the separation of histidine tagged proteins, Ni-NTA gold clusters for their localization using electron microscopy [90] and Ni-NTA lipids for the 2D crystallization of histidine-tagged proteins [91].

Peptides having a histidine tag extension and peptides having a NTA extension could be obtained by standard peptide synthesis and coupling protocols. This will provide new tools to detect and follow histidine-tagged proteins. More importantly, as described in Section 8.3.5.2, it allows an unprecedented control of quantitative labeling through affinity chromatography and opens a new route to multistep synthesis of nanostructures.

### 8.3.5

#### Chromatography of Peptide-capped Nanoparticles

Protein chromatography techniques offer routes to separation based on size, charge, hydrophobicity and affinity. Chromatography media have been optimized to avoid unspecific interactions in the context of protein purification and, thus, are compatible with peptide-capped nanomaterials. This provides a range of protocols to obtain extremely well-defined and pure nanoparticles. Examples of size-exclusion and affinity chromatography are presented below to illustrate the possibilities these techniques offer. Ionic and hydrophobic exchange chromatographies have also been used in purifying peptide-capped nanoparticles.

### 8.3.5.1 Size-exclusion Chromatography

Size-exclusion chromatography on Sephadex G25 provides a rapid means of separating peptide-capped gold nanoparticles from small reagents, including free peptide resulting from the preparation [79]. This process can be scaled up easily for preparative and production purposes. By using a gel with a higher fractionation range, particles of different sizes can be separated (Fig. 8.11).

### 8.3.5.2 Affinity Chromatography

Achieving precise control over the number of functional groups per nanoparticle is an important challenge. Its resolution would open up new opportunities to probe the formation of biological complexes and be an important step towards the preparation of well-defined nanostructures. For DNA-labeled peptide-capped particles, Wang and colleagues have shown that the proportion of labeled peptide in the preparation mixture correlates directly with the amount of label at the nanoparticle surface [85]. Therefore, particles having a mean number of labels well below one can be prepared by using a very low percentage of the labeled peptides. In that case, simple combinatorial arguments show that the labeled particles will be mainly particles having a single label. The problem is then analogous to a simple protein purification problem (separation of labeled and unlabeled particles) and can be solved using IMAC (Fig. 8.12). Particles are loaded on a Ni-NTA column, and particles without a histidine tag do not bind, whereas particles having at least one histidine tag are immobilized and then eluted from the column [92].

### 8.3.6

#### Recognition of Materials

The peptide toolbox provides various molecular tools for the specific recognition of materials (Fig. 8.13, see p. 260). Phage display and cell-surface display are *in vivo* combinatorial biology protocols for identifying biological ligands. The power of such technologies relies on the size and diversity of the library used, combined with the efficiency of the molecular biology tools in allowing easy identification and amplification of the DNA encoding the selected peptide sequences. Libraries are generated by inserting randomized oligonucleotides within certain genes encoded on phage genomes or on bacterial plasmids, leading to the incorporation of a random polypeptide sequence within a protein residing on the surface of the organism (e.g., the coat protein of a phage or an outer membrane or flagellar protein of a cell). Following the pioneering work of Brown on genetically engineered binding of *E. coli* to iron oxide [93], these protocols have been used to select peptides that bind to various inorganic compounds [94]. Peptides with semiconductor binding specificity have been selected by phage display. Selective binding as a function of crystal composition (e.g., binding to GaAs but not to Si) and crystalline face [e.g., binding to (100) GaAs, but not to (111)B GaAs] was obtained [95]. A hexapeptide with specific binding to the surface of titanium was selected by phage display [96]. Gold binding sequences were selected by cell-surface display, and their folding

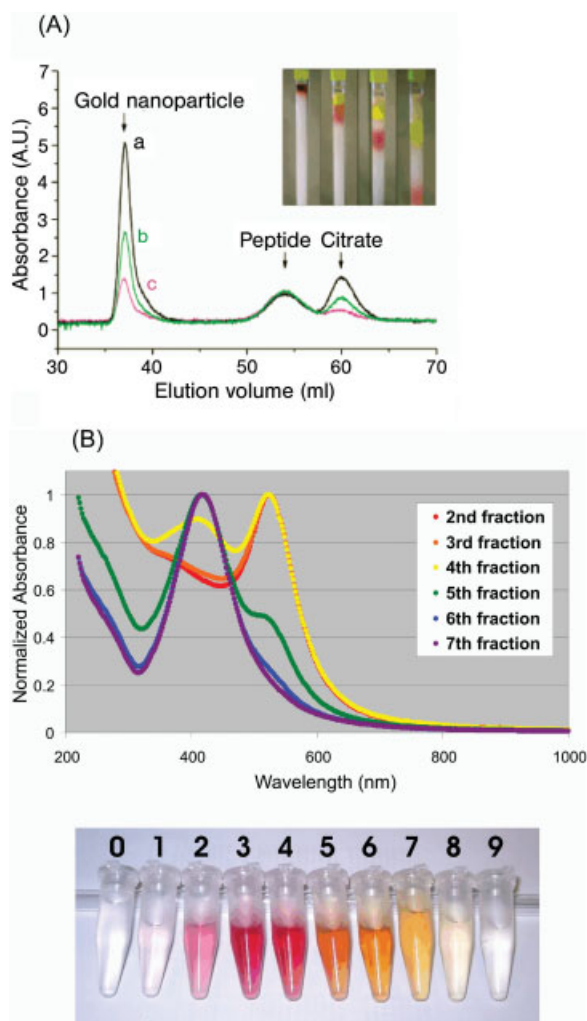


**Fig. 8.11.** Size-exclusion chromatography. (A) Separation of CALNN-capped gold nanoparticles from excess peptide and citrate using Sephadex G25. Inset: separation of CALNN-capped gold nanoparticles (red, diameter  $\sim 12$  nm) from potassium dichromate. (Reprinted with permission

from [79]. Copyright (2004) by ACS.) (B) Separation of CALNN-capped gold nanoparticles from 5 nm PEG-hydroxyl capped silver nanoparticles, (R.C. Doty, unpublished results). Top: absorbance spectra of collected fractions. Bottom: Photograph of collected fractions.

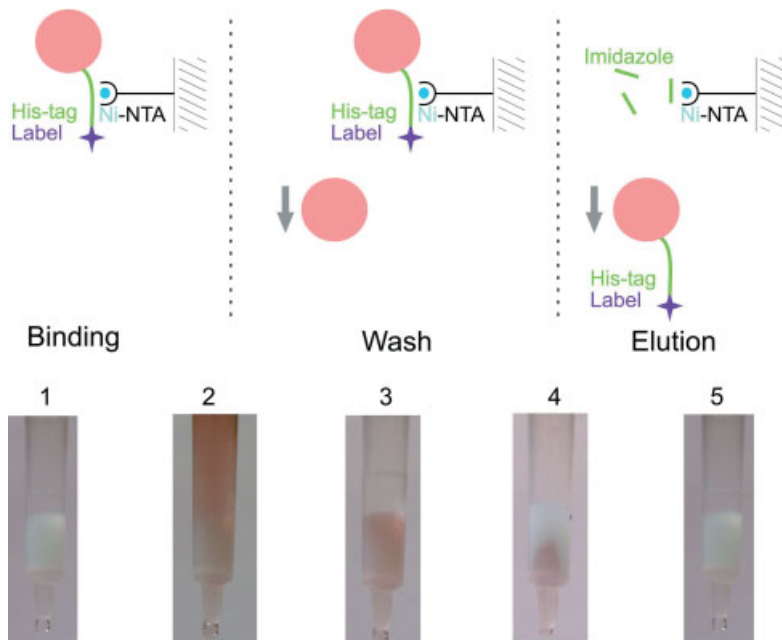


**Fig. 8.12.** Separation of labeled and unlabeled particles using IMAC (R. Lévy, unpublished results). Top: scheme of the main steps of affinity chromatography. Bottom: 1. Clean Ni-NTA gel. 2. Loading of the labeled and unlabeled particles. Only the labeled particles bind to the matrix. 3. Washing; the bound particles remain. 4. Elution with a competitor. 5. Clean Ni-NTA gel.

in the presence of crystalline gold has been investigated by computer modeling [94].

*De novo* design and molecular modeling, another strategy for obtaining affinity towards materials, has been applied successfully to the design of a peptide (nano-1) that binds and solubilizes carbon nanotubes [97, 98]. Nano-1 is designed to fold into an amphiphilic  $\alpha$ -helix and coat carbon nanotubes. The hydrophobic face of the helix was intended to interact noncovalently with the aromatic surface of carbon nanotubes, and the hydrophilic face was designed to promote self-assembly through charged peptide–peptide interactions.

### 8.3.7

#### Peptide-based Linkers

The development of crosslinking systems based on noncovalent interactions facilitates the detection and purification of recombinant proteins [99]. Only a handful of these have been applied in the context of nanomaterials, and new affinity pairs are being developed. The capabilities and versatility of peptide-based linkers are illustrated below for peptide–peptide, peptide–DNA and peptide–synthetic organic molecule linkers.

#### 8.3.7.1 A Peptide-Peptide Linker Based on Leucine-zipper Sequences

The peptide-peptide linker designed by Ryadnov and colleagues consists of three leucine-zipper sequences of *de novo* design: one peptide, “the belt”, templates the co-assembly of the other two half-sized peptides, “the braces” [100]. When mixed, the three peptides reversibly formed a predominantly helical and stable 1:1:1 ternary complex. Surface plasmon resonance experiments demonstrated assembly of the complex on gold surfaces, while the ability of the system to bring together peptide-bound cargo was demonstrated using gold nanoparticles derivatized with the brace peptides before the addition of the belt.

#### 8.3.7.2 A Peptide-DNA Linker Based on Metallopeptides

Metallopeptides of the form Cu(II) or Ni(II) Gly-Gly-His are implicated in nucleic acid recognition and reactivity phenomena. Recently, Fang and colleagues have studied the minor-groove recognition of A/T-rich DNA sites by Ni(II)-(L)-Arg-Gly-His and Ni(II)-(D)-Arg-Gly-His [101]. This study has important implications in understanding protein binding to DNA, but it could also form the basis of new assembly systems for DNA- and peptide-capped nanomaterials.

#### 8.3.7.3 A Peptide-Texas Red Linker Obtained by Phage Display

A library of constrained peptides that form stable folded structures has been screened for aptamers that bind with high affinity to the fluorescent dye Texas red [102]. Two selected clones had binding constants to Texas red of 25 and 80 pM. Thus, minimal, constrained peptides can bind to organic fluorescent dyes in biological contexts, allowing *in vivo* imaging with highly sensitive dyes and some degree of genetic control. It also opens up new routes for the assembly of fluorophores and nanoparticles.

### 8.3.8

#### Biologically Active Peptides

Numerous biologically active peptides have been identified and their potential as biomarkers and drugs are under evaluation [103]. Moreover, phage-display technology provides novel peptides that bind protein targets with high affinity and specificity, offering many opportunities in drug discovery [104]. A review of natural and selected biologically active peptides is far beyond the aim of this chapter. The following example illustrates the benefits of conjugating some of these sequences to nanoparticles. The nanoparticles can play the role of geometrically defined support for the simultaneous presence of multiple sequences as well as the role of optical label for the real-time imaging of these conjugates. Tkachenko and colleagues have prepared peptide-BSA conjugated particles that carry both a receptor-mediated endocytosis peptide and a nuclear localization signal [105]. The particles' localization was monitored inside cells using a combination of video-enhanced color microscopy and differential interference contrast microscopy, revealing an effective targeting of the cell nucleus. Particles bearing only one of the two signal sequences did not target effectively the nucleus. Kanaras and colleagues have demonstrated the



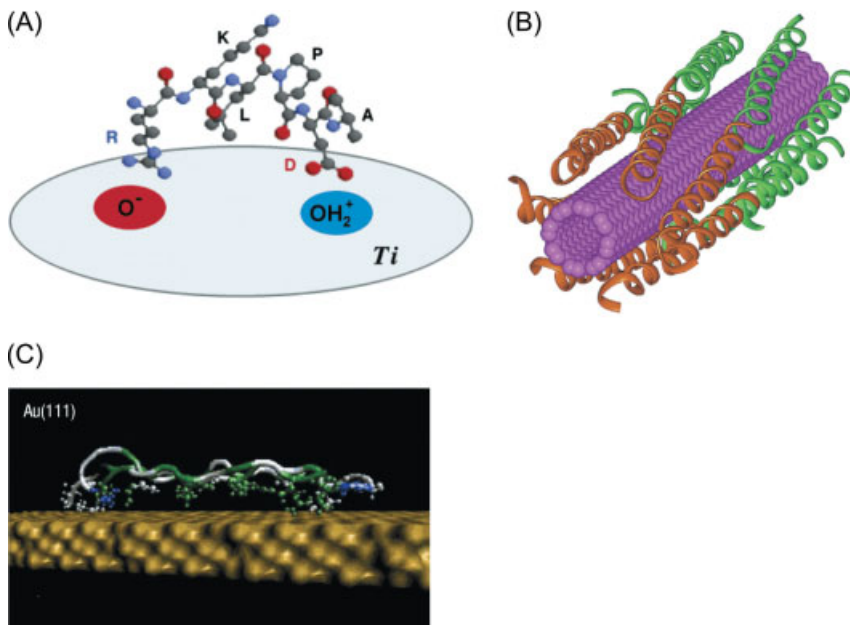


**Fig. 8.13.** Recognition of materials by selected or designed peptides. (A) Peptide selected by phage-display: model of the RKLPGA peptide binding to the surface of titanium. (B) Peptide designed through molecular modeling: model of the peptide Nano-1 wrapping around a carbon nanotube. (C) Peptide selected by cell-surface display: model of a gold binding peptide. (A) reprinted with permission from [96]. Copyright (2003) by ACS. (B) reprinted with permission from [97]. Copyright (2003)

use of DNA processing enzymes (restriction endonucleases, ligase) for multistep nanostructure synthesis using DNA-protected nanoparticles [106]. Similarly, nanoparticles conjugated with peptide sequences comprising enzyme recognition sites (e.g., proteases, kinases or phosphatases) will offer new perspectives for monitoring enzyme activity and for the controlled assembly of nanostructures.

### 8.3.9

#### Self-assembling Peptides

Recently, partly driven by the elucidation of the mechanisms of amyloid fibril formation, a series of articles have revealed the fascinating self-assembly properties of peptides into fibers, nanotubes, micelles, vesicles, and hydrogels (Fig. 8.14) [107–109]. These assemblies exploit various interactions and, eventually, mimic existing biological assemblies. Early work includes the development of biomimetic materials based on self-assembly of ionic self-complementary peptides [110].

##### 8.3.9.1 Fibers and Nanotubes

Alzheimer's beta-amyloid diphenylalanine structural motif has been reported to self-assemble into discrete, stiff nanotubes. Reduction of ionic silver within the

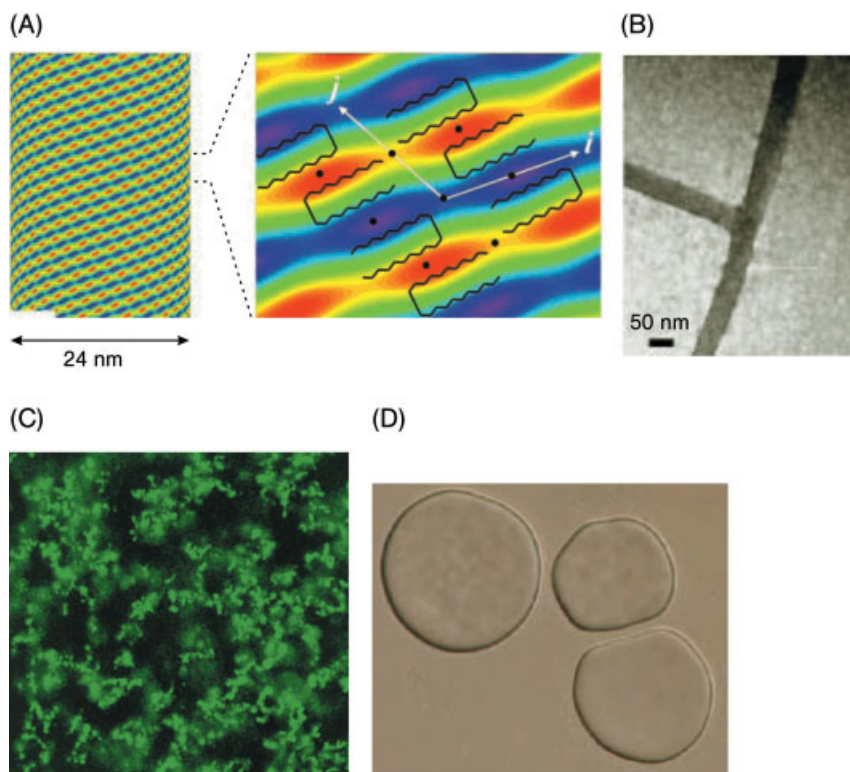


**Fig. 8.14.** Peptide self assemblies.

(A) Nanotubes: crystalline structure of the wall of Lanreotide nanotubes. Left: two-dimensional Patterson function, indicating the main electron density variations of the nanotubes wall. Right: Zoom of the unit cell, showing the beta-hairpin backbone of Lanreotide. The black circles indicate the 2-fold symmetry axes.

(B) Fibers: TEM image of a peptide fiber containing a proportion of a branch-promoting peptide. (C) Hydrogel: Laser scanning confocal microscopy image of hydrogel microstructure

obtained by the assembly of a beta-hairpin designed peptide. Black regions are water-filled pores and channels. (D) Giant vesicles: DIC image of giant vesicles formed by the assembly of amphiphilic block copolyptide.

(A) reprinted with permission from [116]. Copyright (2003) by National Academy of Sciences of the USA. (B) reprinted with permission from [113]. (C) reprinted with permission from [118]. Copyright (2002) by the ACS. (D) reprinted with permission from [120]. Copyright (2002) by the NPG.

nanotubes, followed by enzymatic degradation of the peptide backbone, produced discrete nanowires with a length in the micron range and a diameter of around 100 nm [111].

Woolfson and colleagues have focused on fiber-forming peptides based on the alpha-helical coiled coil, which is a widespread and well-understood protein-protein interaction motif. These peptides form fibers that are over 10  $\mu\text{m}$  long with diameters around 100 nm. Interestingly, a degree of control over their morphology was achieved with mutation-inducing kinks or branching [112–115].

Hierarchical self-assembly of a therapeutic octapeptide, namely Lanreotide, has been revealed at an atomic scale using a combination of characterization tech-

niques (optical and electron microscopies, vibrational spectroscopies, and small and wide-angle X-ray scattering) [116]. This peptide forms hexagonal packing of nanotubes with a high degree of monodispersity in tube diameter (24 nm) and wall thickness ( $\sim 1.8$  nm). The diameter is tunable by suitable modifications of the molecular structure.

#### 8.3.9.2 Peptide-based Amphiphiles

Amphiphilic molecules tend to form well-defined assemblies (e.g., micelles and bilayers) to minimize the contact between the hydrophobic moieties and the aqueous environment. Recent major developments in the design and the structures formed by amphiphilic peptides have been reviewed [117]. Selected papers illustrate the variety of structures formed: One of the attractive properties of these systems is the possibility of easily tuning assembly by external parameters such as the pH and temperature. Kretsinger and colleagues have presented a very elegant way to engineer a stimulus-dependant hydrogel [118]. They have designed a peptide with a pH-dependent intramolecular folding. When folded in a beta-hairpin, this peptide has a propensity to self-assemble into rigid hydrogels with shear-thinning properties and quick mechanical strength recovery. Cryo-transmission electron and laser scanning confocal microscopies revealed a water-filled porous scaffold on both the nano- and microscale. Larger block copolypeptides ( $\sim 200$  amino acids) have been studied by Deming and colleagues [119, 120]. In the first study, the authors used charged amino acids (polylysine and polyglutamate) as hydrophilic blocks. This resulted in hydrogels at very low concentration. In the second study, ethylene glycol-modified amino acid building blocks were used in the hydrophilic domain to give polypeptide segments with stable  $\alpha$ -helical conformations, affording giant vesicles into which functionality could be incorporated.

## 8.4

### Concluding Remarks

With the arrival of new detection systems for metallic nanoparticles, e.g., the photothermal method developed by Lounis and co-workers, restrictions on particle size have been greatly reduced. Previously, single-particle detection was limited to particles with diameters  $> 30$  nm (by light scattering). However, now that particles with a diameter of  $< 5$  nm can be detected photothermally, the emphasis for biological applications of nanotechnology has moved from particle stability to particle functionalization, where it belongs. Peptide capping ligands confer protein-like properties to nanoparticles in terms of water solubility, stability and molecular recognition properties. As a result of their protein-like behavior, functionalized particles can be separated easily from unfunctionalized particles by standard chromatographic techniques, i.e., ion-exchange or metal-ion affinity chromatography. Mixed peptide monolayers on nanoparticles might offer a route towards artificial proteins and enzymes. Peptides offer numerous possibilities in terms of self-assembly, molecular recognition, biological activity, etc., and peptide-capped nano-

particles offer a unique opportunity to integrate these properties into new and complex materials.

## References

- 1 FRENS, G., Controlled nucleation for regulation of particle-size in monodisperse gold suspensions. *Nat. Phys. Sci.* **1973**, *241*, 20–22.
- 2 BROWN, K.R., WALTER, D.G., NATAN, M.J., Seeding of colloidal Au nanoparticle solutions. 2. Improved control of particle size and shape. *Chem. Mater.* **2000**, *12*, 306–313.
- 3 JANA, N.R., GEARHEART, L., MURPHY, C.J., Seeding growth for size control of 5–40 nm diameter gold nanoparticles. *Langmuir* **2001**, *17*, 6782–6786.
- 4 NIKOUBAKHT, B., EL-SAYED, M.A., Preparation and growth mechanism of gold nanorods (NRs) using seed-mediated growth method. *Chem. Mater.* **2003**, *15*, 1957–1962.
- 5 SAU, T.K., MURPHY, C.J., Seeded high yield synthesis of short Au nanorods in aqueous solution. *Langmuir* **2004**, *20*, 6414–6420.
- 6 SAU, T.K., MURPHY, C.J., Room temperature, high-yield synthesis of multiple shapes of gold nanoparticles in aqueous solution. *J. Am. Chem. Soc.* **2004**, *126*, 8648–8649.
- 7 CAO, Y., JIN, R., MIRKIN, C.A., DNA-modified core-shell Ag/Au nanoparticles. *J. Am. Chem. Soc.* **2001**, *123*, 7961–7962.
- 8 JANA, N.R., GEARHEART, L., MURPHY, C.J., Wet chemical synthesis of silver nanorods and nanowires of controllable aspect ratio. *Chem. Commun.* **2001**, 617–618.
- 9 JIN, R., CAO, Y., MIRKIN, C.A., KELLY, K.L., SCHATZ, G.C., ZHENG, J.G., Photoinduced conversion of silver nanospheres to nanoprisms. *Science* **2001**, *294*, 1901–1903.
- 10 CHAN, W.C.W., NIE, S.M., Quantum dot bioconjugates for ultrasensitive nonisotopic detection. *Science* **1998**, *281*, 2016–2018.
- 11 MATTOUSSI, H., MAURO, J.M., GOLDMAN, E.R., ANDERSON, G.P., SUNDAR, V.C., MIKULEC, F.V., BAWENDI, M.G., Self-assembly of CdSe-ZnS quantum dot bioconjugates using an engineered recombinant protein. *J. Am. Chem. Soc.* **2000**, *122*, 12142–12150.
- 12 KANARAS, A.G., KAMOUNAH, F.S., SCHAUMBURG, K., KIELY, C.J., BRUST, M., Thioalkylated tetraethylene glycol: A new ligand for water soluble monolayer protected gold clusters. *Chem. Commun.* **2002**, 2294–2295.
- 13 GERION, D., PINAUD, F., WILLIAMS, S.C., PARAK, W.J., ZANCHET, D., WEISS, S., ALIVISATOS, A.P., Synthesis and properties of biocompatible water-soluble silica-coated CdSe/ZnS semiconductor quantum dots. *J. Phys. Chem. B* **2001**, *105*, 8861–8871.
- 14 SCHROEDTER, A., WELLER, H., Ligand design and bioconjugation of colloidal gold nanoparticles. *Angew. Chem. Int. Ed.* **2002**, *41*, 3218–3221.
- 15 YGUERABIDE, J., YGUERABIDE, E.E., Light-scattering submicroscopic particles as highly fluorescent analogs and their use as tracer labels in clinical and biological applications – I. Theory. *Anal. Biochem.* **1998**, *262*, 137–156.
- 16 YGUERABIDE, J., YGUERABIDE, E.E., Light-scattering submicroscopic particles as highly fluorescent analogs and their use as tracer labels in clinical and biological applications – II. Experimental characterization. *Anal. Biochem.* **1998**, *262*, 157–176.
- 17 MIE, G., Contributions to the optics of turbid media, especially colloidal metal solutions. *Ann. Physik* **1908**, *25*, 377–445.
- 18 WILCOXON, J.P., MARTIN, J.E., PARSAPOUR, F., WIEDENMAN, B., KELLEY, D.F., Photoluminescence from

- nanosize gold clusters. *J. Chem. Phys.* **1998**, *108*, 9137–9143.
- 19 LINK, S., BEEBY, A., FITZGERALD, S., EL-SAYED, M.A., SCHAAFF, T.G., WHETTEN, R.L., Visible to infrared luminescence from a 28-atom gold cluster. *J. Phys. Chem. B* **2002**, *106*, 3410–3415.
- 20 ZHENG, J., PETTY, J.T., DICKSON, R.M., High quantum yield blue emission from water-soluble Au<sub>8</sub> nanodots. *J. Am. Chem. Soc.* **2003**, *125*, 7780–7781.
- 21 ZHENG, J., ZHANG, C., DICKSON, R.M., Highly fluorescent, water-soluble, size-tunable gold quantum dots. *Phys. Rev. Lett.* **2004**, *93*, 077402.
- 22 ZHENG, J., DICKSON, R.M., Individual water-soluble dendrimer-encapsulated silver nanodot fluorescence. *J. Am. Chem. Soc.* **2002**, *124*, 13982–13983.
- 23 PETTY, J.T., ZHENG, J., HUD, N.V., DICKSON, R.M., DNA-templated Ag nanocluster formation. *J. Am. Chem. Soc.* **2004**, *126*, 5207–5212.
- 24 BOYER, D., TAMARAT, P., MAALI, A., LOUNIS, B., ORRIT, M., Photothermal imaging of nanometer-sized metal particles among scatterers. *Science* **2002**, *297*, 1160–1163.
- 25 COGNET, L., TARDIN, C., BOYER, D., CHOQUET, D., TAMARAT, P., LOUNIS, B., Single metallic nanoparticle imaging for protein detection in cells. *Proc. Natl. Acad. Sci. U.S.A.* **2003**, *100*, 11350–11355.
- 26 MIRKIN, C.A., LETSINGER, R.L., MUCIC, R.C., STORHOFF, J.J., A DNA-based method for rationally assembling nanoparticles into macroscopic materials. *Nature* **1996**, *382*, 607–609.
- 27 ALIVISATOS, A.P., JOHNSON, K.P., PENG, X., WILSON, T.E., LOWETH, C.J., BRUCHEZ, J., MARCEL, P., SCHULTZ, P.G., Organization of ‘nanocrystal molecules’ using DNA. *Nature* **1996**, *382*, 609–611.
- 28 JIN, R.C., WU, G.S., LI, Z., MIRKIN, C.A., SCHATZ, G.C., What controls the melting properties of DNA-linked gold nanoparticle assemblies? *J. Am. Chem. Soc.* **2003**, *125*, 1643–1654.
- 29 ELGHANIAN, R., STORHOFF, J.J., MUCIC, R.C., LETSINGER, R.L., MIRKIN, C.A., Selective colorimetric detection of polynucleotides based on the distance-dependent optical properties of gold nanoparticles. *Science* **1997**, *277*, 1078–1081.
- 30 STORHOFF, J.J., LAZARIDES, A.A., MUCIC, R.C., MIRKIN, C.A., LETSINGER, R.L., SCHATZ, G.C., What controls the optical properties of DNA-linked gold nanoparticle assemblies? *J. Am. Chem. Soc.* **2000**, *122*, 4640–4650.
- 31 TATON, T.A., MIRKIN, C.A., LETSINGER, R.L., Scanometric DNA array detection with nanoparticle probes. *Science* **2000**, *289*, 1757–1760.
- 32 TATON, T.A., LU, G., MIRKIN, C.A., Two-color labeling of oligonucleotide arrays via size-selective scattering of nanoparticle probes. *J. Am. Chem. Soc.* **2001**, *123*, 5164–5165.
- 33 PARK, S.J., TATON, T.A., MIRKIN, C.A., Array-based electrical detection of DNA with nanoparticle probes. *Science* **2002**, *295*, 1503–1506.
- 34 MUCIC, R.C., STORHOFF, J.J., MIRKIN, C.A., LETSINGER, R.L., DNA-directed synthesis of binary nanoparticle network materials. *J. Am. Chem. Soc.* **1998**, *120*, 12674–12675.
- 35 MITCHELL, G.P., MIRKIN, C.A., LETSINGER, R.L., Programmed assembly of DNA functionalized quantum dots. *J. Am. Chem. Soc.* **1999**, *121*, 8122–8123.
- 36 FU, A., MICHEEL, C.M., CHA, J., CHANG, H., YANG, H., ALIVISATOS, A.P., Discrete nanostructures of quantum dots/Au with DNA. *J. Am. Chem. Soc.* **2004**, *126*, 10832–10833.
- 37 LOWETH, C.J., CALDWELL, W.B., PENG, X., ALIVISATOS, A.P., SCHULTZ, P.G., DNA-based assembly of gold nanocrystals. *Angew. Chem. Int. Ed.* **1999**, *38*, 1808–1812.
- 38 ZANCHET, D., MICHEEL, C.M., PARAK, W.J., GERION, D., ALIVISATOS, A.P., Electrophoretic isolation of discrete Au nanocrystal/DNA conjugates. *Nano Lett.* **2001**, *1*, 32–35.
- 39 ZANCHET, D., MICHEEL, C.M., PARAK, W.J., GERION, D., WILLIAMS, S.C., ALIVISATOS, A.P., Electrophoretic and structural studies of DNA-directed Au

- nanoparticle groupings. *J. Phys. Chem. B* **2002**, *106*, 11758–11763.
- 40 SUNG, K.-M., MOSLEY, D.W., PEELE, B.R., ZHANG, S., JACOBSON, J.M., Synthesis of monofunctionalized gold nanoparticles by Fmoc solid-phase reactions. *J. Am. Chem. Soc.* **2004**, *126*, 5064–5065.
- 41 WILSON, R., CHEN, Y., AVEYARD, J., One molecule per particle method for functionalising nanoparticles. *Chem. Commun.* **2004**, 1156–1157.
- 42 SHENTON, W., DAVIS, S.A., MANN, S., Directed self-assembly of nanoparticles into macroscopic materials using antibody-antigen recognition. *Adv. Mater.* **1999**, *11*, 449–452.
- 43 THANH, N.T.K., ROSENZWEIG, Z., Development of an aggregation-based immunoassay for anti-protein A using gold nanoparticles. *Anal. Chem.* **2002**, *74*, 1624–1628.
- 44 HALL, S.R., SHENTON, W., ENGELHARDT, H., MANN, S., Site-specific organization of gold nanoparticles by biomolecular templating. *ChemPhysChem* **2001**, *2*, 184–186.
- 45 BERGKVIST, M., MARK, S.S., YANG, X., ANGERT, E.R., BATT, C.A., Bionanofabrication of ordered nanoparticle arrays: Effect of particle properties and adsorption conditions. *J. Phys. Chem. B* **2004**, *108*, 8241–8248.
- 46 PASQUATO, L., PENGO, P., SCRIMIN, P., Functional gold nanoparticles for recognition and catalysis. *J. Mater. Chem.* **2004**, *14*, 3481–3487.
- 47 BOAL, A.K., ROTELLO, V.M., Fabrication and self-optimization of multivalent receptors on nanoparticle scaffolds. *J. Am. Chem. Soc.* **2000**, *122*, 734–735.
- 48 PENGO, P., POLIZZI, S., PASQUATO, L., SCRIMIN, P., Carboxylate-imidazole cooperativity in dipeptide-functionalized gold nanoparticles with esterase-like activity. *J. Am. Chem. Soc.* **2005**, *127*, 1616–1617.
- 49 BALTZER, L., NILSSON, H., NILSSON, J., De novo design of proteins – what are the rules? *Chem. Rev.* **2001**, *101*, 3153–3163.
- 50 VENTURA, S., SERRANO, L., Designing proteins from the inside out. *Proteins-Struct. Funct. Bioinformatics* **2004**, *56*, 1–10.
- 51 VENKATRAMAN, J., SHANKARAMMA, S.C., BALARAM, P., Design of folded peptides. *Chem. Rev.* **2001**, *101*, 3131–3152.
- 52 KAPLAN, J., DEGRADO, W.F., De novo design of catalytic proteins. *Proc. Natl. Acad. Sci. USA* **2004**, *101*, 11566–11570.
- 53 KNEZ, M., BITTNER, A.M., BOES, F., WEGE, C., JESKE, H., MAISS, E., KERN, K., Biotemplate synthesis of 3-nm nickel and cobalt nanowires. *Nano Lett.* **2003**, *3*, 1079–1082.
- 54 NAM, K.T., PEELE, B.R., LEE, S.W., BELCHER, A.M., Genetically driven assembly of nanorings based on the M13 virus. *Nano Lett.* **2004**, *4*, 23–27.
- 55 GOODSSELL, D.S., *Bionanotechnology: Lessons from Nature*, **2004**, Wiley-Liss.
- 56 BRUST, M., WALKER, M., BETHELL, D., SCHIFFRIN, D.J., WHYMAN, R., Synthesis of thiol-derivatized gold nanoparticles in a 2-phase liquid-liquid system. *J. Chem. Soc., Chem. Commun.* **1994**, 801–802.
- 57 WILSON, R., Haptenylated mercaptodextran-coated gold nanoparticles for biomolecular assays. *Chem. Commun.* **2003**, 108–109.
- 58 ZHANG, J., CHI, Q., NIELSEN, J.U., FRIIS, E.P., ANDERSEN, J.E.T., ULSTRUP, J., Two-dimensional cysteine and cystine cluster networks on Au(111) disclosed by voltammetry and in situ scanning tunneling microscopy. *Langmuir* **2000**, *16*, 7229–7237.
- 59 MANDAL, S., PHADTARE, S., SASTRY, M., Interfacing biology with nanoparticles. *Curr. Appl. Phys.* **2005**, *5*, 118–127.
- 60 MANDAL, S., GOLE, A., LALA, N., GONNADE, R., GANVIR, V., SASTRY, M., Studies on the reversible aggregation of cysteine-capped colloidal silver particles interconnected via hydrogen bonds. *Langmuir* **2001**, *17*, 6262–6268.
- 61 SELVAKANNAN, P.R., MANDAL, S., PHADTARE, S., PASRICHA, R., SASTRY, M., Capping of gold nanoparticles by the amino acid lysine renders them water-dispersible. *Langmuir* **2003**, *19*, 3545–3549.

- 62 SELVAKANNAN, P., MANDAL, S., PHADTARE, S., GOLE, A., PASRICHA, R., ADYANTHAYA, S.D., SASTRY, M., Water-dispersible tryptophan-protected gold nanoparticles prepared by the spontaneous reduction of aqueous chloroaurate ions by the amino acid. *J. Colloid Interface Sci.* **2004**, *269*, 97–102.
- 63 JOSHI, H., SHIRUDE, P.S., BANSAL, V., GANESH, K.N., SASTRY, M., Isothermal titration calorimetry studies on the binding of amino acids to gold nanoparticles. *J. Phys. Chem. B* **2004**, *108*, 11535–11540.
- 64 XU, L., GUO, Y., XIE, R., ZHUANG, J., YANG, W., LI, T., Three-dimensional assembly of Au nanoparticles using dipeptides. *Nanotechnology* **2002**, *13*, 725–728.
- 65 ZHONG, Z.Y., LUO, J.Z., ANG, T.P., HIGHFIELD, J., LIN, J.Y., GEDANKEN, A., Controlled organization of Au colloids into linear assemblies. *J. Phys. Chem. B* **2004**, *108*, 18119–18123.
- 66 PENGO, P., BROXTERMAN, Q.B., KAPTEIN, B., PASQUATO, L., SCRIMIN, P., Synthesis of a stable helical peptide and grafting on gold nanoparticles. *Langmuir* **2003**, *19*, 2521–2524.
- 67 ZHANG, F.X., HAN, L., ISRAEL, L.B., DARAS, J.G., MAYE, M.M., LY, N.K., ZHONG, C.J., Colorimetric detection of thiol-containing amino acids using gold nanoparticles. *Analyst* **2002**, *127*, 462–465.
- 68 XIE, H., TKACHENKO, A.G., GLOMM, W.R., RYAN, J.A., BRENNAMAN, M.K., PAPANIKOLAS, J.M., FRANZEN, S., FELDHEIM, D.L., Critical flocculation concentrations, binding isotherms, and ligand exchange properties of peptide-modified gold nanoparticles studied by UV-visible, fluorescence, and time-correlated single photon counting spectroscopies. *Anal. Chem.* **2003**, *75*, 5797–5805.
- 69 BURT, J.L., GUTIERREZ-WING, C., MIKI-YOSHIDA, M., JOSE-YACAMAN, M., Noble-metal nanoparticles directly conjugated to globular proteins. *Langmuir* **2004**, *20*, 11778–11783.
- 70 SCHAAFF, T.G., KNIGHT, G., SHAFIGULLIN, M.N., BORKMAN, R.F., WHETTEN, R.L., Isolation and selected properties of a 10.4 kDa gold: Glutathione cluster compound. *J. Phys. Chem. B* **1998**, *102*, 10643–10646.
- 71 SLOCIK, J.M., MOORE, J.T., WRIGHT, D.W., Monoclonal antibody recognition of histidine-rich peptide encapsulated nanoclusters. *Nano Lett.* **2002**, *2*, 169–173.
- 72 SLOCIK, J.M., WRIGHT, D.W., Biomimetic mineralization of noble metal nanoclusters. *Biomacromolecules* **2003**, *4*, 1135–1141.
- 73 DJALALI, R., CHEN, Y., MATSUI, H., Au nanowire fabrication from sequenced histidine-rich peptide. *J. Am. Chem. Soc.* **2002**, *124*, 13660–13661.
- 74 DJALALI, R., CHEN, Y.F., MATSUI, H., Au nanocrystal growth on nanotubes controlled by conformations and charges of sequenced peptide templates. *J. Am. Chem. Soc.* **2003**, *125*, 5873–5879.
- 75 YU, L.T., BANERJEE, I.A., MATSUI, H., Incorporation of sequenced peptides on nanotubes for Pt coating: Smart control of nucleation and morphology via activation of metal binding sites on amino acids. *J. Mater. Chem.* **2004**, *14*, 739–743.
- 76 MCMILLAN, R.A., HOWARD, J., ZALUZEC, N.J., KAGAWA, H.K., MOGUL, R., LI, Y.-F., PAAVOLA, C.D., TRENT, J.D., A self-assembling protein template for constrained synthesis and patterning of nanoparticle arrays. *J. Am. Chem. Soc.* **2005**, *127*, 2800–2801.
- 77 NAIK, R.R., JONES, S.E., MURRAY, C.J., MCAULIFFE, J.C., VAIA, R.A., STONE, M.O., Peptide templates for nanoparticle synthesis derived from polymerase chain reaction-driven phage display. *Adv. Funct. Mater.* **2004**, *14*, 25–30.
- 78 KRAMER, R.M., LI, C., CARTER, D.C., STONE, M.O., NAIK, R.R., Engineered protein cages for nanomaterial synthesis. *J. Am. Chem. Soc.* **2004**, *126*, 13282–13286.
- 79 LÉVY, R., THANH, N.T.K., DOTY, R.C., HUSSAIN, I., NICHOLS, R.J., SCHIFFRIN, D.J., BRUST, M., FERNIG, D.G., Rational and combinatorial

- design of peptide capping ligands for gold nanoparticles. *J. Am. Chem. Soc.* **2004**, *126*, 10076–10084.
- 80 DOTY, R.C., TSHIKHUDO, T.R., BRUST, M., FERNIS, D.G., Extremely stable water-soluble Ag nanoparticles. Submitted to *Chem. Mater.* **2005**.
- 81 PINAUD, F., KING, D., MOORE, H.-P., WEISS, S., Bioactivation and cell targeting of semiconductor CdSe/ZnS nanocrystals with phytochelatin-related peptides. *J. Am. Chem. Soc.* **2004**, *126*, 6115–6123.
- 82 MICHALET, X., PINAUD, F., BENTOLILLA, L.A., TSAY, J.M., DOOSE, S., LI, J.J., SUNDARESAN, G., WU, A.M., GAMBHIR, S.S., WEISS, S., Quantum dots for live cells, in vivo imaging, and diagnostics. *Science* **2005**, *307*, 538–544.
- 83 REISS, B.D., MAO, C.B., SOLIS, D.J., RYAN, K.S., THOMSON, T., BELCHER, A.M., Biological routes to metal alloy ferromagnetic nanostructures. *Nano Lett.* **2004**, *4*, 1127–1132.
- 84 THANH, N.T.K., PUNTES, V.F., TUNG, L.D., FERNIG, D.G., Peptides as capping ligands for in situ synthesis of water soluble Co nanoparticles for bioapplications. *J. Phys. D – Appl. Phys.* **2005**, in the press.
- 85 WANG, Z., LÉVY, R., FERNIG, D.G., BRUST, M., The peptide route to multifunctional gold nanoparticles. *Bioconjugate Chem.* **2005**, *16*, 457–500.
- 86 SKERRA, A., SCHMIDT, T.G.M., Use of the strep-tag and streptavidin for detection and purification of recombinant proteins. In *Applications of Chimeric Genes and Hybrid Proteins, Pt A* (Vol. 326), **2000**, pp. 271–304.
- 87 HOCHULI, E., DOBELI, H., SCHACHER, A., New metal chelate adsorbent selective for proteins and peptides containing neighbouring histidine residues. *J. Chromatogr.* **1987**, *411*, 177–184.
- 88 GABERC-POREKAR, V., MENART, V., Perspectives of immobilized-metal affinity chromatography. *J. Biochem. Biophys. Methods* **2001**, *49*, 335–360.
- 89 XU, C.J., XU, K.M., GU, H.W., ZHONG, X.F., GUO, Z.H., ZHENG, R.K., ZHANG, X.X., XU, B., Nitritriacetic acid-modified magnetic nanoparticles as a general agent to bind histidine-tagged proteins. *J. Am. Chem. Soc.* **2004**, *126*, 3392–3393.
- 90 HAINFELD, J.F., LIU, W.Q., HALSEY, C.M.R., FREIMUTH, P., POWELL, R.D., Ni-NTA-gold clusters target His-tagged proteins. *J. Struct. Biol.* **1999**, *127*, 185–198.
- 91 VENIEN-BRYAN, C., BALAVOINE, F., TOUSSAINT, B., MIOSKOWSKI, C., HEWAT, E.A., HELME, B., VIGNAIS, P.M., Structural study of the response regulator HupR from *Rhodobacter capsulatus*. Electron microscopy of two-dimensional crystals on a nickel-chelating lipid. *J. Mol. Biol.* **1997**, *274*, 687–692.
- 92 LÉVY, R., Unpublished results, **2005**.
- 93 BROWN, S., Engineered iron oxide-adhesion mutants of the *Escherichia coli* phage-lambda receptor. *Proc. Natl. Acad. Sci. U.S.A.* **1992**, *89*, 8651–8655.
- 94 SARIKAYA, M., TAMERLER, C., JEN, A.K.Y., SCHULTEN, K., BANEXY, F., Molecular biomimetics: Nanotechnology through biology. *Nat. Mater.* **2003**, *2*, 577–585.
- 95 WHALEY, S.R., ENGLISH, D.S., HU, E.L., BARBARA, P.F., BELCHER, A.M., Selection of peptides with semiconductor binding specificity for directed nanocrystal assembly. *Nature* **2000**, *405*, 665–668.
- 96 SANO, K.I., SHIBA, K., A hexapeptide motif that electrostatically binds to the surface of titanium. *J. Am. Chem. Soc.* **2003**, *125*, 14234–14235.
- 97 DIECKMANN, G.R., DALTON, A.B., JOHNSON, P.A., RAZAL, J., CHEN, J., GIORDANO, G.M., MUNOZ, E., MUSSELMAN, I.H., BAUGHMAN, R.H., DRAPER, R.K., Controlled assembly of carbon nanotubes by designed amphiphilic peptide helices. *J. Am. Chem. Soc.* **2003**, *125*, 1770–1777.
- 98 ZORBAS, V., ORTIZ-ACEVEDO, A., DALTON, A.B., YOSHIDA, M.M., DIECKMANN, G.R., DRAPER, R.K., BAUGHMAN, R.H., JOSE-YACAMAN, M., MUSSELMAN, I.H., Preparation and characterization of individual peptide-wrapped single-walled carbon



- nanotubes. *J. Am. Chem. Soc.* **2004**, *126*, 7222–7227.
- 99 TERPE, K., Overview of tag protein fusions: From molecular and biochemical fundamentals to commercial systems. *Appl. Microbiol. Biotechnol.* **2003**, *60*, 523–533.
- 100 RYADNOV, M.G., CEYHAN, B., NIEMEYER, C.M., WOOLFSON, D.N., “Belt and braces”: A peptide-based linker system of de novo design. *J. Am. Chem. Soc.* **2003**, *125*, 9388–9394.
- 101 FANG, Y.Y., RAY, B.D., CLAUSSEN, C.A., LIPKOWITZ, K.B., LONG, E.C., Ni(II)center dot Arg-Gly-His – DNA interactions: Investigation into the basis for minor-groove binding and recognition. *J. Am. Chem. Soc.* **2004**, *126*, 5403–5412.
- 102 MARKS, K.M., ROSINOV, M., NOLAN, G.P., In vivo targeting of organic calcium sensors via genetically selected peptides. *Chem. Biol.* **2004**, *11*, 347–356.
- 103 ADERMANN, K., JOHN, H., STANDKER, L., FORSSMANN, W.G., Exploiting natural peptide diversity: Novel research tools and drug leads. *Curr. Opin. Biotechnol.* **2004**, *15*, 599–606.
- 104 KOLONIN, M., PASQUALINI, R., ARAP, W., Molecular addresses in blood vessels as targets for therapy. *Curr. Opin. Chem. Biol.* **2001**, *5*, 308–313.
- 105 TKACHENKO, A.G., XIE, H., COLEMAN, D., GLOMM, W., RYAN, J., ANDERSON, M.F., FRANZEN, S., FELDHEIM, D.L., Multifunctional gold nanoparticle-peptide complexes for nuclear targeting. *J. Am. Chem. Soc.* **2003**, *125*, 4700–4701.
- 106 KANARAS, A.G., WANG, Z.X., BATES, A.D., COSSTICK, R., BRUST, M., Towards multistep nanostructure synthesis: Programmed enzymatic self-assembly of DNA/gold systems. *Angew. Chem. Int. Ed.* **2003**, *42*, 191–194.
- 107 WRIGHT, E.R., Conticello, V.P., Self-assembly of block copolymers derived from elastin-mimetic polypeptide sequences. *Adv. Drug Deliv. Rev.* **2002**, *54*, 1057–1073.
- 108 ZHANG, S.G., ZHAO, X.J., Design of molecular biological materials using peptide motifs. *J. Mater. Chem.* **2004**, *14*, 2082–2086.
- 109 MACPHEE, C.E., WOOLFSON, D.N., Engineered and designed peptide-based fibrous biomaterials. *Curr. Opin. Solid State Mater. Sci.* **2004**, *8*, 141–149.
- 110 ZHANG, S.G., Emerging biological materials through molecular self-assembly. *Biotechnol. Adv.* **2002**, *20*, 321–339.
- 111 RECHES, M., GAZIT, E., Casting metal nanowires within discrete self-assembled peptide nanotubes. *Science* **2003**, *300*, 625–627.
- 112 RYADNOV, M.G., WOOLFSON, D.N., Engineering the morphology of a self-assembling protein fibre. *Nat. Mater.* **2003**, *2*, 329–332.
- 113 RYADNOV, M.G., WOOLFSON, D.N., Introducing branches into a self-assembling peptide fiber. *Angew. Chem. Int. Ed.* **2003**, *42*, 3021–3023.
- 114 RYADNOV, M.G., WOOLFSON, D.N., Fiber recruiting peptides: Noncovalent decoration of an engineered protein scaffold. *J. Am. Chem. Soc.* **2004**, *126*, 7454–7455.
- 115 SMITH, A.M., ACQUAH, S.F.A., BONE, N., KROTO, H.W., RYADNOV, M.G., STEVENS, M.S.P., WALTON, D.R.M., WOOLFSON, D.N., Polar assembly in a designed protein fiber. *Angew. Chem. Int. Ed.* **2005**, *44*, 325–328.
- 116 VALERY, C., PATERNOSTRE, M., ROBERT, B., GULIK-KRZYWICKI, T., NARAYANAN, T., DEDIEU, J.C., KELLER, G., TORRES, M.L., CHERIF-CHEIKH, R., CALVO, P., ARTZNER, F., Biomimetic organization: Octapeptide self-assembly into nanotubes of viral capsid-like dimension. *Proc. Natl. Acad. Sci. U.S.A.* **2003**, *100*, 10258–10262.
- 117 LOWIK, D.W.P.M., VAN HEST, J.C.M., Peptide based amphiphiles. *Chem. Soc. Rev.* **2004**, *33*, 234–245.
- 118 SCHNEIDER, J.P., POCHAN, D.J., OZBAS, B., RAJAGOPAL, K., PAKSTIS, L., KRETSINGER, J., Responsive hydrogels from the intramolecular folding and self-assembly of a designed peptide. *J. Am. Chem. Soc.* **2002**, *124*, 15030–15037.
- 119 NOWAK, A.P., BREEDVELD, V., PAKSTIS,

- L., OZBAS, B., PINE, D.J., POCHAN, D., DEMING, T.J., Rapidly recovering hydrogel scaffolds from self-assembling diblock copolypeptide amphiphiles. *Nature* **2002**, *417*, 424–428.
- 120 BELLOMO, E.G., WYRSTA, M.D., PAKSTIS, L., POCHAN, D.J., DEMING, T.J., Stimuli-responsive polypeptide vesicles by conformation-specific assembly. *Nat. Mater.* **2004**, *3*, 244–248.

## 9

# Folate-linked Lipid-based Nanoparticles for Tumor-targeted Gene Therapy

Yoshiyuki Hattori and Yoshie Maitani

### 9.1

#### Introduction

Cancer gene therapy has been intensively developed using non-viral vector [1]. Viral vectors such as retroviruses [2], adenoviruses [3], adeno-associated viruses [4] and several other viral types [5], are efficient in transfection, but pose risks to the host from the immunogenicity of viral proteins, a lack of desired tissue selectivity, the potential for oncogenesis due to chromosomal integration, and the generation of infectious viruses due to recombination, making non-viral vectors an attractive alternative. Synthetic vectors such as cationic polymers, liposomes and nanoparticles have been studied widely for DNA delivery due to their potential for tissue-specific targeting, their lack of immunogenicity, the relative safety, and relative ease of large-scale production. For targeted delivery to tumors, vitamin folic acid has been utilized for folate receptor (FR)-mediated drug delivery since the FR is frequently overexpressed on human tumors [6, 7]. Liposomes conjugated to folate ligand have been reported as carriers of chemotherapeutic agents to FR-bearing tumor cells *in vivo* [8–14]. While much has been published on folate-drug conjugates and folate-linked carriers, relatively little is known about the targeting of gene delivery. The use of a folate ligand as a targeting ligand to deliver DNA has also been reported *in vitro* [15–19], but has not been successful in *in vivo* gene therapy [20, 21]. Therefore, in this chapter, we describe the current understanding of tumor-targeting particle vectors and folate-linked lipid-based vectors such as liposomes and nanoparticles. Information pertaining to the formulation of folate-linked lipid-based nanoparticles, their transfection activity *in vitro* and *in vivo* in suicide gene therapy to treat prostate and nasopharyngeal tumors *in vivo* is also included.

### 9.2

#### Gene Delivery and Expression System

Plasmids for gene expression system contain a cDNA coding for either a full gene or minigene and several other genetic elements, including introns, polyadenylation

sequences and transcript stabilizers to control transcription, translation, protein stability and secretion from the host cells [22]. The minimal transcription unit required for expression of a therapeutic protein consists of 5' enhancer/promoter upstream of the gene encoding for the therapeutic protein (e.g., HSV-tk or cytosine deaminase, etc.) and a polyadenylation signal downstream of the gene. Several promoters originating from eukaryotic viruses, such as cytomegalovirus (CMV), simian virus 40 (SV40), Moloney murine leukemia virus (MoMLV), and Rous sarcoma virus (RSV) are widely used. Tumor-specific promoters (e.g., carcinoembryonic antigen (CEA) [23], alpha-fetoprotein (AFP) [24], midkine [25], prostate specific antigen (PSA) [26], etc.) for cancer gene therapy are also designed to interact with transcription factors or other nuclear proteins present in the desired target cells [27].

A major requirement for gene therapy is efficient transport of DNA through the cell membrane by processes that are not well defined. The mechanistic pathway for gene transfection includes the compaction of extended plasmid DNA chain. This process, also known as DNA condensation, has received considerable attention in recent years due to its biological importance in DNA packaging in the development of gene delivery [28, 29]. Multivalent cations such as polyamines (spermidine, spermine), positively charged polymers (polyethylenimine, PEI) and peptides (poly-L-lysine, PLL) provoke the condensation of DNA to nanoparticles [28, 30].

Non-viral particle systems generally entail complex/encapsulation of the gene of interest (present, along with appropriate promoters, etc., in a circular plasmid) with additional molecules, particularly various lipids. These generally display a positive charge and hence interact with the negatively charged DNA molecules. Inside the cytoplasm, endosomes are destabilized and release the plasmid DNA, although this is an inefficient process in many cases [31]. Once plasmid DNA is released into the cytoplasm, it may enter the nucleus. DNA is transported across the nuclear envelope through the nuclear pore. While smaller particles of 25 nm can freely diffuse through the nuclear pore, which is ~55 nm in diameter, larger molecules enter the nucleus through the nuclear pore complex [32, 33]. Finally, therapeutic protein is transcribed and translated from plasmid DNA. Genes introduced into cells using particle vectors are episomal and provide transient expression of transgenes.

### 9.3 Nanoparticles for Gene Delivery System

Systemic administration via intravenous injection rarely achieves meaningful cell transfection. This is most likely due to the high nuclease levels present in serum. Particle vectors can stabilize the DNA, protect it, e.g., from serum nuclease, and ideally interact with the biological system when particles modified with ligands, for example, help target the DNA to particular cells, leading to endocytosis. However, a major limitation of these systems is their inability to cross-intact endothelial barriers and leave general circulation. In general, particle carriers are phagocytosed by the macrophages of the mononuclear phagocytotic cells (MPS), thereby rapidly

localizing predominantly in the liver and spleen [34]. However, sterically stabilized particle carriers such as polyethylene glycol (PEG)-coated nanoparticles have extended circulation times and can remain in the blood [35]. Such nanoparticles, known as long-circulating nanoparticles, tend to accumulate in tumors as a result of increased microvascular permeability and defective lymphatic drainage, a process also referred to as the enhanced permeability and retention (EPR) effect. This is a passive and non-specific process of extravasation that is statically improved by the prolonged residence time of nanoparticles in circulation and repeated passages through the tumor microvascular bed. These ideas have already been realized in liposomal products such as Doxil®.

Liposomes coated with the monoclonal antibodies (mAbs) (immunoliposomes) can provide target-specific binding to the cells [36]. The ligand can be coupled directly to the liposome surface; however, the PEG chains may provide steric hindrance to receptor binding. Alternatively, a bi-functional PEG linker can be used to couple liposomes to one end of PEG chains and ligands to the other end. Steric hindrance is not a problem in the latter approach. The primary focus of their use has been in the targeted delivery of anticancer agents. Hosokawa et al. [37] have reported efficacy of immunoliposomal doxorubicin on cancer models in a cell-surface-antigen-density-dependent manner.

Active targeting increases the affinity of the carrier system for the target site while passive targeting minimizes the non-specific interaction with non-targeted sites by the reticuloendothelial systems (RES). However, gene transfer activity after intravenous injection of a cationic liposome/plasmid DNA complex is most prevalent in the lung [38]. The challenge for tumor-specific targeting using particulate gene delivery systems is to decrease this non-specific gene transfer in the lung while simultaneously maintaining or increasing the level of gene transfer to the tumor tissues. Xu et al. [39] have reported that a cationic immunolipoplex system directed by a single-chain antibody variable region fragment (scFv) against the human transferrin receptor enhanced the transfection efficiency both *in vitro* and *in vivo*. Anti-Her-2 mAb [40], anti-transferrin receptor mAb [39], and growth factor, such as a transferrin, which is a high affinity ligand for the transferrin receptor [41, 42], have been used for tumor-targeting. Other ligands, such as sugar (galactose [43] and glucose [44]), folic acid [45], or RGD-peptide [46], which are associated with asialoglycoprotein receptor on the hepatocyte, folate receptor, and integrin, respectively, in actively growing cells and tumor, can be used.

## 9.4

### Folate-linked Vectors

Folic acid as a targeting ligand offers many potential advantages: (a) a small targeting ligand, often leading to favorable pharmacokinetic properties of the folate conjugates and reduced probability of immunogenicity; (b) convenient availability and low cost; (c) relatively simple and defined conjugation chemistry; (d) high affinity for FR and lack of FR expression in normal tissue; (e) the receptor–ligand complex

can be induced to internalize via endocytosis; and (f) high frequency of FR overexpression among human tumors. Therefore, folate-linked targeting systems show great potential for clinical and therapeutic application.

#### 9.4.1

##### Folate Receptors

Folate receptor (FR) is overexpressed in a wide range of tumors, and is known as a high-affinity membrane folate-binding protein, which mediates uptake of the vitamin by receptor-mediated endocytosis. Therefore, it presents an attractive target for tumor-selective delivery. FR-targeting materials can continuously accumulate into cells due to receptor recycling. FR-targeting imaging agents arrived on the market in 2004. Three isoforms of FR have been identified and two, FR- $\alpha$  and - $\beta$ , are attached to the cell by a glycosylphosphatidylinositol (GPI)-anchor, while FR- $\gamma$  is secreted due to the lack of an efficient signal for GPI modification [7]. The role of FRs in the cellular transport of folate is not well understood, although a potocytosis (caveolin-coated endocytosis) model has been proposed [47]. FR- $\alpha$  was found to be clustered in a membrane region called caveolae or rafts [47]. While an elevated expression of FR has frequently been observed in various types of human tumors, the receptor is generally absent in normal tissues with the exception of the choroid plexus and placenta, with low levels in the lung, thyroid and kidney [48]. FR- $\alpha$  is frequently overexpressed in tumors, including ovarian, colorectal, breast, lung, renal cell carcinomas and brain metastases derived from epithelial cancers [6, 7]. FR- $\beta$  is frequently overexpressed in tumors of non-epithelial cell lineages such as sarcomas and acute myeloid leukemia [49], and FR- $\gamma$  is overexpressed in malignant hemopoietic cells [50]. The causes of FR overexpression in tumors are unclear, but high levels of FR may be associated with increased biological aggressiveness of carcinomas.

#### 9.4.2

##### Folate Receptor-targeting Liposomes

Liposomes used in recent studies have been coated with folate-PEG-lipid to facilitate tumor-targeting by an active mechanism (via FR) and a passive mechanism (prevention/reduction of RES uptake) [20, 51]. PEGylated lipids can significantly reduce non-specific gene transfer activity in the lung, and conjugation of the targeting ligand, folate, to the PEG chain can restore this activity in FR-positive tumors *in vivo* [20]. For intravascular targeting to access tumor cells expressing FR, liposomes must cross the vascular endothelium and diffuse into the interstitial fluid (Fig. 9.1) [51]. The theoretical advantage of FR-targeting over non-targeting is related to a shift in the distribution of the liposomes to the tumor cell compartment and delivery of the genes. The disadvantage of a system targeting a cancer cell receptor such as FR is the difficulty that a large nano-size assembly has in penetrating a solid tumor mass. Many cell types, including most tumor cells, display a low endocytotic capacity. Since the intracellular mechanism of FR-targeted gene deliv-

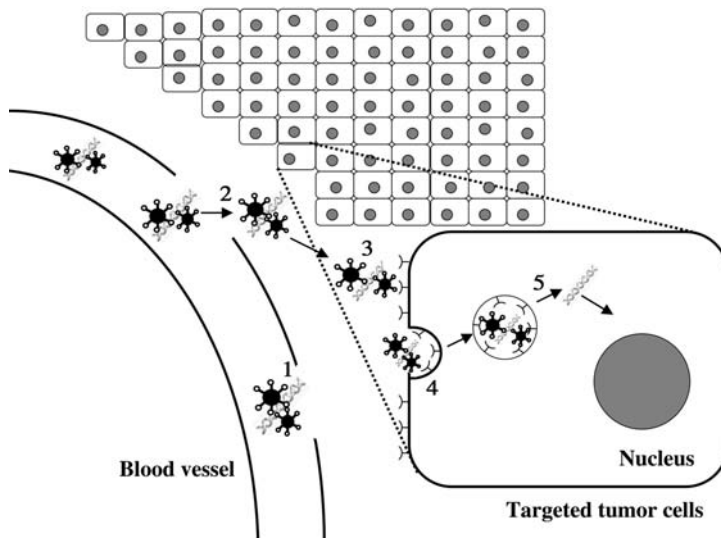


**Fig. 9.1.** Scheme illustrating the concept of using FR-targeting nanoparticles to deliver plasmid DNA to tumor cells. Dots and helices on the nanoparticles represent the folate ligands and plasmid DNA, respectively. The various steps involved in the targeting process are numbered 1–5. Steps 1 and 2 are common to non-targeted and FR-targeting nanoparticles mixed with plasmid DNA (nanoplex). Steps 3–5 are specific to the FR-targeting vector.

(1) long-circulating nanoplexes make more passages through the tumor microvasculature. (2) Increased vascular permeability in tumor tissue enables nanoplexes to extravasate and reach the tumor interstitial fluid. (3) FR-targeting nanoplexes bind to FR expressed on the tumor membrane via the folate ligand. (4) Nanoplexes are internalized by tumor cells via FR. (5) Internalized nanoplexes release their plasmid DNA in the cytoplasm.

ery with liposomes and nanoparticles is endocytosis, this is a serious limitation to the successful application of FR-targeted lipid-based particle delivery systems. The development of suitable delivery vectors for *in vivo* gene transfer is necessary for the clinical application of therapeutic genes.

Several cationic polymer–folate conjugates and/or cationic liposomes, and cationic nanoparticles incorporating folate-derivatives have been developed for FR-targeted gene delivery (Table 9.1). Folic acid retains its receptor-binding and endocytotic properties when covalently linked to a wide variety of molecules. Polyplexes are composed of charged complexes of plasmid DNA and a cationic polymer, such as poly-L-lysine (PLL), polyethylenimine (PEI) and polyamidoamine dendrimers. For FR-targeted gene delivery, PLL-folate [52–54], PLL-PEG-folate [55], PEI-folate [56], PEI-PEG-folate [56, 57], and poly(dimethylaminomethyl methacrylate) (pDMAEMA)-PEG-folate [58] have been synthesized (Fig. 9.2). These folate-conjugates facilitated efficient FR-targeted gene delivery without additional vector components *in vitro*. It appears that the incorporation of a long PEG spacer between folate and the cationic polymer is important for efficient FR-targeted gene delivery [54].

Tab. 9.1. FR-targeted nonviral vectors; all vectors were used in *in vitro* transfection.

Vector	Description	In vivo	Ref.
Polymer	Poly-L-Lys (PLL)	–	52–55
	Polyethylenimine (PEI)	–	56, 57
	Polydimethylamino methyl methacrylate (pDMAEMA)	–	58
Liposome	Cationic	i.v.	15, 17–20, 59
	Incorporating 0.1 mol% folate-PEG <sub>3350</sub> -DOPE, 5 mol% folate-DOPE, 0.5–5 mol% folate-PEG <sub>3400</sub> -DSPE or 5 mol% folate-PEG <sub>4600</sub> -cholesterol into liposome		
LPDI type	Polyplex prepared from protamine was mixed with cationic liposome containing 0.03 mol% folate-PEG <sub>3400</sub> -DSPE or 2 mol% folate-PEG <sub>5000</sub> -DSPE	i.p. i.v.	21, 60
LPDII type	Polyplex prepared from PLL or PEI was mixed with pH-sensitive anionic liposome containing 0.1 mol% folate-PEG <sub>3350</sub> -DOPE or folate-PEG <sub>3350</sub> -DSPE	–	16, 61
Nanoparticle	Polyplex prepared with cationic dithiol-detergent [(C <sub>14</sub> Corr) <sub>2</sub> ] was mixed with 1 or 2 mol% folate-PEG <sub>3400</sub> -DPPE	–	62
NPI-F, NPII-F	Incorporating 2 mol% folate-PEG <sub>2000</sub> -DSPE into cationic nanoparticle based DC-Chol	i.v. i.t.	63, 64, 73
NPIII-F	Incorporating 1 mol% folate-PEG <sub>2000</sub> -DSPE into cationic nanoparticle based OH-Chol	–	68

i.v.: intravenous injection, i.p.: intraperitoneal injection;

i.t.: intratumoral injection.



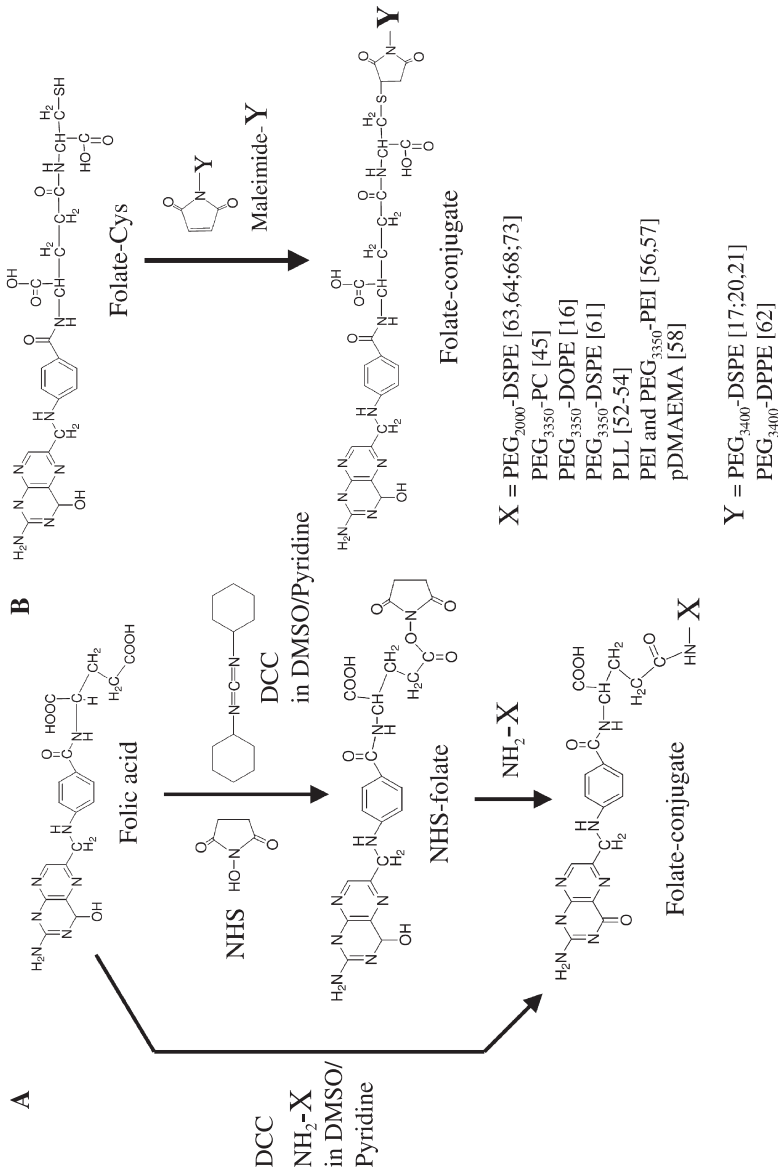


**Fig. 9.2.** Preparations of conjugation with folic acid. (A) N-Hydroxysuccinimidyl ester of folic acid (NHS-folate) is prepared by esterification of folic acid with N-hydroxysuccinimide (NHS) in the presence of 1,3-dicyclohexylcarbodiimide (DCC) and pyridine, and is then conjugated with amino-residues in targeted compounds (X). Alternatively, folic acid can be conjugated directly with compounds (X) in the presence of DCC and pyridine. (B) Folate-cysteine conjugate (Folate-Cys) is reacted with maleimide (MAL) conjugated with targeted compounds (Y).

Lipoplexes are composed of charge complexes of plasmid DNA and cationic liposome. Lipopolyplexes are composed of plasmid DNA attached to both polymers and lipids. Cationic liposomes are generally composed of a cationic lipid, such as dioleoyltrimethylammonium chloride (DOTMA), dioleoyltrimethylammonium propane (DOTAP), or 3-[*N*-(*N,N'*-dimethylaminoethanolamine)carbamoyl]cholesterol (DC-Chol), and a helper lipid, such as dioleoylphosphatidylethanolamine (DOPE) or cholesterol (Chol), which provides fusogenicity and stability to the lipoplex. Depending on the preparation, the lipoplex may not be a single aggregate, but an intricate structure in which the condensed DNA is surrounded by a lipid bilayer. FR-targeting cationic liposomes have been incorporated with folate-derivatives, folate-DOPE [59], folate-PEG-DOPE [15, 16], folate-PEG-DSPE [17–21, 60], folate-PEG-Chol [20], etc. (Fig. 9.2). Hofland et al. [20] have shown that both folate-PEG<sub>3400</sub>-DSPE and folate-PEG<sub>4600</sub>-Chol, when combined with a cationic lipid RPR209120 and DOPE, formed lipoplexes with greatly reduced normal tissue gene transfer and efficient *in vivo* tumor gene transfer.

LPDI-type lipoplexes (lipopolyplex) consist of a ternary complex of cationic liposomes, DNA-condensing polycation, and plasmid DNA. In a report by Reddy et al. [21], polyplexes prepared from protamine were mixed with cationic liposomes containing folate-PEG<sub>3400</sub>-DSPE as a targeting ligand and DOPE as a helper lipid. This vector showed superior transfection activity in FR-positive M109 murine lung carcinoma cells as well as in ascitic cells derived from L1210A murine lymphocytic leukemia cells. LPDII-type lipoplexes (lipopolyplex) consist of a ternary complex of anionic liposomes, DNA-condensing polycation, and plasmid DNA. Lee et al. [16] have reported a formulation of LPDII-type vector, in which DNA was first attached to PLL and then mixed with pH-sensitive anionic liposomes composed of DOPE/CHEMS/folate-PEG<sub>3350</sub>-DOPE. The pH-sensitive liposomes are fusogenic at acidic pH and thus can be used to facilitate endosomal disruption and subsequent release of plasmids in the cytoplasm. Shi et al. [61] have reported efficient gene delivery using an LPDII vector that incorporated PEI as a DNA-condensing agent and a cationic/anionic lipid pair, composed of dimethyldioctadecylammonium bromide (DDAB)/CHEMS/polyoxyethylene sorbitan monooleate (Tween80)/folate-PEG<sub>3350</sub>-DSPE.

## 9.5

### Folate-linked Lipid-based Nanoparticles

Preferential expression of a gene in tumor cells contributes to the safety and efficacy of gene therapy. For FR-targeted gene transfection, the concentrations of folic acid and linker in vectors are important.

#### 9.5.1

##### Formulations

For drug delivery, folate-targeting liposomes contained 0.1–0.5 mol% folate-PEG<sub>2000</sub>-DSPE or folate-PEG<sub>3400</sub>-DSPE for targeting, and about 4 mol% PEG<sub>2000</sub>-

DSPE was used for PEG-coating [8–13]. For gene delivery, FR-targeting liposomes and nanoparticles contained 0.03–5 mol% folate-PEG-lipid. Reddy et al. [21] have reported that a cationic liposome formulated with less than 0.03 mol% of folate-PEG<sub>3400</sub>-DSPE showed the greatest cell association. Folate moieties located at the distal end of the PEG spacers would likely not interact at concentrations lower than 0.03%. Bruckheimer et al. [60] have reported that 2 mol% folate-PEG<sub>3400</sub>-DSPE conjugate increased the cellular association with tumor cells and transfection potency. FR-targeting cationic nanoparticles incorporating 2 mol% folate-PEG<sub>3400</sub>-DPPE showed efficient FR-dependent cellular uptake and transfection [62], and cationic liposomes with 5 mol% folate-PEG<sub>4600</sub>-Chol showed high gene transfer activity into a FR-positive cell line, M109 [20]. Xu et al. [59] have reported specific *in vivo* gene delivery to tumors with a liposome containing about 5 mol% folate-DOPE. Dauty et al. [62] have reported that an FR-targeting cationic nanoparticle incorporating folate-PEG<sub>3400</sub>-DPPE and a cationic dithiol-detergent [dimerized tetradecyl-ornithinyl-cysteine, (C14Corn)<sub>2</sub>] shows efficient FR-dependent cellular uptake and transfection.

As a linker of folate, PEG of  $M_r$  2000–5000 has been used (Table 9.1). A certain distance between the folate moiety and the lipid particles is needed for FR-targeting, due to the need for folate to enter the binding pocket of FR on the cell surface. Lee et al. [45] first described the dependence of folate-liposome targeting on the distance between the folate and liposome, and reported that a PEG<sub>3400</sub> linker was necessary for the targeting. Leamon et al. [17] optimized the targeting activity of the liposomes by modifying the length of the PEG-linker, and found that PEGs as small as  $M_r$  1000 could function as effective linkers. Ward et al. [54] have reported that a folate-linked PEG<sub>800</sub>-polymer-modified PLL/DNA complex did not lead to a significant increase in *in vitro* transgene expression. A PEG spacer with  $M_r > 1000$  might be essential for FR-targeting.

Folate-linked microemulsions have been used composed of 0.24 mol% folate-lipid (F0/M), folate-PEG<sub>2000</sub>-DSPE (F2/M) or folate-PEG<sub>5000</sub>-DSPE (F5/M) for targeting, and 6.7 mol% PEG<sub>2000</sub>-DSPE for PEG-coating and forming emulsion (Fig. 9.3) [14]. Selectivity of folate-linked microemulsions for delivery into KB cells was validated by flow cytometry (Fig. 9.4). The mean fluorescence intensities of F5/M

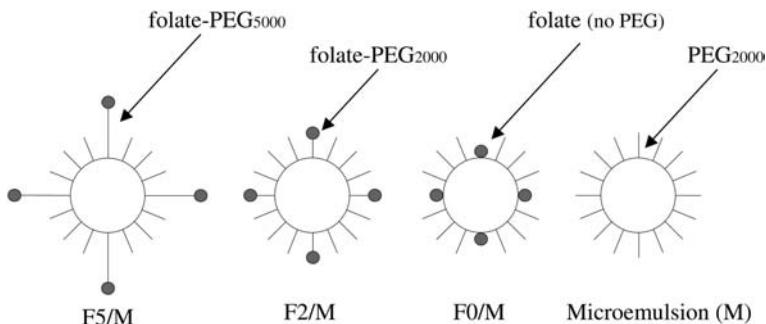
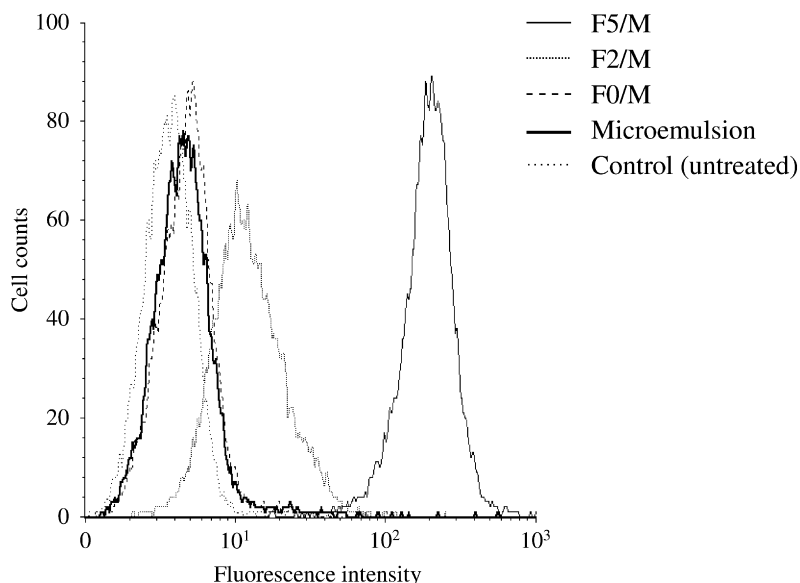


Fig. 9.3. Schematic diagrams of the microemulsion and the folate-linked microemulsions.



**Fig. 9.4.** Association of 1,1'-dioctadecyl-3,3,3',3'-tetramethylindocarbocyanine perchlorate (DiI)-labeled F5/M, F2/M, F0/M and microemulsion with KB cells after 1 h incubation was analyzed by flow cytometry. [14]

and F2/M had ca. 200- and 4-fold greater association than non-folate microemulsion, respectively. In contrast, F0/M showed a similar curve to non-folate microemulsion. These results correspond well with the idea that conjugating folate to a shorter PEG polymer reduces folate exposure by interference with the ability of liposome to interact with FR [9]. Additionally, these increased associations of F5/M and F2/M could be blocked completely by adding 2 mM free folic acid to the medium [14]. Extending the PEG-chain length of the folate-PEG-lipid from 0 to  $M_r$  2000, and  $M_r$  2000–5000, dramatically improved the selective FR-mediated association and the cytotoxicity of folate-linked microemulsions loading anticancer drug *in vitro* [14].

Folate-linked nanoparticles (NPI), consisting of 1 mg mL<sup>-1</sup> DC-Chol as a cationic lipid, 5 mol% conventional Tween 80 (about 50% pure), and 0–1 mol% folate-PEG<sub>2000</sub>-DSPE (f-PEG<sub>2000</sub>-DSPE) or folate-PEG<sub>5000</sub>-DSPE (f-PEG<sub>5000</sub>-DSPE), respectively, have been prepared by a modified ethanol injection method [63, 64]. All nanoparticles were about 100–200 nm in size, with an  $\zeta$ -potential of about 50 mV. Here the definition of a lipid-based nanoparticle is a formula containing no bilayers like liposomes. Cholesterol derivatives are usually unable to form stable bilayers unless used in combination with DOPE or some other neutral lipid. Therefore, these particles may be nanoparticles. Figure 9.5 illustrates some folate-linked nanoparticles.

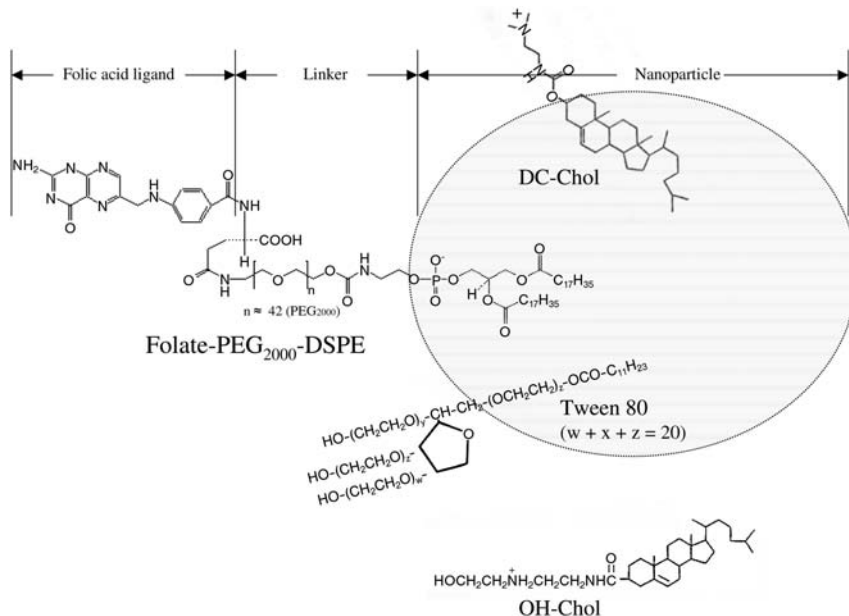


**Fig. 9.5.** Schematic structure of folate-linked nanoparticles composed of folate-PEG<sub>2000</sub>-DSPE, DC-Chol, OH-Chol and Tween 80 (NPI-, NPII-, NPIII-F).

### 9.5.2

#### Nanoplex and Transfection Activity *In Vitro*

Nanoplexes are composed of charged complexes of plasmid DNA and cationic nanoparticles. The size of nanoplexes of NPI with 0.3 mol% f-PEG<sub>2000</sub>-DSPE at a charge ratio (+/-) of cationic nanoparticle to DNA of 3:1 in the presence of 50% serum increased up to 940 nm. Nanoplexes of NPI with 1 mol% f-PEG<sub>5000</sub>-DSPE did not increase greatly in size in serum-containing medium, but showed lower transfection activity than that with 1 mol% f-PEG<sub>2000</sub>-DSPE [63].

Folate-linked nanoparticles (NPII) have been composed with the same composition as NPI with 1–3 mol% f-PEG<sub>2000</sub>-DSPE except for the substitution of Tween 80 (purity 99%) for conventional Tween 80. Each NPII was, on average, ca. 100–200 nm [64] (Table 9.2). Three mol% of f-PEG<sub>2000</sub>-DSPE may not be incorporated in NPII because no reduction in the  $\zeta$ -potential of NPII was seen upon the addition of f-PEG<sub>2000</sub>-DSPE (about 55 mV) [64]. The concentration of f-PEG<sub>2000</sub>-DSPE in an ethanol–water mixture to prepare NPII-2F containing 2 mol% f-PEG<sub>2000</sub>-DSPE, and NPII-3F containing 3 mol% f-PEG<sub>2000</sub>-DSPE, was about 40 and 60  $\mu\text{M}$ , respectively. f-PEG<sub>2000</sub>-DSPE below the critical micelle concentration (c.m.c.) might lead to efficient incorporation into the particles. However, f-PEG<sub>2000</sub>-DSPE above the c.m.c. may help to stabilize micellized f-PEG<sub>2000</sub>-DSPE and lead to inefficient insertion into the particle. The c.m.c. of f-PEG<sub>2000</sub>-DSPE may be between 40 and 60  $\mu\text{M}$

Tab. 9.2. Formulae, particle size and  $\zeta$ -potential of folate-linked nanoparticles (NPII) and their nanoplexes [64].

Formulation	Mol (%)		Nanoparticle		Nanoplex <sup>[a]</sup>		
	DC-Chol	Tween 80	folate-PEG <sub>2000</sub> -DSPE (F)	Size (nm)	$\zeta$ -potential (mV)	Size (nm)	$\zeta$ -potential (mV)
	NPII	95	5	–	117.2 ± 2.0	53.1 ± 2.5	354.9 ± 8.8
NPII-1F	94	5	1	146.1 ± 12.4	43.9 ± 1.7	515.2 ± 32.3	34.2 ± 1.6
NPII-2F (NPII-F)	93	5	2	165.3 ± 22.1	38.6 ± 1.5	233.7 ± 6.5	30.8 ± 1.9
NPII-3F	92	5	3	118.4 ± 4.3	54.8 ± 6.3	396.0 ± 7.8	35.1 ± 0.9

Nanoparticles prepared with lipids [e.g. DC-Chol/Tween 80/ folate-PEG<sub>2000</sub>-DSPE = 94/5/2, molar ratio = 10:1.3:1.3, weight (mg)] in 10 mL of water by a modified ethanol injection method. Nanoparticles consisted of 1 mg mL<sup>-1</sup> DC-Chol and 5 mol% Tween 80 with 0, 1, 2 and 3 mol% folate-PEG<sub>2000</sub>-DSPE (NPII, NPII-1F, NPII-2F and NPII-3F, respectively). The particle size and  $\zeta$ -potential were measured after the nanoparticle and nanoplex were diluted with water. Charge ratio (+/-) of nanoparticle/DNA = 3:1. Each value represents the mean ± SD (*n* = 3).

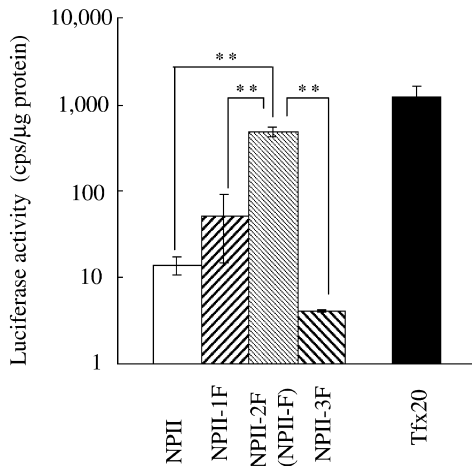


**Fig. 9.6.** Comparison of transfection efficiency in KB cells with luciferase expression between NPII nanoparticles and Tfx20. The NPII nanoplex and the lipoplex were prepared by mixing luciferase plasmid (2 μg) with the luciferase gene under the control of the cytomegalovirus (CMV) promoter, with

nanoparticles and Tfx20, respectively. The luciferase assay was carried out 24 h after incubation of nanoplexes in the medium with 10% serum. Each column represents the mean  $\pm$  S.D. ( $n = 3$ ).  $**P < 0.01$ , compared with NPII-F. NPII-F refers to the formulation in Table 9.2.

and might affect the incorporation of f-PEG<sub>2000</sub>-DSPE in NPII-3F with 3 mol% f-PEG<sub>2000</sub>-DSPE.

In the presence of 10% and 50% serum, NPII-2F with 2 mol% f-PEG<sub>2000</sub>-DSPE (NPII-F) formed injectable-sized nanoplexes (Table 9.2), which showed the highest transfection efficiency among NPII with 0–3 mol% f-PEG<sub>2000</sub>-DSPE, at the optimal charge ratio (+/–) of 3:1 in nasopharyngeal cancer KB cells, being comparable to Tfx20, a commercially available DNA transfection reagent (Fig. 9.6) [64].

### 9.5.3

#### Selectivity of Folate-linked Nanoparticle

NPII-F showed greater transfection efficiency in human prostate cancer LNCaP cells, human prostate adenocarcinoma PC-3 cells, and human cervix carcinoma HeLa cells, than in KB cells, in the comparison with Tfx20 (Fig. 9.7A). There were three FR isoforms,  $\alpha$ ,  $\beta$  and  $\gamma$ , each with a distinctive tissue distribution. FR- $\alpha$  mRNA was expressed strongly in KB and HeLa cells, but not in either LNCaP or PC-3 cells (Fig. 9.7B). FR- $\beta$  and - $\gamma$  mRNAs were not detected in any of the cell lines using the RT-PCR method. Reduced folate carrier (RFC), a carrier-mediated folate transporter, was weakly expressed in all cell lines examined (Fig. 9.7B). Cellular uptake of NPII-F in HeLa and KB cells was mediated via FR- $\alpha$ , following the induction of transfection activity. The selectivity of NPII-F to carry genes into KB cells

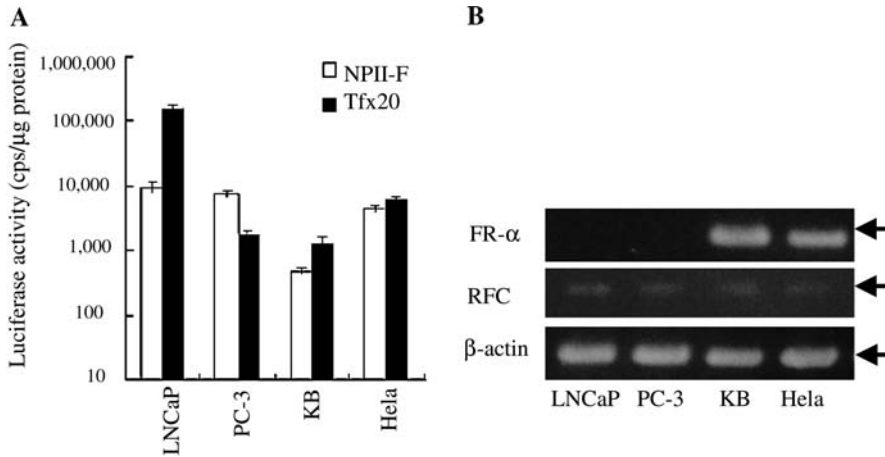


**Fig. 9.7.** Comparison of transfection efficiency between NP11-F and Tfx20 in the NP11-F nanoplexes and Tfx20 lipoplex delivered with the luciferase plasmid into various cell lines (A). Each column represents the mean  $\pm$  S.D. ( $n = 3$ ). FR- $\alpha$ , RFC and  $\beta$ -actin mRNA expression were detected in various cell lines by RT-PCR (B). NP11-F refers to the formulation in Table 9.2.

was validated using FITC-oligodeoxynucleotide (FITC-ODN) from the result of a competitive experiment in the presence of folic acid by flow cytometry [64].

In LNCaP and PC-3 cells, FR mRNAs were not often observed. In the human prostate, a high-affinity folate binding protein has been characterized [65] and folic acid binds to the membrane fraction that cross-reacts with the anti-prostate-specific membrane antigen (PSMA) antibody. PSMA is a transmembrane protein with a pattern of overexpression restricted to malignant human prostate tissue and LNCaP cells [66]. The physiological role of PSMA in prostate cancer remains unknown, but PSMA shows hydrolase enzymatic activity with a folate substrate [66] and is internalized via an endocytic mechanism [67]. If PSMA functions as a receptor mediating the internalization of a putative ligand similar to folic acid, this suggests that the folate-linked nanoparticle binds to PSMA and is then taken up via an endocytic mechanism by LNCaP cells as we reported [63].

In PC-3 cells, our study using RT-PCR confirmed the presence of RFC mRNA, but found no FR or PSMA mRNA [64]. A FITC-labeled folate-BSA conjugate was taken up by PC-3 cells and the cellular association was significantly decreased in the presence of 1 mM folic acid [64]. Xu et al. [59] also reported that a folate-cationic liposome system could mediate gene therapy with p53 antisense DNA in prostate cancer (DU145 cells). We found that NP11-F is a useful vector for transfection in prostate androgen-dependent and -independent cancer cells as well as KB cells.

Nanoparticles composed of cholesteryl-3 $\beta$ -carboxyamidoethylene-*N*-hydroxylamine (OH-Chol) instead of DC-Chol (NP11) could incorporate up to 5 mol% f-PEG<sub>2000</sub>-DSPE (Fig. 9.5). For FR-targeted vectors, NP11-1F (NP11-F), -2F and -5F



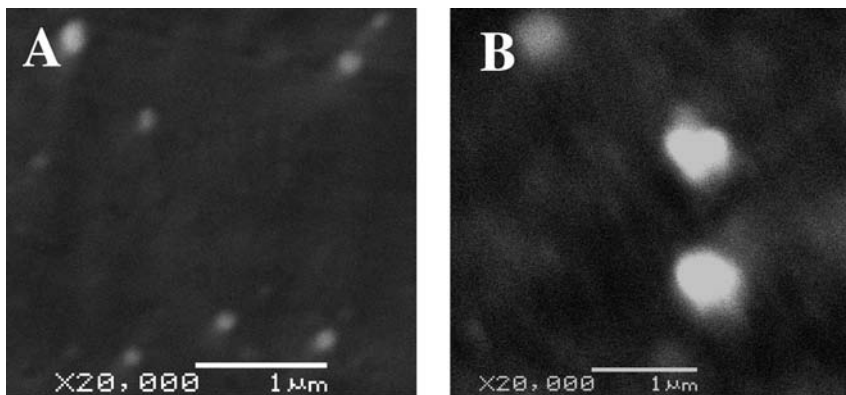


**Fig. 9.8.** Scanning electron micrographs of NPIII-F nanoparticles (A) and NPIII-F nanoplexes (B). In (B), NPIII-F nanoparticles, NPIII with 1 mol% folate-PEG<sub>2000</sub>-DSPE, were mixed for 10 min at a charge ratio (+/–) of 3:1 with plasmid DNA in water. The method used to visualize the nanoparticles and

nanoplexes was adapted [44]. Briefly, aliquots of 10 μL prepared samples were placed on the copper platform and dried. The nanoparticle and nanoplex layers on the copper platform were coated with platinum and observed with a scanning electron microscope (SEM).

consisted of NPIII with 1, 2 and 5 mol% f-PEG<sub>2000</sub>-DSPE, respectively. The average size of each nanoparticle was 100–200 nm (Fig. 9.8A) [68]. When the NPIII nanoparticles were mixed with DNA at a charge ratio (+/–) of 3:1 in water, each NPIII nanoplex increased from 250 to 300 nm (Fig. 9.8B) [68]. When the amount of f-PEG<sub>2000</sub>-DSPE in NPIII was increased, association of plasmid DNA with nanoparticles was inhibited significantly (Fig. 9.9) and a reduction in luciferase activity was observed [68]. A large amount of f-PEG<sub>2000</sub>-DSPE in nanoparticles might prevent enough DNA being carried into the cells, and/or reduce the cellular association with the nanoplex as reported in PEG-lipid [69]. The NPIII-F based on OH-Chol exhibited about 40× higher transfection efficiency than the NP-II-F based on DC-Chol in KB cells [64, 68]. The hydroxyl group of OH-Chol reportedly reduced the stability of the lipoplex, and enhanced transfection efficiency by facilitating the process by which DNA was liberated from the endosome [70].

It is reported that a negatively charged folic acid forms a charge-mediated complex with positively charged particles through its carboxyl groups and has an effect on transfection efficiency [71]. We prepared nanoplexes in water at a charge ratio (+/–) of 1:1 to protect to form complex for co-incubation of the positively charged NPIII with folic acid in the medium, and then incubated them with KB cells. Cellular association of FR-targeting NPIII occurred via FR and the interaction of 1 mol% f-PEG<sub>2000</sub>-DSPE in the NPIII with FR was higher than that of 2 and 5 mol% ones (Fig. 9.10). NPIII-F with 1 mol% f-PEG<sub>2000</sub>-DSPE nanoplexes at a charge ratio (+/–) of NP-F to DNA of 1:1 exhibited higher selectivity to FR, but lower transfection activity relative to that at a charge ratio (+/–) of 3:1 *in vitro*

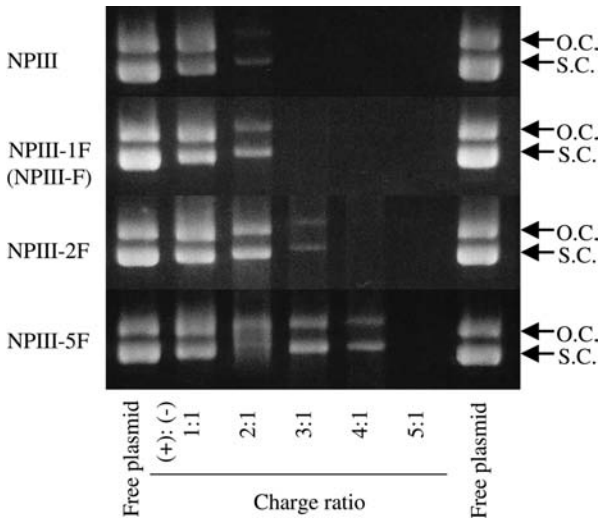


**Fig. 9.9.** Association of plasmid DNA with NPIII nanoplexes formed in water at various charge ratios (+/-), analyzed using agarose gel electrophoresis. One microgram of Plasmid DNA was mixed with aliquots of NPIII at various charge ratios in water. After a 10 min incubation, the nanoplexes were analyzed by 1.5% agarose gel electrophoresis. Charge

ratios (+/-) of nanoparticle:plasmid DNA = 1:1, 2:1, 3:1, 4:1 and 5:1. O.C. indicates open circular plasmid; S.C. indicates supercoiled plasmid. NPIII refers to the formulation in Table 9.2, substituting OH-Chol for DC-Chol. NPIII-F contains NPIII with 1 mol% folate-PEG<sub>2000</sub>-DSPE.

[68]. From a competitive experiment of luciferase assay in the presence of free folic acid in the medium, gene expression of the NPIII-F with 1 mol% f-PEG<sub>2000</sub>-DSPE nanoplexes was reduced [68]. For selectivity and transfection activity in FR-targeted gene delivery, the charge ratio of folate-linked lipid-based nanoparticles to DNA needs to be optimized.

#### 9.5.4

##### **Transfection Activity *In Vivo***

Both systemic and local administration offers several biological opportunities for gene therapy. The systemic route allows non-invasive access to many target cells that are not accessible otherwise by direct administration. Folate-linked liposomes showed efficient FR-dependent cellular uptake and transfection *in vitro*. However, the use of a folate ligand as a targeting ligand to deliver DNA has not been successful in *in vivo* gene therapy [20, 21]. The major limitation of *in vivo* gene therapy using liposomes is the low transfection efficiency. Several factors can adversely affect FR-targeted gene transfer *in vivo*. The first is the presence of endogenous folate in the systemic circulation, which potentially can block FR-binding. Plasma folic acid may interfere with the binding of FR. The human serum folic acid con-

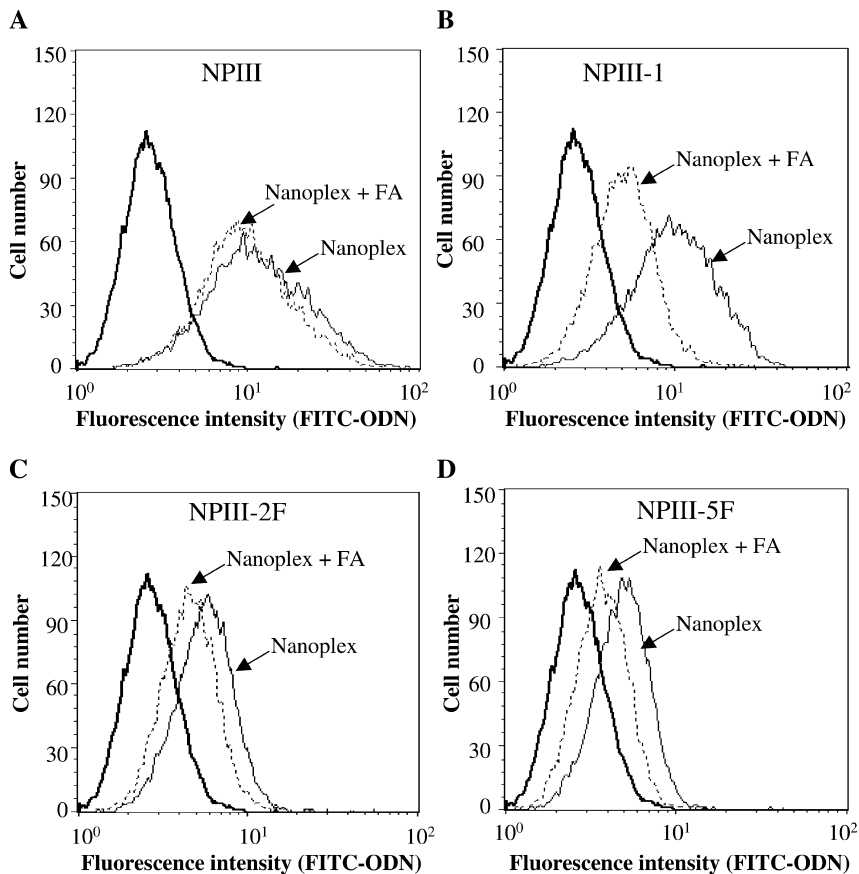


**Fig. 9.10.** Association of FITC-labeled NPIII nanoplex formed in water with KB cells 3 h after transfection in the absence or presence of free folic acid. Each NPIII nanoparticle was mixed with 2  $\mu\text{g}$  of FITC-ODN at a charge ratio (+/-) of 1:1. Association was determined based on FITC-fluorescence by flow cytometry.

Flow cytometry of cells exposed to the nanoplex (continuous line). Dotted line, plus 1 mM folic acid (FA); Bold line, autofluorescence of the cells. NPIII refers to the formulation in Table 9.2, substituting OH-Chol for DC-Chol. NPIII-F contains NPIII with 1 mol% folate-PEG<sub>2000</sub>-DSPE.

centration, following FDA-mandated dietary supplementation, is  $\sim 42$  nM [72]. Earlier reports [45] indicated that serum folic acid at this concentration should not inhibit significantly the binding of FR mediated by liposomes. Our recent study [64] showed that mice on a folate-deficient were actually able to maintain a plasma folate level within the physiologic range of humans diet. In contrast, mice on a normal diet maintained a much higher serum concentration of folic acid. Therefore, mice on a folate-deficient diet should be considered relevant to humans with respect to serum folate levels. A second concern is that the size of gene transfer vectors, escaping the vasculature and intratumoral diffusion, could be limiting to

targeted delivery. To address this issue, formulation parameters can potentially be optimized to improve the pharmacokinetic properties of the vectors. For example, the vector can be PEGylated to reduce plasma protein binding and RES uptake, resulting in an extended systemic circulation time [35]. In addition, the vector should be kept under 300 nm since this is the approximate limit for efficient tumor extravasation. Non-specific cell uptake by the RES (e.g., Kupffer cells in the liver) is expected to be reduced by incorporating PEGylated lipid within the lipid–DNA complex.

When the NP-II-F nanoplex was injected via a tail vein, DNA in the blood was still detectable 4 h later by PCR [73]. Free DNA has an extremely short  $T_{1/2}$  in blood (0.5–1 h), depending on the DNA dose [38, 74]. The NP-II-F seemed to keep the DNA stable in circulation by forming a nanoplex. NP-II-F induced greater gene expression in liver and kidney than NP (unpublished data). FR is on the brush borders of proximal renal tubes and provides for the reabsorption of folate. Recently, Paulos et al. discovered that activated liver-derived macrophages (Kupffer cells) in mice do express the FR [75]. Kupffer cells in the liver and the tubular cells in kidneys of mice may be responsible for capturing NP-II-F by FR. Therefore, FR-targeted delivery of therapeutic genes damages normal cells in organs such as the liver and kidney and may subsequently cause death [13]. For cancer gene therapy, using a tumor-specific promoter to regulate expression transcriptionally in target cancer cells has promise. It will be essential to use a strong and tissue-specific promoter region if a therapeutic gene is to be selectively expressed in the cancer cells.

Intraperitoneal and intratumoral injections of lipoplex and nanoplex have been applied in mice bearing tumors. Reddy et al. [21] have reported that maximum *in vivo* transfection activity of reporter gene (luciferase) occurred with intraperitoneally administered folate-liposome using a disseminated intraperitoneal L1210A tumor model. When the NP-II-F nanoplexes of the luciferase plasmid were injected directly into the nasopharyngeal tumor, KB, xenografts, NP-II-F showed about 100-fold more luciferase activity than Tfx20, suggesting that the NP-II-F nanoplex remained small enough to migrate into the tumorous tissue [64].

## 9.6

### Application of Suicide Gene Therapy

Cancer gene therapy has become an increasingly important strategy for treating various human diseases [1]. Currently, cancer gene therapy is being researched, especially in the field of cancer treatment [76]. Suicide gene therapy is a strategy whereby a gene is introduced into cancer cells, making them sensitive to a drug that is normally non-toxic. The suicide genes used often encode enzymes that metabolize non-toxic prodrugs into toxic metabolites. One of the most frequently used suicide genes is the herpes simplex virus thymidine kinase (HSV-tk) gene [77], which phosphorylates a prodrug, ganciclovir (GCV), into a toxic form (GCV triphosphate, GCV-PPP). GCV, an acyclic analog of natural nucleoside 2'-deoxyguanosine, is an antiviral agent used against human cytomegalovirus, herpes simplex

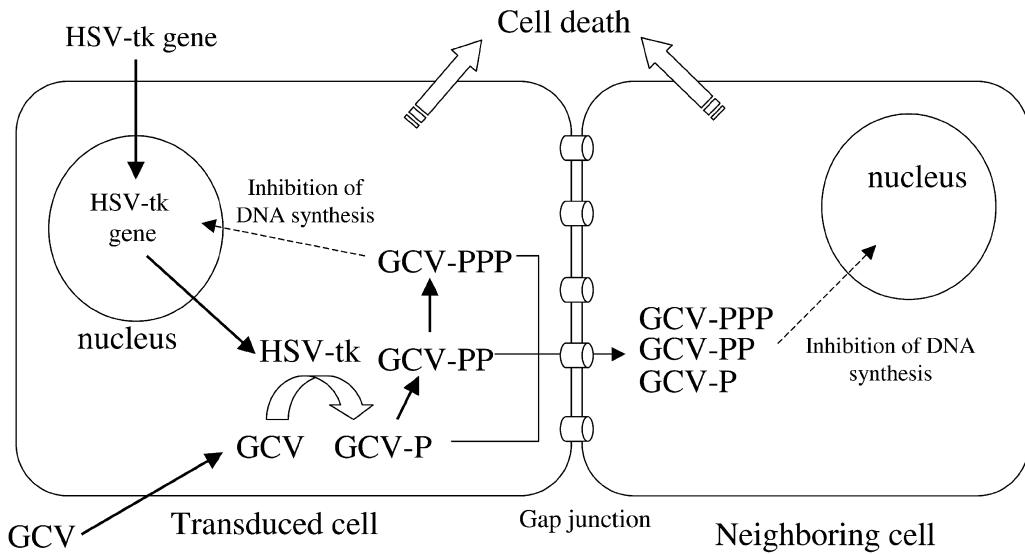


**Fig. 9.11.** Schematic representation of the HSV-tk/GCV system's mode of action and the bystander effect. In HSV-tk-transduced cells, GCV is intracellularly phosphorylated and converted into the triphosphate derivative (GCV-PPP), which acts as a competitive inhibitor of deoxyguanosine triphosphate. The production of GCV monophosphate (GCV-P) appears to be catalyzed by HSV-tk in the transduced cells. Subsequent formation of the

diphosphate and triphosphate GCV derivatives (GCV-PP and -PPP) is catalyzed by cellular guanylate kinase. After incorporation of GCV-PPP into DNA, the synthesis of DNA is immediately inhibited in the cells and this leads to cell death. Cell to cell transfer of HSV-tk-activated GCV between HSV-tk-transduced tumor cells and neighboring cells via gap junctions is a major mechanism of the widespread tumor-cell death (bystander effect).

virus type 1 and 2, varicella zoster virus and Epstein-Barr virus [78]. The effect appears when GCV is intracellularly phosphorylated and converted into the triphosphate derivative GCV triphosphate, which acts as a competitive inhibitor of deoxyguanosine triphosphate (Fig. 9.11) [77]. GCV monophosphate (GCV-P) production appears to be catalyzed in the cells transfected with HSV-tk gene. Subsequent formation of the diphosphate and triphosphate GCV derivatives (GCV-PP and -PPP) is catalyzed by cellular guanylate kinase. GCV-PPP, due to its analogy with the purinic nucleotide 2'-deoxyguanosine triphosphate, becomes substrate for DNA polymerase. Once bound to DNA polymerase, GCV-PPP is either incorporated into DNA or inhibits the polymerase. Consequently, chain termination immediately occurs after GCV incorporation into DNA, and leads to cell death [79].

A powerful characteristic of HSV-tk/GCV therapy is that the transduction of a small fraction of tumor cells with the suicide gene can result in widespread tumor-cell death (bystander effect) (Fig. 9.11). The cell to cell transfer of HSV-tk-activated GCV between HSV-tk-transduced tumor cells and neighboring unmodified cells via gap junctions is a major mechanism of the bystander effect [80, 81]. Gap junctions are composed of connexin subunits and connect the cytoplasmic do-

mains of contacting cells, allowing ionic and metabolic exchange between them [82]. However, many cancer cell lines are deficient in gap junctions [83]. Such a deficiency, which is also found in human tumors [84], can limit the extent of the bystander effect in suicide gene therapy. The bystander effect has been reported to be enhanced by introducing a connexin gene with the HSV-tk gene *in vitro* [81]. In the normal human prostate, the cells communicate via gap junctions, whereas in poorly differentiated prostate cancer the expression of connexin 43 (Cx43) decreased and gap junctional intracellular communication failed [83, 84]. Transfection of the Cx43 gene into a Cx43-deficient prostate cancer cells may enhance the bystander effect, and also has been reported to inhibit cell growth, retard tumorigenicity and induce differentiation [85].

The use of a folate ligand as a targeting ligand to deliver DNA has not been successful in *in vivo* gene therapy [20, 21]. In prostate cancer, suicide gene therapy by local injection using adenoviral vectors has been reported as an alternative treatment [86, 87]. The use of non-viral vectors is a novel approach. A NP-II-F nanoplex of HSV-tk was transiently transfected into KB, LNCaP and PC-3 cells. The first evidence of transfection was that GCV-PPP, the most abundant triphosphate produced, was clearly detected in LNCaP cells transfected with the HSV-tk gene after incubation with GCV by HPLC [73]. These findings were also made in KB and PC-3 cancer cells [64]. Further evidence was that HSV-tk plasmid-transfected LNCaP cells showed significantly greater sensitivity to GCV than the controls ( $IC_{50}$   $9.4 \mu\text{g mL}^{-1}$ ) (Fig. 9.12A). Cx43 plasmid-transfected cells showed significantly higher sensitivity to GCV ( $IC_{50}$   $62.4 \mu\text{g mL}^{-1}$ ) than the controls. Cells co-transfected with HSV-tk and Cx43 plasmids exhibited increased sensitivity to GCV ( $IC_{50}$   $7.9 \mu\text{g mL}^{-1}$ ). This result suggests that HSV-tk and Cx43, individually, induced a cytotoxic effect by GCV in the transfected cells, and that the combination of HSV-tk plus Cx43 genes may display a bystander effect. HSV-tk plasmid-transfected PC-3 cells showed significant sensitivity to GCV ( $IC_{50}$   $6.6 \mu\text{g mL}^{-1}$ ) compared with the controls, but Cx43 plasmid-transfected cells did not (Fig. 9.12B) [64]. Sensitivity to GCV was not enhanced in cells transfected with HSV-tk plus Cx43 plasmids. This result suggests that Cx43 plasmid did not display a bystander effect in PC-3 cells.

The *in vivo* anti-tumor effect of the NP-II-F nanoplex with the HSV-tk gene has been evaluated. First, we determined the anti-tumor effect by direct injection into KB tumor xenografts with the NP-II-F nanoplex of HSV-tk. When KB cells were transiently transfected with the NP-II-F nanoplex using various plasmids, HSV-tk, Cx43 plasmid and combinations thereof, the HSV-tk-transfected cells showed significant sensitivity to GCV compared with the control, but did not with cells co-transfected with HSV-tk and Cx43 plasmids (unpublished data). Therefore, HSV-tk plasmid was used as a therapeutic gene for KB xenograft. When the NP-II-F nanoplex of the HSV-tk plasmid was injected directly into the tumor, the growth of KB nasopharyngeal tumors was inhibited significantly in mice treated with the plasmid on day 13 (Fig. 9.13A). A comparison of tumor weight and appearance after excision also demonstrated that the tumor growth was attenuated in mice treated with the plasmid (Fig. 9.13B and C) [64].

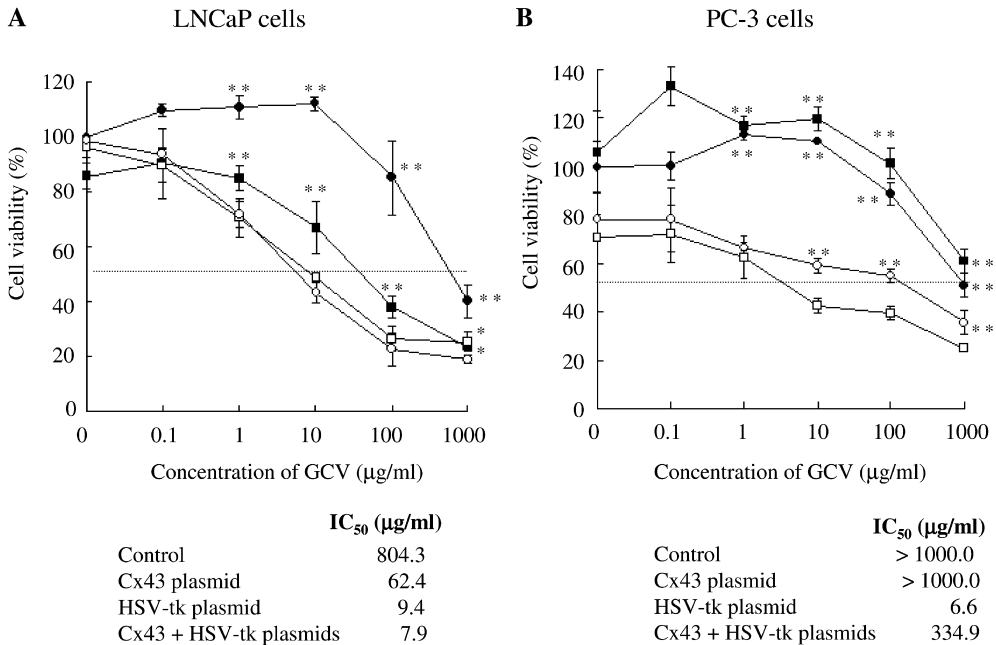


**Fig. 9.12.** Sensitivity of LNCaP (A) and PC-3 (B) cells to GCV. Cells were transfected with various plasmids using NP11-F. After 12 h incubation, the culture medium was replaced with one containing a concentration of GCV ranging from 0.1 to 1000  $\mu\text{g mL}^{-1}$ . Plasmids used were: control plasmid (●), HSV-tk (□), Cx43 (■), and HSV-tk plus Cx43 plasmids (○).

The number of surviving cells was determined with a WST-8 assay after 4 days exposure to the GCV. Data points indicate the mean  $\pm$  S.D. ( $n = 3$ ). \* $p < 0.05$  and \*\* $p < 0.01$ , compared with HSV-tk and Cx43 plasmids in (A). \*\* $p < 0.01$ , compared with HSV-tk plasmid in B [64].

We then evaluated the anti-tumor effect by direct injection into LNCaP tumor xenografts with the NP11-F nanoplex of HSV-tk plus Cx43 plasmid (Fig. 9.14), because this nanoplex was the most effective in *in vitro* experiments with LNCaP cells (Fig. 9.12A). Tumor growth was suppressed in mice treated with the NP11-F nanoplex of HSV-tk plus Cx43 plasmids, but not in the control mice. The mean survival times of the control mice and the mice treated with the nanoplex of HSV-tk plus Cx43 plasmids were 21.5 and 33 days, respectively [64]. The observed reduction in tumor size may not be wholly due to the direct effect of the phosphorylated GCV on the transduced tumor cells. An indirect mechanism (the bystander effect) might be contributing to the antitumor activity. It is reported that a 1–5% *in vivo* transfection efficiency could generate a significant anti-tumoral effect in suicide gene therapy [88]. However, a deficiency of gap junctions is found in human prostate tumors [83, 84], which may limit the extent of the bystander effect in suicide gene therapy. Therefore, to examine the *in vivo* anti-tumor effects of direct injection into LNCaP prostate xenografts, the nanoplex of HSV-tk plus Cx43 plasmids was used, with the result that the tumor growth was suppressed [64] (Fig. 9.14).

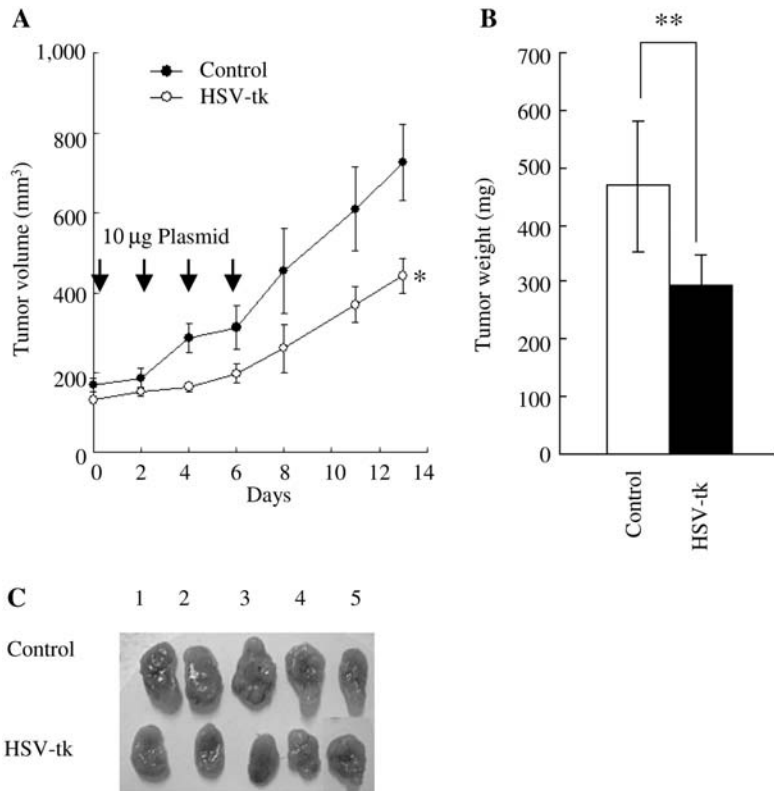


**Fig. 9.13.** *In vivo* suicide gene therapy for KB tumor xenografts with GCV in mice. Mice were divided into two groups: group I, control plasmid (10  $\mu\text{g}$ ); group II, HSV-tk plasmid (10  $\mu\text{g}$ ). NP11-F nanoplexes of the plasmids were injected directly into the tumor four times (day 0, 2, 4, and 6). GCV (25  $\text{mg kg}^{-1}$ ) was administered i.p. at 24 and 36 h after the

injections. Tumor volume (A), excised tumor weight (B) and macroscopic tumor appearance (C) when all the mice in Fig. 9.13(A) were sacrificed at day 14. The results are indicated in (A) and (B) as the mean volume and weight  $\pm$  S.E. or S.D., respectively ( $n = 5$ ). \* $P < 0.05$  and \*\* $P < 0.01$ , compared with control [64].

## 9.7 Conclusions

We have shown that folate-linked lipid-based nanoparticles can deliver DNA with high transfection efficiency and selectivity, inhibiting tumor growth following intratumoral injection into human nasopharyngeal and prostate cancer using an HSV-tk/GCV therapy system. These findings indicate that folate-linked lipid-based nanoparticles have potential as a clinically effective vector in cancer suicide gene therapy. However, several factors have the potential to adversely affect FR-targeted gene transfer *in vivo*. The size of gene transfer vectors, escaping the vasculature and intratumoral diffusion, could be limiting to targeted delivery. They should be



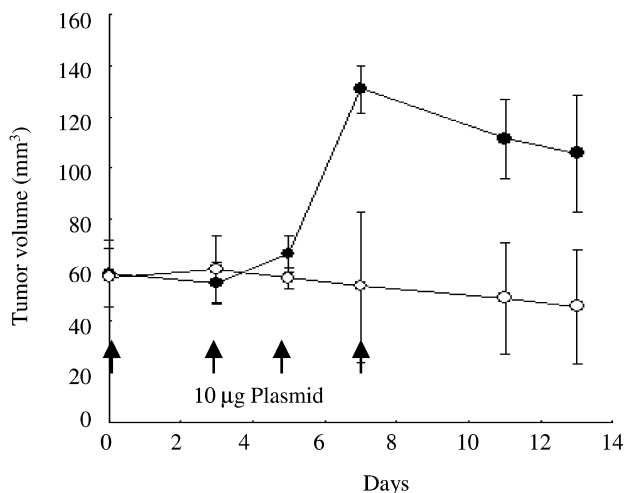


**Fig. 9.14.** Suicide gene therapy for LNCaP tumor xenografts with GCV in mice. Mice were divided into two groups: group I, control plasmid (●); group II, HSV-tk plus Cx43 plasmids (○). NPII-F nanoplexes of the plasmids indicated were injected directly into the tumor four times (day 1, 3, 5, and 7). GCV ( $25 \text{ mg kg}^{-1}$ ) was administered i.p. at 24 and 36 h after the injections. The results are indicated as the mean volume  $\pm$  S.E. ( $n = 6$ ) [64].

kept under 300 nm since this is the approximate limit for long circulation and efficient tumor extravasation. In addition, PEGylated vectors can reduce plasma protein binding and RES uptake, resulting in an extended systemic circulation time. Non-specific cell uptake by the RES (e.g., Kupffer cells in the liver) is expected to be reduced by incorporating PEGylated lipid within the particle/DNA complex. However, PEGylated particles may prevent enough DNA being carried into cells by inhibition of association of plasmid DNA with particles. For gene therapy, a balance of long-circulating vectors and FR-targeting vectors will be key to using folate-PEG-lipid. Further efforts aimed at optimizing FR-targeting vector formulations from a systemic approach should lead to the clinical evaluation of these vectors for cancer gene therapy.

### List of Abbreviations

CHEMS	Cholesteryl hemisuccinate
Chol	Cholesterol
DC-Chol	3-[N-(N',N'-dimethylaminoethane)carbamoyl]cholesterol
DOPE	Dioleoylphosphatidylethanolamine
DPPE	Dipalmitoyl phosphatidylethanolamine
DSPE	Distearoyl phosphatidylethanolamine
FR	Folate receptor

GCV	Ganciclovir
HSV-tk	Herpes simplex virus thymidine kinase
OH-Chol	Cholesteryl-3 $\beta$ -carboxyamidoethylene-N-hydroxylamine
ODN	Oligodeoxynucleotide
PEG	Poly(ethylene glycol)
PEI	Polyethylenimine
PLL	Poly-L-lysine
PEG-DSPE	Poly(ethylene glycol)-distearoylphosphatidylethanolamine
PSMA	Prostate specific membrane antigen
RES	Reticuloendothelial systems
RFC	Reduced folate carrier

## References

- DASS, C. R., BURTON, M. A. Lipoplexes and tumours. A review. *J. Pharm. Pharmacol.*, **1999**, *51*, 755–770.
- ROSENBERG, S. A., AEBERSOLD, P., CORNETTA, K., KASID, A., MORGAN, R. A., MOEN, R., KARSON, E. M., LOTZE, M. T., YANG, J. C., TOPALIAN, S. L. Gene transfer into humans – immunotherapy of patients with advanced melanoma, using tumor-infiltrating lymphocytes modified by retroviral gene transduction. *N. Engl. J. Med.*, **1990**, *323*, 570–578.
- HOFFMAN, M. New vector delivers genes to lung cells. *Science*, **1991**, *252*, 374.
- FLOTTE, T. R., SOLOW, R., OWENS, R. A., AFIONE, S., ZEITLIN, P. L., CARTER, B. J. Gene expression from adeno-associated virus vectors in airway epithelial cells. *Am. J. Respir. Cell Mol. Biol.*, **1992**, *7*, 349–356.
- DACHS, G. U., DOUGHERTY, G. J., STRATFORD, I. J., CHAPLIN, D. J. Targeting gene therapy to cancer: a review. *Oncol. Res.*, **1997**, *9*, 313–325.
- WU, M., GUNNING, W., RATNAM, M. Expression of folate receptor type alpha in relation to cell type, malignancy, and differentiation in ovary, uterus, and cervix. *Cancer Epidemiol. Biomarkers Prev.*, **1999**, *8*, 775–782.
- ANTONY, A. C. Folate receptors. *Annu. Rev. Nutr.*, **1996**, *16*, 501–521.
- LEE, R. J., LOW, P. S. Folate-mediated tumor cell targeting of liposome-entrapped doxorubicin *in vitro*. *Biochim. Biophys. Acta*, **1995**, *1233*, 134–144.
- GABIZON, A., HOROWITZ, A. T., GOREN, D., TZEMACH, D., MANDELBAUM-SHAVIT, F., QAZEN, M. M., ZALIPSKY, S. Targeting folate receptor with folate linked to extremities of poly(ethylene glycol)-grafted liposomes: *in vitro* studies. *Bioconjug. Chem.*, **1999**, *10*, 289–298.
- GOREN, D., HOROWITZ, A. T., TZEMACH, D., TARSHISH, M., ZALIPSKY, S., GABIZON, A. Nuclear delivery of doxorubicin via folate-targeted liposomes with bypass of multidrug-resistance efflux pump. *Clin. Cancer Res.*, **2000**, *6*, 1949–1957.
- PAN, X. Q., ZHENG, X., SHI, G., WANG, H., RATNAM, M., LEE, R. J. Strategy for the treatment of acute myelogenous leukemia based on folate receptor beta-targeted liposomal doxorubicin combined with receptor induction using all-trans retinoic acid. *Blood*, **2002**, *100*, 594–602.
- PAN, X. Q., WANG, H., LEE, R. J. Antitumor activity of folate receptor-targeted liposomal doxorubicin in a KB oral carcinoma murine xenograft model. *Pharm. Res.*, **2003**, *20*, 417–422.
- GABIZON, A., HOROWITZ, A. T., GOREN, D., TZEMACH, D., SHMEEDA, H., ZALIPSKY, S. *In vivo* fate of folate-

- targeted polyethylene-glycol liposomes in tumor-bearing mice. *Clin. Cancer Res.*, **2003**, *9*, 6551–6559.
- 14 SHIOKAWA, T., HATTORI, Y., KAWANO, K., OHGUCHI, Y., KAWAKAMI, H., TOMA, K., MAITANI, Y. Effect of the polyethylene glycol linker chain length of folate-linked microemulsions loading aclacinomycin A on targeting ability and antitumor effect *in vitro* and *in vivo*. *Clin. Cancer Res.*, **2005**, *11*, 2018–2025.
  - 15 REDDY, J. A., DEAN, D., KENNEDY, M. D., LOW, P. S. Optimization of folate-conjugated liposomal vectors for folate receptor-mediated gene therapy. *J. Pharm. Sci.*, **1999**, *88*, 1112–1118.
  - 16 LEE, R. J., HUANG, L. Folate-targeted, anionic liposome-entrapped polylysine-condensed DNA for tumor cell-specific gene transfer. *J. Biol. Chem.*, **1996**, *271*, 8481–8487.
  - 17 LEAMON, C. P., COOPER, S. R., HARDEE, G. E. Folate-liposome-mediated antisense oligodeoxynucleotide targeting to cancer cells: evaluation *in vitro* and *in vivo*. *Bioconjug. Chem.*, **2003**, *14*, 738–747.
  - 18 YANG, L., LI, J., ZHOU, W., YUAN, X., LI, S. Targeted delivery of antisense oligodeoxynucleotides to folate receptor-overexpressing tumor cells. *J. Controlled Release*, **2004**, *95*, 321–331.
  - 19 WANG, S., LEE, R. J., CAUCHON, G., GORENSTEIN, D. G., LOW, P. S. Delivery of antisense oligodeoxyribonucleotides against the human epidermal growth factor receptor into cultured KB cells with liposomes conjugated to folate via polyethylene glycol. *Proc. Natl. Acad. Sci. U.S.A.*, **1995**, *92*, 3318–3322.
  - 20 HOFLAND, H. E., MASSON, C., IGINLA, S., OSETINSKY, I., REDDY, J. A., LEAMON, C. P., SCHERMAN, D., BESSODES, M., WILS, P. Folate-targeted gene transfer *in vivo*. *Mol. Ther.*, **2002**, *5*, 739–744.
  - 21 REDDY, J. A., ABBURI, C., HOFLAND, H., HOWARD, S. J., VLAHOV, I., WILS, P., LEAMON, C. P. Folate-targeted, cationic liposome-mediated gene transfer into disseminated peritoneal tumors. *Gene Ther.*, **2002**, *9*, 1542–1550.
  - 22 PAPADAKIS, E. D., NICKLIN, S. A., BAKER, A. H., WHITE, S. J. Promoters and control elements: designing expression cassettes for gene therapy. *Curr. Gene Ther.*, **2004**, *4*, 89–113.
  - 23 HUMPHREYS, M. J., GHANEH, P., GREENHALF, W., CAMPBELL, F., CLAYTON, T. M., EVERETT, P., HUBER, B. E., RICHARDS, C. A., FORD, M. J., NEOPTOLEMOS, J. P. Hepatic intra-arterial delivery of a retroviral vector expressing the cytosine deaminase gene, controlled by the CEA promoter and intraperitoneal treatment with 5-fluorocytosine suppresses growth of colorectal liver metastases. *Gene Ther.*, **2001**, *8*, 1241–1247.
  - 24 IDO, A., NAKATA, K., KATO, Y., NAKAO, K., MURATA, K., FUJITA, M., ISHII, N., TAMAOKI, T., SHIKU, H., NAGATAKI, S. Gene therapy for hepatoma cells using a retrovirus vector carrying herpes simplex virus thymidine kinase gene under the control of human alpha-fetoprotein gene promoter. *Cancer Res.*, **1995**, *55*, 3105–3109.
  - 25 YOSHIDA, Y., TOMIZAWA, M., BAHAR, R., MIYAUCHI, M., YAMAGUCHI, T., SAISHO, H., KADOMATSU, K., MURAMATSU, T., MATSUBARA, S., SAKIYAMA, S., TAGAWA, M. A promoter region of midkine gene can activate transcription of an exogenous suicide gene in human pancreatic cancer. *Anticancer Res.*, **2002**, *22*, 117–120.
  - 26 SUZUKI, S., TADAKUMA, T., KUNITOMI, M., TAKAYAMA, E., SATO, M., ASANO, T., NAKAMURA, H., HAYAKAWA, M. Liposome-mediated gene therapy using HSV-TK/ganciclovir under the control of human PSA promoter in prostate cancer cells. *Urol. Int.*, **2001**, *67*, 216–223.
  - 27 SAUKKONEN, K., HEMMINKI, A. Tissue-specific promoters for cancer gene therapy. *Expert Opin. Biol. Ther.*, **2004**, *4*, 683–696.
  - 28 VIJAYANATHAN, V., THOMAS, T., THOMAS, T. J. DNA nanoparticles and development of DNA delivery vehicles for gene therapy. *Biochemistry*, **2002**, *41*, 14085–14094.

- 29 BLOOMFIELD, V. A. DNA condensation. *Curr. Opin. Struct. Biol.*, **1996**, *6*, 334–341.
- 30 DE SMEDT, S. C., DEMEESTER, J., HENNINK, W. E. Cationic polymer based gene delivery systems. *Pharm. Res.*, **2000**, *17*, 113–126.
- 31 KAMIYA, H., FUJIMURA, Y., MATSUOKA, I., HARASHIMA, H. Visualization of intracellular trafficking of exogenous DNA delivered by cationic liposomes. *Biochem. Biophys. Res. Commun.*, **2002**, *298*, 591–597.
- 32 NIGG, E. A. Nucleocytoplasmic transport: signals, mechanisms and regulation. *Nature*, **1997**, *386*, 779–787.
- 33 GÖRLICH, D. Nuclear protein import. *Curr. Opin. Cell Biol.*, **1997**, *9*, 412–419.
- 34 ALLEN, T. M., HANSEN, C., RUTLEDGE, J. Liposomes with prolonged circulation times: factors affecting uptake by reticuloendothelial and other tissues. *Biochim. Biophys. Acta*, **1989**, *981*, 27–35.
- 35 KLIBANOV, A. L., MARUYAMA, K., BECKERLEG, A. M., TORCHILIN, V. P., HUANG, L. Activity of amphipathic poly(ethylene glycol) 5000 to prolong the circulation time of liposomes depends on the liposome size and is unfavorable for immunoliposome binding to target. *Biochim. Biophys. Acta*, **1991**, *1062*, 142–148.
- 36 PARK, J. W., HONG, K., KIRPOTIN, D. B., PAPAHOPOULOS, D., BENZ, C. C. Immunoliposomes for cancer treatment. *Adv. Pharmacol.*, **1997**, *40*, 399–435.
- 37 HOSOKAWA, S., TAGAWA, T., NIKI, H., HIRAKAWA, Y., NOHGA, K., NAGAIKE, K. Efficacy of immunoliposomes on cancer models in a cell-surface-antigen-density-dependent manner. *Br. J. Cancer*, **2003**, *89*, 1545–1551.
- 38 MAHATO, R. I., KAWABATA, K., TAKAKURA, Y., HASHIDA, M. *In vivo* disposition characteristics of plasmid DNA complexed with cationic liposomes. *J. Drug Target*, **1995**, *3*, 149–157.
- 39 XU, L., HUANG, C. C., HUANG, W., TANG, W. H., RAIT, A., YIN, Y. Z., CRUZ, I., XIANG, L. M., PIROLLO, K. F., CHANG, E. H. Systemic tumor-targeted gene delivery by anti-transferrin receptor scFv-immunoliposomes. *Mol. Cancer Ther.*, **2002**, *1*, 337–346.
- 40 LEE, C. H., HSIAO, M., TSENG, Y. L., CHANG, F. H. Enhanced gene delivery to HER-2-overexpressing breast cancer cells by modified immunoliposomes conjugated with the anti-HER-2 antibody. *J. Biomed. Sci.*, **2003**, *10*, 337–344.
- 41 JOO, S. Y., KIM, J. S. Enhancement of gene transfer to cervical cancer cells using transferrin-conjugated liposome. *Drug Dev. Ind. Pharm.*, **2002**, *28*, 1023–1031.
- 42 KAKUDO, T., CHAKI, S., FUTAKI, S., NAKASE, I., AKAJI, K., KAWAKAMI, T., MARUYAMA, K., KAMIYA, H., HARASHIMA, H. Transferrin-modified liposomes equipped with a pH-sensitive fusogenic peptide: an artificial viral-like delivery system. *Biochemistry*, **2004**, *43*, 5618–5628.
- 43 NISHIKAWA, M., KAWAKAMI, S., YAMASHITA, F., HASHIDA, M. Glycosylated cationic liposomes for carbohydrate receptor-mediated gene transfer. *Methods Enzymol.*, **2003**, *373*, 384–399.
- 44 HWANG, S. H., HAYASHI, K., TAKAYAMA, K., MAITANI, Y. Liver-targeted gene transfer into a human hepatoblastoma cell line and *in vivo* by sterylglucoside-containing cationic liposomes. *Gene Ther.*, **2001**, *8*, 1276–1280.
- 45 LEE, R. J., LOW, P. S. Delivery of liposomes into cultured KB cells via folate receptor-mediated endocytosis. *J. Biol. Chem.*, **1994**, *269*, 3198–3204.
- 46 HARBOTTLE, R. P., COOPER, R. G., HART, S. L., LADHOFF, A., MCKAY, T., KNIGHT, A. M., WAGNER, E., MILLER, A. D., COUTELLE, C. An RGD-oligolysine peptide: a prototype construct for integrin-mediated gene delivery. *Hum. Gene Ther.*, **1998**, *9*, 1037–1047.
- 47 SABHARANJAK, S., MAYOR, S. Folate receptor endocytosis and trafficking. *Adv. Drug Deliv. Rev.*, **2004**, *56*, 1099–1109.

- 48 WEITMAN, S. D., LARK, R. H., CONEY, L. R., FORT, D. W., FRASCA, V., ZURAWSKI, V. R., JR., KAMEN, B. A. Distribution of the folate receptor GP38 in normal and malignant cell lines and tissues. *Cancer Res.*, **1992**, *52*, 3396–3401.
- 49 SHEN, F., ROSS, J. F., WANG, X., RATNAM, M. Identification of a novel folate receptor, a truncated receptor, and receptor type beta in hematopoietic cells: cDNA cloning, expression, immunoreactivity, and tissue specificity. *Biochemistry*, **1994**, *33*, 1209–1215.
- 50 SHEN, F., WU, M., ROSS, J. F., MILLER, D., RATNAM, M. Folate receptor type gamma is primarily a secretory protein due to lack of an efficient signal for glycosylphosphatidylinositol modification: protein characterization and cell type specificity. *Biochemistry*, **1995**, *34*, 5660–5665.
- 51 GABIZON, A., SHMEEDA, H., HOROWITZ, A. T., ZALIPSKY, S. Tumor cell targeting of liposome-entrapped drugs with phospholipid-anchored folic acid-PEG conjugates. *Adv. Drug Deliv. Rev.*, **2004**, *56*, 1177–1192.
- 52 GOTTSCHALK, S., CRISTIANO, R. J., SMITH, L. C., WOO, S. L. Folate receptor mediated DNA delivery into tumor cells: potosomal disruption results in enhanced gene expression. *Gene Ther.*, **1994**, *1*, 185–191.
- 53 MISLICK, K. A., BALDESCHWIELER, J. D., KAYYEM, J. F., MEADE, T. J. Transfection of folate-polylysine DNA complexes: evidence for lysosomal delivery. *Bioconj. Chem.*, **1995**, *6*, 512–515.
- 54 WARD, C. M., PECHAR, M., OUPICKY, D., ULBRICH, K., SEYMOUR, L. W. Modification of pLL/DNA complexes with a multivalent hydrophilic polymer permits folate-mediated targeting *in vitro* and prolonged plasma circulation *in vivo*. *J. Gene Med.*, **2002**, *4*, 536–547.
- 55 LEAMON, C. P., WEIGL, D., HENDREN, R. W. Folate copolymer-mediated transfection of cultured cells. *Bioconj. Chem.*, **1999**, *10*, 947–957.
- 56 GUO, W., LEE, R. L. Receptor-targeted gene delivery via folate-conjugated polyethylenimine. *AAPS. PharmSci.*, **1999**, *1*, E19.
- 57 BENNS, J. M., MAHATO, R. I., KIM, S. W. Optimization of factors influencing the transfection efficiency of folate-PEG-folate-graft-polyethylenimine. *J. Controlled Release*, **2002**, *79*, 255–269.
- 58 VAN STEENIS, J. H., VAN MAARSEVEEN, E. M., VERBAAN, F. J., VERRIJK, R., CROMMELIN, D. J., STORM, G., HENNINK, W. E. Preparation and characterization of folate-targeted pEG-coated pDMAEMA-based polyplexes. *J. Controlled Release*, **2003**, *87*, 167–176.
- 59 XU, L., PIROLLO, K. F., CHANG, E. H. Tumor-targeted p53-gene therapy enhances the efficacy of conventional chemo/radiotherapy. *J. Controlled Release*, **2001**, *74*, 115–128.
- 60 BRUCKHEIMER, E., HARVIE, P., ORTHEL, J., DUTZAR, B., FURSTOSS, K., MEBEL, E., ANKLESARIA, P., PAUL, R. *In vivo* efficacy of folate-targeted lipid-protamine-DNA (LPD-PEG-Folate) complexes in an immunocompetent syngeneic model for breast adenocarcinoma. *Cancer Gene Ther.*, **2004**, *11*, 128–134.
- 61 SHI, G., GUO, W., STEPHENSON, S. M., LEE, R. J. Efficient intracellular drug and gene delivery using folate receptor-targeted pH-sensitive liposomes composed of cationic/anionic lipid combinations. *J. Controlled Release*, **2002**, *80*, 309–319.
- 62 DAUTY, E., REMY, J. S., ZUBER, G., BEHR, J. P. Intracellular delivery of nanometric DNA particles via the folate receptor. *Bioconj. Chem.*, **2002**, *13*, 831–839.
- 63 HATTORI, Y., MAITANI, Y. Enhanced *in vitro* DNA transfection efficiency by novel folate-linked nanoparticles in human prostate cancer and oral cancer. *J. Controlled Release*, **2004**, *97*, 173–183.
- 64 HATTORI, Y., MAITANI, Y. Folate-linked nanoparticle-mediated suicide gene therapy in human prostate cancer and

- nasopharyngeal cancer with herpes simplex virus thymidine kinase. *Cancer Gene Ther.*, **2005**, in press.
- 65 HOLM, J., HANSEN, S. I., HOIER-MADSEN, M. High-affinity folate binding in human prostate. *Biosci. Rep.*, **1993**, *13*, 99–105.
- 66 PINTO, J. T., SUFFOLETTO, B. P., BERZIN, T. M., QIAO, C. H., LIN, S., TONG, W. P., MAY, F., MUKHERJEE, B., HESTON, W. D. Prostate-specific membrane antigen: a novel folate hydrolase in human prostatic carcinoma cells. *Clin. Cancer Res.*, **1996**, *2*, 1445–1451.
- 67 RAJASEKARAN, S. A., ANILKUMAR, G., OSHIMA, E., BOWIE, J. U., LIU, H., HESTON, W., BANDER, N. H., RAJASEKARAN, A. K. A novel cytoplasmic tail MXXXL motif mediates the internalization of prostate-specific membrane antigen. *Mol. Biol. Cell*, **2003**, *14*, 4835–4845.
- 68 HATTORI, Y., KUBO, H., HIGASHIYAMA, K., MAITANI, Y. Folate-linked nanoparticles formed with DNA complexes in sodium chloride solution enhance transfection efficiency. *J. Biomed. Nanotechnol.*, **2005**, in press.
- 69 SONG, L. Y., AHKONG, Q. F., RONG, Q., WANG, Z., ANSELL, S., HOPE, M. J., MUI, B. Characterization of the inhibitory effect of PEG-lipid conjugates on the intracellular delivery of plasmid and antisense DNA mediated by cationic lipid liposomes. *Biochim. Biophys. Acta*, **2002**, *1558*, 1–13.
- 70 HASEGAWA, S., HIRASHIMA, N., NAKANISHI, M. Comparative study of transfection efficiency of cationic cholesterol-mediated liposomes-based gene delivery. *Bioorg. Med. Chem. Lett.*, **2002**, *12*, 1299–1302.
- 71 GUO, W., LEE, R. J. Efficient gene delivery via non-covalent complexes of folic acid and polyethylenimine. *J. Controlled Release*, **2001**, *77*, 131–138.
- 72 LAWRENCE, J. M., PETITTI, D. B., WATKINS, M., UMEKUBO, M. A. Trends in serum folate after food fortification. *Lancet*, **1999**, *354*, 915–916.
- 73 HATTORI, Y., MAITANI, Y. Folate-linked lipid-based nanoparticle for targeted gene delivery. *Curr. Drug Delivery*, **2005**, *2*, 243–252.
- 74 MAHATO, R. I., KAWABATA, K., NOMURA, T., TAKAKURA, Y., HASHIDA, M. Physicochemical and pharmacokinetic characteristics of plasmid DNA/cationic liposome complexes. *J. Pharm. Sci.*, **1995**, *84*, 1267–1271.
- 75 PAULOS, C. M., TURK, M. J., BREUR, G. J., LOW, P. S. Folate receptor-mediated targeting of therapeutic and imaging agents to activated macrophages in rheumatoid arthritis. *Adv. Drug Deliv. Rev.*, **2004**, *56*, 1205–1217.
- 76 EL ANEED, A. An overview of current delivery systems in cancer gene therapy. *J. Controlled Release*, **2004**, *94*, 1–14.
- 77 FILLAT, C., CARRIO, M., CASCANTE, A., SANGRO, B. Suicide gene therapy mediated by the Herpes Simplex virus thymidine kinase gene/Ganciclovir system: fifteen years of application. *Curr. Gene Ther.*, **2003**, *3*, 13–26.
- 78 FAULDS, D., HEEL, R. C. GANCICLOVIR. A review of its antiviral activity, pharmacokinetic properties and therapeutic efficacy in cytomegalovirus infections. *Drugs*, **1990**, *39*, 597–638.
- 79 ISLEY, D. D., LEE, S. H., MILLER, W. H., KUCHTA, R. D. Acyclic guanosine analogs inhibit DNA polymerases alpha, delta, and epsilon with very different potencies and have unique mechanisms of action. *Biochemistry*, **1995**, *34*, 2504–2510.
- 80 HAMEL, W., MAGNELLI, L., CHIARUGI, V. P., ISRAEL, M. A. Herpes simplex virus thymidine kinase/ganciclovir-mediated apoptotic death of bystander cells. *Cancer Res.*, **1996**, *56*, 2697–2702.
- 81 MESNIL, M., PICCOLI, C., TIRABY, G., WILLECKE, K., YAMASAKI, H. Bystander killing of cancer cells by herpes simplex virus thymidine kinase gene is mediated by connexins. *Proc. Natl. Acad. Sci. U.S.A.*, **1996**, *93*, 1831–1835.
- 82 LAMPE, P. D., LAU, A. F. Regulation of gap junctions by phosphorylation of connexins. *Arch. Biochem. Biophys.*, **2000**, *384*, 205–215.

- 83 TSAI, H., WERBER, J., DAVIA, M. O., EDELMAN, M., TANAKA, K. E., MELMAN, A., CHRIST, G. J., GELIEBTER, J. Reduced connexin 43 expression in high grade, human prostatic adenocarcinoma cells. *Biochem. Biophys. Res. Commun.*, **1996**, *227*, 64–69.
- 84 HABERMANN, H., RAY, V., HABERMANN, W., PRINS, G. S. Alterations in gap junction protein expression in human benign prostatic hyperplasia and prostate cancer. *J. Urol.*, **2002**, *167*, 655–660.
- 85 MEHTA, P. P., PEREZ-STABLE, C., NADJI, M., MIAN, M., ASOTRA, K., ROOS, B. A. Suppression of human prostate cancer cell growth by forced expression of connexin genes. *Dev. Genet.*, **1999**, *24*, 91–110.
- 86 CHEON, J., KIM, H. K., MOON, D. G., YOON, D. K., CHO, J. H., KOH, S. K. Adenovirus-mediated suicide-gene therapy using the herpes simplex virus thymidine kinase gene in cell and animal models of human prostate cancer: changes in tumour cell proliferative activity. *BJU Int.*, **2000**, *85*, 759–766.
- 87 SHALEV, M., MILES, B. J., THOMPSON, T. C., AYALA, G., BUTLER, E. B., AGUILAR-CORDOVA, E., KADMON, D. Suicide gene therapy for prostate cancer using a replication-deficient adenovirus containing the herpesvirus thymidine kinase gene. *World J. Urol.*, **2000**, *18*, 125–129.
- 88 HUBER, B. E., AUSTIN, E. A., RICHARDS, C. A., DAVIS, S. T., GOOD, S. S. Metabolism of 5-fluorocytosine to 5-fluorouracil in human colorectal tumor cells transduced with the cytosine deaminase gene: significant antitumor effects when only a small percentage of tumor cells express cytosine deaminase. *Proc. Natl. Acad. Sci. U.S.A.*, **1994**, *91*, 8302–8306.

## 10 Magnetic Core Conducting Polymer Shell Nanocomposites for DNA Attachment and Hybridization

Jean-Paul Lellouche

### 10.1 Introduction

Micro- and nanosized magnetically responsive particles or particulates have become an important class of micro-/nanomaterials that have found numerous applications in electronics (data storage technology), catalysis, and biotechnology [1–5]. Generally, these nanoparticulate materials display a range of magnetic, electrical, optical, and chemical properties that clearly differ from that of their bulk materials, thus making them very attractive for property-based applications. The main applications of nanosized magnetic particles in biomedical research are magnetism-driven separations of small biological components and cells; magnetic detoxification of undesirable molecules and antigens; magnetic field-guided delivery of drugs (targeting) and genes; relaxation and contrast enhancement in non-invasive magnetic resonance imaging (MRI) of tissues; piezoelectric immunosensors; and magnetic fluid hyperthermia for cancer therapy [6–13].

To exploit the full potential of corresponding magnetic nanoparticles and related nanocomposites, some key general issues need to be consistently addressed regarding their synthesis and further subsequent use. Accordingly, controlling the shape, size, and size distribution of nanoparticles toward spherical or non-spherical anisotropic materials is one significant issue. In addition, magnetic nanoparticles need to be stabilized sterically or by using charge repulsion against aggregation in both organic and/or aqueous media. The versatility of chemical modifications that can be introduced onto particle/composite surfaces is another key question that requires careful investigation. Finally, for *in vivo* use of nanoparticles/related nanocomposites, their biocompatibility profiles and systemic toxicity properties need to be examined in depth.

Related to this field, magnetically responsive core–shell iron oxide-conducting polymer (CP) [14–21] nanosized composites form a relatively recent class of magnetic nanocomposites (NCs) [22, 23]. They display thin outer layers of insoluble CPs, such as doped polypyrrole, that have been oxidatively deposited around nanosized magnetite/magnetite-silica cores. Armes and co-workers, in particular, have



reported the fabrication of colloidal stable core–shell magnetite-silica-polypyrrole NCs with diameters in the range 100–520 nm that are superparamagnetic [24, 25]. Both aqueous oxidants  $\text{H}_2\text{O}_2/\text{Fe}^{3+}/\text{HCl}$  and  $(\text{NH}_4)_2\text{S}_2\text{O}_8$  have been used to chemically oxidize *non-functional* pyrrole around inorganic hybrid magnetite-silica cores (5–20 nm diameter). Nanosized ferromagnetic  $\text{Fe}_3\text{O}_4$ -crosslinked polyaniline NCs have recently been described by the Peng's group using aniline (monomer) and  $(\text{NH}_4)_2\text{S}_2\text{O}_8$  (oxidant) [26]. Related conducting NCs were found polydispersed, 20–30 nm in diameter, and of a core–shell morphology. Consequently, both maghemite ( $\gamma\text{-Fe}_2\text{O}_3$ ) and magnetite ( $\text{Fe}_3\text{O}_4$ ) nanoparticles should be considered as attractive inorganic magnetic cores toward related magnetic CPs-based NCs. These readily prepared iron oxide nanoparticles are prone to minimal oxidation, are of low systemic toxicity, and present a high magnetic susceptibility, in the range of 76–81 and 90–98  $\text{emu g}^{-1}$ , respectively.

Notably, in this related framework, various non-magnetic organic and inorganic cores have been engaged as micro-/nanosized supports to polymerize oxidatively *non-functional* and *functional* CPs monomers in their presence. For example, to develop color visual immunodiagnostic assays, core–shell micrometer-sized polystyrene latex-CPs [27–30] and colloidal nanosized silica-CPs [31–37] composites have been produced by oxidative deposition of insoluble CPs around corresponding cores. Tin(IV) oxide-polypyrrole colloidal NCs have been similarly fabricated by the same group for solid-state conductivity studies [38]. The main CPs studied include polypyrrole, polyaniline, poly(3,4-ethylenedioxythiophene), poly(3-pyrrol-1-yl-propionic acid), poly(3-(1*H*-pyrrol-3-yl)-propionic acid), poly(*N*-succinimidyl ester of 3-pyrrol-1-yl-propionic acid), and related copolymers. Interestingly, the last reported example [37] demonstrated that amine-sensitive *N*-succinimidyl ester of pyrrolyl-3-acetic acid survived the aqueous acidic medium that developed during monomer polymerization onto silica core nanoparticles. The resulting NCs were able to covalently attach proteins without the need for any additional post-polymerization activation step. Gold nanoparticles in a 5–200 nm diameter range have been also used as templating metallic cores to polymerize pyrrole and *N*-methylpyrrole monomers around them [39, 40]. Following core gold etching, hollow nanosized polymeric polypyrrolic capsules were synthesized as useful vehicles for drug physical entrapment and targeted delivery.

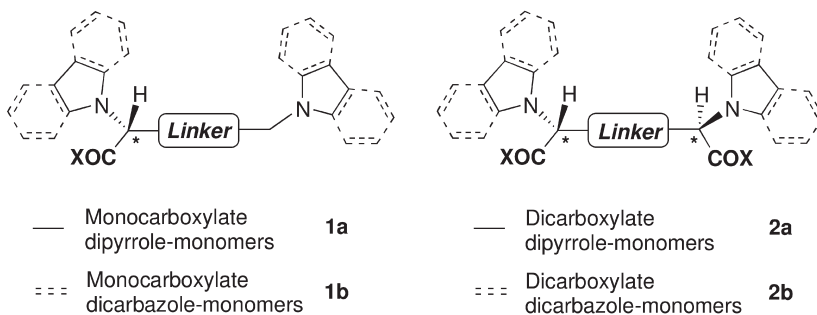
This chapter describes our most recent progress in the field of magnetically responsive new core–shell iron oxide-CPs NCs. It consists of four main sections, dealing with (a) the modular chemical design and synthesis of oxidizable dipyrrole-(DPyr) and dicarbazole- (DCbz) containing monomers to introduce molecular diversity at the monomer level (Sections 10.2 and 10.3); (b) the fabrication of magnetic NCs (chemical polymerization around magnetite cores) and their thorough characterization by means of modern spectral and analytical methods (Section 10.4); and (c) the investigation of covalent/quasi-covalent DNA attachments and hybridizations at NCs surfaces (Section 10.5). Additionally, Section 10.6 contains robust and reliable typical experimental procedures that relate to each separate step.

## 10.2

## Chemical Design of DPyr- and DCbz-containing Monomers: Introduction of Molecular Diversity

Based on the literature considerations cited above, the full potential of magnetically responsive CPs-maghemite/magnetite nanocomposites (NCs) has still to be developed regarding novel (electro-)chemically oxidizable monomers that possess (a) heterocycles different from nonfunctional pyrrole, as well as (b) appropriate functionalities that can be appended by biological species after polymerizing over nanoparticles, e.g., grafting COOH functions that can be readily amidated using well-known amide chemistry. Considering the above points, four generic chemical structures (Fig. 10.1) of mono/dicarboxylate DPyr- and DCbz-containing monomers **1–2a** (index **a** specific for the DPyr-series) and **1–2b** (index **b** specific for the DCbz-series) readily emerged from the indicated planned innovative chemical design. These generic structures have been designed to be modular and clearly accentuated the key roles played by L- or D-amino acid building blocks and appropriate linkers of variable lengths, in order to introduce chirality and molecular diversity [41–43] at the monomer level.  $C_2$ -Symmetrization operations used have been included based on generally high-yielding, stable amide connections between monocarboxylated or monoaminated Pyr- and Cbz-containing building blocks and diaminated or dicarboxylated linkers, respectively. More precisely, molecular diversity at the monomer level should arise from (a) both types of heterocyclic DPyr- and DCbz-units; (b) the existing number of COOH functions (one or two); (c) absolute (*S*) or (*R*) chiralities of asymmetric centers (from L- or D-amino acid building blocks); and, finally, (d) linkers of different chemical types and lengths.

Another notable aspect is that, in these *bis*-heterocyclic generic structures, both pyrrole and carbazole heterocycles of suitable monomers would be simultaneously engaged in polymer chain propagation at positions 2,5 and 5,5', respectively,



X = OH and/or activated esters, Linker definition (see text)

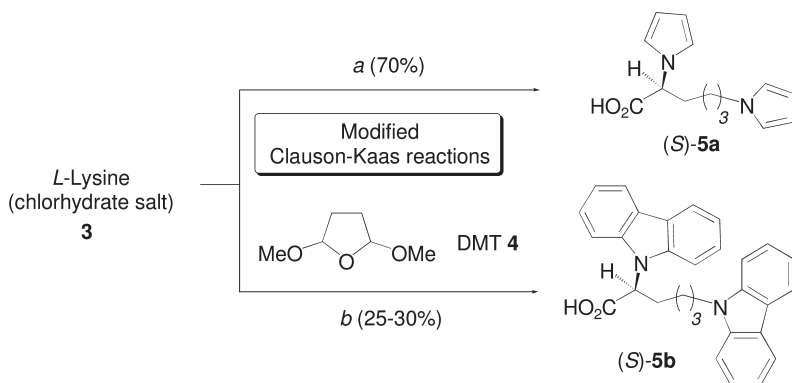
**Fig. 10.1.** Generic structures **1a/2a** and **1b/2b** of optically active mono- and dicarboxylate DPyr- and DCbz-containing oxidizable monomers.

through C–C bond formation, leading to reticulated and more stable polymers. Literature data more particularly emphasized the lack of stability of polycarbazole polymers in the carbazole series of oxidizable monomers. Accordingly, tentative electrosyntheses of polycarbazole films from N-substituted *monocarbazole* monomers resulted chiefly in short tetramers that are soluble in the electrochemical medium [44, 45]. In contrast, our laboratory has overcome this limitation. Electrochemically stable poly(DCbz)-films containing amine-sensitive pentafluorophenol esters have been formed using the electropolymerization of innovative DCbz-monomers synthesized according to the bis-podant bis-heterocyclic design cited above [46]. An example potential applications of these functional polyDCbz-films is the successful covalent attachment of polyphenol and glucose oxidases onto them as a step towards biosensor constructs [47–49].

### 10.3

#### Synthetic Approaches for Mono- and Dicarboxylated DPyr-/DCbz-based Monomers

According to synthetic approaches described below in Schemes 10.1–10.4, a range of *thirteen* enantiomerically pure mono-/dicarboxylated DPyr- and DCbz-monomers has been routinely prepared and used for the fabrication of targeted polyDPyr- and polyDCbz-magnetite NCs. Several key synthetic steps deserve some comments so as to best grasp the power and maneuverability of our planned chemical design for monomers. First, the well-known Clauson-Kaas reaction, a one-step acid-catalyzed transformation of an aromatic or alkyl NH<sub>2</sub> function into a pyrrole heterocycle unit using 2,5-dimethoxytetrahydrofuran (DMT, **4**) (Scheme 10.1) [50], has been modified to moderate reaction conditions (less acidic, salt buffered, solvent diluted, lower temperatures/shorter reaction times) [46]. Similar preparation of carbazole-based monomers generally required higher temperatures for a while

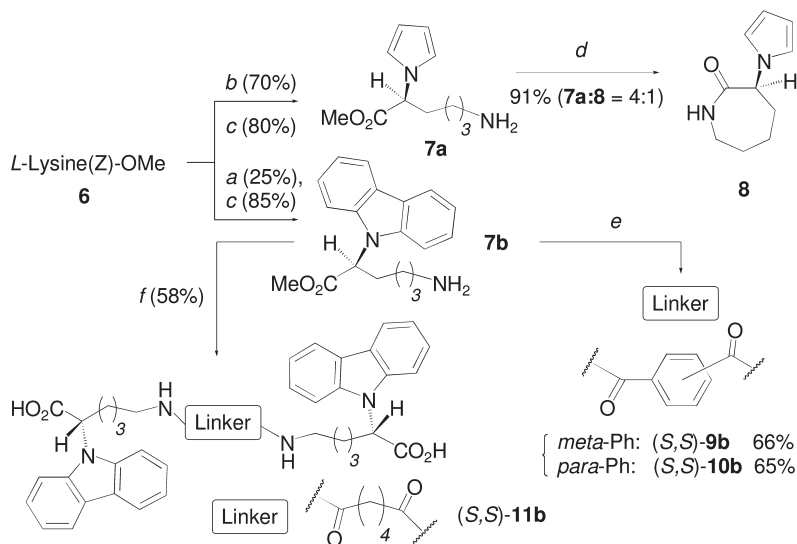


**Scheme 10.1.** Reagents and conditions: (a) 2,5-Dimethoxytetrahydrofuran (DMT, **4**), NaOAc, H<sub>2</sub>O, AcOH–1,2-dichloroethane, 1 h, 76 °C; (b) DMT (**4**), AcOH–dioxane, 3 h at reflux then overnight at 20 °C.

and longer reaction times. Thus, two separate sets of experimental conditions allowed the synthesis of both DPyr- and DCbz-containing monocarboxylated monomers **5a–b**, as well as of intermediates **7a–b**, and **14–17a–b** from enantiomerically pure L-lysine, L-aspartic, and L-glutamic acid derivatives. However, contrary to what was usually observed under harsher conditions, racemization of existing asymmetric centers was nonexistent (*ee* 97–99%, Schemes 10.1–10.4, steps a and b) [46].

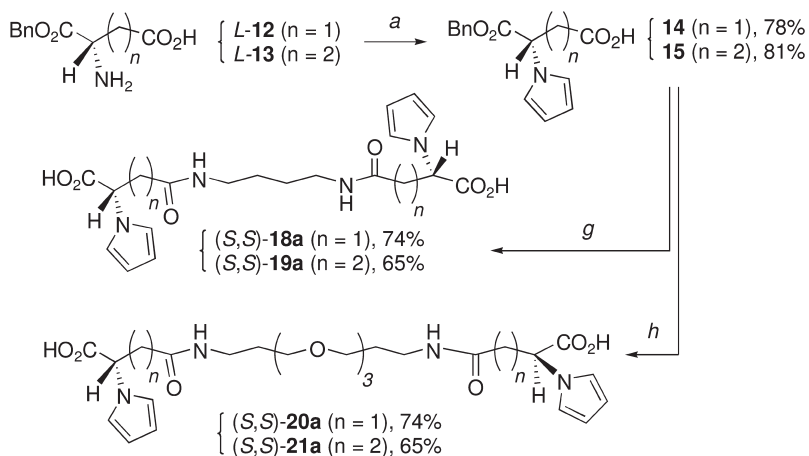
A stability issue has been encountered during the preparation of aminated Pyr-based intermediate **7a**, which readily cyclizes intramolecularly to the corresponding seven-membered lactam **8** (**7a**:**8** = 4:1 assayed by high-field  $^1\text{H}$  NMR for a quasi-quantitative 91% recovery yield after separation from reaction mixture) during chromatographic purifications on silica gel columns. This intramolecular amidation did not, however, occur for the sterically more hindered Cbz-based precursor **7b**, therefore allowing its corresponding  $C_2$ -symmetrization, as described later (Scheme 10.2).

Intermediates and monomer yields were consistently higher in the modified Clauson-Kaas pyrrole synthesis than for the synthesis of carbazoles (70–80% and 25–40%, respectively). In addition,  $C_2$ -symmetrization operations toward bis-heterocyclic oxidizable monomers have been operated straightforwardly, using powerful amide connecting chemistries that do not racemize existing asymmetric centers, e.g., the use of highly reactive diacid dichlorides and of a dicyclohexylcarbodiimide (DCC)/1-hydroxybenzotriazole (HOBT) system in the



**Scheme 10.2.** Reagents and conditions: (a) and (b) same as Scheme 10.1; (c) cyclohexene, MeOH, 10% Pd/C, reflux, 0.5 h; (d) spontaneous cyclization during purification on silica gel column, **7a**:**8a** = 4:1 by  $^1\text{H}$  NMR, 91% recovery; (e) (i)  $\text{CHCl}_3$ – $\text{Et}_3\text{N}$ , terephthaloyl

or isophthaloyl chloride, 2 h, 20 °C, (ii) 1.0 M KOH, 1/1 v/v MeOH– $\text{PhCH}_3$ , reflux, 4 h then 0.1 M HCl; (f) (i)  $\text{CH}_2\text{Cl}_2$ – $\text{Et}_3\text{N}$ , adipoyl chloride, 2 h, 20 °C, (ii) 1.0 M KOH, 1/1 v/v MeOH– $\text{PhCH}_3$ , reflux, 4 h then 0.1 M HCl.



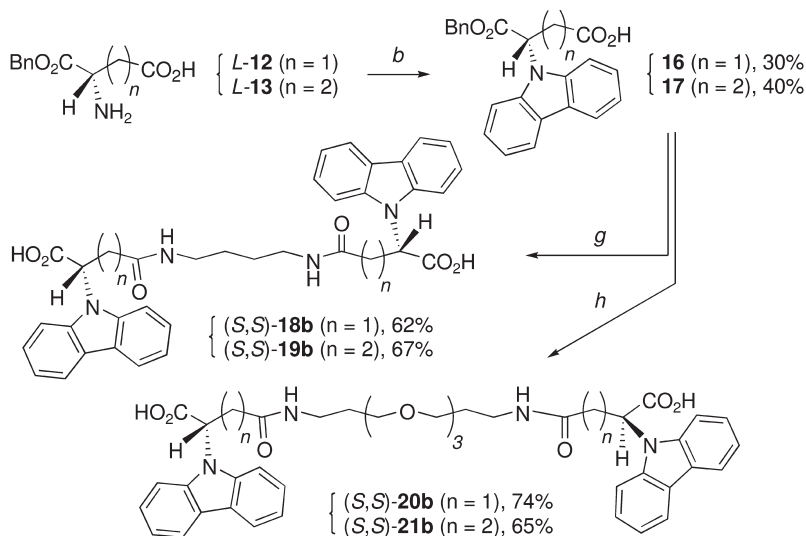
**Scheme 10.3.** Reagents and conditions: (a)–(f): same as Schemes 10.1 and 10.2; (g) (i) Dicyclohexylcarbodiimide (DCC), 1-hydroxybenzotriazole (HOBT),  $\text{CH}_2\text{Cl}_2$ , *N*-methylmorpholine, 1,4-diaminobutane, 3 h,

20 °C, (ii) 1:4 v/v cyclohexene–2-propanol, 10% Pd/carbon, 1.5 h, 20 °C; (h) same conditions as for step g but using a different 1, $\omega$ -diamine, e.g., 4,7,10-trioxatridecane-1,13-diamine.

presence of *N*-methylmorpholine (Schemes 10.2–10.4, Steps e–h). Appropriate monoPyr-/monoCbz-intermediates **7a–b** and **14–17** ( $n = 1$  or  $2$ ) prepared from *L*-lysine(Z)-OMe **6** (Z: benzyloxycarbonyl) and monobenzyl esters of *L*-aspartic/*L*-glutamic acids **12–13** ( $n = 1$  or  $2$ ) presented free  $\text{NH}_2$  and  $\text{COOH}$  groups for  $\text{C}_2$ -symmetrical amide coupling. Diacids as well as diamide linkers variable in length and lipophilicity/hydrophilicity characteristics included aromatic terephthaloyl/isophthaloyl and alkyl adipoyl chlorides, the alkyl 1,4-diaminobutane, and, finally, the more hydrophilic polyoxyethylenyl 1, $\omega$ -diamine 4,7,10-trioxa-1,13-tridecanediamine.

Consequently, these synthetic efforts facilitated routine preparation of five DPyr- and eight DCbz mono-/dicarboxylated homochiral based monomers in a 0.5–1.0 g weight range. From commercially available *L*-amino acid derivatives, and apart from monocarboxylated monomers (*S*)-**5a**/*(S)*-**5b** (Scheme 10.1, *one* synthetic step from **3**, 70 and 25–30% yields), only *three* to *four* synthetic steps were necessary to obtain the entire range of dicarboxylated oxidizable monomers (*S,S*)-**18–21a**, (*S,S*)-**9–11b**, and (*S,S*)-**18–21b** in global 53–58%, 12–14%, and 19–27% yields, respectively (Schemes 10.1–10.4).

All these monomers have been fully characterized, their chemical structures confirmed and their purities checked before fabrication of the corresponding NCs by appropriate analytical means (thin-layer and high-performance liquid chromatographies, optical rotations) and spectroscopic analyses (FT-IR, 1D/2D-high-field  $^1\text{H}/^{13}\text{C}$  NMR, low- and high-resolution FAB-MS). Additionally, and only after completion of synthetic amidations by starting block  $\text{C}_2$ -symmetrization, 1D high-field  $^1\text{H}/^{13}\text{C}$  NMR techniques allowed us to again check that optical purities of resulting



**Scheme 10.4.** Same reagents and conditions as in Schemes 10.1 and 10.3.

monomers were in a 97–98% range, based on the non-detection of meso diastereoisomers arising from asymmetric center racemization.

## 10.4

### Oxidative Polymerization of DPyr-/DCbz-based Monomers around Magnetite Nanoparticles

#### 10.4.1

##### General Considerations

The availability of DPyr- and DCbz-based monomers allowed us to test various oxidative polymerization conditions in the presence of nanosized magnetite particles (Fig. 10.2) towards corresponding magnetic NCs. Numerous methods and related modifications have been reported for the preparation of magnetite nanoparticles, and, significantly, dealing with stabilization against aggregation of the particles [1–4]. With this goal in mind, we modified slightly the original Sugimoto method, and, accordingly, the oxidative hydrolysis of iron(II) sulfate heptahydrate ( $\text{Fe}_2\text{SO}_4 \cdot 7\text{H}_2\text{O}$ ) by  $\text{KNO}_3$  in an alkaline KOH medium under nitrogen [51, 52] (see optimized protocols for NC fabrication in Section 10.6.1) that afforded magnetite sheet-like nanoparticles (mean particle size of 20–40 nm by TEM analysis) as a free-flowing, brilliant black water suspension that can be used immediately or stored under nitrogen if necessary. FT-IR peaks characteristics of pure magnetite ( $\text{Fe}_3\text{O}_4$ ,  $\nu = 410, 510 \text{ cm}^{-1}$ ) confirmed its nature, and, in particular, the absence of contaminating maghemite ( $\gamma\text{-Fe}_2\text{O}_3$ ) [51, 52].

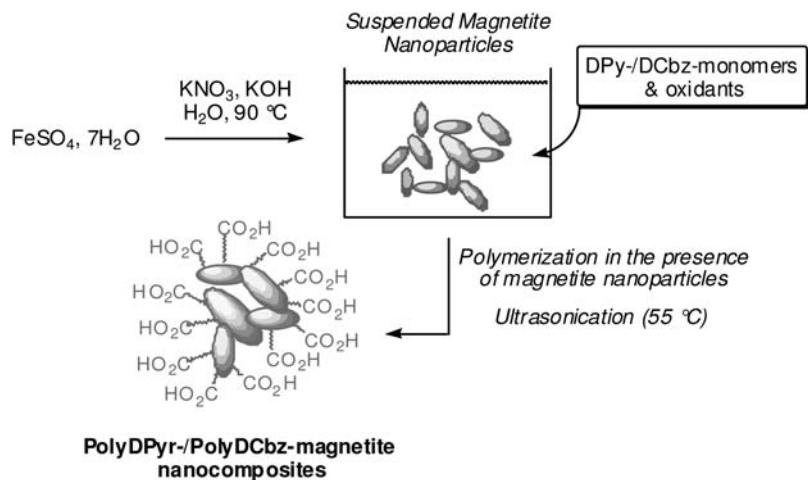


**Fig. 10.2.** Oxidative polymerization of DPyr-/DCbz-based monomers in the presence of magnetite nanoparticles.

Regarding oxidative polymerization of DPyr-/DCbz-based monomers in the presence of nanosized magnetite particles toward corresponding magnetic NCs (Fig. 10.2), several experimental parameters were considered important and, subsequently, examined carefully during extensive screening, keeping in mind the best practicality, reliability, and robustness of NC fabrication protocols. Polymerization parameters examined included different (a) polymerization times; (b) mono- or bi-electronic chemical oxidants; (c) molar/weight ratios of DPyr- and DCbz-monomers/magnetite nanoparticles; (d) polymerization solvents (low-molecular weight alcohols, acetone, acetonitrile, dimethylformamide, and their respective mixtures with water, chloroform, hexane); (e) medium temperatures [25–55 °C when using or not ultrasonic irradiation (ultrasonic cleaner Branson at full 42 kHz power)]; and finally (f) magnetite concentrations (0.5–5% w/v range at constant experiment volume).

Two main problems arose that were successfully solved during this selection process, ending with the delivery of optimized protocols for NC fabrication [53]. First, both DPyr- and DCbz-based oxidizable monomers must be minimally soluble in water, since magnetite nanoparticles had an irreversible strong tendency to aggregate in non-aqueous media. For example, the dicarboxylate DCbz-containing (*S,S*)-**18b** (Scheme 10.4) could not be solubilized in any water-miscible organic solvent mixture and, therefore, could not be polymerized around magnetite nanoparticles. Due to the heterocycle type, DCbz-based monomers are consistently more hydrophobic, or less water-soluble than DPyr-related monomers. Therefore, two different polymerization media have been specifically adapted for monomers of both DPyr- and DCbz-type (water–methanol mixtures and acetone, respectively; see typical procedures for NC fabrication in Section 10.6.1). Secondly, DCbz-based monomers that were expected to polymerize with difficulty under usual chemi-

cal oxidative conditions polymerized efficiently when using the *only* oxidizing Ce(IV) salt CAN  $[(\text{NH}_4)_2\text{Ce}(\text{NO}_3)_6]$  among a range of currently tested oxidants  $[\text{FeCl}_3, \text{Fe}(\text{NO}_3)_3, \text{Fe}(\text{ClO}_4)_3, \text{H}_2\text{O}_2/\text{FeCl}_3/0.1 \text{ M HCl}, \text{CuCl}_2, \text{K}_2\text{Cr}_2\text{O}_7, \text{K}_2\text{S}_2\text{O}_8, (\text{NH}_4)_2\text{S}_2\text{O}_8, \text{I}_2, \text{PbO}_2, \text{etc.}]$  [53].

Conversely, DPyr-based monomers readily polymerize when using  $\text{FeCl}_3$  and ammonium peroxodisulfate,  $(\text{NH}_4)_2\text{S}_2\text{O}_8$ , with the latter oxidant being preferred since it affords much cleaner polyDPyr-magnetite NCs (absence of shorter, water-bleachable, dark colored DPyr-oligomers). Interestingly, the resulting carboxylated polyDPyr-/polyDCbz-magnetite nanocomposites did not always show colloidal stability for the entire range of parameter combinations and during storage (at  $4^\circ\text{C}$  in a neutral PBS phosphate buffer). In fact, preliminary TGA (Thermogravimetric Analysis) analyses over  $200\text{--}750^\circ\text{C}$ , together with FT-IR spectroscopic analyses, helped to confirm successful monomer polymerizations. This large screening towards optimized polymerization parameters rapidly disclosed two separate optimal sets of polymerization conditions specific for each DPyr- and DCbz-series of monomers in the presence of nanosized magnetite. Beyond the use of oxidizers specific to each monomer series, the main protocol differences related to (a) optimal polymerization media, e.g., a 45/55 v/v  $\text{H}_2\text{O}\text{--}\text{CH}_3\text{OH}$  mixture for DPyr-based monomers and pure  $\text{CH}_3\text{COCH}_3$  for more hydrophobic DCbz-based ones, and (b) optimal ultrasound-assisted polymerization times, e.g., 1 h for DPyr-based monomers versus 5 h for DCbz-based ones. Typical preparations of magnetically responsive polyDPyr- and polyDCbz-magnetite NCs are reported in Section 10.6.1.

#### 10.4.2

#### Characterization of Magnetically Responsive PolyDPyr- and PolyDCbz-Magnetite Nanocomposites

Magnetically responsive polyDPyr- and polyDCbz-magnetite NCs have been characterized using a range of analytical and spectroscopic methods that included FT-IR and  $^{57}\text{Fe}$  Mössbauer spectroscopies, C,H,N elemental and TGA analyses, magnetism measurements, and low- and high-resolution TEM microscopies with Energy-Dispersive X-Ray Microanalysis (EDAX). Additionally, as discussed in Section 10.5, a DNA-based biological parallel screening system has also been developed to characterize the fabricated NCs. In fact, NCs have been systematically tested for (a) DNA attachment using both covalent amide and noncovalent streptavidin/biotin linkages, and (b) NC surface-confined DNA hybridizations using an amplifying colored HRP-based enzymatic system (HRP: Horse Radish Peroxidase) towards detection and quantification of optically read signal outputs.

In a first step, carboxylated polyDPyr-/polyDCbz-magnetite NCs have been characterized by TGA analysis (TGA-Mettler apparatus, TG-50 DSS50 model, executed temperature profile:  $25\text{--}130^\circ\text{C}$  at  $20^\circ\text{C min}^{-1}$ ,  $130^\circ\text{C}$  for 15 min, and then  $130\text{--}800^\circ\text{C}$  at  $15^\circ\text{C min}^{-1}$  under nitrogen) and high-resolution FT-IR spectroscopy (Bomen-Hartmann & Braun instrument, KBr pellets,  $4 \text{ cm}^{-1}$  resolution) to check the formation of polyDPyr-/polyDCbz-polymers in the presence of nanosized magnetite nanoparticles. TGA curves showed quite similar two-step profiles, which



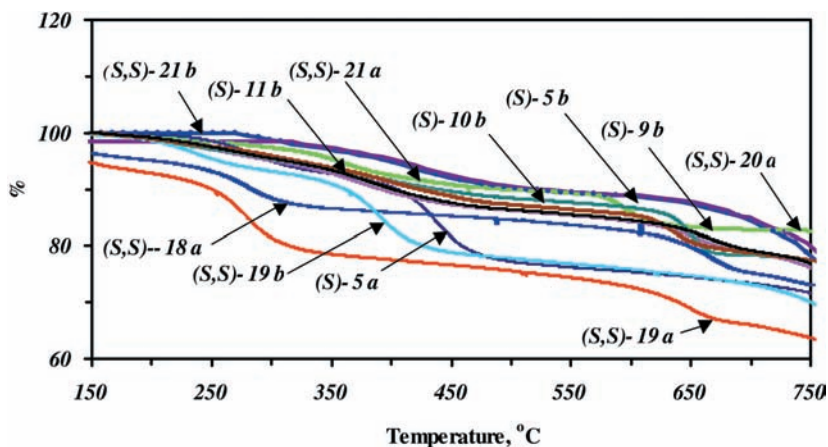


Fig. 10.3. TGA curves of magnetically responsive polyDPyr/polyDCbz-magnetite NCs.

were more or less pronounced depending on NCs over a 200–750 °C temperature range (Fig. 10.3 and Table 10.1). Observed weight losses match up, most likely, to the evaporation of shorter, more volatile polymeric chains followed by final polymer burning. Interestingly, C,H,N elemental analyses (EA 1110/CHNS-O CE instrument) data, corrected for oxygen (Table 10.1), matched with TGA NC composition data and, therefore, allowed us to check for data homogeneity. Both DPyr- and DCbz-based monomers afforded NCs of similar polymer compositions with polymer deposits in a w/w range of 18–30% and 20–32%, respectively. FT-IR spectra

Tab. 10.1. NC compositions from gravimetric measurements (TGA graphs) and from C, H, N elemental analyses.

Nanocomposite poly(monomer)-magnetite	Elemental analysis <sup>[a]</sup> (%)			NC Composition (% w/w) <sup>[a]</sup>	TGA weight loss (% w/w)
	C	H	N		
5a	18.63	2.01	3.20	27	28
18a	15.40	1.71	3.50	25	27
19a	19.37	1.76	2.91	28	30
20a	11.39	1.39	2.11	19	19
21a	13.33	1.65	2.35	22	18
5b	19.52	1.40	2.01	25	24
9b	20.87	1.78	2.41	32	31
10b	21.18	1.67	2.32	30	29
11b	14.11	1.62	1.67	20	23
19b	19.34	1.65	2.48	27	30
21b	13.96	1.39	1.38	20	21

<sup>a</sup> Values corrected for oxygen content.

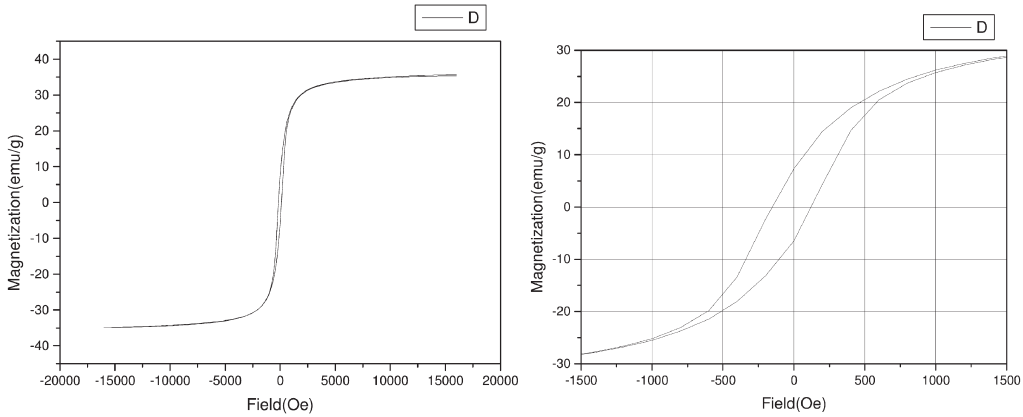
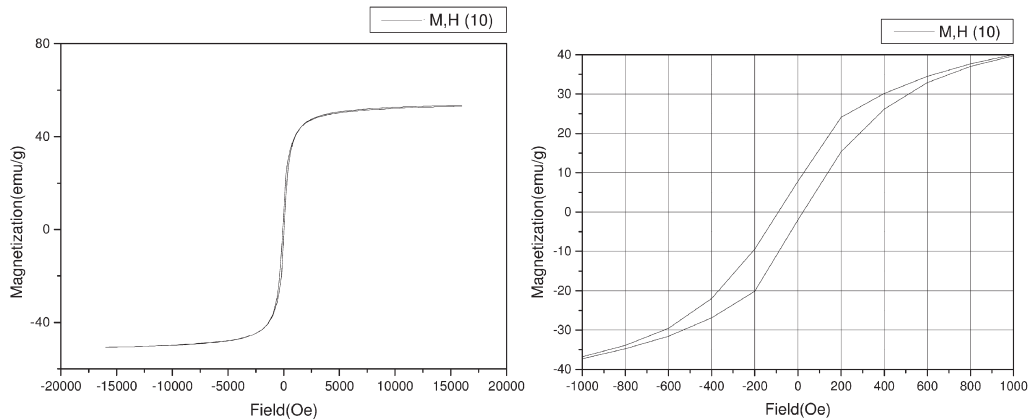
of NCs showed quite similar absorption peaks. They included mixed absorption peaks characteristic of both freshly prepared non-oxidized magnetite ( $\nu = 1083\text{--}1099$ ,  $1017\text{--}1024$ , and  $568\text{--}585\text{ cm}^{-1}$ ) and of polyDPyr- and polyDCbz-polymeric systems [ $\nu = 2850\text{--}2922$  and  $2958\text{--}2964$  ( $\delta_{\text{Csp}^3\text{-H}}$ ),  $1650\text{--}1750$  ( $\nu_{\text{C=O}}$ , carboxyl),  $1454\text{--}1558$  ( $\nu_{\text{Csp}^2\text{-Csp}^2}$ , polypyrrole and polycarbazole aromatics),  $1258\text{--}1264$  ( $\nu_{(\text{C=O})\text{-O}}$ , acid),  $800\text{--}808$  ( $\delta_{\text{Csp}^2\text{-H}}$ , out of plane stretching)  $\text{cm}^{-1}$ ].

Bulk magnetization versus applied magnetic field experiments (Oxford VSM system Magnetometer equipped with an Aerosonic VSM 3001 controller) have been conducted at 300 K on all magnetically responsive, carefully dried NCs. Saturation magnetizations  $M_s$  have been observed in a range of  $32\text{--}55\text{ emu g}^{-1}$ , with coercivity factors  $H_c$  of  $35\text{--}132\text{ Oe}$  (Fig. 10.4 and Table 10.2). Subsequently, these materials cannot be strictly considered as superparamagnetic materials since they presented a low- to medium-range hysteresis. This resulted most likely from the partial oxidation of the former magnetite  $\text{Fe}_3\text{O}_4$  core during the oxidative processes used for monomer polymerizations. In fact, inorganic magnetic cores were formed of nonstoichiometric magnetite,  $\text{Fe}_{3-x}\text{O}_4$  ( $0 \leq x \leq 0.33$ ), or of  $\gamma\text{-Fe}_2\text{O}_3$  (maghemite)–magnetite mixtures as determined by  $^{57}\text{Fe}$  Mössbauer analysis at 300 K (two superposed magnetic subspectra compatible with  $\text{Fe}^{3+}$  and  $\text{Fe}^{2.5+}$  atoms located in tetrahedral and octahedral sites, respectively, with different relative intensities were obtained). For example, polyDCbz(**9b**)- and polyDCbz(**10b**)-magnetite NCs were analyzed and found to contain 30% and 60% maghemite, respectively.

Interestingly, DCbz-containing monomers, which were more difficult to polymerize oxidatively around magnetite particles, mainly afforded NCs of lower  $M_s$  and higher  $H_c$  than similarly prepared polyDPyr-based NCs (Table 10.2). These data are likely to be related to higher contents of less magnetic maghemite/nonstoichiometric magnetite ( $\text{Fe}_{3-x}\text{O}_4$ ) within corresponding NCs, while magnetic spin blocking effects could arise from formation of oxidized magnetite/polymer interfacial domains.

In a second series of analyses, all these NCs were systematically examined by low- and high-resolution transmission electron microscopies TEM (JEOL-1200EX) and HR-TEM (JEOL-JEM 2010 of Oxford Instruments, 200 kV accelerating voltage, Gatan CCD video camera for microphotograph digitization). Even using ultrasonic irradiation, NC fabrication processes were not found to alter the sheet-like morphology of starting magnetite nanoparticles nor the average particle size (20–40 nm). More interestingly, mixed structures of the discrete polyDPyr-/polyDCbz-particulates–magnetite nanoparticle type could not be detected, clearly emphasizing polymerization processes, during which deposition of insoluble polymer chains occurred around magnetite nanoparticles. These observations are consistent with the relatively low quantities of polymers deposited onto magnetite nanoparticles independent of starting DPyr-/DCbz-monomers ( $\sim 18\text{--}32\%$  w/w).

Since polymer–magnetite NC morphology remained a central issue, unambiguous confirmation of the core–shell nature for *all* the fabricated NCs came from HR-TEM analysis combined with EDAX. For illustration, HR-TEM microphotographs of poly(**5a**)-, poly(**10b**)- and poly(**21a**)-magnetite NCs belonging to both poly-

**PolyDCbz(5b)-magnetite Nanocomposite**(specific saturation magnetization  $M_s$ : 35 emu/g, coercivity  $H_c$ : 132 Oe)**polyDCbz(9b)-magnetite NC**(specific saturation magnetization  $M_s$ : 52 emu/g, coercivity  $H_c$ : 35 Oe)**Fig. 10.4.** Magnetism measurements/graphs for polyDCbz(5b)- and polyDCbz(9b)-magnetite NCs.

DPyr- and polyDCbz-series of NCs have been reported that showed clearly amorphous 5.0–7.5 nm thick polyDPyr-/polyDCbz-deposits decorating highly ordered magnetite/maghemite crystals (Fig. 10.5, samples prepared on 400 mesh Au grids free of carbon-containing pollutants). Corresponding elemental compositions have been determined by EDAX microanalysis using an Oxford Instruments X-ray detector and INCA software with electron beams focused at both 15 and 30 nm diameters, depending on the samples. All chemical elements have been analyzed, nor

**Tab. 10.2.** Saturation magnetizations  $M_s$  and coercivities  $H_c$  of polyDPyr-/polyDCbz-magnetite NCs.

<b>Nanocomposite</b> <i>poly(monomer)-magnetite</i>	<b>Saturation magnetization</b> $M_s$ ( $\text{emu g}^{-1}$ )	<b>Coercivity</b> $H_c$ (Oe)
5a	50	55
18a	52	55
19a	55	55
20a	50	40
21a	55	50
5b	35	132
9b	52	35
10b	51	55
11b	35	130
19b	32	130
21b	35	130

malized, and their results obtained in weight percentages. Examples of such EDAX microanalyses are shown for poly(**5a**)- and poly(**21a**)-magnetite NCs in Fig. 10.5, wherein crystal edges have been found to be systematically carbon-rich and iron-poor, while crystal centers appear to be carbon-poor and iron-rich, arguing for the presence of organic polymer deposits around magnetite nanoparticles [poly(**5a**)-magnetite NC, spectrum 1: 55.2 and 18.0% for C and Fe versus spectrum 2: 1.9 and 63.4%; poly(**21a**)-magnetite NC: spectrum 9: 39.6 and 44.1% for C and Fe versus spectrum 6: 1.7 and 48.8%].

## 10.5

### Development of a DNA-based Biological System for Nanocomposite Parallel Screening

Among the critical steps identified for screening the properties and optimization of fabricated polyDPyr-/polyDCbz-magnetite NCs, realization of a reliable highly-parallel (use of 96-well microtiter plates), low cost, less laborious and robust biological screening system were quite essential. Accordingly, a natural choice was to turn to a DNA-based hybridization system, supported on these novel nanosized magnetic NCs, because of the extreme relevance of DNA-based diagnostics using magnetically responsive nanomaterials [54, 55]. Although numerous examples of DNA hybridizations onto various non-planar solid phases have been reported, they are mainly concerned with micrometer-sized beads that generally did not suffer from critical aggregation and non-specific binding (NSB) issues often encountered with nanosized materials [56, 57].

During our studies involving polyDPyr-/polyDCbz-magnetite NCs, two different modes of DNA probe attachments were tested – covalent (via amide bonds) and

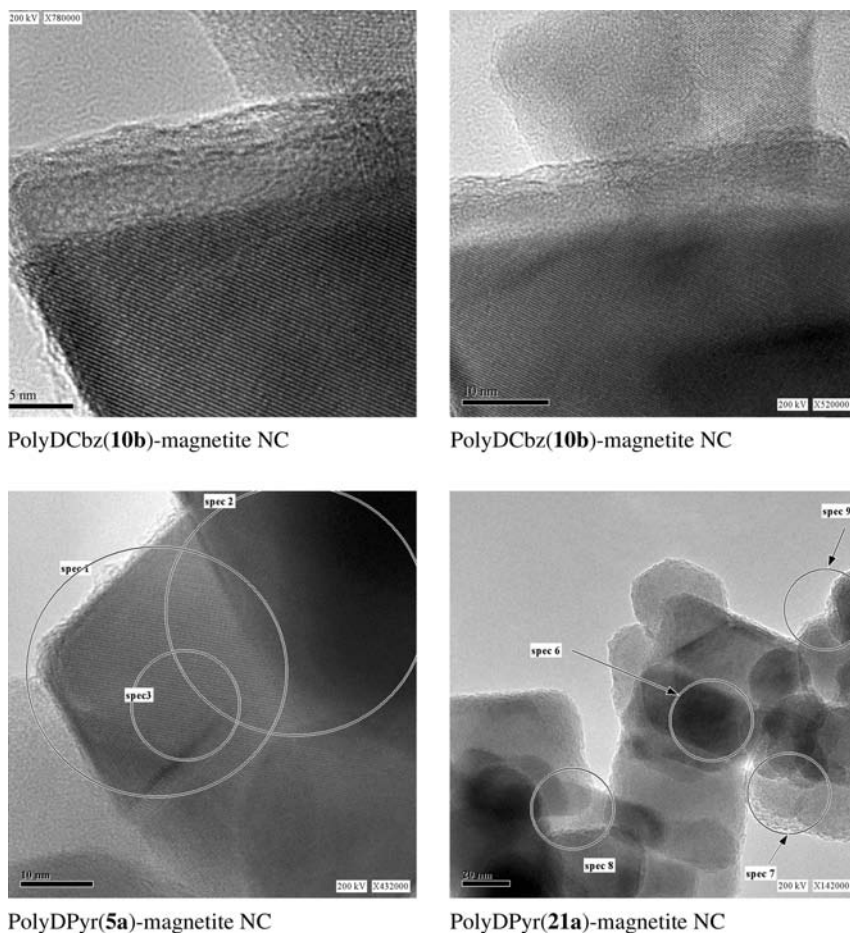


**Fig. 10.5.** High-resolution TEM microphotographs of selected polyDPyr-/polyDCbz-magnetite NCs.

quasi-covalent (via streptavidin–biotin interactions [58–60]). These brought out the great versatility of the chemistry of surface COOH groups of NCs set up by polycarboxylated polyDPyr-/polyDCbz-deposits. After simple chemical activation of COOH groups by water-soluble carbodiimides [61–63], the addition of an  $\text{NH}_2$ -5'-modified DNA sequence as a model molecular DNA probe resulted in covalent attachment of DNA through stable amide bonds. Alternatively, second-generation streptavidin-modified magnetic NCs could be fabricated using a similar activation protocol of polymeric COOH groups followed by incubation with streptavidin. Covalent attachment of streptavidin occurs via amidation of  $\epsilon$ - $\text{NH}_2$  groups of surface lysines of the protein. Then, the same, albeit biotin-5'-modified, DNA sequence will be quasi-covalently (via streptavidin–biotin interactions) attached to modified NCs upon incubation, resulting in the testing and comparison of DNA-decorated

NCs using both probe attachment methodologies. The streptavidin/avidin-biotin system has many advantages [58–60]. Noncovalent streptavidin–biotin supramolecular interactions are very strong ( $K_d \sim 10^{-15}$  M) and, furthermore, the system is more biocompatible, and is therefore less denaturing for DNA/protein molecular probe attachments. Additionally, its great versatility makes it particularly attractive for a wide range of biological and non-biological probes (sugars, peptides, proteins/antibodies, DNA/RNA sequences, and catalysts, small ligands, fluorescent dyes, quantum dots and nanoparticles/clusters).

### 10.5.1

#### Covalent Attachment of an $\text{NH}_2$ -5'-modified 20-mer DNA Probe onto NCs towards DNA-Biofunctionalized NCs. Covalent Amide Bond Chemistry and Resulting NC-Supported DNA Hybridizations

The simple but powerful DNA-based test described in Fig. 10.6 constitutes the basic biological screening system used to investigate the properties of fabricated polyDPyr-/polyDCbz-magnetite NCs in parallel mode [53]. Whether the covalent (amide bond chemistry) or quasi-covalent (streptavidin–biotin system) DNA probe attachments were used in NC functionalization, DNA hybridizations on NC surfaces were characterized and quantified using a blue color-emitting, HRP-based enzymatic amplifying system (HRP: Horse Radish Peroxidase). Resulting hybridization signal outputs were processed in parallel, using 96-well plastic microtiter plates optically read in an Elisa Plate Reader Anthos ht II at 620 nm.

Practically, the amine-modified 20-mer oligonucleotide DNA<sub>1</sub>  $\text{H}_2\text{N}-(\text{CH}_2)_{12}-5'$  GCACTGGGAGCATTGAGGCT that characterized the 20210 mutation in the Human Factor II gene (G → A single oligonucleotide mutation at position 20210) [64, 65] was chosen as a model DNA probe and, through incubation, has been covalently attached to a full range of fabricated NCs after carboxylate activation in

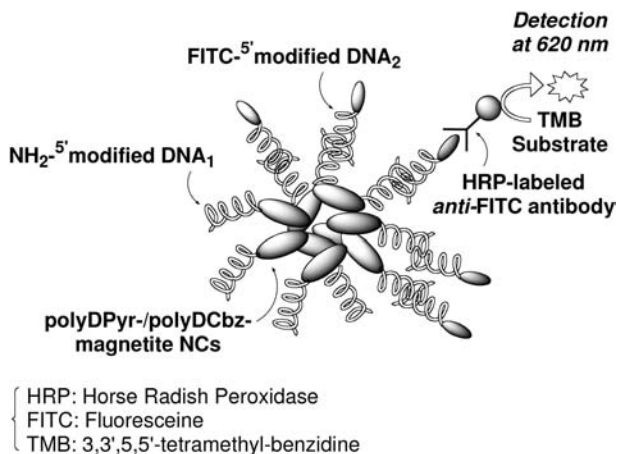


Fig. 10.6. DNA covalent attachment onto polyDPyr-/polyDCbz-magnetite NCs and hybridization.

a 0.4 M MES buffer (pH 5.0) by the water-soluble carbodiimide EDC [63] [EDC: *N*'-(3-dimethylamino-propyl)-*N*-ethylcarbodiimide hydrochloride, 0.4 M MES buffer, 2 h incubation at 20 °C]. NC-supported DNA hybridizations have been performed with the fluoresceine-labeled *anti*-sense 20-mer oligonucleotide FITC-DNA<sub>2</sub> (fluoresceine-5'AGCCTCAATGCTCCCAGTGC, 60 min, 60 °C). After addition of an *anti*-FITC HRP-labeled mouse monoclonal antibody and incubation (20 min, 20 °C), the HRP substrate TMB (3,3',5,5'-tetramethylbenzidine) was added and reacted with the NC-immobilized amplifying enzymatic construct for 1.5 min at the same temperature before visible signal reading at 620 nm (Elisa Plate Reader Anthos ht II). Accordingly, the resulting optical reading data (OD<sub>Total</sub>) allowed the characterization of all the tested DNA-functionalized NCs. These were systematically averaged for six to ten similar parallel experiments for each separate NC, providing minimal signal output variations in a 5–8% range.

Additionally, and for better characterization of DNA-decorated NCs, Non-specific binding (NSB) data were systematically collected during similar averaged parallel experiments, where the complementary FITC-labeled DNA<sub>2</sub> probe was omitted. NSB data allowed us to estimate the affinity of tested DNA-decorated polyDPyr/polyDCbz-magnetite NCs to physically adsorb the reporter *anti*-FITC HRP-labeled antibody. Furthermore, micrometer-sized COOH-Dynabeads<sup>®</sup> M-270 (∅ 2.8 μm, Dynal AS, Oslo, Norway) [66] that are routinely used for magnetism-driven suspension assays were also included in those experiments as an internal standard for comparison.

In a first series of experiments for screening of NC-supported DNA hybridizations, the concentrations of FITC-5' labeled complementary probe FITC-DNA<sub>2</sub> and tested NCs were 10<sup>-7</sup> M and at 50 μg (1.0% w/v), respectively, per microtiter plate well (Fig. 10.7). From patterns of optical signal outputs (OD<sub>Total</sub>) and specific binding (SB = OD<sub>Total</sub> - NSB)/NSB ratios, the three polyDCbz-magnetite NCs, e.g., polyDCbz(**9b**)-, polyDCbz(**10b**)-, and polyDCbz(**19b**)-magnetite NCs, were as efficient as the COOH-Dynabeads tested under similar conditions. Calculated SB/NSB averaged ratios of 19.0–22.8 were in a high range. In contrast, polyDPyr-magnetite NCs were less efficient than standard COOH-Dynabeads with SB/NSB data in a low to medium (4.2–16.3) range. Here, polyDPyr(**19a**) was the most efficient NC in the polyDPyr-based series of NCs (SB/NSB = 16.3 vs. 22.2 for COOH-Dynabeads).

Interestingly, both couples of NCs polyDPyr(**19a**)/polyDCbz(**19b**)- and polyDPyr(**21a**)/polyDCbz(**21b**)-magnetite fabricated from DPyr-/DCbz-monomers **19/21a–b**, possessing an hydrophobic 1,4-diaminobutane and an hydrophilic 4,7,10-trioxa-1,13-tridecaneamine linker, were related. Among the tested NCs, they exhibited the higher and the lower efficiencies, respectively. Confirming this specific trend, the polyDPyr(**20a**)-magnetite NC built on the same hydrophilic 4,7,10-trioxa-1,13-tridecaneamine linker showed the lowest efficiency of all the tested NCs (SB/NSB = 4.2). Additionally, both polyDPyr(**5a**)- and polyDCbz(**5b**)-magnetite NCs arising from the same monocarboxylated L-lysine-based precursor exhibited similar efficiencies (13.2 and 15.4, respectively).

Subsequently, while keeping other assay parameters constant (see the typical

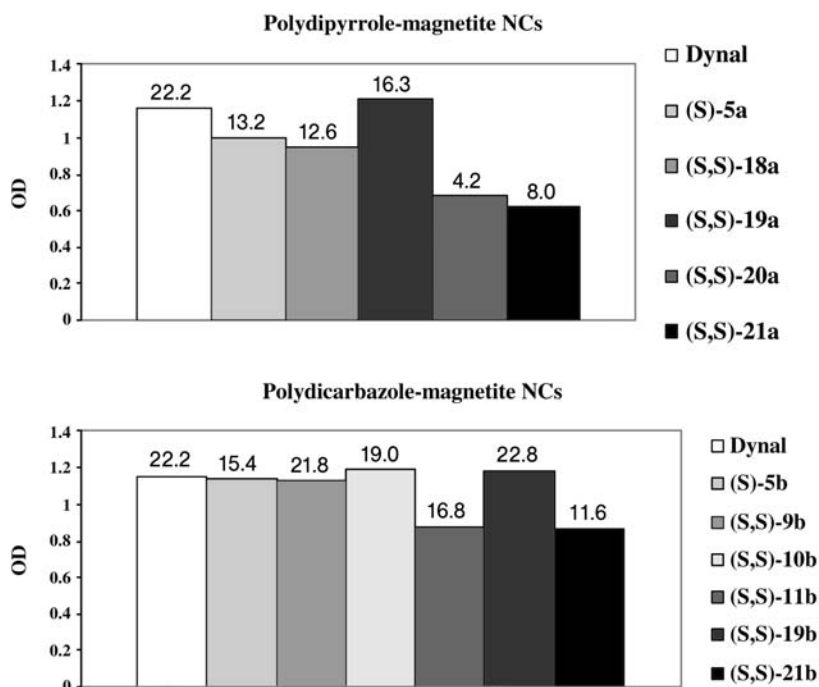
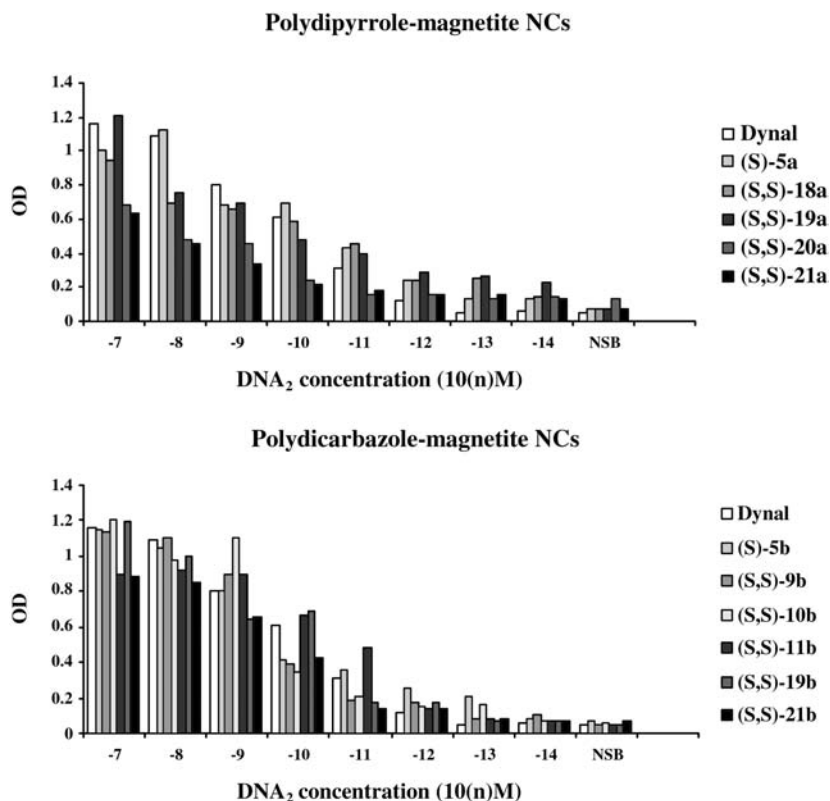


Fig. 10.7. Screening of polyDPyr-/polyDCbz-magnetite NCs at a  $10^{-7}$  M DNA<sub>2</sub> concentration and related specific binding/non-specific binding (SB/NSB) ratios.

procedure reported below), a second larger parallel screening of NC properties was performed to find a minimum assay sensitivity limit to detect the model analyte FITC-labeled DNA<sub>2</sub> (Fig. 10.8). For this purpose, a concentration range of  $10^{-7}$ – $10^{-14}$  M of FITC-labeled DNA<sub>2</sub> was investigated. In this concentration range, NSB averaged data were uniformly observed in a low 0.05–0.09 range for all tested NCs, except for the polyDPyr(20a)-magnetite NC fabricated from the hydrophilic 4,7,10-trioxa-1,13-tridecanediamine (averaged NSB = 0.11). The previously observed trend of being the least efficient system for the SB/NSB ratio was consistent and reproducible for all tested concentrations of FITC-labeled DNA<sub>2</sub>. These data precluded its further use as a sensitive detection of this model analyte. In contrast, three polyDPyr- and three polyDCbz-magnetite NCs were disclosed as the most sensitive NCs, able to achieve reproducible SB/NSB ratios in the range 1.6–2.7, at very low  $10^{-12}$ – $10^{-14}$  M concentrations of FITC-labeled DNA<sub>2</sub>. These NCs were polyDPyr(5a)-, polyDPyr(18a)-, and polyDPyr(19a)-magnetite in the polyDPyr-series and, in the polyDCbz-series, were polyDCbz(5b)-, polyDCbz(9b)-, and polyDCbz(10b)-magnetite. COOH-Dynabeads, tested in parallel under identical concentration range and conditions, were quite inefficient. This emphasized the potential of these novel nanosized magnetic NCs for highly sensitive DNA detec-





**Fig. 10.8.** Sensitivity patterns of PolyDPyr-/polyDCbz-magnetite NCs at decreasing FITC-labeled DNA<sub>2</sub> concentrations.

tion. Interestingly, and among all tested polyDPyr-/polyDCbz-NCs, the unique polyDPyr(**19a**)-magnetite NC was the most sensitive (SB/NSB = 2.7 at  $10^{-14}$  M), while both polyDCbz(**5b**)- and polyDCbz-(**10b**)-magnetite NCs were just an order less sensitive for similar SB/NSB ratios (SB/NSB = 2.0 and 1.6, respectively, at  $10^{-13}$  M).

Importantly, these low-range detection levels were consistently achieved without employing any additional passivating step (Egg albumin, BSA, PEG<sub>1000</sub> or Triton X surfactants, dextran) commonly used in the diagnostic field.

Concentrating on both typical polyDPyr(**5a**)- and polyDCbz(**5b**)-magnetite NCs, sensitivity issues were further examined by investigating the influence of two additional parameters, i.e. minimal amounts of (a) capture NH<sub>2</sub>-modified DNA<sub>1</sub> probe covalently attached onto NCs and (b) NCs used per microtiter plate well to afford reliably quantifiable optical outputs with SB/NSB ratios in a 1.0–1.5 range (Fig. 10.9). First, concentrations of the capture NH<sub>2</sub>-<sup>5'</sup>-modified DNA<sub>1</sub> probe for the covalent functionalization of both NCs were varied in a  $10^{-5}$ – $10^{-16}$  M range. Other

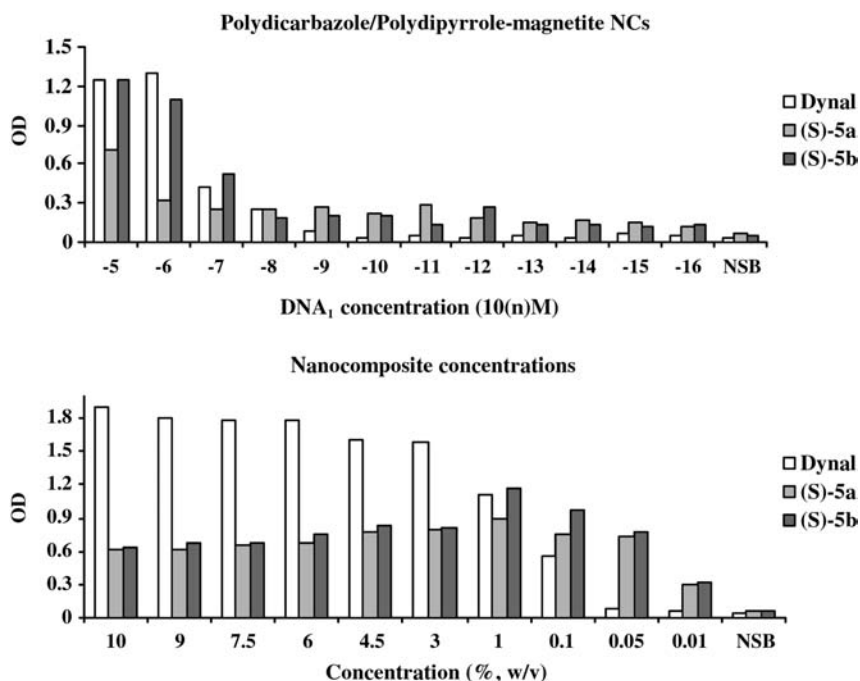


**Fig. 10.9.** Sensitivities of polyDPyr(5a)- and polyDCbz(5b)-magnetite NCs for decreasing DNA<sub>1</sub> and NC concentrations (the value 1% w/v corresponds to 50 µg of NC per microtiter plate well).

protocol parameters were identical to values used in the typical experimental protocol described in Section 10.6.2. For comparison, a DNA<sub>1</sub> concentration of  $10^{-7}$  M for probe attachment onto NCs was used (standardized experimental protocol). Second, variable NC amounts per microtiter plate well were investigated in a  $10^{-2}$ – $10^{-1}$ % w/v range (500.0–0.5 µg) when the same standardized experimental protocol made use of a 1% w/v NC concentration, e.g., use of 50.0 µg of NC per well. The resulting data (Fig. 10.9) led to some interesting conclusions.

A rather wide range of concentrations in NH<sub>2</sub>-5'-modified DNA<sub>1</sub> probe, from  $10^{-9}$  to the very low  $10^{-16}$  M, afforded reliable SB/NSB ratios in a 0.9–4.0 range, depending on NCs and DNA<sub>1</sub> concentrations. In contrast, standard COOH-Dynabeads treated under similar conditions were totally unresponsive. Both polyDPyr(5a)- and polyDCbz(5b)-magnetite NCs were effective even at the lowest tested DNA<sub>1</sub> concentration ( $10^{-16}$  M, SB/NSB = 0.9 and 1.4, respectively). Regarding usable NC concentration per microtiter plate well, only limited decreases in signal outputs were registered when using NC amounts per well as low as 5.0 [0.1% w/v; polyDPyr(5a)- and polyDCbz(5b)-magnetite NCs: SB/NSB = 14.0 and 18.6, respectively] and 0.5 µg [0.01% w/v; polyDPyr(5a)- and polyDCbz(5b)-magnetite NCs: SB/NSB = 13.6 and 14.4, respectively]. In parallel, COOH-Dynabeads af-

forded lower or background-level SB/NSB ratios for both NC concentrations (0.1% w/v: SB/NSB = 13.0; 0.01% w/v: SB/NSB = 0.8).

### 10.5.2

#### **Attachment of a Biotin-<sup>5'</sup>-modified 20-mer DNA Probe to DNA-biofunctionalized NCs. Quasi-covalent Linkage Using the Streptavidin–Biotin System and the Resulting NC-supported DNA Hybridizations**

A second methodology for DNA probe attachment onto polyDPyr(**5a**)/polyDCbz(**5b**)-magnetite NCs has been investigated that exploited the strong quasi-covalent streptavidin–biotin interactions. In the first step, two previously fabricated magnetic polycarboxylated polyDPyr(**5a**)/polyDCbz(**5b**)-magnetite NCs were chemically activated at room temperature by the same water-soluble carbodiimide EDC (COOH activation) in a mixture of neutral PBS and 0.4 M MES (pH 5.0) buffers. This activation step is immediately followed by covalent grafting of a high purity commercial recombinant streptavidin (Roche Inc.), leading to second-generation streptavidin-modified polyDPyr(**5a**)/polyDCbz(**5b**)-magnetite NCs. As usually performed, excess chemical reagents and biological components/buffers were readily eliminated or exchanged by magnetic decantation and appropriate washings before DNA hybridizations (see the typical experimental procedure given below).

In the second step, streptavidin-modified NC-supported DNA hybridizations were similarly tracked using the blue-emitting HRP-based enzymatic amplifying system mentioned previously (Fig. 10.6), providing the use of a biotinylated DNA<sub>1</sub> capture probe biotin–(triethylene glycol) linker-<sup>5'</sup>DNA<sub>1</sub>. Notably, in this particular case, NSB data were attributed to the noncovalent binding affinity of streptavidin-modified NCs (e.g., of protein-decorated, instead of polycarboxylated DNA-decorated, NCs) to physically adsorb the reporter *anti*-FITC HRP-labeled antibody.

Interestingly, efficiency comparisons of both covalent (amide chemistry) and quasi-covalent (streptavidin–biotin system) modes of DNA<sub>1</sub> probe attachment showed a particularly strong dependency on NC concentration (NC weight/Elisa plate well) (Fig. 10.10). For example, at a 1% NC concentration (50.0 μg of NC/Elisa plate well), SB/NSB ratios for streptavidin-modified NCs were in a low to medium range (5.3–10.1), with the streptavidin-modified polyDCbz(**5b**)-magnetite NC being the most efficient system (SB/NSB = 10.1). Streptavidin-modified micrometer-sized Dynabeads, prepared in the same way, were as efficient, with a SB/NSB ratio of 11.0. Though, while in covalent NH<sub>2</sub>-<sup>5'</sup>-linked DNA<sub>1</sub> probe attachment mode, both polyDPyr(**5a**)/polyDCbz(**5b**)-magnetite NCs always exhibited a greater efficiency (SB/NSB = 13.2 and 15.4 respectively), they were not comparable to micrometer-sized DNA<sub>1</sub>-decorated Dynabeads, which performed better as the most efficient support (SB/NSB = 22.2).

Conversely, lowering NC concentration to 0.25% w/v (12.5 μg of NC/Elisa plate well) strongly diminished the previous, detrimentally high NSB, resulting in marked differences. Whatever the covalent or streptavidin/biotin modes of DNA<sub>1</sub> probe attachment, the polyDPyr(**5a**)/polyDCbz(**5b**)-magnetite NCs systematically afforded more efficient responses than that of carboxylated Dynal microbeads

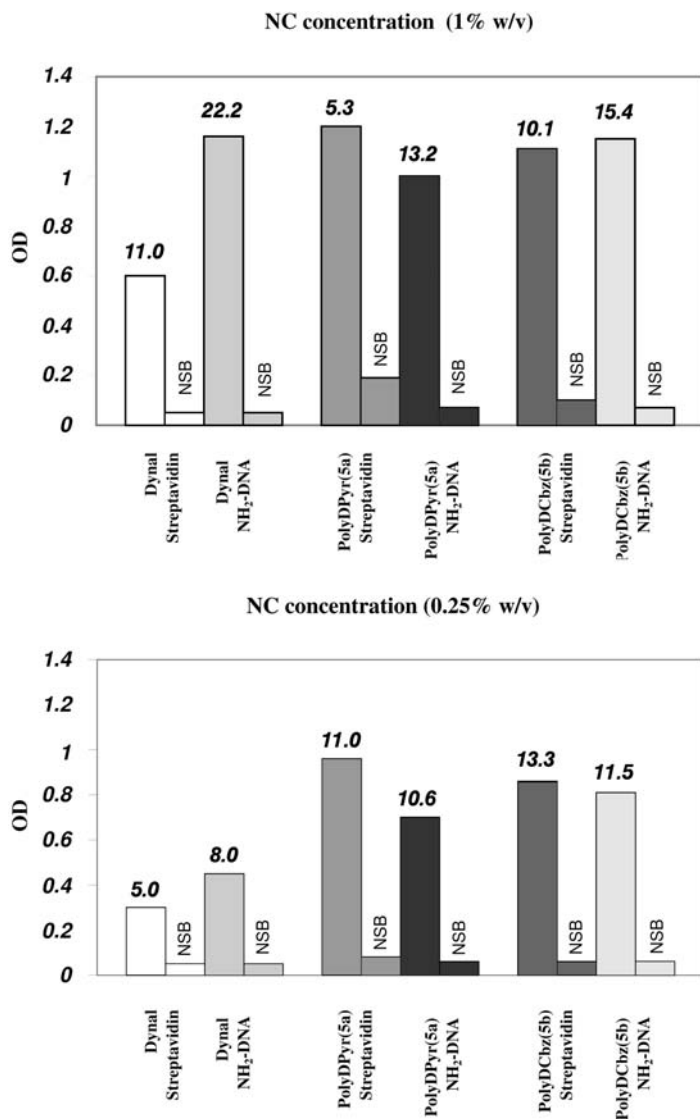


**Fig. 10.10.** Covalent (amide chemistry) and quasi-covalent (streptavidin–biotin system) attachment modes of both NH<sub>2</sub>- and biotin-5'-modified DNA<sub>1</sub> probes onto polyDPyr(5a)- and polyDCbz(5b)-magnetite NCs.

(SB/NSB = 10.6–13.3 vs. 5.0–8.0, respectively). Interestingly for this low NC concentration, both streptavidin-modified polyDPyr(5a)-/polyDCbz(5b)-magnetite NCs displayed better efficiencies than did carboxylated covalently modified ones (SB/NSB = 11.0 and 13.3 vs. 10.6 and 11.5, respectively). These preliminary data featured the important disclosure that optimized conditions dealing with polyDPyr-/polyDCbz-magnetite NCs should be investigated when testing both

types of covalent (amide chemistry) and noncovalent (streptavidin–biotin system) DNA probe attachments.

### 10.5.3

#### Storage: Medium-term Stability of Some PolyDPyr-/PolyDCbz-Magnetite NCs

The colloidal stability of some of these novel polyDPyr-/polyDCbz-magnetite NCs was also examined during storage in a neutral PBS buffer (1% w/v NC concentration) at 4 °C. For this investigation, three freshly prepared polyDPyr- and polyDCbz-magnetite NCs, polyDPyr(**5a**)-, polyDPyr(**19a**)-, polyDPyr(**21a**)-, and polyDCbz-(**5b**)-, polyDCbz(**10b**)-, and polyDCbz(**19b**)-magnetite NCs, and COOH-Dynabeads for reference were stored in the above-described neutral PBS buffer. Regular controls (quadruplicate parallel experiments) were performed on aliquots from these stored NCs on a fifteen day-basis over a period of seven and a half months, using our powerful DNA-based biological screening test. This test was operated using standard conditions of concentrations for DNA<sub>1</sub>, the complementary FITC-labeled DNA<sub>2</sub> and NC components (typical experimental procedure given in Section 10.6.2), for which NSB data were always in a low 0.04–0.05 range.

Importantly, during this period the HRP-based amplifying enzymatic system revealed a slow but regular time-dependent decrease in detection efficiency, probably because of component ageing. This ageing phenomenon, most likely, is due to the natural thermodynamic instabilities of both the HRP-labeled *anti*-FITC antibody (antibody and HRP components), and of the FITC label/epitope of the complementary FITC-labeled DNA<sub>2</sub> (light-induced degradation). Consequently, NC stability data were calculated and presented graphically as ratios of SB data of NCs/SB data of reference COOH-Dynabeads<sup>®</sup> M-270 treated in a similar time-dependent manner. Figure 10.11 depicts the resulting characteristic time-dependent ratio evolutions for each separate NC. More specifically, the three NCs polyDPyr(**5a**)-, polyDPyr(**19a**)- and polyDCbz(**10b**)-magnetite NCs underwent quite noticeable decreases in efficiency (11, 11, and 27%, respectively), most likely due to slow time-dependent NC aggregation. In contrast, the other three NCs belonging to both polyDPyr- and polyDCbz-series displayed reasonable time-dependent stabilities for the examined period and for these specific storage conditions.

## 10.6

### Typical Experimental Procedures for NC Fabrication and NC-Supported DNA Hybridizations

#### 10.6.1

##### Typical Optimized Procedures for NC Fabrication Including Magnetite Preparation

###### 10.6.1.1 Magnetite Preparation Using the Oxidative Hydrolysis of Iron(II) Sulfate in an Alkaline KOH Medium [51, 52]

A solution of iron(II) sulfate heptahydrate (FeSO<sub>4</sub>, 7H<sub>2</sub>O) (17.71 g, 60.0 mmol) in high-purity nitrogen-deoxygenated water (200 mL) was heated at 90 °C in a 1 L

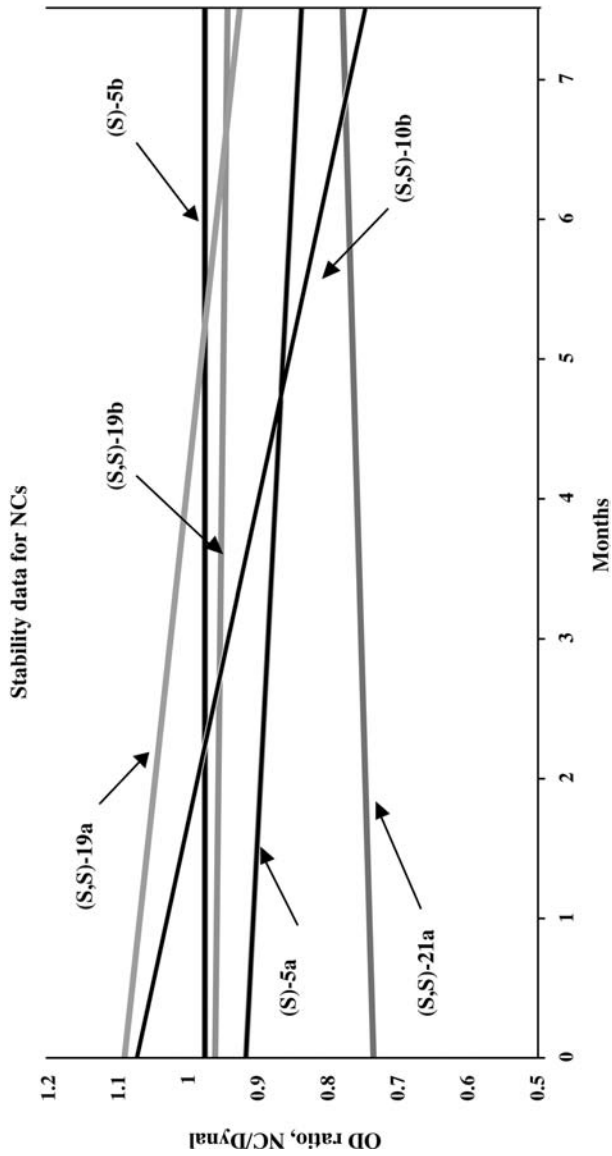


Fig. 10.11. Stability data for polyDPyr-/polyDCbz-magnetite NCs during medium-term storage using a DNA-hybridization screening system.

round-bottomed flask while stirring with an overhead stirrer. In parallel, deoxygenated aqueous solutions of  $\text{KNO}_3$  (10.11 g, 100.0 mmol, 100 mL of  $\text{H}_2\text{O}$ ) and of  $\text{KOH}$  (13.81 g, 250.0 mmol, 50 mL of  $\text{H}_2\text{O}$ ) were prepared and then mixed under nitrogen until complete dissolution of the salts. The resulting basic salt mixture was then slowly added to the  $\text{FeSO}_4$  solution at 90 °C under a constant flow of nitrogen. The oxidative hydrolysis lasted 2 h at 90 °C, affording a brilliant black precipitate of magnetite nanoparticles. After cooling to room temperature (1 h), the black  $\text{Fe}_3\text{O}_4$  nanoparticle suspension was washed twice with  $\text{H}_2\text{O}$  ( $2 \times 2$  L), with 1 M  $\text{HNO}_3$  (2 L), and twice again with  $\text{H}_2\text{O}$  ( $2 \times 2$  L). These washings were repeated if necessary until a visually clear and neutral supernatant aqueous phase was obtained. The suspension volume of precipitated magnetite nanoparticles was adjusted to 1 L with deoxygenated  $\text{H}_2\text{O}$  and kept in a polyethylene storage bottle at 4 °C (stock suspension of magnetite nanoparticles). Preferably, magnetite nanoparticles should be used immediately for polyPyr-/polyCbz-magnetite NC fabrication [final storage concentration of  $\text{Fe}_3\text{O}_4$  nanoparticles: 46 mg (mL of suspension)<sup>-1</sup>].

#### 10.6.1.2 PolyDPyr-Magnetite Nanocomposites

Freshly prepared magnetite nanoparticles (100.0 mg, 2.3 mL of a 3.5% w/v water suspension of magnetite nanoparticles as prepared above) were added with the mono- or dicarboxylated DPyr-monomer (*S*)-**5a** or (*S,S*)-**18–21a** dissolved in MeOH (0.41 mmol, 3.0 mL of MeOH) and sonicated for 1 min (ultrasonic cleaner Bransonic at full 42 kHz power). Thereafter, the oxidizer (ammonium peroxodisulfate,  $(\text{NH}_4)_2\text{S}_2\text{O}_8$ , 98% purity from Riedel-de-Haën, 436.0 mg, 2.05 mmol, 5.0 equiv.) was added in one portion to the sonicated methanolic suspension of magnetite. The resultant fine black suspension (magnetite concentration of 2.0% at constant experiment volume) was then ultrasonicated for 1 h, during which time the medium temperature increased to 55 °C (ultrasound-mediated constant stirring). The resulting brown-black polyDPyr-magnetite NC was magnetically decanted with the help of a powerful external magnet. It was serially washed by  $4 \times 10$  mL of each of the indicated deoxygenated solvents/buffers,  $\text{CH}_3\text{COCH}_3$ , 0.4 M MES buffer (pH 5.0), neutral PBS buffer, TNET buffer (pH 7.5), and, finally, again with neutral PBS buffer to eliminate soluble by-products (inorganic salts, excess oxidants, unreacted monomers, and short, colored monomer-related oligomers). (The preparation of these particular buffers is described in a corresponding typical experimental procedure given in Section 10.6.2.). Colorless supernatants must be obtained at each last separate washing. The resulting magnetically responsive carboxylated polyDPyr-magnetite NCs were suspended in a deoxygenated neutral PBS buffer at a 1% w/v concentration and stored at 4 °C. These colloidal suspensions were stable for at least 2–3 months under these storage conditions.

#### 10.6.1.3 PolyDCbz-Magnetite Nanocomposites [53]

The protocol cited above was modified slightly to take into account the fact that mono- or dicarboxylated DCbz-containing monomers are much more hydrophobic

than DPyr-based ones. Magnetite nanoparticles (same quantity as above) were first magnetically decanted, washed with  $\text{CH}_3\text{COCH}_3$  ( $3 \times 2.0$  mL), and immediately added with the DCbz-based monomer (*S*)-**5b**, (*S,S*)-**9–11b**, or (*S,S*)-**18–21b** solubilized in  $\text{CH}_3\text{COCH}_3$  (0.22 mmol, 2.0 mL of  $\text{CH}_3\text{COCH}_3$ , magnetite concentration of 2.5% at constant experiment volume). After medium sonication for 1 min for best mixing, the ammonium cerium(IV) nitrate oxidizer [CAN:  $(\text{NH}_4)_2\text{Ce}(\text{NO}_3)_6$ ] dissolved in  $\text{CH}_3\text{COCH}_3$  (CAN, 99% purity, Fluka, 0.18 mmol, 100.0 mg, 2.0 mL of  $\text{CH}_3\text{COCH}_3$ ) was added under sonication in one portion. The resultant fine black suspension was ultrasonicated for 5 h at 55 °C (ultrasound-mediated constant stirring). Work-up procedures and storage conditions of the resulting polyDCbz-magnetite NCs were strictly identical to those of the former polymerization protocol.

### 10.6.2

#### Covalent Attachment of an Aminated $\text{NH}_2$ -<sup>5'</sup>-modified DNA Probe. Hybridization Experiments onto PolyDPyr-/PolyDCbz-Magnetite NCs. Typical Experimental Procedures

An appropriate polyDPyr-/polyDCbz-magnetite NC suspension (1% w/v suspension in a neutral PBS buffer, 100  $\mu\text{L}$ , 1.0 mg) was washed by (a) the same PBS neutral buffer ( $3 \times 100$   $\mu\text{L}$ ) and by (b) a 0.4 M MES buffer (pH 5.0, 100  $\mu\text{L}$ ). After magnetically-driven decantation, the supernatant was removed and (a) EDC (0.52 M EDC in 0.4 M MES buffer, 30  $\mu\text{L}$ , 3.0 mg) and (b) the 20-mer amine-modified oligonucleotide DNA<sub>1</sub>  $\text{NH}_2$ - $(\text{CH}_2)_{12}$ -<sup>5'</sup>GCACTGGGAGCATTGAGGCT (0.4 M MES buffer at pH 5.0, 70  $\mu\text{L}$ ,  $1.68 \times 10^{-5}$  M; Danyiel Biotech Ltd, Israel, chemical purity  $\geq 98\%$ ) were added successively at 20 °C. The so-obtained mixture was then incubated at room temperature for 2 h (smooth vortex agitation) for carboxylate activation.

Upon completion, polyDPyr-/polyDCbz-magnetite NCs were washed with  $4 \times 100$   $\mu\text{L}$  of PBS buffer to remove excess DNA<sub>1</sub>. DNA-coated nanocomposites can be stored for weeks at 4 °C at a 1% w/v NC concentration in this same neutral PBS buffer, but containing  $\text{NaN}_3$  (0.02% w/v), without noticeable degradation.

DNA-linked NCs (1.0 mg) were washed in a TNET buffer (100  $\mu\text{L}$ , pH 7.5) and distributed as 5.0  $\mu\text{L}$  (50.0  $\mu\text{g}$ ) portions to the wells of a thermowell polycarbonate non-sterile 96-well microtiter plate, which was then connected to a Dynal MPC<sup>®</sup> magnetic particle concentrator to separate magnetically the nanocomposites. Each well was added with the FITC-labeled *anti*-sense oligonucleotide DNA<sub>2</sub> FITC-<sup>5'</sup>AGCCTCAATGCTCCAGTGC dissolved in a pH 7.5 TNET buffer (50  $\mu\text{L}$ ,  $10^{-7}$  M; Danyiel Biotech Ltd, Israel, chemical purity  $\geq 98\%$ ) and the microtiter plate was incubated for 60 min at 60 °C for hybridization. Hybridized polyDPyr-/polyDCbz-magnetite NCs were washed by a TNET buffer ( $4 \times 100$   $\mu\text{L}$ , pH 7.5) and by 50  $\mu\text{L}$  of a commercially available Assay Solution<sup>®</sup> (Savyon Diagnostics Ltd, Israel) before incubation with the reporter *anti*-FITC HRP-labeled mouse monoclonal antibody (commercially available from Hoffman la Roche Inc., 0.1  $\mu\text{g mL}^{-1}$ , 20 min at 20 °C, 50  $\mu\text{L}$  of an Assay<sup>®</sup> Solution). After magnetically-driven decanta-



tion and plate washings ( $4 \times 100 \mu\text{L}$  of a washing solution), the TMB substrate (0.05% w/w TMB solution in de-ionized water,  $50 \mu\text{L}$ , Savyon Diagnostics Ltd) was added for color development for 1.5 min.

Following decantation, supernatants were removed and  $80 \mu\text{L}$  fractions for each well were transferred to a second PS 96-well microplate for optical reading at 620 nm, using an Elisa plate reader Anthos ht II.

#### 10.6.2.1 Specific Reagents, Buffers and Washing/Assay Solutions

PBS buffer (pH 7.0) prepared from Dubelcco's Phosphate Buffered Saline (Sigma); 0.4 M MES (pH 5.0): prepared using 2-morpholinoethanesulfonic acid hydrate 99%, adjusted to pH 5.0 by addition of 10 M NaOH and stored at  $4^\circ\text{C}$ ; TNET buffer (pH 7.5): prepared from a mixture of 10 mM Tris-HCl, 0.5 M NaCl, 1 mM EDTA and 0.02% Tween-20; washing solution: prepared from a mixture of 3 M NaCl and 2 M Tris-HCl (pH 7.5). Assay solution: prepared from a mixture of 154 mM NaCl, 50 mM Tris-HCl (pH 7.8), 0.5% BSA, and 0.1% Tween 20; EDC: *N*'-(3-dimethylaminopropyl)-*N*-ethylcarbodiimide hydrochloride, >98% purity (Aldrich).

#### 10.6.3

#### Quasi-covalent Attachment of a Biotin-5'-modified DNA Probe and DNA Hybridization Experiments onto Streptavidin-modified PolyDPyr-(5a)/PolyDCbz(5b)-magnetite NCs. Typical Experimental Procedures

Previously prepared polyDPyr(5a)-/polyDCbz(5b)-magnetite NCs (1% w/v suspension in a neutral PBS buffer,  $200 \mu\text{L}$ , 2.0 mg) were first washed by the same neutral PBS buffer ( $3 \times 200 \mu\text{L}$ ), and then gently suspended in a freshly prepared cold 0.4 M MES buffer solution of the activating carbodiimide EDC (100.0 mg EDC/1.0 mL of a 0.4 M MES buffer at pH 5.0,  $60 \mu\text{L}$ ,  $0-4^\circ\text{C}$ ). After 5 min of gentle mixing for carboxylate activation, the commercially available, highly purified recombinant streptavidin dissolved in the same 0.4 M MES buffer [ $0.5 \text{ (mg of protein) mL}^{-1}$  of a 0.4 M MES buffer at pH 5.0,  $140 \mu\text{L}$ ,  $0-4^\circ\text{C}$ , Roche Inc.] was injected for a 1 h of incubation at room temperature (gentle NC mixing/vortexing). The resulting streptavidin-modified NCs were decanted magnetically, washed by a PBS neutral buffer ( $4 \times 200 \mu\text{L}$ ), and finally suspended in the same PBS neutral buffer ( $200 \mu\text{L}$ ) to obtain a 1% w/v suspension of modified NCs ready for use. If necessary, they can be stored at  $4^\circ\text{C}$  for several days without noticeable degradation.

DNA hybridizations operated on streptavidin-modified polyDPyr(5a)-/polyDCbz(5b)-magnetite NCs made use of the 20-mer biotinylated oligonucleotide DNA<sub>1</sub> biotin-(triethylene glycol) linker-5'GCACTGGGAGCATTGAGGCT (1.2 nmol, 0.4 M MES buffer at pH 5.0; Danyiel Biotech Ltd, Israel, chemical purity  $\geq 98\%$  as checked by HPLC analysis, incubation time 2.0 h). DNA hybridizations onto NC surfaces were probed and optically quantified using the same (a) complementary FITC-5'-labeled DNA<sub>2</sub> and (b) HRP-based amplifying enzymatic system, according to the formerly described protocol (covalent amide chemistry). Again, specific (SB) and non-specific binding (NSB) data were averaged values of

three to six parallel experiments so as to minimize dispersion of optical output data.

## 10.7

### Conclusions and Research Outlook

Novel chemically oxidizable COOH-DPyr- and DCbz-monomers have been synthesized using a general modular synthetic route ( $C_2$ -symmetrization of  $NH_2$ -/COOH-amino acid-related building blocks) towards a vast range of functionalized polycarboxylated polyDPyr-/polyDCbz-magnetite NCs. A combination of updated analytical and spectroscopic means has established – without ambiguity – that these magnetically responsive NCs possess a core–shell morphology (sheet-like nanoparticles 20–40 nm in size). This core–shell morphology basically results from chemical oxidative deposition of insoluble polyDPyr-/polyDCbz-polymers from the corresponding DPyr-/DCbz-monomers around magnetite nanoparticles. As a result of NC functionalization [introduction of COOH groups by poly(DPyr)-poly(DCbz)-polymers], DNA attachments and hybridizations have been successfully operated on them under various conditions and attachment formats (covalent and noncovalent) for DNA capture probes. These studies have emphasized their interesting potential for DNA-based diagnostic applications. Additionally, this research clearly offers an original way to combinatorially engineer polyDPyr-/polyDCbz-polymeric shell coverages of these novel magnetic NCs for the optimization of any desired application (NC functionalization by proteins/antibodies/enzymes, small peptides/oligosaccharides, locked nucleic acids, small chemical ligands/receptors). The novel materials, processes, and knowledge produced during this research could also have major applications in materials science and/or sensing technologies. For example, the fabrication of (a) polyDPyr-/polyDCbz-nanorods/nanotubules by template-oxidative polymerization of appropriate monomers within nanosized pores of template membranes, (b) new carbon nanotube–polyDPyr-/polyDCbz NCs, and (c) arrays of nanoporous polyDPyr-/polyDCbz-covered nanoelectrodes for biosensing applications are currently being developed in our laboratory.

### Acknowledgments

This work has been funded under both V<sup>th</sup>/VI<sup>th</sup> Framework European CHEMAG (n° GRD2-2000-30122) and NACBO (n° NMP3-2004-500802-2) projects. J.P.L. warmly acknowledges his close collaborators, Drs. Nurit Perlman, Senthil Govindaraji, Ludmila Buzhanski, and Augustine Joseph for investment in terms of much effort and many ideas during their research period at Bar-Ilan University (Israel). Professor Ian Bruce (Universities of Greenwich, England and of Urbino, Italy), and his main collaborator Dr. M. J. Davies (University of Greenwich, England) contributed much to the success of this research and are particularly

thanked. Many Israeli collaborators/colleagues also supported various aspects of this program, which included specific nanotechnology-related analyses as well as stimulating scientific discussions/support. More particularly, the technical/scientific assistance of Professor Shlomo Margel, Dr. Ishai Bruckental (Departments of Chemistry and Physics, Bar-Ilan University, Israel), and Dr. Erika Rivka Bauminger (Racah Institute of Physics, Hebrew University of Jerusalem, Israel) has been highly appreciated. Drs. Aline Yakir, Nir Navot and Jacob Schlessinger (Savyon Diagnostics Ltd, Ashdod, Israel) are particularly commended for having sensitized us to DNA-based biological techniques.

## References

- 1 R. ARSHADY, D. POULIQUEN, A. HALBREICH, J. ROGER, J. N. PONS, J. C. BACRI, M. DA SILVA, U. HÄFELI, Magnetic nanospheres and nanocomposites in *Microspheres, Microcapsules & Liposomes* (Ed.: R. ARSHADY), Citrus Books, **2002**, Vol. 5, 283–329.
- 2 T. HYEON, Chemical synthesis of magnetic nanoparticles. *Chem. Commun.* **2003**, 927–934.
- 3 M. HILGENDORFF, M. GIERSIG, Synthesis of colloidal magnetic nanoparticles: Properties and applications in the *NATO Science Series, II: Mathematics, Physics and Chemistry*, Springer, **2003**, Vol. 91, 151–161.
- 4 M. A. WILLARD, L. K. KURIHARA, E. E. CARPENTER, S. CALVIN, V. G. HARRIS, Chemically prepared magnetic nanoparticles in the *Encyclopedia of Nanoscience and Nanotechnology* (Ed.: J. A. SCHWARZ, C. CONTESCU, K. PUTYERA), Marcel Dekker, **2004**, Vol. 1, 815–848.
- 5 T. PELLEGRINO, S. KUDERA, T. LIEDL, A. M. JAVIER, L. MANNA, W. J. PARAK, On the development of colloidal nanoparticles towards multifunctional structures and their possible use for biological applications. *Small* **2005**, *1*, 48–63.
- 6 *Scientific and Clinical Applications of Magnetic Carriers*, (Eds.: U. HÄFELI, W. SCHÜTT, J. TELLER, M. ZBOROWSKI), Plenum Press, New York, **1997**.
- 7 I. SAFARIK, M. SAFARIKOVA, Magnetic nanoparticles and biosciences. *Monatsh. Chem.* **2002**, *133*, 737–759.
- 8 R. HERGT, R. HIERGEIST, I. HILGER, W. KAISER, Magnetic nanoparticles for thermoablation in *Recent Res. Develop. Mater. Sc.* **2002**, *3*, 723–742.
- 9 C. C. BERRY, A. S. G. CURTIS, Functionalisation of magnetic nanoparticles for applications in biomedicine. *J. Phys. D: Appl. Phys.* **2003**, *36*, R198–R206.
- 10 K. K. JAIN, Nanodiagnostics: application of nanotechnology in molecular diagnostics. *Expert Rev. Mol. Diagn.* **2003**, *3*, 153–161.
- 11 Q. A. PANKHURST, J. CONNOLLY, S. K. JONES, J. DOBSON, Applications of magnetic nanoparticles in biomedicine. *J. Phys. D: Appl. Phys.* **2003**, *36*, R167–R181.
- 12 S. MORNET, S. VASSEUR, F. GRASSET, E. DUGUET, Magnetic nanoparticle design for medical diagnosis and therapy. *J. Mater. Chem.* **2004**, *14*, 2161–2175.
- 13 A. G. PAYNE, Using immunomagnetic technology and other means to facilitate stem cell homing. *Med. Hypotheses* **2004**, *62*, 718–720.
- 14 G. BIDAN, Electroconducting conjugated polymers: new sensitive matrices to build-up chemical or electrochemical sensors. A review. *Sens. Actuators, B* **1992**, *6*, 45–56.
- 15 A. DERONZIER, J. C. MOUTET, Functionalized polypyrroles as versatile molecular materials for

- electrode modification. A review. *Curr. Top. Electrochem.* **1994**, *3*, 159–200.
- 16 S. COSNIER, Biosensors based on immobilization of biomolecules by electrogenerated polymer films new perspectives. *Appl. Biochem. Biotechnol.* **2000**, *89*, 127–138.
  - 17 A. MALINAUSKAS, Chemical deposition of conducting polymers. *Polymer* **2001**, *42*, 3957–3972.
  - 18 R. GANGOPADHYAY, A. DE, Conducting polymer nanocomposite in the *Handbook of Organic-Inorganic Hybrid Materials and Nanocomposites* (Ed.: H. S. NALWA), American Scientific Publishers: Calcutta, India, **2003**, Vol. 2, 217–263.
  - 19 J. F. RUBINSON, From biology to engineering: The present status of conducting polymers. *ACS Symp. Ser.* **2003**, *832*, 2–15.
  - 20 R. GANGOPADHYAY, Conducting polymer nanostructures in the *Encyclopedia of Nanoscience and Nanotechnology* (Ed.: J. A. SCHWARZ, C. CONTESCU, K. PUTYERA), Marcel Dekker, Sapporo, Japan, **2004**, Vol. 2, 105–131.
  - 21 G. G. WALLACE, P. C. INNIS, L. A. P. KANE-MAGUIRE, Inherently conducting polymer nanostructures in the *Encyclopedia of Nanoscience and Nanotechnology* (Ed.: J. A. SCHWARZ, C. CONTESCU, K. PUTYERA), Marcel Dekker, Wollongong, Australia, **2004**, Vol. 4, 113–130.
  - 22 S. P. ARMES, Conducting polymer colloids. *Curr. Opin. Colloid Interface Sci.* **1996**, *1*, 214–220.
  - 23 R. GANGOPADHYAY, A. DE, Conducting polymer nanocomposites: A brief overview. *Chem. Mater.* **2000**, *12*, 608–622.
  - 24 M. D. BUTTERWORTH, S. P. ARMES, Poly(pyrrole)-silica-magnetite composite colloids. *Polym. Mater.: Sci. Eng.* **1995**, *72*, 300–301.
  - 25 M. D. BUTTERWORTH, S. A. BELL, S. P. ARMES, A. W. SIMPSON, Synthesis and characterization of polypyrrole-magnetite-silica particles. *J. Colloid Interface Sci.* **1996**, *183*, 91–99.
  - 26 J. DENG, X. DING, W. ZHANG, Y. PENG, J. WANG, X. LONG, P. LI, A. S. C. CHAN, Magnetic and conducting Fe<sub>3</sub>O<sub>4</sub>-cross-linked polyaniline nanoparticles with core-shell structure. *Polymer* **2002**, *43*, 2179–2184.
  - 27 S. F. LASCELLES, S. P. ARMES, Synthesis and characterization of micrometer-sized, polypyrrole-coated polystyrene latexes. *J. Mater. Chem.* **1997**, *7*, 1339–1347.
  - 28 C. BARTHET, S. P. ARMES, S. F. LASCELLES, S. Y. LUK, H. M. E. STANLEY, Synthesis and characterization of micrometer-sized, polyaniline-coated polystyrene latexes. *Langmuir* **1998**, *14*, 2032–2041.
  - 29 D. B. CAIRNS, S. P. ARMES, L. G. B. BREMER, Synthesis and characterization of submicrometer-sized polypyrrole-polystyrene composite particles. *Langmuir* **1999**, *15*, 8052–8058.
  - 30 M. A. KHAN, S. P. ARMES, Synthesis and characterization of micrometer-sized poly(3,4-ethylenedioxythiophene)-coated polystyrene latexes. *Langmuir* **1999**, *15*, 3469–3475.
  - 31 S. MAEDA, S. P. ARMES, Preparation of novel polypyrrole-silica colloidal nanocomposites. *J. Colloid Interface Sci.* **1993**, *159*, 257–259.
  - 32 S. MAEDA, S. P. ARMES, Preparation and characterization of novel polypyrrole-silica colloidal nanocomposites. *J. Mater. Chem.* **1994**, *4*, 935–942.
  - 33 S. MAEDA, R. CORRADI, S. P. ARMES, Synthesis and characterization of carboxylic acid-functionalized polypyrrole-silica microparticles. *Macromolecules* **1995**, *28*, 2905–2911.
  - 34 M. R. POPE, S. P. ARMES, P. J. TARCHA, Specific activity of polypyrrole nanoparticulate immunoreagents: Comparison of surface chemistry and immobilization options. *Bioconj. Chem.* **1996**, *7*, 436–444.
  - 35 G. P. MCCARTHY, S. P. ARMES, S. J. GREAVES, J. F. WATTS, Synthesis and characterization of carboxylic acid-functionalized polypyrrole-silica microparticles using a 3-substituted pyrrole comonomer. *Langmuir* **1997**, *13*, 3686–3692.
  - 36 H. M. HAN, S. P. ARMES, Synthesis of

- poly(3,4-ethylenedioxythiophene)/silica colloidal nanocomposites. *Langmuir* **2003**, *19*, 4523–4526.
- 37 A. AZIOUNE, A. BEN SLIMANE, L. A. HAMOU, A. PLEUVY, M. M. CHEHIMI, C. PERRUCHOT, S. P. ARMES, Synthesis and characterization of active ester-functionalized polypyrrole-silica nanoparticles: application to the covalent attachment of proteins. *Langmuir* **2004**, *20*, 3350–3356.
- 38 S. MAEDA, S. P. ARMES, Polypyrrole-tin(IV) oxide colloidal nanocomposites. *Synth. Met.* **1995**, *69*, 499–500.
- 39 S. M. MARINAKOS, J. P. NOVAK, L. C. III BROUSSEAU, A. B. HOUSE, E. M. EDEKI, J. C. FELDHAUS, D. L. FELDHEIM, Gold particles as templates for the synthesis of hollow polymer capsules. Control of capsule dimensions and guest encapsulation. *J. Am. Chem. Soc.* **1999**, *121*, 8518–8522.
- 40 S. M. MARINAKOS, D. A. SHULTZ, D. L. FELDHEIM, Gold nanoparticles as templates for the synthesis of hollow nanometer-sized conductive polymer capsules. *Adv. Mater.* **1999**, *11*, 34–37.
- 41 H. V. MEYERS, Chemical and biological approaches to molecular diversity: Applications to drug discovery in the *Biology-Chemistry Interface* (Ed.: K. NAKANISHI, R. COOPER, J. K. SNYDER III), Marcel Dekker: Framingham, USA, **1999**, 271–287.
- 42 L. WEBER, Molecular diversity analysis and combinatorial library design in *Methods and Principles in Medicinal Chemistry* (Ed.: D. E. CLARK), Wiley-VCH: Weinheim, Germany, **2000**, Vol. 8, 137–157.
- 43 D. L. WRIGHT, R. S. ORUGUNTY, C. V. ROBOTHAM, The role of organic synthesis in the generation of molecular diversity in *Organic Synthesis: Theory and Applications* (Ed.: T. HUDLICKY), JAI Press, **2001**, Vol. 5, 197–254.
- 44 G. HELARY, C. CHEVROT, G. SAUVET, A. SLOVE, Electroactive poly(3,6-carbazole-diyl) with lateral amino-alkyldisiloxane groups. *Polym. Bull.* **1991**, *26*, 131–138.
- 45 A. DESBENE-MONVERNAY, P. C. LACAZE, M. DELAMAR, A quantitative study of cross-linking in electro-deposited carbazole films using tetrabutylammonium tribromide bromination and XPS analysis. *J. Electroanal. Chem.* **1992**, *354*, 241–246.
- 46 K. PÉRIÉ, R. S. MARKS, S. SZUMERITS, S. COSNIER, J.-P. LELLOUCHE, Novel electro-oxidizable chiral *N*-substituted dicarbazoles and resulting electro-active films for covalent attachment of proteins. *Tetrahedron Lett.* **2000**, *41*, 3725–3729.
- 47 S. COSNIER, R. S. MARKS, J.-P. LELLOUCHE, K. PÉRIÉ, D. FOLOGEA, S. SZUMERITS, Electrogenerated poly(chiral dicarbazole) films for the reagentless grafting of enzymes. *Electroanalysis* **2000**, *12*, 1107–1112.
- 48 S. COSNIER, S. SZUMERITS, R. S. MARKS, J.-P. LELLOUCHE, K. PÉRIÉ, Mediated electrochemical detection of catechol by tyrosinase-based poly(dicarbazole) electrodes. *J. Biochem. Biophys. Methods* **2001**, *50*, 65–77.
- 49 S. COSNIER, A. LE PELLE, R. S. MARKS, K. PÉRIÉ, J.-P. LELLOUCHE, A permselective biotinylated polydicarbazole film for the fabrication of amperometric enzyme electrodes. *Electrochem. Commun.* **2003**, *5*, 973–977.
- 50 N. ELMING, N. CLAUSON-KAAS, The preparation of pyrroles from furans. *Acta Chim. Scand.* **1952**, 867–874.
- 51 T. SUGIMOTO, E. MATIJEVIC, Formation of uniform spherical magnetite particles by crystallization from ferrous hydroxide gels. *J. Colloid Interface Sci.* **1980**, *74*, 227–243.
- 52 J. I. TAYLOR, C. D. HURST, M. J. DAVIES, N. SACHSINGER, I. J. BRUCE, Application of magnetite and silica-magnetite composites to the isolation of genomic DNA. *J. Chromatogr., A* **2000**, *890*, 159–166.
- 53 J.-P. LELLOUCHE, N. PERLMAN, A. JOSEPH, S. GOVINDARAJI, L. BUZHANSKY, A. YAKIR, I. BRUCE, New magnetically responsive polydicarbazole-magnetite nano-

- particles. *Chem. Commun.* **2004**, 560–561.
- 54 L. JOSEPHSON, J. M. PEREZ, R. WEISSELEDER, Magnetic nanosensors for the detection of oligonucleotide sequences. *Angew. Chem., Int. Ed.* **2001**, *40*, 3204–3206.
- 55 K. ABDEL-NASSER, J. WANG, Amplified electrical transduction of DNA hybridization based on polymeric beads loaded with multiple gold nanoparticle tags. *Electroanalysis* **2004**, *16*, 101–107.
- 56 D. A. VIGNALI, Multiplexed particle-based flow cytometric assays. *J. Immunol. Methods* **2000**, *243*, 243–255.
- 57 J. WANG, A. ERDEM, An overview to magnetic beads used in electrochemical DNA biosensors in the *NATO Science Series, II: Mathematics, Physics and Chemistry*, Springer: Heidelberg, **2003**, Vol. 102, 297–303.
- 58 E. P. DIAMANDIS, T. K. CHRISTOPOULOS, The biotin-(strept)avidin system: principles and applications in biotechnology. *Clin. Chem.* **1991**, *37*, 625–636.
- 59 M. WILCHEK, E. A. BAYER, Avidin-biotin immobilization systems in *Immobilised Macromolecules: Application Potentials* (Ed.: U. B. SLEYTR, U. BERND), Springer: Heidelberg, **1993**, 51–60.
- 60 E. A. BAYER, M. WILCHEK, The avidin-biotin system. *Immunoassay* **1996**, 237–267.
- 61 J. V. STAROS, *N*-Hydroxysulfosuccinimide active esters: bis(*N*-hydroxysulfosuccinimide) esters of two dicarboxylic acids are hydrophilic, membrane-impermeant, protein cross-linkers. *Biochemistry* **1982**, *21*, 3950–3955.
- 62 F. S. GIBSON, M. S. PARK, H. RAPOPORT, Bis[[4-(2,2-dimethyl-1,3-dioxolyl)]methyl]-carbodiimide (BDDC) and its application to residue-free esterifications, peptide couplings, and dehydrations. *J. Org. Chem.* **1994**, *59*, 7503–7507.
- 63 I. GRAYSON, Water-soluble carbodiimide – an efficient coupling agent for synthesis. *Speciality Chem.* **2000**, *20*, 86–88.
- 64 S. R. POORT, F. R. ROSENDAAL, P. H. REITSMA, R. M. BERTINA, A common genetic variation in the 3'-untranslated region of the prothrombin gene is associated with elevated plasma prothrombin levels and an increase in venous thrombosis. *Blood* **1996**, *88*, 3698–3703.
- 65 V. VICENTE, R. GONZALEZ-CONEJERO, J. RIVERA, J. CORRAL, The prothrombin gene variant 20210A in venous and arterial thromboembolism. *Haematologica* **1999**, *84*, 356–362.
- 66 Dynabeads® M-270 (carboxylic acid form, 2.8  $\mu\text{m}$  diameter, 2–5  $\text{m}^2 \text{g}^{-1}$  specific area) are superparamagnetic beads composed of highly cross-linked polystyrene with a magnetic iron oxide material precipitated and trapped in evenly distributed pores. A hydrophilic outer layer of glycidyl ether provides functional carboxylate groups (150  $\mu\text{mol}$  per g beads). The iron content of the beads is 15% w/w for a magnetic mass susceptibility in a 88–126  $\times 10^{-6} \text{m}^3 \text{g}^{-1}$  range.

## 11 Gelatin Nanoparticles and Their Biofunctionalization

*Sushma Kommareddy, Dinesh B. Shenoy, and  
Mansoor M. Amiji*

### 11.1 Introduction

Progress in nanotechnology and medicine has led to an expansion of novel dosage forms for the delivery of drugs to diseased areas while minimizing toxicity to healthy tissues. Popular nanocarriers include polymeric micelles, dendrimers, micro-nano-emulsions, liposomes, niosomes, supramolecular complexes, nanosuspensions and nanoparticles [1–10]. Most of these can be generally classified as colloidal drug delivery systems (by virtue of their size and physico-chemical properties), each having their own merits and demerits. Nanoparticles, especially those prepared from polymeric materials, enjoy tremendous popularity due to ease of preparation, ease of tuning physico-chemical properties (through an array of polymeric materials), possibility of surface modification, excellent stability and scalability to industrial production. Since their conception in the mid-1970s, nanoparticles have found applicability in almost every section of medicine and biology (besides a host of other fields) in general, in particular for controlled/targeted delivery of drugs and genetic materials [11–21].

Nanoparticles can be categorized as colloidal carrier systems of submicron size that are made from synthetic or natural polymers. Based on the method used for their formation, they could be either nanospheres (or nanoparticles), which are essentially monolithic systems having a solid matrix or nanocapsules that have hollow interior that is filled with the compound of interest and are surrounded by a polymeric shell [16]. Drug-loaded nanoparticles have been developed for almost every route of administration – nasal, ocular, mucosal, inhalation, oral, transdermal and parenteral. Clinically, they have found applications for diagnosing and treating a wide range of pathological conditions.

Polymers used to prepare nanoparticles may be biodegradable or non-biodegradable. An ideal polymer should be biocompatible, biodegradable with minimum toxicity, sterile and non-pyrogenic, and must have a high capacity to accommodate drugs and protect them from degradation. Nanoparticles have been prepared using both natural and synthetic biopolymers. Poly(D,L-lactide-co-

glycolide), poly( $\epsilon$ -caprolactone), polyalkylcyanoacrylates, poly(styrene-co-maleic anhydride), poly(divinylether-co-maleic anhydride), poly(vinyl alcohol), and poly(ethylene glycol) are some of the synthetic, non-immunogenic polymers used extensively for the preparation of nanoparticles [1, 14, 19, 22–25]. Similarly, poly(amino acids), hyaluronic acid, albumin, dextran, chitosan and gelatin are a few of the natural biodegradable polymers [26–32]. While each polymer has its own advantages, nanoparticles can be synthesized with a high degree of reproducibility from most of them; natural polymers, due to their natural origin, are preferred considering non-toxicity and biodegradability. The striking advantage of synthetic polymers is the possibility of synthesizing them reproducibly with well-defined physico-chemical properties. Advances in biotechnology are helping natural polymers overcome this drawback and we can expect a surge in delivery systems based on them. In the sections that follow, the properties of gelatin, its chemical modification, synthesis of nanoparticles using gelatin and its derivatives, characterization of the formed nanoparticles, loading and release of the payload from the nanoparticles and the biocompatibility of gelatin nanoparticles and their conjugates are discussed. Further, the use of these nanoparticles in various drug delivery applications is elaborated.

## 11.2

### Gelatin and Gelatin Derivatives

Gelatin, one of the most versatile, naturally occurring biopolymers, is widely used in food products and pharmaceutical dosage forms. It is a proteinaceous hydrocolloid obtained by partial hydrolysis of collagen. Natural gelatins or recombinant gelatins have been tailored to enhance product performance – thus expanding their applicability in biology and medicine. The following sub-sections give an overview of such gelatins.

#### 11.2.1

##### Gelatin

Gelatin is a heterogeneous mixture of single or multi-stranded polypeptides, each with extended left-handed proline helix conformations and containing between 300 and 4000 amino acids. Figure 11.1 depicts the composition of gelatin in terms of amino acids. The triple helix of type I collagen extracted from skin and bones consists of alpha and beta helical strands together with their oligomers and breakdown (and other) polypeptides and has a molecular mass of  $\sim 95$  kDa, is  $\sim 1.5$  nm wide and  $\sim 0.3$  mm long. It is obtained commercially by acidic or basic cleavage of the intermolecular and intramolecular covalent bonds that stabilize porcine or bovine collagen. Figure 11.2 shows the basic structure of gelatin. Based on the process used for its manufacture, gelatin is obtained either as Type-A or -B. Type-A gelatin is obtained by acidic treatment of collagen and has an isoelectric point (pI) between



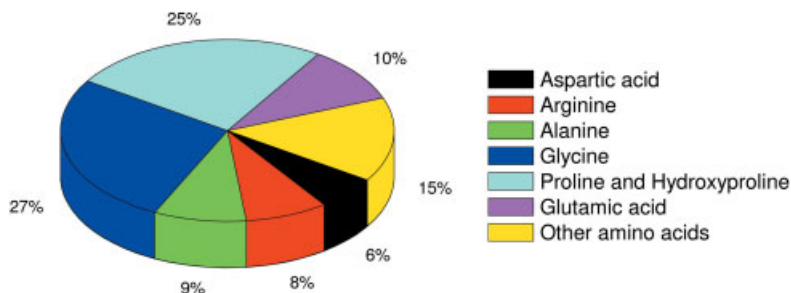


Fig. 11.1. Amino acid composition of gelatin.

7.0 and 9.0. Type-B gelatin, however, is obtained by alkaline hydrolysis of collagen and has a pI between 4.8 and 5.0. [33–35].

Gelatin is a polyampholyte that gels below 35–40 °C. The heterogeneous nature of the molecular weight profile of this biopolymer is affected by pH and temperature, which in turn affects the noncovalent interactions and phase behavior of gelatin in solution [35]. The numerous pendant functional groups throughout the polymeric chain present many opportunities for a pharmaceutical chemist to induce novel functionality via chemical derivatization. The purpose could be as simple as crosslinking and/or hardening or could be as complex as ligand-mediated active targeting at the cellular level.

### 11.2.2

#### Chemical Modification of Gelatin

Different modifications of polymer gelatin are carried out to control the biofunctional properties: biodistribution, targetability and stability of the formulations prepared from the modified polymer [36]. Poly(ethylene glycol) (PEG) conjugation (PEGylation), thiolation and conjugation with other synthetic block copolymers and antibodies are some of the currently studied modifications of gelatin.

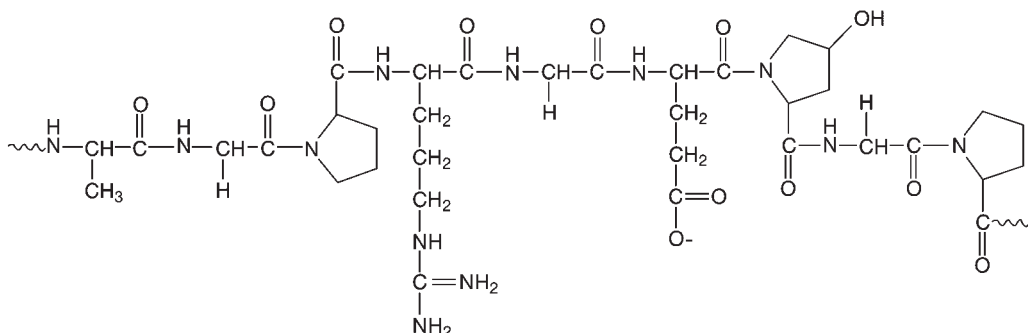


Fig. 11.2. Basic chemical structure of gelatin.

### 11.2.2.1 PEGylation

PEGylation is the simplest and most popular methodology employed to increase the systemic circulation time of colloidal carriers like liposomes, micelles and nanoparticles [37–41]. It is the most widely accepted and commercially utilized technique to improve drug performance by optimizing pharmacokinetics, increasing bioavailability, decreasing immunogenicity and dosing frequency [42–47]. The basic strategy of PEGylation is to hydrophilize the surface and to induce a steric barrier by anchoring long, mobile PEG chains – thus preventing opsonin recognition in the reticuloendothelial system (RES) based blood clearance pathway. Based on the properties of colloids, the stability can be increased by limiting the mutual interactions (hydrophobic, van der Waal's, electrostatic etc.) by usage of hydrophilic and chemically inert polymers that form a protective layer around each particle, resulting in steric stabilization [48]. The major outcome of PEGylation is the significantly increased circulation time, the advantages of which include maintenance of optimal therapeutic concentration of drug in the blood after single administration of the drug carrier, increased probability of extravasation and retention of the colloidal carrier in areas of fenestrated vasculature and enhancement of active targeting ability to areas of diminished blood supply by using a ligand [11]. Besides PEG, polymers such as poly(vinyl alcohol), poly(acryl amide), poly(vinyl pyrrolidone) are also used to modify the physico-chemical properties of colloidal carriers [36].

PEG is a linear or branched polymer with terminal hydroxyl groups and is synthesized by anionic ring-opening polymerization of ethylene oxide initiated by nucleophilic attack of hydroxide ion on epoxide ring. Monomethoxy PEG (mPEG) is another widely used modification where polymerization is initiated by methoxide ion. To conjugate PEG to molecules such as polypeptides, polysaccharides, polynucleotides or other polymers, a derivative of PEG is generally prepared by functionalizing one or both the hydroxyl end groups and then coupled to the reactive amino, hydroxyl or carboxyl groups present on the molecules of interest [42]. The protective action (Stealth<sup>®</sup> property) of PEG is mainly due to the formation of a dense, hydrophilic cloud of long polyethylene chains on the surface of the molecule/colloidal particle. The tethered/chemically anchored PEG chains can undergo spatial conformations, thus preventing the opsonization of particles by the RES of the liver and spleen and hence improving the circulation time of molecules/particles in the blood. In addition, excellent biocompatibility and lack of toxicity/immunogenicity make PEG the polymer of choice for chemically modifying molecule/particles of interest to induce Stealth<sup>®</sup> properties [49–51]. The best known commercial success that employs the PEGylation technology to increase the circulation half-life of an intravenously injected formulation is the Stealth<sup>®</sup> liposomal formulation of doxorubicin (Doxil<sup>®</sup>) [39].

We have prepared PEG-modified gelatin for drug delivery applications by reacting Type-B gelatin with PEG-epoxide according to the scheme depicted in Fig. 11.3 [52]. Carboxylated mPEG can also be prepared, and subsequently coupled to the amine groups of gelatin by the dichlorohexylcarbodiimide method [53]. FTIR and NMR analysis confirmed the carboxylation and coupling reactions, and by estimat-

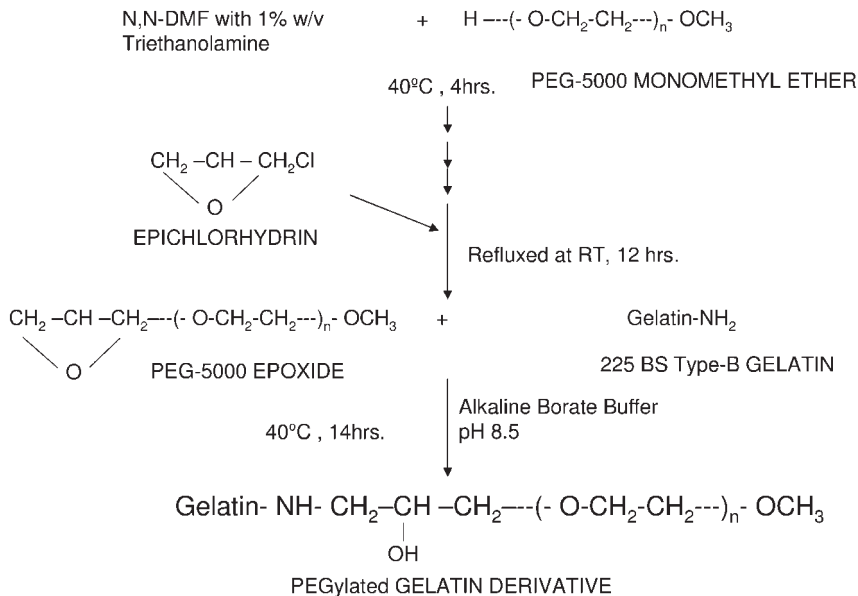


Fig. 11.3. Scheme of poly(ethylene glycol) (PEG) conjugation with Type-B gelatin.

ing the unreacted mPEG it was determined that each molecule of gelatin was coupled to 205 molecules of mPEG. In another study, an ester-activated PEG (mPEG) was coupled to the amino group of gelatin to prepare PEG-grafted gelatin (PEG-gelatin). This PEG-gelatin formed a micellar structure with PEG chains positioned on the outer surface of the micelle [54].

When hydrated in an aqueous medium, the chain-like PEG molecule is swiftly hydrated and set in rapid motion. This extended, quick motion causes the PEG to sweep out a large volume around it, preventing the approach and interference of other molecules/particles. As a result, when attached to a drug or a particle, PEG chains can influence not only inter-molecular/particulate interactions but also protect the underlying core from immune response and other clearance mechanisms, thus sustaining drug bioavailability. The size, molecular weight and shape of the PEG fraction and the linkage used to connect it to the entity of interest determine the consequences of PEGylation in relation to protein adsorption and pharmacokinetics (like volume of distribution, circulation time and renal clearance). When formulated into colloidal particles, the PEG density on the colloidal surface can be changed by using a PEG of appropriate molecular weight (hence length of poly(ethylene glycol) chains) and molar ratio (hence the grafting efficiency) between gelatin and PEG. Longer PEG chains offer greater steric influence around the colloidal entity – similar to increased grafting density with shorter PEG chains. Longer PEG chains may also collapse onto the nanoparticle surface, thus providing a hydrophilic shield.

### 11.2.2.2 Thiolation

Thiolated derivatives of gelatin have been prepared by different methods to create disulfide crosslinked hydrogels that can act as substrates for cell growth, improve the mucoadhesive properties of the nanoparticulate material and to functionalize the gelatin for conjugation with other molecules like antibodies or drugs. Thiolated gelatin can be synthesized by carbodiimide-mediated reaction of the carboxyl groups of gelatin with disulfide-containing dithiobis(propionic hydrazide) (DTP) followed by reduction with dithiothreitol (DTT) (Fig. 11.4) [55]. As this chemical reaction is based on the modification of carboxyl groups of gelatin, the carboxyl rich Type-B gelatin is preferred to Type-A. The reaction is carried out at pH 4.7 to obtain gelatin-DTPH after reduction with DTT [55]. Other thiolation reactions that involve modification of carboxyl residues are activation of carboxyl groups using carbodiimide followed by covalent reaction of a sulfhydryl group containing substrate, like cystaminium dichloride [56].

The  $\epsilon$ -amino groups of the proteins can also be modified to introduce a free thiol group. Traut's reagent (2-iminothiolane) undergoes a ring-opening reaction with amino groups to expose the sulfhydryl group. Reagents like succinimidyl 3-(2-pyridyldithio) propionate (SPDP), succinimidyl 4-(*p*-maleimidophenyl) butyrate (SMPB), *N*-succinimidyl[4-iodoacetyl] aminobenzoate (SIAB), succinimidyl 4-[*N*-maleimidomethyl] cyclohexane-1-carboxylate (SMCC) are also used as bifunctional crosslinkers that react with amino groups of proteins to produce a free sulfhydryl group on the surface. Alternatively, gelatin nanoparticles can be thiolated after crosslinking with glutaraldehyde (post-modification). In such cases, aldehyde groups are quenched with cysteine, which generates free sulfhydryl groups on the surface of gelatin nanoparticles [57]. The disulfide content or the free thiol groups can be determined by Ellman's assay or by  $^1\text{H}$  NMR [56].

Thiolated gelatin obtained by utilizing any of the above-mentioned reactions can be further modified by conjugation with moieties like avidin, which is complexed with biotinylated peptide nucleic acids or biotinylated antibodies [58, 59]. Hyaluronan–gelatin hydrogels have been prepared by disulfide crosslinking of thiol derivatives of hyaluronan and gelatin that were synthesized separately. Such disulfide crosslinked hydrogels have been used as a substrate for cell growth [60].

### 11.2.2.3 Other Conjugates of Gelatin

Gelatin has been conjugated with chitosan by the enzymatic action of tyrosinase on gelatin [61]. The enzyme tyrosinase is an oxidative enzyme that converts phenols into *O*-quinones – hence it reacts with tyrosyl groups present on the telopeptide region of gelatin to convert them into *O*-quinones that react with nucleophilic amino groups of chitosan non-enzymatically. Chemical conjugation of gelatin to chitosan was confirmed by UV/Visible, IR and  $^1\text{H}$  NMR spectroscopy. Viscosity measurements carried out at different reaction conditions also indicated the conjugation of gelatin with chitosan, as it has thermal behavior compared with gels formed by cooling gelatin. These studies indicate that the mechanical properties of tyrosinase-mediated conjugates of gelatin can be further explored for medical and industrial applications [61].

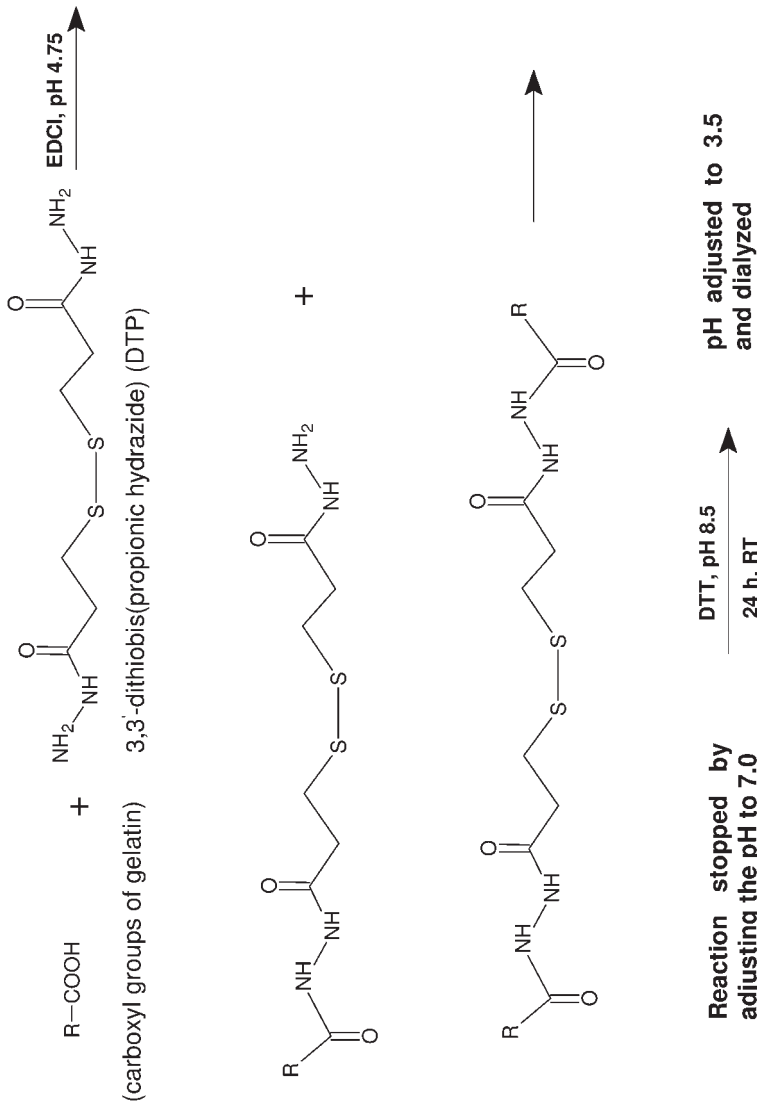


Fig. 11.4. Scheme of thiolation of carboxyl groups of gelatin with disulfide-containing dithiobis(propionic hydrazide) (DTP) mediated by carbodiimide.

Semi-synthetic, biodegradable, amphiphilic copolymers of poly(D,L-lactide) grafted gelatins have been prepared by ring-opening polymerization of D,L-lactide onto gelatin and a trimethylsilyl derivative of gelatin in the presence of a catalyst, tin(II) bis(2-ethylhexanoate), at 80 °C [62]. The solution polymerization was carried out in DMSO and the copolymers formed were characterized by elemental and thermal analysis, and IR and <sup>1</sup>H NMR spectroscopy. Molecular weights of the copolymers were calculated and were found to increase with increasing ratio of D,L-lactide to gelatin, indicating the possibility of fabricating polymers with required properties for tissue engineering [62].

Gelatin nanoparticles have recently been conjugated to antibodies by avidin–biotin complex formation [63, 64]. Following crosslinking, some of the reactive amino groups on the gelatin surface were activated with 2-iminothiolane to introduce reactive sulfhydryl groups. The thiolated nanoparticles were coupled to NeutrAvidin™ (NAv) previously activated by a hetero-bifunctional crosslinker. The NAv-modified nanoparticles were then used for the binding of biotinylated antibodies by avidin–biotin complex formation. The biotinylated antibody attached may be an anti-CD3 antibody that is used for specific drug targeting to T-lymphocytes or trastuzumab (Herceptin), which could be used for targeting HER2 overexpressing tumor cells [63, 64].

### 11.3

#### Nanoparticulate Carriers of Gelatin and Gelatin Derivatives

Preparation of nanoparticles from a pre-formed polymer is, in general, relatively straightforward, having high degree of reproducibility. However, the physico-chemical properties of gelatin, especially its heterogeneity in molecular weight distribution, make it a challenging polymer with which to produce stable nanoparticles. Nonetheless, many groups have successfully prepared nanoparticles, from gelatin and its derivatives, that have been evaluated for a range of biomedical applications [65–70]. Desolvation is the most popular technique for preparing gelatin nanoparticles, followed by techniques such as coacervation and water-in-oil emulsification.

##### 11.3.1

#### Desolvation

Desolvation is the process in which solvents of different polarity and hydrogen bonding, when added to solution of proteins, bring about rolling up or controlled precipitation of proteins due to the displacement of water molecules from the surface of proteins [71]. In solution, the gelatin molecules are well stretched and upon addition of (non-)solvents, such as ethanol, acetone or isopropanol, the solubility of gelatin molecules decreases (as the high hydrogen-bonding capacity of these solvents displaces water molecules), resulting in phase separation of the rolled-up gelatin molecules. These molecules have a size range of 100–200 nm and are further

hardened by crosslinking with aldehydes such as formaldehyde or glutaraldehyde. The pH and stirring conditions affect the size range and yield of these particles [15, 35].

#### 11.3.1.1 Desolvation Using Ethanol

The folding of gelatin in solution is determined by noncovalent interactions with the water molecules and the presence of solvents such as ethanol, which in turn affect these interactions. Marty et al. first observed that the complex phase behavior of gelatin was affected by temperature and other experimental conditions [13]. Farugia et al. have investigated the affect of temperature, pH and ethanol concentration on the molecular weight distribution profile of gelatin in solution in order to develop a robust method for preparing gelatin nanoparticles [35]. The molecular weight profile of gelatin remained unchanged at pH 5.0 to 7.0. However, at pH < 6.0, the gelatin particles lacked a net charge, resulting in aggregation. At pH > 7.5, the increased charge on the particles contributed to increased resistance to dehydration. In addition, the turbidity of the solution during nanoparticles preparation was constant at all temperatures within the pH range, and the percentage of molecular weight fractions precipitated was optimum at ethanol concentrations ranging from 62.5 to 75% w/w [35].

We have standardized preparation procedures for gelatin and PEGylated gelatin nanoparticles using the solvent displacement (based on principles of desolvation) process [52, 72]. Typically, ethanol is used as the non-solvent for gelatin. A 1% w/v solution of gelatin is prepared at 37 °C and the pH adjusted to 7.0 with 0.2 M sodium hydroxide. Nanoparticles are formed when the solvent composition is changed from 100% water to 65% (by volume) hydro-alcoholic solution under continuous stirring. The nanoparticles are further crosslinked with a 40% v/v aqueous solution of glyoxal for the desired time and any unreacted aldehyde is quenched with 12% w/v sodium metabisulfite. Particles so-obtained have a size range of 200–500 nm.

#### 11.3.1.2 Two-step Desolvation

Nanoparticles can be prepared from both Type-A and -B gelatins using this method. In the first step gelatin molecules of low molecular weight are separated (through a first-stage desolvation process) and discarded. The sediment obtained is rich in high-molecular weight gelatin fractions and is resolvated (redissolved in suitable aqueous medium) to carry out a second-stage desolvation process. Gelatin nanoparticles obtained by the two-step desolvation process have high stability (predominantly by virtue of high molecular weight) and do not show any aggregation or flocculation [73–75].

### 11.3.2

#### Coacervation

Coacervation is a process of spontaneous phase separation in the presence of two oppositely charged polyelectrolytes in solution. Electrostatic interaction between the electrolytes and the macromolecules results in the separation of a polymer-

rich phase, the coacervate, and a polymer-poor phase, the supernatant [76]. This concept of coacervation or phase separation can be used for preparing nanoparticles to encapsulate proteins and drugs.

Leong et al. [68, 76, 77] have synthesized gelatin nanoparticles as vehicles for gene delivery, by coacervation brought about by desolvation of water molecules using polyelectrolytes. Gelatin nanoparticles so-obtained form at gelatin concentrations ranging from 1.5 to 5% w/v and sodium sulfate from 0.2 to 1.2% w/v. The conditions of coacervation also depend to a great extent on the mixing conditions and presence or absence of electrolytes in solution. When plasmid DNA was co-encapsulated with endolysolytic agents such as chloroquine the required sodium sulfate concentration was reduced by 10–20% w/v. The uncrosslinked nanoparticles formed were relatively stable in acidic pH; however, as they dissociate at high ionic strength and neutral pH, the formed nanoparticles were separated by centrifugation and crosslinked using  $0.1 \text{ mg mL}^{-1}$  (1-ethyl-3-[3-dimethylamino-propyl]-carbodiimide hydrochloride) (EDC); the excess was quenched using glycine at a concentration of 0.2 M in the final solution.

In other instances, the concept of coacervation was used in combination with phase separation, in which a 1% w/v solution of gelatin containing surfactant (polysorbate 20, at 0.5% w/v) was mixed with sodium sulfate (at 20% w/v) to bring about coacervation followed by phase separation using isopropanol under continuous stirring. The nanoparticles formed were stabilized by crosslinking with glutaraldehyde; the excess aldehyde groups were quenched with sodium metabisulfite. The nanoparticles formed were stabilized by crosslinking with glutaraldehyde; the excess was quenched using sodium metabisulfite. Nanoparticles with an average size of 200 nm were separated from the salts by gel-chromatography using Sephadex G-50 [69, 70, 78].

### 11.3.3

#### **Nano-encapsulation by Water-in-oil Emulsion Method**

Nanoencapsulation involves wrapping small amounts of material in individual coatings or sheaths in discrete, sub-micron sized particles. Materials such as proteins or conventional drugs can be encapsulated, wherein the coatings aid in protecting the encapsulated material and in achieving prolonged or controlled release. Gelatin nanoparticles can be prepared by using the emulsifier-free water-in-oil (W/O) emulsion method either by solvent evaporation [67] or homogenization [79]. The gelling property of gelatin enables the separation of the hydrogel particles that are formed in the emulsion, which can be further stabilized/hardened by glutaraldehyde crosslinking [67]. Typically, a W/O emulsion is prepared with a gelatin solution as the internal aqueous phase and a vegetable oil as the external phase. The payload is incorporated in the internal aqueous phase itself and the two phases are emulsified under high-speed. The emulsion is then cooled to below the gelling point of gelatin to facilitate formation of payload-entrapped hydrogel particles. These are then collected by filtration, the oil phase is washed off with a suitable solvent and the hydrogel particles are then freeze-dried to obtain free flowing gelatin nanoparticles with an average size range of 840 nm [79].



The size distribution of these particles was affected by the nanoencapsulation process – mainly by the time and speed of homogenization and the viscosity of the gelatin solution. The size of these nanocapsules decreased with increasing time and speed of homogenization. However, prolonged homogenization resulted in flocculation of the droplets. The particle size was also increased with increasing viscosity, with a 1–3% w/w gelatin solution having optimum viscosity. The nanoencapsulation process was simple, with mild reaction conditions in the absence of emulsifiers and surfactants that might have harmful effects on the protein and peptide drugs co-encapsulated. The gelatin nanoparticulate system thus produced could be used for controlled delivery of protein and peptide drugs by intravenous, subcutaneous or intramuscular injection [79].

In the method involving solvent evaporation, the external phase is an organic solvent mixture (e.g., a 1:1 mixture of chloroform and toluene) containing a stabilizer [such as poly(methyl methacrylate) (PMMA)] and the internal aqueous phase is gelatin in phosphate-buffered saline (PBS). After high-speed homogenization of the mixture, the internal phase is evaporated under controlled conditions of temperature and pressure to obtain nanoparticles. The particles can then be cross-linked with an aldehyde if necessary. The nanoparticles are collected by centrifugation, washed with toluene to remove any excess of polymer and freeze-dried to obtain a free flowing product with a size range of 100–200 nm. The major advantage of this method is the use of PMMA in the oil phase, which prevents coagulation of the gelatin nanoparticles before and after crosslinking [67].

#### 11.4

#### Characterization of Gelatin and Modified Gelatin Nanoparticles

Gelatin nanoparticles prepared by different methods are generally characterized for size, morphology, surface charge and water content. The mean particle size and size distribution of the gelatin nanoparticles can be measured by photon correlation spectroscopy (PCS) or any suitable technique that is sensitive to detecting particles in the nanometric range. Particle size analysis also helps in ensuring batch-to-batch reproducibility of the nanoparticles and hence can be used as a major quality control tool. Most nanoparticles prepared by the above methods have reported mean sizes ranging from 200 to 400 nm. Colloidal stability, drug encapsulation efficiency, loading capacity, drug release and biodistribution profile, cell internalization kinetics etc. are strongly influenced by the particle size.

Scanning electron microscopy (SEM) is widely used to study the morphology and size of nanoparticles. Nanoparticles separated from suspension either by centrifugation or filtration are dried by lyophilization. Cryoprotectants (such as mannitol, trehalose etc.) can be used if necessary to promote stability of the particle during reconstitution. The dried nanoparticles are mounted on an aluminum sample mount, sputter coated with gold–palladium and observed by SEM. SEM images reveal the morphology of these nanoparticles and their actual diameter when compared with the hydrodynamic diameter obtained by PCS. Hence, nanoparticles

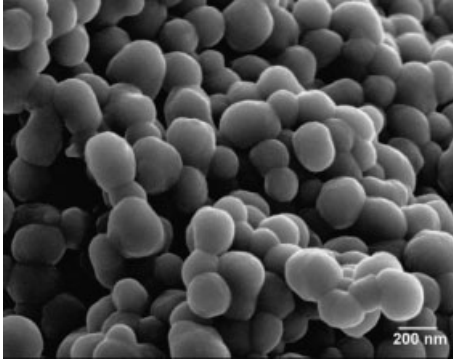


**Fig. 11.5.** Scanning electron microscopy image of non-crosslinked gelatin nanoparticles prepared by desolvation using ethanol.

sized by SEM would be relatively smaller than when determined by PCS [13, 52, 72, 73, 80]. Figure 11.5 shows the SEM image of non-crosslinked gelatin nanoparticles prepared by desolvation using ethanol.

The surface charge on the gelatin nanoparticles is measured by the zeta potential (the electrical potential due to the charged particles on the thin film of liquid bound to the surface of nanoparticles). Measurement of the zeta potential is one of the most important parameters in characterizing colloids, denoting their stability. Colloids with high zeta potentials ( $> \pm 30$  mV) are very stable due to electrostatic repulsions, when the zeta potential is close to zero coagulation and sedimentation of the colloidal particles is faster. The gelatin nanoparticles are dispersed in deionized water (or suitable buffer if necessary) and the zeta potential measured at the default parameters of dielectric constant, refractive index and viscosity of water [81].

Measurement of water content is important for any drug delivery system containing a moisture-sensitive compound like proteins. Gelatin nanoparticles are a kind of nano-hydrogel system that consists of a network of polymer with water molecules incorporated and the polymer crosslinked to enhance stability. The high water content in these systems plays a significant role in their biocompatibility, mechanical strength and drug release. Diffusion of water molecules into the hydrophilic matrix and formation of a gel barrier affects the release of drug from the system [82]. Water molecules can be associated with the hydrophilic polymer gels in three ways: freezing or bound water, freezing interfacial or intermediate water and free water [83]. Each molecule of associated water can exert its influence on the stability and reactivity of the polymeric carrier system in different ways.

Li et al. have determined the water content of hydrogel particles of gelatin prepared by the W/O emulsion method [79]. In this method the nanoparticles were suspended in deionized water and left in a water bath at different temperatures overnight; each sample was then vacuum filtered using a nylon filter membrane and the weight of swollen gelatin nanoparticles was compared with the dry weight

of gelatin nanoparticles to calculate the percentage water content at each temperature. The water content of gelatin was linearly dependent on the temperature, taking up about 51.6% water at 15 °C and 71.4% at 42 °C. NMR spectroscopy and differential scanning calorimetry (DSC) are also widely used to determine the water content of gelatin nanoparticles. In addition, NMR spectroscopy is used to study the structure mobility and hydration properties of the polymers [82].

The nano-structured surfaces of the nanoparticles of gelatin and its derivatives can be characterized by electron spectroscopy for chemical analysis (ESCA) – a surface analysis technique that exploits the photoelectric effect to obtain information about elemental composition and identify the functional groups present within a few nanometers-thick surface layers. This method involves irradiating the sample with photons (mainly low energy X-rays) that interact with the surface of the material and eject electrons, which are then analyzed by a spectrophotometer to identify the elements they come from. We have analyzed gelatin and PEG-modified gelatin nanoparticles prepared in our laboratory by ESCA to provide evidence for the presence of surface PEG chains on the nanoparticles. The results showed surface functional groups identified by high-resolution peak analysis of carbon-1S ( $C_{1S}$ ), oxygen-1S ( $O_{1S}$ ) and nitrogen-1S ( $N_{1S}$ ) envelopes that indicate the presence of ethylene oxide residues of PEG on the surface of modified gelatin [52].

## 11.5

### Loading and Release of Payload from Gelatin Nanoparticles

The payload of drugs or other substances such as proteins or plasmid DNA may be distributed throughout the matrix, or encapsulated in the cavity enclosed by the polymer, or adsorbed on the surface of the nanoparticles. Interaction of gelatin with these substances may be through chemical conjugation, ionic interaction or physical entrapment. The extent of drug loading and encapsulation efficiency of the gelatin nanoparticles depends on the molecular weight and also on the nature of the substance incorporated. Studies by Truong-Le et al. have shown that the encapsulation efficiency of gelatin nanoparticles increases with increasing molecular weight, with some exceptions where charge interactions have a profound affect [68].

The amount of substance incorporated into the gelatin nanoparticles is generally estimated either by assaying the supernatant for the free drug or by determining the amount of drug encapsulated in the particles by subjecting them to enzymatic hydrolysis. We have used tetramethylrhodamine-labeled dextran (TMR-dextran) as a model to represent a hydrophilic macromolecular drug. The TMR-dextran was added to the gelatin solution during nanoparticle preparation, the free drug was separated by centrifugation and the drug-loaded nanoparticles were dissolved in protease ( $0.2 \text{ mg mL}^{-1}$ ) containing PBS. The fluorescence intensity of the resulting solution was measured to account for the amount of drug loaded in the gelatin nanoparticles, and the loading efficiency was found to be 51% [52]. In certain cases the loading of conventional drugs like doxorubicin and proteins like bovine serum

albumin (BSA) was estimated by UV/Visible spectrophotometry and that of plasmid DNA by picogreen assay or by radiolabeling the DNA and accounting for its activity [68, 69, 72, 79].

Drug release from the gelatin nanoparticles may be due to leaching, erosion, rupture or degradation of the particulate material. Generally, it is suggested that the release of the payload is via diffusion and bioerosion for the gelatin nanoparticles [52, 72]. The hydrolysis/biodegradation process is accelerated in presence of enzymes (such as hydrolases or proteases). When the drug is distributed throughout the matrix, slow erosion or degradation can lead to prolonged drug release [15].

*In vitro* release studies of drugs from gelatin nanoparticles is generally carried out in a known amount of PBS, with constant shaking in the presence or absence of protease. Samples are removed at predetermined time intervals to analyze the amount of payload released. Sink conditions are maintained throughout the release study by replenishing the released medium with fresh PBS, and the drug released is calculated as a function of time [52].

Leo et al. have studied the release of doxorubicin from gelatin nanoparticles by dynamic dialysis [78]. The release study was carried out in 0.9% w/v NaCl in both the absence and presence of trypsin in the donor compartment separated by dialysis membrane with a cut-off size of 3.5 kDa. About 9 to 13% of the drug was released in the absence of the enzyme compared with 12.6 to 23.5% in the presence of trypsin [78]. The drug release rate from the gelatin nanoparticles was affected by the degree of crosslinking. This indicated the possibility of achieving controlled release by manipulating the degree of crosslinking. Gel electrophoresis indicated that the crosslinking had no effect on the structure and electrophoretic mobility of the encapsulated DNA [68].

## 11.6 Biocompatibility Studies

Gelatin has several unique properties that support its usability in medicine and biology. However, its animal origin and protein nature make it a material with safety risks, too, especially when intended for medical applications. These safety risks are related to the presence of prions and other infectious contaminations. Currently, there are commercial suppliers that produce gelatin by recombinant DNA technology (refer to the websites of companies like FibroGen, Fuji-Tilburg, etc.).

To evaluate cellular biocompatibility, cytotoxicity assays have been carried out to determine the affect of gelatin and modified gelatin nanoparticles on the viability of the cells in culture. Lactate dehydrogenase (LDH), the enzyme present in the cytosol of the cells, is a marker of membrane integrity of the living cells, and the LDH released by the rupture of the membrane of the dead cells is estimated to determine the affect of nanoparticles on the viability of the cells. Brzoska et al. have compared the cytotoxicity of gelatin nanoparticles with that of human serum albumin (HSA) and poly(hexylcyanoacrylate) nanoparticles by incubating them at concentrations of 0–50  $\mu\text{g mL}^{-1}$  for 6 h with pulmonary epithelial cells, monitoring

the levels of LDH up to 96 h after replacing the supernatant. LDH levels of the cells incubated with gelatin nanoparticles were constant and were comparable with that of negative control. The same group has also looked into the ability of gelatin nanoparticles to initiate the expression of interleukin-8 (IL-8) by the pulmonary epithelial cells. ELISA was used to estimate the concentration of IL-8 in the supernatant after 24 h incubation of nanoparticles. Notably, gelatin nanoparticles did not initiate any expression of IL-8 even at concentrations as high as  $100 \mu\text{g mL}^{-1}$  [75].

One of the most popular methods of estimating cytotoxicity is the MTS assay (commercially available as CellTiter 96<sup>®</sup> AQueous Non-Radioactive Cell Proliferation Assay from Promega). It is based on the principle that when a novel tetrazolium compound [3-(4,5-dimethylthiazol-2-yl)-5-(3-carboxymethoxyphenyl)-2-(4-sulfophenyl)-2H-tetrazolium, inner salt or MTS] is incubated with cells, the metabolically active cell population converts MTS into purple formazan that is soluble in the culture medium (unlike the MTT assay, wherein the formazan salt is not soluble). Mitochondrial dehydrogenase enzymes present in the viable cells cleave the yellow tetrazolium compound to a purple formazan salt that is estimated by calorimetry. We have evaluated the cellular toxicity of gelatin and modified gelatins (PEGylated form) in comparison with polyethyleneimine and lipofectin. Cells incubated with gelatin remained 100% viable even at concentrations up to  $200 \mu\text{g mL}^{-1}$  [52]. These studies indicate that gelatin is biocompatible and non-toxic, and hence is safe and could be used as a vehicle for drug delivery applications.

## 11.7

### Applications of Gelatin and Modified Gelatin Nanoparticles

Gelatin has been widely used for various industrial applications, primarily in food, pharmaceuticals and medicine. It is used extensively in the food industry – confectionary, dairy, meat, desserts, in bakery products as thickening agents, stabilizer and emulsifier. Gelatin is an inexpensive, non-toxic, biocompatible and biodegradable polymer that can be easily formulated – the most popular conventional pharmaceutical dosage form being soft and hard gelatin capsules. Hydrogels, films, micro- and nanoparticles based on gelatin represent a few of the novel formulations, which are being explored widely for pharmaceutical and drug delivery applications.

Gelatin nanoparticles have been used as a carrier for gene delivery applications [84]. Cellular uptake of these nanoparticles is mainly attributed to endocytosis, wherein the cells engulf the nanoparticles, forming a vesicular structure (endosome) that fuses with the lysosomes within the cytoplasmic space. Upon acidification of the endo-lysosomal complex, the nanoparticles degrade and the contents are released into the cytoplasm to exert pharmacological action. Gelatin nanoparticles have several advantages as a non-viral gene delivery vector. They can be conjugated to moieties that stimulate receptor-mediated endocytosis, multiple plasmids or bioactive agents can be encapsulated and the bioactivity of the encapsu-

lated DNA could be improved by preventing digestion by nucleases and by using long-circulating nanoparticles that are modified by PEG [76]. In other instances the DNA is adsorbed onto the surface of the gelatin nanoparticles by modifying the surface of gelatin with cholamine (a quaternary amine) to increase ionic interactions [81].

Gelatin nanoparticles can be crosslinked with dialdehydes (glutaraldehyde, glyoxal etc.) and those aldehyde groups can then be used as chemical handles for further modification. Crosslinking also helps to control the degradation kinetics of the nanoparticles. One limitation of using crosslinked gelatin nanoparticles is that the nature of transfectability of the nanoparticles is reduced due to the reduction in release rate of the DNA from the nanospheres [68, 77].

Nanoparticulate carriers of gelatin have been used for efficient intracellular delivery of the encapsulated payload. Our laboratory is engaged in exploring gelatin and modified gelatin-based nanoparticles for drug delivery. We have carried out cell trafficking studies using gelatin and PEGylated gelatin nanoparticles loaded with TMR-dextran as a model hydrophilic drug in BT-20 cells. We observed the localization of TMR-dextran loaded nanoparticles in the perinuclear region of the cells. The particles were mainly taken up by endocytosis, which later escaped the endosomal system and were found around the perinuclear area in the cytoplasm [52, 72]. In addition, we have reported the gene delivery efficiency of nanoparticles prepared from gelatin and PEGylated gelatin [85]. Most of the administered gelatin and PEGylated gelatin nanoparticles were internalized in NIH-3T3 fibroblast cells within the first 6 h of incubation. A large fraction of the administered nanoparticles was concentrated in the perinuclear region of the cells after 12 h. Green fluorescent protein expression was observed after 12 h of nanoparticle incubation and remained stable for up to 96 h. Flow cytometry results showed that the DNA transfection efficiency with gelatin and PEGylated gelatin nanoparticles was 43% and 61%, respectively, after 96 h. This study illustrates that PEGylated gelatin nanoparticles were rapidly internalized by the cells through nonspecific endocytosis and remained intact in the cytosol for up to 12 h [85]. A similar study was carried out using non-crosslinked gelatin nanoparticles loaded with plasmid DNA; confocal images in Fig. 11.6 show the fluorescence observed at 24 and 96 h post-transfection.

Kushibiki et al. have proven the long-circulation property of PEGylated gelatin by using  $^{125}\text{I}$ -labeled gelatin [54]. The grafted polymer was obtained by incubating succinimidyl succinate methoxy-PEG with gelatin followed by radio-iodination by the chloramine-T method. Nanoparticulates with an average size of 100 nm were prepared by micellization of gelatin and PEGylated gelatin solutions at concentrations ranging from 0.04 to 10 mg mL<sup>-1</sup> in the presence of 5 mM *N*-phenyl-1-naphthylamine (PNA) in methanol. Results of the biodistribution studies indicated a parallel increase in area under the curve (AUC) with an increase in molecular weight of the grafted PEG at the same degree of PEGylation, [54].

We have prepared nanoparticles from gelatin (Type-B) and PEGylated gelatin, radiolabeled with  $^{125}\text{I}$  for *in vivo* biodistribution studies after intravenous (i.v.) administration in mice bearing Lewis lung carcinoma [58]. From the radioactivity in

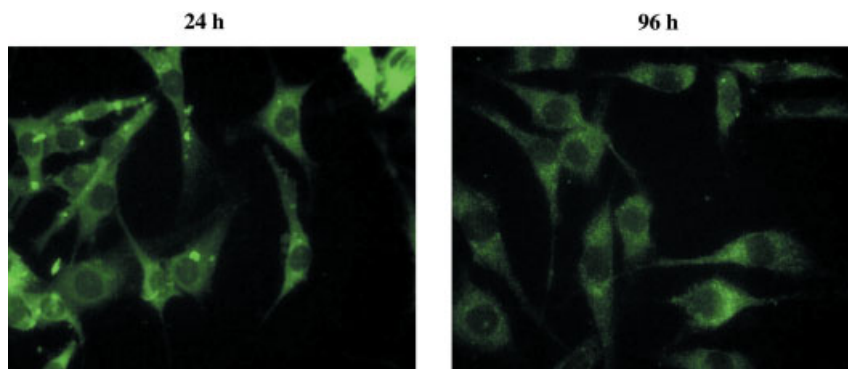


**Fig. 11.6.** Fluorescence confocal microscopy images of NIH-3T3 murine fibroblast cells transfected with enhanced green fluorescent protein plasmid DNA (EGFP-N1)-loaded gelatin nanoparticles after 24 and 96 h post-transfection.

plasma and various organs collected, most PEGylated nanoparticles were evidently present either in the blood pool or taken up by the tumor mass and liver. For instance, after 3 h, the concentrations of PEGylated gelatin nanoparticles were almost two-fold higher in the blood pool than the control gelatin nanoparticles. PEGylated gelatin nanoparticles remained in the blood pool for a longer due to the steric repulsion effect of the PEG chains as compared with the gelatin nanoparticles. In addition, ca. 4–5% of the recovered dose of PEGylated gelatin nanoparticles was present in the tumor mass for up to 12 h. Plasma and the tumor half-lives, mean residence time, and the AUC of the PEGylated gelatin nanoparticles were significantly higher than those for the gelatin nanoparticles. These results showed that PEGylated gelatin nanoparticles possess long-circulating properties and can preferentially distribute in the tumor mass after systemic delivery.

Leong et al. have studied the *in vivo* transfection efficiency of gelatin nanoparticles containing the LacZ plasmid in the tibialis anterior muscle of 6-week-old BALB/c mice; the muscle was isolated and homogenized 3 weeks after injection to assay the expression of  $\beta$ -galactosidase. The gelatin nanoparticles exhibited a more profound and sustained gene expression than the naked plasmid DNA and lipofectamine complexes [76].

Research carried out by Farrugia et al. has indicated the antitumor activity of empty gelatin nanoparticles, which effectively inhibited the formation of melanoma tumors by binding to the fibronectin surfaces that interfere with tumor growth [80]. This property can allow gelatin nanoparticles to be used as a possible alternative to Bacillus Calmette-Guerin vaccine in the treatment of melanoma [80]. In yet another study, nanoparticles of gelatin and PEGylated gelatin, ranging in size from 100–1000 nm, have been prepared via a self-assembly process. These nanoparticles were degraded by collagenase IV within 1 min and the degraded fragments had a molecular weight of 2000 and below, which is smaller than the

cut-off molecular size for the kidney membrane. This indicates the possibility of using these complexes for anticancer therapy wherein the payload is released by the action of matrix metalloproteases (MMPs) at the cancer site. *all-trans*-Retinoic acid has been used as a model drug, and the loading efficiency was found to be about 92% when loaded at 1% weight of polymer. Release studies of the drug-loaded PEGylated gelatin nanoparticles revealed an accelerated release profile in the presence of collagenase IV – an enzyme present in high concentrations in tumor tissues [53].

Gelatin-based nanoparticulate systems have also been used to deliver protein and peptide drugs. Macromolecules such as proteins are degraded in the gastrointestinal tract when administered orally and these drugs require multiple injections to achieve the desired therapeutic effect if administered via the parenteral route. Li et al. have studied gelatin nanoparticles to overcome these hurdles for the delivery of a model protein (BSA) [59, 79].

Gelatin nanoparticles have been explored to encapsulate antitumor drugs, which resulted in increased efficiency, controlled release, and targeting of drugs to the affected area. Paclitaxel-loaded gelatin nanoparticles were used to enhance the solubility of the drug and its partitioning across biological membranes that are sensitive to Cremophor EL, a constituent used to solubilize paclitaxel in commercial formulations. X-Ray diffraction analysis indicated an amorphous state of the entrapped drug, thus confirming its enhanced solubility. These paclitaxel-loaded gelatin nanoparticles were used to treat dogs with intravesical bladder carcinoma and a 2.6× higher drug concentration was achieved in tumors compared with control dogs treated with Cremophor EL containing a commercial paclitaxel injection [86]. Studies have been conducted by injecting doxorubicin-loaded glutaraldehyde-crosslinked gelatin nanoparticles into rats by intraperitoneal injection [69]. The animals were monitored for side effects by electrocardiogram and body weight and the results indicated that control nanoparticles (without any drug) did not show any toxicity. Although the efficiency of the anticancer drug was enhanced, upon repeated administration the formulation (doxorubicin-loaded gelatin nanoparticles) showed high cardiotoxicity. This was attributed to covalent attachment of the drug to the carrier and the toxicity of the degradation products of these drug-peptide conjugates [69, 78]. Michaelis et al. also observed similar results, by conjugating diethylenetriamine pentaacetic acid (DTPA – an extracellular chelator) to gelatin. The attachment to gelatin enhanced cellular uptake and increased the cytotoxic and antiviral activity of DTPA by five- to eight-fold [74].

## 11.8 Conclusions

The unique physical, chemical and biological properties of gelatin and its modified derivatives make it a best possible alternative for drug delivery and therapeutic applications. The safety of traditional gelatins, especially in terms of immunogenicity, presence of biological impurities and other drawbacks associated with



tissue-derived material are some of the reasons why researchers have developed a complete set of new recombinant gelatins. Advances in biotechnology have provided gelatins with well-defined molecular weights, pI, guaranteed lot-to-lot reproducibility, and the ability to tailor the molecule to match a specific application. They are also biodegradable, non-immunogenic, have excellent cell binding properties, and can be delivered with a purity of >99.9%. Thus the new generation recombinant gelatins are the most appropriate materials for a range of medical and pharmaceutical applications, including hydro-gels for controlled release functions, tissue engineering scaffolds, and stabilizing additives of vaccines or bio-pharmaceuticals. It is also evident that gelatin is useful in maintaining the therapeutic activity of biotechnological products such as proteins, peptides and oligonucleotides, in reducing the toxicity of cytotoxic compounds such as doxorubicin and help in improving the targeting ability of various drugs to the diseased site. The examples cited in this chapter show a broad potential for a wide range of clinical and therapeutic applications using gelatin, and ongoing studies should help to improve therapeutic approaches for the effective use of this natural polymer.

### References

- 1 SOPPIMATH, K. S., AMINABHAVI, T. M., KULKARNI, A. R., RUDZINSKI, W. E., Biodegradable polymeric nanoparticles as drug delivery devices. *J. Controlled Release* **2001**, *70* (1–2), 1–20.
- 2 ADAMS, M. L., LAVASANIFAR, A., KWON, G. S., Amphiphilic block copolymers for drug delivery. *J. Pharm. Sci.* **2003**, *92* (7), 1343–1355.
- 3 KATAOKA, K., HARADA, A., NAGASAKI, Y., Block copolymer micelles for drug delivery: design, characterization and biological significance. *Adv. Drug Deliv. Rev.* **2001**, *47* (1), 113–131.
- 4 RAO, G. C., KUMAR, M. S., MATHIVANAN, N., RAO, M. E., Nanosuspensions as the most promising approach in nanoparticulate drug delivery systems. *Pharmazie* **2004**, *59* (1), 5–9.
- 5 UCHEGBU, I. F., VYAS, S. P., Non-ionic surfactant based vesicles (niosomes) in drug delivery. *Int. J. Pharm.* **1998**, *172* (1–2), 33–70.
- 6 DE MIGUEL, I., IOUALALEN, K., BONNEFOUS, M., PEYROT, M., NGUYEN, F., CERVILLA, M., SOULET, N., DIRSON, R., RIEUMAJOU, V., IMBERTIE, L., et al., Synthesis and characterization of supramolecular biovector (SMBV) specifically designed for the entrapment of ionic molecules. *Biochim. Biophys. Acta* **1995**, *1237* (1), 49–58.
- 7 RABINOW, B. E., Nanosuspensions in drug delivery. *Nat. Rev. Drug Discov.* **2004**, *3* (9), 785–796.
- 8 BOAS, U., HEEGAARD, P. M., Dendrimers in drug research. *Chem. Soc. Rev.* **2004**, *33* (1), 43–63.
- 9 SONNEVILLE-AUBRUN, O., SIMONNET, J. T., L'ALLORET, F., Nanoemulsions: a new vehicle for skincare products. *Adv. Colloid Interface Sci.* **2004**, *108–109*, 145–149.
- 10 TENJARLA, S., Microemulsions: an overview and pharmaceutical applications. *Crit. Rev. Ther. Drug Carrier Syst.* **1999**, *16* (5), 461–521.
- 11 TORCHILIN, V. P., Drug targeting. *Eur. J. Pharm. Sci.* **2000**, *11* (Suppl 2), S81–91.
- 12 KREUTER, J., Nanoparticles and nanocapsules – new dosage forms in the nanometer size range. *Pharm. Acta Helv.* **1978**, *53* (2), 33–39.
- 13 MARTY, J. J., OPPENHEIM, R. C., SPEISER, P., Nanoparticles – a new colloidal drug-delivery system. *Pharm. Acta Helv.* **1978**, *53*, 17–23.

- 14 DOUGLAS, S. J., DAVIS, S. S., ILLUM, L., Nanoparticles in drug delivery. *Crit. Rev. Ther. Drug Carrier Syst.* **1987**, *3* (3), 233–261.
- 15 KREUTER, J., Drug targeting with nanoparticles. *Eur. J. Drug Metab. Pharmacokinet.* **1994**, *19* (3), 253–256.
- 16 COUVREUR, P., DUBERNET, C., PUISIEX, F., Controlled drug delivery with nanoparticles: current possibilities and future trends. *Eur. J. Pharm. Biopharm.* **1995**, *41* (1), 2–13.
- 17 RAVI KUMAR, M., HELLMANN, G., LOCKEY, R. F., MOHAPATRA, S. S., Nanoparticle-mediated gene delivery: state of the art. *Expert Opin Biol Ther.* **2004**, *4* (8), 1213–1224.
- 18 MULLER, R. H., RADTKE, M., WISSING, S. A., Solid lipid nanoparticles (SLN) and nanostructured lipid carriers (NLC) in cosmetic and dermatological preparations. *Adv. Drug Del. Rev.* **2002**, *54* (Suppl 1), S131–155.
- 19 MOGHIMI, S. M., HUNTER, A. C., MURRAY, J. C., Long-circulating and target-specific nanoparticles: theory to practice. *Pharmacol. Rev.* **2001**, *53* (2), 283–318.
- 20 ALONSO, M. J., Polymeric nanoparticles: new systems for improving ocular bioavailability of drugs. *Arch. Soc. Esp. Ophthalmol.* **2001**, *76* (8), 453–454.
- 21 KREUTER, J., Nanoparticles and microparticles for drug and vaccine delivery. *J. Anat.* **1996**, *189* (3), 503–505.
- 22 PANYAM, J., LABHASETWAR, V., Biodegradable nanoparticles for drug and gene delivery to cells and tissue. *Adv. Drug Del. Rev.* **2003**, *55* (3), 329–347.
- 23 BARRATT, G., Colloidal drug carriers: achievements and perspectives. *Cell. Mol. Life Sci.* **2003**, *60* (1), 21–37.
- 24 BRIGGER, I., DUBERNET, C., COUVREUR, P., Nanoparticles in cancer therapy and diagnosis. *Adv. Drug Del. Rev.* **2002**, *54* (5), 631–651.
- 25 SPEISER, P. P., Nanoparticles and liposomes: a state of the art. *Methods Find. Exp. Clin. Pharmacol.* **1991**, *13* (5), 337–342.
- 26 LAVASANIFAR, A., SAMUEL, J., KWON, G. S., Poly(ethylene oxide)-block-poly(L-amino acid) micelles for drug delivery. *Adv. Drug Del. Rev.* **2002**, *54* (2), 169–190.
- 27 GOA, K. L., BENFIELD, P., Hyaluronic acid. A review of its pharmacology and use as a surgical aid in ophthalmology, and its therapeutic potential in joint disease and wound healing. *Drugs* **1994**, *47* (3), 536–566.
- 28 CHUANG, V. T., KRAGH-HANSEN, U., OTAGIRI, M., Pharmaceutical strategies utilizing recombinant human serum albumin. *Pharm. Res.* **2002**, *19* (5), 569–577.
- 29 CASCONI, M. G., BARBANI, N., CRISTALLINI, C., GIUSTI, P., CIARDELLI, G., LAZZERI, L., Bioartificial polymeric materials based on polysaccharides. *J. Biomater. Sci. Polym. Ed.* **2001**, *12* (3), 267–281.
- 30 MEHVAR, R., Dextrans for targeted and sustained delivery of therapeutic and imaging agents. *J. Controlled Release* **2000**, *69* (1), 1–25.
- 31 SUH, J. K., MATTHEW, H. W., Application of chitosan-based polysaccharide biomaterials in cartilage tissue engineering: a review. *Biomaterials* **2000**, *21* (24), 2589–2598.
- 32 DJAGNY, V. B., WANG, Z., XU, S., Gelatin: a valuable protein for food and pharmaceutical industries: review. *Crit. Rev. Food Sci. Nutr.* **2001**, *41* (6), 481–492.
- 33 COURTS, A., The N-terminal amino acid residues of gelatin 2. Thermal degradation. *Biochem. J.* **1954**, *58* (1), 74–79.
- 34 FLORY, P. J., WEAVER, E. S., Helix–coil transitions in dilute aqueous collagen solutions. *J. Am. Chem. Soc.* **1960**, *82*, 4518–4525.
- 35 FARRUGIA, C. A., GROVES, M. J., Gelatin behaviour in dilute aqueous solution: designing a nanoparticulate formulation. *J. Pharm. Pharmacol.* **1999**, *51* (6), 643–649.
- 36 TORCHILIN, V. P., How do polymers prolong circulation time of liposomes? *J. Liposome Res.* **1996**, *6* (1), 99–116.
- 37 TORCHILIN, V. P., PEG-based micelles as carriers of contrast agents for

- different imaging modalities. *Adv. Drug Del. Rev.* **2002**, *54* (2), 235–252.
- 38 GREF, R., DOMB, A. J., QUELLEC, P., BLUNK, T., MÜLLER, R. H., VERBAVATZ, J. M., LANGER, R., The controlled intravenous delivery of drugs using PEG-coated sterically stabilized nanospheres. *Adv. Drug Del. Rev.* **1995**, *16* (2–3), 215–233.
  - 39 LEWANSKI, C. R., STEWART, S., Pegylated liposomal adriamycin: a review of current and future applications. *Pharm. Sci. Technol. Today* **1999**, *2* (12), 473–477.
  - 40 REDDY, K. R., Controlled-release, pegylation, liposomal formulations: new mechanisms in the delivery of injectable drugs. *Ann. Pharmacother.* **2000**, *34* (7–8), 915–923.
  - 41 OTSUKA, H., NAGASAKI, Y., KATAOKA, K., PEGylated nanoparticles for biological and pharmaceutical applications. *Adv. Drug Del. Rev.* **2003**, *55* (3), 403–419.
  - 42 ROBERTS, M. J., BENTLEY, M. D., HARRIS, J. M., Chemistry for peptide and protein PEGylation. *Adv. Drug Del. Rev.* **2002**, *54* (4), 459–476.
  - 43 BHADRA, D., BHADRA, S., JAIN, P., JAIN, N. K., Pegnology: a review of PEG-ylated systems. *Pharmazie* **2002**, *57* (1), 5–29.
  - 44 YOWELL, S. L., BLACKWELL, S., Novel effects with polyethylene glycol modified pharmaceuticals. *Cancer Treat. Rev.* **2002**, *28* (Suppl A), 3–6.
  - 45 CRAWFORD, J., Clinical uses of pegylated pharmaceuticals in oncology. *Cancer Treat. Rev.* **2002**, *28* (Suppl A), 7–11.
  - 46 HARRIS, J. M., MARTIN, N. E., MODI, M., Pegylation: a novel process for modifying pharmacokinetics. *Clin. Pharmacokinet.* **2001**, *40* (7), 539–551.
  - 47 FRANCIS, G. E., DELGADO, C., FISHER, D., MALIK, F., AGRAWAL, A. K., Polyethylene glycol modification: relevance of improved methodology to tumour targeting. *J. Drug Target.* **1996**, *3* (5), 321–340.
  - 48 NAPER, D. H., *Polymeric Stabilization of Colloidal Dispersions*. ed., Academic Press, New York, **1983**.
  - 49 TORCHILIN, V. P., Polymer-coated long-circulating microparticulate pharmaceuticals. *J. Microencapsul.* **1998**, *15* (1), 1–19.
  - 50 TORCHILIN, V. P., PAPISOV, M. I., Why do polyethylene glycol-coated liposomes circulate so long? *J. Liposome Res.* **1994**, *4* (1), 725–739.
  - 51 ZALIPSKY, S., Functionalized poly(ethylene glycol) for preparation of biologically revalant conjugates. *Bioconj. Chem.* **1995**, *6*, 150–165.
  - 52 KAUL, G., AMIJI, M., Long-circulating poly(ethylene glycol)-modified gelatin nanoparticles for intracellular delivery. *Pharm. Res.* **2002**, *19* (7), 1062–1068.
  - 53 KIM, K. J., BYUN, Y., Preparation and characterizations of self-assembled PEGylated gelatin nanoparticles. *Biotechnol. Bioprocess Eng.* **1999**, *4*, 210–214.
  - 54 KUSHIBIKI, T., MATSUOKA, H., TABATA, Y., Synthesis and physical characterization of poly(ethylene glycol)-gelatin conjugates. *Biomacromolecules* **2004**, *5* (1), 202–208.
  - 55 SHU, X. Z., LIU, Y., LUO, Y., ROBERTS, M. C., PRESTWICH, G. D., Disulfide crosslinked hyaluronan hydrogels. *Biomacromolecules* **2002**, *3*, 1304–1311.
  - 56 WEBER, C., REISS, S., LANGER, K., Preparation of surface modified protein nanoparticles by introduction of sulfhydryl groups. *Int. J. Pharm.* **2000**, *211* (1–2), 67–78.
  - 57 COESTER, C., KREUTER, J., VON BRIESEN, H., LANGER, K., Preparation of avidin-labelled gelatin nanoparticles as carriers for biotinylated peptide nucleic acid (PNA). *Int. J. Pharm.* **2000**, *196* (2), 147–149.
  - 58 KAUL, G., AMIJI, M., Biodistribution and targeting potential of poly(ethylene glycol)-modified gelatin nanoparticles in subcutaneous murine tumor model. *J. Drug Target.* **2004**, *12* (9–10), 585–591.
  - 59 LI, J. K., WANG, N., WU, X. S., A novel biodegradable system based on gelatin nanoparticles and poly(lactic-co-glycolic acid) microspheres for protein and peptide drug delivery. *J. Pharm. Sci.* **1997**, *86* (8), 891–895.
  - 60 SHU, X. Z., LIU, Y., PALUMBO, F., PRESTWICH, G. D., Disulfide-

- crosslinked hyaluronan-gelatin hydrogel films: a covalent mimic of the extracellular matrix for in vitro cell growth. *Biomaterials* **2003**, *24* (21), 3825–3834.
- 61 CHEN, T., EMBREE, H. D., WU, L. Q., PAYNE, G. F., In vitro protein-polysaccharide conjugation: tyrosinase-catalyzed conjugation of gelatin and chitosan. *Biopolymers* **2002**, *64* (6), 292–302.
- 62 MA, J., CAO, H., LI, Y., LI, Y., Synthesis and characterization of poly(DL-lactide)-grafted gelatins as bioabsorbable amphiphilic polymers. *J. Biomater. Sci. Polymer Ed.* **2002**, *13* (1), 67–80.
- 63 BALTHASAR, S., MICHAELIS, K., DINAUER, N., VON BRIESEN, H., KREUTER, J., LANGER, K., Preparation and characterisation of antibody modified gelatin nanoparticles as drug carrier system for uptake in lymphocytes. *Biomaterials* **2005**, *26* (15), 2723–2732.
- 64 WARTLICK, H., MICHAELIS, K., BALTHASAR, S., STREBHARDT, K., KREUTER, J., LANGER, K., Highly specific HER2-mediated cellular uptake of antibody-modified nanoparticles in tumour cells. *J. Drug Target.* **2004**, *12* (7), 461–471.
- 65 GUPTA, A. K., GUPTA, M., YARWOOD, S. J., CURTIS, A. S., Effect of cellular uptake of gelatin nanoparticles on adhesion, morphology and cytoskeleton organisation of human fibroblasts. *J. Controlled Release* **2004**, *95* (2), 197–207.
- 66 VANDERVOORT, J., LUDWIG, A., Preparation and evaluation of drug-loaded gelatin nanoparticles for topical ophthalmic use. *Eur. J. Pharm. Biopharm.* **2004**, *57* (2), 251–261.
- 67 CASCONI, M. G., LAZZERI, L., CARMIGNANI, C., ZHU, Z., Gelatin nanoparticles produced by a simple W/O emulsion as delivery system for methotrexate. *J. Mater. Sci. Mater. Med.* **2002**, *13* (5), 523–526.
- 68 TRUONG-LE, V. L., AUGUST, J. T., LEONG, K. W., Controlled gene delivery by DNA-gelatin nanospheres. *Hum. Gene Ther.* **1998**, *9* (12), 1709–1717.
- 69 LEO, E., ARLETTI, R., FORNI, F., CAMERONI, R., General and cardiac toxicity of doxorubicin-loaded gelatin nanoparticles. *Farmaco* **1997**, *52* (6–7), 385–388.
- 70 OPPHENEIUM, R. C., Nanoparticulate drug delivery systems based on gelatin and albumin. In: *Polymeric Nanoparticles and Microspheres*, Ed. GUIOT, P., COUVREUR, P., CRC Press, Boca Raton, FL, **1986**, pp. 1–25.
- 71 WEBER, C., COESTER, C., KREUTER, J., LANGER, K., Desolvation process and surface characterisation of protein nanoparticles. *Int. J. Pharm.* **2000**, *194* (1), 91–102.
- 72 KAUL, G., LEE-PARSONS, C., AMIJI, M., Poly(ethylene glycol)-modified gelatin nanoparticles for intracellular delivery. *Pharm. Eng.* **2003**, *23* (5), 1–5.
- 73 COESTER, C. J., LANGER, K., BRIESEN, H. V., KREUTER, J., Gelatin nanoparticles by two step desolvation—a new preparation method, surface modifications and cell uptake. *J. Microencapsul.* **2000**, *17* (2), 187–193.
- 74 MICHAELIS, M., LANGER, K., ARNOLD, S., DOERR, H. W., KREUTER, J., CINATL, J., JR., Pharmacological activity of DTPA linked to protein-based drug carrier systems. *Biochem. Biophys. Res. Commun.* **2004**, *323* (4), 1236–1240.
- 75 BRZOSKA, M., LANGER, K., COESTER, C., LOITSCH, S., WAGNER, T. O., MALLINCKRODT, C., Incorporation of biodegradable nanoparticles into human airway epithelium cells – in vitro study of the suitability as a vehicle for drug or gene delivery in pulmonary diseases. *Biochem. Biophys. Res. Commun.* **2004**, *318* (2), 562–570.
- 76 LEONG, K. W., MAO, H. Q., TRUONG-LE, V. L., ROY, K., WALSH, S. M., AUGUST, J. T., DNA-polycation nanospheres as non-viral gene delivery vehicles. *J. Controlled Release* **1998**, *53*, 183–193.
- 77 TRUONG-LE, V. L., WALSH, S. M., SCHWEIBERT, E., MAO, H. Q., GUGGINO, W. B., AUGUST, J. T.,

- LEONG, K. W., Gene transfer by DNA-gelatin nanospheres. *Arch. Biochem. Biophys.* **1999**, *361* (1), 47–56.
- 78 LEO, E., CAMERONI, R., FORNI, F., Dynamic dialysis for the drug release evaluation from doxorubicin-gelatin nanoparticle conjugates. *Int. J. Pharm.* **1999**, *180*, 23–30.
- 79 LI, J. K., WANG, N., WU, X. S., Gelatin nanocapsulation of protein/peptide drugs using an emulsifier-free emulsion method. *J. Microencapsul.* **1998**, *15* (2), 163–172.
- 80 FARRUGIA, C. A., GROVES, M. J., The activity of unloaded gelatin nanoparticles on murine melanoma B16-F0 growth in vivo. *Anticancer Res.* **1999**, *19* (2A), 1027–1031.
- 81 ZWIOREK, K., KLOECKNER, J., WAGNER, E., COESTER, C., *In Vitro Gene Transfection with Surface Modified Gelatin Nanoparticles*, 2004 International conference on MEMS and NANO and smart systems, Banff, Alberta, Canada, August 25–27, **2004**, pp. 60–63.
- 82 BAUMGARTNER, S., LAHAJNAR, G., SEPE, A., KRISTL, J., Investigation of the state and dynamic of water in hydrogels of cellulose ethers by <sup>1</sup>H NMR spectroscopy. *AAPS Pharm. Sci. Tech.* **2003**, *3* (4).
- 83 HATEKEYAMA, H., HATEKEYAMA, T., Interaction between water and hydrophilic polymers. *Thermochim. Acta* **1998**, *308*, 3–22.
- 84 KAUL, G., AMIJI, M., Protein nanoparticles for gene delivery. In: *Polymeric Gene Delivery: Principles and Applications*, Ed. AMIJI, M., CRC Press LLC, Boca Raton, FL, **2005**, pp. 429–447.
- 85 KAUL, G., AMIJI, M., Cellular interactions and in vitro DNA transfection studies with poly(ethylene glycol)-modified gelatin nanoparticles. *J. Pharm. Sci.* **2004**, *94* (1), 184–198.
- 86 LU, Z., YEH, T. K., TSAI, M., AU, J. L., WIENTJES, M. G., Paclitaxel-loaded gelatin nanoparticles for intravesical bladder cancer therapy. *Clin. Cancer Res.* **2004**, *10* (22), 7677–7684.

## Index

- a**
- $\alpha$ -helix peptide 210
  - $\alpha$ -chymotrypsin 207
  - $\zeta$ -potential, nanoparticles 132–134
  - 1-ethyl-3-(3-dimethylaminopropyl)-  
t-carbodiimide *see* EDC
  - 1-PBA 52
  - 1-pyrenebutanoic acid succinimidyl ester  
*see* 1-PBA
  - absorbance signal 153
  - active ester groups 135–137
  - active ester linkage 138
  - activity, adsorbed proteins 51
  - ADDLs 27
  - a DNA-based Biological System 311
  - adsorption 206
  - adsorption of biomolecules 11
  - aerosol supercritical extraction system 195
  - affinity chromatography 256
  - AFM 62
  - AFM imaging, nanoparticle surface 200
  - Ag *see* silver
  - aligned MWNTs 61
  - Alzheimer's beta-amyloid diphenylalanine  
structural motif 260
  - Alzheimer's disease 27
  - amide linkage 15
  - aminated NH<sub>2</sub>-5'-modified DNA Probe  
323
  - amine, coupling to gold 164
  - amine-ended ligand-protected, gold nano-  
particles 100
  - amine moieties 52
  - amino acid functionalized CNTs 53
  - amino acids, interactions 250
  - aminodextran molecules 246
  - aminosilane groups 87
  - amperometry, hybridization efficiency 156
  - amphiphiles, peptide-based 262
  - amphiphilic biological molecules 50
  - amphiphilic molecules 7
  - amphiphilic peptide 209
  - amplified signal on nanoparticles 138–139
  - amyloid derived diffusible ligands 27, *see also*  
ADDLs
  - animal imaging 28
  - anodic stripping voltammetry 156, *see also*  
ASV
  - ANS 129
  - antibiotics, immobilization 74
  - antibodies 55
    - coupling to gold 166
    - detection 118
  - antibody, anti-CD3 337
  - antibody binding 13
  - antibody denaturation, suppression 144
  - antibody immobilized PMBN/PLA 142
  - anti-CD3 antibody 337
  - anti-*Escherichia coli* 213
  - antigen detection 218
  - anti-prostate-specific membrane antigen 283,  
*see also* PSMA
  - antisolvent process 195
  - antitumor drugs 347
  - anti-tumor effect 289
  - aqueous phase, water-in-oil emulsion 339
  - aqueous solubilization 47
  - aqueous synthesis protocols 235
  - armchair 42
  - array fabrication 151
  - ases 195
  - ASV 156
  - atomic force microscopy *see* AFM
  - atom transfer radical polymerization 78, *see*  
*also* ATRP
  - ATRP 78
  - Au *see* gold
  - autoimmune diseases 140

**b**

- bacteriophage 189
  - ballistic conductors 42
  - BBB 82
  - bidentate enediol 74
  - bifunctional molecule 215
  - bifunctional proteins 112
  - bioactive compounds, specific binding 150
  - biocatalysts 81
  - biochemical synthesis of, therapeutic drugs 80–82
  - biochips 152
  - biocompatibility, polymeric coatings 21
  - biocompatibility studies, gelatin 343–347
  - biocompatible coatings 11
    - design 22
  - biocompatible surfaces 19–20
  - bioconjugate chemistry 162
  - bioconjugate nanoparticles 131
    - design 129–137
  - bioconjugate phospholipid polymer 129
  - bioconjugate phospholipid polymer nanoparticles 132
  - bioconjugation 126
    - chemical reactions 15
    - crosslinker-based 12
    - fluorescent nanoparticles 11
    - key requirements 11
    - phospholipid polymer nanoparticles 136
  - biodegradability 331
  - biodegradable polymer 131
  - biodistribution 332
  - biofunctionalization 161–166
    - carbon nanotubes 41–71
    - gelatin nanoparticles 330–349
    - magnetic nanoparticles 72–98
    - metallic nanoparticles 150–182
    - phospholipid polymeric nanoparticles 125–149
  - biofunctionalization of gold nanoparticles 99
  - biofunctionalized carbon nanotubes 54
  - biofunction on nanoparticles 137–139
  - bio-imaging 82
  - bioinertness, gold 17
  - bioinert surfaces 20
  - bioinorganic nanoparticles 193
  - biointerface 127
  - bio-labeling 72
  - biological applications, gold nanoparticles 118
  - biological imaging 27
  - biological-inorganic materials 189
  - biological ligands, identification 256
  - biologically active peptides 259
  - biological membranes 191
  - biological molecules
    - amphiphilic 50
    - immobilized 51
    - interaction with CNTs 50
  - biological system, DNA-based 311
  - biomedical applications 126–129
  - biomedical imaging 11
  - biomimetic process 188
  - biomolecular detection 150–182
  - biomolecules, specific binding 113–117
  - bionanotechnology, peptide toolbox 249
  - biorecognition 211
  - biosensing 11
  - biosensors 208
    - SPR 155
  - bio-separation 72
  - biotin 73
  - Biotin-<sup>5'</sup>-modified DNA Probe 318, 324
  - biotin–streptavidin crosslinking 194
  - biphasic reduction 9
  - bipyridinium carboxylic acids 73
  - blinking 3
  - blood–brain barrier 82, *see also* BBB
  - blood clearance pathway 333
  - bovine serum albumin *see* BSA
  - brust–schiffrin method 161
  - BSA 4
  - BSA-conjugated nanoparticles 196–197
  - bystander effect 289
- c**
- C2-symmetrization 303
  - CALNN 251, 251, 252
  - cancer gene therapy 270
  - cancer treatment 287
  - candida rugos 81
  - cantilever 158
  - capping ligands 101
    - peptides 249
  - capping magnetic iron oxide cores 76
  - capture agent 114
  - capture molecules 151
  - capture oligonucleotides 152
  - carbodiimide 52
  - carbodiimide-mediated esterification 185
  - carbohydrate-functionalized gold nanoparticles 118
  - carbon nanotube films 45
  - carbon nanotubes 184
    - aqueous solubilization 47
    - biofunctionalization 41–71
    - biofunctionalized 54
    - biological applications 205

- coupling 204–205
- double-walled 42
- formation 205
- multi-walled 42
- self-assembling 56
- semiconducting 42
- single-walled 42
- synthesis 43–46
- types 42–43
- carboxylic acids 211
- catalysts 81
- cavity, polymer 342
- CCMV 193
- cDNA 270
- CDs nanoparticles
  - BSA-conjugated 201–202
  - luminescence spectrum 203
- cell/protein bio-separation 72
- cells 118–124
- cell-surface display 256
- cellular imaging 85
- cellular uptake 282
- chaperonin proteins 186
- chemical design 301
- chemical functionalization 47
- chemical functionalization methods 184–188
- chemical mapping 63
- chemical modifications 47
- chemical polymerization 300
- chemical synthesis, therapeutic drugs 80–82
- chemical vapor deposition 43, *see also* CVD
- chemisorption 11
- chemotherapeutic agents 82
- chiral 42
- chiral index 204
- chiral vector 43
- chitosan 335
- cholesterol derivatives 279
- choline chloride 138
- chromatography 255–256
  - affinity 256
  - size-exclusion 256
- citrate groups, protein coupling 186
- Clauson-Kaas reaction 302
- clustering 3
- CNT electrodes 58
- CNT film-based devices 56
- CNTs 41
  - amino acid functionalized 54
  - electrochemical biosensing 61
  - water-soluble 53
- CNT tips, AFM 62
- coacervation 338–339
- coatings
  - biocompatible 11
  - hydrophilic 4
  - low cytotoxicity 23
  - magnetic metal oxide cores 77
  - nanocore surfaces 78
- colloid, hollow 126
- colloidal carriers, circulation time 333
- colloidal gold 2
  - biofunctionalization 162
- colloidal gold labels 156
- colloidal gold–protein complexes 166
- colloidal nanoparticles 158
- colloidal stability 23
  - PMBN/PLA 145
- colloid gold 99
- compressed antisolvent, precipitation 195
- concentration, biofunctionalized particles 81
- conductance, nanotubes 208
- continuous platinum nanowires 251
- contrast agents 83
  - metallic nanoparticles 160
- core, dielectric 160
- core/shell magnetic nanoparticles 78
- core/shell nanoparticles 79
- core/shell particles 159–160
- core/shell structure, magnetic nanoparticles 73
- core-corona nanoparticles 126
- coupling, carbon nanotubes and proteins 204–205
- coupling agents, carbodiimide 52
- coupling reactions 13
- covalent amide bond chemistry 313
- covalent attachment, DNA Probe 313
- covalent attachment modes 319
- covalent bioconjugation 16
- covalent biofunctionalization 52–54
- covalent BSA-SWNT conjugate, AFM image 214
- covalent functionalization 53–54
- cowpea chlorotic mottle virus 193, *see also* CCMV
- CP 299
- C-reactive antibody-immobilized nanoparticles 141
- C-reactive Protein Detection 139–144
- crosslinked hydrogels 335
- crosslinker-based bioconjugation 12
- crosslinking
  - gelatin nanoparticles 345
  - proteins 188
- crosslinking reaction, adjustable 173
- crosslinking systems 258
- CRP 139



- CT 207
- CTAB 236
- CVD 43
- cysteine 250
- cytotoxicity 4
- cytotoxicity assays 343
  
- d**
- DCbz-based Monomers 305
- DCbz-containing Monomers 301
- deposition 152
- Derjaguin-Landau-Verwey-Overbeek theory 18
- desolvation 337–338
  - two-step 338
- detection
  - detection 26
  - electrochemical 58
  - microarrays 150–182
- detection efficiency, time-dependent decrease 320
- detection methods, biomolecular 153
- dextran-magnetite 82
- diagnosis, high-performance 144–149
- dielectric core 159
- dimerizing nanoparticles 246
- dimers, gold nanoparticles 245
- dimer structures, gold nanoparticles 107
- dispersing agents 48
- DLVO 18
- DNA 162
  - optical detection 118
- DNA/RNA targets 74
- DNA Attachment 299–329
- DNA binding domain 111
- DNA-biofunctionalized nanocomposites 313
- DNA condensation 271
- DNA-conjugated metal nanoparticles 150
- DNA covalent attachment 313
- DNA detection 152
  - microarrays 171
- DNA-directed nanoparticle assemblies 103–111
- DNA hybridization 242
  - detection 26
  - nanocomplex-supported 320
- DNA immobilization 172
- DNA microarrays 152
- DNA molecules, immobilized 57
- DNA-nanoparticle conjugates 165
- DNA probe attachments 311
- DNA sensing 235
- DNA sensors, gravimetric 158
- dopamine 73–75
  
- double-walled carbon nanotubes *see* DWNTs
- DPyr-/DCbz-based Monomers 302
- DPyr- and DCbz-containing monomers, structures 301
- DPyr-based Monomers 305
- DPyr-containing Monomers 301
- drug-polymer systems 196
- drug bioavailability 334
- drug delivery 330
- drug molecules, biosynthesis 72
- drug release 343
- drugs, synthesis 80–82
- drug targeting 82
- ds-DNA 165
- DWNTs 42, 42
- dye-doped nanoparticles 3–5
- dye-doped silica shells 9–10
- dynamic light scattering 134–135
  
- e**
- EDAC 211
- EDAX 307
- EDC 52
- electrical detection 156
  - gold nanoparticles 157
- electric arc discharge 43
- electrochemical detection 156–157
- electronic devices, assembly 54–58
- electronic resonance 158
- electron microscopy 2, *see also* EM
- electron spectroscopy for chemical analysis 342
- electrophoresis 174
- electrostatic coupling, quantum dots 16
- electrostatic interactions, protein coupling 185
- EM 2
- Energy-Dispersive X-Ray Microanalysis, EDAX 307
- engineered proteins 254
- enhanced permeability and retention effect 272, *see also* EPR
- enzymatic activity 81
  - enzymes 207
- enzymatic amplifying system 313
- enzyme inhibition 118
- enzymes, self-assembly 248
- EPR 272
- Epstein-Barr virus 288
- ESCA 342
- Escherichia coli* 191
- esterification, carbodiimide-mediated 185
- ethanol, desolvation 338
- ethylene glycol 102

- eukaryotic viruses 271  
excitons 5  
exfoliation 47
- f**  
fabrication, nano-scaled 125  
FCS 19  
ferritin 206  
ferrofluid 86  
– water-soluble 77  
ferromagnetic nanoparticles, heating 87  
FET *see also* field-effect transistor  
fiber-forming peptides 261  
fibers 260  
fibrinogen 209  
field-effect transistor 60  
field effect transistors 54  
films, carbon nanotube 45  
filtration 56  
flavoenzymes, reconstitution 219  
fluorescence correlation spectroscopy 19, *see also* FCS  
fluorescence probe 129–131  
fluorescence wavelength, phospholipid polymer aggregation 131  
fluorescent nanoparticle probes 2–10  
fluorescent nanoparticles 1  
– biocompatibility 18  
– bioconjugation 11–17  
fluorescent nanoprobe, hybrid architectures 9  
folate ligands 289  
folate-linked nanoparticles  
– NPI 279  
– NPII 280  
– properties 281  
– selectivity 282  
– structure 280  
folate-linked vectors 272  
folate receptors 273  
folate receptor-targeting liposomes 273  
folic acid 85  
– conjugation 276  
FR 273, *see also* folate receptors  
FRET 186  
FRET system, scheme 187  
FR-targeting nanoparticles 274  
functional CPs 300  
functional groups 76  
functionalization 48–49
- g**  
ganciclovir 287–291, *see also* GCV  
GCV monophosphate 288  
gel, pore size 244  
gelatin 331–337  
– amino acid composition 332  
– chemical modification 332–335  
– chemical structure 332  
– conjugates 335–337  
– nanoparticulate carriers 337  
– PEG conjugation 334  
– thiolation 336  
gelatin capsules 344  
gelatin nanoparticles 336  
– applications 344  
– characterization 340–342  
– payload 342–343  
– SEM images 341  
– size distribution 340  
– surface charge 341  
– transfection efficiency 346  
gel barrier 341  
gel electrophoresis 106  
– GST-Zif268 113  
– protein binding 112  
– specific binding 117  
gel electrophoresis analysis 115  
gel filtration separation 106–107  
gels, nanoporous 167  
gene delivery 270  
– gelatin nanoparticles 344  
– vehicles 339  
gene expression system 270  
gene therapy 87  
– tumor-targeted 270–298  
gene transfer vectors, size 287  
glass substrates 56  
globular proteins 17  
glucose, detection 61  
glucose oxidase *see* GO  
glutamate sensor 25  
glutathione s-transferase 112, *see also* GST  
glyconanospheres 22  
GO 60  
gold colloids 161  
gold contacts 55  
gold nanodots, photoluminescence excitation 241  
gold nanoparticle-based microarrays 171  
gold nanoparticles 2  
– biofunctionalization 99  
– biological applications 167  
– dimer structures 108  
– electrolyte-induced aggregation 252  
– geometrical parameters 111  
– images 243  
– ligand-protected 100–103

- gold nanoparticles (*cont.*)
  - metal enhancement 154
  - modification 162
  - oligonucleotide modification 153
  - protected with neutral ligands 102
  - rational design 251
  - strongly ionic ligand-protected 102
  - structures 101
  - surface-bound 153
  - synthesis 99
  - synthesis methods 101
  - trimer structures 109
  - weakly ionic ligand-protected 102
- gold nanospheres 17
- gold spheres, TEM images 237
- graphene cylinders 42
- graphene layer 204
- graphite sensors, screen-printed 62
- gravimetric 158
- GSH 115
- GST 112
- GST protein, specific binding 117
  
- h**
- hepatic clearance 73
- Herpes simplex virus thymidine kinase 287, *see also* HSV-tk
- hierarchical self-assembly 261
- high-pressure carbon monoxide
  - disproportionation 43, *see also* HiPco
- high-resolution transmission electron microscopy 153, *see also* HRTEM
- HiPco 43
- his-tag 254
- histidine-tagged proteins 75
- HIV virus, detection 127
- HL60 214
- HL60 cells, confocal images 215
- hollow protein 193
- hollow protein cages 194
- homobifunctional crosslinkers 12
- horse radish peroxidase 307
- HPA, specific binding 220
- HRP 313
- HRTEM 153
  - microphotographs 309
- HSV-tk 287
- HSV-tk/GCV system's mode 288
- human promyelocytic leukemia 214
- hybrid architectures, fluorescent nano-probes 9
- hybridization
  - DNA 104
  - steric interference 170
- hybrids, nanoparticle–dye 9
- hybrid structures 41
- hydrogels 335
- hydrogen peroxide 138
- hydrophilic coatings 4
- hydrophilic surface modification, quantum dots 8
- hydrophobic interactions 73
- hydrophobic nanoparticles 184
- hydrophobic polymers 3
- hyperthermia treatments 82
  
- i**
- IgE 188
- IgG 13
  - covalent binding 165
  - nanocomposite 74
- IMAC 254
  - particle separation 258
- immobilization, bioactive molecules 72
- immobilization of biocatalysts, support 81
- immobilized biological molecules 51
- immobilized lipase 81
- immobilized metal affinity chromatography 254
- immunoagglutination 140
- immunoassay 140
  - quantum dots 25
- immunocytochemistry 166
- immunological magnetic beads 218
- infectious processes 140
- inflammation marker 140
- inflammatory response 119
- inorganic magnetic cores 309
- inorganic nanoparticles 184
- in situ synthesis 152
- interactions, amino acids with noble metals 250
- intracellular delivery 345
- intravesical bladder carcinoma 347
- ion-exchange chromatography separation 51
- Ionic Ligand-protected gold nanoparticles 102
- Ionic Ligands, gold nanoparticles 102
- iron(ii) sulfate, oxidative hydrolysis 320
- iron oxide nanoparticles 82
- isothermal titration calorimetry 250
  
- k**
- key materials 127–129
  
- l**
- labels, fluorescent nanoparticles 27
- lactate dehydrogenase 343

- Langmuir–Blodgett techniques 169  
lanreotide 261  
large-scale preparation 108  
laser ablation 43  
lattice constant 247  
lattice structure, carbon nanotubes 42  
LDH 343  
lead biosensor 118  
lectin detection 119  
leucine-zipper sequences 259  
ligand 114  
– pentapeptide 167  
ligand-exchange 238  
ligand exchange reaction 103–111  
ligand molecules, immobilization 22  
ligand-protected gold nanoparticles 100–103  
ligands 73  
– activity 15  
– capping 252  
– peptide capping 251  
light emission, metal nanocrystals 239  
light scattering, metal nanocrystals 239  
linkers 184  
– peptide-based 258  
lipid-based nanoparticles 270–298  
lipidic chain 50  
lipids, PEGylated 273  
lipoplexes 277  
lipopolyplex 277  
*Listeria innocua* 193  
liver imaging 84  
low cytotoxicity coatings 23  
lowry assay 201  
luciferase activity 287  
lyophilization 340  
lysine 250  
– coupling to gold 164  
lysozyme, binding with gold nanoparticles 117
- m**  
M13 bacteriophage 189  
mAbs 272  
maghemite nanocomposites 73  
maghemite nanoparticles, structure 74–75  
magnetically responsive nanocomposites 307  
magnetic beads 160  
magnetic core conducting polymer shell nanocomposites 299–329  
magnetic cores, formation 80  
magnetic drug targeting 86  
magnetic fluid hyperthermia 87  
magnetic hyperthermia 160  
magnetic hyperthermia therapy 82  
magnetic nanocomposites, structure 74–75  
magnetic nanoparticles 78  
– biofunctionalization 72–98  
– functionalization 80–82  
magnetic resonance imaging *see* MRI  
magnetism measurements, magnetic nanocomposites 310  
magnetite nanocomposites  
– screening 315  
– sensitivity patterns 316  
– stability 320  
– TEM microphotographs 312  
magnetite nanoparticles 305  
– structure 77  
magnetite preparation 320  
magnetite-silica-poly pyrrole NC 299  
magnetoliposomes 74  
maleimide, coupling to gold 164  
maltose-binding protein 186, *see also* MBP  
maltose sensors 25  
materials, recognition 256  
MBP 186  
MCH 162  
MEONP 129  
– chemical structure 130  
mercaptohexanol 162, *see also* MCH  
metal catalysts 81  
metal colloids 158  
metal–dye 9  
metal enhancement, gold nanoparticles 154  
metal ions, release 20  
metallic nanoparticles  
– biofunctionalization 150–182  
– biological applications 242  
– functionalization 235–269  
– light scattering properties 239  
– optical properties 238  
– overview 236–248  
– stabilization 248  
metallic nanoparticle synthesis, peptides 250  
metallic nanoprobe, bioconjugation 16  
metallic sensors 26  
metallopeptides 259  
metal nanocrystals  
– light emission 239  
– light scattering 239  
metal nanoparticles 7–9  
– biofunctionalization 167  
– DNA-conjugated 150  
– synthesis 9  
metal oxide particles 160  
methacrylate derivative *see* MPC  
MFH 87

- microarrays 152
- gold nanoparticle 171
- microcantilevers 158
- microemulsions 278
- microfluidic chip 26
- microspheres, quantum dots 10
- microstructured biochips 154
- molecular diagnosis 139
- molecular diversity 301
- molecular machine 125
- molecular thin films 169–172
- monoclonal antibodies 272
- monodispersed nanoparticles 134
- monodisperse silica particles 4
- monofunctionalization 246
- monolayer protected, gold nanoparticles 114
- monolayer protected au nanoparticles 104
- monolayer protected nanoparticles, reaction scheme 114
- monolayers, self-assembly 169
- monomethoxy PEG 333, *see also* mPEG
- monomolecular thin films 167
- morphology 134–135
- MPC 127
- chemical structure 127
- mPEG 333
- MPS 73
- MRI 82
- MRI contrast agents 72
- MR Imaging 83–85
- MTS assay 344
- multi-color imaging, quantum dots 28
- multifunctional swnt structures 56
- multi-walled carbon nanotubes *see* MWNTs
- multiplexing, quantum dots 26
- MWNTs 42
- murine fibroblast cells, fluorescence confocal microscopy images 346
- MWNTs 42
- aligned 61
- structure 46
  
- n**
- nanocapsules 330
- size distribution 340
- nanocarriers 330
- nanocomposites
- magnetic core conducting polymer shell 299–329
- magnetically responsive 307
- parallel screening 311
- nanocore surfaces, coating 77
- nanocrystal alignment 191
- nanocrystal ordering 242
- nanocrystals 5
- TOPO-coated 252
- nanocrystal superlattices 193
- nanodevices, bottom-up design 54
- nanodots, metallic 241
- nano-encapsulation 339–340
- nanofabrication 125
- key materials 127–129
- nanomaterials, conjugation with proteins 183–234
- nano-optodes 25
- nanoparticle, synthesis 79
- nanoparticle aggregation 18
- nanoparticle assemblies 103–111
- nanoparticle-based imaging 23
- nanoparticle binding domain 111
- nanoparticle–dye hybrids 9
- nanoparticle probes, fluorescent 2–10
- nanoparticles
- active ester groups 135–137
- amplified signal 138–139
- assembly 202
- bioconjugate 131
- dye-doped 3–5
- fluorescent 1–40
- gold 99
- inorganic 184
- lipid-based 277
- magnetic 72–98
- magnetite 305
- metal 7–9
- metallic 150–182
- peptide-capped 255–256
- phospholipid 125–149
- photochemical activity 7
- polymeric 3
- programmable assembly 111–113
- rare-earth-doped 4
- x-ray photoelectron spectra 133
- nanoparticles for gene delivery system 271
- nanoparticles-proteins interactions 118
- nanoparticle-stabilizing coatings 21
- nanoparticle types 159–161
- nanoparticulate carriers, gelatin 337–340
- nanoplex 280
- nanoporous gels 167
- nanoporous hydrogel 175
- nanoprobes
- photostable 27
- size ranges 3
- nano-scaled processing 126–127
- nanoscale science 248
- nanoscale semiconductors 184

- nanospheres 330
    - silica 4
  - nanotube, electronic structure 205
  - nanotube field-effect transistor 60
  - nanotube functionalization 214
  - nanotubes 260
    - carbon 41–71
    - conductance 208
    - helical wrapping 51
  - nanowires 165
    - platinum 251
  - nanowiring 187
  - nasopharyngeal cancer 291
  - nasopharyngeal tumor 287
  - NC compositions 308
  - NC concentration 318
  - NC Fabrication 320
    - optimized procedures 320
  - NC-Supported DNA Hybridizations 320
  - near-infrared spectroscopy 45, *see also* NIR
  - neuron, live 64
  - neuronal growth 63
  - neurons, cultured 63
  - Neutral Ligands, gold nanoparticles 102
  - NH<sub>2</sub>-5'-normal-modified DNA Probe 313
  - NHS 52
  - N-Hydroxysuccinimide 52, *see also* NHS
  - nickel nitrilotriacetic acid 254
  - Ni-NTA 254
  - nir quantum dots 28
  - NIR spectroscopy 45
  - NMR analysis 115
  - NNLAC 252
  - noble metals 250
  - noncovalent biofunctionalization 50–52
  - non-functional CP 300
  - non-solvent precipitation 104
  - non-specific adsorption, elimination 216
  - nonspecific binding, GSH 115
  - non-specific binding 314
  - nonspecific binding tests 117
  - nonspecific interactions, elimination 113–117
  - non-specific interactions, biosensors 60
  - non-specific protein adsorption 125
  - non-specific protein–nanotube conjugation 209
  - non-viral gene delivery vector 344
  - non-viral particle systems 271
  - nonviral vectors 275
  - NP *see* nanoparticles
  - NPI 279
  - NPII 280
  - NPIII-F nanoparticles, TEM images 284
  - NPIII nanoplexes 286
  - nucleic acids 118
- o**
- oligonucleotide immobilization 170
  - oligonucleotide layers, formation 164
  - oligonucleotide modification, gold nanoparticles 153
  - oligonucleotides 162
    - covalent attachment 163
    - hybridization 55
  - on-chip synthesis 152
  - opsonization process 83
  - optical absorbance 153
  - optical microscopy 1
  - organic ligands 73
  - organic solvents 102
  - organosilane groups 74
  - oxidative polymerization 306
  - oxidative polymerization conditions 305
  - oxidizing agents 47
- p**
- PAA 80
  - PABS 48
  - particle size 134–135
  - pathogen detection sensitivity 213
  - patterned growth 43
  - patterned mwnts 45
  - Patterned SWNT multilayer films 57
  - payload, loading 342–343
  - PBS 340
  - pca 195
  - PCS 340
  - PEBBLEs 25
  - PEG 77
    - aqueous medium 334
  - PEGA 173
  - PEG-coated nanoparticles 272
  - PEG coating 217
  - PEG-linker, length 278
  - peg-magnetite nanoparticles 87
  - PEG-OH 238
  - PEGylation 332–335
  - PEO 48
  - peptide-based amphiphiles 262
  - peptide-based linkers 258
  - peptide-capped nanoparticles 255–256
  - peptide capped particles, binding 255
  - peptide-capped silver nanoparticles 252
  - peptide capping ligands 251
  - peptide chains 17
  - peptide-DNA hybrids 254
  - peptide-DNA Linker 259

- peptide extensions 253–255
- peptide-peptide linker 259
- peptide route 235–269
- peptides 248
  - biologically active 259
  - capping ligands 252
  - reducing agent 250
- peptide self assemblies, images 261
- peptide-texas red linker 259
- peptide toolbox, bionanotechnology 249
- phage display 256, 259
- phage display method 191
- pH conditions 203
- phosphine, coupling to gold 164
- phosphine-protected, gold nanoparticles 100
- phospholipid polar groups 131
- phospholipid polymer, bioconjugate 129
- phospholipid polymeric nanoparticles 125–149
- phospholipid polymer surfaces, bioinert properties 128
- phospholipids 74
- phospholipids polar group 127
- photochemical activity, nanoparticles 7
- photo-initiator 174
- photoluminescence 186
- photon correlation spectroscopy 340, *see also* PCS
- photooxidation, reduction 10
- photostability 5
- photostable nanoprobe 27
- photothermal interference 242
- physisorption 11
- pi-stacking interactions 51
- PLA 131
- plasmid DNA 285
- plasmids 270
- plasmon resonance 158
- PLL 58
- PMBN/PLA
  - antibody immobilized 142
  - colloidal stability 145
- PMBN/PS nanoparticles 131
- PMMA 340
- p-nitrophenyloxycarbonyl poly(oxyethylene) methacrylate 129, *see also* MEONP
- POC 150
- point-of-care diagnostics 150, *see also* POC
- poly(acrylic acid) 22
- polyampholyte 332
- PolyDCbz-Magnetite nanocomposites 322
- polydispersity 4
- PolyDPyr-/PolyDCbz-Magnetite NCs, stability 320
- PolyDPyr-Magnetite nanocomposites 322
- polyelectrolytes 338
- polyethylene glycol *see* PEG
- polyethylene oxide 48, *see also* PEO
- poly(l-lactic acid) 131, *see also* PLA
- poly-l-lysine 58, *see also* PLL
- poly-m-aminobenzene sulfonic acid 48, *see also* PABS
- polymer, biodegradable 131
- polymer chain, folding 248
- polymeric coatings 21
  - biocompatible 82
- polymeric nanoparticles 3
- polymeric polypyrrolic capsules, nanosized 300
- polymeric sensors 25
- polymerization media 307
- polymerization of ethylene oxide 22
- polymer-magnetite nc morphology 309
- polymers 173
  - hydrophobic 3
  - layer-by-layer deposition 78
  - synthetic 331
  - water-soluble 48–49
- polypeptide mixture, gelatin 331
- poly(propionylethylenimine-co-ethylenimine) 49, *see also* PPEI-EI
- polysaccharides 4
- polystyrene 131, *see also* PS
- PPEI-EI 49
- PPO 80
- precipitation with compressed antisolvent 195
- pre-formed synthetic polymers 80
- preparative-scale synthesis 103–111
- probes, fluorescent 2–10
- probes encapsulated by biol. localized embedding 25, *see also* PEBBLEs
- programmable assembly of nanoparticles 111–113
- prostate cancer 270
- protein, isomeric conversion 204
- protein/cell separation 73–80
- protein adsorption 20
- protein binding, gel electrophoresis 112
- protein coat, virus 191
- protein crystal s-layers 192
- protein detection, C-reactive 139–144
- protein isomeric conversion 202
- protein-nanotube conjugation, non-specific 209
- protein recognition 189
- protein-resistant surface 20
- protein-resistivity of, PEG-coated 217

- proteins 248
  - bifunctional 111–113
  - coupling 204–205
  - crosslinkers 188
  - electronic detection 58
  - functional groups 185
  - gold nanoparticles 165
  - gold nanoparticles 166
  - histidine-tagged 75
- protein–SWNT conjugation, indirect 216
- PS 131
- PSMA 283
- purity, CNT material 45
- pyrrole synthesis 303
  
- q**
- QCMs 158
- QD *see* quantum dots
- quantum dots 5–7
  - bioconjugation 15–16
  - biofunctionalized 24
  - emission properties 6
  - microspheres 10
  - multiplexing 26
  - peptide coatings 22
  - surface-functionalized 19
  - synthesis 5–6
  - TOPO-synthesized 7
- quantum dot sensors 25
- quantum dot surface, passivation 23
- quartz-crystal-microbalances 158, *see also*
  - QCMs
- quasi-covalent attachment
  - magnetite NCs 324
  - modes 319
- quasi-covalent linkage 318
  
- r**
- radiotherapeutic agents 82
- raman scattering 155
- rapid expansion of supercritical solutions 195–196, *see also* RESS
- rare-earth-doped nanoparticles 4
- rational design 251
- rayleigh scatterer 2
- receptors, self-assembly 248
- recognition of materials 259
- reduced folate carrier 282, *see also* RFC
- Reducing Agent, peptides 250
- relaxation 84
- relaxation time 83
- RES 333
- RESOLV
  - experimental setup 197
  - process 196
- ress 195
- reticuloendothelial system 83
- reverse microemulsion method 4
- reverse micelle procedures 9
- RFC 282
- Ricinus communis 218
  
- s**
- salmonella antibodies 173
- SAMs 161
- SAR 87
- SAS 195
- Sav-TMR 186
- SAXS 110
- SBP 207
- scaffolds 46
  - CNT-based 43
- scanning electron microscope 134–135
- scanning electron microscopy 63
- scanning tunneling microscopy *see also* STM
- scanometric array 154
- scatchard analysis 166
- scattering cross-sections 239
- SCF 195
- schizophyllan 218, *see also* SPG
- SCMF 20
- screen-printed graphite sensors 62
- SDBS 48
- SDS 48
- SEDS 195
- selenium nanoparticle–antibody conjugates 154
- self-assembly 54
  - monolayers 161, *see also* SAMs
  - peptides 249
  - s-layer 192
  - structures 247
- SEM 340
- semiconductor materials 5
- semiconductor nanoparticles
  - assembly 204
  - BSA-conjugated 197
  - protein-conjugated 202
- semiconductors, nanoscale 184
- sensors, polymeric 25
- separating biomolecules 174
- sequential enzymatic reactions 137–138
  - scheme 138
- SERS 9
- serum, high-performance diagnosis 144–149
- serum-free CRP, calibration curve 142
- silane coupling agents 159



- silanes 7
  - surface modification 171
- silica coatings 81
- silica nanoparticles 4
- silica nanospheres, hollow 4
- silica particles, monodisperse 4
- silica shells, dye-doped 9–10
- silicon oxide 170
- silver coating 118
- silver nanocrystal, light scattering 239
- silver nanocrystals 236
- silver nanodots 241
- silver nanoparticles
  - AFM 203
  - AFM analysis 200
  - BSA-conjugated 198
  - peptide-capped 252
  - synthesis 161
  - TEM-images 199
- single-chain mean field theory 20, *see also* SCMF
- single-domain 72
- single molecule detection 2
- single molecule imaging 1
- single-stranded dna, interaction with CNTs 51
- single-walled carbon nanotubes *see* SWNTs
- size distribution, polymer nanoparticles 135
- size-exclusion chromatography 257
- S-layer, central pore 247
- s-layer lattice types 192
- S-layer proteins 247
- s-layers 191
- small angle x-ray scattering 108, 153, *see also* SAXS
- sodium 1-anilinonaphthalene-8-sulfonate 129, *see also* ANS
- sodium dodecylbenzene sulfonate 48, *see also* SDBS
- sodium dodecyl sulfate *see* SDS
- Sol-gel 77, 186
- solid-phase reactions 246
- solid-state bioapplications 205
- solubilities, SCF 195
- solubility of magnetic nanoparticles 82
- solution 129–131
  - phase characterization 103–111
  - supercritical 195–196
- solution enhanced-dispersion by supercritical fluids 195, *see also* SEDS
- soybean peroxidase 207, *see also* SBP
- spacer molecules 169
- specific absorption rate 87, *see also* SAR
- specific binding 113–117
- specific conjugation 210
  - carbon nanotubes 206
- specific recognition 254
- spectral shift 153
- SPG 218
- spherical colloid 126
- spherical nanocrystals, monodisperse 236
- SPIO *see* superparamagnetic iron oxide
- spleen imaging 84
- spotting systems 174
- SPR 26
- spraying 56
- SPR Imaging 155
- SPRS 169
- ssDNA 51, 165
- stabilization concept, quantum dots 7
- stabilization of nanoparticles 19
- stabilizers 4
- Staphylococcus aureus* 13
- starch polymers 86
- steroid-cyclic disulfide anchoring group 162
- stimulus-dependant hydrogel 262
- STM 153
- Stöber process 77
- strep-tag ii 253
- streptavidin 186
  - nonspecific binding 218
- streptavidin attachment 312
- streptavidin–biotin interactions 318
- streptavidin–biotin system 166
- Streptavidin-modified magnetite NCs 324
- streptavidin recognition 217
- streptavidin-SWNT 60
- substrate biofunctionalization: 168
- substrates, biofunctionalization 167–168
- succinimide, coupling to gold 164
- sugimoto method 305
- suicide gene therapy 291
- supercritical anti-solvent 195, *see also* SAS
- supercritical fluid methods 195–204
- supercritical pressure 195
- superparamagnetic iron oxide 72
- superparamagnetic nanoparticles 74
  - heating 87
- supramolecular assemblies 50
- surface  $\zeta$ -potential 132–134
- surface-bound gold nanoparticles 153
- surface coatings 19
- surface composition 115
- surface elemental analysis 132
- surface-enhanced raman scattering *see* SERS
- surface exchange reaction 76

- surface-initiated polymerization 78  
 surface layers 191, *see also* S-layers  
 surface plasmon absorption 197  
 surface plasmon resonance 26, 239  
 surface plasmon resonance imaging 153  
 surface plasmon resonance spectroscopy  
   169, *see also* SPRS  
 surfactants, water-compatible 47–48  
 SWNT, semiconducting 58  
 SWNT-FET 217  
 SWNT FET devices 209  
 SWNT-FET devices 55  
 SWNT multilayer films, patterned 57  
 SWNT-PEI 65  
 SWNTs 42  
   – aqueous solubilization 213  
   – assembly 59  
   – biosensors 58  
   – noncovalent functionalization 219  
   – self-assembly 47  
   – types 43  
 SWNT structures, assembly 56  
 SWNT tip 63  
   – AFM 62  
 synthesis  
   – carbon nanotubes 43–46  
   – nanoparticle assemblies 103–111  
 synthesizing metal nanoparticles 9  
 synthetic approaches 302  
 synthetic polymers 78  
 synthetic routes 99–103
- t**
- targetability 332  
 targeted drug delivery 86–87  
 targeting ligand 289  
 TEM 164  
 TEM microphotographs, magnetite NCs 312  
 template-directed 191  
 TEOS 77  
 tetraethyl orthosilicate 77, *see also* TEOS  
 tetramethylbenzidine 138, *see also* TMBZ  
 TGA 307  
 therapeutic drugs 80–82  
 thermogravimetric analysis 307  
 thin films 167  
   – molecular 169–172  
 thiol 162  
 thiolation 332  
 thiol coupling 15  
 thiol groups 185  
 three component sandwich assays 244  
 titration calorimetry, isothermal 250
- TMBZ 138  
 tmv 193  
 tobacco mosaic virus *see also* TMV  
 TOPO-coated nanocrystals 252  
 TOPO-synthesized quantum dots 7  
 toxicity 331  
   – carbon nanotubes 65  
 tracking applications 28  
 transfection activity *in vitro* 280  
 transfection activity *in vivo* 285  
 transfection efficiency 282  
   – gelatin nanoparticles 346  
 transgene expression 85  
 transistor devices 58  
 transmission electron microscopy 164, *see also* TEM  
 transmitter dopamine 61  
 trimers, gold nanoparticles 245  
 triple helix 331  
 triton coating 216  
 tumor hyperthermia treatments 82  
 tumor markers 82  
 tumors, growth 289  
 tumor-targeted gene therapy 270–298  
 tyrosinase 335
- u**
- ultrasensitive DNA detection 61  
 ultra-small superparamagnetic nanoparticles  
   84, *see also* USPIO  
 ultrasonication 47  
 USPIO 84
- v**
- vectors, folate-linked 272  
 vegetable oil, water-in-oil emulsion 339  
 viral capsid transitions, monitoring 119  
 viral infection 119  
 viral vectors 270  
 virus 118–124  
 virus protein coat 191
- w**
- water-compatible surfactants 47–48  
 water-in-oil emulsion 339–340  
 watersolubility, quantum dots 7  
 water-soluble CNTs 53  
 water-soluble macromonomers 126  
 water-soluble nanoparticles 102  
 water-soluble polymeric magnetic nanoparticles 79  
 water-soluble polymers 48–49  
 wet-chemical preparation 184

**x**

- x-ray diffraction 153
- x-ray photoelectron spectra, nanoparticles 133
- x-ray photoelectron spectroscopy 132

**z**

- zeta potential, gelatin nanoparticles 341
- Zif268 111
- binding site 112
- zigzag 42
- Zn fingers 111

Nanotechnologies for the Life Sciences

Edited by Challa Kumar

WILEY-VCH

# Biological and Pharmaceutical Nanomaterials



NLS 

## Contents

	<b>Preface</b>	XIV
	<b>List of Contributors</b>	XVII
<b>I</b>	<b>DNA-based Nanomaterials</b>	<b>1</b>
<b>1</b>	<b>Self-assembled DNA Nanotubes</b>	<b>3</b>
	<i>Thom LaBean and Sung Ha Park</i>	
1.1	Introduction	3
1.2	DNA Nanotubes Self-assembled from DX Tiles	4
1.3	3DAE-E DX Tile Nanotubes	5
1.4	DAE-O DX Tile Nanotubes	9
1.5	TX Tile Nanotubes	11
1.6	4 × 4 Tile Nanotubes	14
1.7	6HB Tile Nanotubes	16
1.8	Applications	18
1.9	Summary and Perspectives	19
	References	20
<b>2</b>	<b>Nucleic Acid Nanoparticles</b>	<b>23</b>
	<i>Guy Zuber, Bénédicte Pons and Andrew W. Fraley</i>	
2.1	Introduction	23
2.2	The Chemical and Physical Properties of Therapeutic DNA	25
2.3	Preparation of Nucleic Acid Nanoparticles: Synthesis and Characterization	27
2.3.1	Rationale	27
2.3.2	Synthesis, Characterization and Optimization of Surfactants	31
2.3.3	Organization of the Surfactant–DNA Complexes	35
2.3.4	Quantification of the Stability of Surfactant–DNA Complexes	35
2.4	DNA Functionalization for Cell Recognition and Internalization	37
2.4.1	Strategies for Functionalization	37
2.4.2	Intercalation	38
2.4.3	Triple Helix Formation with Oligodeoxyribonucleotides	39

2.4.4	Peptide Nucleic Acids (PNAs)	41
2.4.5	Interactions of DNA with Fusion Proteins	42
2.4.6	Agents that Bind to the Minor Groove	43
2.5	DNA Nanoparticles: Sophistication for Cell Recognition and Internalization	43
2.5.1	Preparation of DNA Nanoparticles Enveloped with a Protective Coat and Cell Internalization Elements	43
2.5.2	Biomedical Application: Cell Targeting and Internalization Properties of Folate-PEG-coated Nanoparticles	46
2.6	Concluding Remarks	46
	References	47
<b>3</b>	<b>Lipoplexes</b>	<b>51</b>
	<i>Sarah Weisman</i>	
3.1	Introduction	51
3.2	DNA Lipoplexes	51
3.2.1	Composition	51
3.2.2	Nanostructure and Microstructure	52
3.2.2.1	Equilibrium Morphology	52
3.2.2.2	Nonequilibrium Morphology	55
3.2.2.3	Lipoplex Size	57
3.2.3	Lipofection Efficiency	57
3.2.3.1	<i>In Vitro</i>	57
3.2.3.2	<i>In Vivo</i>	59
3.3	ODN Lipoplexes	60
3.4	siRNA Lipoplexes	62
	Acknowledgments	62
	References	62
<b>4</b>	<b>DNA-Chitosan Nanoparticles for Gene Therapy: Current Knowledge and Future Trends</b>	<b>68</b>
	<i>Julio C. Fernandes, Marcio José Tiera and Françoise M. Winnik</i>	
4.1	Introduction	68
4.2	Chitosan as a Carrier for Gene Therapy	69
4.2.1	Chitosan Chemistry	69
4.2.2	General Strategies for Chitosan Modification	71
4.2.3	Chitosan-DNA interactions: Transfection Efficacy of Unmodified Chitosan	71
4.3	Modified Chitosans: Strategies to Improve the Transfection Efficacy	79
4.3.1	The Effects of Charge Density/Solubility and Degree of Acetylation	79
4.3.2	Improving the Physicochemical Characteristics of the Nanoparticulate Systems: Solubility, Aggregation and RES Uptake	80

4.3.3	Targeting Mediated by Cell Surface Receptors	81
4.3.4	Hydrophobic Modification: Protecting the DNA and Improving the Internalization Process	83
4.4	Methods of Preparation of Chitosan Nanoparticles	84
4.4.1	Complex Coacervation	84
4.4.2	Crosslinking Methods	86
4.4.2.1	Chemical Crosslinking	86
4.4.2.2	Ionic Crosslinking or Ionic Gelation	86
4.4.2.3	Emulsion Crosslinking	87
4.4.2.4	Spray Drying	88
4.4.2.5	Other Methods	89
4.5	DNA Loading into Nano- and Microparticles of Chitosan	91
4.6	DNA Release and Release Kinetics	93
4.7	Preclinical Evidence of Chitosan–DNA Complex Efficacy	95
4.8	Potential Clinical Applications of Chitosan–DNA in Gene Therapy	97
4.9	Conclusion	99
	Acknowledgments	99
	References	99
<b>II</b>	<b>Protein &amp; Peptide-based Nanomaterials</b>	<b>115</b>
<b>5</b>	<b>Plant Protein-based Nanoparticles</b>	<b>117</b>
	<i>Anne-Marie Orecchioni, Cécile Duclairoir, Juan Manuel Irache and Evelyne Nakache</i>	
5.1	Introduction	117
5.2	Description of Plant Proteins	118
5.2.1	Pea Seed Proteins	119
5.2.2	Wheat Proteins	119
5.3	Preparation of Protein Nanoparticles	120
5.3.1	Preparation of Legumin and Vicilin Nanoparticles	121
5.3.2	Preparation of Gliadin Nanoparticles	122
5.4	Drug Encapsulation in Plant Protein Nanoparticles	124
5.4.1	RA Encapsulation in Gliadin Nanoparticles	124
5.4.2	VE Encapsulation in Gliadin Nanoparticles	125
5.4.3	Lipophilic, Hydrophilic or Amphiphilic Drug Encapsulation	126
5.5	Preparation of Ligand–Gliadin Nanoparticle Conjugates	127
5.6	Bioadhesive Properties of Gliadin Nanoparticles	129
5.6.1	<i>Ex Vivo</i> Studies with Gastrointestinal Mucosal Segments	130
5.6.2	<i>In Vivo</i> Studies with Laboratory Animals	131
5.7	Future Perspectives	135
5.7.1	Size Optimization	135
5.7.2	Immunization in Animals	136
5.8	Conclusion	137
	References	137

<b>6</b>	<b>Peptide Nanoparticles</b>	<b>145</b>
	<i>Klaus Langer</i>	
6.1	Introduction	145
6.2	Starting Materials for the Preparation of Nanoparticles	146
6.3	Preparation Methods	148
6.3.1	Nanoparticle Preparation by Emulsion Techniques	148
6.3.1.1	Emulsion Technique for the Preparation of Albumin-based Microspheres and Nanoparticles	148
6.3.1.2	Emulsion Technique for the Preparation of Gelatin-based Microspheres and Nanoparticles	151
6.3.1.3	Emulsion Technique for the Preparation of Casein-based Microspheres and Nanoparticles	153
6.3.2	Nanoparticle Preparation by Coacervation	154
6.3.2.1	Complex Coacervation Techniques for the Preparation of Nanoparticles	154
6.3.2.2	Simple Coacervation (Desolvation) Techniques for the Preparation of Nanoparticles	155
6.4	Basic Characterization Techniques for Peptide Nanoparticles	159
6.5	Drug Targeting with Nanoparticles	161
6.5.1	Passive Drug Targeting with Particle Systems	163
6.5.2	Active Drug Targeting with Particle Systems	163
6.5.3	Surface Modifications of Protein-based Nanoparticles	164
6.5.4	Surface Modification by Different Hydrophilic Compounds	164
6.5.5	Surface Modification by Polyethylene Glycol (PEG) Derivatives	165
6.5.6	Surface Modification by Drug-targeting Ligands	166
6.5.7	Different Surface Modification Strategies	168
6.6	Applications as Drug Carriers and for Diagnostic Purposes	169
6.6.1	Protein-based Nanoparticles in Gene Therapy	170
6.6.2	Parenteral Application Route	172
6.6.2.1	Preclinical Studies with Protein-based Particles	172
6.6.2.2	Clinical Studies with Protein-based Particles	172
6.6.3	Topical Application of Protein-based Particles	174
6.6.4	Peroral Application of Protein-based Particles	175
6.7	Immunological Reactions with Protein-based Microspheres	175
6.8	Concluding Remarks	176
	References	176
<b>7</b>	<b>Albumin Nanoparticles</b>	<b>185</b>
	<i>Juan Manuel Irache and Socorro Espuelas</i>	
7.1	Introduction	185
7.2	Serum Albumin	186
7.3	Preparation of Albumin Nanoparticles	187
7.3.1	“Conventional” Albumin Nanoparticles	188
7.3.1.1	Preparation of Albumin Nanoparticles by Desolvation or Coacervation	189



7.3.1.2	Preparation of Albumin Nanoparticles by Emulsification	192
7.3.1.3	Other Techniques to Prepare Albumin Nanoparticles	193
7.3.2	Surface-modified Albumin Nanoparticles	193
7.3.3	Drug Encapsulation in Albumin Nanoparticles	194
7.4	Biodistribution of Albumin Nanoparticles	196
7.5	Pharmaceutical Applications	198
7.5.1	Albumin Nanoparticles for Diagnostic Purposes	198
7.5.1.1	Radiopharmaceuticals	198
7.5.1.2	Echo-contrast Agents	199
7.5.2	Albumin Nanoparticles as Carriers for Oligonucleotides and DNA	199
7.5.3	Albumin Nanoparticles in the Treatment of Cancer	201
7.5.3.1	Fluorouracil and Methotrexate Delivery	201
7.5.3.2	Paclitaxel Delivery	202
7.5.3.3	Albumin Nanoparticles in Suicide Gene Therapy	203
7.5.4	Magnetic Albumin Nanoparticles	204
7.5.5	Albumin Nanoparticles for Ocular Drug Delivery	205
7.5.5.1	Topical Drug Delivery	205
7.5.5.2	Intravitreal Drug Delivery	205
7.6	Concluding Remarks	207
	References	208
<b>8</b>	<b>Nanoscale Patterning of S-Layer Proteins as a Natural Self-assembly System</b>	<b>219</b>
	<i>Margit Sára, D. Pum, C. Huber, N. Ilk, M. Pleschberger and U. B. Sleytr</i>	
8.1	Introduction	219
8.2	General Properties of S-Layers	220
8.2.1	Structure, Isolation, Self-Assembly and Recrystallization	220
8.2.2	Chemistry and Molecular Biology	221
8.2.3	S-Layers as Carbohydrate-binding Proteins	223
8.3	Nanoscale Patterning of S-Layer Proteins	224
8.3.1	Properties of S-Layer Proteins Relevant for Nanoscale Patterning	224
8.3.2	Immobilization of Functionalities by Chemical Methods	225
8.3.3	Patterning by Genetic Approaches	226
8.3.3.1	The S-Layer Proteins SbsA, SbsB and SbsC	226
8.3.3.2	S-Layer Fusion Proteins	228
8.4	Spatial Control over S-Layer Reassembly	241
8.5	S-Layers as Templates for the Formation of Regularly Arranged Nanoparticles	242
8.5.1	Binding of Molecules and Nanoparticles to Functional Domains	242
8.5.2	<i>In Situ</i> Synthesis of Nanoparticles on S-Layers	244
8.6	Conclusions and Outlook	244
	Acknowledgments	245
	References	245

III	<b>Pharmaceutically Important Nanomaterials</b>	253
9	<b>Methods of Preparation of Drug Nanoparticles</b>	255
	<i>Jonghwi Lee, Gio-Bin Lim and Hesson Chung</i>	
9.1	Introduction	255
9.2	Structures of Drug Nanoparticles	257
9.3	Thermodynamic Approaches	257
9.3.1	Lipid-based Pharmaceutical Nanoparticles	258
9.3.2	What is a Lipid?	259
9.3.3	Liquid Crystalline Phases of Hydrated Lipids with Planar and Curved Interfaces	260
9.3.4	Oil-in-water-type Lipid Emulsion	261
9.3.5	Liposomes	261
9.3.6	Cubosomes and Hexosomes	262
9.3.7	Other Lipid-based Pharmaceutical Nanoparticles	263
9.4	Mechanical Approaches	264
9.4.1	Types of Processing	264
9.4.2	Characteristics of Wet Comminution	266
9.4.3	Drying of Liquid Nanodispersions	267
9.5	SCF Approaches	270
9.5.1	SCF Characteristics	270
9.5.2	Classification of SCF Particle Formation Processes	271
9.5.3	RESS	272
9.5.4	SAS	273
9.5.5	SEDS	274
9.6	Electrostatic Approaches	275
9.6.1	Electrical Potential and Interfaces	275
9.6.2	Electrospraying	277
	References	280
10	<b>Production of Biofunctionalized Solid Lipid Nanoparticles for Site-specific Drug Delivery</b>	287
	<i>Rainer H. Müller, Eliana B. Souto, Torsten Göppert and Sven Gohla</i>	
10.1	Introduction	287
10.2	Concept of Differential Adsorption	289
10.3	Production of SLN	292
10.4	Functionalization by Surface Modification	294
10.5	Conclusions	298
	References	299
11	<b>Biocompatible Nanoparticulate Systems for Tumor Diagnosis and Therapy</b>	304
	<i>Mostafa Sadoqi, Sunil Kumar, Cesar Lau-Cam and Vishal Saxena</i>	
11.1	Introduction	304

11.2	Nanoscale Particulate Systems and their Building Blocks/Components	305
11.2.1	Dendrimers	305
11.2.2	Buckyballs and Buckytubes	307
11.2.3	Quantum Dots	309
11.2.4	Polymeric Micelles	310
11.2.5	Liposomes	310
11.3	Biodegradable Nanoparticles	312
11.3.1	Preparation of Nanoparticles	313
11.4	Biodegradable Optical Nanoparticles	314
11.4.1	Optical Nanoparticles as a Potential Technology for Tumor Diagnosis	314
11.4.2	Optical Nanoparticles as a Potential Technology for Tumor Treatment	315
11.5	Optical Imaging and PDT	317
11.5.1	Optical Imaging	317
11.5.1.1	Fluorescence-based Optical Imaging	317
11.5.1.2	NIR Fluorescence Imaging	317
11.5.1.3	NIR Dyes for Fluorescence Imaging	318
11.5.2	PDT	318
11.5.2.1	Basis of PDT	319
11.5.2.2	Photosensitizers for PDT	320
11.5.3	ICG: An Ideal Photoactive Agent for Tumor Diagnosis and Treatment	320
11.5.3.1	Clinical Uses of ICG	320
11.5.3.2	Structure and Physicochemical Properties of ICG	321
11.5.3.3	Binding Properties of ICG	321
11.5.3.4	Metabolism, Excretion and Pharmacokinetics of ICG	322
11.5.3.5	Toxicity of ICG	322
11.5.3.6	Tumor Imaging with ICG	322
11.5.3.7	PDT with ICG	323
11.5.3.8	Limitations of ICG for Tumor Diagnosis and Treatment	324
11.5.3.9	Recent Approaches for Improving the Blood Circulation Time and Uptake of ICG by Tumors	325
11.5.3.10	Recent Approaches for ICG Stabilization <i>In Vitro</i>	326
11.6	PLGA-based Nanoparticulate Delivery System for ICG	327
11.6.1	Rationale of Using a PLGA-based Nanoparticulate Delivery System for ICG	327
11.6.2	<i>In Vivo</i> Pharmacokinetics of ICG Solutions and Nanoparticles	331
11.7	Conclusions and Future Work	336
	References	338
<b>12</b>	<b>Nanoparticles for Crossing Biological Membranes</b>	<b>349</b>
	<i>R. Pawar, A. Avramoff and A. J. Domb</i>	
12.1	Introduction	349

12.2	Cell Membranes	350
12.2.1	Functions of Biological Membranes	351
12.2.2	Kinetic and Thermodynamic Aspects of Biological Membranes	352
12.3	Problems of Drugs Crossing through Biological Membranes	354
12.3.1	Through the Skin	354
12.3.1.1	Mechanical Irritation of Skin	355
12.3.1.2	Low-voltage Electroporation of the Skin	355
12.3.2	Through the BBB	357
12.3.2.1	Small Drugs	359
12.3.2.1.1	Limitations of Small Drugs	359
12.3.2.2	Peptide Drug Delivery via SynB Vectors	360
12.3.3	GI Barrier	360
12.3.3.1	Intestinal Translocation and Disease	361
12.4	Nanoparticulate Drug Delivery	362
12.4.1	Skin	363
12.4.1.1	Skin as Semipermeable Nanoporous Barrier	363
12.4.1.2	Hydrophilic Pathway through the Skin Barrier	363
12.4.2	Solid-Lipid Nanoparticles (SLN) Skin Delivery	364
12.4.2.1	Chemical Stability of SLN	364
12.4.2.2	<i>In Vitro</i> Occlusion of SLN	365
12.4.2.3	<i>In Vivo</i> SLN: Occlusion, Elasticity and Wrinkles	365
12.4.2.4	Active Compound Penetration into the Skin	365
12.4.2.5	Controlled Release of Cosmetic Compounds	365
12.4.2.6	Novel UV Sunscreen System Using SLN	366
12.4.3	Polymer-based Nanoparticulate Delivery to the Skin	366
12.4.4	Subcutaneous Nanoparticulate Antiepileptic Drug Delivery	366
12.4.5	Nanoparticulate Anticancer Drug Delivery	367
12.4.5.1	Paclitaxel	368
12.4.5.2	Doxorubicin	368
12.4.5.3	5-Fluorouracil (5-FU)	369
12.4.5.4	Antineoplastic Agents	369
12.4.5.5	Gene Delivery	369
12.4.5.6	Breast Cancer	370
12.4.6	Nanofibers Composed of Nonbiodegradable Polymer	370
12.4.6.1	Electrostatic Spinning	371
12.4.6.2	Scanning Electron Microscopy	371
12.4.6.3	Differential Scanning Calorimetry (DSC)	371
12.5	Nanoparticulate Delivery to the BBB	371
12.5.1	Peptide Delivery to the BBB	372
12.5.1.1	Peptide Conjugation through a Disulfide Bond	373
12.5.2	Biodegradable Polymer Based Nanoparticulate Delivery to BBB	373
12.5.3	Nanoparticulate Gene Delivery to the BBB	374
12.5.4	Mechanism of Nanoparticulate Drug Delivery to the BBB	375
12.5.5	Nanoparticulate Thiamine-coated Delivery to the BBB	376
12.5.6	Nanoparticle Optics and Living Cell Imaging	376

12.6	Oral Nanoparticulate Delivery	378
12.6.1	Lectin-conjugated Nanoparticulate Oral Delivery	379
12.6.2	Oral Peptide Nanoparticulate-based Delivery	380
12.6.3	Polymer-Based Oral Peptide Nanoparticulate Delivery	381
12.6.3.1	Polyacrylamide Nanospheres	381
12.6.3.2	Poly(alkyl cyanoacrylate) PACA Nanocapsules	381
12.6.3.3	Derivatized Amino Acid Microspheres	382
12.6.4	Lymphatic Oral Nanoparticulate Delivery	382
12.6.5	Oral Nanosuspension Delivery	383
12.6.6	Mucoadhesion of Nanoparticles after Oral Administration	384
12.6.7	Protein Nanoparticulate Oral Delivery	384
	References	385
	<b>Index</b>	<b>394</b>

## Preface

While the recently published first volume of the *NtLS* series, *Biofunctionalization of Nanomaterials*, dealt with approaches to tailoring nanomaterials to be useful in biomedical applications, this second volume of the series, which I am pleased to present to you herewith, focuses on nanomaterials derived from biologically and pharmaceutically important substances. Twelve chapters describe in depth the various nanotechnological aspects behind using DNA, proteins, peptides, chitosan, lipoplexes, lipids and drugs. DNA is the most important and well studied biological molecule which itself is in the nano size regime. One of the attractive features of products containing DNA is the potential for producing materials of biological nature. Although DNA-based nanotechnology is currently in its infancy, it is likely to impact future applications in industrial segments such as electronics, sensors, medicine, and many other fields. The book has four chapters on DNA based nanomaterials. It begins with a chapter entitled *Self-Assembled DNA Nanotubes*, which is a contribution from the laboratories of Thom LaBean and Sung Ha Park from Duke University, USA, on self-assembled one-dimensional (1D) DNA nanotubes with unique design schemes and characteristics. In this chapter, approaches to assembly of artificially designed tiles, DX, TX, 4×4, and 6BH branched-junction tiles to form 1D DNA nanotubes have been described. The second chapter illuminates on the importance of development of effective nucleic acid nanocarriers and provides approaches to prepare DNA nanoparticles containing a single DNA molecule (the minimal particle size possible) as well as their characterization and properties. This chapter, *Nucleic Acid Nanoparticles*, presented by Guy Zuber and co-workers from the Genetic Chemistry Laboratory of Illkirch University, France, reviews strategies for synthesis of DNA nanoparticles and possibilities to functionalize them with cancer cell targeting elements. Mixing DNA with cationic lipids leads to spontaneous self assembly of ordered aggregates known as lipoplexes whose size can range from around 100 nm to several microns depending on preparation conditions. The third chapter, *Lipoplexes*, written by Sarah Weisman from Technion Israel Institute of Technology in Haifa, Israel, gives an overview of the current state of knowledge about lipoplexes, with special attention to their microscopic structure, and the relationships between structure and gene delivery efficiency. Julio C. Fernandes and co-workers from the Medical Faculty of Montreal University, Canada, brought out an exhaustive review on DNA-Chitosan polyplexes presented

in the fourth chapter, *DNA-chitosan Nanoparticles for Gene Therapy: Current Knowledge and Future Trends*. In addition to the basic concepts, the chapter provides information on different procedures to obtain nano- and micro DNA-chitosan particles and their clinical application as non-viral vectors in gene therapy.

Switching gears from DNA to proteins, the book provides a further four chapters on different facets of peptide and protein based nanomaterials. Proteins are a class of natural molecules that have unique functionalities and potential applications in both biological as well as material fields. Nanomaterials derived from proteins, especially protein nanoparticles, are biodegradable, metabolizable and can also be easily amenable for surface modification and covalent attachment of drugs and ligands. In the fifth chapter, Anne-Marie Orecchioni and co-workers from the Laboratory of Galenic Pharmacy of Rouen University, St. Etienne du Rouvray, France, provide an exhaustive account of plant based proteins, their synthesis and applications. This particular chapter, *Plant Protein-based Nanoparticles*, not only provides information on conventional plant protein nanoparticles but also describes 'decorated' (i.e., conjugated) storage protein nanoparticles. Continuing on a similar theme, Klaus Langer from the Biocenter of Frankfurt on Main University, Germany, provides a comprehensive account in chapter six, *Peptide Nanoparticles*, on preparation techniques for peptide and protein-based nanoparticles with focus on their application in drug delivery. Narrowing down from a broad perspective on protein nanoparticles described in chapters two and three, chapter seven has the title *Albumin Nanoparticles*, indicating a review on a specific protein, Serum Albumin, which is extremely important in physicochemical, immunochemical and drug delivery applications. In this chapter, Juan Manuel Irache and Socorro Espuelas from the Galenics Center of Navarra University in Pamplona, Spain, summarize preparation and main applications of albumin nanoparticles for pharmaceutical purposes. Chapter eight, *Nanoscale Patterning of S-Layer Proteins as a Natural Self-Assembly System*, by Margit Sára and co-workers from the Center for Nanobiotechnology of the Agricultural University of Vienna, Austria, provides a survey of the general principles of crystalline bacterial cell surface layer (S-layer) proteins and fusion proteins which are being exploited as building blocks and templates for generating functional nanostructures at the meso- and macroscopic scale for both life and non-life science applications.

Pharmaceutical research and development has recently moved into a new direction thanks to the possibility of obtaining nanoformulation of drugs, i.e. formulation of drugs using nanoparticles. Keeping in tune with this trend a separate chapter specifically on drug nanoparticles has been included in this volume. Chapter nine, *Preparation Methods of Drug Nanoparticles* by Jonghwi Lee and co-workers from the Department of Nano Materials Science at Sejong University in Seoul, Korea, describe methods of preparation of drug nanoparticles, their characterization and advantages over conventional methods. In addition, chapter ten provides a review on Solid-Lipid Nanoparticles delineating the concept of differential protein adsorption as the concept of functionalization of SLN via surface modification from a practical point of view. In this chapter entitled *Production of Biofunctionalized Solid Lipid Nanoparticles for Site-specific Drug Delivery*, Rainer H. Müller and

co-workers from the Department of Pharmaceutical Technology of Free University Berlin, Germany, review methods used for the functionalization of solid lipid nanoparticles by modification of their surface characteristics followed by examples for their application in site-specific drug delivery. Mostafa Sadoqi and co-workers from the Physics Department of St John's University at Jamaica, USA, discuss near-infrared dye (NIR) indocyanine green (ICG) loaded PLGA drug nanoparticles and their application in cancer diagnosis and therapy in chapter eleven, *Biocompatible Nanoparticulate Systems for Tumor Diagnosis and Therapy*. Finally, since membrane transport plays an important role in cellular and subcellular pathways, including multidrug resistance (MDR), cellular signaling and cell-cell communication, an exclusive chapter, placed in twelfth position, discusses general information on cell membranes and the problems encountered by drugs when trying to cross them, and why drug nanoparticles are preferred. This chapter, *Nanoparticles for Crossing Biological Membranes*, is presented by Rajendra P. Pawar, A. Avramoff and Abraham J. Domb from the Department of Medicinal Chemistry of the Hebrew University of Jerusalem, Israel.

I do hope that the information that has been painstakingly accumulated by several researchers in this second volume will help in furthering better understanding of the nanosystems derived from biological materials, leading to new and potent applications. I am very grateful to all the authors for their excellent presentation of their topics, providing timely inputs and corrections in making the second volume a reality. I am always thankful to my employers, family, friends and Wiley-VCH publishers for their continued support and encouragement. Finally, my special thanks to you, the readers, for making attempts to utilize the knowledge base provided in this book. I look forward to receiving your comments and suggestions.

*Baton Rouge, September 2005*

*Challa S. S. R. Kumar*



# I

## DNA-based Nanomaterials



## 1

## Self-assembled DNA Nanotubes

*Thom LaBean and Sung Ha Park*

## 1.1

### Introduction

DNA, well-known as the predominant molecule for the storage of genetic information in biology and biochemistry, has also been recognized as a useful building material in the field of nanotechnology [1–3]. DNA provides basic building blocks for constructing functionalized nanostructures with four major features: molecular recognition, self-assembly, programmability and predictable nanoscale geometry. The limitations of conventional methods of top-down fabrication make bottom-up self-assembled nanostructures using DNA molecules a fascinating and attractive technique for near-term nano/biotechnologies. Recently, self-assembled DNA nanostructures utilizing branched DNA tiles have been reported on (a) various artificial geometrical structures like one- (1-D) and two-dimensional (2-D) periodically patterned structures [4–14], and three-dimensional (3-D) polyhedra [15, 16], and (b) functionalized lattices such as mechanical devices [17–23], molecular computers [24–30] and scaffolds for organizing other functionalized molecules [31–33]. DNA nanostructures are created via self-assembly during the slow annealing of aqueous solutions of carefully designed single-strand DNA, thereby facilitating hybridization of complementary nucleotide sequences, and the formation of double-strand domains and Holliday junction-like crossover points.

In this chapter, we review recent results on self-assembled 1-D DNA nanotubes with unique design schemes and characteristics. DNA nanotubes are characterized by (a) a high aspect ratio, (b) a long, narrow central channel and (c) DNA sidewalls. The 1-D nanotubes are typically made from rolled-up sheets of DNA lattice containing tiles with a variety of motifs: double-crossover (DX) [34], triple-crossover (TX) [35] and four four-arm junctions ( $4 \times 4$ ) [36]. Schematic drawings of four distinct DNA tile motifs which have been used for constructing complex 1-D DNA nanotubes are shown in Fig. 1.1.

The DNA tiles shown in Fig. 1.1 have each been shown to form large two-dimensional lattice sheets up to 10  $\mu\text{m}$  on an edge, as well as nanotubes formed by lattices which curl and close upon themselves. Superstructure morphology

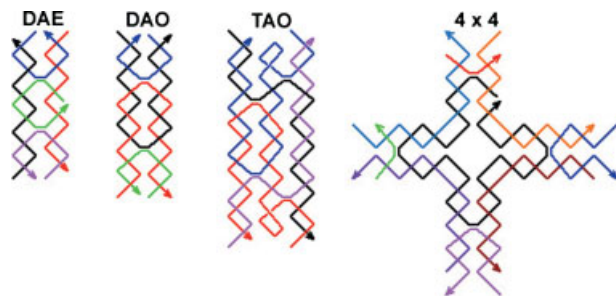


**Fig. 1.1.** Four distinct DNA motifs for constructing complex 1-D DNA nanotubes. The structures DAE, DAO and TAO are named by acronyms describing their basic characteristics. Names begin with “D” for DX (two helical domains) and “T” for TX (three helical domains). The second character indicates the relative orientations of their two double-helical domains. Here, “A” stands for antiparallel and indicates that, upon crossing over, the strands

change direction of propagation along the helical axes. The third character refers to the number of helical half-turns between cross-overs, “E” for an even number and “O” for an odd number. The  $4 \times 4$  tile contains four four-arm branched junctions pointing in four directions (north, south, east and west in the tile plane). Arrows indicate simplified strands running from 5' to 3'.

(sheet versus tube) is controlled in these tiling systems by a variety of means, including counterion concentration, lattice corrugation schemes and disulfide bridge formation. As explained in detail below, curled lattice DNA nanotubes have been observed with either stacked, circular layers of tiles or with spirally wound, chiral configurations. DNA nanotubes have also been intentionally constructed by stacking six-helix bundle (6HB) tiles one on top the other to form tubes with only a single tile per layer and a single double-helix diameter channel through the center [37].

## 1.2 DNA Nanotubes Self-assembled from DX Tiles

Recently, several varieties of nanotubes constructed from DX tiles have been reported [10–12]. Two distinct types of nanotubes made from DNA DX complexes are DAE-E and DAE-O (where the final letter in the acronym indicates the even/odd parity of helical half-turns between neighboring strand-exchange points within inter-tile joints). DAE-E DX tile nanotubes have diameters between 7 and 20 nm and lengths as long as 50  $\mu\text{m}$  with a persistence length of around 4  $\mu\text{m}$ ; they can be programmed to display a variety of patterns. The DAE-O tile lattice can form ribbon structures many micrometers in length and 40–250 nm in width after hybridization.

### 1.3 DAE-E DX Tile Nanotubes

The construction and characterization of programmable DAE-E nanotubes displaying several tiling schemes as well as the kinetics of their assembly have been studied and reported [10, 11]. DX tiles were first described over 10 years ago [34]. DNA tiles can be thought of as having two parts: (a) a central core of duplex DNA (illustrated by rectangles in Fig. 1.2) and (b) four single-stranded sticky ends which allow it to bind to other tiles (shown protruding from the tile corners). In this first case, the tile core is made up of five oligonucleotides strands that form two double-helical domains held in rigid orientation with parallel axes by a pair of strand-exchange crossover points (Fig. 1.3a). In the study, two different sequence assignments were made to yield two different cores, which the authors called RE and SE [10]. Given an appropriate set of sticky ends, a single core yields a single tile and the unique sequences for sticky end allows the interactions between tiles to be

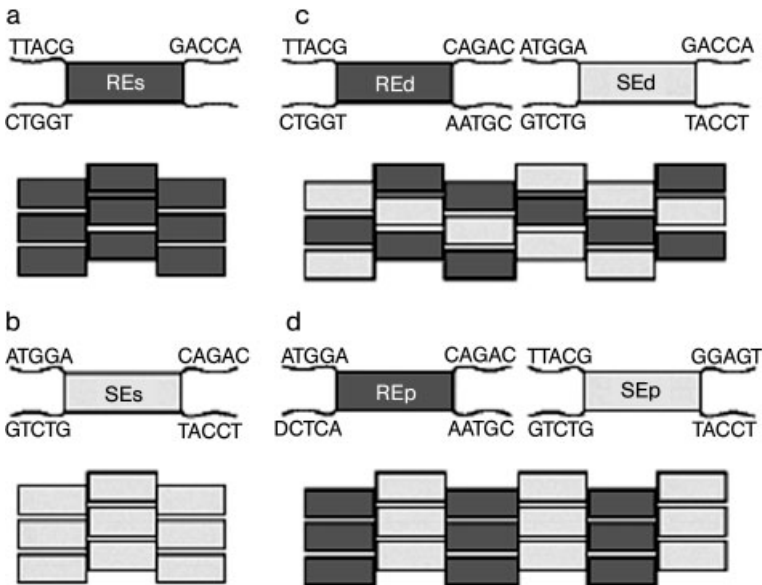


**Fig. 1.2.** Schematics of lattices utilizing DAE-E tiles. (a) Top: a single REs tile, based on the RE core and carrying four sticky ends. Bottom: complementarity between sticky ends directs the tiles to form a regular lattice. (b) A single SEs tile, based on a different core, SE, and its lattice. (c) Two tiles, REd and SEd, which assemble into a lattice with diagonal stripes; alone each tile could assemble into a linear strip. (d) Another pair of tiles, REp and SEp, cannot assemble independently, but together can form a lattice with stripes perpendicular to the long axis of the tiles. Note: lowercase letters “s”, “d” and “p” denote a particular choice of sticky ends and were chosen to represent the pattern generated by the tile set in which they appear: single tile type, diagonally striped or perpendicularly striped lattice. (From Ref. [10].)

programmed (Fig. 1.2). Figure 1.2(c and d) shows how tile sets have been used to create lattices with stripes either diagonal to or perpendicular to the long axis of the tiles. The authors viewed a set of tiles as a program for the construction of a particular structure including a diagonally striped or perpendicularly striped lattice.

In this system, hybridization of complementary sticky end pairs determines whether or not a set of tiles will form a lattice, but the set of sticky ends does not determine whether the lattice will be flat or curved. Curvature is profoundly affected by the choice of lattice symmetry as shown in Fig. 1.3(c–e). The symmetries depicted in Fig. 1.3(c and d) are compatible with flat lattice sheets since deviations

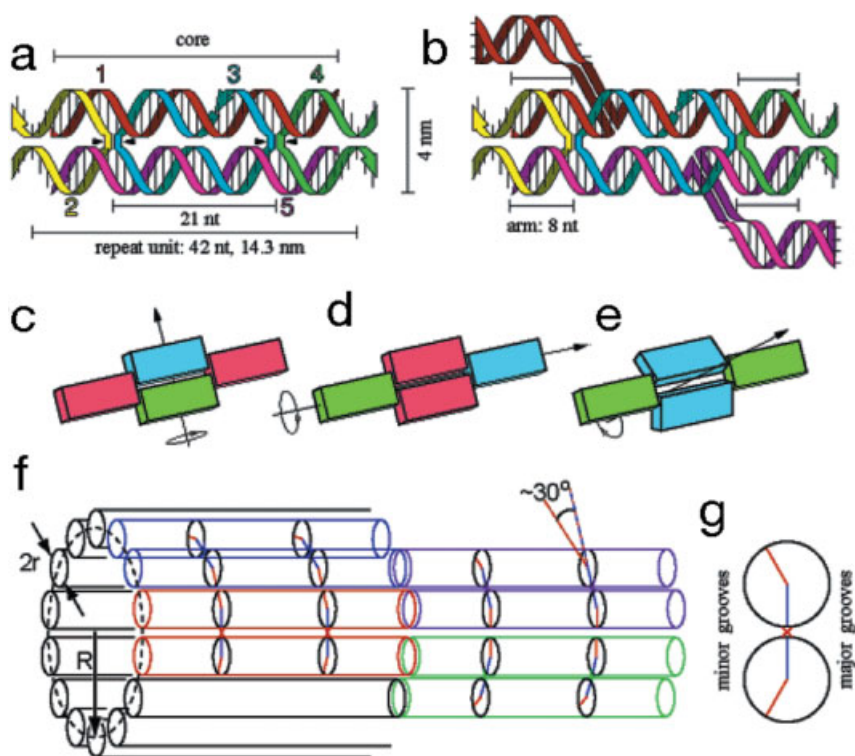


**Fig. 1.3.** (a) Structure of a DAE-E tile showing numbered strands and their paths through the complex. Tiles contain five single strands with 5-nt sticky ends on strands 2 and 4. (b) Tile structure with hairpins (8-nt stem, 4-nt loop) on strands 1 and 5 between nt 14 and 15 from their 5'-ends. Molecular models suggest that these hairpins attach underneath the molecule, as depicted here; in a tube they would be on the outside. (c and d) Two in-plane rotational symmetries that, if satisfied by a patch of tiles, encourage molecular strain to balance, resulting in a flat sheet. (e) A rotational symmetry, satisfied by DAE-E molecules, that permits curvature. (f) Heptagonal tube of radius  $R$ . In each tile, two cylinders of radius  $r$  represent the double helices. Black circles mark crossover points. Blue and orange lines connect the position of phosphate backbones to the center of a helix. The smaller angle between the blue and orange lines defines the minor groove. (g) Cross-section of the red tile from (f) at a crossover point. (From Ref. [10].)

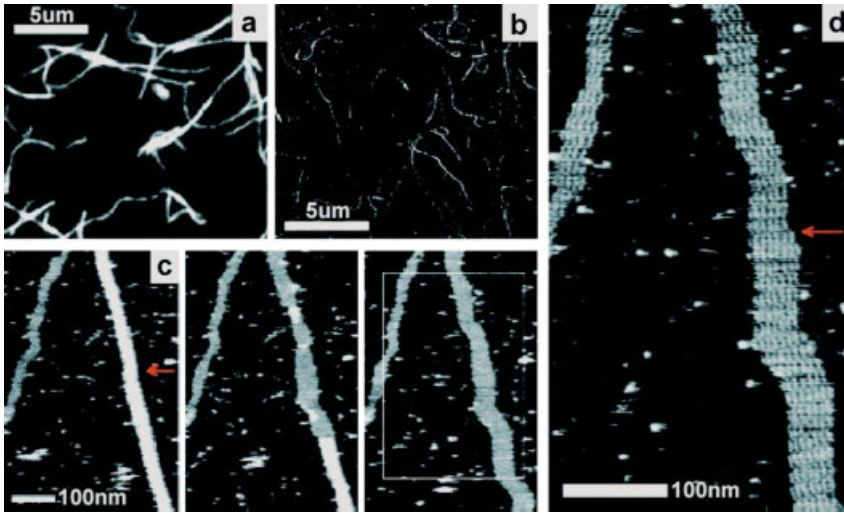


**Fig. 1.4.** Microscopic images of nanotubes. DNA filaments visualized by (a) fluorescence microscopy and (b) AFM. The solution in (a) contains FAM-labeled REp + SEp and in (b) contains REp + SEp. (c) A time series of AFM images indicates that filaments are tubes (REp + SEp). (Left panel) A thick filament (closed tube) runs the length of the image. Heights of closed tubes suggest they are flattened onto the substrate. An already-open

tube is seen on the right. (Center panel) The tube opens progressively from the top, revealing a one-tile-thick lattice. (Right panel) The fully opened tube resembles the lattice on the left. An arrow marks a discrete change in tube width before opening and in the number of tiles after opening, suggesting a defect in the tile lattice. (d) At greater magnification, individual tiles are resolved. (From Ref. [10].)

from planar geometry can be compensated for; thus, molecular strain that could cause curvature may be balanced by symmetric molecular strain elsewhere. Other possible lattice symmetries, such as the one depicted in Fig. 1.3(e), are compatible with intentionally curved lattices and the formation of DNA nanotubes.

DNA nanotubes constructed according to RE- and SE-core tiles were examined by atomic force microscopy (AFM) and by fluorescence microscopy using fluorescein (FAM)-labeled strands. Characterization by AFM showed parallel and diagonal striped patterns, as expected, providing proof that the structural programming functioned properly. AFM studies also revealed that nanotubes flatten out on the mica substrate and were abraded by the AFM tip from double-layer to single-layer structures by imaging repeatedly at the same place on the sample (Fig. 1.4). The dynamic character of the interactions of nanotubes and lattices with mica was seen by re-imaging a sample by AFM under solution over the course of several hours, and observing tubes coming to and diffusing away from the surface. Fragments of lattice were often left on the mica when a nanotube diffused away. For this reason, the dimensions of the filaments were difficult to measure using surface-based AFM.

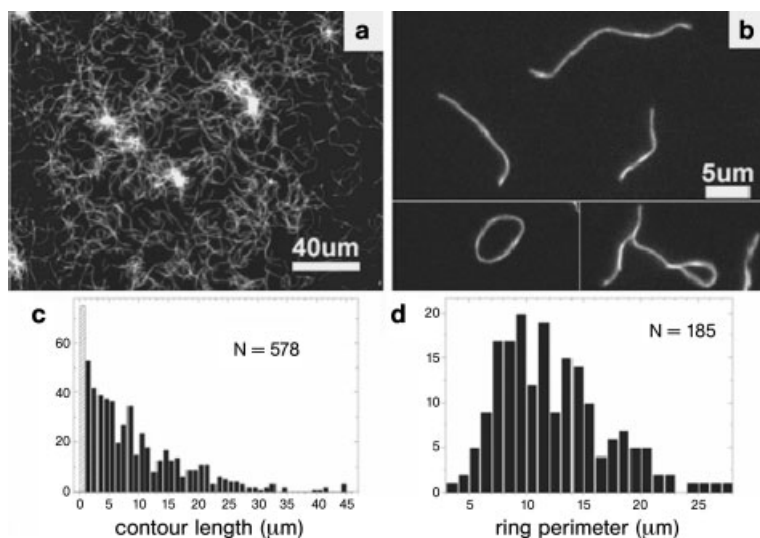


**Fig. 1.5.** Experimental determination of nanotube persistence length. (a) Epifluorescence image of 400 nM solution of FAM-labeled SEs tubes. Tubes were observed diffusing freely in and out of the focal plane. (b) As (a), but diluted to 40 nM. Occasionally, rings (left) and looped structures (right) are found. (c) Histogram of linear tube lengths

with an average of around 7  $\mu\text{m}$ ; approximately 10% are over 15  $\mu\text{m}$  long, consistent with an exponential distribution. Some tubes of around 50  $\mu\text{m}$  were observed. (d) Circularized tubes averaged 12  $\mu\text{m}$  in perimeter with a unimodal distribution. The ring shown is typical; most rings are free of kinks that would indicate local weakness. (From Ref. [10].)

Fluorescence microscopy was used to measure the length and stiffness of DAE-E nanotubes in solution. At the highest concentration (400 nM tiles) the density of tubes was too high to identify individuals and clump-like aggregates were common (Fig. 1.5a). Upon 10-fold dilution, single tubes were well dispersed and occasionally a ring or frayed bundle was seen (Fig. 1.5b). Only short tubes were observed directly following annealing and tube lengths continued to increase until about 16 h later when the distribution appeared to stabilize (at which point data were collected; Fig. 1.5c). The mean tube length was around 7  $\mu\text{m}$  with a small proportion of tubes with lengths up to 50  $\mu\text{m}$  being observed.

Tube stiffness was inferred from the distribution of ring perimeters by assuming that the rate of ring formation for a tube of length  $L$  is approximately proportional to the fraction of time that the ends of the tube are colocalized at equilibrium. Over brief intervals in which the length distribution does not change significantly, this ring closure probability can be calculated a function of tube length  $L$  and persistence length  $p$ . Under these conditions, the distribution of ring perimeters should be the product of the distribution of tube lengths and the ring closure probability. The mean perimeter distance was around 12  $\mu\text{m}$ . Using the distributions of Fig. 1.5(c and d), the persistence length was calculated to be  $3.85 \pm 0.35 \mu\text{m}$ .

Rothemund *et al.* performed the most thorough examination of the program-



mability and structural properties of DNA nanotubes [10]. They were able to identify the tile faces hidden inside and exposed outside the tubes, and drew important conclusions regarding the placement of hairpins on tiles and their effects on lattice stability. A subset of the authors went on to study the breaking and joining reactions among SE tile nanotubes and concluded that the growth of DNA tile nanotubes to multimicron length occurs through joining or fusion of preformed nanotubes rather than by sequential addition of individual tiles [11].

#### 1.4 DAE-O DX Tile Nanotubes

A similar system of DNA tiles which was originally designed to form 2-D flat lattice using DAE-O tiles (Fig. 1.6a) was also observed to form nanotubes either with flat ring layers or with spiral layers producing a range of chiral tubes (Figs. 1.6a and 1.7) [12]. As with the study described above, DX tiles (this time of the DAE-O variety) with the four single-stranded sticky ends on each tile were arranged such that  $\alpha$  and  $\beta$  tiles tessellate as shown in Fig. 1.6(b). The  $\beta$  tiles contained a 5'-biotinylated strand to enable streptavidin binding to be used as an observable marker. Hybridization was accomplished by cooling the solution by a linear gradient from 96 °C to room temperature over the course of 96 h.

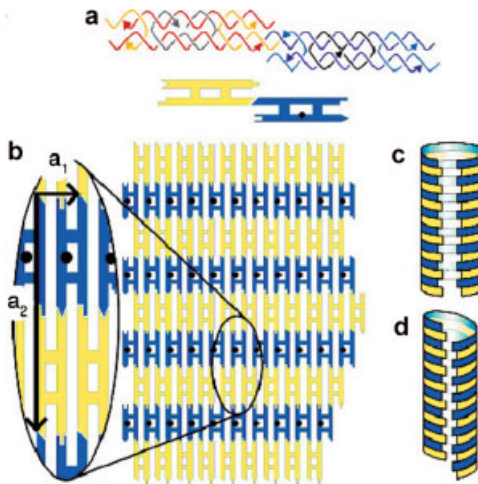


**Fig. 1.6.** Self-assembly of DAE-O tiles into sheets and tubes. (a) Structure of the DX tiles: colored arrows indicate simplified strands running 5' to 3'. The 6-nt single-stranded sticky ends on the  $\alpha$  tile are complementary to those on the  $\beta$  tile (represented schematically by complementary shapes). A 5' biotin label on

the  $\beta$  tile is shown as a black dot. (b) The  $\alpha$  and  $\beta$  tiles can tessellate to form extended 2-D arrays. The 2-D sheets curl and close upon themselves to form tubes, producing either alternating rings (c) or nested helices (d) of  $\alpha$  and  $\beta$  tiles. (From Ref. [12].)

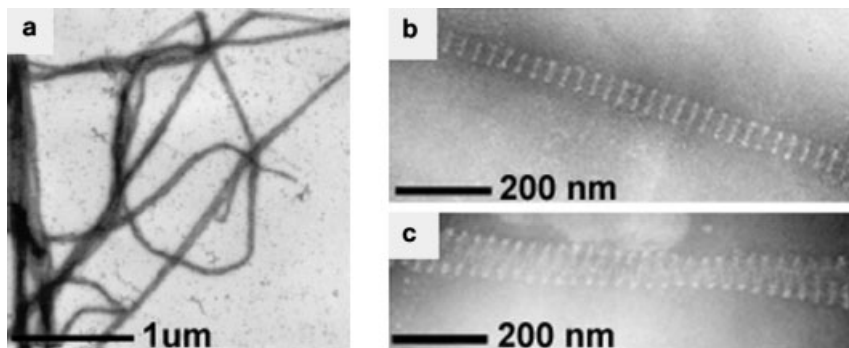


**Fig. 1.7.** Transmission electron micrographs of negatively stained DNA nanotubes and arrays. White features correspond to points of heavy metal stain exclusion where protein labels are bound to the  $\beta$  tiles. (From Ref. [12].)

In a standard  $1 \times \text{TAE}/\text{Mg}^{2+}$  buffer, containing 20 mM Tris–acetate, pH 8.3, supplemented with 12.5 mM  $\text{MgCl}_2$ , the tiles form ribbon structures many micrometers in length and 40–250 nm in width after hybridization (Fig. 1.7a). Higher magnification reveals transverse streptavidin bands with a periodicity of  $31 \pm 2$  nm (Fig. 1.7b and c), consistent with the designed 2-D array structure with the long axis of the tiles aligned along the long axis of the ribbons. A natural explanation for the parallel edges of these structures is that arrays of tiles curl and close upon themselves to form tubes. Unambiguous evidence for the formation of tubes is provided by micrographs such as Fig. 1.7(c) in which lines of streptavidin labels zigzag across a ribbon. In all such cases the line is continuous where it changes direction at the edge of the ribbon, proving they represent helical (spiral) tubes with a structure such as that illustrated in Fig. 1.6(d). Mixed superstructure morphologies (tubes and sheets) were observed in buffer with higher salt concentrations.

The authors point out that, as with carbon nanotubes [38], the structure of a DNA nanotube may be characterized by the indices  $(m, n)$  of the wrapping vector  $\mathbf{c} = m\mathbf{a}_1 + n\mathbf{a}_2$  where  $\mathbf{a}_1$  and  $\mathbf{a}_2$  are basis vectors shown in Fig. 1.6(b), and the tube is formed from a sheet by joining equivalent points separated by  $\mathbf{c}$ . For nonhelical tubes  $n = 0$  (Fig. 1.7b);  $n = 1$  where all labels lie on a single helix (Fig. 1.7c). The short dimensions of the tiles are not resolved (the streptavidin labels are larger than the tile width); assuming  $\mathbf{a}_1 = 4$  nm, then  $m \sim 40$  (Fig. 1.7c). It is likely that tube diameters are determined by nonequilibrium processes, since once a tube has closed, an activation barrier prevents further lateral growth. Tube formation reduces the free energy of a tile array by satisfying all inter-tile bonds except those at the ends of the tube. Intrinsic curvature of the array would facilitate tube formation; however, the odd number of helical half-turns along the arms joining cross-over points on adjacent tiles means that in this system the intrinsic curvatures of  $\alpha$  and  $\beta$  tiles are opposed.

## 1.5

### TX Tile Nanotubes

DNA nanotubes composed of TX tiles have also been constructed and characterized [14]. TX tiles modified with thiol-containing double-stranded DNA stems projected out of the tile plane were used as the basic building blocks. TX nanotubes display a constant diameter of around 25 nm and have been observed with lengths up to 20  $\mu\text{m}$ . In this section, we present high-resolution images of the constructs (TX nanotubes) and experimental evidence of their tube-like nature. DNA nanotubes represent a potential breakthrough in the self-assembly of nanometer-scale circuits for electronics layout because they can be targeted to connect at specific locations on larger-scale structures and can subsequently be metallized to form nanometer-scale metallic wires (see Section 2.6).

TX nanotube self-assemblies were formed from two DNA tile building blocks, a TAO (tile A) and a TAO + 2J (tile B) as shown in Fig. 1.8(a). The B tile contains two extra double-stranded DNA stems, which form junctions with the central helix of the tile such that they project out of the tile plane, with one stem protruding on each side of the tile. The B tiles used here are modified by the replacement of the loop on one protruding stem with a blunt end containing two thiol groups, one on a 3' and the other on a 5' strand terminus. Figure 1.8(b, right) shows a section of the proposed structure of the nanotubes with B tile layers alternating with A tile layers, double-stranded DNA helix axes aligned parallel with the tube axis, and thiol groups are located inside the tubes. Imaging of TX AB flat lattice sheets (Fig. 1.8c, left) demonstrates lattice fragments with widely varying dimensions and often with uneven edges. On the other hand, DNA nanotubes (Fig. 1.8c, right) exhibit uniform widths of around 25 nm for lengths of up to 20  $\mu\text{m}$ .

Figure 1.9(a) shows a typical AFM image (tapping mode in air) of the TX nanotube. Stripes perpendicular to the long axis of the filaments are clearly visible and indicate closed ring structures in successive layers rather than a spiral structure, which would have given stripes with a noticeable diagonal slant. Figure 1.9(b) shows a high-resolution AFM image (tapping mode in buffer) of the TX nanotube in which one can discern three gaps and four tiles in some of the layers. The gaps and tiles are arrayed parallel with the axis of the flattened tube.

Burial of the sulfur moieties within the tubes makes logical sense because disulfide bridges are preferred structures formed by thiol groups under physiologic-like solution conditions such as those used here. The formation of disulfide bonds between neighboring B tiles would cause the lattice to curve and form tubes. The possible existence of free thiols on the outer surface of the nanotubes was probed by using two different gold reagents with reactivity toward sulfur: monomaleimido Nanogold (Nanoprobes, Yaphank, NY) and fresh colloidal gold nanoparticles. The monomaleimido Nanogold failed to react with the tube surfaces, whereas the colloidal gold displayed the interesting reactivity shown in Fig. 1.9(d and e). With very low background levels of unbound gold, the bound gold particles showed a very high probability of attachment to the ends of nanotubes and not to the outer surface anywhere else along the length of the tubes. The indication is that sulfur

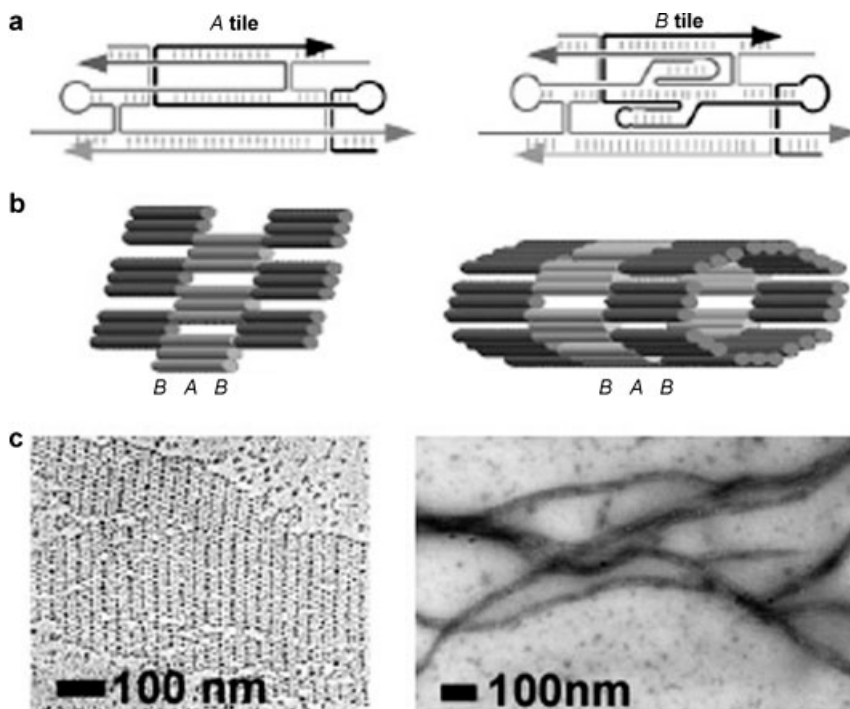


**Fig. 1.8.** (a) Schematic drawings showing the strand traces through the two tile types used in the constructions. Oligonucleotides are shown in different shades of gray and with arrowheads marking the 3'-ends. Short vertical hash marks indicate base pairing within double-helical regions; paired vertical lines represent crossover points. The central helices of both tile types are terminated with  $T_4$  loops. Two extra stem-loops (2J) on the central helix of the B tile are designed to protrude, one into and one out of the tile plane. (b) (Left) Cartoon of a section of TAO flat lattice constructed from A and B tiles. Tubes repre-

sent double-helical regions; for simplicity, the 2J stem-loops on the B tiles are not shown. (Right) Cartoon model of a section of TAO nanotube shown with eight tiles per layer of tube. (c) (Left) TEM image of platinum rotary shadowed TAO lattice. The B tiles appear darker than the A tiles, having picked up more platinum on their protruding 2J stem-loops; alternating stripes of A and B tiles are clearly visible with approximately the expected distance of 28 nm. (Right) TEM image of negative-stained TAO nanotubes. (From Ref. [14].)

which is buried within the tubes is exposed to some extent at the open ends of the nanotubes and available for binding with gold. This observation, in addition to offering evidence of the location of the thiol groups, may also be exploited in future work on targeted binding or formation of electrical contacts with the ends of TX nanotubes. Final evidence of the involvement of disulfide bridges in TX nanotube formation was provided by annealing the DNA in the presence of the reducing agent dithiothreitol and observing a complete lack of tubes.

Figure 1.10 shows a series of *in situ* zoomed images showing a TX nanotube being converted to a flat lattice by the physical effect of the AFM tip. The series of

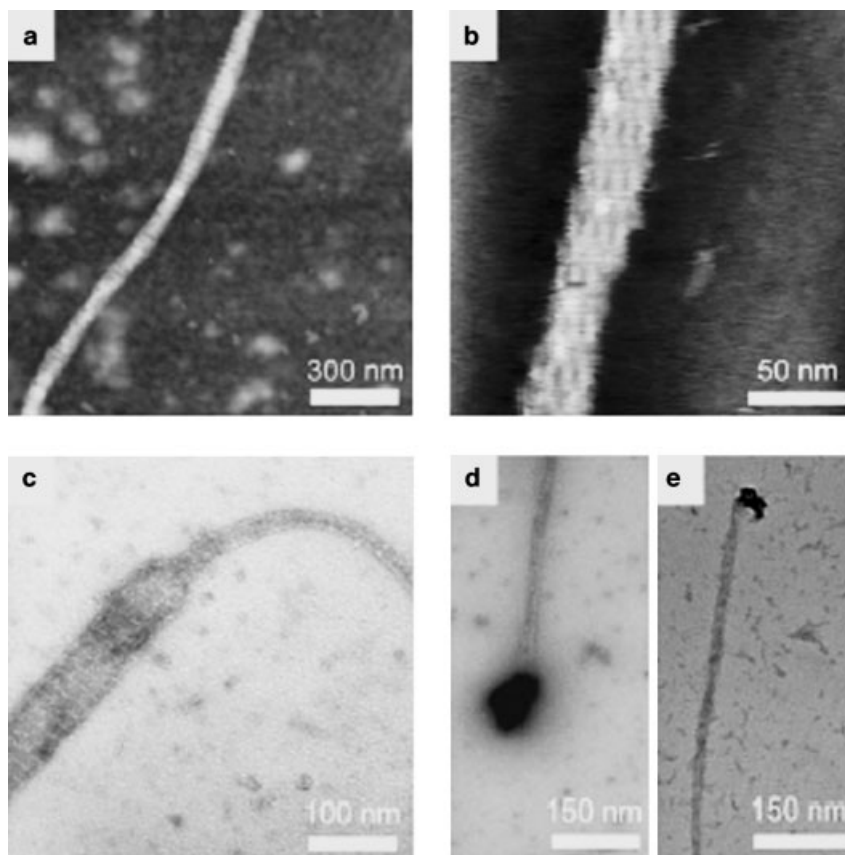


**Fig. 1.9.** (a) AFM image of a TAO nanotube taken by tapping mode in air. The *B* tile layers are visible as brighter stripes (because of increased height) oriented perpendicular to the long axis of the tube. (b) High-resolution image of a nanotube taken by tapping mode under buffer. Single-helix holes between adjacent tiles are visible as darker patches in

several layers. (c) TEM image of a negative-stained sample, showing a section of a nanotube that appears to have split into a flat lattice. (d and e) Negative-stained TEM images of TAO nanotubes with gold nanoparticles attached to the ends, apparently by interaction with thiol sulfurs partially exposed at the tube termini. (From Ref. [14].)

images was collected by repeatedly re-imaging the same nanotube under buffer with an AFM. The high-resolution image in Fig. 1.10(d) shows the detailed nanostructure of the completely torn open DNA nanotube with alternating layers of *A* and *B* tiles clearly discernible. Whole tiles have been scratched away from the opening nanotube by the force of the AFM tip and therefore the tile layers no longer contain all of the tiles that were present in the nanotube. A few layers are seen that still contain six tiles. The combination of the high-resolution AFM images (Fig. 1.9b and 1.10d) provides supporting evidence for the model in which individual tile layers in intact nanotubes contain eight tiles.

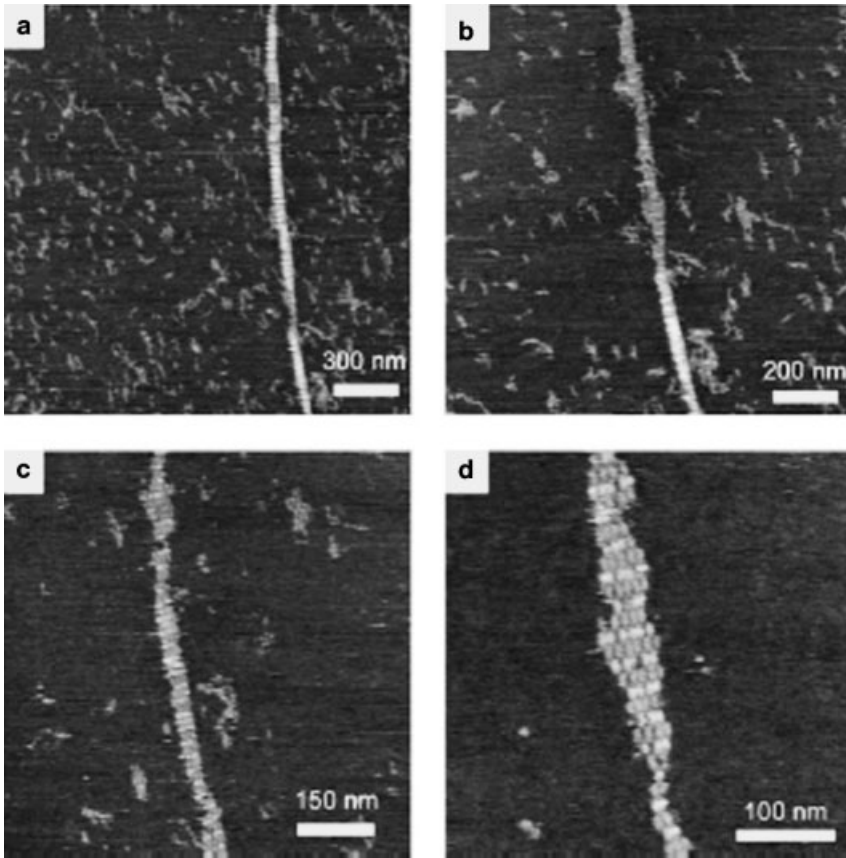


**Fig. 1.10.** A series of AFM images captured by repeatedly re-imaging and zooming in on the same nanotube, which appears mostly tube-like in (a), with increasing wear-and-tear through (b) and (c) until a section of unfolded tube becomes a single-layer, flat lattice (d) displaying stripes composed of lighter (higher) B tiles and darker (shorter) A tiles. (From Ref. [14].)

## 1.6

### 4 × 4 Tile Nanotubes

More complicated 1-D tube-like structure utilizing 4 × 4 tiles has also been reported [36]. Programmable self-assembly of this DNA nanostructure results in a uniform width nanoribbon which displays periodic square cavities. The 4 × 4 DNA tile (Fig. 1.11a) contains four four-armed DNA branched junctions pointing in four directions – north, south, east and west in the tile plane. It is composed of nine strands, with one of the strands participating in every junction. Bulged T<sub>4</sub> loops are placed at each of the four corners inside the tile core in order to decrease the probability of stacking interactions between adjacent four-arm junctions and

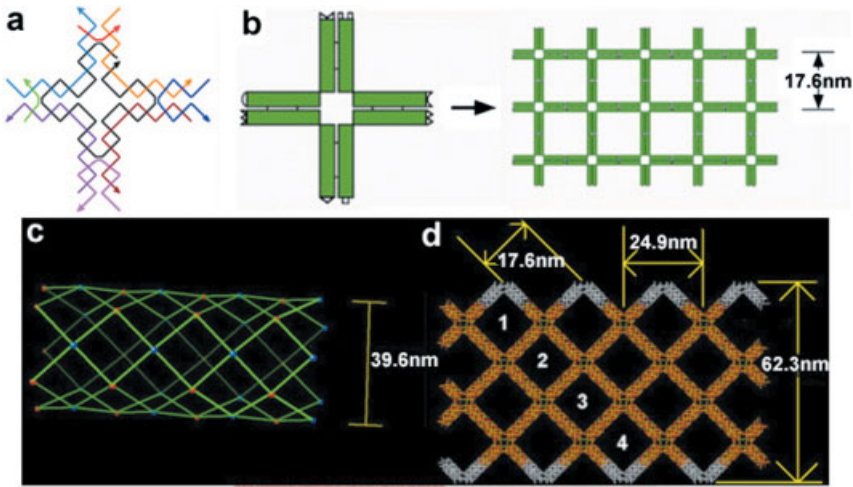


**Fig. 1.11.** Self-assembly of DNA nanoribbons using the  $4 \times 4$  DNA tile. (a) The  $4 \times 4$  tile strand structure. The tile contains nine oligonucleotides, shown as simplified backbone traces in different colors. Each four-arm junction is oriented in four directions. The black strand participates in all four junctions and contains  $T_4$  loops connecting adjacent junctions. (b) Left: double-helical domains are illustrated as rectangles and paired rectangles represent four-arm junctions. Watson–Crick complementary sticky ends are shown as matching geometric shapes. Right: designed structure of the self-assembled lattice. There are four full helical turns between tile centers

so the tiles will be oriented in the same direction in the lattice. (c) Schematic model of the proposed  $4 \times 4$  nanotube. (d) Overhead view of a tube squashed onto the mica substrate and forming a ribbon with four diagonal square cavities with a width of around 62.3 nm. Note the saw-tooth edge formed by folding one row of  $4 \times 4$  tiles along a diagonal running through their most flexible region, the  $T_4$  loops between adjacent arms. The jagged edges along with the  $45^\circ$  diagonal containing four cavities are typically observed in high-resolution AFM images of the ribbons. (From Ref. [36].)

allow the arms to point to four different directions. Characterization of structure formation by nondenaturing gel electrophoresis and thermal transition analysis (see Fig. 1.13 below) shows that the  $4 \times 4$  tile structure is stable and well behaved.

Constructions following the design shown in Fig. 1.11(b) produce a high preponderance of uniform width ribbon structures. In this design the distance between adjacent tiles is an even number of helical half-turns (four full turns) so that the identical face of each tile points toward the same lattice face. Figure 1.12 shows four AFM images of the nanoribbons with lengths of up to around  $20 \mu\text{m}$  and a typical uniform width of around 60 nm. The regularity of the periodic cavities is striking, as well as the observation that some of the nanoribbons revealed a single-layer, flat grid lattice unrolled at the open end of the ribbon (see Fig. 1.12d). This observation strongly suggests that the ribbon structure results from tube-like structures which flatten when the sample is deposited on mica. The AFM image height profile clearly shows that the nanoribbon structure has two layers compared to the flat lattice. Also, the edges of the ribbon appear slightly higher, about 0.12 nm,

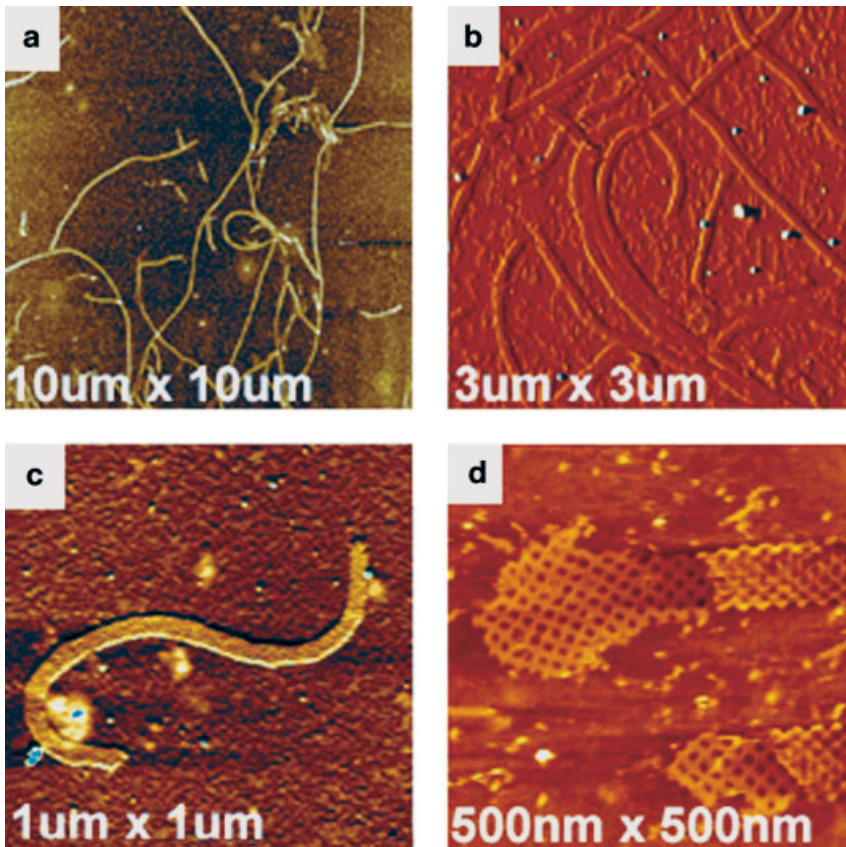


Fig. 1.12. AFM images of  $4 \times 4$  nanoribbons at various scan sizes. (From Ref. [36].)

than the middle, indicating a finite radius of curvature for the squashed tube structure. The formation of tube-like lattices could be due to the fact that each component tile is oriented in the same direction in the designed lattice planes, and therefore any incidental curvature resident in each tile could accumulate and cause circularization of the lattice. This hypothesis is supported by the AFM analysis and by subsequent experiments showing that corrugation schemes where tiles are flipped in the lattice plane to compensate for tile curvature form large flat lattice sheets.

## 1.7

### 6HB Tile Nanotubes

Very recently, a new strategy for the creation of hollow DNA nanotubes was described which made use of tiles that are intrinsically 3-D and formed from a rigid



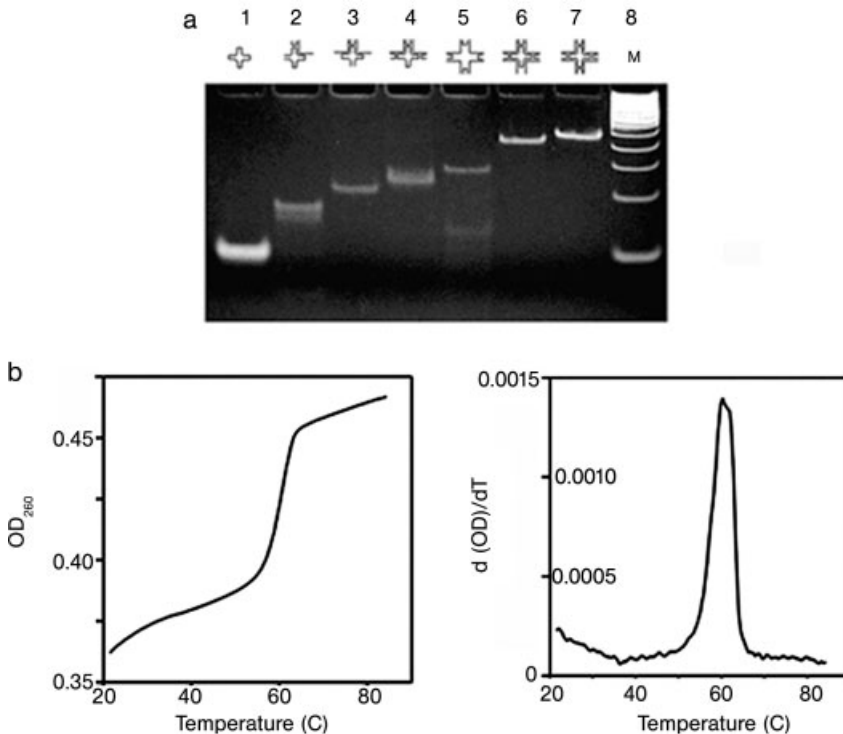


**Fig. 1.13.** Characterization of the  $4 \times 4$  tile structure using nondenaturing electrophoresis and thermal transition experiments. (a) An 8% polyacrylamide gel (ethidium bromide stained) showing association complexes between various equimolar combinations of the  $4 \times 4$  DNA complex component strands. Equimolar mixtures at  $1 \mu\text{M}$  concentration per included strand were annealed and run on the gel at room temperature. Strands included in the annealings are indicated in the drawing above each lane. Lane 8 contains a 50-bp DNA ladder size marker. The  $4 \times 4$  complex runs as a single band on nondenaturing gels, without

any higher-molecular-weight byproducts (from unexpected base pairings between two or more complexes) or lower-molecular-weight byproducts (from dissociated complex), indicating the  $4 \times 4$  tile complex is a stable structure in the buffer used. (b) Thermal transition profile. The left panel shows the relative change in optical density at 260 nm as a function of temperature. The right panel shows the first derivative of the  $4 \times 4$  complex melting data. The results show that the  $4 \times 4$  complex melts cooperatively, as a single transition, with  $T_m \sim 60^\circ\text{C}$ . (From Ref. [36].)

cluster of double-helical domains with a single-helix width pore running down through its entire length [37]. The 6HB (shown schematically in Fig. 1.14) contained six double helices with each pair of neighboring domains linked by strand exchange at each of two crossover points. With complementary pairs of sticky ends appended to each end of the helices, the tiles were induced to assemble into long 1-D arrays with lengths up to around  $15 \mu\text{m}$ . These are the first described DNA nanotubes with perfectly designed widths and tube layers made up of single tiles.

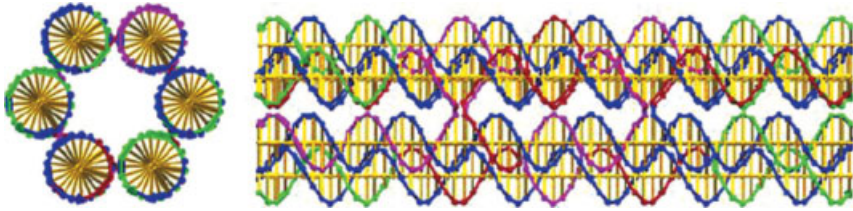


**Fig. 1.14.** Cross-sectional and transverse views of the 6HB tile model. The cross-sectional view emphasizes the cylindrical hole through the center of the tile (From Ref. [37].)

## 1.8 Applications

Self-assembled 1-D nanotubes made from artificially designed tiles show great promise for applications that range from fabrication of nanoelectronic devices to biological studies. Electrical transport in bare DNA molecules has been recognized as an interesting research field for last few decades. Although some of the conductivity experiments of DNA molecules had been shown superconducting [39] or semiconducting [40] properties, DNA molecules mostly show insulating characteristic [41]. The DNA molecule's poor conductivity prevents its direct use in electronic nanodevices. Thus, properly designed DNA lattices can serve as a precisely controllable and programmable scaffold for organizing functionalized nanomaterials in the design and construction of functionalized electronic nanodevices. Nanometer-scale fabrication with reliable DNA-templated metallic nanowires is an example demonstration of DNA's scaffolding capability. Several varieties of DNA tile nanotubes have been shown to be useful templates for the specific chemical deposition of metal for nanowire formation.

Until now, mostly natural  $\lambda$  DNA molecules have been used as a template for fabricating various metallic nanowires such as silver [42], gold [43], palladium [44, 45], platinum [46] and copper [47]. More complex and uniform width 1-D nanotubes can also serve as templates for highly conductive metallic nanowires. One example is shown in Fig. 1.15. Here,  $4 \times 4$  nanoribbons have been metallized with silver using a novel electroless chemical deposition technique [36] and demonstrated electrical measurements through silver nanowires. The resulting nanowires have been characterized by scanning electron microscopy (SEM) and AFM. The metallized nanoribbons have heights of  $35 \pm 2$  nm, widths of  $43 \pm 2$  nm and lengths of up to about 5  $\mu\text{m}$ . The current–voltage curve of the metallic silver  $4 \times 4$  nanoribbon shows linear behavior and the resistance of this sample is around 200  $\Omega$  as measured between the two central contacts at a bias voltage of 0.1 V (Fig. 1.15c). This number corresponds to a bulk resistivity of  $2.4 \times 10^{-6}$   $\Omega\text{m}$ . This nanowire is easily reproducible and has markedly higher conductivity than previously reported double-helix DNA-templated silver nanowires [42]. Other potential uses of DNA nanotubes are inspired by analogy with the roles of nanotubes and nanowires in living cells, e.g. as structural supports for the cytoskeleton, as tracks for

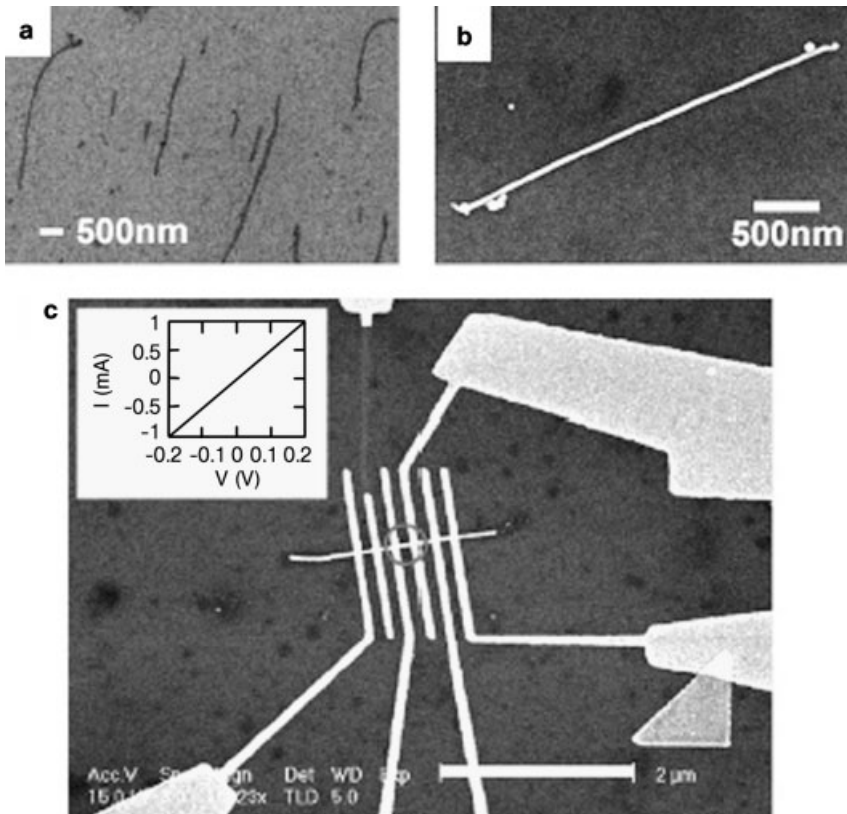


**Fig. 1.15.** Metallization and a conductivity measurement of metallized  $4 \times 4$  nanoribbons. (a) SEM image of nonmetallized  $4 \times 4$  nanoribbons. (b) SEM image of silver-seeded silver nanoribbon. The change in the signal contrast between (a) and (b) is apparent. (c) SEM image of the actual device (scale bar:  $2 \mu\text{m}$ ). (Inset) Current–voltage curve of the metallic silver  $4 \times 4$  nanoribbon. (From Ref. [36].)

the transport of microscopic cargo and as moving parts for cellular motility. DNA nanotubes may eventually be engineered to mimic all these functions.

## 1.9 Summary and Perspectives

DNA-based nanotechnology is currently being developed as a general assembly method for nanopatterned materials that may find use in electronics, sensors, medicine and many other fields. In this chapter, we have described a novel assembly of 1-D nanotubes made from artificially designed tiles, DX, TX,  $4 \times 4$  and 6BH branched junction tiles. Nanotubes, consisting of DAE-E tiles, range from 7 to

20 nm in diameter, grow as long as 50  $\mu\text{m}$  with a persistence length of around 4  $\mu\text{m}$ , and can be programmed to display a variety of patterns. DAE-O DX tiles can form sheets or ribbons with periodic banding controlled by salt concentration. TX nanotubes display a constant diameter of around 25 nm and have been observed with lengths up to 20  $\mu\text{m}$ . Tube formation is controlled by disulfide bonds between tiles augmented with thiol moieties. The  $4 \times 4$  DNA nanoribbon contains four four-armed DNA branched junctions pointing in four directions. The formation of tube-like lattices is due to the fact that each component tile is oriented in the same direction in the designed lattice plane, and therefore any incidental curvature resident in each tile can accumulate and cause circularization of the lattice. The 1-D arrays of 6HB tiles form DNA nanotubes with one tile per tube layer and represent the smallest possible hollow DNA nanotube. Nanotubes formed from DNA tile lattices have been used as metallization templates for the formation of conductive nanowires. Utilizing DNA molecules as scaffolds for making functionalized nanowires offers certain advantages such as site-specific alignment and massive, parallel self-assembly for future electronic nanodevices. It has also been pointed out that DNA nanotubes, by analogy with cellular microtubules, might be useful as tracks along which artificial bionanomachines might transport molecular cargo [10, 12].

## References

- 1 SEEMAN, N. C., DNA in a material world, *Nature* **2003**, 421, 427–431.
- 2 XU, J., LABEAN, T. H., CRAIG, S. L., DNA-based structures and their applications in nanotechnology. In *Supramolecular Polymers 2*, CIFERRI, A. (Ed.), Taylor & Francis, Boca Raton, FL, **2005**, pp. 445–480.
- 3 SEEMAN, N. C., Nucleic acid nanostructures and topology, *Angew. Chem. Int. Ed.* **1998**, 37, 3220–3238.
- 4 SEEMAN, N. C., Nucleic-acid junctions and lattices, *J. Theor. Biol.* **1982**, 99, 237–247.
- 5 SEEMAN, N. C., *De novo* design of sequences for nucleic acid structural engineering, *J. Biomol. Struct. Dyn.* **1990**, 8, 573–581.
- 6 SEEMAN, N. C., WANG, H., YANG, X., LIU, F., MAO, C., SUN, W., WENZLER, L., SHEN, Z., SHA, R., YAN, H., WONG, M. H., SA-ARDYEN, P., LIU, B., QIU, H., LI, X., QI, J., DU, S. M., ZHANG, Y., MUELLER, J. E., FU, T., WANG, Y., CHEN, J., New motifs in DNA nanotechnology, *Nanotechnology* **1998**, 9, 257–273.
- 7 LIU, F., SHA, R., SEEMAN, N. C., Modifying the surface features of two-dimensional DNA crystals, *J. Am. Chem. Soc.* **1999**, 121, 917–922.
- 8 WINFREE, E., LIU, F., WENZLER, L. A., SEEMAN, N. C., Design and self-assembly of two-dimensional DNA crystals, *Nature* **1998**, 394, 539–544.
- 9 MAO, C., SUN, W., SEEMAN, N. C., Designed two-dimensional DNA Holliday junction arrays visualized by atomic force microscopy, *J. Am. Chem. Soc.* **1999**, 121, 5437–5442.
- 10 ROTHEMUND, P., EKANI-NKODO, A., PAPADAKIS, N., KUMAR, A., FYGENSON, D. K., WINFREE, E., Design and characterization of programmable DNA nanotubes, *J. Am. Chem. Soc.* **2004**, 126, 16344–16352.
- 11 EKANI-NKODO, A., KUMAR, A., FYGENSON, D. K., Joining and scission in the self-assembly of nanotubes from DNA tiles, *Phys. Rev. Lett.* **2004**, 93, 2683011–2683014.

- 12 MITCHELL, J. C., ROBIN-HARRIS, J., MALO, J., BATH, J., TURBERFIELD, A. J., Self-assembly of chiral DNA nanotubes, *J. Am. Chem. Soc.* **2004**, *126*, 16342–16343.
- 13 LI, H., PARK, S. H., REIF, J. H., LABEAN, T. H., YAN, H., DNA-templated self-assembly of protein and nanoparticle linear arrays, *J. Am. Chem. Soc.* **2004**, *126*, 418–419.
- 14 LIU, D., PARK, S. H., REIF, J. H., LABEAN, T. H., DNA nanotubes self-assembled from triple-crossover tiles as templates for conductive nanowires, *Proc. Natl Acad. Sci. USA* **2004**, *101*, 717–722.
- 15 ZHANG, Y., SEEMAN, N. C., The construction of a DNA truncated octahedron, *J. Am. Chem. Soc.* **1994**, *116*, 1661–1669.
- 16 SHIH, W. M., QUISPE, J. D., JOYCE, G. F., A 1.7-kilobase single-stranded DNA that folds into a nanoscale octahedron, *Nature* **2004**, *427*, 618–621.
- 17 MAO, C., SUN, W., SHEN, Z., SEEMAN, N. C., A DNA nanomechanical device based on the B–Z transition, *Nature* **1999**, *397*, 144–146.
- 18 YURKE, B., TURBERFIELD, A. J., MILLS, A. P., SIMMEL, F., NEUMANN, J. L., A DNA-fueled molecular machine made of DNA, *Nature* **2000**, *406*, 605–608.
- 19 YAN, H., ZHANG, X., SHEN, Z., SEEMAN, N. C., A robust DNA mechanical device controlled by hybridization topology, *Nature* **2002**, *415*, 62–65.
- 20 TURBERFIELD, A. J., MITCHELL, J. C., DNA fuel for free-running nanomachines, *Phys. Rev. Lett.* **2003**, *90*, 1181021–1181024.
- 21 SHEN, Z., YAN, H., WANG, T., SEEMAN, N. C., Paranemic crossover DNA: a generalized Holliday structure with applications in nanotechnology, *J. Am. Chem. Soc.* **2004**, *126*, 1666–1674.
- 22 PENG, L., PARK, S. H., REIF, J. H., YAN, H., A two-state DNA lattice switched by DNA nanoactuator, *Angew. Chem. Int. Ed.* **2003**, *42*, 4342–4346.
- 23 YIN, P., YAN, H., DANIELL, X. G., TURBERFIELD, A. J., REIF, J. H., A unidirectional DNA walker that moves autonomously along a track, *Angew. Chem. Int. Ed.* **2004**, *43*, 4906–4911.
- 24 ADLEMAN, L., Molecular computation of solutions to combinatorial problems, *Science* **1994**, *266*, 1021–1024.
- 25 WINFREE, E., Algorithmic self-assembly of DNA: theoretical motivations and 2D assembly experiments, *J. Biomol. Struct. Dyn.* **2000**, *11*, 263–270.
- 26 MAO, C., LABEAN, T. H., REIF, J. H., SEEMAN, N. C., Logical computation using algorithmic self-assembly of DNA triple crossover molecules, *Nature* **2000**, *407*, 493–496.
- 27 BENENSON, Y., PAZ-ELIZUR, T., ADAR, R., KEINAN, E., LIVNEH, Z., SHAPIRO, E., Programmable and autonomous computing machine made of biomolecules, *Nature* **2001**, *414*, 430–434.
- 28 RAVINDERJIT, B., CHELYAPOV, N., JOHNSON, C., ROTHMUND, P., ADLEMAN, L., Solution of a 20-variable 3-SAT problem on a DNA computer, *Science* **2002**, *296*, 499–502.
- 29 DWYER, C., POULTON, J., TAYLOR, R., VICCI, L., DNA self-assembled parallel computer architectures, *Nanotechnology* **2004**, *15*, 1688–1694.
- 30 ROTHMUND, P., PAPADAKIS, N., WINFREE, E., Algorithmic self-assembly of DNA Sierpinski triangles, *PLOS Biol.* **2004**, *2*, 2041–2053.
- 31 NIEMEYER, C. M., BURGER, W., PEPLIES, J., Covalent DNA–streptavidin conjugates as building blocks for novel biometallic nanostructures, *Angew. Chem. Int. Ed.* **1998**, *37*, 2265–2268.
- 32 STORHOFF, J. J., MIRKIN, C. A., Programmed materials synthesis with DNA, *Chem. Rev.* **1999**, *99*, 1849–1862.
- 33 BAKER, S. E., CAI, W., LASSETER, T. L., WEIDKAMP, K. P., HAMERS, R. J., Covalently bonded adducts of deoxyribonucleic acid oligonucleotides with single-wall carbon nanotubes, *Nano Lett.* **2002**, *2*, 1413–1417.
- 34 FU, T., SEEMAN, N. C., DNA double-crossover molecules, *Biochemistry* **1993**, *32*, 3211–3220.
- 35 LABEAN, T. H., YAN, H., KOPATSCH, J., LIU, F., WINFREE, E., REIF, J. H., SEEMAN, N. C., Construction, analysis,

- ligation, and self-assembly of DNA triple crossover complexes, *J. Am. Chem. Soc.* **2000**, *122*, 1848–1860.
- 36 YAN, H., PARK, S. H., FINKELSTEIN, G., REIF, J. H., LABEAN, T. H., DNA-templated self-assembly of protein arrays and highly conductive nanowires, *Science* **2003**, *301*, 1882–1884.
- 37 MATHIEU, F., LIAO, S., KOPATSCH, J., WANG, T., MAO, C., SEEMAN, N. C., Six-helix bundles designed from DNA, *Nano Lett.* **2005**, *5*, 661–665.
- 38 DRESSELHAUS, M. S., DRESSELHAUS, G., EKLUND, P. C., *Science of Fullerenes and Carbon Nanotubes*, Academic Press, New York, **1996**.
- 39 KASUMOV, A., KOCIK, M., GUERON, S., REULET, B., VOLKOV, V. T., KLINOV, D. V., BOUCHIAT, H., Proximity-induced superconductivity in DNA, *Science* **2001**, *291*, 280–282.
- 40 PORATH, D., BEZRYADIN, A., DE VRIES, S., DEKKER, C., Direct measurement of electrical transport through DNA molecules, *Nature* **2000**, *403*, 635–638.
- 41 STORM, A., VAN NOORT, J., DE VRIES, S., DEKKER, C., Insulating behavior for DNA molecules between nanoelectrodes at the 100 nm length scale, *Appl. Phys. Lett.* **2001**, *79*, 3881–3883.
- 42 BRAUN, E., EICHEN, Y., SIVAN, U., BEN-YOSEPH, G., DNA-templated assembly and electrode attachment of a conducting silver wire, *Nature* **1998**, *391*, 775–778.
- 43 PATOLSKY, F., WEIZMANN, Y., LIUBASHEVSKI, O., WILLNER, I., Au-nanoparticle nanowires Based on DNA and polylysine templates, *Angew. Chem. Int. Ed.* **2002**, *41*, 2323–2327.
- 44 RICHTER, J., MERTIG, M., POMPE, W., MONCH, I., SCHACKERT, H., Construction of highly conductive nanowires on a DNA template, *Appl. Phys. Lett.* **2001**, *78*, 536–538.
- 45 DENG, Z., MAO, C., DNA-templated fabrication of 1D parallel and 2D crossed metallic nanowire arrays, *Nano Lett.* **2003**, *3*, 1545–1548.
- 46 FORD, W. E., HARNACK, O., YASUDA, A., WESSELS, J., Platinated DNA as precursors to templated chains of metal nanoparticles, *Adv. Mater.* **2001**, *13*, 1793–1797.
- 47 MONSON, C. F., WOOLLEY, A. T., DNA-templated construction of copper nanowires, *Nano Lett.* **2003**, *3*, 359–363.

## 2

# Nucleic Acid Nanoparticles

*Guy Zuber, Bénédicte Pons and Andrew W. Fraley*

### 2.1

#### Introduction

Primarily located in a cell's nucleus, 2'-deoxyribonucleic acid (DNA) provides the cell with the ability to store and copy the genetic information required for the synthesis of proteins that are in charge of all chemical transformations underlying the cell's metabolism. DNA is composed of four 2'-deoxynucleotides connected into a polymer via 5'-3' phosphodiester, where the sequence of the nucleotides allows the encoding of genetic information. The composition and position of heterocyclic functional groups provide a specific arrangement of hydrogen bond donors and acceptors enabling a nucleotide to hydrogen bond (or base pair) with a second nucleotide exhibiting a complementary donor/acceptor arrangement. This allows two strands of DNA to anneal in a sequence-dependent manner, where 2'-deoxyadenosine pairs with 2'-deoxythymidine and 2'-deoxyguanosine pairs with 2'-deoxycytidine, and thus further facilitates a mechanism for DNA replication and RNA transcription. Cellular DNA typically conforms to a B-form helix as first proposed in 1953 by Watson and Crick [1], where the two strands are antiparallel with the hydrophobic bases in the center of the helix and the negatively charged hydrophilic sugar-phosphate backbone on the outside (Fig. 2.1).

Although DNA is composed of only four monomers, prior to the 1970s DNA remained difficult to analyze as the typical eukaryotic cell contains nearly  $3 \times 10^9$  bp of a linear double helix with an extended length of approximately 1 m [2]. Today, nucleic acids are readily manipulated by specific enzymes, produced in large quantities and progress in automation has enabled the sequencing of entire genomes, including the human genome.

Such progress coupled with an increase in the understanding of the molecular mechanisms and genetic implications underlying many diseases has triggered the hope that nucleic acids could treat disease at the source. However, many hurdles remain that must be overcome in order for gene therapy to be of practical use in the clinic. Gene therapy implies the administration of a foreign DNA fragment into a host with subsequent delivery into the nuclei of selected organ cells, where cellular machineries can, in turn, employ the new DNA for production of thera-

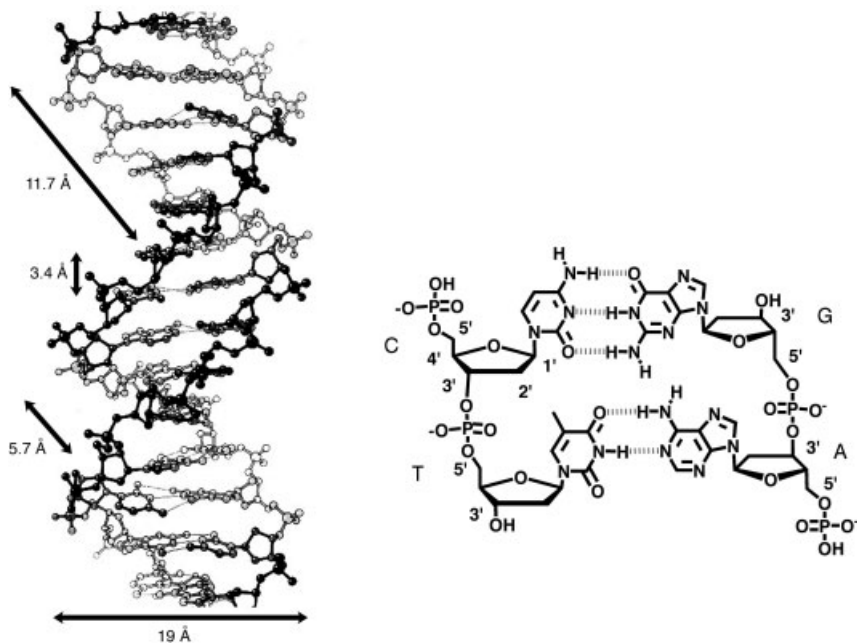


**Fig. 2.1.** Molecular and chemical structure of the DNA double helix. Self-complementation of the helical strands is based on the guanine (G)–cytosine (C) and adenine (A)–thymine (T) Watson–Crick base pairs.

peptic proteins. Although this method is simple in theory, naked DNA is unable to navigate the route from the needle to the nuclei and thus requires other elements to facilitate delivery into the correct cell nucleus while inhibiting the degradation of therapeutic DNA.

Viruses are natural supramolecular assemblies with gene delivery properties. Their diversity and efficiency fulfill most requirements for gene delivery in the clinic [3], but they do have drawbacks [4, 5]. They are by definition infectious and parasitic, and viral shell proteins are understood to elicit adverse immune responses from the host [6]. The production and exploitation of even weakened viral particles has risks because mass production largely exceeds recombination and mutation frequencies. The chance of producing an undesirable and harmful virus increases, and thus can present a significant risk [7]. One alternative is the development of synthetic vectors that interact with DNA in abiotic systems to form virus-like nanoparticles [8]. The requirements for safe DNA transportation into the nucleus have been set by studies on the fate and trafficking of viruses or drug delivery systems at the animal and cellular levels [9]. *In vitro*, gene delivery is predominantly concerned with barriers presented by the cell itself. In an animal, the delivery systems must also be concerned with supracellular barriers that restrict the size of the drug delivery system to less than 100 nm in diameter. Larger par-



ticles introduced in the body intravenously encounter all the blood constituents and cannot cross the blood vessel walls. They are eliminated by hepatic or renal uptake. Local administration, if possible, could circumvent the circulation problems, but particles still encounter barriers in the form of the extracellular matrix that prevent cell accessibility to low-mobility particles. Ligand-mediated cellular uptake might be size dependent as well. It was shown, for instance, that glycolipid-containing liposomes with a size of 30–70 nm were effectively taken up by the asialoglycoprotein receptor *in vitro* and *in vivo*, whereas 90-nm particles were not [10]. The next step, intracellular trafficking and nuclear import, is also a size-restricted process. It was shown by measuring cytoplasmic diffusion of microinjected fluorescent DNA that DNA molecules larger than 1 kbp are essentially immobile. Finally, assisted nuclear pore crossing through nuclear pore complexes (gates between the cytosol and the nucleus) was reported to be restricted to particles up to 39 nm. An ideal vector must interact with a plasmid in such a way to: (a) form particles of minimal size, (b) protect the DNA from nuclease degradation, (c) provide efficient circulation properties in the host, (d) mediate cell-specific internalization, (e) allow mobility in the cytosol and (f) favor intracellular routing into the nucleus, where the genetic material must be effectively liberated from carrier molecules (Fig. 2.2).

The development of effective nucleic acid carriers must consider the above properties, while accounting for the chemical and physical properties of the therapeutic DNA. Section 2.2 gives an overview of the chemical and physical properties of therapeutic DNA. Section 2.3 presents an approach to prepare DNA particles containing a single DNA molecule (the minimal particle size possible) as well as their characterization and properties. Section 2.4 presents strategies for the functionalization of DNA particles and Section 2.5 presents an example of how to prepare DNA nanoparticles with cancer cell targeting elements.

## 2.2

### The Chemical and Physical Properties of Therapeutic DNA

DNA administered into an animal (*in vivo*) must physically contact the surface of a target cell before cellular uptake can occur. The stability, size and charge of the therapeutic DNA coupled with the organization of host tissues into specialized organs seriously complicates the accessibility of targeted cells.

First, native DNA in the blood stream is subjected to fast degradation. Upon injection into a mouse vein, plasmid DNA is removed from the circulation and degraded within a few minutes by hepatic clearance at a rate almost identical to the hepatic plasma flow rate ( $1.6 \text{ mL min}^{-1}$ ) [11]. The delivery of DNA in either *in vivo* or *in vitro* systems is further impeded by the immense mass of DNA that must be delivered (Fig. 2.3). Not only is a gene almost 20 times heavier than the protein it encodes, additional sequences must be added to enable *in vivo* handling and production. To facilitate cellular activity the gene is then cloned into a plasmid, which contains accessory sequences for expression in mammalian cells or cloning into

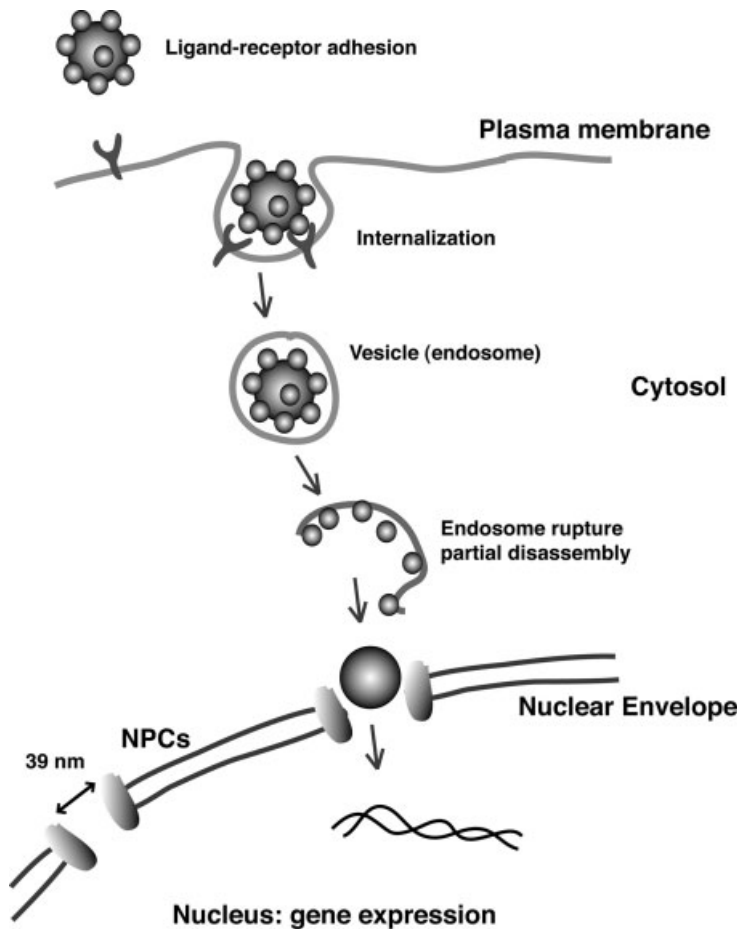
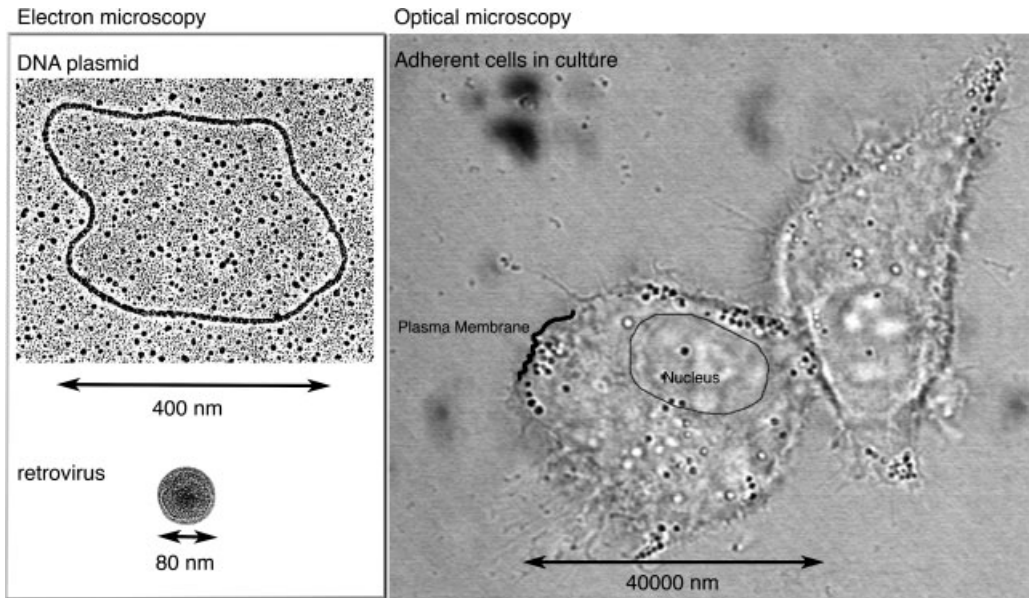


Fig. 2.2. Intracellular pathway for gene delivery. NPC: nuclear pore complexes.

bacteria. Typically, a recombinant plasmid is circular and around 5000 bp in length, with a molar mass of more than 3 MDa. Finally, the polyanionic character of the DNA deoxyribose–phosphate backbone prevents not only passive diffusion across cellular membranes consisting of hydrophobic lipid bilayers, but also the folding of the plasmid into a compact and globular tertiary structure. DNA prefers to exist in a stiff helix that occupies a large volume, which considerably limits mobility [12], particularly in the dense cytoplasm packed with intertwined filaments [13]. Foreign DNA entering fast dividing cells in culture is more readily expressed as it is possible that free and intact DNA plasmids, sitting immobile in the cytoplasm, are transported with chromosomes during mitosis and become incidentally sequestered in the nuclei of daughter cells after reconstruction of the nuclear membrane [14].



**Fig. 2.3.** Comparison of sizes of a plasmid, a virus and a cell. The length of a plasmid and its worm-like behavior in solution, as represented by electron microscopy, greatly limits its diffusion properties. The natural polymer is rather degraded. Optical microscopy shows an epithelial cell in culture.

For its expression, the gene must contact the cell, cross the plasma membrane, diffuse into the cytoplasm and go into the nucleus without being degraded. Its condensation in specialized assemblies such as 80-nm viral particles greatly improves its biodistribution and transport into the cell nuclei.

Theoretically, both *in vivo* biodistribution and intracytoplasmic trafficking of a plasmid into a given nucleus is improved by the condensation of a single plasmid molecule. By calculation, the volume occupied by a plasmid corresponds to a sphere approximately 25 nm in diameter. Single plasmid condensation into minimal size particles may even permit gene delivery into nondividing cells as nuclear localization signal peptide (NLS) sequences derived from the viral SV40 large tumor antigen assist the entry of macromolecules as large as 39 nm in diameter into the nucleus through nuclear pore complexes [15].

## 2.3

### Preparation of Nucleic Acid Nanoparticles: Synthesis and Characterization

#### 2.3.1

##### Rationale

Condensation of the worm-like DNA polymer into a dense particle does not only enhance chemical stability, but additionally improves the dynamic properties of

the polymer with a  $10^4$ – $10^5$  decrease in the effective volume [16]. To give a macroscopic example, a firemen's hose is best transported and handled in a condensed state around a reel, even though the reel adds weight to the system. The compaction of naked DNA into a dense particle is a highly unfavorable process due to the electrostatic repulsion of the charged phosphodiester groups distributed every 7 Å along the backbone. The increase in electrostatic repulsion and competition with other anions could be annihilated by additive effects of Coulomb's interactions using polycationic polymers [16] or cationic surfaces obtained by aggregation of cationic amphiphiles into bilayers or micelles [17]. Although the number and variety of cationic agents are infinite, the formation of DNA condensates is almost entirely driven by electrostatic contributions. Fast kinetic associations of cationic materials with the long DNA polymer typically yield the entrapment of several DNA plasmids and detailed mechanistic studies indicated that DNA condensation proceeds through folding rather than winding. Overall, the nature of the cationic vector dictates the supramolecular organization of the complexes, whereas the stoichiometry and incubation conditions (temperature, ionic forces) impact the final sizes of the DNA condensates [18]. Structural investigations using atomic force microscopy [19, 20] or electron microscopy [21] showed that DNA–cationic polymer complexes display a toroidal or spherical structure of 40–100 nm in diameter. Interaction of DNA with cationic lipid organized in bilayers produces DNA sandwiched into lamellar phases (Fig. 2.4). On the other hand, DNA–cationic lipid complexes adopt an inverted hexagonal phase structure in the presence of DOPE, a lipid well known to induce an inverted hexagonal phase in solution because of its conical shape (Fig. 2.4) [22]. The large contribution of electrostatic interactions also impacts on the colloidal stabilities of these particles. Additional aggregation occurs when ionic surfaces become shielded by other ions (such as physiological conditions) or when the vector/DNA charge ratio approaches the isoelectric point [23, 24]. For transfection into cultured cells, large and positive complexes are advantageous because they sediment onto cells and enter cells by adhesion to ubiquitously expressed anionic receptors present on the cell membranes [25]. Cationic DNA nanoparticles are currently being evaluated for clinical applications [26, 27]. Covalent conjugation of a layer of polyethylene glycol (PEG) onto surfaces greatly enhances the stability and lifespan of biomaterials in the bloodstream [28] or in nasal mucosa [29] by its hindrance and inertness. Inclusion of cell-targeting motifs has further been demonstrated to improve gene delivery to tumors [30] or to liver [31]. Covalent prosthetic groups may interfere with proper DNA condensation [32], complicating these modifications. Theoretically, drastic improvements could be achieved by lowering further the size of the delivery systems to the minimal size (a particle containing a single plasmid) [33].

Cationic detergents, such as cetyltrimethylammonium bromide (CTAB) (see Fig. 2.9 below), have been reported to condense DNA plasmids into homogeneous particles consisting solely of a single plasmid [34]. The formation of these complexes is governed by electrostatic interactions between a single surfactant cationic head and the DNA phosphate group. This initial bimolecular adhesion is immediately followed by aggregation of the surfactant in a highly cooperative manner, leading

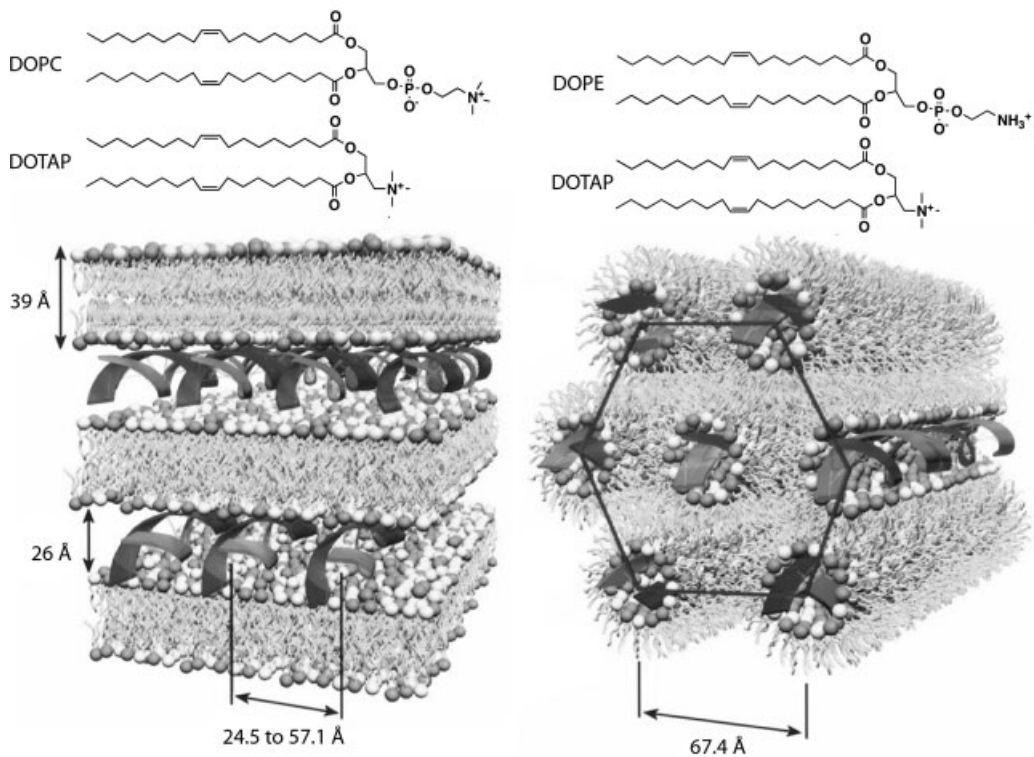


**Fig. 2.4.** Structure of DNA–cationic lipid complexes in lamellar and inverted hexagonal phases. The inverted hexagonal phase is a consequence of the high content of DOPE (70%) in the lipid phase. (Adapted from Ref. [22].)

to single DNA plasmid collapse. However, fast equilibration between monomeric surfactants and micelle domains produces a fast destabilization of surfactant–DNA complexes upon dilution or addition to cellular bilayer membranes.

An appealing solution to this problem is to combine the favorable features of cationic surfactants for DNA condensation and cationic lipids for assembly stability. The chemical transformation of a cationic detergent into an amphiphile within a DNA–vector complex should lead to stable and monomolecular DNA particles. A chemical transformation of this type must remain inert toward the proximal DNA plasmid to ensure the integrity of genetic information. The air-oxidation of two thiols into a disulfide is a suitable answer and has the additional benefit that thiol-based cationic detergents are readily synthesized.

The proof of this concept was demonstrated by Blessing et al. using a cationic detergent containing a cysteine and a  $C_{10}$  alkyl chain ( $C_{10}CysG^+$ ) (Fig. 2.5) [35, 36]. A plasmid was first condensed with a cationic detergent having a free thiol. The concentration of the detergent was kept slightly below its critical micellar con-

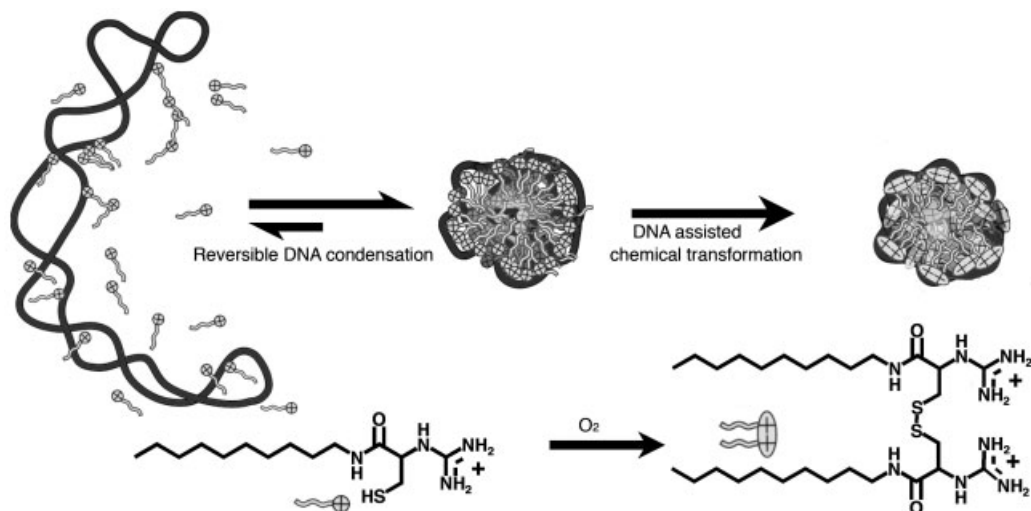


**Fig. 2.5.** Formation of stable 25 nm diameter globular assembly containing a single DNA plasmid. The plasmid is condensed by a thiol-containing detergent ( $C_{10}CysG^+$ ) and the resulting particles are stabilized by template-assisted oxidation of the thiol functions into disulfides.

centration to protect polycationic surfaces from micelle formation and the entrapment of more than one plasmid. Under these conditions, individual phosphate neutralization of the plasmid yields favorable hydrophobic association of detergent molecules into micelle–DNA complexes and the increased concentration of thiol groups around the collapsed DNA polymer in turn favors intracomplex detergent dimerization. According to this theory, oxidative detergent dimerization is expected to be prone to a template effect from the DNA. Kinetic studies confirm this theory – an enhanced thiol oxidation rate was observed in the presence of plasmid DNA (Fig. 2.6).

Upon dimerization of the detergent  $C_{10}CysG^+$ , single plasmids of 5.6 kbp are condensed into a homogeneous population of spherical liponucleic assemblies with a mean diameter of  $25 \pm 4$  nm as determined by transmission electron microscopy. A rough calculation using the volume occupied by a plasmid of 5.6 kbp and  $1.1 \times 10^4$  detergent molecules (the charge equivalent) yields a spherical assembly with a diameter of 28 nm, confirming monomolecular collapse of the plasmid into a single particle. Moreover, diameters of particles resulting from detergent-mediated aerobic collapse of supercoiled pCMVLuc (5.6 kbp) as well as linear phage  $\lambda$  (48 kbp) and phage T4 (166 kbp) were measured by laser light scattering (Fig. 2.7). Particle diameters plotted against the cubic root of the number of DNA base pairs fit a straight line crossing the origin. Since the volume of a sphere varies as the cube of its size, this result provides further evidence of DNA monomolecu-

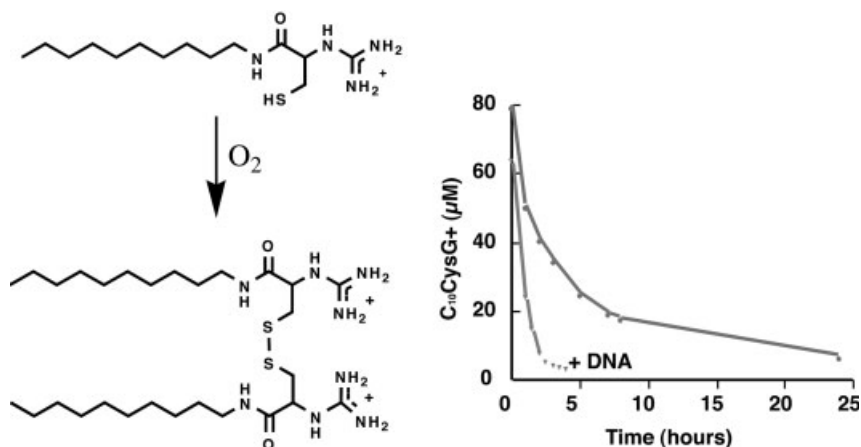


Fig. 2.6. Oxidation of C<sub>10</sub>CysG<sup>+</sup> occurs faster in the presence of template DNA.

lar collapse. Interestingly, the  $\zeta$  potentials of (C<sub>10</sub>CysG<sup>+</sup>)<sub>2</sub>-DNA complexes were found to be negative (−45 to −40 mV) at the isoelectric point. This particular property may be explained by the fact that the DNA backbone constitutes the interface between the aqueous phase and a frozen micellar core. A negative  $\zeta$  potential also suggests that charge repulsion of the nanoparticles may account for the observed colloidal stability. Unfortunately, this short-chain cysteine detergent C<sub>10</sub>CysG<sup>+</sup> and its corresponding gemini cysteine-lipid proved unsatisfactory for biological applications, but led to further investigation of novel amphiphiles.

### 2.3.2

#### Synthesis, Characterization and Optimization of Surfactants

The design of a dimerizable detergent must be tuned so the critical micellar concentration for its monomeric form exceeds the DNA phosphate concentration to elicit monomolecular plasmid collapse. Additionally, once oxidized, the gemini surfactant must also exhibit a low solubility to enable stability in biological conditions. Exploration of dimerizable detergents with the above qualities was accomplished by preserving the cysteine as the reactive agent, but with modification to the polar head group and hydrocarbon chain length. Solid-phase synthesis is well adapted for this investigation and provides a mean for the preparation of a large number of different surfactants (Fig. 2.8) [37].

Fortunately, knowledge of surfactant behavior reduces the possible molecules to only a small quantity (Fig. 2.9). Changing the polar head group to ornithine (two positive charges) or spermine (four positive charges) increases both DNA affinity and detergent solubility (e.g. the critical micellar concentration), while lengthening the hydrocarbon chain, in turn, favors an increase in surfactant association and off-

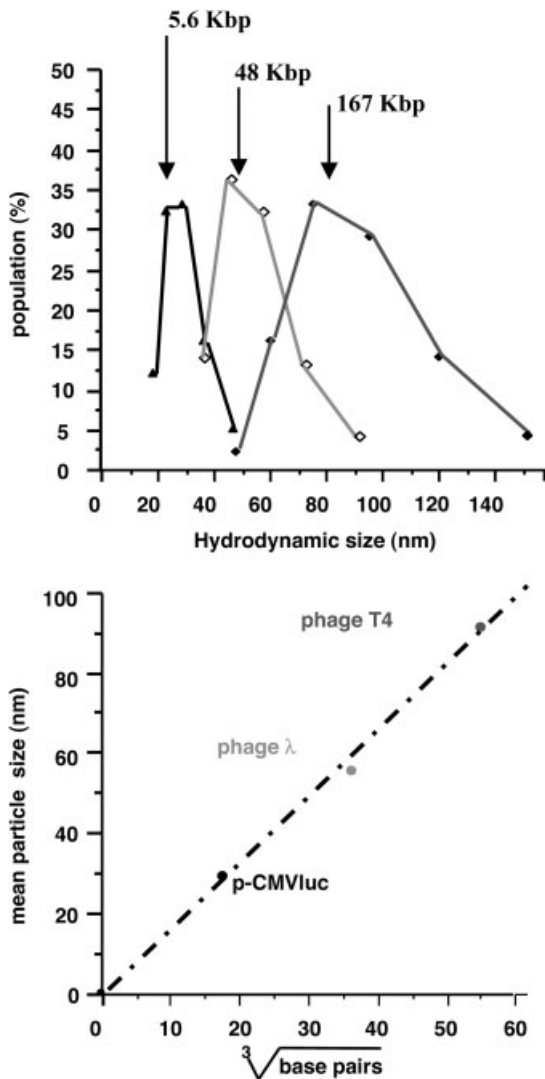
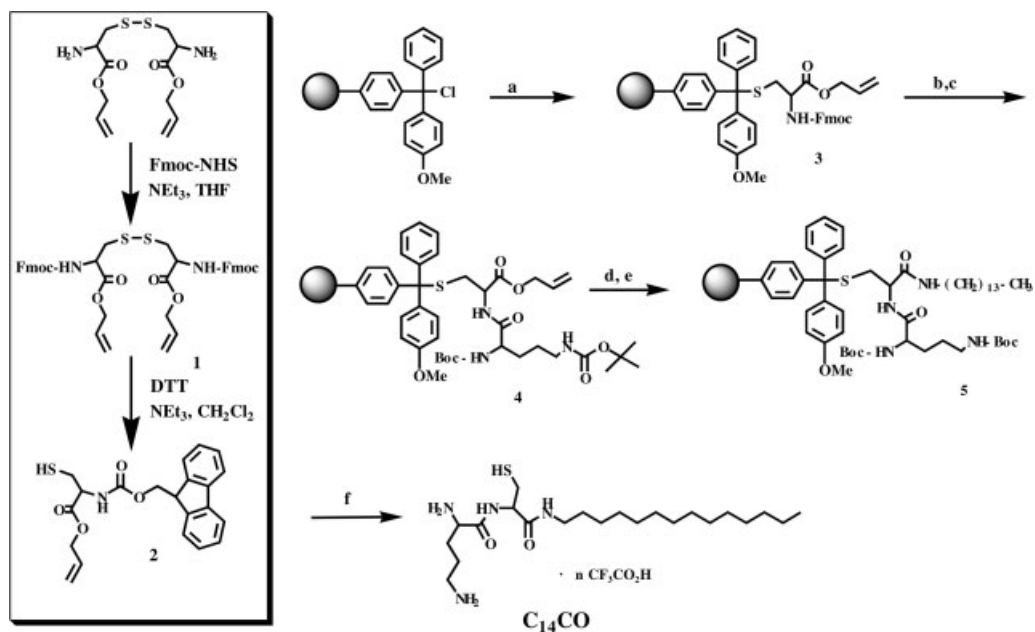


Fig. 2.7. Particle sizes vary as the cubic root of the DNA size, adding more evidence to DNA monomolecular collapse. Particle diameters were determined by light scattering.

sets the increase in solubility (Table 2.1). Typical plasmid concentrations for gene delivery experiments are in the 10–50  $\mu\text{M}$  range, suggesting that  $\text{C}_{14}\text{CO}$  (critical micellar concentration = 45  $\mu\text{M}$ ) is the most likely surfactant/gemini lipid candidate for effective monomolecular plasmid condensation [38].





**Fig. 2.8.** Solid support synthesis of the cationic detergent  $C_{14}CO$ . Inset: preparation of protected cysteine. (a) **2**, DIEA,  $CH_2Cl_2$ ; (b) 20% piperidine, DMF; (c) Bis-Boc-ornithine, PyBOP, DIEA, DMF; (d)  $Pd(PPh_3)_4$ ,  $CHCl_3$ /AcOH/*N*-methylmorpholine (37:2:1); (e) tetradecylamine, PyBOP, DIEA, DMF; (f) TFA. (Adapted from Ref. [37].)

Validation of the  $C_{14}CO$  detergent for stable DNA nanoparticle formation was accomplished by employing a circular 5.6-kbp DNA plasmid with the surfactant at 1/1 charge ratio close to the isoelectric point. The complexes stabilized via DNA-templated air oxidation of the free thiol groups. A gel-retardation assay was used to assess complex formation between plasmid DNA and cationic surfactant (Fig. 2.10). Upon application of an electrical field, molecules or complexes move through the agarose gel at a rate proportional to their charge, but inversely proportional to their volume. Examination of the DNA particle cohesion by agarose gel electrophoresis resulted in a single band with an increase in electrophoretic mobility with respect to the naked plasmid. This result provides evidence that these particles are highly stable in an electric field, where reversible electrostatic interactions would easily be destroyed. Charge neutralization of the DNA phosphate groups and an increase in molecular mass due to the addition of the surfactants should yield a slower migration. However, when one considers that naked DNA tends to move through agarose gel in a snake-like motion, the compaction of the plasmid into a small globular structure can speed migration as there is less entanglement with the gel matrix [37].

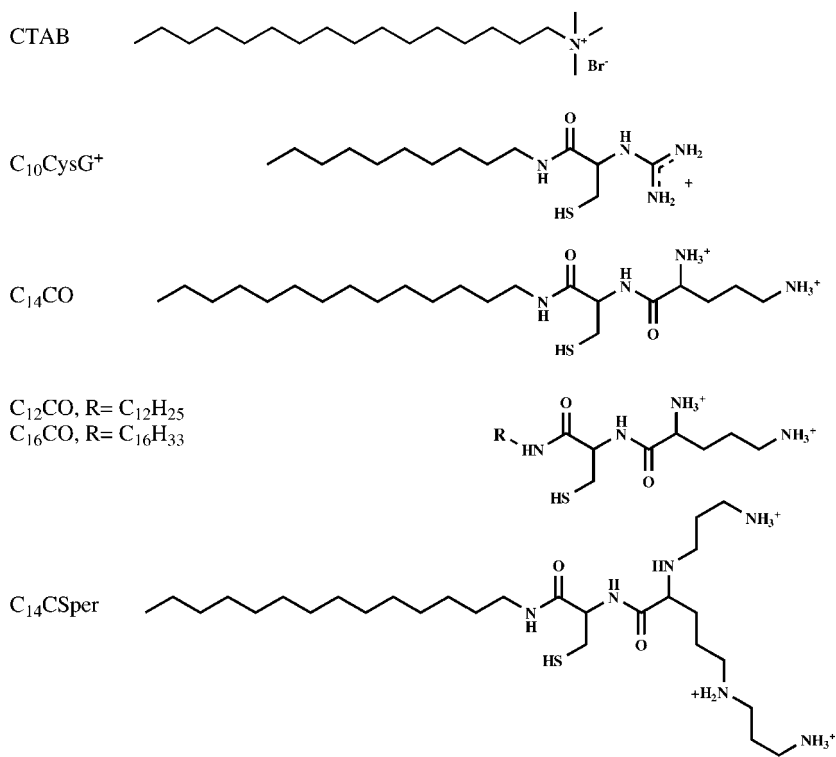


Fig. 2.9. Structure of cationic surfactants.

Tab. 2.1. Parameters describing the stabilities of surfactant–DNA complexes

	<i>Critical micellar concentration (<math>\mu\text{M}</math>)</i> <sup>[a]</sup>	<i>Critical aggregation concentration (<math>\mu\text{M}</math>)</i> <sup>[a]</sup>	$\Delta G$ ( $\text{kJ mol}^{-1}$ ) <sup>[b]</sup>
CTAB	250	5	−28.0
C <sub>10</sub> CysG <sup>+</sup>	100	2.5	−29.5
(C <sub>10</sub> CysG <sup>+</sup> ) <sub>2</sub>		0.4	−33.6
C <sub>14</sub> CO	45	1	−31.9
(C <sub>14</sub> CO) <sub>2</sub>		0.0001	−45.8
C <sub>12</sub> CO	100		
C <sub>16</sub> CO	20		
C <sub>14</sub> Csper	150		

<sup>a</sup>The critical micellar concentration and the critical aggregation concentration are measured in HEPES 20 mM, pH 7.4.

<sup>b</sup> $\Delta G$  is the free energy associated with the binding of the surfactant to DNA. Data adapted from Ref. [40].

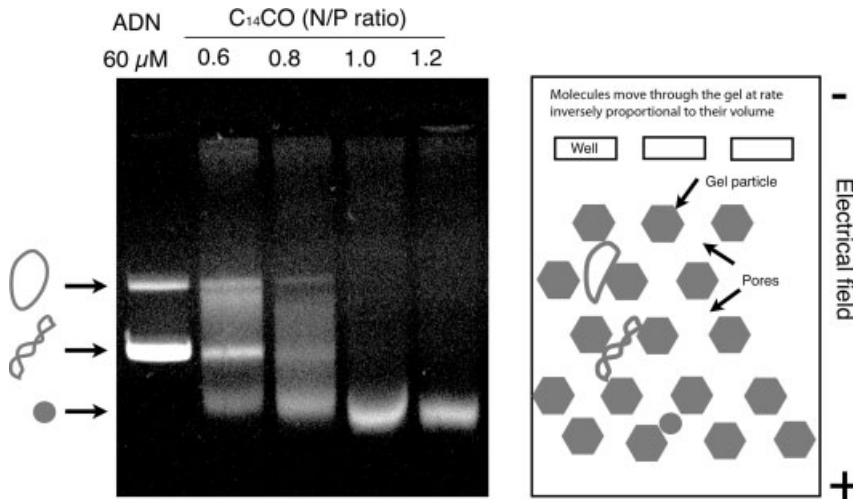


**Fig. 2.10.** Agarose gel electrophoresis of  $(C_{14}CO)_2$ -plasmid complexes and schematic explanation of the difference in mobility.

### 2.3.3

#### Organization of the Surfactant–DNA Complexes

Lipid/surfactant domain stabilities can be further evaluated from examination of morphologies within the lipid phase of DNA complexes. The presence of order within DNA particles indicates strong DNA packing and, by extension, quasi-irreversible amphiphile aggregation. Transmission electron microscopy of oxidized  $(C_{10}CysG^+)_2$ -DNA complexes resulted in a homogeneous population of nearly spherical objects that do not display an internal orderly structure (Fig. 2.11). In contrast, oxidized  $(C_{14}CO)_2$ -DNA particles appeared as a population of 25 nm diameter spheroids that display variable texture from one particle to another. The irregular particle texture appears to be a consequence of close DNA packing induced by quasi-irreversible  $(C_{14}CO)_2$  associations into tubes. A similar ultrastructure was observed previously with lipoplexes formed with another polycationic lipid (Transfectam) [39].

### 2.3.4

#### Quantification of the Stability of Surfactant–DNA Complexes

Association of detergents/amphiphiles with a plasmid can further be characterized by determination of the critical aggregation concentration [40]. The critical aggrega-

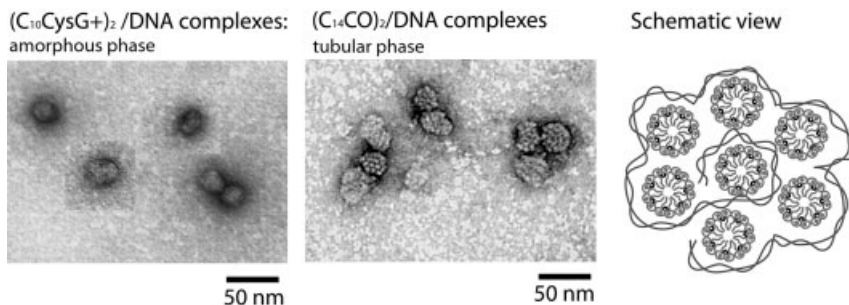


**Fig. 2.11.** Morphology of surfactant–plasmid complexes. Observation was performed by electron microscopy and complexes were stained with uranyl acetate.

gation concentration corresponds to the concentration of free surfactant necessary to initiate the formation of a micelle like domain on the DNA template. This value depends both on the affinity of the cation for DNA phosphate and the ability of the lipid chain to form micellar structures (characterized by the critical micellar concentration). Using fluorescence quenching of the DNA intercalating agent YOYO-1 upon DNA condensation, critical aggregation concentrations of 1, 2.5 and 5  $\mu\text{M}$  were obtained for  $\text{C}_{14}\text{CO}$ ,  $\text{C}_{10}\text{CysG}^+$  and CTAB, respectively. These values followed the same trend as the critical micellar concentration, but shifted to lower values (by a factor of 40–50), highlighting the critical role played by electrostatic interactions in the DNA condensation around micelle domains. The stabilities of the gemini surfactant after DNA-assisted oxidation could be also quantified by determination of their critical aggregation concentration. The critical aggregation concentration of the dimeric surfactant  $(\text{C}_{10}\text{CysG}^+)_2$  is still in the micromolar range and is reduced only by a factor of 3 by comparison to the critical aggregation concentration of the corresponding monomer. On the contrary, the critical aggregation concentration of the dimeric  $(\text{C}_{14}\text{CO})_2$  falls in the nanomolar range and is dramatically reduced by a factor of  $10^3$  by comparison to the critical aggregation concentration of the monomeric  $\text{C}_{14}\text{CO}$ .

One critical aspect in the use of surfactants for gene therapy is the stability of the DNA–surfactant complexes during dilution in the cell culture medium and in the presence of cellular plasma membranes. External and internal leaflets of the plasma lipid bilayer are modeled by using either neutral or anionic lipid vesicles. Surfactant displacement from DNA complexes into bilayers induces, in turn, DNA decondensation that can be easily monitored using fluorescence probes (Fig. 2.12). With CTAB–DNA and  $(\text{C}_{10}\text{CG}^+)_2$ –DNA complexes, the addition of anionic lipid vesicles, and to a lower extend neutral lipid vesicles, leads to almost complete DNA decondensation. In contrast, the addition of both types of vesicles to  $(\text{C}_{14}\text{CO})_2$ –DNA particles is unable to induce DNA release, confirming the stabilities of these particles and their putative biomedical applications.

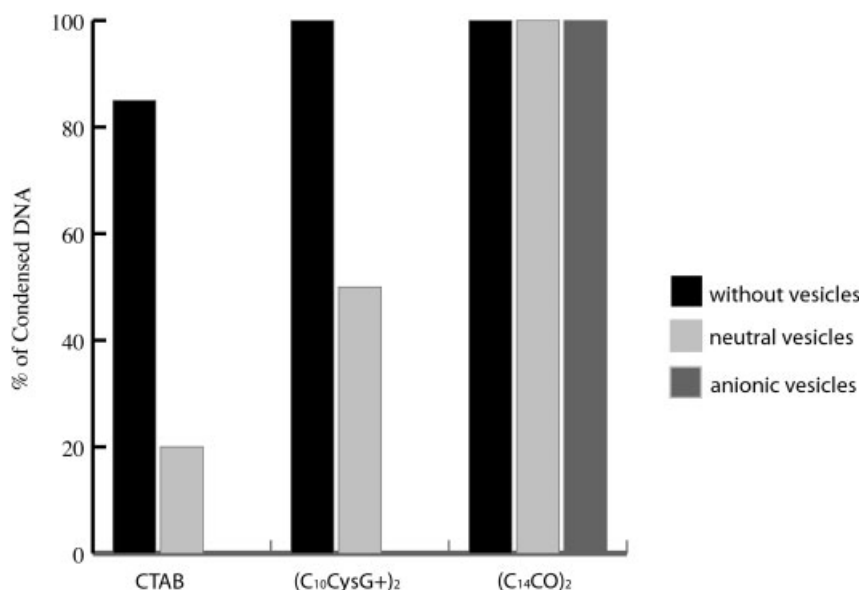


Fig. 2.12. Stability of surfactant–DNA complexes upon interactions with bilayer membranes. (Adapted from Ref. [40].)

## 2.4

### DNA Functionalization for Cell Recognition and Internalization

#### 2.4.1

##### Strategies for Functionalization

Preparation of nanometric DNA vehicles with the minimal size is necessary, but not sufficient, for gene delivery. (C<sub>14</sub>CO)<sub>2</sub>–DNA nanoparticles have overall negative surfaces and are unable to anchor to cell membranes. As a consequence, they do not transfect cells. The use of such scaffolds requires various components for cell-specific internalization. The decoration of surfactant–DNA complexes with components can be accomplished by anchorage within the hydrophilic surfactant core of a lipid bearing a selected ligand or by anchorage to DNA itself. Characterization of stabilized micelle–DNA complexes indicates that the plasmid is at the surface of the particles, which allow possible anchorage to DNA.

The view that DNA is only a polyanionic polymer is in reality a gross oversimplification. Multiple factors such as base stacking, Watson–Crick hydrogen bonding and sugar conformation enable two negatively charged strands of DNA to anneal into the classical B-form helical duplex (Fig. 2.13). The DNA helical structure affords the binding of other molecules by three common motifs. Without disrupting the Watson–Crick base pairing, planar aromatic molecules are able to intercalate between base pairs. The availability of hydrogen bond donors and acceptors in the major groove allows for triple helix formation via Hoogsteen base pair formation.

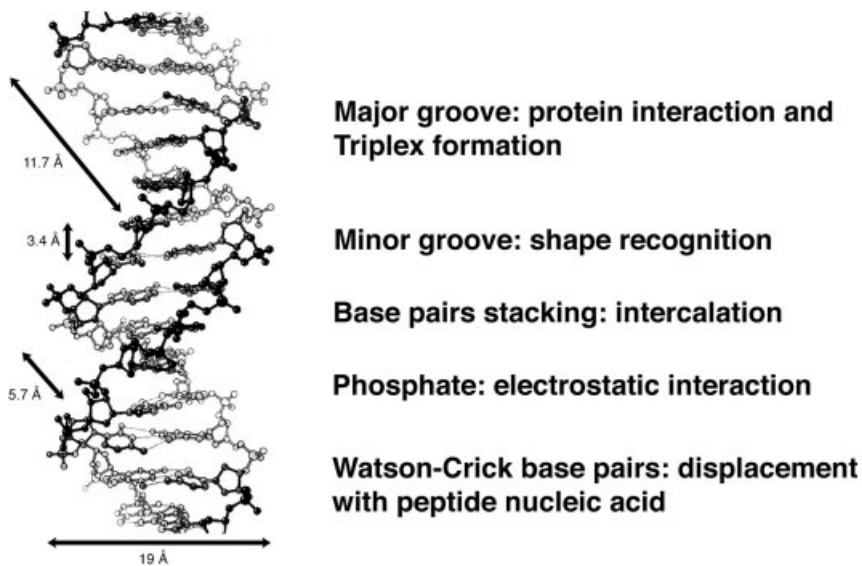


**Fig. 2.13.** DNA recognition by molecules may use (a) the major groove with formation of Hoogsteen base pairs, (b) the phosphate backbone by electrostatic interaction, (c) the minor groove by shape recognition or (d) base pair stacking with intercalation. Alternatively, one strand could be invaded with polymer forming novel Watson–Crick base pairs.

Likewise, the shallow minor groove enables binding of small molecules such as distamycin or Hoechst 33258 [41].

#### 2.4.2

##### Intercalation

Several planar aromatic small molecules are able to intercalate into the DNA duplex [2]. Intercalation occurs generally where the base-pair stacking association is higher and produces a sequence preference binding in between stacked 5'-GC-3' base pairs. The affinity of a single intercalator is relatively weak (in the micromolar range). Kinetic analysis indicates that intercalation is in the millisecond range and is preceded by fast diffusion binding at the outside of the double helix, presumably by interaction in the minor groove. Dimerization of two intercalating agents increases the stability of intercalation to where bis-intercalators are able to be used to fluorescently tag DNA duplexes for cellular trafficking studies [42].

The quasi-irreversible properties of intercalation have been exploited to functionalize plasmids with transferrin, a protein that is understood to facilitate cellular entry via receptor-mediated endocytosis (Fig. 2.14) [43]. Human transferrin tethers two identical carbohydrate chains attached by *N*-glycosylation to asparagines 413 and 611, where the glycans are composed of a mannotriosidodi-*N*-acetylchitobiose core bearing two *N*-acetylneuraminy-*N*-acetylglucosamine units. The glycans do

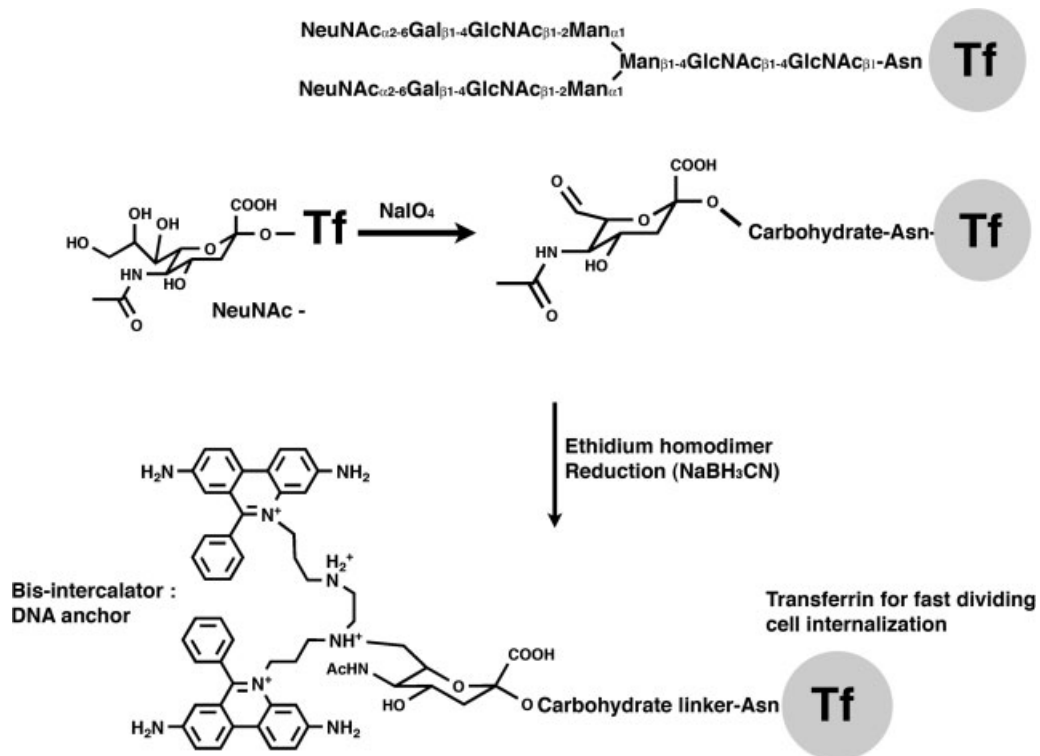


**Fig. 2.14.** Selective conjugation of a strong DNA binding intercalator to the two glycosylation sites of transferrin (Tf). (Adapted from Ref. [43].)

not have any known involvement or influence on cell surface receptor binding and thus have the potential for exploitation as spacers for the site-specific attachment of nucleic acid-binding domains. Within the sugar chain, the terminal *N*-acetyl neuraminic acid has vicinal diols that are readily oxidized by sodium periodate, producing a transferrin displaying aldehyde groups. Reductive amination of the aldehydes with a bis-intercalating ethidium homodimer results in a new transferrin covalently linked to a DNA high-affinity anchor. Although anchorage efficiency was not fully characterized, DNA–transferrin conjugate complexes were observed to enter cells by endocytosis, presumably after transferrin binds to its corresponding cellular membrane receptor.

### 2.4.3

#### Triple Helix Formation with Oligodeoxyribonucleotides

In 1987, Claude Hélène's and Peter Dervan's research groups simultaneously demonstrated that oligodeoxyribonucleotides form stable sequence-specific triple

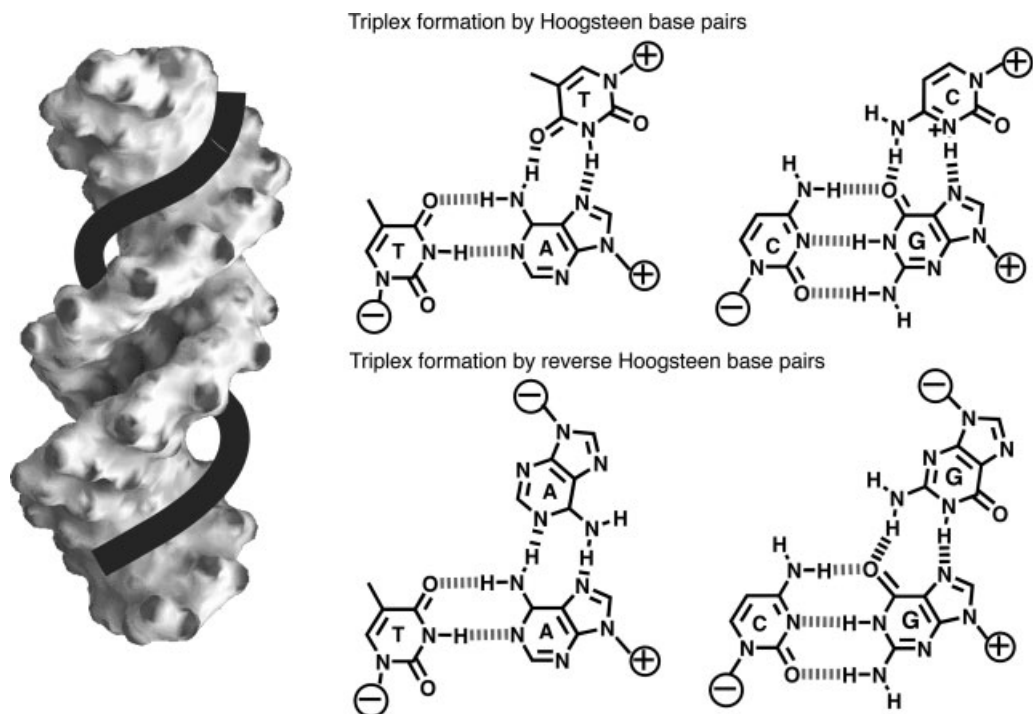


**Fig. 2.15.** DNA recognition from the major groove by triple helix formation with an oligonucleotide forming Hoogsteen or reverse Hoogsteen base pairs.

helices in the major groove of DNA duplexes under conditions close to physiological conditions [44, 45]. DNA triplex formation obeys specific rules imposed by structural constraints; consequently, only a few sequences are viable targets for triplex formation. (Fig. 2.15).

Specifically, homopurine tracts are required for the third strand homopyrimidine to bind via Hoogsteen hydrogen bonds. This binding motif yields the third strand in a parallel orientation to the homopurine strand in the duplex. Additionally, homopurine stands can specifically bind with homopurine tracts in an antiparallel fashion by forming reverse Hoogsteen-type hydrogen bonds between the same nucleobase (recognition of dG by dG and dA by dA) [46]. Thermodynamic and kinetic parameters indicate that selected triplex-forming oligonucleotides of about 20 nucleotides have high affinities for their corresponding duplex targets. In particular, a 24 mer homopurine sequence coupled to the NLS forms a stable triplex with a target duplex at intracellular potassium concentrations with a residence time of 24 h (Fig. 2.16) [8].

DNA third strand–NLS conjugates have further been exploited to functionalize plasmids specifically cloned with several triplex host sequences. Although cova-



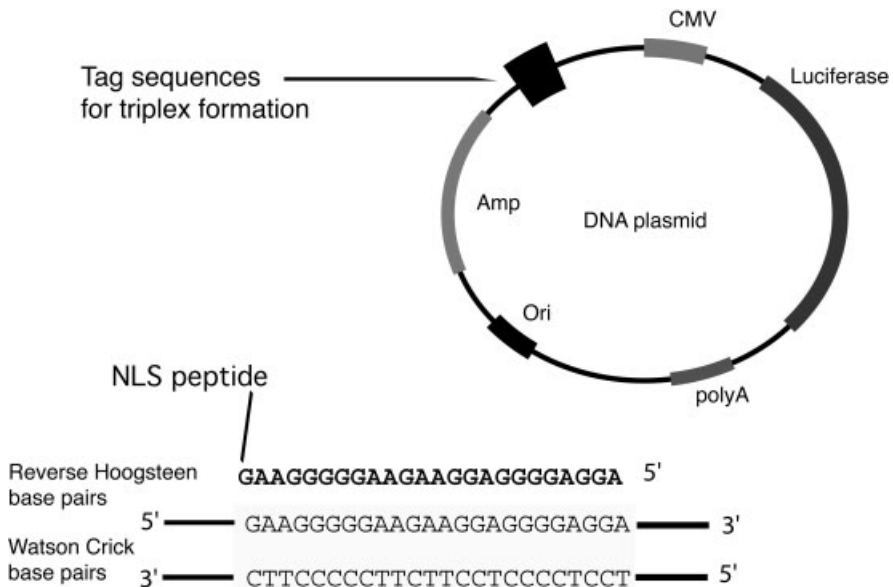


**Fig. 2.16.** Conjugation of a NLS peptide (–PKKKRV–) to a plasmid by triple helix formation. The system requires the preparation of the plasmid with tags for triplex formation in unread regions of the plasmid.

lently functionalized plasmids are not the ideal constructs for gene delivery, triple helix formation may provide a mechanism to sequence specific covalent attachment to plasmids at unread sequences [47]. Covalent sequence-specific peptide conjugation employing triplex formation was accomplished using a psoralen–DNA–peptide conjugate. After triplex formation, the psoralen was in the correct location to adduct formation of a site-specific peptide–DNA conjugate by UV activation.

#### 2.4.4

#### Peptide Nucleic Acids (PNAs)

A PNA is an oligonucleotide analog in which the phosphodiester–sugar backbone is replaced by a polyamide composed of a repeating *N*-(2-aminoethyl)-glycine unit (Fig. 2.17). The nucleobases are attached to the polyamide through methylene carbonyl linkers to produce a polymer remarkably isomorphic in terms of geometry and spacing in comparison to native oligonucleotides. The neutrality of the polyamide favors hybridization to target DNA sequences compared to the charge repulsion of native duplex formation. Plasmid denaturation and annealing in the presence of PNA enables sequence specific PNA hybridization via Watson–Crick base pairing and displacement of the complement strand.

Branden et al. conjugated a NLS peptide to a PNA strand that hybridized to 11

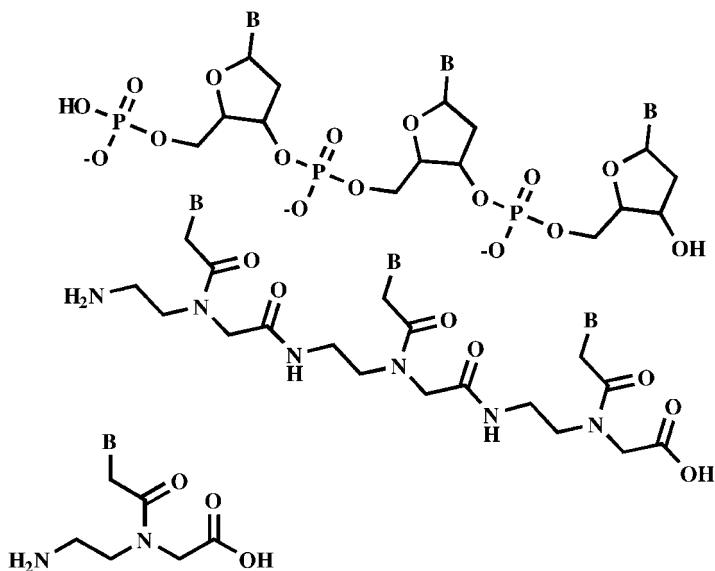


**Fig. 2.17.** Size comparison between a natural DNA strand and its isomorphous “peptide nucleic acid” based on a *N*-(2-aminoethyl)glycine backbone. B: nucleobase.

sites previously cloned into a plasmid containing the gene for the green fluorescent protein (GFP). The NLS–PNA conjugates were docked by a heat-induced denaturation of the plasmid (hybridization by strand displacement), and the (NLS–PNA)<sub>11</sub>–plasmid complexes were delivered into cells using polyethylenimine (PEI) or a cationic lipid formulation. Transfection efficiency was increased 8-fold with respect to the untagged plasmid [48]. Recently, Vaysse et al. reported the employment of a NLS–PNA conjugate for strand invasion at room temperature via a triple-helix motif [49]. Unfortunately, delivery of stable plasmid–NLS–PNA complexes by cationic lipids has not significantly improved gene delivery efficiency when compared to plasmid–PNA complexes lacking NLS peptides. Apart from nuclear targeting, PNAs have also been used to tether transferrin to plasmids [50], where condensation of a plasmid–transferrin–PNA complex with the proton sponge PEI enhanced enzymatic expression of the luciferase gene, a standard reporter, about 4-fold over the plasmid–PEI complex. Competition studies using excess free transferrin resulted in lower transfection, suggesting that DNA–transferrin–PNA–PEI complexes mediated this improvement by binding to the transferrin receptor.

#### 2.4.5

#### Interactions of DNA with Fusion Proteins

Recent progress in biotechnology has enabled the design and production of a variety of fusion proteins, where either whole or subunits of differing proteins have

been cloned together to produce a chimeric protein. Chimeric proteins including cell-anchorage domains, fusogenic peptides, NLS sequence or DNA condensation/recognition elements have been prepared and evaluated as gene delivery agents [51]. Unfortunately, most of the time, *in vitro* reconstruction of viral particles from protein and nucleic acid does not lead to single DNA condensation or nanometric nucleic acid particles [52], but rather to precipitates. Immune response induced by proteins in the host seriously limits the large-scale utilization of exogenous protein [6]. Nonetheless, host-derived protein (as in the case of transferrin) or protein that could be buried within the particles when immune effectors are present, but exposed in the cytoplasm to assist in passage through nuclear pores, could be used. In one study, the fusion between the TetR protein and the NLS peptide exploited the high affinity of the TetR to bind to a short palindromic DNA sequence and the nuclear import capacities of the NLS peptide [49]. Similar to the previous experiment (Fig. 2.16), binding sites for the fusion protein were cloned into a plasmid for NLS anchorage. Gel-shift assays resulted in a lower electrophoretic mobility of the plasmid in the presence of the fusion protein, providing evidence that the TetR protein retains the ability to bind with DNA when conjugated to the NLS peptide. In addition, improved cationic lipid-mediated delivery was observed in mitosis-arrested cell cultures, suggesting that intracellular trafficking to the nucleus mediated by the NLS peptide is improved.

#### 2.4.6

##### **Agents that Bind to the Minor Groove**

The high sequence specificity of PNA, triplex forming oligodeoxynucleotides and proteins to corresponding DNA sequences requires cloning of a target or tag sequence into a nonfunctional section of the plasmid. This hinders not only the target sequence, but further limits the number of elements present on the DNA plasmid. Agents that bind to the minor groove such as distamycin or bisbenzimidazole may overcome the need for tag sequences as they bind with less sequence specificity. Although bisbenzimidazole or distamycin binds in the DNA minor groove with high affinity to AATT sites (dissociation constants in the nanomolar range), they also ramp along the DNA minor groove. Additionally, linking several DNA minor groove binding modules by aliphatic spacers increases DNA duplex affinity and interaction time, but with degenerated sequence selectivity [53].

## 2.5

### **DNA Nanoparticles: Sophistication for Cell Recognition and Internalization**

#### 2.5.1

##### **Preparation of DNA Nanoparticles Enveloped with a Protective Coat and Cell Internalization Elements**

The necessity of DNA protection from aggressive media, such as the blood, demands, at first, particles to be coated with multiple elements. Among the above-

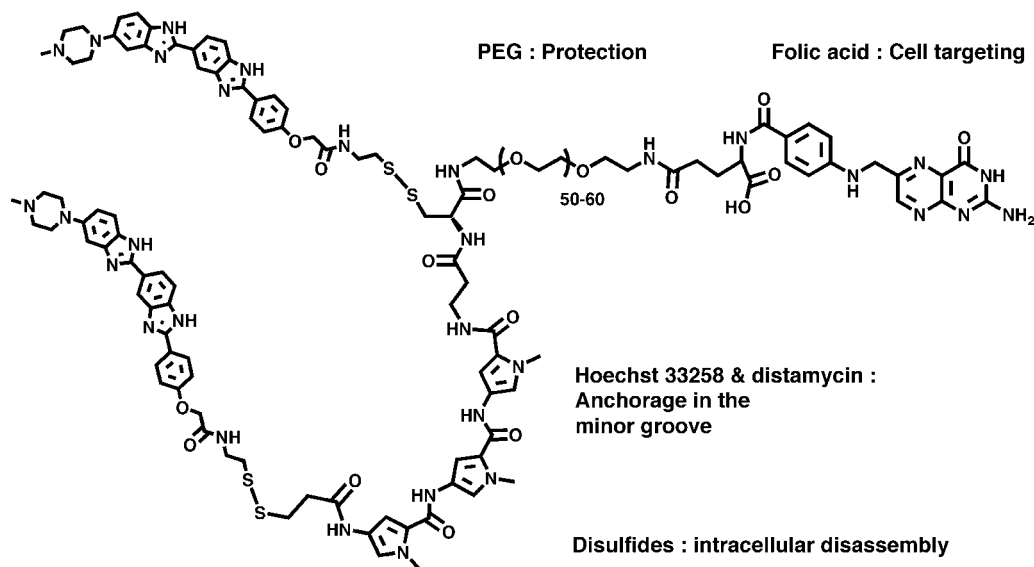


Fig. 2.18. Structure of the DNA anchor 1.

mentioned possible DNA anchors, minor groove agents may prove to be the best choice for noncovalent functionalization of the DNA plasmid with the cell-targeting element. Zuber et al. prepared a minor groove binding anchor (Fig. 2.18, 1) to equip plasmid with folic acid for cell internalization through the folate receptor and PEG to protect the plasmid from degradation in the bloodstream [54].

A distamycin analog and two bisbenzimidazoles were linked by disulfide bond formation, as the presence of disulfide bonds permits the reversion of the anchorage in the cytoplasm by oxidation from glutathione, an intracellular reducing agent. Disulfide bridge cleavage should in turn lead the dissociation of the prosthetic group from the plasmid and therefore facilitate a higher level of expression.

The interaction of 1 with a plasmid of 5.5 kbp was analyzed by agarose gel electrophoresis (Fig. 2.19). Plasmid mobility was reduced and a decrease in ethidium bromide staining was observed in a concentration-dependent manner, suggesting that 1 effectively binds with the plasmid. To test the reversion of the binding in the cytoplasm, glutathione was added to the plasmid–1 complex in solution, resulting in almost complete restoration of plasmid electrophoretic mobility and ethidium bromide staining. The presence of the still-retarded plasmid in lane 4 suggests that some residual bisbenzimidazoles bind to the plasmid; nevertheless, the binding studies indicate the feasibility of release in the cytoplasm.

A PEG–folic acid coat of nanometric DNA particles should not only enhance stability, but further provide cell-targeting and internalization properties. The preparation of monomolecular DNA particles by condensation with lipid-based detergents as previously described in this chapter was accomplished with 1/1 charge equiva-

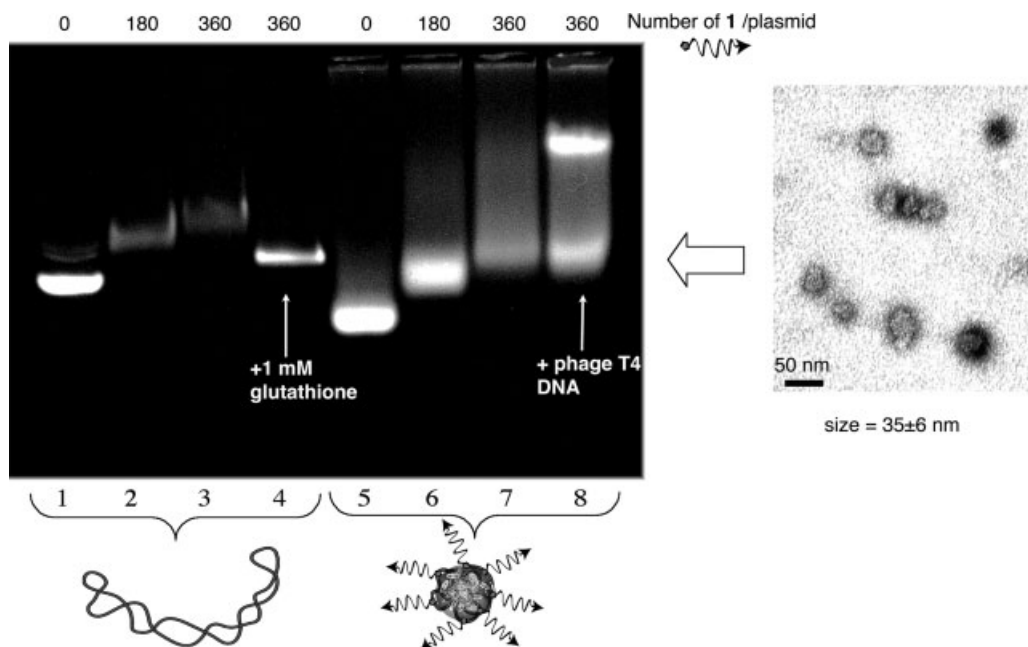


**Fig. 2.19.** Agarose gel electrophoresis shows complex formation between DNA plasmid, the cationic detergent C<sub>14</sub>CO and compound **1**. Plasmid was mixed with increasing amount of **1** as indicated. Lane 4: DNA-**1** complexes were incubated with glutathione for release test. Lanes 5–8: nanometric DNA-(C<sub>14</sub>CO)<sub>2</sub> particles were prepared as described in

**Fig. 2.4.** After overnight incubation, coverage was effected simply by addition of **1** to the particles. Lane 8: a 1-h incubation of the complexes with excess DNA does not displace the anchor. Transmission electron microscopy image of the final DNA-C<sub>14</sub>CO-**1** complexes shows monomolecular DNA condensation into compact particles. (Adapted from Ref. [54].)

lents of the cationic detergent C<sub>14</sub>CO to the plasmid (see Fig. 2.4). After oxidation of the detergent thiols to disulfides, the electrophoretic mobility of the particles through agarose gel was observed to be faster than the corresponding naked DNA (Fig. 2.19). While addition of the PEG-folic acid coat somewhat decreased electrophoretic mobility, competition experiments with excess DNA confirmed quasi-irreversible binding of **1** with the plasmid. Finally, PEG-folate-enveloped DNA particle morphology was observed by transmission electron microscopy. Complexes appeared as a homogeneous population of compact spherical particles with an average diameter of 35 nm. Assuming full DNA association, enveloped particles prepared as in Fig. 2.11 (lane 7) are coated with around 360 molecules of the PEG-folate conjugate, which corresponds to approximately one PEG polymer every 10 nm. This polymer density is sufficient for polymer overlapping onto the surface (termed “weakly overlapping mushroom regime”), [55] and hence should provide both stealth delivery properties and folate receptor-binding properties to the particles.

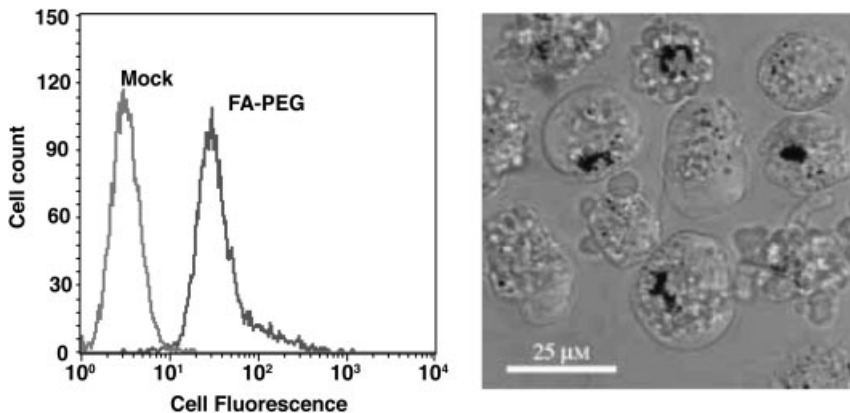


**Fig. 2.20.**  $(C_{14}CO)_2$ -DNA-1 complexes specifically bind to folate receptor-presenting KB cells. Cells were incubated for 3 h with fluorescent DNA complexes. FACS analyses

indicated cellular binding. A Complementary experiment using confocal microscopy indicated that the complexes (darker spots) are further internalized into endosomes.

### 2.5.2

#### **Biomedical Application: Cell Targeting and Internalization Properties of Folate-PEG-coated Nanoparticles**

The abilities of folate-PEG-enveloped DNA particles to carry genes into carcinoma cells were examined using flow cytometry and confocal microscopy (Fig. 2.20). KB cells derived from a human nasopharyngeal cancer were chosen as targets because they conditionally express a large number of folic acid receptors upon folic acid starvation. The  $(C_{14}CO)_2$ -DNA particles were labeled with the fluorescent DNA intercalating dye YOYO and incubated 3 h with the KB cells that expressed large quantity of folate receptors (about  $10^6$  receptors per cell). Flow cytometric analyses show an increased in fluorescence binding to cells with folate-PEG-coated nanoparticles in comparison to untreated cells. To examine whether cell anchorage was followed by endocytosis, the cellular fate of the DNA nanoparticles was observed by confocal fluorescence microscopy. As shown in Fig. 2.20, complexes were internalized in cell perinuclear compartments that very much resemble lysosomes.

## 2.6

### **Concluding Remarks**

Following initial findings from over a decade ago that cationic lipids and polymers carry genes into eukaryotic cells, a lot of effort has been dedicated to improve transfection efficiency by structural modification of the carriers. Exploration of classical pharmacological methods (such as structure and function) has led to molecules capable of transfecting fast dividing cells in culture at a multiplicity of infection of about  $10^6$  gene copies per cell. Their ease of handling as well as their general efficiency for almost all adherent cell lines has made them common tools in cellular

biology. Today, these vectors remain far too simple for *in vivo* gene delivery; the prerequisite to gene therapy. Efforts are currently being made to stabilize these DNA–vector “nanoparticles” in the 100- to 1000-nm range with an inert coat and to equip them with targeting elements [33]. As discussed in this chapter, size restriction of the DNA delivery vehicles is crucial for diffusion *in vivo*. Chemical solutions were found to condense DNA into stable particles with the minimal size (single plasmid condensation). In turn, vehicles incorporating fewer copies of effectors need more activity and specificity. Strategies developed for tethering novel functions onto DNA–surfactant complexes had allowed the preparation of DNA particles having key viral properties such as stability and small size for diffusion and ligands for receptor-mediated endocytosis. However, at this stage, key parameters such as endosome escape or nuclear import are still missing. The pending challenge is in adding these extra functions to the DNA delivery vehicle without interfering with all the other ones. Development of supramolecular systems is still in its infancy and will definitely benefit from a better understanding of biochemistry of the cell and how macromolecules interact together to produce wanted events. Gene therapy relies on the development of effective multicomponent delivery vectors. Following initial findings from over a decade ago that cationic lipids and polymers can facilitate gene transportation into eukaryotic cells, a great deal of effort has been dedicated to improve transfection efficiency by structural modification of the carrier. Exploration of classical pharmacological methods (such as structure and function) has led to molecules capable of transfecting fast dividing cells in culture at a multiplicity of infection of about  $10^6$  gene copies per cell. Their ease of handling as well as their general efficiency for almost all adherent cells lines has made them common tools in cellular biology. The size of a DNA plasmid limits the number of gene copies in delivery vehicles for achieving cell contact in an organism. As discussed in this chapter, stable nanoparticles consisting of a single DNA plasmid can be prepared, and even coated with some functional elements for cell targeting and internalization. Today, DNA nanoparticles are still inefficient in escaping endosomes and require further sophistication. The next obstacle to overcome is the disruption of endosomal membranes, most likely facilitated by the attachment of endosomal disrupting agents such as DOPE or fusogenic peptides. Needless to say, DNA delivery systems with the smallest size incorporate fewer copies of effectors. The implication is that effectors should be more active and specific. The development of nanometric supramolecular systems capable of effective *in vivo* gene delivery is still in its infancy, and will benefit from a better understanding of cellular biochemistry and the interactions between constructed nanoparticles and cellular components.

## References

- 1 WATSON, J. D., CRICK, F. H. C., A structure for deoxyribose nucleic acid, *Nature* 1953, 171, 737–739.
- 2 SAENGER, W., *Principles of Nucleic Acid Structure*, Springer, Berlin, 1983.
- 3 CAVAZZANA-CALVO, M., HACEIN-BEY,

- S., DE SAINT BASILE, G., GROSS, F., YVON, E., NUSBAUM, P., SELZ, F., HUE, C., CERTAIN, S., CASANOVA, J. L., BOUSSO, P., DEIST, F. L., FISCHER, A., Gene therapy of human severe combined immunodeficiency (SCID)-X1 disease, *Science* **2000**, *288*, 669–672.
- 4 HACEIN-BEY-ABINA, S., VON KALLE, C., SCHMIDT, M., LE DEIST, F., WULF-FRAAT, N., MCINTYRE, E., RADFORD, I., VILLEVAL, J. L., FRASER, C. C., CAVAZZANA-CALVO, M., FISCHER, A., A serious adverse event after successful gene therapy for X-linked severe combined immunodeficiency, *N. Engl. J. Med.* **2003**, *348*, 255–256.
  - 5 MARSHALL, E., Gene therapy. Second child in French trial is found to have leukemia, *Science* **2003**, *299*, 320.
  - 6 BALTER, M., Gene therapy on trial, *Science* **2000**, *288*, 951–957.
  - 7 AGUILAR, L. K., AGUILAR-CORDOVA, E., Evolution of a gene therapy clinical trial. From bench to bedside and back, *J. Neurooncol.* **2003**, *65*, 307–315.
  - 8 ZUBER, G., DAUTY, E., NOTHISEN, M., BELGUISE, P., BEHR, J. P., Towards synthetic viruses, *Adv. Drug Deliv. Rev.* **2001**, *52*, 245–253.
  - 9 LEDLEY, F. D., Pharmaceutical approach to somatic gene therapy, *Pharm. Res.* **1996**, *13*, 1595–1614.
  - 10 RENSEN, P. C., SLIEDREGT, L. A., FERNS, M., KIEVIET, E., VAN ROSSENBERG, S. M., VAN LEEUWEN, S. H., VAN BERKEL, T. J., BIESSEN, E. A., Determination of the upper size limit for uptake and processing of ligands by the asialoglycoprotein receptor on hepatocytes *in vitro* and *in vivo*, *J. Biol. Chem.* **2001**, *276*, 37577–37584.
  - 11 KAWABATA, K., TAKAKURA, Y., HASHIDA, M., The fate of plasmid DNA after intravenous injection in mice: involvement of scavenger receptors in its hepatic uptake, *Pharm. Res.* **1995**, *12*, 825–830.
  - 12 CANTOR, C. A., SCHIMMEL, P. R., *Biophysical Chemistry. Part III: The Behavior of Biological Macromolecules*, Freeman, San Francisco, CA, **1980**.
  - 13 VERKMAN, A. S., Solute and macromolecule diffusion in cellular aqueous compartments, *Trends Biochem. Sci.* **2002**, *27*, 27–33.
  - 14 COLLAS, I., COURVALIN, J. C., Sorting nuclear membrane proteins at mitosis, *Trends Cell Biol.* **2000**, *10*, 5–8.
  - 15 PANTE, N., KANN, M., Nuclear pore complex is able to transport macromolecules with diameters of ~39 nm, *Mol. Biol. Cell* **2002**, *13*, 425–434.
  - 16 BLOOMFIELD, V. A., DNA condensation, *Curr. Opin. Struct. Biol.* **1996**, *6*, 334–341.
  - 17 BEHR, J., Gene transfer with synthetic cationic amphiphiles; prospects for gene therapy, *Bioconjug. Chem.* **1994**, *5*, 382–389.
  - 18 VIJAYANATHAN, V., THOMAS, T., THOMAS, T. J., DNA nanoparticles and development of DNA delivery vehicles for gene therapy, *Biochemistry* **2002**, *41*, 14085–14094.
  - 19 DUNLAP, D. D., MAGGI, A., SORIA, M. R., MONACO, L., Nanoscopic structure of DNA condensed for gene delivery, *Nucleic Acids Res.* **1997**, *25*, 3095–3101.
  - 20 VIJAYANATHAN, V., THOMAS, T., ANTONY, T., SHIRAHATA, A., THOMAS, T. J., Formation of DNA nanoparticles in the presence of novel polyamine analogues: a laser light scattering and atomic force microscopy study, *Nucleic Acids Res.* **2004**, *32*, 127–134.
  - 21 SARKAR, T., CONWELL, C. C., HARVEY, L. C., SANTAI, C. T., HUD, N. V., Condensation of oligonucleotides assembled into nicked and gapped duplexes: potential structures for oligonucleotide delivery, *Nucleic Acids Res.* **2005**, *33*, 143–151.
  - 22 KOLTOVER, I., SALDIIT, T., RADLER, J. O., SAFINYA, C. R., An inverted hexagonal phase of cationic liposome–DNA complexes related to DNA release and delivery, *Science* **1998**, *281*, 78–81.
  - 23 MATULIS, D., ROUZINA, I., BLOOMFIELD, V. A., Thermodynamics of cationic lipid binding to DNA and DNA condensation: roles of electrostatics and hydrophobicity, *J. Am. Chem. Soc.* **2002**, *124*, 7331–7342.
  - 24 LUCAS, P., MILROY, D. A., THOMAS, B. J., MOSS, S. H., POUTON, C. W.,



- Pharmaceutical and biological properties of poly(amino acid)/DNA polyplexes, *J. Drug Target.* **1999**, *7*, 143–156.
- 25 KOPATZ, I., REMY, J. S., BEHR, J. P., A model for non-viral gene delivery: through syndecan adhesion molecules and powered by actin, *J. Gene Med.* **2004**, *6*, 769–776.
- 26 LISZIEWICZ, J., TROCIO, J., WHITMAN, L., VARGA, G., XU, J., BAKARE, N., ERBACHER, P., FOX, C., WOODWARD, R., MARKHAM, P., ARYA, S., BEHR, J. P., LORI, F., DermaVir: a novel topical vaccine for HIV/AIDS, *J. Invest. Dermatol.* **2005**, *124*, 160–169.
- 27 OHANA, P., SCHACHTER, P., AYESH, B., MIZRAHI, A., BIRMAN, T., SCHNEIDER, T., MATOUK, I., AYESH, S., KUPPEN, P. J., DE GROOT, N., CZERNIAK, A., HOCHBERG, A., Regulatory sequences of H19 and IGF2 genes in DNA-based therapy of colorectal rat liver metastases, *J. Gene Med.* **2005**, *7*, 366–374.
- 28 ZALIPSKY, S., Functionalized poly(ethylene glycol) for preparation of biologically relevant conjugates, *Bioconjug. Chem.* **1995**, *6*, 150–165.
- 29 KONSTAN, M. W., DAVIS, P. B., WAGENER, J. S., HILLIARD, K. A., STERN, R. C., MILGRAM, L. J., KOWALCZYK, T. H., HYATT, S. L., FINK, T. L., GEDEON, C. R., OETTE, S. M., PAYNE, J. M., MUHAMMAD, O., ZIADY, A. G., MOEN, R. C., COOPER, M. J., Compacted DNA nanoparticles administered to the nasal mucosa of cystic fibrosis subjects are safe and demonstrate partial to complete cystic fibrosis transmembrane regulator reconstitution, *Hum. Gene Ther.* **2004**, *15*, 1255–1269.
- 30 KIRCHEIS, R., BLESSING, T., BRUNNER, S., WIGHTMAN, L., WAGNER, E., Tumor targeting with surface-shielded ligand–polycation DNA complexes, *J. Control Release* **2001**, *72*, 165–170.
- 31 ZHANG, X. Q., WANG, X. L., ZHANG, P. C., LIU, Z. L., ZHUO, R. X., MAO, H. Q., LEONG, K. W., Galactosylated ternary DNA/polyphosphoramidate nanoparticles mediate high gene transfection efficiency in hepatocytes, *J. Controlled Rel.* **2005**, *102*, 749–763.
- 32 ERBACHER, P., BETTINGER, T., BRION, E., COLL, J. L., PLANK, C., BEHR, J. P., REMY, J. S., Genuine DNA/polyethylenimine (PEI) complexes improve transfection properties and cell survival, *J. Drug Target.* **2004**, *12*, 223–236.
- 33 DEMENEIX, B., HASSANI, Z., BEHR, J. P., Towards multifunctional synthetic vectors, *Curr. Gene Ther.* **2004**, *4*, 445–455.
- 34 MEL'NIKOV, S. M., SERGEYEV, V. G., YOSHIKAWA, Y., Transition of double-stranded DNA chains between random coil and compact globule states induced by cooperative binding of cationic surfactants, *J. Am. Chem. Soc.* **1995**, *117*, 9951–9956.
- 35 BLESSING, T., REMY, J.-S., BEHR, J.-P., Monomolecular collapse of plasmid DNA into stable virus-like particles, *Proc. Natl Acad. Sci. USA* **1998**, *95*, 1427–1431.
- 36 BLESSING, T., REMY, J.-S., BEHR, J.-P., Template oligomerization of DNA-bound cations produces calibrated nanometric particles, *J. Am. Chem. Soc.* **1998**, *120*, 8519–8520.
- 37 DAUTY, E., REMY, J. S., BLESSING, T., BEHR, J. P., Dimerizable cationic detergents with a low cmc condense plasmid DNA into nanometric particles and transfect cells in culture, *J. Am. Chem. Soc.* **2001**, *123*, 9227–9234.
- 38 LLERES, D., DAUTY, E., BEHR, J., MELY, Y., DUPORTAIL, G., DNA condensation by an oxidizable cationic detergent. Interactions with lipid vesicles, *Chem. Phys. Lipids* **2001**, *111*, 59–71.
- 39 LABAT-MOLEUR, F., STEFFAN, A. M., BRISSON, C., PERRON, H., FEUGEAS, O., FURSTENBERGER, P., OBERLING, F., BRAMBILLA, E., BEHR, J. P., An electron microscopy study into the mechanism of gene transfer with lipopolyamines, *Gene Ther.* **1996**, *3*, 1010–1017.
- 40 LLERES, D., CLAMME, J. P., DAUTY, E., BLESSING, T., KRISHNAMOORTHY, G., DUPORTAIL, G., MELY, Y., Investigation of the stability of dimeric cationic

- surfactant/DNA complexes and their interaction with model membrane systems, *Langmuir* **2002**, *18*, 10340–10347.
- 41 LOONTIENS, F. G., REGENFUSS, P., ZECHEL, A., DUMORTIER, L., CLEGG, R. M., Binding characteristics of Hoechst 33258 with calf thymus DNA, poly [d(A–T)], and d(CCGGAATCCGG): multiple stoichiometries and determination of tight binding with a wide spectrum of site affinities, *Biochemistry* **1990**, *29*, 9029–9039.
- 42 GLAZER, A. N., PECK, K., MATHIES, R. A., A stable double-stranded DNA–ethidium homodimer complex: application to picogram fluorescence detection of DNA in agarose gels, *Proc. Natl Acad. Sci. USA* **1990**, *87*, 3851–3855.
- 43 WAGNER, E., COTTEN, M., MECHTLER, K., KIRIAPPAS, H., BIRNSTIEL, M. L., DNA-binding transferrin conjugates as functional gene-delivery agents: synthesis by linkage of polylysine or ethidium homodimer to transferrin carbohydrate moiety, *Bioconj. Chem.* **1991**, *2*, 226–231.
- 44 LE DOAN, T., PERROUAULT, L., PRASEUTH, D., HABHOUB, N., DECOUT, J. L., THUONG, N. T., LHOMME, J., HELENE, C., Sequence-specific recognition, photocrosslinking and cleavage of the DNA double helix by an oligo-[alpha]-thymidylate covalently linked to an azidoproflavine derivative, *Nucleic Acids Res.* **1987**, *15*, 7749–7760.
- 45 MOSER, H. E., DERVAN, P. B., Sequence-specific cleavage of double helical DNA by triple helix formation, *Science* **1987**, *238*, 645–650.
- 46 FAUCON, B., MERGNY, J. L., HELENE, C., Effect of third strand composition on the triple helix formation: purine versus pyrimidine oligodeoxynucleotides, *Nucleic Acids Res.* **1996**, *24*, 3181–3188.
- 47 NEVES, C., BYK, G., SCHERMAN, D., WILS, P., Coupling of a targeting peptide to plasmid DNA by covalent triple helix formation, *FEBS Lett* **1999**, *453*, 41–45.
- 48 BRANDEN, L. J., MOHAMED, A. J., SMITH, C. I., A peptide nucleic acid–nuclear localization signal fusion that mediates nuclear transport of DNA, *Nat. Biotechnol.* **1999**, *17*, 784–787.
- 49 VAYSSE, L., HARBOTTLE, R., BIGGER, B., BERGAU, A., TOLMACHOV, O., COUTELLE, C., Development of a self-assembling nuclear targeting vector system based on the tetracycline repressor protein, *J. Biol. Chem.* **2004**, *279*, 5555–5564.
- 50 LIANG, K. W., HOFFMAN, E. P., HUANG, L., Targeted delivery of plasmid DNA to myogenic cells via transferrin-conjugated peptide nucleic acid, *Mol. Ther.* **2000**, *1*, 236–243.
- 51 UHEREK, C., WELS, W., DNA-carrier proteins for targeted gene delivery, *Adv. Drug Deliv. Rev.* **2000**, *44*, 153–166.
- 52 ZUBER, G., MCDERMOTT, J., KARANJIA, S., ZHAO, W., SCHMID, M. F., BARKLIS, E., Assembly of retrovirus capsid-nucleocapsid proteins in the presence of membranes or RNA, *J. Virol.* **2000**, *74*, 7431–7441.
- 53 YOUNGQUIST, R. S., DERVAN, P. B., Sequence-specific recognition of B-DNA by oligo(*N*-methylpyrrole-carboxamide)s, *Proc. Natl Acad. Sci. USA* **1985**, *82*, 2565–2569.
- 54 ZUBER, G., ZAMMUT-ITALIANO, L., DAUTY, E., BEHR, J. P., Targeted gene delivery to cancer cells: directed assembly of nanometric DNA particles coated with folic acid, *Angew. Chem. Int. Ed.* **2003**, *42*, 2666–2669.
- 55 WONG, J. Y., KUHLE, T. L., ISRAELACHVILI, J. N., MULLAH, N., ZALIPSKY, S., Direct measurement of a tethered ligand–receptor interaction potential, *Science* **1997**, *275*, 820–822.

## 3

# Lipoplexes

*Sarah Weisman*

### 3.1

#### Introduction

The introduction of nucleic acids into cells, either plasmid DNA for gene expression or antisense oligodeoxynucleotides (ODN) or small interference RNA (siRNA) for gene silencing, is a valuable tool for biological research and a promising therapeutic treatment for genetic disease. The prevalent means of transport for gene therapy is the use of viral vectors [1]. A synthetic alternative, cationic lipid-mediated nucleic acid delivery (lipofection) [2], has been intensively studied over recent years [3–7]. Lipofection has low efficiency compared to viral vectors, but its advantages include negligible immunogenicity, ease of large-scale production and no limit on the size of the gene transported. Eighty-seven clinical trials of gene therapy via lipofection are currently in progress, aiming to treat cystic fibrosis, arterial disease and many types of cancer [8].

Mixing anionic nucleic acids with cationic lipids leads to spontaneous self-assembly of ordered aggregates known as lipoplexes. Lipoplexes have great potential, but our understanding of the mechanisms of lipoplex function is still incomplete. This chapter will give a brief overview of the current state of knowledge about lipoplexes, with special attention to their microscopic structure, and the relationships between structure and delivery efficiency. The chapter will first address the composition, structure and function of DNA lipoplexes, and then discuss ODN and siRNA lipoplexes in terms of their differences from DNA complexes.

### 3.2

#### DNA Lipoplexes

##### 3.2.1

#### Composition

Cationic lipids do not usually occur in nature, but a wide variety of lipids have been synthesized for the purposes of gene therapy. Cationic lipids contain a cationic

head group, a linker and a hydrophobic moiety, most often two hydrocarbon chains. The effects of variations in lipid structure on the properties of lipoplexes have been recently reviewed elsewhere [7, 9]. The chemical structures of some popular cationic lipids from different families are presented in Table 3.1.

Cationic lipids are often combined with neutral (helper) lipids in order to improve lipofection efficiency. The presence of helper lipids can tune the surface charge density, the preferred microstructure and the stability of lipoplexes. The chemical structures of the three most common helper lipids are presented in Table 3.1. Mixed cationic–neutral lipid systems self-assemble in aqueous solution, usually forming liposomes, which are bilayer membranes closed in upon themselves (Fig. 3.1).

Mixture of anionic DNA with cationic liposomes in aqueous solution leads to spontaneous and nearly instantaneous complexation. The DNA–lipid interaction is endothermic [10, 11]; the driving force for lipoplex formation is the entropy gain from the release of bound counterions [12] and water molecules [13]. The process of lipoplex formation is shown schematically in Fig. 3.1.

DNA in lipoplexes is located in close contact with the lipids and can neutralize the cationic lipid head group charges [14]. In positively charged complexes (with an excess of lipid) the DNA is fully protected from degradation by nucleases or interaction with fluorescent dye [15, 16]. Hence, we infer that DNA is condensed and encapsulated within lipoplexes.

### 3.2.2

#### Nanostructure and Microstructure

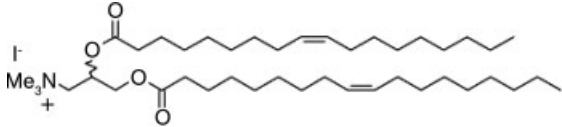
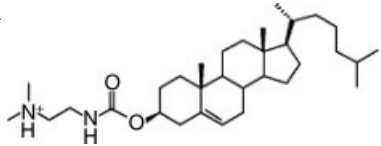
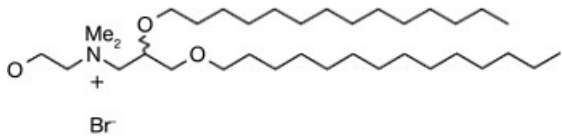
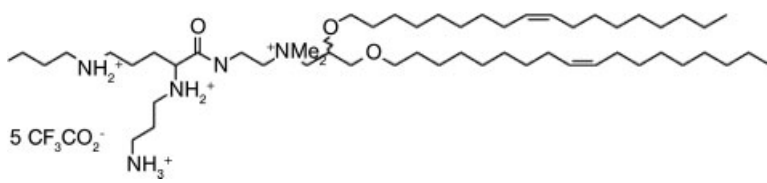
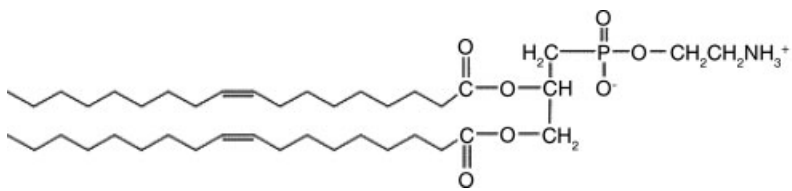
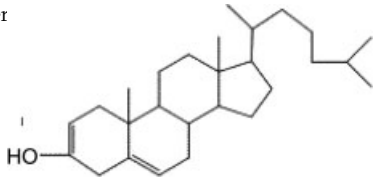
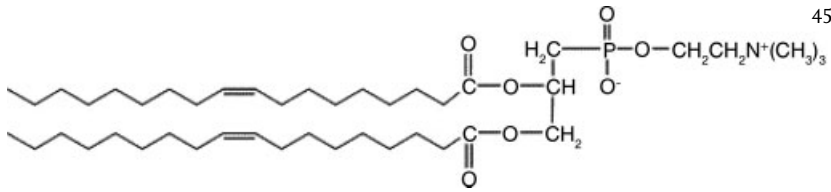
##### 3.2.2.1 Equilibrium Morphology

There are two known supramolecular structures adopted by DNA lipoplexes at equilibrium. The lamellar phase consists of DNA molecules sandwiched between cationic membranes [18, 19]. The inverted hexagonal phase contains DNA molecules coated by monolayers of cationic lipid and arranged in a hexagonal matrix [20, 21]. The different morphologies are shown schematically in Fig. 3.2.

The condensed lamellar ( $L_{\alpha}^C$ ) or “sandwich” phase is characterized by a constant interlamellar water gap,  $w \sim 2.6$  nm, corresponding to the diameter of a DNA helix surrounded by a thin hydration shell [18]. DNA organizes within the monolayer as a lattice of parallel helices. As DNA molecules are rigid, with a persistence length of around 50 nm, this is the only efficient packing regime. The interhelical DNA spacing,  $d$ , is variable, depending on both the membrane charge density and the DNA/lipid charge ratio. Under isoelectric conditions, with full neutralization of lipid and DNA charges,  $d^* = e/(l_0\sigma_M)$ , where  $e$  is the electron charge,  $l_0$  is the distance between anionic charges on the DNA backbone and  $\sigma_M$  is the cationic membrane charge density (dependent on the cationic/neutral lipid ratio). If the cationic membrane includes helper lipids, DNA may induce lipid demixing. Cationic lipids concentrate close to the DNA helices to achieve local charge matching [19].

The inverse hexagonal ( $H_{II}^C$ ) or “honeycomb” phase has a typical water tube diameter of about 2.8 nm, sufficient to contain a hydrated DNA helix [20]. The DNA

Tab. 3.1. Some popular cationic and helper lipids for lipofection

Name	Structure	Literature hits [17]
Cationic lipids [7]		
DOTAP		256
DC-Chol		113
DMRIE		59
DOSPA		16
Helper lipids [9]		
DOPE		389
Cholester		243
DOPC		45

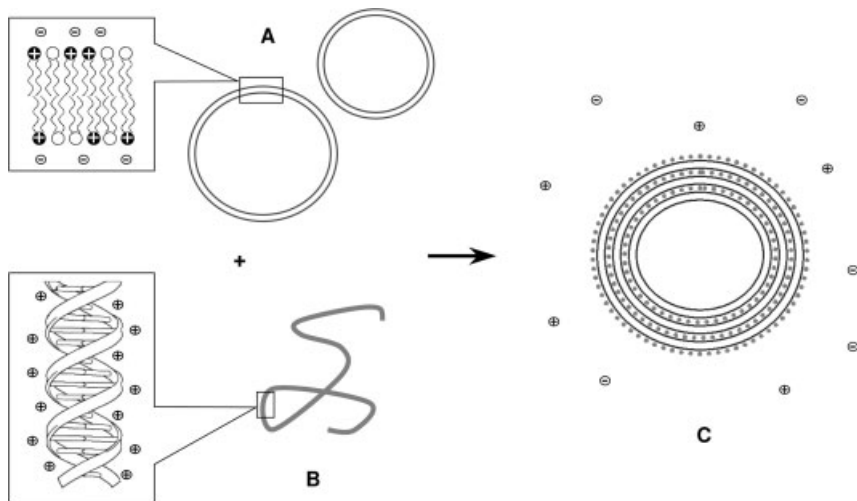


**Fig. 3.1.** Schematic representation of lipoplex formation. (A) Liposomes composed of cationic and neutral lipids. (B) DNA random coil. (C) Condensation of DNA with lipids forms lipoplexes. Complexation is driven by entropy gain due to counterion release.

is tightly and symmetrically enveloped, so this structure can provide very effective charge neutralization. Adding DNA to lamellar lipid bilayers sometimes induces the formation of an inverse hexagonal complex. This phenomenon occurs in soft membranes with low bending rigidity, e.g. systems where short-chain alcohols have been added as cosurfactants.

The preferred structure of lipoplexes consisting of two or more lipid species depends on the packing geometry of the lipid components. Most lipids with two hydrocarbon chains are roughly “cylindrical”, meaning that the cross-sectional areas of their head group and their tail group are comparable. These lipids favor the formation of planar bilayers. Thus, lipoplexes where all lipid molecules are cylindrical usually form only a lamellar complex. Some neutral lipids with small head groups, e.g. DOPE, have “inverse conical” shapes and can promote the formation of an inverse hexagonal phase.

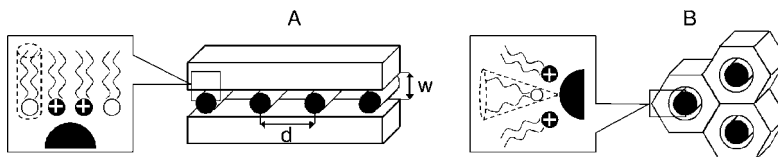


**Fig. 3.2.** Schematic representation of equilibrium structures of lipoplexes. (A) The  $L_x^C$  lamellar phase, promoted by cylindrically shaped helper lipids. (B) The  $H_{II}^C$  inverse hexagonal phase, promoted by inverse conical

helper lipid molecules. In (A),  $w$  is the constant interlamellar water gap,  $d$  is the variable interhelical DNA distance and lipids can locally demix to efficiently neutralize DNA charge. (Adapted from Ref. [5].)

Phase diagrams of DNA lipoplex systems have been constructed both experimentally and theoretically [22–24]. In a mixed lipid system, increasing the mole fraction of DOPE or a similar inverse conical helper lipid can drive a structural transition from lamellar to inverse hexagonal lipoplexes. At high DNA/lipid charge ratios lipoplexes coexist with free DNA and at low DNA/lipid charge ratios lipoplexes coexist with pure lipid phases. Lamellar lipoplexes can be negatively overcharged at excess DNA ( $d < d^*$ ) or positively overcharged at excess lipid ( $d > d^*$ ) and can accommodate different fractions of helper lipid, so there is a single-phase  $L_x^C$  region over a range of component ratios. Inverse hexagonal lipoplexes have no structural or compositional degrees of freedom, thus they only exist as isoelectric complexes in equilibrium with other phases.

Some DNA lipoplex systems that form the condensed lamellar phase have demonstrated three-dimensional interlayer correlations [25–27]. These occur if the cationic lipid membranes are flexible and can partially wrap around the DNA in order to improve charge matching. This produces periodic membrane undulations, as shown in Fig. 3.3. The orientation of DNA helices in different layers is correlated and there is some positional coupling between DNA helices in different layers. The range of the interactions depends on the membrane properties.

The size and sequence of DNA molecules apparently does not affect the lipoplex microstructures formed [28]. The structure of DNA helices within lipoplexes remains in a B-conformation, though in a variant form in which the base–base interactions are perturbed [29].

### 3.2.2.2 Nonequilibrium Morphology

Lipoplex systems under conditions relevant for gene therapy often have not reached thermodynamic equilibrium. Lipoplexes are usually prepared by adding DNA to cationic liposomes. Direct imaging by transmission electron microscopy (TEM) has demonstrated that this procedure can produce a variety of metastable morphologies [30–33]. Slight differences in preparation conditions can apparently cause large variations in the dynamics of complex formation.

Figure 3.4(b) shows a model mechanism for the formation of lamellar lipoplexes [33]. The mechanism suggests that in the first step of complexation anionic DNA coats the surface of cationic liposomes. Following this, liposomes adsorb, rupture and roll over a host liposome, adding layers one by one to form a multilamellar

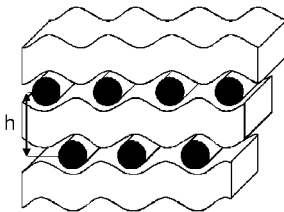


**Fig. 3.3.** Schematic representation of bilayer undulations and interlayer DNA correlations within lamellar lipoplexes. The lamellar repeat distance is denoted by  $h$ . (Adapted from Ref. [5].)

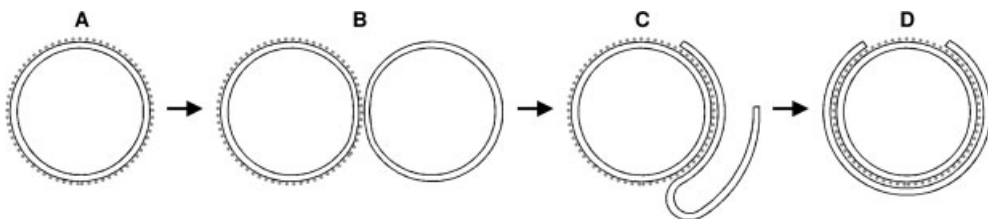
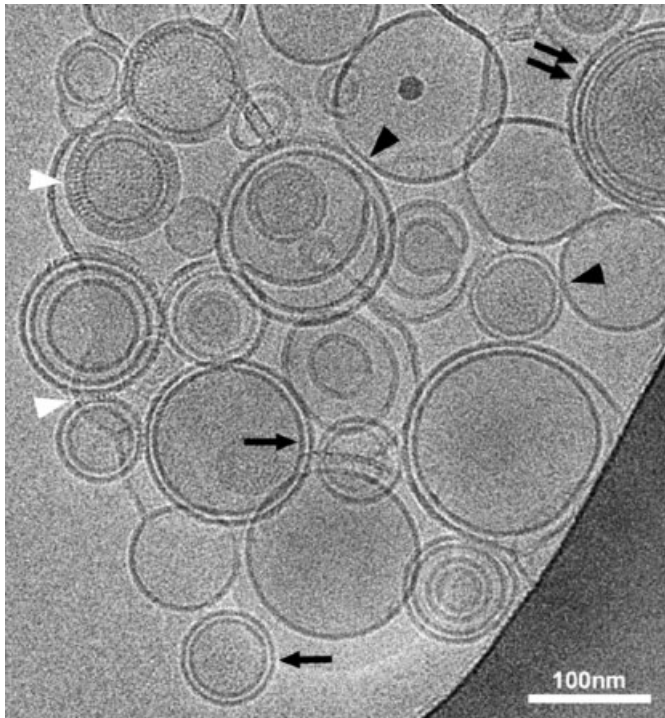


**Fig. 3.4.** (Above) Cryo-TEM image of a DOTAP/DOPC/DNA lipoplex with excess lipid. Black arrowheads indicate liposomes adsorbed to each other; black arrows mark pairs of concentric membranes adsorbed to each other; black double arrows indicate a stack of concentric membranes adsorbed to each other; white arrowheads mark parallel DNA helices clearly visible between adsorbed membranes. (Below) Model mechanism for interactions

between cationic liposomes and DNA. (A) DNA coats a liposome. (B) Two liposomes adsorb to each other. (C) One liposome ruptures after deformation and (D) rolls over the second liposome, yielding a pair of concentric membranes adsorbed to each other, possibly with an open membrane edge. Further layers adsorb similarly. (Adapted from Ref. [33].)

particle. This mechanism is in agreement with calorimetric measurements suggesting that lipoplex formation is a two-step process [34]. A fast exothermic interaction corresponds to DNA binding to liposome surfaces and a slower cooperative endothermic process is probably the reorganization of liposomes into lamellar complexes.



Figure 3.4(a) shows an example of a polymorphous lipoplex, imaged at our laboratory. The lipid composition of the system is expected to favor the lamellar phase at equilibrium. Several of the intermediate stages in the model mechanism of lipoplex formation are observed. The prevalence of metastable structures is a function of the time since preparation. It is also probably promoted by conditions of excess lipid, causing a shortage of free DNA to drive the complexation process forward. In systems with higher DNA charge ratios, multilamellar complexes form much more quickly.

Some DNA lipoplexes have been found to form “spaghetti” tubule structures, with individual DNA molecules coated by cationic lipid bilayers [30]. It has been demonstrated that these structures are metastable [21]; they may be intermediates in the formation of the inverse hexagonal phase.

### 3.2.2.3 Lipoplex Size

Lipoplex particles, with different compositions and under different preparation conditions, range in size from around 100 nm to several microns. At low or high DNA/lipid charge ratios the complexes are charged (with positive or negative  $\zeta$  potential, respectively), and their size is stabilized by electrostatic repulsions. At charge ratios approaching the isoelectric point the  $\zeta$  potential is near zero, and lipoplexes undergo extensive and irreversible aggregation [35]. Size growth is promoted by membrane defects that are believed to result from phase separations between DNA–lipid lamellar domains and uncomplexed bilayers [36].

Increasing mole fraction of helper lipids increases lipoplex size [35]. This is probably due to lower membrane charge density and thus weaker electrostatic repulsions. A medium of high ionic strength masks electrostatic repulsions and facilitates lipoplex growth [37].

Lipoplexes prepared from large cationic liposomes are larger than those prepared from small liposomes [35]. The extent of lipoplex aggregation increases with time.

## 3.2.3

### Lipofection Efficiency

#### 3.2.3.1 *In Vitro*

Lipoplexes must surmount many barriers to successfully deliver DNA to the cell nucleus. A diagram of the most likely mechanism of lipofection is shown in Fig. 3.5. The first stage is binding of a lipoplex to the cell due to nonspecific electrostatic interactions between cationic membranes and anionic proteoglycan residues on the cell surface [38]. Cell association is enhanced for positively charged lipoplexes and for large aggregates, the latter probably due to a faster rate of settling on the cultured cells [39]. The most efficient DNA/lipid mixing ratio for lipofection is a moderate excess of cationic charge [40].

The primary pathway for lipoplex entry into cells is endocytosis [41, 42]. Fusion of lipoplexes with the cell membrane also occurs, but there is no correlation between the degree of lipid mixing and the lipofection efficiency [43]. Possibly a fusion event releases DNA outside the cell, or inside the cell, but too distant from the cell nucleus.

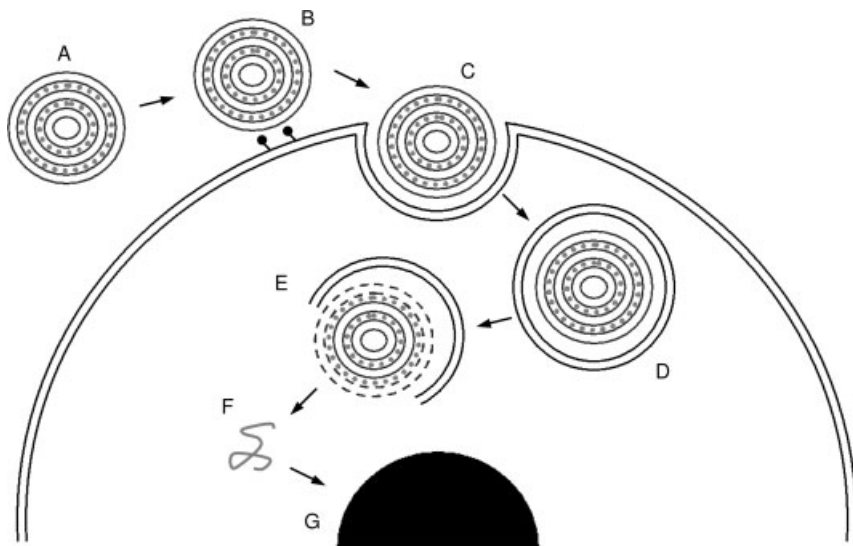


**Fig. 3.5.** Schematic representation of the most likely mechanism of lipofection. (A) A lipoplex approaches the cell. (B) Adsorption to the cell surface due to electrostatic interactions. (C) Entry to the cell by endocytosis. (D) Transport within an endosome. (E) Fusion or disruption of the endosome. (F) Release of DNA. (G) Entry to the nucleus by intracellular trafficking. (Adapted from Ref. [59].)

A recent report has demonstrated that small particles (200 nm or below) enter cells mainly by clathrin-mediated endocytosis and larger particles (around 500 nm) by caveolae-mediated endocytosis, while very large particles (1  $\mu\text{m}$  or above) are not internalized at all [44]. Small particles are delivered to lysosomes for digestion within a few hours, but larger particles have an extended residence time within endosomal compartments, increasing their probability of escape into the cytosol [44]. These results may explain the common empirical finding that lipoplex size has a significant influence on transgene expression. There is an optimal lipoplex size for greatest lipofection efficiency [35, 37, 45].

Release of lipoplexes from endosomal compartments is widely considered a rate-determining step for lipofection. Efficient lipoplex formulations are able to escape from endosomes, while inefficient formulations remain trapped [46, 47]. The endosome membrane can be disrupted by lipid exchange or fusion with lipoplexes. Inverse hexagonal phase lipoplexes are reported to fuse rapidly with anionic membranes, disrupting the membrane and releasing DNA [20] and hexagonal lipoplex structure has been correlated with efficient lipofection [48, 49]. Lipid mixing between cationic lipids and anionic lipids found in the endosomal membrane can also induce local formation of a hexagonal phase, due to ion pair charge neutralization [50, 51]. This destabilization of bilayers is hindered by the presence of cylindrically shaped helper lipid, but is facilitated by inverse conical shaped helper lipid. Formation of a nonbilayer phase in lipoplex–membrane mixtures appears to be critical for efficient endosome escape [51].

A recent report has proposed that the barrier preventing lamellar lipoplex fusion with the anionic endosomal membrane is kinetic rather than thermodynamic [47]. The height of the activation barrier depends on lipoplex membrane bending rigidity and cationic charge density. Efficiency of lipofection increases exponentially with membrane charge density to a plateau, where delivery efficiency of the lamellar phase competes with that of the hexagonal phase [47]. Other studies have suggested that increased membrane fluidity (decreased bending rigidity) enhances lipofection efficiency [52, 53].

DNA may dissociate from lipoplexes during endosomal escape or intact lipoplexes may be released into the cytoplasm [54]. Direct microinjection of lipoplexes into either the cytoplasm or the nucleus results in efficient complex dissociation, so intracellular release of DNA is probably not a limiting step for lipofection [55]. Interestingly, microinjection of lipoplexes or naked DNA into the cytoplasm produces significantly less gene expression than endocytosis-mediated lipofection. Endosomes may play a role in lipofection by transporting the lipoplexes close to the cell nucleus [3].

Transfer of DNA into the nucleus is a very inefficient process. Particles with diameters of up to around 40 nm are able to enter the nucleus by active transport through the nuclear pores [56], but most genes delivered by lipoplexes are much larger than this. Shorter DNA molecules are correlated with increased lipofection efficiency [28]. Dividing cell lines have an alternative nuclear access pathway, as the nuclear envelope fragments during mitosis. Transgene expression is enhanced immediately following mitosis [57], but the duration of the mitosis phase is only around 1 h in a typical cell cycle of 24 h. DNA located in the cytoplasm is degraded by nucleases, with a half-life of approximately 90 min [58].

In general, increasing the lipoplex dose administered improves lipofection efficiency. However, this approach is limited by the toxicity thresholds of cationic lipids [59–61]. Efforts to develop less-toxic lipid formulations for both *in vitro* and *in vivo* applications are in progress.

In addition to the factors described here, lipofection efficiency also depends on the interrelations between cationic/helper lipid formulation, DNA sequence and target cell type. The reasons behind these effects are poorly understood.

### 3.2.3.2 *In Vivo*

The ultimate aim of research in the field of lipoplexes is to achieve effective systemic delivery of therapeutic genes to humans. Unfortunately, lipofection efficiency *in vivo* is much lower than *in vitro*, due to a number of extracellular barriers. Intravenous injection of lipoplexes is followed by unfavorable interactions with blood components and by highly restricted uptake to tissues.

Exposure of cationic lipoplexes to blood serum dramatically inhibits *in vitro* DNA delivery in some systems [62, 63], but not others [64]. Serum does not displace DNA from lipoplexes, but it reverses the  $\zeta$  potential of the complexes due to anionic serum proteins binding to lipoplex surfaces [63]. Incubation with low concentrations of serum can promote bridging and extensive lipoplex aggregation, which is correlated with reduced *in vivo* lipofection efficiency. Incubation with

high concentrations of serum yields homogenous coating of serum proteins and sterically stabilizes lipoplex size [65].

Inclusion of inverse conical helper lipids in lipoplexes significantly reduces their *in vivo* lipofection efficiency [66]. It has been reported that lipoplex structures of this type disintegrate in serum, with penetration and binding of serum proteins to all cationic membranes, inside and out [65]. This both exposes DNA to nucleases in the blood and has detrimental implications for intracellular processing. Even in less extreme cases, serum can interfere with mixture between lipoplexes and anionic liposomes, an analog of endosomal membranes [63]. In agreement, lipoplexes incorporating serum have been shown to fail to escape from endosomes [64].

Long-term incubation (above 30 min) of lipoplexes in blood causes partial degradation of DNA, due to imperfect protection from nucleases [67]. However, this may not be a significant effect, as more than 97% of lipoplexes have been cleared from the blood within 5 min of intravenous injection into mice. At this time the majority of lipoplexes are associated with the lungs, probably partially due to entrapment in the extensive pulmonary microvasculature. Later a large fraction of lung lipoplexes relocates to the liver [67].

Lipoplex particles are, in general, too large to extravasate from the bloodstream. Uptake and expression of lipoplexes in the lungs and most other organs is predominantly by capillary endothelial cells [68]. Uptake of lipoplexes in the liver and spleen is primarily due to elimination of foreign particles by macrophages, which does not lead to significant transgene expression [68]. Some success has been reported in lipofection of tumor tissue, as tumors have a permeable endothelial barrier [69, 70]. An ability to extravasate under these conditions has been attributed to a specific lipoplex structure, bilamellar invaginated vesicles, which yields relatively small and very flexible particles.

Intravenous administration of lipoplexes is an excellent technique for gene delivery to endothelial cells [71]. Efficient targeting of other cell types requires modification of lipoplexes. One current direction of research is development of “stealth lipoplexes”, an analog of well-known stealth liposomes. Lipoplexes are coated with the biocompatible polymer polyethylene glycol (PEG), with the possible addition of a targeting ligand. PEGylation provides steric protection from interactions with serum proteins and reduces nonspecific uptake by the lung endothelial cells, so it greatly extends the residence time of lipoplexes in the circulation [72]. However, PEGylation has been shown to strongly inhibit lipofection in cell culture, due to stabilization of the lamellar phase and preclusion of endosomal escape, unless the PEG molecules desorb [73, 74]. This approach is promising, but needs further work.

### 3.3 ODN Lipoplexes

Antisense ODN, short single-strand DNA molecules, are designed to target and bind a specific messenger RNA, blocking gene expression. Antisense design is

not straightforward, but one ODN drug has been approved and many others are in clinical trials [75]. Cationic lipid-mediated delivery of ODN increases antisense activity by several orders of magnitude [76, 77].

The structure of ODN lipoplexes is similar to that of DNA lipoplexes; both lamellar [78] and inverse hexagonal [79] phases have been observed. In ODN lamellar lipoplexes, however, there is no evidence of ordering within the ODN monolayers. As ODN molecules are relatively short and flexible, they probably orient randomly between the cationic membranes [80].

The thickness of ODN monolayers in the lamellar phase has been measured as around 1.2 nm [80]. This suggests that there is insufficient room for a hydration layer between ODN molecules and cationic membranes as is seen in DNA lipoplexes. In agreement, ODN molecules neutralize cationic lipid charges more efficiently than DNA does, implying that ODN is located in closer contact with the membrane [81, 14]. We consider complete dehydration of ODN unlikely, so we speculate that ODN may adopt a different conformation between cationic mem-

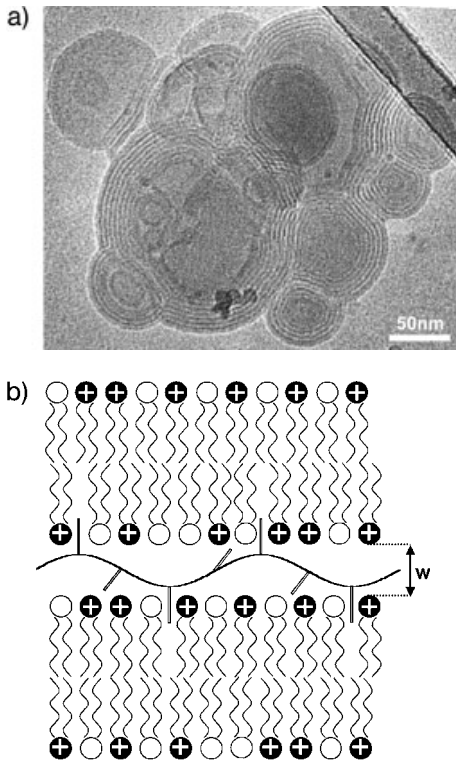


**Fig. 3.6.** (A) Cryo-TEM image of a DOTAP/ODN lipoplex with excess lipid. A condensed multilamellar phase is seen. (B) Schematic representation of the ODN-lipid lamellar phase. The interlamellar water gap is denoted by  $w$ . We speculate that ODN molecule side-groups may penetrate into the lipid bilayer.

branes than in aqueous solution. Instead of a helical backbone with side-groups facing inwards to maximize base-stacking interactions, side-groups may point outwards, leaving a central water tube. Bases would then penetrate into the head-group area of the cationic membranes. Figure 3.6(A) shows an example of a condensed lamellar lipoplex imaged at our laboratory. Figure 3.6(B) shows our suggested model of lamellar structure with ODN bases intercalated between lipid head groups. This hypothesis needs further investigation.

ODN lipoplexes enter cells by endocytosis [77, 82] as DNA lipoplexes do. However, the nuclear membrane is not a major barrier for ODN molecules. After microinjection into the cell, ODN is found to preferentially locate in the nucleus [83], with the rate of uptake inversely proportional to molecular size [84]. ODN is delivered to the nucleus by active transport through nuclear pores [85].

### 3.4

#### siRNA Lipoplexes

siRNA, short double-strand RNA molecules, has recently become a popular tool for gene silencing [86]. Successful cationic lipid-mediated delivery of siRNA has been reported [87], but as yet little research has focused on the properties of siRNA lipoplexes. siRNA lipoplexes would be expected to be similar to DNA lipoplexes, but an early report suggests that the effect of lipoplex size may be less critical for siRNA delivery than for DNA delivery [88].

Nuclear entry is probably not a significant barrier for siRNA lipofection, as RNA interference activity seems to be primarily located in the cytoplasm [86]. Further research into the structure and function of siRNA lipoplexes is needed in order to optimize siRNA delivery and to facilitate the development of this exciting field.

#### Acknowledgments

Cryo-TEM work was performed at the Hannah and George Krumholz Laboratory for Advanced Microscopy at the Technion, part of the Technion Project on Complex Fluids, in collaboration with Y. Talmon, Y. Barenholz and D. Hirsch-Lerner, funded by an Israel Science Foundation grant. Thanks to Y. Talmon for help in editing this manuscript.

#### References

- 1 M. A. KAY, J. C. GLORIOSO, L. NALDINI, Viral vectors for gene therapy: the art of turning infectious agents into vehicles of therapeutics, *Nat. Med.* **2001**, 7, 33–40.
- 2 P. L. FELGNER, T. R. GADEK, M. HOLM, R. ROMAN, H. W. CHAN, M. WENZ, J. P. NORTHROP, G. M. RINGOLD, M. DANIELSEN, Lipofection: a highly efficient, lipid-mediated DNA-transfection procedure, *Proc. Natl Acad. Sci. USA* **1987**, 84, 7413–7417.

- 3 A. ELOUAHABI, J.-M. RUYSSCHAERT, Formation and intracellular trafficking of lipoplexes and polyplexes, *Mol. Ther.* **2005**, *11*, 336–347.
- 4 K. EWERT, N. L. SLACK, A. AHMAD, H. M. EVANS, A. J. LIN, C. E. SAMUEL, C. R. SAFINYA, Cationic lipid–DNA complexes for gene therapy: understanding the relationship between complex structure and gene delivery pathways at the molecular level, *Curr. Med. Chem.* **2004**, *11*, 133–149.
- 5 S. MAY, A. BEN-SHAUL, Modeling of cationic lipid–DNA complexes, *Curr. Med. Chem.* **2004**, *11*, 151–167.
- 6 D. SIMBERG, S. WEISMAN, Y. TALMON, Y. BARENHOLZ, DOTAP (and other cationic lipids): chemistry, biophysics, and transfection, *Crit. Rev. Ther. Drug Carrier Syst.* **2004**, *21*, 257–317.
- 7 I. TRANCHANT, B. THOMPSON, C. NICOLAZZI, N. MIGNET, D. SCHERMAN, Physicochemical optimization of plasmid delivery by cationic lipids, *J. Gene Med.* **2004**, *6*, S24–S35.
- 8 Extensive and current information on clinical trials in the field of gene therapy can be found at <http://www.wiley.co.uk/genetherapy/clinical/>.
- 9 S. ZHANG, Y. XU, B. WANG, W. QIAO, D. LIU, Z. LI, Cationic compounds used in lipoplexes and polyplexes for gene delivery, *J. Controlled Rel.* **2004**, *165*–180.
- 10 M. T. KENNEDY, E. V. POZHARSKI, V. A. RAKHMANOVA, R. C. MACDONALD, Factors governing the assembly of cationic phospholipid–DNA complexes, *Biophys. J.* **2000**, *78*, 1620–1633.
- 11 D. MATULIS, I. ROUZINA, V. A. BLOOMFIELD, Thermodynamics of cationic lipid binding to DNA and DNA condensation: roles of electrostatics and hydrophobicity, *J. Am. Chem. Soc.* **2002**, *124*, 7331–7342.
- 12 K. WAGNER, D. HARRIES, S. MAY, V. KAHL, J. O. RÄDLER, A. BEN-SHAUL, Direct evidence for counterion release upon cationic lipid–DNA condensation, *Langmuir* **2000**, *16*, 303–306.
- 13 D. HIRSCH-LERNER, Y. BARENHOLZ, Hydration of lipoplexes commonly used in gene delivery: follow-up by laurdan fluorescence changes and quantification by differential scanning calorimetry, *Biochim. Biophys. Acta* **1999**, *1461*, 47–57.
- 14 N. J. ZUIDAM, Y. BARENHOLZ, Electrostatic and structural properties of complexes involving plasmid DNA and cationic lipids commonly used for gene delivery, *Biochim. Biophys. Acta* **1998**, *1368*, 115–128.
- 15 S. J. EASTMAN, C. SIEGEL, J. TOUSIGNANT, A. E. SMITH, S. H. CHENG, R. K. SCHEULE, Biophysical characterization of cationic lipid:DNA complexes, *Biochim. Biophys. Acta* **1997**, *1325*, 41–62.
- 16 Y. XU, S.-W. HUI, P. FREDERIK, F. C. SZOKA, Physicochemical characterization and purification of cationic lipoplexes, *Biophys. J.* **1999**, *77*, 341–353.
- 17 Journal papers referring to the applications of a given lipid for gene therapy were found by searching the CAPLUS database in Scifinder®: <http://www.cas.org/SCIFINDER/scicover2.html>.
- 18 J. O. RÄDLER, I. KOLTOVER, T. SALDITT, C. R. SAFINYA, Structure of DNA–cationic liposome complexes: DNA intercalation in multilamellar membranes in distinct interhelical packing regimes, *Science* **1997**, *275*, 810–814.
- 19 D. HARRIES, S. MAY, W. M. GELBART, A. BEN-SHAUL, Structure, stability, and thermodynamics of lamellar DNA–lipid complexes, *Biophys. J.* **1998**, *75*, 159–173.
- 20 I. KOLTOVER, T. SALDITT, J. O. RÄDLER, C. R. SAFINYA, An inverted hexagonal phase of cationic liposome–DNA complexes related to DNA release and delivery, *Science* **1998**, *281*, 78–81.
- 21 S. MAY, A. BEN-SHAUL, DNA–lipid complexes: stability of honeycomb-like and spaghetti-like structures, *Biophys. J.* **1997**, *73*, 2427–2440.
- 22 I. KOLTOVER, T. SALDITT, C. R. SAFINYA, Phase diagram, stability, and overcharging of lamellar cationic lipid–DNA self-assembled complexes, *Biophys. J.* **1999**, *77*, 915–924.

- 23 D. SIMBERG, D. DANINO, Y. TALMON, A. MINSKY, M. E. FERRARI, C. J. WHEELER, Y. BARENHOLZ, Phase behavior, DNA ordering, and size instability of cationic lipoplexes, *J. Biol. Chem.* **2001**, 276, 47453–47459.
- 24 S. MAY, D. HARRIES, A. BEN-SHAUL, The phase behavior of cationic lipid–DNA complexes, *Biophys. J.* **2000**, 78, 1681–1697.
- 25 F. ARTZNER, R. ZANTL, G. RAPP, J. O. RÄDLER, Observation of a rectangular columnar phase in condensed lamellar cationic lipid–DNA complexes, *Phys. Rev. Lett.* **1998**, 81, 5015–5018.
- 26 B. J. BATTERSBY, R. GRIMM, S. HUEBNER, G. CEVC, Evidence for three-dimensional interlayer correlations in cationic lipid–DNA complexes as observed by cryo-electron microscopy, *Biochim. Biophys. Acta* **1998**, 1372, 379–383.
- 27 D. HARRIES, S. MAY, A. BEN-SHAUL, Curvature and charge modulations in lamellar DNA–lipid complexes, *J. Phys. Chem. B* **2003**, 107, 3624–3630.
- 28 P. KREISS, B. CAMERON, R. RANGARA, P. MAILHE, O. AGUERRE-CHARRIOL, M. AIRIAU, D. SCHERMAN, J. CROUZET, B. PITARD, Plasmid DNA size does not affect the physicochemical properties of lipoplexes but modulates gene transfer efficiency, *Nucleic Acids Res.* **1999**, 27, 3792–3798.
- 29 C. S. BRAUN, G. S. JAS, S. CHOOSAKOON-KRIANG, G. S. KOE, J. G. SMITH, C. R. MIDDAGH, The structure of DNA within cationic lipid/DNA complexes, *Biophys. J.* **2003**, 84, 1114–1123.
- 30 B. STERNBERG, F. L. SORGI, L. HUANG, New structures in complex formation between DNA and cationic liposomes visualized by freeze-fracture electron microscopy, *FEBS Lett.* **1994**, 356, 361–366.
- 31 J. GUSTAFSSON, G. ARVIDSON, G. KARLSSON, M. ALMGREN, Complexes between cationic liposomes and DNA visualized by cryo-TEM, *Biochim. Biophys. Acta* **1995**, 1235, 305–312.
- 32 N. S. TEMPLETON, D. D. LASIC, P. M. FREDERIK, H. H. STREY, D. D. ROBERTS, G. N. PAVLAKIS, Improved DNA:liposome complexes for increased systemic delivery and gene expression, *Nat. Biotechnol.* **1997**, 15, 647–652.
- 33 S. HUEBNER, B. J. BATTERSBY, R. GRIMM, G. CEVC, Lipid–DNA complex formation: reorganization and rupture of lipid vesicles in the presence of DNA as observed by cryoelectron microscopy, *Biophys. J.* **1999**, 76, 3158–3166.
- 34 V. PECTOR, J. BACKMANN, D. MAES, M. VANDENBRANDEN, J.-M. RUYSSCHAERT, Biophysical and structural properties of DNA–diC<sub>14</sub>–amidine complexes, *J. Biol. Chem.* **2000**, 275, 29533–29538.
- 35 N. J. ZUIDAM, D. HIRSCH-LERNER, S. MARGULIES, Y. BARENHOLZ, Lamellarity of cationic liposomes and mode of preparation of lipoplexes affect transfection efficiency, *Biochim. Biophys. Acta* **1999**, 1419, 207–220.
- 36 D. HIRSCH-LERNER, Y. BARENHOLZ, Probing DNA–cationic lipid interactions with the fluorophore trimethylammonium diphenylhexatriene (TMADPH), *Biochim. Biophys. Acta* **1998**, 1370, 17–30.
- 37 P. C. ROSS, S. W. HUI, Lipoplex size is a major determinant of *in vitro* lipofection efficiency, *Gene Ther.* **1999**, 6, 651–9.
- 38 K. A. MISLICK, J. D. BALDESCHWIELER, Evidence for the role of proteoglycans in cation-mediated gene transfer, *Proc. Natl Acad. Sci. USA* **1996**, 93, 12349–12354.
- 39 M. T. GIRÃO DA CRUZ, S. SIMÕES, P. P. C. PIRES, S. NIR, M. C. PEDROSA DE LIMA, Kinetic analysis of the initial steps involved in lipoplex–cell interactions: effect of various factors that influence transfection activity, *Biochim. Biophys. Acta* **2001**, 1510, 136–141.
- 40 F. SAKURAI, R. INOUE, Y. NISHINO, A. OKUDA, O. MATSUMOTO, T. TAGA, F. YAMASHITA, Y. TAKAKURA, M. HASHIDA, Effect of DNA/liposome mixing ratio on the physicochemical characteristics, cellular uptake and intracellular trafficking of plasmid DNA/cationic lipid complexes and subsequent gene expression, *J. Controlled Rel.* **2000**, 66, 255–269.



- 41 J. ZABNER, A. J. FASBENDER, T. MONINGER, K. A. POELLINGER, M. J. WELSH, Cellular and molecular barriers to gene transfer by a cationic lipid, *J. Biol. Chem.* **1995**, *270*, 18997–19007.
- 42 D. S. FRIEND, D. PAPAHAJIOPOULOS, R. J. DEBS, Endocytosis and intracellular processing accompanying transfection mediated by cationic liposomes, *Biochim. Biophys. Acta* **1996**, *1278*, 41–50.
- 43 T. STEGMANN, J.-Y. LEGENDRE, Gene transfer mediated by cationic lipids: lack of a correlation between lipid mixing and transfection, *Biochim. Biophys. Acta* **1997**, *1325*, 71–79.
- 44 J. REJMAN, V. OBERLE, I. S. ZUHORN, D. HOEKSTRA, Size-dependent internalization of particles via the pathways of clathrin- and caveolae-mediated endocytosis, *Biochem. J.* **2004**, *377*, 159–169.
- 45 C. KAWAURA, A. NOGUCHI, T. FURUNO, M. NAKANISHI, Atomic force microscopy for studying gene transfection mediated by cationic liposomes with a cationic cholesterol derivative, *FEBS Lett.* **1998**, *421*, 69–72.
- 46 B. MUI, Q. F. AHKONG, L. CHOW, M. J. HOPE, Membrane perturbation and the mechanism of lipid-mediated transfer of DNA into cells, *Biochim. Biophys. Acta* **2000**, *1467*, 281–292.
- 47 A. J. LIN, N. L. SLACK, A. AHMAD, C. X. GEORGE, C. E. SAMUEL, C. R. SAFINYA, Three-dimensional imaging of lipid gene-carriers: membrane charge density controls universal transfection behavior in lamellar cationic liposome–DNA complexes, *Biophys. J.* **2003**, *84*, 3307–3316.
- 48 A. J. LIN, N. L. SLACK, A. AHMAD, I. KOLTOVER, C. X. GEORGE, C. E. SAMUEL, C. R. SAFINYA, Structure and structure–function studies of lipid/plasmid DNA complexes, *J. Drug Target.* **2000**, *8*, 13–27.
- 49 J. SMISTEROVÁ, A. WAGENAAR, M. C. A. STUART, E. POLUSHKIN, G. TEN BRINKE, R. HULST, J. B. F. N. ENGBERTS, D. HOEKSTRA, Molecular shape of the cationic lipid controls the structure of cationic lipid/dioleoylphosphatidylethanolamine–DNA complexes and the efficiency of gene delivery, *J. Biol. Chem.* **2001**, *276*, 47615–47622.
- 50 I. M. HAFEZ, N. MAURER, P. R. CULLIS, On the mechanism whereby cationic lipids promote intracellular delivery of polynucleic acids, *Gene Ther.* **2001**, *8*, 1188–1196.
- 51 I. S. ZUHORN, U. BAKOWSKY, E. POLUSHKIN, W. H. VISSER, M. C. A. STUART, J. B. F. N. ENGBERTS, D. HOEKSTRA, Nonbilayer phase of lipoplex–membrane mixture determines endosomal escape of genetic cargo and transfection efficiency, *Mol. Ther.* **2005**, *11*, 801–810.
- 52 A. E. REGELIN, S. FANKHAENEL, L. GÜRTECH, C. PRINZ, G. VON KIEDROWSKI, U. MASSING, Biophysical and lipofection studies of DOTAP analogs, *Biochim. Biophys. Acta* **2000**, *1464*, 151–164.
- 53 M. E. FERRARI, D. RUSALOV, J. ENAS, C. J. WHEELER, Synergy between cationic lipid and co-lipid determines the macroscopic structure and transfection activity of lipoplexes, *Nucleic Acids Res.* **2002**, *30*, 1808–1816.
- 54 A. EL OUAHABI, M. THIRY, V. PECTOR, R. FUKS, J. M. RUYSSCHAERT, M. VANDENBRANDEN, The role of endosome destabilizing activity in the gene transfer process mediated by cationic lipids, *FEBS Lett.* **1997**, *414*, 187–192.
- 55 S. CORNELIS, M. VANDENBRANDEN, J.-M. RUYSSCHAERT, A. ELOUAHABI, Role of intracellular cationic liposome–DNA complex dissociation in transfection mediated by cationic lipids, *DNA Cell Biol.* **2002**, *21*, 91–97.
- 56 N. PANTÉ, M. KANN, Nuclear pore complex is able to transport macromolecules with diameters of ~39 nm, *Mol. Biol. Cell* **2002**, *13*, 425–434.
- 57 W.-C. TSENG, F. R. HASELTON, T. D. GIORGIO, Mitosis enhances transgene expression of plasmid delivered by cationic liposomes, *Biochim. Biophys. Acta* **1999**, *1445*, 53–64.
- 58 D. LECHARDEUR, K. J. SOHN, M. HAARDT, P. B. JOSHI, M. MONCK, R. W.

- GRAHAM, B. BEATTY, J. SQUIRE, H. O'BRODOVICH, G. L. LUKACS, Metabolic instability of plasmid DNA in the cytosol: a potential barrier to gene transfer, *Gene Ther.* **1999**, *6*, 482–497.
- 59 D. D. LASIC, N. S. TEMPLETON, Liposomes in gene therapy, *Adv. Drug Deliv. Rev.* **1996**, *20*, 221–266.
- 60 C. R. DASS, Lipoplex-mediated delivery of nucleic acids: factors affecting *in vivo* transfection, *J. Mol. Med.* **2004**, *82*, 579–591.
- 61 J.-S. ZHANG, F. LIU, L. HUANG, Implications of pharmacokinetic behavior of lipoplex for its inflammatory toxicity, *Adv. Drug Deliv. Rev.* **2005**, *57*, 689–698.
- 62 V. ESCRIOU, C. CIOLINA, F. LACROIX, G. BYK, D. SCHERMAN, P. WILS, Cationic lipid-mediated gene transfer: effect of serum on cellular uptake and intracellular fate of lipopolyamine/DNA complexes, *Biochim. Biophys. Acta* **1998**, *1368*, 276–288.
- 63 O. ZELPHATI, L. S. UYECHI, L. G. BARRON, F. C. SZOKA, Effect of serum components on the physico-chemical properties of cationic lipid/oligonucleotide complexes and on their interactions with cells, *Biochim. Biophys. Acta* **1998**, *1390*, 119–133.
- 64 I. S. ZUHORN, W. H. VISSER, U. BAKOWSKY, J. B. F. N. ENGBERTS, D. HOEKSTRA, Interference of serum with lipoplex–cell interaction: modulation of intracellular processing, *Biochim. Biophys. Acta* **2002**, *1560*, 25–36.
- 65 D. SIMBERG, S. WEISMAN, Y. TALMON, A. FAERMAN, T. SHOSHANI, Y. BARENHOLZ, The role of organ vascularization and lipoplex–serum initial contact in intravenous murine lipofection, *J. Biol. Chem.* **2003**, *278*, 39858–39865.
- 66 Y. K. SONG, F. LIU, S. CHU, D. LIU, Characterization of cationic liposome-mediated gene transfer *in vivo* by intravenous administration, *Hum. Gene Ther.* **1997**, *8*, 1585–1594.
- 67 R. NIVEN, R. PEARLMAN, T. WEDEKING, J. MACKEIGAN, P. NOKER, L. SIMPSON-HERREN, J. G. SMITH, Biodistribution of radiolabeled lipid–DNA complexes and DNA in mice, *J. Pharm. Sci.* **1998**, *87*, 1292–1299.
- 68 J. W. MCLEAN, E. A. FOX, P. BALUK, P. B. BOLTON, A. HASKELL, R. PEARLMAN, G. THURSTON, E. Y. UMEMOTO, D. M. McDONALD, Organ-specific endothelial cell uptake of cationic liposome–DNA complexes in mice, *Am. J. Physiol.* **1997**, *273*, H387–H404.
- 69 R. RAMESH, T. SAEKI, N. S. TEMPLETON, L. JI, L. C. STEPHENS, I. ITO, D. R. WILSON, Z. WU, C. D. BRANCH, J. D. MINNA, J. A. ROTH, Successful treatment of primary and disseminated human lung cancers by systemic delivery of tumor suppressor genes using an improved liposome vector, *Mol. Ther.* **2001**, *3*, 337–350.
- 70 H. Y. SHI, R. LIANG, N. S. TEMPLETON, M. ZHANG, Inhibition of breast tumor progression by systemic delivery of the maspin gene in a syngeneic tumor model, *Mol. Ther.* **2002**, *5*, 755–761.
- 71 J. D. HOOD, M. BEDNARSKI, R. FRAUSTO, S. GUCCIONE, R. A. REISFELD, R. XIANG, D. A. CHERESH, Tumor regression by targeted gene delivery to the neovasculature, *Science* **2002**, *296*, 2404–2407.
- 72 C. NICOLAZZI, N. MIGNET, N. DE LA FIGUERA, M. CADET, R. T. IBAD, J. SEGUIN, D. SCHERMAN, M. BESSODES, Anionic polyethylene glycol lipids added to cationic lipoplexes increase their plasmatic circulation time, *J. Controlled Rel.* **2003**, *88*, 429–443.
- 73 F. SHI, L. WASUNGU, A. NOMDEN, M. C. A. STUART, E. POLUSHKIN, J. B. F. N. ENGBERTS, D. HOEKSTRA, Interference of poly(ethylene glycol)–lipid analogs with cationic-lipid-mediated delivery of oligonucleotides; role of lipid exchangeability and non-lamellar transitions, *Biochem. J.* **2002**, *366*, 333–341.
- 74 L. Y. SONG, Q. F. AHKONG, Q. RONG, Z. WANG, S. ANSELL, M. J. HOPE, B. MUI, Characterization of the inhibitory effect of PEG–lipid conjugates on the intracellular delivery of plasmid and antisense DNA mediated by cationic lipid liposomes,

- Biochim. Biophys. Acta* **2002**, *1558*, 1–13.
- 75 F. SHI, D. HOEKSTRA, Effective intracellular delivery of oligonucleotides in order to make sense of antisense, *J. Controlled. Rel.* **2004**, *97*, 189–209.
- 76 C. F. BENNETT, M. Y. CHIANG, H. CHAN, J. E. SHOEMAKER, C. K. MIRABELLI, Cationic lipids enhance cellular uptake and activity of phosphorothioate antisense oligonucleotides, *Mol. Pharm.* **1992**, *41*, 1023–1033.
- 77 O. ZELPHATI, F. C. SZOKA, Intracellular distribution and mechanism of delivery of oligonucleotides mediated by cationic lipids, *Pharm. Res.* **1996**, *13*, 1367–1372.
- 78 S. C. SEMPLE, S. K. KLIMUK, T. O. HARASYM, N. D. SANTOS, S. M. ANSELL, K. F. WONG, N. MAURER, H. STARK, P. R. CULLIS, M. J. HOPE, P. SCHERRER, Efficient encapsulation of antisense oligonucleotides in lipid vesicles using ionizable aminolipids: formation of novel small multilamellar vesicle structures, *Biochim. Biophys. Acta* **2001**, *1510*, 152–166.
- 79 I. JÄÄSKELÄINEN, B. STERNBERG, J. MÖNKKÖNEN, A. URTTI, Physicochemical and morphological properties of complexes made of cationic liposomes and oligonucleotides, *Int. J. Pharm.* **1998**, *167*, 191–203.
- 80 S. WEISMAN, D. HIRSCH-LERNER, Y. BARENHOLZ, Y. TALMON, Nanostructure of cationic lipid–oligonucleotide complexes, *Biophys. J.* **2004**, *87*, 609–614.
- 81 V. M. MEIDAN, J. S. COHEN, N. AMARIGLIO, D. HIRSCH-LERNER, Y. BARENHOLZ, Interaction of oligonucleotides with cationic lipids: the relationship between electrostatics, hydration and state of aggregation, *Biochim. Biophys. Acta* **2000**, *1464*, 251–261.
- 82 K. LAPPALAINEN, R. MIETTINEN, J. KELLOKOSKI, I. JÄÄSKELÄINEN, S. SYRJÄNEN, Intracellular distribution of oligonucleotides delivered by cationic liposomes: light and electron microscopic study, *J. Histochem. Cytochem.* **1997**, *45*, 265–274.
- 83 J. P. LEONETTI, N. MECHTI, G. DEGOLS, C. GAGNOR, B. LEBLEU, Intracellular distribution of microinjected antisense oligonucleotides, *Proc. Natl Acad. Sci. USA* **1991**, *88*, 2702–2706.
- 84 G. L. LUKACS, P. HAGGIE, O. SEKSEK, D. LECHARDEUR, N. FREEDMAN, A. S. VERKMAN, Size-dependent DNA mobility in cytoplasm and nucleus, *J. Biol. Chem.* **2000**, *275*, 1625–1629.
- 85 R. HARTIG, R. L. SHOEMAN, A. JANETZKO, S. GRÜB, P. TRAUB, Active nuclear import of single-stranded oligonucleotides and their complexes with non-karyophilic macromolecules, *Biol. Cell* **1998**, *90*, 407–426.
- 86 C. D. NOVINA, P. A. SHARP, The RNAi revolution, *Nature* **2004**, *430*, 161–164.
- 87 J. Q. YIN, J. GAO, R. SHAO, W.-N. TIAN, J. WANG, Y. WAN, siRNA agents inhibit oncogene expression and attenuate human tumor cell growth, *J. Exp. Ther. Oncol.* **2003**, *3*, 194–204.
- 88 S. SPAGNOU, A. D. MILLER, M. KELLER, Lipidic carriers of siRNA: differences in the formulation, cellular uptake, and delivery with plasmid DNA, *Biochemistry* **2004**, *43*, 13348–13356.

## 4

# DNA–Chitosan Nanoparticles for Gene Therapy: Current Knowledge and Future Trends

*Julio C. Fernandes, Marcio José Tiera and Françoise M. Winnik*

### 4.1

#### Introduction

Chitosan is a polysaccharide usually obtained from deacetylation of chitin, which after cellulose is the second most abundant natural biopolymer found in nature. It may be extracted from various sources, particularly from exoskeletons of arthropods such as crustaceans, fungi, insects, annelids, mollusks, coelenterates, etc. [1, 2].

Approximately 1000 clinical trials are listed on the *Journal of Gene Medicine's* online “Gene Therapy Clinical Trials Worldwide” and more than 25% of these use nonviral vectors. This broad category encompasses a variety of technologies, essentially all of which involve complexing and sometimes condensing DNA with an agent that allows it to nonspecifically enter a cell, either by membrane fusion, endocytosis or a membrane-disrupting event. Chitosan is positively charged [1, 2] and thus can be complexed with DNA. It does not need sonication or organic solvents for its preparation, therefore minimizing possible damage to DNA during complexation.

The goal of this chapter is to introduce the reader to chitosan as a DNA carrier, as well as different variables and strategies to improve cellular transfection. The first two sections present the fundamental properties of chitosan as well as how different parameters related to the nonmodified structure affect the transfection efficiency. The third section provides the reader with an understanding of the multiple barriers that must be solved prior to practical use, discussing all the approaches employed and their limitations. The following sections present different procedures to obtain nano- and microparticles for gene therapy, and the potential clinical applications of chitosan–DNA polyplexes.

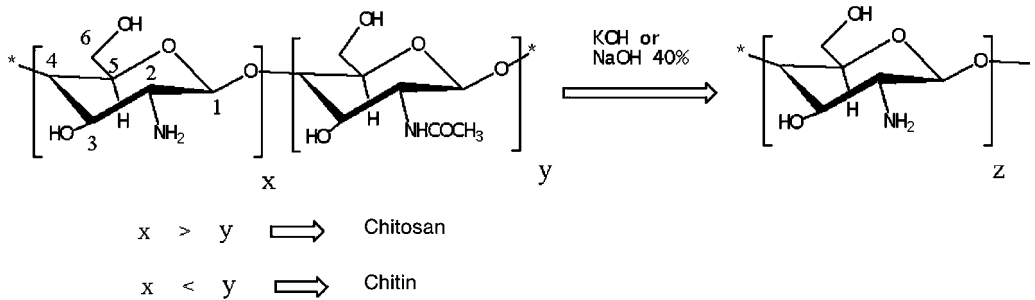


**Fig. 4.1.** Chemical structure of chitin and chitosan, and the deacetylation process to produce the highly deacetylated product. The commonly used numbering for the carbon atoms is shown in the 2-amino-2-deoxy-D-glucopyranose ring.

## 4.2

### Chitosan as a Carrier for Gene Therapy

#### 4.2.1

##### Chitosan Chemistry

The structures of chitin and chitosan correspond to those of poly[ $\beta(1 \rightarrow 4)$ -2-acetamido-2-deoxy-D-glucopyranose] and poly[ $\beta(1 \rightarrow 4)$ -2-amino-2-deoxy-D-glucopyranose], respectively (Fig. 4.1). Chitosan is mainly manufactured from crustaceans (crab, krill and crayfish), primarily because a large amount of the crustacean exoskeleton is available as a byproduct of food processing. In general, the isolation of chitin from crustacean shell waste consists of three basic steps: demineralization (calcium carbonate and calcium phosphate separation), deproteinization (protein separation) and decolorization (removal of pigments). These three steps are the standard procedure for chitin production [3]. Chitosan is obtained after hydrolysis of the acetamide groups of chitin. However, both units are commonly found in the commercialized samples, since chitosans having high degree of deacetylation (DA > 99%) are obtained only through successive hydrolysis with strong bases such as KOH and NaOH, and the degree of deacetylation is strongly dependent of the alkali concentration and temperature (Fig. 4.1) [4]. The source of chitin and the deacetylation process can dramatically change the properties of the final product and deacetylation in alkaline medium leads to depolymerization [5, 6]. However, it has been recently reported that chitin extracted from squid pens can be hydrolyzed under conditions that allow us to obtain chitosans of high molecular weight [7]. The homopolymer is a weak base with a  $pK_a$  value of the D-glucosamine residue of about 6.2–7.0, and is therefore insoluble at neutral and alkaline pH values. In acidic media the amine groups will be positively charged, conferring a high charge density to the polysaccharide. As in all polyelectrolytes, the dissociation constant of chitosan is not constant, but depends on the degree of dissociation at

which it is determined. The  $pK_a$  value can be calculated using Katchalsky's equation [2]:

$$pK_a = \text{pH} + \log[(1 - \alpha)/\alpha] = pK_0 - \varepsilon\Delta\psi(\alpha)/kT$$

where  $\Delta\psi$  is the difference in electrostatic potential between the surface of the polyion and the reference,  $\alpha$  is the degree of dissociation,  $kT$  is Boltzman's constant and  $\varepsilon$  is the electron charge. Extrapolation of the  $pK_a$  values to  $\alpha = 1$ , where the polymer is uncharged and hence the electrostatic potential becomes zero, makes it possible for the value of the intrinsic dissociation constant of the ionizable groups,  $pK_0$ , to be determined. The value obtained does not depend of the degree of *N*-acetylation, whereas the  $pK_a$  value is highly dependent on this parameter, since the electrostatic potential will vary depending on the amount of the free amino groups. The  $pK_0$  value is called the intrinsic  $pK_a$  of the chitosan. However, chitosans of low molecular weight having degrees of deacetylation higher than 0.4 are also easily soluble in weakly acidic solvents such as acetic acid and formic acid [8]. The physicochemical behavior in aqueous solution is highly dependent of the pH and degree of acetylation, and has received more attention only recently. Berth et al., working on chitosans from 95 to 175 kDa, have recently determined the radius of gyration of chitosan ( $R_G$ ) [9, 10]. The  $R_G$  is an alternative measure of the size of the polymer chain and it can be measured by light scattering measurements.  $R_G$  expresses the square mean radius of each one of the elements of the chain measured from its center of gravity. The study established the relationship between the molecular weight and  $R_G$  of chitosan in aqueous solution, and the author indicated that chitosan behaved more like a Gaussian coil instead of the worm-like chain model found in common polyelectrolytes. At the same time the presence of *N*-acetyl groups on the chitosan backbone imparts hydrophobic properties. Schatz et al. [11] have studied a homogeneous series of chitosans with different degrees of acetylation and almost the same degree of polymerization in ammonium acetate buffer. Their results indicate that the aqueous solution behavior depends only on the degree of acetylation. Three distinct domains of degree of acetylation were defined and correlated to the different behaviors of chitosans: (a) a polyelectrolyte domain for DA < 20%, (b) a transition domain for DA = 20–50% where chitosan loses its hydrophilicity and (iii) a hydrophobic domain for DA > 50% where polymer associations can arise. Conformations of chitosan chains varying from 160 to 270 kDa were studied by the calculations of the persistence lengths ( $L_p$ ). The average value was found to be close to 5 nm, in agreement with the wormlike chain model, but no significant variation of  $L_p$  with the degree of acetylation was noticed. Pa et al. [12] have also reported that the particle sizes of chitosan molecules in dilute acetic acid/water solutions increased with decreasing pH. Light scattering studies data also demonstrated that the second virial coefficient ( $A_2$ ) increased with decreasing pH, suggesting that the solubility of chitosan in water increased with increasing acetic acid concentration. Signini et al. [13] have also shown that acid-free aqueous solutions of chitosan hydrochloride

of variable ionic strengths ( $0.06 \leq \mu \leq 0.3 \text{ M}$ ) are free of aggregation as evaluated by the values of the Huggins constants ( $0.31 \leq k \leq 0.63$ ).

As with other polysaccharides, the biodegradation and biocompatibility are important properties of chitosan, making it an attractive polymer for a variety of biomedical and pharmaceutical applications. In addition to the degradation by chitinases [14], chitosanases [15], papain [16–19] and other proteases [20], partially acetylated chitosan may be also degraded by lysozymes of the human serum [21], by oxidative/reductive depolymerization [22] and by acid hydrolysis reactions [23]. In the acid hydrolysis the protonation of the glycosidic oxygen is recognized as the first step of the mechanism, which leads to formation of a cyclic carbonium–oxonium ion, yielding the reducing sugar end group after the addition of water [24, 25]. In addition to enzymatic and acid hydrolysis, alkaline treatment with ultrasonication can be used to obtain either chitosan of decreasing molecular weight [26] or oligomers having a few glucosamine units [27].

#### 4.2.2

##### **General Strategies for Chitosan Modification**

In the chitosan structure, two groups are particularly susceptible to react through nucleophilic attack, i.e. the free amine and/or acetamide groups and the hydroxyl groups linked to the glucopyranose ring. The hydroxyl groups can be modified by substitution of the hydrogen atoms, but their reactivities are smaller than that of the amino group. Various procedures targeting the hydroxyl groups employ a sequence of protection/deprotection reactions aimed at obtaining derivatives with a well-defined structure [28]. However, under appropriate conditions, a variety of other reactions can be easily conducted to selectively modify the free amine groups. The literature presents a wide range of procedures to target the amine group, aiming to improve the properties of chitosan for a particular purpose. The modifications include those aiming at the separation technologies of chiral molecules [29], recovery of metals [30, 31], antimicrobial activity [32], antitumoral carriers [33], biomedical applications [34, 35] and vectors for gene therapy [36–39] (Figs. 4.2 and 4.3). Kumar et al. [40] and Kurita [41] have recently reviewed the procedures for the modification of chitosan, and those of major importance are summarized in Tables 4.1 and 4.2.

#### 4.2.3

##### **Chitosan–DNA interactions: Transfection Efficacy of Unmodified Chitosan**

The first report on chitosan as a possible carrier for gene therapy was made by Mumper et al. in 1995 [125]. Since then it has been reported that besides its immunogenicity, chitosan molecules condense efficiently with DNA to form tight polyplexes avoiding degradation by DNases [126]. However, before using chitosan–DNA nanoparticles *in vivo*, one must study their interaction and cell behavior. Since macrophages play an important role in inflammatory processes, Chellat et al. [127] have investigated the effects of chitosan–DNA nanoparticles on the hu-

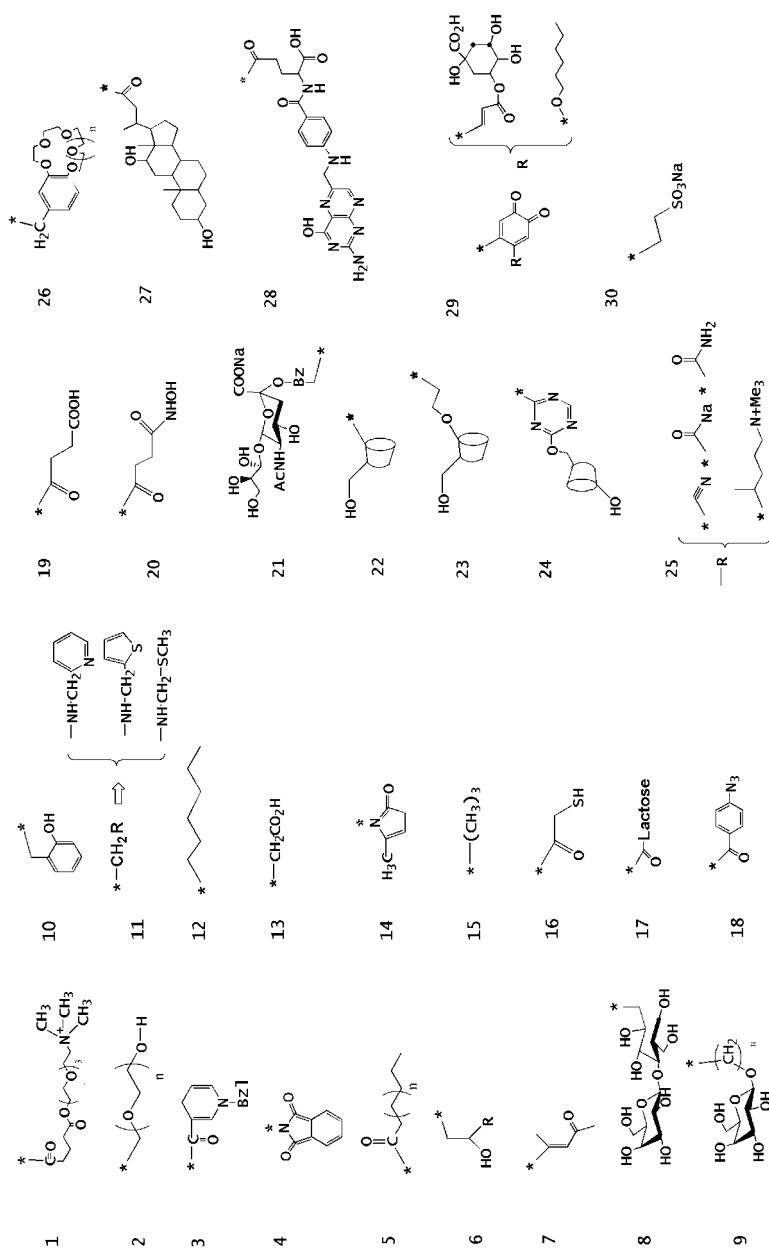
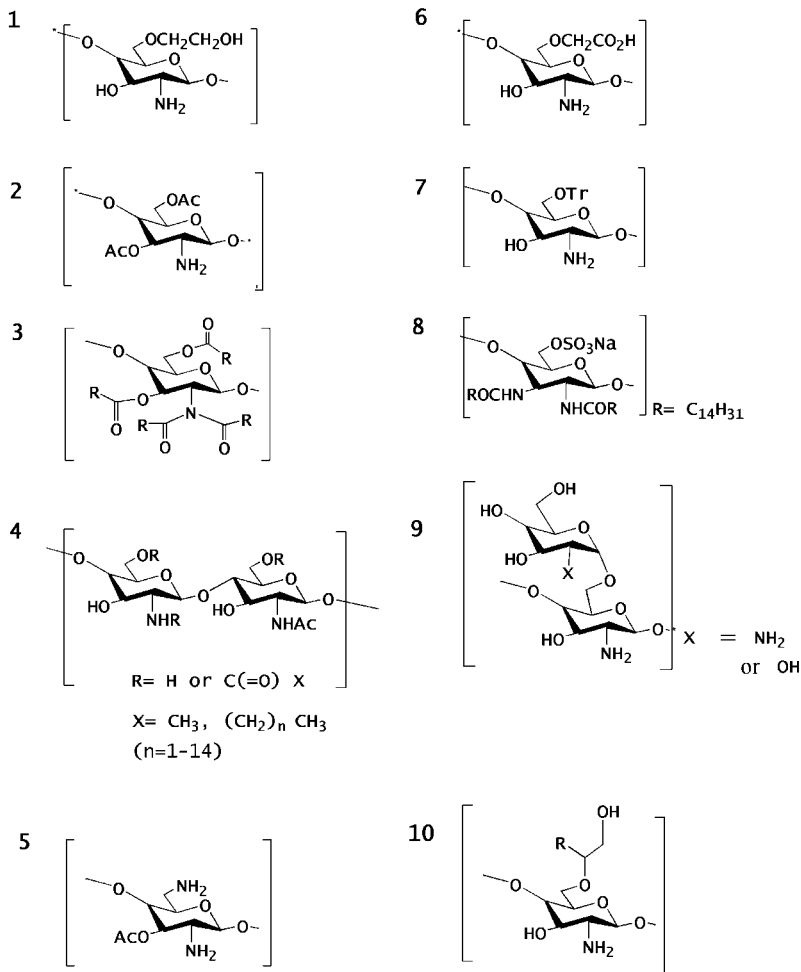


Fig. 4.2. Chemical structure of N-chitosan derivatives. The asterisk indicates the position at which the amino group of chitosan chain is attached. In the 4 and 14 derivatives the nitrogen atom belongs to the main chain of chitosan.





**Fig. 4.3.** Chemical structure of *O*-chitosan derivatives obtained either by regioselective substitution or by controlling the reaction conditions.

man THP-1 cell line. Cytokine [tumor necrosis factor- $\alpha$ , and interleukin (IL)-1b, IL-6 and IL-10] and metalloproteinase (MMP-2 and MMP-9) release as well as their inhibitors (TIMP-1 and TIMP-2) were assessed after incubation with different amounts of nanoparticles. Cytokine secretion was not detected even in the presence of high amounts of nanoparticles. On the contrary, the secretion of MMP-9 in cell supernatants increased significantly after 24 and 48 h in comparison to non-treated cells. MMP-2 secretion was augmented only after 48 h for the highest con-

**Tab. 4.1.** N-Chitosan derivatives and their proposed applications

<b>No.</b>	<b>Derivative</b>	<b>Potential applications</b>	<b>References</b>
1	cationic	protein carrier	42
2	pegylated	protein carrier and gene therapy	43–47
3	nicotinylated	separation technologies	48–50
4	phthaloylation	preparation of chitosan derivatives	51–54
5	acylation	separation technologies	55, 56
6	hydroxyalkylation	components for toiletries	57, 58
7	acylvinyl	metal adsorption	59
8	sugar-modified	drug carrier	60–63
9	sugar-modified	drug carrier	60, 64–65
10	salicylaldehyde	metal adsorption	66
11	phthalaldehyde	metal adsorption	67
12	alkylated	gene therapy	68–71
13	carboxymethylated	drug delivery/metal absorption	72–76
14	methylpyrrolidinone	biomedical applications	77, 78
15	trimethylated	gene therapy	79–85
16	thioglycolic acid	pharmaceutical	86
17	lactobionic acid	biomedical	87–89
18	<i>p</i> -azidebenzoic acid	biomedical	87–89
19	succinylated	drug delivery	90–92
20	hydroxylaminated	drug delivery	90
21	sialic acid	pharmaceutical	93, 94
22	cyclodextrin	drug delivery/cosmetics/analytical chemistry	95, 96
23	cyclodextrin	drug delivery/cosmetics/analytical chemistry	97, 98
24	cyclodextrin	drug delivery/cosmetics/analytical chemistry	99
25	acrylic	drug delivery	43
26	crown-ether bound	metal adsorption	100
27	deoxycholic acid	gene therapy	101–104
28	folic acid	gene therapy	105
29	<i>o</i> -quinones	medical applications	106
30	vinylsulfonate	antimicrobial	107

**Tab. 4.2.** O-Chitosan derivatives and their proposed applications

<b>No.</b>	<b>Derivative</b>	<b>Potential applications</b>	<b>References</b>
1	O-hydroxyethyl	protein carrier/gene therapy	108–110
2	acylation	metal absorption	111
3	acylation	metal absorption	112
4	acylation	electromagnetic shielding materials	113
5	amination	gene therapy	114
6	carboxymethylated	drug carrier/metal absorption	115–118
7	triphenylmethyl	drug carrier	119, 120
8	sulfated/acylated	anticoagulant/antiretroviral agents	121
9	mannoside	antimicrobial agents	122–124
10	acylated	enzyme immobilizers	57, 58

centrations of nanoparticles ( $10$  and  $20$  mg mL<sup>-1</sup> DNA content). The authors have concluded that exposure of THP-1 macrophages to chitosan–DNA nanoparticles did not induce the release of proinflammatory cytokines.

The chitosan–DNA interaction is driven mainly by the electrostatic interaction between the amino groups of chitosan and the charged phosphate groups of DNA [35]. In a slightly acid medium this interaction is fully favored since almost all amine groups will be charged. MacLaughlin et al. [128] have studied the interaction of oligomeric chitosans (8–102 kDa) with plasmids containing a cytomegalovirus (CMV) promoter and a chloramphenicol acetyltransferase. On the basis of transmission electron microscopy they have observed that chitosan of 8 kDa condensed plasmids into toroids and rod-shaped particles. Using the microcalorimetry technique, the interaction could be followed and the exothermic heat output was indicated to provide a significant contribution to the free energy of the interaction. The authors have also observed a small endothermic peak at the ratio of neutrality, which was attributed to an entropic contribution to the free energy. The sizes of the particles were estimated to be 66 nm by light scattering measurements. The sizes of the particles were also shown to be dependent on the chitosan molecular weight and plasmid concentration. Complexes of a 1:6 (+/–) charge ratio showed a decrease in size as the molecular weight of the chitosan decreased and an increase in size was observed by increasing the plasmid concentration [38]. Recently, Danielsen et al. [129], employing atomic force microscopy (AFM), have confirmed that polyplexes made from mixing plasmid DNA (pDNA) with chitosan from 10 to 200 kDa yielded a blend of toroids and rods (Fig. 4.4). The ratios between the fractions of toroids and rods were observed to decrease with increasing degree of acetylation (DA) of the chitosan, indicating that the charge density of chitosan, proportional

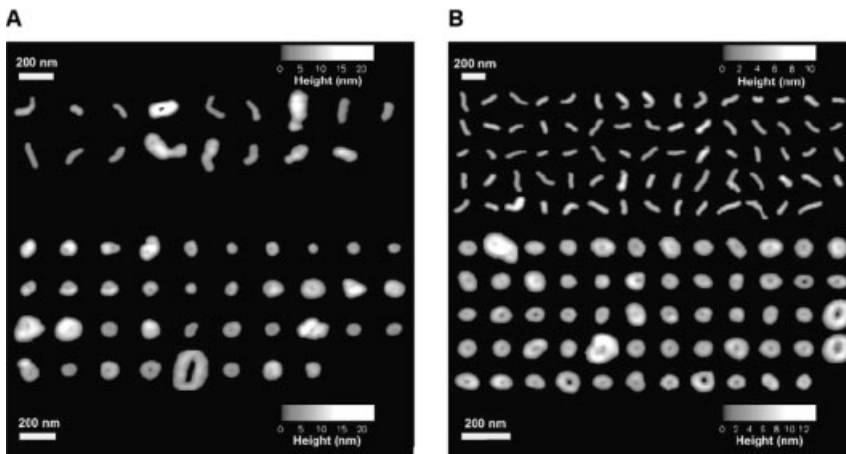


**Fig. 4.4.** Image galleries of toroidal and rod-like ensembles for complexes obtained using chitosan with various degrees of acetylation (DA). The chitosans ( $^*DA = 0.01$ ,  $M_n = 162$  kDa) (A) and ( $^*DA = 0.15$ ,  $M_n = 196$  kDa) (B)

were used to form complexes with pDNA pBR322. cDNA  $4$   $\mu$ g mL<sup>-1</sup> and average charge ratios was adjusted to 1. (Adapted from Ref. [129], with permission.)

to  $(1 - DA)$ , is important in determining the shape of the compacted DNA. The amount of chitosan required to fully compact DNA into well-defined toroidal and rod-like structures was found to be strongly dependent on the chitosan molecular weight, and thus its total charge. A higher charge ratio (+/–) was needed for the shorter chitosans, showing that an increased concentration of the low degree of polymerization (DP) chitosan could compensate for the reduced interaction strength of the individual ligands with DNA. Liu et al. [130] have showed that the charge density is an important parameter by studying the formation of polyplexes at different pH values. Working with 99% deacetylated 5-kDa chitosan their results indicated that upon interacting with chitosan, the DNA molecules retained a B conformation and the binding affinity of chitosan to DNA was dependent on the pH of media. At pH 5.5, highly charged chitosan had a strong binding affinity with DNA; in pH 12.0 medium, only weak interactions existed. However, the authors have reported that no typical toroidal patterns were observed, which was attributed to the strong compaction of DNA caused by highly charged chitosan.

In a recent report, Kiang et al. have showed that in fact the electrostatic interaction with the chitosan chain is very important to efficiently bind DNA. They reported that the charge (+/–) ratio to achieve complete DNA complexation increases for chitosans having smaller degrees of deacetylation, which in turn affects the stabilization of the particles, affecting the transfection *in vitro* and *in vivo* [131]. However, other interactions such as hydrogen bonding and hydrophobic interactions cannot be neglected since hydrophobic interactions have also been detected in aqueous solutions of the polyelectrolyte itself, leading to formation of polymer chain aggregates [132, 133]. Therefore, it is reasonable consider that the formation of polyplexes may result from a combined electrostatic/hydrophobic driving force leading to the packing of chitosan–DNA polyplexes.

Various parameters such as molecular weight, charge (+/–) ratio, pH and particle size have been shown to affect the transfection efficiency. Koping Hoggard et al. [134, 135] prepared monodisperse oligomers of chitosan that were fully deacetylated (6, 8, 10, 12, 14 and 24mers) with very low polydispersity and ultrapure chitosan (UPC) of 154 kDa. Depending on the chain length of chitosan, charge ratio and buffer properties, chitosan–DNA complexes appeared as different physical shapes such as coils, soluble globules, soluble aggregates, precipitated globules and precipitated aggregates. It was shown that only UPC and 24mer chitosans could form stable complexes with DNA, and the 24mer was more efficient in mediating gene expression *in vitro* and *in vivo* than was UPC. Sato et al. [136] have also found that molecular mass of chitosan, pH of medium and serum concentration are very important to promote transfection efficiency. Working on chitosan samples whose average molecular weights were 15, 52 and 100 kDa, they found that transfection efficiency mediated by chitosan of 100 kDa was less than that by chitosan of 15 and 52 kDa, but clearly indicating that a dependence on cell lines was also observed. However, Bozkir et al. [137] have suggested that formulations with high-molecular-weight (HMW) chitosan can be an effective nonviral gene vector in animal studies. The authors have studied the influence of two different prep-

aration methods, i.e. solvent evaporation and complex coacervation method, on the encapsulation of a model plasmid with chitosan. Protection of encapsulated pDNA from nuclease attack offered by these nanoparticles was confirmed by assessing degradation in the presence of DNase I and the transformation of the plasmids with incubated nanoparticles was examined by the  $\beta$ -galactosidase assay. The results obtained showed that pDNA existed as a mixture of both supercoiled (84.2%) and open circular (15.8%) forms, and that the formulation prepared by the complex coacervation method effectively protected the supercoiled form of pDNA. There were no significant changes in nanoparticle size and  $\zeta$  potential values at pH 5.5 for a period of 3 months, but differences in particle sizes were observed after lyophilization with a cryoprotective agent. The efficiency of nanoparticle-mediated transformation to *Escherichia coli* cells was significantly higher than naked DNA or poly-L-lysine (PLL)–DNA polycation complexes. The transfection studies were performed in COS-7 cells. A 3-fold increase in gene expression was produced by nanoparticles as compared to the same amount of naked pDNA.

The charge (+/–) ratio of the polyplexes has also been indicated as important to effectively proceed with the transfection process. Assuming that DNA wrapped in inter-polyelectrolyte complexes is well protected from DNase degradation, the following step is then to reach its target, i.e. the cell. Although the mechanism of internalization contact and crossing of the cell membrane is not fully understood, it is well accepted that the polyelectrolyte complex chitosan–DNA, exhibiting a net positive charge, binds to the negatively charged cell membrane [138]. Therefore, a net positive charge is fundamental in the process and the level of transfection is shown to increase with the charge (+/–) ratio, reaching a maximum and decreasing at higher stoichiometries. It has been reported by Ishi et al. that the level of transfection with plasmid–chitosan complexes was found to be highest when the charge (+/–) ratio was between 3 and 5, and transfection medium contained 10% serum at pH 7.0 [139]. Lee et al. using low-molecular weight (LMW) chitosan found the most efficient transfection was obtained at a charge (+/–) ratio 3:1 [140], while MacLaughlin et al. have reported that the highest level of expression was obtained at a ratio of 2:1 complex made with chitosan 102 kDa [128]. However, it must be considered that the transfection efficiency of chitosan–DNA nanoparticles is also cell-type dependent and the chitosan:plasmid ratio must be controlled to obtain the appropriate particle size when aiming to maximize the transfection [141]. The particle size is recognized as a key parameter since it may affect blood circulation time and cellular uptake. It has been reported that polycation–DNA gene delivery systems mostly enter the cell by endocytosis or pinocytosis, having a size requirement of less than 100 nm [141, 142]. However, the experimental results available are contradictory and reasonable transfection efficiencies were reported for particles having sizes varying from 100 nm [143] to 2.0  $\mu$ m [144]. Recently, on the basis of AFM images, Liu et al. have proposed that chitosan–DNA complexes in the range of several hundreds of nanometers are transferred into the cell mainly via endocytosis [145].

After internalization, the following crucial step in gene delivery with cationic

polymers is the escape of the polymer–DNA complexes from the endosome. The inefficient release of the DNA–polymer complex from endocytic vesicles into the cytoplasm is indicated as one of the primary causes of poor gene deliver. In this respect the approach is to enhance endosomal escape by using cationic polymers with a  $pK_a$  slightly below the physiological pH. The endosomal escape is believed take place through the mechanism named the “proton sponge”, and the importance of this step has been recognized and reviewed recently by Cho et al. [146]. This hypothesis has been proposed to explain the high transfection activity of polyethyleneimine (PEI) [147]. It has been demonstrated that PEI has a buffering capacity over a broad pH range; hence, once PEI-based polyplexes are present in the endosome, they can absorb protons that are pumped into this organelle. Due to repulsion between the protonated amine groups, swelling of the polymer occurs. Moreover, to prevent the build up of a charge gradient due to the influx of protons, an influx of  $Cl^-$  ions also occurs. The influx of both protons and  $Cl^-$  ions increases the osmolarity of the endosome and causes water absorption. The combination of swelling of the polymer and osmotic swelling of the endosome leads to a destabilization of the endosome and release of its contents into the cytoplasm [147]. Subsequently, transport to and uptake in the nucleus as well as dissociation of the polyplex has to occur before transcription of the DNA takes place. However, Funhoff et al., working with a series of synthetic polymers [148], indicated that endosomal escape is not always enhanced by polymer buffering at low pH. In this respect, research focusing on chitosan is scarce, but it is believed that protonation of the free amine groups of chitosan must contribute to the unpacking of the DNA, delivering it in the cytoplasm. Ishi et al. [139] have indicated that when the transfection is performed at pH 6.5 chitosan cannot release from the endosome due to the fact that chitosan is drastically protonated when the pH of medium is altered from pH 7 to 6. Recently, to enhance the transfection efficiency of chitosan, water-soluble chitosan (WSC) was coupled with urocanic acid (UA) and the transfection efficiency was investigated [149]. The authors reported that the transfection efficiency of chitosan into 293T cells was greatly enhanced after coupling with UA and increased with an increase of UA content in the urocanic acid-modified chitosan. Kiang et al. [150] have used poly(propyl acrylic acid) (PPAA) as an approach to enhance the release of endocytosed drugs into the cytoplasmic compartment of the cell. The release of pDNA from the endosomal compartment was enhanced by incorporating this polymer in chitosan nanoparticles. *In vitro* transfection studies confirmed that the incorporation of PPAA into the chitosan–DNA nanoparticles enhanced gene expression in both HEK 293 and HeLa cells compared to chitosan nanoparticles alone. The dose and time at which PPAA was incorporated during the complex formation affected the release of DNA and transfection efficiency. The authors have suggested that the PPAA triggered membrane disruption resulting in the release of DNA from the endosomal compartment.

Therefore neither high cellular uptake, membrane destabilizing activity, endosomal escape nor nuclear localization alone is adequate for high transfection. More studies aiming at a better understanding of these steps as well how the released DNA is expressed will be necessary to improve the transfection efficacy.

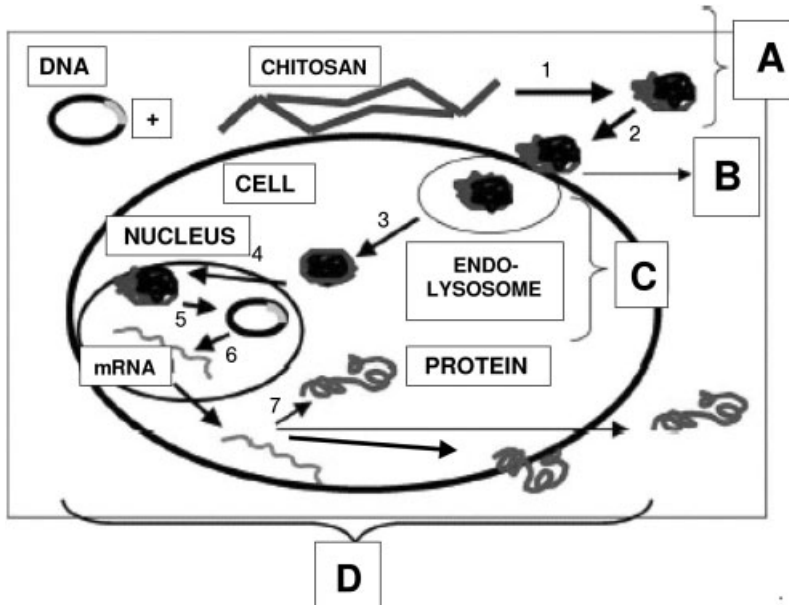


**Fig. 4.5.** Schematic gene therapy mechanism. (A) Bioavailability and extracellular trafficking, and gene-vector complexation (1); (B) internalization and endocytosis by the cell membrane (2); (C) intracellular trafficking and uptake of the vector complex into intracellular endolysosome: (3) DNA–chitosan release from the endosome into the cytoplasm and (4) internalization of the complex into the nucleus; (D) gene expression: (5) DNA dissociation from the vector, (6) mRNA transcription from the gene and (7) protein translation from mRNA. The protein can be secreted out of the cell, released into the cytoplasm or fixed onto the membrane. (Adapted from Ref. [251].)

### 4.3

#### Modified Chitosans: Strategies to Improve the Transfection Efficacy

##### 4.3.1

##### The Effects of Charge Density/Solubility and Degree of Acetylation

Many strategies have been employed to improve the transfection efficiency taking into account the biological steps involved in gene delivery (Fig. 4.5). The literature on this subject shows that the main method is the modification of chitosan structure aiming at providing the necessary capabilities to overcome the barriers previously mentioned, i.e. decreasing the interaction with blood components, vascular endothelial cells and uptake by the reticuloendothelial system (RES), avoiding the degradation of therapeutic DNA by serum nucleases, improving the particle size, internalization, endosomal escape and nuclear import. The attachment of a group or a polymer chain may be either at the main-chain or at the preformed nanoparticles.

The simplest modification in the chitosan structure is to vary the degree of acetylation. This is expected to affect the chitosan–DNA interactions since the charge density is decreased, i.e. the number amino groups is decreased, giving the polymer chain an increased hydrophobic character. Kiang et al. have recently studied the effect of the degree of chitosan deacetylation on the efficiency of gene transfection [131]. They concluded that a decreased degree of deacetylation resulted in a decrease in overall luciferase expression levels in HEK 293, HeLa and SW756 cells due to particle destabilization in the presence of serum proteins. The degree of deacetylation was shown to affect DNA binding, release and gene transfection efficiency *in vitro* and *in vivo*. Various workers aiming to increase the transfection have also investigated trimethylation (quaternization) of the amino groups [81, 84, 151, 152]. The advantage of trimethylated chitosans arises from their higher solubility when compared with the nonmodified polymer. Trimethyl chitosan (TMO) derivatives of 40% (TMO-40) and 50% (TMO-50) degrees of quaternization were synthesized, and examined for their transfection efficiencies in two cell lines: COS-1 and Caco-2 [81, 84]. Results showed that quaternized chitosan oligomers were able to condense DNA and form complexes with a size ranging from 200 to 500 nm. Chitoplexes were shown to transfect COS-1 cells to a lesser extent than DOTAP (*N*-[1-(2,3-dioleoyloxy)propyl]-*N,N,N*-trimethylammonium sulfate)–DNA lipoplexes. Both DOTAP–DNA lipoplexes and chitoplexes resulted in lower transfection efficiency in Caco-2 cell cultures than in COS-1 cells; however, quaternized chitosan oligomers proved to be superior to DOTAP.

#### 4.3.2

##### **Improving the Physicochemical Characteristics of the Nanoparticulate Systems: Solubility, Aggregation and RES Uptake**

After administration, the DNA must be capable of surviving in the bloodstream for a significant length of time so that it can reach the target tissue. Therefore, circulation time is a fundamental factor for reaching the target cells in successful gene delivery, especially in cases of intravenous injection [153]. Nanoparticles will usually be taken up by the liver, spleen and other parts of the RES depending on their surface characteristics. Particles with more hydrophobic surfaces will preferentially be taken up by the liver, followed by the spleen and lungs [154]. Cationic polymer–DNA complexes also show short plasma circulation times with rapid hepatic uptake and accumulation or deposition in organs such as the skin and intestine. Aggregation of cationic particles, such as cationic polymer–DNA complexes, can occur following interaction with blood components. Albumin is known to bind to cationic particles. The binding of albumin may be enough to cause aggregation of particles in the bloodstream, by reducing their  $\zeta$  potential and, hence, reducing the charge repulsion between particles. Extensive aggregation could lead to physical deposition in the capillary bed. Therefore, it is necessary to prevent unwanted interactions between particles and the dynamic environment of the blood circulation by introducing hydrophilic surfaces to the cationic particles. In the absence of a hydrophilic surface, opsonization prepares the particles for uptake by fixed macro-



phages of the mononuclear phagocytic system (MPS). The MPS is a collection of phagocytic cells that are present in tissue of the RES and are collectively responsible for clearance of particles from the circulation. The activity of RES is not to clear charged particles. In practice, typically 80–90% of hydrophobic particles are opsonized and taken up by fixed macrophages of the liver and spleen, often within a few minutes of intravenous administration. Opsonization represents a major biological barrier to the delivery of DNA using condensed particles. Therefore, the modification of chitosan by introducing hydrophilic polymers may create a “cloud” of hydrophilic chains at the particle surface, which may avoid interactions with proteins and phagocytes, thus prolonging the circulation time in the bloodstream [154].

Many hydrophilic groups can be attached to the chitosan backbone or to preformed nanoparticles to improve solubility in water [43–47]. Sashiva et al. [43] have used the Michael reaction of chitosan in water containing acetic acid with various acryl reagents. The modification was controlled by varying the temperature, reaction time and amount of the acryl reagent, and has provided chitosan derivatives showing good biodegradation characteristics. Nanospheres synthesized by salt-induced complex coacervation of cDNA, and gelatin and chitosan were evaluated as gene delivery vehicles [155]. These nanospheres were subsequently modified by introducing PEG<sub>5000</sub> chains. The attachment of these groups avoided the aggregation of particles during lyophilization and storage for 1 month did not alter the properties of the nanospheres. Chitosan–DNA nanospheres were effective in transfecting HEK 293 cells, but not HeLa cells, and the transfection efficiency was not affected by PEG derivatization. Poly(vinyl pyrrolidone) was also grafted on galactosylated chitosan (GCPVP) and showed improved physicochemical properties over the unmodified chitosan [156]. The binding strength of GCPVP 10K–DNA was superior to that of GCPVP 50K–DNA, which was attributable to its higher flexibility due to the smaller size. However, DNase I protection of GCPVP 10K–DNA was inferior to that of GCPVP 50K–DNA. The DNA-binding properties mainly depended on the molecular weight of chitosan and composition of PVP.

#### 4.3.3

##### **Targeting Mediated by Cell Surface Receptors**

It is well known that some kinds of saccharides play important roles in biological recognition on cellular surfaces. Liver parenchymal cells exclusively express large numbers of asialoglycoprotein receptors that strongly bind with galactose [157, 158]. The asialoglycoprotein receptor (ASGP-R) is known to be present only on hepatocytes at a high density of 500 000 receptors per cell and retained on several human hepatoma cell lines [159, 160]. This characteristic may be explored in many ways to target the cells. In a recent study on the biodegradability it was demonstrated that chitosan modification with gluconic acid enhanced susceptibility to lysozyme [161]. D-Gluconic acid is a hydrophilic sugar derivative that may be covalently attached to the chitosan backbone, providing multifunctional properties. As a consequence, by simple modification with gluconic acid and acetic anhydride, it is possible to control the aqueous solubility. The ASGP-R system cannot only bind

galactose-containing ligands, but can also internalize them within membrane-bound vesicles or endosomes [162]. Once a ligand binds to the galactose receptor, the ligand–receptor complex is rapidly internalized and the receptor recycles back to the surface [163, 164], allowing high binding capacity and efficient uptake of galactosylated ligands by liver cells. Murata et al. have suggested that the utilization of a prequaternized and subsequently galactosylated chitosan could be used to transfect cells HepG2 cells [164]. Park et al. have used this specificity to synthesize galactosylated chitosan (GC) in an attempt to transfect HepG2 human hepatoblastoma cells and HeLa human cervix epithelial carcinoma cells [165–167]. The particle sizes for the DNA complexes using GC-13K and GC-18K show a tendency to decrease with increasing charge ratio of GC to DNA, and had minimum values around 240 and 100 nm, respectively, at the charge ratio of 5. The cytotoxicity study showed that GC prepared by water-soluble chitosan had no cytotoxic effects on cells. The results showed that the transfection efficiency into HepG2, which has ASGP-Rs, was higher than that into HeLa without ASGP-Rs. The attachment of PEG to GC (GPC) was also performed in other work by the same group with the aim to improve the stability in water and enhance the cell permeability [168]. In this case it was reported that GCP–DNA complexes were only transfected into HepG2 having ASGP-Rs, indicative of a specific interaction of ASGP-Rs on cells and galactose ligands on GCP. The transfection with GCP–DNA complexes was subsequently investigated by confocal laser scanning microscopy using primary hepatocytes and HepG2 human hepatocarcinoma cell line [169]. The more efficient transfection of the complex occurred in the human-derived HepG2 cells than in primary hepatocytes. Erbacher et al. [170] synthesized lactosylated-modified chitosan derivatives (having various degrees of substitution) and tested their transfection efficiencies in many cell lines. The *in vitro* transfection was found to be cell-type dependent. HeLa cells were efficiently transfected by this modified carrier even in the presence of 10% serum, but neither chitosan nor lactosylated chitosans have been able to transfect HepG2 and BNL CL2 cells. Gao et al. [171] have used highly purified LMW chitosan (LMWC) to attach lactobionic acid (LA) bearing a galactose group. A series of galactosylated LMWC (gal-LMWC) having different group contents was obtained. The transfection efficiency was evaluated in human hepatocellular carcinoma cells (HepG2), L-02, SMMC-7721 and human cervix adenocarcinoma (HeLa) cell lines *in vitro*. The transfection of the gal-LMWC–DNA complex showed a very selective transfection to hepatocytes and the efficiency was shown to increase with the improvement of the degree of galactosylation.

Transferrin is another interesting targeting ligand to attach to the chitosan backbone. Transferrin receptors are found on the surface of most proliferating cells, and, in elevated numbers, on erythroblasts and on many tumors where they have been linked to drug resistance [172]. Leong et al. have reported the conjugation of PEG to preformed nanoparticles of gelatin and chitosan using different procedures [141, 155]. Transferrin was bonded to nanospheres utilizing a sulfhydryl derivative obtained from the protein reaction with 2-iminothyalone, while PEG conjugation was performed utilizing PEG derivatives containing the succinimidyl attached to

the end of the backbone. For the chitosan carrier, the plain nanospheres were reported as effective as the pegylated chitosan-modified nanospheres. However, the conjugation of PEG to the surface of the nanospheres minimized any aggregation in solution [155]. In a subsequent work, Mao et al. attached transferrin to the nanospheres employing two different procedures – periodate oxidation and disulfide linkage [141]. The KNOB protein was also conjugated to the nanoparticles using a bis-succinimidyl PEG derivative. The conjugation of KNOB protein to chitosan–DNA nanoparticles was reported to increase the transfection efficiency 130-fold in HeLa cells and several fold in HEK 293 cells. Chitosan has also been investigated for its ability to form polymeric targeted vesicle drug carriers. Glycol chitosan modified by attachment of a strategic number of fatty acid pendant groups (11–16 mol%) assembles into unilamellar polymeric vesicles in the presence of cholesterol [173, 174]. These polymeric vesicles were found to be biocompatible and hemocompatible, and capable of entrapping water-soluble drugs aiming to target receptors overexpressed in some tumors. Recently, the *in vivo* biological evaluation of doxorubicin formulated in transferrin targeted polymeric vesicles made from palmitoylated glycol chitosan (GCP) was reported. The transferrin-conjugated vesicles showed a statistically significant uptake advantage when compared to the non-targeted vesicles [175].

Use of the folic acid receptor is another approach that can be used to target tumors since cancerous cells divide rapidly and need folic acid to DNA synthesis. This morphological phenomenon is best noted by upregulation of membrane folate binding protein expression for a subsequent increase in folate internalization. The conjugation of folic acid with PEI was done previously by Guo and Lee [176], and more recently by others authors [177, 178]. Guo et al. found that attaching folates to the distal termini of PEG-modified PEI greatly enhanced the transfection activity of the corresponding DNA complexes over polyplexes containing PEG-modified PEI. The enhancements were observed at all charge (+/–) ratios tested and could be blocked partially by coincubation with 200  $\mu\text{M}$  of free folic acid, which suggested the involvement of the folate receptor (FR) in gene transfer. Folate conjugation, therefore, presents a potential strategy for tumor-selective targeted gene delivery. Recently, Mansouri et al. [105] have reported the first conjugation with chitosan. The nanoparticles obtained for folic acid-modified chitosan (FA-CH) showed a very low toxicity and the coacervation process utilized to obtain the FA-CH–DNA did not affect the integrity of the utilized plasmid. These new nanoparticles are currently being tested in transfection studies.

#### 4.3.4

#### **Hydrophobic Modification: Protecting the DNA and Improving the Internalization Process**

Hydrophobic modification is expected to improve the interaction between the DNA and the chitosan since, apart from the electrostatic interactions, the hydrophobic interactions will be increased, which may provide better protection for DNA. *N*-dodecylated chitosan (CS-12) has been synthesized and assembled with DNA to

form a polyelectrolyte complex (PEC) [71]. Dissociation of CS-12–DNA complexes was investigated by the addition of LMW electrolytes and these small molecular salts dissociated the CS-12–DNA complex, inducing the release of DNA. The ability of  $Mg^{2+}$  to dissociate the CS-12–DNA complex was greater than compared to that of  $Na^+$  and  $K^+$ . The incorporation of CS-12 could enhance the thermal stability of DNA and AFM images showed a globule-like structure composed of 40–115 DNA molecules. Lee et al. synthesized deoxycholic acid-modified chitosan (DAMC) which contained 0.6–5.1 deoxycholic acid groups per 100 anhydroglucose units [102]. The mean diameter of DAMC in PBS solution was less than 180 nm with a unimodal size distribution [103, 104]. Complex formation between DAMC and pDNA was confirmed by electrophoresis on an agarose gel. In other work by the same authors the structure of DAMC was found to strongly depend on the molecular weight of chitosan ranging from 5 to 200 kDa [179]. The size of the chitosan aggregates was not precisely controlled by varying the degree of substitution, pH and ionic strength of the medium. Due to the chain rigidity of chitosan, the structure of self-aggregates was suggested to be a cylindrical bamboo-like structure when the molecular weight of chitosan was larger than 40 kDa, which might form a very poor spherical shape of a birdnest-like structure. Complex formation showed a strong dependency on the size and structure of chitosan self-aggregates, and significantly influenced the transfection efficiency of COS-1 cells (up to a factor of 10). Recently, Liu et al. proposed that hydrophobic modification increases internalization process, thus increasing the transfection efficiency [145]. A series of alkylated chitosans (ACSS) derivatives from alkyl bromides was synthesized employing a 99% deacetylated chitosan (CS). The CS and ACSSs were used as vectors for gene transfection, and the effects of hydrophobicity of the alkyl side-chain on the transfection activity were evaluated. It was reported that the complex formation between the ACSSs and DNA requires a relatively smaller amount of ACS compared to unmodified chitosan due to the hydrophobic interaction. The transfection was evaluated in C2C12 cell lines using pcDNA 3.1 plasmid encoding chloramphenicol acetyltransferase. The transfection level was reported to increase upon elongating the alkyl side-chain. The disadvantage of the hydrophobic modification is that the particles are more easily recognized by macrophages of the RES; hence, amphiphilic chitosan may in the future present more advantages than that exhibited by the hydrophobic modification alone [180–182].

#### 4.4

#### Methods of Preparation of Chitosan Nanoparticles

##### 4.4.1

##### Complex Coacervation

Numerous works using different methodologies have been published on the preparation of chitosan micro and nanoparticles; however, for gene therapy, complex coacervation has been the procedure most employed and most of the references

discussed in the previous sections of this chapter relate to this method. The process is a spontaneous phase separation that occurs when two oppositely charged polyelectrolytes are mixed in an aqueous solution. The electrostatic interaction between the two species of macromolecules results in the separation of a coacervate (polymer-rich phase) from the supernatant (polymer-poor phase). This phenomenon can be used to form microspheres and encapsulate a variety of compounds. The encapsulation process can be performed entirely in aqueous solution and at low temperatures, and has a good chance, therefore, of preserving the bioactivity of the encapsulant. In developing an injectable controlled release system, various authors have used the complex coacervation of chitosan and DNA as the main procedure to obtain nanoparticles. In general, chitosan is dissolved in acetic acid/sodium acetate buffer and vortexed rapidly with a pDNA solution at room temperature. Sato et al. [136] reported that complexes of luciferase plasmid (pGL3) with chitosan were prepared only by mixing 100  $\mu\text{L}$  of pGL3 solution ( $1 \text{ mg mL}^{-1}$ ) with a given amount of chitosan solution ( $2.95 \text{ mg mL}^{-1}$ ). The mixtures were gently stirred at room temperature for a couple of hours. Koping-Hoggard et al. [134] reported the preparation chitosan–pDNA complexes were formulated by adding chitosan and then pDNA stock solutions to the solvent (deionized MilliQ water,  $\text{pH } 6.2 \pm 0.1$  or 25 mM acetate buffer,  $\text{pH } 5.0$ ) under intense stirring on a vortex mixer. The sizes of the aggregates (200–3400 nm) were determined by photon correlation spectroscopy, and found to be dependent of the DNA type, chitosan molecular weight and pH. Nanoparticles having sizes ranging from 170 to 180 nm were obtained by Kiang et al. [131] by heating chitosan and DNA solutions separately to 50–55  $^{\circ}\text{C}$ , and then mixing equal volumes of both solutions under high vortexing for 30 s.

It has been reported that, depending of the molecular weight of chitosan, complexes of chitosan–DNA with mean sizes between 50 and 6000 nm can be obtained only by simple mixing followed by incubation [136, 139, 141]. In general, stable complexes are formed only when chitosan is added in molar excess relative to DNA, with  $\zeta$  potential values between 10 and 20 mV, depending upon the degree of excess. Recently, Danielsen et al. [129] reported that the shape of the nanoparticles can vary depending on the degree of acetylation, molecular weight and concentration of chitosan. The DNA stock solution was diluted in  $\text{NH}_4\text{Ac}$  (150 mM,  $\text{pH } 7.4$ ) and complexes were then prepared by adding the chitosan solution to the DNA solution. The average contour length  $\langle L_c \rangle$  of the toroidal and rod-like DNA–chitosan polyplexes was found to be about 130 nm, independent of the linear or toroidal geometry of the complex and the chitosan employed (30–200 kDa). The complex sizes were found less than 1/10 of the contour length of the uncomplexed plasmid (pBR322, 4363 bp; Boehringer Mannheim) of 1.5  $\mu\text{m}$ . Decreasing the charge density of the chitosan resulted in a decrease in the toroid-to-rod ratio, indicating that the strength of the intersegment interaction, mediated by the charge of the chitosan, is important in determining the shape of the DNA–chitosan complexes, with the toroid being the preferred structure for high intersegment attractions. The stability of these DNA–chitosan complexes was studied after exposure to heparin and hyaluronic acid (HA) using AFM and ethidium bromide (EtBr) fluo-

rescence assay. Studies of polyplex stability when challenged by HA showed that whereas HA was unable to dissociate the complexes, the degree of dissociation caused by heparin depended on both the chitosan chain length and the amount of chitosan used for complexation [183].

#### 4.4.2

### Crosslinking Methods

#### 4.4.2.1 Chemical Crosslinking

The crosslinking procedures can be classified as (a) chemical crosslinking and (b) ionic crosslinking. The first involves the formation of covalent bonding between the chitosan chains and the chemical agents. The use of crosslinked nanospheres of chitosan for gene therapy has not been frequently found in the literature because after formation, chitosan–DNA nanoparticles obtained from the coacervation process are reported to be stable. At physiological pH, most of the positive charges would be neutralized and the hydrophobic chitosan becomes insoluble. This unique property ensured that nanoparticles formed at low pH could remain physically stable at physiological pH without chemical crosslinking; however, this was not observed, for example, for gelatin–DNA nanoparticles, which required a crosslinking agent to remain stable [141]. The process involves the precipitation of the polymer followed by chemical crosslinking [184, 185]. Precipitation can be done by sodium sulfate followed by chemical crosslinking using glutaraldehyde, formaldehyde or even using a natural crosslinking agent such as genepin [186, 187]. Recently, glutaraldehyde was used to obtain chitosan microparticles encapsulating an IL-2 expression plasmid [188]. Chitosan microspheres containing recombinant (r) IL-2 were prepared by using the precipitation technique. The rIL-2 encapsulation efficiency in the microspheres was high (75–98%) and the size was reported to vary from 1.45 to 2.00  $\mu\text{m}$ . The authors noted that IL-2 was released from chitosan microspheres over a period of 3 months and remained biologically active, being completely recovered from the release medium. Akbuga et al. [189] have studied the effect of formulation variables (concentration and molecular weight of chitosan, plasmid amount, use of glutaraldehyde as a crosslinker) on microsphere properties. Plasmid-loaded chitosan microspheres were prepared by adding the pDNA to 50 mL of sodium sulfate solution (20% w/v) and this mixture was dropped into 50 mL of acidic solution of chitosan and stirred for 1 h at 500 rpm. The microspheres formed were washed with bidistilled water, separated by centrifugation, freeze-dried and then stored at 4 °C in a desiccator. A high level of IL-2 expression was reported with plasmid-loaded chitosan microspheres in MAT-LyLu, a rat prostate adenocarcinoma cell line, but the authors noted that addition of glutaraldehyde was not necessary for the formulation. Although no damage has been observed in the DNA structure after using glutaraldehyde as a co-crosslinker, it reduced pDNA release from microspheres.

#### 4.4.2.2 Ionic Crosslinking or Ionic Gelation

In ionic crosslinking methods a variety of negatively charged compounds, from small ions to HMW polymers, can be used to produce micro- and nanoparticles

[37]. Ionic crosslinking in aqueous solution occurs due to the electrostatic interaction between the charged amino groups of chitosan and a salt or polyanion. The reactions with negatively charged components, either ions or molecules, can lead to the formation of a network between polymeric chains through ionic bridges. In ionic crosslinking, the entities reacting with chitosan are ions or ionic molecules with a well-defined molecular weight. In contrast, in polyelectrolyte complexation, the entities reacting with chitosan are polymers with a broad molecular weight distribution. In addition to its simplicity [190, 191], the method can be considered a safer alternative, since it avoids chemical crosslinking, and the possible toxicity of reagents and other undesirable effects [192]. There are two salts that have been frequently used in the preparation of chitosan particles by the ionic crosslinking mechanism: sodium tripolyphosphate (PSTP) [193, 194] and sodium sulfate [195]. Li et al. [196] prepared nanoparticles with a size range of 40–200 nm by an ionic gelation procedure using tripolyphosphate, sodium citrate and sodium hydroxide. Chitosan particles formed on the basis of ionic gelation with PSTP were demonstrated to be much more stable than those obtained with sodium citrate and sodium hydroxide. The ability of particles to complex DNA was investigated using gel retardation. Results showed that these chitosan particles have potential as vectors for the transfer of DNA into mammalian cells. Cellular transfection by the chitosan-pGL3-control particles showed a sustained expression of the luciferase gene for about 10 days. Jiang et al. [197] have also prepared chitosan microparticles with tripolyphosphate. The microparticles were tested for nasal vaccination loaded with *Bordetella bronchiseptica* dermonecrototoxin (BBD), a major virulence factor of a causative agent of atrophic rhinitis. The average particle size of the BBD-loaded chitosan microparticles was 4.39  $\mu\text{m}$ . The results reported that released BBD from chitosan microparticles had immune-stimulating activity of the atrophic rhinitis vaccine *in vitro*. Numerous works have been published on ionic crosslinking (ionic gelation) [198–205]; however, these works mainly focused on the various pharmaceutical applications which have been recently reviewed by Kumar et al. [40], Agnoutri et al. [192] and Sinha et al. [37].

#### 4.4.2.3 Emulsion Crosslinking

This method utilizes an acetic acid solution of chitosan, which is added to an organic solvent containing an emulsifier to form a water-in-oil emulsion (w/o). The chitosan solution is added dropwise under different conditions of stirring and temperature. The degree of stirring (i.e. time and speed of stirring during emulsification) determines the size of the dispersed droplets. By varying any one or both of these parameters, the size of droplets can be changed to obtain the product (i.e. chitosan microspheres) in the desired size range. Liquid paraffin is frequently used as the oil phase and, after the formation, the particles are crosslinked using chemical agents as glutaraldehyde or formaldehyde [206]. The literature abounds with reports wherein chitosan microspheres have been prepared for drug delivery. Akbgua and Durmaz [207] prepared chitosan microspheres containing furosemide from a w/o emulsion system using liquid paraffin as the external phase and a solution of chitosan in acetic acid as the disperse phase. Discrete spherical furosemide microspheres having a diameter range of 350–690  $\mu\text{m}$  were produced. Micro-

sphere properties were affected by the preparation variables such as the type and concentration of chitosan, drug concentration, crosslinking process, viscosity of oil, and stirring rate during the preparation. An emulsification/solvent evaporation process was carried out under mild conditions for Genta et al. [208] to entrap the hydrophobic drug ketoprofen. Glutaraldehyde at different concentrations was used as the chemical crosslinking agent on microspheres constituted by different theoretical ketoprofen/chitosan ratios (1:2, 1:4 and 1:6 w/w). Chitosan microspheres were morphologically characterized for shape, surface characteristics and size distribution; chitosan/ketoprofen interactions inside microspheres were investigated by differential scanning calorimetry and powder X-ray diffraction. Recently, Kumbar et al. [209] have used the emulsion crosslinking method to prepare chitosan microspheres to encapsulate diclofenac sodium using three crosslinking agents: glutaraldehyde, sulfuric acid and heat treatment. Microspheres were spherical with smooth surfaces. The size of the microparticles ranged between 40 and 230  $\mu\text{m}$ . Among the three crosslinking agents used, glutaraldehyde crosslinked microspheres showed the slowest release rates, whereas a quick release of diclofenac sodium was observed by the heat crosslinked microspheres. The influence of different parameters as well as the incorporation of different drugs has been extensively studied [210–217], including chitosan-coated systems (hybrid systems) [218, 219]. In these systems emulsions, nanocapsules and nanoparticles are coated by introducing chitosan into the external aqueous phase in which the formation of the colloidal structures take place. The chitosan coating is a result of the ionic interaction with nanoemulsions and nanocapsules, and no crosslinking is needed. In a recent work, Lee et al. [220] used chitosan as a condensing agent to enhance the transfection efficiency of a cationic emulsion-mediated gene delivery vehicle in human hepatoma cells (HepG2). The authors reported that the size of the complexes was reduced after condensation of DNA by chitosan. The results suggested that the use of chitosan enhanced the *in vitro* transfection efficiency and extended the *in vivo* gene transfer.

#### 4.4.2.4 Spray Drying

Spray drying is a method based on drying atomized droplets in a stream of hot air. In this method, chitosan is first dissolved in aqueous acid solution containing a dissolved or dispersed drug, in which a suitable crosslinking agent is added. Particle size depends upon the size of nozzle, spray flow rate, atomization pressure, inlet air temperature and extent of crosslinking. He et al. [221] have prepared crosslinked and noncrosslinked chitosan microspheres. The authors reported that the particle size ranged from 2 to 10  $\mu\text{m}$ , and that the size and  $\zeta$  potential of the particles were influenced by the crosslinking level. The particles sizes as well as the  $\zeta$  potential were observed to increase with decreasing amounts of the crosslinking agents (glutaraldehyde and formaldehyde). Mi et al. [222] have reported the preparation of microspheres with small size and good sphericity. A histological study of the genipin-crosslinked chitosan microspheres injected intramuscularly into the skeletal muscle of a rat model showed a less inflammatory reaction than its glutaraldehyde-crosslinked counterparts. The authors have suggested that the genipin-crosslinked chitosan microspheres may be a suitable polymeric carrier for



long-acting injectable drug delivery. Chitosan microspheres with hydrocortisone and hydrocortisone–hydroxypropyl- $\beta$ -cyclodextrin inclusion complex were studied by Filipovi et al. [223]. Microspheres were studied with respect to particle size distribution, drug content and *in vitro* drug release. The results indicate that the hydrocortisone–hydroxypropyl- $\beta$ -cyclodextrin inclusion complex is more water soluble than hydrocortisone alone. The hydrocortisone release rates from chitosan microspheres were influenced by the drug/polymer ratio in the manner that an increase in the release rate was observed when the drug loading was decreased. The influence of acid type on the release behavior of sodium diclofenac microspheres was studied by Orienti et al. [224]. Among the salts used, glutamic and aspartic salts provided the best control of release. Huang et al. [225] prepared chitosan microspheres by a spray-drying method using type A gelatin and ethylene oxide–propylene oxide block copolymer as modifiers. The microspheres were investigated using scanning electron microscopy (SEM) and microelectrophoresis. The particle shape, size and surface morphology of microspheres were affected by the concentration of gelatin. Betamethasone disodium phosphate (BTM)-loaded microspheres demonstrated good drug stability (less than 1% hydrolysis product), high entrapped efficiency (95%) and a positive surface charge (37.5 mV). The *in vitro* drug release from the microspheres was related to gelatin content. Microspheres containing gelatin/chitosan 0.4–0.6 (w/w) had a prolonged release pattern for 12 h. These formulation factors were correlated to particulate characteristics for optimizing BTM microspheres in pulmonary delivery. Recently, various systems have shown potential application for nasal [226, 227], pulmonary [228] and DNA [229] delivery.

#### 4.4.2.5 Other Methods

Apart from those methods mentioned above, a number of other methods have been reported for the preparation of chitosan micro- and nanoparticles, such as the reverse micellar [231–233], emulsion droplet coalescence [234–238] and sieving [239] methods.

The reverse micellar method is similar to emulsion crosslinking in the sense that in both methods a w/o aggregate is formed; however, the reverse micelles are thermodynamically stable liquid mixtures of water, oil and surfactant. Macroscopically, they are homogeneous and isotropic, structured on a microscopic scale into aqueous and oil microdomains separated by surfactant-rich films. The main advantage of the reverse micellar method is a better control of particle sizes. In the phase diagram of a system in which reverse micelles exist, there is plenty of room to adjust the proportions of the organic solvent and water as well as the surfactant ratio. This allows the dimensions of the reverse micellar particles to be modulated by varying the degree of hydration (molar ratio of  $[\text{H}_2\text{O}]/[\text{surfactant}]$ ) of the system. When the surfactant is kept at a constant concentration, increasing the water content will increase the volume of the reverse micelles. Alternatively, if the water content constant is kept constant, then increasing the surfactant concentration will cause the volume of reverse micellar particles to become smaller. Finally, if both the water and the surfactant concentrations are increased in a constant ratio, the volume of reverse micelles will not change, but the number of vesicles will

increase. Aghnoutri et al. have described this process in the following steps – preparation of the reverse micellar system, adding chitosan and drug, adding cross-linking agent, stirring overnight, evaporation of solvent, and purification [36]. Banerjee et al. [231] reported a procedure to prepare ultrafine crosslinked chitosan nanoparticles in an AOT–*n*-hexane reverse micellar system. They observed that the particle size is influenced by the degree of crosslinking and was found to be 30 nm when 10% of the amino groups in the polymeric chain had been crosslinked, whereas it was 110 nm when all the amino groups were crosslinked. These particles were thoroughly characterized, and electron micrographs reveal that the particles were spherical in shape and that lower crosslinking of the particles leads to smaller aggregates, while highly dense aggregates were formed at 100% crosslinking. The biodistribution of the particles after intravenous injection in mice showed that these particles remain in the blood for a considerable amount of time, and distribute in the heart, liver, kidneys, bladder and vertebral column. Other than these organs, the particles were distributed in the bone marrow, opening the possibility of using these particles for bone imaging and targeting purposes [231]. Andersson and Lofroth [232] investigated a new microemulsion based on heparin–chitosan complex suitable for oral administration. The microemulsion is based on ingredients that are acceptable to humans. These microemulsions were studied with or without biologically active ingredients by dynamic light scattering, turbidity, diffusion nuclear magnetic resonance and conductivity. Appropriate mixing and modifications of these microemulsions lead to nanometer-sized heparin–chitosan complexes [232].

In the emulsion droplet coalescence method, two w/o emulsions are prepared – one containing chitosan and the drug, and other a stable aqueous emulsion of NaOH. The solutions are mixed under high-speed stirring, which leads particle collision, forming solid microparticles that are centrifuged and washed. Gadopentetic acid-loaded chitosan nanoparticles have been prepared by this method for gadolinium neutron capture therapy – a cancer therapy that utilizes  $\gamma$ -rays emitted during the reaction  $^{157}\text{Gd}(n, \gamma)^{158}\text{Gd}$  to kill tumor cells [234, 235]. The bioadhesive characteristics of chitosan and its capacity to recognize, to a certain extent, the tumor cells prompted research on the delivery of gadolinium with the aid of chitosan. Tokumitsu et al. [236] have reported that particles produced using 100% deacetylated chitosan had a mean particle size of 452 nm with 45% drug loading. Nanoparticles were obtained within the emulsion droplet. The size of the nanoparticle did not reflect the droplet size. Since gadopentetic acid is a bivalent anionic compound, it interacts electrostatically with the amino groups of chitosan, which would not have occurred if a crosslinking agent is used that blocks the free amino groups of chitosan. Thus, it was possible to achieve higher gadopentetic acid loading by using the emulsion droplet coalescence method compared to the simple emulsion crosslinking method.

Fully deacetylated chitosan was dissolved in 10% gadolinium diethylenetriamine-pentaacetic acid (GdDTPA) solution to obtain 2.5% chitosan concentration. Then, 1 mL of this solution was added to liquid paraffin (10 mL) with Arlacel 5% and stirred with a homogenizer to form a w/o emulsion. Separately, a similar emulsion

was prepared with NaOH and then the two emulsions were combined to solidify the chitosan droplets. Washing was done with toluene, ethanol and water. The mean particle diameter was around 400 nm and the gadolinium content was around 9%. The GdDTPA chelate was strongly retained by chitosan, so that gadolinium was not released to an isotonic phosphate buffer over 7 days. Actually, the gadolinium concentration in the tumor tissue was about 100 times higher compared to Magnevist controls at the time of the thermal neutron irradiation. Endocytic uptake of nanoparticles, strongly holding GdDTPA, was suggested by transmission electron microscopy studies that indicated that GdDTPA has a high affinity for the cells, contributing to the long retention of gadolinium in tumor tissue. The treatment led to suppression of tumor growth in the *in vivo* studies. In the controls, 14 days after irradiation, the increase of the tumor volume was 20–25%, while the tumor was suppressed in mice treated with the gadolinium preparation; also, the survival time was remarkably prolonged [237–240].

Agnihotri and Aminabhavi [241] have used a sieving method to obtain microparticles. The first step was the crosslinking of chitosan to obtain a nonsticky glassy hydrogel followed by passing through a sieve. A suitable quantity of chitosan was dissolved in 4% acetic acid solution to form a thick glassy hydrogel followed by passing through a sieve. A suitable quantity of chitosan was dissolved in 4% acetic acid solution to form a thick jelly mass that was crosslinked by adding glutaraldehyde. The nonsticky crosslinked mass was passed through a sieve with a suitable mesh size to obtain microparticles. The microparticles were washed with 0.1 N NaOH solution to remove the unreacted excess glutaraldehyde and dried overnight in an oven at around 40 °C. Clozapine was incorporated into chitosan before crosslinking with an entrapment efficiency up to 98.9%. Microparticles were irregular in shape, with average particle sizes in the range 543–698  $\mu\text{m}$ . The *in vitro* release was extended up to 12 h, while the *in vivo* studies indicated a slow release of clozapine.

#### 4.5

#### DNA Loading into Nano- and Microparticles of Chitosan

DNA loading into micro/nanoparticulates of chitosan is mainly done either during the preparation or by adsorption on the preformed particles. The process is very efficient since, as mentioned before, it is mainly driven by electrostatic interactions between the chitosan chain and the charged phosphate groups of DNA. However, the intrinsic characteristics of the carrier (chitosan and its derivatives) may affect the loading, such as the chitosan/DNA ratio and degree of acetylation, molecular weight, as well as experimental conditions like the pH and the presence of additives.

Leong et al. [44] have evaluated the encapsulation efficiency and loading level of DNA into nanospheres having a size range of 200–750 nm. The nanospheres were prepared by complex coacervation in the presence of sodium sulfate aqueous solution, using chitosan 390 kDa and two different pDNAs. The DNA loading level

was determined by the PicoGreen assay (Molecular Probes, Eugene, OR) after the nanospheres were digested with trypsin or chitosanase and lysozyme. The authors reported that over 95% of the DNA was captured by the phase separation, and also that the encapsulation efficiency and loading level were observed to increase with the molecular weight of the encapsulant.

In general, complete binding may be achieved by increasing the amount of chitosan in the formulation. Kiang et al. [131] have evaluated chitosans with various degrees of deacetylation for efficacy of nanoparticle formation, DNA binding efficiency, morphology, and *in vitro* and *in vivo* gene transfection efficiency. The nanoparticles obtained by complex coacervation had a particle size of approximately 150–200 nm. The authors reported that when comparing chitosans with similar degrees of deacetylation, HMW chitosan (390 kDa) with a degree of deacetylation of 90% binds DNA at a charge (+/–) ratio of approximately 3.3, medium-molecular-weight chitosan (209 kDa) with degree of deacetylation of 93% binds DNA at a charge (+/–) ratio of 4.0, while LMW chitosan (138 kDa) with a degree of deacetylation of 85% requires a charge (+/–) ratio of 5.0 to completely bind the DNA. Similarly, at constant molecular weight, when the degree of deacetylation is decreased, the DNA-binding capacity is decreased, i.e. more chitosan is required to completely bind the DNA. This result was observed by comparing gel electrophoresis assays. For HMW chitosan, the charge (+/–) ratio for complete DNA binding increased from 3.3 to 8.0 as the degree of deacetylation decreased from 90 to 62%.

Mao et al. [141] evaluated encapsulation efficiency and DNA loading level by measuring the difference between the total amount of DNA added in the nanoparticle preparation buffer and the amount of nontrapped DNA remaining in the aqueous suspension after the coacervation process. Under optimal conditions, almost all DNA (pRELuciferase, 11.9 kb) and chitosan were captured in the nanoparticles. Using the chitosan (390 kDa)–DNA system, nanoparticles were prepared in the presence of 25 mM Na<sub>2</sub>SO<sub>4</sub> at a charge (+/–) ratio of 3.3, and the encapsulation efficiencies were  $98.0 \pm 2.0$  and  $92.7 \pm 3.7\%$ , respectively, for DNA and chitosan. According to these results, the composition of the nanoparticles was calculated as  $35.6 \pm 0.9$  and  $64.4 \pm 0.9\%$  weight for DNA and chitosan, respectively. Recently, Bozkir and Saka [242] have formulated chitosan–pDNA nanoparticles using complex coacervation and solvent evaporation techniques. The important parameters for the encapsulation efficiency were investigated, including molecular weight and degree of deacetylation of chitosan. They found that the encapsulation efficiency of pDNA is directly proportional to the degree of deacetylation, but there is an inverse proportional relationship with the molecular weight of chitosan. The surface charge of the nanoparticles prepared by the complex coacervation method was slightly positive, with a  $\zeta$  potential of +9 to +18 mV; nevertheless, nanoparticles prepared by the solvent evaporation method had a  $\zeta$  potential around +30 mV. The pDNA–chitosan nanoparticles prepared by using highly deacetylated chitosan having 92.7, 98.0 and 90.4% encapsulation efficiency protected the encapsulated pDNA from nuclease degradation.

Recent studies on DNA-loaded microcapsules have also shown that higher amounts of DNA can be encapsulated into the chitosan particles. Akbuga et al.

[144] have studied pDNA-loaded chitosan microspheres for *in vitro* IL-2 expression. In order to study the effect of formulation variables (concentration and molecular weight of chitosan, plasmid amount, use of glutaraldehyde as a crosslinker, etc.) on microsphere properties, different microsphere formulations were prepared. For microsphere preparation, the pDNA was added to 50 mL of sodium sulfate solution (20% w/v) and this mixture was dropped into 50 mL of acidic solution of chitosan and stirred for 1 h at 500 rpm. Encapsulation efficiency was calculated by measuring the difference between the total amount of DNA added in the preparation medium and the amount of nontrapped DNA remaining in the aqueous supernatant suspension after the coacervation process. For this purpose, the supernatant was spectrophotometrically analyzed at 260 and 280 nm for DNA concentration. Microspheres prepared were about 1.45–2.00 mm in size and spherical in shape. The plasmid encapsulation efficiency of microspheres was about 85%. Plasmid encapsulation efficiency was affected by the initial plasmid amount – a higher encapsulation efficiency was obtained with a lower amount of plasmid. However, the authors reported that other factors (chitosan concentration, using LMW chitosan and the addition of glutaraldehyde) did not affect the encapsulation efficiency significantly.

Aral et al. [243] have prepared chitosan microspheres containing pDNA:PLL complexes. The pDNA:PLL complexes were added to a sodium sulfate solution (20% w/v) before dropping and this mixture was dropped into the chitosan solution (0.35% w/v in 1% Tween 80 and 2% acetic acid) and stirred for 1 h at 500 rpm. The encapsulation efficiency of chitosan microspheres was estimated by measuring the amount of drug in the supernatant after centrifugation. The encapsulation efficiency for pDNA:PLL complexes was about 90% (data not shown). The average sizes of chitosan microspheres were between 3.41 to 3.69  $\mu\text{m}$  and independent of the pDNA:PLL ratio. Chitosan microspheres were evaluated for sustained-release of human rIL-2 and the effects of different formulation factors, such as chitosan and protein concentrations, the volume of sodium sulfate solution, technique of addition of rIL-2, and presence of glutaraldehyde during the encapsulation process, on the microsphere characteristics were investigated [244]. Protein loading of chitosan microspheres was achieved by using two different methods – rIL-2 was added to the sodium sulfate solution during the preparation or it was adsorbed onto the surface of empty microspheres. Spherical microspheres having diameters ranging from 1.11 to 1.59  $\mu\text{m}$  were obtained. The microspheres had a narrow size distribution and the authors reported that higher amounts of rIL-2 could be encapsulated into the chitosan microspheres by both methods (more than 90%).

#### 4.6 DNA Release and Release Kinetics

DNA release from chitosan nanoparticles can be understood as a mechanism occurring through a combination of release from the surface and/or inner of the

nanoparticles and release due to polymer erosion. The definition “kinetics of *in vitro* release” is more commonly used to describe DNA release in a buffer solution, in which salts and/or enzymes are added to test the stability of the particles. Another important subject is the “kinetics of *in vitro* gene expression”, which is a terminology to denote the release process in the presence of targeting cells. Limiting our discussion primarily to kinetics of *in vitro* release from nano- and microparticles, various parameters may affect the release, such as molecular weight of chitosan, charge (+/–) ratio, plasmid size, extent of crosslinking, method of preparation and the presence of additives. Studies on the kinetics of pDNA release from chitosan nanoparticles are not frequently found in the literature, and only recently has more quantitative work been performed on chitosan microparticles. Dastan and Turan [245] have studied the *in vitro* release of DNA microparticles (2.0  $\mu\text{m}$ ) suspended in phosphate buffer at pH 7.4. The suspension was shaken in a water bath at 37 °C, and at defined time intervals the supernatant was collected by centrifugation and microparticles were resuspended in fresh buffer. pDNA (pSV-Gal 6820 bp, pEGFP-N1 4733 bp and pBluescript SK<sup>+</sup> 2961 bp) release into the supernatant was quantified by spectrophotometry. The authors reported that about 10–15% of total DNA loaded into the chitosan microparticles was initially released within the first hour followed by very slow release over 40–50 days. The results obtained showed that the release is dependent on both chitosan and pDNA concentration, as well as of pDNA molecular weight. It was shown that the DNA release rate from microparticles was higher for nanoparticles having a higher pDNA concentration and a lower chitosan concentration. The HMW plasmids were released slower than the smaller ones. Aral and Akubga [243, 246] have also studied the release of pDNA:PLL complexes (pUC18 2.69 kbp, that encoded galactosidase) from chitosan microspheres of about 3.5  $\mu\text{m}$ . Release profiles of the chitosan microspheres were determined by incubating 10 mg samples of microspheres in phosphate-buffered saline (PBS, pH 7.4, BP) at 37 °C. Release studies were continued up to 40 days. All samples were measured spectrophotometrically and fluorometrically using Hoechst 33258 dye that specifically binds to DNA. The release of pDNA:PLL complexes from the microspheres showed no initial burst release. On the first day, 2.1–4.8% of the pDNA:PLL complexes was released from the studied formulations. This was attributed to the high positive charge of chitosan which could hinder the release of surface localized pDNA. At day 40, from 42–70% of the initial drug was released from chitosan microspheres.

Chitosan microspheres containing human rIL-2 were prepared by using the precipitation technique. The average diameter of microspheres was between 1.11 and 1.59  $\mu\text{m}$  [244]. Protein release from chitosan microspheres was determined in PBS buffer in a water bath at  $37 \pm 0.5$  °C. In general, the rIL-2 release profiles were biphasic, characterized by an initial protein burst followed by slow release. Among the different formulation parameters, for some of them the concentration of chitosan as well as the amount of glutaraldehyde affected the release. However, as the protein concentration increased, *in vitro* release significantly decreased. Moreover, the volume of sodium sulfate solution used in the microsphere preparations affected the release pattern of protein from chitosan microspheres. rIL-2 was re-

leased rapidly from chitosan microspheres when a larger volume of sodium sulfate solution was used during the preparation. In other work, Ozbas-Turan et al. [246] have encapsulated two plasmids (pGL2 6046 bp and pMK3 7213 bp) in the same microsphere structure and investigated *in vivo* release and transfection characteristics of chitosan microspheres (1.15–1.28  $\mu\text{m}$ ). They reported that very little burst effect was seen in the release profiles of two plasmid-loaded microspheres and that pDNAs were continuously released from chitosan microspheres. The *in vitro* release of pDNAs from microspheres was dependent on the plasmid amount and chitosan concentration. As the amount of plasmids increased, release decreased significantly. The same results were obtained with microspheres containing different concentrations of chitosan. The authors concluded that there was no significant difference between the release patterns of single- and double-plasmid loaded microspheres. In more a recent paper [144], the same group studied pDNA-loaded chitosan microspheres (1.5–2.0  $\mu\text{m}$ ) for *in vitro* IL-2 expression. They reported that all release profiles of the microspheres were similar and showed a small burst release of about 10–20% in the first 24 h and then slow release at a constant rate. DNA release was reported to change significantly with the chitosan concentration. Microspheres prepared with the highest concentration of chitosan exhibited the lowest DNA release. Microspheres prepared with HMW chitosan exhibit slow DNA release. As the molecular weight of chitosan increased, the release of pDNA from microspheres decreased. The molecular weight of chitosan was previously shown to be important in DNA release as reported by Xu and Du studying the release of bovine serum albumin from chitosan nanoparticles (20–200 nm) [200]. Moreover, DNA release was affected by the amount of plasmid entrapped. An increase in DNA content of microspheres resulted in a decrease in plasmid release.

The studies on the release of chitosan nanoparticles found in the literature mainly focus on the release of proteins and other drugs rather than on pDNAs. The importance of studying the release from nanoparticles is due to the advantages of nanoparticles over microspheres; it has been observed that nanoparticles can enter the cell by endocytosis or pinocytosis, having a size requirement less than 100 nm [141, 142]. Also the number of nanoparticles that cross the epithelium is greater than the number of microspheres [247]. Bozkir and Saka [242] have recently studied the effect of chitosan molecular structure and type of formulation on the release characteristics of chitosan nanoparticles. They found that the release of pDNA from the formulation prepared by complex coacervation was completed in 24 h, whereas the formulation prepared by evaporation technique released pDNA in 96 h; however, these release profiles were not statistically significant compared with formulations with similar structure.

#### 4.7

#### Preclinical Evidence of Chitosan–DNA Complex Efficacy

We have previously demonstrated that chitosan–DNA complexes appear spherical with a mean size of less than 100 nm and a homogenous distribution of DNA

within the particle [249]. Our results are in agreement with previous studies [248]. The size of the complexes is of crucial importance to cellular uptake. Illum et al. have synthesized chitosan–DNA nanoparticles ranging from 20 to 500 nm and thus our complexes are smaller than other polymeric systems [248]. The smaller size complexes have the advantage of entering the cells through endocytosis and/or pinocytosis, and therefore increasing the transfection rate. The transfection efficacy seen *in vitro* is cell-type dependent and cell viability studies following incubation with nanoparticles confirmed the lack of toxicity of chitosan compared to cationic lipids such as lipofectamine [84, 136, 249].

In addition to condensing the pDNA, an efficient gene delivery system is required to transport the gene into the cell and see to its eventual release, leading to gene expression and subsequent protein synthesis (Fig. 4.5). It is thus necessary to test a gene carrier on different cells lines, especially cells that resemble those that will be targeted. We have incubated chitosan–DNA polyplexes with MG63 cells, which have characteristics resembling those of osteoblasts, and with mesenchymal stem cells (MSCs), which are implicated in the formation of tissues such as cartilage, bone, tendons and muscle [250]. Nanoparticles composed of chitosan of molecular weight 400 kDa and a DNA quantity equivalent to 10 mg resulted in a transfection that was statistically significant compared to cells received solely DNA. MG63 cells did not demonstrate the same level of transfection. This can be explained by a delayed internalization of the nanoparticles when compared to HEK 293 cells. In fact, fluorescent microscopy observations undertaken by our group on nanoparticles incubated with human osteoblasts indicate that the particles remain bound to the surface for as long as 1 week following incubation (Fernandes et al., personal observations). However, MSCs did demonstrate gene expression when transfected with chitosan–DNA nanoparticles. This was clearly seen by a number of cells turning blue following X-gal staining; however, their transfection efficacy is not statistically significant when compared to cells receiving solely naked DNA [249].

One major pitfall of *in vitro* studies is their lack of reproducibility *in vivo*. We addressed this question recently by injecting either 0.15 M NaCl (control) or 1 mg of naked or complexed VR1012 plasmid coding for the  $\beta$ -Gal gene (Vical, Anaheim, CA) with chitosan or lipofectamine in the anterior tibialis muscle of 6-week-old male BALB/c mice. One major finding of this pilot study was that chitosan–DNA nanoparticles administered in the anterior tibialis mice muscle revealed a high signal corresponding to  $\beta$ -Gal gene expression within 48 h [251]. In contrast, the administration of naked or DNA–lipofectamine in the anterior tibialis muscle did not reveal any  $\beta$ -Gal gene expression. From these preliminary data, we proposed that chitosan–DNA nanoparticles have the potential ability to transfect muscle cells *in vivo* and lead to protein synthesis.

To improve transfection efficiency, several derivatives of chitosan have been prepared based on reactions with the free amino groups. Mao et al. demonstrated that transferrin and KNOB protein conjugation improved transfection efficiency in HEK 293 and HeLa cells [141]. Trimethylated chitosan is prepared with different degrees of quaternization to increase the solubility of chitosan at neutral pH [84];



deoxycholic group-conjugated chitosan has been synthesized to develop a colloidal carrier for DNA [102]; both quaternarized chitosan and deoxylated modified chitosan have been shown to transfect COS-1 cells effectively *in vitro*. A lactosylated chitosan has also been shown to be able to complex with DNA and effectively transfect HeLa cells [143]. It has been noticed that transfection efficiency also depend on the cell type used and the chitosan derivatives.

Folic acid was chosen by our group as a ligand for targeting cell membrane and allowing nanoparticles endocytosis via the FR for a higher transfection yield. Importantly, the high affinity of folate to bind its receptor (1 nM) [252] and the small size of folate allows its use for specific cell targeting. Moreover, the ability of folic acid to bind the FR that enables endocytosis is not altered by covalent conjugation of small molecules [253–255]. FR is overexpressed on many human cancer cell surfaces [252] and the nonepithelial isoform of FR (FR $\beta$ ) is expressed on activated synovial macrophages present in large numbers in arthritis joints [256]. Folic acid has been used by many researchers like a ligand with cationic liposome and other polymers to target cells expressing FR. For example, Guo et al. showed that folic acid enhanced PEI-mediated transfection activity in the presence of serum into cultured mammalian cells [257]; Reddy et al. showed that folate-mediated endocytosis can be exploited to target transgenes to cancer cells expressing FR and that folate-derivatized DOPE have a high transfection activity [258].

#### 4.8

#### Potential Clinical Applications of Chitosan–DNA in Gene Therapy

The chitosan–DNA system has been used in a novel gene transfer approach against respiratory syncytial virus infection, which at a single dose of about 1 mg/kg body weight is capable of decreasing viral titers by two orders of magnitude (100-fold) on primary infection. The immunologic mechanisms for the effectiveness of this prophylaxis include the induction of high levels of both serum IgG and mucosal IgA antibodies, the generation of an effective control response, and elevated lung-specific production of interferon (IFN)- $\gamma$  with antiviral action. Although effective as a single-dose, it is possible that dose-escalation and prime-booster strategies of the intranasal gene transfer (IGT) vaccine might further enhance its effectiveness. In addition, IGT significantly decreases pulmonary inflammation and does not alter airway hyperresponsiveness, thus making it safe for *in vivo* use [259].

Coxsackievirus B3 (CVB3) infections are common causes of acute and chronic myocarditis for which no effective prophylactic treatment is available. Xu et al. [260] have described a prophylactic strategy using chitosan–DNA intranasal immunization to induce CVB3-specific immune responses. Intranasal administration of a chitosan–DNA complex prepared by votexing DNA with chitosan resulted in transgenic DNA expression in mouse nasopharynx. Mice immunized with chitosan–DNA (pcDNA3-VP1) encoding VP1, major structural protein of CVB3, produced much higher levels of serum IgG and mucosal secretory IgA compared

to mice treated with pcDNA3-VP1 or pcDNA3. Increased virus-specific cytotoxic activity of spleen cells derived from chitosan–DNA-vaccinated mice was also determined. Chitosan–pcDNA3-VP1 intranasal immunization resulted in 42.9% protection of mice against lethal CVB3 challenge and a significant reduction of viral load after acute CVB3 infection. The authors indicated that intranasal delivery of the chitosan–DNA vaccine successfully induced mucosal SIgA secretion and might be a promising vaccine candidate to protect against CVB3 infection.

The zona pellucida (ZP), the extracellular matrix surrounding oocytes, has received considerable attention as a potential target for contraception because of its key role in many reproductive processes, e.g. gamete interaction during fertilization, induction of acrosome reaction. Sun et al. [261] have constructed a eukaryotic expression vector pVAX1-pZP3a as an oral ZP DNA contraceptive vaccine and successfully encapsulated in nanoparticles with chitosan. After 5 days of feeding to mice, the transcription and expression of pZP3a was found in mouse alvine chorion. The authors suggested that the chitosan–pVAX1-pZP3 pDNA nanoparticles can successfully transfect the alvine chorion cells in mice *in vivo*.

In order to investigate the potential of chitosan in the form of an inhaled powder as a gene delivery system, Okamoto et al. prepared powders using pCMV-Luc as a reporter gene and a LM chitosan (3000–30 000) as a cationic vector with supercritical CO<sub>2</sub>. The chitosan–DNA powders obtained were administered to the lungs of mice. The transfection efficiency of these powders was compared with that of DNA solutions and DNA powders without the cationic vector. The gene powder with the cationic polymer was found to be an excellent gene delivery system to the lungs, as evidenced by a high transfection rate and high expression of the luciferase protein. The benefits of the chitosan–DNA powders examined were summarized as follows: (a) the addition of chitosan suppressed the degradation of pCMV-Luc during the supercritical CO<sub>2</sub> process, (b) the addition of chitosan increased the yield of powders and (c) the chitosan–DNA powders increased the luciferase activity in the mouse lung compared with pCMV-Luc powders without chitosan or pCMV-Luc solutions with or without chitosan [262]. Bivas-Benita et al. [263] have proposed chitosan–DNA nanoparticles for pulmonary delivery of a DNA vaccine encoding HLA-A\*0201-restricted T cell epitopes of *Mycobacterium tuberculosis*. The authors used an HLA-A2 transgenic mouse model to investigate the effects of pulmonary delivery of a new pDNA encoding eight HLA-A\*0201-restricted T cell epitopes from *M. tuberculosis* formulated in chitosan nanoparticles. It was shown that the chitosan–DNA formulation was able to induce the maturation of dendritic cells, whereas chitosan solution alone could not, indicating the DNA was released from the particles and was able to stimulate dendritic cells. Pulmonary administration of the pDNA incorporated in chitosan nanoparticles was shown to induce increased levels of IFN- $\gamma$  secretion compared to pulmonary delivery of plasmids in solution or the more frequently used intramuscular immunization route. The authors indicated that pulmonary delivery of DNA vaccines against tuberculosis may provide an advantageous delivery route compared to intramuscular immunization and that increased immunogenicity can be achieved by delivery of this DNA encapsulated in chitosan nanoparticles.

## 4.9

**Conclusion**

Gene therapy offers a promising approach for the treatment of genetic disorders, vaccine development and tissue engineering. However, such opportunities will only be attainable by the development of safe and efficient gene delivery systems. Such systems must protect the DNA, and allow it to enter the targeted cell and reach the nucleus where genetic expression will take place. Several nonviral approaches have been developed and improved for use in different clinical settings. Substantial progress has also been made in improving plasmid expression vectors. It is now possible to achieve gene expression in a controllable manner using gene switch systems. A number of *in vitro* and *in vivo* studies, including ours, showed that chitosan is a suitable material for efficient nonviral gene therapy. Several groups are conducting studies using different strategies that can be linked to chitosan–DNA nanoparticles (including targeting cell membrane receptors) for a higher transfection yield.

Chitosan–DNA nanoparticles, due to their reduced cytotoxicity and ability to transport and release genes intracellularly, where expression of the encoded protein occurs, are considered as a potential candidate for a nonviral gene carrier. Further improvements in nonviral gene therapy will rely on a better understanding of the cellular and *in vivo* barriers to gene transfer.

**Acknowledgments**

This study was supported by a research grant from The Arthritis Society of Canada. J. C. F. holds a clinician scientist scholarship of the Fonds de la recherche en sante du Quebec. M. J. T. holds a post-PhD scholarship from the CAPES program from Brazil.

**References**

- 1 K. KURITA, Controlled functionalization of the polysaccharide chitin, *Prog. Polym. Sci.* **2001**, *26*, 1921–1971.
- 2 G. A. F. ROBERTS, *Chitin Chemistry*, Macmillan, Basingstoke, **1992**.
- 3 H. K. No, S. P. MEYERS, Crawfish chitosan as a coagulant in recovery of organic compounds from seafood processing streams, *J. Agric. Food Chem.* **1989**, *37*, 580–583.
- 4 K. KURITA, T. SANNAN, Y. IWAKURA, Studies on chitin, 4: evidence for formation of block and random copolymers of *N*-acetyl-D-glucosamine and D-glucosamine by hetero- and homogeneous hydrolyses. *Makromol. Chem.* **1977**, *178*, 3197–3202.
- 5 A. DOMARD, M. RINAUDO, Preparation and characterization of fully deacetylated chitosan, *Int. J. Biol. Macromol.* **1983**, *5*, 49–53.
- 6 A. TOLAIMATE, J. DESBRIERES, M. RHAZI, A. ALAGUI, M. VINCENDON, P. VOTTERO, On the influence of deacetylation process on the physicochemical characteristics of chitosan from squid chitin, *Polymer* **2000**, *41*, 2463–2469.

- 7 A. TOLAIMATE, J. DESBRIERES, M. RHAZIA, A. ALAGUI, Contribution to the preparation of chitins and chitosans with controlled physico-chemical properties, *Polymer* **2003**, *44*, 7939–7952.
- 8 K. Y. LEE, W. S. HA, W. H. PARK, Blood compatibility and biodegradability of partially *N*-acylated chitosan derivatives, *Biomaterials* **1995**, *16*, 1211–1216.
- 9 G. BERTHA, H. DAUTZENBERG, M. G. PETER, Physico-chemical characterization of chitosans varying in degree of acetylation, *Carbohydr. Polym.* **1998**, *36*, 205–216.
- 10 G. BERTH, H. DAUTZENBERG, The degree of acetylation of chitosans and its effect on the chain conformation in aqueous solution, *Carbohydr. Polym.* **2002**, *47*, 39–51.
- 11 C. SCHATZ, C. VITON, T. DELAIR, C. PICHOT, A. DOMARD, Typical physicochemical behaviors of chitosan in aqueous solution, *Biomacromolecules* **2003**, *4*, 641–648.
- 12 J. H. PA, T. L. YU, Light scattering study of chitosan in acetic acid aqueous solutions, *Macromol. Chem. Phys.* **2001**, *202*, 985–991.
- 13 R. SIGNINI, J. DESBRIERES, S. P. CAMPANA FILHO, On the stiffness of chitosan hydrochloride in acid-free aqueous solutions, *Carbohydr. Polym.* **2000**, *43*, 351–357.
- 14 T. H. HUNG, Y. M. CHANG, H. Y. SUNG, C. T. CHANG, Purification and characterization of hydrolase with chitinase and chitosanase activity from commercial stem bromelain, *J. Agric. Food Chem.* **2002**, *50*, 4666–4673.
- 15 T. KUROIWA, S. ICHIKAWA, S. SATO, S. MUKATAKA, Improvement of the yield of physiologically active oligosaccharides in continuous hydrolysis of chitosan using immobilized chitosanases, *Biotechn. Bioeng.* **2003**, *84*, 121–127.
- 16 A. B. V. KUMAR, M. C. VARADARAJ, R. G. LALITHA, R. N. THARANATHAN, Low molecular weight chitosans: preparation with the aid of papain and characterization, *Biochim. Biophys. Acta Gen. Sub.* **2004**, *1670*, 137–146.
- 17 H. LIN, H. Y. WANG, C. H. XUE, M. Y. Preparation of chitosan oligomers by immobilized papain, *Enz. Microb. Technol.* **2002**, *31*, 588–592.
- 18 R. A. A. MUZZARELLI, M. TERBOJEVICH, C. MUZZARELLI, O. FRANCESCANGELI, Chitosans depolymerized with the aid of papain and stabilized as glycosylamines, *Carbohydr. Polym.* **2002**, *50*, 69–78.
- 19 M. TERBOJEVICH, A. COSANI, R. A. A. MUZZARELLI, Molecular parameters of chitosans depolymerized with the aid of papain, *Carbohydr. Polym.* **1996**, *29*, 63–68.
- 20 A. B. V. KUMAR, R. N. THARANATHAN, A comparative study on depolymerization of chitosan by proteolytic enzymes, *Carbohydr. Polym.* **2004**, *58*, 275–283.
- 21 K. M. VARURN, M. M. MYHR, R. J. N. HJERDE, O. SMIDSRØD, *In vitro* degradation rates of partially *N*-acetylated chitosans in human serum, *Carbohydr. Res.* **1997**, *299*, 99–101.
- 22 S. MAO, X. SHUAI, F. UNGER, M. SIMONA, D. BI, T. KISSEL, The depolymerization of chitosan: effects on physicochemical and biological properties, *Int. J. Pharm.* **2004**, *281*, 45–54.
- 23 M.-Y. LEE, F. VAR, Y. SHIN-YA, T. KAJIUCHI, J.-W. YANG, Optimum conditions for the precipitation of chitosan oligomers with DP 5–7 in concentrated hydrochloric acid at low temperature, *Proc. Biochem.* **1999**, *34*, 493–500.
- 24 M. L. SINNOTT, Catalytic mechanism of enzymic glycosyl transfer, *Chem. Rev.* **1990**, *90*, 1171–1202.
- 25 V. L. Y. YIP, S. G. WITHERS, Nature's many mechanisms for the degradation of oligosaccharides, *Org. Biol. Chem.* **2004**, *2*, 2707–2713.
- 26 E. S. K. TANG, M. HUANG, L. Y. LIM, Ultrasonication of chitosan and chitosan nanoparticles, *Int. J. Pharm.* **2003**, *265*, 103–114.
- 27 M. L. TSAIH, R. H. CHEN, Effect of degree of deacetylation of chitosan on the kinetics of ultrasonic degradation of chitosan, *J. Appl. Polym. Sci.* **2003**, *90*, 3526–3531.

- 28 K. KURITA, S. ISHII, K. TOMITA, S. NISHIMURA, K. SHIMODA, Reactivity characteristics of squid-chitin as compared with those of shrimp chitin: High potentials of squid chitin as a starting material for facile chemical modifications, *J. Polym. Sci. A Polym. Chem.* **1994**, *32*, 1027–1032.
- 29 P. FRANCO, A. SENSO, L. OLIVEROS, C. MINGUILLON, Covalently bonded polysaccharide derivatives as chiral stationary phases in high-performance liquid chromatography, *J. Chromatogr. A* **2001**, *906*, 155–170.
- 30 E. GUIBAL, Interactions of metal ions with chitosan-based sorbents: a review, *Separ. Purific. Technol.* **2004**, *38*, 43–74.
- 31 A. J. VARMA, S. V. DESHPANDE, J. F. KENNEDY, Metal complexation by chitosan and its derivatives: a review, *Carbohydr. Polym.* **2004**, *55*, 77–93.
- 32 E. I. RABEA, M. E.-T. BADAWY, C. V. STEVENS, G. SMAGGHE, W. STEURBAUT, Chitosan as antimicrobial agent: applications and mode of action, *Biomacromolecules* **2003**, *4*, 1457–1465.
- 33 Y. KATO, H. ONISHI, Y. MACHIDA, N-succinyl-chitosan as a drug carrier: water-insoluble and water-soluble conjugates, *Biomaterials* **2004**, *25*, 907–915.
- 34 J. BERGER, M. REIST, J. M. MAYER, O. FELT, N. A. PEPPAS, R. GURNY, Structure and interactions in covalently and ionically crosslinked chitosan hydrogels for biomedical applications, *Eur. J. Pharm. Biopharm.* **2004**, *57*, 19–34.
- 35 J. BERGER, M. REIST, J. M. MAYER, O. FELT, R. GURNY, Structure and interactions in chitosan hydrogels formed by complexation or aggregation for biomedical applications, *Eur. J. Pharm. Biopharm.* **2004**, *57*, 35–52.
- 36 K. A. JANES, P. CALVO, M. J. ALONSO, Polysaccharide colloidal particles as delivery systems for macromolecules, *Adv. Drug Deliv. Rev.* **2001**, *47*, 83–97.
- 37 V. R. SINHA, A. K. SINGLA, S. WADHAWAN, R. KAUSHIK, R. KUMRIA, K. BANSAL, S. DHAWAN, Chitosan microspheres as a potential carrier for drugs, *Int. J. Pharm.* **2004**, *274*, 1–33.
- 38 W. G. LIU, K. DE YAO, Chitosan and its derivatives – a promising non-viral vector for gene transfection, *J. Controlled Rel.* **2002**, *83*, 1–11.
- 39 G. BORCHARD, Chitosans for gene delivery, *Adv. Drug Deliv. Rev.* **2001**, *52*, 145–150.
- 40 M. N. V. R. KUMAR, R. A. A. MUZZARELLI, C. MUZZARELLI, H. SASHIWA, A. J. DOMB, Chitosan chemistry and pharmaceutical perspectives, *Chem. Rev.* **2004**, *104*, 6017–6084.
- 41 M. N. V. R. KUMAR, A review of chitin and chitosan applications, *React. Func. Polym.* **2000**, *46*, 1–27.
- 42 Y. M. XU, Y. M. DU, R. H. HUANG, L. P. GAO, Preparation and modification of N-(2-hydroxyl) propyl-3-trimethyl ammonium chitosan chloride nanoparticle as a protein carrier, *Biomaterials* **2003**, *24*, 5015–5022.
- 43 H. SASHIWA, N. YAMAMORI, Y. ICHINOSE, J. SUNAMOTO, S.-i. AIBA, Michael reaction of chitosan with various acryl reagents in water, *Biomacromolecules* **2003**, *4*, 1250–1254.
- 44 K. W. LEONG, H.-Q. MAO, V. L. TRUONG-LE, K. ROY, S. M. WALSH, J. T. AUGUST, DNA–polycation nanospheres as non-viral gene delivery vehicles, *J. Controlled Rel.* **1998**, *53*, 183–193.
- 45 M. SUGIMOTO, M. MORIMOTO, H. SASHIWA, H. SAIMOTO, Y. SHIGEMASA, Preparation and characterization of water-soluble chitin and chitosan derivatives, *Carbohydr. Polym.* **1998**, *36*, 49–59.
- 46 T. MUSLIM, M. MORIMOTO, H. SAIMOTO, Y. OKAMOTO, S. MINAMI, Y. SHIGEMASA, Synthesis and bioactivities of poly(ethylene glycol)–chitosan hybrids, *Carbohydr. Polym.* **2001**, *46*, 323–330.
- 47 M. MORIMOTO, H. SAIMOTO, Y. SHIGEMASA, Control of functions of chitin and chitosan by chemical modification, *Trends Glycosci. Glycotecnol.* **2002**, *14*, 205–222.
- 48 K. KURITA, S. IWAWAKI, S. ISHI, S. NISHIMURA, Introduction of poly(L-alanine) side chains into chitin as

- versatile spacer arms having a terminal free amino group and immobilization of NADH active sites, *J. Polym. Sci. A Polym. Chem.* **1992**, *30*, 685–688.
- 49 Y. NISHIYAMA, T. YOSHIDA, T. MORI, S. ISHII, K. KURITA, Asymmetric reduction with chitosan/dihydrionicotinamide conjugates: influence of L-alanine spacer arms on reducing performance, *React. Funct. Polym.* **1998**, *37*, 83–91.
- 50 K. INUI, K. TSUKARNOTO, T. MIYATA, T. URAGAMI, Permeation and separation of a benzene/cyclohexane mixture through benzoylchitosan membranes, *J. Membrane Sci.* **1998**, *138*, 67–75.
- 51 S. NISHIMURA, O. KOHGO, K. KURITA, C. VITAVATVONG, H. KUSUHARA, Syntheses of novel chitosan derivatives soluble in organic-solvents by regioselective chemical modifications, *Chem. Lett.* **1990**, *2*, 243–246.
- 52 S. NISHIMURA, O. KOHGO, K. KURITA, H. KUZUHARA, Chemospecific manipulations of a rigid polysaccharide: syntheses of novel chitosan derivatives with excellent solubility in common organic solvents by regioselective chemical modifications, *Macromolecules* **1991**, *24*, 4745–4748.
- 53 K. KURITA, K. TOMITA, T. TADA, S. NISHIMURA, S. ISHII, Reactivity characteristics of a new form of chitosan – facile *n*-phthaloylation of chitosan prepared from squid beta-chitin for effective solubilization, *Polym. Bull.* **1993**, *30*, 429–433.
- 54 K. KURITA, H. IKEDA, Y. YOSHIDA, M. SHIMOJOH, M. HARATA, Chemospecific protection of the amino groups of chitosan by controlled phthaloylation: facile preparation of a precursor useful for chemical modifications, *Biomacromolecules* **2002**, *3*, 1–4.
- 55 T. SEO, Y. I. GAN, T. KANBARA, T. IJIMA, The selective sorption of D,L-amino acids by chemically modified chitosan gels and its application to liquid chromatography, *J. Appl. Polym. Sci.* **1989**, *38*, 997.
- 56 T. SEO, H. OHTAKE, T. KANBARA, K. YONETAKE, T. IJIMA, Preparation and permeability of chitosan membranes having hydrophobic groups, *Makromol. Chem.* **1991**, *192*, 2447.
- 57 H. YAMADA, T. IMOTO, A convenient synthesis of glycolchitin, a substrate of lysozyme, *Carbohydr. Res.* **1981**, *92*, 160–162.
- 58 G. LANG, G. MARESCH, S. BIRKEL, Hydroxyalkyl chitosans, In R. A. A. MUZZARELLI, M. G. PETER (Eds.), *Chitin Handbook*. Atec Edizioni, Grottammare, **1997**, p. 61.
- 59 M. GOMEZ-GUILLEN, A. GOMEZ-SANCHEZ, M.-E. MARTIN-ZAMORA, A derivative of chitosan and 2,4-pentanedione with strong chelating properties, *Carbohydr. Res.* **1992**, *233*, 255–259.
- 60 L. D. HALL, M. YALPANI, Formation of branched-chain, soluble polysaccharides from chitosan, *J. Chem. Soc. Chem. Commun.* **1980**, 1153–1154.
- 61 M. YALPANI, L. D. HALL, Some chemical and analytical aspects of polysaccharide modifications. III. Formation of branched-chain, soluble chitosan derivatives, *Macromolecules* **1984**, *17*, 272–281.
- 62 M. MORIMOTO, H. SAIMOTO, H. USUI, Y. OKAMOTO, S. MINAMI, Y. SHIGEMASA, Biological activities of carbohydrate-branched chitosan derivatives, *Biomacromolecules* **2001**, *2*, 1133–1136.
- 63 X. LI, Y. TSUSHIMA, M. MORIMOTO, H. SAIMOTO, Y. OKAMOTO, S. MINAMI, Y. SHIGEMASA, Biological activity of chitosan–sugar hybrids: specific interaction with lectin, *Polym. Adv. Technol.* **2000**, *11*, 176–179.
- 64 Y. KATO, H. ONISHI, Y. MACHIDA, Biological characteristics of lactosaminated N-succinyl-chitosan as a liver-specific drug carrier in mice, *J. Controlled Rel.* **2001**, *70*, 295–307.
- 65 K. R. HOLME, L. D. HALL, Chitosan derivatives bearing C10-alkyl glycoside branches: a temperature-induced gelling polysaccharide, *Macromolecules* **1991**, *24*, 3828–3833.
- 66 L. D. HALL, M. YALPANI, Enhancement of the metal-chelating properties of chitin and chitosan, *Carbohydr. Res.* **1980**, *83*, C5–C7.

- 67 R. A. A. MUZZARELLI, F. TANFANI, S. MARIOTTI, M. EMANUELLI, *N*-(*o*-carboxybenzyl) chitosans: Novel chelating polyampholytes, *Carbohydr. Polym.* **1982**, *2*, 145–157.
- 68 S. HIRANO, A facile method for the preparation of novel membranes from *n*-acyl- and *n*-arylidene-chitosan gels, *Agric. Biol. Chem.* **1978**, *42*, 1939–1940.
- 69 R. A. A. MUZZARELLI, F. TANFANI, M. ENAMUELLI, S. MARIOTTI, The characterization of *N*-methyl, *N*-ethyl, *N*-propyl, *N*-butyl and *N*-hexyl chitosans, novel film-forming polymers, *J. Membrane Sci.* **1983**, *16*, 295–308.
- 70 K. KURITA, M. ISHIGURO, T. KATAJIMA, Studies on chitin: 17. Introduction of long alkylidene groups and the influence on the properties, *Int. J. Biol. Macromol.* **1988**, *10*, 124–125.
- 71 W. G. LIU, K. D. KAO, Q. G. LIU, Formation of a DNA/*N*-dodecylated chitosan complex and salt-induced gene delivery, *J. Appl. Polym. Sci.* **2001**, *82*, 3391–3395.
- 72 M. THANOU, M.-T. NIHOT, M. JANSEN, J. C. VERHOEF, H. E. JUNINGER, Mono-*N*-carboxymethyl chitosan (MCC), a polyampholytic chitosan derivative, enhances the intestinal absorption of low molecular weight heparin across intestinal epithelia *in vitro* and *in vivo*, *J. Pharm. Sci.* **2001**, *90*, 38–46.
- 73 Z. JIA, D. SHEN, W. XU, Synthesis and antibacterial activities of quaternary ammonium salt of chitosan, *Carbohydr. Res.* **2001**, *333*, 1–6.
- 74 R. A. A. MUZZARELLI, F. TANFANI, M. EMANUELLI, S. MARIOTTI, *N*-(carboxymethylidene)chitosans and *N*-(carboxymethyl)chitosans: novel chelating polyampholytes obtained from chitosan glyoxylate, *Carbohydr. Res.* **1982**, *107*, 199–214.
- 75 F. DELBEN, R. LAPASIN, S. PRICL, Flow properties of *N*-(carboxymethyl) chitosan aqueous systems in the sol and gel domains, *Int. J. Biol. Macromol.* **1990**, *12*, 9–13.
- 76 R. A. A. MUZZARELLI, M. WECKX, O. FILIPPINI, F. SIGON, Removal of trace metal ions from industrial waters, nuclear effluents and drinking water, with the aid of cross-linked *N*-carboxymethyl chitosan, *Carbohydr. Polym.* **1989**, *11*, 293–306.
- 77 R. A. A. MUZZARELLI, P. ILARI, M. TOMASETTI, Preparation and characteristic properties of 5-methyl pyrrolidinone chitosan, *Carbohydr. Polym.* **1993**, *20*, 99–105.
- 78 R. A. A. MUZZARELLI, G. GIAGINI, M. BELLARDINI, L. SIMONELLI, C. CASTALDINI, G. GRATTO, Osteoconduction exerted by methylpyrrolidinone chitosan used in dental surgery, *Biomaterials* **1993**, *14*, 39–43.
- 79 E. CURTI, D. DEBRITTO, S. P. CAMPANA, Methylation of chitosan with iodomethane: effect of reaction conditions on chemoselectivity and degree of substitution, *Macromol. Biosci.* **2003**, *3*, 571–576.
- 80 J.-I. MURATA, Y. OHYA, T. OUCHI, Design of quaternary chitosan conjugate having antennary galactose residues as a gene delivery tool, *Carbohydr. Polym.* **1997**, *32*, 105–109.
- 81 M. M. THANOU, A. F. KOTZE, T. SCHARRINGHAUSEN, H. L. LUESEN, A. G. DE BOER, J. C. VERHOEF, H. E. JUNGER, Effect of degree of quaternization of *N*-trimethyl chitosan chloride for enhanced transport of hydrophilic compounds across intestinal Caco-2 cell monolayers, *J. Controlled Rel.* **2000**, *64*, 15–25.
- 82 A. B. SIEVAL, M. THANOU, A. F. KOTZE, J. C. VERHOEF, J. BRUSSEE, H. F. JUNGER, Preparation and NMR characterization of highly substituted *N*-trimethyl chitosan chloride, *Carbohydr. Polym.* **1998**, *36*, 157–165.
- 83 M. THANOU, J. C. VERHOEF, S. G. ROMEIJN, J. F. NAGELKERKE, F. W. H. M. MERKUS, H. E. JUNGER, Effects of *N*-trimethyl chitosan chloride, a novel absorption enhancer, on Caco-2 intestinal epithelia and the ciliary beat frequency of chicken embryo trachea, *Int. J. Pharm.* **1999**, *185*, 73–82.
- 84 M. THANOU, B. I. FLOREA, M. GELDOLF, H. E. JUNGER, G. BORCHARD,

- Quaternized chitosan oligomers as novel gene delivery vectors in epithelial cell lines, *Biomaterials* **2002**, *23*, 153–159.
- 85 I. M. LUBBEN, J. C. VERHOEF, G. BORCHARD, H. E. JUNGINGER, Chitosan and its derivatives in mucosal drug and vaccine delivery, *Eur. J. Pharm. Sci.* **2001**, *14*, 201–207.
- 86 C. E. KAST, A. BERNKOP-SCHNURCH, Thiolated polymers – thiomers: development and *in vitro* evaluation of chitosan–thioglycolic acid conjugates, *Biomaterials* **2001**, *22*, 2345–2352.
- 87 M. ISHIHARA, Photocrosslinkable chitosan hydrogel as a wound dressing and a biological adhesive, *Trends Glycosci. Glycotechnol.* **2002**, *14*, 331.
- 88 K. ONO, Y. SAITO, H. YURA, K. ISHIKAWA, A. KURITA, T. AKAIKE, M. ISHIHARA, Photocrosslinkable chitosan as a biological adhesive, *J. Biomed. Mater. Res.* **2000**, *49*, 289–295.
- 89 M. ISHIHARA, K. NAKANISHI, K. ONO, M. SATO, M. KIKUCHI, Y. SAITO, H. YURA, T. MATSUI, H. HATTORI, M. UENOYAMA, A. KURITA, Photocrosslinkable chitosan as a dressing for wound occlusion and accelerator in healing process, *Biomaterials* **2002**, *23*, 833–840.
- 90 K. AIEDEH, M. O. TAHA, Synthesis of iron-crosslinked chitosan succinate and iron-crosslinked hydroxamated chitosan succinate and their *in vitro* evaluation as potential matrix materials for oral theophylline sustained-release beads, *Eur. J. Pharm. Sci.* **2001**, *13*, 159–168.
- 91 Y. KATO, H. ONISHI, Y. MACHIDA, *N*-succinyl-chitosan as a drug carrier: water-insoluble and water-soluble conjugates, *Biomaterials* **2004**, *25*, 907–915.
- 92 Y. KATO, H. ONISHI, Y. MACHIDA, Evaluation of *N*-succinyl-chitosan as a systemic long-circulating polymer, *Biomaterials* **2000**, *21*, 1579–1585.
- 93 R. ROY, D. F. TROPPER, A. ROMANOWSKA, M. LETELLIER, L. COUSINEAU, S. J. MEUNIER, J. BORATYNSKI, Expedient syntheses of neoglycoproteins using phase-transfer catalysis and reductive amination as key reactions, *Glycoconjug. J.* **1991**, *8*, 75–81.
- 94 H. SASHIWA, Y. MAKIMURA, Y. SHIGEMASA, R. ROY, Chemical modification of chitosan: preparation of chitosan–sialic acid branched polysaccharide hybrids, *Chem. Commun.* **2000**, 909–910.
- 95 S. CHEN, Y. WANG, Study on  $\beta$ -cyclodextrin grafting with chitosan and slow release of its inclusion complex with radioactive iodine, *J. Appl. Polym. Sci.* **2001**, *82*, 2414–2421.
- 96 S. VETTER, S. KOCH, A. D. SCHLUTER, Synthesis and polymerization of functionalized dendritic macromonomers, *J. Polym. Sci. A Polym. Chem.* **2001**, *39*, 1940–1954.
- 97 E. FURUSAKI, Y. UENO, N. SAKAIRI, N. NISHI, S. TOKURA, Facile preparation and inclusion ability of a chitosan derivative bearing carboxymethyl- $\beta$ -cyclodextrin, *Carbohydr. Polym.* **1996**, *29*, 29–34.
- 98 T. TOJIMA, H. KATSURA, S. HAN, F. TANIDA, N. NISHI, S. TOKURA, N. SAKAIRI, Preparation of an  $\beta$ -cyclodextrin-linked chitosan derivative via reductive amination strategy, *J. Polym. Sci. A Polym. Chem.* **1998**, *36*, 1965–1968.
- 99 B. MARTLET, M. DEVASSIN, G. CRINI, M. WELTROWSKI, M. BOURDONNEAU, M. MORCELLET, Preparation and sorption properties of a  $\beta$ -cyclodextrin-linked chitosan derivative, *J. Polym. Sci. A Polym. Chem.* **2001**, *39*, 169–176.
- 100 X. H. TANG, S. Y. TAN, Y. T. WANG, Study of the synthesis of chitosan derivatives containing benzo-21-crown-7 and their adsorption properties for metal ions, *J. Appl. Polym. Sci.* **2002**, *83*, 1886–1891.
- 101 Y. H. KIM, S. H. GIHM, C. R. PARK, Structural characteristics of size-controlled self-aggregates of deoxycholic acid-modified chitosan and their application as a DNA delivery carrier, *Bioconjug. Chem.* **2001**, *12*, 932–938.
- 102 K. Y. LEE, I. C. KWON, Y.-H. KIM, W. H. JO, S. Y. JEONG, Preparation of chitosan self-aggregates as a gene



- delivery system, *J. Controlled Rel.* **1998**, *51*, 213–220.
- 103 K. Y. LEE, W. H. JO, I. C. KWON, Y.-H. KIM, S. Y. JEONG, Physicochemical characteristics of self-aggregates of hydrophobically modified chitosans, *Langmuir* **1998**, *14*, 2329–2332.
- 104 K. Y. LEE, W. H. JO, I. C. KWON, Y. H. KIM, S. Y. JEONG, Structural determination and interior polarity of self-aggregates prepared from deoxycholic acid-modified chitosan in water, *Macromolecules* **1998**, *31*, 378–383.
- 105 S. MANSOURI, Synthese et Caracterisation de nanoparticules folate–chitosan–ADN pour la therapie genique. *Memorie de Maitrise*, Universite de Montreal, **2004**.
- 106 G. KUMAR, P. J. SMITH, G. F. PAYNE, Enzymatic grafting of a natural product onto chitosan to confer water solubility under basic conditions, *Biotechnol. Bioeng.* **1999**, *63*, 154–165.
- 107 B. O. JUNG, C. H. KIM, K. S. CHOI, Y. M. LEE, J. J. KIM, Preparation of amphiphilic chitosan and their antimicrobial activities, *J. Appl. Polym. Sci.* **1999**, *72*, 1713–1719.
- 108 H. YAMADA, T. IMOTO, A convenient synthesis of glycolchitin, a substrate of lysozyme, *Carbohydr. Res.* **1981**, *92*, 160–162.
- 109 L. MARTIN, C. G. WILSON, F. KOOSHA, L. TETLEY, A. I. GRAY, S. SENEL, I. F. UCHEGBU, The release of model macromolecules may be controlled by the hydrophobicity of palmitoyl glycol chitosan hydrogels, *J. Controlled Rel.* **2002**, *80*, 87–100.
- 110 S. KWON, J. H. PARK, H. CHUNG, I. C. KWON, S. Y. JEONG, Physicochemical characteristics of self-assembled nanoparticles based on glycol chitosan bearing 5-cholanic acid, *Langmuir* **2003**, *19*, 10188–10193.
- 111 G. K. MOORE, G. A. F. ROBERTS, Reactions of chitosan: 4. Preparation of organosoluble derivatives of chitosan, *Int. J. Biol. Macromol.* **1982**, *4*, 246–249.
- 112 S. FUJII, H. KUMAGAI, M. NODA, Preparation of poly(acyl)chitosans, *Carbohydr. Res.* **1980**, *83*, 389–393.
- 113 H. SASHIWA, N. KAWASAKI, A. NAKAYAMA, E. MURAKI, N. YAMAMOTO, H. ZHU, H. NAGANO, Y. OMURA, H. SAIMOTO, Y. SHIGEMASA, S. ATBA, Chemical modification of chitosan. 13. Synthesis of organosoluble, palladium adsorbable, and biodegradable chitosan derivatives toward the chemical plating on plastics, *Biomacromolecules* **2002**, *3*, 1120–1125.
- 114 T. SATO, T. NAGASAKI, N. SAKAIRI, S. SHINKAI, 6-Amino-6-deoxychitosan. Preparation and application as plasmid vector in COS-1 cells, *Chem. Lett.* **2004**, *33*, 340–341.
- 115 R. TRUJILLO, Preparation of carboxymethylchitin, *Carbohydr. Res.* **1968**, *7*, 483–485.
- 116 Z. i. LI, X. P. ZHUANG, X. F. LIU, Y. L. GUAN, K. DE YAO, Study on antibacterial O-carboxymethylated chitosan/cellulose blend film from LiCl/N,N-dimethylacetamide solution, *Polymer* **2002**, *43*, 1541–1547.
- 117 M. RINAUDO, P. L. DUNG, C. GEY, M. MILAS, Substituent distributions on O,N-carboxymethylchitosans by <sup>1</sup>H and <sup>13</sup>C NMR, *Int. J. Biol. Macromol.* **1992**, *14*, 122–128.
- 118 Xi-G. CHEN, H.-J. PARK, Chemical characteristics of O-carboxymethyl chitosans related to the preparation conditions, *Carbohydr. Polym.* **2003**, *53*, 355–359.
- 119 Y. NISHIYAMA, T. YOSHIKAWA, K. KURITA, K. HOJO, H. KAMADA, Y. TSUTSUMI, T. MAYUMI, K. KAWASAKI, Regioselective conjugation of chitosan with a laminin-related peptide, Tyr-Ile-Gly-Ser-Arg, and evaluation of its inhibitory effect on experimental cancer metastasis, *Chem. Pharm. Bull.* **1999**, *47*, 451.
- 120 Y. NISHIYAMA, T. YOSHIKAWA, K. KURITA, K. HOJO, H. KAMADA, Y. TSUTSUMI, T. MAYUMI, K. KAWASAKI, A conjugate from a laminin-related peptide, Tyr-Ile-Gly-Ser-Arg, and chitosan: efficient and regioselective conjugation and significant inhibitory activity against experimental cancer metastasis, *J. Chem. Soc. Perkin Trans.* **2000**, 1161–1165.

- 121 S. NISHIMURA, Y. MIURA, L. REN, M. SATO, A. YAMAGISHI, N. NISHI, S. TOKURA, K. KURITA, S. ISHII, An efficient method for the syntheses of novel amphiphilic polysaccharides by regioselective and thermoselective modifications of chitosan, *Chem. Lett.* **1993**, 1623–1626.
- 122 K. KURITA, M. KOBAYASHI, T. MUNAKATA, S. ISHII, S. NISHIMURA, Synthesis of nonnatural branched polysaccharides – regioselective introduction of alpha-mannoside branches into chitin, *Chem. Lett.* **1994**, 2063–2066.
- 123 K. KURITA, K. SHIMADA, Y. NISHIYAMA, M. SHIMOJOH, S. NISHIMURA, Nonnatural branched polysaccharides: synthesis and properties of chitin and chitosan having  $\alpha$ -mannoside branches, *Macromolecules* **1998**, *31*, 4764–4769.
- 124 K. KURITA, T. KOJIMA, T. MUNAKATA, H. AKAO, T. MORI, Y. NISHYAMA, M. SHIMOJOH, Preparation of non-natural branched chitin and chitosan, *Chem. Lett.* **1998**, 317–318.
- 125 R. J. MUMPER, J. WANG, J. M. CLASPELL, A. P. ROLLAND, Novel polymeric condensing carriers for gene delivery, *Proc. Int. Symp. Controlled Rel. Bioact. Mater.* **1995**, *22*, 178–179.
- 126 S. C. W. RICHARDSON, H. V. J. KOLBE, R. DUNCAN, Potential of low molecular mass chitosan as a DNA delivery system: biocompatibility, body distribution and ability to complex and protect DNA, *Int. J. Pharm.* **1999**, *178*, 231–243.
- 127 F. CHELLAT, A. GRANDJEAN-LAQUERRIERE, R. LE NAOUR, J. FERNANDES, L'H. YAHIA, M. GUENOUNOU, D. LAURENT-MAQUIN, Metalloproteinase and cytokine production by THP-1 macrophages following exposure to chitosan–DNA nanoparticles, *Biomaterials* **2005**, *26*, 961–970.
- 128 F. R. MACLAUGHLIN, J. MUMPER, J. WANG, J. M. TAGLIAFERRI, I. GILL, M. HINCHCLIFFE, A. P. ROLLAND, Chitosan and depolymerized chitosan oligomers as condensing carriers for *in vivo* plasmid delivery, *J. Controlled Rel.* **1998**, *56*, 259–272.
- 129 S. DANIELSEN, K. M. VARUM, B. T. STOKKE, Structural analysis of chitosan mediated DNA condensation by AFM: influence of chitosan molecular parameters, *Biomacromolecules* **2004**, *5*, 928–936.
- 130 W. LIU, S. SUN, Z. CAO, X. ZHANG, K. YAO, W. W. LU, K. D. K. LUK, An investigation on the physicochemical properties of chitosan/DNA polyelectrolyte complexes, *Biomaterials* **2005**, *26*, 2705–2711.
- 131 T. KIANG, J. WEN, H. W. LIM, K. W. LEONG, The effect of the degree of chitosan deacetylation on the efficiency of gene transfection, *Biomaterials* **2004**, *25*, 5293–5301.
- 132 C. SCHATZ, C. PICHOT, T. DELAIR, C. VITON, A. DOMARD, Static light scattering studies on chitosan solutions: from macromolecular chains to colloidal dispersions, *Langmuir* **2003**, *19*, 9896–9903.
- 133 O. E. PHILIPPOVA, E. V. VOLKOV, N. L. SITNIKOVA, A. R. KHOKHLOV, Two types of hydrophobic aggregates in aqueous solutions of chitosan and its hydrophobic derivative, *Biomacromolecules* **2001**, *2*, 483–490.
- 134 M. KOPING HOGGARD, Y. S. MELNIKOVA, K. M. VARUM, B. LINDMAN, P. ARTURSSON, Relationship between the physical shape and the efficiency of oligomeric chitosan as a gene delivery system *in vitro* and *in vivo*, *J. Gene Med.* **2003**, *5*, 130–141.
- 135 M. KOPING-HOGGARD, K. M. VARUM, M. ISSA, S. DANIELSEN, B. E. CHRISTENSEN, B. T. STROKE, P. ARTUSSON, Improved chitosan-mediated gene delivery based on easily dissociated chitosan polyplexes of highly defined chitosan oligomers, *Gene Therapy* **2004**, *11*, 1441–1452.
- 136 T. SATO, T. ISHII, Y. OKAHATA, *In vitro* gene delivery mediated by chitosan. Effect of pH, serum, and molecular mass of chitosan on the transfection efficiency, *Biomaterials* **2001**, *22*, 2075–2080.
- 137 A. BOZKIR, O. M. SAKA, Chitosan–DNA nanoparticles: Effect on DNA

- integrity, bacterial transformation and transfection efficiency, *J. Drug Target.* **2004**, *12*, 281–288.
- 138 V. CHAN, H. Q. MAO, K. W. LEONG, Chitosan-induced perturbation of dipalmitoyl-*sn*-glycero-3-phosphocholine membrane bilayer, *Langmuir* **2001**, *17*, 3749–3756.
- 139 T. ISHII, Y. OKAHATA, T. SATO, Mechanism of cell transfection with plasmid/chitosan complexes, *Biochim. Biophys. Acta* **2001**, *1514*, 51–64.
- 140 M. LEE, J. W. NAH, Y. KWON, J. J. KOH, K. S. KO, S. W. KIM, Water-soluble and low molecular weight chitosan-based plasmid DNA delivery, *Pharm. Res.* **2001**, *18*, 427–431.
- 141 H.-Q. MAO, K. ROY, V. L. TROUNG-LE, K. A. JANES, K. Y. LIN, Y. W., J. T. AUGUST, K. W. LEONG, Chitosan–DNA nanoparticles as gene carriers: synthesis, characterization and transfection efficiency, *J. Controlled Rel.* **2001**, *70*, 399–421.
- 142 M. A. WOLFERT, L. W. SEYMOUR, Characterization of vectors for gene therapy formed by self-assembly of DNA with synthetic block copolymers, *Human Gene Ther.* **1996**, *3*, 269–73.
- 143 P. ERBACHER, S. ZOU, T. BETTINGER, A.-M. STEFFAN, J.-S. REMY, Chitosan-based vector/DNA complexes for gene delivery: biophysical characteristics and transfection ability, *Pharm. Res.* **1998**, *15*, 1332–1339.
- 144 J. AKBUGA, E. OZBAS-TURAN, N. ERDOGAN, Plasmid-DNA loaded chitosan microspheres for *in vitro* IL-2 expression, *Eur. J. Pharm. Biopharm.* **2004**, *58*, 501–507.
- 145 W. G. LIU, X. ZHANG, S. J. SUN, G. J. SUN, K. DE YAO, *N*-alkylated chitosan as a potential nonviral vector for gene transfection, *Bioconjug. Chem.* **2003**, *14*, 782–789.
- 146 Y. W. CHO, J. D. KIM, K. PARK, Polycation gene delivery systems: escape from endosomes to cytosol, *J. Pharm. Pharmacol.* **2003**, *55*, 721–734.
- 147 O. BOUSSIF, F. LEZOUALCH, M. A. ZANTA, M. D. MERGNY, D. SCHERMAN, B. DEMENEIX, J.-P. BEHR, A versatile vector for gene and oligonucleotide transfer into cells in culture and *in vivo*: polyethylenimine, *Proc. Natl Acad. Sci. USA* **1995**, *92*, 7297–7301.
- 148 A. M. FUNHOFF, C. F. VAN NOSTRUM, G. A. KONING, Endosomal escape of polymeric gene delivery complexes is not always enhanced by polymers buffering at low pH, *Biomacromolecules* **2004**, *5*, 32–39.
- 149 T. H. KIM, J. E. IHM, Y. J. CHOI, J. W. NAH, C. S. CHO, Efficient gene delivery by urocanic acid-modified chitosan, *J. Controlled Rel.* **2003**, *93*, 389–402.
- 150 T. KIANG, C. BRIGHT, C. Y. CHEUNG, P. S. STAYTON, A. S. HOFFMAN, K. W. LEONG, Formulation of chitosan–DNA nanoparticles with poly(propyl acrylic acid) enhances gene expression, *J. Biomater. Sci. Polym. Ed.* **2004**, *15*, 1405–1421.
- 151 M. THANOU, B. I. FLOREA, H. E. JUNGINGER, G. BORCHARD, Quaternized chitosan oligomers as gene delivery vectors *in vitro*, *J. Controlled Rel.* **2003**, *87*, 294–295.
- 152 C. A. JANSMA, M. THANOU, H. E. JUNGINGER, G. BORCHARD, Preparation and characterization of 6-O-carboxymethyl-*N*-trimethyl chitosan derivative as a potential carrier for targeted polymeric gene and drug delivery, *STP Pharm. Sci.* **2003**, *13*, 63–67.
- 153 I. K. PARK, T. H. KIM, S. I. KIM, T. AKAIKE, C. S. CHO, Chemical modification of chitosan for gene delivery, *J. Dispersion Sci. Technol.* **2003**, *24*, 489–498.
- 154 L. B. PEPPAS, J. O. BLANCHETT, Nanoparticle and targeted systems for cancer therapy, *Adv. Drug Deliv. Rev.* **2004**, *56*, 1649–1659.
- 155 K. W. LEONG, H.-Q. MAO, V. L. TROUNG-LE, K. ROY, S. M. WALSH, J. T. AUGUST, DNA-polycation nanospheres as non-viral gene delivery vehicles, *J. Controlled Rel.* **1998**, *53*, 183–193.
- 156 I. K. PARK, J. E. IHM, Y. H. PARK, Y. J. CHOI, S. I. KIM, W. J. KIM, T. AKAIKE, C. S. CHO, Galactosylated chitosan (GC)-graft-poly(vinyl pyrrolidone) (PVP) as hepatocyte-targeting DNA carrier Preparation and

- physicochemical characterization of GC-graft-PVP/DNA complex (1), *J. Controlled Rel.* **2003**, *86*, 349–359.
- 157 G. Y. WU, C. H. WU, Receptor-mediated delivery of foreign genes to hepatocytes, *Adv. Drug Deliv. Rev.* **1998**, *29*, 243–248.
- 158 G. ASHWELL, J. HARFORD, Carbohydrate-specific receptors of the liver, *Ann. Rev. Biochem.* **1982**, *51*, 531–554.
- 159 R. J. FALLON, A. L. SCHWARTZ, Asialoglycoprotein receptor phosphorylation and receptor-mediated endocytosis in hepatoma cells. Effect of phorbol esters, *J. Biol. Chem.* **1988**, *63*, 13159–13166.
- 160 B. B. KNOWLES, C. C. HOWE, D. P. ADEN, Human hepatocellular carcinoma cell lines secrete the major plasma proteins and hepatitis B surface antigen, *Science* **1980**, *209*, 497–499.
- 161 J. H. PARK, Y. W. CHO, H. CHUNG, I. C. KWON, S. Y. JEONG, Synthesis and characterization of sugar-bearing chitosan derivatives: aqueous solubility and biodegradability, *Biomacromolecules* **2003**, *4*, 1087–1091.
- 162 G. ASHWELL, A. MORELL, The role of surface carbohydrates in the hepatic recognition and transport of circulating glycoproteins, *Adv. Enzymol.* **1974**, *41*, 99–128.
- 163 A. CIECHANOVER, A. L. SCHWARTZ, H. F. LODISH, Sorting and recycling of cell surface receptors and endocytosed ligands: the asialoglycoprotein and transferrin receptors, *J. Cell Biochem.* **1983**, *23*, 107–130.
- 164 J.-I. MURATA, Y. OHYA, T. OUCHI, Possibility of application of quaternary chitosan having pendant galactose residues as gene delivery tool, *Carbohydr. Polym.* **1996**, *29*, 69–74.
- 165 Y. K. PARK, Y. H. PARK, B. A. SHIN, E. S. CHOI, Y. R. PARK, T. AKAIKE, C. S. CHO, Galactosylated chitosan-graft-dextran as hepatocyte-targeting DNA carrier, *J. Controlled Rel.* **2000**, *69*, 97–108.
- 166 I. K. PARK, Y. H. PARK, B. A. SHIN, E. S. CHOI, Y. R. KIM, T. AKAIKE, C. S. CHO, Galactosylated chitosan-graft-dextran as hepatocyte-targeting DNA carrier, *J. Controlled Rel.* **2001**, *75*, 433.
- 167 T. H. KIM, I. K. PARK, J. W. NAH, Y. J. CHOI, C. S. CHO, Galactosylated chitosan/DNA nanoparticles prepared using water-soluble chitosan as a gene carrier, *Biomaterials* **2004**, *25*, 3783–3792.
- 168 I. K. PARK, T. H. KIM, Y. H. PARK, B. A. SHIN, E. S. CHOI, E. H. CHOWDHURY, T. AKAIKE, C. S. CHO, Galactosylated chitosan-graft-poly(ethylene glycol) as hepatocyte-targeting DNA carrier, *J. Controlled Rel.* **2001**, *76*, 349–362.
- 169 I. K. PARK, T. H. KIM, S. I. KIM, Y. H. PARK, W. J. KIM, T. AKAIKE, C. S. CHO, *Int. J. Pharm.* **2003**, *257*, 103–110.
- 170 P. ERBACHER, S. M. ZOU, T. BETTINGER, A. M. STEFFAN, J. S. REMY, Chitosan-based vector/DNA complexes for gene delivery: biophysical characteristics and transfection ability, *Pharm. Res.* **1998**, *15*, 1332–1339.
- 171 S. Y. GAO, J. N. CHEN, X. R. XU, Z. DING, Y. H. YANG, Z. C. HUA, J. F. ZHANG, Galactosylated low molecular weight chitosan as DNA carrier for hepatocyte-targeting, *Int. J. Pharm.* **2003**, *255*, 57–68.
- 172 K. BARABAS, W. P. FAULK, transferrin receptors associate with drug-resistance in cancer cells, *Biochem. Biophys. Res. Commun.* **1993**, *197*, 702–708.
- 173 I. F. UCHEGBU, A. G. SCHATZLEIN, L. TETLEY, A. I. GRAY, J. SLUDDEN, S. SIDDIQUE, E. MOSHA, Polymeric chitosan-based vesicles for drug delivery, *J. Pharm. Pharmacol.* **1998**, *50*, 453–458.
- 174 C. DUFES, A. G. SCHATZLEIN, L. TETLEY, A. I. GRAY, D. G. WATSON, J.-C. OLIVIER, W. COUET, I. F. UCHEGBU, Niosomes and polymeric chitosan based vesicles bearing transferrin and glucose ligands for drug targeting, *Pharm. Res.* **2000**, *17*, 1251–1258.
- 175 C. DUFES, J.-M. MULLER, W. COUET, J.-C. OLIVIER, I. F. UCHEGBU, A. G. SCHATZLEIN, Anticancer drug delivery

- with transferrin targeted polymeric chitosan vesicles, *Pharm. Res.* **2004**, *21*, 101–107.
- 176 W. GUO, R. L. LEE, Receptor-targeted gene delivery via folate-conjugated polyethylenimine, *AAPS Pharm. Sci.* **1999**, *1*, E19.
- 177 J. M. BENNS, A. MAHESHWARI, D. Y. FURGESON, R. I. MAHATO, S. W. KIM, Folate-PEG-folate-graft-polyethylenimine-based gene delivery, *J. Drug Target.* **2001**, *9*, 123–139.
- 178 J. M. BENNS, R. I. MAHATO, S. W. KIM, Optimization of factors influencing the transfection efficiency of folate-PEG-folate-graft-polyethylenimine, *J. Controlled Rel.* **2002**, *79*, 255–269.
- 179 Y. H. KIM, S. H. GIHM, C. R. PARK, K. Y. LEE, T. W. KIM, I. C. KWON, H. CHUNG, S. Y. JEONG, Structural characteristics of size-controlled self-aggregates of deoxycholic acid-modified chitosan and their application as a DNA delivery carrier, *Bioconjugate Chem.* **2001**, *12*, 932–938.
- 180 H. S. YOO, J. E. LEE, H. CHUNG, I. C. KWON, S. Y. JEONG, Self-assembled nanoparticles containing hydrophobically modified glycol chitosan for gene delivery, *J. Controlled Rel.* **2005**, *103*, 235–243.
- 181 S. KWON, J. H. PARK, H. CHUNG, I. C. KWON, S. Y. JEONG, Physicochemical characteristics of self-assembled nanoparticles based on glycol chitosan bearing 5-cholanic acid, *Langmuir* **2003**, *19*, 10188–10193.
- 182 W. SUI, G. SONG, G. CHEN, G. XU, Aggregate formation and surface activity property of an amphiphilic derivative of chitosan, *Colloids Surfaces A Physicochem. Eng. Aspects* **2005**, *256*, 29–33.
- 183 S. DANIELSEN, S. STRAND, C. L. DAVIES, B. T. STOKK, Glycosaminoglycan destabilization of DNA–chitosan polyplexes for gene delivery depends on chitosan chain length and GAG properties, *Biochim. Biophys. Acta Gen. Subj.* **2005**, *1721*, 44–54.
- 184 A. BERTHOLD, K. CREMER, J. KREUTER, Preparation and characterization of chitosan microspheres as drug carrier for prednisolone sodium phosphate as model for antiinflammatory drugs, *J. Controlled Rel.* **1996**, *39*, 17–25.
- 185 C. ARAL, S.-TURAN OZBAS, L. KABASAKAL, M. K.-UYSAL, J. AKBUGA, Studies of effective factors of plasmid DNA-loaded chitosan microspheres I. Plasmid size, chitosan concentration and plasmid addition techniques, *STP Pharm. Sci.* **2000**, *10*, 83–88.
- 186 F. L. MI, H. W. SUNG, S. S. SHYU, Drug release from chitosan–alginate complex beads reinforced by a naturally occurring cross-linking agent, *Carbohydr. Polym.* **2002**, *48*, 61–72.
- 187 F. L. MI, H. W. SUNG, S. S. SHYU, C. C. SU, C. K. PENG, Synthesis and characterization of biodegradable TPP/genipin co-crosslinked chitosan gel beads, *Polymer* **2003**, *44*, 6521–6530.
- 188 S. OZBAS-TURAN, J. AKBUGA, C. ARAL, Controlled release of interleukin-2 from chitosan microspheres, *J. Pharm. Sci.* **2002**, *91*, 1245–1251.
- 189 J. AKBUGA, S. OZBAS-TURAN, N. ERDOGAN, Plasmid-DNA loaded chitosan microspheres for *in vitro* IL-2 expression, *Eur. J. Pharm. Biopharm.* **2004**, *58*, 501–507.
- 190 A. POLK, B. AMSDEN, K. D. YAO, T. PENG, M. F. A. GOOSEN, Controlled-release of albumin from chitosan–alginate microcapsules, *J. Pharm. Sci.* **1994**, *83*, 178–185.
- 191 L. S. LIU, S. Q. LIU, S. Y. NG, M. FROIX, T. OHNO, J. HELLER, Controlled release of interleukin-2 for tumour immunotherapy using alginate/chitosan porous microspheres, *J. Controlled Rel.* **1997**, *43*, 65–74.
- 192 S. A. AGNIHOTRI, N. N. MALLIKARJUNA, T. M. AMINABHAVI, Recent advances on chitosan-based micro- and nanoparticles in drug delivery, *J. Controlled Rel.* **2004**, *100*, 5–28.
- 193 H. ZHANG, M. OH, C. ALLEN, E. KUMACHEVA, Monodisperse chitosan nanoparticles for mucosal drug delivery, *Biomacromolecules* **2004**, *5*, 2461–2468.
- 194 P. CALVO, C. REMUNAN-LOPEZ, J. L. VILA-JATO, M. J. ALONSO, Novel

- hydrophilic chitosan–polyethylene oxide nanoparticles as protein carriers, *J. Appl. Polym. Sci.* **1997**, *63*, 125–132.
- 195** H. Q. MAO, K. ROY, S. M. WALSH, J. T. AUGUST, K. W. LEONG, DNA chitosan nanospheres for gene delivery, *Proc. Int. Symp. Controlled Rel. Bioact. Mater.* **1996**, *23*, 401–402.
- 196** X. W. LI, D. K. L. LEE, A. S. C. CHAN, H. O. ALPAR, Sustained expression in mammalian cells with DNA complexed with chitosan nanoparticles, *Biochim. Biophys. Acta* **2003**, *1630*, 7–18.
- 197** H.-L. JIANG, I.-K. PARK, N.-R. SHIN, SANG. G. KANG, H.-S. YOO, S.-I. KIM, S.-B. S., T. AKAIKE, C.-S. CHO, *In vitro* study of the immune stimulating activity of an atrophic rhinitis vaccine associated to chitosan microspheres, *Eur. J. Pharm. Biopharm.* **2004**, *58*, 471–476.
- 198** A. M. DE CAMPOS, A. SANCHEZ, M. J. ALONSO, Chitosan nanoparticles: a new vehicle for the improvement of the delivery of drugs to the ocular surface. Application to cyclosporin A, *Int. J. Pharm.* **2001**, *224*, 159–168.
- 199** L. F. QI, Z. R. XU, Lead sorption from aqueous solutions on chitosan nanoparticles. *Colloids Surfaces A Physicochem. Eng. Aspects* **2004**, *251*, 183–190.
- 200** Y. XU, Y. DU, Effect of molecular structure of chitosan on protein delivery properties of chitosan nanoparticles, *Int. J. Pharm.* **2003**, *250*, 215–226.
- 201** A. VILA, A. SANCHEZA, K. JANES, I. BEHRENSB, T. KISSEL, J. L. V. JATO, M. J. ALONSO, Low molecular weight chitosan nanoparticles as new carriers for nasal vaccine delivery in mice, *Eur. J. Pharm. Biopharm.* **2004**, *57*, 123–131.
- 202** L. QI, Z. XU, X. JIANG, C. HU, X. ZOU, Preparation and antibacterial activity of chitosan nanoparticles, *Carbohydr. Res.* **2004**, *339*, 2693–2700.
- 203** T. LÓPEZ-LEÓN, E. L. S. CARVALHO, B. SEIJO, J. L. ORTEGA-VINUESA, D. BASTOS-GONZÁLEZ, Physicochemical characterization of chitosan nanoparticles: electrokinetic and stability behavior, *J. Colloid Interface Sci.* **2005**, *283*, 344–351.
- 204** K. A. JANES, M. P. FRESNEAU, A. MARAZUELA, A. FABRA, M. J. ALONSO, Chitosan nanoparticles as delivery systems for doxorubicin, *J. Controlled Rel.* **2001**, *73*, 255–267.
- 205** L.-S. LIU, S.-Q. LIU, S. Y. NG, M. FROIX, T. OHNO, J. HELLER, Controlled release of interleukin-2 for tumour immunotherapy using alginate/chitosan porous microspheres, *J. Controlled Rel.* **1997**, *43*, 65–74.
- 206** K. KOFUJI, C.-J. QIAN, Y. MURATA, S. KAWASHIMA, Preparation of chitosan microparticles by water-in-vegetable oil emulsion coalescence technique, *React. Func Polym.* **2005**, *62*, 77–83.
- 207** J. AKBUGA, G. DURMAZ, Preparation and evaluation of cross-linked chitosan microspheres containing furosemide, *Int. J. Pharm.* **1994**, *111*, 217–222.
- 208** I. GENTA, P. PERUGINI, B. CONTI, F. PAVANETTO, A multiple emulsion method to entrap a lipophilic compound into chitosan microspheres, *Int. J. Pharm.* **1997**, *152*, 237–246.
- 209** S. G. KUMBAR, A. R. KULKARNI, T. M. AMINABHAVI, Crosslinked chitosan microspheres for encapsulation of diclofenac sodium: effect of cross-linking agent, *J. Microencapsul.* **2002**, *19*, 173–180.
- 210** S. G. KUMBAR, T. M. AMINABHAVI, Synthesis and characterization of modified chitosan microspheres: Effect of the grafting ratio on the controlled release of nifedipine through microspheres, *J. Appl. Polym. Sci.* **2003**, *89*, 2940–2949.
- 211** A. A. AL-HELW, A. A. AL-ANGARY, G. M. MAHROUS, M. M. AL-DARDARI, Preparation and evaluation of sustained release cross-linked chitosan microspheres containing phenobarbitone, *J. Microencapsul.* **1998**, *15*, 373–82.
- 212** E. B. DENKBAS, M. SEYYAL, E. PISKIN, 5-fluorouracil loaded chitosan microspheres for chemoembolization, *J. Microencapsul.* **1998**, *16*, 741–749.
- 213** B. C. THANOO, M. C. SUNNY, A.

- JAYAKRISHNAN, Cross-linked chitosan microspheres – preparation and evaluation as a matrix for the controlled release of pharmaceuticals, *J. Pharm. Pharmacol.* **1992**, *44*, 283–286.
- 214 C. SANKAR, M. RANI, A. K. SRIVASTAVA, B. MISHRA, Chitosan based pentazocine microspheres for intranasal systemic delivery: development and biopharmaceutical evaluation, *Pharmazie* **2001**, *56*, 223–226.
- 215 S. R. JAMEELA, T. V. KUMARY, A. V. LAL, A. JAYAKRISHNAN, Progesterone-loaded chitosan microspheres: a long acting biodegradable controlled delivery system, *J. Controlled Rel.* **1998**, *52*, 17–24.
- 216 F. BUGAMELLI, M. A. RAGGI, I. ORIENTI, V. ZECCHI, Controlled insulin release from chitosan microparticles, *Arch. Pharm.* **1998**, *331*, 133–138.
- 217 X. PENG, L. ZHANG, Surface fabrication of hollow microspheres from *n*-methylated chitosan cross-linked with glutaraldehyde, *Langmuir* **2005**, *21*, 1091–1095.
- 218 P. CALVO, C. REMUNAN, J. L. VILA JATO, M. J. ALONSO, Development of positively charged colloidal drug carriers: chitosan coated polyester nanocapsules and submicron-emulsions, *Colloid Polym. Sci.* **1997**, *275*, 46–53.
- 219 C. PREGO, M. GARCIA, D. TORRES, M. J. ALONSO, Transmucosal macromolecular drug delivery, *J. Controlled Rel.* **2005**, *101*, 151–162.
- 220 M.-K. LEE, S.-K. CHUN, W.-J. CHOI, J.-K. KIM, S.-H. CHOI, A. KIM, K. t OUNGBHO, J.-S. PARK, W. S. AHN, C.-K. KIM, The use of chitosan as a condensing agent to enhance emulsion-mediated gene transfer, *Biomaterials* **2005**, *26*, 2147–2156.
- 221 P. HE, S. S. DAVIS, L. ILLUM, Chitosan microspheres prepared by spray drying, *Int. J. Pharm.* **1999**, *187*, 53–65.
- 222 F.-L. MI, Y.-C. TAN, H.-F. LIANG, H.-W. SUNG, *In vivo* biocompatibility and degradability of a novel injectable-chitosan-based implant, *Biomaterials* **2002**, *23*, 181–191.
- 223 J. FILIPOVIC-GRICIC, B. PERISSUTTI, M. MONEGHINI, D. VOINOVICH, A. MARTINAC, I. JALSENJAK, Spray-dried carbamazepine-loaded chitosan and HPMC microspheres: preparation and characterisation, *J. Pharm. Pharmacol.* **2003**, *55*, 921–931.
- 224 I. ORIENTI, T. CERCHIARA, B. LUPPI, F. BIGUCCI, G. ZUCCARI, V. ZECCHI, Influence of different chitosan salts on the release of sodium diclofenac in colon-specific delivery, *Int. J. Pharm.* **2002**, *238*, 51–59.
- 225 Y. C. HUANG, M. K. YEH, C. H. CHIANG, Formulation factors in preparing BTM-chitosan microspheres by spray drying method, *Int. J. Pharm.* **2002**, *242*, 239–242.
- 226 T. CERCHIARA, B. LUPPI, F. BIGUCCI, V. ZECCHI, Chitosan salts as nasal sustained delivery systems for peptidic drugs, *J. Pharm. Pharmacol.* **2003**, *55*, 1623–1627.
- 227 C. WITSCHI, R. J. MRSNY, *In vitro* evaluation of microparticles and polymer gels for use as nasal platforms for protein delivery, *Pharm. Res.* **1999**, *16*, 382–390.
- 228 Y. C. HUANG, M. K. YEH, S. N. CHENG, C. H. CHIANG, The characteristics of betamethasone-loaded chitosan microparticles by spray-drying method, *J. Microencapsulation* **2003**, *20*, 459–472.
- 229 H. O. ALPAP, S. SOMAVARAPU, K. N. ATUAH, V. W. BRAMWELL, Biodegradable mucoadhesive particulates for nasal and pulmonary antigen and DNA delivery, *Adv. Drug Deliv. Rev.* **2005**, *57*, 411–430.
- 230 E. S. K. TANG, M. HUANG, L. Y. LIM, Ultrasonication of chitosan and chitosan nanoparticles, *Int. J. Pharm.* **2003**, *265*, 103–114.
- 231 T. BANERJEE, S. MITRA, A. KINGH, R. KHARMA, A. MAITRA, Preparation, characterization and biodistribution of ultrafine chitosan nanoparticles, *Int. J. Pharm.* **2002**, *243*, 93–105.
- 232 M. ANDERSSON, J. E. LOFROTH, Small particles of a heparin/chitosan complex prepared from a pharmaceutically acceptable microemulsion, *Int. J. Pharm.* **2003**, *257*, 305.

- 233 S. MITRA, U. GAUR, P. C. GHOSH, A. N. MAITRA, Tumour targeted delivery of encapsulated dextran–doxorubicin conjugate using chitosan nanoparticles as carrier, *J. Controlled Rel.* **2001**, *74*, 317–23.
- 234 K. KOFUJI, C.-J. QIAN, Y. MURATA, S. KAWASHIMA, Preparation of chitosan microparticles by water-in-vegetable oil emulsion coalescence technique, *Reac. Func. Polym.* **2005**, *62*, 77–83.
- 235 H. SASHIWA, Y. SHIGEMASA, R. ROY, Chemical modification of chitosan part 2 – Novel N-alkylation of chitosan via Michael type reaction, *Chem. Lett.* **2000**, 862–863.
- 236 H. TOKUMITSU, H. ICHIKAWA, Y. FUKUMORI, Chitosan-gadopenetic acid complex nanoparticles for gadolinium neutron-capture therapy of cancer: preparation by novel emulsion-droplet coalescence technique and characterization, *Pharm. Res.* **1999**, *16*, 1830–1835.
- 237 F. SHIKATA, H. TOKUMITSU, H. ICHIKAWA, Y. FUKUMORI, *In vitro* cellular accumulation of gadolinium incorporated into chitosan nanoparticles designed for neutron-capture therapy of cancer, *Eur. J. Pharm. Biopharm.* **2002**, *53*, 57–63.
- 238 H. TOKUMITSU, H. HIRATSUKA, Y. SAKURAI, T. KOBAYASHI, H. ICHIKAWA, Y. FUKUMORI, Gadolinium neutron-capture therapy using novel gadopenetic acid-chitosan complex nanoparticles: *in vivo* growth suppression of experimental melanoma solid tumor, *Cancer Lett.* **2000**, *150*, 177–182.
- 239 H. TOKUMITSU, H. ICHIKAWA, Y. FUKUMORI, Preparation of gadopenetic acid-loaded chitosan microparticles for gadolinium neutron-capture therapy of cancer by a novel emulsion-droplet coalescence technique, *Chem. Pharm. Bull.* **1999**, *47*, 838.
- 240 H. TOKUMITSU, H. ICHIKAWA, T. K. SAHA, Y. FUKUMORI, L. H. BLOCK, Design and preparation of gadolinium-loaded chitosan particles for cancer neutron capture therapy, *STP Pharm. Sci.* **2000**, *10*, 39.
- 241 S. A. AGNIHOTRI, T. M. AMINABHAVI, Controlled release of clozapine through chitosan microparticles prepared by a novel method, *J. Controlled Rel.* **2004**, *96*, 245–259.
- 242 A. BOZKIR, O. M. SAKA, Chitosan nanoparticles for plasmid DNA delivery: effect of chitosan molecular structure on formulation and release characteristics, *Drug Deliv.* **2004**, *11*, 107–112.
- 243 C. ARAL, J. AKBUGA, Preparation and *in vitro* transfection efficiency of chitosan microspheres containing plasmid DNA:poly(L-lysine) complexes, *J. Pharm. Pharm. Sci.* **2003**, *6*, 321–326.
- 244 S. OZBAS-TURAN, J. AKBUGA, C. ARAL, Controlled release of interleukin-2 from chitosan microspheres, *J. Pharm. Sci.* **2002**, *91*, 1245–1251.
- 245 T. DASTAN, K. TURAN, *In vitro* characterization and delivery of chitosan–DNA microparticles into mammalian cells, *J. Pharm. Pharm. Sci.* **2004**, *7*, 205–214.
- 246 S. OZBAS TURAN, C. ARAL, L. KABASAKAL, M. KEYER-UYSAI, J. AKBUGA, Co-encapsulation of two plasmids in chitosan microspheres as a non-viral gene delivery vehicle, *J. Pharm. Pharm. Sci.*, **2003**, *6*, 27–32.
- 247 S. MECLEAN, E. PROCESSER, D. O'MALLEY, N. CLARK, Z. RAMTOOLA, D. BRAYDEN, Binding and uptake of biodegradable poly-DL-lactide micro- and nanoparticles in intestinal epithelia, *Eur. J. Pharm. Sci.* **1998**, *6*, 153–163.
- 248 L. ILLUM, I. JABBAL-GILL, M. HINCHCLIFFE, A. N. FISHER, S. S. DAVIS, Chitosan as a novel nasal delivery system for vaccines, *Adv. Drug Deliv. Rev.* **2001**, *51*, 81–96.
- 249 K. CORSI, F. CHELLAT, L. YAHIA, J. C. FERNANDES, Mesenchymal stem cells, MG63 and HEK 293 transfection using chitosan–DNA nanoparticles, *Biomaterials* **2003**, *24*, 1255–1264.
- 250 A. I. CAPLAN, Mesenchymal stem cells and gene therapy, *Clin. Orthop. Rel. Res.* **2000**, *379* (Suppl.), 67–70.
- 251 S. MANSOURI, P. LAVIGNE, K. CORSI, M. BENDERDOUR, E. BEAUMONT, J. C. FERNANDES, Chitosan–DNA nanoparticles as non-viral vectors in gene therapy: strategies to improve



- transfection efficacy, *Eur. J. Pharm. Biophys.* **2004**, *57*, 1–8.
- 252 A. C. ANTONY, Folate receptors, *Annu. Rev. Nutr.* **1996**, *16*, 501–521.
- 253 S. WANG, J. LUO, D. A. LANTRIP, D. J. WATERS, C. J. MATHIAS, M. A. GREEN, P. L. FUCHS, P. S. LOW, Design and synthesis of [In-111]DTPA-folate for use as a tumor-targeted radiopharmaceutical, *Bioconjug. Chem.* **1997**, *8*, 673–679.
- 254 C. P. LEAMON, P. S. LOW, Delivery of macromolecules into living cells: a method that exploits folate receptor endocytosis, *Proc. Natl Acad. Sci. USA* **1991**, *88*, 5572–5576.
- 255 R. J. LEE, P. S. LOW, Delivery of liposomes into cultured kb cells via folate receptor-mediated endocytosis, *J. Biol. Chem.* **1994**, *269*, 3198–3204.
- 256 M. J. TURK, G. J. BREUR, W. R. WIDMER, C. M. PAULOS, L. C. XU, L. A. GROTE, P. S. LOW, Folate-targeted imaging of activated macrophages in rats with adjuvant-induced arthritis, *Arthritis Rheum.* **2002**, *46*, 1947–1955.
- 257 W. GUO, R. J. LEE, Efficient gene delivery via non-covalent complexes of folic acid and polyethylenimine, *J. Controlled Rel.* **2001**, *77*, 131–138.
- 258 J. A. REDDY, C. ABBURI, H. HOFLAND, S. J. HOWARD, I. VLAHOV, P. WILS, C. P. LEAMON, Folate-targeted, cationic liposome-mediated gene transfer into disseminated peritoneal tumors, *Gene Ther.* **2002**, *9*, 1542–1550.
- 259 M. KUMAR, A. K. BEHERA, R. F. LOCKEY, J. ZHANG, G. BHULLAR, C. PEREZ DE LA CRUZ, L.-C. CHEN, K. W. LEONG, S.-K. HUANG, S. S. MOHAPATRA, Intranasal gene transfer by chitosan–DNA nanospheres protects BALB/c mice against acute respiratory syncytial virus infection, *Hum. Gene Ther.* **2002**, *13*, 1415–1425.
- 260 W. XU, Y. SHEN, Z. JIANG, Y. WANG, Y. CHU, S. XIONG, Intranasal delivery of chitosan–DNA vaccine generates mucosal SIgA and anti-CVB3 protection, *Vaccine* **2004**, *22*, 3603–3612.
- 261 C.-J. SUN, S.-P. PAN, Q.-X. XIE, L.-J. XIAO, Preparation of chitosan-plasmid DNA nanoparticles encoding zona pellucida glycoprotein-3x and its expression in mouse, *Mol. Reprod. Dev.* **2004**, *68*, 182–188.
- 262 H. OKAMOTO, S. NISHIDA, H. TODO, Y. SAKABURA, K. IIDA, K. DANJO, Pulmonary gene delivery by chitosan-pDNA complex powder prepared by a supercritical carbon dioxide process, *J. Pharm. Sci.* **2003**, *92*, 371–380.
- 263 M. BIVAS-BENITA, K. E. VAN MEIJGAARDEN, K. L. M. C. FRANKEN, H. E. JUNGINGER, G. BORCHARD, T. H. M. OTTENHOFF, A. GELUK, Pulmonary delivery of chitosan–DNA nanoparticles enhances the immunogenicity of a DNA vaccine encoding HLA-A\*0201-restricted T-cell epitopes of *Mycobacterium tuberculosis*, *Vaccine* **2004**, *22*, 1609–1615.



## II

### Protein & Peptide-based Nanomaterials



## 5

### Plant Protein-based Nanoparticles

*Anne-Marie Orecchioni, Cécile Duclairoir, Juan Manuel Irache and Evelyne Nakache*

#### 5.1

##### Introduction

Biopolymers, such as proteins, lipids or polysaccharides, are commonly used to encapsulate drugs in order to protect them from rapid degradation by environmental stress (e.g. light, heat, oxygen or pH sensitivity). Drug loading of carriers seems to be an attractive opportunity, especially if they are made from bioacceptable macromolecules, e.g. plant proteins. Colloidal carriers, in the form of nanoparticles with a diameter of 50–500 nm and up to a few micrometers, have the potential to deliver drugs to specific target sites and to achieve sustained drug release. Moreover encapsulation can modify the drug biodistribution and increase its bioavailability [1–4]. Nanoparticles can be formed from a variety of materials including synthetic polymers and biopolymers (i.e. natural compounds), such as proteins, lipids and carbohydrates [5]. Natural macromolecules from vegetable sources appear to be a very promising alternative to synthetic polymers due to their proven safety, especially those that are used as food sources. The selection of a suitable structural material has an important influence on its potential medical use. Comparing plant and animal proteins, it appears that vegetal proteins may be more disposable and cheaper than animal proteins. Moreover, for plant proteins, the purification process might be also simplified.

In general, protein nanoparticles display a number of interesting advantages. Among them, these carriers are biodegradable and metabolizable. Moreover, they can be prepared under “soft” conditions, without the use of toxic organic solvents or materials, and they can incorporate a wide variety of drugs in a relatively non-specific fashion [6]. Moreover, due to their defined primary structure, protein-based nanoparticles may offer various possibilities for surface modification and covalent attachment of drugs and ligands [7, 8].

Taking into account all of these advantages of plant proteins, this chapter will focus solely on the use of storage proteins from pea (legumin and vicilin) and wheat (gliadins) when used as a structural material to prepare nanoparticles, and their possible applications in pharmacy and medicine. These proteins are not the

only ones able to produce nano/microparticles for use as drug carriers – studies have also been performed on other plant proteins like soy glycinin from soybean seeds [9] and zein from corn [10]. However, the numbers of studies with these two proteins are very low. This chapter also includes an overview of the fabrication and applications of both conventional and “decorated” (i.e. conjugated) storage protein nanoparticles.

## 5.2

### Description of Plant Proteins

Plant proteins are characterized by their three-dimensional organization. Two classes can be distinguished:

- Fibrous proteins composed of polypeptide chains joined together along a linear axis. They are involved in the structural material of living organisms.
- Globular proteins composed of one or, more frequently, several polypeptide chains rolled up to give a three-dimensional structure. Most of them are storage proteins.

Most vegetal proteins play an active role in biological processes, e.g. enzymes, and they can be classified by their physicochemical and extraction properties [11]. Four classes are listed:

- Vegetable albumins are hydrosoluble and rich in ionic residues (arginine, glutamic acid, lysine, tryptophan, etc.).
- Globulins are complex molecules and their amino acids composition is similar to that of albumins. However, their solubility needs an electrolyte medium.
- Prolamins are soluble in hydroalcoholic mixtures due to their high content of amino acids with hydrophilic residues.
- Glutelins cannot be dissolved in any of the aforementioned solvents, due to their high molecular mass and the presence of disulfide bonds; they are rich in lipophilic amino acids.

Storage proteins comprise proteins generated mainly during seed production and stored in the seed that serve as nitrogen sources for the developing embryo during germination [12, 13]. It is obviously more effective for the plant to use proteins instead of secondary plant products for this purpose. The average protein content of cereal grains is 10–15% of their dry weight [14], whereas for leguminose seeds it is about 20–25% [15, 16]. In addition to seeds, storage proteins can also be found in root and shoot tubers, e.g. potatoes.

No clear definition exists of what a storage protein is. The term is operational and was coined for all those proteins whose ratio in the total protein amount of the cell is greater than 5%. All of these proteins are characterized by the absence of enzymatic activity, act as a nitrogen source during seed germination and, usually, occur in an aggregated state confined in a membrane [17, 18].

Storage proteins are important for human nutrition (plant proteins), and numerous studies concerning their structure and biosynthesis have been published. For leguminoses, a simplifying rule says that they contain two types of storage proteins – legumin and vicilin. The legumins (as well as the vicilins) are very similar in different leguminose species. However, Gramineae contain a third type of storage proteins – prolamin – and, depending on the origin, it is distinguished between zein (from *Zea mays*) [19], hordein (from *Hordeum vulgare*) [20] and gliadin (from *Triticum aestivum* L.). In contrast to legumins and vicilins that are mainly located in the cotyledons of seeds, prolamines are found in the endosperm [21].

### 5.2.1

#### Pea Seed Proteins

Globulins are the main storage proteins in pea seeds [22]. These globulins were characterized by Osborne [23] according to their insolubility in distilled water and, on the contrary, by their solubility in buffered aqueous neutral salt solutions. When they are fractionated by centrifugation techniques, three different fractions have been described (with sedimentation coefficients of 2, 7 and 11S). The so-called 7 and 11S globulins represent the major pea seeds storage proteins – vicilin and legumin, respectively. These proteins display a number of similarities, including the adopted shape when solved in an aqueous solution and the similar size of the domains of the subunits forming these proteins [24, 25]. However, they can be differentiated by their molecular weight [22, 26] and different behavior at high temperature. In fact, vicilin has a size of about 200 kDa, whereas legumin is about 360 kDa [22, 26]. Furthermore, legumin does not coagulate at high temperature [27].

- Vicilin belongs to the group of so-called 7S globulins. It has a complex globular structure composed of two different types of subunits with molecular weights of about 50 and 60–70 kDa. These subunits form trimeric holoproteins in different combinations [22, 28]. Vicilin is rich in acidic amino acids (aspartic and glutamic acids), leucine and lysine [29, 30].
- Legumin belongs to the group of so-called 11S globulins [26]. This protein has a complex globular structure made of six pairs of subunits. Each of the subunits is composed of disulfide-linked acidic  $\alpha$ -chains (molecular weight 40 kDa) and basic  $\beta$ -chains (molecular weight 20 kDa) [31]. Although the three-dimensional structure of legumin has not been yet determined, the sequence alignment of this protein appears to show some similarities with that of vicilin [24, 32].

### 5.2.2

#### Wheat Proteins

Storage proteins from the wheat seed are able to form a unique viscoelastic network called gluten. The properties of gluten make it useful in the production of food products such as bread, pasta and semolina, and more recently in biopackag-

ing materials [33]. The rheological properties of gluten are dependent on the protein interactions that are formed in the network, and these properties were found to be mainly influenced by physical parameters such as temperature and pressure [34–36].

Two main fractions are present in gluten – gliadin, which is soluble in 70% ethanol, made of single-chain polypeptides with an average molecular weight of 25–100 kDa linked by intramolecular disulfide bonds, and glutenin, an alcohol-insoluble fraction consisting of gliadin-like subunits stabilized by intermolecular disulfide bonds in large aggregates with a molecular weight greater than 106 kDa [37]. Because they account for about half of the total wheat gluten proteins, gliadin constitutes an important class of proteins that are involved in the various properties of the gluten [38, 39]. These proteins are polymorphic, and can be separated and classified on the basis of their electrophoretic mobility at acid pH values [40] in the following four fractions:  $\alpha$  (molecular mass about 25–35 kDa),  $\beta$  (30–35 kDa),  $\gamma$  (35–40 kDa) and  $\omega$  (55–70 kDa) groups [41–44]. All fractions have remarkably low solubility in aqueous solution except at extreme pH. This low water solubility has been attributed to the presence of interpolypeptide disulfide bonds and to the cooperative hydrophobic interactions which cause the protein chains to assume a folded shape. The amino acid composition shows that gliadin has equal amounts of apolar and neutral amino acids, mainly glutamine (about 40%). Furthermore, gliadin also has a high proline content (14%) and a very low proportion of charged amino acids [41, 45].

$\omega$ -Gliadin presents an isoelectric point ( $pI$ ) ranging from 5.5 to 7 and has a few charged molecules with six to 11 basic amino acids per molecule. In contrast,  $\alpha$ -,  $\beta$ - and  $\gamma$ -gliadins, with a  $pI$  range of 6.5–8, are still less charged than  $\omega$ -gliadin [46].

### 5.3

#### Preparation of Protein Nanoparticles

Several methods have been reported in the literature for the preparation of nanoparticles from protein raw materials. Coacervation or controlled desolvation methods have been developed using solvent or electrolyte as the coacervation agent [47, 48] or by adjusting the pH or ionic strength [49, 50]. In the coacervation methods promoted by solvents, the first step consists of dispersing the macromolecules in an adequate solvent, then adding the mixture to a second solvent which is a nonsolvent of the macromolecules. A required condition is that the solvent and the nonsolvent phases are miscible.

The coacervation process is applied to a macromolecular solution to reduce the solubility in the system to such a degree that appropriate phase separation of the macromolecule takes place, i.e. the formation of a macromolecule-rich phase. The desolvation leads to macromolecule precipitation or to coacervate formation. It is assumed that, before phase separation is observed, a conformational change in the macromolecule occurs. The addition of a desolvating agent shrinks the macromolecule coil which becomes smaller and smaller until the phase separation from



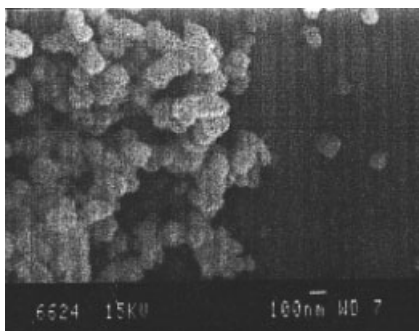


**Fig. 5.1.** Scanning electron micrograph of legumin nanoparticles. (From Ref. [52], permission pending).

the solvent occurs. It is possible to monitor the phenomenon by turbidity measurement. A desolvation agent decreases the turbidity because of the decrease in macromolecular size. To prepare small particles, it is important to maintain the system just outside the coacervation region. The addition of the coacervation agent should stop as soon as the Tyndall effect bounded to aggregation of macromolecules turns the system turbid [7]

### 5.3.1

#### Preparation of Legumin and Vicilin Nanoparticles

Legumin and vicilin have an aqueous solubility that is strongly pH and ionic strength dependent [30]. Nanoparticles from these pea proteins (Figs. 5.1 and 5.2) can be obtained by a simple coacervation or controlled desolvation method [50–52]. It was observed that extreme pH values enable their solubilization in aqueous medium. The coacervating or desolvating agent induces a progressive modification of the tertiary structure of the proteins, giving an increasing hydrophobic material which leads to submicronic aggregates or coacervates [53]. These coacervates are generally unstable and must be hardened for stabilization by physical or chemical

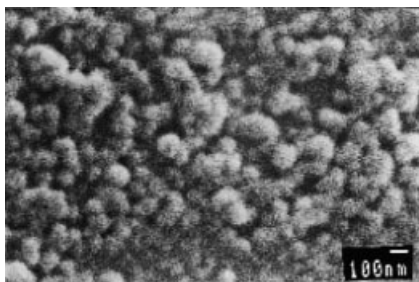


**Fig. 5.2.** Scanning electron micrograph of vicilin nanoparticles. (From Ref. [50]).

crosslinkage. In the case of these pea proteins, a three-step procedure can be employed to obtain nanoparticles.

In a first step, an unstable coacervate is obtained by mixing a solution of the chosen protein (pH 9) with a phosphate buffer solution. In a second step, the coacervates have to be hardened with a crosslinking agent in order to stabilize the just-forming coacervates. The most popular crosslinking agent is glutaraldehyde. This reagent reacts with the amino groups of the proteins, predominantly with the amino group of lysines, to form a Schiff base [54]. Finally, after the crosslinking, for pharmaceutical purposes, the obtained nanoparticles have to be purified. For this purpose, unreacted aldehyde can be neutralized with a sulfite and nanoparticles centrifuged in order to eliminate the nontransformed protein fraction onto particles.

Some comprehensive explanations of nanoparticles formation can be given. It is observed that, at a pH value close to 7, the coacervates show a submicronic size, but the percentages of coacervates yields are under 40% of the added protein. Similarly, the ionic strength of the buffer greatly influences the coacervate size and yield. The best experimental conditions to obtain small-sized particles (average diameter 500 nm) were found to be pH 6.8 and ionic strength 0.15 M for legumin, and pH 6.4 and ionic strength 0.10 M for vicilin [50, 52].

The isoelectric points of the two proteins are about 4.5. Thus, the balance between negative carboxyl groups (from glutamic and aspartic acids) and positive groups (from lysine and arginine) changes when the pH of the protein solution is less or greater than 4.5. Consequently, under environmental conditions close to the isoelectric point, these globulins would present a reduced interfacial charge which may enhance coacervate precipitation and phase separation. In other respects, for neutral pH values, legumin and vicilin would have a charge which may probably act against coacervate formation.

Concerning vicilin, in particular, a hypothesis for protein coacervate formation has been proposed. Under defined conditions, solubilized vicilin (7S form) may associate to yield an 11S insoluble form. This 11S form (probably a dimer of vicilin) may be responsible for the initial precipitation of vicilin which aggregates up to a critical size depending on environmental conditions (pH and ionic strength). The coacervate must be quickly hardened by crosslinkage in order to prevent the aggregates coalescing to a separate phase.

### 5.3.2

#### **Preparation of Gliadin Nanoparticles**

Gliadin nanoparticles (Fig. 5.3) can be prepared by a desolvation method in which a dissolution of gliadin in an organic solvent/water mixture is desolvated by the addition of a nonsolvent aqueous phase [50, 55]. Note that gliadin nanoparticles prepared in this way are stable and further treatment by heat or chemical crosslinking is not necessary to stabilize them. This fact can be explained by the extremely low solubility of gliadin in an aqueous medium and represents an advantage when compared with other protein nanoparticles (i.e. albumin, gelatin).

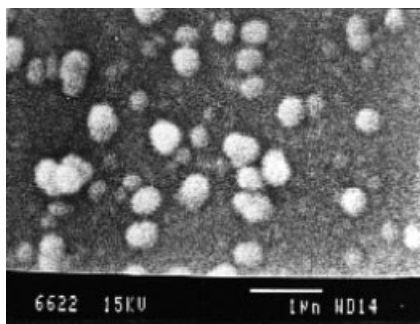


**Fig. 5.3.** Scanning electron micrograph of a gliadin nanoparticle. (From Ref. [8]).

In any case, gliadin nanoparticles can be hardened by chemical stabilization in order to modulate the drug release characteristics of nanoparticles or their *in vivo* distribution and interaction with the body.

Once produced (and eventually hardened by chemical crosslinkage), they have to be purified. The organic solvents are eliminated by evaporation under reduced pressure, whereas the amounts of protein not transformed onto nanoparticles and other impurities (i.e. the chemical crosslinker) are eliminated by dialysis, gel-permeation chromatography or, more frequently, subsequent centrifugations. Finally, nanoparticles can be also lyophilized to preserve their physicochemical properties for a long period of time. For lyophilization of gliadin nanoparticles, a solution of glucose 5% w/v has been proposed as a cryoprotector [56, 57].

In summary, this simple method allows the preparation of reproducible particle sizes with a narrow distribution. The main advantages are the production of nanoparticles in the absence of toxic organic solvents and the possibility of avoiding the chemical stabilization step to obtain stable nanoparticles. The selection of the solvent phase of gliadin has a significant influence on the size of the resulting nanoparticles. In this context, mixtures between either ethanol and water or acetone and water enable production of both smaller particle sizes and reproducible results. Another key factor concerns the nonsolvent of gliadin. In this case, an aqueous solution of NaCl (0.9% w/v) has been proposed [50]. When a mixture of ethanol and water is used, the size of the resulting nanoparticles is close to 450 nm and the yield of the process, determined by gravimetry and reverse-phase high-performance liquid chromatography (RP-HPLC), is about 90% [50, 56].

More recently, in order to understand the influence of environmental parameters governing gliadin nanoparticles size, a thermodynamic approach was investigated, i.e. the determination of the solubility parameter of the protein [58]. According to Hildebrand theory [59], the solubility parameter of gliadin was determined using a panel of solvents or mixtures of them. It is assumed that the solvent which best solubilizes gliadin has the same solubility parameter as the protein [60]. Different mixtures were prepared with bioacceptable solvents such as ethanol, ethylene glycol, propylene glycol and ultra-pure water. These solvents are usually considered

as references for the determination of the solubility parameters of biological compounds.

When a mixture of ethanol and water is used, the size of the resulting nanoparticles is close to 450 nm and the yield of the process, determined by gravimetry and RP-HPLC, is about 90% [50, 56]. However, a mixture of propylene glycol and water (73/27%) appears to be the best selection to obtain small gliadin nanoparticles of about 150 nm [58].

#### 5.4

##### Drug Encapsulation in Plant Protein Nanoparticles

In order to evaluate the encapsulation ability of gliadin nanoparticles, different drugs were tested, chosen for their medical and/or pharmaceutical interest. The objective of this research was to determine the feasibility of nanoparticles loaded with hydrophilic or lipophilic drugs and furthermore in order to obtain as small-sized particles as possible. Attention was focused on the drug release mechanism. Four drugs were chosen – two lipophilic vitamins, i.e. all-*trans* retinoic acid [vitamin A (RA)] and  $\alpha$ -tocopherol [vitamin E (VE)], and two hydrophilic drugs, i.e. a slightly polar mixture of linalool–linalyl acetate (LLA), components of the essential lavender oil, and the cationic amphiphilic benzalkonium chloride (BZC). For all these particulate systems, nanoparticles sizes were determined by scanning electron microscopy or photon correlation spectroscopy.

##### 5.4.1

##### RA Encapsulation in Gliadin Nanoparticles

RA is involved in the proliferation and differentiation of epithelial tissues. This vitamin in acidic form reduces the size of sebaceous glands and sebum secretion, making it an attractive agent for the treatment of skin disorders such as acne, psoriasis, hyperkeratosis, ichthyosis and epithelial tumors [61, 62]. In the treatment of acne, it was demonstrated that RA prevents inflammatory lesions by loosening follicular impactions (microcomedones) and clearing the follicular canal of retained keratin [63]. Furthermore, RA has been proven effective against a range of malignancies in human clinical trials, although many patients relapsed after a remission [64]. *In vivo* studies have shown that RA is active against acute promyelocytic leukemia [65, 66]. Unfortunately, the limited duration of RA activity in this leukemia is a pharmacological adaptation resulting in reduced serum concentration after prolonged treatment [67]. Nevertheless, in spite of a real therapeutic interest, several drawbacks (e.g. teratogenicity) have been reported for the currently available dosage forms [62]. To overcome these inconveniences, and in an attempt to increase the therapeutic efficacy of RA, alternative dosage forms have been suggested – microemulsions [68] and liposomes for intravenous [69] and topical administration [70]. Another system suitable for controlled drug release could be nanoparticles from biopolymers. For this purpose, we have chosen nanoparticles from gliadin

din. They were prepared by the aforementioned desolvation method [50, 58]. These particles can be obtained by using only bioacceptable solvents such as ethanol and water. Their size, which is one of the determinant characteristics for medical purposes, can be optimized. These nanoparticles, showing good stability in phosphate-buffered saline (PBS), were assayed as carriers for RA. They have shown a quite good entrapment efficiency – about 75% of added drug at  $60 \mu\text{g} (\text{mg gliadin})^{-1}$  and a payload of  $74 \mu\text{g} (\text{mg gliadin})^{-1}$  nanoparticles [58]. In order to quantify more precisely the solvent effect, the size diameter was optimized through a solubility parameter study. The smallest size was reached for protein solubility solvent equal to that of gliadin. The average diameter of the particles was about 150 nm [58]. RA was released from these nanoparticles, in a two-step mechanism, characterized by an initial rapid release followed by a continuous diffusion process. The first release was found to be about 20% of the loaded drug and can be related either to the release of the drug entrapped in the peripheral domains of the nanoparticle matrix or to a simple desorption of superficial RA, whilst the second slower period was linear with respect to time and appeared to be a diffusion phenomenon. Furthermore, in this second step, about 20% of the drug was released by diffusion in 3 h.

These observations offer interesting prospects for the preparation of drug-loaded carriers for medical applications.

#### 5.4.2

#### **VE Encapsulation in Gliadin Nanoparticles**

Drug carriers are interesting systems to prevent drawbacks related to the drug itself by decreasing its degradation rate. In order to test the protective power of nanoparticles against environmental stresses, a second lipophilic vitamin, VE, was encapsulated into gliadin nanoparticles. VE is known to act as a strong antioxidant or nitrosamine blocker to prevent the build-up of cellular peroxide [71]. The exposure to free oxygen species induces a rise in lipid peroxidation, which may cause injury at different sites of the body. For instance, the action of free radicals produced by a variety of environmental stresses (among them sun exposure) may promote skin damage, such as premature skin ageing [72], skin fragility and even skin cancers (melanoma or others) [73] related to a decrease in cellular immunity of the skin. VE appears to be one of the strongest free radical scavengers through its action as a chain-breaking antioxidant in membranes [74], preventing acute or chronic damage [75]. In addition to these biological activities, VE also exerts cosmetic functions; notably, it helps delay the progression of aging [76] and possesses a skin moisturizing power [77]. However, VE is degraded by oxygen, and dosage forms must be protected from light, heat and prolonged contact with air. Previous work has shown that the preparation of gliadin nanoparticles could be easily performed by a simple coacervation method. It is for this reason that gliadin has been chosen. Moreover, gliadin possesses the ability to interact with epidermal keratin due to its richness in proline [78]. VE-loaded gliadin nanoparticles have been characterized by their size,  $\zeta$  potential, VE payload and entrapment efficiency.

When loaded, the gliadin particle size is about 900 nm and their charge is close to zero. They are suitable drug carriers with an optimum encapsulation rate of about  $100 \text{ VE } \mu\text{g (mg gliadin)}^{-1}$  with an efficiency of more than 77%. The release behavior of VE-loaded nanoparticles may be interpreted as a “burst” effect, followed by a diffusion process through a homogeneous sphere [3].

#### 5.4.3

#### Lipophilic, Hydrophilic or Amphiphilic Drug Encapsulation

In order to study the influence of drug polarity on nanoparticle characteristics such as particles size, drug loading and drug release, three different drugs with different polarities were chosen [79]. VE, studied in a previous paper [3], was employed as a model of a lipophilic drug, and the slightly polar LLA and the amphiphilic cationic benzalkonium chloride (BZC) as hydrophilic models. Their dielectric constants are, respectively, 4, 8 and 45 [80]. The choice of these drugs was governed by their utilization in pharmaceutical dosage forms:

- VE, widely used as strong antioxidant in many medical and cosmetic applications, is rapidly degraded because of its light, heat and oxygen sensitivity [3].
- Linalool and linalyl acetate are the major components of essential lavender oil used in aromatherapy. They possess antibacterial and antifungal properties [81]. They are used in topical formulations. They may cause skin irritation by reason of a potential caustic power. Gliadin encapsulation could be a fruitful method for LLA formulations. Furthermore, the interaction of gliadin proline with skin keratin associated with the controlled release of LLA may avoid some drawbacks of this drug.
- BZC is a quaternary ammonium used as an antiseptic and bactericide, spermicide [82], and virucide [83]. However, BZC can promote some allergies followed by mucous lesions. It is assumed that encapsulation into gliadin nanoparticles could minimize or avoid lesions promoted by this irritant quaternary ammonium and could improve the dosage form by delaying drug release.

Drug entrapment and efficiency were tested after encapsulation. The results showed that the amount of entrapped VE and LLA is higher than that of the cationic BZC, confirming a strong interaction between gliadins and apolar compounds, due to the apolarity of the proteins. When comparing drug entrapment, results show that the optimal VE concentration is obtained for  $972.0 \text{ VE } \mu\text{g (mg gliadin)}^{-1}$ , with an efficiency of 79.2%, the optimal LLA concentration corresponds to  $980.0 \text{ LLA } \mu\text{g (mg gliadin)}^{-1}$ , with an efficiency of 82.4%, and the optimal BZC concentration corresponds to  $550.3 \text{ BZC } \mu\text{g (mg gliadin)}^{-1}$ , with an efficiency of 52.3% (Table 5.1).

For drug release quantification, only VE and BZC were studied. The reason being that LLA should be studied under a controlled atmosphere and not in a liquid medium. Such differences between media used did not allow an easy comparison to other drugs. For VE and BZC, drug releases were, respectively, 13 and 11% after

Tab. 5.1. Drug encapsulation characteristics in gliadin nanoparticles.

<b>Drug</b>	<b>Polarity (dielectric constant)</b>	<b>Payload (%)</b>	<b>Encapsulation efficacy (%)</b>
VE	Apolar (4)	97.2	79.2
LLA	slightly polar (8)	82.4	98.0
BZC	polar (amphiphilic cationic) (45)	66.0	52.3

1 h, and 30.6 and 11.7% after 30 h. The phenomenon observed can be interpreted as a burst effect completed by a drug diffusion process through a homogeneous sphere. Both release diffusion parts of the profiles have been modeled with a diffusion process in a homogenous sphere. However, the diffusion coefficients are different according to VE or BZC, i.e.  $1.12 \times 10^{-20}$  and  $6.36 \times 10^{-21} \text{ m}^2 \text{ s}^{-1}$ , respectively. This could be related to the different affinity of the gliadin for the two drugs. In organic phases, diffusion coefficients are usually about  $10^{-9} \text{ m}^2 \text{ s}^{-1}$ . Here, the coefficients are clearly much lower, which confirm that the drug is retained by the nanoparticle matrix.

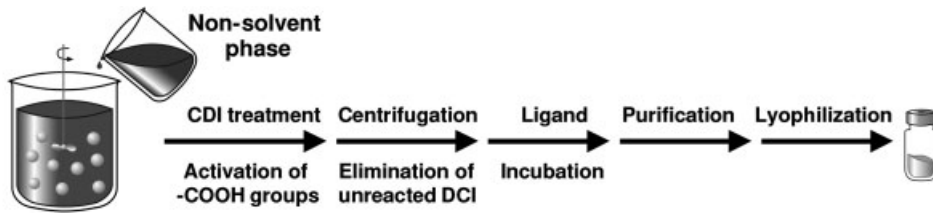
In conclusion, it can be observed that whatever the polar drug character, this gliadin nanoparticulate system is able to entrap the drug with an acceptable payload and encapsulation efficiency [79].

## 5.5

### Preparation of Ligand–Gliadin Nanoparticle Conjugates

In general, proteins produce biodegradable particles whose physicochemical properties can be modulated by the crosslinking process employed for their stabilization. Furthermore, due to the presence of numerous functional groups (i.e. amino and carboxylic residues), proteins are excellent candidates for the preparation of conjugates, formed by the attachment of molecules capable of providing specificity to the surface of nanoparticles. In this context, different ligands have been proposed, including antibodies [84, 85], lectins [86, 87], carbohydrates [88] and other biological ligands, in order to recognize or bind particular molecules [89, 90].

However, the association of ligands with nanoparticles can be achieved by different procedures, including covalent linkage and adsorption processes [91]. Ideally, the ligand should be conjugated to particles through a covalent linkage, which is more stable than adsorption procedures, without affecting its specificity. Noncovalent attachment relies on a fortuitous process. Further, it is difficult to control the amount of ligand which is associated and this process is useful only for those proteins that will associate nonspecifically [92]. Different techniques for covalent attachment may be envisaged, depending on the principal functional groups located on the carrier surface. The most widely used methods of ligand coupling are the use of cyanogen bromide [84, 93] and periodate [94, 95] for hydroxyl



### Protein solvent phase

**Fig. 5.4.** Route for the preparation of ligand–gliadin nanoparticle conjugates by desolvation of gliadin followed by CDI activation and further incubation with the ligand.

groups, glutaraldehyde [96, 97] and ethylene glycol diglycidyl ether [98] for amino groups, and carbodiimide (CDI) for carboxylic groups [99, 100].

This last technique is the one preferred in order to obtain conjugates between a ligand and protein nanoparticles [87, 101–103]. CDI involves the activation of carboxylic acid groups to give NH-activated carboxylic acid groups which can react with free amino groups of the ligand polypeptide chains [104]. In proteins, these carboxylic groups can be found on aspartic and glutamic acid residues. For vicilin, these amino acids represent about 19 groups per 1000 amino acid residues [101]. For gliadin, these amino acids only represent 21 and 71 groups per 1000 amino acid residues, respectively [45, 105]. In spite of gliadin having a very low proportion of these two amino acids, it appears that the coupling reaction is efficient enough to provide acceptable lectin binding.

Figure 5.4 summarizes the preparation of lectin–nanoparticle conjugates. In brief, the first step of the manufacturing protocol involves the activation of the carboxylic groups on the gliadin nanoparticles by addition of a CDI derivative [i.e. 1-(3-dimethylaminopropyl)-3-ethyl-carbodiimide hydrochloride]. After incubation, the suspension of “activated” nanoparticles has to be centrifuged in order to remove the unreacted reagent. Then, the nanoparticles are dispersed in an aqueous medium and incubated with the desired ligand for the coupling reaction by overnight incubation at room temperature [101, 102]. Finally, the resulting conjugates are purified and lyophilized using glucose as a cryoprotector [103].

Different parameters can influence the yield of the process. In spite of the fact that the CDI reaction can effectively occur up to at least pH 7.5 without any significant loss of yield, it has been reported that the optimal pH ranges between 4.7 and 6 [106]. This fact was also observed by Arangoa et al. who showed evidence of superior binding of a *Dolichus biflorus* lectin (DBA) to the surface of gliadin nanoparticles with 2-(*N*-morpholino)ethanesulfonic acid (MES) buffer (1 mM, pH 5.5) rather than with PBS (1 mM, pH 7.4) [103]. This may be explained as being due to the proton of the carboxylic group facilitating the rupture of one double link of the CDI molecule [107], forming the *O*-acylisourea intermediate. This active residue is then able to react directly with primary amines forming amide bonds and



releasing the CDI derivative. Moreover, at neutral pH, the overall charge of both the nanoparticles and the ligand would be negative. Therefore, ligand approaches to a nanoparticle surface and subsequent binding would not be favored by the phenomenon of charge repulsion [108].

Another critical factor affecting ligand binding to the surface of protein nanoparticles is the reaction time between the CDI and the gliadin. Therefore, an increase in the reaction time induced a dramatic decrease in the amount of the ligand binding to the nanoparticle surface. This could be due to the degradation of the reactive *O*-acylisourea complex. In fact, this complex is rapidly hydrolyzed in aqueous solution, having a constant rate measured in seconds [109]. If the target amine does not interact with the *O*-acylisourea intermediate before its hydrolysis, the desired binding cannot occur. This is especially problematic when the target molecule is in low concentration [106], as usually occurs in the binding of active ligands to the surface of nanoparticles. Another possible explanation for the DBA binding decrease could be the formation of the stable *N*-acylurea derivative [110].

However, the amount of CDI used to activate functional groups on the surface of nanoparticles is also important. A low amount of CDI may require longer reaction periods. However, the use of high amounts of CDI may induce irreversible aggregation of nanoparticles. This may be explained by the presence of both carboxylic and amine groups on the surface of the nanoparticles. Therefore, at high CDI concentrations, self-polymerization may take place [106]. In any case, in order to obtain a good binding efficiency, it is necessary to find a balance between the reaction time and the amount of CDI used to activate the nanoparticles.

Finally, another important factor concerns the amount of ligand used in the incubation with the activated nanoparticles. For gliadin nanoparticles, a maximum of ligand binding occurs when the amount of ligand incubated with activated nanoparticles is about  $50 \mu\text{g} (\text{mg gliadin})^{-1}$  nanoparticles [103].

## 5.6

### Bioadhesive Properties of Gliadin Nanoparticles

Bioadhesion is classically defined as the ability of a material to adhere to a biological substrate with the objective of improving the therapeutic efficiency of drugs by increasing the residence time at the site of activity or absorption [111, 112]. It is interesting to note that a number of drugs remain poorly available when administered by the oral route. Among other reasons, this fact can be related either to a low mucosal permeability for the drug or to its low solubility in the mucosal fluids. In both cases, an important fraction of the given dose is eliminated from the alimentary canal prior to being absorbed. The use of bioadhesive nanoparticles can be an adequate strategy to improve drug bioavailability. In fact, these carriers may enhance the drug absorption rate by reducing the diffusion barrier between the dosage form and the site of action or absorption. Similarly, they may prolong the residence time of the drug in the gut and, therefore, increase the time during which absorption can occur.

For bioadhesion studies, gliadin nanoparticles were labeled with carbazole, which is a hydrophobic fluorescent molecule.

### 5.6.1

#### **Ex Vivo Studies with Gastrointestinal Mucosal Segments**

In order to evaluate the bioadhesive capacity of these carriers, nanoparticles were incubated with fresh portions of rat gastrointestinal mucosa using a plate of aluminum with a slit in the center [113]. The mucosa in the slit of the plate was covered with 1 mL of suspensions (containing  $4 \text{ mg mL}^{-1}$  nanoparticles) and the incubation time was fixed for 30 min. After incubation, the suspensions were sucked off and the samples were rinsed with 5 mL 0.9% NaCl solution to eliminate the non-attached particles. Then, the mucus layer including the adsorbed particles was drawn from the membrane and digested with NaOH for 24 h. After total dissolution of mucus, carbazole extraction was performed with 1.5 mL methanol, vortexed for 1 min and centrifuged at  $20\,000 \text{ g}$  for 10 min. Finally, the amounts of adhered nanoparticles or conjugates were estimated by fluorometry [103].

Gliadin nanoparticles were able to develop rapid interaction with the gut mucosa. In fact, the adsorption equilibrium for nanoparticles and conjugates was reached in less than 30 min [103]. Similarly, under the experimental conditions used [ $4 \text{ mg}$  (particles or conjugates)  $\text{mL}^{-1}$ ], no saturation was observed on the apparent surface of mucosa delimited by the device.

Figure 5.5 shows the interactions of gliadin nanoparticles with intestinal mucosa samples. Comparing the different anatomical regions, gliadin nanoparticles

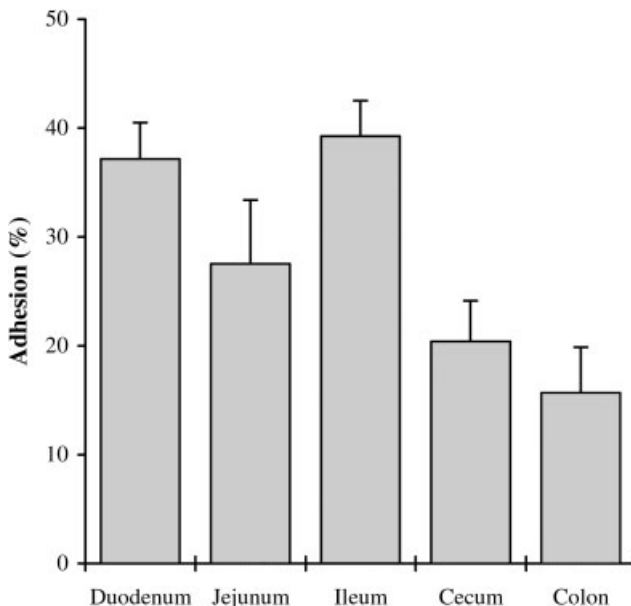


Fig. 5.5. Adhesive interactions of gliadin nanoparticles in isolated intestinal segments ( $n = 4$ ).

showed a high affinity for the small intestine segments. However, no significant differences in the extent of interaction were found between the duodenum, jejunum and ileum ( $P < 0.05$ ). Therefore, for ileum or duodenum portions, the amount of nanoparticles interacting with the mucosa was calculated to be close to  $8 \text{ g m}^{-2}$ , which represents about 40% of the nanoparticles placed in contact with the gastrointestinal tract. In this context, the interaction of poly(styrene) nanoparticles with intestinal segments (under similar experimental conditions) was size dependent and the largest amount of latex able to interact with the mucosa was about  $1 \text{ g m}^{-2}$  [113, 114]. Similarly, gliadin nanoparticles interacted about 8-fold more with the intestinal mucosa than poly(isobutyl cyanoacrylate) nanoparticles [115]. For large intestine portions, the interaction of gliadin nanoparticles strongly decreased. This may be explained by a reduction of both the mucosa surface and the mucin concentration along the gastrointestinal tract. According to these results, it appears that gliadin nanoparticles would be useful for improving the bioavailability of drugs. These powerfully adhesive carriers may prolong the residence time and enhance drug absorption, thus reducing the diffusion pathway.

However, DBA–gliadin nanoparticle conjugates displayed a different ability to develop adhesive interactions with the gut mucosa. In the small intestine, these conjugates showed an adhesive interaction similar to the controls ( $P < 0.05$ ) and, for all segments, this interaction was close to 10% of the initial concentration placed in contact with the mucosa. However, in the large intestine a significant increase of about 100% was found for DBA conjugates. This fact can be explained by the reported capability of DBA to strongly react with the colonic epithelial surface [116, 117] due to the presence of *N*-acetyl-D-galactosamine (specific sugar for DBA) residues, which provide the substrate for their site-specific interaction.

Finally, concerning the interaction of gliadin nanoparticles with Peyer's patches, it was found that gliadin nanoparticles showed 3.5 times more capacity of interaction with these lymphoid tissues than DBA conjugates [103].

All of these results confirmed that gliadin nanoparticles displayed a high interactive potential with biological surfaces. However, the possible interaction between the biological substrate and these nanoparticles is of a nonspecific nature. This fact means that these colloidal systems interact in the same way with a number of components of the biological substrate, without showing target properties for a particular region or cell structure [118].

## 5.6.2

### ***In Vivo* Studies with Laboratory Animals**

In order to evaluate the *in vivo* bioadhesive capacity of gliadin nanoparticles and their influence on the pharmacokinetics of the loaded drug, animals were gavaged with a single dose of nanoparticle formulations dispersed in 0.5 mL water. For the bioadhesion study, the gastrointestinal tract of animals was cut in different portions, rinsed with saline and digested with sodium hydroxide. The fluorescent marker was extracted with methanol and determined by spectrofluorimetry. The amount of carbazole, determined in the mucosa segments, was used for the

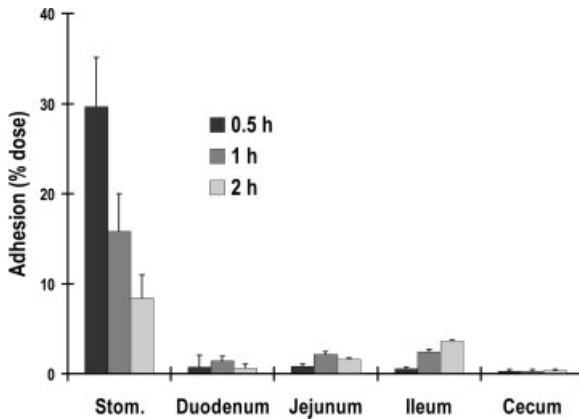


**Fig. 5.6.** Gastrointestinal transit profile of gliadin nanoparticles. Single administration of a single oral dose of 30 mg. Data expressed as the mean  $\pm$  SD ( $n = 4$ ). (Adapted from Ref. [102]).

estimation of the interacted nanoparticulate fractions. For the pharmacokinetics studies, blood samples were taken from the ophthalmic venous plexus, centrifuged and assayed for carbazole content by an HPLC method with fluorescent detection [57]. *In vivo* studies demonstrated that gliadin nanoparticles displayed a high adhesive potential with a clear tropism for the stomach mucosa (Fig. 5.6). Thus, thirty minutes post-administration, about 30% of the initial dose remained adhered within the gut. However, around 90% of the adhered nanoparticles were localized in the stomach. Similarly, 1 h after administration, only 18% of the initial dose could be found in the stomach and their presence in other intestinal regions was also negligible. Finally, at 2 h post-administration, only about 8% of the given dose was found adhered to the mucosa [119]. This profile of bioadhesion (tropism for the stomach mucosa and rapid decline of the adhered fraction over the time) was not significantly affected when nanoparticles were coated with DBA [103].

Nevertheless, in order to study the influence of the degree of crosslinking on the bioadhesive profile of nanoparticles and carbazole absorption, two different formulations were prepared. The first one resulted from the crosslinking of gliadin nanoparticles with glutaraldehyde with 2 h prior purification (CL-NP). The second one (DCL-NP) was obtained after treatment of gliadin nanoparticles with a CDI derivative for 1 h and subsequent treatment with glutaraldehyde for 2 h [57] (Tab. 5.2).

Within the stomach, the bioadhesive profile of gliadin nanoparticles was found to be influenced by the crosslinkage. Thus, noncrosslinked nanoparticles displayed a higher initial ability to develop adhesive interactions than crosslinked nanoparticles. However, the elimination rate of the adhered fraction was higher for noncrosslinked than for stabilized nanoparticles [57, 119]. On the contrary, the crosslinking process allowed a similar amount of carriers adhered to the mucosa to be

**Tab. 5.2.** Physicochemical characteristics of the different formulations based on gliadin nanoparticles ( $n = 6$ ).

	Size (nm)	$\zeta$ potential (mV)	Fixed ligand ( $\mu\text{g mg}^{-1}$ )	Loaded carbazol ( $\mu\text{g mg}^{-1}$ )
NP	460 $\pm$ 19	27.5 $\pm$ 0.8	–	12.6 $\pm$ 1.2
CL-NP	453 $\pm$ 24	24.5 $\pm$ 0.5	–	12.2 $\pm$ 0.8
DCL-NP	478 $\pm$ 31	21.2 $\pm$ 1.3	–	12.1 $\pm$ 1.6
BSA-NP	514 $\pm$ 18	34.7 $\pm$ 1.7	20.8 $\pm$ 1.7	12.5 $\pm$ 0.6
DBA-NP	521 $\pm$ 13	32.4 $\pm$ 0.9	23.5 $\pm$ 2.6	12.6 $\pm$ 0.9

CL-NP: nanoparticles crosslinked with glutaraldehyde; DCL-NP: nanoparticles crosslinked with CDI and glutaraldehyde; BSA-NP: bovine serum albumin–gliadin nanoparticle conjugates (control); DBA-NP: *D. biflorus* lectin–gliadin nanoparticle conjugates.

maintained for at least 1 h, which was calculated to be around 15% of the given dose (Fig. 5.7).

Another interesting point is that, within the stomach, the adhered nanoparticles appear to accumulate in the nonglandular region [119]. In this last region, cross-linked nanoparticles have a 1.5 times higher adhesive intensity than nonhardened nanoparticles. Similarly, the mean residence time of the adhered fraction to the stomach mucosa was about 95 min higher for crosslinked than for conventional gliadin nanoparticles [119].

This high adhesive capacity of gliadin nanoparticles may be explained by the protein composition with a high content of neutral and lipophilic residues. Neutral amino acids may promote hydrogen-bonding interactions with the mucosa, while

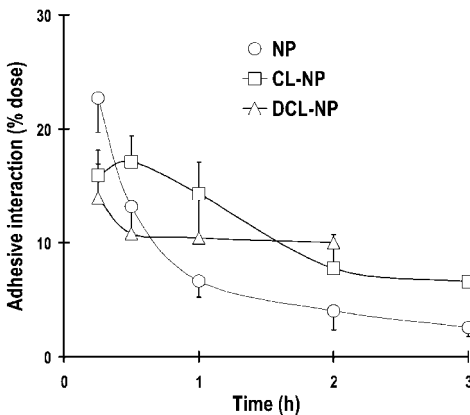


**Fig. 5.7.** Evolution of nonhardened gliadin nanoparticles (NP), nanoparticles crosslinked with glutaraldehyde (CL-NP), and nanoparticles crosslinked with CDI and glutaraldehyde (DCL-NP) in the stomach mucosa, as a function of

time, after single oral administration 20 mg particles ( $1.14 \text{ mg carbazole kg}^{-1}$ ). The results are expressed as the percentage of the given dose ( $n = 6$ ).

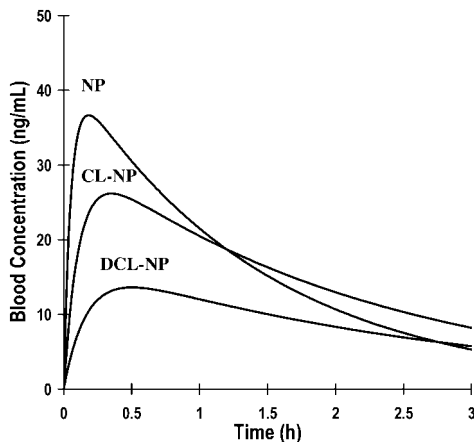


Fig. 5.8. Carbazole plasma levels after the oral administration of a single dose of  $1.14 \text{ mg carbazole kg}^{-1}$  loaded in NP, CL-NP or DCL-NP ( $n = 12$ ).

the lipophilic components may develop hydrophobic interactions with the biological support [115, 118, 120]. On the other hand, a more energetic crosslinking process reduces the ability of nanoparticles to develop adhesive interactions within the mucosa; however, this process would decrease the degradation rate of gliadin nanoparticle and, thus, provide a prolonged residence in the mucosa. For crosslinkage with glutaraldehyde, the adhered fraction of nanoparticles is constant for at least 1 h, whereas for nanoparticles crosslinked with CDI and glutaraldehyde, the adhered fraction (around 10% given dose) remained constant for at least 2 h.

Concerning the pharmacokinetic study, Fig. 5.8 shows the carbazole plasma concentration provided by nonhardened and crosslinked nanoparticles when administered by the oral route. It is interesting to note that when carbazole was formulated as an aqueous suspension it was not possible to determine the  $T_{\max}$ ,  $C_{\max}$  and the elimination rate. Similarly, the area under of curve (AUC) was around zero since their absorption was negligible. This fact is typical for hydrophobic drugs with very poor aqueous solubility [121–124].

However, when formulated in nonhardened nanoparticles, the bioavailability of carbazole was calculated to be about 40% of the dose. For crosslinked nanoparticles, the bioavailability was close to the 50%. Moreover, the crosslinkage enables us to increase the  $T_{\max}$ , and to decrease the  $C_{\max}$  and the elimination rate. Similarly, the mean residence time was significantly increased in comparison with nonhardened nanoparticles and an aqueous solution of carbazole [57].

These pharmacokinetic results can be explained by the ability of gliadin nanoparticles to develop bioadhesive interactions within the stomach mucosa. Once gliadin nanoparticles are adhered to the mucosa, they would release the loaded molecules to the absorbing cell layer, minimizing losses to the luminal environment and increasing the local drug concentration. In this context, the active molecule (carbazole in this study) would be able to show a first-order absorption process. However,

the digestion of nanoparticles either in luminal fluids or adhered in the mucus may provide an instantaneous release component which may be related to a first-order absorption. In fact, the interactions developed by gliadin nanoparticles within the stomach mucosa are the key phenomena influencing carbazole absorption. This hypothesis was confirmed by a deconvolution model [57].

## 5.7

### Future Perspectives

For pharmaceutical dosage forms it is well known that, whatever the administration mode, the principal objectives to be reached are the enhancement of the efficiency associated with a reduced toxicity and controlled drug release. Furthermore, if administered by a parenteral route, it is hoped that a major amount of the drug reaches the target site avoiding undesirable side-effects, i.e. a modification of drug distribution is required [125, 126].

Colloidal carriers in the form of nanoparticles have this potential to deliver drugs to specific target sites and to achieve sustained drug release. The bioacceptability of such nanoparticulate systems is strongly size dependent and, for intravessel administration, the diameter must be smaller than that of the smallest blood capillary. Consequently, size optimization is a very important parameter.

Furthermore, for medical applications, it is of interest to test their potential for parenteral administration, and particularly the humoral and cellular responses of protein particles after injection in animals. The first reports have been published describing these responses for native legumin and legumin nanoparticles after intradermal injection in rats [127].

#### 5.7.1

##### Size Optimization

Bearing in mind this important condition, all the parameters involved in the preparation of gliadin nanoparticles have been optimized (some results have been published [55]; other are in progress). The studied parameters were:

- Choice of the protein solvent
- Protein concentration
- Temperature during the experimental procedure
- Solvent/nonsolvent ratio
- Shear rate imposed during mixing
- Nanoparticle size evolution with time

Concerning the choice of the protein solvent, it was demonstrated that the closer the solubility parameter of the protein is to that of the solvent, the smaller the particle size (and correspondingly higher the amount of protein solubilized), under the experimental conditions chosen.

Other important experimental conditions were the solvent/nonsolvent ratio, the

temperature and the shear rate during the procedure. The data available showed that the best ratio must be less than unity and that an elevated temperature (compatible with protein thermolability, about 35 °C) decreases the particle size. Moreover, an optimum shear rate was observed for each protein concentration in the medium.

Concerning the size evolution of the nanoparticles with time, the first results showed that this parameter is a determinant for high protein concentrations. For instance, for a supersaturated solution of protein, the size increases 10 times in 100 min, ranging from 70 nm after 1 min to about 700 nm after 100 min. This is in favor of a spontaneous nucleation which occurs as soon as the non-solvent is added to the medium. In order to obtain a large range of nanoparticle sizes, it now remains to resolve the stabilization of the particles whatever their size.

In all of these abovementioned works the particle sizes of nanoparticles were greater than 100 nm. There are currently limitations on achieving nanoparticles with a size less than 100 nm and new developments are anticipated in the future.

### 5.7.2

#### **Immunization in Animals**

Preliminary experiments were performed on legumine nanoparticles in order to evaluate the capacities of biodegradable plant protein nanoparticles as drug delivery systems. More particularly, as it is possible to think that these nanoparticulate carriers could be considered as safe for oral or topical administrations, it was of interest to test their potential after injection [127]. In this context, humoral and cell-mediated responses were analyzed in rats. They were immunized with an intradermal injection of legumin or legumin nanoparticles of about 250 nm. Legumin and legumin nanoparticles were suspended in a sterile saline solution mixed with complete Freund's adjuvant (CFA). A control group of rats was inoculated only with saline solution and CFA.

*Humoral responses.* These responses against legumin and legumin nanoparticles were examined by usually appropriate techniques, i.e. Western blot and ELISA [127]. Both techniques showed that sera from rats immunized with legumin strongly expressed antibodies against this protein. On the contrary, serum samples from rats inoculated with legumin nanoparticles did not contain detectable amount of antibodies. Hence, legumin appears to be a potent inductor of the humoral immune response, while the use of legumin nanoparticles seems able to avoid the production of antibodies against them. However, the mechanism implicated in the absence of any humoral response to the legumin nanoparticles is far from clear. Mirshahi et al. [127] suggested some explanations: the chemical cross-linkage with glutaraldehyde [52] may produce some irreversible conformational changes in the protein tertiary structure making it less antigenic than the native protein [128], glutaraldehyde release could modify the surrounding cells and thus the lymphocyte response to antigens [129] or legumin nanoparticles were not sufficiently degraded to allow antigen formation during the period over which



experiment was carried out (1 month). Work is in progress to better understand this behavior.

*Cell-mediated response.* This was evaluated by *in vitro* lymphocyte proliferation assay 10 and 30 days after intradermal injection. Neither legumin nor legumin nanoparticles stimulated an immunogenic response [127]. This absence of response may be explained by a cytostatic effect of legumin. In a previous work (unpublished observations) it was noticed that legumin and legumin nanoparticles have a suppressive effect on *in vitro* fibroblast proliferation. These observations have to be confirmed.

Taking into consideration this cytostatic effect of legumin nanoparticles, it should be interesting to use them as pharmaceutical devices for the delivery of antitumor drugs in local cancer treatment.

Similar experimental work has to be carried out with the other plant proteins, gliadin and vicilin, in order to explore their medical and pharmaceutical potential as drug delivery systems.

From these *in vivo* and *in vitro* results, it can be assumed that plant proteins possess a role exceeding that of inert excipients. They have an influence on the entrapment efficiency of the drug and compatibility with tissues (essentially gliadin). In the future, it will be of interest to test these natural materials as encapsulating agents for the protection of sensitive drug from degradation (peptides, insulin, genes, etc.) and their ability to control drug release.

## 5.8

### Conclusion

The method used to prepare all plant proteins nanoparticles was a controlled desolvation method using only bioacceptable solvents. This procedure, avoiding toxic solvents, allowed the preparation of submicronic nanoparticulate systems with a narrow size distribution, and quite good yields and entrapment efficiency, making them susceptible to scale-up and industrial use. For gliadin, either hydrophilic or lipophilic drugs could be entrapped satisfactorily. Furthermore, gliadin nanoparticles possess a high interactive potential with biological surfaces, as demonstrated by *ex vivo* and *in vivo* animal experimentations. It appears that gliadin nanoparticles are interesting oral carriers to improve bioavailability of drugs. Nevertheless, in the future, efforts should be made to obtain a complete understanding of all the mechanisms implicated in the metabolism of these colloidal systems at the biomolecular level, in order to use them for medical applications.

### References

- 1 F. PUISIEUX, G. BARRATT, G. COURRAZE, P. COUVREUR, J. P. DEVISSAGUET, C. P. DUBERNET, E. FATTAL, H. FESSI, C. VAUTHIER, S. BENITA, Polymeric micro and nanoparticles as drug carriers. In

- Polymeric Biomaterials*, S. DIMITRIU (Ed.), Marcel Dekker, New York, 1994, pp. 747–795.
- 2 M. J. ALONSO, Nanoparticulate drug carrier technology. *Drug Pharm. Sci.* 1996, 77, 203–242.
  - 3 C. DUCLAIROIR, A. M. ORECCHIONI, P. DEPRAETERE, E. NAKACHE, Alpha-tocopherol encapsulation and *in-vitro* release from wheat gliadin nanoparticles. *J. Microencapsul.* 2002, 19, 53–60.
  - 4 S. GOIN, Microencapsulation: industrial appraisal of industrial technologies and trends. *Trends Food Sci. Technol.* 2004, 15, 330–347.
  - 5 E. NAKACHE, N. POULAIN, F. CANDAU, A. M. ORECCHIONI, J. M. IRACHE, Biopolymer and polymer nanoparticles and their biomedical applications. In *Handbook of Nanostructured Materials and Nanotechnology*, H. S. NALWA (Ed.), Vol. 5: *Organics, Polymers and Biological Materials*, Academic Press, New York, 2000, pp. 577–638.
  - 6 P. A. KRAMER, Albumin microspheres as vehicles for achieving specificity in drug delivery. *J. Pharm. Sci.* 1974, 63, 1646–1647.
  - 7 W. LIN, A. G. A. COOMBES, M. C. DAVIES, S. S. DAVIS, L. ILLUM, Preparation of sub 100 nm human serum albumin nanospheres using a pH-coacervation method. *J. Drug Target.* 1993, 1, 237–243.
  - 8 I. EZPELETA, J. M. IRACHE, S. STAINMESSE, C. CHABENAT, J. GUEGUEN, Y. POPINEAU, A. M. ORECCHIONI, Gliadin nanoparticles for the controlled release of all *trans*-retinoic acid. *Int. J. Pharm.* 1996, 131, 191–200.
  - 9 J. LAZKO, Y. POPINEAU, J. LEGRAND, Soy glycinin microcapsules by simple coacervation method. *Colloids Surfaces B.* 2004, 37, 1–8.
  - 10 X. LIU, Q. SUN, H. WANG, L. ZHANG, J. Y. WANG, Microspheres of corn protein, Zein, for an ivermectin drug delivery. *Biomaterials* 2005, 26, 109–115.
  - 11 M. N. MIÈGE, Protein tips and distribution. In *Encyclopedia of Plant Physiology*, D. BOULTER and B. PARTHIER (Eds.), Springer, Berlin, 1982, pp. 291–345.
  - 12 C. DOMONEY, R. CASEY, Measurement of gene number for seed storage proteins in *Pisum*. *Nucleic Acids Res.* 1985, 13, 687–699.
  - 13 M. A. CHOWDHURY, A. E. SLINKARD, Genetic diversity in grass pea (*Lathyrus sativus* L.). *Genet. Resources Crop Evol.* 2000, 47, 163–169.
  - 14 K. S. G. WONG, J. WANG, L. TAO, J. TAN, J. G. ZHANG, D. A. PASSEY, J. YU, compositional gradients in Gramineae genes. *Genome Res.* 2002, 12, 851–856.
  - 15 G. H. MCINTOSH, D. L. TOPPING, Food legumes in human nutrition. In *Proceedings of the Third International Food Legumes Research Conference*, Adelaide, Australia, R. KNIGHT (Ed.), 2000, pp. 655–660.
  - 16 D. W. GRIFFITHS, D. A. LAWES, Variation in the crude protein content of field beans (*Vicia faba* L.) in relation to the possible improvement of the protein content of the crop. *Euphytica* 1978, 27, 487–495.
  - 17 H. LEVANONY, R. RUBIN, Y. ALTSCHULER, G. GALILI, Evidence for a novel route of wheat storage proteins to vacuoles. *J. Cell Biol.* 1992, 119, 1117–1128.
  - 18 I. HOHL, D. G. ROBINSON, M. J. CRISPEELS, G. HINZ, Transport of storage proteins to the vacuole is mediated by vesicles without a clathrin coat. *J. Cell Sci.* 1996, 109, 2539–2550.
  - 19 M. I. GELI, M. TORRENT, D. LUDEVID, Two structural domains mediate two sequential events in  $\gamma$ -zein targeting: protein endoplasmic reticulum retention and protein body formation. *Plant Cell* 1994, 6, 1911–1922.
  - 20 B. G. FORDE, A. HEYWORTH, J. PYWELL, M. KREIS, Nucleotide sequence of a B1 hordein gene and the identification of possible upstream regulatory elements in endosperm storage protein genes from barley, wheat and maize. *Nucleic Acids Res.* 1985, 13, 7327–7339.
  - 21 N. ROSENBERG, Y. SHIMONI, Y. ALTSCHULER, H. LEVANONY, M. VOLOKITA, and G. GALILI, Wheat (*Triticum aestivum* L.)  $\gamma$ -gliadin

- accumulates in dense protein bodies within the endoplasmic reticulum of yeast. *Plant Physiol.* **1993**, *102*, 61–69.
- 22 K. MÜNTZ, Globulins from legume seeds: structure and function during storage and reactivation. In *Plant Proteins from European Crops*, J. GUEGUEN, Y. POPINEAU (Eds.), Springer, Berlin, **1998**, pp. 3–12.
  - 23 T. B. OSBORNE, *The Vegetable Proteins*, 2nd edn., Longmans Green, New York, **1924**.
  - 24 P. ARGOS, S. V. L. NARAYANA, N. C. NIELSEN, Structural similarity between legumin and vicilin storage proteins from legumes. *EMBO J.* **1985**, *4*, 1111–1118.
  - 25 P. E. M. GIBBS, K. B. STRONGIN, A. MCPHERSON, Evolution of legume seed storage protein: a domain common to legumins and vicilins is duplicated in vicilins. *Mol. Biol. Evol.* **1989**, *6*, 614–623.
  - 26 I. A. POPELLO, V. V. SUCHKOV, V. Y. GRINBERG, V. B. TOLTOGUZOV, Liquid/liquid phase equilibrium in globulin/salt/water systems: legumin. *J. Sci. Food Agric.* **1990**, *51*, 345–353.
  - 27 K. D. SCHWENKE, D. ZIRWER, K. GAST, E. GÖRNITZ, K. J. LINOW, J. GUEGUEN, Changes of the oligomeric structure of legumin from pea (*Pisum sativum* L.) after succinylation. *Eur. J. Biochem.* **1990**, *194*, 621–627.
  - 28 J. A. GATEHOUSE, G. W. LYCETT, A. J. DELAUNY, R. R. R. CROY, D. BOULTER, Sequence specificity of the post-translational proteolytic cleavage of vicilin, a seed storage protein of pea (*Pisum sativum* L.). *Biochem. J.* **1983**, *212*, 427–432.
  - 29 E. DERBYSHIRE, D. J. WRIGHT, D. BOULTER, Legumin and vicilin, storage proteins of legume seeds. *Phytochemistry* **1976**, *13*, 3–24.
  - 30 J. GUEGUEN, A. T. VU, F. SCHAEFFER, Large scale purification and characterization of pea globulins. *J. Sci. Food Agric.* **1984**, *35*, 1024–1033.
  - 31 D. CAER, B. COLAS, Protease susceptibility and amino group accessibility to trinitrobenzenesulfonic acid of legumin during its glycosylation. *J. Agric. Food Chem.* **1993**, *41*, 544–546.
  - 32 M. C. LAWRENCE, T. IZARD, M. BEUCHAT, R. J. BLAGROVE, P. M. COLEMAN, Structure of phaseolin at 2.2 Å resolution. Implications for a common vicilin/legumin structure and the genetic engineering of seed storage proteins. *J. Mol. Evol.* **1994**, *238*, 748–776.
  - 33 S. GUILBERT, N. GONTARD, Edible and biodegradable food packaging, in *Foods and Packaging Materials – Chemical Interactions*, P. ACKERMANN, M. JÄGERSTAD, T. OHLSSON (Eds.), Royal Society of Chemistry, Cambridge, **1995**, pp. 159–168.
  - 34 J. HARGREAVES, Y. POPINEAU, M. LE MESTE, M. HEMMINGGA, Molecular flexibility in wheat gluten proteins submitted to heating. *FEBS Lett.* **1995**, *373*, 103–107.
  - 35 A. APICHARTSRANGKON, A. E. BELL, D. A. LEDWARD, J. D. SCOFIELD, Dynamic viscoelastic behavior of high-pressure-treated wheat gluten. *Cereal Chem.* **1999**, *76*, 777–782.
  - 36 J. LEFEBVRE, Y. POPINEAU, G. DESHAYES, L. LAVENANT, Temperature-induced changes in the dynamic rheological behavior and size distribution of polymeric proteins for gluteins from wheat near-isogenic lines differing in HMW-glutenin subunit composition. *Cereal Chem.* **2000**, *77*, 193–201.
  - 37 J. A. BIETZ, J. A. ROTHFUS, Comparison of peptides from wheat gliadin and glutenin. *Cereal Chem.* **1970**, *47*, 381–392.
  - 38 P. R. SHEWRY, Cereal seed storage proteins. In *Seed Development and Germination*, J. KIGEL, G. GALLI (Eds.), NY Bale, Hong Kong, **1995**, pp. 45–72.
  - 39 D. D. KASARDA, Structure and properties of  $\alpha$ -gliadins. *Ann. Technol. Agric.* **1980**, *29*, 151–173.
  - 40 J. H. WOYCHIK, R. A. BOUNDY, R. A. DIMLER, Starch gel electrophoresis of wheat gluten proteins with concentrated urea. *Arch. Biochem. Biophys.* **1961**, *84*, 477–482.
  - 41 M. BYERS, J. MIFFLIN, S. J. SMITH, A quantitative comparison of the extraction of protein fractions from

- wheat grain by different solvents, and of the polypeptide and amino acid composition of the alcohol-soluble proteins. *J. Sci. Food Agric.* **1983**, *34*, 447–462.
- 42 D. L. DU CROS, C. W. WRIGLEY, Improved electrophoretic methods for identifying cereal varieties. *J. Sci. Food Agric.* **1979**, *30*, 785–794.
- 43 C. LARRÉ, Y. POPINEAU, W. LOISEL, Fractionation of gliadins from common wheat by cation exchange FPLC. *J. Cereal Chem.* **1991**, *14*, 231–241.
- 44 H. WIESER, W. SEILMER, H. D. BELITZ, Quantitative determination of gliadin subgroups from different wheat cultivars. *J. Cereal Sci.* **1994**, *19*, 149–155.
- 45 H. HE, R. R. ROACH, R. C. HOSENEY, Effect of nonchaotropic salts on flour bread-making properties. *Cereal Chem.* **1992**, *69*, 366–371.
- 46 Y. POPINEAU, S. DENERY-PAPINI, *Protéines Végétales*, Lavoisier, Paris, **1996**.
- 47 R. BODMEIER, H. CHEN, E. PAERATAKUL, A novel approach to the oral delivery of micro- or nanoparticles. *Pharm. Res.* **1989**, *6*, 413–417.
- 48 M. S. EL-SAMALIGY, P. ROHDEWALD, Reconstituted collagen nanoparticles, a novel drug carrier delivery system. *J. Pharm. Pharmacol.* **1983**, *35*, 537–539.
- 49 D. J. BURGESS, O. N. SINGH, Spontaneous formation of small sized albumin/acacia coacervate particles. *J. Pharm. Pharmacol.* **1993**, *45*, 586–591.
- 50 I. EZPELETA, J. M. IRACHE, S. STAINMESSE, J. GUEGUEN, A. M. ORECCHIONI, Preparation of small-sized particles from vicilin (vegetal protein from *Pisum sativum* L.) by coacervation. *Eur. J. Pharm. Biopharm.* **1996**, *42*, 36–41.
- 51 J. M. IRACHE, L. BERGOUNOUX, I. EZPELETA, J. GUEGUEN, A. M. ORECCHIONI, Optimization and *in vitro* stability of legumin nanoparticles obtained by a coacervation method. *Int. J. Pharm.* **1995**, *126*, 103–109.
- 52 T. MIRSHAHI, J. M. IRACHE, J. GUEGUEN, A. M. ORECCHIONI, Development of drug delivery systems from vegetal proteins: legumin nanoparticles. *Drug Dev. Ind. Pharm.* **1996**, *22*, 841–846.
- 53 J. J. MARTY, R. C. OPPENHEIM, P. SPEISER, Nanoparticles: a new colloidal drug delivery system. *Pharm. Acta Helv.* **1978**, *53*, 17–23.
- 54 I. EZPELETA, J. M. IRACHE, J. GUEGUEN, A. M. ORECCHIONI, Properties of glutaraldehyde cross-linked vicilin nano- and micro-particles. *J. Microencapsul.* **1997**, *14*, 557–565.
- 55 C. DUCLAIROIR, E. NAKACHE, H. MARCHAIS, A. M. ORECCHIONI, Formation of gliadin nanoparticles: influence of the solubility parameter of the protein solvent. *Colloid Polym. Sci.* **1998**, *276*, 321–327.
- 56 M. A. ARANGO, M. A. CAMPANERO, Y. POPINEAU, J. M. IRACHE, Evaluation and characterization of gliadin nanoparticles and isolates by reversed-phase HPLC. *J. Cereal Sci.* **2000**, *31*, 223–228.
- 57 M. A. ARANGO, M. A. CAMPANERO, M. J. RENEDE, G. PONCHEL, J. M. IRACHE, Gliadin nanoparticles as carriers for the oral administration of lipophilic drugs. Relationship between bioadhesion and pharmacokinetics. *Pharm. Res.* **2001**, *18*, 1521–1527.
- 58 C. DUCLAIROIR, J. M. IRACHE, E. NAKACHE, A. M. ORECCHIONI, C. CHABENAT, Y. POPINEAU, Gliadin nanoparticles: formation, all-*trans*-retinoic acid entrapment and release, size optimization. *Polym. Int.* **1999**, *79*, 327–333.
- 59 J. HILDEBRAND, R. SCOTT, *Regular Solutions*, Prentice-Hall, Englewood Cliffs, NJ, **1962**.
- 60 A. F. M. BARTON, *Handbook of Solubility Parameters and Other Cohesion Parameters*, 2nd edn., CRC Press, Boca Raton, FL, **1991**.
- 61 J. T. ELDER, A. ASTROM, U. PETTERSON, A. TAVAKOL, C. E. GRIFFITHS, A. KRUST, P. KASTNER, P. CHAMSON, J. J. VOORHES, Differential regulation of retinoic acid receptors and binding proteins in human skin. *J. Invest. Dermatol.* **1992**, *98*, 673–679.
- 62 A. H. LEWIN, M. E. BOS, F. C. ZUSI, X.

- NAIR, G. WHITING, P. BOURQUIN, G. TETRAULT, F. I. CAROL, Evaluation of retinoids as therapeutic agents in dermatology. *Pharm. Res.* **1994**, *11*, 192–200.
- 63 R. M. LAVKER, J. J. LEYDEN, E. G. THORNE, An ultrastructural study of the effects of topical tretinoin on microcomedones. *Clin. Ther.* **1992**, *14*, 773–780.
- 64 J. DRACH, G. LOPEZ-BERESTEIN, T. MCQUEEN, M. ANDREEFF, K. METHA, Induction of differentiation in myeloid leukemia cells lines and acute promyelocytic leukemia cells by liposomal all-*trans* retinoic acid. *Cancer Res.* **1993**, *53*, 2100–2104.
- 65 S. CASTAIGNE, C. CHOMIENNE, M. T. DANIEL, P. FENAUX, R. BERGER, L. DEGOS, All-*trans* retinoic acid as a differentiation therapy in acute promyelocytic leukemias. I. Clinical results. *Blood*, **1990**, *76*, 1704–1710.
- 66 K. SEITER, W. H. MILLER, E. J. FELDMAN, T. AHMED, Z. ARLIN, Pilot study of all-*trans* retinoic acid as post-remission therapy in patients with acute promyelocytic leukemia. *Leukemia*, **1995**, *9*, 15–18.
- 67 L. DELVA, M. CORNIC, N. BALITRAND, C. CHOMIENNE, Application thérapeutique de l'acide rétinoïque dans la leucémie aiguë promyélocytaire. *Immunoanal. Biol. Spec.* **1991**, *25*, 17–21.
- 68 T. TAKINO, K. KOISHI, Y. TAKAKURA, M. HASHIDA, Long circulating emulsion carrier systems for highly lipophilic drugs. *Biol. Pharm. Bull.* **1994**, *17*, 121–125.
- 69 K. METHA, T. SADEGHI, T. MCQUEEN, G. LOPEZ-BERESTEIN, Liposome encapsulation circumvents the hepatic clearance mechanisms of all-*trans* retinoic acid. *Leuk. Res.* **1994**, *18*, 587–596.
- 70 V. MASINI, F. BONTE, A. MEYBECK, J. WEPIERRE, Cutaneous bioavailability in hairless rats of tretinoin in liposomes or gel. *J. Pharm. Sci.* **1993**, *82*, 17–21.
- 71 B. IDSON, Dry skin moisturizing and emolliency. *Cosm. Toil.* **1992**, *107*, 69–78.
- 72 J. H. EPSTEIN, Photocarcinogenesis, skin cancer and aging. *J. Am. Acad. Dermatol.* **1983**, *9*, 487–502.
- 73 A. J. SOBER, Solar exposure in the etiology of cutaneous melanoma. *Photodermatol.* **1987**, *4*, 23–31.
- 74 A. L. TAPPEL, Vitamin E as the biological lipid antioxidant. *Vitamins Hormones* **1962**, *20*, 493–510.
- 75 L. H. KLIGMAN, A. M. KLIGMAN, Photoaging in dermatology. *Photodermatology* **1986**, *3*, 215–227.
- 76 R. C. WESTER, H. I. MAIBACH, Absorption of tocopherol into and through human skin. *Cosm. Toil.* **1997**, *112*, 53–57.
- 77 P. M. MAYER, W. PITTERMANN, S. WALLAT, The effects of Vitamin E on the skin. *Cosm. Toil.* **1993**, *108*, 99–109.
- 78 A. TEGLIA, G. SECCHI, New protein ingredients for skin detergency: relative wheat protein–surfactant complexes. *Int. J. Cosm. Sci.* **1994**, *16*, 235–246.
- 79 C. DUCLAIROIR, A. M. ORECCHIONI, P. DEPRAETERE, F. OSTERSTOCK, E. NAKACHE, Evaluation of gliadins nanoparticles as drug delivery systems: a study of three different drugs. *Int. J. Pharm.* **2003**, *353*, 133–144.
- 80 A. A. MARYOTT, E. R. SMITH, Table of dielectric constants of pure liquids. In *Circular 514*, National Bureau of Standards, New York, **1951**.
- 81 M. LIS-BALCHIN, S. HART, Studies on the mode of action of the essential oil of lavender (*Lavandula angustifolia* P. MILLER). *Phytother. Res.* **1999**, *13*, 540–542.
- 82 E. AUBENY, J. C. COLAU, A. NANDEUIL, Local spermicidal contraception: a comparative study of the acceptability and safety of a new pharmaceutical formulation of benzalkonium chloride, the vaginal capsule, with a reference formulation, the pessary. *Eur. J. Contracept. Health Care* **2000**, *5*, 61–67.
- 83 M. A. WAINBERG, B. SPIRA, G. BLEAU, R. THOMAS, Inactivation of human immunodeficiency virus type 1 in tissue culture fluid and in genital secretion by the spermicide

- benzalkonium chloride. *J. Clin. Microbiol.* **1990**, *28*, 156–158.
- 84 I. H. AL-ABDULLA, G. W. MELLOR, M. S. CHILDSTONE, A. M. SIDKI, D. S. SMITH, Comparison of three different activation methods for coupling antibodies to magnetisable cellulose particles. *J. Immunol. Methods* **1989**, *122*, 253–258.
- 85 C. WEBER, S. REISS, K. LANGER, Preparation of surface modified protein nanoparticles by introduction of sulfhydryl groups. *Int. J. Pharm.* **2000**, *211*, 67–78.
- 86 C. M. LEHR, J. A. BOUWSTRA, W. KOK, A. B. J. NAACH, A. G. DE BOER, H. E. JUNGINGER, Bioadhesion by means of specific binding of tomato lectin. *Pharm. Res.* **1992**, *9*, 547–553.
- 87 J. M. IRACHE, C. DURRER, D. DUCHÊNE, G. PONCHEL, Preparation and characterization of lectin–latex conjugates for specific bioadhesion. *Biomaterials* **1994**, *15*, 899–904.
- 88 A. MARUYAMA, T. ISHIHARA, N. ADACHI, T. AKAIKE, Preparation of nanoparticles bearing high density carbohydrate chains using carbohydrate-carrying polymers as emulsifier. *Biomaterials* **1994**, *15*, 1035–1042.
- 89 M. ROSER, D. FISCHER, T. KISSEL, Surface-modified biodegradable albumin nano- and microspheres. II: effect of surface charges on *in vitro* phagocytosis and biodistribution in rats. *Eur. J. Pharm. Biopharm.* **1998**, *46*, 255–263.
- 90 K. LANGER, C. COESTER, C. WEBER, H. VON BRIESEN, J. KREUTER, Preparation of avidin-labeled protein nanoparticles as carriers for biotinylated peptide nucleic acid. *Eur. J. Pharm. Biopharm.* **2000**, *49*, 303–307.
- 91 W. LIN, M. C. GARNETT, M. C. DAVIES, F. BIGNOTTI, P. FERRUTI, S. S. DAVIS, L. ILLUM, Preparation of surface-modified albumin nanospheres. *Biomaterials* **1997**, *18*, 559–565.
- 92 G. V. BETAGERI, C. D. V. BLACK, J. SZEBENI, L. M. WAHL, J. N. WEINSTEIN, Fc-receptor-mediated targeting of antibody-bearing liposomes containing dideoxycytidine triphosphate to human monocyte/macrophages. *J. Pharm. Pharmacol.* **1993**, *45*, 48–53.
- 93 N. G. DOLINNAYA, N. I. SOKOLOVA, D. T. ASHIRBEKOVA, Z. A. SHABAROVA, The use of BrCN for assembling modified DNA duplexes and DNA–RNA hybrids; comparison with water soluble carbodiimide. *Nucleic Acids Res.* **1991**, *19*, 3067–3072.
- 94 D. M. BOORSMA, J. G. STREEFKERK, Periodate or glutaraldehyde for preparing peroxidase conjugates? *J. Immunol. Methods* **1979**, *30*, 245–255.
- 95 P. TIJSSEN, E. KURSTACK, Highly efficient and simple methods for the preparation of peroxidase and active peroxidase–antibody conjugates for enzyme immunoassays. *Anal. Biochem.* **1984**, *136*, 451–457.
- 96 S. AVRAMEAS, B. GUILBERT, Enzyme-immunoassay for measurement of antigens using peroxidase conjugates. *Biochimie* **1972**, *54*, 837–842.
- 97 H. OTTO, H. TAKAMIYA, A. VOGT, A two-stage method for cross-linking antibody globulin to ferritin by glutaraldehyde. Comparison between the one-stage and the two-stage method. *J. Immunol. Methods* **1973**, *3*, 137–146.
- 98 S. SANO, K. KATO, Y. IKADA, Introduction of functional groups onto the surface of polyethylene for protein immobilization. *Biomaterials* **1993**, *14*, 817–822.
- 99 R. S. MOLDAY, W. J. DREYER, A. REMBAUM, S. P. S. YEN, New immunolabelled spheres: visual markers of antigens on lymphocytes for scanning electron microscopy. *J. Cell Biol.* **1975**, *64*, 75–88.
- 100 N. R. SHENOY, J. M. BAILEY, J. E. SHIVELY, Carboxylic acid-modified polyethylene: a novel support for the covalent immobilization of polypeptides for C-terminal sequencing. *Protein Sci.* **1992**, *1*, 58–67.
- 101 I. EZPELETA, J. M. IRACHE, S. STAINMESSE, C. CHABENAT, J. GUEGUEN, A. M. ORECCHIONI, Preparation of lectin–vicilin nanoparticle conjugates using the

- carbodiimide coupling technique. *Int. J. Pharm.* **1996**, *142*, 227–233.
- 102 I. EZPELETA, M. A. ARANGO, J. M. IRACHE, S. STAINMESSE, C. CHABENAT, Y. POPINEAU, A. M. ORECCHIONI, Preparation of *Ulex europaeus* lectin–gliadin nanoparticle conjugates and their interaction with gastrointestinal mucus. *Int. J. Pharm.* **1999**, *191*, 25–32.
- 103 M. A. ARANGO, G. PONCHEL, A. M. ORECCHIONI, M. J. RENEDE, D. DUCHENE, J. M. IRACHE, Bioadhesive potential of gliadin nanoparticulate systems. *Eur. J. Pharm. Sci.* **2000**, *11*, 333–341.
- 104 L. H. OLDE DAMINK, P. J. DIJKSTRA, M. J. VAN LUYN, P. B. VAN WACHEM, P. NIEUWENHUIS, J. FEIJEN, *In vitro* degradation of dermal sheep collagen cross-linked using a water-soluble carbodiimide. *Biomaterials* **1996**, *17*, 679–684.
- 105 J. A. EWART, Slow triplet  $\beta$ -gliadin from Capelle-Desprez. *J. Sci. Food Agric.* **1983**, *34*, 653–656.
- 106 G. T. HERMANSON (Ed.), *Zero-length Cross-linkers. Bioconjugate Techniques*, Academic Press, Orlando, FL, **1996**.
- 107 D. BASTOS, J. L. ORTEGA, F. J. DE LAS NIEVES, R. HIDALGO, Carboxylated latexes for covalent coupling antibodies I. *J. Colloid Interface Sci.* **1995**, *176*, 232–239.
- 108 J. L. ORTEGA, D. BASTOS, R. HIDALGO, Comparative studies on physically adsorbed and chemically IgG to carboxylated latexes II. *J. Colloid Interface Sci.* **1995**, *176*, 240–247.
- 109 D. HOARE, D. KOSHLAND, A method for the quantitative modifications and estimation of carboxylic acid groups in proteins. *J. Biol. Chem.* **1967**, *242*, 2447–2453.
- 110 J. V. STAROS, R. W. WRIGHT, D. M. SWINGLE, Enhancement by *N*-hydroxysulfosuccinimide of water soluble carbodiimide-mediated coupling reactions. *Anal. Biochem.* **1986**, *156*, 220–222.
- 111 J. K. VASIR, K. TAMBWEKAR, S. GARG, Bioadhesive microspheres as a controlled drug delivery system. *Int. J. Pharm.* **2003**, *255*, 13–32.
- 112 R. GURNY, J. M. MEYER, N. A. PEPPAS, Bioadhesive intraoral release systems: design, testing and analysis. *Biomaterials* **1984**, *5*, 336–340.
- 113 C. DURRER, J. M. IRACHE, F. PUISIEUX, D. DUCHENE, G. PONCHEL, Mucoadhesion of latexes I. Analytical methods and kinetics studies. *Pharm. Res.* **1994**, *11*, 674–679.
- 114 J. M. IRACHE, C. DURRER, D. DUCHÈNE, G. PONCHEL, Bioadhesion of lectin–latex conjugates to rat intestinal mucosa. *Pharm. Res.* **1996**, *13*, 1714–1717.
- 115 G. PONCHEL, M. J. MONTISCI, A. DEMBRI, C. DURRER, D. DUCHENE, Mucoadhesion of colloidal particulate systems in the gastrointestinal tract. *Eur. J. Pharm. Biopharm.* **1997**, *44*, 25–31.
- 116 P. LANCE, R. LEV, Colonic oligosaccharide structures deduced from lectin-binding studies before and after desialylation. *Hum. Pathol.* **1991**, *22*, 307–312.
- 117 R. SHARMA, U. SCHUMACHER, The influence of diets and gut microflora on lectin binding patterns of intestinal mucin in rats. *Lab. Invest.* **1995**, *73*, 558–564.
- 118 G. PONCHEL, J. M. IRACHE, Specific and non-specific bioadhesive particulate systems for oral delivery to the gastrointestinal tract, *Adv. Drug Del. Rev.* **1998**, *34*, 191.
- 119 M. A. ARANGO, M. A. CAMPANERO, J. M. IRACHE, Potencial bioadhesivo de las nanoparticulas de gliadina en el estómago. *Rev. Colomb. Cien. Quim. Farm.* **2004**, *33*, 38–47.
- 120 J. M. GU, J. R. ROBINSON, H. S. LEUNG, Binding of acrylic polymers to mucin-epithelial surfaces. Structure/property relationship. *Crit. Rev. Ther. Drug Carrier Syst.* **1998**, *5*, 21.
- 121 N. SUBRAMANIAN, S. RAY, S. K. GHOSAL, R. BHADRA, S. P. MOULIK, Formulation design of self-micro-emulsifying drug delivery systems for improved oral bioavailability of celecoxib. *Biol. Pharm. Bull.* **2004**, *27*, 1993–1999.
- 122 A. T. M. SERAJUDDIN, P. C. SHEE, D.

- MUFSON, D. F. BERNSTEIN, M. A. AUGUSTINE, Effect of vehicle amphiphilicity on the dissolution and bioavailability of a poorly water-soluble drug from solid dispersion. *J. Pharm. Sci.* **1988**, *77*, 414–417.
- 123** B. J. AUNGST, N. NGUYEN, N. J. ROGERS, S. ROWE, M. HUSSAIN, L. SHUM, S. WHITE, Improved oral bioavailability of an HIV protease inhibitor using Gelucire 44/14 and Labrasol vehicles. *Bull Tech. Gattefosse* **1994**, *87*, 49–54.
- 124** R. N. GURSOY, S. BENITA, Self-emulsifying drug delivery systems (SEDDS) for improved oral delivery of lipophilic drugs. *Biomed. Pharmacother.* **2004**, *58*, 173–182.
- 125** S. J. DOUGLAS, S. S. DAVIS, L. ILLUM, Nanoparticles in drug delivery. *Crit. Rev. Ther. Drug Carrier System*, **1987**, *3*, 233–261.
- 126** P. ERLICH, *Collected Studies on Immunity*, Wiley, New York, **1906**.
- 127** T. MIRSHAHI, J. M. IRACHE, C. NICOLAS, M. MIRSHAHI, J. P. FAURE, J. GUEGUEN, C. HEQUET, A. M. ORECCHIONI, Adaptive immune responses of legumin nanoparticles. *J. Drug Target.* **2002**, *10*, 625–631.
- 128** O. SCHUSSLER, M. SHEN, L. SHEN, S. M. CARPENTIER, S. KAVERI, A. CARPENTIER, Effect of human immunoglobulins on the immunogenicity of porcine bioprostheses. *Ann. Thorac. Surg.* **2001**, *71*, S396–S400.
- 129** D. WIEBE, J. MEGERMAN, G. J. L'ITALIEN, W. M. ABBOT, Glutaraldehyde release from vascular prosthesis of biologic origin. *Surgery* **1988**, *104*, 26–33.



## 6 Peptide Nanoparticles

Klaus Langer

### 6.1 Introduction

The primary objective of a therapy with pharmacological active compounds is the controlled delivery of the compound to its site of action. After administration most drugs show a certain distribution throughout the body which depends mainly on their physicochemical characteristics. Only a certain fraction of the drug reaches its site of action; the other fraction may be responsible for unwanted or toxic side-effects. Therefore, a lot of concepts and drug delivery systems for the targeting of drugs to their specific site of action have been developed. A promising method is drug loading to colloidal drug carrier systems such as microemulsions, liposomes and nanoparticles. Liposomes, mainly consisting of phospholipids and cholesterol, are characterized by good biocompatibility; however, they suffer from the disadvantage of a short shelf-life and drug leakage. In comparison to liposomes, nanoparticles are solid colloidal particles in the size range between 10 and 1000 nm. They consist of macromolecular material and can be prepared by a polymerization reaction starting with the corresponding monomers or by the dispersion of preformed polymers [1]. In principle, a drug compound can be bound to the surface of such a nanoparticulate system after particle preparation, or can be entrapped or dissolved into the particle matrix (Fig. 6.1).

The ideal colloidal delivery system should be nontoxic and able to be degraded *in vivo* after reaching its site of action. Among the different materials used for the preparation of drug carrier systems, proteins would appear promising, since they can lead to biodegradable and nonantigenic drug carrier systems [2]. Protein-based nanoparticles are relatively easy to prepare and their size distribution can be monitored easily [3]. As a result of the defined primary structure of proteins, the protein-based nanoparticles may offer various possibilities for surface modification as well as the attachment of drugs and compounds for drug-targeting purposes such as antibodies or ligands for cell-specific receptor complexes.

This chapter gives an overview of nanoparticulate, and in some cases microparticulate, systems based on proteins. Only nanoparticles intended to be used as drug carrier systems and in some rare cases for diagnostic purposes will be described.

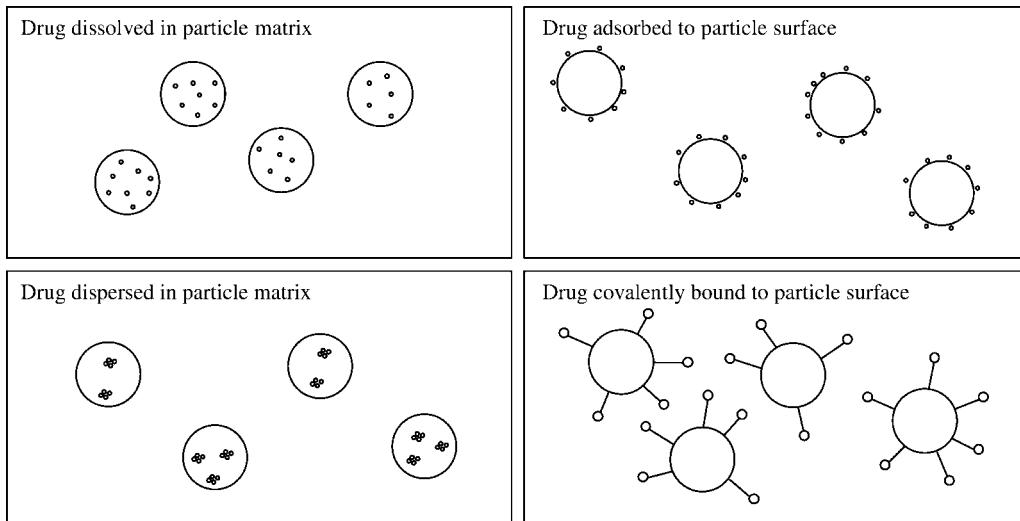


**Fig. 6.1.** Schematic representation of drug binding (small circles) to particulate drug carrier systems (large circles).

The chapter provides an overview of the preparation techniques for protein-based particle systems starting with the first attempts during the 1960s. Based on this earlier work, the attempts to optimize the preparation techniques in order to achieve nanoparticles instead of microparticles are outlined. Different emulsion techniques are compared to the desolvation or coacervation techniques. After the description of the preparation techniques the idea of particle surface modification in order to modify the particle properties under *in vivo* and *in vitro* conditions will be outlined. Nanoparticle systems which focus on cell-specific drug targeting are illustrated. After the preparation and surface modification review, up-to-date applications of protein-based particle systems for clinical studies, therapy and diagnostics are presented.

## 6.2

### Starting Materials for the Preparation of Nanoparticles

Many preparation techniques for nanoparticles were established in the 1970s and 1980s, and these methods were developed further during the following years. The starting materials for particle preparation can be subdivided depending on the preparation technique used [4]:

- I. Preparation by polymerization reactions
  1. Polyacrylamide [5, 6]
  2. Poly(alkyl methacrylates) [7–9]

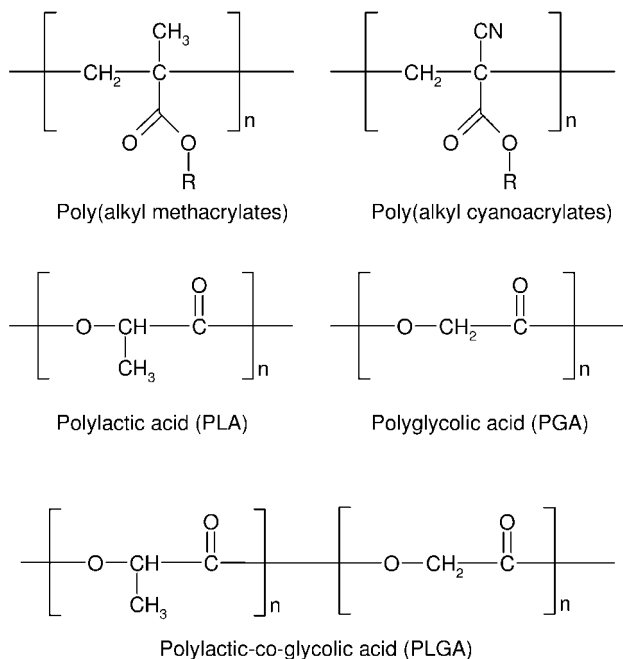


**Fig. 6.2.** Schematic representation of the most important synthetic polymers used for the preparation of nanoparticles as drug delivery systems.

3. Poly(alkyl cyanoacrylates) [10]
  4. Polyglutaraldehyde [11]
- II. Preparation by dispersion of preformed polymers
1. Natural macromolecules: serum albumin, gelatin, alginate [12–14]
  2. Synthetic macromolecules: poly(lactic acid) (PLA), poly(lactic-co-glycolic acid) (PLGA), polyacrylate, poly- $\epsilon$ -caprolactone [15–17]
- III. Preparation by dispersion of solid lipids [18, 19]

The structures of the most important synthetic polymers for the preparation of nanoparticles are outlined in Fig. 6.2. For the preparation of nanoparticles as drug delivery systems, artificial polymers such as poly(alkyl methacrylates) and poly(alkyl cyanoacrylates) were most often used, and nanoparticles were formed by polymerization reactions of the respective monomers. These polymers mainly differ in their biodegradation behavior. Whereas poly(alkyl methacrylates) are poorly biodegradable, the biodegradability of poly(alkyl cyanoacrylates) depends mainly on the length of the ester side-chain [20]. In addition to poor biodegradability, a further disadvantage of nanoparticle preparation by polymerization reactions can be seen in the fact that the resulting drug carrier system may contain unreacted toxic monomers. To avoid this problem and to achieve particle systems of high biocompatibility, preparation techniques involving the use of purified natural

macromolecules or preformed synthetic polymers have been developed. Due to their enhanced biocompatibility, nanoparticles based on PLA, PLGA, solid lipids as well as particle systems based on proteins as starting materials are of growing interest.

### 6.3

#### Preparation Methods

As previously outlined, nanoparticles based on artificial polymers such as poly(alkyl methacrylates) and poly(alkyl cyanoacrylates) are prepared by polymerization reactions starting with the corresponding monomers. Whereas poly(alkyl methacrylate)-based nanoparticles are usually prepared by polymerization in a continuous phase in the presence of a polymerization initiator [7, 21], poly(alkyl cyanoacrylate) nanoparticles are prepared by an emulsion polymerization technique initiated by bases present in the polymerization medium [10]. In comparison to these preparation conditions, nanoparticles based on proteins such as serum albumin, casein or gelatin are prepared by dispersion techniques of the preformed polymer. Different methods for their preparation have been described, based on emulsion formation, desolvation or coacervation. In addition to drug carrier systems consisting of either natural or artificial polymers, recently mixed compositions consisting of bovine serum albumin (BSA) loaded gelatin nanoparticles incorporated in hydrophobic PLGA microspheres have been described [22].

#### 6.3.1

##### Nanoparticle Preparation by Emulsion Techniques

Emulsification of an aqueous drug-containing protein solution in an oily phase was most often used as an established method for the preparation of microspheres (Fig. 6.3). The resulting droplets of the water-in-oil emulsion were stabilized by a crosslinking procedure in the presence of bifunctional aldehydes such as glutaraldehyde or by thermal denaturation. The resulting particle size depends on the droplet size of the protein-containing aqueous phase dispersed within the oily phase. Most of the emulsion techniques described in the literature result in the formation of particles in the size range of several micrometers (i.e. microparticles/microspheres). In some cases the emulsion techniques can be optimized for the preparation of nanoparticles [23]. Most often serum albumin of different origin as well as gelatin have been used as starting materials for the preparations. In the following sections the preparation techniques are divided with regard to the nature of the protein; preparation techniques leading to the formation of microparticles are described as well as methods resulting in the formation of nanoparticles.

##### 6.3.1.1 Emulsion Technique for the Preparation of Albumin-based Microspheres and Nanoparticles

Human serum albumin (HSA) is widely used as a microsphere material since it is considered nonantigenic for human use, biodegradable and readily available. Fur-

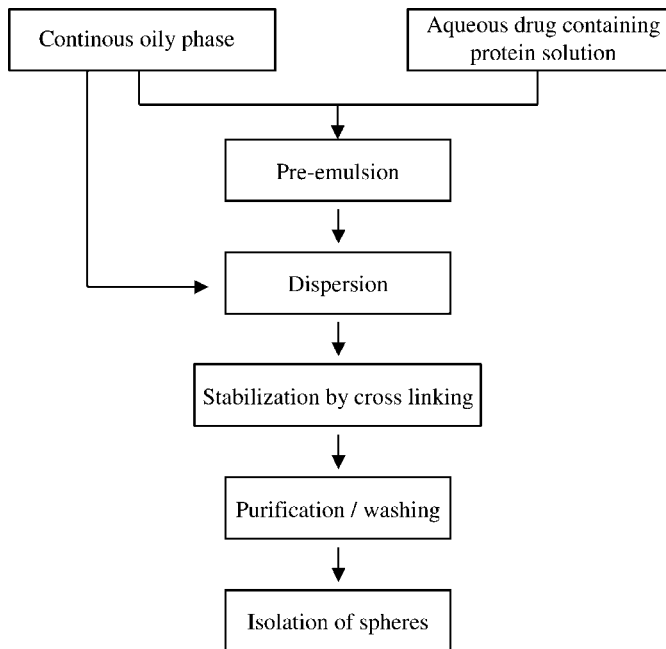


**Fig. 6.3.** Flow chart of nanoparticle preparation by emulsion techniques.

thermore, HSA is a well-defined starting material with a well-known primary structure (Table 6.1) enabling modifications by protein chemistry under stoichiometric conditions. In addition to the use of HSA, other albumin derivatives such as BSA [3] and rabbit serum albumin [24] have been described for the preparation of colloidal drug carrier systems. Although microaggregates and microspheres based on albumin derivatives were reported as early as the 1940s and 1950s, the first descriptions of albumin-based microspheres with a uniform size and predictable physicochemical characteristics were at the end of the 1960s by Rhodes et al. [25] and Zolle et al. [26] who used the system in a radioactive-labeled form for diagnostic purposes. Several further diagnostic applications for such kinds of serum albumin-based microspheres were published in the following years [27–29]. The emulsification methods for the preparation of microspheres had to be modified in order to produce nanoparticulate drug carrier systems instead of microparticles. The group of Scheffel et al. was the first to produce HSA-based particles in the nanometer size range between 300 and 1000 nm, so-called nanospheres, by a modified emulsion technique, and used the system after radioactive labeling to investigate the toxicity and body distribution of such a carrier system [30]. The first description of albumin nanoparticles prepared by a modified method of Scheffel et al. for drug delivery purposes was published by Kramer [31]. In the manuscript the incorporation of the anticancer agent mercaptopurine was outlined, and it was shown that over 85% of the drug present in the original emulsion was associated

**Tab. 6.1.** Quantitative amino acid composition of HSA divided into different properties of amino acid side-chains (the one letter code is given in brackets; amino acids usually used for covalent modification by protein chemistry are outlined in italics)

<b>Amino acid</b>	<b>Number/HSA</b>
Amino acids with hydrocarbon side-chains	
Gly [G]	12
Ala [A]	62
Val [V]	41
Leu [L]	61
Ile [I]	8
Phe [F]	31
Pro [P]	24
Amino acids with nonionic but polar side-chains	
Ser [S]	24
Thr [T]	28
<i>Cys [C]</i>	35
Met [M]	6
Trp [W]	1
Tyr [Y]	18
Asn [N]	17
Gln [Q]	20
Basic amino acids	
<i>Lys [K]</i>	59
Arg [R]	24
His [H]	16
Acidic amino acids	
<i>Asp [D]</i>	36
<i>Glu [E]</i>	62

with the microspheres in the size range between 200 and 1200 nm. Further experiments with the more hydrophilic drug daunorubicin were performed and it was observed that the amount of incorporated drug could be increased with the hydrophilicity of the drug compound. Kramer outlined that such carrier systems are of growing need for drugs with pronounced systemic toxicities and enable drug delivery to target tissues in precise dosages and with minimal interaction with normal tissues.

The main problems with the preparation in an oil-in-water emulsion are the purification of the resulting nanoparticles and the thermal stress for the incorporated drug in the case of particle stabilization by heat denaturation. In most cases the nanospheres have to be washed several times with organic solvents such as diethyl ether and these solvents have to be eliminated prior to the application of the carrier system. To circumvent the problem of the thermal stress during particle stabilization Widder et al. described the chemical crosslinking of HSA microspheres in the size range of about 1  $\mu\text{m}$  by the use of 2,3-butanedione [13]. The group incorpo-

rated doxorubicin into different particle preparations and compared the heat-denatured microspheres with their proposed chemical crosslinked systems, and showed that the stability of both preparations was identical, but that the drug release behavior was mainly influenced by the stabilization procedure. In the following years the group mainly focused on the incorporation of magnetite particles as well as the drug compound into the microsphere matrix in order to achieve drug targeting by magnetic guidance. The applications of such magnetic microspheres were described in the field of diagnostics [32–34] and tumor therapy [35–40].

A complete and systematic study regarding the influence of HSA concentration, emulsification time and power, stirring rate, heat stabilization temperature, and the type of the nonaqueous phase was carried out by Gallo et al. [14]. As an initial procedure for particle preparation they used an aqueous solution of BSA and dispersed this solution in cottonseed oil by ultrasonication. The resultant emulsion was added dropwise to a larger amount of cottonseed oil at 125 °C under stirring in order to stabilize the resulting microspheres by heat denaturation. The influences of different preparation parameters such as albumin concentration, emulsification time, emulsification power and aqueous-to-oil phase volume ratio on the final particle size were evaluated. They found that the procedure for preparing albumin microspheres can withstand a large range of variability until significant changes in the particle characteristics can be observed. Optimal conditions for the preparation of smaller and more uniform microspheres were found by increasing the protein concentration as well as the temperature of heat stabilization. The group of Gupta et al. described in detail the preparation of albumin microspheres loaded with adriamycin [41, 42] as well as adriamycin and magnetite [43]. They focused on the *in vitro* drug release characteristics of these kinds of microspheres and found that the drug release was dependent on the presence of magnetite as well as on the stabilization temperature during the preparation process.

In a systematic study based on a central composite design, Müller et al. proposed a new emulsion method for the preparation of albumin nanoparticles [23]. They established an emulsion method using ultrasound and static mixing for the preparation of sub-200 nm particles. The statistical method used for the evaluation of the different process parameters revealed that only albumin concentration and aqueous phase volume showed a significant influence on the parameters of particle size, polydispersity and yield.

A comprehensive review of the preparation of albumin microspheres by emulsion techniques was given by Gupta and Hung [44–46]. In a methodological review Arshady et al. discussed the main basic features of the preparation procedure such as the crosslinking technique, droplet formation and stabilization, particle size, and size distribution [47].

#### 6.3.1.2 Emulsion Technique for the Preparation of Gelatin-based Microspheres and Nanoparticles

In principle, the emulsion method for the preparation of serum albumin microspheres can be adapted for gelatin microsphere preparation. Gelatin offers some advantages as a matrix material: it is a natural, inexpensive, low-immunogenic,

**Tab. 6.2.** Quantitative amino acid composition of gelatin A divided into different properties of amino acid side chains (the one letter code is given in brackets; amino acids usually used for covalent modification by protein chemistry are outlined in italics)

<b>Amino acid</b>	<b>Amount (%)</b>
Amino acids with hydrocarbon side-chains	
Gly [G]	33.0
Ala [A]	11.2
Val [V]	2.6
Leu [L]	2.4
Ile [I]	1.0
Phe [F]	1.4
Pro [P]	13.2
Amino acids with nonionic but polar side chains	
Ser [S]	3.5
Thr [T]	–
<i>Cys [C]</i>	–
Met [M]	3.6
Trp [W]	–
Tyr [Y]	0.3
Asn [N]	1.6
Gln [Q]	2.5
Basic amino acids	
<i>Lys [K]</i>	2.7
Arg [R]	4.9
His [H]	0.4
Acidic amino acids	
<i>Asp [D]</i>	2.9
<i>Glu [E]</i>	4.8

nontoxic and good biodegradable macromolecule which is registered as an excipient for pharmaceutical formulations. As a protein-based product, gelatin possesses several functional groups which are available for covalent modifications. Due to the preparation of gelatin by hydrolysis of collagen, no defined primary structure can be given and, therefore, the composition of gelatin is most often described by the percentage amount of the respective amino acids (Table 6.2).

The influence of the preparation parameters on the physicochemical characteristics of drug-loaded gelatin microspheres was investigated by Esposito et al. [48]. As model drugs clonidine hydrochloride, TAPP-Br and bromocriptine mesylate were chosen in order to evaluate their encapsulation efficiency and release characteristics. As previously observed for drug incorporation in albumin-based particles [31], the drug loading was mainly dependent on the hydrophilic–hydrophobic balance of the drug molecule, with hydrophobic drugs showing a reduced trapping efficiency. This was due to an increased drug concentration in the oily phase of the emulsion system with increasing hydrophobicity of the drug. The release profile of



the hydrophilic drug TAPP-Br was characterized by a biphasic behavior, whereas the more hydrophobic drugs were released by a fast first-order release mechanism.

The nanoencapsulation of BSA in the matrix of gelatin-based nanoparticles was described by Li et al. [49]. BSA-containing gelatin nanoparticles of a spherical shape and a diameter of 840 nm were achieved. *In vitro* studies revealed BSA release by a diffusion-controlled mechanism. The release kinetic was mainly influenced by the water content of the particles as well as by the temperature of particle stabilization.

### 6.3.1.3 Emulsion Technique for the Preparation of Casein-based Microspheres and Nanoparticles

As well as the application of albumin and gelatin for the preparation of particulate drug carrier systems, the emulsion techniques described so far can also be applied to other proteins. In order to achieve microspheres with an enhanced hydrophilicity, casein was used as a further starting material for microsphere preparation. Chen et al. compared casein and albumin for the preparation of microspheres and their efficiency as a drug carrier system for doxorubicin [50]. They prepared the microspheres based on a water-in-oil emulsion technique in combination with glutaraldehyde stabilization. Compared with albumin, the surface charge of the casein system was more negative and the microspheres exhibited a slower release of drug *in vitro*. Under *in vivo* conditions in a tumor model in rats the casein system showed greater antitumoral potency than did the albumin system at equal amounts of the drug. Due to this observation it was considered that the carrier matrix can influence the potency of the incorporated drug.

The disadvantage of the casein-based microspheres was their poor spherical geometry. Therefore, the preparation of casein microspheres was further optimized by a new emulsion technique using aliphatic polyurethane in a mixture of hexane and dichloromethane as the dispersion medium, which achieved spherical, glutaraldehyde crosslinked microspheres [51, 52]. In comparison to established emulsion techniques, the avoidance of surfactants during particle preparation with this new method was advantageous. The proposed emulsion technique was used for the preparation of microspheres loaded with the cytotoxic drug methotrexate [53]. The versatility of the method was demonstrated by the synthesis of albumin as well as casein microspheres, leading to mean particle sizes of 54 and 172  $\mu\text{m}$ , respectively. They compared both preparations and observed a comparable drug loading as well as a comparable drug release of about 35% in 24 h for both the casein and albumin systems. The applicability of the preparation method of casein microspheres in the presence of the stabilizer polyurethane was demonstrated in combination with different drugs such as methotrexate [53], theophylline [54], 5-fluorouracil [55] and progesterone [56]. Under *in vivo* conditions it was shown that progesterone-loaded casein microspheres hold promise for sustained drug release up to 5 months. After intramuscular injection into rabbits over this time period constant plasma concentrations of 1–2  $\text{ng mL}^{-1}$  were observed without any significant burst release of the drug.

With regard to surface modification, Latha et al. reported that the hydrophilicity

of the casein spheres can be imparted by an end-capping process of the residual aldehyde groups present from the glutaraldehyde crosslinking with glycine or 2-aminoethanol. Comparable end-capping procedures were described earlier by Longo et al. for the preparation of HSA microspheres which were sterically stabilized by the incorporation of artificial polymers such as poly(methyl methacrylate) [57, 58].

### 6.3.2

#### **Nanoparticle Preparation by Coacervation**

As previously described, the disadvantages of the emulsion methods for particle preparation are (a) use of organic solvents for the removal of the oily residues of the preparation process, and (b) removal of surfactants that are used for emulsion stabilization during the preparation and remain on the particle surface. Even in the case of optimized emulsion techniques using aliphatic polyurethane in a mixture of hexane and dichloromethane [51, 52] the resulting nanoparticles have to be purified from the organic compounds of the dispersion medium. In addition to the disadvantage of extensive purification steps, the emulsion techniques preferentially lead to microparticles instead of particles in the nanometer size range, which mostly impedes an intravenous route of administration. Therefore, as alternative methods, the coacervation techniques and desolvation methods, derived from the coacervation method of microencapsulation, have been described for the preparation of nanoparticles. Compared to the emulsion techniques, coacervation methods are simpler and the resulting particles can more easily be cleaned. Beyond these advantages, the resulting particles are mostly in the nanometer size range.

Coacervation is defined as the separation of a colloidal dispersion into a colloid-rich and a colloid-poor phase by careful control of temperature, pH, electrolyte addition or other factors. The coacervate or colloid-rich phase forms as droplets, which makes the system opaque. In principle, coacervation techniques can be subdivided in simple and complex coacervation. Simple coacervation is characterized by the use of only one colloid and involves removal of the associated water from around the dispersed colloid by agents with greater affinity for water, such as various alcohols and salts. The dehydrated molecules of the colloidal dispersion tend to aggregate with surrounding molecules to form the coacervate. Simple coacervation techniques for the preparation of nanoparticles are often described by the term “desolvation”. In contrast, complex coacervation involves the use of more than one colloid. The coacervation is accomplished mainly by charge neutralization of the colloids carrying opposite charges rather than by dehydration.

#### **6.3.2.1 Complex Coacervation Techniques for the Preparation of Nanoparticles**

An example of complex coacervation is the preparation of nanoparticles based on albumin and heparin described by Liu and Leong [59]. The group described a coacervate from complexation of HSA and heparin as the clinically used components for the entrapment, and controlled release of drugs in the molecular weight range between 262 and 67 000 Da. Particle preparation was performed by simply mixing

an acidic HSA solution, which contained the respective drug, with a heparin solution. Due to the opposite charges of both polymers, phase separation under the preparation conditions occurs leading to the formation of nanoparticles. The resulting particles were stabilized by a crosslinking procedure with a carbodiimide derivative. Drug-loading studies were performed with a multitude of compounds showing that a high loading efficiency was observed especially with positively charged drugs. Due to a proteolytic degradation of the carrier system, the *in vitro* release of the drugs was faster in cell culture medium than in phosphate-buffered saline. In addition to the use of albumin, complex coacervation techniques can be carried out with different proteins such as casein [60] and gelatin [61]. In combination with gelatin, complex coacervation was most often used for the incorporation of plasmid DNA in particulate systems. For example, a method for the incorporation of plasmid DNA into a gelatin-based nanoparticle system by salt-induced complex coacervation followed by a crosslinking step with 1-ethyl-3-(3-dimethylamino-propyl)carbodiimide (EDC) was reported [61–64]. Comparable coacervation procedures for the preparation of plasmid DNA-containing nanoparticles based on the polysaccharide chitosan were described by Mao et al. and Roy et al., with the exception that the chitosan–DNA coacervate was stable without any further crosslinking step [65, 66].

#### 6.3.2.2 Simple Coacervation (Desolvation) Techniques for the Preparation of Nanoparticles

As previously outlined, nanoparticle preparation by simple coacervation techniques is often described by the term “desolvation”. Using desolvation techniques, the phase separation of the colloidal solution is carried out by salting out, temperature change, pH variation or addition of water-miscible organic solvents such as alcohols. In the field of nanoparticle preparation, the addition of salts such as sodium sulfate or ammonium sulfate as well as the addition of organic solvents such as alcohols or acetone is most often used. In a second preparation step the nanoparticles have to be stabilized either by chemical crosslinking using bifunctional aldehydes or by thermal denaturation (Fig. 6.4).

The first paper describing desolvation procedures for the preparation of nanoparticles as drug carrier systems was at the end of the 1970s by Marty et al. [12]. The group established a general method for the preparation of nanoparticles based on HSA, BSA, ethylcellulose and casein. In principle, an aqueous macromolecule solution was prepared and the desolvation was performed under the control of turbidimetric measurements by the addition of either a sodium sulfate solution or ethanol. After the addition of a small amount of a resolating agent the resulting nanoparticles were stabilized by chemical crosslinking with glutaraldehyde. The resulting nanoparticles could be purified by a gel-filtration procedure and stored in a solid form after freeze-drying. For the drug loading of the nanoparticles Marty et al. described the incorporation method in which the drug is either added to the aqueous macromolecule solution or to the solution of the desolvating agent. A comparable desolvation procedure was used by El-Samaligy and Rohdewald in order to incorporate triamcinolone diacetate in gelatin-based nanoparticles [67, 68].

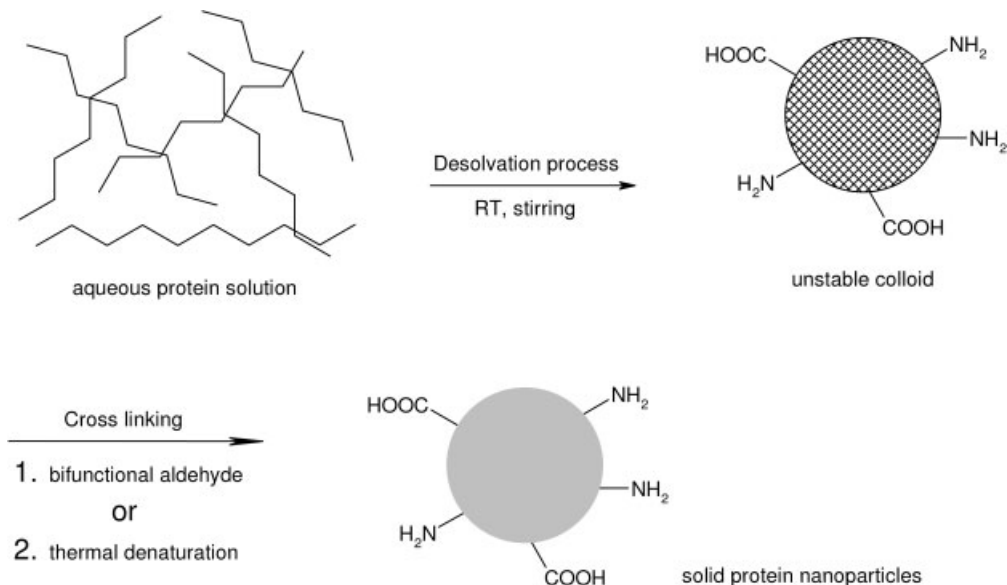


**Fig. 6.4.** Nanoparticle preparation by desolvation (simple coacervation) of an aqueous protein solution followed by particle stabilization by crosslinking.

They prepared nanospheres in the size range of about 200 nm by addition of isopropanol to an ammonium sulfate coacervated HSA system.

The binding and *in vitro* release of the nucleoside analogue ganciclovir (GCV) in combination with BSA prepared by desolvation techniques was studied in several publications [69–72]. The binding of the drug to preformed nanoparticles was compared to the entrapment of GCV during nanoparticle formation. The highest drug-loading capacity was observed for nanoparticles prepared by the addition of the drug to a solution of albumin leading to adsorptive drug binding prior to the formation of the carrier by desolvation. The release profile of the nanoparticle preparations was characterized by a biphasic pattern with an initial and rapid release followed by a slower step for up to 5 days [70]. The amount of rapidly released GCV was highest for nanoparticles with drug bound by adsorption to the preformed carrier. Under cell culture conditions the latter preparation was the most active formulation in the antiviral test assays, whereas the formulation with incorporated drug produced the highest decrease on cytotoxicity of the free drug [72]. The nanoparticles were intended to be used after intravitreal injection as a drug delivery system for therapy of cytomegalovirus infection. Therefore, the ocular disposition after intravitreal injection as well as the toxicity induced by the prolonged presence of BSA nanoparticles was studied [71]. It was observed that a significant amount of the nanoparticles remained in the vitreous cavity for a prolonged period of time in combination with no signs of autoimmune phenomena or alterations in the behavior of ophthalmic cells. The same group investigated nanoparticles pre-

pared by the same techniques for suitability as a drug carrier system for antiviral phosphodiester and phosphorothioate oligonucleotides [73] as well as for their ability to reach the central nervous system in an experimental allergic encephalomyelitis animal model [74].

The suitability of HSA-based nanoparticles to target drugs into cells of the reticuloendothelial system (RES) and to establish a potential therapy of the HIV infection was investigated in a number of studies. The nanoparticles were prepared by desolvation techniques and desolvation was performed by the addition of ethanol. After purification, the nanoparticles were incubated with primary human monocytes/macrophages in order to evaluate cell accumulation. Nanoparticles with a diameter of 200 nm were found to be most useful for targeting antiviral substances such as azidothymidine to macrophages [75]. It was observed that cells infected with a monocytotropic HIV isolate possessed an even higher particle uptake than noninfected cells and thus HSA nanoparticles were recommended as promising carrier systems for targeting drugs into HIV-infected cells of the RES. In an electron microscopy study, the process of cellular particle uptake was demonstrated to be phagocytosis [76]. In this study the intracellular degradation of the nanoparticles was followed and it was observed that particle degradation started within some hours after particle uptake. Within 3 days after particle incubation the process was almost terminated. Based on these observations HSA nanoparticles loaded with the drugs azidothymidine (AZT) and dideoxycytidine (ddC) were tested for their ability to prevent HIV infection in monocytes/macrophages [77]. According to the proposed methods of Marty et al. [12], drug loading was performed by the incorporation method in which the drug is added to the aqueous macromolecule solution prior to protein desolvation. Under cell culture conditions the nanoparticles loaded with the nucleoside analogs were effective against HIV infection, but they showed no superiority in relation to free drug. This was attributed to a fast and easy cellular uptake of the tested substances in free form which does not require drug delivery by nanoparticles.

The suitability of albumin nanoparticles as drug carrier systems for antisense oligonucleotides was studied by Arnedo et al. [78]. Nanoparticles were prepared based on BSA by a simple coacervation process and a phosphodiester oligonucleotide was either incorporated into the particle matrix by incubation with the albumin prior the coacervation process or adsorbed to preformed nanoparticles. Due to the electrostatic interactions that were responsible for drug adsorption to preformed nanoparticles, the adsorbed amount was susceptible to changes in pH and ionic strength of the medium. In comparison to drug loading by adsorption, the incorporation of the drug during nanoparticle formation resulted in a stable entrapment of the antisense oligonucleotide, which complies with earlier results achieved with the nucleoside analog GCV [70]. Only the incorporative method of drug binding was suitable for protection of the antisense compound against enzymatic degradation.

In most of the studies described so far the effective drug loading to the nanoparticles was of major importance, but preparation parameters influencing the physicochemical characteristics of the particles were virtually ignored. The first sys-

tematic investigations for selective control of particle size and size distribution during the desolvation procedure were described in 1993 by Lin et al. [79]. They proposed the preparation of HSA nanoparticles of diameter around 100 nm using a surfactant-free pH-coacervation method. The particles were prepared by the dropwise addition of acetone to an aqueous HSA solution at pH values between 7 and 9, followed by glutaraldehyde crosslinking and purification by gel-permeation chromatography. It was found that particle size was reduced with increasing pH of the HSA solution, apparently due to increased ionization of the HSA (isoelectric point  $pI = 5.3$ ) which leads to repulsion of the HSA molecules and aggregates during particle formation. HSA nanoparticles were obtained in a size range between 90 and 250 nm by adjusting the pH and by controlling the amount of added acetone. The described nanoparticles were of spherical shape, but transmission electron microscopy (TEM) revealed a broad size distribution. No further data concerning the polydispersity of the nanoparticles prepared under different conditions was given. A major shortcoming of the paper is that the pH was adjusted in the absence of salt, whereas it is well known that, under these conditions, pH measurements applying glass electrodes are of limited reliability, in particular in the presence of high concentrations of protein [80].

The process of protein desolvation for the preparation of nanoparticles was adopted and studied in more detail by the group of Langer et al. with the objective to establish particle preparation under well-defined conditions [81–85]. In an earlier study a desolvation method for the preparation of nanoparticles based on HSA and gelatin was described, and the resulting particles were characterized with respect to size,  $\zeta$  potential and number of available amino groups on their surface [81]. In this study the amount of the desolvating agent ethanol in the desolvation process was found to control particle size, but the variability in size at a given ethanol amount was high. The high size variability was confirmed by sedimentation velocity analysis in an analytical ultracentrifuge and electron microscopy [84]. In part, this variability has to be attributed to the manual performance of the desolvation process, characterized by a drop-by-drop addition of the desolvating agent. The conditions of particle stabilization by chemical crosslinking in the presence of the bifunctional compound glutaraldehyde or by heat denaturation showed no influence on the resulting particle size, but the degree of chemical crosslinking mainly influenced the number of amino groups on the surface of HSA nanoparticles as well as the  $\zeta$  potential of the colloid. With regard to a controllable particle size in combination with a reproducible desolvation method, a pump-controlled preparation method was established in a following study which enabled particle preparation under defined conditions (Fig. 6.5) [85]. Based on this new preparation procedure several factors of the preparation process such as rate of ethanol addition, pH value and ionic composition of the HSA solution, protein concentration, and conditions of particle purification were evaluated. Most of the parameters studied showed only a minor influence on the particle characteristics. Only the pH value of the HSA solution prior to the desolvation procedure was identified as the major factor determining particle size. These observations were in good agreement with the earlier work of Lin et al. [79] which was described above. By

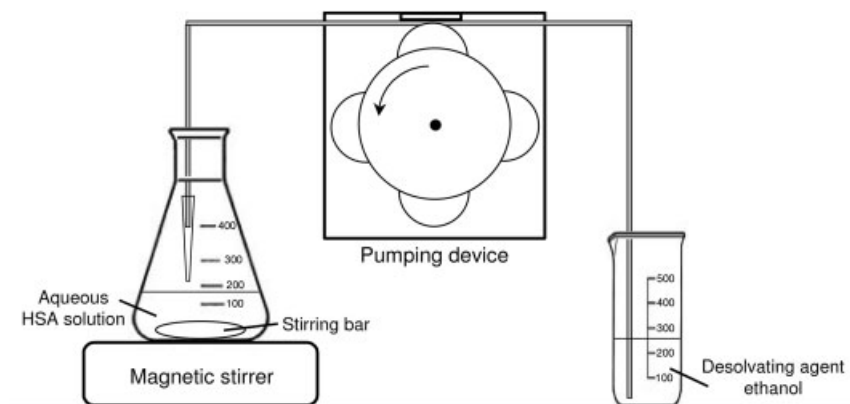


Fig. 6.5. Simple pump-controlled system for reproducible protein desolvation.

sedimentation velocity analysis it was demonstrated that application of a pump-controlled system in combination with a defined pH adjustment leads to well-defined mean particle sizes as well as narrow size distributions.

#### 6.4

#### Basic Characterization Techniques for Peptide Nanoparticles

A rational development of a protein-based colloidal carrier system requires a systematic characterization of the resulting nanoparticles. In particular, physicochemical parameters such as particle size, size distribution,  $\zeta$  potential and surface morphology are of major importance.

Photon correlation spectroscopy (PCS) was used in most of the pharmaceutical studies as the standard method for determination of particle size and size distribution. In principle, PCS uses Brownian motion to measure the size of particles. In brief a diffusion coefficient  $D$  of the particles in suspension is determined by laser light scattering. Based on this coefficient  $D$  and the well-known Stokes–Einstein equation, a “Stokes’ diameter” or hydrodynamic diameter is calculated, which is not equivalent to a weight or number diameter. The advantage of PCS can be seen in a rapid determination of particle size within several seconds or minutes. However, the user has to be aware of the limitations of PCS, such as low resolving power and well-known problems of mathematically ill-conditioned analysis of the autocorrelation function. The resulting particle size distributions can be strongly biased, being critically dependent on the model used for raw data analysis.

As well as PCS, sedimentation velocity analysis in an analytical ultracentrifuge, a standard technique for characterizing particle size distributions in macromolecular chemistry, can also be used in the field of pharmaceuticals as an appropriate technique for particle sizing. In principle, during the centrifugation process the apparent absorbance (turbidity) of the nanoparticle sample versus radius is measured followed by data modeling as a distribution of nondiffusing spherical particles. As

the migration of particles in a gravitational field of an ultracentrifuge shows a stronger size dependence than the diffusion coefficient  $D$  measured by PCS, this method has the potential for significantly higher resolution [86, 87] and therefore is much less mode dependent. Therefore, due to the superior resolving power of this technique more detailed information about the particle size distribution can be obtained. The suitability of ultracentrifugation for characterization of HSA nanoparticles was confirmed by Vogel et al. [84]. The study revealed that HSA nanoparticles prepared by a manual performed desolvation process, characterized by a drop-by-drop addition of the desolvating agent, showed a high variability in particle size. The same technique can also be applied to confirm the reproducibility of particle preparation under optimized preparation conditions [85].

Different microscopic techniques such as electron microscopy (reflection and transmission) and atomic force microscopy (AFM) are useful for determination of particle shape and surface morphology. For example, knowledge of particle shape is a basic requirement for reasonable application of analytical techniques such as PCS and analytical ultracentrifugation – spherical particle shape is an imperative prerequisite for particle size analysis by PCS. In the field of analytical ultracentrifugation, information about particle shape is necessary to apply the proper mathematical model to the apparent absorbance versus radius raw data. For instance, using TEM, it was confirmed that the process of protein desolvation described above for the preparation of HSA nanoparticles led to a spherical particle shape [84]. Therefore, the particle system was well suited for size analysis using PCS or sedimentation velocity analysis. Directly after manual particle preparation and purification, the samples showed a slightly broader size distribution which could be fractionated into narrow distributions by preparative density gradient centrifugation (Fig. 6.6).

In addition to TEM, AFM is another useful technique to obtain more detailed information about surface morphology. AFM is a widely used experimental technique for the characterization of nanostructures. In particular, due to its ability to map variations in material properties with nanometer resolution, AFM is well suited to probe potential subcomponents or substructures of nanoparticles. An AFM picture of HSA nanoparticles prepared by protein desolvation under the same conditions described for the sample in Fig. 6.6 is depicted in Fig. 6.7. The height image of the sample confirms the spherical nature of the nanoparticles, whereas the phase image reveals a substructure in the size range of about 15 nm, showing the crosslinked nature of these particles.

The stability and electrical behavior of nanoparticles can be assessed by determination of the  $\zeta$  potential of the particle colloid under varying pH and buffer conditions. Titration experiments are useful to find the optimal handling and storage conditions for the particle system as well as to determine the isoelectric point of the nanoparticles. For example, the group of Langer et al. used titration experiments for the determination of the  $\zeta$  potential in order to take a more detailed look at the effect of pH and buffer variation on the stability of HSA nanoparticles [85]. They observed positively charged nanoparticles at a pH of 3. With increasing pH value the  $\zeta$  potential was reduced to about  $-50$  mV at pH values between 7 and 10. The salt dependency of the  $\zeta$  potential was determined by titration experiments



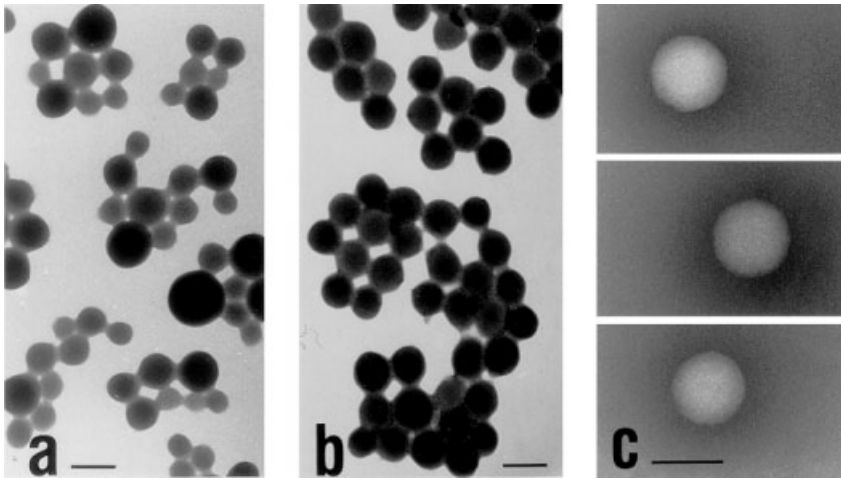


**Fig. 6.6.** Morphology of HSA nanoparticles by means of TEM of negatively stained samples: (a) unfractionated particles, (b) particles in the fraction of highest turbidity from a sucrose gradient and (c) three arbitrary selected particles of sample (b) on films glow discharged for 30 s. Bar length = 200 nm. (From Ref. [84].)

with concentrated buffer systems. As could be expected, due to a shielding of the surface charge with increasing buffer concentration the  $\zeta$  potential of the colloid was reduced. However, it became obvious that a phosphate buffer can be used at least up to concentrations of 150 mM without reducing particle surface charge to a degree that leads to isoelectric aggregation of the particles. Furthermore, the effect of crosslinking on the isoelectric point ( $pI$ ) of HSA nanoparticles was determined. Glutaraldehyde crosslinking of the particle matrix was found to decrease the  $pI$  value of the particles significantly. Such a reduction could be expected for a covalent reaction of glutaraldehyde with lysine side-chains of the protein HSA.

In addition to the basic characterization techniques outlined within this chapter, drug-loading efficiency as well as characterization of the chemical surface structure is of major importance. The influence of drug properties and particle preparation techniques on the drug-loading efficiency was described above within the overview of preparation methods. The analysis of the chemical surface structure depends mainly on the nature of the functional groups on the particle surface or the surface modification strategy used. Different ways of surface modification and the methods suitable for characterization of the resulting particle surface structures are outlined below.

## 6.5

### Drug Targeting with Nanoparticles

Most often nanoparticulate drug carrier systems were prepared in order to modify the body distribution of the entrapped drug and to transport the drug to its site of

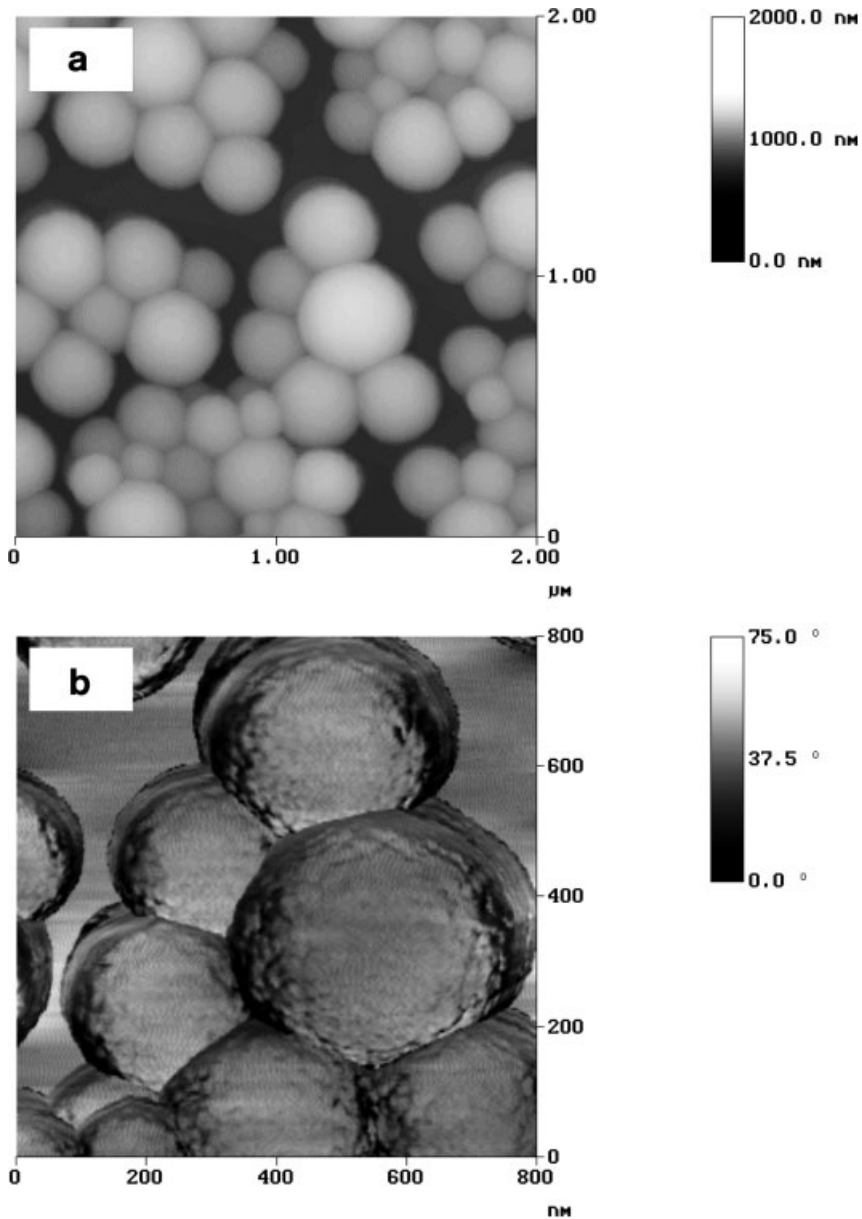


**Fig. 6.7.** Morphology of HSA nanoparticles by means of AFM in tapping mode on a Nanoscope IIIa (Digital Instruments, Santa Barbara, CA) with rotated tapping mode etched silicon probe (RTESP) tips. (a) Height image of nanoparticles on mica. (b) Phase image of the

central part of (a) with crosslinked substructure visible. (From Professor U. S. Schubert, Eindhoven University of Technology, Laboratory of Macromolecular Chemistry and Nanoscience, Eindhoven, The Netherlands.)

action (i.e. drug targeting). When nanoparticles are administered intravenously they are quickly recognized by the mononuclear phagocyte system (MPS) and cleared from the circulation. The size of the nanoparticles as well as the hydrophobicity of their surface determine the *in vivo* fate of the system, with larger particle size and higher hydrophobicity leading to a more pronounced adsorption of blood components (i.e. opsonization) followed by a more rapid clearance from circulation. Therefore, hydrophilic surface structures in combination with small particle sizes (100–200 nm) are crucial parameters for developing nanoparticulate drug carriers with extended half-lives in blood.

### 6.5.1

#### Passive Drug Targeting with Particle Systems

After intravenous injection, unmodified nanoparticles enable passive drug targeting, which is characterized by particle uptake in cells of the MPS. Particle accumulation in macrophages of the liver, spleen and bone marrow as well as in circulating monocytes is observed. The resulting body distribution of the particulate carrier systems is mainly influenced by two physicochemical properties – particle size and surface characteristics [88]. Concerning particle size, the particles should be small enough not to be removed by simple filtration mechanisms in a capillary bed after intravenous injection. On the other hand, surface characteristics such as hydrophilicity/lipophilicity represent the major determinants for protein adsorption in biological fluids and may modify particle interaction with specific plasma membrane receptors, thus leading to elimination of the particles from the systemic circulation. The mechanism of protein adsorption on particle surfaces in conjunction with the recognition of such coated particles by monocytes and macrophages is named opsonization. After intravenous administration of nanoparticle suspensions the particles are normally rapidly coated by adsorption of specific blood components known as opsonins. After this coating the particles are recognized by the MPS and are rapidly eliminated from the central blood circulation. As well as the surface characteristics, the opsonization process seems to be influenced by the surface curvature of the carrier system, with smaller carriers leading to a reduced adsorption of proteins and opsonins, and in turn to a reduced uptake of such systems by phagocytic cells [89].

Therefore, a reduction of the opsonization process leading to a prolongation of the plasma half-life is of major importance in order to achieve a modified body distribution. Coating of the particles with opsonins can be reduced by the introduction of a more hydrophilic surface structure in combination with a reduced particle size. Different techniques to achieve a hydrophilic particle surface are outlined below.

### 6.5.2

#### Active Drug Targeting with Particle Systems

In contrast to passive drug-targeting strategies, active drug targeting enables the transport of the particle system to body compartments not accessible to the un-

modified system. Therefore, in a first step of particle preparation it is required to achieve a more hydrophilic surface structure which leads to a prolongation of the plasma half-life. In a second step, the particle system has to be equipped with ligands, so-called drug-targeting ligands, which enable cell-specific accumulation of the particle system.

### 6.5.3

#### **Surface Modifications of Protein-based Nanoparticles**

In order to achieve a prolonged circulation half-life and to enable active drug targeting the opsonin adsorption has to be reduced by (a) the choice of a suitable particle size and (b) surface modification of the drug carrier system. An appropriate approach in this direction is the modification of the particle surface by different hydrophilic compounds.

As well as modification of the particle surface with hydrophilic compounds in order to modify the pharmacokinetic behavior, surface modification techniques with the aim of enhanced drug loading have also been described. For example, in a paper by Hnatowich and Schlegel, albumin microspheres were synthesized and the particle surface was modified by the covalent attachment of the chelating agents EDTA and DTPA [90]. The resulting particles were used for the attachment of the radionuclide  $^{67}\text{Gd}$  by transcomplexation from a gadolinium acetate solution.

### 6.5.4

#### **Surface Modification by Different Hydrophilic Compounds**

In the field of protein-based nanoparticles the first attempts to achieve a more hydrophilic particle surface were made on the basis of albumin nanoparticles [91, 92]. Based on the method of Longo et al. [57], microspheres were prepared and stabilized by glutaraldehyde crosslinking. Hydrophilic surface modifications were achieved by quenching free aldehyde groups of glutaraldehyde with different amino-functional compounds such as ethanolamine and glycine. The stability of the chemical surface modification was confirmed in fresh human serum and in aqueous solutions of different pH values. Under cell culture conditions the phagocytic uptake of the surface-modified nanoparticles was mainly dependent on the resulting  $\zeta$  potential, with a higher particle charge leading to a more pronounced cellular uptake. Contrary to the results of the cellular uptake study, no differences in blood circulation times and organ accumulation between different nanoparticle preparations were observed after intravenous injection in rats [93]. Therefore, the effect of surface modification by hydrophilic low-molecular-weight compounds remained questionable.

With regard to active drug targeting with nanoparticles (see below), hydrophilic systems with functional groups at their surface are necessary to which ligands such as antibodies can be attached. The emulsion methods for particle preparations employ a lipophilic external phase and therefore produce microspheres with a hydrophobic surface due to the preferential orientation of lipophilic amino acids

of the albumin molecules to the outer lipophilic phase of the water-in-oil emulsion. MacAdam et al. developed a method for the preparation of albumin microspheres which had chemically reactive groups such as carboxylic and amino groups on the surface to which ligands could be attached [3]. Carboxylic groups were introduced by the reaction of amino groups with iodoacetic acid under alkaline conditions. The group described methods for the quantitative determination of these groups at the particle surface using the radioactive probes [ $^{14}\text{C}$ ]glycine ethyl ester and [ $^{14}\text{C}$ ]sodium acetate.

#### 6.5.5

#### Surface Modification by Polyethylene Glycol (PEG) Derivatives

In addition to the modifications with low-molecular-weight compounds described above, several approaches were taken to introduce a hydrophilic steric barrier at the particle surface, i.e. by modification of the particle surface with PEG derivatives. Lin et al. performed several approaches for the introduction of PEG chains onto the surface of HSA nanoparticles. Based on their established preparation method for HSA nanoparticles [79] outlined above, Lin et al. compared HSA nanoparticles either stabilized by the glutaraldehyde method or a novel Dextranox-MPEG crosslinking procedure [94]. Dextranox-MPEG is a methyl PEG-substituted oxidized dextran which created a sterically stabilizing polyethylene oxide surface layer surrounding the nanospheres. They tested the electrolyte- and pH-dependent flocculation of both preparations, and concluded that the higher stability of the proposed nanospheres depended mainly on a hydrated steric barrier surrounding the Dextranox-MPEG crosslinked nanospheres, whereas the glutaraldehyde cross-linked system was mainly stabilized by electrostatic repulsive forces. As an alternative method for steric stabilization of HSA nanoparticles, Lin et al. established a nanoparticle preparation based on two different PEG–HSA conjugates, namely a poly(amidoamine)–poly(ethylene glycol) copolymer grafted HSA (HSA–PAA–PEG) and a poly(thioetheramido acid)–poly(ethylene glycol) copolymer grafted HSA (HSA–PTAAC–PEG) [95]. As with the Dextranox-MPEG crosslinked nanoparticles, they confirmed the existence of a hydrated steric barrier surrounding the nanospheres by electrolyte- and pH-dependent flocculation tests, and showed a reduced plasma protein adsorption on the particle surface compared with unmodified nanoparticles. More recently, Lin et al. developed a third method for surface modification of HSA nanoparticles with PEO chains on the basis of methoxy-PEG modified HSA (HSA–mPEG) and evaluated the resulting nanoparticles as outlined for copolymer grafted HSA [96]. The  $\zeta$  potential of the resulting nanoparticles was significantly lower than that of unmodified nanoparticles and the existence of a hydrated steric barrier was confirmed. The two PEG-modified albumin nanoparticle systems prepared on either HSA–PTAAC–PEG or HSA–mPEG were compared to HSA-based nanoparticles with regard to drug loading and *in vitro* drug release using the model compound rose Bengal [97]. The drug-loading efficiency of HSA–mPEG-based nanoparticles was much lower than that of nanoparticles prepared with unmodified HSA, indicating that less drug–protein binding

sites were available in the HSA–mPEG molecule as compared to the HSA molecule. The *in vitro* drug release of the different particle preparations in the presence of trypsin was mainly dependent on the PEG modification, with a slower drug release in the case of PEG-modified nanoparticles. This observation suggests that not only the behavior in biological systems will be modified by surface modification, but that the existence of a steric barrier on the surface of the nanoparticles mainly influences the enzymatic degradation and consequently the drug release properties of the particles.

#### 6.5.6

#### Surface Modification by Drug-targeting Ligands

In order to achieve a system which enables active drug targeting, in addition to a hydrophilic steric barrier at the particle surface which prevents opsonization, the particle system has to be equipped with drug-targeting ligands. In combination with nanoparticulate systems, in most cases antibodies were described as drug-targeting ligands. The first conjugation reactions between particle surfaces and cell-specific antibodies were described in the 1970s for latex particle systems based on synthetic polyacrylates [98, 99]. The first reports of antigen-specific binding were achieved with these particles. In a further step, the nanoparticles were loaded with magnetite, and were used as magnetic microspheres for labeling and separation of lymphocytes and erythrocytes [100]. In the following years antibody-modified synthetic nanoparticles intended for active drug targeting have been synthesized and characterized in detail [101–104]. Apart from polyacrylate-based nanoparticles, other starting materials such as silica [105], PLA [106] and proteins [107–109] were used for the preparation of ligand-modified nanoparticles in later studies.

A first study with protein-based nanoparticles surface modified with cell-specific antibodies was described by Akasaka et al. [107]. An antitumoral antibody was covalently attached to primary amino groups of BSA nanoparticles prepared with glutaraldehyde crosslinking by covalent linkage (Schiff's base formation) of aldehyde groups at the surface of the nanospheres with amino groups of the antibody. Although in this first study with antibody-modified albumin nanoparticles the specificity of the free antibody for tumor cells was clearly demonstrated, tumor cell binding after conjugation of the respective antibody to the nanoparticles remained unclear. After intravenous administration of the antibody-modified nanoparticles in tumor-bearing mice the carrier system was found to be localized mainly in the liver, lungs and kidneys of the animals.

In a further study, antimucus polyclonal antibodies were covalently linked to the surface of albumin microspheres in order to achieve an oral drug delivery system with delayed gastrointestinal transit [110]. Three different particle systems with either a hydrophobic, a hydrophilic or a carboxymethylated surface were used [3] and the linkage was performed by the carbodiimide reaction using 1-ethyl-3-(3-dimethylaminopropyl)carbodiimide. The group observed that only hydrophilic and carboxymethylated microspheres with surface-attached antibody bound significantly more mucin from suspension. The same particle preparations also showed stronger

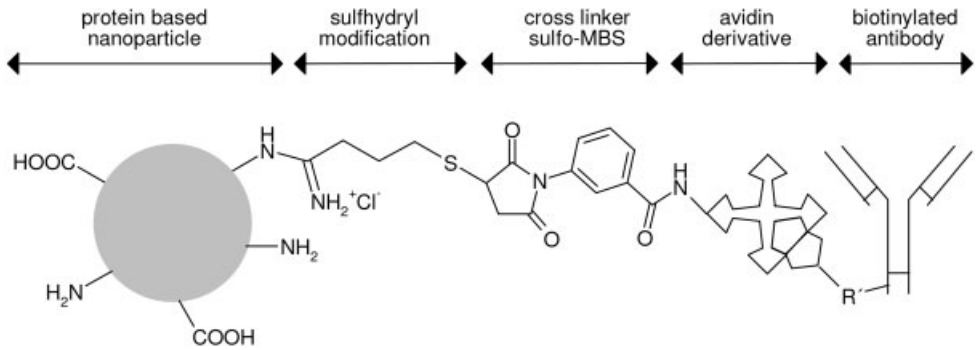


**Fig. 6.8.** Schematic representation of antibody-loaded avidin-modified nanoparticles for cell-type-specific targeting.

binding to isolated gut segments than the other control preparations. The results supported the finding that the combination of a hydrophilic particle surface with a drug-targeting ligand is a precondition for a site-specific carrier system.

In a recent study by Wartlick et al., gelatin as well as HSA nanoparticles were described for cell-type-specific targeting of different breast cancer cells with varying HER2 expression levels [108]. Both particle preparations were prepared by established desolvation techniques and were surface modified in a first step by the covalent attachment of the avidin derivative NeutrAvidin<sup>TM</sup>. The avidin binding was performed with the heterobifunctional PEG-based crosslinker NHS-PEG3400-Mal. The humanized monoclonal antibody trastuzumab (Herceptin<sup>TM</sup>) was used as drug targeting ligand. For the attachment of the antibody to the nanoparticle surface trastuzumab was biotinylated and bound to the particle surface by avidin–biotin complex formation (Fig. 6.8). Under cell culture conditions the resulting antibody-modified nanoparticles showed a highly specific targeting to HER2-overexpressing breast cancer cells. The attachment to the surface of the cells was time and dose dependent, and effective intracellular uptake by receptor-mediated endocytosis was demonstrated. The results indicated that the proposed preparations hold promise for selective drug targeting of tumors expressing a specific tumor antigen.

The same group described a comparable nanoparticulate system based on gelatin for specific drug targeting to T lymphocytes [109]. Using avidin–biotin complex formation a biotinylated anti-CD3 antibody was bound to the surface of NeutrAvidin-modified nanoparticles. The objective of the work was the comprehensive quantification of every chemical reaction step during the preparation procedure of the nanoparticles, including determination of the molecular weight distribution of the starting material gelatin, characterization of the particle surface and determination of the integrity of the covalently attached proteins after conjugation reaction. High compatibility of the nanoparticles with tumor cells was demonstrated under cell culture conditions. The suitability of the proposed particles for receptor-mediated cellular uptake in lymphocytic cells was demonstrated in a separate paper [111].

## 6.5.7

**Different Surface Modification Strategies**

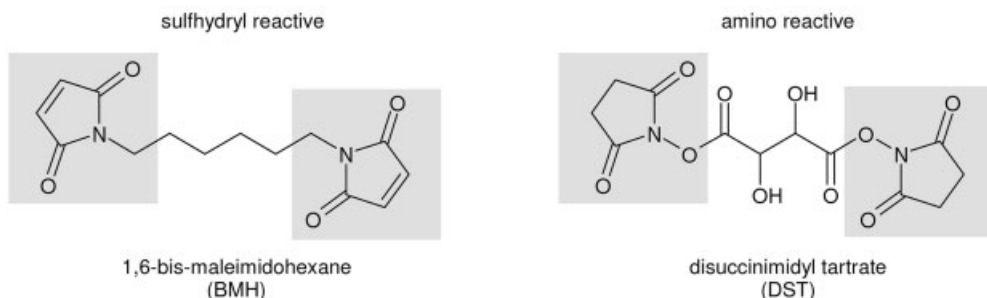
In the case of protein-based nanoparticles the covalent attachment needs a well-defined particle system with functional groups on its surface, which can be used for the respective coupling reaction with the drug-targeting ligand. Therefore, in a number of papers the characterization of the particle surface with regard to functional groups as well as techniques for the introduction of functional groups was described. In the field of protein chemistry, it is mainly amino groups and carboxylic groups that can be used for covalent coupling reactions. In example, proteins such as HSA offer several target sites for covalent modification such as the  $\epsilon$ -amino groups of lysine and the carboxylic groups of asparaginic and glutaminic acid. For glutaraldehyde-stabilized nanoparticles the remaining carbonyl residues of the crosslinker can be used as a further target site.

In a first study by Weber et al., as well as the optimization of the desolvation process for the preparation of HSA and gelatin nanoparticles, the number of available amino groups on the surface of the nanoparticles was determined spectrophotometrically using the reagent 2,4,6-trinitrobenzenesulfonic acid (TNBS) [81]. It was observed that the number of amino groups was mainly dependent on the amount of the crosslinking agent glutaraldehyde used for particle stabilization. As could be expected, increasing amounts of glutaraldehyde led to a decreasing number of available amino groups on the particle surface.

Protein conjugation most often is achieved by the use of established bifunctional crosslinkers, which can be subdivided into homobifunctional and heterobifunctional crosslinkers (Fig. 6.9). Most often heterobifunctional crosslinkers were used which combine two different specific binding sites – one for primary amino groups and one for sulfhydryl groups – in one molecule. Examples for such bifunctional crosslinkers are the homobifunctional substances 1,6-bis-maleinimido-hexane (BMH) [112], disuccinimidyl tartrate (DST) [113] and the heterobifunctional compounds *m*-maleimidobenzoyl-*N*-hydroxysulfosuccinimide ester (sulfo-MBS) [108, 109, 114] or sulfosuccinimidyl-4-*N*-maleimidomethylcyclohexane-1-carboxylate (sulfo-SMCC) [115]. In order to attach an amino group-containing compound to protein-based nanoparticles by the use of such crosslinkers, it is imperative that the nanoparticles expose reactive sulfhydryl groups on their surface. However, as the primary structure of most proteins reveal, there is only a negligibly small number of reactive sulfhydryl groups available in the genuine protein. Therefore, different methods for the introduction of reactive sulfhydryl groups onto the particle surface were described. The objective of a study by Weber et al. was to establish several methods for the introduction of thiol groups onto the surface of HSA nanoparticles [116]. In addition to the  $\epsilon$ -amino groups of lysine, the carboxyl groups of asparaginic and glutaminic acid, and the carbonyl groups of the crosslinker glutaraldehyde were used for the introduction of reactive sulfhydryl groups. In principle, the thiol groups were introduced by the reaction with dithiothreitol or 2-iminothiolane, by quenching reactive aldehyde residues with cystaminiumdichloride, or by coupling L-cysteine and cystaminiumdichloride by the aqueous car-



## 1. homobifunctional cross linkers



## 2. heterobifunctional cross linkers

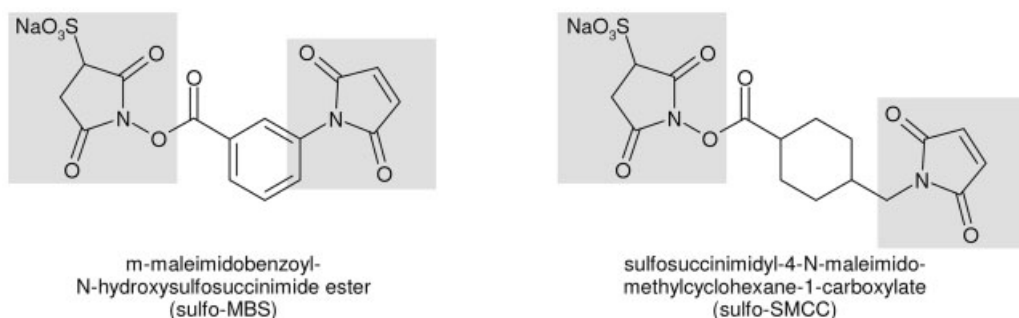


**Fig. 6.9.** Examples of different bifunctional crosslinkers in use for protein chemistry. The reactive groups of the respective crosslinker are outlined in grey.

bodiimide reaction. The resulting nanoparticulate systems were characterized with regard to the number of available sulfhydryl groups and it was shown that the proposed reaction conditions enabled surface modification under well-defined conditions.

In a further step, the sulfhydryl-modified nanoparticles were used for the covalent attachment of functional proteins via bifunctional crosslinkers which reacted in a first step with amino groups of the protein and in a second step with the sulfhydryl groups introduced onto the particle surface [109, 114].

## 6.6

### Applications as Drug Carriers and for Diagnostic Purposes

Protein-based nanoparticles as well as microspheres have been described as drug carrier systems and for diagnostic purposes under *in vitro* and *in vivo* conditions in many studies. A brief overview over the different fields of application will be given below. The main focus is on particle preparations tested under *in vivo* condi-

tions in animals or under clinical conditions in humans; the overview of the *in vivo* studies is divided by the route of application. As well as the often used parenteral application route, topical or peroral administration of the nanoparticles and microspheres was described in some studies.

### 6.6.1

#### Protein-based Nanoparticles in Gene Therapy

The main goal in gene therapy is the formulation of optimal gene delivery vehicles that can achieve efficient gene transfer without immunogenic, cytotoxic and inflammatory effects. In a multitude of previous studies different vectors of viral origin were described, based on either recombinant forms of viruses such as retrovirus, adenovirus or adeno-associated virus (AAV) [117, 118]; however, these systems often suffered from the above-mentioned disadvantages. Nonviral approaches, including lipoplexes, polyplexes and nanoparticles, have advantages over viral systems such as safety, low cost, stability, ease of manufacturing and high flexibility concerning the size of the delivered transgene. However, their lack of specificity and their inability to deliver prolonged gene expression have proved to be drawbacks. Although the current synthetic systems are less efficient than viral vectors, rapid advances have achieved efficient levels of gene transfer. One promising approach is the development of nanoparticles which contain a gene construct inside a protective matrix, which protects them from immune recognition and destruction after systemic application.

In the field of protein-based nanoparticles there are many papers describing the preparation of plasmid DNA-loaded nanoparticles by different coacervation methods, and the subsequent quantification of the transfection efficiency under *in vitro* and *in vivo* conditions. For example, Truong-Le et al. reported a method for the incorporation of plasmid DNA coding for firefly luciferase into gelatin-based nanoparticle system. The nanoparticles were prepared by a salt-induced complex coacervation and were stabilized by crosslinking with EDC [61]. The authors described the incorporation of chloroquine in the particle matrix as well as the binding of transferrin and calcium ions to the resulting system. The transfection efficacy was tested in human kidney epithelial (HEK) 293 cells, and it was shown that the highest gene transfer efficiency was seen when transferrin,  $\text{CaCl}_2$  and chloroquine were simultaneously built into the microspheres.

In 1997, the same group described a crosslinked DNA–gelatin nanosphere preparation containing a  $\beta$ -galactosidase plasmid construct driven by an AAV promoter [62]. The nanospheres showed improved stability of the incorporated DNA in comparison to free DNA in the presence of serum. The *in vivo* application of the plasmid-loaded nanospheres in mice resulted in a 10–30 times higher  $\beta$ -galactosidase expression than that observed for naked DNA whereas the injection of a AAV preparation showed a 50–100 times higher expression. The application of the nanoparticle preparation was characterized by a modest anti- $\beta$ -galactosidase antibody response and a potent cytotoxic T lymphocyte response.

Comparable nanoparticle preparations containing either a cystic fibrosis [cystic

fibrosis transport regulator (CFTR)] or a green fluorescent protein (GFP) gene construct were described by the same group as gene delivery systems for the treatment of cystic fibrosis [119, 120]. The preparations were administered to the lung of rabbits by the use of a bronchoscope. Gene expression of the GFP reporter gene was observed in 43% of the brushed airway epithelial cells from the nanosphere-treated animals. The coencapsulation of sodium 4-phenylbutyrate into DNA–gelatin nanoparticles led to a correction of the cAMP-stimulated chloride conductance in cystic fibrosis epithelial cells. In 1998, Truong-Le et al. described the application of their DNA–gelatin nanospheres for the transfection of HEK 293 cells [63]. The nanospheres were characterized with regard to their DNA encapsulation efficiency, particle size, particle matrix structure as well as their stability in different media. The DNA release was mainly influenced by the nature of the incubation medium as well as by the amount of EDC used for particle stabilization. The highest DNA release was observed in trypsin solution and with low amounts of crosslinking reagent EDC, indicating the possibility to prepare a controlled release nanosphere preparation by variation of the crosslinking conditions. The results of the *in vitro* transfection showed that the most effective nanosphere preparation consisted of a DNA–gelatin coacervate, which was surface modified by the attachment of transferrin, and exhibited incorporated chloroquine and calcium chloride. The cell incubation with the optimal nanosphere preparation achieved a transfection level comparable to Lipofectamine<sup>TM</sup>, Lipofectin<sup>TM</sup> and Ca–DNA coprecipitate techniques. The quantification of *in vivo*  $\beta$ -galactosidase expression subsequent to an intramuscular injection in mice revealed that the nanosphere preparation was much more effective than naked DNA or DNA in Lipofectamine complexes, but that the expression rate was significantly lower than that after DNA delivery with an AAV vector system.

Leong et al. compared the gelatin–DNA nanospheres with chitosan–DNA nanospheres surface modified by the covalent introduction of PEG and transferrin [121]. In comparison to the gelatin–DNA nanospheres the chitosan–DNA nanospheres showed enhanced *in vitro* transfection efficiency in HEK 293 cells, but without further enhancement effects of transferrin or by coencapsulated chloroquine. The authors showed that the optimal DNA delivery preparation mainly depended on the respective cell line and marker gene under evaluation: gelatin–DNA nanospheres were effective in transfecting HeLa cells; however, as mentioned above, when compared to chitosan, nanospheres showed only a reduced effect in HEK 293 cells. The group showed that the transfection efficiency of chitosan–DNA nanospheres was neither influenced by the storage time in suspension nor by a lyophilization step after particle preparation.

In 1999, Truong-Le et al. further characterized the coacervation conditions for the preparation of gelatin–DNA nanospheres of defined physicochemical characteristics [64]. The biological integrity of the proposed nanosphere preparations was demonstrated by a more than 50% transfection of human tracheal epithelial cells with DNA encoding CFTR. The DNA-loaded nanospheres were able to complement human bronchial epithelial cells defective in CFTR-mediated chloride transport activity with a functional CFTR.

Apart from the application of gelatin as the starting material for the preparation of plasmid DNA-loaded systems, nanoparticles based on albumin were described as well. In a study by Rhaese et al., the preparation and characterization of nanoparticles consisting of DNA, HSA and polyethyleneimine was described, and their transfection efficiency was tested in HEK 293 cells [122]. A high transfection efficiency that was nearly in the range of commercially available transfection reagents such as Superfect™ and DOTAP™ was observed when the particles were prepared at a N/P ratio of 6.0. The efficiency was comparable to that exerted by the classical calcium phosphate-mediated transfection.

### 6.6.2

#### Parenteral Application Route

The body distribution of particulate systems after parenteral administration and the modification of the distribution by variation of the particle characteristics have been determined in many studies. Some of these studies that used magnetite-loaded particles under external magnetic guidance have been addressed previously [35–40]. These studies used albumin-based particles as drug carrier systems for cytostatic agents such as doxorubicin for tumor therapy. However, such particles systems are also well suited as superparamagnetic resonance contrast material for the diagnosis of organs of the MPS and tumor diagnosis [34].

##### 6.6.2.1 Preclinical Studies with Protein-based Particles

The influence of covalent surface modification on the body distribution of albumin nanoparticles after intravenous application was studied by Roser et al. [93]. An accumulation of the particles in the central nervous system of rats was observed in an experimental animal model of allergic encephalomyelitis. A later immunohistochemical study of Merodio et al. revealed that circulating macrophages, which migrated to the damaged sites, and resident activated microglial cells were involved in the distribution of the nanoparticles [74].

Albumin-based particles have been used for varying applications. For example, Martodam et al. studied albumin microspheres as drug carriers for an inhibitor of the leukocyte elastase (EC 3.4.21.11) leading to drug accumulation in the lung of rats [123]. Kinsey et al. used albumin particles for transfection under *in vivo* conditions [124]. They described a covalent conjugation between HSA and polyethyleneimine using a reductive cleavable spacer structure. Under elevated temperature and acidic reaction conditions the resulting conjugate was transferred to macroaggregates which were drug loaded with plasmid DNA encoding for GFP. The intravenous application of the preparation in mice resulted in a local transfection in the lung, whereas other tissues were not affected.

##### 6.6.2.2 Clinical Studies with Protein-based Particles

The clinical application of particle systems based on HSA has also been described. In all of these studies the administration of the particle systems was by the parenteral route.

In an early study cisplatin-loaded albumin microparticles were used for clinical chemotherapy. An infusion of the particle system through the lingual artery was performed in seven patients with advanced carcinoma of the tongue [125]. Due to a particle size of about 56  $\mu\text{m}$  an arterial embolism in the tumor area was achieved. Specimens were taken at different time intervals after administration, and it was observed that by the fourth week almost all carcinoma cells were killed and that microspheres were hydrolyzed and vanished within 6 weeks. A combined effect of cytotoxicity and ischemic necrosis of the tumor after microembolism was discussed.

The ability of albumin nanoparticles to act as a carrier system for paclitaxel was investigated in many clinical studies. The albumin-stabilized nanoparticle formulation ABI-007 (American Bioscience, Santa Monica, CA) was designed to overcome insolubility problems encountered with paclitaxel and eliminates the need for toxic solvents such as Cremophor EL, which is part of the commercially available paclitaxel formulation Taxol<sup>TM</sup>. Toxicities and antitumor activity of intra-arterial administration of paclitaxel-loaded albumin nanoparticles were determined in patients with advanced head and neck carcinoma [126]. The intra-arterial administration of the particles to 43 patients was well tolerated by most of the patients and required no premedication. In total, 120 treatment cycles were completed and the cytostatic activity of the particulate preparation was compared with Taxol. The maximum tolerated dose of the particle formulation in a single administration was 270  $\text{mg m}^{-2}$  and most dose levels showed considerable antitumor activity. Complete and partial response was observed in 80.9% of the patients. In a later study, the antitumor activity of the same preparation ABI-007 was studied in patients with advanced squamous cell carcinoma of the tongue [127]. Twenty-three previously untreated patients received intra-arterial therapy with paclitaxel-loaded albumin nanoparticles. Within this study about 78% of the patients had a clinical and radiologic objective response, 13% showed a stable disease, and 9% showed disease progression. The pharmacokinetic behavior and toxicity profile of ABI-007 was studied by Ibrahim et al. [128]. In comparison to the commercially available preparation Taxol, no acute hypersensitivity reactions were observed during the infusion of the nanoparticle formulation. Compared to Taxol, the nanoparticle formulation offered several features of clinical interest such as rapid infusion rate, no requirement for premedication and a high maximum tolerated dose. Further clinical trials in metastatic breast cancer patients were completed, and the evaluation for the treatment of other tumors such as nonsmall lung cancer, ovarian cancer, melanoma and cervical cancers was reported [129, 130]. Based on the promising results of the clinical trials, the FDA recently approved ABI-007 under the trade mark Abraxane<sup>TM</sup> as a new protein-bound breast cancer drug.

In the field of diagnostic applications, protein-based nanoparticles are mainly used as ultrasound contrast agents. The concept of contrast enhancement using gas-filled microspheres was developed during the past two decades. A multitude of clinical trials were performed and different commercially preparations are available. In the field of protein-based systems, Alburnex<sup>TM</sup> was described as air-filled albumin microspheres prepared from sonicated 5% HSA. After intravenous or in-

tracoronary injection the microspheres are ideal agents for myocardial contrast echocardiography. Animal studies showed that although the microspheres are mainly in the size range of several micrometers, Albunex did not alter coronary blood flow, left ventricular function or systemic hemodynamics [131]. Comparable results were achieved under clinical conditions, and it was demonstrated that intravenous injection of Albunex appears to be safe without any adverse hemodynamic and respiratory effects [132]. After intravenous injection the albumin microspheres were found to cross the pulmonary circulation. A further clinical study in 71 patients with three intravenous doses of Albunex showed that all injections were well tolerated and no serious side-effects were noted in any of the patients [133]. An extensive physical and biochemical characterization of Albunex microspheres was described by Christiansen et al. [134]. They found out that the preparation contains mainly air-filled microspheres in a size range from 1 to 15  $\mu\text{m}$  with less than 5% being larger than 10  $\mu\text{m}$ . In particular, the microsphere fraction between 4 and 10  $\mu\text{m}$  was assumed to give the main contribution to the ultrasound signal in the left ventricle of the heart after intravenous injection. Only 1.5% of the total protein in suspension represents the microsphere protein, whereas the remaining protein was soluble albumin molecules. In addition to Albunex, a second preparation based on heat-denatured HSA was licensed as an echocardiographic contrast agent: Optison<sup>TM</sup> consist of gas-filled albumin microspheres, but contains octafluoropropane instead of air entrapped in the particle system. Due to incorporation of the less soluble octafluoropropane the microspheres persist much longer *in vivo* as compared to microspheres filled with air [135].

As well as the diagnostic applications, several attempts have been made at therapeutic applications of gas-filled microspheres such as Albunex, including ultrasound-intensified thrombolysis, tissue targeting and drug delivery [136, 137]. For example, albumin-coated microbubbles were used as a drug carrier system for plasmid DNA [138]. The preparation was injected intramuscularly in mice and even in the absence of ultrasound significantly improved transfection efficiency was observed. In the presence of ultrasound the transfection efficiency was significantly increased in older animals. Therefore, protein-based microbubbles are considered as a promising approach for gene delivery in muscle.

### 6.6.3

#### Topical Application of Protein-based Particles

Apart from parenteral application, other routes such as topical or peroral applications have been described for protein-based particle systems. With regard to topical application, albumin particles were used as drug carrier systems for the ophthalmic administration of pilocarpine [139–141]. After drug binding to the particulate systems a significant prolongation in reduction of the intraocular pressure (IOP) was observed. Based on the kinetic data of IOP reduction and miosis, an increase in pilocarpine bioavailability of 50–70 and 50–90% was calculated, respectively.

#### 6.6.4

#### Peroral Application of Protein-based Particles

At first sight, due an enzymatic degradation in the gastrointestinal tract, peroral administration of protein-based particles seems to be a difficult approach. However, the peroral application was investigated in a number of studies. Widder et al. described a suspension of magnetite-loaded albumin microspheres as a paramagnetic oral magnetic resonance contrast agent [34]. Under *in vitro* conditions the proposed microspheres were stable over a broad range of pH and tolerated proteolytic enzyme exposure over 24 h. The peroral administration of the microspheres was studied under *in vivo* conditions in rabbits and dogs, and the system appeared effective as a small bowel contrast material.

In a further study, protein microspheres were described as adjuvants for oral vaccination [142]. The model antigen ovalbumin was entrapped into gelatin microspheres which were stabilized with different amounts of the bifunctional aldehyde glutaraldehyde. In comparison to ovalbumin in solution, the oral administration of the particulate system in mice led to a significantly increased secretion of anti-ovalbumin IgA antibodies at the intestinal mucosa as well as by urinal excretion. This effect was attributed to an effective accumulation of the particles in immunocompetent regions of the gastrointestinal tract the so called Peyer's patches.

The body distribution after peroral administration of radioactively labeled alginate BSA nanoparticles to rats was investigated by Yi et al. [143]. Nanoparticles about 166 nm and drug loaded with 5-fluorouracil were used for the pharmacokinetic study. After oral administration the nanoparticles were mainly distributed in the liver, spleen, lungs and kidneys of the rats. Using micro-autoradiographic experiments, particle accumulation in Kupffers cells of the liver, liver parenchymal cells and phagocytes of the spleen was observed. Therefore, the group proposed protein-based nanoparticles suitable to enter the body circulation after gastrointestinal passage.

### 6.7

#### Immunological Reactions with Protein-based Microspheres

As was outlined previously, the formulation of a device for the controlled release of biologically active substances has been a goal for many researchers. For injectable preparations it is advantageous to use a matrix material that is well tolerated and produces no adverse immunological reactions. Since protein-based particle systems undergo structural alterations induced during the preparation process of the colloid the formation of new epitopes that may provoke an immunological response in recipients may occur. Different animal and clinical studies have been described in order to access the possible immunogenicity of particulate systems.

In 1981, Lee et al. reported the preparation of hormone-containing albumin microspheres as a sustained release drug delivery system for progesterone [24]. For their immunological studies they prepared a particle matrix based on rabbit serum albumin in the size range of about 100  $\mu\text{m}$ , and injected the resulting spheres in-

tramuscularly and subcutaneously in male rabbits. They described a good tolerance of the carrier system after application. No significant fluctuations of body temperature or weight were observed during the experiment. Rabbits that had received injections for several months did not show any adverse immunological symptoms.

The immune response of Alburnex microspheres was studied by Christiansen et al. [144]. Within this study 34 healthy volunteers received four injections of either Alburnex or 5% HSA at 4-week intervals. Analysis of blood samples did not reveal any formation of IgE or IgG antibodies directed against the microsphere protein or albumin in any of the recipient. Likewise, no adverse reaction was observed when Alburnex was administered to allergic individuals having cat albumin as one of their allergens. The authors concluded from their data that there is no evidence that heat-aggregated albumin of the Alburnex microspheres may provoke an immunological reaction upon repeated injection of the preparation. In a following study, the safety of Alburnex administration was confirmed [145]. Within this study the albumin microspheres were repeatedly administered to 12 healthy volunteers over a period of time long enough to allow development of immune reactions. No formation of microsphere-specific IgE and IgG antibodies was observed after multiple Alburnex exposure.

Clinical evaluations of adverse reactions were performed in the preliminary stages of ABI-007 (Abraxane) approval as a new protein-bound breast cancer drug. Within these studies adverse reactions against the particulate formulation were compared to events after administration of the commercial paclitaxel formulation Taxol. The particulate formulation was characterized by a reduced number of total and severe hypersensitivity reactions.

## 6.8

### Concluding Remarks

Many studies have described nanoparticles and microparticles promising drug carrier systems. Among the different materials used for particle preparation, proteins are especially promising, since they can lead to biodegradable carrier systems for a multitude of application routes. This chapter has summarized the preparation techniques of protein-based particle systems as well as the potentials of surface modifications and drug targeting. The promising results of the particle systems under preclinical and clinical evaluation have been outlined. Recently, the first protein-based particle system was approved by the FDA for tumor therapy. Therefore, there is hope that in future years protein-based particle systems will improve the treatments of several disease and will give patients a better quality of life.

### References

- 1 KREUTER, J., Evaluation of nanoparticles as drug-delivery systems I: preparation methods, *Pharm. Acta Helv.* 1983, 58, 196–209.



- 2 RUBINO, O. P., KOWALSKY, R., SWARBRICK, J., Albumin microspheres as a drug delivery system: relation among turbidity ratio, degree of cross-linking, and drug release, *Pharm. Res.* **1993**, *10*, 1059–1065.
- 3 MACADAM, A. B., SHAFI, Z. B., JAMES, S. L., MARRIOTT, C., MARTIN, C. P., Preparation of hydrophobic and hydrophilic albumin microspheres and determination of surface carboxylic acid and amino residues, *Int. J. Pharm.* **1997**, *151*, 47–55.
- 4 ALLÉMANN, E., GURNY, R., DOELKER, E., Drug-loaded nanoparticles – preparation methods and drug targeting issues, *Eur. J. Pharm. Biopharm.* **1993**, *39*, 173–191.
- 5 BIRRENBACH, G., SPEISER, P. P., Polymerized micelles and their use as adjuvants in immunology, *J. Pharm. Sci.* **1976**, *65*, 1763–1766.
- 6 COUVREUR, P., TULKENS, P., ROLAND, M., TROUET, A., SPEISER, P., Nanocapsules: a new type of lysosomotropic carrier, *FEBS Lett.* **1977**, *84*, 323–326.
- 7 KREUTER, J., SPEISER, P. P., *In vitro* studies of poly(methyl methacrylate) adjuvants, *J. Pharm. Sci.* **1976**, *65*, 1624–1627.
- 8 BERG, U. E., Immunstimulation durch hochdisperse Polymer suspensionen, *Dissertation*, ETH Zürich, **1979**.
- 9 HARMIA, T., SPEISER, P., KREUTER, J., Nanoparticles as drug carriers in ophthalmology, *Pharm. Acta Helv.* **1987**, *62*, 322–331.
- 10 COUVREUR, P., ROLAND, M., SPEISER, P., Biodegradable submicroscopic particles containing a biologically active substance and compositions containing them, *US patent 4,329,332*, **1982**.
- 11 McLEOD, A. D., LAM, F. C., HUNG, C. T., Optimized synthesis of polyglutaraldehyde nanoparticles using central composite design, *J. Pharm. Sci.* **1988**, *77*, 704–710.
- 12 MARTY, J. J., OPPENHEIM, R. C., SPEISER, P., Nanoparticles – a new colloidal drug delivery system, *Pharm. Acta Helv.* **1978**, *53*, 17–23.
- 13 WIDDER, K., FLOURET, G., SENYEI, A., Magnetic microspheres: synthesis of a novel parenteral drug carrier, *J. Pharm. Sci.* **1979**, *68*, 79–82.
- 14 GALLO, J. M., HUNG, C. T., PERRIER, D. G., Analysis of albumin microsphere preparation, *Int. J. Pharm.* **1984**, *22*, 63–74.
- 15 KRAUSE, H. J., SCHWARTZ, A., ROHDEWALD, P., Polylactic acid nanoparticles, a colloidal drug delivery system for lipophilic drugs, *Int. J. Pharm.* **1985**, *27*, 145–155.
- 16 BODMEIER, R., CHEN, H., Indomethacin polymeric nanosuspensions prepared by microfluidization, *J. Controlled Rel.* **1990**, *12*, 223–233.
- 17 ALLÉMANN, E., GURNY, R., DOELKER, E., Preparation of aqueous polymeric nanodispersions by reversible salting-out process, influence of process parameters on particle size, *Int. J. Pharm.* **1992**, *87*, 247–253.
- 18 SPEISER, P., Lipidnanopellets als Trägersystem für Arzneimittel zur peroralen Anwendung, *European patent 0167825*, **1990**.
- 19 MÜLLER, R. H., LUCKS, J. S., Arzneistoffträger aus festen Lipidteilchen (Feste Lipidnanosphären (SLN)), *European patent 0605497 B1*, **1996**.
- 20 VEZIN, W. R., FLORENCE, A. T., *In vitro* heterogeneous degradation of poly(*n*-alkyl alpha-cyanoacrylates), *J. Biomed. Mater. Res.* **1980**, *14*, 93–106.
- 21 BERG, U. E., KREUTER, J., SPEISER, P. P., SOLIVA, M., Herstellung und *In-vitro*-Prüfung von polymeren Adjuvantien für Impfstoffe, *Pharm. Ind.* **1986**, *48*, 75–79.
- 22 LI, J. K., WANG, N., WU, X. S., A novel biodegradable system based on gelatin nanoparticles and poly(lactic-co-glycolic acid) microspheres for protein and peptide drug delivery, *J. Pharm. Sci.* **1997**, *86*, 891–895.
- 23 MÜLLER, G. M., LEUENBERGER, H., KISSEL, T., Albumin nanospheres as carriers for passive drug targeting: An optimized manufacturing technique, *Pharm. Res.* **1996**, *13*, 32–37.
- 24 LEE, T. K., SOKOŁOSKI, T. D., ROYER, G. P., Serum albumin beads: an injectable, biodegradable system for the sustained release of drugs, *Science* **1981**, *213*, 233–235.

- 25 RHODES, B. A., ZOLLE, I., BUCHANAN, J. W., WAGNER, H. N., Radioactive albumin microspheres for studies of the pulmonary circulation, *Radiology* **1969**, *92*, 1453–1460.
- 26 ZOLLE, I., RHODES, B. A., WAGNER, H. N., Preparation of metabolizable radioactive human serum albumin microspheres for studies of the circulation, *Int. J. Appl. Radiat. Isot.* **1970**, *21*, 155–167.
- 27 BURDINE, J. A., SONNEMAKER, R. E., RYDER, L. A., SPJUT, H. J., Perfusion studies with technetium-99m human albumin microspheres (HAM), *Radiology* **1970**, *95*, 101–107.
- 28 MASERI, A., MANCINI, P., CONTINI, C., PESOLA, A., DONATO, L., Method for the estimate of total coronary flow by <sup>99</sup>Tc tagged albumin microspheres, *J. Nucl. Biol. Med.* **1971**, *15*, 58–60.
- 29 RHODES, B. A., STERN, H. S., BUCHANAN, J. A., ZOLLE, I., WAGNER, H. N., Lung scanning with <sup>99m</sup>Tc-microspheres, *Radiology* **1971**, *99*, 613–621.
- 30 SCHEFFEL, U., RHODES, B. A., NATARAJAN, T. K., WAGNER, H. N., Albumin microspheres for study of the reticuloendothelial system, *J. Nucl. Med.* **1972**, *13*, 498–503.
- 31 KRAMER, P. A., Albumin microspheres as vehicles for achieving specificity in drug delivery, *J. Pharm. Sci.* **1974**, *63*, 1646–1647.
- 32 WIDDER, K. J., SENYEI, A. E., OVADIA, H., PATERSON, P. Y., Magnetic protein A microspheres: a rapid method for cell separation, *Clin. Immunol. Immunopathol.* **1979**, *14*, 395–400.
- 33 WIDDER, D. J., GREIF, W. L., WIDDER, K. J., EDELMAN, R. R., BRADY, T. J., Magnetite albumin microspheres: a new MR contrast material, *Am. J. Roentgenol.* **1987**, *148*, 399–404.
- 34 WIDDER, D. J., EDELMAN, R. R., GRIEF, W. L., MONDA, L., Magnetite albumin suspension: a superparamagnetic oral MR contrast agent, *Am. J. Roentgenol.* **1987**, *149*, 839–843.
- 35 WIDDER, K. J., SENYEI, A. E., RANNEY, D. F., Magnetically responsive microspheres and other carriers for the biophysical targeting of antitumor agents, *Adv. Pharmacol. Chemother.* **1979**, *16*, 213–271.
- 36 SENYEI, A. E., REICH, S. D., GONCZY, C., WIDDER, K. J., *In vivo* kinetics of magnetically targeted low-dose doxorubicin, *J. Pharm. Sci.* **1981**, *70*, 389–391.
- 37 WIDDER, K. J., MORRIS, R. M., POORE, G., HOWARD, D. P., SENYEI, A. E., Tumor remission in Yoshida sarcoma-bearing rats by selective targeting of magnetic albumin microspheres containing doxorubicin, *Proc. Natl. Acad. Sci. USA* **1981**, *78*, 579–581.
- 38 WIDDER, K. J., MORRIS, R. M., POORE, G. A., HOWARD, D. P., SENYEI, A. E., Selective targeting of magnetic albumin microspheres containing low-dose doxorubicin: total remission in Yoshida sarcoma-bearing rats, *Eur. J. Cancer Clin. Oncol.* **1983**, *19*, 135–139.
- 39 WIDDER, K. J., MARINO, P. A., MORRIS, R. M., HOWARD, D. P., POORE, G. A., SENYEI, A. E., Selective targeting of magnetic albumin microspheres to the Yoshida sarcoma: ultrastructural evaluation of microsphere disposition, *Eur. J. Cancer Clin. Oncol.* **1983**, *19*, 141–147.
- 40 RETTENMAIER, M. A., STRATTON, J. A., BERMAN, M. L., SENYEI, A., WIDDER, K., WHITE, D. B., DISAIA, P. J., Treatment of a syngeneic rat tumor with magnetically responsive albumin microspheres labeled with doxorubicin or protein A, *Gynecol. Oncol.* **1987**, *27*, 34–43.
- 41 GUPTA, P. K., HUNG, C. T., PERRIER, D. G., Albumin microspheres I. release characteristics of adriamycin, *Int. J. Pharm.* **1986**, *33*, 137–146.
- 42 GUPTA, P. K., HUNG, C. T., PERRIER, D. G., Albumin microspheres II. Effect of stabilization temperature on the release of adriamycin, *Int. J. Pharm.* **1986**, *33*, 147–153.
- 43 GUPTA, P. K., HUNG, C. T., LAM, F. C., PERRIER, D. G., Albumin microspheres III. Synthesis and characterization of microspheres containing adriamycin and magnetite, *Int. J. Pharm.* **1988**, *43*, 167–177.
- 44 GUPTA, P. K., HUNG, C. T., Albumin

- microspheres I: physico-chemical characteristics, *J. Microencapsul.* **1989**, *6*, 427–462.
- 45 GUPTA, P. K., HUNG, C. T., Albumin microspheres II: applications in drug delivery, *J. Microencapsul.* **1989**, *6*, 463–472.
- 46 GUPTA, P. K., HUNG, C. T., Magnetically controlled targeted micro-carrier systems, *Life Sci.* **1989**, *44*, 175–186.
- 47 ARSHADY, R., Albumin microspheres and microcapsules: methodology of manufacturing techniques, *J. Controlled Rel.* **1990**, *14*, 111–131.
- 48 ESPOSITO, E., CORTESI, R., NASTRUZZI, C., Gelatin microspheres: influence of preparation parameters and thermal treatment on chemico-physical and biopharmaceutical properties, *Biomaterials* **1996**, *17*, 2009–2020.
- 49 LI, J. K., WANG, N., WU, X. S., Gelatin nanoencapsulation of protein/peptide drugs using an emulsifier-free emulsion method, *J. Microencapsul.* **1998**, *15*, 163–172.
- 50 CHEN, Y., WILLMOT, N., ANDERSON, J., FLORENCE, A. T., Comparison of albumin and casein microspheres as a carrier of doxorubicin, *J. Pharm. Pharmacol.* **1987**, *39*, 978–985.
- 51 KNEPP, W. A., JAYAKRISHNAN, A., QUIGG, J. M., SITREN, H. S., BAGNALL, J. J., GOLDBERG, E. P., Synthesis, properties, and intratumoral evaluation of mitoxantrone-loaded casein microspheres in Lewis lung carcinoma, *J. Pharm. Pharmacol.* **1993**, *45*, 887–891.
- 52 LATHA, M. S., JAYAKRISHNAN, A., A new method for the synthesis of smooth, round, hydrophilic protein microspheres using low concentrations of polymeric dispersing agents, *J. Microencapsul.* **1995**, *12*, 7–12.
- 53 JAYAKRISHNAN, A., KNEPP, W. A., GOLDBERG, E. P., Casein microspheres: preparation and evaluation as a carrier for controlled release, *Int. J. Pharm.* **1994**, *106*, 221–228.
- 54 LATHA, M. S., JAYAKRISHNAN, A., Glutaraldehyde cross-linked bovine casein microspheres as a matrix for the controlled release of theophylline: *in-vitro* studies, *J. Pharm. Pharmacol.* **1994**, *46*, 8–13.
- 55 LATHA, M. S., JAYAKRISHNAN, A., RATHINAM, K., MOHANTY, M., Casein as a carrier matrix for 5-fluorouracil: drug release from microspheres, drug–protein conjugates and *in-vivo* degradation of microspheres in rat muscle, *J. Pharm. Pharmacol.* **1994**, *46*, 858–862.
- 56 LATHA, M. S., LAL, A. V., KUMARY, T. V., SREEKUMAR, R., JAYAKRISHNAN, A., Progesterone release from glutaraldehyde cross-linked casein microspheres: *in vitro* studies and *in vivo* response in rabbits, *Contraception* **2000**, *61*, 329–334.
- 57 LONGO, W. E., IWATA, H., LINDHEIMER, T. A., GOLDBERG, E. P., Preparation of hydrophilic albumin microspheres using polymeric dispersing agents, *J. Pharm. Sci.* **1982**, *71*, 1323–1328.
- 58 LONGO, W. E., GOLDBERG, E. P., Hydrophilic albumin microspheres, *Methods Enzymol.* **1985**, *112*, 18–26.
- 59 LIU, S. Q., LEONG, K. W., Delivery of protein and low-molecular weight drug by coacervate human serum albumin and heparin, *Proc. Int. Symp. Controlled Rel. Bioact. Mater.* **1997**, *24*, 911–912.
- 60 SANTINHO, A. J., PEREIRA, N. L., DE FREITAS, O., COLLETT, J. H., Influence of formulation on the physicochemical properties of casein microparticles, *Int. J. Pharm.* **1999**, *186*, 191–198.
- 61 TRUONG-LE, V. L., WALSH, S. M., AUGUST, J. T., LEONG, K. W., Gene transfer by gelatin–DNA coacervate, *Proc. Int. Symp. Controlled Rel. Bioact. Mater.* **1995**, *22*, 466–467.
- 62 TRUONG-LE, V. L., HAI-QUAN, M., WALSH, S., LEONG, K. W., AUGUST, J. T., Delivery of DNA vaccine using gelatin–DNA nanospheres, *Proc. Int. Symp. Controlled Rel. Bioact. Mater.* **1997**, *24*, 39–40.
- 63 TRUONG-LE, V. L., AUGUST, J. T., LEONG, K. W., Controlled gene delivery by DNA–gelatin nanospheres, *Hum. Gene Ther.* **1998**, *9*, 1709–1717.
- 64 TRUONG-LE, V. L., WALSH, S. M., SCHWEIBERT, E., MAO, H.-Q., GUGGINO, W. B., AUGUST, J. T.,

- LEONG, K. W., Gene transfer by DNA gelatin nanospheres, *Arch. Biochem. Biophys.* **1999**, *361*, 47–56.
- 65 MAO, H.-Q., ROY, K., TRUONG-LE, V., AUGUST, J. T., LEONG, K. W., DNA-chitosan nanospheres: derivatization and storage stability, *Proc. Int. Symp. Controlled Rel. Bioact. Mater.* **1997**, *24*, 671–672.
- 66 ROY, K., MAO, H.-Q., LEONG, K. W., DNA-chitosan nanospheres: transfection efficiency and cellular uptake, *Proc. Int. Symp. Controlled Rel. Bioact. Mater.* **1997**, *24*, 673–674.
- 67 EL-SAMALIGY, M., ROHDEWALD, P., Triamcinolone diacetate nanoparticles, a sustained release drug delivery system suitable for parenteral administration, *Pharm. Acta Helv.* **1982**, *57*, 201–204.
- 68 EL-SAMALIGY, M. S., ROHDEWALD, P., Reconstituted collagen nanoparticles, a novel drug carrier delivery system, *J. Pharm. Pharmacol.* **1983**, *35*, 537–539.
- 69 MERODIO, M., CAMPANERO, M. A., MIRSHAHI, T., MIRSHAHI, M., IRACHE, J. M., Development of a sensitive method for the determination of ganciclovir by reversed-phase high-performance liquid chromatography, *J. Chromatogr. A* **2000**, *870*, 159–167.
- 70 MERODIO, M., ARNEDE, A., RENEDE, M. J., IRACHE, J. M., Ganciclovir-loaded albumin nanoparticles: characterization and *in vitro* release properties, *Eur. J. Pharm. Sci.* **2001**, *12*, 251–259.
- 71 MERODIO, M., IRACHE, J. M., VALAMANESH, F., MIRSHAHI, M., Ocular disposition and tolerance of ganciclovir-loaded albumin nanoparticles after intravitreal injection in rats, *Biomaterials* **2002**, *23*, 1587–1594.
- 72 MERODIO, M., ESPUELAS, M. S., MIRSHAHI, M., ARNEDE, A., IRACHE, J. M., Efficacy of ganciclovir-loaded nanoparticles in human cytomegalovirus (HCMV)-infected cells, *J. Drug Target.* **2002**, *10*, 231–238.
- 73 ARNEDE, A., IRACHE, J. M., MERODIO, M., ESPUELAS MILLAN, M. S., Albumin nanoparticles improved the stability, nuclear accumulation and anticytomegaloviral activity of a phosphodiester oligonucleotide, *J. Controlled Rel.* **2004**, *94*, 217–227.
- 74 MERODIO, M., IRACHE, J. M., ECLANCHER, F., MIRSHAHI, M., VILLARROYA, H., Distribution of albumin nanoparticles in animals induced with the experimental allergic encephalomyelitis, *J. Drug Target.* **2000**, *8*, 289–303.
- 75 SCHÄFER, V., VON BRIESEN, H., ANDRESEN, R., STEFFAN, A. M., ROYER, C., TRÖSTER, S., KREUTER, J., RÜBSAMEN-WAIGMANN, H., Phagocytosis of nanoparticles by human immunodeficiency virus (HIV)-infected macrophages: a possibility for antiviral drug targeting, *Pharm. Res.* **1992**, *9*, 541–546.
- 76 SCHÄFER, V., VON BRIESEN, H., RÜBSAMEN-WAIGMANN, H., STEFFAN, A. M., ROYER, C., KREUTER, J., Phagocytosis and degradation of human serum albumin microspheres and nanoparticles in human macrophages, *J. Microencapsul.* **1994**, *11*, 261–269.
- 77 BENDER, A., SCHÄFER, V., STEFFAN, A. M., ROYER, C., KREUTER, J., RÜBSAMEN-WAIGMANN, H., VON BRIESEN, H., Inhibition of HIV *in vitro* by antiviral drug-targeting using nanoparticles, *Res. Virol.* **1994**, *145*, 215–220.
- 78 ARNEDE, A., ESPUELAS, S., IRACHE, J. M., Albumin nanoparticles as carriers for a phosphodiester oligonucleotide, *Int. J. Pharm.* **2002**, *244*, 59–72.
- 79 LIN, W., COOMBES, A. G. A., DAVIES, M. C., DAVIS, S. S., ILLUM, L., Preparation of sub-100 nm human serum albumin nanospheres using a pH-coacervation method, *J. Drug Target.* **1993**, *1*, 237–243.
- 80 WESTCOTT, C. C., *pH Measurements*, Academic Press, New York, **1978**, pp. 123–130.
- 81 WEBER, C., COESTER, C., KREUTER, J., LANGER, K., Desolvation process and surface characterisation of protein nanoparticles, *Int. J. Pharm.* **2000**, *194*, 91–102.
- 82 WEBER, C., KREUTER, J., LANGER, K., Desolvation process and surface

- characteristics of HSA-nanoparticles, *Int. J. Pharm.* **2000**, *196*, 197–200.
- 83 COESTER, C. J., LANGER, K., VON BRIESEN, H., KREUTER, J., Gelatin nanoparticles by two step desolvation – a new preparation method, surface modifications and cell uptake, *J. Microencapsul.* **2000**, *17*, 187–193.
- 84 VOGEL, V., LANGER, K., BALTHASAR, S., SCHUCK, P., MÄCHTLE, W., HAASE, W., VAN DEN BROEK, J. A., TZIATZIOS, C., SCHUBERT, D., Characterization of serum albumin nanoparticles by sedimentation velocity analysis and electron microscopy, *Progr. Colloid Polym. Sci.* **2002**, *119*, 31–36.
- 85 LANGER, K., BALTHASAR, S., VOGEL, V., DINAUER, N., VON BRIESEN, H., SCHUBERT, D., Optimization of the preparation process for human serum albumin (HSA) nanoparticles, *Int. J. Pharm.* **2003**, *257*, 169–180.
- 86 MÄCHTLE, W., High-resolution, submicron particle size distribution analysis using gravitational-sweep sedimentation, *Biophys. J.* **1999**, *76*, 1080–1091.
- 87 SCHUCK, P., ROSSMANITH, P., Determination of the sedimentation coefficient distribution by least-squares boundary modeling, *Biopolymers* **2000**, *54*, 328–341.
- 88 MOGHIMI, S. M., HUNTER, A. C., MURRAY, J. C., Long-circulating and target-specific nanoparticles: theory and practice, *Pharm. Rev.* **2001**, *53*, 283–318.
- 89 HARASHIMA, H., SAKATA, K., FUNATO, K., KIWADA, H., Enhanced hepatic uptake of liposomes through complement activation depending on the size of liposomes, *Pharm. Res.* **1994**, *11*, 402–406.
- 90 HNATOWICH, D. J., SCHLEGEL, P., Albumin microspheres labeled with Ga-67 by chelation: concise communication, *J. Nucl. Med.* **1981**, *22*, 623–626.
- 91 KISSEL, T., ROSER, M., Influence of chemical surface-modifications on the phagocytic properties of albumin nanoparticles, *Proc. Int. Symp. Controlled Rel. Bioact. Mater.* **1991**, *18*, 275–276.
- 92 ROSER, M., KISSEL, T., Surface-modified biodegradable nano- and microspheres. I. Preparation and characterization, *Eur. J. Pharm. Biopharm.* **1993**, *39*, 8–12.
- 93 ROSER, M., FISCHER, D., KISSEL, T., Surface-modified biodegradable albumin nano- and microspheres. II: effect of surface charges on *in vitro* phagocytosis and biodistribution in rats, *Eur. J. Pharm. Biopharm.* **1998**, *46*, 255–263.
- 94 LIN, W., COOMBES, A. G. A., GARNETT, M. C., DAVIES, M. C., SCHACHT, E., DAVIS, S. S., ILLUM, L., Preparation of sterically stabilized human serum albumin nanospheres using a novel dextranox-MPEG crosslinking agent, *Pharm. Res.* **1994**, *11*, 1588–1592.
- 95 LIN, W., GARNETT, M. C., DAVIES, M. C., BIGNOTTI, F., FERRUTI, P., DAVIS, S. S., ILLUM, L., Preparation of surface-modified albumin nanospheres, *Biomaterials* **1997**, *18*, 559–565.
- 96 LIN, W., GARNETT, M. C., SCHACHT, E., DAVID, S. S., ILLUM, L., Preparation and *in vitro* characterization of HSA-mPEG nanoparticles, *Int. J. Pharm.* **1999**, *189*, 161–170.
- 97 LIN, W., GARNETT, M. C., DAVIS, S. S., SCHACHT, E., FERRUTI, P., ILLUM, L., Preparation and characterisation of rose Bengal-loaded surface-modified albumin nanoparticles, *J. Controlled Rel.* **2001**, *71*, 117–126.
- 98 MOLDAY, R. S., DREYER, W. J., REMBAUM, A., YEN, S. P. S., Latex spheres as markers for studies of cell surface receptors by scanning electron microscopy, *Nature* **1974**, *249*, 81–83.
- 99 MOLDAY, R. S., DREYER, W. J., REMBAUM, A., YEN, S. P. S., New immunolabelled spheres: visual markers of antigens on lymphocytes for scanning electron microscopy, *J. Cell Biol.* **1975**, *64*, 75–88.
- 100 MOLDAY, R. S., YEN, S. P., REMBAUM, A., Application of magnetic microspheres in labelling and separation of cells, *Nature* **1977**, *268*, 437–438.
- 101 ROLLAND, A., BOUREL, D., GENETET, B., LE VERGE, R., Monoclonal antibodies covalently coupled to

- polymethacrylic nanoparticles: *in vitro* specific targeting to human T lymphocytes, *Int. J. Pharm.* **1987**, *39*, 173–180.
- 102** BOUREL, D., ROLLAND, A., LE VERGE, R., GENETET, B., A new immunoreagent for cell labeling – CD3 monoclonal antibody covalently coupled to fluorescent polymethacrylic nanoparticles, *J. Immunol. Methods* **1988**, *106*, 161–167.
- 103** ILLUM, L., JONES, P. D. E., KREUTER, J., BALDWIN, R. W., DAVIS, S. S., Adsorption of monoclonal antibodies to polyhexylcyanoacrylate nanoparticles and subsequent immunospecific binding to tumour cells *in vitro*, *Int. J. Pharm.* **1983**, *17*, 65–76.
- 104** VELGE-ROUSSEL, F., BRETON, P., GUILLON, X., LESCURE, F., BRU, N., BOUT, D., HOEBEKE, J., Immunochemical characterization of antibody-coated nanoparticles, *Experientia* **1996**, *52*, 803–806.
- 105** SANTRA, S., ZHANG, P., WANG, K., TAPEC, R., TAN, W., Conjugation of biomolecules with luminophore-doped silica nanoparticles for photostable biomarkers, *Anal. Chem.* **2001**, *73*, 4988–4993.
- 106** OLIVIER, J. C., HUERTAS, R., LEE, H. J., CALON, F., PARDRIDGE, W. M., Synthesis of pegylated immunonanoparticles, *Pharm. Res.* **2002**, *19*, 1137–1143.
- 107** AKASAKA, Y., UEDA, H., TAKAYAMA, K., MACHIDA, Y., NAGAI, T., Preparation and evaluation of bovine serum albumin nanospheres coated with monoclonal antibodies, *Drug Des. Deliv.* **1988**, *3*, 85–97.
- 108** WARTLICK, H., MICHAELIS, K., BALTHASAR, S., STREBHARDT, K., KREUTER, J., LANGER, K., Highly specific HER2-mediated cellular uptake of antibody-modified nanoparticles in tumour cells, *J. Drug Target.* **2004**, *12*, 461–471.
- 109** BALTHASAR, S., MICHAELIS, K., DINAUER, N., VON BRIESEN, H., KREUTER, J., LANGER, K., Preparation and characterisation of antibody modified gelatin nanoparticles as drug carrier system for uptake in lymphocytes, *Biomaterials* **2005**, *26*, 2723–2732.
- 110** MACADAM, A. B., SHAFI, Z. B., MARRIOTT, C., MARTIN, G. P., JAMES, S. L., Anti-mucus polyclonal antibody production, purification and linkage to the surface of albumin microspheres, *Int. J. Pharm.* **2000**, *195*, 147–158.
- 111** DINAUER, N., BALTHASAR, S., WEBER, C., KREUTER, J., LANGER, K., VON BRIESEN, H., Selecting targeting of antibody-conjugated nanoparticles to leukemic cells and primary T-lymphocytes, *Biomaterials*, **2005**, *26*, 5898–5960.
- 112** STALTERI, M. A., MATHER, S. J., A cross-linked monoclonal antibody fragment for improved tumor targeting, *Bioconjug. Chem.* **1995**, *6*, 179–186.
- 113** NOVAK, P., YOUNG, M. M., SCHOENIGER, J. S., KRUPPA, G. H., A top-down approach to protein structure studies using chemical cross-linking and Fourier transform mass spectrometry, *Eur. J. Mass Spectrom.* **2003**, *9*, 623–631.
- 114** LANGER, K., COESTER, C., WEBER, C., VON BRIESEN, H., KREUTER, J., Preparation of avidin-labeled protein nanoparticles as carriers for biotinylated peptide nucleic acid, *Eur. J. Pharm. Biopharm.* **2000**, *49*, 303–307.
- 115** HYLARIDES, M. D., MALLETT, R. W., MEYER, D. L., A robust method for the preparation and purification of antibody/streptavidin conjugates, *Bioconjug. Chem.* **2001**, *12*, 421–427.
- 116** WEBER, C., REISS, S., LANGER, K., Preparation of surface modified protein nanoparticles by introduction of sulfhydryl groups, *Int. J. Pharm.* **2000**, *211*, 67–78.
- 117** VERMA, I. M., SOMIA, N., Gene therapy – promises, problems and prospects, *Nature* **1997**, *389*, 239–242.
- 118** FELGNER, P. L., Nonviral strategies for gene therapy, *Sci. Am.* **1997**, *276*, 102–106.
- 119** WALSH, S. M., FLOTTE, T. R., BECK, S., ALLEN, S., GUGGINO, W. B., AUGUST, T., LEONG, K. W., Delivery of CFTR gene to rabbit airways by gelatin–DNA microspheres, *Proc. Int. Symp.*

- Controlled Rel. Bioact. Mater.* **1996**, *23*, 73–74.
- 120** WALSH, S. M., FLOTTE, T. R., TRUONG-LE, V. L., RUBENSTIEN, R., BECK, S., AUGUST, T., ZEITLIN, P., LEONG, K. W., Combination of drug and gene delivery by gelatin nanospheres for the treatment of cystic fibrosis, *Proc. Int. Symp. Controlled Rel. Bioact. Mater.* **1997**, *24*, 75–76.
- 121** LEONG, K. W., MAO, H.-Q., TRUONG-LE, V. L., ROY, K., WALSH, S. M., AUGUST, J. T., DNA-polycation nanospheres as non-viral gene delivery vehicles, *J. Controlled Rel.* **1998**, *53*, 183–193.
- 122** RHAESE, S., VON BRIESEN, H., RÜBSAMEN-WAIGMANN, H., KREUTER, J., LANGER, K., Human serum albumin–polyethylenimine nanoparticles for gene delivery, *J. Controlled Rel.* **2003**, *92*, 199–208.
- 123** MARTODAM, R. R., TWUMASI, D. Y., LIENER, I. E., POWERS, J. C., NISHINO, N., KREJCAREK, G., Albumin microspheres as carrier of an inhibitor of leukocyte elastase: potential therapeutic agent for emphysema, *Proc. Natl Acad. Sci. USA* **1979**, *76*, 2128–2132.
- 124** KINSEY, B., HUA, P., BARRY, M., ORSON, F., Polyethylenimine conjugated to macroaggregated albumin mediates high level transfection *in vitro* and *in vivo*, *Proc. Int. Symp. Controlled Rel. Bioact. Mater.* **1999**, *26*, 5027.
- 125** LI, H., WANG, C., WEN, Y., WU, H., Treatment of squamous cell carcinoma of the tongue using arterial embolism with cisplatin-loaded albumin microspheres: a microstructural and ultrastructural investigation, *Chin. J. Dent. Res.* **1999**, *2*, 61–66.
- 126** DAMASCELLI, B., CANTU, G., MATTAVELLI, F., TAMPLENIZZA, P., BIDOLI, P., LEO, E., DOSIO, F., CERROTTA, A. M., DI TOLLA, G., FRIGERIO, L. F., GARBAGNATI, F., LANOCITA, R., MARCHIANO, A., PATELLI, G., SPREAFICO, C., TICHA, V., VESPRO, V., ZUNINO, F., Intraarterial chemotherapy with polyoxyethylated castor oil free paclitaxel, incorporated in albumin nanoparticles (ABI-007): phase II study of patients with squamous cell carcinoma of the head and neck and anal canal: preliminary evidence of clinical activity, *Cancer* **2001**, *92*, 2592–2602.
- 127** DAMASCELLI, B., PATELLI, G. L., LANOCITA, R., TOLLA, G. D., FRIGERIO, L. F., MARCHIANO, A., GARBAGNATI, F., SPREAFICO, C., TICHA, V. V., GLADIN, C. R., PALAZZI, M., CRIPPA, F., OLDINI, C., CALO, S., BONACCORSI, A., MATTAVELLI, F., COSTA, L., MARIANI, L., CANTU, G., A novel intraarterial chemotherapy using paclitaxel in albumin nanoparticles to treat advanced squamous cell carcinoma of the tongue: preliminary findings, *Am. J. Roentgenol.* **2003**, *181*, 253–260.
- 128** IBRAHIM, N. K., DESAI, N., LEGHA, S., SOON-SHIONG, P., THERIAULT, R. L., RIVERA, E., ESMALI, B., RING, S. E., BEDIKIAN, A., HORTOBAGYI, G. N., ELLERHORST, J. A., Phase I and pharmacokinetic study of ABI-007, a Cremophor-free, protein-stabilized, nanoparticle formulation of paclitaxel, *Clin. Cancer Res.* **2002**, *8*, 1038–1044.
- 129** ABI 007, *Drugs R&D* **2003**, *4*, 303–305.
- 130** ABI 007, *Drugs R&D* **2004**, *5*, 155–159.
- 131** KELLER, M. W., GLASHEEN, W., KAUL, S., Alunex: a safe and effective commercially produced agent for myocardial contrast echocardiography, *J. Am. Soc. Echocardiogr.* **1989**, *2*, 48–52.
- 132** GENY, B., METTAUER, B., MUAN, B., BISCHOFF, P., EPAILLY, E., PIQUARD, F., EISENMANN, B., HABEREY, P., Safety and efficacy of a new transpulmonary echo contrast agent in echocardiographic studies in patients, *J. Am. Coll. Cardiol.* **1993**, *22*, 1193–1198.
- 133** FEINSTEIN, S. B., CHEIRIF, J., TEN CATE, F. J., SILVERMAN, P. R., HEIDENREICH, P. A., DICK, C., DESIR, R. M., ARMSTRONG, W. F., QUINONES, M. A., SHAH, P. M., Safety and efficacy of a new transpulmonary ultrasound contrast agent: initial multicenter clinical results, *J. Am. Coll. Cardiol.* **1990**, *16*, 316–324.
- 134** CHRISTIANSEN, C., KRYVI, H.,

- SONTUM, P. C., SKOTLAND, T., Physical and biochemical characterization of Albunex, a new ultrasound contrast agent consisting of air-filled albumin microspheres suspended in a solution of human albumin, *Biotechnol. Appl. Biochem.* **1994**, *19*, 307–320.
- 135** PODELL, S., BURRASCANO, C., GAAL, M., GOLEC, B., MANIQUIS, J., MEHLHAFF, P., Physical and biochemical stability of Optison, an injectable ultrasound contrast agent, *Biotechnol. Appl. Biochem.* **1999**, *30*, 213–223.
- 136** KASPRZAK, J. D., TEN CATE, F. J., New ultrasound contrast agents for left ventricular and myocardial opacification, *Herz* **1998**, *23*, 474–482.
- 137** CORREAS, J. M., BRIDAL, L., LESAVRE, A., MEJEAN, A., CLAUDON, M., HELENON, O., Ultrasound contrast agents: properties, principles of action, tolerance, and artifacts, *Eur. Radiol.* **2001**, *11*, 1316–1328.
- 138** LU, Q. L., LIANG, H. D., PARTRIDGE, T., BLOMLEY, M. J., Microbubble ultrasound improves the efficiency of gene transduction in skeletal muscle *in vivo* with reduced tissue damage, *Gene Ther.* **2003**, *10*, 396–405.
- 139** ZIMMER, A. K., KREUTER, J., SAETTONI, M. F., ZERBE, H., Size dependency of albumin carrier systems on *in vivo* effects of pilocarpine in the rabbit eye, *Proc. Int. Symp. Controlled Rel. Bioact. Mater.* **1991**, *18*, 493–494.
- 140** ZIMMER, A. K., KREUTER, J., SAETTONI, M. F., ZERBE, H., Evaluation of pilocarpine-loaded albumin particles as controlled drug delivery systems for the eye. I. *In vitro* and *in vivo* characterisation, *J. Controlled Rel.* **1994**, *32*, 57–70.
- 141** ZIMMER, A. K., CHETONI, P., SAETTONI, M. F., ZERBE, H., KREUTER, J., Evaluation of pilocarpine-loaded albumin particles as controlled drug delivery systems for the eye. II. Co-administration with bioadhesive and viscous polymers, *J. Controlled Rel.* **1995**, *33*, 31–46.
- 142** NAKAMURA, N., YAMASHITA, S., TSUME, Y., NADAI, T., SEZAKI, H., KOHNO, T., TABATA, Y., IKADA, Y., Potential efficacy of gelatin microspheres as a new adjuvant for oral vaccination, *STP Pharma Sci.* **1998**, *8*, 64–73.
- 143** YI, Y. M., YANG, T. Y., PAN, W. M., Preparation and distribution of 5-fluorouracil <sup>125</sup>I sodium alginate-bovine serum albumin nanoparticles, *World J. Gastroenterol.* **1999**, *5*, 57–60.
- 144** CHRISTIANSEN, C., VEBNER, A. J., MUAN, B., VIK, H., HAIDER, T., NICOLAYSEN, H., SKOTLAND, T., Lack of an immune response to Albunex, a new ultrasound contrast agent based on air-filled albumin microspheres, *Int. Arch. Allergy Immunol.* **1994**, *104*, 372–378.
- 145** GENY, B., BISCHOFF, P., MUAN, B., PIQUARD, F., THIRANOS, J. C., EPAILLY, E., LAMBRECHS, M., JUELSRUD-VEBNER, A., EISENMANN, B., HABEREY, P., Safety of a new transpulmonary echo-contrast agent (Albunex) in repeated echocardiographic studies in patients, *Clin. Cardiol.* **1997**, *20*, 111–115.



## 7

# Albumin Nanoparticles

*Juan Manuel Irache and Socorro Espuelas*

### 7.1

#### Introduction

Albumin is generally regarded to mean serum albumin or plasma albumin; however, the word albumin is also used to describe a protein or a group of proteins defined by its solubility in water [1, 2]. The albumin literature, already vast, is well served by a number of comprehensive reviews [3–7]. This particular contribution will focus solely on the use of serum albumin as a structural material to prepare nanoparticles, and their possible applications in pharmacy and medicine.

Albumin has substantial value in physicochemical and immunochemical applications. Since serum albumin is so common in the blood and so easy to purify, it was one of the first proteins to be studied by scientists. Its stabilizing and growth supplement properties make albumin ideal for use in cell culture and other commercial applications in which expensive reagents, such as hormones, enzymes and antibodies, require stabilization and/or dilution to maintain their functional integrity for long periods of time [3]. Clinically, albumin is indicated for use as a volume expander for hypovolemia, for treatment of hypoalbuminemia, thermal injuries and certain edematous states, and as an adjunct to cardiopulmonary surgery [8–11]. In North America alone, where it is estimated that the amount of albumin required for a 70-kg patient is approximately 175 g, around 100 000 kg year<sup>-1</sup> are consumed in surgery and shock trauma [12].

Another important field of application is the use of this material in the development of drug delivery systems. In the last 30 years, both bovine serum albumin (BSA) and human serum albumin (HSA) have been widely employed to prepare microparticles and nanoparticles. More than 100 different drugs or diagnostic molecules have been incorporated in albumin particles to be administered by different routes, including intravenous, intramuscular, ophthalmic and nasal routes. A great deal of research has already been conducted in the field of microparticles to determine and evaluate the different possibilities of their use as drug delivery systems and diagnosis tools. Some of these successful efforts have enabled the development of new products as contrast agents for diagnostic purposes (i.e. Optison<sup>TM</sup>). However, albumin nanoparticles, whose development was later than that for mi-

roparticles, are currently being studied by a number of research groups. These carriers appear to offer promising applications, including new therapeutic strategies for both the treatment of cancer and neurological diseases.

This chapter presents an overview of the fabrication and applications of both conventional and “decorated” albumin nanoparticles. After a description of the different preparative processes, representative applications of the albumin nanoparticles are also presented.

## 7.2

### Serum Albumin

Serum albumin or plasma albumin is an abundant, multifunctional protein. It is the major protein component of blood plasma, occurring there at a concentration of around 0.6 mM (range 35–50 g L<sup>-1</sup>), but this represents only approximately 40% of the albumin present in the body. The remainder is found in the extravascular space of tissues.

Serum albumin is a single-chain protein, soluble in water, without any prosthetic groups or covalently bound carbohydrate and lipid [7]. HSA has 585 amino acid residues, whereas BSA is built from 583 amino acid residues [7, 13]. The molecular mass of both molecules is 66.5 kDa. In contrast, the secondary and tertiary structures are not completely known. Based on hydrodynamic experiments [14, 15] and low-angle X-ray scattering [16], serum albumin was postulated to adopt an oblate ellipsoid with dimensions of 140 × 40 Å [17, 18]. However, studies using <sup>1</sup>H nuclear magnetic resonance indicated that this structure was unlikely; rather, a heart-shaped structure has been proposed [19]. This last structure of serum albumin was also confirmed from X-ray crystallographic data [20].

On the basis of the amino acid sequence, Brown proposed a three-domain model for the protein [21]. Each domain is believed to consist of six helices forming a hydrophobic channel with basic and hydrophobic amino acid residues placed at the ends. According to Fourier transform IR (FT-IR) spectra, X-ray crystallographic and differential scanning calorimetry analyses, albumin has about 67%  $\alpha$ -helix, 10% turn and 23% extended chain, but no  $\beta$ -sheet [22, 23]. The analyses have also shown that the three homologous domains (I, II and III) are comprised of two subdomains (A and B) with distinct helical folding patterns that are connected by flexible loops [6, 24]. In addition, albumin domains appear to be stabilized by an internal network of disulfide bonds, bearing a number of ionizable groups with opposite signs [7, 23].

Modifications in the secondary as well as tertiary structures of BSA and HSA occur in dependence of pH, temperature and various kinds of denaturants. A number of studies have been carried out by use of various spectroscopic techniques to explore heat-induced denaturation of albumin [25–29]. The major conclusions reached from them were that conformational changes of the albumin molecule are reversible in the temperature range of 42–50 °C, but unfolding of alpha-helices

are irreversible in the temperature range of 52–60 °C. Above 70 °C, the gel formation by unfolding of albumin advances further [23, 30].

Albumin is synthesized by the liver and released into the circulation, where it possesses a half-life of 19 days [31, 32]. In the blood, serum albumin slowly diffuses across the endothelial linings of the capillaries. The bulk flow of water in the interstitial fluids and lymphatic vessels provides a means of removing albumin from the tissues. Albumin also diffuses into the cerebrospinal fluid, but the rate is so slow compared to the rate of production of the fluid that the concentration is virtually immeasurable [32]. When there is a breakdown in the blood–cerebrospinal fluid barrier, e.g. as occurs in meningitis [33] or multiple sclerosis [34], albumin is found in the fluid as a result of an increased rate of entry.

In mammals, the principal function of albumin is to provide colloid osmotic pressure, preventing plasma loss from the capillaries [6]. Other important functions of serum albumin are to maintain the pH between physiological limits and act as a source for rapid replacement of tissue proteins [35, 36]. Perhaps the most outstanding property of albumin is its ability to bind reversibly to an incredible variety of ligands. Albumin is the principal carrier of fatty acids that are otherwise insoluble in circulating plasma [37]. In fact, each albumin molecule can carry seven fatty acid molecules in deep crevices of the protein, burying their carbon-rich tails safely away from the surrounding water. More recently, serum albumin has been shown to be an important reservoir of the biological regulator and neuro-modulator, nitric oxide [38].

Serum albumin is also a versatile carrier protein, active against a variety of substances with widely differing properties (hydrophobic or hydrophilic, anionic or cationic, etc.). Thus, albumin assists in the distribution, metabolism or regulation of many marginally soluble substances such as calcium ions, tryptophan, various steroid hormones and many drugs [39]. In fact, serum albumin possesses a unique capability to bind, covalently or reversibly, a great number of various endogenous and exogenous compounds. Binding to serum albumin controls the free, active concentration of a drug, provides a reservoir for a long duration of action, and ultimately affects drug absorption, metabolism, distribution and excretion.

### 7.3

#### Preparation of Albumin Nanoparticles

Albumin nanoparticles (Fig. 7.1) have been studied as suitable carriers for drug delivery. The major reported advantages are their biodegradability [40, 41], absence of toxicity [42] and easy preparation by relatively simple methods [43]. Because of their defined primary structure, albumin-based nanoparticles may offer various possibilities for surface modification and covalent attachment of drugs and ligands. Furthermore, the albumin-based nanoparticles could allow the electrostatic adsorption of positively or negatively charged molecules without the requirements of other compounds. In addition, protein nanoparticles can be easily prepared under

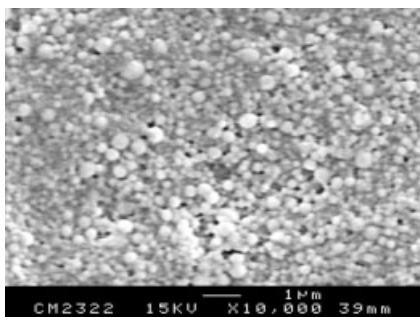


**Fig. 7.1.** Scanning electron microscope image of albumin nanoparticles with an average diameter of about 250 nm. (From Ref. [48].)

soft conditions and incorporate several types of molecules [44, 45]. All of these advantages make albumin one of the most versatile materials to prepare nanoparticles.

### 7.3.1

#### **“Conventional” Albumin Nanoparticles**

Several different methods for the preparation of albumin nanoparticles have been described in the literature; however, many of them are modifications of the two basic techniques – emulsification and coacervation or controlled desolvation.

Emulsification is a relatively simple method to prepare albumin particles; however, control of the particle size is difficult. In fact, albumin particles below 500 nm are difficult to obtain by this procedure [46]. On the other hand, coacervation is more versatile and permits a certain control of the particle size, although careful selection of encapsulation conditions and materials is needed to yield high encapsulation efficiencies.

Once albumin particles have been prepared, the carriers have to be stabilized. Two main methods are used in the stabilization of albumin nanoparticles – thermal treatment at elevated temperatures (95–170 °C) or via the use of chemical reagents. This stabilization or “hardening” process affects the biodegradability and stability of nanoparticles and, thus, their drug release properties [40, 47, 48]. In fact, this step is necessary to prolong the *in vitro* and *in vivo* half-life of the resulting albumin nanoparticles [49].

In heat stabilization, albumin particles are hardened by thermal means, rendering the albumin insoluble by formation of interchain amide links between neighboring amino and carboxylic groups of the protein. [50–52]. This method of stabilization is usually associated with the preparation of nanoparticles by emulsification [40, 43, 47, 53]. The major drawback of the heat-stabilization method relates to the fact that during the formation of the particles and the drug-entrapment

Tab. 7.1. Studies describing the preparation of conventional albumin nanoparticles

Type of albumin	Method of preparation	Desolvating agent	Crosslinking agent	Size (nm)	Yield (%)	Reference
BSA	emulsification with ultrasound and chemical stabilization	–	glutaraldehyde	160–2000	7–99	62
BSA	pH coacervation method (pH 5.5) and chemical stabilization	ethanol	glutaraldehyde	225–300	60–80	48, 63, 64
HSA	pH coacervation method (pH 9) and chemical stabilization	acetone	glutaraldehyde	120–135	ND	44
HSA	pH-coacervation method (pH 7–9) and chemical stabilization	ethanol	glutaraldehyde	150–280	66–95	65
HSA	desolvation and chemical stabilization	ethanol	glutaraldehyde	236	ND	66
HSA	pH control and heat treatment	–	–	240	90	67

ND: not determined.

process, the temperature is sometimes very high. Although a higher temperature may be of little consequence for highly stable drugs, it can potentially lead to degradation and loss of drug efficiency.

To alleviate this problem, room-temperature chemical stabilization methodologies have been developed involving the use of formaldehyde [54, 55], glutaraldehyde [46–48, 50, 51, 56–58], 2,3-butadione [54] and, more recently, methyl polyethylene glycol (PEG)-modified oxidized Dextran (Dextranox-MPEG) [59]. Among all these chemicals, glutaraldehyde is the most popular agent for chemical crosslinkage. The reaction between albumin (proteins in general) and glutaraldehyde leads to the coupling of two amino groups located in the same protein molecule or to form bridges between albumin chains [51]. Glutaraldehyde predominantly reacts with the  $\epsilon$ -amino group on lysine and the N-amino terminal groups of the albumin [47, 60, 61].

Table 7.1 summarizes some of the studies concerning the optimization and preparation of unmodified or conventional albumin nanoparticles.

#### 7.3.1.1 Preparation of Albumin Nanoparticles by Desolvation or Coacervation

The desolvation of albumin with organic solvents followed by chemical crosslinkage is a commonly used method for the preparation of protein nanoparticles. In general, the coacervating agent induces some progressive modifications of the protein's tertiary structure to give an increasingly hydrophobic material, which tends to form submicronic aggregates of desolvated protein (coacervates) [68]. These co-

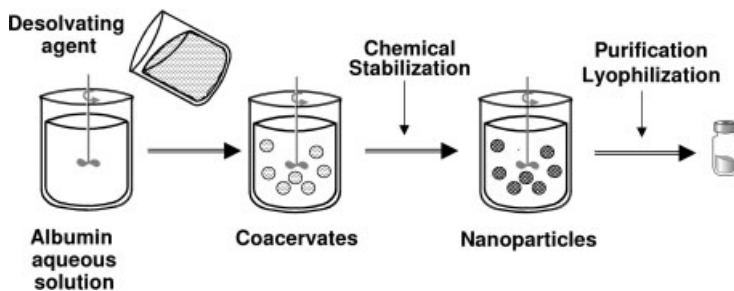


Fig. 7.2. Route for the preparation of albumin nanoparticles by a coacervation method followed by chemical stabilization with glutaraldehyde.

acervates are usually unstable and have to be hardened by physical or chemical crosslinkage. Stabilized coacervates are known as nano- or microparticles depending on their size.

The preparation of albumin nanoparticles by desolvation involves a three-step procedure. In the first step, an unstable dispersed system (coacervates) is obtained by addition of a desolvating agent of albumin (usually, acetone or ethanol) to an aqueous solution of the protein. Then, the coacervates are hardened by thermal stabilization or, more frequently, chemical crosslinkage and, finally, the resulting nanoparticles are purified and lyophilized. Figure 7.2 summarizes this process.

(a) *First step: preparation of albumin coacervates.* Albumin coacervates are obtained from an aqueous solution of the protein and after the addition of a desolvating agent of albumin. Among the different desolvating agents of proteins, acetone and ethanol have been widely employed. The reasons for this selection are their acceptability by pharmaceutical regulations and their easy elimination from the aqueous medium containing the albumin coacervates.

In 1993, Lin et al. described the preparation of HSA nanoparticles using a surfactant-free pH coacervation method [44]. These particles, in a size range between 90 and 250 nm, were prepared by the dropwise addition of acetone to an aqueous albumin solution at pH values between 7 and 9. The size of the resulting nanoparticles appeared to be dependent on the pH and the protein concentration [44].

Another interesting desolvating agent is ethanol. In this case, the addition of ethanol to an aqueous solution of albumin induces the formation of coacervates, whose size increased by increasing the volume of ethanol added up to a ethanol:water ratio of 1.5. Above this ratio, the particle size of albumin coacervates remains constant, but the particle concentration (yield of the process) continues to increase [48, 52]. Similarly, the rate of ethanol addition may influence the width of the particle size distribution – a higher rate of ethanol addition leads to a decrease of the heterogeneity of the albumin coacervates [65].

As a function of the pH and ionic strength of the albumin solution, the appear-

ance of the coacervate changed markedly and it is possible to prepare coacervates with different sizes. Thus, higher pH values lead to smaller nanoparticles; however, the yield of the process decreases [44, 48, 65]. Using acetone as a desolvating agent, the key parameter controlling the size of the resulting nanoparticles appears to be the pH of the medium. It was found that with increasing pH value of the albumin solution, particle size was reduced. This fact can be explained to an increased ionization of the HSA, by increasing the pH of the medium (the isoelectric point of albumin is 5.3) which leads to a repulsion of the albumin molecules and aggregates during particle formation. However, increasing salt concentration of the aqueous solution of the protein induces the formation of large particles. The presence of salts or the use of buffers interferes with the desolvation process. With phosphate buffers (pH 7–8), salt precipitation occurs during desolvation with ethanol. On the contrary, alkaline borate buffers (pH 8–9) or HEPES (pH 7.5) induce the precipitation of albumin in large aggregates [65].

Another important factor affecting the size and yield of nanoparticles produced by desolvation is temperature. Thus, preparation at 4 or 40 °C produces significantly smaller particles than at 20 and 30 °C. In addition, at 30 and 40 °C, clearly more particles are produced than at lower temperatures due to the lower solubility of albumin at higher temperatures under these conditions [52].

(b) *Second step: stabilization of albumin coacervates.* Once albumin coacervates are generated they have to be stabilized to reduce the rate of dissolution of albumin in water. The most popular technique is chemical stabilization with glutaraldehyde. In principle, two factors are important to consider – reagent concentration and duration of the crosslinking process. For the production of stable nanoparticles, the lowest required concentration appears to be at least up to 40% of the theoretical amount of glutaraldehyde that is necessary for the quantitative reaction with the amino groups in the albumin molecule [6, 46, 52]. The crosslinker reacts during variable periods of time ranging from 1 to 24 h. In any case, a large amount of glutaraldehyde or a long reaction time may result in a significant increase in both the size and polydispersion of the resulting nanoparticles [48]. Recently, the chemical stabilization process of albumin nanoparticles was optimized with 1.56 µg glutaraldehyde (mg protein)<sup>-1</sup> for 2 h. Under these conditions, no significant differences in the size, polydispersity and yield of albumin coacervates and nanoparticles were observed [63].

Again, the presence of buffers may negatively affect the stabilization process. Thus, the use of a Tris buffer (pH 8–9), characterized by the presence of amino groups, may negatively affect the efficacy of the crosslinking process with glutaraldehyde [65].

Another possibility is thermal stabilization. Chen et al. described the stabilization of HSA microspheres prepared by desolvation in acetone/water mixtures at 75 °C for 15–30 min [69]. Similar results were obtained by Weber et al. preparing albumin nanoparticles by desolvation with ethanol [52].

(c) *Third step: purification.* Purification of nanoparticles for pharmaceutical purposes is mandatory. The addition of sodium metabisulfite can be a good strategy to block unreacted aldehyde groups [70]. Other possibilities are dialysis, gel-

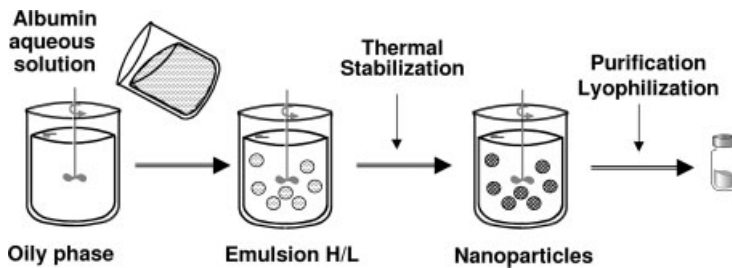


Fig. 7.3. Route for the preparation of albumin nanoparticles by an emulsification method followed by thermal stabilization.

permeation chromatography or, more frequently, subsequent centrifugations to eliminate any remaining protein molecules not transformed onto nanoparticles.

Finally, nanoparticles can be also lyophilized to preserve their physicochemical properties for a long period of time. For lyophilization of albumin nanoparticles, glucose [71], mannose [72] and mannitol [48, 73] have been proposed as cryoprotectors.

In summary, the main advantage of the desolvation process is the absence of toxic organic solvents and its application to the encapsulation of hydrophilic molecules. However, one of the main drawbacks appears to be that there is a close relationship between the size and yield of nanoparticles obtained by this manufacturing method. Therefore, a smaller particle size corresponds to a smaller amount of protein transformed into the nanoparticles.

#### 7.3.1.2 Preparation of Albumin Nanoparticles by Emulsification

Figure 7.3 summarizes a flow diagram of the preparation of albumin nanoparticles by an emulsification technique. For this purpose, an aqueous solution containing the protein is first emulsified in a lipophilic phase (i.e. cotton seed oil or an organic solvent). The two nonmiscible phases are dispersed with the help of high surfactant concentrations and/or energetic stirring procedures (i.e. ultrasounds). Thus, the albumin droplets are thermally stabilized by heating at a temperature higher than 110 °C for a variable period of time (10–30 min) [74, 75]. Then, nanoparticles are centrifuged, washed several times with organic solvents (i.e. diethyl ether or alcohol) and resuspended by sonication to remove residual oil [74, 76, 77].

With respect to emulsion techniques applying serum albumin, a complete and systematic study concerning the influence of protein concentration, emulsification time and power, stirring rate, heat stabilization temperature, and the type of non-aqueous phase was carried out by Gallo et al. [54]. More recently, a method for the preparation of BSA nanoparticles in the sub-200 nm range was described by Müller et al. [62]. In this case the aqueous solution of albumin was injected with a syringe in a solution of organic solvents containing a thickening agent (hydroxypropylcellulose). This emulsion was sonicated and forced to circulate during homogenization through a static mixing device. Finally, nanoparticles were cross-



linked with glutaraldehyde, isolated by centrifugation and washed with *n*-hexane. The emulsification process was carried out in a home-made apparatus, allowing transfer to larger scales [62].

The preparation of nanoparticles by this technique is not easy and involves a number of important drawbacks, including the use of surfactants for emulsion stabilization and the use of organic solvents to eliminate oil residues. In addition, the complete removal of the dispersion agents or oil residues remaining on the particle surface is difficult and time consuming.

#### 7.3.1.3 Other Techniques to Prepare Albumin Nanoparticles

Recently, a new procedure to produce albumin nanoparticles of about 250 nm has been proposed by pH control and heat treatment [67]. In this new procedure, an aqueous solution of albumin at pH 10.65 is heated at 80 °C for a set period. Then, the solution is rapidly cooled to room temperature, the pH of the solution adjusted to 6.04 and the resulting solution stirred for 90 min. Under these conditions, the solution becomes turbid and the albumin nanoparticles are formed.

Another possibility to obtain albumin nanoparticles is by using the sonochemical method. This method was developed by Suslick et al. for the synthesis of non-aqueous liquid-filled microcapsules and air-filled microbubbles [78, 79]. According to this process, the particles are formed by chemically crosslinking cysteine residues of the protein with an HO<sub>2</sub> radical formed around a micrometer-sized gas bubble or a nonaqueous droplet. The chemical crosslinking is responsible for the formation of the albumin particles and is a direct result of the ultrasound radiation on an aqueous medium [80]. However, this technique yields heterogeneous batches with wide size distributions, i.e. between 400 and 2800 nm [81].

#### 7.3.2

#### Surface-modified Albumin Nanoparticles

The surface of albumin nanoparticles possesses several amino and carboxylic groups which are available for covalent modification and drug or protein attachment [82]. These functional groups can be employed to couple targeting ligands such as primary amines [83], avidin [84] and PEG derivatives [59] as well as to covalently bind a variety of drugs.

An interesting approach to modify the surface of albumin nanoparticles is their association with PEG derivatives (or pegylation). PEGs are one of the most popular polymers for surface modification of colloidal drug carriers. In fact, PEGs were found to reduce interactions of the nanoparticles with the cells of mononuclear phagocyte system (MPS), thereby prolonging nanoparticle circulation in the blood stream after parenteral administration [85–87]. The steric repulsion resulting from a loss of conformational entropy of the bound PEG chains upon the approach of a foreign substance and the low interfacial free energy of PEG in water contribute to the extraordinary physiological properties of nanoparticles covered with PEG [85, 88]. Similarly, PEG grafted to surfaces of biomedical devices showed an increase of their biocompatibility [89, 90].

Concerning the preparation of pegylated albumin nanoparticles, little differences with respect of the preparative methods of conventional nanoparticles are observed. The mode of PEG attachment to these nanoparticles is carried out mainly by covalent grafting [91, 92], which is preferable than simple adsorption because of the higher stability of the resulting PEG layer around particle surface. This covalent attachment can be obtained by either synthesis of the PEG–albumin complex before manufacture of nanoparticles or by direct pegylation during the process of nanoparticle formation. The first attempt to prepare pegylated nanoparticles was developed by Lin et al. [59]. In this case HSA nanoparticles with a size of about 170 nm were prepared by a pH coacervation method, using acetone as desolvating agent and crosslinking with Dextranox-MPEG, which created a sterically stabilizing polyethylene oxide surface layer surrounding the nanoparticles.

Later, this same research group proposed the preparation of surface-modified albumin nanoparticles with PEG–albumin conjugates previously synthesized. Thus, pegylated albumin nanoparticles of around 100–140 nm were prepared from either poly(amidoamine)–PEG copolymer-grafted HSA (HSA–PAA–PEG) or poly(thioetheramido acid)–PEG copolymer-grafted HSA (HSA–PTAAC–PEG). These nanoparticles were produced using a pH coacervation method and cross-linked with glutaraldehyde [93].

In all cases, the existence of a hydrated steric barrier surrounding the nanoparticles was confirmed and these pegylated nanoparticles showed reduced plasma protein adsorption on their surface compared with unmodified particles. However, the use of PEG–albumin conjugates, rather than crosslinkage with Dextranox-MPEG, was more useful to obtain nanoparticles with a sole polyoxyethylene barrier on albumin nanoparticles [94]. More recently, pegylated nanoparticles prepared from mPEG–albumin conjugates have been reported [94]. However, when albumin is modified with mPEG, the amphipatic nature of the PEG molecule confers a higher solubility of albumin–PEG conjugates in organic solvents. This fact makes it difficult to induce coacervation of albumin, and thereby form nanoparticles, by using water miscible solvents. To solve this problem, ethyl acetate was introduced in the coacervation method [94]. Table 7.2 summarizes some of the reported methods to prepare pegylated albumin nanoparticles.

### 7.3.3

#### **Drug Encapsulation in Albumin Nanoparticles**

Albumin particles can load a high variety of drugs; however, the best results are obtained with hydrophilic molecules having high albumin-binding abilities. The association of a given drug or active molecule with albumin nanoparticles can be carried out by simple adsorption to the surface of the freshly prepared nanoparticles or during the process of fabrication of these carriers. In any case, the drug-loading efficiency is significantly influenced by the degree of binding between the drug and the albumin molecule [95, 96]. The higher the degree of binding between drug and the albumin molecules, the greater the loading capacity.

Tab. 7.2. Studies describing the preparation of pegylated albumin nanoparticles

Type of albumin	Method of preparation	Desolvating agent	Crosslinking agent	Size (nm)	Reference
HSA	pH coacervation (pH 9) and chemical stabilization	acetone	Dextranox-mPEG	170	59
HSA-PTAAC-PEG	pH coacervation (NaOH 0.5 M, 10 $\mu$ L) and chemical stabilization	acetone	glutaraldehyde	128–130	93
HSA-PAA-PEG	pH coacervation (NaOH 0.5 M, 10 $\mu$ L) and chemical stabilization	acetone	glutaraldehyde	106–138	93
HSA-mPEG	coacervation and chemical stabilization	acetone/ ethylacetate	glutaraldehyde	155	94

The incorporation of a drug (or active molecule) into the albumin nanoparticles by adsorption postparticle preparation can be carried out by simple dispersion of nanoparticles in an aqueous solution of the drug. This process is quite simple and has been used to load pilocarpine nitrate [71, 97] or hydrocortisone [70]. The adsorption capacity of molecules on the surface of albumin nanoparticles appears to be dependent on both their polarizability and hydrophobic properties [98]. For diluted solutions of model dyes (as generally used in drug delivery), the adsorption isotherms of these molecules on unloaded albumin particles exhibited Langmuir behavior suggesting monolayer formation in the initial stages of the sorption process. In addition, the amount of dye adsorbed to the surface of albumin particles increased with increasing hydrophobicity [98].

Adsorption and chemical stabilization can also be performed at the same time. Furthermore, in some cases, chemical crosslinkage can be also used to bind the given drug to the surface of albumin nanoparticles. This fact can be of interest to increase the loading capacity of albumin nanoparticles and to obtain more sustained drug release profiles. This strategy was applied for the loading of urokinase [99], ganciclovir (GCV) [48] and interferon- $\gamma$  [64]. Finally, albumin nanoparticles can be also used as a substrate to covalently bind active molecules by means of other chemical reactions involving different functional groups than that used by glutaraldehyde. This is case for the binding of the chelating agent diethylenetriaminepentaacetic acid [100] and cytochrome *c* [67] to the surface of albumin nanoparticles.

The second possibility consist of simultaneous incubation between the drug and protein before emulsification or desolvation. This strategy was followed for the loading of a number of drugs, including rose Bengal [72], GCV [48], 5-fluorouracil (5-FU) [101], methotrexate [102] and antisense oligonucleotides [63, 103]. An interesting modification of this “incubation step” consist of the use of a complex coacer-

vation method to load DNA. In this case, albumin nanoparticles can be formed by interaction of DNA with albumin in the presence of polyethylenimine (PEI) with the aid of sodium sulfate as a desolvating agent. It is assumed that during complex formation DNA and PEI get entangled into the forming matrix of albumin, thus building up nanoparticles of a spherical shape. The particles were stabilized by using a carbodiimide derivative as crosslinking agent [104]. A more simple method to load oligonucleotides in nanoparticles containing albumin was developed by Vogel et al. [105]. In this case, nanoparticles or proticles (as they were called by the authors) were obtained by simple incubation of protamine, oligonucleotide and albumin in an aqueous solution buffered at pH 7.0.

In general, the incubation method is preferred because it is simpler and gives higher encapsulation efficiencies than the adsorption procedure. Furthermore, this incubation previous to the protein coacervation or emulsification permits the dispersion of drugs or materials with low aqueous solubility and, thus, their incorporation to albumin nanoparticles.

However, the presence of modified albumins or surface “decorated” nanoparticles can also negatively affect the encapsulation or adsorption of the given drug. Thus, Lin et al. reported the lower incorporation of rose Bengal in pegylated nanoparticles when compared with undecorated nanoparticles. This fact appears to be a consequence of the blockage of active binding sites in the albumin molecule by the PEG derivative [72].

#### 7.4

#### Biodistribution of Albumin Nanoparticles

Few biodistribution or pharmacokinetic studies of albumin nanoparticles have been conducted. In healthy animals, no significant differences in the targeting properties of nanoparticles from albumin or from other materials have been reported. Thus, 15 min after the intravenous injection of a single dose of albumin nanoparticles, around 80% of the given dose was localized in the liver [83]. Figure 7.4 shows the capture of fluorescently labeled albumin nanoparticles for phagocyte cells in the liver. Similarly, no significant differences were found in the distribution of albumin nanoparticles when these carriers were coated to render them with positive, neutral or negative surface charges [83].

Nevertheless, the coating of polymer nanoparticles with albumin has been used as strategy to prevent their rapid clearance by mononuclear phagocyte system *in vitro* [106] and *in vivo* [107, 108]. It appears that albumin coating of nanoparticles may impair the adsorption of other serum proteins, such as opsonins C3b or IgG, that promote the receptor-mediated uptake by phagocyte cells. However, some evidence suggests that albumin, during nanoparticles formation, undergoes conformational changes (unpublished data) and the behavior of albumin nanoparticles would not be comparable with albumin-coated particles.

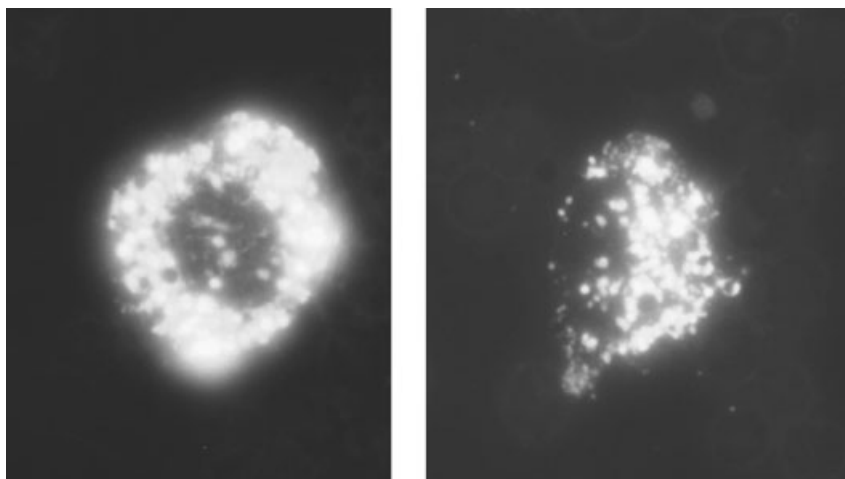


**Fig. 7.4.** Capture of fluorescently labeled albumin nanoparticles by cells of the MPS in the liver.

Merodio et al. studied the distribution of albumin nanoparticles in a model of multiple sclerosis in order to evaluate the potential of these carriers to cross the blood–brain barrier (BBB) [109]. The BBB is a unique membranous barrier that tightly separates the brain from the circulating blood. The capillaries of the brain and spinal cord lack the small pores and fenestrations of general capillaries, and are sealed with tight junctions [110]. The endothelial cells together with glial cells (i.e. astrocytes and pericytes) and the basal membrane constitute this barrier [111]. The result is a complex obstacle for many drugs. Many neurological disorders are characterized by significant alterations in the BBB, such as Alzheimer’s disease, multiple sclerosis, tumors, cytomegalovirus (CMV) or HIV infections [112].

The pathogenesis of multiple sclerosis includes white and grey mater lesions, myelin breakdown, and active inflammation [113]. The study of this disease was extensively performed with the induction in mice of experimental allergic encephalomyelitis (EAE), which displays similar neurological disorders to those observed in the multiple sclerosis disease [114]. Different strategies have been proposed to target pathological tissues within the central nervous system (CNS), including liposomes [115] and recombinant adeno-associated virus [116]. Similarly, Kumagai et al. proposed that cationized albumin is able to traverse the capillary walls of isolated brain capillaries and can be used for brain delivery [117].

More recently, the distribution of albumin nanoparticles (of about 300 nm) in the EAE animal model was carried out [109]. These nanoparticles were administered intraperitoneally, and 4 h after their administration were localized in the damaged and inflamed areas of the CNS, mainly in the lumbar portion of the spinal cord, the optic chiasma or the cerebellar lobules [109]. Immunohistochemical

studies revealed that circulating macrophages, which migrate to the damaged areas within the CNS, and resident activated microglial cells were involved in the distribution of albumin nanoparticles.

## 7.5

### Pharmaceutical Applications

Albumin micro- and nanoparticles have a wide range of biomedical applications, including their use as diagnostic agents, oligonucleotide and DNA delivery, cancer treatment, and ocular drug delivery.

#### 7.5.1

##### Albumin Nanoparticles for Diagnostic Purposes

Albumin nanoparticles have been proposed for imaging purposes because of a number of advantages, including their increased stability, prolonged *in vivo* half-life, reduction of possible adverse effects, concentration of the agent resulting in lower doses and ease of administration [118]. Their main uses are as radiopharmaceuticals and echo-contrast agents.

##### 7.5.1.1 Radiopharmaceuticals

One of the first attempts to use albumin nanoparticles as diagnostic tools was carried out by Scheffel et al. in 1972 [76]. In this case,  $^{99m}\text{Tc}$ -labeled albumin nanoparticles (of about 0.3–1  $\mu\text{m}$  size) were successfully used to visualize the liver and spleen by measuring gamma-rays coming from the isotope with a gamma camera [76]. Later, albumin nanoparticles were proposed for the study of the lymphatic system and identify sentinel nodes in breast cancer [119]. The sentinel node procedure for breast cancer allows for accurate staging of the axilla, while axillary node dissection can be avoided in patients with no sentinel node metastasis [120]. For this purpose, the radioactive tracers most commonly used are  $^{99m}\text{Tc}$  sulfur colloid (US) and  $^{99m}\text{Tc}$ -labeled albumin nanoparticles (Europe) [121]. They are distinctly different in size, and the smaller albumin nanoparticles show earlier retention and higher uptake into the sentinel nodes [122]. Nevertheless, both have been shown to be more effective in the identification of these nodes than microparticles, which show a tendency to remain in the injection site and a lower ability to enter into the lymphatic system [123, 124]. In addition, with albumin nanoparticles the subdermal/intradermal injection appears to be a reliable alternative [125, 126]. These albumin nanoparticles appear also to be effective in the diagnosis of melanoma [127], head and neck squamous cell carcinoma [128], and cervical cancer [129]. Finally, it is interesting to note that these radiopharmaceutical agents have also been proposed for the treatment of solid cancers [130, 131].

### 7.5.1.2 Echo-contrast Agents

Albumin nanoparticles, containing very small amounts of gas, are adequate echo-contrast agents [80, 132, 133]. These particles are prepared by sonication and can be used as an ultrasound contrast agent in echocardiography for the diagnosis of cardiac disease [134] and monitoring of myocardial perfusion [132, 135]. Two-dimensional contrast echocardiography uses the reflection of ultrasound to image heart tissue *in vivo*. To enhance image quality, a solution containing micro- or nanobubbles of albumin (size lower than 10  $\mu\text{m}$ ) may be injected intravenously to perfuse the cardiovascular system; these bubbles change the acoustic impedance of the blood flow, resulting in dramatically improved echo contrast with the surrounding tissues [136].

### 7.5.2

#### Albumin Nanoparticles as Carriers for Oligonucleotides and DNA

Antisense oligonucleotides are very potent drugs for the treatment of important diseases such as oncogene-related cancers or viral infections. Although antisense therapy provides a level of selectivity not available with traditional drugs, their therapeutic potential is currently hampered by their poor biological stability, limited cellular uptake and the poor cytoplasm delivery, where they have to reach their complementary targets. The use of colloidal carriers is a possible strategy to circumvent both stability and permeability problems. Cationic lipids and liposomes have been the most widely exploited, as long as polyanionic oligonucleotides interact spontaneously with positive molecules. However, they are toxic and show instability in presence of serum. Biodegradable nanoparticles made of several types of polymers have been also studied, i.e. polylactic acid (PLA)–PEG, poly(alkylacrylates), chitosan or alginates. Several groups have reported the advantages of using albumin nanoparticles as carriers for oligonucleotides, as compared with other types of polymers [63, 103, 137, 138]. Apart from protecting unmodified oligonucleotides from degradation [63, 138] and improving the cellular uptake [103] protein nanoparticles were able to load appreciable amounts of oligonucleotides without additional positive components [63]. What is more, albumin nanoparticles not only improved the cellular uptake of the oligonucleotides, but led to a significant accumulation of the oligonucleotide in the cytosol compartment of cells, in the absence of endosomolytic agents [103, 138].

The rationale for using albumin nanoparticles for cytoplasmic delivery of oligonucleotides is supported by the spontaneous interaction between these molecules and the protein as well as the fusogenic activity of albumin at low pH. Plasma albumin is their endogenous carrier that governs their transport and tissue distribution. Srinivanan et al. [139] (for HSA) and Arnedo et al. [137] determined values of binding constants that confirmed the high affinity between the protein and the oligonucleotides. It seems that the oligonucleotides bind to site I within the albumin [139]. The affinity was affected by the presence of other molecules associated to the protein (e.g. fatty acids). Also, the length and nature of the backbone in the

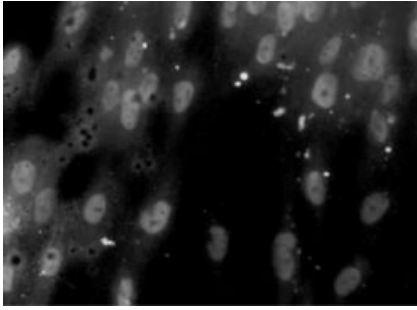


**Fig. 7.5.** Effect of albumin nanoparticles on the subcellular distribution pattern of a fluorescent phosphodiester oligonucleotide loaded in albumin nanoparticles after 24 h incubation time at 37 °C with MRC-5 fibroblasts.

oligonucleotides and the drug/albumin ratio had an influence in the stoichiometry of the interaction [103, 137, 139]. The consequence was that albumin nanoparticles were able to load oligonucleotides by simple incubation between the protein and the polyanions before desolvation, and further crosslinking of the protein coacervates with glutaraldehyde [63, 103]. Also, the adsorption of the oligonucleotides onto preformed nanoparticles was possible [63] and mainly addressed by electrostatic interactions. In addition, albumin nanoparticles encapsulated modified oligonucleotides with more efficiency than unmodified ones in accordance with a higher binding affinity of the native protein with a phosphorotioate backbone [103, 138].

The influence of albumin nanoparticles in cellular uptake and further intracellular distribution has also been evaluated. With an unmodified oligonucleotide Arnedo et al. [138] observed that albumin nanoparticles delayed and decreased the uptake of the oligonucleotide in MRC-5 cells. More important was the effect of albumin nanoparticles in the pattern of intracellular distribution of the oligonucleotide, from a punctate pattern for being concentrated in vesicular compartments to a more diffused cytoplasmic distribution [66, 103, 138]. Figure 7.5 shows this distribution of albumin nanoparticles within the cytoplasm of fibroblasts. This modification in the pattern of intracellular distribution was attributed to fusogenic properties of albumin at low pH, as previously tested in artificial systems with liposomes [140]. Figure 7.6 summarizes the proposed mechanism for the cell internalization and transport of antisense oligonucleotides by albumin nanoparticles.

The oligonucleotides are small molecules that bind to site I in the molecule of native albumin, DNA forms a complex much better with cationized albumin [141]. The system was less toxic than other positive molecules [142], but also it was unable to transfect cells. More frequently, the native protein has been co-associated to DNA-PEI complexes [104] or DNA-protamine lipoplexes [143, 144]. The presence of albumin stabilized the complexes through a decrease in their positive charge that prevented their aggregation in the presence of serum. With similar stabilization role, albumin was also incorporated into oligonucleotide-protamine particles [105].



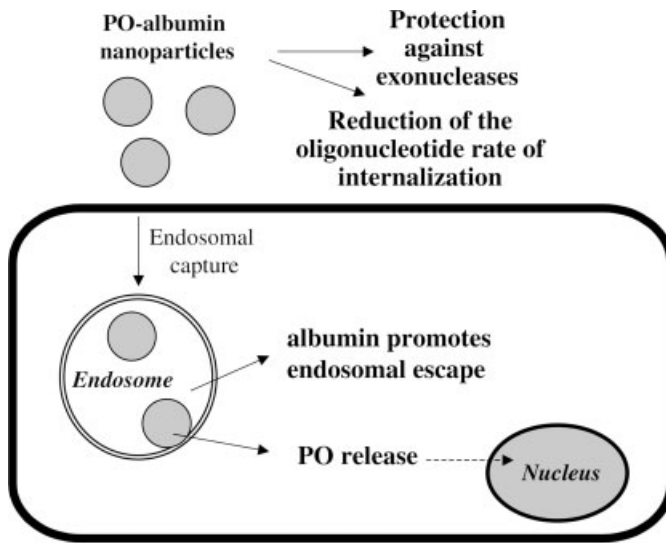


**Fig. 7.6.** Proposed mechanism of the protective effect of albumin nanoparticles on the cell internalization and transport of antisense oligonucleotides (PO).

### 7.5.3

#### Albumin Nanoparticles in the Treatment of Cancer

Albumin nanoparticles have been proposed as carriers for different antitumor drugs, including 5-FU, methotrexate and paclitaxel.

##### 7.5.3.1 Fluorouracil and Methotrexate Delivery

The use of albumin nanoparticles of about 660 nm containing 5-FU for cancer chemotherapy was investigated several years ago [145–147]. Upon intravenous injection into healthy mice, the nanoparticles were found accumulated in the liver and other elements of the MPS. However, when nanoparticles were injected intraperitoneally in Ehrlich ascites carcinoma-bearing mice, phagocytosis of the albumin carriers by tumoral cells was observed and suppression of tumor growth was noted [146]. Furthermore, following injection of multiple doses of 5-FU-loaded albumin nanoparticles, the lifespan of the mice increased by about 30% compared to a control treatment with the free drug [146]. More recently, a similar formulation of 5-FU-loaded albumin nanoparticles (size about 640 nm) was found effective in mice with a 2-fold increase in the antitumor activity of this drug compared with a free 5-FU solution [101]. Another interesting work concerns the ability of sodium alginate–BSA nanoparticles to increase the oral bioavailability of 5-FU. These carriers (about 170 nm) were able, after oral administration, to enter into the circulation and target the tissues rich in phagocytes, such as the liver and spleen [148].

However, albumin nanoparticles induced a markedly different biodistribution of

methotrexate when administered in animals by an intravenous route [102]. In fact, the incorporation of this drug in albumin nanoparticles increased its accumulation in the lungs of animals [102].

#### 7.5.3.2 Paclitaxel Delivery

The more interesting and complete studies of the potential of albumin nanoparticles to deliver antitumor drugs have been carried out with paclitaxel. Paclitaxel (Taxol®) is used extensively in the treatment of breast cancer [149], and, due to its low aqueous solubility, is currently formulated with ethanol and the nonionic surfactant Cremophor EL (polyoxyethylated castor oil) to enhance drug delivery [150]. However, these excipients may contribute to the side-effects associated with the use of paclitaxel, ultimately reducing the quality of life in patients undergoing treatment. Cremophor may contribute to side-effects induced by paclitaxel, as well as the hypersensitivity reactions that occur in 25–50% of patients during infusion that require premedication with histamine blockers and glucocorticoids [151]. Furthermore, the formulation including Cremophor and ethanol leaches plasticizers from PVC bags and infusion sets, resulting in the need for preparation and administration of paclitaxel in glass bottles or non-PVC infusion systems [152].

In order to overcome these drawbacks and to increase its antitumor efficacy, paclitaxel was covalently bound to albumin nanoparticles. This new formulation of about 150 nm allows for a higher concentration of paclitaxel, resulting in a decreased infusion volume and time, and does not require nonstandard infusion sets [149, 153]. In animal models, paclitaxel–albumin nanoparticles resulted in increased delivery of chemotherapeutic drugs to the tumor compared with solvent-based drugs. The mechanism for this advantage is being actively studied and may be related to albumin-activated transport of molecules into tissues by binding to the gp60 albumin receptor on blood vessels with subsequent accumulation of albumin nanoparticles in tumors [154].

In metastatic breast cancer, a pivotal randomized controlled phase III clinical trial was recently completed comparing the safety and efficacy of 260 mg m<sup>-2</sup> of paclitaxel–albumin nanoparticles versus paclitaxel injection (Taxol) at a dose of 175 mg m<sup>-2</sup>. Despite a 50% higher dose of chemotherapy infused over 30 min without premedication for hypersensitivity, paclitaxel–albumin nanoparticles were well tolerated and provided better results than the conventional formulation [154, 155]. In January 2005, the FDA approved this new albumin nanoparticle formulation (Abraxane™) for metastatic breast cancer [156].

Paclitaxel-loaded albumin nanoparticles have also been proved to be effective in the treatment of squamous carcinomas of the head and neck, uterus, and anal canal. In phase I/II studies, complete pathological responses occurred in 1.16, 20 and 18.8% of patients, respectively [157, 158]. In another study, the intra-arterial infusion of paclitaxel incorporated into human albumin nanoparticles for use as induction chemotherapy before definitive treatment of advanced squamous cell carcinoma of the tongue proved to be reproducible and effective to preserve this organ [159]. In fact, 78% of the treated patients had a clinical and radiological objective response (complete, 26%; partial, 52%) and only 9% showed disease progression.

Another interesting attempt concerning the delivery of paclitaxel is its association with pegylated albumin nanoparticles. Due to their low interaction and recognition by the MPS, these pegylated carriers appear to be of interest to passively target inflamed regions within the body, including the CNS and the colon [160].

### 7.5.3.3 Albumin Nanoparticles in Suicide Gene Therapy

In recent years, suicide gene therapy has been proposed for the treatment of a number of cancers. This therapy implies the use of suicide genes that code for enzymes which can transform a prodrug into a cytotoxic product [161]. Thus, the tumoral cell is rendered sensitive to a type of chemotherapy which is relatively nontoxic for the rest of the body [162]. In this context, the therapeutic combination of the herpes virus thymidine kinase (HSV-tk) and GCV has shown great clinical promise as gene therapy for the treatment of a number of cancers including hepatocarcinoma [163], neuroblastoma [164], ovarian [165], pancreatic [166] and prostate cancers [167]. The viral transfection can be carried out by adenoviruses [162, 163, 165, 166] and the expression of this gene in the cell yields the enzyme that converts the nontoxic prodrug GCV into a highly toxic metabolite [168].

In a recent work, the ability of albumin nanoparticles to concentrate GCV in the hepatocytes evidenced by the increase in the antitumoral efficacy of the HSV-tk/GCV combination [169]. In this work, mice were previously treated with  $4 \times 10^{10}$  pfu  $\text{kg}^{-1}$  adenovirus (AdCMV-tk) by intravenous administration and 48 h later received the GCV treatment. The use of albumin nanoparticles demonstrated a higher ability to concentrate this drug in the liver of animals as compared with the conventional formulation. In addition, the histologic analysis of the liver also revealed great cellular damage in terms of necrotizing area and perivascular inflammatory reactions (Fig. 7.7). It seems that the greater and more prolonged hepatic concentration of GCV released from the nanoparticles led to the accumulation of the toxic metabolite of GCV in the liver. These nanoparticulate carriers offered the additional advantage of increasing the plasma half-life of the drug and its tissue distribution, as determined by the pharmacokinetic analysis [169]. There-

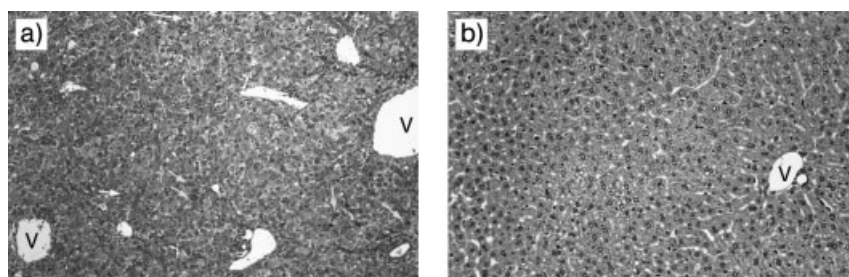


**Fig. 7.7.** (a) Liver section from mice that were treated with  $4 \times 10^{10}$  pfu  $\text{kg}^{-1}$  AdCMV-tk and, 48 h later, received GCV-loaded albumin nanoparticles. (b) Liver section of a nontreated

mouse. Hematoxylin & eosin dye; magnification:  $\times 100$ . Green arrows: ballooning and acidophilic bodies; yellow arrow: apoptotic bodies; V: vessel. (From Ref. [169].)

fore, the use of these nanoparticles permits a higher distribution to the liver, which can be of interest to decrease the drug dose and frequency of administration.

#### 7.5.4

#### **Magnetic Albumin Nanoparticles**

Magnetic drug delivery by particulate carriers is a very efficient method of delivering a drug to a localized disease site. Very high concentrations of chemotherapeutic or radiological agents can be achieved near the target site, such as a tumor, without any toxic effects to normal surrounding tissue or to the whole body [170]. It is thus possible to replace large amounts of freely circulating drug with much lower amounts of drug targeted magnetically to localized disease sites, reaching effective and up to several-fold increased localized drug levels [55, 74, 171, 172].

In magnetically targeted therapy, a cytotoxic drug is attached to a biocompatible magnetic nanoparticle carrier (size in the range of 10–500 nm), such as albumin-coated magnetite [170]. When the particles are administered intravenously, external, high-gradient magnetic fields are used to concentrate the complex at a specific target site within the body. The process of drug localization is based on the competition between forces exerted on the particles by the blood compartment and magnetic forces generated from the magnet, i.e. the applied field. When the magnetic forces exceed the linear blood flow rates in arteries ( $10 \text{ cm s}^{-1}$ ) or capillaries ( $0.05 \text{ cm s}^{-1}$ ), the magnetic particles are retained at the target site and may be internalized by the endothelial cells of the target tissue [173, 174]. The drug can be released from drug/carrier either via enzymatic activity or changes in physiological conditions such as pH, osmolality or temperature [175] and be taken up by the tumor cells. This system, in theory, has major advantages over the normal, non-targeted methods of cytotoxic drug therapy.

The use of magnetic particles for the treatment of liver cancer was proposed for the first time at the end of the 1970s by Widder et al. The intra-arterial injection of these particles containing ultrafine ferroferric oxide and a prototype drug, doxorubicin hydrochloride, in the same target site resulted in 100-fold higher dose compared to free doxorubicin administered intravenously [78, 176–178]. Since those studies, success in cytotoxic drug delivery and tumor remission has been reported by several groups using animals models including pigs [179, 180], rabbits [175] and rats [181]. This technique has also been employed to target cytotoxic drugs to brain tumors [182]. More recently, magnetic albumin nanoparticles containing adriamycin have shown their ability to target a malignant liver tumor in rats [183]. In the presence of the magnetic field, these albumin nanoparticles accumulate in the liver tumor rather than in the normal tissue. Even if the magnetic field is not applied, magnetic albumin nanoparticles in tumor tissues still increase to 2.8 times that of normal liver tissues. In addition, the authors report that, in the presence of magnetic fields, these albumin nanoparticles may drive the drug to the tumoral tissues, preserving normal organs against exposure to chemotherapeutic drugs [183].

### 7.5.5

#### **Albumin Nanoparticles for Ocular Drug Delivery**

##### **7.5.5.1 Topical Drug Delivery**

Ocular administration is associated with rapid elimination of drug formulations from the precorneal area due to drainage through the naso-lacrimal duct and dilution by tear turnover. These processes result in a very low percentage of the drug administered (less than 5%) that could penetrate through the cornea and reach the intraocular tissues. Many studies have demonstrated an enhanced accumulation of nanoparticles in the conjunctival cul-de-sac and better drug bioavailability compared to conventional ophthalmic dosage forms, such as solutions and ointments [184, 185]. The colloidal systems can be administered as simple eye drops and, due to their low viscosity, minimize the temporary hindrance of the patient sight. The frequency of application could be reduced due to sustained drug delivery from the nanoparticle matrix.

Albumin nanoparticles have proved effective for the administration of pilocarpine and hydrocortisone in the interior of the eye [70, 72, 186]. In inflamed conjunctiva, the application of hydrocortisone-coated albumin nanoparticles (size between 100 and 300 nm) led to a higher drug bioavailability than the reference solution, which was rapidly eliminated by lacrimation. In addition, the albumin particles were more efficiently retained at the inflamed area than the normal conjunctiva. Consequently, in the inflamed eye, hydrocortisone-loaded nanoparticles enabled targeting to the precorneal area away from the inner segments of the eye [70].

Similarly, pilocarpine-coated albumin nanoparticles dramatically increased the ocular bioavailability of the drug compared with a reference solution [71]. The association of albumin nanoparticles with bioadhesive polymers was proved effective to increase the residence time of nanoparticles in contact with the eye and, thus, increase drug bioavailability [97]. In the presence of bioadhesives, the nanoparticles induced a significant improved pharmacological response in rabbits (i.e. miotic activity and reduction in the intraocular pressure) when compared with particle dispersions in buffer or free solutions. The best results were obtained with the association of albumin nanoparticles with either bovine submaxillary mucin or carbopol. This fact was due to the higher interaction of these bioadhesive polymers with both nanoparticles and precorneal mucus than other viscosity-enhanced polymers [97].

##### **7.5.5.2 Intravitreal Drug Delivery**

Another problem associated with the treatment of ocular pathologies is the difficulty for a given drug, topically administered, to absorb and reach therapeutic concentrations in the inner tissues of the eye for prolonged periods of time. Sometimes, when chronic treatment is necessary, local intravitreal administration becomes necessary. However, due to the short half-life of the given drugs, frequent injections are necessary to maintain the therapeutic levels. These continuous ad-

ministrations increase the risk of cataracts, retinal detachments, hemorrhages or endophthalmitis [187, 188].

Human CMV (HCMV) is a member of the Herpesviridae family of viruses, which are large DNA viruses that share biological properties of latency and reactivation [189]. In patients with AIDS and those immunocompromised due to hematopoietic stem cell transplantation or solid organ transplantation, HCMV is a major cause of morbidity and mortality [189, 190]. HCMV infections are the major cause of visual loss in these patients. Thus about 20–25% of patients with AIDS develop CMV retinitis during the course of their illness [191]. Without treatment this necrotizing retinitis progresses, resulting in irreversible blindness [192]. In cardiac and liver transplant patients, HCMV infection doubles the 5- and 3-year rates of graft failure, respectively [193]. In the absence of antiviral prophylaxis, symptomatic infections occur in approximately 39% of heart/lung recipients, 25% of heart transplants, 29% of liver transplants and 8% of patients receiving renal transplants [194].

For the treatment of HCMV retinitis, local intravitreal therapy with different antivirals is currently used. In this context, albumin nanoparticles have been proposed as carriers for intravitreal controlled delivery of diethylenetriaminepentaacetic acid (DTPA) [100], GCV [48, 73, 195] and the antisense oligonucleotide fomivirsen [138]. In all cases, these carriers allowed significant increases of the anti-HCMV activity of the loaded drug *in vitro*. These results of antiviral activities seemed to be directly correlated to drug internalization by infected cells [73, 100, 138]. For DTPA-loaded nanoparticles, it appears that these particles were internalized by UKF-NB-3 cells and HFF. This cellular uptake mediated by the drug carrier systems may explain the increased anti-HCMV and cytotoxic effects of DTPA coupled to protein-based drug carrier systems. Another interesting key point is that the improvement of the antiviral activity of GCV when loaded in albumin nanoparticles was not related to any cytotoxic effect on fibroblasts or corneal cells [73].

In order to study the distribution and toxicity of albumin nanoparticles within the eye, these carriers were dispersed in saline and administered to laboratory animals by the intravitreal route [196]. Two weeks after the single injection, a large portion of the administered dose appeared to be localized, quite broadly distributed, overlying the inferior portion of this cavity (see Fig. 7.8). However, some minor fractions were also located in the iris and ciliary body, which can be explained by the higher porosity of these ocular organs and, probably also, by an elimination mechanism of the particles via the ophthalmic anterior chamber. This route of elimination has been described for macromolecules and takes several days to be completed [197]. However, the histological evaluation of the different ocular tissues suggested that albumin nanoparticles are well tolerated after their intravitreal injection. These analyses were confirmed by the absence of cellular infiltrations following the association of the nanoparticles to ocular cells. In addition, no sign of degeneration of the eye receptors was observed [196]. In all cases, the retina kept its cytoarchitecture, with no signs of alteration in the photoreceptor and neuronal

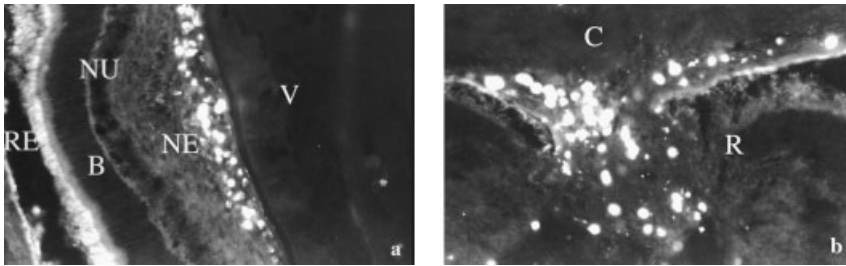


**Fig. 7.8.** Immunofluorescence detection of albumin nanoparticles by streptavidin–FITC staining 2 weeks after their injection in the vitreous cavity (a) and in the blood–aqueous barrier adjacent area and ciliary muscle (b).

Total magnification:  $\times 200$ . B: Bacillary layer; C: ciliary muscle; NE: neuronal interplay area; NU: outer and inner nuclear layers; R: retina; RE: retinal epithelium; V: vitreous cavity. (From Ref. [196].)

layers of the retina. Finally, immunohistochemistry studies also confirmed the lack of ability of albumin nanoparticles to generate autoimmune phenomena, which can stimulate the generation of pathogenic immune responses such as “retinitis pigmentosa” [198] and autoimmune uveoretinitis [199]. In summary, albumin nanoparticles appear to be safe carriers for the intravitreal delivery of drugs.

## 7.6

### Concluding Remarks

This chapter summarizes the preparation and main applications of albumin nanoparticles for pharmaceutical purposes. The use of albumin nanoparticles can offer a number of advantages, including their biodegradability, and the simplicity of preparation in an aqueous environment without the need for harmful solvents and chemicals. Furthermore, the inherent ability of albumin to spontaneously bind a high variety of molecules facilitates their loading in the resulting nanoparticles. In addition, drugs or ligands can also be easily bound to the protein and, thus, modify the surface properties of the resulting nanoparticles. All of these possibilities make albumin nanoparticles versatile carriers for pharmaceutical purposes.

Albumin nanoparticles are currently used as diagnostic tools and as adjuvants to improve the efficacy of the treatment with paclitaxel. However, in the future, the possibility exists that albumin nanoparticles may offer adequate solutions to some pharmaceutical problems such as the delivery of antisense oligonucleotides (and DNA) and the targeting of the CNS for the adequate treatment of neurological disorders.

## References

- 1 OSBORNE, T. B., *The Proteins of the Wheat Kernel*. Publication 84, Carnegie Institute, Washington, DC, 1907.
- 2 SHEWRY, P. R., TATHAM, A. S., FORDE, J., KREIS, M., MIFLIN, B. J., The classification and nomenclature of wheat gluten proteins: a reassessment. *J. Cereal Sci.* **1986**, *4*, 97–106.
- 3 CHUANG, V. T., KRAGH-HANSEN, U., OTAGIRI, M., Pharmaceutical strategies utilizing recombinant human serum albumin, *Pharm. Res.* **2002**, *19*, 569–577.
- 4 PETERS, T., Serum albumin, *Adv. Protein Chem.* **1985**, *37*, 161–245.
- 5 KRAGH-HANSEN, U., Structure and ligand binding properties of human serum albumin, *Dan. Med. Bull.* **1990**, *37*, 57–84.
- 6 CARTER, D. C., HO, J. X., Structure of serum albumin, *Adv. Protein Chem.* **1994**, *45*, 152–203.
- 7 PETERS, T. JR., *All about Albumin: Biochemistry, Genetics and Medical Applications*, Academic Press, San Diego, CA, 1996.
- 8 ERSTAD, B. L., CAMPBELL, D. J., ROLLINS, C. J., RAPPAPORT, W. D., Albumin and prealbumin concentrations in patients receiving post-operative parenteral nutrition, *Pharmacotherapy* **1994**, *14*, 458–462.
- 9 COLGAN, K., Responsible use of blood products in response to supply and demand, *Pharmacotherapy* **2000**, *57*, 2094–2098.
- 10 FLECK, A., SMITH, G., Albumin in intensive care, *Br. J. Intensive Care* **1998**, *8*, 93–95.
- 11 WILKES, M. M., NAVICK, R. J., Albumin verses hydroxyethyl starch in cardiopulmonary bypass surgery: a meta-analysis of postoperative bleeding, *Ann. Thorac. Surg.* **2001**, *72*, 527–534.
- 12 KESHAVJEE, S., Medicine and money: the ethical transformation of medical practice, *Med. Educ.* **2004**, *38*, 271–275.
- 13 WEIJERS, R. N. M., Amino acid sequence in bovine serum albumin, *Clin. Chem.* **1977**, *23*, 1361–1362.
- 14 SQUIRE, P. G., MOSER, P., O'KONSKI, C. T., The hydrodynamic properties of bovine serum albumin monomer and dimer, *Biochemistry* **1968**, *7*, 4261–4272.
- 15 WRIGHT, A. K., THOMPSON, M. R., Hydrodynamic structure of bovine serum albumin determined by transient electric birefringence. *Biophys. J.* **1975**, *15*, 137–141.
- 16 BLOOMFIELD, V., The structure of bovine serum albumin at low pH, *Biochemistry* **1966**, *5*, 684–689.
- 17 BENDEDOUCH, D., CHEN, S. H., Structure and interparticle interactions of bovine serum albumin in solution studied by small-angle neutron scattering. *J. Phys. Chem.* **1983**, *87*, 1473–1477.
- 18 FENG, L., HU, C. Z., ANDRADE, J. D., Scanning tunneling microscopic images of adsorbed serum albumin on highly oriented pyrolytic graphite, *J. Colloid Interface Sci.* **1988**, *126*, 650–653.
- 19 BOS, O. J. M., LABRO, J. F. A., FISCHER, M. J. E., WITLING, J., JANSSEN, L. H. M., The molecular mechanism of the neutral-to-base transition of human serum albumin, *J. Biol. Chem.* **1989**, *264*, 953–959.
- 20 CARTER, D. C., HE, X. M., MUNSON, S. H., TWIGG, P. D., GERNERT, K. M., BROOM, M. B., MILLER, T. Y., Three-dimensional structure of human serum albumin, *Science* **1989**, *244*, 1195–1198.
- 21 BROWN, J. R., Serum albumin, amino acid sequence. In *Albumin: Structure, Function and Uses*, ROSENOER, V. M., ORAZ, M., ROTSHILD, M. A. (Eds.), Pergamon Press, Oxford, 1977, pp. 27–51.
- 22 YAMAZAKI, M., YANO, H., AOKI, K., Differential scanning calorimetric studies on bovine serum albumin: I. Effects of pH and ionic strength, *Int. J. Biol. Macromol.* **1990**, *12*, 263–268.
- 23 MURAYAMA, K., TOMIDA, M., Heat-induced secondary structure and



- conformation change of bovine serum albumin investigated by Fourier transform infrared spectroscopy, *Biochemistry* **2004**, *43*, 11526–11532.
- 24 SUGIO, S., KASHIMA, A., MOCHIZUKI, S., NODA, M., KOBAYASHI, K., Crystal structure of human serum albumin at 2.5 Å resolution, *Protein Eng.* **1999**, *12*, 439–446.
  - 25 WETZEL, R., BECLER, M., BEHLKE, J., BILLWITZ, H., BOHM, S., EBERT, B., HAMAN, H., KRUMBIEGEL, J., LASSMANN, G., Temperature behavior of human serum albumin, *Eur. J. Biochem.* **1980**, *104*, 469–478.
  - 26 GALLER, J., RIVET, P., DE CERTAINES, J., <sup>1</sup>H- and <sup>2</sup>H-NMR study of bovine serum albumin solutions, *Biochim. Biophys. Acta* **1987**, *915*, 1–18.
  - 27 SHIMADA, K., CHEFTEL, J. C., Sulfhydryl group/disulphide bond interchange reactions during heat induced gelation of whey protein isolate, *J. Agric. Food Chem.* **1988**, *37*, 161–168.
  - 28 TAKEDA, K., WADA, A., YAMAMOTO, K., MORIYAMA, Y., AOKI, K., Conformational change of bovine serum albumin by heat treatment, *J. Protein Chem.* **1989**, *8*, 653–659.
  - 29 ZIEGLER, G. R., FOEGEDING, E. A., The gelation of proteins, *Adv. Food Nutr. Res.* **1990**, *34*, 203–298.
  - 30 ROEFS, S. P. F. M., DE KRUIF, K. G., A model for the determination and aggregation of beta-lactoglobulin, *Eur. J. Biochem.* **1994**, *226*, 883–889.
  - 31 PRINSEN, B. H., DE SAIN-VAN DER VELDEN, M. G., Albumin turnover: experimental approach and its application in health and renal diseases. *Clin. Chim. Acta* **2004**, *347*, 1–14.
  - 32 DOWEIKO, J. P., NOMPLEGGI, D. J., Role of albumin in human physiology and pathophysiology, *J. Parenteral Enteral Nutr.* **1991**, *15*, 207–211.
  - 33 QUAGLIARELLO, V. J., MA, A., STUKENBROK, H., PALADE, G. E., Ultrastructural localization of albumin transport across the cerebral microvasculature during experimental meningitis in the rat, *J. Exp. Med.* **1991**, *174*, 657–672.
  - 34 MINAGAR, A., ALEXANDER, J. S., Blood–brain barrier disruption in multiple sclerosis, *Multiple Sclerosis* **2003**, *9*, 540–549.
  - 35 FIGGE, J., ROSSING, T. H., FENCL, V., The role of serum proteins in acid–base equilibria. *J. Lab. Clin. Med.* **1991**, *117*, 453–467.
  - 36 LAIHO, K., Albumin as a marker of plasma transudation in experimental skin lesions. *Int. J. Legal Med.* **2004**, *118*, 282–288.
  - 37 STAMLER, J. S., JARAKI, O., OSBORNE, J., SIMON, D. I., KEANEY, J., VITA, J., SINGEL, D., VALERI, C. R., LOSCALZO, J., Nitric oxide circulates in mammalian plasma primarily as a S-nitroso adduct of serum albumin, *Proc. Natl Acad. Sci. USA* **1992**, *89*, 7674–7677.
  - 38 MURAVSKAYA, E. V., LAFKO, A. G., MURAVSKII, V. A., Modification of transport function of plasma albumin during atherosclerosis and *diabetes mellitus*, *Bull. Exp. Biol. Med.* **2003**, *135*, 433–435.
  - 39 CLARK, A. H., JUDGE, F. J., RICHARDS, J. B., STUBBS, J. M., SUGGETT, A., Electron microscopy of network structures in thermally-induced globular protein gels, *Int. J. Peptide Protein Res.* **1981**, *17*, 380–392.
  - 40 MORIMOTO, Y., FUJIMOTO, S., Albumin microspheres as drug carriers, *Crit. Rev. Ther. Drug Carrier Syst.* **1985**, *2*, 19–63.
  - 41 RUBINO, O. P., KOWALSKY, R., SWARBRICK, J., Albumin microspheres as a drug delivery system: relation among turbidity ratio, degree of cross-linking, and drug release, *Pharm. Res.* **1993**, *10*, 1059–1065.
  - 42 RHODES, B. A., ZOLLE, I., BUCHANAN, J. W., WAGNER, H. N. JR., Radioactive albumin microspheres for studies of the pulmonary circulation, *Radiology* **1969**, *92*, 1453–1460.
  - 43 MACADAM, A. B., SHAFI, Z. B., JAMES, S. L., MARRIOTT, C., MARTIN, G. P., Preparation of hydrophobic and hydrophilic albumin microspheres and determination of surface carboxylic acid and amino residues, *Int. J. Pharm.* **1997**, *151*, 47–55.
  - 44 LIN, W., COOMBES, A. G. A., DAVIES,

- M. C., DAVIS, S. S., ILLUM, L., Preparation of sub 100 nm human serum albumin nanospheres using a pH-coacervation method, *J. Drug Target.* **1993**, *1*, 237–243.
- 45 GESELOWITZ, D. A., NECKERS, L. M., Bovine serum albumin is a major oligonucleotide-binding protein found on the surface of cultured cells, *Antisense Res Dev.* **1995**, *5*, 213–217.
- 46 ROSER, M., KISSEL, T., Surface-modified biodegradable nano- and microspheres. I. Preparation and characterization, *Eur. J. Pharm. Biopharm.* **1993**, *39*, 8–12.
- 47 LEE, T. K., SOKOLOSKI, T. D., ROYER, G. P., Serum albumin beads: an injectable, biodegradable system for the sustained release of drugs, *Science* **1981**, *213*, 233–235.
- 48 MERODIO, M., ARNEO, A., RENELO, M. J., IRACHE, J. M., Ganciclovir-loaded albumin nanoparticles: characterization and *in vitro* release properties, *Eur. J. Pharm. Sci.* **2001**, *12*, 251–259.
- 49 ARSHADI, R., Albumin microspheres and microcapsules: methodology of manufacturing techniques, *J. Controlled Rel.* **1990**, *14*, 111–131.
- 50 WEITZEL, R., BECKER, M., BEHLKE, J., BILLWITZ, H., BOHM, S., EBERT, B., HAMANN, H., KRUMBIEGEL, J., LASSMANN, G., Temperature behavior of human serum albumin, *Eur. J. Biochem.* **1980**, *104*, 469–478.
- 51 BURGESS, D. J., DAVIS, S. S., TOMLINSON, E., Potential use of albumin microspheres as a drug delivery system. I. Preparation and *in vitro* release of steroids, *Int. J. Pharm.* **1988**, *46*, 69–76.
- 52 WEBER, C., COESTER, C., KREUTER, J., LANGER, K., Desolvation process and surface characterisation of protein nanoparticles, *Int. J. Pharm.* **2000**, *194*, 91–102.
- 53 GALLO, J. M., HUNG, C. T., PERRIER, D. G., Analysis of albumin microsphere preparation, *Int. J. Pharm.* **1984**, *22*, 63–74.
- 54 KATTI, D., KRISHNAMURTI, N., Preparation of albumin microspheres by an improved process, *J. Microencapsul.* **1999**, *16*, 231–242.
- 55 WIDDER, K., FLUORET, G., SENYEL, A. E., Magnetic microspheres: synthesis of a novel parenteral drug carrier, *J. Pharm. Sci.* **1979**, *68*, 79–82.
- 56 BURGER, J. J., TOMLINSON, E., DE ROO, J. E., PALMER, J., Technetium-99m labeling of albumin microspheres intended for drug targeting, *Methods Enzymol.* **1985**, *112*, 43–56.
- 57 RATCLIFFE, J. H., HUNNEYBALL, I. M., SMITH, A., WILSON, C. G., DAVIS, S. S., Preparation and evaluation of biodegradable polymeric systems for the intra-articular delivery of drugs, *J. Pharm. Pharmacol.* **1984**, *36*, 431–436.
- 58 EZPELETA, I., IRACHE, J. M., GUEGUEN, J., ORECCHIONI, A. M., Properties of glutaraldehyde cross-linked vicilin nano- and microparticles, *J. Microencapsul.* **1997**, *14*, 557–565.
- 59 LIN, W., COOMBES, A. G., GARNETT, M. C., DAVIES, M. C., SCHACHT, E., DAVIS, S. S., ILLUM, L., Preparation of sterically stabilized human serum albumin nanospheres using a novel Dextranox-MPEG crosslinking agent, *Pharm Res.* **1994**, *11*, 1588–1592.
- 60 HABEEB, A. F. S. A., HIRAMOTO, R., Reaction of proteins with glutaraldehyde, *Arch. Biochem. Biophys.* **1968**, *126*, 16–26.
- 61 PETERS, K., RICHARDS, F. M., Chemical cross-linking: reagent and problems in studies of membrane structure, *Annu. Rev. Biochem.* **1977**, *46*, 523–551.
- 62 MÜLLER, G. M., LEUENBERGER, H., KISSEL, T., Albumin nanospheres as carriers for passive drug targeting: an optimized manufacturing technique, *Pharm. Res.* **1996**, *13*, 32–37.
- 63 ARNEO, A., ESPUELAS, S., IRACHE, J. M., Albumin nanoparticles as carriers for a phosphodiester oligonucleotide, *Int. J. Pharm.* **2002**, *244*, 59–72.
- 64 SEGURA, S., ESPUELAS, S., RENELO, M. J., IRACHE, J. M., Potential of albumin nanoparticles as carriers for interferon-gamma, *Drug Dev. Ind. Pharm.* **2005**, *31*, 271–283.
- 65 LANGER, K., BALTHASAR, S., VOGEL, V.,

- DINAUER, N., VON BRIESEN, H., SCHUBERT, D., Optimization of the preparation process for human serum albumin (HSA) nanoparticles, *Int. J. Pharm.* **2003**, *257*, 169–180.
- 66 BRZOSKA, M., LANGER, K., COESTER, C., LOITSCH, S., WAGNER, T. O., MALLINCKRODT, C., Incorporation of biodegradable nanoparticles into human airway epithelium cells – *in vitro* study of the suitability as a vehicle for drug or gene delivery in pulmonary diseases, *Biochem. Biophys. Res. Commun.* **2004**, *318*, 562–570.
- 67 TAKEOKA, S., TERAMURA, Y., OHKAWA, H., IKEDA, Y., TSUCHIDA, E., Conjugation of Von Willebrand factor-binding domain of platelet glycoprotein Ib $\alpha$  to size-controlled albumin microspheres, *Biomacromolecules* **2000**, *1*, 290–295.
- 68 MARTY, J. J., OPPENHEIMER, R. C., SPEISER, P., Nanoparticles – a new colloidal drug delivery system, *Pharm. Acta Helv.* **1978**, *53*, 17–23.
- 69 CHEN, C. Q., LIN, W., COOMBES, A. G., DAVIS, S. S., ILLUM, L., Preparation of human serum albumin microspheres by a novel acetone-heat denaturation method, *J. Microencapsul.* **1994**, *11*, 395–407.
- 70 ZIMMER, A. K., MAINCENT, P., THOUVENOT, P., KREUTER, J., Hydrocortisone delivery to healthy and inflamed eyes using micellar polysorbate 80 solution or albumin nanoparticles, *Int. J. Pharm.* **1994**, *110*, 211–222.
- 71 ZIMMER, A. K., CHETONI, P., SAETTONI, M. F., ZERBE, H., KREUTER, J., Evaluation of pilocarpine-loaded albumin particles as drug delivery systems for controlled delivery in the eye. I. *In vitro* and *in vivo* characteristics, *J. Controlled Rel.* **1994**, *32*, 57–70.
- 72 LIN, W., GARNETT, M. C., DAVIS, S. S., SCHACHT, E., FERRUTI, P., ILLUM, L., Preparation and characterisation of rose Bengal-loaded surface-modified albumin nanoparticles, *J. Controlled Rel.* **2001**, *71*, 117–126.
- 73 MERODIO, M., ESPUELAS, M. S., MIRSHAHI, M., ARNEADO, A., TRACHE, J. M., Efficacy of ganciclovir-loaded nanoparticles in human cytomegalovirus (HCMV) infected cells, *J. Drug Target.* **2002**, *10*, 231–238.
- 74 WIDDER, K. J., MORRIS, R. M., POORE, G. A., HOWARD, D. P., SENYEI, A. E., Selective targeting of magnetic albumin microspheres containing low-dose doxorubicin – total remission in Yoshida sarcoma-bearing rats, *Eur. J. Cancer Clin. Oncol.* **1983**, *19*, 135–139.
- 75 CHANG, B. S., MAHONEY, R. R., Enzyme thermostabilization by bovine serum albumin and other proteins: evidence for hydrophobic interactions, *Biotechnol. Appl. Biochem.* **1995**, *22*, 203–214.
- 76 SCHEFFEL, U., RHODES, B. A., NATARAJAN, T. K., WAGNER, H. N. JR., Albumin microspheres for studies of reticuloendothelial system, *J. Nucl. Med.* **1972**, *13*, 498–503.
- 77 KRAMER, P. A., Albumin microspheres as vehicles for achieving specificity in drug delivery, *J. Pharm. Sci.* **1974**, *63*, 1646–1647.
- 78 SUSLICK, K. S., GRINSTAFF, M. W., Protein microencapsulation of nonaqueous liquids, *J. Am. Chem. Soc.* **1999**, *112*, 7807–7809.
- 79 SUSLICK, K. S., GRINSTAFF, M. W., Proteinaceous microbubbles: synthesis of an echo contrast agent, *Proc. Natl Acad. Sci. USA* **1991**, *88*, 7708–7710.
- 80 SUSLICK, K. S., GRINSTAFF, M. W., KOLBECK, K. J., WONG, M., Characterization of sonochemically prepared proteinaceous microcapsules, *Ultrason. Sonochem.* **1994**, *1*, S65–S68.
- 81 AVIVI (LEVI), S., NITZAN, Y., DROR, R., GEDANKEN, A., An easy sonochemical route for the encapsulation of tetracycline in bovine serum albumin microspheres, *J. Am. Chem. Soc.* **2003**, *125*, 15712–15713.
- 82 WEBER, C., REISS, S., LANGER, K., Preparation of surface modified protein nanoparticles by introduction of sulfhydryl groups, *Int. J. Pharm.* **2000**, *211*, 67–78.
- 83 ROSER, M., FISCHER, D., KISSEL, T., Surface-modified biodegradable albumin nano- and microspheres. II: effect of surface charges on *in vitro* phagocytosis and biodistribution in

- rats, *Eur. J. Pharm. Biopharm.* **1998**, *46*, 255–263.
- 84 LANGER, K., COESTER, C., WEBER, C., VON BRIESEN, H., KREUTER, J., Preparation of avidin-labeled protein nanoparticles as carriers for biotinylated peptide nucleic acid, *Eur. J. Pharm. Biopharm.* **2000**, *49*, 303–307.
- 85 GREF, R., MINAMITAKE, Y., PERACCHIA, M. T., TRUBETSKOY, V., TORCHILIN, V., LANGER, R., Biodegradable long-circulating polymeric nanospheres, *Science* **1994**, *263*, 1600–1603.
- 86 GREF, R., DOMB, A., QUELLEC, P., BLUNK, T., MULLER, R. H., VERVATZ, J. M., LANGER, R., The controlled intravenous delivery of drugs using PEG-coated sterically stabilized nanospheres, *Adv. Drug Deliv. Rev.* **1995**, *16*, 215–233.
- 87 PERACCHIA, M. T., FATTAL, E., DESMAELE, D., BESNARD, M., NOEL, J. P., GOMIS, J. M., APPEL, M., D'ANGELO, J., COUVREUR, P., Stealth PEGylated polycyanoacrylate nanoparticles for intravenous administration and splenic targeting, *J. Controlled Rel.* **1999**, *60*, 121–128.
- 88 OTSUKA, H., NAGASAKI, Y., KATAOKA, K., PEGylated nanoparticles for biological and pharmaceutical applications, *Adv. Drug Deliv. Rev.* **2003**, *55*, 403–419.
- 89 DEIBLE, C. R., BECKMAN, E. J., RUSSELL, A. J., WAGNER, W. R., Creating molecular barriers to acute platelet deposition on damaged arteries with reactive polyethylene glycol, *J. Biomed. Mater. Res.* **1998**, *41*, 251–256.
- 90 JO, S., PARK, K., Surface modification using silanated poly(ethylene glycol)s, *Biomaterials* **2000**, *21*, 605–616.
- 91 STOLNIK, S., ILLUM, L., DAVIS, S. S., Long circulating microparticulate drug carriers, *Adv. Drug Deliv. Rev.* **1995**, *16*, 195–214.
- 92 YONCHEVA, K., CAMPANERO, M. A., GÓMEZ, S., GAMAZO, C., IRACHE, J. M., Bioadhesive properties of pegylated nanoparticles, *Expert Opin. Drug Del.* **2005**, *2*, 205–218.
- 93 LIN, W., GARNETT, M. C., DAVIES, M. C., BIGNOTTI, F., FERRUTI, P., DAVIS, S. S., ILLUM, L., Preparation of surface-modified albumin nanospheres, *Biomaterials* **1997**, *18*, 559–565.
- 94 LIN, W., GARNETT, M. C., SCHACHT, E., DAVIS, S. S., ILLUM, L., Preparation and *in vitro* characterization of HSA-mPEG nanoparticles, *Int. J. Pharm.* **1999**, *189*, 161–170.
- 95 OPPENHEIM, R. C., Solid colloidal drug delivery systems: nanoparticles, *Int. J. Pharm.* **1981**, *8*, 217–234.
- 96 OPPENHEIM, R. C., GIPPS, E. M., FORBES, J. F., WHITEHEAD, R. H., Development and testing of proteinaceous nanoparticles containing cytotoxics, In *Microspheres and Drug Therapy: Pharmaceutical, Immunological and Medical Aspects*, DAVIS, S. S., ILLUM, L., MCVIE, J. G., TOMLINSON, E. (Eds.), Elsevier, New York, **1984**, pp. 117–128.
- 97 ZIMMER, A. K., ZERBE, H., KREUTER, J., Evaluation of pilocarpine-loaded albumin particles as drug delivery systems for controlled delivery in the eye. II. Co-administration with bioadhesive and viscous polymers, *J. Controlled Rel.* **1995**, *33*, 31–46.
- 98 EGBARIA, K., FRIEDMAN, M., Adsorption of fluorescein dyes on albumin microspheres, *Pharm Res.* **1992**, *9*, 629–635.
- 99 BHARGAVA, K., ANDO, H. Y., Immobilization of active urokinase on albumin microspheres: use of a chemical dehydrant and process monitoring, *Pharm Res.* **1992**, *9*, 776–781.
- 100 MICHAELIS, M., LANGER, K., ARNOLD, S., DOERR, H. W., KREUTER, J., CINATL, J. JR., Pharmacological activity of DTPA linked to protein-based drug carrier systems, *Biochem. Biophys. Res. Commun.* **2004**, *323*, 1236–1240.
- 101 SANTHI, K., DHANARAJ, S. A., JOSEPH, V., PONNUSANKAR, S., SURESH, B., A study on the preparation and anti-tumor efficacy of bovine serum albumin nanospheres containing 5-fluorouracil, *Drug Dev. Ind. Pharm.* **2002**, *28*, 1171–1179.
- 102 SANTHI, K., DHANARAJ, S. A., KOSHY, M., PONNUSANKAR, S., SURESH, B., Study of biodistribution of

- methotrexate-loaded bovine serum albumin nanospheres in mice, *Drug Dev. Ind. Pharm.* **2000**, *26*, 1293–1296.
- 103** WARTLICK, H., SPÄNKUCH-SCHMITT, B., STREBHARDT, K., KREUTER, J., LANGER, K., Tumour cell delivery of antisense oligonucleotides by human serum albumin nanoparticles, *J. Controlled Rel.* **2004**, *96*, 483–495.
- 104** RHAESE, S., VON BRIESEN, H., RUBSAMEN-WAIGMANN, H., KREUTER, J., LANGER, K., Human serum albumin–polyethylenimine nanoparticles for gene delivery, *J. Controlled Rel.* **2003**, *92*, 199–208.
- 105** VOGEL, V., LOCHMANN, D., WEYERMANN, J., MAYER, G., TZIATZIOS, C., VAN DER BROEK, J. A., HAASE, W., WOUTERS, D., SCHUBERT, U. S., KREUTER, J., ZIMMER, A., SCHUBERT, D., Oligonucleotide–protamine–albumin nanoparticles: preparation, physical properties, and intracellular distribution. *J. Controlled Rel.* **2005**, *103*, 99–111.
- 106** THIELE, L., MERKLE, H. P., WALTER, E., Phagocytosis and phagosomal fate of surface-modified microparticles in dendritic cells and macrophages, *Pharm. Res.* **2003**, *20*, 221–228.
- 107** BORCHARD, G., KREUTER, J., The role of serum complement on the organ distribution of intravenously administered poly (methyl methacrylate) nanoparticles: effects of pre-coating with plasma and with serum complement. *Pharm. Res.* **1996**, *13*, 1055–1058.
- 108** OGAWARA, K., FURUMOTO, K., NAGAYAMA, S., MINATO, K., HIGAKI, K., KAI, T., KIMURA, T., Pre-coating with serum albumin reduces receptor-mediated hepatic disposition of polystyrene nanosphere: implications for rational design of nanoparticles, *J. Controlled Rel.* **2004**, *100*, 451–455.
- 109** MERODIO, M., IRACHE, J. M., ECLANCHER, F., MIRSHAHI, M., VILLARROYA, H., Distribution of albumin nanoparticles in animals induced with the experimental allergic encephalomyelitis, *J. Drug Target.* **2000**, *8*, 289–303.
- 110** BODOR, N., BUCHWALD, P., Recent advances in the brain targeting of neuropharmaceuticals by chemical delivery systems, *Adv. Drug Deliv. Rev.* **1999**, *36*, 229–254.
- 111** CORNFORD, E. M., HYMAN, S., Blood–brain barrier permeability to small and large molecules, *Adv. Drug. Deliv. Rev.* **1999**, *36*, 145–163.
- 112** ROUSSEAU, V., DENIZOT, B., LE JEUNE, J. J., JALLET, P., Early detection of liposome brain localization in rat experimental allergic encephalomyelitis, *Exp. Brain Res.* **1999**, *125*, 255–264.
- 113** FILIPPI, M., TORTORELLA, C., ROVARIS, M., BOZZALI, M., POSSA, F., SORMANI, M. P., IANNUCCI, G., COMI, G., Changes in the normal appearing brain tissue and cognitive impairment in multiple sclerosis, *J. Neurol. Neurosurg. Psychiatry* **2000**, *68*, 157–161.
- 114** VILLARROYA, H., MARIE, Y., OUALLET, J. C., LE SAUX, F., TCHELINGERIAN, J. L., BAUMANN, N., Expression of TNF alpha in central neurons of Lewis rat spinal cord after EAE induction, *J. Neurosci. Res.* **1997**, *49*, 592–599.
- 115** STEIN, C. S., ST LOUIS, J., GILBERT, J. J., STREJAN, G. H., Treatment of spinal cord-induced experimental allergic encephalomyelitis in the Lewis rat with liposomes presenting central nervous system antigens, *J. Neuroimmunol.* **1990**, *28*, 119–130.
- 116** GUY, J., QI, X., HAUSWIRTH, W. W., Adeno-associated viral-mediated catalase expression suppresses optic neuritis in experimental allergic encephalomyelitis, *Proc. Natl Acad. Sci. USA* **1998**, *95*, 13847–13852.
- 117** KUMAGAI, A. K., EISENBERG, J. B., PARDRIDGE, W. M., Absorptive mediated endocytosis of cationized albumin and a beta-endorphin-cationized albumin chimeric peptide by isolated brain capillaries. Model system of blood–brain carrier transport, *J. Biol. Chem.* **1987**, *262*, 15214–15219.
- 118** WHEATLEY, M. A., NARAYANA, P., Diagnostic use of microspheres. In *Encyclopedia of Controlled Drug*

- Delivery*, MATHIOWITZ, E., KREITZ, M. R., PEPPAS, L. B. (Eds.), Wiley, New York, 1999, vol. I, p. 340.
- 119 NIEWEG, O. E., JANSSEN, L., VALDES OLMOS, R. A., RUTGERS, E. J., PETERSE, J. L., HOEFNAGEL, K. A., KROON, B. B., Lymphatic mapping and sentinel lymph node biopsy in breast cancer, *Eur. J. Nucl. Med.* **1999**, *4*, S11–S16.
- 120 RAHUSEN, F., PIJPERS, R., VAN DIEST, P., BLEICHRODT, R. P., TORRENGA, H., MEIJER, S., The implementation of the sentinel node biopsy as a routine procedure for patients with breast cancer, *Surgery* **2000**, *128*, 6–12.
- 121 VALDES OLMOS, R. A., TANIS, P. J., HOEFNAGEL, C. A., NIEWEG, O. E., MULLER, S. H., RUTGERS, E. J. Th., KOOI, M. L. K., KROON, B. B. R., Improved sentinel node visualization in breast cancer by optimizing the colloid particle concentration and tracer dosage, *Nucl. Med. Commun.* **2001**, *22*, 579–586.
- 122 VAN DER ENT, F. W., KENGEN, R. A., VAN DER POL, H. A., POVEL, J. A., STROEKEN, H. J., HOOFWIJK, A. G., Halsted revisited: internal mammary sentinel lymph node biopsy in breast cancer, *Ann. Surg.* **2001**, *234*, 79–84.
- 123 WILHELM, A., MIJNHOUT, G., FRANSSSEN, E., Radiopharmaceuticals in sentinel lymph-node detection – an overview, *Eur. J. Nucl. Med.* **1999**, *26*, S36–S42.
- 124 LEIDENIUS, M. H., LEPPANEN, E. A., KROGERUS, L. A., SMITTEN, K. A., The impact of radiopharmaceutical particle size on the visualization and identification of sentinel nodes in breast cancer, *Nucl. Med. Commun.* **2004**, *25*, 233–238.
- 125 HILL, A. D., TRAN, K. N., AKHURST, T., YEUNG, H., YEH, S. D., ROSEN, P. P., BORGES, P. I., CODY, H. S. 3rd., Lessons learned from 500 cases of lymphatic mapping for breast cancer, *Ann. Surg.* **1999**, *229*, 528–535.
- 126 ROUMEN, R. M., GEUSKENS, L. M., VALKENBURG, J. G., In search of the true sentinel node by different injection techniques in breast cancer patients, *Eur. J. Surg. Oncol.* **1999**, *25*, 347–351.
- 127 PIJPERS, R., BORGSTEIN, P. J., MEIJER, S., KRAG, D. N., HOEKSTRA, O. S., GREUTER, H. N., TEULE, G. J., Transport and retention of colloidal tracers in regional lymphoscintigraphy in melanoma: influence on lymphatic mapping and sentinel node biopsy, *Melanoma Res.* **1998**, *8*, 413–418.
- 128 NIEUWENHUIS, E. J., VAN DER WAAL, I., LEEMANS, C. R., KUMMER, A., PIJPERS, R., CASTELIJNS, J. A., BRAKENHOFF, R. H., SNOW, G. B., Histopathologic validation of the sentinel node concept in oral and oropharyngeal squamous cell carcinoma, *Head Neck* **2005**, *27*, 150–158.
- 129 PIJPERS, R., BUIST, M. R., VAN LINGEN, A., DIJKSTRA, J., VAN DIEST, P. J., TEULE, G. J., KENEMANS, P., VERHEIJEN, R. H., The sentinel node in cervical cancer: scintigraphy and laparoscopic gamma probe-guided biopsy, *Eur. J. Nucl. Med. Mol. Imaging* **2004**, *31*, 1479–1486.
- 130 ORDER, S. E., SIEGEL, J. A., LUSTIG, R. A., PRINCIPATO, R., ZEIGER, L. S., JOHNSON, E., ZHANG, H., LANG, P., PILCHIK, N. B., METZ, J., DENITTIS, A., BOERNER, P., BEUERLEIN, G., WALLNER, P. E., A new method for delivering radioactive cytotoxic agents in solid cancers, *Int. J. Radiat. Oncol. Biol. Phys.* **1994**, *30*, 715–720.
- 131 WILDER, R. B., DENARDO, G. L., DENARDO, S. J., Treatment of cancer with intratumoral infusion of radioisotopes, *Int. J. Radiat. Oncol. Biol. Phys.* **1994**, *30*, 737–739.
- 132 TEI, C., KONDO, S., MEERBAUM, S., ONG, K., MAURER, G., WOOD, F., SAKAMAKI, T., SHIMOURA, K., CORDAY, E., SHAH, P. M., Correlation of myocardial echo contrast disappearance rate (“washout”) and severity of experimental coronary stenosis, *J. Am. Coll. Cardiol.* **1984**, *3*, 39–46.
- 133 CHUANG, V. T., KRAGH-HANSEN, U., OTAGIRI, M., Pharmaceutical strategies utilizing recombinant human serum albumin, *Pharm. Res.* **2002**, *19*, 569–577.
- 134 KERBER, R. E., *Echocardiography in Coronary Artery Diseases*, Future, New York, **1988**.

- 135 KAUL, S., GLASHEEN, W. P., OLINER, J. D., KELLY, P., GASCHO, J. A., Relation between anterograde blood flow through a coronary artery and the size of the perfusion bed it supplies: experimental and clinical implications, *J. Am. Coll. Cardiol.* **1991**, *17*, 1403–1413.
- 136 POWSNER, S. M., KELLER, M. W., SANIIE, J., FEINSTEIN, S. B., Quantitation of echo-contrast effects, *Am. J. Physiol. Imaging* **1986**, *1*, 124–128.
- 137 ARNEDO, A., IRACHE, J. M., GONZÁLEZ GAITANO, G., VALGAÑÓN, M., ESPUELAS, S., Bovine serum albumin modified the intracellular distribution and improved the antiviral activity of an oligonucleotide, *J. Drug Target.* **2003**, *11*, 197–204.
- 138 ARNEDO, A., IRACHE, J. M., MERODIO, M., ESPUELAS, S., Albumin nanoparticles: fusogenic carriers that improved the stability, nuclear accumulation and anticytomegaloviral activity of an oligonucleotide, *J. Controlled Rel.* **2004**, *94*, 217–227.
- 139 SRINIVASAN, S. K., TEWARY, H. K., IVERSEN, P. L., Characterization of binding sites, extent of binding, and drug interactions of oligonucleotides with albumin, *Antisense Res. Dev.* **1995**, *5*, 131–139.
- 140 SATO, Y., KANEKO, K., MIKAMI, K., MIZUGAKI, M., SUZUKI, Y., Isolation of bovine serum albumin fragment P-9 and P-9-mediated fusion of small unilamellar vesicles, *Biol. Pharm. Bull.* **1999**, *22*, 1360–1365.
- 141 FISCHER, D., BIEBER, T., BRUSSELBACH, S., ELSASSER, H., KISSEL, T., Cationized human serum albumin as a non-viral vector system for gene delivery? Characterization of complex formation with plasmid DNA and transfection efficiency, *Int. J. Pharm.* **2001**, *225*, 97–111.
- 142 FISCHER, D., LI, Y., AHLEMEYER, B., KRIEGLSTEIN, J., KISSEL, T., *In vitro* cytotoxicity testing of polycations: influence of polymer structure on cell viability and hemolysis, *Biomaterials* **2003**, *24*, 1121–1131.
- 143 FANCA, H., SIMOES, S., PEDROSO DE LIMA, M. C., Association of albumin or protamine to lipoplexes: enhancement of transfection and resistance to serum, *J. Gene Med.* **2004**, *6*, 681–692.
- 144 ZELPHATI, O., UYECI, L. S., BARRON, L. G., SZOKA, F. C. JR., Effect of serum components on the physicochemical properties of cationic lipid/oligonucleotide complexes and on their interactions with cells, *Biochim. Biophys. Acta* **1998**, *1390*, 119–133.
- 145 MORIMOTO, Y., AKIMOTO, M., SUGIBAYASHI, K., NADAI, T., KATO, Y., Drug-carrier property of albumin microspheres in chemotherapy. IV. Antitumor effect of single-shot or multiple shot administration of microsphere-entrapped 5-fluorouracil on Ehrlich ascites or solid tumor in mice, *Chem. Pharm. Bull.* **1980**, *28*, 3087–3092.
- 146 SUGIBAYASHI, K., AKIMOTO, M., MORIMOTO, Y., NADAI, T., KATO, Y., Drug-carrier property of albumin microspheres in chemotherapy. III. Effect of microsphere-entrapped 5-fluorouracil on Ehrlich ascites carcinoma in mice, *J. Pharm. Dyn.* **1979**, *2*, 350–355.
- 147 SUGIBAYASHI, K., MORIMOTO, Y., NADAI, T., KATO, Y., HASEGAWA, A., ARITA, T., Drug-carrier property of albumin microspheres in chemotherapy. II. Preparation and tissue distribution in mice of microsphere-entrapped 5-fluorouracil, *Chem. Pharm. Bull.* **1979**, *27*, 204–209.
- 148 YI, Y. M., YANG, T. Y., PAN, W. M., Preparation and distribution of 5-fluorouracil <sup>125</sup>I sodium alginate-bovine serum albumin nanoparticles, *World. J. Gastroenterol.* **1999**, *5*, 57–60.
- 149 IBRAHIM, N. K., DESAI, N., LEGHA, S., SOON-SHIONG, P., THERIAULT, R. L., RIVERA, E., ESMAELI, B., RING, S., BEDIKIAN, A., HORTOBAGYI, G. N., ELLERHOST, J. A., Phase I and pharmacokinetic study of ABI-007, a cremophor-free, protein-stabilized, nanoparticle formulation of paclitaxel, *Clin. Cancer Res.* **2002**, *8*, 1038–1044.
- 150 DORR, R., Pharmacology and toxicology of Cremophor EL diluent, *Ann. Pharmacother.* **1994**, *28*, S11–S14.
- 151 WEISS, R., DONEHOWER, R., WIERNIK,

- P. H., OHNUMA, T., GRALLA, R. J., TRUMP, D. L., BAKER, J. R. JR., VAN ECHO, D. A., VON HOFF, D. D., LEYLAND-JONES, B., Hypersensitivity reactions from Taxol, *J. Clin. Oncol.* **1990**, *8*, 1263–1268.
- 152 WAUGH, W., TRISSEL, L., STELLA, V., Stability, compatibility, and plasticizer extraction of Taxol (NSC-125973) injection diluted in infusion solutions and stored in various containers, *Am. J. Hosp. Pharm.* **1991**, *48*, 1520–1524.
- 153 KOLODZIE, F. D., JOHN, M., KHURANA, C., FARB, A., WILSON, P. S., ACAMPADO, E., DESAI, N., SOON-SHIONG, P., VIRMANI, R., Sustained reduction of in-stent neointimal growth with the use of a novel systemic nanoparticle paclitaxel, *Circulation* **2002**, *106*, 1195–1198.
- 154 GARBER, K., Paclitaxel formulation hints at new chemotherapy approach, *J. Natl. Cancer Inst.* **2004**, *96*, 90–91.
- 155 BAYES, M., RABASEDA, X., PROUS, J. R., Gateways to clinical trials. *Methods Find. Exp. Clin. Pharmacol.* **2004**, *26*, 211–244.
- 156 NCI Cancer Bull. **2005**, January 18, 2(3), [http://www.cancer.gov/ncicancerbulletin/NCI\\_Cancer\\_Bulletin\\_011805/page5](http://www.cancer.gov/ncicancerbulletin/NCI_Cancer_Bulletin_011805/page5).
- 157 DAMASCELLI, B., CANTÙ, G., MATTAVELLI, F., TAMPLINIZZA, P., BIDOLI, P., LEO, E., DOSIO, F., CERROTTA, A. M., DI TOLLA, G., FRIGERIO, L. F., GARBAGNATI, F., LANOCITA, R., MARCHIANÒ, A., PATELLI, G., SPREAFICO, C., TICHÀ, V., VESPRO, V., ZUNINO, F., Intraarterial chemotherapy with polyoxyethylated castor oil free paclitaxel, incorporated in albumin nanoparticles (ABI-007): phase II study of patients with squamous cell carcinoma of the head and neck and anal canal: preliminary evidence of clinical activity, *Cancer* **2001**, *92*, 2592–2602.
- 158 DAMASCELLI, B., PATELLI, G., LANOCITA, R., DI TOLLA, G., MARCHIANO, A., SPREAFICO, C., FRIGERIO, L. F., GARBAGNATI, F., TICHÀ, V., SOON-SHIONG, P., Intra-arterial paclitaxel in albumin nanoparticles controls squamous carcinoma at various sites, *Proc. Am. Soc. Clin. Oncol.* **2003**, *22*, 509 (abstr 2050).
- 159 DAMASCELLI, B., PATELLI, G. L., LANOCITA, R., DI TOLLA, G., FRIGERIO, L. F., MARCHIANO, A., GARBAGNATI, F., SPREAFICO, C., TICHÀ, V., GLADIN, C. R., PALAZZI, M., CRIPPA, F., OLDINI, C., CALÒ, S., BONACCORSI, A., MATTAVELLI, F., COSTA, L., MARIANI, L., CANTÙ, G., A novel intraarterial chemotherapy using paclitaxel in albumin nanoparticles to treat advanced squamous cell carcinoma of the tongue: preliminary findings, *Am. J. Roentgenol.* **2003**, *181*, 253–260.
- 160 DOSIO, F., ARPICCO, S., BRUSA, P., STELLA, B., CATTTEL, L., Poly(ethylene glycol)–human serum albumin–paclitaxel conjugates: preparation, characterization and pharmacokinetics, *J. Controlled Rel.* **2001**, *75*, 107–117.
- 161 BAILEY, S. M., HART, I., LOHMEYER, L., Ganciclovir and the HSV-tk enzyme prodrug system in cancer therapy, *Drugs of the Future* **1998**, *23*, 401–413.
- 162 QIAN, C., BILBAO, R., BRUÑA, O., PRIETO, J., Induction of sensitivity to ganciclovir in human hepatocellular carcinoma cells by adenovirus-mediated gene transfer of herpes simplex virus thymidine kinase, *Hepatology* **1995**, *22*, 118–123.
- 163 SANGRO, B., QIAN, C., SCHMITZ, V., PRIETO, J., Gene therapy of hepatocellular carcinoma and gastrointestinal tumors, *Ann. NY Acad. Sci.* **2002**, *963*, 6–12.
- 164 BELTINGER, C., FULDA, S., WALCZAK, H., DEBATIN, K. M., Trail enhances thymidine kinase/ganciclovir gene therapy of neuroblastoma cells, *Cancer Gene Ther.* **2002**, *9*, 372–381.
- 165 ALVAREZ, R. D., GÓMEZ NAVARRO, J., WANG, M., BARNES, M. N., STRONG, T. V., ARANI, R. B., ARAFAT, W., HUGHES, J. V., SIEGAL, G. P., CUIRIEL, D. T., Adenoviral-mediated suicide gene therapy for ovarian cancer, *Mol. Ther.* **2000**, *2*, 524–530.
- 166 CARRIO, M., ROMAGOSA, A., MERCADE, E., MAZO, A., NADAL, M., GOMEZ-FOIX, A. M., FILLAT, C., Enhanced pancreatic



- tumor regression by a combination of adenovirus and etrovirus mediated delivery of the HSV/tk gene, *Gene Ther.* **1999**, *6*, 547–553.
- 167 HASSAN, W., SANDFORD, M. A., WOO, S. L., CHEN, S. H., HALL, S. J., Prospects for herpes-simplex-virus thymidine-kinase and cytokine prostate cancer, *World J. Urol.* **2000**, *18*, 130–135.
- 168 LINK, C. J., SEREGINA, T., TRAYNOR, A., BURT, R. K., Cellular suicide therapy of malignant disease, *Oncologist* **2000**, *5*, 68–74.
- 169 MERODIO, M., RUIZ, J., BUSTOS, M., MARTÍNEZ-GALAN, F., CAMPANERO, M. A., IRACHE, J. M., Encapsulation of ganciclovir in albumin nanoparticles enhances the thymidine kinase suicide gene therapy, *J. Drug Deliv. Sci. Technol.* **2005**, *14*, 121–127.
- 170 HÄFELI, U. O., Magnetically modulated therapeutic systems, *Int. J. Pharm.* **2004**, *277*, 19–24.
- 171 WIDDER, K. J., SENYEI, A. E., SCARPELLI, D. G., Magnetic microspheres: a model system specific drug delivery *in vivo*, *Proc. Soc. Exp. Biol. Med.* **1978**, *158*, 141–146.
- 172 WIDDER, D. J., EDELMAN, R. R., GRIEF, W. L., MONDA, L., Magnetite albumin suspension: a superparamagnetic oral MR contrast agent, *Am. J. Roentgenol.* **1987**, *149*, 839–843.
- 173 TIEFENAUER, L. X., TSCHIRKY, A., KUHNE, G., ANDRES, R. Y., *In vivo* evaluation of magnetite nanoparticles for use as a tumor contrast agent in MRI, *Magn. Reson. Imaging* **1996**, *14*, 391–402.
- 174 CHUNFU, Z., JINQUAN, C., DUANZHI, Y., YONGXIAN, W., YANLIN, F., JIAJU, T., Preparation and radiolabeling of human serum albumin (HSA)-coated magnetite nanoparticles for magnetically targeted therapy, *Appl. Radiat. Isot.* **2004**, *61*, 1255–1259.
- 175 ALEXIOU, C., ARNOLD, W., KLEIN, R. J., PARAK, F. G., HULIN, P., BERGEMANN, C., ERHARDT, W., WAGENPFEL, S., LUBBE, A. S., Locoregional cancer treatment with magnetic drug targeting, *Cancer Res.* **2000**, *60*, 6641–6648.
- 176 WIDDER, K. J., SENYEI, A. E., RANNEY, D. F., Magnetically responsive microspheres and other carriers for the biophysical targeting of antitumor agents, *Adv. Pharmacol. Chemother.* **1979**, *16*, 213–271.
- 177 WIDDER, K. J., MORRIS, R. M., POORE, G. A., HODWARD, D. P., SENYEI, A. E., Tumor remission in Yoshida sarcoma-bearing rats by selective targeting of magnetic albumin microspheres containing doxorubicin, *Proc. Natl. Acad. Sci. USA* **1981**, *78*, 579–581.
- 178 WIDDER, K. J., MORINO, P. A., MORRIS, R. M., HODWARD, D. P., POORE, G. A., SENYEI, A. E., Selective targeting of magnetic albumin microspheres to the Yoshida sarcoma: ultrastructural evaluation of microsphere disposition, *Eur. J. Cancer Clin. Oncol.* **1983**, *19*, 141–147.
- 179 GOODWIN, S., PETERSON, C., HOB, C., BITTNER, C., Targeting and retention of magnetic targeted carriers (MTCS) enhancing intra-arterial chemotherapy, *J. Magn. Magn. Mater.* **1999**, *194*, 132–139.
- 180 GOODWIN, S. C., BITTNER, C. A., PETERSON, C. L., WONG, G., Single-dose toxicity study of hepatic intra-arterial infusion of doxorubicin coupled to a novel magnetically targeted drug carrier, *Toxicol. Sci.* **2001**, *60*, 177–183.
- 181 PULLER, S. K., GALLO, J. M., Enhanced brain tumor selectivity of cationic magnetic polysaccharide microspheres, *J. Drug Target.* **1999**, *6*, 215–228.
- 182 PULLER, S. K., CICCOTTO, S. L., GALLO, J. M., Distribution of small magnetic particles in brain tumor-bearing rats, *J. Neurooncol.* **1999**, *41*, 99–105.
- 183 GONG, L. S., ZHANG, Y. D., LIU, S., Target distribution of magnetic albumin nanoparticles containing adriamycin in transplanted rat liver cancer model, *Hepatobiliary Pancreat. Dis. Int.* **2004**, *3*, 365–368.
- 184 GURNY, R., IBRAHIM, H., AEBI, A., BURI, P., WILSON, C. G., WASHINGTON, N., Design and evaluation of controlled release system for the eye, *J. Controlled Rel.* **1987**, *6*, 367–373.

- 185 DESHPANDE, A. A., HELLER, J., GURNY, R., Biodegradable polymers for ocular drug delivery, *Crit. Rev. Ther. Drug Carrier Syst.* **1998**, *15*, 381–420.
- 186 ZIMMER, A., KREUTER, J., Microspheres and nanoparticles used in ocular delivery systems, *Adv. Drug Deliv. Rev.* **1995**, *16*, 61–73.
- 187 HEINEMANN, M. H., *Staphylococcus epidermidis* endophthalmitis complicating intravitreal antiviral therapy of cytomegalovirus retinitis, *Am. J. Ophthalmol.* **1989**, *107*, 643–644.
- 188 COCHEREAU-MASSIN, I., LEHOANG, P., LAUTIER-FRAU, M., ZAZOUN, L., MARCEL, P., ROBINET, M., MATHERON, S., KATLAMA, C., GHARAKHANIAN, S., ROZENBAUM, W., Cytomegalovirus retinitis in AIDS: treatment with intravitreal injections of ganciclovir, *Ophthalmology* **1991**, *98*, 1348–1355.
- 189 NICHOLS, W. G., BOECKH, M., Recent advances in the therapy and prevention of CMV infections, *J. Clin. Virol.* **2000**, *16*, 25–40.
- 190 NOBLE, S., FAULDS, D., Ganciclovir. An update of its use in the prevention of cytomegalovirus infection and disease in transplant recipients, *Drugs* **1998**, *56*, 115–146.
- 191 KEMPEN, J. H., MARTIN, B. K., WU, A. W., BARRON, B., THORNE, J. E., JABS, D. A., The effect of cytomegalovirus retinitis on the quality of life of patients with AIDS in the era of highly active anti-retroviral therapy, *Ophthalmology* **2003**, *110*, 987–995.
- 192 CANTRILL, H. L., HENRY, K., MELROE, N. H., KNOBLOCH, W. H., RAMSAY, R. C., BALFOUR, H. H. JR., Treatment of cytomegalovirus retinitis with intravitreal ganciclovir, *Ophthalmology* **1989**, *96*, 367–374.
- 193 STREBLOW, D. N., KREKLYWICH, C., YIN, Q., DE LA MELENA, V. T., CORLESS, C. L., SMITH, P. A., BRAKEBILL, C., COOK, J. W., VINK, C., BRUGGEMAN, C. A., NELSON, J. A., ORLOFF, S. L., Cytomegalovirus-mediated upregulation of chemokine expression correlates with the acceleration of chronic rejection in rat heart transplants. *J. Virol.* **2003**, *77*, 2182–2194.
- 194 SAGEDA, S., NORDAL, K. P., HARTMANN, A., SUND, S., SCOTT, H., DEGRE, M., FOSS, A., LEIVSTAD, T., OSNES, K., FAUCHALD, P., ROLLAG, H., The impact of cytomegalovirus infection and disease on rejection episodes in renal allograft recipients, *Am. J. Transplant.* **2002**, *2*, 850–856.
- 195 IRACHE, J. M., MERODIO, M., ARNEDO, A., CAMAPANERO, M. A., MIRSHAHI, M., ESPUELAS, S., Albumin nanoparticles for the intravitreal delivery of anticytomegaloviral drugs, *Mini Rev. Med. Chem.* **2005**, *5*, 293–305.
- 196 MERODIO, M., IRACHE, J. M., VALAMANESH, F., MIRSHAHI, M., Ocular disposition and tolerance of ganciclovir-loaded albumin nanoparticles after intravitreal injection in rats, *Biomaterials* **2002**, *23*, 1587–1594.
- 197 MAURICE, D. M., MISHIMA, S., Pharmacology of the eye. In *Handbook of Experimental Pharmacology*, SEARS, M. L. (Ed.), Springer-Verlag, Berlin, 1984, vol. 69, pp. 19–116.
- 198 CASPI, R. R., CHAN, C. C., LEAKE, W. C., HIGUCHI, M., WIGGERT, B., CHADER, G. J., Experimental autoimmune uveoretinitis in mice. Induction by a single eliciting event and dependence on quantitative parameters of immunization, *J. Autoimmun.* **1990**, *3*, 237–246.
- 199 DE KOZAK, Y., MIRSHAHI, M., BOUCHEIX, C., FAURE, J. P., Modulation of experimental autoimmune uveoretinitis by active immunization with autoantigen specific monoclonal antibodies, *Eur. J. Immunol.* **1989**, *17*, 541–547.

## 8

# Nanoscale Patterning of S-Layer Proteins as a Natural Self-assembly System

*Margit Sára, D. Pum, C. Huber, N. Ilk, M. Pleschberger and U. B. Sleytr*

### 8.1

#### Introduction

Nanobiotechnology uses concepts from molecular biology, biochemistry and chemistry to identify components, processes and principles for the construction of self-assembling materials and devices. In particular, biological systems provide an enormous diversity of higher-order functional structures and patterns arising from molecular self-assembly. Most frequently, the initial step of molecular organization into functional units and complex supramolecular structures requires arrangement of molecules into ordered arrays. Recently, considerable efforts have been devoted to exploit natural self-assembly systems and to introduce variations into natural molecules (e.g. proteins and DNA) to achieve basic building blocks for specific structures and applications [1–8].

This chapter is intended to provide a survey of the unique general principles of crystalline bacterial cell surface layer (S-layer) proteins and fusion proteins thereof. In general, S-layer proteins form the outermost cell surface structure of many bacteria and archaea. Monomolecular S-layer protein lattices are composed of single species of protein or glycoprotein subunits with the inherent ability to self-assemble into two-dimensional arrays on the bacterial cell surface, or after isolation, on artificial supports, such as silicon wafers, noble metals, plastics, Langmuir lipid films or liposomes [4–8]. Thus, genetically and/or chemically modified S-layer proteins are exploited as building blocks and templates for generating functional nanostructures at the meso- and macroscopic scale for both life and nonlife science applications. In addition, S-layer-specific heteropolysaccharides are used as biomimetic linkers to solid supports and lipid layers to achieve binding and recrystallization in uniform orientation.

## 8.2

### General Properties of S-Layers

#### 8.2.1

##### Structure, Isolation, Self-Assembly and Recrystallization

Transmission electron microscopic (TEM) studies on the mass distribution of S-layers and subsequent two- and three-dimensional analysis including computer image enhancement led to structural information down to a range of 0.35–1.5 nm [4, 9]. Bacterial S-layer lattices are generally 5–20 nm thick, whereas S-layer lattices of archaea reveal a thickness up to 70 nm. High-resolution images of the surface topography of S-layers under biological conditions were obtained by applying scanning force microscopy (SFM) [4, 9, 10–12]. A common feature of S-layers is, with respect to the orientation on the cell, their smooth outer surface and more corrugated inner surface. The proteinaceous subunits of S-layers are aligned either in lattices with oblique (p1, p2), square (p4) or hexagonal (p3, p6) symmetry with a center-to-center spacing of the morphological units of approximately 3.5–35 nm. Hexagonal lattice symmetry is predominant among archaea [13, 14]. S-layers are highly porous protein lattices with a surface porosity of 30–70%. As S-layers are mostly composed of a single species of subunits, they exhibit pores of identical size and morphology [4]. However, in many S-layer proteins, two or even more distinct classes of pores with diameters in the range of 2–8 nm were identified.

Most techniques for isolation and purification of S-layer proteins involve mechanical disruption of bacterial cells and subsequent differential centrifugation to separate cell wall fragments [4, 15]. Complete solubilization of S-layers into their constituent subunits and release from the bacterial envelope can be achieved by treatment with high concentrations of hydrogen bond breaking agents (e.g. guanidine hydrochloride) or by dramatic changes in the pH value of the environment. Bacterial S-layer proteins are not covalently linked to each other or to the supporting cell wall component. While different combinations of weak bonds (hydrophobic, ionic and hydrogen bonds) are responsible for the structural integrity of S-layers, bonds holding the S-layer subunits together are stronger than those binding S-layer proteins to the underlying cell envelope layer [15, 16]. S-layer proteins reassemble into two-dimensional arrays during removal of the disrupting agent used in the dissolution procedure. Self-assembly products may have the form of flat sheets, open-ended cylinders or closed vesicles [4–8, 15].

Recrystallization of S-layer proteins on technologically relevant substrates, such as silicon wafers, noble metals, plastics, flat lipid layers or liposomes, revealed a broad application potential for these crystalline arrays in micro- and nanotechnology [4–8]. The formation of coherent crystalline arrays strongly depended on the S-layer protein species, the environmental conditions of the bulk phase (e.g. temperature, pH, ion composition and ionic strength) and, in particular, on the surface properties of the substrate [17, 18]. Crystal growth was simultaneously initiated at many randomly distributed nucleation points and proceeded in-plane

until the crystalline domains met, thus leading to a closed, coherent mosaic of individual, several micrometer large S-layer patches [17, 18].

Reassembly of isolated S-layer subunits at the air/water interface and on Langmuir films proved to be an easy and reproducible way for generating coherent S-layer lattices at a large scale [19, 20]. In accordance with S-layer proteins recrystallized on solid surfaces, the orientation of the protein arrays at liquid interfaces was determined by the anisotropy in the physicochemical surface properties of the protein lattice. Electron microscopic examination revealed that recrystallized S-layer proteins were oriented with their outer charge neutral, more hydrophobic surface against the air/water interface and with their negatively charged, more hydrophilic inner surface against the positively charged or zwitterionic head groups of phospholipid or tetraether lipid films [19, 20]. According to the recrystallization on solid supports, a closed mosaic of individual monocrystalline domains was formed.

Furthermore, isolated S-layer proteins were capable to recrystallize on liposomes and on nanocapsules [21–25], thereby forming closed S-layer cages. However, electron microscopic investigations showed that numerous lattice faults were introduced into the crystalline array as necessary for bending the two-dimensional protein lattice.

### 8.2.2

#### Chemistry and Molecular Biology

Chemical analyses and genetic studies revealed that the monomolecular S-layer is the result of the secretion and subsequent crystallization of a single homogeneous protein or glycoprotein species with a molecular mass ranging from 40 to 200 kDa [4, 26]. Most S-layer proteins are weakly acidic with isoelectric points ( $pI$ s) in the range of 4–6 [26]. Exceptions were reported for the S-layer proteins of lactobacilli [27] and that of *Methanothermobacter feravidus* [28] which possess  $pI$ s of 9–11 and 8.4, respectively. Typically, S-layer proteins have a large portion of hydrophobic amino acids (40–60 mol%), possess little or no sulfur-containing amino acids and consist of about 25 mol% charged amino acids. The most frequent posttranslational modification of S-layer proteins is glycosylation [29–31]. The glycan chains of S-layer proteins from Gram-positive bacteria closely resemble the architecture of lipopolysaccharides (LPS) occurring in the outer membrane of Gram-negative bacteria than that of eukaryotic glycan structures.

Information regarding the secondary structure of S-layer proteins is either derived from the amino acid sequence or from circular dichroism (CD) measurements indicating that approximately 20% of the amino acids are organized as  $\alpha$ -helices and about 40% occur as  $\beta$ -sheets. Aperiodic foldings and  $\beta$ -turn content may vary between 5 and 45%. Secondary structure predictions based on protein sequence data revealed that most  $\alpha$ -helical segments are arranged in the N-terminal part.

During the last two decades, numerous S-layer genes from bacteria and archaea of quite different taxonomical position were sequenced and cloned [26]. At least for S-layer proteins of Bacillaceae, common structural organization principles were

identified, as they typically contain three S-layer homology (SLH) motifs [32] on the N-terminal part. Each SLH motif consists of 50–55 amino acids, from which 10–15 are conserved. In most S-layer proteins, three SLH motifs form the SLH domain which specifically recognizes a distinct type of pyruvylated cell wall heteropolysaccharide, termed secondary cell wall polymer (SCWP), as the proper anchoring structure to the rigid cell wall layer [33–41]. This binding mechanism between SLH domains and pyruvylated SCWPs is widespread amongst prokaryotes, and is considered as having been conserved during evolution [40]. The construction of knockout mutants in *Bacillus anthracis* and *Thermus thermophilus* in which the gene encoding a putative pyruvyl transferase was deleted demonstrated that the pyruvic acid residues play an essential role for the binding process [34, 40]. This observation was supported by surface plasmon resonance (SPR) spectroscopy measurements in which native and chemically modified SCWPs devoid of pyruvic acid residues were used for interaction studies [38]. By applying the dissection approach [41], it became apparent that at least in the case of the S-layer protein SbsB of *Geobacillus stearothermophilus* PV72/p2, the SLH domain (rSbsB<sub>32–208</sub>) corresponded to the SCWP-binding domain, whereas the larger C-terminal part (rSbsB<sub>209–920</sub>) represented the self-assembly domain [38, 41].

Although the S-layer proteins SbsA, SbsC and SgsE from *G. stearothermophilus* wild-type strains do not possess an SLH domain on the N-terminal part [42–45], they reveal a highly conserved N-terminal region which specifically recognizes a cell wall heteropolysaccharide containing 2,3-dideoxy-diacetamido mannosamine uronic acid [46] as negatively charged component [42–44]. In these S-layer proteins, arginine and tyrosine typically occurring in carbohydrate binding proteins such as lectins [47] are accumulated on the N-terminal part. In S-layer proteins of *Lactobacillus helveticus*, *L. crispatus* and *L. acidophilus* strains, the conserved C-terminal part was found to be responsible for cell wall anchoring [48], which is most probably mediated by a neutral cell wall polysaccharide [49]. According to the suggestion that S-layer proteins represent cell surface located, carbohydrate-binding, lectin-like proteins [50], the N-terminal region of the S-layer protein from the Gram-negative bacterium *Caulobacter crescentus* recognizes a distinct type of LPS as a binding site to the outer membrane [51, 52]. In *Campylobacter fetus*, a pathogenic organism, two serotypes are distinguished that depend on the type of LPS in the outer membrane. In type A cells, the S-layer protein SapA and its homologs are bound via a conserved N-terminal region to type A LPS, while in type B cells, specific binding was observed between the N-terminal part of SapB and its homologs and type B LPS [53].

For S-layer-carrying bacteria with a generation time of 20 min, about 500 subunits must be synthesized per second, translocated through the plasma membrane and incorporated into the existing protein lattice [15, 16]. Thus, promoters preceding S-layer genes must be very strong [26]. For some S-layer genes, two or even more promoters were identified which are most probably used in different growth stages [26, 27, 37, 43]. With the exception of the S-layer proteins from the Gram-negative bacteria *C. crescentus* and *C. fetus*, all others sequenced so far are produced with an N-terminal secretion signal peptide. For *C. crescentus* and *C. fetus*, type I

secretion signals were detected on the C-terminal part [54]. In contrast, a conserved gene (*abcA*) was identified in the downstream region of the genes encoding the S-layer proteins of the Gram-negative bacteria *Aeromonas salmonicida* and *Aeromonas hydrophila*. This gene encodes a protein that has ATP-binding activity and belongs to the ABC family of transporter proteins, regulates the synthesis of S-layer-specific O-polysaccharide chains in LPS and activates transcription of the S-layer genes [55, 56]. The existence of a translational autoregulation system was reported for *T. thermophilus* [57]. Three genes specifically repressing the expression of the S-layer gene promoter were identified. One of these genes corresponds to the C-terminal fragment of the S-layer protein SlpA which binds to the 5'-untranslated region of the *slpA* mRNA [57].

S-layer variation leads to the expression of alternate S-layer proteins, and was described for pathogens and non-pathogens. In non-pathogens, S-layer variation is frequently induced in response to altered environmental conditions, such as increased oxygen supply [58–60], whereas in pathogens, altered cell surface properties most probably protect the cells from the lytic activity of the immune system [53]. In general terms, two different types of S-layer variation can be distinguished. In the first type, which was observed for *C. fetus* [53, 61] and *G. stearothermophilus* ATCC 12980 [62], only the C-terminal part of the S-layer protein was exchanged, but both the N-terminal region and the S-layer-specific LPS or SCWP remained conserved. In the second type of S-layer variation, which was described for various *G. stearothermophilus* strains, a completely new type of S-layer protein and SCWP was synthesized, and S-layer variation also led to a change in the lattice type [59, 60]. At the molecular level, S-layer variation was either caused by intrachromosomal DNA rearrangement, as observed for *C. fetus* [53, 63], or variant formation depended on recombinational events between a naturally occurring plasmid and the chromosome [64]. In contrast, in *Lactobacillus brevis*, S-layer variation involved activation of transcription by a soluble factor rather than by DNA rearrangement [58]. Regarding the development of S-layer-deficient strain variants, the importance of insertion sequence (IS) elements was demonstrated for various organisms [65–67].

### 8.2.3

#### S-Layers as Carbohydrate-binding Proteins

As described above, the interaction between the N-terminal part of the S-layer proteins SbsB and SbpA and the corresponding SCWP was found to be highly specific [35, 38, 41]. The most detailed interaction studies were carried out with the SLH domain of SbsB (rSbsB<sub>32–208</sub>) and the corresponding SCWP of *G. stearothermophilus* PV72/p2 [38]. Data evaluation from SPR measurements and the setup where the SLH domain was immobilized to the sensor chip indicated the existence of at least two binding sites on a single SCWP molecule with an overall  $K_d = 7.7 \times 10^{-7}$  M. In order to distinguish between the different binding sites, the inverted setup where the SCWP was immobilized to the sensor chip and the SLH domain represented the soluble analyte was investigated. Data analysis was performed according to an extension of the heterogeneous ligand model which allowed us to

**Tab. 8.1.**  $K_d$  values for rSbpA<sub>31–1268</sub>, rSbpA<sub>31–318</sub> and rSbsB<sub>32–209</sub>

S-layer protein	$K_{d1}$	$K_{d2}$	$K_{d3}$
rSbpA <sub>31–1268</sub>	$8.4 \times 10^{-12}$	$7.0 \times 10^{-9}$	$2.1 \times 10^{-4}$
rSbpA <sub>31–318</sub>	$1.2 \times 10^{-11}$	$3.0 \times 10^{-8}$	$2.4 \times 10^{-2}$
rSbsB <sub>32–209</sub>	$6.7 \times 10^{-11}$	$6.1 \times 10^{-8}$	$2.6 \times 10^{-5}$

discriminate between three different kinds of binding sites with low ( $K_d = 2.6 \times 10^{-5}$  M), medium ( $K_d = 6.1 \times 10^{-8}$  M) and high ( $K_d = 6.7 \times 10^{-11}$  M) affinity. Although the existence of three different kinds of binding sites can be explained by structural heterogeneities frequently associated with naturally occurring polysaccharides, it cannot be excluded that the high-affinity binding site resulted from avidity effects caused by binding of at least SLH dimers (Table 8.1) [38]. The existence of three potential binding sites and similar affinity constants were demonstrated for the S-layer protein SbpA and the SCWP of *Bacillus sphaericus* CCM 2177 [35]. However, in the case of SbpA, the three SLH motifs and an SLH-like motif were required for reconstituting the functional SCWP-binding domain (Table 8.1).

For the exploitation of SCWPs as biomimetic linkers to solid supports to guarantee an oriented binding and recrystallization of S-layer proteins, these heteropolysaccharides were extracted from peptidoglycan-containing sacculi with hydrofluoric acid and precipitated with ethanol [68, 69]. After purification by size-exclusion chromatography, the latent aldehyde group of the reducing end of the polymer chain was modified with carbodihydrazide and the Schiff base was reduced with sodium borohydride [38]. Sulfhydryl groups were introduced by reaction of the free amine group with 2-methyl mercaptobutyrimidate (2-iminothiolane). Such modified SCWPs carrying a free terminal sulfhydryl group were used for direct adsorption to gold substrates, as required for SPR [70–72] or surface plasmon field enhanced spectroscopy [73]. For covalent binding to supports carrying free amine groups, the sulfhydryl group of the polymer chain (termed thiolated SCWP) was activated with *m*-maleimidobenzoyl-*N*-hydroxysuccinimide ester (MBS) which, as a heterobifunctional crosslinker, could react with amine groups, e.g. of amine-modified cellulose microbeads [72]. Another possibility to activate thiolated SCWP can be seen in the use of the heterobifunctional crosslinker sulfosuccinimidyl 6-[3'-2-(pyridyldithio)-propionamido]hexanoate (Sulfo-LC-SPDP) [38].

### 8.3

#### Nanoscale Patterning of S-Layer Proteins

##### 8.3.1

##### Properties of S-Layer Proteins Relevant for Nanoscale Patterning

S-layers represent a first order self-assembly system that has been optimized in the course of evolution. As S-layers are composed of single protein or glycoprotein species, they have repetitive (physicochemical) properties down to the subnanometer scale [4–8, 74]. Furthermore, functional groups such as amine and carboxylic acid



groups have identical positions and orientation on each subunit in the protein lattice. In the case of S-layer glycoproteins, the carbohydrate chains are attached to the same amino acid positions in the primary sequence [45]. Isolated S-layer subunits frequently maintain the ability to self-assemble in suspension and to recrystallize into a monomolecular protein lattice on various types of solid supports, such as gold chips, silicon wafers, plastics or glass, as well as on flat lipid layers or liposomes [4–8, 74]. The N-terminal region of S-layer proteins specifically recognizes a distinct type of SCWP as the proper anchoring structure in the rigid cell wall layer. These heteropolysaccharides can be exploited as biomimetic linkers to solid supports [38, 70–72], so that the S-layer subunits attach with their inner surface carrying the N-terminal region. S-layer proteins are ideal candidates for genetic engineering. So far, a single cysteine residue has been inserted at various amino acid positions, leading to numerous mutated S-layer protein forms [75]. As S-layer proteins usually do not possess sulfur-containing amino acids, this modification is particularly attractive, since the whole spectrum of sulfur chemistry can be applied to covalently link functional entities via the cysteine residue to the S-layer subunits. Studies on the structure–function relationship of selected S-layer proteins by producing N- or C-terminally truncated forms revealed that the N-terminal region functions as cell wall anchoring domain, whereas the middle and C-terminal part are responsible for lattice and pore formation [35]. However, in some S-layer proteins even more than 200 amino acids in the C-terminal part could be deleted without any influence on the self-assembly and recrystallization properties [37, 44].

To sum up, S-layer lattices are composed of identical protein or glycoprotein species. This implies that functional sequences introduced by genetic engineering and/or chemical modification are repetitively aligned in exact positions down to the subnanometer scale. This cannot be achieved with amorphous polymers which are three-dimensional networks where only random immobilization can occur [4]. In contrast, functional sequences fused to S-layer proteins or inserted into their primary sequence have identical positions and orientation on each S-layer subunit. Moreover, two or even more sequences with different functionalities can be fused to or inserted into a single S-layer protein, leading to multifunctional S-layer fusion proteins. Another possibility can be seen in the co-recrystallization of different types of engineered S-layer proteins which would also lead to multifunctional protein lattices. Apart from this variability, it is possible that the functional sequences or domains are exposed on the outermost surface of the monomolecular protein lattice and are therefore easily accessible to further binding and reaction partners or they may be inserted inside the pores, which could be advantageous for nanoparticle binding. Thus, S-layer proteins can be considered as an extremely versatile and flexible self-assembly system with considerable application potential in nanobiotechnology.

### 8.3.2

#### **Immobilization of Functionalities by Chemical Methods**

Chemical modification and labeling experiments revealed that S-layer lattices possess a high density of functional groups on the outermost surface. For covalent at-

tachment of foreign (macro)molecules, the carboxylic acid groups originating from either aspartic acid or glutamic acid were activated with carbodiimide and subsequently reacted with free amine groups of functional macromolecules, such as Protein A [76–78], monoclonal antibodies [70, 79–82] or various enzymes [4]. In order to prevent inter- and intramolecular crosslinking reactions, the  $\epsilon$ -amine groups from lysine residues were first modified with monofunctional imidoesters or the S-layer lattice was crosslinked with amine group-specific bifunctional reagents, such as imidoesters or glutaraldehyde. For immobilization of macromolecules, S-layers were either used as self-assembly products which were mostly double layers or as S-layer-carrying cell wall fragments which consisted of the peptidoglycan-containing layer and two mirror-symmetrically arranged S-layer lattices [76]. The amount of monoclonal antibodies, enzymes and streptavidin that could be immobilized to S-layer lattices corresponded approximately to a monolayer of randomly oriented molecules [4]. Quantification of immobilized Protein A, which is extremely elongated, revealed that the molecules were bound in preference with their long axis perpendicularly to the plane of the S-layer lattice [76, 78, 79]. Thus, binding capacities of 290 ng Protein A  $\text{cm}^{-2}$  S-layer lattice were obtained, which was more than 3 times above the theoretical saturation capacity of a planar surface of 90 ng  $\text{cm}^{-2}$  when calculated with the Stoke's radius. S-layer-carrying cell wall fragments deposited on microporous supports and carrying a monolayer of monoclonal antibodies were exploited for the development of novel types of dipstick-style solid-phase immunoassays, which due to the low nonspecific adsorption of S-layer proteins for serum components showed excellent signal-to-noise ratios [80, 81]. In the case of Protein A, affinity microparticles with a size of approximately 1  $\mu\text{m}$  were prepared, which represented cup-shaped structures with a complete outer and inner S-layer arranged in mirror symmetric fashion [76]. Such affinity microparticles were used as IgG-specific adsorbents in affinity crossflow filtration systems for the removal of human IgG from serum [77], as required for blood purification of patients suffering from autoimmune disease [78]. Due to their high surface to volume ratio and the high density of immobilized Protein A, affinity microparticles revealed an excellent binding capacity for IgG which was in the range of 40  $\mu\text{g mg}^{-1}$  wet pellet [76–78].

### 8.3.3

#### Patterning by Genetic Approaches

##### 8.3.3.1 The S-Layer Proteins SbsA, SbsB and SbsC

The S-layer protein SbpA of *B. sphaericus* CCM 2177 consists (including a 30-amino-acid long signal peptide) in total of 1268 amino acids [37]. SbpA self-assembles into a square (p4) lattice structure with a center-to-center spacing of the morphological units of 13.1 nm. The self-assembly process is strongly dependent on the presence of bivalent cations, such as calcium ions [36]. In the absence of bivalent cations, this S-layer protein stays in the water-soluble state. The N-terminal part of SbpA comprises three typical SLH motifs, but for reconstituting the functional SCWP-binding domain, an additional 58-amino-acid long SLH-like

motif located behind the third SLH motif was required [35]. The SCWP of *B. sphaericus* CCM 2177 consists of disaccharide repeating units that are composed of N-acetyl glucosamine (GlcNAc) and N-acetyl mannosamine (ManNAc). The ManNAc residues carry a pyruvate ketal which endows the polymer chains with a negative net charge [36]. Studies on the structure–function relationship revealed that up to 237 C-terminal amino acids could be deleted without influencing the formation of the p4 lattice structure [35, 36]. However, the deletion of 350 C-terminal acids was linked to a change from square (p4) to oblique (p1) lattice symmetry. By producing various C-terminally truncated forms and performing surface accessibility screens, it became apparent that amino acid position 1068 is located on the outer surface of the square lattice [37]. This was the reason why the C-terminally truncated form rSbpA<sub>31–1068</sub> was exploited as base form for the construction of several S-layer fusion proteins [70–72, 83]. An N- and C-terminally truncated form (rSbpA<sub>203–1031</sub>) was capable of self-assembly into the square (p4) lattice structure with a center-to-center spacing of the morphological units and a protein mass distribution similar to that formed by full-length rSbpA [35]. These findings indicated that the segment between amino acids 203 and 1031 is responsible for the self-assembly process and for pore formation.

The S-layer protein SbsB of *G. stearothermophilus* PV72/p2 consists (including a 31-amino-acid long signal peptide) in total of 920 amino acids [84]. By applying the dissection approach, it could be demonstrated that SbsB is composed of the N-terminal SCWP-binding domain which corresponds to the SLH domain and the C-terminal self-assembly domain [38, 41]. As the removal of fewer than 10 C-terminal amino acids led to water-soluble rSbsB forms, the C-terminal part can be considered extremely sensitive against deletions [75, 85]. When the C-terminal end of full-length SbsB was exploited for linking foreign functional sequences, water-soluble S-layer fusion proteins were obtained [85], which recrystallized into the oblique (p1) lattice only on solid supports precoated with SCWP of *G. stearothermophilus* PV72/p2. As demonstrated by SPR spectroscopy, the SLH domain comprising the three SLH motifs specifically recognizes the SCWP of *G. stearothermophilus* PV72/p2 as a binding site [35]. The polymer chains are composed of GlcNAc and ManNAc in the molar ratio of approximately 2:1 [69], and contain pyruvate ketals which provide a net negative charge. The use of chemically modified SCWP in SPR interaction studies clearly showed that it is not the N-acetyl groups of the amino sugars, but the pyruvic acid residues that play a crucial role in the recognition and binding process [38]. Furthermore, thermal as well as guanidine hydrochloride-induced equilibrium unfolding profiles monitored by intrinsic fluorescence and CD spectroscopy allowed us to characterize the SLH domain (rSbsB<sub>32–208</sub>) as an  $\alpha$ -helical protein with a single cooperative unfolding transition. The C-terminal self-assembly domain (rSbsB<sub>209–920</sub>) could be characterized as a  $\beta$ -sheet protein with typical multidomain unfolding and a lower stability as stand-alone protein [41].

Recently, chimeric S-layer proteins either comprising the N-terminal part of SbpA and the C-terminal part of SbsB (rSbpA–SbsB), or vice versa, the N-terminal part of SbsB and the C-terminal part of SbpA (rSbsB–SbpA), have been con-

structed [35]. The aim was to create a spectrum of S-layer proteins that bind to the same type of SCWP, but assemble into different lattice types. Accordingly, rSbsB and rSbsb-SbpA specifically recognized the SCWP of *G. stearothersophilus* PV72/p2 as a binding site, but in contrast to rSbsB which assembled into an oblique (p1) lattice, the chimeric protein rSbsb-SbpA formed a square (p4) lattice structure. In addition, in rSbsB-SbpA the surface-located amino acid position 1068 of the SbpA primary sequence was exploited as a fusion site for foreign functional sequences [37, 74]. However, rSbpA and the chimeric protein rSbpA-SbsB recognized the SCWP from *B. sphaericus* CCM 2177 as a binding site, but they self-assembled into different lattice types, i.e. square (p4) for rSbpA and oblique (p1) for rSbpA-SbsB [35].

SbsC is the S-layer protein of *G. stearothersophilus* ATCC 12980 and consists (including a 30-amino-acid long signal peptide) in total of 1099 amino acids [43]. Isolated SbsC self-assembles into an oblique lattice. SbsC does not possess an SLH domain on the N-terminal part, but reveals a conserved N-terminus region which was also found in S-layer proteins of other *G. stearothersophilus* wild-type strains, such as PV72/p6, DSM 2358 [42] and NRS 2004/3a [45], as well as in a temperature-derived strain variant of strain ATCC 12980 [62]. This type of N-terminal part which comprises amino acids 31–257 specifically recognizes the SCWP that contains 2,3-dideoxy-diacetamido mannosamine uronic acid as a negatively charged component [42, 46]. Studies on the structure–function relationship of SbsC revealed that the N-terminal part is responsible for cell wall anchoring via the specific SCWP. In the C-terminal part, up to 179 amino acids leading to rSbsC<sub>31–920</sub> could be deleted without interfering with the formation of the oblique lattice structure [44]. Further deletion of C-terminal amino acids led to SbsC forms that were still able of self-assembling, but such self-assembly products did not show a regular lattice structure (rSbsC<sub>31–880</sub>), whereas rSbsC<sub>31–844</sub> even represented a completely water-soluble form which was used for three-dimensional crystallization experiments [86].

### 8.3.3.2 S-Layer Fusion Proteins

In general, a broad spectrum of chimeric S-layer fusion proteins was constructed and heterologously expressed in *Escherichia coli*. S-layer fusion proteins were based on the S-layer proteins SbsB, SbpA and SbsC. For generating a universal affinity matrix for binding any kind of biotinylated molecules, S-layer–streptavidin fusion proteins were constructed [73, 85]. The strong interaction between streptavidin and biotin as a biomolecular coupling system is commonly used in biotechnology [86]. Minimum-sized core streptavidin (118 amino acids) was either fused to N- or C-terminal positions of SbsB, the S-layer protein of *G. stearothersophilus* PV72/p2, or to the C-terminal end of rSbpA<sub>31–1068</sub> [37]. The S-layer proteins SbsB and SbpA show different lattice characteristics. SbsB forms an oblique S-layer lattice with p1 symmetry and lattice parameters of  $a = 10.4$  nm,  $b = 7.9$  nm and a base angle of  $\gamma = 81^\circ$ , while SbpA forms a square S-layer lattice with a center-to-center spacing of 13.1 nm.

The genes encoding the fusion proteins and core streptavidin were expressed in-

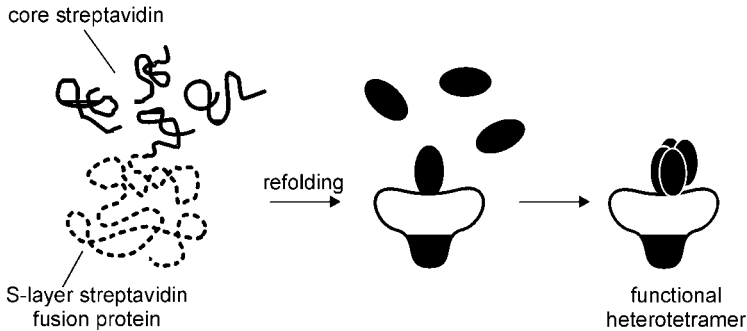


**Fig. 8.1.** Schematic drawing illustrating the disintegration and rapid dilution step leading to functional heterotetramers of a C-terminal S-layer-streptavidin fusion protein.

independently in *E. coli* and isolated from the host cells [73, 85]. To obtain functional heterotetramers, a refolding procedure was developed by subjecting a mixture of fusion protein with excess core streptavidin to denaturing and renaturing (Fig. 8.1). Two dominant tetramer species, one consisting of one molecule of fusion protein and three molecules of streptavidin (heterotetramers), and the other one consisting of four molecules of streptavidin (homotetramers) were formed during rapid dilution. Heterotetramers were separated from homotetramers and from the S-layer-streptavidin fusion protein by gel-permeation and affinity chromatography. In the latter, the pH-dependent affinity of iminobiotin to streptavidin was exploited. The exceptional stability of streptavidin in 5% SDS at room temperature and denaturation upon boiling allowed the application of the gel-shift assay to control rapid dilution and purification (Fig. 8.2). The desired properties of heterotetramers consisting of one chain of S-layer-streptavidin fusion protein and three chains of streptavidin were the maintenance of the recrystallization properties of the S-layer protein moiety, as well as biotin binding.

Recrystallization experiments were either performed in suspension, on peptidoglycan-containing sacculi, on liposomes or on various solid supports, such as silicon or gold chips which were optionally precoated with thiolated SCWP of *B. sphaericus* CCM 2177 or *G. stearothersophilus* PV72/p2. Heterotetramers comprising the N-terminal rSbsB-streptavidin fusion protein formed self-assembly products in suspension, and recrystallized on liposomes and silicon wafers [85], whereas heterotetramers based on the C-terminal rSbpA<sub>31-1068</sub>-streptavidin fusion protein showed dirigible self-assembly formation due to the calcium ion dependency of lattice formation of SbpA. Such heterotetramers recrystallized on gold surfaces which were optionally precoated with SCWP [73] (Fig. 8.3). Analysis of negatively stained preparations of self-assembly products formed by heterotetramers revealed that neither the oblique S-layer lattice of SbsB nor the square lattice of SbpA was changed due to the presence of the fusion partner. Due to unhindered lattice formation and unchanged lattice parameters, the streptavidin moiety was considered as being located above the plane on the outer surface of

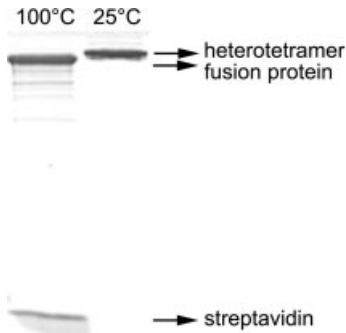


**Fig. 8.2.** Gel-shift assay of SDS extracts from heterotetramers purified by gel-permeation and affinity chromatography. The heterotetramers show the specific property of remaining in the

native state in 5% SDS at 25 °C, but dissociate into the S-layer–streptavidin fusion protein and streptavidin in 5% SDS at 100 °C.

the protein lattice. Digital image reconstructions of self-assembly products of heterotetramers containing the N-terminal rSbsB–streptavidin fusion protein in comparison to the SbsB lattice showed an additional protein mass on the SLH domain which resulted from the fused streptavidin [85] (Fig. 8.4). All self-assembly experiments confirmed that the first of the desired properties was present, i.e. unhindered recrystallization of the fusion protein into a two-dimensional crystalline array.

Since the fusion proteins were constructed from the wild-type streptavidin sequence, the biotin-binding sites were assumed to show the typical high affinity to

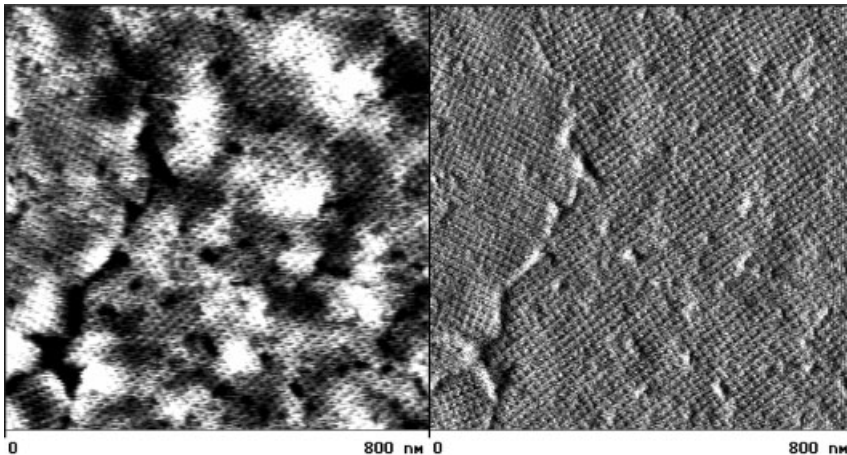


**Fig. 8.3.** SFM image of heterotetramers consisting of one chain of rSbpA<sub>31–1068</sub>–streptavidin fusion protein and three chains of streptavidin. The heterotetramers recrystallized

into the square lattice structure on gold chips precoated with thiolated SCWP of *B. sphaericus* CCM 2177. Right: deflection mode. Left: height mode.

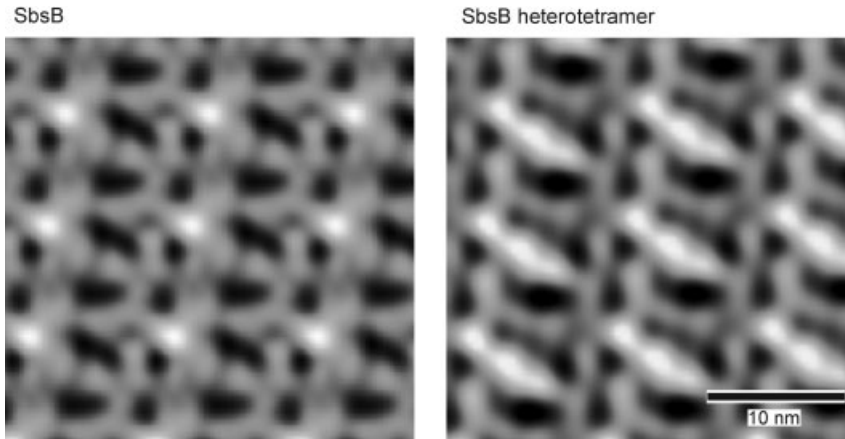


**Fig. 8.4.** Digital image reconstructions of electron micrographs taken of negatively stained preparations of self-assembly products formed by SbsB (left) and heterotetramers consisting of one chain of the N-terminal

rSbsB–streptavidin fusion protein and three chains of streptavidin (right). The streptavidin moiety of the heterotetramers can be seen as the additional protein mass above the plane of the oblique ( $p1$ ) lattice structure.

biotin. However, it remained to be investigated if biotin-binding sites were sterically blocked by the large fusion partner SbsB or SbpA. The biotin-binding ability of soluble heterotetramers was determined by fluorescence quenching of tryptophan residues in the binding pockets of streptavidin upon biotin binding [73, 85, 87, 88]. Biotin, as well as biotinylated insulin ( $M_r$  6 kDa), biotinylated horseradish peroxidase ( $M_r$  44 kDa) and biotinylated serum albumin ( $M_r$  66 kDa) were used for the fluorescence titration experiments. In comparison to free streptavidin which was used as reference protein, heterotetramers showed an even higher binding capacity for D-biotin, biotinylated insulin and biotinylated horseradish peroxidase. For biotinylated serum albumin, a similar binding capacity was determined.

In general, heterotetramers based on S-layer streptavidin fusion proteins are considered a universal affinity matrix for binding biotinylated molecules. As proof-of-principle, heterotetramers comprising C-terminal S-layer streptavidin fusion proteins were recrystallized on peptidoglycan-containing sacculi which were subsequently incubated with biotinylated ferritin as a marker that can be visualized by TEM. As shown in Fig. 8.5, heterotetramers based on the rSbpA<sub>31–1068</sub>–streptavidin fusion protein showed excellent recrystallization properties, as well as high affinity to biotinylated ferritin.

As a first application approach, monolayers of heterotetramers based on the rSbpA<sub>31–1068</sub>–streptavidin fusion protein were recrystallized on gold surfaces which were optionally precoated with thiolated SCWP. The obtained affinity matrix was used to perform hybridization experiments. In a first step, biotinylated oligonucleotides (30mers) were bound to the streptavidin moiety of the heterotetramers. Subsequently, complementary oligonucleotides were hybridized carrying one or two mismatches or they were without any mismatch (Fig. 8.6). Evaluation of the

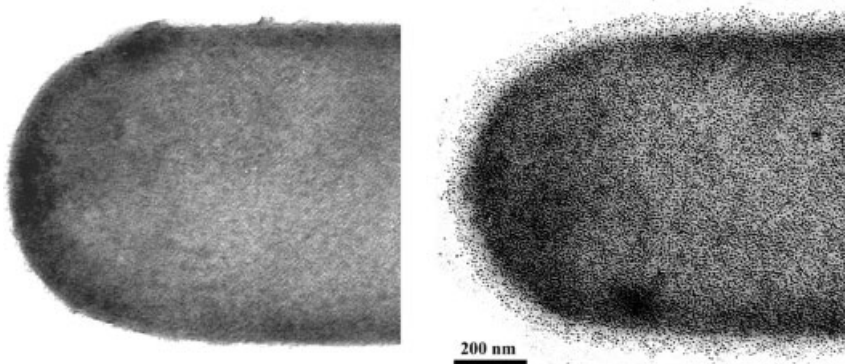


**Fig. 8.5.** Electron micrographs of negatively-stained preparations of heterotetramers consisting of one chain of rSbpA<sub>31-1068</sub>-streptavidin fusion protein and three chains of streptavidin. The heterotetramers were recrystallized on peptidoglycan-containing sacculi of *B. sphaericus* CCM 2177 (left) and subsequently incubated with biotinylated ferritin (right).

hybridization experiments were performed by applying surface-plasmon-field-enhanced fluorescence spectroscopy which combines the advantages of the high optical field intensities of surface plasmon waves with the sensitive detection of fluorescence light emission [89, 90]. For generating functional monomolecular protein lattices, two strategies were pursued – direct recrystallization of heterotetramers on plain gold chips or recrystallization on SCWP-coated gold chips. In both cases, the amount of recrystallized heterotetramers corresponded well to the theoretically calculated value for a monolayer [85]. The advantage of recrystallization on plain gold chips was seen in the strong interaction between the inner surface of the S-layer subunits and gold. This fact could be exploited to regenerate the

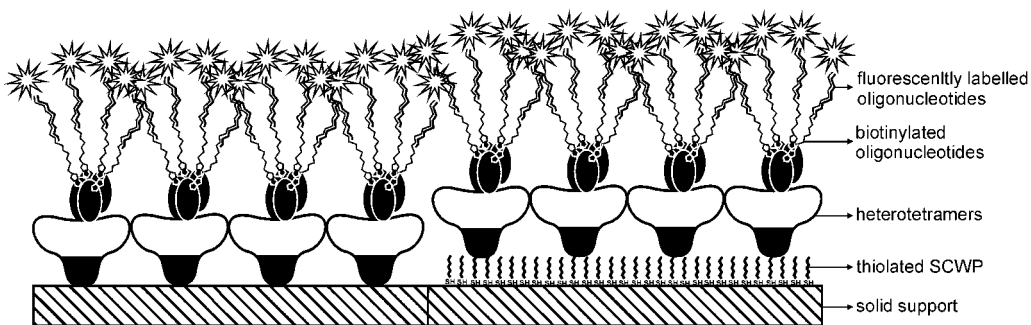


**Fig. 8.6.** Schematic drawing of heterotetramers consisting of one chain of rSbpA<sub>31-1068</sub>-streptavidin fusion protein and three chains of streptavidin, either recrystallized on plain gold chips or on gold

chips precoated with thiolated SCWP. After recrystallization into a monomolecular protein lattice, biotinylated oligonucleotides were bound to which fluorescently labeled oligonucleotides could hybridize.



sensor surface without any loss of heterotetramers, which could not be removed from the gold chip even with ethanol or chaotropic agents such as urea or guanidine hydrochloride. However, the advantage of using SCWP-coated gold chips lies in the unambiguously oriented recrystallization of the heterotetramers via their SCWP-binding domain located on the inner surface, as well in the lower detection limit for fluorescently labeled oligonucleotides. The latter can be explained by the fact that a higher distance between the gold surface and the fluorescently labeled oligonucleotides reduces quenching of fluorescence signals caused by the gold layer. However, monolayers generated on SCWP-coated gold chips were less stable, which was attributed to the rather labile gold-thiol linkage acting between the thiolated SCWP and the gold support. Nonspecific adsorption of DNA did not play a role which could be demonstrated by incubation of the sensor surface with oligonucleotides carrying two mismatches. For hybridization experiments on monolayers generated by recrystallization of heterotetramers on gold chips precoated with thiolated SCWP, fluorescently labeled oligonucleotides carrying one mismatch were used. The fluorescence intensity increased linearly at the beginning of the hybridization reaction, so that the linear slope of the increase in fluorescence intensity plotted versus the concentration of the hybridizing oligonucleotides showed a linear correlation [73]. In a different set of hybridization experiments which were performed on monolayers generated by direct recrystallization of heterotetramers on plain gold chips, the concentration of oligonucleotides carrying one mismatch was stepwise increased. The Langmuir isotherm which indicated that oligonucleotides in solution were in equilibrium with those bound to the monolayer carrying the biotinylated oligonucleotides could be established from the obtained fluorescence intensities (Fig. 8.7) [73]. The detection limit was found to be 1.57 pM on monolayers generated by recrystallization of heterotetramers on gold chips precoated with thiolated SCWP, whereas on plain gold chips the detection limit was determined to be at least 8.2 pM.

To conclude, the results obtained with heterotetramers consisting of one chain of S-layer streptavidin fusion protein and three chains of core streptavidin showed that the self-assembly properties of the S-layer protein moiety could be combined with the biotin-binding properties of streptavidin. First hybridization experiments indicated that a functional sensor surface could be generated by recrystallization of heterotetramers on gold chips, which could find numerous applications in (nano)biotechnology.

In a first approach, an S-layer fusion protein comprising the C-terminally truncated form rSbpA<sub>31-1068</sub> and the variable region of a heavy chain camel antibody directed against lysozyme was constructed. The *Camelidae* is the only taxonomic family known to possess functional heavy chain antibodies lacking light chains and the first constant region. These unique antibody isotypes interact with the antigen by virtue of a single variable domain, termed VHH. A single VHH domain has a molecular mass of only 15 000 and is the smallest known complete antigen-binding fragment from a functional immunoglobulin (Fig. 8.8). The single-domain nature of VHHs gives rise to several unique features as compared to antigen-binding derivatives of conventional antibodies. As well as the advantage of

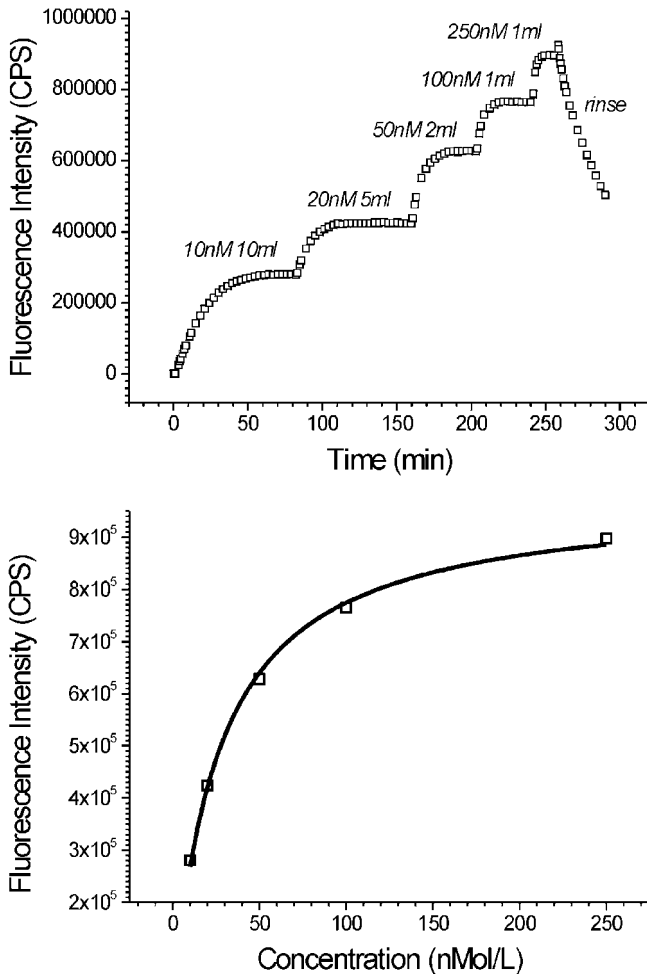


**Fig. 8.7.** Langmuir adsorption isotherm experiment of fluorescently labeled oligonucleotides carrying one mismatch hybridizing to complementary, biotinylated oligonucleotides bound to heterotetramers consisting of one chain of rSbpA<sub>31-1068</sub>-streptavidin fusion protein and three chains of streptavidin. By increasing the concentration of the fluorescently labeled oligonucleotides, higher equilibrium levels were reached (left side). The fluorescence intensities at the equilibrium are plotted against the concentrations of the solutions giving the Langmuir adsorption isotherm (right side).

single-gene cloning and selection from an *in vivo* matured library, recombinant VHs have other technological, functional and physicochemical advantages, such as (a) high expression yields and ease of purification, (b) a highly soluble and stable single domain immunoglobulin fold, (c) the generation of antigen-specific, high-affinity binders, (d) the recognition of unique conformational epitopes with the dominant involvement of its enlarged complementary determining regions, and

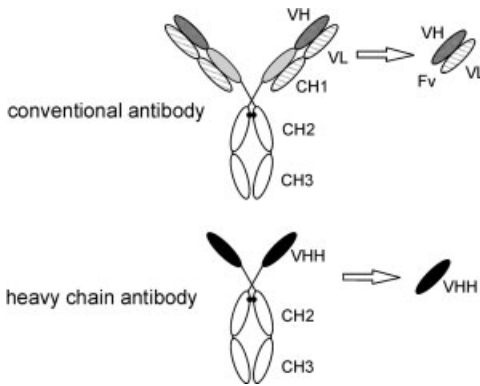


**Fig. 8.8.** Schematic drawing showing conventional (top) and heavy chain IgG antibodies (bottom) present in the serum of *Camelidae*. The complete light chains (dotted areas) and CH1 domains (black areas) are absent in heavy chain camel antibodies. The antigen-binding domains (Fv) of conventional antibodies as obtained after proteolysis or after

expression of the gene encoding VH or VL fragments are shown. The recombinant VHH (curved areas), the variable domain of a heavy chain camel antibody, can be obtained after cloning and expression. The VHH is the minimal intact antigen-binding fragment that can be generated.

(d) the close homology to human VHs (variable domain of the heavy chain) fragments [91, 92]. These features can be expected to lead to a number of applications in which VHHs perform better than conventional antibody fragments, e.g. as enzyme inhibitors, as modular building units for multivalent or multifunctional constructs, or as immunoadsorbents and detection units in biosensors. Due to these properties, VHHs clearly offer an improvement over conventional, more complex, antibody fragments, e.g. in diagnostic applications, for which the stability of the biomolecular probes is critical. Moreover, VHHs constitute ideal modular building blocks for manifold molecular constructs [91, 92]. To explore the potential advantages of camel single-domain antibodies and to gain insight into how they recognize their target, the crystal structure of a camel VHH complexed with hen's egg lysozyme was solved [93].

For construction of an S-layer fusion protein comprising the sequence of a single variable region of a camel heavy chain antibody directed against lysozyme (cAb-Lys3), the C-terminal truncation rSbpA<sub>31-1068</sub> was selected as the base form. The obtained S-layer fusion protein, termed rSbpA<sub>31-1068</sub>/cAb-Lys3 was considered as a model system for the construction of further chimeric proteins, which comprised rSbpA<sub>31-1068</sub> and cAbs directed against various antigens. Independent of the use of soluble or self-assembled rSbpA<sub>31-1068</sub>/cAb-Lys3, the camel antibody sequence remained accessible to lysozyme binding [70]. This was also observed for monolayers which were generated by recrystallization of the S-layer fusion protein on polystyrene substrates or on gold chips precoated with thiolated SCWP. In both cases, cAb-Lys3 was located on the outer S-layer surface and remained functional. As proof-of-principle could be provided with this model system, an S-layer fusion

protein incorporating the sequence of a variable domain of a heavy chain camel antibody (cAb-PSA-N7) directed against the prostate-specific antigen (PSA) was constructed [71]. PSA is a useful marker to screen potential prostate cancer patients. The current diagnostic test systems determine the concentration of total PSA with monoclonal antibodies that recognize free as well as PSA complexed with  $\alpha_1$ -antichymotrypsin (ACT). For their application in a PSA biosensor, VHHs recognizing free and complexed PSA are desired. Moreover, the kinetic requirements in the biosensor impose a high probe density that can probably only be achieved with single domain VHHs.

To generate a PSA-specific sensing layer for SPR measurements, the S-layer fusion protein rSbpA<sub>31-1068</sub>/cAb-PSA-N7 was recrystallized on gold chips precoated with thiolated SCWP [71]. The formation of the monomolecular protein lattice was confirmed by SFM, as well as by the level of the measured SPR signal. As derived from response levels measured for binding of PSA to a monolayer consisting of rSbpA<sub>31-1068</sub>/cAb-PSA-N7, the molar ratio between bound PSA and the S-layer fusion protein was 0.78, which means that at least three PSA molecules were bound per morphological unit of the square S-layer lattice [71]. To summarize, by using thiolated SCWP as a biomimetic linker to gold chips, a sensing layer for SPR could be generated by recrystallization of this S-layer fusion protein (Fig. 8.9). Due to the crystalline structure of the S-layer lattice, the fused ligand sequence showed a well-defined distance in the protein lattice and, according to the selected fusion site in the S-layer protein, they were located on the outermost surface, which reduced diffusion-limited reactions. A further advantage can be seen in the constant and low distance of the ligands from the optically active gold layer, which is exclusively determined by the thickness of the S-layer and lies in the range of only 10–15 nm. Thus, S-layer fusion proteins incorporating camel antibody sequences can be considered as key elements for the development of label-free detection systems such as SPR, surface acoustic wave (SAW) or quartz crystal microbalance (QCM-D), in which the binding event can be measured directly by the mass increase without the need of any labeled molecule.

The sequence encoding rSbpA<sub>31-1068</sub> was also used as a base form for the construction of an IgG-binding fusion protein [72]. As fusion partner, the sequence

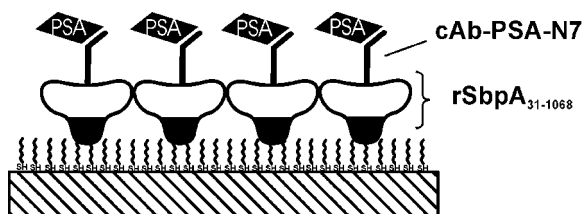


**Fig. 8.9.** Schematic drawing of the S-layer fusion protein rSbpA<sub>31-1068</sub>/cAb-PSA-N7 which was recrystallized on gold chips precoated with the thiolated SCWP. The monomolecular protein lattice was able to specifically bind PSA on the outermost surface.

encoding the Z domain, a synthetic analog of the IgG-binding domain of Protein A from *Staphylococcus aureus* was used. Protein A consists of a cell-wall-targeting domain and five other domains, termed C, B, A, D and E, with C next to the cell wall. X-ray analysis revealed that the B domain of Protein A consists of two contact sites that interact with the Fc part of IgG [94], leaving the Fab regions free for binding the antigen. Based on this knowledge, the synthetic Z domain which is 58 amino acids long and binds to the Fc part of IgG was constructed [95]. To generate the S-layer fusion protein, the 5'-end of the sequence encoding two copies of the Z domain was fused via a short linker to the gene encoding rSbpA<sub>31-1068</sub> [72]. After heterologous expression in *E. coli*, the S-layer fusion protein was isolated from the host cells, purified by size-exclusion chromatography under denaturing conditions in guanidine hydrochloride, dialyzed and recrystallized on SPR gold chips which were precoated with thiolated SCWP of *B. sphaericus* CCM 2177. As shown by SFM, a monomolecular protein lattice with square symmetry was formed. The resonance units indicating the amount of bound protein corresponded to  $4.3 \times 10^{-5}$  nM mm<sup>-2</sup>, which was in good accord with the theoretical value for a monolayer of  $3.9 \times 10^{-5}$  nM mm<sup>-2</sup>. Native monolayers or monolayers crosslinked with the bifunctional imidoester dimethylpimelinimidate (DMP) were finally exploited for binding of human IgG. The amount that could be bound by the native monolayer was  $2.9 \times 10^{-5}$  nM or 4.35 ng IgG mm<sup>-2</sup>, whereas in the case of the DMP-crosslinked monolayer  $2.8 \times 10^{-5}$  nM or 4.20 ng IgG mm<sup>-2</sup> could attach. These values corresponded to 65 and 67% of the theoretical saturation capacity of a planar surface for IgG (6.5 ng mm<sup>-2</sup>) with the Fab regions in the condensed state. As derived from these binding capacities, on average 2.7 and 2.6 IgG molecules were bound per morphological unit of the square S-layer lattice consisting of four identical subunits of the S-layer fusion protein.

For preparing biocompatible microparticles for the microsphere-based detoxification system (MDS) [78] to remove autoantibodies from sera from patients suffering from autoimmune disease, the S-layer fusion protein was recrystallized on SCWP-coated, 3- $\mu$ m cellulose-based microbeads. The MDS is an alternative approach to conventional immunoadsorption systems, in which the plasma does not perfuse on an adsorption column, but is recirculated into a filtrate compartment of a membrane module (Fig. 8.10). The addition of microbeads to the plasma circuit allows the rapid removal of the pathogenic substrates. In the case of microbeads that were covered with a native monolayer, the binding capacity was 1065  $\mu$ g human IgG mg<sup>-1</sup> S-layer fusion protein. For DMP-treated microbeads, a binding capacity of 870  $\mu$ g IgG mg<sup>-1</sup> S-layer fusion protein was determined. These values corresponded to 78 or 65% of the theoretical saturation capacity of a planar surface for IgG having the Fab regions in the condensed state. Bound IgG could be eluted with glycine-HCl buffer at a pH value of 2.2 and the microbeads were used for further IgG-binding experiments [72].

The major birch pollen allergen Bet v1 shares IgE epitopes with all tree pollen allergens from closely related species (e.g. alder hazel, hornbeam, beech). Because of high sequence identities among these allergens and well-studied cross-reactions with B cell epitopes, Bet v1 represents a model allergen [96]. The gene encoding

## Microspheres Based Detoxification-System

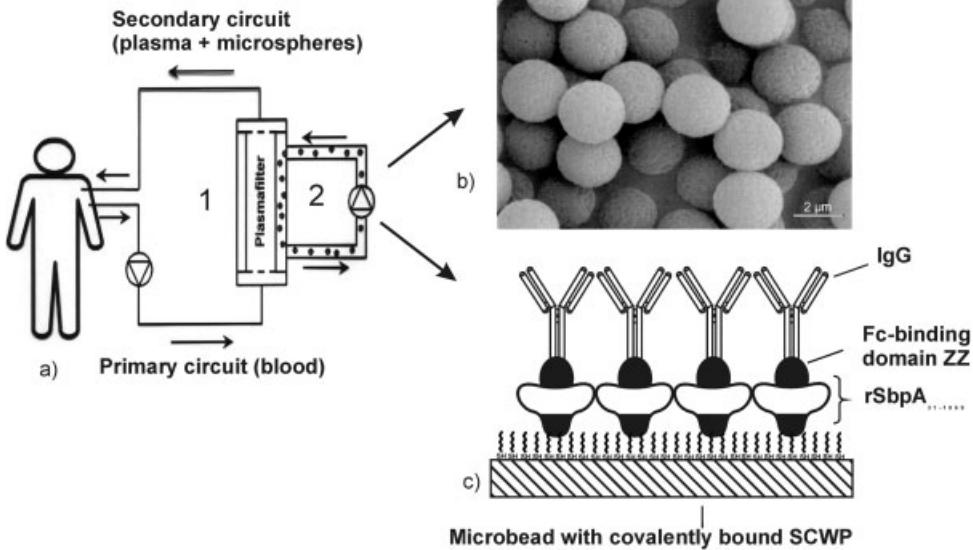


**Fig. 8.10.** (a) Schematic drawing demonstrating the working principle of the MDS. (b) Amine-modified cellulose microspheres. (c) Schematic drawing of microbeads covered with a monolayer consisting of rSbpA<sub>31-1068</sub>/ZZ. The S-layer

fusion protein was recrystallized on amine-modified cellulose microbeads to which thiolated SCWP had been covalently bound before. The fused ZZ domains could bind human IgG via the Fc part.

the chimeric S-layer proteins rSbsC<sub>31-920</sub>/Bet v1 and rSbpA<sub>31-1068</sub>/Bet v1 carrying Bet v1 at the C-terminal end were cloned and expressed in *E. coli*. Ultrathin sections of whole *E. coli* cells induced to express the gene encoding rSbsC<sub>31-920</sub>/Bet v1 revealed the presence of intracellular sheet-like or cylindrical structures [97], whereas rSbpA<sub>31-1068</sub>/Bet v1 accumulated in the form of inclusion bodies in the cytoplasm of the host cells [37]. The fusion proteins maintained the ability to self-assemble, as well as the functionality of the fused allergen to bind a Bet v1-specific monoclonal mouse antibody BIP1 (Fig. 8.11). The location and accessibility of the allergen moiety on the outer surface of the S-layer lattice were demonstrated by immunogold labeling of rSbsC<sub>31-920</sub>/Bet v1 or rSbpA<sub>31-1068</sub>/Bet v1 recrystallized on native peptidoglycan-containing sacculi of *G. stearothermophilus* ATCC 12980 or *B. sphaericus* CCM 2177 [37, 97]. Thereby, the specific interaction between the N-terminal part of the S-layer proteins and the corresponding SCWP was exploited. The aim for the production of these S-layer fusion proteins was to use them for the development of diagnostic test systems to determine the concentration of Bet v1-specific IgE in patients' whole blood, plasma or serum. For that purpose, rSbpA<sub>31-1068</sub>/Bet v1 recrystallized as a monolayer on SCWP-coated plastic foils

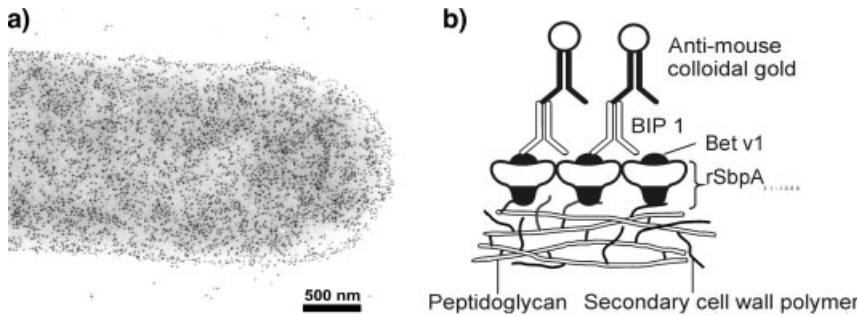


**Fig. 8.11.** (a) Electron micrograph of a negatively stained preparation demonstrating immunogold-labeling of rSbpA<sub>31-1068</sub>/Bet v1 recrystallized on peptidoglycan-containing

sacculi of *B. sphaericus* CCM 2177 using the Bet v1-specific monoclonal mouse antibody BIP1. (b) Schematic drawing of (a).

was used as reaction zone in dipstick-style solid-phase immunoassays for determination of Bet v1-specific IgE in serum samples of patients suffering from atopic allergy. In a recent study, the applicability of rSbsC<sub>31-920</sub>/Bet v1 as a novel approach to design vaccines with reduced allergenicity in combination with strong immunomodulating capacity for immunotherapy of type I allergy was demonstrated [98]. This fusion protein exhibited all relevant Bet v1-specific B and T cell epitopes, but was significantly less efficient in releasing histamine than free Bet v1. In cells of birch pollen-allergic individuals, the fusion protein was capable of modulating the allergen-specific T<sub>H</sub>2-dominated response into a more balanced T<sub>H</sub>1/T<sub>H</sub>0-like phenotype accompanied by enhanced production of interferon- $\gamma$  and interleukin-10 [98]. To conclude, rSbsC<sub>31-920</sub>/Bet v1 could find applications as carrier/adjuvants to design vaccines for specific immunotherapy of type 1 allergy with improved efficacy and safety.

Artificial lipid vesicles termed liposomes are widely used as delivery systems for enhancing the efficiency of various biologically active molecules [99]. S-layer-coated liposomes (S-liposomes) revealed an enhanced stability towards thermal and mechanical stress factors [24], and they represent simple model systems resembling features of virus envelopes. Thus, S-liposomes could find application in drug delivery or in gene therapy. In a recent study, the nucleotide sequence encoding enhanced green fluorescent protein (EGFP), a red-shifted green fluorescent protein (GFP)-derivative possessing a 30 times brighter fluorescence intensity at 488 nm than wild-type GFP [100], was fused to the 3'-end of the sequence encoding the C-terminally truncated form rSbpA<sub>31-1068</sub> [83]. The chimeric gene encoding rSbpA<sub>31-1068</sub>/EGFP was cloned and expressed in *E. coli* host cells. As confirmed by fluorescence microscopy, 1 h after induction of expression an intense EGFP fluorescence was detected in the cytoplasm of the host cells. Expression at 28 °C instead of 37 °C, as usual for *E. coli* expression strains, resulted in clearly increased fluorescence intensity, indicating that the folding process of the EGFP moiety was

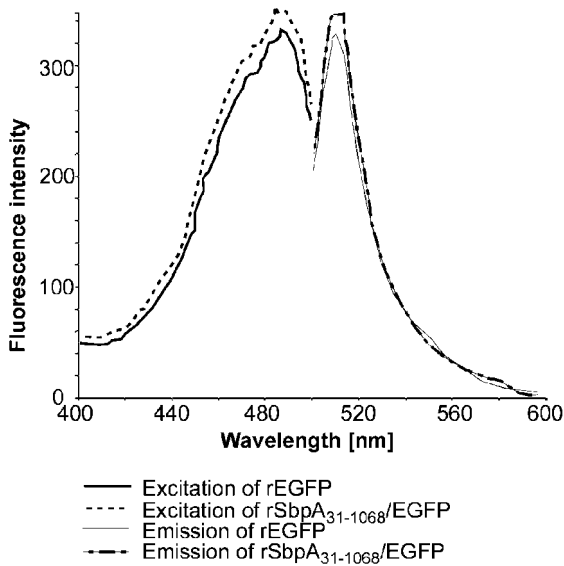


**Fig. 8.12.** Fluorescence excitation and emission spectra of rEGFP and of the fusion protein rSbpA<sub>31-1068</sub>/EGFP. Both proteins were applied in the same molar ratio and exhibited identical excitation peaks at 488 nm and emission peaks at 507 nm.

temperature sensitive. Electron microscopic investigation of ultrathin-sectioned preparations revealed that the S-layer fusion protein was located in inclusion bodies within the cytoplasm of the *E. coli* cells. To protect the EGFP portion against oxidation and to maintain the *in vitro* EGFP fluorescence capability, isolation of rSbpA<sub>31-1068</sub>/EGFP and purification by gel-permeation chromatography was performed in the presence of reducing agents. Comparison of excitation and emission spectra of rEGFP and rSbpA<sub>31-1068</sub>/EGFP indicated identical maxima at 488 and 507 nm, respectively (Fig. 8.12). Because of its intrinsic fluorescence, the fusion protein was recrystallized on positively charged liposomes and their uptake by eukaryotic cells was investigated by confocal laser scanning microscopy. The major part of the liposomes was internalized within 2 h of incubation and entered the HeLa cells by endocytosis [83]. In further studies, the uptake of liposomes coated with rSbpA<sub>31-1068</sub>/EGFP in combination with other S-layer fusion proteins, such as heterotetramers, by target cells and the functionality of transported drugs could be investigated simultaneously without any additional labeling.

Furthermore, this fusion protein was used for recrystallization on silicon wafers covered with polyelectrolytes, as well as for coating of hollow polyelectrolyte capsules. Fluorescence spectroscopy proved that the adsorption of rSbpA<sub>31-1068</sub>/EGFP on hollow capsules did not shift the fluorescence emission of the chromophore [25].



## 8.4 Spatial Control over S-Layer Reassembly

For many technical applications of S-layers, spatial control over reassembly is mandatory. For example, when S-layers are used as affinity matrix for the development of biochips or as templates in the fabrication of nanoelectronic devices, it is not necessary that the monolayer covers the entire area. Micromolding in capillaries is a well known soft-lithographical technique. In this technique, a poly(dimethylsiloxane) (PDMS) mold is first brought in conformal contact with a flat substrate, such as a silicon wafer. Subsequently, the S-layer protein solution is dropped onto the substrate in front of the channel openings of the attached mold and then the solution is sucked in so that the S-layer protein can recrystallize at all surfaces including the silicon. After removal of the mold, a patterned S-layer remains on the support. SFM is best suited to control the crystallinity of the S-layer monolayer and the border line to the blank areas. As micromolding in capillaries restricts the reassembly of the S-layer proteins to certain areas on a solid support, it offers the advantage that all preparation steps can be performed under ambient conditions. Proof-of-principle was shown for patterning the S-layer protein SbpA from *B. sphaericus* CCM 2177 on a silicon wafer with several different line-and-space ratios [101]. The S-layer protein showed perfect long-range order, and no visible leakage of the proteins into the tight interface between substrate and mold.

An alternative to micromolding in capillaries is patterning by conventional optical lithography using deep ultraviolet light (DUV) for exposure. In this approach, the S-layer protein was recrystallized on a silicon wafer covering the entire surface area. In the following step, the S-layer monolayer was dried in a stream of dry nitrogen prior to exposure in order to remove any water layer between the sample and the mask [102]. This is a critical step as denaturation of the S-layer protein and consequently loss of its structural integrity and functionality may occur. Then, a microlithographic mask was brought in conformal contact with the S-layer. The mask is usually made of a patterned chromium layer on quartz glass. Two different wavelengths of DUV were tested: argon fluoride excimer laser radiation (ArF; wavelength 193 nm) and krypton fluoride excimer laser radiation (KrF; wavelength 248 nm). SFM demonstrated that the S-layer protein was completely removed by ArF radiation with two pulses of  $100\text{--}200\text{ mJ cm}^{-2}$  each and retained its structural integrity in the unexposed regions. Section analysis revealed a height difference between exposed and unexposed areas of about 8 nm, clearly demonstrating that the S-layer was completely removed in the exposed areas. According to the well-known paradigm of optics stating that the resolution is determined by the wavelength of the irradiating light, the highest achievable resolution was in the range of 100 nm. In contrast, the S-layer was not ablated by KrF irradiation. Instead, investigation of the irradiated S-layer lattice showed that increasing the electron dose from 10 pulses of about  $100\text{ mJ cm}^{-2}$  to 10 pulses of about  $35\text{ mJ cm}^{-2}$  only led to carbonization, but not to ablation, of the protein lattice.

## 8.5

### S-Layers as Templates for the Formation of Regularly Arranged Nanoparticles

An important key to the fabrication of highly ordered functional arrays of nanoparticles is to provide suitable templates for spatially controlled particle deposition. The application of self-assembly systems for achieving perfect positional control at the molecular level appears feasible, both theoretically and experimentally, and offers striking advantages in the manufacturing process. S-layer proteins seem to be perfectly suited for this purpose as they have the intrinsic property to reassemble into two-dimensional arrays at various interfaces including silicon surfaces. Moreover, functional groups are repeated with the periodicity of the S-layer lattice at a distance of approximately 10 nm, thereby leading to regular arrays (superlattices) of bound foreign molecules and particles.

#### 8.5.1

##### Binding of Molecules and Nanoparticles to Functional Domains

Geometrically confined binding of molecules on S-layer lattices may be induced by noncovalent and covalent forces. The pattern of bound molecules frequently reflects the lattice symmetry, the size of the morphological units and the surface properties of the underlying S-layer. For example, polycationic ferritin (PCF) is a 12 nm large, topographical marker for labeling negatively charged groups for TEM analysis. In several studies, PCF was used to determine the net charge of the outer and inner S-layer surface. In the case of the strictly anaerobic, hyperthermophilic archaeon *Thermoproteus tenax*, PCF was bound to the outer S-layer surface in an absolutely regular manner and reflected the hexagonal symmetry of the underlying S-layer [103]. The distance between the PCF molecules was about 30 nm and corresponded exactly to the center-to-center spacing of the morphological units (Fig. 8.13). The hexagonal super-lattice generated by the bound PCF exhibited the same orientation as the unlabeled S-layer with one axis perpendicularly to the longitudinal axis of the cells. *Methanospirillum hungatei* is a methanogenic archaeon which possesses a hollow tubular sheath that surrounds chains of cells. The sheaths show oblique (p2) lattice symmetry and they are composed of individual hoops [104]. The sheaths could be densely labeled with PCF molecules, which fitted to the widths of the hoops and were thus bound in exact rows. A superlattice of PCF was also observed on the hexagonal S-layer of *Thermoanaerobacter thermohydrosulfuricus* L111-69 after converting the hydroxyl groups from the carbohydrate chain of this S-layer glycoprotein into carboxylic acid groups which was achieved by succinylation [105]. The size of the PCF molecules corresponded well to the center-to-center spacing of the morphological units of the hexagonal lattice of 14.2 nm. Ultrathin-sections of such modified S-layers revealed that due to the length of the carbohydrate chains, the PCF molecules formed even two superimposed layers. In contrast, covalent attachment of ferritin to the carbodiimide-activated carboxylic acid groups of the acidic amino acids led only to small patches of hexago-

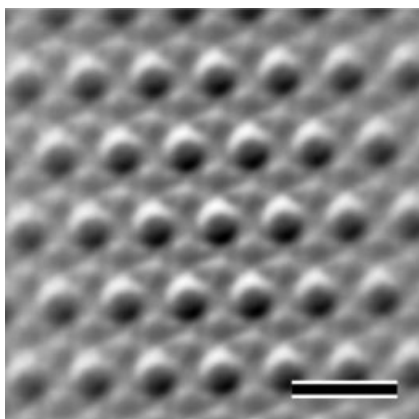


**Fig. 8.13.** TEM image of a freeze-dried preparation of PCF regularly bound to the hexagonally ordered S-layer of *Thermoproteus tenax*. The signal-to-noise ratio was enhanced by crosscorrelation averaging. Bar: 50 nm.

nally ordered ferritin molecules. On the glutaraldehyde-treated, crosslinked outer S-layer surface of the square lattice from *B. sphaericus* CCM 2177 with a lattice constant of 13.1 nm, PCF molecules were bound to the net negatively charged carboxylic acid groups of the acidic amino acids and clearly reflected the square symmetry of the underlying S-layer lattice.

In another approach the S-layer protein SbpA from *B. sphaericus* CCM 2177 was recrystallized on SiO<sub>2</sub>-coated grids [106]. These grids were mimicking the surface properties of silicon wafers, but allowed investigation of the preparations by TEM. In particular, when rendered hydrophilic by oxygen plasma treatment, the S-layer protein formed a monolayer with the outer surface exposed to the environment. It could be demonstrated that after crosslinking the free amine groups in the S-layer lattice with glutaraldehyde and activation of the free carboxylic acid groups with carbodiimide, a close-packed monolayer of 4 nm amino-functionalized CdSe nanoparticles was covalently bound to the protein lattice. However, the amine-functionalized nanoparticles did not resemble the lattice parameters of the S-layer very well as approximately  $1.6 \times 10^6$  carboxylic acid groups  $\mu\text{m}^{-2}$  offered too many equivalent binding sites. Furthermore, for studying the noncovalent binding of nanoparticles, anionic citrate-stabilized gold nanoparticles (5 nm diameter) were used [106, 107]. The negatively charged gold nanoparticles were bound at the inner surface of S-layer self-assembly products. The amount of bound gold nanoparticles per unit area depended on the size of the nanoparticles. Gold nanoparticles with a size of about 10 nm were only randomly bound, whereas 2 nm nanoparticles were densely packed on the S-layer surface. Nevertheless, 5 nm gold nanoparticles were regularly bound, resembling the underlying square S-layer lattice.

## 8.5.2

**In Situ Synthesis of Nanoparticles on S-Layers**

As an alternative to the regular binding of preformed nanoparticles, S-layers can be also used as periodic nanometric templates in the nucleation of inorganic nanoparticles. The very first experiments were performed almost two decades ago and used S-layer fragments deposited onto a solid substrate as a porous mask [108]. In this and the following works [109–111], various metals were evaporated onto the S-layer fragments forming nanoparticles arrays on the substrate due to the periodic arrangement of the pores in the protein lattice. After removal of the S-layer and excess material by ion milling, the regular pattern of metallic nanoparticles became available for further use. It was also demonstrated that S-layer proteins recrystallized on solid supports or S-layer self-assembly products which were deposited on such supports could be used to induce the formation of CdS particles [112] or gold nanoparticles [113]. Inorganic superlattices of CdS with either oblique or square lattice symmetries were fabricated by exposing the S-layer lattices to cadmium ion solutions followed by slow reduction with hydrogen sulfide. Precipitation of the inorganic phase was confined to the pores of the S-layers with the result that CdS superlattices with prescribed symmetries were obtained. In a similar procedure a square superlattice of uniform 4–5 nm gold particles with a 13.1 nm repeat distance was fabricated by exposing a square S-layer lattice which carried thiol groups that had been introduced by chemical modification before to a tetrachloroauric(III) acid solution [113]. TEM analysis showed that the gold nanoparticles were formed in the pore region during electron irradiation of an initially grainy gold coating covering the whole S-layer lattice. The shape of the gold particles resembled the morphology of the pore region of the square S-layer lattice. Electron diffraction patterns revealed that the gold nanoparticles were crystalline, but in the long-range order not crystallographically aligned. Furthermore, this technique was also used for the precipitation of metal nanoparticles from solutions, such as palladium from PdCl<sub>2</sub>, nickel from NiSO<sub>4</sub>, platinum from K<sub>2</sub>PtCl<sub>6</sub>, lead from Pb(NO<sub>3</sub>)<sub>2</sub> and ferrum from KFe [Fe(CN)<sub>6</sub>]. Wet chemistry was also applied for producing platinum nanoparticles on the S-layer of *Sporosarcina ureae* [114–117]. One morphological unit of the S-layer lattice of *S. ureae* revealed seven platinum cluster sites with a diameter of around 1.9 nm. These experiments clearly demonstrated that nanocrystal superlattices can be induced by S-layers as templates with a broad range of particle sizes (5–15 nm diameter), interparticle spacings (up to 30 nm) and lattice symmetries (oblique, square or hexagonal).

## 8.6

**Conclusions and Outlook**

Basic research on the structure, genetics, chemistry, assembly and function of S-layers has led to a broad spectrum of applications in nanobiotechnology and biomimetics. The remarkable intrinsic feature of S-layer proteins and the possibilities for

genetic modifications and combining S-layer lattices with other functional molecules in a spatial predictable way turns them into unique patterning elements for bottom-up strategies. Although, up to now the development of S-layer technologies has primarily focused on life science applications, an important field of future applications concerns nonlife sciences and bioinspired nanomaterials.

## Acknowledgments

This work was supported by the Austrian Science Fonds (FWF; project P17170-MOB) and by the Erwin Schrödinger-Society for Nanosciences.

## References

- 1 CLARK, J., SINGER, E. M., KORNS, D. R., SMITH, S. S., Design and analysis of nanoscale bioassemblies, *BioTechniques* **2004**, *36*, 992–1001.
- 2 NIEMEYER, C. M., MIRKIN, C. A. (Eds.), *Nanobiotechnology: Concepts, Applications and Perspectives*, Wiley-VCH, Weinheim, **2004**.
- 3 SEEMAN, N. C., BELCHER, A. M., Emulating biology: building nanostructures from the bottom up, *Proc. Natl Acad. Sci. USA* **2002**, *99*, 6451–6455.
- 4 SLEYTR, U. B., MESSNER, P., PUM, D., SÁRA, M., Crystalline bacterial cell surface layers (S-layers): from supramolecular cell structure to biomimetics and nanotechnology, *Angew. Chem. Int. Ed.* **1999**, *38*, 1034–1054.
- 5 SLEYTR, U. B., SÁRA, M., PUM, D., Crystalline bacterial cell surface layers (S-layers): a versatile self-assembly system, In *Supramolecular Polymerization*, CIFERRI, A. (Ed.), Marcel Dekker, New York, **2000**, pp. 177–213.
- 6 SLEYTR, U. B., SÁRA, M., PUM, D., SCHUSTER, B., MESSNER, P., SCHÄFFER, C., Self Assembly protein systems: microbial S-layers, In *Biopolymers 7*, STEINBÜCHEL, A., FAHNSTOCK, S. (Eds.), Wiley-VCH, Weinheim, **2003**, pp. 285–338.
- 7 SLEYTR, U. B., PUM, D., SÁRA, M., SCHUSTER, B., Molecular nanotechnology with 2-D protein crystals, In *Encyclopedia of Nanoscience and Nanotechnology 5*, NALWA, H. S. (Ed.), Academic Press, San Diego, CA, **2004**, pp. 693–702.
- 8 SLEYTR, U. B., PUM, D., SCHUSTER, B., SÁRA, M., Molecular nanotechnology and nanobiotechnology with two-dimensional protein crystals (S-layers), In *Nano-Surface Chemistry*, ROSOFF, M. (Ed.), Marcel Dekker, New York, **2001**, pp. 333–389.
- 9 SCHUSTER, B., GYÖRVARY, E., PUM, D., SLEYTR, U. B., Nanotechnology with S-layer proteins, In *Protein Nanotechnology: Protocols, Instrumentation and Applications*, VO-DINH, T. (Ed.), Humana Press, Totowa, NJ, **2005**, pp. 101–124.
- 10 KARRASCH, S., HEGERL, R., HOCH, J., BAUMEISTER, W., ENGEL, A., Atomic force microscopy produces faithful high-resolution images of protein surfaces in an aqueous environment, *Proc. Natl Acad. Sci. USA* **1994**, *91*, 836–838.
- 11 MÜLLER, D. J., BAUMEISTER, W., ENGEL, A., Conformational change of the hexagonally packed intermediate layer of *Deinococcus radiodurans* monitored by atomic force microscopy, *J. Bacteriol.* **1996**, *178*, 3025–3030.
- 12 SCHEURING, S., STAHLBERG, H., CHAMI, M., HOUSSIN, C., RIGAUD,

- J. L., ENGEL, A., Charting and unzipping the surface layer of *Corynebacterium glutamicum* with the atomic force microscope, *Mol. Microbiol.* **2002**, *44*, 675–684.
- 13 KÖNIG, H., Archaeobacterial cell envelopes, *Can. J. Microbiol.* **1988**, *34*, 395–406.
- 14 STETTER, K. O., Hyperthermophilic prokaryotes, *FEMS Microbiol. Rev.* **1996**, *18*, 149–158.
- 15 MESSNER, P., SLEYTR, U. B., Crystalline bacterial cell-surface layers, *Adv. Microbiol. Physiol.* **1992**, *33*, 213–275.
- 16 SLEYTR, U. B., BEVERIDGE, T. J., Bacterial S-layers, *Trends Microbiol.* **1999**, *7*, 253–260.
- 17 PUM, D., SLEYTR, U. B., Monomolecular reassembly of a crystalline bacterial cell surface layer (S-layer) on untreated and modified silicon surfaces, *Supramol. Sci.* **1995**, *2*, 193–197.
- 18 GYÖRVÁRY, E. S., STEIN, O., PUM, D., SLEYTR, U. B., Self-assembly and recrystallization of bacterial S-layer proteins at silicon supports imaged in real time by atomic force, *J. Microsc.* **2003**, *212*, 300–306.
- 19 PUM, D., WEINHANDL, M., HÖDL, C., SLEYTR, U. B., Large-scale recrystallization of the S-layer of *Bacillus coagulans* E38-66 at the air/water interface and on lipid films, *J. Bacteriol.* **1993**, *175*, 2762–2766.
- 20 PUM, D., SLEYTR, U. B., Large scale reconstitution of crystalline bacterial surface layer (S-layer) proteins at the air/water interface and on lipid films, *Thin Solid Films* **1994**, *244*, 882–886.
- 21 KÜPCÜ, S., SÁRA, M., SLEYTR, U. B., Liposomes coated with crystalline bacterial cell surface protein (S-layer) as immobilization structures for macromolecules, *Biochim. Biophys. Acta* **1995**, *1235*, 263–269.
- 22 KÜPCÜ, S., LOHNER, K., MADER, C., SLEYTR, U. B., Microcalorimetric study on the phase behaviour of S-layer coated liposomes, *Mol. Membr. Biol.* **1998**, *15*, 69–74.
- 23 MADER, C., KÜPCÜ, S., SÁRA, M., SLEYTR, U. B., Stabilizing effect of an S-layer on liposomes towards thermal or mechanical stress, *Biochim. Biophys. Acta* **1999**, *1418*, 106–116.
- 24 MADER, C., KÜPCÜ, S., SLEYTR, U. B., SÁRA, M., S-layer-coated liposomes as a versatile system for entrapping and binding target molecules, *Biochim. Biophys. Acta* **2000**, *1463*, 142–150.
- 25 TOCA-HERRERA, J. L., KRASTEV, R., BOSIO, V., KÜPCÜ, S., PUM, D., FERY, A., SÁRA, M., SLEYTR, U. B., Recrystallization of bacterial S-layers on flat polyelectrolyte surfaces and hollow polyelectrolytes capsules, *Small* **2005**, *1*, 339–348.
- 26 SÁRA, M., SLEYTR, U. B., S-Layer proteins, *J. Bacteriol.* **2000**, *182*, 859–868.
- 27 BOOT, H. J., KOLEN, C. P., POWELS, P. H., Identification, cloning, and nucleotide sequence of a silent S-layer protein gene of *Lactobacillus acidophilus* ATCC 4356 which has extensive similarity with the S-layer protein gene of this species, *J. Bacteriol.* **1995**, *177*, 7222–7230.
- 28 BRÖCKL, G., BEHR, M., FABRY, S., HENSEL, R., KAUEWITZ, H., BIENDL, E., KÖNIG, H., Analysis and nucleotide sequence of the genes encoding the surface-layer glycoproteins of the hyperthermophilic methanogens *Methanothermus fervidus* and *Methanothermus sociabilis*, *Eur. J. Biochem.* **1991**, *199*, 147–152.
- 29 MESSNER, P., SCHÄFFER, C., Surface layer glycoproteins of bacteria and archaea, In *Glycomicrobiology*, DOYLE, R. J. (Ed.), Kluwer, New York, **2000**, pp. 93–125.
- 30 SCHÄFFER, C., MESSNER, P., Glycobiology of surface layer proteins, *Biochimie* **2001**, *83*, 591–599.
- 31 NOVOTNY, R., PFÖSTL, A., MESSNER, P., SCHÄFFER, C., Genetic organization of chromosomal S-layer glycan biosynthesis loci of Bacillaceae, *Glycoconj. J.* **2004**, *20*, 435–447.
- 32 ENGELHARDT, H., PETERS, J., Structural research on surface layers: a focus on stability, surface layer homology domains, and surface layer-cell wall interactions, *J. Struct. Biol.* **1998**, *124*, 276–302.
- 33 BRECHTEL, E., BAHL, H., In *Thermo-*

- anaerobacterium thermosulfurigenes* EM1 S-layer homology domains do not attach to peptidoglycan, *J. Bacteriol.* **1999**, *181*, 5017–5023.
- 34 CAVA, F., DE PEDRO, M. A., SCHWARZ, H., HENNE, A., BERENQUER, J., Binding to pyruvylated compounds as an ancestral mechanism to anchor the outer envelope in primitive bacteria, *Mol. Microbiol.* **2004**, *52*, 677–690.
- 35 HUBER, C., ILK, N., RÜNZLER, D., EGELSEER, E. M., WEIGERT, S., SLEYTR, U. B., SÁRA, M., The three S-layer-like homology motifs of the S-layer protein SbpA of *Bacillus sphaericus* CCM 2177 are not sufficient for binding to the pyruvylated secondary cell wall polymer, *Mol. Microbiol.* **2005**, *55*, 197–205.
- 36 ILK, N., KOSMA, P., PUCHBERGER, M., EGELSEER, E. M., MAYER, H. F., SLEYTR, U. B., SÁRA, M., Structural and functional analyses of the secondary cell wall polymer of *Bacillus sphaericus* CCM 2177 that serves as an S-layer-specific anchor, *J. Bacteriol.* **1999**, *181*, 7643–7646.
- 37 ILK, N., VÖLLENKLE, C., EGELSEER, E. M., BREITWIESER, A., SLEYTR, U. B., SÁRA, M., Molecular characterization of the S-layer gene, *sbpA*, of *Bacillus sphaericus* CCM 2177 and production of a functional S-layer fusion protein with the ability to recrystallize in a defined orientation while presenting the fused allergen, *Appl. Environ. Microbiol.* **2002**, *68*, 3251–3260.
- 38 MADER, C., HUBER, C., MOLL, D., SLEYTR, U. B., SÁRA, M., Interaction of the crystalline bacterial cell surface layer protein SbsB and the secondary cell wall polymer of *Geobacillus stearothermophilus* PV72 assessed by real-time surface plasmon resonance biosensor technology, *J. Bacteriol.* **2004**, *186*, 1758–1768.
- 39 MESNAGE, S., TOSI-COUTURE, E., FOUET, A., Production and cell surface anchoring of functional fusions between the SLH motifs of the *Bacillus anthracis* S-layer proteins and the *Bacillus subtilis* levansucrase, *Mol. Microbiol.* **1999**, *31*, 927–936.
- 40 MESNAGE, S., FONTAINE, T., MIGNOT, T., DELEPIERRE, M., MOCK, M., FOUET, A., Bacterial SLH domain proteins are non-covalently anchored to the cell surface via a conserved mechanism involving wall polysaccharide pyruvylation, *EMBO J.* **2000**, *19*, 4473–4484.
- 41 RÜNZLER, D., HUBER, C., MOLL, D., KÖHLER, G., SÁRA, M., Biophysical characterization of the entire bacterial surface layer protein SbsB and its two distinct functional domains, *J. Biol. Chem.* **2004**, *279*, 5207–5215.
- 42 EGELSEER, E. M., LEITNER, K., JAROSCH, M., HOTZY, C., ZAYNI, S., SLEYTR, U. B., SÁRA, M., The S-layer proteins of two *Bacillus stearothermophilus* wild-type strains are bound via their N-terminal region to a secondary cell wall polymer of identical chemical composition, *J. Bacteriol.* **1998**, *180*, 1488–1495.
- 43 JAROSCH, M., EGELSEER, E. M., MATTANOVICH, D., SLEYTR, U. B., SÁRA, M., S-layer gene *sbsC* of *Bacillus stearothermophilus* ATCC 12980: molecular characterization and heterologous expression in *Escherichia coli*, *Microbiology* **2000**, *146*, 273–281.
- 44 JAROSCH, M., EGELSEER, E. M., HUBER, C., MOLL, D., MATTANOVICH, D., SLEYTR, U. B., SÁRA, M., Analysis of the structure-function relationship of the S-layer protein SbsC of *Bacillus stearothermophilus* ATCC 12980 by producing truncated forms, *Microbiology* **2001**, *147*, 1353–1363.
- 45 SCHÄFFER, C., WUGEDITSCH, T., KÄHLIG, H., SCHEBERL, A., ZAYNI, S., MESSNER, P., The surface layer (S-layer) glycoprotein of *Geobacillus stearothermophilus* NRS 2004/3a. Analysis of its glycosylation, *J. Biol. Chem.* **2002**, *277*, 6230–6239.
- 46 SCHÄFFER, C., KÄHLIG, H., CHRISTIAN, R., SCHULZ, G., ZAYNI, S., MESSNER, P., The diacetamidodideoxyuronic-acid-containing glycan chain of *Bacillus stearothermophilus* NRS 2004/3a represents the secondary cell-wall polymer of wild-type *B. stearothermophilus* strains, *Microbiology* **1999**, *145*, 1575–1583.

- 47 WEIS, W. I., Cell-surface carbohydrate recognition by animal and viral lectins, *Curr. Opin. Struct. Biol.* **1997**, *7*, 624–630.
- 48 SMIT, E., OLING, F., DEMEL, R., MARTINEZ, B., POWWELS, P. H., The S-layer protein of *Lactobacillus acidophilus* ATCC 4356: identification and characterisation of domains responsible for S-protein assembly and cell wall binding, *J. Mol. Biol.* **2001**, *305*, 245–257.
- 49 MASUDA, K., KAWATA, T., Reassembly of a regularly arranged protein in the cell wall of *Lactobacillus buchneri* and its reattachment to cell walls: chemical modification studies, *Microbiol. Immunol.* **1985**, *29*, 927–938.
- 50 SÁRA, M., Conserved anchoring mechanisms between crystalline cell surface S-layer proteins and secondary cell wall polymers in Gram-positive bacteria?, *Trends Microbiol.* **2001**, *9*, 47–49.
- 51 AWRAM, P., SMIT, J., Identification of lipopolysaccharide O-antigen synthesis genes required for attachment of the S-layer of *Caulobacter crescentus*, *Microbiology* **2001**, *147*, 1451–1460.
- 52 BINGLE, W. H., NOMELLINI, J. F., SMIT, J., Linker mutagenesis of the *Caulobacter crescentus* S-layer protein: toward a definition of an N-terminal anchoring region and a C-terminal secretion signal and the potential for heterologous protein secretion, *J. Bacteriol.* **1997**, *179*, 601–611.
- 53 DWORKIN, J., BLASER, M. J., Molecular mechanisms of *Campylobacter fetus* surface layer protein expression, *Mol. Microbiol.* **1997**, *26*, 433–440.
- 54 BINGLE, W. H., NOMELLINI, J. F., SMIT, J., Cell-surface display of a *Pseudomonas aeruginosa* strain K pilin peptide within the paracrystalline S-layer of *Caulobacter crescentus*, *Mol. Microbiol.* **1997**, *26*, 277–288.
- 55 NOONAN, B., TRUST, T. J., The leucine zipper of *Aeromonas salmonicida* AbcA is required for the transcriptional activation of the P2 promoter of the surface-layer structural gene, vapA, in *Escherichia coli*, *Mol. Microbiol.* **1995**, *17*, 379–386.
- 56 NOONAN, B., TRUST, T. J., Molecular analysis of an A-protein secretion mutant of *Aeromonas salmonicida* reveals a surface layer-specific protein secretion pathway, *J. Mol. Biol.* **1995**, *248*, 316–327.
- 57 CASTAN, P., DE PEDRO, M. A., RISCO, C., VALLES, C., FERNANDEZ, L. A., SCHWARZ, H., BERENQUER, J., Multiple regulatory mechanisms act on the 5' untranslated region of the S-layer gene from *Thermus thermophilus* HB8, *J. Bacteriol.* **2001**, *183*, 1491–1494.
- 58 JAKAVA-VILJANEN, M., AVALL-JAASKELAINEN, S., MESSNER, P., SLEYTR, U. B., PALVA, A., Isolation of three new surface layer protein genes (*slp*) from *Lactobacillus brevis* ATCC 14869 and characterization of the change in their expression under aerated and anaerobic conditions, *J. Bacteriol.* **2002**, *184*, 6786–6795.
- 59 SÁRA, M., PUM, D., KÜPCÜ, S., MESSNER, P., SLEYTR, U. B., Isolation of two physiologically induced variant strains of *Bacillus stearothermophilus* NRS 2004/3a and characterization of their S-layer lattices, *J. Bacteriol.* **1994**, *176*, 848–860.
- 60 SÁRA, M., KUEN, B., MAYER, H. F., MANDL, F., SCHUSTER, K. C., SLEYTR, U. B., Dynamics in oxygen-induced changes in S-layer protein synthesis from *Bacillus stearothermophilus* PV72 and the S-layer-deficient variant T5 in continuous culture and studies of the cell wall composition, *J. Bacteriol.* **1996**, *178*, 2108–2117.
- 61 DWORKIN, J., TUMMURU, M. K., BLASER, M. J., A lipopolysaccharide-binding domain of the *Campylobacter fetus* S-layer protein resides within the conserved N terminus of a family of silent and divergent homologs, *J. Bacteriol.* **1995**, *177*, 1734–1741.
- 62 EGELSEER, E. M., DANHORN, T., PLESCHBERGER, M., HOTZY, C., SLEYTR, U. B., SÁRA, M., Characterization of an S-layer glycoprotein produced in the course of S-layer variation of *Bacillus stearothermophilus* ATCC 12980 and sequencing and cloning of the *sbsD* gene encoding the protein moiety, *Arch. Microbiol.* **2001**, *177*, 70–80.



- 63 GROGONO-THOMAS, R., BLASER, M. J., AHMADI, M., NEWELL, D. G., Role of S-layer protein antigenic diversity in the immune responses of sheep experimentally challenged with *Campylobacter fetus* subsp. *fetus*, *Infect. Immun.* **2003**, *71*, 147–154.
- 64 SCHOLZ, H. C., RIEDMANN, E., WITTE, A., LUBITZ, W., KUEN, B., S-layer variation in *Bacillus stearothermophilus* PV72 is based on DNA rearrangements between the chromosome and the naturally occurring megaplasmids, *J. Bacteriol.* **2001**, *183*, 1672–1679.
- 65 GUSTAFSON, C. E., CHU, S., TRUST, T. J., Mutagenesis of the paracrystalline surface protein array of *Aeromonas salmonicida* by endogenous insertion elements, *J. Mol. Biol.* **1994**, *237*, 452–463.
- 66 EGELSEER, E. M., IDRIS, R., JAROSCH, M., DANHORN, T., SLEYTR, U. B., SÁRA, M., ISBst12, a novel type of insertion-sequence element causing loss of S-layer-gene expression in *Bacillus stearothermophilus* ATCC 12980, *Microbiology* **2000**, *146*, 2175–2183.
- 67 SCHOLZ, H., HUMMEL, S., WITTE, A., LUBITZ, W., KUEN, B., The transposable element IS4712 prevents S-layer gene (*sbsA*) expression in *Bacillus stearothermophilus* and also affects the synthesis of altered surface layer proteins, *Arch. Microbiol.* **2000**, *174*, 97–103.
- 68 RIES, W., HOTZY, C., SCHOCHER, I., SLEYTR, U. B., SÁRA, M., Evidence that the N-terminal part of the S-layer protein from *Bacillus stearothermophilus* PV72/p2 recognizes a secondary cell wall polymer, *J. Bacteriol.* **1997**, *179*, 3892–3898.
- 69 SÁRA, M., DEKITSCH, C., MAYER, H. F., EGELSEER, E. M., and SLEYTR, U. B., Influence of the secondary cell wall polymer on the reassembly, recrystallization and stability properties of the S-layer protein from *Bacillus stearothermophilus* PV72/p2., *J. Bacteriol.* **1998**, *180*, 4146–4153.
- 70 PLESCHBERGER, M., NEUBAUER, A., EGELSEER, E. M., WEIGERT, S., LINDNER, B., SLEYTR, U. B., MUYLDERMANS, S., SÁRA, M., Generation of a functional monomolecular protein lattice consisting of an S-layer fusion protein comprising the variable domain of a camel heavy chain antibody, *Bioconjug. Chem.* **2003**, *14*, 440–448.
- 71 PLESCHBERGER, M., SAERENS, D., WEIGERT, S., SLEYTR, U. B., MUYLDERMANS, S., SÁRA, M., EGELSEER, E. M., An S-layer heavy chain camel antibody fusion protein for generation of a nanopatterned sensing layer to detect the prostate-specific antigen by surface plasmon resonance technology, *Bioconjug. Chem.* **2004**, *15*, 664–671.
- 72 VÖLLENKLE, C., WEIGERT, S., ILK, N., EGELSEER, E. M., WEBER, V., LOTH, F., FALKENHAGEN, D., SLEYTR, U. B., SÁRA, M., Construction of a functional S-layer fusion protein comprising an immunoglobulin G-binding domain for development of specific adsorbents for extracorporeal blood purification, *Appl. Environ. Microbiol.* **2004**, *70*, 1514–1521.
- 73 HUBER, C., LIU, J., EGELSEER, E. M., MOLL, D., KNOLL, W., SLEYTR, U. B., SÁRA, M., Heterotetramers formed by an S-layer-streptavidin fusion protein and core-streptavidin as nanoarrayed template for biochip development, *SMALL* (accepted).
- 74 SÁRA, M., PUM, D., SCHUSTER, B., SLEYTR, U. B., S-layers as patterning element for nanobiotechnological applications, *J. Nanosci. Nanotechnol.* **2005**, in press.
- 75 HOWORKA, S., SÁRA, M., WANG, Y., KUEN, B., SLEYTR, U. B., LUBITZ, W., BAYLEY, H., Surface-accessible residues in the monomeric and assembled forms of a bacterial surface layer protein, *J. Biol. Chem.* **2000**, *275*, 37876–37886.
- 76 WEINER, C., SÁRA, M., SLEYTR, U. B., Novel protein A affinity matrix prepared from two-dimensional protein crystals, *Biotechnol. Bioeng.* **1994**, *43*, 321–330.
- 77 WEINER, C., SÁRA, M., DASGUPTA, G., SLEYTR, U. B., Affinity cross-flow filtration: purification of IgG with a

- novel protein A affinity matrix prepared from two-dimensional protein crystals, *Biotechnol. Bioeng.* **1994**, *44*, 55–65.
- 78 WEBER, V., WEIGERT, S., SÁRA, M., SLEYTR, U. B., FALKENHAGEN, D., Development of affinity microparticles for extracorporeal blood purification based on crystalline bacterial cell surface proteins, *Ther. Apher.* **2001**, *5*, 433–438.
- 79 BREITWIESER, A., KÜPCÜ, S., HOWORKA, S., WEIGERT, S., LANGER, C., HOFFMANN-SOMMERGRUBER, K., SCHEINER, O., SLEYTR, U. B., SÁRA, M., 2-D protein crystals as an immobilization matrix for producing reaction zones in dipstick-style immunoassays, *Biotechniques* **1996**, *21*, 918–925.
- 80 BREITWIESER, A., MADER, C., SCHOCHER, I., HOFFMANN-SOMMERGRUBER, K., SCHEINER, O., ABERER, W., SLEYTR, U. B., SÁRA, M., A novel dipstick developed for rapid Bet v 1-specific IgE detection: recombinant allergen immobilized via a monoclonal antibody to crystalline bacterial cell-surface layers, *Allergy* **1998**, *53*, 786–793.
- 81 VÖLKELE, D., ZIMMERMANN, K., BREITWIESER, A., SCHEIFLINGER, F., SCHWARZ, H. P., SÁRA, M., SLEYTR, U. B., DORNER, F., Immunochemical detection of prion protein on dipsticks prepared with crystalline bacterial cell-surface layers, *Transfusion* **2003**, *43*, 1677–1682.
- 82 SÁRA, M., SLEYTR, U. B., Crystalline bacterial cell surface layers (S-layers): from cell structure to biomimetics, *Progr. Biophys. Mol. Biol.* **1996**, *65*, 83–111.
- 83 ILK, N., KÜPCÜ, S., MONCAYO, G., KLIMT, S., ECKER, R. C., HOFER-WARBINEK, R., EGELSEER, E. M., SLEYTR, U. B., SÁRA, M., A functional chimeric S-layer-enhanced green fluorescent protein to follow the uptake of S-layer-coated liposomes into eukaryotic cells, *Biochem. J.* **2004**, *379*, 441–448.
- 84 KUEN, B., KOCH, A., ASENBAUER, E., SÁRA, M., LUBITZ, W., Molecular characterization of the *Bacillus stearothermophilus* PV72 S-layer gene *sbsB* induced by oxidative stress, *J. Bacteriol.* **1997**, *179*, 1664–1670.
- 85 MOLL, D., HUBER, C., SCHLEGEL, B., PUM, D., SLEYTR, U. B., SÁRA, M., S-layer-streptavidin fusion proteins as template for nanopatterned molecular arrays, *Proc. Natl Acad. Sci. USA* **2002**, *99*, 14646–14651.
- 86 PAVKOV, T., OBERER, M., EGELSEER, E. M., SÁRA, M., SLEYTR, U. B., KELLER, W., Crystallization and preliminary structure determination of the C-terminal truncated domain of the S-layer protein SbsC, *Acta Crystallogr. D* **2003**, *59*, 1466–1468.
- 87 WILCHEK, M., BAYER, E. A., Foreword and introduction to the book (strept)avidin–biotin system, *Biomol. Eng.* **1999**, *16*, 1–4.
- 88 KURZBAN, G. P., GITLIN, G., BAYER, E. A., WILCHEK, M., HOROWITZ, P. M., Biotin binding changes the conformation and decreases tryptophan accessibility of streptavidin, *J. Protein Chem.* **1990**, *9*, 673–82.
- 89 LIEBERMANN, T., KNOLL, W., Surface-plasmon field-enhanced fluorescence spectroscopy, *Colloids Surfaces A* **2000**, *171*, 115–130.
- 90 LIEBERMANN, T., KNOLL, W., SLUKA, P., HERRMANN, R., Complement hybridization from solution to surface-attached probe-oligonucleotides observed by surface-plasmon-field fluorescence spectroscopy, *Colloids Surfaces A* **2000**, *169*, 337–350.
- 91 MUYLDERMANS, S., Single domain camel antibodies: current status, *Mol. Biotechnol.* **2001**, *74*, 277–302.
- 92 NGUYEN, V. K., DESMYTER, A., MUYLDERMANS, S., Functional heavy-chain antibodies in *Camelidae*, *Adv. Immunol.* **2001**, *79*, 261–269.
- 93 DESMYTER, A., TRANSUE, T. R., GHAHROUDI, M. A., THI, M., POORTMANS, F., HAMERS, R., MUYLDERMANS, S., WYNES, L., Crystal structure of a camel single-domain VH antibody fragment in complex with lysozyme, *Nat. Struct. Biol.* **1996**, *3*, 803–811.
- 94 ELIASSON, M., OLSSON, A.,

- PALMCRANTZ, E., WIBERG, K., INGANAS, M., LINDBERG, M., UHLEN, M., Chimeric IgG-binding receptors engineered from *staphylococcal* protein A and *streptococcal* protein G, *J. Biol. Chem.* **1988**, *263*, 4323–4327.
- 95 NILSSON, B., MOKS, T., JANSSON, B., ABRAHAMSEN, L., ELMBLAD, A., HOLMGREN, E., HEINRICHSON, C., JONES, T. A., UHLEN, M., A synthetic IgG-binding domain based on staphylococcal protein A, *Protein Eng.* **1987**, *1*, 107–113.
- 96 BREITENEDER, H., PETTENBURGER, K., BITO, A., VALENTA, R., KRAFT, D., RUMPOLD, H., SCHEINER, O., BREITENBACH, M., The gene coding for the major birch pollen allergen Betv1, is highly homologous to a pea disease resistance response gene, *EMBO J.* **1989**, *8*, 1935–1938.
- 97 BREITWIESER, A., EGELSEER, E. M., ILK, N., MOLL, D., HOTZY, C., BOHLE, B., EBNER, C., SLEYTR, U. B., SÁRA, M., A recombinant bacterial cell surface (S-layer)-major birch pollen allergen-fusion protein (rSbsC/Bet v1) maintains the ability to self-assemble into regularly structured monomolecular lattices and the functionality of the allergen, *Protein Eng.* **2002**, *15*, 243–249.
- 98 BOHLE, B., BREITWIESER, A., ZWÖLFER, B., JAHN-SCHMID, B., SÁRA, M., SLEYTR, U. B., EBNER, C., A novel approach to specific allergy treatment: the recombinant fusion protein of a bacterial cell surface (S-layer) protein and the major birch pollen allergen Bet v 1 (rSbsC-Bet v 1) combines reduced allergenicity with immunomodulating capacity, *J. Immunol.* **2004**, *172*, 6642–6648.
- 99 LASIC, D. D., PAPAHDJOPOULOS, D., Liposomes revisited, *Science* **1995**, *267*, 1275–1276.
- 100 CORMACK, B. P., VALDIVIA, R. H., FALKOW, S., FACS-optimized mutants of the green fluorescent protein (GFP), *Gene* **1996**, *173*, 33–38.
- 101 GYÖRVARY, E. S., O'RIORDAN, A., QUINN, A., REDMOND, G., PUM, D., SLEYTR, U. B., Biomimetic nanostructure fabrication: non-lithographic lateral patterning and self-assembly of functional bacterial S-layers at silicon supports, *Nano Lett.* **2003**, *3*, 315–319.
- 102 PUM, D., STANGL, G., SPONER, C., FALLMANN, W., SLEYTR, U. B., Deep UV patterning of monolayers of crystalline S-layer protein on silicon surfaces, *Colloids Surfaces B* **1997**, *8*, 157–162.
- 103 MESSNER, P., PUM, D., SÁRA, M., STETTER, K. O., SLEYTR, U. B., Ultrastructure of the cell envelope of the archaeobacteria *Thermoproteus tenax* and *Thermoproteus neutrophilus*, *J. Bacteriol.* **1986**, *166*, 1046–1054.
- 104 STEWART, M., BEVERIDGE, T. J., SPROTT, G. D., Crystalline order to high resolution in the sheath of *Methanospirillum hungatei*: a cross-beta structure, *Mol. Biol.* **1985**, *183*, 509–515.
- 105 SÁRA, M., KÜPCÜ, S., SLEYTR, U. B., Localization of the carbohydrate residue of the S-layer glycoprotein from *Clostridium thermohydro-sulfuricum* L111-69, *Arch. Microbiol.* **1989**, *151*, 416–420.
- 106 GYÖRVARY, E. S., SCHRÖDTER, A., TALAPIN, D. V., WELLER, H., PUM, D., SLEYTR, U. B., Formation of nanoparticle arrays on S-layer protein lattices, *J. Nanosci. Nanotechnol.* **2004**, *4*, 115–120.
- 107 HALL, S. R., SHENTON, W., ENGELHARDT, H., MANN, S., Site-specific organization of gold nanoparticles by biomolecular templating, *Chem. Phys. Chem.* **2001**, *3*, 184–186.
- 108 DOUGLAS, K., CLARK, N. A., ROTHSCHILD, K. J., Nanometer molecular lithography, *Appl. Phys. Lett.* **1986**, *48*, 676–678.
- 109 DOUGLAS, K., DEVAUD, G., CLARK, N. A., Transfer of biological derived nanometer-scale patterns to smooth substrates, *Science* **1992**, *257*, 642–644.
- 110 WINNINGHAM, T. A., GILLIS, H. P., CHOUTOV, D. A., MARTIN, K. P., MOORE, J. T., DOUGLAS, K., Formation of ordered nanocluster arrays by self-assembly on nanopatterned Si(100) surfaces, *Surface Sci.* **1998**, *406*, 221–228.

- 111 MALKINSKI, L., CAMLEY, R. E., CELINSKI, Z., WINNINGHAM, T. A., WHIPPLE, S. G., DOUGLAS, K., Hexagonal lattice of 10 nm magnetic dots, *J. Appl. Phys.* **2003**, *93*, 7325–7327.
- 112 SHENTON, W., PUM, D., SLEYTR, U. B., MANN, S., Synthesis of cadmium sulphide superlattices using self-assembled bacterial S-layers, *Nature* **1997**, *389*, 585–587.
- 113 DIELUWEIT, S., PUM, D., SLEYTR, U. B., Formation of a gold superlattice on an S-layer with square lattice symmetry, *Supramol. Sci.* **1998**, *5*, 15–19.
- 114 POMPE, W., MERTIG, M., KIRSCH, R., WAHL, R., CIACHI, L. C., RICHTER, J., SEIDEL, R., VINZELBERG, H., Formation of metallic nanostructures on biomolecular templates, *Z. Metallkunde* **1999**, *90*, 1085–1091.
- 115 MERTIG, M., KIRSCH, R., POMPE, W., ENGELHARDT, H., Fabrication of highly oriented nanocluster arrays by biomolecular templating, *Eur. Phys. J. D* **1999**, *9*, 45–48.
- 116 WAHL, R., MERTIG, M., RAFF, J., SELENSKA-POBELL, S., POMPE, W., Electron-beam induced formation of highly ordered palladium and platinum nanoparticle arrays on the S-layer of *Bacillus sphaericus* NCTC 9602, *Adv. Mater. Sci. Technol.* **2001**, *13*, 736–741.
- 117 MERTIG, M., WAHL, R., LEHMANN, M., SIMON, P., POMPE, W., Formation and manipulation of regular metallic nanoparticle arrays on bacterial surface layers: an advanced TEM study, *Eur. Phys. J. D* **2001**, *16*, 317–320.

### III

## Pharmaceutically Important Nanomaterials



## 9

**Methods of Preparation of Drug Nanoparticles**

*Jonghwi Lee, Gio-Bin Lim and Hesson Chung*

## 9.1

**Introduction**

The recent rapid progress in techniques supporting drug discovery such as genomics, proteomics, high-throughput methods, etc., has exponentially increased the number of newly introduced potential drug candidates [1]. A new drug candidate undergoes a series of time-consuming investigations. Currently, only about five to 10 drugs among 3000–10 000 candidates go into phase I clinical studies and only one of them finally reaches the market [1]. Among the numerous research steps to launch a new drug, the formulation study is becoming one of the most critical bottlenecks, mainly because of the relatively slow advance of formulation-related technologies. What is worse is that the physical and chemical properties of drugs are being diversified, and so more intelligent and functional drug delivery systems are required. As a consequence, the development of novel drug delivery systems and formulation techniques are critical issues in the pharmaceutical research.

Nanoformulation, i.e. formulation using nanoparticles, is at the center of the recent pharmaceutical research and development. The industrial application of nanoparticles of active pharmaceutical ingredients (API) ranges from traditional simple emulsion [2–5] to solid dispersion systems developed a few years ago mainly with the help of the rapid progress of wet comminution techniques [6–19].

Various benefits have been achieved by using nanoparticles [6–22]. First of all, distinct increases in dissolution rate, bioavailability and rate of absorption have helped the formulation of relatively insoluble API (Figs. 9.1 and 9.2). It is known that, in general, as the size of API particles decreases, their processability decreases and bioavailability increases (Fig. 9.1). The burden of processing difficulty can be released by using advanced nanotechnologies. The increase of surface area as a function of particle size is schematically illustrated in Fig. 9.2, which triggers the increase of dissolution rate and bioavailability. Furthermore, the increases have made the early phase of drug discovery more effective. They also enable higher dose loading into a smaller dosage volume. Nanoparticles can be incorporated into various drug delivery systems for more effective and intelligent delivery [23,

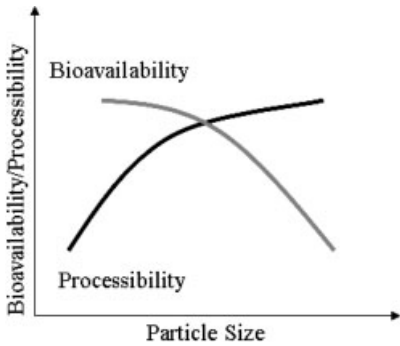


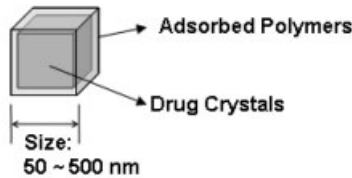
Fig. 9.1. Dependence of bioavailability and processability of a formulation on the particle size of the drug.

24]. Reformulation using nanoparticles often removes harsh excipients, extreme pH and organic solvents currently used. Longer retention in blood and tumors, improvement in the stability of drugs, taste masking, and reduction in fed/fasted variability are often also obtained [24].

As particle size decreases, the extra Gibbs free energy resulting mainly from the surface energy of nanoparticles significantly increases [25]. Therefore, how to deal with the extra Gibbs free energy is the major issue in the preparation and subsequent treatment of nanoparticles. If a nanoparticulate system is considered to be a system having  $N$  smaller noninteracting systems (ensembles), the total Gibbs equation will be:

$$E_t = TS_t - pV_t + \sum \mu_i N_{it} + EN \tag{1}$$

Structure of Drug Nanocrystals



Effect of Size Reduction

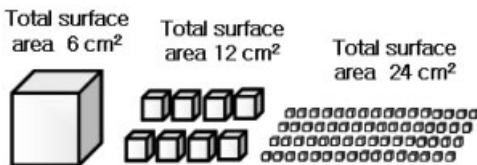


Fig. 9.2. Schematic illustration of the structure of drug nanocrystals, and the relationship between particle size and surface area.



where  $t$  indicates total,  $\mu_i$  is the chemical potential of component  $i$ ,  $N_i$  is the number of molecules of component  $i$  and  $E$  is the “subdivision potential” [25]. The fourth term on the right-hand side is an extra one for the nanosize effects (e.g. surface tension), which increases as API particle size decreases.

Nanoparticle preparation techniques under active development can be categorized into two major routes – kinetic and thermodynamic approaches. The kinetic approach relies on external energies to compensate for the elevated Gibbs free energy of nanoparticles, such as high energy flow, sonication and electrostatic fields. The thermodynamic approach makes use of interfacial energy. For example, the stabilization ability of polymers and surfactants or supercritical fluids (SCFs) can be successfully employed for reducing the fourth term. The stabilizers can cover the surface of nanocrystals, and pay the thermodynamic penalty of the fresh interface between drug and liquid medium. Proteins and lipids can be stable in nanoparticulate forms in water if their conformation makes the fourth term negligible.

In the kinetic approach, the utilization of various energies has been tried to achieve the maximum efficiency. Without the external energies, the resulting particles cannot maintain their stability and so a poststabilization mechanism which remains active after processing is often employed. As a result, the actual processing of nanoparticles often combines both approaches. The combination usually offers better efficiency.

## 9.2

### Structures of Drug Nanoparticles

Pharmaceutical nanoparticles can take various physical forms depending on their final delivery routes and API properties. They can be classified on the basis of their physical states and internal structures. Solid or liquid monolithic nanoparticles are the simplest cases. They require a proper medium to minimize their interfacial energy. Emulsions and lipids have their unique structures to adjust themselves to the surrounding environments. A solid dispersion has a different structure from emulsions and lipids, but the structure is determined by the same thermodynamic origin. By controlling surface/interface energy and kinetic obstacles, various internal structures of nanoparticles from a simple core/shell to more complicated structures can be engineered.

## 9.3

### Thermodynamic Approaches

The interfacial energy related to the preparation of nanoparticles can be minimized by using proper materials in proper regions. Thermodynamic approaches mainly rely on the chemical identity and self-assembly behavior of materials. The micelle structures of traditional surfactants provide good examples, although their pharma-

ceutical applications are often limited due to their poor biocompatibility. Water soluble polymers can form nanoparticles in water by adding a crosslinking agent such as chitosan nanoparticles crosslinked by tripolyphosphate [26, 27], or by simple emulsion or dispersion preparation methods using oil and water mixtures [2–5]. Protein nanoparticles are also available by crosslinking or desolvation [28]. Precipitation by salting-out or solvent evaporation, or other phase separation phenomena, has been intensively investigated to conveniently prepare nanoparticles [29]. Surface active agents such as surfactants or block copolymers can adapt unique structures at the interface, resulting in a reduction in interfacial energy and successful preparation of nanoparticles [30–34]. Lipid systems, which have been intensively examined and widely adapted in the pharmaceutical area, provide typical examples of the thermodynamic approaches. Before moving on to a deeper discussion on lipid systems, it might be helpful to mention that the terminology “thermodynamic approaches” does not necessarily imply that the methods use only thermodynamically stable states.

### 9.3.1

#### **Lipid-based Pharmaceutical Nanoparticles**

Lipid-based drug delivery systems have been used to improve pharmacokinetic profiles, to reduce side-effects and to improve patient compliance. These lipid-based drug delivery systems can utilize various macro- and microstructures that lipids form in a variety of settings. Most popular lipid-based pharmaceutical particles include liposomes and oil-in-water-type lipid emulsions. Parenteral lipid emulsion has been around for more than 40 years to provide nutrition to patients who cannot consume food orally. Parenteral emulsion consists of vegetable oil particles dispersed in an aqueous environment by the use of the natural lipid emulsifier, lecithins. While the oil and lipid themselves or the emulsions as a whole are used to improve the health of the patients, they are used as tools to carry API to the destinations in the body when they are used as drug carriers. The drugs marketed in the form of lipid emulsion-based drug delivery systems include diazepam (Pharmacia) and propofol (Baxter and Astra Zeneca).

It took longer time for liposomes to appear on the market as drug carriers due to the instabilities of the formulation. Commercialization of the liposomal doxorubicin formulation Doxil<sup>®</sup> has been realized by designing a very stable liposome both *in vitro* and *in vivo* [35, 36]. The success has boosted the morale of the scientists working in the field, and has initiated a flurry of research and discovery of novel and innovated lipid-based pharmaceutical particles. Nowadays, new lipid-based drug delivery systems based on original designs appear frequently in the literature. Even though not all of them can be successful drug carriers, they can serve as stepping stones to understand lipid phase behavior and to improve current formulations. In this chapter, the physical characteristics of lipids will be introduced as a background to understand how and why lipids behave as they do, together with frequently encountered lipid-based particulate systems.

## 9.3.2

**What is a Lipid?**

Lipids can be defined as fatty acids, their derivatives and related molecules that are soluble in organic solvents and sparingly soluble in water. The major role of lipids in the living organism is to build the cell membrane. The majority of lipids encountered in nature are amphiphilic in that they embody both polar and apolar elements in one molecule. Dietary lipids are mostly neutral lipids or triglycerides with very low aqueous solubility. There are also classes of lipids that can self-assemble and form a variety of lyotropic liquid crystalline phases having crystalline periodicity and liquid-like molecular diffusibility. This nature of hydrated lipids can help us to design lipid-based nanoparticles.

Lipid phase behavior can be understood by realizing that there exists a lateral pressure function across a lipid monolayer [37–40]. A force profile can be drawn along the direction normal to the lipid monolayer since different forces are dominant in different regions along the lipid molecules (Fig. 9.3). A lipid molecule can be divided roughly into the head group, polar/nonpolar interface and hydrocarbon chain regions. Head groups repel each other due to steric, hydration and electrostatic effects. There is an attractive force in the polar/nonpolar interfacial region in order to minimize the exposure of the interfacial area to the surroundings. Hydrocarbon chains repel each other due to thermally induced rotational motion around the carbon atoms. A lipid monolayer compensates for the imbalance in the lateral stress and can become a planar or curved surface as a result if there exist no other energy terms. In reality, the contributions from other energy terms could easily override the spontaneous tendency of bending the lipid monolayers. These other energy terms include electrostatic interactions, van der Waals interactions and others.

Since the energy of bending is an important energy term to understand in lipid self-assembly, it will be discussed in more detail. The curvature elastic energy describes the energy associated with bending the surface as follows [41]:

$$\Delta G = k_c/2 \langle H - H_0 \rangle^2 - k_g \langle K \rangle \quad (2)$$

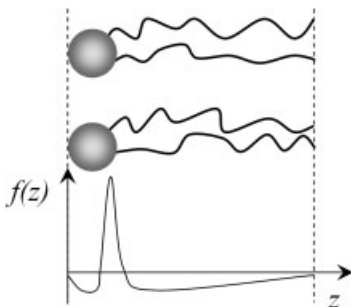


**Fig. 9.3.** The lateral stress profile along a lipid monolayer. A positive value along the  $f(z)$ -axis represents the attractive force.

where  $k_c$  and  $k_g$  are the rigidity or bending modulus and the Gaussian curvature constant, respectively, and  $\langle \rangle$  denotes the average obtained by integrating over a unit surface. Curvature is defined as a reciprocal of the radius of a circle that can be drawn to the tangent of the surface. The principal curvatures  $C_1$  and  $C_2$  are the minimum and maximum of the normal curvatures at a point. Two orthogonal principal curvatures or their average and product values, the mean [ $H = (C_1 + C_2)/2$ ] and the Gaussian ( $K = C_1 C_2$ ) curvatures, can define the curvature of the surface at a given point.

### 9.3.3

#### Liquid Crystalline Phases of Hydrated Lipids with Planar and Curved Interfaces

The vast variety of naturally occurring lipids adopt one or more of the liquid crystalline phases at, or close to, physiological conditions either with planar or curved interfaces. In this section, the lamellar, hexagonal and cubic phases of hydrated lipids will be described although they are bulk phases since they can be micronized into useful pharmaceutical nanoparticles such as liposomes, hexosomes and cubosomes, respectively.

Biomembranes usually incorporate a lipid bilayer structure that has been successfully modeled by the lamellar liquid crystalline ( $L_\alpha$ ) phase at physiological conditions. In the  $L_\alpha$  phase, lipid molecules arrange into stacked sheets (Fig. 9.4). The apolar hydrocarbons are located inside and the head groups line up at the surface of the sheets. Water molecules are located between the layers formed by the head groups. The lamella is a planar structure with zero curvature. The lamellar phase is often described as a frustrated structure since the bilayers cannot overcome an

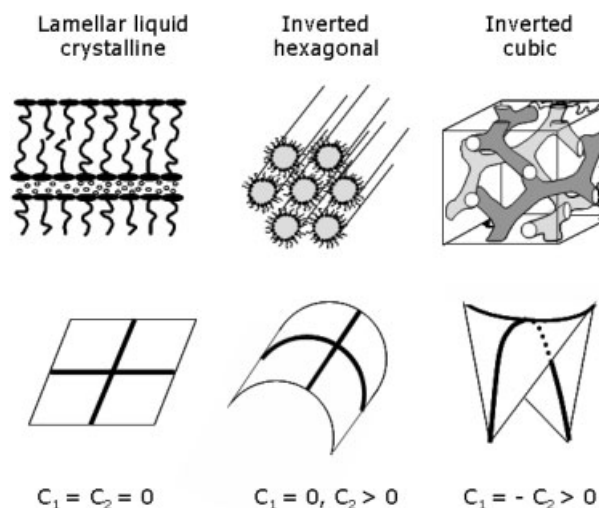


**Fig. 9.4.** Liquid crystalline phases of hydrated lipids and the principal curvatures at the interface between hydrocarbon chain termini.

energy barrier to curl up (called the “packing energy”) even when a curved surface is preferred and, thus, remain flat [42].

The so-called inverted hexagonal ( $H_{II}$ ) phase composed of long cylinders with hexagonally packed aqueous cores is found in hydrated lipids (Fig. 9.4). The lipid head groups coat the surface of the central water-filled cylinders and the hydrocarbon chains constitute the continuous medium. One of the principal curvatures along the cylinder is zero, but the other is around  $0.02 \text{ \AA}^{-1}$ . Another curved liquid crystalline phase encountered in hydrated lipids is the bicontinuous cubic phase [43]. In the bicontinuous cubic phase, each component, lipid or water, forms separate and continuous channels, and the interface between the lipid and water forms the networks of tubes that have three-dimensional cubic symmetry. The interface between the termini of hydrocarbon chains in the cubic phase can be described as the infinite periodic minimal surface whose mean curvature is zero everywhere since the two principal curvatures are identical in quantities with different signs [44, 45].

The appearance and the texture of the hexagonal and the cubic phase are similar to white toothpaste and waxy gel, respectively. They both are very viscous and do not dilute in water. Drugs can be encapsulated in the water channels, hydrocarbon regions as well as interfacial regions.

#### 9.3.4

##### **Oil-in-water-type Lipid Emulsion**

Neutral lipids such as triglycerides phase-separate and form thermodynamically stable bulk oil phases ( $L_2$  phase) in the aqueous system. Fractionizing them into micronized particles would create a large interface between the particles and water. However, this process is entropically favorable – the increased interfacial area between oil and water increases the Gibbs free energy [46]. Emulsification occurs when external energy is provided in the form of stirring, sonicating or microfluidizing. Spontaneous emulsification can also occur when the interfacial energy between oil particles and water is close to zero.

Lipid emulsions have been widely used in pharmaceutical and medical fields as drug carriers. To be applied as parenteral, oral or topical formulations, emulsions must be physically stable and nontoxic [47]. The diameter of oil droplets in stable lipid emulsions is typically less than 500 nm. Many emulsion products are currently on the market, including propofol injectable emulsion (Baxter and Astra Zeneca).

To formulate stable emulsions, suitable emulsifiers should be added to the formulation [48]. It is also important to choose an appropriate oil to increase the stability and biocompatibility of the emulsion [49].

#### 9.3.5

##### **Liposomes**

A liposome is a vesicle made of lipid shells and filled with a portion of an aqueous phase. Liposomes used as drug delivery systems are mostly small unilamellar vesicles (SUV) and smaller-sized multilamellar vesicles (MLV) between 50 and 100

nm in diameter. For pharmaceutical use, a hydrophobic drug can be incorporated in the shell or in the inner aqueous phase. Since a liposome is not a thermodynamically stable system, it can be produced by applying sufficient mechanical force to break up the lamellae and overcome the curvature energy cost to form a closed constrained vesicle from the bulk lamellar liquid crystalline phase [50].

Even though liposomes have been used widely as drug delivery systems, there have been many problems in using conventional liposomes. Phospholipid liposomes are very unstable and form aggregates upon storage. In the blood stream, they are cleared out by the reticuloendothelial system (RES) as they can be recognized as foreign bodies [51, 52]. The breakthrough occurred when long-circulating liposomes were designed by incorporating lipids with covalently attached polyethylene glycol (PEG) [53]. These, so-called, “stealth” liposomes have a relatively long half-life (approximately 1 day) in blood circulation and can be targeted to a desired tissue *in vivo*. The repulsive barrier properties of lipid-grafted PEG polymer chains originate mainly from a steric pressure and this simple polymer steric stabilization is the basis for the extended *in vivo* circulation times observed for polymer-grafted liposomes [53].

Along with “stealth” technology, another novel technique has been put into the development of successful liposome formulations. Conventionally, drug encapsulation efficiency into the liposome has been very low since a liposome is prepared by dispersing the bulk  $L_{\alpha}$  phase in the aqueous system containing drugs. Considering a liposome with a radius of 50 nm and a shell with a single bilayer whose thickness is 5 nm. If the total lipid concentration was 3% (w/w) in the aqueous system at the beginning, a rough calculation gives around 8% (v/v) of the trapped aqueous phase inside the liposome. In reality, the bilayer has one to three layers and therefore the drug trapping efficiency is almost always lower than 8%. A revolutionary technique called remote loading technology was devised to increase the trapping efficiency of drugs [54]. A relatively hydrophobic drug, e.g. doxorubicin, can penetrate the lipid bilayer freely. The inner aqueous phase is rendered acidic with the bulk aqueous phase at a higher pH, then the protonated doxorubicin forms precipitates out inside and cannot escape from the liposome droplet.

When a single lipid species is used to form liposome, different mean curvatures of the outer and inner bilayers could destabilize the liposome. Adding a small amount of lipids with different spontaneous curvature could release the tension by being preferentially distributed in one of the leaflets.

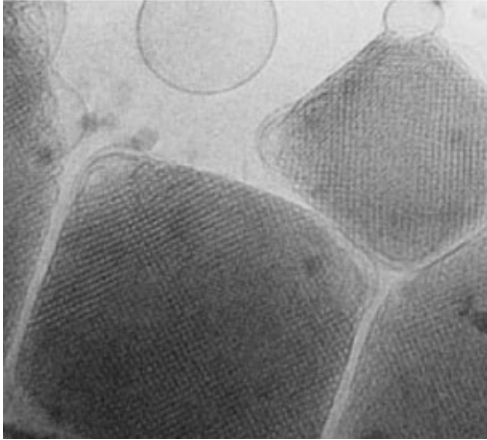
Many attempts have been made to prepare stable liposomes as drug delivery systems and probes to identify proteins by adding the polymerizable lipids with conjugated double or triple bonds that can be polymerized by applying heat or UV light [55] or metal-chelating lipids [56].

### 9.3.6

#### **Cubosomes and Hexosomes**

In the early 1990s, Swedish scientists succeeded in dispersing the lipid cubic phase in water by adding emulsifiers [57, 58]. They have termed the dispersed cubic

## Cubosome



## Hexosome

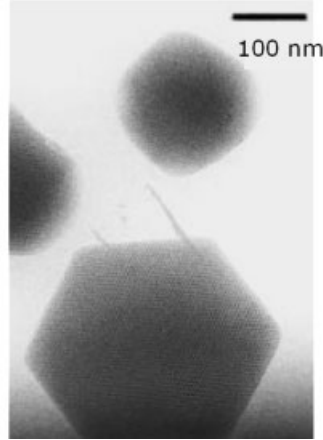


**Fig. 9.5.** Cryo-transmission electron microscopy photograph of cubosomes and hexosomes formed in the monoolein–water system. (Reproduced with permission from Ref. [58].)

phase as a “cubosome”. A cubosome is prepared by micronizing the hydrated lipid cubic phase in water. The interior of a cubosome comprises a thermodynamically stable cubic phase wherein lipid and water components constitute continuous, but separate, three-dimensional channels, and there exists a curved interface between the lipid head group and water (Fig. 9.5). Therefore, cubosome formulations could be advantageous over the conventional emulsion- or liposome-type formulations as they can solubilize amphiphilic as well as hydrophobic and hydrophilic drugs. To increase the stability of cubosome preparation, different preparation procedures have been devised. Precursor type formulation that forms a cubosome spontaneously in the presence of water has been developed [59, 60]. A dry-powder-type formulation was also prepared [61]. Cubosomes have been elegantly described in mathematical terms [62] and have been developed as drug carriers by the scientists in Camurus AB ([www.camurus.se](http://www.camurus.se)). Like liposomes, cubosomes have also been polymerized successfully by utilizing reactive monoglyceride [63]. The term “hexosome” refers to a dispersed hexagonal phase and can also be produced by mechanically micronizing the hydrated hexagonal phase in water (Fig. 9.5).

### 9.3.7

#### Other Lipid-based Pharmaceutical Nanoparticles

A hollow lipid microcylinder has been produced by cooling a liposome solution composed of chiral diacetylenic lipids [64, 65]. Diacetylenic lipids are those with conjugated triple bonds in the middle of hydrocarbon chains. Due to the chirality of the diacetylenic lipid, the bilayer twists to form a tubular structure. Microtubules have a diameter of approximately 0.5  $\mu\text{m}$  and a length ranging up to a few centi-

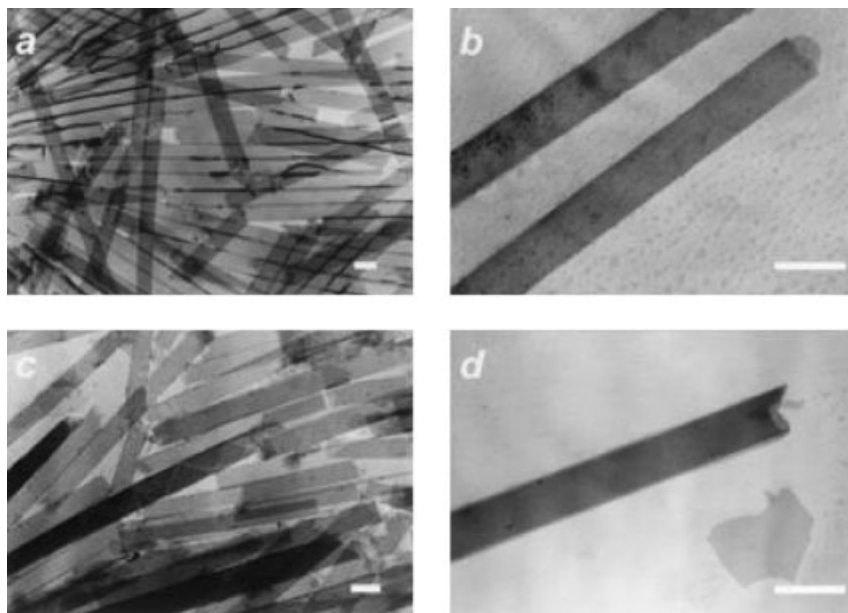


**Fig. 9.6.** Electron micrographs of lipid tubules in methanol/water (7:3) at lipid concentrations of 1 (a and b) and 5 mg ml<sup>-1</sup> (c and d). The scale bar represents 1  $\mu$ m. (Reproduced with permission from *Proc. Natl Acad. Sci. USA* **1996**, 93, 12943–12946.)

meters. The bilayer forms a band arranged like a wrapping paper of a cigar, separated by layers of water (Fig. 9.6). The inside (in the place of the cigar itself) is hollow and filled with water in an excess water environment. Antifouling agents have been encapsulated into the interior of the microtubules and released in a sustained fashion [66].

Lipid cochleates are stable precipitates made from phosphatidylserine and calcium ions [67]. The structure of cochleates consists of a continuous, solid lipid bilayer sheet rolled up in a spiral (Fig. 9.7). Unlike lipid tubules, there is no hollow space for water in the cochleate system. The amphotericin B/cochleate system has been shown to treat *Candida* infection when administered orally [68]. Cochleates have also been used to deliver proteins and peptides for vaccine applications [69].

## 9.4

### Mechanical Approaches

#### 9.4.1

##### Types of Processing

The subdivisional potential penalty in Eq. (1) can be paid by mechanical energy input to produce and maintain nanoparticles. Comminution to prepare pharmaceu-



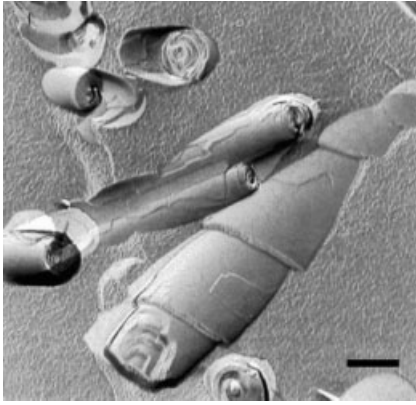


**Fig. 9.7.** Scanning electron micrographs after freeze-fracturing cochleate cylinders. Scale bar: 200 nm. (Reproduced with permission from *J. Controlled Rel.* **2002**, *81*, 7–23.)

tical nanoparticles uses mechanical energy. As the size of particles decreases, the required mechanical energy dramatically increases. To relieve the burden of energy input, additional support by surface active agents is generally used (Fig. 9.2) [9–10]. A series of recent successful commercializations of nanoformulations using this technique proves its efficiency.

Based on the type of mechanical energy employed, two typical types of processing exist – shearing and fracturing [70]. For shear force generation, high-speed stirrers and high-shear mills are commonly used in the processing of low-viscosity systems [71]. When a high-viscosity system is involved, shear force generation requires different types of equipment such as extruders, roll mills, heavy-duty mixers, etc. Fracturing is conveniently triggered by impact mills such as ball and jar mills.

Comminution processes using media such as ceramic balls have commonly been used to reduce the size of API. Both the wet and dry conditions can be used, but individual nanoparticles in the dry state are relatively unstable. When a liquid medium is used, heat dissipation is much more effective, and, more importantly, the surface of nanoparticles can properly be wetted and stabilized by surface active agents. Therefore, wet comminution is more common in pharmaceutical nanoparticle processing. Ball and jar mills, vibratory mills, various attritors, etc., are of this type [18, 19, 70].

In ball milling, grinding media is put into a cylindrical vessel with the drug. The vessel is designed to rotate along an axis and the grinding media undergo a cascading action that provides mechanical energy to reduce the particle size [8]. The critical speed is a speed where cascading stops due to high centrifugal force. Ball milling should use a speed lower than the critical speed to maintain its cascading action. Attrition contributes more to particle size reduction below the critical speed. The shape, size and density of grinding media affect comminution process.

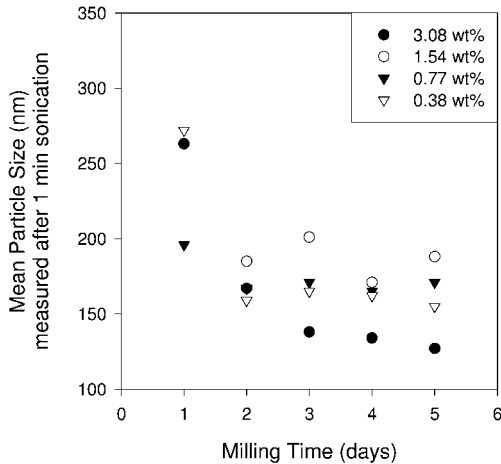


**Fig. 9.8.** Particle size reduction as a function of time during wet milling. The concentration of hydroxypropyl cellulose in the mother liquid is shown. (a) Nanoparticles on a glass slide ( $2 \times 2 \mu\text{m}$ ). (b) Nanoparticulate compact ( $1 \times 1 \mu\text{m}$ ) (compaction pressure = 136 MPa). (Reproduced with permission from Ref. [6].)

An increase in the density and hardness of grinding media usually increases the speed and amount of particle size reduction. A decrease in the size of media produces the same results. Nonetheless, in wet comminution using surface active ingredients, the surface properties of materials appear to be more important than the properties of the grinding media [6]. Figure 9.8 shows a typical result of particle size reduction as a function of milling time in the presence of a polymeric stabilizer.

High-speed stirrers such as blade stirrers and rotor-stator dispersers produce the same high-shear flow to obtain nanoparticles as high-shear mills such as colloid mills, homogenizers, ultrasonic dispersers, etc. [8, 70, 71]. In a typical design of high-pressure homogenization, the initial mainstream of a liquid (a dispersion system) is separated into two liquid streams, and then they collide with each other producing severe deformation and cavitation in the dispersion system [72]. Particle size reduction mainly results from the deformation and cavitation action of high-pressure liquid streams. The final particle size and its distribution significantly depend on the various processing parameters.

#### 9.4.2

##### Characteristics of Wet Comminution

In the wet comminution processes of nanoparticles, comminution continually fractures organic crystals while polymer chains adsorb onto fresh surfaces and stabilize each broken particle. The “primary” particle size produced by wet milling is not necessarily the same as the particle size actually measured in water by a light scattering method (Fig. 9.8). It is possible that some primary particles form aggre-

gates. Ideally, the smallest size of primary particles that can be achieved by mechanical breaking is related to the size of the damage zone ahead of the crack tip. According to the Irwin's equation of linear elastic fracture mechanics, the size of the damage zone ( $r_d$ ) (lower particle size limit) is related to the stress intensity factor ( $K_{IC}$ ) and yield stress ( $\sigma_y$ ) as follows [6, 73]:

$$r_d = 1/6\pi(K_{IC}/\sigma_y)^2 \quad (3)$$

If a set of typical values of  $K_{IC}$  (0.05 MPam<sup>1/2</sup>) and  $\sigma_y$  (50 MPa) for organic crystals is used [6, 74],  $r_d$  is around 50 nm. Accurate calculation is rarely possible due to the anisotropy of crystals and uncertainty in  $\sigma_y$  values, as well as the difficulty in measuring the stress state, loading rate and temperature in wet milling. However, the size of the damage zone ( $r_d$ ) will put a lower limit on the particle size that can be attained by wet comminution [75, 76].

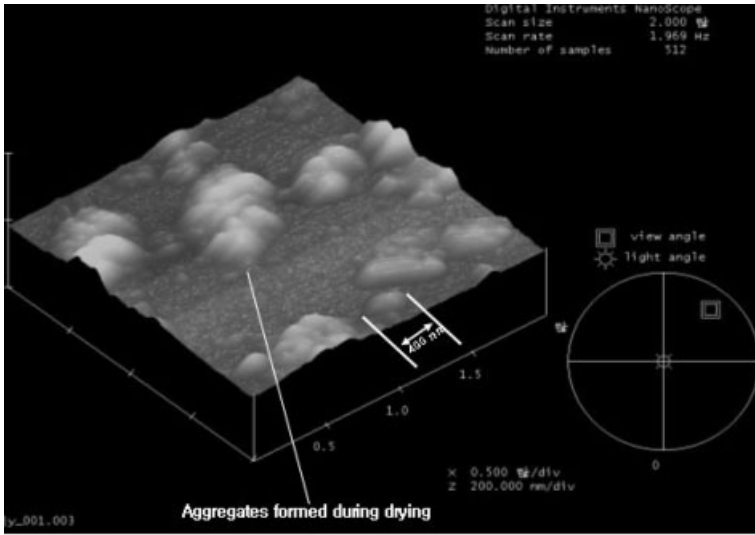
In the actual successful processing as shown in Fig. 9.8, the mean size of drug particles depends more on polymeric stabilizers than on mechanical energies. In semidilute polymer solutions, the adsorption of polymer chains will occur if the free energy reduction associated with adsorption can compensate for the accompanying entropy loss [77]. Since steric stabilization involves adsorption/desorption processes and masking of dispersion forces, it naturally depends on the concentration of polymer in bulk solution (concentration in mother liquid), the size of particles, type of solvent, etc. The amount of adsorbed polymers was found to initially increase with an increase in the concentration of polymer in bulk solution and eventually reach a saturation point [6].

For polymers to provide effective steric stabilization, strong adsorption at full coverage and a long time scale for desorption are necessary [77]. The common minimum layer thickness requirement for stabilization is around  $(0.05\text{--}0.2) \times$  particle size [77] and previous reports showed enough surface coverage based on a simple approximation [6]. When naproxen and hydroxypropyl cellulose were used as a drug and a stabilizer, the surface coverage of hydroxypropyl cellulose in 150-nm particles was estimated to be around  $1.5 \mu\text{g cm}^{-2}$ , which corresponds to an average polymer layer thickness of around 15 nm. It is uncertain whether this result can be generalized for other polymer-stabilized nanocrystal systems. More precise calculation requires an understanding of the polymer morphology on the surface of drugs. Unfortunately, direct measurement of the thickness of polymeric stabilizers has remained unsatisfactory. The atomic force micrographs in Fig. 9.9 clearly show nanoparticles, but no detailed information on polymeric stabilizers.

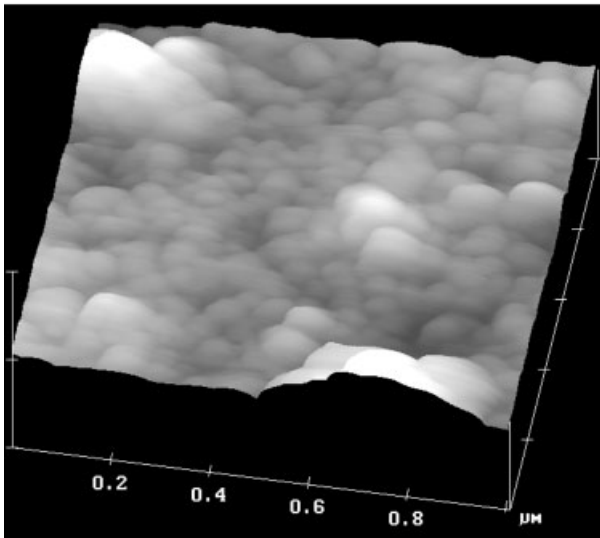
### 9.4.3

#### Drying of Liquid Nanodispersions

In the wet comminution processes, the steric stabilization of polymers is effective only in a liquid medium. While the use of a liquid medium is convenient for nanoparticle preparation, solid dosage forms are generally more important than liquid forms in the pharmaceutical industry. Therefore, a drying process should be em-



a) Nanoparticles on glass slide (2x2  $\mu\text{m}$ )



b) Nanoparticulate compacte (1x1  $\mu\text{m}$ ) (compaction pressure = 136 MPa)

**Fig. 9.9.** Tapping mode atomic force microscopy images of nanoparticles dried on a glass side from an aqueous dispersion (a) and the surface of a nanoparticulate compacte (b). (Reproduced with permission from Ref. [6].)

ployed to connect the wet process and the conventional unit operations of solid dosage formulation. Various drying processes such as spray drying, fluidized bed drying, freeze drying, etc., can be used to prepare dried nanoparticles.

Since the initial thermodynamic and kinetic compensations of the wet comminution process become inactive as drying progresses, nanoparticles easily form aggregates too strong to be dispersed in a liquid medium later. Nanoparticles slowly dried under ambient conditions show their aggregation tendency as can be seen in Fig. 9.9(a). Special care needs to be taken to keep each nanoparticle apart from each other (“re-dispersible”). Otherwise, the advantages of nanof ormulation cannot be fully utilized in solid dosage forms. The drying process of nanoparticle dispersions has become a critical issue in the pharmaceutical industry.

Drying nanoparticle dispersions using conventional processes such as spray drying, freeze drying, etc., is not a trivial process development [16–20]. Solid dosage formulation needs well-dispersed API nanocrystals (Figs. 9.8 and 9.9). For that reason, the key property of dried nanoparticles is their “re-dispersibility”, i.e. whether they can restore their initial nanometer sizes when they are re-dispersed into an aqueous medium. The re-dispersibility can be defined as  $D_0/D$  (%), where  $D_0$  is the initial mean particle size after preparation of the nanoparticle dispersion and  $D$  is the particle size of re-dispersed powder in water. Then, 100% re-dispersibility indicates that dried powders can fully revert to the original nanoparticles upon re-dispersion into water.

Drying certainly increases the chances of aggregation of nanocrystals and polymers. Steric stabilization requires active polymer chain movement in water, which will be restricted as water is frozen or removed. Thus, it is a natural consequence for nanocrystal dispersion to become less stable during drying or freezing (freeze drying). Furthermore, the crystallization (crystal growth) of water in freeze drying tends to exclude foreign particles from crystal regions and lead them to aggregate. Therefore, for better re-dispersibility, fast drying or freezing is necessary and a soluble compound such as a cryoprotectant is frequently added to serve as a medium where solid nanoparticles are dispersed after drying. It was reported that there is a critical freezing rate for a solid dispersion below which its re-dispersibility decreases from 70–100 to 2–3% [78].

Since drug nanoparticles are covered by adsorbed polymer chains, the breaking strength of aggregates into primary nanoparticles would depend on how strongly the polymer chains become entangled during drying [79]. Therefore, to prevent strong entanglement, the frequency and duration time of contacts between nanoparticles need to be minimized by increasing drying speed. In an extreme case of aggregation, API nanoparticles may fuse together. The re-dispersion of fused aggregates can hardly be expected.

For a dispersion system, re-dispersibility might be treated as a result of competition between drying speed and particle collision frequency. The motion of an “ideal” spherical particle could be characterized by using its hydrodynamic diameter,  $d$ . The average apparent velocity of the particle,  $v_{app}$ , is:

$$v_{app} = x/t = (2D/t)^2 \quad (4)$$

where diffusion coefficient,  $D = kT/3\pi\eta d$ ,  $x$  is the average distance traveled by a particle,  $t$  is the time,  $k$  is the Boltzmann constant,  $T$  is the temperature and  $\eta$  is the viscosity [70, 77]. If a set of typical values is employed,  $v_{\text{app}}$  can be obtained for a certain time interval,  $t$ . The apparent velocity  $v_{\text{app}}$  is only an approximation and often fails to describe actual particle motion. However, it seems to hold true that as the concentration increases, the collision frequency increases, resulting in an increase in aggregation tendency. It requires the detailed analysis of interparticle force fields, polymer chain mobility, local heat and mass transfer, etc., to determine how fast a nanoparticle dispersion should be dried.

## 9.5

### SCF Approaches

The use of near critical or SCFs for micro/nanoparticle formation has recently been shown to be good in improving particle characteristics such as size, size distribution, shape and morphology. SCF technology can be an attractive recrystallization method for some difficult-to-comminute materials such as certain explosives, “waxy” or “soft” dyes, polymers and pharmaceutical compounds, etc., that require very small particles and narrow size distribution. Once used, the SCFs can be recycled from dissolved solutes by just depressurizing. Thus, the SCF processes are environmentally benign. The stainless construction, small number of moving part and totally enclosed system are also favorable for the pharmaceutical current good manufacturing practice (cGMP) requirements.

#### 9.5.1

##### SCF Characteristics

More than 100 years ago it was found that SCFs could dissolve nonvolatile compounds [80]. In the pressure–temperature diagram for a pure substance (Fig. 9.10), two nearby phases coexist at the solid curves and three phases (liquid, vapor and solid) exist together at the triple point (TP). “Supercritical” means the state of matter where the temperature and pressure of a single fluid are above the critical point (CP) where the liquid–vapor phase boundaries (equilibrium curve) diminish. The temperature and pressure at the CP are referred to as the critical temperature ( $T_c$ ) and critical pressure ( $P_c$ ), respectively. By literal definition, the SCF is a fluid that is at temperature and pressure higher than those at CP, and the area is called a SCF region. In that region the substance can be brought into the vapor and liquid without an abrupt phase change by lowering the pressure and temperature, respectively. However, due to economic considerations, SCF processing is generally carried out in the vicinity of the CP with reduced temperature ( $T/T_c$ ) in the range of 1.01–1.1 and reduced pressure ( $P/P_c$ ) in the range of 1.0–4.0.

SCFs have advantageous properties of gases and liquids such as a liquid-like density (high solvation power), and gas-like diffusivity and viscosities (high mass transfer rates, i.e. good mixing properties). In addition, near zero surface tension

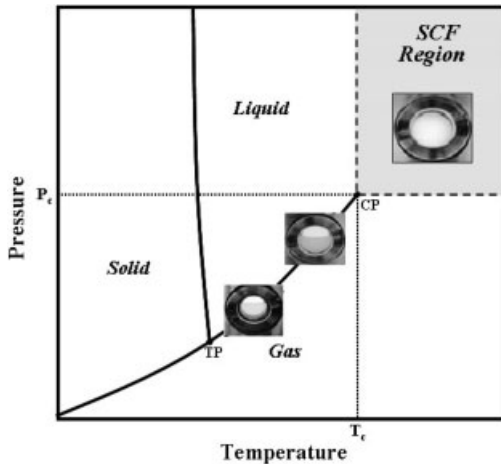


Fig. 9.10.  $P$ - $T$  diagram of a pure substance.

enables SCFs to easily migrate into various microstructures. For particle formation, SCFs are very compressible near the CP, and their density and solvent power can be changed dramatically by a small change of either pressure or temperature. Consequently, their density and solvent power are continuously controlled for selective operation in the SCF region a little distant from the CP. The solvent power can be explained by a high enhancement factor of  $10^4$ – $10^6$  (a dimensionless measure of solvent power defined as the measured solubility of a substance in the solvent divided by the solubility in an ideal gas) [81].

Carbon dioxide is one of the most extensively used SCFs ( $\text{SCCO}_2$ ) due to its relatively low  $T_c$  (31.1 °C) which makes it attractive for processing heat-labile substances such as pharmaceutical ingredients (Fig. 9.11). Additionally, it has a moderate  $P_c$  (73.8 bar) and a good solvation power compared to other SCFs. It is nontoxic, nonflammable and relatively inexpensive (US\$0.11–0.15  $\text{kg}^{-1}$ ) with high purity.

### 9.5.2

#### Classification of SCF Particle Formation Processes

There have been a number of review articles for micro- and nanoparticle formation using SCFs recently [82–88]. In the past 20 years various types of SCF particle formation processes have been developed using different nucleating and growth mechanisms, such as rapid expansion of supercritical solution (RESS), gas antisolvent (GAS) process, supercritical antisolvent (SAS) process, solution-enhanced dispersion by SCFs (SEDS), particles from gas-saturated system (PGSS), etc. Among these techniques, RESS, SAS and SEDS are generally known to achieve nanoparticle formation.

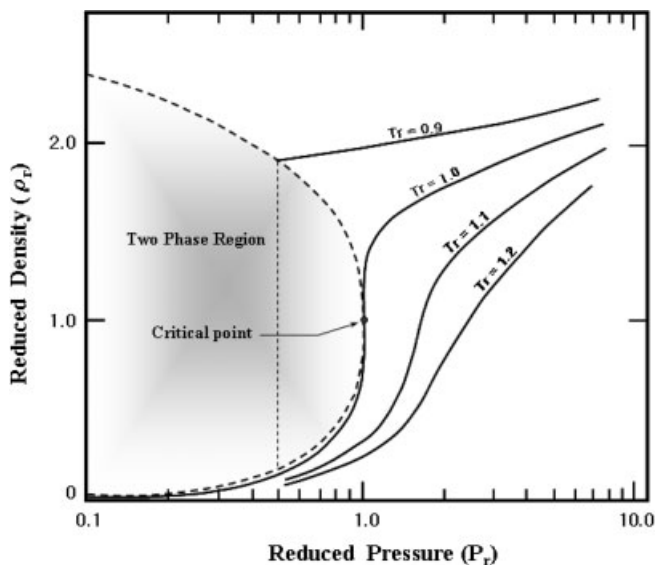


Fig. 9.11. Reduced density–reduced pressure diagram for CO<sub>2</sub> at various reduced temperatures ( $T_r$ ) in the vicinity of the CP.

### 9.5.3

#### RESS

This process is used for materials soluble in a SCF. As shown in Fig. 9.12, the RESS process simply uses a pump, extractor, nozzle and precipitator. Using the compressed SCF, the solutes located in the extractor are dissolved and the supercritical solution is introduced into the precipitator at low pressure (normally atmospheric pressure) through capillary or laser-drilled disk-type nozzles. The resulting rapid pressure drop in solution causes fast evaporation of SCFs and a dramatic decrease in the solvation power of the solution, which leads to a high degree of homogeneous supersaturation and simultaneous formation of very small particles. This high supersaturation ratio, rapidly propagating mechanical perturbation and thermal cooling enable the production of nanoparticles with a narrow size distribution.

This technique can be used without any toxic organic solvent and, thus, is considered a contamination-free process. The general limitation of this process comes from the low solubility of hydrophilic or high-molecular-weight pharmaceuticals, resulting in poor throughput capacity even though a cosolvent is added to improve the solvent power of SCF.

Many works have focused on atomization of pharmaceuticals, either to obtain very fine particles with a narrow size distribution [89–93] or microcapsules which include an API in the carrier [94–96].



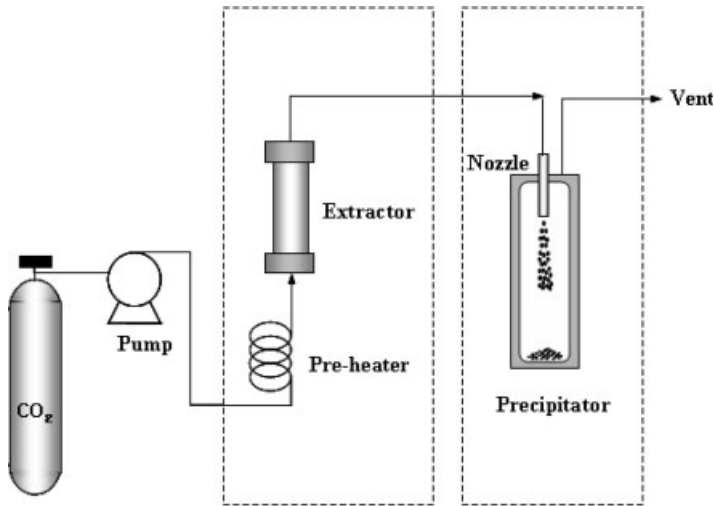


Fig. 9.12. RESS process.

#### 9.5.4

#### SAS

This process can be used for the crystallization of substances insoluble in SCF (Fig. 9.13). Some similar techniques are called the aerosol solvent extraction system (ASES) or precipitation with a compressed antisolvent (PCA) process. Drug and/or carrier are first dissolved into a liquid solvent, and the solution is sprayed from the top of and into a precipitator through a nozzle, where the SCF flows concurrently downward acting as an antisolvent for particle formation (Fig. 9.13). Two particle precipitation mechanisms proceed simultaneously at a high speed, i.e. the diffusion of a SCF into a liquid solution droplet (volumetric expansion of the organic solvent) and the evaporation of the liquid solvent into a SCF (depletion of the solvent from the liquid solution droplet). These phenomena generate a high degree of supersaturation of the solution, resulting in fast nucleation and growth, and consequently produce solute nanoparticles. After collection of a sufficient amount of particles, liquid solution pumping is stopped and pure SCF continues to flow through the vessel to remove residual solvent from particles.

The operation pressure, temperature, jet breakup, droplet size and mass transfer rates between droplets and the antisolvent phase control the particle size and morphology. In this process, the rate of SCF mass transfer into droplets influences particle formation, whereas the rate of solvent mass transfer into the SCF from droplets has an effect on particle agglomeration. This process can also be operated in a continuous mode that facilitates scaleup for the mass production of particles.

Many investigations have been carried out on atomization of pure pharmaceutical components such as insulin [97–100], ascorbic acid [101], pure biopolymer microspheres (dextran [102] and polylactic acid (PLA) [103]), and microcapsules

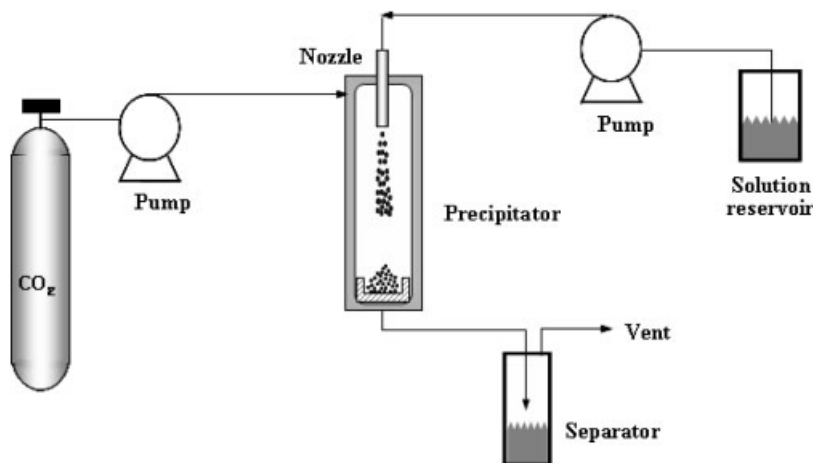
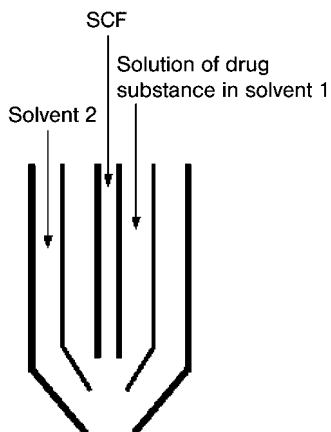


Fig. 9.13. SAS process.

which include an API in the carrier (chemotrypsin in PLA [104], lysozyme in PLA [104] and naproxen in PLA [105]).

#### 9.5.5 SEDS

The SEDS process is a modified version of the SAS. It enhances mixing efficiency by adopting a two- or three-coaxial-channel nozzle (Fig. 9.14) to facilitate smaller particle production. In this process, SCF is used both as an antisolvent and as a



Coaxial nozzle system

Fig. 9.14. Three-coaxial-channel nozzle system for SEDS process.

solution dispersion enhancer. Due to the high velocity of a SCF stream, faster breakup of solution and high mass transfer rates are achieved between the SCF and the solution, and so very fine particles are attained. With a three-coaxial-channel nozzle, one SCF stream and two organic solutions or two SCF streams and one organic solution can be combined. An aqueous solution can also be treated to form particles of water-soluble compounds such as proteins (lysozyme and trypsin [106]) and sugars (lactose, maltose, threhalose and sucrose [107]) using an aqueous solution of API/ethanol or methanol/SCCO<sub>2</sub> system.

## 9.6

### Electrostatic Approaches

The recent advance of spraying techniques under a high electrical field has opened unique possibilities for nanoformulation [108–113]. Electro spraying to prepare monodisperse pharmaceutical nanoparticles is currently being under active investigation and many intriguing successes have been reported. Herein, electro spraying will be briefly introduced as an emerging technology.

#### 9.6.1

##### Electrical Potential and Interfaces

The effect of electrical charges on the surface energy of a solid or liquid has been an interesting subject under thorough investigation. Common electrical charges are generated by the preferential adsorption of ions. In the electro spraying processes, an intentionally applied electrical field can effectively facilitate nanoparticle preparation [70]. When the interface between a solid and water is charged, the interfacial tension is reduced because of the greater interaction with water. This effect is much smaller with an oil drop. The contact angle actually follows the decrease of interfacial tension.

When an electrical field is applied between a nozzle and a collection part in spraying, the size of drop generated from a nozzle is reduced depending on the amount of applied charge (Fig. 9.15). Without an electrical field, the final size of a drop from a nozzle depends on the surface energy and the gravitational force of the drop (dripping mode in Fig. 9.16). With the aid of an electrical field, drops of smaller size overcome their surface energy and detach themselves from the tip of the nozzle (microdripping mode in Fig. 9.16) [114, 115]. As the electrical field increases further, the decrease of drop size reaches a different stage. The charged surface of the drop can no longer sustain its integrity and induces total breakup into droplets of much smaller size (Fig. 9.16). Usually, the droplets are of invisible nanometer size. Transition into this stage is easily confirmed by checking the formation of a Taylor cone (cone-jet in Fig. 9.16) structure at a nozzle tip [114].

The cone-jet mode was successfully explained by Talyor in 1964 [114]. The size of droplets is determined by the hydrostatic balance between electrical and surface tension forces. Further elaboration of the phenomena was later performed by Fer-

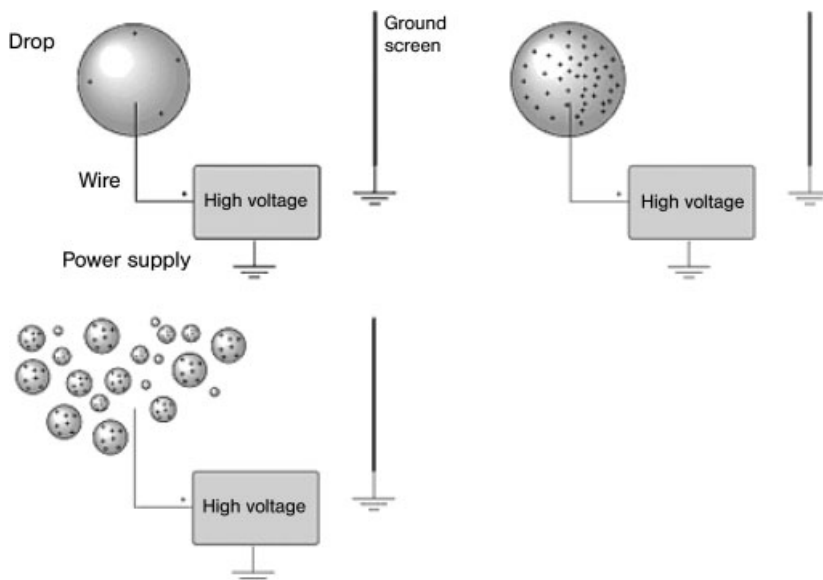


Fig. 9.15. Electro spraying induces the breakup of charged drops by a surface electrostatic force.

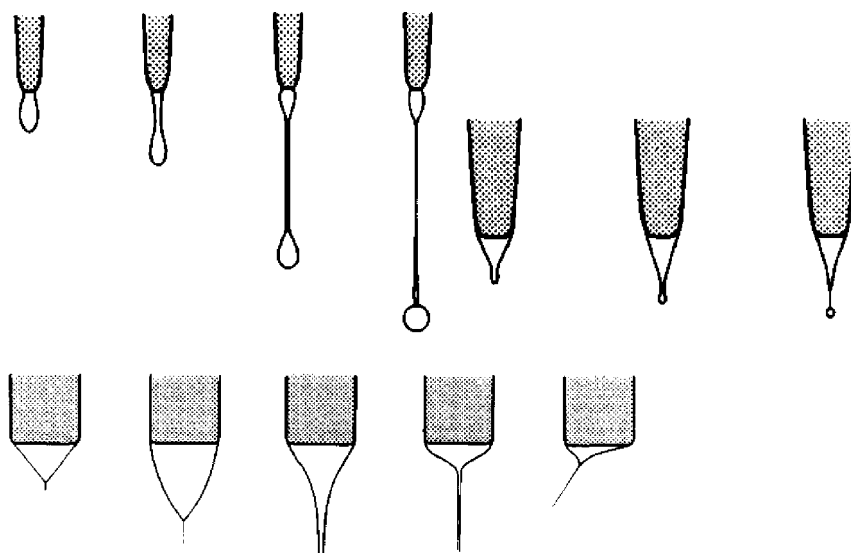


Fig. 9.16. Different stages of electro spraying drops (cyclohexanol): dripping mode (top left), microdripping mode (top right) and cone-jet mode (bottom). (Reproduced with permission from Ref. [115].)

nández de la Mora and Loscertales [116, 117] and Gañán-Calvo *et al.* [118–120]. The detailed relationship between current and flow rate was established depending on the properties of liquids employed. Particle size can be predicted in an ideal case from various parameters such as current, flow rate, permittivity and conductivity, etc. For example, when conductivity and viscosity are relatively low, particle diameter,  $d$ , is:

$$d \sim [(b - 1)^{1/2} Q \epsilon_0 / K]^{1/3} \quad (5)$$

and when both the viscosity and conductivity is high,  $d$  is:

$$d^{3/2} \sim Q/I \quad (6)$$

where  $I$  is the current,  $Q$  is the flow rate,  $b$  is the liquid to vacuum permittivity ratio,  $K$  is the electrical conductivity and  $\epsilon_0$  is the vacuum permittivity [116–120].

When the flow rate is relatively high, a ramified jet results instead of the cone-jet mode (Fig. 9.17). With relatively high conductivity and viscosity, electro spraying works in the spindle mode, which is often used to prepare nanofibers (Fig. 9.17) [114, 115]. Various factors such as flow rate, current, electrical conductivity, permittivity, liquid/gas surface tension, viscosity and density need to be considered to obtain a specific spraying mode, [117, 119–121].

## 9.6.2

### Electrospraying

In a simple electro spraying case, an electrically conductive liquid is slowly injected into a capillary having a potential difference of at least several thousand volts between a plate and itself. Liquids turn into charged droplets out of the “Taylor cone” at the capillary tip (Figs. 15 and 16). Proper posttreatments lead the droplets to form stable pharmaceutical nanoparticles. When a coaxial capillary is used, core/shell-type nanoparticles can be obtained (Fig. 9.18); recently, nanoparticles with more complicated internal structures have been reported [116, 119, 122].

Conventional spraying gives unique advantages for pharmaceutical applications when combined with an electrical field. First, relatively monodisperse pharmaceutical nanoparticles can be conveniently prepared (Fig. 9.19). Since the size of droplets is determined by electrical surface charge, monodispersity can readily be accomplished, and size control is relatively easy. It is also an important bonus that organic solvents are not necessary for this technique. Compared to other preparation methods, electro spraying can be applied to pharmaceutical materials of various physical properties since this method does not significantly rely on the hydrophilicity of solvents and pharmaceutical materials. Proteins can be processed regardless of their surface hydrophilicities. Moreover, protein is known to be stable in high electrical fields. While other methods using organic solvents or mechanical energies often destroy the viability of proteins, electro spraying does not cause such

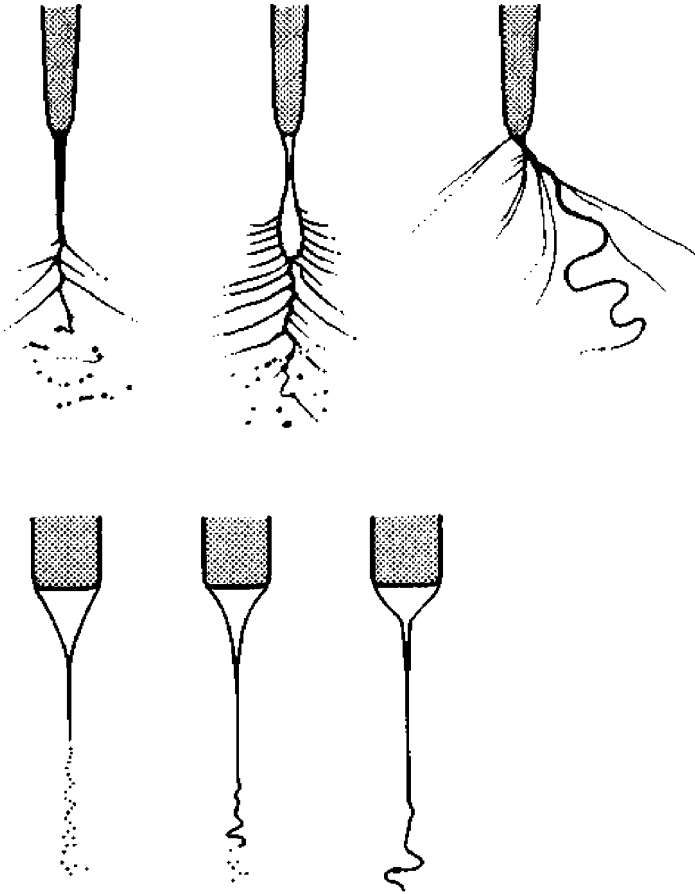


**Fig. 9.17.** Different stages of electro spraying: ramified jet and random spraying (top), and spindle mode (bottom). (Reproduced with permission from Ref. [115].)

problems [123]. As a result, nanoformulation of many different types of drugs, including proteins, can be developed using electro spraying technique.

Core/shell nanoparticles are especially useful for drug delivery systems (Fig. 9.18) [116]. Two liquids are injected into two coaxial capillaries under an electrical field and form nanoparticles as a result of the electrohydrodynamic force. The sizes of two capillaries can range from a few micrometers to several millimeters and the electrical field is applied to the outer capillary. The electrical potential of the inner capillary depends on the electrical conductivity of the liquid in the outer capillary. By changing flow rates and the electrical field, nano-encapsulated particles can be prepared. The size of core/shell particles and the thickness of coating shells depend on the various physical properties of materials, but they are easily controlled by adjusting flow rates of two liquids.

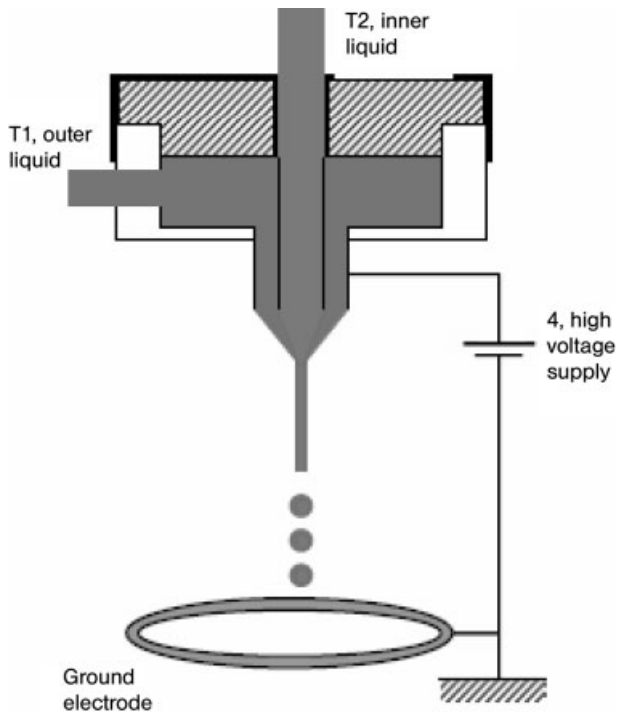


**Fig. 9.18.** Schematic illustration of coaxial electrospaying equipment to prepare core/shell drug particles. (Reproduced with permission from Ref. [116].)

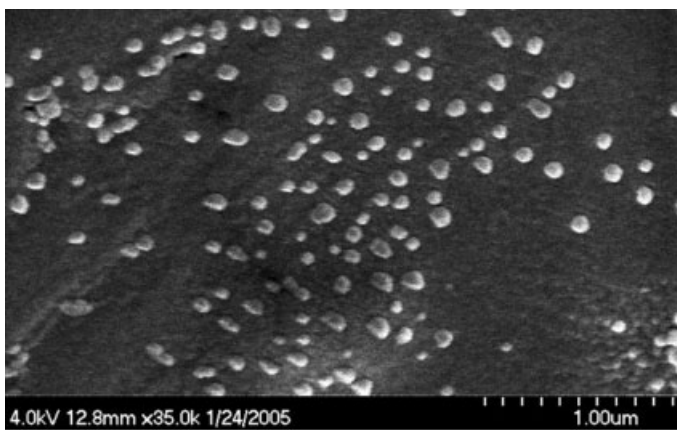


**Fig. 9.19.** Nanoparticles prepared from electrospaying.

The current during coaxial electrospraying mainly relies on the flow rate of more conductive liquid (driving liquid) between the two liquids employed. Whether the driving liquid is injected into the outer or inner capillary affects the core/shell particle formation mechanism. Once it is decided, the flow rate of driving liquid needs to be carefully controlled to obtain a proper current, and resulting particle size and internal structure.

## References

- 1 PhRMA Analysis Reports, *Why Do Medicines Cost So Much?* and *Pharmaceutical Industry Profile*, 2005, <http://www.phrma.org/publications>.
- 2 LI, J. K., WANG, N., WU, X. S., A novel biodegradable system based on gelatin nanoparticles and poly(lactic-co-glycolic acid) microspheres for protein and peptide drug delivery, *J. Pharm. Sci.* **1997**, *86*, 891–895.
- 3 ZAMBAUX, M. F., BONNEAUX, F., GREF, R., DELLACHERIE, E., VIGNERON, C., MPEO–PLA nanoparticles: effect of MPEO content on some of their surface properties, *J. Biomed. Mater. Res.* **1999**, *44*, 109–115.
- 4 MURAKAMI, H., KOBAYASHI, M., TAKEUCHI, H., KAWASHIMA, Y., Evaluation of poly(DL-lactide-co-glycolide) nanoparticles as matrix material for direct compression, *Adv. Powder Technol.* **2000**, *11*, 311–322.
- 5 FOURNIER, E., DUFRESNE, M.-H., SMITH, D. C., RANGER, M., LEROUX, J.-C., A novel one-step drug-loading procedure for water-soluble amphiphilic nanocarriers, *Pharm. Res.* **2004**, *21*, 962–968.
- 6 LEE, J., Drug nano- and microparticles processed into solid dosage forms: physical properties, *J. Pharm. Sci.* **2003**, *92*, 2057–2068.
- 7 GRAU, M. J., KAYSER, O., MÜLLER, R. H., Nanosuspensions of poorly soluble drugs – reproducibility of small scale production, *Int. J. Pharm.* **2000**, *196*, 155–157.
- 8 LIU, R. (Ed.), *Particle Size Reduction in Water-insoluble Drug Formulation*, Interpharm Press, Buffalo Grove, IL, 2000.
- 9 LIVERSIDGE, G. G., CONZENTINO, P., Drug particle size reduction for decreasing gastric irritancy and enhancing absorption of naproxen in rats, *Int. J. Pharm.* **1995**, *125*, 309–313.
- 10 LIVERSIDGE, G. G., CUNDY, K., Particle size reduction for improvement of oral bioavailability of hydrophobic drugs: I. Absolute oral bioavailability of nanocrystalline danazol in beagle dogs, *Int. J. Pharm.* **1995**, *125*, 91–97.
- 11 MERISKO-LIVERSIDGE, E., SARPOTDAR, P., BRUNO, J., HAJJ, S., WEI, L., PELTIER, N., RAKE, J., SHAW, J. M., PUGH, S., POLLIN, L., JONES, J., CORBETT, T., COOPER, E., LIVERSIDGE, G. G., Formulation and antitumor activity evaluation of nanocrystalline suspensions of poorly soluble anticancer drugs, *Pharm. Res.* **1996**, *13*, 272–278.
- 12 SERAJUDDIN, A. T. M., Solid dispersion of poorly water-soluble drugs: early promises, subsequent problems, and recent breakthroughs, *J. Pharm. Sci.* **1999**, *88*, 1058–1066.
- 13 YAMADA, T., SAITO, N., IMAI, T., Effect of grinding with hydroxypropyl cellulose on the dissolution and particle size of a poorly water-soluble drug, *Chem. Pharm. Bull.* **1999**, *47*, 1311–1313.
- 14 ZHENG, J. Y., BOSCH, H. W., Sterile filtration of nanocrystal drug formulation, *Drug Dev. Ind. Pharm.* **1997**, *23*, 1087–1093.
- 15 MERISKO-LIVERSIDGE, E., MCGURK, S. L., LIVERSIDGE, G. G., Insulin nanoparticles: a novel formulation approach for poorly water soluble Zn-



- insulin, *Pharm. Res.* **2004**, *21*, 1545–1553.
- 16 BOSCH, H. W., OSTRANDER, K. D., HOVEY, D. C., Nanoparticulate compositions comprising amorphous cyclosporine and methods of making and using such compositions, *US patent 6,656,504*, **2003**.
- 17 PACE, G. W., MISHRA, A. K., Water-insoluble drug particle process, *US patent 6,682,761*, **2004**.
- 18 RYDE, N. P., RUDDY, S. B., Solid dose nanoparticulate compositions comprising a synergistic combination of a polymeric surface stabilizer and dioctyl sodium sulfosuccinate, *US patent 6,375,986*, **2002**.
- 19 RYDE, N. P., RUDDY, S. B., Nanoparticulate dispersions comprising a synergistic combination of a polymeric surface stabilizer and dioctyl sodium sulfosuccinate, *US patent 6,592,903*, **2002**.
- 20 CHAMBERS, E., MITRAGOTRI, S., Prolonged circulation of large polymeric nanoparticles by non-covalent adsorption on erythrocytes, *J. Controlled Rel.* **2004**, *100*, 111–119.
- 21 SCHMIDT, C., BODMEIER, R., Incorporation of polymeric nanoparticles into solid dosage forms, *J. Controlled Rel.* **1999**, *57*, 115–125.
- 22 AMIDON, G. L., LENNERNÄS, H., SHAH, V. P., CRISON, J. R., A theoretical basis for a biopharmaceutical drug classification: the correlation of *in vitro* drug product dissolution and *in vivo* bioavailability, *Pharm. Res.* **1995**, *12*, 413–420.
- 23 THANOS, C. G., LIU, Z., GODDARD, M., REINEKE, J., BAILEY, N., CROSS, M., BURRILL, R., MATHIOWITZ, E., Enhancing the oral bioavailability of the poorly soluble drug dicumarol with a bioadhesive polymer, *J. Pharm. Sci.* **2003**, *92*, 1677–1689.
- 24 GRET, R., MINAMITAKE, Y., PERACCHIA, M. T., TRUBETSKOY, V., TORCHILIN, V., LANGER, R., Biodegradable long-circulating polymeric nanospheres, *Science* **1994**, *263*, 1600–1603.
- 25 HILL, T. L., A different approach to nanothermodynamics, *Nano Lett.* **2001**, *1*, 273–275.
- 26 AGNIHOTRI, S. A., MALLIKARJUNA, N. N., AMINABHAVI, T. M., Recent advances on chitosan-based micro- and nanoparticles in drug delivery, *J. Controlled Rel.* **2004**, *100*, 5–28.
- 27 XU, Y., DU, Y., HUANG, R., GAO, L., Preparation and modification of *N*-(2-hydroxyl) propyl-3-trimethyl ammonium chitosan chloride nanoparticle as a protein carrier, *Biomaterials* **2003**, *24*, 5015–5022.
- 28 WEBER, C., COESTER, C., KREUTER, J., LANGER, K., Desolvation process and surface characterization of protein nanoparticles, *Int. J. Pharm.* **2000**, *194*, 91–102.
- 29 GOVENDER, T., RILEY, T., EHTEZAZI, T., GARNETT, M. C., STOLNIK, S., ILLUM, L., DAVIS, S. S., Defining the drug incorporation properties of PLA-PEG nanoparticles, *Int. J. Pharm.* **2000**, *199*, 95–110.
- 30 KATAOKA, K., HARADA, A., NAGASAKI, Y., Block copolymer micelles for drug delivery: design, characterization and biological significance, *Adv. Drug Deliv. Rev.*, **2001**, *47*, 113–131.
- 31 TORCHILIN, V. P., Structure and design of polymeric surfactant-based drug delivery systems, *J. Controlled Rel.* **2001**, *73*, 137–172.
- 32 RAO, V. M., STELLA, V. J., When can cyclodextrins be considered for solubilization purposes?, *J. Pharm. Sci.* **2003**, *92*, 927–932.
- 33 ADAMS, M. L., LAVASANIFAR, A., KWON, G. S., Amphiphilic block copolymers for drug delivery, *J. Pharm. Sci.* **2003**, *92*, 1343–1355.
- 34 SOPPIMATH, K. S., TAN, D. C.-W., YANG, Y.-Y., pH-Triggered thermally responsive polymer core-shell nanoparticles for drug delivery, *Adv. Mater.* **2005**, *17*, 318–323.
- 35 LASIC, D. D., Doxorubicin in sterically stabilized liposomes, *Nature* **1996**, *380*, 561–562.
- 36 PAPAHDJOPOULOS, D., ALLEN, T. M., GABIZON, A., MAYHEW, E., MATTHAY, K., HUANG, S. K., LEE, K., WOODLE, M. C., LASIC, D. D., REDEMANN, C., MARTIN, F. J., Sterically stabilized liposomes: improvements in pharmacokinetics and antitumor

- therapeutic efficacy, *Proc. Natl Acad. Sci. USA* **1991**, *88*, 11460–11464.
- 37 SEDDON, J. M., Structure of the inverted hexagonal ( $H_{II}$ ) phase, and non-lamellar phase transitions of lipids, *Biochim. Biophys Acta* **1990**, *1031*, 1–69.
- 38 CANTOR, R. S., Lipid composition and the lateral pressure profile in bilayers, *Biophys. J.* **1999**, *76*, 2625–2639.
- 39 NIELSEN, C., ANDERSEN, O. S., Inclusion-induced bilayer deformations: effects of monolayer equilibrium curvature, *Biophys. J.* **2000**, *79*, 2583–2604.
- 40 SHILLCOCK, J. C., LIPOWSKY, R., Equilibrium structure and lateral stress distribution of amphiphilic bilayers from dissipative particle dynamics simulations, *J. Chem. Phys.* **2002**, *117*, 5048–5061.
- 41 HELFRICH, W., Elastic properties of lipid bilayers: theory and possible experiments, *Z. Naturforsch. C* **1973**, *28*, 693–703.
- 42 ANDERSON, D. M., GRUNER, S. M., LEIBLER, S., Geometrical aspects of the frustration in the cubic phases of lyotropic liquid crystals, *Proc. Natl Acad. Sci. USA* **1988**, *85*, 5364–5368.
- 43 BRIGGS, J., CHUNG, H., CAFFREY, M., The temperature–composition phase diagram and mesophase structure characterization of the monoolein/water system, *J. Phys. II* **1996**, *6*, 723–751.
- 44 SCRIVEN, L. E., Equilibrium bicontinuous structure, *Nature* **1976**, *263*, 123–125.
- 45 HYDE, S. T., ANDERSSON, S., ERICSSON, B., LARSSON, K., A cubic structure consisting of a lipid bilayer forming an infinite periodic minimal surface of the gyroid type in the glycerolmonooleate water system, *Z. Kristallogr.* **1984**, *168*, 213–219.
- 46 BECHER, P., *Encyclopedia of Emulsion Technology: Basic Theory*, Marcel Dekker, New York, **1983**.
- 47 FLOYD, G., Top ten considerations in the development of parenteral emulsions, *Pharm. Sci. Technol. Today* **1999**, *2*, 134–143.
- 48 WHEELER, J. J., WONG, K. F., ANSELL, S. M., MASIN, D., BALLY, M. B., Polyethylene glycol modified phospholipids stabilize emulsions prepared from triacylglycerol, *J. Pharm. Sci.* **1994**, *83*, 1558–64.
- 49 CHUNG, H., KIM, T. W., KWON, M., KWON, I. C., JEONG, S. Y., Oil components modulate physical characteristics and function of the natural oil emulsions as drug or gene delivery, *J. Controlled Rel.* **2001**, *71*, 339–350.
- 50 SZLEIFER, O. V., GERASIMOV, D., THOMPSON, H., Spontaneous liposome formation induced by grafted poly(ethylene oxide) layers: Theoretical prediction and experimental verification, *Proc. Natl Acad. Sci. USA* **1998**, *95*, 1032–1037.
- 51 LIU, Q., HU, Y., SONG, K., Liposome clearance from blood: different animal species have different mechanisms, *Biochim. Biophys. Acta* **1995**, *1240*, 277–284.
- 52 CULLIS, P. R., CHONN, A., SEMPLE, S. C., Interactions of liposomes and lipid-based carrier systems with blood proteins: relation to clearance behaviour *in vivo*, *Adv. Drug Deliv. Rev.* **1998**, *32*, 3–17.
- 53 NEEDHAM, T. J., MCINTOSH, D., LASIC, D., Hydration of polyethylene glycol-grafted liposomes, *Biochim. Biophys. Acta* **1992**, *1108*, 40–48.
- 54 CEH, B., LASIC, D. D., A rigorous theory of remote loading of drugs into liposomes, *Langmuir* **1995**, *11*, 3356–3368.
- 55 RHODES, G., XU, Z., BITTMAN, R., Structure of polymerizable bilayers VII: lateral organization of diacetylenic phosphatidylcholines with short proximal acyl chains, *Biochim. Biophys. Acta* **1992**, *1128*, 93–104.
- 56 ROY, B. C., SANTOS, M., MALLIK, S., CAMPIGLIA, A. D., Synthesis of metal chelating lipids to sensitize lanthanide ions, *J. Org. Chem.* **2003**, *68*, 3999–4007.
- 57 GUSTAFSSON, J., LJUSBERG-WAHREN, H., ALMGREN, M., LARSSON, K., Cubic lipid–water phase dispersed into submicron particles, *Langmuir* **1996**, *12*, 4611–4613.

- 58 GUSTAFSSON, J., LJUSBERG-WAHREN, H., ALMGREN, M., LARSSON, K., Submicron particles of reversed lipid phases in water stabilized by a nonionic amphiphilic polymer, *Langmuir* **1997**, *13*, 6964–6971.
- 59 CHUNG, H., KIM, J., UM, J. Y., KWON, I. C., JEONG, S. Y., Self-assembled nanocubicle as a carrier for peroral insulin delivery, *Diabetologia* **2002**, *45*, 448–451.
- 60 SPICER, P., HAYDEN, K., LYNCH, M., OFORI-BOATENG, A., BURNS, J., Novel process for producing cubic liquid crystalline nanoparticles (cubosomes), *Langmuir* **2001**, *17*, 5748–5756.
- 61 SPICER, P. T., SMALL, W. B., LYNCH, M. L., BURNS, J. L., Dry powder precursors of cubic liquid crystalline nanoparticles (cubosomes), *J. Nanoparticle Res.* **2002**, *4*, 297–311.
- 62 LARSSON, K., On periodic curvature and standing wave motions in cell membranes, *Chem. Phys. Lipids* **1997**, *88*, 15–20.
- 63 YANG, D., O'BRIEN, D. F., MARDER, S. R., Polymerized bicontinuous cubic nanoparticles (cubosomes) from a reactive monoacylglycerol, *J. Am. Chem. Soc.* **2002**, *124*, 13388–13389.
- 64 SCHNUR, J. M., Lipid tubules: a paradigm for molecularly engineered structures, *Science* **1993**, *262*, 1669–1675.
- 65 SPECTOR, M. S., PRICE, R. R., SCHNUR, J. M., Chiral lipid tubules, *Adv. Mater.* **1999**, *11*, 337–340.
- 66 SCHNUR, J. M., PRICE, R., RUDOLPH, A. S., Biologically engineered microstructures: controlled release applications, *J. Controlled Rel.* **1994**, *28*, 3–13.
- 67 PAPAHDJOPoulos, D., VAIL, W. J., JACOBSON, K., POSTE, G., Cochleate lipid cylinders: formation by fusion of unilamellar lipid vesicles, *Biochim. Biophys. Acta* **1975**, *394*, 483–491.
- 68 SANTANGELO, R., PADERU, P., DELMAS, G., CHEN, Z.-W., MANNINO, R., ZARIF, L., PERLIN, D., Oral efficacy of cochleate–amphotericin B (CAMB) in a mouse model with systemic candidiasis, *Antimicrob. Ag. Chemother.* **2000**, *44*, 2356–2360.
- 69 MANNINO, R. J., GOULD-FOGERITE, S., Antigen cochleate formulations for oral and systemic vaccination, In *New Generation Vaccines*, LEVINE, M. M. (Ed.), Marcel Dekker, New York, **1997**, pp. 000–000.
- 70 MORRISON, I. D., ROSS, S., *Colloidal Dispersions*, Wiley, New York, **2002**.
- 71 McDONALD, D. P., Micronization, *Mfg Chem. Aero. News* **1971**, 39.
- 72 YOSHII, H., SOOTTITANTAWAT, A., LIU, X.-D., ATARASHI, T., FURUTA, T., AISHIMA, S., OHGAWARA, M., Flavor release from spray-dried maltodextrin/gum arabic or soy matrices as a function of storage relative humidity, *Inn. Food Sci. Em. Technol.* **2001**, *2*, 55.
- 73 KINLOCH, A. J., YOUNG, R. J., *Fracture Behavior of Polymers*, Elsevier, New York, **1985**.
- 74 DUNCAN-HEWITT, W. C., WEATHERLY, G. C., Evaluating the fracture toughness of sucrose crystals using microindentation techniques, *Pharm. Res.* **1989**, *6*, 373–378.
- 75 SCHONERT, K., Aspects of very fine grinding, In *Challenges in Mineral Processing*, SASTRY, K. V. S., FUERSTENAU, M. C. (Eds.), Society of Mining Engineers, Littleton, CO, **1989**, pp. 155–172.
- 76 SCHONERT, K., Comminution from theory to practice, In *Proceedings of the XIX International Mineral Processing Congress*, Society of Mining Engineers, Littleton, CO, **1995**, pp. 7–14.
- 77 PLOEHN, H. J., RUSSEL, W. B., Interactions between colloidal particles and soluble polymers, *Adv. Chem. Eng.* **1990**, *15*, 137–228.
- 78 LEE, J., CHENG, Y., Critical freezing rate in freeze drying nanocrystal dispersions, *J. Controlled Rel.*, submitted.
- 79 GEDDE, U. W., *Polymer Physics*, Chapman & Hall, London, **1995**.
- 80 HANNAY, J. B., HOGARTH, J., On the solubility of solids in gases, *Proc. Roy. Soc. London* **1879**, *29*, 324.
- 81 McHUGH, M. A., KRUKONIS, V. J., *Supercritical Fluid Extraction*, Butterworth Heinemann, Boston, MA, **1994**.
- 82 TOM, J. W., DEBENEDETTI, P. G., Particle formation with supercritical

- fluids – review, *J. Aerosol Sci.* **1991**, *22*, 555–584.
- 83 SUBRAMANIAM, B., RAJEWSKI, R. A., SNAVELY, K., Pharmaceuticals processing with supercritical carbon dioxide, *J. Pharm. Sci.* **1997**, *86*, 885–890.
- 84 REVERCHON, E., Supercritical antisolvent precipitation of micro- and nano-particles, *J. Supercritical Fluids* **1999**, *15*, 1–21.
- 85 PALAKODATY, S., YORK, P., Phase behavioral effects on particle formation processes using supercritical fluids, *Pharm. Res.* **1999**, *16*, 976–985.
- 86 JUNG, J., PERRUT, M., Particle design using supercritical carbon dioxide, *J. Mater. Chem.* **2001**, *20*, 179–219.
- 87 YE, X., WAI, C. M., Making nano-materials in supercritical fluids: a review, *J. Chem. Educ.* **2003**, *80*, 198–205.
- 88 HAKUTA, Y., HAYASHI, H., ARAI, K., Fine particle formation using supercritical fluids, *Curr. Opin. Solid State Mater. Sci.* **2003**, *7*, 341–423.
- 89 KRUKONIS, V., Supercritical fluid nucleating of difficult-to-comminute solids, Presented at *Annual Meeting of the AIChE*, San Francisco, CA, **1984**.
- 90 MOHAMED, R. S., DEBENEDETTI, P. G., PRUD'HOMME, R. K., Effects of process conditions on crystals obtained from supercritical mixtures, *AIChE J.* **1989**, *325*–332.
- 91 KROBER, H., TEIPEL, U., KRAUSE, H., The formation of small organic particles using supercritical fluids, In *Proceedings (CD-ROM) of the 5th International Symposium on Supercritical Fluids*, ECKERT, C., TEJA, A. (Eds.), Atlanta, GA, **2000**.
- 92 DOMINGO, C., BERENDS, E., VAN ROSMALEN, G. M., Precipitations of ultrafine organic crystals from the rapid expansion of supercritical solutions over a capillary and a frit nozzle, *J. Supercritical Fluids* **1997**, *10*, 39–55.
- 93 FRANK, S. G., YE, C., Small particle formation and dissolution rate enhancement of relatively insoluble drugs using rapid expansion of supercritical solutions (RESS) processing, In *Proceedings (CD-ROM) of the 5th International Symposium on Supercritical Fluids*, ECKERT, C., TEJA, A. (Eds.), Atlanta, GA, **2000**.
- 94 DEBENEDETTI, P. G., TOM, J. W., YEO, S. D., LIM, G.-B., Application of supercritical fluids for the production of sustained delivery devices, *J. Controlled Rel.* **1993**, *24*, 27–44.
- 95 MISHIMA, K., MATSUYAMA, K., UCHIYAMA, H., IDE, M., Microcoating of flavones and 3-hydroxyflavone with polymer using supercritical carbon dioxide, In *Proceedings of the 4th International Symposium on Supercritical Fluids*, Sendai, Japan, **1997**, pp. 267–270.
- 96 MISHIMA, K., MATSUYAMA, K., YAMAUCHI, S., IZUMI, H., FURUDONO, D., Novel control of crystallinity and coating thickness of polymeric microcapsules of medicine by cosolvency of supercritical solution, In *Proceedings (CD-ROM) of the 5th International Symposium on Supercritical Fluids*, ECKERT, C., TEJA, A. (Eds.), Atlanta, GA, **2000**.
- 97 DEBENEDETTI, P. G., LIM, G.-B., PRUD'HOMME, R. K., Formation of protein microparticles by antisolvent precipitation, *European patent 0542314*, **1992**.
- 98 YEO, S. D., LIM, G.-B., DEBENEDETTI, P. G., BERNSTEIN, H., Formation of microparticulate protein powders using a supercritical fluid anti-solvent, *Biotechnol. Bioeng.* **1993**, *41*, 341–346.
- 99 THIERING, R., DEGHANI, F., DILLOW, A., FOSTER, N. R., The influence of operating conditions on the dense gas precipitation of model proteins, *J. Chem. Technol. Biotechnol.* **2000**, *75*, 29–41.
- 100 THIERING, R., DEGHANI, F., DILLOW, A., FOSTER, N. R., Solvent effects on the controlled dense gas precipitation of model proteins, *J. Chem. Technol. Biotechnol.* **2000**, *75*, 42–53.
- 101 WEBER, A., WEISS, C., TSCHERNJAEW, J., KUMMEL, R., Gas anti-solvent crystallization – from fundamentals to industrial applications, In *GVC-Fachausschub "High Pressure Chemical Engineering"*, Karlsruhe, Germany, **1999**, pp. 235–238.

- 102 REVERCHON, E., DE ROSA, I., DELLA PORTA, G., Effect of process parameter on the supercritical anti-solvent precipitation of microspheres of natural polymers, In *GVC-Fachaus-schub "High Pressure Chemical Engineering"*, Karlsruhe, Germany, 1999, pp. 251–258.
- 103 PLA-REVERCHON, E., DELLA PORTA, G., DE ROSA, I., SUBRA, P., LETOURNEUR, D., Biopolymers micronization by supercritical anti-solvent precipitation: the influence of some process parameters, In *Proceedings of the 5th Conference on Supercritical Fluids and their Applications*, Garda, 1999, pp. 473–478.
- 104 ELVASSORE, N., BERTUCCO, A., CALICETI, P., Production of protein-polymer micro-capsules by supercritical anti-solvent techniques. In *Proceedings (CD-ROM) of the 5th International Symposium on Supercritical Fluids*, ECKERT, C., TEJA, A. (Eds.), Atlanta, GA, 2000.
- 105 CHOU, Y. H., TOMASKO, D. L., GAS crystallization of polymer–pharmaceutical composite particles, In *Proceedings of the 4th International Symposium on Supercritical Fluids*, Sendai, Japan, 1997, pp. 55–57.
- 106 SOLAN, R., HOLLOWOOD, M. E., HUMPREYS, G. O., ASHRAF, P., YORK, P., Supercritical fluid processing: preparation of stable protein particles. In *Proceedings of the 5th International Symposium on Supercritical Fluids*, PERRUT, M., SUBRA, P. (Eds.), Nice, France, 1998, Vol. 1, pp. 301–306.
- 107 HANNA, M., YORK, P., Method and apparatus for the formulation of particles, *World patent WO 96/00 610*, 1996.
- 108 AMSDEN, B. G., GOOSEN, M. F. A., An examination of factors affecting the size, distribution and release characteristics of polymer microbeads made using electrostatics, *J. Controlled Rel.* 1997, 43, 183–196.
- 109 YOSHII, H., SOOTTITANTAWAT, A., LIU, X.-D., ATARASHI, T., FURUTA, T., AISHIMA, S., OHGAWARA, M., Flavor release from spray-dried maltodextrin/gum arabic or soy matrices as a function of storage relative humidity, *Inn. Food Sci. Em. Technol.* 2001, 2, 55–61.
- 110 HARDAS, N., DANVIRIYAKUL, S., FOLEY, J. L., NAWAR, W. W., CHINACHOTI, P., Accelerated stability studies of microencapsulated anhydrous milk fat, *Lebensm.-Wiss. U.-Technol.* 2000, 33, 506–511.
- 111 LEE, S. J., ROSEMBERG, M., Whey protein-based microcapsules prepared by double emulsification and heat gelation, *Lebensm.-Wiss. U.-Technol.* 2000, 33, 80–91.
- 112 LEE, Y. H., KIM, C. A., JANG, W. H., CHOI, H. J., JHON, M. S., Synthesis and electrorheological characteristics of microencapsulated polyaniline particles with melamine-formaldehyde resins, *Polymer* 2001, 42, 8277.
- 113 BURLAK, G., KOSHEVAYA, S., SANCHEZ-MONDRAGON, J., GRIMALSKY, V., Electromagnetic eigenoscillations and fields in a dielectric microsphere with multilayer spherical stack, *Opt. Commun.* 2001, 187, 91.
- 114 TAYLOR, G. I., Disintegration of water drops in an electric field, *Proc. Roy. Soc. London Ser. A* 1964, 280, 383.
- 115 CLOUPEAU, M., PRUNET-FOCH, B., Electrohydrodynamic spraying functioning modes: a critical review, *J. Aerosol Sci.* 1994, 25, 1021.
- 116 LOSCERTALES, I. G., BARRERO, A., GUERRERO, I., CORTIJO, R., MA'RQUEZ, M., GAÑÁN-CALVO, A. M., Micro/nano encapsulation via electrified coaxial liquid jets, *Science* 2002, 295, 1695.
- 117 DE LA MORA, F., LOSCERTALES, I. G., The current emitted by highly conducting Taylor cones, *J. Fluid Mech.* 1994, 260, 155.
- 118 GAÑÁN-CALVO, A. M., Generation of steady liquid microthreads and micron-sized monodisperse sprays in gas streams, *Phys. Rev. Lett.* 1997, 80, 285.
- 119 GAÑÁN-CALVO, M., Cone-jet analytical extension of Taylor's electrostatic solution and the asymptotic universal scaling laws in electro spraying, *Phys. Rev. Lett.* 1997, 79, 217.
- 120 GAÑÁN-CALVO, M., Generation of steady liquid microthreads and

- micron-sized monodisperse sprays in gas streams, *Phys. Rev. Lett.* **1998**, *80*, 285.
- 121 GAMERO-CASTANO, M., HRUBY, V., Electric measurements of charged sprays emitted by cone-jets, *J. Fluid Mech.* **2002**, *459*, 245.
- 122 LÓPEZ-HERRERA, J. M., BARRERO, A., LÓPEZ, A., LOSCERTALES, I. G., MÁRQUEZ, M., Coaxial jets generated from electrified Taylor cones-scaling laws, *J. Aerosol Sci.* **2003**, *34*, 535.
- 123 FENN, J. B., MANN, M., MENG, C. K., WONG, S. F., Electrospray ionization for mass spectrometry of large biomolecules, *Science* **1989**, *246*, 64.

## 10

# Production of Biofunctionalized Solid Lipid Nanoparticles for Site-specific Drug Delivery

Rainer H. Müller, Eliana B. Souto, Torsten Göppert and Sven Gohla

### 10.1

#### Introduction

The concept of site-specific drug delivery using particles has greatly benefited from the fast development of nanotechnology to a stage where it is possible not only to produce such small particles (less than 1  $\mu\text{m}$ ) in a very narrow size distribution range, but also to modify the particle surface in order to provide site-specific delivery of drugs.

It is well known that the size of nanoparticles and their surface characteristics are crucial factors to determine the success of the particles when used *in vivo*. With regard to the particle dimensions, it has been shown that nanometer-sized particles could be used for drug targeting, especially to the mononuclear phagocyte system (MPS) and the polymorphonuclear leukocytes, a mechanism that is based on their natural tropism and their biophysical properties [1, 2]. Concerning the surface characteristics, such as hydrophobicity and electrical charge, the internalization of nanoparticles by cells other than MPS cells is severely limited by the short residence time of particles in the blood. The modification of nanoparticle surface induces alterations in cell behavior distinct from the unmodified particles, suggesting that cell response and uptake can be directed via specifically engineered particle surfaces. The surface of nanoparticles can be modified using hydrophilic chains, such as polyethylene glycol (PEG), to prolong the circulation time of those carriers in the blood by resisting protein adsorption, reducing or avoiding the natural blood opsonization process and therefore their intracellular uptake by macrophages from the liver and spleen [2, 3]. The electrical charge of the nanoparticles also affects their *in vivo* fate [4–7].

This approach has been applied to target drug substances incorporated into colloidal drug carriers such as liposomes [8] and polymeric nanoparticles [9]. However, the use of those systems had some disadvantages. In spite of being one of the most extensively investigated drug delivery systems, liposomes show some chemical and physical stability problems that can lead to aggregation and drug degradation or expulsion of drug during storage, limiting their therapeutic performance [10]. Regarding the use of polymeric nanoparticles, the cytotoxicity of polymers

and the problems with polymer chemistry, as well as the need for  $\gamma$ -irradiation for production of sterile formulations, which can cause decomposition of incorporated drug and/or polymer and formation of potentially carcinogenic radicals, are the main disadvantages. Several synthetic polymers, such as poly(lactic acid) (PLA), poly( $\beta$ -hydroxybutyrate) (PHB) and poly(lactide-co-glycolide) (PLGA), have shown good histocompatibility and biodegradability, and their safety has been extensively documented. However, even those polymers which are accepted for use as microparticles and implants can show cytotoxic effects when delivered as nanoparticles or as very small microparticles [11].

Cytotoxic effects can occur both on the outside of the phagocytic cells or after ingestion in the interior of the cell. Therefore, both surfactants and matrix material can lead to cytotoxic degradation products [12, 13]. Furthermore, there is a lack of large-scale production methods for polymeric nanoparticles which are acceptable to the regulatory authorities and at the same time cost-effective. As a consequence – in contrast to liposomes – no polymeric nanoparticulate product is on the market (only polymeric microparticles).

In order to achieve higher viability of cells (i.e. better tolerability) and decrease the risk of toxicity, nanoparticles can be produced by using lipids which are solid both at room and at body temperature. Such systems are called solid lipid nanoparticles (SLN) [14], and they have been recently tested as site-specific carriers particularly for drugs that have a rapid metabolism and are quickly eliminated from the blood, i.e. peptide and protein-loaded SLN [15, 16]. A clear advantage of these particles is the fact that the lipid matrix is composed of physiological lipids, e.g. generally recognized as safe (“GRAS”) status, which decreases the risk of acute and chronic toxicity [17]. SLN prepared with several lipids and emulsifying agents do not exhibit any cytotoxic effects *in vitro* up to concentrations of 2.5% lipid. In fact, it has been shown that even concentrations higher than 10% of lipid phase led to a viability of 80% with human granulocytes in culture [12]. For comparison, PLA nanoparticles showed complete cell death at 0.5% [12, 18]. In addition, a high loading capacity for a broad range of drugs can be achieved, especially if they have lipophilic properties [17, 19].

Due to their physiological and biodegradable properties, SLN have been tested for several administration routes [20], such as the oral and peroral routes [21, 22], pulmonary route, ocular [23], topical, dermal and transdermal administration [24–29], as well as for gene therapy [30–32], as new adjuvants for vaccines [33], and for parenteral delivery [34–38]. Concerning the latter, SLN can accumulate in target tissues based on their natural host cell tropisms and on their biophysical properties (passive targeting). In practice, active targeting to cells other than MPS cells is often insufficient for rapid and specific accumulation in target tissues. Further improvement of tissue selectivity can be achieved by engineering the surface of SLN with hydrophilic polymers [39, 40] or coupling targeting ligands [41–43].

In the present chapter, the concept of differential protein adsorption as well as the concept of functionalization of SLN via surface modification will be defined and discussed from a practical point of view. First, a brief introduction to the concept of differential adsorption after intravenous administration will be given, fol-



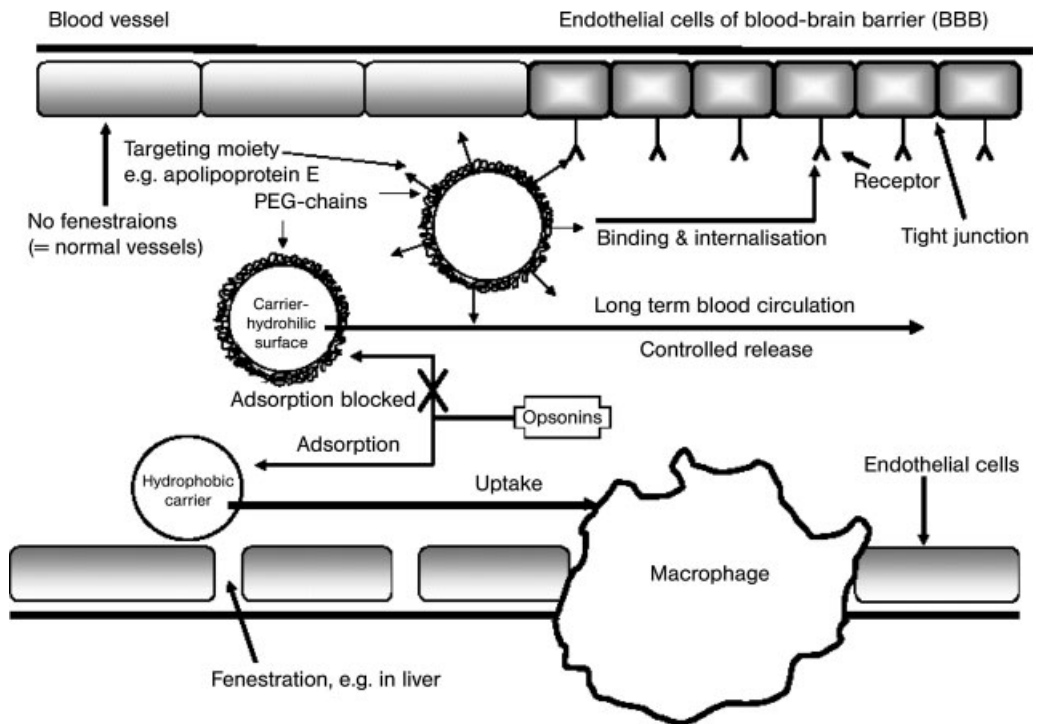


**Fig. 10.1.** Approaches to achieve passive targeting, long-circulating carriers for prolonged drug release and target-specific carriers (active targeting) via the intravenous route. (With permission after Ref. [80].)

lowed by a description of the methods used for the preparation of coated SLN. The last section will focus on the functionalization of SLN by modification of their surface characteristics, where some examples will be presented.

## 10.2 Concept of Differential Adsorption

By far the greatest attention to deliver drugs to selected sites in body has been focused on the intravenous route. Figure 10.1 reviews the main approaches to achieve both passive and active targeting. After injection, hydrophobic carriers will adsorb opsonins leading to uptake by the macrophages. In the liver, the macrophages are located in the layer of the endothelial cells. In case carriers are surface modified with hydrophilic polymers, e.g. PEG chains, the adsorption of opsonins will be minimized or avoided. Long-term blood circulation is achieved with such carriers which can be used, for example, for the controlled release of drugs. By at-

taching targeting moieties to these “stealth” carriers, location at specific cells can be achieved which carry the appropriate receptor and are accessible from the blood, e.g. the endothelial cells of the blood–brain barrier (BBB) or cells which are behind fenestrated blood vessels, such as liver or bone marrow.

Since the 1950s attempts have been made in order to correlate the organ distribution of intravenous injected drug carriers with their physicochemical properties, such as particle size [44] or electrical charge [7]. At the end of the 1980s it was realized that such a complex process like organ distribution could not be explained only by the physicochemical characteristics of the above-mentioned carriers [45]. After intravenous injection colloidal drug carriers immediately interact with plasma proteins, which are adsorbed onto the surface of the carriers. These adsorbed plasma proteins are generally accepted as the determining factor for the *in vivo* fate of the carriers. Drug carriers with different protein adsorption patterns will be recognized by different macrophage subpopulations (“concept of differential adsorption” [45, 46]), carrying proteins such as opsonins, like immunoglobulins or complement factors. When these are preferentially adsorbed onto the carriers’ surface, these carriers are immediately recognized by the MPS as foreign bodies and are therefore “cleared” from the blood. In contrast, when dysopsonins, such as hydrophilic proteins like albumin [47], are enriched on the carriers’ surface the systems will not be so easily recognized by macrophages. Such carriers are useful as circulating depots for the controlled release of drugs. Thus, in order to achieve an active drug targeting with these nonrecognizing carriers, it is important to have an additional enrichment of a protein mediating uptake into the target cells.

The decisive adsorption patterns acquired after intravenous injection depend on the physicochemical properties of the carriers [45, 48]. Therefore, there is a correlation between the physicochemical surface characteristics of the carriers, the plasma protein adsorption patterns and the resulting organ distribution (Fig. 10.2). Knowledge of this basic correlation can be exploited to develop site-specific intravenous carriers in a controlled way.

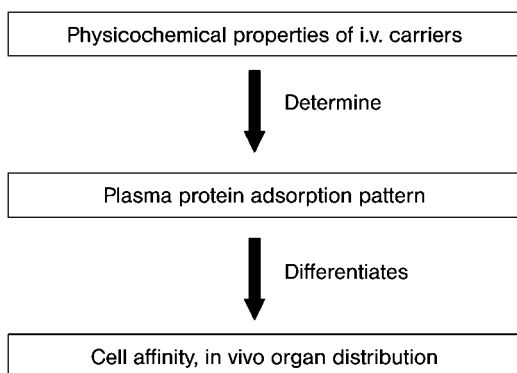


**Fig. 10.2.** Basic correlation exploited in the development of site-specific colloidal drug carriers (concept of “differential protein adsorption”).

In the middle of the 1990s, Kreuter et al. showed the possibility of site-specific targeting of various drugs, such as dalargin, enkephalin, tubocurarine and doxorubicin, into the brain by using polysorbate-coated poly(butyl cyanoacrylate) (PBCA)-nanoparticles [49–52]. The efficiency of drug delivery into the brain depended on the coating of those particles with polysorbate surfactants, particularly polysorbate 80, but also polysorbate 20, 40 and 60. Other surfactants such as poloxamers (e.g. poloxamer 338) led to no effects [53]. Using two-dimensional polyacrylamide gel electrophoresis (2-D PAGE), Müller et al. observed an enrichment of apolipoprotein E (apoE) on the surface of PBCA nanoparticles after incubation in human plasma. No apoE adsorption was seen after incubation with the other surfactants mentioned before [54]. ApoE seemed to play an important role in the transport of lipoproteins into the brain via the low-density lipoprotein receptor at the BBB [55]. Thus, it is possible that apoE-adsorbing drug carriers mimic lipoprotein particles leading to their brain uptake by endocytic processes. This theory was confirmed by turning the negative control in the Kreuter experiments [uncoated PBCA nanoparticles (no polysorbate adsorbed), loaded with dalargin] into a brain-specific carrier. ApoE was preadsorbed prior to injection and then the particles were able to carry dalargin across the BBB. Figure 10.3 summarizes the Kreuter experiments [49, 56].

In the experiments performed by Kreuter et al. the drug was adsorbed onto the surface, leading to a limited loading capacity. Furthermore, these polymeric nanoparticles exhibit the already mentioned toxicity problems. Due to the limited loading capacity, too much matrix material is required to deliver a sufficient amount of the drug to the brain. In addition, the *in vivo* biodegradation will be relatively slow, i.e. depending on the dose, the carrier material might accumulate in the target cell. In addition, the degradation leads to a release of toxicologically problematic formaldehyde [57], whereas it is a controversial discussion if the formaldehyde is really

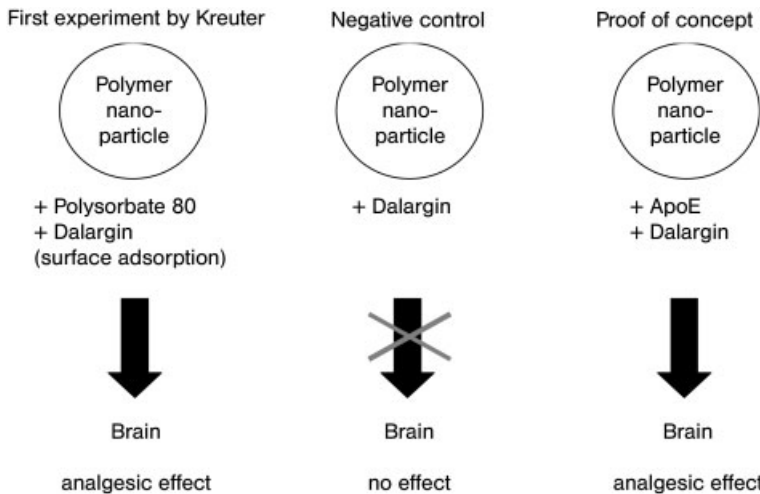


Fig. 10.3. Scheme of the experiments performed by Kreuter et al. (Modified after Ref. [56].)

a problem. Thus, the “concept of differential adsorption” and the analytical methodology to investigate the decisive adsorption patterns were transferred to the *in vivo* well tolerable SLN. Special SLN were produced using different surfactants and the influence on plasma protein adsorption patterns was investigated by 2-D PAGE.

### 10.3

#### Production of SLN

SLN of narrow size ranges can easily be produced and coated with hydrophilic polymers, providing convenient, readily targetable systems [15, 34, 36]. In order to prepare SLN with adsorbed hydrophilic polymers onto their surface, the literature describes three main production methods. These methods are the high-pressure homogenization (HPH) technique developed by Müller and Lucks [14], the microemulsion-based SLN technique developed by Gasco [58] and the solvent emulsification-evaporation technique described by Sjöström and Bergenstahl preparing SLN dispersions by solvent evaporation in oil-in-water (o/w) emulsions [59]. However, methods such as the solvent displacement and the emulsification-diffusion techniques, which have been used to prepare polymeric nanoparticles, have also been tested for SLN preparation [60].

Production of SLN by HPH can be done using either the hot or the cold homogenization technique. For both techniques, the active compound is dissolved or dispersed in the melted lipid prior to HPH [19, 20]. Concerning the hot technique, which is the most frequently applied technique, two different phases are prepared at the same temperature – the lipid phase consisting of melted lipid mixed with drug and the aqueous phase consisting of a hot solution where the hydrophilic coating polymer or protein is dissolved. Both phases are mixed by high-speed stirring or by ultrasound breaking the large droplets of the internal lipid phase into smaller ones yielding a pre-emulsion. This pre-emulsion is then passed through a high-pressure homogenizer applying, for example, a homogenization pressure of 500 bar and one to three homogenization cycles. The obtained nanoemulsion is cooled and solidifies, forming an aqueous SLN dispersion. This technique can process lipophilic and insoluble drugs. Even temperature-sensitive compounds (e.g. retinol) can be incorporated into the SLN matrix by hot HPH once the exposure time to elevated temperatures is relatively short [19]. However, this technique is not suitable for incorporating hydrophilic drugs because they will partition from the melted lipid to the water phase during the homogenization step, resulting in a too low loading capacity.

With regard to the cold technique, the drug-containing lipid melt is cooled and solidified. Dry ice or liquid nitrogen are added to increase the brittleness of the lipid and to ease the further milling procedure. The high cooling rate favors a homogeneous distribution of the drug within the lipid matrix. After solidification, the lipidic mass is ground by means of ball or mortar milling to yield lipid microparticles with a diameter between 50 and 100  $\mu\text{m}$ . The lipid microparticles are then

dispersed in a cold surfactant solution by stirring, yielding a macro-suspension. This suspension is passed through a high-pressure homogenizer at/or below room temperature and the microparticles are broken down to form SLN. The cavitation and shear forces in the homogenization gap are sufficiently high to break the microparticles and to yield SLN. The cold HPH technique minimizes the thermal exposure of the sample, but does not avoid it completely due to the melting of the lipid in the initial step of the process. Therefore, this technique is recommended for extremely temperature-sensitive or hydrophilic drugs, which might partition from the liquid lipid phase to the water phase during hot HPH. SLN prepared by this procedure possess slightly higher mean particle sizes and polydispersity indices compared to those obtained by the hot HPH technique of the same lipid at identical homogenization parameters (pressure, temperature and number of homogenization cycles). To further reduce the mean particle size and to minimize the polydispersity, a higher number of homogenization cycles can be applied. The cold HPH technique can also be employed when the lipid matrix is composed by lipids with high melting points [61]. Note that this technique is less effective in dispersing the lipids. During the production process, the lipid matrix remains mainly in the solid state despite possible high (but extremely short) temperature peaks occurring in the high-pressure homogenizer. The homogenization can be performed slightly below the melting point of the lipid (e.g. 5–10 °C), which seems to lead to a softening of the lipid during the homogenization process. The softened lipid can be more easily dispersed, leading to a more uniform product of smaller mean SLN diameter. The homogenization temperature needs to be carefully selected because otherwise the loss of hydrophilic drugs to the water phase might be too high.

For the preparation of SLN using the microemulsion technique developed by Gasco, the lipid phase is melted and at the same temperature (approximately 60–70 °C) an o/w surfactant/cosurfactant-containing aqueous phase is prepared [58, 62]. Both lipid and aqueous phases are added, and mixed in such a ratio that a microemulsion results. SLN are obtained when the hot microemulsion is diluted into excess of cold water leading to a “breaking” of the microemulsion, converting it into an ultrafine nanoemulsion, which recrystallizes forming SLN. The reasons for the breaking of the emulsion are the dilution with water and the reduction of temperature narrowing the microemulsion region.

Regarding the preparation of SLN by solvent evaporation in o/w emulsions described by Sjöström and Bergenståh, the lipid phase is dissolved in a water-immiscible organic solvent, such as cyclohexane, chloroform or methylene chloride. Then the drug is dissolved or dispersed producing an organic phase containing the drug [63, 64]. This organic phase is emulsified in an o/w surfactant-containing aqueous phase by mechanical stirring. Upon evaporation of the organic solvent from the obtained o/w emulsion under mechanical stirring or reduced pressure, a nanoparticle dispersion is formed by precipitation of the lipid in the aqueous medium.

In the solvent displacement technique described Fessi et al. [65], the lipid phase is dissolved in a semipolar water-miscible solvent, such as ethanol, acetone or

methanol, where the active compound is also dissolved or dispersed. Simultaneously, an o/w surfactant-containing aqueous phase is prepared. The organic phase is injected into the aqueous phase under magnetic stirring. A violent spreading is observed because of the miscibility of both phases. Droplets of solvent of nanometer size are torn from the o/w interface. These droplets are rapidly stabilized by the surfactant molecules presented in the aqueous phase, until diffusion of the solvent is complete and lipid precipitation has occurred. Removal of solvent can be performed by distillation. SLN are formed after total evaporation of the water-miscible organic solvent.

With regard to the emulsification-diffusion methodology described by Quintanar-Gerrero and Fessi, this technique involves the use of a partially water-soluble solvent, such as benzyl alcohol [66] or tetrahydrofuran [67], which is saturated with water to ensure the initial thermodynamic equilibrium between those two liquids (water and solvent). The lipid is dissolved in the saturated solvent producing an organic phase where the drug is added. This organic phase is then emulsified, under vigorous agitation, in an aqueous solution containing a stabilizer agent obtaining an o/w emulsion. The subsequent addition of water to the system, under moderate mechanical stirring, causes solvent diffusion into the external phase and the lipid starts precipitating. Depending on its boiling point, the solvent can be eliminated by distillation or ultrafiltration. After the organic solvent is totally eliminated, an aqueous dispersion of SLN is formed.

Comparing the different methodologies described above, HPH is the most broadly used in different areas and it is also established in pharmaceutical production, e.g. the production of emulsions for parenteral nutrition (Intralipid® and Lipofundin®) [17]. This technique overcomes a major problem of other methods, i.e. large scale production. HPH also leads to nanoparticles with a relatively homogeneous size distribution, which increases the physical stability of the aqueous SLN dispersion.

The microemulsion method has the disadvantage of the dilution of the particle suspension with water, which needs to be removed. However, it avoids the collapse of the hydrophilic chains coating the surface of the particles [20]. Methods requiring solvent evaporation from o/w emulsions have the inconvenience of using organic solvents. In addition, evaporation must be fast in order to avoid collapse of the hydrophilic chains and potential aggregation.

#### 10.4

##### Functionalization by Surface Modification

As already mentioned, targeting of drugs to different sites of the body via intravenous administration requires avoidance of recognition of the carrier system by macrophages of the MPS. To achieve this goal, nanoparticles were engineered by modifying the surface using nonionic surfactants such as poloxamers, poloxamines or polysorbates, reducing adsorption of proteins and blood opsonins compared to uncoated particles [68] (Fig. 10.4).

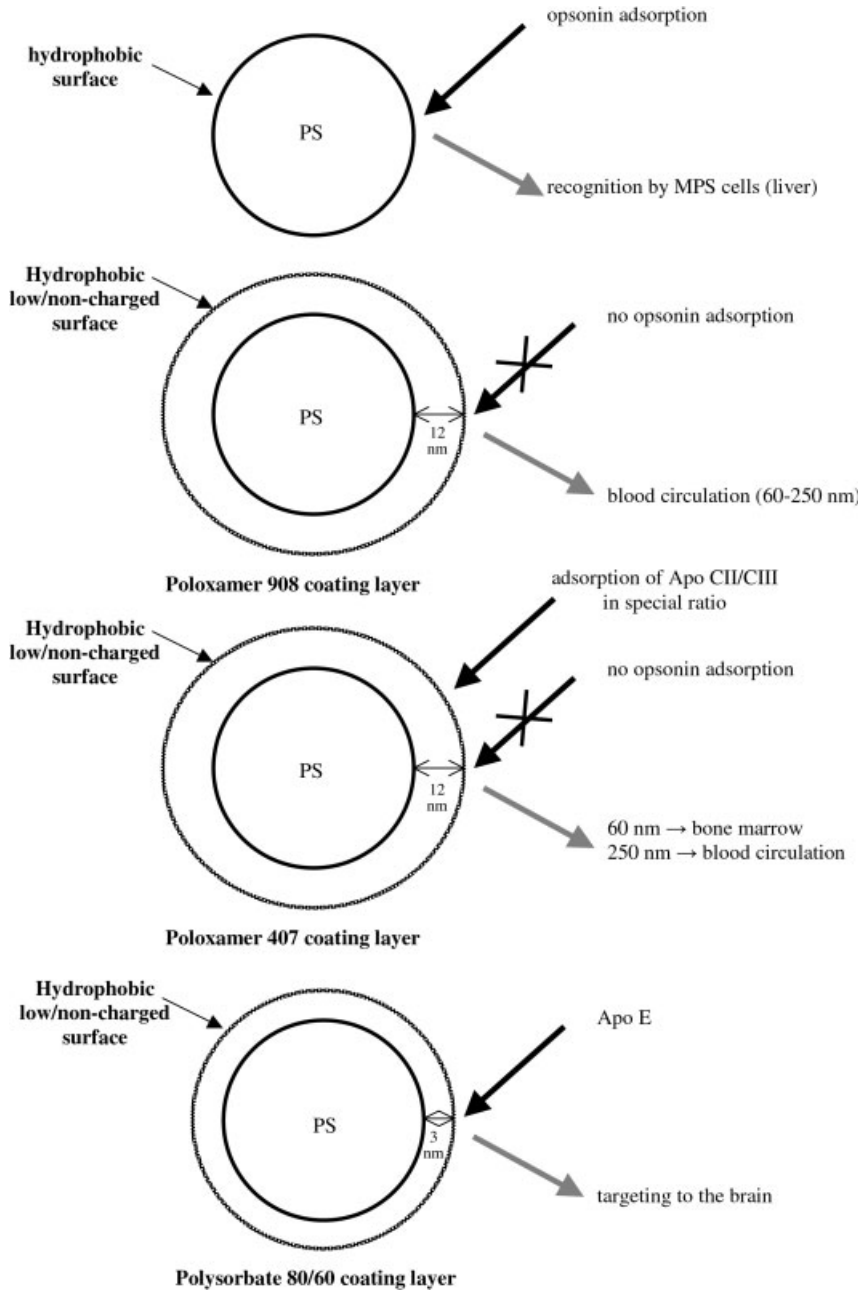


**Fig. 10.4.** Functionalization by surface modification of nanoparticles with poloxamer and polysorbate surfactants and resulting effects obtained *in vivo* (PS, polystyrene particle; PBCH, polybutylcyanoacrylate nanoparticle).

Once the phagocytic uptake is dependent on the surface hydrophilicity, i.e. it increases with the increase of hydrophilicity, it would be beneficial to have an enrichment of hydrophilic proteins (so-called dysopsonins) on the carriers' surface [69–71]. Such dysopsonins are, for example, albumin and apolipoproteins. Apolipoproteins are inherently adsorbed onto the surface of hydrophobic lipids such as triacylglycerols, cholesterol and cholesterol esters, forming lipoproteins in the blood. They show a relatively flexible molecular structure, which is able to change its conformation when adsorbing onto surfaces (“soft proteins”) [72]. This ability of changing its multiple  $\alpha$ -helical segments in the interface in contact to water is the crucial property of these proteins for the efficient removal of nonpolar residues. Therefore, it has been anticipated that apolipoproteins would have a great affinity to SLN as well, because these particles also have a lipid core like lipoproteins. Indeed, a 5-min incubation of different SLN formulations with human plasma at 37 °C and subsequent 2-D PAGE analysis revealed apolipoprotein adsorption of up to 90% of the total amount of proteins adsorbed.

Figure 10.5 shows the plasma protein adsorption patterns obtained after 2-D PAGE analysis (2-D PAGE separation and subsequent silver staining) of cetyl palmitate-based SLN (10% m/m), stabilized with polysorbate 60 (PS60-SLN) and stabilized with poloxamer 338 (1.2% m/m) (PX338-SLN).

The adsorption patterns did not differ greatly with regard to the qualitative aspects of the adsorbed proteins. However, the apolipoproteins showed particularly distinct quantitative changes in the adsorbed amounts, showing the importance of the surfactant used for production of functionalized SLN.

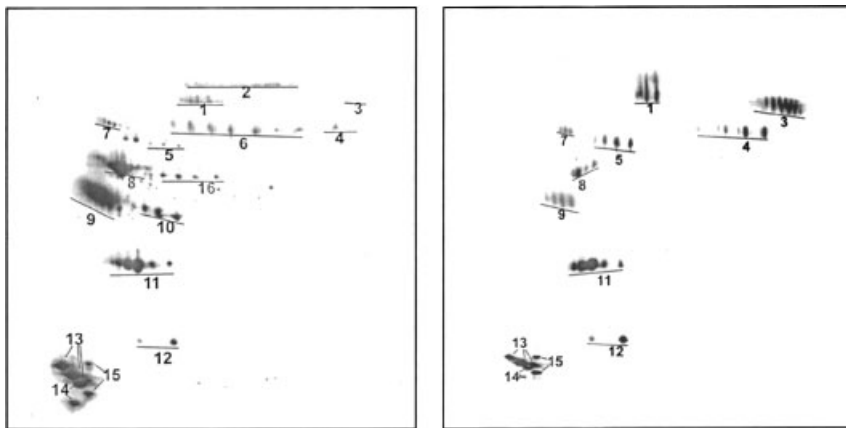


**Fig. 10.5.** Plasma protein adsorption patterns of PS60-SLN (left) and PX338-SLN (right) obtained after 2-D PAGE separation and silver staining. The whole 2-D gels are shown;  $pI$  4.0–9.0 (from left to right, non-linear) molecular weight 250–60 000 Da (top to bottom, non-linear); 1, albumin; 2, IgM  $\mu$

chain; 3, fibrinogen  $\alpha$  chain; 4, fibrinogen  $\beta$  chain; 5, fibrinogen  $\gamma$  chain; 6, apoH; 7,  $\alpha_1$ -antitrypsin; 8, apoA-IV; 9, apoJ; 10, apoE; 11, apoA-I; 12, transthyretin; 13, apoC-III; 14, apoC-II; 15, apoA-II; 16, haptoglobin  $\beta$  chain. (With permission after Ref. [46].)



Interestingly, apoE, which is hardly detectable on 2-D PAGE gels of human plasma, was enriched on the PS60-SLN (Fig. 10.5, left, spot 10), whereas no apoE could be detected on the PX338-SLN. ApoE was also adsorbed onto SLN surface, stabilized by polysorbate 20, 40 and 80 (in similar amounts). This result is in agreement with the findings documented by Müller et al., who investigated the brain specificity of PBCA nanoparticles coated with polysorbates and the lack of brain specificity of PBCA nanoparticles coated with poloxamers (e.g. poloxamer 338) [54].

The spot intensity was evaluated using special software from Bio-Rad (MELANIE III). For data evaluation it has to be taken into account that the silver-staining density is characteristic for each protein [73]. A quantitative comparison between identical protein types on different 2-D PAGE gels is valid, but not between different protein types on an identical gel. Therefore, quantitative 2-D PAGE data assessment is called "semi-quantitative". Nevertheless, it can be used for a reliable approximation of the amount of protein adsorbed.

Typical opsonins, such as immunoglobulins or complement factors, were not detected or were detected in a very low amount (below 5%) on both types of SLN. However, it must be pointed out that PX338-SLN shows higher quantities of fibrinogen adsorbed onto their surface, which has an opsonic function. However, apolipoproteins dominate the protein adsorption patterns (about 86% on PS60-SLN and about 70% on PX338-SLN). From these results, it can be concluded that both SLN types should have the potential to circulate in the blood stream for a prolonged time; in particular, PS60-SLN should be able to target drugs to the brain. The first results of *in vivo* experiments conducted with Nile Red-labeled PS60-SLN indeed nicely showed adherence of particles to the endothelial cells of the brain vessels [74, 75]. Pictures obtained by confocal laser scanning microscopy of the mouse brain tissue showed the particles adhering to the endothelium of the brain vessels, as well as the dye diffusing into the brain tissue. See Fig. 10.6.

Studying a full range of different poloxamer polymers as stabilizers for different SLN formulations revealed that apoE was preferentially adsorbed on the surface of SLN which were stabilized with a poloxamer having a low number of polyethylene oxide (PEO) units. There was an exponential relationship between adsorbed apoE and the PEO chain length, showing highest adsorption of apoE when using poloxamer 184 and poloxamer 235 [76]. These results are in good agreement with the apoE values obtained by Blunk [77] with o/w emulsions (20% w/w soya oil) stabilized with the respective poloxamers (2.5% w/w). Again, highest apoE adsorption occurred when using polymers with short PEO blocks in the molecule.

On cetyl palmitate SLN stabilized with egg lecithin, apoE was enriched up to 5% on their surface [78]. Recently, interesting accumulations in the brain were reported after intravenous injection of SLN with camptothecin [34], paclitaxel [79] and 3',5'-dioctanoyl-5-fluoro-2'-deoxyuridine [15]. All of these workgroups used lecithin as a stabilizer among other surfactants. From this, it can be assumed that apoE was also enriched on the surface of these SLN, leading to their uptake into the endothelial cells of the BBB.

According to these observations, it can be assumed that SLN are suitable car-

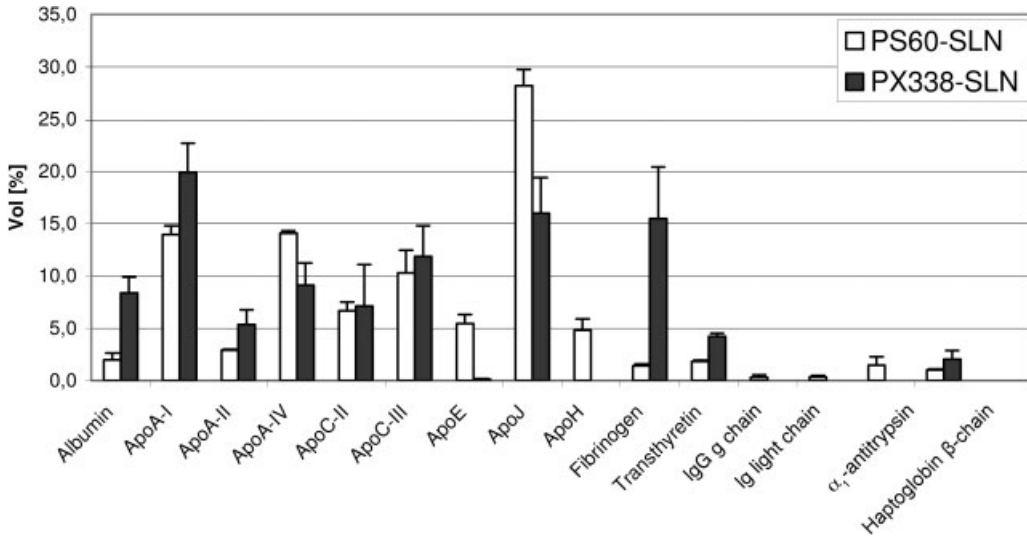


**Fig. 10.6.** Semiquantitative plasma protein composition on PS60-SLN and PX338-SLN expressed in percent (percentage of the overall detected protein pattern); error bars represent the standard deviation ( $n = 2$ ). (With permission after Ref. [46].)

riers, especially when stabilized with polysorbates, to be biofunctionalized with apoE in the blood to have a high potential to deliver drugs to the brain.

## 10.5

### Conclusions

Over recent decades, significant efforts have been made towards the surface modification of various polymeric drug carriers with PEG, not only to improve their biocompatibility and blood circulation times, but also to resist protein adsorption and to increase target cell uptake efficiency.

The surface characteristics of intravenously administered particulate drug carriers decisively influence the protein adsorption, which is regarded as a key factor for the *in vivo* fate of the carriers. It has already been shown that immobilization of PEG on nanoparticles reduces uptake by MPS cells and subsequently increases the amount of nanoparticle uptake into cancer cells in comparison to unmodified nanoparticles. For brain-targeting, substances such as the hexapeptide dalargin, loperamide and doxorubicin have been adsorbed into coated polymeric nanoparticles with a surfactant. In order to reduce toxicological problems of polymeric nanoparticles, biodegradable lipid nanoparticles such SLN can be used. This chapter has given a brief review of the state of the art of biofunctionalized SLN, as well as a brief description of the main production methods of these carriers. *In vivo* data

about achievements in targeting with SLN are summarized. The results obtained with lipid nanoparticles systems are quite promising for further developments in this research field.

## References

- 1 J. KARAJGI, N. K. JAIN, S. P. VYAS, Passive vectoring of a colloidal carrier system for sodium stibogluconate: preparation, characterization and performance evaluation, *J. Drug Target.* **1993**, *3*, 197–206.
- 2 R. H. MÜLLER, *Colloidal Carriers for Controlled Drug Delivery and Targeting*, CRC Press, Boca Raton, FL, **1991**.
- 3 L. ILLUM, S. S. DAVIS, R. H. MÜLLER, E. MAK, P. WEST, The organ distribution and circulation time of intravenously injected colloidal carriers sterically stabilized with a block copolymer – poloxamine 908, *Life Sci.* **1987**, *40*, 367–374.
- 4 A. GESSNER, A. LIESKE, B. R. PAULKE, R. H. MÜLLER, Influence of surface charge density on protein adsorption on polymeric nanoparticles: analysis by two-dimensional electrophoresis, *Eur. J. Pharm. Biopharm.* **2002**, *54*, 165–170.
- 5 L. ILLUM, L. O. JACOBSEN, R. H. MÜLLER, E. MAK, S. S. DAVIS, Surface characteristics and the interaction of colloidal particles with mouse peritoneal macrophages, *Biomaterials* **1987**, *8*, 113–117.
- 6 K. LIND, M. KRESSE, R. H. MÜLLER, Comparison of protein adsorption patterns onto differently charged hydrophilic superparamagnetic iron oxide particles obtained *in vitro* and *ex vivo*, *Electrophoresis* **2001**, *22*, 3514–3521.
- 7 D. J. WILKENS, P. A. MEYERS, Studies on the relationship between the electrophoretic properties of colloids and their blood clearance and organ distribution in the rat, *Br. J. Exp. Pathol.* **1966**, *47*, 568–576.
- 8 W. E. BUCKE, S. LEITZKE, J. E. DIEDRICH, K. BORNER, H. HAHN, S. EHLERS, R. H. MÜLLER, Surface-modified amikacin-liposomes: organ distribution and interaction with plasma proteins, *J. Drug Target.* **1997**, *5*, 99–108.
- 9 P. CALVO, B. GOURITIN, H. VILLARROYA, F. ECLANCHER, C. GIANNAVOLA, C. KLEIN, J. P. ANDREUX, P. COUVREUR, Quantification and localization of PEGylated polycyanoacrylate nanoparticles in brain and spinal cord during experimental allergic encephalomyelitis in the rat, *Eur. J. Neurosci.* **2002**, *15*, 1317–1326.
- 10 G. GREGORIADES, *Liposomes as Drug Carriers*, Wiley, Chichester, **1989**.
- 11 A. SMITH, J. M. HUNNEYBALL, Evaluation of poly(lactic acid) as biodegradable drug delivery system for parenteral administration, *Int. J. Pharm.* **1986**, *30*, 215–220.
- 12 R. H. MÜLLER, S. MAASEN, H. WEYHERS, F. SPECHT, J. S. LUCKS, Cytotoxicity of magnetite-loaded polylactide, poly(lactide/glycolide) particles and solid lipid nanoparticles, *Int. J. Pharm.* **1996**, *138*, 85–94.
- 13 C. LHERM, R. H. MÜLLER, F. PUISIEUX, P. COUVREUR, Alkylcyanoacrylate drug carriers II: cytotoxicity of cyanoacrylate nanoparticles with different alkyl chain length, *Int. J. Pharm.* **1992**, *84*, 13–22.
- 14 R. H. MÜLLER, J.-S. LUCKS, Azneistoff-träger aus festen Lipidteilchen – feste Lipid Nanosphären (SLN), *European patent 0605497*, **1996**.
- 15 J.-X. WANG, X. SUN, Z.-R. ZHANG, Enhanced brain targeting by synthesis of 3'-5'-dioctanoyl-5-fluoro-2'-deoxyuridine and incorporation into solid lipid nanoparticles, *Eur. J. Pharm. Biopharm.* **2002**, *54*, 285–290.
- 16 F. Q. HU, Y. HONG, H. YUAN, Preparation and characterization of solid lipid nanoparticles containing

- peptide, *Int. J. Pharm.* **2004**, *273*, 29–35.
- 17 R. H. MÜLLER, W. MEHNERT, J.-S. LUCKS, C. SCHWARZ, A. ZUR MÜHLEN, H. WEYHERS, C. FREITAS, D. RÜHL, Solid lipid nanoparticles (SLN) – an alternative colloidal carrier system for controlled drug delivery, *Eur. J. Pharm. Biopharm.* **1995**, *41*, 62–69.
  - 18 S. MAAßEN, C. SCHWARZ, W. MEHNERT, J. S. LUCKS, F. YUNIS-SPECHT, B. W. MÜLLER, R. H. MÜLLER, Comparison of cytotoxicity between polyester nanoparticles and solid lipid nanoparticles (SLN), *Proc. Int. Symp. Controlled Rel. Bioact. Mater.* **1993**, *20*, 490–491.
  - 19 R. H. MÜLLER, K. MÄDER, S. GOHLA, Solid lipid nanoparticles (SLN) for controlled drug delivery – a review of the state of art, *Eur. J. Pharm. Biopharm.* **2000**, *50*, 161–177.
  - 20 W. MEHNERT, K. MÄDER, Solid lipid nanoparticles – production, characterization and applications, *Adv. Drug Deliv. Rev.* **2001**, *47*, 165–196.
  - 21 S. YANG, J. ZHU, Y. LU, B. LIANG, C. YANG, Body distribution of camptothecin solid lipid nanoparticles after oral administration, *Pharm. Res.* **1999**, *16*, 751–757.
  - 22 P. M. BUMMER, Physical chemical considerations of lipid-based oral drug delivery solid lipid nanoparticles, *Crit. Rev. Ther. Drug Carrier Syst.* **2004**, *21*, 1–19.
  - 23 R. H. MÜLLER, M. RADTKE, S. A. WISSING, S. A., Solid lipid nanoparticles and nanostructured lipid carriers, In *Encyclopedia of Nanoscience and Nanotechnology*, H. S. NALWA (Ed.), American Scientific Publishers, Stevenson Ranch, CA, **2004**, pp. 43–56.
  - 24 M. KALARIYA, B. K. PADHI, M. CHOUGULE, A. MISRA, Methotrexate-loaded solid lipid nanoparticles for topical treatment of psoriasis: formulation and clinical implications, *Drug Deliv. Technol.* **2004**, *4*, 64–66.
  - 25 A. ILLING, T. UNRUH, Investigation on the flow behavior of dispersions of solid triglyceride nanoparticles, *Int. J. Pharm.* **2004**, *284*, 123–131.
  - 26 M. SCHÄFER-KORTING, W. MEHNERT, Delivery of lipophilic compounds with lipid nanoparticles – applications in dermatics and for transdermal therapy, In *Lipospheres in Drug Targets and Delivery: Approach, Methods and Applications*, C. NORSTRUTTI (Ed.), CRC Press, Boca Raton, FL, **2005**, pp. 127–142.
  - 27 E. B. SOUTO, S. A. WISSING, C. M. BARBOSA, R. H. MÜLLER, Evaluation of the physical stability of SLN and NLC before and after incorporation into hydrogel formulations, *Eur. J. Pharm. Biopharm.* **2004**, *58*, 83–90.
  - 28 E. B. SOUTO, S. A. WISSING, C. M. BARBOSA, R. H. MÜLLER, Development of a controlled release formulation based on SLN and NLC for topical clotrimazole delivery, *Int. J. Pharm.* **2004**, *278*, 71–77.
  - 29 Z. MEI, H. CHEN, T. WENG, Y. YANG, X. YANG, Solid lipid nanoparticle and microemulsion for topical delivery of triptolide, *Eur. J. Pharm. Biopharm.* **2003**, *56*, 189–196.
  - 30 C. OLBRICH, K. TABATT, S. WISSING, N. SCHOELER, R. H. MUELLER, Solid lipid nanoparticles: interaction with cells, cytokine production, and enzymatic degradation, In *Lipospheres in Drug Targets and Delivery: Approach, Methods and Applications*, C. NORSTRUTTI (Ed.), CRC Press, Boca Raton, FL, **2005**, pp. 101–125.
  - 31 K. TABATT, C. KNEUER, M. SAMETI, C. OLBRICH, R. H. MÜLLER, C.-M. LEHR, U. BAKOWSKY, Transfection with different colloidal systems: comparison of solid lipid nanoparticles and liposomes, *J. Controlled Rel.* **2004**, *97*, 321–332.
  - 32 K. TABATT, M. SAMETI, C. OLBRICH, R. H. MÜLLER, C.-M. LEHR, Effect of cationic lipid and matrix lipid composition on solid lipid nanoparticle-mediated gene transfer, *Eur. J. Pharm. Biopharm.* **2004**, *57*, 155–162.
  - 33 C. OLBRICH, R. H. MÜLLER, K. TABATT, O. KAYSER, C. SCHULZE, R. SCHADE, Stable biocompatible adjuvants – a new type of adjuvant based on solid lipid nanoparticles: a

- study on cytotoxicity, compatibility and efficacy in chicken, *Altern. Lab. Anim.* **2002**, *30*, 443–458.
- 34 A. C. YANG, L. F. LU, Y. CAI, J. B. ZHU, B. W. LIANG, C. Z. YANG, Body distribution in mice of intravenously injected camptothecin solid lipid nanoparticles and targeting effect on brain, *J. Controlled Rel.* **1999**, *59*, 299–307.
  - 35 G. P. ZARA, A. BARGONI, R. CAVALLI, A. FUNDARO, D. VIGHETTO, M. R. GASCO, Pharmacokinetics and tissue distribution of idarubicin-loaded solid lipid nanoparticles after duodenal administration to rats, *J. Pharm. Sci.* **2002**, *91*, 1324–1333.
  - 36 G. P. ZARA, R. CAVALLI, A. BARGONI, A. FUNDARO, D. VIGHETTO, M. R. GASCO, Intravenous administration to rabbits of non-stealth and stealth doxorubicin-loaded solid lipid nanoparticles at increasing concentrations of stealth agent: pharmacokinetics and distribution of doxorubicin in brain and other tissues, *J. Drug Target.* **2002**, *10*, 327–335.
  - 37 A. FUNDARO, R. CAVALLI, A. BARGONI, D. VIGHETTO, G. P. ZARA, M. R. GASCO, Non-stealth and stealth solid lipid nanoparticles (SLN) carrying doxorubicin: pharmacokinetics and tissue distribution after i.v. administration to rats, *Pharmacol. Res.* **2000**, *42*, 337–343.
  - 38 S. C. YANG, J. B. ZHU, Preparation and characterization of camptothecin solid lipid nanoparticles, *Drug Dev. Ind. Pharm.* **2002**, *28*, 265–274.
  - 39 T. GÖPPERT, R. H. MÜLLER, Plasma protein adsorption of Tween 80- and Poloxamer 188-stabilized solid lipid nanoparticles, *J. Drug Target.* **2003**, *11*, 225–231.
  - 40 T. GÖPPERT, R. H. MÜLLER, Alternative sample preparation prior to two-dimensional electrophoresis protein analysis on solid lipid nanoparticles, *Electrophoresis* **2004**, *25*, 134–140.
  - 41 W. M. PARDRIDGE, Y. S. KANG, J. L. BUCIAK, J. YANG, Human insulin receptor monoclonal antibody undergoes high affinity binding to human brain capillaries *in vitro* and rapid transcytosis through the blood–brain barrier *in vivo* in the primate, *Pharm. Res.* **1995**, *12*, 807–816.
  - 42 Y. ZHANG, W. M. PARDRIDGE, Rapid transferrin efflux from brain to blood across the blood–brain barrier, *J. Neurochem.* **2001**, *76*, 1597–1600.
  - 43 B. DEHOUCK, M. P. DEHOUCK, J. C. FRUCHART, R. CECHELLI, Upregulation of the low density lipoprotein receptor at the blood–brain barrier: intercommunications between brain capillary endothelial cells and astrocytes, *J. Cell Biol.* **1994**, *126*, 465–473.
  - 44 S. S. DAVIS, Colloids as drug-delivery systems, *Pharm. Technol.* **1981**, *5*, 71–88.
  - 45 R. H. MÜLLER, S. HEINEMANN, Surface modelling of microparticles as parenteral systems with high tissue affinity, In *Bioadhesion – Possibilities and Future Trends*, R. GURNY, H. E. JUNGINGER (Eds.), Wissenschaftliche Verlagsgesellschaft, Stuttgart, **1989**, pp. 202–214.
  - 46 T. BLUNK, D. F. HOCHSTRASSER, J.-C. SANCHEZ, B. W. MÜLLER, R. H. MÜLLER, Colloidal carriers for intravenous drug targeting: plasma protein adsorption patterns on surface-modified latex particles evaluated by two-dimensional polyacrylamide gel electrophoresis, *Electrophoresis* **1993**, *14*, 1382–1387.
  - 47 D. R. ABSOLOM, Opsonins and dysopsonins: an overview, *Methods Enzymol.* **1986**, *132*, 281–318.
  - 48 J. L. BRASH, Protein adsorption at the solid-solution interface in relation to blood–material interactions, In *Proteins at Interfaces: Physicochemical and Biochemical Studies*, J. L. BRASH, T. A. HORBETT (Eds.), ACS, Washington, DC, **1987**, pp. 490–506.
  - 49 R. ALYAUDIN, D. GOTHIER, V. PETROV, D. KHARKEVICH, J. KREUTER, Analgesic activity of the hexapeptide dalargin adsorbed on the surface of polysorbate 80-coated poly(butyl cyanoacrylate) nanoparticles, *Eur. J. Pharm. Biopharm.* **1995**, *41*, 44–48.
  - 50 R. N. ALYAUDIN, E. B. TEZIKOV, P. RAMGE, D. A. KHARKEVICH, D. J.

- BEGLEY, Significant entry of tubocurarine into the brain of rats by adsorption to polysorbate 80-coated polybutylcyanoacrylate nanoparticles: an *in situ* brain perfusion study, *J. Microencapsul.* **1998**, *15*, 67–74.
- 51 A. E. GULYAEV, S. E. GELPERINA, I. N. SKIDAN, A. S. ANTROPOV, G. Y. KIVMAN, J. KREUTER, Significant transport of doxorubicin into the brain with polysorbate 80-coated nanoparticles, *Pharm. Res.* **1999**, *16*, 1564–1569.
- 52 J. KREUTER, R. N. ALYAUDIN, D. A. KHARKEVICH, A. A. IVANOV, Passage of peptides through the blood–brain barrier with colloidal polymer particles (nanoparticles), *Brain Res.* **1995**, *674*, 171–174.
- 53 J. KREUTER, V. E. PETROV, D. A. KHARKEVICH, R. N. ALYAUDIN, Influence of the type of surfactant on the analgesic effects induced by the peptide dalargin after its delivery across the blood brain barrier using surfactant-coated nanoparticles, *J. Controlled Rel.* **1997**, *49*, 81–87.
- 54 R. H. MÜLLER, M. LÜCK, J. KREUTER, Medicament excipient particles for tissue specific application of a medicament, *PCT application PCT/EP98/064299 (P53601)*, **2001**.
- 55 B. DEHOUCK, L. FENART, M. P. DEHOUCK, A. PIERCE, G. TORPIER, R. CECHELLI, A new function for the LDL receptor: transcytosis of LDL across the blood–brain barrier, *J. Controlled Rel.* **1997**, *138*, 877–889.
- 56 R. H. MÜLLER, S. SCHMIDT, PathFinder technology for the delivery of drugs to the brain, *New Drugs* **2002**, *2*, 38–42.
- 57 V. LENAERTS, P. COUVREUR, D. CHRISTIAENS-LEYH, E. JOIRIS, M. ROLAND, B. ROLLMAN, P. SPEISER, Degradation of poly(isobutyl cyanoacrylate) nanoparticles, *Biomaterials* **1984**, *5*, 65–68.
- 58 M. R. GASCO, Solid lipid nanospheres from warm micro-emulsions, *Pharm. Tech. Eur.* **1997**, *9*, 52–58.
- 59 B. SJÖSTRÖM, B. BERGENSTÅHL, Preparation of submicron drug particles in lecithin-stabilized o/w emulsions. I. Model studies of the precipitation of cholesteryl acetate, *Int. J. Pharm.* **1992**, *88*, 53–62.
- 60 E. B. SOUTO, SLN and NLC as drug carriers of clotrimazole for topical formulations, *Master thesis*, Oporto University, **2003**.
- 61 A. ZUR MÜHLEN, E. ZUR MÜHLEN, H. NIEHUS, W. MEHNERT, Atomic force microscopy studies of solid lipid nanoparticles, *Pharm. Res.* **1996**, *13*, 1411–1416.
- 62 M. R. GASCO, Method for producing solid lipid microspheres having a narrow size distribution, *US patent 5,250,236*, **1993**.
- 63 B. SJÖSTRÖM, B. BERGENSTÅHL, B. KRONBERG, A method for the preparation of submicron particles of sparingly water-soluble drugs by precipitation in oil-in-water emulsions. II: influence of the emulsifier, the solvent, and the drug substance, *J. Pharm. Sci.* **1993**, *82*, 584–589.
- 64 B. SJÖSTRÖM, B. KRONBERG, J. CARLFORS, A method for the preparation of submicron particles of sparingly water-soluble drugs by precipitation in oil-in-water emulsions. I: influence of emulsification and surfactant concentration, *J. Pharm. Sci.* **1993**, *82*, 579–583.
- 65 C. FESSI, J. P. DEVISSAGUET, F. PUISIEUX, C. THIES, C., Process for the preparation of dispersible colloidal systems of a substance in the form of nanoparticles, *US patent 5,118,528*, **1992**.
- 66 M. TROTTA, F. DEBERNARDI, O. CAPUTO, Preparation of solid lipid nanoparticles by a solvent emulsification-diffusion technique, *Int. J. Pharm.* **2003**, *257*, 153–160.
- 67 P. SHAHGALDIAN, J. GUALBERT, K. AÏSSA, A. W. COLEMAN, A study of the freeze-drying conditions of calixarene based solid lipid nanoparticles, *Eur. J. Pharm. Biopharm.* **2003**, *55*, 181–184.
- 68 S. M. MOGHIMI, I. S. MUIR, L. ILLUM, S. S. DAVIS, V. KOLB-BACHOFEN, Coating particles with a block copolymer (poloxamine-908) suppresses opsonization but permits the activity of dysopsonins in the serum, *Biophys. Acta* **1993**, *1179*, 157–165.

- 69 S. RUDT, R. H. MÜLLER, *In vitro* phagocytosis assay of nano- and microparticles by chemiluminescence. II. Effect of surface modification by coating of particles with poloxamer on the phagocytic uptake, *J. Controlled Rel.* **1993**, *25*, 51–59.
- 70 R. H. MÜLLER, D. RÜHL, M. LÜCK, B. R. PAULKE, Influence of fluorescent labelling of polystyrene particles on phagocytic uptake, surface hydrophobicity, and plasma protein adsorption, *Pharm. Res.* **1997**, *14*, 18–24.
- 71 R. GREF, M. LÜCK, P. QUELLEC, M. MARCHAND, E. DELLACHERIE, S. HARNISCH, T. BLUNK, R. H. MÜLLER, Stealth corona-core nanoparticles surface modified by polyethylene glycol (PEG): influences of the corona (PEG chain length and surface density) and of the core composition on phagocytic uptake and plasma protein adsorption, *Colloids Surfaces B Biointerfaces* **2000**, *18*, 301–313.
- 72 D. J. GRAHAM, M. C. PHILLIPS, Proteins at liquid interfaces. I., Kinetics of adsorption and surface denaturation, *J. Colloid Interface Sci.* **1979**, *70*, 403.
- 73 H.-M. POEHLING, V. NEUHOF, Visualization of proteins with a silver “stain”: a critical analysis, *Electrophoresis* **1981**, *2*, 141–147.
- 74 C. OLBRICH, O. KAYSER, A. LAMPRECHT, C. KNEUER, C. M. LEHR, R. H. MÜLLER, Interactions of fluorescent solid lipid nanoparticles (SLN) with macrophage-like cells visualized by CLSM, Presented at *3rd World Meeting of APGI/APV*, Berlin, **2000**, pp. 331–332.
- 75 A. GESSNER, C. OLBRICH, W. SCHRÖDER, O. KAYSER, R. M. MÜLLER, The role of plasma proteins in brain targeting: species dependent protein adsorption patterns on brain-specific lipid drug conjugate (LDC) nanoparticles, *Int. J. Pharm.* **2001**, *214*, 87–91.
- 76 T. M. GÖPPERT, R. H. MÜLLER, Protein adsorption patterns on poloxamer- and poloxamine-stabilized solid lipid nanoparticles (SLN), *Eur. J. Pharm. Biopharm.* **2005**, *60*, 361–372.
- 77 T. BLUNK, *Plasmaproteinadsorption auf kolloidalen Arzneistoffträgern*, Department of Pharmacy, Christian-Albrechts-Universität zu Kiel, **1994**.
- 78 T. M. GÖPPERT, R. H. MÜLLER, Solid lipid nanoparticles (SLN) for intravenous drug targeting: comparison of plasma protein adsorption patterns on different SLN detected by two-dimensional polyacrylamide gel electrophoresis (2-D PAGE), Presented at *AAPS Annual Meeting*, Salt Lake City, UT, **2003**, M1002.
- 79 A. MIGLIETTA, R. CAVALLI, C. BOCCA, L. GABRIEL, M. R. GASCO, Cellular uptake and cytotoxicity of solid lipid nanospheres (SLN) incorporating doxorubicin or paclitaxel, *Int. J. Pharm.* **2000**, *210*, 61–67.
- 80 R. H. MÜLLER, C. M. KECK, Challenges and solutions for the delivery of biotech drugs – a review of drug nanocrystal technology and lipid nanoparticles, *J. Biotechnol.* **2004**, *113*, 151–170.

## 11 Biocompatible Nanoparticulate Systems for Tumor Diagnosis and Therapy

*Mostafa Sadoqi, Sunil Kumar, Cesar Lau-Cam and Vishal Saxena*

### 11.1

#### Introduction

Nanotechnology is the development and engineering of materials, devices and systems so small that they can be measured on a molecular scale. This emerging technological field has received considerable attention in the past two decades due to its numerous medical, pharmaceutical, environmental and military applications.

The development of nanoparticles and nanodevices capable of navigating in the bloodstream and of reaching specific destinations remains an attractive and most desirable biomedical endeavor since, for example, it can provide the clinician with an effective and powerful means for detecting and/or treating pathological abnormalities such as solid tumors. Ideally, a nanodevice suitable for diagnostic and therapeutic use should exhibit good physical stability within the biological environment it needs to travel, be fully biocompatible, and show high affinity and selectivity for its final target.

One possible way of maximizing the clinical capabilities of nanodevices is to combine nanotechnology with photonics [1]. For this purpose, nanoparticles carrying a suitable photoexcitable molecule are converted *in situ*, under the activating influence of laser radiation, to a chemical form that will make a tumor more sensitive to the action of conventional chemotherapeutic agents or emit a spectral signal with an output that can be electronically manipulated to provide information on the presence of pathological growth.

This chapter offers an overview of the different methodological approaches that can be used for the fabrication of nanoparticulate systems for medical purposes, of the ways these devices can sense changes within specific biological surroundings and of the medical applications that can be derived from the interaction of loaded nanoparticles within biological matter with laser radiation, particularly as it relates to the imaging and therapy of tumors.

Particular attention will be given to the near-infrared dye (NIR) indocyanine green (ICG), and to the potential of this dye for tumor diagnosis and therapy when administered encapsulated within polymeric nanoparticulate systems. ICG was found to be free of perceptible toxicity, to exhibit good chemical stability within polymeric nanoparticles, to be appreciably taken up by tumor cells following its



delivery as a nanoparticulate formulation and to cause singlet oxygen-induced oxidative damage in target cells when photoexcited. A discussion of the benefits of photodynamic therapy (PDT) with ICG as a means of eradicating unwanted abnormal growths such as tumors will also be presented.

## 11.2

### **Nanoscale Particulate Systems and their Building Blocks/Components**

Nanoscale particulate systems are 100 to 100 000 times smaller than human cells and hair. At present, a vast choice of sensing devices are commercially available for detecting and measuring specific bacteria or hazardous chemicals, for checking acidity levels and for monitoring changes in biological and nonbiological environments. In nanomedicine, nanoscale systems can easily enter most types of cells and can move undisturbed out of blood vessels as they circulate through the body. Furthermore, biomedical nanoscale systems can interact with surface and intracellular biomolecules, can make their way into tissues through capillaries, can get through fenestrations present in epithelial linings such as those of the liver and can diffuse through the blood–brain barrier (BBB) by following openings created at tight junctions by a hyperosmotic mannitol solution [2]. As a result, they can be used to efficiently deliver both low-molecular-weight compounds, such as drugs, and macromolecules such as proteins, peptides and genes, to tissues of interest by either localized or targeted delivery.

In recent years, a great deal of effort has been devoted to the application of nanotechnology to drug delivery, molecular imaging, the assessment of therapeutic efficacy, targeted and multifunctional therapeutics, and the early detection, prevention and control of cancer. Some of the nanoparticulate formulations that have been developed for the delivery of therapeutic agents in a biocompatible form have included nanoparticles, nanocapsules (nanoshells), polymeric micellar systems, buckyballs, nanotubes, dendrimers, quantum dots and immunoconjugates.

Although this chapter will address a select few nanoscale systems, emphasis will be placed on nanoparticle systems of the type developed in our laboratory, since experiments conducted in this laboratory have been focused on the use of nanoparticles to deliver photoexcitable molecules to normal and cancer cells, allowing the study of the interaction of light with the incorporated nanoparticulates in real time and during the earliest stages of the cancer process [3]. In this way, it has been possible to determine that nanoparticles can be used to detect cancer even when the process is still limited to a few cells and that they have the potential as a better alternative to therapy with conventional drug formulations since they can reduce or even eliminate drug side-effects.

#### 11.2.1

##### **Dendrimers**

Dendrimers are a large and complex group of highly branched polymerized macromolecules with well-defined chemical structures and exhibiting monodispersity,

i.e. having the same structure, composition and molecular weight. The three major architectural components of a dendrimer are the core, branches and end groups of the precursor monomeric units. The core is usually an amine, although ammonia, sugars and other molecules can also be used. Regardless of the type of constitutive molecule present, the core exhibits multiple and identical reaction sites. The dendrimer can start with a few branches of atoms, usually three or four, radiating from a central core, with a branch point occurring every six atoms. At each branch point, the current chain of atoms becomes two chains of atoms. As a result, a structure resembling a tree with numerous branches is formed.

In general, a dendrimer consists of layers or shells of branches, each one known as a generation (G), built around a small core molecule. As the number of generations increases to G4, the regular and highly branched architecture of a dendrimer starts to develop into a sphere, whose preferred three-dimensional structure starts to become apparent by G5. Synthetic procedures available for the fabrication of dendrimers allow for the nearly complete control of critical molecular parameters such as size, shape, interior/surface chemistry, flexibility and topology, as well as for a very easy control of the chemical composition and reactivity. Manufacture of cone-shaped, spherical or disk-like dendrimers with a size in the range of 2–12 nm is possible.

The synthesis of a dendrimer is a stepwise iterative process. In its most basic form, it is started by reacting all of the reactive groups of the core molecule with an excess of a monomeric building unit possessing different reactive groups on each end. Reaction of one end of this monomer with the core will produce the first set of branches and reaction of the second end with a different type of monomer, also having two different reactive groups at each end, will generate a second set of branches. At this point, the first shell and the first generation of the dendrimer are complete. The unreacted ends of the first shell will serve as the starting point for new branching and for the next shell.

The two main techniques for the synthesis of dendrimers with a unique combination of properties are the Starburst divergent method [4, 5] and the convergent growth method [6], but a self-assembly method [7] has also been developed. In the divergent method, the dendrimer is started from the periphery (i.e. the tips of the branches) and made to grow inwards. Two of the end tips are connected to a branched monomer to form a dendron (or dendrimer segment) and the process is repeated until a desired size is achieved. In the final step, the interconnected branches are attached to a core molecule. Since the growing dendrimer is undergoing multiple simultaneous reactions, the final product may lack uniformity. Building a dendrimer by a convergent approach requires the same number of steps as by the divergent approach, but starting with a central initiator core around which dendrimer segments are assembled. More importantly, since only two reactions take place at each step of the growing process, the resulting final product is of a high purity.

The self-assembly method, first studied with surfactant molecules in aqueous media, is now being applied to water-soluble dendrimeric polymers and their supra-molecular analogs. Taking advantage of the abundance of surface active end groups on dendrimers, nanoparticulate aggregates having micellar properties can be made

to form from dendrimers at an interface. In turn, these unimolecular micelles can serve as hosts for hydrophobic molecules to enhance solubility in water with an efficiency than may exceed that derived from a conventional surfactant such as sodium dodecylsulfate [8]. By reacting the amino end groups of poly(propylene imine) with various aliphatic acid chlorides it was possible to prepare a series of nonaggregating inverted unimolecular dendritic micelles with a compact hydrophobic shell, a hydrophilic interior and high generation numbers ( $n \geq 4$ ). In contrast to normal micelles, these inverted unimolecular micelles were able to bind hydrophilic molecules in the interior and to solubilize the guest molecule in apolar solvents.

Dendrimers have been more commonly synthesized from polymers such as poly(amidoamine) (PAMAM dendrimers) by a divergent method initiated by ammonia or ethylenediamine as a core or from poly(propylene imine) (PPI dendrimers) by a divergent method initiated by a core of 1,4-diaminobutane, but poly(aminoalcohol), cyclotriphosphazene and phenylacetylene have also been used.

Due to the large number of active chemical groups located at the surface of each generation and to their well-defined chemical structure, dendrimers are good candidates for creating biomedically useful nanodevices. While suitable modifications of the surface properties of dendrimers will allow them to be made electrically charged into a polyelectrolyte or to be linked to biological agents, their cavities can serve as depots or be used as pumping devices for small guest molecules such as organic dyes, drugs and metal clusters [9]. In this respect, a most interesting departure from a conventional dendrimer is the so-called “core dendrimer”, which is synthesized by crosslinking the peripheral groups of the dendrimer and then removing the core by hydrolysis [10].

From a technical and commercial standpoint, some of the most interesting applications of dendrimers are in the pharmaceutical and biomedical fields. For example, sufficient flexibility exists to create dendrimers that are either biologically active or inert and of a sufficiently small size that will permit their entry into cells to deliver drugs, genetic material and organic and inorganic chemical markers without triggering an immune response. In addition, dendrimers can be used to deliver diagnostic and chemotherapeutic agents to target sites for the diagnosis, treatment and eradication of malignant tumors. Medical researchers envision that one day tecto-dendrimers will be used to carry out a five-step task when diagnosing and treating tumors: (a) the search of tumor cells throughout the body, (b) the binding to receptors on tumor cells, (c) the entry into tumor cells upon crossing the cell membranes, (d) the release of chemotherapeutic or radioactive agents inside the tumor cell and (e) the confirmation of the presence, location or death of tumor cells through the use of appropriate medical devices.

### 11.2.2

#### **Buckyballs and Buckytubes**

Buckyballs, also known as  $C_{60}$ , buckminsterfullerenes or fullerenes, are clusters of up to 60 carbon atoms arranged in a series of interlocking hexagons and pentagons to form a structure resembling a soccer ball [11]. In actuality,  $C_{60}$  is a “truncated

icosahedron" consisting of 20 hexagons and 12 pentagons. Buckyballs can be easily manufactured in quantity by heating graphite rods to a high temperature and passing an electric current between them. The crystals of  $C_{60}$  are separated from other carbon compounds, especially  $C_{70}$ , found in the soot fraction. It is the only molecule known to mankind to be composed of a single element and to exist in the form of a hollow spheroid. Possible ways of utilizing a buckyball for biomedical purposes would be to use its spherical structure to carry molecules with diagnostic or therapeutic value in the body after they have been added to its outer surface through chemical reaction or introduced into its cage-like interior. As a delivery system, buckyballs appear well suited because of their nanometer size, and perfectly smooth surface and round shape. In addition, they are inert, nontoxic and, due to their small size, capable of interacting with cells, proteins, and viruses.

Buckytubes, variously designated as nanotubes (NTs) or carbon nanotubes, are molecular-scale nanomaterials of pure carbon that have been prepared in a relatively efficient way by the laser vaporization of graphite in the presence of cobalt nickel catalyst in a furnace at 1200 °C. In this way, a product that can be thought of as a sheet of graphite rolled into a single-wall seamless cylinder and closed at both ends by hemispherical endcaps (SWNTs) can be obtained. In the absence of a catalyst, a group of graphite layers will coil around each other to produce a multi-wall cylinder (MWNTs). Their diameter is in nanometers, their length up to a few millimeters and, depending on their helicity, they can be either electrically conductive (metallic) or semiconductive. In addition to their unusually high strength, buckytubes are light, flexible, with good thermal stability, chemically inert, and have extraordinary electrical conductivity, heat conductivity and mechanical properties. Given their high electrical conductivity and sharpness of their tips, buckytubes are unsurpassed as field emitters, especially at low voltage, and can carry as much as  $10^{13}$  A  $cm^{-2}$  [12].

A demonstration that single-wall buckyballs absorb light and emit it at a single wavelength in the NIR spectrum has opened the door to a new field of potential biomedically related applications for these materials [13]. For the fluorescence to be measurable, however, the buckytubes must be isolated from one another since aggregation into bundles quenches fluorescence and considerably broadens the absorption spectra due to intertube energy transfer from the semiconducting to the metallic nanotubes within each bundle [14], followed by rapid nonradiative carrier cooling in the metallic nanotubes [15]. Time-resolved spectroscopy of these buckyball bundles reveals extremely rapid excited state relaxation [14, 15].

As a result of their small size that allows them to migrate through cell walls, buckyballs could be used as optical biosensors for seeking out specific targets within the body such as tumor cells or inflamed tissues. To increase their specificity toward their targets, buckyballs could be wrapped with proteins that will serve as ligands for surface receptors on target cells. Covalently linked adducts of SWNTs with biomolecules such as biotin or DNA have great potential in biosensing and as a possible means of implementing nanoscale assembly onto selected locations on a surface [16]. By combining buckytubes of a different diameter size one could simultaneously study different target cells. A most promising application of bucky-

tubes has been the imaging of cells. SWNTs were found to be actively ingested by macrophages suspended on a growth medium through phagocytosis and to be held in phagosomes within the macrophages. Cell viability was not affected by the buckytubes and the intracellular fluorescence remained detectable in the harsh oxidizing environment of the phagosomes. These results suggest that the high-contrast NIR detection of SWNTs can lead to valuable methods for tracing the interactions of buckytubes with organisms, and may form the basis for future families of biological contrast agents and fluorescent markers.

On account of the natural fluorescence of SWNTs, and the transparency of human tissues and biological fluids in the NIR region of the spectrum, buckyballs wrapped with a molecular sheath that responds to a particular biological molecule and modulates the optical properties of the buckyball can be constructed. Based on this model, a sensor for tracking blood glucose in diabetics was built by organizing a monolayer of the enzyme glucose oxidase on the surface of SWNTs suspended in water. Reaction of glucose with the enzyme generates hydrogen peroxide which, when exposed to ferricyanide ions, increases the fluorescence emission of the sensor in direct proportion to the concentration of glucose present [17]. In view of their high resistance to degradation, it could be possible to construct buckyballs for implantation into thick tissues or biological fluids for long-term monitoring of specific body components.

### 11.2.3

#### **Quantum Dots**

Quantum dots, also known as nanocrystals, are tiny semiconducting inorganic crystals with unique quantum properties, typically between a nanometer and a few microns in size, and containing from one to several thousand free electrons. The size and the shape of these structures and, hence, the number of electrons they contain, can be precisely controlled. Quantum effects arise from the confinement of electrons and “holes” (an electronless region that behaves as if it were a positively charged particle) in the material. The small size also leads to changes in the electrical and nonlinear optical properties of a material relative to its bulk form. They are made of silicon, germanium, lead, zinc and cadmium salts – materials that can absorb white light and reemit it a couple of nanoseconds later at a higher frequency. The type and intensity of the color is dependent on the size of the crystal. For example, the larger the dot, the redder the light; but as the size shrinks, the wavelength of emission becomes shorter and moves toward the blue or green. Hence, a gamut of colors can be obtained by a simple change in the size of the dot. Moreover, when excited, the smaller the dot the higher the energy and intensity of the emitted light.

These particles represent a convenient alternative to fluorescent dyes in a variety of analytical, biological and biomedical applications since their emitting radiation can be measured over the entire visible spectrum, they have a broader excitation spectrum, and their fluorescence is extremely stable over time. On these bases, a mixture of quantum dots of different sizes can be excited by a light source with a

single wavelength, allowing simultaneous detection and imaging of different biological molecules simultaneously within living organisms. In contrast, the use of more than one organic dye to accomplish the same purpose might meet with difficulties since their spectra may overlap with each other because each dye emits light over a wide range of wavelengths.

The utility of quantum dot nanomaterials as a result of their optoelectronic properties can be further expanded not only by changing their size and composition, but also by incorporating them into a wide variety of polymers and material forms that will make them stable in water. Core quantum dots with fewer surface defects, improved physical stability and enhanced fluorescence brightness are already commercially available. Quantum dots represent a powerful new approach to genetic analysis, disease diagnosis and the monitoring of cell responses to certain drugs or viruses [18, 19]. However, their application to the detection of tumors, in particular, and of cancer, in general, remains to be realized because of their intrinsic toxicity and lack of biocompatibility.

#### 11.2.4

##### **Polymeric Micelles**

Polymeric micelles are a viable form of targeted delivery system for water-insoluble and amphiphilic drugs [20, 21]. Like surfactant-based micelles, polymeric micelles are core/shell structures; however, unlike their traditional counterparts, they are physically more stable and capable of solubilizing substantial amounts of hydrophobic compounds within their inner core. Due to their hydrophilic shell and small size they may prolong the circulation of drugs in body fluids and increase drug accumulation in tissues [20]. The shell is responsible for micelle stabilization and interaction with plasma proteins and cell membranes. The hydrophobic core, usually made from a biodegradable polymer, serves as a reservoir for an insoluble drug and shields the drug from the aqueous surroundings. Polymers used for fabricating polymeric micelles have included pluronics, polyethylene glycol (PEG)-lipid conjugates and pH-sensitive poly(*N*-isopropylacrylamide)-based micelles or polyion complex micelles.

Polymeric micelles have also been used for encapsulating and delivering photosensitizing drugs and dyes. However, the biodistribution characteristics of the polymeric micelle formulations thus far investigated have not been entirely satisfactory. For example, greater selectivity and effectiveness could be gained by introducing targeting ligands and site-controlled releasing capabilities, respectively, and excessive nanoparticulate accumulation and long-term toxic effects could be reduced by utilizing biodegradable polymers with good clearance properties.

#### 11.2.5

##### **Liposomes**

A liposome is a spherical vesicle of colloidal dimensions composed of one or more lipid or phospholipid bilayers. The size of liposomes varies from 20 nm to 100 μm,

although each lipid bilayer is about 4 nm thick. Various amphipathic molecules have been used to fabricate liposomes, especially lecithins from natural or synthetic sources. To increase mechanical stability and decrease the leakage of the contents, charged phospholipids like phosphatidylserine or phosphatidylglycerol and cholesterol can be added. Depending on its physicochemical characteristics, a drug can become trapped in the aqueous space, intercalated or dissolved within the lipid bilayer, or form ionic or hydrophobic complexes with nucleic acids and other macromolecules without physical entrapment [22]. For medical use, a liposome suspension must be precisely defined with respect to drug and lipid concentrations, size distribution, percentage of entrapped drug, pH, osmolarity, conductivity, and presence of degradation products. Specific methods exist to manufacture liposomes of a particular size, morphology and surface characteristics, parameters that together will determine the biologic fate of the liposomes [22].

Due to similarities in both structure and chemical composition to biomembranes, liposomes have been extensively investigated as carriers for enhancing the incorporation of an assortment of drug molecules into target cells [23, 24]. Through the use of liposomes one can achieve a variety of therapeutic goals, including enhanced drug uptake and reduced toxicity. Numerous studies have been conducted on the use of liposomes to deliver chemotherapeutics to tumor cells; however, in spite of some impressive results in animal models, acceptance of liposomes as a drug delivery system for human use has only been realized in a very few instances. In addition to a relatively high cost, additional shortcomings associated with this form of drug delivery are short residency time in the circulation due to rapid removal by phagocytic cells of the reticuloendothelial system (RES), physical and chemical instability on storage, and the lack of generally uniform and applicable techniques for their production on a commercial scale [23, 24].

Conventional liposomes are unstable *in vivo* and show little or no affinity towards tumors. These shortcomings have served as the impetus for the development of more complex liposomal preparations where the surface and/or composition of the structural components have undergone chemical modification. Moreover, in the case of conventional liposomes a significant fraction of the injected dose ends up in organs rich in phagocytic (monocytes, macrophages, Kupffer) cells such as the liver and spleen, which eventually sequester and, thus, reduce the amount of drug that is available for antitumor action. To counteract this situation, liposomal surfaces have been variously modified to limit irrelevant recognition and reduce the uptake of the liposomes into cells of the immune system, thus extending the half-life of drugs in the circulation. Alternatively, these liposomes can be targeted to cells expressing specific receptors by equipping them with specific surface ligands. This delivery modality has been successfully used to provide selective binding and enhanced entry into tumor cells of liposomes loaded with a photosensitizer for PDT purposes and bearing surface tumortropics with the ability to recognize specific target molecules expressed on tumor cell membranes [23, 24].

Through a combination of polymer physics, organic chemistry, biochemistry, pharmacology, ecology and anatomy, sterically stable (“stealth”) liposomes have been developed. This type of lipid-based particles is represented by polymorphic

liposomes designed to change their structure in response to a particular signal such as a change in temperature or pH in the presence of specific molecules. These reactive liposomes can be made to fuse or increase in permeability, or triggered to disintegrate to release their contents upon arrival to the target site. An important breakthrough in chemotherapy with stealth liposomes is the substantial improvement in longevity that is observed in biological systems. This stability arises from the sterile nature of the surface polymer, which limits the clearance of the liposomes from the circulation by opsonization and subsequent macrophage uptake, and by disintegration upon interactions with plasma proteins and lipoproteins. Commercial stealth liposomes of doxorubicin and daunorubicin have received approval by the FDA for the parenteral treatment of Kaposi's sarcoma and solid tumors. Apart from drugs, liposomes can be made to carry a significant load of signal molecules such as dyes, radionuclides or contrast agents for *in vitro* and *in vivo* diagnostic work.

### 11.3

#### Biodegradable Nanoparticles

In recent years, polymeric nanoparticles have received recognition as a promising type of colloidal drug carrier [25]. They have been widely used for controlled drug delivery by the intravenous, ocular and oral routes of administration. An additional positive feature of this form of drug delivery is that they have shown potential as a carrier for anticancer agents. It has been verified that the tissue distribution characteristics, specificity and pharmacokinetic properties of anticancer drugs can be better controlled upon their incorporation into nanoparticles [26, 27]. Furthermore this form of drug delivery may contribute to reducing the side-effects and toxicity normally associated with anticancer drugs, while increasing therapeutic efficacy, and can lead to drug accumulation in the solid tumor since they have been found to escape from the vasculature through the leaky endothelial tissue that surrounds a solid tumor [28, 29].

Nanoparticles can overcome the multidrug-resistance phenotype mediated by P-glycoprotein and bring about an increase in drug content inside neoplastic cells [30]. This finding is of special significance for patients with cancer undergoing treatment with paclitaxel and who, after some time, develop resistance to the drug [31]. Other important advantages derived from the use of nanoparticles include the ease of their preparation, the availability of well-defined biodegradable polymers for their manufacturing [e.g. poly(D,L-lactide-co-glycolide) (PLGA)], and their high stability in biological fluids and during storage [32]. Moreover, nanoparticles can permeate cells and tissues to become internalized and can efficiently deliver a particular drug to its target tissue without clogging the capillaries [33].

The ability of nanoparticles to improve drug diffusion through biological barriers is particularly useful for the delivery of biomarkers and photodynamic agents to the brain without the need for preliminary pharmacological intervention to overcome the BBB [34]. Some studies on nanoparticle-bound antitumor agents have in-



licated that nanoparticles can prolong the retention of the drug by tumors, reduce tumor growth and prolong the survival of tumor-bearing animals [30, 35–37].

### 11.3.1

#### Preparation of Nanoparticles

Several synthetic and natural polymers have been described for the manufacturing of biodegradable nanoparticles [38]. One advantage of synthetic polymers over natural ones is that they can yield nanoparticles with the ability to sustain the release of the encapsulated therapeutic agent over longer periods of times (days to several weeks). However, the use of synthetic polymers in nanoparticle technology is limited by the need to use often toxic organic solvents and relatively harsh formulation conditions. Synthetic polymers for formulating nanoparticles have included polylactic acid and its copolymerization with glycolic acid (PLGA), polyacrylates and polycaprolactones.

Among natural polymers, albumin, gelatin, alginate, collagen and chitosan have been evaluated [38]. Of these polymers, polylactides (PLA) and PLGA are the ones most extensively investigated for achieving controlled release of conventional drug molecules, peptides and proteins. PLGA is the most common choice in pharmaceutical formulations probably because of its good biocompatibility and biodegradability and of its approval by the FDA for use in humans [39]. These polyesters undergo hydrolysis upon implantation in body tissues to biologically compatible and metabolizable moieties (e.g. lactic acid and glycolic acid) that are eventually removed from the body by the citric acid cycle.

In addition, since the biodegradation products are formed at a very slow rate, they appear not to interfere with normal cell functions to a significant extent. Extensive testing for toxicity and safety in laboratory animals has found these polymers to be safe, and, thus, suited for use in humans as contraceptive implants [40, 41], graft materials for artificial organs and, more recently, as supporting scaffolds in tissue engineering research [42–44].

Some of the methods described for the preparation of nanoparticles from preformed biodegradable polymers are solvent evaporation [45], salting out [46], nanoprecipitation [47], extrusion [48], spray drying [49] and supercritical fluid extraction [50].

The most popular method of making nanoparticles is the emulsification-solvent evaporation method, also known as the solvent displacement techniques [51–53]. This methodological approach, schematically shown in Fig. 11.1, usually involves the following major steps: (a) emulsification of a water-immiscible organic solution of the polymer and an organic or inorganic material of interest with an aqueous phase containing stabilizers, (b) stabilization of the particles by chemical crosslinking or by heat, (c) evaporation of the organic solvent to precipitate the encapsulating polymer as nanoparticles, and (d) isolation of the nanoparticles by filtration or centrifugation [54]. This method is suitable for hydrophilic drugs since the drug dissolves in the inner water phase of the double emulsion. In most cases, a stabilizer is added to the formulation to stabilize the emulsion formed during particle

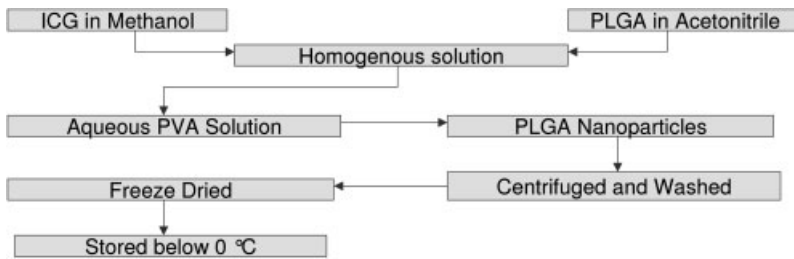


**Fig. 11.1.** Flow diagram of the manufacturing of ICG-loaded PLGA nanoparticles by a modified spontaneous emulsification-solvent diffusion method.

preparation. In this method, the type and concentration of the stabilizer may exert a modifying effect on the properties of the particles being formed. By occupying the boundary between the aqueous and organic phases, the stabilizer can become incorporated onto the surface of the forming particles and, in this way, influence particle properties such as the  $\zeta$  potential and mucoadhesion [55, 56]. In turn, these physicochemical parameters can modify the physical stability of the formulation as well as certain biopharmaceutical properties such as drug release rate, biodistribution and cellular uptake. Although polyvinyl alcohol (PVA) is the stabilizer most often used for the production of PLGA nanoparticles, other available choices are cellulose derivatives such as methylcellulose, hydroxyethylcellulose and hydroxypropylcellulose, gelatin types A and B, carbomer, and poloxamer [57].

One way to construct nanoparticles with long circulating characteristics is to modify their surface with the hydrophilic, flexible and nonionic polymer, PEG [58–60]. The resulting PEG-coated nanoparticles have shown good potential as a biodegradable colloidal type of formulation for the delivery of therapeutic agents to specific sites.

## 11.4

### Biodegradable Optical Nanoparticles

#### 11.4.1

##### Optical Nanoparticles as a Potential Technology for Tumor Diagnosis

Solid tumors and other forms of cancer are commonly localized inside the body by screening diagnostic methods based on imaging techniques or radiology [61–64]. Images of internal parts of the human body can be obtained by using X-rays (tomography, scan or mammography), a powerful magnetic field (magnetic resonance imaging), radioactive isotopes (nuclear scan or radionuclide imaging) and high-frequency sound waves (ultrasound) [65–68]. Examples of nuclear scanning include single-photon emission computed tomography (SPECT) and positron emission tomography (PET) scans. There are also diagnostic methods whose use

is determined by the location of the cancer (e.g. endoscopy for cancers in body openings like the mouth, anus or urethra, tests for measuring estrogen and progesterone receptors in suspected cases of breast cancer, and the Pap smear test for detecting cancers of the cervix and vagina) [69–74]. Once a tumor has been detected in the body by any of the aforementioned screening techniques, confirmatory evidence is gathered by histopathological examination of a tissue sample obtained by biopsy of the suspected area. In spite of their widespread use, these forms of tumor diagnosis suffer from serious limitations. For example, there is a strong safety concern attached to the use of harmful radioactive substances and X-rays, both of which are in themselves risk factors for cancer. Furthermore, harmful adverse reactions may develop from the use of contrast agents, the test may not be sensitive enough to detect very small tumors and the diagnostic procedure may be expensive in comparison to other laboratory medicine procedures.

Nanoparticles loaded with photosensitizer molecules can be an alternative method for tumor diagnosis as well as for drug delivery purposes. Their ability to be readily detected, to show selectivity, and to be easily transported through the blood stream is inherent to the nature of the dye, the specific agent linked to the particulate system (e.g. antibodies) and the physical as well as chemical structure of the polymer used. Nanoparticulate systems have the means to detect the cancer at an early stage and they have the potential as a better alternative to therapy with conventional drug formulations since they can greatly minimize drug side-effects.

#### 11.4.2

#### **Optical Nanoparticles as a Potential Technology for Tumor Treatment**

After detection of a tumor, its treatment usually relies on chemotherapy with specific anticancer agents to ensure that the cancer cells have not metastasized to the other parts of the body [75–83], localized radiation therapy with ionizing radiation such as X-rays and  $\gamma$ -rays [84–87], biologic therapy based on the defense provided by the body's immune system [88–108], and invasive approaches for localized cancer such as surgery [109–111]. Although effective and beneficial, these therapeutic approaches are surrounded by certain drawbacks, among which the main ones are intrinsic toxicity, serious side-effects and damage to healthy tissues by the radiotherapy itself. Consequently, there is a pressing need for simpler, safer, noninvasive imaging systems and technologies than those currently available, offering the required selectivity to detect and/or destroy a tumor while sparing the surrounding areas. At the same time there is also a need for developing diagnostic and therapeutic systems and technologies based on the use of agents that are nontoxic, not requiring systemic distribution or capable of obviating the use of harmful radiation, particularly as it relates to tumors of the skin and breast.

As stated earlier, a nanoparticulate system encapsulating a dye that can be photoexcited to produce singlet oxygen will be a better system for tumor detection and therapy than conventional approaches. The uptake of these nanoparticles by tumor cells can serve as an optical indicator of the presence of the tumor, and can be used

to trigger a laser system for oxidizing and, thus, eradicating tumors or unwanted tissues from the body in a noninvasive manner. Based on these considerations, we have developed nanoparticles loaded with ICG, a photoexcitable molecule with NIR fluorescence properties, good penetrating ability into tumor cells and a long residency time within tissues. The novelty of this approach is to combine the tools and principles of optics, chemistry, physics and engineering for the development and manufacturing of a multifunctional smart nanodevice with the capability of navigating in the blood stream, looking for uptake into abnormal growths such as tumors or for specific areas where to deliver a particular drug. In turn, the drugs thus delivered can emit a measurable signal that can help to locate the abnormality or be made to eliminate the abnormality upon photoactivation with laser radiation via PDT (Fig. 11.2) [3].

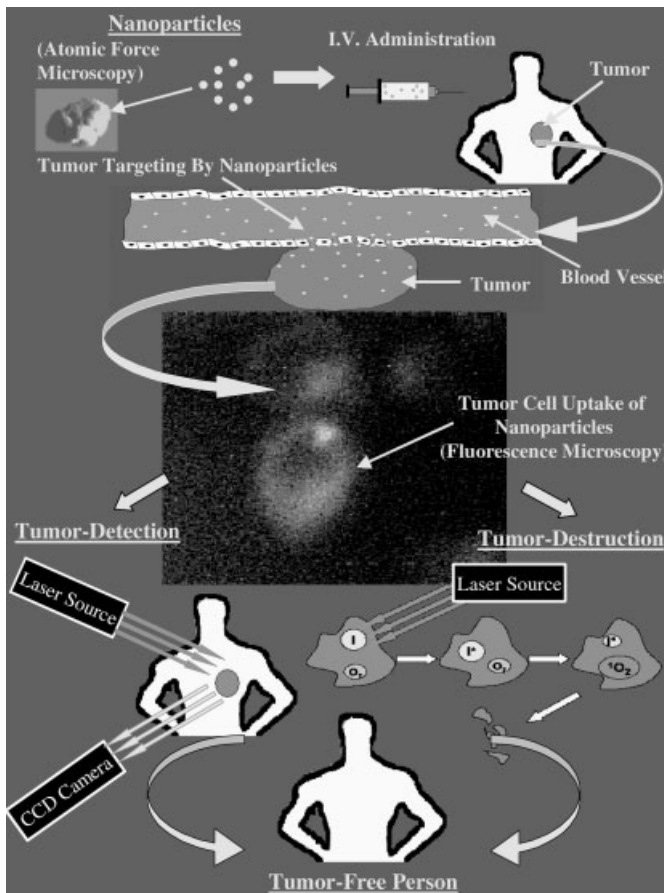


Fig. 11.2. ICG encapsulated in nanoparticles preferentially locates in tumors to allow the noninvasive imaging and destruction of superficial tumors. (from Ref. [3].)

## 11.5

### Optical Imaging and PDT

#### 11.5.1

#### Optical Imaging

Optical imaging is a form of tumor diagnosis based on the interaction between light and biological matter [112]. Two of the most salient advantages this technique can offer to the clinician over traditional diagnostic modalities are a non-reliance on both ionizing radiation and radioactive material, and the wealth of information that it can generate about the structure, dynamics and interactions in biological bulk specimens such as tissues. Optical imaging takes advantage of the spatial variation in the optical properties of a biological specimen, whether it is a cell, a tissue, an organ or an entire live organism [113]. With this diagnostic technique, an optical image is obtained by monitoring the spatial variation of light that is reflected, scattered, absorbed or emitted as fluorescence. The use of lasers as an intense and convenient light source to generate an optical response has considerably expanded the boundaries of optical imaging, particularly as it relates to tumor diagnosis [114–116].

##### 11.5.1.1 Fluorescence-based Optical Imaging

Fluorescence is a radiative phenomenon whereby a molecule becomes excited upon absorbing light of a given wavelength and later on returns to the ground state by emitting light of a longer wavelength. The major advantages of fluorescence detection over other optical imaging techniques are high sensitivity (low signal-to-noise ratio), high speed and safety. In this instance, safety refers to the fact that the sample is neither altered nor destroyed and that no hazardous byproducts are generated in the process [117].

##### 11.5.1.2 NIR Fluorescence Imaging

NIR fluorescence imaging is increasingly gaining importance in the diagnosis of tumors [118, 119]. The NIR region is that portion of the light spectrum extending from 700 to 900 nm. At least four main reasons are responsible for the increasing importance of this imaging technique:

- (a) Blood and other biological tissues are relatively transparent across this spectral wavelength range, thus creating an optical window [113, 119].
- (b) The excitation of chemical agents or dyes for imaging by NIR radiation produces practically no autofluorescence from any endogenous cellular components, a factor that dramatically improves the sensitivity of the detection signal detection, often limited by background autofluorescence [120].
- (c) The NIR excitation and emission wavelengths reduce scattering in tissues, and, thus, increase both the penetration depth and the efficiency of the detection signal [113, 119].

Tab. 11.1. Common NIR dyes

<b>Name</b>	<b>Wavelengths of excitation/emission (nm)</b>
Cy-3 iodoacetamide	565/590
Cy-5 N-hydroxysuccinimide	648/669
Cy-7 isothiocyanate	750/777
Rhodamine 800	680/700
Indocyanine green	782/830
Azure B	638/660
Thiazole orange	735/765
Nile Blue	638/660
Al phthalocyanine	662/680
Oxazine 1	643/658
BODIPY™	665/676

(d) Commercial NIR lasers used as exciting sources are low in cost and convenient to use because of a compact design [113].

#### 11.5.1.3 NIR Dyes for Fluorescence Imaging

The dyes for NIR fluorescence imaging listed in Table 11.1 are either long-wavelength probes such as cyanine, rhodamine, oxazine, phthalocyanine and naphthalocyanine dyes or extended conjugated systems [119, 121–125]. The cyanines, which were initially developed for use as membrane probes, are probably the most commonly used NIR dyes. Typical examples include, in increasing order of wavelength, Cy-3, Cy-5 and Cy-7 [126].

The phthalocyanine and naphthalocyanine dyes are less popular due to their water insolubility, tendency to aggregate, lack of conjugateable forms, and environmental and photochemical instability. Among dyes categorized as extended conjugated systems, ICG has been extensively investigated for use as a long-wavelength probe. By encapsulating this dye within nanoparticles, the authors were recently able to develop a delivery system for the imaging of cancer cells that would overcome most of the problem commonly encountered with other NIR dyes used in biophotonics.

#### 11.5.2

##### PDT

PDT, also referred to as photoradiation therapy, phototherapy or photochemotherapy, is a promising new form of treatment for a variety of oncological, cardiovascular, dermatological and ophthalmic diseases [127, 128]. PDT is an emerging therapy for the treatment of tumors that are accessible to light radiation such as those of the head, neck, digestive tract, skin and breast. PDT has been proposed in several studies as an alternative to overcoming “multidrug resistance phenotype” (MDR), a frequent reason for the failure of conventional chemotherapy. PDT has been approved by the FDA for the treatment of both early- and late-stage lung cancer, for certain types of esophageal cancer and for non-small cell lung cancer, and

most recently it was also approved for the treatment of actinic keratosis, a precancerous skin condition. Clinical trials are currently in progress in the US and abroad to evaluate the effectiveness of PDT in the treatment of several types of cancer and precancerous conditions [113].

PDT is a form of light-activated chemotherapy based on the activation of an exogenous chemical agent, known as the photosensitizer, by light. The photosensitizer is administered either systemically by the intravenous route or locally into the malignant growth, after which light of a specific wavelength is used to irradiate the photosensitizer in a specific part of the body. Upon absorbing light, the photosensitizer will produce reactive oxygen species (ROS) with the ability to destroy the tumor with minimal damage to the surrounding cells [129, 130].

The advantages of PDT are numerous. For example, it circumvents systemic treatment since the light is focused only on the site occupied by the tumor, thus sparing the patient from side-effects commonly associated with conventional chemotherapy such as hair loss, nausea and vomiting. It exhibits more selectivity than conventional chemotherapy and radiotherapy toward tumors because of preferential accumulation of the photosensitizing agent in tumor tissue and the spatially confined photodynamic effects achieved with light radiation. PDT will be a suitable option in patients that cannot undergo removal of a tumor by surgery, e.g. in the upper bronchi, since it can kill cancer cells without damaging adjacent collagenous tissue structures, a situation that allows for the repopulation of these structures by new normal cells. It is expected to be cost-effective and, unlike radiation therapy, amenable to be repeated as many times as deemed necessary, thus providing a way for the long-term management of cancer and the complete removal of the tumor. Additionally, in contrast to surgery, it is a noninvasive form of therapy that does not cause pain or discomfort in the patient or lead to such complications as surgery-related secondary infections.

#### 11.5.2.1 Basis of PDT

In PDT, cytotoxicity by a photosensitizer molecule is attained when the photosensitizer, after undergoing activation by laser light energy, proceeds to return to the ground state by either radiative or nonradiative decay [131–133]. In nonradiative decay, the energy absorbed by the photoactive molecule can be converted to heat (internal conversion) that can then be transferred to nearby intracellular molecules (photooxidation type I) to cause cellular damage by raising the intracellular temperature. Alternatively, the energy absorbed by the photosensitizer can be transferred to molecular oxygen by means of a triplet state (photooxidation type II), to form reactive intermediates such as singlet oxygen that, in turn, can cause irreversible destruction of biological substrates [134, 135]. ROS such as the superoxide anion, and hydroperoxyl and hydroxyl radicals may also be involved in mediating irreversible damage to biologic components [127]. Singlet oxygen possesses a reactive distance of only 0.1  $\mu\text{m}$ , so its cytotoxicity is restricted to the immediate vicinity of the photoactivated drug. When used within their standard doses, neither the photosensitizer nor the light source is active against the target when used independently of each other.

Tab. 11.2. Common photosensitizers

<i>Name</i>	<i>Chemical type</i>	<i>Absorption wavelength (nm)</i>
Photofrin®	porphyrin	630
Bonellin	chlorin	625
MTHPC	chlorin	652
SnET2	chlorin	660
Mono-L-aspartyl chlorine e6	bacteriochlorin	654
HPPH	pyropheophorbide	670
Veteroporphin	benzoporphyrin	690
Protoporphyrin IX	ala	630
Lu-TeX	texaphyrins	732
Indocyanine green	tricyanocyanine	786
AlPcS	phthalocyanine	674
Methylene blue	cationic	660
Tetrabromorhodamine	cationic	540

#### 11.5.2.2 Photosensitizers for PDT

Photosensitizers for PDT are selected taking into account various physiological factors. In brief, an ideal photosensitizer should possess the following properties: (a) ability to selectively accumulate in the cancerous or precancerous tissue, (a) capability of absorbing light significantly in the region of maximum transparency of biological tissues and (c) minimal drug toxicity. Table 11.2 lists some of the common photosensitizers used in PDT [136–149].

#### 11.5.3

#### ICG: An Ideal Photoactive Agent for Tumor Diagnosis and Treatment

Among the photosensitizing agents listed in Tables 11.1 and 11.2, ICG stands out as unique because it possesses both NIR fluorescent properties and PDT capabilities, thus becoming suited for both NIR fluorescence imaging and PDT of tumors. ICG may be more advantageous than other photoactive agents since it causes minimal toxicity, is commercially available in a very pure form, has a low cost, and, more importantly, has been approved by the FDA as a diagnostic agent for use in ophthalmology and other medical specialties. Moreover, in other countries ICG has received approval for use in PDT. On these bases, it would appear that the development of a commercial ICG-based nanoparticulate system for tumor imaging and treatment would meet fewer hurdles for obtaining federal approval for use in humans than would be possible with other related agents.

#### 11.5.3.1 Clinical Uses of ICG

ICG is a photoactive dye approved by the FDA for medical diagnostic studies, and is widely used in the clinical setting for the evaluation of cardiac output, liver function and microcirculation of skin flaps, the visualization of the retinal and choro-



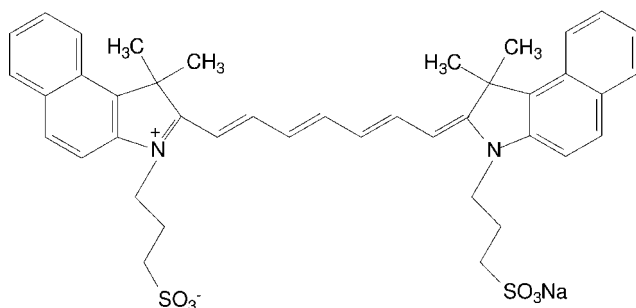


Fig. 11.3. Chemical structure of ICG.

dal vasculatures, in pharmacokinetic analysis, to localize objects within tissues, as a fluorescence probe for enzyme and proteins, and in tissue welding [150, 151].

#### 11.5.3.2 Structure and Physicochemical Properties of ICG

Chemically ICG (FW 775) is a tricyanocyanine dye containing an extended conjugated system. The structure of ICG, shown in Fig. 11.3, is made up of two polycyclic moieties, each known as a benzoindotricarbocyanin, connected to each other by a carbon chain. While the polycyclic moieties are responsible for the lipophilic properties of ICG, the sulfate groups attached to each polycyclic component impart hydrophilicity. As a result, ICG is, overall, amphiphilic in nature and, because of its amphiphilicity, ICG is soluble in organic solvents [e.g. methanol and dimethylsulfoxide (DMSO)] and in aqueous media, including buffers.

#### 11.5.3.3 Binding Properties of ICG

ICG binds rapidly and almost completely (98%) to most plasma proteins. Thus, in the circulation it binds to albumin, globulins and lipoproteins. Due to its amphiphilic nature, ICG can interact with both lipophilic and hydrophilic molecules. Furthermore, because of its three-dimensional structure, ICG can simultaneously bind to the lipophilic and hydrophilic parts of amphiphiles such as phospholipids.

ICG binds to human serum albumin (HSA) through its hydrophobic core. In this case, about one or two molecules of ICG become bound to one molecule of HSA [152]. ICG has also been found to bind to  $\alpha_1$ -lipoproteins and  $\beta$ -lipoproteins [153] in human serum. In general, the binding of ICG to plasma proteins will impact negatively on its potential intracellular effects since the bound form will be primarily confined to the vascular compartment and hindered from entering tumors [154–156]. Numerous reports have described the binding of ICG to phospholipids [157–159]. These binding interactions are relevant to photoimaging since the emission spectrum and fluorescence yield of ICG are influenced by the resulting quenching [158, 160–163].

Several studies have been carried out on the interactions of ICG with model membranes. It was observed that ICG is able to interact with phospholipid bilayers and that the binding takes place at the interface of the model membrane. The

physicochemical and fluorescence spectral characteristics of ICG in aqueous solution have been evaluated in the presence of micelles and liposomes [162]. ICG was found to be tensioactive, and to aggregate or become embedded at the interface of micelles and liposomes. The fluorescence of ICG was very low in the aggregated form due to quenching and very high when embedded at the interface.

#### 11.5.3.4 Metabolism, Excretion and Pharmacokinetics of ICG

The excretion of ICG follows a hepatobiliary route in the human body. After intravenous injection, most of the circulating ICG is taken up into the liver where, rather than being metabolized, it is excreted as part of the bile into the intestinal tract. Upon reaching the intestine it is neither reabsorbed through the intestinal mucosa nor put through the enterohepatic circulation [156]. Negligible uptake of the dye occurs in the kidneys, lungs and peripheral tissues. ICG does not undergo significant renal excretion [164] and it is not detected in the cerebrospinal fluid [156].

The metabolic fate and excretion of ICG correlate well with its lipophilic characteristics. As a result, ICG is rapidly eliminated from the circulation after an intravenous injection, with the plasma half-life being about 2–4 min [164–167]. The plasma disappearance rate of ICG in healthy human subjects is from 18 to 24%  $\text{min}^{-1}$ . The normal biological half-life has been determined to be from 2.5 to 3 min, so single blood samples taken from healthy subjects 20 min after an intravenous injection should contain not more than 4% of the initial concentration of dye [168].

Spectrophotometric studies on ICG have shown the blood levels of this dye to follow a biexponential decay curve following intravenous injection. The plasma clearance of ICG is biphasic, showing a rapid initial phase with a half-life of 3–4 min and a secondary phase with a half-life of more than 1 h at low concentrations [165, 169, 170].

#### 11.5.3.5 Toxicity of ICG

ICG produces minimal toxicity in animals and its  $\text{LD}_{50}$  after intravenous administration ranges from 50 to 80  $\text{mg kg}^{-1}$  [171]. Although no equivalent data exists for humans, the maximum recommended human dose is 5  $\text{mg kg}^{-1}$ . The safety of intravenous ICG in humans is well documented, with severe adverse reactions occurring in only 0.05% of recipients [172].

#### 11.5.3.6 Tumor Imaging with ICG

ICG is rapidly gaining acceptance as a diagnostic agent for tumor imaging purposes due to its NIR fluorescence characteristics. Li et al. [173] have studied the efficiency of ICG as a sensitive contrast agent for tumor detection and localization. These authors assessed the differences in fluorescence signals of ICG between opposite tumor-bearing and tumor-free areas after the intravenous administration of a low, 80  $\mu\text{g kg}^{-1}$  body weight, dose of ICG to rats implanted with a tumor in one leg. In this way it was possible to determine that a difference in fluorescence exists between the tumor side and tumor-free side, and that the difference was detectable

even when the tumor was very small (about  $0.15 \text{ cm}^3$ ). During the exponential growth phase of the tumor, the ratio of these two signals was approximately 2.5 and the ratio of the initial ICG clearance velocity in the tumor leg to that in the control leg was about 3.

Preliminary investigations with human subjects affected with breast tumors were conducted using an ICG dose of  $400 \mu\text{g kg}^{-1}$  body weight. The results of this study indicated the existence of differences in the fluorescence emanating from a tumor-bearing breast and that from a tumor-free breast. Additional evidence in support of the use of ICG in the imaging of breast tumors has been gathered in dogs [174]. By using a gain-modulated, image-intensified, charge-coupled, camera these authors were able to obtain intensity-modulated fluorescence signals from canine mammary tumors. By means of a continuous wave diffuse optical tomography apparatus, Intes et al. [175] have demonstrated the usefulness of ICG as a diagnostic tool for differentiating benign from malignant pathologies in breast cancer patients.

A number of studies have also reported on the use of ICG as a fluorescence contrast imaging agent to obtain two- or three-dimensional images from experimental phantoms, rats and synthetic samples [176]. It is quite clear that a great deal of interest exists in finding new diagnostic applications for ICG by NIR imaging, optical spectroscopy and tomography, and that there is still room for improving the sensitivity, specificity and cost-effectiveness of currently available ICG-based optical techniques, especially of those intended for the detection of breast and skin tumors.

#### 11.5.3.7 PDT with ICG

Due to its photosensitizing properties, ICG has great potential for application in PDT. An important reason for using ICG in PDT is that its strongest absorption and emission bands occur at around 800 and 820 nm, respectively [177, 178]. Since these two wavelengths are the wavelengths at which blood and other tissues are relatively transparent, and at which the penetration depth of light in biological tissue is at its maximum (5 mm or more) [179, 180], they confer ICG an advantage over comparable chemical agents that work in the visible spectral range. In addition, like other second-generation photosensitizers, ICG demonstrates those features that are considered desirable in PDT, including rapid biodistribution, low skin phototoxicity, and ease of administration and monitoring [181].

Fickweiler et al. [182] were the first to provide concrete evidence on the photodynamic action of ICG. Using HaCaT cells, an immortalized human keratinocyte cell line, they were able to examine the dose-dependent phototoxic effects of ICG *in vitro*. In their experiments, keratinocytes were incubated with 0–50  $\mu\text{M}$  aqueous solutions of ICG for 24 h, after which the cells were irradiated with diode laser (805 nm) of a different energy density (0, 12, 24 and 48  $\text{J cm}^{-2}$ ). Under these conditions, photoactivated ICG demonstrated a cell killing effect at concentrations above 5  $\mu\text{M}$ . In addition, the participation of ROS in the cell killing process was suggested by the results of an experiment in which sodium azide, a quencher of ROS, protected against the cytotoxicity of ICG [182].

A different approach was later used by Baumler et al. [135] to elucidate the mechanism responsible for the cytotoxicity of ICG in PDT. In their study, HT-29 cells, an immortalized human colon carcinoma cell line, were first incubated with different concentrations of ICG (10–100  $\mu\text{M}$ ) for 24 h and next irradiated with a continuous wave diode laser (805 nm, 30  $\text{J cm}^{-2}$ ). Apart from demonstrating light-induced cytotoxicity, these investigators also observed that the cytotoxicity increased when heavy water ( $\text{D}_2\text{O}$ ) was used in place of normal water. These results were interpreted as indicative of the production and participation of singlet oxygen during laser irradiation of ICG since  $\text{D}_2\text{O}$  is known to prolong the lifetime of singlet oxygen. Moreover, evidence for the occurrence of lipid peroxidation upon the addition of  $\text{D}_2\text{O}$  was gathered from the concomitant elevation of the levels of malondialdehyde, a marker of lipid peroxidation. This line of thought was further examined with quenchers of singlet oxygen species such as sodium azide, histidine, and with specific quenchers of superoxide anion and hydroxyl radical such as mannitol. Since only sodium azide and histidine protected against the photodynamic killing effect of ICG on HT-29 cells, the participation of singlet oxygen and of lipid peroxides, but not of superoxide anion and hydroxyl radicals, was inferred. Virriale et al. [183] have also provided proof of the involvement of singlet oxygen in the photodynamic antitumor action of ICG. In photosensitization experiments performed by this research group, irradiation of U-937 human monocytes (histiocytic lymphoma, CRL-1593), a leukemia cell line, with a diode laser (805 nm) source providing a dose of radiation of 18  $\text{J cm}^{-2}$  in the presence of 12  $\mu\text{M}$  of ICG and dithiothreitol, an oxidizable substrate, caused the cells to undergo programmed cell death (apoptosis).

Urbanska et al. [184] have reported the potential utility of ICG as a photosensitizer for the treatment of melanoma, a common type of skin cancer. PDT with ICG is particularly suited to control melanoma because the melanin present in these cells absorbs the wavelength of visible light commonly used for photodynamic effect but not the NIR wavelengths at which ICG exerts its cytotoxic effects. In this study a very high photosensitizing efficiency was demonstrated for ICG upon exposing SKMEL 188 cells, a human melanoma cell line, to 100  $\mu\text{M}$  of ICG followed by irradiation with a diode laser (830 nm) delivering a radiation dose of 30–100  $\text{J cm}^{-2}$ . Costa et al. [181] have described an *in vivo* photodynamic study on ICG that demonstrated the potential utility of the dye in the occlusion of choroidal neovascularization. Using pigmented rabbits as an animal model, doses of ICG between 10–20  $\text{mg kg}^{-1}$  and an activating light dose of 6.3  $\text{J cm}^{-2}$  from a diode laser, ICG was shown to be effective in occluding choriocapillaries.

#### 11.5.3.8 Limitations of ICG for Tumor Diagnosis and Treatment

The *in vivo* value of ICG in tumor imaging and treatment is severely limited by two intrinsic characteristics – a very high tendency to bind to plasma proteins (95–98%) and a rapid elimination from the body (plasma  $t_{1/2} = 2\text{--}4$  min) [158, 178]. As a result, a very small amount of ICG will accumulate in tumor tissue following intravenous dosing since the dye will remain largely confined in the blood before its removal by the liver for eventual rapid elimination into the small intestinal

tract. Needless to say that for both imaging and PDT applications, it will be essential to deliver a substantially higher quantity of ICG to the tumor site than it is possible with a conventional aqueous solution and that this objective will be only realized when its limiting characteristics are appropriately minimized.

Another important factor that limits the clinical use of ICG is extreme instability in aqueous media. In addition to preventing its storage for a significant period of time, aqueous solutions of ICG are only suitable for conducting *in vivo* imaging and other types of diagnostic procedures for a short time [150, 185]. The chemical stability of ICG at ambient temperature has been found to decrease in inverse proportion to its concentration [177, 186], and it can be easily monitored by following the changes of its visible absorption spectrum over time [177, 186–188]. Light appears to be the major determining factor in the stability of ICG since degradation is much greater for samples exposed to ordinary light than for samples kept in the dark [186, 189]. A similar photodegradation has been verified with aqueous solutions of ICG that were exposed to laser radiation [185]. Since most current clinical applications of ICG are carried out with aqueous solutions, the development of a more stable preparation for parenteral use is clearly warranted.

#### 11.5.3.9 Recent Approaches for Improving the Blood Circulation Time and Uptake of ICG by Tumors

No specific mechanism has been described for the localization of ICG in tumors [190]. Moreover, since ICG lacks tumor selectivity, its use as a diagnostic tool for differentiating among various types of tumor will not be reliable. Several approaches have been tested as ways of attaining greater tumor selectivity with ICG. One attempt has been to synthesize dye–peptide conjugates that are receptor specific [190]. The experimental results suggest that small dye–peptide conjugates are effective as contrast agents for optical imaging purposes. Even when covalently united to each other, the dye and the peptide were found to retain the native fluorescence characteristics and the affinity for peptide receptors, respectively. These newly synthesized conjugates, identified as Cytate and Cybesin, preferentially localized for over 24 h in tumors known to overexpress somatostatin and bombesin receptors, respectively. In contrast, the dye moiety was not retained in these two tumor models when they were no longer conjugated to a peptide [190]. This behavior and the lack of data on the chemical stability of dye–peptide combinations *in vitro* and *in vivo* represent a significant impediment to the potential commercialization of dye–peptide conjugates.

Devoisselle et al. [191] have developed an emulsion formulation to increase the blood circulation time of ICG. To test this formulation, Wistar rats were intravenously dosed with 7.5 mg kg<sup>-1</sup> body weight of ICG, given as either an aqueous solution or as an oil-in-water emulsion formulation. It was verified that the emulsion increased the plasma clearance time of ICG in the first 15–60 min and the residence time in the skin as compared to an equipotent dose of an aqueous solution. However, no information was given on the chemical stability of ICG in water or in an *o/w* emulsion *in vitro* and no experiments were conducted to determine the efficiency of an emulsion in tumor targeting under *in vivo* conditions.

#### 11.5.3.10 Recent Approaches for ICG Stabilization *In Vitro*

An early way of ensuring the stability of ICG in solution was to substitute water by nonaqueous solvents. For this purpose, methanol, 1,2-propanediol and dimethylformamide were evaluated [192]. It was found that under ordinary conditions of illumination, ICG was more stable in methanol than in any of the other solvents. Moreover, the thermostability of ICG was greater in methanol and 1,2-propanediol than in dimethylformamide. A later study examined the photodegradation and thermodegradation of ICG in a wide variety of aqueous and organic solvents [185]. This study indicated that ICG exhibited a low photostability in water, D<sub>2</sub>O and aqueous sodium azide (NaN<sub>3</sub>) solutions, and a good photostability in methanol, DMSO and human plasma. In addition, the thermal stability of ICG was moderate in water, D<sub>2</sub>O and aqueous NaN<sub>3</sub>, and very high in human plasma, methanol and DMSO. Thus, excluding human plasma, ICG appears to remain quite stable in organic solvents. Unfortunately these results are of no value in trying to develop an appropriate photostable, thermostable and biocompatible injectable solution of ICG for use in human subjects inasmuch as they all possess intrinsic toxicity.

A different solution to improving the stability of ICG in aqueous media has been to complex the dye with water-soluble cyclodextrins [193]. The stability of ICG in water increases because the dye can fit in the torus of  $\gamma$ -cyclodextrin to form an inclusion complex at pH 6.0 and 25 °C that will somewhat shield the dye from the external environment. Although in this manner the stability of ICG increases in aqueous media, the effect is short-lived due to the tendency of ICG to leave the cavity of  $\gamma$ -cyclodextrin to form an equilibrium mixture with its complexed form. Also, complexation of ICG with a cyclodextrin will make accurate assessment of the thermostability of ICG a difficult task.

The stability of ICG in aqueous solutions has also been achieved by conjugating it noncovalently with a polymeric carrier molecule [151, 194]. The conjugate is formed by gently stirring a solution of ICG plus the anionic polymer sodium polyaspartate (PASP), added in a respective molar ratio of 1:2.6, at ambient temperature. Under ordinary conditions of illumination and ambient temperature, an aqueous solution of conjugated ICG emitted a fluorescence that remained quite stable for up to 24 days. In contrast, the fluorescence of a solution of plain ICG was only stable for 4 days. However, this gain is offset by the failure of the ICG–PASP conjugate to show a sufficiently long blood clearance rate for ICG that would allow the dye to accumulate in tumors in a therapeutically effective concentration.

A more recent attempt to prevent the photodegradation of ICG has been to place this compound in close proximity to colloidal gold [195]. Although the interaction of ICG with colloidal gold allows ICG to form a metallic conjugate with better photostability than plain ICG, the utilization of metallic nanoparticles raises concerns about the biodegradability and biocompatibility of the formulation. An additional concern is the efficiency and effectiveness of this type of conjugate under *in vivo* conditions since none of these issues has, thus far, been experimentally substantiated.

## 11.6

### PLGA-based Nanoparticulate Delivery System for ICG

#### 11.6.1

##### Rationale of Using a PLGA-based Nanoparticulate Delivery System for ICG

From the foregoing statements, it is apparent that the use of ICG in tumor diagnosis and treatment will only become a reality when its present shortcomings in terms of chemical stability in solution, circulation half-life and adequate uptake by tumor cells are solved.

One attractive and novel approach to achieving these objectives may be to encapsulate ICG within a biocompatible and biodegradable nanoparticulate system. Among possible candidates for use in the preparation of nanoparticles for drug delivery purposes, PLGA and several of its derivatives stand out since they meet the requirements of biocompatibility and biodegradability, and, in addition, have been extensively used by the pharmaceutical industry. Further advantages to be gained from the use of PLGA in nanoparticles are, among others, (a) enhanced uptake into a tumor site because of increased endocytosis and of leakiness of the vasculature permeating a tumor, i.e. they are suited for the passive targeting of tumors [196], (b) amenability to surface modification by special targeting moieties such as antibodies to enhance specificity toward a target site, i.e. active targeting [196], (c) attainment of a long circulation half-life (14 min, which is about 3–7 times that of plain ICG [197], and which can be increased further by coating the surface of the nanoparticles with specific polymers such as PEG [198]), (d) confirmation by *in vitro* studies with PLGA nanoparticles of their ability to be enter human cell lines such as arterial smooth muscle cells (HASMC) and vascular smooth muscle cells (VSMC), and accumulate at the tumor site [199, 200], (e) demonstrable stability in aqueous media for intravenous delivery and which, unlike that of micelles and liposomes, is independent of surfactant/lipid concentrations, and (f) ease of preparation which, unlike the synthesis of delivery systems based on a antibody–drug conjugate, does not entail the formation of covalent linkages. It is expected that as a result of future advances in nanotechnology, fully biocompatible and biodegradable PLGA-based nanoparticles will be engineered on an industrial scale to meet the clinical demands imposed by human tumors.

PLGA was used to entrap ICG into nanoparticles. The amount of each ingredient was varied to represent ratios of dye to polymer ranging from 1:10 to 1:800. The ICG content appeared to vary within a narrow range (0.17–0.29%) regardless of the dye to polymer ratio (Table 11.3) [201–203]. A similar trend was noted for the particle size and polydispersity of the nanoparticles (Table 11.4). The  $\zeta$  potential was more negative with a dye to polymer ratio of 1:800 than with the other ratios used (Table 11.4). The surface of the nanoparticles was porous in nature (Fig. 11.4), a feature that may facilitate the fairly rapid release of the dye into an aqueous environment during the first 8 hours (Fig. 11.5). The incorporation of ICG into nanoparticles not only isolated the dye from a potentially hostile external environment, but at the same time contributed to enhance its chemical stability to the degrading

**Tab. 11.3.** Effect of formulation parameters on ICG entrapment efficiency, ICG content and nanoparticle recovery

<b>Formulation number</b>	<b>Amount of ICG in formulation (mg)</b>	<b>Amount of polymer in formulation (mg)</b>	<b>ICG content (%)<sup>[a]</sup></b>	<b>ICG entrapment (%)<sup>[a]</sup></b>	<b>Nanoparticle recovery (%)</b>
1	1	100	0.21 ± 0.06	9.92 ± 2.68	48.0
2	5	100	0.29 ± 0.04	2.92 ± 0.40	49.4
3	10	100	0.17 ± 0.01	1.14 ± 0.08	65.3
4	1	800	0.20 ± 0.01	74.47 ± 0.74	45.7

<sup>a</sup> Values are given as mean ± SD for  $n = 3$ .

action of an aqueous medium, ambient light and heat (Figs. 11.6–11.8, and Tables 11.5 and 11.6) [202].

The uptake of PLGA nanoparticles into cells is by endocytosis and this uptake mechanism appears to take place even at low concentrations of ICG. As shown in Fig. 11.9, the amount of ICG taken up as nanoparticles into B16-F10 and C-33A cells, two types of cancer cells, increased in liner proportion to the concentration of extracellular ICG and the rate of uptake was greater into B16-F10 cells than into C-33A cells.

Figure 11.10 compares the uptake of ICG into B16-F10 and C-33A cells from aqueous solutions and from nanoparticles. For each type of formulation, the uptake of ICG was always slightly better into B16-F10 cells than into C-33A cell and the resulting uptake versus concentration profiles were virtually parallel to each other. Irrespective of the extracellular concentration of ICG used (0.0005–50 μM), in all instances ICG was better taken up into cells as nanoparticles than in the free form [204].

The entry of a nanoencapsulated compound into the cytoplasm was investigated by fluorescence microscopy after incubating B16-F10 cells with PLGA nanoparticles loaded with coumarin 6 serving as a fluorescence probe (mean diameter  $300 \pm 10$  nm, polydispersity index = 0.01). There were three main reasons for using coumarin 6 in place of ICG to make the nanoparticles for cell uptake studies. First, since ICG fluoresces in the NIR portion of the light spectrum, it cannot be detected using an ordinary fluorescence microscope. Second, coumarin 6 emits a

**Tab. 11.4.** Size and  $\zeta$  potential values of various nanoparticle formulations

<b>Formulation number</b>	<b>Nanoparticle size (nm)<sup>[a]</sup></b>	<b>Polydispersity</b>	<b><math>\zeta</math> potential (mV)<sup>[a]</sup></b>
1	405 ± 05	0.01	−7.2 ± 1.0
2	338 ± 12	0.04	−7.8 ± 0.8
3	307 ± 08	0.02	−10.3 ± 2.1
4	357 ± 21	0.06	−16.3 ± 1.5

<sup>a</sup> Values are given as mean ± SD for  $n = 3$ .



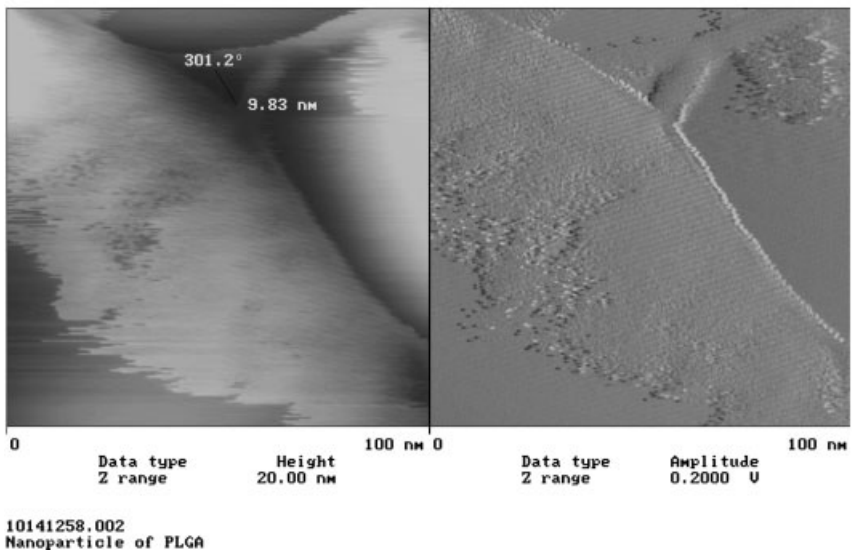
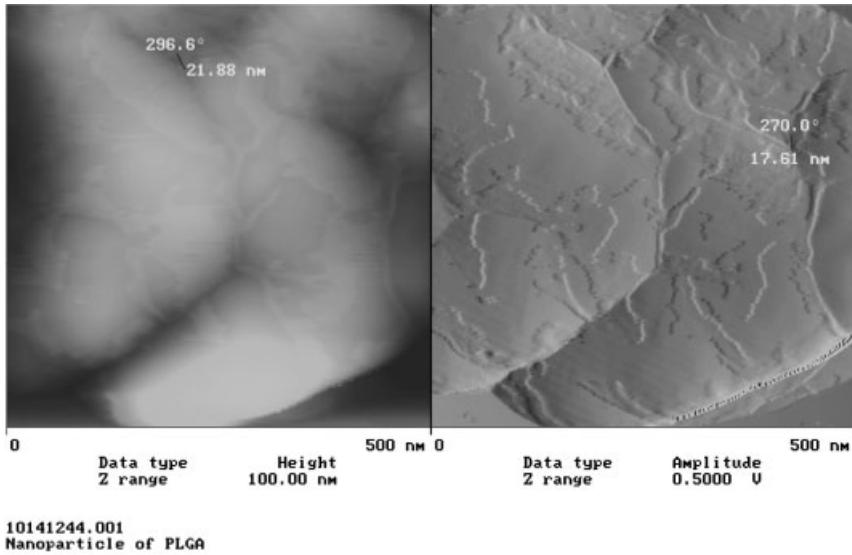


Fig. 11.4. Different views of the surface of ICG-loaded PLGA nanoparticles.

characteristic green fluorescence when excited with red light, thus becoming suited for detection by fluorescence microscopy [200]. Third, due to a higher degree of lipophilicity than ICG, coumarin 6 tends to remain longer within PLGA nanoparticles exposed to an aqueous environment than ICG [202, 205, 206]. As seen in Fig. 11.11, coumarin 6 was found to be evenly distributed throughout

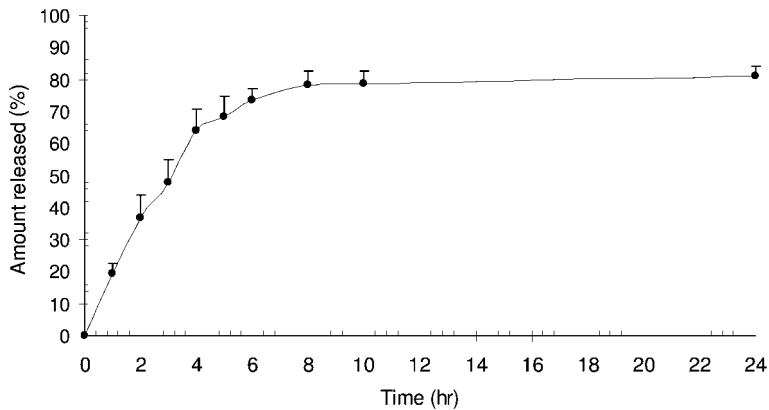


Fig. 11.5. Release profile of ICG from nanoparticles (mean  $\pm$  SD,  $n = 3$ ).

the cytoplasm apart from the nucleus, and to bind to intracellular proteins and structures.

Incubating B16-F10 cancer cells in the dark with either ICG added as an aqueous solution or as nanoparticles was without apparent effect on cell viability at all concentrations of ICG examined (Figs. 11.12 and 11.13). Irradiating the cancer cells with a laser source emitting at 786 nm had no apparent effect on the viability of cells incubated with various doses (1–100  $\mu$ M) ICG as a solution (Fig. 11.14) or with empty nanoparticles (Fig. 11.15), but reduced viability by 22 and 24% in cells incubated with ICG nanoparticles providing 11 and 22  $\mu$ M of dye, respectively (Fig. 11.15) [205].

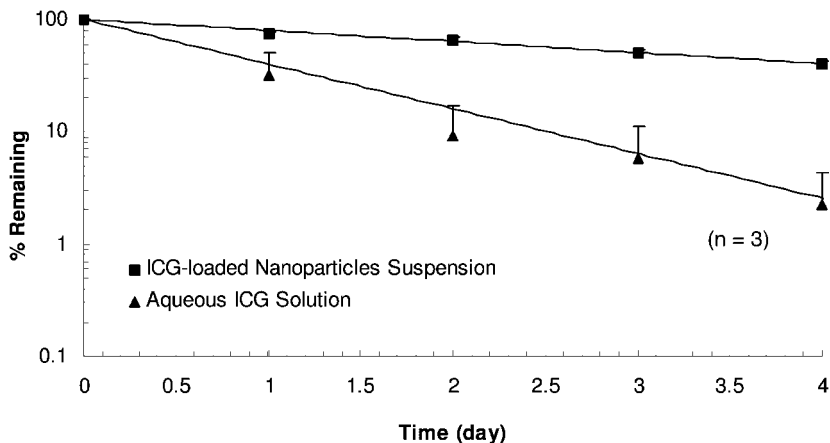


Fig. 11.6. Chemical stability of ICG in an aqueous solution and as a nanoparticle suspension in distilled water after storage at 22  $^{\circ}$ C in the dark.

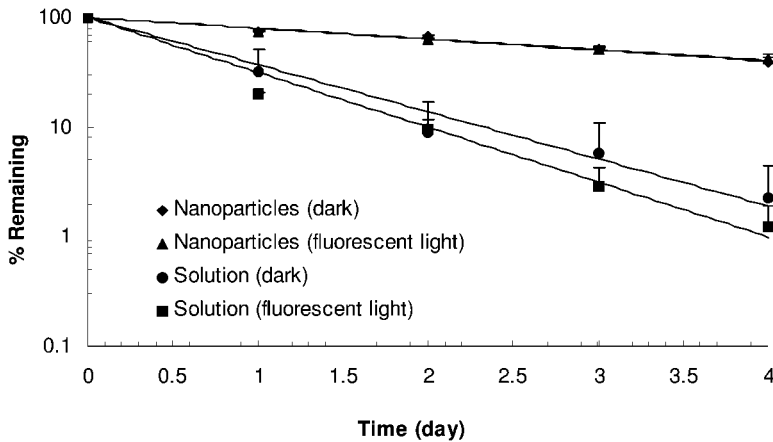


Fig. 11.7. Chemical stability of ICG in an aqueous solution and as a nanoparticle suspension in distilled water after storage at 22 °C in the dark and under fluorescent light.

#### 11.6.2

#### *In Vivo* Pharmacokinetics of ICG Solutions and Nanoparticles

Assessment of the plasma kinetics and biodistribution of ICG following administration as an aqueous solution and as a nanoparticle suspension was conducted in mice. This type of study will also be of help in the future optimization of ICG-containing nanoparticulates in terms of dye load, and selectivity for and improved uptake into target sites.

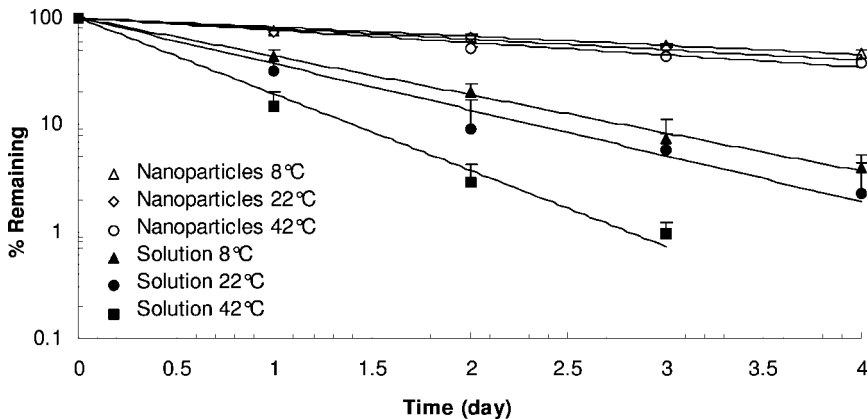


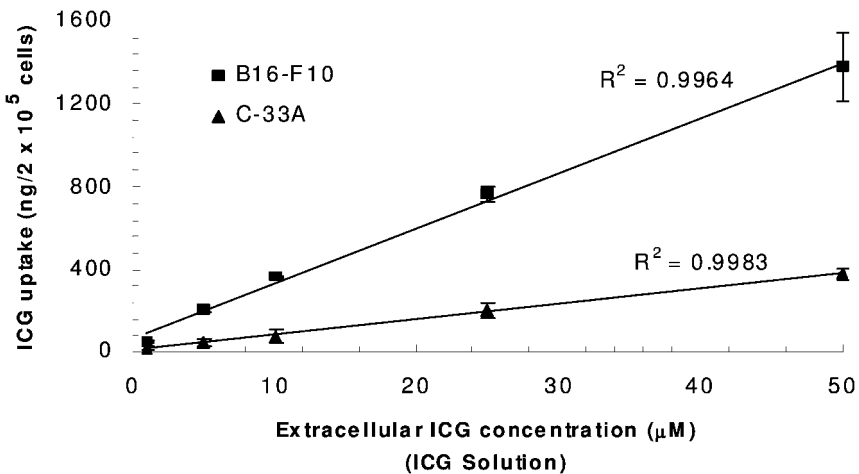
Fig. 11.8. Chemical stability of ICG in an aqueous solution and as a nanoparticle suspension in distilled water stored at different temperatures in the dark.

**Tab. 11.5.** Degradation rate constants,  $k_{obs}$  and degradation half-lives,  $t_{1/2}$  of ICG aqueous solution and aqueous nanoparticle suspension (mean  $\pm$  SD,  $n = 3$ )

Formulation	Experimental conditions	$k_{obs}$ ( $h^{-1}$ )	$t_{1/2}$ (h)	$R^2$
ICG aqueous solution (ICG concentration $1 \mu\text{g mL}^{-1}$ )	dark at 22 °C	$0.0412 \pm 0.0038$	$16.8 \pm 1.5$	$0.972 \pm 0.023$
	room light at 22 °C	$0.0480 \pm 0.0052$	$14.4 \pm 2.4$	$0.979 \pm 0.016$
	dark at 8 °C	$0.0344 \pm 0.0027$	$20.1 \pm 1.6$	$0.997 \pm 0.006$
	dark at 42 °C	$0.0684 \pm 0.0043$	$10.1 \pm 0.6$	$0.984 \pm 0.063$
ICG loaded nanoparticles aqueous suspension (ICG concentration $1 \mu\text{g mL}^{-1}$ )	dark at 22 °C	$0.0096 \pm 0.0008$	$72.2 \pm 6.1$	$0.986 \pm 0.023$
	room light at 22 °C	$0.0094 \pm 0.0009$	$73.7 \pm 7.5$	$0.979 \pm 0.019$
	dark at 8 °C	$0.0082 \pm 0.0006$	$84.5 \pm 6.3$	$0.981 \pm 0.009$
	dark at 42 °C	$0.0111 \pm 0.0003$	$62.4 \pm 1.7$	$0.960 \pm 0.011$

**Tab. 11.6.** Extent of ICG degradation in solution and as nanoparticles after 4 days of storage under different conditions (mean  $\pm$  SD,  $n = 3$ )

Storage condition	ICG remaining (% of initial)	
	Aqueous solution	Nanoparticles
Darkness, 22 °C	$97.8 \pm 0.8$	$60.5 \pm 3.2$
Ambient light, 22 °C	$98.8 \pm 0.7$	$57.8 \pm 4.1$
Darkness, 8 °C	$96.1 \pm 1.3$	$53.4 \pm 3.7$
Darkness, 42 °C	$99.2 \pm 0.3$	$62.8 \pm 0.9$

**Fig. 11.9.** Effect of the extracellular concentration of ICG (1–50  $\mu\text{M}$ ) on the uptake of ICG into B16-F10 and C-33A cells.

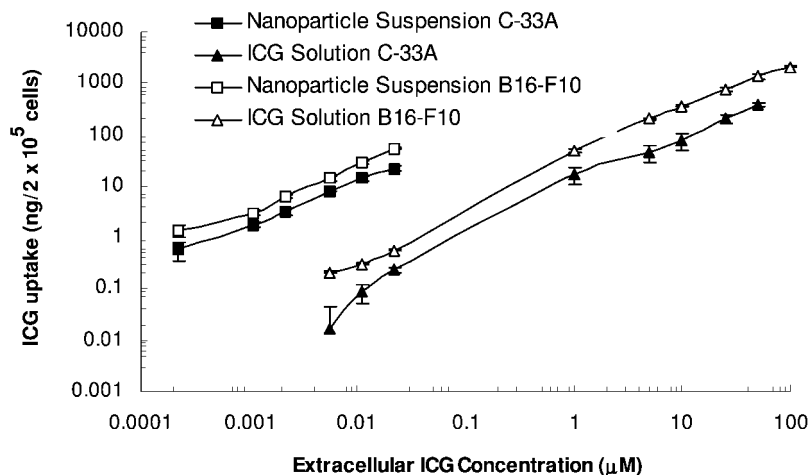


**Fig. 11.10.** Uptake of ICG from a solution and a suspension of nanoparticles into B16-F10 and C-33A cells (mean  $\pm$  SD,  $n = 3$ ). Extracellular concentration of ICG: 0.0005–50  $\mu\text{M}$ .

The temporal changes of ICG in plasma and in various tissues that follow a single intravenous dose of ICG (10  $\mu\text{g}$  per mouse) as a solution and as nanoparticles was investigated. The results of these studies are presented in Figs. 11.16 and 11.17. For the ICG solution, the highest levels of ICG were found in the liver, followed in decreasing order in the kidney, spleen, heart and lung. These data confirm the role of the liver as the major organ for the removal of ICG from the general circulation and supports the clinical use of ICG as a test for liver function. In

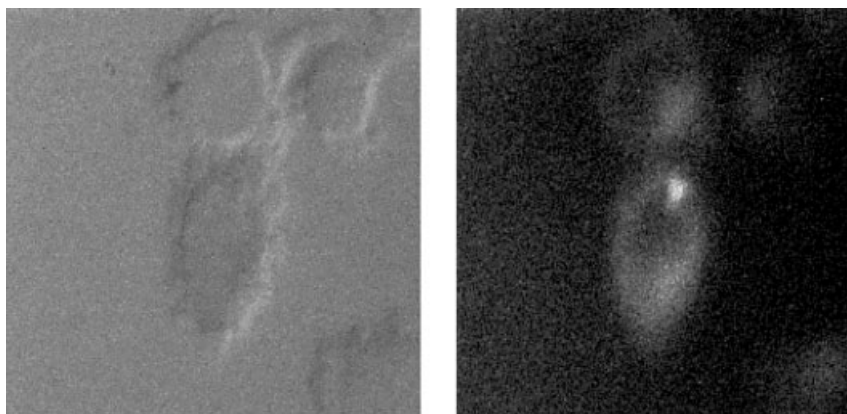


**Fig. 11.11.** Fluorescence microscopic images of B16-F10 cells incubated with 0.1  $\text{mg mL}^{-1}$  coumarin-6-loaded nanoparticle suspension. Differential contrast image (left) and fluorescence image (right). A Nikon 100/1.40 oil lens was used.

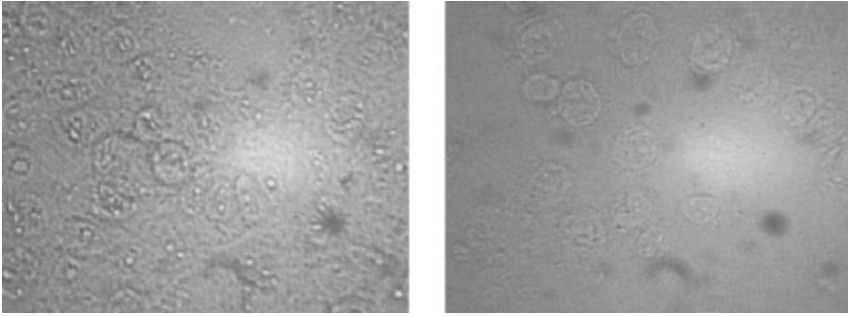


**Fig. 11.12.** Subcellular localization of ICG in C-33A cancer cells (using free ICG solution). Treated cells incubated with 100  $\mu\text{M}$  ICG (left) and control cells without ICG (right).

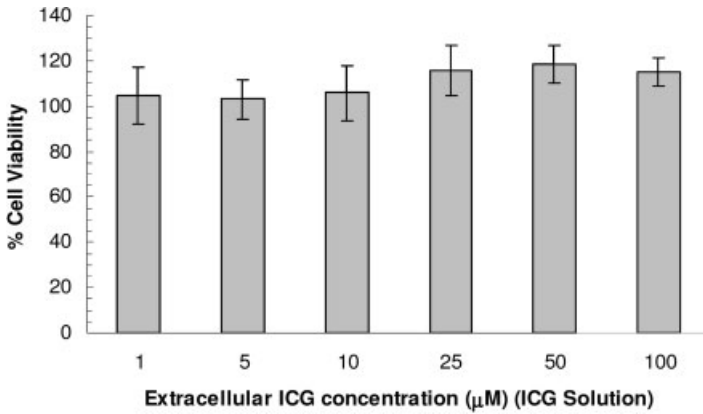


**Fig. 11.13.** Effect of ICG in solution on the viability of B16-F10 cells (mean  $\pm$  SD,  $n = 5$ ). Extracellular concentration of ICG: 1–100  $\mu\text{M}$ .

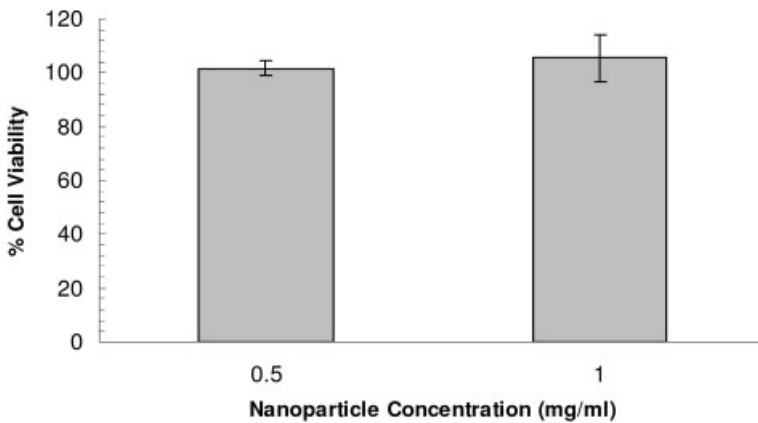


**Fig. 11.14.** Effect of ICG-loaded nanoparticles on the viability of B16-F10 cells (mean  $\pm$  SD,  $n = 5$ ). Nanoparticle concentration: 0.5 and 1  $\text{mg mL}^{-1}$ .

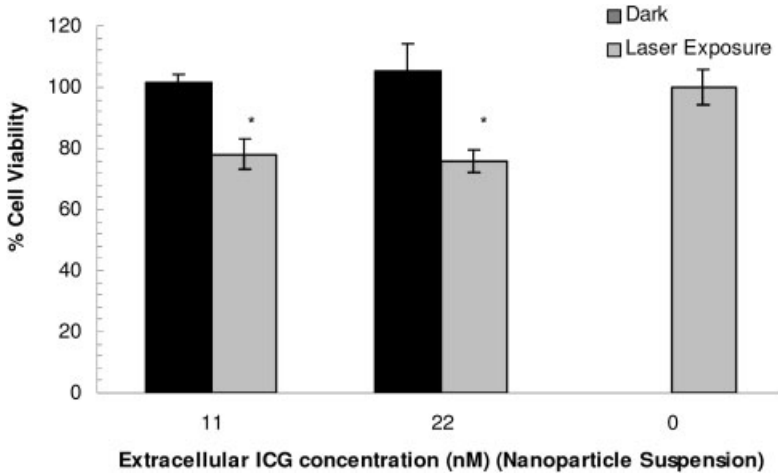


**Fig. 11.15.** Photodynamic activity of ICG-loaded nanoparticles on the viability of B16-F10 cells (mean  $\pm$  SD,  $n = 5$ ). Extracellular concentration of ICG was 11 and 22 nM. \*Significantly different from dark at  $p < 0.05$ .

the case of ICG nanoparticles, while the liver again accumulated the highest concentrations of dye, the biodistribution pattern for other organs was somewhat different than with a solution, since the concentrations decreased in the order spleen, lungs, heart and kidneys. It is evident that ICG nanoparticles are preferentially taken up into liver and spleen, two organs that form part of the RES that is responsible for the removal of foreign particles from the blood through an active phagocytic activity.

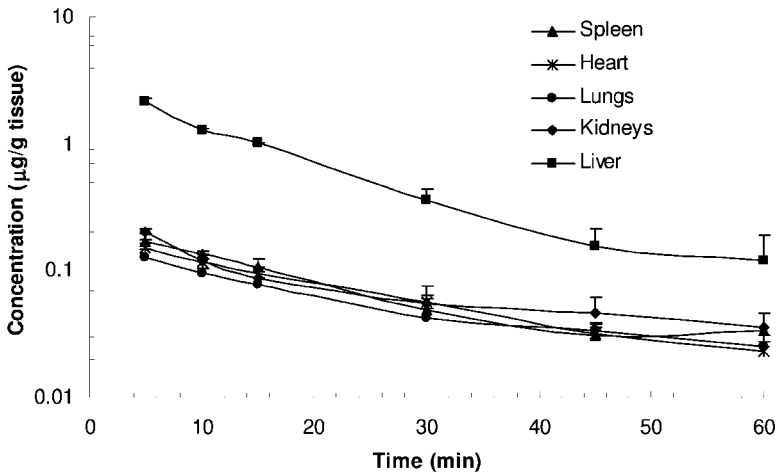


**Fig. 11.16.** Biodistribution of ICG (solution) in mouse tissues following an intravenous dose of ICG (10  $\mu\text{g}$  per mouse).

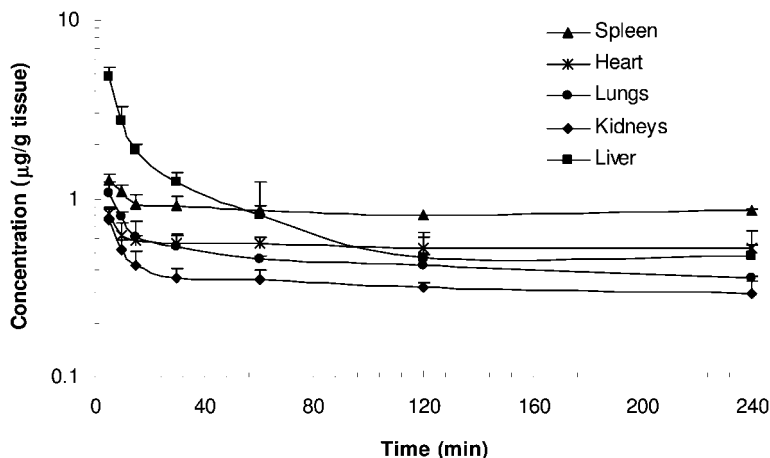


Fig. 11.17. Biodistribution of ICG (nanoparticles) in mouse tissues following an intravenous dose of ICG (10 µg per mouse).

Interestingly, the administration of ICG as a nanoparticle formulation led to a blood ICG level that was significantly higher than from a solution and which remained elevated for up to 4 h posttreatment. We believe that these results reflect the slower hepatic clearance of circulating ICG nanoparticles than of free ICG [155]. Also, nanoparticles may enhance the entry and retention of ICG into organs since the levels of ICG in organs were higher from a suspension of nanoparticles than from an equivalent aqueous solution. This feature should be of particular value in the targeting of tumors with ICG-loaded nanoparticles. In the body, the elimination of ICG appears to follow a biphasic pattern, with a rapid initial phase of maximum dye removal followed later by a slower removal phase.

## 11.7

### Conclusions and Future Work

Nanoparticulate systems can serve as an ideal carrier system for drugs used in tumor imaging and PDT. By forming a wall around the drug they contain, nanoparticles can effectively protect the drug from the altering effects of the surrounding aqueous environment and from potential degradation by light and temperature. Taking advantage of the leaky vasculature of tumors, nanoparticles can enhance the passive uptake into and ultimate accumulation of antitumor drugs at the target site by an enhanced permeation and retention effect. Furthermore, in comparison to a drug solution, nanoparticles can provide a longer half-life and retention of a drug in the body due to their size and surface characteristics. Finally, nanoparticulates loaded with photoactive antitumor drugs can show photodynamic activity in tumor cells.



We have shown the feasibility of manufacturing PLGA nanoparticles of ICG with good potential as an agent for the diagnosis and treatment of tumors. These nanoparticles should be viewed primarily as a foundation for the development of new nanoparticles with improved pharmaceutical and therapeutic features. In pursuit of this goal, future work on this area will be addressed to, among other things, compare different types of PLGA (e.g. 25/75, 30/70, 75/25) for their suitability in manufacturing ICG nanoparticles with enhanced entrapment efficiency and dye content. Another idea worthy of a future investigation is to test polymeric materials such as albumin, chitosan, and PEGs (including PEG 2000, 5000 and 20 000). In an effort to minimize the opsonization of the nanoparticles *in vivo* and, hence, to prolong the plasma half-life of ICG, the application of an external coating with a hydrophilic polymer may be warranted. Furthermore, to magnify the selectivity of the nanoparticles to particular target sites, one could explore the possibility of modifying the nanoparticle surface by the attachment of antibodies and other types of ligands with the ability to interact with specific types of tumors.

Another important aspect of nanotechnology applied to drug delivery using polymeric nanoparticles that will need to be considered is the scale-up of the production from the laboratory to an industrial scale, with particular attention to uniformity of particle size, reproducible solute entrapment efficiency and stability on storage under a variety of environmental conditions. Efforts will need to be directed to investigating the porosity characteristics of the nanoparticle surface (including pore size, pore shape and number of pores per surface area) and its relevance to solute release in a biological environment. In addition, to reduce the dose of ICG as ICG nanoparticles for applications like imaging and PDT, future developmental work on this type of formulation should concentrate in finding ways to enhance the fluorescence signal of a dye after undergoing intracellular uptake. The use of nanoparticles containing both silver ions and ICG is an attractive alternative that merits future consideration.

At the cellular level, a vast amount of work remains to be carried out with ICG nanoparticles using cell culture systems. In this regard, the use of new tumor cell lines will provide a better picture of the type of cancers that can be treated with ICG, especially cell lines of breast and skin cancers. The effectiveness of PDT for each of the cancer cell lines will only be established by evaluating the effects of critical factors such as light dose and ICG dose, which will eventually have to be optimized. A detailed investigation will have to be conducted to elucidate the mechanism of PDT activity on different tumor cell lines and the role of singlet oxygen in this process. The location of nanoparticles in the cell, their movement within the cells and the delivery of the nanoparticle contents to various cell organelles are also important subjects for future studies.

To more accurately define the biodistribution patterns and pharmacokinetic profiles of ICG delivered as nanoparticles, further investigation of this type of formulation could be done in higher animal models such as the rat and rabbit. Furthermore, testing the nanoparticles in tumor-bearing animal models will provide us with a clearer picture of the therapeutic and diagnostic effectiveness of the nanoparticles under more realistic conditions, particularly as it relates to tumor imaging

and PDT applications. Again, the results of these studies will be of great help in optimizing the test formulations.

## References

- 1 SHEN, Y., FRIEND, C. S., JIANG, Y., JAKUBCZYK, J., PRASAD, P. N., Nanophotonics: interactions, materials and applications, *J. Phys. Chem.* **2000**, *104*, 7577–7587.
- 2 KROLL, R. A., PAGEL, M. A., MULDOON, L. L., ROMAN-GOLDSTEIN, S., FIAMENGO, S. A., NEUWELT, E. A., Improving drug delivery to intercerebral tumor and surrounding brain in a rodent model: a comparison of osmotic versus bradykinin modification of the blood–brain and/or blood–tumor barriers, *Neurosurgery* **1998**, *43*, 879–886.
- 3 SAXENA, V., SADOQI, M., SHAO, J., KUMAR, S., Tiny bubbles, *SPIE's OE Mag (Special Focus): Biotechnology* **2004**, *Sept*, 21–23.
- 4 TOMALIA, D. A., BAKER, H., DEWALD, J., HALL, M., KALLOS, G., MARTIN, S., ROECK, J., RYDER, J., SMITH, P., A new class of polymers: starburst-dendritic macromolecules, *Polym. J.* **1985**, *17*, 117–132.
- 5 TOMALIA, D. A., NAYLOR, A. M., GODDARD III, W. A., Starburst dendrimers: molecular-level control of size, shape, surface chemistry, topology, and flexibility from atoms to macroscopic matter, *Angew. Chem. Int. Ed.* **1990**, *29*, 138–175.
- 6 FRECHET, J. M. J., HAWKER, C. J., WOOLEY, K. L., The convergent route to globular dendritic macromolecules – a versatile approach to precisely functionalized 3-dimensional polymers and novel block-copolymers, *J. Macromol. Sci. Pure Appl. Chem.* **1994**, *A31*, 1627–1645.
- 7 ZIMMERMAN, S. C., ZENG, F., REICHERT, D. E. C., KOLOTUCHIN, S. V., Self-assembling dendrimers, *Science* **1996**, *271*, 1095–1098.
- 8 FRECHET, J. M. J., Functional polymers and dendrimers: reactivity, molecular architecture, and interfacial energy, *Science* **1994**, *263*, 1710–1715.
- 9 MEIJER, E. W., Macro-organische chemie, supramoleculaire architectuur van functionele materialen, *Chem. Mag.* **1994**, *May*, 2002–2005.
- 10 WENDLAND, M. S., ZIMMERMAN, S. C., Synthesis of cored dendrimers, *J. Am. Chem. Soc.* **1999**, *121*, 1389–1390.
- 11 WEBER, S., Application of the five-dimensional maximum entropy method to the structure refinement of decagonal Al–Mn–Pd quasicrystals, *Doctoral thesis*, University of Tsukuba, Japan, **1997**.
- 12 WEI, B. Q., VAJTAI, R., AJAYAN, P. M., Reliability and current carrying capacity of carbon nanotubes, *Appl. Phys. Lett.* **2001**, *79*, 1172.
- 13 O'CONNELL, M. J., BACHILO, S. M., HUFFMAN, C. B., MOORE, V. C., STRANO, M. S., RIALON, K. L., BOUL, P. J., NOON, W. H., KITRELL, C., MA, J. P., HAUGE, R. H., WEISMAN, R. B., SMALLEY, R. E., Band gap fluorescence from individual single-walled carbon nanotubes, *Science* **2002**, *297*, 593–596.
- 14 HERTEL, T., FASEL, R., MOOS, G., Charge-carrier dynamics in single-wall carbon nanotube bundles: a time-domain study, *Appl. Phys. A Mater. Sci. Process.* **2002**, *75*, 449–465.
- 15 LAURET, J. S., VOISIN, C., CASSABOIS, G., DELALANDE, C., ROUSSIGNOL, Ph., JOST, O., CAPES, L., Ultrafast carrier dynamics in single-wall carbon nanotubes, *Phys. Rev. Lett.* **2003**, *90*, 057404.
- 16 BAKER, S. E., LASSETER, T. L., SMITH, L. M., HAMERS, R. J., Covalently bonded adducts of deoxyribonucleic acid (DNA) oligonucleotides with single-wall carbon nanotubes: synthesis and hybridization, *Nano Lett.* **2002**, *2*, 1413–1417.
- 17 STRANO, M. S., Probing chiral selective reactions using a revised Kataura plot

- for the interpretation of single-walled carbon nanotube. *J. Am. Chem. Soc.* **2003**, *125*, 16148–53.
- 18 BALLOU, B., ERNST, L. A., WAGGONER, A. S., Fluorescence imaging of tumors *in vivo*, *Curr. Med. Chem.* **2005**, *12*, 795–805.
  - 19 VOURA, E. B., JAISWAL, J. K., MATTOUSSI, H., SIMON, S. M., Tracking metastatic tumor cell extravasation with quantum dot nanocrystals and fluorescence, emission-scanning microscope, *Nat. Med.*, **2004**, *10*, 993–998.
  - 20 JONES, M. C., LEROUX, J. C., Polymeric micelles – a new generation of colloidal drug carriers, *Eur. J. Pharm. Biopharm.* **1999**, *48*, 101–11.
  - 21 NOSTRUM, C. F., Polymeric micelles to deliver photosensitizers for photodynamic therapy, *Adv. Drug Deliv. Rev.* **2004**, *56*, 9–16.
  - 22 LASIC, D. D., Doxorubicin in sterically stabilized liposomes, *Nature* **1996**, *381*, 630–630.
  - 23 KIM, S., Liposomes as carriers of cancer chemotherapy: current status and future prospects, *Drugs* **1993**, *46*, 618–638.
  - 24 DERYCKE, A. S. L., DE WITTE, P. A. M., Liposomes for photodynamic therapy, *Adv. Drug Deliv. Rev.* **2004**, *56*, 17–30.
  - 25 SOPPIMATH, K. S., AMINABHAVI, T. M., KULKARNI, A. R., RUDZINSKI, W. E., Biodegradable polymeric nanoparticles as delivery devices, *J. Controlled Rel.* **2001**, *70*, 1–20.
  - 26 COUVREUR, P., KANTE, B., LENAERTS, V., SCAILTEUR, V., ROLAND, M., SPEISER, P., Tissue distribution of antitumor drugs associated with polyalkylcyanoacrylate nanoparticles, *J. Pharm. Sci.* **1980**, *69*, 199–202.
  - 27 ROLLAND, A., Clinical pharmacokinetics of doxorubicin in hepatoma patients after a single intravenous injection of free or nanoparticle-bound anthracycline, *Int. J. Pharm.* **1989**, *54*, 113–121.
  - 28 LEROUX, J. C., DOELKER, E., GURNY, R., The use of drug-loaded nanoparticles in cancer chemotherapy, In *Microencapsulation: Methods and Industrial Applications*, BENITA, S. (Ed.), Marcel Dekker, New York, **1996**, pp. 535–575.
  - 29 MONSKY, W. L., FUKUMURA, D., GOHONGI, T., ANCUKIEWCZ, M., WEICH, H. A., TORCHILIN, V. P., YUAN, F., JAIN, R. K., Augmentation of transvascular transport of macromolecules and nanoparticles in tumors using vascular endothelial growth factor, *Cancer Res.* **1999**, *59*, 4129–4135.
  - 30 BENNIS, S., CHAPEY, C., COUVREUR, P., ROBERT, J., Enhanced cytotoxicity of doxorubicin encapsulated in polyisohexylcyanoacrylate nanospheres against multidrug-resistant cells in culture, *Eur. J. Cancer* **1994**, *30*, 89–93.
  - 31 ROWINSKY, E. K., and DONEHOWER, R. C., Drug therapy: paclitaxel, *N. Engl. J. Med.* **1995**, *332*, 1004–1014.
  - 32 MAGENHEIM, B., and BENITA, S., Nanoparticle characterization: a comprehensive physicochemical approach, *STP Pharma Sci.* **1991**, *1*, 221–241.
  - 33 MU, L., FENG, S. S., A novel controlled release formulation for the anticancer drug paclitaxel (Taxol®): PLGA nanoparticles containing vitamin E TPGS, *J. Controlled Rel.* **2003**, *86*, 33–48.
  - 34 BRIGGER, I., DUBERNET, C., COUVREUR, P., Nanoparticles in cancer therapy and diagnosis, *Adv. Drug Deliv. Rev.* **2002**, *54*, 631–651.
  - 35 VERDUN, C., BRASSEUR, F., VRANOKX, H., COUVREUR, P., ROLAND, M., Tissue distribution of doxorubicin associated with polyisohexylcyanoacrylate nanoparticles, *Cancer Chemother. Pharmacol.* **1990**, *26*, 13–18.
  - 36 SIMEONOVA, M., ILARIONOVA, M., IVANOVA, T., KONSTANTINOV, C., TODOROV, D., Nanoparticles as drug carriers for vinblastine. Acute toxicity of vinblastine in a free form and associated to polybutylcyanoacrylate nanoparticles, *Acta Physiol. Pharmacol. Bulg.* **1991**, *17*, 43–49.
  - 37 BECK, P., KREUTER, J., RESZKA, R., FICHTNER, I., Influence of polybutylcyanoacrylate nanoparticles and liposomes on the efficacy and toxicity of the anticancer drug mitoxantrone in

- murine tumor models, *J. Microencapsul.* **1993**, *10*, 101–114.
- 38 MOGHIMI, M. S., HUNTER, C. A., MURRAY, C. J., Long-circulation and target-specific nanoparticles: theory to practice, *Pharmacol. Rev.*, **2001**, *53*, 283–318.
  - 39 ANDERSON, J. M., SHIVE, M. S., Biodegradation and biocompatibility of PLA and PLGA microspheres, *Adv. Drug Deliv. Rev.* **1997**, *28*, 5–24.
  - 40 HANAFUSA, S., MATSUSUE, YASUNAGA, T., YAMMAMURO, T., OKA, M., SHIKINAMI, Y., IKADA, Y., Biodegradable plate fixation of rabbit femoral shaft osteotomies. A Comparative study, *Clin. Orthop.* **1995**, *315*, 262–271.
  - 41 MATSUSUE, Y., HANAFUSA, S., YAMMAMURO, T., SHIKINAMI, Y., IKADA, Y., Tissue reaction of biodegradable ultra high strength poly(L-lactide) rod. A long-term study in rabbits, *Clin. Orthop.* **1995**, *317*, 246–253.
  - 42 LANGER, R., Tissue engineering: a new field and its challenges, *Pharm. Res.* **1997**, *14*, 840–841.
  - 43 MOONEY, D. J., SANO, K., KAUMANN, P. M., MAJAHOD, K., SCHLOO, B., VACANTI, J. P., LANGER, R., Engraftment of hepatocytes transplanted on biodegradable polymer sponges, *J. Biomed. Mater. Res.* **1997**, *37*, 413–420.
  - 44 EISELT, P., KIM, B. S., CHACKO, B., ISENBERG, B., PETERS, M. C., GREENE, K. G., ROLAND, W. D., LOEBSACK, A. B., BURG, K. J., CULBERSON, C., HALBERSTADT, C., HOLDER, W. D., MOONEY, D. J., Development of technologies aiding large-tissue engineering, *Biotechnol. Progr.* **1998**, *14*, 134–140.
  - 45 GURNY, R., PEPPAS, N. A., HARRINGTON, D. D., BANKER, G. S., Development of biodegradable and injectable lattices for controlled release of potent drugs, *Drug Dev. Ind. Pharm.* **1981**, *7*, 1–25.
  - 46 BINDSCHAELDER, C., LEONG, K., MATHIOWITZ, E., LANGER, R., Poly(hydroxy acid) microsphere formulation by solvent-extraction, *J. Pharm. Sci.* **1988**, *77*, 696–698.
  - 47 FESSI, H., PUISIEUX, F., DEVISSAGUET, J. P., AMMOURY, N., BENITA, S., Nanocapsule formation by interfacial polymer deposition following solvent displacement, *Int. J. Pharm.* **1989**, *55*, R1–R4.
  - 48 ZHANG, X., WISS, U. P., PICHORA, D., GOOSSEN, M. F., A mechanistic study of antibiotic release from biodegradable poly(D,L-lactide) cylinders, *J. Controlled Rel.* **1994**, *31*, 128–144.
  - 49 O'HARA, P., HICKNEY, A. J., Respirable PLGA microspheres containing rifampicin for the treatment of tuberculosis: manufacture and characterization, *Pharm. Res.* **2000**, *17*, 955–961.
  - 50 KOMPELLA, U. B., KOUSHIK, K., Preparation of drug delivery systems using supercritical fluid technology, *Crit. Rev. Ther. Drug. Carrier Syst.* **2001**, *18*, 2173–2199.
  - 51 JAIN, R. A., The manufacturing techniques of various drug loaded biodegradable poly(lactide-co-glycolide) devices, *Biomaterials* **2000**, *21*, 2475–2490.
  - 52 O'DONNELL, P. B., MCGINITY, J. W., Preparation of microspheres by the solvent evaporation technique, *Adv. Drug Deliv. Rev.* **1997**, *28*, 25–42.
  - 53 MURAKAMI, H., KOBAYASI, M., TAKEUCHI, H., KAWASHIMA, Y., Preparation of poly(DL-lactide-co-glycolide) nanoparticles by modified spontaneous emulsification solvent diffusion method, *Int. J. Pharm.* **1999**, *187*, 143–152.
  - 54 CLELAND, J. L., JONES, A. J. S., Stable formulations of recombinant human growth hormone and interferon-gamma for microencapsulation in biodegradable microspheres, *Pharm. Res.* **1996**, *13*, 1464–1475.
  - 55 SCHOLLES, P. D., COOMBS, A. G. A., ILLUM, L., DAVIS, S. S., WATTS, J. F., USTARIZ, C., VERT, M., DAVIS, M. C., Detection and determination of surface levels of proloxamer and PVA surfactant on biodegradable nanospheres using SSIMS and XPS, *Int. J. Pharm.* **1999**, *59*, 261–278.
  - 56 FENG, S., HUANG, G., Effects of emulsifiers on the controlled release

- of paclitaxel (taxol) from nanospheres of biodegradable polymers, *J. Controlled Rel.* **2001**, *71*, 53–69.
- 57 VANDERVOORT, J., LUDWIG, A., Biocompatible stabilizers in the preparation of PLGA nanoparticles: a factorial design study, *Int. J. Pharm.* **2002**, *238*, 77–92.
- 58 GREF, R., MINAMITAKE, Y., PERACCHIA, M. T., TRUBETSKOY, V., TORCHILIN, V., LANGER, R., Biodegradable long-circulating polymeric nanospheres, *Science* **1994**, *263*, 1600–1603.
- 59 STOLNIK, S., FELUMB, N. C., HEALD, C. R., GARNETT, M. C., ILLUM, L., DAVIS, S. S., Adsorption behavior and conformation of selected poly(ethylene oxide) copolymers on the surface of a model colloidal drug carrier, *Colloids Surfaces A: Physicochem. Eng. Aspects* **1997**, *122*, 151–159.
- 60 TOBIO, M., GREF, R., SANCHEZ, A., LANGER, R., ALONSO, M. J., Stealth PLA–PEG nanoparticles a protein carriers for nasal administration, *Pharm. Res.* **1998**, *1*, 270–275.
- 61 THOMAS, G. M., Improved treatment for cervical cancer – concurrent chemotherapy and radiotherapy, *N. Engl. J. Med.* **1999**, *340*, 1198–1200.
- 62 WHARTON, J. T., TORTOLERO-LUNA, G., Neoplasms of the cervix, In *Cancer Medicine*, BAST, R. C., KUFFE, D. W., POLLOCK, R. E., WEICHSELBAUM, R. R., HOLLAND, J. F., FREI, E. (Eds.), BC Decker, Hamilton, **2000**, pp. 1631–1666.
- 63 EIFEL, P. J., BEREK, J. S., THIGPEN, J. T., Cancer of the cervix, vagina, and vulva, In *Cancer: Principles and Practice of Oncology*, DeVITA, V. T., HELLMAN, S., ROSENBERG, S. A. (Eds.), Lippincott Williams & Wilkins, Philadelphia, PA, **2001**, pp. 1526–1572.
- 64 FIELDS, A. L., JONES, J. G., THOMAS, G. N., RUNOWICZ, C. D., Gynecologic cancer, In *Clinical Oncology*, LENHARD, R. E., OSTEEEN, R. T., GANSLER, T. (Eds.), American Cancer Society, Atlanta, GA, **2001**, pp. 455–496.
- 65 STECKEL, R. J., Principles of imaging, In *Cancer Medicine*, BAST, R. C., KUFFE, D. W., POLLOCK, R. E., WEICHSELBAUM, R. R., HOLLAND, J. F., FREI, E. (Eds.), BC Decker, Hamilton, **2000**, pp. 400–439.
- 66 YARBRO, C. H., FROGGE, M., GOODMAN, M., GROENWALD, S. L. (Eds.), *Cancer Nursing: Principles and Practice*, 5th edn., Jones and Bartlett, Sudbury, MA, **2000**.
- 67 COLEMAN, R. E., TESAR, R. D., Diagnostic aspects of radiopharmaceuticals. In *Radiopharmaceuticals in the Diagnosis and Treatment of Cancer, Oncol. Issues (Suppl.)* **2001**, *16*, 7–8.
- 68 FISHMAN, E. K., URBAN, B. A., Cancer diagnosis: imaging, In *Cancer: Principles and Practice of Oncology*, DeVITA, V. T., HELLMAN, S., ROSENBERG, S. A. (Eds.), Lippincott Williams & Wilkins, Philadelphia, PA, **2001**, pp. 659–720.
- 69 MORRA, M., POTTS, E., *Choices*, Avon Books, New York, **1994**.
- 70 DOLLINGER, M., ROSENBAUM, E. H., CABLE, G., *Everyone's Guide to Cancer Therapy*, 3rd edn., Somerville House Books, Toronto, **1997**.
- 71 RUNOWICZ, C. D., PETREK, J. A., GANSLER, T. S., *Women and Cancer*, Villard, New York, **1999**.
- 72 ABELOFF, M. D., ARMITAGE, J. O., LICHTER, A. S., NIEDERHUBER, J. E., *Clinical Oncology*, 2nd edn., Churchill Livingstone, Philadelphia, PA, **2000**.
- 73 DeVITA, JR. V. T., HELLMAN, S., ROSENBERG, S. A. (Eds.), *Cancer: Principles and Practice of Oncology*, Lippincott Williams & Wilkins, Philadelphia, PA, **2001**.
- 74 MURPHY, G. P., MORRIS, L. B., LANGE, D., *Informed Decisions: The Complete Book of Cancer Diagnosis, Treatment, and Recovery*, 2nd edn., American Cancer Society, Viking Press, New York, **2002**.
- 75 VARRICCHIO, C., PIERCE, M., WALTER, C. L., ADES, T. B., *A Cancer Source Book for Nurses*, 7th edn., American Cancer Society, Atlanta, GA, **1977**.
- 76 COOPER, G. M., *The Cancer Book: A Guide to Understanding The Causes, Prevention, and Treatment of Cancer*, Jones and Bartlett, Boston, MA, **1993**.

- 77 BURKE, M. B., WILKES, G. M., INGWERSEN, K., BEAN, C. K., BERG, D., A nursing process approach, In *Cancer Chemotherapy*, 2nd edn., Jones and Bartlett, Boston, MA, 1996.
- 78 GUY, J. L., INGRAM, B. A., Medical oncology: the agents, In *Cancer Nursing: A Comprehensive Textbook*, MCCORKLE, R., GRANT, M., FRANK-STROMBORG, M., BAIRD, S. B. (Eds.), Saunders, Philadelphia, PA, 1996, pp. 359–394.
- 79 CAMP-SORRELL, D., Chemotherapy: toxicity management, In *Cancer Nursing: Principles and Practice*, 4th edn., GROENWALD, S. L., FROGGE, M. H., GOODMAN, M., YARBRO, C. H. (Eds.), Jones and Bartlett, Boston, MA, 1997, pp. 387–425.
- 80 GOODMAN, M., RILEY, M. B., Chemotherapy: principles of administration, In *Cancer Nursing: Principles and Practice*, 4th edn., GROENWALD, S. L., FROGGE, M. H., GOODMAN, M., YARBRO, C. H. (Eds.), Jones and Bartlett, Boston, MA, 1997, pp. 31–386.
- 81 TROTICE, P. V., Chemotherapy: principles of therapy, In *Cancer Nursing: Principles and Practice*, 4th edn., GROENWALD, S. L., FROGGE, M. H., GOODMAN, M., YARBRO, C. H. (Eds.), Jones and Bartlett, Boston, MA, 1997, pp. 283–316.
- 82 YASKO, J. M., *Nursing Management of Symptoms Associated with Chemotherapy*, Meniscus Health Care Communications, Bala Cynwyd, PA, 1998.
- 83 LABRIOLA, D., LIVINGSTON, R., Possible interactions between dietary antioxidants and chemotherapy, *Oncology* 1999, 13, 1003–1008.
- 84 MOSS, W. T., COX, J. D., *Radiation Oncology: Rationale, Technique, Results*, Mosby, St. Louis, MO, 1994.
- 85 COIA, L., MOYLAN, D., *Introduction to Clinical Radiation Oncology*, 3rd edn., Medical Physics Publishing, Madison, WI, 1998.
- 86 PEREZ, C. A., BRADY, L. W., *Principles and Practice of Radiation Oncology*, 3rd edn., Lippincott-Raven, Philadelphia, PA, 1998.
- 87 STROHL, R., Radiation therapy, In *Oncology Nursing: Assessment & Clinical Care*, MIASKOWSKI, C., BUCHSEL, P. (Eds.), Mosby, St. Louis, MO, 1999, pp. 59–81.
- 88 RIETHMULLER, G., SCHNEIDER-GADICKE, E., SCHLIMOK, G., Randomised trial of monoclonal antibody for adjuvant therapy of resected Dukes' C colorectal carcinoma, *Lancet* 1994, 14, 1177–1183.
- 89 CANEVARI, S., STOTER, G., ARIENTI, F., Regression of advanced ovarian carcinoma by intraperitoneal treatment with autologous T lymphocytes retargeted by a bispecific monoclonal antibody, *J. Natl Cancer Inst.* 1995, 87, 1463–1469.
- 90 DISIS, M. L., GRABSTEIN, K. H., SLEATH, P. R., CHEEVER, M. A., Generation of immunity to the HER-2 *neu* oncogenic protein in patients with breast and ovarian cancer using a peptide-based vaccine, *Clin. Cancer Res.* 1999, 5, 1289–1297.
- 91 FOON, K. A., CHAKRABORTY, M., JOHN, W. J., SHERRATT, A., KOHLER, H., BHATTACHARYA-CHATTERJEE, M., Immune response to the carcino-embryonic antigen in patients treated with an anti-idiotypic antibody vaccine, *J. Clin. Invest.* 1995, 96, 334–342.
- 92 FUJITA, K., IKARASHI, H., TAKAKUWA, K., Prolonged disease-free period in patients with advanced epithelial ovarian cancer after adoptive transfer of tumor-infiltrating lymphocytes, *Clin. Cancer Res.* 1995, 501–507.
- 93 HSU, F. J., CASPAR, C. B., CZERWINSKI, D., Tumor-specific idiotype vaccines in the treatment of patients with B-cell lymphoma long-term results of a clinical trial, *Blood* 1997, 89, 3129–3135.
- 94 TOURANI, J. M., PFISTER, C., BERDAH, J. F., Outpatient treatment with subcutaneous interleukin-2 and interferon alfa administration in combination with fluorouracil in patients with metastatic renal cell carcinoma: results of a sequential nonrandomized phase II study, *J. Clin. Oncol.* 1998, 16, 2505–2513.

- 95 GEZ, E., MEKORI, T., STRUMINGER, L., T-cell subpopulation in patients with metastatic renal cell carcinoma treated by recombinant interleukin-2, recombinant interferon-alpha, 5-fluorouracil, and vinblastine, *Cancer Invest.* **1999**, *17*, 259–263.
- 96 GRETEN, T. F., JAFFEE, E. M., Cancer vaccines, *J. Clin. Oncol.* **1999**, *17*, 1047–1060.
- 97 HADDEN, J. W., The immunology and immunotherapy of breast cancer: an update, *Int. J. Immunopharmacol.* **1999**, *21*, 79–101.
- 98 HEMILLA, M. R., CHANG, A. E., Clinical implications of the new biology in the development of melanoma vaccines, *J. Surg. Oncol.* **1999**, *70*, 263–274.
- 99 HSUEH, E. C., NATHANSON, L., FOSHAG, L. J., Active specific immunotherapy with polyvalent melanoma cell vaccine for patients with in-transit melanoma metastases, *Cancer* **1999**, *85*, 2160–2169.
- 100 SANDMAIER, B. M., OPARIN, D. V., HOLMBERG, L. A., REDDISH, M. A., MACLEAN, G. D., LONGENECKER, B. M., Evidence of a cellular immune response against sialyl-Tn in breast and ovarian cancer patients after high-dose chemotherapy, stem cell rescue, and immunization with Theratope STn-KLH cancer vaccine, *J. Immunother.* **1999**, *22*, 54–66.
- 101 TJOA, B. A., SIMMONS, S. J., ELGAMAL, A., Follow-up evaluations of a phase II prostate cancer vaccine trial, *Prostate* **1999**, *40*, 125–129.
- 102 BAST, R. C., ZALUTSKY, M. R., KREITZMAN, R. J., SAUSVILLE, E. A., FRANKEL, A. R., Monoclonal serotherapy, In *Cancer Medicine*, BAST, R. C., KUFU, D. W., POLLOCK, R. E., WEICHELBAUM, R. R., HOLLAND, J. F., FREI, E. (Eds.), 5th edn., Williams & Wilkins, Baltimore, MD, **2000**, pp. 860–875.
- 103 GRIMM, E. A., Cytokines: biology and applications in cancer medicine, In *Cancer Medicine*, BAST, R. C., KUFU, D. W., POLLOCK, R. E., WEICHELBAUM, R. R., HOLLAND, J. F., FREI, E. (Eds.), 5th edn., Williams & Wilkins, Baltimore, MD, **2000**, pp. 825–834.
- 104 RAVINDRANTH, M. H., MORTON, D. L., Active specific immunotherapy with vaccines, In *Cancer Medicine*, BAST, R. C., KUFU, D. W., POLLOCK, R. E., WEICHELBAUM, R. R., HOLLAND, J. F., FREI, E. (Eds.), 5th edn., Williams & Wilkins, Baltimore, MD, **2000**, pp. 800–814.
- 105 SALGALLER, M. L., Immune adjuvants, In *Principles and Practice of the Biologic Therapy of Cancer*, ROSENBERG, S. A. (Ed.), 3rd edn., Lippincott Williams & Wilkins, Philadelphia, PA, **2000**, 584–601.
- 106 KREITZMAN, R. J., WILSON, W. H., BERGERON, K., Efficacy of the anti-CD22 recombinant immunotoxin BL22 in chemotherapy-resistant hairy-cell leukemia, *N. Engl. J. Med.* **2001**, *345*, 241–247.
- 107 RESTIFO, N. P., SZYNOL, M., OVERWIJK, W. W., Therapeutic cancer vaccines, In *Cancer: Principles and Practice of Oncology*, DeVITA, V. T., HELLMAN, S., ROSENBERG, S. A. (Eds.), Lippincott Williams & Wilkins, Philadelphia, PA, **2001**, pp. 3195–3217.
- 108 DUDLEY, M. E., WUNDERLICH, J. R., ROBBINS, P. F., YANG, J. C., HWU, P., SCHWARTZENTRUBER, D. J., TOPALIAN, S. L., SHERRY, R., RESTIFO, N. P., HUBICKI, A. M., ROBINSON, M. R., RAFFELD, M., DURAY, P., SEIPP, C. A., ROGERS-FREEZER, L., MORTON, K. E., MAVROUKAKIS, S. A., WHITE, D. E., ROSENBERG, S. A., Cancer regression and autoimmunity in patients after clonal repopulation with antitumor lymphocytes, *Science* **2002**, *298*, 850–854.
- 109 PAZDUR, R., COIA, L. R., HOSKINS, W. J., WAGMAN, L. D., *Cancer Management: A Multidisciplinary Approach, Medical Surgical and Radiation Oncology*, PRR, Huntington, NY, **1996**.
- 110 LENHARD, R. E., OSTEEN, R. T., GANSLER, T. (Eds.), *Clinical Oncology*, American Cancer Society, Atlanta, GA, **2001**.
- 111 EYRE, H. J., LANGE, D., MORRIS, L. B., *Informed Decisions*, 2nd edn.,

- American Cancer Society, Atlanta, GA, 2002.
- 112 GAYEN, S. K., ALFANO, R. R., Emerging biomedical imaging techniques, *Opt. Photon. News* **1996**, *7*, 17–22.
  - 113 PRASAD, P. N., *Introduction to Biophotonics*, 1st edn., Wiley-Interscience, New York, **2003**.
  - 114 MITRA, K., KUMAR, S., Development and comparison of models for light pulse transport through scattering-absorbing media, *Appl. Optics* **1999**, *38*, 188–196.
  - 115 GUO, Z., ABER, J., GARETZ, B., KUMAR, S., Monte Carlo Simulation and experiments of pulsed radiative transfer, *J. Quant. Spec. Radiat. Transfer* **2002**, *73*, 159–168.
  - 116 WAN, S. K., GUO, Z., KUMAR, S., ABER, J., GARETZ, B. A., Noninvasive detection of inhomogeneities in turbid media with time-resolved log-slope analysis, *J. Quant. Spec. Radiat. Transfer* **2004**, *84*, 493–500.
  - 117 SADOQI, M., RISEBORO, P., KUMAR, S., Analytical models for pulse laser fluorescence imaging in tissues, *Phys. Med. Biol.* **2001**, *46*, 2725–2743.
  - 118 GAYEN, S. K., ZEVALLOS, M. E., AERUBAIEE, M., ALFANO, R. R., Near-infrared laser spectroscopic imaging: a step towards diagnostic optical imaging of human tissue, *Laser Life Sci.* **1999**, *98*, 187–198.
  - 119 LAKOWICZ, J. R., *Principles of Fluorescence Spectroscopy*, 2nd edn., Kluwer, New York, NY, **1999**.
  - 120 THOMPSON, R. B., Red and near-infrared fluorometry, In *Topics in Fluorescence Spectroscopy 4: Probe Design and Chemical Sensing*, LAKOWICZ, J. R. (Ed.), Plenum Press, New York, NY, **1994**, 151–222.
  - 121 LEZNOFF, C. C., LEVER, A. B. P., *Phthalocyanines: Properties and Applications*, VCH, New York, NY, **1989**.
  - 122 MATSUOKA, M., *Infrared Absorbing Dyes*, Plenum Press, New York, NY, **1990**.
  - 123 RAHAVENDRAN, S. V., KARNES, H. T., Application of rhodamine 800 for reversed phase liquid chromatographic detection using visible diode laser induced fluorescence, *Anal. Chem.* **1996**, *68*, 3763–3768.
  - 124 FLANAGAN, J. H., ROMERO, S. E., LEGENDRE, B. L., HAMMER, R. P., SOPER, A., Heavy-atom modified near-IR fluorescent dyes for DNA sequencing applications: synthesis and photophysical characterization, *SPIE Proc.* **1997**, *2980*, 328–337.
  - 125 OWENS, C. V., DAVIDSON, Y. Y., KAR, S., SOPER, S. A., High-resolution separation of DNA restriction fragments using capillary electrophoresis with near-IR diode-based, laser-induced fluorescence detection, *Anal. Chem.* **1997**, *69*, 1256–1261.
  - 126 SOUTHWICK, P. L., ERNST, L. A., TAURIELLO, E. W., PARKER, S. R., MAJUMDAR, R. B., MAJUMDAR, S. W., CLEVER, H. A., WAGGONER, A., Cyanine dye labeling reagents – carboxymethylindocyanine succinimidyl esters, *Cytometry* **1990**, *11*, 418–430.
  - 127 HENDERSON, B., DOUGHERTY, T., How does photodynamic therapy work?, *J. Photochem. Photobiol. B Biol.* **1992**, *55*, 145–157.
  - 128 FISHER, A. M. R., MURPHREE, A. L., GOMER, C. J., Clinical and preclinical photodynamic therapy, In *Laser Surgery and Medicine*, PULIAFITO, C. A. (Ed.), Wiley-Liss, New York, NY, **1996**, pp. 339–368.
  - 129 BHAWALKAR, J. D., KUMAR, N. D., ZHAO, C. F., PRASAD, P. N., Two-photodynamic therapy, *J. Clin. Laser Med. Surg.* **1997**, *15*, 201–204.
  - 130 OCHSNER, M., Photophysical and photobiological processes in the photodynamic therapy of tumors, *J. Photochem. Photobiol. B Biol.* **1997**, *39*, 1–18.
  - 131 SCHMIDT-ERFURTH, U., HASAN, T., Mechanisms of action of photodynamic therapy with Verteporfin for the treatment of age-related macular degeneration, *Surv. Ophthalmol.* **2000**, *45*, 195–214.
  - 132 KONAN, Y. N., GURNY, R., ALLEMANN, E., State of the art in the delivery of photosensitizers for photodynamic therapy, *J. Photochem. Photobiol. B Biol.* **2001**, *66*, 89–106.



- 133 MORGAN, J., OSEROFF, A. R., Mitochondria based photodynamic anti-cancer therapy, *Adv. Drug Deliv. Rev.* **2001**, *49*, 71–86.
- 134 GORMAN, A. A., RODGERS, M. A. J., Current perspectives of singlet oxygen detection in biological environments, *J. Photochem. Photobiol. B Biol.* **1992**, *14*, 159–176.
- 135 BAUMLER, W., ABELS, C., KARRER, S., WEIB, T., MESSMANN, H., LANDTHALER, M., SZEIMIES, R. M., Photo-oxidative killing of human colonic cancer cells using indocyanine green and infrared light, *Br. J. Cancer* **1999**, *80*, 360–363.
- 136 JOHNSON, L. V., WALSH, M. L., BOCHUS, B. J., CHEN, L. B., Monitoring of relative mitochondrial membrane potential in living cells by fluorescence microscopy, *J. Cell Biol.* **1981**, *88*, 526–535.
- 137 DOUGHERTY, T. J., GOMER, C. J., HENDERSON, B. W., Photodynamic therapy, *J. Natl. Cancer Inst.* **1998**, *32*, 889–368.
- 138 STERNBERG, E. D., DOLPHIN, D., BROCKNER, C., Porphyrin-based photosensitizers for use in photodynamic therapy, *Tetrahedron* **1998**, *54*, 4151–4202.
- 139 MORGAN, A. R., GARBO, G. M., KECK, R. W., SELMAN, S. H., New photosensitizers for photodynamic therapy: combined effect of metallopyrin derivatives and light on transplantable bladder tumors, *Cancer Res.* **1998**, *48*, 194–198.
- 140 VOGTEL, F., Dendrimers, *Curr. Chem.* **1998**, *197*, 1–228.
- 141 COLUSSI, V. C., FEYES, D. K., MULIVHILL, J. W., Phthalocyanine 4 (Pc4) photodynamic therapy of human OVCAR-3 tumor xenografts, *Photochem. Photobiol.* **1999**, *69*, 236–241.
- 142 FISHER, M., VOGTEL, F., Dendrimers from design to applications: a progress report, *Angew. Chem. Int. Ed. Engl.* **1999**, *38*, 884–905.
- 143 HORNUNG, R., FEHR, M. K., MONTIFRAYNE, J., Highly selective targeting of ovarian cancer with the photosensitizer PEG–m-THPC in a rat model, *Photochem. Photobiol.* **1999**, *70*, 624–629.
- 144 SHARMAN, W. M., ALLEN, C. M., VAN LIER, JR. J. E., Photodynamic therapeutics, *Drug Discov. Today* **1999**, *4*, 507–517.
- 145 PANDEY, R. K., SUMLIN, A. B., CONSTANTINE, S., AOUA, M., POTTER, W. R., HENDERSON, B. W., RODGERS, M. A., DOUGHERTY, T. J., Alkyl ether analogs of chlorophyll-a derivatives, part 1: synthesis, photophysical properties and photodynamic efficacy, *Photochem. Photobiol.* **1996**, *64*, 194–204.
- 146 SESSLER, J. L., and MILLE, R. A., Texaphyrins – new drugs with diverse clinical applications in radiation and photodynamic therapy, *Biochem. Pharmacol.* **2000**, *59*, 733–739.
- 147 PIFFERI, A., TARONI, P., TORRICELLI, A., VALENTINI, G., COMELLI, D., D'ANDREA, C., ANGELINI, V., CANTI, G., Fluorescence imaging during photodynamic therapy of experimental tumors in mice sensitized with disulfonated aluminium phthalocyanine, *Photochem. Photobiol.* **2000**, *72*, 690–695.
- 148 BATTAH, S. H., CHEE, C. E., NAKANISHI, H., GERSCHER, S., MACROBERT, A. J., EDWARDS, C., Synthesis and biological studies of 5-aminolevulinic acid-containing dendrimers for photodynamic therapy, *Bioconjug. Chem.* **2001**, *12*, 980–988.
- 149 HACKBARTH, S., HORNEFFER, V., WIEHE, A., HILLENKAMP, F., and RÖDER, B., Photophysical properties of pheophorbide-a substituted diamino-butane polypropyleneamine imine dendrimer, *Chem. Phys.* **2001**, *269*, 339–346.
- 150 PHILIP, R., PENZKOFER, A., BAUMLER, W., SZEIMIES, R. M., and ABELS, C., Absorption and fluorescence spectroscopic investigation of indocyanine green, *J. Photochem. Photobiol. A Chem.* **1996**, *96*, 137–148.
- 151 MAAREK, J. M. I., HOLSCHNEIDER, D. P., HARIMOTO, J., Fluorescence of indocyanine green in blood: intensity dependence on concentration and stabilization with sodium poly-

- aspartate, *J. Photochem. Photobiol. B Biol.* **2001**, *65*, 157–164.
- 152** ZHOU, J. F., CHIN, M. P., SCHAFFER, S. A., Aggregation and degradation of indocyanine green, In *Laser Surgery: Advanced Characterization, Therapeutics and Systems IV*, ANDERSON, R. (Ed.), SPIE, Bellingham, CA, **1994**, pp. 495–505.
- 153** KAMISAKA, K., YATSUJII, Y., YAMADA, H., KAMEDA, H., The binding of indocyanine green and other organic anions to serum proteins in liver diseases, *Clin. Chim. Acta* **1974**, *53*, 225–264.
- 154** BAKER, K. J., Binding of sulfobromophthalein (BSP) sodium and indocyanine green (ICG) by plasma alpha-1 lipoprotein, *Proc. Soc. Exp. Biol. Med.* **1966**, *122*, 957–963.
- 155** PAUMGARTNER, G., PROBST, P., KRAINES, R., and LEEVY, C. M., Kinetics of indocyanine green removal from the blood, *Ann. NY Acad. Sci.* **1970**, *170*, 134–147.
- 156** PAUMGARTNER, G., The handling of indocyanine green by the liver, *Schweiz. Med. Wochenschr.* **1975**, *105*, 1–30.
- 157** CHANG, A. A., MORSE, L. S., HANDA, J. T., Histologic localization of indocyanine green dye in aging primate and human ocular tissues with clinical angiographic correlation, *Ophthalmology* **1998**, *105*, 1060–1068.
- 158** MORDON, S., DEVOISSELLE, J. M., SOULIE-BEGU, S., DESMETTRE, T., Indocyanine green: physicochemical factors affecting its fluorescence *in vivo*, *Microvasc. Res.* **1998**, *55*, 146–152.
- 159** YONEYA, S., SAITO, T., KOMATSU, Y., KOYAMA, I., TAKAHASHI, K., DUVOLLYOUNG, J., Binding properties of indocyanine green in human blood, *Invest. Ophthalmol. Vis. Sci.* **1998**, *39*, 1286–1290.
- 160** YONEYA, S., NOYORI, K., Improved visualization of the choroidal circulation with indocyanine green angiography, *Arch. Ophthalmol.* **1993**, *111*, 1165–1166.
- 161** DESMETTRE, T., MORDAN, S., SOULIE, S., Shift of the fluorescence peak of Indocyanine green (ICG) after injection: *in vivo* study on a vascular model, *Invest. Ophthalmol. Vis. Sci.* **1996**, *36*, S1127.
- 162** DEVOISSELLE, J. M., MORDON, S., SOULIE, S., DESMETTRE, T., MAILLOLS, H. C., Fluorescence properties of indocyanine green, Part 1: *in vitro* study with micelles and liposomes, In *Advances in Fluorescence Sensing Technology III*, LAKOWICZ, J. R., THOMPSON, J. B. (Eds.), SPIE, Bellingham, CA, **1997**, pp. 530–537.
- 163** ITO, S., MUGURUMA, N., HAYASHI, S., Developments of agents for reinforcement of fluorescence on near-infrared ray excitation for immunohistological staining, *Bioorg. Med. Chem.* **1998**, *6*, 613–618.
- 164** CHERRICK, G. R., STEIN, S. W., LEEVY, C. M., DAVIDSON, C. S., Indocyanine green: observation on its physical properties, plasma decay and hepatic extraction, *J. Clin. Invest.* **1960**, *39*, 592–600.
- 165** HOLLINS, B., NOE, B., HENDERSON, J. M., Fluorometric determination of Indocyanine green in plasma, *Clin. Chem.* **1987**, *33*, 765–768.
- 166** McEVoy, G. K., *AHFS 97 Drug Information*, American Society of Health-System Pharmacists, Bethesda, MD, **1997**.
- 167** FLOCK, S. T., JACQUES, S. L., Thermal damage of blood vessels in a rat skin flap window chamber using ICG and a pulsed alexandrite laser: a feasibility study, *Laser Med. Sci.* **1993**, *8*, 185–196.
- 168** VILLENEUVE, J. P., HUOT, R., MARLEAU, D., HUET P. M., The estimation of hepatic blood flow with Indocyanine green: comparison between the continuous infusion and single injection methods, *Am. J. Gastroenterol.* **1982**, *77*, 233–237.
- 169** BOLLINGER, A., SAESSELLI, B., HOFFMANN, U., FRANZECK, U. K., Intravital detection of skin capillary aneurysms by videomicroscopy with indocyanine green in patients with progressive systemic sclerosis and related disorders, *Circulation* **1991**, *83*, 546–551.
- 170** OTT, P., KEIDING, S., JOHNSEN, A. H.,

- Bass, L., Hepatic removal of two fractions of indocyanine green after bolus injections in anesthetized pigs, *Am. J. Physiol.* **1994**, *266*, 1108–1122.
- 171 LUTTY, G. A., The acute intravenous toxicity of biological stains, dyes, and other fluorescent substances, *Toxicol. Appl. Pharmacol.* **1978**, *44*, 225–249.
- 172 HOPE-ROSS, M., YANNUZZI, L. A., GRAGOUDAS, E. S., Adverse reactions due to indocyanine green, *Ophthalmology* **1994**, *101*, 529–533.
- 173 LI, X., BEAUVOIT, B., WHITE, R., NIOKA, S., CHANCE, B., YODH, A. G., Tumor localization using fluorescence of indocyanine green (ICG) in rat models, Abstract. Optical Tomography, Photon migration, and spectroscopy of tissue and model media theory, human studies and instrumentation, *SPIE Proc.* **1995**, *2389*, 789–797.
- 174 REYNOLDS, J. S., TROY, T. L., MAYER, R. H., THOMPSON, A. B., WATERS, D. J., CORNELL, K. K., SNYDER, P. W., SEVICK-MURACA, E. M., Imaging of spontaneous canine mammary tumors using fluorescent contrast agents, *Photochem. Photobiol.* **1999**, *70*, 87–94.
- 175 INTES, X., RIPOLL, J., CHEN, Y., NIOKA, S., YODH, A. G., CHANCE, B., *In vivo* continuous-wave optical breast imaging enhanced with ICG, *Med. Phys.* **2003**, *30*, 1039–1047.
- 176 NTZIACHRISTOS, V., CHANCE, B., Accuracy limits in the determination of absolute optical properties using time-resolved NIR spectroscopy, *Med. Phys.* **2001**, *28*, 1115–1124.
- 177 LANDSMAN, M. L., KWANT, G., MOOK, G. A., ZIJLSTRA, W. G., Light-absorbing properties, stability and spectral stabilization of indocyanine green, *J. Appl. Physiol.* **1976**, *40*, 575–583.
- 178 DESMETTRE, T., DEVOISSELLE, J. M., MORDON, S., Fluorescence properties and metabolic features of indocyanine green (ICG) as related to angiography, *Surv. Ophthalmol.* **2000**, *45*, 15–27.
- 179 ANDERSON, R., HU, J., PARRISH, J., Optical radiation transfer into human skin, In *Bioengineering and the Skin*, MARKS, R., and PAYNE, P. (Eds.), MTP, Boston, MA, **1991**, pp. 253–265.
- 180 GROSSWEINER, L., *Science of Phototherapy*, CRC Press, London, **1994**.
- 181 COSTA, R. A., FARAH, M. E., FREYMIER, E., MORALES, P. H., SMITH, R., CARDILLO, J. A., Choriocapillaries photodynamic therapy using indocyanine green, *Am. J. Ophthalmol.* **2001**, *132*, 557–565.
- 182 FICKWEILER, S., SZEIMIES, R. M., BAUMLER, W., STEINBACH, P., KARRER, S., GOETZ, A. E., ABELS, C., HOFSTADTER, F., LANDTHALER, M., Indocyanine green: intracellular uptake and phototherapeutic effects *in vitro*, *J. Photochem. Photobiol. B Biol.* **1997**, *38*, 178–183.
- 183 VARRIALE, L., CRESCENZI, E., PABA, V., DE CELSO, B. M., Selective light-induced modulation of Bcl-X<sub>L</sub> and Bax expressions in indocyanine green-loaded U937 cells: effects of continuous or intermittent photosensitization with low IR-light using a 805-nm diode laser, *J. Photochem. Photobiol.* **2000**, *57*, 66–75.
- 184 URBANSKA, K., ROMANOWSKA-DIXON, B., MATUSZAK, Z., OSZAJCA, J., NOWAK-SLIWINSKA, P., STOCHEL, G., Indocyanine green as a prospective sensitizer for photodynamic therapy of melanomas, *Acta Biochim. Polon.* **2002**, *49*, 387–391.
- 185 HOLZER, W., MAUERER, M., PENZKOFER, A., SZEIMIES, R. M., ABELS, C., LANDTHALER, M., BAUMLER, W., Photostability and thermal stability of indocyanine green, *J. Photochem. Photobiol. B Biol.* **1998**, *47*, 155–164.
- 186 GATHJE, J., STEUER, R. R., NICHOLAS, K. R. K., Stability studies on indocyanine green dye, *J. Appl. Physiol.* **1970**, *29*, 181–185.
- 187 OWEN, V. M. J., Laboratory note: estimation of indocyanine green concentrations, *Clin. Biochem.* **1973**, *6*, 132–135.
- 188 HEINTZ, R., SVENSSON, C. K., STOECKEL, K., POWERS, G. L., Indocyanine green: pharmacokinetics in the rabbit and relevant studies of its stability and purity, *J. Pharm. Sci.* **1986**, *75*, 398–402.

- 189 SAXENA, V., SADOQI, M., SHAO, J., Degradation kinetics of indocyanine green in aqueous solution, *J. Pharm. Sci.* **2003**, *92*, 2090–2097.
- 190 BUGAJ, J. E., ACHILEFU, S., DORSHOW, R. B., RAJAGOPALAN, R., Novel fluorescent contrast agents for optical imaging of *in vivo* tumors based on a receptor-targeted dye-peptide conjugate platform, *J. Biomed. Optics* **2001**, *6*, 122–133.
- 191 DEVOISSELLE, J. M., SOULIE, S., MORDON, S., DESMETTRE, T., MAILLOLS, H., A preliminary study of the *in vivo* behavior of an emulsion formulation of indocyanine green, *Lasers Med. Sci.* **1998**, *13*, 279–282.
- 192 BJORNSSON, O. G., MURPHY, R., CHADWICK, V. S., BJORNSSON, S., Physicochemical studies on indocyanine green: molar lineic absorbance, pH tolerance, activation energy and rate of decay in various solvents, *Clin. Chem. Clin. Biochem.* **1983**, *21*, 453–458.
- 193 JEJURKAR, P., Effects of  $\gamma$ -cyclodextrin on stability of indocyanine green in aqueous solution, *MS thesis*, St. John's University, New York, NY, **1997**.
- 194 RAJAGOPALAN, R., UETRECHT, P., BUGAJ, J. E., ACHILEFU, S. A., DORSHOW, R. B., Stabilization of the optical tracer agent indocyanine green using noncovalent interactions, *Photochem. Photobiol.* **2000**, *7*, 347–350.
- 195 GEDDES, C. D., CAO, H., LAKOWICZ, J. R., Enhanced photostability of ICG in close proximity to gold colloids, *Spectrochim. Acta A* **2003**, *59*, 2611–2617.
- 196 PANYAM, J., LABHASETWAR, V., Biodegradable nanoparticles for drug and gene delivery to cells and tissue, *Adv. Drug Deliv. Rev.* **2003**, *55*, 329–347.
- 197 LI, Y. P., PEI, Y. Y., ZHANG, X. P., GU, Z. H., ZHOU, Z. H., YUAN, W. F., ZHOU, J. J., ZHU, J. H., GAO, X. J., PEGylated PLGA nanoparticles as protein carriers: synthesis, preparation and biodistribution in rats, *J. Controlled Rel.* **2001**, *71*, 203–211.
- 198 AVGOUSTAKIS, K., BELETSI, A., PANAGI, Z., KLEPETSANIS, P., LIVANIOU, E., EVANGELATOS, G., ITHAKISSIOS, D. S., Effect of copolymer composition on the physicochemical characteristics, *in vitro* stability, and biodistribution of PLGA–mPEG nanoparticles, *Int. J. Pharm.* **2003**, *259*, 115–127.
- 199 SAHOO, S. K., PANYAM, J., PRABHA, S., LABHASETWAR, V., Residual polyvinyl alcohol associated with poly(DL-lactide-co-glycolide) nanoparticles affects their physical properties and cellular uptake, *J. Controlled Rel.* **2002**, *82*, 105–114.
- 200 PANYAM, J., SAHOO, S. K., PRABHA, S., BARGAR, T., LABHASETWAR, V., Fluorescence and electron microscopy probes for cellular and tissue uptake of poly(D,L-lactide-co-glycolide) nanoparticles, *Int. J. Pharm.* **2003**, *262*, 1–11.
- 201 SAXENA, V., SADOQI, M., SHAO, J., Indocyanine green loaded biodegradable nanoparticles: preparation, physicochemical characterization and *in-vitro* release, *Int. J. Pharm.* **2004**, *278*, 293–301.
- 202 SAXENA, V., SADOQI, M., KUMAR, S., SHAO, J., Novel near-infrared nanoparticulate biomarker: preparation and stability studies, *SPIE Proc.* **2004**, *5329*, 269–275.
- 203 SAXENA, V., SADOQI, M., KUMAR, S., SHAO, J., Novel multifunctional near-infrared fluorescent nanoparticles: integrating nanotechnology and biophotonics, *SPIE Proc.* **2004**, *5331*, 29–35.
- 204 SAXENA, V., SADOQI, M., SHAO, J., Enhanced photo stability, thermal stability and aqueous-stability of indocyanine green in polymeric nanoparticulate systems, *J. Photochem. Photobiol. B Biol.* **2004**, *74*, 29–38.
- 205 SAXENA, V., SADOQI, M., KUMAR, S., SHAO, J., Long circulating near-infrared fluorescent nanoparticles for diagnosis and photodynamic therapy of cutaneous cancers, *SPIE Proc.* **2004**, *5312*, 41–46.
- 206 SAXENA, V., SADOQI, M., SHAO, J., Enhanced intracellular uptake of indocyanine green by polymeric nanoparticulate delivery systems, *J. Biomed. Nanotechnol.* **2005**, *1*, 168–215.

## 12 Nanoparticles for Crossing Biological Membranes

*R. Pawar, A. Avramoff and A. J. Domb*

### 12.1 Introduction

Membrane transport plays an important role in cellular and subcellular pathways, including multidrug resistance (MDR), cellular signaling and cell–cell communication. Membrane transport mechanisms, such as the membrane permeability and extrusion machinery, lead to accumulation of specific intracellular substances and MDR. The introduction of the polymerase chain reaction resulted in the designing of new laboratory devices and analysis of amplified DNA fragments. In addition, a number of studies have been conducted related to mimicking living systems as well as developing nanodevices such as biomolecular sensors and artificial cells. The potential of nanotechnology has been studied in health care and medicine, including the development of nanoparticles for diagnostic and screening purposes [1].

New therapeutic agents are naturally occurring compounds like peptides, proteins, carbohydrates or oligonucleotides. The main problems faced in the utilization of these compounds are efficient and targeted drug delivery. Oral, nasal, transdermal and buccal routes are generally used for the administration of protein drug delivery. In such administration, the absorption of sufficient amount of drug through a particular barrier is expected in order to achieve a pharmacological response.

In therapeutic drug delivery, drugs generally should pass through barriers like the skin, blood–brain barrier (BBB) and gastrointestinal (GI) tract via cell membranes. These barriers can be overcome by using nanoparticle drug delivery. This chapter discusses general information on cell membranes and the problems encountered by drugs when trying to cross them. To circumvent such barriers in drug delivery, nanoparticulate drug delivery is preferred through the skin, BBB and orally.

In nanoparticle drug delivery through the skin the encapsulation of hydrophobic carriers with penetration enhancers is used to increase the hydrophobicity. Encapsulation involves the entrapment of a polypeptide drug within a polymeric, phospholipid or carbohydrate particulate delivery system such as nanoparticles, micro-

spheres and liposomes [2]. The BBB acts as an insurmountable barrier for a large number of drugs like central nervous system (CNS)-active drugs and antibiotics. It is also used as a major component in the regulation of the internal environment of the brain. A number of attempts have been made to overcome such a barrier, including the osmotic opening of tight junctions and the use of prodrugs or carrier system like nanoparticles/liposomes. Prodrugs can efficiently penetrate and transport across the lipophilic endothelial barrier or the efflux pump systems [3]. The best carriers for oral administration are nanoparticles and microspheres. A wide range of polymers of different sizes have been employed to investigate particle uptake. An encapsulation technique is used for the entrapment of hydrophilic or hydrophobic fluorochromes.

Nanoparticulate drug delivery has become a popular route of administration due to its penetrating and fast-acting capacity. Nanomaterials used in drug delivery created by nanotechnology research range from 1 to 100 nm in size. Nanomaterials have the potential to solve unique biological challenges such as dealing with inorganic materials, detecting electrical changes from biological molecules and treating disease.

## 12.2

### Cell Membranes

Cell membranes are composed of lipid bilayers, proteins and lipopolysaccharides attached to the membrane surface. Due to the amphipathic nature of the lipid molecules, the lipid bilayer has charged (phosphate) groups on the water-faced surface and hydrophilic carbon inside the chains. The membrane proteins are either partially or fully integrated into the membrane bilayer or attached to its surface. Protein-free lipid bilayers are freely permeable to water and small nonpolar molecules, such as  $O_2$  and  $N_2$ , but impermeable to ions. For this reason, cells have evolved special ways of transferring water-soluble molecules across the membranes [4].

Understanding membrane transport has been an important goal for more than a century because it governs many aspects of life. All membranes work as gatekeepers to cells. They are responsible for signaling in the nervous system, and for coordination of the contraction of skeletal muscle and the heart, forcing its muscle to function as a pump. Membranes contain receptors or effectors for many drugs and natural substances that control the life of cells. Some other important functions like energy storage and signal transduction are also mediated through biological pores via ion flow.

One major group of transport drugs is the ion channel proteins. The mechanism and properties of ion transport through these channel proteins are subjects of wide current interest [5–9]. These ion channels provide gates for ions like  $Na^+$ ,  $Cl^-$ ,  $K^+$  and  $Ca^{2+}$  to enter or leave the cell. The channel and carrier proteins allow solutes to cross the membrane passively in a so-called “facilitated diffusion”. These transport processes occur in the direction of a concentration gradient or according to

different transmembranal potentials [10] without requiring any cell energy. However, certain membrane proteins can also act as ion pumps, transporting ions actively against a concentration gradient using energy equivalents such as ATP. By regulating the passage through these gates, cells can maintain the desired internal ion concentrations (which are often quite different from their concentrations in the surrounding solutions).

Transport processes across membranes are experimentally studied with the patch-clamp recording technique, which has revolutionized research in this field. Transport through a single molecule of a channel protein can be studied in a small patch of membrane covering the mouth of a micropipette using this technique [4]. Patch-clamp recording enables us to observe the current flow through the channel depending on the applied voltage and voltage or transmitter-induced channel gating states.

Gap junctions are clusters of closely packed intercellular membrane channels embedded in the plasma membranes of two adjoining cells [11]. They are unique systems among ion channels because two hemi-channels are connected to span two cell membranes. They facilitate a form of intercellular communication by permitting the regulated passage of ions and small molecules from one cell to another. Intercellular communication through gap junction channels has functional roles in cell survival, development, differentiation, metabolism, morphogenesis and mutagenesis [12–15]. Gap junctions permit action potential propagation in electrically excitable synapses and help to maintain homeostasis in vascular systems, such as the lens and ovarian follicles [16]. The two hemi-channels are a structure of connexon hexamers, each consisting of six connexin proteins. They dock to form a sealed cell-to-cell passageway [17]. The interlocking of the two channels occurs extracellularly in a narrow 3.5 nm “gap” separating the junctional membranes. This channel–channel interaction is known to be selective between connexins [18]. So far, the secondary and tertiary structural organization of the connexins has been solved at 7–21 Å resolution [19]. The outer diameter of the connexon is about 70 Å and it narrows at the extracellular domains, creating a “waist” in the appearance of the intercellular channel in the gap region of an outer diameter of about 50 Å [11]. The channel pore narrows from an apparent 40 Å diameter at the cytoplasmic side to 15 Å at the extracellular side of the bilayer and then widens to 25 Å in the extracellular region. The gap junction channels can be opened and closed by various physiological stimuli and experimental treatments (gating processes). They are permeable to ions and neutral molecules up to a size of about 1 kDa or 1.5 nm diameter, including secondary messengers and metabolites. Trans-junctional voltages or those between the cytoplasm and exterior affect junctions the most [12, 16].

### 12.2.1

#### Functions of Biological Membranes

The main functions of biological membranes are to: (a) provide an enclosure for the cells, (b) allow the exchange of materials, (c) act as sites of biological reactions

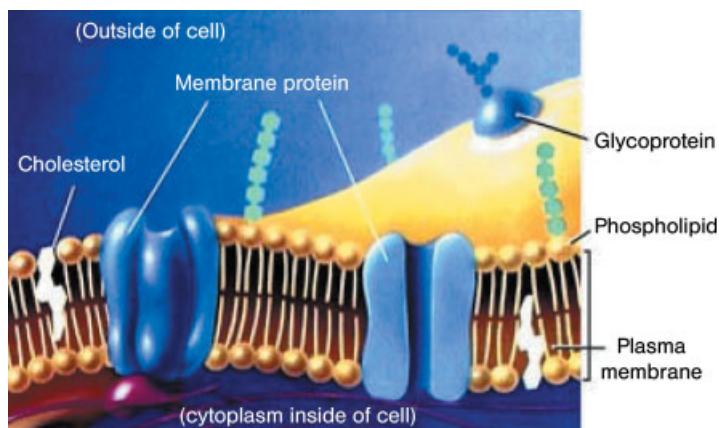


Fig. 12.1. Schematic view of a typical cell membrane [20b].

including photosynthesis, electron transfer and oxidative phosphorylation, (d) facilitate cell motion, and (e) enable recognition and cell fusion.

The biological membrane has proved to be vital in countless mechanisms necessary for cell survival. The phospholipid bilayer performs the simpler functions of compartmentalization, protection and osmoregulation. The proteins perform a wider range of functions such as extracellular interactions and metabolic processes. The carbohydrates are found in conjunction with both the lipids and proteins, and therefore enhance the properties of both. This may vary from recognition to protection.

Overall, the biological membrane is an extensive, self-sealing, fluid, asymmetric, selectively permeable and compartmental barrier essential for the correct functioning of a cell or organelles, and for a cell survival [20a]. See Fig. 12.1 for a schematic view of a typical cell membrane.

### 12.2.2

#### Kinetic and Thermodynamic Aspects of Biological Membranes

Plasma membranes of eukaryotic cells show a pronounced asymmetry with respect to the distribution of the major lipid components between the two protein monolayers. The aminophospholipids phosphatidylserine (PS) and phosphatidylethanolamine (PE) are predominantly located on the cytoplasmic leaflet, whereas the phospholipids phosphatidylcholine (PC) and sphingomyelin (SM) are mainly found on the external leaflet. Evidence for the distribution of cholesterol as another membrane component is still contradictory. Some researchers found a preference for cholesterol for the cytoplasmic layer of the red blood cell membrane, whereas other results indicated a rather symmetrical distribution.

The asymmetrical distribution of the aminophospholipids may be understood by an ATP-dependent translocation of these components from the external to the



cytoplasmic layer. The response of the membrane to this directed transport will concern not only the counter-directed movement of PS and PE, but also a redistribution of PC, SM and cholesterol. Furthermore, a change in membrane curvature may occur because of geometrical restrictions and corresponding mechanical forces caused by the coupling of the monolayer surfaces. This reasoning shows that the membrane asymmetry is determined by a multitude of processes, depending on (a) the metabolic state of the cell, (b) the mechanism of active translocation, (c) the transmembrane concentration differences of lipids and (d) mechanical forces.

Studies have attempted to gain a complete understanding of the phenomena of transbilayer lipid movement by finding an appropriate phenomenological description of the lipid fluxes. The steady-state asymmetrical lipid distribution is governed by dynamic equations. A reference simulation with a minimal set of phenomenological parameters yields qualitative restrictions to the many possible translocation mechanisms. Relations between phenomenological and kinetic model parameters serve, furthermore, as guidelines for the selection of kinetic constants in a quantitative way. It can be shown how the mechanical driving forces of the phenomenological model are to be incorporated into a kinetic model of lipid translocation.

Active transport based on a kinetic scheme involving competitive binding of PS and PE has been developed. It is clear that besides the kinetic parameters of passive translocation, mechanical forces affect those of active transport. However, the presented mechanism of active transport is not sufficient to allow for a proper treatment of mechanical effects because ATP binding, ATP hydrolysis, ADP release and lipid translocation are lumped into single irreversible translocation steps for PS and PE. Despite this, the proposed equations for active translocation are compatible with present knowledge about the kinetic properties of active lipid translocation in erythrocytes. This is particularly noted in the competition of PS and PE for the same binding site with a 10-fold higher affinity of PS on the external monolayer. The latter property results in a pronounced difference in the time constants of active transport of these two lipids.

The effect of proteins on membrane asymmetry has been taken into account in the mechanism of active translocation, in the kinetic approach and in the mechanism of facilitated lipid transport. However, possible effects of the mechanical properties of the membrane proteins have not been analyzed in detail. It may be an oversimplification that a rather high proportion of the membrane surface (around 50% for erythrocytes) is occupied by proteins. It would be straightforward to extend the mechanical energy of the monolayers by incorporating compressible protein components. Thus, the net effect of proteins on the mechanical force constants is taken into account, at least qualitatively. In addition to mechanical forces, transmembrane electric potential gradients may also affect the translocation kinetics of lipids, depending on their ionization states under physiological conditions. The present model neglects the effects of lateral organization of cell membranes that could result from specific lipid–lipid interactions, e.g. the pronounced interaction of cholesterol and SM and the protein–lipid interactions. These interactions would give rise to a more general expression for the free energy of mixing. Prelim-

inary results, based on the Bragg–Williams approximation, indicate that no qualitative changes regarding the simulation of the overall transversal lipid distributions occur, at least in the limits of that approximation [21].

### 12.3

#### Problems of Drugs Crossing through Biological Membranes

##### 12.3.1

##### Through the Skin

The skin is an extremely efficient barrier that minimizes water loss from the body. Drug absorption across the skin is potentially more limiting, and the relationship between drug physiochemical properties and epidermal permeability is less ambiguous than for the mucosal barriers. The body skin surface area in humans is approximately  $1.5 \text{ m}^2$  and represents a readily accessible surface for the application of drug delivery systems. The skin is structured in three layers: the epidermis, the dermis and the subcutaneous layer. The outer layer of the epidermis and the stratum corneum cover the entire outside of the body, and contain dead cells only, those that are strongly keratinized. For most chemicals, the stratum corneum is the rate-limiting barrier to percutaneous absorption. The skin of mammalian species is, on most parts of the body, covered with hair. At the sites where hair follicles grow, the barrier capacity of the skin differs slightly from the “normal” stratified epidermis. Most studies concerning penetration of materials into the skin have focused on whether or not drugs penetrate through the skin using different formulations containing chemicals and particulate materials as a vehicle.

The main types of particulate materials commonly used are: liposomes, inorganic compounds such as zinc and  $\text{TiO}_2$ , polymer particulates and solid lipid nanoparticles (SLN).  $\text{TiO}_2$  particles are often used in sunscreens to absorb UV light and therefore protect skin against sunburn or genetic damage. The micrometer-sized particles of  $\text{TiO}_2$  penetrate through the human stratum corneum and even into some hair follicles (including their deeper parts) [22]. The observation of penetration into living layers of the skin is not considered, since this part of the follicular channel (the acroinfundibulum) is covered with a horny barrier layer. In a recent review, Kreilgaard argued that “very small  $\text{TiO}_2$  particles (e.g. 5–20 nm) penetrate into the skin and can interact with the immune system”. Particles of  $0.5\text{--}1.0 \text{ }\mu\text{m}$ , in conjunction with motion, penetrate the stratum corneum of human skin, and reach the epidermis and, occasionally, the dermis. The lipid layers within the cells of the stratum corneum form a pathway through which the particles can move into the skin and be phagocytosed by the Langerhans cells [23]. The penetration of particles is limited to particle diameter of  $1 \text{ }\mu\text{m}$  or less.

Penetration of nonmetallic solid materials such as biodegradable poly(D,L-lactic-co-glycolic acid) (PLGA) microparticles,  $1\text{--}10 \text{ }\mu\text{m}$  with a mean diameter of  $4.61 \pm 0.8 \text{ }\mu\text{m}$ , was studied after application on to porcine skin. The number of microparticles in the skin decreased with the depth (measured from the airside

towards the subcutaneous layer). At 120  $\mu\text{m}$  depth (where the viable dermis is present), a relatively high number of particles was found. At 400  $\mu\text{m}$  depth (dermis), some microparticles were still seen. At 500  $\mu\text{m}$  depth, no microparticles were found. Soil microparticles frequently of 0.4–0.5  $\mu\text{m}$  and some large particles 25  $\mu\text{m}$  diameter were found in the dermis of the foot in a patient with endemic elephantiasis. The particles are seen to be in the phagosomes of macrophages or in the cytoplasm of other cells. The failure to conduct lymph to the nodes produces a permanent deposit of silica in the dermal tissues (a parallel is drawn with similar deposits in the lung in pneumoconiosis). This indicates that soil particles penetrate through (damaged) skin, most probably in every individual, and are normally removed through the lymphatic system [24]. Liposomes penetrate through the skin in a size-dependent manner. Micron-sized, and even submicron-sized, liposomes do not easily penetrate into the viable epidermis, whereas liposomes with an average diameter of 272 nm can reach into the viable epidermis and some are found in the dermis. Smaller-sized liposomes of 116 and 71 nm were found in higher concentration in the dermis. Submicron emulsion particles such as liposomes and nonionic surfactant vesicles (niosomes), with a diameter of 50 nm to 1  $\mu\text{m}$ , were detected in the epidermis in association with the cell membranes after application to human skin. The single molecules that make up the particles penetrate the intercellular spaces at certain regions in the stratum corneum, and are able to accumulate and reform into microspheres. The formulation used allowed the penetration of the spheres into melanoma cells, even to the nucleus [25]. The uptake of metals through the skin is difficult because of both exogenous factors (e.g. dose, vehicle, protein reactivity, valence) and endogenous factors (e.g. age of skin, anatomical site, homeostatic control). Penetration of metals through the skin still needs to be determined separately for each of metal species, either by *in vitro* or *in vivo* assays.

#### 12.3.1.1 Mechanical Irritation of Skin

Glass and rockwool fibers are widely distributed manmade mineral fibers, and have many applications, mainly as insulation materials. They are used as a substitute for asbestos fibers. In contact with the skin, these fibers can induce dermatitis through mechanical irritation. These fibers are strong irritants and thus were not examined in detail. In occlusion with irritant patch tests in humans, rockwool fibers with a diameter of  $4.20 \pm 1.96 \mu\text{m}$  were more irritating than those with a mean diameter of  $3.20 \pm 1.50 \mu\text{m}$ . The fact that “small” fibers can cause strong skin irritation has been known for a long time. It is also commonly accepted that some types of manmade fibers can easily induce nonallergic dermatitis. It is not clear what makes these fibers irritants. No information is available on skin irritation caused by fibers with a diameter of less than 100 nm, indicating that more research is needed on this problem [26].

#### 12.3.1.2 Low-voltage Electroporation of the Skin

The skin is an effective barrier against toxic chemicals and pathogens. The uppermost layer of skin, the stratum corneum, is impermeable to almost all water-

soluble substances. It also constitutes a formidable obstacle to transdermal delivery of drugs and genetic material. The transdermal route, if available, provides an alternative, convenient and noninvasive pathway for local and systemic delivery of drugs, especially with respect to time release and the avoidance of degradation or metabolism in the GI tract or liver. The stratum corneum is crossed by many appendages like hair follicles and sweat glands. The lining of these appendage ducts, consisting of two layers of epithelial cells, is much less resistant than the stratum corneum for drug transport.

Many biophysical approaches have been suggested to facilitate the transport of selected chemicals across the skin barrier. The most well-known method used is iontophoresis. In this approach, a low DC voltage (normally below 5 V) is applied across the skin. Charged molecules to be delivered are placed under an appropriate electrode, and driven through the skin barrier by electrophoresis and electroosmosis [27, 28]. The electrical impedance spectra of the skin are well characterized and transport by iontophoresis has been analyzed by macroscopic theory [29].

About 20 years ago, reversible electroporation of biological membranes was recognized to deliver materials into living cells [30]. This method is based on the resilience of the cell membrane to resealing after a temporary electrical breakdown. Due to the low electric conductivity across the membrane, as compared with that of the cytoplasm and the external media, the major potential drop across the cell is concentrated across the plasma membrane “poles” facing the electric field direction. This leads to the electroporation of the membrane, whereas the rest of the cell experiences a much lower potential gradient. The same advantage applies to the electroporation of the skin barrier in which the major potential drop develops across the highly resistive stratum corneum – the target for electroporation. This was recognized recently and the technique has been applied, although sometimes in an irreversible sense, to permeabilize the skin for drug delivery.

A paradox is realized that if electroporation occurs when a potential of 1 V is applied across a cell membrane, the membranes of the epithelial cell layers lining the skin appendages are porated, as soon as the low iontophoretic voltage (above 4 V) is applied to the skin. Molecular transport by iontophoresis is considered, as there is consequence of electroporation of the epithelial layers of the skin appendages. This alternative interpretation is complicated because the potential drop along narrow hair follicles or sweat glands is taken into account in calculating the net potential drop across the epithelial cell layers at different depths from the skin surface. Furthermore, the response and resealing times of the membrane to the applied electric field are unknown. The difficulties arise in modeling the low field electroporation if a pulse or AC voltage is applied in the traditional iontophoretic setting [31].

The analysis and the experimental support given provide a broad picture of what happens when a low electric voltage is applied to the skin with appendages. The initial event, characterized by the charging of the skin capacitor and the subsequent poration of the appendage lining, is clearly depicted. It bridges the gap between the theories of iontophoresis and electroporation. This work paves the way for the future development of combined high- and low-voltage protocols

designed to enhance transdermal transport that will play an increasingly important role in drug and gene delivery [32].

### 12.3.2

#### Through the BBB

Despite enormous advances in brain research, brain and CNS disorders remain the world's leading cause of disability. More hospitalization and prolonged care is necessary in CNS disorders than almost all other diseases. The major problem in drug delivery to the brain is the presence of the BBB. Effective drugs against the CNS disease reach the brain via the blood compartment, which must pass through the BBB. It is important to understand the mechanisms involved in uptake into and efflux from the brain. Various cells present at the level of the BBB dynamically regulate the function of the BBB. This realization implies a better understanding of the relationship of transport at the BBB to drug structure and physicochemical properties. Despite successful drug delivery to the CNS, only some drugs have reached the phase where they can provide safe and effective human applications. As pharmacological strategies improve, there will be less need for invasive procedures for treating CNS diseases. Considerable advances are being made in intravascular delivery and neurosurgical invasive procedures to deliver therapeutic substances into the brain. The failure of systemically delivered drugs to effectively treat many CNS diseases can be rationalized by considering a number of barriers that inhibit drug delivery to the CNS.

The CNS consists of blood capillaries which are structurally different from the blood capillaries in other tissues. These structural differences result in a permeability barrier between the blood within brain capillaries and the extracellular fluid in brain tissue. Blood capillaries of the vertebrate brain and spinal cord lack small pores and allow rapid movement of solutes from the circulation into other organs. These capillaries are lined with a layer of special endothelial cells that lack fenestrations and are sealed with tight junctions. Tight epithelium, similar in nature to this barrier, is also found in other organs (skin, bladder, colon and lung) [33].

Ependymal cells lining the cerebral ventricles and glial cells are of three types. Astrocytes form the structural framework for the neurons and control their biochemical environment. Astrocyte foot processes or limbs spread out and meet one other, encapsulate the capillaries to form the BBB. Oligodendrocytes are responsible for the formation and maintenance of the myelin sheath, which surrounds axons and is essential for fast transmission by salutatory conduction. The tight junctions between endothelial cells result in a very high transendothelial electrical resistance of 1500–2000  $\Omega \text{ cm}^2$  compared to 3–33  $\Omega \text{ cm}^2$  of other tissues, which reduces the aqueous based paracellular diffusion observed in other organs [34, 35].

Microvessels cover an estimated 95% of the total surface area of the BBB and represent the principal route through which chemicals enter the brain. Vessels in the brain are found to have a somewhat smaller diameter and thinner wall than vessels in other organs. The mitochondrial density in brain microvessels was also

found to be higher than in other capillaries, not because of more numerous or larger mitochondria, but because of the small dimensions of the brain microvessels and, consequently, the smaller cytoplasmic area. In brain capillaries, intercellular cleft, pinocytosis and fenestrae are virtually nonexistent; transcellular exchange is preferred. Lipid-soluble solutes can only freely diffuse through the capillary endothelial membrane and may cross the BBB. In capillaries of other parts of the body, such exchange is overshadowed by other nonspecific exchanges. Despite the estimated total length of 650 km and total surface area of 12 m<sup>2</sup> of capillaries in human brain, this barrier is very efficient and makes the brain practically inaccessible for lipid-insoluble compounds such as polar molecules and small ions.

Therefore, the therapeutic value of many promising drugs is diminished and cerebral diseases have proved to be most refractory to therapeutic interventions. All drugs used for disorders of the brain are lipid soluble and readily cross the BBB following oral administration. Although antimicrobial  $\beta$ -lactam antibiotics, when administered intracerebroventricularly, cause severe convulsion, these antibiotics do not cause such CNS side-effects when administered intravenously or orally, due to their limited transport across the BBB. Further, in spite of being well distributed into various tissues, a lipophilic new quinolone antimicrobial agent, grepafloxacin, cannot enter the brain. It results in CNS side-effects such as headache and dizziness due to the displacement of  $\gamma$ -aminobutyric acid (GABA) from the GABA receptor binding sites. Benzodiazepines such as diazepam are used as sedative hypnotic agents because these lipophilic drugs readily cross the BBB. However, the BBB transport of an immunosuppressive agent, cyclosporin A, that is more lipophilic than diazepam is highly restricted. Similarly, almost all of the lipophilic anticancer agents such as doxorubicin, epipodophylotoxin and Vinca alkaloids (e.g. vincristine and vinblastine) hardly enter the brain, causing difficulty in the treatment of brain tumors. L-DOPA, used for the treatment of Parkinson's disease, is very hydrophilic and it can readily penetrate the BBB. What mechanisms underlie these diverse BBB transport characteristics of drugs that are apparently structurally and pharmacologically unrelated? Drug transport across the BBB of small-molecular drugs by carrier-mediated transport and of peptide drugs through adsorptive-mediated transcytosis is possible. The regions adjacent to the ventricles of the brain are termed circumventricular organs (CVOs). The CVOs include the choroid plexus, median eminence, neurohypophysis, pineal gland, organum vasculosum of the lamina terminalis, subfornical organ, subcommissural organ and area postrema. Although the capillaries in the CVO brain regions are more permeable to solutes, the epithelial cells of the choroid plexus and the tanycytes of other regions form tight junctions to prevent transport from the abluminal extracellular fluid (ECF) to the brain ECF. The choroid plexus is very important for the transport of peptide drugs. Although it is the major site of cerebrospinal-fluid (CSF) production, both the CSF and brain ECF are freely exchanged with each other [36]. BBB enzymes are well known and recognized for rapid degradation of almost all peptides, including naturally occurring neuropeptides. Solutes crossing the cell mem-

branes are subsequently exposed for enzyme degradation present in large numbers inside endothelial cells. These contain large densities of mitochondria and metabolically highly active organelles. The BBB is further reinforced by a high concentration of P-glycoprotein, an active drug-efflux transporter protein in the luminal membranes of the cerebral capillary endothelium. This efflux transporter actively removes a broad range of drug molecules from the endothelial cell cytoplasm before they cross into the brain parenchyma [37].

### 12.3.2.1 Small Drugs

The majority of drugs do not cross the brain capillary wall which forms the BBB *in vivo*. Only small molecules with high lipid solubility and a low molecular mass ( $M_r$ ) below 400–500 Da cross the BBB [38]. However, only few diseases of the brain consistently respond to this category of small-molecule drugs [39, 40]. These include depression, affective disorders, chronic pain and epilepsy. In contrast, many other serious disorders of the brain do not respond to conventional lipid-soluble molecular therapeutics. These include Alzheimer's disease, stroke/neuroprotection, brain and spinal cord injury, brain cancer, HIV infection of the brain, various ataxia-producing disorders, amyotrophic lateral sclerosis, Huntington's disease, Parkinson's disease, multiple sclerosis and childhood inborn genetic errors affecting the brain. Although L-DOPA therapy has been available for decades to treat Parkinson's disease, there has been no neuroprotective drug available for Parkinson's disease that halts the inexorable neurodegeneration of this disorder. Patients with multiple sclerosis have benefited from cytokine drug therapy that acts on the peripheral immune system. However, no drug is available to stop the inevitable demyelination within the CNS caused by multiple sclerosis. Many of the CNS disorders that are refractory to small-molecule drug therapy might be treated with large-molecule drugs including recombinant proteins and gene-based medicines; however, several obstacles, both biochemical and economic, are inhibiting their development.

#### 12.3.2.1.1 Limitations of Small Drugs

Only 12% of drugs are active in the CNS and only 1% of the total number of drugs are active in the CNS for diseases other than affective disorders [41]. The rate-limiting role of the BBB is illustrated by the small molecule histamine. Histamine, however, does not cross the BBB, but the inability of histamine to penetrate the brain is illustrated [42]. Histamine has too many hydrogen-bond-forming functional groups and the BBB penetration is inversely related to the number of hydrogen bonds that a drug forms with solvent water. Large-molecule drugs are not suitable for brain treatment because of the BBB problem. Indeed, if a large-molecule drug is found to be effective for the brain, the molecule is generally abandoned for a small-molecule peptidomimetic. However, with the exception of where the endogenous ligand itself is a small molecule, no small-molecule peptidomimetics have been discovered to date that are capable of transport across the BBB. There-

fore, the small-molecule peptidomimetics still have to be reformulated for BBB transport. The development of a small-molecule drug targeting the BBB is challenging and requires more work in this field.

#### 12.3.2.2 Peptide Drug Delivery via SynB Vectors

Cells poorly take up a large number of hydrophilic molecules such as peptides, proteins and oligonucleotides, since they do not efficiently cross the lipid bilayer of the plasma membrane. Peptide neuromodulators failed to affect their target cells within the brain when administered peripherally. This is due to the existence of the BBB. The most important factors determining the extent to which a molecule is delivered from the blood into the CNS are lipid solubility, molecular mass and charge. Simply based on lipid solubility and molecular mass, peptide- or oligonucleotide-based neuropharmaceuticals are impeded by the BBB. To overcome the limitation in accessing the drugs to the brain, some strategies need to be developed to achieve BBB penetration [43, 44]. In the past decade, several peptides have been described such as penetratin [45, 46], a basic segment of the transcription-activating factor (Tat), and SynB vectors [44] that allow the intracellular delivery of polar, biologically active compounds *in vitro* and *in vivo*. Since the peptides penetrate into the cells by a receptor-independent nonendocytotic process, the interaction of some of them with the lipid matrix of the plasma membrane could play a key role in their cell uptake [43].

#### 12.3.3

##### GI Barrier

The GI barrier plays an important role in the organism – protecting against toxic substances, and transferring nutrients and xenobiotics from the lumen to the blood. Since the oral route of administration is the most common route, the absorption and metabolism of a chemical in the intestinal mucosa is particularly important. These processes affect the bioavailability of a chemical, i.e. the fraction of an oral dose that reaches the systemic circulation [47]. Absorption across the intestinal lining includes passive diffusion across the cell membrane and cytoplasm (transcellular transport). The uptake transporters includes the sodium-dependent bile transporter, peptide transporters, the glucose transporter and organic anion transporters. Some of the export transporters includes ATP-dependent P-glycoprotein, and multi drug resistance (MDR) proteins 1 and 2 (MRP1 and MRP2). These represent well-characterized transporters in the apical membrane of the intestinal mucosal epithelium, which actively pump substrates back into the intestinal lumen after absorption into the intestinal epithelial cells [48, 49]. The current *in vitro* models of the intestinal barrier have been recently made available for investigating the principal mechanisms of absorption [50, 51]. The advantage of *in vivo* models is that they integrate all the factors that can influence chemical partitioning. The disadvantage is that it is very difficult to separate these variables during absorption. The advantage of *in vitro* models over *in vivo* models is that



it is possible to study the mechanisms of absorption *per se*, and to bypass stomach and liver metabolism. The rate and extent of drug absorption from the small intestine depends on the release of the active ingredient from a dosage form, its solubility in the liquid phase of the GI contents, and the transport of the dissolved compound or the intact dosage form from the stomach into the duodenum. In dynamic systems such as dosing to the GI tract, drug absorption is dependent on the residence time of the drug in solution at an absorption site. As such, gastric emptying and intestinal motility can be critical determinants of drug absorption.

The oral route of administration for protein and nucleic acid drugs is quite problematic because in addition to proteolysis in the stomach, the high acidity of the stomach destroys them before they can reach the intestine for absorption. Polypeptides and protein fragments, produced by the action of gastric and pancreatic enzyme, are further cleaved by exo- and endopeptidases in the intestinal brush border membrane to yield di- and tripeptides, even if proteolysis by pancreatic enzymes is avoided. Polypeptides are mostly degraded by brush border peptidases. Any peptide that survives and passes through the stomach is further metabolized in the intestinal mucosa, where the penetration barrier prevents entry into cells [52].

#### 12.3.3.1 Intestinal Translocation and Disease

Crohn's disease is characterized by transmural inflammation of the GI tract. It is of unknown etiology, and it has been suggested that a combination of genetic predisposition and environmental factors plays a role. Particles (0.1–1.0  $\mu\text{m}$ ) are associated with the disease and indicated as potent adjuvants in model antigen-mediated immune responses. In a double-blind randomized study, a low particle diet (low in calcium and exogenous microparticles) alleviated the symptoms of Crohn's disease [53]. However, there is a clear association between particle exposure, their uptake and Crohn's disease. The exact role of the phagocytosis cells in the intestinal epithelium is not known. The disruption of the epithelial barrier function by apoptosis of enterocytes is a possible trigger mechanism for mucosal inflammation. Diseases other than of gut origin also have marked effects on the ability of the GI tract to translocate particles. The absorption of 2- $\mu\text{m}$  polystyrene particles from the PP of rats with experimentally induced diabetes is increased up to 100-fold (10% of the administered dose) compared to normal rats [54]. However, the diabetic rat displayed a 30% decrease in the systemic distribution of the particles. The possible explanation for this discrepancy is the increased density of the basal lamina underlying the GI mucosa of diabetic rats that may impede particle translocation into deeper villous regions. This uncoupling between enhanced intestinal absorption and reduced systemic dissemination has been observed in dexamethasone-treated rats [55].

From the literature it is clear that engineered nanoparticles are taken up via the GI tract. In general, the intestinal uptake of particles is better understood and has been studied in more detail than pulmonary and skin uptake. Because of this advantage, it is possible to predict the behavior of some particles in the intestines,

with some precautions. Nanoparticles designed for food or to drug delivery via intestinal uptake needs to follow strict rules before marketing.

## 12.4

### Nanoparticulate Drug Delivery

Drug delivery at a simplistic level has been dominated by the theme of noninjected peptide delivery. Efforts to combine peptides with novel mucoadhesive polymers and to encapsulate them in nanoparticles are being renewed. This is done by increasing intestinal permeability and increasing solubility. In last 10 years, scientists have discovered nanoparticles that favor uptake by immune surveillance systems in the intestine and in the dermis of the skin. This led to an increase in vaccine delivery research with novel antigens and adjuvants. The nanoparticles and liposomes discovered can access the brain, which has potential for targeting them to the BBB. It is worth noting that 95% of all drugs discovered for Alzheimer's disease, Parkinson's disease and stroke have poor brain-penetrating capability. There are a number of advanced transdermal systems in the research phase, including iontophoresis, sonophoresis and patches with probes. Peptide delivery via the skin is back in vogue, although the devices are simpler and cheaper. A complete range of new bioadhesive and mucoadhesive polymers is being produced, and they have unique properties to increase organ retention. Such polymers, of which the glucosamine-based chitosan was a pioneer, can lead to increased localization and retention of a conjugated drug.

Several types of nanomaterials created by nanotechnology research range are used in drug delivery, ranging in size from 1 to 100 nm:

- Fullerenes are pure carbon molecules composed of at least 60 atoms of carbon. Fullerene has a shape similar to a soccer ball or a geodesic dome (also known as a "buckyball").
- Nanotubes are a sequence of nanoscale  $C_{60}$  atoms arranged in a long, thin cylindrical structure. They are related to two other carbon crystal forms – graphite and diamonds. They often look like rolls of graphite chicken wire. However, as member of the fullerene family, they are buckyballs expanded from the center into cylinders.
- Quantum dots are nanoscale crystalline structures made up of cadmium selenide that absorb white light and then reemit it within a couple of nanoseconds later in a specific color.
- Dendrimers are synthetic, three-dimensional macromolecules formed using a nanoscale fabrication process. A dendrimer is formed from monomers, with new branches added in steps until form a tree-like structure.
- Nanoshells are concentric sphere nanoparticles consisting of a dielectric (typically gold sulfide or silica) core and a metal (gold) shell. They are a very special kind of nanoparticle because they combine IR optical activity with the uniquely biocompatible properties of gold colloids. In simple words, they are spheri-

cal glass particles with an outer shell of gold. Their size is about 100 nm in diameter.

#### 12.4.1

##### **Skin**

Mammalian skin is a complex transport barrier with an anatomical organization and chemical structure. The important region of skin is the stratum corneum, which comprises columns of tightly packed corneocytes organized into clusters of up to a dozen cells. Mammalian stratum corneum consists of 15 corneocyte layers, with a total thickness of 0.3–0.8  $\mu\text{m}$ . The corneocytes merge together with desmosomes and are sealed tightly with intercellular lipids, attached to plasma membranes. The quality and crystallinity of lipids in the stratum corneum determine the skin barrier characteristics. The fine structure of the skin and epidermal refractivity to molecular diffusion differ at different body sites [56–58].

##### **12.4.1.1 Skin as Semipermeable Nanoporous Barrier**

The skin behaves as a mechanical nanoporous barrier perforated by a large number of probably gap-like or quasi-semicircular pathways. The reported estimates for such passage widths range from 0.4 to 36 nm. Detailed information on the distribution of hydrophilic transcutaneous path widths in the skin is unavailable to date. Arguably, pore size distribution is nonsymmetrical, with a peak around 20 nm and decline on the low size side. Only one hydrophilic (circular) pathway exists between two corneocytes in the stratum corneum. The maximum number of passages through the barrier is calculated to be between  $10^{10} \text{ cm}^{-2}$  (in the case of 0.4-nm pores) and  $4.5\text{--}10^8 \text{ cm}^{-2}$  (for 20-nm pores). The most likely, realistic “open pore” density in the skin is  $10^8\text{--}10^9 \text{ cm}^{-2}$ . Pore density of a comparable order of magnitude was determined by analyzing the results of transcutaneous electrical current (iontophoresis) and water flux (streaming potential) measurements. The funnel-like pathway shape close to the skin surface minimizes the impact of such geometrical factors. Experiments accordingly reveal that a much higher proportion of the epicutaneously applied material is transported through the skin, at least under suitable conditions [59, 60].

##### **12.4.1.2 Hydrophilic Pathway through the Skin Barrier**

The hydration and stress-dependent pathways within each cluster of cells have relatively high transport resistance, and typically lead between intercellular lipid (multi) lamellae and/or such lamellae and the proximal corneocyte envelope. In contrast, the hydrophilic pathways between clusters of corneocytes in the stratum corneum have a lower transport resistance and are sparser. The hydrophilic path between the skin cells clusters acts as a transcutaneous shunt, which is typically wider than 30 nm and permanently open. Transepidermal shunts thus cover a broad spectrum of widths, encompassing anything between a relatively wide inter-cluster gap (width greater than 5  $\mu\text{m}$ ), a hair follicle (width greater than 5  $\mu\text{m}$ ) and a cutaneous gland (width greater than 50  $\mu\text{m}$ ) [61].

## 12.4.2

**Solid-Lipid Nanoparticles (SLN) Skin Delivery**

The liposomal and emulsion solid particles possess several advantages like protection of incorporated active compounds from chemical degradation and flexibility in modulating the release of the compound. Liposomes and emulsions are composed of well-tolerated excipients and are used as a carrier for drug delivery. Solid-Lipid Nanoparticles (SLN) were realized simply by exchanging the liquid lipid (oil) of the emulsion by a solid lipid at room temperature. Solid-Lipid Nanoparticles (SLN) focused exclusively on pharmaceutical applications mainly for nondermal administration routes, e.g. oral and parenteral administration. In the last few years Solid-Lipid Nanoparticles (SLN) have been used in topical formulations for pharmaceutical and cosmetic products [62, 63]. In addition, generally recognized as safe (“GRAS”) substances were also used, which provide a broad variety of lipids and surfactants/polymers for the formulation of Solid-Lipid Nanoparticles (SLN) dispersions. The production of Solid-Lipid Nanoparticles (SLN) is done using hot or cold homogenization techniques. The cold homogenization technique is commonly used for extremely temperature-sensitive and hydrophilic compounds [64].

**12.4.2.1 Chemical Stability of SLN**

With regard to polymeric nanoparticles, the active compounds were incorporated into the solid matrix of SLN to protect them from degradation. The coenzyme Q10 incorporated in SLN composed of cetyl palmitate is stabilized with 1.2% Tego Care 450 as a surfactant [65]. Similarly, under the influence of light and oxygen, the sensitive cosmetic molecule retinol is decomposed to different epoxyretinoids. The stabilization effect of SLN on retinol was investigated using different lipids as matrix and different surfactants. The study of the stabilization effect between lipids indicates the lipids have to be selected carefully for sensitive molecules. The smallest particles with a large interface area had the most pronounced stabilization effect. Obviously, retinol located in the surface layer and an optimal surfactant showed highest stability. This indicates that the smallest particles provided the largest interfacial area for retinol and led to the highest stabilization.

The homogeneous matrix with dispersed drug molecules is present in amorphous clusters when the cold homogenization method is applied and when the lipophilic drug molecules are incorporated in SLN by the hot homogenization method. In the cold homogenization method, the bulk lipid contains the dissolved drug in dispersed form, which breaks up under high pressure and leads to nanoparticles having a homogeneous matrix structure [66]. Fast release is attained if the application of SLN to the skin should increase the drug penetration, using the occlusive effect of SLN. A core with an active compound is formed when the active compound starts precipitating and the shell has fewer drugs. This leads to a membrane-controlled release governed by the law of diffusion. It indicates that the structure of the SLN formed depends on the chemical nature of the active compounds and excipients. The release profile of SLN is often biphasic. The initial burst release is followed by a prolonged release. The burst release is high when produced at high temperature by hot homogenization.

#### 12.4.2.2 *In Vitro* Occlusion of SLN

An adhesive effect is claimed for small-sized liposomes, forming a film on the skin after application. The occlusivity of SLN in the form of the occlusion factor has been investigated using the de Vringer model of a water beaker covered by a filter paper [67]. In this study, the particle size should be small-sized nanoparticles. Admixing of the SLN increased the occlusivity to maintain the light characters of day cream, avoiding the glossiness of occlusive night cream. Highly occlusive night cream was composed of lipid nanoparticles of high lipid concentration.

#### 12.4.2.3 *In Vivo* SLN: Occlusion, Elasticity and Wrinkles

A study on the effect of *in vivo* SLN on skin hydration and elasticity has been performed. Using several volunteers, the cosmetic formulation was applied to one arm and the same formulation with 4% SLN was applied to other arm twice a day for 4 weeks. The addition of SLN with the commercial formulation increased the skin hydration by 32%, while in pure formulation the skin hydration increased by 24% [68]. Little or no increase in elasticity was observed in young volunteers. The effect on wrinkle depth was found effective in wrinkle treatment using established formulations with SLN. Detection of adhesive SLN on human skin was done by the Tesa strip test. The SLN were found to stick to the skin surface, forming a film and increasing the skin hydration.

#### 12.4.2.4 Active Compound Penetration into the Skin

The penetration of active compounds into human skin involves coenzyme Q10 and retinol. SLN are found to be more efficient in promoting penetration into the stratum corneum. In cosmetic products the active compounds should stay in the skin, penetrating sufficiently deep, but not too deep so as to affect systemic availability. Penetration study with drugs in pharmaceutical dermal formulations revealed that the degree of penetration depends on the chemical composition of the formulation. The film formation, skin hydration, SLN lipids interaction and surfactants with the skin lipids are considered the factors affecting the degree of penetration [65].

Depending on the composition of SLN, different penetration profiles were obtained [69]. In the optimized formulation, a therapeutically desired enrichment in the upper layer of the skin was obtained with systemic uptake minimization.

#### 12.4.2.5 Controlled Release of Cosmetic Compounds

Perfume was incorporated in SLN and the release study compared to a nanoemulsion of the same lipid and surfactant composition. Initially the release was same due to the presence of perfume in the outer shell of the SLN. During the follow-up period to 8 h the release from SLN was delayed. This technique is used for developing longer-lasting perfume formulations based on the prolonged release of the perfume from the solid lipid matrix [70].

Prolonged release is also desired for insect repellents, while the carrier should be also released from the adhesive SLN carrier system to stick firmly to the skin. The insect repellent DEET (*N,N*-diethyl-4methyl Benzamide) was incorporated in different SLN formulations. A loading of 10% was achieved in stearic acid SLN stabi-

lized with Tween 80 as a surfactant. The particles were physically stable for a long period when incorporated into a gel [71, 72].

#### 12.4.2.6 Novel UV Sunscreen System Using SLN

The reduction of the ozone layer has increased the need for effective UV protection systems with minimum side-effects. The main UV protection systems are molecular UV blockers (sunscreens) and particulate compounds like  $\text{TiO}_2$ . The molecular blockers showed side-effects such as photoallergies and phototoxic effects; therefore, the particulate blockers systems are now used. The mechanism of the protection is simply the scattering of UV rays. However, the very small  $\text{TiO}_2$  particles penetrate into the skin and interact with the immune system [73]. The crystalline solid lipid nanoparticles also act as particulate UV blockers by scattering the light efficiently. To enhance the UV protection further, a molecular sunscreen was incorporated into the solid lipid matrix. The fixation of the molecular sunscreen inside the solid matrix minimized the side-effects due to penetration of the molecular sunscreen into the skin. Incorporation of the molecular sunscreen into the SLN matrix led to a synergetic protective effect. This means that the total amount of molecular sunscreen in the formulation was reduced with a minimization of the side-effects.

The release of the sunscreen from oil-in-water nanoemulsions and SLN dispersions was studied. A membrane-free release model used an oil phase above the aqueous nanoemulsion or aqueous SLN dispersion in a test tube. After 4 h, 6.5% of the sunscreen was released from the nanoemulsion; however, only 3.1% of the sunscreen was released from the SLN dispersion [74].

#### 12.4.3

##### Polymer-based Nanoparticulate Delivery to the Skin

Poly(alkyl cyanoacrylate) (PACA) nanoparticles have been used as controlled release devices for peptide delivery after subcutaneous administration. Radiolabeled poly(isobutyl cyanoacrylate) (PIBCA) nanospheres injected subcutaneously revealed a progressive reduction of staining in muscular tissue suggesting that the nanospheres were progressively biodegraded [75a]. These nanospheres were used to release growth releasing factor in a sustained manner and to improve its bioavailability. After association with the nanospheres, the peptide was partially protected from enzymatic degradation, whereas it was very rapidly metabolized at the injection site when administered with the free drug.

A proposed mechanism for the reversion of MDR by means of doxorubicin-loaded PACA nanospheres is shown in Fig. 12.2.

#### 12.4.4

##### Subcutaneous Nanoparticulate Antiepileptic Drug Delivery

Antiepileptic drugs are rarely administered subcutaneously due to their slowness and unreliability. In extraordinary circumstances such as end of life palliative

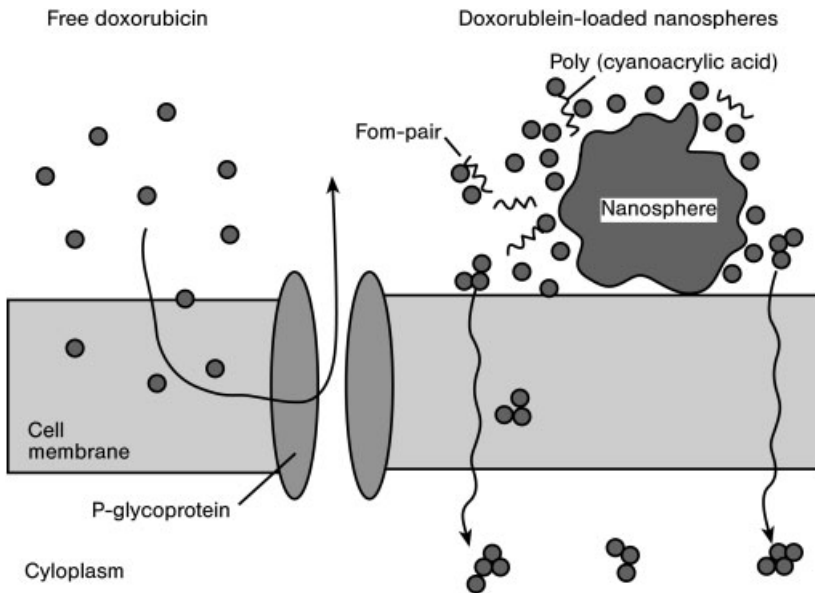


**Fig. 12.2.** Proposed mechanism for the reversion of MDR by means of doxorubicin-loaded PACA nanospheres. Given as free drug, doxorubicin is pumped out of the cell by P-glycoprotein (A). When given as PACA nanospheres, doxorubicin and degradation

products such as poly(cyanoacrylic acid) are released locally from the nanospheres adsorbed on the cell membrane. Together they can form ion pairs, which facilitate the penetration of doxorubicin into resistant cells [75b].

care, subcutaneous administration is advocated. Subcutaneous delivery of insulin by programmable infusion or on-demand linked to a glucose sensor has proved promising [76]. The idea of a subcutaneous antiepileptic drug implant is attractive. The low solubility, high alkaline pH in solution and low potency of most antiepileptic drugs make such implants bulky and impractical. Benzodiazepines have high potency, but exhibit tachyphylaxis with continuous use. All most all antiepileptic drugs have a relatively narrow therapeutic/toxic range, allowing for little variations in release rates from the implant. Transdermal patches are used to deliver many medications like nitroglycerine, antiemetics and nicotine. Significant transdermal penetration through the stratum corneum by medicines usually requires chemical enhancers like oxazolidinones, propylene glycol and epidermal enzymes [77]. Despite the limits of solubility and potency, antiepileptic drug patches remain an attractive option.

#### 12.4.5

#### Nanoparticulate Anticancer Drug Delivery

Cancer therapy usually involves intrusive processes including application of catheters to allow chemotherapy to shrink any cancer present, surgery to then remove

the tumor followed by more chemotherapy and radiation. The purpose of the chemotherapy and radiation is to kill the tumor cells, which are more susceptible to the action of the drugs and methodologies, due to their faster growth rate than healthy cells. Current research areas include development of carriers to allow alternative dosing routes, new therapeutic targets such as blood vessels fueling tumor growth (angiogenesis) and targeted therapeutics that are more specific in their activity. The effectiveness of the treatment is directly related to the treatment's ability to target and kill the cancer cells while affecting as few healthy cells as possible. Currently, cancer patients' selectivity in their treatment is related to the inherent nature of the chemotherapeutic drugs to work on a particular type of cancer cell more intensely than on healthy cells. However, by administering bolus doses of these intense drugs systematically some side-effects will always occur and sometimes these are so intense that the patient must discontinue therapy before the drugs have a chance to eradicate the cancer [78]. Advances in the treatment of cancer are progressing quickly both in terms of new agents against cancer, and new ways of delivering both old and new agents. Some new methods for delivering therapies, both old and new, with a focus on nanoparticle formulations and ones that specifically target tumors are discussed in the following subsections.

#### 12.4.5.1 Paclitaxel

Paclitaxel is a microtubule-stabilizing agent that promotes polymerization of tubulin causing cell death by disrupting the dynamics necessary for cell division. It has neoplastic activity against primary epithelial ovarian carcinoma, breast, colon and non-small cell lung cancers. Paclitaxel is poorly soluble in aqueous solutions, but soluble in many organic solvents such as alcohols. The currently available formulation includes Cremophor EL (polyethoxylated castor oil) and ethanol for solubilization; however, Cremophor EL is a toxic substance which shows side-effects such as hypersensitivity reactions, nephrotoxicity and neurotoxicity [79]. Biodegradable nanoparticle formulations of PLGA have been used. Paclitaxel is incorporated at very high loading efficiencies, about 100%, by a nanoprecipitation method using acetone and PLGA [80]. These nanoparticles, 117–160 nm diameter, released over half of their drug *in vitro* in the first 24 h.

#### 12.4.5.2 Doxorubicin

It is the most potent and widely used anticancer drug and works by inhibiting the synthesis of nucleic acids within cancer cells [81]. Doxorubicin has a number of undesirable side-effects like cardiotoxicity and myelosuppression, which leads to a very narrow therapeutic index. Various researchers have studied different ways to target doxorubicin delivery to cancer tissues with minimum side-effects. Conjugates of dextran and doxorubicin have been encapsulated in chitosan nanoparticles of around 100 nm diameter. Mice injected intravenously with both dextran-doxorubicin conjugates and the conjugates encapsulated in chitosan nanoparticles showed a decrease in tumor volume. Treatment with doxorubicin alone did not decrease the tumor volume. Another method used for cancer treatment is neutron capture therapy using gadolinium [82]. *In vitro* cellular studies of chitosan-



encapsulated gadopentetic acid in nanoparticles has shown that the nanoparticles will be taken up by L929 fibroblast cells, B16F10 melanoma cells and SCC-VII squamous cell carcinoma cells through endocytosis. Doxorubicin was also conjugated with PLGA and formed nanoparticles from these conjugates [81]. Nanoparticles of 200–250 nm diameter were prepared, with *in vitro* release for up to 1 month. *In vivo* analysis of injected nanoparticles as compared with daily doxorubicin injections shows a single injection of doxorubicin–PLGA conjugate nanoparticles could suppress tumor growth for up to 12 days.

#### 12.4.5.3 5-Fluorouracil (5-FU)

Incorporation of 5-FU is achieved using dendrimers of poly(amidoamine) modified with mPEG-500. The hydrophilicity of the 5-FU is allowed to complex with the dendrimers. Simply incubate the polymer with the drug. In *in vitro* studies, pegylated formulations showed release over 144 h (6 days), while non-pegylated formulations had completed their release within 1 day. Intravenously administered formulations in rats showed that free 5-FU was cleared from the bloodstream within 1.75 h. Those given dendrimer formulations, however, showed 5-FU clearance only after 7 h for non-pegylated systems and 13 h for pegylated systems. This confirms the formulation ability to control the 5-FU release *in vivo* and the extension of release by pegylation of the polymers in the formulation [83].

#### 12.4.5.4 Antineoplastic Agents

Camptothecin-based drugs, specifically irinotecan (Camptosar) and topotecan (Hycamptin), have been approved by the FDA, and are used most often either in conjunction with 5-FU as first-line therapy or sometimes used alone after 5-FU has failed. Analogs of these molecules have shown up to 1000-fold higher activity, but the great challenge to their delivery is their extreme hydrophobicity [84]. Lipid-based nanoparticles of 100–375 nm diameter were prepared with the SN-38 analog of irinotecan. The weight of tumors was followed for mice injected twice weekly for 2 weeks (four doses) or daily for 10 days (10 doses) with Camptosar as compared with encapsulated SN-38 twice weekly for 2 weeks (four doses) at two different particle sizes. The longest tumor regression and survival was seen for mice injected with nanoparticles around 375 nm in diameter (65 days survival, 1.98 mg SN-38 per mouse), followed by those injected daily with Camptosar (51 days survival, 9 mg irinotecan per mouse) and those injected with nanoparticles around 100 nm diameter (48 days survival, 1.51 mg SN-38 per mouse). The control mice survival was 22 days.

#### 12.4.5.5 Gene Delivery

Other ligands which show a selective targeting to cancer cells are transferrin (Tf) and epidermal growth factor (EGF) [85, 86]. Complexes for DNA delivery composed of poly(ethyleneimine) linked to PEG coated with either Tf or EGF were prepared with nanoparticle diameters ranging from 49 to 1200 nm. The plasmid pCMV-Luc which codes for luciferase production was incorporated into these nanoparticles and *in vivo* studies in mice showed the gene expression from admin-

istration of targeted systems was 10–100 higher in tumors than in other organs [87].

A new class of biosensors has been developed which recognizes and detects specific DNA sequences and genetic mutations in laboratory experiments. The technology could lead to a new method of cancer detection or drug development. The nanosensors, called “smart nanoparticle probes”, work by attaching short pieces of DNA (oligonucleotides) to 2.5-nm gold nanocrystals, which serve both as scaffolds and as “quenchers” for fluorescence. The oligonucleotide molecule forms into an arch-like shape labeled with a fluorescent dye at one end and a sulfur atom at the other end. The new nanoparticle probes will be more effective than conventional molecular beacons because their unique shape is better suited to binding with target molecules and their fluorescence changes very little with changes in temperature.

Nanoparticles are used to trace specific proteins in cells for early cancer diagnosis and to monitor the effectiveness of drug therapy. The nanoparticles are also used to quantify and identify gene sequences, proteins, infectious organisms and genetic disorders. The particles might be able to profile a large number of genes and proteins simultaneously, allowing physicians to individualize cancer treatments based on the molecular differences in the cancers of various patients. Because of their novel structural and optical properties, these nanobeacons open new opportunities in biomolecular sensing and bioengineering [88].

#### 12.4.5.6 Breast Cancer

A research study used Doxil (a commercial liposomal doxorubicin formulation from Alza) in which a modified PEG conjugated to antibody F5 had been incubated to form a coupled liposome system. Comparison *in vivo* in mice treated with Doxil or F5-coupled Doxil showed a faster and greater regression in tumor volume for F5-containing Doxil over unmodified Doxil [89].

#### 12.4.6

#### Nanofibers Composed of Nonbiodegradable Polymer

The incorporation of a drug into water-insoluble nonbiodegradable polyurethane has been performed to make the drug amorphous. To achieve this goal, electrostatic spinning was applied [90, 91] resulting in the formation of nanodimension fibers. The application of this technology to drug-based delivery systems has been examined only to a limited extent [92–95]. To generate drug delivery systems based on this approach, a drug is incorporated along with the polymer in the solution to be electrospun. In this process, three general variable types determine the diameter and morphology of the filaments – solution parameters, equipment-controlled parameters and environmental parameters [96, 97]. Such treatments form fibers ranging in diameter from 100 nm to several Ångstroms, which are cylindrical and uniform ranging to beaded fibers of homogeneous size. The large surface area associated with nanospun fabrics allows fast and efficient solvent evaporation, giving

limited time to recrystallize the incorporated drug for the formation of amorphous dispersions or solid solutions [92]. The electrostatic spinning of poorly water-soluble drugs in a water-insoluble nonbiodegradable polymer may generate useful delivery forms. Two drug models, itraconazole and ketanserin, were evaluated using a polyurethane carrier. Oral itraconazole is widely used for the treatment of tinea pedis and other superficial fungal infections. The compound is highly water insoluble and does not penetrate into the dermis to any significant extent after topical application to explant human skin in traditional vehicles [98, 99]. Ketanserin is a selective 5<sub>2</sub>-serotonin antagonist which accelerates wound healing in the treatment of diabetic foot ulcers [100, 101].

#### 12.4.6.1 Electrostatic Spinning

A high voltage Spellman DC current supply was used for the experiments in an electrostatic spinner. The voltage applied was set to 16 kV. All the experiments were done at ambient temperature and humidity. The solutions were prepared by dissolving the drug and polymer in a suitable organic solvent. The solution was fed to the glass spinneret and a high voltage was applied to the solution. On completion of the spinning nonwoven spun fabric was removed and characterized.

#### 12.4.6.2 Scanning Electron Microscopy

The electrostatic spun fibers surface was analyzed using a scanning electron microscope. In the method of analysis the spun fibers were placed in a center of an aluminium stud. A very thin layer of gold was applied to the fibers and placed in the microscope chamber connected to a high vacuum. Surface morphology study was done at 5–10 kV mode.

#### 12.4.6.3 Differential Scanning Calorimetry (DSC)

The Differential Scanning Calorimetry (DSC) study was done using a DSC instrument connected with a thermal analysis controller. The samples were analyzed in covered aluminum pans under dry nitrogen. Approximately 5 mg of crystalline compound was heated from 25 to 200 °C and then cooled at room temperature.

A second heating cycle was applied on the sample starting at room temperature upto 200 °C. For the electrospun materials, approximately 5 mg was weighed in the DSC pan.

## 12.5

### Nanoparticulate Delivery to the BBB

Nanoparticles represent a tool to transport essential drugs across the BBB that are normally unable to cross this barrier. Drugs that have successfully been transported into the brain using nanoparticles include the hexapeptide dalargin, the dipeptide kytorphin, loperamide, tubocurarine, the NMDA receptor antagonist MRZ 2/576 and doxorubicin. Nanoparticles may be especially helpful for the treatment

of disseminated and very aggressive brain tumors. The first promising result in this direction was obtained in rats. The mechanism of nanoparticle-mediated transport of drugs across the BBB needs further elucidation. The most likely mechanism seems to be receptor-mediated endocytosis by the endothelial cells lining the brain blood capillaries [35], following adsorption of apolipoprotein (apo) B and E from the blood after intravenous injection.

By increasing bioavailability, nanoparticles can increase the drug development and help to treat previously untreatable conditions. Because of the BBB, many new chemical entities aimed at treating brain disorders have not proved clinically useful. In contrast, nanoparticles have been used to cross the BBB with little difficulty. Several systems have been developed, capable of reaching the brain for anesthesia (Dalargin, an analgesic), cancer drugs and other different therapeutics. There are several advantages over existing systems, including (a) no requirement to open the BBB, (b) the ability to use hydrophilic or hydrophobic drugs, and (3) the drug does not need to be modified. Researchers at the University of Texas at Austin have also described means of using nanospheres for oral drug delivery. These nanosphere carriers are derived from hydrogels – highly stable organic compounds that swell when their environment becomes more acidic. These are successfully formulated into controlled release tablets and capsules, which release active drug compounds.

#### 12.5.1

##### **Peptide Delivery to the BBB**

Nanoparticles are used as transport vectors for peptide drugs. The nanoparticles are colloidal polymer particles of poly(butyl cyanoacrylate) with the desired peptide absorbed onto the surface and then coated with polysorbate 80. Nanoparticles are also used as a vector for delivering the hexapeptide dalargin (an enkephalin analog). Intravenous injections of the vector-dalargin produce analgesia, while dalargin alone does not [102]. Drugs successfully transported across the BBB with nanoparticles include loperamide, tubocerin and doxorubicin [103, 104]. The mechanism of nanoparticulate transport was not completely elucidated. The most probable transport pathway seems to be endocytosis by the blood capillary endothelial cells following adsorption of blood plasma components, most likely apoE after intravenous injection. These particles interact with the low-density lipoproteins (LDL) receptors on the endothelial cells and are then internalized. After internalization by the brain capillary endothelial cells, the drug is released by desorption or degradation of the nanoparticles and diffuses into the residual brain. Alternatively, transport may occur by transcytosis of the nanoparticles with the drug across the endothelial cells. The coating of nanoparticles with polysorbate led to adsorption of apoE and possibly other plasma components. This interacts with the LDL receptors of the brain endothelial cells, which could lead to their endocytosis [105]. In addition to these processes, polysorbates are capable of inhibiting the efflux pump. This inhibition could contribute to the brain transport properties of

the nanoparticles. However, the possibility of a general toxic effect is also a serious impediment.

#### 12.5.1.1 Peptide Conjugation through a Disulfide Bond

Short peptide sequences, known as protein transduction domains (also known as cell-penetrating peptides), have become important tools to internalize impermeant molecules into cells. The transduction domain from the HIV TAT protein has been the most widely used and characterized. The ability of the TAT protein to cross the plasma membrane has since been shown to reside primarily in a highly basic region composed of nine amino acid residues.

A microanalytical instrument is used to provide quantitative data on cargo transported into the cytoplasm of living. Fluorescently labeled peptides, kinases, were conjugated to a TAT-derived peptide. Two strategies were employed to introduce a cleavage site between the TAT and the substrate cargo – a disulfide bond and a photolabile moiety. Cytosolic concentrations of the released substrates were detectable at approximate concentrations of less than  $10^{-20}$  moles. These substrate peptides were used as probes of cytoplasmic kinase activity in single cells, with their phosphorylation providing a measure of their accessibility to cytoplasmic kinases. The percentage of phosphorylation of a TAT-loaded substrate peptide was compared to determine whether the free peptide released from the TAT conjugate was efficiently phosphorylated. The conjugated peptides were also used to determine the kinetics and temperature dependence of TAT-mediated delivery of kinase-accessible peptide to the cytosol [106].

#### 12.5.2

#### Biodegradable Polymer Based Nanoparticulate Delivery to BBB

Polymeric lipid-based devices that can deliver drug molecules at defined rates for specific periods are making a tremendous impact in clinical medicine. Drug delivery to the brain interstitium using polyanhydride can circumvent the BBB. The drug is released directly to an intracranial target in a sustained fashion for an extended period of time. The fate of a drug delivered to the brain interstitium from the biodegradable polymer was predicted by a mathematical model based on (a) rates of drug transport via diffusion and fluid convection, (b) rates of elimination from the brain via degradation, metabolism and permeation through capillary networks, and (c) rates of local binding and internalization [107]. Such models are used to predict the intracranial drug concentrations, results from 1,3-bis(2-chloroethyl)-1-nitrosourea (BCNU)-loaded pCPP:SA (1,3-bis-para-carboxyphenoxypropane:sebacic acid) as well as other drug–polymer combinations, paving the way for the rational design of drugs specifically for intracranial polymeric delivery.

Conjugation of a polymerically delivered chemotherapeutic agent to a water-soluble macromolecule increases drug penetration into the brain by increasing the period of drug retention. Recently, interleukin-2-loaded biodegradable polymer microspheres were developed for local cytokine delivery to improve the immuno-

therapeutic approach to brain tumor treatment [108]. Polymeric cytokine delivery has several advantages over delivery from transduced cells, including obviating need for transecting cytokine genes, producing longer periods of cytokine release *in vivo*, yielding more reproducible cytokine release profiles and total cytokine dose. Microparticles are easily implanted by stereotaxy in discrete, precise and functional areas of the brain without damaging the surrounding tissue. This type of implantation avoids the inconvenient insertion of large implants by open surgery, which may lead to repeat operations [109]. The feasibility of polymer-mediated drug delivery by the standard chemotherapeutic agent BCNU showed local treatment of gliomas. This method is effective in animal models of intracranial tumors. Obviously, such an invasive approach is only useful in a limited number of patients; however, it does prolong survival of patients with recurrent glioblastoma multiform brain tumors. Nevertheless, because of diffusion problems the therapeutic agent is likely to reach only nearby sites.

Polymeric nanoparticles are interesting colloidal systems to enhance the therapeutic efficacy and reduces the toxicity of a large variety of drugs [110]. Nanoparticles are helpful for the treatment of the disseminated and aggressive brain tumors. Intravenously injected doxorubicin-loaded polysorbate 80-coated nanoparticles produced 40% cure in rats with intracranially transplanted glioblastomas [103]. Another study shows that pegylated PHDCA (*n*-hexadecylcyanoacrylate) nanoparticles made by pegylated amphiphilic copolymer penetrate into the brain better than all the other tested nanoparticle formulations, without inducing any modification of BBB permeability [111]. Two important requirements are necessary in design of adequate brain delivery systems – long-circulating properties of the carrier and appropriate surface characteristics to permit interactions with endothelial cells. Valproic acid-loaded nanoparticles showed reduced toxic side-effects of valproate therapy, not by reducing the therapeutically necessary dosage, but by inhibiting the formation of toxic metabolites [112]. In conclusion, the capacity of biodegradable polymer delivery methodology to deliver drugs directly to the brain interstitium is extensive.

### 12.5.3

#### **Nanoparticulate Gene Delivery to the BBB**

Another strategy to achieve interstitial drug delivery involves releasing drugs from biological tissues. The simplest approach to this technique is to implant into the brain a tissue which naturally secretes a desired therapeutic agent. This approach is useful in the treatment of Parkinson's disease. Transplanted tissue often did not survive due to a lack of neovascular innervation. Recently, enhanced vascularization and microvascular permeability in cell-suspension embryonic neural grafts related to solid grafts has been demonstrated [113]. An alternative for this method is to use gene therapy to develop optimized biological tissue for interstitial drug delivery. Before implantation, cells are modified genetically to synthesize and release specific therapeutic agents. The therapeutic potential of this technique in the treatment of brain tumors has been demonstrated [114]. The use of nonneuronal cells

for therapeutic protein delivery to the CNS has been recently reviewed. The survival of foreign tissue grafts may be improved by advancements in techniques for culturing distinct cell types. Co-grafted cells engineered to release neurotropic factors with cells engineered to release therapeutic proteins may enhance the survival and development of foreign tissue [115].

It is possible to perform *in vivo* genetic engineering to cause specific endogenous brain tissue to express a desired protein, circumventing the ischemic and immunogenic complications encountered with the implantation of foreign tissue grafts. One such technique that has been successfully used for the treatment of CNS malignancies involves *in vivo* tumor transduction with the herpes simplex virus thymidine kinase (HSV-tk) gene followed by the treatment with anti-herpes drug ganciclovir. It was achieved by intratumoral injection of retroviral vector-producing cells containing the HSV-tk gene, rendering the transfected tumor cells susceptible to treatment with ganciclovir [116]. Other vector systems used in CNS gene transfer studies include retroviruses, adenoviruses, adeno-associated viruses, encapsulation of plasmid DNA into cationic liposomes, and neutral and oligodendrial stem cells. Although this approach holds remarkable therapeutic potential in the treatment of CNS diseases, several obstacles hinder its efficacy – restriction to the delivery of vector systems across the BBB, inefficient transfection of host cells, nonselective expression of the transgene and deleterious regulation of the transgene by the host [117].

#### 12.5.4

#### **Mechanism of Nanoparticulate Drug Delivery to the BBB**

The mechanism of drug delivery across the BBB has not been completely elucidated, even several possibilities are existing to explain it [103, 118]:

- (a) An increased retention of the nanoparticles in the brain blood capillaries is combined with adsorption to the capillary walls. A higher concentration gradient is responsible for enhancing the transport across the endothelial cell layer and it results in delivery to the brain.
- (b) A general surfactant effect characterized by a solubilization of the endothelial cell membrane lipids leads to membrane fluidization and enhanced drug permeability through the BBB.
- (c) The nanoparticles could lead to an opening of the tight junctions between the endothelial cells. The drug permeates through the tight junctions in free form or together with the nanoparticles.
- (d) The nanoparticles may be endocytosed by the endothelial cells followed by the release of the drugs within these cells and delivery to the brain.
- (e) The nanoparticles bound with drugs are transcytosed through the endothelial cell layer.
- (f) The polysorbate 80 used as the coating agent could inhibit the efflux system, especially P-glycoprotein.

## 12.5.5

**Nanoparticulate Thiamine-coated Delivery to the BBB**

Thiamine is a water-soluble micronutrient essential for normal cell function, growth and development. The consideration of thiamine as a cell-specific ligand for targeted delivery is rationalized since all eukaryotic cells have a specified transport mechanism for thiamine. The effectiveness of using the thiamine ligand in tumor targeting has been studied. Thiamine-coated gadolinium nanoparticles had specific association with human breast cancer cells, which expressed the thiamine transporters THTR1 and THTR2 [119]. The thiamine ligands bind to the BBB thiamine transporter and subsequently increase the number of nanoparticles at the BBB interface. Based upon BBB thiamine transport capacity and kinetics, it is referred to as a brain drug delivery vector [120]. The thiamine-coated nanoparticles (thiamine nanoparticles) specifically favor the brain uptake either by facilitating transport mechanisms or by increased passive diffusion, secondary to an increased concentration gradient of the nanoparticles located at the BBB interface due to association with the thiamine transporter. The thiamine-coated nanoparticles are engineered directly from microemulsion precursors. Brain uptake and distribution of nanoparticles with and without thiamine as a brain targeting ligand were investigated.

## 12.5.6

**Nanoparticle Optics and Living Cell Imaging**

Optical properties of silver nanoparticles depend on their size and shape and on the dielectric constant of the embedded medium [121–123]. The surface plasmon resonance of nanoparticles is excited by propagating light waves leading to the selective absorption and scattering of light. Therefore, the colors [localized SPRs (LSPRs)] of silver nanoparticles are correlated with the sizes of nanoparticles, while the shape of nanoparticles and their embedded medium remain unchanged [124, 125]. Unique size-dependent optical properties allow us to use the color index of nanoparticles (violet, blue, green, red) as nanometer-size index probes for real-time sizing of the change of living cellular membrane permeability and porosity at the nanometer scale. Individual silver nanoparticles are extremely bright under dark-field optical microscope and directly imaged by a digital or CCD camera through the dark-field microscope.

These nanoparticles do not photo-decompose and are used as probes to continuously monitor dynamics and kinetics of membrane transport in living cells for an extended time (hours). In addition, these nanoparticles are used to determine the sizes of substrates transported in and out of the living cellular membrane in real time. The scattering intensity of the nanoparticles decreases as nanoparticles enter the cell membrane and move into the cytoplasmic space. The cellular membrane and matrix absorbs the light of the microscope illuminator and reduces its intensity. The intracellular nanoparticles are surrounded by a cellular matrix (e.g. proteins, lipids) inside the cells and hence the reflection coefficient of intracellular



silver nanoparticles is smaller than the extracellular silver nanoparticles [121, 123]. The imaging system is sufficiently sensitive to detect single fluorescence dye molecules [126], and intracellular and extracellular single silver nanoparticles with diameters of 20–100 nm. Since the size of the nanoparticles and the thickness of the cellular membrane are under the optical diffraction limit (200 nm), the intracellular nanoparticles are accumulated on the membrane. However, these nanoparticles appear blurry and dimmer than extracellular nanoparticles, indicating that the blurry nanoparticles are inside the cells.

Transmission electron microscopy (TEM) is used to confirm the intracellular nanoparticles inside the cells. TEM images of ultrathin cross-sections of cells with nanoparticles unambiguously illustrate that nanoparticles up to 80 nm in diameter are observed inside the cells in the absence of chloramphenicol. The majority of nanoparticles (20–80 nm) are in the cytoplasmic space of the cells, whereas some of nanoparticles are right underneath the cellular membrane. It suggests that the outer and inner membrane of *Pseudomonas aeruginosa* permeate substrates with sizes up to 80 nm, which are 50 times larger than conventional antibiotics and detergents. Bulk cells are monitored simultaneously at single-cell resolution using single-living-cell imaging. Accumulation kinetics of nanoparticles in living cells is measured in real time using single nanoparticle optics. Even though these nanoparticles look larger than their actual sizes due to the optical diffraction limit, the sizes of nanoparticles are determined using their colors (LSPRS). As chloramphenicol concentration increases to 25 and 250  $\mu\text{g mL}^{-1}$ , more nanoparticles are observed in the cells, suggesting that the membrane permeability and porosity increase. The sizes of individual intracellular nanoparticles are distinguished using their colors (LSPRS) even in the presence of 250  $\mu\text{g mL}^{-1}$  of chloramphenicol, suggesting the chloramphenicol increases membrane permeability, but does not completely disrupt the cell walls. Chloramphenicol's primary target is ribosomal peptidyl transferase, where it acts competitively to inhibit normal substrate binding and protein synthesis [127]. These new insights further demonstrate the unique advantages of using single nanoparticle as probes for the study of function of antibiotics and membrane transport.

The MexAB–OprM has a wide spectrum of substrates, such as antibiotics, dyes, detergents and chemotoxic materials, and works by using proton motive force as the energy source [128]. Therefore, it is plausible to suggest that the transport mechanism of nanoparticles through the living cellular membrane is that nanoparticles enter the cells through passive diffusion and are extruded out of the cells by the extrusion mechanism of bacteria. Even though the sizes of silver nanoparticles seem 50 times larger than the pore sizes of membrane pumps (MexAB–OprM), the substrate (nanoparticles) can induce the assembly of the pumps in real time and define the pore sizes of the pumps. Currently, the crystal structure of the membrane pump is unavailable and the extrusion mechanism of the pump is still unknown [129]. Silver nanoparticles may enter the cells and be extruded out of the cells through unidentified pathways.

Ethidium bromide (EtBr) has been widely used as a fluorescence probe for the study of membrane permeability and extrusion machinery of bacterial cells [130,

131]. EtBr emits weaker fluorescence in an aqueous environment (outside the cells), and becomes 10 times more strongly fluorescent as it enters the cells and intercalates with DNA in the cells [132]. EtBr enters the cells through passive diffusion and is extruded out of cells by efflux pumps of *P. aeruginosa* using proton motive force as an energy source. The fluorescence spectra of EtBr indicate that the emission peak at 590 nm remains unchanged after a 2-h incubation of EtBr with the living cells. The time-dependent fluorescence intensity transients also show the mutant dependence. It indicates the mutant devoid of MexAB–OprM ( $\Delta$ ABM) accumulates EtBr most rapidly, whereas the mutant with overexpression of MexAB–OprM (nalB-1) accumulates EtBr most slowly. MexAB–OprM plays an important role in the accumulation of substrate (EtBr) in the cells. Taken together, accumulation kinetics measured using EtBr is consistent with those observed using single nanoparticles, eliminating the concern of the possible steric and size effects. The minimum inhibitory concentrations (MICs) of chloramphenicol in the presence of 10  $\mu$ M EtBr or 1.3 pM silver nanoparticles show mutant dependence, indicating a MIC of 12.5, 25 and 250  $\mu$ g mL<sup>-1</sup> for  $\Delta$ ABM, wild-type and nalB-1, respectively [133]. See Fig. 12.3.

## 12.6

### Oral Nanoparticulate Delivery

The oral route is the preferred route for drug delivery. However, numerous drugs remain poorly absorbed after oral administration. This can be due to (a) low mucosal permeability of a drug, (b) permeability restricted to a region of the GI tract, (c) low solubility of the compound results in low dissolution in the mucosal fluids and (d) lack of stability in the GI environment, resulting in degradation of the compound prior to its absorption (e.g. peptides, oligonucleotides). Drug delivery associated with nanoparticle systems has been investigated to overcome these problems. Several oral administration experiments are known which help to improve the pharmacokinetics of the drugs [134, 135]. See Fig. 12.4.

Orally administered drugs with nano- and microparticles follow different pathways and undergo: (a) direct transit and fecal elimination, (b) bioadhesion, and (c) oral absorption. Those pathways are important to determine an efficient drug delivery strategy. Some techniques are used for macroscopic controlled-release dosage forms for the accurate control of the drug delivery successfully transported via nanoparticles [136]. Micro- or nanoparticles orally administered in the form of a suspension diffuse into the liquid media and rapidly encounter the mucosal surface. The particles are immobilized at the intestinal surface by an adhesion mechanism referred as to as “bioadhesion”. More specifically, when adhesion is restricted to the mucus layer lining the mucosal surface, the term “mucoadhesion” is employed. The direct contact of particles with intestinal cells through a bioadhesion phase is the first step before particle absorption. The oral absorption pathway is investigated in the work of Volkheimer [137].

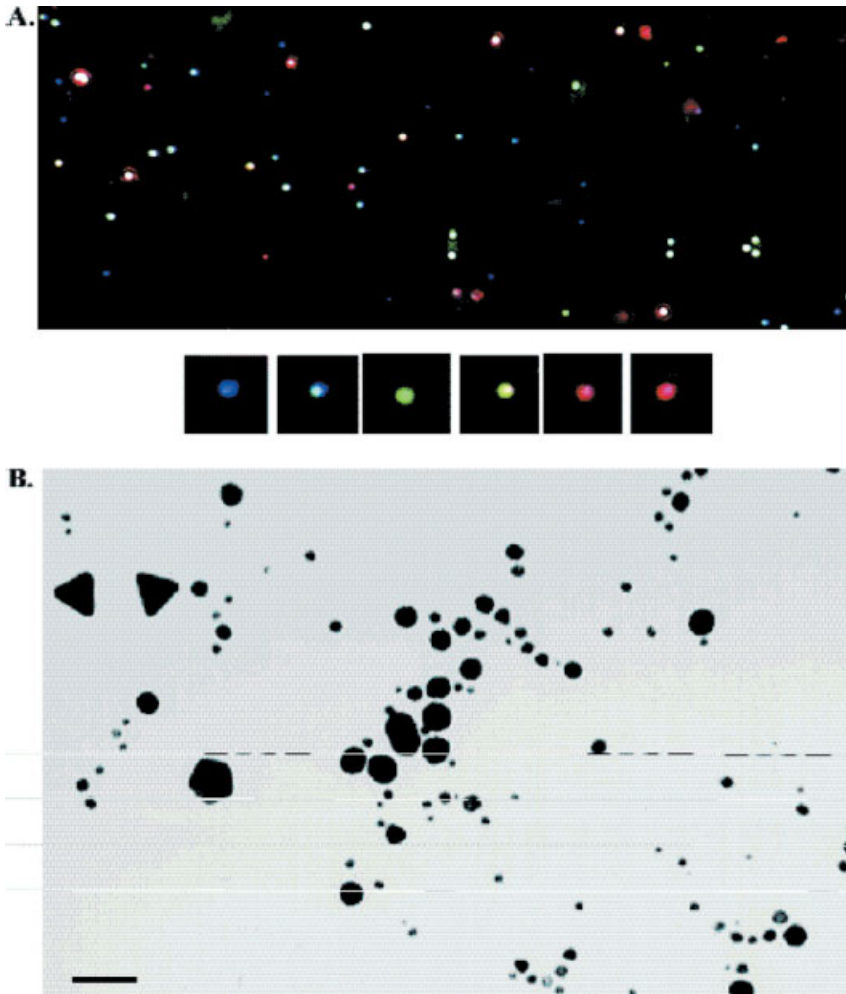


**Fig. 12.3.** Characterization of color index and size index of silver nanoparticles. (A) The representative full-frame optical image of silver nanoparticles taken from a 0.4-nM silver nanoparticle solution in a microchannel by a digital color camera through the dark-field optical microscope. Optical images of single silver nanoparticles selected from the full

frame image show the color index of silver nanoparticles. The optical images of nanoparticles look larger than their actual sizes because of the optical diffraction limit (200 nm). (B) Representative TEM images of silver nanoparticles from the solutions in (A) show the sizes and shapes of nanoparticles. The scale bar represents 40 nm [133].

### 12.6.1

#### Lectin-conjugated Nanoparticulate Oral Delivery

The association of ligands (i.e. lectins) with particulate systems is achieved by different procedures, including covalent linkage and adsorption processes. The ligand

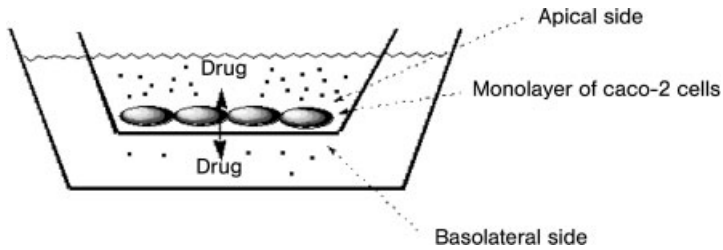


Fig. 12.4. Problems inherent in developing peptides as drugs [134b].

should be bound to particles through a covalent linkage, which is more stable than simple adsorption. It is difficult to control the amount of ligand associated, which is not sufficient to assure its efficacy [138]. Most of the conjugates have been prepared from polystyrene nanoparticles. Polystyrene latexes are interesting models from an experimental point of view, because polystyrene particles are not degradable in biological media and are easily detected by turbidimetry [139] or fluorescent labeling. However, it is probably unacceptable as a drug carrier because of the non-degradability of the polymer after a probable translocation of a fraction of the particles after administration. For conjugates based on polystyrene nanoparticles (latex), the binding procedure is by covalent attachment. Depending on the chemical nature of the functional groups located on the carrier surface, glutaraldehyde and carbodiimide, are used for lectin coupling. Recently, some lectin conjugates based on a biodegradable particulate system were described. The carbodiimide technique was successfully used for the covalent attachment of lectins to vicilin (feed vegetal protein from *Pisum sativum*) and gliadin (protein fraction from wheat gluten) nanoparticles [140]. The procedure used for the preparation of the lectin–vicilin nanoparticle conjugates is illustrated elsewhere [141, 142].

#### 12.6.2

#### Oral Peptide Nanoparticulate-based Delivery

Nanospheres have a matrix-type structure, where active compounds (e.g. peptides) are adsorbed at their surface entrapped or dissolved in the matrix. The development of oral therapeutic peptide formulations with these substances is a challenging opportunity for researchers. The GI tract is designed to degrade dietary proteins and facilitate absorption of single amino acids or oligopeptides. For therapeutic compounds, however, the molecules have to remain intact when they reach the systemic circulation. Due to the presence of an acidic environment, pepsins, peptides and proteins are hydrolyzed in the stomach. In the intestine, peptides are confronted with pancreatic proteases, such as trypsin, chymotrypsin, elastase and carboxypeptidase A [143]. Furthermore, the peptides are exposed to brush border proteases and finally have to cross the epithelium. Degradation by enzymes is also possible during the absorption step. Several approaches, such as site-specific delivery systems, chemical modification of peptides (e.g. lipophilic derivatives, synthesis

of peptidomimetics), bioadhesive systems and concomitant administration of penetration enhancers or protease inhibitors, have been investigated to improve the oral delivery of peptides [143]. The use of particulate systems aims to improve the delivery of peptides by the oral route. Incorporating or encapsulating peptides in polymeric particles should have at least one effect. Depending on the nature of the particles used (type of polymer, size, adjuvant substances added), these systems enhance oral peptide absorption by other mechanisms. How the drug-loaded particulate systems are translocated from the intestinal mucosa to the systemic circulation after oral administration is still unknown [144, 145]. Many studies mention that not more than 5% of the ingested dose of submicron particles can be absorbed.

### 12.6.3

#### **Polymer-Based Oral Peptide Nanoparticulate Delivery**

Calcitonin is a peptide comprising 32 amino acids with high species-to-species sequence variations. It is soluble in water (1:5) and methanol (1:10), and is almost insoluble in acetone, alcohol, chloroform and ether. Calcitonin-loaded polyacrylamide nanospheres have been prepared by a reported method [146]. Particles containing hydrophilic peptide have also been prepared by interfacial polymerization, leading to the formation of nanocapsules [147, 148].

##### **12.6.3.1 Polyacrylamide Nanospheres**

Calcitonin-loaded nanospheres are prepared by the method of Birrenbach and Speiser [149]. This method involves polymerization in an inverse microemulsion (water-in-oil) method. It requires a large amount of solvent (e.g. hexane). The particles are isolated by several washings with ethanol and finally are freeze-dried. The nanospheres obtained with this technique had a size below 50 nm, but their loading efficiency remained low (5%). The peptide was immediately released from the particles after rehydration, thus impeding the protection against protease degradation.

##### **12.6.3.2 Poly(alkyl cyanoacrylate) PACA Nanocapsules**

The interfacial polymerization technique was used to encapsulate calcitonin in poly(isobutyl cyanoacrylate) PICBA nanocapsules [146]. The isobutyl cyanoacrylate (IBCA) monomers and calcitonin were dissolved in ethanol solution containing an oil (Mygliol 812). This phase was added dropwise into stirred water containing poloxamer 188. Anionic polymerization took place at the surface of the Mygliol droplets as soon as IBCA reached the oil/water interface, thus forming nanocapsules of a mean size ranging from 100 to 300 nm. Preparation additives were subsequently removed by diafiltration. Surprisingly, the calcitonin incorporated with an efficiency of 90%. The hydrophilic peptide has marked hydrophobic regions in its structure. This probably enables calcitonin to interact with the Mygliol oil. When incorporated into PIBCA nanocapsules, calcitonin was significantly more resistant to protease degradation than the free peptide [146]. However, in the pres-

ence of bile salts, the protection was significantly reduced, but still higher than a solution of free peptide. The authors suggested that calcitonin molecules diffused at the oil/water interface, together with IBCA and the poloxamer. This localization would then render the peptide susceptible to enzymes. Taking into account that peptides are highly water soluble it leads to the formation of nanocapsules with a complete inner aqueous core facilitates the incorporation of hydrophilic compounds [147, 148].

#### 12.6.3.3 Derivatized Amino Acid Microspheres

The releasing of the peptide at a specific site of the GI tract is done using dissolved nanoparticles of substrate. Microparticles sensitive to pH were prepared by using derivatized amino acids [150, 151]. Benzoylated and phenylsulfonylated single amino acids are novel, low-molecular-weight and self-assembling molecules. At low pH, these molecules aggregate to form microspheres that dissolved readily under neutral conditions. For example, modified soybean amino acids, dissolved in water, form microparticles when poured into a 1.7 N citric acid solution containing salmon calcitonin. This technique is used for the entrapment of nearly 60% of the dissolved peptide.

#### 12.6.4

#### Lymphatic Oral Nanoparticulate Delivery

The lymphatic pathway has not been investigated in many studies, possibly due to the difficulty, complexity and expense encountered in cannulating the major lymph ducts in laboratory animals. The evaluation of 80-nm solid lipid nanoparticles administered intraduodenally shows primarily their presence in the thoracic lymph duct [152]. Incorporation of the highly lipophilic drug cyclosporin in solid lipid microspheres increases lymphatic absorption 46-fold compared to conventional formulations. In another study, cyclosporin A formulated in stearic acid nanoparticles (300 nm) had a relative bioavailability of nearly 80% over the cyclosporin reference solution; however, it was unclear whether this was primarily lymphatic absorption [153]. Bioactive peptides such as insulin, calcitonin, luteinizing hormone-releasing hormone [154] and cyclosporin have been the typical peptides delivered as GI tract-labile drugs using nanoparticulate systems. Further, alteration in the physiology and metabolism of an animal is found in diseased states. In insulin-deficient streptozotocin-treated rats, the intestine is hypertrophic, and the synthesis and transport of cholesterol are increased. The increased load of cholesterol is transported through the mesenteric lymph in chylomicrons to developed oral formulations for insulin using steroidal lipids [155]. Liposome compositions of soybean sterols showed higher uptake than cholesterol, but this has been attributed to the increased stability of vesicles prepared by forming rigid liposomes [156]. All these attempts to deliver insulin orally using nanoparticles have been successful. In the oral administration of a very similar system, but dispersed in an oily phase, a 50% decrease of fasted glycemia was achieved from 2 h up to 10–13 days in rats [157]. This effect was shorter (2 days) or absent when nanospheres were dispersed in wa-

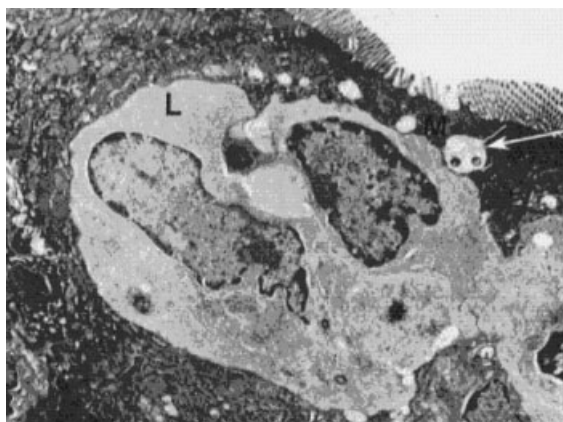


**Fig. 12.5.** Electron photomicrograph of semi-thin sections of rat Peyer's patch of a ligated intestinal segment after exposure to liposomes. Gold particles are indicated by the arrow. Notice the relatively small area of the M-cell apical surface sandwiched between the regular villi of the enterocytes. The presence of a large intraepithelial lymphocyte that approaches the apical surface is a conspicuous feature of the M-cell [158].

ter with and without surfactants. The results suggest primarily a lymphatic route of absorption with the nanoparticles being lodged in some way in the intestinal mucosa. A similar result has been reported for recombinant human erythro protein administered in liposomes composed of soyabean sterols. See Fig. 12.5.

#### 12.6.5

#### Oral Nanosuspension Delivery

The problems to find a suitable formulation are even greater in the case of drugs that are poorly soluble in aqueous media and in organic media.

Simple examples reflecting this problem of poor solubility combined with low absorption are the experimental compound bupravaquone and the recently approved drug atovaquone (Wellvone), used for the treatment of opportunistic *Pneumocystis carinii* infections in HIV patients. Oral administration of nanosuspensions can overcome the problem of the poor solubility of drug. This is because of the high adhesiveness of drug particles, sticking on biological surfaces of the epithelial gut wall. When atovaquone formulated as a nanosuspension is given orally to *Leishmania*-infected mice, the parameter for increased absorption is related to the infectivity score of each animal or it is related to the reduction of the parasite load in the liver. In comparison to Wellvone-treated mice, containing a micronized drug, nanosuspensions of atovaquone at equivalent doses reduced infectivity from 40 to 15% at a reduced concentration of only  $7.5 \text{ mg kg}^{-1}$  [158, 159]. Another example of the effectiveness of nanosuspensions for improving bioavailability is the application of amphotericin B. When amphotericin B is given orally in approved drugs for the treatment of GI tract mycosis, the drug is not, or only to a minor ex-

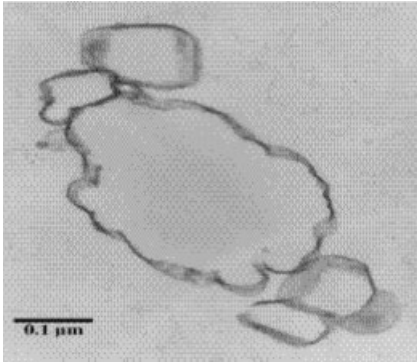


**Fig. 12.6.** Transmission electron micrographs of a atovaquone nanosuspension (size: 468 nm) [161].

tent, absorbed. Formulating this antimycotic and leishmanicidal drug as a nanosuspension and administering it orally, the number of *L. donovani* parasites *in vivo* was reduced significantly, indicating a high uptake of the drug in the GI tract. When given amphotericin B nanosuspensions orally, the infectivity score was determined at 25% (control = 100% parasite growth) [160]. See Fig. 12.6.

#### 12.6.6

##### **Mucoadhesion of Nanoparticles after Oral Administration**

Considering the different phenomena occurring after oral administration of a suspension of colloidal particles via the oral route, the following general dynamic description is given. First, a suspension of particles is administered and immediately contacts the oral mucosa. From this moment on, the concentrated suspension acts as a reservoir of particles and, very rapidly, an adsorption process takes place, leading to the adsorption of a fraction of the available particles. Adsorption occurring with the mucous layer is an irreversible process. However, the luminal particle suspension transits through the intestine, progressively sweeping the whole mucosa. The simultaneous adsorption process results in a progressive covering of the intestinal mucosa by adhering particles. Finally, detachment of the particles from the mucosa begins to occur in the proximal region and is progressively extended to the distal region. Nonadhering particles from the lumen pool are detached from the mucoadherent pool and are finally eliminated in the feces. Quantitatively, particle translocation through the intestinal mucosa remains a secondary phenomenon [161].

#### 12.6.7

##### **Protein Nanoparticulate Oral Delivery**

Protein nanoparticles are incorporated into biodegradable polymer microspheres/nanospheres as a controlled release depot or for oral delivery. In proteinaceous



therapeutics, the generation of nanoparticles is problematic. Existing practices have difficulties in achieving the desired particle size for distribution. Protein nanoparticles technology avoids most of these difficulties. The process exploits the ability of superfluids to penetrate the protein aggregates and then utilizes the expansive energy of superfluids to disaggregate protein crystals into monodisperse nanoparticles. Superfluid protein nanoparticles technology is not constrained by limited solubility in benign solvents such as ethanol [162].

## References

- 1 KUBIK T., BOGUNIA K., SUGISAKA M., Nanotechnology on duty in medical applications, *Curr. Pharm. Biotechnol.* 6, 2005, 17–33.
- 2 FOLDVARI M., BECA-ESTRADA M. E., HE Z., HU J., ATTAH-POKU S., KING M., Dermal and transdermal delivery of protein pharmaceuticals: lipid-based delivery systems for interferon, *Biotechnol. Appl. Biochem.* 30, 1999, 129–137.
- 3 KREUTER J., Transport of drugs across the blood–brain barrier by nanoparticles, *Curr. Med. Chem. CNS Ag.* 2, 2002, 241–249.
- 4 ALBERTS B., BRAY D., LEWIS J., RAFF M., ROBERTS K., WATSON J. D., *Molecular Biology of the Cell*, 3rd edition, Garland Publishing, New York, 1994, pp. 195–212.
- 5 COOPER K. E., GATES P. Y., EISENBERG R. S., Surmounting barriers in ionic channels, *Q. Rev. Biophys.* 21, 1988, 331–364.
- 6 EISENBERG B., Ionic channels in biological membranes – electrostatic analysis of a natural nanotube [Review], *Contemp. Phys.* 39, 1998, 447–466.
- 7 EISENBERG R. S., From structure to function in open ionic channels, *J. Membr Biol.* 171, 1999, 1–24.
- 8 FISHMAN G. I., MORENO A. P., SPRAY D. C., LEINWAND L. A., Functional analysis of human cardiac gap junction channel mutants, *Proc. Natl Acad. Sci. USA* 88, 1991, 3525–3529.
- 9 ILLE B., ARMSTRONG C. M., MACKINNON R., Ion channels: from idea to reality, *Nat. Med.* 5, 1999, 1105–1109.
- 10 NOSSAL R., LECAR H., *Molecular and Cell Biophysics*, Addison-Wesley, San Francisco, CA, 1991.
- 11 SOSINSKY G., PERKINS G., Electron crystallographic methods for investigating gap junction structure, *Methods* 20, 2000, 140–155.
- 12 BENNETT D. L., VERSELIS V., Biophysics of gap junctions, *Semin. Cell Biol.* 3, 1992, 29–47.
- 13 DERMETZEL R., HWANG T. K., SPRAY D. S., The gap junction family: structure, function and chemistry, *Anat. Embryol. (Berl.)* 182, 1990, 517–528.
- 14 FRASER I. D., SCOTT J. D., Modulation of ion channels: a “current” view of AKAPs, *Neuron* 23, 1999, 423–426.
- 15 GILULA N. B., Topology of gap junction protein and channel function, *Ciba Found. Symp.* 125, 1987, 128–139.
- 16 BAIGENT S., STARK J., WARNER A., Modeling the effect of gap junction nonlinearities in systems of coupled cells, *J. Theor. Biol.* 186, 1997, 223–239.
- 17 UNGER V. M., KUMAR N. M., GILULA N. B., YEAGER M., Expression, two-dimensional crystallization, and electron cryo-crystallography of recombinant gap junction membrane channels, *J. Struct. Biol.* 128, 1999, 98–105.
- 18 PERKINS G., GOODENOUGH D., SOSINSKY G., Three-dimensional structure of the gap junction connexon, *Biophys. J.* 72, 1997, 533–544.
- 19 SOSINSKY G. E., PERKINS G. A.,

- Electron crystallographic methods for investigating gap junction structure. *Methods* 20, 2000, 140–155.
- 20 (a) *Studyworld Studynotes, Reports & Essays: Science – Biological, Components of Biological Membranes*. (b) <http://www.biosci.uga.edu/almanac/bio>.
  - 21 FRICKENHAUS S., HEINRICH R., Kinetic and thermodynamic aspects of lipid translocation in biological membranes, *Biophys. J.* 76, 1999, 1293–1309.
  - 22 LADEMANN J., WEIGMANN H., RICKMEYER C., BARTHELMES H., MUELLER G., STERRY W., Penetration of titanium dioxide microparticles in a sunscreen formulation into the horny layer and the follicular orifice, *Skin Pharmacol. Appl. Skin Physiol.* 12, 1999, 247–256.
  - 23 MENON G. K., ELIAS P. M., Morphologic basis for a pore-pathway in mammalian stratum corneum, *Skin Pharmacol.* 10, 1997, 235–246.
  - 24 BLUNDELL G., HENDERSON W. J., PRICE E., Soil particles in tissues of the foot in endemic elephantiasis of the lower legs, *Ann. Trop. Med. Parasitol.* 83, 1989, 381–385.
  - 25 SAUNDERS J., DAVIS H., COETZEE L., BOTHA S., KRUGER A., GROBLER A., A novel skin penetration enhancer: evaluation by membrane diffusion and confocal microscopy, *J. Pharm. Pharm. Sci.* 2, 1999, 99–107.
  - 26 HOEF F. H., HOHLFELD I. B., SALATA O. V., Nanoparticles – known and unknown health risks, *J. Nanobiotechnol.* 2, 2004, 12.
  - 27 OH S. Y., LEUNG L., BOMMANNAN D., GUY R. H., POTTS R. O., Effect of current, ionic strength and temperature on the electrical properties of skin, *J. Controlled Rel.* 27, 1993, 115–125.
  - 28 CULLANDER C., What are the pathways of iontophoretic current flow through mammalian skin?, *Adv. Drug Deliv. Rev.* 9, 1992, 119–135.
  - 29 EDWARDS D. A., LANGER R., A linear theory of transdermal transport phenomena. *J. Pharm. Sci.* 83, 1994, 1315–1334.
  - 30 CHANG D. C., CHASSY B. M., SAUNDERS J. A., SOWERS A. E. (Eds.), *Handbook of Electroporation and Electrofusion*. Academic Press, New York, 1992.
  - 31 GALLO S. A., OSEROFF A. E., JOHNSON P. G., HUI S. W., Characterization of electric pulse induced permeabilization of porcine skin using surface electrodes, *Biophys. J.* 72, 1997, 2805–2811.
  - 32 HUI S. W., Low voltage electroporation of the skin, or is it iontophoresis?, *Biophys. J.* 74, 1998, 679–680.
  - 33 CRONE C., The blood–brain barrier: a modified tight epithelium, In *The Blood–Brain Barrier in Health and Disease*, SUCKLING A. J., RUMSBY M. G., BRADBURY M. W. B. (Eds.), Ellis Harwood, Chichester, 1986, pp. 17–40.
  - 34 BRIGHTMAN M., Ultrastructure of brain endothelium, In *Physiology and Pharmacology of the Blood–Brain Barrier*, BRADBURY M. W. B. (Ed.), Springer, Berlin, 1992, pp. 1–22.
  - 35 LO E. H., SINGHAL A. B., TORCHILIN V. P., ABBOTT N. J., Drug delivery to damaged brain, *Brain. Res. Rev.* 38, 2001, 140–148.
  - 36 DAVSON H., SEGAL M. B., *Physiology of the CSF and Blood–Brain Barriers*, CRC Press, Boca Raton, FL, 1995.
  - 37 MISRA A., GANESH S., SHAHIWALA A., SHAH S. P., Drug delivery to the central nervous system: a review, *J. Pharm. Pharm. Sci.* 6, 2003, 252–273.
  - 38 PARDRIDGE W. M., *Brain Drug Targeting: The Future of Brain Drug Development*, Cambridge University Press, Cambridge, 2001.
  - 39 AJAY, BEMIS G. W., MURCKO M. A., Designing libraries with CNS activity, *J. Med. Chem.* 42, 1999, 4942–4951.
  - 40 GHOSE A. K., VISWANADHAN V. N., WENDOLOSKI J. J., A knowledge-based approach in designing combinatorial or medicinal chemistry libraries for drug discovery. 1. A qualitative and quantitative characterization of known drug databases, *J. Comb. Chem.* 1, 1999, 55–68.
  - 41 LIPINSKI C. A., Drug-like properties and the causes of poor solubility and poor permeability, *J. Pharmacol. Toxicol. Methods* 44, 2000, 235–249.

- 42 PARDRIDGE W. M., Biochemistry of the human blood-brain barrier, *Ann. Intern. Med.* 105, 1986, 82-95.
- 43 JOLLIET-RIANT P., TILLEMENT J. P., Drug transfer across the blood-brain barrier and improvement of brain delivery, *Fundam. Clin. Pharmacol.* 13, 1999, 16-26.
- 44 TEMSAMANI J., ROUSSELLE C., REES A. R., SCHERRMANN J. M., Vector-mediated drug delivery to the brain, *Expert Opin. Biol. Ther.* 1, 2001, 773-782.
- 45 LINDGREN M., HÄLLBRINK M., PROCHIANZ A., LANGEL U., Cell-penetrating peptides, *Trends Pharmacol. Sci.* 21, 2000, 99-103.
- 46 LANGEL U., *Cell Penetrating Peptides: Processes and Applications*, CRC Press, New York, 2002.
- 47 STANLEY S. D., WILDING I. R., Oral drug absorption studies: the test model for man is man, *Drug Discov. Today* 6, 2001, 127-128.
- 48 AYRTON A., MORGAN P., Role of transport proteins in drug absorption, distribution and excretion, *Xenobiotica* 31, 2001, 469-470.
- 49 LI A. P., Screening for human ADME/Tox drug proteins in drug discovery, *Drug Discov. Today* 6, 2001, 357-366.
- 50 UNGELL A. L., *In vitro* absorption studies and their relevance to absorption from the GI tract, *Drug Dev. Ind. Pharm.* 23, 1997, 879-892.
- 51 LENNERNAS H., Human intestinal permeability, *J. Pharm. Sci.* 87, 1998, 403-410.
- 52 MAHATOO R., Biological membranes and barriers, In *Biomaterials for Delivery and Targeting of Proteins and Nucleic acids*, CRC Press, New York, 2005.
- 53 LOMER M. C., THOMPSON R. P., POWEL J. J., Fine and ultrafine particles of the diet: influence on the mucosal immune response and association with Crohn's disease, *Proc. Nutr. Soc.* 61, 2002, 123-130.
- 54 MCMINN L. H., HODGES G. M., CARR K. E., Gastrointestinal uptake and translocation of microparticles in the streptozotocin-diabetic rat, *J. Anat.* 189, 1996, 553-559.
- 55 LIMPANUSSORN J., SIMON L., DAYAN A. D., Intestinal uptake of particulate material by dexamethasone-treated rats: use of a novel technique to avoid intestinal mucosal contamination, *J. Pharm. Pharmacol.* 50, 1998, 745-751.
- 56 BODERKE P., SCHITTKOWSKI K., WOLF M., MERKLE H. P., Modeling of diffusion and concurrent metabolism in cutaneous tissue, *J. Theor. Biol.* 204, 2000, 393-407.
- 57 JOHNSON M., BLANKSCHTEIN D., LANGER R., Evaluation of solute permeation through the stratum corneum: lateral bilayer diffusion as the primary transport mechanism, *J. Pharm. Sci.* 86, 1997, 1162-1172.
- 58 DOUCETO G. N., ROSDY M., FARTASCH M., ZASTROW L., Critical events in the barrier development of reconstructed epidermis, *Perspect. Percutaneous Penetration* 5, 1997, 141-144.
- 59 FARTASCH I. D., BASSUKAS T. L., SCHÄTZLEIN A., CEVC G., Non-uniform cellular packing of the stratum corneum and permeability barrier function of intact skin: a high-resolution confocal laser scanning microscopy study using highly deformable vesicles (Transfersomes), *Br. J. Dermatol.* 138, 1998, 583-592.
- 60 VAN DEN BERGH, B. A. I., VROOM J., GERRITSEN H., JUNGINGER H. E., BOUWSTRA J. A., Interactions of elastic and rigid vesicles with human skin *in vitro*: electron microscopy, *Biochim. Biophys. Acta* 1461, 1999, 155-173.
- 61 ZHAI H., MAIBACH H. I., Effects of skin occlusion on percutaneous absorption: an overview, *Skin Pharmacol. Appl. Skin Physiol.* 14, 2001, 1-10.
- 62 MULLER R. H., MEHNERT W., LUCKS J. S., SCHWARZ C., ZUR MUHLEN A., WEYHERS H., FREITAS C., RUHL D., Solid lipid nanoparticles (SLN) - an alternative colloidal carrier system for controlled drug delivery, *Eur. J. Pharm. Biopharm.* 41, 1995, 62-69.
- 63 MULLER R. H., MADER K., GOHLA S., Solid lipid nanoparticles (SLN) - a review of the state of the art, *Eur. J. Pharm. Biopharm.* 50, 2000, 161-177.

- 64 WEYHERS H., Feste Lipid-Nanopartikel (SLN) für die gewebsspezifische Arzneistoffapplikation, *PhD thesis*, Free University of Berlin, 1995.
- 65 MULLER R. H., DINGLER A., Feste Lipid-Nanopartikel (Lipopearls) als neuartiger Carrier für kosmetische und dermatologische Wirkstoffe, *PZ Wiss.* 49, **1998**, 11–15.
- 66 ZUR MUHLEN A., MEHNERT W., Drug release and release mechanism of prednisolone loaded solid lipid nanoparticles, *Pharmazie* 53, **1998**, 552.
- 67 DE VRINGER T., Topical preparation containing a suspension of solid lipid particles, *European patent application EP 0506197 A1*, **1992**.
- 68 WISSING S. A., MULLER R. H., The influence of solid lipid nanoparticles (SLN) on skin hydration and viscoelasticity: *in vivo* study, *Eur. J. Pharm. Biopharm.* **2002**, submitted.
- 69 SANTOS MAIA C., MEHNERT W., SCHAFFER-KORTING M., Solid lipid nanoparticles as drug carriers for topical glucocorticoids, *Int. J. Pharm.* 196, **2000**, 165–167.
- 70 WISSING S. A., MADER K., MULLER R. H., Solid lipid nanoparticles (SLN) as novel carrier system offering prolonged release of the perfume Allure (Chanel), *Int. Symp. Controlled Rel. Bioact Mater.* 27, **2000**, 311–312.
- 71 YAZIKSIZ-ISCAN Y., HEKIMOGLU S., SARGON M. F., KAS S., HINCAL A. A., *In vitro* release and skin permeation of DEET incorporated solid lipid particles in various vehicles, In *Proceedings of the 4th World Meeting, ADRITELF/APGI/APV*, **2002**, 1183–1184.
- 72 YAZIKSIZ-ISCAN Y., WISSING S. A., MULLER R. H., HEKIMOGLU S., Different production methods for solid lipid nanoparticles (SLN) containing the insect repellent DEET, In *Proceedings of the 4th World Meeting, ADRITELF/APGI/APV*, **2002**, 789–790.
- 73 HAGEDORN-LEWEKE U., LIPPOLD B. C., Accumulation of sunscreens and other compounds in keratinous substrates, *Eur. J. Pharm. Biopharm.* 46, **1998**, 215–221.
- 74 WISSING S. A., MULLER R. H., Solid lipid nanoparticles as carrier for sunscreens: *in vitro* release and *in vivo* skin penetration, *J. Controlled Rel.* **2002**, 81 (3), 225–233.
- 75 (a) GAUTIER J. C., GRANGIER J. L., BARBIER A., DUNPONT P., DUSSOSSY D., PASTOR G., COUVREUR P., Biodegradable nanoparticles for subcutaneous administration of growth hormone releasing factor (hGRF), *J. Controlled Rel.* 3, **1992**, 205–210. (b) DE VERDIERE A. C., DUBERNET C., NEMATI F., SOMA E., APPEL M., FERTE J., BERNARD S., PUISIEUX F., COUVREUR P., Reversion of multidrug resistance with poly-alkylcyanoacrylate nanoparticles: towards a mechanism of action, *Br. J. Cancer* 76, **1997**, 198–205.
- 76 MANIATIS A. K., KLIGENSMITH G. J., SLOVER R. H., Continuous subcutaneous insulin infusion therapy for children and adolescents: an option for routine diabetes care, *Pediatrics* 107, **2001**, 351–356.
- 77 ASBILL C. S., EL-KATTAN A. F., MICHNAIK B., Enhancement of transdermal drug delivery: chemical and physical approaches, *Crit. Rev. Ther. Drug Carrier Syst.* 17, **2000**, 621–625.
- 78 FENG S. S., CHIEN S., Chemotherapeutic engineering: application and further development of chemical engineering principles for chemotherapy of cancer and other diseases, *Chem. Eng. Sci.* 58, **2003**, 4087–4114.
- 79 SINGLA A. K., GARG A., AGGARWAL D., Paclitaxel and its formulations, *Int. J. Pharm.* 235, **2002**, 179–192.
- 80 FONSECA C., SIMÕES S., GASPARI R., Paclitaxel-loaded PLGA nanoparticles: preparation, physicochemical characterization and *in vitro* anti-tumoral activity, *J. Controlled Rel.* 83, **2002**, 273–286.
- 81 YOO H. S., PARK T. G., *In vitro* and *in vivo* anti-tumor activities of nanoparticles based on doxorubicin-PLGA conjugates, *Polym. Prep.* 41, **2000**, 992–993.
- 82 SHIKATA F., TOKUMITSU H., ICHIKAWA H., FUKUMORI Y., *In vitro* cellular

- accumulation of gadolinium incorporated into chitosan nanoparticles designed for neutron-capture therapy of cancer, *Eur. J. Pharm. Biopharm.* **53**, **2002**, 57–63.
- 83 BHADRA D., BHADRA S., JAIN S., JAIN N. K., A PEGylated dendritic nanoparticulate carrier of fluorouracil, *Int. J. Pharm.* **257**, **2003**, 111–124.
- 84 WILLIAMS J., LANSDOWN R., SWEITZER R., ROMANOWSKI M., LABELL R., RAMASWAMI R., UNGER E., Nanoparticle drug delivery system for intravenous delivery of topoisomerase inhibitors, *J. Controlled Rel.* **91**, **2003**, 167–172.
- 85 KIRCHEIS R., KICHLER A., WALLNER G., KURSA M., OGRIS M., FELZMANN T., BUCHBERGER M., WAGNER W., Coupling of cell-binding ligands to polyethylenimine for targeted gene transfer, *Gene Ther.* **4**, **1997**, 409–418.
- 86 OGRIS M., STEINLEIN P., CAROTTA S., BRUNNER S., WAGNER E., DNA/polyethylenimine transfection particles: influence of ligands, polymer size, and PEGylation on internalization and gene expression, *AAPS PharmSciTech.* **3**, **2001**, 21.
- 87 OGRIS M., WALKER G., BLESSING T., KIRCHEIS R., WOLSHEK M., WAGNER E., Tumor-targeted gene therapy: strategies for the preparation of ligand-polyethylene glycol-polyethyleneimine/DNA complexes, *J. Controlled Rel.* **91**, **2003**, 173–181.
- 88 HOLLY K., Biomedical engineer constructs illuminating nanoparticles for medical imaging and gene detection, Emory University Health Sciences Center. Public release date: 27 March 2003.
- 89 NIELSEN U. B., KIRPOTIN D. B., PICKERING E. M., HONG K., PARK J. W., SHALABY M. R., SHAO Y., BENZ C. C., MARKS J. D., Therapeutic efficacy of anti-ErbB2 immunoliposomes targeted by a phage antibody selected for cellular endocytosis, *Biochim. Biophys. Acta* **1591**, **2002**, 109–118.
- 90 RENEKER D. H., CHUN I., Nanometre diameter of polymer, produced by electrospinning, *Nanotechnology* **7**, **1996**, 216–223.
- 91 DOSHI J., RENEKER D. H., Electrospinning process and applications of electrospun fibers, *J. Electrostat.* **35**, **1995**, 151–160.
- 92 VERRECK G., CHUN I., PEETERS J., ROSENBLATT J., BREWSTER M. E., Preparation and characterization of nanofibers containing amorphous drug dispersion generated by electrostatic spinning, *Pharm. Res.* **20**, **2003**, 810–817.
- 93 KENAWY E. R., BOWLIN G. L., MANSFIELD K., LAYMAN J., SIMPSON D. G., SANDERS E. H., WNEK G. E., Release of tetracycline hydrochloride from electrospun poly(ethylene-co-vinylacetate), poly(lactic acid), and a blend, *J. Controlled Rel.* **81**, **2002**, 57–64.
- 94 IGNATIOUS F., BALDONI J. M., Electrospun pharmaceutical compositions, *WO 0154667*, 2001.
- 95 ZONG X., KIM K., FANG D., RAN S., HSIAO B. S., CHU B., Structure and process relationship of electrospun bioabsorbable nanofiber membranes, *Polymer* **43**, **2002**, 4403–4412.
- 96 LEE K. H., KIM H. Y., KHIL M. S., RA Y. M., LEE D. R., Characterization of nano-structured poly( $\epsilon$ -caprolactone) nonwoven mats via electrospinning, *Polymer* **44**, **2003**, 1287–1294.
- 97 SHIN Y. M., HOHMAN M. M., BRENNER M. P., RUTLEDGE G. C., Experimental characterization of electrospinning: the electrically forced jet and instabilities, *Polymer* **42**, **2001**, 9955–9967.
- 98 PEETERS J., NEESKENS P., TOLLENAERE J. P., VAN REMOORTERE P., BREWSTER M. E., Characterization of the interaction of 2-hydroxypropyl-hydroxyethylcyclodextrin with itraconazole at pH 2, 4 and 7, *J. Pharm. Sci.* **91**, **2002**, 1414–1422.
- 99 MEIS J. F. G. M., VERWEIJ P. E., Current management of fungal infections, *Drugs* **61**, **2001**, 13–25.
- 100 MARTINEZ-DE JESUS F. R., MORALES-GUZMAN M., CASTANEDA M., PEREZ-MORALES A., GARCIA-ALONSO J., MEDIOLA-SEGURA I., Randomized

- single-blind trial of topical ketanserin for healing acceleration of diabetic foot ulcers, *Arch. Med. Res.* 28, 1997, 95–99.
- 101 APELQVIST J., CASTENFORS J., LARSSON J., STENSTROM A., PERSSON G., Ketanserin in the treatment of diabetic foot ulcer with severe peripheral vascular disease, *Int. Angiol.* 9, 1990, 120–124.
- 102 KREUTER J., ALYAUTDIN R. N., KHARKEVICH D. A., IVANOV A. A., Passage of peptides through the blood–brain barrier with colloidal polymer particles (nanoparticles). *Brain Res.* 674, 1995, 171–174.
- 103 KREUTER J., Nanoparticulate systems for brain delivery of drugs, *Adv. Drug. Deliv. Rev.* 47, 2001, 65–81.
- 104 KREUTER J., Transport of drugs across the blood–brain barrier by nanoparticles, *Curr. Med. Chem.* 2, 2002, 241–249.
- 105 LUCK M., Plasma protein adsorption als Moglicher Schlusselfaktor fur eine kontrollierte Arzneistoffapplikation mit partikularen Tragern, *PhD thesis*, Freie Universitat Berlin, 1997.
- 106 SOUGHAYER J. S., WANG Y., LI H., CHEUNG S., ROSSI F. M., STANBRIDGE E. J., SIMS C. E., ALLBRITTON N. L., Characterization of TAT-mediated transport of detachable kinase substrates, *Biochemistry* 43, 2004, 8528–8540.
- 107 FUNG L. K., EWEND M. G., SILLS A., SIPOS E. P., THOMPSON R., WATTS M., COLVIN O. M., BREM H., SALTZMAN W. M., Pharmacokinetics of interstitial delivery of carmustine, 4-hydroperoxycyclophosphamide and paclitaxel from a biodegradable polymer implant in the monkey brain, *Cancer Res.* 58, 1998, 672–684.
- 108 HANES J., BATYCKY R. P., LANGER R., EDWARDS D. A., A theoretical model of erosion and macromolecular drug release from biodegrading microspheres, *J. Pharm. Sci.* 86, 1997, 1464–1477.
- 109 JEAN-PIERRE B., NATHALIE F., MARIE-CLAIRE V. J., PHILIPPE M., Development of microspheres for neurological disorders: from basics to clinical applications, *J. Controlled Rel.* 65, 2000, 285–296.
- 110 COUVREUR P., DUBERNET C., PUISIEUX F., Controlled drug delivery with nanoparticles: current possibilities and future trends, *Eur. J. Pharm. Biopharm.* 41, 1995, 2–13.
- 111 PILAR C., BRUNO G., HELENE C., DIDIER D., JEAN A., JENE-PIERRE N., DOMINIQUE G., ELIAS F., JEAN A. P., PATRICK C., Long-circulating PEGylated polycyanoacrylate nanoparticles as new drug carrier for brain delivery, *Pharm. Res.* 18, 2001, 1157–1166.
- 112 JOERG D., FRANK M. P., BERNHARD S. A., ULRIKE S., Influence of nanoparticles on the brain-to-serum distribution and the metabolism of valproic acid in mice, *J. Pharm. Pharmacol.* 562, 2000, 1043–1047.
- 113 LEIGH K., ELISEVICH K., ROGERS K. A., Vascularization and microvascular permeability in solid versus cell-suspension embryonic neural grafts, *J. Neurosurg.* 81, 1994, 272–283.
- 114 LAL B., INDURTI R. R., COURAUD P. O., GOLDSTEIN G. W., LATERRA J., Endothelial cell implantation and survival within experimental gliomas, *Proc. Natl Acad. Sci. USA* 91, 1994, 9695–9699.
- 115 YUREK D. M., SLADEK J. R., Dopamine cell replacement: Parkinson's disease, *Annu. Rev. Neurosci.* 13, 1990, 415–440.
- 116 RAFFEL C., CULER K., KOHN D., NELSON M., SIEGEL S., GILLIS F., LINK C. J., VILLABLANCA J. G., ANDERSON W. F., Gene therapy for the treatment of recurrent pediatric malignant astrocytomas with *in-vivo* tumor transduction with the herpes simplex thymidine kinase gene/ganciclovir system, *Hum. Gene Ther.* 5, 1994, 863–890.
- 117 ZLOKOVIC B. V., APUZZO M. L., Cellular and molecular neurosurgery: pathways from concept to reality – part II: vector systems and delivery methodologies for gene therapy of the central nervous system, *Neurosurgery* 40, 1997, 805–812.
- 118 KREUTER J., SHAMENKOV D., PETROV

- V., RAMGE P., CYCHUTEK K., KOCH-BRANDT C., ALYAUTDIN R., Apolipoprotein-mediated transport of nanoparticle-bound drugs across the blood-brain barrier, *J. Drug Target.* **10**, **2002**, 317–325.
- 119 OYEWUMI M. O., LIU S., MOSCOW J. A., MUMPER R. J., Specific association of thiamine-coated gadolinium nanoparticles with human breast cancer cells expressing thiamine transporters, *Bioconjug. Chem.* **14**, **2003**, 404–411.
- 120 SMITH Q. R., Drug delivery to the brain and the role of carrier mediated transport, In *Frontiers in Cerebral Vascular Biology: Transport and its Regulation*, DREWES L. R., BETZ A. L. (Eds.), Plenum, New York, **1993**, pp. 83–93.
- 121 KREIBIG U., VOLLMER M., *Optical Properties of Metal Clusters*, Springer, Berlin, **1995**.
- 122 HAYNES C., VAN DUYN R., Nanosphere lithography: a versatile nanofabrication tool for studies of size-dependent nanoparticle optics, *J. Phys. Chem. B* **105**, **2001**, 5599–5611.
- 123 MIE G., Beitrag zur optik trüber medien, speziell kolloidaler metrallösungen, *Ann. Phys.* **25**, **1908**, 377–445.
- 124 KYRIACOU S. V., BROWNLOW W., XU X.-H. N., Nanoparticle optics for direct observation of functions of antimicrobial agents in single live bacterial cells, *Biochemistry* **43**, **2004**, 140–147.
- 125 XU X.-H. N., CHEN J., JEFFERS R., KYRIACOU S., Direct measurement of sizes and dynamics of single living membrane transporters using nano-optics, *Nano Lett.* **2**, **2002**, 175–182.
- 126 STEEL C., WAN Q., XU X.-H. N., Single living cell imaging of chromosomes in chloramphenicol-induced filamentous *P. aeruginosa*, *Biochemistry* **43**, **2004**, 175–182.
- 127 GREENWOOD D., Modes of action in antibiotic and chemotherapy, In *Antibiotic and Chemotherapy: Anti-infective Agents and Their Use in Therapy*, O'GRADY F., LAMBERT H. P., FINCH R. G., GREENWOOD D. (Eds.), 7th edn., Churchill Livingstone, New York, **1997**, pp. 10–21.
- 128 MASEDA H., YONEYAMA H., NAKAE T., Assignment of the substrate-selective subunits of the MexEF–OprN multi-drug efflux pump of *Pseudomonas aeruginosa*, *Antimicrob. Ag. Chemother.* **44**, **2000**, 658–664.
- 129 RYAN B. M., DOUGHERTY T. J., BEAULIEU D., CHUANG J., DOUGHERTY B. A., BARRETT J. F., Efflux in bacteria: what do we really know about it?, *Expert Opin. Invest. Drugs* **10**, **2001**, 1409–1422.
- 130 YONEYAMA H., MASEDA H., KAMIGUCHI H., NAKAE T., Function of the membrane fusion protein, MexA, of the MexA,B–OprM efflux pump in *Pseudomonas aeruginosa* without an anchoring membrane, *J. Biol. Chem.* **275**, **2000**, 4628–4634.
- 131 XU X. H., WAN Q., KYRIACOU S., BROWNLOW W., NOWAK M., Direct observation of substrate induction of resistance mechanism in *Pseudomonas aeruginosa* using single live cell imaging, *Biochem. Biophys. Res. Commun.* **305**, **2003**, 941–949.
- 132 MORGAN A. R., LEE J. S., PULLEYBLANK D. E., MURRAY N. L., EVANS D. H., Review: ethidium fluorescence assays. Part 1. Physicochemical studies, *Nucleic Acids Res.* **7**, **1979**, 547–569.
- 133 XU X. H., BROWNLOW W. J., KYRIACOU S. V., WAN Q., VIOLA J. J., Real-time probing of membrane transport in living microbial cells using single nanoparticle optics and living cell imaging, *Biochemistry* **43**, **2004**, 10400–10413.
- 134 (a) DAMGE C., MICHEL C., APRAHAMIAN M., COUVREUR P., DEVISSAGUET J. P., Nanocapsules as carriers for oral peptide delivery, *J. Controlled Rel.* **13**, **1990**, 233–239. (b) PAULETTI G. M., GANGWAR S., SIAHAAN T. J., AUBÉ J., BORCHARDT R. T., Improvement of oral peptide bioavailability: peptidomimetics and prodrug strategies, *Adv. Drug Deliv. Rev.* **27**, **1997**, 235–256.
- 135 AMMOURY N., FESSI H., DEVISSAGUET J. P., DUBRASQUET M., BENITA S.,

- Jejunal absorption, pharmacological activity, and pharmacokinetic evaluation of indomethacin-loaded poly(D,L-lactide) and poly(isobutylcyanoacrylate) nanocapsules in rats, *Pharm. Res.* 8, 1991, 101–105.
- 136 LEROUX J. C., COZENS R., ROESEL J. L., GALLI B., KUBEL F., DOELKER E., GURNY R., Pharmacokinetics of a novel HIV-1 protease inhibitor incorporated into biodegradable enteric nanoparticles following intravenous and oral administration to mice, *J. Pharm. Sci.* 84, 1996, 1387–1391.
- 137 VOLKHEIMER G., SCHULZ F. H., The phenomenon of persorption, *Digestion* 1, 1968, 213–218.
- 138 BETAGERI G. V., BLACK C. D., SZEBENI J., WAHL L. M., WEINSTEIN J. N., Fc-receptor-mediated targeting of antibody-bearing liposomes containing dideoxycytidine triphosphate to human monocyte/macrophages, *J. Pharm. Pharmacol.* 45, 1993, 48–53.
- 139 IRACHE J. M., DURRER C., PONCHEL G., DUCHENE D., Determination of particle concentration in latexes by turbidimetry, *Int. J. Pharm.* 90, 1993, R9–R12.
- 140 EZPELETA I., Potentialites de proteines vegetales comme materiau pour la fabrication de vecteurs particulaires, *These*, l'Universite de Rouen, 1996.
- 141 EZPELETA I., IRACHE J. M., STAINMESSE S., CHABENAT C., GUEGUEN J., ORECCHIONI A. M., Preparation of lectin–vicilin nanoparticle conjugates using the carbodiimide coupling technique, *Int. J. Pharm.* 142, 1996, 227–233.
- 142 EZPELETA I., IRACHE J. M., STAINMESSE S., GUEGUEN J., ORECCHIONI A. M., Preparation of small-sized particles from vicilin (vegetal protein from *Pisum sativum* L.) by coacervation, *Eur. J. Pharm. Biopharm.* 42, 1996, 36–41.
- 143 BANGA A. K., *Therapeutic Peptides and Proteins*, Technomic, Lancaster, 1995.
- 144 FLORENCE A. T., HILLERY A. M., HUSSAIN N., JANI P. U., Nanoparticles as carriers for oral peptide absorption: studies on particle uptake and fate, *J. Controlled Rel.* 36, 1995, 39–46.
- 145 DESAI M. P., LABHASETWAR V. D., AMIDON G. L., LEVY R. J., Gastrointestinal uptake of biodegradable micro-particles: effect of particle size, *Pharm. Res.* 13, 1996, 838–1845.
- 146 LOWE P. J., TEMPLE C. S., Calcitonin and insulin in isobutylcyanoacrylate nanocapsules: protection against proteases and effect on intestinal absorption in rats, *J. Pharm. Pharmacol.* 46, 1994, 547–552.
- 147 VRANCKX H., DEMOUSTIER M., DELEERS M., A new formulation with hydrophilic core: application to the oral administration of salmon calcitonin, *Eur. J. Pharm. Bionanocapsules Pharm.* 42, 1996, 345–347.
- 148 VRANCKX H., DEMOUSTIER M., DELEERS M., Pharmaceutical compositions containing nanocapsules, *US patent* 5,500,224, 1996.
- 149 BIRRENBAACH G., SPEISER P. P., Polymerized micelles and their use as adjuvants in immunology, *J. Pharm. Sci.* 65, 1976, 1763–1766.
- 150 LEONE-BAY A., MCINNIS C., WANG N., DEMORIN F., ACHAN D., LERCARA C., SARUBBI D., HAAS S., PRESS J., BARANTSEVICH E., O'BROIN B., MILSTEIN S., PATON D., Microsphere formation in a series of derivatized alpha-Amino acids: properties, molecular modeling, and oral delivery of salmon calcitonin, *J. Med. Chem.* 38, 1995, 4257–4262.
- 151 MILSTEIN S. J., BARANTSEVICH E. N., GRECHANOVSKI V. A., SARUBBI D. J., pH-dependent microspheres from modified soybean protein hydrolysate, *J. Microencapsul.* 13, 1996, 651–665.
- 152 BARGONI A., CAVALLI R., CAPUTO O., FUNDARO A., GASCO M. R., ZARA G. P., Solid lipid nanoparticles in lymph and plasma after duodenal administration to rats, *Pharm. Res.* 15, 1998, 745–750.
- 153 ZHANG Q., YIE G., LI Y., YANG Q., NAGAI T., Studies on the cyclosporin A loaded stearic acid nanoparticles, *Int. J. Pharm.* 200, 2000, 153–159.
- 154 HILLERY A. M., TOTH I., FLORENCE A. T., Biological activity of luteinizing hormone releasing hormone after oral dosing with a novel nanoparticulate



- delivery system: co-polymerised peptide particles, *Pharm. Sci.* 2, 1996, 281–283.
- 155 MARTINS J., SAINSBURY A. J., MAMO J. C., REDGRAVE T. G., Lipid and apolipoprotein B48 transport in mesenteric lymph and the effect of hyperphagia on the clearance of chylomicron-like emulsions in insulin-deficient rats. *Diabetologia* 37, 1994, 238–246.
- 156 MURAMATSU K., MAITANI Y., NAGAI T., Dipalmitoylphos phatidylcholine liposomes with soybean-derived sterols and cholesterol as a carrier for the oral administration of insulin in rats, *Biol. Pharm. Bull.* 19, 1996, 1055–1058.
- 157 (a) MICHEL C., APRAHAMIAN M., DEFONTAINE L., COUVREUR P., DAMGE C., The effect of site of administration in the gastrointestinal tract on the absorption of insulin from nano-capsules in diabetic rats. *J. Pharm. Pharmacol.* 43, 1991, 1–5. (b) HUSSAIN N., JAITLEY V., FLORENCE A. T., Recent advances in the understanding of uptake of microparticulates across the gastrointestinal lymphatics, *Adv. Drug Deliv. Rev.* 50, 2001, 107–142.
- 158 MULLER R. H., BECKER R., KRUSS B., PETERS K., Pharmaceutical nano-suspensions for medicament administration as system of increased saturation solubility and rate of solution, *US patent* 5,858,410, 1998.
- 159 KAYSER O., WATER R. W., UPTON S. J., JACOBS C., KEITHLY J. S., Anticryptosporidial activity of bupravaquone and development of a mucoadhesive drug delivery system for improving its *in vivo* efficacy. *J. Drug Target.* 2000, submitted.
- 160 MULLER R. H., JACOBS C., KAYSER O., Nanosuspensions as particulate drug formulations in therapy: rationale for development and what we can expect for the future. *Adv. Drug Deliv. Rev.* 47, 2001, 3–19.
- 161 PONCHEL G., MONTISCI M. J., DEMBERI A., DURRER C., DUCHENE D., Mucoadhesion of colloidal particulate systems in the gastrointestinal tract, *Eur. J. Pharm. Biopharm.* 44, 1997, 25–31.
- 162 CASTOR T. P., Protein Nanoparticles, *NSTI Nanotechnology Conference of Trade Show*, 2005.

## Index

### a

- acetylation, effect on chitosan transfection efficiency 79–80
- acroinfundibulum 354
- active compound penetration, skin 365
- active drug targeting 163–164
- active pharmaceutical ingredients (API) 255
  - carriers 258
- active targeting 289
- adhesive capacity, gliadin nanoparticles 133
- adhesive interactions, gliadin nanoparticles 130
- adsorption, association of ligands with nanoparticles 127
- adsorption equilibrium 130
- AFM *see* atomic force microscopy
- agarose gel electrophoresis
- (C<sub>14</sub>CO)<sub>2</sub>–plasmid complexes 35
- DNA anchor 44–45
- aggregation
  - lipoplexes 57
  - modified chitosans 80
- aggregation concentration, critical 35–36
- albumin
  - clinical indication 185
  - nanoparticle preparation 154
  - principal function 187
- albumin microspheres 151
  - hormone-containing 175
- albumin nanoparticles 185–218
  - biodistribution 196–198
  - carrier system 173
  - chemical stabilization 195
  - conventional 187–193
  - diagnostic purposes 198–200
  - distribution 199–201
  - drug encapsulation 194–196
  - emulsification 192–193
  - immunochemical detection 207
  - magnetic 204
  - ocular drug delivery 205–207
  - preparation 187, 189–193
  - protective effect 201
  - Scanning electron microscope image 188
  - surface-modified 193–196
  - three-step procedure 190
  - toxicity 206
- Albunex 173
  - immune response 176
- alkyl cyanoacrylate nanocapsules 381–382
- all-*trans* retinoic acid (RA) 124–125
- amino acid microspheres 382
- amino groups
  - interaction of chitosan amino group with DNA 75
  - N-chitosan 72
  - trymethylation (quaternization) 80
- γ-aminobutyric acid (GABA) 358
- amphiphilic drug encapsulation 126–127
- antibody, variable domain of the light chain 235
- antibody response, nanoparticle preparation 170
- anticancer agent, mercaptopurine 149
- antiepileptic drug delivery 366–367
- antimucous polyclonal antibodies 166
- antineoplastic agents 369
- antisense oligonucleotides 199–201
- API *see* active pharmaceutical ingredients
- apoE *see* apolipoprotein E
- apolipoprotein E, enrichment 291
- array structure, DNA nanotubes 10
- artificial lipid vesicles, liposomes 239
- ASGP-R *see* asialoglycoprotein receptor
- asialoglycoprotein receptor (ASGP-R) 81–82
- atomic force microscopy (AFM)
  - chitosan–DNA complexes 75
  - DNA nanotubes 7, 12–14

- atovaquone 383  
 azidothymidine (AZT) 157  
 AZT *see* azidothymidine
- b**
- B16-F10 cells  
 – fluorescence microscopic images 333  
 – viability 334  
 BALB/c mice 96  
 ball milling 265  
 BBB, crossing 357  
 BBD *see* *Bordetella bronchiseptica* dermonecrotin  
 benzalkonium chloride (BZC), amphiphilic model 126–127  
 betamethasone disodium phosphate (BTM), included in chitosan microspheres 89  
 bifunctional crosslinkers 168  
 – structure 169  
 bilayer undulations, lamellar lipoplexes 55–56  
 bioadhesion 129  
 bioadhesive properties, gliadin nanoparticles 129–135  
 bioavailability, drug particle size dependence 256  
 biocompatibility, chitosan 71  
 biocompatible nanoparticulate systems for tumor diagnosis 304–348  
 biodegradable, plant protein-based nanoparticles 117  
 biodegradable nanoparticles 312–314  
 biodegradable polymer, delivery to BBB 373–374  
 biodegradation, chitosan 71  
 biodistribution  
 – albumin nanoparticles 196  
 – in vivo 26–27  
 biofunctionalized solid lipid nanoparticles, production 287–303  
 biological membranes  
 – asymmetry 353  
 – crossing by nanoparticles 349–393  
 – drugs crossing problems 354–362  
 – functions 351–352  
 – kinetics 352–354  
 – lipid bilayer structure 260  
 – thermodynamics 352–354  
 – *see also* cell membrane  
 biomembranes *see* biological membranes  
 bionanomachines 19  
 1,6-bis-maleinimido-hexane (BMH) 168  
 blood circulation time, ICG 325  
 blood opsonization process, reduction 287  
 blood–brain barrier  
 – crossing of albumin nanoparticles 197  
 – diffusion of nanoparticles 305  
 bloodstream, surviving of chitosan–DNA nanoparticles 80  
 BMH *see* 1,6-bis-maleinimido-hexane  
 body distribution  
 – drug carrier systems 163  
 – peroral administration 175  
*Bordetella bronchiseptica* dermonecrotin (BBD) 87  
 bovine serum albumin *see* BSA  
 breast cancer 370  
 bromocriptine mesylate, drug-loaded gelatin microspheres 152  
 BSA (bovine serum albumin) 187  
 – incorporated in hydrophobic PLGA microspheres 148  
 – nanoencapsulation 153  
 – release from chitosan nanoparticles 95  
 BTM *see* betamethasone disodium phosphate  
 buckyballs 307–309  
 buckytubes 307–309  
 building blocks, nanoscale particulate systems 305–312  
 burst effect, in chitosan microsphere DNA release 95  
 2,3-butadione, albumin nanoparticles chemical stabilization 189  
 BZC *see* benzalkonium chloride
- c**
- C<sub>10</sub>CysG+ 29–30  
 – structure 31, 34  
 C<sub>14</sub>CO, structure 34  
 C<sub>14</sub>CSper, structure 34  
 (C<sub>14</sub>CO)<sub>2</sub>–plasmid complexes, mobility 35  
 cancer treatment, albumin nanoparticles 201–204  
 capillary endothelial cells, lipoplex uptake 60  
 carbazole, hydrophobic fluorescent molecule 130–132, 134  
 carbodiimide (CDI)  
 – crosslinked with gliadin nanoparticles 133  
 – preparation of ligand–gliadin nanoparticle conjugates 128  
 carbohydrate-binding, S-layer 223–224  
 carbon nanotubes 308  
 carcinogenic radicals 288  
 carriers  
 – albumin nanoparticles 199  
 – DNA 69–79  
 cationic lipid-mediated nucleic acid delivery *see* lipofection

- cationic lipids 51–53
- cationic liposomes, interactions with DNA 56
- cationic surfactants, structure 34
- caveolae-mediated endocytosis 58
- CDI *see* carbodiimide
- cell internalization elements, DNA nanoparticles 43–46
- cell-mediated response, legumin nanoparticles 137
- cell membrane 350–354
  - fusion with lipoplexes 57
  - *see also* biological membranes
- cell membrane crossing, DNA-nanoparticles 77
- cell recognition, DNA nanoparticles 43–47
- cell surface receptors, mediation of gene carrier targeting 81–83
- cellular trafficking studies 38
- CFTR *see* cystic fibrosis transport regulator
- cGMP *see* pharmaceutical current good manufacturing practice
- charge density, effect on chitosan transfection efficiency 79–80
- chemical crosslinking, chitosan nanoparticle preparation 86
- chimeric proteins 43
- chitin 68
  - structure 69
- chitosan 258
  - *N*-dodecylated chitosan (CS-12) 83–84
  - biocompatibility 71
  - carrier for gene therapy 69–79
  - chemistry 69–71
  - deoxycholic acid-modified chitosan (DAMC) 84
  - DNA–chitosan nanoparticles 68–99
  - galactosylated chitosan (GC) 81–82
  - GCPVP 81
  - genipin-crosslinked microspheres 88
  - heparin–chitosan complex 90
  - hydrophobic modification 83–84
  - $pK_a$  70
  - proposed applications 74
  - schematic gene therapy mechanism 79
  - structure 69
  - *see also* modified chitosan, unmodified chitosan
- chitosan nanoparticles
  - chemical crosslinking 86
  - complex coacervation 84–86
  - DNA loading 91–93
  - DNA release and release kinetics 93–95
  - emulsion crosslinking 87–88
  - emulsion droplet coalescence 90
  - ionic crosslinking/gelation 86–87
  - preparation methods 84–91
  - release of bovine serum albumin 95
  - reverse micellar method 89
  - sieving method 91
  - spray drying 88–89
- chitosan–DNA complex
  - atomic force microscopy (AFM) 75
  - incorporation by inhaled powder 98
  - potential clinical applications 97–98
  - preclinical evidence of efficacy 95–97
  - therapy of respiratory syncytial virus infection 97
- chitosan–DNA interactions 71
- cholester, structure 53
- circular dichroism (CD) measurements, S-layers 221
- circumventricular organs (CVO) 358
- clathrin-mediated endocytosis 58
- clinical studies, protein-based particles 172
- clinical uses, ICG 320–321
- coacervation, albumin nanoparticles 187, 189–192
  - nanoparticle preparation 120, 154–159
- coacervation techniques
  - complex 154–155
  - simple 155–159
- cochleate cylinders 265
- cochleates, lipid 263
- colloidal carriers 117
- colloidal drug carriers 287
- comminution
  - pharmaceutical nanoparticle processing 265–266
  - wet 266–267
- compaction, of DNA by highly charged chitosan 76
- complex coacervation, chitosan nanoparticle preparation 84–86
- condensation, DNA polymer 27–28
- condensed lamellar phase, lipoplexes 52–54
- conductivity, self-assembled 1-D nanotubes 18
- confocal microscopy, nanoparticle internalization 46
- connexin proteins, gap junctions 351
- connexon hexamers, gap junctions 351
- contrast enhancement, gas-filled microspheres 173
- convergent growth method, dendrimer synthesis 306
- copolymer grafted HSA 165
- core dendrimer 307
- core/shell nanoparticles 278

- cosmetic compounds, controlled release 365–366
- covalent linkage, association of ligands with nanoparticles 127
- coxsackievirus B3 (CVB3) 97–98
- CP *see* critical point
- Cremonophor 202
- Cremonophor EL 173, 368
- Crick, F. H. C. 23
- critical aggregation concentration 35–36
- critical point (CP) 270
- Crohn's disease 361
- crosslinkage, protein nanoparticles 122
- crosslinking, HSA (Human serum albumin) 150
- crosslinking agent, tripolyphosphate 258
- crustaceans 69
- crystalline bacterial cell surface layer *see* S-layer
- crystalline phases, liquid 260–261
- CS-12 (*N*-dodecylated chitosan) 83–84
- CTAB 36
- structure 34
- cubosomes 262–263
- curvature elastic energy, lipids 259–260
- CVB3 *see* coxsackievirus B3
- CVO *see* circumventricular organs
- Cybesin 325
- cyclosporin 382
- cystic fibrosis transport regulator (CFTR) 171
- Cytate 325
- cytokine, secretion in presence of nanoparticles 73
- cytotoxicity
- chitosan–DNA nanoparticles 99
- decrease 156
- galactosylated chitosan (GC) 82
- ICG 323–324
- photosensitizer molecule 319
- d**
- DAE, DNA structure 4–10
- Dalargin 372
- DAMC *see* deoxycholic acid-modified chitosan
- DAO, DNA structure 4, 9–10
- daunorubicin, hydrophilic drug 150
- DBA *see Dolichus biflorus* lectin
- DBA-gliadin nanoparticle conjugates 131
- DC-Chol, structure 53
- DDC *see* dideoxycytidine
- deacetylation, in chitosan production 69
- DEET (*N,N*-diethyl-4methyl benzamide) 365
- dendrimers 305–307, 362
- synthesis 306
- deoxycholic acid-modified chitosan (DAMC) 84
- derivatives
- *N*-chitosan *see* *N*-chitosan derivatives
- *O*-chitosan *see* *O*-chitosan derivatives
- PEG *see* PEG derivatives
- derivatized amino acid microspheres 382
- Dervan, Peter 39
- desolvation 155–159
- albumin nanoparticles 189–192
- gliadin nanoparticles 122
- protein nanoparticles 121
- detergent, C<sub>10</sub>CysG+ 29–31, 36
- C<sub>14</sub>CO 33, 36, 45
- cationic 27–29, 33
- lipid-based 44
- dextranox-MPEG *see* methyl polyethylene glycol (PEG)-modified oxidized dextran
- diagnostics
- albumin nanoparticles 198–200
- protein-based nanoparticles 169–175
- dideoxycytidine (ddC) 157
- diethylenetriaminepentaacetic acid (DTPA) 206
- differential adsorption 289–292
- differential scanning calorimetry 371
- direct microinjection
- lipoplexes 59
- ODN lipoplexes 62
- distamycin 38
- anchorage in minor groove 44
- disuccinimidyl tartrate (DST) 168
- disulfide bond, peptide conjugation 373–374
- DMRIE, structure 53
- DNA
- carriers 199
- chemical structure 24
- interactions with chitosan 71
- interactions with cationic liposomes 56
- interactions with fusion proteins 42–43
- DNA anchor 1, structure 44
- DNA based nanomaterials 1–99
- DNA binding intercalator 39
- DNA compaction, by highly charged chitosan 76
- DNA functionalization 37–43
- strategies 37–38
- DNA lipoplexes 51–60
- DNA loading, in chitosan micro- and nanoparticles 91–93
- DNA nanoparticles 43–47
- transfection efficiency 46
- DNA nanotubes, persistence length and stiffness 8

- DNA plasmid, size in comparison to virus and cell 27
- DNA polymer, condensation 27–28
- DNA recognition
  - by molecules 38
  - major groove 40
  - minor groove 43
- DNA release, burst effect 95
- DNA–chitosan nanoparticles 93–95
  - gene therapy 68–99
- DNA–transferrin conjugate complexes 39
- N*-dodecylated chitosan (CS-12) 83–84
- Dolichus biflorus* lectin (DBA) 128
- DOPC, structure 53
- DOPE 28, 47
  - structure 53
- DOSPA, structure 53
- DOTAP, structure 53
- DOTAP/DOPC/DNA lipoplex 56
- DOTAP/ODN lipoplex, Cryo-TEM 61
- DOTAP–DNA lipoplexes 80
- Doxil 258
- doxorubicin 368–369
  - drug carrier system 153
- droplet size, electrical field 275–277
- drug binding, in drug carrier systems 146
- drug candidates, investigations. 255
- drug carrier systems, drug binding in 146
- drug carriers
  - colloidal 287
  - doxorubicin 153
  - protein-based nanoparticles 169–175
- drug delivery 205–207
  - anticancer 367–370
  - antiepileptic 366–367
  - nanoparticulate 367
  - peptide 360
  - solid lipid nanoparticles 287–303
  - topical 205
- drug delivery systems, lipid-based 258
- drug encapsulation
  - albumin nanoparticles 194–196
  - characteristics in gliadin nanoparticles 127
  - in plant protein nanoparticles 124–127
- drug nanoparticles
  - preparation 255–286
  - structures 257
- drug particles, mean size 267
- drug targeting
  - active 163–164
  - nanoparticles 161–169
  - passive 163
- drug-targeting ligands, surface modification 166
- drugloading efficiency, albumin nanoparticles 194
- drugs crossing biological membranes, problems 354–362
- DSC 371
- DST *see* disuccinimidyl tartrate
- DTPA *see* diethylenetriaminepentaacetic acid
- DUV, deep ultraviolet light 241
- DX tile nanotubes 4–10
- dye, encapsulated 315
- dysopsonins 290, 296
- e**
- ECF 358
- echo-contrast agents, albumin nanoparticles 199
- EDC *see* 1-ethyl-3-(3-dimethylaminopropyl) carbodiimide
- EGF *see* epidermal growth factor
- EGFP *see* enhanced green fluorescent protein
- electrical field, droplet size 275
- electroless chemical deposition 18
- electron micrography, heterotetramers 232
- electronic nanodevices 18
- electroporation, low-voltage 355–357
- electrospraying 277
  - coaxial 279
  - stages 276, 278
- electrostatic approaches, nanoformulation 275
- electrostatic spinning 371
- emission spectrum
  - rEGFP 240
  - rSbpA<sub>31a1068</sub>/EGFP 240
- emulsification, albumin nanoparticles 187, 192–193
- emulsification-diffusion, SLN production 294
- emulsion crosslinking, chitosan nanoparticle preparation 87–88
- emulsion droplet coalescence, chitosan nanoparticle preparation 90
- emulsion technique 151–154
  - flowchart 149
  - nanoparticle preparation 148–154
- emulsions
  - drug carriers 258
  - oil-in-water-type 261
- encapsulation efficiency, chitosan nanoparticle preparation 92–93
- endocytosis
  - lipofection 57–58
  - ODN lipoplexes 62
  - receptor-mediated 38, 372

- endosomal escape, gene carriers 78  
 endosomal membrane 59  
 energy of bending, lipids 259  
 enhanced green fluorescent protein (EGFP) 239–240  
 ependymal cells, cerebral ventricles 357  
 epidermal growth factor (EGF) 369  
 equilibrium structure, lipoplexes 52–55  
*Escherichia coli* 77  
 EtBr *see* ethidium bromide  
 ethidium bromide (EtBr) 377  
 1-ethyl-3-(3-dimethylaminopropyl) carbodiimide (EDC) 155  
 extracellular barriers, lipofection 59  
 extracellular fluid 358  
 extracellular trafficking 79
- f**
- FAM-labeled strands, DNA nanotubes 7–8  
 fibrous proteins, characteristics 118  
 fluorescein labeled strands, DNA nanotubes 7–8  
 fluorescence  
 – FAM 7–8  
 – YOYO 36, 46  
 fluorescence excitation  
 – rEGFP 240  
 – rSbpA<sub>31a1068</sub>/EGFP 240  
 fluorescence imaging, NIR 317–318  
 fluorescence microscopy, DNA nanotubes 7–8  
 fluorescent molecules, carbazole 130–132  
 fluorescently labeled albumin nanoparticles 197  
 5-Fluorouracil 369  
 Fluorouracil delivery 201–202  
 folate receptor (FR) 83, 97  
 folate–peg-coated nanoparticles, biomedical applications 46  
 folic acid receptor 83  
 formaldehyde, albumin nanoparticles chemical stabilization 189  
 FR *see* folate receptor  
 freeze drying, nanoparticles 269  
 5-FU *see* 5-Fluorouracil  
 5-FU-loaded albumin 201  
 fullerenes 362  
 functional domains, Binding of Molecules and Nanoparticles 242–243  
 functionalization, DNA 37–43  
 fusion, lipoplexes with cell membrane 57  
 fusion proteins, interactions with DNA 42–43  
 fusogenic peptides 47
- g**
- G *see* generation  
 $\gamma$ -aminobutyric acid (GABA) 358  
 GABA *see*  $\gamma$ -aminobutyric acid  
 $\beta$ -galactosidase assay 77  
 galactosylated chitosan (GC) 81–82  
 $\beta$ -Gal gene, vivo release 96  
 ganciclovir (GCV) 156, 195  
 – cancer treatment 203  
 gap junctions 351  
 gastrointestinal mucosal segments  
 – *ex vivo* studies of drug carriers 130–131  
 – *in vivo* studies of drug carriers 132–135  
 gastrointestinal transit profile, gliadin nanoparticles 132  
 GC *see* galactosylated chitosan  
 GCPVP 81  
 GCV *see* ganciclovir  
 gel electrophoresis, agarose 35, 44–45  
 gel-shift assay, SDS 230  
 gelatin A, amino acid composition 152  
 gelatin-based microspheres  
 – drug-loaded 152  
 – emulsion technique 151–153  
 gelatin–DNA nanospheres 171  
 gene carrier targeting, mediation by cell surface receptors 81–83  
 gene carriers, endosomal escape 78  
 gene delivery 369–370  
 – BBB 374–375  
 gene delivery system, inhaled powder 98  
 gene expression 26  
 – blocked by ODN 60  
 gene therapy  
 – DNA–chitosan nanoparticles 68–99  
 – potential clinical applications of chitosan–DNA complex 97–98  
 – protein-based nanoparticles 170–172  
 – use of surfactants 36  
 – viral vectors 51  
*in vivo* gene transfer 88  
 gene-vector complexation 79  
 generation (G), dendrimers 306  
 genipin-crosslinked chitosan microspheres 88  
 GFP *see* green fluorescent protein  
 GI Barrier 360–362  
 Gibbs equation, including nanoparticles 256  
 Gibbs free energy, drug particles 256  
 GlcNAc, N-acetyl glucosamine 227  
 gliadin, wheat proteins 120  
 gliadin nanoparticles  
 – *ex vivo* studies of bioadhesive properties 130–131

- gliadin nanoparticles (*cont.*)
    - *in vivo* studies of bioadhesive properties 132–135
    - adhesive interactions 130
    - bioadhesive properties 129–135
    - gastrointestinal transit profile 132
    - ligand–gliadin nanoparticle conjugates 127–129
    - particle size optimization 135–136
    - preparation 122–124
    - RA encapsulation 124–125
    - scanning electron micrograph 123
    - VE encapsulation 125–126
  - globular assembly, plasmid 30
  - globular proteins, characteristics 118
  - globulins
    - characteristics 118
    - pea seed proteins 119
  - glutaraldehyde, albumin nanoparticles
    - chemical stabilization 189
  - glutaraldehyde, crosslinking 155
  - glutelins, characteristics 118
  - gluten, wheat proteins 120
  - glutenin, wheat proteins 120
  - glycolic acid, nanoparticle preparation 313
  - glycoprotein, S-layer 219
  - gold chips 233
  - GRAS, safe substances 364
  - green fluorescent protein 42
  - guanidine hydrochloride 220
- h**
- H<sub>II</sub>C-phase, lipoplexes 52–54
  - HCMV *see* Human CMV
  - head groups, lipids 259
  - heat-induced plasmid denaturation 42
  - heavy water, cytotoxicity of ICG 324
  - HEK 293 cells 78–83, 96, 170–172
  - HeLa cells 78–83, 96, 171, 240
  - Hélène, Claude 39
  - helper lipids 52–53
  - hemispherical endcaps nanotubes 308
  - heparin, nanoparticle preparation 154
  - heparin–chitosan complex, emulsion droplet coalescence 90
  - HepG2 cells 82, 88
  - herpes virus thymidine kinase (HSV-tk), cancer treatment 203
  - heterotetramers
    - functional 229
    - fusion protein 230
    - rSbpA 232, 234
    - SbsB 231
  - hexosomes 262–263
  - high-molecular-weight (HMW) chitosan 76, 92, 95
  - high-pressure homogenization (HPH), SLN production 292–294
  - Hildebrand theory, solubility parameter of gliadin 123
  - HIV-infection, potential therapy 157
  - HMW chitosan *see* high-molecular-weight chitosan
  - Hoechst 33258 38
    - anchorage in minor groove 44
  - homotetramers, streptavidin 229
  - “honeycomb” phase, lipoplexes 52–54
  - Hoogsteen base pairs 40
  - HPH *see* high-pressure homogenization
  - HSA 187
    - acid solution 155
    - copolymer grafted 165
    - ICG binding 321
    - microsphere and nanoparticle material 148
    - quantitative amino acid composition 150
  - HSA nanoparticles, morphology 161–162
  - HSA system, ammonium sulfate coacervated 156
  - HSA–PAA–PEG 194
  - HSA–PTAAC–PEG 194
  - HSV-tk *see* herpes virus thymidine kinase
  - human CMV, pathology 206
  - human rIL-2, included in chitosan microspheres 94
  - human serum albumin *see* HSA
  - humoral responses, legumin nanoparticles 136
  - hydrated lipids, liquid crystalline phases 260–261
  - hydrocarbon chains, lipids 259
  - hydrocortisone 195
    - included in chitosan microspheres 89
  - hydrophilic compounds, surface modification 164–165
  - hydrophilic drug encapsulation 126–127
  - hydrophilic pathway, skin barrier 363
  - hydrophobic, carbazole 130–132
  - hydrophobic modification, chitosan 83–84
  - hydrophobic PLGA microspheres 148
  - hydroxypropylcellulose, thickening agent 192
- i**
- ICG 304, 320
    - binding properties 321–322
    - biodistribution 335
    - blood circulation time 325
    - chemical stability in aqueous solution 330–331



- degradation 332
  - encapsulated in nanoparticles 316
  - excretion 322
  - metabolism 322
  - nanoparticle pharmacokinetics 331–336
  - nanoparticulate delivery system 327–336
  - pharmacokinetics 322
  - physicochemical properties 321
  - release profile 330
  - solution pharmacokinetics 331–336
  - stabilization *in vitro* 326
  - structure 321
  - subcellular localization 334
  - tumor imaging 322–323
  - uptake 333
  - uptake by tumors 325
  - ICG-loaded nanoparticles, photodynamic activity 335
  - ICG-loaded PLGA nanoparticles
    - manufacturing 314
    - surface views 329
  - IgC antibodies, *Camelidae* 235
  - IL-2, expression plasmid 86, 93–95
    - included in chitosan microspheres 94
  - immunization in animals, legumin nanoparticles 136–137
  - immunological reactions, protein-based microspheres 175–177
  - immunotherapy, type I allergy 239
  - in situ* synthesis, nanoparticles 244–244
  - in vivo* biodistribution 26–27
  - indocyanine green 304
    - *see also* ICG
  - inhaled powder, gene delivery system 98
  - intercalating dye, YOYO 36, 46
  - intercalation 38–39
  - intercalator, DNA binding 39
  - interfaces, lipids 260–261
  - interfacial energy, nanoparticles 257
  - interfacial tension 275
  - interferon- $\gamma$  195
  - interlayer DNA correlations, lamellar lipoplexes 55–56
  - interleukin *see also* cytokine, IL2, 239, 373
    - secretion in presence of nanoparticles 73
  - internalization
    - chitosan–DNA complexes 83–84
    - DNA nanoparticles 43–47
  - intestinal disease 361–362
  - intestinal translocation 361–362
  - intracellular trafficking 79
  - intracytoplasmic trafficking 26–27
  - intravitreal drug delivery 205–207
  - inverse hexagonal phase, lipoplexes 52–54
  - ion channel proteins 350
  - ionic crosslinking, chitosan nanoparticle preparation 86–87
  - ionic gelation, chitosan nanoparticle preparation 86–87
  - iontophoresis 356
  - Irwin's equation 267
- k**
- Katchalsky's equation 70
  - ketoprofen 87
  - kinetic approaches, nanoparticle preparation 257
  - KNOB protein 83, 96
- l**
- L-DOPA 359
  - (L<sub>α</sub>C)-phase, lipoplexes 52–54
  - lamellar lipoplexes, formation 55
  - Langmuir adsorption, oligonucleotides 234
  - lateral stress profile, lipid monolayer 259
  - lectin-conjugated nanoparticles, oral delivery 379–380
  - legumin, pea seed proteins 119
  - legumin nanoparticles
    - cell-mediated response 137
    - humoral responses 136
    - immunization in animals 136–137
    - preparation 121–122
  - leguminoses, source of plant proteins 119
  - ligand–gliadin nanoparticle conjugates, preparation 127–129
  - light chain antibody, variable domain 235
  - linalool–linalyl acetate (LLA) 124
    - hydrophilic model 126–127
  - lipid-based pharmaceutical nanoparticles 258–259
  - lipid emulsion, oil-in-water-type 261
  - lipid nanoparticles, site-specific drug delivery 287–303
  - lipid tubules 264
  - lipids
    - cationic 51–52
    - definition 259–260
    - hydrated 260–261
  - lipofection 51
    - direct microinjection 59
    - efficiency 57–60
    - endocytosis 57–58
    - extracellular barriers 59
    - most likely mechanism 58
    - tumor tissue 60
    - *in vitro* lipofection 57–59
    - *in vivo* lipofection 59–60

- lipophilic drug encapsulation 126–127
  - lipoplexes 51–62
    - composition 51–52
    - DOTAP–DNA 80
    - equilibrium structure 52–55
    - formation 54–55
    - fusion with cell membrane 57
    - nonequilibrium structure 55–57
    - polymorphous 56
    - size 57
  - liposomes 52, 239, 261–262, 310–312
    - conventional 262
    - drug carriers 258
    - stealth 262
  - liquid crystalline phases 260–261
    - lamellar 260
  - liquid nanodispersions, drying 267–270
  - liquid solution droplet, supercritical fluids 273
  - liver cancer, magnetic treatment 204
  - living cell imaging 376–378
  - LLA *see* linalool–linalyl acetate
  - LMW chitosan *see* low-molecular weight chitosan
  - localized SPRs, living cell imaging 376
  - low-density lipoproteins receptors 372
  - low-molecular weight (LMW) chitosan 77, 82, 92
  - low-voltage electroporation, skin 355–357
  - luciferase 170
  - lymphatic oral nanoparticulate delivery 382–384
- m**
- m-maleimidobenzoyl-N-hydroxysulfosuccinimide ester 168
  - magnetic albumin nanoparticles 204
  - major groove, DNA recognition 40
  - ManNAc, N-acetyl mannosamine 227
  - MDR *see* multi drug resistance
  - MDS *see* microsphere-based detoxification system
  - mechanical approaches 264–270
  - mechanical irritation, skin 355
  - membranes *see* biological membranes
  - mercaptopurine, anticancer agent 149
  - messenger RNA 60
  - metabolizable plant protein-based nanoparticles 117
  - metallization
    - 4 × 4 nanoribbons 18
    - TX tile nanotubes 11
  - metastable morphology, lipoplexes 55
  - metastatic breast cancer, albumin nanoparticles 202
  - Methanothermobacter ferredoxigenes*
  - Methotrexate delivery 201–202
  - methyl polyethylene glycol (PEG)-modified oxidized Dextran 165
    - albumin nanoparticles chemical stabilization 189
  - MexAB–OprM 377
  - MG63 cells 96
  - mica, interaction with nanotubes 7–8
  - micelle–DNA complexes, stabilized 37
  - microbeads 238
  - microcylinder, lipid 263
  - microemulsion technique, SLN production 293
  - microscopic techniques, nanoparticle size 160
  - microspheres
    - casein-based 153–154
    - gelatin-based 151–153
    - stability 153
    - uniform 151
  - microsphere-based detoxification system 237–238
  - microstructure, lipoplexes 52–55
  - microtubules, lipid 263
  - milling 265
  - minor groove
    - agents binding to 43
    - anchorage 44
  - MLV *see* multilamellar vesicles
  - MMP-9, secretion in presence of nanoparticles 73
  - modified chitosan 71
    - targeting mediated by cell surface receptors 81–83
    - transfection efficiency 79–74
  - monomolecular DNA condensation 45
  - mononuclear phagocytic system (MPS) 81
  - MPS *see* mononuclear phagocytic system
  - mucoadhesion, nanoparticles 384–385
  - multi drug resistance (MDR) proteins 360
    - reversion 367
  - multicomponent delivery vectors 47
  - multilamellar vesicles (MLV) 261
  - multiple sclerosis, pathogenesis 197
  - multiwall cylinder nanotubes (MWNT) 308
  - MWNT *see* multiwall cylinder nanotubes
- n**
- N-chitosan derivatives
    - proposed applications 74
    - structure 72
  - nanodispersions, drying 267–270
  - nanoelectronic devices 18

- nanofibers 370–371
  - nanoformulation, drug candidates 255
  - nanomaterials
    - DNA based 1–99
    - plant protein-based 117–137
    - protein-/peptide-based 115–245
  - nanoparticle crosslinkage, physico-chemical 122
  - nanoparticle optics 376–378
  - nanoparticle preparation 313–314
    - coacervation 154–159
    - mechanical energy input 264–265
    - methods 148–159
    - simple coacervation (desolvation) techniques 155–159
    - starting materials 146
    - thermodynamic approaches 257–264
  - nanoparticles
    - biodegradable 312–314
    - casein-based 153–154
    - coacervation techniques 154–155
    - crossing biological membranes 349–393
    - desolvation yield 191
    - DNA–chitosan 68–99
    - drug targeting 161–169
    - drying 268
    - gelatin-based 151–153
    - nucleic acid 23–50
    - peptide 159–161
    - peptide-based 145–176
    - pharmaceutical 258–259
    - protein-based 164
  - nanoparticulate drug delivery 362
    - anticancer 367–370
    - BBB 371–378
    - mechanisms 375
    - PLGA-based 327–336
    - skin 366
    - subcutaneous 366–367
  - nanoparticulate systems, tumor diagnosis 304
  - nanoporous barrier, semipermeable 363
  - 4 × 4 nanoribbons 18–19
    - metallization 18
  - nanoscale particulate systems, components 305–312
  - nanosensors 370
  - nanoshells 362
  - nanostructure, lipoplexes 52–55
  - nanosuspension delivery, oral 383–384
  - nanotubes (NT) 308, 362
    - self-assembled 3–22
  - nanowires 18
  - naphthalocyanine dyes, fluorescence imaging 318
  - natural self-assembly system, nanoscale
    - patterning of S-layer proteins 219–252
  - NHS-PEG3400-Ma, PEG-based crosslinker 167
  - NIR dyes 318
  - NIR fluorescence imaging 317–318
  - NLS peptide 27
    - fusion with TetR protein 43
  - NLS peptide conjugation, triple helix formation 41
  - nonbiodegradable polymer 370–371
  - nonequilibrium structure, lipoplexes 55–57
  - NPC *see* nuclear pore complexes
  - NT *see* nanotubes
  - nuclear localization signal peptide *see* NLS peptide
  - nuclear pore complexes (NPC) 26
  - nucleic acid drugs, oral route 361
  - nucleic acid nanoparticles 23–50
    - synthesis 27–31
  - nucleus, gene expression 26
- o**
- O-chitosan derivatives
    - proposed applications 74
    - structure 73
  - ocular drug delivery, albumin nanoparticles 205–207
  - ODN
    - antisense 60–61
    - monolayers 61
    - triple helix formation 39–41
  - ODN lipoplexes 60–62
  - ODN–lipid lamellar phase 61
  - oligodeoxyribonucleotides *see* ODN
  - oligomeric chitosans 75
  - oligonucleotides
    - carriers 199
    - PNAs 41
  - optical imaging 317–326
    - fluorescence-based 317
  - optical nanoparticles, biodegradable 314–316
  - oral delivery, lectin-conjugated nanoparticles 379–380
  - oral nanoparticulate delivery 378–385
  - oral nanosuspension delivery 383
  - oral route, nucleic acid drugs 361
  - oral vaccination, protein microspheres 175
  - oxidation, C<sub>10</sub>CysG<sup>+</sup> 31
- p**
- pK<sub>a</sub>, chitosan 70
  - PACA *see* poly(alkyl cyanoacrylate)

- paclitaxel 368
- albumin nanoparticles 202–203
- carrier system 173
- PAMAM *see* poly(amidoamine) dendrimers
- parenteral application route 172–174
- parenteral lipid emulsion 258
- particle size
  - reduction 266
  - surface energy 256
  - wet comminution 266
- particle size distribution, gliadin nanoparticles 123
- particle size optimization, gliadin nanoparticles 135–136
- particle systems
  - active drug targeting 163–164
  - passive drug targeting 163
- particulate systems, nanoscale 305–312
- PASP *see* sodium polyaspartate
- passive drug targeting 163
- passive targeting 289
- patch–clamp recording technique, cell transport 351
- patterning, S-layer proteins 219–252
- PBCA 290–291
- PBCA nanoparticles, brain specificity 297
- PC *see* phosphatidylcholine
- PCF *see* polycationic ferritin
- PCS *see* photon correlation spectroscopy
- pDNA:PLL complexes, included in chitosan microspheres 93
- PDT 317–326
  - ICG 323
  - photosensitizers 320
- PE *see* phosphatidylethanolamine
- pea seed proteins 119
- PEG 28, 82–83, 262
  - lipoplex coating 60
  - nanoparticle surface modification 287
  - protective coat 44–46, 60
- PEG derivatives, surface modification 165–166
- PEG–HSA conjugates 165
- PEG–lipid conjugates, polymeric micelles 310
- pegylation, albumin nanoparticles 193
- PEI *see* polyethylenimine
- PEO *see* polyethylene oxide
- peptide-based nanomaterials 115–245
- peptide conjugation 373–374
- peptide delivery, BBB 372–373
- peptide drug delivery 360
- peptide nanoparticles
  - oral delivery 380–381
  - polymer-based 381
- peptide nanoparticles 145–176
  - characterization techniques 159–161
- peptide nucleic acids *see* PNAs
- peptides
  - fusogenic 47
  - nanoparticles 145–176
  - NLS 27, 43
- peroral administration, body distribution 175
- peroral application, protein-based particles 175
- persistence length, DNA nanotubes 8
- Peyer's patch, electron photomicrograph 383
- PGA *see* polyglycolic acid
- pharmaceutical applications, albumin nanoparticles 198–207
- pharmaceutical current good manufacturing practice (cGMP) 270
- pharmaceutical nanoparticles
  - comminution 265
  - lipid-based 258–259, 263
  - monodisperse 277
- pharmacokinetics
  - gliadin nanoparticles 132
  - ICG 322, 331–336
- phase behavior, lipids 259–261
- phase separation phenomena, nanoparticle preparation 258
- phosphatidylcholine (PC) 352
- phosphatidylethanolamine (PE) 352
- phosphatidylglycerol, liposomes 310
- phosphatidylserine (PS) 352
  - liposomes 310
- photoactive agent, ICG 320
- photodegradation, ICG 326
- photon correlation spectroscopy (PCS), particle size 159
- photoradiation therapy (PDT) 318
- photosensitizer molecules 314
- photosensitizers, PDT 320
- phthalocyanine dyes, fluorescence imaging 318
- physicochemical characteristics, gliadin nanoparticles 133
- PIBCA *see* poly(isobutyl cyanoacrylate)
- PicoGreen assay 92
- pilocarpine, ophthalmic administration 174
- pilocarpine-coated albumin nanoparticles, topical drug delivery 205
- pilocarpine nitrate 195
- pinocytosis 77, 95–96, 358
- plant protein-based nanoparticles 117–137
  - drug encapsulation 124–127
- plant proteins, characteristics 118–120

- plasma protein composition 298  
 plasmid DNA, incorporation 155  
 plasmids  
 – globular assembly 30  
 – heat-induced denaturation 42  
 – size in comparison to virus and cell 27  
 plasmid–transferrin–PNA complex 42  
 PLGA, structure 147  
 PLGA microspheres, hydrophobic 148  
 PLGA nanoparticles, uptake 328  
 PNAs 41–42  
 – plasmid–transferrin–PNA complex 42  
 – size in comparison to natural DNA 42  
 poloxamer 338 296  
 poly(alkyl cyanoacrylates) 366  
 – structure 147  
 poly(alkyl methacrylates), structure 147  
 poly(amidoamine) dendrimers 307  
 poly(D,L lactic-co-glycolic acid) 354  
 poly(D,L-lactide-co-glycolide) 312  
 poly(isobutyl cyanoacrylate) 366  
 poly(N-isopropylacrylamide), polymeric micelles 310  
 poly(propylene imine) dendrimers 307  
 poly(thioetheramido acid)–PEG copolymer-grafted HSA 194  
 poly(vinyl pyrrolidone) 81  
 polyacrylamide nanospheres 381  
 polycationic ferritin (PCF) 242–243  
 polyclonal antibodies 166  
 polyethylene glycol *see* PEG  
 polyethylene oxide (PEO) 297  
 polyethylenimine (PEI) 196  
 polyglycolic acid (PGA), structure 147  
 polylactic acid, nanoparticle preparation 313  
 polylactic-co-glycolic acid *see* PLGA  
 polymer-based nanoparticulate delivery, skin 366  
 polymer erosion, DNA release 93–94  
 polymer nanoparticles, albumin coating 196  
 polymeric micelles 310  
 polymeric stabilizers 267  
 polymers  
 – nonbiodegradable 370–371  
 – stabilization ability 257  
 polymorphous lipoplex 56  
 polysaccharide 68  
 polysorbate 60 296  
 polysorbate 80 372  
 polysorbate-coated poly(butyl cyanoacrylate) *see* PBCA  
 PPI *see* poly(propylene imine) dendrimers  
 precipitation technique, chitosan nanoparticle preparation 94  
 preclinical studies, protein-based particles 172  
 processability, drug particle size dependence 256  
 progesterone, drug delivery system 175  
 prolamins, characteristics 118  
 protective coat, DNA nanoparticles 43–46  
 protein, KNOB 83  
 protein-based microspheres, immunological reactions 175–177  
 protein-based nanomaterials 115–245  
 protein-based nanoparticles  
 – preparation 120–124  
 – surface modifications 164  
 protein-based particles  
 – clinical studies 172  
 – oral delivery 384–385  
 – peroral application 175  
 – preclinical studies 172  
 – topical application 174–175  
 protein desolvation 158  
 proteins, chimeric 43  
 PS *see* phosphatidylserine  
 PS60-SLN 296  
*Pseudomonas aeruginosa* 377–378  
 psoralen–DNA–peptide conjugate 41  
 P–T diagram, pure substance 271  
 pure pharmaceutical components, atomization 273  
 purification, nanoparticles 154, 191  
 PVP (Poly(vinyl pyrrolidone)) 81  
 PX338-SLN 296
- q**  
 quantum dots 309–310, 362  
 quaternization, chitosan amino groups 80
- r**  
 RA (all-*trans* retinoic acid, vitamin A) 124–125  
 RA encapsulation, gliadin nanoparticles 124–125  
 rabbit serum albumin 149  
 radioactive tracers 198  
 radionuclide <sup>67</sup>Gd, attachment to nanoparticles 164  
 radiopharmaceuticals 198  
 rapid expansion of supercritical solution 272–273  
 re-dispersibility, dried nanoparticles 269  
 reactive groups, albumin microspheres 165  
 reactive oxygen species (ROS) 319  
 receptor  
 – asialoglycoprotein 81–82  
 – folic acid 83

- receptor-mediated endocytosis 38
- release kinetics, chitosan nanoparticles 93–95
- remote loading technology, drug trapping 262
- RES 262
- RES uptake, modified chitosans 80
- respiratory syncytial virus infection, gene therapy with chitosan–DNA complex 97
- RESS *see* rapid expansion of supercritical solution
- reticuloendothelial system *see* RES
- retinitis, HCMV 206
- reverse Hoogsteen base pairs 40
- reverse micellar method, chitosan nanoparticle preparation 89
- ribbon structure, DNA nanotubes 10
- ROS *see* reactive oxygen species
  
- S**
- S-layer fusion proteins 228–240
  - rSbpA<sub>31a1068</sub> 239
  - rSbpA<sub>31a1068</sub>/cAb-Lys3 235
  - rSbpA<sub>31a1068</sub>/cAb-PSA-N7 236
- S-layer lattices, thickness 220
- S-layer proteins
  - archaeae 219
  - bacteria 219
  - immobilization 225–226
  - nanoscale patterning 219–252
  - properties 220–225
  - SbsA 226–227
  - SbsB 227–228
  - SbsC 228–229
  - S-layer homology (SLH) motifs 222
- S-layer reassembly, spatial control 241–241
- S-layer streptadivin *see* streptadivin
- S-layer variation 223
- S-layers
  - carbohydrate-binding 223–224
  - chemistry and molecular biology 221–223
  - formation of regularly arranged nanoparticles 242–244
  - glycoprotein 219
  - glycosylation 221
  - heterogeneous ligand model 223–224
  - isoelectric point 221
  - isolation 220–221
  - monomolecular protein lattices 219
  - nanoparticles on 244–244
  - recrystallization 220–221
  - recrystallization experiments 229
  - symmetry 220
- S-liposomes, S-layer-coated liposomes 239
- “sandwich” phase, lipoplexes 52–54
- SAS *see* supercritical antisolvent
- scanning electron micrograph
  - gliadin nanoparticles 123
  - vicilin nanoparticles 121
- scanning electron microscopy (SEM) 89, 371
- SCF
  - approaches 270–275
  - characteristics 270–271
  - particle formation 271–272
- SCWP
  - biomimetic linkers 224
  - formation from 3 SLH motifs 222
  - secondary cell wall polymer 222
  - thiolated SCWP 224
- secondary cell wall polymer *see* SCWP
- SEDS *see* solution-enhanced dispersion by SCFs
- self-assembled DNA nanotubes 3–22
- self-assembly, DAE-O tiles 9
- self-assembly method, dendrimer synthesis 306
- self-assembly system, nanoscale patterning of S-layer proteins 219–252
- semipermeable nanoporous barrier, skin 363
- serum albumin 187–196
  - three-domain model 187
- SFM
  - heterotetramers 230
  - surface topography of S-layers 220
- side-effects, doxorubicin 368
- sieving method, chitosan nanoparticle preparation 91
- silver nanoparticles, color index 379
- simple coacervation 155–159
- siRNA lipoplexes 62
- site-specific drug delivery, solid lipid nanoparticles 287–303
- skin 363
  - drugs crossing problems 354–357
  - low-voltage electroporation 355–357
  - mechanical irritation 355
- SLH, S-layer homology 222
- SLN *see* solid lipid nanoparticles
- SM *see* sphingomyelin
- small drugs, BBB crossing 359
- small unilamellar vesicles (SUV) 261
- smart nanoparticle probes 370
- sodium alginate–BSA nanoparticles 201
- sodium azide, cytotoxicity of ICG 323
- sodium polyaspartate (PASP), ICG stabilization 326
- sodium sulfate, use in ionic crosslinking 87
- sodium tripolyphosphate (PSTP), use in ionic crosslinking 87
- solid-lipid nanoparticles (SLN) 288, 354

- *in vitro* occlusion 365
  - *in vivo* elasticity 365
  - *in vivo* occlusion 365
  - *in vivo* wrinkles 365
  - biofunctionalized 287–303
  - chemical stability 364
  - production 292–294
  - skin delivery 364
  - UV sunscreen 366
  - solubility
    - chitosan 70
    - effect on chitosan transfection efficiency 79–80
  - solubility parameter of gliadin, Hildebrand theory 123
  - solution-enhanced dispersion by SCFs (SEDS) 274–275
    - nozzle system 274
  - sonochemical method, albumin nanoparticles 193
  - “spaghetti” tubule structures, lipoplexes 57
  - sphingomyelin (SM) 352
  - SPR-spectroscopy, SCWP
  - spray drying, chitosan nanoparticle preparation 88–89
  - stabilization
    - albumin coacervates 191
    - albumin nanoparticles 187
    - ICG 326
  - stabilization ability, polymers 257
  - stabilizers, polymeric 267
  - starburst divergent method, dendrimer synthesis 306
  - starting materials, nanoparticle preparation 146
  - stealth carriers 290
  - stealth liposomes 262
  - sticky ends 5
  - stiffness, DNA nanotubes 8
  - Stokes’ diameter, nanoparticles 159
  - stomach mucosa, bioadhesion of gliadin nanoparticles 132–135
  - storage proteins, characteristics 118
  - streptavidin 229
    - biotin-binding properties 233
  - suicide gene therapy, albumin nanoparticles 203–204
  - sulfo-MBS 168
  - sulfo-SMCC 168
  - sulfosuccinimidyl-4-N-maleimidomethylcyclohexane-1-carboxylate (sulfo-SMCC) 168
  - supercritical antisolvent 273–274
  - supercritical fluids *see* SCF
  - supercritical nanoparticles 270
  - surface energy, drug particles 256
  - surface modification
    - drug-targeting ligands 166
    - functionalization 294–298
    - hydrophilic compounds 164–165
    - polyethylene glycol 165–166
    - protein-based nanoparticles 164
    - strategies 168–169
    - surfactants 295
  - surface plasmon resonance spectroscopy *see* SPR-spectroscopy
  - surfactant–DNA complexes 34
    - biomedical applications 36
    - organization 35
    - stability 35–37
    - ultrastructure 35
  - surfactant–plasmid complexes, morphology 36
  - surfactants
    - cationic 34
    - CTAB 36
    - reverse micellar method 89
    - stabilization ability 257
    - surface modification 295
    - synthesis 31–35
  - SUV *see* small unilamellar vesicles
  - SWNT *see* hemispherical endcaps nanotubes
  - SynB vectors, peptide drug delivery 360
  - synthesis
    - nanoparticles 244–244
    - nucleic acid nanoparticles 27–31
    - surfactants 31–35
- t**
- TAO, DNA structure 4
  - TAPP-Br, drug-loaded gelatin microspheres 152
  - target specific carriers 289
  - TAT protein 373
  - Taxol 173
  - TEM *see* transmission electron microscopy
  - TetR protein, fusion with NLS peptide 43
  - Tf *see* transferrin
  - therapeutic DNA, chemical and physical properties 25–27
  - therapy, magnetically targeted 204
  - thermodegradation, ICG 326
  - thermodynamic approaches, nanoparticle preparation 257–264
  - thiamine-coated delivery, BBB 376
  - thickening agent, albumin emulsification 192
  - three-domain model, serum albumin 187
  - 4 × 4 tile nanotubes 14–15

- 6HB tile nanotubes 16–17
  - TNBS *see* 2,4,6-trinitrobenzenesulfonic acid
  - $\alpha$ -tocopherol (vitamin E, VE) 124–125
    - lipophilic model 126–127
  - toxicity, ICG 322
  - TP *see* triple point
  - trafficking, intracytoplasmic 26–27
  - transbilayer lipid movement 353
  - transfection efficiency
    - chitosan 76
    - DNA nanoparticles 46
    - modified chitosans 79–84
    - unmodified chitosan 71
  - transfection reagents, commercially available 172
  - transferrin (Tf) 38–39, 82, 96, 369
    - plasmid–transferrin–PNA complex 42
  - transmission electron microscopy (TEM)
    - DNA nanotubes 10
    - mass distribution of S-layers 220
    - monomolecular DNA condensation 45
  - trastuzumab 167
  - 2,4,6-trinitrobenzenesulfonic acid, nanoparticle surfaces 168
  - trimethylation, chitosan amino groups 80
  - triple helix formation 41
    - with oligodeoxyribonucleotides 39–41
  - triple point (TP) 270
  - tripolyphosphate, crosslinking agent 258
  - tubules, lipid 264
  - tumor diagnosis 304
    - ICG 320
    - ICG limitations 324–325
    - optical nanoparticles 314–315
  - tumor imaging, ICG 322–323
  - tumor necrosis factor- $\alpha$ , secretion in presence of nanoparticles 73
  - tumor tissue, lipofection 60
  - tumor treatment
    - ICG 320
    - ICG limitations 324–325
    - optical nanoparticles 315–316
  - TX tile nanotubes 11–13
    - metallization 11
- u**
- UA (urocanic acid), coupled with water-soluble chitosan 78
  - ultrastructure, surfactant–DNA complexes 35
  - unmodified chitosan, schematic gene therapy mechanism 79
  - uptake by tumors, ICG 325
  - urocanic acid (UA), coupled with water-soluble chitosan 78
  - urokinase 195
  - UV sunscreen, solid-lipid nanoparticles 366
- v**
- $K_d$  values 224
  - variable domain, light chain antibody 235
  - VE ( $\alpha$ -tocopherol, vitamin E) 124–125
    - lipophilic model 126–127
  - VE encapsulation, gliadin nanoparticles 125–126
  - vectors
    - multicomponent delivery 47
    - viral 170
  - vegetable albumins, characteristics 118
  - VH 235
  - VHH, antibody isotype 233
  - vicilin, pea seed proteins 119
  - vicilin nanoparticles
    - preparation 121–122
    - scanning electron micrograph 121
  - viral vectors, gene therapy 51
  - virus infection, respiratory syncytial 97
  - vitamin A (all-*trans* retinoic acid, RA) 124–125
  - vitamin E ( $\alpha$ -tocopherol, VE) 124–125
    - lipophilic model 126–127
  - VL 235
- w**
- w/o *see* water-in-oil emulsion
  - water-in-oil emulsion (w/o) 87
  - water-soluble chitosan 78
  - water soluble polymers 258
  - Watson, J. D. 23
  - weakly overlapping mushroom regime, DNA nanoparticle protection 45
  - wet comminution 266–267
  - wheat proteins 119–120
  - wrapping vector 10
- y**
- yield, nanoparticles 191
  - YOYO, intercalating dye 36, 46
- z**
- zona pellucida (ZP) 98
  - ZP *see* zona pellucida

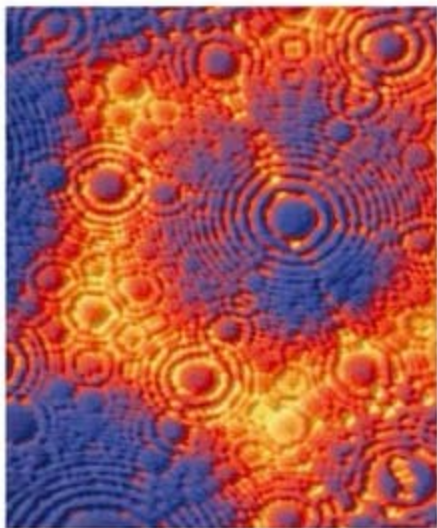


Nanotechnologies for the Life Sciences

Edited by Challa Kumar

 WILEY-VCH

# Nanosystem Characterization Tools in the Life Sciences



**NLS** 

# 1

## Fluorescence Imaging in Biology using Nanoprobes

*Daniele Gerion*

### 1.1 Introduction and Outlook

#### 1.1.1 A New Era in Cell Biology

Fluorescence is ubiquitous in biology. Indeed, any biology textbook contains a multitude of colorful images, most of which would not disfigure an art gallery [1]. For decades, biologists have mastered the use of fluorescently labeled molecules to stain cells in cultures or tissues. They developed the tools to target different compartments inside the cells, such as the nucleus and mitochondria, and subcompartment structures, such as chromosomes and the telomeres using light-emitting organic markers. These traditional approaches permitted the unraveling of a wealth of information on organs and tissues and, to a smaller scale, on the cell organization and its functioning. Images of cellular division captured by fluorescence microscopy are breathtaking, particularly the movement of the duplicated chromosomes along the spindle apparatus towards the two poles of the parent cell. Similar examples abound in the scientific literature and in fluorescent dye catalogs to the point that biology may convey a false sense of completeness. Indeed, an engineer or a physicist like myself may have the impression that everything interesting in biology has been already discovered and that only a few blanks remain to be filled.

Yet, in recent years, biology has witnessed an extraordinary revolution. Modern biology looks beyond responses to stimuli or the morphological description of structures. Modern biology does not satisfy itself with the successful sequencing of the human genome because a list of four repeating letters does not reveal a biological function. Modern biology is much more ambitious. It seeks to understand how biological and chemical processes work together to make cells and living organisms [2]. The journey towards this “Holy Grail” of biology depends on our ability to decipher interconnected cellular networks, mainly by observing molecular pathways of proteins and other metabolites in living organisms. The ultimate goal is to know where and when proteins and metabolites are expressed, how and at

which level they are distributed in time and space and how are signals generated and transmitted to maintain cell vitality [3].

### 1.1.2

#### **Nanotechnology and its Perspectives for Fluorescence Imaging in Cell Biology**

It is instructive to describe a problem of primary interest for biologists that illustrates the importance of knowing the entire pathway of a biological process and exemplifies how nanotechnology may enter the game. The example concerns double-stranded silencing RNA (siRNA [4–6]), a potent agent able to temporarily knockdown selected genes in mysterious fashion. Elucidation of this process is of considerable importance because it may reveal new routes that regulate the expression of genes and lead to the development of drugs with the ability to selectively keep the “good” genes on and turn the “bad” ones off. To study the mechanism by which siRNA works, a simple strategy would be to follow its path when it travels through the cell. This can be done by labeling it with a fluorescent chromophore and following its path with a fluorescence microscope. The double strand nature of the duplex raises the possibility that siRNA opens up at some point and that only one of the strands becomes the active agent that knocks down the gene expression. Where and when does it happen? A partial answer can be gained by labeling each strand of the siRNA duplex with a different fluorophore and following each of them separately. However, the colocalization of both strands with a resolution of a few nanometers far exceeds the diffraction limit of conventional microscopes, and therefore the very idea of observing the siRNA denaturation needs a different strategy. An elegant approach would be to use fluorescence resonance energy transfer or FRET [7] between two fluorophores, each located on a different strand of the siRNA duplex. When the duplex is intact, the fluorescence of the donor is resonantly transferred to the acceptor. Therefore, the donor fluoresce is “low” and the acceptor emission is “high”. The opening up of the molecule manifests itself by the switching off of the FRET mechanism with the consequence that the donor fluorescence becomes “high” while the acceptor fluorescence goes to “low”. Such a plan to study siRNA cannot rely on organic dyes. They bleach too rapidly under continuous illumination, especially at the single molecule level where the time window to observe them is limited to a few seconds. In addition, the photobleaching is generally associated with the formation of reactive oxygen radicals, which are a major cause of DNA damage and may result in the poisoning and death of the cell [8].

Enter nanotechnology. Over the past ten years, chemists have learned how to make fluorescent colloidal nanocrystals [9], also called quantum dots, and how to solubilize them in water, and to functionalize them with biomolecules [10, 11]. What makes these quantum dots interesting is their remarkable optical properties [12] and the fact that live cells seem to tolerate them quite well [13–15]. Quantum dots could represent an ideal solution to the shortcomings of organic dyes for labeling siRNA in live cells. The fate of siRNA is only one of a handful of problems where quantum dots can play a decisive role in biology or medicine. Other exam-

ples are described below. In fact, nanotechnology could represent a platform that would feed biologist's requests for more sophisticated tools to see smaller and smaller units with faster and better resolution. Whether chemists' dreams of using quantum dots to label live cells and solve important problems will come true is an open issue; but as the number of scientists working in nanoscience grows, new horizons open and the role of nanotechnology in biology is likely to expand in directions not yet been foreseen.

This chapter presents one area in which nanotechnology is rapidly establishing itself, namely fluorescence imaging. It seeks to describe different imaging techniques, and how new types of fluorescent probes, i.e., quantum dots, can be used in the context of biolabeling. In Section 1.2, I review some fundamentals of fluorescence by summarily describing the properties of several types of fluorescent probes. A brief section describes a few ways to excite the fluorescent probes and some principles of detection that will illustrate the potential of qdots for bioimaging. Section 1.3 considers how sources and detectors can be assembled to allow the observation of fluorescent signals in live organisms. Then I will take a brief tour and describe different strategies to make images, insisting on the advantages that nanoparticles may offer (Section 1.4). Section 1.5 then presents some example applications where quantum dots may indeed be the probes that biologists have been looking for.

## 1.2 Fundamentals of Fluorescence

### 1.2.1 Basic Principles

Fluorescence is the result of molecules emitting photons after an excitation. The fluorescence process is generally illustrated by the Jablonski diagram [16] (Fig. 1.1), a schematic based on the energy levels of the molecules. The molecule can be excited from a ground electronic state to a higher energy electronic state by the absorption of a photon whose energy is in resonance with the transition energy. Very rapidly, internal conversion takes place. During this process the molecule dissipates some excess energy into the vibrational states and falls to the bottom of the electronic excited state. There, the molecule still needs to dissipate some of its excess of energy, which is too large to go only through the vibrational modes. The return to the ground state can use different channels, which are described in details in the caption of Fig. 1.1. One possible relaxation channel proceeds through the emission of a photon (black arrows  $K_R$ ) and constitutes what is called "fluorescence". The emission energy is always lower than the excitation energy, which translates into the fact that the wavelength of the emission is always red-shifted compared with that of the excitation. This difference in wavelength is called the Stokes shift. The Stokes shift depends on the nature of the molecules and on their environment (i.e., the solvent), but it is in the order of 10–20 nm. A large Stokes

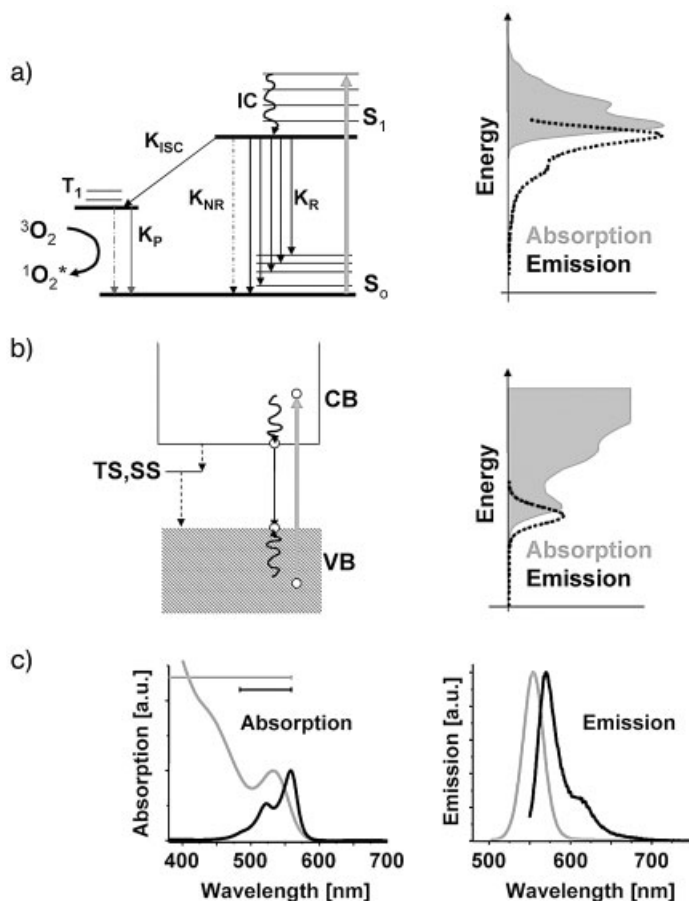


**Fig. 1.1.** Optical properties of organic dyes and qdots. (A) Jablonski diagram for organic dyes. Upon absorption of a photon of appropriate energy (light gray arrow), a molecule in a vibrational sublevel of the electronic ground state ( $S_0$ ) is promoted to a vibrational sublevel of the first excited electronic state ( $S_1$ ). This excess energy supplied by the photon is relaxed partially into vibrational modes by internal conversion (IC). IC is a radiation-less process that brings the molecule to the lowest  $S_1$  sublevel within picoseconds. The remaining excess energy is too large to be dissipated only into vibrational modes. Thus, the dye emits one photon to reach one sublevel of  $S_0$  (black arrows,  $K_R$ ). Emission takes place a few nanoseconds after excitation. This is the fluorescence mechanism of an organic dye. The energy can also be dissipated through collisions with other molecules in solution and,

in this case, there is no need to emit a photon (black dotted arrow,  $K_{NR}$ ). A third route is possible in organic molecules: intersystem crossing to the first triplet state ( $T_1$ ,  $K_{ISC}$ ). The electronic transition from  $T_1$  to  $S_0$  is spin-forbidden and, therefore, requires the assistance of phonons or external collisions. Consequently, relaxation to the ground state is in the microsecond to the millisecond range. It can take place through emission of a photon (phosphorescence) or through a nonradiative process. Note also that oxygen reacts readily with the triplet state ( $T_1$ ) of the dye, producing quenching of the emission. In this reaction, the ground state oxygen molecule,  $^3O_2$  (a triplet), is excited into a singlet state,  $^1O_2^*$ . This singlet state can initiate chemical reactions that lead to bleaching of the dye and its phototoxicity. The right-hand panel shows the absorption band of an organic dye (Cy3B) as a

shift is desirable for imaging because it facilitates separation between the excitation light and the emission (Section 1.3).

The precedent emission properties are shared by all organic dyes because their electronic structure is composed of discrete electronic states with vibrational envelopes. Nanotechnology has brought along new types of fluorescent systems that differ markedly from dyes. These systems are nanometer-size crystals made of semiconductor materials [12, 17]. In bulk semiconductors, the electronic states merge into bands, a valence band and a conduction band, separated by a bandgap [18]. In the ground state, the valence band is fully occupied and the conduction band is empty. Any photon of energy superior to the bandgap can excite the semiconductor by forming an exciton, i.e., by bringing one electron in the conduction band and leaving a hole in the valence band. Both electrons and holes release part of their energy by relaxing to the bottom of the conduction band and the top of the valence band, respectively. Once there, one possible energy relaxation mechanism is a recombination process where the electron recombines with the hole and the excess of energy is released as a photon. The photon energy corresponds to the value of the bandgap. In confined systems of nanometer size dimension, the same overall picture applies except that the bandgap varies with the diameter of the nanoparticles: the smaller the particle, the larger the bandgap [17, 19]. Therefore, the fluorescence of a quantum dot is size tunable. Similarly to the fluorescence process in organic molecules, the energy of the emitted photon is lower

function of photon energy along with the associated fluorescence emission. Note the limited extension of the absorption band, the redshift of the emission maximum compared to the maximum of absorption and the tail in the fluorescence emission extending towards low energies. The tail represents the contribution of photons relaxing into vibrational levels of  $S_0$ .

(B) A diagram similar to the Jablonski plot can be drawn for quantum dots. In a qdot, the electronic energy levels merge into two bands called valence and conduction bands. They are separated by an energy gap. In the ground state, the valence band is full and the conduction band is empty. Upon absorption of a photon with energy larger than the bandgap, an electron is promoted to the conduction band, leaving a hole in the valence band. Both electrons and holes can easily relieve energy by relaxing to the bottom of the conduction band or the top of the valence band, a process analogous to internal conversion in organic dyes (although involving electronic states of qdots and not vibrations). At this stage, there are no more electronic states available and the

excess energy would be too large to be dissipated through vibrations of the qdot. Therefore, qdots emit a photon, whose energy corresponds to the bandgap. As in organic dyes, qdots also undergo nonradiative processes. For instance, a nonradiative channel is induced by surface/trap states (defect at the surface of the dots) that create discrete energy levels within the bandgap. The right-hand panel shows the absorption spectrum of qdots along with its emission spectra. Unlike dyes, the absorption is a continuous band not limited to a specific energy range. The fluorescence emission is also redshifted compared with the absorption band. Remarkably, the position of the emission is independent of the excitation energy, although its amplitude depends on it.

(C) Absorption spectra of a qdots solution (light gray) and the organic dye Cy3B (in black). Horizontal lines at the top of the figure represent the range of wavelengths that can effectively excite the chromophores. In the emission spectra, notice the symmetry of the qdot emission and the tail in that of dyes at higher wavelengths.

than that of the absorbed photon and, therefore, the fluorescence light has a longer wavelength than the excitation.

A marked difference between a quantum dot and an organic dye is in their absorption spectra. For a dye, the absorption is centered around bands, conveying the discrete nature of the electronic states. In quantum dots, the absorption is a continuum from the band-edge up, mapping the continuous nature of the conduction band of the material. A continuous excitation spectrum represents clear advantages for imaging purposes. First, a main issue concerns the filtering out of the excitation source. When the excitation and emission are close in wavelength, as with organic dyes, the excitation light can be filtered out but a fair amount of the emission is also blocked. The possibility to excite quantum dots far from their emission greatly improves fluorescent detection. Second, it becomes possible to excite all sizes of quantum dots with just one single wavelength and therefore obtained all colors of emission with one excitation. Similarly, the emission of organic dyes exhibits a red tail resulting from transitions from the bottom of the excited state into the various vibrational levels of the ground state (black arrows  $K_R$  in Fig. 1.1). In contrast, quantum dots have symmetric and narrower emission patterns, because the energies of the radiated photons are determined solely by the size of the bandgap. Those properties represent distinct advantages for multicolor labeling, as the rest of this chapter will show.

### 1.2.2

#### A Few Types of Fluorescent Probes

Now that the mechanism of fluorescence has been described in general terms, it is worth looking in more detail into the nature of fluorescent molecules encountered in biology.

##### 1.2.2.1 Small Luminescent Units and Autofluorescence of Living Organisms

Fluorescence in organic molecules comes from delocalized  $\pi$  orbital states of conjugated double bonds [16, 20]. Thus, most aromatic molecules exhibit a natural emission. This is the case of tryptophan, an amino acid, NADH (nicotinamide adenine dinucleotide), an important coenzymes found in cells used extensively in glycolysis and in the citric acid cycle of cellular respiration, and other coenzymes such as flavins and some forms of pyridoxyl. Because these fluorophores are natural, cells and tissues fluoresce when excited with a UV source; this is the source of autofluorescence. The dominant autofluorescence from biological samples usually occurs below 500 nm.

Autofluorescence represents a fair amount of light. Unfortunately, these natural fluorophores do not possess properties that are useful for biolabeling. Most proteins contain a few tryptophan amino acids and therefore all proteins emit to a certain extent. Because autofluorescence may easily overshadow other unnatural fluorescent labels, it must be removed by an appropriate combination of filters, or by the implementation of detection techniques that selectively eliminate autofluorescence (Section 1.4.3).

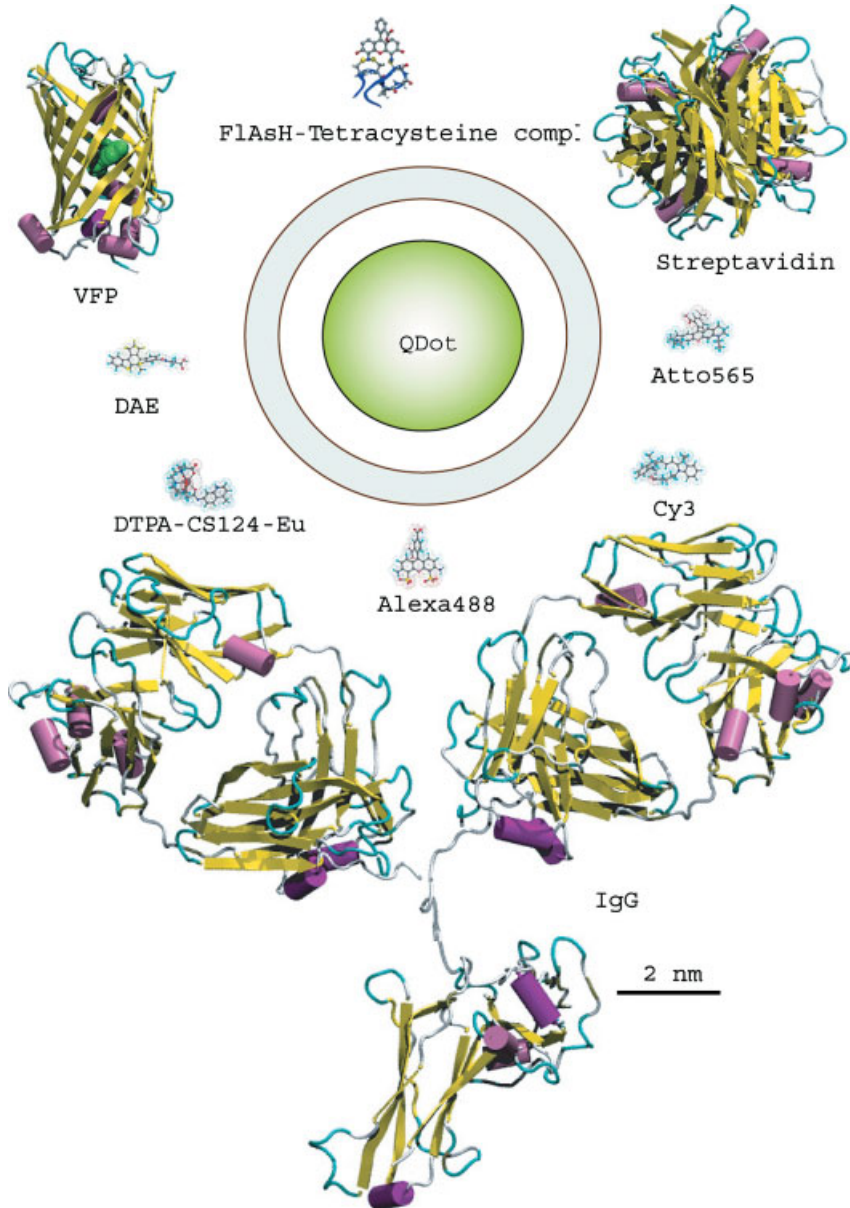


**Fig. 1.2.** Structure of commonly used organic dyes, fluorescent proteins, qdots and bio-molecules, and the comparative sizes of common fluorophores, fluorescent proteins, qdots, some protein carriers and antibodies. The scale bar applies to all molecules. Organic dyes (FLAsH tetracysteine complex, DAE, DTPA-CS124-Eu, alexa, Cy3 and atto) are organic

conjugated structures 1–2 nm in size. Qdots passivated to become water-soluble are ~10 nm – comparable to proteins such as streptavidin and VFP (violet fluorescent proteins) – but are smaller than a typical IgG antibody. (Copyright 2004 Nature Publishing Group. Reproduced with permission from Ref. [7].)



#### 1.2.2.2 A few Organic Dyes and their Limitation in Live Cell Labeling

A plethora of unnatural organic dyes cover the whole range of desirable emissions and have unique optical signatures. Fluorescein, cyanine, rhodamine, alexa or atto are among the most popular. Figure 1.2 shows the structure of organic dyes and compares their size with other fluorescent probes and biological units. Organic dyes consist of aromatic conjugated structures of 2 to 10 units providing different degrees of electron delocalization, and hence colors of emission. The emission of an organic dye has a full-width at half-maximum (fwhm)  $>50$  nm and exhibits a red tail (Fig. 1.1C). The quantum yield, the ratio of the number of photons emitted to the number of photons absorbed, can be close to one, but it is quite dependent on the local environment of the dye. Alteration of the media pH, buffer components, solvent polarity, or dissolved oxygen can affect or even quench an organic probe. For instance, in an environment below pH 7, fluorescein is significantly quenched. Similarly, the solubility of the dyes depends on the solvent and not all dyes are soluble in aqueous environment. The fluorescence decay time or lifetime of most organic fluorophores falls in a narrow range of 1 to 5–10 ns, a time window shared by autofluorescence lifetime. This limits the use of time-gated detection methods to distinguish between the fluorescence of an unnatural dye and the autofluorescence (Section 1.4.3). These properties represent an inconvenience for the use of organic dyes as biolabels. But, in fairness, the dye industry has managed to downplay these issues by synthesizing alternative or new types of probes that minimize these effects.

A more serious shortcoming that has not been solved yet is photostability. Dyes bleach after the emission of  $10^6$ – $10^8$  photons [21]. The exact physical bases for bleaching are not entirely clear in all cases. The dye is not physically destroyed, but rather it is altered so that it can no longer emit. One cause of photobleaching is the oxidative reaction between atmospheric oxygen and the triplet state of the dye (Fig. 1.1 and its caption). Photobleaching of the dye produces radical oxygen species (ROS) that may poison and kill the cell in a short while [8]. One way to markedly reduce photobleaching consists in using antioxidants, an oxygen-free atmosphere or oxygen scavengers (such as the enzyme glucose oxidase along with glucose and catalase). Such approaches work well for studying conformation change of biomolecules, catalytic activity of ribosomes adsorbed on surfaces or fixed (dead) cells [22]. However, they are inadequate for the study of live organisms that need oxygen to survive.

#### 1.2.2.3 Green Fluorescent Protein and its Cousin Mutants

Green fluorescent protein (GFP) is a natural fluorescent protein produced by the jellyfish *Aequorea victoria* [23]. It has 238 amino acids and a molecular weight of 27 or 30 kDa. The gene responsible for this protein was identified in 1961 [24] and cloned in 1992 [23]. GFP has a barrel-shape enclosing a short polypeptide fluorescent unit (Fig. 1.2). The nature of the polypeptide determines the color of emission. Biologists have selectively modified this short amino acid sequence and have been able to clone mutants that emit at different wavelengths. The proteins are called YFP (yellow fluorescent protein), BFP (blue), RFP (red), or CFP (cyan).

All exhibit, however, a fairly large emission spectrum with a fwhm larger than 50 nm and the distinctive red tail common to all organic dyes. Fluorescent proteins are relatively stable in the very diverse environments of the cells, although their fluorescence properties may be affected. GFP for instance remains fully fluorescent at pH above 6, below which the fluorescence decreases dramatically.

By applying the powerful methods of DNA recombinant technology it is possible to link together a specific gene of interest, for instance a therapeutic gene, with the GFP gene, and to transfect a mammalian cell or a whole organism with this engineered DNA. The cell machinery can translate this DNA into the protein of interest tagged with GFP. The protein complex is fluorescent but, amazingly, the tagged protein maintains the same function as the natural protein. Biologists have, therefore, a fluorescent complex whose location in space and time can be monitored. This is a marked improvement over traditional antibody labeling techniques that work on fixed (dead) cells. The ability to fuse the GFP gene to any protein brings biologists very close to what we called the promised land in the introduction.

Yet GFP and its cousin mutants are still cumbersome to construct. GFP fluorescence is the final product of a long, complex pathway involving transcription, translation, and post-translational modifications. Moreover, GFP and its mutants tend to form dimeric structures, and there have been questions on the feasibility of using GFP in certain conditions, for instance for gene expression studies under tumor conditions [25]. As a result, although GFP and its cousins allowed a huge step forward for molecular imaging, there is still room and need for alternative probes.

#### 1.2.2.4 Quantum Dots

Quantum dots, often abbreviated qdots, are nanometer-size crystals made of semiconductor materials [12, 17]. The most widely used and studied quantum dots consist of a core of cadmium selenide or CdSe [9]. Colloidal chemistry allows the synthesis of nanoparticles with a very narrow size distribution (<10%) and in (milli)-gram quantities (Fig. 1.3a). The dimension of the core determines the bandgap and hence the color of emission of the nanoparticles. For instance, emission of CdSe quantum dots covers the visible spectrum from green (520 nm, ~2.3 nm dots) to red (650 nm, ~5 nm dots). It is possible to cover the near-IR and IR spectrum by synthesizing quantum dots made from other materials such as CdTe [26], InP [27], InAs [28], PdS [29], PbSe [30, 31] but most of these chemical syntheses do not allow the degree of control reached in the case of CdSe. In principle though, the emission of qdots can be coarse-tuned by the choice of the material and later fine-tuned by playing with the size of the core (Fig. 1.3b).

The emission of the qdots presents many advantages over that of organic dyes and GFP. For instance, the emission of a batch of CdSe qdots is symmetrical and its fwhm is generally around 30–35 nm, although experienced groups can reach an fwhm as low as 22–25 nm. Moreover, the position of the qdot emission does not depend on the excitation wavelength. If qdots are excited at 360, 400 or at 500 nm, the emission will occur at the same wavelength (but the intensity will vary). All together, these relatively narrow and symmetric emissions that can be excited by a single excitation wavelength are ideal candidates for multiplexing detection

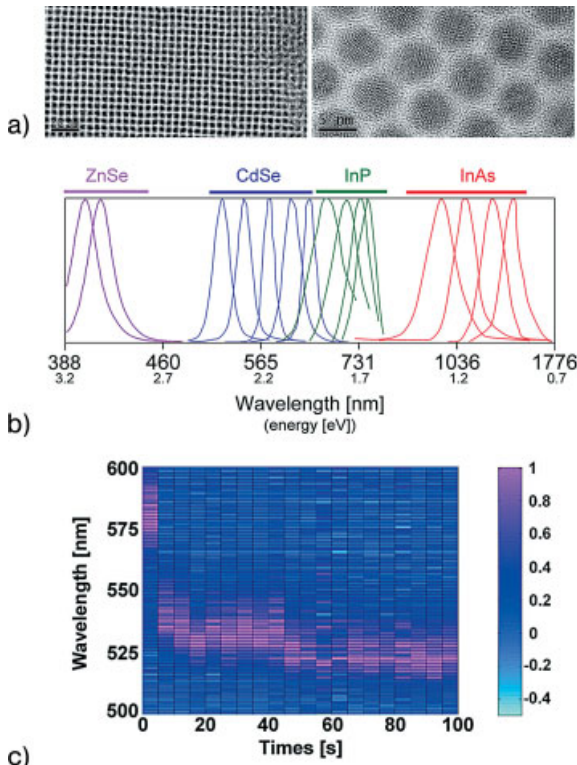


**Fig. 1.3.** Overview of CdSe qdots and their optical properties. (A) Low-resolution transmission electron microscope (TEM) image of CdSe qdots, showing an ordered lattice of CdSe nanocrystals, called a superlattice. The superlattice extends over a few microns. Scale bar: 20 nm. Right-hand side: high-resolution TEM view of the superlattice, revealing the internal structure of the CdSe qdots. Scale bar: 5 nm. Note the different alignment of qdots and the homogeneous particle size. (Image courtesy of Dr Natalia Zaitseva, Lawrence Livermore National Laboratory.) (B) Fluorescence emission of qdots spans from the UV to the IR. Different materials emit in different bands. For a given material, the emission can be fine-tuned by the size of the qdots. For instance, with CdSe, the maximum emission is at 530, 550, 590, 620 and 640 nm for qdots of 2.1, 2.4, 3.1, 3.6, 4.6 nm respectively. (C) Comparison

of the photostability of an organic dye (Cy3B) and a silica-coated CdSe/ZnS qdot in phosphate buffer. The qdot–dye conjugate was synthesized as a model system to study FRET. The conjugate was illuminated continuously with a picosecond laser diode (400 nm) and its emission spectrum collected every 5 s with a CCD camera. The dye emits at 579 nm and the qdot emits at ~530 nm. In the first 5 s of illumination, the qdot is not seen because it transfers its emission energy to the dye through a FRET process (Section 1.4.4). However, after <5 s, the dye photobleaches, the FRET channel closes and the qdot shows up. The qdot emission remains strong throughout the measurement, with only a slight blue-shift. The long-lasting emission of single dots is the basis of long-term monitoring of molecular processes in live cells (Section 1.5.2).

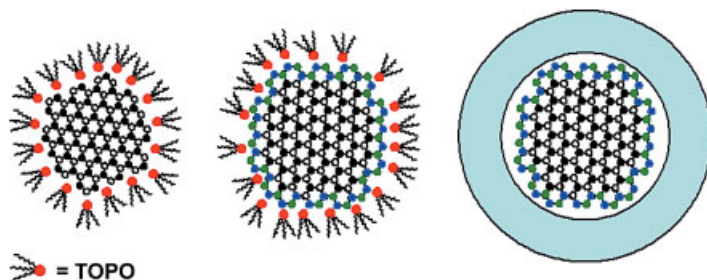


**Fig. 1.4.** CdSe, CdSe/ZnS and water-soluble qdots. Schematic of qdot cores, core/shell and water-soluble particles used in bioapplications (drawing not to scale). Left: a core of CdSe surrounded by TOPO (tri-octylphosphine oxide). The phosphine oxide head of TOPO (red ball) sticks to the Se atoms of the qdot. Middle: a thin shell of ZnS passivates the CdSe core. The shell increases the fluorescence emission of the core. The quantum yield of core/shell qdots is 30–50%. Since TOPO

molecules are hydrophobic, core and core/shell are not soluble in water, where biology takes place. An additional shell makes the interface between the inorganic qdot and the organic/water outside (right-hand side). If the shell is made of glass, functional groups on the glass surface allow bioconjugation of the qdots to biomolecules. Note that, regardless of the solubilization method, the final size of water-soluble qdots is close to or above 10 nm, even if the active CdSe core is only 2–3 nm.

with minimal or no cross-talk between detection channels. In a proof-of principle experiment, five orthogonal channels have been simultaneously detected within the visible range using a single laser excitation [32], but under more realistic conditions, which use ligand–receptor interactions mediated by single-stranded DNA, only four qdot channels could be unambiguously sorted out [33].

In general, qdots grown by colloidal methods have surface trap states that reduce their emission to a few percents. However, these trap states can be removed by passivating the surface with a few layers of a second semiconductor material with a larger bandgap. For instance, a few monolayers of zinc sulfide (ZnS) can be grown on top of a CdSe core (Fig. 1.4) [34]. The core/shell CdSe/ZnS are about 20–50× brighter than CdSe cores and their quantum yield can reach 30–50%, although certain laboratories with more experience in the art of growing core/shell qdots can reach quantum yields above 80–90% by further doping the shell. Core/shell qdots do not bleach as fast as organic dyes. In fact, qdots in solutions can be excited continuously well over 4 h with an Ar<sup>+</sup> laser excitation and their emission remains fairly stable [35]. Eventually, over the long term, photobleaching occurs. It is easier to quantify the resistance to photobleaching at the single molecule level. With organic dyes exposed to air, photobleaching occurs in a matter of seconds, even for Cy3B, one of the most robust dyes (Fig. 1.3C). Under similar excitation conditions, qdots can emit for well over a few minutes and in some cases for over 20 min. The photostability of qdots is the major advantage that could allow the tracking of single molecules over extended periods (see Section 1.5.2).

Qdots are characterized by very high photoabsorption cross-sections. Chemists prefer to use the extinction coefficients, which measure the absorption of a 1 M

solution along a 1 cm path. Extinction coefficients scale roughly as the volume of the qdots and range from  $\sim 1.5 \times 10^5 \text{ M}^{-1} \text{ cm}^{-1}$  for CdSe qdots of 2 nm up to over  $5 \times 10^5 \text{ M}^{-1} \text{ cm}^{-1}$  for qdots of 5 nm [36]. For comparison, extinction coefficients of organic dyes vary from less than  $1 \times 10^5$  to  $1.5 \times 10^5$ . High extinction coefficients mean that a lower amount of light is needed to excite them, a particularly beneficiary thing for the study of delicate systems such as live cells. Similarly, two-photon cross sections of CdSe/ZnS qdots exceed by far the values of organic dyes. In fact, two-photon cross-sections of qdots are two to three orders of magnitude larger than those of organic dyes and one order of magnitude larger than those of molecules designed specifically for enhanced two-photon absorption [37]. These high values enable the imaging of organs and tissues at greater depth and lower power than with any other dyes. A further improvement may come from the use of IR-qdots whose emitted photons are more transparent to tissues (Section 1.5.3).

Other optical signatures that distinguish organic dyes and qdots are lifetime and polarization. Qdots have a lifetime of  $\sim 10\text{--}20$  ns, which is significantly larger than the lifetime of organic dyes (1–5 ns) or the lifetime of autofluorescence [38]. This longer lifetime provides an efficient way to reduce the autofluorescence background by time-gating the detection (Section 1.4.3). Conversely, a negative point of qdots vs. dyes is the lack of strong polarization of the emitted photons. In fact, elongated qdots, also called nanorods, do emit photons polarized along the long axis of the rod [39]. But as the ratio between the long axis and the short axis of the rod approaches one, the polarization vanishes. Since chemical procedures to solubilize nanorods are not perfected yet, the present qdot technology does not allow orientational sensing. Further developments in the post-processing of nanorods will likely lift this limitation.

Although qdots have photophysical properties that surpass organic dyes in many aspects, they have one big shortcoming: quantum dots are not water-soluble. Qdots are generally synthesized in organic solvents and are passivated with hydrophobic molecules. It is possible to modify the surface of the qdots to render them hydrophilic. Many methods have been developed and there is probably no consensus on which one works best. The most promising solubilization methods for bioapplications consist in embedding the qdots into a shell or surfactant layer that cannot be further exchanged. The reason is that the shell/layer represents a protection that masks the true hydrophobic nature of the qdots. Examples of solubilization strategies include ligand exchange by thiol-containing molecules [40], oligomeric phosphines [41], dendrons [42], or two-domain peptides [43]. Other solubilizations proceed through encapsulation of the qdots by layers of phospholipids micelles [14], amphiphilic diblock [44], or triblock copolymers [45], polymer [46] or silica shells [35] and amphiphilic polysaccharides [47]. Regardless of the solubilization strategy, the difficulty to interface these inorganic objects with the bioworld is a major concern for biolabeling applications, and is likely to require constant improvement in forthcoming years.

As with organic dyes, water-soluble qdots can be conjugated to biomolecules using standard bioconjugation approaches [48]. Biologists have developed covalent conjugation schemes based on thiol, amine, and carboxylic group chemistries (the

natural functional groups found in amino acids) to crosslink proteins together. It turns out that similar schemes can be used to link qdots to any biomolecule. Most biomolecules (DNA, oligonucleotides [14, 33, 49, 50], peptides [13, 43], antibodies [44], virus peptides [13], proteins [45]) have been linked to water-soluble qdots and, surprisingly, the binding has no effect either on the qdot optical signature or on the functionality of the biomolecules. For instance, a single strand of DNA of 24 bases long ( $\sim 7$  nm) linked to a qdot of  $\sim 10$  nm is able to find its perfect complement within a pool of competing stands. Even a single base mismatch does not produce hybridization [51]. In addition, the DNA strand does not modify the emission of the qdot. Similarly, qdots linked to antibodies for surface receptor proteins indeed find their target on the cell membranes without losing their optical properties [43]. It is remarkable that a 10 nm qdot does not perturb the function of a biomolecule and conversely that a biomolecule does not modify the emission of the qdot, although it does change the local dielectric constant around the dot. It becomes therefore possible to envision studying biomolecules in their native cellular environment (Section 1.5.2) [2].

#### 1.2.2.5 Toxicity Issues of Nanomaterials

So far, we have described the benefits of using qdots for *in vivo* labeling applications. In fact, a major issue for biologists is the toxicity of the qdots for live organisms. Because qdots are made of toxic chemicals, they have to be toxic, or so the rationale goes. This has sparked a debate that encompasses the general theme of the environmental impact of nanotechnology [52, 53]. An extreme position calls for a ban on nanoscience until its environmental impact is assessed. A wiser position may consist in taking seriously the potential toxicity of these new nanoprobe and studying in parallel benefits and shortfalls of this technology. There are no benefits in banning nanoscience all together. However, there are strong merits in warning against the potential toxicity of the nanomaterials, while we await the results of long-term cytotoxicity or genotoxicity studies.

Besides its unknown long-term effects, short-term toxicity is an important factor for live cell labeling, because the markers must not interfere with the regular cell cycle. For instance, the presence of qdots in the cell cytoplasm should not impede the cellular division, nor should it switch off vital cell–cell communication channels. So far, the toxicity of qdots towards live cells has been studied only through simple experiments where the survival rate of cells transfected with different types of foreign material was quantified [15, 54, 55]. The major result in all those studies is that surface functionalization plays the key role in nanoparticle toxicity. For instance, an apparently inert molecule like  $C_{60}$ , with a well-defined surface and no available dangling bonds, is extremely harmful to cells even at low doses because  $C_{60}$  is an excellent electron acceptor that can readily react with available oxygen and water and generate free radicals [56]. These radicals eventually cause oxidative damage to the cellular membrane.  $C_{60}$  derivatized with hydroxyl groups showed much lower toxicity because derivatized fullerenes are less efficient in producing oxygen radicals. A similar situation exists for water-soluble CdSe/ZnS. These qdots tend to release  $Cd^{2+}$  into the cellular environment, due to photooxidation, which

leads to the death of the cells by poisoning. If these qdots are solubilized by ligand exchange with a mercaptoacid [40] the particles present low solubility and a high toxicity in the cells, essentially because the bond between the qdot and the mercapto-surfactant is weak, dynamic and unable to prevent diffusion of dissolved  $\text{Cd}^{2+}$ . In contrast, qdots embedded in a cross-linked silica shell have greatly reduced toxicity [55]. However, even in such cases, the overall toxicity is a function of surface functionalization. Silica-coated qdots with negatively-charged phosphate groups at the surface cause a higher rate of cell death than silica-coated qdots with neutral PEG groups. Such experiments tell us a lot about the compatibility of the probes to live organisms, but they lack the ability to discriminate further than the simple toxic/less toxic/non-toxic conclusions. A classification of the effects of nanomaterials on the expression of genes in live cells would help clarify the potential dangers of nanomaterials. Those experiments are likely underway.

### 1.2.3

#### Sources and Detectors

With a toolkit of bioconjugated qdots in hand, the doors to biology get closer. But before going there, let us tour the world of sources and detectors that could be used for imaging qdots. There are many ways to excite fluorescent probes and similarly there are many different ways of detecting them. The selection of a particular type of source and detector is dictated by the type of experiments and the information that one wants to access. Imaging time-resolved and dynamic events puts a stronger constraint on the equipment than the imaging of a static field of fluorescent probes. In the next section, we look briefly into the different types of light sources and detectors commonly used in fluorescence microscopy.

##### 1.2.3.1 Light Sources

Light sources commonly used for fluorescent microscopy are arc lamps and lasers. Lasers are essentially used for confocal microscopy where an important aspect is to focus the excitation source (Section 1.3.2). For wide-field (Section 1.3.1) illumination, however, biologists tend to prefer arc lamps because of their lower price, relative flexibility (i.e., any wavelength may be selected – an important factor when using two different dyes) and the lack of interference fringes from reflections inside the optical system.

**Arc Lamps** These include mercury lamps or xenon lamps. Mercury lamps exhibit a compact arc, with some lines dominating the whole spectrum. They can reach very high flux densities, mainly concentrated in the wavelengths of the mercury lines. When a broader, more homogenous excitation spectrum is needed, xenon lamps are the sources of choice. They have a fairly flat spectrum with only a few lines in the blue and IR region. A main disadvantage of arc lamps is the need of optical filters to block the excitation light from the fluorescence light. Considering the broad excitation that often overlaps with the emission of the probes, complete removal of the excitation source also reduces the fluorescent signal that reaches the detector. This is a problem when one wants to detect a few labels inside a cell. In

that case, every photon counts. Arc lamps also lack coherence properties. Because of their wide spectrum, different wavelengths going through an objective are focused at different locations in the sample. This is one source of chromatic aberrations in the excitation arm of the microscope. One consequence is that two different dyes, excited by two different wavelengths, may show up at the same location on the recorded image even though they are physically far apart. As a result, high precision colocalization of two fluorophores cannot be achieved with an arc lamp. A high level of localization requires coherent light sources.

**Lasers** Lasers are coherent, monochromatic light sources. While it becomes experimentally easier to get rid of the excitation light using interference filters, lasers present the inconvenience that not all organic dyes can be excited by a single wavelength, so a second excitation wavelength is needed; and the story continues. However, qdots have a broad absorption band and therefore a single wavelength can produce the emission of all qdot colors at once. For instance, with a simple Ar<sup>+</sup> laser emitting at 488 nm and a shortpass filter with cutoff below 500 nm, it is easy to observe the glowing of five different colors of CdSe qdots simultaneously and record it with a color consumer-grade CCD camera. A decided advantage of monochromatic excitation is that chromatic aberrations in the excitation path are suppressed altogether. This opens up the possibility of colocalizing multiple qdots with nanometer precision (Section 1.5.1). A disadvantage of a laser source over an arc lamp is the smaller area that can be illuminated. A Xe lamp can cover an area of a few cm<sup>2</sup>. In contrast, a defocused laser beam can illuminate an area of a few tens of μm<sup>2</sup> only [33, 57].

### 1.2.3.2 Detectors

Fluorescence microscopy uses digital imaging due to the high sensitivity that such detectors can reach. The detection of fluorescence signals is often a trivial task, especially if the signals are strong. This is the case when the nucleus of a cell is stained with DAPI dyes or when the cell membrane is stained with fluorescent markers. In these cases, the fluorescence signal is easily observable even to naked eyes, and can be captured by low-tech techniques such as the traditional emulsion-based films. Most of today applications, however, look intensively to fluorescence signals coming from rare events where only a handful of probes emit. One example concerns the expression of proteins in live cells following an external stimulus. Often, these proteins are expressed at a low level (a few hundred to a thousand of copies per cells) and their localization is spread all around the cell cytoplasm. Detecting them is like finding a nail in a haystack. In addition, irreversible photobleaching imposes an additional constraint on the quality of the detector, because not only there are a few emitting probes, but the time window to detect them is limited. The detection of weak signals becomes therefore a central piece in biomedical applications. Fortunately, the field of optics has developed ultrasensitive detection devices for all sorts of single-molecule applications that encompass the field of materials science, chemistry, physics and biology. Broadly defined, there are two classes of detectors: point detectors and two-dimensional arrays. The next two sections discuss their properties.



**Point Detectors** These detectors include photomultiplier tubes (PMT) and photodiodes (PD). Both devices employ a photosensitive surface that captures the impinging photons and generates electronic charges that are amplified and sensed. Therefore, a common feature of these single-elements detectors is the lack of spatial resolution.

In a PMT, the impinging photon strikes a photocathode that releases secondary electrons that get amplified by a series of dynodes. PMT sensitivity depends on the composition of the photocathode [58]. Photocathodes made of gallium-arsenide-phosphide (GaAsP) are sensitive in the range of 250–650 nm and GaAs photocathodes are sensitive to 300–800 nm. InGaAs photocathodes extend the sensitivity from 900 to 1700 nm in the IR range, but they are less common or available in regular laboratories. The output signal from a dynode is proportional to the number of impinging photons and a gain of up to  $10^6$  can be obtained. Because PMTs do not store charge, and respond to changes in photon fluxes within a few nanoseconds, they can be used to monitor extremely fast events such as photon bursts. A limiting factor of PMTs is their low quantum efficiency (QE), i.e., the ability to generate a signal from the percentage of incident photons. It ranges from 20% for GaAs up to 40% for GaAsP photocathodes. In contrast, PMTs have a large detection area, on the order of  $1 \times 1$  cm. Such a large area is a great experimental advantage because it does not require tedious alignment of the microscope on a daily basis.

Avalanche photodiodes (APDs) are an alternative to PMTs with greater efficiencies. They consist for instance in p-n junctions or heterojunctions operated at reverse biases close to avalanche breakdown voltage to enable the multiplication of photogenerated carriers [58]. APDs have generally higher QEs (up to 95% for silicon APDs) and a relatively flat response over the entire visible range (400–850 nm). APDs have been fabricated in many semiconductor materials. While Si APDs have a 90% QE up to  $\sim 850$  nm, their efficiency is greatly diminished in the 1000–1600 nm range. For this wavelength range, APDs made of Ge or other III–V compounds are used. The temporal response of APDs is comparable to PMTs but the sensing surface area is much smaller (a few hundreds of microns in diameter). Although PMTs offer higher gain, APDs feature better quantum efficiency, lower noise, higher linearity, and compact packaging.

**Two-dimensional Array Detectors** Two-dimensional detectors consist of a dense array of photodiodes that collect simultaneously the light coming from an area several microns or millimeters in size. These detectors are used for imaging a wide field in a single shot. There are several variations on the same principle, but the most popular 2D detector used in fluorescence microscopy is the CCD (charge couple device). A photosensor called a pixel is coupled to a charge storage region that is connected to an amplifier. The amplifier reads out the quantity of accumulated charge.

The spectral sensitivity of CCD camera is usually lower than that of a simple photodiode, because the CCD surface has channels used for charge transfer that are shielded by polysilicon electrodes. These structures do absorb in the blue region. This reduces the quantum efficiency of the device down to  $\sim 40\%$  in the

case of a Si chip. A marked improvement consists in using a back-illuminated CCD. In this configuration, the light impinges on the back of the CCD on a surface that has been thin-etched to the point of being transparent ( $\sim 10\text{--}15\ \mu\text{m}$ ). This results in quantum efficiencies of  $\sim 90\%$  over the entire visible spectrum. In addition, when CCD cameras are cooled to liquid nitrogen temperature, the background noise can be reduced to a few counts per second, making it possible to detect single emitters spread on a surface in a heartbeat.

The limiting factor of CCD cameras, beside their cost, is the transfer rate, i.e., the speed at which the collected frames are read out and transferred to the computer. CCD cameras are often termed slow-scan cameras because their standard frame rate is usually less than that of a video camera. This is because the data readout is performed pixel row by pixel row. The fastest full resolution readout time reaches a few hundreds of milliseconds or about 10 frames per second in the case of frame-transfer cameras. As a result, CCD cameras are not appropriate to monitor time-dependent events occurring on a timescale of millisecond or below. For instance, the dynamics of proteins folding, the lifetime emission of fluorophores and time-correlated events are too fast for CCD detection, but can be caught quite easily with a PMT/APD.

### 1.3 Microscope Configurations

So far, we have discussed how to excite a fluorescent probe and how to detect its emission. Let us now look at how to assemble these devices into a custom-made microscope to acquire images. The next few sections discuss the advantages and disadvantages of each configuration (Fig. 1.5).

#### 1.3.1

#### Wide-field Methods: Epi-, and Total Internal Reflection (TIR)

Most fluorescence detection techniques in biology use a wide-field illumination. As the name indicates, a laser or an arc lamp illuminates a large area of interest and the fluorescence from the whole field of view is collected.

##### 1.3.1.1 Epifluorescence Illumination

By far the simplest microscope uses an epifluorescence configuration in which the excitation and the emission pass through the same objective (Fig. 1.5). The excitation light, usually a mercury or xenon source, or in rarer cases a defocused laser beam [33, 57], is directed through an objective by a dichroic mirror and illuminates the sample. The fluorescence emission is captured back through the same objective, and passes through an appropriate long pass filter that further removes any residual excitation light scattered back from the surface. The fluorescent light is then detected. The simplicity of such a setup has made it the most commonly used fluorescent imaging technique.

Epifluorescence microscopy has certain limitations. For instance, the samples are illuminated along the whole path of the excitation light and therefore probes

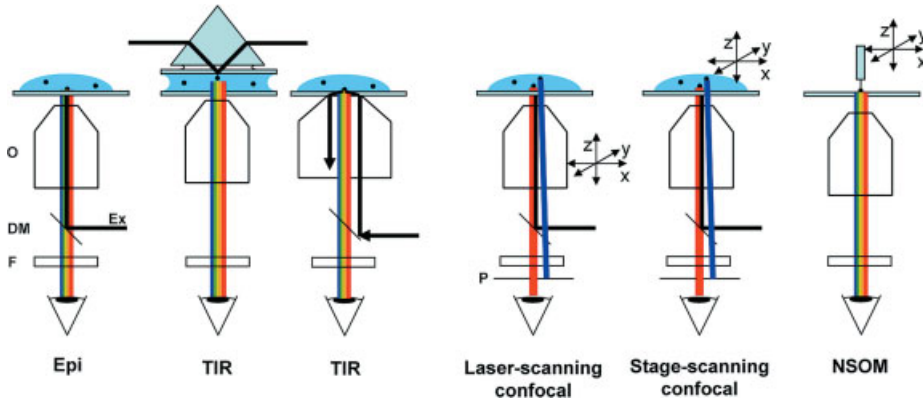


**Fig. 1.5.** A qdot sample can be illuminated in many ways. Excitation light is represented by the black line. The most popular illumination is *epifluorescence*, where the excitation source (arc lamp or laser) and the fluorescence emission go through the same objective. A dichroic mirror (DM) is used to direct the excitation in the back of the objective. The back-scattered excitation light is further blocked by a bandpass filter (F) that is transparent to the fluorescence emission that is directed to the detector. Total internal reflection (TIR) uses an evanescent wave at the interface of two phases of different refractive indexes to excite the probes. It is, therefore, used to study structures close to interfaces. TIR illumination can use either a prism or a special objective configuration. In both cases, excitation and emission paths

are disconnected. The detection arm of a TIR microscope is similar to that of an epifluorescence microscope. In a scanning *confocal* microscope, a focused light source, i.e., a laser, is scanned over the surface at a fixed height. Although all probes crossing the laser beam will emit, emissions from outside the focal plane of the objective are blocked by a pinhole (P). By varying the focal depth, sections of the samples can be isolated and imaged. In a stage-scanning confocal microscope, the stage is scanned while the objective is kept fixed. This configuration allows the removal of chromatic aberration in the excitation arm. Finally, in a near-field scanning optical microscope (NSOM), the tip of a fiber is brought in close to the sample and is scanned over it.

that are slightly out of the objective focal plane emit light that can reach the detector. This results in images that contain a fair amount of background signal. As a consequence, epifluorescence imaging lacks the sectioning ability and has a limited spatial resolution. It does not allow discrimination between a probe on the membrane of the cell or a probe engulfed in the cytoplasm.

### 1.3.1.2 Total Internal Reflection (TIR) Illumination

One strategy to decrease the background and increase the spatial resolution is to eliminate fluorescence from outside the focal plane. Various strategies are employed to restrict the excitation and detection of fluorophores to a thin region of the specimen. Among them, total internal reflection (TIR) is one way to reduce the background signal while maintaining the wide-field illumination. Confocal microscopy is a second option, which will be discussed in Section 1.3.2.1.

The principle of TIR is simple and illustrated in Fig. 1.5. A light beam, incident on an interface with different refractive indexes for the two phases, is totally reflected if the incident angle exceeds a critical angle. While the light is totally reflected, a portion of the radiation exists in the distal phase called the evanescent wave. The evanescent wave will continue to travel into the medium of higher refractive index, but its strength will decay exponentially. The TIR illumination system takes advantage of the evanescent wave to specifically illuminate only a range of 100–200 nm from the coverslip. The result is that only probes located within such distance from the surface are excited. This provides an optical sectioning capability of a few hundreds of nanometers, at least  $5\times$  thinner than any existing confocal microscope (Section 1.3.2).

In general, TIR illumination has potential benefits in any applications requiring imaging of minute structures or single molecules in specimens having large numbers of fluorophores located outside the optical plane of interest. Since the excitation light is completely reflected away from the detection, one can easily discriminate the fluorescence signal from the excitation light and achieve very high sensitivities and detection limits. This capability is particularly useful in many types of applications. For instance, TIR fluorescence is very helpful in monitoring the interaction between an intracellular protein and the substrate, especially in cases where the intracellular protein is of very high abundance in the cytoplasm, which will inevitably generate very high internal noise using a conventional epillumination. Another important application of TIR is in the characterization of forces exerted on the substrate during cell motility. For instance, the observation of points of contacts or focal adhesions between the cell and the substrate holds information on how the traction forces are transmitted [59]. Finally, by varying the illumination incidence angle, and consequently the penetration depth of the evanescent wave, fluorophores can be distinguished by depth on a nanometric scale. If one were able to vary rapidly the evanescent field depth, target vesicles or other structures can be tracked at different depths and their positions accurately determined.

The main limitation of TIR, however, resides in the small penetration depth of the evanescent field. Imaging chromophores inside cells becomes exponentially difficult and requires a different strategy.

### 1.3.2

#### Scanning Methods for Microscopy

##### 1.3.2.1 Laser-scanning or Stage-scanning Confocal Microscopy

Traditionally, biologists have physically sliced through specimens to look at internal structures with a conventional light or electron microscope. The *laser-scanning* confocal microscope allows optical sectioning through a whole intact sample. Its principle is illustrated in Fig. 1.5. A computer-controlled laser beam is tightly focused and scanned over the surface at a fixed depth (in fact the objective is scanned). For each position of the light beam, the emission light is collected back through the same objective. By using a pinhole in the path to the detector, the fluorescence

light coming from outside the objective focal plane is rejected, thus providing a high-resolution image at that depth. By progressively changing the plane of focus, one can section the entire specimen optically, producing a sharp image of the fluorescently marked components for many different depths. A confocal reconstruction is produced when all these layers are put together to provide a two-dimensional representation of the three-dimensional information. The slicing resolution of a confocal microscope is of the order of  $\sim 1 \mu\text{m}$ , i.e., about  $5\times$  the  $z$ -resolution achievable by TIR illumination (Section 1.3.1.2). However, the ability to probe entire cells or organisms instead of only their contact point with the surface makes confocal microscopy the method of choice for many applications. One inconvenience of a confocal microscope is the time needed to acquire an image. Considering an integration time of a few tens of milliseconds per pixel, it takes a few minutes to capture a high resolution image.

In a laser-scanning confocal microscope, the spatial resolution is limited by the optics and by the size of the focused laser beam. In particular, diffraction limits its size so that a tightly focus beam of wavelength  $\lambda$  still has a spot with extension of roughly  $\lambda/2$ . Considering that excitation wavelengths are in the 400–500 nm range, the spot of a focused laser beam is at least 200 nm wide. Two point-like sources closer than this distance will be excited simultaneously by the focused beam, and one will not be able to distinguish them. There are two strategies to reduce the resolution limit of a confocal microscope. First, the excitation volume can be narrowed. This can be achieved through interference methods [60] or by stimulated emission depletion [61]. Resolutions beyond the Rayleigh limit have been achieved, although these methods are cumbersome to implement. The second strategy is useful when one is interested in the relative distance between two point-like sources with different emissions rather than the exact location of each object separately [32]. In this case, one can acquire the diffraction-limited shape of each point-like source in separate channels, also called point spread function or PSF, and determine the position of the center of each PSF [62]. This requires a signal strong enough to accurately fit the PSFs. An additional critical point here is to make sure that both objects are excited identically. Usually, wavelength-dependent properties of the objective produce different  $z$ -focuses for different wavelengths. In addition, spherical aberrations and uneven flatness of the back of the objective will produce distortions in beams scanned off-axis. Finding the exact positions of the PSFs in these conditions requires an impractical characterization of the whole system. One way to circumvent these problems is to use a monochromatic excitation and move the stage instead of the laser beam. This constitutes the principle of the *stage-scanning confocal* microscope. By keeping the laser beam fixed with respect to the optical setup, chromatic aberrations in the excitation path are removed. With such a setup, colocalization of two chromophores with distinct emission spectra in the nanometer range has been reported [32, 62, 63].

### 1.3.2.2 Near-field Scanning Optical Microscopy (NSOM)

An alternative way to beat the Rayleigh diffraction limit is to use near-field methods [21, 64]. Near-field optics uses laser spots and tiny fibers with an aperture di-

ameter smaller than the diffraction limit. If the light that leaks through the fiber tip is captured in close proximity of the aperture, the excitation spot size is on the order of the aperture size, i.e., it has a subwavelength dimension. Transmitted and fluorescence light are collected in the far-field through conventional optics and detectors. To make an image, the tip is scanned over the surface and an image is built pixel by pixel.

To obtain a high-resolution image of a specimen, the tip has to be positioned within a few nanometers of the sample surface all along the scanning process. This requires a feedback mechanism, usually based on shear force. Although NSOM has been successful in imaging biological specimens on surfaces, it still presents a tremendous challenge to image unfixed cells under buffered conditions. An additional limitation of NSOM comes from the delicate process of manufacturing the fiber tips. These are brittle and may break easily if in contact with rough surfaces. In addition, the near-field regime disappears quickly in the  $z$ -direction, preventing observations in the cell interior. Finally, the experimental challenges in NSOM often overcome by far its benefits over confocal microscopy.

## 1.4 Strategies for Image Acquisition

There are different strategies to collect information and form an image. Each photon encodes a wealth of information: it has a wavelength, a polarization, and an arrival time. Each of these properties can be used to create an image. It is also possible to use a combination of detectors to measure multiple properties of the photons simultaneously, i.e., the location of multiple chromophores, their spectra, their polarization and their lifetime, provided there are enough photons to generate a signal.

### 1.4.1 Intensity Imaging

The simplest method to acquire an image is to attribute to each pixel a value proportional to the intensity of light impinging on the detector. In its simplest form, such approach is color-blind since one green photon and one red photon are not discriminated by a PMT/APD or a CCD camera. However, with the appropriate use of bandpass filters, it is possible block all photons outside a spectral window and leave only a few selected photons to reach the detector. By sequentially using different filters with orthogonal spectral windows, images corresponding to each spectral window are collected and then overlaid to produce a false-color image. Figure 1.6(A) illustrates this procedure. It shows a field of HeLa cells whose nucleus is stained with DAPI, an organic dye, and whose cytoplasm is stained with qdots. Cells are observed under epifluorescence illumination using a Hg lamp. Since DAPI emission occurs at  $\sim 450\text{--}550$  nm and the qdots emission is centered around 620 nm, the two channels of emission present minimal spectral overlap. By insert-

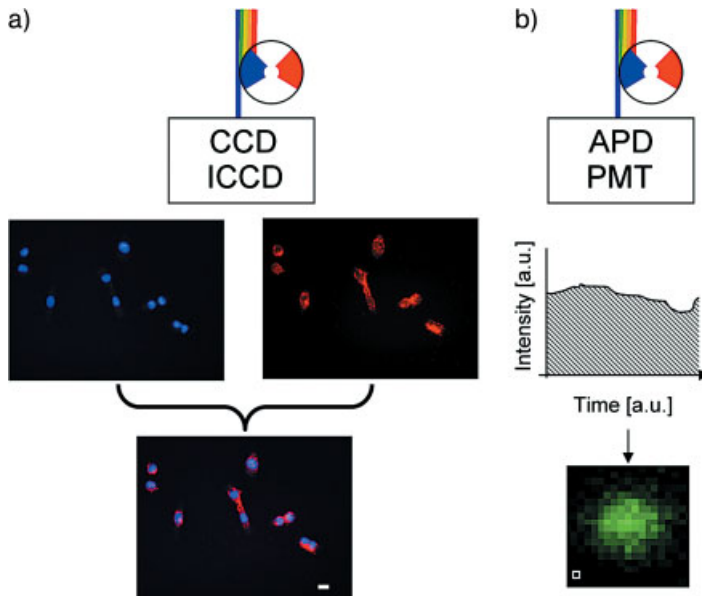


**Fig. 1.6.** A simple option for making images – Intensity imaging. (A) The simplest method of image making is to collect the fluorescence light in a CCD or intensified CCD camera. To discriminate different colors, filters are inserted in the emission path to block undesired colors. By changing filters, the same CCD camera can record, sequentially, different emissions from the same area. A color image is created by overlaying individual images. In the example shown, HeLa cells are imaged through epifluorescence illumination with an Hg lamp. The nuclei of the cells were stained with a blue dye (DAPI) and the cytoplasm stained with red qdots. Scale bar: 5 nm. (B) If a PMT or an APD

were used, one would have measured a time-dependent signal with no encoded spatial information. The integrated intensity over a period of time may be used for imaging. If a focused laser beam is scanned over a surface, each position of the objective can be translated into a pixel. The value of the pixel is proportional to the integrated intensity. This is illustrated by measuring the spot produced by a single qdot. Note that the qdot spot is diffraction-limited even if the emitter is a point source. The white square represents a single pixel. Pixel size: 50 nm, integration time: 100 ms pixel<sup>-1</sup>.

ing the appropriate bandpass filters (for instance a short pass filter with cutoff at 520 nm and a long pass with cutoff at 580 nm), a blue image of the nuclei and a red image of the cell cytoplasm can be recorded separately and then overlaid. When multiple chromophores with closer emission wavelengths are used, a clear distinction between channels is not always possible, and spectral imaging (Section 1.4.2) can represent one way to minimize the overlaps. This is especially true for organic dyes where the emissions are broad (>50 nm) and tailed to the red; but it also applies to qdots with narrower and more symmetric emission spectra.

If the CCD camera were replaced by a PMT or APD detector, one would acquire a trace similar to that shown in Fig. 1.6(B). There is no spatial resolution in this case but a time dependence of the signal, which represents the amount of photons

emitted from all over the illuminated area that reach the detector. For imaging purposes, epifluorescence illumination using an arc lamp and PMT detection is of limited use. However, things are different if a cw or pulsed laser is used. Here, the coherence of the laser allows its focusing down to a tiny spot. The fluorescence intensity from the illuminated spot is proportional to the integrated signal reaching the PMT/APD detector. If the laser spot is scanned over the surface, and the out-of-focus light blocked by a pinhole (Section 1.3.2.1), an image of the emitters can be constructed pixel by pixel. For example, Fig. 1.6(B) shows the confocal image of a single CdSe/ZnS qdot. Although the qdot is less than 10 nm in diameter, its image is diffraction-limited because it maps the point-spread function of the excitation. With a sufficient signal-to-noise ratio, the PSF can be accurately fitted and its center determined (Sections 1.3.2.1 and 1.5.1) [32, 62]. Because of the scanning nature of the acquisition process and because typical integration times of a few tens of millisecond per pixel are needed, the acquisition of a  $256 \times 256$  pixels image necessitates a few minutes. The use of a pulsed excitation affords additional imaging modalities. It allows correlation of the arrival time of the photon onto the PMT/APD detector to an external clock (i.e., the pulse of the laser), which constitutes the basis for measuring the lifetime of a chromophore (Fig. 1.8 and Section 1.4.3 below).

#### 1.4.2

#### **Spectral Imaging**

A general problem with organic chromophores is their relatively broad emission spectra. This makes the spectral separation by bandpass filters difficult and impractical, especially when multiple chromophores with close emissions are used. It is often impossible to avoid the leaking of one color channel into another one. It is then advantageous to use spectral imaging. These methods collect all photons together and record an emission spectrum. Because fluorescence is incoherent, the total signal is simply the sum of every individual photon. The knowledge of the emission properties of each single fluorophore permits the deconvolution of the signal into diverse contributions.

Spectral imaging is illustrated in Fig. 1.7. Green-emitting qdots (emission at 540 nm) are covalently linked to several Cy3B, an organic dye with emission at about 575 nm. These conjugates are model systems for FRET imaging that will be discussed in Section 1.4.4. A tightly focused laser excites the conjugates. The fluorescence emission is spectrally resolved using a grating and collected by a CCD camera. The spectrum clearly shows two components, corresponding to qdots and dyes, respectively. Notice the narrower contribution of the qdot. A deconvolution of the spectrum into qdot and dye components allows the encoding of this pixel into several colors. If the same procedure is repeated for other pixels, a multicolor map can be constructed. In the simple case of Fig. 1.7, the deconvolution is a trivial task because the chromophores have almost non-overlapping emissions. However, spectral imaging may become quite complex as the number of chromophores increases and their spectra start to overlap. With CdSe/ZnS qdots, four colors of



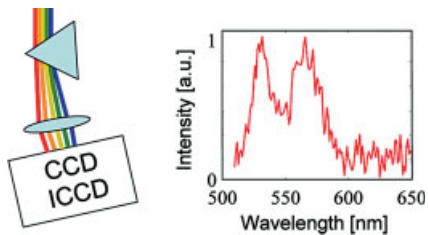


**Fig. 1.7.** Another simple option for making images is spectral imaging. Instead of using filters to separate the different emissions, the entire beam can be split through a prism or a grating and detected with a CCD camera or an intensified CCD camera. Here, the wavelength of the photon is encoded into the area of the CCD chip. The spectrum on the right shows

the emission of a complex made of a single CdSe/ZnS qdot (emission  $\sim 530$  nm) linked to several Cy3B, an organic dye (emission  $\sim 580$  nm). By scanning the surface and deconvoluting the spectrum into these two components for each pixel, a multicolored map can be created with a single scan.

emission in the visible range could be specifically coded and detected by linking single-stranded DNA to each color of emission [33]. The use of qdots with emissions in the IR (Fig. 1.3B) can provide additional detection channels while preserving the simplicity of the excitation/detection schemes.

#### 1.4.3

#### Lifetime and Time-gated Imaging

Lifetime is another property of fluorophores that can be used for imaging because it allows high-sensitivity and background-free imaging (Fig. 1.8). After excitation by a laser pulse, most organic fluorophores emit one photon within a characteristic time of a few nanoseconds. Two distinct fluorophores are likely to have different

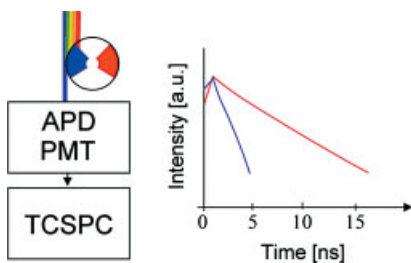


**Fig. 1.8.** Lifetime imaging is a further simple option for making images. A PMT/APD can also be used to map the lifetime of the emission. The arrival time is correlated with the firing of the laser by a time correlated single-photon counter (TCSPC). The example

shown here compares the lifetimes of Cy3B, an organic dye (blue curve,  $\sim 2$  ns), and qdots (red curve,  $\sim 10$ – $17$  ns). The large difference allows electronic gating as a way of increasing the signal-to-noise ratio.

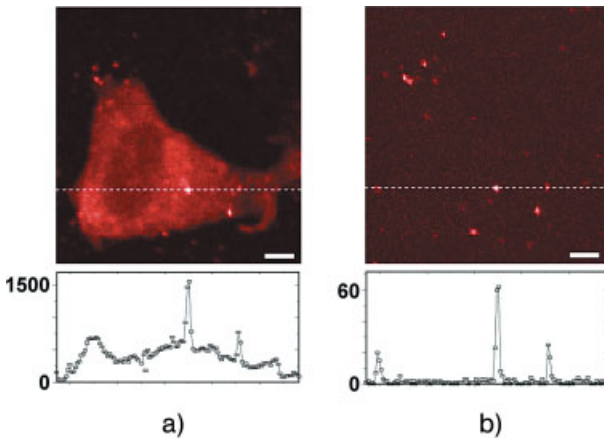


**Fig. 1.9.** Time-gate detection. The long lifetime of qdot permits suppression of the fluorescence of short-lived species, for instance autofluorescence and emission from other organic dyes. In this example, 3T3 mouse fibroblasts were incubated with red qdots. Imaging was performed using a confocal microscope (10 ms integration per pixel, lifetime window of 0–150 ns after the laser

pulse, 5 MHz repetition rate). (A) All photons have been used to create the image. (B) Only photons arriving after the disappearance of the autofluorescence background were retained (30–65 ns after the laser pulse). Even though the total signal decreases markedly, the signal-to-noise ratio increases from 3 to 45. (Adapted with permission from Ref. [38]. Copyright 2001, Optical Society of America.)

lifetimes and a simple idea is to harness this difference to encode the image. Often, however, the difference in lifetime is too small to allow a proper discrimination between two distinct fluorophores. For instance moieties responsible for the autofluorescence background of cells and conventional organic dyes have very close lifetimes and it is difficult to isolate and remove only the background contribution. Other types of fluorophores have lifetimes of the orders of milliseconds (chelated lanthanide, metal ligand complexes), but this slow emission process results in a low turnover rate, i.e., a few photons emitted per second. Qdots combine the advantage of a high turnover rate with a long lifetime (10–20 ns) that seems more amenable for high-sensitive or background-free imaging. Lifetime imaging can be implemented by using either a time correlated single-photon counter (TCSPC) [65] or a time-gated ICCD camera [38]. In this latter case, the camera is electronically gated to detect only photons emitted after a certain time window after the laser pulse and reject all other photons.

Figure 1.9 shows an implementation of lifetime imaging of a cell using qdots to increase the signal-to-noise ratio [38]. 3T3 epithelial cells were transfected with qdots and imaged with a stage-scanning confocal microscope (Section 1.3.2). Figure 1.9(A) shows the image of the cell constructed from all photons reaching the APD detector. A major contribution comes from autofluorescence background that masks partially the qdot contribution. The electronically gated image con-

structured from photons that arrived 35–65 ns after the laser pulse is shown in Fig. 1.9(B). The autofluorescence background is suppressed but the emission of the qdots is still visible. The linescan shows that the time-gated imaging, allowed by the long lifetime of the qdots, considerably increases the signal-to-noise ratio.

#### 1.4.4

#### **Other Imaging Modalities: Polarization and FRET Imaging**

Polarization imaging can be achieved by splitting the emission according to the polarizations of the photons. This can be achieved through the use of a polarizing beam-splitter or through the use of a 50/50 beam-splitter and the insertion of polarizers in front of the detector. Similarly, imaging based on fluorescence resonance energy transfer (FRET) can also be performed [66]. In a FRET process, a fluorescent donor molecule is excited but, instead of relaxing through the emission of a photon, it transfers its energy into an acceptor molecule. Emission comes from the acceptor although excitation was provided by the donor. The FRET process efficiency is very sensitive to the distance between the donor and the acceptor and vanishes for distances larger than  $\sim 10$  nm. Therefore FRET can resolve molecular interactions, because even though both donor and acceptor probes cannot be localized below the diffraction-limit individually the fact that FRET occurs is an indication that donor and acceptor are less than 10 nm apart. The detection of FRET usually proceeds through the detection in parallel of two different channels, corresponding to the donor and acceptor probes. Several protein interactions have been demonstrated in cells by FRET microscopy [67]. In fact, FRET imaging has been performed only with pairs of organic dyes or pairs of fluorescent proteins (CFP and YFP) [68] because the use of qdots as FRET pairs has not yet been established. CdSe/ZnS qdots are excellent donors even at the single molecule level, as Fig. 1.3(C) indicated. Whether they also can act as acceptors is an open issue. It may well be that, because of their size and optical properties (Section 1.2.2.4), qdots will not be efficient probes neither as FRET pairs nor for polarization imaging.

### 1.5

#### **Qdots in Biology: A Few Selected Examples**

So far, we have focused on generic aspects of qdot fluorescence, by insisting on the properties that distinguish them from organic dyes. We have described several ways to excite and detect them, and several modalities for imaging them. It is time to consider their use in life sciences applications. In fact, qdot technology has generated a great deal of excitement in chemistry and material sciences communities for all their wonderful properties, but biologists have yet to embrace it. One reason is that the interface between the bioworld and the inorganic world is still a complex field. For example, live organisms have developed defense mechanisms to fight foreign intruders. Forcing them to tolerate unnatural inorganic probes may require tricks such as masking the surface of qdots with natural moi-

eties. This section goes through some examples that illustrate how qdots can provide unique detection signatures in biology. The examples will give an overview of the possibilities of qdots for biolabeling. We will start by describing briefly the problematic that biologists are facing and how qdot technology may help solve those issues.

### 1.5.1

#### Ultra-high Colocalization of Qdots for Genetic Mapping

An important issue in genetic disease screening and diagnostics is the ability to detect DNA abnormalities in high-throughput. Many diseases result from deletions, additions or rearrangements of short segments of DNA, some of them only a few bases long. Although single nucleotide polymorphisms can be detected by DNA microarray methods using either dyes [69] or qdots [51], when the length of the abnormalities gets bigger, so do the challenges to detect and map them. A new approach was proposed in the mid-1990s by combining a technique to stretch the full genome on a glass slide with a technique to hybridize short fluorescently labeled oligonucleotides along the DNA backbone at selected locations [70]. This new approach was named dynamic molecular combing, or DMC. It features a homogenous stretching of the DNA (2  $\mu\text{m}$  per kilobase) that allows the conversion of physical distances into genetic units. DMC measures the gap between loci labeled with two different dyes. Loci can be chosen to be contiguous of a specific gene and, therefore, the measured gap between loci holds information on the length of the gene. By comparing the gap measured on the normal allele with the gap measured on the abnormal allele, the size of the deletion/addition can be determined. DMC proved to be successful in observing kilobase deletions in *tuberous sclerosis 2* gene on patients' DNA [70].

Detection of smaller abnormalities using DMC requires a method that can localize two distinct sets of probes distance of 10 to 200 nm. This range of distances lies between the range of FRET detection (1–10 nm) and the Rayleigh resolution limit of conventional optical microscopes. Two recent methods promised to reach this goal. In the first approach, resolutions down to the 5–10 nm range have been reported using organic dyes, TIR illumination and a CCD camera [60]. The method makes use of the photobleaching behavior of one of the two probes. By fitting images collected both before and after photobleaching of one of the dyes, it is possible to localize both dyes separately and compute their distance. The method has been validated by using two identical Cy3 dyes linked by a double stranded DNA [60] or multicolor dyes that are more amenable for DNA mapping [71]. Colocalization by photobleaching requires that all random and individual photobleaching events are resolved. Besides, the numerical methods used to compute the relative distances may affect the precision of the localization.

The second approach does not rely on such constraints but builds on the strengths of fluorescent probes: it uses the photostability of qdots. The approach is based on stage-scanning confocal microscopy with a single excitation source that allows the imaging of qdots free of chromatic aberrations (Section 1.3.2.1)

[32]. A laser beam is focused onto a sample sitting on a stage that can be positioned and moved with nanometer precision. For each position of the stage, the intensity of fluorescence is collected, directed into an APD, and converted into a pixel value. Pixel by pixel, an image of the emitting object is constructed as illustrated in Fig. 1.6(B). By using two APDs/PMTs, each recording the light in an orthogonal fashion, it is possible to image simultaneously two point sources emitting at different wavelengths. Because the excitation arm is fixed, it does not produce chromatic aberrations. Comparison of the positions of the two PSFs allows the determination of their relative distances. Using such a stage-scanning confocal setup and qdots, two qdots have been localized with better than 10 nm resolution. Advances in nanometer-localization imaging are likely to open new doors for DNA mapping. It may be envisioned that such fluorescence techniques would yield physical maps of single nucleotide polymorphisms of the whole genome adsorbed on a surface a few inches wide.

### 1.5.2

#### **Dynamics of Biomolecules in a Cellular Environment**

The ability to track molecules directly in live cells is an important issue in biology that may lead to an integrative view of cellular function [2, 3]. Indeed, seeing the whole pathway of a molecule in its native environment, seeing how it works, where it goes and what it does may reveal precious information on its function and its communication with the rest of the interconnected cellular network. One way to study the motion of a biomolecule is to label it with a chromophore and acquire a succession of fluorescence images that are recombined in a movie. The first experiments of fluorescence tracking of lipids on cell surfaces were reported in 2000, using TIR fluorescence microscopy [72]. Since then, ion channels, cell-adhesion proteins [73], virus infection pathways [74] and other biological processes have been visualized at the single molecule level in live cells. Most of the measurements provide a low contrast and, above all, a time window for observation limited to a few seconds before the dye or GFP bleaches out [3, 57, 75].

The photostability of qdots provides a bright and long-lasting photon source that can be used to monitor biomolecular motion either on cell membranes [11, 76, 77] or directly inside cells [13] with a high signal-to-noise ratio for many minutes. The use of an epifluorescence illumination with a CCD detector is a good compromise between the necessity to monitor an area of a few tens/hundreds of micron square, a reasonable signal-to-noise ratio, and the time resolution of  $\sim 100$  ms required to monitor moving molecules. In fact, the monitoring of molecular motion through fluorescence only reveals changes in the location of a fluorescent spot. It is then necessary to analyze its position as a function of time and relate it to a physical or biological process. Traditionally, this has been analyzed in terms of diffusion constants. An example of a physical process is Brownian motion, which is characterized by a single diffusion coefficient and a mean square travel distance that depends linearly on time. If linearity is not observed, it may be a sign that an underlying biological process is at play.

### 1.5.2.1 Trafficking of Glycine Receptors in Neural Membranes of Live Cells

The first example of molecule tracking using qdots concerns the study of the membrane structure of spinal neurons. This is achieved by tracking the dynamics of qdot-labeled glycine receptors (GlyR) for long periods [76, 77]. In general, membrane neurotransmitter receptors, such as GlyR, are free to diffuse in the membrane. However, they can accumulate at synaptic sites by interacting with sub-synaptic scaffold proteins. The number of neurotransmitter receptors at synaptic sites is an important parameter because it determines synapse plasticity and the strength of synaptic transmission. For example, removal of glutamate receptors from synapses is involved in long-term depression while their insertion contributes to long-standing synaptic efficiency. Generally, immunocytochemistry methods used to study variations in receptors distribution provide a static view of the neurotransmitter receptors and give no information on their dynamics. To study the dynamics of neurotransmitter receptors, a simple strategy consists in labeling them with fluorescent latex beads and tracking their motions with a simple epifluorescence illumination and a CCD detector. The size of the latex beads ( $\sim 500$  nm) prevented them from accessing the synaptic cleft. Things change by replacing beads with qdots. Because of their much smaller size ( $\sim 10$ – $20$  nm), qdots can be used to study the lateral movement of individual GlyR in great detail.

Figure 1.10 shows an example of QD-GlyR motion over the neural surface. Synaptic buttons are labeled in red using an organic dye (FM4-64) while GlyR are labeled with green qdots using a bridge of biotinylated antibodies and streptavidin coated qdots. The sequence of images shows one QD-GlyR (in the white circle) moving from one synaptic button to another one about  $4 \mu\text{m}$  away. In the first 30 s (top row), QD-GlyR diffuses freely in the synaptic membrane, it then docks at the synaptic button (bottom row). Further quantitative information is obtained by analysis of QD-GlyR motions over more than 20 min. The diffusion coefficients reveal three types of behavior: some receptors diffuse freely and cover large areas

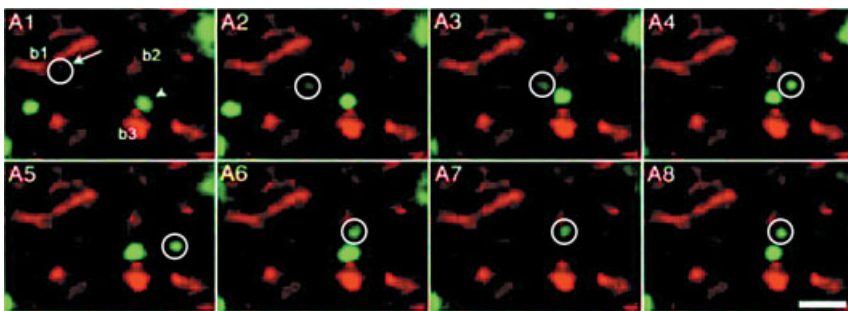


**Fig. 1.10.** Dynamics of glycine receptors revealed by qdots tracking: The example here shows the movement of a single membrane glycine receptor (circle). The receptor is labeled by a single green qdot moving from one synaptic button, labeled b1, to another

labeled b2. The synaptic buttons are labeled with a red dye. Images on the panel are selected snapshots from a 20 min sequence. (Reproduced with permission from Ref. [76]. Copyright 2003, The American Association for the Advancement of Science.)

on the membrane, other receptors remain at the synapse, whereas a final pool of receptors move in a confined space around the synapse. This leads to the classification of the neural membrane in three domains (extrasynaptic, synaptic and perisynaptic, respectively) with distinct diffusion properties. This beautiful work of Dahan and co-workers underlies the advantages of using robust qdot probes for tracking small biomolecules and illustrates the potential of qdots for the study of membrane dynamics.

#### 1.5.2.2 Dynamics of Labeled Nuclear Localization Sequences Inside Living Cells

The observation of dynamical events directly inside live cells adds one layer of complexity because the cytoplasmic environment is vastly different from conditions found outside the cell. Live cells have various kinds of inner membranes that maintain compartmental organization and they have developed various defense mechanisms to protect themselves against foreign intruders [1]. Whether exogenous qdot labels are compatible with the cell cytoplasm environment is largely unknown.

Only a handful of preliminary targeting studies using qdots in live cells have been performed. Perhaps, the simplest approach is to target the largest and most distinctive organelle of a cell: its nucleus. Nature provides the drive on how to do that. For example, viruses are hollow particles containing infectious RNA. Their

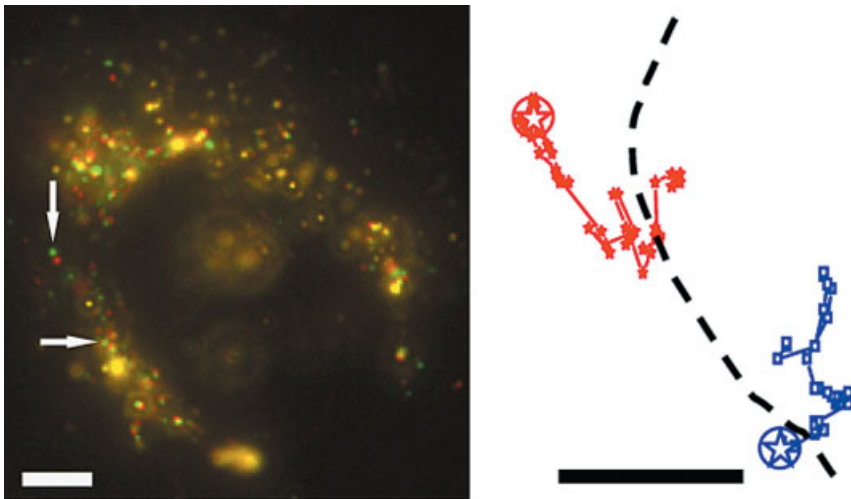


**Fig. 1.11.** Dynamics of labeled biomolecules inside live cells. HeLa cells were transfected with qdots linked to a nuclear localization signal (NLS). The NLS–qdots localize around the nucleus of the cell, and attempt to penetrate the nuclear envelope. The nucleus of a single cell is visible in the image. The image is an overlay of two frames taken 10 s apart that show how the qdots move during these 10 s (green is at time  $t$ , red at  $t + 10$  s, yellow

is the overlay, 700 ms integration time). Scale bar: 5 nm. The motions of the two NLS–qdots indicated by the arrows are shown on the right of the image. Positions at the beginning of the imaging process are indicated by stars. The nuclear membrane is shown as a dashed line. The NLS–qdot conjugates jiggle around the membrane and eventually cross it. Scale bar: 5 nm.

envelope contains peptide sequences, called nuclear localization signals (NLSs), that are recognized by the cell machinery and ferried towards the nucleus by motor proteins. It is possible to link a NLS sequence derived from a virus SV40 [78] to a silanized qdot [13]. Figure 1.11 shows the end stage of the infection process where NLS-qdots attempt to penetrate through the nuclear pores of a live cell. In a movie sequence that lasts well over 15 min, the somewhat chaotic jiggling of qdots can be observed. Some qdots get stuck at the nuclear membrane, while others manage to cross the nuclear membrane. Two examples of such NLS-qdots are highlighted on the right of the figure.

Although fluorescence imaging shows qdots concentrated around the nucleus, the fate of the NLS peptide is not known. The presence of the qdot exogenous agent is likely to activate the defense mechanisms of the cells. This may result in the cleavage of the qdot from the NLS peptide with the obvious consequence that the tracking of the fluorescent probe does not mimic the molecular pathway of the biomolecule. This is an obvious concern that needs to be addressed in forthcoming years when, no doubt, people will start tracking biomolecules inside live cells using qdots.

### 1.5.3

#### ***In Vivo* and Non-invasive Detection Using Qdot Reporters**

A final example concerns the observation of fluorescent qdots inside small animals through non-invasive imaging. In general, biomedical imaging in living tissues requires the use of exogenous contrast agents. These include MRI contrast agents, radioactive PET reporters, or infrared photons that can penetrate deeper into tissues than visible photons. In particular, the use of IR or near-IR probes would provide submicron spatial resolution and high sensitivity with simple and cost-effective detector technologies. Unfortunately, the requirements of absorption cross section, quantum yield and stability are not met by conventional organic fluorophores emitting in the IR. However, infra-red qdots may be efficient alternatives.

The fact that IR core/shell CdTe/CdSe qdots may be useful probes for non-invasive detection was demonstrated in early 2004 by mapping the sentinel lymph nodes in mice [79]. This allowed a major cancer surgery to be performed in an animal under complete image guidance. A subsequent step forward was achieved when near-IR CdSe/ZnS dots functionalized with a cancer targeting antibody were used to detect non-invasively the location of cancerous metastasis in live mice [45]. These two preliminary reports open new windows of opportunities for nanotechnology in medicine. The area of non-invasive imaging using qdots is likely to grow, as chemists get better at synthesizing IR probes.

## 1.6

### **Outlook: Is there a Role for Nanoscience in Cellular Biology and in Medicine?**

In this chapter we have focused on fluorescence detection, a central diagnostics in biology and medicine. Fluorescence imaging has reached an incredible level of



sensitivity, mainly fueled by the desire of some pioneers to watch single molecules. Today, researchers want to see more than single molecules, they want to see them rock'n roll (as beautifully phrased by Xavier Michalet [80]), and possibly in an *in vivo* environment. Moreover, as other examples discussed in this chapter have shown, biology and medicine have very ambitious plans to observe molecular events directly in their native environment. What limits such experiments today is the availability of appropriate probes, probes that are non-toxic, probes that do not bleach, probes that can be functionalized. Organic dyes, and to a lesser extent engineered fluorescent proteins, have certain limitations. Their shortcomings will likely not be compensated by an upgrade of current technologies. Future breakthroughs will rely on the development of advanced technologies based on a radically different platform. Nanotechnology can provide this platform.

Biology and nanoscience have come to a crossroads after a long courtship. Driven by the intellectual challenge of addressing the properties of particles with a finite size (first enounced by Feynman [81] and later addressed theoretically by Ryogo Kubo [82] and Terrell L. Hill [83] in the early 1960s), experimentalists started working on the production of small particles in the late 1960s and early 1970s. Over the course of two decades, synthetic methods have been perfected and the range of material synthesized has been expanded. In the 1990s, the use of chemical routes permitted the synthesis of semiconductor, metallic and oxide nanoparticles with excellent crystallinity, and with controlled size and shape [17]. In particular, semiconductor nanocrystals, whose flag carrier is cadmium selenide, exhibited remarkable optical properties, described in an earlier section, that attracted the interest of biologists as possible biolabels. Eight years after the first two reports [40, 84], the use of fluorescent nanocrystals in biology is still limited. This is largely due to the difficulty of interfacing inorganic nanoobjects with the bioworld. Yet, chemists and physicists are learning how to do it at a fast pace, and it is likely that fluorescent particles will emerge as useful tools for biology.

We can dream that qdot technology will provide highly integrated probes that can be customized to perform many tasks at once. For instance, qdots would be synthesized to carry diagnostics (they fluoresce), functional (they may be programmed to recognize tumoral cells), and therapeutics properties (they may kill tumoral cells). Qdots could be linked to MRI or PET active compounds to allow non-invasive imaging. Because qdots are made of heavy elements they are easily observable in electron microscopy and through synchrotron radiation, which will provide access to high-resolution cellular localization. We may imagine that further developments will allow the tagging of stem cells with qdots, their transplantation in live animal models, and the remote detection of their differentiation *in vivo*. One may argue that the view expressed here is much too optimistic, and even wonder whether nanotechnology will have a real impact in biology and medicine. Only time can tell.

### Acknowledgments

I would like to thank Fanqing Chen (Lawrence Berkeley Laboratory), Balaji Kannan (UC Berkeley) and Xavier Michalet (UCLA) for many discussions and collabora-

tions over the years. I want to thank Natalia Zaitseva, Giulia Galli and Sirine Fakra for their support and Maxime Dahan, Thomas Jobin and Elizabeth Jares-Erijman for permission to reproduce their figures. This work was performed under the auspices of the US Department of Energy by the University of California at the LLNL under contract no W-7405-Eng-48.

## References

- 1 H. LODISH, D. BALTIMORE, A. BERK, S. L. ZIPURSKI, P. MATSUDAIRA, J. DARNELL. *Molecular Cell Biology* (Scientific American Books, New York, NY, 1995).
- 2 R. Y. TSIEN. Imagining imaging's future. *Nat. Cell Biol.* **2003**, SS16–SS21.
- 3 Y. SAKO, T. YANAGIDA. Single-molecule visualization in cell biology. *Nat. Rev. Mol. Cell Biol.* **2003**, 4, SS1–SS5.
- 4 R. C. C. RYTHYER, A. S. FLYNT, J. A. I. PHILLIPS, J. C. PATTON. siRNA therapeutics: big potential from small RNAs. *Gene Therap.* **2004**, 1–7.
- 5 D. SEMIZAROV, P. KROEGER, S. FESIK. siRNA-mediated gene silencing: a global genome view. *Nucl. Acids Res.* **2004**, 32, 3836–3845.
- 6 G. MEISTER, T. TUSCHL. Mechanisms of gene silencing by double-stranded RNA. *Nature* **2004**, 431, 343–349.
- 7 E. A. JARES-ERIJMAN, T. M. JOVIN. FRET imaging. *Nat. Biotechnol.* **2003**, 21, 1387–1395.
- 8 E. C. FRIEDBERG, G. C. WALKER, W. SIEDE. *DNA Repair and Mutagenesis* (American Society for Microbiology, Washington, D.C., 1995).
- 9 C. B. MURRAY, D. J. NORRIS, M. G. BAWENDI. Synthesis and characterization of nearly monodisperse CdE (E = S, Se, Te) semiconductor nanocrystallites. *J. Am. Chem. Soc.* **1993**, 115, 8706–8715.
- 10 P. ALIVISATOS. The use of nanocrystals in biological detection. *Nat. Biotechnol.* **2004**, 22, 47–52.
- 11 X. MICHALET, F. F. PINAUD, L. A. BENTOLILA, J. M. TSAY, S. DOOSE, J. J. LI, G. SUNDARESAN, A. M. WU, S. S. GAMBHIR, S. WEISS. Quantum dots for live cells, in vivo imaging, and diagnostics. *Science* **2005**, 307, 538–544.
- 12 A. P. ALIVISATOS. Perspectives on the physical chemistry of semiconductor nanocrystals. *J. Phys. Chem.* **1996**, 100, 13226–13239.
- 13 F. Q. CHEN, D. GERION. Fluorescent CdSe/ZnS nanocrystal-peptide conjugates for long-term, nontoxic imaging and nuclear targeting in living cells. *Nano Lett.* **2004**, 4, 1827–1832.
- 14 B. DUBERTRET, P. SKOURIDES, D. J. NORRIS, V. NOIREAUX, A. H. BRIVANLOU, A. LIBCHABER. In vivo imaging of quantum dots encapsulated in phospholipid micelles. *Science* **2002**, 298, 1759–1762.
- 15 J. K. JAISWAL, H. MATTOUSSI, J. M. MAURO, S. M. SIMON. Long-term multiple color imaging of live cells using quantum dot bioconjugates. *Nat. Biotechnol.* **2003**, 21, 47–51.
- 16 J. R. LAKOWICZ (ed.). *Principles of Fluorescence Spectroscopy*, P. Press, (New York, NY, 1986).
- 17 W. J. PARAK, L. MANNA, F. C. SIMMEL, D. GERION, A. P. ALIVISATOS. In *Nanoparticles: From Theory to Application*, ed. G. SCHMID, pp 4–49 (Wiley-VCH Verlag GmbH & Co KGaA, Weinheim, 2004).
- 18 C. KITTEL. *Introduction to Solid State Physics* (Wiley and Sons, Inc., New York, NY, 1996).
- 19 A. L. ERFOS, M. ROSEN. The electronic structure of semiconductor nanocrystals. *Annu. Rev. Mater. Sci.* **2000**, 30, 475–521.
- 20 J. R. LAKOWICZ. Fluorescent analogues in biological research. *Encyclopedia of Life Sciences* **2001**, 1–11.
- 21 W. E. MOERNER, D. P. FROMM. Methods of single-molecule fluores-

- cence spectroscopy and microscopy. *Rev. Sci. Instrum.* **2003**, *74*, 3597–3619.
- 22 S. C. BLANCHARD, H. D. KIM, R. L. GONZALEZ, J. D. PUGLISI, S. CHU. tRNA dynamics on the ribosome during translation. *Proc. Natl. Acad. Sci. U.S.A.* **2004**, *101*, 12 893–12 898.
  - 23 D. C. PRASHER, V. K. ECKENRODE, W. W. WARD, F. G. PRENDERGAST, M. J. CORMIER. Primary structure of the *Aequorea victoria* green fluorescent protein. *Gene* **1992**, *111*, 229–233.
  - 24 O. SHIMOMURA, F. H. JOHNSON, Y. SAIGA. Extraction, purification and properties of aequorin, a bioluminescent protein from the luminous hydromedusa, *Aequorea*. *J. Cell. Comparative Physiol.* **1962**, *59*, 223–239.
  - 25 C. CORALLI, M. CEMAZAR, C. KANTHOU, G. M. TOZER, G. U. DACHS. Limitations of the reporter green fluorescent protein under simulated tumor conditions. *Cancer Res.* **2001**, *61*, 4784–4790.
  - 26 W. W. YU, Y. A. WANG, X. PENG. Formation and stability of size-, shape-, and structure-controlled CdTe nanocrystals: Ligand effects on monomers and nanocrystals. *Chem. Mater.* **2003**, *15*, 4300–4308.
  - 27 A. A. GUZELIAN, J. E. B. KATARI, A. V. KADAVANICH, U. BANIN, K. HAMAD, E. JUBAN, A. P. ALIVISATOS, R. H. WOLTERS, C. C. ARNOLD, J. R. HEATH. Synthesis of size-selected, surface-passivated InP nanocrystals. *J. Phys. Chem.* **1996**, *100*, 7212–7219.
  - 28 A. A. GUZELIAN, U. BANIN, A. V. KADAVANICH, X. PENG, A. P. ALIVISATOS. Colloidal chemical synthesis and characterization of InAs nanocrystal quantum dots. *Appl. Phys. Lett.* **1996**, *69*, 1432–1434.
  - 29 L. BAKUEVA, I. GORELIKOV, S. MUSIKHIN, X. S. ZHAO, E. H. SARGENT, E. KUMACHEVA. PbS quantum dots with stable efficient luminescence in the near-IR spectral range. *Adv. Mater.* **2004**, *16*, 926–929.
  - 30 J. M. PIETRYGA, R. D. SCHALLER, D. WERDER, M. H. STEWART, V. I. KLIMOV, J. A. HOLLINGSWORTH. Pushing the band gap envelope: Mid-infrared emitting colloidal PbSe quantum dots. *J. Am. Chem. Soc.* **2004**, *126*, 11752–11753.
  - 31 R. B. VASILIEV, S. G. DOROFEEV, D. N. DIRIN, D. A. BELOV, T. A. KUZNETSOV. Synthesis and optical properties of PbSe and CdSe colloidal quantum dots capped with oleic acid. *Mendeleev Commun.* **2004**, 169–171.
  - 32 T. D. LACOSTE, X. MICHALET, F. PINAUD, D. S. CHEMLA, A. P. ALIVISATOS, S. WEISS. Ultrahigh-resolution multicolor colocalization of single fluorescent probes. *Proc. Natl. Acad. Sci. U.S.A.* **2000**, *97*, 9461–9466.
  - 33 D. GERION, W. J. PARAK, S. C. WILLIAMS, D. ZANCHET, C. M. MICHEEL, A. P. ALIVISATOS. Sorting fluorescent nanocrystals with DNA. *J. Am. Chem. Soc.* **2002**, *124*, 7070–7074.
  - 34 M. A. HINES, P. GUYOTSIENNET. Synthesis and characterization of strongly luminescing ZnS-capped CdSe nanocrystals. *J. Phys. Chem.* **1996**, *100*, 468–471.
  - 35 D. GERION, F. PINAUD, S. C. WILLIAMS, W. J. PARAK, D. ZANCHET, S. WEISS, A. P. ALIVISATOS. Synthesis and properties of biocompatible water-soluble silica-coated CdSe/ZnS semiconductor quantum dots. *J. Phys. Chem. B* **2001**, *105*, 8861–8871.
  - 36 W. W. YU, L. H. QU, W. Z. GUO, X. G. PENG. Experimental determination of the extinction coefficient of CdTe, CdSe, and CdS nanocrystals. *Chem. Mater.* **2003**, *15*, 2854–2860.
  - 37 D. R. LARSON, W. R. ZIPFEL, R. M. WILLIAMS, S. W. CLARK, M. P. BRUCHEZ, F. W. WISE, W. W. WEBB. Water-soluble quantum dots for multiphoton fluorescence imaging in vivo. *Science* **2003**, *300*, 1434–1436.
  - 38 M. DAHAN, T. LAURENCE, F. PINAUD, D. S. CHEMLA, A. P. ALIVISATOS, M. SAUER, S. WEISS. Time-gated biological imaging by use of colloidal quantum dots. *Opt. Lett.* **2001**, *26*, 825–827.
  - 39 J. T. HU, L. S. LI, W. D. YANG, L. MANNA, L. W. WANG, A. P. ALIVISATOS. Linearly polarized emission from

- colloidal semiconductor quantum rods. *Science* **2001**, *292*, 2060–2063.
- 40 W. C. W. CHAN, S. M. NIE. Quantum dot bioconjugates for ultrasensitive nonisotopic detection. *Science* **1998**, *281*, 2016–2018.
  - 41 S. KIM, M. G. BAWENDI. Oligomeric ligands for luminescent and stable nanocrystal quantum dots. *J. Am. Chem. Soc.* **2003**, *125*, 14652–14653.
  - 42 W. Z. GUO, J. J. LI, Y. A. WANG, X. G. PENG. Conjugation chemistry and bioapplications of semiconductor box nanocrystals prepared via dendrimer bridging. *Chem. Mater.* **2003**, *15*, 3125–3133.
  - 43 F. PINAUD, D. KING, H. P. MOORE, S. WEISS. Bioactivation and cell targeting of semiconductor CdSe/ZnS nanocrystals with phytochelatin-related peptides. *J. Am. Chem. Soc.* **2004**, *126*, 6115–6123.
  - 44 X. Y. WU, H. J. LIU, J. Q. LIU, K. N. HALEY, J. A. TREADWAY, J. P. LARSON, N. F. GE, F. PEALE, M. P. BRUCHEZ. Immunofluorescent labeling of cancer marker Her2 and other cellular targets with semiconductor quantum dots. *Nat. Biotechnol.* **2003**, *21*, 41–46.
  - 45 X. H. GAO, Y. Y. CUI, R. M. LEVENSON, L. W. K. CHUNG, S. M. NIE. In vivo cancer targeting and imaging with semiconductor quantum dots. *Nat. Biotechnol.* **2004**, *22*, 969–976.
  - 46 T. PELLEGRINO, L. MANNA, S. KUDERA, T. LIEDL, D. KOKTYSH, A. L. ROGACH, S. KELLER, J. RADLER, G. NATILE, W. J. PARAK. Hydrophobic nanocrystals coated with an amphiphilic polymer shell: A general route to water soluble nanocrystals. *Nano Lett.* **2004**, *4*, 703–707.
  - 47 F. OSAKI, T. KANAMORI, S. SANDO, T. SERA, Y. AOYAMA. A quantum dot conjugated sugar ball and its cellular uptake on the size effects of endocytosis in the subviral region. *J. Am. Chem. Soc.* **2004**, *126*, 6520–6521.
  - 48 G. T. HERMANSON. *Bioconjugate Techniques* (Academic Press, Inc., San Diego, CA, 1996).
  - 49 W. J. PARAK, D. GERION, D. ZANCHET, A. S. WOERZ, T. PELLEGRINO, C. MICHEEL, S. C. WILLIAMS, M. SEITZ, R. E. BRUEHL, Z. BRYANT, C. BUSTAMANTE, C. R. BERTOZZI, A. P. ALIVISATOS. Conjugation of DNA to silanized colloidal semiconductor nanocrystalline quantum dots. *Chem. Mater.* **2002**, *14*, 2113–2119.
  - 50 S. PATHAK, S. K. CHOI, N. ARNHEIM, M. E. THOMPSON. Hydroxylated quantum dots as luminescent probes for in situ hybridization. *J. Am. Chem. Soc.* **2001**, *123*, 4103–4104.
  - 51 D. GERION, F. Q. CHEN, B. KANNAN, A. H. FU, W. J. PARAK, D. J. CHEN, A. MAJUMDAR, A. P. ALIVISATOS. Room-temperature single-nucleotide polymorphism and multiallele DNA detection using fluorescent nanocrystals and microarrays. *Anal. Chem.* **2003**, *75*, 4766–4772.
  - 52 V. L. COLVIN. Sustainability for nanotechnology. *Scientist* **2004**, *18*, 26–27.
  - 53 V. L. COLVIN. The potential environmental impact of engineered nanomaterials (vol. 21, p. 1166, 2003). *Nat. Biotechnol.* **2004**, *22*, 760–760.
  - 54 A. M. DERFUS, W. C. W. CHAN, S. N. BHATIA. Probing the cytotoxicity of semiconductor quantum dots. *Nano Lett.* **2004**, *4*, 11–18.
  - 55 C. KIRCHNER, T. LIEDL, S. KUDERA, T. PELLEGRINO, A. MUÑOZ JAVIER, H. E. GAUB, S. STÖLZLE, N. FERTIG, W. J. PARAK. Cytotoxicity of colloidal CdSe and CdSe/ZnS nanoparticles. *Nano Lett.* **2005**, *5*, 331–338.
  - 56 C. M. SAYES, J. D. FORTNER, W. GUO, D. LYON, A. M. BOYD, K. D. AUSMAN, Y. J. TAO, B. SITHARAMAN, L. J. WILSON, J. B. HUGHES, J. L. WEST, V. L. COLVIN. The differential cytotoxicity of water-soluble fullerenes. *Nano Lett.* **2004**, *4*, 1881–1887.
  - 57 J. DEICH, E. M. JUDD, H. H. MCADAMS, W. E. MOERNER. Visualization of the movement of single histidine kinase molecules in live *Caulobacter* cells. *Proc. Natl. Acad. Sci. U.S.A.* **2004**, *101*, 15921–15926.
  - 58 A. S. SEDRA, K. C. SMITH. *Micro-electronic Circuits* (Oxford University Press, New York, NY, 1998).
  - 59 P. ROY, Z. RAJFUR, P. POMORSKI,

- K. JACOBSON. Microscope-based techniques to study cell adhesion and migration. *Nat. Cell Biol.* **2002**, *4*, E91–E96.
- 60 J. T. FROHN, H. F. KNAPP, A. STEMMER. True optical resolution beyond the Rayleigh limit achieved by standing wave illumination. *Proc. Natl. Acad. Sci. U.S.A.* **2000**, *97*, 7232–7236.
- 61 T. A. KLAR, S. JAKOBS, M. DYBA, A. EGNER, S. W. HELL. Fluorescence microscopy with diffraction resolution barrier broken by stimulated emission. *Proc. Natl. Acad. Sci. U.S.A.* **2000**, *97*, 8206–8210.
- 62 X. MICHALET, T. D. LACOSTE, S. WEISS. Ultrahigh-resolution colocalization of spectrally separable point-like fluorescent probes. *Methods* **2001**, *25*, 87–102.
- 63 X. MICHALET, F. PINAUD, T. D. LACOSTE, M. DAHAN, M. P. BRUCHEZ, A. P. ALIVISATOS, S. WEISS. Properties of fluorescent semiconductor nanocrystals and their application to biological labeling. *Single Mol.* **2001**, *2*, 261–276.
- 64 R. C. DUNN. Near-field scanning optical microscopy. *Chem. Rev.* **1999**, *99*, 2891–2928.
- 65 W. BECKER, A. BERGMANN, K. KOENIG, U. TIRLAPUR. Picosecond fluorescence lifetime microscopy by TCSPC imaging. *Proc. SPIE* **2001**, *4431*, 414–419.
- 66 W. BECKER, K. BENNDORF, A. BERGMANN, C. BISKUP, K. KONIG, U. TIRLAPUR, T. ZIMMER. FRET measurements by TCSPC laser scanning microscopy. *Proc. SPIE* **2001**, *4431*, 94–98.
- 67 F. S. WOUTERS, P. J. VERVEER, P. I. H. BASTIAENS. Imaging biochemistry inside cells. *Trends Cell Biol.* **2001**, *11*, 203–211.
- 68 A. G. HARPUR, F. S. WOUTERS, P. I. H. BASTIAENS. Imaging FRET between spectrally similar GFP molecules in single cells. *Nat. Biotechnol.* **2001**, *019*, 167–169.
- 69 P. O. BROWN, D. BOTSTEIN. Exploring the new world of the genome with DNA microarrays. *Nat. Genet.* **1999**, *21*, 33–37.
- 70 X. MICHALET, R. EKONG, F. FOUGEROUSSE, S. ROUSSEAU, C. SCHURRA, N. HORNIGOLD, M. VANSLEGTHENHORST, J. WOLFE, S. POVEY, J. S. BECKMANN, A. BENSIMON. Dynamic molecular combing: Stretching the whole human genome for high-resolution studies. *Science* **1997**, *277*, 1518–1523.
- 71 X. H. QU, D. WU, L. METS, N. F. SCHERER. Nanometer-localized multiple single-molecule fluorescence microscopy. *Proc. Natl. Acad. Sci. U.S.A.* **2004**, *101*, 11298–11303.
- 72 G. J. SCHUTZ, G. KADA, V. P. PASTUSHENKO, H. SCHINDLER. Properties of lipid microdomains in a muscle cell membrane visualized by single molecule microscopy. *Embo J.* **2000**, *19*, 892–901.
- 73 R. IINO, I. KOYAMA, A. KUSUMI. Single molecule imaging of green fluorescent proteins in living cells: E-cadherin forms oligomers on the free cell surface. *Biophys. J.* **2001**, *80*, 2667–2677.
- 74 G. SEISENBERGER, M. U. RIED, T. ENDRESS, H. BUNING, M. HALLEK, C. BRAUCHLE. Real-time single-molecule imaging of the infection pathway of an adeno-associated virus. *Science* **2001**, *294*, 1929–1932.
- 75 M. GOULIAN, S. M. SIMON. Tracking single proteins within cells. *Biophys. J.* **2000**, *79*, 2188–2198.
- 76 M. DAHAN, S. LEVI, C. LUCCARDINI, P. ROSTAING, B. RIVEAU, A. TRILLER. Diffusion dynamics of glycine receptors revealed by single-quantum dot tracking. *Science* **2003**, *302*, 442–445.
- 77 M. DAHAN. Watching the dynamics of individual proteins in live cells using quantum dots. *J. Histochem. Cytochem.* **2004**, *52*, S18–S18.
- 78 D. A. JACKSON, R. H. SYMONS, P. BERG. Biochemical method for inserting new genetic information into DNA of Simian Virus 40: Circular SV40 DNA molecules containing lambda phage genes and the galactose operon of *Escherichia coli*. *Proc. Natl. Acad. Sci. U.S.A.* **1972**, *69*, 2904–2909.
- 79 S. KIM, Y. T. LIM, E. G. SOLTESZ, A. M. DE GRAND, J. LEE, A. NAKAYAMA, J. A.

- PARKER, T. MIHALJEVIC, R. G. LAURENCE, D. M. DOR, L. H. COHN, M. G. BAWENDI, J. V. FRANGIONI. Near-infrared fluorescent type II quantum dots for sentinel lymph node mapping. *Nat. Biotechnol.* **2004**, *22*, 93–97.
- 80 X. MICHALET, A. N. KAPANIDIS, T. LAURENCE, F. PINAUD, S. DOOSE, M. PFLUGHOEFFT, S. WEISS. The power and prospects of fluorescence microscopies and spectroscopies. *Annu. Rev. Biophys. Biomol. Struct.* **2003**, *32*, 161–182.
- 81 R. P. FEYNMAN. There's plenty of room at the bottom. <http://www.zyvex.com/nanotech/feynman.html> **1959**.
- 82 R. KUBO. Electronic properties of metallic fine particles. *J. Phys. Soc. Jpn.* **1962**, *17*, 975–986.
- 83 T. L. HILL. Thermodynamics of small systems. *J. Chem. Phys.* **1962**, *36*, 3182–3197.
- 84 M. BRUCHEZ, M. MORONNE, P. GIN, S. WEISS, A. P. ALIVISATOS. Semiconductor nanocrystals as fluorescent biological labels. *Science* **1998**, *281*, 2013–2016.

## 2 Characterization of Nanoscale Systems in Biology using Scanning Probe Microscopy Techniques

*Anthony W. Coleman, Adina N. Lazar, Cecile F. Rousseau,  
Sebastien Cecillon, and Patrick Shahgaldian*

### 2.1 Introduction

The numerous variants of Scanning Probe Microscopies (SPM) that have appeared since the invention of Scanning Tunneling Microscopy (STM) in 1982 [1] have opened up a new world for the visualization and characterization of surfaces. Their application to the biological sciences has allowed imaging of a vast range of systems hitherto unseen and the spin-offs of SPM have allowed biologists to probe the forces [2], mechanical properties of biological entities [3] and, with the use of SPM derived cantilever arrays, develop novel bio-sensors [4–8].

However, this meeting of physics, biology, chemistry and micro-technology was and still remains, in my opinion, not quite the universal solution to the imaging of the nano-world of biology. The problems would appear to stem from the near immiscibility of the scientific rigor of biology and physics, and this chapter has been approached from the point of view of a tool user not a tool maker, but one who has been over the last ten years confronted by the need to characterize and understand complex structures interacting with biological systems while using physical methods. As a sideline, I have also spent the last ten years translating between the scientific languages and habits of biologists, physicists, chemists and microsystems scientists.

Thus this chapter is oriented not to the theory of Scanning Probe Microscopies but rather to how to obtain, using SPM, useful and valid information about biological systems at all levels. The physics of SPM has been widely treated in several excellent texts and readers are referred to the list of books given in Appendix 1. Similarly, an extensive body of reviews exists on the imaging of biological systems (Appendix 2).

With regard to the use of SPM on biological samples, the questions to ask are really: what information can one obtain from SPM; how can one best set up the bio-SPM experiment to maximize the chances of success; how can one avoid obtaining skewed information from a bio-SPM experiment and finally, and most importantly, does the information obtained have a real biological sense?

**Tab. 2.1.** The various microscopies available to the bio-sciences, and their characteristics.

	<i>Optical microscope</i>	<i>SEM</i>	<i>SPM</i>	<i>SNOM-NSOM</i>	<i>Confocal microscopy [9, 10]</i>	<i>Environmental electron microscopy</i>
Sample operating environment	Air, liquid or vacuum	Vacuum	Gas, liquid or vacuum	Gas, liquid or vacuum	Gas, liquid or vacuum	Gas <sup>[a]</sup> (up to 10 Torr)
Depth of field	Small	Large	Medium	Medium	Small	Large
Depth of focus	Medium	Large	Small	Small	Medium	Large
Resolution: $x, y$ (nm)	1000	5	1–10 AFM; atomic for STM	20–80	200	5–7
Resolution: $z$ (nm)	N/A	N/A	0.1 AFM 0.01 STM	1	200	N/A
Magnification	$1-2 \times 10^3 X$	$10-10^8 X$	$5 \times 10^2-10^8$			$15-5 \times 10^5 X$
Sample preparation requirement	Little	Little to substantial	Little or none	Little to substantial	Little to substantial	Little
Characteristics required for sample	Sample opaque to light	Sample must be vacuum compatible	Local variations in surface height $< 10 \mu\text{m}$		Incorporation of a fluorescent dye	–

<sup>a</sup> Possible in wet environments; suitable for hydrated specimens (cells, plant samples, tissue, etc.).

In view of these questions we will treat the various SPM methods in terms of the information they generate and also their limitations, some general thoughts on sample preparation and how this may affect the experiment, the pitfalls that may arise from various artifacts, before looking at selected examples of imaging, probing and analyzing biological systems. [Evidently, rarely are artifacts published but I know that the image files of anyone involved in the field are full of various types of artifacts, but with biological samples sometimes the seeming artifact may in fact be real and just seem to be an artifact.] There remains one final question; why carry out a bio-SPM experiment? To start to answer that question, Table 2.1 presents various microscopy methods with their experimental conditions, sample treatments, resolutions, etc.

## 2.2 The Scanning Probe Microscopy Experiment

The basis of all SPM experiments is simple: a probe is scanned across a surface to generate an image of some type. To obtain the image there must exist a localized interaction between the probe and the surface, in this way the signal obtained will be dominated only by the small part of the probe closest to the surface. Hence it is implicit that there is a strong distance dependence of the interaction so that



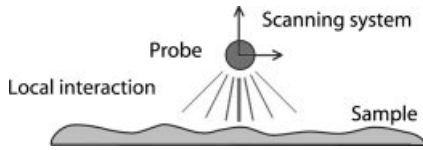


Fig. 2.1. Principle of probe–sample interaction in SPM. (Courtesy of JPK GmbH.)

only those nearest parts of the probe can contribute to the measured signal (Fig. 2.1).

Thus the SPM experiment can be defined as requiring:

$$\text{Signal} = f(d)^n$$

and effectively the resolution will be governed both by the size of the probe and the distance dependence, allowing, for example in STM where both tip size is very small and the distance dependence very strong, imaging at the atomic level.

While the physical basis of the family of Scanning Probe Microscopies is relatively straightforward, and indeed the basis of Scanning Near-Field Optical Microscopy was proposed by Syngge in 1926 in a letter to Einstein [11], the technical problems involved in the construction of a working high-resolution SPM system were the real challenge. It was thus only in the 1980s, with the development of working piezoelectric materials [12] and the computing power to implement control over the system, that working systems became available. Even then, their application to biological materials was at first hesitant.

In the following sections the basic modes of imaging, use of force–distance measurements and other SPM derived methods will be discussed with particular emphasis on the information that may be obtained and on the limitations of the various techniques towards imaging biological systems.

### 2.3

#### Scanning Tunneling Microscopy Imaging

Scanning Tunneling Microscopy is based on the principle of “tunneling current” flowing between a metallic tip and a conducting material (when the distance is small enough, typically around 1 nm) (Fig. 2.2). This current is the result of the overlapping wave functions between the tip atom and surface atom – electrons can tunnel across the vacuum barrier separating the tip and sample in the presence of a small bias voltage. This current is amplified (7 to 10 orders of magnitude) and allows the distance between the tip and the sample to be kept constant. It is mandatory to do this amplification as close as possible to the tip because any noise incorporated before the amplifier would be amplified with the relevant signal. If the tunneling current goes over its set-point the distance between tip and sample is increased, if it falls below this value then the distance is decreased.

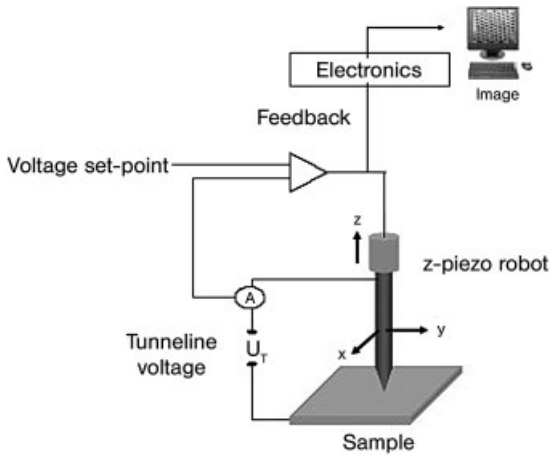


Fig. 2.2. Principle of scanning tunneling microscopy (STM) imaging.

Tunneling current originates from the wavelike properties of particles (electrons, in this case) in quantum mechanics. When a small voltage,  $V$ , is applied between the tip and the sample, the overlapped electron wave function permits quantum mechanical tunneling and a current flows across the vacuum gap (Fig. 2.3).

## 2.4

### Atomic Force Microscopy

#### 2.4.1

##### Generalities

Atomic Force Microscopy (AFM) and its various imaging modes is the most widely used member of the SPM family in the study of biological systems (Fig. 2.4). The interactions used in AFM are the local attractive and repulsive forces occurring between a tip attached to a flexible cantilever and the sample surface. A typical curve of tip-sample interaction is given below (Fig. 2.5) along with one of the more generally used scanning conformations. As the tip approaches the surface from an infinite distance, firstly attractive forces are present and due to the flexible nature of the cantilever it deflects toward the surface; at close ranges repulsive forces will dominate and the cantilever will deflect away from the surface. By use of a laser beam reflected from the surface of the cantilever (where the tip is mounted) onto a four quadrant Position Sensitive Device (PSD) the deflection of the cantilever can be measured and a feedback loop can be activated to position the cantilever with regard to the surface (Fig. 2.4). Obviously, the choice of the deflection at a set point to set in place the feedback loop along with the spring constant of the cantilever allows the forces applied to the surface to be determined.

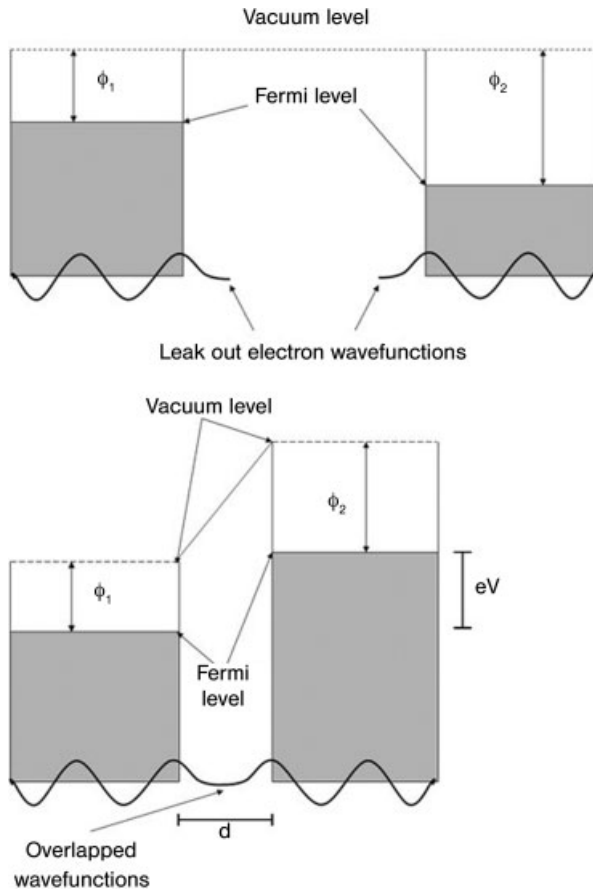


Fig. 2.3. Metal–vacuum–metal tunneling junction.

The schematic shown in Fig. 2.4 is one of two possible configurations of the microscope set up; here the piezo-ceramic scanners used to move in the  $x$ ,  $y$  and  $z$  dimensions are positioned to move the sample with the cantilever and the tip is held in a constant position. The second configuration has the piezo-ceramic scanners positioned above the sample to move the cantilever and the tip. Evidently both configurations present advantages and disadvantages; for a moving sample stage the rigidity and, hence, stability of the tip positioning can be maximized (however, access from below to the sample is blocked); this configuration also requires sealed fluid cells to prevent leakage into the piezo-ceramics when scanning in liquid systems. The use of a moving cantilever assembly above the sample will be less rigid and so more prone to “noise” in the images; however, for biological samples the advantage of being able to couple the AFM to a conventional optical microscope far outweighs the possible noise problem. There is also in this configuration much more experimental flexibility with regard to working in liquids.

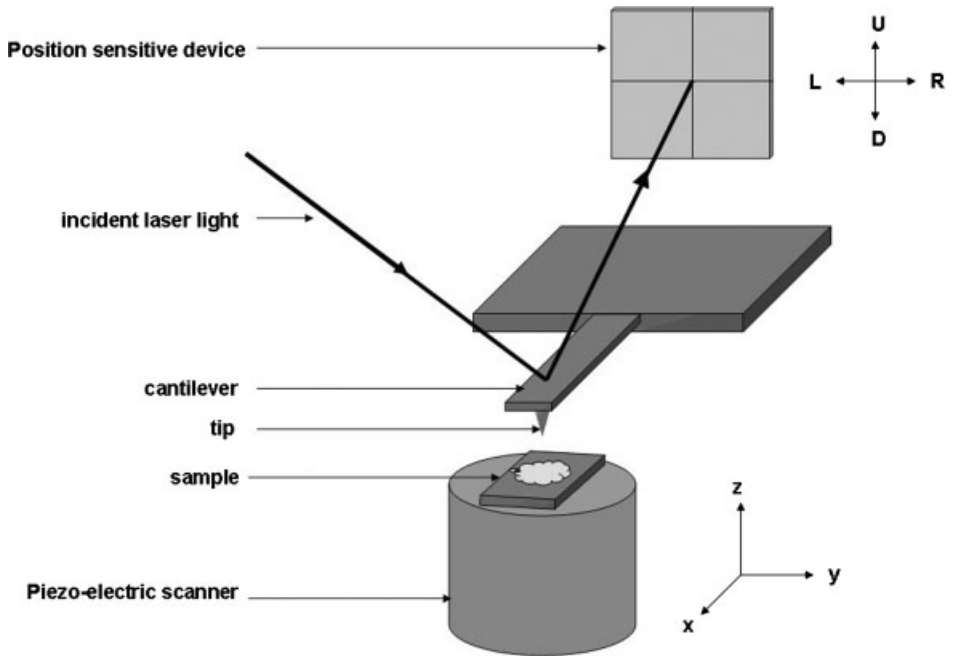


Fig. 2.4. Schematic of the atomic force microscope measurement system using the light deflection mode.

The most used imaging modes in AFM are the contact, force modulation, non-contact and intermittent contact modes. They may be best defined with regard to their positioning along the tip-sample interaction curve (Fig. 2.5).

For both contact and force modulation modes the interactions remain entirely in the repulsive zone of the curve and hence there is no part of the experiment in

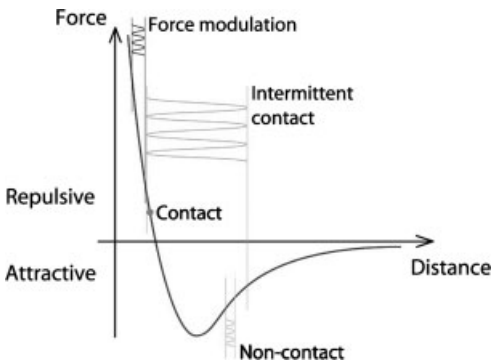


Fig. 2.5. Force curve as function of the distance between the tip and the surface. (Courtesy of JPK GmbH.)

which the tip is not touching the surface. In non-contact mode the interactions remain entirely in the attractive part of the curve, while for intermittent contact (often termed the “tapping” mode) the point will oscillate between attractive and repulsive parts of the curve.

At this point it is necessary to consider the hydration of a surface in air. Effectively, all surfaces, even highly hydrophobic ones, have a thin “contamination” layer of water associated with them, which is generally of the order of 1–5 nm high. Hence, experimentally, contact and force modulation modes of SPM imaging will be with the tip within the aqueous layer, while intermittent contact will involve the tip moving in and out of the water layer. However, for the non-contact mode it is possible to position the tip either within the water layer or when there is high cohesion of this layer to come into feedback at the surface of the aqueous layer; such positioning can modify the images obtained.

The water layer has a second effect. By capillarity, water will move up the tip to form a meniscus, and hence generate secondary drag effects when the tip scans the surface. These capillary forces may often be greater than the applied tip–sample forces and are often a cause of sample distortion or damage (cf. Section 2.6 on artifacts).

#### 2.4.2

##### Tips and Cantilevers

The SPM experiment is, in reality, simply a mean to position, move and observe the probe across a surface – hence the key to the experiment is the probe or tip.

SPM probes generally consist of a sharp (or ultra-sharp) tip mounted on the end of small flexible cantilevers [13]. Obviously, the shape and the geometry (and also the quality) of the tip will determine the resolution of the SPM image. They are generally produced from Si or  $\text{Si}_3\text{N}_4$  by micro-fabrication techniques.

Two basic shapes of cantilevers are commercially available, the V-shaped and the beam cantilever (Fig. 2.6). Because of higher mechanical stability, V-shaped cantilevers are generally preferred for contact-mode imaging (Fig. 2.7). When mechanical properties (torsion or friction forces) are studied, beam cantilevers would be preferred. For each type of cantilever, a force (spring) constant could be determined and depends on its geometry, dimensions and the material from which it is fabricated.



Fig. 2.6. V-shaped and beam SPM cantilevers.

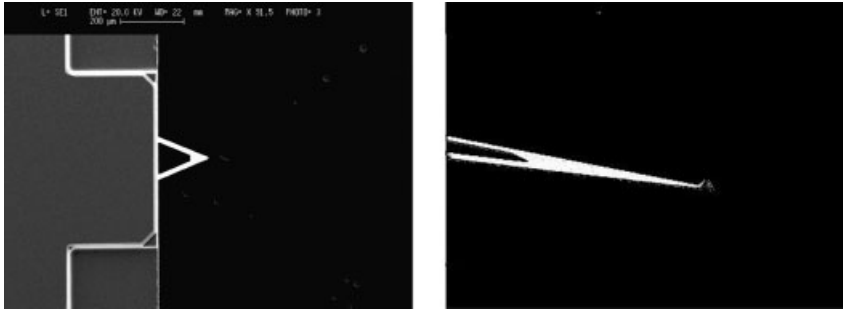


Fig. 2.7. SEM images of V-shaped pyramidal cantilevers. (Courtesy of Dr A. Wirth.)

Table 2.2 summarizes typical physical data for various commercially available cantilevers for contact and dynamic modes of SPM.

AFM tips are usually made of the same material as the cantilever as both are usually fabricated in the same time. The geometry of the tip depends on the micro-fabrication technique [14]; two main tip geometries exist: pyramidal and cone-shaped (Fig. 2.8). These tips may be submitted to additional treatments to sharpen [15] or chemically modify them [16].

Very high aspect ratios may be obtained with electron beam deposited (EBD) tips, which are AFM tips modified to grow a narrow tip-on-the-tip (Fig. 2.9). Normally, shaped silicon intermittent-contact cantilevers are modified in scanning electron microscopes. The electron beam focused on top of the tip deposits a small column of carbon, leading to a tip with narrow radius and high aspect ratio. The

Tab. 2.2. Physical characteristics of commercial cantilevers used in different modes of operation in SPM.

<b>Contact mode cantilevers</b>		
<b>Technical data</b>	<b>Typical value</b>	<b>Range</b>
Thickness ( $\mu\text{m}$ )	2	1.5–2.5
Mean width ( $\mu\text{m}$ )	50	45–55
Length ( $\mu\text{m}$ )	450	445–455
Force constant ( $\text{N m}^{-1}$ )	0.2	0.07–0.4
Resonant frequency (kHz)	13	9–17
<b>Non-contact and intermittent contact mode cantilevers</b>		
<b>Technical data</b>	<b>Typical value</b>	<b>Range</b>
Thickness ( $\mu\text{m}$ )	4	3.5–4.5
Mean width ( $\mu\text{m}$ )	30	25–35
Length ( $\mu\text{m}$ )	125	120–130
Force constant ( $\text{N m}^{-1}$ )	42	21–78
Resonant frequency (kHz)	320	250–390

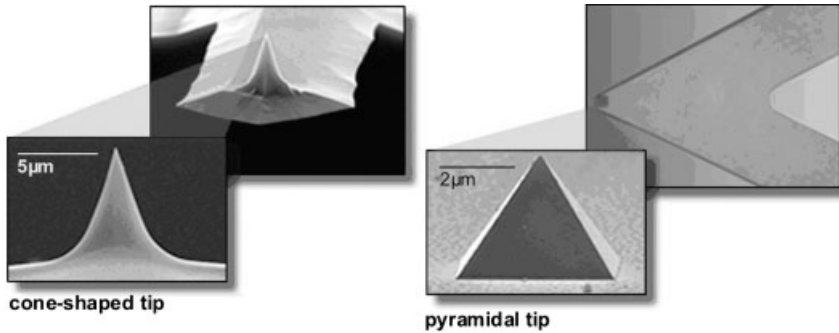


Fig. 2.8. SEM images of pyramidal and cone-shaped SPM tips. (Courtesy of JPK GmbH.)

carbon arises from hydrocarbon contamination in the vacuum chamber of the SEM. The high aspect ratio of the tip allows imaging of structures such as grooves or troughs, which are not properly imaged by tips with conventional shapes and aspect ratios [17].

#### 2.4.3

##### Contact Mode AFM

In the contact mode the tip is in continuous contact with the surface (Fig. 2.10); consequently, very high resolution imaging becomes possible. On crystalline surfaces atomic level resolution is routine for mineral systems. With well-organized two-dimensional crystals molecular imaging of proteins with sufficient resolution to show sub-units can be achieved (see Section 2.7.2 on protein imaging).

The force exerted by the tip on the sample can readily be controlled by modification of the set point value; given that this is generated by the deflection of the cantilever a lower value will evidently lead to lower interaction forces.

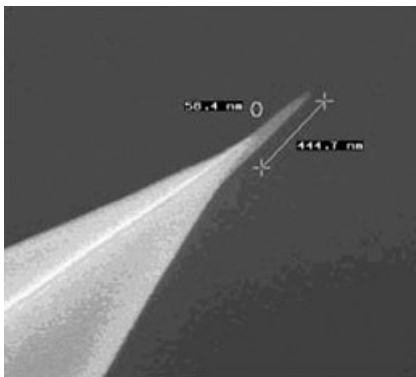
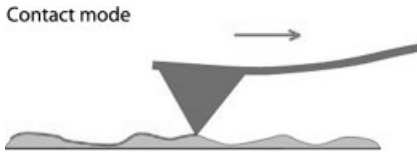


Fig. 2.9. Electron beam deposited (EBD) modified tip. (Courtesy of JPK GmbH.)



**Fig. 2.10.** Contact mode imaging; physical contact between the tip and the sample. (Courtesy of JPK GmbH.)

However, lateral forces will also be present as the tip is effectively dragged across the surface and these will, for imaging in air, be combined with effects from the capillary forces of the water contamination layer. This may generate, in systems having low adhesion to the surface on which the sample is placed, movement of all or parts of the sample; similarly, samples having low cohesion may be moved. The problem of capillary forces may be removed by carrying out the imaging in water.

Cantilevers used in contact mode imaging have, in general, low spring constants with resonance frequencies of about 10 kHz.

In nanolithography this effect is taken to its extreme and in fact becomes a useful tool, as by increasing the set point and hence the forces applied to the surface material may be voluntarily removed from the surface. This has been used to measure the heights of Langmuir–Blodgett films and also to remove self-assembled monolayers to allow deposition of other molecular layers.

#### 2.4.4

#### Dynamic Modes

##### 2.4.4.1 Generalities

In the various non-contact or dynamic modes the cantilever vibrates and it is this oscillation of the cantilever that is measured to generate the image rather than direct tip deflection. Various methods can be used to cause oscillation of the cantilever, for imaging in air these are usually mechanical, magnetic or piezoelectric, but in liquid imaging the cantilever is driven acoustically.

The resonant frequency  $f$  of the cantilever is defined by Eq. (1).

$$\text{Res. Freq. } f = \frac{1}{2\pi} \sqrt{\frac{k}{m}} \quad (1)$$

where  $k$  is the spring constant of the cantilever and  $m$  is the mass. Evidently, as the frequency passes through a resonant condition the amplitude of the oscillation increases to a maximum value before decreasing. This peak in the oscillation of the amplitude is accompanied by a switch in phase of the detected oscillation. Hence two modes of detection are possible: either via the amplitude directly or via measurement of the phase shift of the signal.



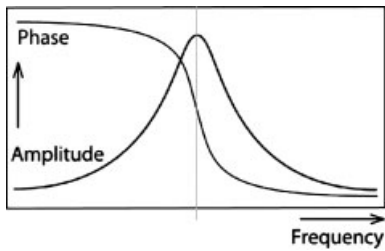


**Fig. 2.11.** First resonance frequency of a cantilever measured with optical detection. (Courtesy of JPK GmbH.)

Experimentally the situation is seldom as clear as presented in Fig. 2.11 and, often, several resonance peaks are available for use. It is also often not clear which of the resonances will generate the best image!

As the tip approaches the surface the effective mass of the cantilever will change due to the attractive forces acting on the point and hence the resonant frequency will vary. By setting the signal acquisition close to the resonant frequency and defining the set point in terms of the signal amplitude the feedback loop is engaged.

#### 2.4.4.2 Non-contact Mode

In non-contact mode (Fig. 2.12) the tip remains at all times in the attractive part of the interaction curve and the tip is scanned at a small distance (a few nanometers) above the surface with a relatively small amplitude. A clear problem with this mode is that the tip may jump into contact with the surface if the attractive forces exerted are greater than the spring constant of the cantilever, and thus much stiffer cantilevers are required. Generally, cantilevers with resonance frequencies in the range 150–300 kHz are used. True non-contact mode is almost unusable in liquid systems as the damping of the small cantilever oscillations by water or other liquids is too large and the signal disappears.

Resolution is also reduced in non-contact imaging, with a minimum value of around 1 nm. However, this may be compensated in the case of very soft samples by the lack of any contact between the tip and the sample, which may allow more accurate information in the z-axis, i.e., on the height.

#### Non-contact mode

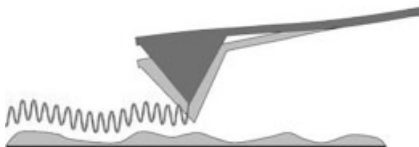


**Fig. 2.12.** Non-contact mode imaging based on oscillation of the cantilever due to interaction of the tip with the surface. (Courtesy of JPK GmbH.)

### Intermittent contact

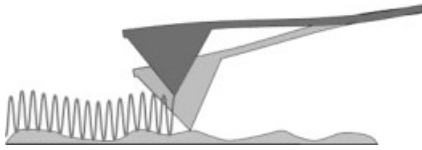


**Fig. 2.13.** Intermittent contact mode imaging characterized by oscillation with high amplitudes. (Courtesy of JPK GmbH.)

#### 2.4.4.3 Intermittent Contact Mode

In intermittent contact mode, or as it is often termed the tapping mode, the cantilever moves rapidly with a large oscillation between the repulsive and attractive regimes of the interaction curve (Fig. 2.13). Here the maximum orthogonal forces applied to the surface may be lower or higher than those experienced in the contact mode but such forces are not applied constantly, thus lowering drag forces on the sample and reducing to some extent the possibility of sample damage. However, care must be taken with regard to very soft samples in terms of compression and possible distortion of height information.

Again stiff cantilevers, generally with resonant frequencies in the range 200–400 kHz, are used to allow the tip to break free of the water contamination layer. With regard to imaging using intermittent contact mode in water the problem of capillary forces is removed and much softer cantilevers, often contact mode, are generally used. However, again severe damping will occur. Technically this problem is overcome by driving the cantilever at the resonant frequency of the liquid cell or of the acoustic cell used.

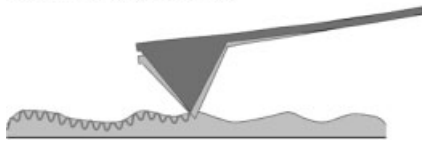
As noted above, there will be a shift between the phase of the drive signal and that observed by the lock-in amplifier of the detector. This phase signal is highly sensitive to the tip–sample interaction and can generate information on the mechanical properties of the sample. Such phase shifting may occur via adhesion between the tip and the sample or by a viscoelastic response of the sample. This can be particularly useful to analyze samples in which a phase separation has occurred between two components of a sample having the same height.

#### 2.4.4.4 Force Modulation Mode

This mode combines the oscillation of the cantilever with scanning in the contact mode (Fig. 2.14). The cantilever is now oscillated at very low frequencies, normally between 1 and 5 kHz, and thus much below the resonant frequency of even the cantilevers used in contact mode imaging.

The information extracted concerns the mechanical and viscoelastic properties of the sample, and again is useful for extracting information on samples containing composite materials but which have no topographical differentiation between the components.

However, the forces applied to the sample can be very high and this mode is often damaging to both sample and tip.

**Force modulation mode**

**Fig. 2.14.** Force modulation mode imaging based on the vertical motion of the scanner undergoing a “feeling out” of the surface by the cantilever. (Courtesy of JPK GmbH.)

## 2.4.5

**Friction Force Mode or Lateral Force Mode**

As noted in Section 2.4.1, the experimental setup of the AFM experiment uses a four quadrant detector. Thus information is not only available about the topography of the sample via the cantilever deflection in the vertical axis but also concerning twisting of the cantilever in the horizontal axis. This information concerns the friction forces occurring between the tip and the surface.

Gel surfaces that do not contribute to topographical information can be observed in the lateral mode image.

## 2.4.6

**Force–Distance Analysis**

If, in place of scanning, the tip is placed at a fixed point on the sample and now moved in the vertical direction to the surface and then retracted from the surface the deflection of the cantilever as it moves can be measured as shown in Fig. 2.15. The deflection of the cantilever will provide information on the mechanical properties of the material during the part of the approach and the retraction when it is in the repulsive, contact region of the cycle, and also on the adhesion interactions between the tip and the surface as it tries to disengage from the sample. This is termed force–distance measurement.

When the sample is hard and incompressible, as would be seen with glass, ceramics or metallic surfaces (Fig. 2.16a and b), the tip will simply approach the surface, jump into contact and then bend; the retraction curve will be the same, although scanning in air will induce adhesion of the tip to the sample by the water layer. To remove these water adhesion effects, which can be of the order of several to hundreds of nano-Newtons, force–distance measurements are normally carried out in a fluid system.

For more compressible samples the curve will be expected to resemble that in Fig. 2.16(c) and information on the mechanical properties of the sample may be extracted. However, care must be taken as effects of the sample substrate may also be observed. Often, during retraction hysteresis will be seen, particularly if the sample is not perfectly elastic.

However, now suppose that a molecule has been coupled to the tip and a recep-

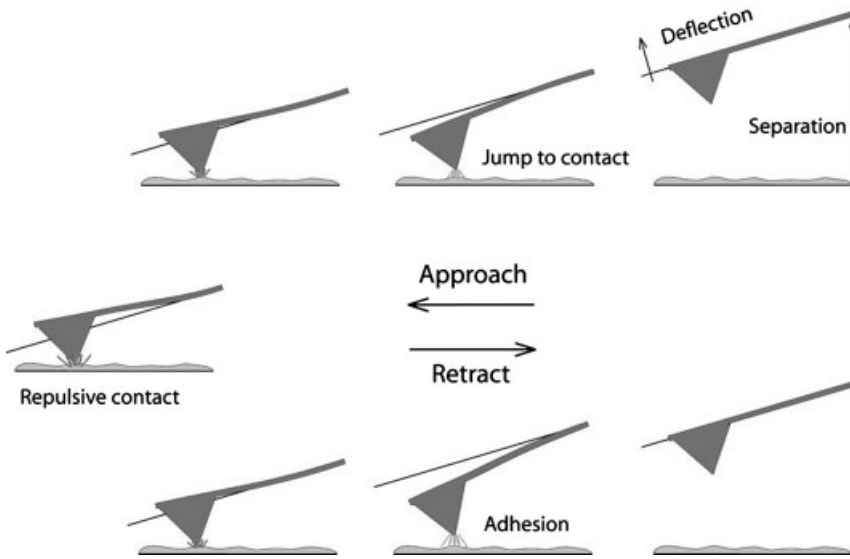


**Fig. 2.15.** Schematic diagram of vertical tip movement during the approach and retract parts of a force spectroscopy experiment. (Courtesy of JPK GmbH.)

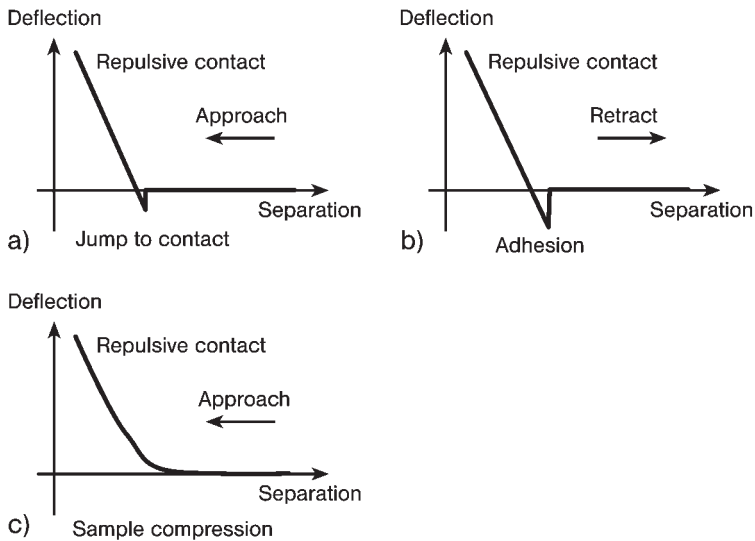


**Fig. 2.16.** Typical force–distance curves, showing, left to right, no adhesion on a hard surface, adhesion on a hard surface and non-adhesion on a soft surface in a liquid. (Courtesy of JPK GmbH.)

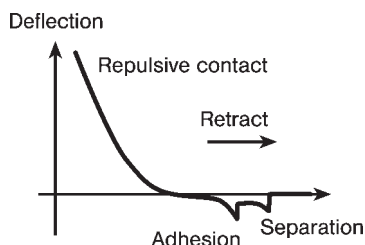


**Fig. 2.17.** Force–distance measurement in water between a ligand fixed to a coated AFM tip and the receptor present on the sample. (Courtesy of JPK GmbH.)

tor is present on the sample. When the tip is in contact with the surface there will be ligand–receptor coupling; as the tip is retracted, force will be applied to the complex until, eventually, the applied force is greater than the interaction force. At this point the tip will snap off. As the area of the tip is considerably greater than that of a single molecule one cannot be certain that the rupture of the complex is due to a single molecular event, and so multiple analysis and deconvolution of the force–distance curves (Fig. 2.17) are required to calculate a single molecule interaction force. However, where knowledge of the forces involved in single molecular complexes is not required, assuming that a set of tips are roughly the same size and using receptors of the same size, e.g., antibodies, the experiment may be used to analyze whether there is recognition between a ligand and a biomolecule [18].

Interaction forces have been calculated for a wide range of molecular interactions, varying from the streptavidin–biotin complex, which has the strongest non-covalent interaction known for biological systems at  $340 \pm 120$  pN [26], down to carboxylic acid–carboxylic acid interactions where forces are in the range of 17 pN [20]. Table 2.3 gives typical values of molecular interactions forces for biological molecules and interaction forces for cells.

AFM has also been used to evaluate the strength of a covalent bond (Si–C) under an external load [36].

For biological molecules other events may be associated with force–distance curves, including unraveling of the molecule, as has been observed for polysaccharides [37, 38], DNA [39–42] and proteins [43–49].

#### 2.4.7

#### Chemical Force Imaging

In Chemical Force Microscopy the tip is modified chemically, either directly by using organo-silane chemistry or by alkylthiol chemistry after first coating the tips with a thin layer of gold. In this way charged (ammonium or carboxylate), hydrogen bonding (hydroxyl) or non-interacting hydrophobic (alkane) surfaces may be grafted onto the tips, Fig. 2.18 [50].

Tab. 2.3. Intermolecular forces derived from force spectroscopy.

Receptor	Ligand	Force (pN)	Ref.
Thymine	Adenine	54	19
Carboxylic acid	Carboxylic acid	16.6	20
Biotin	Avidin	160	21
Iminobiotin	Avidin	85	21
Adhesion glycoprotein CsA	Adhesion glycoprotein CsA	23	22
Concavalin-A (lectin)	Mannose	47 ± 9	23
Meromyosin	Actin	15–25	24
Biotin	Streptavidin	200–257	25, 26
		340 ± 120	
20 Base pairs DNA	Complementary strand	1520	27
16		1110	
12		830	
Cell-adhesion proteoglycans	Cell-adhesion proteoglycans	40–125	28
Biotin	Antibiotin antibody	60	29
Anti-HAS, other antibody	HAS, other antigen	49–244	30, 31
P-selectin	Glycoprotein ligand-1	165	32
Cell receptor	RGD	35–120	33
Uterine epithelium	Trophoblast	1000–16000	34
Uncoated surface	Cell-adhesion proteoglycans	19000–100000	35
Coated surface	Cell	100000–220000	35

Obviously, in the case of gold-coated tips the resolution of the experiment will reduce convolution effects due to the tip.

Scanning in the lateral force mode allows chemical imaging of structures present on the surface due to differences in interactions between the tip and the sample. Figure 2.19 shows the results of scanning with alkyl carboxylic acid or alkane

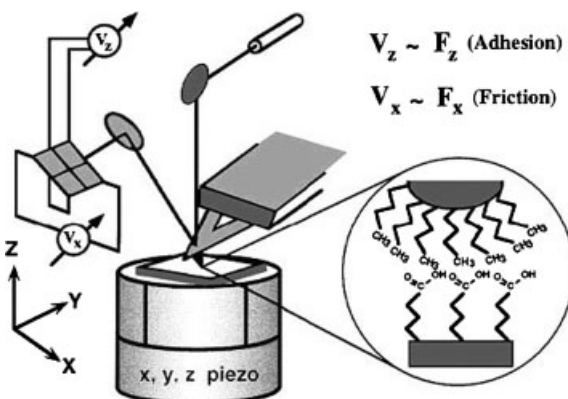
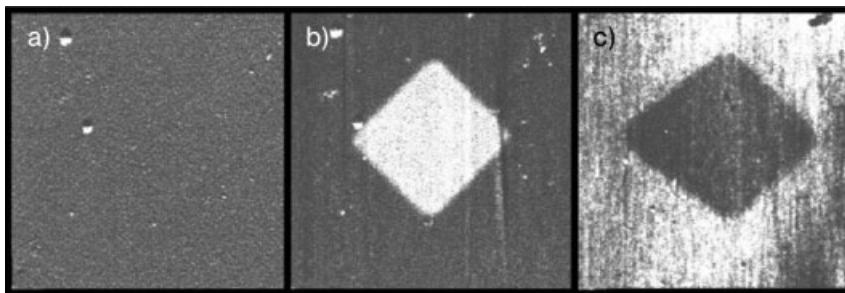


Fig. 2.18. Schematic of the principle of chemical force microscopy (CFM). (Reprinted with permission from Ref. [50]. Copyright (1997) Annual Review of Materials Science.)



**Fig. 2.19.** Force microscopy images of a photo-patterned SAM sample. The  $10 \times 10 \mu$  square region terminates in COOH, and the surrounding region terminates in CH<sub>3</sub>. The images are of (A) topography, (B) friction force using a tip modified with a COOH-terminated

SAM, and (C) friction force using a tip modified with a CH<sub>3</sub>-terminated SAM. (Reprinted with permission from Ref. [50]. Copyright (1997) Annual Review of Materials Science.)

modified points on patterned surfaces in which a square pattern of an alkylcarboxylic acid has been deposited. The topographic image in Fig. 2.19(A) clearly shows that there are no variations in layer heights. Figure 2.19(B) presents a friction force image using a tip modified with a COOH-terminated SAM, and Fig. 2.19(C) a friction force image using a tip modified with a CH<sub>3</sub>-terminated SAM. Light regions in Figs. 2.19(B) and (C) indicate high friction, and dark regions indicate low friction [50].

#### 2.4.8

##### **Dip-pen Lithography**

In a further extension of SPM derived techniques, the use of AFM tips to directly “write” structures on surfaces has been demonstrated [51–53]. Based on the soft lithography of Whitesides [54] a suitable molecule is adsorbed by capillary forces onto the AFM tip. This is then used in the contact-mode to scan pre-determined patterns on a given surface (Fig. 2.20). The use of suitable programming allows features of any shape and form to transfer to the surface with a resolution of 30 to 100 nm [53]. The choice of molecular ink to be transferred depends on the particular surface chemistry of the substrate, the application of alkane thiols onto gold surfaces being the most generally used chemistry.

#### 2.4.9

##### **Cantilever Array Sensors**

In contrast to all SPM derived methods, cantilever sensors [8] are based not on probe–sample interactions but rather on direct interaction of the sample with tip-less cantilevers. Signal detection is based on measurement of the mechanical response of the thin Si beams, arranged in a micro-fabricated array (Fig. 2.21).

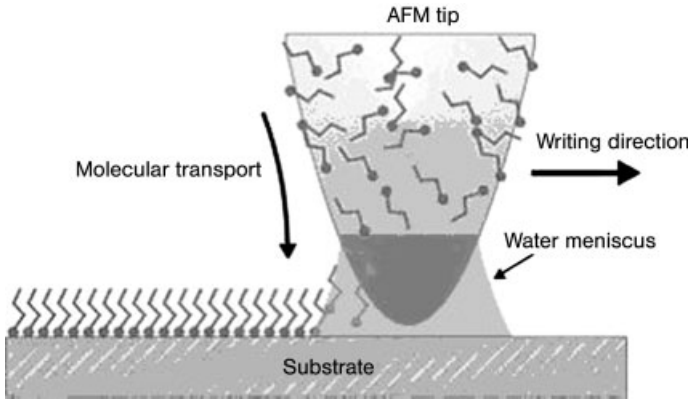


**Fig. 2.20.** Schematic of the principle of dip-pen lithography. (Reprinted with permission from Ref. [53]. Copyright (1999) Science.)

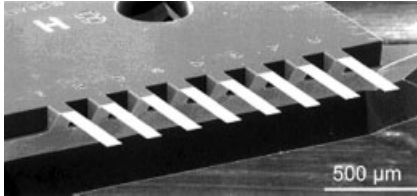


**Fig. 2.21.** Microfabricated Si cantilever array. (Reprinted with permission from Ref. [8]. Copyright (2000) Elsevier.)

Cantilever sensor arrays experiments can be performed in either static or dynamic mode. In the static mode, only one side of the cantilever is chemically modified (with a receptor molecule); contact with the analyte is responsible for surface stress that causes a bending of the cantilever. In dynamic mode, both sides of the cantilever may be modified and detection is based on mass-dependant resonance frequency (or phase) shifts of the cantilever.

Detection is either by deflection of the laser on the standard AFM photo-detector or by resonance shifts as detected with dynamic AFM modes (Fig. 2.22).

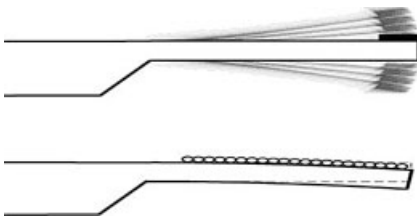


**Fig. 2.22.** Schematic of the detection principle. (Reprinted with permission from Ref. [5]. Copyright (2001) Elsevier.) ■AQ3■



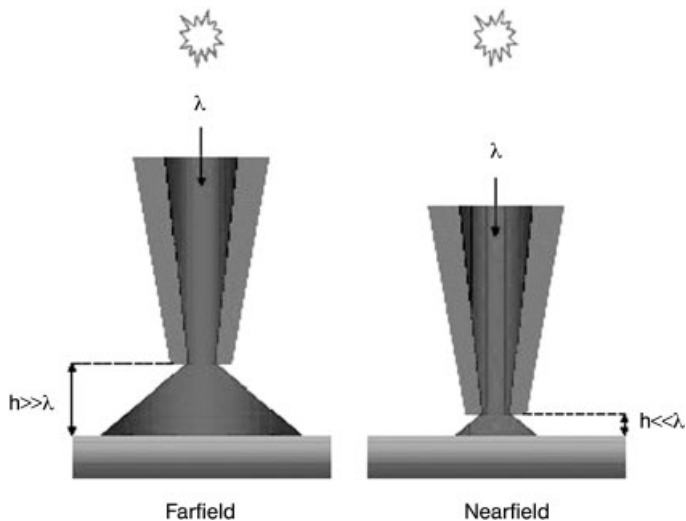


Fig. 2.23. Schematic of far-field and near-field microscopies, and probe positioning.

## 2.5

### Near-field Scanning Optical Microscopy

Near-field illumination of a sample with visible light can resolve features well beyond the resolution of conventional, far-field microscopes [55–58]. Near-field Scanning Optical Microscopy (NSOM) thus has the potential of extending the resolution of techniques such as fluorescent labeling, yielding images of cell structures and molecules on the nanoscale (Fig. 2.23).

The spatial resolution of ordinary light microscopes is limited to about 250 nm, the objective lens or equivalent, at a distance from the object observed that is several times the wavelength,  $\lambda$ , of the illuminating light. At this distance the high spatial frequencies in the image components giving information about the smallest features of the object are not collected by the imaging optics and do not contribute to image formation. It is this phenomenon, rather than the physics of light itself, that sets the  $\lambda/2$  diffraction limit. If the collecting or the illuminating optics can be brought closer to the object, to a distance less  $\ll \lambda$  from its surface (Figure 23, right-hand side), then the high spatial frequencies can be resolved, at the price of reconstructing the image from the scan of the optics across the sample. The most efficient way to do this is to bring an aperture with diameter  $\ll \lambda$  to within a few nm of the object surface. Positioning at this distance allows collection of light from the sample that otherwise would be lost to far-field collection. Conversely, illuminating through the aperture means that the incident light reaches the sample and interacts with it before it can be diffracted and lost. Thus, NSOM, like scanning confocal microscopy or AFM, builds an image by registering intensity for each point of the scan. Like confocal microscopy, NSOM uses visible light. Like AFM, it achieves super-resolution by means of a very small probe. All of the

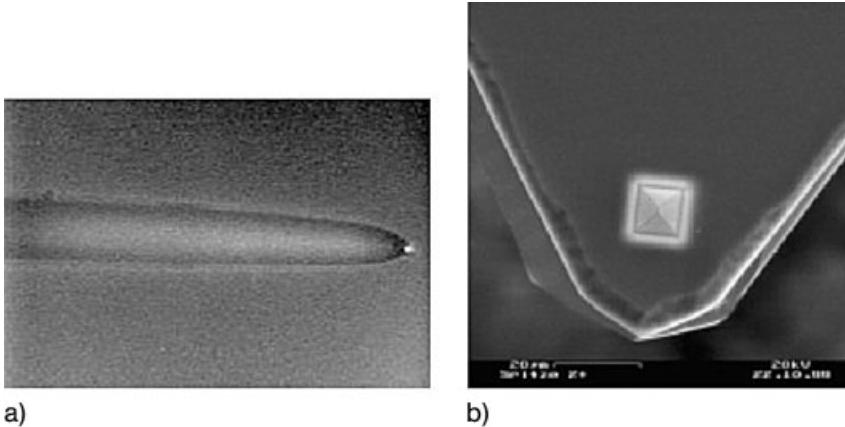


**Fig. 2.24.** The two forms of NSOM tips: (a) a pulled optical fiber with aluminum cladding and (b) an etched aperture in a standard AFM cantilever.

problems and the promise of NSOM then turn on the problems of fabricating the aperture, and scanning across the sample surface while keeping it within near-field distance of the surface.

Two main forms of NSOM tips exist (Fig. 2.24): pulled optical fibers covered with an aluminum layer and AFM tips into which the aperture is etched. Fiber tips have a better theoretical resolution, below 20 nm, while that for etched AFM tips is higher, around 50 nm; however, such resolution is not generally achieved.

In practice, fiber tips are much more fragile than AFM cantilever based tips. With regard to scanning in liquids, often a condition for biological samples, feedback control is easily obtained for the AFM tips in either contact or dynamic modes; however, fiber tips use either shear-force or an attached tuning fork for feedback, and damping of the signal is generally very high, making the experiment difficult.

## 2.6 Artifacts

### 2.6.1 Artifacts Related to Tip Size and Geometry

The shape of an AFM tip can modify considerably, with both the geometry and the radius of the tip causing artifacts. Figure 2.25 shows the effects of tip geometry on the form of the observed image of a vertical step.

None of these tip geometries can accurately give a true image of the step, indeed only a truly two-dimensional tip could image correctly such a feature. The image will always contain elements arising from a combination of tip shape and the true topography of the surface. While long thin tips will clearly best reproduce the

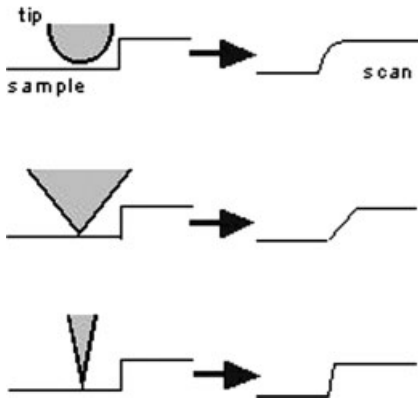


Fig. 2.25. Tip geometry effects on the image of a sharply stepped surface.

topography, there is a trade-off between the mechanical strength of the tip and the quality of the image, with sharp narrow tips being much more fragile and apt to break, which can then lead to other artifacts (see below).

Tip artifacts arising from the geometry can be modeled in terms of the cone angle of the main pyramid forming the tip and the radius of the tip end. Thus images of small sharp objects will be dominated by the tip radius, leading to sizes in the  $x$  and  $y$  dimensions that effectively measure the tip size. However, the information in the  $z$ -axis is correct and may be used to obtain the correct size of spherical or cylindrical objects. For larger objects the artifacts will be dominated by the cone angle, as noted above.

The relationship between the observed width  $W$  of a feature and the diameter of the probe tip can be calculated for an idealized tip shape, such as the one shown in Fig. 2.26, where  $x^2 = R^2 - (R - d)^2$ . For  $R \gg d$ ,  $W = \sqrt{8dR}$  and  $d = (W^2/8R)$ . For  $R = 10$  nm and  $d = 5$  nm, the observed width  $W$  would be 20 nm.

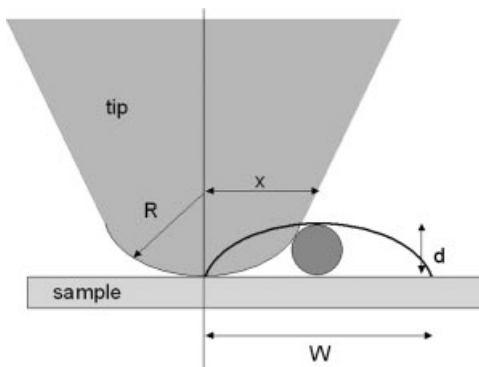
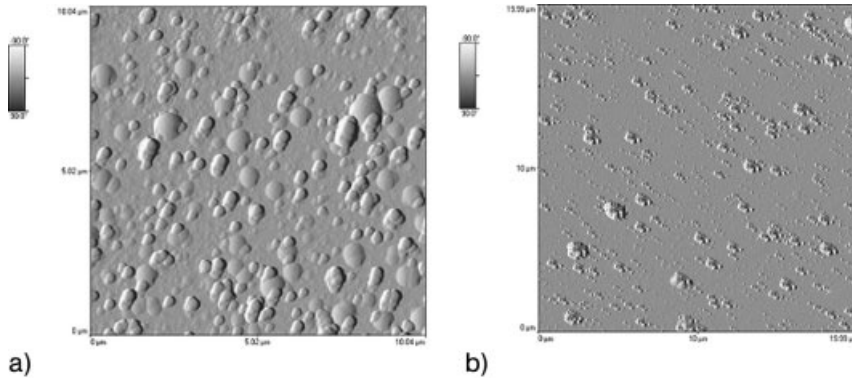


Fig. 2.26. Geometries used in investigating tip deconvolution effects.



**Fig. 2.27.** Artifacts arising from (a) a blunt tip with triangular geometry and (b) a broken tip with at least double tips.

### 2.6.2

#### Artifacts from Damaged Tips

Sometimes the tip will be damaged during use or during the fabrication process, leading to the occurrence of double or multiple tips. Such tips will generate images in which features will be present as pairs or larger multiples. These are normally relatively easy to identify (Fig. 2.27). Other damaged tips may simply have non-pyramidal shapes – again these can be identified by the presence of repeating geometries of all the features.

### 2.6.3

#### Artifacts from Tip–Sample Interactions

Artifacts may also occur when tip–sample interactions are greater than the mechanical strength of the sample being imaged. This is often encountered in the contact mode imaging of soft surfaces, or when the response times of the feedback loop are incorrectly set. This often occurs when there are rapid changes in the height of the sample in certain areas of the sample and the feedback loop values have been set on a flat part of the surface.

### 2.6.4

#### Sample Artifacts

Biological samples scanned in air are prone to sample artifacts arising from the presence of buffers in the solution used to prepare the sample. On drying, the buffer may crystallize, yielding dendritic patterns (Fig. 2.28a). By careful washing the buffer can often be selectively removed. However, some care may be taken to determine whether the patterns observed arise from the buffer, the sample or from highly complex structures arising from self-assembly (Fig. 2.28b). Here the

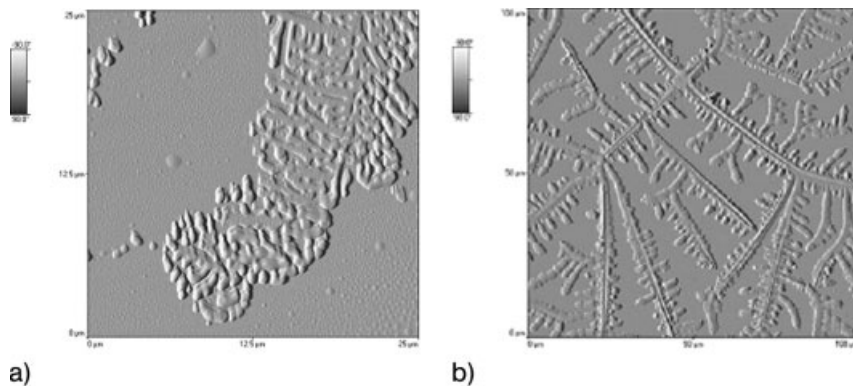


**Fig. 2.28.** (a) Artifact caused by phosphate buffer; dendritic crystallization is evident in the upper left of the image, (b) Non-artifactual patterns in a bovine serum albumin–sodium chloride mesocomposite.

apparently dendritic patterns are not “true artifacts” but arise from the protein, in this case bovine serum albumin, controlling crystallization of composite structures containing salt–protein complexes [59]. A similar problem was observed in the self-assembly of cowpea mosaic virus particles into highly ordered comb-structures with a spacing of 6  $\mu\text{m}$  [60].

## 2.7

### Using the Tools

In this section we attempt to illustrate how the various methods of SPM can be applied to the study of biological systems, using selected examples for each type of system. Evidently, due to space requirements, the presentations will not be exhaustive, but rather represent my personal choice (A.W.C.). So, in advance, I apologize to any author who feels left out in the examples presented.

#### 2.7.1

##### DNA

DNA has been imaged with a wide range of SPMs since the very debut of such experiments, firstly by STM [61] and then by AFM [62]. Subsequent experiments have involved various types of manipulation of DNA and determination of the recognition properties [63] and the mechanical unraveling of DNA strands [64]. Application of SPM to DNA has been widely reviewed (see Appendix 2).

##### 2.7.1.1 Topographic Imaging of DNA

In a series of single molecule experiments with different methods of AFM, Anselmetti et al. [65] observed topographically various DNA topologies (Fig. 2.29). Linear

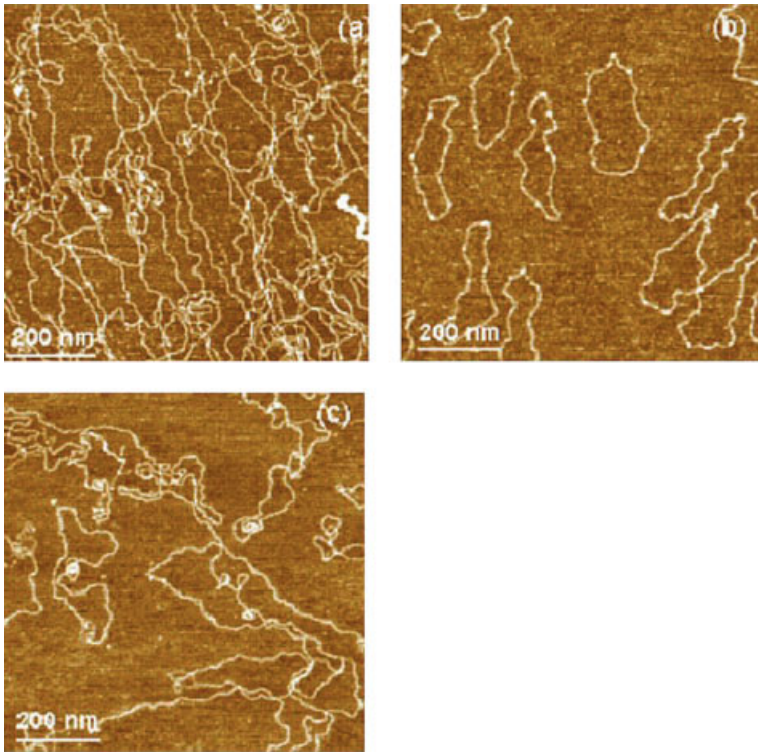


**Fig. 2.29.** Topographic images of various DNA topologies. (a) Linear  $\lambda$ -DNA (48.5 kbp), (b) non-twisted circular DNA plasmids (vector 3.2 kbp) and (c) circular supercoiled DNA with twists and writches due to internal supercoiling (supercoiled DNA ladder 2–16 kbp). Intermittent contact mode, vertical scale 3 nm. (Reprinted with permission from Ref. [65]. Copyright (2000) Wiley.)

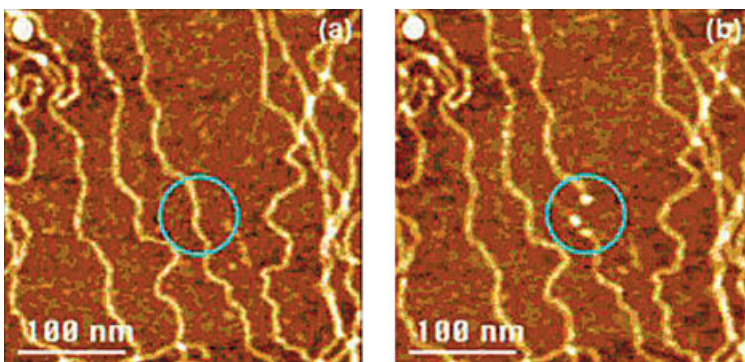


**Fig. 2.30.** Topographic images of  $\lambda$ -DNA: (a) Before and (b) after cutting a dsDNA strand. Intermittent contact mode, vertical scale 3 nm. (Reprinted with permission from Ref. [65]. Copyright (2000) Wiley.)

double strand DNA, circular plasmids and supercoiled DNA were observed. The measured widths of the strands were in the range 3–7 nm, which can be compared to the known radius of 2 nm [66]; thus the size of the imaged DNA is controlled by the tip convolution effects cited in Section 2.6.1. In comparison the observed height was 1 nm.

The experiments were further expanded to use the AFM tip as a cutting tool to locally cut the DNA strands. By using much higher tip-surface forces than normally used for scanning of soft material and repeatedly scanning at a predefined point on the DNA strand, the authors were able to use the AFM tip as a mechanical restriction endonuclease (Fig. 2.30).

As discussed above in Section 3.4.4.3, both topographic and phase difference information are available from the intermittent contact imaging AFM mode. By using carefully controlled humidity conditions Lee et al. [67] were able to image very short oligonucleotide strands (a biotinylated 21 mer 5'-biotinGAGGAGTTGGGG-GAGCACATT-3') attached to streptavidin on a gold surface. Under normal conditions such short strands of DNA-oligonucleotides are impossible to image and even here at low humidity little information is obtained. However, as shown in Fig. 6.31, localized signals arising from higher hydration of the oligonucleotide were observed. Normal phase differences are of the order of  $10^\circ$ ; however, phase differences in the range of  $70$ – $100^\circ$  were obtained (Fig. 2.31c). These show a typical adsorption curve as a function of concentration, implying saturation of available streptavidin–biotin binding sites.

#### 2.7.1.2 Imaging DNA Translocation

Atomic force microscopy imaging in liquids allows observation in almost real time (scan speeds are now such that an image can be acquired in about 1 min) of biological processes. This recognition was applied by Firman et al. [68] to translocation of DNA by Type 1 restriction-modification enzymes. Here large DNA fragments (2364 and 724 bp) both containing a single recognition site at 175 bp were used. Figure 2.32 shows the images obtained after fixed incubation times. Both DNA and the protein are clearly present. By using a large body of images the amount of translocated DNA associated with loop formation was analyzed. Single loops observed for the R1–DNA complex were determined. Evidently, the size of the loop increased with time. The authors were able to determine the velocity of the translocation process, which proved to be much lower than that previously measured [69, 70]. Prudently, the authors note that this may be due to sample surface interactions leading to an artificially slow translocation process. With the R2–DNA complex, two loops were formed (Fig. 2.32) – the difference in size between the loops was postulated to arise from the switch from the recognition to translocation process occurring independently in the two sub-units of the enzyme.

#### 2.7.1.3 DNA Interactions and Stretching

The double stranded DNA may interact with drugs, specific pharmacological functions being strongly dependent on the nature of the binding of the two systems.

Single-molecule force spectroscopy can discriminate between different interaction modes that modulate the binding of the small molecules to the DNA, by measuring the mechanical properties of DNA [71]. Several structure transitions are characterized upon stretching of double stranded DNA; it was observed, at a level of a single molecule, that the binding of a small molecule on to the DNA strongly affects these transitions (Fig. 2.33).

DNA occurs in solution as an entropic coil. When a DNA molecule attached between an AFM-tip and a surface is stretched it exerts a restoring force (see black curve in the Fig. 2.33). Up to a certain limit, these force–extension characteristics may be described by the worm-like chain model. On further increasing the applied force, the molecule undergoes an important structural transition (corresponding to a plateau in the force–extension profile). Initially, this transition plateau was thought to correspond to a structural modification of B-DNA to an overstretched S-DNA structure. One study [72] explains the plateau in the force–extension curves by a mere melting of the double helix, implying also the breakage of hydrogen bonds in the overstretching transition. After stretching beyond this melting transition the double stranded molecule is finally separated into two single strands, one of which remains tethered between tip and surface. The relaxation trace does not resemble the extension trace and single stranded DNA mechanical properties prevail. At lower forces ( $<150$  pN), partial melting of the DNA molecule can occur and is observable as a deviation of the relaxation trace from the stretching traces (melting hysteresis). This model, however, predicts that the overstretching force should be related to the thermal melting temperature and that the force range over which overstretching occurs should be related to the width of the thermal melting transition.

Ethidium bromide is a well-characterized dye that intercalates into DNA without sequence specificity. Insertion of a single dye molecule increases the base pair rise by  $3.4 \text{ \AA}$  and unwinds the double helix by  $26^\circ$ . Typical force–extension traces obtained on DNA in the presence of ethidium bromide show that low concentrations ( $0.44 \mu\text{g mL}^{-1}$  or ca. 1 molecule of ethidium per 10 bp) (Fig. 2.33 curve b) markedly affect the overstretching plateau. The increased slope of the transition regime is indicative of a reduction in cooperativity as compared to the curve obtained on the very same molecule before ethidium was added (Fig. 2.33 curve a). The force is reduced in the beginning of the transition while at the end it rises above 110 pN, almost twice the force at the end of the overstretching transition in non-complexed molecules. The melting transition, however, is still observed and hysteresis between stretching and relaxation remains. At elevated concentrations (Fig. 2.33 curve c), the plateau vanishes and a steadily rising force is observed that begins at larger extensions. Furthermore, the sharpness of the end of the overstretching plateau is lost, and it is difficult to precisely identify the beginning or end of the overstretching transition. The mechanical energy that can be deposited in the DNA double helix before force-induced melting occurs was found to decrease with increasing temperature. This energy correlates with the base-pairing free enthalpy  $\Delta G(\text{bp})(T)$  of DNA. Experiments with pure poly(dG-dC) and poly(dA-dT) DNA



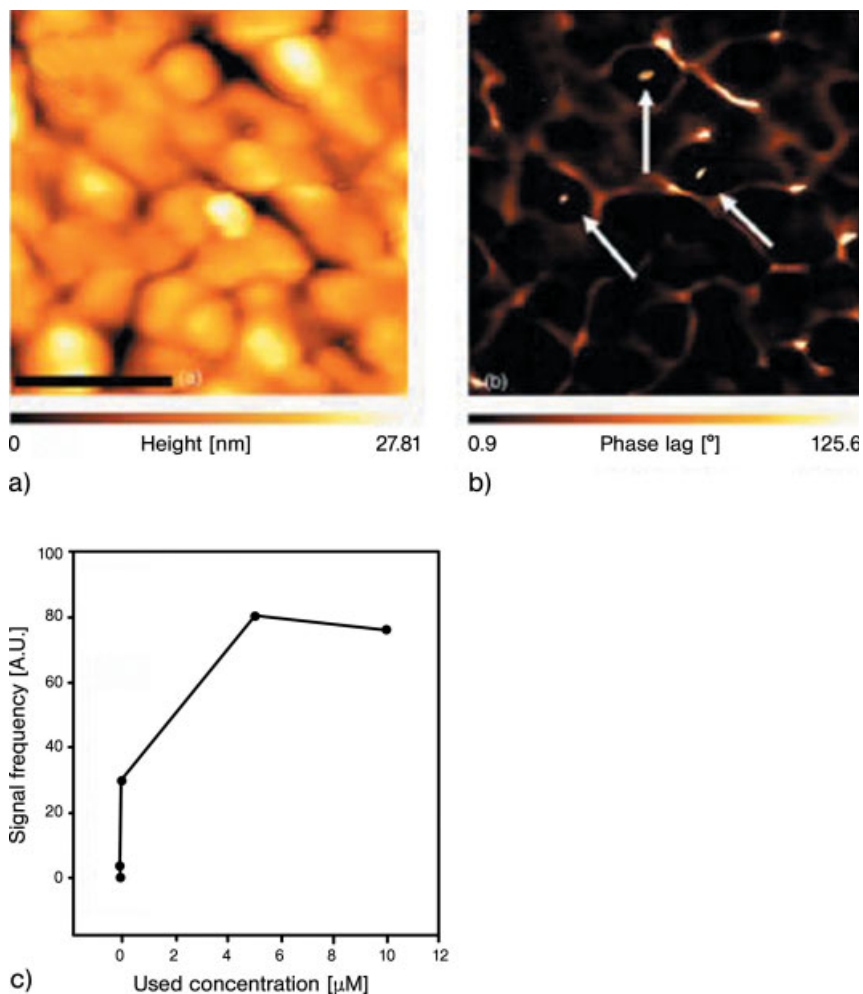


**Fig. 2.31.** (a) Topographic image of oligonucleotide complex, (b) phase shift image, (c) phase shift variation as a function of oligonucleotide concentration. Image size  $250 \times 250$  nm. (Reprinted with permission from Ref. [67]. Copyright (2004) Elsevier.)

sequences again revealed a close correlation between the mechanical energies at which these sequences melt with base pairing free enthalpies  $\Delta G(\text{bp})(\text{sequence})$  (Fig. 2.34): while the melting transition occurs between 65 and 200 pN in  $\lambda$ -phage DNA, depending on the loading rate, the melting transition is shifted to  $\sim 300$  pN for poly(dG-dC) DNA, whereas poly(dA-dT) DNA melts at a force of 35 pN [73].

The force at which the melting transition occurs depends on the pulling velocity, ranging from 68 pN at  $0.15 \mu\text{m s}^{-1}$  to 300 pN at  $3 \mu\text{m s}^{-1}$ .

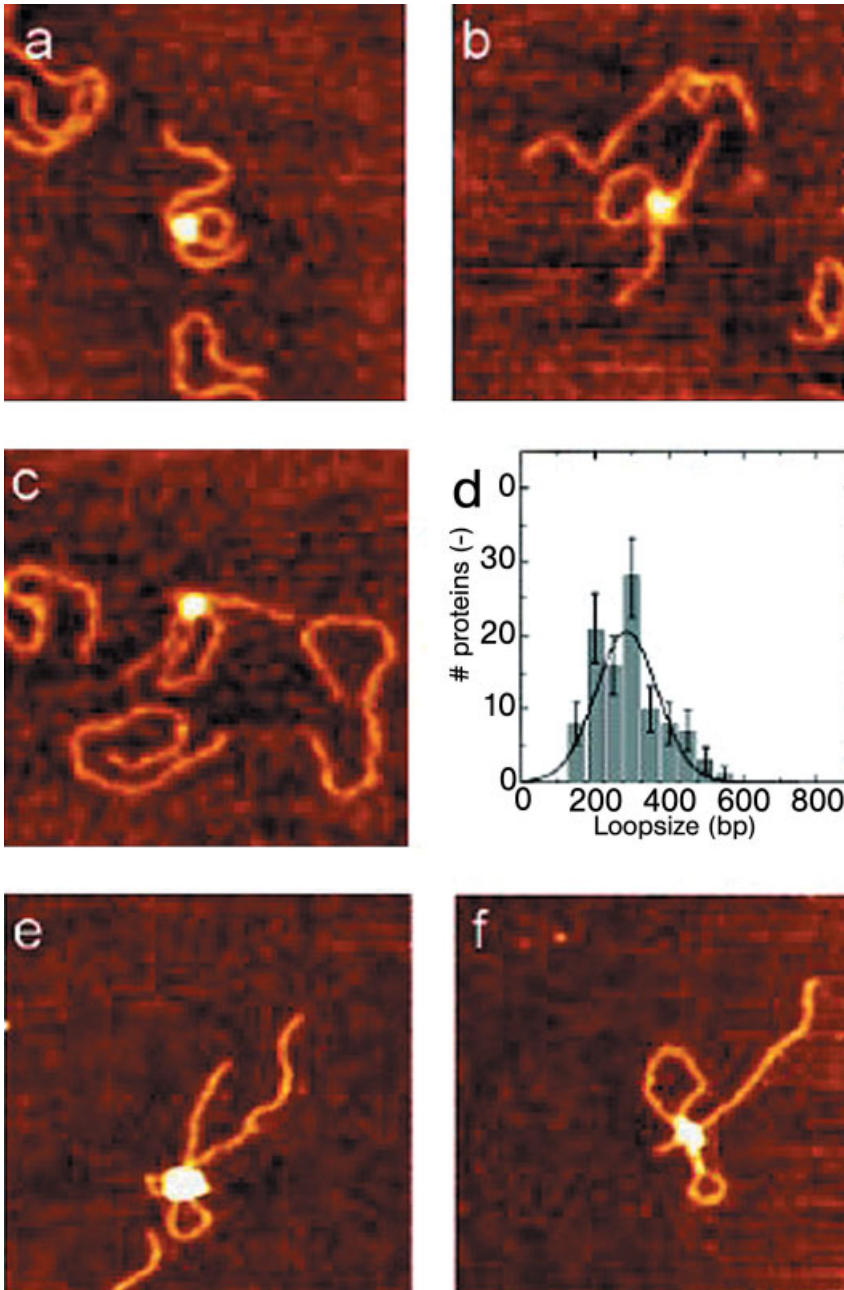


**Fig. 2.32.** AFM images of DNA translocation. (a)–(c) Scans taken after 10, 30 and 60 s incubation, respectively, with  $R_1$ -complex. Scan  $250 \times 250$  nm, height scale 3 nm. (d) Loop

size distribution for images taken after 10 s. (e, f) Double loops of DNA translocated by  $R_2$ -complexes. (Reprinted with permission from Ref. [68]. Copyright (2004) Oxford Journals.)

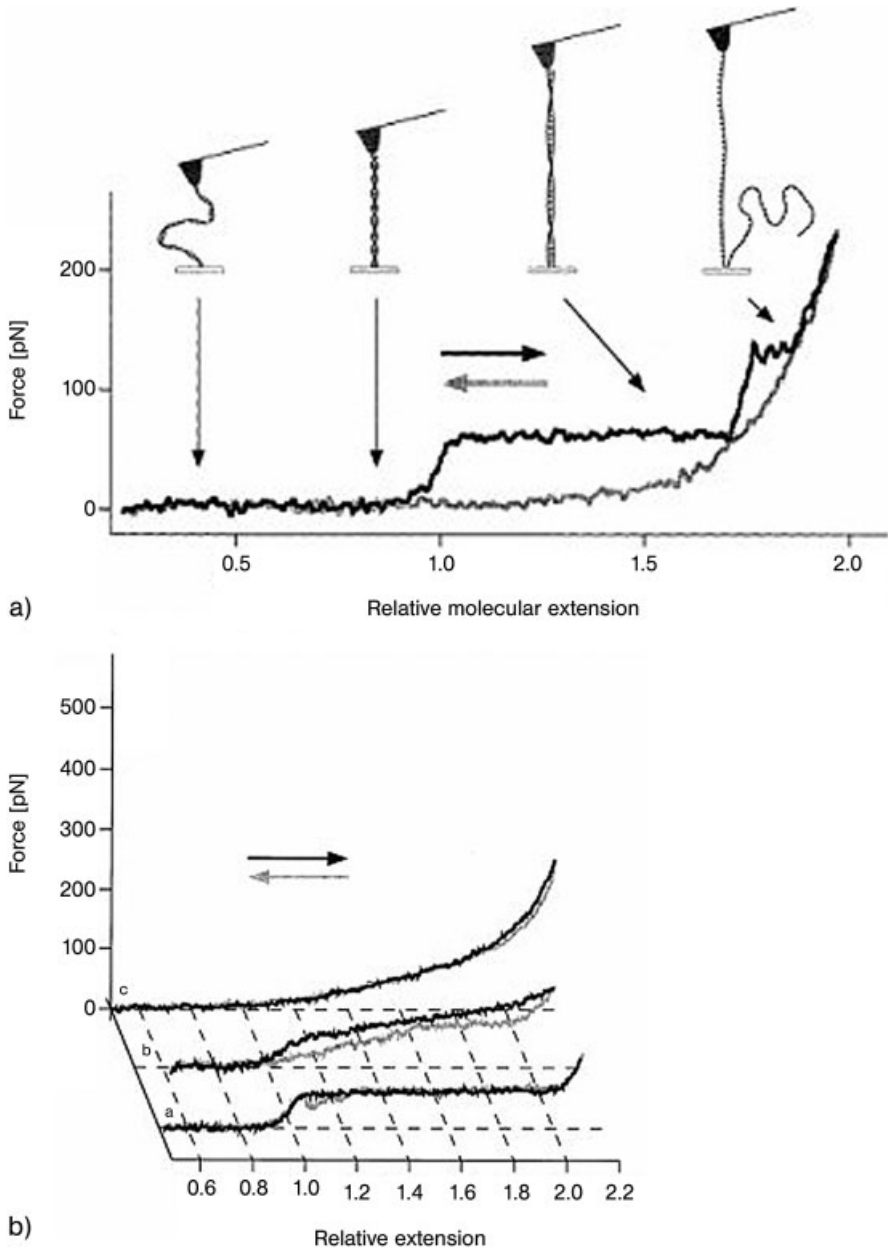


**Fig. 2.33.** Schematic of the force–extension characteristics of DNA (A): at 65 pN the molecule is overstretched to about  $1.7\times$  its contour length; at 150 pN the double strand separates into two single strands, one of which remains attached between tip and surface. (B) Force vs. extension curve of a single molecule of DNA in pure buffer (a) and in the presence of (b) 0.44 and (c)  $2.2 \mu\text{g mL}^{-1}$  ethidium

bromide. With increasing ethidium bromide concentration the overstretching plateau shortens while the force at the end of the transition increases to 110 pN. At high concentrations, hysteresis between stretching and relaxation is drastically reduced. (Reprinted with permission from Ref. [71]. Copyright (2002) Elsevier.)

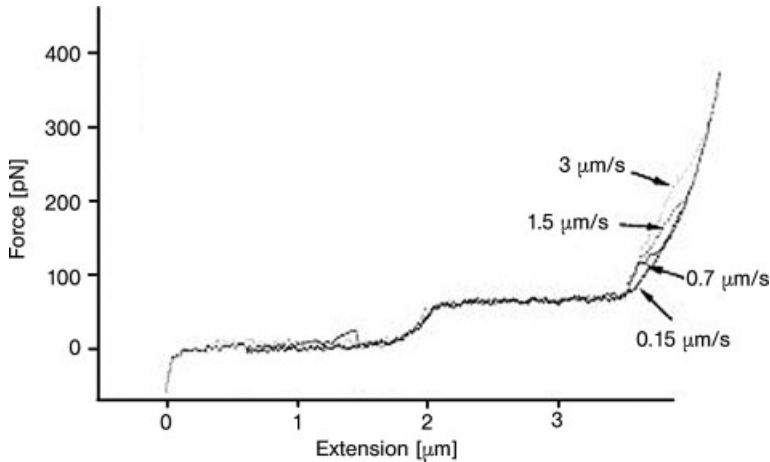


**Fig. 2.34.** Superposition of four extension traces of the same piece of  $\lambda$ -BstE II digest at different pulling velocities: 3, 1.5, 0.7 and  $0.15 \mu\text{m s}^{-1}$ . (Reprinted with permission from Ref. [73]. Copyright (2002) Biophysical Society.)

Apparently the flexibility of DNA and RNA molecules depends on the D+C content. More than that, it was observed [74] that the stacking forces are stronger in RNA than in DNA, as an increased transition force is noted for RNA molecules.

## 2.7.2

### Proteins

#### 2.7.2.1 Topographic Imaging of Proteins

Collagen presents the archetypal protein for AFM imaging first observed by Lees et al. in 1994 [75]; the bands of collagen spaced at 67 nm is often the first experiment encountered on entering the field of bio-AFM.

AFM high resolution imaging of membrane, reconstituted in high concentrations in lipid domains, is proving to be one of the major tools for obtaining structural information on these proteins, which represent a major difficulty for classical methods, such as X-ray diffraction, of structural analysis.

Contact mode AFM in liquids allows resolution at a level of individual sub-units of assembled arrays of proteins (Fig. 2.35) for the case of chloroplast ATP-synthase [76]. The image shows the protein to be formed of 14 sub-units arranged cylindrically. There are alternating cylinder diameters of  $5.9 \pm 0.3$  and  $7.4 \pm 0.3$  nm, with both having the same internal diameter of  $3.5 \pm 0.3$  nm. Given that SDS-PAGE reveals only a single sharp band at 100 kDa, the authors propose that there is alternating presentation of the extra- and intra-cellular faces of the protein. Furthermore the sub-units project by differing amounts from the lipid bilayer,  $1.7 \pm 0.3$  nm for the wider face and  $1.5 \pm 0.3$  nm for the narrower face.

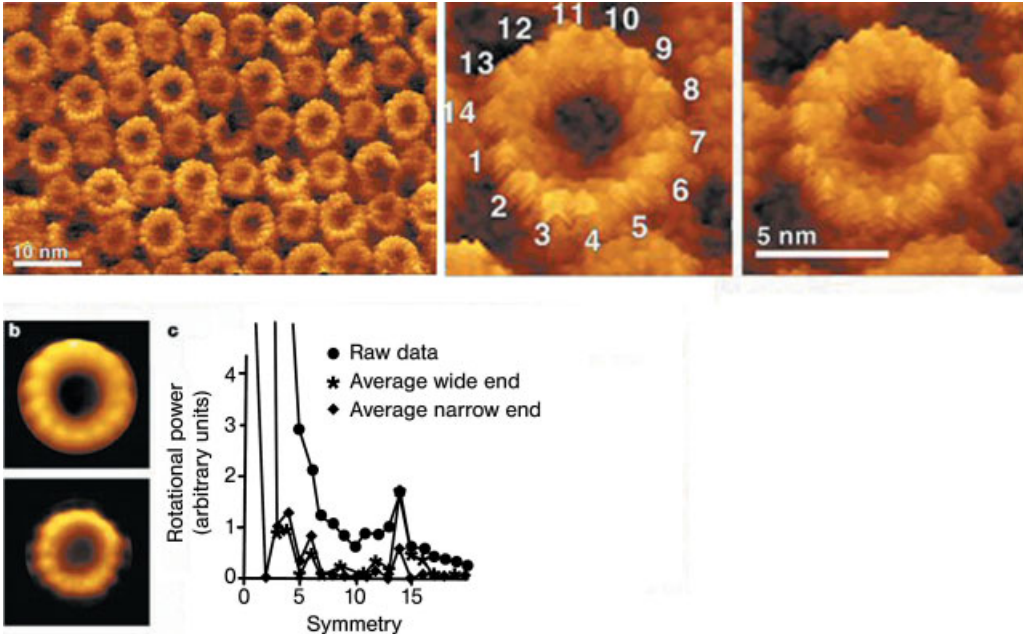


**Fig. 2.35.** (a) High-resolution AFM contact-mode images of images of chloroplast ATP-synthase, showing the fourteen-fold symmetry; (b) wide and narrow faces; (c) power spectrum

analysis, showing the peak for fourteen-fold symmetry. (Reprinted with permission from Ref. [76]. Copyright (2000) Nature.)

Combining AFM with cryo-electron crystallography provides a means to enhance the structural data that may be obtained from molecular resolution AFM topographic imaging of proteins.

The lens major intrinsic protein (MIP) has been studied by Engel et al. [77], using reconstituted purified ovine lens MIP and exogenous lipids to obtain crystalline sheets. The sheets show two surfaces, one smooth and the other rough, Fig. 2.36(A) and (B). From the high level of organization, Fourier transform analysis allowed determination of the unit cell and the presence of a tetrameric structure. The rough surface was imaged by mechanical removal of the smooth part using high tip-surface forces.

Careful analysis of the geometry of the protrusions present on the surfaces of the rough and smooth faces, along with analysis of carboxypeptidase Y digestion, which permitted identification of the smooth face as being cytoplasmic, allowed the authors to propose a tongue and groove fit between the two surfaces, showing MIP assembles as a two-layer system (Fig. 2.36). Use of cryo-electron microscopy projection maps allowed confirmation of a two-layer structure of the crystalline sheets.

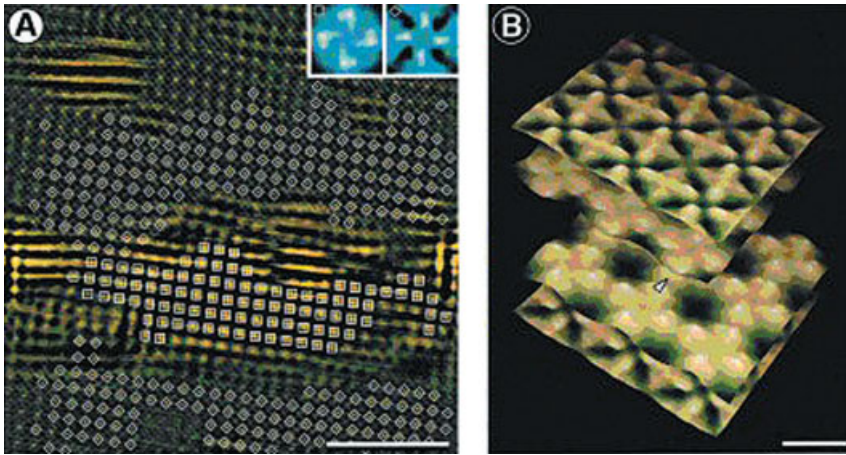


**Fig. 2.36.** Treated images of MIP from lens fiber cells. (A) Both rough and smooth surfaces are visible after using the point to remove the upper layer. (B) Model of the tongue and groove fit of the two layers. (Reprinted with permission from Ref. [77]. Copyright (2000) Elsevier.)

### 2.7.2.2 Dip-pen Nanolithography Patterning of Proteins

The use of Dip-pen nanolithography to allow deposition of various geometries of protein arrays on negatively charged  $\text{SiO}_2$  surfaces has been demonstrated by Mirkin (Fig. 2.37) [78].

Arrays of 450 nm spots of anti-rabbit IgG with 350 nm spacing were generated in under 5 min, using a deposition time of 3 s. While not as rapid as conventional robotic systems, the spatial resolution is much higher. However, this is counter-balanced by the maximum standard AFM displacement of about  $100 \times 100 \mu\text{m}$ . Individual spots of size as low as 55 nm can be generated by using shorter contact times (0.5 s) with low contact forces (0.5 nN). Such arrays were used to validate immuno-recognition with suitably labeled fluorescent antibodies.

### 2.7.2.3 Protein–Protein and Protein–Ligand Interactions

In the classical first experiment on force–distance measurement between a ligand and a protein, avidin was coupled to a bovine serum albumin coated tip and reacted with biotin or iminobiotin attached to agarose beads. The force required to separate a single avidin–biotin interaction was 160 pN, and 85 pN was required for a single avidin–iminobiotin complex (Figs. 2.38 and 2.39) [79].

The function of a protein derives from the specific folding of the polypeptide chain. In the case of muscles or cytoskeletal proteins, the folding is designed to maintain a certain structure under varying load conditions. Thus, single-molecule force spectroscopy, in which one end of the protein is attached to the AFM tip and

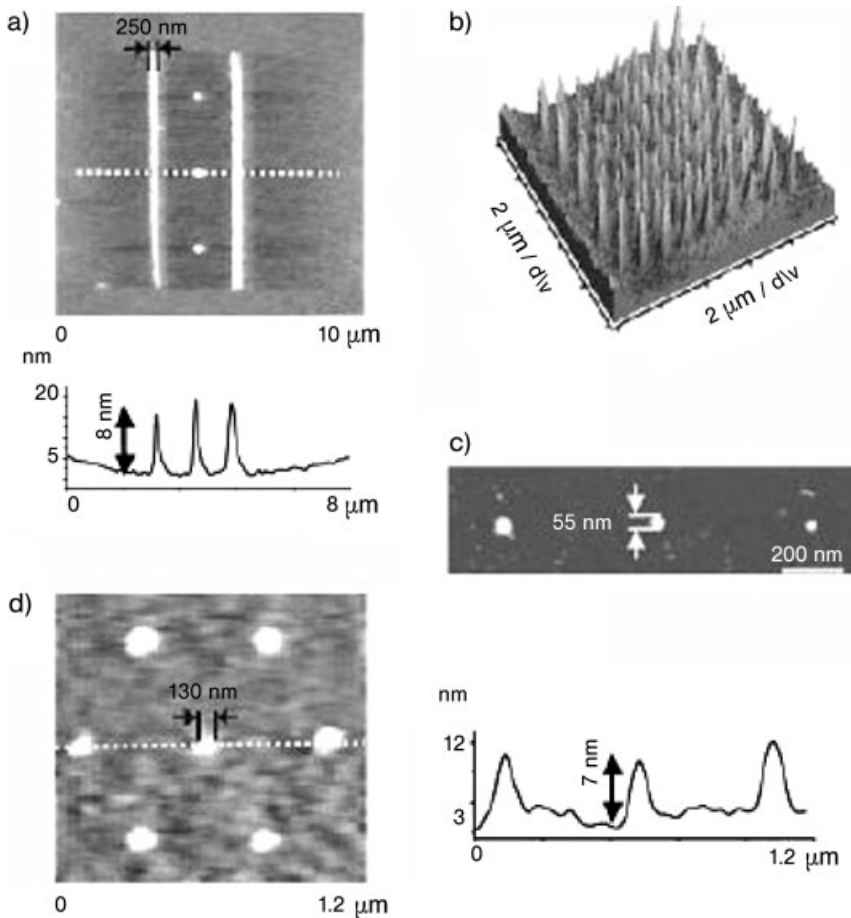


**Fig. 2.37.** Various arrays produced from IgG deposition on negatively charged Si surfaces. (Reprinted with permission from Ref. [78]. Copyright (2003) Wiley.)

the other end to the surface, provides a unique method of studying single molecular unfolding and folding under controlled loading.

The study by Gaub of reversible unfolding of titin immunoglobulin domains is a textbook example [80]. Titin was first chemisorbed onto a gold surface that was then adsorbed by contact onto the AFM tip. Retraction of the tip from the surface produced, as shown in Fig. 2.40, force–distance curves that show a saw tooth form extending to over 1  $\mu\text{m}$  from the surface.

The initial high force peak may arise from tip–gold interactions. Periodicity between the peaks is between 25 and 28 nm. Using a retraction velocity of 1  $\mu\text{m s}^{-1}$ , maximum forces observed in the saw tooth curves are between 100 and 300 pN. The periodicity is close to the 31 nm expected for unraveling of an Ig domain.

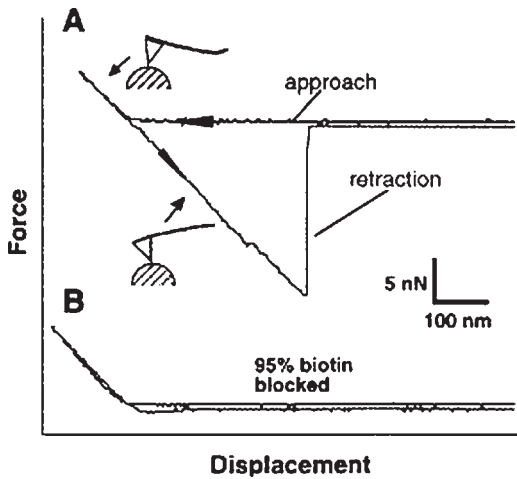


**Fig. 2.38.** Force–distance curves for avidin–biotin interaction. (Reprinted with permission from Ref. [79]. Copyright (1999) Elsevier.)

This was confirmed using constructs of four or eight Ig domains (Fig. 2.41), which exhibited a strict 25 nm periodicity measured at 100 pN.

Interestingly, the slope of the rising half of the curves, representing the stiffness of the protein, decreases from peak to peak. This implies that the stiffness of the stretched protein decreases, and that the stiffness is dominated by a spring that softens on unfolding of the Ig domains. The data fits to a worm-like chain model. Repeated stretching–relaxation cycles showed that refolding occurs when the construct is allowed to fully retract (Fig. 2.42).

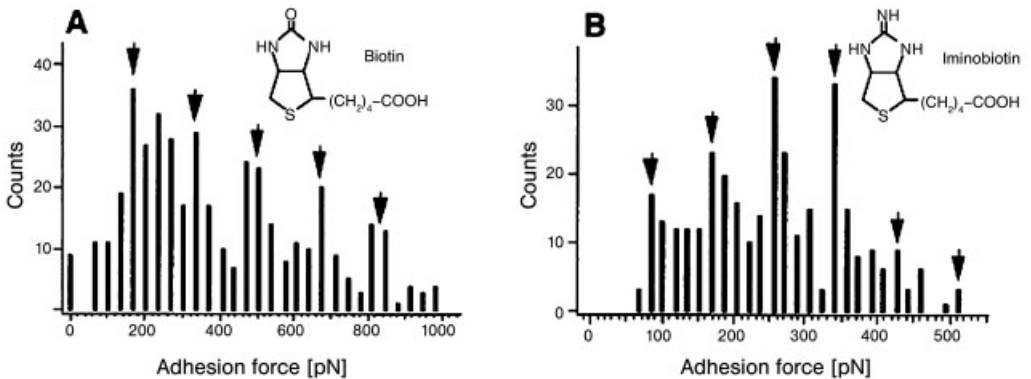


**Fig. 2.39.** Histograms of (A) biotin–avidin and (B) iminobiotin–avidin rupture forces. The arrows point to the locations of peaks in the histograms as determined by autocorrelation analysis. (Reprinted with permission from Ref. [79]. Copyright (1999) Elsevier.)



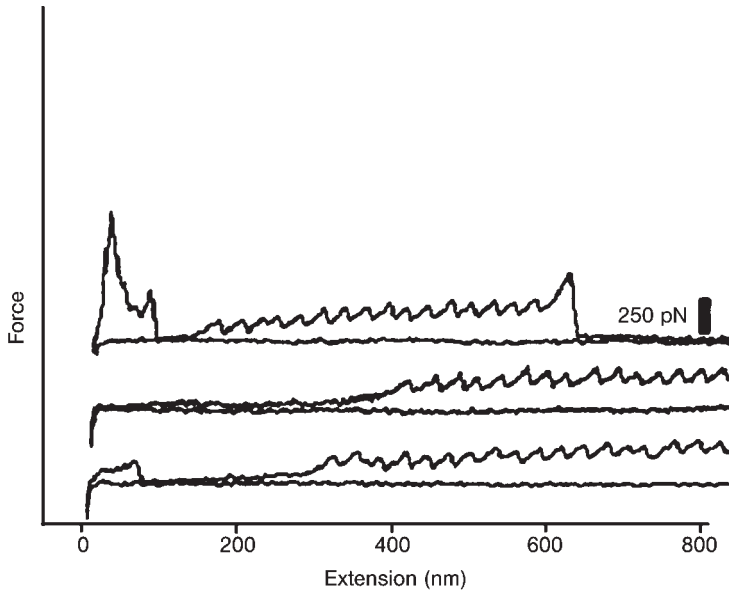


**Fig. 2.40.** Force–extension curves obtained by stretching titin proteins; three typical approach and retract cycles are shown: the AFM tip approaches the surface covered with the protein (lower trace), and segments of the adsorbed titin are picked up at random by an AFM tip and then stretched (upper trace). (Reprinted with permission from Ref. [80]. Copyright (1997) Science.)

### 2.7.3

#### Polysaccharides

##### 2.7.3.1 Proteoglycan Topographic Imaging

AFM topographic imaging at the molecular level can be used as a structural tool for the study of biological molecules that prove resistant to methods such as X-ray crystallography and NMR.

Ortiz et al. have achieved molecular resolution imaging of individual aggrecan proteoglycans [81]. The non-glycosylated N-terminal region was identified, along

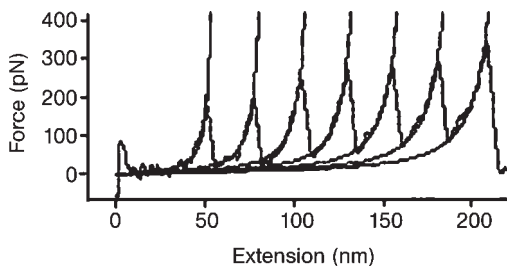


**Fig. 2.41.** Force–extension curve obtained by stretching of a single Ig8 titin fragment. (Reprinted with permission from Ref. [80]. Copyright (1997) Science.)

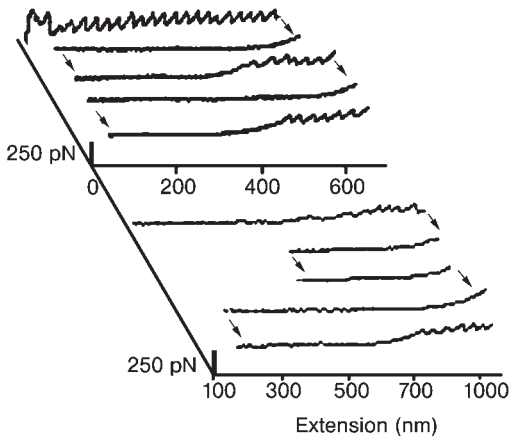


**Fig. 2.42.** Stretching–relaxation cycles of titin in the force extension experiment. Upper trace: full relaxation yields the same saw tooth pattern. Lower trace: after half relaxation the sawtooth pattern disappears. (Reprinted with permission from Ref. [80]. Copyright (1997) Science.)

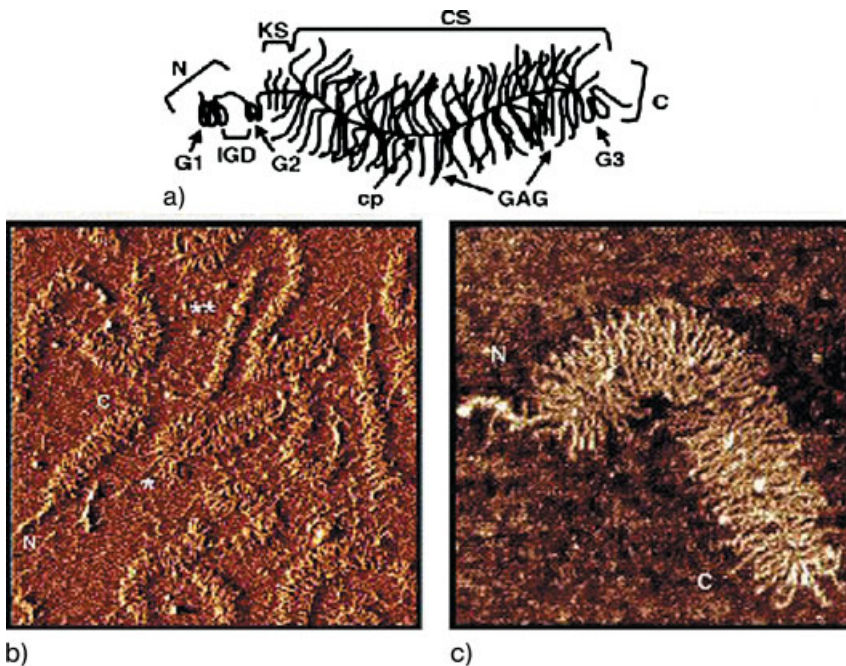


**Fig. 2.43.** (a) Schematic of the structure of aggrecan, showing the protein core and keratin sulfate (KS) and chondroitin sulfate (CS) chains. (b and c) Molecular resolution images of aggrecan, where N is the N-terminus of the

protein and C the C-terminus. Image sizes are  $1 \times 1 \mu\text{m}$  (B) and  $325 \times 325 \text{ nm}$  (C). (Reprinted with permission from Ref. [81]. Copyright (2003) Elsevier.)

with nanometer resolution of the keratin sulfate and chondroitin sulfate chains, and their spacing. Figure 2.43(a) shows a schematic of the structure of aggrecan. Figure 2.43(b) shows an image of the individual aggrecan molecules and Fig. 2.43(c) shows the GAG side chains. For fetal aggrecan, both the protein core ( $400 \pm 60$  nm) and the GAG side chains ( $41 \pm 7$  nm) were significantly longer than in mature aggrecan [protein core ( $350 \pm 90$  nm) and GA chain length ( $32 \pm 5$  nm)]. The high quality of the imaging showed that the GAG spacing increased from  $3.2 \pm 0.8$  to  $4.4 \pm 1.2$  nm on going from fetal to mature aggrecan.

#### 2.7.4

#### Lipid Systems

Scanning probe microscopies have become key methodologies in the study of the various types of lipid assemblies, including liposomes [82], solid lipid nanoparticles (SLNs) [83] and supported lipid bilayers (SLBs), and also of functioning membrane proteins contained in these assemblies. Such assemblies are highly fragile and often contain water, which hinders their study by conventional electron microscopies. Their structures are generally perturbed by insertion of fluorescent probes, effectively eliminating confocal microscopy for their study.

##### 2.7.4.1 Liposomes

A series of articles [84a,b] by Paquet and Morel on the assembly of the NADPH oxidase complex in liposomes demonstrates the utility of AFM to investigate highly complex assembly processes involving membrane proteins in their native lipid environment (Fig. 2.44). The use of functioning proteins allowed the authors to combine information from the AFM experiments with biological activity data and hence, as with the work of Firman on DNA-restriction enzymes, to determine the underlying mechanisms.

The system is particularly complicated as the NADPH oxidase complex involves assembly of different proteins: the cytochrome  $b_{558}$  an integral membrane protein composed by two sub-units p22-phox and gp91-phox; three cytosolic activating proteins p67-phox, p47-phox and p40-phox; three monomeric G proteins Rac1 or 2 participating in activation, and Rap1A a regulation factor.

Initial experiments involved simple imaging of the liposomes containing the  $b_{558}$  complex, where gp91-phox was native or enzymatically deglycosylated. Interestingly, while oxidase turnover rates and liposome heights were identical for both systems, the liposome diameter decreased from 150 nm for the native system to 68 nm for the deglycosylated system, thus showing the glycosylation is associated not just with recognition processes but also with structural properties.

As the proteins remained active in the liposomes, activation with arachidonic acid to generate the NADPH complex was achieved (Fig. 2.44), and, using height measurement, the size of the active complex was proposed to be 4 nm.

Correlating the height information and the biological activity allowed the authors to probe the role of the cytosolic proteins in the assembly and functioning of the

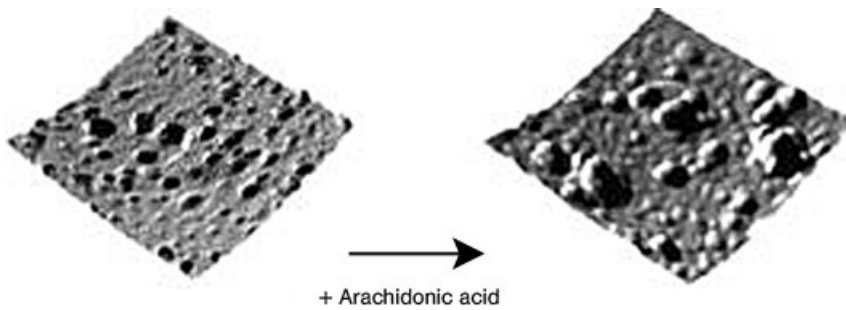


**Fig. 2.44.** Topographic images showing NADPH oxidase containing liposomes before (left) and after (right) activation. (Reprinted with permission from Ref. [84]. Copyright (2000) American Chemical Society.)

NADPH complex (Table 2.4). The data demonstrated that rp67-phox alone is able to mediate both assembly (change in liposome height, 6 nm) and activation. The role of p40-phox was determined; it acts to decrease the turnover rate, and with p67-phox and p47-phox alone leads to assembly (giving height changes of 6 and 4 nm, respectively, prior to activation). In the full set of cytosolic proteins this pre-activation assembly is absent.

The study was extended in a second paper to conformational changes in the cytochrome  $b_{558}$  complex, mediated by the proteins MRP8 and MRP14.

In the final paper, the use of force–distance measurements was applied to antibody recognition. The authors chose to use a “global” force–distance measurement; here it is assumed that tip size variation is not greater than experimental error, and thus associated with the use of molecules of the same size (antibodies) to assume that the total number of interaction events will be roughly constant. Hence the use of distribution curves (Fig. 2.45A) allows determination of whether the antibody–antigen recognition process occurs. The observed histograms show

**Tab. 2.4.** Correlation of assembly and activation steps of the NADPH-oxidase complex.

System	Liposome height (nm)		Oxidase turnover [[mol of O <sub>2</sub> s <sup>-1</sup> (mol of heme b) <sup>-1</sup> ]
	Before activation	After activation	
Cyt $b_{558}$ (PMN) + rRac1 +	5 ± 1	6 ± 2	20 ± 4
rp67-phox + rp47-phox +	5 ± 2	11 ± 2	95 ± 8
rp67-phox + rp40-phox-GST +	4 ± 1	12 ± 3	14 ± 5
rp67-phox + rp47-phox +	10 ± 2	13 ± 3	35 ± 4
rp40-phox-GST + rp47-phox +	5 ± 2	12 ± 3	42 ± 3
rp40-phox-GST	9 ± 2	9 ± 3	–

**Tab. 2.5.** Atomic force microscopy study to investigate the interaction of MRP8/MRP14 with cytochrome  $b_{558}$  liposomes; measurements of cytochrome  $b_{558}$  liposome height in the presence or absence of MRP8/MRP14.

Systems	Liposome height (nm)	
	-AA	+AA
Cyt $b_{558}$ PMN	$5 \pm 2$	$6 \pm 2$
Cyt $b_{558}$ EBV-BL	$7 \pm 2$	$6 \pm 4$
Cyt $b_{558}$ PMN + MRP8/MRP14 ( $\text{Ca}^{2+}$ )	$3 \pm 2$	$5 \pm 2$
Cyt $b_{558}$ PMN + MRP8/MRP14 ( $\pm\text{AA}$ )	$8 \pm 3$	$10 \pm 2$
Cyt $b_{558}$ EBV-BL + MRP8/MRP14 ( $\text{Ca}^{2+}$ )	$5 \pm 1$	$15 \pm 5$

a bimodal form with an interval control, as imprecision in the positioning often generates an antibody–mica contact (Fig. 2.45B). Again work was carried out using native and deglycosylated cytochrome  $b_{558}$ .

The results present several interesting points (Table 2.6). Firstly, interaction between the antibody Ab54.1 and the protein are significant even though the epitope is on the intracellular surface of the protein; this implies that orientation of the protein with regard to the membrane is statistical on reconstruction. Secondly, in the case of the mAb11C12 antibody, directed against neutrophil associated cyt- $b_{558}$  recognition occurs for both native and deglycosylated protein, while for EBV-BL–cyt  $b_{558}$  for the native protein no recognition is observed; deglycosylation leads to a strong recognition event, implying that here the epitope is present but hidden by the carbohydrate chains. The glycosylation is also related to the biological activity of the complex in the EBV-BL cell lines.

AFM is widely used to investigate the mode of liposomes formation, their size, the transition of attached liposomes to bilayers patches, and the complexes they form with biological molecules such as DNA or proteins. The following is the

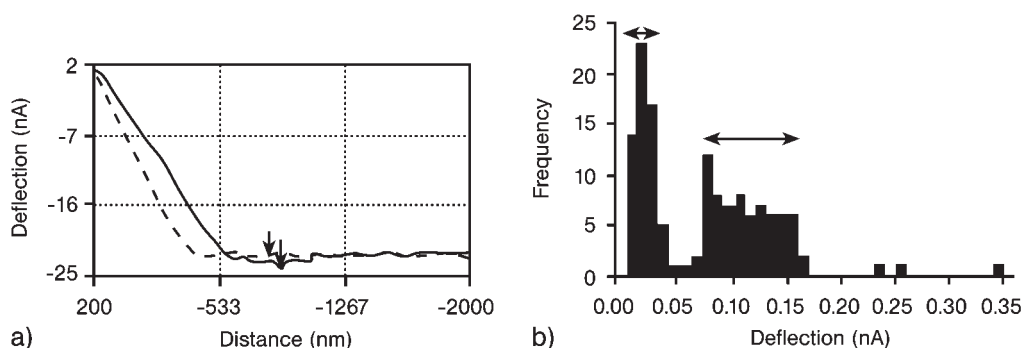


**Fig. 2.45.** (A) Typical force–distance curve. (B) Histogram of frequency against deflection for antibody–antigen interaction (0.1–0.15 nA) are visible. (Reprinted with permission from Ref. [18]. Copyright (2001) FEBS.)

**Tab. 2.6.** Measures of interaction forces between specific antibodies and purified native (N) or deglycosylated (D) cytochrome  $b_{558}$ .

Antibody	Interaction (nN)				
	Mica	Neutrophil cyt. $b_{558}$		EBV-BL cyt. $B_{558}$	
		N	D	N	D
Negative control	$9 \pm 5$	$16 \pm 5$	$8 \pm 4$	$9 \pm 5$	$9 \pm 4$
54.1	$10 \pm 5$	$39 \pm 11$	$26 \pm 10$	$12 \pm 2$	$9 \pm 4$
11C12	$4 \pm 1$	$25 \pm 21$	$23 \pm 7$	$16 \pm 12$	$28 \pm 11$
(562–569)	$5 \pm 2$	$16 \pm 2$	–	$8 \pm 3$	–
44.1	$9 \pm 3$	$13 \pm 5$	–	$5 \pm 4$	–

work of Vermette et al. [85] on interaction forces between a silica particle and immobilized liposomes layers. The experiments were performed according to the colloid probe method developed by Ducker et al. [86]. Thus, a spherical colloidal particle of pure silica (diameter 4–5  $\mu\text{m}$ ) is attached to the microfabricated, gold-coated AFM cantilever spring via an epoxy adhesive. The liposomes had biotinylated PEG lipids. The resultant biotin moieties on the outer surface of the liposomes were capable of docking onto NeutrAvidin molecules immobilized onto the hydrogel interlayers. The intention was to provide a platform for binding NeutrAvidin molecules, at the same time minimizing nonspecific adsorption events as well as the disruption of liposomes upon contact with the surface. Compression of liposome layers by an approaching silica colloid sphere, mounted on the AFM cantilever, can be quantified by comparing the force vs. distance curves measured with a spherical silica particle approaching NeutrAvidin (on hydrogel interlayers) surfaces and putative immobilized liposome surfaces. Comparison of the release characteristics of fluorescent dye from liposomes in solution and liposomes bound to the three different hydrogel interlayers showed that the release characteristics were little affected, indicating that there was minimal disruption of the liposomes upon surface binding. By blocking surface-immobilized NeutrAvidin it was shown that there exists a physicochemical attractive force of non-negligible magnitude between PEGylated liposomes and hydrogel surfaces decorated with NeutrAvidin, and this physicochemical binding mechanism can surface-attach liposomes when the biologically specific biotin–avidin mechanism is absent.

The utility of AFM for measuring the mechanical properties of adsorbed small liposomes and stability changes in liposomes has been demonstrated by Liang et al. [87]. They investigated the effects of cholesterol concentration on the micro-mechanical properties of the small unilamellar EggPC liposomes adsorbed to mica. These liposomes are stable and maintain their vesicular form without fusion when deposited on a mica surface. The elastic properties are revealed by force curves between an AFM tip and an adsorbed vesicle obtained in the contact mode. Figure 2.46 presents the types of tip–sample interactions.

AFM analyses quantified the Young's modulus ( $E$ ) and bending modulus ( $K_c$ )

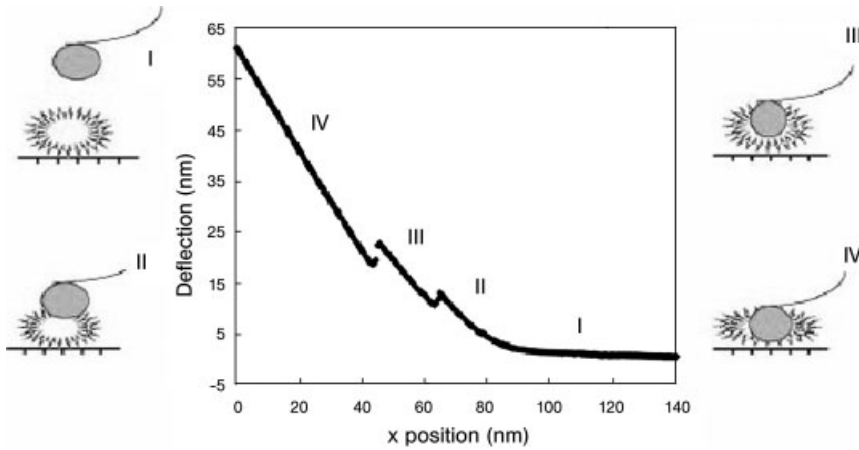


**Fig. 2.46.** Deflection versus  $z$  position approaching curve. Zero separation is not defined as described previously. The force curve was obtained on the EggPC/cholesterol. Zone I is non-contact. Zones II–IV illustrate different on-contact stages of tip and sample interaction. Region II illustrates elastic deformation of the vesicle under tip

compression. Region III corresponds to further tip compression after the tip penetrates the top bilayer. Region IV: tip at the top of the mica substrate; the steep slope (0.9946) indicates mica is an infinitely hard surface without deformation. (Reprinted with permission from Ref. [87]. Copyright (2004) Elsevier.)

for those unilamellar vesicles (Table 2.7). The analyses showed an increase in both  $E$  and  $K_c$  with increasing quantity of cholesterol incorporation into pure EggPC. This may be explained by the fact that the presence of cholesterol molecules enhances the rigidity of the EggPC vesicles.

#### 2.7.4.2 Solid Lipid Nanoparticles (SLNs)

Atomic force microscopy is the most used technique for the size characterization of nanoparticles, generally in conjunction with Dynamic Light Scattering (DLS).

Atomic force microscopy (FMM and LFM) has been shown to be a key tool for imaging nanoparticles incorporated in gels of biological interest [88]. It was seen that SLNs do not aggregate in gels and the use of lateral force and force modulation modes in addition to the classical topographic mode provides additional information on the gel structuring (Figure 2.47).

**Tab. 2.7.** Comparison of Young's modulus ( $E$ ) and bending modulus ( $K_c$ ) of liposome with different cholesterol and lipid ratios.

	<i>Cholesterol:lipid ratio</i>				
	<i>Pure eggPC</i>	<i>85:15</i>	<i>80:20</i>	<i>70:30</i>	<i>50:50</i>
$E \times 10^6$ Pa	$1.97 \pm 0.75$	$12.07 \pm 1.53$	$10.77 \pm 0.64$	$10.4 \pm 4.06$	$13.0 \pm 2.97$
$K_c \times 10^6$ Pa	$0.27 \pm 0.10$	$1.68 \pm 0.21$	$1.49 \pm 0.09$	$1.44 \pm 0.56$	$1.81 \pm 0.41$

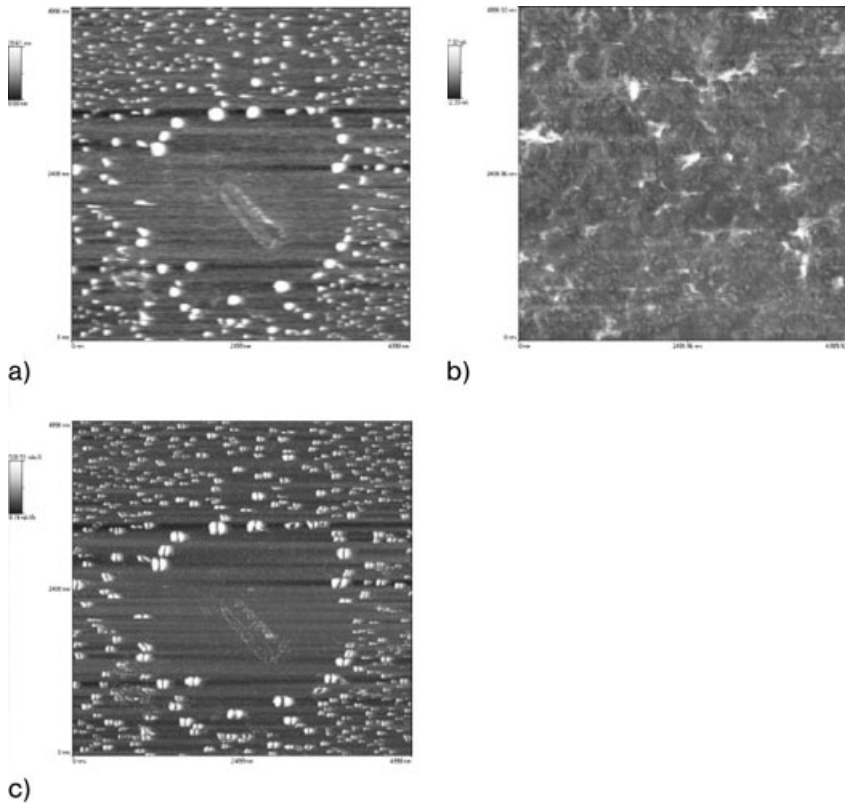


**Fig. 2.47.** Images of carbopol 2020 containing nanoparticles in topographic (a), lateral force (b) and force modulation (c) modes; average particle diameter is 150 nm and the average height is 120 nm. (Reprinted with permission from Ref. [88]. Copyright (2003) Elsevier.)

To proceed to the use of SLNs in intravenous administration, it is important to verify that they do not aggregate in the presence of albumins. Gualbert et al. performed AFM studies on the interaction of SLNs based on amphiphilic calix[4]arene with one of the major circulatory proteins, serum albumin (Fig. 2.48) [89].

The results show that no aggregation occurs between the SLNs and the serum albumin. The difference in diameter and height of the particles (155 and 15 nm, respectively) with respect to the size of nanoparticles without protein (250 nm in diameter and 55 nm in height) may be explained by the fact that the nanoparticles are included in the protein gel (only the protruding parts being measured). The more circular shape proves a protective action of BSA, i.e., capping the particles, preventing their flattening.

AFM and SEM (Scanning Electron Microscopy) analyses were performed by Dubes et al. [83] on SLNs derived from  $\beta$ -CD21C6 (Fig. 2.49). Comparison of the



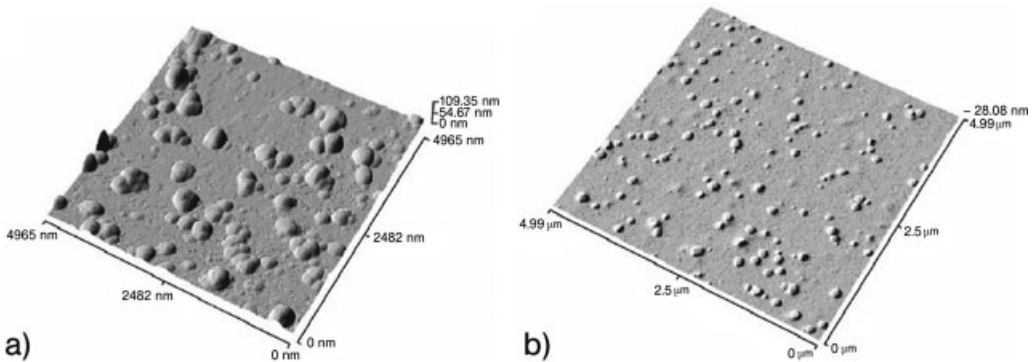


**Fig. 2.48.** Non-contact mode AFM images of *para*-decanoyl-calix[4]arene-based solid lipid nanoparticles without (a) and with BSA ( $20 \text{ g L}^{-1}$ ) (b) on a mica surface. (Reprinted with permission from Ref. [89]. Copyright (2003) Elsevier.)

results shows that the vacuum drying technique used in sample preparation for SEM causes shrinkage in the size of the SLNs, whereas the deposition method used for AFM causes the nanoparticles to form small clusters.

Both techniques confirm that the SLNs are circular. With images obtained from AFM, the SLNs tend to be organized as clusters of 15–30 nanoparticles. This is probably due to the sample preparation method, where the colloidal suspension is slowly dried. At the same time, shrinkage of the nanoparticles analyzed by SEM

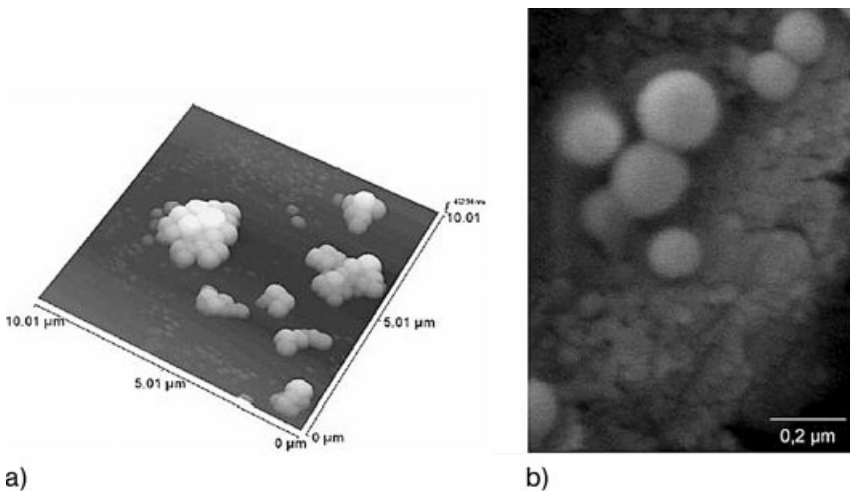


**Fig. 2.49.** Non-contact mode AFM images of  $\beta$ -CD21C6-derived solid lipid nanoparticles (SLNs) at a scan range of 5  $\mu\text{m}$  (a). SEM images of the  $\beta$ -CD21C6-derived SLNs, scale 0.2  $\mu\text{m}$  (b). (Reprinted with permission from Ref. [83]. Copyright (2003) Elsevier.)

**Tab. 2.8.** Measured diameters on images provided by two analysis techniques.

	<i>Diameter (nm)</i>
SEM	$212 \pm 12$
AFM	
Diameter	$359 \pm 50$
Height	$140 \pm 27$

was observed (Table 2.8). This might have been caused by the freeze-drying treatment prior to analyzing.

The advantage of AFM is the simple sample preparation as no vacuum is needed during operation and the sample does not undergo high vacuum treatment leading to dehydration and shrinkage.

### 2.7.4.3 Supported Lipid Bilayers and Monolayers

Supported lipid bilayers (SLBs) are formed by the spreading and unfolding of liposomes on surfaces. Their formation was first demonstrated by Brian and McConnell [90] in 1984. The mechanism of their formation was proposed from AFM imaging by Jass et al. [91] (Fig. 2.50).

More recently, Richter et al. investigated the adsorption and conformational changes of unilamellar vesicles adsorbed on silica by AFM in real time studies [92]. They proved that the process of vesicle deposition onto surfaces is more complicated and depends strongly on the nature of the component lipids. Zwitterionic, negatively charged and positively charged lipids were used for this investigation.

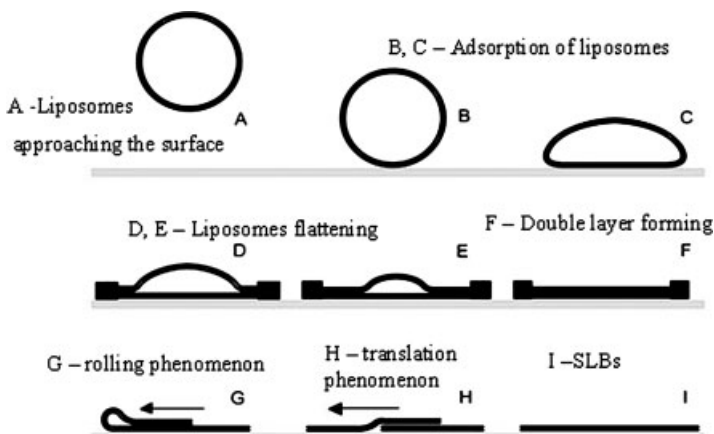


**Fig. 2.50.** Schematic representation of supported lipid bilayer formation. (Reprinted with permission from Ref. [91]. Copyright (2000) Biophysical Society.)

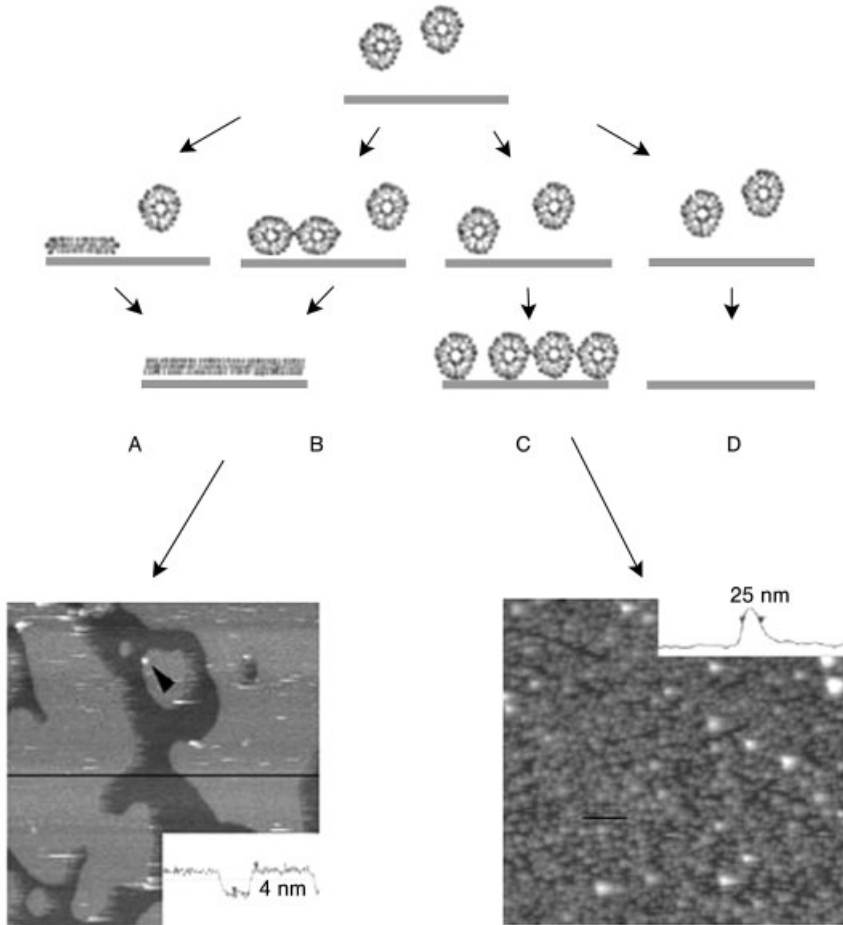


**Fig. 2.51.** AFM imaging determination of supported lipid bilayer (SLB) formation; (left) image shows SLBs, (right) image of liposomes. Insets: heights of the structure. (Reprinted with permission from Ref. [92]. Copyright (2003) Biophysical Society.)

Based on AFM analysis, a schema of the pathway of vesicles deposition was proposed (Fig. 2.51).

Table 2.9 exemplifies the types of vesicle deposition, as function of the lipid ratio and composition.

The height of the SLBs did vary evidently with lipid composition. Bilayers about 4 nm high described the SLBs film.

The reported existence of microdomains in plasma membranes has prompted considerable recent interest. Microdomains of a similar composition to lipid rafts

Tab. 2.9. Dependence of vesicle deposition pathway on the lipid ratio.

Lipid ratio			Vesicle deposition pathway
DOTAP	DOPC	DOPS	
1	–	–	SLB (I)
1	4	–	SLB (II)
–	1	–	SLB (II)
–	4	1	SLB (II)
–	2	1	SLB (II)
–	1	1	SVL
–	1	2	No adsorption
1	–	–	SLB (I)
1	4	–	SLB (II)
–	1	–	SLB (II)
–	4	1	SLB (II)
–	2	1	SLB (II)
–	1	1	SLB (II), restructuring
–	1	2	SLB (II), restructuring

have been shown to form in lipid bilayers, providing a model to investigate raft formation [93] (Fig. 2.52).

Many studies led to the conclusion that mixed lipid bilayers generate lipid rafts that are enriched in sphingomyelin and cholesterol. These two lipid components are thought to exist in a liquid-ordered phase or gel phase.

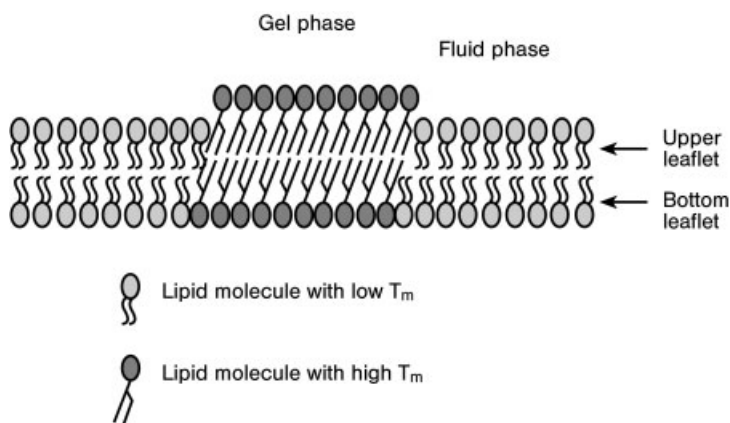
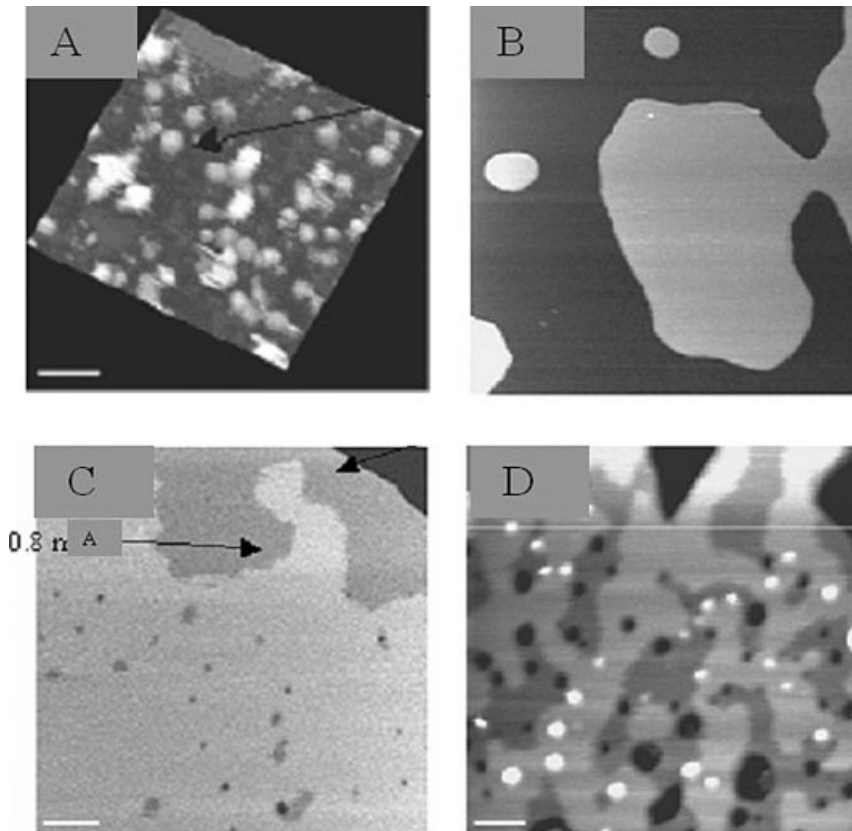


Fig. 2.52. Schematic of a lipid membrane with gel and fluid phase separation. The height difference due to lipid packing is such that AFM topographic imaging can distinguish the zones. (Reprinted with permission from Ref. [93]. Copyright (2003) acsmb@bmb.leeds.ac.uk.)



**Fig. 2.53.** (A) Protein film; (B) SLB containing sphingomyelin and cholesterol; (C) SLB containing sphingomyelin, cholesterol and phosphatidylcholine; (D) protein containing lipid rafts (sphingomyelin, cholesterol and phosphatidylcholine). (Reprinted with permission from Ref. [97]. Copyright (2004) Biochemical Society.)

More evidence about lipids rafts existing in biological membranes is brought by AFM studies that provide high-resolution imaging under physiological conditions [94]. Apparently, crucial cellular functions depend on preferential association of proteins with rafts [95, 96].

*Helicobacter pylori* vacuolating toxin–SLBs interaction and the preferential association of this protein with rafts [97] are presented below (Fig. 2.53).

The VacA film shows particles 7 nm high with an outer diameter of 30 nm (Fig. 2.53a). Supported lipid bilayers, formed of sphingomyelin and cholesterol, and raft formation (when phosphatidylcholine is added) are observed in Fig. 2.53(b) and (c). The film based on cholesterol and sphingomyelin is about 4 nm high. The presence of phosphatidylcholine in the lipids induces the formation of rafts. Differences of 0.8 nm in height protrude from the lipid bilayer. Analyzing the film of mixed lipids (all three components) in the presence of VacA (Fig. 2.53d), particles

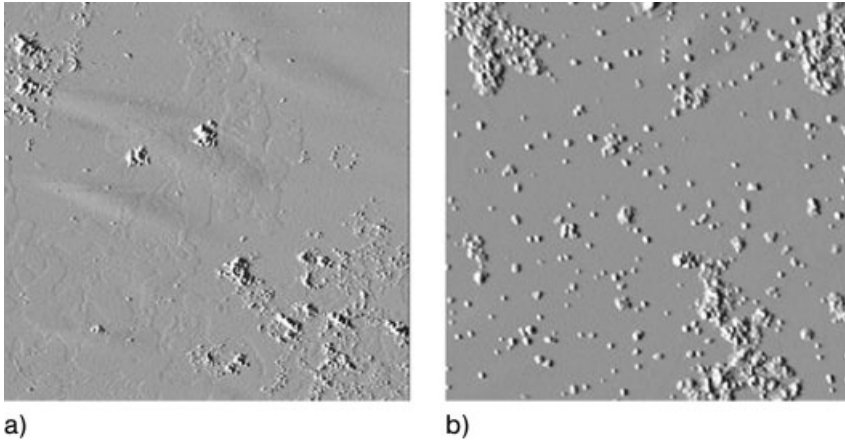


**Fig. 2.54.** AFM imaging of DRM-enriched membrane bilayers. (A) 60% cholesterol depleted; (B) after repletion with cholesterol. (Reprinted with permission from Ref. [98]. Copyright (2005) Biophysical Society.)

corresponding to the protein, 2 nm higher than the SLB and of much smaller diameter (25 nm), prove that the protein is inserted and traverses the lipid bilayer. The VacA obviously associates preferentially with rafts.

Barakat et al. proved [98], in a similar study on P-glycoprotein in a DRM-enriched membrane bilayer, that the depletion of cholesterol from the rafts induces protein translocation and aggregation outside rafts (Fig. 2.54). Approximately the same height differences (about 0.7 nm) were found for the protruding rafts. Repletion of the sample with cholesterol allows the reinsertion of P-gp in the rafts, probably recovering its P-gp ATPase activity.

Thus, cholesterol appears to be an essential component of DRMs for maintaining a structure of P-gp that is compatible with its optimal activity.

### 2.7.5

#### SNOM Imaging

Scanning near-field optical microscopy is generally used complementary to AFM to enrich the structural details of supported lipid monolayers and bilayers (Fig. 2.55). The two techniques can detect the presence of domains on the submicron scale on the supported lipid bilayers. The initial supposition was that a defect in the lipid layer occurred. Further analysis of these structures simultaneously by high-resolution fluorescence and topography measurements confirmed that they arise from coexisting liquid condensed and liquid expanded lipid phases. NSOM is the only reliable technique able to observe the lipid domains. Hollars et al., using NSOM fluorescence measurements, showed that lipid domains are quantitatively similar when formed in lipid bilayers or monolayers [99].

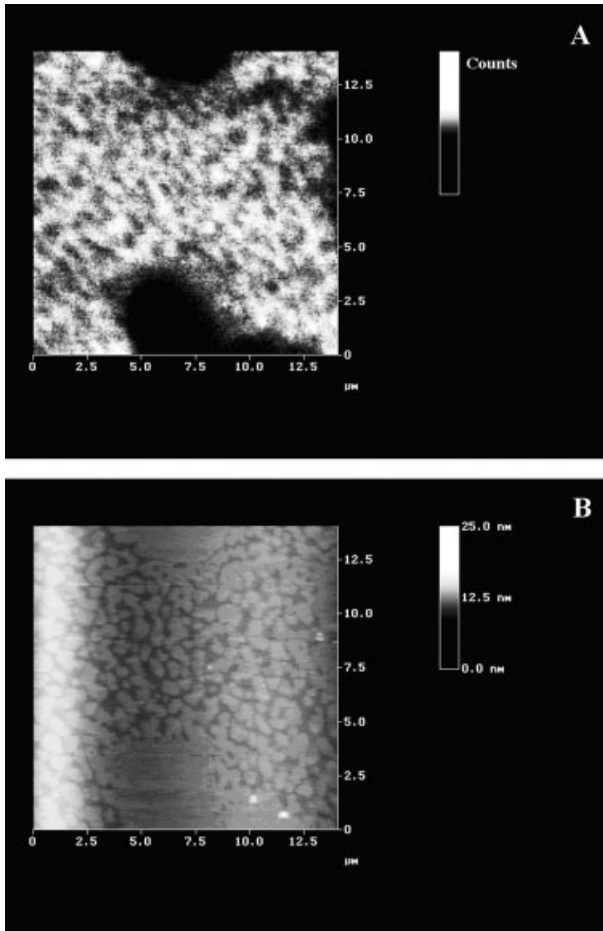


**Fig. 2.55.** (A) NSOM images and (B) AFM topographic images of monolayers, showing phase separation. The fluorescence is situated in the liquid expanded zones, as shown by the correlation with lower height in the AFM image. (Reprinted with permission from Ref. [99]. Copyright (1998) Biophysical Society.)

Apparently these domains are common features of the sample, regardless of the nature of the substrate.

The formation of phase domains can be influenced by the deposition conditions. As exemplified in Fig. 2.56, the surface pressure at the moment of deposition influences the distribution of the phase domains on the lipidic film [100].

Taken together, these results prove that SNOM might be a unique technique sensitive enough to observe phase structures present in lipid bilayers at the nanometer scale and may provide new clues to the existence of lipid phase domains in natural biomembranes.

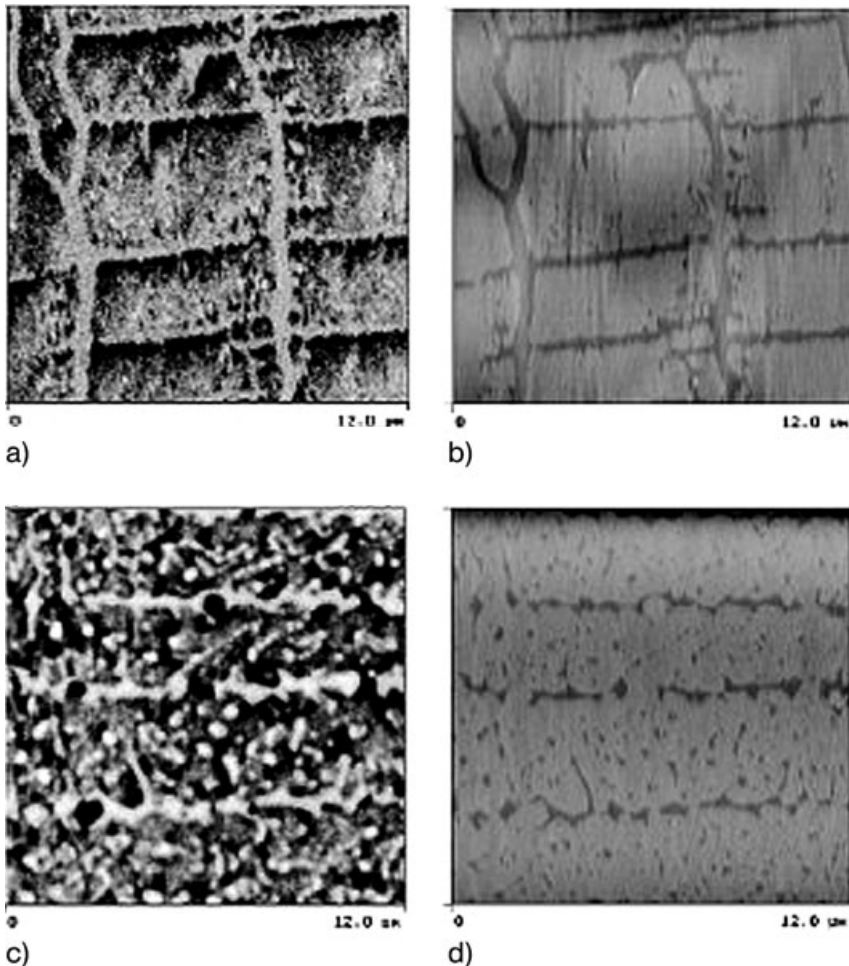


**Fig. 2.56.** (A, C) NSOM fluorescence images of mixed DPPC, diC18 monolayers; (B, D) corresponding AFM topographic images. (Reprinted with permission from Ref. [100]. Copyright (1999) American Chemical Society.)

### 2.7.6

#### Viruses

Figure 2.57 presents typical images of the Moloney murine Leukemia virus emerging from the surfaces of infected NIH 3T3 cells [101]. The viral particles have an average diameter of 145 nm, but with a degree of polydispersity. The surfaces of the virions are studded with projections (tufts) of proteins, which display a range of packing densities. The tufts are generally 11–12 nm in size and often show a



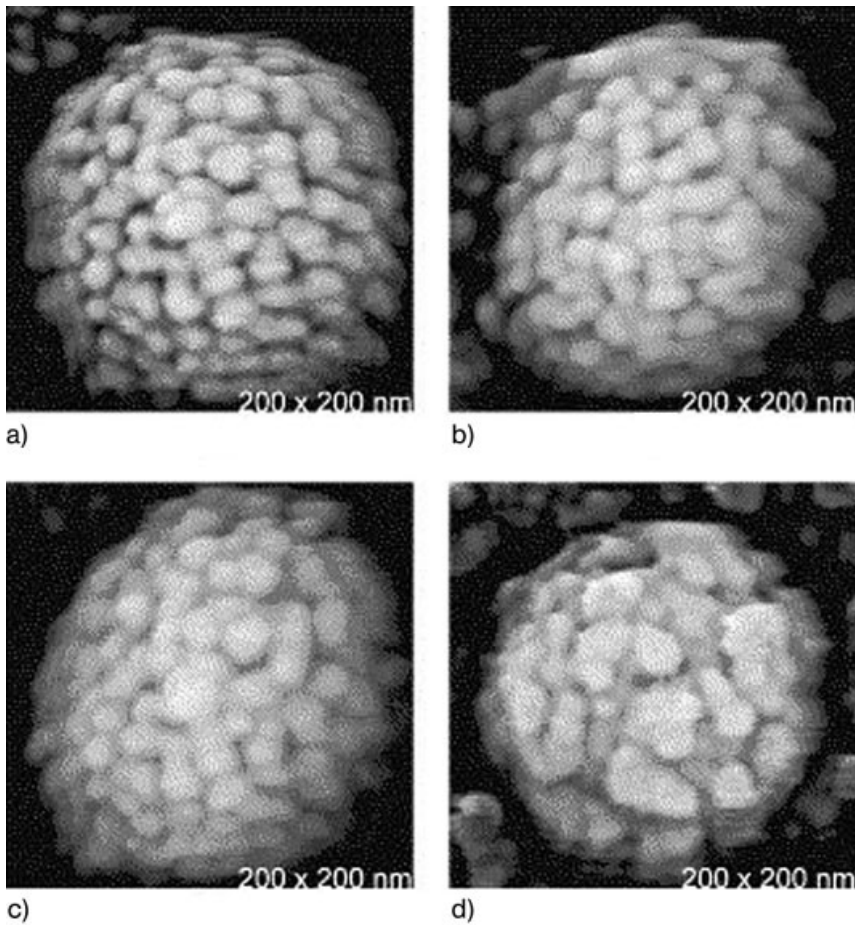


**Fig. 2.57.** (a–c) Typical AFM images of the surfaces of Moloney murine leukemia virion, showing the dense packing of protein projections. (d) AFM image of a virus particle, showing a low density of protein projection. (Reprinted with permission from Ref. [101]. Copyright (2002) Blackwell.)

high density of surface packing. The authors postulated that these projections are aggregates of SU protein. In view of the varying aggregation, the variation in size and geometry can be explained. Moloney murine leukemia virus (M-MuLV) lacking the gene for the envelope glycoprotein ( $env^-$ ) was produced in NIH 3T3 cells and investigated using atomic force microscopy (AFM). The particles were compared with similarly produced wild-type virions, some of which had been exposed to a monoclonal antibody against the surface component of the envelope protein (SU protein).

## 2.7.7

### Cells

#### 2.7.7.1 Topographic Imaging

Optimized methods were realized to study the complex system *Shewanella oneidensis* (Gram negative). We exemplify here the work of Micic [102] which correlated tapping-mode AFM and confocal microscopy (FLIM) to analyze living bacterial cells. As this technique allows imaging of bacterial cells in their native environment, Gram-negative *Shewanella oneidensis* MR-1 cells were spread on poly-L-lysine coated surfaces or agarose gel coated surfaces for analyzing, confining them a wet environment, which is propitious for *in vivo* imaging conditions. Figure 2.58 depicts a topographic image ( $256 \times 256$  pixels) of MR-1 bacterial cells. To reduce image noise, the imaging was acquired in a slow mode, with a raster-scan frequency of 0.1 Hz.

Single cells images were obtained only by diluting the sample and using a poly-L-lysine coated substrate. Images of live MR-1 cells bearing flagella of high resolution were obtained. The topographic image shown in Fig. 2.59(A) demonstrates that the ends of these elongated cells are thicker than the central portion. However, more information and structural details are presented by phase imaging (Fig. 2.59B).

The utility of correlated AFM–FLIM imaging on MR-1 cells expressing the MCP–YFP fusion is presented as follows (Fig. 2.60) by AFM height image, fluorescence intensity image, and fluorescence lifetime image of single cells.

The fluorescence images show higher intensities at both ends of the cells, which suggest polar localization of the SO0584–YFP fusion protein. The same information is obtained by the AFM image on both ends of the cells, allowing correlation between the polar localization of the SO0584–YFP fusion protein and surface protuberances in MR-1 cells.

#### 2.7.7.2 Interactions and Mechanical Properties

Essential for multicellular development are cell–cell adhesions mediated by specific cell-surface molecules. By combining single-molecule force spectroscopy with genetic manipulation and by controlling the interactions between single cells it is possible to quantify de-adhesion forces at the resolution of an individual cell.

Presented here as a prototype of cell-adhesion properties are the measurements of Benoit et al. [22] on a glycoprotein, contact site A (csA), expressed in aggregating cells of *Dictyostelium discoideum*, which are engaged in development of a multicellular organism proteins. A simple mechanism of cell addition is used (Fig. 2.61): a cantilever-mounted cell is positioned on a target cell deposited on a Petri dish. The two elements were brought in contact until a certain repulsive force is detected and were then held in this position for a certain time, allowing the establishment of cell addition.

When retracting the cantilever, force vs. distance measurements were recorded, until the rupture of the contact between cells.

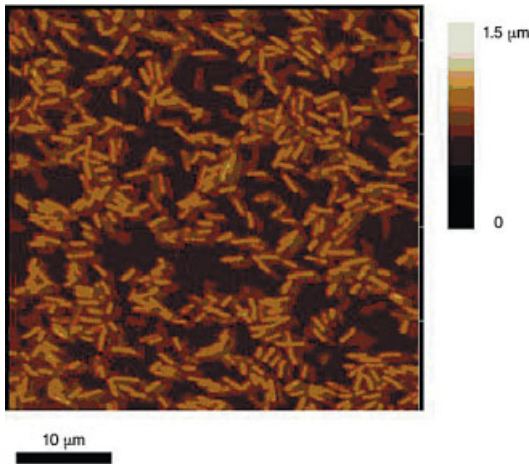


**Fig. 2.58.** Low magnification, tapping-mode image of an *S. oneidensis* colony in agarose. (Reprinted with permission from Ref. [102]. Copyright (2004) Elsevier.)

Force spectra of  $\text{Ca}^{2+}$ -dependent adhesion between cells in the growth phase were realized. In this particular case, cell–cell contacts were maintained for  $20\text{ s}$  at  $150 \pm 20\text{ pN}$  and the rupture was induced at a speed of  $1.5\text{ mm s}^{-1}$ . Strong de-adhesion forces and stepwise separation of cells in the  $\text{Ca}^{2+}$  trace are notable. When replacing  $\text{Ca}^{2+}$  by EDTA, adhesion forces are markedly reduced (Fig. 2.62a). Thus it was proved that, in the case of *Dictyostelium discoideum* cells, cell–

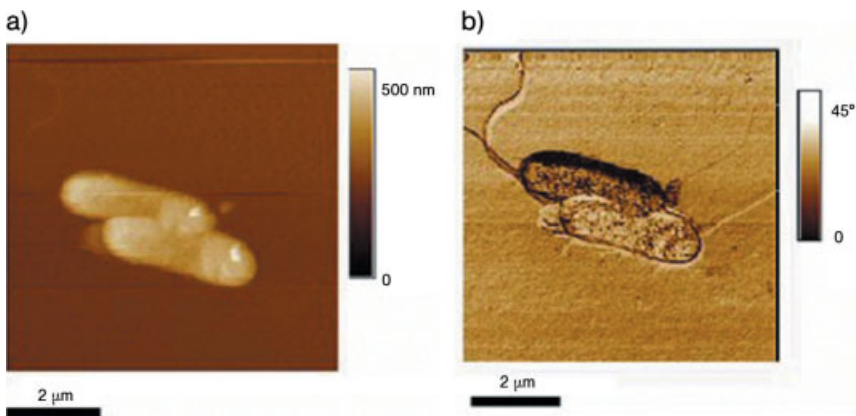


**Fig. 2.59.** AFM tapping-mode images of a pair of *S. oneidensis* on a poly-L-lysine surface: (A) topographic height image and (B) phase image. (Reprinted with permission from Ref. [102]. Copyright (2004) Elsevier.)

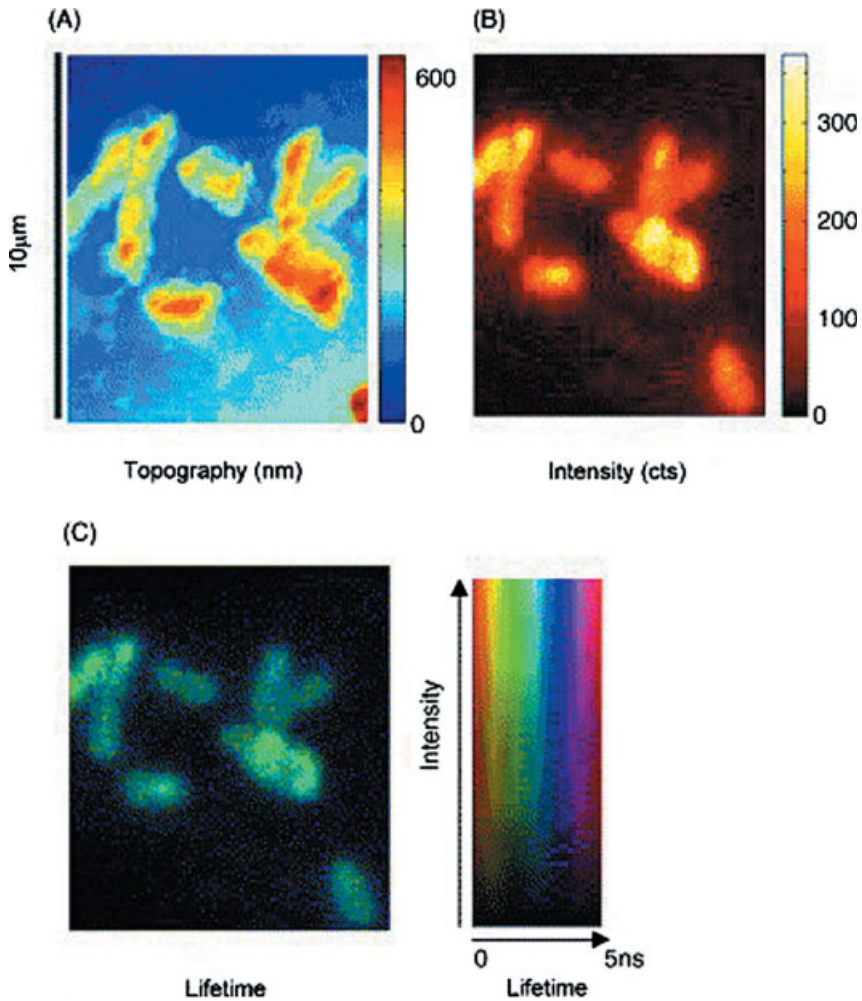


**Fig. 2.60.** Composite correlated AFM-confocal FLIM image of *S. oneidensis* bacterial cells on poly-L-lysine surface: (A) topographic AFM image, (B) confocal fluorescence intensity, and (C) confocal fluorescence lifetime image. The differences in fluorescence intensity and lifetime are presented by the brightness and color (inset), respectively. (Reprinted with permission from Ref. [102]. Copyright (2004) Elsevier.)

cell adhesion of undeveloped cells depends on the presence of  $\text{Ca}^{2+}$ . For the de-addition process, significant de-addition occurred predominantly in a single step (Fig. 2.62b).

### 2.7.7.3 NSOM Imaging

Protein–protein interactions are difficult to elucidate by classical techniques, as it is difficult to obtain an accurate localization of proteins within the substructure of

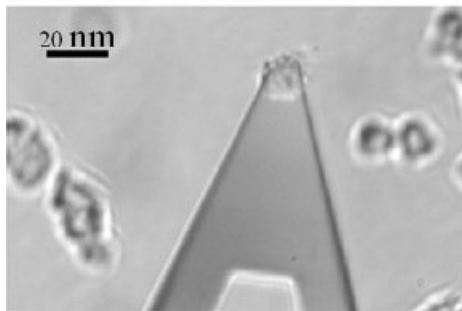
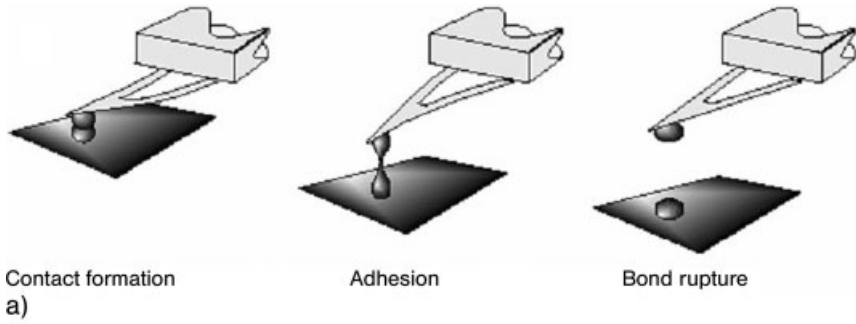


**Fig. 2.61.** (a) Experimental procedure for cell–cell adhesion; (b) light-microscopic image of a cantilever-mounted cell before being brought into contact with another cell. (Reprinted with permission from Ref. [22]. Copyright (2000) Nature.)

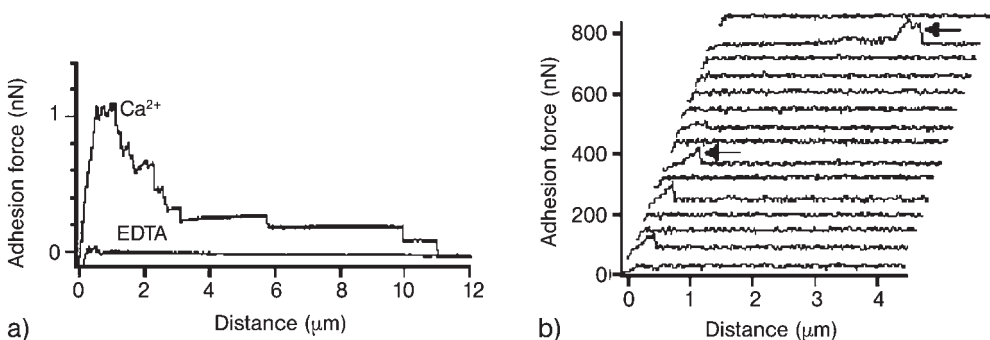


**Fig. 2.62.** (a) Force spectroscopy traces for *D. discoideum* cells. Cell–cell contacts were maintained for 20 s at  $150 \pm 20$  pN and the cells were subsequently pulled apart at  $1.5$  mm s<sup>-1</sup>. (b) Force spectroscopy traces for cell–cell contacts maintained for 0.2 s at  $35 \pm 5$  pN. (Reprinted with permission from Ref. [22]. Copyright (2000) Nature.)

cells and cellular organelles. Enderle et al. have described the use of near-field scanning optical microscopy (NSOM) for mapping and detection of colocalized proteins within a cell, simultaneously and at high resolution [103]. The system of interest was that of human red blood cells invaded by the human malaria parasite *Plasmodium falciparum*. This parasite expresses proteins, during intra-erythrocytic growth, that are transported across the erythrocyte cell membrane and associate with the host skeletal proteins. Specifically, these colocalization studies of the protein pairs of mature parasite-infected erythrocyte surface antigen (MESA)(parasite)/protein 4.1 (host) and *P. falciparum* histidine-rich protein (PfHRP1)(parasite)/protein 4.1 (host) have been analyzed by dual color excitation and NSOM fluorescence detection. A thin blood smear of the trophozoite infected erythrocytes was fixed, then reacted with antibodies against PfHRP1, and labeled with tetramethylrhodamine (Fig. 2.63).

While all three cells are imaged in topography, only the one in the lower right corner was infected and is visible in the fluorescence image. The results imply that the malarial protein MESA interacts with erythrocyte protein in membranes of infected red blood cells, whereas PfHRP1 does not interact with protein 4.1.

### 2.7.8

#### Cantilever Arrays as Biosensors

The application of cantilever arrays to the detection of biomolecules may open the way to a new range of biosensors capable of detecting extremely low concentrations of the order of 10 nM of analytes. Figure 2.64 shows three sets of experiments [7].

Firstly, the effect of a base pair mismatch in oligonucleotide–oligonucleotide recognition was demonstrated (Fig. 2.64A). Here the difference between full complementarity and the single mismatch is clearly seen. The detection limit is demonstrated in Fig. 2.64(B), where decreasing concentrations of oligonucleotide were used. Given the differences between 12 mer oligonucleotides and proteins, it may be expected that even lower concentration limits can be attained with protein. Figure 2.64(C) demonstrates the use of a cantilever array for immunodetection. Here differential signals between a cantilever coated with protein A and a second one coated with BSA to allow removal of signals from non-specific binding were used. Some caution must be taken over the use of cantilever arrays as the microfabrication of such systems generally leads to arrays having different cantilever thicknesses and hence differing spring constants. Thus, much care is required to validate the reproducibility of the biosensors.

## 2.8

### Conclusion

This chapter has illustrated the various types of scanning probe microscopy available to the biological community. The examples presented in the section on using

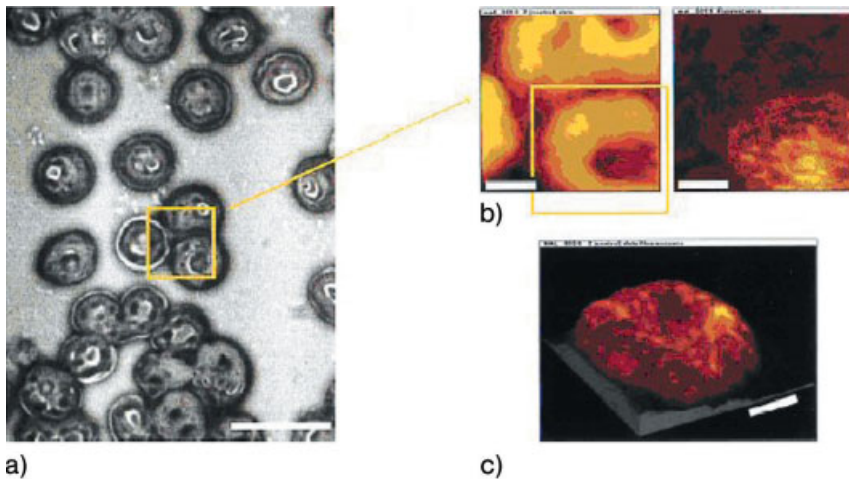


**Fig. 2.63.** (a) Bright-field image of a blood smear; (b) result of NSOM imaging in topography (left) and fluorescence (right) ( $128 \times 128$  pixels,  $60 \text{ nm pixel}^{-1}$ ); (c) Zoom around the infected cell seen in the lower right corner of (b) ( $128 \times 128$  pixels,  $52 \text{ nm pixel}^{-1}$ ). The

fluorescence signal is superimposed as a color value (brightness scale goes from black via red to yellow) to the topography to show the distribution of PfHRP1 in the erythrocyte membrane. (Reprinted with permission from Ref. [103]. Copyright (1997) PNAS.)

the tools are there to stimulate interest in imaging biological systems, and to try and answer the question posed in the introduction. Why use scanning probe microscopies in biology?

The final question is where do we go from here? The reply would seem to be towards integrated studies using SPM as one tool along with the wide panoply of other physical techniques to probe biological activity in its environment.

### Acknowledgments

We gratefully acknowledge JPK GmbH of Berlin for allowing us to use many figures from their handbook. We wish to thank the Fondation pour la Recherche Medicale for funding our AFM. S.C. thanks BioMerieux and A.N.L. thanks Delta Proteomics for financial support.

### References

- 1 G. BINNING, H. ROHRER, C. GERBER, E. WEIBEL, Surface studies by scanning tunneling microscopy *Phys. Rev. Lett.* **1982**, 49, 57–61.
- 2 J. K. H. HOERBER, M. J. MILES, Scanning probe evolution in biology *Science* **2003**, 302, 1002–1005.
- 3 K. D. JANDT, Atomic force microscopy

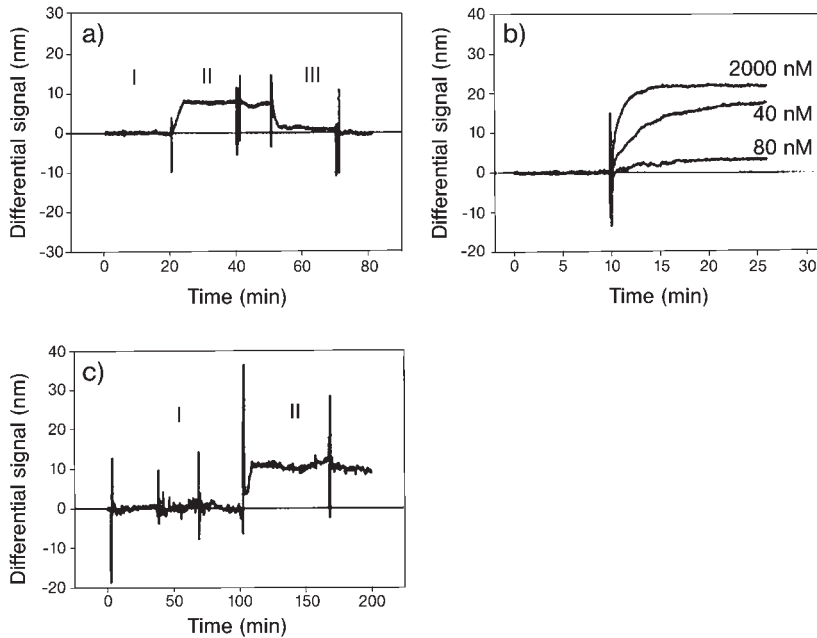


**Fig. 2.64.** (A) Differential signal of a hybridization experiment, showing detection of a single base mismatch in 12 mer oligonucleotides. Two cantilevers were functionalized with sequences differing only in one base: 59-CTATGTCAGCAC-39 (first oligonucleotide), 59-CTATGTAAGCAC-39 (second oligonucleotide). Injection of the first complementary oligonucleotide increases the differential signal (interval II); injection of the second complementary oligonucleotide decreases the differential signal (interval III). (B) Three successive hybridization experiments with different 12 mer oligonucleotide concentrations, using one array. The concen-

tration detection limit was calculated to be 10 nm, on the basis of a deflection noise of 0.5 nm. (C) Differential signal from a protein-protein interaction. One cantilever was functionalized with protein A and the other with BSA as a reference. First, as a negative control, buffer and then buffer containing goat IgG were injected. In both cases (interval I), no change of the differential signal was detected. In contrast, injection of rabbit IgG increased the differential signal by 12 nm within minutes (interval II). The signal persisted after the liquid cell was purged again with buffer. (Reprinted with permission from Ref. [7]. Copyright (2000) Science.)

of biomaterials surfaces and interfaces *Surf. Sci.* **2001**, *491*, 303–332.

- 4 R. MCKENDRY, J. ZHANG, Y. ARNTZ, T. STRUNZ, M. HEGNER, H. P. LANG, M. K. BALLER, U. CERTA, E. MEYER, H.-J. GUNTHERODT, C. GERBER, Multiple label-free biodetection and quantitative DNA-binding assays on a nanomechanical cantilever array *Proc. Natl. Acad. Sci. U.S.A.* **2002**, *99*, 9783–9788.
- 5 F. M. BATTISTON, J. P. RAMSEYER,

H. P. LANG, M. K. BALLER, C. GERBER, J. K. GIMZEWSKI, E. MEYER, H. J. GUNTHERODT, A chemical sensor based on a microfabricated cantilever array with simultaneous resonance-frequency and bending readout *Sens. Actuators, B* **2001**, *B77*, 122–131.

- 6 J. FRITZ, M. K. BALLER, H. P. LANG, T. STRUNZ, E. MEYER, H. J. GUNTHERODT, E. DELAMARCHE, C. GERBER, J. K. GIMZEWSKI, Stress at the solid-liquid interface of self-assembled



- monolayers on gold investigated with a nanomechanical sensor *Langmuir* **2000**, *16*, 9694–9696.
- 7 J. FRITZ, M. K. BALLER, H. P. LANG, H. ROTHUIZEN, P. VETTIGER, E. MEYER, H. J. GUNTHERODT, C. GERBER, J. K. GIMZEWSKI, Translating biomolecular recognition into nanomechanics *Science* **2000**, *288*, 316–318.
  - 8 M. K. BALLER, H. P. LANG, J. FRITZ, C. GERBER, J. K. GIMZEWSKI, U. DRECHSLER, H. ROTHUIZEN, M. DESPONT, P. VETTIGER, F. M. BATTISTON, J. P. RAMSEYER, P. FORNARO, E. MEYER, H. J. GUNTHERODT, A cantilever array-based artificial nose *Ultramicroscopy* **2000**, *82*, 1–9.
  - 9 S. W. PADDOCK (ed.), *Confocal Microscopy Methods and Protocols*, Methods Mol. Biol., vol. 122, Humana, Totowa, **1999**.
  - 10 S. PADDOCK, Tech sight: Optical sectioning-slices of life *Science* **2002**, *295*, 1319–1321.
  - 11 E. H. SYNGE, A suggested method for extending microscopic resolution into the ultra-microscopic region *Phil. Mag.* **1928**, *6*, 356–62.
  - 12 Z. OUNAIES, Piezoelectric materials, in *Encyclopedia of Biomaterials and Biomedical Engineering*, vol. 2, eds. G. E. WNEK, G. L. BOWLIN, Marcel Dekker, New York, **2004**.
  - 13 R. L. SMITH, G. S. ROHRER, The preparation of tip and sample surfaces for scanning probe experiments, in *Scanning Probe Microscopy and Spectroscopy. Theory, Techniques and Applications*, 2<sup>nd</sup> edn, ed. D. A. BONNEL, Wiley & Sons, New York, **1993**.
  - 14 M. J. MADOU, *Fundamentals of Microfabrication: The Science of Miniaturization*, 2<sup>nd</sup> edition, CRC Press, Boca Raton, **2002**.
  - 15 M. TOMITORI, T. ARAI, Tip cleaning and sharpening processes for non-contact atomic force microscope in ultrahigh vacuum *Appl. Surf. Sci.* **1999**, *140*, 432–438.
  - 16 D. WOUTERS, U. S. SCHUBERT, Nanolithography and nanochemistry: probe-related patterning techniques and chemical modification for nanometer-sized devices *Angew. Chem. Int. Ed.* **2004**, *43*(19), 2480–2495.
  - 17 H. F. KNAPP, W. WIEGRÄBE, M. HEIM, R. ESCHRICHT, R. GUCKENBERGER, Atomic force measurements and manipulation of Langmuir-Blodgett films with modified tips *Biophys. J.* **1995**, *69*, 708–715.
  - 18 M.-H. PACLET, A. W. COLEMAN, J. BURRITT, F. MOREL, NADPH oxidase of Epstein-Barr-virus immortalized B lymphocytes. Effect of cytochrome b558 glycosylation *Eur. J. Biochem.* **2001**, *268*, 5197–5208.
  - 19 T. BOLAND, B. D. RATNER, Direct measurement of hydrogen bonding in DNA nucleotide bases by atomic force microscopy *Proc. Natl. Acad. Sci. U.S.A.* **1995**, *92*(12), 5297–301.
  - 20 T. HAN, J. M. WILLIAMS, T. P. JR. BEEBE, Chemical bonds studied with functionalized atomic force microscopy tips *Anal. Chim. Acta* **1995**, *307*(2–3), 365–76.
  - 21 E. L. FLORIN, V. T. MOY, H. E. GAUB, Adhesion forces between individual ligand-receptor pairs *Science* **1994**, *264*, 415–417.
  - 22 M. BENOIT, D. GABRIEL, G. GERISCH, H. E. GAUB, Discrete interactions in cell adhesion measured by single-molecule force spectroscopy *Nat. Cell Biol.* **2000**, *2*(6), 313–317.
  - 23 T. V. RAITO, K. C. LANGRY KEVIN, R. E. RUDD, R. L. BALHORN, M. J. ALLAN, M. W. McELFRESH, Force spectroscopy of the double-tethered concanavalin-A mannose bond *Biophys. J.* **2004**, *86*(4), 2430–2437.
  - 24 H. NAKAJIMA et al., Scanning force microscopy of the interaction events between a single molecule of heavy meromyosin and actin *Biochem. Biophys. Res. Commun.* **1997**, *234*, 178–182.
  - 25 V. T. MOY, E. L. FLORIN, H. E. GAUB, Intermolecular forces and energies between ligands and receptors *Science* **1994**, *266*, 257–259.
  - 26 G. U. LEE, D. A. KIDWELL, R. J. COLTON, Sensing discrete streptavidin-biotin interactions with atomic force microscopy *Langmuir* **1994**, *10*, 354–357.
  - 27 G. U. LEE, L. A. CHRISEY, R. J. COLTON, Direct measurement of the forces between complementary

- strands of DNA *Science* **1994**, *266*, 771–773.
- 28 U. DAMMER, O. POPESCU, P. WAGNER, D. ANSELMETTI, H. J. GUNTHERODT, G. N. MISEVIC, Binding strength between cell adhesion proteoglycans measured by atomic force microscopy *Science* **1995**, *267*, 1173–1175.
  - 29 U. DAMMER, M. HEGNER, D. ANSELMETTI, P. WAGNER, M. DREIER, W. HUBER, H. J. GUNTHERODT, Specific antigen/antibody interactions measured by force microscopy *Biophys. J.* **1996**, *70*, 2437–2441.
  - 30 P. HINTERDORFER, W. BAUMGARTNER, H. J. GRUBER, K. SCHILCHER, H. SCHINDLER, Detection and localization of individual antibody-antigen recognition events by atomic force microscopy *Proc. Natl. Acad. Sci. U.S.A.* **1996**, *93*, 3477–3481.
  - 31 S. ALLEN, X. CHEN, J. DAVIES, M. C. DAVIES, A. C. DAWKES, J. C. EDWARDS, C. J. ROBERTS, J. SEFTON, S. J. TENDLER, P. M. WILLIAMS, Detection of antigen-antibody binding events with the atomic force microscope *Biochemistry* **1997**, *36*, 7457–7463.
  - 32 J. FRITZ, A. G. KATOPODIS, F. KOLBINGER, D. ANSELMETTI, Force-mediated kinetics of single P-selectin/ligand complexes observed by atomic force microscopy *Proc. Natl. Acad. Sci. U.S.A.* **1998**, *95*, 12283–12288.
  - 33 P. P. LEHENKARI, M. A. HORTON, Single integrin molecule adhesion forces in intact cells measured by atomic force microscopy *Biochem. Biophys. Res. Commun.* **1999**, *259*, 645–650.
  - 34 M. THIE, R. ROSPEL, W. DEITMANN, M. BENOIT, M. LUDWIG, H. E. GAUB, H. W. DENKER, Interactions between trophoblast and uterine epithelium: monitoring of adhesives forces *Hum. Reprod.* **1998**, *13*, 3211–3219.
  - 35 G. SAGVOLDEN, I. GIAEVER, E. O. PETTERSEN, J. FEDER, Cell adhesion force microscopy *Proc. Natl. Acad. Sci. U.S.A.* **1999**, *96*, 471–476.
  - 36 C. BUSTAMANTE, D. A. ERIE, D. KELLER, Biochemical and structural applications of scanning force microscopy *Curr. Opin. Struct. Biol.* **1994**, *4*, 750–760.
  - 37 M. GRANDBOIS, M. BEYER, M. RIEF, H. CLAUSEN-SCHAUMANN, H. E. GAUB, How strong is a covalent bond? *Science* **1999**, *283*, 1727–1730.
  - 38 H. LI, M. RIEF, F. OESTERHELT, H. E. GAUB, Force spectroscopy on single xanthan molecules *Appl. Phys. A: Mater. Sci. Process.* **1999**, *68*, 407–410.
  - 39 C. BUSTAMANTE, Z. BRYANT, S. B. SMITH, Ten years of tension: single-molecule DNA mechanics *Nature* **2003**, *421*, 423–427.
  - 40 C. BUSTAMANTE, S. B. SMITH, J. LIPHARDT, D. SMITH, Single-molecule studies of DNA mechanics *Curr. Opin. Struct. Biol.* **2000**, *10*, 279–285.
  - 41 U. BOCKELMANN, Single-molecule manipulation of nucleic acids *Curr. Opin. Struct. Biol.* **2004**, *14*, 368–373.
  - 42 M. HEGNER, W. GRANGE, Mechanics and imaging of single DNA molecules *J. Muscle Res. Cell Motility* **2002**, *23*, 367–375.
  - 43 J. VAN NOORT, Unraveling bacteriorhodopsin *Biophys. J.* **2005**, *88*, 763–764.
  - 44 R. ROUNSEVELL, J. R. FORMAN, J. CLARKE, Atomic force microscopy: mechanical unfolding of proteins *Methods* **2004**, *34*, 100–111.
  - 45 R. B. BEST, D. J. BROCKWELL, J. L. TOCA-HERRERA, A. W. BLAKE, D. A. SMITH, S. E. RADFORD, J. CLARKE, Force mode atomic force microscopy as a tool for protein folding studies *Anal. Chim. Acta* **2003**, *479*, 87–105.
  - 46 R. B. BEST, J. CLARKE, What can atomic force microscopy tell us about protein folding? *Chem. Commun.* **2002**, 183–192.
  - 47 M. LUDWIG, M. RIEF, L. SCHMIDT, H. LI, F. OESTERHELT, M. GAUTEL, H. E. GAUB, AFM, a tool for single-molecule experiments *Appl. Phys. A: Mater. Sci. Process.* **1999**, *A68*, 173–176.
  - 48 D. P. ALLISON, P. HINTERDORFER, W. HAN, Biomolecular force measurements and the atomic force microscope *Curr. Opin. Biotechnol.* **2002**, *13*, 47–51.
  - 49 T. BASCHE, S. NIE, J. M. FERNANDEZ, Single molecules *Proc. Natl. Acad. Sci. U.S.A.* **2001**, *98*, 10527–10528.
  - 50 A. NOY, D. V. VEZENOV, C. M. LIEBER, Chemical force microscopy *Annu. Rev. Mater. Sci.* **1997**, *27*, 381–421.

- 51 M. SU, V. P. DRAVID, C. A. MIRKIN, Direct patterning of solid-state and organic materials by dip-pen nanolithography *Abstracts of Papers, 224th ACS National Meeting, Boston, MA, United States, August 18–22, 2002*, COLL-092.
- 52 S. HONG, J. ZHU, C. A. MIRKIN, Multiple ink nanolithography: Toward a multiple-pen nano-plotter *Science* **1999**, *286*, 523–525.
- 53 R. D. PINER, J. ZHU, F. XU, S. HONG, C. A. MIRKIN, “Dip-pen” nanolithography *Science* **1999**, *283*, 661–663.
- 54 B. GATES, Q. XU, J. C. LOVE, D. B. WOLFE, G. M. WHITESIDES, Unconventional nanofabrication. *Annu. Rev. Mater. Res.* **2004**, *34*, 339–372.
- 55 E. A. ASH, G. NICHOLLS, Super-resolution aperture scanning microscope *Nature* **1972**, *237*, 510–512.
- 56 E. BETZIG, R. J. CHICHESTER, Near-field optics: microscopy, spectroscopy, and surface modification beyond the diffraction limit *Science* **1992**, *257*, 189–195.
- 57 E. BETZIG, R. J. CHICHESTER, Single molecules observed by near-field scanning optical microscopy *Science* **1993**, *262*, 1422–1425.
- 58 R. C. DUNN, Near-field optical microscopy *Chem. Rev. Wash DC.* **1999**, *99*(10), 2891–2927.
- 59 A. N. LAZAR, P. SHAHGALDIAN, A. W. COLEMAN, Anion recognition effects in the structuring of bovine serum albumin films. *J. Supramol. Chem.* **2001**, *1*, 193–199.
- 60 J. FANG, C. M. SOTO, T. LIN, J. E. JOHNSON, B. RATNA, Complex pattern formation by cowpea mosaic virus nanoparticles *Langmuir* **2002**, *18*(2), 308–310.
- 61 T. P. BEEBE, T. E. WILSON, D. F. OGLETREE, J. E. KATZ, R. BALHORN, M. B. SALMERON, W. J. SIEKHAUS, Direct observation of native DNA structures with the scanning tunneling microscope *Science* **1989**, *243*, 370–372.
- 62 S. GOULD, B. DRAKE, C. B. PRATER, A. L. WEISENHORN, S. M. LINDSAY, P. K. HANSAMA, Imaging polymers, proteins and DNA in aqueous solutions with atomic force microscope *Proc. of the 47<sup>th</sup> Electron Microscopy Society of America* **1989**, 32–33.
- 63 W. GRANGE, T. STRUNZ, I. SCHUMAKOVITICH, H.-J. GUNTHERODT, M. HEGNER, Molecular recognition and adhesion of individual DNA strands studied by dynamic force microscopy, *Single Molecules* **2001**, *2*, 75–78.
- 64 K. UMEMURA, T. OKADA, R. KURODA, Cooperativity and intermediate structures of single-stranded DNA binding-assisted RecA-single-stranded DNA complex formation studied by atomic force microscopy *Scanning* **2005**, *27*, 35–43.
- 65 D. ANSELMETTI, J. FRITZ, B. SMITH, X. FERNANDEZ-BUSQUETS, Single molecule DNA biophysics with atomic force microscopy *Single Mol.* **2000**, *1*, 53–58.
- 66 T. THUNDAT, X.-Z. ZHENG, S. L. SHARP, D. P. ALLISON, R. J. WARMACK, D. C. JOY, T. L. FERRELL, *Scanning. Microsc.* **1992**, *6*, 903–910.
- 67 J. M. KIM, H. S. JUNG, J. WAN PARK, H. Y. LEE, T. KAWAI, AFM phase lag mapping for protein–DNA oligonucleotide complexes *Anal. Chem. Acta* **2004**, *525*, 151–157.
- 68 J. VAN NOORT, T. VAN DER HEIJDEN, C. F. DUTTA, K. FIRMAN, C. DEKKER, Initiation of translocation by Type I restriction modification enzymes is associated with a short DNA extrusion *Nucl. Acids Res.* **2004**, *32*, 6540–6547.
- 69 K. FIRMAN, M. SZCZELKUN, Measuring motion on DNA by the type I restriction endonuclease EcoR124I using triplex dissociation *EMBO J.* **2000**, *19*, 2094–2102.
- 70 R. SEIDEL, J. VAN NOORT, C. VAN DER SCHEER, J. G. P. BLOOM, N. H. DEKKER, C. F. DUTTA, A. BLUNDELL, T. ROBINSON, K. FIRMAN, C. DEKKER, Real-time observation of DNA translocation by the type I restriction-modification enzyme EcoR124I *Nat. Struct. Mol. Biol* **2004**, *11*, 838–843.
- 71 R. KRAUTBAUER, L. H. POPE, T. E. SCHRADER, S. ALLEN, H. E. GAUB, Discriminating small molecule DNA binding modes by single molecule

- force spectroscopy *F.E.B.S. Letters* **2002**, *510*, 7(3), 154–158.
- 72 H. CLAUSEN-SCHAUMANN, M. RIEF, C. TOLKSDORF, H. E. GAUB, Mechanical stability of single DNA molecules *Biophys. J.* **2000**, *78*, 1997–2007.
- 73 M. BONIN, R. ZHU, Y. KLAUE, J. OBERSTRASS, E. OESTERSCHULZE, W. NELLEN, Analysis of RNA flexibility by scanning force spectroscopy *Nucl. Acids Res.* **2002**, *30*(16), e81.
- 74 M. RIEF, H. CLAUSEN-SCHAUMANN, H. E. GAUB, Sequence-dependent mechanics of single DNA molecules *Nat. Struct. Biol.* **1999**, *6*, 346–349.
- 75 S. LEES, K. S. PROSTAK, V. K. INGLE, K. KJOLLER, The loci of mineral in turkey leg tendon as seen by atomic force microscope and electron microscopy *Calcified Tissue International* **1994**, *55*(3), 180–189.
- 76 H. SEELERT, A. POETSCH, N. A. DENCHER, A. ENGEL, H. STAHLBERG, D. J. MÜLLER, Proton-powered turbine of a plant motor *Nature* **2000**, *405*, 418–419.
- 77 D. FOTIADIS, L. HASLER, D. J. MULLER, H. STAHLBERG, J. KISTLER, A. ENGEL, Surface tongue-and-groove contours on lens MIP facilitate cell-to-cell adherence *J. Mol. Biol.* **2000**, *300*, 779–789.
- 78 J.-H. LIM, D. S. GINGER, K.-B. LEE, J. HEO, J.-M. NAM, C. A. MIRKIN, Direct-write dip-pen nanolithography of proteins on modified silicon oxide surfaces, *Angew. Chem. Int. Ed.* **2003**, *42*, 2309–2312.
- 79 J. WONG, A. CHILKOTI, V. T. MOY, Direct force measurements of the streptavidin–biotin interaction *Biomol. Eng.* **1999**, *16*, 45–55.
- 80 M. RIEF, M. GAUTEL, F. OESTERHELT, J. M. FERNANDEZ, H. E. GAUB, Reversible unfolding of individual titin immunoglobulin domains by AFM *Science* **1997**, *276*(5315), 1109–1112.
- 81 L. NG, A. J. GRODZINSKY, P. PATWARI, J. SANDY, A. PLAAS, C. ORTIZ, Individual cartilage aggrecan macromolecules and their constituent glycosaminoglycans visualized via atomic force microscopy *J. Struct. Biol.* **2003**, *14*, 242–257.
- 82 F. TOKUMASU, A. J. JIN, G. W. FEIGENSON, J. A. DVORAK, Atomic force microscopy of nanometric liposome adsorption and nanoscopic membrane domain formation, *Ultramicroscopy* **2003**, *97*, 217–227.
- 83 A. DUBES, H. PARROT-LOPEZ, A. WASSIM, G. DEGOBERT, H. FESSI, P. SHAHGALDIAN, A. W. COLEMAN, Scanning electron microscopy and atomic force microscopy imaging of solid lipid nanoparticles derived from amphiphilic cyclodextrins, *Eur. J. Pharm. Biopharm.* **2003**, *55*, 279–282.
- 84 a: M. H. PACLET, A. W. COLEMAN, S. VERGNAUD, F. MOREL, P67-phox-mediated NADPH oxidase assembly: imaging of cytochrome b558 liposomes by atomic force microscopy, *Biochemistry* **2000**, *39*, 9302–9310.
- 85 H. BROCHU, A. POLIDORI, B. PUCCI, P. VERMETTE, Drug delivery systems using immobilized intact liposomes: A comparative and critical review, *Curr. Drug Delivery* **2004**, *1*, 299–312.
- 86 W. A. DUCKER, T. J. SENDEN, R. M. PASHLEY, Direct measurement of colloidal forces using an atomic force microscope *Nature* **1991**, *353*, 239–241.
- 87 X. LIANG, G. MAO, K. Y. S. NG, Mechanical properties and stability measurement of cholesterol-containing liposome on mica by atomic force microscopy *J. Colloid Interface Sci.* **2004**, *278*, 53–62.
- 88 P. SHAHGALDIAN, L. QUATTROCCHI, J. GUALBERT, A. W. COLEMAN, P. GORELOFF, AFM imaging of calixarene based solid lipid nanoparticles in gel matrices *Eur. J. Pharm. Biopharm.* **2003**, *55*, 107–113.
- 89 J. GUALBERT, P. SHAHGALDIAN, A. W. COLEMAN, Interactions of amphiphilic calix[4]arene based solid-lipid-nanoparticles with bovine serum albumin *Int. J. Pharm.* **2003**, *257*(1–2), 69–73.
- 90 A. A. BRIAN, H. M. MCCONNELL, Allogenic stimulation of cytotoxic tcells by supported planar membranes, *Proc. Natl. Acad. Sci. U.S.A.* **1984**, *81*, 6159–6163.

- 91 J. JASS, T. TJÄRNHAGE, G. PUU, From liposomes to supported, planar bilayer structures on hydrophilic and hydrophobic surfaces: An atomic force microscopy study *Biophys J.* **2000**, 79, 3153–3163.
- 92 R. RICHTER, A. MUKHOPADHYAY, A. BRISSON, Pathways of lipid vesicle deposition on solid surfaces: A combined QCM-D and AFM study *Biophys. J.* **2003**, 85, 3035–3047.
- 93 A. GARNER, S. CONNELL, G. LI, A. SMITH, J. COLYER, N. HOOPER, Atomic force microscopy of microdomains in lipid bilayers, <http://www.astbury.leeds.ac.uk/Report/2003/Report/46smith-AFM.pdf>, **2003**.
- 94 T. BERGE, D. J. ELLIS, D. T. F. DRYDEN, J. M. EDWARDSON, R. M. HENDERSON, Translocation-independent dimerization of the EcoKI endonuclease visualized by atomic force microscopy *Biophys. J.* **2000**, 79(1), 479–484.
- 95 D. E. SASLOWSKY, J. LAWRENCE, X. REN, D. A. BROWN, R. M. HENDERSON, J. M. EDWARDSON, Placental alkaline phosphatase is efficiently targeted to rafts in supported lipid bilayers *J. Biol. Chem.* **2002**, 277, 26966–26970.
- 96 H. HA, H. B. KWAK, S. K. LEE, D. S. NA, C. E. RUDD, Z. H. LEE, H. H. KIM, Membrane rafters play a crucial role in receptor activator of nuclear factor Kappa B (Rank) signaling and osteoclast function *J. Biol. Chem.* **2003**, 278, (20), 18573–18580.
- 97 N. A. GEISSE, T. L. COVER, R. M. HENDERSON, T. M. EDWARDSON, Targeting of *Helicobacter pylori* vacuolating toxin to lipid raft membrane domains analyzed by atomic force microscopy *Biochem. J.* **2004**, 381, 911–917.
- 98 S. BARAKAT, L. GAYET, G. DAYAN, S. LABIALLE, A. LAZAR, V. OLEINIKOV, A. W. COLEMAN, L. G. BAGGETTO, Multidrug-resistant cancer cells contain two populations of P-glycoprotein with differently stimulated P-gp ATPase activities. Evidence from atomic force microscopy and biochemical analysis, *Biochem. J.* **2005**, 388, 563–571.
- 99 C. W. HOLLARS, R. C. DUNN, Submicron structure in L- $\alpha$ -dipalmitoylphosphatidylcholine monolayers and bilayers probed with confocal, atomic force, and near-field microscopy *Biophys. J.* **1998**, 75, 342–353.
- 100 H. SHIKU, R. C. DUNN, Domain formation in thin lipid films probed with near-field scanning optical microscopy *J. Microsc.* **1999**, 194, 455–460.
- 101 Y. G. KUZNETSOV, A. LOW, H. FAN, A. MCPHERSON, Atomic force microscopy investigation of wild-type Moloney murine leukaemia virus particles and virus particles lacking the envelope protein *Virology* **2004**, 323, 189–196.
- 102 M. MICIC, D. HU, Y. D. SUH, G. NEWTON, M. ROMINE, H. P. LU, Correlated atomic force microscopy and fluorescence lifetime imaging of live bacterial cells, *Colloids Surf., B: Biointerfaces* **2004**, 34(4), 205–212.
- 103 T. H. ENDERLE, T. HA, D. F. OGLETREE, D. S. CHEMLA, C. MAGOWAN, S. WEISS, Membrane specific mapping and colocalization of malarial and host skeletal proteins in the *Plasmodium falciparum* infected erythrocyte by dual-color near-field scanning optical microscopy *Proc. Natl. Acad. Sci. U.S.A.* **1997**, 94, 520–525.

## Appendix 1 Books on Scanning Probe Microscopies Reviews on Scanning Probe Microscopies in Biology

- M. ALLEGRI, N. GARCIA, O. MARTI (2001). *Nanometer Scale Science and Technology*. Amsterdam, IOS Press.
- G. ATTARD, C. BARNES (1998). *Surfaces*. Oxford, Oxford University Press.
- C. BAI (2000). *Scanning Tunneling Microscopy*

- and Its Application. Heidelberg, Springer Verlag.
- J. D. BATTEAS, G. C. MICHALES (2005). *Applications of Scanned Probe Microscopy to Polymers*. Oxford, Oxford University Press.
- R. J. BEHM, H. ROHRER, N. GARCIA (1990). *Scanning Tunneling Microscopy and Related Methods Proceedings*. New York, Kluwer Academic Publishers.
- G. BENEDEK (1992). *Surface Properties of Layered Structures*, New York, Kluwer Academic Publishers.
- B. BHUSHAN (2003). *Applied Scanning Probe Methods*. Heidelberg, Springer Verlag.
- K. S. BIRDI (2003). *Scanning Probe Microscopes Applications in Science and Technology*. Boca Raton, FL, CRC Press.
- P. C. BRAGA, D. RICCI (2003). *Atomic Force Microscopy Biomedical Methods and Applications*. Totowa, Humana Press.
- H. BUBERT, B. JENETT (2002). *Surface and Thin Film Analysis Compendium of Principles, Instrumentation and Applications*. New York, Wiley-VCH.
- S. H. COHEN (1995). *Atomic Force Microscopy/ Scanning Tunneling Microscopy*. New York, Kluwer Academic Publishers.
- D. A. BONNELL (2000). *Scanning Probe Microscopy and Spectroscopy: Theory, Techniques, and Applications*. New York, Wiley-VCH.
- A. DE STEFANIS, A. A. G. TOMLINSON (2001). *Scanning Probe Microscopies From Surface Structure to Nano-scale Engineering*. Zurich, Trans Tech Publications Ltd.
- N. J. DINARDO (2004). *Nanoscale Characterization of Surfaces and Interfaces*. New York, Wiley-VCH.
- G. DOYEN, D. DRAKOVA (2004). *The Physical Principles of STM and AFM Operation*. New York, Wiley-VCH.
- P. L. GAI (1997). *In-Situ Microscopy in Materials Research Leading International Research in Electron and Scanning Probe*. New York, Kluwer Academic Publishers.
- M. GENTILI, C. GIOVANNELLA (1994). *Nanolithography A Borderland Between STM, EB, IB and X-Ray Lithographies*. New York, Kluwer Academic Publishers.
- A. A. GEWIRTH, H. SIEGENTHALER (1995). *Forces in Scanning Probe Methods*. New York, Kluwer Academic Publishers.
- H.-J. GUNTHERODT, R. WIESENDANGER (1995). *Scanning Tunneling Microscopy*. Berlin and Heidelberg, Springer Verlag.
- H. NEDDERMEYER (1993). *Scanning Tunneling Microscopy*. New York, Kluwer Academic Publishers.
- B. P. JENA, J. K. HEINRICH HOBER (2002). *Atomic Force Microscopy in Cell Biology (Methods in Cell Biology, vol 68)*. London, Elsevier.
- S. KAWATA, M. OHTSU, M. IRIE (2002). *Nano-Optics*. Heidelberg, Springer Verlag.
- D. LANGE, O. BRAND, H. BALTES (2002). *Cantilever-Based CMOS Nano-Electro-Mechanical Systems Atomic-Force Microscopy and Gas Sensing Applications*. New York, Springer-Verlag.
- X. Y. LIU, J. J. DE YOREO (2004). *Nanoscale Structure and Assembly at Solid-Fluid Interfaces*. New York, Kluwer Academic Publishers.
- W. J. LORENZ, W. PLEITH (1999). *Electrochemical Nanotechnology: In Situ Local Probe Techniques at Electrochemical Interfaces*. New York, Wiley-VCH.
- O. MARTI, M. AMREIN (1993). *STM and SFM in Biology*. London, Elsevier Academic Press.
- F. MAYER, M. HOPERT (2003). *Microscopic Techniques in Biotechnology*. New York, Wiley-VCH.
- S. MORITA, R. WIESENDANGER, E. MEYER (2002). *Non Contact Atomic Force Microscopy*. Heidelberg, Springer-Verlag.
- V. J. MORRIS, A. R. KIRBY, A. P. GUNNIN (2000). *Atomic Force Microscopy for Biologists*. London, Imperial College Press.
- M. NIETO-VESPERINAS, N. GARCIA (1996). *Optics at the Nanometer Scale Imaging and Storing with Photonic Near Fields*. New York, Kluwer Academic Publishers.
- A. PERIASAMY (2001). *Methods in Cellular Imaging*. Oxford, Oxford University Press.
- R. H. TEMPLER, R. LEATHERBARROW (2003). *Biophysical Chemistry: Membrane and Proteins*. Cambridge, The Royal Society of Chemistry.
- R. VANSELOW (1990). *Chemistry and Physics of Solid Surfaces*. Heidelberg, Springer Verlag.
- T. VO-DINH (2004). *Protein Nanotechnology Protocols, Instrumentation, and Applications*. Totowa, Humana Press.
- R. WIESENDANGER (1994). *Scanning Probe Microscopy and Spectroscopy Methods and Applications*. Cambridge, Cambridge University Press.

## Appendix 2 Reviews on Scanning Probe Microscopies in Biology

- N. I. ABU-LAIL, T. A. CAMESAN, Polysaccharide properties probed with atomic force microscopy *J. Microsc.* **2003**, 212(3), 217–238.
- W. M. ALBERS, I. VIKHOLM, et al., Interfacial and materials aspects of the immobilization of biomolecules onto solid surfaces *Handbook Surf. Interfaces Mater.* **2001**, 5, 1–31.
- S. ALLEN, S. M. RIGBY-SINGLETON, et al., Measuring and visualizing single molecular interactions in biology *Biochem. Soc. Trans.* **2003**, 31(5), 1052–1057.
- D. P. ALLISON, P. HINTERDORFER, et al., Biomolecular force measurements and the atomic force microscope *Curr. Opin. Biotechnol.* **2002**, 13(1), 47–51.
- M. AMREIN, H. GROSS, Scanning tunneling microscopy of biological macromolecular structures coated with a conducting film *Scanning Microsc.* **1992**, 6(2), 335–344.
- M. AMREIN, H. GROSS, et al., STM of proteins and membranes *STM SFM Biol.* **1993**, 127–175.
- J. E. T. ANDERSEN, J. ULSTRUP, et al., Imaging of electrochemical processes and biological macromolecular adsorbates by in-situ scanning tunneling microscopy *Electrochem. Nanotechnol.* **1998**, 27–44.
- T. ANDO, Atomic force microscope: Application to life science *Seikagaku* **2002**, 74(11), 1329–1342.
- T. ANDO, Real-time AFM imaging of protein motions *Farumashia* **2002**, 38(6), 508–512.
- T. ANDO, High-speed atomic force microscope: High-speed imaging of nanometer-scale dynamics of biological molecules *Oyo Butsuri* **2003**, 72(10), 1304–1308.
- T. ANDO, High speed AFM observes motor protein movement *Kagaku* **2004**, 59(1), 28–29.
- T. ANDO, N. KODERA, et al., A high-speed atomic force microscope for studying biological macromolecules in action *ChemPhysChem* **2003**, 4(11), 1196–1202.
- O. N. ANTZUTKIN, Amyloidosis of Alzheimer's Ab peptides: Solid-state nuclear magnetic resonance, electron paramagnetic resonance, transmission electron microscopy, scanning transmission electron microscopy and atomic force microscopy studies *Magn. Resonan. Chem.* **2004**, 42(2), 231–246.
- M. AOKI, M. ITOH, Methods for kinetic analysis of protein-protein interaction *Tanpakushitsu Kakusan Koso* **2004**, 49(17, Zokan), 2780–2785.
- H. ARAKAWA, Mechanical property of protein measured with AFM *Denshi Kenbikyō* **2003**, 38(2), 86–89.
- P. G. ARSCOTT, V. A. BLOOMFIELD, Scanning tunneling microscopy in biotechnology *Trends Biotechnol.* **1990**, 8(6), 151–156.
- Y. BABA, Micro- and nanobiochip technology *Oyo Butsuri* **2002**, 71(12), 1481–1487.
- K. BALASHEV, T. R. JENSEN, et al., Novel methods for studying lipids and lipases and their mutual interaction at interfaces. Part I. Atomic force microscopy *Biochimie* **2001**, 83(5), 387–397.
- M. L. BENNINK, D. N. NIKOVA, et al., Dynamic imaging of single DNA-protein interactions using atomic force microscopy *Anal. Chim. Acta* **2003**, 479(1), 3–15.
- M. BENOIT, Cell adhesion measured by force spectroscopy on living cells *Methods Cell Biol.* **2002**, 68, 91–114.
- P. BERLIN, D. KLEMM, et al., Film-forming aminocellulose derivatives as enzyme-compatible support matrices for biosensor developments *Cellulose* **2003**, 10(4), 343–367.
- J. A. BLACH-WATSON, G. S. WATSON, et al., Characterization of biological materials on the nano/meso-scale by force microscopy *Mater. Technol.* **2004**, 19(1), 12–16.
- E. BUZANEVA, A. GORCHYNSKY, et al., Nanotechnology of DNA/NANO – Si and DNA/carbon nanotubes/nano – Si chips *NATO Sci. Ser., II: Mathematics, Physics and Chemistry* **2002**, 57, 191–212.
- G. CHARRAS, P. LEHENKARI, et al., Biotechnological applications of atomic force microscopy *Methods Cell Biol.* **2002**, 68, 171–191.
- A. A. CHERNOV, P. N. SEGRE, et al., Crystallization physics in biomacromolecular solutions *Crystal Growth: From Fundamentals to Technology, [International Summer School of Crystal Growth], 12th, Berlin, Germany* **2004**, 95–113.

- C. R. CLEMMER, T. P. BEEBE, JR., A review of graphite and gold surface studies for use as substrates in biological scanning tunneling microscopy studies *Scanning Microsc.* **1992**, 6(2), 319–333.
- L. T. COSTA, S. THALHAMMER, et al., Atomic force microscopy as a tool in nanobiology. Part II: Force spectroscopy in genomics and proteomics *Cancer Genom. Proteom.* **2004**, 1(1), 71–76.
- W. V. DASHEK, Methods for atomic force and scanning tunneling microscopies *Methods Plant Electron Microsc. Cytochem.* **2000**, 215–221.
- J. J. DAVIS, D. A. MORGAN, et al., Scanning probe technology in metalloprotein and biomolecular electronics *IEE Proc.: Nanobiotechnol.* **2004**, 151(2), 37–47.
- J. M. DE LA FUENTE, S. PENADES, Understanding carbohydrate-carbohydrate interactions by means of glyconanotechnology *Glycoconj. J.* **2004**, 21(3–4), 149–163.
- F. DE LANGE, A. CAMBI, et al., Cell biology beyond the diffraction limit: near-field scanning optical microscopy *J. Cell Sci.* **2001**, 114(23), 4153–4160.
- V. DECKERT, Near-field imaging in biological and biomedical applications *Biomed. Photonics Handbook* **2003**, 12/1–12/19.
- E. DELAIN, D. MICHEL, et al., Near-field microscopy: from the isolated molecule to the living cell *Morphologie: Bull. Assoc. Anatomistes* **2000**, 84(265), 25–30.
- D. E. DISCHER, P. CARL, New insights into red cell network structure, elasticity, and spectrin unfolding – a current review *Cell. Mol. Biol. Lett.* **2001**, 6(3), 593–606.
- C. M. DRAIN, J. D. BATTEAS, et al., Designing supramolecular porphyrin arrays that self-organize into nanoscale optical and magnetic materials *Proc. Natl. Acad. Sci. U.S.A.* **2002**, 99(9, Suppl. 2), 6498–6502.
- R. C. DUNN, Near-field scanning optical microscopy *Chem. Rev. (Washington, D.C.)* **1999**, 99(10), 2891–2927.
- J. A. DVORAK, The application of atomic force microscopy to the study of living vertebrate cells in culture *Methods (San Diego, CA)* **2003**, 29(1), 86–96.
- A. EBNER, F. KIENBERGER, et al., Molecular look at the cell nucleus *Bioforum* **2004**, 27(12), 48–49.
- M. EDDIN, Near-field scanning optical microscopy, a siren call to biology *Traffic (Copenhagen)* **2001**, 2(11), 797–803.
- M. FIRTEL, T. J. BEVERIDGE, Scanning probe microscopy in microbiology *Micron (Oxford, England)* **1995**, 26(4), 347–362.
- C. S. FOKAS, Scanning near-field optical microscopy (SNOM) *Nachrichten Chem., Technik Lab.* **1999**, 47(6), 648–652.
- D. FOTIADIS, S. SCHEURING, et al., Imaging and manipulation of biological structures with the AFM *Micron* **2002**, 33(4), 385–397.
- P. L. T. M. FREDERIX, T. AKIYAMA, et al., Atomic force bio-analytics *Curr. Opin. Chem. Biol.* **2003**, 7(5), 641–647.
- J. K. GIMZEWSKI, Scanning tunneling microscopy of surface structures NATO ASI Ser., Ser. C: *Mathematical Phys. Sci.* **1991**, 328, 203–215.
- D. G. GRAY, Investigations of cellulose and pulp fiber surfaces by atomic force microscopy *Preprints – International Paper and Coating Chemistry Symposium, 5th, Montreal, QC, Canada* **2003**, 47–49.
- J.-B. D. GREEN, A. IDOWU, et al., Modified tips: molecules to cells *Mater. Today* **2003**, 6(2), 22–29.
- L. GUO, T. ZHAO, et al., Carbon nanotube tip for AFM and its application in the biology *Gaojishu Tongxu*, **2002**, 12(4), 36–41.
- L. HAGGERTY, A. M. LENHOFF, STM and AFM in biotechnology *Biotechnol. Progr.* **1993**, 9(1), 1–11.
- P. K. HANSMA, V. B. ELINGS, et al., Scanning tunneling microscopy and atomic force microscopy: application to biology and technology *Science* **1988**, 242(4876), 209–216.
- H. G. HANSMA, Surface biology of DNA by atomic force microscopy *Annu. Rev. Phys. Chem.* **2001**, 52, 71–92.
- H. G. HANSMA, K. KASUYA, et al., Atomic force microscopy imaging and pulling of nucleic acids *Curr. Opin. Struct. Biol.* **2004**, 14(3), 380–385.
- M. HARA, New stage in STM/AFM for use in organic and biological studies *Kagaku* **1993**, 48(2), 142–143.
- M. HARA, K. NAKAJIMA, et al., Single molecular measurement using a scanning probe microscope: for nanofishing *Hikari Nanotekunoroji: Seimei Kagaku e no Tenkai, Nippon Bunko Ga kkai Igaku Seibutsugaku Kenkyu Bukai Shinpojumu, Chiba, Japan, Sept. 5, 2002*, 8–12.



- M. HEGNER, A. ENGEL, Single molecule imaging and manipulation *Chimia* **2003**, 56(10), 506–514.
- M. HIBINO, I. HATTA, STM observation of organic molecules *Nippon Butsuri Gakkaishi* **1998**, 53(1), 32–36.
- K. HIZUME, S. YOSHIMURA, et al., The connection between biochemistry and morphology: imaging of DNA and proteins *Denshi Kenbikyō* **2003**, 38(2), 74–77.
- J. K. H. HORBER, Local probe techniques in biology *Proc. Int. School of Physics "Enrico Fermi"* **2001**, 144, 221–246.
- M. HORTON, G. CHARRAS, et al., Analysis of ligand-receptor interactions in cells by atomic force microscopy, *J. Receptors Signal Transduct.* **2002**, 22(1–4), 169–190.
- M. A. HORTON, P. P. LEHENKARI, et al., Probing cellular structure and function by atomic force microscopy, *Special Publication – Royal Society of Chemistry* **2002**, 283, 31–49.
- O. HOSHI, T. USHIKI, Three-dimensional structure of human chromosomes by image analysis using atomic force microscopy, *Denshi Kenbikyō* **2003**, 38(2), 78–82.
- J. HU, J.-H. LU, et al., Nano-manipulation of single DNA molecules *Nucl. Sci. Tech.* **2004**, 15(3), 140–143.
- J. L. HUFF, M. P. LYNCH, et al., Label-free protein and pathogen detection using the atomic force microscope *J. Biomol. Screen.* **2004**, 9(6), 491–497.
- A. IKAI, Biological applications. Studies on DNA structure by STM/AFM *Nippon Kessho Gakkaishi* **1993**, 35(2), 157–158.
- A. IKAI, Study of organic compounds and biological samples by STM/AFM *Gendai Kagaku* **1995**, 289, 24–30.
- A. IKAI, STM and AFM of bio/organic molecules and structures *Surf. Sci. Rep.* **1997**, 26(8), 261–332.
- A. IKAI, Nanomechanics of surface immobilized protein molecules *Hyomen Kagaku* **2001**, 22(9), 620–626.
- A. IKAI, Methods for the analysis of surface adsorbed proteins *Tanpakushitsu Kakusan Koso* **2004**, 49(11, Zokan), 1740–1744.
- A. IKAI, R. AFRIN, Toward mechanical manipulations of cell membranes and membrane proteins using an atomic force microscope: An invited review *Cell Biochem. Biophys.* **2003**, 39(3), 257–277.
- A. IKAI, R. AFRIN, et al., Nano-mechanics of protein molecules and cellular structures: A review of recent work done in the laboratory of biodynamics, Tokyo Institute of Technology *Recent Res. Develop. Appl. Phys.* **2003**, 6(Pt. 2), 717–732.
- A. IKAI, R. AFRIN, et al., Nano-mechanical methods in biochemistry using atomic force microscopy *Curr. Protein Peptide Sci.* **2003**, 4(3), 181–193.
- A. IKAI, R. AFRIN, et al., Measurement of mechanical properties and adsorption of protein molecules *Oyo Butsuri* **2003**, 72(10), 1300–1303.
- A. IKAI, T. OKAJIMA, et al., Mechanical stretching and rheological study of single protein molecules *Toraiborojisuto* **2004**, 49(1), 49–55.
- S. IWABUCHI, E. TAMIYA, Bioimaging using a scanning near-field optical/atomic-force microscope (SNOAM) *Maku* **1998**, 23(4), 169–176.
- K. D. JANDT, Atomic force microscopy of biomaterials surfaces and interfaces *Surf. Sci.* **2001**, 491(3), 303–332.
- A. JANICIJEVIC, D. RISTIC, et al., The molecular machines of DNA repair: scanning force microscopy analysis of their architecture *J. Microsc.* **2003**, 212(3), 265–272.
- B. P. JENA, S.-J. CHO, The atomic force microscope in the study of membrane fusion and exocytosis *Methods Cell Biol.* **2002**, 68(Atomic force microscopy in cell biology), 33–50.
- N. KATAOKA, K. HASHIMOTO, et al., Nano/micromechanics analysis of vascular endothelial cells related to genesis of arteriosclerosis *Okayama Igakkai Zasshi* **2004**, 116(2), 97–101.
- A. KAWAI, Adhesion and coagulation interpretation of micro-solids by atomic force microscope *Setchaku no Gijutsu* **2003**, 23(2), 11–15.
- H. KAWAKAMI, Nano-structure control of protein in microarray fabrication by dip-pen nanolithography *Kagaku* **2004**, 59(6), 62–63.
- S. KIDOAKI, T. MATSUDA, Mechanistic aspects of protein/material interactions probed by atomic force microscopy *Colloids Surf., B: Biointerfaces* **2002**, 23(2–3), 153–163.
- J. H. KINDT, J. C. SITKO, et al., Methods for biological probe microscopy in aqueous fluids *Methods Cell Biol.* **2002**, 68, 213–229.
- O. I. KISELYOVA, I. V. YAMINSKY, Scanning

- probe microscopy of proteins and protein-membrane complexes *Colloid J.* **1999**, *61*(1), 1–19.
- K. KITAGAWA, T. MORITA, et al., Single molecule observation of helix peptide, and its electron mediator function *Kyoto Daigaku Nippon Kagaku Sen'i Kenkyusho Koenshu* **2004**, *61*, 27–32.
- T. KOBORI, M. YOKOKAWA, et al., Atomic force microscopy, passport to nanobiology *Seibutsu Butsuri* **2004**, *44*(6), 255–259.
- T. S. KOFFAS, E. AMITAY-SADOVSKY, et al., Molecular composition and mechanical properties of biopolymer interfaces studied by sum frequency generation vibrational spectroscopy and atomic force microscopy *J. Biomater. Sci., Polym. Edn.* **2004**, *15*(4), 475–509.
- K. KOGURE, Application of AFM to marine microorganisms *Denshi Kenbikyo* **2003**, *38*(2), 83–85.
- H. KONDO, Scanning tunneling microscopic observation of biorelated substances *Idemitsu Giho* **1992**, *35*(2), 224–227.
- S. i. KURODA, T. OKAJIMA, et al., A new pinpoint gene delivery system using genetically engineered hepatitis B virus envelope L particles *Mater. Integration* **2002**, *15*(7), 12–17.
- R. M. LEBLANC, V. KONKA, Langmuir and Langmuir-Blodgett films of chlorophyll a and photosystem II complex *Surfactant Sci. Ser.* **2001**, *95*, 641–648.
- J. LEGLEITER, T. KOWALEWSKI, Tapping, pulling, probing: atomic force microscopy in drug discovery *Drug Discovery Today: Technol.* **2004**, *1*(2), 163–169.
- S. H. LEUBA, J. ZLATANOVA, Single-molecule studies of chromatin fibers: A personal report *Arch. Histol. Cytol.* **2002**, *65*(5), 391–403.
- A. LEWIS, The optical near-field and cell biology *Seminars Cell Biol.* **1991**, *2*(3), 187–192.
- A. LEWIS, A. RADKO, et al., Near-field scanning optical microscopy in cell biology *Trends Cell Biol.* **1999**, *9*(2), 70–73.
- G. LI, W. FUDICKAR, et al., Rigid lipid membranes and nanometer clefts: Motifs for the creation of molecular landscapes *Angew. Chem., Int. Ed.* **2002**, *41*(11), 1828–1852.
- M. Q. LI, Scanning probe microscopy (STM/AFM) and applications in biology *Appl. Phys. A: Mater. Sci. Processing* **1999**, *A68*(2), 255–258.
- A. P. LIMANSKII, Atomic force microscopy: from DNA and protein imaging to measurement of intermolecular interaction force *Uspekhi Sovremennoi Biol.* **2003**, *123*(6), 531–542.
- Y. L. LYUBCHENKO, DNA structure and dynamics: An atomic force microscopy study *Cell Biochem. Biophys.* **2004**, *41*(1), 75–98.
- T. MAJIMA, Soft X-ray imaging of living cells in water: flash contact soft X-ray microscope *Trends Anal. Chem.* **2004**, *23*(7), 520–526.
- R. E. MARCHANT, I. KANG, et al., Molecular views and measurements of hemostatic processes using atomic force microscopy *Curr. Protein Peptide Sci.* **2002**, *3*(3), 249–274.
- S. J. MARSHALL, M. BALOOCH, et al., The dentin-enamel junction – a natural, multilevel interface *J. Eur. Ceram. Soc.* **2003**, *23*(15), 2897–2904.
- J. MASAI, T. SHIBATA, et al., Observation of biological materials by STM/AFM – principles and present status of applications *Tanpakushitsu Kakusan Koso. Protein, Nucleic Acid, Enzyme* **1993**, *38*(4), 741–752.
- L. MATYUS, A. JENEI, et al., Atomic force microscopy in cell biology, in *Fluorescence Microscopy and Fluorescent Probes, (Based on the Proceedings of the Conference on Fluorescence Microscopy and Fluorescent Probes)*, 2nd, Prague, Apr. 9–12, **1998**, 41–46.
- A. J. MEIXNER, H. KNEPPE, Scanning near-field optical microscopy in cell biology and microbiology *Cell. Mol. Biol.* **1998**, *44*(5), 673–688.
- B. MICHEL, STM in biology *NATO ASI Ser., Ser. B: Phys.* **1991**, *285*, 549–572.
- P. E. MILHET, M.-C. GIOCONDI, et al., AFM imaging of lipid domains in model membranes *Sci. World* **2003**, *3*(3), 59–74.
- V. J. MORRIS, Probing molecular interactions in foods *Trends Food Sci. Technol.* **2004**, *15*(6), 291–297.
- D. J. MUELLER, A. ENGEL, Conformations, flexibility, and interactions observed on individual membrane proteins by atomic force microscopy *Methods Cell Biol.* **2002**, *68*, 257–299.
- D. J. MUELLER, H. JANOVJAK, et al., Observing

- structure, function and assembly of single proteins by AFM *Progr. Biophys. Mol. Biol.* **2002**, 79(1–3), 1–43.
- D. J. MUELLER, H. JANOVIK, et al., Folding, structure and function of biological nanomachines examined by AFM *AIP Conference Proc.* **2003**, 696, 158–165.
- R. MUKHOPADHYAY, Molecular level structural studies of metalloproteins/metalloenzymes by scanning tunneling microscopy: Scopes and promises *Curr. Sci.* **2003**, 84(9), 1202–1210.
- H. MURAMATSU, J.-M. KIM, DNA-immobilization on surface of mica and image analysis by scanning near-field optical microscopy *Hyomen Gijutsu* **2002**, 53(12), 909–911.
- K. NAGAI, K. SUZUKI, Observation of microorganisms and genes using atomic force microscope *Farumashia* **2003**, 39(2), 133–136.
- C. NAKAMURA, Application of AFM to the lithographic processing of biochips and the measurement of molecular interaction on the biochip *Baiochippu Saishin Gijutsu Oyo* **2004**, 72–80.
- H. OBERLEITHNER, H. SCHILLERS, et al., Nanoarchitecture of plasma membrane visualized with atomic force microscopy *Ion Channel Localization* **2001**, 405–424.
- T. OHTANI, Nano-measurement of genome by atomic force microscope *Kagaku Seibutsu* **2003**, 41(2), 129–135.
- A. L. OLIVEIRA, I. B. LEONOR, et al., Surface treatments and pre-calcification routes to enhance cell adhesion and proliferation *NATO Sci. Ser., II: Mathematics, Phys. Chem.* **2002**, 86, 183–217.
- E. OROUDJEV, S. DANIELSEN, et al., Surface biology: analysis of biomolecular structure by atomic force microscopy and molecular pulling *Nanobiotechnology* **2004**, 387–403.
- T. OSADA, H. UEHARA, et al., Clinical laboratory implications of single living cell mRNA analysis *Adv. Clinical Chem.* **2004**, 38, 239–257.
- R. E. PALMER, Q. GUO, Imaging thin films of organic molecules with the scanning tunneling microscope *PhysChemChemPhys* **2002**, 4(18), 4275–4284.
- L. PAULINO DA SILVA, Atomic force microscopy and proteins *Protein Peptide Lett.* **2002**, 9(2), 117–125.
- R. D. S. PEREIRA, Atomic force microscopy as a novel pharmacological tool *Biochem. Pharmacol.* **2001**, 62(8), 975–983.
- P. PERFETTI, A. CRICENTI, et al., Scanning probe microscopy applied to materials science and biology *Surf. Rev. Lett.* **2000**, 7(4), 411–422.
- O. POPESCU, I. CHECIU, et al., Quantitative and qualitative approach of glycan-glycan interactions in marine sponges *Biochimie* **2003**, 85(1/2), 181–188.
- L. A. PUGNALONI, E. DICKINSON, et al., Competitive adsorption of proteins and low-molecular-weight surfactants: computer simulation and microscopic imaging *Adv. Colloid Interface Sci.* **2004**, 107(1), 27–49.
- J. P. RABE, Molecules at interfaces: STM in materials and life sciences *Ultramicroscopy* **1992**, 42–44 (Pt A), 41–54.
- A. RAZATOS, Application of atomic force microscopy to study initial events of bacterial adhesion *Methods Enzymol.* **2001**, 337, 276–285.
- A. P. RAZATOS, G. GEORGIOU, Evaluating bacterial adhesion using atomic force microscopy *Handbook Bacterial Adhesion* **2000**, 285–296.
- C. K. RIENER, G. KADA, et al., Bioconjugation for biospecific detection of single molecules in atomic force microscopy (AFM) and in single dye tracing (SDT) *Recent Res. Develop. Bioconj. Chem.* **2002**, 1, 133–149.
- C. J. ROBERTS, S. ALLEN, et al., Quantification and mapping of protein-ligand interactions at the single molecule level by atomic force microscopy *Protein–Ligand Interactions: Structure Spectrosc.* **2001**, 407–423.
- D. B. RODRIGUEZ-AMAYA, M. SABINO, Mycotoxin research in Brazil: the last decade in review *Braz. J. Microbiol.* **2002**, 33(1), 1–11.
- M. SALMERON, T. BEEBE, et al., Imaging of biomolecules with the scanning tunneling microscope: problems and prospects *J. Vac. Sci. Technol., A: Vacuum, Surf. Films* **1990**, 8(1), 635–641.
- M. SALMERON, D. F. OGLETREE, et al., Imaging of biological material with STM/AFM *Proc. SPIE – Int. Soc. Optical Eng.* **1992**, 1556, 40–54.
- N. C. SANTOS, M. A. R. B. CASTANHO, An overview of the biophysical applications of atomic force microscopy *Biophys. Chem.* **2004**, 107(2), 133–149.
- H. SASABE, Modification, characterization and

- handling of protein molecules as the first step to bioelectronic devices *Electron. Biotechnol. Adv. (EL.B.A.) Forum Ser.* **1996**, *2*, 157–174.
- C. SHANNON, Y. DONG, Bioanalytical applications of the atomic force microscope *Genomic/Proteomic Technol.* **2002**, *2*(5), 36–39.
- X. SHENG, M. D. WARD, et al., Adhesion between molecules and calcium oxalate crystals: Critical interactions in kidney stone formation *J. Am. Chem. Soc.* **2003**, *125*(10), 2854–2855.
- J. M. SLOAN, W. F. SMITH, Contrast mechanisms for scanning tunneling microscopy of biological molecules *Probe Microsc.* **1997**, *1*(1), 11–21.
- D. A. SMITH, S. D. CONNELL, et al., Chemical force microscopy: applications in surface characterization of natural hydroxyapatite *Anal. Chim. Acta* **2003**, *479*(1), 39–57.
- H. STAHLBERG, A. ENGEL, et al., Assessing the structure of membrane proteins: combining different methods gives the full picture *Biochem. Cell Biol.* **2002**, *80*(5), 563–568.
- O. M. STUKALOV, Application of atomic force microscopy in protein and DNA biochips development *NATO ASI Ser., II: Mathematics, Phys. Chem.* **2002**, *57*, 331–340.
- V. SUBRAMANIAM, A. K. KIRSCH, et al., Scanning near-field optical imaging and spectroscopy in cell biology *Emerging Tools Single-Cell Anal.* **2000**, 271–290.
- H. SUMI, Y. HORI, Direct measurement of redox-reorganization energies of electron-transfer proteins by V-I characteristics of photoinduced scanning tunneling microscopy currents *Hyomen Kagaku* **2003**, *24*(1), 8–12.
- O. TAKEUCHI, S. YASUDA, et al., Analysis of single molecular interaction by using scanning probe microscope *Toraiborjisuto* **2004**, *49*(1), 42–48.
- I. TANIGUCHI, Design of functional surfaces of electrodes for bioelectrochemical sensing *Chem. Sensors* **1998**, *14*, 161–164.
- H. TATSUMI, Near-field microscope *Byori Rinsho* **1998**, *16*(6), 717–721.
- S. THALHAMMER, W. M. HECKL, Atomic force microscopy as a tool in nanobiology. Part I: Imaging and manipulation in cytogenetics *Cancer Genomics Proteomics* **2004**, *1*(1), 59–70.
- G. TRAVAGLINI, M. AMREIN, et al., Imaging and conductivity of biological and organic material *NATO ASI Ser., Ser. E: Appl. Sci.* **1990**, *184*, 335–347.
- K. TSUNODA, H. YAJIMA, et al., Excimer laser ablation of collagen film *Kokagaku* **2002**, *33*(1), 18–25.
- K. UOSAKI, Scanning tunneling microscopy *Bunseki* **1990**, *9*, 675–681.
- K. UOSAKI, Scanning tunneling microscope and related techniques *Kagaku Kogaku* **1991**, *55*(10), 785–786.
- D. W. URRY, T. M. PARKER, Mechanics of elastin: molecular mechanism of biological elasticity and its relationship to contraction *J. Muscle Res. Cell Motility* **2002**, *23*(5–6), 543–559.
- T. USHIKI, O. HOSHI, et al., The structure of human metaphase chromosomes: Its histological perspective and new horizons by atomic force microscopy *Arch. Histol. Cytol.* **2002**, *65*(5), 377–390.
- H. C. VAN DER MEI, P. KIERS, et al., Measurements of softness of microbial cell surfaces *Methods Enzymol.* **2001**, *337*, 270–276.
- J. VAN NOORT, Unraveling bacteriorhodopsin *Biophys. J.* **2005**, *88*(2), 763–764.
- P. G. VEKILOV, Microscopic, mesoscopic, and macroscopic lengthscales in the kinetics of phase transformations with proteins *Nanoscale Struct. Assembly Solid-Fluid Interf.* **2004**, *2*, 145–199.
- J. A. VEERMAN, O. WILLEMSSEN, Scanning microscopes. Looking with other eyes *Natuur & Techniek (Beek, Netherlands)* **1997**, *65*(9), 66–73.
- S. WANG, S.-X. CAI, et al., Mechanism and progress on protein crystal growth by atomic force microscopy *Chongqing Daxue Xuebao, Ziran Kexueban* **2004**, *27*(7), 36–39.
- H.-S. XIA, Q. WANG, Advances in nanotechnology *Gaofenzi Cailiao Kexue Yu Gongcheng* **2001**, *17*(4), 1–6.
- Y. YANG, H. WANG, et al., Quantitative characterization of biomolecular assemblies and interactions using atomic force microscopy *Methods (San Diego, CA)* **2003**, *29*(2), 175–187.
- M. YOKOKAWA, S. H. YOSHIMURA, et al., The observation of biological samples by atomic force microscopy *Tanpakushitsu Kakusan Koso* **2004**, *49*(11, Zokan), 1607–1614.
- E. YONEMOCHI, Assessment of drug characteristics by atomic force microscope (AFM) *Yakuzaigaku* **2003**, *63*(3), 129–132.

- T. YOSHIO, T. OHTANI, Application of SNOW/AFM to biomaterials *Denshi Kenbikyo* **2003**, 38(2), 94–97.
- L. YU, A. WU, et al., Deoxyribonucleic acid sample preparation in scanning probe microscope *Fenxi Huaxue* **2001**, 29(12), 1470–1477.
- J. A. ZASADZINSKI, Scanning tunneling microscopy with applications to biological surfaces *BioTechniques* **1989**, 7(2), 174–187.
- A. H. ZEWAAL, Femtochemistry. Atomic-scale dynamics of the chemical bond using ultrafast lasers *Prix Nobel* **2000**, 110–203.
- J. ZHANG, Q. CHI, et al., Organization and control of nanoscale structures on Au(111) *Probe Microsc.* **2001**, 2(2), 151–167.
- J. ZHANG, Q. CHI, et al., Electronic properties of functional biomolecules at metal/aqueous solution interfaces *J. Phys. Chem. B* **2002**, 106(6), 1131–1152.
- J. ZHANG, Q. CHI, et al., Organized monolayers of biological macromolecules on Au(111) surfaces *Russ. J. Electrochem. (Transl. of Elektrokimiya)* **2002**, 38(1), 68–76.
- J. ZHANG, M. GRUBB, et al., Electron transfer behavior of biological macromolecules towards the single-molecule level *J. Phys.: Condensed Matter* **2003**, 15(18), S1873–S1890.
- J. ZHANG, Y. WANG, et al., Atomic force microscopy of actin *Shengwu Huaxue Shengwu Wuli Xuebao* **2003**, 35(6), 489–494.
- X. ZHANG, A. CHEN, et al., Probing ligand-receptor interactions with atomic force microscopy *Protein–Protein Interactions* **2002**, 241–254.
- T. J. ZIEZIULEWICZ, D. W. UNFRICHT, et al., Shrinking the biologic world – nanobiotechnologies for toxicology. *Toxicol. Sci.* **2003**, 74(2), 235–244.
- J. ZLATANOVA, S. H. LEUBA, Chromatin structure and dynamics: lessons from single molecule approaches *New Comprehensive Biochem.* **2004**, 39, 369–396.
- G. ZUCCHERI, A. BERGIA, et al., Scanning force microscopy studies of the structure of biological macromolecules *Seminars Org. Synth. Summer School “A. Corbella”*, 27th, Gargnano, Italy, June 17–21 **2002**, 7–15.

### 3

## Quartz Crystal Microbalance Characterization of Nanostructure Assemblies in Biosensing

*Aren E. Gerdon, David W. Wright, and David E. Cliffler*

### 3.1

#### Introduction

The characterization of functional nanostructures is crucial in determining their efficacy for life sciences. Nanostructure design requires careful consideration of recognition units and material properties, while synthesis can be meticulous, but evaluation and characterization of the system is equally challenging and important. Nanostructure creation can not easily be deemed successful without analytical evaluation. Furthermore, it may not be used to its potential if it is not well defined and well understood. The design and development of analytical tools and techniques for nanocharacterization is, therefore, imperative. A widely-used and effective tool for structure assembly evaluation is the quartz crystal microbalance (QCM). QCM is a sensitive technique based on the propagation of evanescent acoustic waves, which are affected by adsorption processes as well as local changes in density and viscosity of the contact liquid. Real-time analyte adsorption is monitored through simultaneous measurement of the quartz crystal's resonant frequency of oscillation and the damping resistance caused by liquid loading. One of the paramount applications of QCM has been the study of adsorption of biomolecules on functionalized surfaces. It has also been used in various other applications and is particularly suited to the study of nanoscale materials [1]. This chapter addresses the principles and operational aspects of QCM (Section 3.1.1), followed by important QCM applications to the life sciences (Section 3.1.5). The importance of interfaces between biology and nanoscale materials will be discussed (Section 3.2) and will precede examples of QCM-nanoparticle sensors for chemical (Section 3.3), biological (Section 3.4), and immunological systems (Section 3.5).

#### 3.1.1

##### Principles of QCM

The quartz crystal microbalance relies on the converse-piezoelectric effect, reported by the Curie brothers in 1880. Piezoelectricity describes the electrical charge produced by pressure applied to solids having certain geometries, while the converse

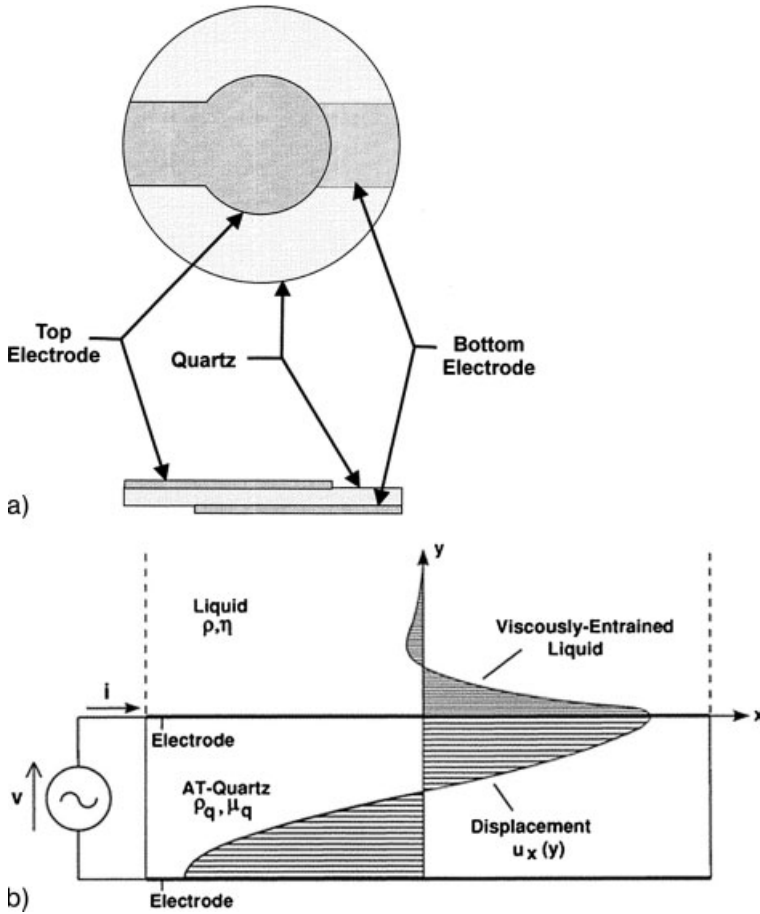


**Fig. 3.1.** Top and side view of a QCM resonator (a and b) and cross sectional view of a QCM resonator in contact with a liquid (bottom). Wave propagation is relatively loss-less in the piezoelectric material, but becomes evanescent in the viscous liquid [7]. (Reprinted with permission the American Chemical Society.)

effect produces a strain on the crystal when an electric field is applied [2]. Coupling the crystal to an oscillating circuit provides crystal oscillation at a resonant frequency (Fig. 3.1).

These quartz resonators have been widely used in communication devices, commercial acoustic electronics, and sonar [2, 3]. Sauerbrey first demonstrated the usefulness of this effect for analytical chemistry by showing a linear relationship between mass deposited on the crystal and the frequency of oscillation [Eq. (1)] [1, 2].

$$\Delta f = -C_f \Delta m \tag{1}$$

Initially, QCM was used in the gas phase, where oscillator resistance is low and mass adsorption is rigid. The device was improved in 1982 by the advent of circuitry capable of crystal operation in liquids. While this advancement introduced QCM to the world of bioanalytical chemistry, it also introduced new difficulties. The first is that operation in liquid slows the mass transport of analyte to the sensor surface. The second is that many binding events in liquid, especially those biological in nature, are not static but tend to be in equilibrium. The third is resonator damping and viscous loading (Fig. 3.1). The density and viscosity of the contact solution affects crystal frequency response, convolutes mass measurements, and requires modification of the Sauerbrey equation [Eq. (1)] [2, 4]. Careful consideration of simultaneous mass and liquid loading by Kanazawa [5] and Martin [6] has shown that  $\Delta f$  relates to adsorbed mass and the density and viscosity of the contact liquid according to Eq. (2) [6].

$$\Delta f \approx C_f \Delta m - C_f (\Delta \rho \eta / 4\pi f_o)^{1/2} \quad (2)$$

It is, therefore, impossible to distinguish mass loading from liquid loading by frequency measurements alone. Fortunately, the independent term of liquid loading resistance,  $R_L$ , depends solely on density and viscosity [Eq. (3)] [6].

$$\Delta R_L \approx (\eta_q / [c_{66} C_1]) + (N\pi C_1)^{-1} (\Delta \rho \eta / \pi f_o c_{66} \rho_q)^{1/2} \quad (3)$$

Measuring both changes in frequency and resistance provides a means for decoupling mass and liquid loading effects, though different methods have been described [1, 2, 5–9]. Applying Eqs. (2) and (3) to frequency and resistance measurements to reliably calculate adsorbed mass has proven to be non-trivial. A simple approach to a reliable mass measurement has been to create a calibration curve of change in frequency as a function of change in resistance for a system in which mass loading is minimal. In one case, sucrose, a hydrophilic molecule that will not independently adsorb to the QCM electrode, was dissolved in DI water at 0, 5, 10, 20, and 40% by weight. Sequential addition of these five solutions to the QCM sensor provided simultaneous changes in frequency and resistance that were due to density and viscosity effects only (Fig. 3.2) [1]. The relationship between frequency and resistance within this range is linear and provides an accurate calibration. Above ~40% sucrose, the relationship deviates from linearity, making this approach only applicable to systems in which the resistance changes by less than 500  $\Omega$  [5, 10]. Problems also occur with this calibration, as in any QCM measurement, when coupling to the sensor is non-rigid and the analyte has its own viscous properties. Calibration allows for the calculation of  $\Delta m$  through simultaneously solving Eqs. (2) and (3) and using a sensitivity factor,  $C_f$ , of 56.6 Hz cm<sup>2</sup>  $\mu\text{g}^{-1}$ , which is known for a 5 MHz crystal [11]. Decreasing the crystal thickness increases the resonant frequency and can provide enhanced sensitivity.

Since his study of simultaneous QCM mass and liquid loading in 1991 [6], Stephen Martin from Sandia National Laboratory and collaborators at Leicester University have continued to contribute experimental and theoretical-based insight



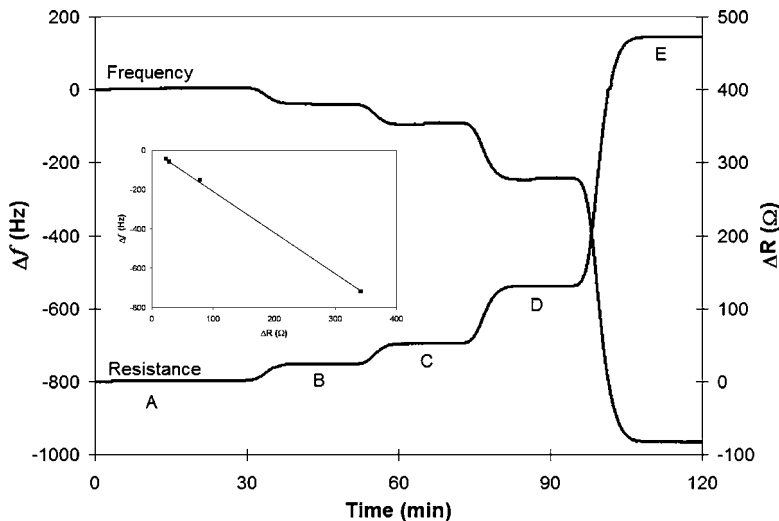


**Fig. 3.2.** Practical QCM mass calibration using a non-mass loading system. Frequency and resistance changes mirror each other upon the addition of deionized (DI) water with (A) 0, (B) 5, (C) 10, (D) 20 and (E) 40% sucrose. Inset: linear calibration curve of change in frequency vs. change in resistance [1].

into the details of QCM measurement in liquids. Four contributions, since 1997, have covered resonator response to liquid loading [7], the modeling of resonator response under loading conditions [12], the modeling of viscoelastic film response [13], and a model for wetting characteristics of roughened surfaces [14]. This collective work has provided a better understanding of loading responses in QCM and has supported more rigorous evaluation of important systems.

Another area of QCM sensor development has been multi-channel QCM. Using arrays of resonators or micro-fluidics to partition individual resonators could provide the simultaneous measurements needed for multi-analyte detection strategies. A significant challenge in multi-channel QCM is the isolation of each electrode. Circuit shorting or resonance overlap from electrode to electrode could cause considerable problems. Two approaches to this problem have made use of electrode miniaturization [15] and the restriction of oscillation to indented areas surrounded by thicker quartz [16]. Both approaches have had success in the construction of a multi-channel QCM instrument.

### 3.1.2

#### QCM Wave Penetration Depth

QCM works well with 3D substrates and multilayer adsorptions often encountered in materials applications [1]. QCM acoustic shear waves are evanescent and decay exponentially in the contact liquid, causing a loss of sensitivity at distances from

the sensor surface (Fig. 3.1). Mass that is rigidly coupled to the sensor propagates the wave without loss, whereas viscous material causes immediate wave decay [8]. The depth at which these waves penetrate the contact liquid affects instrument sensitivity. QCM, at 5 MHz, has a calculated penetration depth of 250 nm [2], with a total decay length of 1  $\mu\text{m}$  [8], though experiments have shown no loss of sensitivity for layers as large as 400 nm [1, 8, 17, 18]. In comparison, surface plasmon resonance spectroscopy (SPR) has a calculated penetration depth of only 150 nm and has shown significant peak broadening with layers less than 200 nm [19, 20]. Examples of peak broadening in SPR come from the use of metal nanoclusters for signal amplification [21–23]. Antibody-presenting gold nanoclusters binding to immobilized anti-IgG increased the SPR shift as compared to free antibody [21, 22]. This also caused broadening of the SPR curve, which increased in width as the density or diameter of the colloidal gold was increased [23]. QCM has not suffered from this sensitivity loss, even at extensive adsorption [1].

### 3.1.3

#### QCM Sensor Specificity

A challenge in QCM, and in many biosensors, is sensor functionalization for improved specificity. While the gold QCM electrode imparts almost no specificity of its own, it provides a substrate for various functionalizations. The gold electrode is amenable to hydrophobic interactions, is well-suited for self-assembled monolayer (SAM) formation, and enables electrochemical surface reactions. Approaches to improve specificity in QCM have used SAMs [24–26], ionic interactions [27–30], electrochemical deposition [31, 32], and protein adsorption (Fig. 3.3) [33–35]. These methods allow for the immobilization of various biological species and nanostructures and permit various detection schemes. SAMs have been studied extensively [26, 36, 37] and feature a defined orientation, high aerial density, and programmability in the exposed head-group. They have recently been used for the covalent immobilization of oligosaccharides [24] and peptide epitopes [38].

Ionic layering, using polyelectrolyte [28–30] or SAMs with ionic head-groups [27], has allowed for effective immobilization and orientation of various nanoparticles. Though the interaction is generally non-specific, relying on electrostatic and van der Waals interactions, layer-by-layer growth is highly tunable according to concentration, ionic strength, and pH. This promotes high-affinity binding, reversibility, and high packing density, and has been used for single layer deposition and multilayer nanorainbow assembly [28, 30].

Electrode functionalization and nanoparticle immobilization has also been pursued with electrochemical deposition, using an electrochemical quartz crystal microbalance (EQCM). Viologens, such as *N*-methyl-*N'*-ethylamine-viologen dinitrate (MEAV), have been previously studied [32] as electroactive species and adhere to electrodes upon reversible reduction of the [viologen]<sup>2+/1+</sup> couple. Attachment of MEAV to nanoclusters allows similar adhesion to electrodes, thereby immobilizing the nanocluster on the QCM surface [31].

Another route employs Protein A for immobilization of antibodies in an accom-

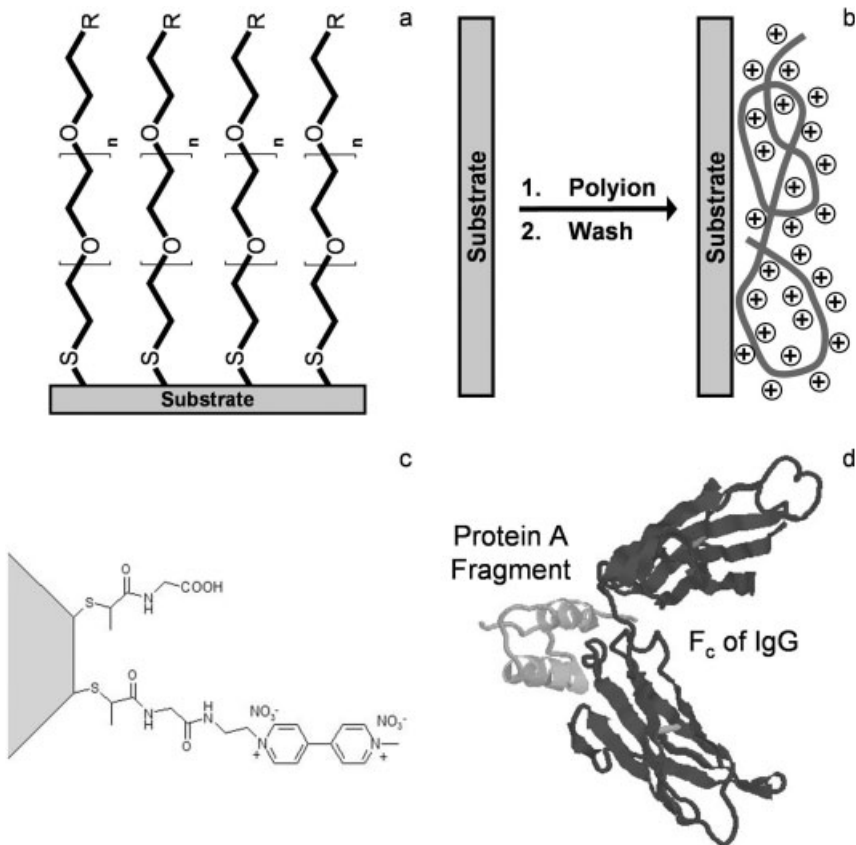


**Fig. 3.3.** Examples of QCM functionalization techniques to impart specificity: (a) Self-assembled monolayers immobilize ligands in a high density, and often use poly(ethylene glycol) spacers. (b) A polyelectrolyte provides a thin layer of charge (positive or negative) for ionic interactions. (c) Viologen functionalized electroactive nanoclusters can be electrochemically deposited on the QCM surface. (d) X-ray crystal structure of a Protein A fragment commonly used in the immobilization of antibody [35].

modating conformation. Protein A is a cell wall protein that forms stable complexes with gold through van der Waals interactions ( $K_a \sim 10^8 \text{ M}^{-1}$ ) [33] and contains five tandem domains that bind the Fc region of IgG with high affinity and selectivity. These properties optimize the presentation of antibodies such that both antigen binding regions (Fab) are unobstructed (see also Figs. 3.4 and 3.6) [33–35].

#### 3.1.4

#### Calculation of Equilibrium and Kinetic Constants

An important advantage of real-time binding measurements is the ability to derive equilibrium binding constants and kinetic rate constants. These constants provide valuable information concerning the affinity or avidity of one material for another,

the rate at which they interact, and the interaction order. A molecule's affinity is defined through the equilibrium association constant ( $K_a$ ) for the interaction and is generally valid for monovalent, one-to-one interactions. Avidity is related to the same equilibrium process ( $K_v$ ), but describes multivalent processes. For example, at low ligand concentrations a multivalent ligand could bind to several monovalent receptors, increasing the affinity of the ligand for the receptor. There are also cases of multivalent receptors with monovalent ligands as well as multivalent receptors with multivalent ligands [39]. The complexity of these interactions can be daunting, especially for molecules like lectins that are designed for increased affinity through multivalency. The simplest case would be the interaction of a monovalent ligand (e.g., an antigen) with a monovalent receptor (e.g., a ScFv antibody):  $\text{Ag} + \text{Ab} \leftrightarrow \text{Ag-Ab}$ . The elementary equilibrium expression for the formation of the complex is [Eq. (4)],

$$K_a = [\text{Ag-Ab}] / ([\text{Ab}][\text{Ag}]) \quad (4)$$

where  $K_a$  is the equilibrium association constant and is generally in the range of  $10^6$  to  $10^{12} \text{ M}^{-1}$  for monoclonal antibody interactions, indicating a large equilibrium shift to product formation when antigen is in the presence of antibody. If this association and equilibrium shift occurs at a surface, where the first component adsorbs to the surface-supported second component, the equilibrium expression can be rearranged to an adsorption isotherm. The adsorption isotherm represents the connection between the amount of substance adsorbed, the concentration of the bulk solution, and the equilibrium constant,  $K_a$ . The Langmuir isotherm is commonly used and relies on three important assumptions: (1) there is no lateral interaction between adsorbed species; (2) the surface is homogeneous; (3) the maximum adsorption is saturation to a monolayer. Adsorption isotherms are sometimes written in terms of fractional coverage ( $\Theta$ ) or percent of monolayer formation. A generalized Langmuir isotherm in this form is given by Eq. (5).

$$\Theta / (1 - \Theta) = K_a C \quad (5)$$

For QCM studies, the fractional coverage is related to the change in mass ( $\Delta m$ ) and the initial concentration of surface immobilized antibody is related to the maximum change in mass ( $\Delta m_m$ ). Rearranging to solve for  $\Delta m$  provides a commonly used form of the Langmuir isotherm [Eq. (6)].

$$\Delta m = \Delta m_m [K_a C / (1 + K_a C)] \quad (6)$$

Plotting  $\Delta m$  as a function of bulk concentration ( $C$ ) shows a steep increase in adsorption that levels off with increasing concentration as a complete monolayer is achieved (Fig. 3.9d below). This line can be fit to nonlinear regressions, but does not provide a simple means for extracting the equilibrium constant. Instead a reciprocal plot can be used to obtain a straight line fit. There is more than one way to obtain a reciprocal plot by rearranging the Langmuir isotherm [Eq. (6)]. Two options are Eqs. (7) and (8).

$$\Delta m = -(K_a)^{-1}(\Delta m/C) + \Delta m_m \quad (7)$$

$$C/\Delta m = (\Delta m_m)^{-1}(C) + (\Delta m_m K_a)^{-1} \quad (8)$$

With Eq. (7),  $\Delta m$  is plotted against  $\Delta m/C$  and the inverse of the slope provides  $K_a$ . With Eq. (8)  $C/\Delta m$  is plotted against  $C$  and the  $K_a$  must be extracted from a combination of the slope and  $y$ -intercept. Both techniques have been used in the literature and provide reliable  $K_a$  [1, 24, 40–42]. Once the equilibrium association constant is known, it can be used to calculate both the fractional coverage at an infinite time point [ $\Theta_\infty$ , Eq. (9)] and the Gibbs free energy of adsorption [ $\Delta G_{\text{ads}}$ , Eq. (10)].

$$\Theta_\infty = C/(C + K_a^{-1}) \quad (9)$$

$$\Delta G_{\text{ads}} = -RT \ln K_a \quad (10)$$

This method offers a simple way to determine equilibrium constants for systems that generally follow the assumptions outlined for a Langmuir isotherm, though variations on the Langmuir isotherm can account for more complex systems.

Equilibrium association constants for antibody/antigen interactions can be determined in different ways, not necessarily involving real-time measurements. Kinetic information, however, requires time-resolved information. The rate at which an interaction takes place can be valuable in evaluating component efficacy. The time course for monolayer formation is given by Eq. (11).

$$\Theta(t) = [C/(C + K_a^{-1})]\{1 - \exp[-(k_f C + k_r)t]\} \quad (11)$$

According to Eq. (9),  $\Theta_\infty$  can be substituted in and the exponent can be simplified by calling  $(k_f C + k_r)$  equal to the time constant  $(\tau^{-1})$  [Eq. (12)],

$$\Theta(t) = \Theta_\infty[1 - \exp(-\tau^{-1}t)] \quad (12)$$

For a given concentration of the bulk solution ( $C$ ),  $\Theta(t)$  is related to  $\Delta m$  at a particular time and  $\Theta_\infty$  is related to the maximum change in mass [ $\Delta m_m$ , Eq. (13)],

$$\Delta m_t = \Delta m_m[1 - \exp(-\tau^{-1}t)] \quad (13)$$

Fitting Eq. (13) to each time point in the real-time adsorption binding curve yields the time constant. Knowing the concentration of the bulk solution allows the extraction of forward ( $k_f$ ) and reverse ( $k_r$ ) rate constants. The ratio of these kinetic constants is equal to the equilibrium constant ( $K_a = k_f/k_r$ ) and can be used for comparison with isotherm methods.

### 3.1.5

#### QCM Application to Life Sciences

The benefits of QCM and detailed functionalization strategies have allowed the study of many biological and chemical systems [2, 43]. An early and notable exam-

ple of a chemical study is the direct kinetic measurements of thiolate molecules self-assembling on two-dimensional gold surfaces [37]. This helped provide a foundation for QCM kinetic studies and was quickly followed by a kinetic study of anti-fluorescyl antibody binding to fluorescein lipids in Langmuir–Blodgett films [41]. The fluorescein hapten was coupled to lipids and mixed with unfunctionalized lipids to form a bilayer with ~5% fluorescein lipid. Through QCM measurements, monoclonal antibody was found to have an affinity ( $K_a$ ) in the range  $10^7$ – $10^8$   $M^{-1}$  and forward and reverse rate of reaction constants of approximately  $2 \times 10^5$   $M^{-1} s^{-1}$  and  $2 \times 10^{-3}$   $s^{-1}$ , respectively.

More recently, Zeng et al. conducted two immunoassay experiments using QCM [24, 44]. The first was a study of  $\alpha$ -Gal carbohydrate antigen as anti-Gal antibodies are of interest for therapeutics in xenotransplantation. Thiolated trisaccharides were immobilized on the surface of the QCM through the formation of a self-assembled monolayer and exposed to polyclonal anti-Gal antibodies, a lectin from *Griffonia simplicifolia*, and a lectin from *Marasmius oreades*. The antibody displayed the strongest binding, with a dissociation constant ( $K_d$ ) three orders of magnitude greater than either of the lectins. They concluded that this QCM approach is competitive with established label-free techniques [24]. The second immunoassay made use of single-chain fragment variable (ScFv) antibodies to increase the surface density of antigen binding sites (Fig. 3.4). The recombinant antibodies were genetically engineered to contain a linker arm and cysteine residue to ensure self-assembly in a defined orientation. Considering their size (27 kDa) and ease of engineering, they have a considerable advantage over Fab fragments or full-sized IgG for the detection of antigen. The ScFv antibodies were initially expressed and evaluated using SDS-PAGE and Western blot analysis. After immobilization on the QCM gold electrode, the monolayer assembly was verified electrochemically with cyclic voltammetry and electrochemical impedance. This confirmed surface coverage, but provided no information on antibody orientation. The ScFv rabbit anti-IgG antibody was successful in detecting rabbit IgG down to 1.1 nM, which is more than 7 times lower than that detected with an anti-IgG Fab fragment sensor. Another benefit of this system is the reversibility of IgG binding coupled with the

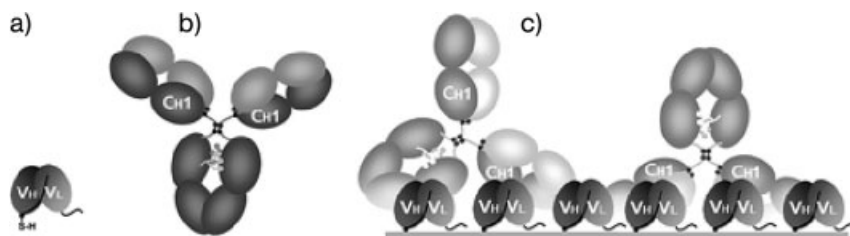


**Fig. 3.4.** (a) Single-chain fragment variable recombinant antibody with cysteine incorporated into the linker; (b) rabbit IgG; (c) interaction between immobilized ScFv and rabbit IgG. (Reprinted with permission from the American Chemical Society.)

stability of the ScFv monolayer to allow regeneration and reusability of the sensor [44].

A piezoelectric immunosensor has also been developed to detect aerosolized SARS-associated coronavirus [45]. Since the introduction of circuitry able to operate QCM in liquids, gas phase measurements have primarily been used in metal vapor deposition techniques, rather than biological studies. A functionalized QCM crystal could be used as a biological “nose” for the detection of aerosolized agents, such a coronavirus. In this example, polyclonal anti-SARS-CoV was presented on the gold QCM electrode through a specific Protein A intermediate. Antigen powder was then reconstituted in the saliva of a healthy volunteer and aerosolized in the presence of the sensor. The antigen bound quickly to the antibody and was detected at concentrations down to  $0.60 \text{ mg mL}^{-1}$ .

Many other interesting and pertinent biological systems have been studied, including the use of glycosphingolipids for detection of ricin [46], the use of high resonant frequency quartz crystals (39 to 110 MHz) for the detection of phages [47], and the study of annexin A1 binding to solid-support membranes [48]. A complete review of QCM applications to the life sciences is not the scope of this chapter, though other sources can be consulted for further examples [2, 43].

### 3.2

#### Interface Between Biology and Nanomaterials

Fundamental advances in chemistry and biology have allowed biotechnology and materials science to develop over the past decades. Biotechnology has attempted to emulate naturally occurring functional assemblies, from the double helix of DNA to the multi-subunit protein cage, ferritin, while material science has taken advantage of chemical methods for the miniaturization of functional devices. Further evolution of these disciplines into the emerging field of bionanotechnology depends on the successful development and evaluation of structurally well-defined interfaces that bridge biology and inorganic materials chemistry. Interdisciplinary collaboration between these fields will allow for improved biological components to generate new materials while advanced materials will be used to ameliorate biological problems [49]. The design, synthesis, and characterization of readily programmable, structurally well-defined biological interfaces for inorganic materials represent significant challenges for the realization of these goals.

Progress has been made towards the development of such interfaces, though many options have yet to be explored. Some encouraging synthetic attempts have used DNA, semiconductor-binding peptides, genetically-engineered viruses, and silica-precipitating peptides. Specifically, synthetic single-stranded oligonucleotides coordinated to nanoparticles have been shown to self-assemble with the appropriate complement to form higher ordered structures (Fig. 3.5a) [50]. Phage-display libraries have been used in the successful selection of 12-mer peptides that specifically bind to the 100 face of GaAs single crystals (Fig. 3.5b). Bivalent peptides of this nature could be used in the directed assembly of nanoscale components [51].

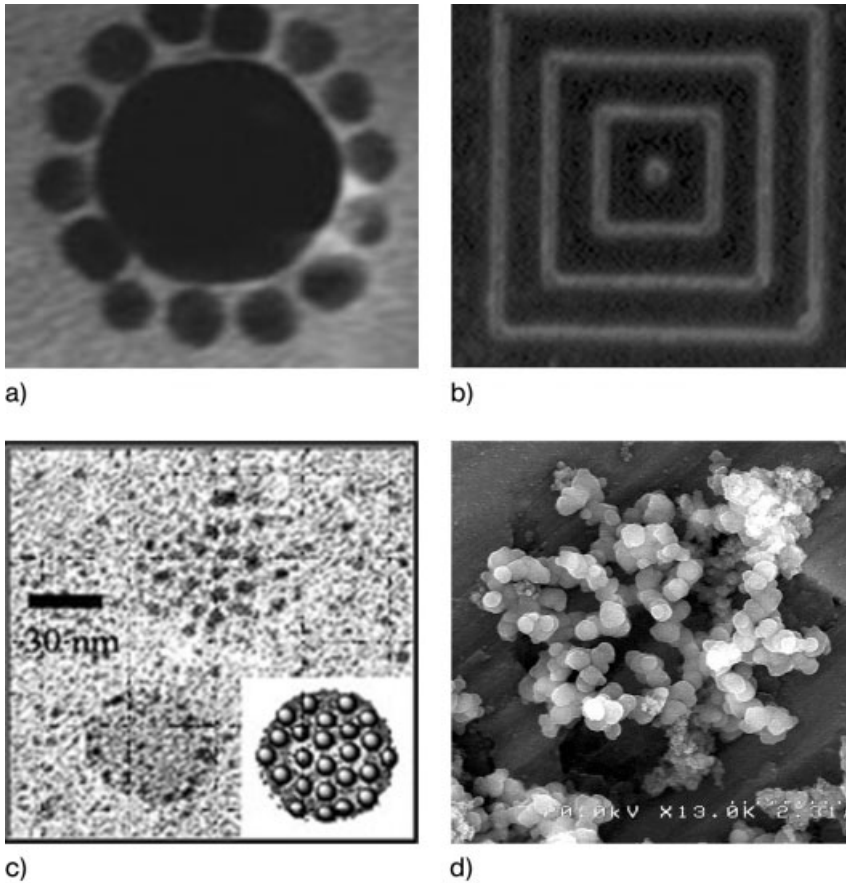


**Fig. 3.5.** Examples of successful interfaces between biology and inorganic materials: (a) TEM of 8 nm diameter Au nanoparticles connected to a 31 nm diameter Au nanoparticle through complementary strands of DNA [50]. (Reprinted with permission from the American Chemical Society.) (b) Fluorescently labeled antibody bound to peptide presenting phage, which specifically

recognized the 100 face of GaAs [51]. (Reprinted with permission from Nature Publishing Group.) (c) TEM of virus templated synthesis of Au<sup>0</sup> nanoparticles [52]. (Reprinted with permission from the Royal Society of Chemistry.) (d) Electron micrograph of silica particles precipitated via a synthetic peptide [53]. (Reprinted with permission from the Royal Society of Chemistry.)

Recently, the iron-storage protein ferritin, which contains its own interface between biology and inorganic iron oxide, has been used as inspiration for the design of a genetically-engineered viral cage that can precipitate nanoclusters. The virus, cowpea chlorotic mottle virus, was engineered with HRE peptide epitopes on its surface and provided a template for the symmetry-directed synthesis of Au<sup>0</sup> nanoparticles (Fig. 3.5c) [52]. Another attempt at interfacing biology and inorganic materials has made use of a synthetic peptide based on silaffin from various eukary-



otic algae or diatoms. This peptide was shown to efficiently precipitate silica under mild conditions, mimicking diatom activity (Fig. 3.5d) [53]. These functional materials have enjoyed success in the assembly of nanoscale materials, but have not shown results for sensor applications. Still, they have succeeded at interfacing biology and inorganic materials and have served as inspiration for the subsequent design of sensor interfaces.

One biomolecular recognition method that has not been widely employed in the assembly of nanoscale materials is immunomolecular recognition. Immunoglobulin (IgG) antibodies have affinities (association constant,  $K_a$ ) on the order of  $10^6$ – $10^{12} \text{ M}^{-1}$  and have been well studied for sensor applications [54–57]. Applications of such immunoassays have had a tremendous impact on medical diagnosis and the treatment and understanding of disorders and diseases. Interfacing immunology and nanomaterials will expand these applications and provide potential for improvements on existing assays and treatments. There are several cases where immunology and inorganic materials have been successfully brought together to provide a ground work for further development.

Progress began with the non-specific immobilization of antibody on micron-sized, hydrophobic, latex beads [58–60]. Antigen binding to immunoreactive beads causes agglutination, which can be quantified by changes in solution turbidity [60]. Similarly, antibodies have been non-specifically immobilized on 11 nm diameter colloidal gold particles. These particles were used in traditional sandwich immunoassays, where the gold particle provided signal amplification when binding was detected with surface plasmon resonance spectroscopy (SPR) [21]. More recently, Nam et al. created an immunoassay using micron-diameter immuno-magnetic particles in conjunction with 13 nm diameter DNA/antibody derivatized gold clusters. Magnetization allowed for facile separation of agglutinated particle, while double stranded DNA provided an amplification avenue through polymerase chain reaction (PCR) [61]. Other strategies have used nanocluster/antibody interfaces as a means for multiplexing and amplification [62–64]. Another approach made use of a peptide epitope known to bind monoclonal antibody associated with the human malarial parasite, *Plasmodium falciparum*, and was the first example of antigen encapsulated nanoclusters assembling with antibodies through the antibody (paratope)/antigen (epitope) interface [65]. This important advancement appears to provide a robust, functional nanostructure that has the potential of successfully mimicking a biological entity. Together these interface-dependent techniques have suggested new routes for the study and detection of human IgG, prostate specific antigen, hepatitis B surface antigen, and the human malarial parasite.

### 3.2.1

#### Antibodies

Extraordinary binding affinities, ease of use, and relevance to medical disorders make antibodies attractive analytical reagents and recognition units for interfacing with nanoscale materials. The classic IgG immunoglobulin has a prototypical Y-shape made up of two heavy and light chains (Fig. 3.6). The antigen binding

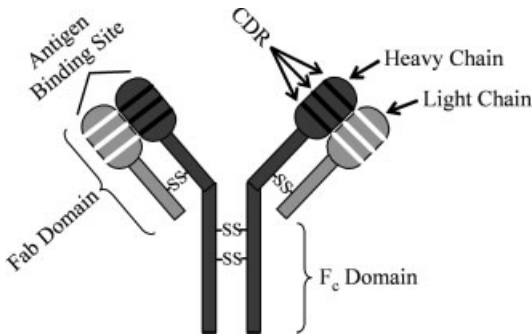


**Fig. 3.6.** Cartoon structure of a typical IgG antibody, highlighting heavy and light chains joined by disulfides, a constant fragment (Fc), two fragments of antigen binding (Fab), and complementarity determining regions (CDRs).

site (paratope), within the Fab (fragment of antigen binding), is formed by the three-dimensional (3D) arrangement of the complementarity determining regions (CDR). In antibodies, this is the key region of immunorecognition and results in the proteins valency. Three different types of antibody preparations are in use for immunoassays: polyclonal, monoclonal, and single chain fragment variable (ScFv). Polyclonal antibodies (pAb) are generally collected from animals and result as a response to the injection of an antigen. They are produced by many different B lymphocytes and recognize different epitopes within the same antigen, resulting in a mixture of antibodies, with only a subset of total IgG recognizing the epitope of interest. Monoclonal antibodies (mAb), however, are produced in a colony of identical B cells. Each antibody binds to the same epitope and the mAb sample is homogeneous [54]. Single chain fragment variable (ScFv) antibodies represent the smallest functional domain of a traditional monoclonal or polyclonal antibody as they consist of one linked Fab domain [44, 66]. Phage-display recombinant antibody technology has produced high-quality, antigen-specific ScFv antibodies with affinities (binding strengths) comparable or greater than those of traditional antibodies [51]. This technique and these antibodies are particularly useful for antigens that are poorly immunogenic, readily degrade, or for which monoclonal or polyclonal antibodies are difficult to obtain. These three types of antibodies provide a range of options for interfacing immunology with nanoscale materials.

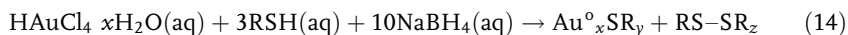
### 3.2.2

#### Nanoparticles

The interface between biology and inorganic materials has manifested in many different forms, covering the range of biological systems and the range of inorganic materials. Immunology has interfaced with many substrates, including two-dimensional (2D) surfaces [24, 38, 44], organic polymers [58, 60, 61], large metal particles [21, 65], semiconductor quantum dots [67], and small, ligand-capped

metal cores [1]. The interface of antibodies with each of these substrates has produced interesting functional materials, though ligand-capped noble-metal clusters (monolayer-protected clusters, MPC) have received attention for their unique consolidation of self-assembly techniques and metal nanoparticle chemistry [68–70]. Furthermore, their chemical, electronic, and physical properties, a lack of air and water sensitivity, and convenient characterization make them robust materials [65, 71–74]. Programmed specificity through the introduction of biologically relevant molecules is one of their most promising features and lends to the development of an immuno-interface [75, 76].

Synthesis and assembly of MPCs can occur through several routes, using various metals (Au, Ag, Cu, Pt, CdS, ZnS, Ag<sub>2</sub>S) [77], reductants (citrate, Na<sub>2</sub>S, NaBH<sub>4</sub>), and capping ligands (thiolate, disulfide, amine, imidazole, carboxylic acid, phosphine, iodine). Surfactants, templates, and physical methods (photochemistry, sonochemistry, radiolysis, thermolysis) have also been employed [78]. Conventional methods have primarily been based on the Brust–Schiffrin method, published in 1994 [79]. This was originally a two-phase synthesis with stabilization by organic soluble thiolates and reduction by NaBH<sub>4</sub> (Fig. 3.7a). This method was subsequently adjusted for the synthesis of water-soluble MPCs, which is generally a one-phase synthesis and follows a simple equation [Eq. (14)] [72].



Templeton et al. have reported the synthesis of water-soluble tiopronin [*N*-(2-mercaptopropionyl)glycine] MPCs  $1.8 \pm 0.7$  nm in diameter by this method. Characterization of these nanoclusters follows from traditional materials techniques, as previously described in depth [69, 72, 80]. Figure 3.7(b) and (c) shows examples of a transmission electron microscopy (TEM) picture and proton nuclear magnetic resonance spectroscopy (<sup>1</sup>H NMR) spectrum, respectively. Daniel et al. have recently published a more complete review of gold nanoparticle synthesis, characterization, and applications [78].

One of the most promising features of MPCs is their ability to exchange thiolate ligands with ligands in solution. This allows for the specific introduction of biologically active molecules, programmable specificity, and the synthesis of functional nanoclusters. In this way, nanoscale inorganic materials make potentially interesting solid supports for the immobilization and presentation of antibody or antigen, leading to a successful interface with an immunological system. Place exchange of free thiol onto 3D MPCs is a relatively facile process that is regulated by solvent, reaction temperature, reaction time, and properties and concentration of original and replacement thiol [75]. Investigation of the dynamics, kinetics, and mechanism of place exchange are abundant and generally support an associative, S<sub>N</sub>2 mechanism [75, 76, 81, 82]. Place exchange on MPCs has been compared to preceding studies of place exchange on 2D self-assembled monolayers. Exchange is more likely to occur on 3D surfaces (MPCs) than 2D surfaces (SAMs) due to the higher propensity for defect sites in structures with a substantial radius of curvature [36, 75, 83]. Another important feature of place exchange reactions is the

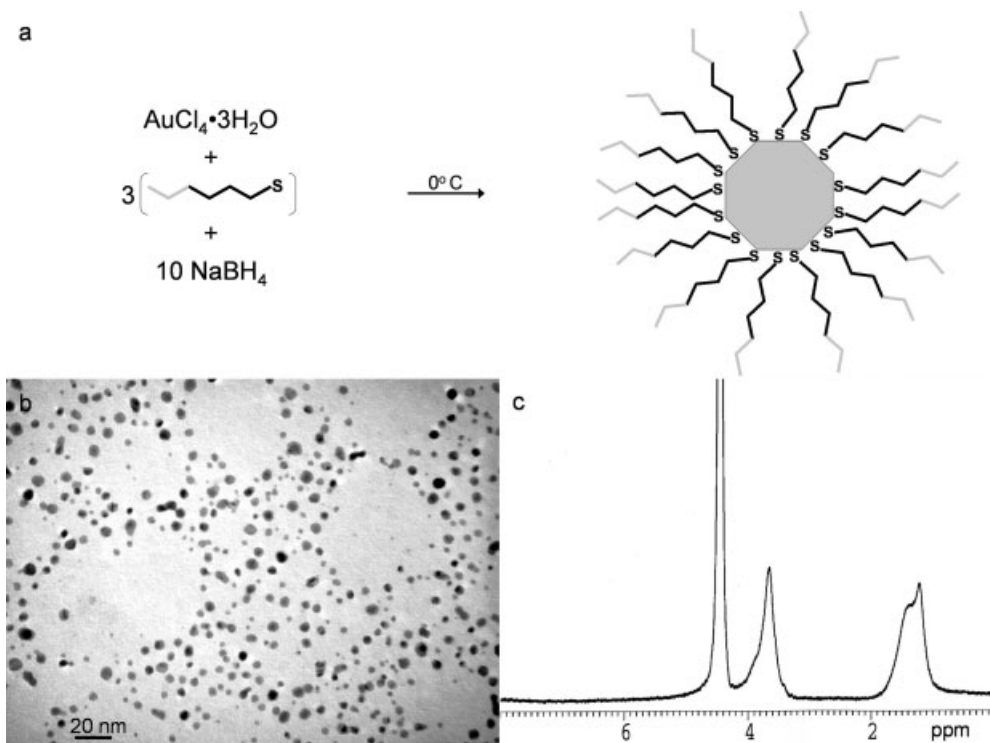


**Fig. 3.7.** Representative synthesis and characterization for a tiopronin (*N*-2-mercapto)propionylglycine)-protected cluster. (a) Synthesis conditions based on a modified Brust method and cartoon schematic of a monolayer-protected cluster (MPC). MPC ligands are connected through thiolate

moieties at one end and generally have a functional group at the opposing end (gray). (b) TEM image of MPC showing spherical shape and size dispersity. (c)  $^1\text{H}$  NMR of tiopronin MPC, showing broad  $-\text{CH}_3$  ( $\sim 1$  ppm) and  $-\text{CH}_2-/-\text{CH}-$  ( $\sim 3.5$  ppm) peaks. The water peak is at 4.8 ppm.

idea that fast-exchange sites are not static. Evidence for this has come from the exchange of several different ligands onto the same MPC [69, 76] and from an inability to completely remove ligand that had been previously exchanged on a cluster [75, 76]. A significant implication of these results is the ability of a thiolate to migrate across the monolayer of an MPC and position itself for an optimal interface [83].

There are many examples of successful place exchange and coupling reactions with organic and water-soluble MPCs, resulting in functional nanostructures. For example, Templeton et al. [76] used traditional amide coupling techniques to attach 12 different functional ligands to nanoclusters, introducing spin labels, amino acids, fluorophores, sugars, and electroactive moieties. Place exchange has also introduced fluorescein and an electroactive viologen species. Electrochemical quartz crystal microbalance of this MPC showed redox activity of the viologen as well

as deposition of the MPC upon viologen reduction [31]. Antimicrobial nanoclusters have been prepared by functionalization with vancomycin [84], glutathione-protected nanoclusters have been shown to interact with the enzyme glutathione transferase [85], and biotinylated nanoclusters bind to streptavidin [85]. This type of MPC functionalization produces nanostructures with specific activity and suggests potential for further nanocluster modulation in the design of bioreactive materials.

### 3.3

#### QCM Nanoparticle-based Chemical Sensors

The evaluation of interfaces between biology and nanotechnology has been an area of recent research interest, but originally started through the early development of chemical sensors. Originally, QCM was designed for gas-phase measurements and has been used in the control of metal vapor deposition. QCM continues to be used for gas-phase measurements, but has employed polymer and nanoparticle films for organic vapor sensing [86–88]. In 2001, dodecanethiol MPCs of 2 and 5 nm diameter were covalently assembled on a QCM substrate through dithiol linkages or non-covalently through carboxylic acid hydrogen bonding [86]. The nanoparticle thin-layers were then studied for their ability to partition toluene, hexane, methanol, ethanol, and water vapors. Vapor sorption was detected by simultaneous monitoring of frequency and resistance. Results suggested the viability of nanostructure films for vapor sensing and highlighted similarities and differences between the size of MPC used and the assembly technique.

Shortly thereafter, Zamborini et al. used electrochemical QCM to simultaneously measure conductivity and vapor partitioning in MPC films [87]. This approach used small (1.6 nm diameter) nanoclusters with mixed monolayers of alkanethiolate and  $\omega$ -carboxyalkanethiolate. The free carboxylic acid was used in conjunction with  $\text{Cu}^{2+}$  ions to assemble a network polymer of carboxylate- $\text{Cu}^{2+}$ -carboxylate bridges. These ion bridges allowed for electron transport through the polymer, though film swelling due to vapor partitioning (ethanol or dichloromethane) diminished electron flow.

Another example [88] made use of a greater variety of nanoclusters, protected with dodecanethiol, benzenethiol, 4-chlorobenzenethiol, 4-bromobenzenethiol, 4-(trifluoromethyl)benzenethiol, 4-hydroxybenzenethiol, and 4-aminobenzenethiol. Nanoparticle films were spray coated onto a QCM substrate and monitored by QCM to a final change in frequency of  $\sim 10\,000$  Hz. It was important to deposit a film with a thickness large enough to partition vapor, but small enough to rigidly couple the entire film to the sensor, maintaining an accurate sorption response. Motional resistance was monitored during film deposition to ensure rigidity as resistance is related to film viscoelastic properties. Results implied that different nanocluster films had increased sensitivity for different vapors (hexane, toluene, butanone, and butanol) and compared with vapor partitioning into organic polymers.

### 3.4

#### QCM Nanoparticle-based Biosensors

Inspired by the success of QCM bioassays (Section 3.1.5) and bionanotechnology, researchers have developed nanoparticle-based detection schemes using QCM for improved sensitivity. A popular area of analytical biochemistry involves the detection of DNA for a range of applications from gene analysis to forensic applications, where low detection limits are required. Willner et al. have developed three amplification paths for the detection of single-base mismatches in DNA with QCM detection [89–91]. Each path begins with the immobilization of ssDNA (25 bases) through SAM technology. Its complementary strand with an extra 16 bases is then introduced and allowed to base pair. In some cases a complement DNA strand with a single base-pair mismatch is purposely assembled. This allows for a single nucleotide, coupled with biotin, to bind at the mismatch site. At this point, three different approaches can be used: (1) free avidin can bind to the base-pair biotin, followed by biotin-labeled liposome binding; (2) avidin-labeled nanocluster can bind, followed by controlled nanoparticle growth for amplification; (3) avidin-labeled alkaline phosphatase can bind and catalyze the precipitation of an insoluble organic product for amplification. These methods lead to mismatch detection with detection limits ranging from  $10^{-12}$  to  $10^{-16}$  M<sup>-1</sup>. QCM gravimetry is well-suited for such precipitation/amplification schemes.

A similar approach to DNA hybridization detection and amplification also uses avidin-labeled alkaline phosphatase (as above). In this case, the enzyme catalyzes the production of the reducing agent, *p*-aminophenol, from a *p*-aminophenyl phosphate precursor. The reducing agent reduces Ag<sup>+</sup> ions in solution, which biomineralize into Ag nanoparticles on the DNA strand or on the QCM sensor surface, causing QCM signal amplification. The deposited silver can then be used in anodic stripping voltammetry to further confirm DNA binding, down to 100 aM concentrations.

Another example involves a glucose oxidase-based glucose sensor, which results from a complex nanostructure assembly. In this case, the QCM sensor was not used in the final analyte detection, but is a good example of the ability to assemble and monitor the assembly of complex nanostructures. First, polyethyleneimine (PEI) was immobilized, followed successively by 9–45 nm silica nanoparticles and PEI until several layers were assembled. This provided a roughened surface that allowed the immobilization and increased density of glucose oxidase enzyme. QCM was used to monitor these depositions and provided information for subsequent layer-by-layer construction on latex particles.

### 3.5

#### QCM Nanoparticle-based Immunosensors

The design, synthesis, and assembly of functional nanostructures are important challenges in the interface with immunology. Finding key recognition units and

presenting them in the appropriate environment and conformation are crucial to programming material specificity and affinity. A unique and creative idea for interface assembly may provide a good starting point, but redesign and optimization is difficult without a method for evaluating the proposed interface. The understanding of an interaction places interface development and application within reach. Traditional techniques have supplied qualitative information on antibody recognition for interface design and are widely used. Nanotechnology has expanded immunoassay options for the study of more diverse systems and, combined with QCM, provides a label-free, quantitative alternative. These analytical techniques can determine structural integrity of assembled nanoarchitectures, can provide equilibrium and kinetic binding constants of biological entities, and can detect analytes (antibodies, toxins, etc.) for medical diagnostic applications.

### 3.5.1

#### **Traditional Immunoassays**

Radiolabeled immunoassays were one of the first techniques used in the detection of antibody or antigen in biological systems. In this assay, radioisotopes, commonly  $^{125}\text{I}$ , were used to label the antibody or antigen, and scintillation counters measured the gamma or beta emission of the isotope. This provided the low detection limits needed for immunoassays, but regulation of radioactive isotopes made this technique inconvenient [92].

Another standard immunoassay is the enzyme-linked immunosorbent assay (ELISA). Its success comes from the ability to amplify binding through an enzyme reaction, which produces a spectroscopic signal. There are many formats for an ELISA experiment, though the indirect sandwich assay format has been widely accepted. In this format, the primary antibody is immobilized on a solid support (typically a well-plate) and antigen is allowed to bind. A second, polyclonal antibody for the antigen from a different species than that used as the primary antibody is then added and binds to the other side of the immobilized antigen, creating a "sandwich". An antibody that recognizes the second antibody (an anti-antibody) is functionalized with an enzyme (typically horseradish peroxidase) and allowed to bind. Finally, a substrate for the enzyme is introduced, which produces an enzyme product that is chromogenic. The chromophore is detected by conventional spectroscopic methods [57]. While the signal amplification from the enzyme reaction is beneficial, there are certain limitations to ELISA experiments. A lack of simple quantitation and excessive time required to assemble the complex immunomolecular biosensor, as in the case of an indirect sandwich assay, are poignant drawbacks. An example is the recent development of a quantitative ELISA assay for the detection of human IgG, which requires 19 hours from analyte immobilization to chromophore detection [93]. Other limitations include the need for labeling with a bulky enzyme, which could interfere with the antibody/antigen interaction, and the nonspecific adsorption of analyte to a hydrophobic well plate could lead to random orientation of binding sites and possible denaturation of substrate [57].

Surface plasmon resonance spectroscopy (SPR) has recently been used to detect

antibody binding. Details of SPR phenomena have been previously outlined [20, 94]. Briefly, SPR is an optical technique that takes advantage of plasmon excitation in bulk metal by wave vector matched photons. The photons induce oscillations of free electrons in the metal, which then propagate an additional field into the contacting dielectric medium. The plasmon excitation requires a transfer of energy from the photons, which can be observed through the sharp minimum of reflectivity during resonance, leading to an SPR signal [94]. Therefore, measuring the change in reflection angle provides real-time, label-free detection of antigen/antibody interaction. SPR has been used to study several different systems, an example being the characterization of FLAG peptide epitope arrays [38]. Important drawbacks of the SPR method are the complicated and expensive optics required for operation, loss of sensitivity at distances from the sensor, and interference from molecules with high molar absorptivity.

### 3.5.2

#### **Immunoassays using Nanotechnology**

Radiolabeling, ELISA, and SPR are important and effective techniques for the evaluation of traditional antibody/antigen interactions. Inorganic materials, such as nanoclusters, offer useful spectroscopic and microscopic properties that can make analysis convenient, but can also introduce added challenges. One of the first interfaces between materials and antibodies [58] was designed because radiolabel immunoassays were cumbersome and enzyme immunoassays require delicate procedures [59]. The potential of materials was harnessed to design a simpler method and successfully used antibody-functionalized latex beads and turbidity measurements to detect agglutination [58, 60]. Improvements to this method quickly followed, using electric pulses to promote antibody/antigen interaction and decrease reaction time [59].

A similar, though more recent, nanoimmunoassay also used antibody-functionalized particles. These 70 nm diameter silica particles had exterior antibody functionalization and interior fluorophore entrapment. Fluorescent-labeling techniques have enjoyed long-lived success, though low fluorescence intensity and photostability have been recurring problems. Encapsulation of  $\text{Ru}(\text{bpy})_3^{2+}$  fluorophore in silica nanoparticles yielded high intensity fluorescence and increased photostability due to exclusion of damaging oxygen [95]. These nanoparticles were compared to popular quantum dots (Qdots), which are semiconductor nanoparticles with intense intrinsic fluorescence, and were found to have similar intensity and stability. Antibody-functionalized Qdots have also been used as fluorescent tags for the imaging of live cells [67, 96].

Metal nanoparticles have been used as electrochemical labels for the simultaneous detection of four antigens,  $\beta_2$ -microglobulin, IgG, bovine serum albumin, and C-reactive protein [64]. In this experiment, a large magnetic bead was functionalized with four types of antibodies corresponding to the four different antigens. After binding antigen to the antibody on the magnetic bead, antibody with unique nanoparticle labels bound to the immobilized antigen. Collection of the



nanoparticle-labeled antibody and detection with square-wave stripping voltammetry provided four unique signals from the reduction of four unique metal nanoparticles [64].

A microscopic technique often used in nanocluster characterization, but not in immunoassay, is transmission electron microscopy (TEM). Metal nanoclusters absorb electrons, making them visible in TEM, while small carbon-based molecules do not. In a recent study, antibody-functionalized nanoparticles were incubated with pathogens *Staphylococcus saprophyticus* and *S. aureus* and examined with TEM. Functionalized nanoclusters bound to antibody binding sites and were detected. Furthermore, bacteria-bound magnetic particles were collected, thereby concentrating target pathogens [63].

Success with traditional immunoassay formats prompted SPR research in the area of nanoimmunotechnology. In 1998, Natan's group showed SPR signal amplification of antibody-nanocluster complex binding as compared to free antibody [21]. These results were confirmed with the detection of human complement factor 4 (C4) and C4 attached to colloidal Au particles [97].

These techniques, along with others, have had some success in the evaluation of interfaces between immunology and nanoscale materials. They also have their drawbacks. Many suffer from a lack of sensitivity and use large diameter particles (50–1000 nm) with relatively low surface area. Others rely on labeling to provide a detectable signal, which can interfere with recognition events and change the immunoassay dynamics. With SPR, nanoparticle labeling is used to acquire enhanced binding signals. Unfortunately, this also significantly broadens peaks, leading to a loss of sensitivity, complicated time-resolved measurements, and limited structural information [19, 20]. Efforts to develop a label-free, time-efficient, quantitative assay format that allows for 3D substrates and multilayer adsorptions have involved the quartz crystal microbalance (QCM) [1].

### 3.5.3

#### **QCM Nanoparticle-based Immunosensors**

Piezoelectric biosensors developed since 1990 have gained ground on traditional labeling experiments and on competing label-free instrumentation such as SPR [2, 98, 99]. The field of QCM immunosensors has also developed rapidly [43]. Considering the age of the new, though explosive, field of nanotechnology (the Brust nanoparticle synthesis was published in 1994), QCM immunosensors for nanotechnology applications are limited. One example used gold nanoparticle growth to amplify antibody-mediated lung carcinoma cell detection using QCM [100]. In these experiments a monoclonal antibody to cell surface antigen was immobilized on a polystyrene film and captured lung carcinoma cells. The same antibody conjugated to 10 nm diameter citrate-reduced gold nanoparticles bound to the immobilized cell in a typical sandwich scheme. Auric acid and  $\text{NH}_2\text{OH}$  were then introduced, reacted with the pre-existing gold nanoparticle, and caused the nanoparticle to grow. This growth created an increased QCM signal and allowed for the detection of cells at levels as low as  $100 \text{ cells mL}^{-1}$ . This method provided results similar to ELISA, but was less time consuming.

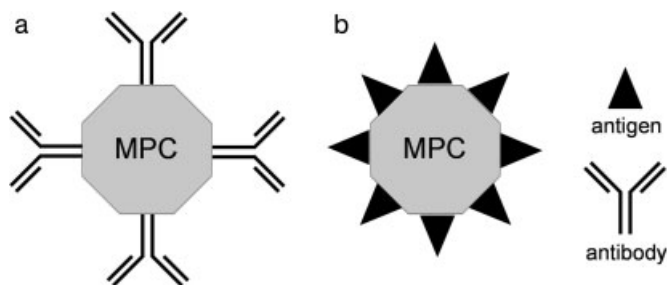


**Fig. 3.8.** Cartoon schematic of (a) nanocluster presenting antibody (antibody mimic) and (b) nanocluster presenting antigen (antigen mimic). Epitope antigens are generally smaller than antibodies and can be presented at a higher aerial density than antibodies.

Another example used polymer immobilized colloidal gold particles ( $\sim 15$  nm diameter) as an alternative approach to antibody immobilization [101]. Thiol-terminated Fab' antibody fragments will often denature on an unprotected hydrophobic gold QCM electrode, but retained activity when bound to the polymer/nanogold mixture. This nanoparticle-based immunosensor supplied a means for phenotyping leukemia cells for medical diagnostics with detection limits of  $6000$  cells  $\text{mL}^{-1}$ . An important technical detail of this work was the ability to detect four different phenotypes simultaneously using an array of QCM sensors. Other nanoparticle-based QCM immunosensors have made use of peptide epitope functionalized nanoclusters.

### 3.5.3.1 Antigen Mimic Design

There are two ways that functionalized nanoclusters can interface with immunology through paratope/epitope recognition: an antibody can be covalently attached to an MPC or an MPC can play the role of the antigen (Fig. 3.8). Antibody/nanocluster complexes have been previously studied as mentioned above. Briefly, immunoassays for human IgG have been developed using antibody bound latex beads [59, 60], signal amplification was observed with antibody bound gold nanoclusters in SPR immunoassays [21], and antibody bound magnetic microparticles have been used as capture agents [61]. There is further interest in using nanoparticle labeled antibodies as nanoprobables [102].

An alternative approach would be to attach an antigen to an MPC or functionalize an MPC with a peptide epitope (Fig. 3.8b). An epitope is the antigenic determinant of a protein and corresponds to the region of the protein that is specifically recognized by the antibody [103]. Accordingly, epitopes are only defined in an operational or functional sense: anything that is bound by an antibody is, by definition, an epitope. Therefore, epitope regions from proteins have been synthesized and expressed as smaller functional units and have been shown to bind antibodies. Examples of these would be the FLAG or E tags commonly used in expressed proteins [38, 44]. The current approach to this type of antigen mimetics is to synthesize the linear epitope and rely on primary structure (amino acid sequence) to

provide specificity. Combining this type of mimetics with nanoscale materials produced the first example of antigen encapsulated nanoclusters assembling with antibodies through the paratope/epitope interface. A linear peptide epitope known to bind monoclonal antibody associated with the human malarial parasite, *P. falciparum*, was used in the assembly of a robust, functional nanostructure that successfully mimicked a biological entity [65]. A more recent example used glutathione-protected nanoclusters and polyclonal anti-glutathione antibodies. This approach confirmed the ability to assemble epitope-protected nanoclusters with antibodies and provided quantitative binding information through improved analytical techniques [1].

These two examples used nanoclusters with peptide epitopes completely covering their surface and were synthesized with large amounts of the ligand, rather than specifically functionalized with small amounts of peptide. The next step in antigen mimic design was to functionalize pre-existing nanoclusters through place exchange reactions described above. This type of assembly provided a more complex nanostructure with three or more components and allowed for the use of more complicated linear and conformational epitopes. In a very recent study a linear peptide epitope, from the hemagglutinin (HA) protein related to influenza, has been synthesized and specifically presented at a controlled density on the surface of a pre-existing tiopronin-protected cluster [104]. This mimic of the HA protein was shown to interface with monoclonal anti-HA antibody and was compared to a self-assembled monolayer of the same peptide epitope.

Linear peptide epitopes used in the malaria, glutathione, and HA examples rely on primary amino acid sequence to provide antigenicity and specificity. This does not take into account the complex secondary structure (local conformation) exhibited by native proteins, which is essential to antibody recognition. Cyclization of peptides to approximate a loop structure has been used to introduce epitope conformation [105], but the development and presentation of a peptide epitope that reconstitutes a physiological conformation is an interesting alternative. This was recently achieved through the bidentate presentation of a peptide epitope from a loop region in the protective antigen (PA) of *B. anthracis* [83]. The conformational antigen mimic was able to interface with monoclonal anti-PA antibodies and showed a greater than two-fold increase in affinity over a linear antigen mimic.

This variety of antigen mimics using small molecule, linear, and conformational epitopes suggests multiple routes to interfacing inorganic nanoclusters with biological antibodies. Many other options are also available and, together, supply a “toolbox” of interfaces that can be used and studied in a multitude of systems. The three examples of GSH-MPC, HA-MPC, and PA-MPC are reviewed in further detail below.

### 3.5.3.2 Glutathione-protected Nanocluster

This research aimed to develop an immunoassay to study the test case of anti-glutathione antibody recognition of glutathione-protected nanocluster. The immunoassay was designed to be label-free, time-efficient, and quantitative and allow 3D substrates, multilayer adsorptions, and non-rigid biological recognition. QCM tech-

nology was used for many of the reasons previously mentioned, including high sensitivity, real-time detection, low cost, and a large wave penetration depth. Glutathione (GSH) monolayer-protected clusters (MPC) were used for their ease of synthesis, water solubility, high surface area and ligand valency, and the commercial availability of polyclonal anti-GSH antibody. Both GSH and tiopronin (Tiop), a glycine derivative and truncate of the GSH tripeptide, nanoclusters were synthesized according to a modified Brust method and characterized. The GSH-MPC had an average diameter of  $3.7 \pm 1.2$  nm, average composition of  $\text{Au}_{953}\text{GS}_{199}$ , and average molecular weight of 220 kDa.

The immunosensor consisted of the gold QCM electrode, Protein A, bovine serum albumin (BSA), and polyclonal anti-GSH antibody (Fig. 3.9a). Protein A was used to conveniently immobilize the antibody on the sensor surface in a defined orientation and BSA was used to block any exposed gold that might contribute to non-specific binding. Protein A bound to the gold electrode as a multilayer, BSA binding was minimal, and IgG bound specifically to Protein A, completing the immunosensor assembly (Fig. 3.9b). One drawback of this immunosensor design is the lack of reversibility and the need to reassemble the immunosensor structure before each experiment.

Analyte, GSH-MPC, was detected in a dose-dependent manner that was designed to limit non-specific adsorption and aggregation. Samples of different concentration were introduced to the immunosensor in short (5 min) doses and provided changes in mass that fit a logarithmic curve, revealing saturation of the immunosensor (Fig. 3.9d). This showed that the antibody was able to recognize the glutathione tripeptide epitope presented on the surface of a nanocluster. Furthermore, control experiments showed a lack of antibody binding to Tiop-MPC, suggesting antibody recognition of the  $\gamma$ -glutamic acid portion of GSH as opposed to the glycine portion (Fig. 3.9c). Equilibrium and kinetic constants for polyclonal anti-GSH antibody binding to GSH-MPC were calculated from Langmuir isotherm fits (Fig. 3.9e) and from individual binding curves (Fig. 3.9c and f). The equilibrium association constant,  $K_a$ , was found to be  $3.6 \pm 0.2 \times 10^5 \text{ M}^{-1}$ , the rate of forward reaction,  $k_f$ , was  $5.4 \pm 0.7 \times 10^1 \text{ M}^{-1} \text{ s}^{-1}$ , and the rate of reverse reaction,  $k_r$ , was  $1.5 \pm 0.4 \times 10^{-4} \text{ s}^{-1}$ . These values are reasonable, considering the use of polyclonal antibody. These results confirm the usefulness of a QCM immunosensor and suggest that epitope-presenting nanoclusters can be immunoreactive materials.

### 3.5.3.3 Hemagglutinin Mimic Nanocluster

Hemagglutinin (HA) and neuraminidase are two virus glycoproteins that are responsible for influenza infection and are targets for antibody neutralization. A peptide epitope-presenting nanocluster was designed to mimic one aspect of HA (Fig. 3.10a) and a QCM immunosensor was developed to examine the interface between monoclonal anti-HA and the HA-MPC. The peptide spanning amino acids 98–106 in the protein amino acid sequence (sequence: YPYDVPDYA) have been involved in influenza vaccine studies [106, 107]. The HA mimic was assembled by specific presentation of the synthetic peptide epitope on the surface of a pre-formed Tiop-

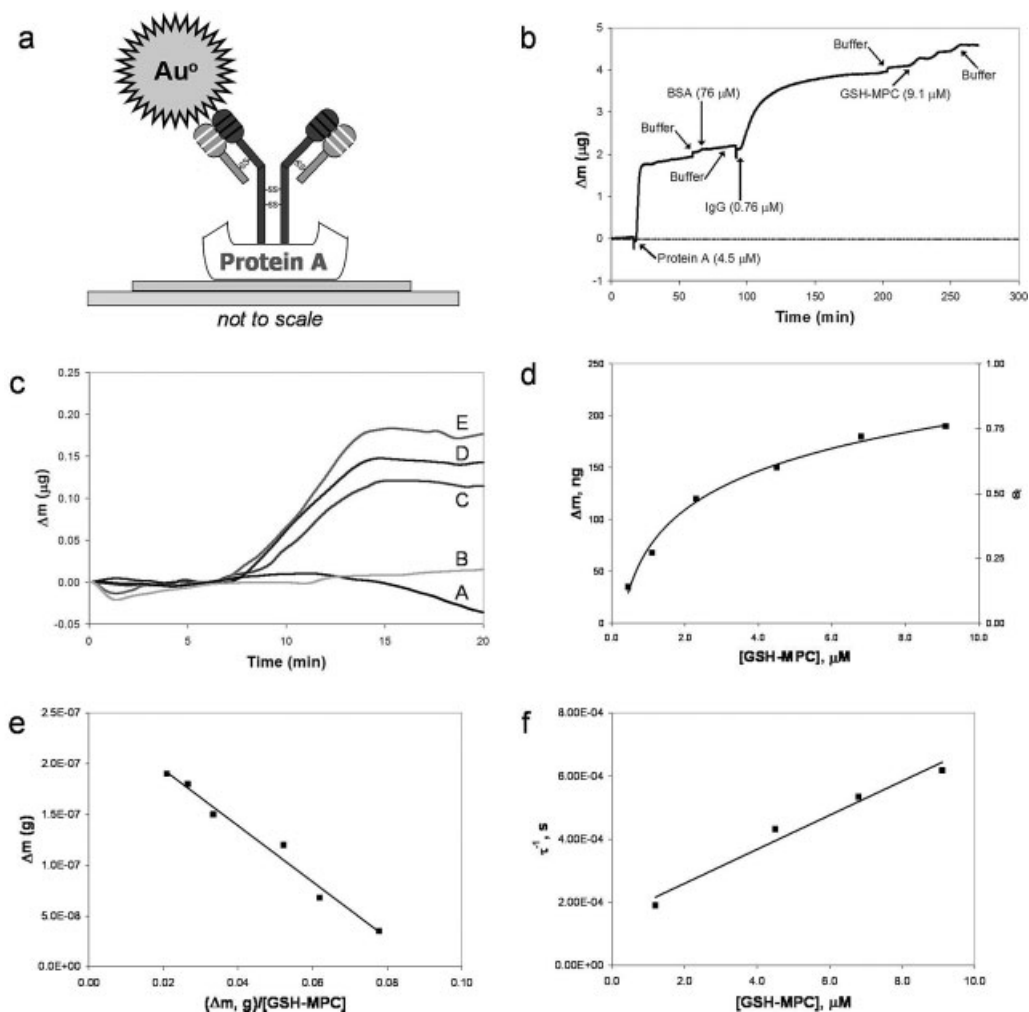


**Fig. 3.9.** (a) Cartoon schematic of immunosensor assembly using Protein A. (b) Representative total immunosensor assembly showing Protein A binding, BSA blocking, IgG capture, and MPC detection. (c) Binding curves (A) 1 mM free GSH, showing mass stripping; (B) 4.1  $\mu\text{M}$  tiopronin-MPC; (C) 2.3

$\mu\text{M}$  GSH-MPC; (D) 4.5  $\mu\text{M}$  GSH-MPC; (E) 9.1  $\mu\text{M}$  GSH-MPC. (d)  $\Delta m$  vs. [GSH-MPC] with logarithmic fit, showing saturation of the biosensor. (e) Linear Langmuir adsorption isotherm. (f) Adsorption kinetics. (Reprinted with permission from the American Chemical Society.)

MPC through place exchange reaction. This produced a three-component system consisting of  $3.5 \pm 1.0$  nm colloidal gold, tiopronin ligand, and HA peptide, with a final composition of  $\text{Au}_{807}\text{T}_{242}\text{HA}_4$ . A QCM immunosensor was then used in the evaluation of the interface between HA-MPC and anti-HA antibody.

In this immunoassay, a different assembly technique was used than for the

preceding GSH-MPC experiments. This approach made use of ionic interactions to immobilize the nanocluster and detect antibody binding. One reason for using this approach was the available option of analyzing complex samples containing one more antibody and various other components. The immunosensor consisted of the gold QCM electrode, a positively charged polyelectrolyte [poly(diallyldimethylammonium chloride)], nanocluster, and BSA (Fig. 3.10b). Polyelectrolyte had been previously used in the multi-layering of quantum dots and provided a thin layer of positive charge on the surface of the QCM. Negatively charged HA-MPC bound non-specifically and was immobilized for antibody binding. Before analyte was introduced, BSA was used to block non-specific polyelectrolyte binding sites (Fig. 3.10b). Again, a limitation of this immunoassay approach is the lack of reversibility and the time required to reassemble the sensor before each experiment.

This immunosensor was used for two applications, the first being an examination of antibody binding as related to the density of peptide presented on the Tiop-MPC. Three nanoclusters with 4, 11, and 33 peptides per cluster were examined and suggested that the lower density of peptide allowed the highest ratio of antibody to peptide interaction. The second application was a thorough study of the antibody interface with the HA-MPC displaying four peptides per cluster. Samples with different concentrations of antibody were introduced to the sensor in dose amounts and produced changes in mass that fit a logarithmic curve and showed saturation of the biosensor. This suggested that the antibody did recognize the peptide epitope specifically presented on the surface of a nanocluster. Control experiments using Tiop-MPC presenting no peptide showed a lack of antibody binding, signifying the specificity of the antibody for the epitope. Preliminary calculations have suggested an equilibrium binding constant ( $K_a = 1.0 \pm 0.3 \times 10^7 \text{ M}^{-1}$ ) and kinetic rate constants ( $k_f = 5.1 \pm 0.6 \times 10^5 \text{ M}^{-1} \text{ s}^{-1}$  and  $k_r = 9.4 \pm 0.7 \times 10^{-2} \text{ s}^{-1}$ ) for the association of anti-HA and HA-MPC.

These results were compared to traditionally used peptide epitope arrays. Self-assembled monolayers (SAMs) consisting of tiopronin ligand and mixed-monolayers of both peptide and tiopronin were formed on the QCM gold electrode. Antibody was introduced to the mixed-monolayer peptide array in dose amounts and bound in a manner similar to that seen with the functionalized nanocluster (Fig. 3.10c). Preliminary equilibrium association constant ( $K_a = 4.1 \pm 0.7 \times 10^6 \text{ M}^{-1}$ ) and kinetic constants ( $k_f = 1.4 \pm 0.2 \times 10^5 \text{ M}^{-1} \text{ s}^{-1}$ ,  $k_r = 3.5 \pm 0.2 \times 10^{-2} \text{ s}^{-1}$ ) were calculated and compared to those for the antigen mimic HA-MPC. The  $K_a$  for the nanocluster is more than double that for the SAM, indicating a more accurate reconstitution of the peptide epitope on the surface of the MPC.

#### 3.5.3.4 Protective Antigen of *B. anthracis* Mimic Nanocluster

This study [83] made use of a QCM immunosensor, four independently functionalized nanoclusters, and monoclonal antibodies to effectively map one antibody clone to one peptide epitope. Not only did the identified antibody distinguish between three different peptide epitopes from the protective antigen (PA) of *B. anthracis*, it had an increased affinity for a conformational epitope as compared to a linear version with the same amino acid sequence. Epitopes from PA were used for

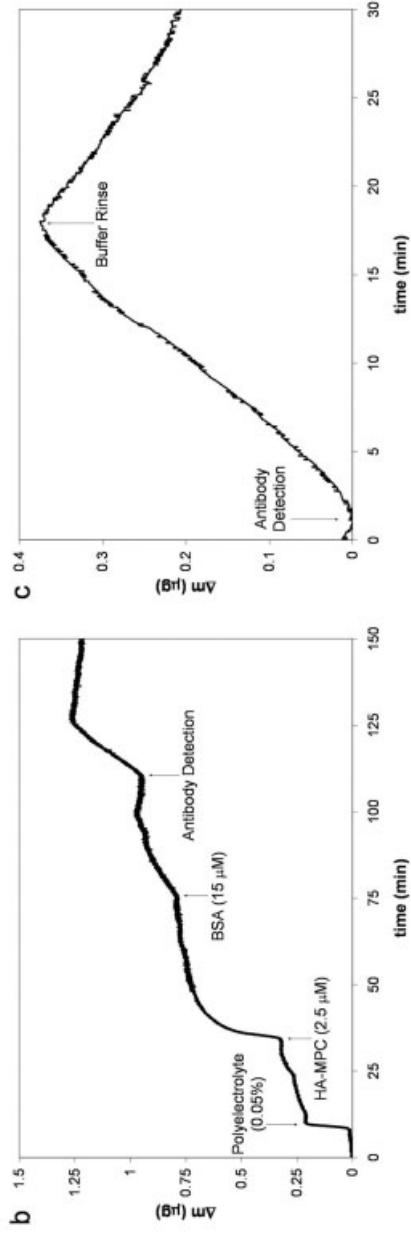
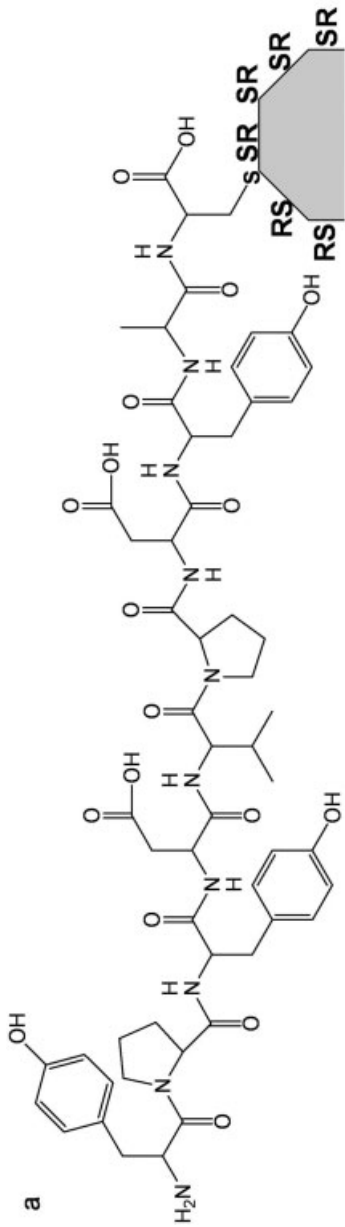


**Fig. 3.10.** (a) Schematic of a HA peptide epitope-functionalized MPC (not to scale). (b) Representative total immunosensor assembly, showing polyelectrolyte and MPC binding, BSA blocking, and antibody detection. (c) Representative antibody detection using HA/tiopronin SAM.

four reasons: (1) epitopes had been previously identified through various mapping techniques; (2) PA has been a target for immunological studies, as anti-PA antibodies confer immunity to anthrax; (3) PA has both conformational and linear epitopes; (4) anthrax has been identified as a potential bioterrorism agent. Identified PA peptide epitopes [108–111] span amino acids 680–692 (PA680), 703–722 (PA703), and 730–735 (PA730) in the intact protein, and were each synthesized for use in antigen mimic design. The functional nanostructures were assembled by specifically presenting conformational or linear epitopes on the surface of pre-existing Tiop-MPCs through place exchange reactions. Four antigen mimics had final peptide densities of 4 (PA680B, conformational), 4 (PA680M, linear), 8 (PA703B, conformational), and 10 (PA730M, linear) peptides per MPC. A cartoon schematic of PA680B-MPC and the crystal structure of PA [109] are given in Fig. 3.11(a). Labeling experiments suggested the bidentate attachment of loop epitopes to MPCs, implying the formation of conformational antigen mimics. Increased antibody affinity for the conformational over the linear epitope provided a strong case for faithful reconstitution of the loop structure.

The QCM immunoassay used ionic interactions for the immobilization of MPC, similar to that used with HA-MPC (Section 3.5.3.3). Polyelectrolyte acted as an intermediate between the gold electrode and the MPC for successful immobilization (Fig. 3.11b). Again, BSA was used to block non-specific binding sites. This immunosensor assembly was used for two different studies, the first being the screening of seven monoclonal anti-PA antibodies against the four antigen mimics. The antibodies were known to bind the full-sized 83 kDa PA protein, but had not been tested for neutralization ability [112]. Screening provided qualitative binding information and pointed to one antibody as being specific for the conformational antigen mimic, PA680B-MPC. The magnitude of antibody binding as a function of antibody concentration was the second system studied. Antibody did not bind to PA703B-MPC or PA730M-MPC, but PA680B-MPC ( $K_a = 5.9 \pm 0.7 \times 10^6 \text{ M}^{-1}$ ) and PA680M-MPC ( $K_a = 2.6 \pm 0.9 \times 10^6 \text{ M}^{-1}$ ) were evaluated to obtain equilibrium association constants. Both were also evaluated in buffer of high ionic strength. In this system, PA680B-MPC had a  $K_a$  similar to that previously reported, though PA680M-MPC showed no binding. Kinetic studies of antibody binding for PA680B-MPC yielded forward and reverse reaction rate constants of  $9 \pm 2 \times 10^3 \text{ M}^{-1} \text{ s}^{-1}$  and  $2.3 \pm 0.5 \times 10^{-3} \text{ s}^{-1}$ , respectively. Free peptide (amino acids 680–692), unencumbered or unconstrained by nanocluster or protein scaffold, showed only non-specific binding to the antibody. In this immunoassay, anti-PA antibody was immobilized using Protein A, as previously described (Section 3.5.3.2), and free peptide was introduced. This implies that the peptide epitope was presented in a more accommodating conformation on the surface of the MPC, as opposed to being free in solution.

These results point out that peptide epitopes and monolayer protected nanoclusters can be brought together in the successful assembly of an immunoreactive material and be interfaced with biological antibodies. They also show the screening and effective mapping of an antibody to a peptide epitope, as well as differentiation between conformational and linear presentation.



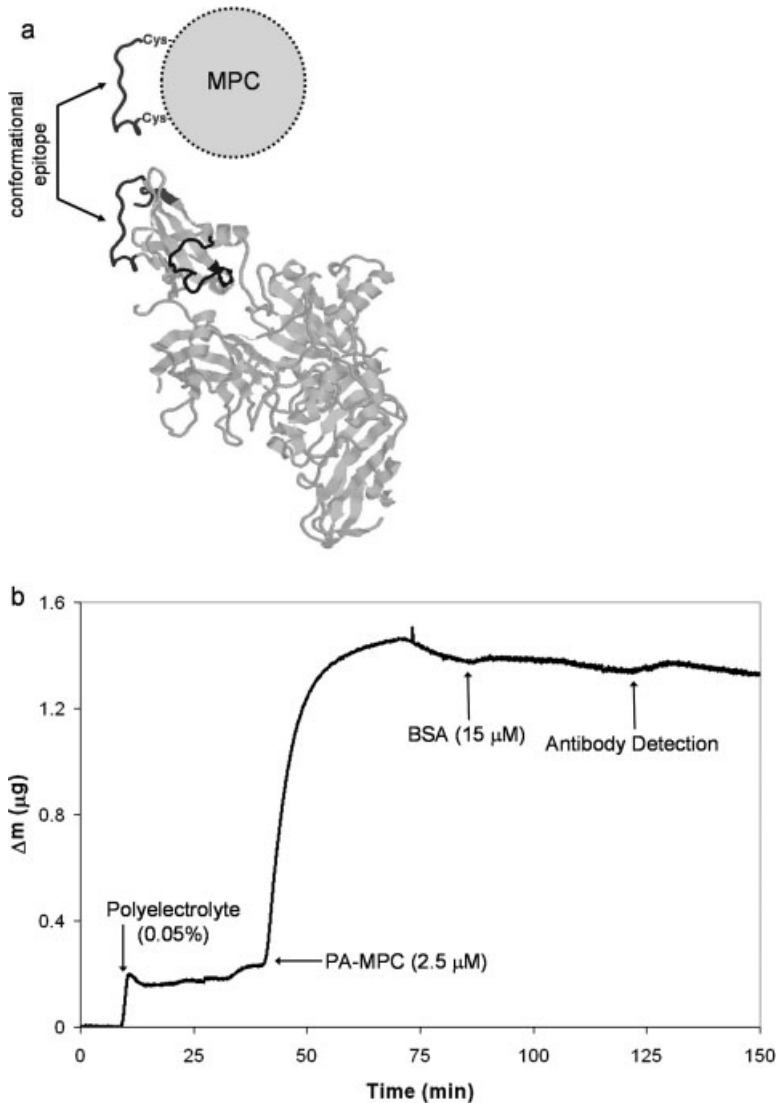


**Fig. 3.11.** (a) X-ray crystal structure of the protective antigen (PA) of *B. anthracis* with epitope regions highlighted (dark). Schematic of PA680B-MPC antigen mimic, highlighting conformational peptide epitope. (b) Representative total immunosensor assembly, showing polyelectrolyte and MPC binding, BSA blocking, and antibody detection.

### 3.6 Conclusions and Future Directions

The future of bionanotechnology lies at the interface between biology and inorganic nanomaterials and relies on the ability to probe and evaluate that interface. Many analytical techniques outlined in this chapter, including AFM, TEM, NMR,

and molecular imaging, have been developed for this very purpose, for the analysis of all types of interfaces. The quartz crystal microbalance is another technique that has evolved to become a central tool in the study of both biological and nanomaterials applications. QCM has principal advantages for the investigation of bionanotechnology over existing immunological techniques: low cost and ease of operation, quantitation, real-time measurements, and large wave penetration depth, to name a few. For these reasons QCM technology has been applied to the exploration of various life science applications. QCM nanoparticle-based immunoassay is a relatively new field, but has been designed for the evaluation of several antigen mimics. Specifically, QCM has shown that antibody can recognize and interface with immunoreactive nanomaterials designed with linear and conformational peptide epitopes presented on the surface of monolayer-protected clusters. This is only one interface that QCM has successfully characterized. Given the virtues of this technique and the vast number of possible combinations between biology and nanotechnology, more systems will doubtlessly be studied.

The prospects of biotechnology and nanomaterials science are most promising at their interface, where they overlap in the emerging field of bionanotechnology. This interfacial discipline further relies on analytical techniques that can probe the boundary where they meet. The quartz crystal microbalance is certain to be an integral tool in the exploration of this frontier. Specifically, QCM can expand its applicability through the design of new immobilization strategies for repeated, reversible interactions. An improved, commercially available, multichannel detection apparatus will improve throughput and multiplexing. In the realm of medical diagnostics and defense-based toxin detection, a blood sample, water-way, or gaseous area could be largely characterized through multi-analyte detection. This is possible because of the portability, low cost, and ease of use of existing QCM instruments and potential devices. Furthermore, advances in nanotechnology and improved understanding of biology will produce smart sensors and functional devices capable of carrying out an environmental analysis or capable of modulating an environment. Continued research on advanced nanomaterials in a biological paradigm using an effective QCM transducer can make this a reality.

### Acknowledgments

A.E.G. would like to thank the Chemical Biology Interface Training Grant (T32 GM065086) and the Vanderbilt Institute of Nanoscale Science and Engineering (VINSE) for support. D.W.W. acknowledges support from the SouthEast Regional Center of Excellence for Biodefense (NIH U54 AI57157-03).

### Symbols

- A      area of the QCM electrode
- [C]    concentration of a bulk solution
- [C]<sub>0</sub>   initial concentration, initial concentration of surface immobilized analyte

$C_1$	motional capacitance of the unperturbed crystal
$c_{66}$	piezoelectrically stiffened quartz elastic constant
$C_f$	Sauerbrey sensitivity factor, $2f_o^2/A(c_{66}\rho_q)^{1/2}$
$f_o$	frequency of crystal in air (unperturbed) (Hz)
$k_f$	forward kinetic rate constant
$k_r$	reverse kinetic rate constant
$N$	overtone number
$R$	gas constant ( $8.3145 \text{ J K}^{-1} \text{ mol}^{-1}$ )
$R_L$	loading resistance
$T$	temperature (K)
$\Delta f$	change in frequency (Hz)
$\Delta G_{\text{ads}}$	Gibbs free energy of adsorption
$\Delta m$	change in mass (g)
$\Delta \eta$	change in viscosity
$\Delta \rho$	change in density
$\eta_q$	effective quartz viscosity
$\Theta$	fractional coverage of a surface by a species
$\Theta_\infty$	fractional coverage at infinite time
$\rho_q$	quartz mass density
$\tau^{-1}$	kinetic time constant, equal to $k_f C + k_r$

## References

- GERDON, A.E., WRIGHT, D.W., CLIFFEL, D.E. Quartz crystal microbalance detection of glutathione-protected nanoclusters using antibody recognition, *Anal. Chem.* **2005**, *77*, 304–310.
- JANSHOFF, A., GALLA, H.J., STEINEM, C. Piezoelectric mass-sensing devices as biosensors – an alternative to optical biosensors?, *Angew. Chem. Int. Ed.* **2000**, *39*, 4004–4032.
- CADY, W.G., *Piezoelectricity*. **1946**, New York: McGraw-Hill.
- NOMURA, T., OKUHARA, M. Frequency shifts of piezoelectric quartz crystals immersed in organic liquids, *Anal. Chim. Acta* **1982**, *142*, 281–284.
- KANAZAWA, K.K., GORDON, J.G. Frequency of a quartz microbalance in contact with liquid, *Anal. Chem.* **1985**, *57*, 1770–1771.
- MARTIN, S.J., GRANSTAFF, V.E., FRYE, G.C. Characterization of a quartz crystal microbalance with simultaneous mass and liquid loading, *Anal. Chem.* **1991**, *63*, 2272–2281.
- MARTIN, S.J., SPATES, J.J., WESSENDORF, K.O., SCHNEIDER, T.W. Resonator/oscillator response to liquid loading, *Anal. Chem.* **1997**, *69*, 2050–2054.
- RICKERT, J., BRECHT, A., GOPEL, W. QCM operation in liquids: constant sensitivity during formation of extended protein multilayers by affinity, *Anal. Chem.* **1997**, *69*, 1441–1448.
- CHAGNARD, C., GILBERT, P., WATKINS, A.N., BEELER, T., PAUL, D.W. An electronic oscillator with automatic gain control: EQCM applications, *Sens. Actuators B* **1996**, *32*, 129–136.
- Maxtek, Inc. Home Page, <http://www.maxtekinc.com>, **2003**.
- HILLIER, A.C., WARD, M.D. Scanning electrochemical mass sensitivity

- mapping of the quartz crystal microbalance in liquid media, *Anal. Chem.* **1992**, *64*, 2539–2554.
- 12 BANDEY, H.L., MARTIN, S.J., CERNOSEK, R.W., HILLMAN, A.R. Modeling the responses of thickness-shear mode resonators under various loading conditions, *Anal. Chem.* **1999**, *71*, 2205–2214.
  - 13 MARTIN, S.J., BANDEY, H.L., CERNOSEK, R.W. Equivalent-circuit model for the thickness-shear mode resonator with a viscoelastic film near film resonance, *Anal. Chem.* **2000**, *72*, 141–149.
  - 14 THEISEN, L.A., MARTIN, S.J., HILLMAN, A.R. A model for the quartz crystal microbalance frequency response to wetting characteristics of corrugated surfaces, *Anal. Chem.* **2004**, *76*, 796–804.
  - 15 HUNG, V.N., ABE, T., MINH, P.N., ESASHI, M. High-frequency one-chip multichannel quartz crystal microbalance fabricated by deep RIE, *Sens. Actuators A* **2003**, *108*, 91–96.
  - 16 TATSUMA, T., WATANABE, Y., OYAMA, N. Multichannel quartz crystal microbalance, *Anal. Chem.* **1999**, *71*, 3632–3636.
  - 17 FAWCETT, N.C., CRAVEN, R.D., ZHANG, P., EVANS, J.A. QCM response to solvated, tethered macromolecules, *Anal. Chem.* **1998**, *70*, 2876–2880.
  - 18 THOMPSON, M., KIPLING, A.L., DUNCAN-HEWITT, W.C. Thickness-shear-mode acoustic wave sensors in the liquid phase, *Analyst* **1991**, *116*, 881–890.
  - 19 WIJEKON, W.M.K.P., ASGHARIAN, B., CASSTEVENS, M., SAMOC, M., TALAPATRA, G.B., PRASAD, P.N., GEISLER, T., ROSENKILDE, S. Electrooptic effect in Langmuir–Blodgett films of 2-(docosylamino)-5-nitropyridine probed by surface plasmon waves, *Langmuir* **1992**, *8*, 135–139.
  - 20 SALAMON, Z., MACLEOD, H.A., TOLLIN, G. Surface plasmon resonance spectroscopy as a tool for investigating the biochemical and biophysical properties of membrane protein systems. II: Applications to biological systems, *Biochim. Biophys. Acta* **1997**, *1331*, 131–152.
  - 21 LYON, L.A., MUSICK, M.D., NATAN, M.J. Colloidal Au-enhanced surface plasmon resonance immunosensing, *Anal. Chem.* **1998**, *70*, 5177–5183.
  - 22 LYON, L.A., MUSICK, M.D., SMITH, P.C., REISS, R.D., PENA, D.J., NATAN, M.J. Surface plasmon resonance of colloidal Au-modified gold films, *Sens. Actuators B* **1999**, *54*, 118–124.
  - 23 LYON, L.A., PENA, D.J., NATAN, M.J. Surface plasmon resonance of Au colloid-modified Au films: particle size dependence, *J. Phys. Chem. B* **1999**, *103*, 5826–5831.
  - 24 ZHANG, Y., TELYATNIKOV, V., SATHE, M., ZENG, X., WANG, P.G. Studying the interactions of  $\alpha$ -Gal carbohydrate antigen and proteins by quartz-crystal microbalance, *J. Am. Chem. Soc.* **2003**, *125*, 9292–9293.
  - 25 BAIN, C.D., WHITESIDES, G.M. Formation of monolayers by the coadsorption of thiols on gold: variation in the length of the alkyl chain, *J. Am. Chem. Soc.* **1989**, *111*, 7164–7175.
  - 26 PALE-GROSDÉMANGE, C., SIMON, E.S., PRIME, K.L., WHITESIDES, G.M. Formation of self-assembled monolayers by chemisorption of derivatives of oligo(ethylene glycol) of structure HS(CH<sub>2</sub>)<sub>11</sub>(OCH<sub>2</sub>CH<sub>2</sub>)<sub>m</sub>OH on gold, *J. Am. Chem. Soc.* **1991**, *113*, 12–20.
  - 27 TEMPLETON, A.C., ZAMBORINI, F.P., WUELFING, W.P., MURRAY, R.W. Controlled and reversible formation of nanoparticle aggregates and films using Cu<sup>+2</sup>-carboxylate chemistry, *Langmuir* **2000**, *16*, 6682–6688.
  - 28 MAMEDOV, A.A., BELOV, A., GIERSIG, M., MAMEDOVA, N.N., KOTOV, N.A. Nanorainbows: graded semiconductor films from quantum dots, *J. Am. Chem. Soc.* **2001**, *123*, 7738–7739.
  - 29 DECHER, G. Fuzzy Nanoassemblies: toward layered polymeric multicomposites, *Science* **1997**, *277*, 1232–1237.
  - 30 HICKS, J.F., SEOK-SHON, Y., MURRAY, R.W. Layer-by-layer growth of polymer/nanoparticle films containing

- monolayer-protected gold clusters, *Langmuir* **2002**, *18*, 2288–2294.
- 31 TEMPLETON, A.C., CLIFFEL, D.E., MURRAY, R.W. Redox and fluorophore functionalization of water-soluble, tiopronin-protected gold clusters, *J. Am. Chem. Soc.* **1999**, *120*, 4845–4849.
  - 32 KATZ, E., DE LACY, A.L., FIERRO, J.L.G., PALACIOS, J.M., FERNANDEZ, V.M. Covalent binding of viologen to electrode surfaces coated with poly(acrylic acid) formed by electropolymerization of acrylate ions, *J. Electroanal. Chem.* **1993**, *358*, 247–259.
  - 33 DAVIS, K.A., LEARY, T.R. Continuous liquid-phase piezoelectric biosensor for kinetic immunoassays, *Anal. Chem.* **1989**, *61*, 1227–1230.
  - 34 BOHINSKI, R.C. Immunoprecipitation of serum albumin with protein A-Sepharose, *J. Chem. Educ.* **2000**, *77*, 1460–1462.
  - 35 DEISENHOFER, J. Crystallographic refinement and atomic models of a human fc fragment and its complex with fragment B of protein A from *Staphylococcus aureus* at 2.9- and 2.8-Å resolution, *Biochemistry* **1981**, *20*, 2361–2370.
  - 36 BAIN, C.D., TROUGHTON, E.B., TAO, Y.T., EVALL, J., WHITESIDES, G.M., NUZZO, R.G. Formation of monolayer films by the spontaneous assembly of organic thiols from solution onto gold, *J. Am. Chem. Soc.* **1989**, *111*, 321–335.
  - 37 KARPOVICH, D.S., BLANCHARD, G.J. Direct measurement of the adsorption kinetics of alkanethiolate self-assembled monolayers on a microcrystalline gold surface, *Langmuir* **1994**, *10*, 3315–3322.
  - 38 WEGNER, G.J., LEE, H.J., CORN, R.M. Characterization and optimization of peptide arrays for the study of epitope-antibody interactions using surface plasmon resonance imaging, *Anal. Chem.* **2002**, *74*, 5161–5168.
  - 39 LAUFFENBURGER, D.A., LINDERMAN, J.J., *Receptors: Models for Binding, Trafficking, and Signaling*. **1996**, New York: Oxford University Press.
  - 40 EBARA, Y., ITAKURA, K., OKAHATA, Y. Kinetic studies of molecular recognition based on hydrogen bonding at the air-water interface by using a highly sensitive quartz-crystal microbalance, *Langmuir* **1996**, *12*, 5165–5170.
  - 41 EBATO, H., GENTRY, C.A., HERRON, J.N., MULLER, W., OKAHATA, Y., RINGSDORF, H., SUCI, P.A. Investigation of specific binding of anti-fluorescein antibody and Fab to fluorescein lipids in Langmuir–Blodgett deposited films using quartz crystal microbalance methodology, *Anal. Chem.* **1994**, *66*, 1683–1689.
  - 42 SMITH, E.A., THOMAS, W.D., KIESSLING, L.L., CORN, R.M. Surface plasmon resonance imaging studies of protein-carbohydrate interactions, *J. Am. Chem. Soc.* **2003**, *125*, 6140–6148.
  - 43 SU, X., CHEW, F.T., LI, S.F.Y. Design and application of piezoelectric quartz crystal-based immunoassay, *Anal. Sci.* **2000**, *16*, 107–114.
  - 44 SHEN, Z., STRYKER, G.A., MERNAUGH, R.L., YU, L., YAN, H., ZENG, X. Single-chain fragment variable antibody piezoimmunosensors, *Anal. Chem.* **2005**, *77*, 797–805.
  - 45 ZUO, B., LI, S., GUO, Z., ZHANG, J., CHEN, C. Piezoelectric immunosensor for SARS-associated coronavirus in sputum, *Anal. Chem.* **2004**, *76*, 3536–3540.
  - 46 STINE, R., PISHKO, M.V., SCHENGRUND, C.-L. Comparison of glycosphingolipids and antibodies as receptor molecules for ricin detection, *Anal. Chem.* **2005**, *77*, 2882–2888.
  - 47 UTTENTHALER, E., SCHRAML, M., MANDEL, J., DROST, S. Ultrasensitive quartz crystal microbalance sensors for detection of M13-phages in liquids, *Biosens. Bioelectron.* **2001**, *16*, 735–743.
  - 48 KASTL, K., ROSS, M., GERKE, V., STEINEM, C. Kinetics and thermodynamics of annexin A1 binding to solid-supported membranes: A QCM study, *Biochemistry* **2002**, *41*, 10087–10094.
  - 49 NIEMEYER, C.M. Nanoparticles, Proteins, and nucleic acids: biotechnology meets materials science, *Angew. Chem. Int. Ed.* **2001**, *40*, 4128–4158.
  - 50 STORHOFF, J.J., MIRKIN, C.A.

- Programmed materials synthesis with DNA, *Chem. Rev.* **1999**, *99*, 1849–1862.
- 51 WHALEY, S.R., ENGLISH, D.S., HU, E.L., BARBARA, P.F., BELCHER, A.M. Selection of peptides with semiconductor binding specificity for directed nanocrystal assembly, *Nature* **2000**, *405*, 665–668.
- 52 SLOCIK, J.M., NAIK, R.R., STONE, M.O., WRIGHT, D.W. Viral templates for gold nanoparticle synthesis, *J. Mater. Chem.* **2005**, *15*, 749–753.
- 53 KNECHT, M.R., WRIGHT, D.W. Functional analysis of the biomimetic silica precipitating activity of the R5 peptide from *Cylindrotheca fusiformis*, *Chem. Commun.* **2003**, *24*, 3038–3039.
- 54 NELSON, D.L., COX, M.M., *Lehninger Principles of Biochemistry*. Third edn., **2000**, New York: Worth Publishers.
- 55 MORRIS, G.E., Choosing a method for epitope mapping, in *Epitope Mapping Protocols*. **1996**, Humana Press: Totowa, NJ. pp. 1–9.
- 56 MERNAUGH, R., MERNAUGH, G., *Molecular Methods in Plant Pathology*, ed. SINGH, R.P., SINGH, U.S. **1995**, Boca Raton: CRC Lewis Publishers.
- 57 CROWTHER, J.R., *The ELISA Guidebook*. Methods in Molecular Biology. vol. 149. **2001**, Totowa, New Jersey: Humana Press.
- 58 BERNARD, A.M., LAUWERYS, R.R. Comparison of turbidimetry with particle counting for the determination of human B2-microglobulin by latex immunoassay (LIA), *Clin. Chem. Acta* **1982**, *119*, 335–339.
- 59 TAMIYA, E., WANTANBE, N., MATSUOKA, H., KARUBE, I. Pulse immunoassay for human immunoglobulin G using antibody bound latex beads, *Biosensors* **1988**, 139–146.
- 60 ORTEGA-VINUESA, J.L., MOLINA-BOLIVAR, J.A., HIDALGO-ALVAREZ, R. Particle enhanced immunoaggregation of F(ab')<sub>2</sub> molecules, *J. Immunol. Methods* **1996**, *190*, 29–38.
- 61 NAM, J.-M., THAXTON, C.S., MIRKIN, C.A. Nanoparticle-based bio-bar codes for the ultrasensitive detection of protein, *Science* **2003**, *301*, 1884–1886.
- 62 TANG, D.P., YUAN, R., CHAI, Y.Q., ZHONG, X., LIU, Y., DAI, J.Y., ZHANG, L.Y. Novel potentiometric immunosensor for hepatitis B surface antigen using a gold nanoparticle-based biomolecular immobilization method, *Anal. Biochem.* **2004**, *333*, 345–350.
- 63 HO, K.-C., TSAI, P.-J., LIN, Y.-S., CHEN, Y.-C. Using biofunctionalized nanoparticles to probe pathogenic bacteria, *Anal. Chem.* **2004**, *76*, 7162–7168.
- 64 LIU, G., WANG, J., KIM, J., JAN, M.R. Electrochemical coding for multiplexed immunoassays of proteins, *Anal. Chem.* **2004**, *76*, 7126–7130.
- 65 SLOCIK, J.M., MOORE, J.T., WRIGHT, D.W. Monoclonal antibody recognition of histidine-rich peptide encapsulated nanoclusters, *Nano Lett.* **2002**, *2*, 169–173.
- 66 BIRD, R.E., HARDMAN, K.D., JACOBSON, J.W., JOHNSON, S., KAUFMAN, B.M., LEE, S.-M., LEE, T., POPE, S.H., RIORDAN, G.S., WHITLOW, M. Single-chain antigen-binding proteins, *Science* **1988**, *242*, 423–426.
- 67 BENTZEN, E.L., HOUSE, F., UTLEY, T.J., CROWE, J.E.J., WRIGHT, D.W. Progression of respiratory syncytial virus infection monitored by fluorescent quantum dot probes, *Nano Lett.* **2005**, *5*, 591–595.
- 68 HOSTETLER, M.J., GREEN, S.J., STOKES, J.J., MURRAY, R.W. Monolayers in three dimensions: synthesis and electrochemistry of  $\omega$ -functionalized alkanethiolate-stabilized gold cluster compounds, *J. Am. Chem. Soc.* **1996**, *118*, 4212–4213.
- 69 INGRAM, R.S., HOSTETLER, M.J., MURRAY, R.W. Poly-hetero- $\omega$ -functionalized alkanethiolate-stabilized gold cluster compounds, *J. Am. Chem. Soc.* **1997**, *119*, 9175–9178.
- 70 WUELFING, W.P., ZAMBORINI, F.P., TEMPLETON, A.C., WEN, X., YOON, H., MURRAY, R.W. Monolayer-protected clusters: molecular precursors to metal films, *Chem. Mater.* **2001**, *13*, 87–95.
- 71 SCHAAF, T.G., KNIGHT, G., SHAFIGULLIN, M.N., BORKMAN, R.F., WHETTEN, R.L. Isolation and selected properties of a 10.4 kDa gold:

- glutathione cluster compound, *J. Phys. Chem. B* **1998**, *102*, 10643–10646.
- 72 TEMPLETON, A.C., CHEN, S., GROSS, S.M., MURRAY, R.W. Water-soluble, isolable gold clusters protected by tiopronin and coenzyme A monolayers, *Langmuir* **1999**, *15*, 66–76.
- 73 ALVAREZ, M.M., KHOURY, J.T., SCHAAF, T.G., SHAFIGULLIN, M.N., VEZMAR, I., WHETTEN, R.L. Optical absorption spectra of nanocrystal gold molecules, *J. Phys. Chem. B* **1997**, *101*, 3706–3712.
- 74 LEE, D., DONKERS, R.L., WANG, G., HARPER, A.S., MURRAY, R.W. Electrochemistry and optical absorbance and luminescence of molecule-like Au<sub>38</sub> nanoparticles, *J. Am. Chem. Soc.* **2004**, *126*, 6193–6199.
- 75 HOSTETLER, M.J., TEMPLETON, A.C., MURRAY, R.W. Dynamics of place-exchange reactions on monolayer-protected gold cluster molecules, *Langmuir* **1999**, *15*, 3782–3789.
- 76 TEMPLETON, A.C., HOSTETLER, M.J., WARMOTH, E.K., CHEN, S., HARTSHORN, C.M., KRISHNAMURTHY, V.M., FORBES, M.D.E., MURRAY, R.W. Gateway reactions to diverse, polyfunctional monolayer-protected gold clusters, *J. Am. Chem. Soc.* **1998**, *120*, 4845–4849.
- 77 SLOCIK, J.M., KNECHT, M.R., WRIGHT, D.W., *Biogenic Nanoparticles*. Encyclopedia of Nanoscience and Nanotechnology, ed. NALWA, H.S. vol. 1. **2004**, Stevenson Ranch: American Scientific Publishers. pp. 293–308.
- 78 DANIEL, M.-C., ASTRUC, D. Gold nanoparticles: Assembly, supramolecular chemistry, quantum-size-related properties, and applications towards biology, catalysis, and nanotechnology, *Chem. Rev.* **2004**, *104*, 293–346.
- 79 BRUST, M., WALKER, M., BETHELL, D., SCHIFFRIN, D.J., WHYMAN, R. Synthesis of thiol-derivatized gold nanoparticles in a two-phase liquid-liquid system, *Chem. Commun.* **1994**, *7*, 801–802.
- 80 HOSTETLER, M.J., WINGATE, J.E., ZHONG, C.-J., HARRIS, J.E., VACHET, R.W., CLARK, M.R., LONDONO, J.D., GREEN, S.T., STOKES, J.J., WIGNALL, G.D., GLISH, G.L., PORTER, M.D., EVANS, N.D., MURRAY, R.W. Alkanethiolate gold cluster molecules with core diameters from 1.5 to 5.2 nm: core, monolayer properties as a function of core size, *Langmuir* **1998**, *14*, 17–30.
- 81 MONTALTI, M., PRODI, L., ZACHERONI, N., BAXTER, R., TEOBALDI, G., ZERBETTO, F. Kinetics of place-exchange reactions of thiols on gold nanoparticles, *Langmuir* **2003**, *19*, 5172–5174.
- 82 SONG, Y., MURRAY, R.W. Dynamics and extent of ligand exchange depend on electronic charge of metal nanoparticles, *J. Am. Chem. Soc.* **2002**, *124*, 7096–7102.
- 83 GERDON, A.E., WRIGHT, D.W., CLIFFEL, D.E. Epitope mapping of the protective antigen of *B. anthracis* using nanoclusters presenting conformational peptide epitopes, **2005**, *J. Am. Chem. Soc.*, submitted.
- 84 GU, H., HO, P.L., TONG, E., WANG, L., XU, B. Presenting vancomycin on nanoparticles to enhance antimicrobial activities, *Nano Lett.* **2003**, *3*, 1261–1263.
- 85 ZHENG, M., HUANG, X. Nanoparticles comprising a mixed monolayer for specific bindings with biomolecules, *J. Am. Chem. Soc.* **2004**, *126*, 12047–12054.
- 86 HAN, L., DANIEL, D.R., MAYE, M.M., ZHONG, C.-J. Core-shell nanostructured nanoparticle as chemically sensitive interfaces, *Anal. Chem.* **2001**, *73*, 4441–4449.
- 87 ZAMBORINI, F.P., LEOPOLD, M.C., HICKS, J.F., KULESZA, P.J., MALIK, M.A., MURRAY, R.W. Electron hopping conductivity and vapor sensing properties of flexible network polymer films of metal nanoparticles, *J. Am. Chem. Soc.* **2002**, *124*, 8958–8964.
- 88 GRATE, J.W., NELSON, D.A., SKAGGS, R. Sorptive behavior of monolayer-protected gold nanoparticle films: implications of chemical vapor sensing, *Anal. Chem.* **2003**, *75*, 1868–1879.
- 89 WILLNER, I., PATOLSKY, F., WEIZMANN, Y., WILLNER, B. Amplification

- detection of single-base mismatches in DNA using microgravimetric quartz-crystal-microbalance transduction, *Talanta* **2002**, *56*, 847–856.
- 90 WEIZMANN, Y., PATOLSKY, F., WILLNER, I. Amplified detection of DNA and analysis of single-base mismatches by the catalyzed deposition of gold on Au-nanoparticles, *Analyst* **2001**, *126*, 1502–1504.
- 91 PATOLSKY, F., LICHTENSTEIN, A., WILLNER, I. Amplified microgravimetric quartz-crystal-microbalance assay of DNA using oligonucleotide-functionalized liposomes or biotinylated-liposomes, *J. Am. Chem. Soc.* **2000**, *122*, 418–419.
- 92 PRICE, C.P., NEWMAN, D.J., *Principles and Practice of Immunoassay*, ed. PRICE, C.P., NEWMAN, D.J. **1991**, New York: Stockton Press. pp. 265–295.
- 93 QUINN, C.P., SEMENOVA, V.A., ELIE, C.M., ROMERO-STEINER, S., GREENE, C., LI, H., STAMEY, K., STEWARD-CLARK, E., SCHMIDT, D.S., MOTHERSHED, E., PRUCKLER, J. Specific, sensitive, and quantitative enzyme-linked immunosorbent assay for human immunoglobulin G antibodies to anthrax toxin protective antigen, *Emerging Infectious Dis.* **2002**, *8*, 1103–1110.
- 94 SALAMON, Z., MACLEOD, H.A., TOLLIN, G. Surface plasmon resonance spectroscopy as a tool for investigating the biochemical and biophysical properties of membrane protein systems. I: Theoretical principles, *Biochim. Biophys. Acta* **1997**, *1331*, 117–129.
- 95 LIAN, W., LITHERLAND, S.A., BADRANE, H., TAN, W., WU, D., BAKER, H.V., GULIG, P.A., LIM, D.V., JIN, S. Ultra-sensitive detection of biomolecules with fluorescent dye-doped nanoparticles, *Anal. Biochem.* **2000**, *334*, 135–144.
- 96 WU, X., LIU, H., LIU, J., HALEY, K.N., TREADWAY, J.N., LARSON, J.P., GE, N., PEALE, F., BRUCHEZ, M.P. Immuno-fluorescent labeling of cancer marker Her2 and other cellular targets with semiconductor quantum dots, *Nat. Biotechnol.* **2003**, *21*, 41–46.
- 97 LIU, X., SUN, Y., SONG, D., ZHANG, Q., TIAN, Y., BI, S., ZHANG, H. Sensitivity-enhancement of wavelength-modulation surface plasmon resonance biosensor for human complement factor 4, *Anal. Biochem.* **2004**, *222*, 99–104.
- 98 KOSSLINGER, C., UTTENTHALER, E., DROST, S., ABERL, F., WOLF, H., BRINK, G., STANGLMAIER, A., SACKMANN, E. Comparison of the QCM and the SPR method for surface studies and immunological applications, *Sens. Actuators B* **1995**, *24–25*, 107–112.
- 99 SPANGLER, B.D., WILKINSON, E.A., MURPHY, J.T., TYLER, B.J. Comparison of the Spreeta surface plasmon resonance sensor and a quartz crystal microbalance for detection of *Escherichia coli* heat-labile enterotoxin, *Anal. Chim. Acta* **2001**, *444*, 149–161.
- 100 MA, Z., WU, J., ZHOU, T., CHEN, Z., DONG, Y., TANG, J., SUI, S.-F. Detection of human lung carcinoma cell using quartz crystal microbalance amplified by enlarging Au nanoparticles, *New J. Chem.* **2002**, *26*, 1795–1798.
- 101 WANG, H., ZENG, H., LIU, Z., YANG, Y., DENG, T., SHEN, G., YU, R. Immunophenotyping of acute leukemia using an integrated piezoelectric immunosensor array, *Anal. Chem.* **2004**, *76*, 2203–2209.
- 102 HAINFELD, J.F., POWELL, R.D. New frontiers in gold labeling, *J. Histochem. Cytochem.* **2000**, *484*, 471–480.
- 103 VAN REGENMORTEL, M.H.V. The concept and operational definition of protein epitopes, *Phil. Trans. R. Soc. London B* **1989**, *323*, 451–466.
- 104 GERDON, A.E., WRIGHT, D.W., CLIFFEL, D.E. Epitope presentation on monolayer-protected clusters for multi-component functional nanostructures, *Biomacromolecules* **2005**, accepted.
- 105 MISUMI, S., ENDO, M., MUKAI, R., TACHIBANA, K., UMEDA, M., HONDA, T., TAKAMUNE, N., SHOJI, S. A novel cyclic peptide immunization strategy for preventing HIV-1/AIDS infection



- and progression, *J. Biol. Chem.* **2003**, *278*, 32335–32343.
- 106** MULLER, G.M., SHAPIRA, M., ARNON, R. Anti-influenza response achieved by immunization with a synthetic conjugate, *Proc. Natl. Acad. Sci. U.S.A.* **1982**, *79*, 569–573.
- 107** LU, Y., DING, J., LIU, W., CHEN, Y.-H. A candidate vaccine against influenza virus intensively improved the immunogenicity of a neutralizing epitope, *Int. Arch. Allergy Immunol.* **2002**, *127*, 245–250.
- 108** LEPPLA, S., ROBBINS, J., SCHNEERSON, R., SHILOACH, J. Development of an improved vaccine for anthrax, *J. Clin. Invest.* **2002**, *109*, 141–144.
- 109** PETOSA, C., COLLIER, R.J., KLIMPEL, K.R., LEPPLA, S.H., LIDDINGTON, R.C. Crystal structure of the anthrax toxin protective antigen, *Nature* **1997**, *385*, 833–838.
- 110** SANTELLI, E., BANKSTON, L.A., LEPPLA, S.H., LIDDINGTON, R.C. Crystal structure of a complex between anthrax toxin and its host cell receptor, *Nature* **2004**, *430*, 905–908.
- 111** WILD, M.A., XIN, H., MARUYAMA, T., NOLAN, M.J., CALVELEY, P.M., MALONE, J.D., WALLACE, M.R., BOWDISH, K.S. Human antibodies from immunized donors are protective against anthrax toxin in vivo, *Nat. Biotechnol.* **2003**, *21*, 1305–1306.
- 112** Biodesign International, <http://www.biodesign.com>, **2004**.

## 4 NMR Characterization Techniques – Application to Nanoscaled Pharmaceutical Carriers

*Christian Mayer*

### 4.1 Introduction

The use of nanoparticles for biomedical applications has been widely discussed in recent years. Among their wide variety, organic nanoparticles in stable aqueous dispersions are most promising candidates for pharmaceutical carrier systems. Controlled release and drug targeting are the main issues motivating their development [1–6]. In many cases, the preparation of these dispersions is quite straightforward, even on a technical scale. However, the analysis and detailed characterization of nanoparticle systems still represent a considerable challenge for common analytical methods. Most problems are connected to the fact that the particle structures are evidently nanoscopic, sensitive to many types of sample preparation techniques and often represent inhomogeneous and quite complex systems. Different approaches of transmission and electron microscopy can be applied successfully, but are often complicated by the necessity of tedious sample preparation. Atomic force microscopy is an important tool for studies on the particle assembly, but, as for electron microscopy, this method asks for isolated particles on a surface, a condition that may easily induce the formation of artifacts and destroy sensitive structures.

With the desire to analyze the particles in their “natural habitat”, the liquid dispersion, researchers are left to choose from a selection of spectroscopic methods. While most spectroscopic measurements do not differentiate between solid and liquid components, i.e., the particles and the surrounding or encapsulated liquid, nuclear magnetic resonance spectroscopy is a notable exception. Its unique ability to simultaneously detect chemical structure together with the lateral and rotational molecular mobility of every single system component makes it perfectly suitable for the study of particle dispersions [7–15]. This particular advantage of NMR spectroscopy is especially helpful in studying pharmaceutical carrier systems [16–22]. As most NMR methods are run under extremely mild physical conditions, measurements on nanoparticle dispersions may be extended over long periods under a wide variety of chemical and thermal influences. This allows for long-term time-resolved observations and opens up the possibility for continuous monitoring of

slow release and degradation processes. In most cases, the influence of the NMR measurement on the particle system can be completely neglected. The main disadvantage of NMR spectroscopy, its significant lack of sensitivity, is compensated by increasing the particle concentrations or sample volumes.

Clearly, NMR is not a routine technique for process or quality control and will always require special equipment and experimental skills. However, it may play a key role for the development and design of nanoscaled pharmaceutical carriers. Unlike any other single method, it yields comprehensive data on the structure and the function of these systems under a large variety of conditions. The combination between high resolution and solid-state NMR together with the application of pulsed field gradient (PFG) turns out to be especially promising. The experimental techniques are quite straightforward and can be performed on standard commercial NMR spectrometers. Analysis of the resulting data is often complicated by the fact that slow rearrangements on the nanometer scale, e.g. rotational diffusion of the particles, affect line shapes and require numerical simulation of the spectra. However, these phenomena offer the chance to study motions on the microsecond scale such as particle tumbling. Thus, NMR becomes a valuable tool for the time-dependent observation of processes like particle degradation or agglomeration.

In the following, examples are presented that demonstrate the power and versatility of NMR spectroscopy in its application to nanoparticle dispersions. They include studies on basic particle characteristics such as the nanoparticle structure, phase transitions of the particle matrix, exchange processes on the particle surface, permeability of nanocapsule walls, release and particle degradation. Analysis of the NMR data is performed using adapted simulation procedures based on rotational and lateral diffusion of nanoparticles and their individual system components.

## 4.2 Structural Analysis of Nanoparticles

The unique power of NMR spectroscopy lies in its ability to simultaneously detect the chemical nature and molecular mobility of individual chemical components in a complex system. Identification of the chemical composition of a substance in the liquid or solid phase is a well-known feature of NMR and is practiced on a routine basis. With solid components, it requires solid-state techniques, with magic-angle spinning (MAS) as the most prominent representative. In addition, broad line NMR techniques and relaxation measurements have been applied for the analysis of rotational molecular mobility. Recently, commercial NMR instruments have also acquired the capability of detecting lateral motion, a method that generally combines classical echo sequences with pulsed magnetic field gradients. All three approaches may be successfully combined for studies on dispersed nanoparticles.

In a spectrum of a static sample, all solid constituents (like the particle matrix and capsule walls) are easily identified by their wide spectral lines, whereas all liquid and dissolved components yield relatively narrow signals due to their

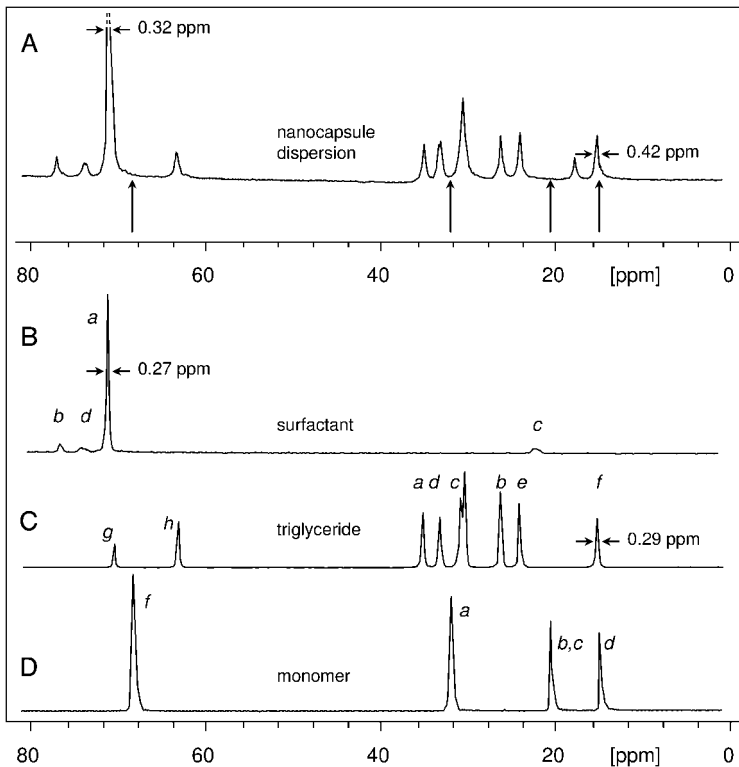


**Fig. 4.1.** Comparison of a directly excited  $^{13}\text{C}$  spectrum of dispersed poly-n-butylcyanoacrylate nanocapsules (A) with the corresponding spectra of dissolved surfactant (B), of liquid triglyceride (C) and of a solution of the monomer used for capsule formation (D) [8].

Capsule spectrum A shows no traces of the resonances of spectrum D (arrows), proving the absence of any residual monomer after capsule formation. For assignment of the signals see Fig. 4.2.

rapid isotropic rotational diffusion. Due to their spectral widths, the signals of the solid components usually appear at very small amplitude and often remain undetectable.

Figure 4.1(A) shows an example of a directly excited  $^{13}\text{C}$  spectrum of dispersed nanoparticles. It was obtained on an aqueous dispersion of poly-n-butylcyanoacrylate nanocapsules, a capsule system where the liquid core is formed by a commercial triglyceride (Miglyol®) and which is stabilized by a block-copolymer surfactant (Synperonic F68®) [9, 23–25]. The spectrum lacks all traces of the polymer forming the solid capsule walls, but clearly shows all liquid and dissolved components [8]. A comparison with reference spectra of the individual system components (Fig. 4.1B and C) allows for the identification of all capsule constituents in the liquid phase. The complete absence of the monomer signals (spectrum D in Fig. 4.1) proves the completion of the polymerization process dur-

ing capsule formation. The increased line widths in the presence of the capsules are assigned to partial immobilization of molecules on the capsule surface and the local inhomogeneity of the magnetic field.

To enhance the spectral contribution of the solid material, the  $(^1\text{H})$ - $^{13}\text{C}$  cross-polarization (cp) technique may be applied, which strongly amplifies signals from molecules with slow tumbling mobility [8, 17, 26] and therefore allows for the simultaneous observation of all constituents. The resulting  $(^1\text{H})$ - $^{13}\text{C}$  cp spectrum of the dispersion clearly shows relatively narrow signals superimposed on the characteristic wide line of the solid polymer (Fig. 4.2A). The broad contribution to the capsule spectrum is reproduced by a cp solid-state spectrum of a bulk sample of poly-n-butylcyanoacrylate (Fig. 4.2B). The positions of the narrow lines of the cap-

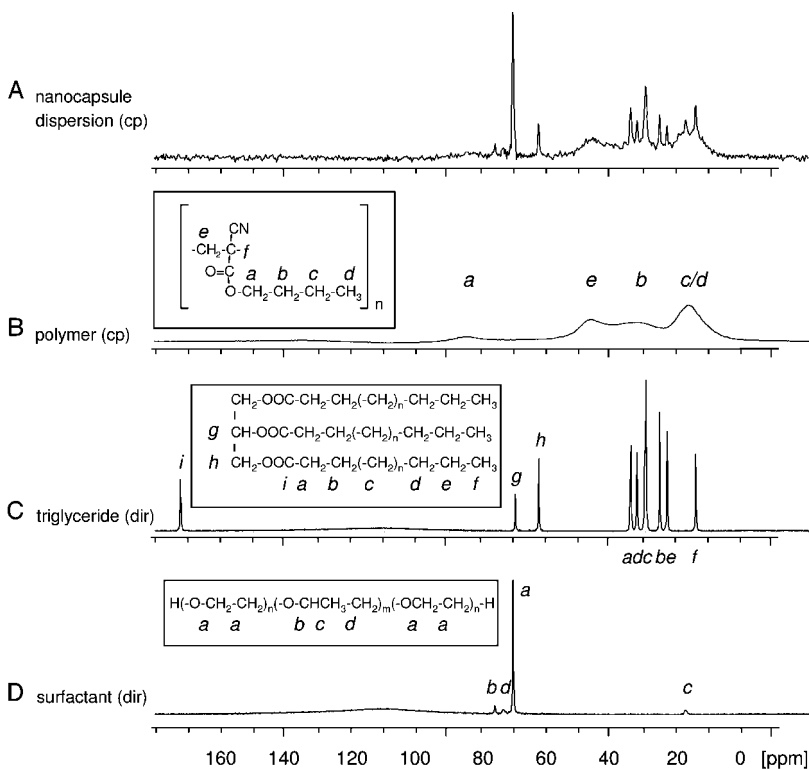


**Fig. 4.2.** Comparison of a  $(^1\text{H})$ - $^{13}\text{C}$  cross-polarization spectrum of dispersed poly-n-butylcyanoacrylate nanocapsules (A) with a corresponding spectrum of bulk solid poly-n-butylcyanoacrylate (B) and directly excited  $^{13}\text{C}$ -spectra of liquid triglyceride (C) and of an aqueous solution of the surfactant (D). All system components (B–D) are detectable in

the capsule spectrum A; their line widths depend strongly on their phase state (see text). The carbonyl signal of the triglyceride (signal *i* in spectrum C) and two carbon signals of the polymer remain invisible in cp spectra A and B due to lack of hydrogen at these positions. Signal assignments are given in the inserts.

sule spectrum are in good agreement with those of reference spectra of the liquid oil phase and the dissolved surfactant (Fig. 4.2C and D). Again, an increase in line width is detected in the presence of the capsules.

Clearly, identification of the solid components is difficult given the low resolution of the corresponding wide signals. Spectral amplitude and resolution can be improved significantly using sample spinning conditions such as magic-angle spinning (MAS), which has been widely used for bulk samples of solid polymers [27–29]. For particle dispersions, one generally faces the problem that a typical sample spinning process induces a gravitational field similar to the conditions of a centrifugation experiment [7]. However, if the dispersion is sufficiently stable, or the density of the particles is matched to the density of the liquid phase, the method can be applied to particle dispersions [7, 18].

Figure 4.3 shows an example for a sample-spinning experiment on a nanosized carrier system [18, 30]. The spectrum was obtained on an aqueous dispersion of

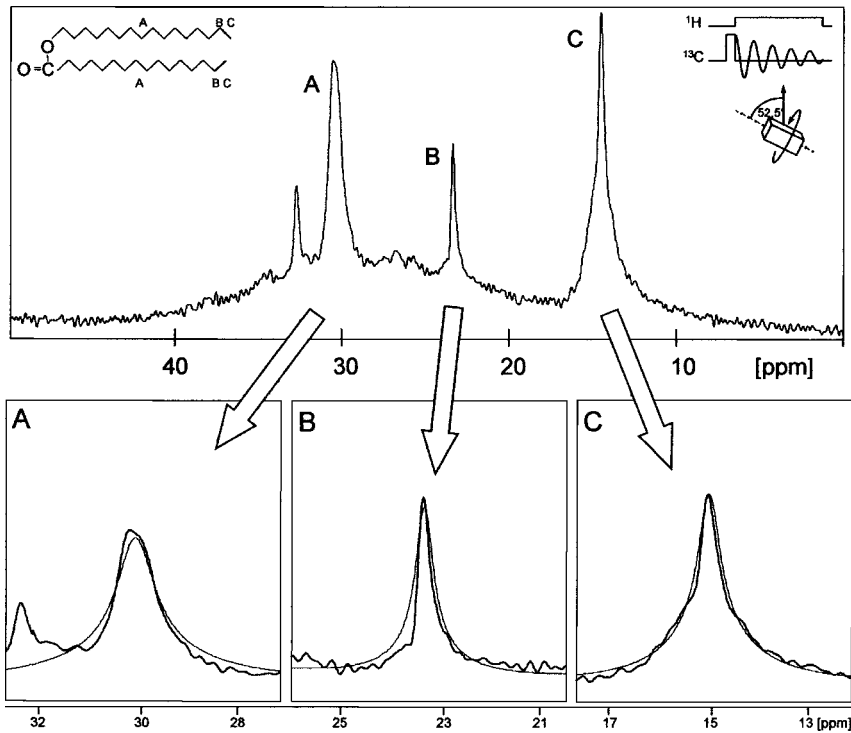


**Fig. 4.3.** Top: Result of a sample-spinning experiment of an aqueous dispersion of cetyl palmitate nanoparticles (SLN) obtained under direct excitation on  $^{13}\text{C}$  nuclei. The sample was spun at a rate of  $\omega_r/2\pi = 1660$  Hz and at an angle of  $52.5^\circ$ , which deviates from the magic angle. Signals A–C can be assigned to the central methylene, end methylene and end

methyl groups, respectively. Due to incomplete relaxation, the integrals of the signals do not reflect the corresponding number of nuclei. Bottom: comparison between signal line shapes A–C and their simulated fits based on the expected rotational diffusion of the particles.

solid lipid nanoparticles (SLNs) that consist of cetyl palmitate nanospheres with diameters between 100 and 200 nm [31]. Sample spinning was performed at a spinning rate of  $\omega_r/2\pi = 1660$  Hz and at an angle of  $52.5^\circ$ , which differs slightly from the magic angle ( $54.74^\circ$ ). Under these conditions, one obtains sufficient resolution for the assignment of the signals to the central methylene, end methylene and end methyl groups (signal A, B, and C, respectively, in Fig. 4.3). At the same time, the deviation from the magic angle leads to a characteristic variation of line shape that depends on the rate of rotational diffusion of the particles [18, 30]. Thus, the chemical composition of the particles can be studied together with their rotational diffusion. However, the influence of isotropic tumbling on signal line shapes is not at all straightforward. Analysis of the effect on the NMR spectrum requires a numeric simulation procedure that has been developed based on a finite element scheme: the time axis as well as the orientation in space is segmented into a set of discrete numbers and positions, such that the NMR time signal can be numerically calculated based on given sets of system parameters and experimental data [26, 32, 33]. The influence of rotational diffusion of the molecules is approximated by a corresponding spin exchange between adjacent “sites”, with rate constants depending on the equilibrium population, orientation and rotational diffusion constant. After Fourier transformation, the simulation procedure yields sets of NMR spectra that can be compared with experimental ones. A typical example for the end methyl group of cetyl palmitate under the experimental parameters given above is shown in Fig. 4.4. It refers to correlation times of isotropic rotational diffusion from 15 ms (front) to 15  $\mu$ s (back), showing the strong dependence of line shape on the rate of the motion [7, 18].

In some cases, the particle matrix undergoes local phase separations, leading to an inhomogeneous solid phase on the nanometer scale. On these occasions, analy-

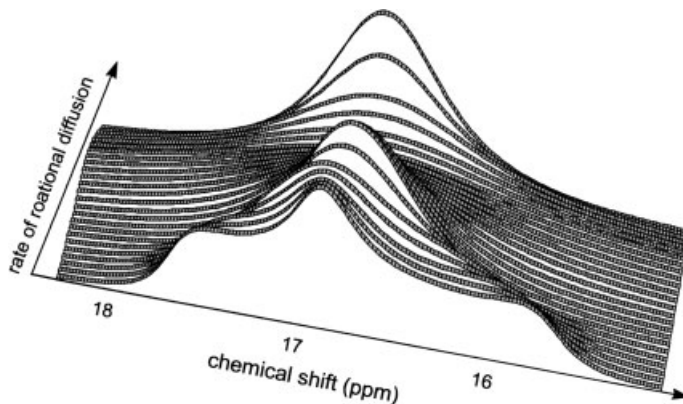


**Fig. 4.4.** Set of simulated  $^{13}\text{C}$  spectra for the end methyl group of cetyl palmitate (signal C in Fig. 4.3) for different rates of isotropic rotational diffusion. The correlation time varies from 15 ms (front) to 15  $\mu$ s (back). Rotational sidebands are weak and not included in the

given frequency window [7, 18]. For all spectra, the simulated sample spinning has been adjusted to a frequency of  $\omega_r/2\pi = 1660$  Hz. The spinning axis is tilted at  $52.5^\circ$  with respect to the direction of the external magnetic field.

sis of spin diffusion between different components of the matrix material allows for the detection of inhomogeneous distribution and the determination of domain sizes [21]. Due to spin diffusion between all protons in the solid phase, only a single common relaxation curve is observed for all proton signals of a homogeneous matrix domain. As soon as different domains with sizes exceeding approximately 5 nm are formed, it is possible to identify different decay curves for the proton spin–lattice relaxation ( $T_{1\rho}$ ) in the rotating frame. Hereby, phase separations between a solid matrix and a solid active ingredient may be detected and quantified [21].

The methods introduced so far allow for the identification of chemical components together with their assignment to the liquid and to the solid phase. However, with nanocapsules, we often deal with two separate liquid compartments: the continuous (solvent) phase and the encapsulated liquid domain. The widths of the spectral signals or their development in a cross polarization spectrum does not differentiate between the two, as their rotational diffusion is within the same order of magnitude. The only physical property that differs between the two liquid compartments is represented by the characteristics of lateral self-diffusion. While molecules of the continuous phase undergo almost free self-diffusion, lateral motion of the encapsulated counterparts is strongly hindered by the capsule walls. Let us assume that we can observe the average lateral dislocation of the molecules in the liquid phase. If the observation period is very short, the difference between free and encapsulated becomes almost negligible as the number of molecules that collide with the capsule boundaries is very small. On extending the observation period, the number of wall collisions increases and the difference between the inner and the outer phase becomes increasingly evident. Finally, the residual mobility of the molecules in the capsule content appears to be identical to the mobility of the capsules as a whole.

In NMR, this theoretical consideration is experimentally reproduced by application of the pulsed field gradient (PFG) technique. In combination with echo sequences, like the Hahn or the stimulated echo, it allows the determination of mean-square displacements over given time intervals  $\Delta$ , which can be varied over a wide range [34–37]. This method has served for the characterization of heterogeneous systems such as emulsions [36, 38, 39]. Figure 4.5 shows an example for the application to poly-n-butylcyanoacrylate nanocapsules [9]. The basic pulse sequence (insert in Fig. 4.5) consists of a so-called stimulated echo sequence that produces a proton echo signal after three pulses of equal duration. In combination with two gradient pulses (FG) of a given duration ( $\delta$ ), the amplitude of the signal (and of the corresponding line spectrum) depends on the gradient strength and on the average lateral dislocation during the gradient pulse spacing  $\Delta$ . While the dependence on the gradient strength  $G_{\max}$  allows one to determine the average dislocation pattern, the variable  $\Delta$  determines the time window for the observation. The resonance signals shown in Fig. 4.5 correspond to different liquid or dissolved components in the capsule system: water, ethanol, triglyceride and the block-copolymer surfactant. With increasing gradient strength  $G_{\max}$ , the signals of water and ethanol show rapid decay, indicating free, efficient lateral self-diffusion. The



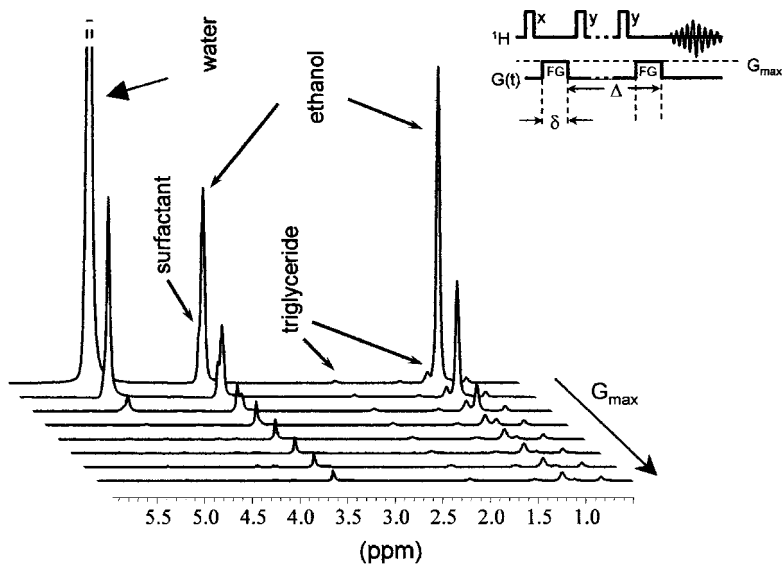


**Fig. 4.5.** Set of proton spectra obtained in a pulsed field gradient experiment on a dispersion of poly-n-butylcyanoacrylate nanocapsules. The pulse sequence (insert) consists of a stimulated echo sequence on protons combined with two gradient pulses FG. All signals in the displayed region can be assigned to liquid or dissolved system components: water, ethanol, triglyceride and

surfactant. The dependence of signal intensity on gradient strength ( $G_{\max}$ ) indicates lateral dislocation of the molecules within the given time window of  $\Delta = 30$  ms. Efficient self-diffusion leads to strong decays of the signals for water and ethanol, while those of the large surfactant molecules and the encapsulated oil show much smaller dependencies [9].

signal for the surfactant exhibits a much shallower decay, caused by slower self-diffusion connected to its much larger molecular mass. An even smaller dependence is observed for the triglyceride signal, which almost stays constant on the given scale. As the molecular mass of the triglyceride is much smaller than that of the surfactant, this observation strongly hints that the triglyceride oil is enclosed inside the capsule walls.

This becomes more evident if the echo decay of the triglyceride signal at 2.1 ppm is studied under variation of the diffusion time  $\Delta$ . Figure 4.6 shows a plot of the negative logarithmic echo intensity ( $-\ln I_{\text{rel}}$ ) vs. the parameter  $\gamma^2 G_{\max}^2 \delta^2 (\Delta - \delta/3)$ , with  $\gamma$  standing for the gyromagnetic ratio of the observed nucleus [9]. This type of plot yields linear dependencies with slopes identical to the apparent self-diffusion constant  $D_{\text{app}}$ . Evidently, the resulting apparent diffusion constant strongly depends on the diffusion time  $\Delta$  (Fig. 4.7). For very short observation periods ( $\Delta < 10$  ms), it comes close to the value of  $2.3 \times 10^{-11} \text{ m}^2 \text{ s}^{-1}$  found for a bulk triglyceride sample [9]. On this time scale, we observe local dislocations where the presence of the capsule walls affects only a small fraction of the oil molecules. Consequently, there is little difference between the behavior of free and encapsulated oil. On increasing

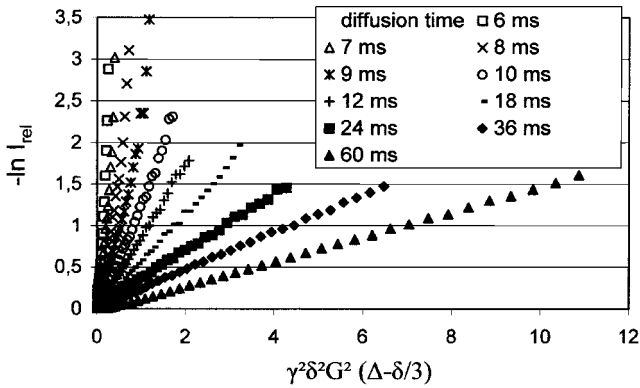


**Fig. 4.6.** Reciprocal echo decay plots for the triglyceride signal from an aqueous dispersion of poly-n-butyrylcyanoacrylate nanocapsules. Negative logarithmic echo intensities are plotted vs. the parameter  $\gamma^2 \delta^2 G^2 (\Delta - \delta/3)$  as derived from the triglyceride  $^1\text{H}$  signal at 2.1

ppm (Fig. 4.5). As typical for restricted diffusion, the observed slopes depend strongly on the diffusion time  $\Delta$ . Apparent diffusion constants  $D_{\text{app}}(\Delta)$  are determined from the slopes of the individual plots (Fig. 4.7).

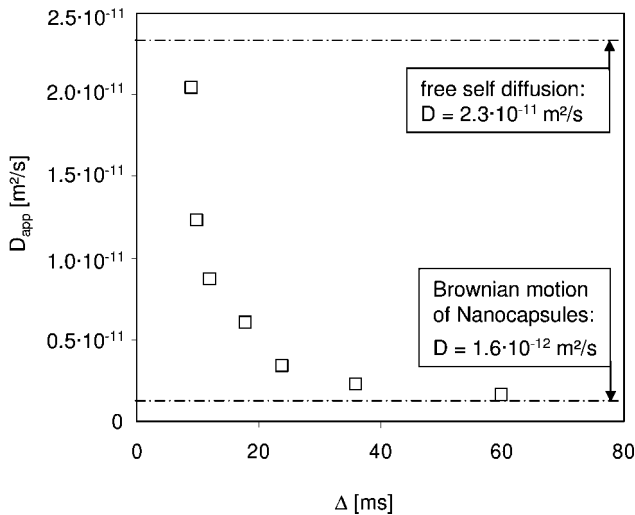


**Fig. 4.7.** Dependence of the apparent self-diffusion constant ( $D_{\text{app}}$ ) of the triglyceride oil component on the observation time interval  $\Delta$  (diffusion time). For short  $\Delta$ ,  $D_{\text{app}}$  comes close to the self-diffusion coefficient of the bulk oil

( $D = 2.3 \times 10^{-11} \text{ m}^2 \text{ s}^{-1}$ , top line). For long diffusion times,  $D_{\text{app}}$  approaches the diffusion constant that describes the Brownian motion of the capsules in aqueous medium ( $D = 1.6 \times 10^{-12} \text{ m}^2 \text{ s}^{-1}$ , bottom line).

diffusion time, the apparent diffusion constant decreases significantly and finally approaches the value for the Brownian motion of the capsules in the aqueous dispersion (Fig. 4.7) [9]. In this case, the lateral shift of the encapsulated molecules becomes seriously restricted by the capsule walls. Finally, for  $\Delta > 50$  ms, the position of all oil molecules average out in the capsule center and we observe the mobility of the complete capsules.

The similarity between the apparent oil diffusion constant for short time intervals with that observed for the bulk oil can serve as proof that we actually deal with “hollow” capsules with obviously no diffusion barriers in the internal volume. This important structural information could hardly have been obtained with other techniques. In summary, the NMR approach allows chemical identification of the solid matrix and the external liquid as well as the liquid-encapsulated components. In addition, it yields data about the molecular dynamics of the system, from which further conclusions on the particle structure can be derived.

### 4.3

#### Phase Transitions of the Particle Matrix

Even if we restrict ourselves to solid particle matrices, we still have to consider certain varieties of the solid phase. A prominent example is the gel phase formed by extensively swollen polymers, which is often encountered when particles are formed by polymer precipitation [40]. This gel phase may be reversibly or irreversibly transformed into a “real” solid state by removal of the solvent. An example of an irreversible phase transition is represented by poly- $\epsilon$ -caprolactone nanoparticles formed by the emulsion-diffusion process [20, 41] (Fig. 4.8). Preparation starts with the polymer being dissolved in the organic phase of an o/w emulsion, the continuous water phase being saturated with the organic solvent ethyl acetate. In the next step, the aqueous phase is diluted, causing the ethyl acetate to diffuse from the droplets into the surrounding water. Hereby, the polymer, which is dissolved in ethyl acetate at the maximum concentration, precipitates and forms nanospheres (Fig. 4.8, left-hand column). In the presence of a hydrophobic oil component, the process leads to nanocapsules with the oil forming the liquid core (Fig. 4.8, right-hand column). In both cases, the organic solvent is subsequently removed by evaporation.

Initially, the solid matrix of the particles consists of a physically crosslinked network that is swollen by water and some residual ethyl acetate. A solid-state  $^{13}\text{C}$  NMR spectrum of the freshly prepared nanospheres (Fig. 4.9, top) reveals a very high degree of local mobility for the polymer chains. Compared with a solid-state spectrum of the bulk polymer (Fig. 4.9, bottom), the spectrum of the particles exhibits relatively narrow lines that are consistent with rotational diffusion on the microsecond time scale [7]. This means that, on a local scale, most of the polymer behaves as though in a dissolved state while it still forms the framework of a solid particle on the sub-micrometer size range. This apparent contradiction is explained

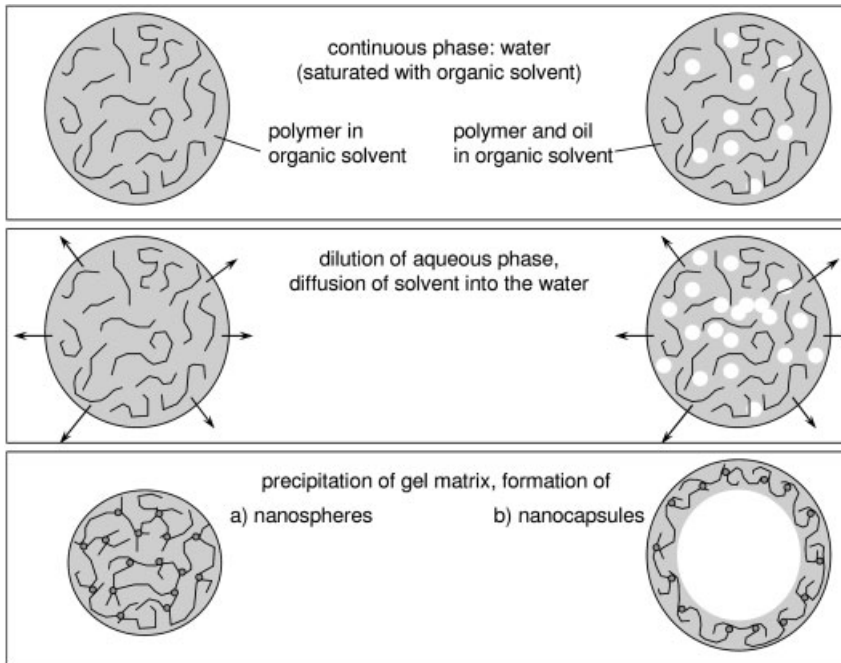


**Fig. 4.8.** Schematic representation of processes leading to the formation of gel phase nanospheres (left) and nanocapsules (right) by the emulsion-diffusion process. Top: a polymer dissolved in an organic solvent (optionally containing an oil component, right-hand column) is dispersed in an aqueous phase. Center: water is added to the dispersion, causing the organic solvent to

diffuse into the aqueous phase in connection with reestablishment of the distribution equilibrium. Bottom: polymer precipitation is induced by loss of solvent in the organic phase, forming gel nanospheres (a) or gel nanocapsules (b). In both cases, the polymer becomes physically crosslinked and is swollen beyond the point that accords with the thermodynamic swelling equilibrium [7, 20].

by assuming a gel state of the polymer induced by a high water content that is much beyond the value expected from the swelling equilibrium.

On removing the water, an irreversible phase transformation is observed (Fig. 4.10). Careful evaporation under lowered pressure induces the appearance of an increasing contribution of polymer in the classical solid state. At the same time, the process is accompanied by a slight decrease in particle diameter [20]. The transformation is irreversible, as addition of water does not lead back to the gel state. Alternatively, removal of water from the particle matrix can be induced by simple freezing of the sample [7, 20]. At all stages of water removal, the amount of polymer in both phase states can be quantitatively determined by solid-state NMR [7].

This phenomenon opens up the possibility for an interesting application of gel particles: the matrix of nanospheres or nanocapsules in the gel state may be re-

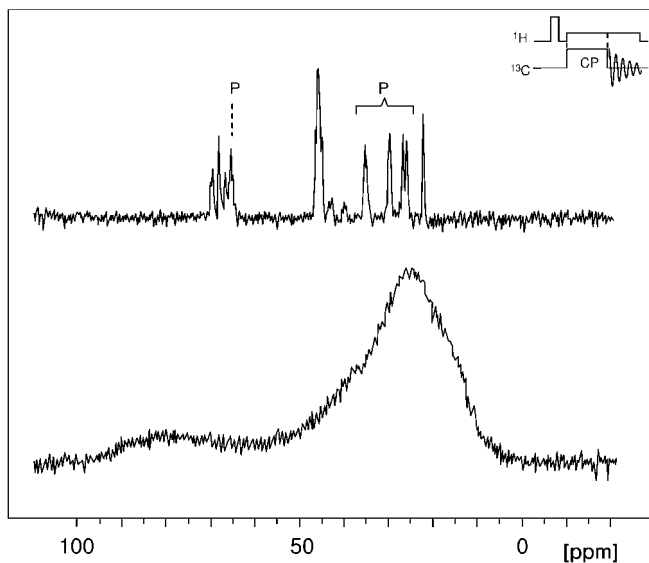


**Fig. 4.9.** Comparison of a  $(^1\text{H})\text{--}^{13}\text{C}$  cross-polarization spectrum of freshly prepared poly- $\epsilon$ -caprolactone nanospheres (top) with a corresponding spectrum of the bulk polymer (bottom). Obviously, the dispersed particles do not contain organic material in the classical solid state [7, 20]. A high degree of local chain mobility leads to narrow signals that can be assigned to the polymer (P). All other peaks derive from the surfactant [poly(vinyl alcohol)] and small amounts of poly(vinyl acetate). The insert indicates the pulse sequence used.

garded as an “open” carrier system, allowing ingredients to diffuse into or through the matrix. After the particles are loaded, they may be irreversibly “sealed” by a simple freezing step that turns the gel matrix into a relatively dense, impermeable solid polymer, a state that is preserved after melting the dispersion. The whole process of phase transition of the polymer and encapsulation of an active ingredient may be conveniently monitored by NMR spectroscopy.

#### 4.4

##### Adsorption to the Particle Surface

For medical applications of nanoparticles, it is of special interest to elucidate adsorption phenomena on the external particle surface. The most important adsorbent is the surfactant used to stabilize the particle dispersion. Additional components, such as encapsulated ingredients, may also adsorb to the particle surface. Surface adsorption usually means an equilibrium state, where adsorption and desorption processes take place simultaneously at equal rates. NMR offers an experimental approach for the study of adsorption phenomena and the molecular exchange connected to a continuous adsorption–desorption process [7, 17].

The use of cross-polarization in solid-state NMR generally favors the spectral

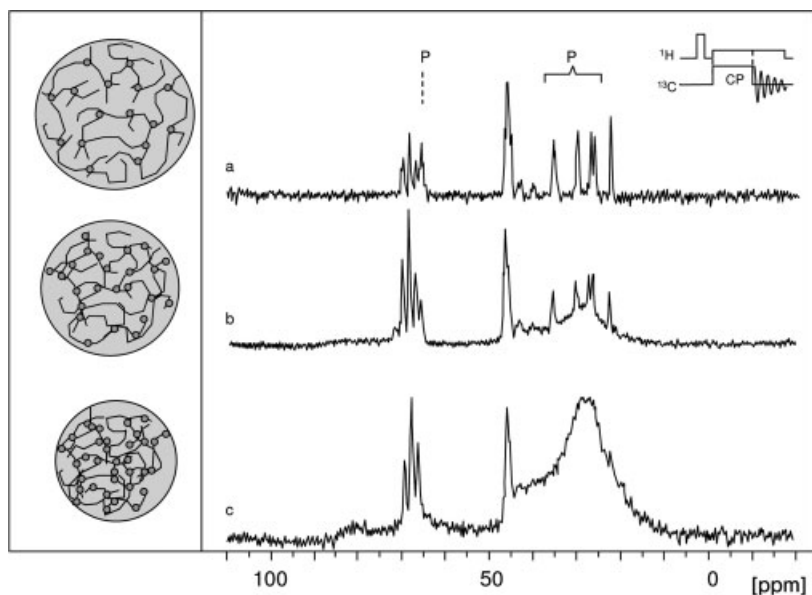


**Fig. 4.10.**  $(^1\text{H})\text{-}^{13}\text{C}$  cross-polarization spectra of dispersed poly- $\epsilon$ -caprolactone nanospheres in different stages of irreversible dehydration. With the original water content after the emulsion-diffusion process (a), all polymer signals (P) indicate a high degree of local mobility. After removal of ca. 50% of the swelling water (c), the complete polymer content has transformed into a rigid state. Spectrum (b) represents an intermediate situation [7, 20]. Pictograms on the left symbolize the corresponding stages of network formation.

contribution of solid constituents. It requires reduced mobility of the molecular environment and is therefore quite inefficient for dissolved molecules. However, there is a notable exception: if dissolved molecules become temporarily adsorbed to a solid surface, they remain relatively immobilized for a time interval in the millisecond range, which is sufficient to efficiently allow for the polarization transfer, e.g., between protons and carbon nuclei. The small adsorbed fraction is usually not directly detectable by NMR. However, after the molecules desorb, they again undergo rapid rotational diffusion and their cross-polarization induced carbon signal becomes a dominant contribution to the spectrum (Fig. 4.11).

In an aqueous dispersion of poly-*n*-butylcyanoacrylate nanocapsules, this phenomenon is observed for the block-copolymer surfactant as well as, to a somewhat smaller degree, for the encapsulated oil [7, 17]. Indications for an unusual mechanism of cross-polarization are obvious from the characteristics of cross-polarization development. While the solid-state signal of the nanocapsule wall material is already fully developed after a cross-polarization period of 0.1 ms, the narrow signals of the triglyceride and the surfactant still gain intensity after 1 ms and reach their maximum only after 5 ms [7]. After 10 ms of cross-polarization, the polymer signal is almost fully relaxed, while the signals for the triglyceride and the surfactant re-

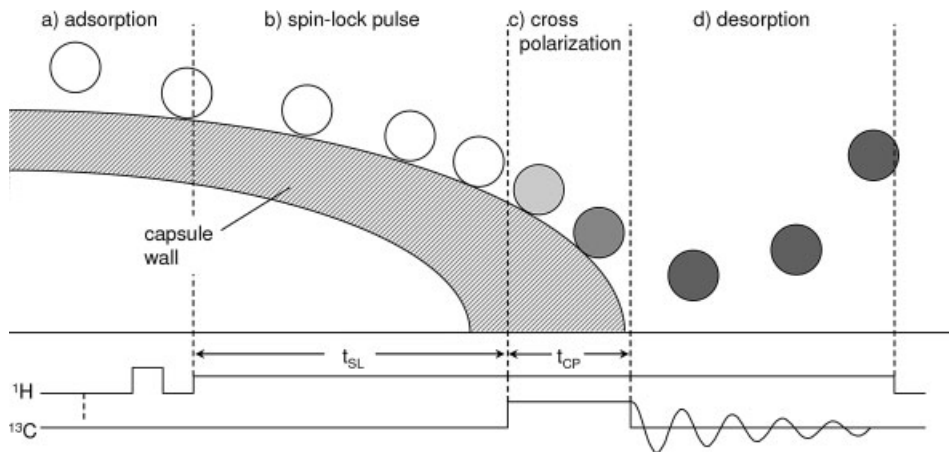


**Fig. 4.11.** Schematic representation of the process of  $(^1\text{H})$ - $^{13}\text{C}$  cross-polarization induced by temporary adsorption of dissolved molecules to a nanocapsule wall. The degree of polarization is indicated by the intensity of the grey shading of the symbol. First, we focus on a molecule adsorbed shortly after an initial pulse is set to the proton nuclei (a). A spin-lock pulse may be included at this time to study spin-lattice relaxation [7, 17] (b). Later,

during the period of adsorption, simultaneous pulses on  $^1\text{H}$  and  $^{13}\text{C}$  nuclei are adjusted to fulfill the Hartmann-Hahn condition, which allows for an efficient  $(^1\text{H})$ - $^{13}\text{C}$  polarization transfer within the immobilized molecules (c). Finally, the molecule is desorbed, taking the strong polarization of the  $^{13}\text{C}$  nuclei into the fluid state, where it can be easily detected [7, 17] (d).

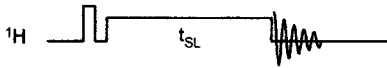
main constant for more than 30 ms. Such a cross-polarization and relaxation pattern is quite uncommon and indicates a special mechanism of polarization transfer.

Studies under variation of the spin-lock time have been performed to elucidate this polarization phenomenon, assuming an adsorption-desorption cycle on the capsule walls (Fig. 4.12). For comparison, corresponding relaxation curves obtained under direct excitation have been measured that focus on the triglyceride and surfactant molecules in the liquid phase. In this case, all data could be fitted assuming a mono-exponential decay and long relaxation times between 34 and 79 ms for the

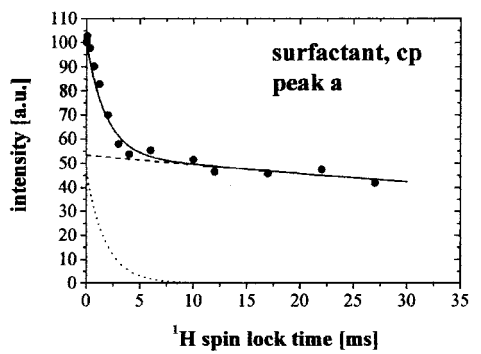
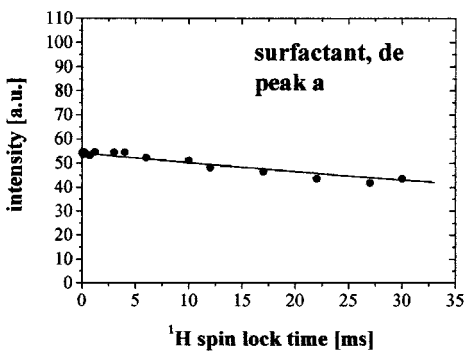
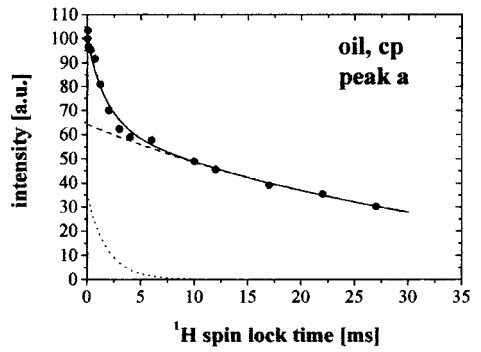
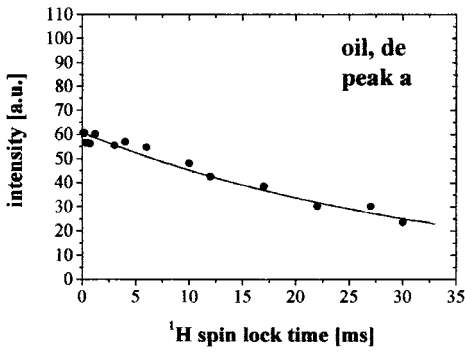
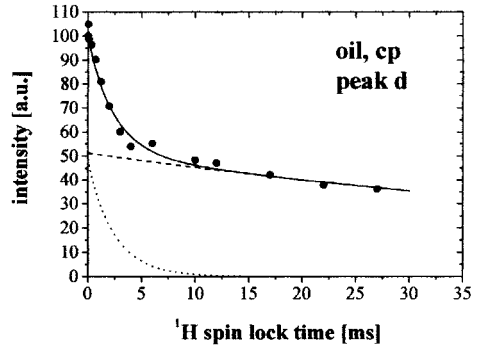
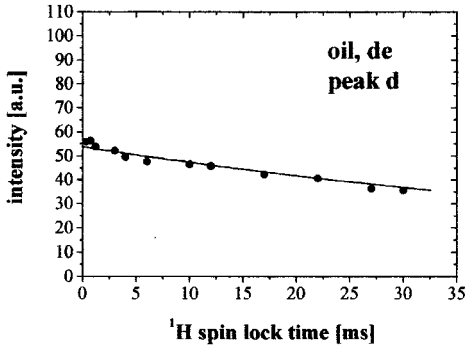
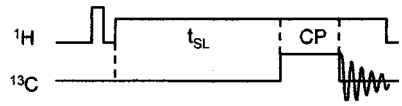
**Fig. 4.12.** Relaxation curves showing the dependence of two aliphatic signals of triglyceride oil (top and center) and a single aliphatic signal of the surfactant (bottom) on the duration of a spin-lock period. With direct excitation experiments (left-hand column), the spin-lock period follows the initial pulse on the protons. All resulting relaxation curves can be fitted mono-exponentially. For cross-polarization experiments (right-hand column)

the spin-lock pulse is set before the cp period (see phase b in Fig. 4.11) and the signal intensity is observed via the corresponding carbon signals. The resulting relaxation curves are bi-exponential and consist of an initial steep decay, which corresponds to immobilized molecules (dotted line), and a subsequent shallow decay that can be assigned to molecules in the liquid phase (dashed line). Pulse sequences are indicated schematically at the top of each column [17].

direct measurement of  $T_{1\rho}^H$ :



indirect measurement of  $T_{1\rho}^H$  via cp:





triglyceride oil and 131 ms for the strongest signal of the surfactant [17]. With cross-polarization experiments (right-hand column in Fig. 4.12), the spin-lock pulse is set prior to the cp period (see Fig. 4.11b) and the signal intensity is observed via the corresponding carbon signals. No significant change in the resonance line shapes is observed during the full course of the experiment [17]. However, all resulting relaxation curves are distinctly bi-exponential and consist of an initial steep decay and a following shallow section of the relaxation curve. The latter is very similar to the results obtained by direct excitation with relaxation times that differ only slightly from those mentioned above [17]. This part clearly corresponds to the fraction of molecules in the desorbed state. The initial steep decay is connected to relaxation times of 1–2 ms, which resemble those of the solid polymer. This contribution obviously reflects the fraction of molecules that are in the adsorbed state. The complete signal decay curves from the cp experiment can be analyzed for adsorption–desorption characteristics using a relatively simple expression for relaxation under molecular exchange [42].

Figure 4.13 summarizes the results of the best fit to the complete set of relaxation data. They reveal that the average duration ( $\tau_{\text{ads}}$ ) of the adsorption step of an individual molecule is around 1 ms for the surfactant and 3 ms for the oil component. The overall signal intensities for both components consist of the signal

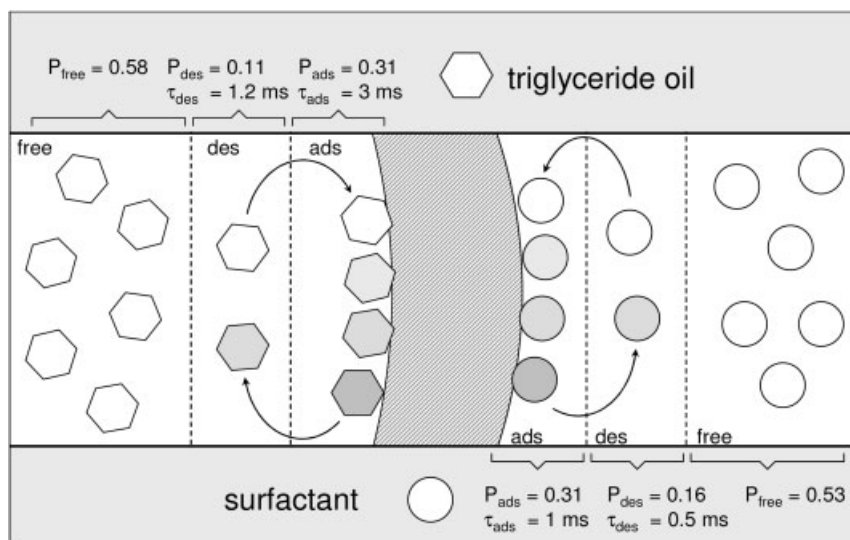


**Fig. 4.13.** System parameters obtained from a least-squares fit on the data shown in Fig. 4.12, based on an analytical expression for relaxation under molecular exchange [42].  $\tau_{\text{ads}}$  and  $\tau_{\text{des}}$  for the triglyceride oil and the surfactant refer to the average duration of adsorbed and desorbed states, respectively, of molecules taking part in the adsorption–desorption cycle.  $P_{\text{ads}}$ ,  $P_{\text{des}}$ , and  $P_{\text{free}}$  stand for signal contributions of the adsorbed, desorbed and “free” molecules, respectively. The latter fraction derives from those molecules in the liquid phase that do not take part in the adsorption–desorption cycle during the observation period.

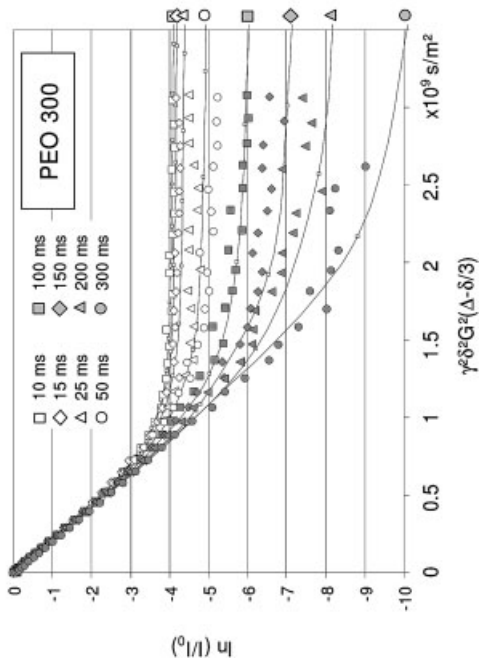
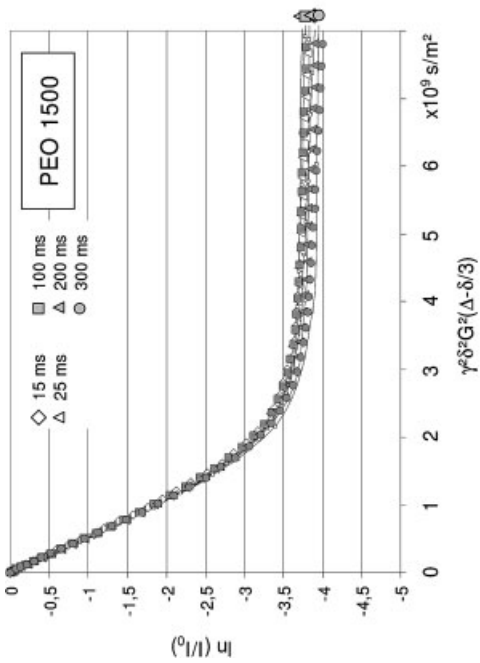
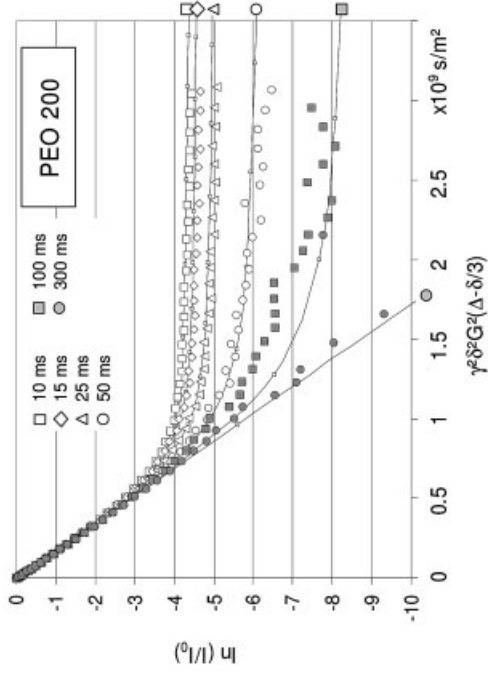
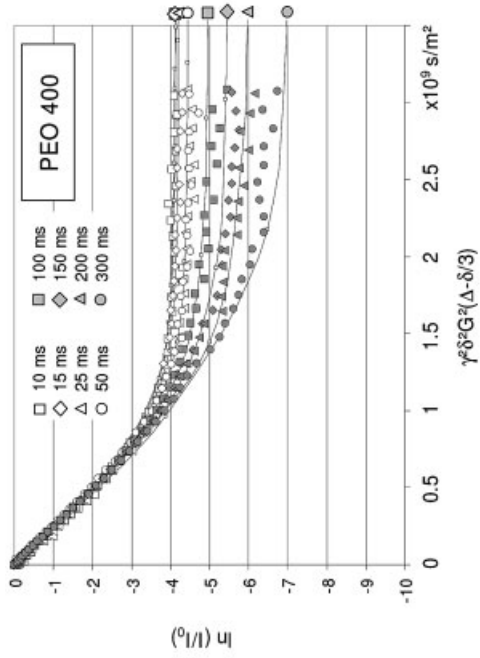
fraction  $P_{\text{ads}}$  of the adsorbed molecules, the signal fraction  $P_{\text{des}}$  of the desorbed molecules, and finally the fraction  $P_{\text{free}}$  of the molecules that take no part in the adsorption–desorption cycle during the observation period. Notably, these fractions are relative signal contributions and do not reflect the actual number of molecules involved in these processes. The resulting average residence times of molecules on the particle surface compare well with results on similar systems obtained with pulsed field gradient NMR [43, 44]. Using comparable non-ionic surfactants, residence times between 7.0 and 13.4 ms were detected. These values were obtained with much lower surfactant concentrations than for the results illustrated in Fig. 4.13; it was also shown that the residence time decreases with increasing surfactant concentration. Therefore, the value of 1 ms found for the highly concentrated block-copolymer on the poly-*n*-butylcyanoacrylate nanocapsules is within the expected range.

Principally, cross-polarization NMR (as well as pulsed field gradient experiments) offers another promising experimental approach for the study of adsorption phenomena on surfaces. In contrast to field gradient techniques where lateral diffusion is the key parameter, it distinguishes adsorbed molecules from molecules in the fluid phase by their degree of rotational diffusion. As the immobilized fraction is only observed indirectly after desorption into the fluid phase, it is generally more sensitive in its detection. However, there is also a significant disadvantage. As cross polarization is involved, there is no possibility of quantitative analysis of the adsorbed and desorbed molecules. Conversely, the cp experiment gives access to the time scale of the adsorption–desorption cycle of all system components. Such adsorption–desorption phenomena on the nanoparticle surface are of key importance for the primary physiological response to nanoparticles when applied to living organisms.

#### 4.5 Molecular Exchange through Nanocapsule Membranes

According to the nomenclature of Kreuter [40], nanocapsules are nanoparticles that form a shell-like wall, encapsulating a generally liquid content. Nanocapsule walls can be very thin, with thicknesses down to few nanometers. For polymer capsule walls, this corresponds to only a few molecular layers. Obviously, this can not be considered as an impermeable barrier for compounds of small molecular weight. At the same time, the main purpose of nanocapsules is based on their ability to separate two fluid domains and to block the diffusion of encapsulated components into the continuous phase. Therefore, the capsule wall permeability represents a key parameter for the characterization of the capsule system.

A very straightforward approach for a physico-chemical determination of the capsule wall permeability involves fluorescent labels and the use of a dialysis cell. In many cases, however, transfer through the capsule membranes is too rapid to be followed in this manner. On these occasions, NMR offers an extremely versatile and reliable technique for the study of trans-membrane exchange in capsule dis-



persions. It relies on the fact that free and encapsulated molecules can be separated by the characteristics of their lateral diffusion (Section 4.2). This criterion can be used to follow release processes in a time-resolved manner, similar to experiments using fluorescent labels. In addition, for rapid exchange through capsule membranes, this method offers an especially promising alternative. It allows for the observation of trans-membrane exchange of a tracer molecule in the equilibrium state, a method that has been successfully applied to nanocapsules [9], micellar carriers [45, 46] and vesicles [47].

The basic idea of this experimental approach may be shown by the example of block-copolymer vesicles [48, 49]. The result of a pulsed field gradient (PFG) measurement on vesicles from poly(2-vinylpyridine-*block*-ethylene oxide) [47] is represented in Fig. 4.14. The external as well as the internal domain are completely identical in their chemical composition and mainly made up from water. Polyethylene oxide (PEO) molecules of variable molecular mass are used as water-soluble tracers to sample the permeability of the vesicle membrane. Figure 4.14 displays four of the resulting echo decay curves (cf. Figs. 4.5 and 4.6), showing dramatic changes of the exchange pattern depending on molecular mass of the PEO tracer. All echo intensities were obtained from the proton signal at 3.2 ppm and are plotted logarithmically in relation to the original echo intensity  $I_0$ . In the absence of trans-membrane exchange, interpretation of the plots is quite straightforward. In general, the steep initial decay corresponds to the free molecules, while the encapsulated fraction of the tracer is represented by the subsequent plateau. The level of the plateau indicates the fraction of encapsulated molecules, e.g., a  $\ln(I/I_0)$  of  $-4$  corresponds to a relative fraction of  $\exp(-4) = 0.0183$ , which means that 1.83% of the tracer is in the encapsulated state. The slope of the initial decay is identical to the negative self-diffusion coefficient of the tracer in the continuous phase, while the slope of the final plateau is dominated by the (relatively slow) Brownian motion of the vesicles themselves.

For tracers with high molecular mass (e.g., PEO-1500 with  $M_w = 1500 \text{ g mol}^{-1}$ ), the result of the PFG measurement basically follows this simple interpretation. As expected from impermeable vesicle membranes, the decay curves show no significant dependence on the diffusion time: for  $\Delta = 15$  to 300 ms, the plots are more or less identical. With both fluid domains strictly separated, the experimental result is not affected by a change in observation period. This result changes dramatically for a PEO tracer with  $M_w = 400 \text{ g mol}^{-1}$ . Here, the plateau value decreases with  $\Delta$ . This is due to the relatively high permeability of the vesicle membrane for PEO-400. With increasing time period ( $\Delta$ ), more and more of the initially encapsulated

**Fig. 4.14.** Experimental and simulated echo decay curves for a block-copolymer vesicle dispersion containing poly(ethylene oxide) tracer molecules of different molecular mass: PEO-1500 ( $M_w = 1500 \text{ g mol}^{-1}$ ), PEO-400 ( $M_w = 400 \text{ g mol}^{-1}$ ), PEO-300 ( $M_w = 300 \text{ g mol}^{-1}$ ), and PEO-200 ( $M_w = 200 \text{ g mol}^{-1}$ ). Echo intensities are plotted as  $\ln(I/I_0)$  vs.  $\gamma^2 \delta^2 C^2 (\Delta - \delta/3)$  such that the resulting slope is equivalent to the negative self-diffusion coefficient for free diffusion. Calculated curves (solid lines) are assigned by the symbols on the right-hand axis. Table 4.1 lists the parameters for the simulated curves [47].

PEO molecules will be exchanged with those from the external domain, which already have suffered a large lateral dislocation. Therefore, the resulting slope is determined by a certain mix of the external self-diffusion constant, the apparent constant for the restricted diffusion in the confined space and the Brownian motion of the vesicles. The influence of the exchange is increasingly relevant with increasing observation period  $\Delta$ . As expected, this dependence is even more dominant for PEO-300 and PEO-200, with  $M_w = 300$  and  $200 \text{ g mol}^{-1}$ , respectively. Finally, with PEO-200 and  $\Delta = 300 \text{ ms}$ , the rapid exchange does not allow for an experimental distinction between external and encapsulated tracer molecules and the encapsulated fraction is not detectable.

All in all, detailed analysis of the PFG data yields extensive information on the exchange characteristics of the different tracer molecules. However, such an analysis is not always straightforward. For very small nanocapsules where, to a first approximation, the internal diffusion may be neglected it is possible to use an analytical approach for molecular exchange between two domains with different signal decay properties [9, 45, 46], similar to that developed for magnetic relaxation [42]. If internal self-diffusion of the encapsulated tracer is significant, restricted diffusion within the nanocapsules has to be accounted for. Analysis of PFG NMR measurements for restricted diffusion in a spherical confinement has been treated analytically [50–52]. However, in combination with molecular exchange through the capsule walls, there is no simple solution to this problem [53]. This again asks for a numerical analysis approach that is once more based on a finite element approximation [7, 47]. In this case, the external as well as the internal volume is segmented into small finite elements in space along the axis of the field gradient. Lateral diffusion is then approximated by an exchange of spins between adjacent space elements with rates defined by the diffusion constant. An additional spin exchange between space elements for the internal and those for the external domain accounts for the simultaneous transfer of molecules through the capsule walls [47]. Except for the exchange of spin contributions, all processes are assumed to be in steady state equilibrium, therefore the net flow during the simulated tracer diffusion is zero.

The result of a simulated best fit to the experimental data is shown by solid lines in Fig. 4.14 [47]. Basically, all plots for a given PEO tracer are fitted by a single parameter that is the average exchange rate constant  $\bar{k}_{\text{ex}}$ . The encapsulated fraction  $x_{\text{in}}$  of the tracer, which is identical to the partial volume of the vesicles, can be determined from the echo decay plots as well as by independent measurements. The complete set of simulation data (including one for PEO-600, which is not shown in Fig. 4.14) is listed in Table 4.1. As expected, the trans-membrane exchange rate decreases with increasing molecular mass of the tracer. For the given mass range, the rates vary between  $0.05$  and  $1.6 \text{ s}^{-1}$ , which is equivalent to half-life times of the encapsulated state between  $13.8 \text{ s}$  and  $430 \text{ ms}$ . Of course, all molecules that leave the encapsulated domain are simultaneously replaced by molecules from the external domain in an equilibrium exchange. With exchange rates in the given range, the equilibrium state between the internal and the external domain is sufficiently established within minutes after addition of the tracer. So the actual experiment is

**Tab. 4.1.** Simulation parameters used for the numerical reproduction of the echo decay curves shown in Fig. 4.14 (including data for PEO-600) [47].

Tracer molecule	Approx. molar mass ( $\text{g mol}^{-1}$ )	Encapsulated fraction ( $x_{in}$ )	Exchange rate ( $\bar{k}_{ex}$ ) ( $\text{s}^{-1}$ )
PEO-200	200	$0.022 \pm 0.001$	$1.6 \pm 0.2$
PEO-300	300	$0.023 \pm 0.001$	$0.85 \pm 0.05$
PEO-400	400	$0.0205 \pm 0.001$	$0.38 \pm 0.02$
PEO-600	600	$0.015 \pm 0.001$	$0.075 \pm 0.01$
PEO-1500	1500	$0.028 \pm 0.001$	$0.05 \pm 0.01$

kept quite simple: the tracer is added to a given vesicle dispersion, the PFG-NMR experiment is started after a waiting period of approximately one hour. After completion of the measurement, the tracer A can be removed by successive washing/dialysis cycles and be replaced by a tracer B.

A systematic study of wall permeability using a series of tracers plays a significant role in a general characterization of capsule membranes. For block-copolymer vesicles, it is used to understand the mechanism of the molecular transfer through the vesicle walls. Figure 4.15 shows a logarithmic plot of the average exchange constant  $\bar{k}_{ex}$  vs. hydrodynamic radius of the PEO molecules in aqueous solution [47]. For molecular masses between 200 and 600  $\text{g mol}^{-1}$ , the plot shows a roughly linear dependence between  $\log \bar{k}_{ex}$  and the hydrodynamic radius. Based on the Arrhenius law, this indicates that the activation energy of the molecular transfer through the vesicle membrane is proportional to the radius of the molecule. Possibly, the energy barrier for the transfer is connected to a local disruption of the membrane

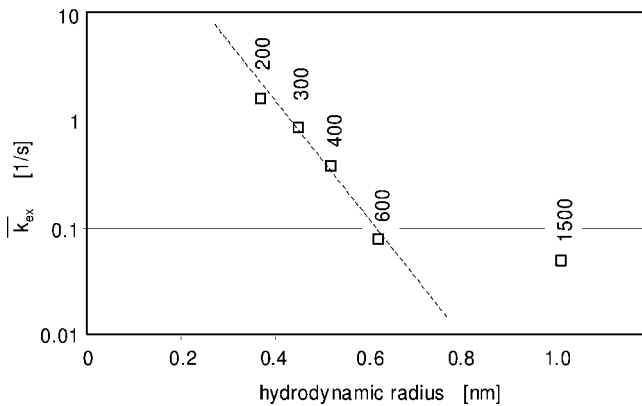


**Fig. 4.15.** Logarithmic plot of rate constants ( $\bar{k}_{ex}$ ) for the trans-membrane exchange (Table 4.1) vs. hydrodynamic radii of PEO tracers in aqueous solution. For molecular masses between 200 and 600  $\text{g mol}^{-1}$ , the dependence

of  $\log \bar{k}_{ex}$  on hydrodynamic radius is nearly linear, indicating that the activation energy for the membrane transfer is proportional to the size of the molecule [47].

– one that grows linearly with increasing size of the tracer molecule. Obviously, the tracer PEO-1500 does not obey this rule. This could be linked to a specific unfolding mechanism necessary for the transfer of larger molecules. In general, the use of tracers under systematic variation of size, polarity, conformational flexibility etc. leads to specific information on the membrane characteristics. Such information is crucial for the capsule design in order to optimize the stability, permeability and release properties.

## 4.6

### Particle Degradation and Release

The final steps during the life cycle of a particulate carrier system usually consist in the release of the active ingredients and, more or less simultaneously, degradation of the particles. Given the ability of NMR to distinguish between chemical components that are embedded in nanospheres, confined in nanocapsules or part of the continuous phase, it is not surprising that it gives easy access to release profiles. In general, all techniques described in Section 4.2 can be applied in a time-resolved manner; therefore, NMR represents an efficient method to follow structural changes such as the release of an active ingredient over time.

Figure 4.16 shows an example of a simple time-resolved measurement on polyelectrolyte nanospheres containing poly(ethylene oxide) as a model ingredient [54]. After dispersion in an aqueous environment, the directly-excited  $^1\text{H}$  signal of the PEO is followed over time in occasional measurements. While the solid PEO inside the nanospheres is practically invisible under these conditions, it is possible to determine the amount of dissolved PEO by detecting the integral of the single

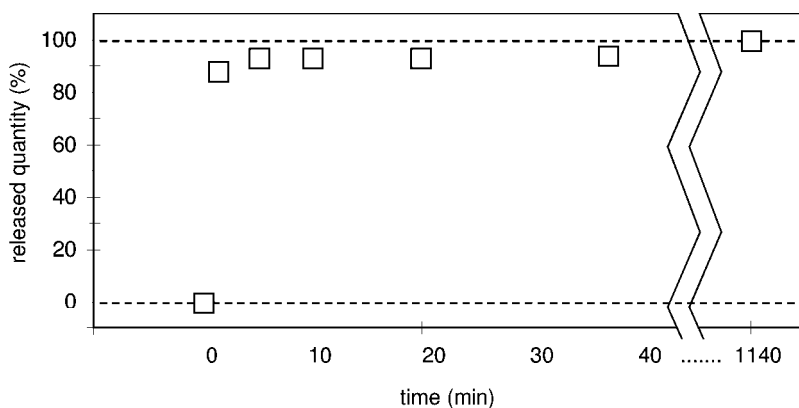


**Fig. 4.16.** Time-resolved observation of the  $^1\text{H}$  signal of the model compound PEO incorporated in polyelectrolyte nanospheres. The signal is obtained under direct excitation, therefore only the released fraction of PEO is detected as a function of time after the addition of water at  $t = 0$ .

$^1\text{H}$  peak at 3.2 ppm. In direct excitation, the signal integral is strictly proportional to the quantity of the observed component. In the given case, the variation in peak intensity over time clearly shows a phenomenon that was quite undesired: on addition of water, the system undergoes a burst release of  $\sim 90\%$  of the model active ingredient within the first 3 min. The residual 10% of the PEO then slowly escapes into the fluid phase within the following 20 h. This observation yields the release profile, but also gives a certain clue about the particle structure. Most probably, the largest part (90%) of the PEO is loosely adsorbed onto the particle surface; only about 10% seems to be integrated into the particle matrix.

The solid matrix of nanospheres and nanocapsules is subject to various degradation processes. They take place during storage as well as during their *in vivo* application and may be connected to chemical as well as physical phenomena. They all affect the solid contribution to the magnetic resonance spectrum, so cross polarization is a promising technique to study particle degradation. However, some mechanisms of matrix decay also lead to the formation of low molecular weight components in the liquid phase. In this case, the direct excitation approach is especially suitable. Of course, both experimental methods can be combined to yield a complete analysis of the degradation process.

Figure 4.17 shows an example for such an analysis on an aqueous dispersion of poly-*n*-butylcyanoacrylate nanocapsules. It refers to thermal decomposition of the dispersion induced by storage for 3 h at different temperatures (50, 100, 130 °C) [55]. As mentioned before, the cp spectra (left-hand column of Fig. 4.17) focus on the solid matrix of the capsules. While the broad solid-state spectrum is virtually unchanged after treatment at 50 °C (a), it shows increasing loss in intensity after storage at 100 °C (b) and completely disappears after 3 h storage at 130 °C (c). The narrow peaks assigned to the triglyceride and the surfactant remain visible but suffer significant losses at higher temperatures. Their residual cp signal intensity corresponds to the fraction  $P_{\text{free}}$  (Fig. 4.13), which is independent of polarization transfer on the particle surface. Clearly, the solid-state components have vanished after 3 h treatment at 130 °C. Since obviously no new solid phase has been generated, the material that originally formed the solid matrix has to show up in the liquid phase. Traces of it can be seen in the directly excited spectrum (right-hand column in Fig. 4.17) after heat treatment at 130 °C (c, arrows). Figure 4.18 shows a scaled-up comparison between the “new” signals (top) and the counterparts from a spectrum of the monomer *n*-butylcyanoacrylate (bottom). Obviously, these “new” signals show up near corresponding peaks expected for the product of depolymerization. The slight deviations for the chemical shifts of 1 to 3 ppm may derive from differences in the chemical environment: the reference spectrum was taken in  $\text{CDCl}_3$  as a solvent, while the depolymerization product was dissolved in an aqueous environment containing some residual ethanol. Hence, the loss in solid polymer seems to be accompanied by the appearance of monomer in the fluid phase. This indicates that the matrix has been subject to a thermally induced depolymerization that finally leads to complete disintegration of the particles.

At this point, two varieties of particle defragmentation are possible: (a) depolymerization of the matrix could cause the capsule to separate into smaller solid



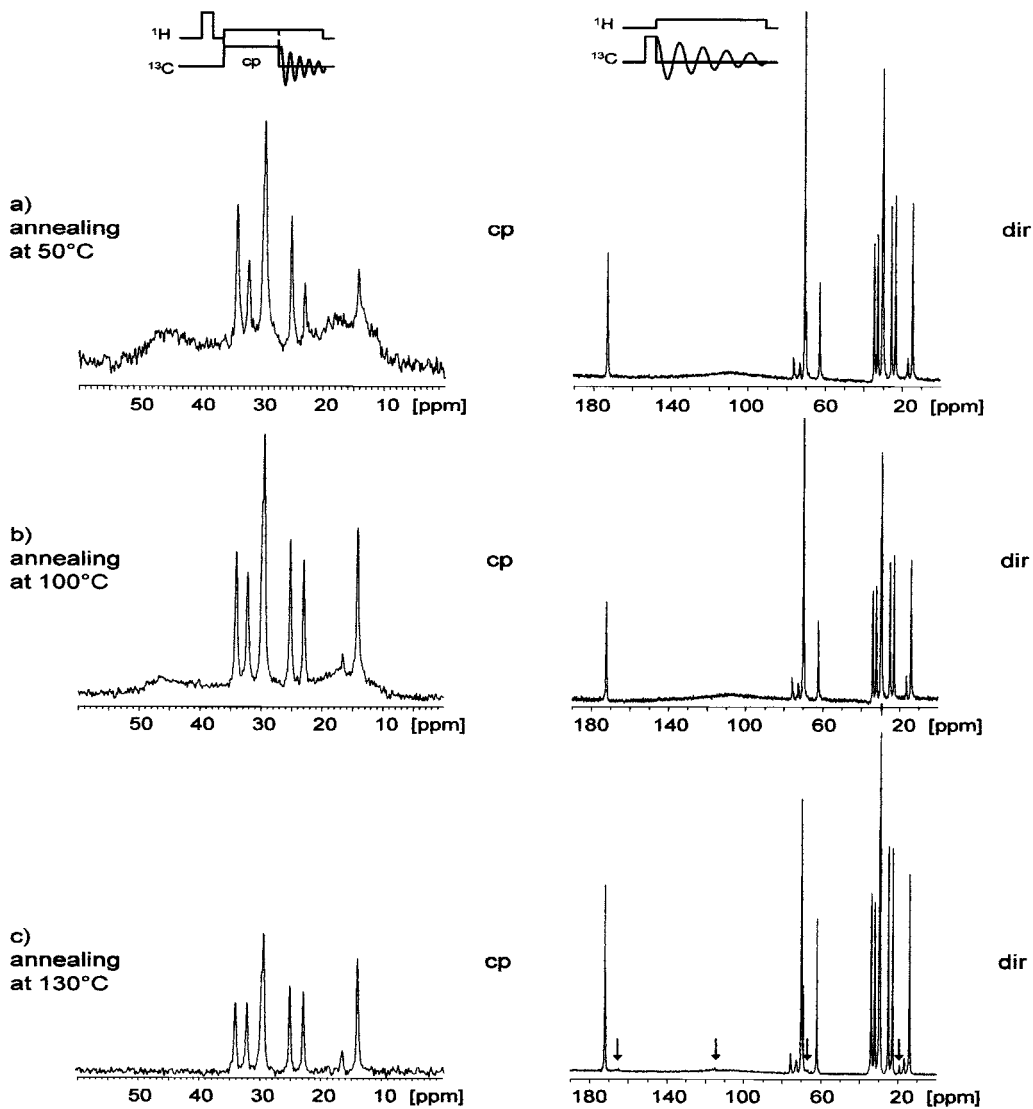


**Fig. 4.17.** Proton-decoupled  $^{13}\text{C}$  spectra of aqueous dispersions of poly-n-butylcyanoacrylate nanocapsules after heat treatment for 3 h at (a) 50 (b) 100 and (c) 130 °C. Wide lines in the ( $^1\text{H}$ )– $^{13}\text{C}$  cross-polarization spectra (left-hand column) indicate the loss of solid matrix material at higher temperatures. The superimposed narrow signals derive partially from adsorption

of liquid components to the capsule walls, and partially from the residual cp in the liquid phase. Direct excitation spectra (right-hand column) show the liquid and dissolved components and, for  $T = 130$  °C (c, arrows), indicate the formation of a depolymerization product (Fig. 4.18). Insets: pulse sequences used for cross-polarization and direct excitation experiments.

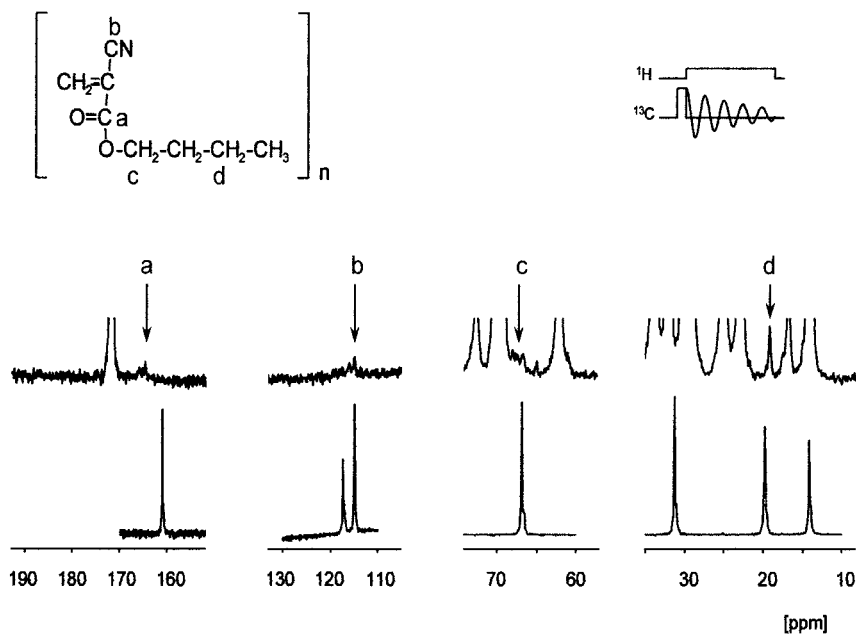


**Fig. 4.18.** Comparison between enlarged sections of direct excitation <sup>13</sup>C spectra obtained on poly-n-butylcyanoacrylate nanocapsules after heat treatment for 3 h at 130 °C (top line) and on a solution of n-butylcyanoacrylate in CHCl<sub>3</sub> (bottom line). The “new” signals a–d can be assigned to traces of

monomer resulting from depolarization of the capsule matrix. The obvious variation of the chemical shifts could result from the different solvent environments. Inserts: signal assignments and pulse sequence used for direct excitation.

fragments or (b) the capsule could essentially preserve its spherical geometry while the capsule wall corrodes and finally disappears. In the first case, the smaller solid fragments should lead to an increase in the tumbling rate, leading to a corresponding narrowing of the cp resonance lines of the solid-state spectrum. Figure 4.19 shows that this is clearly not the case: direct comparison of the spectra after annealing at 100 and 130 °C shows that the solid line shapes are virtually identical – no indications for a motional narrowing of the cp signal are found. This leaves the second alternative: while suffering increasing material loss, the capsule sphere preserves its overall geometrical shape and therefore keeps its original low tumbling rate.

One of the principal advantages of decomposition studies based on NMR detection is its variability for chemical and physical conditions. The NMR experiment can be performed under a wide variety of thermal, chemical or other influences on the sample during the time-resolved observation. At the same time, the impact caused by the static NMR measurement itself is insignificant, which allows for undisturbed and extended measurements over long periods.

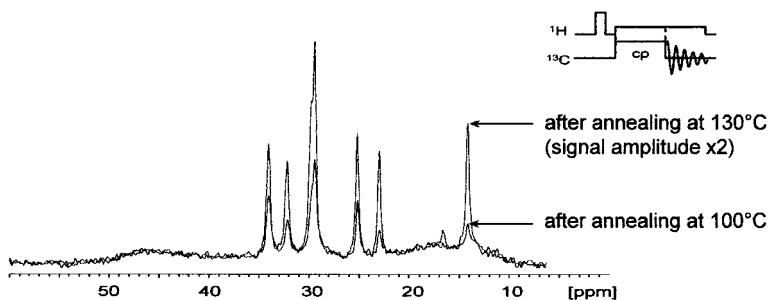


**Fig. 4.19.** Comparison between enlarged sections of cross-polarization spectra of dispersed poly-n-butylcyanoacrylate nanocapsules after heat treatment for 3 h at 100 and 130 °C. The spectrum for 130 °C has been vertically expanded to match that for 100 °C in its solid-state contribution. Both solid-state line shapes (superimposed by narrow signals for the triglyceride and surfactant) are virtually identical. For the solid matrix, no motional narrowing is detected that would indicate the formation of smaller fragments with increased tumbling rate. Insert: pulse sequence used for the cp measurement.

#### 4.7

#### Summary and Outlook

This selection of NMR experiments on nanoparticles is meant to show the power of NMR in this field. Unlike any other analytical technique, it combines a distinctly non-invasive character with the ability to analyze for a chemical composition as well as for local mobility of individual system components. Its main disadvantages, most prominently represented by its relatively low sensitivity and the time consuming acquisition of experimental data, can be overcome by a suitable choice of pulse sequences and experimental conditions. Applied to nanoscaled pharmaceutical carrier systems, it gives access to several important structural details and system parameters. Table 4.2 gives an overview of various experimental NMR techniques that are suitable for studies focusing on different particle characteristics. Evidently, this scheme is by no means complete, but it may serve as a starting point to elucidate further approaches in NMR in this field.

One new technique that is presently under development may serve as an example: Studies are in progress that focus on the characterization of magnetic nanoparticles in liquid dispersion (magnetofluids) [56–61] used for medical applications, e.g., for the magnetically controlled local application of drug-loaded organic carriers. Here, the local perturbation of the magnetic field caused by the nano-sized magnets is detected by the observation of spins in the solid or fluid environment of the particles. It is used to characterize system parameters such as the magnetism of the particles and their distribution in space. The particle-induced magnetic perturbation may also be used in the opposite sense: by creating a very strong local field gradient it could allow for the observation of lateral molecular mobility on a very small scale. As for many other approaches of this kind, analysis of such experimental data requires a numerical simulation procedure that accounts for the local structures on the nanometer scale. Such algorithms are being developed based on the idea of small-scale susceptibility effects [61].

Tab. 4.2. Overview of the application of different NMR techniques for the analysis of different particle system characteristics.

	Direct excitation (incl. multi-dimensional NMR)	Cross polarization	Magic-angle spinning	Pulsed field gradient NMR	Relaxation curves ( $T_1, T_{1\rho}, T_2, \dots$ )
Identification of structural elements	Identification of fluid components	Observation of solid matrix	Identification of solid matrix	Identification of capsule contents	
Heterogeneity of the solid matrix					Detection of solid domain sizes
Phase transitions	Detection of new fluid components	Detection of new solid components	Identification of new solid matrix		
Adsorption to particle surface		Identification of adsorbed components		Time scale of adsorption–desorption cycle	Time scale of adsorption–desorption cycle
Permeability of capsule membranes				Detection of exchange rates	
Release	Release from nanospheres			Release from nano-capsules	
Degradation	Detection of fluid degradation products	Observation of disappearing solid components			

## References

- 1 W. MEHNERT, K. MÄDER, Solid lipid nanoparticles – production, characterization and applications, *Adv. Drug Deliv. Rev.* 47, 165–196 (2001).
- 2 P. COUVREUR, G. BARRAT, E. FATTAL, P. LEGRAND, C. VAUTHIER, Nano-capsule technology: a review, *Critical Rev. Therap. Drug Carrier Systems* 19, 99–134 (2002).
- 3 G. BARRATT, Colloidal drug carriers: achievements and perspectives, *Cell. Mol. Life Sci.* 60, 21–37 (2003).
- 4 J. K. VASIR, K. TAMBWEKAR, S. GARG, Bioadhesive microspheres as a

- controlled drug delivery system, *Int. J. Pharm.* 255, 13–32 (2003).
- 5 F. MARCUCCI, F. LEFOULON, Active targeting with particulate drug carriers in tumor therapy: fundamentals and recent progress, *Drug Discovery Today* 9, 219–228 (2004).
  - 6 M. J. ALONSO, Nanomedicines for overcoming biological barriers, *Biomed. Pharmacother.* 58, 168–172 (2004).
  - 7 C. MAYER, NMR on dispersed nanoparticles, *Prog. NMR Spectrosc.* 40, 307–366 (2002).
  - 8 C. MAYER, D. HOFFMANN, M. WOHLGEMUTH, Structural analysis of nanocapsules by nuclear magnetic resonance, *Int. J. Pharm.* 242, 37–46 (2002).
  - 9 M. WOHLGEMUTH, C. MAYER, Pulsed field gradient NMR on polybutyl-cyanoacrylate nanocapsules, *J. Colloid Interface Sci.* 260, 324–331 (2003).
  - 10 K. JORES, W. MEHNERT, K. MÄDER, Physicochemical investigations on solid lipid nanoparticles and on oil-loaded solid lipid nanoparticles: a nuclear magnetic resonance and electronic spin resonance study, *Pharm. Res.* 20, 1274–1283 (2003).
  - 11 M. GARCIA-FUENTES, D. TORRES, M. MARTIN-PASTOR, M. J. ALONSO, Application of NMR spectroscopy to the characterization of PEG-stabilized lipid nanoparticles, *Langmuir* 20, 8839–8845 (2004).
  - 12 M.-H. CHEN, R. KUMAR, V. S. PARMAR, J. KUMAR, L. A. SAMUELSON, A. C. WATTERSON, Self-organization of amphiphilic copolymers into nanoparticles: study by  $^1\text{H}$  NMR longitudinal relaxation time, *J. Macromol. Sci., Part A: Pure Appl. Chem.* A41(12), 1489–1496 (2004).
  - 13 M. GARCIA-FUENTES, D. TORRES, M. MARTIN-PASTOR, M. J. ALONSO, Application of NMR spectroscopy to the characterization of PEG-stabilized lipid nanoparticles, *Langmuir* 20(20), 8839–8845 (2004).
  - 14 J. KRIZ, J. PLESTIL, H. POSPISIL, P. KADLEC, C. KONAK, L. ALMASY, A. I. KUKLIN,  $^1\text{H}$  NMR and small-angle neutron scattering investigation of the structure and solubilization behavior of three-layer nanoparticles, *Langmuir* 20(25), 11255–11263 (2004).
  - 15 Y. ZHANG, Q. ZHANG, L. ZHA, W. YANG, C. WANG, X. JIANG, S. FU, Preparation, characterization and application of pyrene-loaded methoxy poly(ethylene glycol)-poly(lactic acid) copolymer nanoparticles, *Colloid Polym. Sci.* 282(12), 1323–1328 (2004).
  - 16 K. WESTESEN, A. GERKE, M. H. J. KOCH, Characterization of native and drug-loaded human density lipoproteins, *J. Pharm. Sci.* 84, 139–147 (1995).
  - 17 D. HOFFMANN, C. MAYER, Cross polarization induced by temporary adsorption: NMR investigation on nanocapsule dispersions, *J. Chem. Phys.* 112, 4242–4250 (2000).
  - 18 C. MAYER, G. LUKOWSKI, Solid state NMR investigations on nanoparticulate carrier systems, *Pharm. Res.* 17, 486–489 (2000).
  - 19 H. Y. HUANG, K. L. WOOLEY, J. SCHAEFER, REDOR determination of the cross-linked amphiphilic core-shell nanoparticles and the partitioning of sequestered fluorinated guests, *Macromolecules* 34, 547–551 (2001).
  - 20 S. GUINEBRETIERE, S. BRIANCON, J. LIETO, C. MAYER, H. FESSI, Study on the emulsion-diffusion process: formation and characterization of nanoparticles, *Drug Develop. Res.* 57, 18–33 (2002).
  - 21 S. WISSING, R. MÜLLER, L. MANTHEI, C. MAYER, Structural characterization of Q10-loaded SLN by nuclear magnetic resonance, *Pharm. Res.* 21, 400–405 (2004).
  - 22 P. A. BERTIN, K. J. WATSON, S. T. NGUYEN, Indomethacin-containing nanoparticles derived from amphiphilic polynorbornene: a model ROMP-based drug encapsulation system, *Macromolecules* 37(22), 8364–8372 (2004).
  - 23 P. COUVREUR, B. KANTE, M. RD, P. GUIOT, P. BAUDHUIN, P. SPEISER, *J. Pharm. Pharmacol.* 31, 331 (1979).
  - 24 A. T. FLORENCE, T. L. WHATELEY, D. A. WOOD, *J. Pharm. Pharmacol.* 31, 422 (1979).

- 25 M. WOHLGEMUTH, W. MÄCHTLE, C. MAYER, Improved preparation and physical studies of polybutylcyanoacrylate nanocapsules, *J. Microencapsulation* 17, 437–448 (2000).
- 26 C. MAYER, Calculation of cross-polarization spectra influenced by slow molecular tumbling, *J. Magn. Reson.* 145, 216–229 (2000).
- 27 M. MEHRING, High resolution NMR spectroscopy in solids, in *NMR Basic Principles and Progress*, P. DIEL, E. FLUCK, R. KOSFELD (eds.), Springer Verlag, Berlin (1976).
- 28 V. J. MCBRIERTY, K. J. PACKER, *Nuclear Magnetic Resonance in Solid Polymers*, Cambridge University Press, Cambridge (1993).
- 29 K. SCHMIDT-ROHR, W. SPIESS, *Multidimensional Solid-State NMR and Polymers*, Academic Press, London (1994).
- 30 G. LUKOWSKI, D. HOFFMANN, P. PFLEGEL, C. MAYER, *Solid State NMR Investigations On Nanosized Carrier Systems*, Proc. 3<sup>rd</sup> World Meeting APV/APGI Berlin (2000).
- 31 R. H. MÜLLER, K. MÄDER, S. GOHLA, Solid lipid nanoparticles (SLN) for controlled drug delivery – a review of the state of the art, *Eur. J. Pharm. Biopharm.* 50, 161–178 (2000).
- 32 C. MAYER, Lineshape calculations on spreadsheet software, *J. Magn. Reson.* 138, 1–11 (1999).
- 33 C. MAYER, Calculation of MAS spectra influenced by slow molecular tumbling, *J. Magn. Reson.* 139, 132–138 (1999).
- 34 E. O. STEJSKAL, J. E. TANNER, *J. Chem. Phys.* 42, 288 (1965).
- 35 E. O. STEJSKAL, J. E. TANNER, *J. Chem. Phys.* 43, 3597 (1965).
- 36 J. E. TANNER, E. O. STEJSKAL, *J. Chem. Phys.* 49, 1768 (1968).
- 37 R. KIMMICH, *NMR Tomography Diffusometry Relaxometry*, Springer Verlag, Berlin (1997).
- 38 I. LÖNNQVIST, A. KHAN, O. SÖDERMANN, *J. Colloid Interface Sci.* 144, 401 (1990).
- 39 O. SÖDERMANN, *Progr. Colloid Polym. Sci.* 106, 34 (1997).
- 40 J. KREUTER, Nanoparticles, in *Colloidal Drug Delivery Systems*, J. KREUTER (ed.), Marcel Dekker, New York (1994).
- 41 D. QUINTANAR-GUERRERO, Etude du mecanisme de formation de nanoparticules polymériques d'émulsification-diffusion, *Colloid Polym. Sci.* 275, 640–647 (1997).
- 42 D. E. WOESSNER, Relaxation effects of chemical exchange, in *Encyclopedia of Magnetic Resonance*, Wiley, New York (1996), Vol. 6, pp. 4018–4028.
- 43 M. SCHÖNHOF, O. SÖDERMANN, PFG-NMR diffusion as a method to investigate the equilibrium adsorption dynamics of surfactants at the solid/liquid interface, *J. Phys. Chem. B* 101, 8237–8242 (1997).
- 44 M. SCHÖNHOF, O. SÖDERMANN, Exchange dynamics of surfactants in adsorption layers investigated by PFG NMR diffusion, *Magn. Reson. Imag.* 16, 683–685 (1998).
- 45 K. I. MOMOT, P. W. KUCHEL, B. E. CHAPMAN, D. WHITTAKER, NMR study of the association of propofol with nonionic surfactants, *Langmuir* 19, 2088–2095 (2003).
- 46 K. I. MOMOT, P. W. KUCHEL, Pulsed field gradient nuclear magnetic resonance as a tool for studying drug delivery systems, *Concepts Magn. Reson. Part A* 19, 51–64 (2003).
- 47 A. RUMPLECKER, S. FÖRSTER, M. ZÄHRES, C. MAYER, Molecular exchange through vesicle membranes: a pulsed field gradient NMR study, *J. Chem. Phys.* 120, 8740–8747 (2004).
- 48 D. E. DISCHER, A. EISENBERG, Polymer vesicles, *Science* 297, 967–973 (2002).
- 49 E. KRÄMER, S. FÖRSTER, C. GÖLTNER, M. ANTONIETTI, Synthesis of nanoporous silica with new pore morphologies by templating the assemblies of ionic block copolymers, *Langmuir* 14, 2027–2031 (1998).
- 50 B. BALINOV, B. JÖNSSON, P. LINSE, O. SÖDERMANN, The NMR self-diffusion method applied to restricted diffusion. Simulation of echo attenuation from molecules in spheres and between planes, *J. Magn. Reson. A* 104, 17–25 (1993).
- 51 P. T. CALLAGHAN, Pulsed-gradient

- spin-echo NMR for planar, cylindrical, and spherical pores under conditions of wall relaxation, *J. Magn. Reson. A* 113, 53–59 (1995).
- 52 S. L. CODD, P. T. CALLAGHAN, Spin echo analysis of restricted diffusion under generalized waveforms: planar, cylindrical, and spherical pores with wall relaxivity, *J. Magn. Reson.* 137, 358–372 (1999).
- 53 J. PFEUFFER, U. FLÖGEL, W. DREHER, D. LEIBFRITZ, Restricted diffusion and exchange of intracellular water: theoretical modelling and diffusion time dependence of  $^1\text{H}$  NMR measurements on perfused glial cells, *NMR Biomed.* 11, 19–31 (1998).
- 54 D. HOFFMANN, M. ZÄHRES, unpublished result.
- 55 D. HOFFMANN, PhD thesis, University of Duisburg (2000).
- 56 E. K. JANG, I. YU,  $^1\text{H}$  NMR of water influenced by suspended magnetic particles, *Colloids Surf. A* 72, 229–235 (1993).
- 57 C. E. GONZALEZ, D. J. PUSIOL, A. M. F. NETO, M. RAMIA, A. BEE, Nuclear magnetic resonance study of the internal magnetic field distribution in water base ionic and surfactated ferrofluids, *J. Chem. Phys.* 109, 4670–4674 (1998).
- 58 S. SAITO, M. OHABA, Proton nuclear magnetic resonance and optical microscopic studies of magnetic fluids, *J. Phys. Soc. Jpn.* 68, 1357–1363 (1999).
- 59 A. TERHEIDEN, M. MICHAELSEN, G. DYKER, C. MAYER, Nuclear magnetic resonance as a tool for the characterization of magnetic fluids, *Magneto hydrodynamics* 39, 17–22 (2003).
- 60 A. TERHEIDEN, C. MAYER, NMR study on colloidal magnetic fluids of various viscosities, *Phase Transitions* 77, 81–87 (2004).
- 61 C. MAYER, A. TERHEIDEN, Numerical simulation of magnetic susceptibility effects in nuclear magnetic resonance spectroscopy, *J. Chem. Phys.* 118, 2775–2782 (2003).

## 5 Characterization of Nano Features in Biopolymers using Small-angle X-ray Scattering, Electron Microscopy and Modeling

*Angelika Krebs and Bettina Böttcher*

### 5.1

#### Introduction

Biological molecules and systems have several attributes that make them highly suitable for nanotechnology applications. For example, proteins fold into precisely defined three-dimensional (3D) shapes, and nucleic acids assemble according to structural rules. Antibodies are highly specific in recognizing and binding their ligands, and biological assemblies such as molecular motors can perform transport operations. Because of these, and other favorable properties, they are ideal for applications in nanotechnology. Gaining structural information of such complexes is crucial for understanding their functionality and for their successful incorporation in nano technologies.

Various techniques are available that provide information at various degrees of reliability and detail. Protein crystallography and multidimensional NMR are well-established methods that provide models of biological macromolecules on an atomic scale. With small-angle X-ray scattering the structure of macromolecules in solution can be investigated. Typical samples range from small proteins (from 5–10 kDa) to multi-domain proteins and protein complexes (up to MDa). The scattering data are sensitive to domain orientations and conformational changes and/or flexibility as well as to molecular associations; atomic resolution, however, will not be achieved. The technique is most powerful when used as a complementary tool with other structural techniques, such as three-dimensional electron microscopy (3D-EM). Three-dimensional image reconstructions from electron micrographs have become important in recent years, because near atomic resolution has been achieved with cryo-EM for several important systems. At the moment, low-resolution EM structures are obtained almost routinely for complex biopolymers and this information can be used advantageously in combination with other methods. One example is the merging of complex structures determined by EM at medium resolution with high-resolution crystal structures of their components. Another possibility, which is the scope of this chapter, is the merging of structural information obtained by EM with information obtained from SAXS.

After a general introduction to SAXS and EM, this chapter explains how both



methods together can be used successfully to gain structural information on the nanoscale.

## 5.2

### Small-angle X-ray Scattering

Small-angle X-ray scattering is a well-established technique for structural investigations of proteins on the nanometer length scale (1–300 nm), having its origins more than 50 years ago [1–4]. Recently, biological SAXS has gained additional importance, mainly due to outstanding hardware and software development. Very important in this context are new SAXS instruments and advanced methods to analyze SAXS data from macromolecular solutions (e.g., *ab initio* low-resolution structure analysis and rigid body refinement). Common applications in nanotechnology are the investigation of micro-emulsions or liquid crystals, the particle sizing of suspended nano-powders or investigations concerning structural information of polymer films and fibers. Applications in life science and biotechnology mainly deal with proteins, viruses and DNA complexes, whereby the border between nanotechnology and life science constantly diminishes.

#### 5.2.1

##### Scattering Technique

###### 5.2.1.1 Scattering Phenomenon

X-rays are photons with wavelengths in the range 0.1–100 Å and, depending on the frequency of electromagnetic waves, different interactions with matter are observable. They are usually generated by bombarding a target with electrons of energies of 10 000 eV or more. Upon collision, these high-energy electrons can knock electrons out of the target atoms, leaving vacancies in atomic shells. If, for example, a vacancy is produced in the innermost (K) shell of an atom, it rapidly will be filled by an electron descending from the next (L) shell, or one from the one after that (M). The photons emitted as a result of these transitions are the X-rays; they vary in wavelength according to the path of the electron. Copper is commonly used as a target, where  $\text{CuK}_\alpha$  radiation is emitted by electrons propagating from the L to the K shell and  $\text{CuK}_\beta$  is the radiation emitted by an electron changing from the M to the K shell.

X-rays interact with matter in different ways, i.e., absorption, elastic and inelastic scattering (Fig. 5.1). Elastic scattering is the basic event for X-ray scattering techniques. There, the incident X-ray photons undergo perfectly elastic collisions with the electron, leaving their energy unchanged and leading to radiation propagating away from the sample in all directions [1, 3–5].

The event behind that is the following: When a beam of electromagnetic radiation strikes an electron, some of the energy is momentarily absorbed and the electron becomes displaced from its unperturbed position due to the force exerted on it by the electric field. As a result, the electron is set into periodic motion with a fre-

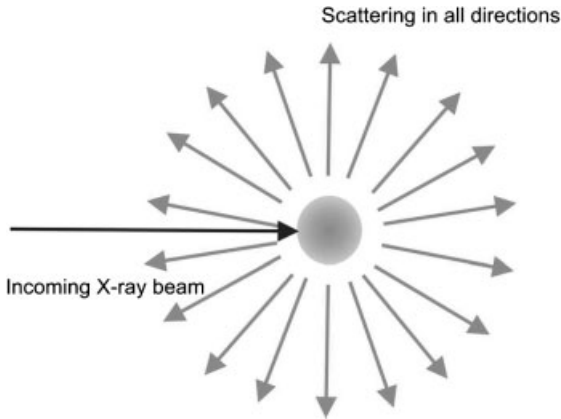


**Fig. 5.1.** Scattering phenomenon. When a beam of electromagnetic radiation strikes an atom it is mainly the electrons that react. Some of the energy is momentarily absorbed and the electron becomes displaced from its unperturbed position due to the force exerted on it by the electric field. As a result, the electron is set into periodic motion with a frequency equal to that of the exciting

radiation. Since, according to the Maxwell equations, any accelerating or decelerating charge must radiate an electromagnetic wave in all directions, and since the radiation reemitted by the electron has the same frequency as the exciting radiation, experimental observation gives the impression that the incident radiation is scattered in all directions by the electron.

quency equal to that of the exciting radiation. Since, according to the Maxwell equations, any accelerating or decelerating charge must radiate an electromagnetic wave in all directions and since the radiations reemitted by the electron has the same frequency as the exciting radiation, the experimental observation gives the impression that the incident radiation is scattered in all directions by the electron. Thus the electrons can be considered as centers of secondary waves and the wavelength of the incident and the scattered radiation is the same (elastic scattering).

The amount of scattering is described by the Thomson equation [Eq. (1)], which states that scattered intensity from a single independent electron  $I(\theta)$  is given by:

$$I(\theta) = I_0 \frac{e^4}{m_0^2 c^4 a^2} \left\{ \frac{1 + \cos^2(2\theta)}{2} \right\} \quad (1)$$

where  $e$  is the electronic charge,  $m$  is the mass of the electron,  $c$  is velocity of light,  $a$  is the sample–detector distance and  $2\theta$  is the scattering angle. The product  $e^4/m_0^2 c^4$  is known as the electronic scattering factor (also termed electron-scattering cross section and Thomson’s constant), and the quantity in parentheses is known as polarization factor. The angle  $\theta$  is defined as one-half the angle of deflection of the incident beam relative to the scattered beam. In so-called reciprocal space the scattering vector  $h$  ( $\text{nm}^{-1}$ ) is usually used [Eq. (2)], where with  $\lambda$  is the wavelength.

$$h = (4\pi/\lambda) \sin \theta \quad (2)$$

While scattering from a single electron is extremely weak, in real systems, such as a protein in aqueous solution, we measure the total scattering from all electrons in the irradiated volume (which is of the order of 0.1 mL). Since the dimensions of macromolecules are always large relative to the wavelength of the incident X-ray radiation, interference occurs between the radiation scattered from individual electrons. Thus the spatial distribution of electrons in one molecule leads to several secondary waves that are able to interfere. The phase difference of the scattered waves depends on the path distance of the electrons in the molecule. This path difference increases with larger scattering angles and is the cause of diminishing scattering at larger angles. At very large scattering angles the scattered intensity is 0. This is why we observe small-angle X-ray scattering.

### 5.2.1.2 Scattering Curve and Pair Distance Distribution Function

In general, because electrons are not localized, it is better to describe an electron density  $\rho(\mathbf{r})$  in a volume element  $dV$ ; the scattering then is proportional to  $\rho(\mathbf{r}) dV$ . Therefore, for a continuous electron distribution, the sum of all secondary (scattered) waves  $e^{-ihr}$  is replaced by an integral [Eq. (3)].

$$F(h) = \int_V \rho(\mathbf{r}) e^{-ihr} dV \quad (3)$$

The integral is over the entire sample. This equation is the single fundamental equation that governs all X-ray scattering and diffraction. If the electron density distribution  $\rho(\mathbf{r})$  of a sample is known, one can compute the structure factor, and from this one can compute the expected X-ray scattering for all scattering geometries.

In solution small-angle X-ray scattering, however, the information contained in the 3D electron-density distribution  $\rho(\mathbf{r})$ , which describes the whole structure of the particle, is reduced to a one-dimensional distance distribution function  $p(r)$ , because the particles we measure are non-oriented in solution. [For solution scattering  $\rho(\mathbf{r})$  stands for the difference in electron density between sample and solvent.] The  $p(r)$  function is proportional to the number of lines with length  $r$  that connect any volume element  $i$  with any volume element  $k$  of the same particle. The spatial orientation of these connection lines is not important and the connection lines  $r$  are weighted by the product of the number of electrons situated in the volume elements  $i$  and  $k$  respectively. Each distance between two electrons of the sample as part of the function  $p(r)$  leads to an angular dependent scattering intensity. This physical process of scattering can be mathematically expressed by a Fourier transformation that defines how the information in real space (distance distribution function) is transferred into reciprocal space (scattering function) [Eq. (4)], with  $\gamma(r)$  as a measure of the probability of finding two points with the distance  $r$  within the particle of interest (correlation function).

$$I(h) = 4\pi \int_0^\infty \gamma(r) r^2 \frac{\sin hr}{hr} dr \quad (4)$$

The correlation function can be calculated from the scattering intensity using a Fourier transform [Eq. (5)].

$$\gamma(r) = \frac{1}{2\pi^2} \int_0^\infty I(h) h^2 \frac{\sin hr}{hr} dh \quad (5)$$

With  $p(r) = \gamma(r)r^2$  one can calculate the pair distance distribution function from the scattering intensity according to Eq. (6).

$$p(r) = \frac{r^2}{2\pi^2} \int_0^\infty I(h) h^2 \frac{\sin hr}{hr} dh \quad (6)$$

### 5.2.1.3 Determination of Scattering Parameters

SAXS parameters, such as the radius of gyration  $R_G$ , maximum particle size  $D_{\max}$ , volume  $V$  and molecular weight  $MW$  can be determined directly from the scattering behavior of the sample. In the following the procedures are outlined briefly:

(a) The radius of gyration,  $R_G$ , i.e., the root-mean-square of the distances of all the electrons of the particle from its center of electronic mass, is a characteristic geometric parameter of any particle. It can be determined according to a Guinier plot [ $\ln I(h)$  vs.  $h^2$ ] [Eq. (7), with  $I(0)$  as scattering intensity at zero angle].

$$I(h) = I(0)e^{-(h^2 R_G^2/3)} \quad (7)$$

Another way is to use the information given by the distance distribution function [Eq. (8)].

$$R_G = \sqrt{\frac{\int_V \rho(\mathbf{r}) r^2 dV}{\int_V \rho(\mathbf{r}) dV}} = \sqrt{\frac{1}{2} \frac{\int_V \rho(r) r^2 dr}{\int_V p(r) dr}} \quad (8)$$

(b) The maximum diameter  $D_{\max}$  of a particle can be determined by a linear diagram of  $p(r)$  vs. distance  $r$ .  $D_{\max}$  is then given by the crossover of the  $p(r)$  function with the  $x$ -axis.

(c) The hydrated volume can be assessed according to Eq. (9), with  $Q = \int I(h) h^2 dh$  being the invariant according to Porod.

$$V = 2\pi^2 \frac{I(0)}{Q} \quad (9)$$

(d) Finally, the relation of the scattered intensity to the primary intensity is a measure of the molecular weight of the biological sample [Eq. (10)].

$$MW = \frac{I(0)a^2}{N_A T_e P_0 (z_2 - v_2' \rho_1)^2 dc} \quad (10)$$

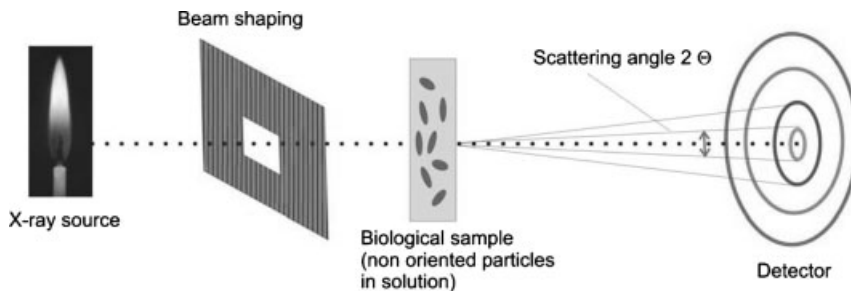


Fig. 5.2. Typical SAXS experiment.

where  $P_0$  is the primary intensity of the X-ray beam,  $N_A$  is the Loschmidt number,  $T_e$  is the Thomson factor, ( $7.9 \times 10^{-26} \text{ cm}^2$ ),  $z_2$  is the number of electrons per gram of the soluble sample in ( $\text{mol g}^{-1}$ ),  $\rho_1$  is the electron density of the solvent in ( $\text{mol mL}^{-1}$ ),  $v'_2$  is the isopotential specific volume in ( $\text{mL g}^{-1}$ ),  $d$  is the thickness of the sample in cm, and  $c$  is the concentration ( $\text{g mL}^{-1}$ ).

#### 5.2.1.4 Experimental Setup

With solution SAXS it is possible to study monodisperse as well as polydisperse systems. For monodisperse systems one can determine size, shape, interparticle interactions and internal structure of the particles. For polydisperse systems a size distribution can be calculated under the assumption that all particles have the same shape. In the SAXS experiments, the sample is irradiated by a well-defined, monochromatic X-ray beam (Fig. 5.2).

There exist laboratory instruments based on more conventional sources and synchrotron-based instrumentation. Synchrotron radiation sources with their intense brightness and natural collimation are ideal because biological materials are very poor scatterers. There is always some form of beam shaping required to maintain the small cross-section in going from the source to the sample and to reduce distortions from parasitic scattering from whatever obstacles, including air, are encountered. This is where much of the experimental effort is required and additional mathematical corrections take care of the non-ideal circumstances of a normal scattering experiment. A sample stage that may or may not involve heating/cooling elements then follows, ideally all within an in-vacuum path. No preparation such as staining of the material is required (in contrast to EM), and thicknesses of the biological sample between 1 and 3 mm are usually sufficient. Most commonly, small vials are used. As shown here the SAXS technique is performed in transmission mode. An extended sample–detector distance is usually required to give the barely scattered photons room to spread out from the main beam and also to reduce the detected X-ray background. Finally, a proportional counter, a scintillation counter, or a position sensitive detector, ideally two-dimensional, is required to measure the scattered intensity. As can be seen here, the black spot would be the beamstop that is absolutely essential to block the

main beam. To reduce errors, measurements are performed repeatedly, because the statistical error is inversely proportional to the square root of the counts.

## 5.2.2

### Interpretation of Data

#### 5.2.2.1 Direct Methods

Interpreting SAXS data can be very difficult, unless one is very lucky and the sample fits one of the many idealized models developed over the years. Regular wide-angle X-ray scattering tends to focus on the location, width, shifts, etc. of Bragg peaks that arise from crystalline lattice structures. One can still observe Bragg peaks in SAXS but these will result from regular spacings that are of the order of hundreds of angstroms. Most of the time, however, the observed curves tend to be apparently featureless.

Direct methods of analysis give us information based on interpretation of the clean (background corrected) data with no further manipulation [6]. All of these parameters are based on well-defined assumptions, such as the existence of uniform density within our particle, uniform density in the background, sharp interfaces between the two, etc.

At very small angles, the slope of the scattering in the so-called Guinier region (Fig. 5.3) can be used to get an idea of the radius of gyration of any distinct structure [see Eq. (7)]. For unisometric particles the radius of gyration of the cross-section and the radius of gyration of the thickness can be determined with equations similar to Eq. (7) (for further details see Ref. [4], p. 155). At higher angles, if we have a system of relatively identical particles, dilute enough for there to be no interactions, we may be able to see broad peaks that give us information on

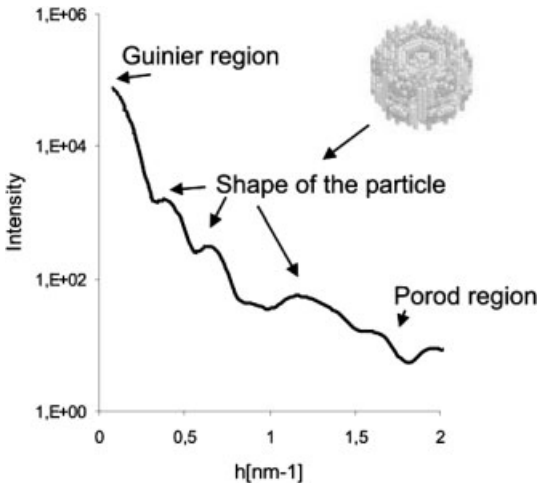


**Fig. 5.3.** Scattering curve and SAXS model from a biopolymer on the nanometer scale (hemoglobin from the earthworm *Lumbricus terrestris*).

**Tab. 5.1.** Experimental SAXS data and model data of *Lumbricus terrestris* hemoglobin.

<i>Lumbricus terrestris</i> hemoglobin				
	<i>Experimental SAXS data</i> <sup>[a]</sup>	<i>SAXS "consensus model"</i> <sup>[b]</sup>	<i>EM model "expected volume"</i> <sup>[c]</sup>	<i>EM model "hydrated volume"</i> <sup>[d]</sup>
$R_G$ (nm)	$10.71 \pm 0.02$	$10.68 \pm 0.04$	11.30	10.73
$D_{\max}$ (nm)	$29.37 \pm 0.21$	$29.61 \pm 0.05$	29.39	29.03
$V$ (nm <sup>3</sup> )	$6200 \pm 200$	$6200 \pm 400$	4500	7200
MW (MDa)	$3.5 \pm 0.2$			
Number of spheres		6844	11671	23021
Radius of spheres (nm)		0.66	0.45	0.426

<sup>a</sup> Experimental data are taken from Ref. 90.

<sup>b</sup> Mean values and standard deviations result from averaging the 22 models included in the consensus model shown in Fig. 5.3.

<sup>c</sup> Threshold = 171, voxel-size =  $0.726 \times 0.726 \times 0.726$ .

<sup>d</sup> Threshold = 115, voxel-size =  $0.687 \times 0.687 \times 0.687$ .

the shape of the particles. At still higher angles, the so-called Porod region, the shape of the curve is useful in obtaining information on the surface-to-volume ratio of the scattering objects. This can also be used to gain information on the dimensions of our scattering particles. The area under the curve gives us the invariant, which is a measure of how much scattering material is seen by the beam and allows us to estimate the hydrated volume according to Eq. (9). The volume is a very important parameter, which we can determine with SAXS [the scattering amplitude is well defined according to Eq. (1)], whereas this is not easy in EM. Changes in the invariant can be used, for instance, to monitor the crystallization process in polymer materials. Finally, the shape of the  $p(r)$  function gives additional information on the size and overall structure of the particle as well as the maximum diameter. Thus we gain useful information rather quickly by careful analysis of the scattering behavior of the particle (Table 5.1).

### 5.2.2.2 Indirect Methods

For further interpretation purposes, it may be helpful if we propose specific structures and simulate their scattering behavior. The model-scattering data are then compared with the experimental data and the fit is a measure of the quality of the proposed structure. This approach, however, tends to imply that we already know the answer. Another possibility, therefore, if we don't really have any clear order to base our interpretation on, would be to assume a strongly disordered structure and to change this structure as long as it takes to gain a similar scattering behavior of the model and the experiment. This then is the basis of any indirect interpretation. In recent decades, various indirect modeling techniques have been described, including simple whole-body approaches, multi-body procedures and advanced *ab initio* modeling techniques (Fig. 5.4) (for summaries see Refs. [7, 8]).

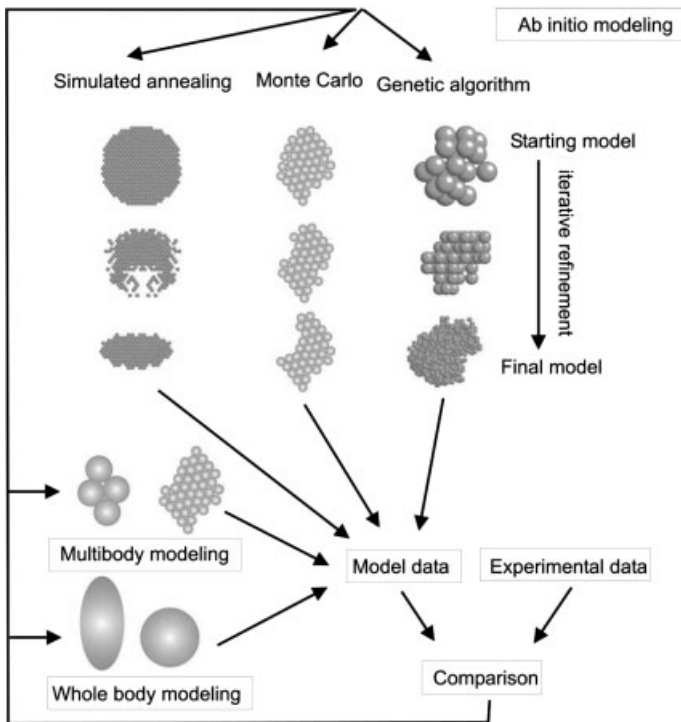


Fig. 5.4. Modern SAXS modeling techniques.

**Conventional Whole-body and Multi-body Modeling Approaches** As a first approximation, biopolymers can be modeled as spheres, prolate or oblate ellipsoids or triaxial bodies with unequal axes. Approaches along this line are called whole-body modeling [9–11]. They consider hydration contributions by using experimental molecular properties such as the hydrated volume,  $V$ , which can be directly obtained by SAXS (see above). The surface of whole-body models is entirely smooth and therefore whole-body approaches are not used to determine structural details on the nanoscale.

For nano-applications the use of an assembly of spheres (beads) instead of a single geometrical body seems appropriate, e.g., Refs. [7, 12–18], because proteins and other types of biopolymers are often composed of various constituents. In multi-body modeling approaches the target experimental profile is simulated by a finite element method (“bead modeling”) and we can either use a small number of objects (each object would then simulate a subunit of the whole protein complex under investigation) or a large number of small spheres (in that case the spheres might be chosen to represent single amino acids or slightly larger details of the nano particle). Model scattering curves are usually calculated by means of Debye’s formula [4].



An example of a two-step multi-body approach is the consensus model of a giant multisubunit protein complex with a diameter of about 30 nm; this complex with a molecular weight of about 3600 kDa and an overall  $D_6$  symmetry [19, 20] is responsible for oxygen transport in the earthworm *Lumbricus terrestris* (Fig. 5.3). Due to considerable differences in mass estimations, the exact stoichiometry of the components was unclear for a long time [21, 22]. Two models have been proposed to explain the architecture of *Lumbricus* Hb: The first consists of 24 octameric subassemblies of globin chains and 24 linker chains [23]. In the second, the so-called “bracelet model” [21, 24–26] 12 dodecameric 200 kDa subunits, each composed of 3 monomeric and 3 trimeric heme-containing globin chains, and 36 heme-deficient linker chains form the HBL complex with a total mass of about 3.6 MDa. Several 3D reconstructions from cryo-EM have been presented [27–29] and the crystal structure at 5.5 Å resolution has been published [30], revealing an organization of 144 oxygen-binding hemoglobin subunits and 36 non-hemoglobin linker subunits, similar to the bracelet model.

Solution SAXS studies and subsequent multi-body modeling led to the consensus model, which consists of 6844 spheres of equal size (radius 0.66 nm) but unequal weight. In the first step, about 600 different models, all biased to represent the biopolymer structure in eclipsed arrangement (top and bottom half exactly on top of each other), were generated by trial and error and tested for equivalence in scattering with the protein complex. In the second step, the 22 best-fitting models were superimposed and averaged, a procedure that resulted in spheres of different weights according to the different occupation densities of positions [18]. No structural bias other than hexagonal symmetry (known from early EM studies) was imposed in the model calculations. The model shown here is an early example of generation of a SAXS model that allows us to determine better and worse defined areas of the model. This is an important step to produce more reliable SAXS models. The scattering behavior of this model is compared with the experimental data in Table 5.1.

**Structure Reconstruction by *Ab Initio* Modeling Approaches** A fascinating aspect of modern evaluation procedures for SAXS data is the possibility to establish *ab initio* reconstructions of low-resolution biopolymer shapes [7, 31–35], even without resorting to any kind of spatial information. Among these highly advanced methods, in particular the approaches based on simulated annealing [36–38], a genetic algorithm [39], Monte-Carlo approaches [40, 41] or a molecular-dynamics algorithm [42] need to be addressed.

In the simulated annealing approach [37] models from densely packed dummy atoms (beads) are established. Each dummy atom is ascribed either to the particle or the solvent. Starting from a random initial configuration in a chosen search space (in general a sphere of diameter exceeding slightly the particle diameter, or a chain-like ensemble of dummy residues to mimic the backbone of the protein structure and dummy water molecules to simulate hydration), simulated annealing is used as a global minimization algorithm to find a configuration matching the SAXS data. In the beginning symmetry information or other information on the

shape of the particle (from other methods, such as EM) may be introduced to increase the reliability of the generated models.

Using the genetic algorithm the scattering curves may also be iteratively fitted [39, 43]. There, a population of genes codifying a given mass distribution on a hexagonal lattice in a confined volume (e.g., an ellipsoidal search space of selected dimensions) is randomly generated. From each genotype the obtained model structure is compared to the observed SAXS data (by calculating the scattering profile of the model body by the Debye approach) and a fitness criterion is used to generate the next population by genetic operators (crossover and mutation), until, as a consequence of the selection pressure, the system converges, i.e., the best-fitting model is found. The fitting starts with a low number of large spheres and uses, incipiently, only the innermost portion of the scattering curve; during the run, the size of the spheres is gradually scaled down and the limit of resolution is increased by addition of further portions of the scattering curve. Monte Carlo approaches add and remove beads on a lattice until an optimum fit to the experimental SAXS profile is reached and the value of the score is at its minimum [40, 41].

In general, a thorough analysis to develop a structural model from SAXS data requires the execution of multiple runs for each condition chosen (e.g., bead radius, i.e., resolution) to avoid misinterpretations owing to unfavorable or ill-posed calculation conditions. A comparison of the results requires visualization, alignment and superimposing of the obtained models, followed by some kind of averaging and filtering. In any case, the resultant models cannot guarantee absolute uniqueness. In particular, for very complex structures or if considerable particle inhomogeneities exist, a note of caution is advised. In such cases, structural knowledge from other methods (such as EM) is extremely helpful for the creation of SAXS models and should therefore be introduced at the beginning of the model calculations.

**Generation of Averaged Models** Averaging of SAXS models is a legitimate procedure to point out structural tendencies by emphasizing the most persistent features [17, 44]. In this way, important, recurring features in the protein structure can be spotted and interpreted accordingly. Structural details at high resolution, however, may be lost during the averaging procedure and the averaged model may also provide a worse fit of the experimental data. Despite these reservations, averaging can be a valuable tool to reduce the problem of uniqueness of shape reconstructions and, nowadays, best-matching alignment and superposition of the bead models and subsequent averaging may be done automatically [44, 45].

### 5.3 Electron Microscopy

As we have seen in preceding paragraphs, interpretation of SAXS data greatly benefits from the incorporation of a priori knowledge of the structural organization of the nano-particles. Here EM can provide useful information on size and shape.

In addition, merging of different views allows reconstruction of the 3D image information. Such image reconstructions provide quite accurate phase information of the object but often show a modulation of the amplitude profile, which, in turn, can be corrected by combination with SAXS measurements.

### 5.3.1

#### Image Formation

Microscopy, as other methods, relies on the interference of electromagnetic radiation with the object. In contrast to diffraction methods, images contain the complete image information, consisting of amplitude and phase information. In EM the source of electromagnetic radiation is electrons accelerated by high voltage in a vacuum. The velocity of these electrons is close to the speed of light. With a typical accelerating voltage of 200 kV the electrons already reach a speed of 210 000 km s<sup>-1</sup>, which is ~70% of the velocity of light. At these high relativistic speeds, electrons can be considered as waves with wavelengths of the order of a few picometer (2.5 pm at 200 kV).

##### 5.3.1.1 Interference of Electrons with Matter

Electron waves interfere with an object in several modes (Fig. 5.5). Most of the incoming electrons pass a thin object without interference. A certain fraction of electrons is elastically scattered by small angles and interferes with the unscattered

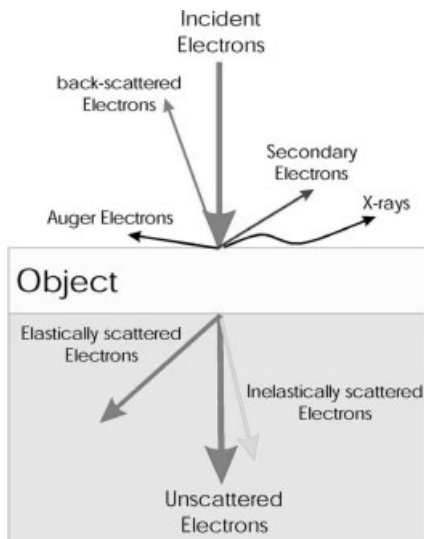


**Fig. 5.5.** Interaction of electrons with the object in EM. Phase contrast, which is the main source of contrast for thin unstained specimens composed of elements with low atomic numbers, is generated by interaction of the elastically scattered electrons with the unscattered electrons.

beam. These electrons contribute to the phase contrast, which is the main source of contrast in transmission EM of thin objects. Another fraction of electrons is scattered by higher angles and does not reach the back-focal plane. These electrons contribute to amplitude contrast. Some of the incoming electrons are scattered inelastically and deposit energy on the object, which leads to beam-damage and consequently to loss of high-resolution information. The event of inelastic scattering is not highly localized. Therefore, the inelastically scattered electrons do not contribute to the high-resolution information but contain image information at low spatial frequencies [46].

The cross-section of atoms in the sample for scattering electrons increases with the atomic number. Heavy metal atoms have much larger cross-sections than carbon, oxygen or nitrogen atoms, which are the main building blocks of biopolymers and organic polymeric materials. Therefore, heavy metal compounds play a crucial role as stains in EM. As a consequence of their larger cross-sections more electrons are scattered and contribute to the phase contrast. The stronger interaction also increases the number of electrons scattered by larger angles, leading to an increase in amplitude contrast. For a thin stained catalase crystal the amplitude contrast is of the order of 37% [47] whereas for unstained biological samples the amplitude contrast is only about 7% [48].

The cross-section for the inelastic scattering also depends on the atomic number. Up to an atomic number of about 10 the inelastic cross section is larger than the elastic cross section [49], meaning that for every elastic scattering event, which contributes to phase or amplitude contrast, at least one or more electrons are scattered inelastically and contribute to beam damage. Especially for biological objects and organic polymers, which consist mainly of elements with low atomic numbers, this leads to a serious limitation in resolution by beam damage. For example, in carbon, for each electron that is elastically scattered, three electrons are inelastically scattered (for an accelerating voltage of 100 kV), depositing an average energy between 10 and 25 eV on the sample. Therefore, to recover high-resolution information, electron doses are limited to about 5–10 e  $\text{\AA}^{-2}$ . However, at these small doses images are noisy. At large spatial frequencies the signal is much lower than the noise level. To recover the high-resolution information the image information of many low-dose images has to be merged. In theory the combination of only 3000–10000 individual images [50, 51] is sufficient to calculate a 3D image reconstruction to 3  $\text{\AA}$  resolution.

#### 5.3.1.2 Contrast Transfer Function

These considerations assume perfect transfer of contrast in the electron microscope. However, this is far from the real situation, where image contrast is modulated, depending on different parameters. In theory a thin object can be considered as a weak phase, weak amplitude object. Interference of the electron wave with the phase object introduces a phase shift  $\chi$ . This phase shift depends on the defocus  $\Delta$ , the spatial frequency  $R$  and the wavelength of the electrons  $\lambda$ . With a perfect lens a pure phase object in focus has no contrast. However, electron lenses are far from perfect. They deflect electrons much more strongly further from the optical axis

than in their centre. This causes an aberration, which introduces an additional phase shift that depends on the “hardware” of the electron microscope, such as the spherical aberration of the lens  $C_s$ , the wavelength of the electrons ( $\lambda$ ) and the spatial frequency  $R$ . The phase-shift  $\chi$  is given by Eq. (11).

$$\chi = \frac{\pi}{2}(c_s \lambda^3 R^4 - 2\Delta\lambda R^2) \quad (11)$$

In phase contrast the contrast is proportional to the sine of the phase shift, whereas amplitude contrast is proportional to the cosine. For an accurate description of the image information the exact ratio of amplitude and total contrast ( $a$ ) has to be known. For most conditions it is a sufficient approximation to assume that the ratio between amplitude and phase contrast is constant over the spatial frequencies. For the contrast transfer function (CTF) it follows that

$$\text{CTF} = a \cos(\chi) + \sqrt{1 - a^2} \sin(\chi) \quad (12)$$

According to Eq. (12), a pure phase object has almost no contrast at low spatial frequencies, whereas a pure amplitude object shows optimal contrast.

At high spatial frequencies, additionally to the modulation of the contrast-transfer due to the phase-shift, a decrease in contrast transfer occurs that is caused by imperfections of the electron optics such as spherical and chromatic aberrations. This dampening of contrast transfer can be described by exponential decay functions [52]. For spherical aberration, the function depends on the defocus and the illumination half-angle. This has serious implications for high-resolution imaging of low contrast phase objects. Usually, micrographs are taken with a defocus of 2–5  $\mu\text{m}$  to increase contrast at low spatial frequencies (visibility of the particles). At this defocus and with moderate exposure times of 1–2 s, the dampening of contrast transfer is already evident at spatial frequencies of about  $1/(2 \text{ nm})$  in electron microscopes with thermionic guns. For better contrast-transfer at higher spatial frequencies either electron microscopes with brighter electron sources such as field emission guns or longer exposure times, which require extremely stable sample holders, have to be used.

### 5.3.2

#### Sample Preparation

In contrast to SAXS, sample preparation in EM is an important issue. Sample preparation has three major aims: (1) The object has to be reduced to a suitable size (40–500 nm thick, less than 3  $\mu\text{m}$  in diameter). (2) The object has to be stabilized to resist the high vacuum inside the electron microscope. (3) The structure has to be preserved to withstand beam-damage over a high electron dose.

#### 5.3.2.1 Vitrification of Biological Specimens

Nano-particles such as biological complexes, viruses or artificial polymeric materials are in general small enough to be imaged as a whole. However, the high vac-

uum inside the electron microscope makes it impossible to image these particles in an aqueous environment, where the vacuum leads to instant evaporation of the solution. This evaporation can be avoided by lowering the vapor pressure of the water by cooling the sample [53]. However, slow cooling leads to the formation of ice crystals, which can destroy the fine-structure of the object. Therefore, the aim of preservation is to maintain a state of water that is as close to liquid as possible. Such a state is the vitrified form of water, where water solidifies in an amorphous modification [54–57]. Vitrification is achieved by high cooling rates, which are of the order of  $3 \times 10^6 \text{ K s}^{-1}$  [58]. These cooling rates are so rapid that water does not form sizeable ice crystals. Electron diffraction patterns of vitrified solutions show smooth rings, demonstrating the amorphous nature, with some variability in the average spacing between molecules [54]. The average nearest neighbor distance between two oxygen atoms in the vitrified state is 2.76 Å. The structural model, which had been proposed for the vitrified form of water, is based on cubic ice but with a greater variation of the second nearest neighbor distance [59].

In practice, vitrified samples are prepared by forming a thin film of particle suspension and plunge freezing it in liquid ethane. To form the thin film, 2–5  $\mu\text{L}$  of particle suspension are applied to a carbon-coated copper grid. The carbon film is used as support for the sample. Because strong interactions between the object and the carbon film can lead to distortions and the carbon adds an undesirable background, instead of a continuous film, often a film with holes (diameter 1–5  $\mu\text{m}$ ) is used, where the particle suspension spreads over the holes. For a good spread of particles and an even thickness of the vitrified water, a hydrophilic surface of the support film is required, which is achieved by mild plasma etching.

For formation of the thin film most of the sample is removed with filter paper. The thickness of the remaining film is ideally between 20 and 100 nm. Thicker films are possible but usually lead to micrographs of poor quality (low contrast, multiple scattering, charging). This is a major limitation for the investigation of large nano-particles, which are thicker than 100 nm. If the thickness of the film is below the diameter of the object, the particle experiences a considerable pressure, forcing it out of the aqueous environment into the air. This pressure can be so large that deformation (e.g., liposomes) or even bursting of the object (e.g., whole cells) occurs.

**Freezing Apparatus** Immediately after film formation the sample is rapidly frozen by plunging it into liquid ethane. The cooling rates in ethane are sufficient to prevent formation of ice crystals. The vitrified modification is stable and can be stored below the devitrification temperature of about 150–160 K for a prolonged time. To date, different types of apparatus have been used for vitrification. The simplest one is a guillotine in which the forceps holding the grid are mounted [57]. The sample is applied to the grid and then removed by pressing a filter paper against the liquid. Exact observance of the area where filter paper and sample touch allows determination of the best moment when the film has the right thickness. Then the guillotine is released and the forceps with the grid are plunged into a pot with liquid ethane, which is cooled by a surrounding bath of liquid nitrogen.

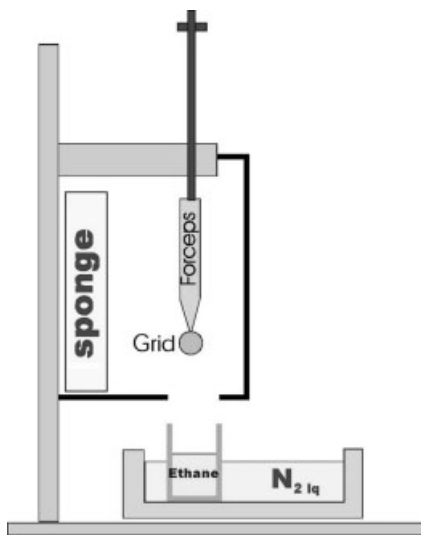


**Fig. 5.6.** Freezing apparatus for vitrifying samples. Forceps holding the grid are mounted in a humidified chamber (water soaked sponges). After release the grid is plunged by a spring driven mechanism into liquid ethane, which is cooled by a bath of liquid nitrogen.

The timing for blotting depends on ambient humidity, viscosity of the sample and concentration of solutes and requires some experience before reproducible results are achieved. Furthermore, evaporation of the sample leads to an increase of solute concentrations and a measurable drop in temperature. Evaporation can be reduced by surrounding the sample with a humidified chamber (Fig. 5.6), which can be temperature controlled if necessary [60]. Here blotting times are constant and no longer depend on ambient parameters. Alternatively, evaporation can be minimized by blotting the sample from both sides (e.g., Ref. [61]) where the surrounding filter paper wetted with the sample provides a defined microenvironment.

The ethane pot also requires special attention in the setup. At liquid nitrogen temperature ethane is solid. After condensation of ethane gas, ethane freezes within a relatively short time when cooled by a bath of liquid nitrogen. This provides only a short time window in which the thin film has to be formed before plunge freezing. This period can be increased if cooling is slowed by surrounding the ethane pot with an insulating layer. Alternatively, ethane can be heated with a thermo-foil to just above its freezing point. This provides constant conditions over long periods.

After freezing, the sample has to be transferred from the ethane tank to liquid nitrogen, where it is stored. During transfer, the grid is vulnerable to accumulating surface contaminations such as small hexagonal ice crystals formed by condensa-

tion of ambient humidity. Therefore, a dry environment for the transfer is desirable, which can easily be achieved by increasing the height of the walls of the surrounding nitrogen bath above the top of the ethane pot. Evaporation of liquid nitrogen forms a dry nitrogen atmosphere, which is usually sufficient to minimize surface contamination.

Vitrification preserves the sample in an environment that is similar to the aqueous phase. However, there are also important differences, such as the density of the vitrified phase, which is more similar to cubic ice than to liquid water [56, 59]. Consequently, the packing density of the water molecules must have decreased during the short period of freezing. Whether this sudden change in the structure of the water induces structural alterations in the nano-particles is still unclear. For the many biological objects investigated so far, there is no evidence that vitrification by itself induces damage. The change in density from the liquid to vitrified state increases the contrast between the nano-particle and the solvent. This has to be taken into account when combining data from EM and SAXS.

During imaging of vitrified samples constant cooling below the devitrification temperature is required. This cooling has the advantageous effect that beam damage is significantly reduced compared to that at room temperature [62–65]. One reason for this reduction is the decreased mobility of breakdown products at lower temperatures. Consequently, at even lower temperatures (4–10 K) this protective effect is further increased, permitting higher doses [66] without losing high-resolution information. In the past, this has been exploited in acquiring high-resolution information (2.8–4 Å) of two-dimensional crystals of membrane proteins (e.g., Refs. [67–71]). However, at low resolution (>20 Å) the protective effect is not evident; on the contrary, with increasing dose a massive loss in contrast occurs. This is most likely caused by an increase in density of the solute that surrounds the particles. The cause for such a change can be either a change in the modification of the water by a transition to a high density vitrified state [56] or/and the beam-induced enrichment of high density break down fragments, which usually evaporate at higher temperatures and therefore do not alter the contrast. These changes in density have to be taken into account when merging data from EM and SAXS.

### 5.3.3

#### **Two-dimensional Merging of Electron Microscopic Data**

To preserve a certain resolution of an organic or biological material the permissible dose is limited to about 5–20 e Å<sup>-2</sup>. At higher doses, in vitrified samples bubbles form at the surface of protein or carbon [54]. This event marks severe damage to the gross structure and defines the highest tolerable dose for structure determination. As a consequence, micrographs have to be taken with low electron doses, which results in poor counting statistics. To improve the signal-to-noise ratio, and thus recover the high-resolution information, many images of different particles have to be merged. As a prerequisite for a coherent merging of the data, particles must exist in multiple identical copies. For many biological complexes, which have



defined stoichiometries and assembly pathway, this is fulfilled. For artificially created nano-particles made of organic polymeric material the exact stoichiometry and shape is often not precisely determined. In this case, the assumption that the particles exist in multiple identical copies is no longer valid. For such particles, which are usually similarly sensitive to radiation as biological complexes, high-resolution structure determination becomes impossible.

### 5.3.3.1 Cross Correlation Function

Another prerequisite for coherent merging of image data is that the particle images show the same view of the object. If this is the case, the images are only variable by in-plane operations such as image-shift and image-rotation ( $x$  and  $y$  for the origin of the particle and  $\phi$  for the in-plane-rotation). These parameters can be calculated by cross-correlation functions between the noisy particle images and a common reference (Fig. 5.7). The relative image shift between the reference and the raw image is determined from the position of the maximum of the cross-

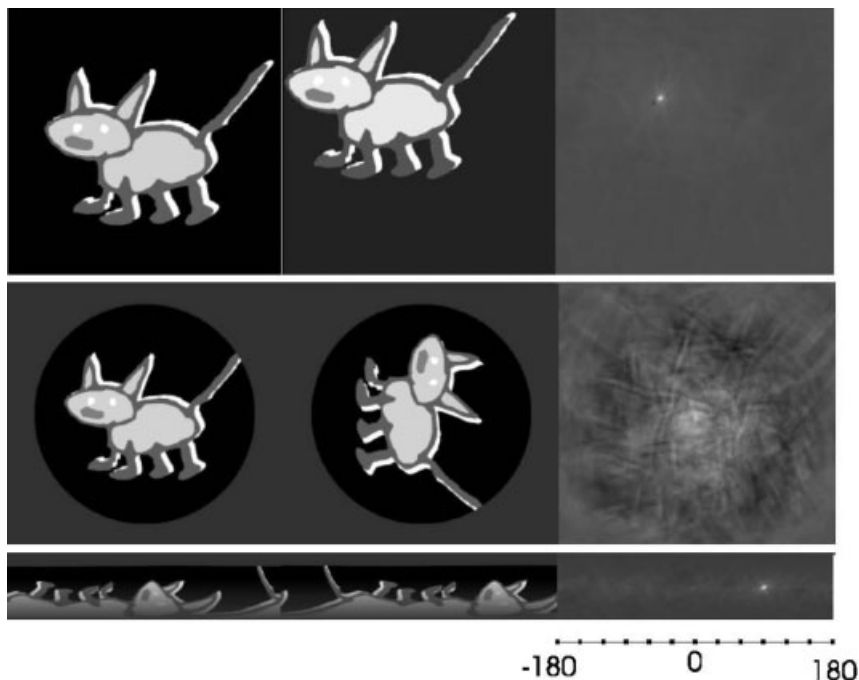


**Fig. 5.7.** Cross correlation function: Upper row: The cat on the left is correlated to the cat in the central panel. The cross-correlation function between the two cats shows a sharp peak (right-hand side). The position of this peak relative to the centre gives the translational shift between the two cats. Central row: The two cats vary by their in-plane

rotation. The correlation function between the two cats (right-hand panel) shows a broad peak. Lower row: Cats from the central row are transformed into cylindrical coordinates. The cross-correlation function (right-hand panel) shows a defined peak. The position of the peak relative to the centre gives the relative in-plane rotation.

correlation function relative to the image-centre. The height of the peak above background is a direct measure for the correlation and thus for the signal-to-noise ratio. If the reference and raw image do not match, the peak is broad without a well-defined shape. In this case, determination of the common origin from the cross correlation function becomes unreliable. A direct measure of how well the reference and raw image agree is the cross correlation coefficient, which ranges between  $-1$  and  $+1$ , where  $0$  means no correlation and  $1$  indicates that the compared images are identical. If the two images have opposite contrast, the cross-correlation coefficient becomes negative.

The rotational angle between reference and raw image is also determined by a cross correlation function but this time a polar-coordinate grid is used (Fig. 5.7). The position of the maximum in the cross-correlation function in this coordinate system gives the relative rotational angle. Exact determination of the rotational angle requires that reference image and raw image have the same origin. However, precise determination of the origin also requires the same rotational angle between the two compared images. To solve this dilemma, both origin and rotational angle are often searched alternately in an iterative process.

If all particle images in the data set are brought to a common origin and have the same in-plane rotation, the images can be averaged pixel-wise. Noise has random distribution whereas image information has the same position in all aligned images. By averaging many images the signal from the localized image information grows much faster than the one from the randomly distributed noise, increasing the signal-to-noise ratio.

For precise alignment of very noisy images the choice of reference plays a crucial role. Alignment of pure noise to a well-defined reference reproduces the basic features of the reference in the average [72, 73]. Averaging large numbers of pure noise images preserves the features of the reference over many iterative steps. This makes it difficult to spot whether a certain feature in an average is a genuine feature of the particle or arises from noise correlation. Recently, several strategies have been suggested to test data for such artifacts. One possibility is the exclusion of certain bands of spatial frequencies from the reference image. If the correlation in this resolution band is only due to noise correlation, after alignment to a reference with the missing spatial frequencies, the correlation will drop to levels below significance in this band. Another possibility is to mask off small areas in the reference image. If, after alignment, the feature in this “blind” spot of the reference is reproduced faithfully in the average, it represents a real feature of the particle and is not solely caused by noise correlation.

#### 5.3.3.2 Identification of the Different Views

Particles prepared for EM only rarely assume a single unique orientation – an exception is two-dimensional crystals. For single particle preparations a unique orientation of particles is uncommon. Instead particles usually have different orientations and often show a random distribution of views. This creates the problem of identifying the different views and merging only those particle images that represent the same view. Identification of the different views requires statistical

analysis of the image data, in which differences caused by noise are separated from those related to overall changes in shape related to a difference in particle orientation. The most common approach is a statistical method, which is similar to the principal component analysis used in the analysis of correlated data. The basic idea is that certain details of an image that are related to positional variations change in a concerted way, whereas noise varies independently across the image.

For the analysis of similarity between images, each particle image is represented as a single point in a multidimensional space. The space is defined by linear independent axes that point into the directions of the major differences between all images in the data set [74, 75]. The advantage of this representation is that comparable particle images will be in close proximity whereas images of different views will be further apart. Therefore, the distance between particle images can be directly used to group particle images according to similarity. The axes of the coordinate system can also be regarded as images (Eigenimage), representing the major changes between different views, and are therefore quite informative to identify common properties of the images. For example, in data of centered particles with random in plane rotation, rotational symmetry can be easily spotted in the Eigenimages [76]. In this case two of the major Eigenimages will show a ring of alternating bright and dark areas, which have the same rotational symmetry. Another property of the particles, which can be easily identified by analysis of the Eigenimages, is heterogeneity in size distribution [77]. Representation of particle images in Eigenimage space is the bases for the subsequent grouping of particles. Classification algorithms sort particle images in close proximity into the same class. These images represent approximately the same view and therefore fulfill the requirements for coherent merging, which leads to improvement of the signal-to-noise ratio.

For particle images representing different views (or different types of conformations or architectures), a single reference is no longer the best choice for alignment. Instead, multiple references, which represent all characteristic views, are more suitable and allow a more precise alignment. Appropriate sets of references can be generated from class averages to which each noisy particle image is aligned. As origin and rotational angle for the raw image the parameters from the alignment to the reference image with the highest cross correlation coefficient are chosen.

To reduce the bias introduced by the choice of an unrepresentative first reference a combination of classification and multi-reference alignment is favorable. This strategy was coined alignment by classification [76]. The basic idea is to classify a data-set of pre-centered particle images. A first set of references is generated from selected class-averages. By doing so only representative views are used as references and biasing by choosing an unsuitable single reference image is avoided. The limitations of this approach are connected to the accuracy of pre-centering. For approximately spherical particles quite accurate pre-centering is achieved by alignment to a rotationally averaged mean of all particle images. However, for elongated particles, where the different views vary significantly in their dimensions or

for spherical particles belonging to different size classes this gives unsatisfactory results.

Alternatively to the alignment by classification, neuronal networks are used to generate self-organizing maps to avoid biasing by the first reference [78]. Although this is a quite promising stable approach, it also relies on accurately pre-centered particles.

#### 5.3.4

#### Merging of EM-data in Three Dimensions

Due to the high depth of field caused by the small permissible apertures, an electron micrograph can be considered a good approximation of a projection of particle density. Consequently, no 3D information is obtained if the object is imaged from only one side. This is in contrast to light microscopy where the depth of field is much smaller than the thickness of the object. Here 3D image information is reconstructed by stacking consecutive focus layers.

##### 5.3.4.1 Sinogram Correlation

To reconstruct a three-dimensional volume from electron micrographs different projections have to be combined. With single particles, where the object has random orientations, the class averages can be considered as random projections of the object. A prerequisite for reconstructing the 3D volume is that the relative orientations of the projected particles are known. These orientations can be determined in real space by sinogram correlation [79] or in Fourier space by the equivalent method of cross common lines [80].

In 3D-Fourier space the 2D-Fourier-transform of a projection is a single plane. Fourier transforms of different projections have the same origin but different orientations, which depend on the direction of projection in real space. The planes in Fourier-space intersect along lines at which the phases and amplitudes in the two intersecting Fourier transforms are equal. These lines are called cross-common lines. The position of the cross-common lines in a pair of intersecting transforms reflects the angular relationship between the two projections in real space. Pair wise comparison of three transforms is sufficient to allow the determination of the complete angular relationship to which further projections can be fitted. The relative orientation of the first three projections can be determined by an exhaustive search. For finding the orientation of further projections, the cross-common lines between the transform of the projection with the unknown orientation and the set of transforms with known spatial relationship are searched for all possible orientations.

The real space approach uses sinograms [79], which are stacks of regularly angular-spaced 1D-line-projections of a 2D projection. Two different 2D-projections will share one 1D-line-projection with the same profile (Fig. 5.8). This line can be identified by sinogram correlation. The position of this 1D-line projection in the two sinograms depends on the angular relationship between the 2D projections.

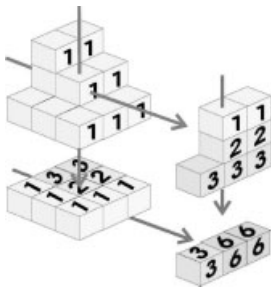


**Fig. 5.8.** Sinogram-correlation: Two 2D-projections of the same object share a common 1D-line projection.

The common 1D-line-projection in sinograms is equivalent to the cross-common lines between the two Fourier transforms in the cross common line approach.

For asymmetric particles these two approaches are problematic because only a very small part of the image information is used for determining the relative angular relationship between the different projections (three pairs of line projections in real space or three pairs of cross-common lines in Fourier space). Therefore, this method is only reliable for very accurate projections, which have a very high signal-to-noise ratio and are centered precisely. To cover the space optimally three approximately orthogonal views should be chosen for the first three projections.

Other approaches for the determination of orientations work with multiple micrographs of the same object where the relative tilt angle between consecutive images and the position of the tilt axis are known. These methods are much more robust for determining the initial orientations from projections of asymmetric particles. One example of these strategies is the conical tilt reconstruction [81], where two micrographs of the same object are recorded. In the first micrograph the object is highly tilted (preferably  $60\text{--}70^\circ$ ) and in the second micrograph it is un-tilted. The same particles are selected pair wise from both micrographs. When the orientation of the tilt axis and the tilt angle are known the relative spatial orientation between the two projections of the particle can be calculated. For unambiguous determination of the spatial orientations only those particle images are considered that show the same projection in the un-tilted micrograph.

For a particular view the in-plane rotation of the particles is determined by standard alignment procedures of the images of the un-tilted object. Knowing the tilt axis and tilt angle gives the complete information on the relative spatial orientations for the complementing tilted images.

#### 5.3.4.2 Reconstruction of the Three-dimensional Model

The next step is to reconstruct the 3D model from the different projections with known orientations. This can be either done in real space or in Fourier space. In real space the back-projection is used [82], where each projection is projected back to a three-dimensional volume. The direction for the back-projections is the same as the original direction of projections. For a single projection, back-projection

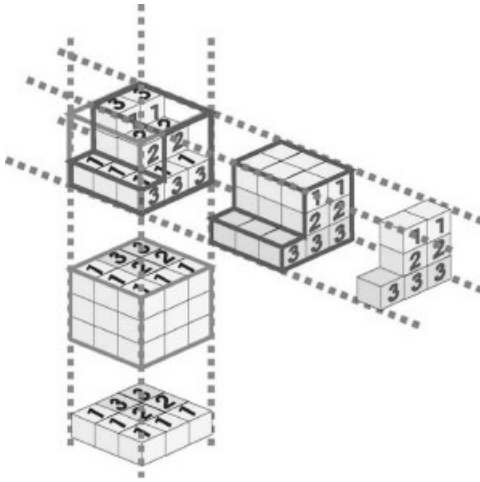


**Fig. 5.9.** Back-projection: 2D-projections are projected back into 3D space using the same direction for back-projection as that initially used for generating the 2D-projections. Averaging of the back-projected volumes regenerates the original volume.

results in a prism, where the image information is smeared out in the direction of projection (Fig. 5.9). Many of these back-projected volumes are averaged to reconstruct the three-dimensional volume.

This approach leads to an overestimation of the low spatial frequencies, resulting in a blurred appearance. To reduce this problem filter algorithms are employed that take the angular spread of projections and the resulting degree of over-sampling into account. This leads to a faithful representation of the 3D volume.

Alternatively to reconstruction in real space, reconstruction can also be carried out in Fourier space. Here, for the different projections, Fourier-transforms are calculated, which are combined in 3D-Fourier space. The 2D-Fourier-transforms in 3D-Fourier space are given the same orientations as determined for the corresponding projections in real space. Fourier synthesis provides the final reconstructed three-dimensional volume [83]. As in real space, over-sampling of the low-resolution information occurs and has to be properly corrected. For an object that is tilted around a single axis the maximal obtainable resolution  $d$  is given by the diameter  $D$  of the particle and the number  $n$  of evenly spaced views between  $-90^\circ$  and  $+90^\circ$  [Eq. (13)].

$$d = \pi \frac{D}{n} \quad (13)$$

For a nano-particle of 50 nm diameter, for instance, about 80 regularly spaced projections are needed to reconstruct the volume at 2 nm resolution. At higher resolution the Fourier-space is under-sampled and can therefore not be reconstructed

properly. According to the formula thinner objects need less independent projections. Importantly, resolution depends not only on these spatial considerations but also on the signal-to-noise ratio, which is related to the cumulative number of scattered electrons [51] and the general quality of the micrograph.

Often the projections are not equally spaced over the asymmetric unit but cover only a certain area. In this case the resolution is no longer isotropic and is worse in the direction where views are missing. Such image reconstructions look blurred and elongated in one direction.

For further refinement of orientations, reference-based approaches are chosen where the 3D model is taken into account. For example, in sinogram correlation the orientation of a projection is determined by sinogram correlation against a set of sinograms of equally spaced “anchor”-projections of the three-dimensional volume. Alternatively a projection matching algorithm is employed, where the volume is projected in different directions and the particle images are aligned by multi-reference alignment to this set of references. After alignment the particle is assigned the same orientation as the direction of projection of the reference image to which the particle correlated best [84]. A similar approach is followed in Fourier-space. Here Fourier transforms of the particle images are compared to the 3D-Fourier-transform of the reference-volume, testing different orientations for the best match [85].

For high-resolution image reconstructions, the transfer of contrast by the electron microscope plays an important role. This modulation is described by the contrast transfer function. Depending on the defocus and other imaging conditions this function has zeros at certain spatial frequencies, where no information is transferred and pass-bands at other spatial frequencies, where the information is transferred alternately with positive or negative contrast. In the pass-bands the strength of contrast transfer varies between no transfer and complete transfer of information. The simplest approach to correction is the contrast-inversion in every other pass-band, which leads to transfer of image information with the same contrast. Doing that is sufficient for obtaining image reconstructions where the phases are accurately preserved but the amplitudes show a clear deviation from their true values. Especially at low spatial frequencies the amplitudes are severely underestimated (e.g., no phase contrast transfer at 0 spatial frequencies). More sophisticated approaches also attempt to correct for the amplitude information. However, at spatial frequencies, where the overall contrast transfer is close to zero or zero, the information is often too noisy and should not be amplified by huge factors. This problem is solved by a Wiener filtering algorithm in which a maximal permissible amplification factor is set (e.g., Ref. [86]). The choice of maximal amplification factor depends on the signal-to-noise ratio and is chosen close to 1 when correction for the contrast transfer function is done on raw images and can be considerably higher (e.g., 10; Ref. [86]) if the correction is done on averaged images. Even with these more sophisticated approaches to contrast transfer correction, low spatial frequencies are usually underestimated. Therefore, the amplitude profile is not correctly maintained. However, the relative amplitudes in a certain resolution band are preserved accurately.

## 5.4 Merging of Methods

### 5.4.1

#### Comparison of EM and SAXS Data

SAXS data provides information on the accurate amplitude profile. For a combination with electron microscopic data a relative scaling of the amplitude profiles is required. For such scaling it is necessary to understand the underlying mechanisms that influence the amplitude profile in the electron microscopic data. We have already discussed in detail the effect of the contrast transfer function. An exact knowledge of if and how it was corrected is a prerequisite for the interpretation of the amplitude profile. In addition, at low spatial frequencies the contrast between particles and solvent determines the amplitude profile. Here differences in density between water in the SAXS measurements and vitrified water in the electron microscopic measurements have to be taken into account. Furthermore, in many image reconstructions of electron microscopic images band-pass filtering of the data has been used to suppress information at low and high spatial frequencies. Again the exact filter parameters and the shape of the filter have to be known to reproduce the true amplitude profile. Another serious effect on the amplitude profile is decay in contrast-transfer at higher spatial frequencies, which is best described by a temperature factor, similar to the one known from X-ray crystallography. Many parameters contribute to this overall temperature factor, such as spherical and chromatic aberration of the microscope, stability of the holder, beam damage, charging, inaccuracy in the determination of particle orientations, effects of interpolation in image processing, and the modulation transfer function of the CCD or the photographic film and scanner. Typical cumulated temperature factors have been estimated to range between ca. 500 and 1000 Å<sup>2</sup> [51, 87], which is considerably larger than those observed in X-ray crystallography. Accurate estimates of the temperature factors in the raw data come from comparison of the amplitude profile from electron micrographs and SAXS measurements on Herpes Simplex Virus [88]. These temperature factors ranged between 50 and 200 Å<sup>2</sup>, depending on the defocus.

To illustrate that, we discuss here a direct comparison of SAXS and EM data from *Lumbricus terrestris* hemoglobin. SAXS data include the scattering curve,  $I(h)$ , pair distance distribution function,  $p(r)$ , radius of gyration,  $R_G$ , hydrated volume,  $V$  and the maximum diameter of the particle,  $D_{\max}$ . EM data provide information on the 3D electron density distribution (Table 5.1). For direct comparison the EM data need to be converted into data suitable for SAXS model calculations. As outlined in previous sections, in SAXS models, the protein mass is simulated with a large number of small spheres. Accordingly, to compare EM data with SAXS profiles, EM data are used to calculate models with a large number of small spheres, whereby the position of the spheres is given by the EM model coordinates. Then model scattering functions, pair distance distribution functions and molecular parameters (radius of gyration, maximum particle diameter, volume) of the EM



model can be calculated in a way similar to the calculation of the SAXS models (Table 5.1). To convert the EM electron density in a meaningful weighting scheme for the model calculations, the weight of spheres is chosen to represent density values between 0.3345 (electron density of water) and 0.4395 (averaged electron density of a protein). Here the value for the electron density of water was chosen, because vitrified water, as used in the EM experiment, forms no ice crystals (see above). Additionally, appropriate rescaling is necessary to fit the positions of the maxima of the experimental scattering curve and the model parameters (scaling due to magnification differences).

A common problem in EM is the exact determination of the volume of the biological sample and here knowledge from SAXS studies may help. Figure 5.10

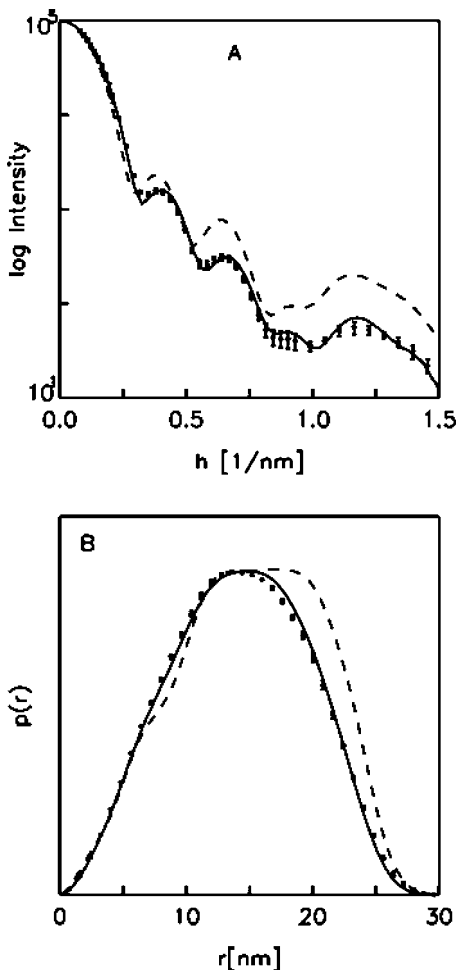


Fig. 5.10. Comparison EM (dashed line) and SAXS data (experimental data dotted with error bars; model data solid line) for *Lumbricus terrestris* hemoglobin.

shows that the threshold of the EM model has to be chosen in a way that the model represents the hydrated particle volume rather than the “expected” volume of the protein to give good agreement of data. The “expected” particle volume is calculated by the molecular weight of the protein, and the partial specific volume. This is usually much smaller than the hydrated volume [18].

We see that SAXS and EM data agree very well up to a scattering angle of  $h = 1.2 \text{ nm}^{-1}$ . Careful analyses of the scattering curves reveal that the 1st minimum of the experimental scattering curve is not fitted within the limits of error by the scattering curve calculated from the EM data. The minimum of the model scattering curve seems to be more pronounced than the minimum of the experimental curve. This, however, must not be taken too seriously. In scattering experiments the randomly oriented particles in solution together account for the observed scattering and the structural information from all the particles in solution is summarized in one scattering curve. This summarizing of structural information may lead to an additional “smearing” of the minima of the scattering curve. If, on the other hand, the scattering curve of a model (e.g., an EM model) is calculated, the information of only one particle is present, giving rise to a very “clear” scattering curve. Therefore, model scattering curves sometimes show more pronounced minima than the experimental curves and consequently, as long as the positions of the minima and the heights and positions of the maxima are fitted correctly by the model data, this does not decrease the quality of a model.

The observed differences in the outer part of the scattering curve, however, may be due to slightly different structures of the protein observed in vitreous ice and in solution. Another explanation might be the contrast transfer of the magnetic lens of the electron microscope or the application of an additional filtering procedure during the EM reconstruction (as mentioned above).

In general, it is important to state that the value of the hydrated volume can only be determined with sufficient certainty from the SAXS data, whereas information on the 3D electron density distribution is contained in the EM data. Thus, both methods together give maximal information.

#### 5.4.2

#### **SAXS Modeling Approaches using EM Information**

We have seen that SAXS modeling is not unique and therefore SAXS data are usually interpreted by comparing the experimental data with model profiles. The creation of model profiles is not trivial and, as stated above, it is very useful to implement structural knowledge from other methods to increase the reliability of any SAXS modeling attempt. As an example we want to discuss here an indirect incorporation of information gained by EM into automated SAXS modeling: In this approach, first templates are created using the structural information gained by EM. Subsequently, those templates are used as starting models for the automated SAXS model creation.

In Fig. 5.11 different models of the hemoglobin from the leech *Macrobdella decora* are shown. Overall the protein complex is related to the hemoglobin from

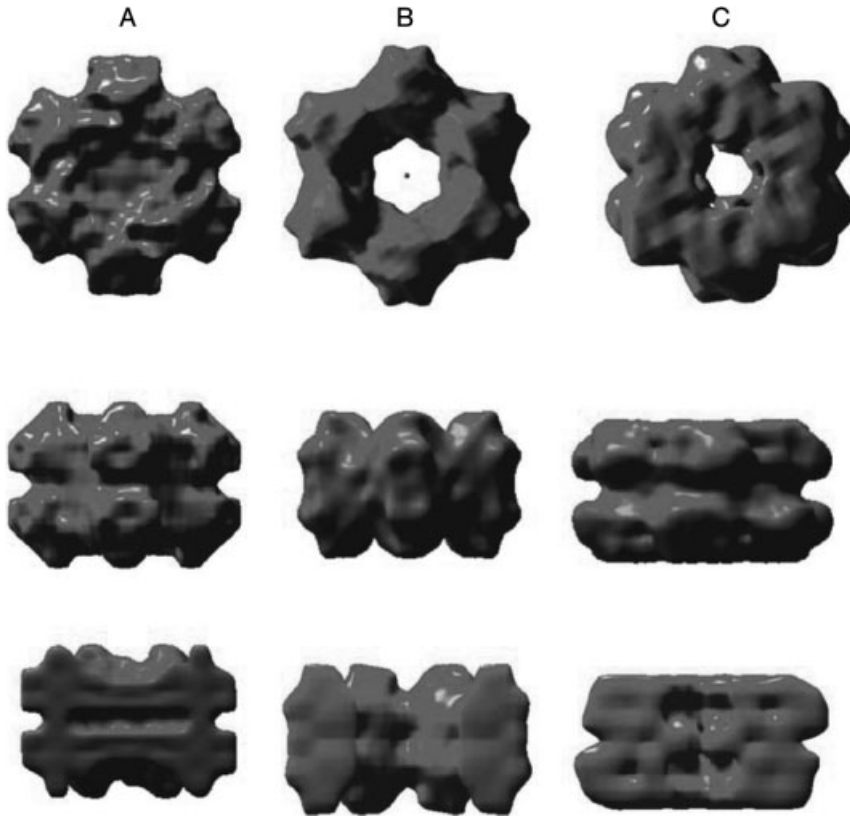


**Fig. 5.11.** Models of *Macrobdella decora* hemoglobin: (A) two-step trial-and-error SAXS model, (B) automatic generation without information other than  $D_6$  symmetry, (C) automatic generation employing a template created with information from EM data.

*Lumbricus terrestris* and it has a similar appearance (hexagonal bilayer architecture). In Fig. 5.11 the trial-and-error approach from SAXS multi-body modeling is shown in part (A) (similar to the approach shown earlier for *L. terrestris* hemoglobin). Fig. 5.11(B) shows the automatically generated SAXS model calculated without structural information other than  $D_6$  symmetry (*ab initio* modeling). For Fig. 5.11(C) additional information concerning shape and internal structure was incorporated in the calculations by the use of a template derived from 3D EM reconstructions [89]. Clearly, this final example shows that SAXS modeling procedures can be increased in accuracy and reliability through the use of suitable EM templates. SAXS and EM model values are given in Table 5.2.

In conclusion, if characterization of a nano-particle is attempted by either SAXS or EM, a combination of knowledge gained by different methods is advisable. Although such approaches are not yet well established, the results shown here illustrate that this is the way forward for nano applications.

**Tab. 5.2.** Experimental SAXS parameters and data of SAXS models of *Macrobdella decora* hemoglobin.

	<i>Exp.</i> <sup>[a,b]</sup>	<i>Two-step model</i> <sup>[c]</sup>	<i>Automatic generation with D6</i>	<i>Automatic generation with EM template</i>
$R_G$ (nm)	$10.75 \pm 0.01$	$10.73 \pm 0.02$	$10.79 \pm 0.01$	$10.78 \pm 0.01$
$D_{\max}$ (nm)	$29.54 \pm 0.02$	$29.6 \pm 0.1$		
$V$ (nm <sup>3</sup> )	$5800 \pm 300$	$6000 \pm 300$	$5895 \pm 155$	$5746 \pm 111$
$r_b$ (nm)		0.66	0.8	0.8
$d_z$ (nm) <sup>[d]</sup>		$19.4 \pm 1.7$	$22.5 \pm 2.2$	$17.6 \pm 0.0$
Consensus model:				
Number of models included ( $N_m$ )		4	11	8
Total number of spheres ( $N_b$ )		5970	$1662 \pm 44$	$1620 \pm 31$

<sup>a</sup>Experimental data taken from Ref. 90.

<sup>b</sup>Mean values and standard deviations result from averaging experimental data.

<sup>c</sup>Mean values and standard deviations result from averaging the four models included in the consensus model shown in Fig. 5.11.

<sup>d</sup>Values for  $d_z$  refer to the largest dimension in the z direction, obtained from the difference of sphere coordinates by adding the diameter of one sphere.

## References

- GUINIER, A., FOURNET, J., *Small-angle Scattering of X-rays*, 1995, Wiley, New York.
- PESSON, H., KUMOSINSKI, F., TIMASHEFF, S.N., Small-angle X-ray scattering, *Methods Enzymol.* **1973**, 27, part D, 151–209.
- PILZ, I., GLATTER, O., KRATKY, O. Small-angle X-ray scattering, *Methods Enzymol.* **1979**, 61, 148.
- GLATTER, O., KRATKY, O. (eds), *Small-angle X-ray Scattering*, 1982, Academic Press, New York, London.
- KRATKY, O., PILZ, I. Recent advances and applications of diffuse X-ray small-angle scattering on biopolymers in dilute solutions. *Quart. Rev. Biophys.* **1972**, 5, 481–537.
- FEIGIN, L.A., SVERGUN, D.I. *Structure Analysis by Small-Angle X-ray and Neutron Scattering*, 1987, Plenum Press, New York.
- ZIPPER, P., DURCHSCHLAG, H. Modeling of protein solution structures. *J. Appl. Crystallogr.* **2003**, 36, 509.
- DURCHSCHLAG, H., ZIPPER, P. Modeling the hydration of proteins: prediction of structural and hydrodynamic parameters from X-ray diffraction and scattering data. *Eur. Biophys. J.* **2003**, 32, 487.
- KUMOSINSKI, T.F., PESSON, H. Estimation of sedimentation coefficients of globular proteins: an application of small-angle X-ray scattering. *Arch. Biochem. Biophys.* **1982**, 219, 89.
- DURCHSCHLAG, H., ZIPPER, P. Calculation of structural parameters from hydrodynamic data. *Prog. Colloid Polym. Sci.* **1999**, 113, 87.
- DURCHSCHLAG, H., ZIPPER, P. Prediction of hydrodynamic

- parameters of biopolymers from small-angle scattering data. *J. Appl. Crystallogr.* **1997**, *30*, 1112.
- 12 BYRON, O. Hydrodynamic bead modeling of biological macromolecules. *Methods Enzymol.* **2000**, *321*, 278.
  - 13 SVERGUN, D., BARBERATO, C., KOCH, M.H.J. CRY SOL – a program to evaluate X-ray solution scattering of biological macromolecules from atomic coordinates. *J. Appl. Crystallogr.* **1995**, *28*, 768.
  - 14 PERKINS, S.J., ASHTON, A.W., BOEHM, M.K., CHAMBERLAIN, D. Molecular structures from low angle X-ray and neutron scattering studies. *Int. J. Biol. Macromol.* **1998**, *22*, 1.
  - 15 ZIPPER, P., KREBS, A., DURCHSCHLAG, H. Comparative modeling of giant annelid hemoglobins. *Prog. Colloid Polym. Sci.* **2004**, *127*, 126.
  - 16 ZIPPER, P., KREBS, A., DURCHSCHLAG, H. Prediction of hydrodynamic parameters of *Lumbricus terrestris* hemoglobin from small-angle X-ray and electron microscopic structures. *Prog. Colloid Polym. Sci.* **2002**, *119*, 141.
  - 17 KREBS, A., DURCHSCHLAG, H., ZIPPER, P. Small angle X-ray scattering studies and modeling of *Eudistylia vancouverii* chlorocruorin and *Macrobdeella decora* hemoglobin. *Biophys. J.* **2004**, *87*, 1173.
  - 18 KREBS, A., LAMY, J., VINOGRADOV, S.N., ZIPPER, P. *Lumbricus terrestris* hemoglobin: a comparison of small-angle x-ray scattering and cryoelectron microscopy data. *Biopolymers* **1998**, *45*, 289.
  - 19 ROYER, W.E. JR, HENDRICKSON, W.A. Molecular symmetry of *Lumbricus erythrocrurorin*. *J. Biol. Chem.* **1998**, *263*, 13762.
  - 20 BOEKEMA, E.J., VAN HEEL, M. Molecular shape of *Lumbricus terrestris* erythrocrurorin studied by electron microscopy and image analysis. *Biochim. Biophys. Acta* **1988**, *957*, 370.
  - 21 MARTIN, P.D., KUCHUMOV, A.R., GREEN, B.N., OLIVER, R.W.A., BRASWELL, E.H., WALL, J.S., VINOGRADOV, S.N. Mass spectrometric composition and molecular mass of *Lumbricus terrestris* hemoglobin: a refined model of its quaternary structure. *J. Mol. Biol.* **1996**, *255*, 154.
  - 22 ZHU, H., OWNBY, D.W., RIGGS, C.K., NOLASCO, N.J., STOOPS, J.K., RIGGS, A.F. Assembly of the gigantic hemoglobin of the earthworm *Lumbricus terrestris*. *J. Biol. Chem.* **1996**, *271*, 30007.
  - 23 OWNBY, D.W., ZHU, H., SCHNEIDER, K., BEAVIS, R.C., CHAIT, B.T., RIGGS, A.F. The extracellular hemoglobin of the earthworm, *Lumbricus terrestris*. Determination of subunit stoichiometry. *J. Biol. Chem.* **1993**, *268*, 13539.
  - 24 VINOGRADOV, S.N., LUGO, S.D., MAINWARING, M.G., KAPP, O.H., CREWE, A.V. Bracelet protein: a quaternary structure proposed for the giant extracellular hemoglobin of *Lumbricus terrestris*. *Proc. Natl. Acad. Sci. U.S.A.* **1986**, *83*, 8034.
  - 25 VINOGRADOV, S.N., SHARMA, P.K., QABAR, A.N., WALL, J.S., WESTRICK, J.A., SIMMONS, J.H., GILL, S.J. A dodecamer of globin chains is the principal functional subunit of the extracellular hemoglobin of *Lumbricus terrestris*. *J. Biol. Chem.* **1991**, *266*, 13091.
  - 26 MARTIN, P.D., EISELE, K.L., DOYLE, M.A., KUCHUMOV, A.R., WALZ, D.A., ARUTYUNYAN, E.G., VINOGRADOV, S.N., EDWARDS, B.F.P. Molecular symmetry of the dodecamer subunit of *Lumbricus terrestris* hemoglobin. *J. Mol. Biol.* **1996**, *255*, 170.
  - 27 SCHATZ, M., ORLOVA, E.V., DUBE, P., JÄGER, J., VAN HEEL, M. Structure of *Lumbricus terrestris* hemoglobin at 30 Å resolution determined using angular reconstitution. *J. Struct. Biol.* **1995**, *114*, 28.
  - 28 TAVEAU, J.-C., BOISSET, N., VINOGRADOV, S.N., LAMY, J.N. Three-dimensional reconstruction of *Lumbricus terrestris* hemoglobin at 22 Å resolution: intramolecular localization of the globin and linker chains. *J. Mol. Biol.* **1999**, *289*, 1343.
  - 29 MOUCHE, F., BOISSET, N., PENCZEK, P.A. *Lumbricus terrestris* hemoglobin – the architecture of linker chains and

- structural variation of the central toroid. *J. Struct. Biol.* **2001**, *133*, 176.
- 30 ROYER, W.E. JR, STRAND, K., VAN HEEL, M., HENDRICKSON, W.A. Structural hierarchy in erythrocyrin, the giant respiratory assemblage of annelids. *Proc. Natl. Acad. Sci. U.S.A.* **2000**, *97*, 7107.
- 31 SVERGUN, D.I. Advanced solution scattering data analysis methods and their applications. *J. Appl. Crystallogr.* **2000**, *33*, 530.
- 32 SVERGUN, D.I., KOCH, M.H.J. Advances in structure analysis using small-angle scattering in solution. *Curr. Opin. Struct. Biol.* **2002**, *12*, 654.
- 33 KOCH, M.H.J., VACHETTE, P., SVERGUN, D.I. Small-angle scattering: a view on the properties, structures and structural changes of biological macromolecules in solution. *Quart. Rev. Biophys.* **2003**, *36*, 147.
- 34 HAMMEL, M., KRIECHBAUM, M., GRIES, A., KOSTNER, G.M., LAGGNER, P., PRASSL, R. Solution structure of human and bovine beta(2)-glycoprotein I revealed by small-angle X-ray scattering. *J. Mol. Biol.* **2002**, *321*, 85.
- 35 TAKAHASHI, Y., NISHIKAWA, Y., FUJISAWA, T. Evaluation of three algorithms for *ab initio* determination of three-dimensional shape from one-dimensional solution scattering profiles. *J. Appl. Crystallogr.* **2003**, *36*, 549.
- 36 SVERGUN, D.I. Restoring low resolution structure of biological macromolecules from solution scattering using simulated annealing. *Biophys. J.* **1999**, *76*, 2879.
- 37 SVERGUN, D.I., PETOUKHOV, M.V., KOCH, M.H.J. Determination of domain structure of proteins from X-ray solution scattering. *Biophys. J.* **2001**, *80*, 2946.
- 38 PETOUKHOV, M.V., SVERGUN, D.I. New methods for domain structure determination of proteins from solution scattering data. *J. Appl. Crystallogr.* **2003**, *36*, 540.
- 39 CHACÓN, P., MORÁN, F., DÍAZ, J.F., PANTOS, E., ANDREU, J.M. Low-resolution structures of proteins in solution retrieved from X-ray scattering with a genetic algorithm. *Biophys. J.* **1998**, *74*, 2760.
- 40 WALTHER, D., COHEN, F.E., DONIACH, S. Reconstruction of low-resolution three-dimensional density maps from one-dimensional small-angle X-ray solution scattering data for biomolecules. *J. Appl. Crystallogr.* **2000**, *33*, 350.
- 41 VIGIL, D., GALLAGHER, S.C., TREWHELLA, J., GARCÍA, A.E. Functional dynamics of the hydrophobic cleft in the N-domain of calmodulin. *Biophys. J.* **2001**, *80*, 2082.
- 42 KOJIMA, M., TIMCHENKO, A.A., HIGO, J., ITO, K., KIHARA, H., TAKAHASHI, K. Structural refinement by restrained molecular-dynamics algorithm with small-angle X-ray scattering constraints for a biomolecule. *J. Appl. Crystallogr.* **2004**, *37*, 103.
- 43 CHACÓN, P., DÍAZ, J.F., MORÁN, F., ANDREU, J.M. Reconstruction of protein form with X-ray solution scattering and a genetic algorithm. *J. Mol. Biol.* **2000**, *299*, 1289.
- 44 ZIPPER, P., DURCHSCHIAG, H., KREBS, A. Modeling of biopolymers, **2005**, in SCOTT, D.J., HARDING, S.E., ROWE, A.J. (eds.) *Modern analytical ultracentrifugation: techniques and methods*. Royal Society of Chemistry, Cambridge, U.K.
- 45 VOLKOV, V.V., SVERGUN, D.I. Uniqueness of *ab initio* shape determination in small-angle scattering. *J. Appl. Crystallogr.* **2003**, *36*, 860.
- 46 LANGMORE, J.P., SMITH, M.F. Quantitative energy-filtered electron microscopy of biological molecules in ice. *Ultramicroscopy*, **1992**, *46*, 349–373.
- 47 ERICKSON, H.P., KLUG, A. Measurement and compensation of defocusing and aberrations by Fourier processing of electron micrographs. *Phil. Trans. Roy. Soc. Lond. B*, **1971**, *261*, 105–118.
- 48 TOYOSHIMA, C., UNWIN, N. Contrast transfer for frozen-hydrated specimens: determination from pairs of defocused images. *Ultramicroscopy*, **1988**, *25*, 279–291.

- 49 COLLIEX, C., JEANGUILLAUME, C., MORY, C. Unconventional modes for STEM imaging of biological structures. *J. Ultrastruct. Res.*, **1984**, *88*, 177–206.
- 50 HENDERSON, R. The potential and limitations of neutrons, electrons and X-rays for atomic resolution microscopy of unstained biological molecules. *Quart. Rev. Biophys.*, **1995**, *28*, 171–193.
- 51 ROSENTHAL, P.B., HENDERSON, R. Optimal determination of particle orientation, absolute hand, and contrast loss in single-particle electron cryomicroscopy. *J. Mol. Biol.*, **2003**, *333*, 721–745.
- 52 WADE, R.H. A brief look at imaging and contrast transfer. *Ultramicroscopy*, **1992**, *46*, 145–156.
- 53 TAYLOR, K.A., GLAESER, R.M. Electron diffraction of frozen, hydrated protein crystals. *Science*, **1974**, *186*, 1036–1037.
- 54 DUBOCHET, J., LEPAULT, J., FREEMAN, R., BERRIMAN, J., HOMO, J.C. Electron microscopy of frozen water and aqueous solutions. *J. Microscop.*, **1982**, *128*, 219–237.
- 55 DUBOCHET, J., ADRIAN, M., CHANG, J.J., HOMO, J.C., LEPAULT, J., McDOWALL, A.W., SCHULTZ, P. Cryo-electron microscopy of vitrified specimens. *Q. Rev. Biophys.*, **1988**, *21*, 129–228.
- 56 HEIDE, H.G. Observation on ice layers. *Ultramicroscopy*, **1984**, *14*, 271–278.
- 57 HEIDE, H.G., ZEITLER, E. The Physical Behaviour of solid water at low temperatures and the embedding of electron microscopical specimens. *Ultramicroscopy*, **1985**, *16*, 151–160.
- 58 BALD, W.B. On crystal size and cooling rate. *J. Microsc.*, **1986**, *143* (Pt 1), 89–102.
- 59 NARTEN, A.H. Diffraction pattern and structure of amorphous solid water at 10 and 77 K. *J. Chem. Phys.*, **1976**, *64*, 1106–1120.
- 60 BELLARE, J.R., DAVIS, H.T., SCRIVEN, L.E., TALMON, Y. Controlled environment vitrification system: An improved sample preparation technique. *J. Electron. Microsc. Techn.*, **1988**, *10*, 87–111.
- 61 WHITE, H.D., THIRUMURUGAN, K., WALKER, M.L., TRINICK, J. A second generation apparatus for time-resolved electron cryo-microscopy using stepper motors and electrospray. *J. Struct. Biol.*, **2003**, *144*, 246–252.
- 62 EGERTON, R.F. Chemical measurement of radiation damage in organic samples at and below room temperature. *Ultramicroscopy*, **1980**, *5*, 521–523.
- 63 KNAPEK, E., DUBOCHET, J. Beam damage to organic material is considerably reduced in cryo-electron microscopy. *J. Mol. Biol.*, **1980**, *141*, 147–161.
- 64 LAMVIK, M.K. Radiation damage in dry and frozen hydrated organic material. *J. Microscop.*, **1991**, *161*, 171–181.
- 65 SIEGEL, G. Der Einfluß tiefer temperature auf die Strahlenschädigung von organischen kristallen durch 100 keV-elektronen. *Z. Naturforsch.*, **1971**, *27*, 325–332.
- 66 STARK, H., ZEMLIN, F., BOETTCHER, C. Electron radiation damage to protein crystals of bacteriorhodopsin at different temperatures. *Ultramicroscopy*, **1996**, *63*, 75–79.
- 67 BALDWIN, J.M., HENDERSON, R., BECKMAN, E., ZEMLIN, F. Images of purple membrane at 2.8 Å resolution obtained by cryo-electron microscopy. *J. Mol. Biol.*, **1988**, *202*, 585–591.
- 68 HENDERSON, R., BALDWIN, J.M., CESKA, T.A., ZEMLIN, F., BECKMANN, E., DOWNING, K.H. Model for the structure of bacteriorhodopsin based on high-resolution electron cryo-microscopy. *J. Mol. Biol.*, **1990**, *213*, 899–929.
- 69 KÜHLBRANDT, W., WANG, D.N., FUJIYOSHI, Y. Atomic model of plant light-harvesting complex by electron crystallography. *Nature*, **1994**, *367*, 614–621.
- 70 MIYAZAWA, A., FUJIYOSHI, Y., UNWIN, N. Structure and gating mechanism of the acetylcholine receptor pore. *Nature*, **2003**, *423*, 949–955.
- 71 MURATA, K., MITSUOKA, K., HIRAI, T.,

- WALZ, T., AGRE, P., HEYMAN, J.B., ENGEL, A., FUJIYOSHI, Y. Structural determinants of water permeation through aquaporin-1. *Nature*, **2000**, *407*, 599–605.
- 72 SHAIKH, T.R., HEGERL, R., FRANK, J. An approach to examining model dependence in EM reconstructions using cross-validation. *J. Struct. Biol.*, **2003**, *142*, 301–310.
- 73 STEWART, A., GRIGORIEFF, N. Noise bias in the refinement of structures derived from single particles. *Ultramicroscopy*, **2004**, *102*, 67–84.
- 74 VAN HEEL, M. Multivariate statistical classification of noisy images (randomly oriented biological macromolecules). *Ultramicroscopy*, **1984**, *13*, 165–183.
- 75 VAN HEEL, M., FRANK, J. Use of multivariate statistics in analysing the images of biological macromolecules. *Ultramicroscopy*, **1981**, *6*, 187–194.
- 76 DUBE, P., TAVARES, P., LURZ, R., VAN HEEL, M. The portal protein of bacteriophage SPPI: a DNA pump with 13-fold symmetry. *Embo J.*, **1993**, *12*, 1303–1309.
- 77 WHITE, H.E., SAIBIL, H.R., IGNATIOU, A., ORLOVA, E.V. Recognition and separation of single particles with size variation by statistical analysis of their images. *J. Mol. Biol.*, **2004**, *336*, 453–460.
- 78 PASCUAL-MONTANO, A., DONATE, L.E., VALLE, M., BARCENA, M., PASCUAL-MARQUI, R.D., CARAZO, J.M. A novel neural network technique for analysis and classification of EM single-particle images. *J. Struct. Biol.*, **2001**, *133*, 233–245.
- 79 VAN HEEL, M. Angular reconstitution: A posteriori determination of projection directions for 3D reconstructions. *Ultramicroscopy*, **1987**, *21*, 110–113.
- 80 DEROSIER, D.J., KLUG, A. Reconstruction of three dimensional structures from electron micrographs. *Nature*, **1968**, *217*, 130–134.
- 81 RADERMACHER, M. Three-dimensional reconstruction of single particles from random and nonrandom tilt series. *J. Electron. Microsc. Tech.*, **1988**, *9*, 359–394.
- 82 HOPPE, W., SCHRAMM, H., STURM, M., HUNSMANN, N., GASSMAN, J. 3-dimensional electron-microscopy of individual biological objects. 1. Methods. *Z. Naturforsch.*, **1976**, *A31*, 645–655.
- 83 CROWTHER, R.A., KLUG, A. Structural analysis of macromolecular assemblies by image reconstruction from electron micrographs. *Annu. Rev. Biochem.*, **1975**, *44*, 161–182.
- 84 SANDER, B., GOLAS, M.M., STARK, H. Corrim-based alignment for improved speed in single-particle image processing. *J. Struct. Biol.*, **2003**, *143*, 219–228.
- 85 GRIGORIEFF, N. Three-dimensional structure of bovine NADH:ubiquinone oxidoreductase (complex I) at 22 Å in ice. *J. Mol. Biol.*, **1998**, *277*, 1033–1046.
- 86 BÖTTCHER, B., CROWTHER, R.A. Difference imaging reveals ordered regions of RNA in turnip yellow mosaic virus. *Structure*, **1996**, *4*, 387–394.
- 87 BÖTTCHER, B., WYNNE, S.A., CROWTHER, R.A. Determination of the fold of the core protein of hepatitis B virus by electron cryomicroscopy. *Nature*, **1997**, *386*, 88–91.
- 88 SAAD, A., LUDTKE, S.J., JAKANA, J., RIXON, F.J., TSURUTA, H., CHIU, W. Fourier amplitude decay of electron cryomicroscopic images of single particles and effects on structure determination. *J. Struct. Biol.*, **2001**, *133*, 32–42.
- 89 DE HAAS, F., BOISSET, N., TAVEAU, J.-C., LAMBERT, O., VINOGRADOV, S.N., LAMY, J. Three-dimensional reconstruction of *Macrobodella decora* (Leech) hemoglobin by cryoelectron microscopy. *Biophys. J.* **1996**, *70*, 1973–1984.
- 90 KREBS, A., ZIPPER, P., VINOGRADOV, S.N. Lack of size and shape alteration of oxygenated and deoxygenated *Lumbricus terrestris* hemoglobin? *Biochim. Biophys. Acta* **1996**, *1297*, 115.



## 6

# ***In Situ* Characterization of Drug Nanoparticles by FTIR Spectroscopy**

*Michael Türk and Ruth Signorell*

### 6.1

#### **Introduction**

Infrared (IR) spectroscopy is an important tool to characterize nanomaterials in life sciences. Refs. [1–10] highlight only a few recent examples in this large field, including catalysis using nanoparticles, the targeted synthesis of nanoparticles, the use of nanoparticles as biosensors, and the characterization of drug nanoparticles. This chapter focuses on particulate matter built from molecules and in particular on drug nanoparticles. For the characterization of these molecular nanoparticles IR spectroscopy is particularly well suited. It is relatively sensitive and non-invasive, which is decisive for instance for the investigation of sensitive molecular particles. Furthermore, IR spectroscopy can be used for different kinds of particulate samples (aerosols, particles on a holder, or particles in a matrix) and under a broad range of different experimental conditions (temperature, pressure, etc.). For molecular particles, it opens a direct window to the characteristic intermolecular and intramolecular vibrational dynamics. The vibrational spectra of such large aggregates contain a wealth of information not only about the chemical composition or the phase behavior of the particles, but also about intrinsic particle properties such as the particle size, the particle shape, or structural changes in the particles' surface.

Approximately 80% of all pharmaceutical products are in solid dosage form. Thus, in biomedical applications both the size and shape of the solid particles are important quantities to know, for instance because they can affect the bioavailability of drug particles. The size of the particles manifests itself in the IR extinction spectra by scattering phenomena. They lead to slanted baselines and to a dispersion shape of the absorption bands. To determine the size distribution for a particle ensemble directly from the infrared spectrum it is crucial to know the frequency-dependent optical data (indices of refraction) of the particles. Nowadays, few databases provide refractive index data for particulate systems and most of these data bases focus more on molecular ice particles than on biomolecular substances. Since the optical properties of particles can differ markedly from those of the solid bulk, corresponding bulk data are often not suitable either. This clearly illustrates the need for optical data of particles, especially for substances of biomolecular in-

terest. The particles' shape can lead to characteristic band structures in IR extinction spectra. These phenomena, however, are pronounced only for very strong vibrational transitions. The structure and position of weak absorption bands are dominated by rather local effects, i.e., by interactions with neighboring molecules, such as the formation of specific hydrogen-bonded networks in the particles.

The main focus of this chapter lies in the *in situ* characterization of nanoparticles by Fourier-transform infrared (FTIR) spectroscopy. Most often, off-line techniques are used to investigate particles, which have, consequently, first to be collected on a holder. This approach is not only very slow, but the process of collecting can also affect the particles' properties. *In situ* characterization by contrast is quick, thus allowing us to investigate and control the particle properties during their formation. We compare and complement the results from direct absorption FTIR spectroscopy *in situ* with particle sizing using a scanning mobility particle sizer, with 3-wavelengths-extinction measurements, with scanning electron microscopy, with differential scanning calorimetry, and with X-ray diffraction.

The infrared investigations are combined here with two different particle generation methods, *viz.* Rapid Expansion of Supercritical Solutions (RESS) and electro-spraying. Rapid expansion of supercritical CO<sub>2</sub> solutions is a particularly useful method to micronize thermally labile drugs, which often consist of lipophilic compounds. The main advantage of the solvent CO<sub>2</sub> lies in its low critical data and in the fact that it can easily be separated from the product after particle formation. As an example, the mixing/coating of phytosterol with polymers (Eudragit®, L-PLA) is discussed. Encapsulation of drugs with polymers is especially attractive to avoid agglomeration and to control drug release in the body. Electro-spraying of aqueous or alcoholic solutions allows us to generate nanoscale particles of hydrophilic compounds. Here, the particle formation of sugar-like substances is discussed. This class of substances is attractive as carrier for administering drugs in solid dosage form.

## 6.2

### Particle Generation Methods

#### 6.2.1

#### Rapid Expansion of Supercritical Solutions (RESS)

The potential of RESS for the micronization of molecular substances has been demonstrated previously [11–15]. The key idea behind RESS is to dissolve the solute of interest in a supercritical fluid followed by a rapid expansion of the supercritical solution. This leads to an extremely fast phase change from the supercritical to the gas-like state, resulting in high supersaturation in the supersonic free jet and the formation of submicron particles. Since the solvent is a dilute gas after expansion, the RESS process offers a highly pure final product. Dissolution experiments demonstrate that the RESS processing of Griseofulvin leads to a signifi-

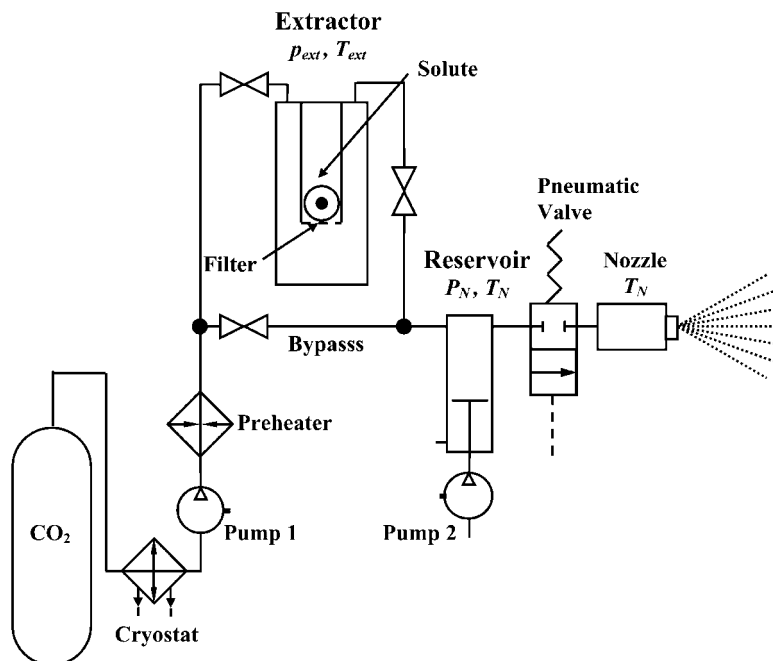


Fig. 6.1. Scheme of the RESS apparatus.

cantly better dissolution rate of the drug, resulting in an improved bioavailability [14].

We have built up several types of RESS apparatuses [14–18], which differ in size (continuous and batch RESS apparatuses) and in the mode of expansion, i.e. continuous expansion versus pulsed expansion. A general scheme of a RESS apparatus is depicted in Fig. 6.1. Our setup is designed for experiments in the temperature range 300–600 K and for pressures up to 60 MPa. The gaseous solvent ( $\text{CO}_2$ ,  $\text{N}_2\text{O}$ ,  $\text{CHF}_3$ ) is taken from a reservoir, liquefied by a cryostat, and pressurized (pump 1: diaphragm pump or pneumatic pump) to the desired pressure in the extractor ( $p_{\text{ext}}$ ). For the formation of nanoscale particles of thermally labile drugs,  $\text{CO}_2$  is a particularly suitable solvent since it has low critical data ( $T_{\text{crit}} = 304$  K,  $p_{\text{crit}} = 7.38$  MPa), is non-toxic, and can be easily separated from the particulate phase after particle formation. The extractor is a heated ( $T_{\text{ext}}$ ) high-pressure autoclave that is packed with the solute. For continuous operation, the supercritical solution is expanded directly through the pinhole nozzle. For pulsed operation, a heatable high-pressure reservoir ( $T_N$ ,  $p_N$ ) is filled with the solution first. Expansion then takes place from this reservoir, the pressure of which is kept constant during the pulses (duration  $t_{\text{puls}} > 100$  ms) by a movable piston connected to pump 2. The length of the pulses is controlled by the pneumatic valve in front of the nozzle. The pinhole nozzles used have variable inner diameters of 20–200  $\mu\text{m}$  and lengths of

50–300  $\mu\text{m}$ . The nozzle is positioned in the expansion chamber, as further explained in Section 6.3.1.1 and depicted in Fig. 6.3 below.

Particle generation by RESS can be used, in principle, for a wide range of different solutes [11–14]. This statement, however, has to be qualified to some extent for thermally labile substances such as drugs for which the solvent has to meet special requirements. Here, carbon dioxide is often the only suitable solvent so that the application of RESS is restricted to compounds with reasonable solubility in supercritical  $\text{CO}_2$ . Micronization with RESS, in general, produces particles with rather broad size distributions [geometric standard deviation  $\sigma > 1.5$ , see Eq. (2)]. In this context, an important factor is the agglomeration of the primary particles, which leads to a broadening of the size distribution. Different methods (RESSAS, CORESS, CPD) for stabilizing the primary particles against agglomeration have recently been realized [19–26]. They are discussed briefly in Section 6.5.

## 6.2.2

### Electro-Spraying

Electro-spraying is a method of generating particles of molecular compounds that are preferentially soluble in polar solvents such as water or different alcohols. A scheme of the Electro Spray Aerosol Generator (EAG, TSI 3480) is depicted in Fig. 6.2 (see also Refs. [9, 27–30] for further information). The compound of interest is

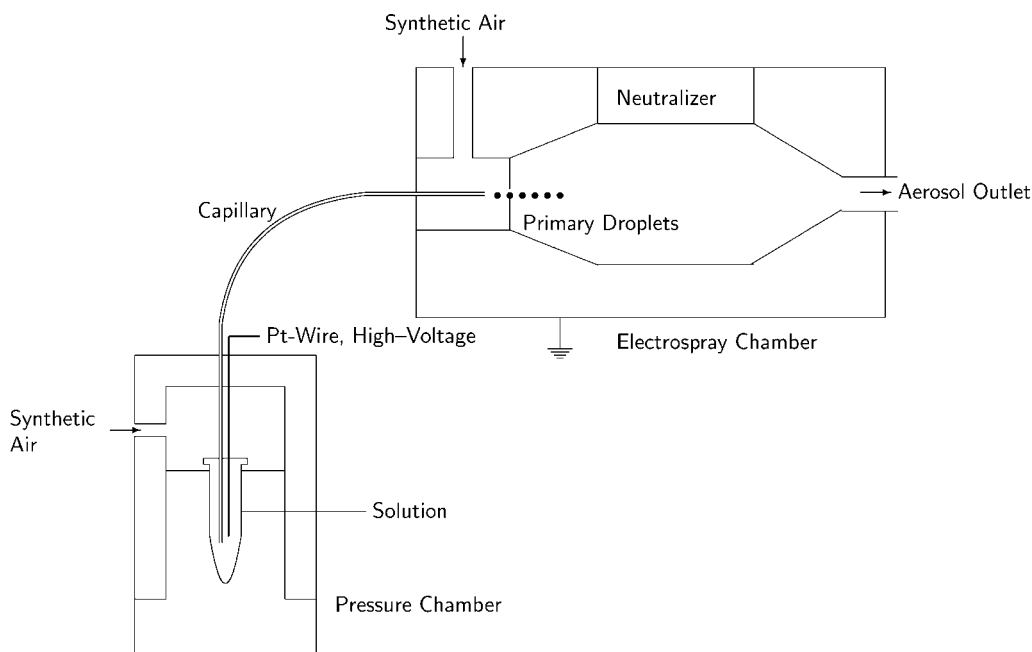


Fig. 6.2. Scheme of the electro spray.

dissolved in an aqueous buffer solution (ammonium acetate/ammonium hydroxide in  $\text{H}_2\text{O}$ ). The buffer solution serves to adjust the pH and to increase the electric conductivity of the solution (usually,  $500\text{--}2000\ \mu\text{S cm}^{-1}$ ). Typical concentrations of the solute lie between 2 and 10 vol%. The solute concentration determines the diameters of the final particles, which lie below  $\sim 100\ \text{nm}$ . The setup consists of a capillary that is immersed in the solution. The solution is driven through the capillary ( $\sim 70\ \text{nL min}^{-1}$ ) by a pressure gradient. Between the capillary tip and an electrode with a pinhole, a high voltage is applied so that highly charged primary droplets of the solution (diameters  $\sim 150\ \text{nm}$ ) are formed. The droplets are neutralized by a radioactive source and the solvent evaporates from these primary droplets in a sheath-flow of clean dry synthetic air ( $\text{N}_2/\text{O}_2$ ;  $\sim 2\ \text{L min}^{-1}$ ). The neutralized aerosol flow then enters the multireflection sheath-flow cell described in Section 6.3.1.1.

The electrospray generates small particles with relatively narrow size distributions. Typical geometric standard deviations amount to  $\sigma = 1.3$ . This is a great advantage over many other particle generation methods, which for molecular substances often lead to particles with fairly broad distributions ( $\sigma > 2$ ). As monodisperse products exhibit much more homogeneous properties they are usually highly preferred over polydisperse particle ensembles. However, particle generation by electro-spraying has two major disadvantages. One concerns the separation of the solvent. The commonly used solvents are liquid at atmospheric conditions and thus can easily condense on the particles collected from the gas phase. The second more severe problem is the clogging of the capillary, especially of the capillary tip. This reduces the general applicability of electro-spraying for particle generation to substances that are slow to crystallize at the capillary tip (i.e., with a tendency to form supersaturated solutions).

## 6.3 Particle Characterization Methods

### 6.3.1

#### *In Situ* Characterization with FTIR Spectroscopy

##### 6.3.1.1 Experimental Setup

Figure 6.3 shows the experimental setup for the *in situ* characterization with Fourier transform infrared spectroscopy (FTIR). The nozzle of the RESS apparatus (see Section 6.2.1 and Fig. 6.1) is positioned in the expansion chamber and is connected to the reservoir of the RESS apparatus with a high-pressure hose. The expansion chamber and the buffer volume are connected vacuum chambers with a total volume of  $0.8\ \text{m}^3$ . The buffer volume helps to limit the increase of pressure,  $p_c$ , in the expansion chamber. The whole vacuum part is evacuated to  $p_c = 0.03\ \text{mbar}$  by two rotary piston vacuum pumps (Leybold DK 100 and E 250) connected in parallel. With the  $50\ \mu\text{m}$  nozzle and a reservoir pressure of  $p_R = 400\ \text{bar}$ , the pressure in the chamber typically increases to  $0.16\ \text{mbar}$  after a pulse of  $0.5\ \text{s}$  duration. A pulse duration of  $2\ \text{s}$  leads to  $p_c = 0.55\ \text{mbar}$ . The IR spectra of nanoparticles were

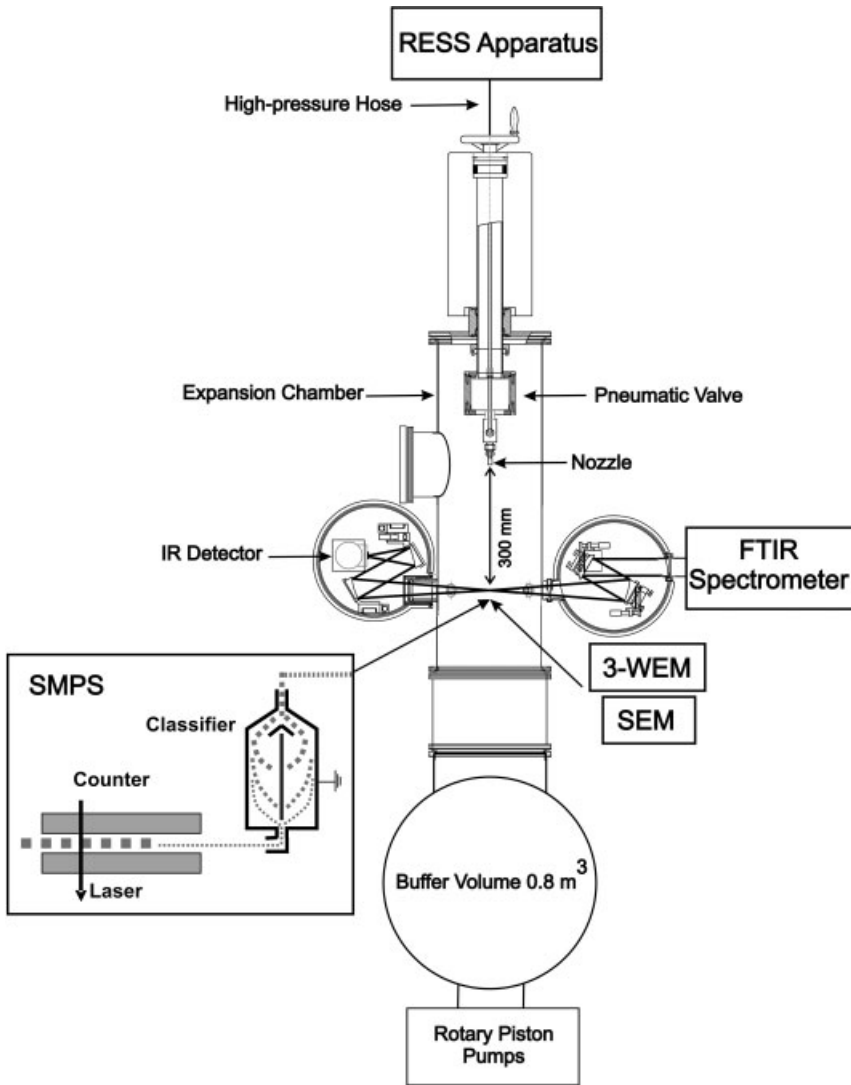


Fig. 6.3. Scheme of the vacuum apparatus for the *in situ* characterization with FTIR.

recorded *in situ* using a Bruker IFS 66v/S FTIR spectrometer. As depicted in Fig. 6.3, the supersonic flow is probed radially by the infrared beam. The infrared beam from the Globar light source is focused into the center of the expansion by a first off-axis parabolic mirror (327 mm focal length). After passing the expansion, the light is collected by a second off-axis parabolic mirror (327 mm focal length) and a third parabolic mirror (109 mm focal length) focusses the light onto a liquid nitrogen cooled MCT detector. The spectrometer and detector chamber are

separated from the expansion chamber by two KBr windows. The rapid-scan mode of the spectrometer allows us to synchronize the acquisition of IR spectra with the pulsed expansion. With a scanner velocity of 280 kHz, one scan is recorded in 30 ms at a resolution of  $2\text{ cm}^{-1}$ , which means that several scans can be made during one pulse (pulse duration  $> 100\text{ ms}$ ). To get a good signal-to-noise ratio, we typically accumulate more than 500 scans. A similar combination of direct absorption FTIR spectroscopy with intense fluid pulses through a slit-nozzle into the vacuum has been realized for the first time by Suhm and coworkers [31, 32] to study the vibrational dynamics of small clusters.

The investigation of particles during their generation in the aerosol phase by *in situ* FTIR spectroscopy has many advantages. First of all, IR spectra contain information about various particle properties such as the size distribution, chemical composition, and structural aspects. Therefore, the combination with rapid characterization *in situ* represents a very useful method for process control. With the setup described here, the particles do not have to be collected first but can be continuously analyzed during their generation. This allows us, for instance, to control their size by changing the process parameters such as the temperature, pressure, or concentration of the supercritical solution. It also enables us to control the portion of different components in the final product if supercritical solutions with several solutes are used. This is of interest for the coating of drug particles or for the generation of mixed drug/matrix particles (see also Section 6.5.3). In addition, with the vacuum option we can change the generation conditions of the particles by varying the pressure  $p_c$  in the expansion chamber. With phenanthrene particles, particles generated under vacuum conditions have smaller mean sizes but broader distributions than those generated at ambient pressure (see Ref. [10] and Section 6.5.1). Section 6.3.1.2 demonstrates that our setup can also be used to study the region of the expansion before the Mach disc, which is essential for a better understanding of the RESS and is crucial to verify corresponding theoretical predictions [12, 33–38].

Particles generated in the electrospray (Fig. 6.2) are investigated spectroscopically in a multireflection sheath-flow cell [30, 39]. The cell consists of two concentric cylinders. The carrier gas is introduced into the gap between the two, enters the inner cylinder through a large number of small holes, and is finally pumped off at the bottom. This creates a smooth sheath-flow for samples injected coaxially at the top of the inner cylinder. The cell is operated at room temperature with a sheath-flow of 1.5 L He per minute. The sheath-flow serves to guide the aerosol through the flow tube and to minimize contaminations of the mirrors. The cell is equipped with White optics with an optical path length of about  $h = 16\text{ m}$ .

#### 6.3.1.2 Characterization of the RESS Process

The mole fraction of the solute in supercritical  $\text{CO}_2$  typically lies below 0.1–0.01 [40]. In other words, the supercritical solution expanded in the RESS process mainly consists of  $\text{CO}_2$ . Evidently, the influence of  $\text{CO}_2$  on particle formation is not negligible. Due to the high supersaturation, one expects that not only the solute with its low volatility but also the  $\text{CO}_2$  itself condenses into small particles within

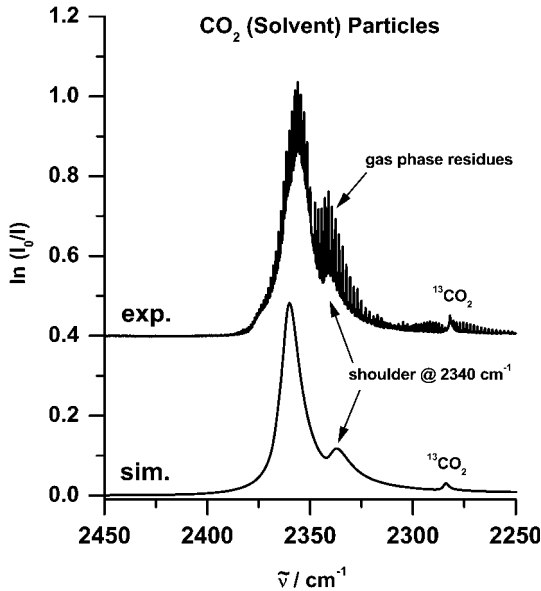


**Fig. 6.4.** Upper trace: Experimental IR spectrum of  $\text{CO}_2$  particles recorded in the collision-free region before the Mach disc. Experimental conditions: nozzle diameter  $d = 50 \mu\text{m}$ ,  $p_R = 400 \text{ bar}$ ,  $T_N = 298 \text{ K}$ . The sharp peaks arise from residual gas phase  $\text{CO}_2$

in the expansion. Lower trace: Calculated  $\text{CO}_2$  particles spectrum. For the fit we have used the refractive index data from Ref. [44], a Mie-model [42], and a log-normal distribution [Eq. (2)].  $\tilde{\nu}$  is the transition wavenumber.

the nozzle and some nozzle diameters downstream [12, 33–38]. Figure 6.4 shows that these solvent particles really can be observed in the collision-free region before the Mach disc. The experimental IR spectrum in the region of the antisymmetric stretching vibration  $\nu_3$  of  $\text{CO}_2$  is depicted in the upper trace. The sharp peaks superimposed on the broad band have nothing to do with the solvent particles, they arise from residual gas-phase  $\text{CO}_2$  in the expansion. The appearance of the broad band is characteristic of  $\text{CO}_2$  particles [41]. It allows us to estimate the size of the solvent particles [10] since both the width and the shoulder at about  $2340 \text{ cm}^{-1}$  strongly depend on the particle size. As a rough rule one can say that for larger particles the band broadens and the intensity of the shoulder increases. The size is an important quantity to know since the condensation/evaporation behavior of the solvent influences the particle formation processes. It is also of interest to verify corresponding theoretical predictions [12, 33–38]. The sizes are estimated by fitting calculated extinction spectra to the experimental IR spectrum. For that, we have assumed Mie theory [42] and a log-normal size distribution that is characterized by the mean particle radius ( $r_0$ ), the geometric standard deviation ( $\sigma$ ) and the particle number concentration ( $N$ ) [see Eq. (2)]. The refractive index data have been taken from Refs. [43, 44]. Typical parameters for expansions at temperatures between 298–398 K and pressures between 100–400 bar are listed in Table 6.1. As



**Tab. 6.1.** Geometric standard deviation  $\sigma$ , mean particle radius  $r_0$ , and particle number concentration  $N$  [see Eq. (2)]. Data from IR spectra have been obtained from a fit to the experimental data using Mie theory and two different sets of refractive index data [43, 44]. Since  $r_0$  and  $\sigma$  are strongly correlated, the value for  $\sigma$  has been fixed [10].

$p_N$ /(bar)	$T_N$ /(K)	$\sigma$	$r_0$ /(nm)	$N^{[a]}$ /( $10^8 \text{ cm}^{-3}$ )
400	298	1.4	300	0.2
100	298	1.4	180	0.1
400	360	1.4	210	0.2
400	298	2.1	70	3.9

<sup>a</sup> Values for  $N$  for a path length of  $h = 1 \text{ cm}$ .

expected, we find a systematic decrease of  $r_0$  with decreasing reservoir pressure ( $p_N$ ) and with increasing temperature. The values of the radii of the solvent particles in Table 6.1 lie well above 100 nm. However, because the parameters  $\sigma$  and  $r_0$  turned out to be highly correlated we have fixed the value of  $\sigma$  at 1.4 during the refinement procedure. For comparison, the last row of Table 6.1 gives one example with the geometric standard deviation fixed at  $\sigma = 2.1$ . Comparison with the first row shows that the mean size decreases if a broader distribution is assumed. Independent of the widths of the distribution, however, we can finally state that the mean particle radius of the solvent particles lies clearly above  $r_0 = 50 \text{ nm}$  for temperatures between 298 and 398 K and pressures between 100 and 400 bar [10].

In the collision-free region of the expansion,  $\text{CO}_2$  and the solute both exist as small particles due to the supersaturation and subsequent condensation upon expansion. This result is in good agreement with the modeling results published by Helfgen et al. [38]. From these calculations it follows that the decrease of pressure and temperature in the supersonic free-jet can lead to solvent condensation. Depending on the pre-expansion conditions, the condensate mass fraction goes up to around 30% for  $\text{CO}_2$  and 25% for  $\text{CHF}_3$ . As mentioned above, the mole fraction of the solute in supercritical  $\text{CO}_2$  lies below 0.1–0.01 so that the amount of condensed  $\text{CO}_2$  is much higher than that of condensed solute. But it is not clear whether the two components form (statistically) mixed particles or whether the solute condenses first to small particles that then act as condensation nuclei for the more volatile  $\text{CO}_2$  (coated particles). We have investigated this question for an expansion of a n-nonadecane/ $\text{CO}_2$  solution. Figure 6.5 shows the corresponding IR spectrum in the region of the CH-stretching vibrations of n-nonadecane ( $\text{C}_{19}\text{H}_{40}$ ) particles. The region of the antisymmetric stretching vibration of the  $\text{CO}_2$  particles is not shown again. It looks the same as already depicted in Fig. 6.4. The shape and the band positions in the spectrum of the nonadecane particles in Fig. 6.5 are the same as those for pure nonadecane particles [10]. We consider this fact a hint that coated particles rather than mixed particles exist in the collision-free region before the Mach disc. The preference of coated particles, however, is much more plausible since nonadecane is much less volatile than  $\text{CO}_2$  and thus condenses first, probably already within the nozzle [12, 33–38].

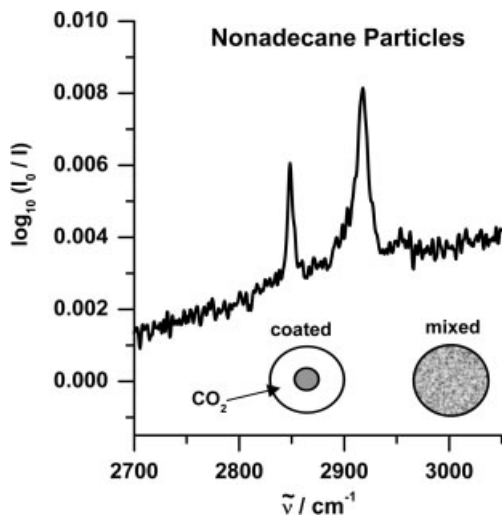


**Fig. 6.5.** Experimental IR spectrum of nonadecane in the region of the CH-stretching vibrations. The spectrum was recorded in the collision-free region before the Mach disc. In this region both nonadecane and the solvent  $\text{CO}_2$  condense to small particles.  $\tilde{\nu}$  is the transition wavenumber.

The conditions and processes before the Mach disc described in this section certainly influence the properties of the final particles. But the processes taking place at and after the Mach disc and the manner in which the particles are collected are much more important factors, for instance for the size of the final particles. All these factors can lead to coagulation and agglomeration of primary particles. The sudden temperature and pressure increase taking place at the Mach disc leads to evaporation of the solvent particles so that after the Mach disc only pure solute particles are present. However, we have shown previously [10] that complete evaporation of the solvent particles takes some seconds. Since agglomeration and coagulation seem to be important it is not astonishing that the electron microscopy images of the final products, which are further discussed in Section 6.5, often show agglomerates consisting of relatively small (50–100 nm) primary particles. One possibility to avoid this subsequent agglomeration is by coating the particles as discussed in Section 6.5.3.

### 6.3.2

#### ***In Situ* Characterization with 3-WEM**

In continuous particle formation processes, fast *in situ* measurement techniques for on-line particle size determination are desirable. In contrast to the usual off-line examination techniques, the particles are therefore measured in the expansion

chamber on-line and *in situ* with the Three-Wavelengths-Extinction (3-WEM) measurement technique (see Fig. 6.3). The 3-WEM measuring devices used are equipped with three lasers emitting at wavelengths of 405, 633, and 1064 nm (home-built device) and of 674, 814, and 1311 nm (WIZARD-DQ, Wizard Zahoransky KG, Todtnau, Germany), respectively. The fiber-coupled transmitter of the latter device is placed at the optical access of the test volume. The remaining light is detected with the opposite receiver. The relative transmissions of the three different wavelengths  $I/I_0$  are used for the evaluation on a PC. According to Mie theory [42], the system allows the measurement of particle diameters in a range from 0.2 to 4  $\mu\text{m}$  and particle concentrations ranging from  $10^5$  to  $10^8$  particles per  $\text{cm}^3$  [10, 45]. The advantages of the 3-WEM measurement technique are that it is a suitable method for measuring particle size and number concentration under sub-, near-, and supercritical conditions. In addition, the 3-WEM enables on-line process control because particle characteristics can be determined within  $10^{-6}$  s. However, for non-spherical and/or agglomerated particles the 3-WEM measurement technique can lead to incorrect results for the particle size distribution. To overcome this, a combination of different measurement methods has to be used to accumulate sufficient information on the size and structure of the particles investigated. Therefore, samples for additional SEM examination (see Section 6.3.3) were taken 300 mm from the nozzle exit directly behind the 3-WEM-probe. A more detailed description of the apparatus and the experimental procedure is given elsewhere [16].

### 6.3.3

#### Characterization with SMPS and SEM

The number size distribution of the aerosol is also measured on-line with a Scanning Mobility Particle Sizer (SMPS), which can be connected to the RESS expansion chamber (Fig. 6.3) or to the electro-spray (Fig. 6.2). The SMPS consists of a differential mobility analyzer (TSI 3080L/N), which classifies the particles according to their mobility in an electric field, and of a condensation nuclei counter (TSI 3022A), where the particles are counted optically. The SMPS only works at atmospheric pressure and at room temperature and, therefore, can only be used for a limited range of experiments. Compared with 3-WEM and IR spectroscopy it leads to more detailed size distributions since it measures the number of particles for each single size and does not rely on any assumption about the type of the size distribution (e.g., log-normal distribution). However, the SMPS is much slower than 3-WEM or IR spectroscopy. Typical acquisition times lie around 2 min. Examples for size distributions measured with the SMPS are given in Section 6.5.

To visualize the shape of nanoparticles and also to determine their approximate size, we use Scanning Electron Microscopy (SEM). This off-line characterization requires collection of the particles first, which often leads to agglomeration. We collect them either on a polycarbonate membrane or on a silicon holder previously covered with a thin gold layer (11 nm). After collecting, the sample is covered with a second gold layer (7 nm) to avoid evaporation of substances inside the SEM apparatus. Examples of SEM images are depicted in Section 6.5.

## 6.4

### Determination of Refractive Index Data in the Mid-infrared Region

Knowledge of the frequency-dependent complex refractive index  $n + ik$  of the solute particles is a prerequisite for *in situ* characterization with FTIR spectroscopy. Therefore, we have started to derive corresponding optical data from the measured infrared extinction spectra of organic aerosols and from size distributions determined experimentally with the SMPS and with 3-WEM (Section 6.3). The formalism is given below by Eqs. (1–5). The refractive index data thus derived are collected in Ref. [46] together with a short description and an estimate of their accuracy. There exist other databases for refractive indices in the mid-infrared region (see for instance Refs. [47–49]) which are, however, focussed more on molecular ices rather than on particles of biomolecular interest.

Our data are obtained from particle spectra and not from thin films. It is more difficult to derive accurate data from particle spectra than from thin films since it is often very difficult to get accurate information about the correct size distribution or the shape of the particles. On the other hand, the structure and even the chemical composition of the particles (crystalline/amorphous, modified structure of the particle surface [9, 30, 41, 50–52]) can strongly depend on the generation method and conditions. The latter aspect clearly illustrates the need for optical data obtained directly from particle spectra. Ref. [46] contains an accurate description of the methods used, but due to the limited information about size and shape of the particles the tabulated data only provide a first starting point towards the determination of more accurate data. Although we use three different methods (SEM, SMPS, and 3-WEM) for the characterization of the size and shape it is nearly impossible to get very accurate experimental data for these properties. The main disadvantage of SEM is that, upon collecting, the particles often agglomerate. Analysis with SMPS and 3-WEM relies on assumptions for the particle shape or the size distribution. Moreover, the derivation of the infrared optical data is based on models [see Eqs. (1–5)]. The Mie theory used for that purpose gives the solutions for the scattering and absorption of light by spherical particles. The assumption of a spherical shape is often regarded as an adequate approximation even for non-spherical particles. But this is more of an assertion than a fact and would have to be tested for each case [42, 53]. For instance, Mie theory fails for non-spherical particles in the case of strong vibrational transitions when transition dipole coupling is dominant [41, 54, 55]. We also neglect multiple scattering, which will not lead to major errors as long as the particle density is not too high.

The frequency-dependent complex refractive index  $n + ik$  of solute particles has been determined directly from the experimental extinction spectrum of the corresponding aerosols in the mid-infrared region by following two alternative approaches: (a) a Lorentz model fit and (b) a Kramers–Kronig inversion. Both proceed via the complex refractive index to characterize the optical properties of the particulate phase. We employed Mie theory for spherical particles [42] to calculate the observed extinction spectrum. The refractive index of the surrounding medium (different gases) was set to unity. The frequency dependent extinction cross section

( $C_j$ ) is calculated separately for each value of the particle radius ( $r_j$ ). The calculated total absorbance ( $A_{\text{calc}}$ ) is obtained by summing over all different radii using the experimentally determined particle size distribution:

$$A_{\text{calc}} = h \sum_j N_j C_j \quad (1)$$

where  $h$  is the optical pathlength and  $N_j$  is the number density of aerosol particles with size  $r_j$ . The experimental size distribution is determined either by the SMPS (Section 6.3.3), by 3-WEM (Section 6.3.2), or by a combination of both [9, 10, 15, 29, 30, 41]. The classifier of the SMPS determines the particle radii ( $r_j$ ) for different size intervals  $j$ . Each decade of particle size is divided into 64 equidistant logarithmic intervals. The particle counter of the SMPS then measures the particle number concentration ( $N_j$ ) in each interval  $j$ . The measurement range of the SMPS is limited to the region 7–1000 nm. Size distributions that exceed this range are extrapolated by using a log-normal distribution. A log-normal distribution for the particle radii ( $r$ ) is also assumed for the interpretation of the 3-WEM experiments. Its form is given by [56]:

$$df = \frac{1}{\sqrt{2\pi} \ln \sigma} \exp \left\{ -\frac{[\ln(r/u) - \ln(r_0/u)]^2}{2(\ln \sigma)^2} \right\} d[\ln(r/u)] \quad (2)$$

with the mean particle radius ( $r_0$ ) and the geometric standard deviation ( $\sigma$ ) as parameters;  $u$  is the unit radius. The product  $N \cdot h$  of the particle number concentration ( $N$ ) and the pathlength ( $h$ ) is determined by the absolute values measured for the extinction [Eq. (1)].

In the first approach to determine the complex refractive index of the nanoparticles we assume a model function for the (complex, frequency dependent) dielectric function ( $\varepsilon$ ) of the solute particles. The empirical parameters of this function are determined from a nonlinear least-squares fit of the calculated extinction,  $A_{\text{calc}}$  [Eq. (1)], to the experimental aerosol spectra. In this study we have used the so-called Lorentz model, which describes the optical properties of the solid by a collection of isotropic damped harmonic oscillators coupled to the electromagnetic field of the light by their effective charge. Solution of the classical equations of motion leads to the Kramers–Heisenberg dielectric function [42, 57]:

$$\varepsilon = \varepsilon_1 + i\varepsilon_2 = \varepsilon_e + \sum_s \frac{\tilde{\nu}_{sJ}^2 f_s}{\tilde{\nu}_s^2 - \tilde{\nu}^2 - i\gamma_s \tilde{\nu}} \quad (3)$$

The dielectric function is directly related to the complex index of refraction ( $n, k$ ):

$$n = \sqrt{\frac{\sqrt{\varepsilon_1^2 + \varepsilon_2^2} + \varepsilon_1}{2}} \quad k = \sqrt{\frac{\sqrt{\varepsilon_1^2 + \varepsilon_2^2} - \varepsilon_1}{2}} \quad (4)$$

The parameter  $\varepsilon_e$  is the dielectric function at frequencies that are high compared with the vibrational excitations considered (but low compared with electronic excitations, which are neglected here). Eq. (3) sums over all oscillators in the spectral region of interest. They are characterized by their resonance wavenumber ( $\tilde{\nu}_s$ ), their reduced oscillator strength ( $f_s$ ) and a width ( $\gamma_s$ ) resulting from the damping of the oscillator.

To the extent that a Lorentz oscillator can be compared to a molecular oscillator (e.g., a molecular normal mode),  $\tilde{\nu}_s^2 f_s$  is proportional to the absorbance  $\int A(\tilde{\nu}) d\tilde{\nu}$  integrated over the corresponding absorption band (also termed integrated intensity). Eq. (3), however, neglects any local field correction, i.e., it assumes that each oscillator experiences the external electric field, which is not necessarily a good approximation in the condensed phase. An approximate local field correction for isotropic media leads to a formally identical expression [58], but with shifted resonance wavenumbers and modified effective reduced oscillator strengths. For the relatively small values of the reduced oscillator strengths found in the vibrational spectrum of many of the solutes, the wavenumber shifts can be neglected. The modification of the reduced oscillator strengths significantly changes their absolute values, thus affecting their interpretation in terms of molecular transition moments [58]. The relative values, however, remain approximately unchanged by the local field correction.

In the second approach, we exploit the Kramers–Kronig relation between the real ( $n$ ) and the imaginary ( $k$ ) part of the complex refractive index [42, 57]. The optical constants can thus be derived from the experimental extinction spectrum without assuming any particular model. In its so-called subtractive form the Kramers–Kronig relation [59–61] is given by Eq. (5).

$$n(\tilde{\nu}') = n(\tilde{\nu}_r) + \frac{1}{\pi} \int_{\tilde{\nu}_{\min}}^{\tilde{\nu}_{\max}} \left( \frac{k(\tilde{\nu})}{\tilde{\nu} + \tilde{\nu}'} - \frac{k(\tilde{\nu})}{\tilde{\nu} + \tilde{\nu}_r} + \frac{k(\tilde{\nu})}{\tilde{\nu} - \tilde{\nu}'} - \frac{k(\tilde{\nu})}{\tilde{\nu} - \tilde{\nu}_r} \right) d\tilde{\nu} \quad (5)$$

Eq. (5) requires knowledge of the real index of refraction at some reference point,  $\tilde{\nu}_r$ . Although in principle arbitrary, it is best (for numerical reasons) chosen to lie within the spectral region of interest. Starting with some guess for the real part  $n$  of the refractive index its imaginary part  $k$  is adjusted (by bisection) so that the Mie scattering calculation reproduces the experimentally measured extinction separately for each value of the wavenumber  $\tilde{\nu}$ . Eq. (5) is then applied to  $k(\tilde{\nu})$  to produce an improved guess for  $n(\tilde{\nu})$ . The Cauchy principal value of the integral in Eq. (5) was calculated on a grid as described in Ref. [61] with the difference, however, that  $k(\tilde{\nu})$  was expanded to fourth order around the singularity at  $\tilde{\nu} = \tilde{\nu}'$ . The whole procedure is repeated until convergence is reached. Since the reference value  $n(\tilde{\nu}_r)$  of the real index of refraction cannot be determined through this procedure it enters as the only free parameter. Here it was set to the value obtained from the Lorentz model fit at  $2000 \text{ cm}^{-1}$ , where the experimentally measured extinction vanishes. Otherwise this second approach to the determination of optical constants constitutes an inversion of the experimental spectrum rather than a fit.

## 6.5

## Examples

## 6.5.1

## Phenanthrene Particles: Size, Shape, Optical Data

Phenanthrene ( $C_{14}H_{10}$ ) serves here as a model system to demonstrate the different aspects of the particle generation and characterization methods described in Sections 6.2–6.4. Phenanthrene has been used as a representative compound in the modeling of particle formation processes with RESS [33, 36, 37]. Polycyclic aromatic hydrocarbons such as phenanthrene are of importance as pollutants in the atmosphere [62, 63] and have also been discussed in astrophysics as carriers of the “unidentified” infrared bands [64, 65].

We have generated phenanthrene particles with the RESS apparatus (Section 6.2.1) under various experimental conditions. In summary, we find that the phenanthrene particles are nearly spherical, as depicted in the SEM image in Fig. 6.6(a). Various SEM images also show that the tendency to form agglomerates is only minor for this substance, which is in contrast to the behavior of phytosterol particles discussed in Section 6.5.3. For phenanthrene, we found no major differences in the properties of the particles by changing the pre-expansion conditions (temperatures between 298 and 350 K, pressures between 20 and 40 MPa, and for different nozzle diameters). In this context we also mention the partly contradictory discussions in Refs. [15, 66–70]. One parameter that affects the size of the particles is the pressure  $p_c$  in the expansion chamber: Particles generated under vacuum conditions ( $p_c = 0.03$  mbar) have smaller mean diameters by about 30% but larger geometric standard deviation by about 30% than those formed at  $p_c = 960$  mbar. Whether this is a general trend for other substances as well remains to be seen.

Typical size distributions for the expansion against  $p_c = 1000$  mbar ( $T_{\text{ext}} = T_N = 298$  K,  $p_R = 400$  bar) are depicted in Fig. 6.6. From different SEM images recorded under equivalent conditions, we have determined a rough size distribution, which is shown by the bars in Fig. 6.6(a). Each bar represents the relative number of particles in the corresponding size interval. This size distribution is obviously very coarse and, in particular, it does not contain any information about the particle number concentration ( $N$ ) of the corresponding aerosol from which the SEM samples were collected. This information is important for the derivation of optical data from corresponding IR spectra as discussed below. Detailed information about the particle number concentration and the size can be obtained with the SMPS. The corresponding experimental number size distribution is shown by the bars in Fig. 6.6(b). The circles represent a fit to the measured distribution assuming a log-normal distribution [Eq. (2)]. This fit allows us to extrapolate the distribution beyond the measurement range (see Section 6.4) and leads to the following typical data for the phenanthrene particles:

$$r_0 \sim 120 \text{ nm}, \quad \sigma \sim 2.2, \quad \text{and} \quad N \sim 5 \times 10^6 \text{ cm}^{-3} \quad (6)$$

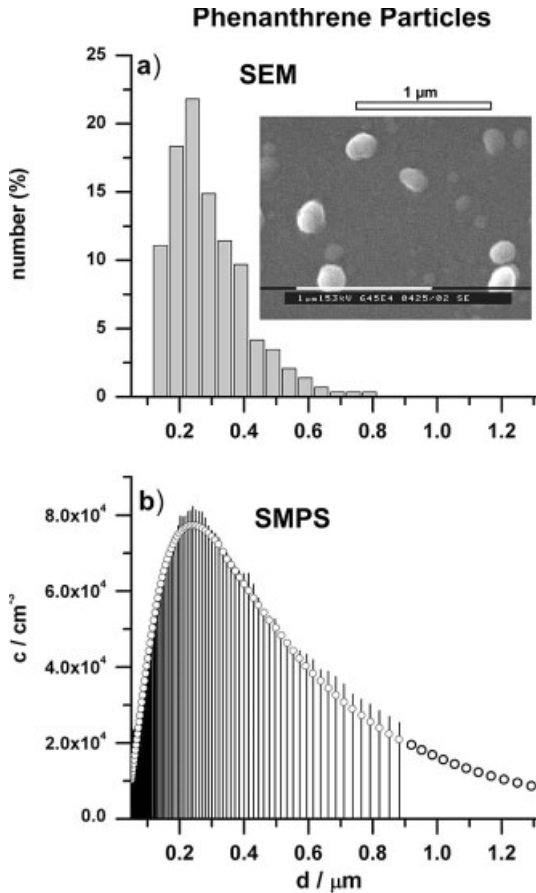


**Fig. 6.6.** (a) Bars: Size distribution of phenanthrene particles obtained from SEM measurements. Ordinate: Percentage of particles with sizes in size intervals of 50 nm. Inset: Typical SEM image. (b) Bars: Number size distribution of phenanthrene particles measured on-line with the SMPS.  $c$  is the

number concentration per logarithmic sampling interval. Bars indicate the center of the intervals. Circles: Fit to the measured distribution assuming a log-normal distribution [Eq. (2)]. Conditions for particle formation:  $T_{\text{ext}} = T_N = 298$  K,  $p_{\text{ext}} = p_N = 400$  bar.

Comparison of Fig. 6.6(a) and (b) shows that the size distribution from SEM and from SMPS are in good agreement. Since the phenanthrene particles are nearly spherical the 3-WEM should also lead to similar results as SEM and SMPS. In contrast to this expectation, the 3-WEM leads to larger mean radii (40%) and smaller geometric standard deviations (20%) than the two other methods. Similar behavior has already been observed in previous studies that compared 3-WEM with other sizing methods [16, 45, 71]. At the moment we cannot finally explain the origin of this deviation but it is, presumably, due to assumptions implicit in the analysis of the 3-WEM data (Section 6.3.2).



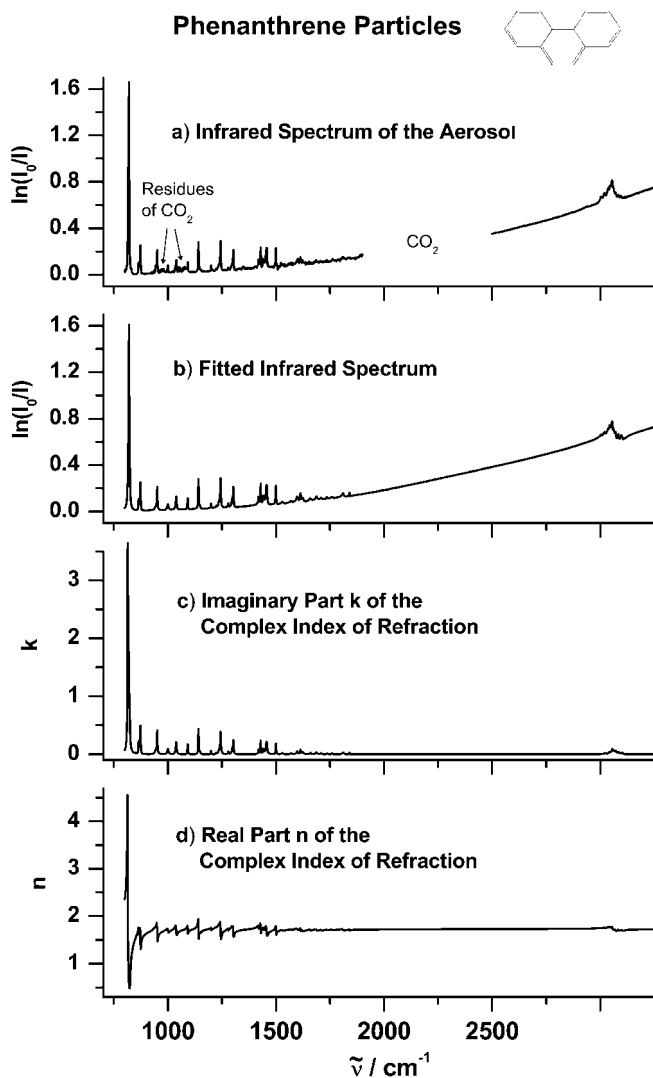


**Fig. 6.7.** (a) Experimental IR spectrum of phenanthrene aerosol particles. (b) Fitted infrared spectrum (see Section 6.4). (c) Imaginary part  $k$  of the complex index of refraction. (d) Real part  $n$  of the complex index of refraction.  $\tilde{\nu}$  is the transition wavenumber.

The size information is also contained in the IR spectrum of the aerosol depicted in Fig. 6.7(a). Thus, the scattering by the particles leads to the slanted baseline, which is characteristic for the size distribution of the particle ensemble. Note that the strong bands from gas-phase  $\text{CO}_2$  (residues of the solvent) below  $800 \text{ cm}^{-1}$  and between  $1900$  and  $2500 \text{ cm}^{-1}$  have been cut from this spectrum. The determina-

tion of the particle size distribution from the experimental mid-infrared spectrum requires knowledge of the corresponding refractive index data  $n + ik$  for the solute in this region (Section 6.4). Since these data were not known for phenanthrene particles, we have derived them from a fit to the experimental spectrum using the experimentally measured size distributions from the SMPS (Fig. 6.6b). We assumed Mie theory for spherical particles and a Lorentz model for the optical properties [Eqs. (3, 4), and [42]]. More details of this procedure can be found in Refs. [15, 30, 42]. According to Eq. (3) each Lorentz oscillator is characterized by three parameters: The resonance wavenumber, the oscillator strength, and the damping width. The number of oscillators is not determined *a priori*. It depends on the number of intra- and intermolecular vibrations and on interactions between them. The phenanthrene spectrum in Fig. 6.7(a) consists of sharp resolved absorptions. Therefore, we have assigned one Lorentz oscillator to each of these bands. The results from our Lorentz fit are depicted in Fig. 6.7(b–d). Trace (b) shows the fitted IR spectrum, which reproduces the experimental spectrum quite well. The region below  $2000\text{ cm}^{-1}$  is dominated by the strong absorption of the CH out-of-plane bending at  $819\text{ cm}^{-1}$ . All other vibrations in the mid-infrared region are rather weak. The region below  $2000\text{ cm}^{-1}$  consists of well-resolved individual transitions whereas the CH-stretching transitions around  $3100\text{ cm}^{-1}$  strongly overlap. Trace (c) shows the imaginary part  $k$  and trace (d) the real part  $n$  of the complex index of refraction. The corresponding fitted parameters and refractive index data together with a description of the estimated uncertainties ( $\sim 20\%$ ) are available in Ref. [46]. With these data the determination of the size distribution now becomes possible directly from IR spectra for phenanthrene aerosols.

Apart from the size, the IR spectrum also contains information about the chemical composition, about the structure (crystalline, amorphous), and sometimes about the particle shape. Comparison of the experimental spectrum in Fig. 6.7(a) with corresponding spectra for crystalline phenanthrene reveals the crystalline character of the phenanthrene particles [72]. Fig. 6.7(c) and (d) show that there exists a spectral range around  $819\text{ cm}^{-1}$  where  $n$  is small and  $k$  varies widely. In classical scattering theory, this is the condition for the occurrence of shape effects in particle spectra [42]. We have pointed out previously [44] that on a molecular level this can be explained by exciton coupling (transition dipole coupling), which elucidates that shape effects only occur for bands with relatively large molecular transition dipoles ( $\delta\mu > 0.1\text{--}0.2\text{ D}$ ). For phenanthrene this is fulfilled only for the band at  $819\text{ cm}^{-1}$ , which is shown in an expanded view in Fig. 6.8(a). By different examples [52, 54, 55, 73] we have illustrated that different particle shapes lead to different band structures for such strong absorption bands in the IR spectra. Figure 6.8(a) shows the band at  $819\text{ cm}^{-1}$  for spherical phenanthrene particles as depicted in the SEM image of Fig. 6.6(a). To modify the shape of the phenanthrene particles we have produced a layer of particles on a NaCl window and recorded its IR spectrum, which is depicted in Fig. 6.8(b). This layer no longer consists of single spherical particles but of strongly agglomerated/coagulated primary particles, as illustrated by the SEM image in trace (b). The deviation from the spherical shape obviously leads to a completely different band shape in the IR spectrum of the par-

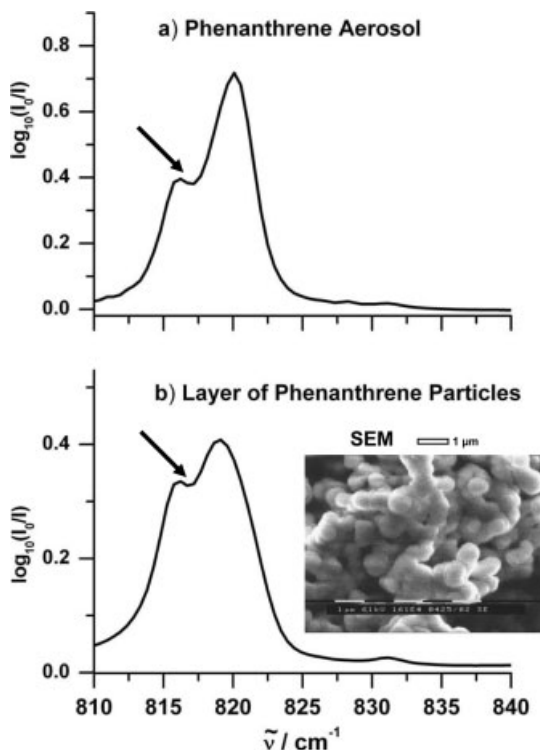


**Fig. 6.8.** (a) Expanded view of the IR spectrum of phenanthrene aerosol shown in Fig. 6.7(a) in the region of the band at  $819 \text{ cm}^{-1}$ . (b) IR spectrum of a layer of particles on a NaCl window together with the

corresponding SEM image of this layer. The different band shapes in traces a and b most likely arise from the different particle shapes of the two samples.  $\tilde{\nu}$  is the transition wavenumber.

particle layer (trace in Fig. 6.8b) compared with the aerosol (trace a). In accordance with the explanations above, we do not observe such deviations between the two different spectra for the weak absorption bands.

### 6.5.2

#### Sugar Nanoparticles

Sugar-like substances such as cyclodextrins are attractive carriers for drugs to administer them in solid dosage form and improve their dissolution. Cyclodextrins are cyclic oligosaccharides of D-glycopyranose units able to form inclusion complexes with many drugs [74, 75]. Controlled particle deposition (CPD, [74, 76]) is one possibility to produce such complexes. In CPD the solute of interest is dissolved in supercritical  $\text{CO}_2$ . This solution then permeates the pores of the carrier where the drug precipitates after a fast drop of the pressure. Another possibility is to generate mixed particles with an electro-spray or with RESS by using a solution

of both the drug and the carrier (CORESS [19–22, 24, 74, 76]). This results in encapsulation of the drug by or mixing of the drug with the carrier. In this section we show some results concerning particle formation of different sugar-like substances with the electro-spray (Section 6.2.2) and with RESS (Section 6.2.1). The complicated network of hydrogen bonds in such sugar particles gives rise to various amorphous and crystalline forms that can affect their use in nanoparticle technology. Infrared spectroscopy again proves to be useful to elucidate the complex inter- and intramolecular hydrogen-bond dynamics in these particles.

We have investigated different sugar particles generated with the electro-spray, including glycolaldehyde, hydroxyacetone, glyceraldehyde dimer, dihydroxyacetone and its dimer, glucose, fructose, saccharose, ribose, 2-deoxyribose, and erythrose [9, 29, 30, 51]. Figure 6.9 shows, from top to bottom, the IR spectra of fructose particles ( $C_6H_{12}O_6$ ), glucose particles ( $C_6H_{12}O_6$ ), ribose particles ( $C_5H_{10}O_5$ ), and 2-deoxyribose particles ( $C_5H_{10}O_4$ ). Common to all of these spectra are the relatively broad absorption bands, which clearly indicate that the aerosol particles are amorphous and not crystalline. This statement has been further corroborated by comparing the particle spectra with spectra of the crystalline substances. In contrast to the particles the latter exhibit narrow bands in the IR spectra, as illustrated for 2-deoxyribose by Fig. 6.10(b), with the corresponding particle spectrum shown in Fig. 6.10(a). Comparison of the four spectra in Fig. 6.9 also shows that the finger-

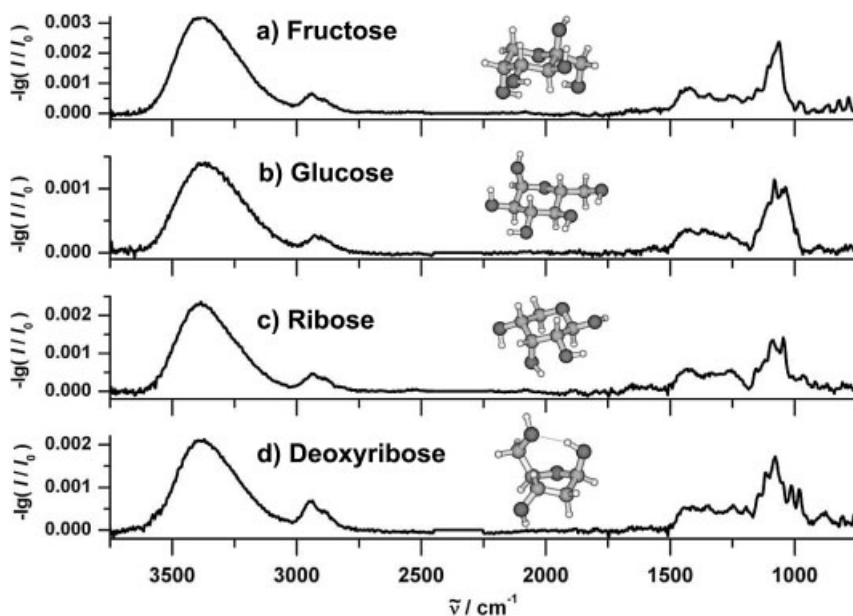


**Fig. 6.9.** Infrared spectra of aerosol particles of (a) fructose, (b) glucose, (c) ribose, and (d) deoxyribose. Fructose, glucose, and ribose molecules form pyranose rings in the particles, as indicated by the molecular structures. For

deoxyribose a furanose ring is shown, but it is not clear in this case whether the particles consist of furanose or pyranose rings.  $\tilde{\nu}$  is the transition wavenumber.

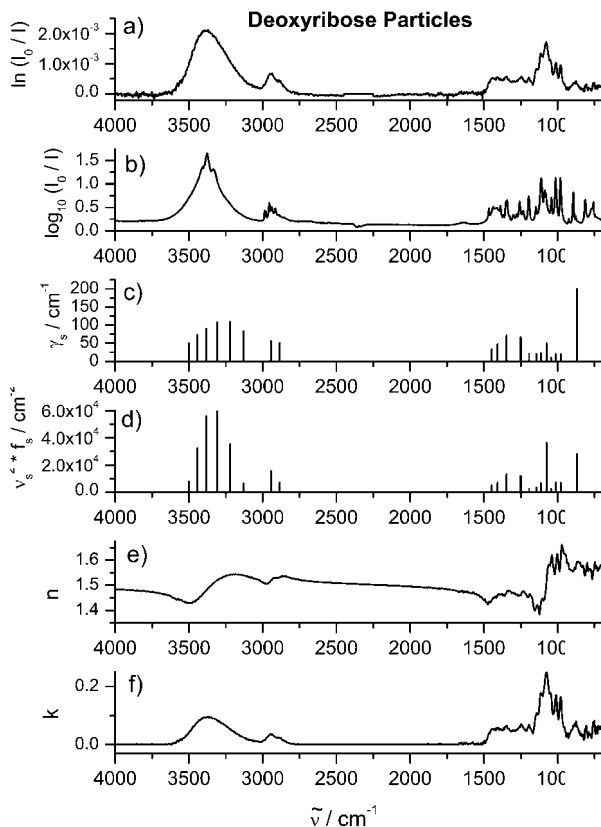


**Fig. 6.10.** (a) Experimental IR spectrum of deoxyribose aerosol particles. (b) Experimental IR spectrum of crystalline deoxyribose in KBr. (c) Optimized damping constants  $\gamma_s$  and (d) optimized relative transition intensities  $\tilde{\nu}_s^2 f_s$  from the Lorentz model [Eq. (3)]. (e) Real part  $n$  and (f) imaginary part  $k$  of the complex refractive index obtained by a Kramers–Kronig inversion of the experimental particle spectrum [Eq. (5)].  $\tilde{\nu}$  is the transition wavenumber.

print region below  $1800\text{ cm}^{-1}$  is characteristic for each compound, even for compounds as similar as the two isomers fructose and glucose. The fingerprint region does not only allow us to distinguish between different sugars, it even provides information about the structure of the molecules in the particles. For instance the missing carbonyl band (expected at  $1750\text{ cm}^{-1}$ ) in all four spectra proves that the sugar molecules are not present in their open form but that they form ring structures in the particles. In addition, from comparison of the IR spectra with quantum chemical calculations it is possible, for some sugars, to make statements about the kind of ring structure (e.g., furanose or pyranose). For fructose, glucose, and ribose the pyranose rings seem to be predominant, as indicated by the molecular structures (insets) in Fig. 6.9. For deoxyribose, however, it is not clear from the analysis of the IR spectra whether the particles consist of pyranose or furanose rings.

In contrast to the fingerprint region, the OH-stretching region around  $3300\text{ cm}^{-1}$  looks almost identical for all four sugars. It is characterized by a single, unstructured, very broad band, which is shaded towards lower frequencies. This spectral region is strongly influenced by the formation of inter- and intramolecular hydrogen bonds. The characteristic band shape seems to reflect a more general behavior that is common to all four carbohydrate particles. To elucidate this phenomenon we have performed a band shape analysis assuming a Lorentz model that leads to the dielectric function given by Eq. (3). The relation to the refractive index data is given by Eq. (4). The same procedure as described in the previous section for phenanthrene particles was used to determine the optical data. As a result, we obtained the oscillator strengths ( $\tilde{\nu}_s^2 f_s$ ) and the damping widths ( $\gamma_s$ ) of the different Lorentz oscillators with resonance wavenumbers ( $\tilde{\nu}_s$ ). For deoxyribose, the values for  $\gamma_s$  are depicted in Fig. 6.10(c) and the values for  $\tilde{\nu}_s^2 f_s$  in 6.10(d). Here, we are mainly interested in the OH-stretching region. The sequence of oscillator strengths and widths found in this region for the particle spectra reveals a hierarchy of different hydrogen bonds: large redshifts ( $\tilde{\nu}_s$ ) of OH-stretch transitions are accompanied by an increase in transition intensity ( $\tilde{\nu}_s^2 f_s$ ) and a stronger coupling to the environment ( $\gamma_s$ ). We interpret this observation as a result of a certain degree of short-range order in the amorphous solid particles caused by intermolecular hydrogen bonds. Since the other three sugars give the same qualitative results as discussed here for deoxyribose this hints at similarities in the kind of short range order for the different sugar-like substances. The band shape analysis with the Lorentz model also yields refractive index data. We have further improved these data by a Kramers–Kronig inversion [Eq. (5)]. The final refractive index data  $n$  and  $k$  are listed in Ref. [46] and are shown in Fig. 6.10(e) and (f) respectively. With these data, the determination of the size distribution now becomes possible for deoxyribose aerosols.

In addition to the electro-spray generation, a batch RESS apparatus has been used to investigate the formation of submicron sugar particles. This apparatus is designed for experiments in the temperature range from 270 to 370 K and pressures up to 25 MPa. The RESS experiments were performed at a pre-expansion temperature of 338 K and a pre-expansion pressure of 20 MPa. In all experiments the extraction conditions were  $T_{\text{ext}} = 323\text{ K}$  and  $p_{\text{ext}} = 20\text{ MPa}$ . Figure 6.11 shows, on the left-hand side, maltodextrin particles and, on the right-hand side, lactose particles produced by RESS. These SEM pictures are typical examples of the products obtained and show that the spherical particles are less than 300 nm in diameter. However, notably, due to the very low solubility of both maltodextrin and lactose in supercritical  $\text{CO}_2$  a co-solvent should be used in further investigations to enhance the solubility of the sugars in  $\text{CO}_2$ .

### 6.5.3

#### Drug Nanoparticles

One main problem arising from the micronization of drugs with RESS is that in the final products the small primary particles often coagulate or agglomerate to

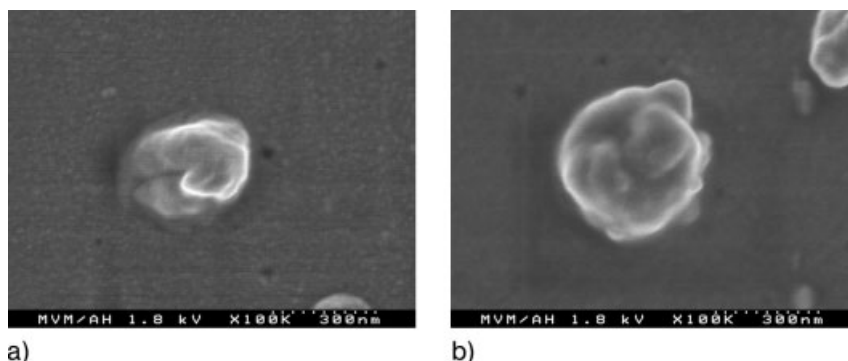


**Fig. 6.11.** Maltodextrin particles (left) and lactose particles (right) produced by RESS. The particles are 300 nm in diameter.

form much larger aggregates. These processes can take place either upon particle formation, or upon collecting the particles, or during storage of the powders. Coagulation and agglomeration leads to a decrease of the active surface and thus reduces the dissolution rate and the bioavailability of drugs. This can be overcome by mixing with or encapsulating by a second substance that avoids or at least reduces agglomeration. For instance, this can be achieved by rapid expansion of a ternary supercritical mixture which leads to co-precipitation of the two solutes (CORESS). Until now, much work has been done on producing particles of pure solutes by RESS, but only a few studies have been devoted to the simultaneous co-precipitation of two solutes [19–22, 24, 26, 74, 76]. Another way to prevent particle growth through coagulation and agglomeration and to stabilize the particles is to spray the supercritical solution directly into an aqueous surfactant solution (RESSAS [14, 18, 23, 25]). Encapsulation of particles is not only of interest for stabilizing primary particles, it is also a promising way for controlled drug delivery in the body. For instance, the coating can allow for targeted drug release in different intestinal regions (pH-dependent release). We have investigated such aspects for different pharmaceutical agents such as griseofulvin (oral antifungal drug), ibuprofen (anti-inflammatory drug), and phytosterol [10, 14, 18, 24, 74, 76]. In this section, we discuss the agglomeration behavior of phytosterol particles generated with RESS and the influence of co-expanding a polymer in the supercritical solution (CORESS). Phytosterol is a mixture of 85%  $\beta$ -sitosterol, 10% stigmasterol, and 5% campesterol. The main component  $\beta$ -sitosterol can be used as an additive for cosmetic substances or as an agent to reduce the amount of cholesterol in the human blood.

Pure phytosterol particles generated by RESS have a strong tendency to coagulate/agglomerate. This is documented by the two SEM images in Fig. 6.12. The survey in trace (a) shows that micronized phytosterol has a spongy structure that consists of coagulated/agglomerated primary particles. This can be seen best in trace (b), which represents an expanded view of trace (a). The agglomerated

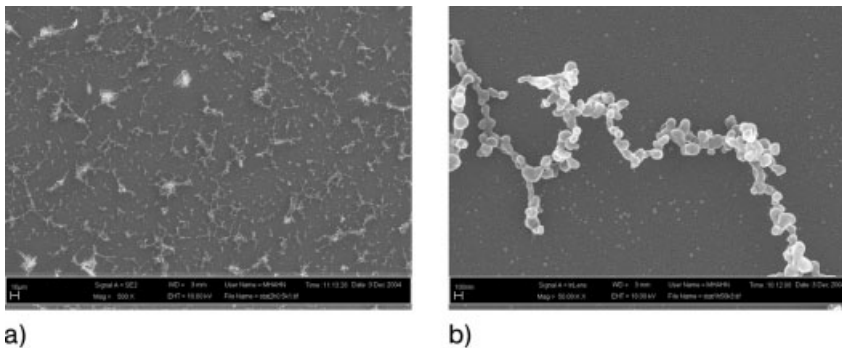


**Fig. 6.12.** SEM images of pure phytosterol particles produced by RESS. (a) Survey and (b) detailed view.

spongy structure consists of primary particles with diameters between 50 and 150 nm. With our *in situ* characterization methods we have tried to find out where the agglomeration of the phytosterol particles takes place. In principle, the particles can agglomerate before and at the Mach disc, after the Mach disc in the gas phase, or during the particle collection on the sample holder for the SEM examination. From our measurements, we cannot make firm statements about agglomeration processes taking place before and at the Mach disc, but the 3-WEM at least indicates that the phytosterol particles are quite small ( $r_0 \sim 50$  nm,  $\sigma \sim 1.8$ ) immediately after the pulse and after all  $\text{CO}_2$  has evaporated. After the pulse has finished, however, we can observe the behavior of the aerosol in the expansion chamber as a function of time. For the very large agglomerated particles depicted in Fig. 6.12(a), we would expect a decrease of the extinction in the IR spectra and a decrease of the extinction signals recorded for the 3-WEM with increasing time. The reason for that is the settling of the agglomerates. For comparison, settling of the phenanthrene particles with mean diameters around 400 nm leads to a decrease of the extinction by 70% already after 10 min. In contrast to these expectations, both the infrared signal and the 3-WEM signal are almost completely constant for more than 15 min after the end of the pulse. This is shown in Fig. 6.13(a) and (b). Both figures show only a minor change of the signal with time. This means that most of the particles in the gas phase are very small and stay small (no agglomeration). Bigger particles or agglomerates would settle down in our chamber and thus lead to a decrease in the extinctions for FTIR and 3-WEM. This is a clear experimental hint that the agglomeration takes place predominantly during the sample collection for the SEM measurements.

Based on a modified RESS-process (CORESS [19–22, 24, 74, 76]), additional experiments were performed with biodegradable polymers [Eudragit® and poly-L-lactic-acid (L-PLA)] and phytosterol as solutes. In these experiments both phytosterol and the polymer are thoroughly mixed and weighed out and then packed into the extraction vessel. Experiments with Eudragit® were performed with the batch apparatus (see Section 6.2.1) at pre-expansion temperatures between 310



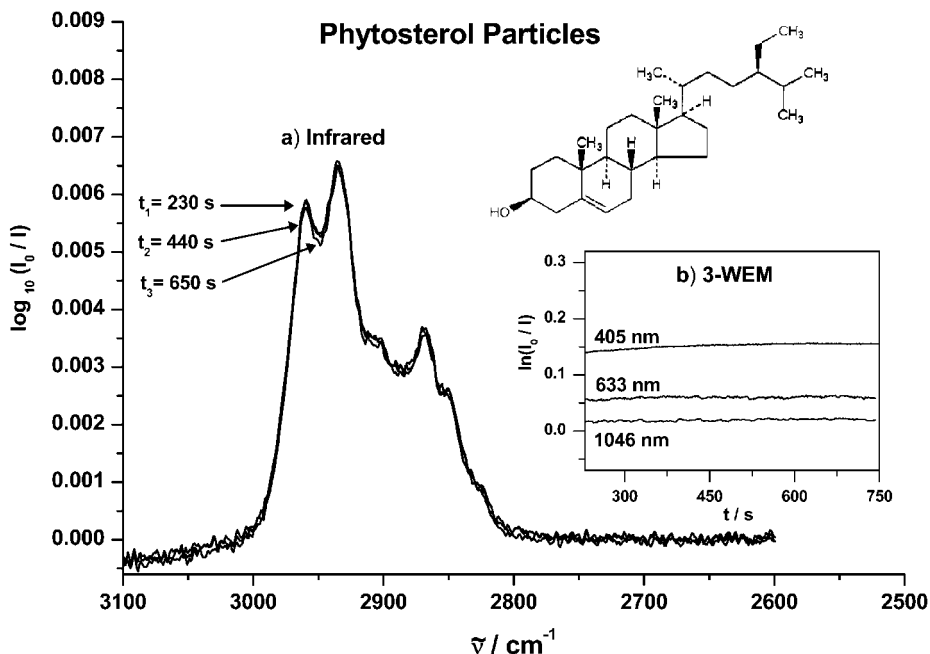
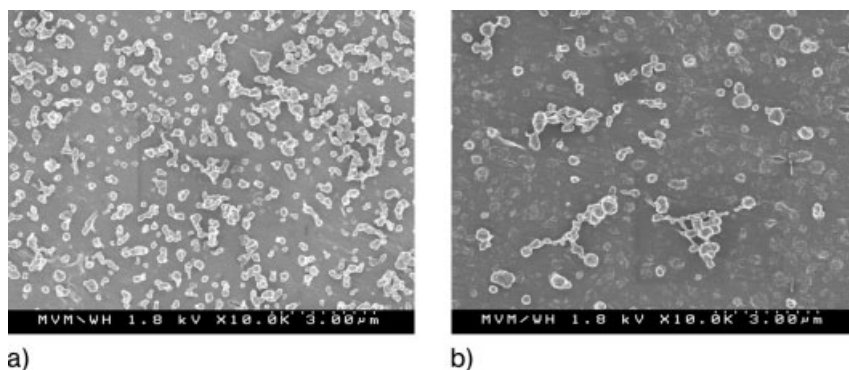


Fig. 6.13. (a) Infrared spectra of pure phytosterol aerosol particles recorded at  $t_1 = 230$ ,  $t_2 = 440$ , and  $t_3 = 650$  s after the end of the expansion pulse ( $t = 0$  s).  $\tilde{\nu}$  is the transition wavenumber. (b) Extinction signals

from 3-WEM for the three lasers with wavelengths  $\lambda_1 = 405$ ,  $\lambda_2 = 633$ , and  $\lambda_3 = 1064$  nm. The signals remain nearly constant as a function of time ( $t$ ) after the end of the expansion pulse.

and 340 K and a pre-expansion pressure of 20 MPa. With L-PLA the continuous RESS apparatus was used. These experiments were performed at an extraction temperature of 313 K, pre-expansion temperatures between 348 and 388 K and a pre-expansion pressure of 20 MPa. To avoid clogging, the nozzle temperature was 10 K higher than the respective pre-expansion temperature. These pre-expansion conditions were chosen to prevent particle precipitation inside the capillary nozzle. SEM was used to observe the morphology of the particle surface. The size of the particles produced by CORESS was measured online with 3-WEM. Differential Scanning Calorimetry (DSC) was used for physical characterization (melting point, heat of fusion, and crystallinity) of the original and the processed materials. The decrease of the heat of fusion obtained in the first heating-run allowed us to estimate the amount of polymer in the mixture. In addition, the unprocessed and the processed substances were characterized by X-ray diffraction (XRD).

Figure 6.14 shows, on the left, typical results for the co-precipitated phytosterol/Eudragit® particles. As mentioned above, the pure phytosterol particles are usually agglomerated and show a spongy structure. Contrary to these results the CORESS experiments performed with mixtures of phytosterol/Eudragit® (mass ratios of 1:1 and 1:10) lead to finely dispersed particles with diameters in the range of 250 nm.



**Fig. 6.14.** Phytosterol/Eudragit<sup>®</sup> particles (left) and phytosterol/L-PLA particles (right) produced by CORESS. The amount of Eudragit<sup>®</sup> is ~10 wt% and the amount of L-PLA is ~12 wt%.

The particles thus obtained were analyzed by DSC and compared with the unprocessed materials to determine the amount of polymer in the particles. The melting temperature and the heat of fusion of the original phytosterol were found to be 413 K and 56.9 J g<sup>-1</sup>, respectively. These values differ markedly from those of the submicron phytosterol/Eudragit<sup>®</sup> particles (407 K and 37.1 J g<sup>-1</sup>, respectively, for a mass ratio of 1:10). Depending on the initial mass ratio of the mixture in the extraction vessel, the amount of Eudragit<sup>®</sup> in the particles varies from ~10 to ~35 wt%. Additional FTIR analysis of the phytosterol/Eudragit<sup>®</sup> particles obtained confirm these results.

Additional CORESS experiments were performed with mixtures of phytosterol/L-PLA (mass ratios of 1:5 and 1:8). As shown in the right-hand part of Fig. 6.14, the experiments again lead to dispersed particles 250 nm in diameter. The product was characterized by DSC and XRD. Both the melting temperature and the heat of fusion were reduced in comparison to pure phytosterol. Typical DSC curves of pure phytosterol particles, of phytosterol/L-PLA particles, and of pure L-PLA particles are depicted in Fig. 6.15. The curve of pure phytosterol shows a melting peak in the range between 403 and 415 K while the curve of the phytosterol/L-PLA particles shows a broad peak between 388 and 411 K, corresponding to the microencapsulation of phytosterol. Depending on the initial mass ratio of the mixture in the extraction vessel, the amount of L-PLA varied from 12 to 40 wt%. Figure 6.16 displays typical XRD patterns of pure phytosterol particles, of phytosterol/L-PLA particles, and of pure L-PLA particles. For both the pure phytosterol and the phytosterol/L-PLA mixture diffraction peaks characteristic for crystalline phytosterol are obtained. These diffraction peaks disappear for the submicron L-PLA particles. Thus, the L-PLA particles are in the amorphous state. This result is in good agreement with the DSC analyses where no melting peak of crystalline L-PLA was observed (Fig. 6.15).

IR spectroscopy allows us to determine and thus to control the amount of L-PLA

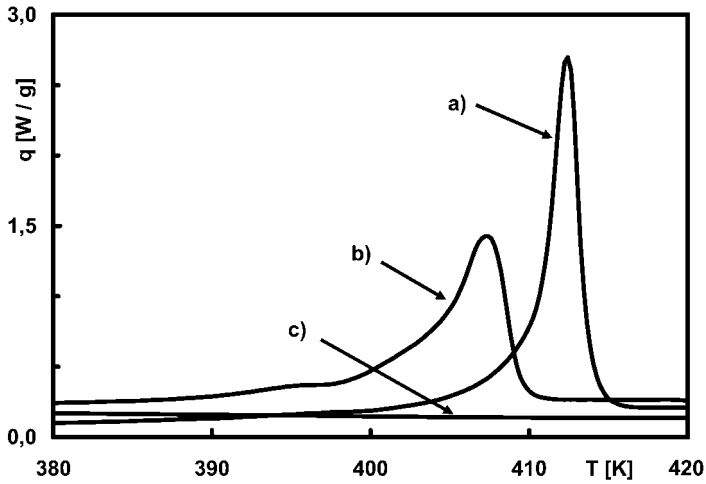


Fig. 6.15. DSC curves of (a) pure phytosterol particles, (b) phytosterol/L-PLA particles, and (c) pure L-PLA particles.

*in situ* during particle formation. This is much faster and simpler than the analysis with DSC and allows us to optimize the amount of polymer by adjusting the process parameters during particle formation. Figure 6.17 compares the IR spectrum of pure phytosterol particles (trace a) with two spectra of mixed phytosterol/L-PLA particles (traces b and c). The spectrum of pure phytosterol particles has strong absorption bands in the OH/CH-stretching region around  $2900\text{ cm}^{-1}$  but only weak absorption bands in the fingerprint region below  $1800\text{ cm}^{-1}$ . Although there are many bands in this region, they are barely visible due to their weakness. Traces

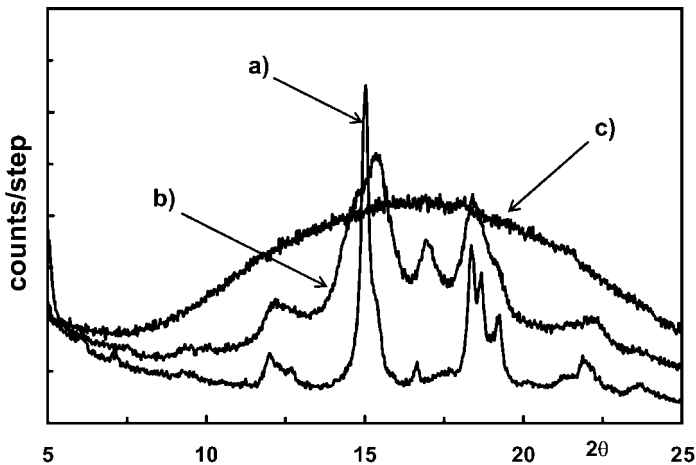
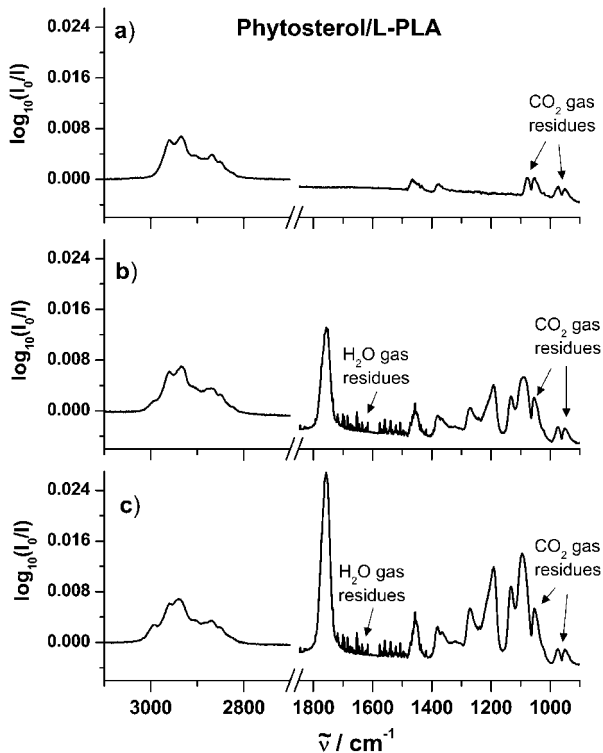


Fig. 6.16. XRD patterns of (a) pure phytosterol particles, (b) phytosterol/L-PLA particles, and (c) pure L-PLA particles.



**Fig. 6.17.** (a) Infrared spectrum of pure phytosterol aerosol particles. (b) and (c) IR spectra of mixed phytosterol/L-PLA aerosol particles. There is  $\sim 70\%$  more polymer in the particles of trace (c) than in trace (b).  $\bar{\nu}$  is the transition wavenumber.

(b) and (c) show that the strongest band of L-PLA in the fingerprint region is the carbonyl stretching-band around  $1765\text{ cm}^{-1}$ . In contrast to the other absorption bands of L-PLA in the fingerprint region it is well separated and does not overlap with phytosterol bands or  $\text{CO}_2$  bands. Moreover, L-PLA shows no significant absorbance above  $2800\text{ cm}^{-1}$ . Therefore, the ratio of its carbonyl band intensity to that of the phytosterol OH/CH absorption is well suited to determine the relative content of L-PLA in the particles. From trace (b) to trace (c) the amount of L-PLA in the particles increases by  $\sim 70\%$ .

In summary, these results illustrate that the simultaneous co-precipitation of two solutes is a promising method to produce composite particles. The particles obtained from the CORESS process appear as a drug core encapsulated in a polymer coating. This encapsulation helps to prevent agglomeration and to control drug release, which both depend on the amount of polymer in the particles. The easiest way to control the amount of polymer is by *in situ* FTIR spectroscopy during particle formation.

## 6.6

### Summary and Conclusion

FTIR spectroscopy provides a wealth of information about molecular nanoparticles, which makes it an particularly powerful method for the characterization of such systems. Vibrational spectra of particulate systems allow us to draw conclusions about the chemical composition, the size, the shape, and about structural properties of the particles. Especially attractive is the use of *in situ* direct absorption FTIR spectroscopy, which allows us to characterize and control the particle properties during or shortly after their generation. For these investigations it is crucial that *in situ* FTIR spectroscopy is fast, that it can be combined with various particle generation methods, and that it can be used under very different experimental conditions.

The different examples in this chapter document the general applicability of this characterization method and the wide range of information it provides for biomolecular particles. This comprises different aspects of particle characterization. One example is the investigation of the particle formation process itself. In agreement with previous modeling results the RESS experiments show that, depending on the pre-expansion conditions, condensation of the solvent CO<sub>2</sub> can occur in the initial stage of particle formation. Such information is very useful for the evaluation of the obtained particles since the condensation/evaporation behavior of the solvent has a strong influence on particle formation and therewith on the properties of the final solid particles. Another example is the on-line control of particle composition. This is crucial, for instance, for polymer encapsulated drugs when a well defined amount of polymer in the particles has to be maintained.

A prerequisite for a successful analysis of the information contained in the IR spectra is the knowledge of the corresponding refractive index data. These data provide information, for instance, about the size effects and the shape effects to be expected in extinction spectra. We have demonstrated that the determination of accurate optical data from experimental IR spectra is not easy. The main reason lies in the lack of accurate information about the size, shape, and number concentration of the particles and in the model assumptions used in the derivation of the optical data. Therefore, it is not astonishing that, nowadays, only a few databases provide optical data for particulate systems and nearly none for nanoparticles of interest in life sciences. The lack of these data certainly represents one of the major restrictions for the routine application of FTIR spectroscopy for particle characterization. To alleviate that restriction is one of the most important challenges in the field.

### Acknowledgment

Our special thanks go to to our coworkers Dr A. Bonnamy, G. Firanescu, D. Hermsdorf, P. Hils, M. Jetzki, Ch. Kornmayer, M. Meier, R. Ueberschaer, and D. Vollmar. We gratefully acknowledge collaboration with Professor Dr M. A. Suhm and PD Dr S. Beuermann. Financial support was provided by the Deutsche For-

schungsgemeinschaft (grant Nrs. SI 833/1-1,2 and Tu 94/5-1,2; SFB 602; and GRK 782) and by the Fonds der Chemischen Industrie.

## References

- 1 D. LIU, J. GAO, C. J. MURPHY, C. T. WILLIAMS. In situ attenuated total reflection infrared spectroscopy of dendrimer-stabilized platinum nanoparticles adsorbed on alumina. *J. Phys. Chem. B*, 108, 12911–12916, 2004.
- 2 J. HOLMAN, S. YE, D. J. NEIVANDT, P. B. DAVIES. Studying nanoparticle-induced structural changes within fatty acid multilayer films using sum frequency generation vibrational spectroscopy. *J. Am. Chem. Soc.*, 126, 14322–14323, 2004.
- 3 F. MAILLARD, E. R. SAVINOVA, P. A. SIMONOV, V. I. ZAIKOVSKII, U. STIMMING. Infrared spectroscopic study of CO adsorption and electro-oxidation on carbon-supported Pt nanoparticles: interparticle versus intraparticle heterogeneity. *J. Phys. Chem. B*, 108, 17893–17904, 2004.
- 4 V. STAMENKOVIĆ, M. ARENZ, P. N. ROSS, N. M. MARKOVIĆ. Temperature-induced deposition method for anchoring metallic nanoparticles onto reflective substrates for in situ electrochemical infrared spectroscopy. *J. Phys. Chem. B*, 108, 17915–17920, 2004.
- 5 F. S. MANCIU, R. E. TALLMAN, B. D. MCCOMBE, B. A. WEINSTEIN, D. W. LUCEY, Y. SAHOO, P. N. PRASAD. Infrared and Raman spectroscopies of InP/II–VI core–shell nanoparticles. *Physica E*, 26, 14–18, 2005.
- 6 J. L. BURT, C. GUTIÉRREZ-WING, M. MIKI-YOSHIDA, M. JOSÉ-YACAMÁN. Noble-metal nanoparticles directly conjugated to globular proteins. *Langmuir*, 20, 11778–11783, 2004.
- 7 J. M. MERRITT, G. E. DOUBERLY, R. E. MILLER. Infrared–infrared double resonance spectroscopy of cyanoacetylene in helium nanodroplets. *J. Chem. Phys.*, 121, 1309–1316, 2004.
- 8 S. A. KALELE, S. S. ASHTAPUTRE, N. Y. HEBALKAR, S. W. GOSAVI, D. N. DEOBAGKAR, D. D. DEOBAGKAR, S. K. KULKARNI. Optical detection of antibody using silica–silver core–shell particles. *Chem. Phys. Lett.*, 404, 136–141, 2005.
- 9 M. JETZKI, R. SIGNORELL. The competition between hydrogen bonding and chemical change in carbohydrate nanoparticles. *J. Chem. Phys.*, 117, 8063–8073, 2002.
- 10 A. BONNAMY, D. HERMSDORF, R. UEBERSCHAER, R. SIGNORELL. Characterization of the rapid expansion of supercritical solutions by FTIR spectroscopy in situ, accepted. *Rev. Sci. Instrum.*, 76(5), Art. No 053904 (published online).
- 11 D. W. MATSON, J. L. FULTON, R. C. PETERSEN, R. D. SMITH. Rapid expansion of supercritical fluid solutions: solute formation of powders, thin films, and fibers. *Ind. Eng. Chem. Res.*, 26, 2298–2306, 1987.
- 12 J. W. TOM, P. G. DEBENEDETTI. Particle formation with supercritical fluids – a review. *J. Aerosol. Sci.*, 22, 555–584, 1991.
- 13 J. JUNG, M. PERRUT. Particle design using supercritical fluids: Literature and patent survey. *J. Supercrit. Fluids*, 20, 179–219, 2001.
- 14 M. TÜRK, P. HILS, B. HELFGEN, K. SCHABER, H.-J. MARTIN, M. A. WAHL. Micronization of pharmaceutical substances by rapid expansion of supercritical solutions (RESS): a promising method to improve bioavailability of poorly soluble pharmaceutical agents. *J. Supercrit. Fluids*, 22, 75–84, 2002.
- 15 D. HERMSDORF, A. BONNAMY, M. A. SUHM, R. SIGNORELL. Infrared spectra of phenanthrene particles generated by pulsed rapid expansion of CO<sub>2</sub>

- solutions. *Phys. Chem. Chem. Phys.*, 6, 4652–4657, 2004.
- 16 S. CIHLAR. *Mikronisierung organischer Feststoffe durch schnelle Expansion überkritischer Lösungen*. Doctoral Thesis, VDI Verlag GmbH (Düsseldorf), 2000.
  - 17 M. TÜRK. Formation of small organic particles by RESS: Experimental and theoretical investigations. *J. Supercrit. Fluids*, 15, 79–89, 1999.
  - 18 M. TÜRK, B. HELFGEN, P. HILS, R. LIETZOW, K. SCHABER. Micronization of pharmaceutical substances by Rapid Expansion of Supercritical Solutions (RESS): Experiments and modeling. *Particle Particle Systems Characteriz.*, 19, 327–335, 2002.
  - 19 J. W. TOM, P. G. DEBENEDETTI. Formation of bioerodible polymeric microspheres and microparticles by rapid expansion of supercritical solutions. *Biotechnol. Prog.*, 7, 403–411, 1991.
  - 20 J. W. TOM, G.-B. LIM, P. G. DEBENEDETTI, R. K. PRUD'HOMME. Applications of supercritical fluids in the controlled release of drugs. *ACS Symp. Ser.*, 514, 238–257, 1993.
  - 21 J. W. TOM, P. G. DEBENEDETTI. Precipitation of poly(L-lactic acid) and composite poly(L-lactic acid)–pyrene particles by rapid expansion of supercritical solutions. *J. Supercrit. Fluids*, 7, 9–29, 1994.
  - 22 J.-H. KIM, T. E. PAXTON, D. L. TOMASKO. Microencapsulation of naproxen using rapid expansion of supercritical solutions. *Biotechnol. Prog.*, 12, 650–661, 1996.
  - 23 M. TÜRK. Herstellung organischer Nanopartikel und deren Stabilisierung in wässrigen Lösungen (RESSAS). *Chem. Ing. Techn.*, 75, 792–795, 2003.
  - 24 M. TÜRK. Untersuchung zum coating von submikronen partikeln mit dem CORESS-Verfahren. *Chem. Ing. Techn.*, 76, 835–838, 2004.
  - 25 M. TÜRK, R. LIETZOW. Stabilized nanoparticles of phytosterol by rapid expansion from supercritical solutions into aqueous solution. *AAPS PharmSciTech*, 5:Article 56, 2004.
  - 26 Kh. HUSSEIN, M. TÜRK, M. A. WAHL. Preparation and evaluation of drug/ $\beta$ -cyclodextrin solid inclusion complexes by supercritical fluid technology. I. KIKIC, M. PERRUT (eds.), *Proceedings of the 9<sup>th</sup> Meeting on Supercritical Fluids*, Trieste, Italy, June 13–16, 2004.
  - 27 D.-R. CHEN, D. Y. H. PUI, S. L. KAUFMAN. Electrospraying of conducting liquids for monodisperse aerosol generation in the 4 nm to 1.8  $\mu$ m diameter range. *J. Aerosol Sci.*, 26, 963–977, 1995.
  - 28 S. L. KAUFMAN, R. CALDOW, F. D. DORMAN, K. D. IRWIN, A. PÖCHER. Conversion efficiency of the TSI model 3480 electrospray aerosol generator using sucrose. *J. Aerosol Sci.*, 30, S373–S374, 1999.
  - 29 R. SIGNORELL, M. K. KUNZMANN, M. A. SUHM. FTIR investigation of non-volatile molecular nanoparticles. *Chem. Phys. Lett.*, 329, 52–60, 2000.
  - 30 R. SIGNORELL, D. LUCKHAUS. Aerosol spectroscopy of dihydroxyacetone: Gas phase and nanoparticles. *J. Phys. Chem. A*, 106, 4855–4867, 2002.
  - 31 Th. HÄBER, U. SCHMITT, C. EMMELUTH, M. A. SUHM. Ragout-jet FTIR spectroscopy of cluster isomerism and cluster dynamics: from carboxylic acid dimers to N<sub>2</sub>O nanoparticles. *Faraday Discuss.*, 118, 331–359, 2001.
  - 32 Th. HÄBER, U. SCHMITT, M. A. SUHM. FTIR-spectroscopy of molecular clusters in pulsed supersonic slit-jet expansions. *Phys. Chem. Chem. Phys.*, 1, 5573–5582, 1999.
  - 33 P. G. DEBENEDETTI. Homogeneous nucleation in supercritical fluids. *AIChE J.*, 36, 1289–1298, 1990.
  - 34 M. TÜRK. Influence of thermodynamic behaviour and solute properties on homogeneous nucleation in supercritical solutions. *J. Supercrit. Fluids*, 18, 169–184, 2000.
  - 35 B. HELFGEN, P. HILS, Ch. HOLZKNECHT, M. TÜRK, K. SCHABER. Simulation of particle formation during the rapid expansion of supercritical solutions. *J. Aerosol Sci.*, 32, 295–319, 2001.
  - 36 M. WEBER, L. M. RUSSELL, P. G. DEBENEDETTI. Mathematical modeling

- of nucleation and growth of particles formed by the rapid expansion of supercritical solution under subsonic conditions. *J. Supercrit. Fluids*, 23, 65–80, 2002.
- 37 M. WEBER, M. C. THIES. Understanding the RESS Process. In Y.-PING SUN, ed., *Supercritical Fluid Technology in Material Science and Engineering*, pp. 387–437. Marcel Dekker, New York, 2002.
- 38 B. HELFGEN, M. TÜRK, K. SCHABER. Hydrodynamic and aerosol modelling of the rapid expansion of supercritical solutions (RESS-process). *J. Supercrit. Fluids*, 26, 225–242, 2003.
- 39 M. K. KUNZMANN, R. SIGNORELL, M. TARASCHEWSKI, S. BAURECKER. The formation of N<sub>2</sub>O nanoparticles in a collisional cooling cell between 4 and 110 K. *Phys. Chem. Chem. Phys.*, 3, 3742–3749, 2001.
- 40 K. D. BARTLE, A. A. CLIFFORD, S. A. JAFAR, G. F. SHILSTONE. Solubilities of solids and liquids of low volatility in supercritical carbon dioxide. *J. Phys. Chem. Ref. Data*, 20, 713–756, 1991.
- 41 R. SIGNORELL. Infrared spectroscopy of particulate matter: between molecular clusters and bulk. *Mol. Phys.*, 101, 3385–3399, 2003.
- 42 C. F. BOHREN, D. R. HUFFMAN. *Absorption and Scattering of Light by Small Particles*, Wiley-Interscience, New York, 1998.
- 43 J. A. ROUX, B. E. WOOD, A. M. SMITH. *IR Optical Properties of Thin H<sub>2</sub>O, NH<sub>3</sub>, and CO<sub>2</sub> Cryofilms*. AEDC-TR-79-57 (AD-A074913), September, 1979.
- 44 A. BONNAMY, M. JETZKI, R. SIGNORELL. Optical properties of molecular ice particles from a microscopic model. *Chem. Phys. Lett.*, 382, 547–552, 2003.
- 45 J. MEYER, M. KATZER, E. SCHMIDT, S. CIHLAR, M. TÜRK. Comparative particle size measurements in lab-scale nanoparticle production processes. J. BRIDGEWATER (ed.), *Proceedings of the World Congress on Particle Technology* 3, July 6–9, 1998, Brighton, UK.
- 46 <http://www.user.gwdg.de/~rsignor/refindex.htm>.
- 47 D. M. HUDGINS, S. A. SANDFORD, L. J. ALLAMANDOLA, A. G. G. M. TIELENS. Mid- and far-infrared spectroscopy of ices: optical constants and integrated absorbances. *Astron. Astrophys. Suppl. Ser.*, 86, 713–722, 1993.
- 48 Th. HENNING, V. B. IL'IN, N. A. KRIVOVA, B. MICHEL, N. V. VOSHCHINIKOV. WWW database of optical constants for astronomy. *Astron. Astrophys. Suppl. Ser.*, 136, 405–406, 1999.
- 49 L. S. ROTHMAN et al. The HITRAN molecular spectroscopic database and HAWKS (HITRAN Atmospheric Workstation): 1996 edn. *J. Quant. Spectrosc. Radiat. Transfer*, 60, 665–710, 1998.
- 50 M. K. KUNZMANN, S. BAURECKER, M. A. SUHM, R. SIGNORELL. Spectroscopic characterization of N<sub>2</sub>O aggregates: from clusters to the particulate state. *Spectrochim. Acta A*, 59, 2855–2865, 2003.
- 51 M. JETZKI, D. LUCKHAUS, R. SIGNORELL. Fermi resonance and conformation in glycolaldehyde particles. *Can. J. Chem.*, 82, 915–924, 2004.
- 52 M. JETZKI, A. BONNAMY, R. SIGNORELL. Vibrational delocalization in ammonia aerosol particles. *J. Chem. Phys.*, 120, 11775–11784, 2004.
- 53 M. I. MISHCHENKO, J. W. HOVENIER, L. D. TRAVIS. *Light Scattering by Nonspherical Particles*, Academic Press, San Diego, 2000.
- 54 R. SIGNORELL. Verification of the vibrational exciton approach for CO<sub>2</sub> and N<sub>2</sub>O nanoparticles. *J. Chem. Phys.*, 118, 2707–2715, 2003.
- 55 R. SIGNORELL, M. K. KUNZMANN. Isotope effects on vibrational excitons in carbon dioxide particles. *Chem. Phys. Lett.*, 371, 260–266, 2003.
- 56 W. C. HINDS. *Aerosol Technology*, Wiley Interscience, New York, 1999.
- 57 H. KUZMANY. *Solid-State Spectroscopy*, Springer-Verlag, Berlin, 1998.
- 58 J. E. BERTIE, S. L. ZHANG, C. D. KEEFE. Infrared intensities of liquids XVI. Accurate determination of molecular band intensities from infrared refractive index and dielectric



- constant spectra. *J. Mol. Struct.*, 324, 157–176, 1994.
- 59 R. Z. BACHRACH, F. C. BROWN. Exciton-optical properties of TlBr and TlCl. *Phys. Rev. B*, 1, 818–831, 1970.
- 60 R. K. AHRENKIEL. Modified Kramers–Kronig analysis of optical spectra. *J. Opt. Soc. Am.*, 61, 1651–1655, 1971.
- 61 J. P. HAWRANEK, P. NEELAKANTAN, R. P. YOUNG, R. N. JONES. The control of errors in i.r. spectrophotometry – IV. Corrections for dispersion distortion and the evaluation of both optical constants. *Spectrochim. Acta A*, 32, 85–98, 1976.
- 62 B. J. FINLAYSON-PITTS, J. N. PITTS. *Chemistry of the Upper and Lower Atmosphere*, Academic Press, San Diego, 2000.
- 63 H. SCHÖNBUCHNER, G. GUGGENBERGER, K. PETERS, H. BERGMANN, W. ZECH. Particle-size distribution of PAH in the air of a remote Norway spruce forest in northern bavaria. *Water, Air, Soil Pollut.*, 128, 355–367, 2001.
- 64 A. LI, B. T. DRAINE. Infrared emission from interstellar dust. II. The diffuse interstellar medium. *Astrophys. J.*, 554, 778–802, 2001.
- 65 M. SCHNAITER, H. MUTSCHKE, J. DORSCHNER, Th. HENNING. Matrix-isolated nano-sized carbon grains as an analog for the 217.5 nanometer feature carrier. *Astrophys. J.*, 498, 486–496, 1998.
- 66 E. M. BERENDS, O. S. L. BRUINSMA, G. M. VAN ROSMALEN. Nucleation and growth of fine crystals from supercritical carbon dioxide. *J. Cryst. Growth*, 128, 50–56, 1993.
- 67 G.-T. LIU, K. NAGAHAMA. Application of rapid expansion of supercritical solutions in the crystallization separation. *Ind. Eng. Chem. Res.*, 35, 4626–4634, 1996.
- 68 G.-T. LIU, K. NAGAHAMA. Solubility and RESS experiments of solid solution in supercritical carbon dioxide. *J. Chem. Eng. Jpn.*, 30, 293–301, 1997.
- 69 C. DOMINGO, E. BERENDS, G. M. VAN ROSMALEN. Precipitation of ultrafine organic crystals from the rapid expansion of supercritical solutions over a capillary and a frit nozzle. *J. Supercrit. Fluids*, 10, 39–55, 1997.
- 70 D. M. GINOSAR, W. D. SWANK, R. D. MCMURTREY, W. J. CARMACK. Flow-field studies of the RESS process. *Proceedings of the 5<sup>th</sup> International Symposium on Supercritical Fluids*, Atlanta, USA, April 8–12, 2000.
- 71 R. UEBERSCHAER. Charakterisierung der Partikelbildung bei der schnellen Expansion überkritischer Lösungen. In *Diploma Thesis*. University of Göttingen, 2004.
- 72 E. T. PETERS, A. F. ARMINGTON, B. RUBIN. Lattice constants of ultrapure phenanthrene. *J. Appl. Phys.*, 37, 226–227, 1966.
- 73 A. BONNAMY, R. GEORGES, E. HUGO, R. SIGNORELL. Infrared signatures of (CO<sub>2</sub>)<sub>N</sub> clusters: size, shape, and structural effects. *Phys. Chem. Chem. Phys.*, 7, 963–969, 2005.
- 74 M. TÜRK, P. HILS, K. HUSSEIN, M. WAHL. Utilization of supercritical fluid technology for the preparation of innovative carriers loaded with nanoparticulate drugs. In U. TEIPEL, ed., *Produktgestaltung in der Partikeltechnologie*, pp. 337–386, Fraunhofer-IRB-Verlag, Stuttgart, 2004.
- 75 J. SZEJTLI. Introduction and general overview of cyclodextrin chemistry. *Chem. Rev.*, 98, 1753–1753, 1998.
- 76 M. TÜRK, M. WAHL. Utilization of supercritical fluid technology for the preparation of innovative carriers loaded with nanoparticulate drugs. In S. E. PRATSINIS (ed.), *Proceedings of the International Congress for Particle Technology, PARTEC 2004, Nürnberg, March 16–18 (2004)*.

## 7

# Characterization of Nanoscaled Drug Delivery Systems by Electron Spin Resonance (ESR)

*Karsten Mäder*

### 7.1

#### Introduction

Nanoscaled drug delivery systems (nano-DDS) have been heavily investigated due to their large potential to make drug therapy more efficient. After years of intense research, they have entered the pharmaceutical market and many systems have reached the late clinical state. Nano-DDS are only defined by their submicron size. They are made from different materials (e.g., lipid or polymer based) and include very different kinds of associates and particles. Examples include (mixed) micelles, polymer micelles, liposomes, microemulsions, polymer nanoparticles, solid lipid nanoparticles, nanocapsules. The main applications are in peroral and parenteral drug delivery, although nano-DDS are also considered for other administration routes (dermal, pulmonal). In peroral drug delivery, higher absorption rates and decreased variabilities of poorly soluble drugs are achieved. Nano-DDS make the i.v. injection of poorly soluble drugs feasible and help to push drug targeting strategies from the conception to reality.

The performance of nano-DDS strongly depends on many parameters, including composition, particle size, surface charge and the physical state of the matrix. Appropriate characterization of nanoparticle systems is a serious challenge due to following reasons:

- the submicron size of the objects;
- the sensitivity of many Nano-drug delivery systems to environmental changes, including drying, freezing or dilution;
- the coexistence of several colloidal species;
- the importance of dynamic phenomena;
- material properties might differ significantly from bulk material.

Some commonly used methods require tedious sample preparation (electron microscopy) or fixing of the particles (AFM). Fixation by drying of the samples composed of soft matter such as lipid nanoparticles, however, will change considerably the sample characteristics. Therefore, there is a need for methods that are can char-

acterize Nano-drug delivery systems with no or minimized sample preparation. NMR spectroscopy, fluorescence and other optical techniques, Raman-spectroscopy and ESR are methods that offer possibilities to conduct such studies. The challenge of appropriate characterization is considerable higher for characterization in biological surroundings *in vitro* or *in vivo*. Most techniques are not capable of *in vivo* measurements. Radiolabeling techniques are used to monitor the distribution of Nano-drug delivery systems in the body of animals and man; however, they provide no information about the physicochemical changes of the drug delivery system caused by interaction with the environment or metabolic processes. Consequently, our knowledge of the detailed fate of the drug and drug carrier *in vivo* is still rather limited. This chapter will discuss how ESR can contribute to shedding more light on nanoscaled drug delivery systems. The basic requirements of ESR will be discussed. Examples will show which information can be extracted from the spectra and how this information can be used to characterize drug delivery systems. Finally, the opportunities and limits of ESR for the *in vivo* characterization will be shown.

## 7.2

### ESR Basics and Requirements

Electron Spin Resonance (ESR) or synonymously Electron Paramagnetic Resonance (EPR) can be regarded as a sister method for Nuclear Magnetic Resonance (NMR). Both methods were first described about 60 years ago and both require the presence of a magnetic moment. In NMR, the magnetic moment comes from the nuclear spin (e.g.,  $^1\text{H}$ ,  $^{13}\text{C}$ ,  $^{19}\text{F}$ ), in ESR it derives from unpaired electrons. Sources of unpaired electrons are free radicals and certain oxidations states of transition metals.

The basic magnetic resonance experiment (NMR and EPR) requires the positioning of the sample in a homogenous magnetic field. The applied magnetic field leads to parallel or anti-parallel alignment of the spins. Irradiation of the sample with an appropriate frequency (= resonance frequency) leads the spins to switch between both states. Under such conditions, part of the energy is absorbed and a signal observed. Higher magnetic fields lead to higher sensitivity and need higher frequencies. Typical NMR frequencies are radiofrequencies (e.g., 20–600 MHz), whereas typical ESR frequencies are in the microwave range (10 GHz). However, the recent development of high-field NMR (800 MHz and higher) and low-frequency ESR (1 GHz and 300 MHz) have led to partial overlapping of the NMR and ESR frequency ranges. Due to the high dielectric loss, the standard ESR frequency of 10 GHz penetrates only 1–2 mm in water-containing samples (e.g., biological tissue). The development of low frequency ESR was necessary to make possible the investigation of larger samples with high water content. It permits ESR experiments on whole living mammals (mice and rats). Refs. [1, 2] give a broad coverage of basic ESR and biological related applications.

NMR is per se less sensitive than ESR due to the smaller magnetic moment of

Tab. 7.1. Comparison of NMR and ESR.

	ESR	NMR
Prerequisite	Electron spin	Nuclear spin
Examples	Free radicals, $\text{Cu}^{2+}$ , $\text{Mn}^{2+}$ , $\text{Fe}^{3+}$	$^1\text{H}$ , $^{13}\text{C}$ , $^{19}\text{F}$ , $^{35}\text{P}$
Magnetic moment ( $\text{J T}^{-1}$ )	Larger: $\mu_{e^-} = 9.274 \times 10^{-24}$	Smaller: $\mu_{\text{H}} = 5.051 \times 10^{-27}$
Typical frequency	9–10 GHz	100–800 MHz
Mode of operation	Continuous wave	FT-NMR
Typical line widths	MHz	<Hz
“Time window” (s)	$10^{-9}$ – $10^{-11}$	$10^{-5}$ – $10^{-9}$

the nuclear spin. However, this disadvantage is compensated by the much higher concentrations of nuclear spins and the development of pulsed NMR. Most ESR spectrometers work in the continuous mode because most radicals relax very rapidly and, therefore, pulsed methods are difficult or impossible to apply. Table 7.1 summarizes the main features of NMR and ESR.

The basic instrumentation of ESR requires a magnet, a microwave bridge, and a resonator with phase sensitive detection. Of course, modern spectrometers are operated via a computer interface. Most spectrometers operate at 9 to 10 GHz (X-band). Due to the high dielectric loss, the measurement of samples with high water content is limited to a size  $< 1$ – $2$  mm. Recent progress in the design of instruments has resulted in small, sensitive benchtop spectrometers at reasonable prices (Fig. 7.1). Larger objects with high water content (tablets or small animals) can be assessed by spectrometers that work at lower frequencies, e.g., 0.3 or 1 GHz (Fig. 7.2).

We will focus only on drug delivery and will not consider other important applications such as ESR oximetry [3], the measurement of nitric oxide [4] or the direct detection [5] of radical metabolites. Spin trapping is a method that transfers very reactive radical intermediates into more stable spin adducts [6]. However, very careful preparation of the experiments and interpretation of the results is necessary to avoid artifacts [7, 8]. Artifacts might be caused by impurities of the com-



Fig. 7.1. Benchtop 9 GHz ESR-spectrometer (X-band) with temperature unit (below the spectrometer).

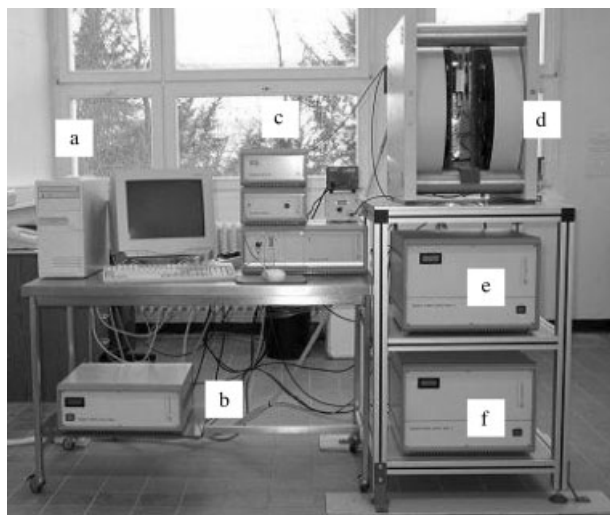


**Fig. 7.2.** L-band (1 GHz) ESR spectrometer with imaging possibility. The lower frequency of the L-band permits noninvasive measurement of larger samples with high water content, including mice and rats. The

spectrometer consists of a computer (a), a magnet power supply (b), a microwave bridge (c), the magnet with resonator (d) and power supply for the imaging gradients (e).

mercial spin traps, non-radical reactions or instability of the spin adduct. Inexperienced researchers often misinterpret the experimental results due to their poor knowledge of the reactivity of the radical, the trapping efficiency, the instability of the trap under the experimental conditions and the adduct stability. ESR spin trapping has been used recently to detect the radical formation from  $\text{TiO}_2$  nanoparticles [9] and the antioxidant potential of selenium nanoparticles [10].

Paramagnetic species that can be detected by ESR are free radicals and certain oxidation states of metal ions. ESR spectra of metal ions (e.g.,  $\text{Fe}^{3+}$ ,  $\text{Cu}^{2+}$ ,  $\text{Mn}^{2+}$ ) are in most cases very broad due to short relaxation times and magnetic interactions. Sometimes, their detection requires study at very low temperatures (77 K and below). ESR spectroscopy of metal ions permits the characterization of enzymes and organs, but it is of low importance in drug delivery. Some materials like bentonite and kaolin contain  $\text{Fe}^{3+}$  as impurity. Nearly all ESR studies in the field of drug delivery are based on the detection of free radicals, because most samples are ESR silent. Endogenous radicals could be present in the case of gamma sterilized or mechanical treated samples, if the delivery matrix or the drug is in the crystalline state and has a high melting point [11, 12]. Gamma irradiation induced radicals will rapidly decay in liquid and semisolid matrices and in polymers with a low glass transition temperature, but they can be detected and quantified by

spin-trapping techniques or at low temperatures [13]. Gamma irradiation induced radicals can be used to follow water penetration in biodegradable polymers *in vitro* and *in vivo*, if they have sufficient thermostability (e.g., slow decay rates at 37 °C) [14].

Magnetite is a very important material for both diagnostic and therapy, and exhibits endogenous ESR signals. Magnetite is used as an MRI contrast agent as well as for local hyperthermia. Magnetite has very broad ESR lines. These can be used to quantify and characterize the material, including the uptake in cells and tissue [15, 16, 17].

However, most samples are ESR silent and require the addition of radicals. For this reason, the addition of radical probes is a necessity. In most cases, nitroxide radicals are used. A large variety of nitroxides with different hydrophobicity, charge and functional groups is commercially available. Most nitroxides derive from piperidine, pyrrolidine or imidazolidine structures. Examples of nitroxide radicals are illustrated in Fig. 7.3.

The numerous different structures (hydrophilic, hydrophobic, charged, uncharged, aliphatic or aromatic) permit one to choose a molecule with the desired

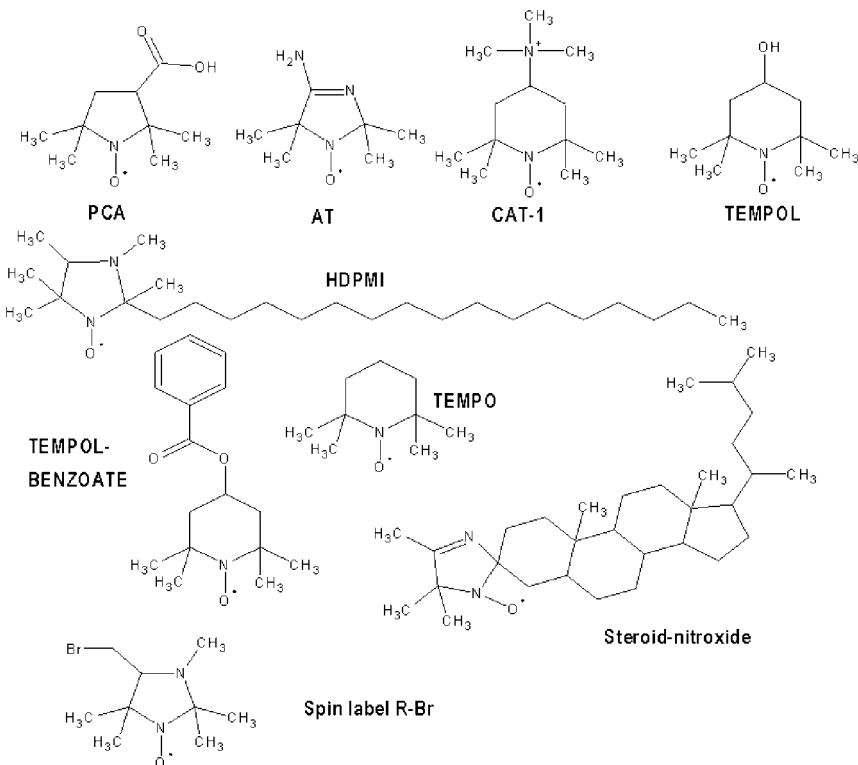


Fig. 7.3. Examples of nitroxide radicals with different hydrophilicities.

physicochemical properties. Nitroxides can be used as spin probes (= model drugs) to monitor processes of drug delivery *in vitro* and *in vivo*. Larger molecules (e.g., proteins, PVA, chitosan) can be spin labeled by the covalent linking of a chemically activated nitroxide to a suitable group of the macromolecule (e.g., amino, hydroxyl, carboxyl groups). For most macromolecules, the spin labeling procedure will lead to small and insignificant changes in the properties the molecules; however, this has to be verified. Spin labeling of low molecular weight compounds will lead to significant changes in molecular properties because the nitroxide moiety contributes significantly to the whole molecule.

### 7.3

#### Information from ESR Spectroscopy and Imaging

The following information can be obtained by EPR spectroscopy and imaging:

1. nitroxide concentration
2. micropolarity and microviscosity
3. microacidity
4. distribution of radicals and spatial resolution of parameters 1–3 (by imaging techniques or using different nitroxide isotopes).

Let us consider the information content step by step.

#### 7.3.1

##### Nitroxide Concentration

Nitroxide concentrations can be used to follow the release and distribution kinetics of drug carriers. ESR spectra are recorded in most cases in the form of the first derivative. Therefore, the nitroxide concentration can be obtained by double integration of the spectra. The signal intensity depends on the radical concentration, the parameters of measurement (microwave power, modulation amplitude, resonator type, filling factor, sample positioning, temperature etc.) and the dielectric loss of the sample. Samples with higher dielectric loss will give lower signal intensities for equal radical concentrations. It is highly recommended to use internal standards for quantitative measurements and to take great care about the positioning of the sample, reproducible filling factors, and sufficient scan width.

The hydrophilic ascorbic acid reduces piperidine nitroxides rapidly to the EPR silent hydroxylamines, and the loss of the EPR signal intensity indicates the accessibility of the nitroxide to the aqueous outer phase (Fig. 7.4). Solid lipid nanoparticles (SLN) and nanostructured lipid carriers (NLC) are less protective, respectively, than a nanoemulsion. This finding can be explained by the platelet structure of the SLN and the expulsion of foreign molecules during lipid crystallization.

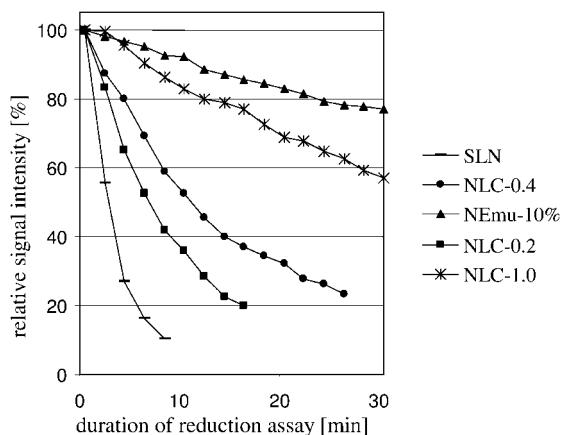


**Fig. 7.4.** Kinetics of nitroxide reduction of different colloidal lipid carriers. The lipophilic nitroxide TEMPOLBENZOATE is reduced more rapidly from solid lipid nanoparticles (SLN) and nanostructured lipid carriers (NLC) than with a standard nanoemulsion.

### 7.3.2

#### Micropolarity and Microviscosity

The unpaired electron of the nitroxide group is distributed between the nitrogen and oxygen of the nitroxyl group. Mesomeric forms of the distribution are illustrated in Fig. 7.5.

The nitrogen nucleus has a nuclear spin of 1. Magnetic interaction between the electron and nuclear spins of the nitrogen leads to a splitting of the ESR signal into three lines, which is also called hyperfine splitting (Hfs). Hfs is given by the Hfs constant  $a_N$  (Fig. 7.6).

The oxygen atom has no nuclear spin and therefore does not contribute to the splitting. Polar solvents (e.g., water) will favor the left-hand form in Fig. 7.5 and increase the spin density (= density of the unpaired electron) at the nitrogen. Non-polar solvents (e.g., oil) will increase localization of the spin at the oxygen and, therefore, decrease the spin density at the nitrogen. As a result, a smaller hyperfine coupling constant  $a_N$  will be observed (Fig. 7.6). Figure 7.7 shows quantitative values of hyperfine splitting in different solvents of pharmaceutical relevance.

For nitroxides, hyperfine coupling between the electron and nuclear spins is anisotropic. The  $a_N$ s are smaller for the  $x$  and  $y$  direction (around 0.6 mT) than

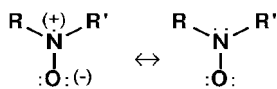


**Fig. 7.5.** Mesomeric forms of the nitroxyl group. The free electron is distributed between the nitrogen and oxygen atom.



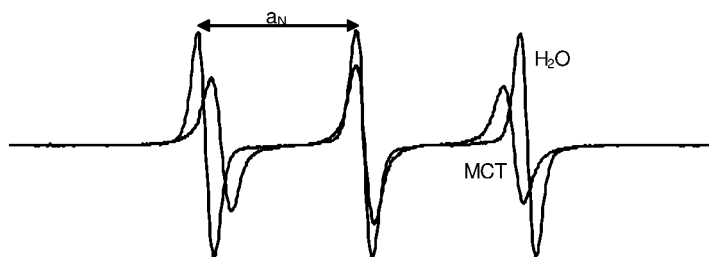


**Fig. 7.6.** ESR spectra of the spin probe TEMPOL in middle chain triglycerides (MCT) (oil) and water. Note the larger hyperfine splitting ( $a_N$ ) in the solvent with higher polarity.

for the  $z$  direction (around 3.3 mT). The anisotropy is averaged by rapid movement of the nitroxide in low viscous environments and an isotropic Hfs of around 1.5 mT results:  $a_{N\text{-iso}} = (0.6 + 0.6 + 3.3 \text{ mT})/3 = 1.5 \text{ mT}$ .

Viscous or even solid environments permit only partial or no averaging of the anisotropy. Incomplete averaging of the Hfs results in changes of the spectral shape and increased linewidths (Fig. 7.8). Initially, increased line widths, but no changes in line positions, are observed. The third line is most sensitive for mobility changes and shows the largest broadening, which leads to the smallest amplitude (see spectrum at 15 °C). If mobility of the nitroxides is further restricted, the line shape changes and anisotropic spectra are observed (Fig. 7.8). If the nitroxide tumbling is very slow (e.g., microseconds and below), no averaging occurs and the ESR spectrum depends on the orientation of the nitroxide axis to the magnetic field. Typical “powder” ESR spectra are recorded if the nitroxide is randomly orientated (Fig. 7.8,  $-30 \text{ }^\circ\text{C}$ ).

The following examples demonstrate how the sensitivity of ESR spectra to micro-polarity and microviscosity might be used to characterize nanosized drug delivery systems.

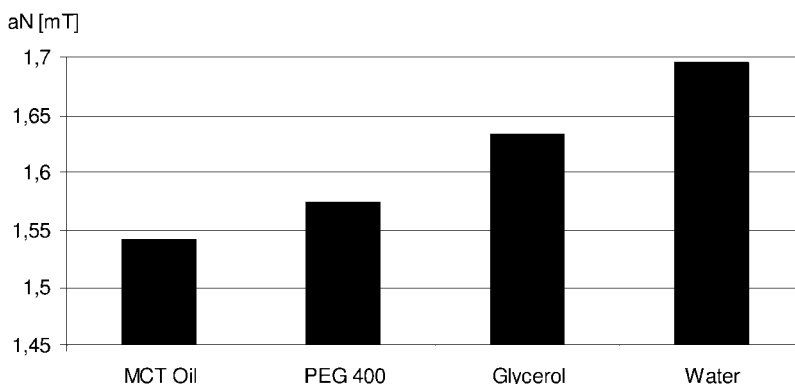


**Fig. 7.7.** Hyperfine coupling constants of TEMPOL in different solvents of pharmaceutical relevance.

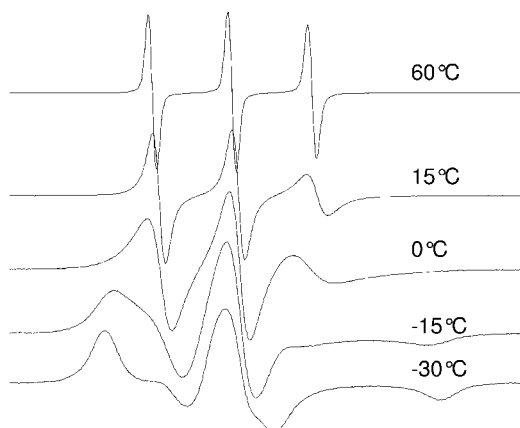


**Fig. 7.8.** Influence of temperature on ESR spectra of TEMPOL in poly(oxyethylene-pentaerythrol): Lower temperatures increase the viscosity and lead to a decreased averaging of the anisotropy of the hyperfine coupling. The high mobility of TEMPOL at 60 °C leads to a nearly isotropic shape; higher viscosities at lower temperatures lead to imperfect averaging (15 to -15 °C) of the anisotropy. At -30 °C, no averaging occurs on the ESR timescale and fully anisotropic spectra are recorded.

Nitroxide mobility might differ in different environments of heterogeneous systems. It will also change with time due to water penetration or degradation of the delivery matrix. Figure 7.9 shows simulated spectra and their integrative forms of different ratios of samples where immobilized and mobile nitroxide molecules

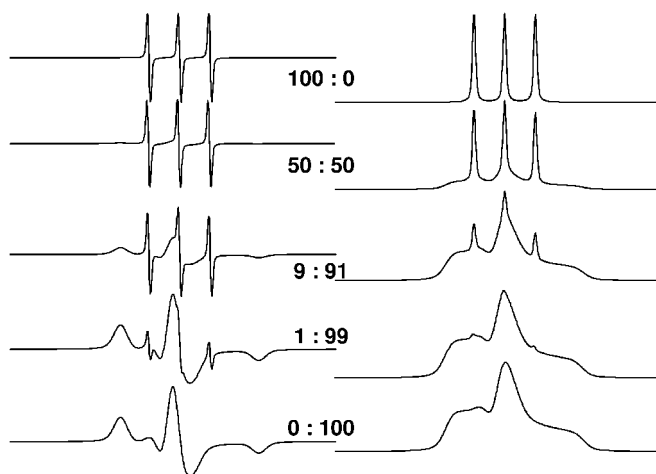


**Fig. 7.9.** Simulated ESR spectra of nitroxides with high and low mobility. The ratio indicates the ratio of mobile to immobile nitroxide molecules. Simulated ESR spectra (left) and their integrals (right) of different ratios of both components are represented.

coexist. The ESR spectra (= 1<sup>st</sup> derivative) are very sensitive to narrow lines and, therefore, mobile (= solubilized) nitroxides are detected below 1%. Immobilized nitroxides are more difficult to detect due to their broad lines and low signal amplitudes. They are easily overlooked in the ESR spectra if their concentration is below 50% of the total content. It is recommended that ESR spectra are integrated to make them more visible (Fig. 7.9).

The surface properties of nanoparticles play a significant role *in vivo*. Chauvierre et al. have used covalent ESR spin labeling of the dextran coat to investigate the surface properties of poly(isobutylcyanoacrylate) nanoparticles. They found a superposition of different nitroxide mobilities (similar to Fig. 7.9) and a dependency on the method used for particle synthesis [18]. The authors measured the mobile and immobile compartments in a quantitative manner. Italian scientists have used ESR to characterize the influence of lipid composition and the chain length of PEG on the characteristics of pegylated liposomes [19].

ESR can not only be used to characterize drug delivery systems before their use, it is also a method to shed more light on the release mechanisms themselves. The method can give unique and important information because different release mechanisms lead to different changes in spectral intensity and shape. Pure surface erosion will lead to a decrease in signal intensity, but no changes in spectral shape. In contrast, diffusion-controlled drug release can be recognized by changes in spectral shape due to increased mobility of the incorporated nitroxide.

The next example investigates the influence of temperature on the polarity of Poloxamer 188 solutions. Figure 7.10 shows ESR spectra of the lipophilic spin probe TEMPOLBENZOATE in 2% Poloxamer solutions. The ESR spectrum recorded at 25 °C indicates that the nitroxide is localized in a polar environment. The spectrum can be simulated with one species with a Hfs constant of  $a_N = 1.66$  mT. Heating the sample to 60 °C leads to significant changes in spectral shape, which are most visible in the region of the third line. Obviously, the experimental spectrum is now a superposition of at least two ESR spectra from TEMPOLBENZOATE localized in different microenvironments. Simulation results for the ESR spectrum show that about 25% of the probe is localized in a polar environment ( $a_N = 1.66$  mT, third spectrum from top from Fig. 7.10). This environment is highly polar and very similar to the one and only environment observed at 25 °C. About 75% of the spin probe, however, is localized in a less polar, more viscous environment ( $a_N = 1.568$  mT, bottom spectrum in Fig. 7.10). This environment was not observed at 25 °C. Therefore, heating Poloxamer 188 solutions results in a new hydrophobic environment, in which lipophilic molecules accumulate. Experimental results demonstrate the thermal reversibility of this process. The temperature-induced formation of this hydrophobic environment has to be kept in mind if heating of Poloxamer solutions takes place (e.g., DSC).

The usefulness of ESR to get more insights has also been demonstrated for colloidal lipid carriers. The results indicate that the loading capacity of colloidal solid lipid dispersions is very low due to the crystalline nature of the lipid. They also showed that solid lipid nanoparticles (SLN) and nanostructured lipid carriers (NLC, composed of solid and liquid lipids) do not offer the proposed advantages in

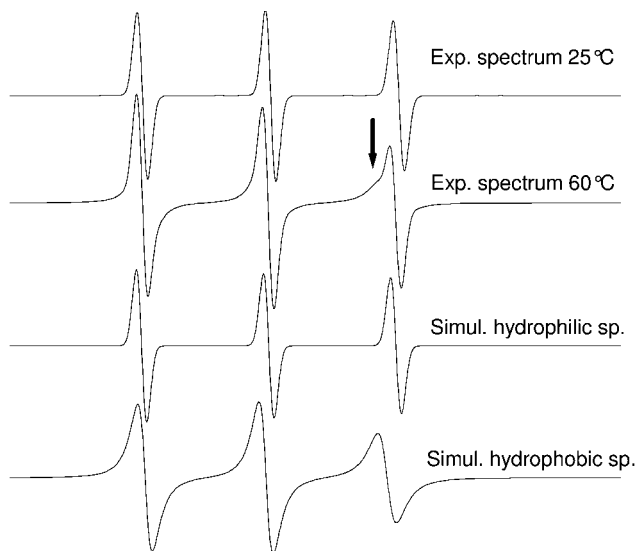


**Fig. 7.10.** ESR spectra of TEMPOLBENZOATE in 2% (w/w) Poloxamer 188 solutions at 25 and 60 °C. Note the different line shape at 60 °C, as indicated by the arrow. The bottom spectra are the result of simulating the experimental 60 °C spectrum, indicating the distribution of the nitroxide in two environments with different polarity.

comparison with a submicron emulsion, because lipid crystallization leads to expulsion of the lipophilic nitroxide into the aqueous phase. Detailed analysis of the ESR spectra shows that about  $\frac{2}{3}$  of TEMPOLBENZOATE were exposed to a polar environment in a 10% colloidal dispersion of Compritol (a mixture of different glycerolbehanates) – which demonstrates the poor performance of SLN (Fig. 7.11) [20]. Incorporation into the lipid is even worse if the lipid crystal is more perfect. The incorporation rate of lipophilic nitroxides in cetylpalmitate is close to zero (own unpublished results).

Lipid crystallization might be retarded in nanosized systems due to the small size. Therefore, sample storage might greatly influence the lipid crystallization and localization of the incorporated drug. Figure 7.12 shows that the nitroxide TEMPO distributes in a ratio of 1:3 between the polar (aqueous) and nonpolar (lipid) environment, if the sample is stored at room temperature. Data from NMR, DSC and X-ray measurements show that the lipid matrix does not crystallize under such conditions. Storage at low temperatures induces crystallization of the lipid, at least partially. The lipid crystallization is connected with a redistribution of the nitroxide into a more polar environment and a 1:1 distribution is observed. Clearly, solid lipids can accommodate only traces of foreign molecules, because the concentration of the spin probe is rather low ( $3 \text{ mmol kg}^{-1}$ ).

An important aspect of colloidal drug delivery systems is dynamic phenomena, e.g., the kinetics of distribution processes. The dilution assay monitors the change in spectral shape after further addition of the outer phase (Fig. 7.13). Current re-

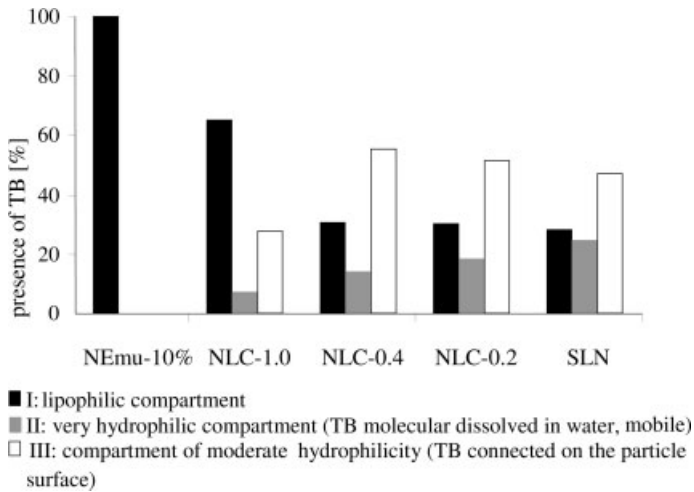


**Fig. 7.11.** Localization of the lipophilic spin probe TEMPOLBENZOATE (TB) in different colloidal lipid carriers. Note that the nitroxide is almost exclusively localized in liquid lipids and only partially in solid lipid nanoparticles (SLN) and nanostructured lipid carriers (NLC).

sults obtained from different colloidal carriers (SLN, NLC, nanoemulsions, nanocapsules and polymeric nanoparticles) suggest that distribution processes take place in the range from seconds to minutes for nitroxides with moderate lipophilicity ( $\log P < 4$ ). This is not surprising with respect to the very short diffusion length within the particles and the very small thickness (e.g., 10 nm) of the shell of nanocapsules [21]. Nitroxides with very high hydrophobicity such as HDPMI (Fig. 7.3) can be simulated with one component before and after dilution. They do

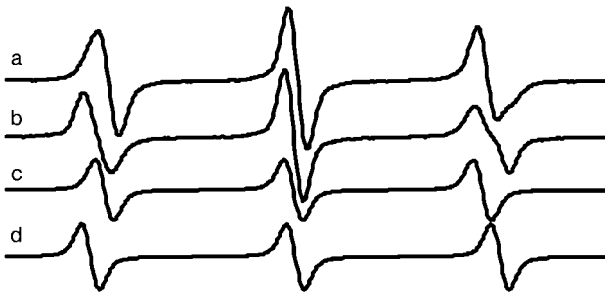


**Fig. 7.12.** 2.1 GHz ESR spectra of TEMPO loaded (20% w/w) WITEPSOL (mixtures of triglycerides and partial glycerides) dispersions, (a) experiment: sample stored at room temperature, (b) experiment: stored at refrigerator, (c) simulation: lipophilic component, (d) simulation: hydrophilic component.

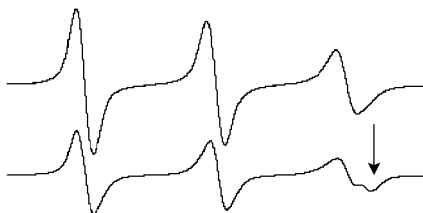


**Fig. 7.13.** ESR spectra of TEMPOLBENZOATE loaded nanocapsules before (top) and after (bottom) 1:4 dilution with the outer phase. The change in spectral shape is caused by increased localization of the probe in the aqueous environment.

not change their spectral shape due to their high preferential localization in the lipophilic environment.

ESR has been used to follow the pH-induced micelle-to-vesicle transformation of oleic acid in more detail [22]. Changes in the ESR spectra can also be used to follow the interaction between colloidal drug carriers and colloidal lipid dispersions with cells. Slovenian scientists found that the transfer depends on the spin probe, colloid matrix, and surfactant [23].

### 7.3.3

#### Monitoring of Microacidity

The development of pH-sensitive nitroxides offers the opportunity to monitor microacidity in drug delivery systems *in vitro* and *in vivo*. Figure 7.14 illustrates the principle.

Kroll et al. reported the first pharmaceutical application, monitoring drug degradation induced pH changes inside nontransparent w/o-ointments [24]. The pH is of crucial importance in the field of biodegradable polymers, because commonly used materials such as polyhydroxyesters, polyanhydrides and polyorthoesters are hydrolyzed to acids. The pH might affect the stability and solubility of incorporated drugs and, furthermore, also the degradation rate of many polymers to a large extent. The first *in vivo* measurement of the pH inside degrading PLGA implants was published in 1996 [ ]. The pH drops to as low as 2 inside subcutaneous PLGA implants in mice.

EPR has also been used to determine the acidity in PLGA-PEG microparticles designed for protein release [26]. For this purpose, albumin was covalently linked to a pH-sensitive label. Another study describes the influence of drugs and buffer substances on the acidity within the microparticles. Gentamicine base and sodium acetate are able to increase the pH inside the particles [27]. ESR is, therefore, a useful tool to monitor the success of a formulation measure in influencing the pH inside drug delivery systems. The principles of pH-measurement by ESR can also be applied to colloidal drug carriers and I am sure that we will soon witness further applications in this field.

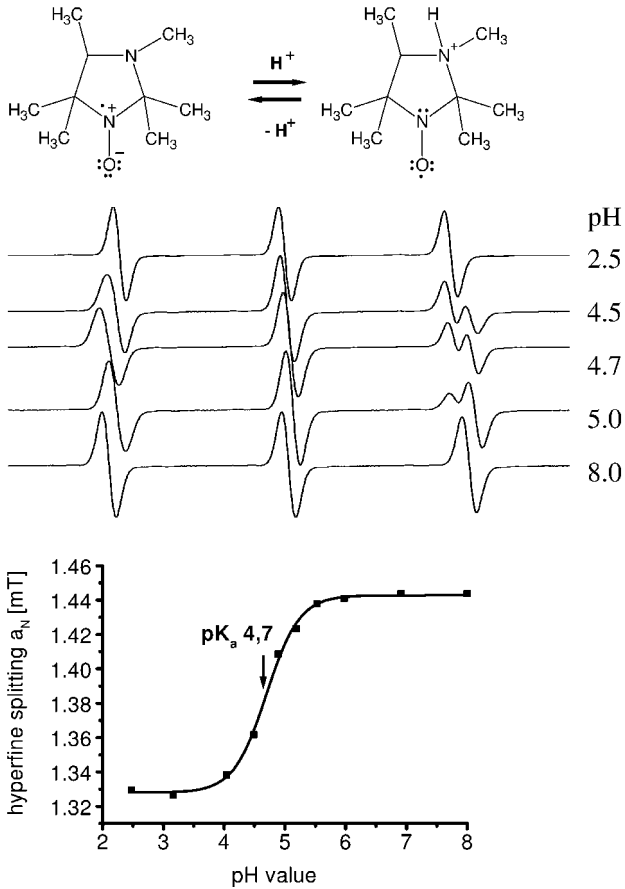


**Fig. 7.14.** Principle of pH measurement by imidazolidine nitroxides. Protonation of the nitrogen at position 3 leads to significant changes in the spin density and hyperfine coupling constant. At  $pK_a$  4.7, the ESR

spectrum results from equal contributions of protonated (small Hfs) and unprotonated (larger Hfs) forms of the nitroxide. The influence of pH on Hfs is shown in the lower part of the figure.

#### 7.3.4

#### ESR Imaging

From the ESR spectrum, conclusions can be drawn on the nitroxide concentration, micropolarity, microviscosity and (using appropriate nitroxides) pH. Deeper insight into drug delivery processes is possible if the information can be attributed to a certain layer of the delivery system. Spectral-spatial information can be obtained by ESR imaging techniques. For example, pH gradients of almost two units within a distance of a few micrometers have been found in degrading polyanhydrides [28]. A more recent study showed the formation of pH gradients in polymers composed of polyorthoester and polylactide units [29]. Another study demon-

strated that commercial ointments can modify the microacidity in human skin *in vitro*, leading to pH gradients in the skin [30]. The resolution of ESR imaging, in the range of a few microns, is insufficient to monitor distributions inside nano-scaled systems. However, it can be used to follow the fate of nanostructures with a macroscopic controlled release system (e.g., tablets that release nanoparticles) or, even more interestingly, to follow the fate of nanocarriers in mice and rats.

#### 7.4

##### ***In Vivo* ESR**

The development of low-frequency spectrometers and imagers has made noninvasive ESR studies on mice and rats possible. *In vivo* applications include the characterization of antacid induced pH changes of the stomach in mice [31].

Correlation of *in vitro* and *in vivo* data is very important for the development and quality control of delivery systems. Major differences may arise from decreased water accessibility *in vivo*, different pH or buffer capacities or the involvement of enzymes. EPR is a useful tool to figure out whether the general release mechanism *in vitro* corresponds to the *in vivo* situation in a small mammal. For example, incomplete release of a water-soluble nitroxide has been found *in vivo* due to encapsulation of the polymer implant [32].

EPR observations show that release processes from biodegradable polyesters and polyanhydrides are rather complex [25, 33]. A surface erosion front mechanism with zero-order kinetics has been observed for P(CPP-SA) 20:80 polyanhydrides. The *in vivo* release was 1.5× slower than for *in vitro* experiments [33]. Substitution of the aromatic dicarboxylic acid CPP by long-chain aliphatic dicarboxylic acids (FAD) leads to increased mobility inside the manufactured polyanhydride and a more complex release pattern with partially diffusion-controlled processes [32]. For P(FAD-SA) implants, an intermediate increase in viscosity inside the degrading polymer has been observed, which was caused by precipitation of the dicarboxylic acids. EPR spectra of nitroxide-loaded poly(lactide-co-glycolide) implants did not change in shape or intensity during the first week, indicating an initial lag time. During the second week, a small portion of the nitroxides became solubilized within the polymer. The ratio of solubilized/immobilized nitroxides increased with time and a rapid, almost pulse-like release was observed after four weeks. The authors were able to distinguish release processes of the core from the outer layers by manufacturing sandwich implants that contained <sup>14</sup>N-nitroxides in the outer layers and <sup>15</sup>N-nitroxides in the core [33]. These studies show the possibility of obtaining unique information about drug delivery processes *in vivo*.

#### 7.5

##### **Summary and Outlook**

ESR can be applied to samples that are otherwise difficult to assess, e.g., nontransparent, solid or multiphase samples, or samples with heterogeneities in the nano-



meter range. This allows monitoring of the distribution kinetics and protection capacity of nanoscaled drug delivery systems.

Technical developments now permit sensitive ESR spectroscopy and imaging of mice and rats. An increasing number of *in vivo* spectrometers are being built, and I am sure that we shall soon see many papers that focus on the *in vivo* characterization of nanoscaled drug delivery systems by ESR spectroscopy and imaging.

### Acknowledgment

I thank the former and present members of my group, S. Liedtke, K. Jores, A. Rube, C. Augsten, and R. K. Narayanan for the measurement of samples and discussions.

### References

- 1 C.P. POOLE, *Electron Spin Resonance: a Comprehensive Treatise on Experimental Techniques*, 2<sup>nd</sup> Edn. New York: John Wiley & Sons, 1983.
- 2 L.J. BERLINER ed., *In Vivo EPR (ESR): Theory and Applications*, New York: Kluwer Academic/Plenum Publishers, 2003.
- 3 S.S. VELAN, R.G.S. SPENCER, J.L. ZWEIER, P. KUPPUSAMY. Electron paramagnetic resonance oxygen mapping (EPROM): Direct visualization of oxygen concentration in tissue, *Magn. Reson. Med.* 43 (2000) 804–809.
- 4 T. YOSHIMURA, S. FUJII, H. YOKOYAMA, H. KAMADA. In-vivo electron-paramagnetic-resonance imaging of NO-bound iron complex in a rat head, *Chem. Lett.* (1995) 309–310.
- 5 K. MÄDER, G. BACIC, H.M. SWARTZ. In vivo detection of anthralin derived free radicals in the skin of hairless mice by low frequency electron paramagnetic resonance spectroscopy, *J. Investigative Dermatol.* 104 (1995) 514–517.
- 6 R. MASON, M.B. KADIISKA. Ex vivo detection of free radical metabolites of toxic chemicals and drugs by spin trapping, in L.J. BERLINER (ed) *In Vivo EPR(ESR): Theory and Applications, Biological Magnetic Resonance* 18, New York: Kluwer Academic/Plenum Publishing, pp. 309–323, 2003.
- 7 M.J. BURKITT, R.P. MASON. Direct evidence for in vivo hydroxyl-radical generation in experimental iron overload: an ESR spin-trapping investigation. *Proc. Natl. Acad. Sci. U.S.A.* 88, (1991) 8440–8444.
- 8 G.S. TIMMINS, K.J. LIU. Spin trapping: facts and artifacts, in *In Vivo EPR: Theory and Applications*, L.J. BERLINER (ed), New York: Kluwer Academic/Plenum Publishers, pp. 285–308, 2003.
- 9 T.A. KONOVALOVA, J. LAWRENCE, L.D. KISPERT. Generation of superoxide anion and most likely singlet oxygen in irradiated TiO<sub>2</sub> nanoparticles modified by carotenoids, *J. Photochem. Photobiol. A: Chem.*, 162 (2004) 1–8.
- 10 X. GAO, J. ZHANG, L. ZHANG. Hollow sphere selenium nanoparticles: their in-vitro anti hydroxyl radical effect. *Adv. Mater. (Weinheim)*, 14(4) (2002) 290–293.
- 11 D. TEOMIM, K. MÄDER, A. BENTOLILA, A. MAGORA, A.J. DOMB. Gamma-irradiation stability of saturated and unsaturated aliphatic polyanhydrides-ricinoleic acid based polymers. *Biomacromolecules* 2 (2001) 1015–1022.
- 12 J. RAFFI, S. GELLY, L. BARRAL, F. BURGER, P. PICCERELLE, P. PRINDERRE, M. BARON, A. CHAMAYOU. Electron paramagnetic resonance of

- radicals induced in drugs and excipients by radiation or mechanical treatments, *Spectrochim. Acta Part A* 58 (2002) 1313–1320.
- 13 M.B. SINTZEL, K. SCHWACH-ABDELLAOUI, K. MÄDER, R. STÖSSER, J. HELLER, C. TABATABAY, R. GURNY. Influence of irradiation sterilization on semi-solid poly(ortho ester). *Int. J. Pharm.* 175 (1998) 165–176.
  - 14 K. MÄDER, A. DOMB, H.M. SWARTZ. Gamma sterilization induced radicals in biodegradable drug delivery systems. *Appl. Radiation Isotopes*, 47 (1996) 1669–1674.
  - 15 O. MYKHAYLYK, N. DUDCHENKO, A. DUDCHENKO. Doxorubicin magnetic conjugate targeting upon intravenous injection into mice: High gradient magnetic field inhibits the clearance of nanoparticles from the blood. *J. Magn. Magn. Mat.*, 293 (2005) 473–482.
  - 16 P. SMIRNOV, F. GAZEAU, M. LEWIN, J.C. BACRI, N. SIAUVE, C. VAYSETTES, C.A. CUENOD, O. CLEMENT. In vivo cellular imaging of magnetically labeled hybridomas in the spleen with a 1.5-T clinical MRI system, *Magn. Reson. Med.* 52 (2004) 73–79.
  - 17 C. WILHELM, F. GAZEAU, J. ROGER, J.N. PONS, J.-C. BACRI. Interaction of anionic superparamagnetic nanoparticles with cells: Kinetic analyses of membrane adsorption and subsequent internalization, *Langmuir* 18 (2002) 8148–8155.
  - 18 C. CHAUVIERRE, C. VAUTHIER, D. LABARRE, H. HOMMEL. Evaluation of the surface properties of dextran-coated poly(isobutylcyanoacrylate) nanoparticles by spin-labelling coupled with electron resonance spectroscopy, *Colloid Polym. Sci.* 282 (2004) 1016–1025.
  - 19 R. BARTUCCI, S. BELSITO, L. SPORTELLI. Spin-label electron spin resonance studies of micellar dispersions of PEGs-PES polymer-lipids, *Chem. Phys. Lipids* 124 (2003) 111–122.
  - 20 K. JORES, W. MEHNERT, K. MÄDER. Physicochemical investigations on solid lipid nanoparticles (SLN) and on oil-loaded solid lipid nanoparticles: a NMR- and ESR-study, *Pharm. Res.* 20(8) (2003) 1274–1283.
  - 21 A. RÜBE, K. MÄDER. An electron spin resonance study on the dynamics of polymeric nanocapsules, *J. Biomed. Nanotechnol.* 1 (2005) 208–213.
  - 22 H. FUKUDA, A. GOTO, H. YOSHIOKA, R. GOTO, K. MORIGAKI, P. WALDE. Electron spin resonance study of the pH-induced transformation of micelles to vesicles in an aqueous oleic acid/oleate system, *Langmuir* 17 (2001) 4223–4231.
  - 23 J. KRISTL, B. VOLK, P. AHLIN, K. GOMBAC, M. SENTJURC. Interactions of solid lipid nanoparticles with model membranes and leukocytes studied by EPR, *Int. J. Pharm.* 256 (2003) 133–140.
  - 24 C. KROLL, K. MÄDER, R. STÖESSER, H.-H. BORCHERT. Nondestructive determination of pH values in nontransparent W/O systems by means of EPR spectroscopy, *Eur. J. Pharm. Sci.* 3 (1995) 21–26.
  - 25 K. MÄDER, B. GALLEZ, K.J. LIU, H.M. SWARTZ. Noninvasive in vivo characterization of release processes in biodegradable polymers by low frequency electron paramagnetic resonance spectroscopy, *Biomaterials* 17 (1996) 459–463.
  - 26 K. MÄDER, B. BITTNER, Y. LI, W. WOHLAUF, T. KISSEL. Monitoring microviscosity and microacidity of the albumin microenvironment inside degrading microparticles from polylactide-co-glycolide (PLG) or ABA-triblock polymers containing hydrophobic poly(lactide-co-glycolide) A blocks and hydrophilic poly(ethylenoxide) B blocks, *Pharm. Res.* 15 (1998) 787–793.
  - 27 A. BRUNNER, K. MÄDER, A. GÖPFERICH. The microenvironment inside biodegradable microspheres: changes in pH and osmotic pressure, *Pharm. Res.* 16 (1999) 847–853.
  - 28 K. MÄDER, S. NITSCHKE, R. STÖSSER, H.-H. BORCHERT, A. DOMB. Non-destructive and localised assessment of acidic microenvironments inside biodegradable polyanhydrides by spectral spatial electron paramagnetic

- resonance imaging (EPRI), *Polymer* 38 (1997) 4785–4794.
- 29 S. CAPANCIONI, K. SCHWACH-ABDELLAOUI, W. KLOETI, W. HERRMANN, H. BROSIK, H.H. BORCHERT, J. HELLER, R. GURNY. In vitro monitoring of poly(ortho ester) degradation by electron paramagnetic resonance imaging, *Macromolecules* 36 (2003) 6135–6141.
- 30 C. KROLL, W. HERRMANN, R. STÖSSER, H.H. BORCHERT, K. MÄDER. Influence of drug treatment on the microacidity in rat and human skin – an in vitro electron spin resonance imaging study, *Pharm. Res.* 18 (2001) 525–530.
- 31 B. GALLEZ, K. MÄDER, H.M. SWARTZ. Non-invasive measurement of the pH inside the gut using pH-sensitive nitroxides. An in vivo EPR study, *Magn. Reson. Med.* 36 (1996) 694–697.
- 32 K. MÄDER, Y. CREMMILLEUX, A. DOMB, J.F. DUNN, H.M. SWARTZ. In vitro/in vivo comparison of drug release and polymer erosion from biodegradable P(FAD-SA) polyanhydrides – a non-invasive approach by the combined use of electron paramagnetic resonance spectroscopy and nuclear magnetic resonance imaging, *Pharm. Res.* 14 (1997) 820–826.
- 33 K. MÄDER, G. BACIC, A. DOMB, O. ELMALAK, R. LANGER, H.M. SWARTZ. Noninvasive in vivo monitoring of drug release and polymer erosion from biodegradable polymers by EPR spectroscopy and NMR imaging, *J. Pharm. Sci.* 86 (1997) 126–134.

## 8

## X-ray Absorption and Emission Spectroscopy in Nanoscience and Lifesciences

Jinghua Guo

## 8.1

### Introduction

The properties of matter at nanoscale dimensions can be dramatically different from the bulk or the constituent molecules. The differences arise through quantum confinement, altered thermodynamics or changed chemical reactivity. In general, electronic structure ultimately determines the properties of matter, and it is therefore natural to anticipate that a complete understanding of the electronic structure of nanoscale systems will lead to progress in nanoscience and bioscience, not inferior to that seen in recent years.

The ability to control the particle size and morphology of nanoparticles is of crucial importance, both from a fundamental and industrial point of view, considering the tremendous amount of high-tech applications of nanostructured metal oxide materials devices such as dye-sensitized solar cells, displays and smart windows, chemical, gas and biosensors, lithium batteries, supercapacitors. Controlling the crystallographic structure and the arrangement of atoms along the surface of nanostructured material will determine most of its physical properties.

So far the electronic structure and dynamics in biological systems have been little investigated. Synchrotron-based X-ray diffraction has been used to determine the molecular geometry that in many cases can determine the biological function of the molecule. Unfortunately, as crystallography was unable to address the local structural geometry of a chemisorbed molecule on surface, disordered biological systems may be a challenge too. When studying biological systems it is necessary to perform the experiments in a natural environment, i.e., in water/liquid solutions. We show later in this chapter that X-ray photon-in and photon-out spectroscopy can be used for *in situ* spectroscopic studies of wet systems.

X-rays originate from an electronic transition between a localized core state and a valence state. By the second half of the twentieth century, technological advances in detector and X-ray spectrometry produced a renaissance of interest in X-ray spectroscopy as an analytical tool in chemical analysis and as a tool for studying the solid state in general [1]. The parallel development of computational methods in solid-state physics and quantum chemistry, abetted by modern high-speed com-

puters, enabled theoreticians to return to the many unrevolved problems in X-ray spectroscopy. Thus, the last decade has seen a rebirth of effort in expanding the methods of X-ray spectroscopy as well as applications to a growing lists of studies in various fields of science.

Soft X-ray spectroscopy has some basic features that are important to consider [2]. As a core state is involved, elemental selectivity is obtained because the core levels of different elements are well separated in energy, meaning that the involvement of the inner level makes this probe localized to one specific atomic site, around which the electronic structure is reflected as a partial density-of-states contribution. The participation of valence electrons gives the method chemical state sensitivity and, further, the dipole nature of the transitions gives particular symmetry information.

An introduction to soft X-ray absorption spectroscopy (XAS) along with soft X-ray emission spectroscopy (XES) is given in Section 8.2, and their chemical sensitivity in nanostructured and molecular materials is discussed in Section 8.3. A number of examples, including some recent findings, then illustrate the potential of XAS and XES applications in the nanoscience (Section 8.4) and bioscience (Section 8.5).

## 8.2

### Soft X-ray Spectroscopy

Synchrotron radiation has become an indispensable tool in many areas of science. Synchrotron radiation is the light emitted by electrons as they circulate around a high-energy accelerator. This light covers the spectrum from hard (short wavelength) X-rays through soft (long wavelength) X-rays, ultraviolet (UV), visible, and infrared. The use of synchrotron radiation has grown to a powerful research tool in science in the last decade. Vacuum ultraviolet and X-ray photons emerging from storage rings are now among the most frequently used probes for advanced investigation of the electronic and geometric structure of matter.

The newly developed theoretical methods in band theory and quantum chemistry, as well as the use of different instrumentation, set the soft X-ray community apart from hard X-ray spectroscopists [3]. This separation has long been symbolized by the existence of separate triannual international conference series on Vacuum Ultraviolet Radiation Physics [4] and X-ray Physics and Inner Shell Ionization [5].

The utility of hard X-ray absorption spectroscopy as a probe of chemical identity in the biological, environmental and biomedical sciences is well documented [6–12]. Metals in enzymes can be probed in all oxidation states and spin states, and environmental samples can be examined in a chemically undisturbed form. In appropriate cases, intact tissues or even an entire organism can be examined. For example, a 23 amino-acid synthetic lytic peptide (Hecate) has been covalently linked to magnetite nanoparticles, and the lytic peptide-bound nanoparticles characterized by X-ray absorption near-edge structure spectroscopy [13]. In recent years, the ad-

vent of synchrotron sources as the best source for both X-ray regions has greatly reduced the barriers between the two communities [14]. Soft X-ray absorption fine structure, or NEXAFS technique, has become a powerful tool to study molecules bonded on surfaces [15].

Current developments in synchrotron radiation techniques have led to extremely bright undulator sources. The use of synchrotron radiation for the excitation of soft X-ray emission spectra adds several important qualities to this spectroscopic method. Firstly, it provides a very intense photon-excitation source. Secondly, monochromatized soft X-ray photons offer a higher degree of energy selectivity than do electrons. Thirdly, synchrotron radiation offers the possibility of exciting soft X-ray spectroscopy by polarized light.

### 8.2.1

#### Soft X-ray Absorption Edges

The X-ray absorption spectrum of a given element consists of series of edges, each corresponding to excitation of a different core electron. Electron levels with the quantum number  $n$  equal to 1–4 are named as K, L, M, N levels, respectively. K-edges arise from the innermost 1s orbital, L-edges from the second shell, M-edges from the third and N-edges from the fourth. While there is only one K-edge, the higher order edges are further divided by the angular momentum of the resulting core electron vacancy. Hence, there are three L-edges, denoted  $L_1$ ,  $L_2$  and  $L_3$ , arising from 2s,  $2p_{1/2}$  and  $2p_{3/2}$  final states, respectively. Similarly, there are five M-edges and seven N-edges. These edges are well separated in energy. With  $\text{Fe}_2\text{O}_3$ , for example, the O K-edge is at 530 eV, and the Fe  $L_2$  and  $L_3$ -edges are close together at 720 and 707 eV, while the observable M-edge has a very low energy of 52 eV.

The soft X-ray region ranges from about 50 to 1200 eV. Much of biological and environmental science can be based on soft X-ray spectroscopy measurements. This is because the X-ray edges in this region offer routes to chemical information not readily obtained by other techniques. Edges in the soft X-ray region include: the light element K-edges, including C, N, O, F, Si; the first transition metal L-edges, including Ti, Cr, Mn, Fe, Co, Ni, Cu, Zn; the M-edges of Fe through to the lanthanides, and N-edges of the lanthanides etc. All the absorption edges can be found on a website of the Center for X-ray Optics, Lawrence Berkeley National Laboratory [16], and some of the edges are illustrated in Fig. 8.1.

### 8.2.2

#### Soft X-ray Emission Spectroscopy

In soft X-ray emission, the core vacancy left by the excited 1s electron is filled by a valence-orbital electron, thereby also giving direct information about the chemical bonding. Characteristic X-ray emission spectra consist of spectral series with lines having a common initial state with the vacancy in the inner level. The emission intensity from a disordered sample is given by the formula

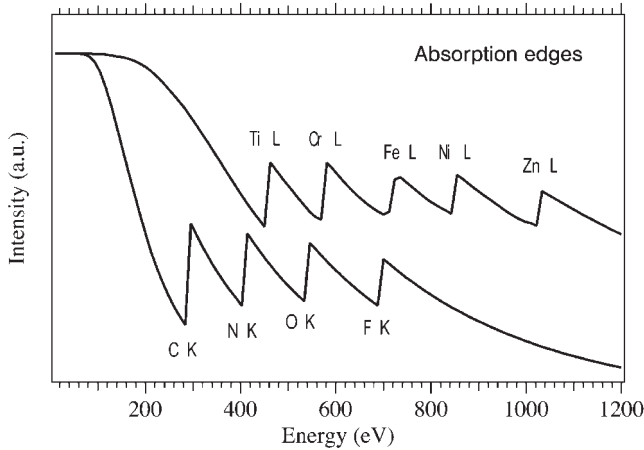


**Fig. 8.1.** Schematic illustration of X-ray absorption edges from the K-edges of some light elements and L-edges from some transition metals.

$$I \propto \sum_f \omega_{if}^3 |\mathbf{r}_{if}|^2 \Delta(\omega' - \omega_{if}, \Gamma) \quad (1)$$

Eq. (1) can be further simplified in the one-electron approximation. To be specific let us consider the K-emission of atom  $n$  in a molecule. The transition matrix element  $\mathbf{r}_{if}$  describes now the one-electron transition between the  $1s_n$  core orbital and occupied molecular orbital (MO)  $i$ , the effective wavefunction of which can be written as

$$\phi_i = \sum_n \chi_n c_{in} \quad (2)$$

where  $\chi_n$  is the p-orbital of the atom  $n$ . Thus, the intensity Eq. (1) becomes

$$I \propto \sum_i c_{ni}^2 \Delta(\omega' - \omega_{i,1s}, \Gamma). \quad (3)$$

where  $\omega_{i,1s} \approx \varepsilon_i - \varepsilon_{1s}$ ,  $\varepsilon_i$  and  $\varepsilon_{1s}$  are the energies of the  $1s$  electron and MO  $i$ .

Further simplification could be made by retaining only the first term in the expansion of the exponential function, i.e., the so-called *dipole approximation*. This important approximation assumes  $kr \ll 1$ . Such an approximation works well for soft X-ray radiation. As result of the dipole approximation, K-emission probes the p-character of a molecular orbital  $\phi_i$ , while L-emission probes the contributions of s and d atomic orbitals in  $\phi$ . One can map the MO  $\phi$  by measuring spectra of all series (K, L, M, ...) of all atoms.

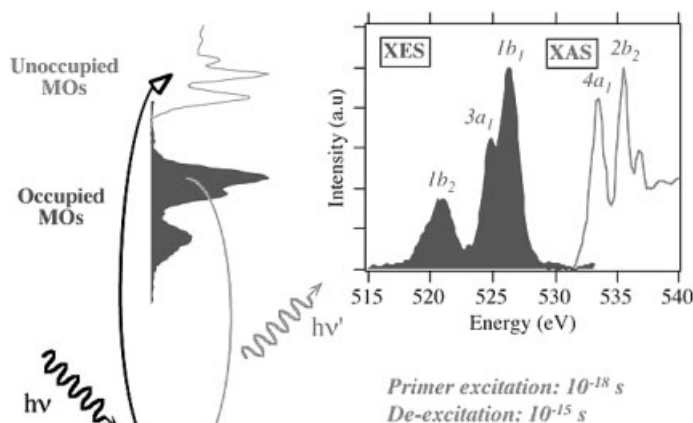


Fig. 8.2. Left: schematic illustration of X-ray absorption and emission spectroscopy. Right: X-ray absorption and emission of a water molecule.

### 8.2.3

#### Soft X-ray Absorption Spectroscopy

A soft X-ray absorption spectrum provides information about the unoccupied states. For example, in the oxygen K-edge absorption, the oxygen 1s electron is excited to empty electronic states in the water unoccupied molecular orbitals, and the dipole selection rule provides a tool to study locally the O 2p character of these unoccupied valence band (Fig. 8.2). The atomic nature of the core hole implies elemental and site selectivity. The probability of such a transition is related to the X-ray absorption cross section. The intensity of these secondary electrons or the photons can be measured as a function of incoming photon energy. This will reflect the absorption cross section as the intensity of the secondary electrons/emitted photons are proportional to the absorbed intensity. Because of the short mean free path of electrons, the electron-yield-detection method is very surface sensitive. If the out-coming photons are detected (fluorescence yield), the X-ray absorption becomes bulk probing (about 100–200 nm) due to the comparatively larger attenuation lengths.

The photoabsorption transition probability for a transition from an initial state  $|i\rangle$  to a final state  $|f\rangle$  is governed by Fermi's "Golden Rule":

$$P_{if} = \frac{2\pi}{\hbar} |\langle f|V|i\rangle|^2 \Delta(\omega - \omega_{fi}, \Gamma_{if}), \quad \omega_{fi} = \varepsilon_f - \varepsilon_i \quad (4)$$

where  $\varepsilon_f$  and  $\varepsilon_i$  are energies of final and initial states of the system, and  $\Gamma_{if}$  is the width of the spectral transition,  $V$  describes the interaction between molecule and light, and  $\Delta(\varepsilon, \Gamma)$  is the Lorentzian function



$$\Delta(\varepsilon, \Gamma) = \frac{\Gamma}{\pi(\varepsilon^2 + \Gamma^2)} \quad (5)$$

The final electron state  $|f\rangle$  could be a bound or a continuum state, depending on the photon frequency  $\omega$ .

Thus, the expression for the X-ray absorption (XAS) cross section is obtained as Eq. (6).

$$\sigma = \frac{4\pi^2}{m^2} \frac{e^2}{c} \frac{1}{\omega} |\langle f | \mathbf{e} \cdot \mathbf{p} | i \rangle|^2 \Delta(\omega - \omega_{fi}, \Gamma_{if}) \quad (6)$$

#### 8.2.4

#### Resonant Soft X-ray Emission Spectroscopy

The big improvement in the performance of synchrotron radiation based soft X-ray spectroscopy during the last decade is the high brightness of the third generation source combined with high quality optical systems for refocusing the monochromatized soft X-ray beam. The new generation synchrotron radiation sources producing intense tunable monochromatized X-ray beams has opened up new possibilities for soft X-ray spectroscopy. X-ray absorption and emission have been traditionally treated as two independent processes, with the absorption and emission spectra providing information on the unoccupied and occupied electronic states, respectively.

The possibility to select the energy of the excitation has created an extra degree of freedom compared with traditional spectroscopy pursued with high-energy electron or characteristic X-ray excitation. The energy selectivity makes it possible to perform resonant excitation, i.e., exciting to particular empty states [28–30]. The introduction of selectively excited soft X-ray emission has opened a new field of study by disclosing many new possibilities of soft X-ray resonant inelastic scattering (RIXS). Among the new tools available with this technique are site selectivity in high- $T_c$  superconducting materials [31], femtosecond dynamics [32] and chemical bonding mechanism [33] by detuning from resonance, etc.

Resonant inelastic X-ray scattering at core resonances has become a new tool for probing the optical transitions in transition metal oxides. The scheme of RIXS process is presented in Fig. 8.3. For the hard X-ray K-edge RIXS process, the intermediate state in a transition metal is the same as the final state in a K absorption measurement, while the RIXS final state (when scanning the  $K\alpha$  region) is the same as in L absorption spectroscopy [21, 22]. For L-edge and M-edge RIXS, the final states are typical d–d or f–f excitations [23, 24].

Final states probed via such a channel, RIXS or XRS, are related to eigenvalues of the ground state Hamiltonian. The core–hole lifetime is not a limit on the resolution in this spectroscopy. According to the many-body picture, an energy of a photon, scattered on a certain low-energy excitation, should change by the same amount as a change in an excitation energy of the incident beam, so that inelastic

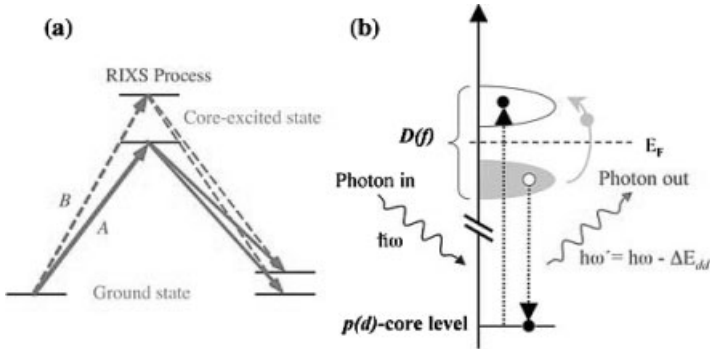


Fig. 8.3. Schematic representation of RIXS process (a), soft X-ray RIXS in study of dd (ff) excitations (b).

scattering structures have constant energy losses and follow the elastic peak on the emitted-photon energy scale.

The formulations of RIXS lead to a Kramers–Heisenberg type dispersion formula for the cross section, with generally only the resonant part of the scattering process taken into account [17–20]. Second-order perturbation theory for the RIXS process leads to the Kramers–Heisenberg formula for the resonant X-ray scattering amplitude. Using this starting point RIXS has been analyzed in periodic solids as a momentum conserving process, suggesting that it can be used as a novel “band-mapping” technique in diamond and graphite [25–27].

The spectral and polarization properties of the RIXS process can be described by a double differential cross section

$$\frac{d^2\sigma}{d\omega' d\Omega} = \sum_v \sum_n \frac{\omega'}{\omega} |F_{vn}(\omega)|^2 \Delta(\omega - \omega' - \omega_{vn}, \Gamma_{vn}) \Phi(\omega - \omega_0) \quad (7)$$

where  $\omega$  and  $\omega'$  are the frequencies of incident and scattered X-ray photons, respectively.  $\Gamma_{vn}$  is the final-state lifetime broadening.  $\Phi(\omega - \omega_0)$  is the spectral profile of the incoming beam. The broadening of the core excitations  $\Gamma_{vk}$  is much larger than the lifetime broadening  $\Gamma_{vn}$  of optical transitions  $n \rightarrow v$ . It is thus reasonable to assume that  $\Gamma_{vn} = 0$ , replacing the  $\Delta$  function by a Dirac  $\delta$ -function. This is the basis for super-highly resolved X-ray spectroscopy, which allows us to record X-ray fluorescence resonances without the lifetime broadening [18]. Further discussion on resonant soft X-ray emission spectroscopy is beyond the scope of this chapter, but it can be found in earlier reviews [34–37].

### 8.2.5

#### Experimental Details

An outline of an undulator beamline, such as beamline 7.0.1 of the Advanced Light Source [38], is presented in Fig. 8.4, showing its principle elements. It consists of a

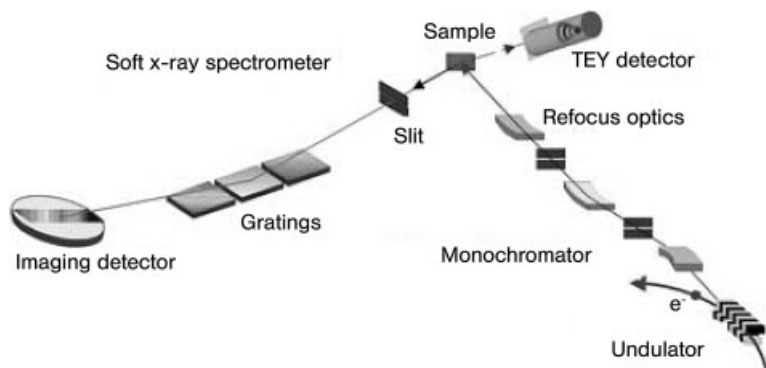


**Fig. 8.4.** Outline of an undulator beamline, including an undulator, monochromator and a Rowland circle geometry grating spectrometer and channeltron for soft X-ray fluorescence detection.

5 m, 5-cm period undulator and a spherical grating monochromator (SGM) covering the spectral range from 60 to 1200 eV. It is designed for high resolution operation with maximum photon flux and a small spot size (typically, 50–100 mm) at the sample, matched to the acceptance of the experiment spectrometers.

The experimental set-up at a synchrotron radiation beamline is called the end-station, since it constitutes an interchangeable experiment at the end of the beamline. The end-station consists of three main parts: analysis chamber, preparation chamber and loadlock chamber, separated by valves [39].

X-ray absorption spectra are recorded in total-electron-yield (TEY) mode or fluorescence-yield (FY) mode. TEY is measured from sample drain current, and the FY is obtained from a channeltron. X-ray emission spectra are recorded by using a grazing incidence grating spectrometer. Figure 8.5 shows a common experimental set-up for soft X-ray spectroscopy.

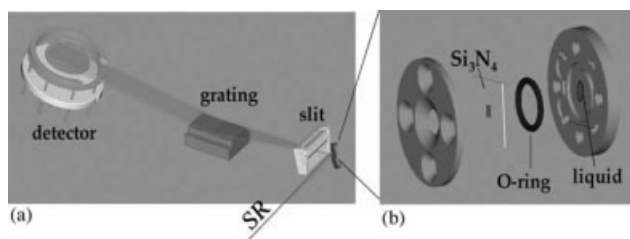


**Fig. 8.5.** A Rowland circle geometry grating spectrometer (a) and a static liquid cell (b) for soft X-ray spectroscopic study of liquid samples.

The high-resolution grating spectrometer was mounted parallel to the polarization vector of the incident photon beam to detect the emitted X-ray (Fig. 8.5a). The grazing-incidence grating spectrometer is based on Rowland geometry. It consists of slit, gratings and detector. Three spherical gratings are optimized to cover an operation range of 50–1000 eV. The gratings are mounted at angles of incidence to have a joint fixed slit, and the emitted X-rays are detected using a two-dimensional detector that can be positioned and oriented tangentially to the pertained Rowland circle. The detector consists of multi-channel plates and a resistive anode with a four-electrode readout.

Solid-state samples can be studied by placing the solid sample in front of the spectrometer slit, as shown in Fig. 8.5(a). While for the liquid (or wet) samples, a liquid cell has to be used. The liquid cell has a window to attain compatibility with UHV conditions of the spectrometer and beamline. The synchrotron radiation enters the liquid cell through a 100 nm thick silicon nitride window and the emitted X-rays exit through the same window. The thin silicon nitride window is commercially available [42]. The test showed that a 100 nm thin  $\text{Si}_3\text{N}_4$  membrane of  $2.25 \times 2.25 \text{ mm}^2$  could hold one atmosphere pressure. The liquid cell (Fig. 8.5b) consists of a metal container and a  $1 \times 1 \text{ mm}^2$  and 100 nm thin  $\text{Si}_3\text{N}_4$  membrane, which can withstand the differential pressure between the liquid on one side and UHV on another side. The transmission of X-rays at the C, O K-edge, and Fe L-edge for a 100 nm thick window is about 46%, 66%, and 82%, respectively. Silicon nitride membranes are not the best choice when compared to other materials with respect to their transmission of X-rays in the energy region 80–1000 eV, but their mechanical properties and fabrication process make them the only candidate at present. They also allow experiments to be performed at a vacuum pressure of less than  $1 \times 10^{-9}$  Torr.

### 8.3 Chemical Sensitivity of Soft X-ray Spectroscopy

The region from 200 to 700 eV covers the K-edges of the biologically relevant light elements carbon, nitrogen, oxygen and fluorine. The useful properties of soft X-ray spectroscopy stem from the electric dipole nature of the transitions involved. The emission originates from an electronic transition between a localized core state and a valence state. The energy of the emitted X-ray is equal to the difference in energy of the two states. Involvement of the inner level makes this probe localized to one specific atomic site, around which the electronic structure is reflected as a partial density-of-states (DOS) contribution. Chemical sensitivity is obtained when the resolution of the detected emission lines is high enough to resolve fine structure. The line shapes are determined by the valence electron distribution and the transitions are governed by dipole selection rules. For solids, essentially a partial DOS mapping is obtained. This is exemplified by the carbon  $K\alpha$  emission spectra of the carbon solids shown in Fig. 8.6 (see also Fig. 8.8a).

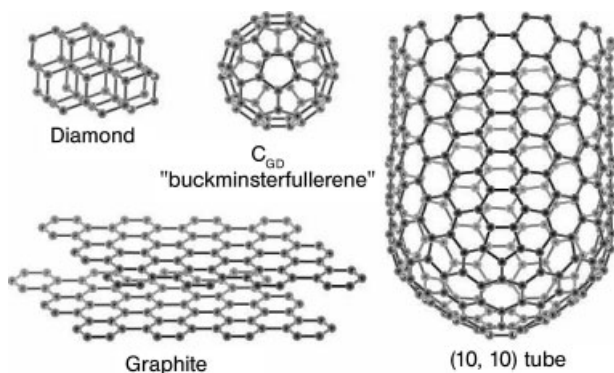


**Fig. 8.6.** Schematic representation of carbon in different allotropic forms: diamond, graphite, C<sub>60</sub>, and nanotubes. (From Ref. [41].)

### 8.3.1

#### Electronic Structure and Geometrical Structure

The difference in structural arrangement of these allotropic forms (Fig. 8.6) of carbon gives rise to the wide differences in their physical properties. Carbon has an atomic number of 6 and has a  $1s^2 2s^2 2p^2$  configuration in the electronic ground state. The atoms in diamond are tetrahedrally bonded to their four nearest-neighbors using linear combinations of  $2s$ ,  $2p_x$ ,  $2p_y$ , and  $2p_z$  orbitals in an  $sp^3$  configuration. In contrast, in graphite, strong in-plane bonds are formed between a carbon atom and its three nearest-neighbors from  $2s$ ,  $2p_x$ , and  $2p_y$  orbitals; this bonding arrangement is denoted by  $sp^2$ . The remaining electron with a  $p_z$  orbital provides only weak interplanar bonding, but it is responsible for the semi-metallic electronic behavior of graphite.

The  $sp$ -orbital, and the  $sp^3$ -hybrid orbital indicate rotational symmetry. Bonds of this kind are called  $\sigma$ -bonds. The electrons involved in such bonds are called  $\sigma$ -electrons. With double bonds, so-called  $\pi$ -orbitals occur with corresponding  $\pi$ -electrons. Such orbitals are not symmetrical with regard to their bonding orientation. Figure 8.7 displays X-ray absorption spectra of highly oriented pyrolytic graphite (HOPG) recorded at different incidence angles [40]. When the polarization vector of the incident beam is parallel to the basal plane only excitations to  $\sigma$  states are possible. Excitations to  $\pi$  states become more likely the more perpendicular to the basal plane the polarization vector is. Thus, one can see that the main feature below 292 eV has mainly  $\pi$  character, while the  $\sigma$  states are observed at energies above 292 eV. Notably, the sharp absorption feature appearing at 292.0 eV is not due to the band structure but to an excitonic state, which has been discussed in detail elsewhere [26].

The normal carbon  $K_\alpha$  XES spectra of diamond, graphitic carbon, C<sub>70</sub>, C<sub>60</sub>, and benzene are presented in Fig. 8.8(a), where large differences in spectral profile are observed. The spectra of diamond and graphitic carbon show a wide band with

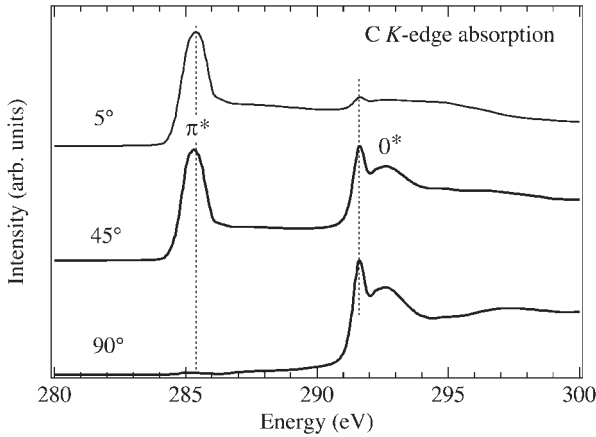


Fig. 8.7. Polarization dependent X-ray absorption spectra of HOPG.

some shoulder structures, where the energy positions of the peak maximum and band shapes are largely different. In some studies related to vapor deposition the XES spectral profile has been used as a means to identify certain chemical states [34]. In contrast, the spectra of benzene,  $C_{60}$ , and  $C_{70}$  exhibit clearly resolved emission peaks, indicating strong molecular character in their solid phases. The marked resolved emission features in benzene can find their counterpart in the emission spectra of  $C_{60}$  and  $C_{70}$ , and all the fine structures are washed out in diamond and graphite.

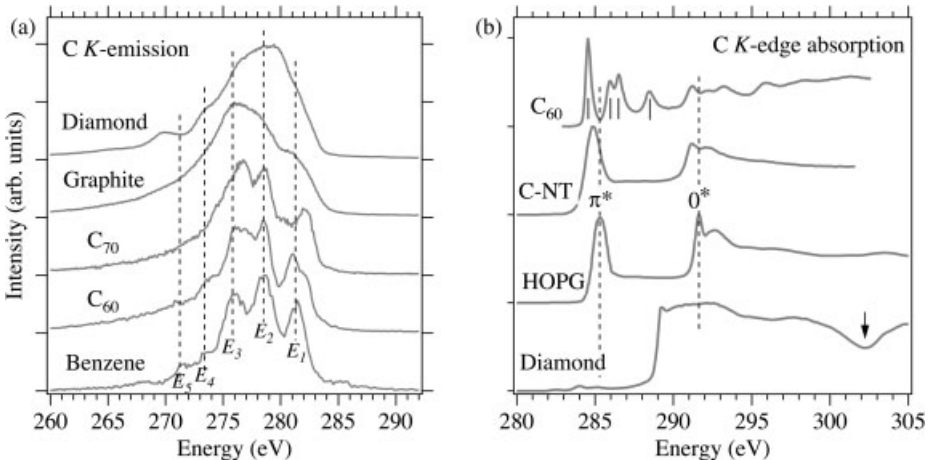


Fig. 8.8. (a) Non-resonant carbon  $K\alpha$  SXES spectra of diamond, amorphous carbon (graphitic),  $C_{70}$ ,  $C_{60}$ , and benzene; (b) X-ray absorption spectra of  $C_{60}$ , carbon nanotubes, HOPG, and diamond.

Figure 8.8(b) shows the X-ray absorption spectra of  $C_{60}$ , carbon nanotubes (C-NT), HOPG, and diamond. The X-ray absorption spectral shape of carbon nanotubes is similar to that of HOPG, which is different to that of  $C_{60}$ . The  $\pi^*$  shows a shift towards low photon energy in the X-ray absorption of C-NT.  $C_{60}$  gives more resolved absorption features, which indicate a strong molecular character of  $C_{60}$ . Non-resonant carbon  $K\alpha$  XES spectra of carbon nanotubes and  $C_{60}$  show a similar shape, but resonantly excited XES spectra reveal large differences in the electronic structure of these two systems. The XAS spectrum of diamond shows no  $\pi^*$  contribution, and the absorption feature at 288.85 eV is the diamond exciton. The 2nd bandgap at 302 eV is also clearly observed.

### 8.3.2

#### Hydrogen Bonding Effect

A very important but hitherto less addressed question is that of the hydrogen bond effect on the electronic structure. This effect is essential for understanding the physical and chemical properties of many chemical and biological systems. The reason for this neglect, however, is the limited experimental access to the electronic structure of liquids. The application of spectroscopic methods to study the electronic structure of liquids has been hampered by the incompatibility of wet samples and high-vacuum conditions. Hence, even understanding the properties of pure liquid water remains a challenge.

Water is the most abundant substance on our planet, and it is the principal constituent of all living organisms. Chemical reactions taking place in liquid water are essential for many important processes in electrochemistry, environmental science, pharmaceutical science, and biology in general. Many models have been proposed to view the details of how liquid water is geometrically organized by a hydrogen bond network. Hydrogen bonding is an attractive interaction from a link of a hydrogen atom and one of the highly electronegative and non-metallic elements that contain a lone pair of electrons. Although H-bonds are much weaker than conventional chemical bonds, they have important consequences on the properties of water. Diffraction of X-rays [43] and neutrons [44] provides strong evidence that tetrahedral hydrogen-bond order persists beyond the melting transition, but with substantial disorder present [45]. Important questions remain about the precise nature of the disorder and how it is spatially manifested.

A network with four hydrogen bonds connects most of the water molecules in the liquid phase. Such a network can often be terminated by local structures with three or even two hydrogen bonds.

Soft-X-ray emission spectroscopy is essentially bulk sensitive, since the attenuation length of photons in this energy range is typically hundreds of nanometers in solid matter. The penetration depth offers a few experimental opportunities not present in electron-based spectroscopy. Figure 8.9 shows XAS and XES spectra of water in the gas phase and liquid phase at room temperature.

Another X-ray absorption study of liquid water [46] suggests that the four hydrogen-bonding networks mainly contribute to a single broad feature, while a shoulder located at 534.7 eV suggests the presence of the broken hydrogen bonds.

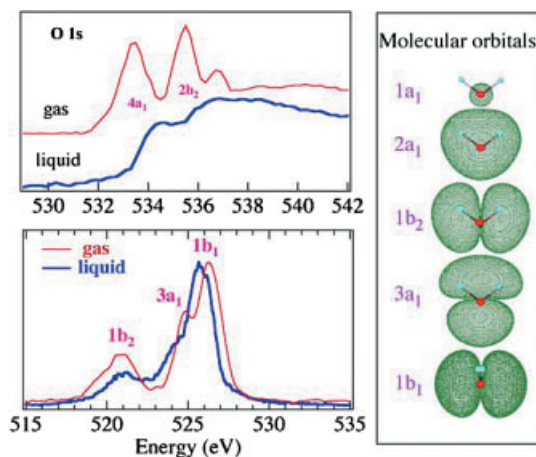


**Fig. 8.9.** X-ray emission spectra of the water molecules and liquid water, formed as electrons from the three outermost occupied molecular orbitals, schematically depicted in the right panel, fill a vacancy in the  $1a_1$  core-

level. The excitation-energy is 543 eV, well above the ionization limit but sufficiently low so that the emission from multiply excited states can be neglected.

Indeed, recent theoretical simulations assign this pre-edge structure to a particular three-hydrogen bond structure with one missing hydrogen bond at the hydrogen site.

### 8.3.3

#### Charge and Spin States of Transition Metals

Many metals that play important roles in biological and environmental sciences lack the partially filled d-shells used for UV-visible spectroscopy. Still, there are always soft X-ray resonances that can be exploited.

First transition metal L-edge spectroscopy is a relatively new technique for biological samples. L-edge spectra can be analyzed through theoretical simulation using ligand field multiplet theory (LFMT). LFMT is a multi-electron approach that describes the initial and final states as multiplets that are mixed and split by the symmetry of the ligand field [47–51].

The experimental Fe- $L_{2,3}$  absorption spectra for  $K_4[Fe(CN)_6]$  ( $Fe^{2+}$ ) and  $K_3[Fe(CN)_6]$  ( $Fe^{3+}$ ) are displayed in Fig. 8.10. The first peak at 704.5 eV is observed in the ( $Fe^{3+}$ ) derivative but not in the ( $Fe^{2+}$ ) one. It corresponds to the excitation  $2p^6t_{2g}^5 \leftrightarrow 2p^5t_{2g}^6$  which is absent in the  $Fe^{2+}$  configuration ( $t_{2g}^6$  ground state). This peak is a signature of the  $Fe^{3+}$  configuration [52]. The other peaks between 707 and 715 eV correspond to multiplet structures arising from transitions from  $2p$  to  $e_g$  orbitals.

The second peak, which corresponds to the transition from  $2p_{3/2}$  to empty  $e_g$  orbitals, exhibits at least five structures, which have to be analyzed with a multiplet model, taking into account the exchange interaction between the  $2p$  hole and  $3d$  electrons [51]. Note that the splitting of the  $L_3$  line is related, but not directly scaled, to the  $10Dq$  crystal field strength parameter (energy separation between



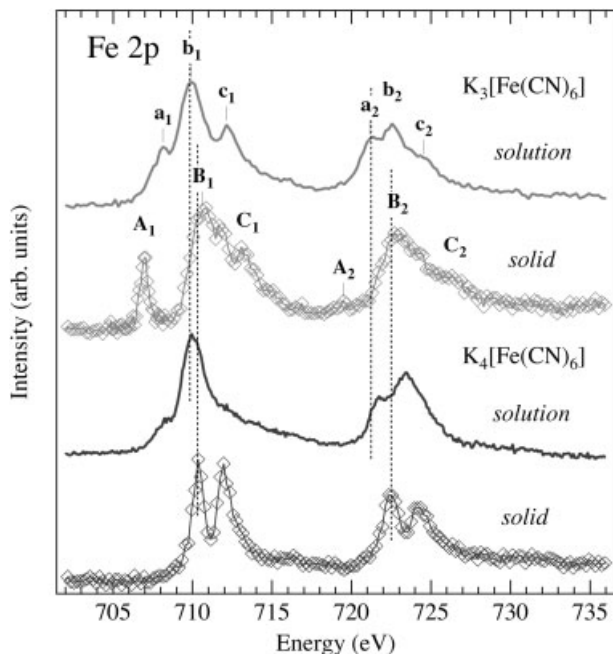


**Fig. 8.10.** Fe  $L_{2,3}$ -edges absorption from  $K_3[Fe(CN)_6]$  and  $K_4[Fe(CN)_6]$  in both solid state and water solutions. The peak labeled “ $A_1$ ” corresponds to a singlet excitation.

the levels  $t_{2g}$  and the center of mass of the  $e_g$  levels). The Fe L-edge of both complexes,  $K_3[Fe(CN)_6]$  and  $K_4[Fe(CN)_6]$  presented the significant changes in the spectral profile when they were dissolved in water solutions.

The Ni L-edge XAS and RIXS spectra of NiO and  $(Ph_4As)_2Ni[S_2C_2(CF_3)_2]$  are shown in Fig. 8.11 [53]. NiO is a typical high-spin  $Ni^{2+}$ , and the complex of  $(Ph_4As)_2Ni[S_2C_2(CF_3)_2]$  is a Ni dithiolene, which has a low-spin  $Ni^{2+}$ . The dd and charge-transfer excitations can be observed along with some contributions of normal emission. The transition of dd excitations in the high-spin compound NiO was within 3.0 eV, while the low-spin system shows dd excitations with larger energies. Examination of these Ni models will serve as a first step in measuring real biological nickels, and one can create a spectral data base for use in future biological spectra analysis. Preliminary experiments on a small number of Ni compounds also confirm the feasibility.

#### 8.4 Electronic Structure and Nanostructure

In the nano-regime, two effects dominate the chemical and physical properties: (a) increasing contribution of surface atoms (surface effect). The surface atom to bulk

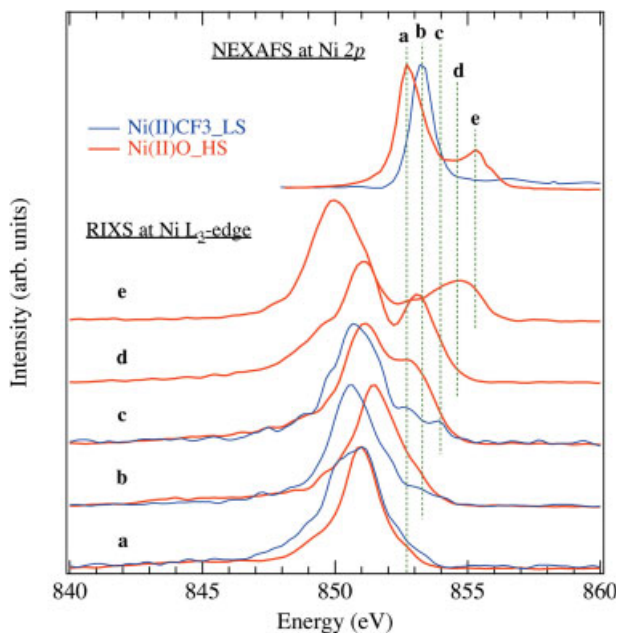


Fig. 8.11. X-ray absorption and RIXS spectra of NiO ( $\text{Ni}^{2+}$  in high spin) and  $(\text{Ph}_4\text{As})_2\text{Ni}[\text{S}_2\text{C}_2(\text{CF}_3)_2]$  ( $\text{Ni}^{2+}$  in low spin).

atom ratio increases dramatically as the particles size decreases. For a 30-nm particle, about 5% of all the atoms are on the surface, while for 3 nm particle, up to 50% of the atoms are on the surface, (b) quantum confinement as nanoclusters decrease down to a few nanometers (size effect), where electrons begin to feel the effects of quantum confinement when the size of the structure becomes comparable to the electron wavelengths.

Synchrotron radiation with photon energy at or below 1 keV is giving new insight into such areas as wet cell biology, condensed matter physics and extreme ultraviolet optics technology. In the soft X-ray region, the question tends to be, what are the electrons doing as they migrate between the atoms? [54].

#### 8.4.1

#### Wide Bandgap Nanostructured Semiconductors

Soft X-ray spectroscopy has proved useful in probing the electronic structure of nanostructured solids [55, 56]. The development of the electronic band structure of solids from discrete localized atomic states is one of the key points of interest in cluster physics. As the size of nanocrystal extends into a truly molecular regime, such as cadmium thiolate  $[\text{Cd}_8(\text{SR})_{16}]$  units, the optical excitation energies for the dissolved particles increase from 2.5 eV for CdS bulk to around 4.7 eV for Cd thiolate [57–59].

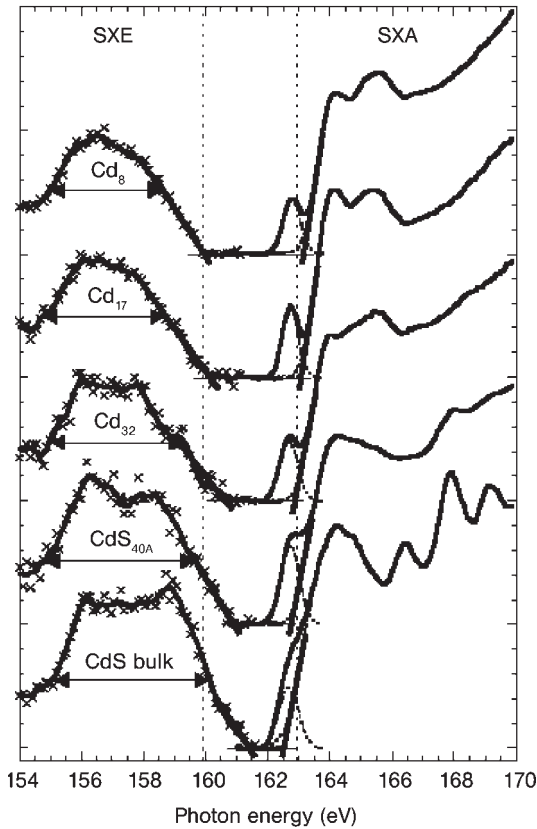


**Fig. 8.12.** Right: S L-edge XAS spectra of CdS bulk and Cd nanocrystallites. The dotted lines show the separation into excitonic and LPDOS excitation. Left: S L3 SXE spectra mapping the local DOS of the upper VB. Gray bars indicate the linear extrapolation of the emission cutoffs and the LPDOS absorption onsets, respectively. Courtesy of [60].

Figure 8.12 shows the S L-edge XAS and XES spectra for different samples (labeled by the number of Cd atoms per cluster) [60]. For decreasing particle size, an increase of the bandgap was observed. This opening of the bandgap can be separated into valence band and conduction band contributions.

X-ray absorption spectra have also been used to measure the band edges of silicon nanocrystals, with average diameters ranging from 1 to 5 nm [61]. The conduction band (CB) edge shift (from XAS measurements) and the valence band (VB) edge shift (from photon emission measurements) vary as a function of nanocrystal diameter. If the observed VB or CB shifts are due to quantum confinement, one would expect the size of the band shifts to increase as the particle size of the nanocrystalline Si is decreased. Other X-ray absorption studies of quantum confinement have examined CdSe and InAs nanocrystals [62], nanodiamonds [63], and porous silicon [64], etc.

## 8.4.2

**Cu Nanoclusters**

Copper nanoclusters have been studied due to potential applications in optics, magneto-electronics and catalyst systems [65–67]. Silicon carbide provides a structurally and chemically stable support for such nanoclusters due to its stability against copper [68]. Although there are some studies on copper island formation on silicon carbide, the reports relied on the indirect spectroscopic results, mainly focusing on the stability of Cu/SiC interfaces [69–71]. Recently, we have observed the morphology of copper nanoclusters by high-resolution transmission electron microscopy (TEM) where copper nanoclusters had an ellipsoid shape inside a SiC matrix [72]. XAS studies can give a detailed description of the size dependence of the electronic structure of the copper nanoclusters in order to understand the nature of chemical bonds due to size effects.

Figure 8.13 shows the Cu L-edge XAS spectra of a series of Si/Ta(100 nm)/[Cu(0.5–3 nm)/SiC(2 nm)]<sub>10</sub>/Ta(5 nm) and the reference Cu. The bulk Cu sample shows three distinct features in the L<sub>3</sub>-edge region, which are associated with the unoccupied 3d states in Cu. In a free Cu atom, the 3d orbital is fully occupied. In contrast, a solid Cu is characterized by a re-mixing of the valence wave functions in the ground state, gaining a small amount of non-vanishing 3d hole. According to dipole-selection rules, the dominant transition in XAS of Cu is from the Cu 2p<sub>3/2</sub> and 2p<sub>1/2</sub> states to the unoccupied Cu 3d states [73]. Thus, the peak at the onset of the L<sub>3</sub>-edge is associated with the Cu 3d-derived character due to 3d–4s hybridization, giving a sharp 2p → 3d transition superimposed on the smooth 2p → 4s transitions. The peak at 939 eV and the peak at 943 eV are attributed to transitions

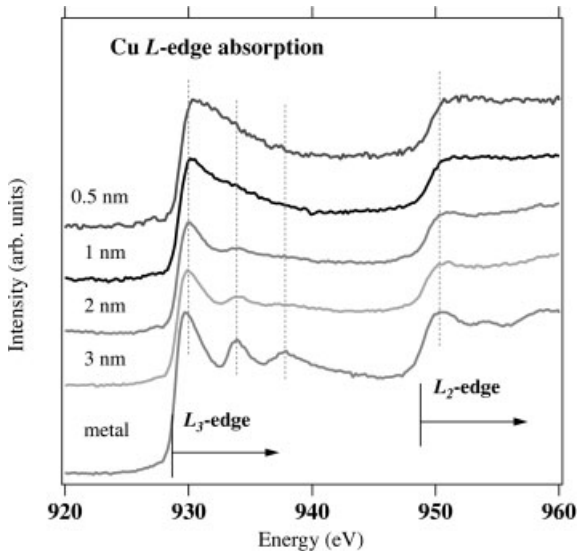


Fig. 8.13. XAS spectra of Cu L-edge with different nanocluster sizes.

towards empty states, mainly mixed with s, p characters. As the nanocluster size decreases, two distinct changes occur. First, the peaks move slightly to higher energy. Second, the peaks at 939 and 943 eV drastically decrease in intensity. The decrease of these peaks indicates that the s–p–d hybridization becomes weaker. This behavior can be attributed to the surface effect. The Cu atoms at surface have lower coordination number and see fewer Cu neighboring atoms, giving rise to a reduction in Cu–Cu interaction. The Cu–Cu interaction is mainly determined by d–d interaction and stronger Cu d–d interaction favors s–p–d re-hybridization [12, 13]; reduction of the d electron will weaken the hybridization.

#### 8.4.3

#### ZnO Nanocrystals

ZnO, a wide band-gap semiconductor, has attracted considerable attention recently due to its potential technological applications such as, for instance, highly efficient vacuum fluorescent displays (VFD) and field-emission displays [76]. ZnO has also been used for short wavelength laser devices [77], high power and high frequency electronic devices [78], and light-emitting diodes (LED) [79, 80]. ZnO shows many advantages: (a) it has a larger exciton energy (60 meV) than GaN (23 meV); (b) the band-gap is tunable from 2.8 to 4 eV [81, 82]; (c) wet chemical synthesis is possible; (d) low power threshold at room temperature; (e) dilute Mn-doped ZnO shows room temperature ferromagnetism [83]. Recently, quantum size effects on the exciton and band-gap energies were observed in semiconductor nanocrystals [61, 84].

The controlled synthesis of ZnO nanostructures and in-depth understanding of their chemical/physical properties and electronic structure are the key issues for the future development of ZnO based nanodevices.

The XES spectra of bulk and nanostructured ZnO are displayed together with the corresponding XAS spectrum in Fig. 8.14 [85]. The O K-edge emission spectrum reflects the O 2p occupied states (valence band), and the O K-edge absorption spec-

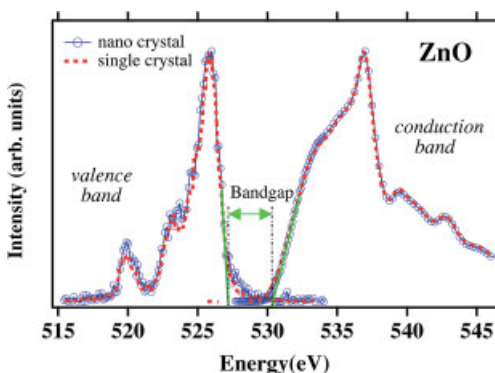


**Fig. 8.14.** Oxygen X-ray absorption–emission spectrum reflected conduction band and valence band near the Fermi-level of ZnO nanoparticles in comparison with bulk ZnO.

trum reflects the O 2p unoccupied states (conduction band). In the photon energy region of 530–539 eV, the X-ray absorption can be mainly assigned to the O 2p hybridized with Zn 4s states. In the region 539–550 eV the spectrum is mainly attributed to O 2p hybridized with Zn 4p states. Above 550 eV, the contribution comes mainly from O 2p–Zn 4d mixed states [86]. Stronger s–p–d hybridization was revealed in nanostructured ZnO since the contributions of features at 520 and 523 eV are enhanced. A well-defined band-gap can be observed between the valence-band maximum and conduction-band minimum. Our absorption–emission spectrum yields a fundamental band-gap energy of 3.3 eV.

## 8.5

### Electronic Structure and Molecular Structure

Our microscopic understanding of a liquid is based very much on the study of spatial and of spatio-temporal correlation functions. This is the main bequest by the liquid state to the whole of physics: think in terms of correlations, be these between molecules in water or between galaxies in the cosmos. The study of correlations allows us to appreciate the local organization of one molecule around others, and to unravel the microscopic dynamics. Neutron diffraction and scattering have and continue to play a major role in these studies. X-ray diffraction is important as well, and very recently X-ray inelastic scattering has become available. We should add to these the soft X-ray spectroscopy experiments.

Using X-ray absorption and selectively excited X-ray emission spectroscopy to probe unoccupied and occupied electronic states, one can establish a firm interpretation for the unusual thermodynamic properties of molecular liquids. Furthermore, one can elucidate finer details of their structural properties. XAS and XES spectra reflect the local electronic structure of the various conformations; in this case, the oxygen lineshape is sensitive to the hydrogen bonding configurations.

#### 8.5.1

##### Hydrogen Bonding in Liquid Water

The local structure of liquid water is still under debate. Soft X-ray emission spectra, emanating from the radiative decay, subsequent to core excitation, can be useful in assigning structures in XAS spectra [87–90], and especially we have, earlier, shown that resonantly excited XES spectra of liquid water are compatible with the traditional view that three and four hydrogen bonds dominate in the structure [89]. Here we show that a theory that assumes that most water molecules in liquid water only make two hydrogen bonds fails to reproduce the experimental XES spectra.

Both the experiment and calculation have been described earlier [89], and the salient results are shown in Fig. 8.15. At excitation high above threshold (545.5 eV), the XES spectrum is well described by a calculation both with symmetric four-fold coordination, and conformations with one broken hydrogen bond. Thus, at high

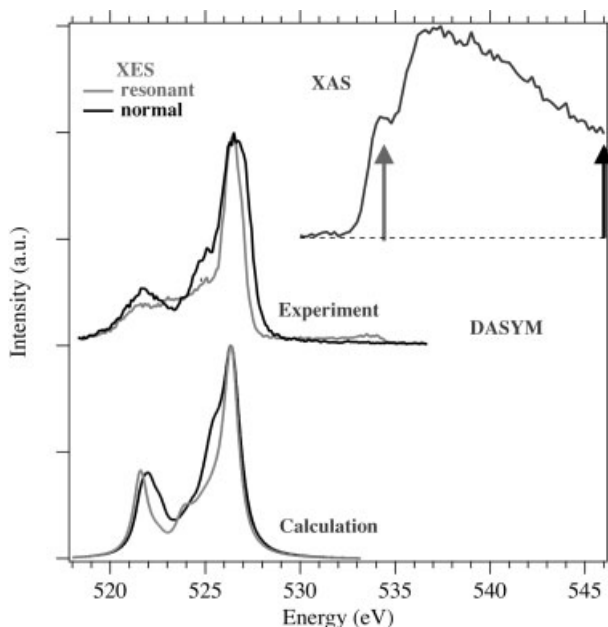


**Fig. 8.15.** Resonantly (excitation energy at 534.7 eV) and non-resonantly (at 545.5 eV) excited XES spectra of liquid water, compared to calculations for the SYM and DASYM species. Excitation energies are marked in the XAS spectrum.

excitation energy the spectra are not predicted to be sensitive to the breaking of a single hydrogen bond. When tuning the excitation energy to the pre-peak at 534.7 eV, the spectral changes comply with what is expected when structures with one broken hydrogen bond at the hydrogen donor site (DASYM) [46, 89] are resonantly excited. We have shown elsewhere that a thorough analysis of XES spectra excited in the threshold region can give further details on the contributions by various structures to the XAS spectrum [91].

### 8.5.2

#### Molecular Structure in Liquid Alcohol and Water Mixture

Near-edge X-ray absorption spectra of water, methanol and a mixture of the two are displayed in Fig. 8.16. The X-ray absorption spectra of all samples present a similar shape: a strong pre-edge at 534.5 eV (B) and a broad main absorption threshold arising from 537.0 eV (C). The pre-edge (B) in liquid water has been the fingerprint of the particular water cluster with a broken hydrogen bond at the hydrogen side [89]. In methanol, the ring-structure configuration contributes mostly to the pre-edge (B) and the chain-structure configuration contributes mostly to the main threshold (C) of the absorption spectra [92]. Upon mixing water and methanol, a small X-ray absorption peak (A) appears at 531.5 eV, below the known X-ray ab-

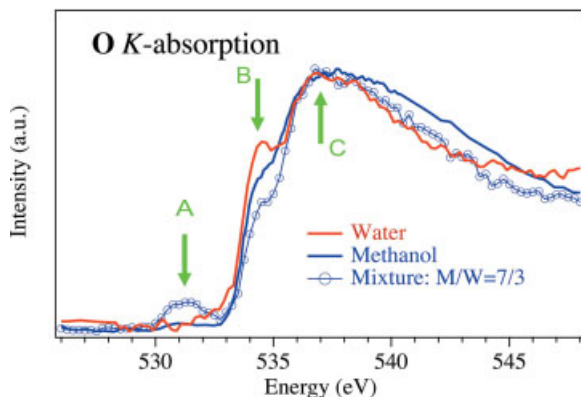


Fig. 8.16. X-ray absorption spectra of liquid water, methanol and a mixture of molar concentration 7:3.

sorption pre-edge (B). The new absorption peak (A) suggests direct interaction between water molecules and methanol molecules.

To understand the origin of the pre-peaks in X-ray absorption spectra, resonant X-ray emission measurements were performed (Fig. 8.17). Structures of rings and chains for methanol and mixtures of water clusters and methanol are fully optimized at the hybrid density functional theory B3LYP level with 6-31G basis set using GAUSSIAN 98 [92]. The theoretical X-ray emission spectra of methanol were generated by the group theory formulation [20], using the adiabatic approximation (ground state electronic structure) for intensities as established for molecules and clusters [93]. All transition moments and orbital energies were calculated at the canonical Hartree–Fock level with the Sadlej basis set by using the DALTON program [94].

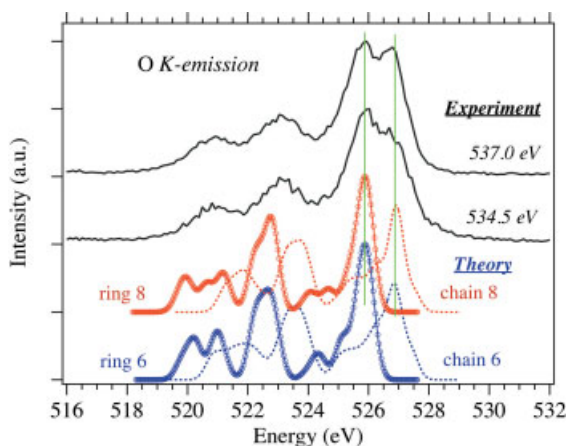


Fig. 8.17. Experimental and calculated X-ray emission spectra of liquid methanol.



The double structure emission band centered at 527 eV indicates two major different chemical species (molecular structure) in the alcohol and water mixtures. Comparison between experiment and theory shows that the two species originate from the combination of methanol rings and chains. These two peaks clearly have different origins: the one at higher energy side is from the chains, and the other from the rings. From the intensity distribution, it was found that the chains and rings have a similar size with same portion.

As to the mixtures of liquid water and methanol, when selecting the excitation energies around the pre-peak (A) in the X-ray absorption, the main emission band becomes very narrow and shifts towards higher photon energy, opposite to the shifting of the elastic peak. Is the interaction between water molecules and these chains or rings be responsible for the sharp spectral features in the resonantly excited X-ray emission spectra? We learnt previously [90] that the dominant chain and ring structures in methanol are those with 6 and 8 molecules. Of course, we do not know if this is the answer or just one of the possibilities. Notably, when methanol mixes with water, the ring and chain become the same. The results from alcohol–water mixtures of different concentrations are prerequisites to support the experimental findings from the equimolar study [11]. Thus, we know that the exact mixing level is not critical to our conclusions.

This study shows that, when a few water molecules interact with chains, the chains start to bend over to form open-ring structures. By adding water, the alcohol structures become more compact. The formation of such ordered molecular structure upon mixing provides evidence that the entropy of the alcohol and water mixture is not less than expected for ideal solutions.

We find a strong involvement of hydrogen bonding in the mixing of water and methanol molecules. The local electronic structure of water and methanol clusters, where water cluster is bridging within a six-membered open-ring structured methanol cluster, is separately determined. The experimental findings suggest an incomplete mixing of water–alcohol systems and a strong self-association between methanol chain and water cluster through hydrogen bonding. The enhancement of joint water–methanol-ring structure explains the loss of entropy of the aqueous solutions.

The answer to this specific question is likely to be of interest to a much broader scientific community of readers. The novelty of this work is that it relies on a spectroscopic probe to investigate problems that have, largely, been the territory of scattering methods. This technique could have great impact to the extent that this approach can be generalized to investigate other solvent mixtures.

### 8.5.3

#### **Electronic Structure and Ion Solvations**

Ion solvation is a phenomenon that is of fundamental interest in many chemical contexts because solvated ions are almost omnipresent on Earth. Hydrated ions occur in aqueous solution in many chemical and biological systems [95, 96]. Metal-ion transport in both aqueous- and polymer-solvent media involves continual

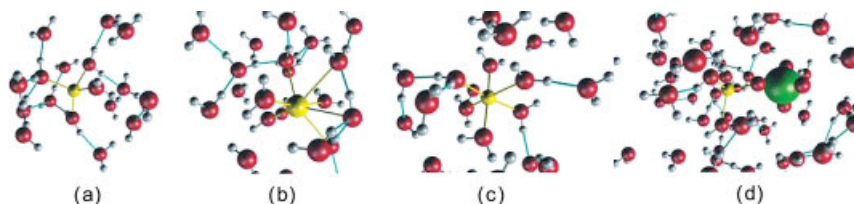


**Fig. 8.18.** Sample snapshots showing configurations with water molecules in the first and second solvation shells for (a)  $\text{Li}^+$ , (b)  $\text{Na}^+$ , (c)  $\text{Mg}^{2+}$ , and (d) ion pair water solutions.

solvent–ligand exchange. Metal-ion coordination chemistry is therefore fundamental to these phenomena where a dramatic exchange of ligand occurs. Alternatively, the effects of solvated cations could be monitored via examining the spectra of solvent. The great advantage of this approach is that the restriction to cations no longer applies. For example, it can be used in studying what happens when salts of the alkali and alkaline earth metals are added to aqueous solvent.

An ion in solution disturbs the local solvent structure. The local structure around a  $\text{Li}^+$  ion central water molecule, a  $\text{Na}^+$  ion, and a  $\text{Mg}^{2+}$  ion in water solutions as obtained using the polarizable MD model is shown in Fig. 8.18. The influences of cations on the water molecular structure can be seen as the threshold shifts towards higher energy in the X-ray absorption spectra; the mixing of molecular orbital in  $3a_1$  symmetry is reinforced as the intensity of  $3a_1$  is further reduced. We find that the charge difference of the cations may not be the only factor that accounts for the interactions between the cations and water molecules.

Figure 8.19 reports the O K-edge absorption spectra of liquid water and  $\text{NaCl}$ ,  $\text{MgCl}_2$ ,  $\text{AlCl}_3$  water solutions. The pre-peak (marked as  $\alpha$ ) in XAS spectrum of

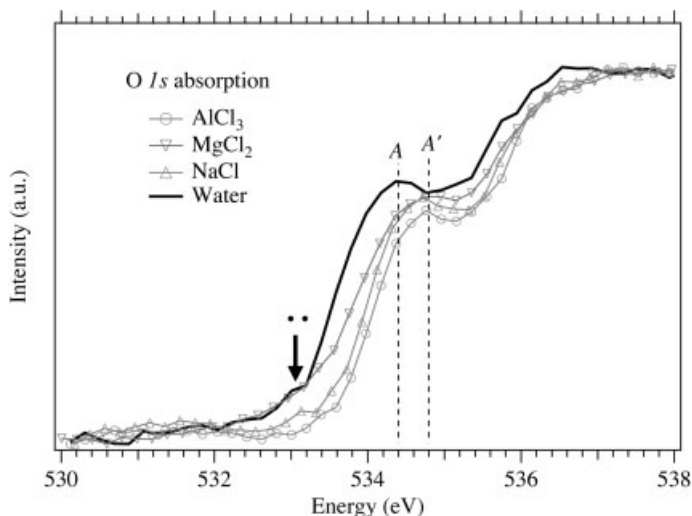


**Fig. 8.19.** X-ray absorption spectra of liquid water and  $\text{NaCl}$ ,  $\text{MgCl}_2$ ,  $\text{AlCl}_3$  water solutions.

water has partly  $4a_1$  symmetry. The major difference on going from pure water to ion–water solutions can be seen as a shift of 0.4 eV for the absorption pre-peak (A), which is probably a result of a higher degree ionic character of the chemical bonding between cations and oxygen. The front slope of the absorption threshold has shifted most away from that of pure water for  $\text{Al}^{3+}$ -water, followed by  $\text{Na}^+$ -water, while  $\text{Mg}^{2+}$ -water shows a tendency to resemble that of pure water in the region marked by A. For the monovalent  $\text{Na}^+$ , the distance between the water molecules in the first and second solvation shells is long, 2.40–2.50 Å [97], and rather unaffected by the ion. For  $\text{Mg}^{2+}$  and  $\text{Al}^{3+}$ , the distances are substantially shorter, 2.00–2.14 Å and 1.87–1.90 Å, respectively. Thus, the changes observed XAS spectra are not in line with the charge order of the cations:  $\text{Na}^+$ ,  $\text{Mg}^{2+}$ , and  $\text{Al}^{3+}$ .

#### 8.5.4

##### Drugs in Water Solution

All orally administered drugs must be dissolved, absorbed, and transported by the blood stream to the site of action. It is a pharmaceutical challenge to establish predictive models for this complex process. One essential aspect of the problem is the lack of understanding of solubility on the microscopic level. Especially when hydrogen bonding is involved, the situation is often too complex for reliable predictions.

It is possible to understand drug solubility by applying X-ray spectroscopy to substances in solid phases, in aqueous solution, and in the gas-phase (Fig. 8.20). The influence of the molecular surrounding on the local electronic structure is reflected in soft X-ray absorption fine structure, and in site-selectively excited X-ray emission spectra.

The overall shapes of the XAS spectra recorded at the nitrogen and oxygen K edges of atenolol and nadolol are similar (Fig. 8.21), apart from some remarkable exceptions. In atenolol there is an additional sharp resonance that is virtually absent in nadolol, both at the oxygen and nitrogen edge. These resonances can be assigned to excitations at specific sites by considering the structure of the molecules (Fig. 8.21). Nadolol has a single nitrogen site, ( $-\text{NH}-$ ), whereas atenolol contains an additional amino-group nitrogen ( $-\text{NH}_2$ ). It is, therefore, straightforward to assign the additional peak at 400.5 eV to excitations at this site. The smaller resonance at 398.5 eV can be assigned to the ( $-\text{NH}-$ ) site, as it is present in both molecules. Similarly, the atenolol resonance at around 532 eV in the oxygen spectrum can be assigned to the ( $=\text{O}$ ) site, which is unique to this molecule. Regions in the spectra with less pronounced features cannot be assigned without theory, and, especially at higher energies, overlapping intensity from several non-equivalent sites is difficult to disentangle.

#### 8.5.5

##### Electronic Structure of Bases in DNA Duplexes

Characterization of electronic states near the Fermi level of DNA duplexes has been desired to clarify the mechanisms of long-range charge migration in DNA [98–103].

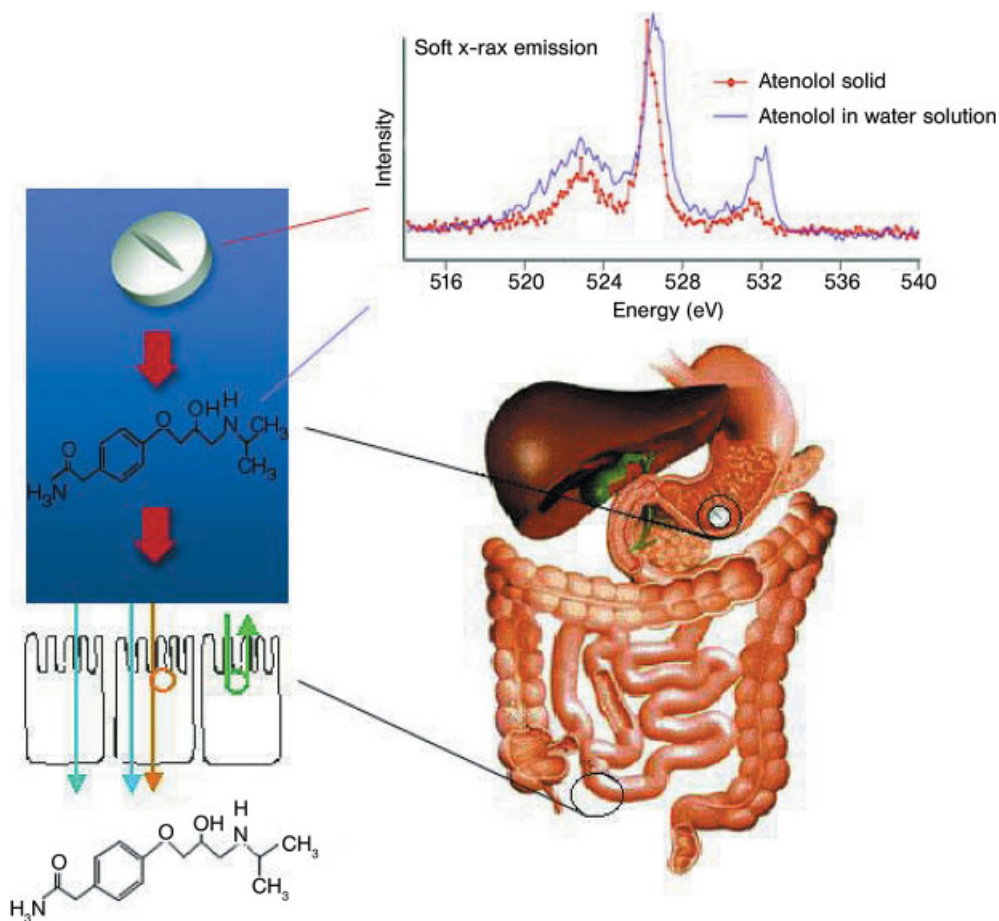


Fig. 8.20. X-ray emission spectra of atenolol in solid powder and water solution.

It was recently reported that the N K-edge XAS and Resonant Photoemission (RPE) spectroscopy characterized the electronic structure near the Fermi level of DNA duplexes to specify the charge migration mechanism [104]. The samples were thick GC- and AT-DNA films on  $\text{SiO}_2/\text{p-Si}(111)$  substrates. Since N atoms are included in only bases in DNA duplexes, the RPE spectra excited from N 1s to unoccupied states purely extract the electronic orbital features of the bases in DNA. It was concluded that the charge-hopping model is suitable for electric conduction in DNA duplexes rather than the charge-transfer model via delocalized states when electrons pass through the  $\pi^*$  states of DNA bases.

Soft X-ray absorption and emission spectroscopies have been applied to study the nitrogen bonding structure in poly(dC) ··· poly(dG) [105]. The three sharp peaks at 398.5, 399.5, and 400.9 eV (Fig. 8.22a) indicate that absorption features originate from the well-defined structures. From previous studies of carbon nitride films [88, 106], the nitrile structure ( $\text{N}_1$ -site) aligns very well with the peak of 399.5 eV.

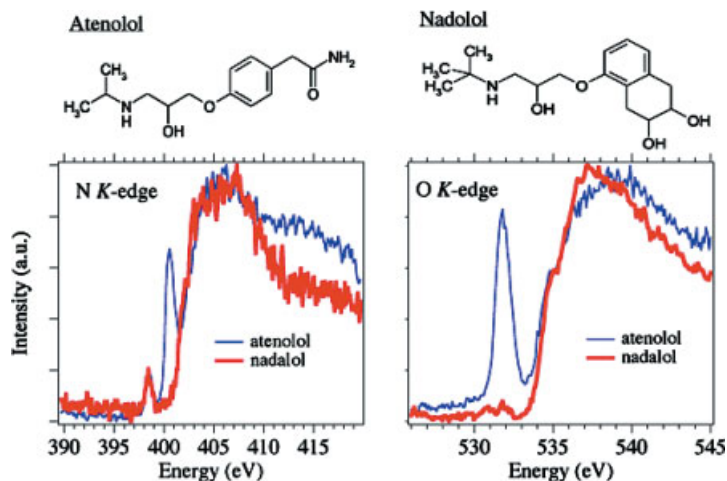
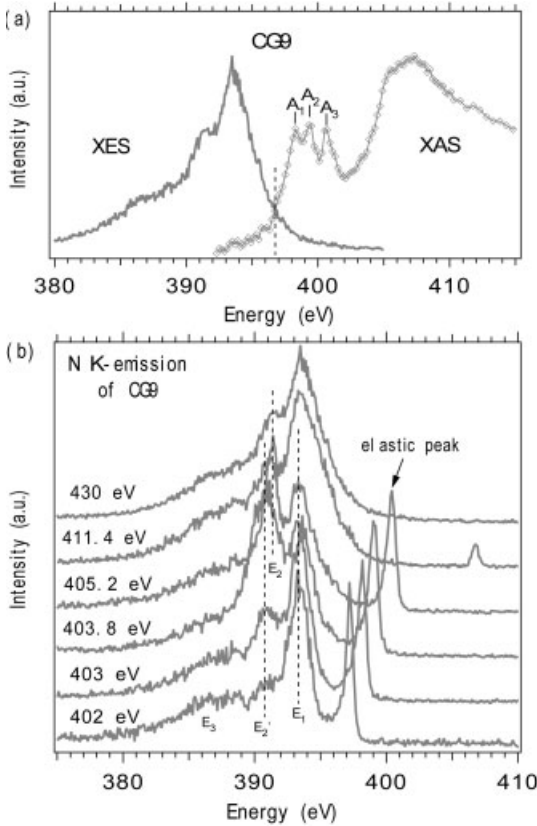


Fig. 8.21. XAS spectra of atenolol and nadolol, measured at the nitrogen and oxygen K edges.

Since the nitrile bond predominantly has p-character, this peak appears strong in the  $\pi^*$  region. The 398.5 eV peak corresponds to pyridine-like N ( $N_2$ -site). The spectra for graphite-like  $N_3$ -site shows a peak at 401.7 eV, with a shoulder to the low energy side. This could be a low-energy  $\sigma^*$  resonance; however, with the complex structure in DNA it is difficult to separate the  $\pi$  and  $\sigma$  bonds. This structure together with pyridine-like N are, possibly, the origin of the absorption peak at 400.9 eV in XAS spectrum.

Nitrogen K-emission spectra are shown in Fig. 8.22(b). The excitation energies were selected to correspond to the absorption features in the XAS spectrum. The fact that N atoms in different bonding environments are excited depending on the photon energy is clearly reflected by the differences in XES spectra. For the lowest excitation energy (398.5 eV), presumably corresponding to the  $1s \leftrightarrow \pi^*$  transition of pyridine-like N, the main emission line is centered at 393.5 eV. The overall spectral shape is similar to that of pyridine. When the excitation energy is increased to 399.5 eV, mainly nitrogen in the  $N_1$  structure should be excited. However, the emission spectra indicate that a large fraction of the pyridine-like N atoms are also excited at this energy. This can be explained by a relatively broad signal corresponding to pyridine-like N due to shifts that depend on the second nearest neighbors. Thus the emission spectrum can be modeled by a superposition of the  $N_1$  and  $N_2$  spectra. The excitation energy of 400.9 eV, however, mainly excites the  $N_1$  structure.

X-ray transitions, where a core-level vacancy is filled by a valence-orbital electron, give direct information about the chemical bonding. While such transitions have been analyzed using X-ray spectrometers since the late 1920s, interest in the technique is presently booming due to the advent of third generation synchrotron radiation sources. Today the method is frequently applied in research fields ranging



**Fig. 8.22.** (a) N K-edge absorption and emission spectra of poly(dC) ··· poly(dG). (b) N K-edge emission spectra recorded at selected excitation energies.

from atomic and molecular physics to materials research. Understanding protein functionality is of fundamental importance in biochemistry. Soft-X-ray absorption and emission study of poly(dC) ··· poly(dG) can elucidate the relation between the structure and functionality of proteins.

### Acknowledgments

This chapter would not exist without the contributions from my collaborators. I acknowledge some of them for their support over the years, to name a few: Y. Luo, J. Nordgren, J.-E. Rubensson, A. Augustsson, C. L. Dong, S. Kashtanov, C. L. Chang, L. Vayssieres, S. Butorin, L. Duda, C.-J. Englund, S. H. Yang, D. W. Shin, J. Söderström, P.-A. Glans, T. Learmonth, K. Smith, etc. Preparation of the manuscript for

this chapter was also supported by the office of Science, Basic Energy Sciences, and the Department of Energy under contract DE-AC03-76SF000098 at Lawrence Berkeley National Laboratory.

## References

- 1 LEONID V. AZAROFF, ed. *X-ray Spectroscopy*. (McGraw-Hill Inc., 1974).
- 2 TSUN-KONG SHAM, ed. *Chemical Applications of Synchrotron Radiation* (World Scientific, Singapore, 2002). Chapter 10 Soft X-ray fluorescence spectroscopy for materials science and chemical physics, J. NORDGREN, S. M. BUTORIN, L. C. DUDA, J.-H. GUO, J. E. RUBENSSON, p. 517.
- 3 J. A. SAMSON, D. L. EDERER, ed. *Vacuum Ultraviolet Spectroscopy*. (Academic Press, London, 2000). Chapter 13, Soft X-ray fluorescence spectroscopy, T. A. CALLCOTT, p. 279.
- 4 Twelve International Conferences on Vacuum Ultraviolet Radiation Physics have been held since 1965, the most recent being VUV12 in San Francisco in 1998.
- 5 Seventeen International Conferences on X-ray Physics and Inner Shell Ionization have been held, the most recent being X-96 in Prague, Czechoslovakia in 1996.
- 6 S. P. CRAMER, K. O. HODGSON, Bioinorganic applications of X-ray absorption spectroscopy, *Prog. Inorg. Chem.* 25, 1 (1979).
- 7 D. KONIGSBERGER, R. PRINS, ed. *Extended X-ray Absorption Fine Structure*, (Plenum: New York, 1988). Chapter Biochemical Applications of X-ray Absorption Spectroscopy, S. P. CRAMER, pp. 257–320.
- 8 J. TELSER, ed. *Paramagnetic Resonance of Metallobiomolecules*, (American Chemical Society, Washington D.C., 2003). Chapter X, X-Ray Magnetic Circular Dichroism – A Primer for Chemists, S. P. CRAMER.
- 9 M. V. ALDRICH, J. L. GARDEA-TORRESDEY, J. R. PERALTA-VIDEA, J. G. PARSONS, Uptake and Resuction of Cr(VI) to Cr(III) by mesquite (Prosopis spp.): chromate-plant interaction in hydroponics and solid media studied using XAS, *Environ. Sci. Technol.* 37, 1859 (2003).
- 10 JORGE L. GARDEA-TORRESDEY, EDUARDO GOMEZ, JOSE R. PERALTA-VIDEA, JASON G. PARSONS, HORACIO TROIANI, MIGUEL JOSE-YACAMAN, Alfalfa Sprouts: A Natural Source for the Synthesis of Silver Nanoparticles, *Langmuir* 19, 1357 (2003).
- 11 J. GOULON, A. ROGALEV, G. GOUJON, Ch. GAUTHIER, E. MOGUILINE, A. SOLE, S. FEITR, F. WHIHELM, N. JAOUEN, Ch. GOULON-GINET, P. DRESSLER, P. ROHR, M.-O. LAMPERT, R. HENCK, Advanced detection systems for X-ray fluorescence excitation spectroscopy, *J. Synchro. Rad.* 12, 57 (2005).
- 12 S. ROUX, B. GARCIA, J.-L. BRIDOT, M. SALOME, C. MARQUETTE, L. LEMELLE, P. GILLET, L. BLUM, Pascal Perriat, Olivier Tillement, Synthesis, characterization of dihydroliipoic acid capped gold nanoparticles, and functionalization by the electroluminescent luminol, *Langmuir* 21, 2526 (2005).
- 13 CHALLA S. S. R. KUMAR, C. LEUSCHNER, E. E. DOOMES, L. HENRY, M. JUBAN, J. HORMES, Efficacy of lytic peptide-bound magnetite nanoparticles in destroying breast cancer cells, *J. Nanosci. Nanotechnol.* 4, 245 (2004).
- 14 FRANK DE GROOT, High-resolution X-ray emission and X-ray absorption spectroscopy, *Chem. Rev.* 101, 1779 (2001).
- 15 JOACHIM STÖHR, *NEXAFS Spectroscopy*. (Springer-Verlag, Berlin Heidelberg, 1992).
- 16 <http://www.cxro.lbl.gov/opticalconstants/>
- 17 F. Kh. GEI'MUKHANOV, L. N.

- MAZALOV, A. V. KONTRATENKO, A theory of vibrational structure in the X-ray spectra of molecules, *Chem. Phys. Lett.* 46, 133 (1977).
- 18 F. Kh. GEL'MUKHANOV, H. ÅGREN, Resonant inelastic X-ray scattering with symmetry-selective excitation, *Phys. Rev. A* 49, 4378 (1994).
- 19 F. Kh. GEL'MUKHANOV, H. ÅGREN, Channel interference in resonance elastic X-ray scattering, *Phys. Rev. A* 50, 1129 (1994).
- 20 Y. LUO, H. ÅGREN, F. Kh. GEL'MUKHANOV, Symmetry assignments of occupied and unoccupied molecular orbitals through spectra of polarized resonance inelastic X-ray scattering, *J. Phys. B: At. Mol. Phys.* 27, 4169 (1994).
- 21 K. HAMALAINEN, D. P. SIDDONS, J. B. HASTINGS, L. E. BERMAN, Elimination of the inner-shell lifetime broadening in X-ray-absorption spectroscopy, *Phys. Rev. Lett.* 67, 2850 (1991).
- 22 K. HAMALAINEN, C. C. KAO, J. B. HASTINGS, D. P. SIDDONS, L. E. BERMAN, V. STOJANOFF, S. P. CRAMER, Spin-dependent X-ray absorption of MnO and MnF<sub>2</sub>, *Phys. Rev. B* 46, 14274 (1992).
- 23 S. M. BUTORIN, J.-H. GUO, M. MAGNUSON, P. KUIPER, J. NORDGREN, Low-energy *d-d* excitations in MnO studied by resonant X-ray fluorescence spectroscopy, *Phys. Rev. B* 54, 4405 (1996).
- 24 P. KUIPER, J.-H. GUO, C. SÄTHE, L.-C. DUDA, J. NORDGREN, J. J. M. POTHUIZEN, F. M. F. DE GROOT, G. A. SAWATZKY, Resonant X-ray Raman spectra of Cu *dd* excitations in Sr<sub>2</sub>CuO<sub>2</sub>Cl<sub>2</sub>, *Phys. Rev. Lett.* 80, 5204 (1998).
- 25 Y. MA, N. WASSDAHL, P. SKYTT, J.-H. GUO, J. NORDGREN, P. D. JOHNSON, J.-E. RUBENSSON, T. BÖSKE, W. EBERHARDT, S. D. KEVAN, Soft-X-ray resonant inelastic scattering at the C K edge of diamond, *Phys. Rev. Lett.* 69, 2598 (1992).
- 26 Y. MA, P. SKYTT, N. WASSDAHL, P. GLANS, D. C. MANCINI, J.-H. GUO, J. NORDGREN, Core excitons and vibronic coupling in diamond and graphite, *Phys. Rev. Lett.* 71, 3725 (1993).
- 27 J. A. CARLISLE, E. L. SHIRLEY, E. A. HUDSON, L. J. TERMINELLO, T. A. CALCOTT, J. J. JIA, D. L. EDERER, R. C. C. PERERA, F. J. HIMPSEL, Probing the graphite band structure with resonant soft-X-ray fluorescence, *Phys. Rev. Lett.* 74, 1234 (1995).
- 28 J. NORDGREN, N. WASSDAHL, Soft X-ray fluorescence spectroscopy using tunable synchrotron radiation, *J. Electron Spectrosc. Relat. Phenom.* 72, 273 (1995).
- 29 E. J. NORDGREN, Soft X-ray emission spectroscopy in the nineties, *J. Electron Spectrosc. Relat. Phenom.* 78, 25 (1996).
- 30 J. NORDGREN, P. GLANS, K. GUNNELIN, J.-H. GUO, P. SKYTT, C. SÄTHE, N. WASSDAHL, Resonant soft X-ray fluorescence spectra of molecules, *Appl. Phys. A* 65, 97 (1997).
- 31 J.-H. GUO, S. M. BUTORIN, N. WASSDAHL, P. SKYTT, J. NORDGREN, Y. MA, Electronic structure of La<sub>2-x</sub>Sr<sub>x</sub>CuO<sub>4</sub> studied by soft-X-ray-fluorescence spectroscopy with tunable excitation, *Phys. Rev. B* 49, 1376 (1994).
- 32 P. SKYTT, P. GLANS, J.-H. GUO, K. GUNNELIN, C. SÄTHE, J. NORDGREN, F. Kh. GEL'MUKHANOV, A. CESAR, H. ÅGREN, Quenching of symmetry breaking in resonant inelastic X-ray scattering by detuned excitation, *Phys. Rev. Lett.* 77, 5035 (1996).
- 33 M. NYBERG, YI LUO, L. QIAN, J.-E. RUBENSSON, C. SÄTHE, D. DING, J.-H. GUO, T. KÄÄMBRE, J. NORDGREN, Bond formation in titanium fulleride compounds studied through X-ray emission spectroscopy, *Phys. Rev. B* 63, 115117 (2001).
- 34 J.-H. GUO, J. NORDGREN, Resonant C K $\alpha$  X-ray emission of some carbon allotropes and organic compounds, *J. Electron Spectrosc. Relat. Phenom.* 110–111, 105–134 (2000).
- 35 S. M. BUTORIN, Resonant inelastic X-ray scattering as a probe of optical scale excitations in strongly electron-correlated systems: quasi-localized view, *J. Electron Spectrosc. Relat. Phenom.* 110–111, 213–233 (2000).



- 36 S. M. BUTORIN, J.-H. GUO, N. WASSDAHL, J. E. NORDGREN, Tunable-excitation soft X-ray fluorescence spectroscopy of high-Tc superconductors: an inequivalent-site seeing story, *J. Electron Spectrosc. Relat. Phenom.* 110–111, 235–273 (2000).
- 37 A. KOTANI, S. SHIN, Resonant inelastic X-ray scattering spectra for electrons in solids, *Rev. Mod. Phys.* 73, 203 (2001).
- 38 T. WARWICK, P. HEIMANN, D. MOSSISSIAN, W. MCKINNEY, H. PADMORE, Performance of a high resolution, high flux density SGM undulator beamline at the ALS, *Rev. Sci. Instrum.* 66, 2037 (1995).
- 39 J.-H. GUO, N. WASSDAHL, P. SKYTT, S. M. BUTORIN, L.-C. DUDA, C. J. ENGLUND, J. NORDGREN, End station for polarization and excitation energy selective soft X-ray fluorescence spectroscopy, *Rev. Sci. Instrum.* 66, 1561 (1995).
- 40 P. SKYTT, P. GLANS, D. C. MANCINI, J.-H. GUO, N. WASSDAHL, J. NORDGREN, Y. MA, Angle-resolved soft-X-ray fluorescence and absorption study of graphite, *Phys. Rev. B* 50, 10457 (1994).
- 41 Allotropic figures are downloaded from <http://cnst.rice.edu/pics.html>.
- 42 Silson Ltd, JBJ Business Park, Northampton Road, Blisworth, Northampton, NN7 3DW, England. (Email: peter.anastasi@silson.com).
- 43 A. H. NARTEN, H. A. LEVY, Liquid water: molecular correlation functions from X-ray diffraction, *J. Chem. Phys.* 55, 2263 (1971).
- 44 A. H. NARTEN, Liquid water: atom pair correlation functions from neutron and X-ray diffraction, *J. Chem. Phys.* 56, 5681 (1972).
- 45 F. H. STILLINGER, Water revisited, *Science* 209, 451 (1980).
- 46 S. MYNENI, Y. LUO, L. Å. NÄSLUND, M. CAVALLERI, L. OJAMÄE, OGASAWARA, A. PELMENSCHIKOV, Ph. WERNET, P. VÄTERLEIN, C. HESKE, Z. HUSSAIN, L. G. M. PETERSSON, A. NILSSON, Spectroscopic probing of local hydrogen-bonding structures in liquid water, *J. Phys. Condensed Matter* 14, L213 (2002).
- 47 T. YAMAGUCHI, S. SHIBUYA, S. SUGA, S. SHIN, Inner-core excitation spectra of transition-metal compounds: II. *p-d* absorption spectra, *J. Phys. C* 15, 2641 (1982).
- 48 B. T. THOLE, G. VAN DER LAAN, P. H. BUTLER, Spin-mixed ground state of Fe phthalocyanine and the temperature-dependent branching ratio in X-ray absorption spectroscopy, *Chem. Phys. Lett.* 149, 295 (1988).
- 49 G. VAN DER LAAN, B. T. THOLE, G. A. SAWATZKY, M. VERDAGUER, Multiplet structure in the  $L_{2,3}$  X-ray-absorption spectra: A fingerprint for high- and low-spin  $Ni^{2+}$  compounds, *Phys. Rev. B* 37, 6587 (1988).
- 50 F. M. F. DE GROOT, J. C. FUGGLE, B. T. THOLE, G. A. SAWATZKY,  $L_{2,3}$  X-ray-absorption edges of d0 compounds:  $K^+$ ,  $Ca^{2+}$ ,  $Sc^{3+}$ , and  $Ti^{4+}$  in  $O_h$  (octahedral) symmetry, *Phys. Rev. B* 41, 928 (1990).
- 51 F. M. F. DE GROOT, J. C. FUGGLE, B. T. THOLE, G. A. SAWATZKY,  $2p$  X-ray absorption of  $3d$  transition-metal compounds: An atomic multiplet description including the crystal field, *Phys. Rev. B* 42, 5459 (1990).
- 52 C. CARTIER DIT MOULIN, P. RUDOLF, A.-M. FLANK, C. T. CHEN, Spin transition evidenced by soft X-ray absorption spectroscopy, *J. Phys. Chem.* 96, 6196 (1992).
- 53 J.-H. GUO, H. WANG, S. CRAMER, Resonant Soft X-ray Emission Spectroscopy of Some Ni Complexes, in preparation (2005).
- 54 N. SMITH, Science with Soft X Rays, *Physics Today*, January, 29 (2001).
- 55 L. PAVESI, E. BUZANEVA, ed., *Frontier of Nano-Optoelectronic Systems*, (Kluwer Academic Publishers, Netherlands, 2000). Soft X-ray spectroscopy as a probe of the electronic structure of nanostructured solids, S. EISEBITT and W. EBERHARDT, p. 347–362.
- 56 J. GUO, Synchrotron radiation, soft-X-ray spectroscopy and nanomaterials, *Int. J. Nanotechnol.* 1–2, 193 (2004).
- 57 T. VOSSMEYER, G. RECK, B. SCHULZ, L. KATSIKAS, H. WELLER, Double-layer superlattice structure built up of  $Cd_{32}S_{14}(SCH_2CH(OH)CH_3)_{36}\cdot 4H_2O$

- clusters, *J. Am. Chem. Soc.* 117, 12881 (1995).
- 58 T. VOSSMEYER, G. RECK, L. KATSIKAS, E. T. K. HAUPT, B. SCHULZ, H. WELLER, A double diamond superlattice built up of  $\text{Cd}_{17}\text{S}_4(\text{SCH}_2\text{CH}_2\text{OH})_{26}$  clusters, *Science* 267, 1476 (1995).
- 59 T. VOSSMEYER, G. RECK, L. KATSIKAS, E. T. K. HAUPT, B. SCHULZ, H. WELLER, A new three dimensional crystal structure of a cadmium thiolate, *Inorg. Chem.* 34, 4926 (1995).
- 60 J. LÜNINGA, J. ROCKENBERGER, S. EISEBITT, J.-E. RUBENSSON, A. KARL, A. KORNOWSKI, H. WELLER, W. EBERHARDT, Soft X-ray spectroscopy of single sized CdS nanocrystals: size confinement and electronic structure, *Solid State Commun.* 112, 5 (1999).
- 61 T. VAN BUUREN, L. N. DINH, L. L. CHASE, W. J. SIEKHAUS, L. J. TERMINELLO, Changes in the electronic properties of Si nanocrystals as a function of particle size, *Phys. Rev. Lett.* 80, 3803 (1998).
- 62 K. S. HAMAD, R. ROTH, J. ROCKENBERGER, T. VAN BUUREN, A. P. ALIVISATOS, Structural disorder in colloidal InAs and CdSe nanocrystals observed by X-ray absorption near-edge spectroscopy, *Phys. Rev. Lett.* 83, 3474 (1999).
- 63 J.-Y. RATY, GIULIA GALLI, C. BOSTEDT, T. VAN BUUREN, L. J. TERMINELLO, Quantum confinement and fullerene-like surface reconstructions in nanodiamonds, *Phys. Rev. Lett.* 90, 37401 (2003).
- 64 T. VAN BUUREN, T. TIEDJE, S. N. PATITSAS, W. WEYDANZ, Effect of thermal annealing on the conduction- and valence-band quantum shifts in porous silicon, *Phys. Rev. B* 50, 2719 (1994).
- 65 R. L. ZIMMERMAN, D. ILA, E. K. WILLIAMS, B. GASIC, A. ELSAMADICY, A. L. EVELYN, D. B. POKER, D. K. HENSLEY, D. J. LARKIN, Gold, silver and copper nanocrystal formation in SiC by MeV implantation, *Nucl. Instrum. Meth. B* 166/167, 892 (2000).
- 66 H. FUKUZAWA, H. YUASA, S. HASHIMOTO, K. KOI, H. IWASAKI, M. TAKAGISHI, Y. TANAKA, M. SAHASHI, MR ratio enhancement by NOL current-confined-path structures in CPP spin valves, *IEEE, Trans. Magn.* 40, 2236 (2004).
- 67 P. L. HANSEN, J. B. WAGNER, S. HELVEG, J. R. ROSTRUP-NIELSEN, B. S. CLAUSEN, H. TOPSE, Atom-resolved imaging of dynamic shape changes in supported copper nanocrystals, *Science* 295, 2053 (2002).
- 68 K. NISHIMORI, H. TOKUTAKA, S. NAKANISHI, S. KISHIDA, N. ISHIHARA, Off-Angle SiC(0001) Surface and Cu/SiC Interface Reaction, *Jpn. J. Appl. Phys. Lett.* 28, L1345 (1989).
- 69 Z. AN, A. OHI, M. HIRAI, M. KUSAKA, M. IWAMI, Study of the reaction at Cu/3CPSiC interface, *Surf. Sci.* 493, 182 (2001).
- 70 Z. AN, M. HIRAI, M. KUSAKA, T. SAITOH, M. IWAMI, Analysis of nanostructure formation using photon/electron spectroscopies: Cu on SiC substrates, *Jpn. J. Appl. Phys. Part 1* 40/3B, 1927 (2001).
- 71 I. DONTAS, S. LADAS, S. KENNOU, Study of the early stages of Cu/6HPSiC(000-1) interface formation, *Diamond Relat. Mater.* 12, 1209 (2003).
- 72 D. W. SHIN, S. X. WANG, A. MARSHALL, W. KIMURA, C. L. DONG, A. AUGUSTSSON, J.-H. GUO, Growth and characterization of copper nanoclusters embedded in SiC matrix, *Thin Solid Films* 473, 267 (2005).
- 73 H. H. HSIEH, Y. K. CHANG, W. F. PONG, J. Y. PIEH, P. K. TSENG, T. K. SHAM, I. COULTHARD, S. J. NAFTEL, J. F. LEE, S. C. CHUNG, K. L. TSANG, Electronic structure of Ni-Cu alloys: The *d*-electron charge distribution, *Phys. Rev. B* 57, 15204 (1998).
- 74 S. SHIONOYA, W. M. YEN, eds. *Phosphor Handbook*, (CRC Press, Boca Raton, FL, 1999), p. 255.
- 75 J. NAUSE, S. GANESAN, B. NEMETH, V. MUNNE, A. VALENCIA, P. KEISEL, H. MORKOC, D. LOOK, From sunscreen and diaper ointment to wide band gap optoelectronics: ZnO-based homoepitaxial device technology, *III-Vs Rev.* 12, 28 (1999).
- 76 M. W. SHIN, R. J. TREW, GaN

- MESFETs for high-power and high-temperature microwave applications, *Electron. Lett.* 31, 498 (1995).
- 77 F. HAMDANI, A. E. BOTCHKAREV, H. TANG, W. KIM, H. MORKOC, Effect of buffer layer and substrate surface polarity on the growth by molecular beam epitaxy of GaN and ZnO, *Appl. Phys. Lett.* 71, 3111 (1997).
- 78 T. DETCHPROHM, K. HIRAMATSU, H. AMANO, I. AKASAKI, Hydride vapor phase epitaxial growth of a high quality GaN film using a ZnO buffer layer, *Appl. Phys. Lett.* 61, 2688 (1992).
- 79 R. D. VISPUTE, V. TALYANSKY, S. CHOOPUN, R. P. SHARMA, T. VENKATESAN, M. HE, X. TANG, J. B. HALPERN, M. G. SPENCER, Y. X. LI, L. G. SALAMANCA-RIBA, A. A. ILIADIS, K. A. JONES, Heteroepitaxy of ZnO on GaN and its implications for fabrication of hybrid optoelectronic devices, *Appl. Phys. Lett.* 73, 348 (1998).
- 80 A. OHTOMO, M. KAWASAKI, T. KOIDA, H. KOINUMA, Y. SAKURAI, Y. YOSHIDA, M. SUMIYA, S. FUKE, T. YASUDA, Y. SEGAWA, Double heterostructure based on ZnO and  $Mg_xZn_{1-x}O$ , *Mater. Sci. Forum* 264, 1463 (1998).
- 81 P. SHARMA, A. GUPTA, K. V. RAO, F. J. OWENS, R. SHARMA, R. AHUJA, J. M. OSORIO GUILLEN, B. JOHANSSON, G. A. GEHRING, Ferromagnetism above room temperature in bulk and transparent thin films of Mn-doped ZnO, *Nat. Mater.* 2, 673 (2003).
- 82 Y. K. CHANG, H. H. HSIEH, W. F. PONG, M.-H. TSAI, F. Z. CHIEN, P. K. TSENG, L. C. CHEN, T. Y. WANG, K. H. CHEN, D. M. BHUSARI, J. R. YANG, S. T. LIN, Quantum confinement effect in diamond nanocrystals studied by X-ray-absorption spectroscopy, *Phys. Rev. Lett.* 82, 5377 (1999).
- 83 C. L. DONG, C. PERSSON, L. VAYSSIERES, A. AUGUSTSSON, T. SCHMITT, M. MATTESINI, R. AHUJA, C. L. CHANG, J.-H. GUO, Electronic structure of nanostructured ZnO from X-ray absorption and emission spectroscopy and the local density approximation, *Phys. Rev. B* 70, 195325 (2004).
- 84 J.-H. GUO, L. VAYSSIERES, C. PERSSON, R. AHUJA, B. JOHANSSON, J. NORDGREN, Polarization-dependent soft-X-ray absorption of highly oriented ZnO microrod arrays, *J. Phys. Condens. Matter* 14, 6969 (2002).
- 85 K. GUNNELIN, P. GLANS, P. SKYTT, J.-H. GUO, J. NORDGREN, H. ÅGREN, Assigning X-ray absorption spectra by means of soft-X-ray emission spectroscopy, *Phys. Rev. A* 57, 864 (1998).
- 86 N. HELLGREN, J.-H. GUO, C. SÄTHE, A. AGUI, J. NORDGREN, Y. LUO, H. ÅGREN, J.-E. SUNDGREN, Nitrogen bonding structure in carbon nitride thin films studied by soft X-ray spectroscopy, *Appl. Phys. Lett.* 79, 4348 (2001).
- 87 J.-H. GUO, Y. LUO, A. AUGUSTSSON, J.-E. RUBENSSON, C. SÄTHE, H. ÅGREN, H. SIEGBAHN, J. NORDGREN, X-ray emission spectroscopy of hydrogen bonding and electronic structure of liquid water, *Phys. Rev. Lett.* 89, 137402 (2002).
- 88 J.-H. GUO, Y. LUO, A. AUGUSTSSON, S. KASHTANOV, J.-E. RUBENSSON, D. SHUH, H. ÅGREN, J. NORDGREN, The molecular structure of alcohol-water mixtures, *Phys. Rev. Lett.* 93, 157401 (2003).
- 89 A. AUGUSTSSON, S. KASHTANOV, Y. LUO, J.-H. GUO, C.-L. DONG, C. L. CHANG, H. ÅGREN, J.-E. RUBENSSON, J. NORDGREN, Conformations and core-excitation dynamics in liquid water, in preparation (2005).
- 90 M. J. FRISCH et al., Gaussian 98, 1998, Gaussian Inc., Pittsburgh PA, 1998. See <http://www.gaussian.com>.
- 91 T. PRIVALOV, F. GEL'MUKHANOV, H. ÅGREN, Role of relaxation and time-dependent formation of X-ray spectra, *Phys. Rev. B* 64, 165 115 (2001).
- 92 T. HELGAKER et al., Dalton, An ab initio electronic structure program, Release 1.0 (1997). See <http://www.kjemi.uio.no/software/dalton/dalton.html>.
- 93 D. T. RICHENS, *The Chemistry of Aqua Ions*. (Wiley, Chichester, 1997).
- 94 W. KAIM, B. SCHWEDERSKI, *Bioinorganic Chemistry: Inorganic*

- Elements in the Chemistry of Life: An Introduction and Guide.* (Wiley, Chichester, 1994).
- 95 H. OHTAKI, T. RADNAI, Structure and dynamics of hydrated ions, *Chem. Rev.* 93, 1157 (1993).
- 96 E. BRAUN, Y. EICHEN, U. SIVAN, G. BEN-YOSEPH, DNA-templated assembly and electrode attachment of a conducting silver wire, *Nature (London)* 391, 775 (1998).
- 97 P. J. DE PABLO, F. MORENO-HERRERO, J. COLCHERO, J. GÓMEZ HERRERO, P. HERRERO, A. M. BARÓ, P. ORDEJÓN, J. M. SOLER, E. ARTACHO, Absence of dc-Conductivity in  $\lambda$ -DNA, *Phys. Rev. Lett.* 85, 4992 (2000).
- 98 D. PORATH, A. BEZRYADIN, S. DE VRIES, C. DEKKER, Direct measurement of electrical transport through DNA molecules, *Nature (London)* 403, 635 (2000).
- 99 K.-H. YOO, D. H. HA, J.-O. LEE, J. W. PARK, J. KIM, J. J. KIM, H.-Y. LEE, T. KAWAI, H. Y. CHOI, Electrical conduction through Poly(dA)-Poly(dT) and Poly(dG)-Poly(dC) DNA molecules, *Phys. Rev. Lett.* 87, 198 102 (2001).
- 100 H. FINK, C. SCHÖNENBERGER, Electrical conduction through DNA molecules, *Nature (London)* 398, 407 (1999).
- 101 A. YU. KASUMOV, M. KOCIK, S. GUÉRON, B. REULET, V. T. VOLKOV, D. V. KLINOV, H. BOUCHIAT, Proximity-induced superconductivity in DNA, *Science* 291, 280 (2001).
- 102 H. S. KATO, M. FURUKAWA, M. KAWAI, M. TANIGUCHI, T. KAWAI, T. HATSUI, N. KOSUGI, Electronic structure of bases in DNA duplexes characterized by resonant photoemission spectroscopy near the Fermi level, *Phys. Rev. Lett.* 93, 86403 (2004).
- 103 J.-H. GUO, S. KASHTANOV, J. SÖDERSTRÖM, H. CHENG, P.-A. GLANS, T. LEARMONTH, K. SMITH, J. NORDGREN, Y. LUO, The electronic structure of Bases in DNA Duplexes studied by soft-X-ray absorption and emission spectroscopy, in preparation (2005).
- 104 N. HELLGREN, J. GUO, Y. LUO, C. SÄTHE, A. A. S. KASHTANOV, J. NORDGREN, H. ÅGREN, J.-E. SUNDGREN, Electronic structure of carbon nitride thin films studied by X-ray spectroscopy techniques, *Thin Solid Films* 471, 19 (2005).

## 9

# Some New Advances and Challenges in Biological and Biomedical Materials Characterization

*Filip Braet, Lilian Soon, Thomas F. Kelly, David J. Larson, and  
Simon P. Ringer*

### 9.1 Introduction

The three sections of this chapter identify new and recent advances as well as challenges in the microscopy of selected biological and biomedical materials using (1) atom probe tomography, (2) atomic force microscopy and (3) cryo-transmission electron microscopy.

Section 9.2 describes the fundamental principles of atom probe tomography, a time-of-flight mass spectroscopy method that exploits the quantum-mechanical tunneling phenomenon that occurs when many conducting solids are raised to very high electric fields. The resultant ionization associated with the tunneling liberates an ion with a specific mass-to-charge ratio that is subsequently accelerated towards a position-sensing detector. Time-of-flight data is transformed into mass-to-charge ratios in a way that provides identification of the individual isotopes of the elements, as well as molecular species. This section also provides the results of recent applications of atom probe to biomedical materials that are used as human-prosthetic devices and components. These applications demonstrate the core competency of the atom probe technique in analyzing three-dimensional (3D) atomic-level compositional information of materials. Probing interfaces using compositional profiles, identifying the presence, or otherwise, of chemical heterogeneities within phases and measuring the local composition near and within nanoscale precipitate phases are key areas where this technique can contribute to the science and technology of biomedical materials. Applications data are also presented for biological materials after a brief review of work to date. This section concludes with some of the challenges facing the field in terms of sample preparation issues, specimen stability issues under high fields and the challenge of interpreting mass spectra from complex molecules.

Sections 9.3 and 9.4 provide a correlative microscopy context for fenestral studies in the hepatic endothelial cell model. Section 9.3 focuses on atomic force methods and Section 9.4 focuses on electron microscopy approaches and data. The result is a new insight into the morpho-function and structure of the liver sieve.

## 9.2

### Modern Atom Probe Tomography: Principles, Applications in Biomaterials and Potential Applications for Biology

#### 9.2.1

##### The Need for an Ideal Microscope

The length scale at which human knowledge and endeavor operates is directly linked to the scale of our microscopies. Though people have long been able to conjecture about the nature and significance of length scales beyond our ability to observe, be they microscopical or astronomical, practical technologies always require observations and measurements that can transform such conjecture into fact. Examples include the postulation of the very concept of the atom [1], the potential for a double helix DNA structure [2] and the notion that crystal defects (dislocations) were the origin of the discrepancy between the observed and theoretical strength of metals and alloys [3]. As we enter the century of nanotechnology, the need for the “ideal” microscope will grow because the critical dimensions of materials and devices trend towards the truly atomic. Modern atom probe microscopy is coming closer to this ideal than any other microscopy. In this section, the modern instrument is reviewed and some of the significant challenges and potential opportunities of the technique and its application in both biomaterials and in biological science are discussed.

##### 9.2.1.1 Field Ion Microscopy and the Modern Atom Probe Instrument

As introduced above, Greek philosophers were, interestingly, able to hypothesize the existence of atoms, but it took 25 centuries before they were first observed by humans with, in fact, a field ion microscope (FIM) pioneered by Erwin Müller [4]. The technique is mentioned here because of its potential significance in imaging molecules and the close relation to the atom probe technique. Miller et al. [5] provide a detailed explanation of the FIM, and Panitz [6] has provided a detailed review of the technique as applied to molecules. Essentially, a high positive potential is applied as a standing voltage to a cryogenically cooled specimen-tip in a controlled ultra-high vacuum (UHV) chamber. An inert gas such as He, Ne or Ar is leaked into the chamber to fill a back pressure of  $\sim 10^{-3}$  Pa and, in the presence of the applied field, the gas atoms are field polarized and so are gradually drawn towards the tip. The gas atoms eventually make contact with the specimen tip and migrate, though a series of collisions towards positions of low potential energy. Once these gas atoms have lost most of their kinetic energy and are trapped by the very high field of the specimen, they may be field ionized by electron tunneling processes. Such ions are repelled from the tip and projected in an almost radial direction towards a fluorescent screen. Field ionization occurs preferentially at the atomic steps and terrace positions and so forms a stereographic-like projection image of the material surface with atomic resolution. A tungsten (W) FIM image is

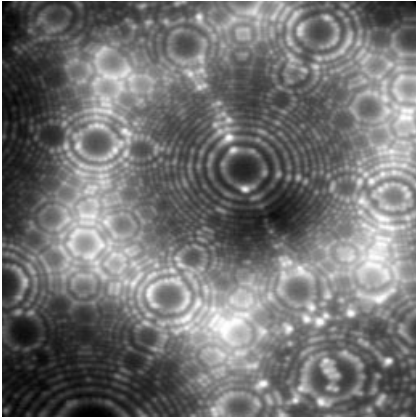


**Fig. 9.1.** Field ion micrograph of W atoms imaged using Ne. Each bright dot is an individual atom.

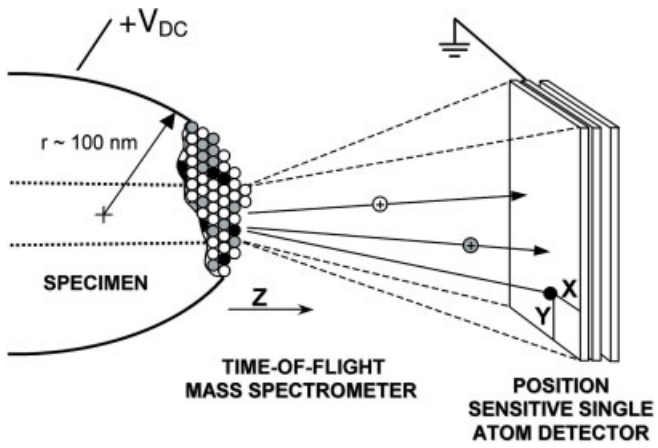
provided in Fig. 9.1, where each bright dot corresponds to an individual atom. The concentric circles around low-index crystallographic poles correspond to the outer atoms of atomic planes, one atop another.

Figure 9.2(a) is a simplified schematic of the atom probe principle, showing how the application of a positive high voltage pulse,  $V_{\text{pulse}}$ , to a sharp needle-shaped specimen under a standing positive voltage,  $V_{\text{dc}}$ , can raise the local field on the sample so as to render some of the surface atoms as ions, through the quantum mechanical process of electron tunneling. This field-induced ionization of the surface atoms results in their “evaporation” from the specimen along trajectories close to normal to the tangent to the sample surface. These ions eventually strike a single-ion detector and this *stop* signal is compared to the *start* of the initial pulse to generate an ion flight-time. The mass-to-charge ( $m/n$ ) ratio of the ion is determined by equating the potential energy of the ion just prior to field evaporation to the kinetic energy just after, such that

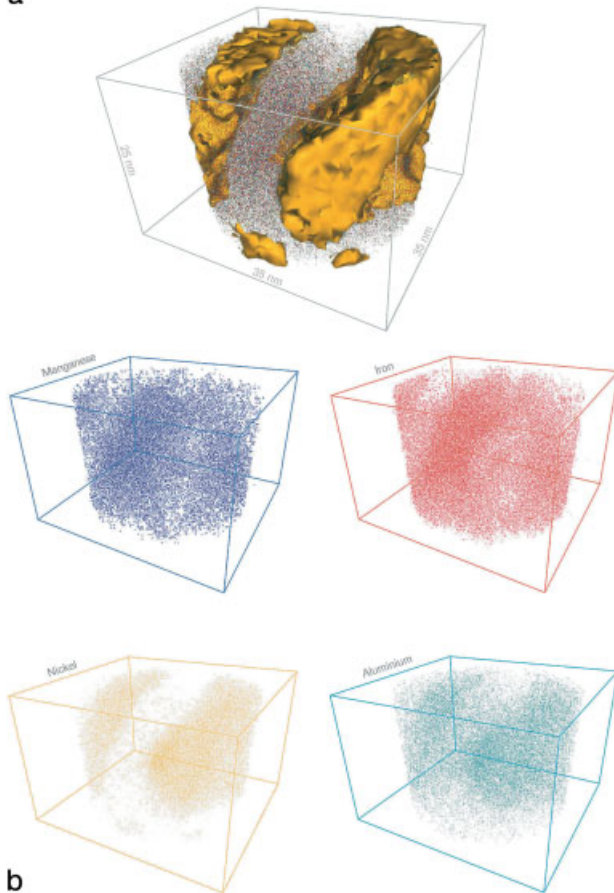
$$neV = \frac{1}{2}mv^2$$

**Fig. 9.2.** (a) Atom probe principle: individual atoms are field ionized from the sample surface and accelerated towards a detector. Time-of-flight mass spectroscopy is used to identify the atom species and this is correlated to spatial orientation ( $x, y$ ) by the position-sensitive detector. Tomographic data is generated when the 2D image slices are

correctly reconstructed along  $z$ . (b) Atom probe tomography from a spinodal alloy, revealing a spinodal interface with separate Fe- and Ni-rich regions [7, 8]. Isoconcentrational surfaces for 10 at% Ni are charted in the upper 3D atom map ( $30 \times 30 \times 25$  nm). Blue = Mn, red = Fe, yellow = Ni and teal = Al.



a



b



and so

$$\frac{m}{n} = KV \frac{t^2}{d^2} \quad (1)$$

where  $n$  is the number of electrons removed in the field ionization,  $e$  is the elementary charge,  $V$  is the total electric field on the specimen,  $m$  and  $v$  are the mass and velocity of the ion, respectively,  $d$  is the flight distance from the specimen to the detector and  $K$  is a constant. The identity of the ion is then correlated spatially to the hit-position ( $x, y$ ) on the detector and the depth  $z$  within the sample. Figure 9.2(b) is an example of 3D atom probe tomographic data. Within this analysis volume is a spinodal interface decorated with solute atoms of Fe, Ni, Mn and Al, revealing nanoscale phase separation into the Fe-rich and Ni-rich phases. In this way, researchers can view a tomographic reconstruction of materials, since 3D images of the internal structure are generated by the reconstruction along  $z$  of thousands of 2D  $x$ - $y$  slices. This approach to nanostructural analysis has taken microscopy and materials characterization into a new era and is opening up new directions for materials research and development [5–9]. Excellent texts on the workings, instrumentation, historical development and applications of conventional 1D and 3D atom probe techniques are available [5, 6, 9].

The current state-of-the art of atom probe employs a local electrode ahead of the specimen to mediate extraction of ions (Fig. 9.3). Figure 9.3(a) is drawn so as to emphasize that the sample may be an individual needle or tip or may be composed of an array of many tips (Fig. 9.3b). Such arrays have the advantage that they can present geometrically similar tips to the local electrode and so effectively normalize many of the stochastic field evaporation issues. Arrays will also allow statistical evaluations of structures in the same way that cryo-electron microscopy enables single-particle image analysis, via thousands of images of randomly-oriented individual protein molecules. Figure 9.3(b) is a schematic that emphasizes this approach and conveys the importance of the proximity or “local” effects of the counter electrode with the specimen [10–12]: hence the name, local electrode atom probe or LEAP®. Here, the cryogenically cooled needle-shaped specimen, Fig. 9.3(c) – or planar array specimen (Fig. 9.3d) – is mounted on a nanopositioning stage and pointed towards a funnel-shaped local electrode. The specimen is aligned to the aperture of the local electrode with the aid of a pair of orthogonal long-range optical microscopes. The initially detected field evaporated ions are used to finalize the alignment.

For a specimen positioned close to a local electrode aperture of  $\sim 20$ – $30 \mu\text{m}$  in diameter, the field at the specimen apex is very high even at relatively low voltages. It is viable to build suitable pulsers (2 ns fwhm pulse with amplitudes of up to 2000 V) that can operate at pulse repetition rates of up to 200 kHz. This rate is two orders of magnitude faster than previous instruments. In addition, the ions that are field evaporated from the specimen reach the local electrode in a significantly shorter time (tens of picoseconds) and thereafter are shielded from time-varying fields as the  $V_{\text{pulse}}$  decays. This eliminates the major source of energy defi-

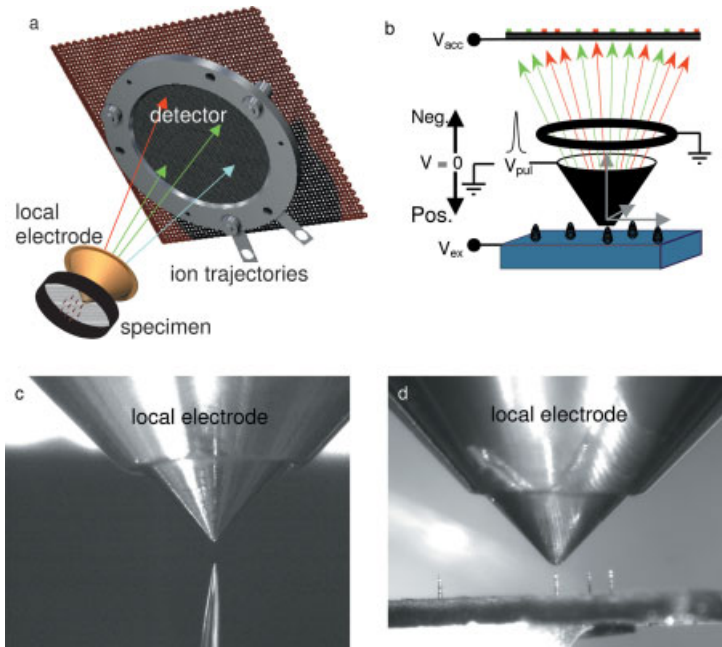


**Fig. 9.3.** (a) LEAP<sup>TM</sup> principle: individual atoms are field ionized from the sample surface and accelerated towards a detector. (b) The local electrode enhances the field on the specimen, permitting lower applied voltages  $V_{ex}$  and  $V_{pulse}$ , which allow a much higher pulsing frequency. In addition, having a small  $V_{ex}$  and a large  $V_{accel}$  effects an acceleration of the ions through the local electrode that provides for highly sensitive mass separation (high mass resolution time-of-flight mass

spectroscopy). The time-of-flight mass spectroscopy is used to identify the atom species and this is correlated to spatial orientation ( $x$ ,  $y$ ) by the position-sensitive detector. Tomographic data is generated when the 2D image slices are correctly reconstructed along  $z$ . (c) Close-up optical image of a sharpened tip in the vicinity of the local electrode. (d) Demonstration application of an array of tips.

cits. Therefore, the local electrode atom probe can achieve high mass resolution (better than  $\Delta m/m$  of 1/500) over a 1.5 steradian field of view. This mass resolution is sufficient to separate the individual isotopes of all the elements. The wide field of view permits up to  $\sim 10^8$  atoms to be collected routinely from a specimen.

To position correctly ions at these higher pulse rates, a novel crossed delay line (CDL) detector is used. The CDL detector features a pair of delay lines, placed perpendicularly, in place of the phosphor screen or anodes used in the other variants of 3DAP. When electrons from the microchannel plate strike the delay line at some location, they travel to each end of the line. The position of the ion's impact is therefore determined from the arrival times measured at each end of the delay line. These times are converted into true  $x$  and  $y$  distances on the detector. A crossed delay line detector and high speed digital timing system that provides

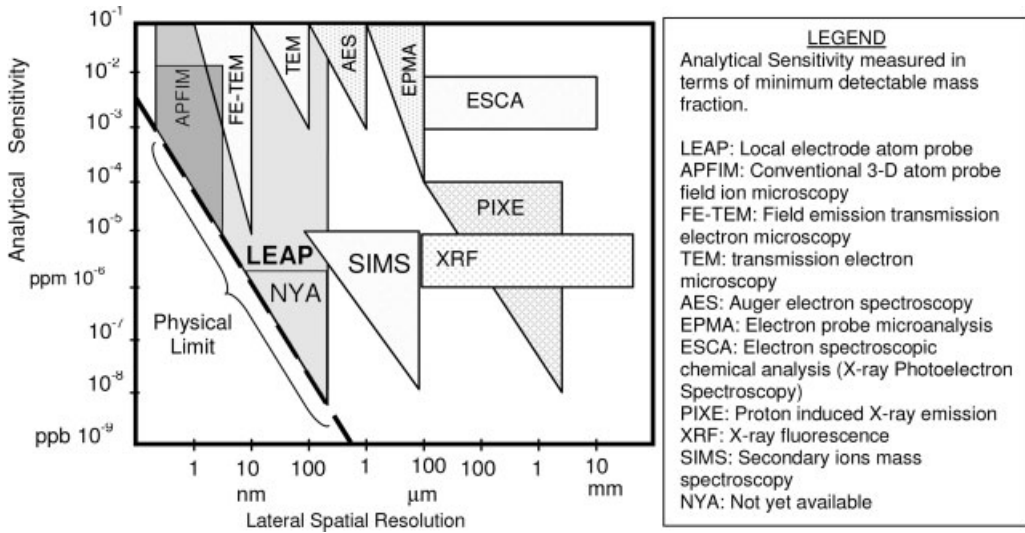


Fig. 9.4. Potential for a modern atom probe (LEAP) to be combined with other analytical techniques so as to probe the structure and, in particular, chemical composition of materials.

600 × 600 pixels at rates up to 25 000 ions per second has been developed by Imago.

The new features – local electrode, high speed pulser and high speed single atom sensitive CDL detector – are incorporated in a commercial instrument [12] that achieves the high-performance gains originally envisioned for this geometry. The Imago LEAP® microscope can collect data at sustained rates of up to 20 000 correctly positioned ions per second (one million ions per minute). These developments have dramatically improved the overall performance of atom probe tomography for a wide range of materials. In particular, the characterization of planar specimens in addition to traditional needle-shaped specimens is now practical [13].

Figure 9.4 is a survey of a range of analytical microscopy techniques and shows the analytical capacity of the modern atom probe in the context of related techniques. The strengths of the LEAP are clear and the potential for solving problems over various length-scales by a correlative microscopy approach, such as is advocated in this chapter, is very high. There are interesting opportunities and significant challenges for those working in biological science and technology and some of these will now be introduced.

#### 9.2.1.2 Applications in Biomaterials

As other chapters in this volume affirm, the term “biomaterials” is very broad. One important class of biomaterials is those used as implants that replace or augment components of the human body such as tissue, organs, skeletal or the like. The most common examples include the use of medical grade austenitic 316 stainless

steels, which are used as implanted spinal fixation devices, bone screws, cardiovascular and neurological stents, and as critical components of minimally invasive surgical devices. These applications are made possible due to suitable physical and mechanical properties, good corrosion resistance in biological environments, reasonable biocompatibility, and ease of manufacture [14].

These steels are thermomechanically processed so as to ensure the thermodynamic stability of the austenite ( $\gamma$ ) phase at high temperatures and to suppress the formation of martensite at lower (near ambient) temperatures. The typical composition of these alloys is (wt%): Fe, <0.03 C, 16–18.5 Cr, 10–14 Ni, 2–3 Mo, <2 Mn, <1 Si, <0.045 P, <0.03 S and they possess yield strengths of at least 170 MPa. Elements that stabilize the  $\gamma$ -phase include Ni, Mn and N, usually in some combination [15, 16]. The relatively common allergy affects attributed to Ni and the potential for carcinogenic effects associated with this element have driven the development of Ni-free 316 grade stainless steel. In more general terms, the conventional theory of Cr-oxide passivation applies to these steels and is the main protection mechanism that results in their high corrosion resistance. However, other corrosion processes, such as crevice corrosion and pitting, can be very damaging in biomaterials applications. Therefore, much of the design of composition and thermomechanical processing for these alloys aims to mitigate or overcome these damage mechanisms by minimizing precipitation of a second phase that is electrochemically active with respect to the  $\gamma$ -phase. This requires suppression of precipitation of carbides, nitrides, or even body-centered-cubic  $\alpha$  or  $\delta$  ferrite. This is effected by lowering the amount of C and N that remains in the  $\gamma$ -phase. This, in turn, can be achieved by alloying with strong carbo-nitride forming elements such as Ti and Nb, so that these elements preferentially scavenge the interstitials and form highly stable, electrochemically inactive carbo-nitride M (CN) precipitates. This approach is particularly effective in avoiding the deleterious process of sensitization where Cr-based carbo-nitrides nucleate heterogeneously on  $\gamma/\gamma$  grain boundaries and so deplete the capacity of Cr to protect the surface of the component (resulting in severe local attack). Therefore, the electrochemical activity of the grain boundaries must be kept low and it is essential to minimize any localized changes in alloy chemistry that can produce electrochemical interaction with body fluids.

This is a formidable materials requirement and effectively requires the control of nanostructure and composition of the material. For example, the surface of such alloys will be especially critical since biological responses and corrosion occur at the material–environment interface. In addition, precise control of the chemistry and structure of buried interfaces such as grain boundaries and other chemical heterogeneities is critically important. Such characterization requires microscopy in three-dimensions (3D) at high resolution: reference to the foregoing discussion and to Fig. 9.2(b) reveals that the modern atom probe can provide key insights into these issues.

Figure 9.5(a–d) presents recent research on both the nanostructure of surfaces and buried interfaces in medical device 316L stainless steel. Figure 9.5(a) and (b) show a 3D atom map reconstruction of a 316L grade, chemically modified at Med-

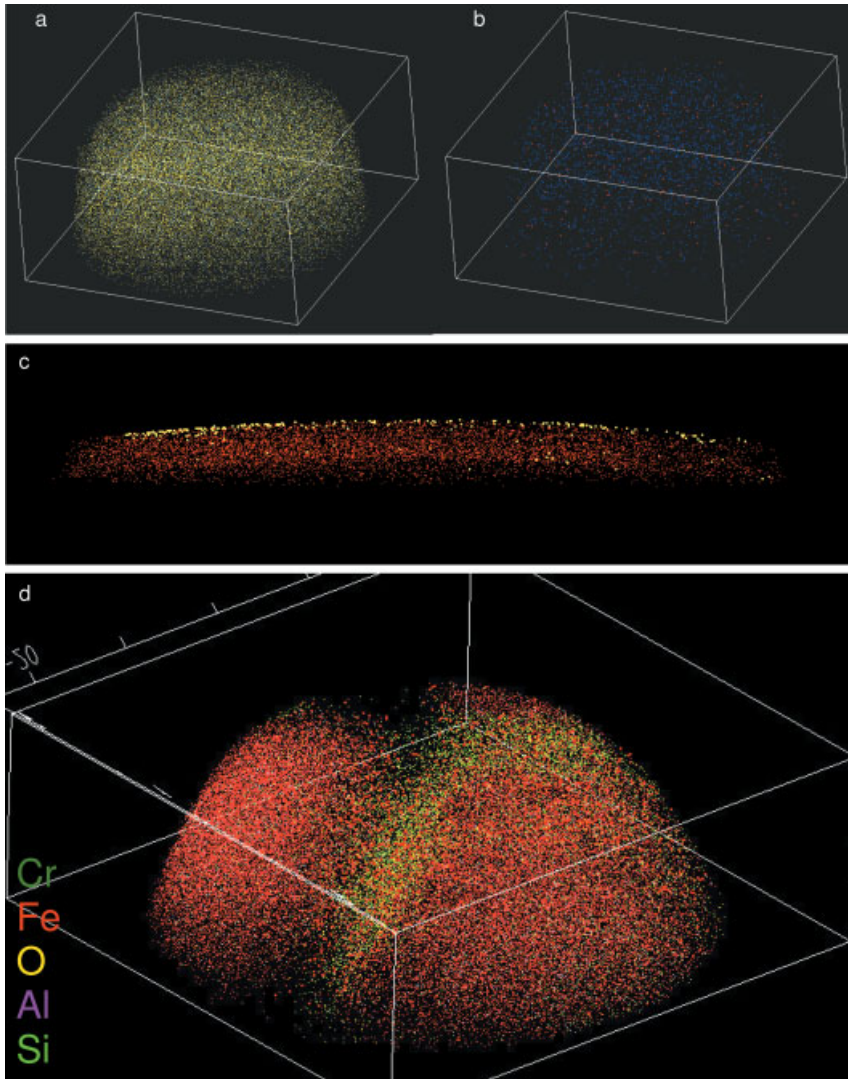


**Fig. 9.5.** (a, b) Bulk structure of a Medtronic 316L specimen. Each color-coded dot shows the location of an individual atom. Cr is in yellow, Ni in light blue, Si in blue and Cu in red. Image is 20 nm wide and 10 nm high. (c) Near-surface structure of a 316L wire specimen; Cr in red, oxygen in gold. The image is about 25 nm wide. (d) Region that is thought to be a grain boundary triple point in a 316L wire specimen, showing clear enrichment of O.

tronic [14]. To determine the bulk structure of the Medtronic sheet specimens, segments were cut from the interior volume and polished. These were then mounted in holders, electropolished with 10% perchloric acid in acetic acid at 8–20 V DC to a nominal end radius of 20–50 nm, to provide the necessary needle-shape for atom

probe analysis. The bulk atomic composition and structure of this material was then studied with a LEAP microscope. All anticipated elements were located in the specimen, including Fe, Cr, Ni, C, P, Si, Mo, and Cu, with a uniform elemental distribution and without precipitates or grain boundaries in the analyzed regions. This is highly significant because of the relation between biocompatibility, related performance as a biomaterial and the uniformity of the solid solution  $\gamma$ -phase. Figure 9.5(c) provides 3D atom map reconstructions from a commercial 316L grade procured as wire 0.38 mm in diameter, 1/8 hard, from a commodity supplier. The commodity 316L wires were electropolished as described above. During electropolishing and subsequent air exposure, a thin oxide naturally forms on the surface of the sharpened wire. This oxide was used to develop specimen preparation methods for analysis of oxides on medical-grade 316L samples. Notably, there is relatively little atom probe work examining metal oxide surfaces with atom probe microscopes. To prepare the surface oxide for LEAP analysis, a  $\sim 15$  nm thick capping layer of Ni was applied to the sharpened wire specimens by argon (Ar) ion sputtering to protect the surface during the first stages of atom probe analysis. Analyses demonstrated that such coatings provided some preservation of the oxide layer, enabling the imaging of the oxide–stainless steel interface, Fig. 9.5(c). Note the presence of oxygen (O) at the stainless steel surface (for clarity, Ni atoms species are not shown in this projection). Although the volume and total number of atoms in this image are limited, there is a clear oxygen-rich layer on the specimen surface.

Significantly, this data gives access to the body fluid/oxide/ $\gamma$ -phase interface chemistry, since it is the first 20–50 nm of the biomaterial (in this case 316L stainless steel) over which ionic mass transport occurs and is almost always mediated via an oxide layer. An understanding of surface roughness, oxide thickness and elemental compositional profiles near these oxides is essential for thorough characterization of biomaterials interfaces. In Fig. 9.5(c), the oxide is seen to be  $\sim 1$  nm thick, and [O] atoms are also observed deeper into the  $\gamma$ -phase. Roughness indices on both sides of the oxide interface can be developed, as can concentration profiles.

Figure 9.5(d) provides a 3D atom map reconstruction from the commodity 316L wire-stock, revealing a significant oxide-based chemical heterogeneity within the analyzed volume, which is thought to be a grain boundary. Such chemical heterogeneities at the grain boundaries of biomaterials are very serious for reasons explained above, since they have the potential to increase the potency of these sites for heterogeneous nucleation, leading ultimately to sensitization of the steel. Moreover, depending on the proximity of these O/Cr/Si enriched boundaries to the body fluids, there is the risk of developing a localized electro-active region that leaches toxic elements into the body and stimulates a corrosion reaction. The regions of 316L such as presented in Fig. 9.5(d) are inferior to those such as in Fig. 9.5(a) and (b), where the degree of chemical homogeneity is much higher.

### 9.2.1.3 Applications and Challenges for Biological Science

It is almost 50 years since Erwin Müller first observed the flicker of individual atoms on a phosphor (P) screen from field ion microscopy, along with his work shortly after in pioneering the atom probe to select individual atoms from the

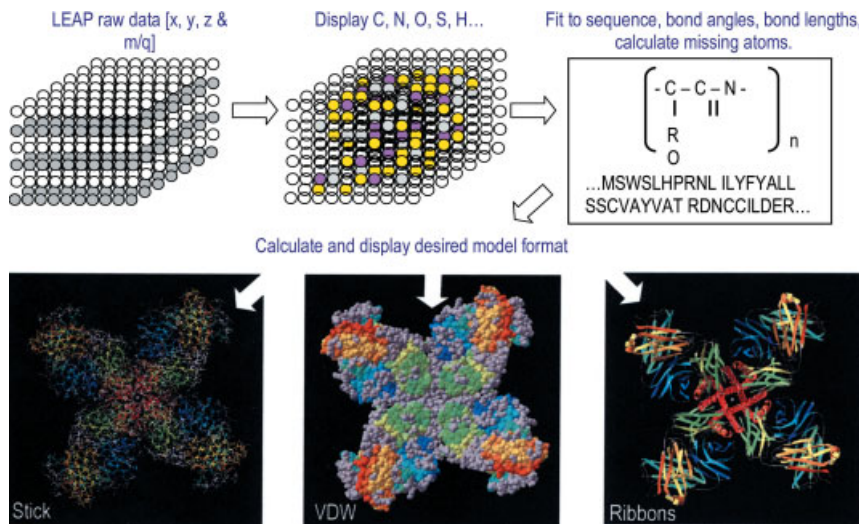


**Fig. 9.6.** Idealized atom probe experiment of biological material. The LEAP acquires positional ( $x$ ,  $y$  &  $z$ ) and atom identity data, via  $m/q$ . Specific individual atoms are identified and displayed, and an informatics-like algorithm would fit and identify the molecular structure, which could be displayed in the appropriate format.

FIM image and analyze them [17]. Today, we see the core-competence of the atom probe in analyzing multi-million atom data-sets and representing a premium high-resolution analytical technique for materials metrology and characterization. The examples provided in Figs. 9.2 and 9.5 demonstrate this.

Having discussed the capacity of the atom probe to analyze individual atoms in 3D in the inorganic context of biomaterials, it is appropriate to also examine the capacity of this instrument to solve complex problems in organic biological materials. From the preceding discussion on the analysis of alloy biomaterials, where individual atoms can be mapped in 3D, lattice-plane by lattice-plane, the biologist might be tempted to view the instrument as something akin to an atom-level confocal microscope. The possibility of reconstructing molecular conformation in 3D, such as is performed, albeit with some experimental difficulty using cryo-electron microscopy (see, e.g., Ref. [18]), is highly attractive. Questions related to the structure of proteins and macromolecular complexes, proteins at interfaces, virus structures, ligand binding, protein membrane structure and so on represent seminal questions in modern structural biology. The concept here is outlined in Fig. 9.6. In this experiment, individual light elements are displayed and mathematical filters applied to the data that display selected atoms (C, N, O, S, H etc.) with specific coordination in terms of angles, density or simple proximity [19]. These could then be fitted to the molecular sequence and ultimately display complete biological structures [20]. This approach is not unlike the computational methods applied to X-ray synchrotron and cryo-electron microscopy data and, in particular, to the computational data-fitting that has recently become so successful in nuclear magnetic

**Tab. 9.1.** Biological specimen preparation methods and relevance to atom probe.

<i>Method</i>	<i>Comment for atom probe</i>
Chemical fixation	Not suitable for all biological samples
Dry specimens	Use of low-tension solvents, freeze drying
Embedded and crosslinked samples	Offer possibilities for stabilizing molecules under the electric field
Provide electrical conductivity	Metal coatings, OsO <sub>4</sub> , RuO <sub>4</sub> or conductive embedding agents can assist the molecules to field ionize via electrically pulsed atom probe

resonance (NMR). However, there are access, sample preparation and cost issues with these types of characterization, which require significant equipment installations, and the experiments are non-trivial. The idealized atom probe experiment described above requires the following research and development in at least three specific areas.

**Sample Fabrication Issues** Biomolecules need to be stabilized for imaging under high vacuum conditions, since these conditions are far from their natural state. Fortunately, electron microscopists have developed numerous technologies to address this issue, many of which seem relevant here. Indeed, such has been the recent progress in biological specimen preparation that this is no longer the limiting factor for achieving high resolution. In fact, destructive electron-beam specimen interactions are more limiting.

Table 9.1 lists various biological specimen preparation methods and mentions some of the issues that require attention in assessing these methods for atom probe. Certainly, with respect to stabilizing the specimens for UHV, there seem to be excellent prospects of adapting a method for atom probe tips or tip arrays.

**Stability of the Specimen under High Electric Fields** The response of biomolecules to the very high applied electric fields that occur with an atom probe is one of the most complex and problematic aspects of these experiments. However, Panitz has examined Poly(GC) DNA using FIM [21] and Machlin has published FIM images that are reported to come from tRNA [22]. Other work has appeared on synthetic polymers, including polypyrrole [23] and octacyanophthalocyanine metal complexes [24]. These pioneering experiments have shown that the stability of the molecules under the field can be resolution-limiting. Figure 9.7(a) provides schematic images that describe the preparation of a specimen of human immunoglobulin G via FIM: a W tip is Au-coated before application of the IgG. This was chemically fixed and examined in the FIM (Fig. 9.7b shows the results). Individual bright dots are seen in the images that may correlate to individual molecules or groups thereof. Progressive evaporation of the sample revealed systematic changes in the FIM image until, eventually, the IgG material was all evaporated and the substrate Au became visible (Fig. 9.7b, final two images). These FIM images are



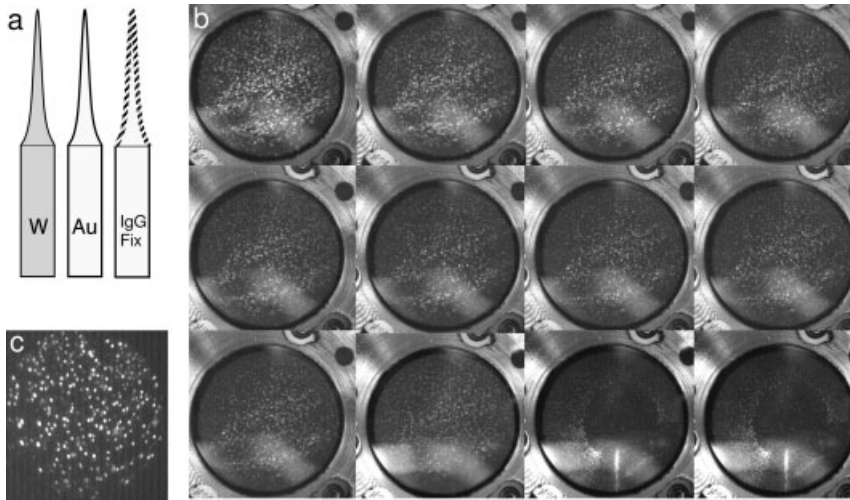


**Fig. 9.7.** (a) Schematic showing the three stages of specimen preparation for a human IgG specimen: a polished W tip is sputter-coated with a few nm of Au, offering excellent bonding for the IgG-fixed molecule. (b) Series of FIM images recorded with Ne imaging gas.

The series show self-consistent and uniform contrast: progressive evaporation of what are thought to be the biomolecules continues until the substrate Au is revealed. (c) Ne FIM image of amorphized alloy. The uniform contrast of amorphous alloys provides similar contrast.

very similar to the image (Fig. 9.7c) to a Cu-Co multi-layer film device amorphized by a Ga focused ion beam [25]. In this respect, amorphous inorganic materials represent closer analogies to organic molecular samples than their crystalline counter-parts and the so comparison is of interest. Whereas the bright contrast in the image in Fig. 9.7(c) arises, almost certainly, from individual atoms on the alloy surface, a contrast theory for the series of images in Fig. 9.7(b) is not available: bright spots may be individual atoms or could be particular functional groups or the domains thereof. There are numerous other artifacts that could, in principle, also explain the contrast observed in these early experiments. Nevertheless, the systematic character of the images suggests that there is some local equilibrium at the surface of these tips and that we are observing molecular species. It is unlikely that the images are from Au metal or any oxide thereof. The challenge is to reproduce such images and to understand them in terms of the primitive molecular structure of the specimen. The recent discussion by Panitz [26] also supports the notion that stable images may be formed from biomolecules in FIM. As powerful as the atom probe technique is, it is suggested that a significantly better understanding of FIM images such as those provided in Fig. 9.7 is required and that stable FIM imaging may be a necessary precursor to sound atom probe analysis.

**Mode of Field Evaporation: Notion of the Molecular Probe** As described earlier, atom probe experiments usually involve the application of energy pulses to a sam-

ple under an applied standing voltage so that the surface atoms are field evaporated as ions that can be identified by time-of-flight mass spectroscopy. The energy is usually transmitted via a high voltage pulse although it can be transmitted via a laser to effect, e.g., a thermally-induced evaporation process. In any case, there are at least three modalities by which one can imagine the field evaporation of a biomolecule may occur.

*Type I* field evaporation involves, predominantly, the liberation of individual atoms from the molecule surface. In this case, the mass spectra are closely similar to those obtained for inorganic materials.

*Type II* field evaporation involves, predominantly, the liberation of molecular fragments. An enormous range of molecular bonds may be sheared from the sample, providing C, C–C, C–C–C, C–H, C–H–H etc. In this case, the mass spectra will be very complex. Clearly, a major challenge in developing atom probe science to solve problems in biology is to provide a system for understanding the mass spectra.

*Type III* field evaporation involves predominantly the liberation of rational molecular fragments, as recognizable functional groups. In this scenario, an enormous range of molecular bonds may also be sheared from the sample. However, conceivably, the proposed *molecular probe* could apply look-up tables of known molecular species that correspond to specific mass-charge ratios, in the same way that *atom probe* uses the charge state of the isotope abundances to develop range files that window signals from the individual elements in the specimen.

Clearly, the exact effect of the energy pulse on biomolecules is a fertile area for new research. Such efforts will need to use both modeling and experiments and also utilize the rapidly developing knowledge-base arising from the success of other spectroscopic techniques, particularly SIMS and nanoSIMS, XPS and MALDI (matrix-assisted laser desorption/ionization). Figure 9.8 provides one representation of these techniques, where the different modalities of signal generation are emphasized. Whereas the high-energy ion beam in SIMS generates variable fragments of the initial molecular specimen (closer to type II field evaporation), XPS causes an emission of characteristics electrons, and MALDI causes ionization of whole molecules (closer to type III). We expect an atom probe to cause field evaporation across all three types listed above.

Figure 9.9 is the mass spectrum for a C<sub>18</sub> self-assembled-monolayer (SAM). Here, the raw number of counts of detector-events is plotted as a function of  $m/q$ . The mass spectrum is “indexed” by attributing the known or expected molecular fragments to the significant peaks. In the same way that we have presented indicative early-stage FIM data in Fig. 9.7 from quite new experiments that demonstrate the challenges in comprehensive interpretation of FIM images, Fig. 9.9 reveals the opportunities and challenges for molecular probing of these sorts of samples. An encouraging aspect of Fig. 9.9 is the clear success of the instrument in probing the molecular species of the specimen, since discrete peaks of organic matter are identified in the mass spectra, as opposed to Au peaks etc. Prima facie, most of the peaks can be plausibly identified and labels are provided. Moreover, the data can be reconstructed in 3D (Fig. 9.9c). Here, the outer surface is displayed in the 3D

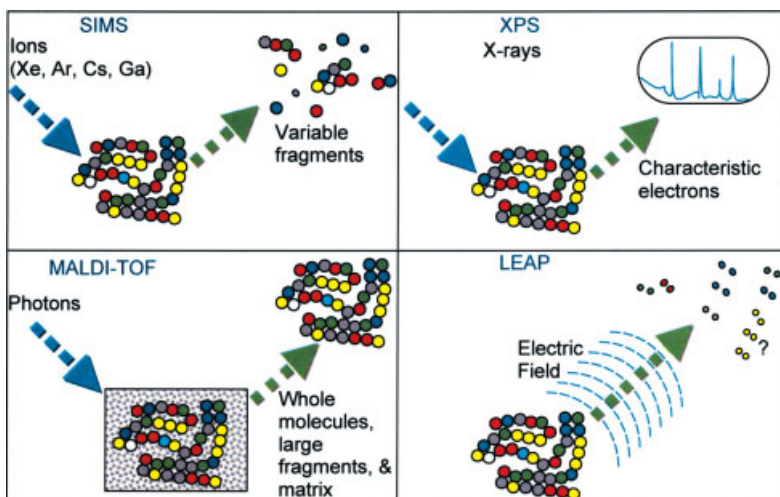


**Fig. 9.8.** Schematic representation of signal modalities from a selection of molecular analysis techniques. The SIMS technique is a mixture of type II and type III evaporation, liberating variable fragments of the original molecule. XPS uses characteristic electrons. MALDI (matrix-assisted laser desorption/ionization) TOF is capable of ionizing whole molecules.

reconstruction-cube, and the species are clearly located at the surface. As a method of probing biointerfaces, this approach seems promising. However, a key uncertainty in such data, which will require unequivocal resolution, is the specific identity of mass spectra peaks. In Fig. 9.9, for example, we have left a significant peak at  $m/q = 22$  unidentified. Also, the significance of the particular type of molecular species that occur in the mass spectra is uncertain, since certain species clearly evaporate more readily than others. Another important question relates to the effect of molecular size and asymmetric charge distribution on trajectory aberrations. Since the ultimate molecular properties depend on coordination, orientation and bond angles, it is strongly desired that these characteristics are preserved when the molecules hit the position-sensing detector. Nevertheless, the results of initial experimentation with these ideas using the LEAP, taken together with other pioneering work attempting FIM and atom probe of organics referred to here, suggests that, under certain circumstances, biomolecules may be imaged and analyzed using these techniques. Clearly, much experimentation and development remains.

**Future Developments** Figure 9.10 reveals the common range of bond energies, comparing ionic, covalent and the dispersion bond forces. One of the intriguing characteristics of biomolecular atom probe specimens is the way that they can, potentially, present an enormously diverse range of bond energies to the instrument. The fact that the field evaporation process must occur across such a range of inter-atomic or inter-molecular forces would seem to imply that a substantial range of fragmentation will occur in response to the pulse. Figure 9.10 also lists some of

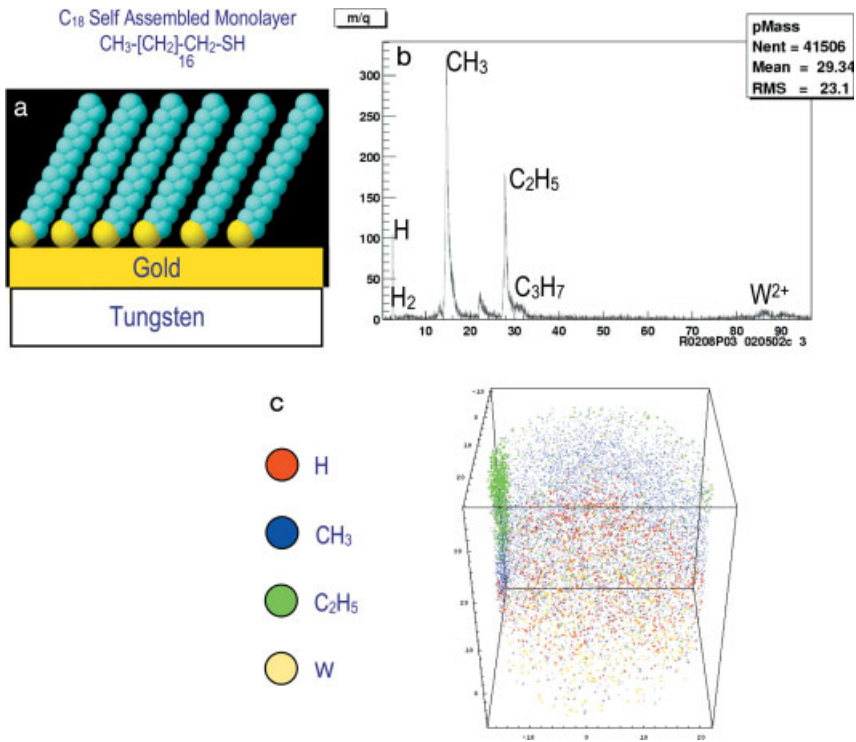


**Fig. 9.9.** (a) Schematic of a  $C_{18}$  self-assembled monolayer chemisorbed on an Au-coated W-tip via the thiol headgroup. (b) A LEAP mass spectrum. (c) 3D atom map reconstructed from the mass spectrum in (b).

the key interatomic bond energies that are so prevalent in biomolecular materials. As shown, the probe pulse must rupture significant interatomic bond energies before individual atoms are ionized and detected as single events on the detector. A theme of developments in this area will be to mitigate the effects of the variety of bond-energies through specimen preparation strategies.

## 9.3

### Atomic Force Microscopy

#### 9.3.1

##### Introduction

In 1986, Binnig et al. [28] revolutionized microscopy through the invention of the atomic force microscope (AFM). Marketable instruments of this new imaging technique began to appear in the five years following its discovery. In the early 1990s,

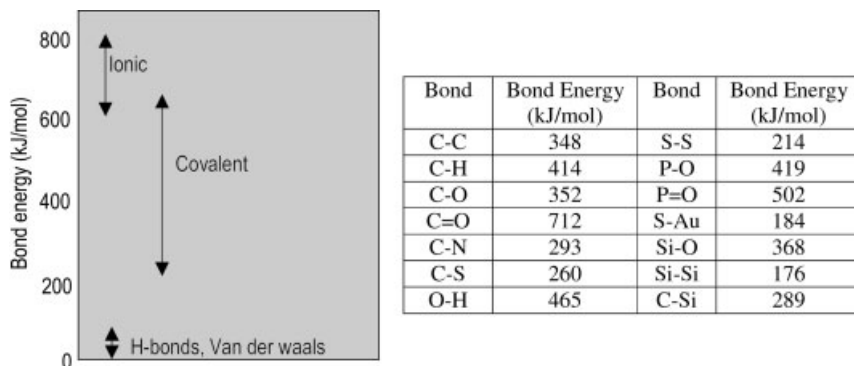


**Fig. 9.10.** Range of bond energies in organic and inorganic materials, together with a table summarizing the more significant interatomic bond energies in organic materials such as biomolecules [27].

Henderson et al. [29] and Radmacher et al. [30] both illustrated the potential of the instrument to image biological preparations in real time under near physiological conditions with nanometer resolution. From then onwards the AFM has fascinated biologists and the number of publications describing biological applications of AFM has grown swiftly [31].

Atomic force microscopy is becoming a valuable tool for determining biological structure and function [32]. It can be operated *in vitro* on live cells without the necessity for further specimen preparation such as fixation or staining [33]. Atomic force microscopy potentially provides for nanometer-scale resolution [34, 35]. Recently, it has been combined with simultaneous confocal laser scanning microscopic imaging [35]. It also can be used to image individual isolated cellular complexes (i.e., proteins, DNA, organelles, etc.) [36]. In addition, biomolecular probing with functionalized tips can be used to generate force versus displacement curves, providing the capability to obtain single-molecule bond-strength information [37]. Furthermore, the elasticity or softness or compliance of biological samples can be assessed [38].

### 9.3.2

#### Instrumentation

A range of materials, methods and notes have appeared with regard to imaging cultured cells with the AFM [39]. In general, maintenance of steady-state culture conditions involves a high degree of thermal stability ( $37 \pm 0.5$  °C), continual renewal of the culture medium (osmolarity of  $\pm 320$  mOsmol per kg-H<sub>2</sub>O) and a neutral pH ( $7.4 \pm 0.3$ ), stabilized by the use of 20 mM HEPES buffer and/or a flow of CO<sub>2</sub> through the AFM cell chamber to maintain a steady-state concentration of 5%. Fluctuations in temperature, osmotic pressure and pH have severe af-

fects on cell viability and structure, making consistent AFM imaging difficult [40]. Commercial liquid cells for studying biological samples under controlled conditions are available, but are only useful for a limited number of special application problems. Therefore, biologists have designed their own set-ups and, consequently, various home-made systems, which differ from laboratory to laboratory, are found when reviewing the literature.

Our AFM studies used (a) the Topometrix Explorer™ TMX equipped with a 100 μm XY/12 μm Z TrueMetrix Linearized Liquid Scanner installed on a Zeiss IM 35 inverted microscope with a home-made XY specimen stage adaptation; and (b) a home-made fluid cell in combination with a heating stage. This design allows positioning of the cantilever in the optical axis of the inverted microscope, movement of the sample via the inverted microscope independently of the AFM, and minimizes cantilever drift by controlling temperature-induced variations. Time-lapse images of living cells in contact [33, 41–43] or non-contact mode [43, 44] have been obtained over 2–3 h, before peripheral parts of the cytoplasm started to detach from the substrate or before cell viability started to decrease as determined by the trypan blue exclusion test [38].

#### 9.3.2.1 Live Cell Imaging

The major advantages of AFM over scanning electron microscopy (SEM) for imaging cells are that no coating and no vacuum are required, electrons are avoided and imaging can be carried out in an aqueous environment. As a result, living cell studies under near physiological conditions can be performed. Evidence for the successful application of AFM for biological imaging comes from abundant studies in the past decade, where the dynamic behavior of living cells at a resolution comparable with SEM has been imaged and analyzed (for reviews see Refs. [31] and [32]). In our set-up, images of living cells in contact mode could be obtained repeatedly over a period of 1 h (Fig. 9.11) and more [33, 43] depending on the cell type used, and at the same time we observed no scanning-induced artifacts such as lateral deformation. Instead, attention-grabbing cell biological processes such as moving membrane sheets at the rim of the cytoplasm of rat hepatocytes could be observed, illustrating lamellipodial activity (Fig. 9.11, 0–60 min). In some instances, prolonged AFM-imaging of cells may result in removal of parts of cells or even cells *in toto* from the substrate due to repeated tip contact (Fig. 9.11, 75 min). Therefore, to assure optimal viability of the cells, scanning of the sample should be carried out for a maximum of 2(–3) hours, after which the sample should be replaced. At the end of the experiment, the viability should be checked routinely with the aid of the trypan blue and/or the propidium iodide test. In our combined AFM-light microscope set-up the overall viability usually drops by ~6% with every hour. In addition, the combined AFM/inverted microscope allows the cell and AFM tip to be seen by the optical microscope at all times during the scanning process. By doing so, the morphology of the cells during AFM imaging can be easily judged and tip-induced alterations such as detachment or removal of the peripheral parts of the cytoplasm can be easily observed. These tip-induced changes are typical morphological signs for the onset of decreased cell viability.

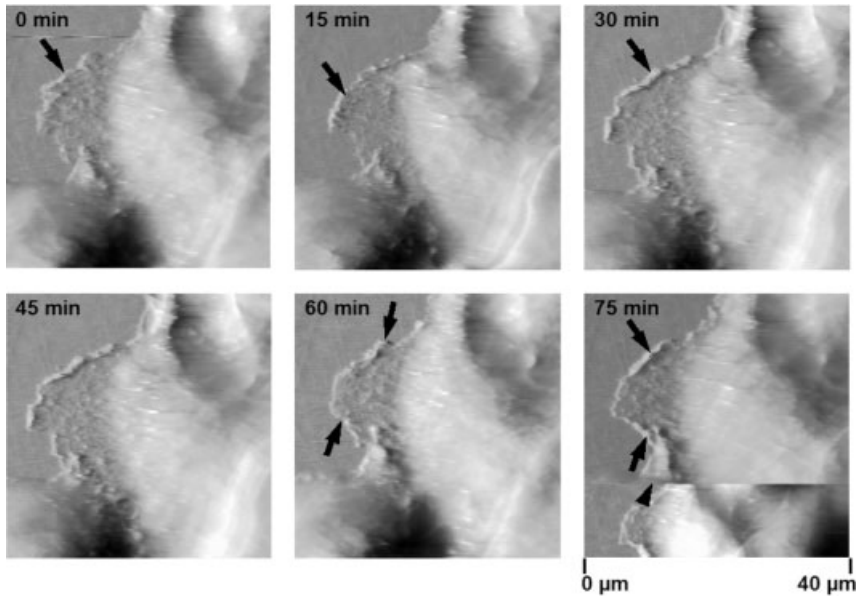
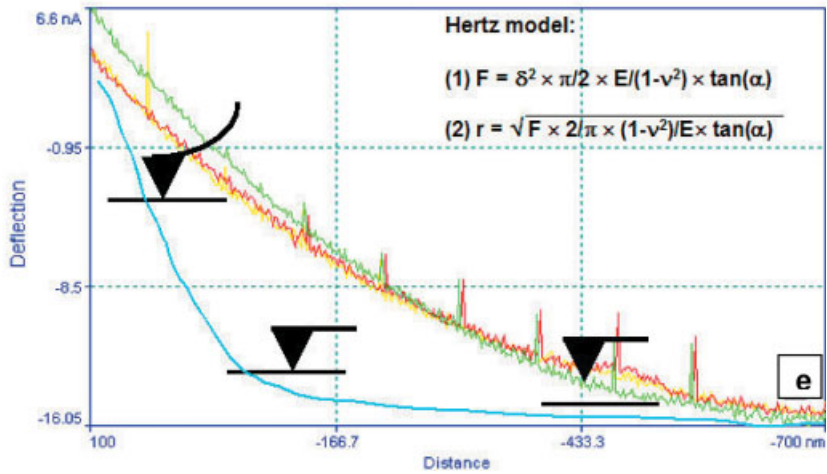
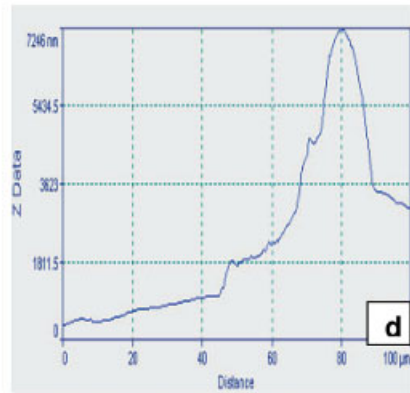
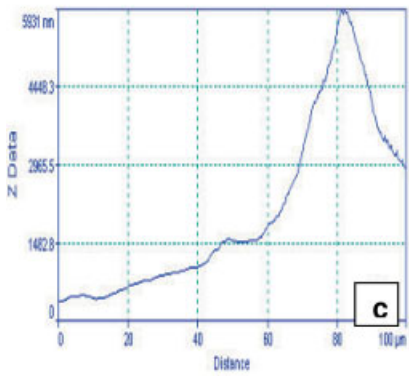
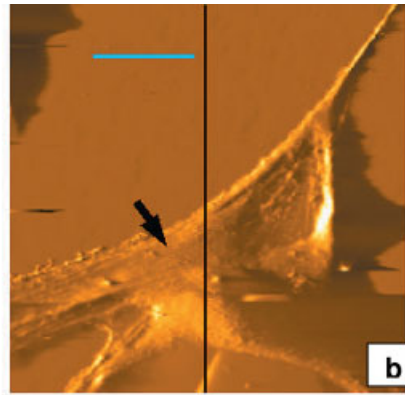
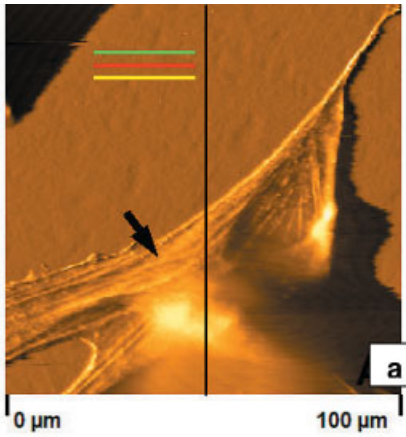


**Fig. 9.11.** Rat liver parenchymal cells. Time-lapse AFM series of moving membrane sheets at the rim of the cytoplasm in living rat liver parenchymal cells (hepatocytes). Arrows denote the lamellipodial activity observed at

the rim of the cytoplasm of the hepatocytes over time. Note that prolonged scanning resulted in artifactual smearing and even removal of cell parts (arrowhead).

The AFM can gather, simultaneously, correlative topology and submembranous structures on the same cell at high resolution [33]. Sample deformation is an important component of the contrast mechanism in the visualization of living cells by AFM, and originates from local variations in stiffness when the tip palpates the cell membrane [29]. The cell stiffness or elasticity is determined mainly by the various organelles lying in the cytoplasm of the cell, and high-resolution imaging of submembranous cell compartments in the past was only possible when cells underwent detergent-extraction, fixation and/or immunocytochemical staining, thereby precluding dynamic studies [38, 40]. Therefore, indirect AFM imaging of organelles underneath the plasma membrane is a powerful tool to probe subcellular dynamics at nanometer resolution in intact living cells without the necessity of further preparative steps. The most prominent submembranous structure that can be probed with the AFM is the cytoskeleton of cells. An example is given in Fig. 9.12(A), illustrating the presence of long actin fibers with a straight outline in rat liver fibroblasts. We previously reported cytoskeletal changes in living rat skin fibroblasts for up to one hour after applying the microfilament-disrupting drug latrunculin A [33]. Interestingly, when cells underwent short fixation with 0.1% glutaraldehyde the morphology of the cell surface changed drastically (Fig. 9.12B); i.e., (i) there was an increase in cell height (Fig. 9.12C versus 12D); (ii) underlying





cytoskeleton structures and clearly depicted cell contours could no longer be observed, even when the imaging force was increased 10-fold; and (iii) images were dominated by topographic information (Fig. 9.12A versus 9.12B). The latter two points can be explained by the fact that the stiffness of the cell membrane is much higher after fixation than the spring constant of the AFM-cantilever used, resulting in less deformation of the membrane around rigid submembranous structures. This is confirmed by the softness (i.e., elasticity) measurements performed on living versus fixed fibroblasts (Fig. 9.12E). The elasticity of those cells, as calculated by the Hertz model, increased  $\sim 12$ -fold, i.e., from 10 kPa for the living cell to more than 120 kPa for the fixed status.

### 9.3.3

#### Summary

Finally, much can be expected from the recent integration of atomic force and confocal fluorescence microscopies in one instrument, combining the high-resolution topographical imaging of probe microscopy with the reliable biomolecular identification capabilities of optical microscopy [35].

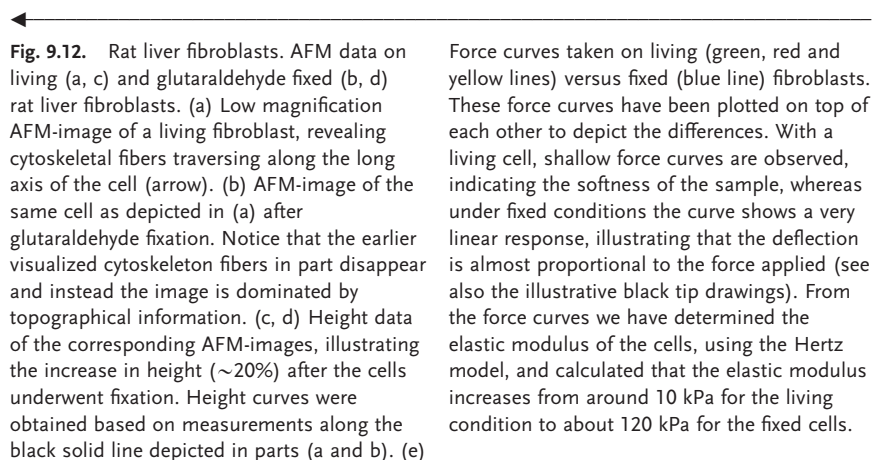
## 9.4

### Cryo-electron Microscopy

#### 9.4.1

##### Introduction

Cryo-electron microscopy has seen an increase in biological applications in the past fifteen years with the advent of significant technical innovation [45]. This microscopy method incorporates both vitrification, a freezing process that subverts



crystalline ice formation, and image acquisition under cryo-conditions. The cryo-fixation process is rapid, of the order of 0.1 ms, which is  $10^4$  times faster than conventional infiltration methods [46, 47], and preserves spatial as well as temporal biological states. In addition, sample preparation methods such as high-pressure freezing allow vitrification of specimens up to 200  $\mu\text{m}$  thick. Significant achievements have also been made in the understanding and technology of freezing thin samples such as hepatic endothelial monolayers that are vulnerable to osmotic and temperature effects, as described in following section.

#### 9.4.2

##### Instrumentation

Chemical fixation, dehydration and drying or embedding/sectioning of cells can induce image artifacts, resulting in different observations when different preparation techniques are applied [48]. In cryo-electron microscopy, living cells are physically fixed by rapid cooling, enabling their study as whole mounts without the necessity of further preparation steps. However, transmission electron microscopy of thin cells *in toto* (whole mount) has long been tried and considered impossible or extremely difficult due to the mass-thickness of the specimen. This view is usually substantiated by failures reported in the literature. Culturing cells as a single layer thick on grids, beam-specimen interaction resulting in specimen damage, and problems associated with cryo-specimen preparation have all been held responsible for this failure, depending on the spirit of the time. Over ten years ago the possibilities of cryo-electron microscopy on whole-mounted cells was discussed. By that time, the isolation and culture of hepatic endothelial cells on electron microscopy grids had become established [49], and cryo-electron microscopy had become an accepted approach for cellular imaging, as supported by the cryo-observations on intact blood platelets [50] and bacteria [51], revealing subcellular details such as organelles, membranous structures and cytoskeleton elements. It was argued, based on preliminary atomic force microscopy data [52], that the thickness of hepatic endothelial cells was of the same dimensional order as blood platelets and bacteria, and thus cryo-electron microscopy imaging could be expected using intermediate voltages. This holds especially for the thin fenestrated areas of cultured hepatic endothelial cells, which are less than 100 nm thick. As a result, electron beam-related problems (damage) or electron optical limitations were not expected. By that time, the development of an automated, computer-controlled vitrification system had begun that ultimately culminated in the Vitrobot<sup>TM</sup> [53–55] and a temperature and humidity controlled glove box in conjunction with a Vitrobot<sup>TM</sup> [55–57].

##### 9.4.2.1 Cryo-electron Microscopy Imaging

The use of a temperature and humidity controlled glove box in conjunction with a Vitrobot<sup>TM</sup> is essential for the manipulation of whole-mount hepatic endothelial cells from culture conditions in preparation for cryo-electron microscopy investigation [56, 57]. The fenestrae and surrounding cytoskeleton elements and different

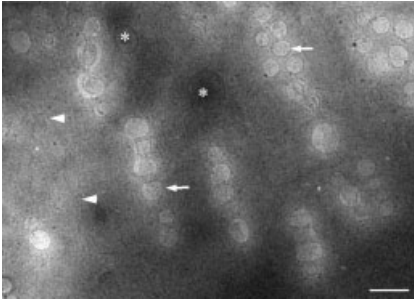


**Fig. 9.13.** High magnification image of the fenestrated cytoplasm of a vitrified hydrated whole-mounted hepatic endothelial cell obtained under controlled sample handling conditions by using a temperature and humidity controlled glove box in combination with the Vitrobot™, as described previously

[35, 36], showing fenestrae and the associated cytoskeleton rings (arrow). Note the cytoskeleton elements (arrowhead) running next to the fenestrae and membrane-bound vesicles (asterisk). Scale bar: 500 nm. (Courtesy of Dr Peter Frederik & Paul Bomans, University of Maastricht, The Netherlands).

membrane-bound organelles are easily observed in these types of cryo-images without the presence of preparation-induced artifactual gaps (Fig. 9.13), indicating that our earlier observations on the fenestrae-associated cytoskeleton are not an artifact introduced by chemical fixation, partial extraction or other preparation procedure [57]. Further improvements in cryo-imaging may be expected when higher accelerating voltages are used (300 instead of 120 kV) in conjunction with electron tomography [45].

#### 9.4.3

#### Summary

Once a biological sample is vitrified correctly the challenge becomes to extract all the available 3D information and in the time-domain. Tomography at the cryo-electron microscopy level can resolve details at a 3D resolution better than 3 nm in a specimen of 100 nm thick, providing a solid basis for tomography as an emerging 3D technology that may greatly contribute to the 3D study of intact cells at the (supra-)molecular level [58].

### 9.5

#### Conclusions

Imaging in biology has seen increasingly improved resolutions over the decades with the advent of new microscopical techniques. Applications of high-resolution microscopy span different sectors, from medical to biotechnology to fundamental-type research; analytical surveys serve as measures of quality control and materials improvement in medical technology; and the nano-world of basic biology bridges

the structure–function relationship at several levels, from macromolecular to cellular and physiological, as seen with the wide use of AFM and cryo-EM. Soon, atomic resolutions from the atom probe will allow better device diagnostics and the generation of new questions and fields in biology appropriate for this new level of analysis. There will also be a continued need for correlative microscopy to develop control measures and for cross-referencing of methodologies from sample preparation to software development for data interpretation and rendering.

## Acknowledgments

The facilities, scientific and technical assistance from staff in the NANO Major National Research Facility at the Electron Microscope Unit, the University of Sydney are gratefully appreciated. We gratefully acknowledge the staff of Imago Scientific Instruments, in particular Mr Tom Kunicki for helpful discussions and insights, and Dr Steve Goodman now at 10H, Inc. Consulting ([www.10htech.com](http://www.10htech.com)) for contributions to experimental data and illustrations. With respect to the cryo-electron microscopy data, the authors gratefully acknowledge the work of Drs Peter Fredrik and Paul Bomans (University of Maastricht, The Netherlands).

## References

- 1 ALLEN, R.E., FURLEY, D. *Studies in Presocratic Philosophy*. Routledge, New York, 1975.
- 2 WATSON, J.D. *The Double Helix: A Personal Account of the Discovery of the Structure of DNA*. Simon & Schuster Adult Publishing Group, 2001.
- 3 HIRTH, J.P., LOTHE, J. *Theory of Dislocations*. Wiley, New York, 1982.
- 4 MÜLLER, E.W., Field ion microscopy. *Science*, 1965, 149, 591.
- 5 MILLER, M.K., CEREZO, A., HETHERINGTON, M.G., SMITH, G.D.W. *Atom Probe Field Ion Microscopy*. Oxford University Press, Oxford, 1996.
- 6 PANITZ, J. Point-projection microscopy of macromolecular contours. *J. Microsc.*, 1982, 125, 3.
- 7 SAXEY, D.W., HANNA, J., ZHENG, R.K., MARCEAU, R.K.W., BAKER, I., RINGER, S.P. Nanonstructural analysis of advanced alloys in a local electrode atom probe. Proceedings of Conference: Microsc. Microanal., Honolulu, Hawaii, USA, Supplement to *J. Microsc. Microanal.*, 2005, 11, 872CD.
- 8 RINGER, S.P., RATINAC, K. On the role of characterisation in the design of interfaces in nanoscale materials technology. *Microsc. Microanal.*, 2004, 10, 324–335.
- 9 MILLER, M.K. *Atom Probe Tomography*. Kluwer Academic/Plenum Press, New York, 2001.
- 10 NISHIKAWA, O., OHTANI, Y., MAEDA, K., WATANABLE, M., TANAKA, K. Development of the scanning atom probe and atomic level analysis. *Mater. Char.* 2000, 44, 29–57.
- 11 KELLY, T.F., LARSON, D.J. Local electrode atom probes. *Mater. Char.* 2000, 44, 59–85.
- 12 KELLY, T.F., GRIBB, T.T., OLSON, J.D. OLTMAN, E., WIENER, S.A., LENZ, D.R., SHEPARD, J.D., MARTENS, R.L., ULFIG, R.M., STRENNEN, E.M., BUNTON, J.H., STRAIT, D.R., KUNICKI, T.C., PAYNE, T. and WATSON, J. Configuration and performance of a local electrode atom probe. *Microsc. Microanal.* 2003, 9, 564–565.

- 13 LARSON, D.J., PETFORD-LONG, A.K., MA, Y.Q., CEREZO, A. Overview No. 138: Information storage materials: nanoscale characterisation by three-dimensional atom probe analysis. *Acta Mater.*, **2004**, *52*, 2847–2862.
- 14 GOODMAN, S.L., MENGELT, T.J., ALI, M., ULFIG, R.M., ISTEPHANOUS, N., KELLY, T.F. Atomic structure and compositional analysis of 316L stainless steel medical device materials with the local electrode atom probe. Proceedings of Conference: Microsc. Microanal., Savannah, Georgia, USA, Supplement. *J. Microsc. Microanal.*, **2004**, *10*, Suppl. 2, 541.
- 15 PEKNER, D., BERNSTEIN, I.M. *Handbook of Stainless Steel*. McGraw-Hill, New York, **1977**.
- 16 See: [www.azom.com](http://www.azom.com).
- 17 MÜLLER, E.W., PANITZ, J.A., MCLANE, S.B. The atom-probe field ion microscope. *Rev. Sci. Instrum.*, **1968**, *39*, 83–86.
- 18 ZHOU, Y., MORAIS-CABRAL, J.H., KAUFMAN, A., MACINNON, R. Chemistry of ion coordination and hydration revealed by a K<sup>+</sup> channel-Fab complex at 2.0 Å resolution. *Nature*, **2001**, *414*, 43–48.
- 19 GUEX, N., PEITSCH, M.C. SWISS-MODEL and the Swiss-PdbViewer: An environment for comparative protein modeling. *Electrophoresis*, **1997**, *18*, 2714–2723.
- 20 UNGER, V.M., KUMAR, N.M., GILULA, N.B., YEAGER, M. Three-dimensional structure of a recombinant gap junction membrane channel. *Science*, **1999**, *283*, 1176–1180.
- 21 PANITZ, J. Point-projection imaging of unstained ferritin clusters. *Ultramicroscopy*, **1982**, *7*, 3.
- 22 MACHLIN, E.S., FREILICH, A., AGRAWAL, D.C., BURTON, J.J., BRIANT, C.L. Field ion microscopy of biomolecules. *J. Microsc.* **1975**, *104*, 127–168.
- 23 MARUYAMA, T., NISHI, T., HASEGAWA, Y., SAKURAI, T. *Interfaces in Polymer, Ceramic and Metal Matrix Composites*. ed.: ISHIDA, M., Elsevier, Amsterdam, **1988**, p. 73.
- 24 IWATSU, F., MORIKAW, H., TERAU, T. FIM of phthalocyanines. *J. Phys.*, **1984**, *45–C9*, 471.
- 25 LARSON, D.J., FOORD, D.T., PETFORD-LONG, A.K., ANTHONY, T.C., ROZDILSKY, I.M., CEREZO, A., SMITH, G.W.D. Focused ion beam milling for atom probe field ion microscopy specimen preparation: Preliminary experiments. *Ultramicroscopy*, **1998**, *75*, 147–159.
- 26 PANITZ, J. In search of the chimera: molecular imaging in the atom-probe. Proceedings of Conference: Microsc. Microanal. Honolulu, Hawaii, USA, Supplement to *J. Microsc. Microanal.*, **2005**, *11*, 92.
- 27 *Handbook of Chemistry and Physics*, 85<sup>th</sup> edition, CRC Press, Boca Raton, FL, **2004–2005**.
- 28 BINNING, G., QUATE, C.F., GERBER, C.H. Atomic force microscope. *Phys. Rev. Lett.* **1986**, *56*, 930–933.
- 29 HENDERSON, E., HAYDON, P.G., SAKAGUCHI, D.S. Actin filament dynamics in living glial cells imaged by atomic force microscopy. *Science*, **1992**, *257*, 1944–1946.
- 30 RADMACHER, M., TILLMAN, R.W., FRITZ, M., GAUB, H.E. From molecules to cells: imaging soft samples with the atomic force microscope. *Science*, **1992**, *257*, 1900–1905.
- 31 HORBER, J.K., MILES, M.J. Scanning probe evolution in biology. *Science*, **2003**, *302*, 1002–1005.
- 32 SANTOS, N.C., CASTANHO, M.A. An overview of the biophysical applications of atomic force microscopy. *Biophys. Chem.* **2004**, *107*, 133–149.
- 33 BRAET, F., SEYNAEVE, C., DE ZANGER, R., WISSE, E. Imaging surface and submembranous structures with the atomic force microscope: a study on living cancer cells, fibroblasts and macrophages. *J. Microsc.* **1998**, *190*, 328–338.
- 34 FREDERIX, P., AKIYAMA, T., STAUFER, U., GERBER, C.H., FOTIADIS, D., MULLER, D.J., ENGEL, A. Atomic force bio-analytics. *Curr. Opin. Chem. Biol.* **2003**, *7*, 641–647.
- 35 KASSIES, R., VAN DER WERF, K.O., LENFERINK, A., HUNTER, C.N., OLSEN,

- J.D., SUBRAMANIAM, V., OTTO, C. Combined AFM and confocal fluorescence microscope for applications in bio-nanotechnology. *J. Microsc.* **2005**, *217*, 109–116.
- 36 IKAI, A., AFRIN, R. Toward mechanical manipulations of cell membranes and membrane proteins using an atomic force microscope: an invited review. *Cell Biochem. Biophys.* **2003**, *39*, 257–277.
- 37 ROUNSEVELL, R., FORMAN, J.R., CLARKE, J. Atomic force microscopy: mechanical unfolding of proteins. *Methods Enzymol.* **2004**, *34*, 100–111.
- 38 RADMACHER, M. Measuring the elastic properties of living cells by the atomic force microscope. *Methods Cell Biol.* **2002**, *68*, 67–90.
- 39 NAGAO, E. and DVORAK, J.A. An integrated approach to the study of living cells by atomic force microscopy. *J. Microsc.* **1998**, *191*, 8–19.
- 40 RADMACHER, M. Measuring the elastic properties of biological samples with the AFM. *IEEE Eng. Med. Biol. Mag.* **1997**, *16*, 47–57.
- 41 BRAET, F., ROTSCH, C., WISSE, E., RADMACHER, M. AFM imaging and elasticity measurements on living rat liver macrophages. *Appl. Phys.* **1998**, *66*, S575–S578.
- 42 BRAET, F., DE ZANGER, R., SEYNAEVE, C., BAEKELAND, M., WISSE, E. A comparative atomic force microscopy study on living skin fibroblasts and liver endothelial cells. *J. Electron Microsc.* **2001**, *50*, 283–290.
- 43 BRAET, F., VERMIJLEN, D., BOSSUYT, V., DE ZANGER, R., WISSE, E. Early detection of cytotoxic events between hepatic natural killer cells and colon carcinoma cells as probed with the atomic force microscope. *Ultramicroscopy*, **2001**, *89*, 265–273.
- 44 BRAET, F., DE ZANGER, R., KÄMMER, S., WISSE, E. Noncontact versus contact imaging: An atomic force microscopic study on hepatic endothelial cells *in vitro*. *Int. J. Imaging Syst. Technol.* **1997**, *8*, 162–167.
- 45 KOSTER, A.J., KLUMPERMAN, J. Electron microscopy in cell biology: integrating structure and function. *Nat. Rev. Mol. Cell Biol.* **2003**, Supp, S56–S510.
- 46 SITTE, H., EDELMAN L., NEUMANN, K. *Cryotechniques in Biological Electron Microscopy*. eds.: STEINBRECHT, R.A., ZIEROLD, K., Springer-Verlag, Berlin, **1987**, pp. 87–113.
- 47 SITTE, H., EDELMAN, L., NEUMANN, K. Cryofixation without pretreatment at ambient pressure. *Cryotechniques in Biological Electron Microscopy*. ed. R.A. STEINBRECHT, K. ZIEROLD, Springer-Verlag, Berlin, **1987**, pp. 87–113.
- 48 KING, M. Dimensional changes in cells and tissues during specimen preparation for the electron microscope. *Cell Biophys.* **1991**, *18*, 31–55.
- 49 BRAET, F., DE ZANGER, R., BAEKELAND, M., CRABBÉ, E., VAN DER SMISSEN, P., WISSE, E. Structure and dynamics of the fenestrae-associated cytoskeleton of rat liver sinusoidal endothelial cells. *Hepatology*, **1995**, *21*, 180–189.
- 50 FREDERIK, P., STUART, M.C., BOMANS, P., BUSING, W., BURGER, K., VERKLEIJ, A. Perspective and limitations of cryo-electron microscopy. From model systems to biological specimens. *J. Microsc.* **1991**, *161*, 253–262.
- 51 FREDERIK, P., BOMANS, P., STUART, M. The ultrastructure of cryo-sections and intact vitrified cells – the effects of cryoprotectants and acceleration voltage on beam induced bubbling. *Scanning Microsc.* **1991**, *5*, S43–S51.
- 52 BRAET, F., KALLE, W., DE ZANGER, R., DE GROOTH, B., RAAP, A., TANKE, H., WISSE, E. Comparative atomic force and scanning electron microscopy: an investigation on fenestrated endothelial cells *in vitro*. *J. Microsc.* **1996**, *181*, 10–17.
- 53 FREDERIK, P., BOMANS, P., BRAET, F., WISSE, E. *Cells of the Hepatic Sinusoid* eds.: WISSE, E., KNOOK, D.L., BALABAUD, C. Kupffer Cell Foundation, Leiden, **1997**, 476–478.
- 54 FREDERIK, P., BOMANS, P., FRANSSSEN, V., LAEVEN, P. *Proceedings of the 12th European Congress on Electron Microscopy*, ed. JANISH, R., LECH, S., Brno, Reklamní Atelier Kupa, **2000**, pp. B383–B384.

- 55 FREDERIK, P., HUBERT, D.H. Cryo-electron microscopy of liposomes. *Methods Enzymol.* **2005**, 391, 431–448.
- 56 BRAET, F., BOMANS, P., WISSE, E., FREDERIK, P. The observation of intact hepatic endothelial cells by cryo-electron microscopy. *J. Microsc.* **2003**, 212, 175–185.
- 57 BRAET, F., WISSE, E., FREDERIK, P., GEERTS, W., KOSTER, A., SOON, L., RINGER, S. Contribution of high-resolution correlative imaging techniques in the study of the hepatic sieve in three-dimensions. *Microsc. Res. Tech.* **2005**, in press.
- 58 BAUMEISTER, W. From proteomic inventory to architecture. *FEBS Lett.*, **2005**, 579, 933–937.

## 10

# Dynamic Light Scattering Microscopy

*Rhonda Dzakpasu and Daniel Axelrod*

### 10.1

#### Introduction

We describe here a novel imaging technique for optical microscopy based on dynamic light scattering. Conventional dynamic light scattering (DLS, also known as quasielastic light scattering, QELS) is a well-established laser-based nonmicroscopic, nonimaging technique commonly used to measure diffusion coefficients of proteins in solution [1, 2]. DLS is based on the time-dependent interference among electric fields emanating from scattering centers in relative motion and is sensitive to relative motions that are six times smaller than the optical resolution of the microscope. We have adapted DLS to microscopy (DLSM) and, with the use of a CCD camera in a line-streaking mode, we use the rate of data readout transfer as the rate of data collection. This allows us to image rapid motions over submicroscopic distances. Rather than creating images based on static index of refraction variations, spatial maps based on the rates of motions are produced. This can provide valuable insight into the processes imaged in biological systems.

The theory of DLSM is presented here, followed by a description of a detection system that uses a slow scan (a few Hz exposure rate) CCD to record the rapid (kHz range) fluctuations of DLS, and finally followed by tests on a model system (small polystyrene beads in suspension) and a living cell system (macrophages). The goal of the tests on macrophages is not to answer any particular biological question at this point, but rather to verify the applicability of DLSM to cell biological systems.

Previously reported applications of DLS in a microscope have been limited to a single point (rather than spatial mapping) measurement of diffusion coefficients and flow rates (velocimetry) [3–15]. These works did not address the theoretical question as to how intensity fluctuations can occur from scattering centers mutually close enough to fall within the optical resolution distance of the microscope; this question is addressed here.

DLSM in its present form is chemically nonspecific, as are dark field, phase contrast, and differential interference contrast. Unlike those techniques that detect spatial but temporally static variations in local refractive index, DLSM detects tem-



porally dynamic variations in a spatially resolved format. We discuss possible extensions of the technique that might increase its chemical specificity while preserving its ability to detect rapid motions in submicroscopic regions.

This chapter is divided into five further sections: Section 10.2 presents the theoretical solution for the functional form of the scattered electric field from a single and then a collection of scattering centers. The temporal and spatial autocorrelation function is derived for the intensity at the image plane of the microscope. We show there can be significant intensity fluctuations due to the relative motion of scattering centers within the optical resolution of the microscope. In addition, we show that fast time scale fluctuations can be measured with this technique.

Section 10.3 describes the experimental realization of the technique for our control system of polystyrene beads and the first application to cell biology, macrophage cells.

Section 10.4 describes the data analysis performed on the intensity fluctuations obtained from the experimental system.

Section 10.5 presents results for the two experimental systems. We show that the rates of motion obtained for different bead sizes agree with those expected from hydrodynamic theory for such beads and are in relative agreement based on their size ratio. In addition, we also show that we can observe spatially resolved differences in the decay rates in macrophages, both untreated and treated by a pharmacological agent.

Section 10.6 discusses the experimental and theoretical results stemming from this work. It also presents possible applications of the technique and suggests potential improvements.

## 10.2

### Theory

This section presents a theoretical derivation of the functional form of the scattered electric field at the image plane of a microscope (which is modeled as a simple lens), first from a single scattering center and then from a collection of centers. From the resulting intensity, the temporal and spatial autocorrelation functions are derived. The theory is essentially a combination of scalar diffraction theory for a simple lens and a generalization of the conventional DLS theory as presented in Ref. [16].

The optical resolution of a microscope specifies the minimum separation of two objects in object space required to form distinctly separated images. If the separation is greater than the resolution distance, then clearly little interference can occur in the image plane. We show here that for scattering centers spaced closer than the optical resolution distance, sufficient phase variations still exist to create intensity fluctuations in the image plane.

As individual scattering centers can enter and/or leave an imaged region monitored by a single pixel in the detector, additional intensity fluctuations are created due to the change in particle number. These intensity fluctuations would occur even for incoherent light scattering (e.g., fluorescence). We derive an expression

that includes the effect of intensity fluctuations due to both phase and number variations.

The characteristic decay time of the temporal intensity autocorrelation function guides what is the minimum sample time that should be employed in the detection system. The characteristic decay distance of the spatial autocorrelation function guides what is the maximum pixel size that should be employed in the detection system.

### 10.2.1

#### Single Scattering Center

We first consider the electric field as it scatters from a single particle toward the objective lens, refracts through the lens, and propagates to the image plane. The scattering center is assumed to be much smaller than the wavelength of the incident light  $\lambda$  (the Rayleigh scattering limit); the polarization of the incident light is assumed to be linear and the polarization of the scattered light is assumed to be the same as the incident light. The electric fields are thereby represented as (complex) scalars rather than vectors. All of the light (incident and scattered) is monochromatic so the common factor  $\exp(i\omega t)$  is everywhere suppressed.

The coordinate systems are depicted in Fig. 10.1. Scattering center (object) space, objective lens space, and image space coordinates are unprimed, primed, and double primed, respectively. The optical axis of the microscope is defined as the  $z$ -axis. The incident light is formed from a collimated laser beam propagating in the  $y$ - $z$  plane and passing through a cylindrical lens. This lens focuses in the  $x$ -dimension only and leaves the incident light as a thin stripe along the  $y$ -direction, although still much larger in every dimension than the optical resolution. Therefore, the illumination electric field amplitude  $E_0$  can be considered constant over a region competent for mutual interference at one detector pixel. The direction of propagation and focusing is such that no direct incident light reaches the objective (i.e., essentially dark field). If  $\mathbf{k}_0$  is the incident wave vector and  $\mathbf{r}$  is the location of a

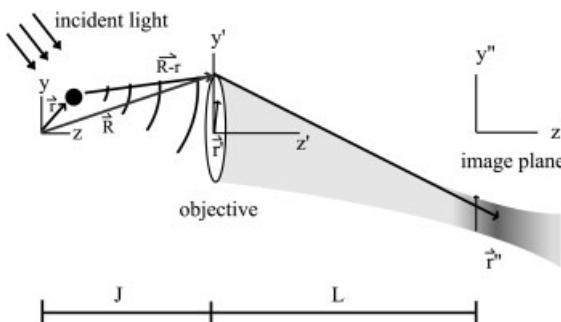


**Fig. 10.1.** Coordinate systems used in Section 10.2. The object is shown as a discrete black dot, and the point spread intensity in the image region as a blur. The origin in image

space is located in the plane of the detector. The origin in object space is chosen at a point on the optical axis such that its focused image is centered at the origin in image space.

particular scattering center in object space, then the incident electric field  $E(\mathbf{r})$  at a single scattering center is:

$$E(\mathbf{r}) = E_0 \exp(i\mathbf{k}_0 \mathbf{r}) \quad (1)$$

At the position of the objective lens (before propagating through it), the scattered light will produce an electric field  $E'(\mathbf{r}')$  with amplitude proportional to both  $E(\mathbf{r})$  and some scattering efficiency factor dependent upon the polarizability of the scattering center. However, this scattering efficiency factor is assumed constant among all scattering centers and also isotropic over the range of angles gathered by the lens, so its appearance will be suppressed in the expression for  $E'(\mathbf{r}')$ :

$$E'(\mathbf{r}') = E(\mathbf{r}) \exp(ik_s |\mathbf{R} - \mathbf{r}|) \quad (2)$$

where  $\mathbf{R}$  is the vector from the origin in  $\mathbf{r}$ -space to a point on the objective lens represented by two-dimensional vector  $\mathbf{r}'$  in the plane of the lens;  $|\mathbf{R} - \mathbf{r}|$  is the distance from the scattering center to that point on the objective; and  $k_s = |\mathbf{k}_s|$  is the amplitude of the scattered wave vector.

The electric field  $E''(\mathbf{r}'', z'')$  in the image region (with positions denoted in cylindrical coordinates) is given in Ref. [17]:

$$E''(\mathbf{r}'', z'') = \frac{\exp(ik_0 L)}{i\lambda L} \iint E'(\mathbf{r}') \exp\left(\frac{-ik_0 r'^2}{2f}\right) \times \exp\left\{\frac{ik_0 r'^2}{2} \left[\frac{1}{L} \left(1 - \frac{z''}{L}\right)\right] - \frac{ik_0 \mathbf{r}' \cdot \mathbf{r}''}{L}\right\} d^2 \mathbf{r}' \quad (3)$$

where  $f$  is the focal length of the objective lens,  $k_0 \equiv |\mathbf{k}_0|$  and  $L$  is the distance from the objective to the image plane. Assuming a small angle (i.e., small numerical aperture) approximation, the term  $\exp(-ik_0 r'^2/2f)$  corresponds to the phase shift imposed by the objective lens. The factor

$$\exp\left\{\frac{ik_0 r'^2}{2} \left[\frac{1}{L} \left(1 - \frac{z''}{L}\right)\right] - \frac{ik_0 \mathbf{r}' \cdot \mathbf{r}''}{L}\right\}$$

describes the phase alteration as the field propagates in the empty space from the objective lens to the image region.

Combining Eqs. (1-3), noting that  $\mathbf{k}_s$  is oriented in the same direction as  $\mathbf{R} - \mathbf{r}$  with  $k_s \approx k_0$ , and regrouping, we obtain:

$$E''(\mathbf{r}'', z'') = E_0 \frac{\exp(ik_0 L)}{i\lambda L} \exp(i\mathbf{k}_0 \cdot \mathbf{r}) \iint \exp\left\{ik_0 |\mathbf{R} - \mathbf{r}| - \frac{ik_0 \mathbf{r}' \cdot \mathbf{r}''}{L} - \frac{ik_0 r'^2}{2} \left[\frac{1}{f} - \frac{1}{L} \left(1 - \frac{z''}{L}\right)\right]\right\} d^2 \mathbf{r}' \quad (4)$$

For  $r \ll R$ , we can substitute an approximation for  $|\mathbf{R} - \mathbf{r}|$ :

$$|\mathbf{R} - \mathbf{r}| = \left\{ R^2 \left[ 1 + \left( \frac{r}{R} \right)^2 - \frac{2\mathbf{r} \cdot \mathbf{R}}{R^2} \right] \right\}^{1/2} \cong R + \frac{1}{2} \left( \frac{r^2}{R} \right) - \frac{\mathbf{r} \cdot \mathbf{R}}{R} \quad (5)$$

Since  $\mathbf{R} = \mathbf{r}' + J\hat{\mathbf{z}}$ , where  $J$  is the object distance,  $1/R$  can be written in the small aperture approximation ( $r' \ll J$ ) as:

$$\frac{1}{R} = (r'^2 + J^2)^{-1/2} \cong \frac{1}{J} \left[ 1 - \frac{1}{2} \left( \frac{r'}{J} \right)^2 + \dots \right] \quad (6)$$

Substituting Eqs. (5) and (6) into Eq. (4), and noting that  $\frac{1}{f} = \frac{1}{J} + \frac{1}{L}$ , the electric field in the image region becomes:

$$E''(\mathbf{r}'', z'') = E_0 \frac{\exp ik_0(L+J)}{i\lambda L} \int \exp ik_0 \left( -\mathbf{r} \cdot \mathbf{Q}(\mathbf{r}') + \frac{r'^2 \gamma(r'')}{2J} - \frac{\mathbf{r}' \cdot \mathbf{r}''}{L} - \frac{z'' r'^2}{2L^2} \right) d^2 \mathbf{r}' \quad (7)$$

where

$$\gamma(r') \equiv 1 - \frac{r'^2}{2J^2} \quad (8)$$

and

$$\mathbf{Q}(\mathbf{r}') \equiv \gamma \left( \frac{\mathbf{r}'}{J} + \hat{\mathbf{z}} \right) - \hat{\mathbf{k}}_0 \quad (9)$$

Vector  $k_0 \mathbf{Q}$  is a generalized conventional scattering vector, analogous to  $\mathbf{q}$  ( $\equiv \mathbf{k}_s - \mathbf{k}_0$ ) in conventional nonimaging DLS. Here,  $\mathbf{Q}$  additionally takes into account the range of scattering angles gathered by the microscope objective lens.

To simplify Eq. (7) further, we assume that the detector is located in the image plane ( $z'' = 0$ ). The scattering centers imaged within the same optical resolution area are then very close to the origin in object space so that  $r \ll r'$  for almost the entire range of the integral. Therefore, the exponent term  $\mathbf{r} \cdot \mathbf{Q} \gg r^2 \gamma / 2J$ , implying that the factor  $\exp(-ik_0 \mathbf{r} \cdot \mathbf{Q})$  in Eq. (7) varies much more rapidly than  $\exp(-ik_0 r^2 \gamma / 2J)$  over the range of the  $r'$ , so that the latter factor can be assumed constant and close to unity. Eq. (7) then becomes:

$$E''_{z''=0}(\mathbf{r}, \mathbf{r}'') = E_0 \frac{\exp ik_0(L+J)}{i\lambda L} \int \exp ik_0 \left( -\mathbf{r} \cdot \mathbf{Q} - \frac{\mathbf{r}' \cdot \mathbf{r}''}{L} \right) d^2 \mathbf{r}' \quad (10)$$

## 10.2.2

**Multiple Scattering Centers**

Each scattering center  $i$  located at position  $\mathbf{r}_i$  produces an electric field at  $z'' = 0$  according to Eq. (10). The total electric field  $E$  and the consequent intensity  $I$  at the image plane depend on the set of all the  $\mathbf{r}_i$  positions ( $I = 1, \dots, N$ ) as follows:

$$E(\{\mathbf{r}_i\}, \mathbf{r}'', t) = \sum_i^N b_i(t) E_{z''=0}''(\mathbf{r}_i, \mathbf{r}'') \quad (11)$$

$$I(\{\mathbf{r}_i\}, \mathbf{r}'', t) = E * E \quad (12)$$

To understand the meaning of the  $b_i(t)$  parameters, we define an “equivalent volume”  $v_{\text{pix}}$  in object space that contains all of the  $\mathbf{r}$  positions that contribute to the intensity observed by a single CCD camera pixel at one position in the image plane. (Of course, the actual region from which scattered light is gathered has graded rather than sharp edges.) We also define an arbitrarily larger volume  $V$  that subsumes  $v_{\text{pix}}$  and contains the  $N$  scattering centers included in the sum in Eq. (11). The occupation number  $b_i(t)$  equals unity if scattering center  $i$  is in  $v_{\text{pix}}$  at time  $t$  and zero otherwise. We assume that the positions  $\mathbf{r}_i$  are statistically independent and randomly time-dependent (e.g., due to Brownian motion). These random motions cause  $E$  to fluctuate in both phase and amplitude, and the resulting intensity to fluctuate in amplitude. The temporal and spatial behavior of the intensity fluctuations can be investigated through autocorrelation functions.

## 10.2.3

**Temporal Autocorrelation of Intensity**

The temporal autocorrelation is defined as

$$\Gamma(\tau) = \langle I(t_1)I(t_2) \rangle \quad (13)$$

where  $\tau \equiv t_2 - t_1$ , the intensities at the two times are measured at the same  $\mathbf{r}''$  position in the image plane, and the ensemble average indicated by the brackets is taken over all possible  $\{\mathbf{r}_i\}$  configurations. Because the system is assumed to be in equilibrium,  $\Gamma$  depends only on the time difference  $\tau$  and not the absolute times. After substituting Eqs. (10–12) into Eq. (13), we get Eq. (14).

$$\begin{aligned} \Gamma(\tau) = & \left( \frac{|E_0|}{i\lambda L} \right)^4 \sum_{i,j,k,l}^N \langle b_i(t_1)b_j(t_1)b_k(t_2)b_l(t_2) \rangle \\ & \times \iiint \left\langle \exp(-ik_0\mathbf{r}_i(t_1) \cdot \mathbf{Q}_a) \exp(ik_0\mathbf{r}_j(t_1) \cdot \mathbf{Q}_b) \right. \\ & \left. \exp(ik_0\mathbf{r}_k(t_2) \cdot \mathbf{Q}_c) \exp(-ik_0\mathbf{r}_l(t_2) \cdot \mathbf{Q}_d) \right\rangle \end{aligned}$$

$$\begin{aligned}
& \times \exp\left(-\frac{ik_0\mathbf{r}'_a \cdot \mathbf{r}''}{L}\right) \exp\left(\frac{ik_0\mathbf{r}'_b \cdot \mathbf{r}''}{L}\right) \exp\left(\frac{ik_0\mathbf{r}'_c \cdot \mathbf{r}''}{L}\right) \\
& \times \exp\left(-\frac{ik_0\mathbf{r}'_d \cdot \mathbf{r}''}{L}\right) d^2\mathbf{r}'_a d^2\mathbf{r}'_b d^2\mathbf{r}'_c d^2\mathbf{r}'_d
\end{aligned} \tag{14}$$

The phase fluctuations (arising from the complex exponential factors) are uncorrelated with number fluctuations (arising from the  $b$  factors); this is why the single ensemble average in Eq. (13) can be separated into a product of two ensemble averages (number and phase) in Eq. (14).

The summation in Eq. (14) can be separated according to the relationships among the summation indices  $i, j, k, l$  such that

$$\Gamma = \left(\frac{|E_0|}{i\lambda L}\right)^4 \sum_{m=1}^6 (\sum_m \Gamma_m^{\text{num}} \Gamma_m^{\text{ph}}) \tag{15}$$

where  $\Gamma_m^{\text{num}}$  and  $\Gamma_m^{\text{ph}}$  are the number and phase fluctuation factors, respectively, and  $\sum_m$  represents sums over  $i, j, k, l$  restricted as shown in Table 10.1.

#### 10.2.4

##### Phase Fluctuation Factors

In the first three cases ( $m = 1, 2, 3$ ) at least one index is unique from all of the others. In such cases, a factor  $\langle \exp(-ik_0\mathbf{r} \cdot \mathbf{Q}) \rangle$  with the unique index on the  $\mathbf{r}$  vector can be factored out from the overall ensemble average since the motions of the scattering centers are mutually independent. That factor can be handled as follows (written here for a particular scattering index  $i$ ):

$$\langle \exp(-ik_0\mathbf{r}_i(t_1) \cdot \mathbf{Q}_a) \rangle = \int \chi_i(\mathbf{r}_i) \exp(-ik_0\mathbf{r}_i \cdot \mathbf{Q}_a) d^3\mathbf{r}_i \tag{16}$$

where  $\chi_i$  is the probability density that the particle is located in the vicinity of position  $\mathbf{r}_i$ . The scattering centers  $i$  are assumed to be uniformly distributed over the volume  $v_{\text{pix}}$  imaged by an individual pixel in  $r$ -space so that  $\chi_i(\mathbf{r}_i) = \chi = 1/v_{\text{pix}}$ . Eq. (16) becomes:

**Tab. 10.1.** Number of unique indices.

$m$ Index	Scattering center indices	Number of unique indices
1	$i \neq j \neq k \neq l$	4
2	$i \neq j \neq k = l$	2
3	$i \neq j = k = l$	1
4	$i = j \neq k = l$	0
5	$i = k \neq j = l$	0
6	$i = j = k = l$	0

$$\langle \exp(-ik_0 \mathbf{r}_i(t_1) \cdot \mathbf{Q}_a) \rangle = \frac{1}{v_{\text{pix}}} \int \exp(-ik_0 \mathbf{r}_i \cdot \mathbf{Q}_a) d^3 \mathbf{r}_i = \frac{(2\pi)^{3/2}}{v_{\text{pix}}} \delta(k_0 \mathbf{Q}_a) \quad (17)$$

The integral over  $\mathbf{r}'_a$  in Eq. (14) then becomes:

$$\begin{aligned} & \int \langle \exp(-ik_0 \mathbf{r}_i(t_1) \cdot \mathbf{Q}_a) \rangle \exp\left(-\frac{ik_0 \mathbf{r}'_a \cdot \mathbf{r}''}{L}\right) d^2 \mathbf{r}'_a \\ &= \frac{(2\pi)^{3/2}}{v_{\text{pix}}} \int \delta(k_0 \mathbf{Q}_a) \exp\left(-\frac{ik_0 \mathbf{r}'_a \cdot \mathbf{r}''}{L}\right) d^2 \mathbf{r}'_a \\ &= \frac{(2\pi)^{3/2}}{v_{\text{pix}}} \left(\frac{J}{k_0 \gamma}\right)^2 \int \delta(k_0 \mathbf{Q}_a) \exp\left(-\frac{ik_0 \mathbf{r}'_a \cdot \mathbf{r}''}{L}\right) d^2(k_0 \mathbf{Q}_a) \end{aligned} \quad (18)$$

The integral has a nonzero value only when  $k\mathbf{Q}_a = 0$ . From the definition of  $\mathbf{Q}_a$  in Eq. (9), we can obtain the  $\mathbf{r}'_a$  for which this condition is satisfied:

$$\mathbf{r}'_a|_{\mathbf{Q}_a=0} = \frac{J}{\gamma} \hat{\mathbf{k}}_0 - J\dot{\mathbf{z}} \quad (19)$$

This particular  $\mathbf{r}'_a$  is located where the extension of the incident beam crosses the plane of the objective lens. Since our experimental setup was designed so that the incident light misses the objective, the integral over  $\mathbf{r}'_a$  in Eq. (18) (which is limited to the area of the objective) does not include  $\mathbf{r}'_a|_{\mathbf{Q}_a=0}$ . Thus, those terms in the sum of Eq. (15) with at least one unique summation index (i.e.,  $m = 1, 2, 3$ ) are zero.

The phase term for the  $m = 4$  case from Eq. (15) is given by Eq. (20).

$$\begin{aligned} \Gamma_4^{\text{ph}} &= \iint \langle \exp ik_0 [\mathbf{r}_i(t_1) \cdot \Delta \mathbf{Q}_{ab}] \rangle \exp\left(\frac{ik_0 \Delta \mathbf{r}'_{ab} \cdot \mathbf{r}''}{L}\right) d^2 \mathbf{r}'_a d^2 \mathbf{r}'_b \\ &\quad \times \iint \langle \exp -ik_0 [\mathbf{r}_k(t_2) \cdot \Delta \mathbf{Q}_{cd}] \rangle \exp\left(\frac{-ik_0 \Delta \mathbf{r}'_{cd} \cdot \mathbf{r}''}{L}\right) d^2 \mathbf{r}'_c d^2 \mathbf{r}'_d \\ &= \left| \iint \langle \exp ik_0 [\mathbf{r}_i(t_1) \cdot \Delta \mathbf{Q}_{ab}] \rangle \exp\left(\frac{ik_0 \Delta \mathbf{r}'_{ab} \cdot \mathbf{r}''}{L}\right) d^2 \mathbf{r}'_a d^2 \mathbf{r}'_b \right|^2 \end{aligned} \quad (20)$$

where  $\Delta \mathbf{Q}_{\alpha\beta} \equiv \mathbf{Q}_\beta - \mathbf{Q}_\alpha$  and  $\Delta \mathbf{r}'_{\alpha\beta} \equiv \mathbf{r}'_\beta - \mathbf{r}'_\alpha$ . The terms of the form  $\langle \exp ik_0 [\mathbf{r}(t_1) \cdot \Delta \mathbf{Q}] \rangle$  are similar to that in Eq. (17), except for the factor  $\Delta \mathbf{Q}$  instead of  $\mathbf{Q}$ . Therefore, the integral in Eq. (20) can be reduced to:

$$\begin{aligned} & \frac{1}{v_{\text{pix}}} \iint \left( \int \exp ik_0 [\mathbf{r}_i(t_1) \cdot \Delta \mathbf{Q}_{ab}] dx_i dy_i dz_i \right) \exp\left(\frac{ik_0 \Delta \mathbf{r}'_{ab} \cdot \mathbf{r}''}{L}\right) d^2 \mathbf{r}'_a d^2 \mathbf{r}'_b \\ &= \frac{I_{\text{pix}}(2\pi)}{v_{\text{pix}}} \iint \delta(k_0 \Delta \mathbf{Q}_{ab}) \exp\left(\frac{ik_0 \Delta \mathbf{r}'_{ab} \cdot \mathbf{r}''}{L}\right) d^2 \mathbf{r}'_a d^2 \mathbf{r}'_b \end{aligned}$$

$$\begin{aligned}
&= \frac{(2\pi)}{s_{\text{pix}}} \left( \frac{J}{k_0\gamma} \right)^4 \iint \delta(k_0\Delta\mathbf{Q}_{ab}) \exp\left(\frac{ik_0\Delta\mathbf{r}'_{ab} \cdot \mathbf{r}''}{L}\right) d^2(k_0\mathbf{Q}_a) d^2(k_0\mathbf{Q}_b) \\
&= \frac{(2\pi)}{s_{\text{pix}}} \left( \frac{J}{k_0\gamma} \right)^4 \iint \left[ \exp\left(\frac{ik_0\Delta\mathbf{r}'_{ab} \cdot \mathbf{r}''}{L}\right) \right] \Big|_{a=b} d^2(k_0\mathbf{Q}_b) \\
&= \frac{(2\pi)}{s_{\text{pix}}} \left( \frac{J}{k_0\gamma} \right)^4 \int d^2(k_0\mathbf{Q}) = \frac{(2\pi)}{s_{\text{pix}}} \left( \frac{J}{k_0\gamma} \right)^2 \int d^2\mathbf{r}' = \frac{(2\pi)}{s_{\text{pix}}} \left( \frac{J}{k_0\gamma} \right)^2 A \quad (21)
\end{aligned}$$

where  $l_{\text{pix}}$  is the  $z$ -dimension of the observed volume  $v_{\text{pix}}$ ;  $s_{\text{pix}}$  is the area of the observed volume; and  $A$  is the area of the objective. Therefore,

$$\Gamma_4^{\text{ph}} = \frac{(2\pi)^2}{s_{\text{pix}}^2} \left( \frac{J}{k_0\gamma} \right)^4 A^2 \quad (22)$$

For the  $m = 5$  term in Eq. (15),

$$\begin{aligned}
\Gamma_5^{\text{ph}} &= \left| \iint \langle \exp ik_0[\mathbf{r}_i(t_2) \cdot \mathbf{Q}_c - \mathbf{r}_i(t_1) \cdot \mathbf{Q}_a] \rangle \right. \\
&\quad \times \left. \exp\left(-\frac{ik_0\mathbf{r}'_a \cdot \mathbf{r}''}{L}\right) \exp\left(\frac{ik_0\mathbf{r}'_c \cdot \mathbf{r}''}{L}\right) d^2\mathbf{r}'_a d^2\mathbf{r}'_c \right|^2 \\
&= \left| \iint \langle \exp(-ik_0\Delta\mathbf{r}_i \cdot \mathbf{Q}_c) \exp(-ik_0\mathbf{r}_i(t_2) \cdot \Delta\mathbf{Q}_{ac}) \rangle \right. \\
&\quad \times \left. \exp\left(-\frac{ik_0\Delta\mathbf{r}'_{ac} \cdot \mathbf{r}''}{L}\right) d^2\mathbf{r}'_a d^2\mathbf{r}'_c \right|^2 \\
&= \left| \iint \langle \exp(-ik_0\Delta\mathbf{r}_i \cdot \mathbf{Q}_c) \rangle \langle \exp(-ik_0\mathbf{r}_i(t_2) \cdot \Delta\mathbf{Q}_{ac}) \rangle \right. \\
&\quad \times \left. \exp\left(-\frac{ik_0\Delta\mathbf{r}'_{ac} \cdot \mathbf{r}''}{L}\right) d^2\mathbf{r}'_a d^2\mathbf{r}'_c \right|^2 \quad (23)
\end{aligned}$$

where  $\Delta\mathbf{r}_i \equiv \mathbf{r}_i(t_2) - \mathbf{r}_i(t_1)$ . The term  $\langle \exp(-ik_0\mathbf{r}_i(t_2) \cdot \Delta\mathbf{Q}_{ac}) \rangle$  reduces to a  $\delta$ -function, so we obtain:

$$\begin{aligned}
\Gamma_5^{\text{ph}} &= \left| \frac{(2\pi)}{s_{\text{pix}}} \left( \frac{J}{k_0\gamma} \right)^4 \iint \left[ \delta(k_0\Delta\mathbf{Q}_{ac}) \exp\left(-\frac{ik_0\Delta\mathbf{r}'_{ac} \cdot \mathbf{r}''}{L}\right) d^2(k_0\mathbf{Q}_a) \right] \right. \\
&\quad \times \left. \langle \exp(-ik_0\Delta\mathbf{r}_i \cdot \mathbf{Q}_a) \rangle d^2(k_0\mathbf{Q}_c) \right|^2 \\
&= \left| \frac{(2\pi)}{s_{\text{pix}}} \left( \frac{J}{k_0\gamma} \right)^2 \int \langle \exp(-ik_0\Delta\mathbf{r}_i \cdot \mathbf{Q}) \rangle d^2\mathbf{r}' \right|^2 \quad (24)
\end{aligned}$$

where the subscript “ $c$ ” on the  $\mathbf{r}'_c$  factors has been suppressed. The ensemble average in Eq. (24) can be rewritten as:



$$\langle \exp(-ik_0 \Delta \mathbf{r}_i \cdot \mathbf{Q}) \rangle = \int p[\Delta \mathbf{r}_i(\tau)|0] \exp(-ik_0 \Delta \mathbf{r}_i \cdot \mathbf{Q}) d^3 \Delta \mathbf{r}_i \quad (25)$$

where  $p[\Delta \mathbf{r}_i(\tau)|0]$  is the conditional probability of finding a particle at position  $\Delta \mathbf{r}_i$  at time  $\tau$  given that it was at the origin ( $\Delta \mathbf{r}_i = 0$ ) at  $\tau = 0$ . The right-hand side of Eq. (25) is the Fourier transform of  $p[\Delta \mathbf{r}_i(\tau)|0]$ :

$$\langle \exp(-ik_0 \Delta \mathbf{r}_i \cdot \mathbf{Q}) \rangle = (2\pi)^{3/2} \tilde{p}(\mathbf{Q}) \quad (26)$$

where  $\tilde{p}(\mathbf{Q})$  is the Fourier transform of  $p[\Delta \mathbf{r}_i(\tau)|0]$  into  $\mathbf{Q}$ -space.

We assume that the scattering centers are undergoing random diffusive motion. Taking the Fourier transform of the diffusion equation  $\partial p / \partial \tau = D \nabla^2 p$  from  $\Delta \mathbf{r}_i$ -space to  $\mathbf{Q}$ -space gives:

$$\frac{\partial \tilde{p}}{\partial \tau} = -D k_0^2 \mathbf{Q}^2 \tilde{p} \quad (27)$$

so that

$$\tilde{p}(\mathbf{Q}) = (2\pi)^{-3/2} \exp(-D \mathbf{Q}^2 k_0^2 \tau) \quad (28)$$

and therefore, in combination with Eq. (26):

$$\langle \exp(-ik_0 \Delta \mathbf{r}_i \cdot \mathbf{Q}) \rangle = \exp(-D \mathbf{Q}^2 k_0^2 \tau) \quad (29)$$

Eq. (24) then becomes:

$$\Gamma_5^{\text{ph}} = \frac{(2\pi)^2}{s_{\text{pix}}^2} \left( \frac{J}{k_0 \gamma} \right)^4 A^2 \left| \frac{1}{A} \int \exp(-D \mathbf{Q}^2 k_0^2 \tau) d^2 \mathbf{r}' \right|^2 \quad (30)$$

For the  $m = 6$  term in Eq. (15),

$$\begin{aligned} \Gamma_6^{\text{ph}} &= \iiint \langle \exp ik_0 [\mathbf{r}_i(t_1) \cdot \Delta \mathbf{Q}_{ab}] \exp ik_0 [\mathbf{r}_i(t_2) \cdot \Delta \mathbf{Q}_{cd}] \rangle \\ &\quad \times \exp\left(\frac{ik_0 \Delta \mathbf{r}'_{ab} \cdot \mathbf{r}''}{L}\right) \exp\left(\frac{ik_0 \Delta \mathbf{r}'_{cd} \cdot \mathbf{r}''}{L}\right) d^2 \mathbf{r}'_a d^2 \mathbf{r}'_b d^2 \mathbf{r}'_c d^2 \mathbf{r}'_d \\ &= \iiint \langle \exp ik_0 [\mathbf{r}_i(t_1) \cdot (\Delta \mathbf{Q}_{ab} + \Delta \mathbf{Q}_{cd})] \exp ik_0 [\Delta \mathbf{r}_i(\tau) \cdot \Delta \mathbf{Q}_{cd}] \rangle \\ &\quad \times \exp\left(\frac{ik_0 \Delta \mathbf{r}'_{ab} \cdot \mathbf{r}''}{L}\right) \exp\left(\frac{ik_0 \Delta \mathbf{r}'_{cd} \cdot \mathbf{r}''}{L}\right) d^2 \mathbf{r}'_a d^2 \mathbf{r}'_b d^2 \mathbf{r}'_c d^2 \mathbf{r}'_d \\ &= \frac{1}{v_{\text{pix}}} \iiint \left( \int \exp ik_0 [\mathbf{r}_i(t_1) \cdot (\Delta \mathbf{Q}_{ab} + \Delta \mathbf{Q}_{cd})] dx_i dy_i dz_i \right) \end{aligned}$$

$$\begin{aligned}
& \times \langle \exp ik_0[\Delta\mathbf{r}_i(\tau) \cdot \Delta\mathbf{Q}_{cd}] \rangle \exp\left(\frac{ik_0\Delta\mathbf{r}'_{ab} \cdot \mathbf{r}''}{L}\right) \\
& \times \exp\left(\frac{ik_0\Delta\mathbf{r}'_{cd} \cdot \mathbf{r}''}{L}\right) d^2\mathbf{r}'_a d^2\mathbf{r}'_b d^2\mathbf{r}'_c d^2\mathbf{r}'_d \\
& = \frac{(2\pi)l_{\text{pix}}}{v_{\text{pix}}} \left(\frac{J}{k_0\gamma}\right)^2 \iiint \left[ \int \delta(\mathbf{Q}_b - \mathbf{Q}_a + \mathbf{Q}_d - \mathbf{Q}_c) \right. \\
& \quad \left. \times \exp\left(\frac{ik_0\mathbf{r}'' \cdot (\Delta\mathbf{r}'_{ab} + \Delta\mathbf{r}'_{cd})}{L}\right) d^2(k_0\mathbf{Q}_a) \right] \\
& \quad \times \langle \exp ik_0[\Delta\mathbf{r}_i(\tau) \cdot \Delta\mathbf{Q}_{cd}] \rangle d^2\mathbf{r}'_b d^2\mathbf{r}'_c d^2\mathbf{r}'_d \\
& = \frac{(2\pi)}{s_{\text{pix}}} \left(\frac{J}{k_0\gamma}\right)^2 \iint \langle \exp ik_0[\Delta\mathbf{r}_i(\tau) \cdot \Delta\mathbf{Q}_{cd}] \rangle d^2\mathbf{r}'_c d^2\mathbf{r}'_d \int d^2\mathbf{r}'_b \\
& = \frac{(2\pi)}{s_{\text{pix}}} \left(\frac{J}{k_0\gamma}\right)^2 A \iint \exp(-Dk_0^2\Delta Q^2\tau) d^2\mathbf{r}'_c d^2\mathbf{r}'_d \quad (31)
\end{aligned}$$

### 10.2.5

#### Number Fluctuation Factors

The total volume of the imaged sample is  $V$  and the total number of scattering centers in that volume is  $N$ . The volume “imaged” by a single pixel is  $v_{\text{pix}}$ . The number of particles  $M(t)$  (assumed  $\ll N$ ) and its expectation value in the volume  $v_{\text{pix}}$  can be written:

$$M(t) = \sum_i^N b_i(t) \quad (32)$$

$$\langle M \rangle = \left\langle \sum_i b_i(t) \right\rangle = \sum_i \langle b_i(t) \rangle = N \langle b_i \rangle \quad (33)$$

The variance of  $M$  can be derived from Eqs. (32) and (33):

$$\text{var } M = N \text{ var } b_i \quad (34)$$

The assumption that  $\langle b_i \rangle \ll 1$  implies that  $M$  follows a Poisson distribution and, therefore,  $\text{var } M$  equals  $\langle M \rangle$ . Therefore,

$$\text{var } b_i = \langle M \rangle / N = \langle b_i \rangle \quad (35)$$

and the temporal autocorrelation function for  $b_i$  can be written as:

$$\langle b_i(t_1)b_i(t_1 + \tau) \rangle = (\text{var } b_i)g_{\text{num}}(\tau) + \langle b_i \rangle^2 \approx \frac{\langle M \rangle}{N} g_{\text{num}}(\tau) \quad (36)$$

where  $g_{\text{num}}(\tau)$  is a normalized number fluctuation autocorrelation function such that

$$g(0) = 1 \quad \text{and} \quad g(\infty) = 0$$

We are now set to consider the terms  $\Gamma_m^{\text{num}}$  that appear in Eq. (15). Since the  $m = 1, 2, 3$  terms in Eq. (15) are forced to zero by their phase fluctuation factors, we need consider only  $\Gamma_{4,5,6}^{\text{num}}$ . We make the approximations that  $N \gg \langle M \rangle \gg 1$ .

For the  $m = 4$  term of Eq. (15),

$$\begin{aligned} \Gamma_4^{\text{num}} &= \sum_{i \neq k}^N \langle b_i^2(t_1) b_k^2(t_1 + \tau) \rangle = \sum_{i \neq k}^N \langle b_i(t_1) b_k(t_1 + \tau) \rangle = \sum_{i \neq k}^N \langle b_i(t_1) \rangle \langle b_k(t_1 + \tau) \rangle \\ &= (N^2 - N) \langle b_i \rangle^2 \approx \langle M \rangle^2 \end{aligned} \quad (37)$$

For the  $m = 5$  term,

$$\begin{aligned} \Gamma_5^{\text{num}} &= \sum_{i \neq j}^N \langle b_i(t_1) b_i(t_1 + \tau) b_j(t_1) b_j(t_1 + \tau) \rangle \\ &= \sum_{i \neq j}^N \langle b_i(t_1) b_i(t_1 + \tau) \rangle \langle b_j(t_1) b_j(t_1 + \tau) \rangle \\ &= (N^2 - N) \langle b_i(t_1) b_i(t_1 + \tau) \rangle^2 \approx \langle M \rangle^2 g_{\text{num}}^2(\tau) \end{aligned} \quad (38)$$

For the  $m = 6$  term,

$$\begin{aligned} \Gamma_6^{\text{num}} &= \sum_i^N \langle b_i^2(t_1) b_i^2(t_1 + \tau) \rangle = \sum_i^N \langle b_i(t_1) b_i(t_1 + \tau) \rangle \\ &= N \langle b_i(t_1) b_i(t_1 + \tau) \rangle \approx \langle M \rangle g_{\text{num}}(\tau) \end{aligned} \quad (39)$$

The  $m = 6$  term is smaller than the  $m = 4$  and  $m = 5$  terms by a factor of  $\langle M \rangle$ ; therefore, it will be neglected. The complete temporal autocorrelation function thereby becomes:

$$\Gamma(\tau) = \langle I \rangle^2 \left\{ 1 + g_{\text{num}}^2(\tau) \left[ \frac{1}{A} \int \exp(-DQ^2 k_0^2 \tau) d^2 \mathbf{r}' \right]^2 \right\} \quad (40)$$

where  $\langle I \rangle$  is the mean intensity observed at a pixel from the  $\langle M \rangle$  scattering centers in its view:

$$\langle I \rangle = \left( \frac{|E_0|}{i\lambda L} \right)^2 \frac{(2\pi)}{s_{\text{pix}}} \left( \frac{J}{k_0 \gamma} \right)^2 A \langle M \rangle \quad (41)$$

To compare the result given in Eq. (40) with experimentally obtained autocorrelation functions, we construct the normalized temporal autocorrelation function:

$$g_T(\tau) \equiv \frac{\Gamma(\tau) - \langle I \rangle^2}{\langle I \rangle^2} \quad (42)$$

Combining Eqs. (40) and (42) shows that  $g_T(\tau)$  monotonically decays to zero:

$$g_T(\tau) = g_{\text{num}}^2(\tau) \left[ \frac{1}{A} \int \exp(-DQ^2 k_0 \tau) d^2 \mathbf{r}' \right]^2 \quad (43)$$

### 10.2.6

#### Characteristic Times and Distances

Figure 10.2(a) shows  $g_T(\tau)$  [Eq. (43)] plotted as a function of the unitless time variable  $Dk_0^2 \tau$  with the indicated integration performed numerically for the particular case where the objective numerical aperture NA equals 0.4 (as used in the experimental setup).

The characteristic decay time  $Dk_0^2 \tau_c$ , defined as the time required for  $g_T(\tau)$  to reach its  $e^{-1}$  value, is  $Dk_0^2 \tau_c \approx 0.52$  for this particular numerical aperture. In that time, the mean distance  $r_c$  the particle travels laterally by three-dimensional diffusion is:

$$r_c \equiv (4D\tau_c)^{1/2} = (4 \cdot 0.52/k_0^2)^{1/2} = 0.23\lambda \quad (44)$$

This characteristic distance is about a factor of six smaller than the resolution of the microscope, which according to the Raleigh criterion is  $r_{\text{res}} = 0.61\lambda/\text{NA} = 1.5\lambda$  for  $\text{NA} = 0.4$ . This proves that dynamic light scattering intensity fluctuations of significant amplitude do occur amongst scattering centers within a resolution distance of each other.

The actual characteristic time  $\tau_c$  can be estimated for an aqueous suspension of 200 nm diameter polystyrene nanospheres as used in some of our experiments. Hydrodynamics predict  $D = 2.2 \times 10^{-8} \text{ cm}^2 \text{ s}^{-1}$  for such spheres. For  $\lambda = 632.8 \text{ nm}$ , the characteristic time of the temporal intensity autocorrelation function would be  $\tau_c = 2.4 \text{ ms}$ . The experimental detection system must be able to observe these fast time-scale fluctuations.

### 10.2.7

#### Spatial Autocorrelation of Intensity

We define the spatial correlation region to be the spatial extent of the intensity fluctuations at the image plane. It is measured as the characteristic distance of the spatial autocorrelation function and determines the maximum pixel size allowable for measuring the temporal behavior of the intensity fluctuations. For example, if a pixel is larger than several characteristic spatial correlation regions, then the rela-

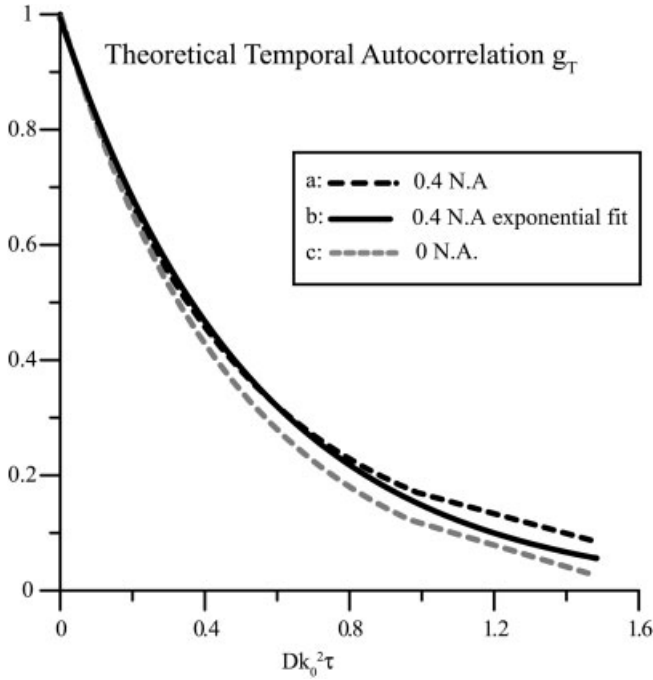


**Fig. 10.2.** Theoretical temporal autocorrelation function of the scattered light intensity [as calculated from Eq. (43)] vs. the unitless time parameter  $Dk_0^2\tau$ . Three curves are plotted. (a) The black dashed line curve is obtained from a numerical integration of Eq. (43) for a 0.4 numerical aperture objective. (b) The black solid curve is a single exponential decay, fitted to the points obtained from the numerical integration. (c) The grey dashed line is the pure exponential decay obtained from the zero aperture limit.

tive size of the observed fluctuations will be greatly reduced, compromising the signal-to-noise ratio. Ideally, a pixel should cover less than one spatial correlation region.

We start the calculation of the spatial autocorrelation function in a manner similar to the temporal autocorrelation function [Eq. (14)] except here using the intensities at two different *positions*  $\mathbf{r}_{1,2}''$ , recorded at the same time. (Because of the similarity of the mathematical procedures, we will skip most of the details here.) We count only those scattering centers that are actually present in the illuminated region at one snapshot of time, so all the  $b_i(t)$  factors can be set equal to unity.

$$\begin{aligned}
 \Gamma_S(\Delta\mathbf{r}'') = & \left(\frac{|E_0|}{i\lambda L}\right)^4 \left\langle \sum_{i,j,k,l}^N \int \exp(-ik_0\mathbf{r}_i(t_1) \cdot \mathbf{Q}_a) \exp(ik_0\mathbf{r}_j(t_1) \cdot \mathbf{Q}_b) \right. \\
 & \left. \times \exp(ik_0\mathbf{r}_k(t_1) \cdot \mathbf{Q}_c) \exp(-ik_0\mathbf{r}_l(t_1) \cdot \mathbf{Q}_d) \right\rangle
 \end{aligned}$$

$$\begin{aligned}
& \times \exp\left(-\frac{ik_0\mathbf{r}'_a \cdot \mathbf{r}''_1}{L}\right) \exp\left(\frac{ik_0\mathbf{r}'_b \cdot \mathbf{r}''_1}{L}\right) \exp\left(\frac{ik_0\mathbf{r}'_c \cdot \mathbf{r}''_2}{L}\right) \\
& \times \exp\left(-\frac{ik_0\mathbf{r}'_d \cdot \mathbf{r}''_2}{L}\right) d^2\mathbf{r}'_a d^2\mathbf{r}'_b d^2\mathbf{r}'_c d^2\mathbf{r}'_d
\end{aligned} \tag{45}$$

As in the calculation for the temporal autocorrelation function, the spatial autocorrelation function terms corresponding to  $m = 1, 2, 3$  (see Table 10.1) produce zero values and the  $m = 4, 5, 6$  terms produce non-zero values. In the latter terms, an integral appears that can be related to a first-order Bessel function:

$$\int \exp\left(\frac{-ik_0\mathbf{r}' \cdot \Delta\mathbf{r}''}{L}\right) d^2\mathbf{r}' = \frac{2J_1(\mu)}{\mu} \tag{46}$$

where  $\Delta\mathbf{r}'' \equiv \mathbf{r}''_2 - \mathbf{r}''_1$  and  $\mu = k_0 r_o' \Delta\mathbf{r}''/L$  and  $r_o'$  is the radius of the objective.

The final form of the spatial autocorrelation function becomes:

$$\Gamma_S(\Delta\mathbf{r}'') = \langle I \rangle^2 \left\{ \left[ 1 + \left( \frac{2J_1(\mu)}{\mu} \right)^2 \right] + \langle M \rangle^{-1} \left[ \left( \frac{2J_1(\mu)}{\mu} \right)^4 - \left( \frac{2J_1(\mu)}{\mu} \right)^2 - 1 \right] \right\} \tag{47}$$

For large  $\langle M \rangle$ , the  $\langle M \rangle^{-1}$  term is small and is not included in further calculations. The leading term of the spatial autocorrelation function has the same distance dependence as the point spread function of the microscope objective at the image plane (an Airy disk). In analogy with Eq. (42), a normalized form of  $\Gamma_S(\Delta\mathbf{r}'')$  can be written as

$$g_S(\Delta\mathbf{r}'') = \frac{\Gamma_S(\Delta\mathbf{r}'') - \langle I(\mathbf{r}'') \rangle^2}{\langle I(\mathbf{r}'') \rangle^2} \tag{48}$$

The characteristic spatial correlation distance is qualitatively the average distance in the image plane from constructive to destructive interference [18, 19]. It can be defined quantitatively as the distance  $l_c$  in  $\mathbf{r}''$ -space corresponding to  $\mu = 1$ . Parameter  $\mu$  [see after Eq. (46)] can be rewritten in terms of the numerical aperture (NA) and magnification (mag) of the objective (in the low aperture, air immersion case) as:

$$\mu = \left( \frac{2\pi}{\lambda} \right) \left( \frac{\text{NA}}{\text{mag}} \right) \Delta\mathbf{r}'' \tag{49}$$

Thus the spatial correlation distance  $l_c$  is:

$$l_c = \Delta\mathbf{r}''_c = \left( \frac{\lambda}{2\pi} \right) \left( \frac{\text{mag}}{\text{NA}} \right) \cong 8 \mu\text{m} \tag{50}$$

The size of the CCD camera pixel in the experiments reported here is  $6.3 \mu\text{m}$ , so that approximately one spatial correlation distance is observed in each pixel.

### 10.2.8

#### Variance of Intensity Fluctuations: Mobile Fraction

We define the mobile fraction  $\beta$  to be the ratio of the scattered intensity from the mobile scattering centers  $\langle I \rangle_{\text{mob}}$  to the total scattering intensity  $\langle I \rangle$  in the collection volume of each pixel:

$$\beta = \frac{\langle I \rangle_{\text{mob}}}{\langle I \rangle} \quad (51)$$

where

$$\langle I \rangle = \langle I \rangle_{\text{mob}} + \langle I \rangle_{\text{fix}} \quad (52)$$

and  $\langle I \rangle_{\text{fix}}$  arises from fixed scattering centers (such as the sample substrate). The mobile fraction  $\beta$  can be estimated from the variance of the intensity fluctuations, which is the difference between the extrapolated values of the temporal autocorrelation function values at  $\tau = 0$  and at  $\tau = \infty$ . Combining the definition of  $\Gamma$  in Eq. (13) with Eq. (52), we get

$$\begin{aligned} \Gamma(\tau) = & \langle I_{\text{mob}}(t)I_{\text{mob}}(t+\tau) \rangle + \langle I_{\text{mob}}(t)I_{\text{fix}}(t+\tau) \rangle \\ & + \langle I_{\text{fix}}(t)I_{\text{mob}}(t+\tau) \rangle + \langle I_{\text{fix}}(t)I_{\text{fix}}(t+\tau) \rangle \end{aligned} \quad (53)$$

The first term in the above equation can be reduced to  $\langle I \rangle_{\text{mob}}^2 + g(\tau)\langle I \rangle_{\text{mob}}^2$  where  $g(0) = 1$  and  $g(\infty) = 0$ . The next two terms are each  $\langle I \rangle_{\text{mob}}\langle I \rangle_{\text{fix}}$  and the last term is  $\langle I^2 \rangle_{\text{fix}} = \langle I \rangle_{\text{fix}}^2$  since the scattering due to the immobile intensity does not fluctuate. Therefore,

$$\Gamma(0) = 2\langle I \rangle_{\text{mob}}^2 + 2\langle I \rangle_{\text{mob}}\langle I \rangle_{\text{fix}} + \langle I \rangle_{\text{fix}}^2 \quad (54)$$

and

$$\Gamma(\infty) = \langle I \rangle_{\text{mob}}^2 + 2\langle I \rangle_{\text{mob}}\langle I \rangle_{\text{fix}} + \langle I \rangle_{\text{fix}}^2 = \langle I \rangle^2 \quad (55)$$

and therefore

$$\beta^2 = \frac{\langle I \rangle_{\text{mob}}^2}{\langle I \rangle^2} = \frac{\Gamma(0) - \Gamma(\infty)}{\Gamma(\infty)} \quad (56)$$

## 10.3 Experimental Design

### 10.3.1 Optical Setup

Light from a CW helium neon laser (15 mW, 632.8 nm) was focused through an 8-mm focal length cylindrical lens and propagated down towards the sample (at  $\sim 60^\circ$  from the vertical) such that the direct incident light missed the objective (Fig. 10.3a). The resulting illumination region was a thin line, 2  $\mu\text{m}$  full-width at half-maximum and oriented so that the stripe was in the plane of incidence.

A Leitz Diavert inverted microscope with a 0.4 NA, 32X long working distance objective collected the scattered light from the sample. The objective focused the scattered light at an image plane above the microscope at which a 5  $\mu\text{m}$  wide slit was located. Lens L in the path between the image plane and the face of the CCD camera refocused the scattered light and image plane slit onto the CCD array of a digital camera with no additional magnification. The image plane slit served to select a clean-edged line of scattered light that illuminated only a single column of pixels in the CCD camera (Fig. 10.3b). The image plane slit also created a confocal-like effect, reducing the out-of-focus light at the camera.

The sample chamber containing either cells or beads (see below) was placed on a motorized stage (Maerzhaeuser Wetzlar, Germany) that could be translated step-wise in the direction transverse to the illumination stripe.

Emission path filters (Chroma Technology, Corp., Brattleboro, VT) were chosen depending upon whether light scattering (for DLSM experiments) or fluorescence (for number fluctuation experiments) was performed. For DLSM, a  $632 \pm 10$  nm laser narrow bandwidth filter was used. For the number fluctuation experiments, a long pass 650 nm filter was used to block scattered excitation light and transmit fluorescence from dye-labeled beads.

### 10.3.2 Data Acquisition

During an image acquisition period, the camera shutter remained open. The progressive scan cooled CCD camera (Pentamax-KAF-1400, Roper Scientific, Trenton, NJ, pixel size  $6.8 \times 6.8 \mu\text{m}$ ) reads out data column-by-column such that the intensities recorded in each pixel column shifts one column (Fig. 10.4) every 300  $\mu\text{s}$ . The shifting continues until the full frame of the CCD array is read. Therefore, each pixel along the column of illumination formed by the image plane slit in our optical setup gave rise to a temporal streak of intensity fluctuations with a “bin time” of 300  $\mu\text{s}$ .

Custom PC software written in LabView and interfaced to a data acquisition board (National Instruments, Austin, TX) coordinated the image acquisition with the microscope stage controller (Lang MCL-2, Huttenberg, Germany). Images



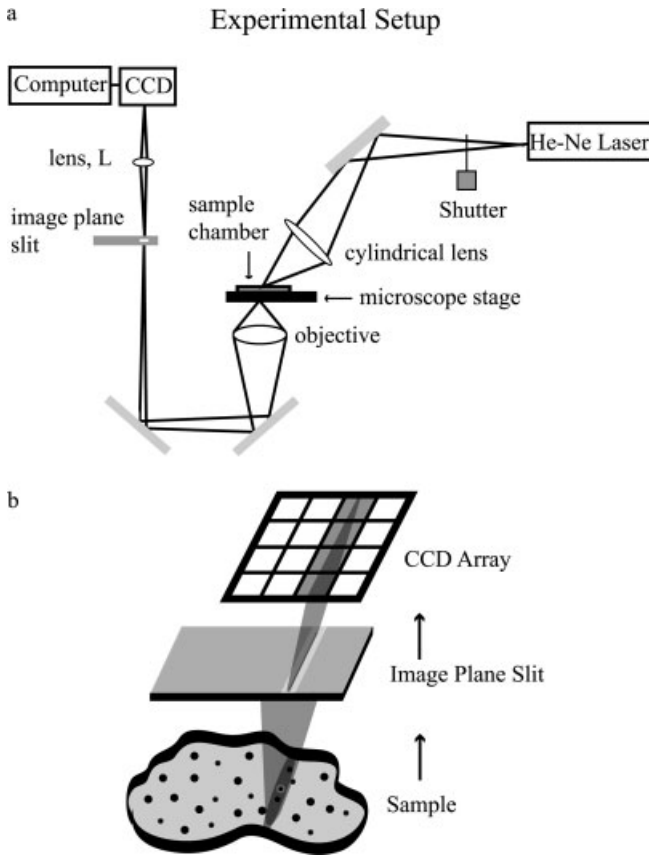


**Fig. 10.3.** Schematic drawing of experimental setup. (a) A cylindrical lens focuses the beam from a He-Ne laser to create a thin stripe of illumination (oriented in the page plane here) on the sample. A motorized stage controls the motion of the sample and the sample is moved in the  $x$ -direction only (normal to the page plane). A 32X, 0.4 NA, objective gathers the scattered light from the sample and focuses it onto a  $5\ \mu\text{m}$  wide slit placed in the image plane and oriented in the direction of

the illumination stripe. A lens (L) re-images the slit onto the face of a CCD camera without additional magnification. (b) Detail of the imaging on the CCD array, with lenses omitted from the drawing. The slit excludes out-of-focus light and creates a well-defined focused line of scattered illumination that gets mapped onto a single column of the CCD camera array. Other columns of the CCD camera array are not illuminated.

were taken every 500 ms, followed by the advancement of the microscope stage to a new position on the sample. The sequence was repeated until the entire sample had been stepped through, resulting in a stack of images containing the intensity fluctuations from every point in the sample. Images were stored using a Windows 98, 600 MHz Intel P-III computer running WinView (Roper Scientific, Trenton, NJ).

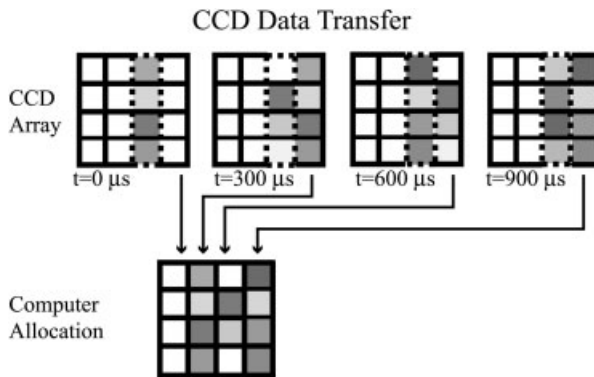


**Fig. 10.4.** Schematic of CCD readout mechanism. The dashed rectangle represents the column of the CCD array that is constantly exposed to the scattered light. The CCD array readout shift register is represented by the column of pixels at the extreme right. (Between the illuminated columns and the shift register there may be intermediate columns but these are not shown.) The (progressive scan) camera is operated in its normal readout mode, except with the camera shutter always open. At the end of every  $300 \mu\text{s}$  interval, accumulated intensity data in the illuminated column of pixels is advanced rightward column-by-column toward the shift register. At the same time, blank counts from the pixel columns to

the left are shifted into the illuminated column, effectively clearing it, and data in the shift register is read into an array in the computer memory. This process continues until the shift register has read every column of the CCD array, thereby completing image acquisition for a single stage position of the sample. The final “image” as recorded in the computer consists of a time sequence ( $\Delta t = 300 \mu\text{s}$ ) of 800 intensity readings at each pixel along the illuminated pixel column. The next streak-like image is acquired after the motorized microscope stage has advanced to the next position on the sample. The whole image acquisition process is complete when the stage has stepped through the entire sample.

### 10.3.3

#### Sample Preparation: Polystyrene Beads

For dynamic light scattering experiments, 200 and 500 nm diameter polystyrene nanospheres (Duke Scientific, Palo Alto, CA) were tip-sonicated (to break up large clusters) and loaded at their undiluted aqueous suspension concentrations of  $2.1 \times 10^{12}$  particles  $\text{mL}^{-1}$  (200 nm) and  $1.4 \times 10^{11}$  particles  $\text{mL}^{-1}$  (500 nm) into separate rectangular cross-section glass microcapillary tubes (inner thickness  $0.05 \times 0.5$  mm wide, Wilmad Specialty Glass, Buena, NJ) by capillary action. The two microcapillary tubes containing the two bead sizes were placed side-by-side on a plastic holder and oriented at a diagonal across the microscope field of view so that laser light line illuminated both microcapillary tubes simultaneously. Vacuum grease was used to seal the ends of the microcapillary tubes and to adhere them to the holder. For number fluctuations measurements, 200 nm carboxylate-modified fluorescent dark red FluoSpheres were obtained from Molecular Probes (Eugene, OR). FluoSpheres were drawn into microcapillary tubes at their undiluted concentration of  $5.3 \times 10^{12}$  particles  $\text{mL}^{-1}$  and mounted similarly.

The CCD camera acquired 40 images of the polystyrene beads assembly, each of which represented a line position 10  $\mu\text{m}$  apart on the sample.

#### 10.3.4

##### **Sample Preparation: Living Macrophages**

Coverslips (25 mm diameter, #2 thickness, and 32.5 mm diameter, #1.5 thickness) were treated for several hours in concentrated  $\text{H}_2\text{SO}_4$  in a porcelain holder and then rinsed for 2 h in distilled water and oven dried overnight at 130 °F. This treatment greatly reduced the light scattering from the coverslips.

Two aqueous buffers, Ringer (RB) (155 mM NaCl, 5 mM KCl, 2 mM  $\text{CaCl}_2$ , 1 mM  $\text{MgCl}_2$ , 2 mM  $\text{NaH}_2\text{PO}_4$ , 10 mM HEPES, pH 7.2, 10 mM glucose) and Ringers with acetate (ARB) (80 mM NaCl, 70 mM sodium acetate, 5 mM KCl, 2 mM  $\text{CaCl}_2$ , 1 mM  $\text{MgCl}_2$ , 2 mM  $\text{NaH}_2\text{PO}_4$ , 10 mM HEPES pH 6.8, 10 mM glucose) were prepared for use during the experiment.

Monoclonal mouse macrophage cultures (RAW 264.7, American Type Tissue Culture, Manassas, VA) were obtained from the laboratory of Dr Joel Swanson (Department of Immunology, University of Michigan Medical School). The cultures were maintained in 60 mm diameter polystyrene tissue culture dishes in 10 mL of a 0.2  $\mu\text{m}$  filtered (Millipore, Bedford MA) solution of Dulbecco's modified Eagle's medium containing 10% heat-inactivated fetal bovine serum, high glucose, L-glutamate and sodium pyruvate (DMEM, Grand Island Biological Company, Grand Island, NY) and penicillin–streptomycin. For replating onto the glass coverslips, cells were dislodged by vigorous trituration. A 1:30 dilution of the resulting suspension in DMEM was prepared, plated onto 32.5 mm coverslips (pre-cleaned as described above) in polystyrene dishes, and incubated for two days at 37 °C. Macrophage cells on a glass coverslip can spread to  $\sim 80$   $\mu\text{m}$  diameter circular shapes, with thicknesses of a couple of microns at the periphery and about 5  $\mu\text{m}$  in the center.

The cell sample chamber consisted of a 25 mm diameter, 50  $\mu\text{m}$  thick Teflon spacer ring, cut into two slightly separated halves to provide a channel for easy fluid exchange by capillary action. These spacers were placed on top of the 32.5 mm coverslip with adherent cells. A 25 mm diameter coverslip was then placed over the spacers to create a cell sandwich chamber, which was clamped with plastic clips over a drilled hole in a plastic plate. The cells in the chamber were gently rinsed with 1 mL of RB.

#### 10.3.5

##### **Buffer Changes during Data Acquisition**

The CCD camera first took 120 successive streak images of the cell in RB with a 5  $\mu\text{m}$  step stage motion between each image. Subsequently, 1 mL of ARB was exchanged into the cell coverslip sandwich and incubated for 20 min before a second similar round of streak image recording was initiated over the same cell area. A final 1 mL of RB buffer was exchanged into the sample chamber, another 20 min of

incubation time elapsed, and the camera acquired a final similar sequence of 120 streak images over the same area.

## 10.4 Data Analysis

The two types of intensity autocorrelation functions – temporal and spatial – for each pixel along an illuminated line can be calculated from the width and height, respectively, of the same streak image (Fig. 10.5a).

### 10.4.1 Temporal Intensity Autocorrelation Function

Normalized temporal autocorrelation functions  $g_T(\tau)$  of the experimental intensity fluctuations [see Eq. (42)] were calculated along the rows for each point on the line of illumination.

The theoretically expected temporal autocorrelation function [Eq. (43)] can be integrated numerically and fit to a single exponential (Fig. 10.2b). The close agreement between the fitted function and the numerical integration justifies approximating the experimental data with a single exponential. However, DLSM is very sensitive to extraneous sources of noise, such as table and acoustic vibrations and laser source fluctuations. To remove these largely periodic noise effects, the obtained temporal autocorrelation functions were fit to a sum of a single exponential, three sine waves, and a constant:

$$g_{\text{fit}}(\tau) = A_0 e^{-A_1 \tau} + A_2 \cos(2A_3 \pi \nu \tau) + A_4 \cos(2A_5 \pi \nu \tau) + A_6 \cos(2A_7 \pi \nu \tau) + A_8 \quad (57)$$

where  $A_{0-8}$  are the fitting parameters. The  $A_1$  decay rate parameter was assigned a pseudocolor for each pixel to create a spatial map of the fluctuation decay rates. The mean value of the decay rates for each bead size was used to calculate the apparent diffusion coefficients using  $Dk_0^2 \tau_c \approx 0.52$  where  $\tau_c = 1/A_1$ .

### 10.4.2 Spatial Intensity Autocorrelation Function

We calculated the normalized spatial autocorrelation function  $g_s(\Delta \mathbf{r}'')$  [see Eq. (48)] along each of the columns of a streak image of the intensity fluctuations from polystyrene bead suspensions. To obtain a single spatial autocorrelation function for comparison with theory, all of the  $g_s(\Delta \mathbf{r}'')$  were averaged over all of the columns. The result was not fit to the theoretical function, but the characteristic decay distance was compared with theory [see Eqs. (49) and (50)].

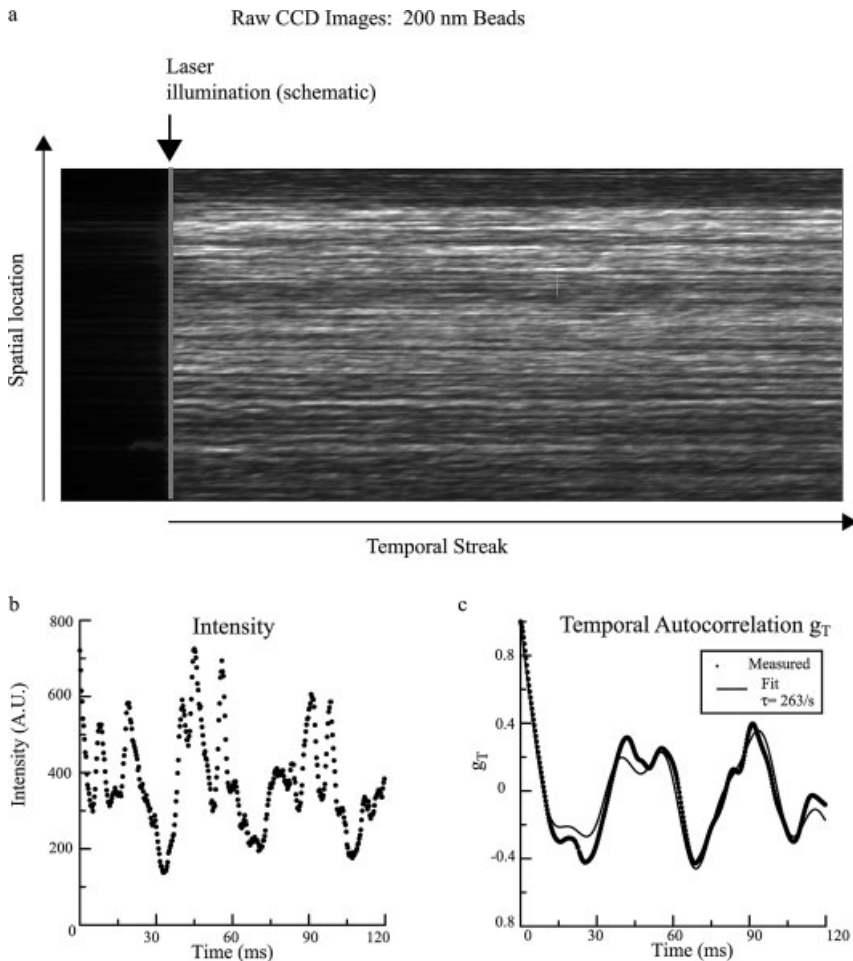


**Fig. 10.5.** (a) Example of an image recorded by the CCD camera of a 200 nm polystyrene bead suspension. The image is recorded from a single stage position on the sample. The vertical column corresponds to spatial positions on the sample illuminated by the thin line. Each horizontal row is the temporal streak recorded during the readout process of

the CCD camera at this location. (b) An example of a recorded intensity fluctuation along one of the rows. (c) The autocorrelation function of the intensity time course shown in (b), based directly on the experimental intensities (dotted line) and then subsequently fitted with the form of Eq. (43) (solid line).

#### 10.4.3

##### Mobile Fraction

Mobile fraction  $\beta$  was calculated pixel-by-pixel from  $\Gamma(0)$  and  $\Gamma(\infty)$  [Eq. (56)], and the calculated values were assigned different pseudocolors for display. Eq. (56) assumes that phase fluctuations are the only contributors to  $\Gamma(\tau)$ . However, in an actual experiment,  $\Gamma(\tau)$  can also be affected by other factors, as follows.

- (a) *Photon shot noise* contributes to the amplitude of  $\Gamma(\tau)$ , but only at  $\tau = 0$  since the photon arrival times are uncorrelated. Thus, to obtain an accurate estimate of  $\Gamma(0)$  apart from shot noise, a linear extrapolation was performed from the values of  $\Gamma(1)$  and  $\Gamma(2)$ .
- (b) *Number fluctuations* were recorded on a sample that produces no coherent phase fluctuations: fluorescent beads. Here, the variance was very small, only marginally above the noise level in  $\Gamma(\tau)$ , and  $\Gamma(0)$  was estimated as  $\Gamma(1)$ .
- (c) *Overly large pixels size* can decrease the recorded variance; pixels should be smaller than the spatial correlation distance, as indeed occurs here (see Section 10.2).

## 10.5

### Experimental Results

Polystyrene beads were used to quantitatively test the DLSM technique and compare the experimental values of the mean decay rates and mobile fractions with values predicted from theory. DLSM was then applied to macrophage cells as a test on a living biological system. Macrophages are very motile and their motility can be altered pharmacologically.

#### 10.5.1

##### Polystyrene Beads: Temporal Phase Autocorrelation

An example of scattered light intensity fluctuations along with the corresponding autocorrelation function is displayed in Figs. 10.5(b) and (c). The temporal autocorrelation functions were fit to a linear combination of a single exponential and three sine waves [Eq. (57)]. The sine waves were added to the fitting function because the obtained autocorrelation functions exhibited some pseudo-oscillatory behavior with varying frequencies in addition to the expected exponential decay. An average of the ( $\sim 1000$ ) temporal autocorrelation functions obtained from the rows of a single streaked image of 200 nm polystyrene beads is displayed in Fig. 10.6. This average exhibits only an exponential decay, indicating that the pseudo-oscillations in some individual rows are random noise arising from the low number of correlation times in the time represented by a streak (240 ms).

Figure 10.7(b) shows a DLSM decay rate pseudocolor spatial map of a section of two adjacent microcapillary tubes containing 200 and 500 nm diameter beads, respectively. Although the range of colors suggests a wide distribution of decay rates in each tube, there are more pixels with shorter decay rates for the system of 200 nm beads than for 500 nm beads, as can be seen in normalized histograms of the decay rates for both sonicated and unsonicated beads of both sizes (Fig. 10.8). Fluctuation decay rates are generally much faster for the 200 nm beads. In addition, sonication resulted in an increase of the average decay rates towards the theoretical values. Average values of decay rates measured with our technique were 209 and 256  $s^{-1}$  (non-sonicated and sonicated, respectively) for the 200 nm beads and

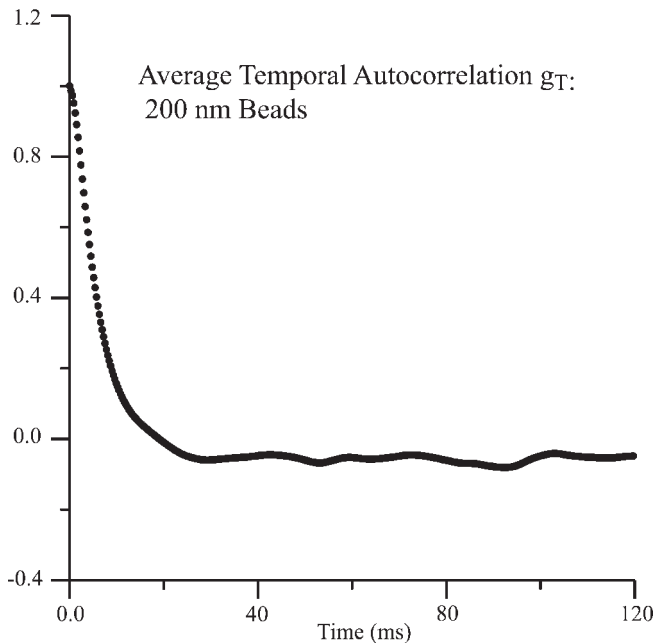


**Fig. 10.6.** Temporal autocorrelation function of 200 nm polystyrene beads, averaged over all the rows of the streaked image shown in Fig. 10.5(a).

107 and  $144 \text{ s}^{-1}$  (non-sonicated and sonicated, respectively) for the 500 nm beads. These decay rates correspond to diffusion coefficients of  $1.35 \times 10^{-8}$  and  $8.75 \times 10^{-9} \text{ cm}^2 \text{ s}^{-1}$  for the sonicated 200 and 500 nm beads, respectively. Table 10.2 compares the experimentally obtained results with the theoretically predicted values. The experimental results are in good agreement with the hydrodynamic theory values for the 500 nm sonicated beads and about 40% lower than the theoretical expectation for the 200 nm sonicated beads. There is no obvious correlation between variations in the local decay rates and the local mean scattered light intensity (data not shown).

### 10.5.2

#### Variance of Intensity Fluctuations on Beads: Phase Fluctuations

A qualitative representation for the size of the intensity fluctuations can be obtained by visual inspection of an image from the CCD camera. Figure 10.9 shows a raw streaked image recorded by the CCD camera for scattered light (DLSM fluctuations, Fig. 10.9a) and for fluorescence (number fluctuations, Fig. 10.9c), both recorded from 200 nm carboxylate-modified dark red FluoSpheres. Figure 10.9(b) shows the normalized temporal autocorrelation function,  $g_T(\tau)$ , for a typical row in the DLSM streaked image depicted in Fig. 10.9(a). Figure 10.9(d) shows a corre-

## Polystyrene Beads: Spatial Maps

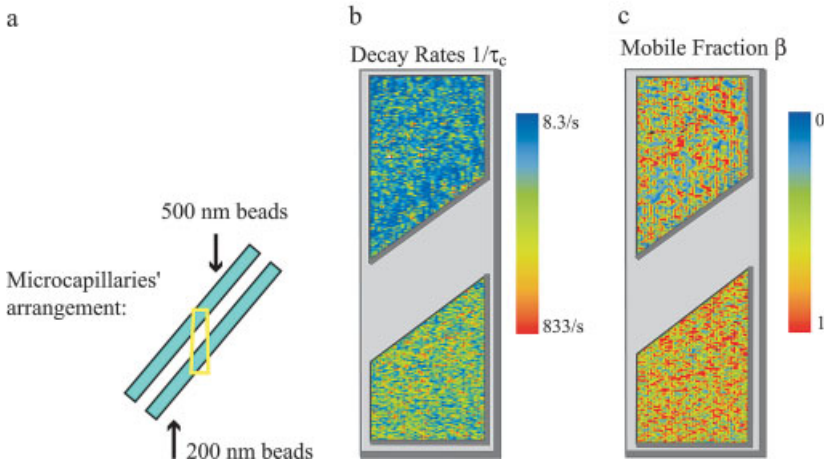


**Fig. 10.7.** Experimental spatial maps for the polystyrene beads. (a) Two different sizes of polystyrene beads were used in a single experiment: 200 and 500 nm. The beads were in separate microcapillary tubes oriented at an angle with respect to the optical axis and mounted on a homemade microscope sample chamber. The yellow box represents the field of view of the microscope. (b) Spatial map of the decay rates in the field of view. Note the faster diffusion of the 200 nm beads, as expected. (c)

Spatial map of the mobile fractions, obtained using Eq. (56), in the same field of view. A zero on the scale implies that most of the scattering centers are immobile whereas unity implies all of the scattering centers are mobile. Both bead sizes show a large mobile fraction: for the 200 nm beads  $\beta_{avg} = 0.63$ , and for the 500 nm beads  $\beta_{avg} = 0.42$ . The 200 nm beads show a smaller spread of the degree of mobility than the 500 nm beads.

sponding normalized temporal autocorrelation function for the number fluctuation experiment of Fig. 10.9(c). The relative variance of phase fluctuations is much larger than the relative variance of number fluctuations.

In principle, the amplitude of the normalized autocorrelation function for an entirely mobile DLSM sample should be unity. But, as can be seen from Fig. 10.9(b), the experimental value is  $\sim 0.6$ . This decreased amplitude is probably due to a fixed scattering background and a consequent “mobile fraction” that is less than unity.

## 10.5.3

**Polystyrene Beads: Number Fluctuations**

Number fluctuations without contamination by phase interference effects could be autocorrelated from streaked images of the fluorescence from labeled polystyrene beads. The average value of the normalized variance for all of the temporal autocorrelation functions from number fluctuations was only  $10^{-3}$ . Thus, we conclude that the fluctuations observed at 632 nm were due almost exclusively to dynamic light scattering phase fluctuations rather than number fluctuations of particles dif-



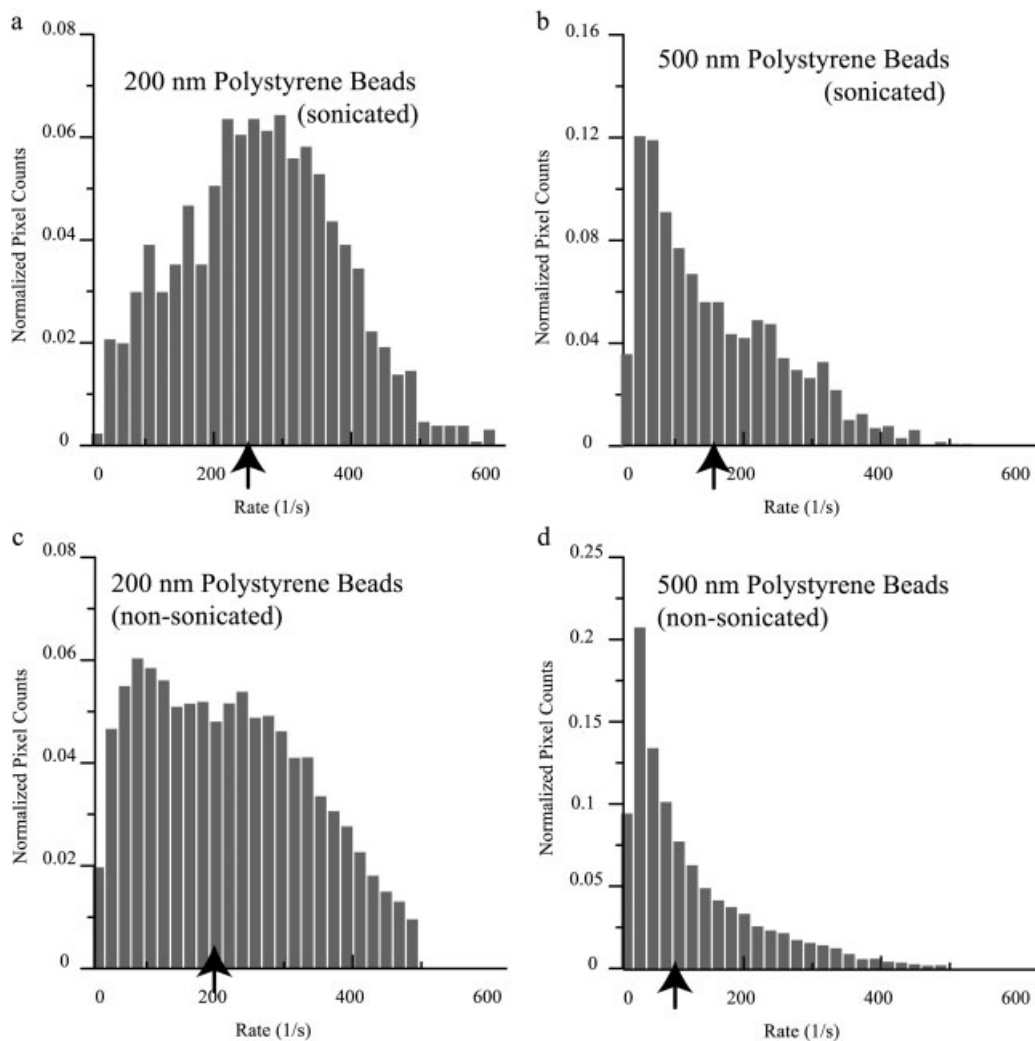


**Fig. 10.8.** Histograms of the decay rates for the polystyrene beads. (a, c) 200 nm beads (sonicated and unsonicated). (b, d) 500 nm beads (sonicated and unsonicated). Arrows indicate mean values.

**Tab. 10.2.** Mean diffusion coefficients of polystyrene beads (average experimentally measured diffusion coefficients for 200 and 500 nm beads along with expected values from hydrodynamic theory).

<i>Diffusion coefficient</i> ( $10^{-8} \text{ cm}^2 \text{ s}^{-1}$ ) $\pm$ S.E.	<i>200 nm sonicated beads</i> ( $2.1 \times 10^{12} \text{ particles mL}^{-1}$ )	<i>500 nm sonicated beads</i> ( $1.4 \times 10^{11} \text{ particles mL}^{-1}$ )
Experimental	$1.35 \pm 0.03$	$0.875 \pm 0.03$
Theoretical	2.23	8.76

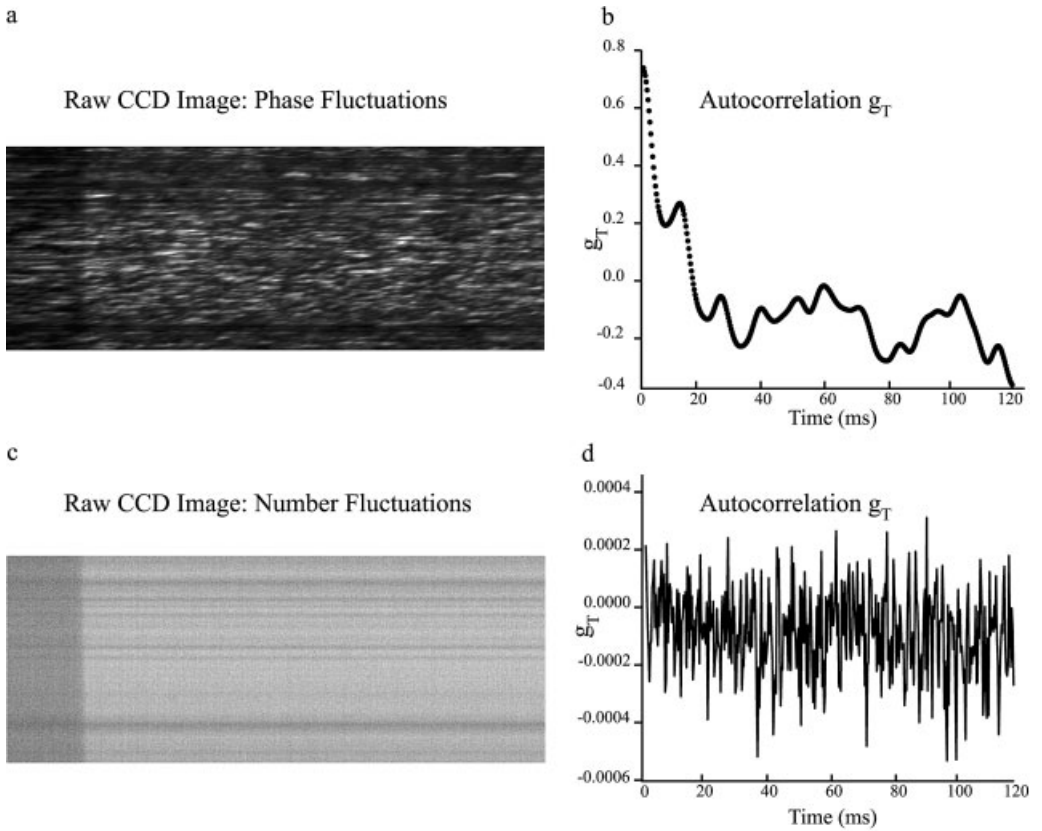


**Fig. 10.9.** CCD camera images and their corresponding autocorrelation functions of intensity fluctuations from 200 nm carboxylate-modified dark red FluoSpheres. (a) Raw streak image from dynamic light scattering measurement. (b) Normalized temporal autocorrelation function for panel a, calculated using Eq. (43). The large variations in intensity across the raw image imply a large amplitude in the temporal autocorrelation function. (c) Image from the number fluctuation experiment

is taken from the same sample as in panel a, but with a long pass 650 nm filter placed in the emission path. The image is very smooth, indicating small intensity variations. (d) Normalized temporal autocorrelation function for panel c. The function has a very small amplitude, implying that the contribution from particle number variations to the DLSM intensity fluctuations seen in panels a and b is very small.

fusing in and out of the volume observed by a pixel. The intensity fluctuations resulting from the fluorescence emission were so small that decay rates could not be reliably extracted from the temporal autocorrelations.

#### 10.5.4

##### Polystyrene Beads: Spatial Autocorrelation

Figure 10.10 shows the spatial autocorrelation function obtained for the 200 nm sonicated polystyrene beads along with the theoretically predicted one [Eq. (48)].

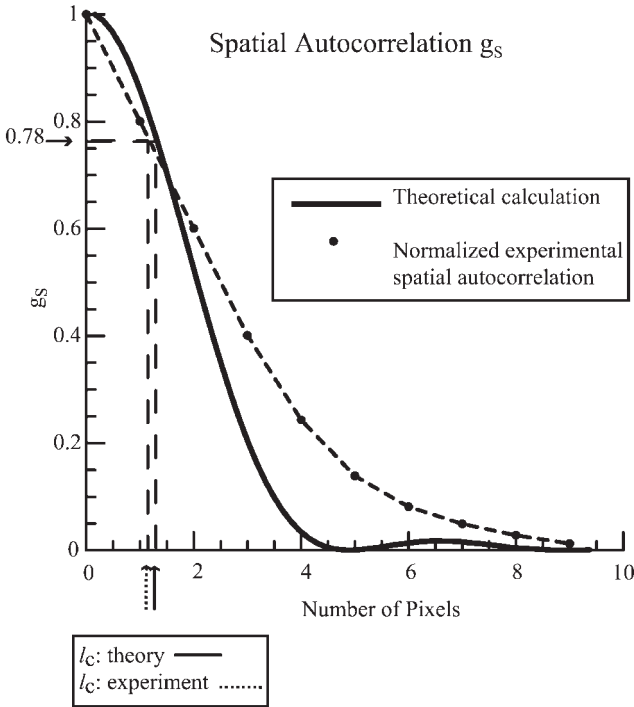


**Fig. 10.10.** Normalized spatial autocorrelation function for the 200 nm polystyrene beads. The experimentally obtained spatial autocorrelation function is depicted by black dots connected by dashed lines. The theoretical spatial autocorrelation function [based on Eq. (48)] is depicted by the solid line. The characteristic decay distance of the spatial autocorrelation function (where  $\mu = 1$ ) is marked for both the experimentally and theoretically obtained curves.

The amplitude at which the characteristic distance is defined ( $\mu = 1$ ) is indicated, from which the spatial correlation distance  $l_c$  can be derived [Eq. (50)]. The spatial correlation distance obtained from the theoretical curve is approximately  $l_c = 1.27$  pixels, which corresponds to  $8 \mu\text{m}$ , whereas the value calculated from the experimentally obtained spatial autocorrelation function is  $l_c = 1.1$  pixels, which corresponds to  $6.93 \mu\text{m}$ . Thus, the experimentally obtained value of the spatial correlation distance agrees well with the theoretically derived one. In addition, since the size of the CCD camera pixel is  $6.3 \mu\text{m}$ , each pixel will observe intensity fluctuations from approximately one spatial correlation area.

### 10.5.5

#### Polystyrene Beads: Mobile Fractions

Mobile fractions were calculated using Eq. (56). Figure 10.7(c) shows the spatial map of the mobile fractions obtained from the dynamic light scattering intensity

fluctuation measurements for the 200 and 500 nm beads. The 200 nm beads show a higher overall relative mobility than the 500 nm beads. This is because the concentration of the 200 nm beads is an order of magnitude larger than that of the 500 nm beads, which caused the mean light scattering intensity to be larger from the smaller beads. Thus, scattering from the smaller beads constituted a larger fraction of the total scattering in the experimental system, which includes background scattering from the microcapillary tubes and optics.

### 10.5.6

#### Living Macrophage Cells: Temporal Autocorrelation

DLSM experiments were performed on a total of 21 macrophage cells as follows: (a) 10 min after the cell was removed from the incubator and washed with Ringers

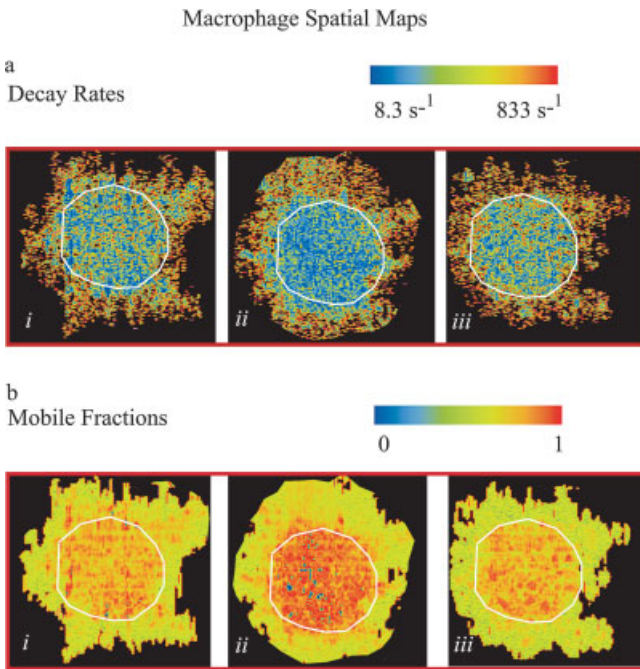


**Fig. 10.11.** Experimental spatial maps of a macrophage cell. For both panels a and b, each map depicts one of the three treatments on the cell: (i) Cell was flushed with 1 mL of Ringer's buffer (RB); (ii) cell was flushed with 1 mL of an acetate-containing RB (ARB) and incubated for 20 min; (iii) the ARB was washed out with RB and the cell was incubated for 20 min. (a) Spatial map of the temporal autocorrelation intensity fluctuation decay

rates. There is a noticeable decrease in motility of the acetate-treated cell. Washing out the acetate reverses this attenuated motility, restoring the cell to its initial state. Black pixels occur where the scattering intensity was too low to obtain useful data. (b) Spatial map of the mobile fractions  $\beta$  of macrophages. The mobile fraction data are plotted on a logarithmic scale. Most of the motion occurs in the central interior portion of the cells.

buffer; (b) 20 min after the acetate-containing Ringers buffer was introduced; and (c) 20 min after Ringers buffer with acetate was replaced with plain Ringers buffer to remove the acetate. Figure 10.11(a) shows pseudocolor spatial maps of the fluctuation decay rates created for the three conditions for a typical cell.

A white overlay line divides the cell image into outer and inner regions. In all three maps, the outer region of the cell shows faster motility than the inner region. Additionally, the center of the cell shows a noticeable decrease in the macrophage motility when acetate is added. The original motility seems to be restored when acetate is washed out. The black areas within the periphery of the cell region represent the locations at which the decay rates could not be reliably calculated because the scattered intensity was too low.

#### 10.5.7

##### **Living Macrophage Cells: Mobile Fraction**

Figure 10.11(b) shows the spatial maps of the mobile fractions on a log scale for the three treatments described above. Overall, the mobile fraction is quite low, especially in the outer region where the mean scattering intensity from the cell is a smaller fraction of the background scattering.

## 10.6

### **Discussion**

We have demonstrated that the dynamic light scattering imaging technique presented here is a viable method to observe and image small relative motions among nearby scattering centers in a microscope [20, 21]. These relative motions, visualized as intensity fluctuations, are detected in both non-biological and biological systems using a slow scan CCD camera. Fluctuations as fast as  $250 \text{ s}^{-1}$  were measured and relative motions between scattering centers on the order of a fraction of a wavelength were spatially mapped. The technique provides information about the relative motion of the scattering centers (rather than their relative location as with conventional microscopy) without sacrificing optical resolution.

#### 10.6.1

##### **Polystyrene Beads**

The experimental diffusion coefficients were relatively correct for the ratio of 200 vs. 500 nm polystyrene beads with the values for the 200 nm beads slower than expected. However, both were somewhat lower than theoretically predicted from hydrodynamics. This discrepancy can be explained by the fact that aggregates were most likely present in both samples, forming particles with larger effective sizes and therefore lowering their diffusion rate. Sonication of the bead suspensions increased the diffusion rates towards the theoretical value.

Because of the high concentration of beads in these samples, we would expect that number fluctuations should be small, as was experimentally confirmed. Also, because the relevant characteristic volume for number fluctuations (i.e., the effective volume observed by a pixel) is typically larger than the characteristic volume leading to phase fluctuations, number fluctuations are likely to be slower than phase fluctuations, as was also experimentally confirmed. Number fluctuations do not contribute much to the DLSM streaked images observed here.

Although not relevant to our experimental conditions, extreme cases could show interesting number fluctuation effects, according to the theory. In the limit of one scattering center, the only contribution to the intensity autocorrelation function will arise entirely from number fluctuations and so there will not be a contribution due to phase fluctuations. If the number fluctuations occur on a faster time scale than the phase fluctuations, there would be an appreciable decay of the autocorrelation function before a phase fluctuation took place. Thus, only if the phase fluctuations occur on a faster time scale than the number fluctuations will any phase fluctuations be detected.

The spread in diffusion rates is in part due to the noisiness of the temporal autocorrelation function. This effect arises from the fact that the temporal autocorrelation function is computed over a relatively small number of coherence times. The coherence time of the intensity fluctuations for the 200 nm polystyrene beads ( $\tau_c$ ) was approximately 3 ms and the intensity fluctuations were collected over a 240 ms period ( $T$ , the time duration of a streak in the CCD record). The signal-to-noise in the autocorrelation function is thereby expected to be

$$(T/\tau_c)^{1/2} \approx 9$$

As an alternative approach to estimating the spread of autocorrelation decay rates arising solely from a finite experimental time  $T$ , we calculated the temporal autocorrelation function from an ensemble of numerically generated “telegraph” signals, over the same number of coherence times as in the experiment. A telegraph signal has transitions between +1 and -1 at completely uncorrelated times (but at a certain average rate) and has an exponentially decaying autocorrelation function [22].

Figure 10.12(a) shows the experimentally obtained distribution of decay rates for 200 nm polystyrene beads. Figure 10.12(b) is the distribution of decay rates from the autocorrelation function of the telegraph signal. The mean decay rate of the telegraph signal was scaled to match that of the experimental data. Comparison of the two confirms that much of the spread of experimental characteristic rates on the beads is due to an insufficient number of correlation times in  $T$ . However, the width of the distribution of the decay rates for the beads is still somewhat wider than that for the noise signal and it is skewed towards the slower decay rates. This indicates that the width of the distribution for the beads is in due in part to spatial heterogeneity of different sized aggregates in the 240 ms time scale of the experiments.

The theoretical calculation indicates that the amplitude of the normalized tem-

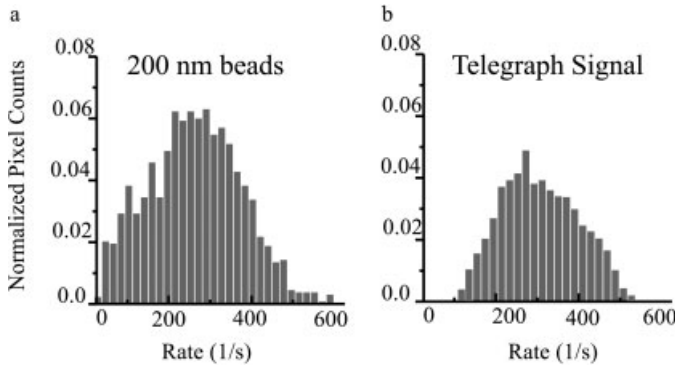


**Fig. 10.12.** Comparison of distribution of decay rates for the 200 nm polystyrene beads and for a numerically generated telegraph signal with the same average rate and number of coherence times for calculation. (a) Normalized intensity fluctuation decay rates for 200 nm polystyrene beads. (b) Normalized intensity fluctuation decay rates for the telegraph signal. The finite number of coherence times results in a spread in the intensity fluctuation decay rates for both the experimental data as well as the numerically generated noise signal.

poral autocorrelation function should be unity. However, the amplitude of the experimentally obtained autocorrelation function for polystyrene beads is significantly less. This amplitude reduction could arise for two reasons. First, there is a large background of immobile scattering emanating from the collection optics. This background does not contribute to the intensity fluctuation decay of the autocorrelation function, but does increase in the overall light intensity. Secondly, since the spatial correlation distance covered a region less than two pixels in size, not all the parts of a single pixel will see the same intensity, thereby decreasing the pixel-to-pixel variance of the recorded intensities.

The “proof-of-concept” experiments were performed on 200 and 500 nm polystyrene beads. However, notably, this technique is limited not by the size of the scattering center, but by the “scattering power”. If the scattering center is large but has the same index of refraction as the surrounding environment it will not be detected, but if the scattering center is extremely small but index mismatched to the surrounding environment it will be detected. If, in a microscope resolution region, the scattering center emits less light than the Rayleigh scattering of the water, it will not produce much of a DLSM effect.

### 10.6.2

#### Macrophages

Macrophages are immune system cells well known for their high motility. They are found in all tissues and in the blood. They are scavenger cells, acting as the first line of defense in recognizing and killing foreign microorganisms through phago-

cytosis [23]. During phagocytosis, the macrophage invaginates foreign material and breaks it down enzymatically.

Previous work on macrophages showed there are two distinct regions of the cell, a thin outer section and a thicker central section [24]. The DLSM spatial maps of the fluctuation decay rates of the imaged cells confirm this finding. Those maps indicate that the outer zone has faster fluctuations than the center of the cell. This result is particularly interesting because previous experiments from this lab, using polarized total internal reflection fluorescence microscopy, [25] showed the plasma membrane in the outer zone to be rather flat and inert whereas the plasma membrane of the central zone was quite bumpy and dynamic. Evidently, other intracellular scattering centers in that outer zone are moving rapidly.

Treatment with acetate-containing buffer reduced the rate of motion of scattering centers in the interior zone (Fig. 10.11). Previous studies have shown that exposure of the macrophage to acetate-containing Ringer's buffer acidifies the cell and causes the lysosomes concentrated in the center of the cell to migrate radially outward to the cell edge [26]. This causes certain regions within the cell to switch from high activity to quiescence.

The studies on macrophages here show that DLSM is feasible on living cells. It essentially provides contrast in unlabeled cells based on rapid rates of submicroscopic motion rather than static refractive index gradients. However, background scattering can be significant and can make some of the least-scattering regions of a cell unusable for DLSM.

### 10.6.3

#### **Improvements for DLSM**

Further improvements in DLSM should aim to increase its spatial and chemical specificity. Our current optical setup works in an epi-illumination mode. Since the depth of the focal region is approximately  $2\ \mu\text{m}$ , the entire thickness of the cell is illuminated. Therefore, the scattered light intensity comes from multiple layers of scattering centers in the region of illumination. To begin to understand the various physical processes contributing to the intracellular motion causing the phase fluctuations, the illuminated region should be better defined to a thin optical slice, such as obtainable with total internal reflection (TIR) illumination [27]. With TIR illumination, the cell membrane and submembrane structure would be the major component in the region of illumination.

Another improvement to DLSM would be to increase its chemical specificity while maintaining the coherent scattering necessary for intensity phase fluctuations. One possibility is to combine DLSM with second harmonic generation imaging microscopy (SHIM) [28]. Second harmonic generation (SHG) is a second-order optical process such that the monochromatically scattered light is coherent but is double the frequency of the incident light. SHG signals can only arise from scattering centers lacking a center of symmetry. Cell membranes and many highly ordered structural proteins intrinsically lack this symmetry center and can be imaged via SHIM. In addition, chemical dyes are available having the required second-



order optical nonlinearities. The dyes can be specifically bound to target organelles and have been used to increase the SHG resolution and contrast within the membrane of the cell [29].

Another technique that could be combined with DLSM is a modification of resonance light scattering microscopy (RLS) [30, 31]. RLS in its current form produces highly monochromatic scattered light from gold particles in suspension illuminated by a xenon lamp, with the scattered color dependent upon the size of the particles. In an application to cell biology, these gold particles could be biochemically modified to specifically label organelles within a cell. The gold particles have a high light-scattering power and are unbleachable. Illumination with a wavelength-tunable laser tuned to the resonance of the gold particles would produce coherent scattered light emanating mainly from the gold particles. Phase intensity fluctuations would occur between neighboring gold particles; these fluctuations could then be autocorrelated to measure relative motions among specifically constituents in the cell.

### Acknowledgments

We thank Drs Kenneth Christensen, Adam Hoppe, and Joel Swanson for macrophage cell culturing assistance.

### References

- 1 PECORA, R., Doppler shifts in light scattering from pure liquids and polymer solutions. *J. Chem. Phys.* **1964**, *40*, 1604–1614.
- 2 CUMMINS, H. Z., KNABLE, N., YEH, Y., Observation of diffusion broadening of Rayleigh scattered light. *Phys. Rev. Lett.* **1964**, *12*, 150–153.
- 3 MAEDA, T. and FUJIME, S., Quasi-elastic light scattering under optical microscope. *Rev. Sci. Instrum.* **1972**, *43*, 566–567.
- 4 MISHINA, H., ASAKURA, T., NAGAI, S., A laser Doppler microscope. *Opt. Commun.* **1974**, *11*, 99–102.
- 5 COCHRANE, T., EARNSHAW, J. C., Practical laser Doppler microscopes. *J. Phys. E: Sci. Instrum.* **1978**, *11*, 196–198.
- 6 HERBERT, T. J., ACTON, J. D., Photon correlation spectroscopy of light scattered from microscopic regions. *Appl. Opt.* **1979**, *18*, 588–590.
- 7 NISHIO, I., TANAKA, T., IMANISHI, Y., OHNISHI, S. T., Hemoglobin aggregation in single red blood cells of sickle cell anemia. *Science* **1983**, *220*, 1173–1174.
- 8 BLANK, P. S., TISHLER, R. B., CARLSON, F. D., Quasielastic light scattering microscope spectrometer. *Appl. Opt.* **1987**, *26*, 351–356.
- 9 PEETERMANS, J., NISHIO, I., OHNISHI, S. T., TANAKA, T., Light-scattering study of depolymerization kinetics of sickle hemoglobin polymers inside single erythrocytes. *Proc. Natl. Acad. Sci. U.S.A.* **1986**, *83*, 352–356.
- 10 PEETERMANS, J. A., FOY, B. D., TANAKA, T., Accumulation and diffusion of crystallin inside single fiber cells in intact chicken embryo lenses. *Proc. Natl. Acad. Sci. U.S.A.* **1987**, *84*, 1727–1730.
- 11 PEETERMANS, J. A., MATTHEWS, E. K., NISHIO, I., TANAKA, T., Particle

- motion in single acinar cells observed by microscope laser light scattering spectroscopy. *Eur. Biophys. J.* **1987**, *15*, 65–69.
- 12 PEETERMANS, J. A., NISHIO, I., OHNISHI, T., TANAKA, T., Single cell laser light scattering spectroscopy in a flow cell: repeated sickling of sickle red blood cells. *Biochim. Biophys. Acta* **1987**, *931*, 320–325.
  - 13 TISHLER, R. B., CARLSON, F. D., A study of the dynamic properties of the human red blood cell membrane using quasi-elastic light scattering spectroscopy. *Biophys. J.* **1993**, *65*, 2586–2600.
  - 14 WONG, A., WILTZIUS, P., Dynamic light scattering with a CCD camera, *Rev. Sci. Instrum.* **1993**, *64*, 2547–2549.
  - 15 KAPLAN, P. D., TRAPPE, V., WEITZ, D. A., Light scattering microscope, *Appl. Opt.* **1999**, *38*, 4151–4157.
  - 16 CUMMINS, H. Z., CARLSON, F. D., HERBERT, T. J., WOODS, G., Translational and rotational diffusion constants of tobacco mosaic virus from Rayleigh linewidths. *Biophys. J.* **1969**, *9*, 518–546.
  - 17 KLEIN, M. V., *Optics*. Wiley, New York, **1970**.
  - 18 JAKEMAN, E., OLIVER, C. J., PIKE, E. R., The effects of spatial coherence on intensity fluctuation distributions of Gaussian light. *J. Phys. A* **1970**, *3*, L45–L48.
  - 19 CANTRELL, C. D., FIELDS, J. R., Effect of spatial coherence on the photoelectric counting statistics of Gaussian light. *Phys. Rev. A* **1973**, *7*, 2063–2069.
  - 20 DZAKPASU, R., AXELROD, D., Dynamic light scattering microscopy: A novel optical technique to image submicroscopy motions I: Theory, *Biophys. J.* **2004**, *87*, 1279–1287.
  - 21 DZAKPASU, R., AXELROD, D., Dynamic light scattering microscopy: A novel optical technique to image submicroscopy motions II: Experimental applications, *Biophys. J.* **2004**, *87*, 1288–1297.
  - 22 DAVENPORT, W. and ROOT, W., *An Introduction to the Theory of Random Signals and Noise*. McGraw Hill, New York, **1958**.
  - 23 CANNON, G. J. and SWANSON, J. A., The macrophage capacity for phagocytosis. *J. Cell Sci.* **1992**, *101*, 907–913.
  - 24 SWANSON, J. A., LOCKE, A., ANSEL, P., HOLLENBECK, P. J., Radial movement of lysosomes along microtubules in permeabilized macrophages. *J. Cell Sci.* **1992**, *103*, 201–209.
  - 25 SUND, S. E., SWANSON, J. A., AXELROD, D., Cell membrane orientation visualized by polarized total internal reflection fluorescence. *Biophys. J.* **1999**, *77*, 2266–2283.
  - 26 HEUSER, J., Changes in lysosome shape and distribution correlated with changes in cytoplasmic pH. *J. Cell Biol.* **1989**, *108*, 855–864.
  - 27 AXELROD, D., Total internal reflection fluorescence microscopy in cell biology. *Methods Enzymol.* **2003**, *361*, 1–33.
  - 28 CAMPAGNOLA, P. J., CLARK, H. A., MOHLER, W. A., LEWIS, A., LOEW, L. M., Second harmonic imaging microscopy of living cells. *J. Biomed. Opt.* **2001**, *6*, 277–286.
  - 29 CAMPAGNOLA, P., MILLARD, A., TERASAKI, M., HOPPE, P., MALONE, C., MOHLER, W., Three-dimensional high-resolution second-harmonic generation imaging of endogenous structural proteins in biological tissues. *Biophys. J.* **2002**, *82*, 493–508.
  - 30 YGUERABIDE, J. and YGUERABIDE, E., Light-scattering submicroscopic particles as highly fluorescent analogs and their use as tracer labels in clinical and biological applications I. theory. *Anal. Biochem.* **1998**, *262*, 137–156.
  - 31 YGUERABIDE, J. and YGUERABIDE, E., Light-scattering submicroscopic particles as highly fluorescent analogs and their use as tracer labels in clinical and biological applications II. Experimental characterization. *Anal. Biochem.* **1998**, *262*, 157–176.

## 11

# X-ray Scattering Techniques for Characterization of Nanosystems in Lifesciences

*Cheng K. Saw*

### 11.1 Introduction

This chapter aims to provide the basics of using X-ray diffraction techniques to obtain information on the structure and morphology of nanosystems, and also to point out some of its strengths and weaknesses when compared to other characterization techniques. X-ray scattering techniques cover a wide range of density domains, from a tenth to a thousandth of an angstrom. Essentially, this covers a whole range of condensed matter, including the structure and morphology of nanosystems, which is particularly useful for examining nanostructures in the life-sciences. This range of domain size requires both wide-angle X-ray scattering (WAXS) and small-angle X-ray scattering (SAXS) techniques. Roughly, WAXS covers from 2 nm down, and SAXS covers from 0.5 to 100 nm and possibly 1000 nm for a finely tuned instrument. A brief theoretical description of both WAXS and SAXS is given in this chapter. WAXS is a powerful technique in providing information on the crystallographic structure, or lack of structure, atomic positions and sizes in a unit cell and, to some extent, chemical compositions and chemical stoichiometry. Examples of such experiments will also be given. To describe the technique of X-ray scattering, some historical and theoretical background will be given in the hope of making this subject both interesting and simple.

Over the past 10 to 20 years, the major development in this scattering technique is in the instrumentation. Better and faster detectors have been developed. Solid-state detectors and position sensitive detectors clearly play an important role in energy discrimination and high-speed data acquisition. The X-ray beams are conditioned with the latest technology in monochromators, mirrors and multi-layers and they can also be made to focus or collimate to the desired probe sizes without significant reduction in X-ray flux. X-ray optics have been improved drastically. Improvements in data quality have also been demonstrated. The basic theory regarding X-ray diffraction and interactions of X-ray with matter developed in the early nineteenth hundreds remains. The arrival of synchrotron radiation for materials probe afforded a quantum leap in all aspects of diffraction capabilities (Section 11.13). Some examples are given in the later part of this chapter.

By and large, X-ray diffraction capability is a major, and necessary, component in any modern characterization laboratory. In most cases, several diffraction instruments are needed for numerous reasons, e.g., high through-put, different X-ray optics for high resolution requirements, different incident energies may be needed, different scan types and so on. Some of these will be more apparent in the later part of this chapter. In general, X-ray scattering is the quickest and cheapest method to obtain a great deal of structural information. For example, identification of crystalline phases, phase impurities, additional disordered phases and the quality of the phases as well as lack of phases. It is also non-destructive and requires very little, or no, major sample preparation. In today's technological world, structural information is required on very different sample types, e.g., thin films, multilayers, very small amounts of samples, specific crystalline orientations, residual stresses and so on. X-ray diffraction has also played an important part in protein crystallography where high quality data with an enormous number reflections are needed for analysis to determine the structure of the protein. Clearly, with such sophisticated demands the experimental setups have to be somewhat unique for each investigation. This chapter also points out the experimental difficulties and ways to compensate and optimize the scattering properties when carrying out these types of experiments on different nanosystems. These small and unique changes in the set-up determine the quality of data and, thus, the success of the experiment.

X-ray scattering techniques also play a major role in obtaining information on both the structure and morphology of materials in nanosystems in the lifesciences. Clearly, the understanding of structure and morphology of materials is a basic requirement for one to design and generate materials with particular desired functions. Other characterization techniques, well established over the years for materials science, also play major roles in characterizing nanosystems for lifescience applications.

Experiments requiring higher resolution or sensitivity can be carried out using more sophisticated national facilities, like the synchrotron and neutron sources at several major research facilities. In fact, the development of synchrotron sources for characterization purposes represents a major advancement for X-ray scattering techniques. Experiments that are either not possible or very difficult to perform using in-house sources can now be easily carried out on one of the beamlines at a synchrotron source. It has greatly enhanced X-ray scattering capabilities. Most national facilities are open to general users around the world. Synchrotron radiations are also X-rays. In this case, the X-rays are highly collimated, polarized, tunable and also have enormous brightness. Many new techniques, e.g., absorption spectroscopy, anomalous scattering, elastic scattering and diffraction at different energies and high spatial resolution techniques (microprobes), to name a few, are being developed. To enhance atomic speciation, anomalous WAXS and SAXS have also been developed and are often used in advanced laboratories. This arises from the tunability of the X-ray to the desired energies close to the absorption edges to enhance the scattering power by taking advantage of anomalous scattering factors. These techniques are covered elsewhere in this volume (e.g. Chapter 8).

In general, nanostructures are crystalline structures with very small crystallite

sizes in the nanometer range. However, they can also be disordered in the angstrom domains but highly ordered in the nanometer range. If the crystallites are small enough, the diffraction peaks are essentially very broad. As the size decreases, the material goes from paracrystalline to, eventually, the amorphous state. This chapter will describe the concept of small crystallite size, paracrystallinity and, briefly, “structures” in an amorphous state.

Nanostructures in the application of nanostructure technology, very often, are formed with some kind of coating around each particle to prevent agglomeration or the fusing of the particles to form a bigger crystallite size. Characterization of this size domain is generally well suited and carried out using the SAXS technique. SAXS is also used to examine morphology and molecular ordering in lifesciences, particularly with proteins, micelles and lipids. Essentially, SAXS is used in two major cases: dilute and highly correlating systems. A dilute system refers to non-interacting nanostructure entities, e.g., proteins and micelles in solutions. Highly correlating systems, for example, can be lipids and collagen where the overall molecules are highly ordered. In other situations, particularly polymer chains, mass fractal analysis is required. This will not be discussed here. Readers are encouraged to examine foundation books listed in the reference section. Several fundamental X-ray diffraction books used in formulating this chapter are listed in the reference section [1–13].

## 11.2

### **Brief Historical Background and Unique Properties**

In 1895, Wilhelm Konrad Röntgen, while experimenting with electric discharges in a tube noted that a barium platinocyanide treated paper lit up as a result of fluorescence induced by unknown so-called X-rays. The X-rays originated from the tube and showed great penetration power, which is inversely proportional to the atomic number. The earliest application of X-ray was in radiography in surgical operations, which clearly revolutionized the medical field. For this discovery, Röntgen won the Nobel Prize in 1901. Another prominent discovery was by C. G. Barkla, who noted that there is a homogeneous energy component in the emitted X-ray operating under certain conditions and is characteristic of the target elements. He also noted that there are two main groups of emission lines, known as K and L lines, which clearly play a major role in Niels Bohr atomic model. For this he won the Nobel Prize of 1917. As the theory developed, X-rays were found to be electromagnetic radiation with a wavelength in the range of atomic spacing. Friedrich and Knipping first recorded the diffraction diagram of a copper sulfate crystal. With this information Laue formulated the theory of diffraction, which won him the Nobel Prize in 1914.

W. L. Bragg explained and correlated the X-ray spots with the atomic spacing and suggested that the diffraction of X-rays is caused by planes of atoms arranged in a lattice. Together with his son, W. H. Bragg, he built the first X-ray spectrometer and carefully recorded the quantitative diffracted intensity and angular positions.

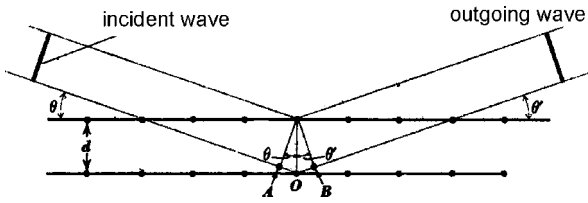


Fig. 11.1. Diagram showing the constructive interference of monochromatic X-rays.

As a result, the concept of diffraction was described and Bragg's law was introduced. These findings won them the Nobel Prize of 1915.

This phenomenon is explained by supposing that the wave property of X-rays is scattered by individual atoms, spherically, in the lattice (Fig. 11.1). The scattered waves then interfere either constructively or destructively at some distance away in space. Therefore, it is a phase issue. For the waves to add up constructively, the Bragg condition has to be satisfied, i.e.,

$$n\lambda = 2d \sin \theta \quad (1)$$

where  $n$  is the order of reflection,  $\lambda$  is the incident wavelength,  $\theta$  is the observed angle and  $d$  is the interatomic spacings. The right-hand side of Eq. (1) is essentially the difference in path lengths when the waves are scattered at positions  $O$  and  $O'$  (see Fig. 11.1). These  $d$ -spacings are generated by the atomic locations of positions in lattices. As a result, many crystal structures were found, lattice spacings were accurately measured and, also, characteristic X-rays from different elements were found and better defined. This is indeed a big advance in materials science and fundamental atomic physics.

Energy is often used to describe the X-ray, instead of wavelength, and is related by

$$E(\text{keV}) = h\nu = \frac{hc}{\lambda(\text{Å})} \quad (2)$$

where  $hc = 12.4$ ;  $h$  is Planck's constant and  $c$  is the speed of light.

### 11.3 Scattering of X-rays

To see how scattering theory developed, it is important to start by describing the scattering of X-rays by a charged particle, say an electron. This result can then be carried over to represent the scattering intensity of an assembly of electrons, say in an atom, and then to a larger volume of mass. Because matter is essentially surrounded by electrons, X-ray scattering is accomplished by X-ray–electron interac-

tions. Basically, there are two major components of scattered X-rays, coherent and incoherent, assuming monochromatic incident X-ray beam. Coherent refers to scattered X-rays that have the same wavelength (energy) as the incident X-rays. Incoherent refers to those X-rays that change wavelength (energy), implying that the incident X-rays imparted part of their energy to the charged particle. The incoherent component (also referred to as inelastic) is a slowly varying function over the scattering angles. The coherent component, which eventually interacts via diffraction, is the elastic component, and will be considered in this chapter.

Classically, an X-ray is described as a wave and is represented by the electric and magnetic field components. The wave is then incident on a charged electron, is then modified, either coherently or incoherently, and is then spherically scattered. The X-ray intensity is proportional to the square of the amplitude. The intensity of X-ray scattering by a charged particle is given by the classic Thomson formula [14],

$$I_e = I_o \frac{e^4}{m^2 c^4 R^2} \left( \frac{1 + \cos^2 2\theta}{2} \right) \quad (3)$$

where  $e$  is the electron charge,  $m$  is the mass of the electron,  $c$  is the velocity of light, and  $R$  is the distance between the observer or detector and the electron. The component in parenthesis is referred to as polarization factor. As Warren [10] has pointed out, the component to the left is the scaling number of the order of  $10^{-26}$  for 1 electron; however, even in milligram amounts of sample there are  $10^{20}$  electrons. The scattering by an individual atom with atomic number  $Z$  can be written as the summation of individual electron scattering.

This is not totally correct, since the electrons are not located at a point. There is an electronic distribution function around an atom. Hence, the structure factor  $f$  is introduced into the scattering equation. This factor is an integral of the electronic density distribution function, generally derived by empirical means. Without going into details of the derivation, the structure factor is given by Eq. (4), where  $k = (4\pi \sin \theta)/\lambda$ ,  $\lambda$  is the X-ray wavelength, and  $\rho(r)$  is the electronic density distribution.

$$f = \frac{4\pi}{e} \int_0^\infty r^2 \rho(r) \frac{\sin kr}{kr} dr \quad (4)$$

Thus,  $f$  is proportional to the atomic number  $Z$  at an angle of  $0^\circ$  and diminishes at higher angles. Notably, Eq. (4) is valid only if the distribution is truly spherical and the energy of the incident X-ray is not close to the absorption edge. Due to the anharmonicity of the electron distribution function and the wavelengths near the absorption edges, the structure factor is more complicated and has two additional modifying terms,

$$f = f_o + \Delta f' + i\Delta f'' \quad (5)$$

where  $f'$  and  $f''$  are, respectively, the real and imaginary components, often re-

ferred to as the anomalous dispersion. Derivation of these factors will not be discussed here. These values are also tabulated in the *International Table of Crystallography* [15].

#### 11.4 Crystallography

As the result of the development of X-ray diffraction and the complexity of Bragg's planes, a method of defining the X-ray peak positions and intensities is need. This is essentially accomplished by mathematical development through space groups. Again, the results of this work have been accurately tabulated, in the four-volume series *International Table for X-ray Crystallography*, a widely used reference. More detailed descriptions of crystallography appear in many fundamental X-ray diffraction books.

The crystallographic planes generated by lattices defined by the space groups are correlated to the X-ray scattering peaks. Hence, it is important to know where the atoms are located and what kind of planes they generate, in order to calculate the peak positions. Crystallography describes the atomic arrangements in a lattice, which are defined by atomic translations and rotations forming some kind of periodic arrangements. The smallest unique atomic arrangement used to generate the crystal by rotations and translations is called the unit cell. Unit cell parameters are defined by three axes and three angles defined by the axes. There are seven forms of large subgroups of crystallographic systems and 14 unique Bravais lattices for the atoms to arrange themselves in. The seven systems are triclinic, monoclinic, orthorhombic, tetragonal, hexagonal, rhombohedral and cubic. Essentially, they are defined by the relationship of the lattice parameters of three axes  $a$ ,  $b$  and  $c$ , and three axial angles  $\alpha$ ,  $\beta$  and  $\gamma$  defined by the axes. Table 11.1 lists the crystal structures and characteristic parameters of the axes and angles.

With the atoms placed in the unit cell positions, 14 unique systems can then be described. In the cubic system, there are three lattices, namely simple, body-centered, and face-centered cubic. There are two tetragonal structures (simple and body-centered), four orthorhombic structures (simple, body-centered, end-centered

Tab. 11.1. Crystal systems and their axes [16].

System	Axes	Axial angle
Triclinic	$a \neq b \neq c$	$\alpha \neq \beta \neq \gamma \neq 90^\circ$
Monoclinic	$a \neq b \neq c$	$\alpha = \gamma = 90^\circ, \beta \neq 90^\circ$
Orthorhombic	$a \neq b \neq c$	$\alpha = \beta = \gamma = 90^\circ$
Tetragonal	$a = b \neq c$	$\alpha = \beta = \gamma = 90^\circ$
Hexagonal	$a = b \neq c$	$\alpha = \beta = 90^\circ, \gamma = 120^\circ$
Rhombohedral	$a = b = c$	$\alpha = \beta = \gamma \neq 90^\circ$
Cubic	$a = b = c$	$\alpha = \beta = \gamma = 90^\circ$



and face-centered), and two monoclinic (simple and end-centered). Additional atoms can be placed in each of the unit cells; however, these positions are simple equivalent positions.

These lattices generally have a unique set of  $d$ -spacings; hence, in X-ray diffraction experiments, these spacings are reflected in the intensity of the scattered X-ray at specific Bragg angles by these unique planes. Eventually, X-ray diffraction from crystals progressed to such a level that a simpler way of identifying these planes had to be developed. This is accomplished by so-called Miller indices ( $hkl$ ). X-ray peak positions can be correlated to the type of lattices or space group.

## 11.5

### Scattering from a Powder Sample

The most common X-ray diffraction experiments are carried out on powder or bulk material with random crystalline orientation. Single-crystal diffraction experiments are also performed quite often; however, they have to be carried out using a four-circle goniometer. When the unit cell is complex with a large number of atoms, a single crystal experiment may be the only way to extract the desired structural information. Single-crystal experiments are generally far more complicated and difficult to perform without significant experience. Also, when the samples are prepared they are polycrystalline. Therefore, the selection of a single homogeneous crystal is often very tedious and difficult.

The total intensity from a powder pattern for a particular ( $hkl$ ) at the angle  $2\theta$  is generally given by the scattering power [10],

$$P = I_o \left( \frac{e^4}{m^2 c^4} \right) \frac{V \lambda^3 m |F_{hkl}|^2}{4v_a^2} \left( \frac{1 + \cos^2 2\theta}{2 \sin \theta} \right) \quad (6)$$

where  $I_o$  is the intensity of the primary beam,  $e$ ,  $m$ ,  $c$ ,  $\lambda$  and  $\theta$  take their usual meaning,  $V$  is the effective volume of the crystalline material in the powder sample,  $m$  is the multiplicity for that reflection and  $|F_{hkl}|^2$  is the structure factor squared. The term in brackets on the right is known as the Lorentz polarization factor. For an actual experiment using a diffractometer, the scattering power is divided per unit length of the diffraction circle.

In an actual experiment, Compton scattering needs to be subtracted, a temperature factor needs to be added and the scattering power per unit detection length calculated. In most cases, with slits, the sample-detector distance is kept the same. Then, the scattering power is given by Eq. (7),

$$P = Km_{hkl}|F_{hkl}|^2(\text{LP})_{hkl} \quad (7)$$

where  $K$  is a constant with intensity proportional to the multiplicity  $m_{hkl}$ , structure factor square  $|F_{hkl}|^2$  and Lorentz polarization factor  $(\text{LP})_{hkl}$ . The structure factor is essentially,

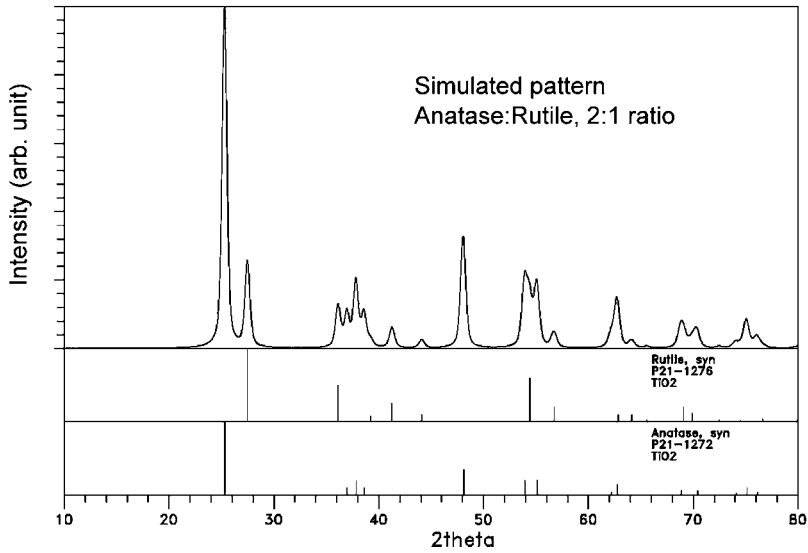


Fig. 11.2. Simulated XRD pattern for two phases of titanium oxide.

$$F_{hkl} = \sum_n f_n e^{2\pi i(hx_n + hy_n + lz_n)} \quad (8)$$

where  $f_n$  is the scattering factor, which is directly dependent on the atomic number, and  $e^{2\pi i(hx_n + hy_n + lz_n)}$  is the form factor, which has the sinusoidal property and turns the intensity on or off. There are some exceptions to this rule, which will be described below.

Figure 11.2 shows a typical diffraction pattern for a simulated pattern of two phases of titanium oxide; the major phase is anatase and the minor is rutile. Along with the plots are the reported peak intensities and positions from the ICDD database. Both phases are tetragonal, with different cell parameters. Thus, phases can be identified even for the same compound. Such results are common.

The structure factor as described in Eq. (8) is summed over all the atoms in the unit cell. For example, in the face-centered cubic (FCC) cell, for simplicity, there are four atoms, located at  $(0, 0, 0)$ ,  $(0, \frac{1}{2}, \frac{1}{2})$ ,  $(\frac{1}{2}, 0, \frac{1}{2})$  and  $(\frac{1}{2}, \frac{1}{2}, 0)$ . Eq. (8) will become,

$$F_{hkl} = [1 + e^{\pi i(h+k)} + e^{\pi i(h+l)} + e^{\pi i(k+l)}] \quad (9)$$

noting that  $e^{\pi im} = (-1)^m$  when  $m$  is an integer. Hence, it can be concluded that  $F_{hkl} = 4$  if the indices  $hkl$  are all odds or evens, and  $F_{hkl} = 0$  when the indices are mixed. Turning our attention to a body-centered cubic (BCC) structure, with two atoms  $(0, 0, 0)$  and  $(\frac{1}{2}, \frac{1}{2}, \frac{1}{2})$  per unit cell. Eq. (8) becomes

$$F_{hkl} = [1 + e^{\pi i(h+k+l)}] \quad (10)$$

For  $F_{hkl}$  to be non-zero,  $(h + k + l)$  must be even. Hence, in FCC, reflections occur when  $hkl$  are all even or all odd, but with a BCC structure,  $(h + k + l)$  has to be even. For another FCC system, for example, the rock salt structure of sodium chloride, having four Na atoms and four Cl atoms per unit cell, the summation in Eq. (8) will result in slightly different  $F_{hkl}$ . Again, the simple rule applied here is that  $hkl$  have to be all evens or all odds. However, for the even case,  $F_{hkl}$  will be four times the sum of the scattering factors, whereas for the odd case  $F_{hkl}$  will be four times the difference of the scattering factors.

In the order-disordered structure of non-monatomic systems, it is possible to violate the above  $hkl$  requirements. This is because, even though the atomic positions are periodic, the atomic species may not be. The scattering factors do not completely cancel out, resulting in the observation of non-allowed peaks. A good example is the well-known  $\text{Cu}_3\text{Au}$  alloy [10]. Another system that needs to be considered is materials with antiphase domains where the atoms of different species have been interchanged, resulting in super structures and X-ray diffraction peaks not normally allowed.

## 11.6

### Scattering by Atomic Aggregates

In practice, not all matter in life has atoms arranged in nice lattices. The most interesting of these materials are those with complex atomic connectivity and having long atomic chains and no kind of ordering in the unit cell range. Examples of such systems are given Section 11.11, which describes the component of amorphous and highly disordered scatterings. It is often very difficult to distinguish between an amorphous structure, similar to liquid or gas, and an extremely small crystallite state, also sometimes referred as a “paracrystalline” state. For nanostructures, it may be important to determine whether the structure is amorphous or simply paracrystalline.

For time average scattering of non-interacting scatterers like mono-atomic gases, the scattering is given by the Debye equation,

$$I_{cu} = \sum_m \sum_n f_m f_n \frac{\sin kr_{mn}}{kr_{mn}} \quad (11)$$

where  $f_m, f_n$  are the scattering factors and  $r_{mn}$  are the interatomic distances. This equation is represented in Fig. 11.3 for  $r_{mn} = 1$ . This result clearly shows that even for a non-interacting system there is a ripple effect, which declines very rapidly on going from low to high scattering angles. For polyatomic systems, the result is the same except that the ripples are much broader.

For a condensed system like a liquid, the summation from Eq. (11) can be simplified to

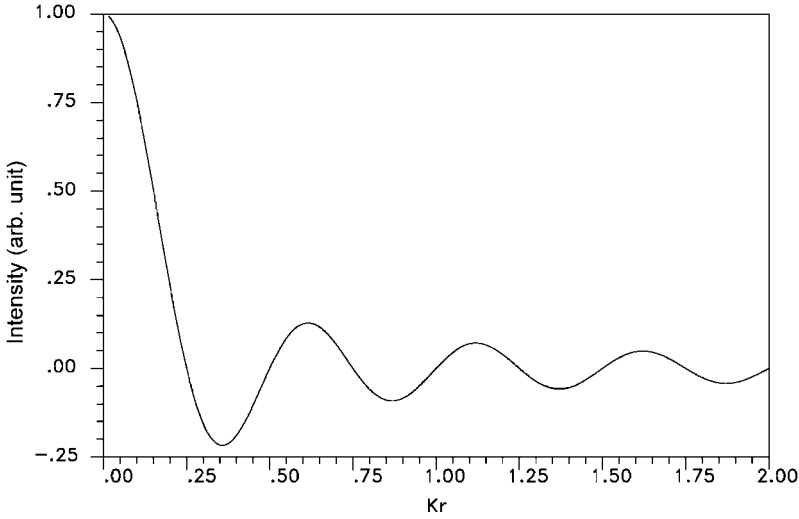


Fig. 11.3. Intensity function of a monatomic gas.

$$I_{eu} = Nf^2 \left( 1 + \sum_m \frac{\sin kr_{mn}}{kr_{mn}} \right) \quad (12)$$

where the 1<sup>st</sup> term is the summation onto itself and the 2<sup>nd</sup> is the interacting term. This equation can then be converted into an integral [Eq. (13)].

$$I_{eu} = Nf^2 \left[ 1 + \int 4\pi\rho(r) \frac{\sin kr}{kr} dr \right] \quad (13)$$

Using algebraic manipulation and defining  $\rho(r) = [\rho(r) - \rho_0] + \rho_0$ , Eq. (13) becomes

$$k[i(k)] = 4\pi \int_0^\infty r[\rho(r) - \rho_0] \sin kr dr \quad (14)$$

Where  $i(k) = [I_{eu}/(N - f^2)]/f^2$ , for simplicity, and by using the theorem of Fourier's conversion we can write the radial distribution function as Eq. (15).

$$4\pi r^2 \rho(r) = 4\pi r^2 \rho_0 + \frac{2r}{\pi} \int_0^\infty k[i(k)] \sin kr dk \quad (15)$$

Eq. (15) provides a mean of converting the intensity function, which is in  $k$  space, into the radial distribution function in real space. In this formulation, the atoms are arranged in completely random fashion, giving an amorphous state. There are

broad diffraction peaks, which belong to the amorphous structure. Unlike crystals, there is no crystallographic ordering. Several papers have demonstrated on model calculations from ideal random atomic arrangements and then determined the radial distribution functions. The density distribution function can be converted into the intensity or interference distribution function and be compared to the experiments [17]. For binary systems, with atoms of A and B species, for example, the intensity function  $i(k)$  is a composite of the three partial functions  $i_{A-A}(k)$ ,  $i_{A-B}$  and  $i_{B-B}(k)$ . It is, therefore, impossible to extract each partial density distribution function without further experiments. Because of differences in scattering factors for X-ray, neutrons and electrons, partial distribution functions can be extracted using a combination of the three experiments. Anomalous scattering experiments can and have also been performed to extract the partial distribution functions. By using the dense random packed models and comparing the calculated  $i_{\text{total}}(k)$  with the experimental observations, the partial functions can be determined [18]. This is particularly useful in the understanding of atomic and chemical short-range order. Clearly, for ternary systems the functions get very complex.

## 11.7

### Crystallite Size and Paracrystallinity

Paracrystalline is a term used to describe small size ordering. Essentially, when the crystalline size is small enough, the resulting diffraction peaks will be broadened; however, the peak positions, if they can be deconvoluted, will fall precisely at the crystalline positions. Extraction of the crystallite size from the peak widths can never be accurate. Hence, in most cases crystallite size is generally an estimate. There are many factors that impact on the peak width, e.g., lattice distortions possibly due to the thermal vibrations, micro-strains, nature of the paracrystallinity. In general, to improve the precision of extracting the crystallite size, the instrumentation broadening component can be subtracted out by performing an exact experiment on a highly ordered structure like silicon powder. Instrument factors are due to misalignment, horizontal divergence (on a vertical goniometer), energy spread of the incident beam, interference of the  $\alpha_1$  and  $\alpha_2$  doublets, and also absorption of the X-rays by the sample. Notably, instrument broadening does not remain constant with all  $2\theta$  but, rather, increases with increasing angle. For this discussion, we are only concerned with determining the estimated crystallite size  $D_{hkl}$  of nanoparticles; it is generally given by the Scherrer equation,

$$D_{hkl} = \frac{K\lambda}{\beta \cos \theta_{hkl}} \quad (16)$$

where  $\beta$  is the peak broadening with the inherent instrument broadening subtracted out,  $\theta_{hkl}$  is the Bragg angle measured at  $hkl$  reflection.  $K$  is normally taken to be 0.9 or unity, depending on the crystal shapes. For details on different values of  $K$ , refer to Refs. [3, 4]. Figure 11.4 shows a plot of crystal size against X-ray peak

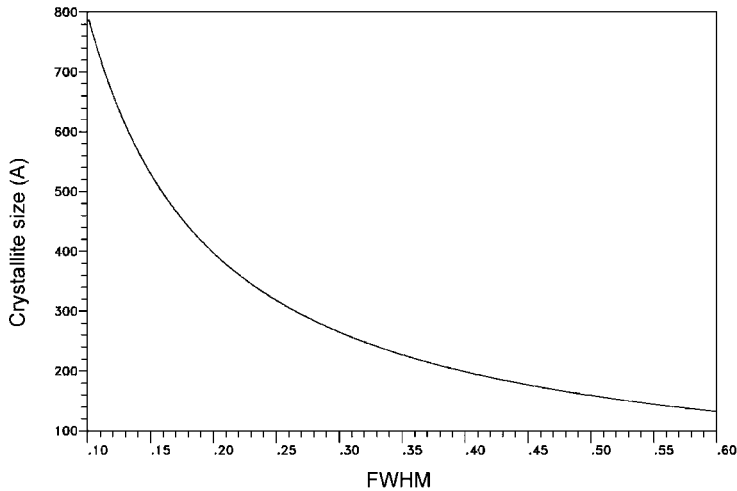


Fig. 11.4. Crystallite size versus FWHM.

broadening (fwhm – full-width at half-maximum) using Eq. (16) and assuming  $2\theta_{hkl} = 20^\circ$ , indicating the sensitivity in the measurement of small crystallites but not large ones. That is, a small change in fwhm translates into a large change in crystallite size in the small width region and a small change in crystallite size in the large width region. Very often, due to uncertainty in the measurements, “apparent crystallite size” is used.

As the crystallite size decreases, the peak broadens. Figure 11.5(a) and (b) compare the simulated diffraction spectra of crystalline hexagonal and cubic Co as a function of crystallite size, calculated using Jade software (MDI) for copper  $K_\alpha$  radiation. Multiple peaks are observed in the hexagonal structure for crystallite sizes of 40 Å and above. Below 40 Å, the three distinct peaks between 40 and 50° ( $2\theta$ ) diminish; hence it is not so clear whether the Co is either cubic or hexagonal phase. Moreover, without significant features, it can be concluded that the Co may be essentially amorphous. In this case, above 40 Å should not be a problem in making the distinction.

## 11.8 Production of X-rays

It is important to understand the production and properties of the X-ray used in the probe. X-rays are generated when electrons emitted from a tungsten filament are accelerated with sufficiently high energy onto a specific target. Typically, X-ray tube voltages are set at 20 to 50 keV. Interaction between the electrons and the electrons of the target materials results in a broad continuous X-ray spectrum. This radiation is often referred to as white radiation or the Bremsstrahlung (German for braking) radiation. This radiation is useful in the energy dispersive type of diffrac-

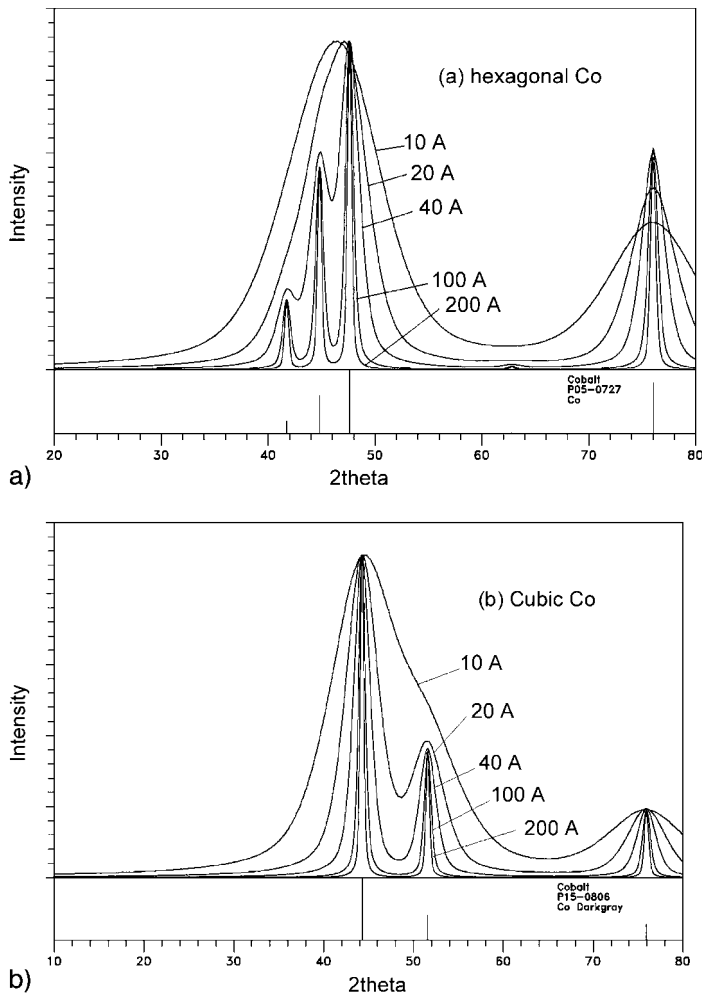


**Fig. 11.5.** Simulated spectra of crystalline hexagonal (a) and cubic (b) cobalt of different crystallite sizes.

tion experiment or a Laue experiment for single crystals but is a nuisance when monochromatic radiation is needed. The energies and intensity of the Bremsstrahlung radiation are affected by changing the tube voltage.

With sufficiently high kinetic energy, the electrons can kick out bound (orbital) electrons from the target. Subsequently, the decay of higher bound state electrons to the lower bound state results in the release of energy by emitting X-rays of characteristic energies and wavelengths, referred to as the K series, with  $K_{\alpha 1}$ ,  $K_{\alpha 2}$ ,  $K_{\beta 1}$  and  $K_{\beta 2}$  radiations. The population of the  $\alpha$  series is much greater than that of the  $\beta$  series. In general, most diffraction experiments are carried out using  $K_{\alpha}$  radiation, and  $K_{\beta}$  radiation is masked off by several techniques.

Less than 1% of the energy incident on the target is converted into X-rays. Hence, this is a very inefficient method. Most of the energy is dissipated as heat at the target. This heat needs to be removed immediately otherwise the targets can melt away. Generally, targets are designed to be on top of a highly thermal conducting heat sink, which is also under constant cooling. Because of this heating issue, there is a limiting power at which the X-ray generator can operate. This clearly depends on the tube design to achieve optimum cooling of the targets. Another target design, which allows for higher power setting, is the rotating anode X-ray generator. The target element is deposited on a highly thermal conducting rotating drum (usually made of copper), which is constantly cooled. The drum rotates at a very high speed, thus constantly changing the target position where the electrons hit. This design alleviates the heat dissipation problem and, therefore, a higher power setting can be achieved, resulting in higher X-ray flux. Unfortunately, maintaining vacuum conditions with a rotating shaft is a challenge.

## 11.9

### Absorption of X-rays

It is also important to understand the absorption behavior of X-rays through opaque materials. In general, X-rays are absorbed whenever they pass through matter. The equation governing this rule is simply

$$I = I_0 e^{-\mu\tau} \quad (17)$$

where  $I_0$  is the incident intensity,  $I$  is the transmitted intensity,  $\mu$  is the linear absorption coefficient ( $\text{cm}^{-1}$ ) and  $\tau$  is the thickness (cm) of the absorber. This is assuming that the X-ray energy is far from the absorption edge. For convenience, the mass absorption coefficients  $\mu/\rho$  ( $\text{cm}^2 \text{g}^{-1}$ ) are used and have been tabulated [15].

$$I = I_0 e^{-(\mu/\rho)\rho\tau} \quad (18)$$

Hence, the mass absorption coefficient is independent of density, and the overall absorption coefficient will just be the summation of the coefficients weighted according to the composition. For X-ray energies close to the absorption edges, the coefficient of absorption changes abruptly. This is directly related to the work function required to knock electrons from their original shells. The absorption coefficient can also be calculated empirically [15].

## 11.10

### Instrumentation: WAXS

Crystallographic structural information on nanoparticles has to be obtained using conventional X-ray diffraction techniques. In general, the most common diffraction



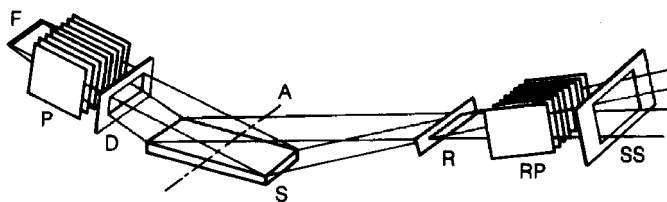


Fig. 11.6. Para-focusing Bragg-Brentano geometry.

experiments are carried out on bulk and powder samples. Again, most materials are polycrystalline. Occasionally, single-crystal experiments are very useful for obtaining detailed structural information, small lattice anisotropy and complex unit cell or cells with a large number of atoms. Single crystal experiments have to be carried out on a four-circle goniometer and will not be described here. Also, there are times when special scans are needed, e.g., to measure residual stress, pole figures, rocking curves etc. a four-circle X-ray goniometer is needed.

The most common and widely used X-ray powder diffraction technique is the Bragg-Brentano method. It is self-focusing and optimizes for intensity and resolution using the conventional in-house X-ray sources. Figure 11.6 shows the X-ray optics. Such diffractometers are essentially very versatile. The distance from the source F to the sample and from the sample to the receiving slit is always kept equal and constant at all scattering angles. Parallel vertical slits P and RP are added to improve the scattering signal. D is the defining slit and R is the receiving slit. Because of the focusing requirement, alignment of the sample is critical for accurate peak position measurements. To help in alignment and calibration, a known standard is used, e.g., a well-characterized silicon powder standard from NIST.

Traditionally, the X-rays are detected using high sensitivity film. In some cases, they are still used. The films are then processed and read by a digitizer, which is essentially a measurement of transmitted light over the spatial positions on the films. X-ray films are also used when examining two-dimensional scattering. Because of the difficulty in processing the film, the modern image plate was invented. Here, an image reader is needed.

For pulse counting techniques, a gas ionization counter, also known as a Geiger-Müller counter, is used. Essentially, it consists of exposing a gas-filled region, normally a noble gas like argon, krypton or xenon mixed with a small amount of quenching gas, held at high potential to the X-rays. Normally, this region is protected by an X-ray-transparent window. When an X-ray enters the compartment it ionizes the gas, producing electrons. These electrons are accelerated to the anode, thus creating a current pulse. The quantum efficiency of this detector greatly depends on the design and type of gas it uses. The energy resolution is poor and the detector can be saturated without going to very high count rates.

A more convenient scintillation has also been developed. This type of detector depends greatly on the fluorescence of certain crystals, e.g., sodium iodide or cesium iodide crystal doped with thallium. Other crystals are also used. These crys-

tals emit light when exposed to X-rays. The light is then converted into an electron pulse via a set of multiplier plates that can then be counted by the electronics. In this case, the dead time is much shorter and counting for higher count rates can be achieved.

The energy resolution of the above two counts is not optimal for normal diffraction techniques. The  $K_\beta$  radiation and other background radiations, e.g., contamination from the X-ray tube, need to be discriminated. Traditionally, foil filters are used. Selection of the foils is based on the absorption edges, e.g., when using copper  $K_\alpha$  radiation a nickel filter foil of 0.0158 mm is needed, which will absorb 98.4% of the  $K_\beta$  radiation [4].

Another way of removing background radiation is the commonly used analyzing crystal (also called diffracted beam monochromator), which is placed in front of the detector (which can either be the gas proportional counter or the scintillation counter) and after the receiving slit. The choice of crystal is based on the crystal mosaic, for energy selectivity and efficiency. The most widely used energy discriminator is usually graphite for efficiency without significantly sacrificing X-ray intensity. For experiments with more stringent energy discrimination, a LiH monochromator is used. In most cases, the analyzing crystal does not have sufficient resolution to remove the  $K_{\alpha 2}$  radiation.

Another way of improving the scattering signal is to use a solid-state detector (SSD). Normally, the detector consists of Si(Li) (silicon-lithium drifted) or Ge(Li) (germanium-lithium drifted) held at liquid nitrogen temperature. When an X-ray impinges on the detector, an electron-hole pair is created and the number of electron-hole pairs is proportional to the energy. Hence, in this case, the energy resolution is roughly about 130 eV.  $K_\beta$  radiation can be eliminated as well as other background radiations and fluorescence from the sample.

The high energy-resolution of the solid-state detector permits energy dispersive diffraction. Essentially, this takes advantage of the full broad energy spectrum of X-rays coming from the tube because of the Bremsstrahlung radiation and, by having the detector at specific angle, a full range of Bragg scattering can be obtained from the energy dispersion. The advantage here is that there is no moving part when conducting the experiment. It makes use of the full range of X-rays and counting statistics can be greatly improved. The drawbacks are that Bragg peak is significantly broader than that of the conventional scanning technique. The detector is big and clumsy, and has to be constantly cooled with liquid nitrogen. However, a newer version of SSD known as a Peltier detector is electrically cooled. This is also rather heavy and clumsy.

A normal mono-energetic experiment makes use of the strong  $K_\alpha$  radiations, which consist of  $K_{\alpha 1}$  (8.04778 keV) and  $K_{\alpha 2}$  (8.02783 keV) energies [19]. For copper  $K_\alpha$  radiation,  $K_{\alpha 2}$  intensity is about half that of  $K_{\alpha 1}$ .  $K_{\alpha 2}$  radiation is an unwanted component of the incident beam. The difference in energies is about 20 eV. However, if a more stringent monochromator is used, the intensity will be drastically reduced. Most powder diffraction experiments simply ignore it. However, when one examines nanostructures where the crystallite size is very small, the presence of  $K_{\alpha 2}$  will not be a factor. On the other hand, if one chose to use higher energetic

radiation, like molybdenum, the difference is about 105 eV. Normally, the best solid-state detectors have a resolution of 130–150 eV.

Unfortunately, this setup is not favorable for samples with elements excitable by the incident X-ray with energy 8.04 keV for copper  $K_\alpha$  radiation, e.g., magnetic nanoparticles Fe and Co-containing samples. In these situations, some form of tighter discrimination is needed to extract the coherently scattered X-rays and not the fluorescence from the sample, which is essentially noise for the diffraction experiment. A way around this problem is to change the probe radiation to that of  $CoK_\alpha$  for cobalt-containing samples and  $FeK_\alpha$  for iron-containing samples. In this way the X-ray probe energies will not be sufficient to cause fluorescence. By changing incident X-ray energies, one has to be aware that the penetration depth is decreased and the energy discrimination needs to be readjusted. Another way to carry out diffraction experiments on highly fluorescent samples is to ensure that the incident energies are sufficiently far from the fluorescence of the samples, e.g., using  $MoK_\alpha$  radiation on iron- and cobalt-containing samples. In this way, the diffracted beam crystal can easily filter out the fluorescent signals.

### 11.11

#### Small Angle X-ray Scattering

The regime covered by small angle X-ray scattering techniques typically covers 0.5 to 100 nm and, according to Bragg's equation, this turns out to be only a few degrees in  $2\theta$ . This regime also turns out to be very useful for examining many types of nanostructures. In general, for the application of nanostructures, it is customary to have a layer of polymer coated on each particle. Information on size, shapes, interparticle correlations and density fluctuations of nanostructure are of importance and can be obtained using this technique. In lifesciences, for example, biological cells and cell tissues, proteins and protein folding, colloids, micelles, bacteria and viruses can also be investigated using SAXS. This technique has also been widely used in examining tumors and cancerous cells, and distinctions in the diffraction patterns between healthy and cancerous cells have been shown. It is the information on the macro-scale, the connectivity and arrangement of the local domains, that is critical in understanding the behavior of these systems. For example, a SAXS study examining healthy and cancerous human breast tissues found that the collagens have very different structures [20]. It has also been widely used to examine tumors and cancerous cells [21], and, again, distinctions have been drawn between healthy and cancerous cells. Further research by many groups is continuing to try to understand the causes of cancer. Even so, by combining SAXS and WAXS characterization techniques, experiments can be carried out on well chosen cell tissue samples that will provide information for the understanding of disease processes evolution. This represents a new form of diagnostic capability for health sciences.

Information on the nanostructure, size, shapes, interparticle correlations, density fluctuations are of importance and can be obtained. In the lifesciences, most systems, such as those listed above, are highly disordered at the local level (ang-

stroms) and at times they are even semi-crystalline. Clearly, they are very complex and in most cases consist of interpenetrating components of the different make-up of molecules. These molecules, which can have odd shapes, essentially hinder the formation of unit cell arrangements. Again, the macro-crystalline arrangements are critical in the generation of properties.

Another example of X-ray scattering experiments in lifesciences is in understanding the structure and morphology of bone. Bones are made up of fibrillar collagens with nano-particles of crystalline hydroxyapatite distributed in the macro-structure. It is this macro-arrangement of the collagen and the crystalline component that provides the optimal compression strength for the load bearing of the anatomy [22]. A network of collagen fibers is deposited and grown within and between the collagen fibrils [23]. SAXS experiments can provide information on the macro-domains. One area in lifesciences that SAXS will play an important role is in understanding the cell membrane. Information on the structure of the lipid moieties in the cell membrane essentially defines the functionality of the membrane [24]. Even though lipids are considered to have bilayer structures, monolayer structures do exist. Of particular interest is understanding lipid behavior in solvent, which again can be carried out using SAXS. Depending on the acquisition time, *in situ* experiments as a function of temperature or time decay can also be carried out.

For nanostructures in biological materials SAXS analysis is used to extract information relating to the macro-lattice on highly correlating domains, which often can be periodic. A typical example for this is the tendons. Many biological systems also possess periodic structures, e.g., animal tail tendons and myelin membranes in the nerve. In polymers, the scattering signal arises from the stacking of lamellar crystals and block copolymers having segregating density domains.

Laboratory prepared nanoparticles (or crystals), e.g., cobalt [25] when coated with organic layers, can self-assemble into superstructures. The structure and dimension of these superstructures have also been examined using both WAXS and SAXS, thus providing a full description of the overall structure. The superstructure of biomaterials like colloidal particles of glycolipids has also been examined using SAXS. The technique was able to provide information on the structure of the dispersed particles [26].

The analysis of SAXS data can be divided into three groups: dilute systems, highly correlating systems and fractals. In dilute systems, when the structures are non-interacting, information on the shape, size and mass of the molecules can be obtained. For highly correlating systems, the basic formulation follows Bragg's law. The fractal component is generally useful for polymers and polymer chains and will not be discussed here. The reader is encouraged to refer to other sources [7, 12].

### 11.11.1

#### **Dilute Systems**

The scattering for dilute systems assumes that the scattering from each particulate is independent. Hence, it is critical for the sample to have an appropriate thickness

so that no multiple scattering can occur. The X-ray interacts with the electron fluctuations surrounding the particulates and the total intensity is merely the sum of all the individual scattering components. Therefore, information on sizes, shapes and mass can be obtained. The generalized scattering function is essentially given as

$$I(k) = (\rho_0 v)^2 F^2(k) \quad (19)$$

where  $\rho_0$  is the density difference over total volume  $v$ , and  $F(k)$  is the structure factor. The form factor is simply represented by

$$F(k) = \int \rho(r) e^{ikr} dr \quad (20)$$

where the integral is over the electron density over each particulate and the exponential component is the form factor. By expanding the form factor and dropping out the higher order terms, Guinier has shown that the intensity function is

$$I(k) = \rho_0^2 v^2 \exp\left(-\frac{1}{3} k^2 R_g^2\right) \quad (21)$$

or

$$I(k) = I(0) \exp\left(-\frac{1}{3} k^2 R_g^2\right) \quad (22)$$

where  $I(0)$  is the scattering at zero angle. Essentially, this function is Gaussian. Very often,  $\ln I(k)$  is plotted against  $k^2$  and the radius of gyration  $R_g$  can be extracted from the resultant slope. Shape information is obtained from  $R_g$ ; the value of  $R_g$  for many forms of particulate has been calculated and will not be discussed here. Actually,  $R_g$  is defined as in Eq. (23) and described as the root-mean-square distance of all points in the particle from the center of mass weighted accordingly.

$$R_g^2 = \frac{\int_0^\infty \rho(r) r^2 dr}{\int_0^\infty \rho(r) r dr} \quad (23)$$

The size of the particle is conveniently expressed by  $R_g$  and, assuming the shape is known, the radius of gyration can be extracted accurately. The radius of gyration for some common shapes has been tabulated in many review articles. By knowing or assuming the shape of the particle examined, the dimension of the particle can be gotten by solving for the radius of gyration. Extrapolation of the Guinier plot to scattering at zero angle results in  $\rho_0^2 v^2$ , which provides information on the particle molecular weight and volume. However, in this case, accurate intensity of the main beam is needed.

For homogenous particles with distinct boundaries between the particles and the matrix, which can be a solution or another media with different density, e.g., in

polymers with crystalline and amorphous components, Porod has indicated that the scattering  $I(k)$  should decrease as  $k^{-4}$  for large  $k$  and the proportionality constant is related to the total area  $S$  occupied by the boundaries and is expressed as

$$I(k) \rightarrow \frac{2\pi\rho_0^2 S}{k^4} = \frac{P}{k^4} \quad (24)$$

By plotting  $\log(I(k))$  versus  $\log(k)$  and extrapolating to  $k = 0$ , the  $P$  (Porod constant) can be extracted. When this parameter is divided by the “invariant”, which is the scattering intensity for the total volume, the surface area to volume ratio can be gotten. When this parameter is divided by the density, the total surface area (m/g) resulted. The information is particularly useful, especially in the area of catalysis when the amount of surface area controls the property of the material.

### 11.11.2

#### Highly Correlating Systems

Most systems in lifesciences are highly correlated or rather densely packed with significant density fluctuation and are also highly oriented. For example, collagens are very well packed in a fibrillar fashion and the diffraction pattern shows many orders of reflections. The peaks are also very sharp, with a dimension of 67 nm for native rat tendon [26]. Obviously, for densely packed systems, the scattering theory is governed by Bragg's law.

Collagens are common in lifescience. It is a major constituent in tendon, bone, skin, cornea, cartilage and other parts that require strength and flexibility. Clearly, the packing and deformation of collagens will reveal the state of the matter when compared with healthy tissue. The arrangement of collagen is believed to be liquid-crystalline-like as well as having large scale triple helices arrangements for roughly 300 nm [27, 28]. The change in packing indicates some kind of mineralization that prevents proper function of the component. It is indeed a mystery that collagen, which is abundant in our anatomy, has so many functions. It is the arrangement on the macro-scale that changes its properties [29].

As described earlier [24], examination of protein bilayers is of great importance in biological science. Essentially, these are highly correlated systems. Clearly, the structure and makeup of these bilayers constitute the working of the membranes, peptides etc. There are enormous numbers of biological systems for which both SAXS and WAXS can be utilized for understanding their behavior. Biological systems are normally very complex.

## 11.12

### SAXS Instrumentation

A SAXS experiment, in principle, has a very simple geometry (Fig. 11.7); however, improperly arranged and aligned components will result in all kinds of problems, e.g., parasitic scattering, calibrations, peak profiles and background noise. The

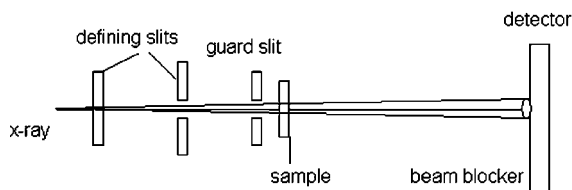


Fig. 11.7. Optics for carrying out SAXS experiment using the three-slit system.

quality of the instrument greatly depends on the level of noise because the diffuse scattering intensity for most samples can be very weak for different reasons. A very well-defined X-ray beam is needed for this application.

Numerous SAXS instrumentations are available commercially. Essentially, there are two types of configuration, pin-hole and the line source technique, each with its own strengths and weaknesses. The pin-hole technique is useful for examining anisotropic materials, e.g., fibers, films and any sample with orientations. However, there is an inherent loss in intensity, resulting in long data acquisition time. A two-dimensional detector system is required, e.g., conventional highly sensitive X-ray film, image plate, 2D proportional gas detector and even the CCD (charge coupled device) detector systems. Both the film and image plate require X-ray exposure and then have to be processed and read by some kind of digitizer or image reader. In this way, some level of spatial resolution and dynamic range will be lost. When small peaks are of interest or accurate intensity function is required, these are not the desired techniques. Moreover, real-time experiments or experiments performed as a function of temperature will be extremely tedious and inefficient.

A basic requirement for a good experimental setup for SAXS is in the collimation. This is because SAXS is a measurement of extremely small intensity at very small angle, next to a very strong incident main beam. Hence, the scattering around the incident beam has to be as clean as possible and protected against parasitic scattering caused by the defining slits and beam blocker. Commonly used in the pin-hole technique for the in-house systems is the three pin-hole slits system with different sizes (Fig. 11.7). They have to be properly arranged and matched with the size of the beam blocker to obtain the clean primary beam and reach to the lowest angle. The third slit is the guard slit that filters out the parasitic scattering from the defining slits. Not that the beam diverges from the source. To avoid air scattering, the beam path has to be under vacuum, which inherently introduces two X-ray windows. The weakly scattered X-ray from the sample has to penetrate these windows without changing in energy and direction. The advantage of the pin-hole technique is that anisotropic samples can be examined, e.g., fibers and films. By translating the sample, localized spot examination can also be carried out.

The more advanced 2D gas proportional detector system has also been used. The heart of the detector is the multi-wire grid; the spatial resolution is limited to the

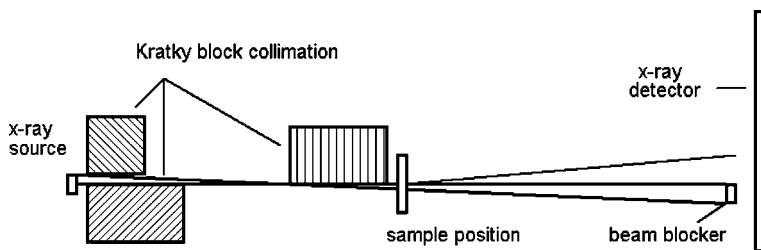


Fig. 11.8. Kratky block collimation system.

wire spacings. Normally, this is limited to about 1 mm, even though some advances have been made (0.2–0.3 mm) through electronic and software developments. As a consequence, pin-hole SAXS instruments require long path lengths to expand the image for the detector to receive.

To increase the intensity, the second method, using a line source, is often used. The optics are essentially similar to the pin-hole system shown in Fig. 11.7. This method increases the flux of the incident beam; however, only isotropic sampling can be carried out. Unfortunately, because of the fixed slit, desmearing of the data is needed. Again, three line slits properly arranged are used to minimize parasitic scattering. Adjustments to these slits are often very sensitive and difficult. Consequently, the Kratky block collimation (Fig. 11.8) was introduced and is still used today. It is easier to align and there are not too many adjustments. It can also achieve much smaller  $k$  ( $\text{\AA}^{-1}$ ) than the normal three-slit system.

Another method of increasing the incident beam flux and improving the spatial resolution is by using focusing mirrors and monochromators. To achieve even smaller in  $k$ , the Bonse-Hart technique is used. By taking advantage of a tighter energy filter, an even smaller angle can be achieved. This is accomplished by having the X-ray bounce several times through a channel cut crystal on the incident end as well as the diffracted end. This technique also requires significant alignments, which are normally set up at dedicated beam lines at synchrotron sources. Again, this is also a line source and the issue of desmearing will have to be considered.

### 11.13 Synchrotron Radiation

Undoubtedly, synchrotron radiation has played a major role in extending X-ray scattering capabilities. As pointed out in the introduction, unlike in-house X-ray sources, synchrotron radiation has unique properties. The generation of synchrotron radiation will not be covered here. The X-rays generated by a synchrotron source are highly collimated, highly polarized, tunable, and have high brightness. The probe size can be made small, down to 2  $\mu\text{m}$ , which essentially provides an insight into the composition of biological cell and local structure that is not possible using in-house sources.



The high collimation enables diffraction experiments to be carried out with improved precision. The peak width spread will be extremely small. The fwhm will be essentially due to the character of the sample and not the instrument. Divergence will be extremely small. By using an incident monochromator, unlike the in-house source, only a mono-energetic beam is allowed to pass the incident monochromator. Because of the small divergence of the beam, SAXS experiments can be better set up.

To enhance atomic speciation, anomalous WAXS and SAXS have also been developed and often used in advanced laboratories. This arises from the tunability of the X-ray to the desired energies close to the absorption edges to enhance the scattering power by taking advantage of anomalous scattering factors. These techniques are covered elsewhere in this volume (see Chapter 8). Clearly, there are more examples of utilizing the advantages of performing X-ray diffraction experiments using a synchrotron source.

#### 11.14

##### **Concluding Remarks**

In the field of materials characterization, X-ray scattering stands out as the preferred method for obtaining information on the structure and morphology of all sorts of materials. Essentially, X-rays are scattered by electrons, and all matter has electrons. The domain size that fits both wide angle and small angle X-ray scattering ranges from a fraction of a nm to 100 nm. At the low end, X-ray diffraction has provided information on atomic positions, lattices, bond lengths, atomic speciation and structure. By carefully examining the character of the scattering, secondary information, like the crystallite size, lattice distortion and occupancy, can also be extracted. The penetration depth of an X-ray is also sufficiently high compared with X-ray photoemission or electron scattering, hence X-ray scattering can be considered as bulk probing.

With the theory and technique firmly understood, the method has been used on more complex organic and polymeric systems. Unfortunately, in general, these systems are not fully crystalline. They are semi-crystalline and, more often, it is this semi-crystallinity that provides the unique properties of polymers, essentially controlling their morphology. This is one of the reasons for the development of small angle X-ray scattering.

Both the wide angle and small angle techniques are quite well developed. Basically, these characterization techniques have been extended to different aspects of biological and lifescience. The structure of cells and cell tissues, lipid membranes, proteins and protein behavior, the building blocks of many organs in our anatomy, are now being examined using both the wide angle and small angle X-ray techniques.

Structures or nanostructures in biological and lifescience are generally very complex. However, with the advancement of computing power, high energy and the spatial resolution of synchrotron sources, experiments on tissues, like cancer, tu-

mors or sclerosis, are now possible. Clearly, X-ray scattering, together with synchrotron and neutron scattering, covers a whole range of characterization for organic and inorganic condensed matter, crystalline and semi-crystalline, and amorphous structures. These experiences have also developed into the biological field and lifesciences.

### Acknowledgment

This work was performed under the auspices of the U.S. Department of Energy by the University of California, Lawrence Livermore National Laboratory under Contract W-7405-Eng-48. Thanks are given to Dr Art Nelson for reviewing the manuscript.

### References

The subject presented has been reviewed in several fundamental books. Listed are some of the books used in writing this chapter.

- 1 GUINIER, A., *X-ray Diffraction*, Freeman and Company, San Francisco, 1963.
- 2 BALTA-CALLEJA, F.J., VONK, C.G., *X-ray Scattering of Synthetic Polymers*, Elsevier, New York, 1989, chapter 7.
- 3 WANG, J.I., HARRISON, I.R., *Methods of Experimental Physics: Volume 16: Polymers*, Ed. FAVA, R.A., Academic Press, New York, 1980.
- 4 KLUG, H.P., ALEXANDER, L.E., *X-ray Diffraction Procedures*, John Wiley & Sons, New York, 1973.
- 5 ALEXANDER, L., *X-ray Diffraction Methods in Polymer Science*, Wiley-Interscience, New York, 1969.
- 6 AZAROFF, L.V., *Elements of X-ray Crystallography*, McGraw-Hill Book Company, New York, 1968.
- 7 ROE, R.J., *Methods of X-Ray and Neutron Scattering in Polymer Science*, Oxford University Press, New York, 1999.
- 8 KOSTORZ, G., *Treatise on Materials Science and Technology*, Academic Press Inc., New York, 1979, pp. 15, 227–286.
- 9 RICHTMYER, F.K., KENNARD, E.H., COOPER, J.N., *Introduction to Modern Physics-6<sup>th</sup> Ed.*, McGraw-Hill, New York, 1969.
- 10 WARREN, B.E., *X-ray Diffraction*, Addison-Wesley Publishing Co., Reading, MA, 1969.
- 11 SCHWARTZ, L.H., COHEN, J.B., *Diffraction from Materials*, Springer, New York, 1981.
- 12 GLATTER, O., KRATKY, O., *Small Angle X-ray Scattering*, Academic Press, London, 1982, p. 156.
- 13 BALTA-CALLEJA, F.J., VONK, C.G., *X-ray Scattering of Synthetic Polymers*, Elsevier, New York, 1989, chapter 7.
- 14 THOMSON, J.J., *Conduction of Electricity Through Gases*, 2<sup>nd</sup> edn., Cambridge University Press, Cambridge, 1928–33, p. 321, and COMPTON, A.H. and ALLISON, S.K., *X-rays in Theory and Experiment*, 2<sup>nd</sup> edn. Van Nostrand-Reinhold, Princeton, NJ, 1935.
- 15 *International Table of Crystallography*, vols. 1–4, by The International Union of Crystallography, ed. N.F.M. HENRY and K. LONSDALE, The Kynoch Press, Birmingham, England, 1952.
- 16 SPRUELL, J.E. and CLARK, E.S., *Methods of Experimental Physics*, chapter 6: X-ray Diffraction, ed. FAVA, R.A., Academic Press, New York, 1980.
- 17 BENNETT, C.H., Serially deposited amorphous aggregates of hard spheres, *J. Appl. Phys.* 1972, 43, 2727–2734; BOUDREAUX, D.S., GREGOR,

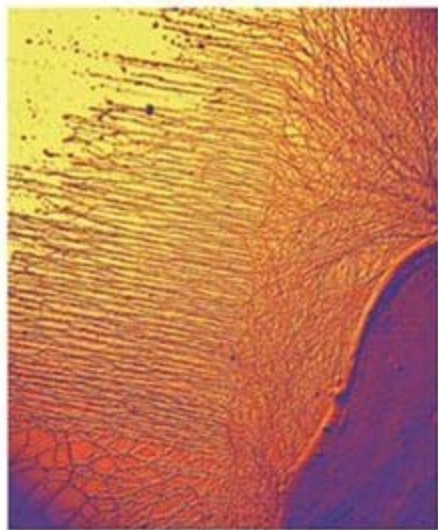
- J.M., Structure simulation of transition-metal-metalloid glasses. III, *J. Appl. Phys.*, **1977**, *48*, 5057–5061.
- 18 SAW, C.K. and SCHWARZ, R.B., Chemical short-range order in dense random-packed models, *J. Less-Common Metals*, **1988**, *140*, 385–393.
- 19 VAUGHAN, D. (ed), *X-ray Data Booklet*, Center for X-ray Optics, Lawrence Berkeley Laboratory, Berkeley, CA, 1986, and DYSON, N.A., *X-rays in Atomic and Nuclear Physics*, Longman, London, **1973**, chapter 3.
- 20 FERNANDEZ, M., KEYRILAINEN, J., SERIMAA, R., TORKKELI, M., KARJALAINEN-LINDSBERG, M.-L., TENHUNEN, M., THOMLINSON, W., URBAN, V. and SUORTTI, P., Small-angle x-ray scattering studies of human breast tissue samples, *Phys. Med. Biol.*, **2002**, *47*, 577–592.
- 21 LEWIS, R.A., ROGERS, K.D., HALL, C.J., TOWNS-ANDREWS, E., SLAWSOM, S., EVANS, A., PINDER, S.E., ELLIS, I.O., BOGGIS, C.R.M., HUFTON, A., DANCE, D.R., Breast cancer diagnosis using scattered x-rays, *J. Synchrotron Rad.* **2000**, *7*, 348–352, JAMES, V., Synchrotron fibre diffraction identifies and locates foetal collagenous breast tissue associated with breast carcinoma, *J. Synchrotron Rad.*, **2002**, *9*, 71–76.
- 22 JASCHOUZ, D., PARIS, O., ROSCHGER, P., HWANG, H.S., FRATZL, P., Pole figure analysis of mineral nanoparticles orientation in individual trabecula of human vertebral bone, *J. Appl. Cryst.*, **2003**, *36*, 494–498.
- 23 JAGER, I., FRATZL, P., Mineralized collagen fibrils: A mechanical model with a staggered arrangement of mineral particles, *Biophys. J.*, **2000**, *79*, 1737–1746.
- 24 LAGGNER, P., *Physicochemical Methods in the Study of Biomembranes: Subcellular Biochemistry*, ed. HILDERSON, H.J., RALSTON, G.B., Plenum Press, New York, **1994**, pp. 23, 11, 451–491.
- 25 MURRAY, C.B., KAGAN, C.R., BAWENDI, M.G., Synthesis and characterization of monodisperse nanocrystals and closed-packed nanocrystals assemblies, *Annu. Rev. Mater. Sci.*, **2000**, *20*, 545–610.
- 26 STUHRMANN, H.B., MILLER, A., Small-angle scattering of biological structures, *J. Appl. Cryst.* **1978**, *11*, 325–345.
- 27 FRATZL, P., Cellulose and collagen: from fibres to tissues, *Curr. Opin. Colloid Interface Sci.*, **2003**, *8*, 32–39.
- 28 FRATZL, P., GUPTA, H.S., PASCHALIS, E.P., ROSCHGER, P., Structure and mechanical quality of the collagen-mineral nano-composite in bone, *J. Mater. Chem.*, **2004**, *14*, 2115–2123.
- 29 ABRAHAM, T., MASAKATSU, H., HIRAI, M., Glycolipid based cubic nanoparticles: preparation and structural aspects, *Colloids Surf. B: Biointerfaces*, **2004**, *35*, 107–117.

Nanotechnologies for the Life Sciences

Edited by Challa Kumar

WILEY-VCH

# Nanodevices for the Life Sciences



**ntLS** The logo for the Nanotechnology Life Sciences (NLS) program. It features the lowercase letters 'ntLS' in a bold, sans-serif font. To the right of the text is a vertical graphic element consisting of a series of red and white wavy lines, resembling a DNA double helix or a spring, with a central vertical line.

## Contents

**Preface** XIII

**List of Contributors** XVII

<b>1</b>	<b>The Physics and Modeling of Biofunctionalized Nanoelectromechanical Systems</b>	<b>1</b>
	<i>Mark R. Paul and Jerry E. Solomon</i>	
1.1	Introduction	1
1.2	The Stochastic Dynamics of Micro- and Nanoscale Oscillators in Fluid	4
1.2.1	Fluid Dynamics at Small Scales	4
1.2.2	An Exact Approach to Determine the Stochastic Dynamics of Arrays of Cantilevers of Arbitrary Geometry in Fluid	8
1.2.3	An Approximate Model for Long and Slender Cantilevers in Fluid	11
1.2.4	The Stochastic Dynamics of a Fluid-coupled Array of (BIO)NEMS Cantilevers	16
1.3	The Physics Describing the Kinetics of Target Analyte Capture on the Oscillator	19
1.4	Detecting Noise in Noise: Signal-processing Challenges	24
1.5	Concluding Remarks	25
	Acknowledgments	26
	References	26
<b>2</b>	<b>Mathematical and Computational Modeling: Towards the Development and Application of Nanodevices for Drug Delivery</b>	<b>29</b>
	<i>John P. Sinek, Hermann B. Frieboes, Balakrishnan Sivaraman, Sandeep Sanga, and Vittorio Cristini</i>	
2.1	Introduction	29
2.2	RES Avoidance	30
2.2.1	A Statistical Model of Nanovector Surface Coverage	31
2.2.2	Modeling the Forces Mediating Protein Approach and Binding	35
2.3	Tumoral Vasculature and Hemodynamics	35

2.3.1	An Invasion Percolation Model of Vasculogenesis and Hemodynamics	37
2.3.2	Flow Simulations Using Anderson and Chaplain's Model	40
2.3.3	Particle Dynamics within the Tumoral Vasculature	45
2.4	Receptor–Ligand-mediated Binding	47
2.4.1	Bell's Deterministic Model	49
2.4.2	A Stochastic Model	52
2.5	Intratumoral and Cellular Drug Kinetics and Pharmacodynamics	54
2.5.1	A Two-Dimensional Model of Chemotherapy	55
2.5.2	Refinements of the Model	57
2.6	Conclusion	61
	References	62

### 3 Nanolithography: Towards Fabrication of Nanodevices for Life Sciences 67

*Johnpeter Ndiangui Ngunjiri, Jie-Ren Li, and Jayne Carol Garno*

3.1	Introduction: Engineering Surfaces at the Nanoscale	67
3.2	Immobilization of Biomolecules for Surface Assays	69
3.2.1	Strategies for Linking Proteins to Surfaces	69
3.2.1.1	Electrostatic Immobilization	70
3.2.1.2	Covalent Immobilization	70
3.2.1.3	Molecular Recognition and Specific Interactions	71
3.2.1.4	Nonspecific Physical Adsorption to Surfaces	71
3.2.2	SAM Chemistry	74
3.3	Methods for Nanolithography with Proteins	76
3.3.1	Bias-induced Nanolithography of SAMs	78
3.3.2	Force-induced Nanolithography of SAMs	82
3.3.3	DPN of SAMs and Proteins	87
3.3.4	Latex Particle Lithography with Proteins	91
3.4	Detection of Protein Binding at the Nanoscale	94
3.5	Future Directions	96
3.5.1	Advantages of Nanoscale Detection	96
3.5.2	Development of Cantilever Arrays	97
3.5.3	Concluding Remarks	101
	References	101

### 4 Microcantilever-based Nanodevices in the Life Sciences 109

*Horacio D. Espinosa, Keun-Ho Kim, and Nicolaie Moldovan*

4.1	Introduction	109
4.2	Microcantilevers	111
4.2.1	Microfabrication of Miniaturized Probes	112
4.2.2	Cantilever Probes for Nanopatterning	116
4.2.3	Elastomeric AFM Probes	121
4.2.4	Monolithically Fabricated Conductive Diamond Probes	122
4.3	Cantilevers with Integrated Micro- and Nanofluidics	126

4.3.1	Apertured Pyramidal Tips	126
4.3.2	Open-channel Cantilevered Microspotters	128
4.3.3	Closed-channel Cantilevered Nanopipettes	133
4.3.4	Micromachined Hypodermic Needle Arrays	136
4.3.5	NFPs	137
4.4	Applications	141
4.4.1	Patterning of DNA	141
4.4.2	Patterning of Proteins	142
4.4.3	Patterning of Viruses	143
4.5	Conclusions and Outlook	143
	References	144
<b>5</b>	<b>Nanobioelectronics</b>	<b>150</b>
	<i>Ross Rinaldi and Giuseppe Maruccio</i>	
5.1	Introduction	150
5.2	Bio-self-assembly and Motivation	150
5.3	Fundamentals of the Bio-building Blocks	153
5.3.1	DNA	153
5.3.2	Proteins	154
5.4	Interconnection, Self-assembly and Device Implementation	155
5.4.1	Interconnecting Molecules	157
5.4.2	Delivering Molecules	158
5.5	Devices Based on DNA and DNA Bases	160
5.5.1	Charge Transfer in DNA	161
5.5.2	DNA Conductivity	164
5.5.2.1	Near-ohmic Behavior (Activated Hopping Conductor)	164
5.5.2.2	Semiconducting (Bandgap) Behavior	168
5.5.2.3	Insulating Behavior	169
5.5.2.4	Discussion of DNA Conductivity	170
5.5.2.5	Other Applications of DNA in Molecular Electronics	173
5.6	Devices Based on Proteins	177
5.7	Conclusions	183
	Acknowledgments	183
	References	184
<b>6</b>	<b>DNA Nanodevices: Prototypes and Applications</b>	<b>189</b>
	<i>Friedrich C. Simmel</i>	
6.1	Introduction	189
6.2	DNA as a Material for Nanotechnology	189
6.2.1	Nanoscale Science	189
6.2.2	Biophysical and Biochemical Properties of Nucleic Acids	190
6.2.3	DNA Nanoconstruction	193
6.3	Simple DNA Devices	193
6.3.1	Conformational Changes Induced by Small Molecules and Ions	193
6.3.2	Hybridization-driven Devices	196

6.4	Towards Functional Devices	198
6.4.1	Walk and Roll	199
6.4.2	Interaction with Proteins	202
6.4.3	Information Processing	206
6.4.4	Switchable Networks and Hybrid Materials	207
6.5	Autonomous Behavior	209
6.5.1	Driving Devices with Chemical Reactions	209
6.5.2	Genetic Control	210
6.6	Conclusion	212
	Acknowledgments	213
	References	213
<b>7</b>	<b>Towards the Realization of Nanobiosensors Based on G-protein-coupled Receptors</b>	<b>217</b>
	<i>Cecilia Pennetta, Vladimir Akimov, Eleonora Alfinito, Lino Reggiani, Tatiana Gorojankina, Jasmina Minic, Edith Pajot-Augy, Marie-Annick Persuy, Roland Salesse, Ignacio Casuso, Abdelhamid Errachid, Gabriel Gomila, Oscar Ruiz, Josep Samitier, Yanxia Hou, Nicole Jaffrezic, Giorgio Ferrari, Laura Fumagalli, and Marco Sampietro</i>	
7.1	Introduction	217
7.2	Preparation and Immobilization of GPCRs on Functionalized Surfaces	220
7.3	Signal Techniques	221
7.4	Theoretical Approach	222
7.5	The Impedance Network Model	224
7.6	Equilibrium Fluctuations	231
7.7	Conclusions	235
	Acknowledgments	236
	References	236
<b>8</b>	<b>Protein-based Nanotechnology: Kinesin–Microtubule-driven Systems for Bioanalytical Applications</b>	<b>241</b>
	<i>William O. Hancock</i>	
8.1	Introduction	241
8.2	Kinesin and Microtubule Cell Biology and Biophysics	242
8.2.1	Kinesin Motility Assays	244
8.3	Theoretical Transport Issues for Device Integration	245
8.3.1	Diffusion versus Transport Times	247
8.4	Interaction of Motor Proteins and Filaments with Synthetic Surfaces	249
8.4.1	Motor Adsorption	249
8.4.2	Microtubule Immobilization	251
8.5	Controlling the Direction and Distance of Microscale Transport	252
8.5.1	Directing Kinesin-driven Microtubules	252
8.5.2	Movement in Enclosed Microchannels	255



8.5.3	Immobilized Microtubule Arrays	257
8.6	Cargo Attachment	259
8.6.1	Maximum Cargo Size	261
8.7	System Design Consideration	262
8.7.1	Protein Stability and Lifetime	262
8.7.2	Sample Introduction and Detection	264
8.7.3	Analyte Detection and Collection	265
8.8	Conclusion	265
	Acknowledgments	266
	References	266
<b>9</b>	<b>Self-assembly and Bio-directed Approaches for Carbon Nanotubes: Towards Device Fabrication</b>	<b>272</b>
	<i>Arianna Filoramo</i>	
9.1	Introduction	272
9.2	CNTs: Basic Features, Synthesis and Device Applications	274
9.2.1	Basic Features	274
9.2.2	Synthesis of Nanotubes	276
9.2.3	Device Applications	277
9.3	Fabrication of CNT Transistors and Self-assembly Approaches	278
9.4	<i>In situ</i> CVD Growth	280
9.5	Selective Deposition of CNTs by SAM-assisted Techniques	281
9.5.1	Methodology and Key Parameters	282
9.5.2	Performance of CNTFETs Fabricated by the SAM Method	288
9.6	DNA-directed Self-assembly	291
9.6.1	The Assembly of the Scaffold	292
9.6.2	Selective Attachment of the DNA Scaffold on the Surface Microscale Electrodes	294
9.6.3	Positioning of Nano-objects or Nanodevices on the Scaffold	295
9.6.4	Realization of Electrical Connections and Circuitry	298
9.6.5	Fabrication of DNA-directed CNT Devices	303
9.7	Conclusion	304
	References	305
<b>10</b>	<b>Nanodevices for Biosensing: Design, Fabrication and Applications</b>	<b>317</b>
	<i>Laura M. Lechuga, Kirill Zinoviev, Laura G. Carrascosa, and Miguel Moreno</i>	
10.1	Introduction	317
10.2	From Biosensor to Nanobiosensor Devices	318
10.2.1	Overview	318
10.2.2	Biological Functionalization of Nanobiosensors	320
10.3	Nanophotonic Biosensors	321
10.3.1	Overview	321
10.3.2	Integrated Mach–Zehnder Interferometer (MZI) Nanodevice	322
10.3.2.1	Design and Fabrication	323
10.3.2.2	Characterization and Applications	325

10.3.3	Integration in Microsystems	329
10.4	Nanomechanical Biosensors	330
10.4.1	Overview	330
10.4.2	Working Principle	330
10.4.3	Detection Systems	332
10.4.4	Design of a Standard Microcantilever Sensor	333
10.4.4.1	Fabrication of a Standard Microcantilever Sensor	334
10.4.4.2	Optical Waveguide Microcantilever: Design and Fabrication	337
10.4.4.2.1	Principle of Operation and Theoretical Analysis	338
10.4.4.2.2	Fabrication and Characterization	339
10.4.5	Biosensing Applications of Nanomechanical Sensors	342
10.5	Conclusions and Future Goals	344
	Acknowledgments	344
	References	344
<b>11</b>	<b>Fullerene-based Devices for Biological Applications</b>	<b>348</b>
	<i>Ginka H. Sarova, Tatiana Da Ros, and Dirk M. Guldi</i>	
11.1	Introduction	348
11.2	Solubility	348
11.3	Toxicity	350
11.4	DNA Photocleavage	351
11.4.1	Photodynamic Therapy (PDT)	353
11.4.2	Fullerene-mediated Electron Transfer Across Membranes	358
11.4.3	Neuroprotective Activity via Radical Scavenging	362
11.4.4	Enzyme Inhibition and Antiviral Activity	367
11.4.5	Antibacterial Activity	369
11.4.6	Fullerenes as Nanodevices in Monoclonal Immunology	371
11.4.7	Fullerenes as Radiotracers	373
11.4.8	Fullerenes as Vectors	375
	Acknowledgments	376
	References	376
<b>12</b>	<b>Nanotechnology for Biomedical Devices</b>	<b>386</b>
	<i>Lars Montelius</i>	
12.1	Introduction	386
12.2	Nanotechnologies	388
12.2.1	Overview of Nanotechnologies and Nanotools	388
12.2.1.1	NIL	393
12.2.1.2	Other Lithography Techniques	393
12.2.1.3	Scanning Probes	395
12.3	Applications	397
12.3.1	Introduction	397
12.3.2	Biomedical Applications based on Nanostructured Passive Surfaces	397
12.3.2.1	Separation, Concentration and Enriching Structures	398

12.3.2.2	Molecular Motors Transported in Nanometer Channels	400
12.3.2.3	Topographical Structures, Cells and Guidance of Neurons	401
12.3.3	Biomedical Applications utilizing Active Nanostructured Surfaces	405
12.3.4	Protein Chips	409
12.3.5	Protein Interactions	412
12.3.6	Biomedical Applications using Nanowires	415
12.3.7	Biomedical Applications using Nanoparticles	416
12.3.8	Biomedical Applications using SPM Technology	416
12.3.8.1	Imaging of Biomolecules using SPM	418
12.3.8.2	Force Detection of Single Molecular Events	418
12.3.8.3	Cantilever-based Detection of Molecular Events	418
12.4	Discussion and Outlook	423
	Acknowledgments	424
	References	425
<b>13</b>	<b>Nanodevices in Nature</b>	<b>436</b>
	<i>Alexander G. Volkov and Courtney L. Brown</i>	
13.1	Introduction	436
13.2	Multielectron Processes in Bioelectrochemical Nanoreactors	437
13.3	Cytochrome Oxidase: A Nanodevice for Respiration	438
13.3.1	Nanodevice Architectonics	441
13.3.2	Activation Energy and Mechanism of Oxygen Reduction	442
13.3.3	Proton Pump	443
13.4	Photosynthetic Electrochemical Nanoreactors, Nanorectifiers, Nanoswitches and Biologically Closed Electrically Circuits	443
13.5	Phototropic Nanodevices in Green Plants: Sensing the Direction of Light	448
13.6	Membrane Transport and Ion Channels	451
13.7	Molecular Motors	453
13.8	Nanodevices for Electrorception and Electric Organ Discharges	455
13.9	Neurons	456
	References	456
	<b>Index</b>	<b>460</b>



## Preface

Welcome to the world of nanoscale devices! The fourth volume of the series on Nanotechnologies for the Life Sciences is in front of you, providing glimpses of the exciting possibilities that exist in the world of tiny devices. Nanotechnology and nature are intimately intertwined. Such an intimate partnership is critical for reaping the benefits of nanotechnology by unraveling the mysteries of nature. Therefore, this volume, *Nanodevices for the Life Sciences*, is timely and provides a broader perspective to this partnership and enlightens us on the theory, physics, chemistry, biology and engineering of nanodevices that are being constructed in the laboratory as well those that are already being utilized by nature. See for example a recent article in *Science* (Vol 312, pp 860–861, 2006) that describes the possibilities to utilize biomolecular motors in nanometer-scale devices to perform mechanical work. Three chapters (chapters 7, 8 & 13) in the book are specifically dedicated to provide glimpses of the power of such natural nanoscale devices and I am certain that these chapters will catalyze development of new ideas and tools for non-biologists interested in utilizing the underlying principles.

Theory and experiments will have to go hand in hand as deeper understanding of the complexities associated with nanoscale devices bring us a step closer to designing devices that are as efficient as in nature. Therefore, the first two chapters have been dedicated to provide theoretical and computational understanding of nanoscale devices with potential applications in life sciences. The first chapter illuminates on *The Physics and Modeling of Biofunctionalized Nanoelectromechanical Systems*. Two leading theoreticians, M. R. Paul from Virginia Polytechnic Institute and State University in Virginia, USA, and J. E. Solomon from the California Institute of Technology in Pasadena take readers to the realm of theoretical challenges associated with modeling of BioNEMS. I have no doubt that the information provided in this chapter will form a strong basis for deeper understanding of many other nanoscale systems that one encounters in our laboratories as well as in biological systems. The second chapter is a contribution from the laboratories of Vittorio Cristini from the University of California at Irvine delving on intricacies of modeling various components associated with nanoscale drug delivery for the treatment of cancer. The chapter, *Mathematical and Computational Modeling: Towards the Development and Application of Nanodevices for Drug Delivery*, is a great source of information on mathematical models and computer simulations of important steps in the journey of intravenously injected nanovectors into tumoral

tissue in order to deliver drug in the most effective manner. This chapter is a must for all those interested in utilizing nanotechnologies for drug delivery.

Moving from utilizing theory, modeling and computational tools for fabrication of nanodevices, the rest of the book is a testimony to the rapid advances being made in the application of a variety of experimental techniques and tools for building nanoscale devices and for application of such devices in a number of fields ranging from biosensors to bioelectronics. In the third chapter, which is contributed by J. C. Garno and co-workers from Louisiana State University in Baton Rouge, USA, a detailed description is given of how scanning probe techniques are proving to be versatile tools for fabricating arrays of self-assembled monolayers (SAMs) and proteins. In this chapter, *Nanolithography: Towards Fabrication of Nanodevices for the Life Sciences*, the authors describe how nanolithography is revolutionizing the fabrication of nanoscale biomolecular devices in general and proteins in particular through precise control over chemical functionality, shape, dimensions and spacing on the nanometer scale. Continuing on a similar theme, H. D. Espinosa, K.-H. Kim and N. Moldovan from Northwestern University in Illinois, USA, have carried out a remarkable job in delineating the importance of microcantilevers for biopatterning and biosensing in scanning probe microscopy (SPM)-based techniques. Their contribution in the fourth chapter, entitled *Microcantilever-based Nanodevices in the Life Sciences*, is very unique in the sense that it covers not only various approaches for fabrication of microcantilevers but also their applications in the emerging field of bionanotechnology. The chapter clearly demonstrates the fact that microcantilevers are fundamental tools for biopatterning and biosensing in SPM-based techniques, and with the possibility of integrating micro/nanofluidics into microcantilevers, they are in the process of revolutionizing the field of bioanalytical nanodevices.

The fifth chapter in this volume, *Nanobioelectronics*, is a testimony to the fact that there have been several advances made in the field of molecular electronics over the last decade particularly in utilizing biomolecules for fabrication of molecular-scale devices and integrated computers. The authors from the University of Lecce in Italy, R. Rinaldi and G. Maruccio reviewed these advances in the field of nanobiomolecular electronics describing the fabrication of devices such as rectifiers, amplifiers, information storage devices based on biomolecules in general and DNA and proteins in particular. Highlight of the chapter is the information on interconnecting biomolecules and exploitation of their self-assembly properties leading to nanobiodevices. It is particularly heartening to see that the progress made so far in the field of nanobioelectronics is very promising and is likely to fill the void in the face of current limitations with CMOS devices and post-optical lithographies. While the fifth chapter focuses on electronic devices using DNA, the sixth chapter provides complete information on the most important properties of DNA and how these properties are being exploited in building functional devices such as DNA-based molecular motors and automata with possible applications in the life sciences. Friedrich Simmel from Ludwig-Maximilians-Universität München, Germany, has provided an up to date review on this subject and is very optimistic that the recent advances are likely to lead to the development of autonomous molecular-scale devices which can sense environmental information, perform compu-

tations and act independently as molecular motors, drug reservoirs, or as signal transducers. The chapter is aptly titled as *DNA Nanodevices: Prototypes and Applications*. While the fifth and sixth chapters provide a broader perspective to build nanoscale devices from DNA and proteins, the next two chapters contain very specific information on nanodevices made from G-protein coupled receptors and Kinesin-microtubule systems respectively. The seventh chapter, *Towards the Realization of Nanobiosensors Based on G-protein-coupled Receptors*, a contribution from the laboratories of Cecilia Pennetta, also from Lecce University, provides a thorough review on G-protein-coupled receptors (GPCRs) including different techniques to prepare and immobilize them on a substrate, followed by utilization of the electrochemical impedance spectroscopy (EIS) technique for the detection of biosensing events at the electrodes. A very unique aspect of the chapter is that it covers several theoretical aspects investigating the current response to an applied AC voltage of a nanodevice realized by a single GPCR embedded in its membrane and in contact with two functionalized metallic nanoelectrodes. The chapter is extremely valuable for nanotechnologists exploring applications in life sciences as GPCRs are one of the widest groups of receptor proteins known and they can be activated by a large variety of extracellular signals, such as light, odorant molecules, hormones, peptides, lipids, neurotransmitters and nucleotides. GPCRs mediate the sense of vision, smell, taste and pain, and are involved in an extraordinary number of physiological processes. Competing for prominence with GPCRs are the Kinesin-microtubule-driven systems as they hold significant potential as molecular motors due to their compactness, high efficiency in vitro in extracting energy from the aqueous environment. The eighth chapter, *Protein-based Nanotechnology: Kinesin-Microtubule-driven Systems for Bioanalytical Applications*, assumes enormous importance in this volume as it has valuable information on how kinesin molecular motors can be integrated with microtubule tracks into microdevices for bioanalytical applications. The chapter is an important contribution for the book as the author, William Hancock from Pennsylvania State University, USA, covers wide-ranging topics from cell biology and biophysics, in vitro assays, theoretical aspects, biofunctionalization of the kinesin-microtubule system in addition to experimental approaches to integrating into functional microscale devices for potential analytical applications.

Carbon Nanotubes (CNTs) are finding extraordinary applications in the field of life sciences especially in biosensing, drug delivery, diagnosis, imaging and so on. These applications are further complimented by recent efforts in fabricating CNT-based nanodevices especially field-effect transistors (FETs) having very interesting performance characteristics. The ninth chapter, *Self-assembly and Bio-directed Approaches of Carbon Nanotubes: Towards Device Fabrication*, begins with a review on important characteristic of CNTs followed by the synthesis methods reported in the literature. The central theme of the chapter, written by Arianna Filoramo from the Laboratory of Electronic Materials in Gif sur Yvette, France, is however the utilization of self-assembly approaches (bio as well as non-bio directed) for fabrication of CNT devices for application in the electronics industry. Alternative strategies to CMOS technologies such as bio-inspired technologies for nanoscale devices as described in this chapter as well as in chapter five are likely to revolutionize the electronics industry in the near future. Focusing primarily on biosensing, chapter

ten explores the possibility of fabricating nanodevices based on nanophotonic/optoelectronic platforms and on nanomechanical platforms. The chapter, *Nanodevices for Biosensing: Design, Fabrication and Applications*, contributed by L. M. Lechuga and co-workers from the Microelectronics National Center (CNM) in Spain, is a valuable source of information for design, fabrication and testing of nanosensors and their integration with microfluidics, optical and electronic functions on a single chip. Chapter eleven, *Fullerene-based Devices for Biological Applications*, written by Dirk M. Guldi from Friedrich Alexander University in Erlangen-Nürnberg, Germany, and his collaborators is complimentary to the ninth chapter, describing in detail the solubility, toxicity and major biological applications of fullerenes and their potential application in nanoscale devices. It provides a basic framework for fabricating fullerene-based nanoscale devices in near future. A more general approach for utilization of nanotechnological principles for the fabrication of biomedical devices is presented in the twelfth chapter, wherein Lars Montelius from Lund University in Sweden describes various types of nanotechnologies that are employed in the biomedical field in general and biomedical engineering in particular, together with suitable examples. The chapter, *Nanotechnology for Biomedical Devices*, provides a fundamentally strong backbone for the realization of nanoscale devices for biomedical applications.

Finally, the book ends with a chapter dedicated to providing an overview of nanoscale devices that nature utilizes. Chapter thirteen, *Nanodevices in Nature*, written by Alexander Volkov and Courtney Brown from Oakwood College in Huntsville, USA, complements more specialized information in chapters seven and eight. The chapter elegantly delineates the role of various nanodevices in a wide variety of biological processes focusing more specifically on cytochrome oxidase, photosynthesis and phototropism, membrane transport, molecular motors, and electroreceptors. In my view the last chapter is a grand finale to the excellent source of information that the authors of this book gathered and reminds me of a great statement from *Vedas*, one of the oldest Indian scriptures, which describes universal power as the smallest of the smallest and biggest of the biggest. Truly, the power that encompasses the universe comes from nanodevices!

As I conclude this preface, there is no doubt in my mind that a book of this magnitude and high quality would not have been possible without the timely contributions of all authors, and I am always grateful to them for sharing my vision for this book as well as for the rest of the series. I am glad to let you know that Volumes 1–3 and 5–6 of this exciting series have already been published and you might have seen them in your library or obtained a personal copy. The remainder of the series, volumes 7–10, is currently in press and will be available to you before the year ends. In addition to the authors, a project of this magnitude is not possible but for unwavering support from my employer, family, friends and Wiley-VCH publishers. This is yet another opportunity for me to convey my thanks to them. Before I take leave, I would like to request you, the reader, who is sharing the knowledge with me and rest of the authors, to let me know your comments, suggestions and constructive criticism to make further improvements to this exciting series.



## 1

## The Physics and Modeling of Biofunctionalized Nanoelectromechanical Systems

Mark R. Paul and Jerry E. Solomon

## 1.1

### Introduction

Experimental fabrication and measurement are rapidly approaching the nanoscale (see, e.g. Refs. [1–4]). With this comes the potential for many important discoveries in both the physical and life sciences, with particularly intense attention in the fields of medicine and biology [5]. As Richard Feynman famously predicted in the early 1960s, there is indeed plenty of room at the bottom [6, 7]. A particularly promising avenue of research with the potential to make significant contributions is that involving what we will call biofunctionalized nanoelectromechanical systems [(BIO)NEMS]. This is a large and burgeoning field, and we do not attempt to present a survey, but rather we have picked an interesting example of a (BIO)NEMS device in order to highlight the dominant physics and types of modeling issues that arise.

This is not to imply that molecular-scale science is something new – scientists and engineers have been manipulating atoms and molecules for decades. (For an interesting discussion about where nanotechnology fits in with molecular science, see Ref. [8].) However, one new and exciting feature is the ability to fabricate micro- and nanoscale structures that can be used to manipulate, interact and sense biological systems at the single-molecule level.

For a better perspective of the length scales in question it is useful to place micro- and nanometers on biological scales; a human hair has a diameter of about 1 mm, a red blood cell has a diameter of about 10  $\mu\text{m}$  ( $1 \mu\text{m} = 1 \times 10^{-6} \text{ m}$ ), the diameter of the bacteria *Escherichia coli* is about 1  $\mu\text{m}$ , the diameter of the protein lysozyme is about 5 nm ( $1 \text{ nm} = 1 \times 10^{-9} \text{ m}$ ) and the diameter of a single hydrogen atom is about 0.1 nm. When viewed in this context, a device with a characteristic length scale of 100 nm falls in the middle of these biological length scales, i.e. the device is quite large compared to single atoms, yet quite small when compared to single cells or large molecules. It is important to consider this when modeling these systems, as we illustrate below.

The force landscape descriptive of biological and chemical interactions occurs at the piconewton scale ( $1 \text{ pN} = 10^{-12} \text{ N}$ ). Biologically relevant force magnitudes are

related to the breaking and manipulation of chemical bonds. For example it takes hundreds of piconewtons to break covalent bonds, and on the order of 10 pN to break a hydrogen bond or to describe the entropic elasticity of a polymer (see, e.g. Refs. [9, 10]).

The dominant biological time scales of small numbers of molecules are also dictated by their chemical interactions. The time scales of chemical reactions vary over many orders of magnitude, e.g. protein conformational changes can take of the order of milliseconds, binding reactions such as those that occur between transcription factors and genes or between enzymes and substrates are of the order of seconds, covalent bond modifications such that occur with phosphorylation is of the order of minutes, and new protein synthesis in a cell can take tens of minutes.

With these biological length, force and time scales in mind it becomes clear that a major challenge facing the successful development of a single-molecule biosensor is to measure on the order of tens of piconewtons on microsecond time scales. Despite the rapid advancement of new technologies such as surface plasmon resonance [11], optical tweezers [12, 13], microneedles [14, 15] and scanning force microscopy [16–19], detailed knowledge of the real-time dynamics of biomolecular interactions remains a current challenge.

An attractive device with the potential to measure the biophysical properties of a single molecule is based upon the dynamics of nanoscale cantilevers in fluid. In discussing the physics and modeling of (BIO)NEMS we will focus on this type of device. In some aspects this device can be thought of as the miniaturization of atomic force microscopy (AFM) which depends upon the response of micron-scale cantilevers. The invention of AFM [20] has revolutionized surface science, paving the way for direct measurements of intermolecular forces and topographical mapping with atomic precision for a wide array of materials, including semiconductors, polymers, carbon nanotubes and (CNTs) biological cells (see Refs. [21, 22] for current reviews). AFM is most commonly performed in one of three different driven modalities; contact mode, noncontact mode and tapping mode. In contact mode, the cantilever remains in contact with the surface and direct measurements are made based upon the cantilever response as it interacts with the sample. Despite its great success, contact-mode microscopy raises concerns about strong adhesive forces, friction and the damage of soft materials. In response to these issues emerged the noncontact- and tapping-mode modalities which are often referred to as dynamic AFM [23–28].

In noncontact mode, an oscillating cantilever never actually makes impact with the surface, yet its response alters due to an interaction between the cantilever tip and surface forces. The noncontact mode allows the measurement of electric, magnetic and atomic forces. In tapping mode, the cantilever oscillates near the sample surface making very short intermittent contact. Commonly the oscillation amplitude is held fixed through a feedback loop and as the cantilever moves over topographical features of the sample, the change in deflection is measured and related to the surface features. As a result of this minimal impact, and by greatly reducing the effects of adhesion and friction, the tapping mode has become the method of

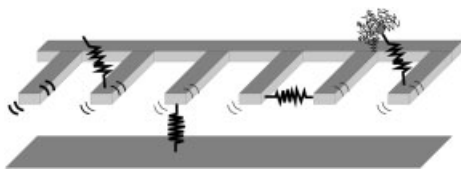


**Figure 1.1.** Schematic illustrating possible single-molecule detection modalities using small-scale cantilevers immersed in fluid.

choice for high-resolution topographical measurements of soft and fragile materials that are difficult to examine otherwise.

We would like to focus here upon something quite different – the stochastic dynamics of a passive cantilever in fluid. By passive we mean that the cantilever is not being dragged along a surface or forced to tap a surface, but that the cantilever is simply immersed in the fluid. However, recall that at microscopic length scales there is a sea of random thermal molecular noise. Experimental measurement is often limited by this inherent thermal noise; however, with current technology this noise can be exploited to make extremely sensitive experimental measurements [29] including the highly sensitive measurements to be made by gravitational wave detectors [30].

The basic idea is illustrated in Fig. 1.1. A small cantilever placed in fluid will exhibit stochastic dynamics due to the continual buffeting by water molecules that are in constant thermal motion (Brownian motion). In Fig. 1.1, all of the cantilevers will exhibit such oscillations; the four dark lines around each cantilever tip are meant to indicate these oscillations and their degree of shading represents the relative magnitude of these oscillations. One way to measure such oscillations in the laboratory would be through the use of optical methods. The cantilever on the far left is bare and is simply a reference cantilever placed in fluid. The adjacent cantilevers suggest various detection modalities that could also be considered. The fundamental idea is that in the presence of a biomolecule, either attached directly to a single cantilever or between the a cantilever and something else, the cantilever response will change. Measuring this change can then be used to detect the presence of a single biomolecule or, in more prescribed situations, details of the response will yield information about the dynamics of the molecule being probed.

An important advantage of this approach is that small cantilevers have large resonant frequencies, allowing the measurement of these dynamics on natural chemical time scales. In fact, nanoscale cantilevers immersed in water can have resonant frequencies in the megahertz range. The last cantilever on the right shows the case where the target biomolecule is bound between the cantilever and a very large molecule. The purpose of this would be to take advantage of its large surface area and, as a result, its increased fluid drag to enhance the change in response.

An additional complication is that the stochastic dynamics of cantilevers placed in an array, such as those shown in Fig. 1.1, will become coupled to one another through the resulting fluid motion. In other words, if one cantilever moves this

will cause the fluid to move, which will cause the adjacent cantilevers to move and *vice versa*. At first this may appear as just another component of background noise to contend with. However, it is interesting to point out that this correlated noise can be exploited to significantly increase the sensitivity of these measurements. Consider measuring the cross-correlation of the fluctuations between two cantilevers in fluid supporting a tethered biomolecule. By examining only the correlated motion of the two cantilevers we have effectively eliminated the random uncorrelated component of the noise acting on each cantilever. In fact, this approach has been used to measure femtonewton forces ( $1 \text{ fN} = 10^{-15} \text{ N}$ ) on millisecond time scales between two micron-scale beads placed in water [12]. Additionally, this approach was used to quantify the Brownian fluctuations of an extended piece of DNA tethered between the beads leading to the resolution of some long-standing issues concerning the dynamics of single biomolecules in solution [13].

Whatever the manner in which the measurements will actually be made in the laboratory, it will be essential to have a firm understanding of the complex and sometimes counterintuitive physics at work on these scales in order to interpret them (for an excellent introduction to the modeling of micro- and nanoscale systems, see Ref. [31]).

The purpose of this chapter is to shed some light upon this for the particularly illustrative case where the Brownian noise of small cantilevers in fluid is exploited for potential use as a single-molecule biosensor. Before these measurements can be made and understood, the following questions must be answered:

- (a) What are the stochastic dynamics of an array of nanoscale cantilevers immersed in fluid in the absence of the target biomolecules?
- (b) How much analyte will arrive at the sensor and what are the time scales for its capture?
- (c) Successful measurements will require the discernment between the noise when the biomolecule is attached and the background noise. What signal processing schemes can be used to make these measurements?

We address these questions in the following sections.

## 1.2

### The Stochastic Dynamics of Micro- and Nanoscale Oscillators in Fluid

#### 1.2.1

##### Fluid Dynamics at Small Scales

The dynamics of fluid motion at small scales contains many surprises when compared with what we are accustomed to in the macroscopic world. In fact most of life involves the interactions of small objects in fluidic environments (see Ref. [32] for an introduction or Refs. [33, 34] for a detailed discussion).

At the molecular scale a fluid is clearly composed of individual molecules. How-

ever, most fluid analysis is done assuming that the fluid is a *continuum*. What this implies is that at any particular point in space (no matter how small) the properties of the fluid (velocity, pressure, etc.) are well defined and well behaved. Another way to think of this is that for any experimental measurement in question we assume that our probe is effectively sampling the average behavior of many molecules.

As our domain of interest becomes smaller it is clear that this assumption will eventually break down. This raises the difficult question – at which point does the continuum approximation become invalid? An approximate answer can be provided by physical reasoning. In the continuum limit one would like the mean free path of collisions of the fluid molecules to be much smaller than a characteristic fluid length scale. This idea is captured by the Knudsen number  $\text{Kn} = \lambda/L$ , where  $\lambda$  is the mean free path and  $L$  is a characteristic length scale. For the case of water, and of liquids in general, the molecules are always in very close contact with one another and the characteristic mean free path can be approximated by the diameter of a single molecule. For water this yields  $\lambda \approx 0.3$  nm.

For the stochastic oscillations of small cantilevers we will use the cantilever half-width  $w/2$  as the characteristic length. This is because while a cantilever oscillates most of the fluid flows around spanwise over the cantilever. Assuming the cantilever has a width of  $w = 1$   $\mu\text{m}$  and is immersed in water yields  $\text{Kn} \approx 6 \times 10^{-4}$ . Since  $\text{Kn} \ll 1$  this indicates that the continuum approximation is good for the fluid dynamics even at these small scales. A quantitative understanding of when the continuum approximation breaks down and what the effects will be is currently an active and exciting area of research with many open questions (see, e.g. Ref. [35]).

The classical equations of fluid dynamics in the continuum limit are the well-known Navier–Stokes equations (see Ref. [36] for a thorough treatment):

$$R_\omega \frac{\partial \vec{u}}{\partial t} + R_u \vec{u} \cdot \vec{\nabla} \vec{u} = -\vec{\nabla} p + \nabla^2 \vec{u}, \quad (1)$$

$$\vec{\nabla} \cdot \vec{u} = 0 \quad (2)$$

Equation (1) is an expression of the conservation of momentum (we have neglected the body force due to gravity). Equation (2) expresses the conservation of mass for an incompressible fluid. We have written the equations in nondimensional form using  $L$ ,  $U$  and  $T$  as characteristic length, velocity and time scales, respectively. Two nondimensional parameters  $R_\omega$  and  $R_u$  emerge in Eq. (1) that multiply the two inertial terms on the left-hand side.

It is worthwhile discussing these two parameters in more detail, which will lend some insight into the dominant physics at small scales in fluids. The parameter:

$$R_u = \frac{UL}{\nu_f} \quad (3)$$

expresses the ratio between convective inertial forces and viscous forces (where  $\nu_f$  is the kinematic viscosity of the fluid, for water  $\nu_f \approx 1 \times 10^{-6}$   $\text{m}^2 \text{s}^{-1}$ ). This is the

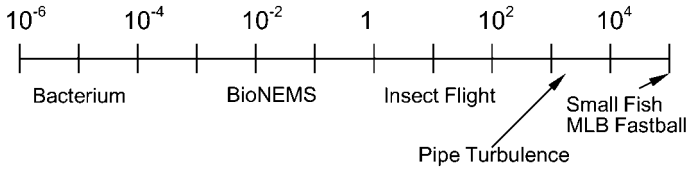


**Figure 1.2.** Examples of different phenomena occurring over a range of 10 orders of magnitude in the velocity-based Reynolds number,  $R_u$ .

velocity-based Reynolds number. It is clear that for micron or nanoscale devices both the characteristic velocity and length scales become quite small, resulting in what is commonly referred to as the low Reynolds number regime. A precise definition of what is meant by “low” is not clear. For perspective, Fig. 1.2 illustrates the Reynolds numbers for some particular cases of interest. Note the vast range of phenomena that occurs over 10 orders in magnitude of the Reynolds number. As the Reynolds number decreases, the effects of viscosity dominate inertial effects. For example, if a 1- $\mu\text{m}$  microorganism swimming in water at  $10 \mu\text{m s}^{-1}$  suddenly turns off its source of thrust, say by flagellar or cilia motion, it will come to rest in the fraction of an angstrom. This is nothing like what we are used to on the macro-scale. An important consequence when  $R_u \ll 1$  is that the nonlinear convective inertial term  $\vec{u} \cdot \nabla \vec{u}$  becomes negligible. As a result, the equations become linear, greatly simplifying the analysis. The parameter:

$$R_\omega = \frac{L^2}{\nu_f T} \quad (4)$$

expresses the ratio between inertial acceleration forces and viscous forces. Notice that if we take the characteristic velocity to be simply  $L/T$ , the frequency and the velocity-based Reynolds numbers become equivalent. However, it is useful not to make this assumption here because we want to consider further the case where the oscillations are imposed externally and the inverse frequency of these oscillations is taken as the time scale. The result is the frequency-based Reynolds number,

$$R_\omega = \frac{\omega w^2}{4\nu_f} \quad (5)$$

where again we have used the cantilever half-width,  $w/2$ , as the characteristic length scale.

The frequency-based Reynolds is the appropriate Reynolds number to describe micro- or nanoscale cantilevers immersed in fluid. Let us consider further the type of cantilever currently under consideration for the next generation of biosen-

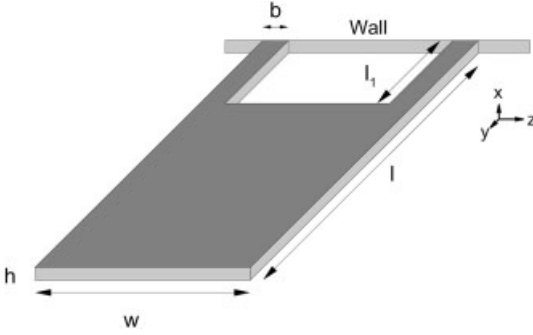


**Figure 1.3.** Schematic of a proposed cantilever geometry for use as a single-molecule biosensor (not drawn to scale):  $l = 3 \mu\text{m}$ ,  $w = 100 \text{ nm}$ ,  $l_1 = 0.6 \mu\text{m}$ ,  $b = 33 \text{ nm}$ . The cantilever is silicon with a density  $\rho_s = 2330 \text{ kg m}^{-3}$ , Young's modulus  $E_s = 125 \text{ GPa}$  and spring constant,  $k = 8.7 \text{ mN m}^{-1}$  [2, 41].

sors. Approximate values for the cantilever geometry are a width  $w \approx 1 \mu\text{m}$ , height  $h \approx 100 \text{ nm}$ , resonant frequency  $\omega \approx 2\pi \times 1 \text{ MHz}$  and we will assume water is the working fluid. As we show later, the maximum cantilever deflection due to Brownian motion will be of the order of  $0.01h$  (and often much less depending upon the particular geometry in question). Using these numbers the characteristic velocity is  $U = 0.01h\omega$ , which yields a velocity-based Reynolds number of  $R_u = 3 \times 10^{-3}$ . Since  $R_u \ll 1$ , the nonlinear inertial term can be neglected. However, the frequency-based Reynolds number is  $R_\omega = 1.6$ . As a result, the first inertial term must be kept in Eq. (1), making the resulting linear analysis more difficult. The governing equations are now:

$$R_\omega \frac{\partial \vec{u}}{\partial t} = -\vec{\nabla} p + \nabla^2 \vec{u} \quad (6)$$

$$\vec{\nabla} \cdot \vec{u} = 0 \quad (7)$$

These equations are known as the time-dependent Stokes equations. In what follows we will drop the subscript  $\omega$  on  $R_\omega$  and assume that  $R$  represents the frequency-based Reynolds number. Although these equations are linear it is still a formidable challenge to derive an analytical solution for all but the simplest scenarios. One such example is when the cantilever is modeled as an oscillating two-dimensional (2-D) cylinder (discussed in more detail in Section 1.2.3). However, even in simple cases the fluid-coupled motion of arrays of oscillating objects still presents a challenge. This is in addition to the fact that most experimental geometries are not simple, which further complicates the analysis (e.g., see Fig. 1.3). This has led to the development of an experimentally accurate numerical approach to calculate the stochastic dynamics of small-scale cantilevers [37] (discussed below).

## 1.2.2

**An Exact Approach to Determine the Stochastic Dynamics of Arrays of Cantilevers of Arbitrary Geometry in Fluid**

At first sight the determination of the stochastic dynamics of an array of fluid-coupled nanoscale oscillators appears quite challenging. Considering the nature of the equations (a system of coupled partial differential equations) and the complex geometries under consideration for experiments, the appeal of a numerical solution is apparent. However, the important question then arises of how to carry out such a numerical investigation? One approach that may come to mind is to perform stochastic simulations of the precise geometries in question that resolves the Brownian motion of the fluid particles as well as the motion of the cantilevers. In principle, this could be done in the context of a molecular dynamics simulation. However, this would be extremely difficult, if possible at all. Two major problems with this approach are:

- (a) There are simply too many molecules. A small box with side length of  $L = 10 \mu\text{m}$  will contain of the order of  $10^{13}$  water molecules. For low Reynolds number flows fluid disturbances are long range and will be of the order of microns even if the oscillators are nanoscale. The length scale of the fluid disturbance scales as approximately  $\sqrt{\nu_F/\omega}$ . This length scale describes the distance from the oscillating cylinder over which the bulk of the fluid momentum is able to diffuse.
- (b) There are vastly disparate time scales. For every oscillation of the cantilever, many water collisions will have had to occur. On average, a water molecule undergoes a collision every picosecond ( $1 \text{ ps} = 1 \times 10^{-12} \text{ s}$ ). However, the cantilever oscillates about once per microsecond. In other words, a million water molecules collide with the cantilever for every single cantilever oscillation – imposing considerable overhead upon our numerical scheme. To make matters worse, in order to get good statistics the numerical solution will have to run for many cantilever oscillations or, equivalently, many numerical simulations will have to be run for different initial conditions and averaged.

However, there is a much better approach if one exploits the fact that the system is in *thermodynamic equilibrium*. This allows the use of powerful ideas from statistical mechanics and, in particular, the fluctuation–dissipation theorem, which relates equilibrium fluctuations with the way a system, that has been slightly perturbed out of equilibrium, returns to equilibrium. In other words, if one understands how a systems dissipates near equilibrium, one understands how that same system fluctuates at equilibrium. The fluctuation–dissipation theorem was originally discussed by Callen and Greene [38, 39]; also see Chandler [40] for an accessible introduction.

It has recently been shown that the fluctuation–dissipation theorem allows for the calculation of the stochastic equilibrium fluctuations of small-scale oscillators using only standard *deterministic* numerical methods [37]. For the case of small



cantilevers in fluid, the dissipation is mostly due to the viscous fluid although internal elastic dissipation of the cantilever could be included if desired.

We will introduce the use of this approach for the case of two opposing cantilevers as shown in Fig. 1.7(a). Consider one dynamic variable to be the displacement of the cantilever on the left  $x_1(t)$ . This is a classical system, so  $x_1(t)$  will be a function of the microscopic phase space variables consisting of  $3N$  coordinates and conjugate momenta of the cantilever, where  $N$  is the number of particles in the cantilever. We now take the system to a prescribed excursion from equilibrium and observe how the system returns to equilibrium, which, in effect, quantifies the dissipation in the system. A particularly convenient way to accomplish this is to consider the situation where a force  $f(t)$  has been applied to the cantilever on the left at some time in the distant past and is removed at time zero. The step force is represented by:

$$f(t) = \begin{cases} F_1 & \text{for } t < 0 \\ 0 & \text{for } t \geq 0 \end{cases} \quad (8)$$

This force couples to  $x_1(t)$  causing a deflection in the cantilever. For this case the Hamiltonian of the system  $H$  is given by:

$$H = H_0 - fx_1 \quad (9)$$

We only consider the case of small  $f$  so the response of  $x_1(t)$  remains in the linear regime. In the linear response regime, the change in the average value of a second dynamical quantity  $X_2(t)$  (here we will use the displacement of the cantilever on the right, which is again a function of the  $3N$  coordinates and conjugate momenta) from its equilibrium value in the absence of  $f$  is given by:

$$\Delta X_2(t) = \frac{F_1}{k_B T} \langle \delta x_1(0) \delta x_2(t) \rangle_0 \quad (10)$$

where  $k_B$  is Boltzmann's constant ( $k_B = 1.38 \times 10^{-23} \text{ J K}^{-1}$ ) and  $T$  is the absolute temperature. The equilibrium fluctuations are given by:

$$\delta x_1 = x_1 - \langle x_1 \rangle_0 \quad (11)$$

$$\delta x_2 = x_2 - \langle x_2 \rangle_0 \quad (12)$$

where the average  $\langle \rangle_0$  denotes the equilibrium average in the absence of the force  $f$ . However, for our case the cantilevers fluctuate about an equilibrium of zero deflection,  $\langle x_1 \rangle_0 = \langle x_2 \rangle_0 = 0$ , which then implies that  $\delta x_1 = x_1$  and  $\delta x_2 = x_2$ . The average behavior of the cantilever deflection in the linear response regime is:

$$\Delta X_2(t) = X_2(t) - \langle x_2(t) \rangle_0 \quad (13)$$

However, as just mentioned,  $\langle x_2(t) \rangle_0 = 0$ , which also implies  $\Delta X_2(t) = X_2(t)$  and yields:

$$X_2(t) = \frac{F_1}{k_B T} \langle x_1(0)x_2(t) \rangle_0 \quad (14)$$

Using this result we can calculate a general equilibrium cross-correlation function in terms of the linear response as:

$$\langle x_1(0)x_2(t) \rangle_0 = \frac{k_B T}{F_1} X_2(t) \quad (15)$$

Similarly, the autocorrelation of the fluctuations is given by:

$$\langle x_1(0)x_1(t) \rangle_0 = \frac{k_B T}{F_1} X_1(t) \quad (16)$$

where  $X_1(t)$  is the average behavior of the deflection of the cantilever in which the force was applied. The spectral properties of the correlations can be found by taking the cosine Fourier transform of the auto- and cross-correlation functions. This yields the noise spectra,  $G_{11}(\nu)$  and  $G_{12}(\nu)$ , given by:

$$G_{11}(\nu) = \int_0^\infty \langle x_1(0)x_1(t) \rangle \cos(\omega t) dt, \quad (17)$$

$$G_{12}(\nu) = \int_0^\infty \langle x_1(0)x_2(t) \rangle \cos(\omega t) dt \quad (18)$$

where  $\nu$  is the frequency defined by  $\omega = 2\pi\nu$ . The noise spectra are important because they are precisely what would be measured in an experiment.

This result is exact with the only assumptions being classical mechanics and linear behavior. Equations (15) and (16) are extremely useful in that they relate the *stochastic* cantilever dynamics on the left-hand side to its *deterministic* response to the removal of a step force on the right-hand side. In other words, Eq. (16) relates the equilibrium fluctuations of the cantilever to its average deflection as it returns to equilibrium from a prescribed excursion to a nonequilibrium state.

With this in mind, the remaining challenge is to calculate the deterministic quantities  $X_1(t)$  and  $X_2(t)$  for use in Eqs. (15) and (16). Since the dynamic variables of interest are macroscopic (after all they are the cantilever deflections  $X_1$  and  $X_2$ ), they can be calculated using the deterministic macroscopic equations which govern the fluid and solid dynamics. This can be from analytics, simplified models or large-scale numerical simulation.

To summarize, the scheme consists of the following steps in a deterministic calculation:

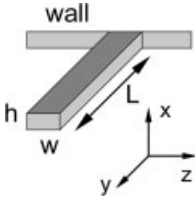


**Figure 1.4.** Schematic of a simple cantilevered beam of length  $L$ , width  $w$  and height  $h$ .

- (a) Apply an appropriate force  $f$  that is constant in time and small enough so that the response remains linear. An appropriate force is one that couples to the variable of interest  $X_1$ . After applying the force, allow the system to come to steady state.
- (b) Turn off the force at a time labeled  $t = 0$ .
- (c) Measure some dynamical variable  $X_2(t)$  (which might be the same as  $X_1$  to yield an autocorrelation function) to yield the correlation function of the equilibrium fluctuations via Eqs. (15) and (16).

For the case of small cantilevers in fluid, the fluid motion can be calculated using the incompressible Navier–Stokes equations and the dynamics of the solid structures can be computed from the standard equations of elasticity. Using the sophisticated numerical tools developed for such calculations it is possible to find accurate results for realistic experimental geometries that may be quite complex, e.g. the triangular cantilever design often used in commercial AFM or the paddle geometries currently under investigation for use as detectors of single biomolecules as shown in Fig. 1.3.

### 1.2.3

#### An Approximate Model for Long and Slender Cantilevers in Fluid

Let us first consider a long and slender cantilever ( $L \gg w, h$ ) that is fixed at its base and free at its tip with the simple beam geometry as shown in Fig. 1.4. This configuration is particularly useful because this geometry is commonly used for AFM. A simplified and effective model analysis is available for this case [42, 43]. In this model, the dynamics of the beam motion is described using classical elasticity theory:

$$\mu \frac{\partial^2 w(y, t)}{\partial t^2} + EI \frac{\partial^4 w(y, t)}{\partial y^4} = F_f(y, t) \quad (19)$$

where  $w(y, t)$  is the displacement of the beam as a function of distance  $y$  along the length of the beam and time  $t$ ,  $\mu$  is the mass per unit length of the cantilever,  $E$  is Young's modulus,  $I$  is the moment of inertia of the cantilever, and  $F_f$  is the force acting on the cantilever due to the fluid. In this expression we have neglected internal dissipation in the elastic body, tensile forces leading to a stressed or strained

state when the cantilever is at equilibrium and gravity forces (it is straightforward to show that small cantilevers do not bend significantly in a gravitational field). It is important to note that Eq. (19) is coupled with the fluid equations Eqs. (6) and (7) through the force  $F_f$ , and that the coupled system of equations are linear. The equations governing beam dynamics are well studied and well understood (see Ref. [44] for an excellent reference on the theory of elasticity). The viscous dissipation in a low Reynolds number fluid is quite large and will dominate any other modes of dissipation such as internal elastic dissipation in the beam itself.

This leaves the important question of how to determine the flow field. Since the beam is long and slender, most of the fluid will interact with the beam by flowing around the sides as opposed to flowing over the beam tip. In this case one can assume that the cantilever is infinite in length and consider only the flow over a 2-D cross-section of the beam [42]. It can then be shown that it is a small correction to then assume that the usually rectangular cross-section of the beam is cylindrical. This is particularly convenient because an analytical solution for the flow field over an oscillating cylinder is available. In fact, the fluid problem was first solved in 1851 by Stokes; however, for a modern treatment, see Ref. [45].

Since the fluidic damping dominates the cantilever motion we can further simplify the analysis by considering only the fundamental mode of the beam dynamics (the higher harmonics will be damped out by the fluid). This additional simplification aids in clarifying the approach without significantly affecting the results (for the analysis using the full beam equation, see Ref. [42]). The equation of motion describing the fundamental mode of a beam immersed in fluid then becomes:

$$m_e \ddot{x} + kx = F_f + F_B \quad (20)$$

where  $x$  represents the deflection of the cantilever tip,  $m_e$  is the effective mass of the beam in vacuum,  $k$  is the effective spring constant of the beam and  $F_B$  is the random force due to Brownian motion. Notice that  $F_f$  contains both the fluid damping as well as the fluid loading due to the additional fluid mass that the beam “carries” as it moves.

It is convenient to transform into frequency space by taking the Fourier transform of this equation to give:

$$(-m_e \omega^2 + k) \hat{x} = \hat{F}_f + \hat{F}_B \quad (21)$$

where:

$$\hat{F}_f = m_{\text{cyl},e} \omega^2 \Gamma(\omega) \hat{x} \quad (22)$$

and:

$$m_{\text{cyl},e} = 0.243 m_{\text{cyl}} = 0.243 \rho_1 \left( \frac{\pi}{4} w^2 L \right) \quad (23)$$

which is the effective mass of a fluid cylinder of radius  $w/2$ , where  $\rho_1$  is the fluid density. The prefactor of 0.243 ensures that mode-shape mass is equivalent for the mass of the cantilever, the fluid loaded mass and the fluid damping. The Fourier transform convention we are using is:

$$\hat{x}(\omega) = \int_{-\infty}^{\infty} x(t)e^{-i\omega t} dt \quad (24)$$

$$x(t) = \frac{1}{2\pi} \int_{-\infty}^{\infty} \hat{x}(\omega)e^{i\omega t} \quad (25)$$

Here,  $\Gamma(\omega)$  is the hydrodynamic function and is defined to be:

$$\Gamma(\omega) = 1 + \frac{4iK_1(-i\sqrt{iR})}{\sqrt{iR}K_0(-i\sqrt{iR})} \quad (26)$$

where  $K_1$  and  $K_0$  are Bessel functions. Note that by this definition the arguments on the right-hand side are  $R$  and not the frequency  $\omega$ . The cantilever is effectively loaded by the fluid which can be characterized by an effective mass,  $m_f$ , larger than  $m_e$  that takes into account the fluid mass that is also being moved. The fluid also damps the motion of the cantilever, which can be expressed as an effective damping  $\gamma_f$ . Relations for  $m_f$  and  $\gamma_f$  can be found by expanding  $\Gamma(\omega)$  into its real and imaginary parts  $\Gamma_r$  and  $\Gamma_i$  in Eq. (21), and rearranging such that:

$$-m_f(\omega)\omega^2\hat{x} - i\omega\gamma_f(\omega)\hat{x} + k\hat{x} = \hat{F}_B \quad (27)$$

to give:

$$m_f = 0.243m_c(1 + T_0\Gamma_r) \sim \Gamma_r(\omega) \quad (28)$$

$$\gamma_f = 0.243m_{\text{cyl}}\omega\Gamma_i \sim \omega\Gamma_i(\omega) \quad (29)$$

Notice that both the fluid loaded mass of the cantilever and the fluidic damping are functions of frequency. The ratio of the mass of the fluid-loaded cantilever to the effective mass of the cantilever in vacuum,  $m_e$ , as a function of frequency is shown in Fig. 1.5. The cantilever has a mass of nearly 20 times the effective value at  $R \approx 1$ . Over 4 orders of magnitude in frequency the mass changes by a factor of about 200. The fluidic damping is shown in Fig. 1.5. There is a slight frequency dependence, over 4 orders of magnitude in frequency the damping changes by a factor of 7, which is much less than the frequency dependence of the mass loading.

From the fluctuation–dissipation theorem the spectral density of the fluctuating force,  $G_{F_B}(v)$ , can be related to the dissipation due to the fluid and is given by:

$$G_{F_B}(v) = 4k_B T m_e T_0 \omega \Gamma_i(\omega) \quad (30)$$

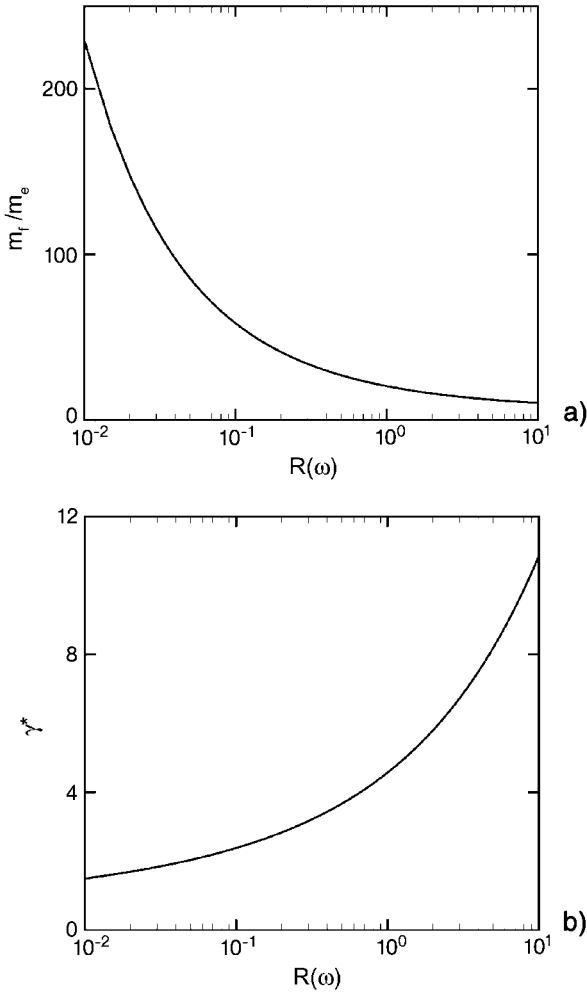


**Figure 1.5.** (a) The ratio of the mass of a fluid-loaded cantilever to the effective mass of the cantilever in vacuum as a function of the frequency-based Reynolds number. (b) The fluidic damping of a cantilever immersed in fluid as a function of the frequency-based Reynolds number. Shown is the nondimensional damping  $\gamma^* = R\Gamma_1(R)$ .

where  $T_0$  is the ratio of the mass of fluid contained in a cylindrical volume of radius  $w/2$  to the mass of the cantilever. The analysis of Ref. [42] does not take into account the frequency dependence of the damping and assumes that the numerator is constant. Although the frequency dependence of the damping is not large as shown in Fig. 1.5, it should be accounted for. Solving for the spectral density of the displacement fluctuations,  $G_x(v)$ , from Eqs. (21) and (30) yields:

$$G_x(v) = \frac{4k_B T}{k} \frac{1}{\omega_0} \frac{\tilde{\omega} T_0 \Gamma_i(R_0 \tilde{\omega})}{[(1 - \tilde{\omega}^2(1 + T_0 \Gamma_r(R_0 \tilde{\omega})))^2 + (\tilde{\omega}^2 T_0 \Gamma_i(R_0 \tilde{\omega}))^2]}$$

where  $\tilde{\omega} = \omega/\omega_0$  is the frequency relative to the vacuum resonance frequency  $\omega_0 = \sqrt{k/m}$  and  $R_0$  is the frequency-based Reynolds number using  $\omega_0$ . Using the equipartition of energy theorem and applying it to the cantilever's potential energy, we arrive at:

$$\frac{1}{2} k \langle x^2 \rangle = \frac{1}{2} k_B T \quad (31)$$

Using this we scale  $G_x(v)$  in Eq. (31) such that:

$$\int_0^\infty |\hat{x}(\omega)|^2 d\omega = \frac{k_B T}{k} \quad (32)$$

The value of  $\omega$  at the maximum value of  $|\hat{x}(\omega)|^2$  yields a theoretical prediction of the fundamental frequency in fluid  $\omega_f$ . Once  $\omega_f$  is known, an approximation for the quality factor of the oscillator,  $Q$ , is:

$$Q \approx \frac{\frac{1}{T_0} + \Gamma_r(\omega)}{\Gamma_i(\omega)} \quad (33)$$

Equation (33) is valid only for  $Q \gtrsim 1/2$  because it neglects to account for the frequency dependence of the mass and fluid loading in Eq. (27) (by considering only the explicit frequency dependence) which become very important for highly overdamped cantilevers (i.e.  $R \lesssim 1$ ).

Using what we have discussed so far let us quantify the stochastic dynamics of an AFM placed in water. We consider a cantilever with the simple beam geometry as shown in Fig. 1.4. The cantilever dimensions are length  $L = 197 \mu\text{m}$ , width  $w = 29 \mu\text{m}$  and height  $h = 2 \mu\text{m}$ . These are chosen so that we can compare with the analytical and experimental results of Ref. [43]. From beam theory, the effective spring constant of a cantilever is:

$$k = \frac{3EI}{L^3} \quad (34)$$

which, for the cantilever in question, yields  $k = 1.3 \mu\text{N m}^{-1}$ . Using the approach described in Section 1.2 we use a step force  $F_1 = 26 \text{ nN}$  and calculate the deterministic response of the cantilever,  $X_1(t)$ , as it returns to equilibrium. For detailed information on the particular computation algorithm we used to solve the deterministic fluid–solid equations, see Refs. [46, 47]. The value of  $\langle x_1(0)x_1(0) \rangle^{1/2}$  is interesting in that it yields the magnitude of the deflections that would be expected

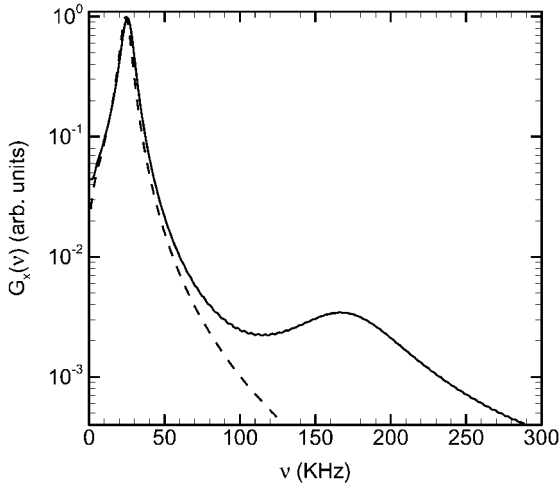


**Figure 1.6.** The noise spectrum as calculated from full finite element deterministic numerical simulation (solid line) and the noise spectrum from the approximate analytical theory (dashed line) for an AFM immersed in water (for experimental results see cantilever c2 in Ref. [43]). The full numerical simulations include all of the cantilever modes including two that are shown in the frequency range of the figure identified by the two peaks in the simulation results. The analytical model only considers the

fundamental mode of the cantilever oscillation resulting in only one peak. Note that more modes could be included if desired; however, as shown in the figures, the higher-frequency modes are strongly damped and will not be significant in experiment. The micron-scale cantilever used for this calculation is of the geometry shown in Fig. 1.4, and has a length  $l = 197 \mu\text{m}$ , width  $w = 29 \mu\text{m}$  and height  $h = 2 \mu\text{m}$ . The applied step force is  $F_1 = 26 \text{ nN}$ .

in an experiment. For this case we find that  $\langle x_1(0)x_1(0) \rangle^{1/2} = 3.16 \times 10^{-21} \text{ m}^2$ . This indicates that the deflection of the cantilever due to Brownian motion in an experiment is about 0.056 nm or about 0.003% of the thickness of the cantilever – an extremely small value even on an atomistic scale. Multiplying this quantity by the spring constant gives an estimate of the force sensitivity of 73.1 pN, which is clearly too large to be used as a biological force detector (recall biological force scales are around 10 pN). The noise spectrum is shown in Fig. 1.6, where there is good agreement with the approximate analytical theory available for this case.

#### 1.2.4

#### The Stochastic Dynamics of a Fluid-coupled Array of (BIO)NEMS Cantilevers

We now use this approach to find the auto- and cross-correlation functions for the equilibrium fluctuations in the displacements of the tips of two nanoscale cantilevers with the experimentally realistic geometries depicted in Fig. 1.3. For this case we would like to emphasize that no analytical expressions or simplified models are currently available. However, we can again use full numerical simulations and exploit the fluctuation theorem, which remains exact.



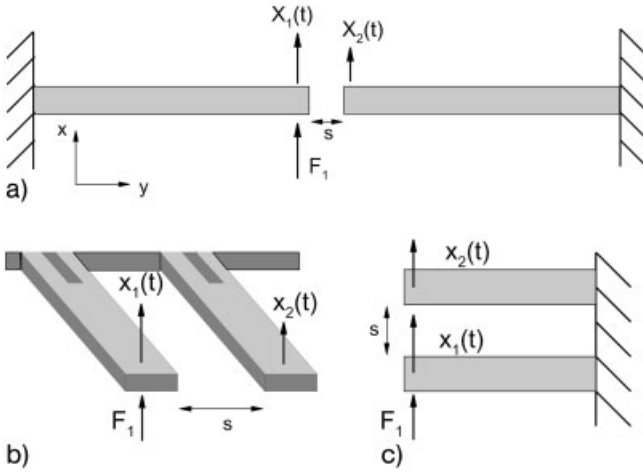


**Figure 1.7.** Schematic showing various cantilever configurations. In all configurations the step force  $F_1$  is released at  $t = 0$ , resulting in the cantilever motion referred to by  $X_1(t)$ . The motion of the neighboring cantilever is

$X_2(t)$  and is driven through the response of the fluid. (a) Two cantilevers with ends facing, (b) side-by-side cantilevers and (c) cantilevers separated along the direction of the oscillations.

To do this we again calculate the deterministic response of the displacement of each cantilever tip, which we call  $X_1(t)$  and  $X_2(t)$  after switching off at  $t = 0$  a small force applied to the tip of the first cantilever,  $F_1$ , given by Eq. (8). Various possible cantilever configurations are shown in Fig. 1.7(a–c); however, we will only consider the case where two cantilevers face one another end-to-end as shown in Fig. 1.7(c).

Again, the equilibrium auto- and cross-correlation functions for the fluctuations  $x_1$  and  $x_2$  are given by Eqs. (15) and (16), and the noise spectra  $G_{11}(\nu)$  and  $G_{12}(\nu)$  are given by Eqs. (17) and (18). The cantilever autocorrelation function and the two cantilever cross-correlation function are shown in Fig. 1.8(b and c, respectively). The value of  $\langle x_1(0)x_1(0) \rangle$  is  $0.471 \text{ nm}^2$ , indicating that the deflection of the cantilever due to Brownian motion in an experiment would be  $0.686 \text{ nm}$  or about 2.3% of the thickness of the cantilever. Multiplying this quantity by the spring constant gives an estimate of the force sensitivity of  $6 \text{ pN}$ ; therefore, a (BIO)NEMS cantilever with this geometry is capable of detecting the breakage of a single hydrogen bond, indicating its potential as a single-molecule biosensor. The cross-correlation of the Brownian fluctuations of two facing cantilevers is small compared with the individual fluctuations. The largest magnitude of the of the cross-correlation is  $-0.012 \text{ nm}^2$  for  $s = h$  and  $-0.0029 \text{ nm}^2$  for  $s = 5h$ . The noise spectra for both the one- and two-cantilever fluctuations are shown in Fig. 1.9(a and b).

The variation in the cross-correlation behavior with cantilever separation as shown in Fig. 1.8(c) can be understood as an inertial effect resulting from the non-zero Reynolds number of the fluid flow. The flow around the cantilever can be separated into a long-range potential component that propagates instantaneously in

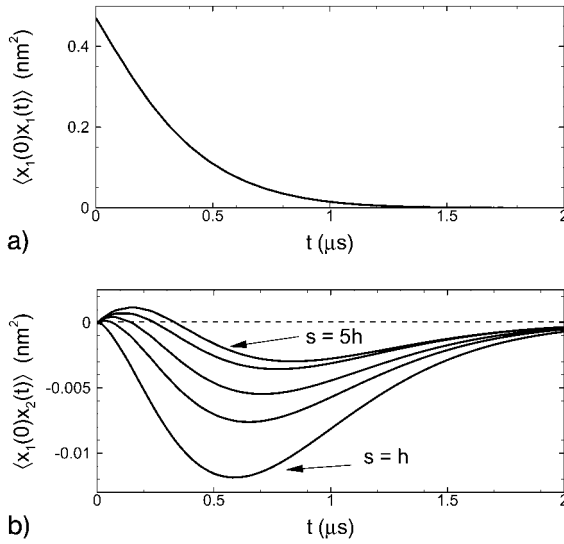


**Figure 1.8.** Predictions of the auto- and cross-correlation functions of the equilibrium fluctuations in displacement of the cantilevers shown in Figs. 1.3 and 1.7(a). The step force applied to the tip of the first cantilever is  $F_1 = 75$  pN. (a) Autocorrelation and (b) cross-correlation of the fluctuations (5 separations are shown for  $s = h, 2h, 3h, 4h$  and  $5h$ , where only  $s = h$  and  $5h$  are labeled, and the remaining curves lie between these values in sequential order).

the incompressible fluid approximation and a vorticity containing component that propagates diffusively with diffusion constant given by the kinematic viscosity  $\nu_f$ . For step forcing, it takes a time  $\tau_v = s^2/\nu_f$  for the vorticity to reach distance  $s$ . For small cantilever separations the viscous component dominates, for nearly all times,

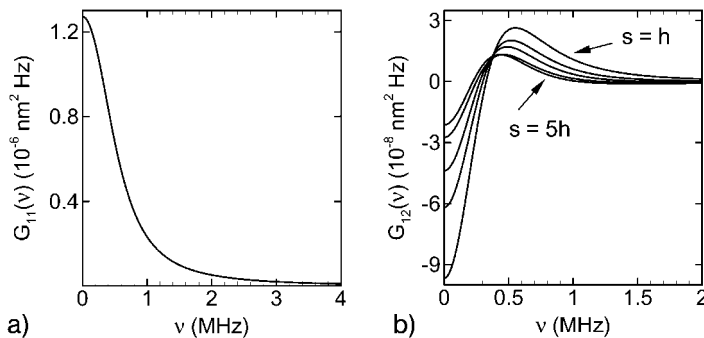


**Figure 1.9.** (a) The noise spectrum  $G_{11}(\nu)$  and (b) the noise spectrum  $G_{12}(\nu)$  as a function of cantilever separation  $s$  for two adjacent experimentally realistic cantilevers. Five separations are shown for  $s = h, 2h, 3h, 4h$  and  $5h$ , where only  $s = h$  and  $5h$  are labeled, and the remaining curves lie between these values in sequential order.

and results in the anticorrelated response of the adjacent cantilever in agreement with [12]. However, as  $s$  increases, the amount of time where the adjacent cantilever is only subject to the potential flow field increases, resulting in the initial correlated behavior.

The complex fluid interactions between individual cantilevers in an array are still an area of active research. Nevertheless, using the thermodynamic approach described here it is now possible to describe quantitatively, with experimental accuracy, the stochastic dynamics of micro- and nanoscale oscillators in fluid. A compelling feature about these results is that the proposed experiments are just beyond the reach of current technologies, making the theoretical results that much more important, as the insight gained will be critical in guiding future efforts.

### 1.3

#### The Physics Describing the Kinetics of Target Analyte Capture on the Oscillator

Now that we have developed the methods necessary to understand the stochastic dynamics of small cantilevers in fluid we turn to the physics describing the capture of target analyte. In order to provide analyte specificity, cantilever surfaces are generally *functionalized* to contain an array of receptor molecules complementary to the target analyte (ligand). This functionalization is carried out by constructing a self-assembling monolayer (SAM), consisting of alkanethiol chains, to which specific receptor molecules are linked. Among other things, the overall performance of (BIO)NEMS cantilever-type sensors will depend on the analyte–receptor capture kinetics and we now discuss a number of issues related to this problem. The basic situation for analyte binding to the functionalized surface of a cantilever is shown in Fig. 1.10.

The binding of analyte from bulk solution to a fixed array of receptors located on a cantilever tip can be described by the kinetic equations relevant to the case of ligand binding to cell surface-bound receptors [48–50], i.e.:

$$\frac{dB}{dt} = [k_{\text{on}}L_oR_o - (k_{\text{on}}L_o + k_{\text{off}})B] \left[ 1 + \frac{k_{\text{on}}(R_o - B)}{k_+} \right]^{-1} \quad (35)$$

where  $B$  is the number of analyte–receptor bound complexes,  $L_o$  is the analyte concentration and  $R_o$  is the total number of receptors in the functionalized array. This model equation describes the reversible biochemical reaction:



The parameters  $k_{\text{on}}$  and  $k_{\text{off}}$  are the usual forward and reverse rate constants for analyte–receptor binding, and  $k_+$  is the so-called diffusion rate constant, which for the case at hand is just  $k_+ = 4\pi\mathcal{D}a_c$ . The quantity  $\mathcal{D}$  is the analyte diffusion coefficient and  $a_c$  is a length which characterizes the size of the functionalized area,

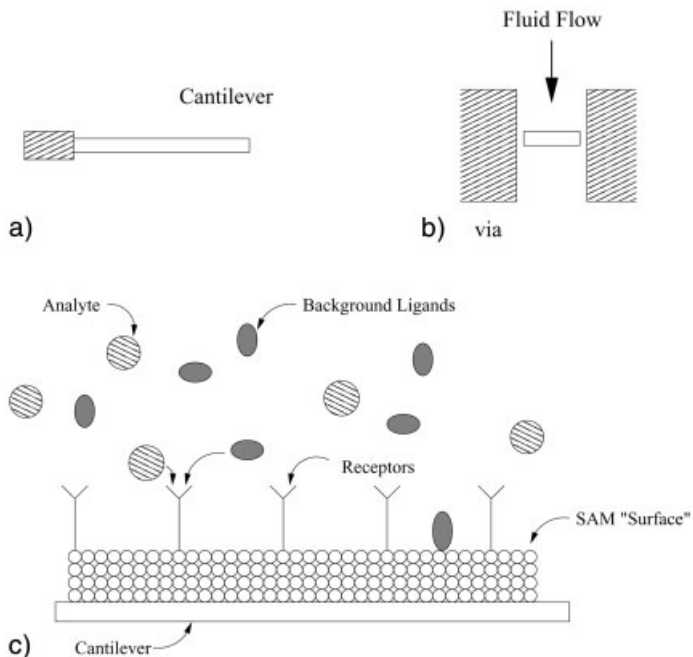


**Figure 1.10.** (a) The side view of a single cantilever. (b) A schematic placing the cantilever in a via. Fluid flows through the via and around the cantilever shown as a rectangular box in the center. (c) A closeup view of a cantilever tip that has been biofunctionalized.

e.g. its width. Defining new variables,  $u = B/R_o$  and  $\tau = k_{\text{off}}t$ , this equation may be put into the more useful nondimensional form:

$$\frac{du}{d\tau} = \frac{K' - (1 + K')u}{[1 + \beta(1 - u)]} \quad (37)$$

with dimensionless parameters  $K' = L_o k_{\text{on}}/k_{\text{off}}$  and  $\beta = R_o k_{\text{on}}/k_{\text{+}}$ . This rather simple kinetic equation describes the analyte–receptor binding under reaction–diffusion conditions, where the parameter  $\beta$  indicates the extent to which the binding is reaction limited ( $\beta \ll 1$ ) or diffusion limited ( $\beta \gg 1$ ).

To give the reader some quantitative insight into this problem, consider the case of biotin–streptavidin ligand–receptor binding. The functionalized region of the cantilever tip is taken to have an area of  $1 \mu\text{m}^2$ , with a total of  $10^4$  receptors linked to the SAM surface. Note that receptor densities achievable using SAM construction are several orders of magnitude larger than those observed for specific receptors found on biological cell surfaces. The forward binding rate constant is approximately  $k_{\text{on}} = 5 \times 10^6 \text{ M}^{-1} \text{ s}^{-1}$ , with a reverse rate constant of  $k_{\text{off}} \sim 10^{-3} \text{ s}^{-1}$ . In

addition, we find that  $k_+ \approx 10^{12} \text{ M}^{-1} \text{ s}^{-1}$ ; thus,  $\beta = 0.05$  and the ligand–receptor binding process is essentially reaction limited. In fact, for cantilever-type devices designed for detection of biomolecules, we find that the capture process is almost invariably reaction limited. This means that the capture kinetics is dominated by the  $k_{\text{on}}$  and  $k_{\text{off}}$  rates of the analyte–receptor pair.

There are two issues of importance when it comes to evaluating the performance of these devices:

- (a) The ultimate sensitivity, which will depend on the total number of analytes captured on the cantilever surface;
- (b) The time required to achieve a specified sensitivity, which is determined by the capture kinetics.

If no other processes of significance are involved in analyte capture, then ultimate sensitivity can be estimated from a steady-state solution of the model equation given above. Thus, at steady-state, the fraction of total surface receptors that are bound by analyte is given by:

$$u_s = \frac{L_o K_a}{(1 + L_o K_a)} \quad (38)$$

where  $K_a$  is the analyte–receptor binding *affinity*. However, depending on the actual analyte–receptor rate constants and the analyte concentration, this may take a considerable time to achieve.

In addition to the basic model equation describing the capture of analyte from bulk solution to surface-bound receptors, there are at least two additional processes that should be considered in connection with sensor performance evaluation:

- (a) The effects of background *contaminant* biomolecules;
- (b) possible surface-enhanced analyte–receptor binding.

Interference by contaminant biomolecules may arise from two distinct mechanisms. The first of these is by *competitive* binding with the surface receptors, thus lowering the number of receptors available for analyte capture. Competitive binding effects may be analyzed by using a straightforward extension of the basic model equation discussed above. Results of such analyses show that these effects may generally be neglected even for background biomolecule concentrations approaching 10 times the analyte concentration. This is of course largely due to the fact that binding affinities for such biomolecules are 1–3 orders of magnitude smaller than the analyte–receptor binding affinities. The second mechanism involves non-specific binding of contaminant biomolecules to the SAM surface itself and would be important if analyte detection were accomplished by mass-loading effects. Even though achievable receptor surface densities for these devices approach  $10^{12} \text{ cm}^{-2}$ , a molecule in solution still “sees” mostly bare SAM surface. Thus, contaminant biomolecules may become attached to the cantilever through nonspecific surface

binding. If one treats the alkanethiol end groups as discrete binding sites on the SAM surface, then this problem may be handled by a model equation analogous to the analyte–receptor capture kinetics equation.

Since the concept was first introduced by Adam and Delbruck [51], the possibility of so-called surface-enhanced ligand–receptor binding has been studied by a number of investigators [48, 52, 53]. This mechanism involves a two-step process:

- (a) Nonspecific binding of ligand from bulk solution to a surface;
- (b) Ligand–receptor binding following 2-D diffusion along the surface.

Although this process may easily be modeled by a pair of coupled kinetic equations, actual quantitative assessment is made difficult by the lack of reliable values for the relevant parameters, i.e. surface nonspecific binding rate and the so-called *collision-coupling* rate constant,  $k_c$  [48]. The parameter  $k_c$  is the rate constant for a surface-diffusing ligand to bind with a surface-bound receptor and is a difficult quantity to measure experimentally. Nevertheless, it may be useful to attempt to estimate the magnitude of this effect for a particular device implementation since it can result in significant enhancement of the analyte capture efficiency for certain combinations of parameters.

Without considering the parameters of a fully specified sensor it is difficult to give general estimates for cantilever capture performance. However, if we consider the  $k_{\text{on}}$ ,  $k_{\text{off}}$  rates of the biotin–actin system described above, then the binding affinity will be  $K_a = 5 \times 10^9 \text{ M}^{-1}$ . Thus, the steady-state receptor coverage is expected to be 33% for an analyte concentration of 0.1 nM. While this represents a very substantial capture efficiency, it should be noted that for these parameter values it will take many 10s of seconds to approach this coverage. This simple example points up an important issue that often arises when attempting to implement specific sensors of this type: One must usually make a trade-off between achievable sensitivity and the time required to make a measurement. A number of applications of these sensors require that detection of the presence of analyte be accomplished in times that are less than 1 s; not infrequently one wishes to achieve millisecond (or less) detection times.

So far the discussion has assumed that analyte transport to the cantilever is accomplished by diffusion only; however, most proposed cantilever sensor implementations involve the use of a microfluidic system to provide constant flow of analyte in a carrier fluid. Thus, in principle, one must consider analyte capture in the context of a reaction–diffusion–convection problem and examine the impact of convection on analyte capture efficiency. Given the previous discussion regarding the reaction rate-limited nature of the analyte capture process, one expects that convection will not have a significant impact on capture efficiency. We can also arrive at this conclusion based on two different fluid dynamics arguments. If one can show that diffusion effects dominate over convection effects in the system, then our previous argument regarding the reaction-limited character of the process still holds and convection cannot contribute significantly to analyte capture. A dimensionless parameter, the Peclet number:

$$\text{Pe} = \frac{LU}{\mathcal{D}} \quad (39)$$

measures the relative importance of convective flow versus diffusive transport; here,  $L$  is a characteristic length of the system,  $U$  is the flow velocity and  $\mathcal{D}$  is the diffusion coefficient. For example, if we take  $L = 1 \mu\text{m}$ ,  $U = 10 \mu\text{s}^{-1}$ , and  $\mathcal{D} = 100 \mu\text{m}^2 \text{s}^{-1}$ , then we have  $\text{Pe} = 0.1$ , and diffusion is the dominant transport process. We may also observe that for laminar flow perpendicular to the cantilever surface a diffusion boundary layer of thickness  $\delta$  is formed. This boundary layer thickness is given approximately by:

$$\delta \approx L(1/\text{Pe})^{1/3} \quad (40)$$

For the parameter values just used this yields a diffusion boundary layer thickness of about  $2.2 \mu\text{m}$ ; thus, at this flow rate essentially all analyte transport to the cantilever surface must be by diffusion. Of course one may also consider significantly increasing the fluid flow velocity; however, nanoscale cantilevers can easily be damaged by high flow rates. Even if the flow velocity is not high enough to actually damage a cantilever, it can result in a “bending bias” of the cantilever which can interfere with detection of binding events. We should point out, however, that these arguments should be re-examined when considering specific sensor implementations.

The use of mass-action-derived kinetic equations for the purpose of analyzing analyte capture performance is completely adequate for analyte concentrations down to about  $0.1\text{--}1.0 \text{ nM}$ . However, when we consider analyte concentrations in the picomolar (or smaller) range, concentration fluctuations may become important in describing the overall performance of the sensor system. Recall that an analyte concentration of  $1 \text{ nM}$  corresponds to a molecular density of slightly less than  $1 \text{ molecule } \mu\text{m}^{-3}$ . In this event one must resort to stochastic methods for describing the reaction–diffusion process of analyte capture. For this case we mention an approach originally developed by Gillespie [54, 55] for “exact” stochastic simulation of coupled chemical reactions. Since the approach has been extended by Stundzia and Lumsden [56] to incorporate diffusion effects, the combined algorithm is suitable for providing a stochastic analysis of the analyte capture problem.

The Gillespie approach is based on the fact that at the microscopic level chemical reactions consist of discrete events that may be described by a joint probability density function (PDF). Thus, given a total of  $\mu = 1, 2, \dots, M$  coupled reactions, consisting of a total of  $\nu = 1, 2, \dots, N$  species, the appropriate joint PDF is  $P(\mu, \tau)$ , where  $\tau$  is the time interval between reactions. This is simply the joint probability that the  $\mu$ th reaction occurs after a time interval of  $\tau$ , which may be written as  $P(\mu, \tau) = P(\mu)P(\tau)$ . Expressions for the individual probabilities are readily derived; these expressions may then be used to implement a rather simple computer algorithm that simulates the evolution of the discrete species concentrations as a function of time, thus yielding the stochastic kinetics for the system. As Gillespie has shown [57], the resulting algorithm is an “exact” simulation of the stochastic master equation describing the coupled chemical system.

As mentioned above, as long as analyte concentrations are expected to be in a range where concentration fluctuations are not important, i.e. greater than about 0.1–1.0 nM, then use of the usual mass-action-derived kinetic equations is perfectly satisfactory in estimating the capture kinetics of the sensors considered here. However, since by its nature the mass-action-derived kinetics computes average values, this method cannot give one any insight into the stochastic behavior of the system. While there are no well-defined rules as to when one must consider fluctuations, it is generally true that when the total number of reactant molecules (ligands) in the reaction volume is only of the order of several hundred, then one should begin to suspect that fluctuations may play an important role in the system behavior. In such cases it is advisable to investigate this possibility through the use of a stochastic simulation algorithm such as the one described above.

#### 1.4

#### Detecting Noise in Noise: Signal-processing Challenges

Although space does not permit a detailed analysis of the various signal-processing methods that may be used in conjunction with (BIO)NEMS cantilever-type sensors, we present a simple analysis of the most basic signal detection method that one might employ. For this analysis we assume a single passive cantilever that utilizes a piezoresistive transducer to sense the fluctuations in the cantilever tip. As discussed before, the term passive simply means that we do not actively drive the cantilever motion in order to provide for a lock-in detector-type processing system. Under these assumptions, and with no analyte bound to the cantilever, the mean-square displacement of the cantilever tip due to fluid fluctuations is given by:

$$\langle x^2(t) \rangle = \frac{4k_B T \gamma_e}{k^2} \quad (41)$$

where  $k_B$  is Boltzmann's constant,  $T$  is the temperature,  $\gamma_e$  is the effective damping constant for the cantilever and  $k$  is the effective spring constant for the cantilever. The mean-square voltage signal into the front end of a signal-processing system is then just:

$$\langle v^2(t) \rangle = |\mathcal{G} \cdot I|^2 \langle x^2(t) \rangle \quad (42)$$

with  $\mathcal{G}$  being the transducer conversion coefficient and  $I$  being the piezoresistive bias current.

We next assume that the presence of bound analyte on the cantilever tip appears as a change in the effective cantilever damping constant, i.e.  $\gamma_e \rightarrow \gamma_e^b$ . Note that in this situation our “signal” appears as a change in the mean-square fluctuations of the cantilever tip. From a signal detection theory standpoint we are attempting to discriminate against the presence of two random voltages, both being Gaussian



distributed but having different variances. Our expressions for the mean-square voltage fluctuations yield a (power) signal-to-noise ratio,  $(\text{SNR})_p$ , of:

$$(\text{SNR})_p = \frac{\gamma_e^b}{\gamma_e} \quad (43)$$

Note that since our expression for the mean-square displacement fluctuations was essentially derived from a fluctuation–dissipation theorem, these expressions are for a system with infinite bandwidth. Our expression for  $\text{SNR}_p$  may thus be called an *inherent* signal-to-noise ratio for this detection modality. The simplest possible processing of this signal then amounts to sending it through a low-noise root mean square (r.m.s.) detector with threshold. The threshold is set to achieve the desired balance between probability of detection and false-alarm probability (*cf.* Ref. [58]).

Of course, since it is usually required that one achieve the highest possible system sensitivity, more sophisticated signal-processing techniques than the simple r.m.s. detector are usually required. We will mention only two such possibilities:

- (a) Passive detection using a *reference* cantilever;
- (b) Active detection using a reference cantilever and lock-in (phase) detection.

In the first case we incorporate an additional cantilever, which is *not* functionalized, into the system. One may then use a technique which is analogous to one developed in the early days of radio astronomy. In this implementation one periodically switches between the reference and sensing cantilevers to make what amounts to a phase-detection measurement of the “signal” power. The method allows one to eliminate the front-end electronics noise and to make a much better estimate of the no-signal power, thus allowing an improved signal-to-noise ratio. In the second approach we move to an active system where the reference and sensing cantilevers are subjected to periodic deflection forces that are  $90^\circ$  out of phase. This allows one to directly utilize lock-in amplifier (phase detector) technology to achieve significant enhancements to the achievable signal-to-noise ratio. For details on these and other more sophisticated signal-processing approaches to the detection of cantilever sensor signals, the reader is referred to Refs. [58–60].

## 1.5

### Concluding Remarks

The physics and modeling of (BIO)NEMS devices poses many theoretical challenges that must be faced as experiment continues to push measurement to the nanoscale. In this chapter we have just scratched the surface of this exciting new field. In picking one particular example to focus upon it was our intent to leave the reader with an idea of some of the physics and modeling issues that one may encounter.

## Acknowledgments

Our research in the modeling of MEMS and NEMS has benefited from many fruitful discussions with the Caltech BioNEMS effort (M. L. Roukes, PI) and we gratefully acknowledge extensive interactions with this team.

## References

- 1 M. B. VIANI, T. E. SCHÄFFER, A. CHAND. Small cantilevers for force spectroscopy of single molecules. *J. Appl. Phys.* 86, 2258–2262, 1999.
- 2 M. L. ROUKES. *Nanoelectromechanical Systems*. condmat/0008187, 2000.
- 3 C. BUSTAMANTE, J. C. MACOSKO, G. J. L. WUITE. Grabbing the cat by the tail: manipulating molecules one by one. *Nature* 1, 130–136, 2000.
- 4 C. WANG, M. MADOU. From MEMS to NEMS with carbon. *Biosens. Bioelectron.* 20, 2181–2187, 2005.
- 5 C. ZANDONELLA. The tiny toolkit. *Nature* 423, 10–12, 2003.
- 6 R. P. FEYNMAN. There is plenty of room at the bottom. *J. Microelectromech. Syst.* 1, 60–66, 1992.
- 7 R. P. FEYNMAN. Infinitesimal machinery. *J. Microelectromech. Syst.* 2, 4–14, 1993.
- 8 G. M. WHITESIDES. The ‘right’ size in nanbiotechnology. *Nat. Biotechnol.* 21, 1161–1165, 2003.
- 9 H. CLAUSEN-SCHAUMANN, M. SEITZ, R. KRAUTBAUER, H. E. GAUB. Force spectroscopy with single biomolecules. *Curr. Opin. Chem. Biol.* 4, 524–530, 2000.
- 10 M. DOI, S. F. EDWARDS. *The Theory of Polymer Dynamics (International Series of Monographs on Physics 73)*. Oxford Science Publications, Oxford, 1986.
- 11 C. TASSIUS, C. MOSKALENKO, P. MINARD, M. DESMADRIL, J. ELEZGARAY, F. ARGOU. Probing the dynamics of a confined enzyme by surface plasmon resonance. *Physica A* 342, 402–409, 2004.
- 12 J.-C. MEINERS, S. R. QUAKE. Direct measurement of hydrodynamic cross correlations between two particles in an external potential. *Phys. Rev. Lett.* 82, 2211–2214, 1999.
- 13 J.-C. MEINERS, S. R. QUAKE. Femtonewton force spectroscopy of single extended DNA molecules. *Phys. Rev. Lett.* 84, 5014–5017, 2000.
- 14 A. KISHINO, T. YANAGIDA. Force measurements by micromanipulation of a single actin filament by glass needles. *Nature* 334, 74–76, 1988.
- 15 A. ISHIJIMA, H. KOJIMA, H. HIGUCHI, Y. HARADA, T. FUNATSU, T. YANAGIDA. Multiple- and single-molecule analysis of the actomyosin motor by nanometer piconewton manipulation with a microneedle: unitary steps and forces. *Biophys. J.* 70, 383–400, 1995.
- 16 M. RADMACHER, M. FRITZ, H. HANSMA, P. K. HANSMA. Direct observation of enzymatic activity with the atomic force microscope. *Science* 265, 1577–1579, 1994.
- 17 N. H. THOMSON, M. FRITZ, M. RADMACHER, J. CLEVELAND, C. F. SCHMIDT, P. K. HANSMA. Protein tracking and detection of protein motion using atomic force microscopy. *Biophys. J.* 70, 2421–2431, 1996.
- 18 M. B. VIANI, L. I. PIETRASANTA, J. B. THOMPSON, A. CHAND, I. C. GEBESHUBER, J. H. KINDT, M. RICHTER, H. G. HANSMA, P. K. HANSMA. Probing protein–protein interactions in real time. *Nat. Struct. Biol.* 7, 644–647, 2000.
- 19 D. A. WALTERS, J. P. CLEVELAND, N. H. THOMSON, P. K. HANSMA, M. A. WENDMAN, G. GURLEY, V. ELINGS. Short cantilevers for atomic force microscopy. *Rev. Sci. Instrum.* 67, 3583–3590, 1996.
- 20 G. BINNIG, C. F. QUATE, Ch. GERBER.

- Atomic force microscope. *Phys. Rev. Lett.* 56, 930–933, 1986.
- 21 F. J. GIESSBL. Advances in atomic force microscopy. *Rev. Mod. Phys.* 75, 949–983, 2003.
  - 22 N. JALILI, K. LAXMINARAYANA. A review of atomic force microscopy imaging systems: applications to molecular metrology and biological sciences. *Mechatronics* 14, 907–945, 2004.
  - 23 Y. MARTIN, C. C. WILLIAMS, H. K. WICKRAMASINGHE. Atomic force microscope force mapping and profiling on a sub 100-Å scale. *J. Appl. Phys.* 61, 4723–4729, 1987.
  - 24 T. R. ALBRECHT, P. GRUTTER, D. HORNE, D. RUGAR. Frequency-modulation detection using high-Q cantilevers for enhanced force microscope sensitivity. *J. Appl. Phys.* 69, 668–673, 1991.
  - 25 M. RADMACHER, R. W. TILLMAN, M. FRITZ, H. E. GAUB. From molecules to cells: imaging soft samples with the atomic force microscope. *Science* 257, 1900–1905, 1992.
  - 26 Q. ZHONG, D. INNISS, K. KJOLLER, V. B. ELINGS. Fractured polymer/silica fiber surface studied by tapping mode atomic force microscopy. *Surf. Sci.* 290, L688–L692, 1993.
  - 27 P. K. HANSMA, J. P. CLEVELAND, M. RADMACHER, D. A. WALTERS, P. E. HILLNER, M. BENZANILLA, M. FRITZ, D. VIE, H. G. HANSMA, C. B. PRATER, J. MASSIE, L. FUKUNAGE, J. GURLEY, V. ELINGS. Tapping mode atomic force microscopy in liquids. *Appl. Phys. Lett.* 64, 1738–1740, 1994.
  - 28 R. GARCIA, R. PEREZ. Dynamic atomic force microscopy methods. *Surf. Sci. Rep.* 197–301, 2002.
  - 29 S. KOS, P. LITTLEWOOD. Hear the noise. *Nature* 431, 29, 2004.
  - 30 Y. LEVIN. Internal thermal noise in the LIGO test masses: a direct approach. *Phys. Rev. D* 57, 659–663, 1998.
  - 31 J. A. PELESKO, D. H. BERNSTEIN. *Modeling MEMS and NEMS*. Chapman & Hall/CRC, London, 2003.
  - 32 E. M. PURCELL. Life at low Reynolds number. *Am. J. Phys.* 45, 3–11, 1977.
  - 33 J. HAPPEL, H. BRENNER. *Low Reynolds Number Hydrodynamics*. Springer, Berlin, 1983.
  - 34 C. POZRIKIDIS. *Boundary Integral and Singularity Methods for Linearized Viscous Flow*. Cambridge University Press, Cambridge, 1992.
  - 35 G. KARNIADAKIS, A. BESKOK, N. ALURU. *Micro Flows*. Springer, Berlin, 2001.
  - 36 R. L. PANTON. *Incompressible Fluid Flow*. Wiley, New York, 2005.
  - 37 M. R. PAUL, M. C. CROSS. Stochastic dynamics of nanoscale mechanical oscillators in a viscous fluid. *Phys. Rev. Lett.* 92, 235501, 2004.
  - 38 H. B. CALLEN, T. A. WELTON. Irreversibility and generalized noise. *Phys. Rev.* 83, 34–40, 1951.
  - 39 H. B. CALLEN, R. F. GREENE. On a theorem of irreversible thermodynamics. *Phys. Rev.* 86, 702–710, 1952.
  - 40 D. CHANDLER. *Introduction to Modern Statistical Mechanics*. Oxford University Press, Oxford, 1987.
  - 41 J. ARLETT et al. BioNEMS: biofunctionalized nanoelectromechanical systems. To be published.
  - 42 J. E. SADER. Frequency response of cantilever beams immersed in viscous fluids with applications to the atomic force microscope. *J. Appl. Phys.* 84, 64–76, 1998.
  - 43 J. W. M. CHON, P. MULVANEY, J. SADER. Experimental validation of theoretical models for the frequency response of atomic force microscope cantilever beams immersed in fluids. *J. Appl. Phys.* 87, 3978–3988, 2000.
  - 44 L. D. LANDAU, E. M. LIFSHITZ. *Theory of Elasticity*. Butterworth-Heinemann, London, 1959.
  - 45 L. ROSENHEAD. *Laminar Boundary Layers*. Oxford University Press, Oxford, 1963.
  - 46 H. Q. YANG, V. B. MAKHIJANI. A strongly-coupled pressure-based CFD algorithm for fluid–structure interaction. In: *AIAA-94-0179*, pp. 1–10, 1994.

- 47 CFD Research Corp., Huntsville, AL 35805.
- 48 D. A. LAUFFENBURGER, J. J. LINDERMAN. *Receptors*. Oxford University Press, New York, 1993.
- 49 H. C. BERG, E. M. PURCELL. Physics of chemoreception. *Biophys. J.* 20, 193–219, 1977.
- 50 O. G. BERG, P. H. VON HIPPEL. Diffusion-controlled macromolecular interactions. *Annu. Rev. Biophys. Biophys. Chem.* 14, 131–160, 1985.
- 51 G. ADAM, M. DELBRUCK. *Structural Chemistry and Molecular Biology*. A. RICH, N. DAVIDSON (Eds.). Freeman, San Francisco, CA, 1968.
- 52 D. WANG, S.-Y. GOU, D. AXELROD. Reaction rate enhancement by surface diffusion of adsorbates. *Biophys. Chem.* 43, 117–137, 1992.
- 53 D. AXELROD, M. D. WANG. Reduction-of-dimensionality kinetics at reaction-limited cell surfaces. *Biophys. J.* 66, 588–600, 1994.
- 54 D. T. GILLESPIE. A general method for numerically simulating the stochastic time evolution of coupled chemical reactions. *J. Appl. Phys.* 22, 403–434, 1976.
- 55 D. T. GILLESPIE. Exact stochastic simulation of coupled chemical reactions. *J. Phys. Chem.* 81, 2340–2361, 1977.
- 56 A. B. STUNDZIA, C. J. LUMSDEN. Stochastic simulation of coupled reaction–diffusion processes. *J. Comp. Phys.* 127, 196–207, 1996.
- 57 D. T. GILLESPIE. Concerning the validity of the stochastic approach to chemical kinetics. *J. Stat. Phys.* 16, 311–318, 1977.
- 58 H. L. VAN TREES. *Detection, Estimation, and Modulation Theory: Part I*. Wiley, New York, 2001.
- 59 A. D. WHALEN. *Detection of Signals in Noise*. Academic Press, New York, 1971.
- 60 J. L. STENSBY. *Phase-Locked Loops: Theory and Applications*. CRC Press, Boca Raton, FL, 1997.

## 2

# Mathematical and Computational Modeling: Towards the Development and Application of Nanodevices for Drug Delivery

*John P. Sinek, Hermann B. Frieboes, Balakrishnan Sivaraman,  
Sandeep Sanga, and Vittorio Cristini*

### 2.1

#### Introduction

Within recent decades, quickening research and development of liposomal and nanoparticle delivery systems has made Paul Ehrlich's dream of *zauberkugeln* – therapeutic magic bullets – a reality. Although these bilipid and polymeric fabrications of the modern laboratory never received the scrutiny of his microscope, their potential to seek out and destroy specific pathogens while leaving the body's healthy tissues relatively unharmed promises to fulfill the paradigm of targeted drug delivery that he envisaged. A critical advantage afforded by the use of molecularly targeted nanovectors over conventional free-drug and antibody-based therapy is highly tunable selectivity, which greatly increases the therapeutic index of any given drug.

A plethora of excellent experimental work has been undertaken ranging from surface modification to prolong circulation, to ligand–particle conjugation to augment selectivity [1–17]. Mathematical and computational modeling can complement this experimental work by providing insight and guidance in both the fabrication and the performance of nanotechnology. A popular concern of such modeling is exemplified in work [18, 19] in which drug-release behavior of nanodevices is modeled according to the laws of mass balance and Fickian diffusion. However, the performance of micro- and nanodevices must be considered in the context of a dynamic biological environment, spanning several scales and modes, including the intravascular, the intratumoral and even the intracellular. Therefore, it is not merely what such devices do in isolation that requires investigation, but also what they do in the body, and what the body does, or attempts to do, to them. From this perspective, a principal consideration in the optimization of nanodevice performance is a thorough understanding of those bodily environments and systems with which the devices will interact. Thus, we do not merely use mathematics and computation to model the nanodevice, but rather to model the performance of the nanodevice/body system. The implications for improvement in not only the devices themselves, but also modes of delivery and possible adjuvant treatments to maximize performance (see, e.g. Ref. [20]), can be readily appreciated.

The treatment of cancer employing liposomes and nanoparticles provides fertile

ground for demonstrating this approach. For example, the modeling and simulation of vasculogenesis and hemodynamics [21–23] point out difficulties in homogeneously delivering nanovectors to tumoral lesions. This has consequences for their design specifications, such as circulation time, loading and release kinetics. Furthermore, fundamental performance limitations imposed by the biological environment must be defined in order for the direction of future development to be determined. Work on opsonization prevention by authors such as Torchilin and coworkers [24], and work on receptor–ligand binding by Bell [25] and Cozens-Roberts and coworkers [26, 27], has a direct influence on the design of liposomes and nanoparticles. Overprotection from protein adsorption may interfere with desirable receptor–ligand binding and therefore both potentials must be mutually optimized. Alternately, methods could be developed that circumvent interference. As yet another example, *in silico* modeling of nanoparticle chemotherapy, such as that performed by Sinek and coworkers [28], can demonstrate potential strengths as well as weaknesses in the particle-vectored delivery paradigm. Knowing the obstacles and options along one’s path is at least half of what is required in planning one’s journey.

The treatment of cancer motivates the lion’s share of nanodevice drug delivery research and provides excellent modeling opportunities in the spirit of what has been discussed above. In this chapter we identify four critical scales or environments which intravenously injected nanovectors must navigate in order to extravasate in sufficient quantity into tumoral tissue and deliver drug in the most efficacious manner. The corresponding functions at each of the scales they must successfully perform are

- To avoid uptake by the reticuloendothelial system (RES) while in circulation.
- To navigate irregularities of tumoral vasculature and homogeneously extravasate.
- To selectively bind to cancer cells and undergo endocytosis.
- To release drug at a level and on a timescale that optimizes cell kill without precipitating tumoral fragmentation.

Mathematical models and computer simulations regarding each of the four phases are discussed in the following sections. The mathematics used ranges from simple force-balance systems to stochastic processes and sophisticated reaction–diffusion solvers. To our knowledge, while facets of nanodevice drug delivery modeling have been expertly treated, no attempt has been made at integrated modeling encompassing the many scales of the problem. Defining those scales while providing examples of models that address each of them is a beginning to unification.

## 2.2 RES Avoidance

The RES is a system of macrophages and specialized cells lining the liver, spleen, bone marrow and lymphatic tissue. Unprotected colloidal moieties, including lipo-

somes and nanoparticles, are sequestered and removed from circulation by the RES too rapidly for them to be effective [29]. A representative accumulation due to sequestration by the reticuloendothelial system is in the liver (60–90% of injected dose), spleen (2–10%), lungs (3–20%) and bone marrow (above 1%) [30, 31]. Not only does removal from circulation prevent particles from reaching their intended target, but also the accumulation in unintended sites could present a toxic threat.

A critical factor in avoiding this uptake is the prevention of opsonization, i.e. the accrual of proteins on the particle surface. The principal way in which this is achieved is by making suitable surface modifications to the particles [12]. Developments chiefly revolve around coating particles with hydrophilic polymers and surfactants. In an early study, Wilkins and Myers [1–3] treated polystyrene particles with polylysyl gelatin and gum Arabic, resulting in an altered distribution throughout the RES, but ultimately the same total sequestered fraction as with untreated particles. Later, Tröster and coworkers [4] and Tröster and Kreuter [5] performed an extensive study of 13 surfactants and polymers as coatings for nanoparticles, and were able to significantly reduce total RES uptake at 30 min post-injection, with uptake increasing to the same level as with uncoated nanoparticles after 7 days. Bazile and coworkers [6] developed nanoparticles based on methoxy poly(ethylene glycol) (PEG)–poly(lactic acid) (PLA) blends, and, by employing  $^{14}\text{C}$  labeling, demonstrated a reduction in their capture by cultured THP-1 monocytes. Poloxamine- and poloxamer-coated nanoparticles have also been studied with respect to liver and spleen uptake and circulation longevity in rabbits and rodents with favorable results [7–11]. Today, popular coating materials are PEG, poly(ethylene oxide) (PEO), poloxamer, poloxamine, polysorbate (Tween-80) and lauryl ethers (Brij-35) [12].

Insight can be gained in modeling the mechanisms by which polymers like PEG and PEO reject protein adhesion to nanovectors. Lasic and coworkers [32] offer a qualitative model of particle rejection in which steric repulsion is generated by a surface of hydrated PEG chains that “brush” away incoming macromolecules. Indeed, the term “steric stabilization” has become standard in describing polymer-mediated protection. In what follows, we present models by Torchilin and coworkers [24] and Jeon and coworkers [33]. In the former, statistical simulations demonstrate the area of coverage of polymer chains as functions of their flexibility and length. The optimization of these parameters as well as the surface coating density is one goal. The latter model focuses on the balance of forces keeping proteins removed from the particle or liposome surface.

### 2.2.1

#### **A Statistical Model of Nanovector Surface Coverage**

Torchilin and coworkers [24] model nanoparticle protection as statistical “clouds” produced by surface-grafted PEG chains that rapidly transit within a “space” of conformations. The surface covered by these clouds is unavailable for blood protein binding, and therefore the density and area of coverage produced by each polymer chain is of interest.

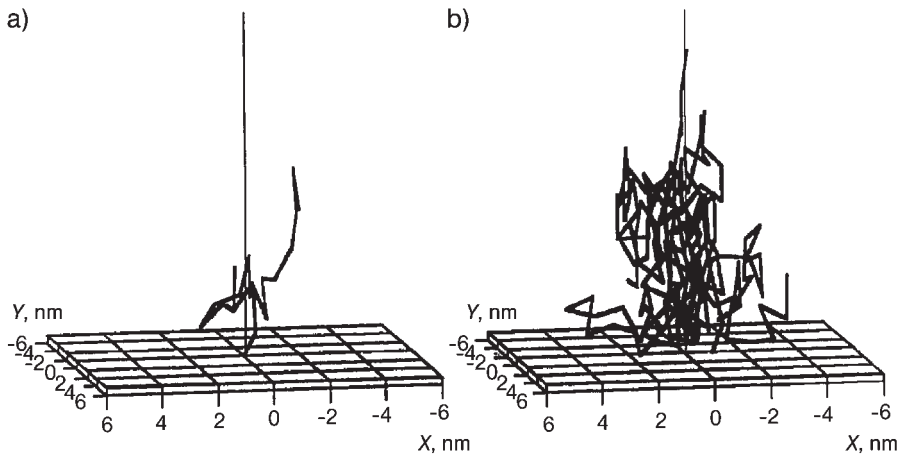


**Figure 2.1.** Model of a polymer chain attached to the particle or liposome surface. (a) Single conformation of one chain. (b) Superposition of 11 random conformations. (Reprinted from Ref. [24], p. 14, © 1994, with permission from Elsevier.)

A single polymer chain is modeled as being composed of a number of segments (e.g. 20), each a fixed unit in length (e.g. 1 nm). Each joint can be selectively articulated and, reckoning from joint 0 anchored into the particle, the mass of each segment is assumed to be concentrated at the distal end (Fig. 2.1). By simulating numerous conformations, an empirical probability distribution in the space directly above the liposome surface can be constructed. By coupling this distribution with the rate of conformation change, the apparent density of the cloud and, therefore, its ability to sterically hinder proteins can be known. Three parameters are critical – the degrees of freedom (or flexibility, as Torchilin calls it) of the polymer chain, its length and its rate of conformation change. To simulate a flexible polymer chain (one having many degrees of freedom), one would allow complete articulation at each joint. To simulate a less-flexible chain, some of the joints would be locked. The probability distributions in Fig. 2.2 show the effects of chain length and flexibility.

Torchilin's model can be used to optimize steric protection, which must be balanced against targeting affinity, if this is desired (see Section 2.4). In general, density and area of coverage increase as the length (weight) and flexibility of polymer chains increase. From the model simulations, the number of polymer chains to be attached to a given nanovector required for a specified degree of coverage, while still providing for accessibility to targeting ligands, can be calculated. Results are given in Fig. 2.3 and are in agreement with experimental data [24–35].



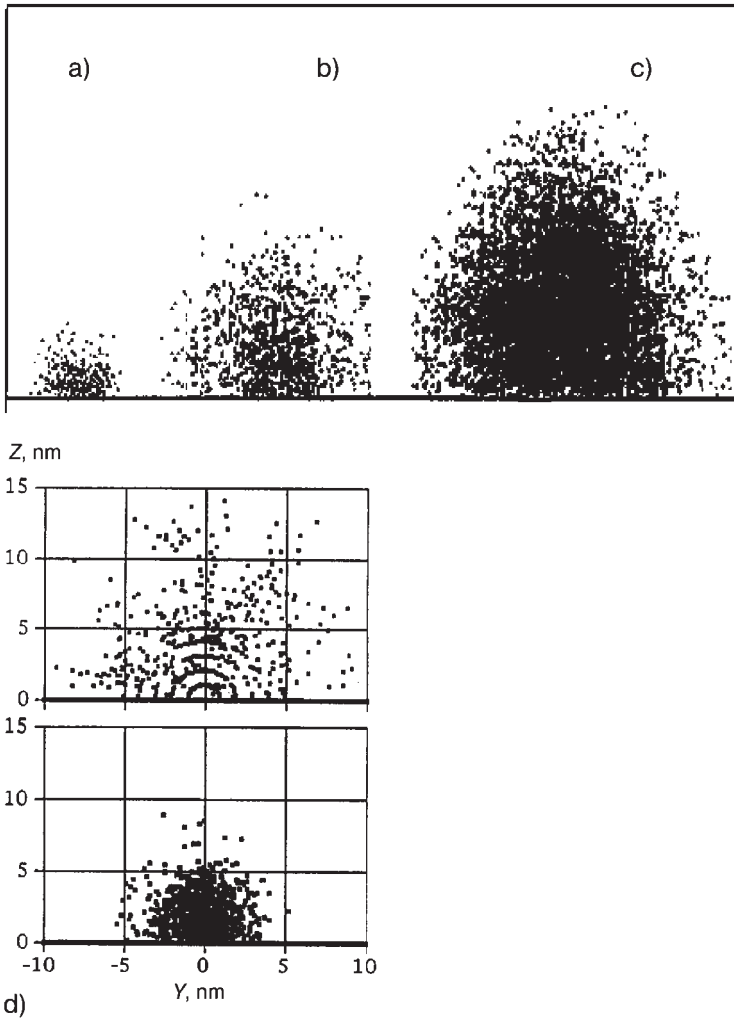


**Figure 2.2.** Simulated distributions of polymer conformations in space directly above the particle surface. (a–c) Effect of polymer length. (a) Short-chain polymer provides little protection. (b) Optimal chain length provides adequate protection while leaving enough surface exposed for receptor–ligand interaction. (c) Excessive length hinders the function of potential targeting ligands on the polymer surface. (d) Rigid polymer is

simulated in the upper panel by assuming four segments of 5 nm each. Although the area of protection appears large, the density of coverage is compromised. Flexible polymer is simulated in the lower panel by assuming 20 segments of 1 nm each. All simulations assume the density of the segments is concentrated in their distal ends. (Reprinted from Ref. [24], pp. 16 and 15, © 1994, with permission from Elsevier.)

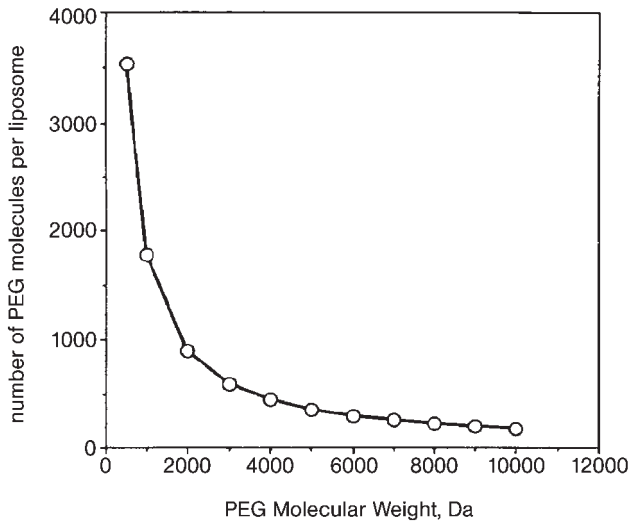


**Figure 2.3.** Model predictions for the minimum number of PEG molecules of a given weight needed for 100% coverage of a liposome of radius 100 nm. (Reprinted from Ref. [24], p. 17, © 1994, with permission from Elsevier.)

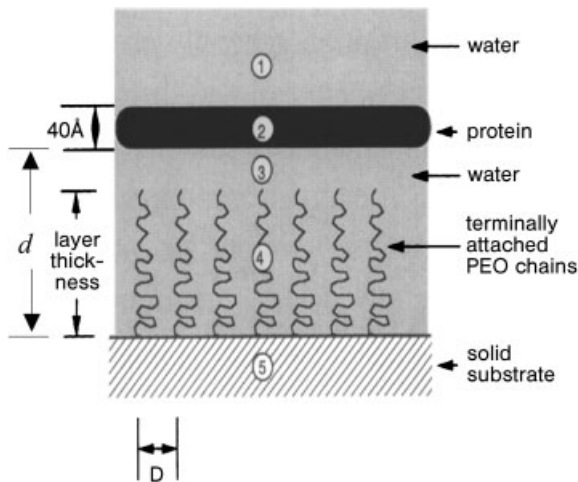


**Figure 2.4.** Pictorial description of the model used by Jeon and coworkers. The two principal forces that mediate binding are steric repulsion due to compression of the PEO chains, and

hydrophobic attraction between the protein and solid substrate. Van der Waals attraction plays a minor role. (Reprinted from Ref. [33], p. 150, © 1991, with permission from Elsevier.)

## 2.2.2

**Modeling the Forces Mediating Protein Approach and Binding**

While surface availability is one determinant of opsonization, ultimately it is the forces between a particle and approaching protein that determine whether it binds. Jeon and coworkers [33] model the approach of a protein with a hydrophobic patch to a hydrophobic particle substrate surfaced with PEO chains as in Fig. 2.4.

The principal forces considered are steric repulsion due to compression of the PEO chains and hydrophobic attraction between the protein and the substrate, although van der Waals attraction plays a minor role. These forces are functions of PEO chain separation distance  $D$  (a measure of density) and polymerization  $N$  (a measure of length). Their corresponding free energies are given as:

$$F_{\text{St}} = K_1 N D^{-11/3} \left[ \left( \left( \frac{K_2 N D^{-2/3}}{d} \right)^{5/4} - 1 \right) + \frac{5}{7} \left( \left( \frac{d}{K_2 N D^{-2/3}} \right)^{7/4} - 1 \right) \right]$$

$$F_{\text{Hyd}} = -K_3 e^{-d/14}$$

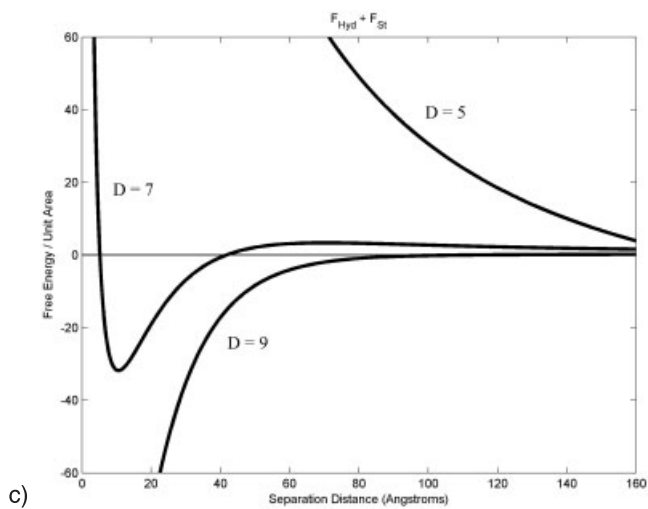
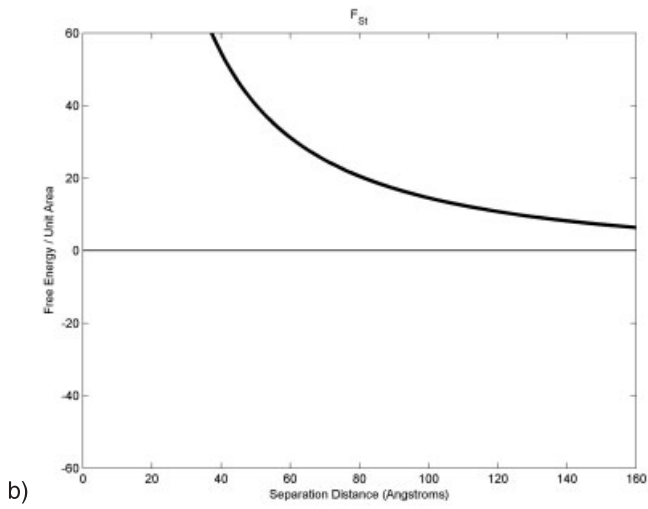
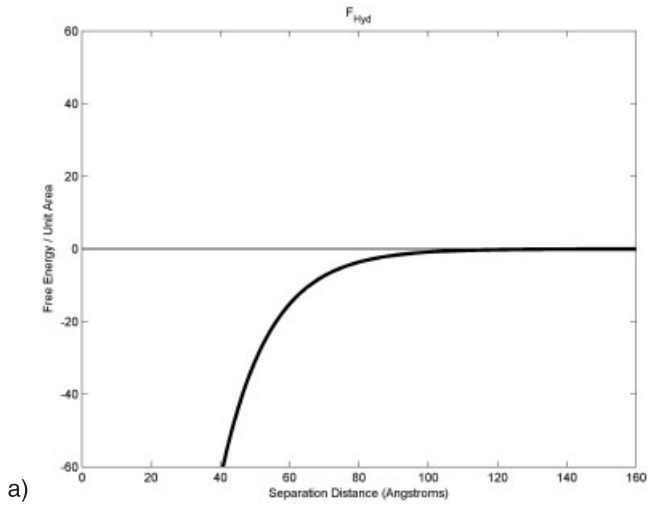
where the  $K$ 's are positive constants, and  $d$  is the separation of protein and polymeric substrate.

Consulting Fig. 2.5, as the protein approaches the PEO-coated substrate, it experiences hydrophobic and, to a lesser extent, van der Waals attraction. The hydrophobic attraction free energy is negative and decreasing with approach, as shown in Fig. 2.5(a). However, strong repulsive steric forces generated by compression of the PEO chains are soon encountered and dominate (Fig. 2.5(b)). Depending on  $D$  and  $N$ , the sum of their free energies can produce an energy well as illustrated in Fig. 2.5(c). It is the depth of this well that determines how tightly bound the protein becomes. As might be expected, high surface density (low values of  $D$ ) and long chain length of PEO (high values of  $N$ ) are desirable for optimal protein resistance, with surface density having a greater effect. Furthermore, PEO retains an advantage among water-soluble synthetic polymers due to its low refractive index, resulting in low van der Waals interaction with the protein.

## 2.3

**Tumoral Vasculature and Hemodynamics**

All systemically administered drug therapy, whether free or nanovectored, relies upon the tumoral vasculature to gain access to malignant cells. As the quantity and uniformity of extravasated nanovectors is of pivotal importance to the success of therapy, models of tumoral vasculogenesis and hemodynamics are indispensable. However, the tumor vasculature is notorious for its irregularity [20, 36, 37]. The tumor vasculature does not follow the normal organizational pattern in which an artery connects to an arteriole to a capillary to a postcapillary venule to a venule to a vein. Instead, a tumor venule may connect to another venule via capillaries or



postcapillary venules. The organization may also be spatially and temporally heterogeneous. The blood flow in tumors grown in transparent windows has been investigated and found to be intermittent, periodically abating and reversing [37, 38]. Tumor vessels are also dilated, saccular and hyper-fenestrated, often containing cancer cells within the vessel endothelial lining. Hobbs and coworkers [39] found that the pore sizes in one human and five murine tumors ranged from 380 to 780 nm, significantly higher than in normal tissue. While this pore size is used to advantage in the preferential extravasation of particles at lesion sites, it also leads to increased fluid extravasation and interstitial pressure. As extravasation from the vasculature depends in part on convection, this increased pressure may unfavorably influence transport. In addition to interstitial fluid pressure, a tumor has a separate mechanical pressure associated with cellular proliferation. Padera and coworkers [40] found that this mechanical stress plays a key role in the collapse of tumor vessels and further restriction of the blood supply in the tumor.

Mathematical models have revealed that the topology of the tumoral vasculature may have a significant impact on blood flow through the network. Secomb and Hsu [41] suggested that irregularities in the vascular geometry could lead to a 2-fold increase in the vascular resistance, relative to the resistance measured in a uniform tube with the same mean diameter. Baish and coworkers [22] have found similar characteristics. In a later work, Baish and coworkers [42] showed that the excessive compliance and leakiness of tumoral vasculature causes blood flow to be diverted from the center of the tumor to its periphery. Recently, Sinek and coworkers [28] have demonstrated that vasculature irregularities are as detrimental to particulate drug delivery systems as to free-drug administration. Results such as these suggest the need for therapies designed to “normalize” the vasculature [22, 20]. Pruning immature and inefficient blood vessels may lead to a more normal vasculature of vessels reduced in diameter, density and permeability, with the potential of restoring more normal hemodynamics.

We next consider models and simulations of both vasculogenesis as well as hemodynamics [21–23]. We furthermore review work performed [43] regarding erythrocyte and leukocyte dynamics within capillaries, which is highly nonlinear and cannot be inferred solely from the dynamics of a strictly Newtonian fluid.

### 2.3.1

#### An Invasion Percolation Model of Vasculogenesis and Hemodynamics

Baish and coworkers [22] used an invasion percolation model of vasculogenesis to investigate the heterogeneity of vessel perfusion and resistance to flow. The principle of invasion percolation is that vascular growth follows the gradient of a sub-

---

←

**Figure 2.5.** (a) Free energy due to hydrophobic attraction and (b) free energy of steric repulsion. Depending on the values of  $D$  and  $N$ , an energy well can be created as in panel (c). The depth of the well determines the force of binding. For low values of  $D$  (high density), steric repulsion dominates; for higher values, energy wells are produced. Strongest binding occurs for  $D = 9$  or above. (Panel c reprinted from Ref. [33], p. 157, © 1991, with permission from Elsevier.)

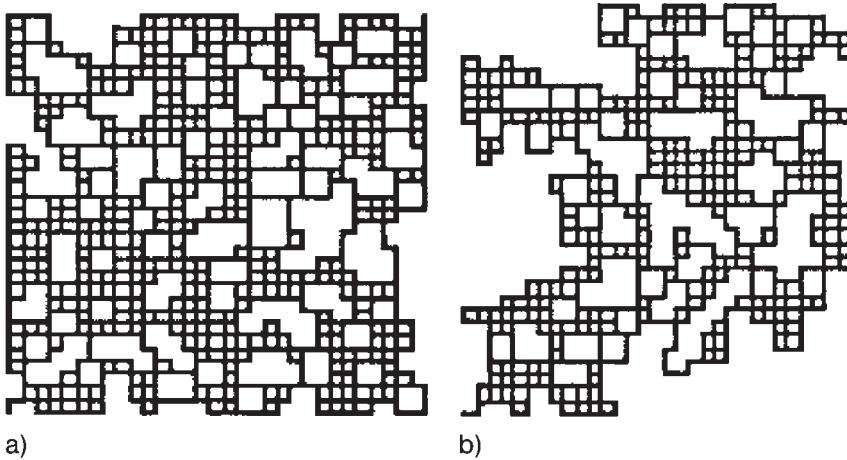


**Figure 2.6.** Examples of two networks produced by the invasion percolation model of Baish and coworkers, showing the network produced when 80 (a) or 60% (b) vessel occupancy is specified. (Reprinted from Ref. [22], p. 332, © 1996, with permission from Elsevier.)

strate’s material weakness rather than responds to a physiological stimulus, such as the gradient of oxygen. To simulate the network, the model begins with a square array of lattice points to which material “strengths” are assigned. The network is then “seeded” at the lower left point. In subsequent iterations it extends to, or invades, the point adjacent to the network that has the lowest strength. This is repeated until a desired vessel “occupancy” (density) is attained (Fig. 2.6).

The structure of their simulated networks was characterized by two measurements propounded earlier by Gazit and coworkers [44] in their studies on mice – the fractal dimension  $d_{\text{vasculature}}$  and the minimum path length  $d_{\text{min}}$ . The table reprinted here as Fig. 2.7 compares several known network growth processes to

Dimension	Known Growth Processes			Observed <i>in vivo</i>		
	Space-filling growth	Diffusion limited aggregation	Invasion percolation	Normal capillaries	Normal arteries and veins	Tumor vessels
$d_{\text{vasculature}}$	2.00	1.71	1.90	$1.99 \pm 0.01$	$1.70 \pm 0.03$	$1.88 \pm 0.04$
$d_{\text{min}}$	1.00	1.00	1.13	$1.00 \pm 0.02$	$0.99 \pm 0.02$	$1.10 \pm 0.04$

**Figure 2.7.** A comparison of the values of  $d_{\text{vasculature}}$  and  $d_{\text{min}}$  for several known growth processes and processes observed *in vivo*. Note the agreement between the invasion percolation model and tumor vessels. (Reprinted from Ref. [22], p. 331, © 1996, with permission from Elsevier.)

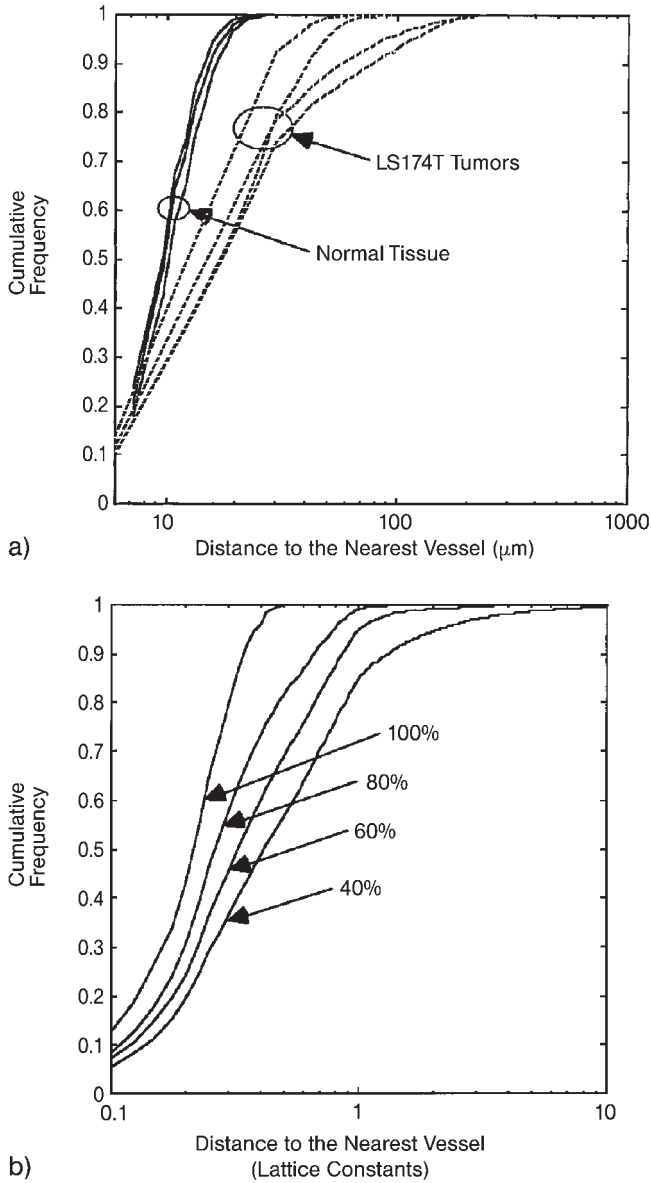


**Figure 2.8.** (a) Probability distributions of distance from the nearest vessel for both normal and tumoral tissue. (b) Probability distributions produced by the invasion percolation model set to various vessel

occupancies. The long “tail” of the distributions is a hallmark of tumoral tissue and is well reproduced in the model simulations. (Reprinted from Ref. [22], pp. 334 and 335, © 1996, with permission from Elsevier.)

those observed *in vivo* by Gazit and coworkers [44], and demonstrates the close correspondence between the results of invasion percolation and tumoral vessels.

With respect to the heterogeneity of perfusion, Fig. 2.8 shows typical probability distributions of distance from the nearest vessel. The important characteristic here is the long tail seen in tumoral vasculature distributions, which is qualitatively reproduced by the percolation model. This means that a significant portion of tumoral tissue is distant from vessels, not only reducing oxygenation, but also the transport of chemotherapeutic agents, especially particles that are expected to deliver their death signal via endocytosis.

The percolation model also predicts inefficient and heterogeneous flow as well as the increased resistance found in tumoral vasculature. In contrast to the fairly uniform fluid flux found in a regular mesh, a few of the vessels of a percolation network carry a disproportionately large flux, while some of the vessels are almost stagnant. In line with this, tumors are typically associated with a higher flow resistance than normal tissue even though they contain a higher proportion of large-diameter vessels [38, 45–48]. For example, tumoral vessels are typically 50% greater in diameter than those of normal tissue. Since flow resistance varies inversely with the fourth power of diameter, one would expect the resistance to be 20% of that in normal tissue. Even decreasing the vascular density by half would only increase resistance 2-fold, still yielding a net 40% of resistance found in normal tissue. According to the percolation model, however, halving the vascular density increases the resistance *7-fold* – more than enough to offset the vessel diameter advantage.

### 2.3.2

#### Flow Simulations Using Anderson and Chaplain's Model

Unlike the previous angiogenesis model [22], Anderson and Chaplain's model [21] relies heavily upon physiological stimuli. In order to produce veridical networks, they note that tumor angiogenic factors (TAFs), such as vascular endothelial growth factor, and fibronectin, a large, non-diffusing molecular constituent of the extracellular matrix, play key roles. TAFs, produced by perinecrotic cells starved of nutrients, induce a chemotactic response in endothelial cells (the essential component of blood vessels), causing them to degrade their parent vessel's basement membranes and migrate towards the tumor. Fibronectin, existing naturally in most tissues and also produced and degraded by endothelial cells, forms an adhesive matrix upon which they can migrate. As the endothelial cells move chemotactically up the gradient of TAFs towards the tumor, consumption of fibronectin produces lateral gradients enabling them to spread via haptotaxis. The interaction of endothelial cells with the extracellular matrix is crucial to the model. In particular, without the interaction of endothelial cells and fibronectin, the lateral motion of the cells, necessary to form vessel loops, requires a much higher random diffusivity than is experimentally measured.

Anderson and Chaplain's is a hybrid continuum–discrete model. Endothelial cell density  $e$ , along with TAF  $c$  and fibronectin  $f$ , are modeled with a system of continuum reaction–diffusion equations incorporating chemotaxis and haptotaxis:



$$\frac{\partial e}{\partial t} = D_e \nabla^2 e - \nabla \cdot (\alpha e \nabla e) - \nabla \cdot (\beta e \nabla f)$$

$$\frac{\partial f}{\partial t} = v_f e - \eta_f e f$$

$$\frac{\partial c}{\partial t} = -\eta_c e c$$

The first term on the right-hand side in the first equation represents cell diffusion (relatively weak) with diffusivity  $D_e$ , while the second and third represent chemotaxis up the TAF gradient and haptotaxis up the fibronectin gradient.  $\alpha$  and  $\beta$  can be constant; however, it is more realistic to have  $\alpha$  be a decreasing function of TAF [21]. The terms in the second equation represent production and uptake of fibronectin by endothelial cells, with  $v_f$  and  $\eta_f$  being constant. The term in the last equation represents uptake of TAF, with constant rate  $\eta_c$ . Initial conditions for endothelial cell density are set by seeding several small regions of high-density “sprouts” along a parental vessel (see below in Fig. 2.10). Initial fibronectin and TAF are assumed to be produced from the parental vessel and the perinecrotic rim just within the tumor, respectively. This results in concentrations decaying with distance from their sources. (Evolution of endothelial cell density is shown in Fig. 2.10.)

The discrete portion of the model is a reinforced random walk of blood vessel tips that begin at the endothelial sprouts. These tips probabilistically follow endothelial cell density as shown in Fig. 2.9. Higher densities of cells bias the random walk of the tip in their direction. Further rules determine capillary branching and

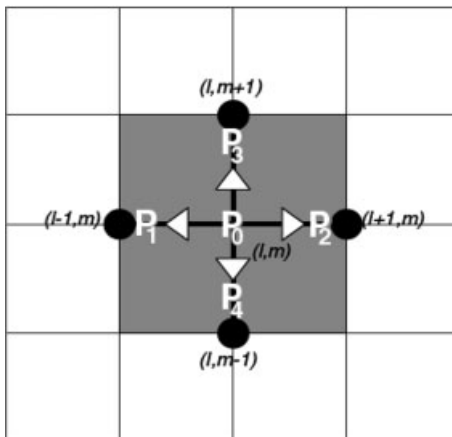
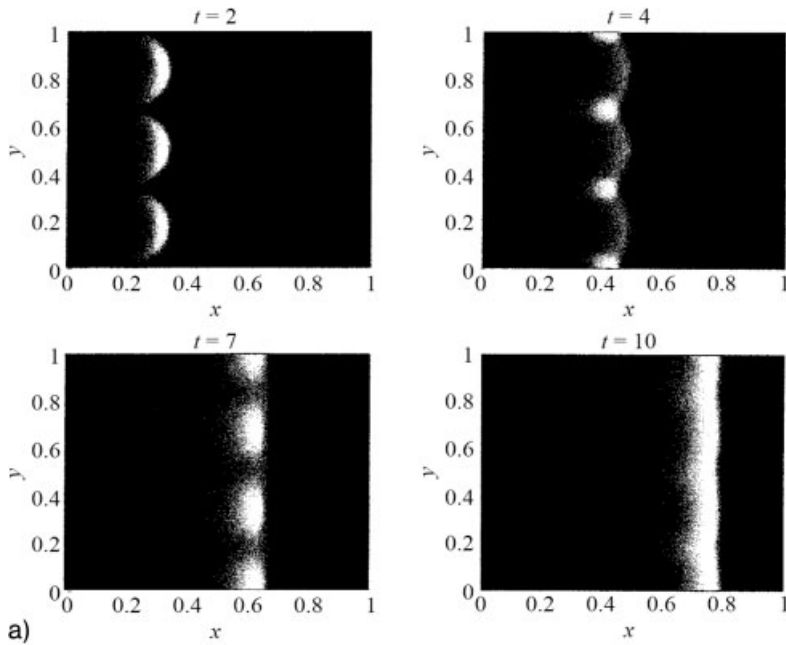
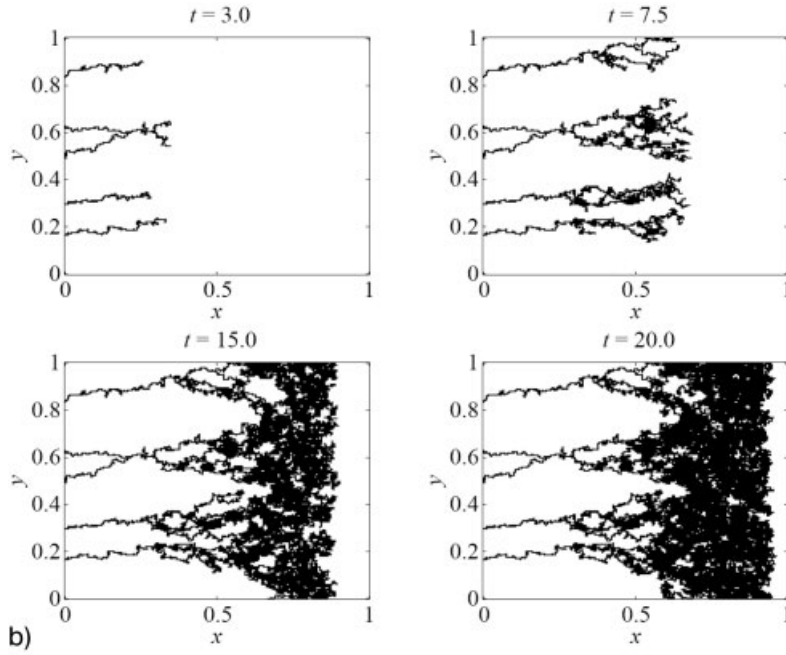


**Figure 2.9.** The vessel tip is initially in the middle. At the next time step it transits to one of the four neighboring grid points with probabilities  $P_1$ – $P_4$  or it stays at its present location

with probability  $P_0$ . The probabilities are determined by the underlying endothelial cell density as shown in Fig. 2.10. (Reprinted from Ref. [23], p. 679, © 2002, with permission from Elsevier.)



a)



b)

**Figure 2.10.** (a) The evolution of endothelial cell density of Anderson and Chaplain's model, beginning with three dense regions (sprouts) in the top left. Density proceeds across the region up the gradient of TAF towards the tumor, whose boundary is assumed on the right edge. Consumption of fibronectin

produces gradients that allow for the lateral spreading of the cell density. (b) The evolution of the actual vessels, whose tips probabilistically follow endothelial cell density. (Reprinted from Ref. [21], pp. 870 and 883, © 1998, with permission from Elsevier.)

the formation of loops (anastomoses) enabling circulation. The result is a realistic capillary network with its essential dendritic structure as well as the reproduction of the experimentally observed “brush border”, whereby extensive branching is observed just before the network penetrates the tumor [49, 50].

McDougall and coworkers [23] used Anderson and Chaplain’s model to simulate blood and drug flow to tumors. They analyzed effects of blood viscosity, pressure drop across parental vessel, mean radius of capillaries and radius of parental vessel by tracking the total quantity of drug within the vasculature in time.

The specifics of the model are as follows. A network is generated using Anderson and Chaplain’s algorithm as in Fig. 2.10, which is then mapped to a Cartesian grid. Then a radius  $R_{ij}$  is randomly assigned from a probability distribution to each element (vessel segment) joining nodes  $i$  and  $j$  on the grid. At each node  $i$  there exists a pressure  $P_i$ , and through each element joining nodes  $i$  and  $j$  there exists a flux  $Q_{ij}$ . This flux is assumed to obey Poiseuille’s law:

$$Q_{ij} = \frac{\pi R_{ij}^4 \Delta P_{ij}}{8\mu L_{ij}}$$

where  $L_{ij}$  is the length of element  $ij$  and  $\mu$  is fluid viscosity. Imposing mass conservation at each node  $i$  via:

$$\sum_{1 \leq j \leq 4} Q_{ij} = 0$$

where  $j$  varies over the four adjacent lattice nodes results in an exactly determined system of linear equations given the pressure drop across the parental vessel. The parental vessel feeds all capillaries going into the tumor.

To analyze drug flow, total drug mass  $M$  within the vasculature is tracked in time for values of four important parameters: blood viscosity, pressure drop across parental vessel, mean radius of capillaries and radius of parental vessel. A steady-state infusion as well as a bolus injection is shown in Fig. 2.11 for a base set of parameter values. The graph of  $M$  in time is shown for the continuous infusion and is compared to other graphs that result when, for example, mean capillary radius or viscosity are changed. When viscosity is raised, although the same limiting amount of drug mass is eventually reached within the vasculature  $M_\infty$ , the time required to reach that level is greater. Lowering the mean radius of the capillary bed, however, decreases the carrying capacity of the network so that  $M_\infty$  is, itself, reduced.

It is apparent that understanding results such as these is crucial to optimizing nanovector delivery. With increasing precision of measurement of the tumoral environment so as to provide more accurate input parameters, such simulations may improve to the point that they can quantitatively model a given patient’s lesion and contemplated therapy, bringing to bear the full weight of intervention on the disease.

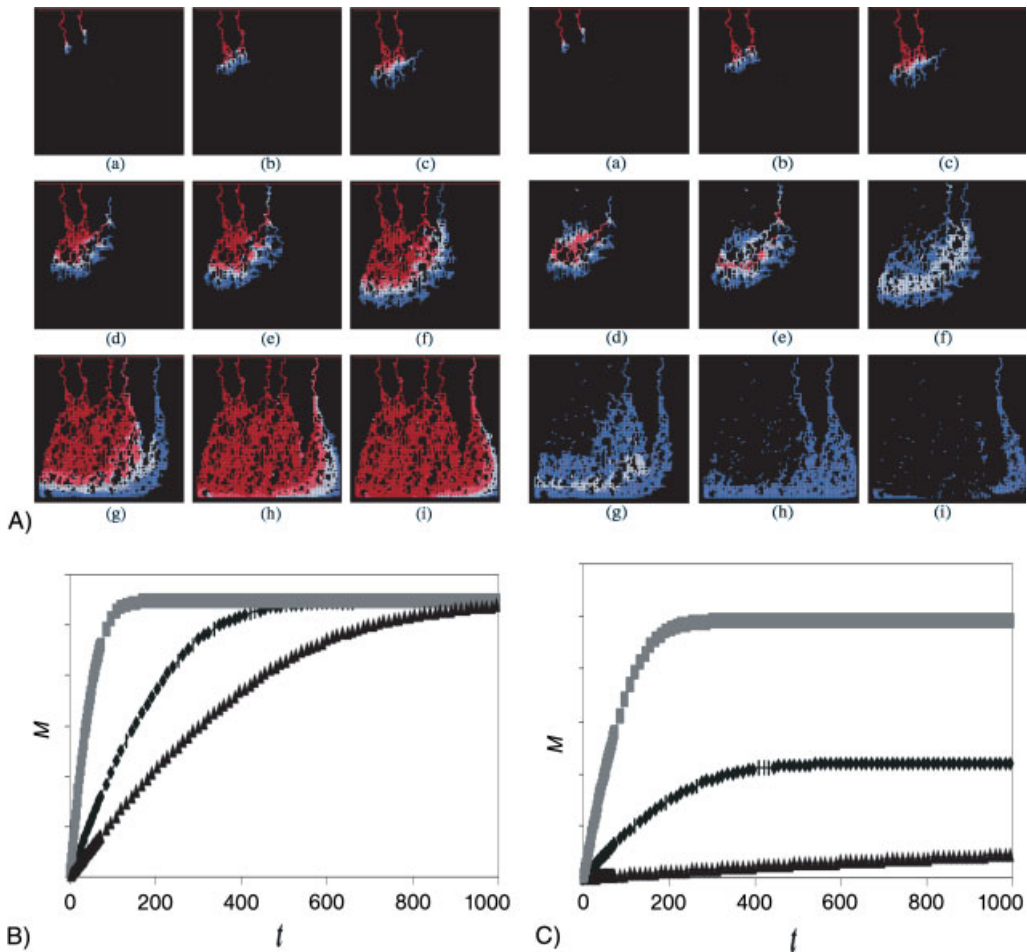


**Figure 2.11.** Simulations of drug delivery. The parental vessel runs across the top, with blood flowing from left to right. The tumor boundary runs along the bottom. (A) The left upper set of panels show a continuous infusion for a base set of parameters (blood viscosity, pressure drop across parental vessel, mean radius of capillaries and radius of parental vessel). Blood begins to flow into the vascular bed through the first two vessels in (b) and (c). It begins to flow out of the bed back towards the parental vessel in frames (d)–(f). Steady-state is reached by frame (i). The right upper set of panels show a bolus injection for

the same base set of parameters. The lower set of graphs shows the effects of changing parameter values on the amount of drug in the vasculature  $M$  in scaled time  $t$  (continuous infusion). (B) From top to bottom shows the effect of increasing viscosity of blood: time to vascular saturation is lengthened although the saturation level remains constant. (C) From top to bottom shows the effect of decreasing the mean capillary radius: saturation capacity is severely reduced. (Reprinted from Ref. [23], pp. 689, 696, 690 and 691, © 2002, with permission from Elsevier.)

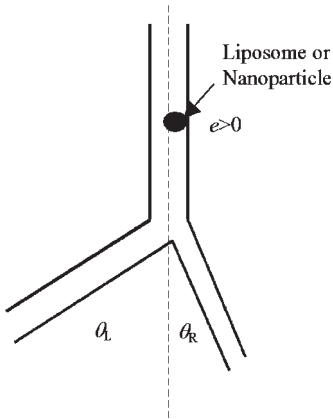


**Figure 2.12.** Diagram of a vessel bifurcation. Some important parameters are the branching angles  $\theta_L$  and  $\theta_R$ , the radii of the daughter vessels, and the eccentricity of the approaching liposome or particle. The latter is defined as axial displacement divided by vessel radius.

### 2.3.3

#### Particle Dynamics within the Tumoral Vasculature

The fluid flow dynamics discussed above become even more complex when particulate carriers are involved. Schmid-Schönbein and coworkers [43] model the flow of blood cells at vascular branches and find that the distribution of cells at a vessel bifurcation is nonlinearly related to bulk fluid flow through the branches. The analysis easily extends to liposomes and, to a lesser extent, nanoparticles. Figure 2.12 depicts the situation where a parental vessel splits into two daughter vessels. Here, important parameters are the left and right angles of separation  $\theta_L$  and  $\theta_R$  and the radii of the daughter vessels  $r_L$  and  $r_R$ . A particle that approaches the bifurcation may not be centered in the vessel, thus we measure its eccentricity  $e$ , defined as its distance from the centerline divided by the radius of the parental vessel. Letting the proportions of particles that enter either the left or right daughter vessel of a symmetric bifurcation ( $\theta_L = \theta_R$  and  $r_L = r_R$ ) be denoted by  $\varphi_L$  and  $\varphi_R$  ( $\varphi_L + \varphi_R = 1$ ), and also letting the proportions of total flow (all particulate matter and plasma) that enter each daughter be  $\psi_L$  and  $\psi_R$ , we can write particulate distribution as a function of total flow distribution and eccentricity  $\varphi = \varphi(\psi, e)$ , “R” and “L” subscripts having been dropped. Note that in the symmetric case it is not necessary that  $\psi_L = \psi_R = 0.5$  since blockages may exist downstream of one of the daughters. In the general case, this function will also depend upon the branching angles, daughter vessel radii and possibly other geometric information.

Several important results are obtained, perhaps the most notable being the nonlinear relationship shown in Fig. 2.13 in the case of symmetric branching. For particles whose diameter is small compared with the diameter of the vessel,  $\varphi_R = \psi_R$ .

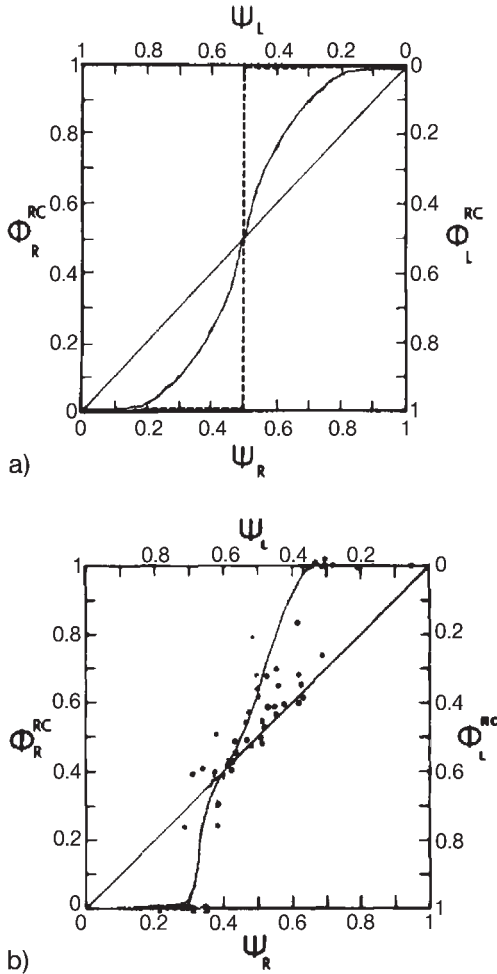


**Figure 2.13.** Relationship between bulk flow distribution into left and right daughter vessels ( $\psi_L$  and  $\psi_R$ ) and particle flow distribution ( $\phi_L$  and  $\phi_R$ ). (a) For particles that are small in comparison to vessel radius, bulk flow distribution and particle flow distribution are the same (diagonal line). As the relative particle size grows, a sigmoidal relationship

becomes evident. At the limit, the step function results where  $\phi_R = 1$  for  $\psi_R > 0.5$ .

(b) Data from an experiment performed by Schmid-Schönbein and coworkers on red blood cells (dots) together with a least-squares fit (solid curve). (Adapted from Ref. [43], pp. 24 and 27, © 1980, with permission from Elsevier.)

Otherwise,  $\phi_R$  is very sensitive to deviations in  $\psi_R$  from 0.5, resulting in the steep curve. In the limit where the diameter of the particle is almost equal to the diameter of the vessel, this curve becomes vertical, so that for  $\psi_R > 0.5$ , all particles flow to the right, i.e.  $\phi_R = 1$ . However, there are notable exceptions for particles that cling to the endothelium, such as leukocytes. In some experiments performed by

Schmid-Schönbein and coworkers [40], in spite of a high percentage of the bulk flow to the right ( $\psi_R \geq 73\%$ ), white blood cells that were biased to the left, with some rolling along the endothelium, still entered the left branch. Although the eccentricity of the cells had an effect, this behavior was far less pronounced for red blood cells under similar conditions.

## 2.4

### Receptor–Ligand-mediated Binding

Much effort has been devoted to conjugating cell-targeting ligands on nanoparticles and liposomes in an attempt to improve specificity. The objective is that particles whose surface is covered by a layer of “adhesive molecules” (ligands) will tether to target cells expressing receptors for the ligands. These targets may be cells of tumor endothelium or the tumor cells themselves, which typically overexpress certain receptors, e.g. folate receptors, in comparison to normal cells. Lee and Low [51] were among the first to suggest that liposomes could be targeted to cancerous KB cells by conjugating them with folic acid (Fig. 2.14). Folate conjugates have a high affinity for cell-surface folate receptors ( $K_D \sim 10^{-10}$  M) [52]. Additionally, folate is inexpensive, stable during storage and *in vivo* circulation, and nontoxic. The steps in the folate-targeting of liposomes to cancer cells are shown in Fig. 2.15 and are as follows [17]:

- Liposomes pass through the tumor microvasculature.
- The increased vascular permeability of the tumor tissue enables the liposomes to extravasate into the tumor interstitial fluid.

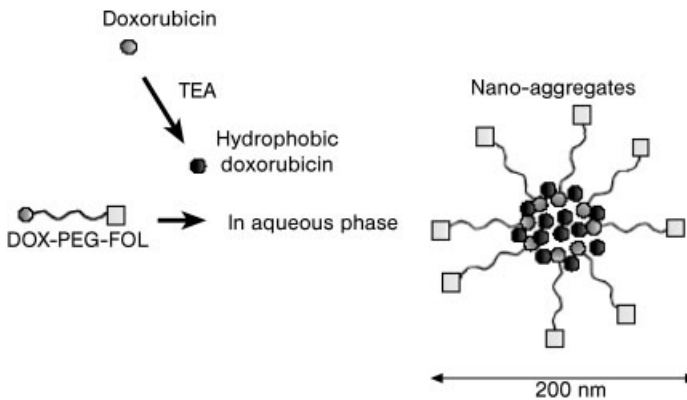
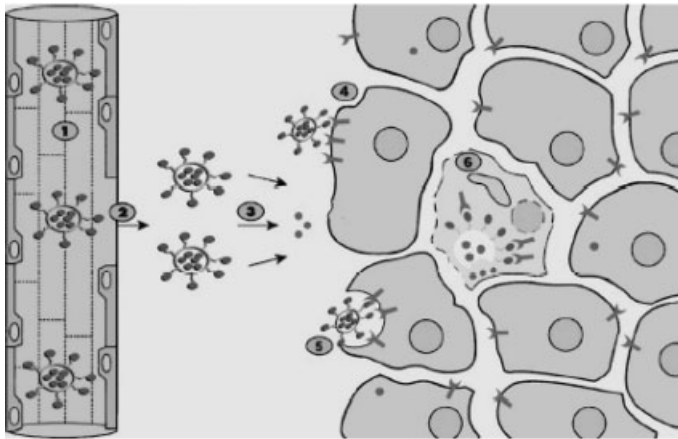
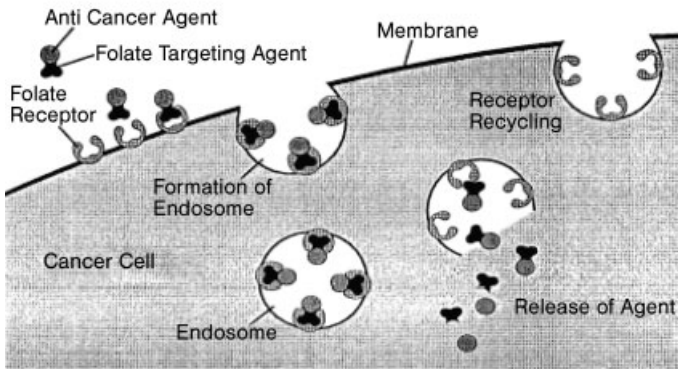


**Figure 2.14.** Scheme for creating folate-targeted doxorubicin(DOX-PEG-FOL) Nan conjugates. The folate-targeting moieties at the end of the PEG chains improve the targeting efficiency of the nano-aggregates. (Reprinted from Ref. [15], p. 248, © 2004, with permission from Elsevier.)



a)



b)

**Figure 2.15.** (a) Schematic diagram illustrating the concept of folate-targeting of liposomes to cancer cells. After preferential extravasation from hyper fenestrated tumoral vasculature, conjugates bind to tumor cells and are endocytosed. (Reprinted from Ref. [17], p. 1179, © 2004, with permission from Elsevier.)

(b) Folate receptor-mediated endocytosis of nanovectors containing anticancer drugs. The formation of endosomes that encapsulate the conjugates protects them from P-glycoprotein, MRP, GS-X and other efflux proteins. (Adapted from Ref. [53], p. 40, © 1998, with permission from Elsevier.)

- Drug is released gradually from the liposomes that remain in the interstitial fluid, enters the tumor cells as free drug, and exerts a cytotoxic effect.
- The other liposomes bind to the folate receptors on the surface of tumor cells via the folate ligand. It is important to note that due to the limited diffusion capacity of the liposomes, generally only the tumor cells closest to the blood vessels are associated with this binding.
- These liposomes are then internalized by the tumor cells via folate receptor-mediated endocytosis.



- The internalized liposomes then release the drug, which is free to exert its cytotoxic effect on the cells.

Research has shown that conjugates can overcome the multidrug resistance effect of the P-glycoprotein efflux pump due to their cellular uptake via folate receptor-mediated endocytosis [54]. According to Turek and coworkers [52], the process of endocytosis consists of receptor–ligand binding followed by internalization in clathrin-coated pits (clathrin is a protein that is the major constituent of the “coat” of the coated pits that are formed during the endocytosis of materials at the surface of cells) or “uncoated” caveolae (small invaginations in the plasma membrane that play a role in endocytosis as well as signal transduction and are observed especially in endothelial cells). As seen in Fig. 2.15, when the receptors bind to their target molecules, the pit deepens until a clathrin-coated vesicle is released into the cytosol. Due to the fact that the liposomes are encapsulated in these endosomal vesicles, they escape being effluxed by the P-glycoprotein efflux pumps.

Understanding the kinetics of receptor-mediated cell attachment would be of service in the design and optimization of ligand-conjugated nanovectors. An important question is, what are the strength and density of bonds needed to achieve adequate adhesion under various stresses? Bell [25] developed a deterministic model for cell attachment in the absence of fluid stress and cell detachment in the presence of fluid stress. We give an account of his work first, followed by a stochastic reanalysis. Another stochastic treatment of receptor–ligand binding can be found in Cozens-Roberts and coworkers [26].

#### 2.4.1

##### Bell's Deterministic Model

Once a cell and nanoparticle or liposome have been brought into proximity via non-specific interactions such as Brownian motion and van der Waals forces, receptor–ligand bond formation may occur. The proximate cell and particle surface, each with its associated protein receptor or ligand available for contact, are shown in Fig. 2.16. The cell's receptor and liposome's ligand are free to diffuse in the plane of the phospholipid bilayer, while for a polymeric nanoparticle ligand is presumably limited to local gyrations. The most elementary formulations assume single receptor–ligand binding.



**Figure 2.16.** Proximate cell and particle or liposome surfaces with some free and bound receptors and ligands.

Letting  $N_1$  and  $N_2$  be the densities of total available receptor and ligand, respectively, and letting  $X_t$  be the density of bound receptor–ligand complex at time  $t$  with  $N_1 \gg X_t$  for all  $t$  to simplify the exposition, bond formation is governed by:

$$\frac{dX_t}{dt} = k^+ N_1 (N_2 - X_t) - k^- X_t \quad (1)$$

where  $k^+$  and  $k^-$  are the forwards and backwards kinetic rate constants. At equilibrium, we have:

$$X_\infty = \alpha N_2 (1 + \alpha)^{-1} \quad (2)$$

where  $\alpha = KN_1$  and  $K = k^+/k^-$  and is the association constant.

The forwards and backwards rate constants can in theory be derived from the planar diffusion constants  $D_1$  and  $D_2$  of membrane-bound receptor and ligand, although rotation and gyration of species also play a part. In order to do this, the binding is assumed to take place according to the two-step reaction:



where  $R \circ L$  represents an “encounter complex” in which receptor and ligand are within some critical radius  $C$ , and  $RL$  represents bound receptor–ligand. The  $d$ 's and  $r$ 's represent directional reaction rates for the steps. The former are related to the receptor and ligand planar diffusion constants according to:

$$\begin{aligned} d^+ &= 2\pi(D_1 + D_2) \\ d^- &= 2(D_1 + D_2)C^{-2} \end{aligned} \quad (4)$$

In many cases the rate of change of the encounter complex is negligible. Setting  $d[R \circ L]/dt = 0$  then allows for the net reaction rates in (1) to be approximated as  $k^+ = d^+ r^+ / (d^- + r^+)$  and  $k^- = d^- r^- / (d^- + r^-)$ . If, furthermore,  $r^+ \gg d^-$ , as is the case for receptors and ligands in a viscous membrane, then these rates reduce to  $k^+ = d^+$  and  $k^- = d^- r^- / r^+$ .

This, then, provides the basis for determining the strength of bonding between, for example, a ligand-conjugated liposome and a receptor-rich cell. The question can be asked, what force is required to break a bound particle–cell complex? To answer this question, we assume that a force  $F$  is applied to separate the surfaces in Fig. 2.16. Under this condition kinetic theory provides that the reverse reaction rate  $k^-$  in Eq. (1) is modified to  $k^- \exp(AF/X_t)$ , where  $A$  is a constant, so that the equation becomes:

$$\frac{dX_t}{dt} = k^+ N_1 (N_2 - X_t) - k^- \exp(AF/X_t) X_t \quad (5)$$

From this expression it can be seen that as the force is increased, so does the reverse reaction rate and therefore the equilibrium number of bonds will be decreased. However, this rate also increases as the number of bonds  $X_t$  decreases because the force is being applied over fewer bonds. This is reflected by the presence of  $X_t$  in the denominator of the exponential. Therefore, the dynamics will be different than for the case of no applied force; for forces in excess of a critical minimum  $F_c$ , the net rate of bond formation  $dX_t/dt$  will always be negative.

This can be seen from Fig. 2.17, which shows  $dX_t/dt$  as a function of  $X_t$  for four different forces, all other parameters being held constant. In all cases (possibly unstable) equilibrium occurs where the curve crosses the horizontal axis. The upper curve represents the case where no force is applied. The three other curves in descending order represent the effects of a subcritical force  $F_{\text{sub}}$ , the critical force  $F_c$  and a supercritical force  $F_{\text{sup}}$ . For all curves, net bond formation is positive above the horizontal axis and we move to the right along the curve. Net bond formation is negative below the horizontal axis and we move to the left. It can be appreciated that for  $F_{\text{sup}}$  the curve is completely negative so that no new equilibrium can be reached, i.e. the particle–cell complex separates. The critical force  $F_c$  results in a curve that just touches the axis, but otherwise is completely negative, and any force greater than this results in separation. Assuming the association constant  $K = 1$  and fixing the density of receptors at  $N_1 = 10^3 \mu\text{m}^{-2}$ , Bell calculates a representa-

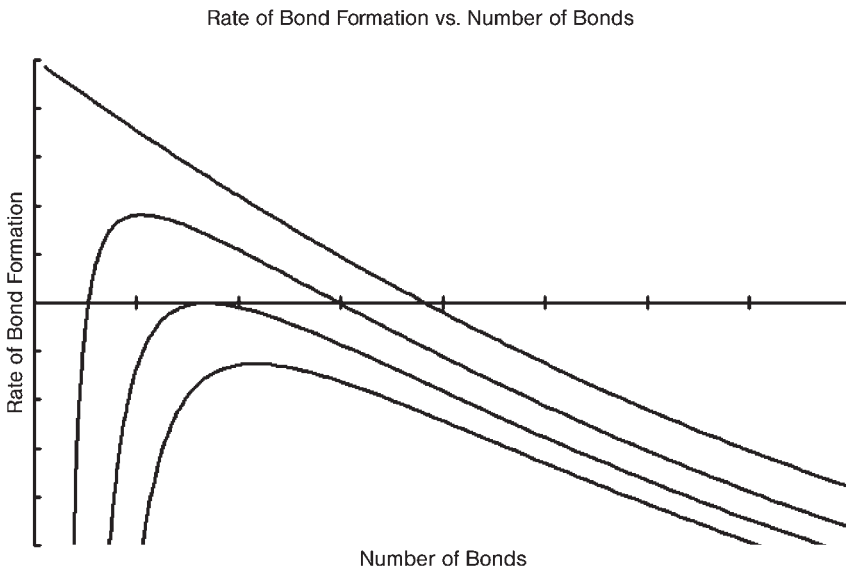


**Figure 2.17.** The  $y$ -axis is the right-hand side of Eq. (5) and represents the rate of bond formation under various separation forces. In all cases, when above the axis, the dynamics

moves to the right along the curve; otherwise, it moves to the left. Forces represented from top to bottom are: none, a subcritical force  $F_{\text{sub}}$ , the critical force  $F_c$  and a supercritical force  $F_{\text{sup}}$ .

tive value of  $F_c/N_2 \sim 4 \times 10^{-6}$  dynes per total available ligand. In the foregoing we have abused notation in that  $N_2$  is here being used as the absolute number of available ligands in a specific  $1\text{-}\mu\text{m}^2$  patch.

This critical force can be compared to other biologically relevant forces, such as the stress created by a fluid flowing past a bound liposome or nanoparticle. Stokes' law says that for a spherical body of radius  $r$  the force generated by a fluid flowing past at velocity  $v$  is given by  $F = 6\pi\eta rv$ , where  $\eta$  is fluid viscosity. For a liposome of radius  $4\text{ }\mu\text{m}$  this is calculated to be  $5.3 \times 10^{-5}v$  dynes. Using the values of  $K$  and  $N_1$  above, and again abusing notation, we set  $4 \times 10^{-6} = F_c/N_2 = 5.3 \times 10^{-5}v/N_2$  to yield  $N_2 \sim 13v$  potential bonding sites. Thus, the liposome would need only 13 available ligands to resist a fluid velocity of  $1\text{ cm s}^{-1}$ .

#### 2.4.2

##### A Stochastic Model

Stochastic formulations may be more appropriate for receptor–ligand binding, especially when the bonds are few. Again we base our model upon the deterministic equation (5) with the understanding that  $N_1 \gg X_t$  at all times. This time, though, we must recognize that  $X_t$  is a stochastic process. Most importantly, this means that rather than assuming any particular value at a given time, it is a probability *distribution* of bonds. Even after having attained equilibrium as  $t \rightarrow \infty$ , it becomes a limiting distribution  $X_\infty$ . In what follows we limit our attention to one square unit of area, since otherwise the values of  $X_t$  are not discrete. Nonetheless, the results are completely general. Following Bailey [55] and letting  $X_{\Delta t} \equiv X_{t+\Delta t} - X_t$  we have, for  $1 \leq X_t \leq N_2 - 1$ :

$$P[X_{\Delta t} = j|X_t] = \begin{cases} k^+ N_1(N_2 - X_t)\Delta t + o(\Delta t) & \text{if } j = 1 \\ k^- \exp(AF/X_t)X_t\Delta t + o(\Delta t) & \text{if } j = -1 \end{cases} \quad (6)$$

Making appropriate adjustments for  $X_t = 0$  and  $X_t = N_2$ , this results in the system of partial differential equations for the discrete probabilities  $p_i(t) \equiv P[X_t = i]$ :

$$\begin{aligned} \frac{\partial p_0(t)}{\partial t} &= k^- \exp(AF) p_1(t) - k^+ N_1 N_2 p_0(t) \\ \frac{\partial p_i(t)}{\partial t} &= k^+ N_1(N_2 - (i - 1)) p_{i-1}(t) + (i + 1)k^- \exp\left(\frac{AF}{i+1}\right) p_{i+1}(t) \\ &\quad - \left(k^+ N_1(N_2 - i) + ik^- \exp\left(\frac{AF}{i}\right)\right) p_i(t) \quad \text{for } 0 < i < N_2 \\ \frac{\partial p_{N_2}(t)}{\partial t} &= k^+ N_1 p_{N_2-1}(t) - N_2 k^- \exp\left(\frac{AF}{N_2}\right) p_{N_2}(t) \end{aligned} \quad (7)$$

With the further restriction that  $\sum p_i = 1$  we can find the distribution of  $X_\infty$  by solving for the steady-state solution of the above, yielding:

$$\begin{aligned}
 p_i(\infty) &= \frac{N_2!}{(N_2 - i)!} \frac{\alpha^i p_0(\infty)}{\prod_{1 \leq j \leq i} i \exp(\frac{\Delta E}{i})} \\
 p_0(\infty) &= \left( \sum_{0 \leq i \leq N_2} \frac{N_2!}{(N_2 - i)!} \frac{\alpha^i}{\prod_{1 \leq j \leq i} i \exp(\frac{\Delta E}{i})} \right)^{-1}
 \end{aligned} \tag{8}$$

where  $\alpha = KN_1$  and  $K = k^+/k^-$  is the association constant. In the case of no separating force, the probability generating function  $P(\theta) = \sum_{i \geq 0} p_i \theta^i$  is discovered from this to be the Taylor expansion of  $(1 + \alpha)^{-N_2} (1 + \alpha \theta)^{N_2}$ . A quick check on the mean yields  $\bar{X}_\infty = P'(1) = \alpha N_2 (1 + \alpha)^{-1}$ , in agreement with (2).

Although the variance as well as any chosen moment could also be calculated, it is perhaps of more interest to calculate the probability of complete disengagement of all bonds under various values of  $F$ . This means we are interested in  $p_0$  (henceforth understanding this to mean  $p_0(\infty)$ ), which, in the case of no applied force, is simply  $(1 + \alpha)^{-N_2}$ . For the values of  $\alpha = 10^3$  and  $N_2 = 13$  used for the example in Section 2.4.1 this yields  $9.9 \times 10^{-40}$ , hardly consequential. However, in contrast to the deterministic analysis, the stochastic analysis demonstrates that even a sub-critical force that is little more than *half* of the critical force is sufficient to dislodge the liposome. Consulting Fig. 2.18, we see three curves that result from using the aforementioned values of  $\alpha$  and  $N_2$ , and three different forces: none,  $F_{\text{sub}}$  ( $\sim 0.5F_c$ ) and  $F_c$ . (Strictly speaking, these are *scaled* curves of the rate of bond formation (Eq. (5)) because we do not know  $k^+$  or  $k^-$  independently. Moreover, we

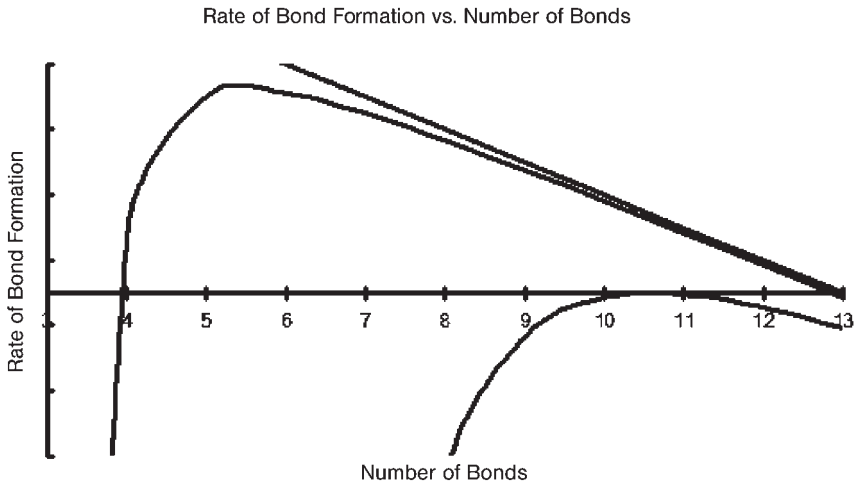


**Figure 2.18.** The example from Section 2.4.1 reanalyzed ( $\alpha = 10^3$  and  $N_2 = 13$ ). The top curve has no separation force applied. The bottom curve results from applying  $F_c$ . The middle curve results from applying

$F_{\text{sub}} \sim 0.5F_c$ . The deterministic model predicts no separation until  $F_c$  is reached; however, the stochastic model predicts the probability of separation for  $F_{\text{sub}}$  to be greater than 0.9958.

do not quote units of force. Nonetheless, for the relevant computations to find probabilities at equilibrium,  $k^+$  and  $k^-$  only enter as a ratio, and  $AF$ , as a product. Only one value of this product will result in a critical force curve. The two product values used in the calculations were  $AF_c = 57.5$  and  $AF_{\text{sub}} = 30$ .) While it is no surprise to learn that  $F_c$  results in  $p_0 = 1$  to more than 20 decimals, it may yet be surprising that  $F_{\text{sub}}$  results in  $p_0 > 0.9958$ .

The application of both the deterministic and stochastic models to the optimization of receptor–ligand binding is apparent. Subtle differences in the models may become significant in light of the necessity of balancing binding affinity with protein rejection needed to avoid RES uptake (Section 2.2).

## 2.5

### Intratumoral and Cellular Drug Kinetics and Pharmacodynamics

Once nanovectors have successfully evaded the RES, navigated the tortuous topology of tumoral vasculature and extravasated at their intended site, cellular-level drug kinetics and pharmacodynamics determine modeling concerns. Liposomes are too large to penetrate much more than two or three cell layers into tumoral interstitium, while most nanoparticles fair no better. In many cases, lesion tissue is within 100  $\mu\text{m}$  of the nearest vessel and a typical cell diameter is about 10  $\mu\text{m}$ . Thus, for ligand-conjugated vectors, expected to enter into individual cells, penetration into and destruction of three cell layers means that 30% of the tumor can hypothetically be eradicated with one treatment. If, furthermore, as tissue is destroyed, inner layers are next exposed to unspent particles, more cell kill is potentially possible. For “plain” nanovectors, it is not penetration that is the issue, but rather the sustained release of sufficient concentration of drug. This may also be an issue for ligand-conjugated vectors, since some of their charge will be released into tumoral interstitium.

The physics of liposomal and nanoparticle drug release is well researched, with the Higuchi, power law and Weibull models sometimes used as phenomenological approximations. Although these models are not considered to be mechanistic, Kosmidis and coworkers [19] make the case for such an interpretation of the Weibull model, which is a single exponential asymptotically approaching 100% release in time. In fact, nanoparticle release profiles frequently evince a simple bi-exponential release pattern described by  $C_t = C_\infty - (Ae^{-\alpha t} + Be^{-\beta t})$ , where  $C_\infty$  is the total drug,  $C_t$  is the amount of drug released by time  $t$ ,  $A$  is the rapidly released portion of drug with rate constant  $\alpha$ , and  $B = C_\infty - A$  is the slowly released portion of drug with rate constant  $\beta$  [28, 29, 56]. If the release can be sustained long enough, then the bi-exponential becomes approximately linear with release rate  $B\beta$ .

Even with the above simplification, cellular-level drug kinetics and transport is highly nonuniform not only because of the inhomogeneous transport of vectors through and extravasation from tumoral vasculature discussed in Section 2.3, but also because of drug gradients due to cellular uptake and metabolism. Below, we present models and simulations of chemotherapy [28, 57] that highlight intratumoral and cellular-level drug release and kinetics.

## 2.5.1

**A Two-Dimensional Model of Chemotherapy**

In 2004, Sinek and coworkers simulated nanoparticle-mediated chemotherapy and tumor response using a two-dimensional multiscale tumor simulator due to Zheng and coworkers [58]. The simulator is built upon continuum-scale reaction–diffusion equations for its growth component following the previous work of Byrne and Chaplain [59, 60] and Cristini and coworkers [61], together with a combined continuum–discrete model of angiogenesis based upon the work of Anderson and Chaplain [21]. It is capable of tracking cancer progression from its avascular stage, through the transition from avascular to vascular growth and into the later stages of invasion of normal tissue. Sinek’s group focused on the case of glioblastoma multiforme by using microphysical parameters characterizing malignant glioma cells obtained from *in vitro* experiments by Frieboes and Cristini [62] and clinical data. Glioblastoma is an aggressive brain tumor that may present as the last stage of astrocytoma progression or *de novo*. It is extremely recalcitrant to all forms of therapy, whether surgical, genetic, chemical or radiological. This is in part due to the high motility of glial cells, rendering the tumor highly diffuse on the periphery [63].

They first simulated the growth of a highly perfused lesion of glioma. This was then exposed to simulated chemotherapy in which nanoparticles were assumed to remain at their point of extravasation from the vasculature and function as a constant source of drug along the vessels. Extravasation, diffusion and cellular uptake of both drug and nutrient was simulated according to the quasi-steady-state reaction–diffusion equations:

$$\begin{aligned} 0 &= v_s \delta_V + D_s \nabla^2 s - \eta_s s \\ 0 &= v_n \delta_V + D_n \nabla^2 n - \eta_n s \end{aligned} \quad (9)$$

where  $s$  and  $n$  are the local concentrations of drug and nutrient, respectively, the  $v$ ’s are (spatially and temporally variable) production rates related to release of drug and supply of nutrient, the  $\eta$ ’s are uptake rates by cancer cells, and the  $D$ ’s are diffusion coefficients.  $\delta_V$  is the Dirac delta function indicating the location of the vasculature. Drug action was then modeled as cell kill being proportional to normalized drug concentration  $\bar{s}$  acting on the fraction of cycling cells, given by the normalized nutrient  $\bar{n}$ . When combined with the growth of cells, modeled as the product of a mitosis constant and normalized nutrient  $\lambda_M \bar{n}$ , the net local growth or regression of tumor cells (the velocity field divergence) becomes:

$$\nabla \cdot \mathbf{u} = \lambda_M \bar{n} - \lambda_D \bar{s} \bar{n} \quad (10)$$

where  $\lambda_D$  is the killing power of the drug.

Sinek’s group performed two classes of simulations. The first recognized extravasational difficulties due not only to irregular vascular topology generated using Anderson and Chaplain’s model (Section 2.3.2), but also pressure variations within tumor interstitium. The latter was accomplished by using  $v_n =$

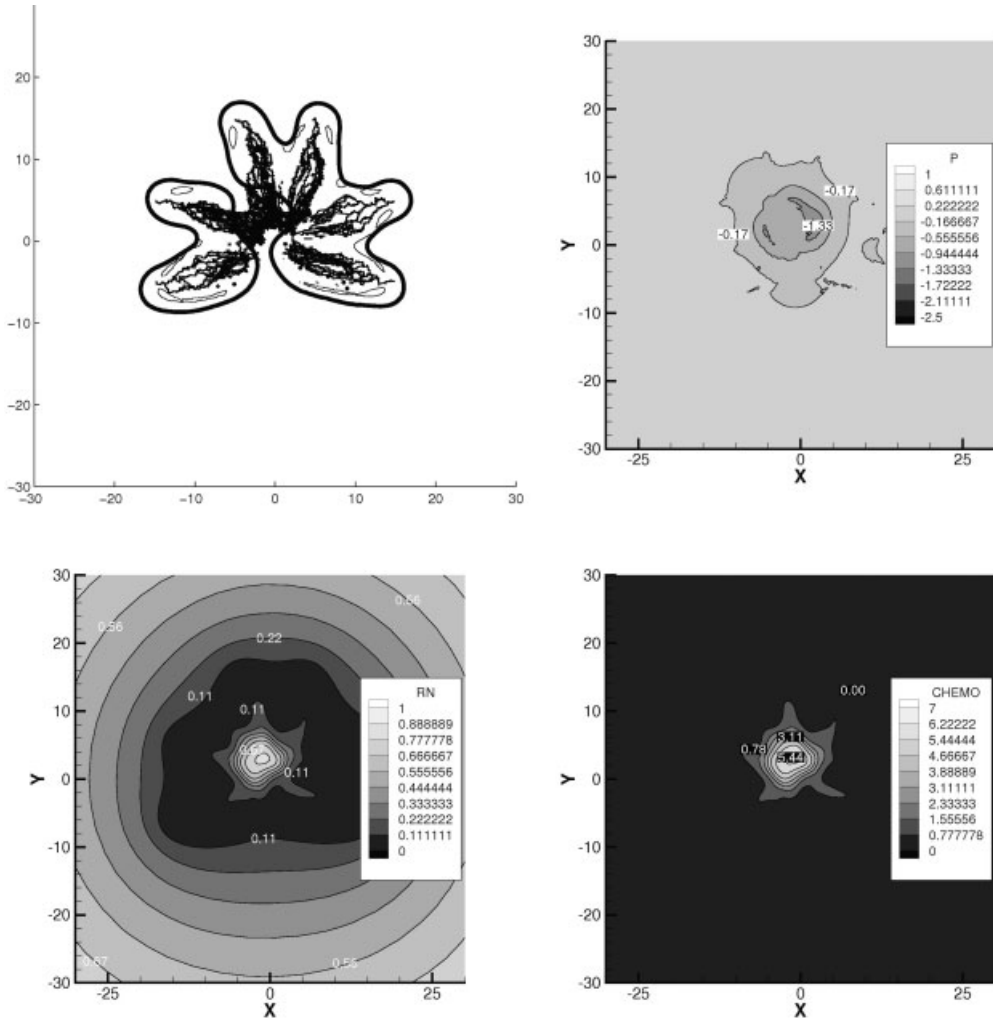


**Figure 2.19.** Simulations of nanoparticle chemotherapy. Clockwise, from upper left corner: tumor at equilibrium after many months of simulated continuous therapy, pressure contours, drug concentration contours and nutrient contours. Inhomogeneities in nutrient delivery and initial

nanoparticle extravasation and subsequent diffusion and uptake of drug result in stable equilibrium at significant tumor mass. (Adapted from Ref. [28], Fig. 4(b), © 2004 Kluwer Academic Publishers. With kind permission from Springer Science and Business Media.)

$v'_n(p_V - p)(n_V - n)$  in Eq. (9), where  $v'_n$  is constant,  $p_V$  and  $p$  are the pressures in the vasculature and tumor, respectively, and  $n_V$  and  $n$  are the nutrient concentration in the vasculature and tumor, respectively. A similar function for  $v_s$  was used for the initial extravasation of particles. This model qualitatively demonstrated that inhomogeneities in drug delivery and action, even using nanoparticles releasing



drug at a constant rate, had the potential to diminish chemotherapeutic efficacy, still leaving substantial regions of tumor unharmed after months of simulated therapy (Fig. 2.19).

The second class of simulations addressed the possible benefits of improving drug delivery via the use of adjuvant antiangiogenic drugs to “normalize” tumor vasculature [20, 40, 64]. To do this, Sinek’s group let  $v_s$  in Eq. (9) be constant so that the source of drug was uniform along the vasculature. Again, although cell kill was significantly greater, inhomogeneities due to drug diffusion and cellular uptake resulted in nonuniform tumor regression, and eventually fragmentation at significant equilibrium masses (Fig. 2.20). These results compare favorably with experimental data. Antiangiogenic and chemotherapeutic treatments have been observed to induce tumor mass fragmentation, cancer cell migration and tissue invasion [65–67]. Cristini and coworkers [68] have termed this behavior “diffusional instability”. It is a phenomenon known to materials scientists and is analogous to the processes whereby dendritic ice crystals form or water droplets in ice migrate via a melt-and-freeze process over an imposed temperature gradient. The existence of this phenomenon with regard to tumor response would have significant influence on the design of all modes of chemotherapy.

### 2.5.2

#### Refinements of the Model

In Eq. (9), the two parameters  $D_s$  and  $\eta_s$  are critical to the penetration of drug into the tumor. One criticism of the previously described simulations is that, although drug gradients formed for the values chosen, these values were not experimentally measured. If the ratio  $D_s/\eta_s$  should actually be relatively high, then drug would be uniformly presented to tumor cells and it is possible that the simulations would have revealed complete tumor regression with no fragmentation. A subsequent work of Sinek and coworkers [57] obtains values of the drug diffusion coefficient  $D_s$ , the uptake rate  $\eta_s$  and the killing power  $\lambda_D$  for the drugs, cisplatin and doxorubicin.

In order to more accurately model the cellular drug kinetics of cisplatin and doxorubicin, compartmental models were constructed by Sinek and coworkers [57] following earlier work of Dordal and coworkers [69, 70], Jackson [71] and El-Kareh and Secomb [72]. Three compartments are assumed (Fig. 2.21): Compartment 1 is extracellular interstitium, Compartment 2 is intracellular free drug and Compartment 3 is intracellular DNA-bound drug. For cisplatin, the system of equations determining drug kinetics is:

$$\begin{aligned}\frac{\partial s_1}{\partial t} &= v_s \delta_V + D_s \nabla^2 s_1 - k_{12} s_1 + k_{21} s_2 \\ \frac{\partial s_2}{\partial t} &= k_{12} s_1 - k_{21} s_2 - k_{23} s_2 \\ \frac{\partial s_3}{\partial t} &= k_{23} s_2 - k_3 s_3\end{aligned}\tag{11}$$

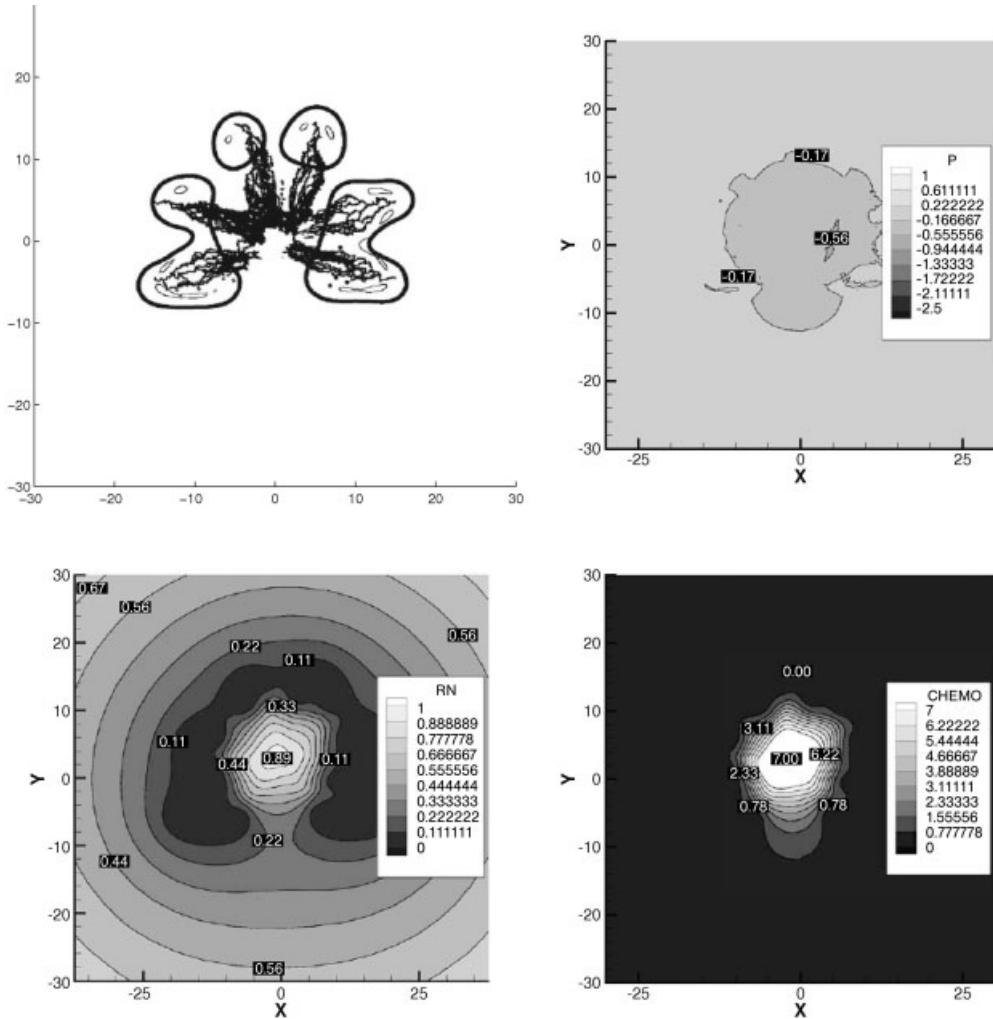


**Figure 2.20.** Nanoparticle chemotherapy after antiangiogenic “normalization”, simulated by making drug release constant along the vasculature. Clockwise, from upper left: tumor at equilibrium after many months of simulated continuous therapy, pressure contours, drug concentration contours and nutrient contours.

Although tumor kill is greater than that in Fig. 2.19, diffusional instability (see text) results in fragmentation and aggressive phenotype. (Adapted from Ref. [28], Fig. 5, © 2004 Kluwer Academic Publishers. With kind permission from Springer Science and Business Media.)

where  $s_i$  is drug concentration in Compartment  $i$ , and the  $k_{ij}$ 's are transfer rates from Compartment  $i$  to  $j$ . In particular,  $k_{12}$  is determined by the “inward” cell membrane permeability,  $k_{21}$  by the “outward” permeability and  $k_{23}$  by the drug–DNA binding affinity.  $k_3$  is a repair rate of DNA platinum adducts. The system for

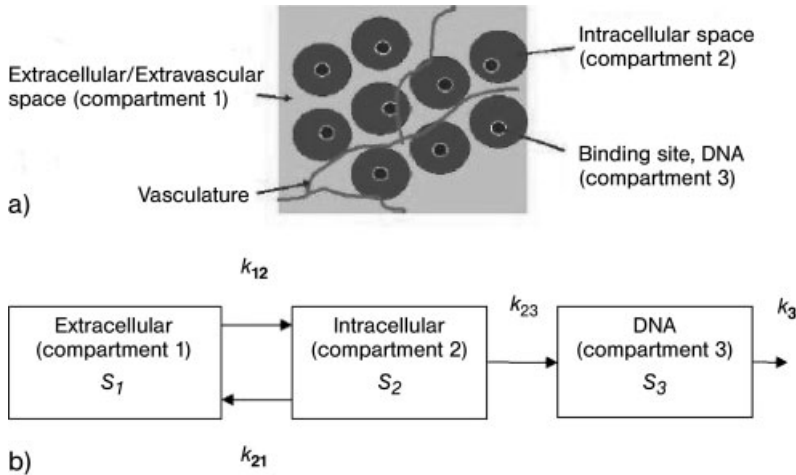


**Figure 2.21.** The compartment model used by Sinek and coworkers [28].  $k$ 's represent transfer rates, while  $s$ 's represent concentrations. Cell death is ultimately due to  $s_3$ .

doxorubicin is similar; for purposes of illustration we shall refer to the cisplatin model.

It is well established that cisplatin induces apoptosis by forming DNA–platinum adducts and that doxorubicin kills cells via DNA intercalation [73, 74]. Thus, of critical importance is the value of  $s_3$ . If we reduce the situation to one dimension with a boundary condition at  $x = 0$  representing the vessel source, then the steady-state form of Eq. (11) can be written in terms of  $s_3$  alone:

$$0 = D_s(k_{21} + k_{23}) \frac{d^2 s_3}{dx^2} - k_{12} k_{23} s_3 \quad (12)$$

The solution of this equation is  $s_3 = C_1 e^{-ax} + C_2 e^{ax}$ , where:

$$a = \sqrt{\frac{k_{12}}{D_s(k_{21}/k_{23} + 1)}}$$

The constants are determined according to the boundary value of drug at the vessel source along with a no-flux condition at approximately 100  $\mu\text{m}$  from the vessel (since another vessel is assumed to exist approximately 200  $\mu\text{m}$  from the one being modeled). It is the negative exponential in which we are most interested, with high values of  $a$  resulting in gradients. Thus, high cell permeabilities ( $k_{12}$ ) as well as poor interstitial diffusion ( $D_s$ ) result in gradients and, thus, presumably poor lateral penetration into tumor (Fig. 2.22). This is in line with studies that demonstrate doxorubicin penetration is particularly poor (severe gradients) in comparison with cisplatin penetration. Doxorubicin enters cells much more rapidly than cispla-

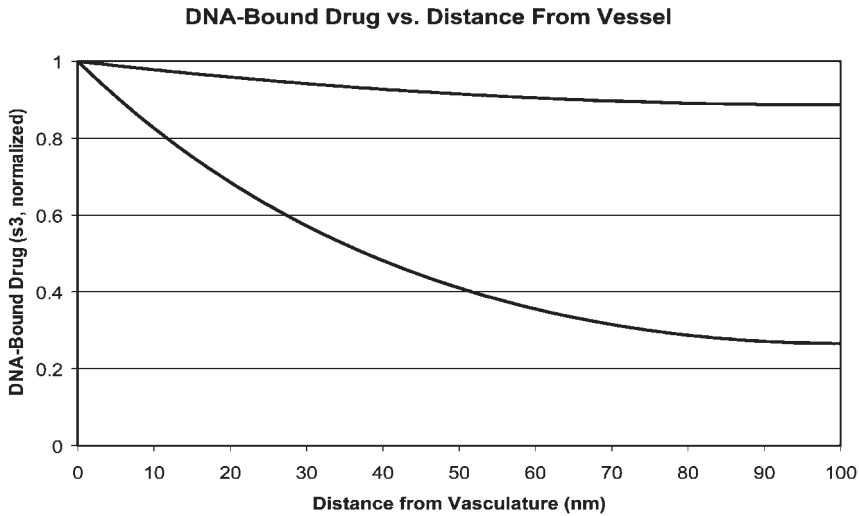


**Figure 2.22.** The normalized steady-state DNA-bound drug ( $s_3$ ) as a function of distance from nearest vessel (located at distance = 0). Gradients are sensitive to drug-cell permeability. A drug like doxorubicin, which penetrates cells quickly and possesses high affinity for cell endosomes and DNA, would give rise to the lower graph.

tin, and it has particularly high affinities for cell endosomes and DNA [69, 70, 75–79].

The apparent paradox that high cell permeability should result in poor tissue penetration underscores the power of mathematical modeling in overcoming the prejudice of intuition. Upon reflection it can be appreciated that if drug is removed from interstitium quickly due to high cell permeability as it diffuses from its originating vessel, there will be correspondingly less to continue further along, hence low penetration. It should be noted, however, that significant *lateral* penetration at the expense of insignificant *cellular* penetration is also undesirable, but rather an optimal balance of the two must be sought.

Values of the transfer and repair rates in Eq. (11) can be obtained via several techniques including measuring the time uptake of intracellular and bound cisplatin concentrations for cells in monolayer exposed to constant serum drug concentrations. The repair rate  $k_3$  is estimated from two different experiments performed by Sadowitz and coworkers [80], wherein the adducts per million nucleotides fell in 2 h from 75 to 5 in one case and from 185 to 40 in the other. Using the exponential repair model  $s'_3 = -k_3 s_3$ ,  $k_3$  is estimated to be between 0.013 and 0.023  $\text{min}^{-1}$ . An initial estimate of  $k_{23}$  is made as follows. Sadowitz shows that cells incubated in 7  $\mu\text{M}$ , in 2 h cells accumulate about 25 DNA adducts per million nucleotides. This converts to  $1.03 \times 10^{-19}$  moles of platinum docked on the DNA. Neglecting the cell membrane and supposing the DNA to be exposed directly to the *cis* solution, we solve the ODE  $s'_3 = 7k_{23} - k_3 s_3$ , substituting 0.015  $\text{min}^{-1}$  for  $k_3$ .  $k_{23}$  is thereby estimated to be  $2.6 \times 10^{-16}$   $\text{min}^{-1}$ . Finally,  $k_{12}$  and  $k_{21}$  are estimated by

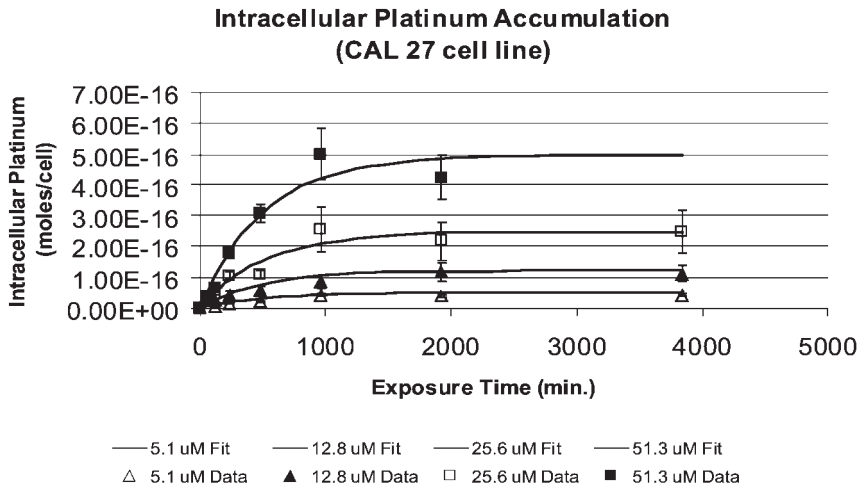


**Figure 2.23.** Troger and coworkers [81] plotted total intracellular ( $s_2 + s_3$ ) platinum versus time for cells exposed as monolayers to four different concentrations of cisplatin. Curves represent best fits obtained by adjusting  $k_{12}$  and  $k_{21}$  in the second two equations of (11). In the equations,  $s_1$  is set to the concentrations that Troger used. (Adapted from Sinek and coworkers [57].)

fitting the second two equations in (11) with intracellular cisplatin time-uptake data of Troger and coworkers [81]. They exposed cells in monolayer to four different concentrations of cisplatin and then measured the total intracellular platinum content at selected times. The graph in Fig. 2.23 shows Troger and coworker's data (symbols) along with the fits (lines) for four different extracellular concentrations. For this purpose, in the equations  $s_1$  was set to be constant and equal to the concentrations that Troger and coworkers used. Then the sum  $s_2 + s_3$  was plotted, with values for  $k_{12}$  and  $k_{21}$  chosen to provide the best fits. Although these parameters are obtained from different experiments using different cell lines, they provide a starting point for producing quantitatively accurate simulations.

## 2.6 Conclusion

We have identified four critical phases of nanovector performance, each requiring a thorough understanding in order to optimize delivery and anticancer action. In the service of this understanding, mathematics and computation provides its own laboratory of pencil, paper and silicon chip, lending insight, providing guidance and offering testable prediction. The models of protein rejection in Section 2.2, in conjunction with the models of ligand binding in Section 2.4, can facilitate optimized surface preparation, yielding particles and liposomes that reject opsonization and therefore circulate long, yet bind effectively when finally presented to target cells.

The models of tumoral vasculature and hemodynamics presented in Section 2.3 reveal the “nature of the beast”, at once starkly exposing the tremendous difficulties in homogenous nanovector delivery and extravasation, while offering hope in quantifying the improvement that proposed therapies, such as vascular normalization, might bring. Finally, multiscale models of nanoparticle chemotherapy in Section 2.5, incorporating vasculogenesis, particle extravasation, nutrient and drug diffusion and uptake, and cellular-level phenomena such as DNA repair, suggest the existence of powerful mechanisms, such as diffusional instability, that can possibly be tempered, or even used to advantage, with the right approach.

Biological systems are “murky”, rarely providing simple, solid boundaries. Rather, their behavior is the sum of myriad processes spanning the scales of the whole body, tissues, cells and molecules. The nascent field of mathematical biology in conjunction with nanoscale therapeutics development is therefore presented with great opportunities. New technological designs and paradigms provide exciting grist for the mathematical mill. In turn, advanced mathematical methods along with computational techniques shine a bright and promising light on the future potential of technology. We hope that the foregoing has offered illuminating ideas that will guide this potential to fruition.

## References

- 1 WILKINS, D. J., MYERS, P. A. Studies on the relationship between the electrophoretic properties of colloids and their blood clearance and organ distribution in the rat. *Br. J. Exp. Pathol.* **1966**, *47*, 568–576.
- 2 WILKINS, D. J. The biological recognition of foreign from native particle as a problem in surface chemistry. *J. Colloid Interface Sci.* **1967**, *25*, 84.
- 3 WILKINS, D. J. Interaction of charged colloids with the RES. In: *The Reticuloendothelial System and Arteriosclerosis*, DI LUZIO, N. R., PAOLETTI, R. (Eds.). New York: Plenum Press, **1967**, p. 25.
- 4 TRÖSTER, S. D., MULLER, U., KREUTER, J. Modification of the body distribution of poly(methyl methacrylate) nanoparticles in rats by coating with surfactants. *Int. J. Pharm.* **1990**, *61*, 85–100.
- 5 TRÖSTER, S. D., KREUTER, J. Influence of the surface properties of low contact angle surfactants on the body distribution of 14-C-poly(methyl methacrylate) nanoparticles. *J. Microencapsul.* **1992**, *9*, 19–28.
- 6 BAZILE, D., PRUD HOMME, C., BASSOULET, M., MARLARD, M., SPENLEHAUER, G., VEILLARD, M. Stealth Me-PEG–PLA nanoparticles avoid uptake by the mononuclear phagocyte system. *J. Pharm. Sci.* **1995**, *84*, 493–498.
- 7 ILLUM, L., DAVIS, S. S. Effect of the nonionic surfactant poloxamer 338 on the fate and deposition of polystyrene microspheres following intravenous administration. *J. Pharm. Sci.* **1983**, *72*, 1086–1089.
- 8 ILLUM, L., DAVIS, S. S. The organ uptake of intravenously administered colloidal particles can be altered using a non-ionic surfactant (poloxamer 338). *FEBS Lett.* **1984**, *167*, 79–82.
- 9 RUDT, S., MULLER, R. H. *In vitro* phagocytosis assay of nano- and microparticles by chemiluminescence. III. Uptake of differently sized surface-modified particles, and its correlation to particle properties and *in vivo* distribution. *Eur. J. Pharm. Sci.* **1993**, *1*, 31–39.
- 10 MOGHIMI, S. M., GRAY, T. A. Single dose of IV-injected poloxamine coated

- long-circulating particle triggers macrophage clearance of subsequent doses in rats. *Clin. Sci.* **1997**, *93*, 371–379.
- 11 DEMOY, M., ANDREUX, J. P., WEINGARTEN, C., GOURITIN, B., GUILLOUX, V., COUVREUR, P. Spleen capture of nanoparticles: influence of animal species and surface characteristics. *Pharm. Res.* **1999**, *16*, 37–41.
  - 12 SOPPIMATH, K. S., AMINABHAVI, T. M., KULKARNI, A. R., RUDZINSKI, W. E. Biodegradable polymeric nanoparticles as drug delivery devices. *J. Controlled Rel.* **2001**, *70*, 1–20.
  - 13 SAPRA, P., ALLEN, T. M. Ligand-targeted liposomal anticancer drugs. *Prog. Lipid Res.* **2003**, *42*, 439–462.
  - 14 WANG, S., LEE, R. J., CAUCHON, G., GORENSTEIN, D. G., LOW, P. S. Delivery of antisense oligodeoxynucleotides against the human epidermal growth factor receptor into cultured KB cells with liposomes conjugated to folate via polyethylene glycol. *Proc. Natl Acad. Sci. USA* **1995**, *92*, 3318–3322.
  - 15 YOO, H. S., PARK, T. G. Folate-receptor-targeted delivery of doxorubicin nano-aggregates stabilized by doxorubicin–PEG–folate conjugate. *J. Controlled Rel.* **2004**, *100*, 247–256.
  - 16 MATSUMURA, Y., GOTOH, M., MURO, K., YAMADA, Y., SHIRAO, K., SHIMADA, Y., OKUWA, M., MATSUMOTO, S., MIYATA, Y., OHKURA, H., CHIN, K., BABA, S., YAMAO, T., KANNAMI, A., TAKAMATSU, Y., ITO, K., TAKAHASHI, K. Phase I and pharmacokinetic study of MCC-465, a doxorubicin (DXR) encapsulated in PEG immuno-liposome, in patients with metastatic stomach cancer. *Ann. Oncol.* **2004**, *15*, 517.
  - 17 GABIZON, A., SHMEEDA, H., HOROWITZ, A. T., ZALIPSKY, S. Tumor cell targeting of liposome-entrapped drugs with phospholipid-anchored folic acid–PEG conjugates. *Adv. Drug Deliv. Rev.* **2004**, *56*, 1177–1192.
  - 18 JO, Y. S., KIM, M.-C., KIM, D. K., KIM, C.-J., JEONG, Y.-K., KIM, K.-J., MUHAMMED, M. Mathematical modelling on the controlled-release of indomethacin-encapsulated poly(lactic acid-co-ethylene oxide) nanospheres. *Nanotechnology* **2004**, *15*, 1186–1194.
  - 19 KOSMIDIS, K., ARGYRAKIS, P., MACHERAS, P. A reappraisal of drug release laws using Monte Carlo simulations: the prevalence of the Weibull function. *Pharmac. Res.* **2003**, *20*, 988–995.
  - 20 JAIN, R. K. Normalizing tumor vasculature with anti-angiogenic therapy: a new paradigm for combination therapy. *Nat. Med.* **2001**, *7*, 987–989.
  - 21 ANDERSON, A., CHAPLAIN, M. Continuous and discrete mathematical models of tumor-induced angiogenesis. *Bull. Math Biol.* **1998**, *60*, 857–900.
  - 22 BAISH, J. W., GAZIT, Y., BERK, D. A., NOZUE, M., BAXTER, L. T., JAIN, R. K. Role of tumor vascular architecture in nutrient and drug delivery: an invasion percolation-based network model. *Microvasc. Res.* **1996**, *51*, 327–346.
  - 23 MCDUGALL, S., ANDERSON, A., CHAPLAIN, M., SHERRAIT, J. Mathematical modeling of flow through vascular networks: implications for tumour-induced angiogenesis and chemotherapy strategies. *Bull. Math. Biol.* **2002**, *64*, 673–702.
  - 24 TORCHILIN, V. P., OMELYANENKO, V. G., PAPISOV, M. I., BOGDANOV, JR., A. A., TRUBETSKOY, V. S., HERRON, J. N., GENTRY, C. A. Poly(ethylene glycol) on the liposome surface: on the mechanism of polymer-coated liposome longevity. *Biochim. Biophys. Acta* **1994**, *1195*, 11–20.
  - 25 BELL, G. I. Models for the specific adhesion of cells to cells. *Science* **1978**, *200*, 618–627.
  - 26 COZENS-ROBERTS, C., QUINN, J. A., LAUFFENBURGER, D. A. Receptor-mediated cell attachment and detachment kinetics. I. Probabilistic model and analysis. *Biophys. J.* **1990**, *58*, 841–856.
  - 27 COZENS-ROBERTS, C., LAUFFENBURGER, D. A., QUINN, J. A. Receptor-mediated cell attachment and detachment

- kinetics. II. Experimental model studies with the radial-flow detachment assay. *Biophys. J.* **1990**, *58*, 857–872.
- 28 SINEK, J. P., FRIEBOES, H. B., ZHENG, X., CRISTINI, V. Two-dimensional chemotherapy simulations demonstrate fundamental transport limitations involving nanoparticles. *Biomed. Microdevices* **2004**, *6*, 297–309.
- 29 KREUTER, J. (Ed.), *Colloidal Drug Delivery Systems*. Dekker, New York, **1994**.
- 30 KREUTER, J. Evaluation of nanoparticles as drug-delivery systems II: comparison of the body distribution of nanoparticles with the body distribution of microspheres, liposomes, and emulsions. *Pharm. Acta Helv.* **1983**, *58*, 217.
- 31 KREUTER, J. Factors influencing the body distribution of polyacrylic nanoparticles. In: *Drug Targeting*, BURI, P., GUMMA, A. (Eds.). Elsevier, Amsterdam, **1985**, p. 51.
- 32 LASIC, D. D., MARTIN, F. J., GABIZON, A., HUANG, S. K., PAPAHDJOPOULOS, D. Sterically stabilized liposomes: a hypothesis on the molecular origin of the extended circulation times. *Biochim. Biophys. Acta* **1991**, *1070*, 187–192.
- 33 JEON, S. I., LEE, J. H., ANDRADE, J. D., DE GENNES, P. G. Protein–surface interactions in the presence of polyethylene oxide, I: simplified theory. *J. Colloid Interface Sci.* **1991**, *142*, 149–158.
- 34 TORCHILIN, V. P., KLIBANOV, A. L., HUANG, L., O'DONNELL, S., NOSSIFT, N. D., KHAW, B. A. Targeted accumulation of polyethylene glycol-coated immunoliposomes in infarcted rabbit myocardium. *FASEB J.* **1992**, *6*, 2716–2719.
- 35 ALLEN, T. M., HANSEN, C. Pharmacokinetics of stealth versus conventional liposomes: effect of dose. *Biochim. Biophys. Acta* **1991**, *1068*, 133–141.
- 36 HAROON, Z., PETERS, K. G., GREENBERG, C. S., DEWHIRST, M. W. Angiogenesis and blood flow in the solid tumors. In: *Antiangiogenic Agents in Cancer Therapy*, TEICHER, B. (Ed.). Humana Press, Totowa, NJ, **1999**, pp. 3–21.
- 37 JAIN, R. K. Physiological barriers to delivery of monoclonal antibodies and other macromolecules in tumors. *Cancer Res. (Suppl.)* **1990**, *50*, 814s–819s.
- 38 JAIN, R. K. Determinants of tumor blood flow: a review. *Cancer Res.* **1988**, *49*, 2641–2658.
- 39 HOBBS, S. K., MONSKY, W. L., YUAN, F., ROBERTS, W. G., GRIFFITH, L., TORCHILIN, V. P., JAIN, R. K. Regulation of transport pathways in tumor vessels: Role of tumor type and microenvironment. *Proc. Natl Acad. Sci. USA* **1998**, *95*, 4607–4612.
- 40 PADERA, T. P., STOLL, B. R., TOOREDMAN, J. B., CAPEN, D., DI TOMASO, E., JAIN, R. K. Cancer cells compress intratumour vessels. *Nature* **2004**, *427*, 695.
- 41 SECOMB, T. W., HSU, R. Motion of red blood cells in capillaries with variable cross-sections. *J. Biomech. Eng.* **1996**, *118*, 538–544.
- 42 BAISH, J. W., NETTI, P. A., JAIN, R. K. Transmural coupling of fluid flow in microcirculatory network and interstitium in tumors. *Microvasc. Res.* **1997**, *53*, 128–141.
- 43 SCHMID-SCHÖNBEIN, G. W., SKALAK, R., USAMI, S., CHIEN, S. Cell distribution in capillary networks. *Microvasc. Res.* **1980**, *19*, 18–44.
- 44 GAZIT, Y., BERK, D., LEUNIG, M., BAXTER, L. T., JAIN, R. K. Scale-invariant behavior and vascular network formation in normal and tumor tissue. *Phys. Rev. Lett.* **1995**, *75*, 2428–2431.
- 45 DEWHIRST, M. W., TSO, C. Y., OLIVER, R., GUSTAFSON, C. S., SECOMB, T. W., GROSS, J. F. Morphologic and hemodynamic comparison of tumor and healing normal tissue microvasculature. *Int. J. Radiat. Oncol. Biol. Phys.* **1989**, *17*, 91–99.
- 46 LESS, J. R., POSNER, M. C., SKALAK, T. C., WOLMARK, N., JAIN, R. K. Geometric resistance and microvascular network architecture of human colorectal carcinoma. *Microcirculation* **1997**, *4*, 25–33.



- 47 LEUNIG, M., YUAN, F., MENGER, M. D., BOUCHER, Y., GOETZ, A. E., MESSMER, K., JAIN, R. K. Angiogenesis, microvascular architecture, microhemodynamics, and interstitial fluid pressure during early growth of human adenocarcinoma LS174T in SCID mice. *Cancer Res.* **1992**, *52*, 6553–6560.
- 48 SKINNER, S. A., TUTTON, P. J. M., O'BRIEN, P. E. Microvascular architecture of experimental colon tumors in the rat. *Cancer Res.* **1990**, *50*, 2411–2417.
- 49 GIMBRONE, M. A., COTRAN, R. S., LEAPMAN, S. B., FOLKMAN, J. Tumor growth and neovascularization: an experimental model using the rabbit cornea. *J. Natl Cancer Inst.* **1974**, *52*, 413–427.
- 50 AUSPRUNK, D. H., FOLKMAN, J. Migration and proliferation of endothelial cells in preformed and newly formed blood vessels during tumour angiogenesis. *Microvasc. Res.* **1977**, *14*, 53–65.
- 51 LEE, R. J., LOW, P. S. Delivery of liposomes into cultured KB cells via folate receptor-mediated endocytosis. *J. Biol. Chem.* **1994**, *269*, 3198–3204.
- 52 TUREK, J. J., LEAMON, C. P., LOW, P. S. Endocytosis of folate-protein conjugates: ultrastructural localization in KB cells. *J. Cell Sci.* **1993**, *106*, 423–30.
- 53 WANG, S., LOW, P. S. Folate-mediated targeting of antineoplastic drugs, imaging agents, and nucleic acids to cancer cells. *J. Controlled Rel.* **1998**, *53*, 39–48.
- 54 YOO, H. S., LEE, K. H., OH, J. E., PARK, T. G. *In vitro* and *in vivo* anti-tumor activities of nanoparticles based on doxorubicin-PLGA conjugates. *J. Controlled Rel.* **2000**, *68*, 419–431.
- 55 BAILEY, N. T. J. *The Elements of Stochastic Processes*. Wiley, New York, **1964**.
- 56 FENG, S. S., CHIEN, S. Chemo-therapeutic engineering: application and further development of chemical engineering principles for chemo-therapy of cancer and other diseases. *Chem. Eng. Sci.* **2003**, *58*, 4087–4114.
- 57 SINEK, J. P., CRISTINI, V. Modeling and simulation of multi-drug resistance mechanisms. In preparation.
- 58 ZHENG, X., WISE, S. M., CRISTINI, V. Nonlinear simulation of tumor necrosis, neo-vascularization and tissue invasion via an adaptive finite-element/level-set method. *Bull. Math. Biol.* **2005**, *67*, 211–259.
- 59 BYRNE, H., CHAPLAIN, M. Growth of nonnecrotic tumors in the presence and absence of inhibitors. *Math. Biosci.* **1995**, *130*, 151–181.
- 60 BYRNE, H., CHAPLAIN, M. Growth of necrotic tumors in the presence and absence of inhibitors. *Math. Biosci.* **1996**, *135*, 187–216.
- 61 CRISTINI, V., LOWENGRUB, J., NIE, Q. Nonlinear simulation of tumor growth. *J. Math. Biol.* **2003**, *46*, 191–224.
- 62 FRIEBOES, H. B., ZHENG, X., SUN, C.-H., TROMBERG, B., GATENBY, R., CRISTINI, V. An integrated computational experimental model of tumor invasion. *Cancer Res.* **2006**, *66*, 1597–1604.
- 63 MAHER, E., FURNARI, F., BACHOO, R., ROWITCH, D., LOUIS, D., CAVENEE, W., DE-PINHO, R. Malignant glioma: genetics and biology of a grave matter. *Genes Dev.* **2001**, *15*, 1311–1333.
- 64 JAIN, R. K. Delivery of molecular medicine to solid tumors: lessons from *in vivo* imaging of gene expression and function. *J. Controlled Rel.* **2001**, *74*, 7–25.
- 65 PENNACCHIETTI, S., MICHIELI, P., GALLUZZO, M., MAZZONE, M., GIORDANO, S., COMOGLIO, P. Hypoxia promotes invasive growth by transcriptional activation of the met protooncogene. *Cancer Cell* **2003**, *3*, 347–361.
- 66 BELLO, L., LUCINI, V., COSTA, F., PLUDERI, M., GIUSSANI, C., ACERBI, F., CARRABBA, G., PANNACCI, M., CARONZOLO, D., GROSSO, S., SHINKARUK, S., COLLEONI, F., CANRON, X., TOMEI, G., DELERIS, G., BIKFALVI, A. Combinatorial administration of molecules that simultaneously inhibit angiogenesis and invasion leads to increased

- therapeutic efficacy in mouse models of malignant glioma. *Clin. Cancer Res.* **2004**, *10*, 4527–4537.
- 67 KUNKEL, P., ULBRICHT, U., BOHLEN, P., BROCKMANN, M. A., FILLBRANDT, R., STAVROU, D., WESTPHAL, M., LAMSZUS, K. Inhibition of glioma angiogenesis and growth *in vivo* by systemic treatment with a monoclonal antibody against vascular endothelial growth factor receptor-2. *Cancer Res.* **2001**, *61*, 6624–6628.
- 68 CRISTINI, V., FRIEBOES, H. B., GATENBY, R., CASERTA, S., FERRARI, M., SINEK, J. P. Morphological instability and cancer invasion. *Clin. Cancer Res.* **2005**, *11*, 6772–6779.
- 69 DORDAL, M. S., WINTER, J. N., ATKINSON JR., A. J. Kinetic analysis of P-glycoprotein-mediated doxorubicin efflux. *J. Pharmacol. Exp. Ther.* **1992**, *263*, 762–766.
- 70 DORDAL, M. S., HO, A. C., JACKSON-STONE, M., FU, Y. F., GOOLSBY, C. L., WINTER, J. N. Flow cytometric assessment of the cellular pharmacokinetics of fluorescent drugs. *Cytometry* **1995**, *20*, 307–314.
- 71 JACKSON, T. L. Intracellular accumulation and mechanism of action of doxorubicin in a spatio-temporal tumor model. *J. Theor. Biol.* **2003**, *220*, 201–213.
- 72 EL-KAREH, A. W., SECOMB, T. W. A mathematical model for cisplatin cellular pharmacodynamics. *Neoplasia* **2003**, *5*, 161–169.
- 73 JOHNSON, N. P., LAPETOULE, P., RAZAKA, H., VILLANI, G. Biological and biochemical effects of DNA damage caused by platinum compounds. In: *Biochemical Mechanisms of Platinum Antitumour Compounds*, McBRIEN, D. C. H., SLATER, T. F. (Eds.). IRL Press, Oxford, 1986, pp. 1–28.
- 74 ROBERTS, J. J., KNOX, R. J., FRIEDLOS, F., LYDALL, D. A. DNA as the target for the cytotoxic and antitumour action of platinum co-ordination complexes: comparative *in vitro* and *in vivo* studies of cisplatin and carboplatin. In: *Biochemical Mechanisms of Platinum Antitumour Compounds*, McBRIEN, D. C. H., SLATER, T. F. (Eds.). IRL Press, Oxford, 1986, pp. 28–64.
- 75 PAUL, C., PETERSON, C., GAHRTON, G., LOCKNER, D. Uptake of free and DNA-bound daunorubicin and doxorubicin into human leukemic cells. *Cancer Chemother. Pharmacol.* **1979**, *2*, 49–52.
- 76 ERLANSON, M., DANIEL-SZOLGAY, E., CARLSSON, J. Relations between the penetration, binding and average concentration of cytostatic drugs in human tumour spheroids. *Cancer Chemother. Pharmacol.* **1992**, *29*, 343–353.
- 77 TANNOCK, I. F., LEE, C. M., TUNGGAL, J. K., COWAN, D. S. M., EGORIN, M. J. Limited penetration of anticancer drugs through tumor tissue: a potential cause of resistance of solid tumors to chemotherapy. *Clin. Cancer Res.* **2002**, *8*, 878–884.
- 78 JEKUNEN, A. P., SHALINSKY, D. R., HOM, D. K., ALBRIGHT, K. D., HEATH, D., HOWELL, S. B. Modulation of cisplatin cytotoxicity by permeabilization of the plasma membrane by digitonin *in vitro*. *Biochem. Pharmacol.* **1993**, *45*, 2079–2085.
- 79 DEMANT, E. J. F., FRICHE, E. Kinetics of anthracycline accumulation in multidrug-resistant tumor cells: relationship to drug lipophilicity and serum albumin binding. *Biochem. Pharmacol.* **1998**, *56*, 1209–1217.
- 80 SADOWITZ, P. D., HUBBARD, B. A., DABROWIAK, J. C., GOODISMAN, J., TACKA, K. A., AKTAS, M. K., CUNNINGHAM, M. J., DUBOWY, R. L., SOUID, A.-K. Kinetics of cisplatin binding to cellular DNA and modulations by thiol-blocking agents and thiol drugs. *Drug Metab. Dispos.* **2002**, *30*, 183–190.
- 81 TROGER, V., FISCHER, J. L., FOMENTO, P., GIOANNI, J., MILANO, G. Effects of prolonged exposure to cisplatin on cytotoxicity and intracellular drug concentration. *Eur. J. Cancer* **1992**, *28*, 82–86.

### 3

## Nanolithography: Towards Fabrication of Nanodevices for Life Sciences

*Johnpeter Ndiangui Ngunjiri, Jie-Ren Li, and Jayne Carol Garno*

### 3.1

#### Introduction: Engineering Surfaces at the Nanoscale

Tools for nanofabrication have begun to provide important contributions for life sciences investigations, for developing biochip and biosensing technologies, as well as supplying basic research in protein–protein interactions and protein function. Scanning probe microscopy (SPM) supplies tools for visualization, physical measurements and precise manipulation of atoms and molecules at the nanometer scale. Nanoscale studies can facilitate the development of new and better approaches for immobilization and bioconjugation chemistries, which are key technologies in manufacturing biochip and biosensing surfaces.

Protein patterning is essential for the integration of biological molecules into miniature bioelectronic and sensing devices. To fabricate nanodevices for the life sciences it is often necessary to attach biomolecules to surfaces with retention of structure and function. For example, controlling the interaction of proteins, biomolecules and cells with surfaces is important for the development of new biocompatible materials. Precisely engineered surfaces can be used for the exploration of biochemical reactions in controlled environments. Spatially well-defined regions of surfaces can be constructed with reactive or adhesive terminal groups for the attachment of biomolecules. Micropatterning of proteins has been applied for biosensors and biochips [1–4]. Direct applications of protein patterning include biosensing, medical implants, control of cell adhesion and growth, and fundamental studies of cell biology [5–7]. Protein patterning has been accomplished at the micrometer level using microcontact printing [8–13], photolithography [14–16] and microfluidic channels [17, 18]. Thus, the capabilities for micrometer-scale methods for controlling the spatial arrangements of biomolecules have been well established and offer valuable new research methodologies for life sciences investigations. Collectively, these techniques provide a means for assembling proteins at a size scale of hundreds of nanometers or larger.

To progress to even smaller sizes, atomic force microscopy (AFM)-based lithography can be applied to pattern surfaces at nanometer dimensions. Scanning probe lithography (SPL) provides versatile approaches for designing the chemistry of sur-

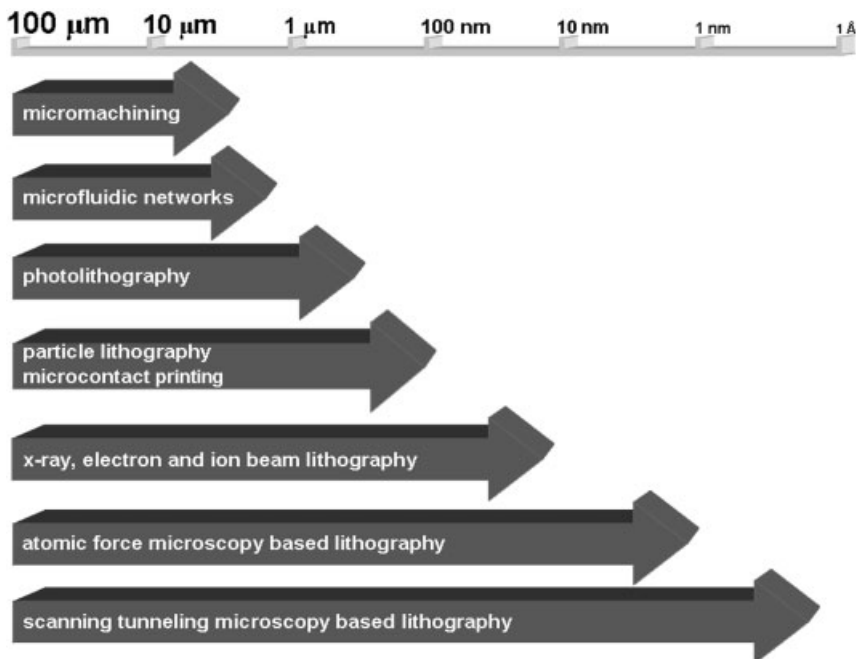


**Figure 3.1.** Overview of the hierarchy of dimensions which can be achieved using various micro- and nanopatterning methods.

faces at the nanoscale. Figure 3.1 shows the dimensions which can be achieved using various micro- and nanopatterning methods. Arrays of self-assembled monolayers (SAMs) and proteins can be fabricated via SPL, with precise control over chemical functionality, shape, dimensions and spacing on the nanometer scale. Combined with the capabilities for high-resolution imaging and characterization, SPM enables a molecular-level approach for directly investigating changes that occur on surfaces during biochemical reactions. The tools of SPL are accessible to investigators across a broad range of disciplines and do not require costly instrument modifications.

Cutting-edge research has begun to apply nanolithography for studying proteins on surfaces, possibly at the level of single-molecule detection. At present, nanodevices constructed by SPM-based lithography are being conceptualized and, to the best of our knowledge, SPL has not yet been applied for making nanodevices. Readers are referred to recent reviews which discuss potential nanoscale devices [19, 20]. Although there are also many studies which investigate peptides, DNA and cells, we limit the focus of this chapter to studies which apply nanoscale lithography to proteins and to applications using SPL for nanoscale protein assays. This chapter provides an overview of advances in the application of nanolithography using SPM and latex particle lithography for protein patterning. Beginning with a general introduction of the chemistry for immobilization of proteins on sur-

faces, the application of SAMs for coupling proteins to surfaces is presented. Nanolithography methods including bias-induced lithography, AFM-based force-induced nanolithography, “dip-pen” nanolithography (DPN) and latex particle lithography are described, including examples of protein nanopatterning. The chapter concludes with a discussion of nanoscale detection of protein binding and future directions in cantilever array technology.

## 3.2

### Immobilization of Biomolecules for Surface Assays

A number of factors need to be considered for choosing a successful protein-immobilization strategy, such as the efficiency and rate of binding, potential side-reactions, and the strength and resilience of the attachment. For protein assays, the binding site recognized by immunoglobulin G (IgG) on an antigen is relatively small; consisting of only 5–6 amino acids or several sugar residues. The recognition element is referred to as an antigenic determinant or epitope. Proteins must be attached in such an orientation that their active sites or binding domains are accessible for binding and not buried or blocked by the surface. The binding site is only a small part of the total surface area of the protein. Adsorption on a surface may impair or prevent the protein’s activity. The eventual orientation of proteins on surfaces is determined by multiple factors such as the type of binding, the positions and composition of external residues on the protein surface, the isoelectric point of the protein, and the pH of buffers used during application.

Proteins have a three-dimensional (3-D) structure which is critical to their function and activity. Most proteins have both positively and negatively charged regions that interact with surfaces. Upon encountering a surface, intramolecular forces within proteins can be disrupted, causing the proteins to unfold and become denatured. Some proteins are known to lose activity when bound to a solid surface, due to a loss of tertiary structure. For example, the strong polarization forces at metal surfaces along with ionic or covalent interactions on many inorganic metal oxides and semiconductor surfaces may cause denaturation of biomolecules [21]. For retention of activity, chemistries for protein arrays should permit the immobilization of proteins on surfaces such that perturbation to the native 3-D structure is minimized. Using a spacer or linker molecule on the sensor surface often enables biomolecules to retain their functionality and 3-D structure. The tools of organic chemistry provide a wealth of chemical strategies and binding motifs for conjugating biomolecules such as proteins to solid surfaces [22, 23].

#### 3.2.1

##### Strategies for Linking Proteins to Surfaces

Increasingly, researchers have begun to use the self-assembly of functionalized alkanethiol and alkylsilane molecules as model surfaces for protein binding. The terminal moieties of SAM surfaces mediate the type of binding, such as through

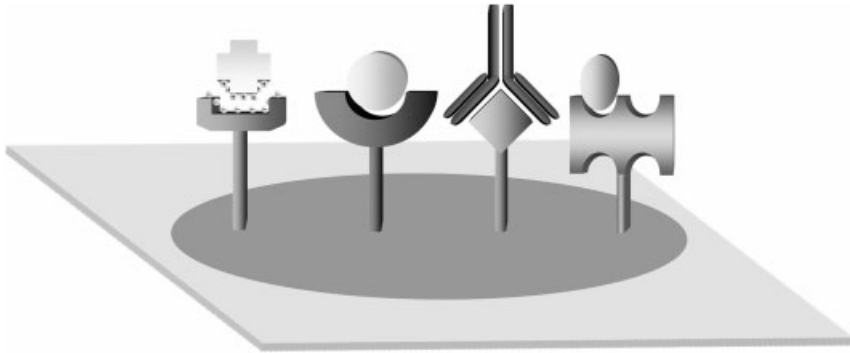


**Figure 3.2.** Strategies for linking proteins to surfaces include electrostatic interactions, covalent bonding, antigen–antibody recognition and biotin–streptavidin specific interactions.

electrostatic interactions, covalent binding, molecular recognition or via specific interactions (Fig. 3.2). The following sections introduce representative examples of chemical immobilization strategies which have been applied for protein patterning.

#### 3.2.1.1 Electrostatic Immobilization

The strategy of functionalizing a surface through electrostatic assembly is often used to immobilize biomolecules on surfaces. Electrically charged amino acids are found mostly on the exterior of proteins and can mediate assembly on charged surfaces. Proteins contain both positively and negatively charged domains that interact with surfaces via long-range electrostatic forces. The electrostatic attraction between oppositely charged molecules is nonspecific and surfaces are negatively or positively charged, depending on the solution pH.

Electrostatic binding is physically mediated and proteins often retain their activity after immobilization. It is a direct, simple method for attaching proteins to surfaces without requiring multiple steps for chemical activation. Binding is reversible, since certain buffers and detergents can remove proteins from surfaces. However, a potential disadvantage of electrostatic immobilization is that the resulting orientation of proteins on surfaces is random; electrostatic-mediated binding does not provide a means for directing the protein assembly in a designed conformation. Representative examples of chemistries for the electrostatic immobilization of proteins which have been applied for nanopatterning proteins are summarized in Tab. 3.1. For example, alkanethiols or alkylsilanes terminated with functional groups, such as  $\text{NH}_2$  or  $\text{COOH}$ , have been used to immobilize biomolecules through electrostatic interactions.

#### 3.2.1.2 Covalent Immobilization

Covalent immobilization is important for applications in which displacement or desorption of proteins can be a problem. Covalent bonds occur when two molecules share atoms and form the strongest chemical bonds for surface immobiliza-

tion. The methods of covalent attachment are boundless – thousands of proteins have been immobilized on hundreds of different solid supports for affinity-capture assays [22]. The best choice for covalent immobilization will depend on the functionalities of both the protein and the surface. Several amino acids provide suitable functional groups for covalent modification. Common functional groups of amino acids used for covalent immobilization include: amino groups from the side-chains of lysine and the N-terminus; carboxyl groups from the C-terminus, aspartic and glutamic acids; sulfhydryl groups of cysteine; hydroxyl groups of serine and threonine; and the phenyl groups of phenylalanine and tyrosine. Since proteins typically present a number of these groups, the chemical nature of the solid surface becomes a primary consideration. A specific chemical reaction is chosen to activate the surface and then proteins are immobilized upon exposure to the active surface groups. Examples of chemistries for covalent immobilization of proteins include activation of surface hydroxyl groups, carboxyl groups and amines. Also, bifunctional crosslinking reagents such as glutaraldehyde have been used to covalently couple proteins to various surfaces. Further examples of covalent immobilization chemistries are listed in Tab. 3.1.

An important factor to be considered in covalent attachment of proteins is the possibility of chemically altering the protein in such a way that its reactivity is reduced. For example, covalent approaches may be hindered by competing side-reactions. It is possible that groups associated with the active site or binding site of a protein could be involved in the reaction. In addition, chemical crosslinking within protein domains could occur, causing damage to the protein's tertiary structure.

#### 3.2.1.3 Molecular Recognition and Specific Interactions

Highly specific interactions between binding pairs can be used effectively for protein immobilization. Examples include affinity capture ligands such as biotin–streptavidin binding and molecular recognition through antigen–antibody recognition. Such affinity ligands require either physical or covalent immobilization of one moiety of the affinity pair onto the surface. Small-molecule receptors such as biotin offer viable strategies for the immobilization of proteins. Further examples are listed in Tab. 3.1. A strong advantage of specific immobilization is to provide a means for directing the protein assembly in a designed conformation. The orientation of proteins on surfaces can be designated by selectively targeting certain amino acid residues of the protein for specific coupling.

#### 3.2.1.4 Nonspecific Physical Adsorption to Surfaces

By far the most widely used method of protein immobilization for protein arrays uses nonspecific adsorption of proteins dried on solid supports. Forces which nonspecifically influence the binding of proteins to almost any substrate include ion bridging, hydration forces, hydrophobic forces and short-range attractive or repulsive forces. This approach produces randomly oriented proteins, some of which may be denatured. Surface assays typically include a blocking step, such as with the adsorption of bovine serum albumin (BSA) to prevent nonspecific binding of

Tab. 3.1 Strategies used for biomolecule immobilization applied for nanopatterning proteins.

Type of interaction	Surface derivatization	Proteins studied	Surface	SPL method	Dimensions	Reference
Chemisorption	S-Au attachment of C-terminal thiol groups	bundle metalloproteins	Au(111)	nanografting	100 nm	80
Chemisorption	gold surface	thiolated collagen	Au(111)	DPN	30–50 nm	92
Covalent	3-mercaptopropional patterns in a decanethiol resist	lysozyme, IgG	Au(111)	nanografting	40–350 nm	74
Covalent	MHA passivated with EG <sub>3</sub> -SH, then activated to form aldehyde groups	elastin-like polypeptide	Au(111)	DPN	200 nm dots	91
Covalent	1,2-diols cleaved to produce aldehydes	acetylcholine esterase–insulin	Au(111)	nanografting	50–200 nm	79
Covalent and specific	EDC activation of mixed hydroxyl and carboxyl SAMs, then biotin–streptavidin binding	anti-IgG, protein G	Au(111)	uCP	10 $\mu$ m	10
Electrostatic	MHA SAM decanethiol resist	lysozyme	Au(111)	nanografting	100–400 nm	74
Electrostatic	MHA and dodecanethiol SAMs	lysozyme	Au(111)	natural assembly	<1 $\mu$ m	137
Electrostatic	MHA passivated with ethylene glycol SAM	rabbit IgG, lysozyme	Au(111)	DPN	100–350 nm	86
Electrostatic	MHA	mouse anti-p24 HIV-1 p24 antigen	Au(111)	DPN	60 nm	108
Electrostatic	gold surface	cytochrome <i>c</i>	Au(111)	DPN	200 nm dots	87



Electrostatic	mercaptoundecanoic acid passivated with octanethiol and glycol SAMs	rabbit IgG anti-rabbit IgG	Au(111)	nanografting	500 nm–1 $\mu\text{m}$	78
Electrostatic	mercaptohexanol, mercaptopropionic acid, N-(mercapto)hexylpyridinium bromide thiols in matrix terminated with hexa(ethylene glycol) resist	lysozyme, bovine carbonic anhydrase, rabbit IgG	Au(111)	nanografting	200–400 nm	77
Electrostatic and specific	biotin–streptavidin on MHA, with oligoethylene glycol SAM passivation	biotinylated BSA	Au(111)	DPN	100–230 nm	89
Physical adsorption	PDMS stamping onto glass surfaces	rabbit IgGs, BSA, avidin	glass	uCP	40–100 nm	138
Physical adsorption	nickel oxide surface	ubiquitin and thioredoxin	nickel oxide	DPN	80 nm	95
Physical adsorption	direct writing on bare gold; passivation with PEG	lysozyme, rabbit IgG	Au(111)	DPN	45–200 nm	94
Physical adsorption	direct writing on modified $\text{SiO}_2$	IgG, anti-rabbit IgG	$\text{SiO}_2$	DPN	55–550 nm	93
Specific avidin–biotin	oligo-(ethylene glycol) SAM	avidin–biotin–BSA	Si(111)	bias-induced SPL	90 nm	66
Specific avidin–biotin	oxidized regions of PMMA layer spin-coated onto p-doped silicon wafer	biotin IgG–avidin	Si wafer	bias-induced SPL	0.5–1.5 $\mu\text{m}$	61
Specific maleimide–cysteine	maleimide substituted SAM as ink for specific immobilization of cysteine-labeled biomolecules	virus capsid particles	Au(111)	DPN	150 nm	90

proteins. BSA is a globular serum protein which is often used in bioassays to back-fill uncovered areas of surfaces where proteins did not attach.

### 3.2.2

#### SAM Chemistry

SAMs provide a chemical method for creating well-defined surfaces with controllable surface functionality [24]. Due to their stability, ease of preparation and well-ordered surface structures, SAMs of alkanethiols and alkylsilanes provide excellent models for studying protein binding, since layers of defined thickness and designed properties can be generated [25, 26]. Thiol endgroups of *n*-alkanethiols bond via chemisorption to metal surfaces. SAM surface properties can be flexibly controlled by changing the functional (head) groups of the alkyl chain (Fig. 3.3) and these end groups can also be used for further chemical reactions. The acidity, adhesion, wetting and structural properties of surfaces can be modified by choosing specific chemical headgroups (such as  $\text{NH}_2$ ,  $\text{OH}$ ,  $\text{COOH}$ ,  $\text{CH}_3$ , glycol, etc.) [27, 28]. For example, surfaces can be made hydrophilic by introducing SAMs with polar moieties such as hydroxyl or carboxyl groups. Nonpolar functionalities such as methyl-terminated groups yield hydrophobic surfaces. The preparation, characterization and properties of SAMs have been described and reviewed previously [28–32]. SAMs have promising applications in biosensing, corrosion inhibition, lubrication, surface modification and molecular device fabrication. This section introduces the chemistry and structure of SAMs of alkanethiols and alkylsilanes (Fig. 3.3), which are often applied for nanolithography with proteins.

Close-packed *n*-alkanethiol SAMs can be readily prepared with high reproducibility to present functional groups such as alkyls, amides, esters, alcohols, etc., on

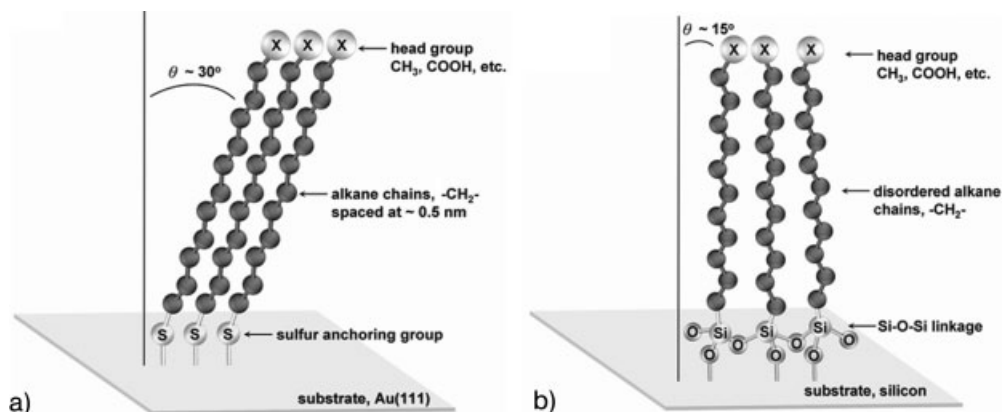


**Figure 3.3.** General structural features of self-assembled monolayers of (A) *n*-alkanethiols/Au(111) and (B) *n*-alkylsilanes/Si(111).

surfaces of gold or coinage metals. Typically, alkanethiol SAMs are formed by soaking gold thin films in dilute (0.1–1.0 mM) solutions of thiols dissolved in solvents such as 2-butanol, hexane or ethanol. Typically, substrates can be stored in a thiol solution for 1–7 days at room temperature to ensure the formation of mature monolayers. Alkanethiols on Au(111) form a close packed, commensurate ( $\sqrt{3} \times \sqrt{3}$ )R30° lattice on Au(111) surfaces [33–36]. In surface assemblies of alkanethiol SAMs, according to studies by IR, near-edge X-ray absorption fine structure (NEXAFS) spectroscopy and grazing incidence X-ray diffraction (GIXD), the alkyl chains of thiol molecules are tilted approximately 30° from surface normal (Fig. 3.3A) [36–38]. The sulfur atoms of alkanethiol molecules are considered to bind at the triple hollow sites of Au(111) lattices [29].

STM and AFM studies have confirmed the long-range order and periodicity of alkanethiol monolayers, and have provided a direct view of defects such as domain boundaries, etch pits, steps and dislocations within SAM films [29, 39]. SPM images visualize the intricate details of the surface topography of SAMs. Figure 3.4 displays a typical topographic view of an octadecanethiol SAM/Au(111) acquired in ethanol by AFM. These molecular landscapes may appear somewhat rough, because at the atomic scale most surfaces are not truly smooth and flat, and contain defects. Considering that the height of gold steps is 0.25 nm, the overall surface roughness of the underlying gold substrates for these images is less than 1 nm. The monolayer surfaces consist of domains of closely packed thiol molecules decorated with etch pits. Readers are referred to several works using STM for a more detailed discussion of the morphology and packing of *n*-alkanethiol SAMs [29, 39–41].

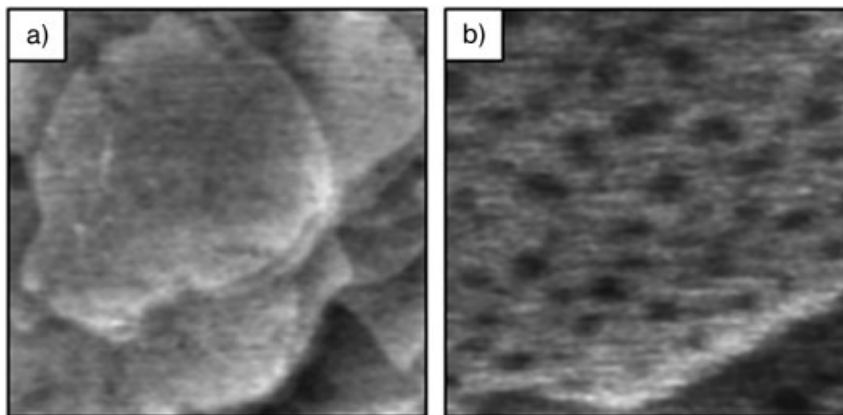


**Figure 3.4.** Contact-mode AFM topographs of an octadecanethiol self-assembled monolayer on Au(111). (A) Terrace arrangement of flat gold steps coated with octadecanethiol SAM ( $400 \times 400 \text{ nm}^2$ ). (B) Zoom-in view displays etch pits ( $80 \times 80 \text{ nm}^2$ ).

Similar to alkanethiols, the chain length and terminal moieties of alkylsilane SAMs can be tailored to meet experimental requirements; however, the properties of alkylsilane assemblies are quite different from SAMs of alkanethiols. SAMs of alkylchlorosilanes, alkylalkoxysilanes and alkylaminosilanes require hydroxylated surfaces to form polysiloxane, which is connected to surface silanol groups ( $-\text{SiOH}$ ) through a network of  $\text{Si}-\text{O}-\text{Si}$  bonds. Substrates on which silane SAMs have been prepared include silicon oxide, aluminum oxide, quartz, glass, mica, zinc selenide and germanium oxide [32]. High-quality alkylsilane SAMs are not as simple to produce as thiol SAMs, because of the need to carefully control the presence of water in solutions. Reproducibility can be a problem, since the quality of the monolayers formed is very sensitive to reaction conditions. Silane monolayers on mica typically consist of domains separated by boundaries. Within domains, silane molecules form structures without long-range order or periodicity [42–44]. The headgroups of silane SAMs crosslink into a  $\text{Si}-\text{O}$  network and the chains are estimated to tilt  $15^\circ$  from surface normal (Fig. 3.3B) [42, 43].

Mixed SAM surfaces can be engineered to avoid nonspecific protein adsorption, yet make specific interactions with targeted proteins to be assayed, by choosing the appropriate buffered conditions as well as an effective matrix layer, resistive to protein adsorption (such as glycol-terminated SAMs). Very few surfaces resist protein adsorption and it remains a challenge to understand the mechanisms that contribute to protein resistance or adhesion to surfaces. To prepare monolayers that resist protein adsorption, the groups of Whitesides [45–48], Mrksich [49] and Grunze [50] have conducted systematic studies of functionalized SAMs to determine the molecular characteristics that impart resistance to protein adsorption. The factors that determine the resistance to protein adsorption were found to include characteristics such as the hydrophilicity of the terminal group, lateral packing density, the presence of hydrogen bond accepting groups and the absence of hydrogen bond donor groups, and terminal groups with overall electrical neutrality.

Approaches which use chemical methods for the activation of SAM surfaces are beginning to gain importance for the surface coupling of biomolecules. Thus far, most reactions for the surface activation of SAMs for protein adsorption have been accomplished after the SAM has been formed with monolayers terminated with carboxyl, amino or hydroxyl groups. Hundreds of synthetic pathways can be applied for *in situ* activation chemistry, including reagents such as *N*-hydroxysuccinimide (NHS), 1-ethyl-3-(3-dimethylaminopropyl)carbodiimide hydrochloride (EDC) and dithiobis(succinimidyl undecanoate) (DSU) [10, 51].

### 3.3 Methods for Nanolithography with Proteins

With the invention and continuing development of scanning probe techniques, such as scanning tunneling microscopy (STM) [52] and AFM [53], surface changes became evident when too much force was applied by an AFM tip, or if the applied bias voltages exceeded certain thresholds using STM or conductive AFM imaging.

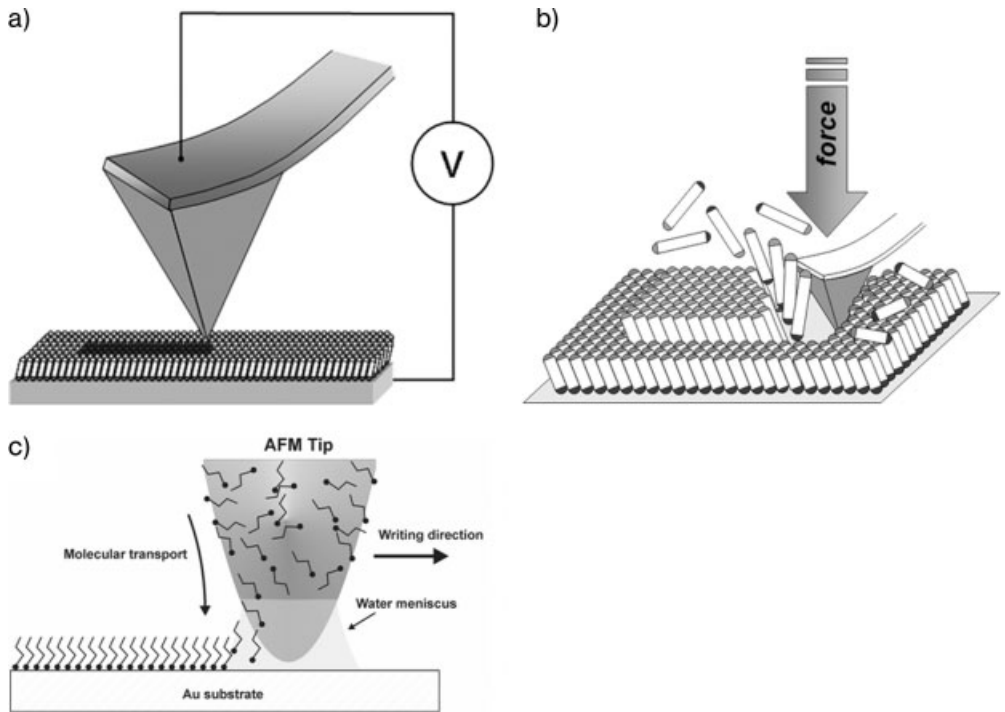


**Figure 3.5.** Schematic representations of three AFM-based nanofabrication techniques: (A) bias-induced lithography, (B) force-induced nanolithography (nanografting) and (C) DPN. (Panel C reproduced with permission from Ref. [56].)

Researchers began experimenting to deliberately and selectively control these alterations. Molecules of SAMs can be written precisely on surfaces using a variety of different SPL methods. Figure 3.5 illustrates the fabrication principles of the three most predominant SPL methods applied for patterning proteins. SPL provides flexible and convenient approaches to construct SAM nanopatterns with designated functionalities in selected nanosized areas. These nanoengineered surfaces can then be used to selectively immobilize desired proteins through covalent, electrostatic or specific recognition approaches.

A common feature of all SPL methods is that an SPM tip is used as a tool for both nanofabrication and characterization of surfaces. A helpful analogy for describing SPL methods with SAMs is an SPM tip (pen) which writes with molecules (ink) on various surfaces (paper). SPL provides exquisite control of surface chemistry including parameters such as the spatial arrangement, chemical composition and the written density of molecular ligands. The shape and dimensions of the tip dictate the detailed resolution of written nanostructures – SAM patterns as small as 5 nm have been reported and it has become routine to achieve patterns

of 20–50 nm (or larger). Since the dimensions of proteins range from tens to hundreds of nanometers, SPL methods are ideally suited for surface studies of protein binding. Particle lithography is another promising method for protein nanopatterning, which can produce arrays of protein nanostructures. Table 3.2 provides a comparison of approaches which have been successfully applied for protein patterning. The next sections of this chapter present further details of these nanolithography methods, including nanografting [54], bias-induced lithographies [55], DPN [56] and latex particle lithography [57].

As a tool for high-resolution characterization, the same SPM tips used to write nanopatterns on surfaces are also used to explore the morphology of nanopatterns after protein adsorption. Both AFM and STM are highly suitable, well-established methods for visualizing surfaces with high resolution. The new tools of AFM and STM have emerged as significant and powerful techniques for imaging surfaces at the molecular scale. Unlike electron microscopy methods which require high vacuum environments and conductive coating of specimens, *in situ* AFM/STM experiments can be accomplished under physiological conditions in aqueous buffered environments. Experiments using SPM provides exquisite resolution for the detailed characterization of molecular structures, has versatility in imaging modes and can be used for local modification of surfaces by lithography. Topographic images provide direct visualization of changes on surfaces after proteins bind to nanopatterns. Commercial advances continue to improve SPM resolution by providing consistently higher-quality probes at lower cost and by the ongoing development of imaging modes for viewing chemical contrast differences for surfaces. Various AFM imaging modes can be applied for probing friction, softness, surface charge, polarizability, magnetic domains and viscoelasticity at the atomic scale.

### 3.3.1

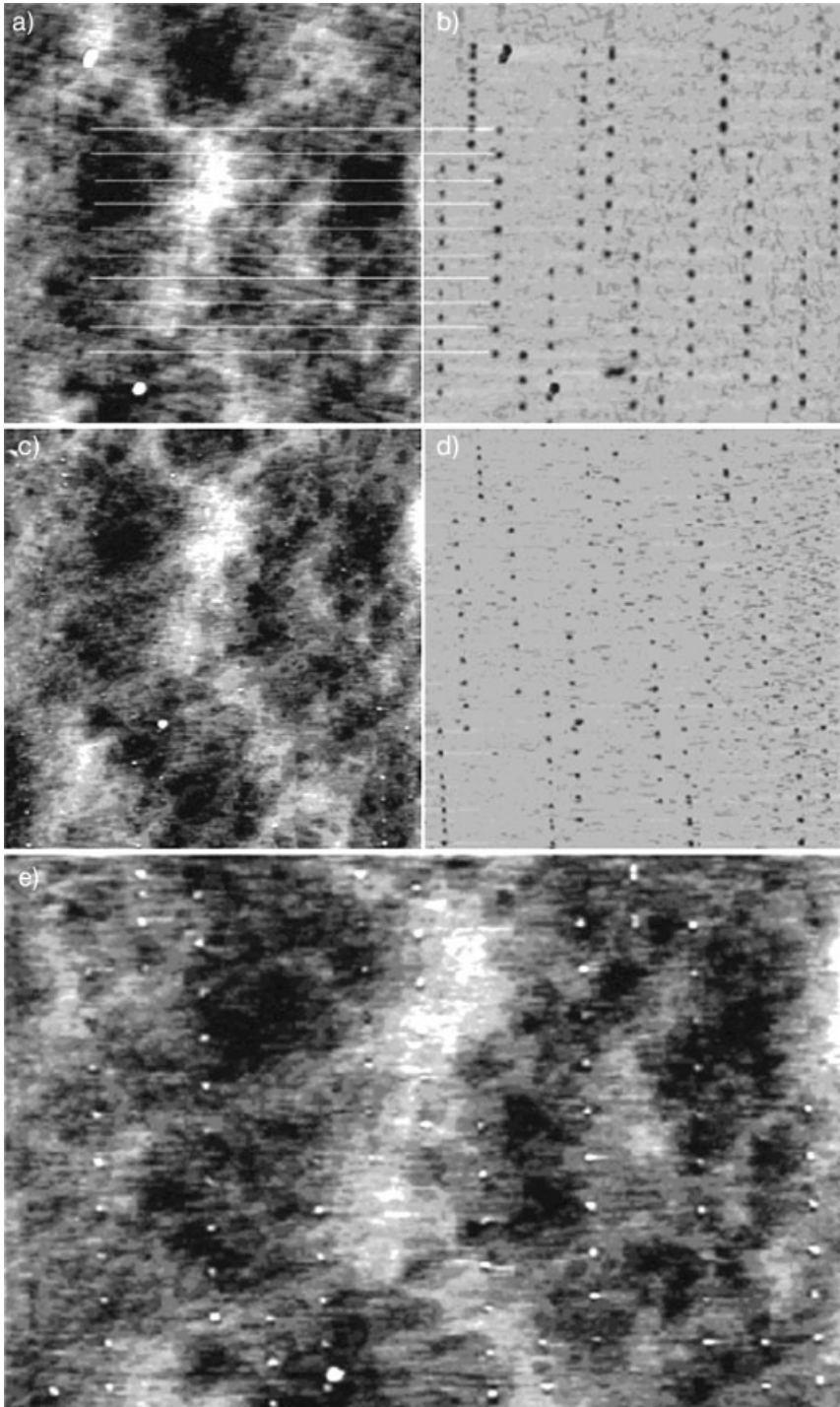
#### **Bias-induced Nanolithography of SAMs**

When an electric field is applied at elevated bias voltages between a conductive SPM tip and sample, local chemical or physical changes occur in the area under the tip. Depending on the nature of the surface and environmental conditions (ambient versus UHV), the “bias-induced” changes may result from electrochemistry (oxidation) at either the tip or sample which occurs from electric field effects [58], or the changes may result from ohmic heating, which induces evaporation or desorption of organic layers [59, 60]. This section describes the method of bias-induced lithography and then presents an example of bias-induced nanofabrication applied for protein nanopatterning.

Figure 3.5(A) displays the general principle of bias-induced lithography. For bias-induced SPL, short (microsecond to millisecond) pulses of bias voltage are applied between a conductive SPM tip placed very near, but not in contact with, the surface. The size of the surface features are determined by the duration and magnitude of the electric field, and also by the dimensions of the area probed by the SPM tip. Often, with bias-induced oxidation, the chemical changes produced by an electric field do not manifest height changes and thus are not detectable by top-

Tab. 3.2 Comparison of methods applied for nanopatterning proteins.

Nanopatterning method	Pen	Paper	Mechanism	Surface chemistry	Reference
Bias-induced oxidation	biased tip STM/AFM	conductive or semiconductive substrate	surface oxidation	oxidization of surfaces or SAM terminal groups	66
Bias-induced replacement lithography	biased tip STM/AFM in solution	conductive or semiconductive substrate with SAM	displacement of SAMs under elevated bias	replace matrix SAM with new molecules	55, 62
Nanografting	bare AFM tip in a SAM solution	thiol SAMs	force and solution replacement	replace matrix with diverse functional groups of new SAMs	75, 80
DPN	ink-coated AFM tip in air	clean, uncoated surface	meniscus liquid transfer	write diverse functional groups of SAMs and other nanomaterials	86
Latex particle lithography	(not an SPL-based method)	mica(0001)/Au(111)	physical adsorption	self-ordering of monodisperse spheres as a structural template	57





ographic imaging. However, SPM imaging modes which display contrast between different terminal groups, such as force modulation, lateral force imaging and current/electrical force images, can clearly differentiate areas that are modified based on chemical changes.

Bias-induced lithography is emerging as a flexible and convenient means for nanofabrication of designed surface components, using either silane or thiol SAMs. Requirements for bias-induced nanofabrication include a conductive or semiconductive substrate and a conductive SPM probe. To prepare conductive AFM tips, a thin film of metal (usually gold) is sputter-coated onto the surface of probes precoated with a precursor binding layer of chromium or titanium. Conductive tips and cantilevers comprised of doped silicon exhibit sufficient electrical conductivity for bias-induced modification of surfaces without requiring metal coatings. Bias-induced SPL methods are now accessible techniques for most SPM users, as a result of improvements in instruments, and in the quality, cost and availability of commercial AFM probes, which now include coatings of cobalt, diamond-like carbon, doped diamond, platinum, platinum/iridium, tungsten carbide, titanium nitride and nickel.

Researchers have begun to apply biased-induced SPL to pattern proteins. Bias-induced lithography was used directly for protein patterning by attachment of IgG–biotin to an array of 30-dot patterns generated using 1-ms voltage pulses (40–80 V) [61]. The substrate was a poly(methyl methacrylate) (PMMA) layer spin-coated on polished p-doped silicon wafer. Differences in hydrophobicity between the patterned areas and the substrate provided a driving force for the selective electrostatic deposition of proteins on nanopatterns. After reaction with avidin–fluorescein isothiocyanate (FITC), micron-sized patterned regions could then be imaged by fluorescence microscopy.

To further extend the capabilities of bias-induced lithography for patterning SAMs with designated surface chemistries, methods which include replacement or addition of new molecules from solution have recently been developed [55]. After voltage pulsing, small areas of the surface were exposed for adsorption of new molecules using bias-induced replacement lithography [62–64]. In another approach, bias conditions which selectively oxidize SAM terminal groups (tip-induced electro-oxidation) were used to generate surface oxides of SAMs. Oxidized areas then were used to chemically attach new molecules with desired functional groups [58, 65]. Nanopatterned protein arrays were fabricated by Cai and co-workers using bias-induced oxidation followed by protein adsorption (Fig. 3.6) [66]. Bias-induced SPL was applied to oxidize the headgroups of monolayers of

**Figure 3.6.** More than 100 protein dots produced by bias-induced nanofabrication. (A) AFM height and (B) friction image of nanoholes produced by bias-induced nanofabrication after treatment with EDAC/avidin ( $4 \times 4 \mu\text{m}^2$ ). The lines provide a reference for corresponding features. The dots are approximately 90 nm in diameter. (C) Topography and (D) friction images of the same area after incubation with biotinylated BSA. (E) After the nanopatterns of biotinylated BSA were reacted with avidin a positive height was observed for the nanodot arrays. (Reproduced with permission from Ref. [66].)

$\alpha$ -hepta(ethylene glycol) methyl  $\omega$ -undecenyl ether on Si(111) substrates. Bursts of 1-ms pulses of +17 V were applied to the sample, to generate rows of spots (90 nm diameter) separated by about 270 nm. The nanopatterned templates were then used to attach avidin followed by biotinylated BSA.

Although bias-induced lithography has not yet been widely applied for nanopatterning proteins, the newly introduced capabilities of customizing surface chemistry by tethering coupling agents to oxidized surfaces holds promise for new applications of bias-induced lithography in future investigations.

### 3.3.2

#### Force-induced Nanolithography of SAMs

Nanofabrication of SAMs can be accomplished by applying mechanical force to an AFM tip during scans. An intrinsic advantage of AFM instruments is the superb control of forces applied between the tip and sample, ranging from pico- to nanonewtons. For high-resolution and faithful imaging of surface topography it is critical to apply minimal, nondestructive forces. When too much force is applied by an AFM tip, areas of the surface can be swept clean or “nanoshaved” [59]. Nanografting was first invented in 1997 and combines nanoshaving with the simultaneous replacement of matrix SAM molecules by the self-assembly of new molecules [54, 67]. A broad range of thiolated molecules have been nanografted to provide tremendous flexibility in choosing the desired molecular lengths and terminal groups for experimental designs [68–72]. This section describes the procedure for nanografting SAMs, presents an example using automated nanografting with SAMs and then reviews examples which apply force-induced lithography (nanografting) for protein patterning.

Nanografting (Fig. 3.5B) is accomplished in dilute SAM solutions containing the selected molecule to be patterned by exerting a high local force on an AFM tip, pushing through the matrix SAM to contact the underlying gold surface. During scanning, pressure between the tip and surface displaces the SAM matrix molecules underneath the tip. As matrix molecules are removed, new thiol molecules from solution immediately adsorb onto the uncovered areas of the substrate to form nanopatterns, following the scanning track of the tip. SPM controllers can be programmed for automated lithography, to rapidly and consistently generate desired surface arrangements of arrays of SAM nanopatterns [73]. Commercial instruments typically include software with capabilities to control the length, direction, speed, bias pulse duration, residence time and the applied force of the scanning motion of the SPM tip, analogous to a pen-plotter. Automated SPL offers tremendous advantages for the speed and reproducibility of nanopatterning, and can produce highly sophisticated pattern arrangements and geometries, with superb precision and reproducibility for the alignment, spacing and shapes of nanopatterns. Examples of SAM nanopatterns generated by force-induced AFM-based lithography (nanografting) are shown in Fig. 3.7.

The AFM contact-mode topograph (Fig. 3.7A) displays 16 nanopatterns of 11-mercaptopundecanoic acid (11-MUA) written within a resist of octadecanethiol.

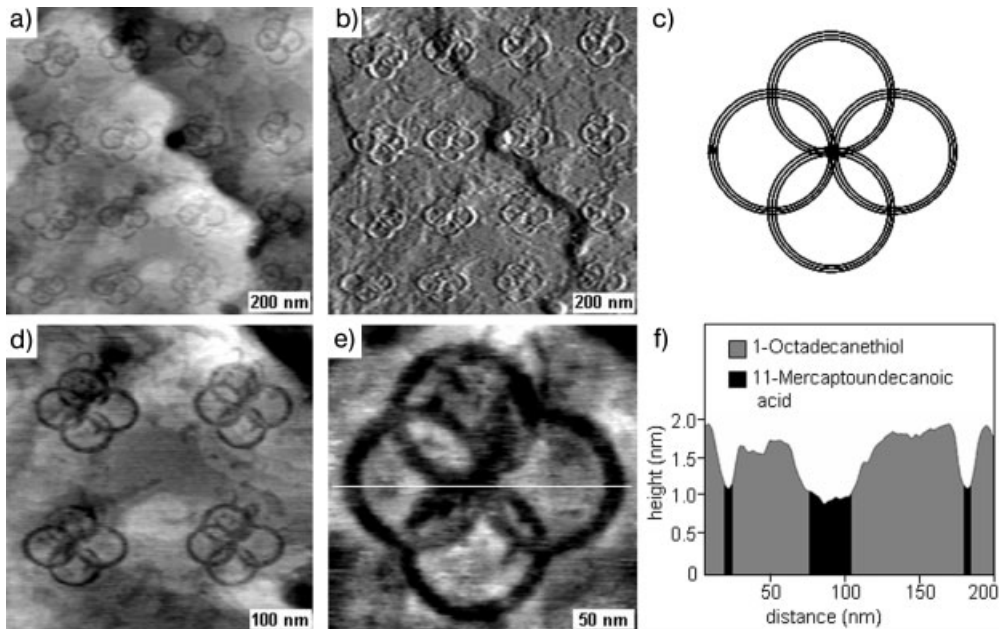


**Figure 3.7.** Nanopatterned array generated by automated nanografting. (A) Topography and (B) corresponding friction images ( $1.0 \times 1.0 \mu\text{m}^2$ ) of nanopatterns of 11-mercaptoundecanoic acid grafted in octadecanethiol/

Au(111). (C) Design of nanopatterned (100 nm) ring elements. (D) Close-up view of four patterns. (E) Zoom-in view of a single pattern ( $250 \times 250 \text{ nm}^2$ ). (F) Cross-section taken along the line in (E).

The corresponding frictional force image (Fig. 3.7B) more clearly displays the arrangement and shapes for the nanopatterned array of circular designs. Nanografting was executed using a programmable computer module interfaced to the AFM controller for translating the tip rapidly and uniformly across the surface to create designed arrangements of nanopatterns (controllers from RHK Technology, Troy, MI). A computer script (written in-house) was used to apply a higher load on the tip to inscribe the pretzel-shaped designs. Each design was generated by writing four 100-nm diameter rings as in Fig. 3.7(C). The rings were inscribed by outlining each circle 3 times with the AFM tip, beginning with the bottom ring and moving in a clockwise direction around the center intersection. It required approximately three minutes to complete the entire  $4 \times 4$  array, (around 12 s to write each pattern). After nanografting, AFM images were acquired under normal imaging conditions using minimal force. Figure 3.7(D) displays a close-up view of four nanopatterns, exhibiting nearly perfect alignment and symmetry. The high-resolution topograph of a single nanopattern in Fig. 3.7(E) reveals the exquisite capabilities of AFM-based nanolithography to write and visualize surface details. The height difference between the (ODT) nanopattern and the 11-MUA matrix SAM is indicated by the cursor profile (Fig. 3.7F) to be approximately  $0.7 \pm 0.1 \text{ nm}$ , in close

agreement with the theoretical height difference (0.7 nm). The line width of the rings is approximately 10 nm. Commercial silicon nitride cantilevers with an average spring constant of  $0.58 \text{ N m}^{-1}$  were used for both imaging and lithography (Veeco Probes, Santa Barbara, CA). The patterning and imaging experiments for Fig. 3.7 were conducted *in situ*, in a liquid environment.

Typically, it requires less than 1 min to fabricate individual nanopatterns using force-induced SPL such as nanoshaving and nanografting. Hundreds of nanopatterns can be written during an experiment without evidence of tip damage, provided that a minimal threshold force is applied. The fabrication forces used for force-induced SPL typically range from 2 to 30 nN, depending on the system under investigation and the geometries and spring constants of the cantilevers. Of course, if far too much force is applied the tip or substrate can be damaged, so it is critical to determine the minimum force for nanofabrication with each experiment. Commercially available soft  $\text{Si}_3\text{N}_4$  cantilevers have mostly been used for nanofabrication by mechanical force, with force constants ranging from 0.03 to  $2.0 \text{ N m}^{-1}$ . When imaging in liquid, the total force applied typically is less than 1 nN, to prevent damage to substrate layers.

The first studies using nanografting to immobilize proteins were conducted in 1999 by Gang-Yu Liu and coworkers using either electrostatic or covalent interactions to immobilize lysozyme, rabbit IgG and BSA on SAM nanopatterns [74]. Since then, a growing number of investigators have taken advantage of the flexibility of nanografting in liquids for surface studies with biomolecules. The typical general steps of an *in situ* protein binding experiment are (a) to fabricate nanopatterns of adhesive tethering molecules, (b) bind proteins to these nanopatterns and (c) test the activity of the immobilized proteins by introducing a second antibody or protein that will bind specifically to the surface-bound protein.

An important advantage of nanografting is the capability to conduct experiments *in situ*, viewing the successive changes in surface topography after the steps of nanopatterning SAMs, rinsing, and introducing buffers and proteins. With *in situ* nanografting, the protein patterns are not subjected to air exposure, and remain in a carefully controlled environment by rinsing and exchanging solutions within the liquid cell. As molecules bind to nanopatterns, *sequential real-time AFM images expose reaction details at a molecular level*, uncovering critical details of the adsorption of proteins to nanostructured surfaces. Figure 3.8 illustrates the basic steps of an *in situ* protein adsorption experiment using nanografting.

In the initial investigations of protein immobilization on nanografted SAMs, Liu et al., used functionalized alkanethiol SAMs to mediate electrostatic and covalent binding of IgG and lysozyme [74]. The reactivity and stability of protein nanopatterns was studied in further reports, and included investigation of the retention of specific activity of the immobilized proteins for binding antibodies [75, 76]. Protein patterns sustained washing with buffer and surfactant solutions and were stable for at least 40 h of AFM imaging. The smallest protein feature yet produced by nanografting is a  $10 \times 150 \text{ nm}^2$  line containing three proteins [74, 76].

The first *in situ* antigen–antibody binding AFM experiment with nanofabricated SAMs was conducted using nanografting to direct protein immobilization [75].

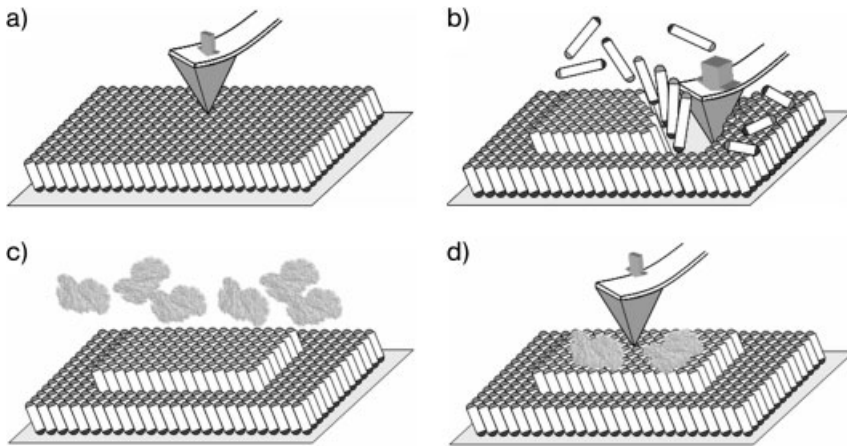


**Figure 3.8.** Steps for nanopatterning proteins using force-induced lithography. (A) A flat area is chosen for writing nanopatterns by imaging at low, nondestructive forces. (B) Nanofabrication is accomplished by applying higher force to write new SAM molecules. (C) Proteins are introduced by exchanging liquids. (D) Protein nanostructures can be characterized under low force.

The activity of covalently immobilized rabbit IgG was tested by reactivity toward mouse anti-rabbit IgG. AFM topographs of protein binding on nanografted patterns of an aldehyde-terminated SAM are shown in Fig. 3.9. Several aldehyde-terminated nanopatterns, a1–a5, were first grafted into a dodecanethiol SAM matrix. The depth of these patterns measured  $0.8 \pm 0.2$  nm and images display dark contrast where the rectangular patterns were inscribed (Fig. 3.9A). After injecting rabbit IgG and rinsing with a surfactant solution, selective adsorption was observed on all six nanopatterns (Fig. 3.9B) in which the bright contrast indicates heights taller than the matrix SAM. In the next step, mouse anti-rabbit IgG was introduced (Fig. 3.9C), showing further height increases. By comparing the height of nanopatterns before and after secondary IgG binding, it was observed that immobilized IgG may adopt various configurations (Fig. 3.9G).

Several investigators have applied nanografting to write nanopatterns for protein immobilization. Abell and coworkers conducted a side-by-side comparison of protein adsorption on multifunctionalized surfaces at the nanoscale using nanografting. Protein adsorption on three differently charged linkers nanografted within a hexa(ethylene glycol) terminated alkanethiol resist SAM was monitored *in situ* by AFM at various pH values [77]. The adsorption of proteins onto nanografted patterns ( $400 \times 400$  nm<sup>2</sup>) of 6-mercaptohexan-1-ol (MCH), *n*-(6-mercapto hexyl) pyridinium bromide (MHP) and 3-mercaptopropionic acid (MPA) was studied with lysozyme, IgG and carbonic anhydrase II. They conclude that in addition to the overall charge of protein molecules, the charge of local domains of the proteins plays a role in immobilization. In the same paper, Abell and coworkers used nanografting to assemble multilayered protein G/IgG/anti-IgG nanostructures through

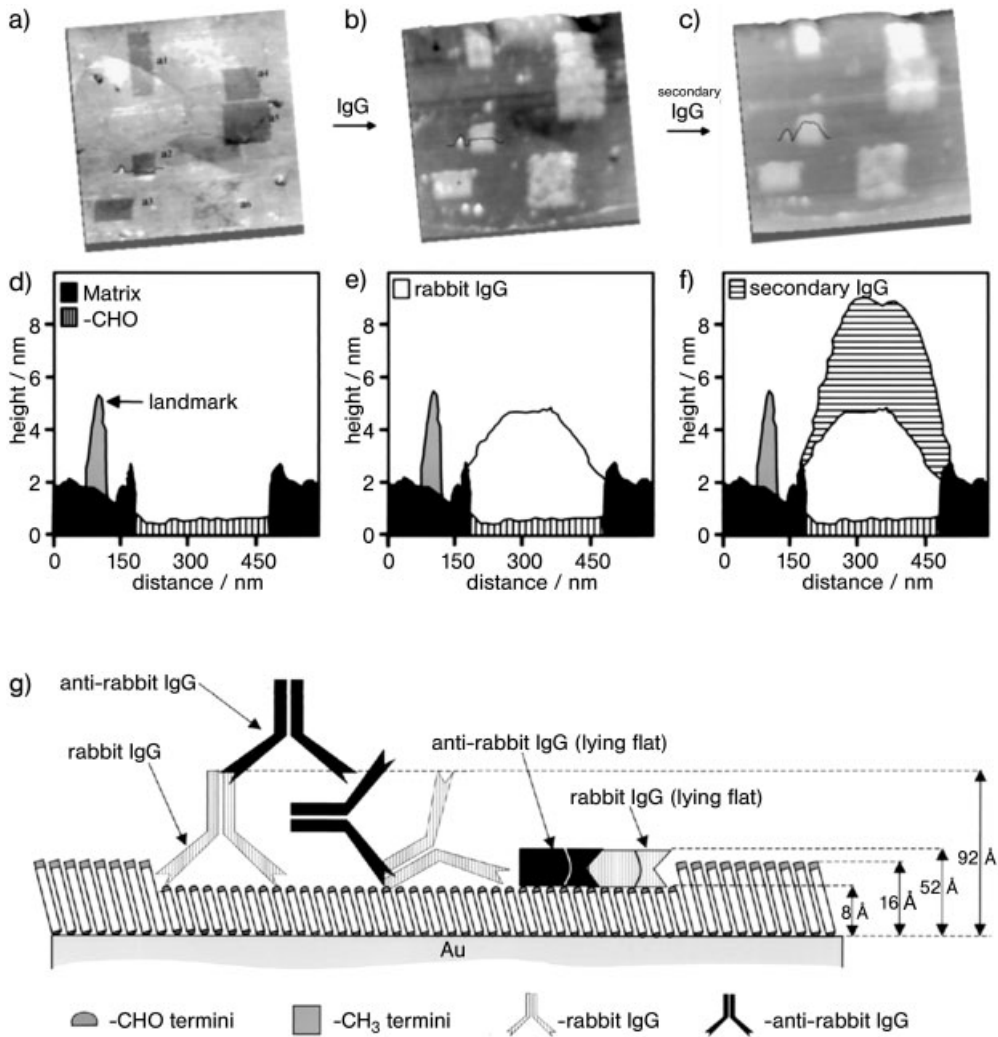


**Figure 3.9.** The steps of protein binding and molecular recognition with nanografted patterns captured by AFM topographic images. (A) Five nanopatterns of 3-mercaptopropional were written in a dodecanethiol SAM. (B) The image contrast changed after rabbit IgG bound covalently to the aldehyde-terminated nanopatterns. (C) After introducing mouse anti-rabbit IgG, the patterns display

further height changes, indicating the antibody binds specifically to the protein nanopatterns. Cursor traces across pattern a2 indicate the height changes (D) after nanografting, (E) after injecting IgG and (F) after introducing anti-rabbit IgG. (G) Map for understanding the evolution of molecular height changes during the steps of this *in situ* experiment. (Reproduced with permission from Ref. [75].)

electrostatic interactions as a potential means to orient IgG molecules for antibody-based biosensor surfaces.

Using force-induced SPL methods of nanografting and nanoshaving, Porter and coworkers compared three approaches for protein patterning [78]. They successfully combined force-induced SPL with immobilization of IgG via EDC activation of 11-mercaptopundecanoic acid; through direct adsorption of Fab'-SH fragments to nanoshaved regions of an EG<sub>3</sub>-OMe matrix, and through chemisorption of a disulfide coupling agent, DSU. Ducker and coworkers applied nanografting to immobilize insulin and acetylcholinase esterase on nanografted 1,2-diols which were activated by sodium periodate to produce aldehyde groups [79]. Retention of catalytic activity was demonstrated for nanopatterned enzymes. Nanografting was applied to directly pattern designed metalloproteins by Au-S chemisorption by Scoles and coworkers [80]. The bundle protein structure was designed to present the C-termini of three helices, terminated with D-cysteine residues for assembly in a vertical orientation, normal to the Au(111) substrate.

A potential disadvantage for nanografting is that exchange takes place between solution molecules and the surface matrix SAM for some systems of alkanethiols. Natural self-exchange is an issue particularly when nanografting longer chain thiols into a shorter chain matrix layer, thus it is important to use very dilute (below 0.1 mM) solutions for nanografting. Exchange can be detected within 2–4 h (depending on the age of the matrix SAM) when molecules from solution adsorb onto defect sites and at step edges.

Although not yet practical for high-throughput applications and manufacturing, combining SPL with protein immobilization enables new approaches for directly investigating changes that occur on surfaces during biochemical reactions. Nano-engineered surfaces are useful for viewing antigen-antibody binding at the nanometer scale, to assess the specificity of selective binding, and to evaluate protein orientation and the accessibility of ligands for binding. Advantages of force-induced SPL include the ability to precisely produce nanometer-sized patterns of bioreceptors, and to successively image and conduct fabrication *in situ*, within well-controlled environments. For protein nanopatterning, force-induced SPL can be applied to either directly write proteins on surfaces via nanoshaving, or can be applied to write molecules for attaching proteins to surfaces through electrostatic, covalent or specific binding chemistries.

### 3.3.3

#### **DPN of SAMs and Proteins**

DPN, developed by Chad Mirkin and coworkers in 1999, has emerged as an important and versatile method for producing multicomponent arrays of SAM nanopatterns, as well as other molecules and nanomaterials [81]. This section describes the DPN nanofabrication method and then presents examples of DPN applied for protein nanopatterning. Protein nanopatterning has been accomplished by several different approaches via DPN. For SAM molecules written directly by DPN, proteins may be attached to nanopatterns through electrostatic, covalent or specific interac-

tions on nanopatterns after surface passivation. Another strategy is to use surface activation of nanopatterned amine, carboxylate or hydroxyl groups for protein immobilization. Direct writing of proteins has also been accomplished by DPN using modified AFM tips.

In DPN, an AFM tip (pen) is coated with a molecular “ink” to write on clean gold substrates or “paper” under ambient conditions in air [56, 82]. Ink molecules migrate from the coated AFM tip through a capillary meniscus to the substrate by diffusion (Fig. 3.5C). Capillary transport of molecules from the AFM tip to the substrate can be used to directly write arrays of SAM nanopatterns. Additional mechanical force is not applied to the AFM tip or “pen.” When an AFM tip is used in air to image a surface, the narrow gap between the tip and surface forms a tiny capillary meniscus from the condensation of water. Nanopatterns such as individual lines, dots, grids and arrays of alkanethiols have been written on bare gold surfaces [56, 83, 84]. The size of the water meniscus that bridges the tip and substrate depends on the tip shape and the relative humidity [85]. In DPN, the meniscus is used to transport molecules from the tip to the surface. The resolution of DPN depends on several parameters, such as the geometry of the AFM tip, the humidity of the ambient environment, as well as the duration over which the inked tip is placed in contact with the surface – typically of the order of approximately 1–10 s. With commercial cantilevers, DPN routinely generates feature sizes down to 15 nm.

Protein arrays were produced with DPN by patterning 16-mercaptohexadecanoic acid (MHA) for immobilizing lysozyme and IgG through electrostatic interactions by Mrksich and coworkers (Fig. 3.10) [86]. After writing MHA dots (diameter 100–350 nm) the gold surface was passivated with 11-mercaptoundecyl-tri(ethylene glycol). The MHA patterns were exposed to proteins by immersing substrates in a solution containing the desired protein. The arrays were then rinsed with buffer and imaged in air by tapping-mode AFM. The reaction of IgG patterns with rabbit antibody and with mixtures of proteins was also studied using AFM to investigate and detect nonspecific binding to nanopatterns and to passivated areas of the substrate. In another study, Choi and coworkers immobilized cytochrome *c* through electrostatic adsorption on nanopatterns of MHA written by DPN [87]. The areas surrounding the MHA nanopatterns were passivated with octadecanethiol.

Covalent attachment of synthetic peptides was accomplished by Ivanisevic and Cho using DPN [88]. First, nanopatterns of amine-terminated silane molecules (3-aminopropyl-triethoxysilane) (APTES) were written on  $\text{SiO}_x$  surfaces by DPN. Next, the heterobifunctional cross-linker *N*-hydroxysuccinimide ester (SMPB) was conjugated to the APTES nanopatterns. In the final step, a TAT peptide was covalently linked to SMPB via a cysteine residue in the peptide sequence.

The molecular recognition-mediated, stepwise fabrication of patterned protein nanostructures was accomplished by Zauscher and colleagues using DPN [89]. First, a SAM of MHA was patterned on gold by DPN, shown in Fig. 3.11. Next, the surrounding regions were passivated with a protein-resistant oligoethylene glycol-terminated alkanethiol SAM [11-mercaptoundecyl-tri(ethylene glycol) ( $\text{EG}_3\text{-SH}$ )]. Nonspecific adsorption of proteins on the background was prevented by pas-



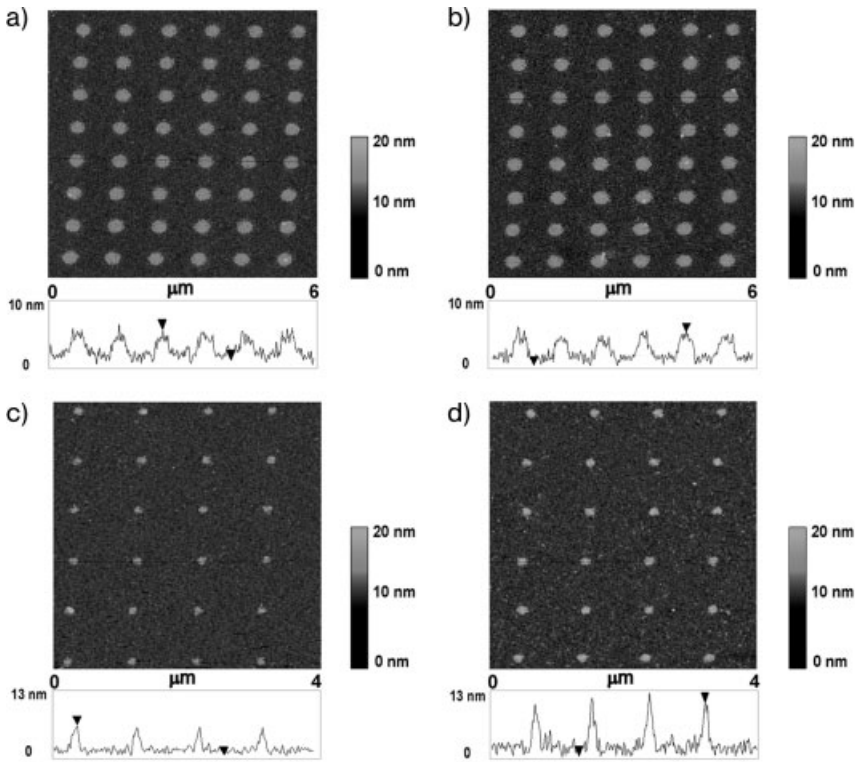


**Figure 3.10.** Snapshots of protein patterns generated by DPN captured *ex situ* by tapping mode AFM images in air and corresponding AFM height profiles. (A) MHA dot array written by DPN after rabbit IgG adsorption. (B) Same IgG array after treatment with a mixture of lysozyme, retronectin, goat/sheep anti-IgG and human IgG. No height change or nonspecific

adsorption is detected. (C) A rabbit IgG array before and (D) after treatment with a mixture containing lysozyme, goat/sheep anti-IgG, human anti-IgG and rabbit anti-IgG. The height of the nanopatterns increased from  $6.5 \pm 0.9$  to  $12.1 \pm 1.3$  nm, indicating the binding of anti-IgG onto IgG nanopatterns. (Reproduced with permission from Ref. [86].)

sivation with EG<sub>3</sub>-SH. In the third step, an amine-terminated biotin derivative was covalently conjugated with the MHA nanopatterns through a reaction with NHS and 1-ethyl-3-(dimethylamino)propyl carbodiimide (EDAC). The surface was then incubated with streptavidin in a fourth step, mediated by molecular recognition between biotin and streptavidin. In the final step, protein nanopatterns were fabricated by molecular recognition-mediated immobilization of biotinylated protein (BSA) in solution. This method provides a generic platform for immobilization of biotin-tagged molecules mediated by biospecific interactions of biotin–streptavidin ligands.

For the specific immobilization of cysteine-labeled cowpea mosaic virus (CPMV) capsid particles, Mirkin and coworkers applied DPN to write a mixture of two dia-

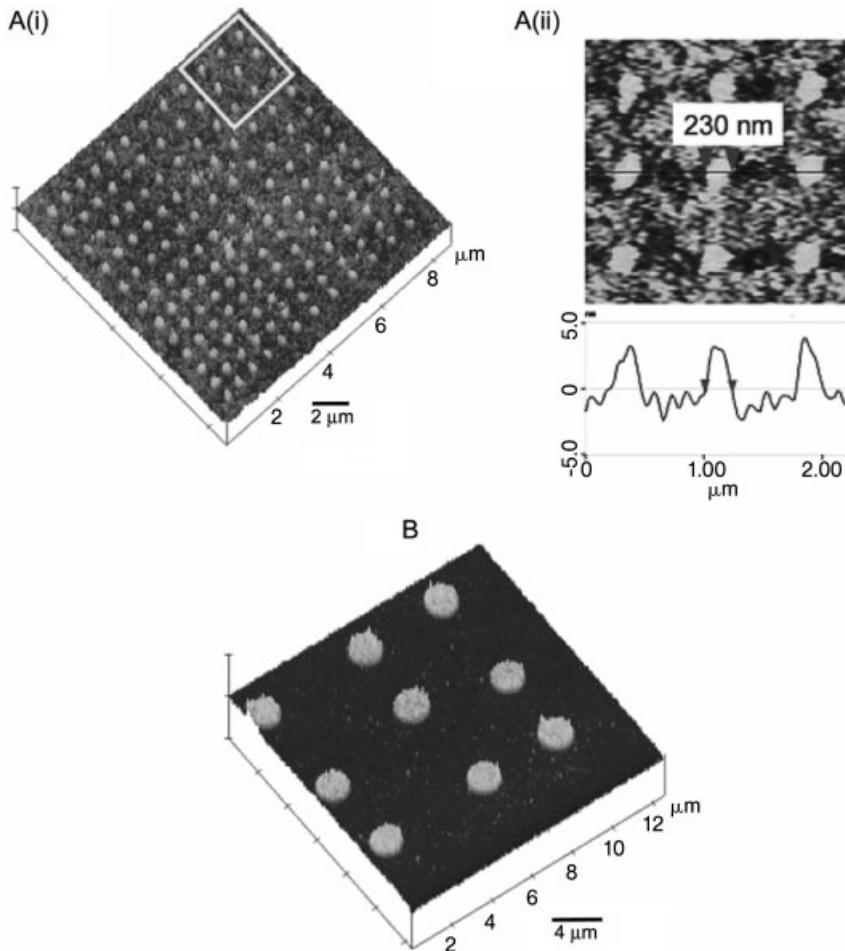


**Figure 3.11.** Nanopatterns of biotin–BSA imaged by tapping mode AFM. [A(i)] An array of 144 dots written by DPN; [A(ii)] zoom-in view of the area within the frame, showing the size of the dots. (B) The 3-D dot array with 1- $\mu\text{m}$  features. (Reproduced with permission from Ref. [89].)

lky disulfides as ink [90]. The areas surrounding the nanopatterns were passivated with penta(ethylene glycol) groups. The density of maleimide groups provided efficient thiol capture through Michael addition of the thiol from cysteine residues of engineered CPMV particles to the nanopatterned maleimide groups.

Surface activation of nanopatterns of MHA written by DPN was used by Zauscher and coworkers to fabricate nanostructures of stimulus-responsive elastin-like polypeptide (ELP) [91]. First, patterns of MHA were written directly using DPN. The surface was then passivated with 11-mercaptoundecyl-tri(ethylene glycol). Next, the COOH groups of the nanopatterned MHA were reacted with

NHS and EDAC to covalently conjugate ELP to the surface. ELP was end-grafted to the surface through an amine group to dictate the surface orientation.

Mirkin and colleagues have presented several studies with direct writing of proteins using DPN. Thiolated collagen was used as ink for direct writing of collagen nanopatterns on gold substrates [92]. Using a modified AFM tip, IgG was written directly on either negatively charged SiO<sub>2</sub> or on aldehyde-modified SiO<sub>2</sub> surfaces by DPN [93]. Tips were coated with 2-[methoxypoly(ethyleneoxy)propyl]trimethoxysilane (Si-PEG), which forms a biocompatible and hydrophilic surface layer on AFM tips for protein inking. Protein arrays of IgG and lysozyme were nanopatterned by direct writing using metallized AFM tips (gold) with a thioctic acid coating, for protein adsorption [94]. Humidity is a critical variable in transporting proteins from tips to a surface, for direct writing of proteins; optimum results were obtained in a glove box at 80–90% humidity to achieve consistent transport properties. Direct writing of proteins on nickel oxide surfaces also was accomplished using tips modified with nickel. For direct write DPN, AFM tips were coated with 5 nm of nickel to facilitate transfer of histidine-tagged proteins (ubiquitin and thioredoxin) as inks [95]. High humidity enabled diffusion from the tip to the surface and also served to minimize the denaturation of protein structures on nickel substrates. Oxidized nickel has a high affinity for polyhistidine residues and patterns could not be generated for protein inks without histidine tags. The binding activity of the nanopatterns was investigated by reaction with fluorescently labeled antibodies, indicating that surface structures remained active for fluorescent labeling.

Another strategy for DPN nanopatterning is accomplished by combining bias-induced electrochemistry and DPN [96]. Electrochemical DPN (E-DPN) was used to immobilize histidine-tagged proteins on nickel substrates [97]. Silicon AFM probes were coated with polyhistidine-tagged peptides, proteins and free-base porphyrins for nanopatterning. By applying a negative bias (–2 to –3 V) to the coated AFM tips, nanopatterns could be written on nickel surfaces using tapping-mode AFM. Without an applied potential, protein deposition was not observed.

DPN provides methods for directly writing chemical inks on surfaces for complex, multistep fabrication of nanostructures of proteins. Chemical reagents can be delivered directly to nanosized areas of a surface and then the surrounding uncovered areas can be passivated with resistive SAMs. The DPN method is amenable to conducting experiments at ambient temperatures in air and ink transfer is facilitated by controlling humidity. After each reaction step, samples can be characterized *ex situ* by AFM imaging. Different molecules can be deposited by exchanging tips to produce multicomponent arrays of nanopatterns. For protein nanopatterning, DPN can be applied to either directly write proteins on surfaces using modified tips or to nanopattern SAM molecules for attaching proteins to surfaces through electrostatic, covalent or specific binding.

#### 3.3.4

#### Latex Particle Lithography with Proteins

Particle or nanosphere lithography is an approach for nanopatterning which uses physical adsorption of materials to surfaces. Monodisperse latex particles self-

assemble into periodic structures on flat surfaces, which have then been used as structural templates or photomasks for defining the deposition of proteins or other materials. The latex particles are removed by various approaches, such as calcination, solvent dissolution or simple rinsing with water. Particle lithography has been successfully applied for patterning metals, sols, polymers and inorganic materials [98–102]. Researchers have also applied colloidal lithography with latex beads as photomasks to construct functional surfaces for selective protein adsorption on lithographically defined regions [102, 103]. This section describes a method of particle lithography which can be applied directly for controlling the organization of proteins on surfaces through physical adsorption [57].

Particle lithography can be used to construct arrays of protein nanostructures on surfaces, with superb control of the distribution of proteins within a single layer over micron-sized areas [57]. An outline of the steps for patterning proteins using latex particle lithography is shown in Fig. 3.12. First, the protein and latex are mixed together in an aqueous solution. For best results, the solution containing protein and latex should be allowed to remain at room temperature for time intervals not longer than 4 h. (To maintain protein activity the solutions should be freshly prepared and to minimize contaminants the latex particles should be pre-washed to ensure that the particles are free of surfactants.) In the second step, a small volume ( $10 \mu\text{L cm}^{-2}$ ) of the colloidal suspension is deposited at the center of the substrate surface, using a pipette. The liquid spreads out into a thin layer across the surface as it dries. The protein and latex mixture forms ordered assem-

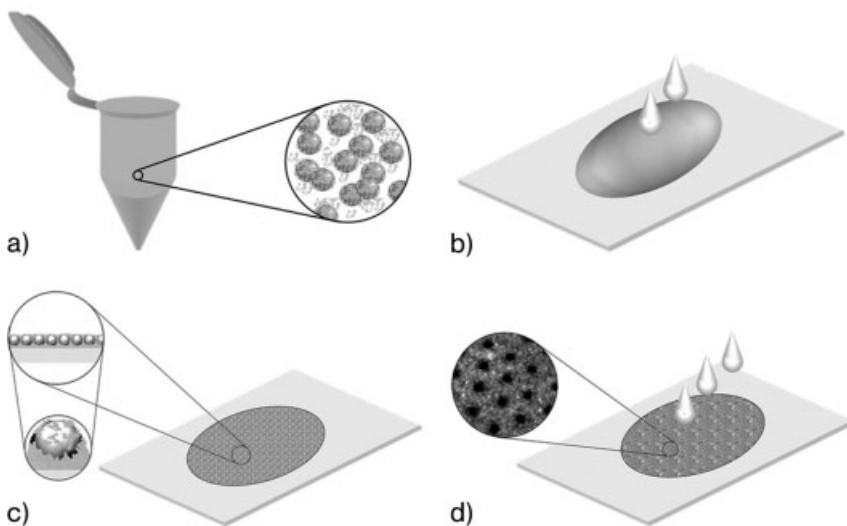


**Figure 3.12.** Fabrication steps for creating arrays of protein nanostructures via particle lithography. (A) Monodisperse latex particles are mixed with protein. (B) The mixture is deposited on a flat surface such as

mica(0001). (C) After the droplet dries, an ordered crystalline layer is formed. (D) Latex are removed by rinsing with deionized water, leaving a layer of protein nanostructures on the surface.

blies supported by mica or gold. During drying, the convective motion of water as it evaporates pulls the latex together into close-packed assemblies. After the deposits have dried, the latex is rinsed away with deionized water to leave a single layer of protein nanostructures on the surface. The assembly of latex particles and the protein nanostructures can be characterized using AFM throughout the fabrication process.

Example images of BSA arrays formed from 500- and 200-nm diameter spheres are shown in Fig. 13(A and B, respectively). The 2-D AFM topographs reveal an organized arrangement of circular dark holes (uncovered areas of mica) surrounded by clusters of BSA. The periodicity of the resulting nanopatterns depends on the separation of latex spheres, which is observed to be 10–15% smaller than the original latex diameters. This is likely attributable to the shrinking and deformation of latex particles during drying. Using 500 nm particles, the ratio of BSA:latex was 55 000:1 which roughly corresponds to a single layer of proteins encapsulating a sphere. For the 200 nm particles, the ratio of BSA:latex was 9000:1, also corresponding to a monolayer shell. The ratios for successful lithography have

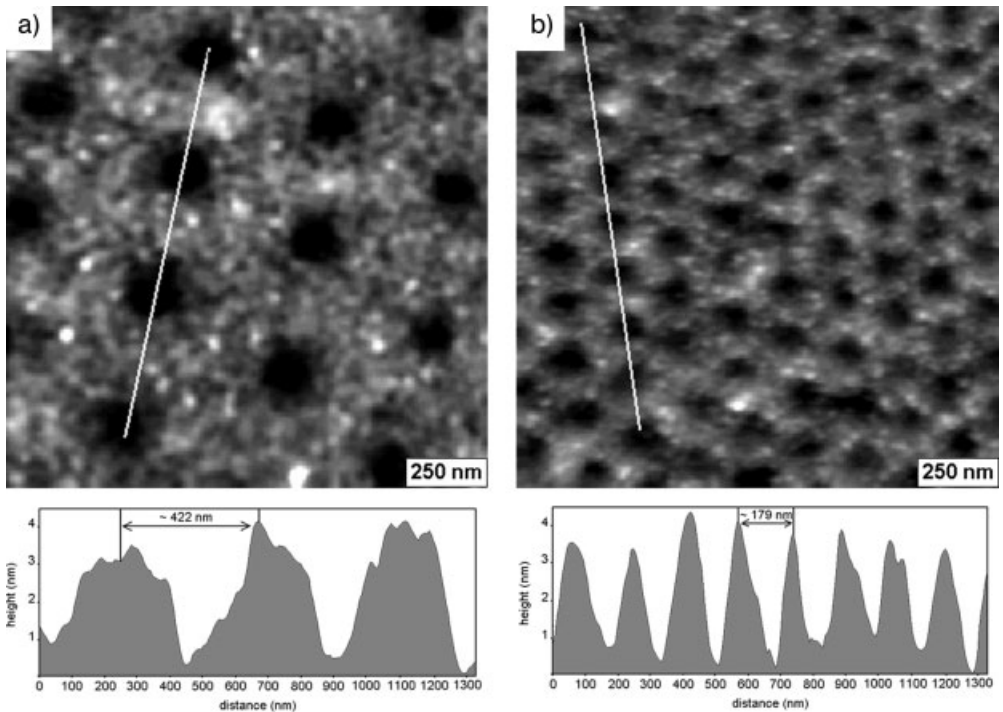


**Figure 3.13.** Periodic arrays of BSA nanostructures generated with latex nanoparticle lithography. (A) BSA nanopatterns from 500-nm particles, using a BSA:latex ratio of 55 000:1. The corresponding cursor indicates the period-

icity of the BSA nanostructures is  $422 \pm 33$  nm. (B) BSA nanostructures generated using 200-nm particles and a BSA:latex ratio of 9000:1. The periodicity of the BSA nanostructures measured  $179 \pm 21$  nm.

ranged from approximately half of monolayer coverage of spheres to that of two layers, yielding different distributions and surface morphologies. Particle lithography uses mild conditions (ambient temperatures, buffers), yet provides nanometer-level control of the spatial distribution of proteins organized within a single surface layer. Particle lithography was also successfully applied for nanopatterning rabbit IgG [57]. Both IgG and BSA nanopatterns retained the ability to bind corresponding specific antibodies.

Particle lithography is a highly reproducible and robust method for patterning proteins, and serves as an excellent starting point for continuing to develop more complex bioassays with different surfaces and proteins. Using latex particles to control the arrangement of proteins on surfaces is a practical technology which is amenable to microspotting or immersion methods used for protein microarrays and biochips. Latex bead immobilization has been applied in spotting solutions to create microarrays for detection of antibodies [104]. Particle lithography offers the advantages of nanometer precision and high throughput, since a small vial of solution can produce hundreds of replicate samples. Future investigations will address the suitability of particle lithography to other surfaces and to other proteins, for application in surface-bound immunoassays.

### 3.4

#### Detection of Protein Binding at the Nanoscale

Nanoengineering approaches for the development of nanoscale bioassays capitalize on the unique *in situ* and high-resolution capabilities of SPM. Designed surfaces can be created with precisely placed proteins, which are subsequently monitored during the binding of secondary antibodies. SPM can be applied directly for detection, measuring changes in the heights of nanopatterns with protein binding. The height changes indicate the side-on or end-on orientation of immobilized proteins (Fig. 3.14) [74]. In some investigations, fluorescent labels were conjugated to antibodies for microscopic examination of samples. Optical microscopy can detect changes in fluorescence after antigen–antibody binding. An important question to address is whether or not the tagging entity hinders the affinity and efficiency of antigen–antibody binding. Many fluorescent dyes currently used are hydrophobic, which substantially decreases the solubility of protein–dye conjugates. This could adversely influence signal intensity for fluorescent detection [105]. Nanoscale studies can be applied to refine critical parameters used to link and organize proteins on surfaces of biochips and biosensors. SPM images of protein binding can be beneficial for evaluating the effectiveness of different bioconjugation chemistries for biomarkers.

At the core of biosensing is detection of biomolecular binding events with high selectivity and sensitivity. Typically, bioassays for surface-bound proteins are not as sensitive as approaches which use solution chemistry, due in part to the accessibility of molecules for binding. Pressing the limits of protein patterning to the nanometer scale will furnish direct views of the differences in immobilization chemis-

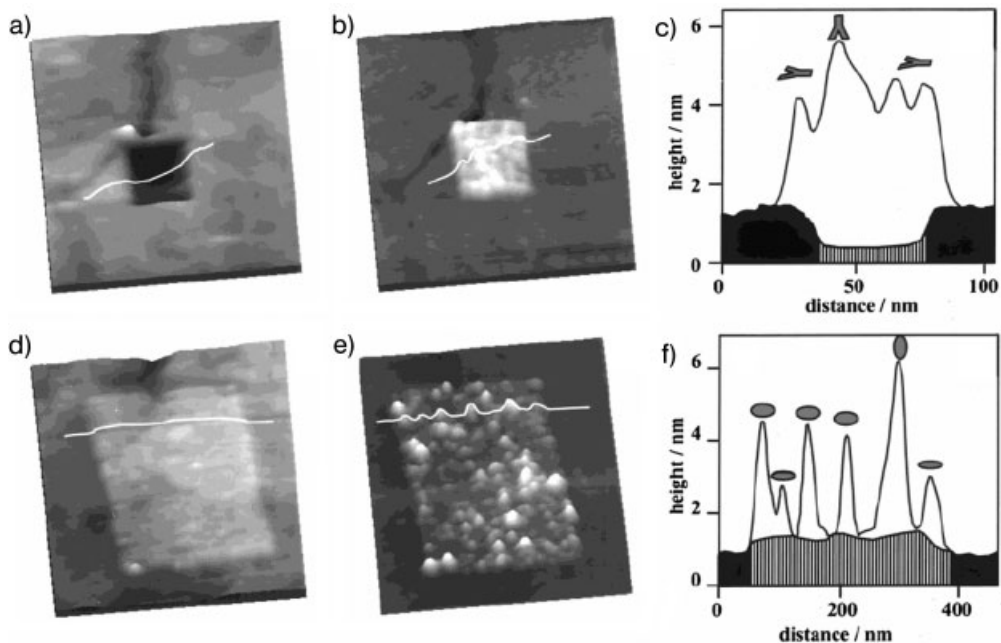


**Figure 3.14.** Nanografted patterns of aldehyde-terminated SAMs were used to covalently immobilize proteins via imine bonds. (A) Nanopattern of 3-mercaptopropanal ( $150 \times 150 \text{ nm}^2$ ) written in decanethiol; (B) after *in situ* immersion in buffer containing rabbit IgG; (C) combined cursor profiles for lines in (A) and (B). (D) Nanografted rectangle

of mercaptodecanal ( $340 \times 300 \text{ nm}^2$ ) written in hexanethiol; (E) after immersion in lysozyme solution. (F) Corresponding cursor profiles across (D) and (E). The ellipsoidal lysozyme and Y-shaped IgG molecules may adopt various orientations, as shown in the schematics above the cursor plots. (Reproduced with permission from Ref. [74].)

tries. Conventionally, biosensors and biochips rely on microspotting or solution deposition to place proteins on various surfaces, without control of the placement and arrangement of target proteins. There is a requirement for efficient yet mild immobilization chemistries which preserve tertiary structure and maximize the activity of fragile biomolecules.

Biomolecules immobilized on a surface serve as the receptor and in some cases as the signal transducer in biosensors. Therefore, the placement of biological ligands in precisely defined locations can increase the density of sensor elements and lead to improved detection limits with molecular-level control of the surface reactivity [106, 107]. As a proof-of-concept, Wolinsky and Mirkin have reported a nanometer-scale antibody array prepared by DPN to test for the presence of the human immunodeficiency virus type 1 (HIV-1) in blood samples [108]. The HIV-1 antibodies were immobilized on the MHA nanopatterns for hybridizing (HIV-1 p24) antigen and bound proteins. With a nanoarray of 100-nm features written by DPN, the three-component sandwich assay exceeded the limit of detection of con-

ventional enzyme-linked immunosorbent assay (ELISA) based immunoassays by 1000-fold.

### 3.5

#### Future Directions

It can be anticipated that array-based technologies in proteomics including protein-based biochip and biosensing devices will significantly advance biotechnology, clinical diagnostics, tissue engineering and targeted drug delivery [109–111]. Ultra-small protein patterns can be used in biosensing, control of cell adhesion and growth and in biochip fabrication [5, 6, 112]. Methods of high-throughput protein analysis offer immense potential for fast, direct and quantitative detection, including the possibility of screening thousands of proteins within a single sample to test for protein, ligand and drug interactions. Improved binding to surfaces onto which capture proteins are arrayed and improved sensitivity of detection are technical challenges advancing protein microarray technology. The next section first discusses the motivation for advancing beyond microtechnology to the nanoscale frontier and then describes new technologies which are being developed for multiplexing AFM systems for parallel processes.

#### 3.5.1

##### Advantages of Nanoscale Detection

Tools for nano- and microfabrication will provide important contributions in developing biochip and biosensing technologies, as well as supply basic research in protein–protein interactions. With the rapid progress in development of large sets of characterized antibodies, protein and antibody arrays will provide tremendous advantages for diagnostics and medical science. Miniaturization provides rewards of reduced quantities of analytes and reagents, increased density of sensor and chip elements, and more rapid reaction response [107, 113–115]. Multiplex screening of many interactions in a parallel fashion reduces analysis time and gives insight into the multiplicity of factors involved in diseases. Protein microarrays used in experiments based on AFM detection may soon reach capabilities for routinely achieving single-molecule detection.

Nanotechnology offers advantages not only for array production, but also for sample detection for bioarrays. In the nanoscale size regime, material properties are different than at macroscopic scales, exhibiting phenomena such as electromagnetic field enhancement, narrow emission band fluorescence, surface plasmon resonance, and conductivity and signal amplification. These properties enable new signaling and recognition capabilities for use in sensor systems. For example, bioconjugates of nanoparticles and quantum dots may provide improved stability and sensitivity for quantitative fluorescence detection with advantages over the conventional approach of fluorescent staining which suffers from the disadvantage of photobleaching [116]. With regard to biomolecule detection, new strategies based on



functionalized metal nanoparticles, in combination with magnetic detection have been reported, using superparamagnetic beads coated with antibodies for detection [117].

### 3.5.2

#### Development of Cantilever Arrays

Using SPM-based nanofabrication, the single pen-and-ink approach is far too slow for cost-effective manufacturing of protein arrays. AFM-based lithography offers the ultimate capabilities for nanometer-scale control of surfaces with extremely high spatial precision; however, it has the limitation of relatively low throughput by fabricating each pattern individually. If higher throughput can be accomplished for nanoscale biochips, such arrays would offer immense capabilities. Miniaturization of protein sensing to nanodimensions will require techniques for rapid, efficient and high-throughput writing of biomolecules and SAMs. New designs for AFM probe arrays are being developed which will provide parallel and multiplexing capabilities for surface characterization and fabrication. Readers are referred to two recent reviews which detail the developments in multiple probe systems [81, 118].

Successful lithography with probe arrays has been demonstrated by several researchers, and representative examples are summarized in Tab. 3.3. Initial designs of tip arrays used feedback from a single cantilever for operation. This can sometimes be problematic for lithography because of variations in tip geometries and difficulties for precise alignment [119]. Micromachined arrays of cantilevers operated in parallel ( $2 \times 1$ ,  $5 \times 1$ ,  $10 \times 1$ ,  $32 \times 1$  and  $50 \times 1$ ) were used for bias-induced oxidation of silicon as reported by Quate and coworkers [119–121]. Proof-of-concept experiments were presented for operation of parallel AFM probes for bias-induced lithography using as many as 50 probes. Arrays with integrated  $z$ -axis control were found to improve the quality and reproducibility of writing. There are several approaches for control and actuation of individual probes within cantilever arrays, including piezoelectric sensing [121–123], optical interferometric detection [124], thermal actuation of bimetallic tips [125–129] and conductivity sensing of tip–surface contact [130].

DPN has been advanced to parallel processes through the use of 1-D cantilever arrays [131, 132]. Control of the horizontal and vertical movements of AFM probes can be achieved using the laser signal feedback of a closed-loop AFM scanner. Using an eight-cantilever array, a miniaturized combinatorial chemical sensor was produced with DPN by writing multiple inks as sensor elements [133]. Also, examples have been reported using tip arrays for simultaneously writing multiple patterns of octadecanethiol using DPN [128–130].

Two-dimensional cantilever arrays have been developed and tested, including designs which combine passive (feedback from deflection of a single tip) and active control through actuation of multiple tips [134]. A group at IBM has implemented an addressable  $32 \times 32$  probe array designed for high-density data storage [135, 136]. The “Millipede” array format with 1024 cantilevers measures  $3 \times 3 \text{ mm}^2$

**Tab. 3.3** Examples of AFM probe arrays which have been successfully demonstrated for AFM imaging/lithography applications.

Year	Array size	Tip actuation method	Application	Reference
1995	2 × 1	integrated piezoelectric sensor and piezoresistive sensor for both tips	parallel constant-force AFM imaging	139
1995	2 × 1, 5 × 1	single tip feedback (piezoresistive levers)	bias-induced oxidation of silicon (100–200 nm line patterns)	119
1996	2 × 1	integrated piezoelectric actuators for each tip	bias-induced oxidation of silicon (micron patterns)	121
1998	10 × 1, 32 × 1, 50 × 1	thermal actuation of individual probes, piezoresistive sensors and integrated ZnO actuators	bias-induced oxidation of silicon (1.1- $\mu$ m line patterns) and parallel AFM imaging	120
1999	5 × 5	integrated piezoresistive sensing using five actuators	multiplexed AFM imaging	134
2000	2 × 1	thermal bimorph actuator, metal-oxide-semiconductor (MOS) electronics	AFM imaging with constant height mode, tapping mode, constant force mode	126
2000	2 × 4	piezoresistive deflection sensors	parallel AFM imaging	123
2000	32 × 32	thermal actuation, corner sensors for z-feedback control of entire chip	data storage read/write operations	135, 136
2001	5 × 1	optical interferometric detection	parallel AFM imaging, constant height mode	124
2002	2 × 2, 2 × 7	piezoresistive sensing with integrated electrical interconnects	parallel contact-mode imaging of large sample areas	122

2002	8 × 1, 32 × 1	single tip actuation and optical deflection feedback	DPN with octadecanethiol/gold	131
2003	8 × 1	single tip actuation and optical deflection feedback	DPN with sol inks for chemical sensing	133
2003	10 × 1	conductivity-based sensing of tip–surface contact	simultaneous DPN writing with eight probes	130
2004	10 × 1	integrated thermal actuation of probes with piezoresistive stress sensors	parallel constant-force AFM imaging	127
2004	12 × 1	thermal actuation of bimetallic probes, piezoresistive Wheatstone bridge detection	AFM imaging and force–distance measurements	125
2004	10 × 1	individual tip control by thermal actuation of bimorph probes	simultaneous DPN writing with 10 probes	128, 129

---

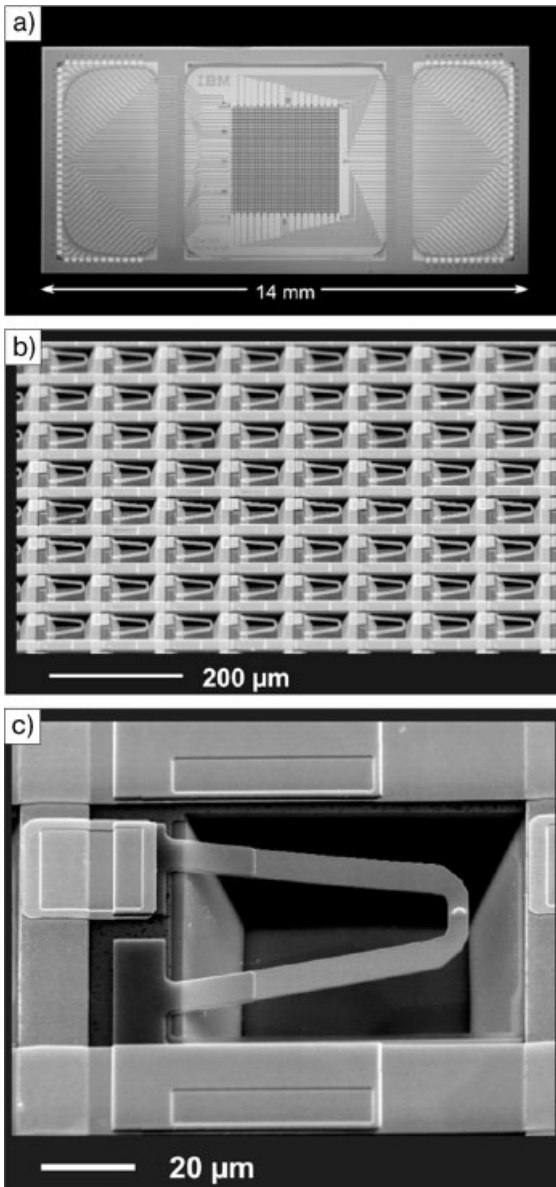


**Figure 3.15.** The “Millipede” array of 1024 cantilevers. (A) Photograph of the entire chip. (B) SEM images of cantilevers of the  $32 \times 32$  array. (C) A single cantilever with integrated silicon tip. (Reproduced with permission from Ref. [135].)

and each cantilever is assigned to read and write areas of  $100 \times 100 \mu\text{m}^2$ . The Millipede approach is not based on individual  $z$ -feedback for each cantilever; feedback control is applied for the whole chip. This design requires stringent control of tip fabrication parameters via micromachining to generate uniform probe dimensions (Fig. 3.15). Although the Millipede design is intended for read/write data storage, other applications can be envisaged using SPL.

### 3.5.3

#### Concluding Remarks

Fundamental understanding of the interactions of protein binding to substrates or antibodies is essential for developing workable technologies for life sciences. The new capabilities to study and control processes on the nanometer scale are emerging as valuable assets in both fundamental and applied research. At present, SPM and SPL are primarily used as research tools in laboratories rather than as tools for manufacturing. However, in the future, nanoscale technology in manufacturing is predicted to bring an even greater impact and benefit to society than present-day microfabrication technologies. Potential applications include the development of a new generation of chemical and biosensors, biochips, and molecular electronic devices. We anticipate that nanoscale research will define new directions in areas such as biosensing, biomimetic surfaces for drug delivery and biomolecule-based electronics. This chapter provides insight on the tremendous versatility of several new SPL methods applied for protein nanopatterning. In addition, there are many new nanofabrication methods being developed which may be suitable in the future for engineering surfaces for nanoscale protein assays.

Applying the *in situ* tools of lithography with proteins will enable systematic evaluation of the differences in bioaffinity for various chemical immobilization strategies, with direct views of how the morphology and geometry of nanoengineered surfaces direct and influence the binding of antibodies and proteins. Conceptually, by arranging and orienting proteins on well-defined surfaces, the selectivity and sensitivity of surface-based protein assays can be substantially improved. These studies will facilitate the development of new and better approaches for immobilization and bioconjugation chemistries – key technologies used in manufacturing biochip and biosensing surfaces.

#### References

- O'BRIEN, J. C., JONES, V. W., PORTER, M. D. Immunosensing platforms using spontaneously adsorbed antibody fragments on gold. *Anal. Chem.* **2000**, *72*, 703–710.
- DELAMARCHE, E., SUNDARABABU, G., BIEBUYCK, H., MICHEL, B., GERBER, C., SIGRIST, H., WOLF, H., RINGSDORF, H., XANTHOPOULOS, N., MATHIEU, H. J. Immobilization of antibodies on a photoactive self-assembled monolayer on gold. *Langmuir* **1996**, *12*, 1997–2006.
- ROWE, C. A., TENDER, L. M., FELDMAN, M. J., GOLDEN, J. P., SCRUGGS, S. B., MACCRAITH, B. D.,

- CRAS, J. J., LIGLER, F. S. Array biosensor for simultaneous identification of bacterial, viral, and protein analytes. *Anal. Chem.* **1999**, *71*, 3846–3852.
- 4 LYNCH, M., MOSHER, C., HUFF, J., NETTIKADAN, S., JOHNSON, J., HENDERSON, E. Functional protein nanoarrays for biomarker profiling. *Proteomics* **2004**, *4*, 1695–1702.
- 5 SCOUTEN, W. H., LUONG, J. H. T., BROWN, R. S. Enzyme or protein immobilization techniques for applications in biosensor design. *Trends Biotechnol.* **1995**, *13*, 178–185.
- 6 ZHANG, S. G., YAN, L., ALTMAN, M., LASSLE, M., NUGENT, H., FRANKEL, F., LAUFFENBURGER, D. A., WHITESIDES, G. M., RICH, A. Biological surface engineering: a simple system for cell pattern formation. *Biomaterials* **1999**, *20*, 1213–1220.
- 7 DILLMORE, W. S., YOUSAF, M. N., MRKSICH, M. A photochemical method for patterning the immobilization of ligands and cells to self-assembled monolayers. *Langmuir* **2004**, *20*, 7223–7231.
- 8 KANE, R. S., TAKAYAMA, S., OSTUNI, E., INGBER, D. E., WHITESIDES, G. M. Patterning proteins and cells using soft lithography. *Biomaterials* **1999**, *20*, 2363–2376.
- 9 JAMES, C. D., DAVIS, R. C., KAM, L., CRAIGHEAD, H. G., ISAACSON, M., TURNER, J. N., SHAIN, W. Patterned protein layers on solid substrates by thin stamp microcontact printing. *Langmuir* **1998**, *14*, 741–744.
- 10 LAHIRI, J., OSTUNI, E., WHITESIDES, G. M. Patterning ligands on reactive SAMs by microcontact printing. *Langmuir* **1999**, *15*, 2055–2060.
- 11 BERNARD, A., RENAULT, J. P., MICHEL, B., BOSSHARD, H. R., DELAMARCHE, E. Microcontact printing of proteins. *Adv. Mater.* **2000**, *12*, 1067–1070.
- 12 BERNARD, A., DELAMARCHE, E., SCHMID, H., MICHEL, B., BOSSHARD, H. R., BIEBUYCK, H. Printing patterns of proteins. *Langmuir* **1998**, *14*, 2225–2229.
- 13 WHITESIDES, G. M., OSTUNI, E., TAKAYAMA, S., JIANG, X., INGBER, D. E. Soft lithography in biology and biochemistry. *Annu. Rev. Biomed. Eng.* **2001**, *3*, 335–373.
- 14 BLAWAS, A. S., OLIVER, T. F., PIRRUNG, M. C., REICHERT, W. M. Step-and-repeat photopatterning of protein features using caged-biotin–BSA: characterization and resolution. *Langmuir* **1998**, *14*, 4243.
- 15 NICOLAU, D. V., TAGUCHI, T., TANIGUCHI, H., YOSHIKAWA, S. Micron-sized protein patterning on diazonaphthoquinone/novolac thin polymeric films. *Langmuir* **1998**, *14*, 1927–1936.
- 16 DONTA, N., NOWALL, W. B., KUHR, W. G. Generation of biotin/avidin/enzyme nanostructures with maskless photolithography. *Anal. Chem.* **1997**, *69*, 2619–2625.
- 17 DELAMARCHE, E., BERNARD, A., SCHMID, H., BIETSCH, A., MICHEL, B., BIEBUYCK, H. Microfluidic networks for chemical patterning of substrate: design and application to bioassays. *J. Am. Chem. Soc.* **1998**, *120*, 500–508.
- 18 PATEL, N., SANDERS, G. H. W., SHAKESHEFF, K. M., CANNIZZARO, S. M., DAVIES, M. C., LANGER, R., ROBERTS, C. J., TENDLER, S. J. B., WILLIAMS, P. M. Atomic force microscopic analysis of highly defined protein patterns formed by microfluidic networks. *Langmuir* **1999**, *15*, 7252–7257.
- 19 KINBARA, K., AIDA, T. Toward intelligent molecular machines: directed motions of biological and artificial molecules and assemblies. *Chem. Rev.* **2005**, *105*, 1377–1400.
- 20 FORTINA, P., KRICKA, L. J., SURREY, S., GRODZINSKI, P. Nanobiotechnology: the promise and reality of new approaches to molecular recognition. *Trends Biotechnol.* **2005**, *23*, 168–173.
- 21 KASEMO, B. Biological surface science. *Surf. Sci.* **2002**, *500*, 656–677.
- 22 WONG, S. S. *Chemistry of Protein Conjugation and Cross-linking*. CRC Press, Boca Raton, FL, **1991**.
- 23 HERMANSON, G. T. *Bioconjugate Techniques*. Academic Press, San Diego, CA, **1996**.
- 24 NUZZO, R. G., ALLARA, D. L. Adsorption of bifunctional organic

- disulfides on gold surfaces. *J. Am. Chem. Soc.* **1983**, *105*, 4481–4483.
- 25 SCHREIBER, S. L. Self-assembled monolayers: from “simple” model systems to biofunctionalized interfaces. *J. Phys.: Condens. Matter* **2004**, *16*, R881–R900.
  - 26 SAGIV, J. Organized monolayers by adsorption – formation and structure of oleophobic mixed monolayers on solid surfaces. *J. Am. Chem. Soc.* **1980**, *102*, 92–98.
  - 27 ULMAN, A. *An Introduction to Ultrathin Organic Films: From Langmuir–Blodgett to Self-Assembly*. Academic Press, Boston, MA, **1991**.
  - 28 WITT, D., KLAJN, R., BARSKI, P., GRZYBOWSKI, B. A. Applications, properties and synthesis of *w*-functionalized *n*-alkanethiols and disulfides – the building blocks of self-assembled monolayers. *Curr. Org. Chem.* **2004**, *8*, 1–35.
  - 29 POIRIER, G. E. Characterization of organosulfur molecular monolayers on Au(111) using scanning tunneling microscopy. *Chem. Rev.* **1997**, *97*, 1117–1127.
  - 30 SCHREIBER, F. Structure and growth of self-assembling monolayers. *Prog. Surf. Sci.* **2000**, *65*, 151–256.
  - 31 DUBOIS, L. H., NUZZO, R. G. Synthesis, structure and properties of model organic surfaces. *Annu. Rev. Phys. Chem.* **1992**, *43*, 437–463.
  - 32 ULMAN, A. Formation and structure of self-assembled monolayers. *Chem. Rev.* **1996**, *96*, 1533–1554.
  - 33 PORTER, M. D., BRIGHT, T. B., ALLARA, D. L., CHIDSEY, C. E. D. Spontaneously organized molecular assemblies. 4. Structural characterization of normal-alkyl thiol monolayers on gold by optical ellipsometry, infrared-spectroscopy, and electrochemistry. *J. Am. Chem. Soc.* **1987**, *109*, 3559–3568.
  - 34 FENTER, P., EBERHARDT, A., EISENBERGER, P. Self-assembly of *n*-alkyl thiols as disulfides on Au(111). *Science* **1994**, *266*, 1216–1218.
  - 35 SCHWARTZ, P. K. Mechanisms and kinetics of self-assembled monolayer formation. *Ann. Rev. Phys. Chem.* **2001**, *52*, 107–137.
  - 36 FENTER, P., EBERHARDT, A., LIANG, K. S., EISENBERGER, P. Epitaxy and chainlength dependent strain in self-assembled monolayers. *J. Chem. Phys.* **1997**, *106*, 1600–1608.
  - 37 DANNENBERGER, O., WEISS, K., HIMMEL, H. J., JAGER, B., BUCK, M., WOLL, C. An orientation analysis of differently endgroup-functionalised alkanethiols adsorbed on Au substrates. *Thin Solid Films* **1997**, *307*, 183–191.
  - 38 NUZZO, R. G., DUBOIS, L. H., ALLARA, D. L. Fundamental studies of microscopic wetting on organic surfaces. 1. Formation and structural characterization of a self-consistent series of polyfunctional organic monolayers. *J. Am. Chem. Soc.* **1990**, *112*, 558–569.
  - 39 QIAN, Y., YANG, G., YU, J., JUNG, T. A., LIU, G.-Y. Structures of annealed decanethiol self-assembled monolayers on Au(111): an ultrahigh vacuum scanning tunneling microscopy study. *Langmuir* **2003**, *19*, 6056–6065.
  - 40 CAMILLONE III, N., EISENBERGER, P., LEUNG, T. Y. B., SCHWARTZ, P., SCOLES, G., POIRIER, G. E., TARLOV, M. J. New monolayer phases of *n*-alkane thiols self-assembled on Au(111): preparation, surface characterization, and imaging. *J. Chem. Phys.* **1994**, *101*, 11031–11036.
  - 41 YANG, G., LIU, G.-Y. New insights for self-assembled monolayers of organothiols on Au(111) revealed by scanning tunneling microscopy. *J. Phys. Chem. B* **2003**, *107*, 8746–8759.
  - 42 XIAO, X.-D., LIU, G. Y., CHARYCH, D. H., SALMERON, M. Preparation, structure, and mechanical stability of alkylsilane monolayers on mica. *Langmuir* **1995**, *11*, 1600–1604.
  - 43 PEANASKY, J., SCHNEIDER, H. M., GRANICK, S. Self-assembled monolayers on mica for experiments utilizing the surface forces apparatus. *Langmuir* **1995**, *11*, 953–962.
  - 44 SCHWARTZ, D. K., STEINBERG, S., ISRAELACHVILI, J., ZASADZINSKI, J. A. N. Growth of a self-assembled monolayer

- by fractal aggregation. *Phys. Rev. Lett.* **1992**, *63*, 3354–3357.
- 45 CHAPMAN, R. G., OSTUNI, E., TAKAYAMA, S., HOLMLIN, R. E., YAN, L., WHITESIDES, G. M. Surveying for surfaces that resist the adsorption of proteins. *J. Am. Chem. Soc.* **2000**, *122*, 8303–8304.
- 46 OSTUNI, E., CHAPMAN, R. G., LIANG, M. N., MELULENI, G., PIER, G., INGBER, D. E., WHITESIDES, G. M. Self-assembled monolayers that resist the adsorption of proteins and the adhesion of bacterial and mammalian cells. *Langmuir* **2001**, *17*, 6336–6343.
- 47 HOLMLIN, R. E., CHEN, X., CHAPMAN, R. G., TAKAYAMA, S., WHITESIDES, G. M. Zwitterionic SAMs that resist nonspecific adsorption of protein from aqueous buffer. *Langmuir* **2001**, *17*, 2841–2850.
- 48 OSTUNI, E., CHAPMAN, R. G., HOLMLIN, R. E., TAKAYAMA, S., WHITESIDES, G. M. A Survey of structure–property relationships of surfaces that resist the adsorption of protein. *Langmuir* **2001**, *17*, 5605–5620.
- 49 LUK, Y.-Y., KATO, M., MRKSICH, M. Self-assembled monolayers of alkanethiolates presenting mannitol groups are inert to protein adsorption and cell attachment. *Langmuir* **2000**, *16*, 9604–9608.
- 50 HERRWERTH, S., ECK, W., REINHARDT, S., GRUNZE, M. Factors that determine the protein resistance of oligoether self-assembled monolayers – internal hydrophilicity, terminal hydrophilicity, and lateral packing density. *J. Am. Chem. Soc.* **2003**, *125*, 9359–9366.
- 51 TENGVALL, P., JANSSON, E., ASKENDAL, A., THOMSEN, P., GRETZER, C. Preparation of multilayer plasma protein films on silicon by EDC/NHS coupling chemistry. *Colloids Surf. B* **2003**, *28*, 261–272.
- 52 BINNIG, G., ROHRER, H., GERBER, C. Surface studies by scanning tunneling microscopy. *Phys. Rev. Lett.* **1982**, *49*, 57.
- 53 BINNIG, G., QUATE, C. F., GERBER, C. Atomic force microscope. *Phys. Rev. Lett.* **1986**, *56*, 930.
- 54 XU, S., LIU, G. Y. Nanometer-scale fabrication by simultaneous nano-shaving and molecular self-assembly. *Langmuir* **1997**, *13*, 127–129.
- 55 GORMAN, C. B., FUJERER, R. R., KRAMER, S. Scanning probe lithography using self-assembled monolayers. *Chem. Rev.* **2003**, *103*, 4367–4418.
- 56 PINER, R. D., ZHU, J., XU, F., HONG, S., MIRKIN, C. A. “Dip-pen” nanolithography. *Science* **1999**, *283*, 661–663.
- 57 GARNO, J. C., AMRO, N., WADU-MESTHRIGE, K., LIU, G.-Y. Production of periodic arrays of protein nanostructures using particle lithography. *Langmuir* **2002**, *18*, 8186–8192.
- 58 LIU, S., MAOZ, R., SAGIV, J. Planned nanostructures of colloidal gold via self-assembly on hierarchically assembled organic bilayer template patterns with in-situ generated terminal amino functionality. *Nano Lett.* **2004**, *4*, 845–851.
- 59 LIU, G.-Y., XU, S., QIAN, Y. Nanofabrication of self-assembled monolayers using scanning probe lithography. *Acc. Chem. Res.* **2000**, *33*, 457–466.
- 60 LEWIS, M. S., GORMAN, C. B. Scanning tunneling microscope-based replacement lithography on self-assembled monolayers. Investigation of the relationship between monolayer structure and replacement bias. *J. Phys. Chem. B* **2004**, *108*, 8581–8583.
- 61 NAUJOKS, N., STEMME, A. Using local surface charges for the fabrication of protein patterns. *Colloids Surf. A* **2004**, *249*, 69–72.
- 62 CHEN, J., REED, M. A., ASPLUND, C. L., CASSELL, A. M., MYRICK, M. L., RAWLETT, A. M., TOUR, J. M., VANPATTEN, P. G. Placement of conjugated oligomers in an alkanethiol matrix by scanned probe microscope lithography. *Appl. Phys. Lett.* **1999**, *75*, 624–626.
- 63 GORMAN, C. B., CARROLL, R. L., HE, Y., TIAN, F., FUJERER, R. Chemically well-defined lithography using self-assembled monolayers and scanning



- tunneling microscopy in nonpolar organothiol solutions. *Langmuir* **2000**, *16*, 6312–6316.
- 64 ZHAO, J., UOSAKI, K. Formation of nanopatterns of a self-assembled monolayer (SAM) within a SAM of different molecules using a current sensing atomic force microscope. *Nano Lett.* **2002**, *2*, 137–140.
- 65 MAOZ, R., COHEN, S. R., SAGIV, J. Nanoelectrochemical patterning of monolayer surfaces: toward spatially defined self-assembly of nanostructures. *Adv. Mater.* **1999**, *11*, 55–61.
- 66 GU, J., YAM, C. M., LI, S., CAI, C. Nanometric protein arrays on protein-resistant monolayers on silicon surfaces. *J. Am. Chem. Soc.* **2004**, *126*, 8098–8099.
- 67 XU, S., LAIBINIS, P. E., LIU, G.-Y. Accelerating the kinetics of thiol self-assembly on gold – a spatial confinement effect. *J. Am. Chem. Soc.* **1998**, *120*, 9356–9361.
- 68 XU, S., MILLER, S., LAIBINIS, P. E., LIU, G.-Y. fabrication of nanometer scale patterns within self-assembled monolayers by nanografting. *Langmuir* **1999**, *15*, 7244–7251.
- 69 HACKER, C. A., BATTEAS, J. D. B., GARNO, J. C., MARQUEZ, M., RICHTER, C. A., RICHTER, L. J., VAN ZEE, R. D., ZANGMEISTER, C. D. Structural and chemical characterization of monofluoro-substituted oligo(phenylene-ethynylene) thiolate self-assembled monolayers on gold. *Langmuir* **2004**, *20*, 6195–6205.
- 70 LIU, J.-F., CRUCHON-DUPEYRAT, S., GARNO, J. C., FROMMER, J., LIU, G.-Y. Three-dimensional nanostructure construction via nanografting: positive and negative pattern transfer. *Nano Lett.* **2002**, *2*, 937–940.
- 71 BROWER, T. L., GARNO, J. C., ULMAN, A., LIU, G.-Y., YAN, C., GOLZHAUSER, A., GRUNZE, M. Self-assembled multilayers of 4,4-dimercaptobiphenyl formed by Cu(II) oxidation. *Langmuir* **2002**, *18*, 6207–6216.
- 72 LIU, M., AMRO, N. A., CHOW, C. S., LIU, G. Y. Production of nanostructures of DNA on surfaces. *Nano Lett.* **2002**, *2*, 863–867.
- 73 CRUCHON-DUPEYRAT, S., PORTHUN, S., LIU, G.-Y. Nanofabrication using computer-assisted design and automated vector-scanning probe lithography. *Appl. Surf. Sci.* **2001**, *175–176*, 636–642.
- 74 WADU-MESTHRIGE, K., XU, S., AMRO, N. A., LIU, G.-Y. Fabrication and imaging of nanometer-sized protein patterns. *Langmuir* **1999**, *15*, 8580–8583.
- 75 WADU-MESTHRIGE, K., AMRO, N. A., GARNO, J. C., XU, S., LIU, G.-Y. Fabrication of nanometer-sized protein patterns using atomic force microscopy and selective immobilization. *Biophys. J.* **2001**, *80*, 1891–1899.
- 76 LIU, G.-Y., AMRO, N. A. Positioning protein molecules on surfaces: a nanoengineering approach to supramolecular chemistry. *Proc. Natl Acad. Sci. USA* **2002**, *99*, 5165–5170.
- 77 ZHOU, D., WANG, X., BIRCH, L., RAYMENT, T., ABELL, C., AFM study on protein immobilization on charged surfaces at the nanoscale: toward the fabrication of three-dimensional protein nanostructures. *Langmuir* **2003**, *19*, 10557–10562.
- 78 KENSETH, J. R., HARNISCH, J. A., JONES, V. W., PORTER, M. D. Investigation of approaches for the fabrication of protein patterns by scanning probe lithography. *Langmuir* **2001**, *17*, 4105–4112.
- 79 JANG, C.-H., STEVENS, B. D., PHILLIPS, R., CALTER, M. A., DUCKER, W. A. A Strategy for the sequential patterning of proteins: catalytically active multiprotein nanofabrication. *Nano Lett.* **2003**, *3*, 691–694.
- 80 CASE, M. A., MCLENDON, G. L., HU, Y., VANDERLICK, T. K., SCOLES, G. Using Nanografting to achieve directed assembly of *de novo* designed metalloproteins on gold. *Nano Lett.* **2003**, *3*, 425–429.
- 81 GINGER, D. S., ZHANG, H., MIRKIN, C. A. The evolution of dip-pen nanolithography. *Angew. Chem. Int. Ed. Engl.* **2004**, *43*, 30–45.
- 82 HONG, S., ZHU, J., MIRKIN, C. A. A new tool for studying the *in situ* growth processes for self-assembled

- monolayers under ambient conditions. *Langmuir* **1999**, *15*, 7897–7900.
- 83 HONG, S., MIRKIN, C. A. A nanoplotter with both parallel and serial writing capabilities. *Science* **2000**, *288*, 1808–1811.
- 84 MIRKIN, C. A., HONG, S., DEMERS, L. Dip-pen nanolithography: controlling surface architecture on the sub-100 nanometer length scale. *ChemPhysChem* **2001**, *2*, 37–39.
- 85 SHEEHAN, P. E., WHITMAN, L. J. Thiol diffusion and the role of humidity in “dip pen nanolithography”. *Phys. Rev. Lett.* **2002**, *88*, 1561041–1561044.
- 86 LEE, K.-B., PARK, S.-J., MIRKIN, C. A., SMITH, J. C., MRKSICH, M. Protein nanoarrays generated by dip-pen nanolithography. *Science* **2002**, *295*, 1702–1705.
- 87 KWAK, S. K., LEE, G. S., AHN, D. J., CHOI, J. W. Pattern formation of cytochrome *c* by microcontact printing and dip-pen nanolithography. *Mater. Sci. Eng. C* **2004**, *24*, 151–155.
- 88 CHO, Y., IVANISEVIC, A. SiO<sub>x</sub> surfaces with lithographic features composed of a TAT peptide. *J. Phys. Chem. B* **2004**, *108*, 15223–15228.
- 89 HYUN, J., AHN, S. J., LEE, W. K., CHILKOTI, A., ZAUSCHER, S. Molecular recognition-mediated fabrication of protein nanostructures by dip-pen lithography. *Nano Lett.* **2002**, *2*, 1203–1207.
- 90 SMITH, J. C., LEE, K.-B., WANG, Q., FINN, M. G., JOHNSON, J. E., MRKSICH, M., MIRKIN, C. A. Nanopatterning the chemospecific immobilization of cowpea mosaic virus capsid. *Nano Lett.* **2003**, *3*, 883–886.
- 91 HYUN, J., LEE, W.-K., NATH, N., CHILKOTI, A., ZAUSCHER, S. Capture and release of proteins on the nanoscale by stimuli-responsive elastin-like polypeptide “switches”. *J. Am. Chem. Soc.* **2004**, *126*, 7330–7335.
- 92 WILSON, D. L., MARTIN, R., HONG, S., CRONIN-GOLOMB, M., MIRKIN, C. A., KAPLAN, D. L. Surface organization and nanopatterning of collagen by dip-pen nanolithography. *Proc. Natl Acad. Sci. USA* **2001**, *98*, 13660–13664.
- 93 LIM, J.-H., GINGER, D. S., LEE, K.-B., HEO, J., NAM, J.-M., MIRKIN, C. A. Direct-write dip-pen nanolithography of proteins on modified silicon oxide surfaces. *Angew. Chem. Int. Ed. Engl.* **2003**, *42*, 2309–2312.
- 94 LEE, K.-B., LIM, J.-H., MIRKIN, C. A. Protein nanostructures formed via direct-write dip-pen nanolithography. *J. Am. Chem. Soc.* **2003**, *125*, 5588–5589.
- 95 NAM, J.-M., HAN, S. W., LEE, K.-B., LIU, X., RATNER, M. A., MIRKIN, C. A. Bioactive protein nanoarrays on nickel oxide surfaces formed by dip-pen nanolithography. *Angew. Chem. Int. Ed. Engl.* **2004**, *43*, 1246–1248.
- 96 LI, Y., MAYNOR, B. W., LIU, J. Electrochemical AFM “dip-pen” nanolithography. *J. Am. Chem. Soc.* **2001**, *123*, 2105–2106.
- 97 AGARWAL, G., NAIK, R. R., STONE, M. O. Immobilization of histidine-tagged proteins on nickel by electrochemical dip pen nanolithography. *J. Am. Chem. Soc.* **2003**, *125*, 7408–7412.
- 98 HAYNES, C. L., VAN DUYN, R. P. Nanosphere lithography: a versatile nanofabrication tool for studies of size-dependent nanoparticle optics. *J. Phys. Chem. B* **2001**, *105*, 5599–5611.
- 99 FREY, W., WOODS, C. K., CHILKOTI, A. Ultraflat nanosphere lithography: a new method to fabricate flat nanostructures. *Adv. Mater.* **2000**, *12*, 1515–1519.
- 100 XIA, Y. N., GATES, B., YIN, Y. D., LU, Y. Monodispersed colloidal spheres: old materials with new applications. *Adv. Mater.* **2000**, *12*, 693–713.
- 101 JIANG, P., HWANG, K. S., MITTLEMAN, D. M., BERTONE, J. F., COLVIN, V. L. Template-directed preparation of macroporous polymers with oriented and crystalline arrays of voids. *J. Am. Chem. Soc.* **1999**, *121*, 11630–11637.
- 102 DENIS, F. A., HANARP, P., SURTHERLAND, D. S., DUFRENE, Y. F. Nanoscale chemical patterns fabricated by using colloidal lithography and self-assembled monolayers. *Langmuir* **2004**, *20*, 9335–9339.

- 103 MICHEL, R., REVIKINE, I., SUTHERLAND, D., FOKAS, C., CSUCS, G., DANUSER, G., SPENCER, N. D., TEXTOR, M. A novel approach to produce biologically relevant chemical patterns at the nanometer scale: selective molecular assembly patterning combined with colloidal lithography. *Langmuir* **2002**, *18*, 8580–8586.
- 104 MARQUETTE, C. A., DEGIULI, A., IMBERT-LAURENCEAU, E., MALLET, F., CHAIX, C., MANDRAND, B., BLUM, L. J. Latex bead immobilisation in PDMS matrix for the detection of p53 gene point mutation and anit-HIV-1 capsid protein antibodies. *Anal. Bioanal. Chem.* **2005**, *381*, 1019–1024.
- 105 MACBEATH, G. Protein microarrays and proteomics. *Nat. Genet. (Suppl.)* **2002**, *32*, 526–532.
- 106 EGGERS, M., HOGAN, M., REICH, R. K., LAMTURE, J., EHRLICH, D., HOLLIS, M., KOSICKI, B., POWDRILL, T., BEATTIE, K., SMITH, S., VARMA, R., GANGADHARAN, R., MALLIK, A., BURKE, B., WALLACE, D. Microchip for quantitative detection of molecules utilizing luminescent and radioisotope reporter groups. *Biotechniques* **1994**, *17*, 516.
- 107 KUNZ, R. E. Miniature integrated optical modules for chemical and biochemical sensing. *Sens. Actuators B* **1997**, *38*, 13–28.
- 108 LEE, K.-B., KIM, E.-Y., MIRKIN, C. A., WOLINSKY, S. M. The use of nanoarrays for highly sensitive and selective detection of human immunodeficiency virus type 1 in plasma. *Nano Lett.* **2004**, *4*, 1869–1872.
- 109 WILSON, D. S., NOCK, S. Functional protein microarrays. *Curr. Opin. Chem. Biol.* **2002**, *6*, 81–85.
- 110 TEMPLIN, M. F., STOLL, D., SCHRENK, M., TRAUB, P. C., VOHRINGER, C. F., JOOS, T. O. Protein microarray technology. *Trends Biotechnol.* **2002**, *20*, 160–166.
- 111 SCHWEITZER, B., KINGSMORE, S. F. Measuring proteins on microarrays. *Curr. Opin. Chem. Biol.* **2002**, *13*, 14–19.
- 112 BLAWAS, A. S., REICHERT, W. M. Protein patterning. *Biomaterials* **1998**, *19*, 595–609.
- 113 BERGVELD, P. The future of biosensors. *Sens. Actuators A* **1996**, *56*, 65–73.
- 114 TEMPLIN, M. F., STOLL, D., SCHWENK, J. M., PÖTZ, O., KRAMER, S., JOOS, T. O. Protein microarrays: promising tools for proteomic research. *Proteomics* **2003**, *3*, 2155–2166.
- 115 WALT, D. R. Miniature analytical methods for medical diagnostics. *Science* **2005**, *308*, 217–219.
- 116 CHAN, W., C. W., NIE, S. Quantum dot bioconjugates for ultrasensitive nonisotopic detection. *Science* **1998**, *281*, 2016–2018.
- 117 BASELT, D. R., LEE, G. U., COLTON, R. J. Biosensor based on force microscope technology. *J. Vac. Sci. Technol. B* **1996**, *14*, 789–793.
- 118 WOUTERS, D., SCHUBERT, U. S. Nanolithography and nanochemistry: probe-related patterning techniques and chemical modification for nanometer-sized devices. *Angew. Chem. Int. Ed. Engl.* **2004**, *43*, 2480–2495.
- 119 MINNE, S. C., FLUECKIGER, P., SOH, H. T., QUATE, C. F. Atomic force microscope lithography using amorphous silicon as a resist and advances in parallel operation. *J. Vac. Sci. Technol. B* **1995**, *13*, 1380–1385.
- 120 MINNE, S. C., ADAMS, J. D., YARALIOGLU, G., MANALIS, S. R., ATALAR, A., QUATE, C. F. Centimeter scale atomic force microscope imaging and lithography. *Appl. Phys. Lett.* **1998**, *73*, 1742–1744.
- 121 MINNE, S. C., MANALIS, S. R., ATALAR, A., QUATE, C. F. Independent parallel lithography using the atomic force microscope. *J. Vac. Sci. Technol. B* **1996**, *14*, 2456–2461.
- 122 CHOW, E. M., YARALIOGLU, G., QUATE, C. F., KENNY, T. W. Characterization of a two-dimensional cantilever array with through-wafer electrical interconnects. *Appl. Phys. Lett.* **2002**, *80*, 664–666.
- 123 CHOW, E. M., SOH, H. T., LEE, H. C., ADAMS, J. D., MINNE, S. C., YARALIOGLU, G., ATALAR, A., QUATE, C. F., KENNY, T. W. Integration of through-wafer interconnects with a

- two-dimensional cantilever array. *Sens. Actuators A* **2000**, *83*, 118–123.
- 124** SULCHEK, T., GROW, R. J., YARALIOGLU, G., MINNE, S. C., QUATE, C. F. Parallel atomic force microscopy with optical interferometric detection. *Appl. Phys. Lett.* **2001**, *78*, 1787–1789.
- 125** HAFIZOVIC, S., BARRETTINO, D., VOLDEN, T., SEDIVY, J., KIRSTEIN, K.-U., BRAND, O., HIERLEMANN, A. Single-chip mechatronic microsystem for surface imaging and force response studies. *Proc. Natl Acad. Sci. USA* **2004**, *101*, 17011–17015.
- 126** AKIYAMA, T., STAUFER, U., DEROOIJ, N. F., LANGE, D., HAGLEITNER, C., BRAND, O., BALTES, H., TONIN, A., HIDBER, H. R. Integrated atomic force microscopy array probe with metal-oxide-semiconductor field effect transistor stress sensor, thermal bimorph actuator, and on-chip complementary metal-oxide-semiconductor electronics. *J. Vac. Sci. Technol. B* **2000**, *18*, 2669–2675.
- 127** VOLDEN, T., ZIMMERMAN, M., LANGE, D., BRAND, O., BALTES, H. Dynamics of CMOS-based thermally actuated cantilever arrays for force microscopy. *Sens. Actuators A* **2004**, *115*, 516–522.
- 128** BULLEN, D., CHUNG, S.-W., WANG, X., ZOU, J., MIRKIN, C. A., LIU, C. Parallel dip-pen nanolithography with arrays of individually addressable cantilevers. *Appl. Phys. Lett.* **2004**, *84*, 789–791.
- 129** WANG, X., BULLEN, D., ZOU, J., LIU, C., MIRKIN, C. A. Thermally actuated probe array for parallel dip-pen nanolithography. *J. Vac. Sci. Technol. B* **2004**, *22*, 2563–2567.
- 130** ZOU, J., BULLEN, D., WANG, X., LIU, C., MIRKIN, C. A. Conductivity-based contact sensing for probe arrays in dip-pen nanolithography. *Appl. Phys. Lett.* **2003**, *83*, 581–583.
- 131** ZHANG, M., BULLEN, D., CHUNG, S.-W., HONG, S., RYU, K. S., FAN, Z., MIRKIN, C. A., LIU, C. A MEMS nanoplotter with high-density parallel dip-pen nanolithography probe arrays. *Nanotechnology* **2002**, *13*, 212–217.
- 132** HONG, S., MIRKIN, C. A. Multiple ink nanolithography: toward a multiple-pen nano-plotter. *Science* **1999**, *286*, 523–525.
- 133** SU, M., LI, S., DRAVID, V. P. Miniaturized chemical multiplexed sensor array. *J. Am. Chem. Soc.* **2003**, *125*, 9930–9931.
- 134** LUTWYCHE, M., ANDREOLI, C., BINNIG, G., BRUGGER, J., DRECHSLER, U., HABERLE, W., ROHRER, H., ROTHUIZEN, H., VETTIGER, P., YARALIOGLU, G., QUATE, C. F.  $5 \times 5$  2D AFM cantilever arrays a first step towards Terabit storage device. *Sens. Actuators A* **1999**, *73*, 89–94.
- 135** KING, W. P., KENNY, T. W., GOODSON, K. E., CROSS, G. L. W., DESPONT, M., DURIG, U. T., ROTHUIZEN, H., BINNIG, G., VETTIGER, P. Design of atomic force microscope cantilevers for combined thermomechanical writing and thermal reading in array operation. *J. Microelectricalmech. Syst.* **2002**, *11*, 765–774.
- 136** VETTIGER, P., DESPONT, M., DRECHSLER, U., DURIG, U. T., HABERLE, W., LUTWYCHE, M., ROTHUIZEN, H., STUTZ, R., WIDMER, R., BINNIG, G. K. The “Millipede” – one thousand tips for future AFM data storage. *IBM J. Res. Dev.* **2000**, *44*, 323–340.
- 137** LI, L., CHEN, S., JIANG, S. Protein adsorption on alkanethiolate self-assembled monolayers: nanoscale surface structural and chemical effects. *Langmuir* **2003**, *19*, 2974–2982.
- 138** RENAULT, J. P., BERNARD, A., BIETSCH, A., MICHEL, B., BOSSHARD, H. R., DELAMARCHE, E., KREITER, M., HECHT, B., WILD, U. P. Fabricating arrays of single protein molecules on glass using microcontact printing. *J. Phys. Chem.* **2003**, *107*, 703–711.
- 139** MINNE, S. C., MANALIS, S. R., QUATE, C. F. Parallel atomic force microscopy using cantilevers with integrated piezoresistive sensors and integrated piezoelectric actuators. *Appl. Phys. Lett.* **1995**, *67*, 3918–3920.

## 4

# Microcantilever-based Nanodevices in the Life Sciences

*Horacio D. Espinosa, Keun-Ho Kim, and Nicolaie Moldovan*

### 4.1

#### Introduction

Microcantilevers were initially developed for atomic force microscopy (AFM), where precise force sensing is critical for atomic-resolution imaging [1, 2]. Microcantilevers were required to have a low force constant and a high mechanical resonance frequency for a superior signal-to-noise ratio. Such requirements were met by cantilevers made by microfabrication techniques, which had been originally developed for integrated circuit (IC) process technology, but were later on applied to micrometer-scale silicon sensors and actuators [3, 4]. Microfabrication also permitted the integration of sharp tips at the free ends of microcantilevers for high lateral resolution in AFM scanning and manipulation. Microfabrication techniques further tailored microcantilevers to broaden the AFM techniques for probing, material delivery, manipulation, biomaterial sensing and lithography. Most of such applications take advantage of the high-precision positioning and subnanometer deflection-detection capabilities of scanning probe microscopy (SPM), which includes scanning tunneling microscopy (STM), AFM, near-field scanning optical microscopy (NSOM) and a plethora of conductive, capacitive, magnetic or thermal probing techniques. Among the extended use of microcantilever applications, patterning of biological materials at the submicron scale is of great importance to fabricating ultra-miniaturized bioanalytical tests and devices. Patterning using biological materials at the miniaturized scale has been pursued by many methods such as ink-jet printing [5, 6], photolithography [7], microcontact printing [8–10], microfluidic devices [11, 12] and “dip-pen” nanolithography (DPN) [13–15]. To date, the DPN technique, an AFM-based direct-write lithographic method, provides the best resolution. Features smaller than 100 nm in size containing patterned biomolecules have been obtained. In such direct-write patterning techniques, the tip sharpness is critical. Through micromachining, tip radii as small as a few nanometers have been obtained [16].

In the initial application of the DPN technique, microcantilevers were used to pattern self-assembled monolayers (SAMs) formed by the adsorption of alkanethiols onto gold surfaces [13]. The SAMs have extraordinary utility to control inter-

facial characteristics, such as the adsorption of proteins and the attachment of cells, and for use in biological analysis including array-based high-throughput screening and diagnostic applications [14, 15]. Also, SAM-coated microcantilevers can detect specific chemical interactions via an optical beam-deflection technique [17]. Direct delivery of biomaterials without the use of a SAM as a binding agent has also been pursued. In biopatterning applications, it is usually required to maintain and transport biomaterials in a liquid environment. Hence, the incorporation of microfluidic systems has been attempted. For example, a commercial AFM tip with a small opening at its apex was reported [18]. These tips allow the on-demand deposition of small single droplets at a predetermined location on a sample. The demand to use liquid as a transport medium has created versatile micro- and nanofluidic tools, specifically engineered for biopatterning, based on the popular microcantilever architecture. Micromachining techniques made the development of such useful structures possible.

Practical implementation of biopatterning and sensing by SPM techniques requires high throughput. This is being pursued by means of microcantilever parallelization [19, 20]. A two-dimensional (2-D) array of independently addressable microcantilevers was developed for high-density data storage [21]. Although this design was conceived for thermal patterning, it is possible to imagine similar tools for biopatterning. With such a massively parallel biopatterning tool, the feature sizes of DNA [22] or protein [23] chips can be further miniaturized, leading to nanoscale assays. For instance, specialized microfluidic probes arranged in a 2-D array would be able to produce ultra-miniaturized, high-density assays, requiring only extremely small analyte volumes, and allowing the simultaneous processing and massively parallel integration of proteins. The massive parallelization at the nanoscale benefits the technique by decreasing the reaction time and by drastically increasing the statistical significance of the experiments. This has the potential to have a huge impact on applications in the life sciences, such as drug discovery and diagnosis devices.

In this chapter we describe how microfabrication techniques were utilized to build micro- and nanoscale devices which facilitated research and development in the life sciences. Microfabrication techniques in general are now available from many sources; books dedicated to topics of microfabrication for versatile SPM cantilever probes have also been published [16, 24, 25]. Furthermore, versatile principles and applications of the SPM techniques have been reviewed [26–30]. Without claiming to exhaust the field, we include a list of currently available books and review articles related to the construction and working principles of general microcantilever probes in Tab. 4.1 for easy reference. However, none of the existing books and reviews bring together the microfabrication aspects and life sciences applications, to discuss them in their close, technologically-targeted relationship. For example, the microfabrication of apertured tips was introduced [16], but their applications in life sciences were not considered for delivering biosamples. Similarly, articles on principles/applications lack information on how the microcantilevers were constructed. In addition, since the development of microfluidic probes for bio-nano applications is an emerging field, to the best of our knowledge, there are

**Tab. 4.1.** Books and review articles on microcantilever-based applications in the life sciences.

Subjects covered	Reference
Fabrication of cantilever probes for near-field optical applications	16
Principles of cantilever sensors for vibrating and force sensing applications; parallelization of recording; chemical surface sensing with nanochemical functionalized probes	24
Arraying probes and integration of sensing and actuation	25
Microfabrication	4
Artificial nose	32
AFM force spectroscopy	26–28
DPN applications	30
SPM for surface patterning	27–29
SPM imaging techniques	26, 28

no current review articles or books that provide a systematic treatment. We hope that this book chapter helps researchers to broaden their viewpoints in this hot topic, organize their thoughts to rise from microfabrication to principles and stimulate new ideas.

Our focus is on devices and methods for surface patterning that typically involve SPMs, although some other interesting devices and concepts will be briefly introduced, such as integration of microchannels. Section 4.2 gives a description of how conventional types of microcantilevers have been microfabricated and used in biotechnology. Beyond the use of conventional microcantilevers, many efforts have been made to integrate microfluidic systems in micro- and nanocantilever devices. Microfluidic systems are of interest because most applications in life sciences require liquid samples to be delivered or probed. Such advanced microcantilevers involving microfluidics are in Section 4.3 and their applications in biopatterning are presented in Section 4.4. Conclusions and outlook are given in Section 4.5.

## 4.2 Microcantilevers

The most commonly used cantilevers in SPM-based biopatterning and sensing are rectangular or V-shaped. The preferred materials in microcantilever fabrication are thin films, such as silicon oxide, silicon nitride, single crystal silicon, diamond or metals. Sharp protruding tips are necessary at the free end of the cantilever for

high-resolution imaging or manipulation, allowing the interaction area between the tip and the sample surface to be minimized. The force constant of microcantilevers used in AFM has been accustomed by practical experience to be in the range from  $10^{-2}$  to  $10^2$  N m<sup>-1</sup> in order to achieve atomic resolution in the contact mode. The force constant  $k$  of a rectangular cantilever with fixed-free boundary condition is defined as follows:

$$k = \frac{Ewt^3}{4L^3} \quad (1)$$

where  $E$  is the modulus of elasticity,  $w$  is the width,  $t$  is the thickness and  $L$  is the length of the cantilever. Surface micromachining techniques are typically used to fabricate micro- and nanoscale cantilevers with or without integrated tips. The fundamental fabrication methods for AFM microcantilevers were established in the late 1980s and their basic concepts are still being used, but with improved features. However, since AFM started to be used for purposes other than for surface profiling, many modified and specific designs have been proposed, leading to a large diversity of micro- and nanocantilever probes. For example, microcantilevers with an apertured pyramidal tip were used to pattern surfaces with liquid contained in a small reservoir just above the tip.

In this section we describe microfabrication techniques of versatile micro/nanocantilevers and their applications in life sciences.

#### 4.2.1

##### **Microfabrication of Miniaturized Probes**

The fabrication methods of cantilevers can be basically divided into two classes [31]. The first uses thin films deposited or diffused into a silicon substrate; in the second fabrication method, all parts of the cantilevered are micromachined out of bulk materials. In the first method, cantilevers beams were commonly formed from thin films such as silicon nitride and silicon oxide. Thin films were deposited on a (100) silicon substrate and then patterned through lithographic processes to define the cantilever shape. The cantilevers were released by etching the substrate, e.g. in aqueous potassium hydroxide (KOH) solutions or ethylenediamine/pyrocatechol/water mixtures (EDP) [4]. Depending on the requirements, sharp tips can be integrated on the cantilever, as discussed later.

Rectangular microcantilevers were employed as biological or biochemical detectors utilizing the bending by adsorption-induced surface stress. The advantage of cantilever-based biosensors is label-free detection and subnanometer deflection sensitivity. In biological sensing applications, the cantilever generates either a static deflection or a change in the resonance frequency when target molecules are adsorbed on the surface of the cantilever [32]. Measurements of such changes can be achieved by either electrical or optical means. Electrical methods include capacitance and piezoresistive sensing, whereas optical techniques include optical lever and interferometric methods.



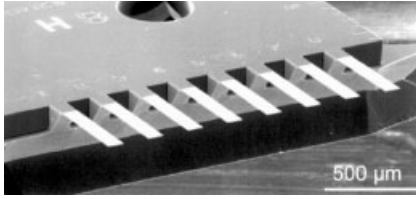


Figure 4.1. SEM image of a microcantilever sensor array [33].

Arrays of silicon cantilevers were produced by a combination of dry and wet etching techniques [33], to form an “artificial nose”, working on the principle of bending stress induced by surface adsorbed molecular species. Individual cantilevers were made (Fig. 4.1) with rectangular dimensions of 500  $\mu\text{m}$  in length, 100  $\mu\text{m}$  in width and 0.8  $\mu\text{m}$  in thickness, resulting in a typical spring constant of 0.02  $\text{N m}^{-1}$ .

A thiol-gold immobilization system [34] was used to form stressed monolayers to induce bending of the cantilevers in detection schemes for vapor thiols. For this application, silicon nitride cantilevers with a 20-nm gold layer evaporated on one side were used as sensors for gas-phase adsorption of alkanethiols [35]. The optical detection scheme of an AFM was used to measure deflections down to the picometer scale. Alkanethiol vapors were generated by placing a few microliters of alkanethiol in a closed glass beaker. After thermal equilibrium was reached, the cantilever was exposed to the alkanethiol vapor. The deflection was measured as a function of time to show how the chemisorbed alkanethiols caused compressive surface stress during the progressive self-assembly. With the same methodology, single-strand (ss) DNA [36, 37] and proteins [38, 39] were detected utilizing DNA hybridization and antigen–antibody interaction as a mechanism to cause surface stress change. The biomaterials were delivered onto the cantilever in liquid environment.

In addition to deflection detection, the change in resonance frequency was used for the detection of target materials adsorbed on a cantilever [40–42]. The cantilever was driven close to the resonance frequency by a piezoelectric actuator. The oscillation was detected by the AFM optical detection. The deposited material increased the mass of the cantilever system, thus decreased the resonance frequency. Assuming there is negligible stiffness change of the cantilever due to the layer of adsorbed materials, the mass change  $\Delta m$  can be calculated from the following equation [40]:

$$\Delta m = \frac{k}{0.72\pi^2} \left( \frac{1}{f_1^2} - \frac{1}{f_2^2} \right) \quad (2)$$

where  $k$  is the spring constant of the cantilever, and  $f_0$  and  $f_1$  are the resonance frequencies before and after adsorption, respectively. Simultaneous use of deflection and resonance frequency detection was also reported [43].

Furthermore, the force exerted by conformational changes of a surface-tethered DNA system was investigated on microfabricated cantilevers [44]. The ability to manipulate the direction and amplitude of bending of cantilevers envisioned potential for micromechanical machinery, including valves, switches and actuators triggered by molecular shape.

In order to integrate tips onto thin film cantilevers, molds for tips needed to be fabricated on the silicon substrate prior to the deposition of the thin film [45]. Either pits or convexities produced on a substrate were exploited as molds. Since molds were employed for tip integration, those types of techniques for thin-film cantilevers were frequently referred to as micromolding or microcasting techniques.

The fabrication of molding-pit cantilevers started with the formation of pits on a (100) silicon surface by an anisotropic etchant such as KOH solutions with a circular or square opening on a mask layer. Such an anisotropic etching produced a pyramidal pit delineated by (111) planes. Subsequently, a thin film was deposited to conformally coat the pit and patterned to delineate the cantilever shape. By removing the whole silicon substrate underneath the cantilever, a protruding tip integrated on the cantilever was obtained [45, 46]. Hybrid tip/cantilever structures were reported by replacing the tip materials with metals, such as tungsten [45] and gold [47], while keeping the cantilever body made of silicon nitride, with better mechanical properties. In a different design, Rasmussen and coworkers [48] reported having all parts of the probe, including the tip, cantilever and support, made out of electroformed metal. The general disadvantage of this type of molding technique is that the fabricated tips point into the substrate, which makes the substrate impractical to use as a chip handling body. Thus, the addition of an extra handling body is needed on the opposite side of the tip, prior to the releasing step. Wafer bonding [45] or electroplating techniques [48] were used to form a handling body. The sharpness of the released tip is determined by that of the molding pit on the silicon substrate, whose final tip angle is around  $70^\circ$  due to the characteristic of anisotropic etching of silicon [3]. However, the sharpness, as well as the aspect ratio, of the tips can be improved by sharpening the molding pit using thermal oxidation at around  $950^\circ\text{C}$  [49]. Oxidation at such a low temperature caused the growth of a nonuniform silicon dioxide film in the pit, resulting in a narrower angle between the walls of the pit, giving a sharper molded tip. With modified pits, tips with curvature radii as low as  $110\text{ \AA}$  were obtained [49].

Convex tip molds were also used to integrate tips onto microcantilevers [45]. In this fabrication scheme, a precursor cap and isotropic etching were used to create a molding tip out of the silicon substrate. For this purpose, a masking layer ( $\text{SiO}_2$  or  $\text{Si}_3\text{N}_4$ ) was deposited on a (100) silicon wafer, followed by lithographically patterning the layer to produce a tip mask of square or circular shape. During a subsequent etching process, the tip mask was undercut to form a silicon post underneath. The silicon etching was a combination of isotropic and anisotropic plasma etching. Extended etching formed a sharp tip with the cap detached. Subsequent thermal oxidation at  $1100^\circ\text{C}$  forms a silicon oxide layer incorporating the tip. A cantilever was lithographically formed on the silicon oxide layer and finally re-

leased by removing the silicon substrate in a KOH solution. When a protruding tip is used as a mold, the molded tip faces in the opposite direction of the silicon substrate, which allows the substrate to be used to form a handling chip. An oxidation sharpening technique can also improve the geometry of convex-molded tips [50, 51]. This technique is based on an experimental study showing that the oxide growth is about 30% slower at silicon step edges than on flat surfaces at temperatures ranging between 900 and 950 °C [50, 51]. The effect is related to the stress-induced diffusion anisotropy of oxygen in silicon oxide, which allows oxidation sharpening to be used both for sharpening concave and convex silicon molds. The low temperature during the oxidation process is important, since at above 950 °C silicon oxide suffers a softening and flow, thus eliminating the stress and the diffusion anisotropy.

As for the materials for a cantilever/tip structure other than silicon oxide, single-crystal silicon doped with boron was used [52]. Also, a silicon nitride layer deposited onto a convex mold was reported [53].

Instead of thin film cantilevers, whole parts of the structure (i.e. tips, cantilevers and handling chips) can be micromachined entirely out of bulk silicon. In the scheme reported by Wolter and coworkers [31], the fabrication was done by etching a (100) silicon wafer through a rectangular etch widow in a mask layer on the reverse side until a thickness of twice the desired thickness of the cantilever remained. The cantilever was subsequently defined on a mask layer on the front side of the wafer, followed by resumed KOH etching until both sides met. The tip integration was achieved with a precursor and undercut. The thickness of the cantilever was controlled by the etching time in KOH. Accurate geometry control by timing the etching is generally impeded by the following factors: (a) the etching is not uniform on a wafer due to stirring-induced flow, liquid flow induced by bubble generation and strong proximity effects, and (b) the etch rate cannot be precisely controlled on every batch. Hence, etch stop techniques, such as boron doping [54, 55] and buried oxide [56, 57], were pursued to precisely define the cantilever thickness.

The molding techniques are particularly important for fabricating tips and cantilevers out of materials hard to pattern directly, such as diamond, silicon carbide, platinum, silicon elastomers, resins, etc. Some of these cases will be treated in more depth in the following sections.

Sharp integrated tips are essential in many SPM-based applications including lithography and manipulation of nano-objects in order to produce smaller nanopatterned or assembled structures. For example, such tips integrated on cantilevers allowed the manipulation of single molecules, and measurements of intermolecular [58–60] and intramolecular [61–63] forces. Force spectroscopy with SPM was typically achieved by functionalizing a tip with a partner suitable for specific interaction with a target molecule bound onto a substrate. When the tip and substrate were brought into contact, the molecular partners interacted. Subsequently, the cantilever was retracted to stretch the target molecule. Mechanical properties of the intermolecular bond established between partners were identified for biomolecular combinations including biotin–streptavidin, antibody–antigen, complemen-

**Tab. 4.2.** Types of fabrication methods for tip integration on cantilevers.

Fabrication type	Notes	Reference
Molding on a pyramidal pit	monolithic tip/cantilever	48, 83
	hybrid tip/cantilever	45, 47, 77
Molding on a convexity	pyramidal convexity	20, 53
	conical convexity	91
Monolithic etching	doping for etch stop	20, 54, 55
	buried oxide for etch stop	56, 57

tary strands of DNA and interactions between proteins. By stretching molecules bound between a tip and a substrate, unfolding events were measured to determine rupture forces associated with various numbers of base pairings [61, 62]. Many applications in SPM force microscopy may be found in the literature [26].

The fabrication methods of the aforementioned types of cantilevers with integrated tips are summarized in Tab. 4.2. In the following sections we discuss how microcantilevers with integrated tips have been used for nanofabrication and manipulation.

#### 4.2.2

#### **Cantilever Probes for Nanopatterning**

Tips integrated on microcantilevers may function as pens or quills, to locally deliver molecules previously present on the tip surface. The tip sharpness allows sub-100 nm patterning with various molecular species. The domain becomes relevant for life sciences if these molecules achieve a local functionalization of the surfaces, such that specific biochemical experiments can be conducted at these length scales. DPN is a direct-write lithographic technique which uses AFM tips to locally deposit materials on a variety of surfaces [13, 30]. The deposited material and the substrate usually have to be paired, such that a chemical reaction occurs upon delivery, or a SAM is formed, so that a reading is possible using the same AFM technique. In some cases, this reaction or SAM formation is not needed, such as the case of simple patterning with fluorescent dyes, when the reading can be achieved optically. In the DPN technique, the species form a thin molecular layer on the tip surface, such that the tip geometry is not significantly altered. When the tip is placed in contact with a target surface, the molecules migrate from the tip onto the surface and the time of surface contact directly correlates with the amount of materials transferred. DPN was originally reported to pattern gold surfaces with a solution of alkanethiols [13], and its applications have been subsequently extended

to patterning surfaces with versatile types of materials such as biomolecules [14, 15, 64], polymers [65], small organic materials [66], sol precursors [67] and metal salts [68]. One of the advantages of the DPN technique is that biomolecules, such as DNAs or proteins, can be patterned both by direct-write and indirect assembly [14, 15, 69–72], which can be utilized to build nanoscale biomolecular sensor arrays with higher sensitivity and selectivity due to much smaller sample volumes. For example, modified ssDNAs with a thiol group on one end were patterned on a gold surface and used to capture complementary DNA sequences tagged with nanoparticles [14]. In this way a pattern of gold particles could be assembled (bottom up) on the surface, in a completely different way than by thin film deposition and etching or lift-off (traditional top-down techniques). Feature sizes ranging from a few micrometers to less than 100 nm were achieved.

The water meniscus formed by capillary condensation was suggested as the mechanism of molecular transfer from a tip to a substrate in DPN and the formation of such a meniscus was recently confirmed using an environmental scanning electron microscopy (SEM) technique [73]. Once transferred to the substrate, the molecules spread across the surface depending on the humidity, temperature, reactivity of the ink with the substrate and contact radius of the tip. Assuming the environmental conditions and types of ink and substrate are optimized, the patterning of small feature sizes is critically dependent on the radius of curvature of the tips integrated on AFM cantilevers. The most commonly used probes in the DPN technique are made of silicon nitride with integrated pyramidal tips, which are typically fabricated using the pyramidal-pit-molding technique [45]. For higher resolution of DPN writing, sharper tips improved by the oxidation-sharpening technique [49] are usually employed. The dimensions of the cantilevers meet the reported range of desired force constants of the cantilever  $0.03\text{--}0.3\text{ N m}^{-1}$  [74].

Once a tip is coated with molecules of interest, patterning is typically controlled by commercially available AFM instruments to precisely deposit desired amounts of molecules at controlled locations. DPN writing has been typically performed with a single probe; however, patterning large areas with a single tip, due to its serial nature and limited AFM scan size, is very inefficient. In an effort to improve the throughput of the DPN technique, the feasibility of parallel DPN patterning with a commercially available tip array was demonstrated in a commercially available AFM [74].

Furthermore, linear arrays of high-density probes with integrated tips for DPN were microfabricated [19, 20]. Two types of DPN probe arrays were developed using surface micromachining techniques. The first type, or type-1 probe array, was made out of thin-film silicon nitride using the molding technique with a protruding tip, whereas the second type, or type-2 probe array, was fabricated from heavily boron-doped silicon (Fig. 4.2). The type-1 probe array consists of 32 straight probes in a 1-D arrangement with the space between consecutive probes being  $100\text{ }\mu\text{m}$ . The dimensions of an individual cantilever were  $400\text{ }\mu\text{m}$  long,  $50\text{ }\mu\text{m}$  wide and  $0.6\text{ }\mu\text{m}$  thick. The type-2 array had eight probes separated from each other by a

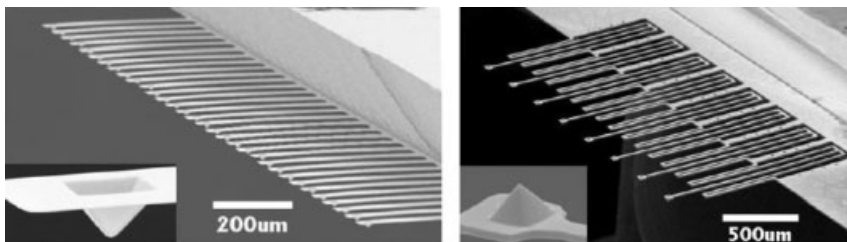


**Figure 4.2.** SEM micrographs of DPN probe arrays with the type-1 (left) and type-2 (right) arrays [20].

spacing of 310  $\mu\text{m}$ , whereas each cantilever was in a multifold configuration. The dimensions are 1400  $\mu\text{m}$  long, 15  $\mu\text{m}$  wide and 10  $\mu\text{m}$  thick.

The fabrication of the type-1 probe started with growing a thin oxide film on a (100) silicon wafer. The oxide film on the front side was patterned to serve as precursor caps for the subsequent etching (Fig. 4.3a). Anisotropic etching in KOH solution undercut the precursors to create tips protruding out of the silicon substrate until the tips had small flat top surfaces (Fig. 4.3b). Subsequently, a thermal oxidation process sharpened the tip and removed the precursor cap (Fig. 4.3c). As a result, uniform sharpness was obtained for the produced tip array. A layer of silicon nitride film was deposited through a low-pressure chemical vapor deposition (LPCVD) process and then patterned to form the shanks of the individual probes (Fig. 4.3d). The cantilevers were released in the ensuing anisotropic wet etching in ethylene-diamine pyrocatechol (EDP) solution at 95  $^{\circ}\text{C}$  (Fig. 4.3e).

The fabrication of the type-2 probes started from a silicon wafer having two extra layers on the top, consisting of a 10- $\mu\text{m}$  layer heavily doped with boron and a 10- $\mu\text{m}$  silicon layer grown epitaxially on top of the doped layer. The wafer was thermally oxidized to form a 500-nm oxide layer, from which tip precursors were lithographically patterned (Fig. 4.4a). Tips were created from the epitaxial silicon layer by underetching the silicon oxide precursor caps (Fig. 4.4b). Thermal oxidation followed to sharpen the tips (Fig. 4.4c). Another layer of oxide film was formed to protect the front side during the subsequent etching (Fig. 4.4d). The bulk silicon substrate was etched away using EDP until the boron-doped etch-stop layer was reached (Fig. 4.4e). A final reactive ion etching (RIE) process was performed to define the cantilever shape (Fig. 4.4f).

This fabricated array of probes was used to pattern gold surfaces with 16-mercaptohexadecanoic acid (MHA) and octadecanethiol (ODT), and to demonstrate parallel DPN capabilities in a conventional AFM. Only one cantilever was monitored by the optical beam-deflection scheme of the AFM, while the others in the array followed in a passive manner. Eight duplicate copies of patterns with a 60-nm feature size were generated by parallel-writing, while only one cantilever was used for the deflection sensing.

In addition, a linear array of 26 tips was operated in a parallel fashion to deposit patterns of MHA on a gold surface to form a mask for a subsequent gold-etching

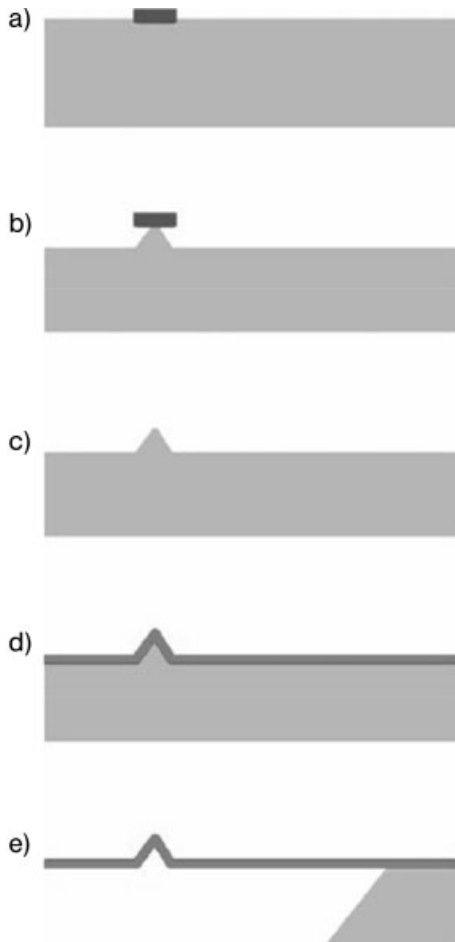


**Figure 4.3.** Fabrication process of a type-1 probe array [20]. The sequence is described in detail in the text.

step [75] (Fig. 4.5). Results obtained demonstrated that the line widths were nearly identical without any writing failure at individual tips (Fig. 4.6). Patterning with an array of three 26-tip arrays produced more than 34 000 dot features in 7.3 min. Furthermore, arrays containing up to 250 probes performed parallel DPN writing in a high-throughput fashion over the centimeter length scale. Patterning of multilayer organic thin films was also demonstrated in parallel fashion [76].

By addressing the throughput issue of DPN with microcantilever arrays, it was envisaged that parallel-probe lithography would lead to many applications in high-resolution patterning over large areas with the aforementioned versatile inks such as biomolecules, organic materials, polymers, sol precursors, metal salts, etc. [30].

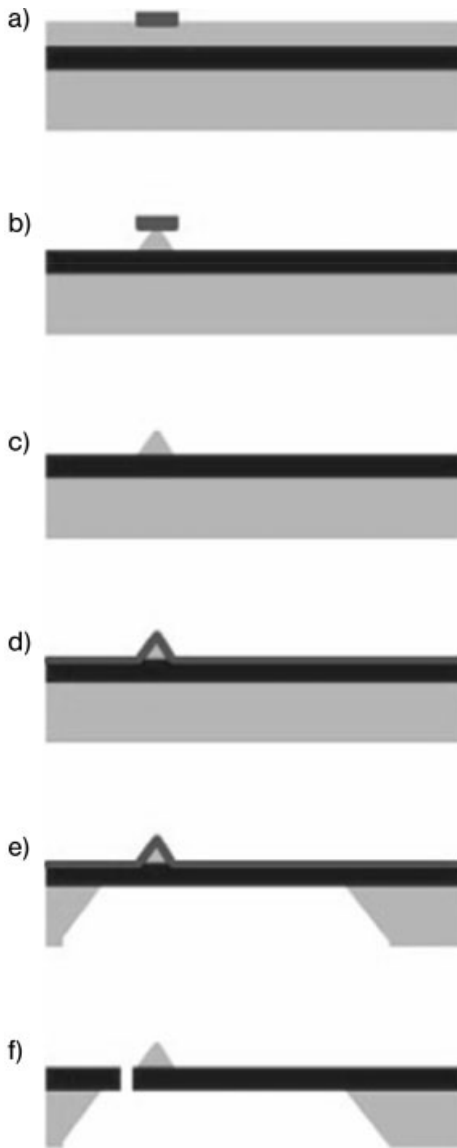


**Figure 4.4.** Fabrication process of a type-2 probe array [20]. The sequence is described in detail in the text.



**Figure 4.5.** Optical micrograph of a 26-pen array [75].



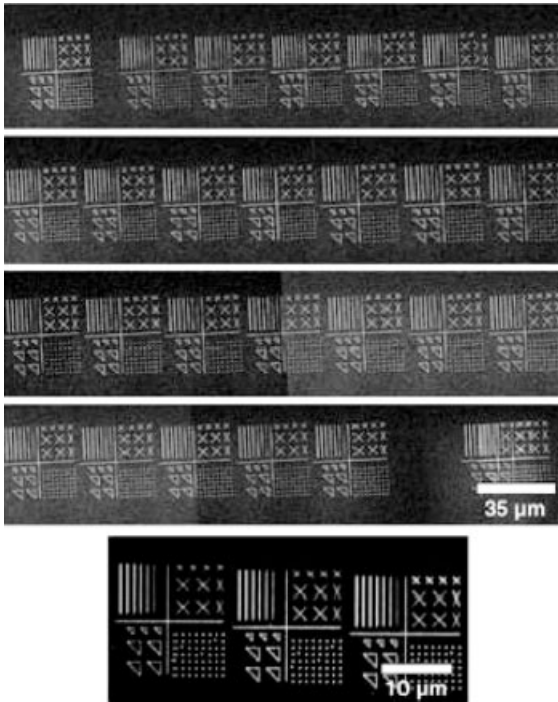


**Figure 4.6.** SEM image of gold patterns generated through the parallel DPN technique using a linear 26-pen array [75].

#### 4.2.3

##### **Elastomeric AFM Probes**

Hard materials, especially silicon nitride, have been the preferred tip materials for DPN patterning probes. However, tips made of soft materials such as silicon elastomers were also reported [77]. Poly(dimethylsiloxane) (PDMS) has been widely used in microcontact printing, and is known to be compatible with a wide range of chemicals and biological media [78]. A molded AFM tip was made of PDMS and integrated at the end of a polyimide cantilever (Fig. 4.7). The microfabricated tip demonstrated DPN patterning capabilities with ODT as ink and achieved dot sizes as small as 330 nm in diameter.

The fabrication sequence of the PDMS probe is presented in Fig. 4.8. A tip mold was made on a (100) silicon wafer using an oxide mask layer via wet etching in EDP (Fig. 4.8a). After the oxide layer was etched, an aluminum film was deposited as a sacrificial layer (Fig. 4.8b). A 10:1 mixture of Sylgard 184 silicone elastomer base and curing agent was coated on the wafer (Fig. 4.8c). Excessive liquid-state PDMS was plowed out using a rubber blade leaving the PDMS only in the pit and curing was performed at 90 °C for 30 min (Fig. 4.8d). A thin polyimide layer was spin-coated over the processed surface and patterned to define a cantilever shape

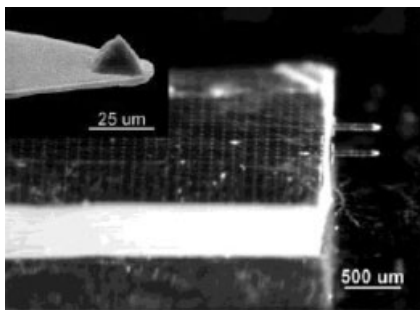


**Figure 4.7.** Optical micrograph of a probe chip with two cantilevers with elastomeric tips. Inset shows a SEM image of the integrated PDMS tip [77].

(Fig. 4.8e). A thick PDMS piece was bonded on the patterned polyimide layer as a handling body (Fig. 4.8f). An aluminum etchant removed the sacrificial aluminum layer to release the cantilever/tip structure without damaging either the PMDS tip (Fig. 4.8g) or the silicon mold, which could be reused after cleaning.

The polyimide cantilever in this example was 400  $\mu\text{m}$  long, 100  $\mu\text{m}$  wide and 4  $\mu\text{m}$  thick. The minimal printed ODT dot diameter was consistent with the PDMS probe radius of curvature of 300 nm.

Another use of PDMS for DPN printing was reported by Zhang and coworkers, who coated commercially available silicon nitride tips with PDMS and used them to pattern surfaces with sub-100-nm resolution [79]. The advantage of using PDMS as the tip material is that it provides higher coating efficiency, especially when the inks are macromolecules such as biomolecules and polymers, for which rich experience is available from the domain of microcontact printing with PDMS stamps [78, 80]. The advantage comes at the expense of a serious decrease in writing resolution, due to the soft nature of the contact between the tip and substrate. In contrast, DPN with silicon nitride tips needed functionalization of the tip surface to improve ink-coating efficiency when used for DNA patterning [14, 81], but achieved 100-nm resolution.

#### 4.2.4

#### **Monolithically Fabricated Conductive Diamond Probes**

Since DPN is performed in contact-mode operation, wear of tips is expected during extended use. Tips made of the aforementioned materials such as silicon nitride, silicon oxide, silicon and PDMS would be good enough for laboratory-level experiments; however, the use of wear-resistant tips is of great importance to probe arrays for high-throughput manufacture of bioassays. Hard materials are typically employed to enhance the wear characteristics and diamond is the hardest known material. Furthermore, tailoring its surface properties would allow diamond to become a platform material to construct bioinorganic interfaces [82].

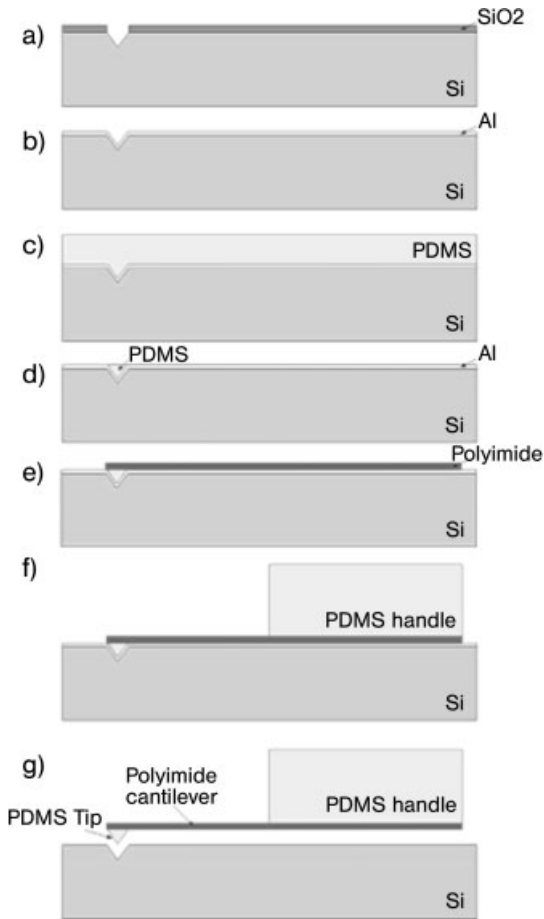


**Figure 4.8.** Fabrication process of the cantilever with an integrated elastomeric tip [77]. The sequence is described in detail in the text.

A wear-resistant probe for contact-mode AFM techniques was fabricated using ultra-nanocrystalline diamond (UNCD) [83]. The all-diamond probe demonstrated molecular writing capability in DPN mode and potential use in scratch-based lithography. The probe was monolithically microfabricated with a pyramidal tip utilizing the molding technique on pits. Electroplating was utilized to form a handling body. The diamond was microfabricated to be either electrically conductive by nitrogen doping or nonconductive. The growth of diamond film was achieved by microwave plasma CVD (MPCVD) using a methane/argon mixture, which also contained nitrogen in the case of nitrogen-doped films [84]. This doped film permits AFM potentiometry and a large variety of conductive AFM techniques [85, 86] with an extended tip life cycle. Furthermore, diamond is chemically and biolog-

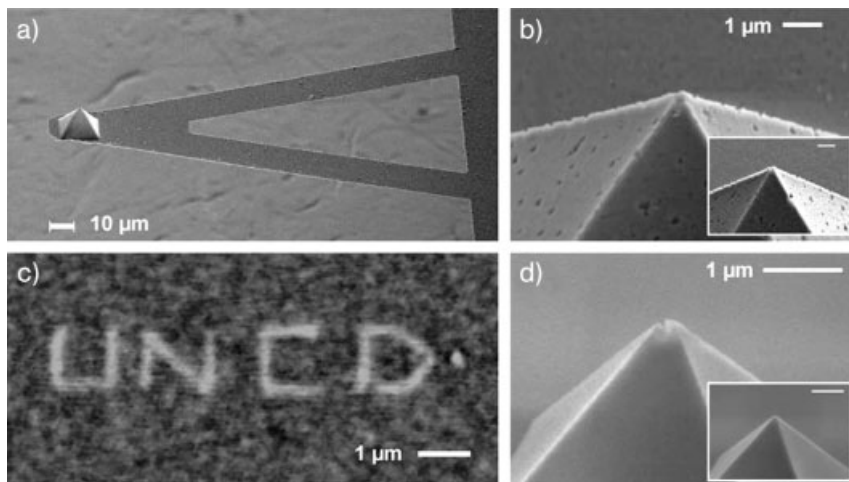


**Figure 4.9.** (a) SEM image of a UNCD cantilever with a tip. (b) SEM image of a UNCD tip after 1 h of scanning on a diamond substrate. Inset shows the tip before scanning. (c) Frictional AFM image of alkanethiol monolayer patterned on a gold substrate by a UNCD tip. (d) SEM image of a commercially available silicon nitride tip after 1 h of scanning with the same parameters used for the UNCD tip in (b). It shows damage at the tip apex; the inset shows the tip prior to the test.

ically inert, and forms an excellent electrode for electrochemical applications. It also has a tunable hydrophobicity that can be achieved by surface functionalization [82].

Two types of cantilevers were fabricated: V-shaped and arrow-shaped. The lengths and thicknesses of both cantilevers were 170 and 0.8–1.4  $\mu\text{m}$ , respectively. The arm width of the V-shaped cantilever was 18.8  $\mu\text{m}$ , whereas the rectangular one was 12  $\mu\text{m}$  wide. The V-shape cantilevers had a stiffness of around 2  $\text{N m}^{-1}$ , and were better suited for contact and tapping mode AFM techniques, while the rectangular cantilevers had a stiffness of around 1  $\text{N m}^{-1}$  and performed well in lateral force imaging, well-suited for imaging DPN patterns. The fabrication started by forming of a thermal oxide on a (100) silicon wafer to be used as a mask in subsequent microfabrication steps and patterning square holes into it lithographically. Pyramidal pits were formed by KOH etching to be used as a molds for the future tips (Fig. 4.10a) and then sharpened by thermal oxidation utilizing the nonuniform growth of the oxide in the pit (Fig. 4.10b). The wafer was immersed in a diamond powder solution in methanol, followed by ultrasonication for uniform seeding. The growth of a diamond layer was achieved by MPCVD using a combination of argon and methane gases, with or without nitrogen gas (Fig. 4.10c). An aluminum layer was deposited by electron beam evaporation and then patterned to define cantilevers (Fig. 4.10d). The UNCD film was etched using the aluminum as a mask by oxygen RIE (Fig. 4.10e), followed by the removal of the aluminum mask (Fig. 4.10f). An etch window was patterned on the reverse side

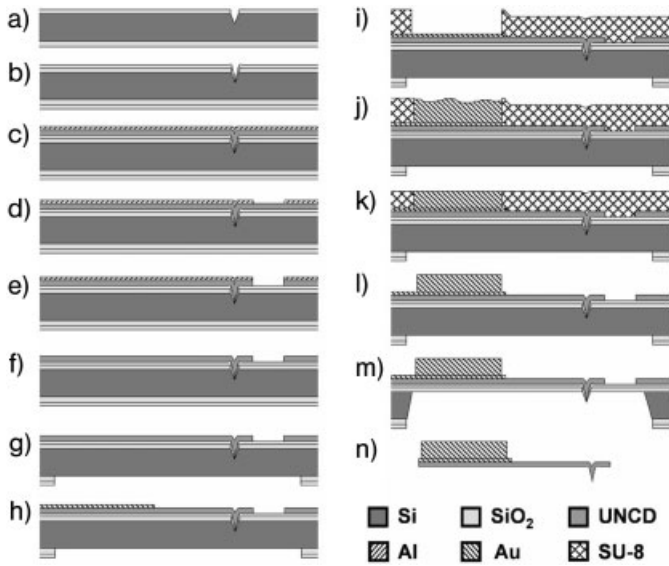


**Figure 4.10.** Microfabrication steps for UNCD probe [83]. Detailed steps are described in the text.

oxide layer for subsequent release of the cantilevers and chips (Fig. 4.10g). A seeding layer for electroplating was deposited and patterned on the front side (Fig. 4.10h). A thick photoresist (SU-8) was spin-coated and patterned to form a mold for the handling body of the chip (Fig. 4.10i). A layer of gold was then electroplated up to 300  $\mu\text{m}$  thickness onto the seed layer to form the chip body (Fig. 4.10j). The top side of the gold was then flattened by polishing (Fig. 4.10k). After removing the photoresist (Fig. 4.10l), the chip was released in KOH solution (Fig. 4.10m).

The DPN compatibility of the diamond probe was tested. A commercial AFM (Digital Instruments; Dimension 3100) was used for the writing test using MHA as ink and gold substrates to write on. Lines produced were around 200 nm wide, whereas the smallest dots generated had a diameter of around 80 nm. In addition to the compatibility with the DPN technique, the UNCD probe demonstrated AFM imaging capabilities of topography and lateral force when used for scanning right after the patterning (Fig. 4.9c). Surface scratch testing was also performed, promising a favorable tool for scratch nanolithography. Furthermore, the scalability of the probes batch-fabricated with the integration of diamond films could lead to 1- and 2-D arrays of probes that could be used for massively parallel DPN-based fabrication of nanostructures. Such probes have the potential to perform DPN for long working times, virtually wear free.

We have described microfabrication aspects of simple microcantilevers in several applications related to the fabrication and manipulation of nanostructures and the detection of minute volumes of substances. Although microcantilevers are relatively simple structures, they have served as powerful tools for such purposes.

However, advanced applications demand more functionality from the devices. In the next section we discuss advanced microcantilevers that allow delivery of fluid materials and suspensions.

### 4.3

#### **Cantilevers with Integrated Micro- and Nanofluidics**

Material delivery in suspension has many potential applications, especially when the materials are macromolecules, such as biomolecules and polymers, nanoparticles, catalysts, and nanotubes. Controlled delivery of such materials would permit the fabrication of complicated nanostructures and nanoelectromechanical systems (NEMS). Also, in life sciences, it is oftentimes required to deliver large-size molecules and it is challenging to carry out scanning probe-based lithography with such molecules if the microcantilevers are not equipped with microfluidic systems. The implementation of micro- and nanofluidics into microcantilevers has been pursued to achieve material delivery in suspension as well as surface patterning with high resolution. Dispensing femtoliter or smaller volumes was achieved with a modified version of a conventional silicon nitride microcantilever [53]. Split-pin-type spotters for the fabrication of gene chips have been further miniaturized by microfabrication [87, 88]. Micro- and nanopipette-based AFM probes were used to deliver minute amounts of liquids [89]. Micropipette arrays with buried microchannels were micromachined for drug injection [90]. A nanofountain probe (NFP) was fabricated and tested, having an on-chip reservoir, cantilevers with embedded microchannels and high-resolution dispensing tips [91, 92].

In this section we describe microfabrication techniques for micro- and nanofluidic cantilevers and their applications along with their potential impact in life sciences.

#### 4.3.1

##### **Apertured Pyramidal Tips**

The on-demand dispensing of single liquid attoliter droplets using AFM probes was demonstrated with modified tips containing a simple orifice. Meister and co-workers [18] created an aperture at the apex of a commercially available probe using focused ion beam (FIB) milling. The hollow reverse side of the pyramidal tip was used as a reservoir to store the liquid. Flow of the liquid was initiated simply by contacting the pipette with a surface and stopped by lifting it from the surface. Created features had dimensions of 100 nm and below. As the FIB process is serial in nature and precludes high-volume production, microfabrication techniques were employed to build directly apertured pyramidal tips integrated on cantilevers [53]. The device has potential applications in nanofabrication for the direct deposition of versatile materials, including biomolecules, catalysts, etch resists and nanoparticle suspensions. With the reservoir on the reverse side, extended writing was possible without reloading.

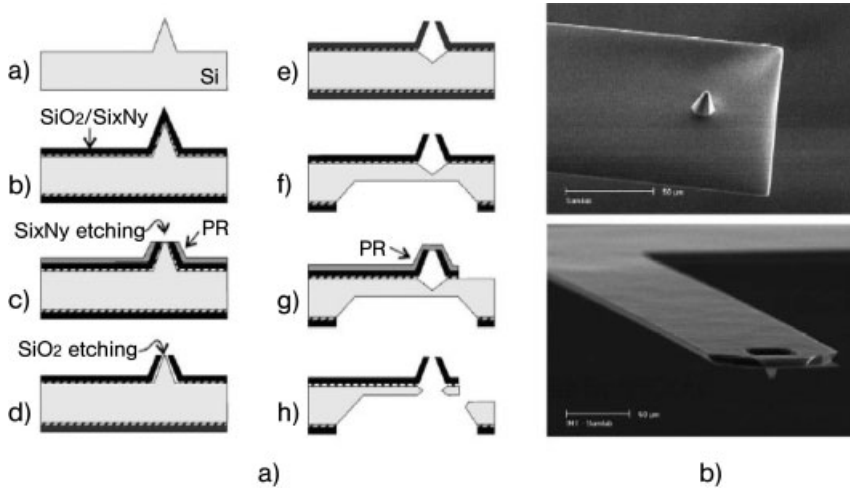


**Figure 4.11.** Microfabrication process for cantilevered probes with apertured tips [53]. Detailed steps are described in the text.

The fabrication process for the cantilevers with the apertured tips is illustrated in Fig. 4.11. The probes consisted of a hollow silicon nitride tip on a compound cantilever of silicon and silicon nitride. The molding technique on a pyramid was employed to integrate the tip on the cantilever. A molding tip was first fabricated on a silicon (110) wafer by underetching a precursor cap (Fig. 4.11A-a). The wafer was thermally oxidized, followed by LPCVD deposition of a silicon nitride layer to form a mold (Fig. 4.11A-b). Photoresist was spin-coated in such a manner that the tip apex was uncovered. With this opening at the tip apex, only that portion of the silicon nitride layer was etched by RIE (Fig. 4.11A-c). Through the opening of the silicon nitride layer, hydrofluoric acid etched the underlying silicon oxide layer (Fig. 4.11A-d) and, subsequently, KOH etching removed the underlying mold pyramid to produce an empty space surrounded by a pyramidal silicon nitride shell (Fig. 4.11A-e). A combination of photolithography and RIE patterned the silicon nitride and silicon oxide layers on the reverse side to open an etching window on the reverse side (Fig. 4.11A-f), while a cantilever was defined on the compound layer from the front side (Fig. 4.11A-g). Etching in KOH solution not only released the cantilever, but also opened a hole on the silicon portion of the hollow space of the tip to be used as a reservoir (Fig. 4.11A-h). The final thickness of the cantilever was 7–8  $\mu\text{m}$ .

The patterning of the microfabricated probe was tested using alkanethiols to be deposited on gold substrates as well as Cy3 fluorescent dye in glycerol to be deposited on glass. The loading of the hollow probe was done by hand pipetting under an optical microscope. The probe had a pre-patterned loading area to avoid wetting the entire cantilever while loading the solution. A lower limit on the size of the deposition was given by the diameter of the aperture (around 100 nm to 1.5  $\mu\text{m}$ ). In

addition, it was a challenge to routinely load ink into the reservoir island located at the end of the cantilever. Furthermore, evaporation constituted a major problem in this approach, preventing long-term writing.

#### 4.3.2

#### Open-channel Cantilevered Microspotters

In microspotting technologies, a biochemical sample is loaded into a spotting pin by capillary action, and a small volume is transferred to a solid surface by physical contact between the pin and the solid substrate [93]. Other than microspotting pins, capillaries or tweezers can act as a printhead of biochemical samples. Printheads are moved by an  $xyz$  motion control system and brought into a contact with a surface to transfer pre-made substances. In an effort to fabricate massively parallel, high-density DNA, protein and cell chips, microfabricated cantilevers have been used as printheads (Fig. 4.12). Microcantilever spotters were used for depositing biological samples [87, 94] and nanoparticles [95].

Arrays of microcantilevers were also produced by microfabrication techniques. Deposition was achieved by direct contact between the cantilevers and the surface by capillary transport. An electrowetting technique for controlling surface tension was applied for the loading of the liquid. A passivated aluminum layer integrated on the cantilevers was employed as an electrode for the electrowetting. The sample loading required a droplet of a solution containing biological samples to be placed on a conductive solid substrate. After the end of cantilevers was dipped into a droplet of liquid to be deposited, an electric field was applied between the electrode and the substrate to increase the affinity of the liquid. The electric-field introduced a modified charge distribution that changed the free energy, causing the liquid to spread and wet the surface of the cantilevers [96]. As a result, the height of liquid rise on the cantilever surface was increased.

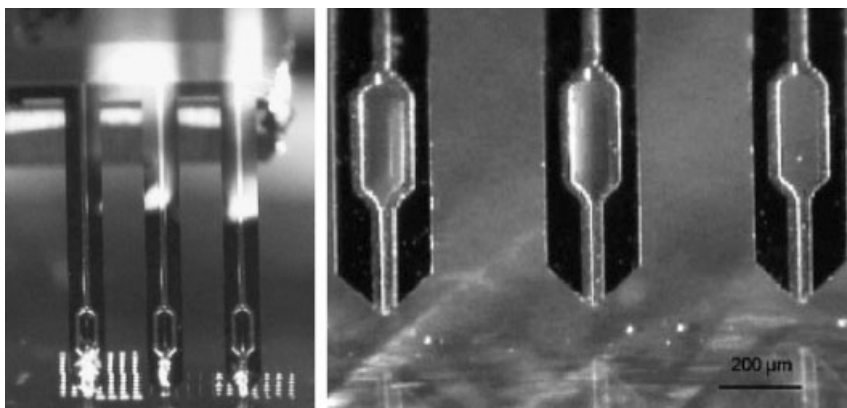


**Figure 4.12.** Optical photographs of microfabricated cantilever spotters [87, 95].



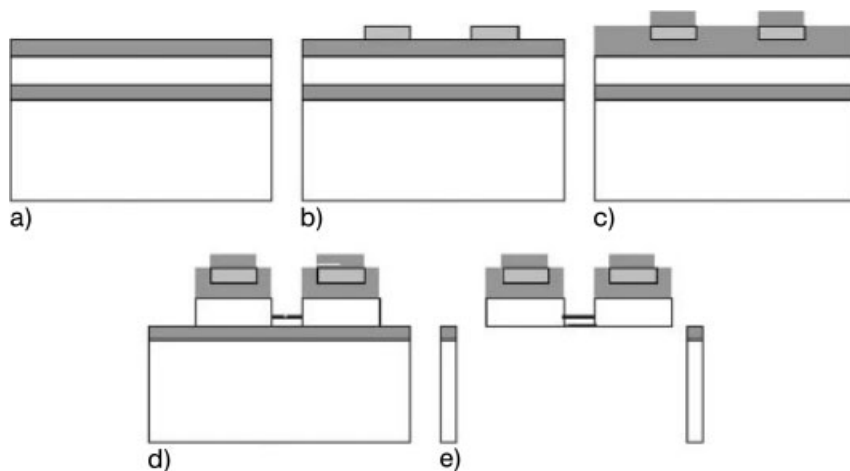


**Figure 4.13.** Microfabrication process of cantilevers [87]. Detailed steps are described in the text.

Figure 4.13 illustrates the fabrication steps of the cantilever microspotter as described by Belaubre and coworkers [87]. The microfabrication used a silicon-on-insulator (SOI) substrate with a 5- $\mu\text{m}$  thick top silicon layer. First, a layer of low-temperature silicon oxide (LTO) was deposited by LPCVD (Fig. 4.13A). Aluminum electrodes were defined by a lift-off process (Fig. 4.13B). A second layer of LTO was deposited for passivation purposes (Fig. 4.13C). Cantilever shanks were defined by photolithography to be used as a mask for the following etching of the LTO layers by RIE. Subsequently, the top silicon layer of the SOI wafer was etched by another RIE step (Fig. 4.13D), in which microchannels and microreservoirs were formed on the cantilevers. Finally, the reverse side of the wafer was removed through etch windows in a deep RIE step. Etching was stopped by the buried oxide layer of the wafer. The silicon oxide layer was then etched from the reverse side by RIE to release the cantilevers (Fig. 4.13E). Arrays of cantilevers, with a spacing of 450  $\mu\text{m}$ , were microfabricated, where each cantilever was 2 mm long, 210  $\mu\text{m}$  wide and 5  $\mu\text{m}$  thick.

The microfabricated cantilevers were used to pattern a glass slide with 1-pL volumes of a solution containing Cy3-labeled oligonucleotides (15mers) [94]. In addition, protein, anti-goat IgG (rabbit), microarrays were generated on a glass slide coated with dendrimer molecules as crosslinkers. With both molecules, 30- $\mu\text{m}$  diameter spots were obtained. It was also demonstrated that two different biological samples were deposited with the same cantilevers using a cleaning procedure, in which no cross-contamination was observed.

Furthermore, microspotter cantilevers were used to deposit functionalized amorphous silica nanospheres on coated silicon surfaces by Leichle and coworkers [95]. Colloidal solutions, containing poly(ethylene glycol) (PEG)-600 and aminopropyltriethoxysilane (APTS) nanoparticles with diameters of around 300 and 150 nm,

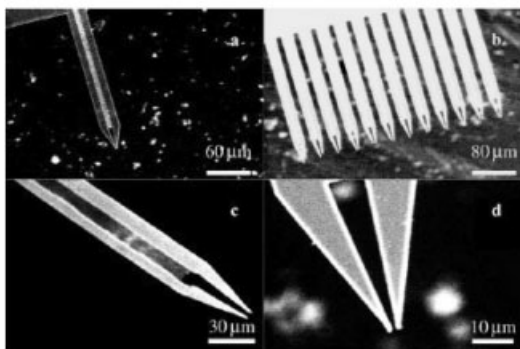
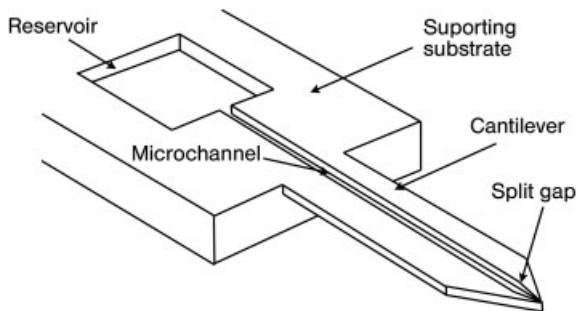


**Figure 4.14.** Schematic of the quill-type cantilever and SEM images of fabricated cantilever [88].

respectively, were deposited on surfaces to form spots of various diameters ranging from around 10 to more than 100  $\mu\text{m}$ .

The minimum spot size writable with a common cantilever spotter is around 10  $\mu\text{m}$  in diameter. To achieve higher resolution, cantilever microspotters were further miniaturized. A microcantilever-based tool with a 1- $\mu\text{m}$  wide split gap at the end (Fig. 4.14) has been reported by Xu and coworkers [88]. Named the surface patterning tool (SPT), this device had integrated on-chip sample reservoirs and fluid transportation microchannels, which addressed limitations inherent in the use of the conventional AFM probes. An SPT consisted of a cantilever with a split gap at the end, a reservoir on the handling chip, and a 1- $\mu\text{m}$  deep transportation microchannel connecting the gap and the reservoir. Sample loading was carried out by filling the reservoir with sample solutions as well as by dipping the cantilever end into sample fluid. These new designs, dedicated to biomolecular patterning, allowed reliable patterning of large molecular species and reduced reloading requirements.

The length of the SPT cantilevers ranged between 200 and 300  $\mu\text{m}$ , and the width between 20 and 40  $\mu\text{m}$ . The split gap was around 1  $\mu\text{m}$  wide and around 40  $\mu\text{m}$  long. At the fixed end of the cantilever, a 10- $\mu\text{m}$  deep rectangular reservoir was located on the handling substrate. The depth and width of the microchannel

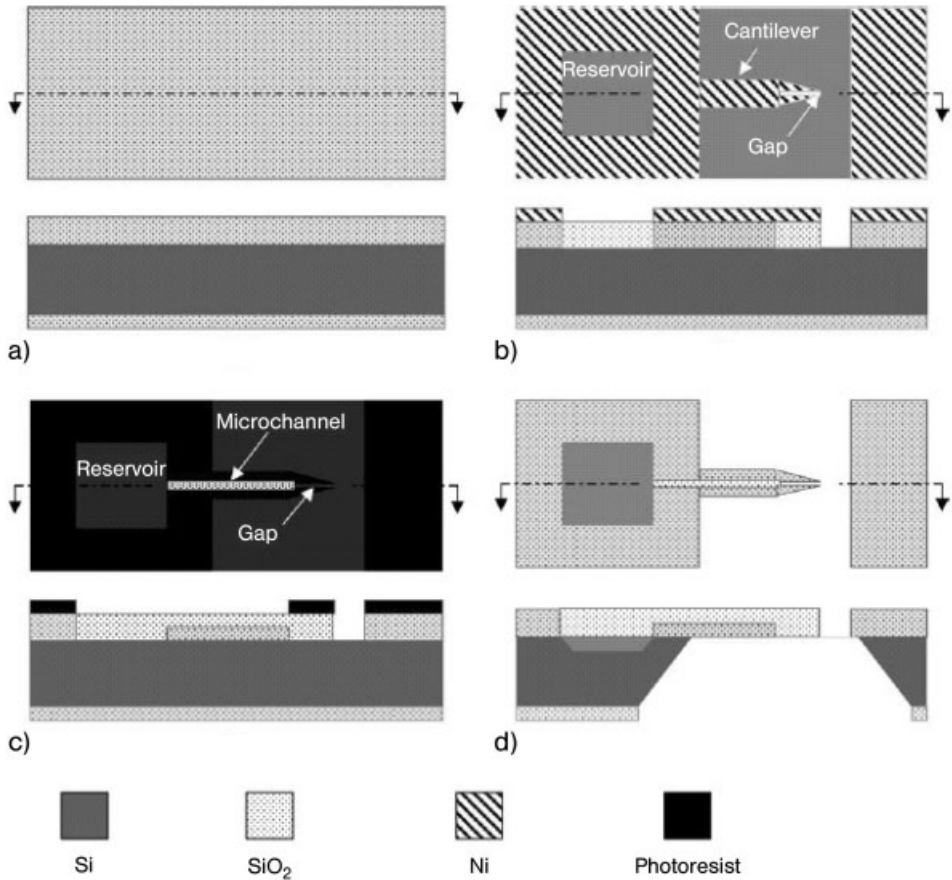


**Figure 4.15.** Schematic diagram of the microfabrication processes for the quill-type SPT [88].

were 1 and 1–10  $\mu\text{m}$ , respectively. Silicon oxide was selected as the material for the cantilever due to its advantages in terms of mechanical properties, fabrication requirements and biocompatibility.

The fabrication steps of the SPT are shown in Fig. 4.15. A (100) double-side polished silicon wafer was thermally oxidized to have a thickness of 2–3  $\mu\text{m}$ . The front side oxide layer was lithographically processed to define a cantilever shank, a split gap and a reservoir. In order to fabricate the cantilever with the 1- $\mu\text{m}$  gap using conventional photolithography, a nickel layer was electroplated on top of the oxide to be used as mask, using a negative photoresist pattern. The oxide layer was then anisotropically etched by RIE with a gas mixture of  $\text{CHF}_3$  and  $\text{SF}_6$  (50:1  $\text{cm}^2$ ) and power of 50 W at 50 mTorr pressure. After patterning the cantilever and the gap, a 1- $\mu\text{m}$  deep microchannel was etched by RIE. Finally, a window was patterned on the backside layer of  $\text{SiO}_2$ , followed by releasing the cantilever in KOH solution of concentration 35 wt%, at 80 °C.

Testing of the fabricated SPTs was performed using a dedicated commercial instrument called a NanoArrayer (BioForce Nanosciences, Ames, IA). This instrument was equipped with a precision motion control system and an environmental chamber. Although this instrument used an optical lever deflection scheme employed in an AFM, it did not scan or acquire images. SPTs were mounted to form a  $12^\circ$  angle with the deposition substrates such that only the tip end was in contact with the substrate. Patterning was demonstrated using Cy3–streptavidin in a standard protein patterning application [88]. The Cy3–streptavidin sample solution was loaded into the reservoir using a micropipette, prior to mounting the SPT into the NanoArrayer. Spots were patterned on a dithiobis(succinimidyl undecanoate) (DSU) monolayer coated on a gold surface. Fluorescence microscopy was utilized to analyze the patterned features. A  $10 \times 10$  array of spots with a diameter of 2–3  $\mu\text{m}$  was routinely obtained. With a single loading, more than 3000 spots could be printed in about 1 h. It was also demonstrated that quantum dots conjugated to streptavidin could be deposited in patterns of lines and spots using the SPT [97]. Those features had line widths of around 150 nm to 7  $\mu\text{m}$  and spot diameters of 3–5  $\mu\text{m}$ .

Multiple cantilever-based SPTs for multiplexed biomolecular arrays were also reported by Xu and coworkers [98]. Their SPT featured a 1-D array of microcantilevers and a corresponding microfluidic network that was capable of transporting multiple fluid samples from macro-scale reservoirs located on the SPT substrate through micro-scale channels to the distal end of the cantilevers. Five cantilevers and five reservoirs were arranged in a chip so that multiple biological samples could be transferred from the reservoirs to the SPT cantilever array. The overall size of an SPT chip was  $3 \times 6 \text{ mm}^2$ . Each cantilever was 250  $\mu\text{m}$  long, 30  $\mu\text{m}$  wide and 2  $\mu\text{m}$  thick, and consecutive cantilevers were separated by a spacing of 50  $\mu\text{m}$ . The microchannel on each cantilever was 15  $\mu\text{m}$  wide and 1  $\mu\text{m}$  deep.

The fabrication steps for the multiple-cantilever SPT are illustrated in Fig. 4.16. A double-side polished (100) silicon wafer was first thermally oxidized to form a 2.2- $\mu\text{m}$  thick oxide film. The oxide layer on the front side was photolithographically patterned to define the cantilevers, reservoirs and channels, and etched by RIE (Fig. 4.16a). Subsequently, a 1- $\mu\text{m}$  deep microchannel was etched on the cantilevers by overlay photolithography and follow-up RIE (Fig. 4.16b). In the next step, the oxide layer on the reverse side was patterned to form an etching window and the cantilevers were released by KOH etching (30 wt%). A wafer holder was used to protect the front side oxide pattern during the KOH step. Finally, once leakage began to occur through the wafer holder in the KOH etching bath, the wafer was released from the hold and dipped in a 40 wt% KOH solution to form the reservoirs and microchannels (Fig. 4.16c).

The multiple ink loading and patterning were tested using two types of fluorescent proteins: Cy2–donkey anti-goat IgG and Texas Red–donkey anti-rabbit IgG. These two proteins were diluted in phosphate-buffered saline (PBS) and alternatively loaded into the five reservoirs by hand pipetting. The solutions transferred from the reservoirs to the distal end of each channel by capillary action and the fluids were confined inside the microchannels without observed cross-contamination. A DSU/gold surface was patterned to generate  $10 \times 10$  multiple

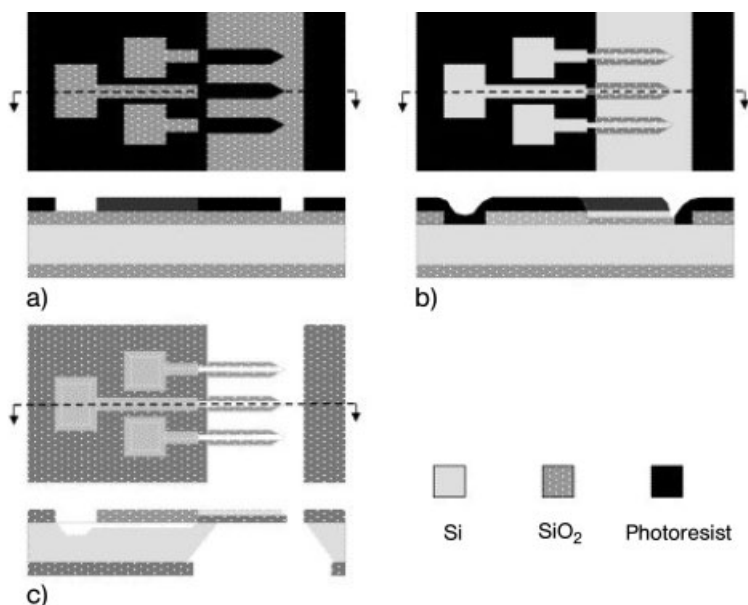


Figure 4.16. Fabrication steps for an array of SPT cantilevers [98].

ink dot arrays, with the mean spot diameter being about 12  $\mu\text{m}$ . The SPTs generated biological arrays with a routine spot size of 2–3  $\mu\text{m}$ . Several thousand spots could be printed without reloading. It was reported that the minimum spot size of the SPT was mainly limited by its gap width. The gap size can be further reduced with a higher-resolution lithography technique.

The SPTs have open microchannels integrated on cantilevers. This type of open channel has advantages of being clog-free, and allowing easy cleaning and simple microfabrication. However, such open microfluidic elements including microchannels and reservoirs are prone to cross-contamination via vapor by different types of samples, especially when loaded in arrays of cantilevers [99]. Also, evaporation may be critical in some applications, although its rate can be reduced with environmental conditioning. Enclosed microchannels are beneficial in such cases, although they are relatively difficult to microfabricate and the clogging issue needs to be addressed. Pipettes are conventionally used microfluidic devices with enclosed channels. Microneedles with embedded microchannels were also demonstrated to deliver liquid materials. In the following subsections, microcantilever devices with enclosed microchannels are described.

#### 4.3.3

##### Closed-channel Cantilevered Nanopipettes

Pipettes are essential tools in biomedical applications in order to precisely manipulate and deliver fluidic samples, and they have been miniaturized for applications

of local delivery of liquid/gaseous materials at the nanometer scale. It was reported that apertures as small as 3 nm at the tip with outer diameters at the tip of 10 nm were produced [89]. Such nanopipettes permit delivering or probing liquid samples in small volumes. In addition to delivering precise volumes of samples, accurate positioning is pivotal in biomedical applications. Nanopipettes were used in AFM for precise positioning to deliver liquid or gaseous materials on surfaces for localized chemistry [89, 100–104]. Nanopipette-based probes were used to deliver minute amounts of materials such as Cr etchant [89], photoresist [103], DNA [104], proteins [100] and enzymes [101, 102]. They are capable of continuous sample feeding through the capillary. In certain applications, nanopipettes were bent to have a cantilevered portion so that they could be used in AFM. The deflection, or contact force, of such cantilevered micropipettes was regulated by the AFM optical beam-deflection scheme, whereas straight nanopipettes, not compatible with the optical deflection scheme of AFM, employed other techniques such as shear-force feedback control [103] or an electrical current between the pipette and solution [104].

Protein solutions readily flowed through cantilevered nanopipettes to be directly deposited on a surface with dot diameters of around 200 nm [100]. A proteolytic enzyme was used to locally break a layer of bovine serum albumin (BSA) [101, 102]. Photoresist was delivered through the aperture formed at the end of a pulled nanopipette [103]. In this case, direct-write with photoresist replaced conventional photolithographic steps including spin-coating, mask alignment, exposure to UV light and developing. A nanopipette was used in a solution environment, whereas the tip-sample separation was controlled by the feedback signal of the ionic current established between two electrodes – one in the pipette and the other in the solution [104].

Production of cantilevered pipettes is based on pulling quartz capillary tubes by computerized systems called micropipette pullers. These pullers apply a controlled axial load on the capillaries, while heating them locally with a flame, electrical solenoid or, for better control, a laser beam. Two pipettes can be obtained after the pulled capillary breaks. A desired bending can be produced to make the probes usable in scanning probe systems [105, 106] (see Fig. 4.17).

The bending can be obtained close to the tip by heating the micropipette over a microflame. The operation can be performed in specialized tools called bevelers. Such cantilevered glass micropipettes can be coated with metals in order to allow the optical deflection detection scheme of AFM to function (Fig. 4.17). The diameter of the cantilevered portion of the micropipette can be around 12  $\mu\text{m}$  and the cantilever length around 300  $\mu\text{m}$ . Such dimensions of the glass cantilevers resulted in resonance frequencies up to 400 kHz and force constants ranging from tenths to tens of Newtons per meter. It was also reported that a filament made of metal thread was installed inside a pipette to mechanically strengthen the pulled tapered region [103]. The filament improves the wetting characteristics of the inner wall of the pipette such that the liquid can spontaneously fill the pipette lumen.

Taha and coworkers [100] reported micropipette printing of a yeast protein onto aldehyde-coated glass slides, in which an aldehyde group on the surface reacted

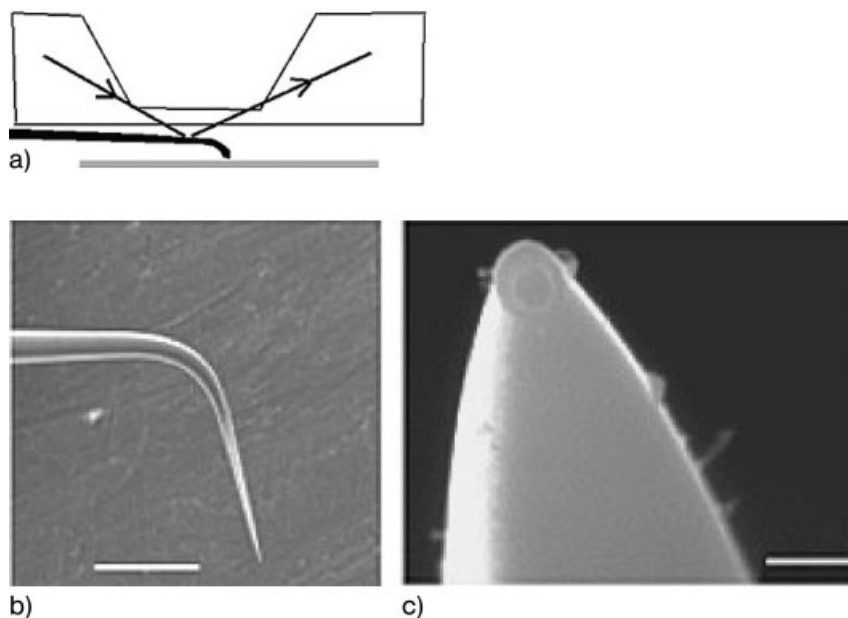


**Figure 4.17.** (a) Experimental setup of the cantilevered nanopipette in an AFM. (b) SEM image of a cantilevered nanopipette. Scale bar: 100  $\mu\text{m}$ . (c) Close-up of the tapered end of a 50-nm aperture nanopipette. Scale bar: 500 nm [101].

preferentially with the primary amino group of the N-terminus of the protein for immobilization as described in Ref. [23]. A solution of the protein in PBS 100  $\mu\text{M}$  with 10% glycerol to keep the proteins hydrated was prepared and manually loaded from the large end of the pipette with a syringe. The capillary action delivered the solution to the end of the pipette. Subsequently, the nanopipette deposited a line of the protein which was around 500 nm wide and around 40 nm thick. The experiment was performed at room temperature without humidity control. The same type of pipette was also used to pattern dots and lines of green fluorescent protein (GFP) on BSA-coated glass slides, resulting in dot diameters of around 250 nm and line widths of around 450 nm. This method demonstrated that the feature size can be made 1000 times smaller than with conventional spot arrays.

A nanopipette filled with a solution of DNA or protein was utilized by Bruckbauer and coworkers [104] to pattern surfaces in an aqueous environment with a voltage applied between the pipette and surface. This method was based on scanning ion conductance microscopy (SICM) [107]. In this report, a pipette was filled with a solution of 100 nM DNA or protein and the pipette tip was inserted into a bath of ionic solution. The ion current was used to control the dispensing rate of molecules as well as the tip-to-surface distance. Spots of ssDNA labeled with Rhodamine Green were deposited on a streptavidin-coated glass surface and the mea-

sured full width at half-maximum (FWHM) was  $830 \pm 80$  nm. Spots of Protein G were also patterned onto a positively charged glass surface utilizing electrostatic interaction as an immobilization mechanism. Measured feature sizes were 1.3  $\mu\text{m}$ .

Although pulled micropipettes are capable of delivering small volumes of samples with precise positioning, it is a challenge to accomplish reproducibility and scalability when expansion to arrays is required, which is essential for tools in bio-nano applications, e.g. to fabricate microarrays or nanoarrays. Micromachined pipettes in the following section will give an idea how microcantilevers with channels can be microfabricated to address the reproducibility and scalability of conventionally produced micropipettes.

#### 4.3.4

#### **Micromachined Hypodermic Needle Arrays**

Microcantilevers with closed microchannels were microfabricated to be used as micropipettes and microneedles for drug injection applications. The applications of micromachined cantilevered needles are different from the microcantilevers discussed in the preceding sections in terms of size (larger) and functionality (not for surface patterning). However, they are integrated with microchannels to effectively deliver biofluid into a body via injection and the microfabrication approach is worth discussing because it can be utilized to create embedded microchannels in microcantilevers. Microcantilever-based hypodermic needles are sometimes referred to as in-plane microneedles since they are fabricated in the plane of a silicon wafer as contrasted to out-of-plane needles, where short microneedles are microfabricated normal to the plane of the wafer surface [108, 109]. Microcantilever-based needles have been fabricated using several structural materials such as silicon [110, 111], polysilicon [112] and metals [90, 113].

Micromachined pipette arrays were reported by Papautsky and coworkers [90]. They have integrated microchannels on cantilevers as well as dispensing apertures at the end of the cantilevers. The cantilevers were 1.5 mm long and 400  $\mu\text{m}$  wide, and the microchannels had an inner cross-sectional area of  $400 \times 30 \mu\text{m}^2$  ( $W \times H$ ). For fabrication, a (100) silicon wafer was doped with boron to form a 4–6- $\mu\text{m}$   $p^+$  layer, which later served as an etch stop. Then, a silicon nitride layer was deposited by plasma CVD to be used as a mask during the following anisotropic etching in KOH (Fig. 4.18a). Next, a palladium layer was selectively electroplated onto the silicon wafer to form the undersides of the needles (Fig. 4.18b). A thick photoresist layer (P4620) was deposited and photolithographically patterned as a sacrificial layer to define the inner lumen of the needles (Fig. 4.18c). A palladium layer was sputter-deposited to conformally cover the patterned thick photoresist layer, this was followed by the electrodeposition of a thin additional layer of palladium on top of the sputtered metal. The primary structural material was then electroformed to complete the top and side walls of the pipette (Fig. 4.18d). The sacrificial photoresist was dissolved by immersing the wafer in acetone (Fig. 4.18e). The  $p^+$  membrane was removed by plasma etching with  $\text{SF}_6$  gas from the reverse side to release the micropipettes (Fig. 4.18f).



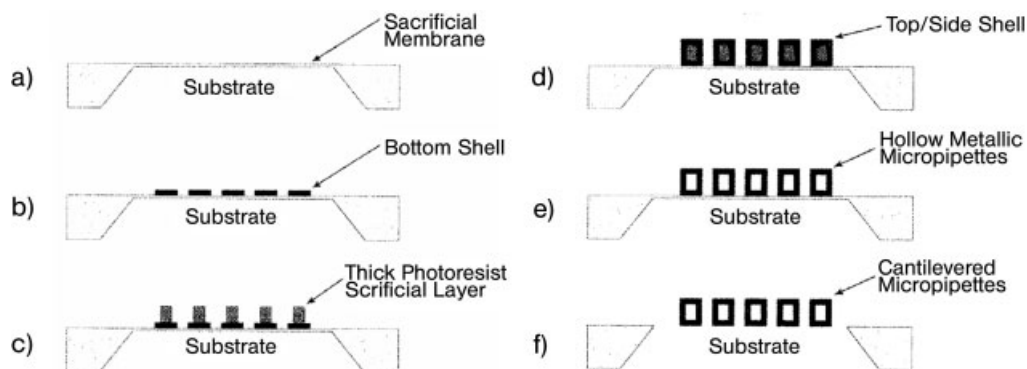


Figure 4.18. Fabrication steps for microneedle arrays [90].

The microfabricated microneedles were used for high lane density slab-gel electrophoresis. Capillary action was utilized to load samples into the microneedle. The samples were dispensed into wells of electrophoretic micro-gels using a syringe pump demonstrating a 2-fold increase in the number of theoretical plates and a 6-fold reduction in lane spacing compared to standard mini-gel separations. Although the micromachined pipettes were not intended for surface patterning, their closed microchannels demonstrated a means to effectively deliver biofluid by capillary action.

#### 4.3.5

##### NFPs

NFPs can be defined as microfluidic dispensing probes that incorporate a reservoir, continuously feeding the ink to the tip, which can write with sub-100-nm resolution [91, 114]. On-chip reservoirs were met in several applications already described. Apertured pyramidal tips incorporated a small reservoir at the hollow back of each tip [53]. Cantilever microspotters were capable of containing liquid samples in the split at the end of the cantilever [87], while SPTs had on-chip reservoirs for storing larger volumes of samples [88]. However, the minimum resolution of all those tools was limited by the size of the aperture or the width of the gap. It seemed to be challenging to make patterns in the sub-100-nm region. Also, the open microfluidic components in the aforementioned devices resulted in restricted control of evaporation and possible cross-contamination when multiple tips/inks are used. From such a point of view, nanopipette-based probes showed advantages [89]. Since nanopipettes are fabricated by individual glass capillary pulling, difficulties arise in fabricating arrays of uniform probes. Also, the minimum feature size patterned by nanopipettes is limited since it depends critically on the aperture size, which typically leads to a larger dimension of the patterns due to the formation of an external liquid meniscus around the pipette tip during patterning.

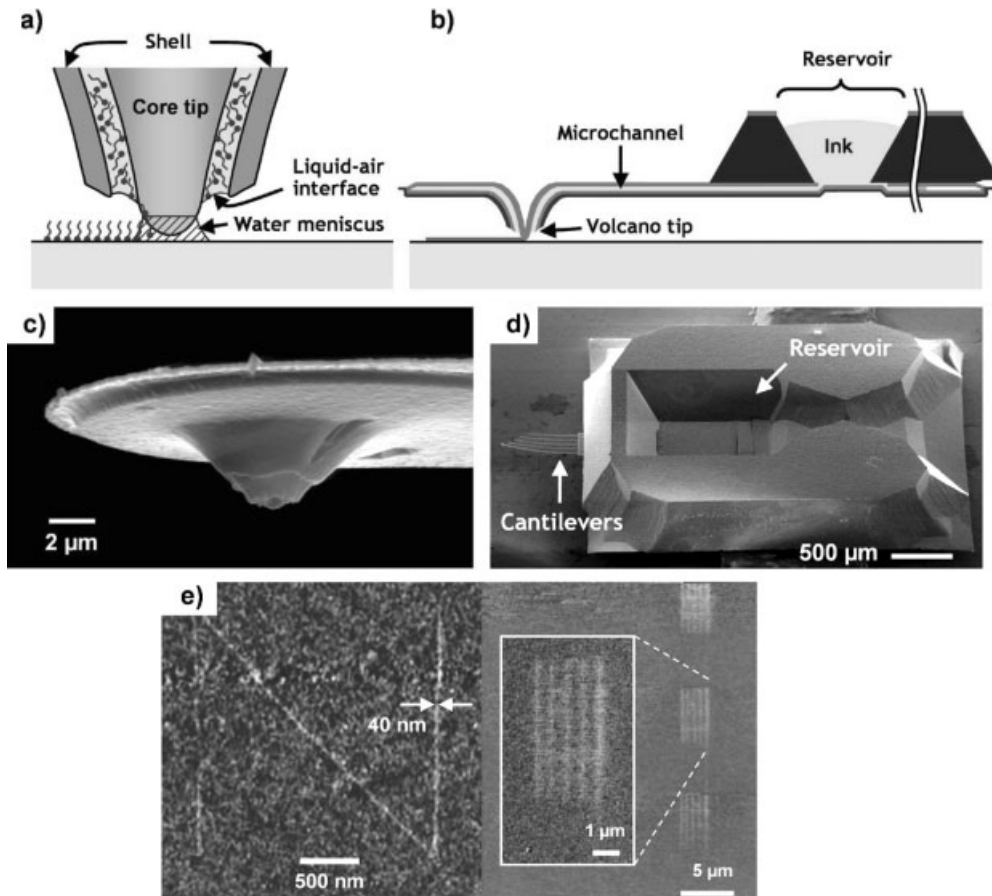


**Figure 4.19.** (a) Writing mechanism of the NFP device. A molecular ink drawn from an on-chip reservoir forms a liquid–air interface at the annular aperture of the volcano-like dispensing tip. Molecules are transferred by diffusion from the interface to a substrate and a water meniscus is formed by capillary condensation. (b) Liquid from the reservoir is

delivered to the dispensing tip via capillary force. (c) SEM image of a dispensing tip. (d) SEM image of an NFP chip showing cantilevers and an on-chip reservoir. (f) Frictional AFM images of features patterned by an NFP. Patterns with line widths as small as 40 nm have been successfully generated.

Both high-resolution patterning and continuous sample feeding through closed microchannels were achieved by NFP. Figure 4.19 illustrates a first-generation microfabricated NFP device and its molecular-writing results. A volcano-like dispensing tip was configured to have a ring-shaped aperture through which samples were dispensed to generate sub-100-nm lines on a routine basis. Features with a line width as small as 40 nm were patterned, which experimentally demonstrated high-resolution fountain-pen-mode writing, i.e. a writing mode in which ink is

transported from the on-chip reservoir to the substrate. An embedded microchannel and an on-chip reservoir continuously replenished the tip with liquid samples. Due to the unique volcano-like dispensing tip of the NFP, both continuous feeding and high-resolution writing were possible. The resolution of the NFP was controlled by the radius of the tip since it preserved the DPN-mode writing, compared to other techniques, where the aperture size or the gap width were considered as the dominant factors limiting the resolution. While the nanopipettes, apertured pyramidal tips and quill-type SPTs work by the formation of an outer meniscus between the probe and substrate, the NFP forms a meniscus between the ultra-sharp AFM-like tip and substrate, like traditional DPN.

The batch-fabrication processes developed for the NFP chips provided straightforward scaling-up to NFP arrays. Using standard microfabrication technologies, chips with five fountain-pen probes were batch-fabricated (Fig. 4.20). The fabrication steps started with the conventional tip formation process using a precursor cap defined by mask M1 (Fig. 4.20a). During the oxidation sharpening process, the precursor tip fell off (Fig. 4.20b). A silicon nitride film with a thickness of around  $0.3\ \mu\text{m}$  was deposited by LPCVD to form the floor of the channels. Mask M2 defined the space through which the on-chip reservoir would be connected to the channels. Layers of silicon oxide with a thickness of around  $0.5\ \mu\text{m}$  and silicon nitride with a thickness of  $0.3\text{--}0.5\ \mu\text{m}$  were deposited by LPCVD to form the sacri-

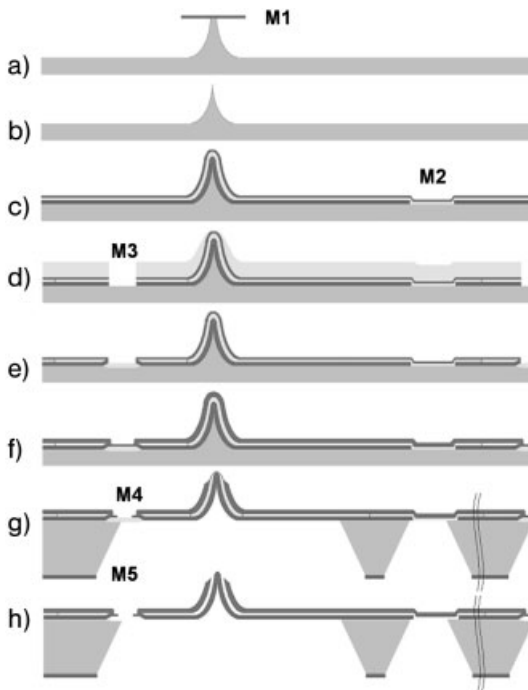
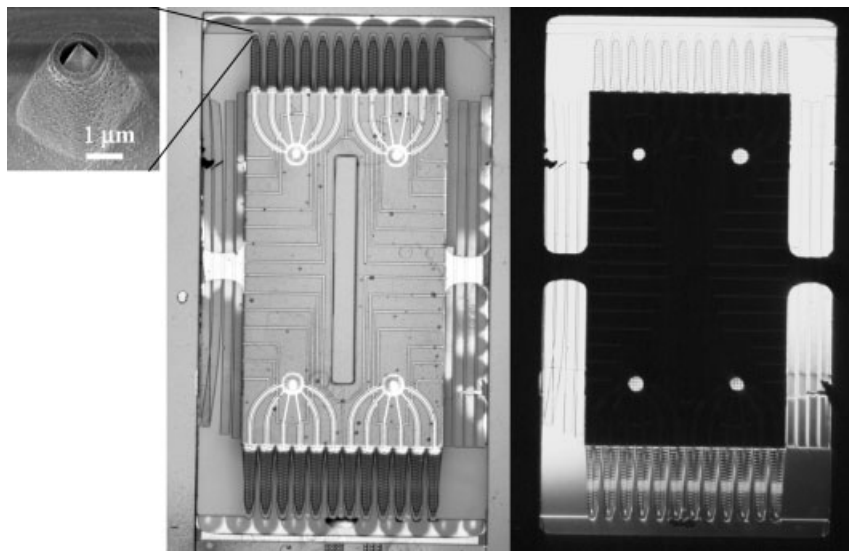


Figure 4.20. Microfabrication steps of NFP [114].

ficial layer and the ceiling layer of the microchannels, respectively (Fig. 4.20c). Lithography with mask M3 followed by RIE in  $\text{CF}_4$  plasma defined the in-plane geometry of the channels, where the channels follow the edges of the pattern comprised in mask M3. A buffered oxide etching (BOE) solution was used for a controlled underetching of the structures, to provide the lumen of the microchannels (Fig. 4.20d). Subsequently, the lateral openings of the channels were closed by bird's beak oxidation (Fig. 4.20e). Sealing of the channels followed using either an LPCVD silicon nitride layer or an electron-beam evaporated gold layer (Fig. 4.20f). Lithography with mask M4 was conducted to pattern the sealing layer with the geometry of the cantilevers and chip boundaries. The reverse-side nitride was lithographically processed with mask M5 and subsequently etched by  $\text{CF}_4$  RIE. Anisotropic etching in KOH solution formed the on-chip reservoir and the handling body (Fig. 4.20g). After the removal of the oxide, the chip remained suspended by small, easy-to-break silicon bridges, to provide good wafer-level maneuverability (Fig. 4.20h). After this step, a thin gold layer was deposited on the reverse side of the cantilevers to provide sufficient reflectivity for the optical beam-deflection sensing system of the AFM.

With the expansion to 1- or 2-D NFP arrays incorporating multiple on-chip reservoirs, simultaneous patterning of surfaces with multiple biological inks can be carried out. Potential applications include high-throughput manufacturing of nanosensors and nanoarrays. For example, in the DPN technique, a substrate was patterned with a MHA monolayer and subsequently antibodies were attached to be



**Figure 4.21.** Second-generation NFP chip. Left: reflected light optical micrograph of the top side of the chip, showing two reservoirs feeding each six microchannels on each side of

the chip. Right: transmitted light optical micrograph, showing the reservoir wells. Inset shows a SEM detail of the dispensing volcano-shape tip.

ready to sense antigens. With the NFP, most of the intermediate steps may not be necessary. It is also important to emphasize that NFP patterning does not require repeated dipping of the tip and specific treatment of the substrate for protein printing. A second-generation NFP device was recently fabricated by the same group, allowing two on-chip reservoirs, each feeding a linear array of six cantilevers with nanodispensing probes (Fig. 4.21). The new chip presents some advantages regarding channel sealing and fabrication, an increased uniformity and sharpness of the nanodispensing tips, a better control of the longitudinal and lateral bending stiffness of the cantilever and the possibility to add independent actuation of the probes and electrical contacts for conductive NFP lithography and voltamography.

#### 4.4 Applications

We now describe applications of cantilevers for patterning biomolecules, including DNA, protein and viruses.

##### 4.4.1 Patterning of DNA

Silicon nitride DPN tips created nanoscale patterns of oligonucleotides on both metallic and insulating substrates [14]. Hexanethiol-modified oligonucleotides were used as ink for DPN patterning on gold substrates with features ranging from 50 nm to several micrometers in size. The patterned surface was subsequently used to direct the assembly of complementary oligonucleotide-modified gold nanoparticles. The immobilization of the DNA was achieved by the covalent bonding between the hexanethiol group of the DNA and the gold surface. Prior to the patterning, the surface of the silicon nitride AFM cantilever was modified with 3'-aminopropyltrimethoxysilane in order to improve the coating of the DNA on the surface of the tip. The modified tip surface was readily wetted by the DNA ink solution when dipped. In addition to utilizing the gold-thiol immobilization for DNA patterning, modified silicon oxide surfaces were demonstrated to work as a DPN substrate. Since gold surfaces prevented the study of electrical or optical characteristics of the DPN-patterned nanostructures due to the conductivity and quenching, respectively, of the surface, the use of silicon oxide opened the door to such studies. The silicon oxide surface was treated with 3'-mercaptopropyltrimethoxysilane (MPTMS) and the oligonucleotides were modified with acrylamide groups in order to utilize the covalent link between the pendant thiol groups of the MPTMS and the acrylamide moieties of the DNA as an immobilization mechanism. The biological activity of the patterned oligonucleotides was confirmed in an ensuing hybridization process.

In DPN, functionalization of the tip surface is required to efficiently coat the DNA ink. However, the NFP did not need such tip modification due to the direct delivery of the DNA ink in suspension from the on-chip reservoir to the tip.

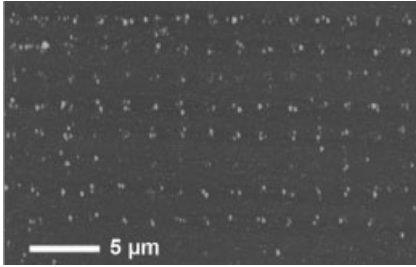


**Figure 4.22.** AFM topography image of an array of DNA dots patterned by fluidic spotting using an NFP probe.

Hexanethiol-modified oligonucleotides were deposited on a gold substrate in a fountain-pen fashion using the device presented in Fig. 4.21. An array of dots was patterned and verified by AFM topography scanned with a commercially available silicon nitride tip as shown in Fig. 4.22.

#### 4.4.2

##### **Patterning of Proteins**

DPN was used to fabricate a nanoarray for the HIV-1 immunoassay as a proof-of-concept DPN-based biodetection [15]. DPN-generated dots of MHA on a thin gold film were used to immobilize anti-HIV-1 p24 antibodies. When immersed into a sample containing HIV-1 p24, the nanoarray reacted with the antigens leading to a height difference of the MHA features due to the bound antigens. This height difference is not easily detectable by AFM. Hence, the height difference was amplified by gold nanoparticles that were functionalized with the same antibody. The DPN-generated nanoarray with the double-sandwich immunoassay demonstrated the capability to detect and measure antigens with unprecedented sensitivity. The important feature of this approach is the high number and small size of individual dots, which reduces the time necessary for antigens to travel and bind to antibodies, and also provides the necessary redundancy for a correct statistics.

An enhanced tool was introduced by Lynch and coworkers [115] for fast and large-area patterning. One of the improvements consisted of replacing the AFM piezotube with a piezoelectric inchworm stage capable of 20-nm resolution over 25 mm of  $xy$  travel. Although the stage did not provide as high lateral resolution as the piezotube, it performed better in terms of repeatable movements over several centimeters. A second improvement was the shortening of the tip–surface contact time for patterning by applying precisely timed bursts of wet or dry air directly to the tip–surface interface. With this scheme, protein transfer could be achieved in less than 100 ms, which was an improvement upon the  $250 \text{ s } \mu\text{m}^{-1}$  in DPN [15]. For patterning, a commercially available AFM probe was mounted on the tool for building protein nanoarrays. In demonstrated experiments, an array of antigen (mouse IgG) was spotted with approximately 700-nm diameter spots on

a pretreated substrate [115]. The specific binding of Cy3-labeled goat anti-mouse antibody was verified with minimal nonspecific background binding. It was demonstrated that nanoarray assays could be produced in a rapid fashion and the miniaturized size would lead to a reduced sample volume of the protein for bioanalysis. For example, each 1- $\mu\text{m}$  dot in the nanoarray would cover less than 1/1000 of the surface area of a conventional microarray dot while maintaining enough antibodies to provide a useful dynamic range [115].

#### 4.4.3

#### **Patterning of Viruses**

AFM was utilized to identify viruses utilizing type-specific immunocapture and the morphological properties of the capture viruses by Nettikadan and coworkers [116, 117]. Multiple virus-specific antibody capture domains were constructed on a chip using ink-jet protein arraying technology. The chip, termed ViriChip, was constructed with 600- $\mu\text{m}$  diameter antibody domains. The ViriChips were individually exposed to each of six group B coxsackieviruses [116]. Each of the six group B coxsackievirus types bound extensively to their specific ViriChip with little or no binding observed on the nonspecific chips. Counting of the number of bound viruses was performed using AFM inspection.

Substrates for the chips were prepared from diced silicon wafers ( $4 \times 4 \text{ mm}^2$ ). After ultrasonic cleaning in water and ethanol, metal films of 5-nm chromium and 10-nm gold were sequentially sputter coated. Target areas (600  $\mu\text{m}$  diameter) were created using copper electron microscopy grids as masks during sputtering. A SAM layer was coated by immersing the substrate in an alkanethiolate solution. The target areas were covered with recombinant Protein A/G followed by blocking the unreacted alkanethiol groups. The chip was completed by placing 1  $\mu\text{l}$  of antiviral antibody on the Protein A/G domain of a substrate, followed by incubation and rinsing. Each virus sample (1  $\mu\text{l}$ ) of the six group B coxsackieviruses was applied onto the antibody-coated domains. AFM scanning operated in tapping mode was used to obtain morphological and counting information on the viruses.

It was inferred that a reduction of the antibody domain size to 2–5  $\mu\text{m}$  should increase the sensitivity of the assay [116] based on the previous study on the phenomenon of analyte harvesting [23, 118]. Further, it was verified that the efficiency of virus capture increases dramatically with decreased sample volume. With microfluidic delivery of samples to the capture domain, the capture efficiency would likely be increased.

#### 4.5

#### **Conclusions and Outlook**

Since they have been used in AFM for imaging, microcantilevers have evolved to meet the requirements from many life sciences applications. Microcantilevers are fundamental tools for biopatterning and biosensing in SPM-based techniques. Dif-

ferent materials targeting the biochemical applications were integrated and used for fabricating the tips and cantilevers. Massive parallel arrays are being pursued in an attempt to increase the throughput. Efforts have been made to integrate microfluidics into microcantilevers, which include apertured pyramidal tips, miniaturized spotters with nib-type reservoirs, open and closed microchannels, on-chip reservoirs, and complex systems with several of the previously mentioned features. Microcantilevers may serve to create ultra-miniaturized bioanalytical devices and testing methodologies in which the efficiency relies on the higher detection speed, higher accuracy and increased statistical significance of the results.

## References

- 1 BINNIG G., QUATE C. F., GERBER C. Atomic force microscope, *Phys. Rev. Lett.* **1986**, *56*, 930–933.
- 2 ALBRECHT T. R., QUATE C. F. Atomic resolution imaging of a nonconductor by atomic force microscopy, *J. Appl. Phys.* **1987**, *62*, 2599–2602.
- 3 PETERSEN K. E. Silicon as a mechanical material, *Proc. IEEE* **1982**, *70*, 39–76.
- 4 MADOU M. J. *Fundamentals of Microfabrication*. CRC Press, Boca Raton, FL, **2002**.
- 5 BLANCHARD A. P., KAISER R. J., HOOD L. E. High-density oligonucleotide arrays, *Biosens. Bioelectron.* **1996**, *11*, 687–690.
- 6 BIETSCH A., HEGNER M., LANG H. P., GERBER C. Inkjet deposition of alkanethiolate monolayers and DNA oligonucleotides on gold: evaluation of spot uniformity by wet etching, *Langmuir* **2004**, *20*, 5119–5122.
- 7 FODOR S. P. A. DNA sequencing – massively parallel genomics, *Science* **1997**, *277*, 393–395.
- 8 JAMES C. D., DAVIS R. C., KAM L., CRAIGHEAD H. G., ISAACSON M., TURNER J. N., SHAIN W. Patterned protein layers on solid substrates by thin stamp microcontact printing, *Langmuir* **1998**, *14*, 741–744.
- 9 BERNARD A., DELAMARCHE E., SCHMID H., MICHEL B., BOSSHARD H. R., BIEBUYCK H. Printing patterns of proteins, *Langmuir* **1998**, *14*, 2225–2229.
- 10 LANGE S. A., BENES V., KERN D. P., HORBER J. K. H., BERNARD A. Microcontact printing of DNA molecules, *Anal. Chem.* **2004**, *76*, 1641–1647.
- 11 DELAMARCHE E., BERNARD A., SCHMID H., MICHEL B., BIEBUYCK H. Patterned delivery of immunoglobulins to surfaces using microfluidic networks, *Science* **1997**, *276*, 779–781.
- 12 BERNARD A., MICHEL B., DELAMARCHE E. Micromosaic immunoassay, *Anal. Chem.* **2001**, *73*, 8–12.
- 13 PINER R. D., ZHU J., XU F., HONG S., MIRKIN C. A. “Dip-pen” nanolithography, *Science* **1999**, *283*, 661–663.
- 14 DEMERS L. M., GINGER D. S., PARK S.-J., LI Z., CHUNG S.-W., MIRKIN C. A. Direct patterning of modified oligonucleotides on metals and insulators by dip-pen nanolithography, *Science* **2002**, *296*, 1836–1838.
- 15 LEE K.-B., PARK S.-J., MIRKIN C. A., SMITH J. C., MRKSICH M. Protein nanoarrays generated by dip-pen nanolithography, *Science* **2002**, *295*, 1702–1705.
- 16 MINH P. N., TAKAHITO O., MASAYOSHI E. *Fabrication of Silicon Microprobes for Optical Near-Field Applications*. CRC Press, Boca Raton, FL, **2002**.
- 17 LANG H. P., BERGER R., BATTISTON F., RAMSEYER J. P., MEYER E., ANDREOLI C., BRUGGER J., VETTIGER P., DESPONT M., MEZZACASA T., SCANDELLA L., GUNTHERODT H. J., GERBER C., GIMZEWSKI J. K. A chemical sensor based on a micromechanical cantilever array for the identification of gases and vapors, *Appl. Phys. A* **1998**, *66*, S61–S64.



- 18 MEISTER A., LILEY M., BRUGGER J., PUGIN R., HEINZELMANN H. Nanodispenser for attoliter volume deposition using atomic force microscopy probes modified by focused-ion-beam milling, *Appl. Phys. Lett.* **2004**, *85*, 6260–6262.
- 19 BULLEN D., WANG X., ZOU J., HONG S., CHUNG S., RYU K., FAN Z., MIRKIN C., LIU C. Micromachined arrayed dip pen nanolithography probes for sub-100 nm direct chemistry patterning. Presented at: *16th IEEE International Micro Electro Mechanical Systems Conference*, Kyoto, **2003**.
- 20 ZHANG M., BULLEN D., CHUNG S.-W., HONG S., RYU K. S., FAN Z., MIRKIN C. A., LIU C. A MEMS nanoplotter with high-density parallel dip-pen nanolithography probe arrays, *Nanotechnology* **2002**, *13*, 212–217.
- 21 VETTIGER P., DESPONT M., DRECHSLER U., DURIG U., HABERLE W., LUTWYCHE M. I., ROTHUIZEN H. E., STUTZ R., WIDMER R., BINNIG G. K. The “Millipede” – more than one thousand tips for future AFM data storage, *IBM J. Res. Dev.* **2000**, *44*, 323–340.
- 22 RAMSAY G. DNA chips: state-of-the-art, *Nat. Biotechnol.* **1998**, *16*, 40–44.
- 23 MACBEATH G., SCHREIBER S. L. Printing proteins as microarrays for high-throughput function determination, *Science* **2000**, *289*, 1760–1763.
- 24 LANGE D., BRAND O., BALTES H. *CMOS Cantilever Sensor Systems*. Springer, Berlin, **2002**.
- 25 MINNE S. C., MANALIS S. R., QUATE C. F. *Bringing Scanning Probe Microscopy Up to Speed*. Kluwer, Boston, MA, **1999**.
- 26 ALESSANDRINI A., FACCI P. AFM: a versatile tool in biophysics, *Meas. Sci. Technol.* **2005**, *16*, R65–R92.
- 27 SAMORI P. Scanning probe microscopy beyond imaging, *J. Mater. Chem.* **2004**, *14*, 1353–1366.
- 28 GREENE M. E., KINSER C. R., KRAMER D. E., PINGREE L. S. C., HERSAM M. C. Application of scanning probe microscopy to the characterization and fabrication of hybrid nanomaterials, *Microsc. Res. Tech.* **2004**, *64*, 415–434.
- 29 WOUTERS D., SCHUBERT U. S. Nanolithography and nanochemistry: probe-related patterning techniques and chemical modification for nanometer-sized devices, *Angew. Chem. Int. Ed. Engl.* **2004**, *43*, 2480–2495.
- 30 GINGER D. S., ZHANG H., MIRKIN C. A. The evolution of dip-pen nanolithography, *Angew. Chem. Int. Ed. Engl.* **2004**, *43*, 30–45.
- 31 WOLTER O., BAYER T., GRESCHNER J. Micromachined silicon sensors for scanning force microscopy, *J. Vac. Sci. Technol. B* **1991**, *9*, 1353–1357.
- 32 RAITERI R., GRATTAROLA M., BUTT H.-J., SKLÁDAL P. Micromechanical cantilever-based biosensors, *Sens. Actuators B* **2001**, *79*, 115–126.
- 33 BALLER M. K., LANG H. P., FRITZ J., GERBER C., GIMZEWSKI J. K., DRECHSLER U., ROTHUIZEN H., DESPONT M., VETTIGER P., BATTISTON F. M., RAMSEYER J. P., FORNARO P., MEYER E., GUNTHERODT H. J. A cantilever array-based artificial nose, *Ultramicroscopy* **2000**, *82*, 1–9.
- 34 BAIN C. D., TROUGHTON E. B., TAO Y. T., EVALL J., WHITESIDES G. M., NUZZO R. G. Formation of monolayer films by the spontaneous assembly of organic thiols from solution onto gold, *J. Am. Chem. Soc.* **1989**, *111*, 321–335.
- 35 BERGER R., DELAMARCHE E., LANG H. P., GERBER C., GIMZEWSKI J. K., MEYER E., GUNTHERODT H. J. Surface stress in the self-assembly of alkanethiols on gold, *Science* **1997**, *276*, 2021–2024.
- 36 FRITZ J., BALLER M. K., LANG H. P., ROTHUIZEN H., VETTIGER P., MEYER E., GUNTHERODT H.-J., GERBER C., GIMZEWSKI J. K. Translating biomolecular recognition into nanomechanics, *Science* **2000**, *288*, 316–318.
- 37 WU G., JI H., HANSEN K., THUNDAT T., DATAR R., COTE R., HAGAN M. F., CHAKRABORTY A. K., MAJUMDAR A. Origin of nanomechanical cantilever motion generated from biomolecular interactions, *Proc. Natl Acad. Sci. USA* **2001**, *98*, 1560–1564.
- 38 WU G., DATAR R. H., HANSEN K. M., THUNDAT T., COTE R. J., MAJUMDAR A. Bioassay of prostate-specific antigen

- (PSA) using microcantilevers, *Nat. Biotechnol.* **2001**, *19*, 856–860.
- 39 ARNTZ Y., SEELIG J. D., LANG H. P., ZHANG J., HUNZIKER P., RAMSEYER J. P., MEYER E., HEGNER M., GERBER C. Label-free protein assay based on a nanomechanical cantilever array, *Nanotechnology* **2003**, *14*, 86–90.
  - 40 THUNDAT T., WACHTER E. A., SHARP S. L., WARMACK R. J. Detection of mercury-vapor using resonating microcantilevers, *Appl. Phys. Lett.* **1995**, *66*, 1695–1697.
  - 41 THUNDAT T., CHEN G. Y., WARMACK R. J., ALLISON D. P., WACHTER E. A. Vapor detection using resonating microcantilevers, *Anal. Chem.* **1995**, *67*, 519–521.
  - 42 WACHTER E. A., THUNDAT T. Micro-mechanical sensors for chemical and physical measurements, *Rev. Sci. Instrum.* **1995**, *66*, 3662–3667.
  - 43 BATTISTON F. M., RAMSEYER J. P., LANG H. P., BALLER M. K., GERBER C., GIMZEWSKI J. K., MEYER E., GUNTHERODT H. J. A chemical sensor based on a microfabricated cantilever array with simultaneous resonance-frequency and bending readout, *Sens. Actuators B* **2001**, *77*, 122–131.
  - 44 SHU W., LIU D., WATARI M., RIENER C. K., STRUNZ T., WELLAND M. E., BALASUBRAMANIAN S., MCKENDRY R. A. DNA molecular motor driven micromechanical cantilever arrays, *J. Am. Chem. Soc.* **2005**, *127*, 17054–17060.
  - 45 ALBRECHT T. R., AKAMINE S., CARVER T. E., QUATE C. F. Microfabrication of cantilever styli for the atomic force microscope, *J. Vac. Sci. Technol. A* **1990**, *8*, 3386–3396.
  - 46 WATANABE S., FUJII T. Micro-fabricated piezoelectric cantilever for atomic force microscopy, *Rev. Sci. Instrum.* **1996**, *67*, 3898–3903.
  - 47 YAMAMOTO T., SUZUKI Y., MIYASHITA M., SUGIMURA H., NAKAGIRI N. Development of a metal patterned cantilever for scanning capacitance microscopy and its application to the observation of semiconductor devices, *J. Vac. Sci. Technol. B* **1997**, *15*, 1547–1550.
  - 48 RASMUSSEN J. P., TANG P. T., SANDER C., HANSEN O., MOLLER P. Fabrication of an all-metal atomic force microscope probe. In: *Proceedings of the International Conference on Solid-State Sensors and Actuators*, Chicago, IL, **1997**, pp. 463–466.
  - 49 AKAMINE S., QUATE C. F. Low temperature thermal oxidation sharpening of microcast tips, *J. Vac. Sci. Technol. B* **1992**, *10*, 2307–2310.
  - 50 RAVI T. S., MARCUS R. B., LIU D. Oxidation sharpening of silicon tips, *J. Vac. Sci. Technol. B* **1991**, *9*, 2733–2737.
  - 51 MARCUS R. B., RAVI T. S., GMITTER T., CHIN K., LIU D., ORVIS W. J., CIARLO D. R., HUNT C. E., TRUJILLO J. Formation of silicon tips with <1 nm radius, *Appl. Phys. Lett.* **1990**, *56*, 236–238.
  - 52 BOISEN A., HANSENYAN O., BOUWSTRA S. AFM probes with directly fabricated tips, *J. Micromech. Microeng.* **1996**, *6*, 58–62.
  - 53 MEISTER A., JENEY S., LILEY M., AKIYAMA T., STAUFER U., DE ROOIJ N. F., HEINZELMANN H. Nanoscale dispensing of liquids through cantilevered probes, *Microelectron. Eng.* **2003**, *67–68*, 644–650.
  - 54 FAROQUI M. M., EVANS A. G. R., STEDMAN M., HAYCOCKS J. Micro-machined silicon sensors for atomic force microscopy, *Nanotechnology* **1992**, *3*, 91–97.
  - 55 FAROQUI M. M., EVANS A. G. R. Silicon sensors with integral tips for atomic force microscopy: a novel single-mask fabrication process, *J. Micromech. Microeng.* **1993**, *3*, 8–12.
  - 56 ITOH J., TOHMA Y., SHIMIZU S., KA K. Fabrication of an ultrasharp and high-aspect-ratio microprobe with a silicon-on-insulator wafer for scanning force microscopy, *J. Vac. Sci. Technol. B* **1995**, *13*, 331–334.
  - 57 FOLCH A., WRIGHTON M. S., SCHMIDT M. A. Microfabrication of oxidation-sharpened silicon tips on silicon nitride cantilevers for atomic force microscopy, *J. Microelectromech. Syst.* **1997**, *6*, 303–306.
  - 58 FLORIN E. L., MOY V. T., GAUB H. E. Adhesion forces between individual

- ligand–receptor pairs, *Science* **1994**, *264*, 415–417.
- 59 LEE G. U., KIDWELL D. A., COLTON R. J. Sensing discrete streptavidin biotin interactions with atomic-force microscopy, *Langmuir* **1994**, *10*, 354–357.
- 60 KRAUTBAUER R., RIEF M., GAUB H. E. Unzipping DNA oligomers, *Nano Lett.* **2003**, *3*, 493–496.
- 61 RIEF M., OESTERHELT F., HEYMANN B., GAUB H. E. Single molecule force spectroscopy on polysaccharides by atomic force microscopy, *Science* **1997**, *275*, 1295–1297.
- 62 RIEF M., GAUTEL M., OESTERHELT F., FERNANDEZ J. M., GAUB H. E. Reversible unfolding of individual titin immunoglobulin domains by AFM, *Science* **1997**, *276*, 1109–1112.
- 63 FISHER T. E., OBERHAUSER A. F., CARRION-VAZQUEZ M., MARSZALEK P. E., FERNANDEZ J. M. The study of protein mechanics with the atomic force microscope, *Trends Biochem. Sci.* **1999**, *24*, 379–384.
- 64 WILSON D. L., MARTIN R., HONG S., CRONIN-GOLOMB M., MIRKIN C. A., KAPLAN D. L. Surface organization and nanopatterning of collagen by dip-pen nanolithography, *Proc. Natl Acad. Sci. USA* **2001**, *98*, 13660–13664.
- 65 MAYNOR B. W., FILOCAMO S. F., GRINSTAFF M. W., LIU J. Direct-writing of polymer nanostructures: poly(thiophene) nanowires on semiconducting and insulating surfaces, *J. Am. Chem. Soc.* **2002**, *124*, 522–523.
- 66 IVANISEVIC A., MIRKIN C. A. “Dip-pen” nanolithography on semiconductor surfaces, *J. Am. Chem. Soc.* **2001**, *123*, 7887–7889.
- 67 SU M., DRAVID V. P. Colored ink dip-pen nanolithography, *Appl. Phys. Lett.* **2002**, *80*, 4434–4436.
- 68 LI Y., MAYNOR B. W., LIU J. Electrochemical AFM “dip-pen” nanolithography, *J. Am. Chem. Soc.* **2001**, *123*, 2105–2106.
- 69 LIM J.-H., GINGER D. S., LEE K.-B., HEO J., NAM J.-M., MIRKIN C. A. Direct-write dip-pen nanolithography of proteins on modified silicon oxide surfaces, *Angew. Chem. Int. Ed. Engl.* **2003**, *42*, 2309–2312.
- 70 LEE K.-B., LIM J.-H., MIRKIN C. A. Protein nanostructures formed via direct-write dip-pen nanolithography, *J. Am. Chem. Soc.* **2003**, *125*, 5588–5589.
- 71 AGARWAL G., SOWARDS L. A., NAIK R. R., STONE M. O. Dip-pen nanolithography in tapping mode, *J. Am. Chem. Soc.* **2003**, *125*, 580–583.
- 72 AGARWAL G., NAIK R. R., STONE M. O. Immobilization of histidine-tagged proteins on nickel by electrochemical dip pen nanolithography, *J. Am. Chem. Soc.* **2003**, *125*, 7408–7412.
- 73 WEEKS B. L., VAUGHN M. W., DEYOREO J. J. Direct imaging of meniscus formation in atomic force microscopy using environmental scanning electron microscopy, *Langmuir* **2005**, *21*, 8096–8098.
- 74 HONG S., MIRKIN C. A. A nanoplotter with both parallel and serial writing capabilities, *Science* **2000**, *288*, 1808–1811.
- 75 SALAITA K., LEE S. W., WANG X., HUANG L., DELLINGER T. M., LIU C., MIRKIN C. A. Sub-100 nm, centimeter-scale, parallel dip-pen nanolithography, *Small* **2005**, *1*, 940–945.
- 76 LEE S. W., SANEDRIN R. G., OH B.-K., MIRKIN C. A. Nanostructured polyelectrolyte multilayer organic thin films generated via parallel dip-pen nanolithography (p NA), *Adv. Mater.* **2005**, *17*, 2749–2753.
- 77 WANG X., RYU K. S., BULLEN D. A., ZOU J., ZHANG H., MIRKIN C. A., LIU C. Scanning probe contact printing, *Langmuir* **2003**, *19*, 8951–8955.
- 78 XIA Y. N., WHITESIDES G. M. Soft lithography, *Angew. Chem. Int. Ed. Engl.* **1998**, *37*, 551–575.
- 79 ZHANG H., ELGHANIAN R., AMRO N. A., DISAWAL S., EBY R. Dip pen nanolithography stamp tip, *Nano Lett.* **2004**, *4*, 1649–1655.
- 80 XIA Y. N., ROGERS J. A., PAUL K. E., WHITESIDES G. M. Unconventional methods for fabricating and patterning nanostructures, *Chem. Rev.* **1999**, *99*, 1823–1848.

- 81 CHUNG S. W., GINGER D. S., MORALES M. W., ZHANG Z. F., CHANDRASEKHAR V., RATNER M. A., MIRKIN C. A. Top-down meets bottom-up: dip-pen nanolithography and DNA-directed assembly of nanoscale electrical circuits, *Small* **2005**, *1*, 64–69.
- 82 JIAN W., FIRESTONE M. A., AUCIELLO O., CARLISLE J. A. Surface functionalization of ultrananocrystalline diamond films by electrochemical reduction of aryldiazonium salts, *Langmuir* **2004**, *20*, 11450–11456.
- 83 KIM K.-H., MOLDOVAN N., KE C., ESPINOSA H. D., XIAO X., CARLISLE J. A., AUCIELLO O. Novel ultrananocrystalline diamond probes for high-resolution low-wear nanolithographic techniques, *Small* **2005**, *1*, 866–874.
- 84 KRAUSS A. R., AUCIELLO O., GRUEN D. M., JAYATISSA A., SUMANT A., TUCEK J., MANCINI D. C., MOLDOVAN N., ERDEMIR A., ERSOY D., GARDOS M. N., BUSMANN H. G., MEYER E. M., DING M. Q. Ultrananocrystalline diamond thin films for MEMS and moving mechanical assembly devices, *Diamond Rel. Mater.* **2001**, *10*, 1952–1961.
- 85 HERSAM M. C., HOOLE A. C. F., O'SHEA S. J., WELLAND M. E. Potentiometry and repair of electrically stressed nanowires using atomic force microscopy, *Appl. Phys. Lett.* **1998**, *72*, 915–917.
- 86 TRENKLER T., STEPHENSON R., JANSEN P., VANDERVORST W., HELLEMANS L. New aspects of nanopotentiometry for complementary metal-oxide-semiconductor transistors, *J. Vac. Sci. Technol. B* **2000**, *18*, 586–594.
- 87 BELAUBRE P., GUIRARDEL M., LEBERRE V., POURCIEL J. B., BERGAUD C. Cantilever-based microsystem for contact and non-contact deposition of picoliter biological samples, *Sens. Actuators A* **2004**, *110*, 130–135.
- 88 XU J., LYNCH M., HUFF J. L., MOSHER C., VENGASANDRA S., DING G., HENDERSON E. Microfabricated quill-type surface patterning tools for the creation of biological micro/nano arrays, *Biomed. Microdevices* **2004**, *6*, 117–123.
- 89 LEWIS A., KHEIFETZ Y., SHAMBRODT E., RADKO A., KHATCHATRYAN E., SUKENIK C. Fountain pen nanotechnology: atomic force control of chrome etching, *Appl. Phys. Lett.* **1999**, *75*, 2689–2691.
- 90 PAPAUTSKY I., BRAZZLE J., SWERDLOW H., WEISS R., FRAZIER A. B. Micro-machined pipette arrays, *IEEE Trans. Biomed. Eng.* **2000**, *47*, 812–819.
- 91 KIM K.-H., MOLDOVAN N., ESPINOSA H. D. A nanofountain probe with sub-100 nm molecular writing resolution, *Small* **2005**, *1*, 632–635.
- 92 MOLDOVAN N., KIM K.-H., ESPINOSA H. D. Multi-ink linear array of nanofountain probes, submitted to *J. Micromech. Microeng.* **2006**.
- 93 SCHENA M., HELLER R. A., THERIAULT T. P., KONRAD K., LACHENMEIER E., DAVIS R. W. Microarrays: biotechnology's discovery platform for functional genomics, *Trends Biotechnol.* **1998**, *16*, 301–306.
- 94 BELAUBRE P., GUIRARDEL M., GARCIA G., POURCIEL J. B., LEBERRE V., DAGKESSAMANSKAIA A., TREVISIOL E., FRANCOIS J. M., BERGAUD C. Fabrication of biological microarrays using microcantilevers, *Appl. Phys. Lett.* **2003**, *82*, 3122–3124.
- 95 LEICHLER T., SILVAN M. M., BELAUBRE P., VALSESIA A., CECCONE G., ROSSI F., SAYA D., POURCIEL J. B., NICU L., BERGAUD C. Nanostructuring surfaces with conjugated silica colloids deposited using silicon-based microcantilevers, *Nanotechnology* **2005**, *16*, 525–531.
- 96 LEE J., MOON H., FOWLER J., SCHOELLHAMMER T., KIM C. J. Electrowetting and electrowetting-on-dielectric for microscale liquid handling, *Sens. Actuators A* **2002**, *95*, 259–268.
- 97 VENGASANDRA S. G., LYNCH M., XU J., HENDERSON E. Microfluidic ultra-microscale deposition and patterning of quantum dots, *Nanotechnology* **2005**, *16*, 2052–2055.
- 98 XU J., LYNCH M., NETTIKADAN S., MOSHER C., VENGASANDRA S., HENDERSON E. Microfabricated “biomolecular ink cartridges” –

- surface patterning tools (SPTs) for the printing of multiplexed biomolecular arrays, *Sens. Actuators B* **2005**, *113*, 1034–1041.
- 99 BIETSCH A., ZHANG J. Y., HEGNER M., LANG H. P., GERBER C. Rapid functionalization of cantilever array sensors by inkjet printing, *Nanotechnology* **2004**, *15*, 873–880.
- 100 TAHA H., MARKS R. S., GHEBER L. A., ROUSSO I., NEWMAN J., SUKENIK C., LEWIS A. Protein printing with an atomic force sensing nanofountainpen, *Appl. Phys. Lett.* **2003**, *83*, 1041–1043.
- 101 IONESCU R. E., MARKS R. S., GHEBER L. A. Nanolithography using protease etching of protein surfaces, *Nano Lett.* **2003**, *3*, 1639–1642.
- 102 IONESCU R. E., MARKS R. S., GHEBER L. A. Manufacturing of nanochannels with controlled dimensions using protease nanolithography, *Nano Lett.* **2005**, *5*, 821–827.
- 103 HONG M.-H., KIM K. H., BAE J., JHE W. Scanning nanolithography using a material-filled nanopipette, *Appl. Phys. Lett.* **2000**, *77*, 2604–2606.
- 104 BRUCKBAUER A., YING L. M., ROTHERY A. M., ZHOU D. J., SHEVCHUK A. I., ABELL C., KORCHEV Y. E., KLENERMAN D. Writing with DNA and protein using a nanopipet for controlled delivery, *J. Am. Chem. Soc.* **2002**, *124*, 8810–8811.
- 105 SHALOM S., LIEBERMAN K., LEWIS A., COHEN S. R. A micropipette force probe suitable for near-field scanning optical microscopy, *Rev. Sci. Instrum.* **1992**, *63*, 4061–4065.
- 106 LIEBERMAN K., LEWIS A., FISH G., SHALOM S., JOVIN T. M., SCHAPER A., COHEN S. R. Multifunctional, micropipette based force cantilevers for scanned probe microscopy, *Appl. Phys. Lett.* **1994**, *65*, 648–650.
- 107 HANSMA P. K., DRAKE B., MARTI O., GOULD S. A. C., PRATER C. B. The scanning ion-conductance microscope, *Science* **1989**, *243*, 641–643.
- 108 McALLISTER D. V., ALLEN M. G., PRAUSNITZ M. R. Microfabricated microneedles for gene and drug delivery, *Annu. Rev. Biomed. Eng.* **2000**, *2*, 289–313.
- 109 ZAHN J. D., DESHMUKH A., PISANO A. P., LIEPMANN D. Continuous on-chip micropumping for microneedle enhanced drug delivery, *Biomed. Microdevices* **2004**, *6*, 183–190.
- 110 LIN L. W., PISANO A. P. Silicon-processed microneedles, *J. Microelectromech. Syst.* **1999**, *8*, 78–84.
- 111 PAIK S. J., BYUN A., LIM J. M., PARK Y., LEE A., CHUNG S., CHANG J. K., CHUN K., CHO D. D. In-plane single-crystal-silicon microneedles for minimally invasive microfluid systems, *Sens. Actuators A* **2004**, *114*, 276–284.
- 112 ZAHN J. D., TALBOT N. H., LIEPMANN D., PISANO A. P. Microfabricated polysilicon microneedles for minimally invasive biomedical devices, *Biomed. Microdevices* **2000**, *2*, 295–303.
- 113 CHANDRASEKARAN S., BRAZZLE J. D., FRAZIER A. B. Surface micromachined metallic microneedles, *J. Microelectromech. Syst.* **2003**, *12*, 281–288.
- 114 MOLDOVAN N., KIM K.-H., ESPINOSA H. D. Design and fabrication of a novel microfluidic nanoprobe, *J. Microelectromech. Syst.* **2006**, *15*, 204–213.
- 115 LYNCH M., MOSHER C., HUFF J., NETTIKADAN S., JOHNSON J., HENDERSON E. Functional protein nanoarrays for biomarker profiling, *Proteomics* **2004**, *4*, 1695–1702.
- 116 NETTIKADAN S. R., JOHNSON J. C., VENGASANDRA S. G., MUYS J., HENDERSON E. ViriChip: a solid phase assay for detection and identification of viruses by atomic force microscopy, *Nanotechnology* **2004**, *15*, 383–389.
- 117 NETTIKADAN S. R., JOHNSON J. C., MOSHER C., HENDERSON E. Virus particle detection by solid phase immunocapture and atomic force microscopy, *Biochem. Biophys. Res. Commun.* **2003**, *311*, 540–545.
- 118 MACBEATH G. Protein microarrays and proteomics, *Nat. Genet.* **2002**, *32*, 526–532.

## 5 Nanobioelectronics

*Ross Rinaldi and Giuseppe Maruccio*

### 5.1 Introduction

Nanobiotechnology has been boosted by the advancements in fabrication technologies, which enable the construction of artificial structures in the size range of biological entities. The fascinating world of the bio-self-assembly provides new opportunities and directions for future electronics, opening the way to a new generation of computational systems based on biomolecules and biostructures. Here, we review the advances in the field of nanobiomolecular electronics, starting from the description of a few selected bio-units up to the implementation of hybrid devices. Possible applications of bioelectronic devices to standard electronics, such as rectification, amplification and storage, as well as novel functionalities will be discussed on the basis of recent concept studies.

The chapter is organized as follows: Section 5.2 is dedicated to the motivations of nanobioelectronics research, Section 5.3 summarizes the fundamentals of bio-building blocks for nanoelectronics (DNA and proteins), and Section 5.4 deals with how to interconnect biomolecules and exploit their self-assembly properties for the implementation of nanobiodevices. Sections 5.5 and 5.6 are dedicated, respectively, to the investigation of DNA and proteins for nanobioelectronics applications. Finally, some conclusions are drawn and possible future research directions are forecast in Section 5.7.

### 5.2 Bio-self-assembly and Motivation

Moore's Law (Fig. 5.1), the 1965 prediction by Intel co-founder Gordon Moore that manufacturers would double the number of transistors on a chip every 18 months, with resulting declining prices and increasing performances, has been fulfilled for four decades by the semiconductor industry. However, the latest editions of the annual International Technology Roadmap for Semiconductors [1] – a joint effort of worldwide semiconductor industry associations predicting the main trends in the

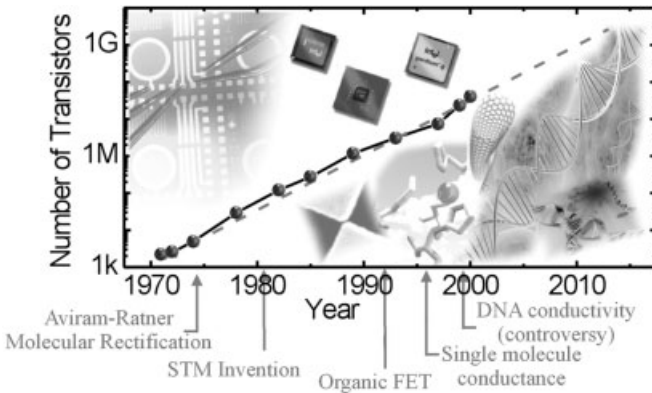


**Figure 5.1.** Moore's law – number of transistors as a function of time (points refer to the various processors introduced by Intel: 4004, 8008, 8080, 8086, 286, 386, 486, Pentium, Pentium II, Pentium III and Pentium 4, respectively). The concomitant occurrence of some milestones of molecular electronics is also indicated. In 1965, Gordon Moore, co-founder of Intel, first observed and then predicted that the number of transistors per integrated circuit grew exponentially. So far, this prediction has been fulfilled thanks to the continuous advances in miniaturization driven by the

progress in lithographic techniques. However, it now seems to be in serious danger and modern electronics has to face the restrictions dictated by the laws of physics when the minimum feature size of a chip approaches 100 nm, at least with current technologies. Thus, gaining the nanometer scale and/or further enhancing the computational capabilities requires a turning point, a change in architecture and the development of conceptually new devices exploiting spin, quantum mechanics and/or molecular building blocks. (Adapted from Ref. [2].)

semiconductor industry spanning 15 years into the future – lists reasons for thinking that this may soon change.

The Roadmap explores “technology nodes” – advances needed to keep shrinking the so-called DRAM half-pitch, i.e. half the spacing between cells in memory chips. Currently, the industry is moving to a DRAM half-pitch of 90 nm, about 2/1000 the width of the proverbial human hair. Analyzing various aspects of chipmaking, the Roadmap forecasts that researchers should lower that figure to 35 nm by 2014, continuing doubling the number of transistors per integrated circuit. This miniaturization trend is expected to continue for another 15–20 years, but the down-scaling with the usual top-down approach (i.e. thanks to the improvement of the lithographic techniques) is becoming increasingly difficult because of physical limitations including size of atoms, wavelengths of radiation used for lithography, interconnect schemes, etc. Three fundamental limits exist [2]: (a) the energy needed to write a bit must be bigger than the average energy of the thermal fluctuations ( $kT$ ) to avoid bit errors (thermal limit), (b) the energy necessary to read or write a bit and the frequency of the circuits are limited by the uncertainty principle (quantum limit), and (c) a maximum tolerable power density exists (power dissipation limit).

Although minimum feature sizes in the few nanometers range have been demonstrated in various laboratories and a number of new lithographic solutions [such as extreme UV, X-ray proximity, and electron (EBL)- and ion-beam lithography (IBL)] have been proposed as post-optical techniques, to a large extent these tools are not suitable for mass production and/or capable of meeting the requirements of the Roadmap, and no known solutions currently exist for these problems.

Thus, the Roadmap underlines the pressing need for developing beyond-CMOS devices and post-optical lithographies, together with the necessity to engineer manufacturable interconnection schemes compatible with the new materials and processes recently proposed. Gaining the nanometer scale and/or further enhancing computational capabilities is expected to require a turning point, a change in architecture and the development of conceptually new devices [2–5].

One of the potential roadblocks to continue the scaling beyond the 50-nm node is molecular electronics. Having the final goal of using interconnected molecules to perform the basic functions of digital electronics, molecular electronics (for a review see Ref. [2]) has recently attracted much interest as a different approach to maintain the historical trend of reducing the cost/function ratio by around 25–30% per year. The concept of molecular electronics can be traced back to the Aviram–Ratner prediction [6] that molecules having a donor–spacer–acceptor structure would exhibit rectifying properties when placed between two electrodes.

A bottom-up approach is promising for building nanodevices from molecular building blocks instead of carving lithographically bigger pieces of matter into smaller and smaller chunks, since it provides a new solution to miniaturization. In fact, although it needs a cross-disciplinary effort (merging chemical, biological and physical expertise), the molecular approach offers important advantages of high reproducibility and small size of the molecular building blocks (naturally identical and with well-defined sizes and electronic levels), along with their thermodynamically driven self-assembly and self-recognition properties [7]. From this perspective, the fascinating world of biomolecules (accurately optimized by nature over billions of years of evolution) provides new opportunities and directions for further miniaturization. While engineers and scientists have long been aspiring to manipulate structures controllably and specifically at the micro- and nanometer scale, nature has been performing these tasks with great accuracy and high efficiency using highly specific biological molecules such as DNA and proteins. One of the biggest drivers behind nanotechnology's enthusiasm for biological systems revolves around the organism's impressive ability to manufacture complex molecules (like DNA and proteins) with atomic precision. However, the strongest motivation for using biomolecules as building blocks for the construction of artificial computational systems lies in their self-assembly properties, which open the way for a new generation of devices and fabrication strategies [8]. The self-assembly properties of biological units can be defined as “the self-organization of one or more entities without any external source of information about the structure to be formed as the total energy of the system is minimized to result in a more stable state” [9]. This process inherently implies (a) some mechanism driving movement



of entities like diffusion, electric fields, etc., and (b) the concept of “recognition” between different elements, or “bio-linkers”, that drives the self-assembly and results in binding of elements dictated by forces (electrical, covalent, ionic, hydrogen bonding, van der Waals, etc.), such that the final physical placement of the entities originates a state of lowest energy [10].

Researchers are now looking at biology as a source of inspiration, and working to join biology and nanotechnology, fusing useful biomolecules to man-made structures in order to fabricate devices that mimic nature in sensing [11], performing complex computational tasks [5], transferring electrons [12], relaying, processing and storing information and producing energy (e.g. biofuel cells exploiting enzymes that extract energy from compounds such as glucose to power life) [13], as well in creating multifunctional systems and molecular-scale motors [14] capable of performing mechanical movements. The result is a merger that attempts to blend biology’s ability to assemble complex structures with the nanoscientist’s capacity to build useful devices or the chemist’s ability to synthesize complex systems (up to hundreds of atoms in size) controlling the position of every atom without too much trouble or fusing useful biomolecules to chemically synthesized nanoclusters in arrangements that do everything from emitting light to storing tiny bits of magnetic data.

Over the last decade there have been dramatic advances toward the realization of molecular-scale devices and integrated computers at the molecular scale [2, 15]. First pioneering experiments were performed demonstrating that individual molecules can serve as nanorectifiers [16] and switches [17, 18], 1000 times smaller than those on conventional microchips. Very recently, the assembly of tiny computer logic circuits built from such molecular-scale devices has been demonstrated [19, 20]. Moreover, molecular electronics is expected to also develop nanodevices exhibiting new functionalities, which exploit peculiar properties of engineered molecules [21] or of biomolecules capable of performing efficiently a lot of different functions.

## 5.3

### Fundamentals of the Bio-building Blocks

#### 5.3.1

#### DNA

DNA is the basic building block of life. It has a double-stranded helical structure. The famous double-helix structure discovered by Watson and Crick in 1953 [22] consists of two strands of DNA wound around each other (Fig. 5.2). Each strand is about 2 nm wide, and has a long polymer backbone built from repeating sugar molecules and phosphate groups. Each sugar group is attached to one of four “bases”. The four bases – guanine (G), cytosine (C), adenine (A) and thymine (T) – form the genetic alphabet of the DNA and their order or “sequence” along the



**Figure 5.2.** (a) Diagram of the DNA double-stranded helical structure. (b) Possible interconnection of DNA fragment with two electrodes or an acceptor and a donor group for transport studies.

molecule constitutes the genetic code. Two single-strand (ss) DNA molecules can join together through hydrogen bonding to form a double-strand (ds) DNA. This process is called hybridization. The chemical bonding is such that an A can only pair with a T, while a G is always paired with a C. The base pairs look like the rungs of a helical ladder. Since the phosphate groups on the backbone are negatively charged, the DNA is usually surrounded by positive “counterions”. The negative charges produce electrostatic repulsion of the two strands, so that positive ions are needed to neutralize the negative charges and keep them together. DNA molecules have been proposed as molecular wires because some of the electron orbitals belonging to the bases overlap quite well with each other along the long axis of the molecule. Such so-called stacking interactions also underlie many one-dimensional (1-D) molecular conductors, including one of the most widely studied organic conductors – tetrathiafulvalene-tetracyano-*p*-quinodimethane (TTF-TCNQ).

### 5.3.2

#### Proteins

Proteins have a vital role in all living systems. The biological function of proteins is determined by the interaction with other molecules. The ability of proteins to interact with the outside world is based on their 3-D structure and conformational flexibility. Proteins are encoded by DNA. The primary structure of the protein determines how a protein will fold into a functional 3-D shape. A scheme concerning

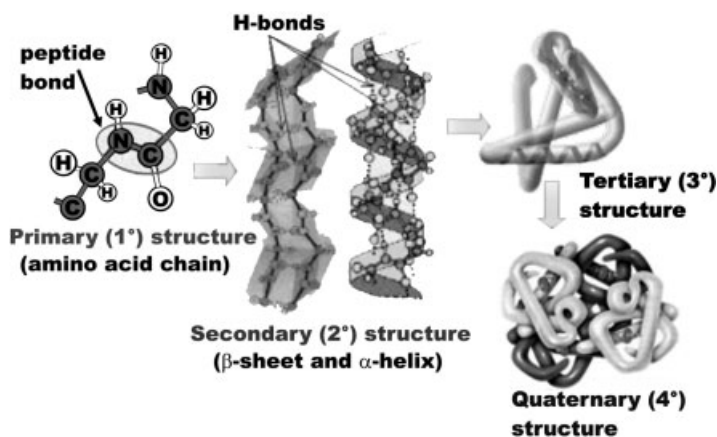


Figure 5.3. Fundamentals of protein structure.

the fundamentals of protein structure is reported in Fig. 5.3. The folded (native-state) protein consists of hydrophilic (polar) residues on the inside and hydrophobic (nonpolar) residues on the outside. In solution, the polar residues are usually in contact with the solvent, whereas the nonpolar residues are protected from solvent in a hydrophobic core. The hydration shell in aqueous solution, where the  $\text{H}_2\text{O}$  molecules forms hydrogen bonds onto the protein surface, solvates the protein.

Proteins play a fundamental role in all biological processes, as they may have different functionalities such as enzymatic catalysis, ionic and electron transfer, coordinated moving, mechanical support, immunization, production and transmission of neuronal pulses, growth and transformation control, etc. Typical examples are hemoglobin that transports oxygen in the erythrocytes and myoglobin that plays the same role in the muscles, whereas iron is carried in the blood by the transferrin and is deposited in the liver by means of a complex with a different protein, ferritin.

In particular, proteins capable of charge transport can most likely be used for building bioelectronic devices. For example, blue copper proteins like Azurin from *Pseudomonas aeruginosa* and poplar plastocyanin are involved in the bacterial respiratory phosphorylation and in some steps on the photosynthesis of green plants, respectively. They show little differences in molecular mass (14 000–10 500) and in the structure of the copper active site (distorted trigonal bipyramid for Azurin and distorted tetrahedral for plastocyanin), which plays the role of an electron reservoir in the electron transfer process. Both of them are redox proteins whose functionality in physiological conditions consists of performing electron transfer between other metalloproteins [cytochrome  $c_{551}$  and nitrite reductase for Azurin and cytochrome *bf* and photosystem I (PS I) for plastocyanin].

## 5.4

**Interconnection, Self-assembly and Device Implementation**

To date, a fully biological device, presumably operating in a living (liquid) environment, is far from being realistic. An intermediate and necessary step is to fabricate hybrid devices in which the functionality of the biological molecules is exploited through the interconnection with a more conventional solid-state inorganic device. This is the case, for instance, of a field-effect transistor (FET) whose gate channel consists of a self-assembled biomolecular layer.

Although at the early stage, such technology is very fundamental for the understanding of biomolecular systems and for the exploration of their potentialities. The processes for the implementation of hybrid biodevices are based on two fundamental steps:

- The nanofabrication of a pattern which interconnects the bio-entity to the external world (load, power supply, circuit, etc.), following a typical “top-down” lithographic approach. This is a general issue concerning all molecular electronics (see Section 5.4.1).
- The self-assembling of the biomolecules (“bottom-up” fabrication) to immobilize the biosystem in the pattern. A possible systematic approach to build complex biomolecular devices is to start from well-characterized clean substrates [such as Si(100), SiO<sub>2</sub> or Au(111) single crystal surfaces] and deposit submonolayers of spatially isolated molecules or biomolecular functional units. The self-assembly of the biological units on the substrate can follow different pathways like (a) bulk (polymer) entrapment, i.e. absorption, (b) surface absorption (physisorption), (c) nondirected covalent binding to the surface (chemisorption), (d) electrostatic adsorption, (e) covalent binding at defined (molecularly engineered) sites of the biocompound or (f) binding by bio-specific interactions (Fig. 5.4) [23]. See Section 5.4.2 for further details.

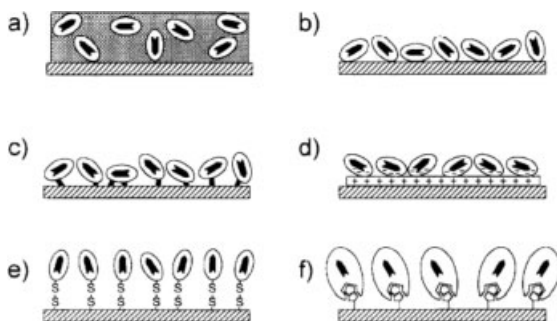


**Figure 5.4.** Schematic of the different self-assembling mechanisms of biological units onto a substrate. (reprinted with permission from W. Göpel, *Biosensor and Bioelectronics* 1995, 10, 35–39. Copyright 1995 Elsevier Science Ltd.)

## 5.4.1

**Interconnecting Molecules**

A major challenge in molecular electronics is how to interconnect single molecules and probe molecular conductivity in real devices working at the nanoscale (both two- and three-terminal devices). This issue requires the fabrication of nanometer-spaced electrodes. Since optical lithography suffers from physical limitations (mainly related to diffraction effects), new techniques are needed for patterning below 100 nm. Even though none of the proposed methods equals the advantages of photolithography for low cost and high throughput, a number of lithographic solutions (extreme UV lithography [24], X-ray proximity lithography, and EBL and IBL) are available, and new techniques have been developed to produce very close electrodes. For instance, Reed and coworkers [25] have investigated charge transport through molecules of benzene-1,4-dithiol self-assembled onto the two facing gold electrodes of a mechanically controllable break junction fabricated by the gentle fracture of an electrode by means of mechanical deformation. Another possibility is to constrain molecules in free-standing junctions, which consist of suspended electrodes used to electrostatically trap molecules and/or nanoparticles by monitoring the current and interrupting the trapping fields at the first increase in conductivity. Among these various alternatives, planar nanojunctions – consisting of two facing metallic electrodes separated by an insulating medium and fabricated by EBL and lift-off processes – are ideal to implement molecular devices since they have a high process yield (typically more than 90% of the nanojunctions are good with an open-circuit resistance around 1 T $\Omega$ ) and provide the opportunity to perform transport experiments on molecules and/or nanostructures self-assembled at the surface of a solid, as well as to fabricate field-effect devices by adding a third electrode at the bottom of the device. Recently, Kervennic and coworkers [26] succeeded in producing pairs of platinum electrodes with a separation down to 3.5 nm by combining EBL and chemical electrodeposition. The separation between EBL-fabricated electrodes is reduced to atomic separation by monitoring the interelectrode conductance and stopping the electrodeposition process at predefined conductance values. In the particular case of DNA, the conductance has been measured using nanofabricated electrodes, atomic force microscopy (AFM), scanning tunneling microscopy (STM) and low-energy electron point source (LEEPS) microscopy. See Tab. 5.1.

**Tab. 5.1.** Transport characterization techniques.

Scanning probe techniques	STM	Conductive-probe AFM	Mercury drop electrodes
Nanojunctions for devices	break junctions	free standing junctions	planar junctions

## 5.4.2

**Delivering Molecules**

Molecular-scale assembly of individual components in working devices is another challenge. In the last few years, great attention has been focused on the development of techniques capable of fabricating molecular layers and patterns [evaporation, spin-coating, Langmuir–Blodgett techniques, thermodynamically driven self-assembly (TDSA) and soft lithography] or to deliver molecules to specific locations (electrostatic trapping, dip-pen and related techniques, and optical tweezers). All these strategies have their own advantages and disadvantages. For example, evaporation usually is not suitable for delicate biomolecules, while spin-coating is fast and cheap, but films are strongly anisotropic and inhomogeneous. TDSA is particularly attractive for bioelectronics applications since it opens the way for the fabrication of engineered highly ordered layers, taking advantage of the specific reactivity of biomolecules having functional groups with affinity for specific surface atoms and/or molecular sites [7]. Although a detailed knowledge of the positions, identities and affinities of the functional groups is required in order to develop a reasonable linkage strategy, TDSA allows us to fully exploit all the intrinsic advantages of the biomolecular approach. Recently, soft lithographies (consisting of different fabrication techniques embracing imprint and stamping methods) have also been attracting considerable attention since they are biocompatible and allow us to create patterns on a surface of interest using a pattern-transfer element (a rigid stamp) made of an elastomer, a thermoplastic polymer network that deforms under an applied force and recovers its shape when the force is released.

In addition to these techniques (parallel and static), a number of scanning methods (serial or parallel) have been developed to place molecules in specific, well-established locations (e.g. in the gap between two nanoelectrodes). “Dip-pen” nanolithography (DPN), proposed by Mirkin’s group [27], is a powerful resistless nanopatterning technique allowing the delivery of molecules to a suitable substrate from a solvent meniscus. The concept of DPN is quite simple. A conventional silicon nitride AFM tip literally draws molecules of virtually any material from the solvent meniscus to a surface of interest (“paper”). The molecular “ink” consists of a chemically reactive material placed on the tip. The fine controls of the tip position and the chemisorption of ink molecules as the tip is scanned across the substrate enables the deposition of organic molecules in a nanometer-scale region. Using DPN it is currently possible to achieve high-resolution patterns (linewidths as small as 15 nm and less than 10-nm spatial resolution). The main parameters affecting the nanopatterning results are the diffusion and the relative humidity. When deposited onto solid surfaces, molecules diffuse out, therefore dramatically influencing the spatial resolution. The relative humidity controls the dimension of the naturally formed water droplet between the substrate and the AFM tip, and thus the effective contact area. Another limiting parameter is the tip radius of curvature. Due to the high resolution and the possibility to use the same apparatus to image and to write a pattern, DPN is a very powerful tool for molecular electronics. More recently, Mirkin’s group has also developed an eight-pen nanoplotter capable

of performing parallel DPN [28] using a dense array of AFM tips and has employed DPN to generate DNA-based templates capable of guiding the assembly of nanoscale building blocks [29]. This technique opens the way to placing molecules and/or nanostructures at established positions. Another interesting tool for molecular delivery is the optical tweezer where light is used to move matter and manipulate nanoscopic objects, exploiting photons momentum. For examples, nanoparticles can be trapped in the focus of a laser beam and serially moved. The force felt by the trapped particle is primarily given by the dipole and by the gradient force due to the interaction of a dielectric object with light and lies in the piconewton range, therefore allowing the manipulation of very fragile structures. Recently, MacDonald and coworkers have constructed 3-D trapped structures within an optical tweezers setup using an interferometric pattern between two laser beams. These results point towards the creation of extended 3-D crystalline structures [30]. Assembling functional molecular devices with this serial manipulation approach is, however, extremely slow, and thus technologically unattractive and not suitable for mass production. An alternative, promising strategy to produce large-scale functional circuits at the molecular level is so-called “molecular lithography” directly exploiting self-recognition and self-assembly of biomolecules on surfaces (a parallel process), as described in Section 5.5.

In particular, in order to attach single DNA molecules to metal electrodes, DNA oligomers have been functionalized with thiol groups (SH) [31] or other sulfur-gold interactions have been exploited [32–34], such as derivatizing oligonucleotides with disulfide groups. Electrostatic trapping has been also employed [35, 36] to align DNA molecules between the electrodes. See Tab. 5.2.

**Tab. 5.2.** Nanopatterning and molecular delivery methods.

Local/scanning	Static/large area	Type
Optical tweezers	extreme UV and X-ray proximity lithography	light-based
Electrostatic trapping; EBL and IBL		electromagnetic
AFM nanolithography, AFM storage, “Millipede”	nanoimprint lithography	thermomechanical
AFM nanostencil, membrane nanostencil	evaporation, spin-coating, Langmuir–Blodgett technique	deposition
DPN and parallel DPN	soft lithography	molecular delivery
Molecular lithography	self-assembled monolayers	self-assembly/self recognition

## 5.5

### Devices Based on DNA and DNA Bases

DNA plays a crucial role in biology as the carrier of genetic information in all living species. Recently, however, physicists and chemists have become increasingly interested in the electronic properties of the “molecule of life”, as demonstrated by the large number of fundamental and applied works published in the recent years, mainly concerning its charge transfer properties. Such considerable interest is largely explained by the number of possible applications ranging from electronic devices to long-range detection of DNA damage.

Despite the current hot debate, the subject is far from new. Soon after the Watson-Crick discovery of the double-helix structure of DNA in 1953, Eley and Spivey suggested that DNA could serve as an electronic conductor [37], as the result of interbase hybridization and  $\pi$ - $\pi$  interactions in the stacked base pairs of double-stranded DNA. If  $z$  is the direction of the DNA helical axis (i.e. perpendicular to the base plane), atomic  $p_z$  orbital can originate delocalized  $\pi$  bonding and  $\pi^*$  antibonding orbitals, enabling charge transport along the helical axis (similar stacked aromatic crystals, such as the Bechgaard salt, are indeed metallic). (Note that although DNA bases are also aromatic, there are important differences such as the nonperiodic nature of biological DNA and the expectation of Anderson localization for the electronic states. Moreover, the chemical surroundings and molecular vibrations have also to be taken into account in the case of DNA.)

The advent of measurements on single DNA molecules recently revived the field. In particular, measuring the fluorescence produced by an excited molecule, the Barton's group at the California Institute of Technology [38] found that it no longer emitted light if attached to a DNA molecule and ascribed this fluorescence quenching to the charge transfer from the excited donor molecule to a nearby acceptor molecule along the DNA strand. In other words, DNA would act as a conducting molecular wire, mediating long-range transport on fast timescales. Moreover, they reported a profound sensitivity of long-range charge transfer to stacking and a significant reduction of electron migration as the result of the presence of base mismatches or other stacking perturbations [38].

It is worth noting how these results could have deep implications in the fundamental understanding of important biological processes such as the mechanisms for sensing DNA damage in living organisms, which unlike the DNA repairing processes still present various open-points. For example, in response to DNA-damaging agents, cells induce the expression of DNA-repair enzymes, activate cell-cycle checkpoints, inhibit DNA replication and mitosis and promotes DNA repair, recombination, or, under some circumstances, undergo apoptosis (in the case of fatally damaged DNA, cells are triggered to self-destruct so that they cannot cause cancer). However, the mechanisms by which these cellular responses are activated are not completely understood. Proteins moving along the DNA could be responsible for DNA damage recognition, but in such case the screening of the genome would be quite inefficient since this process is expected to be highly time-consuming and very slow along, for example, the 2 m of DNA in the human



genome. However, if DNA is a conducting molecular wire, as reported by Barton and coworkers, the presence of damaged regions could be electronically detected exploiting DNA-mediated long-range charge transport, by two proteins (a transmitter and a receiver) working as a donor group at one end and an acceptor at the other end. If a damaged region intervenes between them, a significant reduction of charge transfer is expected and the transmitter could simply move along the DNA until the identification of the site of damage, which is then marked for repair [39].

After much initial controversy, the chemists studying charge transfer in DNA are now moving towards a common view [40, 41] and it is generally accepted that charge carriers can hop along the DNA over distances of few nanometres. On the contrary, the understanding of physicists investigating transport through DNA molecules is much less clear and the issue of DNA conductivity still presents some open-points, since the experimental results of different worldwide groups are surprisingly contrasting and range from an insulating [31–33, 42], semiconducting [35, 43] or ohmic [34, 36, 43–46] up to a proximity-induced superconducting behavior [47].

### 5.5.1

#### Charge Transfer in DNA

The process of charge transfer (intermolecular from one molecule to another or intramolecular from one end to the other of the same molecule) is one of the most fundamental in chemistry and materials science and has been extensively studied in extended molecules, like DNA, with a donor group at one end and an acceptor at the other end. Experimental and theoretical studies have shown that the electron-transfer reactions within such a single molecule can occur by two main mechanisms. The first consists of a single-step quantum mechanical tunnelling (QMT) from the donor to the acceptor, a coherent process since no energy is exchanged between the electron and the molecule during the transfer and the electron is never localized. QMT is quantitatively described by the Marcus theory [48] and characterized by a rate decreasing exponentially with the distance. As a consequence, it is possible only for short distances events, while for very long distances, it is expected to be insignificant. The second possible mechanism is thermal hopping, an incoherent process involving several uncorrelated events resulting in a random multi-step walk. In this case, the electron is localized on the molecule and exchanges energy with it. Hopping is predominant for long-distance electron transfer.

Shortly, the main factors influencing the electron transfer (ET) rate are [49]: (1) the distance between the donor and acceptor (in QMT the ET rate decreases exponentially with distance, whereas in hopping it is inversely related to the distance); (2) the nature of the micro-environment separating the donor and the acceptor (which mediates the virtual state or provides intermediate states, respectively); (3) the reorganization energy  $\lambda$ , i.e. the energy required for all structural adjustments (in the reactants and in the surrounding molecules) that are needed for the transfer of the electron [50]; (4) the driving force.

In the past, electron transfer in DNA was largely studied by means of various techniques. However, it was the important work of the Barton's group at Caltech [38] and the Turro's group at Columbia University [51] to revive the field, investigating its distance dependency and reporting the apparent coherent transfer over distances as long as 4 nm. As a result, DNA became a new paradigm for electron transfer, with possible applications as a molecular wire. In this respect, the extensive chemical variability of DNA (including differences in sequence, structures – kinks, bends, bulges and distortions – as well as the polyelectrolyte character of the double helix with the possible flow of positively charged counterions along the negatively charged phosphate backbone) opens large possibilities for tuning electron transport in DNA. On the other hand, the same variability is at the origin of the different results reported in DNA charge-transfer experiments. However, a common view about the basic mechanisms (coherent tunnelling and thermal hopping) involved in DNA charge-transfer was laboriously achieved in the last years thanks to extensive experimental and theoretical work.

To understand why the DNA sequence makes a difference, we have to compare the relative energies of the G-C and A-T base pairs obtained from computational models, photoemission experiments and electrochemical measurements. Since the thermal energy of the charge carrier is substantially smaller than the energy difference between these two base pairs, a hole will localize on G-C pairs while the A-T pairs act as barriers. Hole transfer is thus possible by tunnelling or hopping between G-C sites, with the second mechanism dominant for large distances due to the different distance dependencies.

Both the charge-tunnelling and the thermal-hopping mechanisms have been verified in experiments, notably by Bernd Giese and co-workers [52, 53]. In their experiment (Fig. 5.5), the charge transfer between G bases, separated by adenine-thymine  $(A \bullet T)_n$  bridges of various lengths, in double DNA strands was measured using gel electrophoresis. They found that from being a coherent superexchange charge transfer (tunnelling) process at short distances, the mechanism becomes a thermally induced hopping process for long  $(A \bullet T)_n$  sequences, where the adenines are involved as charge carriers (A-hopping). A switch between these reaction mechanisms occurs because the tunnelling rates decrease considerably as the distance increases. Therefore, in DNA strands where the guanines are separated by long  $(A \bullet T)_n$  sequences (more than three), endothermic transfer of the positive charge from a guanine radical cation ( $G^+$ ) to an adjacent adenine becomes faster than the direct transfer of this charge to the distant guanine. The subsequent migration of the positive charge between the adenines (A-hopping) is so rapid that the length of the  $(A \bullet T)_n$  sequence plays only a minor role. Note that charge transfer (and transport) in DNA strongly depends on the base-stacking characteristics, the dynamic structural distortion of the DNA, the base sequence and the different redox potentials of the bases (Fig. 5.6). In this scenario, having the smallest oxidation potential between the DNA bases, guanines (G) or sequences of guanines are easily oxidizable sites. Thus, once holes are created on the DNA chain, then the charge transport can occur among discrete G sites or delocalized GGG domains (e.g., polaron). This means also that they represent easy targets for many oxidizing

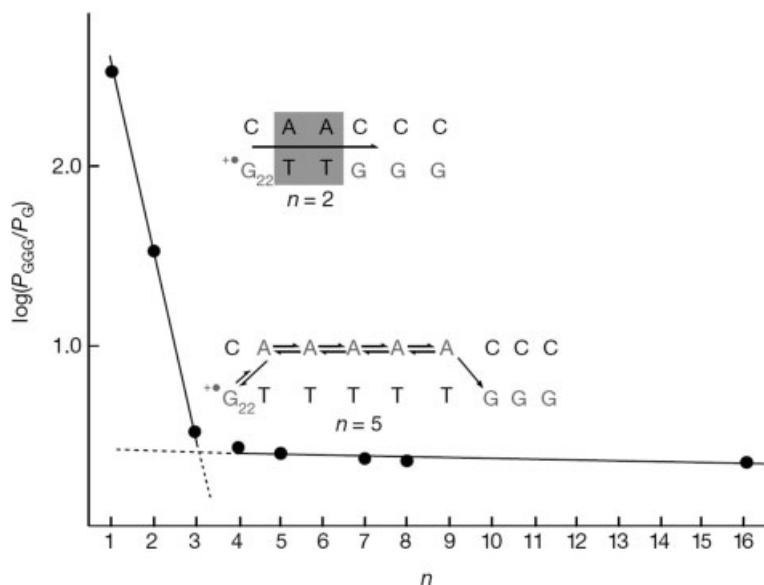


**Figure 5.5.** Electron transfer between a GGG sequence and a guanine radical cation, separated by  $(AT)_n$  base pairs. The ratio  $P_{GGG}/P_G$  is a measure of the efficiency of the electron transfer. (reprinted with permission from B Giese et al., *Nature* 2001, 412, 318. Copyright 2001 Macmillan Publishers Ltd.)

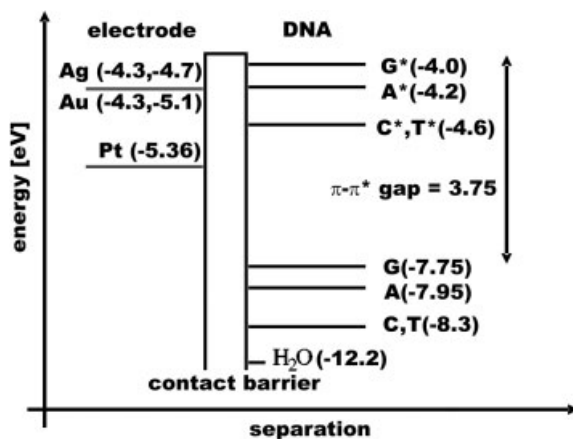


**Figure 5.6.** Energy levels for DNA bases and some metal work functions. (reprinted with permission from R. G. Endres et al., *Rev. Mod. Phys.* 2004, 76, 195. Copyright 2004 American Physical Society)

agents and guanine-rich regions of DNA could serve as “cathodic” protectors against oxidation for genes which are in electrical contact with them [54].

Meanwhile, Lewis and coworkers, at Northwestern University, have directly observed both thermal hopping and coherent transfer [55], while Barton and Zewail, at Caltech, also explained their fluorescence-quenching experiments using these two mechanisms [56]. For a more detailed description of the theory of charge transfer, see Ref. [57]. Most of the reported examples of charge transfer in DNA are in liquid environment.

### 5.5.2

#### DNA Conductivity

While chemists are now converging towards a common view, among physicists there is still a hot debate about the issue of DNA conductivity due to the conflicting results yielded in direct electrical measurements by different groups worldwide. This is a quite new field which in the last years took advantage of the nanotechnology tools (such as electron beam lithography and scanning probe microscopy) to image samples at the molecular level and probe conduction in single DNA molecules by interconnecting them between two metal electrodes.

##### 5.5.2.1 Near-ohmic Behavior (Activated Hopping Conductor)

In 1999, Fink and Schönemberger at the Basel University [44] carried out the first direct electrical measurements on small bundles of DNA developing a special high-vacuum low-energy electron microscope able to image thin free-standing bundles of DNA stretched across a hole in a membrane. The molecules were placed onto a regular array of 2- $\mu\text{m}$  holes in a carbon foil by cast deposition of a drop of water containing 0.3  $\mu\text{g}/\text{ml}$  of  $\lambda$ -DNA onto the sample holder. This procedure usually resulted in  $\lambda$ -DNA networks spanning the sample-holder holes with DNA strands associated into a rope and only very occasionally individual DNA molecules were obtained. The DNA conductance was then measured in a vacuum environment ( $\sim 10^{-7}$  mbar) by touching the DNA bundles with an additional tip (Fig. 5.7) placed at an electrical potential  $U$  with respect to the grounded sample holder and used to achieve mechanical contact to a specific site of the DNA rope, to break the ropes at a certain distance from the rim of the hole, and to apply a voltage bias to one end of the ropes (while the other one is grounded). These manipulations were performed *in situ* while observing the projection images of the molecules on a TV monitor and the sample holder was covered with a gold layer to improve the electrical contact to the molecules. The result of this experiment was quite unexpected: a single DNA rope of 600 nm in length was found to behave like a ohmic conductor with a resistivity of the order of 1  $\text{m}\Omega\text{cm}$ , while two DNA ropes simultaneously interconnected behaved like two resistors in parallel (with the overall measured resistance reduced by a factor of 2). Contrarily, in the simplest picture one expects DNA to behave like a semiconductor with a large energy gap between the valence and conduction bands.

Results from the groups of Tran, Rakitin, Cai, Hartzell and Yoo [45, 43, 36, 34,

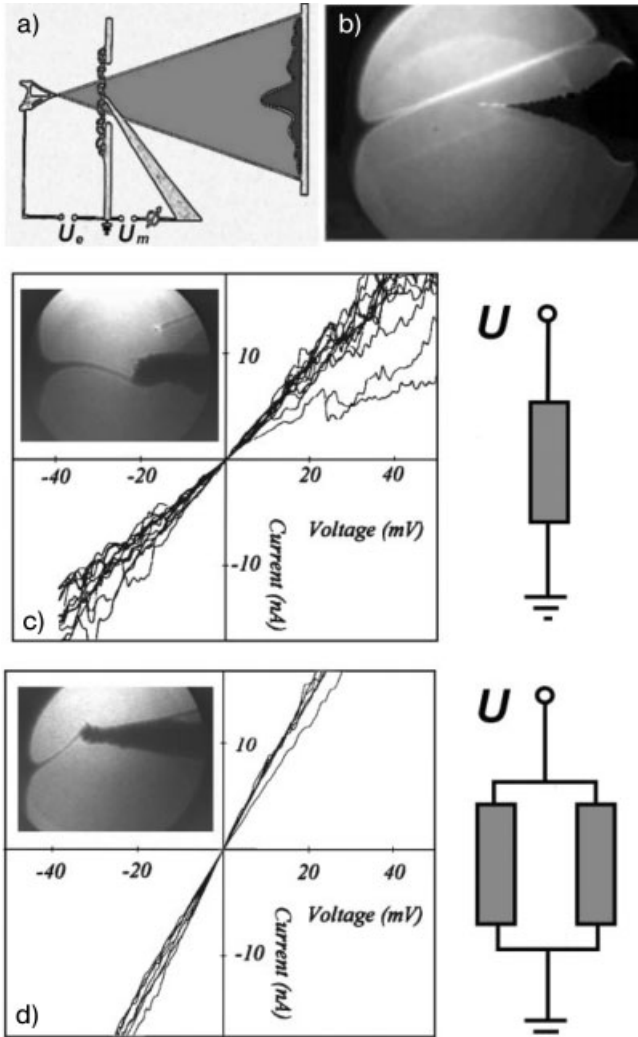


**Figure 5.7.** (a) The experimental setup used by Fink and Schonberger to probe the conductivity of DNA. (b) A 2-mm hole spanned by a single DNA rope and the shadow image of the manipulation tip. (c and d)  $I$ - $V$

characteristics of an individual DNA rope and two DNA ropes in parallel. (reprinted with permission from H. W. Fink et al., *Nature* 1999, 398, 407. Copyright 1999 Macmillan Publishers Ltd.)

46] also suggested almost ohmic conductance at room temperature by means of very different experimental techniques. In all these studies DNA bundles, networks of bundles or supercoiled samples were investigated (see Tab. 5.3).

In particular, due to the numerous open points and difficulties concerning the contact effects and charge injection into DNA, Tran and coworkers measured the

**Tab. 5.3.** Summary of recent measurements of DNA conductivity (adapted with permission from Ref. [57], Copyright 2004 American Physical Society).

Class	Group	DNA sample	Result	Electrodes	Method	Ions
1. Anderson insulator	Storm et al. (2001)	single $\lambda$ -DNA/poly(G)–poly(C)	insulating (at room temperature) (DNA height: 0.5 nm)	Pt/Au	on SiO <sub>2</sub> , mica surface	Mg <sup>2+</sup>
	Braun et al. (1998)	single $\lambda$ -DNA	insulating (at room temperature)	Au	free hanging (gluing technique)	Na <sup>+</sup>
	Zhang et al. (2002) de Pablo et al. (2000)		(conducting if doped)		SFM, on mica	
2. Bandgap insulator	Porath et al. (2000)	single poly(G)–poly(C) (only 30 base pairs)	wide bandgap semiconductor (at room temperature)	Pt	free hanging	Na <sup>+</sup>
	Rakitin et al. (2001)	single, short oligomer- $\lambda$ -DNA	(at room temperature)	Au	(gluing technique)	
3. Activated hopping conductor	Rakitin et al. (2001)	bundles of $\lambda$ -DNA	narrow “bandgap”	Au	free hanging	Na <sup>+</sup>
	Yoo et al. (2001)	supercoiled poly(G)–poly(C)/poly(A)–poly(T)	linear ohmic at room temperature insulating at low temperature	Au/Ti	on SiO <sub>2</sub>	
	Cai et al. (2000)	networks of bundles poly(G)–poly(C)/poly(A)–poly(T)	linear ohmic (at room temperature)	Au	SFM, on mica	
	Tran et al. (2000) Fink and Schonenberger (1999)	supercoiled dry and wet $\lambda$ -DNA bundles of $\lambda$ -DNA	hopping conductivity conducting (doped) (at room temperature)	None Au	microwave absorption free hanging	
4. Conductor	Kasumov et al. (2001)	few $\lambda$ -DNA molecules	induced superconductivity ( $T < 1$ K)	Re/C	on mica	Mg <sup>2+</sup>

temperature dependence of the AC conductivity in a contact-less configuration by evaluating the absorption in a microwave resonant cavity [45]. The measured conductivity was found to be only weakly frequency dependent and influenced by the environment of the double helix (with larger values in buffer). They interpreted the observed temperature dependence by means of a crossover between two transport

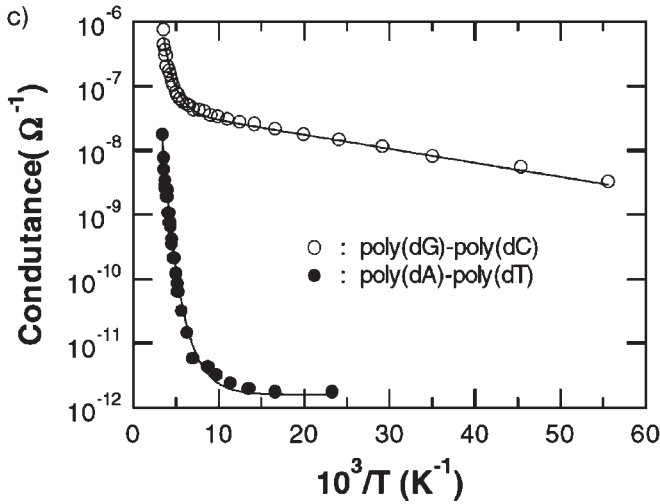


**Figure 5.8.** Temperature dependence of the conductance for poly(dA)–poly(dT) and poly(dG)–poly(dC). (reprinted with permission from Yoo et al., Phys. Rev. Lett. 2001, 87, 198102. Copyright 2001 American Physical Society)

mechanisms: ionic conduction due to the counterions at low temperatures and carrier excitations across single particle gaps or temperature-driven hopping transport processes at high temperatures. Notably, the same temperature dependence was observed by Yoo and coworkers (Fig. 5.8 [46]), which proposed an explanation in terms of a small polaron hopping model over the whole temperature range (the same model predicting a dependence of  $I \propto \sinh(bV)$  also fits their  $I$ – $V$  data very well).

Yoo and coworkers investigated transport in poly(dA)–poly(dT) and poly(dG)–poly(dC) DNA molecules and reported room-temperature resistances of 100 and 1.3 MΩ, respectively. Other interesting differences were observed like the much weaker temperature dependence for poly(dG)–poly(dC) and its behavior as a p-type semiconductor, while poly(dA)–poly(dT) acts as a n-type semiconductor under the effect of a gate voltage. Tran and coworkers reported a resistivity of 0.005 Ωcm for the dry λ-DNA, while Yoo and coworkers estimated a value of 0.025 Ωcm in the case of poly(dG)–poly(dC).

Other experimental results came from the Kawai group at Osaka University [36]. They used scanning probe microscopy and a conductive tip to inject current in DNA bundles connected to a metal strip at different positions in order to determine the length dependence of the current. The resistance was found to increase exponentially with the distance, from  $10^9$  ohm to  $10^{12}$  ohm (Fig. 5.9). Moreover, DNA made of C and G bases were more conductive than DNA with A and T bases [36] (estimated resistivity for poly(dG)-poly(dC) around 1 Ωcm). The increasing of the resistance with the length was attributed to the number of defect in the molecules, while they proposed that the more compact base-stacking structure of

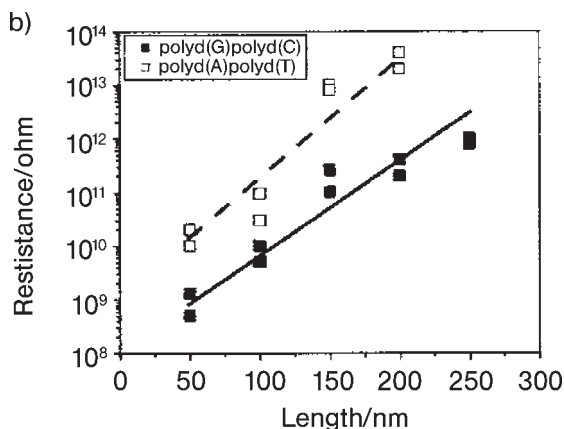


**Figure 5.9.** Resistance versus DNA length for poly(dA)–poly(dT) and poly(dG)–poly(dC). (reprinted with permission from Cai et al., *Appl. Phys. Lett.* 2000, 77, 3105. Copyright 2000 American Institute of Physics)

poly(dG)-poly(dC) (crystal structure data indicates that the helical rises of residues are 2.88 Å and 3.22 Å for poly(dG)-poly(dC) and for poly(dA)-poly(dT), respectively [36]) can also contribute to its better conductance as compared to poly(dA)-poly(dT). In the same group, in a four probes current voltage measurement [58] the effect of oxygen doping was tested on poly(dG)–poly(dC) DNA and poly(dA)-poly(dT) DNA samples. The authors found that the conductance of the DNA samples increases by orders of magnitudes due to oxygen hole doping and that the poly(dG)–poly(dC) DNA samples behave like a p-type semiconductor, whereas the poly(dA)–poly(dT) ones are more likely n-type semiconductors. This difference was attributed to the lower oxidation potential of dG with respect to dA. In this experiment the spacing between the electrodes was varied from 100 to 200 nm.

Finally, Hartzell and coworkers [34] compared the conduction in nicked and repaired  $\lambda$ -DNA, showing a gap up to  $\pm 3$  V and almost ohmic behavior (it is worth noting, once again, the important possible implications in DNA damage recognition). Moreover, Kasumov and coworkers [47] reported proximity induced superconductivity in long  $\lambda$ -DNA, which in their experiment exhibits metallic behavior down to very low temperature (this would be the proof of the existence of true extended states). However, this result has not been independently reproduced and will not be further discussed here.

### 5.5.2.2 Semiconducting (Bandgap) Behavior

The role of the DNA sequence on transport was investigated at the nanoscale for the first time by Porath and co-workers at Delft University, who measured very short DNA molecules consisting of two strands containing only G and C bases, respectively, in order to probe the importance of G-C pairs in hole transfer through



DNA [35]. Using electrostatic trapping from a dilute aqueous buffer containing about one molecule per  $(100 \text{ nm})^3$ , Porath and co-workers placed individual double-stranded poly(G)-poly(C) DNA molecules between two nanoelectrodes only 8 nm apart. The DNA molecule was 10.4 nm long to span the two closely spaced metal nanoelectrodes as a linear, nearly stiff structure. After a DNA molecule was trapped from the solution, the device was dried in a flow of nitrogen and electrical transport was measured. On applying a voltage to the device, they first observed an insulating gap (i.e. no current) at low voltage followed by a conduction onset above 1 V. The low-current region widened as the temperature increased. Two different peaks were present in the differential conductance curves and suggested a molecular-band-mediated transport mechanism and a wide-gap semiconductor behavior, as expected for short DNA molecules if we assume that DNA bases have a rather large highest occupied–lowest unoccupied molecular orbital (HOMO–LUMO) gap (4 eV) and the metal work function lies in the gap. In this case, in fact, a very large electric field is needed to drive transport and allow charge carriers to enter the DNA by aligning the molecular energy bands with the energy levels in the electrodes. The reported  $dI/dV$  curve is thus a measure of the DOS, while the voltage gap (1–2 eV) can be related to the energy difference between the metal work function and the nearest molecular level available for conduction (either the guanine HOMO or the cytosine LUMO). Porath and coworkers [35] interpreted their results as reasonable evidence of the existence of coherent electronic states extended across the molecule. It is worth noting that, in this experiment, transport through DNA molecules only a few base pairs long is probed: the persistence length in dsDNA is about 100 base pairs at room temperature, thus the investigated molecules are reasonably free of the kinks and defects that would lead to an interruption of the  $\pi$ – $\pi$  interactions [57]. This experimental finding was confirmed by the model developed by Cuniberti and coworkers [59] on a similar DNA short sequence.

More recently, Watanabe et al. at Xerox in Japan [60] performed other experiments on single DNA molecules by means of a triple probe atomic force microscope in which two conductive carbon nanotube (CNT) electrodes were employed as source and drain electrodes to interconnect a DNA molecule and a third CNT (fixed to the AFM probe) served as the gate electrode. Due to the small drain-source distance (25 nm), also in this case only few base pairs were probed. Experiments were carried out under nitrogen atmosphere at room temperature and non linear  $I_{DS}$ - $V_{DS}$  characteristics with a non-conducting gap decreasing from 2 to 0.2 V with increasing  $V_G$  from 0 to 5 V were observed. Electrical measurements with drain-source distance of only 5 nm showed equally spaced steps in the  $I_{DS}$ - $V_{DS}$  curve with a period of 80 meV and a gap of 400 meV at  $V_G = 2$  V.

### 5.5.2.3 Insulating Behavior

The electronic conduction at length scales of 40 nm and longer was measured at Delft University by Storm and co-workers with different electrode shape [31]. They obtained clear AFM images of DNA molecules interconnecting the nanoelectrodes, but did not observe any conduction for such long lengths of DNA

with applied bias voltages up to 10 V and also with an additional gate voltage in the range between  $-50$  V and 50 V. They used both individual DNA molecules and small DNA bundles (mixed sequence and poly(dG)-poly(dC)) and employed a cast deposition technique to deposit the molecules between the electrodes. Although under their conditions DNA self-assembles into networks similar to those obtained by Cai and coworkers, Storm and colleagues measured a higher resistance in all their experiments of around  $1\text{ T}\Omega$ , which was observed to increase in a flow of dry nitrogen gas ( $>10^{13}\ \Omega$ , i.e.  $10\text{ T}\Omega$ ). Thus, they suggested that the observed conduction was due to the thin water layer on the hydrophilic mica. These findings clearly contrast with the Basel results (and other high-conductance reports), but they confirm earlier measurements by Braun and coworkers at Technion in Israel [32], who also observed insulating behavior for DNA over a scale length of about  $16\ \mu\text{m}$  in length, and results of de Pablo and coworkers [42], who measured the DNA conductivity using a scanning force microscopy (SFM) tip covered by gold (they reported a lower bound of  $10^6\ \Omega\text{cm}$  for the resistivity). The discrepancy between the Storm lower value ( $1\text{ T}\Omega$ ) and the conductivity reported by Cai and coworkers [about  $200\ \text{G}\Omega$  for bundles of poly(dG)-poly(dC) at a length scale of  $200\ \text{nm}$ ] is, however, not so large.

de Pablo and coworkers [42] also presented “first principles” electronics structures calculations for a double helix of infinite length in acidic dry conditions, which supported the picture of an insulating behavior for the  $\lambda$ -DNA. They started by considering a poly(C)-poly(G) sequence and then analyzed the effect of swapping guanine and cytosine bases in one of every 11 base pairs of their unit cell. This resulted in a dramatic change of the electronic structure of the chain and in a cut in the HOMO-state channel (more or less the same happens for the unoccupied band), as shown in Fig. 5.10. Thus, Anderson localization (over very few base pairs) and an exponential decay of the conductance with the length are expected in biological DNA, due to the nonperiodic nature of its base sequence. Residual conduction by hopping mechanisms (polaronic or not) is still possible, but it should exhibit a marked dependence on temperature and frequency [42]. Taking into account the electronic structure obtained for poly(C)-poly(G), de Pablo and coworker’s results could be consistent with those of Porath, but are strongly in contrast with those of Fink and Schonberger (whose resistivity is 10 orders of magnitude lower). An insulating behavior for a  $\lambda$ -DNA molecule on the micron scale has been also reported by Zhang and coworkers [33] (resistivity higher than  $10^6\ \Omega\text{cm}$ ).

#### 5.5.2.4 Discussion of DNA Conductivity

Despite the large worldwide efforts, the issue of DNA conductivity is, thus, still subject of intense debate and rather unsettled. Assessing and understanding DNA transport properties, with all their facets, it is crucial to gain a deep insight inside important life mechanisms (like DNA damage recognition and reparation) as well as for a variety of applications in molecular electronics and biotechnology, e.g. the implementation of DNA chips with an electronic readout. Microarrays for the de-

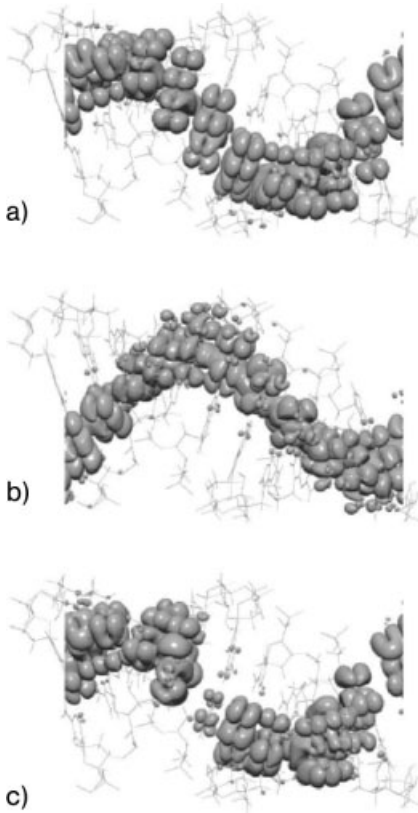


**Figure 5.10.** Isosurfaces of constant density for (a and b) the 11 highest occupied and lowest unoccupied states of poly(G)–poly(C), and (c) the 11 highest occupied states when swapping a guanine and a cytosine base in

one of every 11 base pairs of the unit cell. (reprinted with permission from de Pablo et al., *Phys. Rev. Lett.* 2000, 85, 4992. Copyright 2000 American Physical Society)

tection of nucleic acids (DNA chips) are widely used for DNA sequencing, disease screening and gene expression analysis since they allow us to obtain information on nucleic acid sequences in a manner that is faster, simpler and cheaper than traditional methods [61]. Currently, the readout schemes for such devices are optical and involve the use of fluorescent dyes, but the exploitation of DNA conductivity (if large enough, after hybridization, in well-stacked dsDNA as compared to floppy, insulating single strands of DNA) or of its self-assembly properties (for the delivery of conductive elements between pairs of electrodes in large arrays) could enable in the near future the development of an electronic readout which is expected to allow a significant increase in the number of different probe sites (whose density would be no more resolution limited) per unit area, and thus a potentially faster and more efficient sequence analysis.

The main difficulties in addressing the DNA conductivity lie in the complexity of the system and in making clean (i.e. fully controllable) experiments, due to three main issues:

- (a) Differences in the DNA molecules: sequence, length, character (single molecules or ropes).
- (b) Influence of the molecular environment (hardly controllable and possibly preparation dependent): water molecules, counterions, substrate, physisorbed/chemisorbed DNA. For example, the number of water molecules per base is believed to influence the DNA structure [62].
- (c) The detection scheme and the role (nature and quality) of contacts between electrodes and molecules. It is very difficult to have an ideal ohmic molecule-metal contact and the organic-inorganic interfaces usually produce tunnel barriers that can strongly influence the results. Only the metal work function is typically known.

Even theoretically, the situation is quite confused with the large unit cell limiting computational approaches [57], and a number of proposed transport models involving electrons, holes [63], polarons [64] and solitons [65].

However, recently, some progress in the analysis and understanding of the wide range of experimental results has been done [57]. We will try to provide a more unitary as possible discussion of the literature. As noted above, there has been only one group reporting proximity-induced superconductivity in long  $\lambda$ -DNA, thus these results will not be discussed here (Zhang and coworkers [33] proposed contamination from carbon or rhenium to explain such results).

Although the contact-less detection scheme of Tran and coworkers could detect very short dissipative regions embedded in an insulating DNA molecule [33] and de Pablo and coworkers [42] demonstrated that in Fink and Schonberger's experiment [44] the measured DNA conductivity was affected by the irradiation with the imaging electron beam of the LEEPS microscope (resulting in a contamination layer with subsequent increase of conduction), the different experimental evidence of conducting DNA molecules needs an explanation in a comprehensive framework, which also takes into account the observed semiconducting and insulating behaviors. In this respect, it is worth noting how all reports of near-ohmic behavior concern DNA bundles, networks of bundles or supercoiled samples, while insulating behavior was observed in single molecules and short molecules were found to be semiconducting.

The possible stabilization of floppy single DNA molecules by the bundles or condensed water and counterions trapped between the DNA molecules (leading to a different pathway for charge transport) could explain the observed near-ohmic behavior [57] and also the dependence of the conductance on humidity (the contribution of the alternative pathway to conduction would be of course strongly influenced by the water content, but the more regular structure of DNA at high humidity could also contribute) as well as the lack of anisotropy seen in films of oriented DNA molecules [62].

A 1-D pathway through stacked base pairs could be argued from the weak sequence dependence reported by Yoo and coworkers; however, this could also be related to the different helical rises of poly(G)–poly(C) and poly(A)–poly(T) DNA, which could lead to a different contribution from water and counterions. In this scenario, small molecules could easily exhibit a semiconductor behavior, as observed by Porath and coworkers. The effects of the water solvent on the electronic states are accurately discussed in [57].

#### 5.5.2.5 Other Applications of DNA in Molecular Electronics

The interest in DNA for molecular electronics, however, does not stop at its conduction properties, but also lies in its self-assembly ability. For example, in Rinaldi's group at the National Nanotechnology Laboratory, a single modified DNA base, the lipophilic deoxyguanosine, was adopted to fabricate electronic devices. Guanosine was chosen due to the lowest oxidation potential among the DNA bases, which favors transport, and its self-assembling properties related to its peculiar sequence of hydrogen-bond donor and acceptor groups [66]. Using this approach, Maruccio and coworkers [67], from the same group, succeeded in the fabrication of a prototype FET based on this modified DNA base (Fig. 5.11) with a maximum voltage gain of 0.76. Unlike other molecular electronics devices based on CNTs, this prototype FET is based on ordered and self-assembled layers, instead of a single molecule with tremendous interconnection problems [68]. The transistor was fabricated by cast deposition of a droplet of the deoxyguanosine derivative in chloroform solution between the source and drain contacts consisting of two EBL-fabricated chromium/gold electrodes separated by a distance of 20–100 nm, while the control electrode was a layer of silver deposited on the reverse of the Si/SiO<sub>2</sub> substrate. The guanosine-based FET operated at room temperature and ambient pressure, and exhibited a voltage threshold for the conduction which could be modulated by the gate voltage. The electrical characteristics were explained in terms of resonant tunneling, the threshold voltage being defined by the alignment between the molecular minibands and the Fermi level in the electrodes.

DNA exhibits a surprising range of structural forms and possible modifications. One interesting example is the replacement of certain hydrogen atoms in the base pairs of the DNA with metal ions (Zn<sup>2+</sup>) as reported by Rakitin and co-workers at Brown University in the US [43], in collaboration with researchers at the University of Saskatchewan in Canada. Specifically, they prepared and investigated four types of  $\lambda$ -DNA samples:

- (1) *B*-DNA in standard buffer at pH 7.5.
- (2) *M*-DNA where the imino-proton of each base pair was substituted with a metal ion (Zn<sup>2+</sup>).
- (3) *B*-DNA samples in which the sticky ends of the DNA were attached to surface-bound oligomers.
- (4) *B*-DNA at pH 7.5 with 0.1 mM of Zn<sup>2+</sup>, since at this pH *M*-DNA does not form but the contribution of DNA surface-bound Zn<sup>2+</sup> ions on the measured electrical characteristics can be determined.

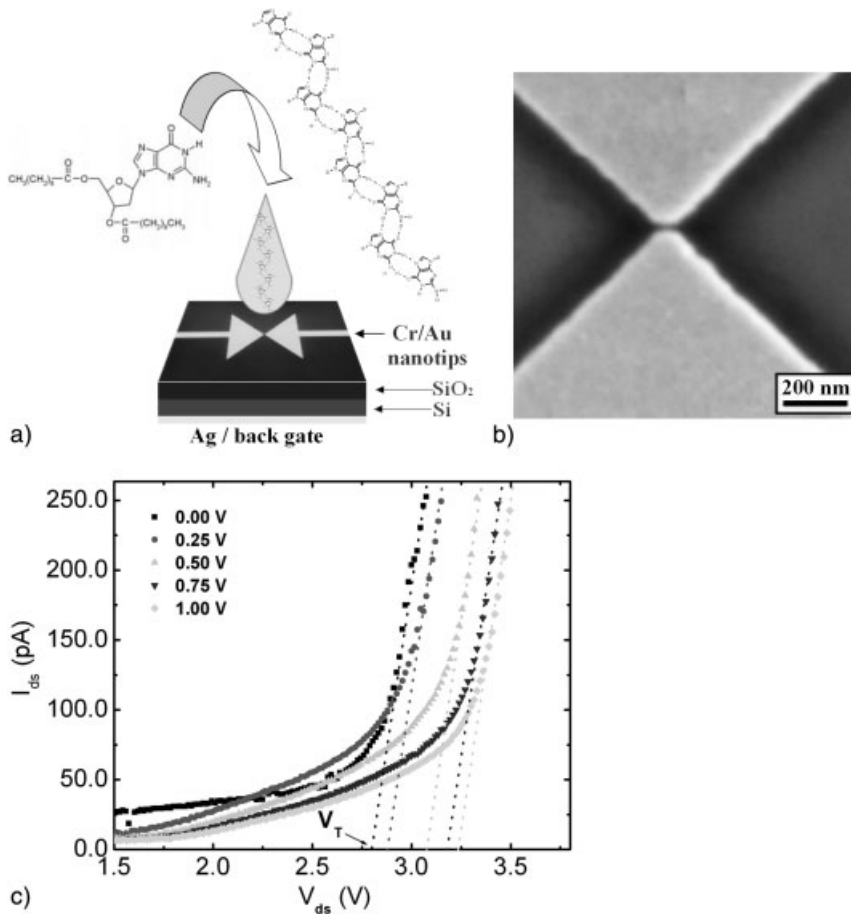


**Figure 5.11.** (a) Self-assembly and cast deposition of dG(C<sub>10</sub>)<sub>2</sub> on the three-terminal device, consisting of two arrow-shaped Cr/Au electrodes on a SiO<sub>2</sub> substrate and a third Ag back electrode (not to scale). (b) High-magnification SEM image of two Cr/Au nanotips with a separation of 20 nm. (c) Characteristics of the FET at different gate voltages ( $V_G$ ). The dashed lines extrapolate

the voltage threshold  $V_T$  for any  $V_G$  value. By changing the gate voltage,  $V_T$  can be modulated since the alignment condition for resonant tunneling is modified due to a shift in the energy of the molecular band. (reproduced with permission from G. Maruccio et al., *Nanoletters*, 2003, 3, 479–483. Copyright 2003 American Chemical Society)

The subsequent exposure of the samples to “freeze-dry” methods could not rule out the ionic contribution because of the existence of salt bridges formed on the substrate surface between electrodes. To solve this problem a new design for the contact was implemented by placing DNA between two electrodes separated by a physical gap of width 1–30  $\mu\text{m}$  and practically infinite depth. A metallic-like con-

duction was observed in 15  $\mu\text{m}$  long *M*-DNA, while a semiconducting behavior with a few hundred meV band gap was obtained in the case of *B*-DNA before conversion into *M*-DNA. Finally, a decrease in the zero bias conductance of about three orders of magnitude with respect to *M*-DNA was found in sample (4). The possibility to achieve such drastic change in conductivity could have important applications in molecular electronics.

An entirely different use of DNA was proposed by Braun and co-workers at the Technion and is based on the exploitation of its unrivaled assembly properties [32]. In fact, a strategy for the assembly of integrated circuits is still missing in molecular electronics and in this respect the highly specific binding between DNA strands may provide a key tool to control the geometry and connectivity of future electronic circuits without the use of destructive lithography techniques. Inspired by this, the Braun group firstly assembled DNA between two electrodes adding sticky ends to DNA fragments and then replaced the counterions with silver ions demonstrating that DNA can be used as a linear template to grow a thin metallic wire. The same approach was followed by Richter at Dresden to build up highly conductive palladium nanowires on a DNA template [69]. Moreover, the group of Erez Braun developed also the so-called sequence-specific molecular lithography [8], an alternative and promising strategy to produce large-scale functional circuits at the molecular level exploiting self-recognition and self-assembly of DNA (a parallel process). The information encoded in the DNA molecules replaces the masks used in conventional lithography, while a RecA protein serves as the resist. This technique enables high resolution, the fabrication of three-way junctions (branch-points) and the sequence-specific positioning of molecular objects. More recently, Keren and coworkers [70] reported the fabrication of a carbon nanotube FET, self-assembled using a DNA scaffold molecule to provide the address for precise localization of the nanotube as well as the template for the extended metallic wires contacting it (Fig. 5.12). Besides DNA and proteins, genetically engineered viruses have also been employed to order nanostructures [71].

Recently Williams and coworkers at Delft joined the conducting properties of single-walled carbon nanotubes (SWNTs) with the specific molecular-recognition features of DNA by coupling SWNTs to peptide nucleic acid (PNA, an uncharged DNA analogue) and hybridizing these macromolecular wires with complementary DNA [72]. The oligonucleotide adducts imparted recognition properties, used to programme the attachment of SWNTs to each other and to the electrodes. This general approach can be exploited in the field of biosensors.

DNA can be also combined with specific chemical side groups, providing the basis for new functional devices and accurate biosensors. For example, nanocomposite structures made of gold nanoparticles covered with single-strand DNA fragments were prepared by the Alivisatos's group at Berkeley [73] and Mirkin and coworkers at Northwestern [74] with the spacing between the nanoparticles controlled statically (by using different sticky ends) or dynamically (by exploiting the melting properties of DNA with changes in temperature or solvent). Moreover, DNA has the potential for assembling intricate spatial structures and networks with a variety of geometries, as those produced by Seeman and co-workers at New

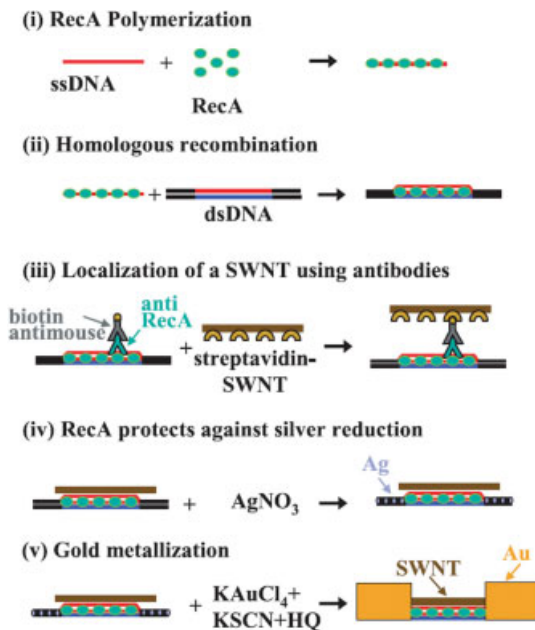


**Figure 5.12.** Assembly of a DNA-templated FET by molecular lithography. (i) Polymerization of RecA monomers on a ssDNA molecule, resulting in the formation of a nucleoprotein filament. (ii) Binding of the nucleoprotein filament at a desired address by homologous recombination. (iii) Delivery of a streptavidin-functionalized SWNT on the DNA-bound RecA by means of a primary antibody to RecA and a biotin-conjugated secondary antibody.

(iv) Incubation in an AgNO<sub>3</sub> solution and formation of silver clusters on segments unprotected by RecA. (v) Formation of two DNA-templated gold wires to contact the SWNT by electroless gold deposition (the silver clusters are used as nucleation centers). (reproduced with permission from K. Keren et al., *Science*, 2003, 302, 1380–1382. Copyright 2003 American Association for the Advancement of Science)

York University, including loops, knots, one- and two-dimensional arrays, three-dimensional cubes and nanolattices based on synthetic DNA structures [75].

As previously discussed, an important application of the assembly properties of DNA are the DNA chips which make use of many parallel DNA (single strands) probes to check whether certain genetic codes are present in a given specimen of DNA. Their read out schemes are currently optical, but an electronic read-out possibly exploiting the electron-transfer properties of DNA or using single-strands with sticky ends attached to electrically active molecular elements (such as metal clusters, fullerenes or certain molecular switches) could enable further miniaturization. The different electrochemical responses of single- and double-strand DNA molecules that attach to a surface can be also used in this frame [76].

Finally, concerning the applications of DNA self-assembly, we have of course to mention the DNA computation and its proof-of-concept by Adleman's group in 1994 [5], which demonstrated that the recombinant properties of DNA can be ex-



ploited to solve problems appropriately encoded into single DNA strands, using five simple operations: (a) synthesis of a large numbers of oligonucleotides, (b) annealing/hybridization of oligonucleotides to produce dsDNA molecules, (c) extraction of molecules containing a given sequence of bases, (d) detection of DNA molecules and (e) amplification of DNA molecules. The massive parallelism intrinsic in this approach allowed Adleman's group to solve a problem that had resisted conventional methods. The problem-specific technique of Adleman's group has been recently extended theoretically to more general Boolean operations.

In conclusion, although the advantages to use DNA as a molecular wire in electronic devices have probably to be evaluated in more detail, its unique assembly and recognition properties seem destined to be a major tool in molecular electronics.

## 5.6 Devices Based on Proteins

Besides DNA, proteins have been also intensively investigated in the last years for application in molecular electronics, molecular motors and biosensors, since their nature-tailored functions presents clear advantages for a number of specific applications. For example, the potential of photochromism has generated great interest in the synthesis of new photosensitive materials and in the development of new techniques for their use. Some biological systems, like bacteriorhodopsin and the green fluorescent protein (GFP) of the *Aequorea Victoria* jelly fish, offer naturally evolved optimized structures with unique properties that can further be tailored for specific applications by genetic engineering. The green fluorescent protein (GFP) is very interesting for optoelectronic applications since it exists in two distinct configurations (bright and dark) and has a very efficient fluorescence emission that makes possible also single-molecule detection. Moreover, genetic engineering allows producing mutants with modified spectral characteristics, enhanced brightness, photostability, quantum yield, and other properties tailored for specific applications. In particular, two GFP mutants – EGFP (enhanced GFP) and E<sup>2</sup>GFP (obtained by a single point mutation T203Y of EGFP) – were recently investigated by the Beltram group [77] who achieved optical control of transition between the bright and dark states in E<sup>2</sup>GFP by means of two laser beams with different wavelengths ( $\lambda = 476$  nm and 350 nm). Both the investigated proteins exhibited in solution absorption peaks at 400 and 515 nm, ascribed respectively to the protonated neutral and deprotonated anionic forms (states A and B) of the chromophore. A weak emission was observed for both mutants after excitation of state A and was ascribed to excited-state photoconversion from A to B. Moreover, the authors observed a reversible turning on and off (blinking) of the emission and its ultimate switching off (photobleaching) into a long-lasting dark state (C) within a few seconds after excitation at 476 nm. In the case of E<sup>2</sup>GFP mutants, it was possible to achieve a reversible photoconversion from state C back into state B by irradiation at 350 nm. Since unlimited optically controllable cycles between the bright

and dark configurations were reported, these results open the way to the use of the E<sup>2</sup>GFP mutant in memory devices by employing the states B and C to encode a (0, 1) bit. In fact, information can be stored and manipulated and the basic required operations (write, read and erase data) are performed at the single molecule level. According to the authors, one possible implementation is to use photoconversion from the dark to bright state by irradiation at 350 nm as WRITE step, fluorescence emission following weak excitation at 476 nm as READ step and photobleaching as ERASE step.

As discussed above, another interesting protein is the Bacteriorhodopsin (BR), a trans-membrane protein found in the cellular membrane of *Halobacterium salinarium*, which functions as a light-driven proton pump and thus is expected to be useful as photonic material. Due to its peculiar properties, its use as the active component in memory devices was investigated (for a recent review on Bacteriorhodopsin-based applications see [78]), in particular in holographic associative memories and branched-photocycle three-dimensional optical memories. More in detail, the proposed holographic associative memories were based on a Fourier transform optical loop and the real-time holographic properties of a BR films. On the other hand, in the branched-photocycle three-dimensional optical memories, parallel write, read, and erase processes were performed exploiting a sequential multiphoton process and an unusual branching reaction that creates a long-lived photoproduct. A very broad range of applications was proposed, from electronics to optoelectronics and computing including random access thin film memories, neural-type logic gates, photon counters and photovoltaic converters, artificial retinas, picosecond photodetectors, multilevel logic gates optical computing, and different kinds of memories (see [78] for further details).

Then, very recently, Yasutomi and coworkers at the Kyoto University [79] reported the fabrication of a molecular photodiode that can switch photocurrent direction by changing the wavelength of an irradiating light (Fig. 5.13). Their device was based on bicomponent SAMs of two helical peptides carrying different chromophores (thus selectively activable) and having opposite direction of dipole moments (when immobilized on gold). Since at a certain range of the applied potentials the direction of the photocurrent is determined by the direction of the dipole moment, photocurrent can be switched from anodic to cathodic alternating photoirradiation at 351 nm and 459 nm. The optimum voltage for photocurrent switching was determined by investigating the dependence of photocurrents on applied potential for the unicomponent SAMs.

The Greenbaum group reported on the generation of exogenous photovoltages by the Photosystem I (PSI) reaction centers, nanometer-size robust supramolecular structures that can be isolated and purified from green plants. A diode laser at  $\lambda = 670$  nm was used to illuminate heterostructures composed of PSI and organosulfur molecules onto gold substrates, while the photovoltage was measured by Kelvin force probe microscopy. Under illumination, the potentials of the central region of the PSIs were found to be typically more positive than the periphery by 6–9 kT, where kT is the Boltzmann energy at room temperature [80]. Possible applications of the PSI to the implementation of artificial retina are currently under exper-

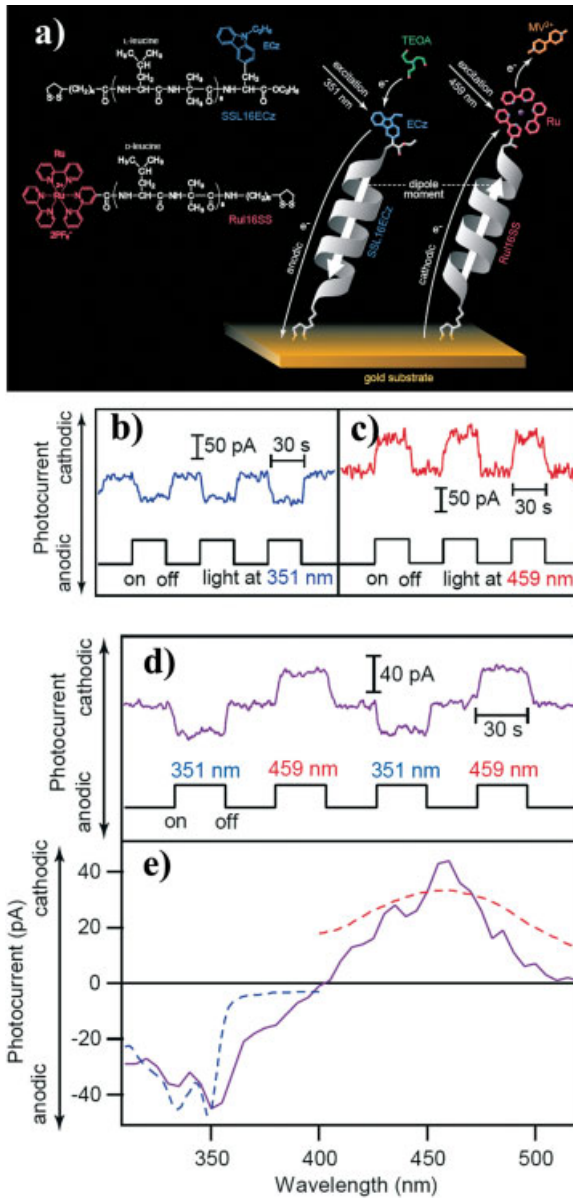


**Figure 5.13.** (a) Molecular structures of the two kinds of hexadecapeptides employed (SSL16ECz and Ru16SS) whose dipole moments (with opposite directions) determine the photocurrent switching from anodic to cathodic under selective photoexcitation of the sensitizer (an ECz or Ru group respectively) when the peptides are coassembled in a highly-ordered bicomponent SAM on a gold substrate via an Au-S linkage. (b-c) Periodic photocurrent generation by the SSL16ECz (Ru16SS) SAM upon photoirradiation at

351 nm (459 nm) in a 50 mM TEOA ( $MV^{2+}$ ) aqueous solution. (d) Time course of photocurrent switching upon alternating photoirradiation at 351 and 459 nm. (e) The action spectra (purple solid line) consists of anodic and cathodic photocurrent regions, which agree with the absorption spectra of SSL16ECz (blue dashed line) and Ru16SS (red dashed line) in ethanol, respectively. (reproduced with permission from S. Yasutomi et al. *Science*, 2004, 304, 1944. Copyright 2004 American Association for the Advancement of Science)

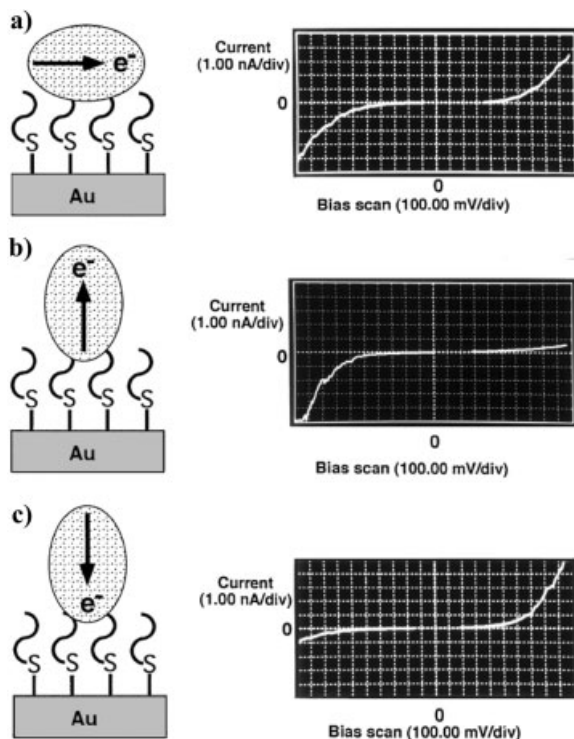


**Figure 5.14.** Orientation-dependent STS characteristics of individual PS I reaction centers. (a) If a PS I is oriented parallel to the electrode surface, a semiconductor-like behavior with a bandgap of around 1.8 eV can be observed. (b and c) If a PS I is anchored

perpendicular to the gold surface, a diode-like (current rectification)  $I$ - $V$  curve can be observed. (reproduced with permission from I. Lee et al., *Phys. Rev. Lett.* 1997, 79, 3294–97. Copyright 1997 American Physical Society)

imentation in the same group. Moreover, they also explored two-dimensional vectorial arrays of functional PSI reaction centers (prepared on atomically flat derivatized gold surfaces) by STS [12]. The nature and extent of PSI orientation were controlled by chemical modification of the surface derivative and checked by STS. When gold electrodes were treated with mercaptoacetic acid, 83% of the electron transport vectors were parallel to the electrode surface and a semiconductor-like  $I$ - $V$  curve with a band gap of  $\approx 1.8$  eV (corresponding to the first excited singlet state of chlorophyll) was observed (Fig. 5.14a). On the other hand, using 2-mercaptoethanol, 70% were oriented perpendicularly in the “up” position and only 2% were in the “down” position and current-rectification (i.e. diode-like behavior) was observed (Fig. 5.14b–c). Authors ascribed the asymmetry of the  $I$ - $V$  characteristics to either a difference in electronic energy (in analogy with a solid-state p-n junction) or a difference in the tunneling distance for each end.

A novel example of protein-based active electronic device has been recently dem-

onstrated by the group of Rinaldi and coworkers at NNL, taking advantage of the redox properties and of the functional groups of the blue copper protein Azurin, that, *in vitro*, is able to mediate electron transfer (ET) from cytochrome  $c_{551}$  to nitrite reductase from the same organism [81]. Azurin from *P. aeruginosa* is a 14.6 kDa blue-copper protein existing in two stable configurations – Cu(I) and Cu(II) – and its ET capability depends on the equilibrium between these two oxidation states by means of the reversible redox reaction  $\text{Cu}^{2+} + \text{e}^- \rightleftharpoons \text{Cu}^{1+}$ , which converts continuously the Cu(II) copper oxidized state into the Cu(I) reduced state and *vice versa*. A disulfide bridge (Cys-3-Cys-26) located at a distance of  $\approx 2.6$  nm from the copper site [82] allows the chemisorption of Azurin in oriented monolayers onto crystalline gold or other suitably functionalized surfaces [83, 84]. Since protein adsorption on surfaces may lead to denaturation, in their recent publication, Maruccio and co-workers [49] examined the integrity of proteins in dry monolayers after immobilization by non-contact atomic-force microscopy and by intrinsic fluorescence (the fluorescence of aromatic residues in proteins is strongly influenced by their microenvironment) concluding that neither the covalent binding to the functionalized  $\text{SiO}_2$  surface nor the application of strong electric fields induce gross denaturation and/or conformational transitions in Azurin. Their prototype device consists of a planar metal-insulator-metal nanojunction, fabricated by EBL [85] and connected by the self-assembled protein monolayer, and a silver back gate electrode in a field-effect transistor configuration. An oriented protein monolayer was formed in a two-step procedure involving (a) the self-assembly of 3-mercaptopropyltrimethoxysilane (3-MPTS) and (b) the reaction of the free thiol groups of 3-MPTS with the unique surface disulfide bridge of Azurin. The current-voltage characteristic ( $I_{\text{ds}}-V_{\text{ds}}$ ) exhibited a low-current plateau at low field and then rises up to hundreds of pA (see Fig. 5.15). The transfer characteristic exhibited a pronounced resonance centered at  $V_{\text{g}} = 1.25$  V. This feature gradually disappeared after some gate sweeps. From an electronic viewpoint, their device switches from a n-MOS FET behavior before resonance to a p-MOS FET after resonance. Although among all the fabricated nanodevices, only a limited group exhibited a clear gate effect over a number of gate sweeps (whereas the others failed during the first few sweeps – the ageing of nanodevices is a general issue of molecular electronics [16, 85, 87]), this is a key result because it would allow to exploit the advantages of a complementary logic, fabricating both p-type and n-type devices on the same chip.

The authors ascribed these results to the unique transport mechanism of their biomolecular devices. The transport of electrons through systems containing redox sites may occur via physical displacement of the redox molecules and/or electron hopping from one reduced molecule to an adjacent oxidized molecule [88]. The authors discarded the first mechanism since the proteins were covalently bound to the substrate. Thus, they ascribed electron transport in the Pro-FET to hopping from one reduced (Cu(I)) protein to an adjacent oxidized (Cu(II)) protein, which behave as a redox pair. For electrons to flow, therefore, both reduced and oxidized Azurins must be present and their relative proportion determines the ET rate. The authors proposed that the Azurin redox state is regulated by  $V_{\text{g}}$ : the higher is

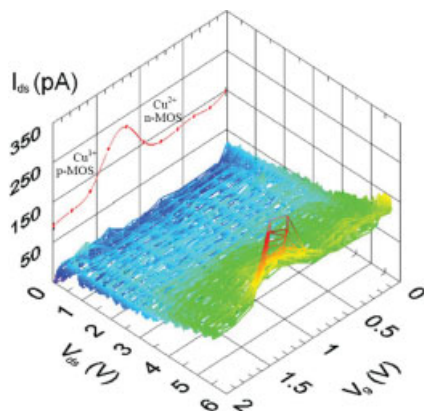


**Figure 5.15.** Characteristic of the Pro-FET: 3-D plot of the drain–source current as a function of the drain–source bias ( $V_{DS}$ ) and gate bias ( $V_G$ ) measured in the dark and at room temperature. No leakage current was observed to flow between the planar electrodes and the back-gate (values as low as few picoamperes and a negligible variation with  $V_G$  up to 8 V).

A pronounced resonance centered at  $V_G = 1.25$  V is present (see also the transfer characteristic at  $V_{DS} = 5.5$  V in the projection). (Reproduced with permission from G. Maruccio et al., *Towards Protein Field-Effect Transistors: Report and Model of a Prototype*, *Adv. Mater.*, 2005, 17, 816–822)

$V_g$ , the greater is the fraction of reduced Azurins. At a particular value of  $V_g$  the fraction of oxidized molecules will equal that of reduced molecules and therefore ET will be maximal. In their model the change in the protein oxidation state was ascribed to the influence of the applied electric field on the redox energy levels of the proteins. To verify whether such model based on a hopping mechanism between neighbouring proteins was compatible with their experimental findings, they performed numerical simulations of the current flowing in the device as a function of the applied potentials. The basic features of the experimental curves were exhibited also in the results of their simulation. Moreover, the proposed model is also consistent with the interpretation of the redox peak in cyclic voltammetry curves and in electrochemical STM experiments [84, 89] performed on Azurins chemisorbed on Au(111) substrates. The key role of the copper atom in electron transfer was further supported by a comparison with the current-voltage curves measured in devices implemented with two Azurin variants (the first with the Cu atom replaced by a Zn atom, the second without metal atom), where the flowing currents were significantly lower and no modulation was observed between  $-6$  and  $6$  volts.

The same metalloprotein has been investigated also at Oxford, where Davis and coworkers acquired current–voltage characteristics by means of conductive-probe AFM and studied the dependence of the conductance from the force load, finding that forces larger than  $3$  nN were necessary to achieve a reliable contact to the protein [90].

Before concluding, we would also like to mention the work of Yu and coworkers, who succeeded in the construction of ordered neuronal networks by positioning neurons on a bioelectronic chips by means of a negative dielectrophoretic force [91].

## 5.7

### Conclusions

We have briefly discussed the present status of the research in the field of nanobioelectronics, with special emphasis on DNA- and protein-based devices.

Although this field is rather young and very open, the worldwide results obtained so far are promising, and deserve further studies to determine the actual potentiality of biodevices and to further investigate a number of important issues, such as:

- Interconnection of biomolecules and inorganic devices
- Molecular engineering and self-organization
- Transport mechanisms
- Reproducibility and ageing of biomolecular devices
- Biochemical driven implementation of fully biomolecular nanodevices

On the basis of recent progress in the field of nanobioelectronics we feel as though we are just at the beginning of a great journey that will have many unexpected findings. There is no turning back and we cannot even envisage the future developments of this field and where it will take us.

There is much work under way actively pursuing molecular and biomolecular engineering, and the building of composite materials at the nanoscale to be joined together, but there is still an enormous challenge ahead. Building materials from the bottom up requires a multidisciplinary approach. This arena is unquestionably in the nano-dimension, where all fields of science and engineering meet. New ideas will be fostered from collaboration among scientists with diverse backgrounds. As Francis Crick put it, “In nature, hybrid species are usually sterile, but in science the reverse is often true. Hybrid subjects are often astonishingly fertile, whereas if a scientific discipline remains too pure it usually wilts”.

### Acknowledgments

We are thankful for the invaluable support and exciting collaboration by various colleagues. We would like to thank Elisa Molinari, Rosa Di Felice, Francesca De Rienzo, Stefano Corni and Paolo Facci at S<sup>3</sup>-CNR-INFN research center in Modena (Italy), Gerard Canters and Martin Verbeet at Leiden University (The Netherlands), Salvatore Masiero, Tatiana Giorgi, Gianpiero Spada and Giovanni Gottarelli at University of Bologna (Italy), Roberto Cingolani, Valentina Arima, Adriana Biasco, Alessandro Bramanti, Franco Calabi, Stefano D’Amico, Eliana

D'Amone, Antonio Della Torre, Pier Paolo Pompa and Paolo Visconti at NNL-CNR-INFM research center in Lecce (Italy). Financial support by NNL-CNR-INFM, EC through SAMBA project and Italian MIUR (FIRB molecular devices) is gratefully acknowledged.

## References

- 1 The Internet Technology Roadmap for Semiconductors (ITRS) is available at <http://public.itrs.net>.
- 2 MARUCCIO, G., CINGOLANI, R., RINALDI, R. Projecting the nanoworld: concepts, results and perspectives of molecular electronics, *J. Mater. Chem.* **2004**, *14*, 542–554 and references therein.
- 3 WOLF, S. A., AWSCHALOM, D. D., BUHRMAN, R. A., DAUGHTON, J. M., VON MOLNAR, S., ROUKES, M. L., CHITCHELKOVA, A. Y., TREGGER, D. M. SPINTRONICS: a spin-based electronics vision for the future, *Science* **2001**, *294*, 1488–1495.
- 4 (a) STEANE, A. Quantum computing, *Rep. Prog. Phys.* **1998**, *61*, 117–173; (b) DE MARTINI, F., BUZEK, V., SCIARRINO, F., SIAS, C. Experimental realization of the quantum universal NOT gate, *Nature* **2003**, *419*, 815–818.
- 5 (a) ADLEMAN, L. M. Molecular computation to solutions of combinatorial problems, *Science* **1994**, *266*, 1021; (b) BRAICH, R. S., CHELYAPOV, N., JOHNSON, C., ROTHMUND, P. W. K., ADLEMAN, L. Solution of a 20-variable 3-SAT problem on a DNA computer, *Science* **2002**, *296*, 499–502.
- 6 AVIRAM, A., RATNER, M. A. Molecular rectifiers, *Chem. Phys. Lett.* **1974**, *29*, 277–283.
- 7 LEHN, J. M. *Supramolecular Chemistry – Concept and Perspectives*. VCH, Weinheim, **1995**.
- 8 KEREN, K., KRUEGER, M., GILAD, R., BEN-YOSEPH, G., SIVAN, U., BRAUN, E. Sequence-specific molecular lithography on single DNA molecules, *Science* **2002**, *297*, 72–75.
- 9 MARUCCIO, G., VISCONTI, P., BIASCO, A., BRAMANTI, A., DELLA TORRE, A., POMPA, P. P., FRASCERRA, V., ARIMA, V., D'AMONE, E., CINGOLANI, R., RINALDI, R. Nano-scaled biomolecular field-effect transistors: prototypes and evaluations, *Electroanalysis* **2004**, *16*, 1853–1862.
- 10 BASHIR, R. DNA-mediated artificial nanobiostructures: state of the art and future directions, *Superlattices Microstruct.* **2001**, *29*, 1–16.
- 11 LOOGER, L. L., DWYER, M. A., SMITH, J. J., HELLINGA, H. W. Computational design of receptor and sensor proteins with novel functions, *Nature* **2003**, *423*, 185–190.
- 12 LEE, I., LEE, J. W., GREENBAUM, E. Biomolecular electronics: vectorial arrays of photosynthetic reaction centers, *Phys. Rev. Lett.* **1997**, *79*, 3294–3297.
- 13 CHEN, T., CALABRESE BARTON, S., BINYAMIN, G., GAO, Z., ZHANG, Y., KIM, H., HELLER, A. A miniature biofuel cell, *J. Am. Chem. Soc.* **2001**, *123*, 8630–8631.
- 14 GIMZEWSKI, J. K., JOACHIM, C., SCHLIETTLER, R. R., LANGLAIS, V., TANG, H., JOHANNSEN, I. Rotation of a single molecule within a supramolecular bearing, *Science* **1998**, *281*, 531–533.
- 15 JOACHIM, C., GIMZEWSKI, J. K., AVIRAM, A. Electronics using hybrid-molecular and mono-molecular devices, *Nature* **2000**, *408*, 541.
- 16 METZGER, R. M., CHEN, B., HOPFNER, U., LAKSHMIKANTHAM, M. V., VUILLAUME, D., KAWAI, T., WU, X., TACHIBANA, H., HUGHES, T. V., SAKURAI, H., BALDWIN, J. W., HOSCH, C., CAVA, M. P., BREHMER, L., ASHWELL, G. J. Unimolecular electrical rectification in hexadecylquinolinium tricyanoquinodimethanide, *J. Am. Chem. Soc.* **1997**, *119*, 10455–10466.



- 17 REED, M. A., CHEN, J., RAWLETT, A. M., PRICE, D. W., TOUR, J. M. Molecular random access memory cell, *Appl. Phys. Lett.* **2001**, *78*, 3735.
- 18 ROTH, S., JOACHIM, C. *Atomic and Molecular Wires*. Kluwer, Dordrecht, **1997**.
- 19 BACHTOLD, A., HADLEY, P., NAKANISHI, T., DEKKER, C. Logic circuits with carbon nanotube transistors, *Science* **2001**, *294*, 1317–1320.
- 20 HUANG, Y., DUAN, X., CUI, Y., LAUHON, L. J., KIM, K., LIEBER, C. M. Logic gates and computation from assembled nanowire building blocks, *Science* **2001**, *294*, 1313–1317.
- 21 ROCHA, A. R., GARCIA-SUAREZ, V. M., BAILEY, S. W., LAMBERT, C. J., FERRER, J., SANVITO, S. Towards molecular spintronics, *Nat. Mater.* **2005**, *4*, 335.
- 22 WATSON, J., CRICK, F. A structure for deoxyribose nucleic acid, *Nature* **1953**, *171*, 737.
- 23 GÖPEL, W. Controlled signal transduction across interfaces of “intelligent” molecular systems, *Biosens. Bioelectron.* **1995**, *10*, 35–59.
- 24 GWYN, C. W., STULEN, R., SWEENEY, D., ATTWOOD, D. Extreme ultraviolet lithography, *J. Vac. Sci. Technol. B* **1998**, *16*, 3142–3149.
- 25 REED, M. A., ZHOU, C., MULLER, C. J., BURGIN, T. P., TOUR, J. M. Conductance of a molecular junction, *Science* **1997**, *278*, 252–254.
- 26 KERVENNIC, Y. V., VAN DER ZANT, H. S. J., MORPURGO, A. F., GUREVICH, L., KOUWENHOVEN, L. P. Nanometer-spaced electrodes with calibrated separation, *Appl. Phys. Lett.* **2002**, *80*, 321–323.
- 27 PINER, D., ZHU, J., XU, F., HONG, S., MIRKIN, C. A. Dip-Pen nanolithography, *Science* **1999**, *283*, 661–663.
- 28 (a) HONG, S., ZHU, J., MIRKIN, C. A. Multiple ink nanolithography: towards a multiple-pen nanoplotter, *Science* **1999**, *286*, 523–525; (b) HONG, S., MIRKIN, C. A. A nanoplotter for soft lithography with both parallel and serial writing capabilities, *Science* **2000**, *288*, 1808–1811.
- 29 DEMERS, L. M., GINGER, D. S., PARK, S. J., LI, Z., CHUNG, S. W., MIRKIN, C. A. Direct patterning of modified oligonucleotides on metals and insulators by dippen nanolithography, *Science* **2002**, *296*, 1836–1838.
- 30 MACDONALD, M. P., PATERSON, L., VOLKE-SEPULVEDA, K., ARLT, J., SIBBETT, W., DHOLAKIA, K. Creation and manipulation of three-dimensional optically trapped structures, *Science* **2002**, *296*, 1101–1103.
- 31 STORM, A. J., VAN NOORT, J., DE VRIES, S., DEKKER, C. Insulating behavior for DNA molecules between nanoelectrodes at the 100 nm length scale, *Appl. Phys. Lett.* **2001**, *79*, 3881.
- 32 BRAUN, E., EICHEN, Y., SIVAN, U., BEN-YOSEPH, G. DNA-templated assembly and electrode attachment of a conducting silver wire, *Nature* **1998**, *391*, 775.
- 33 ZHANG, Y., AUSTIN, R. H., KRAEFT, J., COX, E. C., ONG, N. P. Insulating behavior of  $\lambda$ -DNA on the micron scale, *Phys. Rev. Lett.* **2002**, *89*, 198102.
- 34 (a) HARTZELL, B., MCCORD, B., ASARE, D., CHEN, H., HEREMANS, J. J., SOGHOMONIAN, V. Comparative current–voltage characteristics of nicked and repaired  $\lambda$ -DNA, *Appl. Phys. Lett.* **2003**, *82*, 4800. (b) HARTZELL, B., MCCORD, B., ASARE, D., CHEN, H., HEREMANS, J. J., SOGHOMONIAN, V. Current–voltage characteristics of diversely disulfide terminated  $\lambda$ -deoxyribonucleic acid molecules, *J. Appl. Phys.* **2003**, *94*, 2764.
- 35 PORATH, D., BEZRYADIN, A., DE VRIES, S., DEKKER, C. Direct measurement of electrical transport through DNA molecules, *Nature* **2000**, *403*, 635.
- 36 CAI, L., TABATA, H., KAWAI, T. Self-assembled DNA networks and their electrical conductivity, *Appl. Phys. Lett.* **2000**, *77*, 3105.
- 37 ELEY, D. D., METCALFE, E., WHITE, M. P., Semiconductivity of organic substances. Part 17. – Effects of ultraviolet and visible light on the conductivity of the sodium salt of deoxyribonucleic acid, *J. Chem. Soc., Faraday Trans. 1*, **1975**, *71*, 955.

- 38 (a) HALL, D. B., HOLMLIN, R. E., BARTON, J. K. Oxidative DNA damage through long-range electron transfer, *Nature* **1996**, *382*, 731; (b) DANDLIKER, P. J., HOLMLIN, R. E., BARTON, J. K. Oxidative thymine dimer repair in the DNA helix, *Science* **1997**, *275*, 1465; (c) KELLEY, S. O., HOLMLIN, R. E., STEMPE, E. D. A., BARTON, J. K. Photoinduced electron transfer in ethidium-modified DNA duplexes: dependence on distance and base stacking, *J. Am. Chem. Soc.* **1997**, *119*, 9861; (d) KELLEY, S. O., BARTON, J. K. Electron transfer between bases in double helical DNA, *Science* **1999**, *283*, 375.
- 39 RAJSKI, S. R., JACKSON, B. A., BARTON, J. K. DNA repair: models for damage and mismatch recognition, *Mutat. Res.* **2000**, *447*, 49.
- 40 DEKKER, C., RATNER, M. A. Electronic properties of DNA, *Phys. World* **2001**, *14*, 29.
- 41 E. K. WILSON, DNA Charge Migration: No Longer An Issue, *Chemical & Engineering News* **2001**, *79*, 1.
- 42 DE PABLO, P. J., MORENO-HERRERO, F., COLCHERO, J., GOMEZ HERRERO, J., HERRERO, P., BAR, A. M., ORDEJON, P., SOLER, J. M., ARTACHO, E. Absence of dc-conductivity in lambda-DNA, *Phys. Rev. Lett.* **2000**, *85*, 4992.
- 43 RAKITIN, A., AICH, P., PAPADPOULOS, C., KOZAR, YU., VEDENEV, A. S., LEE, J. S., XU, J. M. Metallic conduction through engineered DNA: DNA nanoelectronic building blocks, *Phys. Rev. Lett.* **2001**, *86*, 3670.
- 44 FINK, H. W., SCHÖNENBERGER, C. Electrical conduction through DNA molecules, *Nature* **1999**, *398*, 407.
- 45 TRAN, P., ALAVI, B., GRUNER, G. Charge transport along the lambda-DNA double helix, *Phys. Rev. Lett.* **2000**, *85*, 1564.
- 46 YOO, K. H., HA, D. H., LEE, J. O., PARK, J. W., KIM, J., KIM, J. J., LEE, H. Y., KAWAI, T., CHOI, H. Y. Electrical conduction through poly(dA)-poly(dT) and poly(dG)-poly(dC) DNA molecules, *Phys. Rev. Lett.* **2001**, *87*, 198102.
- 47 KASUMOV, A. Y., KOCAK, M., GUERON, S., REULET, B., VOLKOV, V. T. Proximity-induced superconductivity in DNA, *Science* **2001**, *291*, 280.
- 48 (a) MARCUS, R. A. On the theory of oxidation-reduction reactions involving electron transfer: I, *J. Chem. Phys.* **1956**, *24*, 966; (b) MARCUS, R. A. Electrostatic free energy and other properties of states having nonequilibrium polarization. I, *J. Chem. Phys.* **1956**, *24*, 979; (c) MARCUS, R. A. Electron transfer reactions in chemistry. Theory and experiment, *Rev. Mod. Phys.* **1993**, *65*, 599; (d) MARCUS, R. A. Ion pairing and electron transfer, *J. Phys. Chem. B* **1998**, *102*, 10071.
- 49 MARUCCIO, G., BIASCO, A., VISCONTI, P., BRAMANTI, A., POMPA, P. P., CALABI, F., CINGOLANI, R., RINALDI, R., CORNI, S., DI FELICE, R., MOLINARI, E., VERBEET, M. P., CANTERS, G. W. Towards protein field-effect transistors: report and model of a prototype, *Adv. Mater.* **2005**, *17*, 816-822.
- 50 IUPAC Compendium of Chemical Terminology, 2nd edn. IUPAC, Research Triangle Park, NC, **1997**.
- 51 ARKIN, M. R., STEMPE, E. D. A., TURRO, C., TURRO, N. J., BARTON, J. K. Luminescence quenching in supramolecular systems: a comparison of DNA- and SDS micelle-mediated photoinduced electron transfer between metal complexes, *J. Am. Chem. Soc.* **1996**, *118*, 2267.
- 52 GIESE, B., AMAUDRUT, J., KÖHLER, A. K., SPORMANN, M., WESSELY, S. Direct observation of hole transfer through DNA by hopping between adenine bases and by tunneling, *Nature* **2001**, *412*, 318.
- 53 GIESE, B., WESSELY, S., SPORMANN, M., LINDEMANN, U., MEGGERS, E., MICHEL-BEYERLE, M. E. On the mechanism of long-range electron transfer through DNA, *Angew. Chem. Int. Ed. Engl.* **1999**, *38*, 996.
- 54 HELLER, A. Spiers Memorial Lecture. On the hypothesis of cathodic protection of genes, *Faraday Discuss.* **2000**, *116*, 1.
- 55 (a) LEWIS, F. D., WU, T. F., ZHANG, Y. F., LETSINGER, R. L., GREENFIELD, S. R., WASIELEWSKI, M. R. Distance-

- dependent electron transfer in DNA hairpins, *Science* **1997**, *277*, 673;
- (b) LEWIS, F. D., WU, T. F., LIU, X. Y., LETSINGER, R. L., GREENFIELD, S. R., MILLER, S. E., WASIELENWSKI, M. R. Dynamics of photoinduced charge separation and charge recombination in synthetic DNA hairpins with stilbenedicarboxamide linkers, *J. Am. Chem. Soc.* **2000**, *122*, 2889.
- 56 FIEBIG, T., WAN, C. Z., KELLEY, S. O., BARTON, J. K., ZEWAHL, A. H. Femtosecond dynamics of the DNA intercalator ethidium and electron transfer with mononucleotides in water, *Proc. Natl Acad. Sci. USA* **1999**, *96*, 1187.
- 57 ENDRES, R. G., COX, D. L., SINGH, R. R. P. Colloquium: the quest for high-conductance DNA, *Rev. Mod. Phys.* **2004**, *76*, 195.
- 58 LEE, H., TANAKA, H., OTSUKA, Y., YOO, K., LEE, J., KAWAI, T. Control of electrical conduction in DNA using oxygen hole doping, *Appl. Phys. Lett.* **2002**, *80*, 1670.
- 59 CUNIBERTI, G., CRACO, L., PORATH, D., DEKKER, C. Backbone-induced semiconducting behavior in short DNA wires, *Phys. Rev. B* **2002**, *65*, 241314.
- 60 WATANABE, H., MANABE, C., SHIGEMATSU, T., SHIMOTANI, K. Single molecule DNA device measured with triple-probe atomic force microscope, *Appl. Phys. Lett.* **2001**, *79*, 2462.
- 61 PIRRUNG, M. C. How to make a DNA chip, *Angew. Chem. Int. Ed. Engl.* **2002**, *41*, 1276–1289.
- 62 WARMAN, J. M., DE HAAS, M. P., RUPPRECHT, A. DNA: a molecular wire?, *Chem. Phys. Lett.* **1996**, *249*, 319.
- 63 BERATAN, D. N., PRIYADARSHY, S., RISSER, S. M. DNA: insulator or wire?, *Chem. Biol.* **1997**, *4*, 3.
- 64 CONWELL, E. M., RAKHMANOVA, S. V. Polarons in DNA, *Proc. Natl Acad. Sci. USA* **2000**, *97*, 4556.
- 65 HERMON, Z., CASPI, S., BEN-JACOB, E. Prediction of charge and dipole solitons in DNA molecules based on the behavior of phosphate bridges as tunnel elements, *Europhys. Lett.* **1998**, *43*, 482.
- 66 GOTTARELLI, G., MASIERO, S., MEZZINA, E., PIERACCINI, S., RABE, J. P., SAMORI, P., SPADA, G. P. The self-assembly of lipophilic guanosine derivatives in solution and on solid surfaces, *Chem. Eur. J.* **2000**, *6*, 3242.
- 67 MARUCCIO, G., VISCONTI, P., ARIMA, V., D'AMICO, S., BIASCO, A., D'AMONE, E., CINGOLANI, R., RINALDI, R., MASIERO, S., GIORGI, T., GOTTARELLI, G. Field effect transistor based on a modified DNA base, *Nano Lett.* **2003**, *3*, 479–483.
- 68 LEFEBVRE, J., LYNCH, J. F., LLAGUNO, M., RADOSAVLJEVIC, M., JOHNSON, A. T. Single-wall carbon nanotube circuits assembled with an atomic force microscope, *Appl. Phys. Lett.* **2002**, *75*, 3014–3016.
- 69 RICHTER, J., MERTIG, M., POMPE, W., MÖNCH, I., SCHCKERT, H. K. Construction of highly conductive nanowires on a DNA template, *Appl. Phys. Lett.* **2001**, *78*, 536.
- 70 KEREN, K., BERMAN, R. S., BUCHSTAB, E., SIVAN, U., BRAUN, E. DNA-templated carbon nanotube field-effect transistor, *Science* **2003**, *302*, 1380–1382.
- 71 LEE, S., MAO, C., FLYNN, C. E., BELCHER, A. M. Ordering of quantum dots using genetically engineered viruses, *Science* **2002**, *296*, 892–895.
- 72 WILLIAMS, K. A., VEENHUIZEN, P. T. M., DE LA TORRE, B., ERITJA, R., DEKKER, C. Nanotechnology: carbon nanotubes with DNA recognition, *Nature* **2002**, *420*, 761.
- 73 ZANCHET, D., MICHEEL, C. M., PARAK, W. J., GERION, D., WILLIAMS, S. C., ALIVISATOS, A. P. Electrophoretic and structural studies of DNA-directed Au nanoparticle groupings, *J. Phys. Chem. B* **2002**, *106*, 11758.
- 74 TATON, T. A., MIRKIN, C. A., LETSINGER, R. L. Scanometric DNA array detection with nanoparticle probes, *Science* **2000**, *289*, 1757.
- 75 WINFREE, E., LIU, F. R., WENZLER, L. A., SEEMAN, N. C. Design and self-assembly of two-dimensional DNA crystals, *Nature* **1998**, *394*, 539.

- 76 PARK, S. J., TATON, T. A., MIRKIN, C. A. Array-based electrical detection of DNA with nanoparticle probes, *Science* **2002**, 295, 1503.
- 77 CINELLI, R. A. G., PELLEGRINI, V., FERRARI, A., FARACI, P., NIFOSI, R., TYAGI, M., GIACCA, M., BELTRAM, F. Green fluorescent proteins as optically controllable elements in bioelectronics, *Appl. Phys. Lett.* **2001**, 79, 3353.
- 78 BIRGE, R. R., GILLESPIE, N. B., IZAGUIRRE, E. W., KUSNETZOW, A., LAWRENCE, A. F., SINGH, D., SONG, Q. W., SCHMIDT, E., STUART, J. A., SEETHARAMAN, S., WISE, K. J. Biomolecular electronics: protein-based associative processors and volumetric memories, *J. Phys. Chem. B* **1999**, 103, 10746.
- 79 YASUTOMI, S., MORITA, T., IMANISHI, Y., KIMURA, S. A molecular photodiode system that can switch photocurrent direction, *Science* **2004**, 304, 1944.
- 80 LEE, I., LEE, J. W., STUBNA, A., GREENBAUM, E. Measurement of electrostatic potentials above oriented single photosynthetic reaction centers, *J. Phys. Chem. B* **2000**, 104, 2439.
- 81 VIJGENBOOM, E., BUSCH, J. E., CANTERS, G. W. *In vivo* studies disprove an obligatory role of azurin in denitrification in *Pseudomonas aeruginosa* and show that azu expression is under control of rpoS and ANR, *Microbiology* **1997**, 143, 2853.
- 82 FARVER, O., PECHT, I., Long range intramolecular electron transfer in azurins, *J. Am. Chem. Soc.* **1992**, 114, 5764.
- 83 CHI, Q., ZHANG, J., NIELSEN, J. U., FRIIS, E. P., CHORKENDORFF, I., CANTERS, G. W., ANDERSEN, J. E. T., ULSTRUP, J. Molecular monolayers and interfacial electron transfer of *Pseudomonas Aeruginosa* azurin on Au(111), *J. Am. Chem. Soc.* **2000**, 122, 4047.
- 84 ALESSANDRINI, A., GERUNDA, M., CANTERS, G. W., VERBEET, M. P., FACCI, P. Electron tunneling through azurin is mediated by the active site Cu ion, *Chem. Phys. Lett.* **2003**, 376, 625.
- 85 MARUCCIO, G., VISCONTI, P., D'AMICO, S., CALOGIURI, P., D'AMONE, E., CINGOLANI, R., RINALDI, R. Planar nanotips as probes for transport experiments in molecules, *Microelectron. Eng.* **2003**, 67–68, 838.
- 86 PARK, J., PASUPATHY, A. N., GOLDSMITH, J. I., CHANG, C., YAISH, Y., PETTA, J. R., RINKOSKI, M., SETHNA, J. P., ABRUNA, H. D., MCEUEN, P. L., RALPH, C. Coulomb blockade and the Kondo effect in single-atom transistors, *Nature* **2002**, 417, 722.
- 87 (a) LEE, J., LIENTSCHNIG, G., WIERTZ, F., STRUIJK, M., JANSSEN, R. A. J., EGBERINK, R., REINHOUDT, D. N., HADLEY, P., DEKKER, C. Absence of strong gate effects in electrical measurements on phenylene-based conjugated molecules, *Nano Lett.* **2003**, 3, 113; (b) KAGAN, C. R., AFZALI, A., MARTEL, R., GIGNAC, L. M., SOLOMON, P. M., SCHROTT, A. G., EK, B. Evaluations and considerations for self-assembled monolayer field-effect transistors, *Nano Lett.* **2003**, 3, 119.
- 88 BLAUCH, D. N., SAVEANT, J. M. Dynamics of electron hopping in assemblies of redox centers. Percolation and diffusion, *J. Am. Chem. Soc.* **1992**, 114, 3323.
- 89 FACCI, P., ALLIATA, D., CANNISTRARO, S. Potential-induced resonant tunneling through a redox metalloprotein investigated by electrochemical scanning probe microscopy, *Ultramicroscopy* **2001**, 89, 291.
- 90 ZHAO, J., DAVIS, J. J., SANSOM, M. S. P., HUNG, A. Exploring the electronic and mechanical properties of protein using conducting atomic force microscopy, *J. Am. Chem. Soc.* **2004**, 126, 5601–5609.
- 91 YU, Z., XIANG, G., PAN, L., HUANG, L., YU, Z., XING, W., CHENG, J. Negative dielectrophoretic force assisted construction of ordered neuronal networks on cell positioning bioelectronic chips, *Biomed. Microdevices* **2004**, 6, 311–324.

## 6

# DNA Nanodevices: Prototypes and Applications

*Friedrich C. Simmel*

### 6.1

#### Introduction

The unique biochemical and biophysical properties of DNA can be utilized to construct artificial, machine-like molecular structures which can perform simple mechanical or computational tasks, or both. This chapter gives an overview over the first prototypes of such “DNA nanodevices” as well as over recent developments towards functional DNA machines. In contrast to earlier review articles on this subject, particular emphasis is put on possible applications of DNA nanodevices in the life sciences – DNA devices interacting with proteins, as biosensors or as components of drug delivery systems.

The outline of this chapter is as follows. Section 6.2 gives a short introduction into the most important properties of DNA which make this molecule so interesting for nanoscale science and technology. Section 6.3 deals with “simple DNA devices” – prototype devices which can perform simple movements on the nanoscale. Section 6.4 focuses on more recent developments of “functional” nanodevices with an emphasis on possible applications in the life sciences. DNA-based molecular motors and automata will be discussed as well as the interaction of DNA devices with proteins. Section 6.5 deals with problems related to the construction of autonomous or “free-running” DNA devices and discusses a variety of different concepts to achieve such autonomous behavior. Section 6.5 closes the chapter with a few concluding remarks.

### 6.2

#### DNA as a Material for Nanotechnology

##### 6.2.1

#### Nanoscale Science

One of the main goals of nanotechnology is the manipulation of matter at the level of single molecules or atoms. Such ultimate control could lead to the development

of new functional materials and devices which obtain their functionality from the ordered assembly of components on the molecular scale. In the life sciences, such molecularly ordered systems could lead to extremely sensitive and even autonomous sensors and to intelligent drug delivery units.

One approach towards nanoscale control – often termed the “top-down” approach – is the manipulation of matter using macroscopic machines. Using scanning probe techniques, for example, the manipulation of single atoms or molecules has already been demonstrated during the last decade [1, 2]. Even though such examples show impressively the degree of control on the atomic level that has been achieved so far, it is not clear how scanning probe or other “top-down” techniques could be used for fast and efficient assembly of a large number of nanoscale components.

A different approach to molecular-scale engineering does not involve the “direct” manipulation of molecules and atoms with the help of a macroscopic device, but rather the utilization of self-assembly and self-organization principles. This approach is inspired by biological systems which often serve as “prototypes” for self-assembled nanotechnological structures.

In biological systems, complex and comparatively large structures are formed from smaller and simpler building blocks by “molecular recognition” events – usually the cooperative action of a multitude of weak bonds between two or more molecules which result in strong and highly specific interactions. Molecular construction is often assisted by “molecular machines” or enzymes – themselves self-assembled macromolecular complexes – which, among others, catalyze reactions, assist molecular transport or transduce signals. In addition, the molecules in a living cell are intimately linked within complex interaction networks which give rise to fascinating “emergent” properties.

Naturally, all these features would be highly desirable for artificial nanosystems. For these reasons, researchers in the field are trying to utilize the molecular recognition properties of biological molecules for the construction of nonbiological structures. Furthermore, first attempts have been made to construct artificial analogs of biological molecular machines and motors. One of the most interesting and most widely used biomolecules in this context is the famous molecule of heredity – DNA.

### 6.2.2

#### **Biophysical and Biochemical Properties of Nucleic Acids**

There are a number of good – and practical – reasons for the utilization of DNA in nanoscience (summarized in Fig. 6.1). The main feature of interest, of course, is the base-pairing interaction between complementary DNA bases which was discovered more than 50 years ago [3]. DNA molecules are composed of so-called nucleotides which themselves consist of a sugar unit (2'-deoxyribose) with a phosphate group and a “base” attached to it. The bases in DNA are the purines adenine (A) and guanine (G) and the pyrimidines thymine (T) and cytosine (C). In the Watson–Crick (WC) base-pairing scheme, the bases A and T bind together

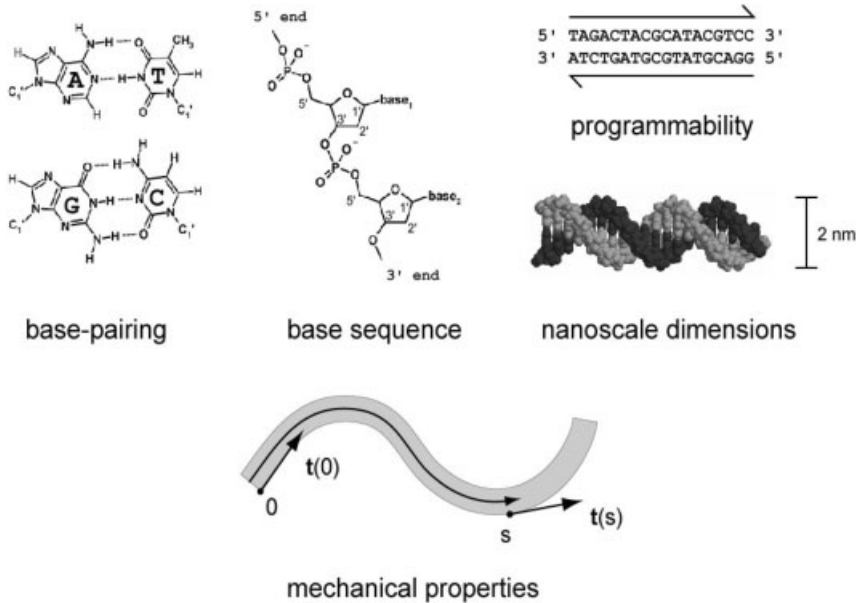


**Figure 6.1.** The most important features of DNA for nanoscience. *Base-pairing:* The specific binding between adenine (A) and thymine (T), on the one hand, and guanine (G) and cytosine (C), on the other hand, is the basis of the unique molecular recognition properties of DNA. *Base sequence:* In ssDNA, nucleotides which consist of deoxyribose, phosphate and a base are linked together. The bases can be chosen arbitrarily and therefore large numbers of distinct DNA molecules with different base sequences are possible. *Programmability:* If two

DNA sequences are complementary, they may bind together to form a DNA duplex structure, i.e. sequence determines structure. *Nanoscale dimensions:* Under normal conditions DNA duplexes are right-handed double-helices with a diameter of 2 nm. *Mechanical properties:* On the nanoscale, DNA is a rigid molecule. The persistence length, i.e. the length over which the correlation between the tangential vector  $t(s)$  decays, is of the order of 50 nm or 150 base pairs.

via two hydrogen bonds, whereas G and C are connected via three such bonds. In DNA, the nucleotides are linked together by the phosphate groups which connect the 3' position of deoxyribose of one nucleotide with the 5' position of the sugar ring of the following nucleotide. This linkage endows the DNA strand with a “direction”, e.g. 5'-AG-3' and 5'-GA-3' (where the sequence is read from the 5' end of the first nucleotide to the 3' end of the last nucleotide) are two different molecules. If two DNA molecules with “complementary” sequences are brought together, they can bind to each other and form a DNA duplex. Here it is important that the two strands have opposite directionality, i.e. a DNA strand with sequence 5'- $N_1N_2 \dots N_{n-1}N_n$ -3' will bind to a strand with sequence 5'- $\underline{N}_n\underline{N}_{n-1} \dots \underline{N}_2\underline{N}_1$ -3', where  $\underline{N}_i$  denotes the WC complement of  $N_i$ . Under standard buffer conditions, the DNA duplex will adopt a double-helical structure with a diameter of 2 nm and a helix pitch of roughly 10.5 base pairs. The base pairs stack upon each other and

are “hidden” within the double helix. The planes defined by the base pairs are oriented roughly perpendicularly to the axis of the helix, whereas the sugar units with the negatively charged phosphates point radially away from it. The vertical distance between two subsequent base pairs is approximately 0.34 nm. The phosphate linkages make DNA a highly negatively charged polyelectrolyte. Due to the double-helical structure and this high charge density, duplex DNA is a relatively rigid molecule. In terms of polymer science, the persistence length  $L_p$  of double-helical DNA is of the order of 50 nm or 150 base pairs. This is a measure for how far one has to follow the contour of a polymer until the original orientation is lost – essentially this is a measure of its flexibility. More technically,  $L_p$  is the correlation length of the tangent vector of the polymer. In the worm-like chain (WLC) polymer model, we have  $\langle \vec{t}(s) \cdot \vec{t}(0) \rangle = \exp(-s/L_p)$ , where  $s$  is the coordinate along the polymer and  $\vec{t}(s)$  is the tangent vector at position  $s$ . An  $L_p$  of 50 nm makes DNA a considerably less flexible molecule than most synthetic polymers. For nano-construction, DNA can thus simply be regarded as a stiff molecular rod. At the same time, DNA is much more flexible than other biopolymers such as the cytoskeletal F-actin or microtubuli. It is therefore not straightforward to produce ordered micron-scale structures with DNA.

By the proper choice of DNA sequences, one can also *avoid* the formation of duplex structures. To this end, sequences have to be chosen in such a way that they are not complementary to any other DNA molecule – or to itself – over stretches of more than a few bases. In contrast to double-stranded (ds) DNA, single-stranded (ss) DNA is a much more flexible polymer with a persistence length on the order of 1 nm. By “programming” DNA molecules to form partly double-stranded and partly single-stranded regions, one can therefore construct molecular networks consisting of rigid and flexible elements.

Unlike the folding of amino acid chains in proteins, the formation of secondary and tertiary structure in nucleic acids is hierarchical and sequential [4] – the binding energies for base-pairing are much larger than the energies for other interactions between remote residues, and therefore DNA and RNA folding are dominated by secondary structure formation. The prediction of the formation of base-paired regions within one DNA molecule or those formed between several DNA molecules therefore represents a major step in accurate structure prediction for nucleic acids structures. In the absence of significant three-dimensional (3-D) interactions between distant sections of a DNA or RNA molecule, it is already the final step. This property makes the relation between DNA sequence and structure much more transparent than in proteins and therefore a “rational” design of DNA structures can be achieved much easier.

This rational design is also facilitated by the wealth of thermodynamic data available for nucleic acids structures. Based on these data, thermodynamic quantities such as the free energy of formation of DNA structures or useful experimental parameters such as the melting temperature of a given DNA duplex (the temperature at which half of the duplexes are dissociated into single strands) can be calculated relatively reliably. In a given set of DNA molecules, strands may also hybridize to each other in several alternative configurations and here thermodynamic calcula-



tions aid in the design of structures which mainly self-assemble into one specific, desired structure.

Maybe one of the most important practical features of DNA, however, is the availability of automated synthesis methods which allow the production of reasonable quantities of DNA with virtually any desired base sequence. A designed DNA structure can therefore be readily translated from a sequence on your computer to a real molecule.

### 6.2.3

#### **DNA Nanoconstruction**

The unique properties of DNA summarized in the previous section have indeed already been utilized for the realization of a number of impressive supramolecular constructions. Starting with the synthesis of a DNA molecule with the topology of a cube by Seeman and coworkers in 1991 [5]. DNA has been used to construct molecules with the structure of a truncated octahedron [6], DNA catenanes [7], tetrahedra and octahedra [8, 9], and other geometrical objects [10]. DNA has also been used to construct 2-D molecular networks from DNA branched junctions [11, 12]. When these networks fold back to themselves, they can also form DNA “nanotubes” [13–15]. Recently, such networks have even been utilized to arrange nanoparticles and proteins in two dimensions [16–18]. Attempts to extend these structures into the third dimension are currently being made in a number of laboratories.

## 6.3

### **Simple DNA Devices**

The biochemical and mechanical properties of DNA cannot only be used for the construction of static supramolecular structures, but they can also be utilized to achieve motion on the nanometer scale. So far, one can discern essentially two strategies. Some of the devices rely on conformational changes of the DNA molecules themselves which occur under certain buffer conditions. Other devices exploit the different rigidity of ssDNA and dsDNA, and switch back and forth between several structures by the addition or removal of DNA “fuel” or “set” strands.

### 6.3.1

#### **Conformational Changes Induced by Small Molecules and Ions**

The presence of multiply charged cations can lead to marked changes in DNA structure. DNA strands with a sequence of repeating CG residues, for example, may undergo a transition to the so-called Z form of DNA in the presence of cobalt hexammine. Z-DNA is a left-handed helical conformation of DNA and the transition from B form DNA (the “usual” right-handed double-helical DNA conformation) is therefore associated with a change in helicity of the molecule. In the “B–Z

device” [19], the B–Z transition has been utilized to produce nanoscale rotatory motion. To this end, the DNA sequence  $d(CG)_{10}$  which tends to undergo the B–Z transition, was flanked by two DNA supramolecular structures which do not. When the  $d(CG)_{10}$  sequence was switched into the Z form, the two flanking parts rotated with respect to each other. Experimentally this could be proved by fluorescence resonance energy transfer (FRET) measurements between two strategically attached fluorescent dyes. In FRET, excitation energy is transferred from one donor fluorophore to another chromophore in close proximity. The strong distance dependence of this effect in the nanometer range makes it extremely valuable for the characterization of nanoscale motions. Consequently, it is the most commonly used experimental technique – apart from gel electrophoresis – to characterize the operation of DNA nanodevices.

Another example where the presence of cations influences DNA structure is related to the phenomenon of DNA condensation – even though duplex DNA is highly negatively charged, two DNA helices can overcome their mutual electrostatic repulsion in the presence of multivalent cations such as  $Mg^{2+}$ , putrescine, cobalt hexammine, spermidine or spermine [20]. In Ref. [21], magnesium ions were utilized to switch a network of biotinylated DNA molecules linked by streptavidin from an uncondensed into a condensed structure, in which neighboring DNA duplexes formed supercoils. This was accompanied by a movement of the nodes of the network with respect to each other.

The presence of protons may also induce a DNA conformational change. At low pH values the DNA bases adenine and cytosine, for example, are protonated at their N6 or N4 positions, respectively. Protonated cytidine ( $pK_a = 4.2$ ) participates in a number of unconventional DNA secondary structures, e.g. the DNA “i-motif” and a DNA triplex structure. The i-motif [22] can form between DNA strands with repetitive stretches of cytosine residues and is held together by hemiprotonated cytosine pairs (Fig. 6.2a). The intramolecularly formed i-motif shown in Fig. 6.2(b)

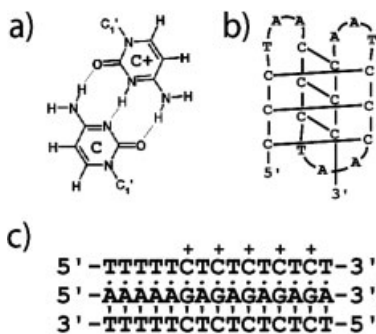


**Figure 6.2.** Unusual DNA structures which form with protonated cytosine residues. (a) A hemiprotonated CC+ base pair. (b) A C-rich strand of DNA forms the so-called “i-motif” at low pH values due to intramolecular CC+ base-pairing. (c) Protonated cytosine also plays

a role in DNA triplex formation. Here, the lower two DNA strands bind to each other in standard WC mode, whereas the upper strand binds to the middle strand in the “Hoogsteen” mode. This is only possible when the cytosines are protonated.

has recently been utilized for a simple proton-driven DNA device [23]. Upon the addition of a small amount of hydrochloric acid to a solution of the DNA device strand 5'-CCCTAACCCTAACCCTAACC-3', the molecule folds into the *i*-motif. When the pH is subsequently raised by the addition of sodium hydroxide, the molecule unfolds again. At neutral pH, the DNA strand is available for hybridization and it can form a DNA duplex with its complement strand. During one operation cycle, the 5' and 3' ends of the device strand therefore move from a proximate position with a distance on the order of 1 nm to a position where they are separated by roughly 6 nm.

Under certain conditions DNA can also form triplex structures. In a triplex, two strands bind with each other in conventional WC mode while the third strand binds to the duplex via other base-pairing interactions. One such triplex structure is based on the binding of two homopyrimidine strands to one homopurine strand. In the example in Fig. 6.2(c), the homopurine strand contains the repetitive sequence  $d(GA)_n$ . One homopyrimidine strand [with the sequence  $d(TC)_n$ ] binds to the homopurine strand by WC base-pairing while the other homopyrimidine strand binds via “Hoogsteen” base-pairing [24]. The latter binding mode is only possible when the cytosine residues are protonated. One can therefore switch between a duplex and a triplex DNA structure by lowering or raising the pH value [25]. This duplex–triplex transition has already been utilized to drive the simple DNA mechanical device depicted in Fig. 6.3 [26]. Here, a long DNA strand L has been hybridized to two shorter DNA strands F and S. The strands F and L form a struc-

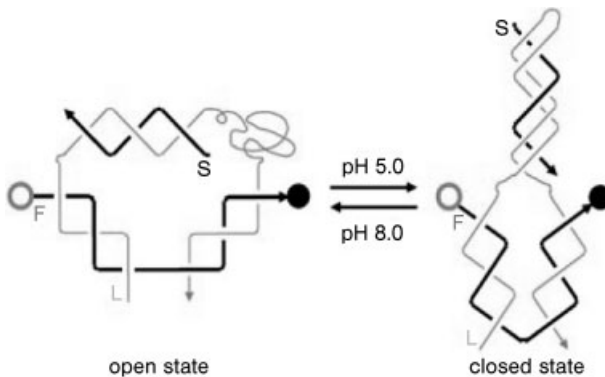


**Figure 6.3.** A proton-driven DNA nanodevice based on the duplex–triplex transition. The device consists of three DNA strands L, F and S. L and F form two rigid double-stranded “arms” connected by a flexible single-stranded hinge. Strand S is also hybridized to L and contains a DNA sequence which is able to form a triplex structure. The sequence which can bind to the duplex formed by S and L is contained in the unhybridized section schematically depicted as a “random coil” in the open

state. At low pH, the cytosine residues in this coil region are protonated and this section of L can bind to the S–L duplex in Hoogsteen mode, thereby forming a triplex structure. This closes the arms of the structure. The structure can be cycled between the open, duplex state and the closed, triplex state by changing the pH value of the reaction solution between pH 8 and pH 5. (Reprinted with permission from Ref. [26], © 2004, Wiley-VCH.)

ture characterized by two rigid arms connected by a short flexible hinge (very similar to the structure of other, hybridization-driven devices to be discussed in the next section). Strand S also hybridizes to a section of L, while a part of L remains unhybridized at high pH values. S contains a hompurine sequence and can form a triplex structure with L at low pH values. As shown in Fig. 6.3, in the triplex configuration strand L folds back on itself and therefore moves the two arms of the device with respect to each other.

Another (maybe the earliest) example of a DNA nanomechanical device, demonstrated by the Seeman group, was based on the influence of the intercalating dye ethidium bromide on DNA structure [27]. Here, the position of base pairs in a cruciform DNA junction embedded into a circular dsDNA construct could be shifted by applying torsional stress to the DNA circle via the incorporation of the intercalator.

One great disadvantage of the devices based on conformational changes caused by small molecules or ions is the fact that here DNA only plays a structural role – the DNA code is only utilized for the construction of the devices, but not for their control. Hence all of the devices in a reaction volume are affected by a buffer change simultaneously and they cannot be addressed individually. This issue is, at least in principle, resolved in hybridization-driven devices.

### 6.3.2

#### Hybridization-driven Devices

A very different operation principle underlies hybridization-driven DNA devices. Here, the conformational change of a DNA supramolecular structure is brought about by the hybridization of “fuel strands” with single-stranded “motor” sections. “DNA tweezers” were the first prototype of this kind of device [28]. Their operational principle is shown in Fig. 6.4. In the open state, the DNA tweezers consist of three strands of DNA. One 40-nucleotide long strand is hybridized to two other, 42-nucleotide strands in such a way that together they form two 18-base pair (6-nm), rigid duplex “arms” connected by a 4-nucleotide, single-stranded flexible “hinge”. In the open state, each of the 42-nucleotide strands still has 24-nucleotide (i.e. 42–18 nucleotides) single-stranded extensions available for hybridization. The addition of a 56-nucleotide “fuel” strand which is complementary to these extensions can then be used to close the tweezers structure, i.e. the two arms are forced together by the hybridization with the fuel strand. A “trick” is used to switch the device back to its original configuration. In the closed state, from the 56 nucleotides of the fuel strand, 8 nucleotides are deliberately left single-stranded. These 8 nucleotides serve as a “toehold” for another “anti-fuel” or “reset” strand which is exactly complementary to the fuel strand. A biochemical process known as “branch migration” unzips the structure, when fuel and anti-fuel try to bind with each other. After completion of this process, a stable 56-base pair “waste” duplex is formed and the DNA tweezers are in their open configuration once more. The device can be operated cyclically by the alternate addition of set and reset strands.

The same operation principle has since been used in many other DNA devices: a

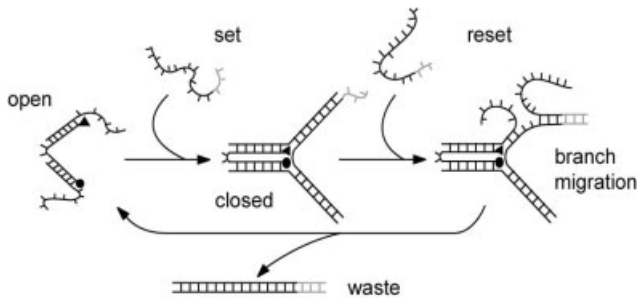


**Figure 6.4.** Operation cycle of the DNA tweezers (*cf.* Ref. [28]). In the open state, the DNA tweezers consist of three DNA strands which together form a “tweezers”-like structure consisting of two double-stranded arms connected by a flexible single-stranded hinge. The arms have two single-stranded extensions to which a “set” or “fuel” strand can attach. The hybridization of the fuel strand with these extensions closes the tweezers structure. Another fuel strand which is completely

complementary to the first one can reset the tweezers to the open state. When the tweezers are in the closed state, the reset strand attaches to the single-stranded “toehold” region of the set strand (gray) and displaces the set strand from the tweezers by “branch migration”. After completion of this process, a double-stranded waste product is formed by the set and reset strand, while the open state of the tweezers is restored.

simple variation of the DNA tweezers is the DNA actuator device [29, 30] shown in Fig. 6.5. Here, instead of two single-stranded extensions, the arms of the tweezers were connected by a single-stranded loop. Depending on the sequence of the fuel strands, the device could either be closed similarly to the tweezers or stretched into an elongated conformation. Whereas the intermediate configuration is a rather floppy structure (like the open tweezers), the closed and the stretched configurations are much more rigid. The distance between the fluorescent dyes attached to the arms of the actuator is switched from roughly 2 nm in the closed state to approximately 14 nm in the stretched state.

A rotatory DNA device based on multiple crossover molecules (complex supramolecular DNA structures in which DNA strands are shared between two or more DNA duplexes) was demonstrated by Yan and coworkers [31]. Their DNA structure could be switched between a “paranemic crossover” (PX) conformation and a “juxtaposed” ( $JX_2$ ) configuration (Fig. 6.6). The PX motif is a four-stranded DNA structure in which two neighboring duplexes exchange strands of the same directionality at every possible site [32]. If parts of this motif are removed and replaced by DNA sections without crossover, molecules such as the juxtaposed  $JX_2$  structure result in which two helices are rotated with respect to the corresponding PX structure (Fig. 6.6). In the PX- $JX_2$  device, the central section of a supramolecular structure based on the PX motif was created with DNA molecules which could be removed by the same branch migration “trick” as used for the operation of the DNA tweezers. After removal, these molecules could be replaced by DNA strands which switched the device to a  $JX_2$  configuration. Again using branch migration, the device could be switched back to the original PX structure.

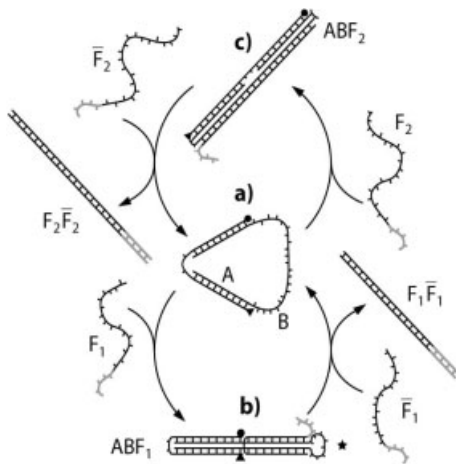


**Figure 6.5.** Operation cycle of a DNA actuator [30] switchable between three mechanical states. The actuator is similar to the tweezers and consists of two DNA strands (A and B) which hybridize together to form a circular structure as depicted in (a). By the addition of appropriate fuel or removal strands  $F_1$ ,  $\bar{F}_1$ ,  $F_2$  or  $\bar{F}_2$ , the device can be switched between a relaxed state (a), a closed state (b) and a stretched state (c). Removal strands can bind to the toehold sections depicted in gray of the fuel strands and remove them by branch migration. The ends of the arms (circular and triangular symbols stand for fluorescent dyes which are used for characterization) are switched from a short distance of a few nanometers in the closed state (b) to almost 14 nm in the stretched state (c). (Reprinted with permission from Ref. [30], © 2002, American Institute of Physics.)

Other devices utilizing branch migration were based on unusual DNA structures such as guanine quartets (“G quartets”). In a G quartet, four guanine bases bind to each other into a cyclical configuration via non-WC base-pairing interactions. In the experiments described by Li and Tan [33] and by Alberti and Mergny [34], ssDNA structures formed by several stacked intramolecular G quartets were switched to an elongated duplex structure by the addition of a complementary DNA fuel strand. This transition could be reversed by removing the fuel strand using branch migration. The overall effect was a detectable change in distance between the 5' and 3' ends of the device strand from about 2 nm in the quadruplex state to 7 nm in the duplex state.

#### 6.4 Towards Functional Devices

With the prototype devices described in the previous section it was established that it is possible to construct DNA structures which can perform movements on the nanometer scale. Except for their building material, these structures are nonbiological and completely “designed”. Their realization can therefore be regarded as an

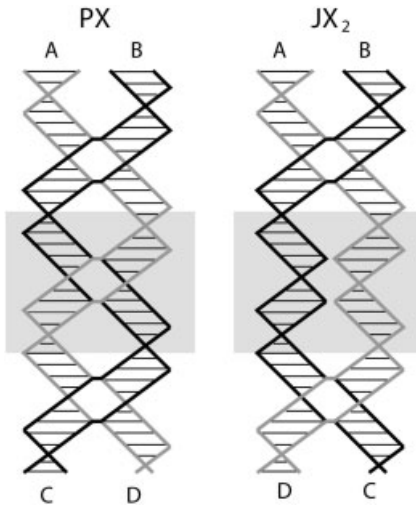


**Figure 6.6.** The transition between the PX and the  $JX_2$  structure forms the basis of a nanomechanical device by Yan and coworkers [31]. Both structures are formed by two DNA duplexes which share common DNA strands. In the PX (paranemic crossover) structure, the two DNA double-helices exchange strands wherever it is possible, whereas in the  $JX_2$  (juxtaposed) structure strands do not cross over in the middle part of the structure. Note

that in the  $JX_2$  structure, the helices C and D have a different position than in the PX structure. In Ref. [31], Yan and coworkers managed to switch the inner section of these structures (gray) using removable DNA strands and branch migration. This leads to a switchable transition between the PX and the  $JX_2$  form. The corresponding “rotation” of the duplexes C and D with respect to each other can be observed.

important step towards the realization of complex artificial molecular machinery. However, the tasks these prototype devices could perform were not particularly “useful”. In fact, their movements (rotation or stretching) were mostly idle, i.e. the motion was just an internal rearrangement of parts. To lift DNA devices to the next level of complexity, it is important to design structures that can perform specific tasks and interact with their environment. There are a number of different approaches towards such functional devices. One is to achieve directed motion rather than idle movements with the goal to produce artificial molecular motors. Another possibility for functional devices is to couple DNA devices to nanoscale structures like other biomolecules or nanoparticles. Such hybrid structures could be particularly interesting for applications in biotechnology and the life sciences.

#### 6.4.1

##### Walk and Roll

Among the most fascinating biological molecular machines are molecular motors such as kinesin, dynein or the myosins [35]. Kinesin and dynein motors walk along cytoskeletal microtubuli, whereas myosin motors walk on supramolecular

tracks made from actin. Kinesin, dynein and certain kinds of myosin help to actively transport vesicles within cells. Myosin motors are also responsible for other kinds of active movement in eukaryotic cells, including muscle contraction in higher eukaryotes. Many other enzymes like DNA or RNA polymerases can also be regarded as biological molecular motors. Clearly, the ability to actively transport molecular components or to exert forces on a molecular scale would also be highly desirable for nanotechnological applications or in biotechnology. However, building an artificial molecular motor is not an easy task.

Molecular motors work very differently from macroscopic machines as all movements on the molecular scale are dominated by Brownian motion. The energies available for the operation of molecular motors are only slightly higher than the thermal energy and they are therefore subjected to large fluctuations. Research on biological molecular motors has shown that these tiny machines do not work against Brownian motion, but rather utilize it for their operation. In many cases, a “Brownian ratchet” mechanism seems to be at work, where an irreversible chemical step is utilized to “rectify” the undirected Brownian motion [36]. The general features of such biological motors now serve as a guideline for the construction of artificial DNA motors.

Three different concepts to achieve directional motion in DNA-based systems are depicted schematically in Fig. 6.7. They correspond to the DNA walkers by Shin and Pierce [37] and Sherman and Seeman [38], the molecular “gears” by Tian and Mao [39], and the enzyme-assisted walker by Yin and coworkers [40]. The first simple DNA walker was introduced by Shin and Pierce [37]. A double-stranded DNA scaffold with ssDNA “docking positions” attached to it serves as a track for the DNA walker. The walker itself is a DNA duplex with two single-stranded “feet”. As explained in Fig. 6.7(a), DNA fuel strands are used to connect the single-stranded feet to the docking positions on the track. The connector strands are equipped with single-stranded toehold sections and can be displaced from the device by removal strands via branch migration. The free DNA foot can then be connected to the next free position on the track. This can be repeated several times with the appropriate connector and removal strands to move the walker to arbitrary positions on the track.

A similar walking device based on more complex DNA structures was realized by Sherman and Seeman [38]. In their work, the walker consists of two DNA duplexes joined by flexible single-stranded linkers. The walker can be translocated along a track which consists of a triple crossover molecule (“TX”, three double helices connected by shared DNA strands) which contains single-stranded position labels. Similar to the walker by Shin and Pierce, the duplexes of the Sherman and Seeman walker also contain single-stranded “feet” and can be attached to the docking positions on the TX track via DNA linker molecules. Again, these connections can be removed by branch migration and the free foot can be connected to the next position.

As shown in Fig. 6.7(b), the same principle can be applied to achieve a different kind of unidirectional motion. In the “molecular gears” system realized by Tian and Mao [39], two DNA “circles” roll against each other driven by hybridization



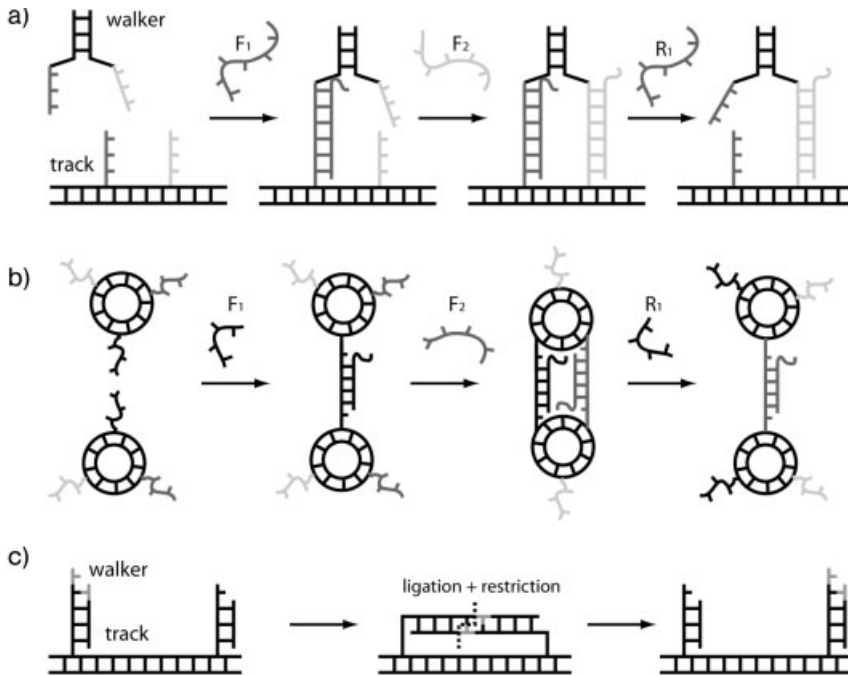


**Figure 6.7.** Three examples for unidirectional motion realized with DNA devices. (a) A simple walker system. A walker, which consists of a DNA duplex (or a more complex structure) and single-stranded “feet”, can attach to a dsDNA track from which single-stranded binding positions or “footholds” extend. The attachment of the feet is achieved with DNA fuel strands  $F_1$  and  $F_2$ , which are partly complementary to the footholds and partly complementary to the feet. The connection between the walker and track can be broken again with removal strands which can remove the fuel strands by branch migration. Using a different fuel strand the free foot can be attached to another position on the track. This walking principle has been applied in Refs. [37, 38]. (b) Essentially the same principle as in (a) can be used to make two DNA circles roll against

each other. The two circles with single-stranded extensions can be connected to each other with one or two fuel strands. Using fuel and removal strands in the correct order, the circles can roll against each other (corresponds to the device in Ref. [39]). (c) An autonomous enzyme-driven “walker” (cf. Ref. [40]). The walker system consists of a dsDNA track with double-stranded position strands. Initially, the first two neighboring position strands have sticky ends which may hybridize with each other. The two position strands can be ligated together and cut with a restriction enzyme. This creates new sticky ends on the position strands. The net effect is the transfer of a few DNA bases from one position to the next (depicted in gray). Using two different restriction enzymes, transport of the bases can autonomously occur over a longer track with many positions.

and branch migration. The two circles consist of a closed single strand to which three strands are hybridized containing flexible hinges made of thymine residues and single-stranded extensions (“teeth”). The two circles can be connected by DNA linker strands which are partly complementary to one “tooth” of one circle and another tooth of the other circle. Due to the flexible hinges, two circles can be con-

nected by two linker strands simultaneously. As in the case of the walkers, the linker strands contain single-stranded toehold sections at which removal strands can attach and displace the linker strands from the device. By the alternate addition of linker and removal strands in the correct order, the two circles can be made to roll against each other in one direction.

A different concept to achieve unidirectional motion in a DNA-based system was demonstrated by Yin and coworkers [40]. In contrast to the other walkers, their system needs the help of DNA-modifying enzymes, but it walks “autonomously”. The basic idea is depicted in Fig. 6.7(c). Again, the walker (which now consists of only a few DNA bases) sits on a DNA track which consists of double-helical DNA with duplex position strands. These position strands have short, single-stranded ends. If the ends of neighboring strands are complementary, they can hybridize with each other and can then be ligated by a DNA ligase. The sequences of these duplexes are chosen such that in the ligated state the recognition sequence for a restriction endonuclease is formed. Upon the addition of the endonuclease, the connected neighboring position duplexes are cut and a new pair of sticky ends is produced. In this way, the DNA bases representing the “walker” are transferred from one to the next position. Using two different restriction enzymes, the system can be designed to unidirectionally transport the walker bases along a track without ever stepping back [40].

Quite recently, several improvements on these systems could be demonstrated. Turberfield and coworkers could realize an autonomous walker system similar to the system by Yin and coworkers, but now driven by the action of a nicking enzyme and branch migration [41]. In this new system, a longer DNA fragment is passed from one binding position to the next. In a different approach, Mao and coworkers could utilize the action of a DNA enzyme (*cf.* Section 6.5.1) to achieve autonomous unidirectional motion along a track [42].

The DNA walker systems demonstrated so far essentially belong to the “Brownian” type. The walkers diffusively find a binding position on a track and a chemical reaction (hybridization or enzymatic ligation, restriction, etc.) is used to fix the position. Directionality is introduced by the choice of the base sequence of the track positions and the walkers. So far, the walkers also move without load – so nothing can be said about the efficiency of these systems. It will be very interesting to see in the future how DNA walkers behave when they have to carry something, i.e. when they have to perform work.

#### 6.4.2

##### **Interaction with Proteins**

The numerous advantages of DNA mentioned in Section 6.1.1, i.e. its controllability, programmability and stability, allow us to rationally construct artificial molecular devices which are (by their very nature) “automatically” biocompatible. The life sciences should therefore be a particularly interesting and fruitful area for the application of ideas developed in the context of DNA-based nanodevices: moving molecular components, sensing, information processing, etc.

Exciting possibilities arise, for example, when DNA nanodevices are made to interact with proteins. This interaction can be achieved in a variety of different ways: proteins can be coupled to DNA chemically or biochemically, proteins may be utilized which naturally bind to DNA, and proteins can bind to “aptamers” – nucleic acids which fold into a specific structure in which they strongly bind to a protein.

Many interesting examples for biochemically coupled protein–DNA conjugates come out of the Niemeyer lab. One example, not directly related to DNA nanomechanical devices, is the utilization of DNA recognition in the so-called immunopolymerase chain reaction (PCR) technique [43]. Here biotinylated antibodies are linked to biotinylated DNA molecules via streptavidin. These DNA–protein constructs can then be used to detect a primary antibody–antigen recognition event by the amplification of the DNA fragment with the PCR. Another very interesting example for supramolecular constructs produced from biotinylated DNA and proteins is the assembly of bienzymic complexes from NADH:FMN oxidoreductase and bacterial luciferase [44]. NADH:FMN oxidoreductase reduces flavin mononucleotide (FMN) to FMNH<sub>2</sub>, which binds to luciferase. Luciferase in turn oxidizes an aldehyde to a carboxylic acid and emits blue light. As bacterial luciferase needs FMNH<sub>2</sub> for the reaction, holding the NADH:FMN oxidoreductase in close proximity greatly enhances its activity. Such a concept may allow one to tune biochemical activity by controlling the distance between enzymes in DNA-scaffolded multi-enzyme complexes.

There are also many proteins which naturally interact with DNA: nucleases, ligases, polymerases, recombination proteins, transcription factors, to name but a few. In many cases these DNA-binding proteins recognize specific DNA sequences and in some cases they also distort the structure of DNA. Seeman and coworkers demonstrated recently that DNA devices can be used to estimate the work performed by a DNA-binding protein when it distorts the double helix [45]. As protein, the *Escherichia coli* integration host factor (IHF) was used which bends the DNA double helix by more than 160°. The binding site for IHF was sandwiched between two DNA TX structures which were fluorescently labeled with a FRET pair (Fig. 6.8). The bending of the construct can be monitored with the FRET signal. To measure the work performed by the enzyme upon bending, cohesive ends of various lengths were also attached to the TX units. Upon bending the DNA, IHF also has to disrupt the duplex formed by these cohesive ends. The work can therefore be determined from the free energy of formation of the duplex. Interestingly, this concept is very similar to a recently demonstrated DNA-based force sensor [46], but here the “measuring device” itself is also on the molecular scale.

A different approach to DNA–protein hybrid devices is not to utilize proteins which bind to DNA, but rather to evolve specific DNA or RNA sequences which bind to proteins. Such so-called “aptamers” can be isolated in *in vitro* selection experiments (SELEX) for a large variety of proteins and also small ligands such as ATP [47]. Aptamers bind specifically to their targets and in many cases have comparable binding constants as antibodies with their antigens. The great advantage of aptamers as compared to antibodies is their simple preparation and their stability. In particular, once isolated, DNA aptamers can be easily synthesized using the

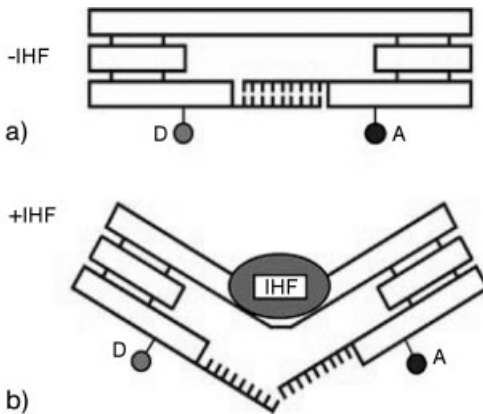


**Figure 6.8.** A DNA device that can be used to measure the work performed by a DNA-binding protein which distorts the double-helix. (a) The device consists of two connected triple-crossover (TX) constructs (left and right part; these are similar to the structures in Fig. 6.6, but with three interconnected double helices). The upper domains of the TX structures are connected by a DNA duplex which contains the recognition site for the DNA-binding protein IHF. The lower domains are connected by a

cohesive part which consists of two complementary single-stranded sections of DNA. (b) When IHF binds to its recognition site it distorts the DNA duplex connecting the TX structures. However, to be able to do so it has to perform additional work to disrupt the cohesive tract connecting the lower domains of the device. Using cohesive tracts of varying lengths one can estimate the maximum work the protein is able to perform. (Reprinted with permission from Ref. [45], © 2004, Wiley-VCH.)

automated DNA synthesis methods mentioned before. In the context of DNA nanodevices, one additional advantage is that they can be incorporated into DNA nanomechanical devices or supramolecular structures.

Recently, Dittmer and coworkers [48] applied the concept of switching a DNA device between two conformations using branch migration to a DNA aptamer structure. The operation principle of this device is explained in Fig. 6.9. The nanodevice is based on a DNA aptamer selected to bind the human blood-clotting protein, thrombin. The 15-base DNA sequence 5'-GGTTGGTGTGGTTGG-3' folds into a secondary structure consisting of two G-quartets, in the presence of potassium ions (Fig. 6.9). The device in its standard state binds thrombin. Release of the protein can be triggered by the addition of a single-stranded effector DNA containing a sequence that is complementary to a portion of the aptamer sequence, resulting in an unfolding of the aptamer to form a duplex, which is unable to bind the protein. The protein can be bound once again by the addition of another DNA strand, fully complementary to the previously added strand, which removes the effector by branch migration. The aptamer is thus allowed to return to its protein-binding quadruplex form. By the alternate addition of effector strands, the DNA device can repeatedly made to bind or release the protein – the device can therefore be thought of as a “nanohand”. In principle, similar devices can be constructed to bind other proteins and ligands if an appropriate aptamer exists.

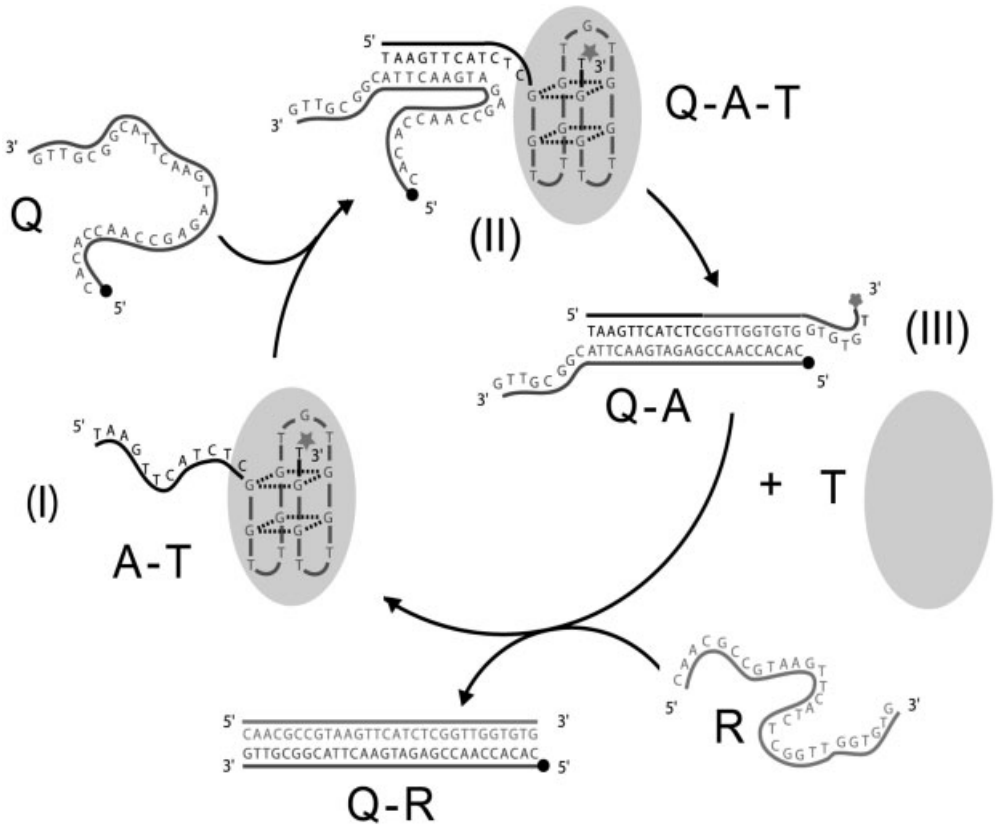


**Figure 6.9.** A DNA device based on a DNA aptamer. The aptamer sequence 5'-GTTGGTGGTGGTGG-3' folds into a structure characterized by two stacked guanine quartets. In this structure, the aptamer binds strongly and specifically to the protein thrombin. To be able to switch this aptamer efficiently between a protein-binding and a non-binding conformation, it has been extended by a 12-nucleotide "toehold" section. In the folded state (I) the aptamer device A binds to the protein thrombin (T). In (II), the opening

strand Q attaches to the 12-nucleotide toehold section of the device and displaces the protein. In the stretched duplex conformation (III), the device cannot bind to thrombin. The removal strand R can attach to a second toehold section in strand Q and displace Q from A by branch migration. Strand A then refolds and binds the protein thrombin again. Alternate addition of Q and R strands allows repeated release and binding of the protein. (Reprinted with permission from Ref. [48], © 2004, Wiley-VCH.)

The examples mentioned in this section should give an impression of the potential of hybrid systems composed of DNA nanodevices and proteins. Such systems can have many interesting applications in the life sciences. DNA structures can be used to arrange proteins into certain geometries to fine-tune or study their interactions. DNA nanodevices can also be used as sensors which measure the work performed by DNA-binding proteins. Finally, DNA aptamers can be combined with

switchable DNA nanostructures to control the binding or release of molecules. This may find applications in biosensors or in intelligent drug delivery systems.

### 6.4.3

#### Information Processing

In biology DNA is used for the storage of genetic information. For artificial applications, this information-carrying nature of DNA has been utilized in the field of “DNA computing” for the solution of computational problems such as the “Hamiltonian path problem” [49], satisfiability problems [50–52] and many others. One more recent development in DNA computing is the construction of molecular automata which do not solve hard computational problems, but which can autonomously perform simple logical operations based on molecular inputs. This should be particularly interesting in the context of intelligent drug delivery systems. Here, one would like to construct autonomous molecular devices which can sense environmental information, perform a simple computation and decide which action to take, e.g. whether to release a specific molecule or not.

One approach towards autonomous information processing by DNA-based devices was taken by Benenson and coworkers [53–55]. In their work, the DNA-cleaving properties of the class IIS restriction endonuclease *FokI* were utilized to build the molecular realization of the computer-theoretical concept of “finite state machines” or “finite automata”. Finite automata are computing machines with a finite number of internal states which can undergo transitions between these states according to certain rules. A program for such an automaton consists of a series of such transitions. The operation of the automaton is based on the fact that the enzyme *FokI* cleaves a dsDNA substrate 9 and 13 nucleotides offset from its recognition, creating a 4-nucleotide sticky end. Hence, the states and input symbols for the automaton are represented by different 4-nucleotide sequences. In Ref. [53], *FokI* is used to sequentially cleave off pieces of a double-stranded program and thereby create a series of transitions between the various states of the automaton. Finite automata are related to Turing machines, but have limited computing power. In Ref. [53], Benenson and coworkers used their DNA automata to make simple decisions such as to determine whether a given input symbol occurs at least once. Keinan and coworkers recently used another class IIS endonuclease, *BbvI*, to perform similar molecular computations in a chip-based approach [56].

Benenson and coworkers, on the other hand, were able to demonstrate how their *FokI*-based DNA automaton could actually find application in autonomous diagnosis and drug delivery systems [57]. To this end, the transition molecules for a *FokI*-based DNA automaton were designed to be active only in the presence of specific mRNA molecules. With these transition molecules, a molecular computer was realized which could decide whether the levels of certain mRNA molecules were high or low. Depending on the decision, a short DNA strand was released as a “drug”. This DNA drug was chosen as an antisense molecule, which in principle could inhibit the synthesis of a cancer-related protein by binding to its corresponding mRNA.

A different approach towards autonomous computing with DNA is based on DNA enzymes. Similar to DNA aptamers, DNA enzymes are another example of DNA molecules which have functional properties in addition to their structural properties. They also fold into specific secondary and tertiary structures in which they exhibit catalytic activity. DNA enzymes (and their RNA counterparts, i.e. ribozymes) catalyze reactions such as RNA cleavage, ligation and even peptide bond formation. In Ref. [58], Stojanovic and coworkers realized several logic gates based on the action of the RNA cleaving deoxyribozymes E6 [59] and 8–17 [60, 61]. These DNA enzymes cleave RNA molecules or, alternatively, chimeric DNA/RNA hybrid molecules with an RNA base at the appropriate position, when these are bound to their substrate recognition sections. In Ref. [58], the recognition sequences are protected by self-hybridized stem–loop modules. By base-pairing with a DNA strand complementary to the loop sequence, the stem–loop modules can be opened. This makes the substrate recognition sequence accessible for the substrate, which is subsequently cleaved. By combining controlling and catalytic modules, Stojanovic and coworkers realized simple logic gates such as AND or XOR [58], a DNA half-adder [62] and a molecular computer which autonomously could play the game “Tic Tac Toe” [63]. A combination of autonomous DNA-based computers with aptamer-based molecular devices (as introduced above) seems natural. In fact, Kolpashchikov and Stojanovic recently introduced a molecular “robotic” system in which DNA logic gates controlled the binding state of a DNA aptamer for the chromophore malachite green [64].

#### 6.4.4

#### Switchable Networks and Hybrid Materials

The properties of DNA nanomechanical devices may also be utilized to switch larger DNA nanostructures such as DNA-linked nanoparticle networks or DNA-based supramolecular networks between several states.

Yan and coworkers could show recently that the topology of large supramolecular DNA networks could be switched by nanomechanical actuators incorporated into these networks [65]. Again, switching between two different states was accomplished with DNA fuel strands and by using the branch migration mechanism. In a different publication, Yan and coworkers recently also demonstrated the incorporation of aptamer sequences into DNA supramolecular structures [18], which facilitated the spatial arrangement of proteins bound by the aptamers. Based on this work and ideas put forward above [44, 48], supramolecular structures are now conceivable on which several interacting proteins are held by different aptamer sequences and their distance (and hence their interactions) is regulated by actuating elements incorporated into the structures.

Similar structures can be realized which can switch the distance between inorganic nanoparticles rather than proteins. As a first example, Niemeyer and coworkers demonstrated a switchable network composed of gold nanoparticles and DNA molecules [66]. The experimental concept is displayed in Fig. 6.10. Two batches of gold nanoparticles are first tagged with thiolated oligonucleotides with

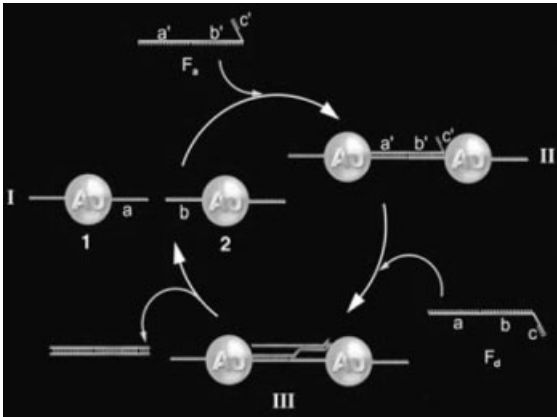


**Figure 6.10.** DNA can be used to reversibly control the aggregation of gold nanoparticles. Two species of gold nanoparticles (1 and 2) tagged with different single-stranded “address labels” can be connected using DNA strands  $F_a$  complementary to these labels. This leads to an aggregation of the nanoparticles which can be monitored, e.g. in the absorption characteristics of the sample. Removal strands  $F_d$

complementary to  $F_a$  can attach to the toehold section  $c'$  of  $F_a$  and remove the connecting strands from the aggregate by branch migration. This leads to a deaggregation of the DNA-linked nanoparticle network. By the alternate addition of  $F_a$  and  $F_d$ , the aggregation–deaggregation cycle can be performed many times. (Reprinted with permission from Ref. [66], © 2004, Wiley-VCH.)

different sequences. Two nanoparticles with different tags can then be connected by linker oligonucleotides which are partly complementary to the tags on one species of nanoparticle and partly complementary to the other. This leads to the formation of a crosslinked network of gold nanoparticles. To make the system switchable, the crosslinking oligonucleotides are equipped with a DNA “toehold” (as in the original “tweezers” system [28]) at which a DNA strand complementary to the crosslinker can attach. The crosslinker is then removed by branch migration and the nanoparticles are disconnected. By the alternate addition of crosslinkers and removal strands, the system can be driven through several operation cycles during which the mean distance between the particles is switched. In the case of metallic nanoparticles, the distance between the particles influences the coupling between surface plasmon excitations within the particles, and aggregation of the nanoparticles results in an observable shift in the absorbance of the reaction sample. This color change upon aggregation has already been applied in a variety of biosensors [67, 68] and such switchable networks may also find application in this area.

Apart from biosensing applications, switchable hybrid structures composed of DNA actuators and nanoparticles may also help to answer more fundamental questions regarding the coupling of excitations in nanoparticles, and to tune energy and charge transfer rates between them.



## 6.5

### Autonomous Behavior

Most of the devices described so far could not operate autonomously, with the exception of the autonomous walkers by Yin and coworkers [40], Bath and coworkers [41], and Tian and coworkers [42], and the computing devices by Benenson and coworkers [53] and Stojanovic and coworkers [63]. Usually, an external operator had to intervene at each step of the operation cycle of the devices and add DNA “fuel” or “effector” strands, or change the buffer conditions. While this may be no hindrance in simple applications, in many cases it might be desired to have free-running devices rather than “clocked” devices. For example, for applications in intelligent drug delivery or in nanofabrication, the devices should respond to environmental stimuli by a complex series of actions without guidance by an external operator.

#### 6.5.1

##### Driving Devices with Chemical Reactions

The successful concept of “fuel strands + branch migration” for the operation of DNA-based nanodevices has one drawback when it comes to autonomous operation: complementary fuel and removal strands cannot be added simultaneously to the reaction solution as they would immediately react with each other rather than driving a device through its states. A possible solution for this problem has been proposed by Turberfield and coworkers [69] based on the inhibition of hybridization between complementary strands by the formation of secondary structures. In Ref. [69] it is shown that the hybridization between two complementary strands can be slowed down considerably by forcing the strands into hairpin conformations using “protection strands”. Hybridization can be sped up again by DNA “catalysts” which can open these hairpin structures. To construct free-running devices using this concept, such catalyst strands would have to be incorporated into DNA nanomechanical structures. These would then be continuously driven through their states by the consumption of the metastable protected “fuel” strands. These fuel molecules could be added simultaneously as now the reaction with the DNA device would be much faster than a direct reaction.

Another realization of a self-running device was demonstrated by Chen and coworkers with a machine consisting of a DNA actuator [29] modified with an RNA-cleaving DNA enzyme [70] similar to the DNA enzymes used for computing by Stojanovic and coworkers. In its standard state, the DNA enzyme is in a compact form and the actuator assumes its closed state (Fig. 6.11). In the presence of its substrate (a DNA/RNA chimera), the enzyme extends to its catalytically active structure as it forms a duplex with the substrate and the arms of the actuator are pushed apart from each other. When the substrate is cleaved by the DNA enzyme, two short fragments remain hybridized to the device instead of one long substrate strand. The two short duplexes are thermodynamically less stable and the cleaved

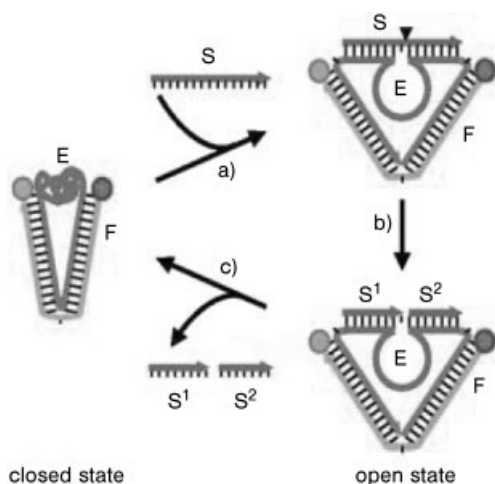


**Figure 6.11.** An autonomous DNA device based on the action of a DNA enzyme. The sequence for an RNA-cleaving DNA enzyme has been incorporated into a DNA actuator similar to the one shown in Fig. 6.5. When a chimeric RNA/DNA substrate  $S$  binds to the DNA enzyme section  $E$ , the two arms of the device are pushed apart from each other. After

cleavage of the substrate the resulting shorter DNA fragments  $S^1$  and  $S^2$  unbind from  $E$ , and the device collapses into the closed state. This opening–closing motion can continue as long as substrate strands are available. (Reprinted with permission from Ref. [70], © 2004, Wiley-VCH.)

substrate is released from the device leading to the collapse of the enzyme section and thus an automatic closure of the actuator. The device will run through its operation cycle autonomously as long as the substrate is present. When using a noncleavable DNA substrate, the device can also be deliberately forced into a stalled configuration [71]. The recently demonstrated free-running walker by Tian and coworkers [42] is also based on this operation principle.

A different concept to autonomously operate buffer-driven DNA nanodevices has been demonstrated by Liedl and Simmel. It could be shown that the pH-sensitive conformational transition of a cytosine-rich DNA strand between a random coil conformation and the i-motif (Fig. 6.2b) could be driven by the oscillating proton concentration generated by a chemical oscillator [72]. In this system, the states of the DNA devices are synchronized by the dynamics of a nonlinear dynamical system rather than by an external operator.

### 6.5.2

#### Genetic Control

A very different possibility for the autonomous operation of DNA-based devices opens up when one considers the production of DNA or RNA effector molecules “on the run”. RNA molecules are produced, of course, when a gene is transcribed into mRNA by an RNA polymerase. It is therefore quite natural to think about

the utilization of genetic transcription for the operation of DNA nanomechanical devices.

It is well established that biochemical reaction networks have information-processing properties [73, 74]. This is particularly obvious in genetic networks which control the expression level of proteins through complex interactions between regulatory molecules and genes. The textbook example for a genetic switch is the *lac* operon in *E. coli* bacteria in which the expression of the protein  $\beta$ -galactosidase is regulated by the relative concentrations of lactose and glucose. Many other gene regulatory motifs with a variety of tasks and responsibilities have been found since the discovery of the *lac* operon and biochemical analogs of switches, oscillators, filters, components with memory functions and others have been identified [74].

Recently, the knowledge about these motifs has also been used to construct artificial genetic networks. By transferring circuit designs known from electrical engineering to artificial regulatory networks, such functions as a bistable genetic switch [75], a genetic oscillator [76], or a sender–receiver system [77] could be synthetically implemented in bacteria and similarly *in vitro* [78]. An overview of the developments in “synthetic biology” is given in Refs. [79, 80].

It is a tempting idea to use similar artificial genetic networks to drive DNA nanodevices through their mechanical states. One could imagine a genetic oscillator periodically producing RNA fuel strands which switch a DNA actuator from one conformation into another and back, possibly dependent on environmental variables which modulate the genetic activity. A first step in this direction was taken in Ref. [81] in which the DNA tweezers introduced in Section 6.2.2 were operated by an mRNA fuel strand which was transcribed from an artificial “fuel gene”. More recently, the transcription of fuel strands was also put under the control of simple gene regulatory mechanisms [82]. One example is shown in Fig. 6.12, where the closure of DNA tweezers by RNA fuel is controlled by the Lac repressor and the inducer IPTG. In the presence of the repressor protein LacI, fuel transcription is suppressed and the DNA tweezers are in their open state. When the inducer isopropyl-D-thiogalactoside (IPTG) is added to the transcription solution, it binds to LacI, which in turn cannot bind to the DNA substrate in this form. Consequently, fuel transcription is switched on and the tweezers close. In Ref. [82], the transcription of an appropriate removal strand has also been put under the control of a second repressor (LexA). Closed tweezers are opened by RNA fuel only in the absence of this repressor. To achieve genetic control over a series of movements, in the future the temporal order of the transcription events will have to be regulated using transcriptional cascades or feedback loops.

These initial steps demonstrate that it is indeed possible to control the action of DNA-based nanomechanical devices by gene regulatory mechanisms. It should therefore be possible to program DNA devices to perform a complex series of tasks in response to certain environmental influences. It is also conceivable to construct similar DNA or RNA structures which act in response to naturally occurring mRNA molecules. This again could be interesting in the context of biosensing or drug delivery. For example, one could construct aptamer-based devices which

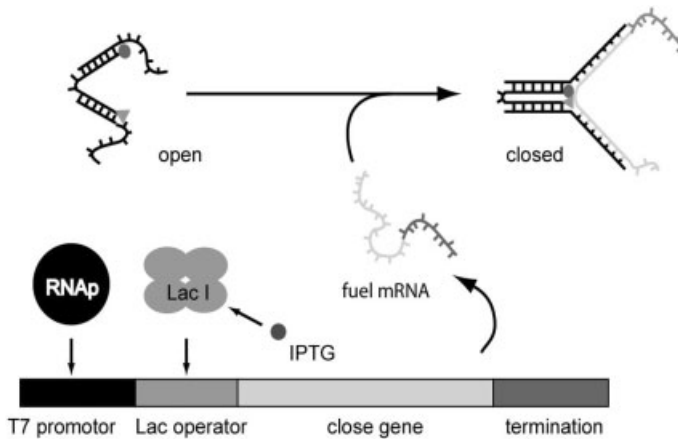


**Figure 6.12.** Gene regulatory control of DNA devices. A gene construct contains the instructions to close opened DNA tweezers (close gene). Its transcription will lead to the production of a fuel mRNA strand which can close the tweezers. In the construct, the promoter of the gene is put under the control of the Lac operator directly downstream of the promoter.

When the repressor protein LacI binds to the operator, transcription extension by T7 polymerase is blocked. However, when the “inducer” IPTG binds to LacI, it cannot bind to the operator sequence. Then transcription is switched on, fuel mRNA is produced and the DNA tweezers are closed. (Reprinted with permission from Ref. [81], © 2005, Wiley-VCH.)

release their molecular load in response to the presence of specific mRNA molecules.

## 6.6 Conclusion

Apart from their original biological role, DNA molecules can be used as highly versatile building blocks for the construction of nanoscale structures and devices. The first simple prototype devices based on DNA could only perform simple movements such as stretching or rotation. Based on these prototypes and combining them with other concepts from nanotechnology and the life sciences, a variety of more functional DNA nanodevices has recently been demonstrated. The first examples of “DNA walkers” capable of unidirectional motion have been given; the interaction of DNA devices and proteins has been utilized for sensors, for the control of biochemical reaction rates and for the controlled binding and release of proteins; ideas from DNA computing have been integrated to logically control the action of DNA-based devices; and, finally, the action of DNA devices has been coupled to the genetic machinery.

These developments represent the first steps towards autonomous molecular-scale devices which can sense environmental information, perform computations and act independently as molecular motors, drug reservoirs or signal transducers.

As such, they are expected to have a significant impact on the development of advanced biosensors or as components for intelligent drug delivery systems.

## Acknowledgments

The author gratefully acknowledges funding by the Deutsche Forschungsgemeinschaft through its Emmy Noether program.

## References

- 1 M. F. CROMMIE, C. P. LUTZ, D. M. EIGLER. Confinement of electrons to quantum corrals on a metal-surface, *Science* **1993**, 262, 218–220.
- 2 S. W. HLA, L. BARTELS, G. MEYER, K. H. RIEDER. Inducing all steps of a chemical reaction with the scanning tunneling microscope tip: towards single molecule engineering, *Phys. Rev. Lett.* **2000**, 85, 2777–2780.
- 3 C. DENNIS, P. CAMPBELL. The eternal molecule, *Nature* **2003**, 421, 396–396.
- 4 I. TINOCO, C. BUSTAMANTE. How RNA folds, *J. Mol. Biol.* **1999**, 293, 271–281.
- 5 J. H. CHEN, N. C. SEEMAN. Synthesis from DNA of a molecule with the connectivity of a cube, *Nature* **1991**, 350, 631–633.
- 6 Y. W. ZHANG, N. C. SEEMAN. Construction of a DNA-truncated octahedron, *J. Am. Chem. Soc.* **1994**, 116, 1661–1669.
- 7 C. D. MAO, W. Q. SUN, N. C. SEEMAN. Assembly of Borromean rings from DNA, *Nature* **1997**, 386, 137–138.
- 8 R. P. GOODMAN, R. M. BERRY, A. J. TURBERFIELD. The single-step synthesis of a DNA tetrahedron, *Chem. Commun.* **2004**, 1372–1373.
- 9 W. M. SHIH, J. D. QUISPE, G. F. JOYCE. A 1.7-kilobase single-stranded DNA that folds into a nanoscale octahedron, *Nature* **2004**, 427, 618–621.
- 10 M. SCHEFFLER, A. DORENBECK, S. JORDAN, M. WÜSTEFELD, G. V. KIEDROWSKI. Self-assembly of trisoligonucleotidyls: the case for nano-acetylene and nano-cyclobutadiene, *Angew. Chem. Int. Ed. Engl.* **1999**, 38, 3311–3315.
- 11 E. WINFREE, F. R. LIU, L. A. WENZLER, N. C. SEEMAN. Design and self-assembly of two-dimensional DNA crystals, *Nature* **1998**, 394, 539–544.
- 12 T. H. LABEAN, H. YAN, J. KOPATSCH, F. R. LIU, E. WINFREE, J. H. REIF, N. C. SEEMAN. Construction, analysis, ligation, and self-assembly of DNA triple crossover complexes, *J. Am. Chem. Soc.* **2000**, 122, 1848–1860.
- 13 D. LIU, S. H. PARK, J. H. REIF, T. H. LABEAN. DNA nanotubes self-assembled from triple-crossover tiles as templates for conductive nanowires, *Proc. Natl Acad. Sci. USA* **2004**, 101, 717–722.
- 14 J. C. MITCHELL, J. R. HARRIS, J. MALO, J. BATH, A. J. TURBERFIELD. Self-assembly of chiral DNA nanotubes, *J. Am. Chem. Soc.* **2004**, 126, 16342–16343.
- 15 P. W. K. ROTHMUND, A. EKANI-NKODO, N. PAPADAKIS, A. KUMAR, D. K. FYGENSON, E. WINFREE. Design and characterization of programmable DNA nanotubes, *J. Am. Chem. Soc.* **2004**, 126, 16344–16352.
- 16 H. YAN, S. H. PARK, G. FINKELSTEIN, J. H. REIF, T. H. LABEAN. DNA-templated self-assembly of protein arrays and highly conductive nanowires, *Science* **2003**, 301, 1882–1884.
- 17 J. MALO, J. C. MITCHELL, C. VENIEN-BRYAN, J. R. HARRIS, H. WILLE, D. J. SHERRATT, A. J. TURBERFIELD. Engineering a 2D protein–DNA

- crystal, *Angew. Chem. Int. Ed. Engl.* **2005**, *44*, 3057–3061.
- 18 Y. LIU, C. X. LIN, H. Y. LI, H. YAN. Protein nanoarrays – aptamer-directed self-assembly of protein arrays on a DNA nanostructure, *Angew. Chem. Int. Ed. Engl.* **2005**, *44*, 4333–4338.
  - 19 C. D. MAO, W. Q. SUN, Z. Y. SHEN, N. C. SEEMAN. A nanomechanical device based on the B–Z transition of DNA, *Nature* **1999**, *397*, 144–146.
  - 20 W. M. GELBART, R. F. BRUINSMA, P. A. PINCUS, V. A. PARSEGGIAN. DNA-inspired electrostatics, *Phys. Today* **2000**, *53*, 38–44.
  - 21 C. M. NIEMEYER, M. ADLER, S. LENHERT, S. GAO, H. FUCHS, L. F. CHI. Nucleic acid supercoiling as a means for ionic switching of DNA–nanoparticle networks, *ChemBioChem* **2001**, *2*, 260–264.
  - 22 K. GEHRING, J. L. LEROY, M. GUERON. A tetrameric DNA-structure with protonated cytosine–cytosine base-pairs, *Nature* **1993**, *363*, 561–565.
  - 23 D. S. LIU, S. BALASUBRAMANIAN. A proton-fuelled DNA nanomachine, *Angew. Chem. Int. Ed. Engl.* **2003**, *42*, 5734–5736.
  - 24 V. A. BLOOMFIELD, D. M. CROTHERS, I. TINOCO, JR. *Nucleic Acids*. University Science Books, Sausalito, CA, **2000**.
  - 25 M. BRUCALE, G. ZUCCHERI, B. SAMORI. The dynamic properties of an intramolecular transition from DNA duplex to cytosine–thymine motif triplex, *Org. Biomol. Chem.* **2005**, *3*, 575–577.
  - 26 Y. CHEN, S. H. LEE, C. D. MAO. A DNA Nanomachine based on a duplex–triplex transition, *Angew. Chem. Int. Ed. Engl.* **2004**, *43*, 5335–5338.
  - 27 X. P. YANG, A. V. VOLOGODSKII, B. LIU, B. KEMPER, N. C. SEEMAN. Torsional control of double-stranded DNA branch migration, *Biopolymers* **1998**, *45*, 69–83.
  - 28 B. YURKE, A. J. TURBERFIELD, A. P. MILLS, F. C. SIMMEL, J. L. NEUMANN. A DNA-fuelled molecular machine made of DNA, *Nature* **2000**, *406*, 605–608.
  - 29 F. C. SIMMEL, B. YURKE. Using DNA to construct and power a nanoactuator, *Phys. Rev. E* **2001**, *6304*, 041913.
  - 30 F. C. SIMMEL, B. YURKE. A DNA-based molecular device switchable between three distinct mechanical states, *Appl. Phys. Lett.* **2002**, *80*, 883–885.
  - 31 H. YAN, X. P. ZHANG, Z. Y. SHEN, N. C. SEEMAN. A robust DNA mechanical device controlled by hybridization topology, *Nature* **2002**, *415*, 62–65.
  - 32 Z. Y. SHEN, H. YAN, T. WANG, N. C. SEEMAN. Paranemic crossover DNA: A generalized Holliday structure with applications in nanotechnology, *J. Am. Chem. Soc.* **2004**, *126*, 1666–1674.
  - 33 J. W. J. LI, W. H. TAN. A single DNA molecule nanomotor, *Nano Lett.* **2002**, *2*, 315–318.
  - 34 P. ALBERTI, J. L. MERGNY. DNA duplex–quadruplex exchange as the basis for a nanomolecular machine, *Proc. Natl Acad. Sci. USA* **2003**, *100*, 1569–1573.
  - 35 J. HOWARD. *Mechanics of Motor Proteins and the Cytoskeleton*, 1st edn. Sinauer, Sunderland, MA, **2001**.
  - 36 C. BUSTAMANTE, D. KELLER, G. OSTER. The physics of molecular motors, *Acc. Chem. Res.* **2001**, *34*, 412–420.
  - 37 J. S. SHIN, N. A. PIERCE. A synthetic DNA walker for molecular transport, *J. Am. Chem. Soc.* **2004**, *126*, 10834–10835.
  - 38 W. B. SHERMAN, N. C. SEEMAN. A precisely controlled DNA biped walking device, *Nano Lett.* **2004**, *4*, 1203–1207.
  - 39 Y. TIAN, C. D. MAO. Molecular gears: a pair of DNA circles continuously rolls against each other, *J. Am. Chem. Soc.* **2004**, *126*, 11410–11411.
  - 40 P. YIN, H. YAN, D. X. G., A. J. TURBERFIELD, J. H. REIF. A unidirectional DNA walker that moves autonomously along a track, *Angew. Chem. Int. Ed. Engl.* **2004**, *43*, 4906–4911.
  - 41 J. BATH, S. J. GREEN, A. J. TURBERFIELD. A free-running DNA motor powered by a nicking enzyme, *Angew. Chem. Int. Ed. Engl.* **2005**, *44*, 4358–4361.
  - 42 Y. TIAN, Y. HE, Y. CHEN, P. YIN, C. D. MAO. Molecular devices – A DNzyme that walks processively and auto-

- mously along a one-dimensional track, *Angew. Chem. Int. Ed. Engl.* **2005**, *44*, 4355–4358.
- 43 C. M. NIEMEYER, M. ADLER, R. WACKER. Immuno-PCR: high sensitivity detection of proteins by nucleic acid amplification, *Trends Biotechnol.* **2005**, *23*, 208–216.
  - 44 C. M. NIEMEYER, J. KOEHLER, C. WUERDEMANN. DNA-directed assembly of bienzymic complexes from *in vivo* biotinylated NAD(P)H:FMN oxidoreductase and luciferase, *Chem-biochem* **2002**, *3*, 242–245.
  - 45 W. Q. SHEN, M. F. BRUIST, S. D. GOODMAN, N. C. SEEMAN. A protein-driven DNA device that measures the excess binding energy of proteins that distort DNA, *Angew. Chem. Int. Ed. Engl.* **2004**, *43*, 4750–4752.
  - 46 C. ALBRECHT, K. BLANK, M. LALIC-MULTHALER, S. HIRLER, T. MAI, I. GILBERT, S. SCHIFFMANN, T. BAYER, H. CLAUSEN-SCHAUMANN, H. E. GAUB. DNA: a programmable force sensor, *Science* **2003**, *301*, 367–370.
  - 47 D. S. WILSON, J. W. SZOSTAK. *In vitro* selection of functional nucleic acids, *Annu. Rev. Biochem.* **1999**, *68*, 611–647.
  - 48 W. U. DITTMER, A. REUTER, F. C. SIMMEL. A DNA-based machine that can cyclically bind and release thrombin, *Angew. Chem. Int. Ed. Engl.* **2004**, *43*, 3550–3553.
  - 49 L. M. ADLEMAN. Molecular computation of solutions to combinatorial problems, *Science* **1994**, *266*, 1021–1024.
  - 50 K. SAKAMOTO, H. GOZU, K. KOMIYA, D. KIGA, S. YOKOYAMA, T. YOKOMORI, M. HAGIYA. Molecular computation by DNA hairpin formation, *Science* **2000**, *288*, 1223–1226.
  - 51 D. FAULHAMMER, A. R. CUKRAS, R. J. LIPTON, L. F. LANDWEBER. Molecular computation: RNA solutions to chess problems, *Proc. Natl Acad. Sci. USA* **2000**, *97*, 1385–1389.
  - 52 R. S. BRAICH, N. CHELYAPOV, C. JOHNSON, P. W. K. ROTHMUND, L. ADLEMAN. Solution of a 20-variable 3-SAT problem on a DNA computer, *Science* **2002**, *296*, 499–502.
  - 53 Y. BENENSON, T. PAZ-ELIZUR, R. ADAR, E. KEINAN, Z. LIVNEH, E. SHAPIRO. Programmable and autonomous computing machine made of biomolecules, *Nature* **2001**, *414*, 430–434.
  - 54 Y. BENENSON, R. ADAR, T. PAZ-ELIZUR, Z. LIVNEH, E. SHAPIRO. DNA molecule provides a computing machine with both data and fuel, *Proc. Natl Acad. Sci. USA* **2003**, *100*, 2191–2196.
  - 55 R. ADAR, Y. BENENSON, G. LINSHIZ, A. ROSNER, N. TISHBY, E. SHAPIRO. Stochastic computing with biomolecular automata, *Proc. Natl Acad. Sci. USA* **2004**, *101*, 9960–9965.
  - 56 M. SORENI, S. YOGEV, E. KOSOY, Y. SHOHAM, E. KEINAN. Parallel biomolecular computation on surfaces with advanced finite automata, *J. Am. Chem. Soc.* **2005**, *127*, 3935–3943.
  - 57 Y. BENENSON, B. GIL, U. BEN-DOR, R. ADAR, E. SHAPIRO. An autonomous molecular computer for logical control of gene expression, *Nature* **2004**, *429*, 423–429.
  - 58 M. N. STOJANOVIC, T. E. MITCHELL, D. STEFANOVIC. Deoxyribozyme-based logic gates, *J. Am. Chem. Soc.* **2002**, *124*, 3555–3561.
  - 59 R. R. BREAKER, G. F. JOYCE. A DNA enzyme with Mg<sup>2+</sup>-dependent RNA phosphoesterase activity, *Chem. Biol.* **1995**, *2*, 655–660.
  - 60 S. W. SANTORO, G. F. JOYCE. A general purpose RNA-cleaving DNA enzyme, *Proc. Natl Acad. Sci. USA* **1997**, *94*, 4262–4266.
  - 61 J. LI, W. C. ZHENG, A. H. KWON, Y. LU. *In vitro* selection and characterization of a highly efficient Zn(II)-dependent RNA-cleaving deoxyribozyme, *Nucleic Acids Res.* **2000**, *28*, 481–488.
  - 62 M. N. STOJANOVIC, D. STEFANOVIC. Deoxyribozyme-based half-adder, *J. Am. Chem. Soc.* **2003**, *125*, 6673–6676.
  - 63 M. N. STOJANOVIC, D. STEFANOVIC. A deoxyribozyme-based molecular automaton, *Nat. Biotech.* **2003**, *21*, 1069–1074.
  - 64 D. M. KOLPASHCHIKOV, M. N. STOJANOVIC. Boolean control of

- aptamer binding states, *J. Am. Chem. Soc.* **2005**, *127*, 11348–11351.
- 65 L. P. FENG, S. H. PARK, J. H. REIF, H. YAN. A two-state DNA lattice switched by DNA nanoactuator, *Angew. Chem. Int. Ed. Engl.* **2003**, *42*, 4342–4346.
- 66 P. HAZARIKA, B. CEYHAN, C. M. NIEMEYER. Reversible switching of DNA-gold nanoparticle aggregation, *Angew. Chem. Int. Ed. Engl.* **2004**, *43*, 6469–6471.
- 67 J. J. STORHOFF, R. ELGHANIAN, R. C. MUCIC, C. A. MIRKIN, R. L. LETSINGER. One-pot colorimetric differentiation of polynucleotides with single base imperfections using gold nanoparticle probes, *J. Am. Chem. Soc.* **1998**, *120*, 1959–1964.
- 68 J. W. LIU, Y. LU. Adenosine-dependent assembly of aptazyme-functionalized gold nanoparticles and its application as a colorimetric biosensor, *Anal. Chem.* **2004**, *76*, 1627–1632.
- 69 A. J. TURBERFIELD, J. C. MITCHELL, B. YURKE, A. P. MILLS, M. I. BLAKEY, F. C. SIMMEL. DNA fuel for free-running nanomachines, *Phys. Rev. Lett.* **2003**, *90*.
- 70 Y. CHEN, M. S. WANG, C. D. MAO. An autonomous DNA nanomotor powered by a DNA enzyme, *Angew. Chem. Int. Ed. Engl.* **2004**, *43*, 3554–3557.
- 71 Y. CHEN, C. D. MAO. Putting a brake on an autonomous DNA nanomotor, *J. Am. Chem. Soc.* **2004**, *126*, 8626–8627.
- 72 T. LIEDL, F. C. SIMMEL. Switching the conformation of a DNA molecule with a chemical oscillator, *Nano Lett.* **2005**, *5*, 1894–1898.
- 73 A. ARKIN, J. ROSS. Computational functions in biochemical reaction networks, *Biophys. J.* **1994**, *67*, 560–578.
- 74 D. M. WOLF, A. P. ARKIN. Motifs, modules and games in bacteria, *Curr. Opin. Microbiol.* **2003**, *6*, 125–134.
- 75 T. S. GARDNER, C. R. CANTOR, J. J. COLLINS. Construction of a genetic toggle switch in *Escherichia coli*, *Nature* **2000**, *403*, 339–342.
- 76 M. B. ELOWITZ, S. LEIBLER. A synthetic oscillatory network of transcriptional regulators, *Nature* **2000**, *403*, 335–338.
- 77 R. WEISS, T. F. KNIGHT, JR. Engineering communications for microbial robotics, in: *DNA Computing: 6th International Workshop on DNA-Based Computers, Lecture Notes in Computer Science 2054*, A. E. CONDON, G. ROZENBERG (Eds.). Springer, Berlin, **2000**, pp. 1–16.
- 78 V. NOIREAUX, R. BAR-ZIV, A. LIBCHABER. Principles of cell-free genetic circuit assembly, *Proc. Natl Acad. Sci. USA* **2003**, *100*, 12672–12677.
- 79 J. HASTY, D. McMILLEN, J. J. COLLINS. Engineered gene circuits, *Nature* **2002**, *420*, 224–230.
- 80 S. A. BENNER, A. M. SISMOUR. Synthetic biology, *Nat. Rev. Genet.* **2005**, *6*, 533–543.
- 81 W. U. DITTMER, F. C. SIMMEL. Transcriptional control of DNA-based nanomachines, *Nano Lett.* **2004**, *4*, 689–691.
- 82 W. U. DITTMER, S. KEMPTER, J. O. RÄDLER, F. C. SIMMEL. Using gene regulation to program DNA-based molecular devices, *Small* **2005**, *1*, 709–712.



## 7

## Towards the Realization of Nanobiosensors Based on G-protein-coupled Receptors

*Cecilia Pennetta, Vladimir Akimov, Eleonora Alfinito, Lino Reggiani,  
Tatiana Gorojankina, Jasmina Minic, Edith Pajot-Augy,  
Marie-Annick Persuy, Roland Salesses, Ignacio Casuso,  
Abdelhamid Errachid, Gabriel Gomila, Oscar Ruiz, Josep Samitier,  
Yanxia Hou, Nicole Jaffrezic, Giorgio Ferrari, Laura Fumagalli, and  
Marco Sampietro*

## 7.1

### Introduction

Among membrane proteins, G-protein-coupled receptors (GPCRs) are of special importance because they form one of the widest groups of receptor proteins [1–6]. As they can be activated by a large variety of extracellular signals, such as light, odorant molecules, hormones, peptides, lipids, neurotransmitters and nucleotides, GPCRs mediate the sense of vision, smell, taste and pain [1–8], and are involved in an extraordinary number of physiological processes [1–8]. For the same reasons, GPCRs are also implicated in a number of pathologies and they constitute one of the most important classes of pharmacological targets [1–6]. Accordingly, many efforts in the field of nanobiotechnology are devoted to the realization of nanobiosensors based on a single or a few GPCRs and aimed at detecting the specific ligands [9–18]. In the cell, the detection and transduction process begins with the conformational change of the GPCRs associated with the capture of the specific ligand [1, 7]. This conformational transition then activates the so-called G-proteins, giving rise to a complex sequence of biological mechanisms which ends in the production of an electric pulse by neurons (action potential) [1, 7].

It must be noted that different ligands may induce and stabilize distinct conformational states among the various structures available, and thus promote different G protein activation and receptor desensitization/internalization [19–22]. Moreover, GPCRs can interact with other proteins through their C-terminal domains. They can also give rise to homodimers and heterodimers with other membrane-bound proteins involved in their function and pharmacology [23]. Of course, understanding these mechanisms is crucial for new drug design. However, the drug-discovery process and the research of novel GPCR-based therapeutics require a large body of data to allow the identification of new receptor ligands. Therefore,

there is an increasing need to develop genetic and chemical high-throughput screening (HTS) methods for an efficient sorting of compounds with pharmaceutical potential [3, 24–26]. In this context, the production of nanobiosensors based on GPCRs can provide a very useful tool.

In nanobiosensors, the detection process bypasses the complicated sequence of biological events which follows G protein activation; rather, the goal is to achieve sensitive and reliable monitoring of the conformational change by direct analysis of the optical or the electrical response of the nanodevice itself.

The first difficulty to be faced in developing such chip-based sensors is to prepare and immobilize the receptors in such a manner as to preserve their function, i.e. their ability of undergoing the appropriate conformational transition. The second difficulty consists in achieving sensitive and reliable monitoring of the conformational change, by analysis of the optical or electrical response of the device. Of course, this analysis requires the development of suitable tools, both experimental and theoretical.

This development represents a true challenge. In particular, here we discuss the possibility of studying the detection process of a single receptor device by direct measurement of its electrical properties [16, 17]. Actually, most of efforts in the literature focus on optical or atomic force microscopy (AFM) techniques to monitor the ligand detection process (see Section 7.3). Only a few attempts [16–18] based on electrical measurements have been made until now, as a consequence of the difficulty arising from the very low values expected for currents, which requires very advanced amplification techniques. Thus, the method adopted here and illustrated in this chapter represents a very innovative approach. Concerning this point, we further underline the novelty of the theoretical model that, uniquely in the literature, uses an impedance network for the description of the electrical properties of a single protein device.

It is important to note that all the members of the GPCR superfamily [1] share a common molecular topology consisting of seven transmembrane helical domains ( $\alpha$ -helices), connected by three intracellular and three extracellular loops (Fig. 7.1). This feature of the GPCR superfamily plays an important role in the development of theoretical and computational models of these receptors [1]. Actually, while the primary structure (amino acid sequence) is known for many GPCRs [27], the detailed atomic positions are available only in the case of rhodopsin, the rod cell photoreceptor that mediates light vision, where they can be measured by X-rays diffraction experiments performed in the protein crystalline state [27–31]. Indeed, the natural abundance and availability of rhodopsin, in contrast to other GPCRs, typically expressed at a very low level in the cell, results in the fact that only rhodopsin crystals have been obtained and studied at high resolution [27–33]. For all these reasons, rhodopsin is the best-studied GPCR, and it is often selected as a model protein for biological and biophysical studies of this kind of receptor [34–36]. Rhodopsin also serves as a pilot receptor for establishing biotechnological platforms for chip-based screening technologies, to characterize the function and interactions of GPCRs [37].

A three-dimensional structure for the activated state of rhodopsin, i.e. metarhodopsin II [19, 31, 37], was obtained at medium resolution by combining elements

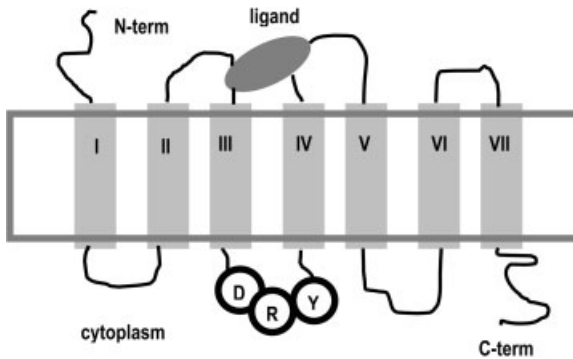


**Figure 7.1.** Schematic drawing of a GPCR. The big dark-grey rectangular box represents the cellular membrane which separates the extracellular region (above) from the cytoplasmic region (below). The seven grey vertical rectangles show the seven transmembrane  $\alpha$ -helical domains of the receptor, while the loops and the two termini (N- and C-terminus) are shown by black lines. The three black circles represent the three subunits of the G-protein and, finally, the grey ellipse on the top shows a ligand captured by the receptor.

of secondary structure with experimental, long-range distance constraints inducing rigid body movements of secondary structures relative one to another. As a result, the metarhodopsin II state of the receptor exhibits a spatial organization different from the ground state rhodopsin [31].

In this chapter, we first briefly review some of the different techniques that have been previously developed to prepare and immobilize the receptors on the substrate. Then, we consider the detection process as characterized by the response of the device. In particular, we discuss the electrochemical impedance spectroscopy (EIS) technique, which is emerging as a very effective technique for the detection of biosensing events at the electrodes [38–42]. The largest part of this chapter is devoted to illustrating a recent theoretical model [17, 43–45] which studies the current response to an applied AC voltage of a nanodevice realized by a single GPCR embedded in its membrane and in contact with two functionalized metallic nanoelectrodes.

This model, based on a coarse-grained approach [17, 46, 47], describes the protein as a network [48] of elementary impedances. The model starts with the construction of a time-independent (static) network, corresponding to an ideally frozen protein, in which all the atomic positions are fixed at the equilibrium values [17]. The nodes of this static network correspond to the positions of the  $\alpha$  carbons ( $C_\alpha$ ) atoms of the rhodopsin amino acids, in the ground or in the activated state (metarhodopsin II), as taken from the protein data bank [27]. Then, an elementary impedance is associated with each link between a pair of amino acids, established according to a length cut-off criterion [46]. The elementary impedances, which mimic the electrical interactions among the protein amino acids, are taken dependent on the amino acid distance and on other parameters which account for the different physical and chemical properties of the amino acids [17]. The solution of the equivalent circuit determines the global impedance of the network itself. The

results of this static-network model, applied to the case of rhodopsin and OR-17 (rat olfactory receptor) [49], predict a detectable change of the global impedance associated with the conformational change of the receptor due to the sensing action [17, 45]. Afterwards, the frozen protein approximation is relaxed and the thermal fluctuations of the atomic positions are included in the model, first by adopting a single-force-constant approximation [43, 50, 51], as the simplest level of modeling, and then a two-force-constant approximation [44]. This last update in the model is introduced to describe the different flexibility of the atomic bonds within the  $\alpha$ -helices and within the loops [1]. The protein thermal fluctuations result in an impedance noise which is calculated as a function of the temperature. The implications of this impedance noise on the ligand detection process are then discussed.

## 7.2

### Preparation and Immobilization of GPCRs on Functionalized Surfaces

The first requirement to develop receptor-based nanobiosensors is the immobilization of receptors in such a manner as to preserve their function. Since GPCRs are composed of seven transmembrane  $\alpha$ -helices [1], they are extremely hydrophobic and require a lipidic or detergent environment to keep their native conformation and function. Generally, membrane receptors are expressed in heterologous cells, solubilized, and then purified in an appropriate detergent before being reconstituted in proteoliposomes and immobilized on a sensor surface [52–54]. Although many such successful procedures have been reported, the method requires substantial effort for purification of GPCRs prior to analysis. This cannot be considered for the majority of GPCRs because of their very low expression level, even in recombinant systems. Furthermore, the receptor function can be influenced by its lipidic environment as shown for rhodopsin [55] and  $\mu$ -opioid receptor [56]. Therefore, enormous care must be taken to avoid modification of the activity of the receptor during its solubilization and reconstruction.

The possibility of building bilayers harboring previously purified GPCRs on sensor surfaces has been demonstrated for rhodopsin [54, 57],  $\beta_2$ -adrenergic receptor [58, 59] and  $\mu$ -opioid receptor [60, 61]. On-surface reconstitution of rhodopsin in lipidic membranes has also been achieved from mixed detergent/lipid micelles, with a high density of functional receptors [15]. However, one of the most promising strategies for the preparation of GPCRs seems to produce lipid vesicles by breaking membranes where GPCRs have been expressed [18, 42]. Indeed, this procedure bypasses the difficulties implied in the purification of GPCRs and in their subsequent insertion into the reconstituted membranes.

For what concerns the immobilization of GPCRs, the self-assembled multilayer technique appears to be the most suitable and effective for the construction of well-ordered and ultra-thin organic films, since it allows the required control at a molecular level. Actually, starting from the pioneering works of Nuzzo and Allara [62], the field of self-assembled monolayers (SAMs) has experienced an explosive growth [63]. The simplicity in the production of SAMs, their adaptability and the

possibility of controlling the orientation of biomolecules on the surface ascribe to the SAM technique a central role in the construction of artificial biomolecular recognition surfaces, particularly in the development of biosensors [64–66]. The construction of self-assembled multilayers from biological components has been investigated intensively due to its potential application for biosensors [13, 14, 67, 68]. In particular, it has been found that the avidin–biotin system works very well as a bridge to anchor a bioreceptor, since the biotinylation of a biomolecule does not affect its biological activity. Furthermore, the noncovalent complex between avidin and biotin is characterized by a very high affinity constant of  $10^{15} \text{ mol}^{-1} \text{ L}$ . Once formed, the bond is stable even if the pH of the solution is changed and it can easily resist multiple washings [69].

In recent studies, a mixed SAM formed by 16-mercaptohexadecanoic acid (MHDA) and biotinyl-PhosphoEthanolamine, inserted and bound to MHDA, has been produced on gold electrodes [18, 42]. Neutravidin was then used to anchor biotin-labeled, receptor-specific antibodies. Such a multilayer system using biotin/avidin pairs acting as binding agents is of relevance for biosensor research, to immobilize a membrane receptor. Immobilization of the prototypical GPCR, rhodopsin, in its native membranes was thus achieved on functionalized surfaces [18, 42], which represents the first prerequisite for elaborating a GPCR-based biosensor. The rhodopsin membrane fraction preparations were obtained by simple sonication of the natural rod outer segments membranes. Negative-staining electron microscopy of the sample showed that the fragments are circularized into microsome, although unclosed membrane fragments are still present and the suspension is mostly constituted of vesicles with diameters of 40–100 nm. This procedure provides samples of rather uniform size, which fit the geometrical requirements of the nanobiosensor supports. Moreover, as the receptor remains at all times in its native environment, this procedure offers the advantage of avoiding the risks of altering or loosing receptor activity as a consequence of the purification and reconstitution of the GPCR in artificial membranes or liposomes. Furthermore, this specific immobilization methodology can be very useful to develop molecular arrays of other GPCRs that, in contrast to rhodopsin, are usually present in a low amount in the membrane fraction. Therefore, this form of *in situ* purification and immobilization on biostructured solid supports can overcome the difficulties usually encountered in studying most of the GPCRs and that arise from a low expression level.

### 7.3

#### Signal Techniques

Different techniques have been developed in recent years. A particularly important role in this field is played by optical techniques which, in most cases, make use of visible fluorescent proteins (VFPs) [70] and of confocal microscopy analysis, as in fluorescence resonance energy transfer (FRET) and fluorescence lifetime imaging (FLIM) techniques [71–73].

Other important tools for the investigation of this kind of system are offered by

surface plasmon resonance (SPR) [18, 54, 58] and AFM. This last technique, in particular, represents a very powerful tool for structural biology studies since it gives access to the molecular architecture [74, 75], and it can also be used to follow and characterize receptor immobilization on the selected biostructured surfaces.

EIS has become one of the most effective electrochemical techniques for the characterization of biomaterial-functionalized electrodes and of biocatalytic transformations at electrode surfaces; specifically, for the detection of biosensing events at electrodes [38–42]. Compared to other electrochemical techniques, one of the great advantages of EIS is the small amplitude of the perturbation from the steady state, which makes it possible to treat the response theoretically by linearized or otherwise simplified current–potential characteristics [38–42]. Therefore, EIS has been performed extensively to characterize the fabrication of biosensors and to monitor biomolecular recognition [12, 38–41, 76]. Very recently, electrochemical impedance measurements have demonstrated the sensitivity and selectivity of self-assembled multilayer systems for the specific grafting of the rhodopsin membrane fraction [18, 42].

#### 7.4

#### Theoretical Approach

The theoretical study of the electrical response to an external voltage of a GPCR-based device is a hard task. Thus, we limit ourselves to consider a “simple” two-terminal device, made by a single receptor embedded in a small portion of its native membrane and inserted between two ohmic electrical contacts (functionalized metallic layers) through which an AC voltage is applied. The device is placed within a physiological buffer solution, necessary to keep the protein in the correct conformation. This device is sketched in Fig. 7.2, where, without loss of generality,

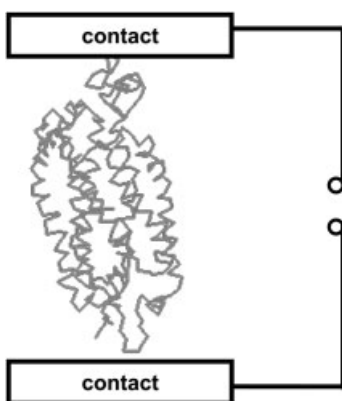


**Figure 7.2.** Representation of a single receptor device: the receptor is contacted between two functionalized electrodes through which an external AC voltage is applied.

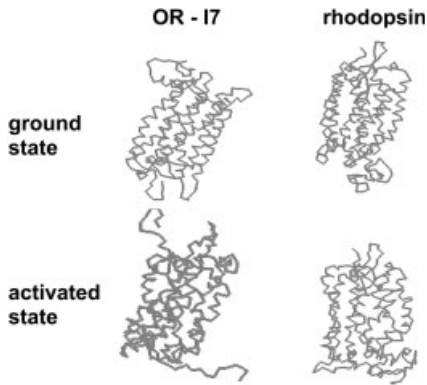


**Figure 7.3.** Schematic representation of the ground and activated states of OR-17 and rhodopsin.

a vertical configuration of the electrodes has been assumed (other configurations can also be considered).

As discussed before, the main mechanism by which GPCRs perform their biological functions is associated with the conformational transition undergone as consequence of the interaction and capture of the ligands [1, 9]. Thus, the main task of a theoretical study of the electrical properties of a GPCR-based device consists in estimating the magnitude of the difference of the electrical response to the external voltage in the two receptor conformations. The GPCR conformational transitions have been intensively studied [27, 31, 32, 46, 77–82], especially by experiments [27, 31, 32, 77–80], and it has been realized that the activation of the receptor involves a release of constraints in the transmembrane helix bundle, resulting in the opening of a cleft at its cytoplasmic end [19, 37], and in a net volume change of the protein [79]. In particular, a lot of information is available concerning the most stable light-activated state of rhodopsin, known as metarhodopsin II [27, 31, 32], where the available information also includes the coordinates of the atomic positions. To illustrate qualitatively the conformational change of GPCRs, Fig. 7.3 shows a schematic representation of the ground and activated states of rhodopsin and of the rat OR-17. Apart from these large-scale conformational transitions, it is well known that proteins are not rigid, but instead they sample a variety of conformations in the neighborhood of their native conformation [82]. These fluctuations within different conformations, all near to the equilibrium one, are called equilibrium fluctuations [82].

Both the complicated relationship between structure and functions of the proteins and the details of the molecular motion in the folded state can, in principle, be studied by molecular dynamics (MD) simulations and normal-mode analysis, by using classical MD or “*ab initio*” quantum MD, or even hybrid schemes [81, 83–85]. These last mix a quantum treatment of a limited number of atoms and a classical treatment of the remaining atoms, thus allowing the study of large biological molecules [81, 83–85]. However, the use of these atomic approaches becomes computationally very heavy and inefficient with increasing protein size [46].

Recently, alternative methods have been proposed, based on coarse-grained models of proteins and simplified force fields [50, 51]. Successively, many other studies have shown the success and the effectiveness of these kinds of models in describing protein dynamics, particularly for the case of large proteins composed by more than several thousands of amino acids [46, 47].

Therefore, in developing a theoretical model of the electrical properties of a GPCR-based device we have also followed a coarse-grained approach, by formulating it in terms of an electric network of impedances [17, 43–45] instead of the usual elastic network of springs, considered in the above cited works [46, 47, 50, 51]. In the following we illustrate in detail the procedure and we discuss the results for the case of rhodopsin. Moreover, we also show results concerning OR-17 [49]. However, it is important to note that, in addition its computational simplicity, an important advantage of this coarse-grained network approach [17, 46, 47, 50, 51] is given by the fact that, by focusing mainly on protein topology, it represents an appropriate tool for providing predictions for the other GPCRs, for which detailed information on the atomic positions is missing.

## 7.5

### The Impedance Network Model

We start by considering an ideally frozen bovine rhodopsin molecule, in which no fluctuation occurs and all the atoms occupy the equilibrium positions [17]. We describe this protein as a static network made of elementary impedances (in this context, a static network means a network made of time-independent elements). The network is built in the following manner [17].

First, we have to choose the nodes of the networks, i.e. we have to choose a reference position within each amino acid (residue). By following a choice largely adopted in the literature [46, 47, 51], we assume the  $C_\alpha$  atoms present in any amino acid as nodes of the network. Accordingly, we have taken the atomic coordinates of bovine rhodopsin from the Protein Data Bank (PDB) [27], where several sets of data from independent experiments are present in the standard PDB file format. We have used PDB with IDs 1F88 [28] and 1JFP [32] for the rhodopsin ground state, and the data set II (PDB ID 1LN6) [31] (engineered data) for meta-rhodopsin II. Then, we have extracted the spatial coordinates of the  $C_\alpha$  atoms of each amino acid (348 for bovine rhodopsin) from the PDB file.

We assume that the amino acids interact electrically between each other and that charge transfers between neighboring residues [78, 86] and/or changes of their electronic polarization [87] affect these interactions. Accordingly, a link is drawn between any pair of nodes,  $i$  and  $j$  separated by a distance  $l_{i,j}$  less than a given cut-off value,  $d = 2R_a$ , where  $R_a$  is an electrical interaction radius (Fig. 7.4). Moreover, we introduce two extra nodes (contact nodes) which mimic the electrodes. These contact nodes are linked to a given set of amino acids, depending on the particular geometry of the contacts in the real device (each electrode is linked at least to one amino acid). A representation of this interaction network for the case



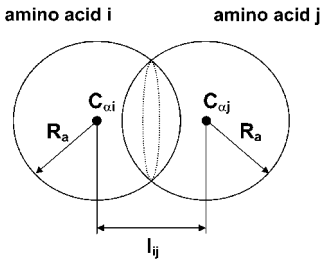


**Figure 7.4.** A link is drawn between the nodes  $i$  and  $j$ , which stay at the positions of the  $\alpha$  carbon atoms  $C_{\alpha i}$  and  $C_{\alpha j}$  of the  $i$ th and  $j$ th amino acid, when their relative distance is less than twice the interaction radius  $R_a$ .

of a hypothetical protein made of 18 residues is shown in Fig. 7.5. We note that the solution and the membrane are not directly taken into account at this stage of the model (however, as the main effect of the membrane is to keep the protein in the folded state, this effect is implicitly accounted for by taking the coordinates of the  $C_\alpha$  corresponding to a given folded conformation of the protein).

The next step of the model consists of associating an elementary impedance  $Z_{i,j}$  with the link between the nodes  $i$  and  $j$  [17]. We take this elementary impedance as the impedance of a RC parallel circuit (the most usual passive AC circuit) and we denote as  $R_{i,j}$  and  $C_{i,j}$ , respectively, the resistance and the capacitance of the link between the nodes  $i$  and  $j$ . Different expressions can be adopted for  $Z_{i,j}$ . Here, we discuss three possibilities, corresponding to an increasing level of complexity. The first possibility, model (i), is the simplest one: all the impedances are taken to be equal:  $Z_{i,j} = Z_0$ . The second possibility, model (ii), consists of assuming that  $R_{i,j}$  and  $C_{i,j}$  are, respectively, the resistance of a simple ohmic resistor and the capacitance of a planar homogeneous capacitor. Thus,  $R_{i,j} \propto l_{i,j}$  and  $C_{i,j} \propto l_{i,j}$ . Consequently,  $Z_{i,j}$  takes the expression [17]:

$$Z_{i,j} = l_{i,j} \frac{\rho}{A(1 + i\rho\omega\epsilon\epsilon_0)} \quad (1)$$



**Figure 7.5.** Interaction network associated with a hypothetical protein made of 18 residues: the full circles show the nodes positioned at the  $\alpha$  carbon atom of each amino acid and the lines represent the links arising

from electrical interactions between a pair of amino acids with a relative distance shorter than a cut-off value. The open circles represent two extra nodes associated with the electrodes.

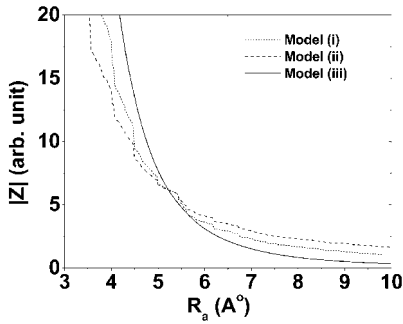


**Figure 7.6.** Modulus of the network impedance as a function of the interaction radius: the dotted curve is obtained from model (i), the dashed curve from model (ii) and the solid curve from model (iii). The impedance is expressed in arbitrary units and the interaction radius is in Ångstroms.

where  $A$  is the cross-sectional area of the capacitor and of the resistor,  $\rho$  is the resistivity,  $\varepsilon$  the relative dielectric constant,  $\varepsilon_0$  is the vacuum dielectric permittivity,  $\omega$  is the angular frequency of the external AC voltage. The third choice, model (iii), consists of taking the cross-sectional area of the resistor and of the capacitor equal to the area of the cross-section defined by the overlap of the two spheres pertaining to the given amino acids, as shown in Fig. 7.4. Thus:

$$A = \pi \left[ R_a^2 - \frac{l_{i,j}^2}{4} \right] \quad (2)$$

To compare these three models, we plot in Fig. 7.6 the modulus of the total network impedance,  $|Z|$ , calculated by using models (i), (ii) and (iii) as a function of the interaction radius  $R_a$ . The total network impedance  $Z$  is calculated by solving Kirchhoff's node equations. We note that in the case of an irregular network, with complex topology [48], the solution of the circuit by node equations is particularly convenient with respect to the use of loop equations. The systematic decrease of  $|Z|$  shown in Fig. 7.6 at increasing values of  $R_a$  reflects the increasing importance of parallel connections with respect to series connections. One can see that the curves of the first two models show a step-like behavior related to the sharp discontinuity in the value of  $|Z|$  when  $R_a$  becomes equal to  $l_{i,j}$ . However, the curve obtained by using model (iii) shows a continuous behavior. Furthermore, model (iii) appears to be more sensitive to a variation of the number of links in the networks.

Of course, an improvement in the description of the protein is expected if the physical and chemical properties of the different amino acids are accounted for in the expression of  $Z_{i,j}$ . At a simplest level, this can be done by considering  $\varepsilon$  and/or  $\rho$  as dependent on the indices  $i$  and  $j$ . For this purpose, we have taken [17] the following expression  $\varepsilon_{i,j} = 1 + g(\bar{\alpha} - 1)$  for the dielectric constant of the capacitor associated with the pair  $i$  and  $j$  of amino acids, where  $\bar{\alpha} \equiv (\alpha_i + \alpha_j)/2$  is the average

intrinsic polarizability of the pair, and  $\alpha_i$  and  $\alpha_j$  are the intrinsic polarizabilities of the  $i$ th and  $j$ th amino acid, respectively. Actually, by describing a protein in solution as a set of polarizable dipoles embedded in a dielectric medium of solvent molecules, Song [87] has calculated a set of values for the intrinsic polarizabilities of the 20 amino acids, portable for all the proteins in nature. Finally, we have chosen the value of  $g$  in the expression of  $\varepsilon_{i,j}$  in such a manner as to obtain the values of  $\varepsilon_{i,j}$  distributed between 1 and 80 (vacuum and water) proportionally to  $\bar{\alpha}$ . Thus, with the last update, model (iii) provides for  $Z_{i,j}$  the expression [17]:

$$Z_{i,j} = \frac{l_{i,j}}{\pi(R_a^2 - l_{i,j}^2/4)} \cdot \frac{1}{(\rho^{-1} + i\omega\varepsilon_{i,j}\varepsilon_0)} \quad (3)$$

In the following we will show and discuss results obtained by using this expression of  $Z_{i,j}$ .

An important feature characterizing the topology of a network is represented by the degree distribution, i.e. the distribution function of the node connectivity [48]. Figure 7.7 shows the degree distribution of the interaction networks of rhodopsin and OR-17 obtained for two values of the interaction radius,  $R_a = 4$  and  $5 \text{ \AA}$ . The degree distribution is found to be only roughly described by a Poissonian curve. Indeed, secondary peaks are present for both rhodopsin and OR-17. This behavior of the degree distribution characterizes a pseudo-random network [48]. We note that for the values of  $R_a$  considered in Fig. 7.7 the width of the distribution increases by increasing the interaction radius. The contrary will occur at the highest values of  $R_a$ . In particular, above a given maximum value of the radius,  $R_{a,\max}$ , of the order of the size of the receptor, each node will be connected with all the other nodes and the degree (number of links) of all the nodes will be become  $(N_{\text{am}} - 1)$ ,

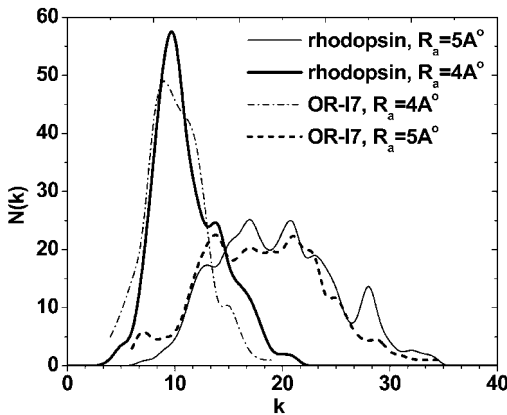


**Figure 7.7.** Degree distribution (distribution function of the node connectivities) of the interaction network of rhodopsin and OR-17. The thin and thick solid curves are obtained in

the case of rhodopsin by taking  $R_a = 4$  and  $5 \text{ \AA}$ , respectively; the dot-dashed and the dashed curves are obtained in the case of OR-17 by taking  $R_a = 4$  and  $5 \text{ \AA}$ .

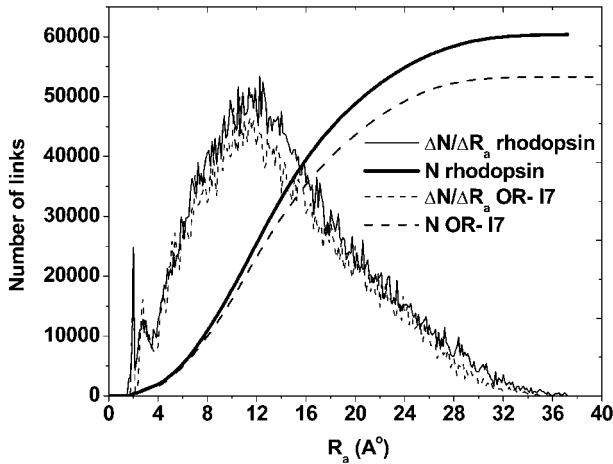


**Figure 7.8.** Total number of links in the network,  $N$ , and relative increment as a function of the interaction radius. The thin thick solid and the grey short-dashed curves show  $N$  for the interaction network corresponding to the

basic state of rhodopsin and OR-17. The thin solid and the grey short-dashed curves show the relative increment of  $N$ . The interaction radius is expressed in Ångstroms.

where  $N_{am}$  is the number of amino acids. Consequently, for  $R_a \geq R_{a,max}$  the degree distribution will become a  $\delta$  function independently of  $R_a$ .

Figure 7.8 reports the total number of links,  $N$ , existing in the network, as a function of the interaction radius. The data concerning the ground state of rhodopsin and OR-17 are shown by the thick solid and the grey dashed curves, respectively. We can see that for any value of  $R_a$ , the number of links in the interaction network of rhodopsin is higher than that existing in the case of OR-17. Moreover, the difference in the link number is rather significant (about 10%) for values of  $R_a \geq 8 \text{ \AA}$ . Figure 7.8 also displays as a function of  $R_a$  the behavior of the relative increment of the number of links,  $\Delta N/\Delta R_a$ , for the ground state of rhodopsin (black solid curve) and OR-17 (grey short-dashed curve). Thus, from Fig. 7.8 we can conclude that when  $R_a \sim 8\text{--}18 \text{ \AA}$  the connectivity of the network is very sensitive to the value of the interaction radius. On the other hand, by comparing the behavior versus  $R_a$  of  $N$  and  $\Delta N/\Delta R_a$  in the ground and in the activated state of rhodopsin, it has been found [17] that the range of values  $R_a \sim 8\text{--}18 \text{ \AA}$  corresponds to the maximum sensitivity of the network to conformational changes.

This statement is also confirmed by the analysis of the dependence of the total network impedance,  $Z$ , on the interaction radius in the case of rhodopsin and metarhodopsin, as shown in Fig. 7.9. Precisely, in Fig. 7.9 we report the difference of the impedance modulus,  $|Z|$ , calculated in the case of rhodopsin and metarhodopsin. This difference has been normalized to the impedance modulus of the rhodopsin network. We can see that when  $R_a \sim 8\text{--}18 \text{ \AA}$  the total network impedance depends strongly on the conformation of the protein. It must be noted that this

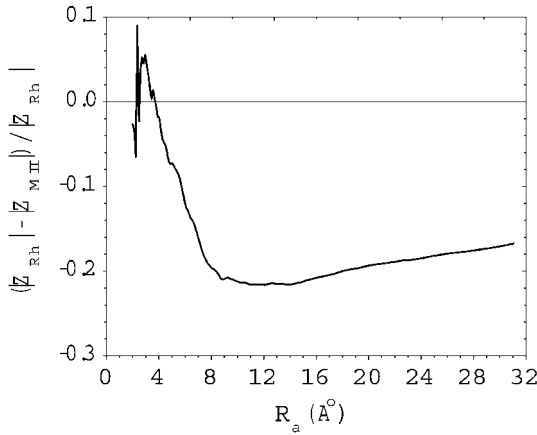


**Figure 7.9.** Relative difference of the values of the impedance modulus in the ground state (Rh) and in the activated state (MII) of rhodopsin as a function of the interaction radius ( $R_a$  expressed in Ångstroms).

sensitivity of the total network impedance to the conformational changes arises not only from the above discussed sensitivity of  $N$  to the protein conformation, but also from the fact that the elementary impedances  $Z_{i,j}$  are assumed to be functions of the distances  $l_{i,j}$ .

To provide a prediction of the expected electrical response of the GPCR-based nanodevice and to test our model in a direct comparison with the results of EIS measurements [38–42], we have calculated the network impedance as a function of the frequency of the applied AC voltage. Figure 7.10 shows the Nyquist plot of the network impedance calculated in the case of rhodopsin. Precisely, Fig. 7.10 displays the opposite of the imaginary part of the network impedance versus the real part, where both these quantities are calculated in the frequency range  $0 \div 1$  kHz. The three curves reported in Fig. 7.10 are obtained for  $R_a = 2$  Å (short-dashed curve),  $R_a = 5$  Å (long-dashed curve) and  $R_a = 12.5$  Å (solid curve). In all cases, we have taken  $\rho = 10^9 \Omega\text{m}$  while the amplitude of the applied voltage,  $V_0$ , is  $V_0 = 1$  V. Moreover, the real and the imaginary parts of the impedance have been normalized to the static value of the real part,  $\text{Re}[Z(\omega = 0)]$ , which takes the values  $\text{Re}[Z(\omega = 0)] = 302 \text{ G}\Omega$ ,  $11.2 \text{ G}\Omega$  and  $1.67 \text{ M}\Omega$ , respectively, for  $R_a = 2, 5$  and  $12.5$  Å. As a general trend, when  $R_a \geq 5$  Å, the shape of the Nyquist plot is indistinguishable from that corresponding to a single RC parallel circuit (semicircle). In contrast, when  $R_a < 5$  Å, the Nyquist plot deviates from this behavior. In particular, when  $R_a = 2$  Å, the degree of most of the nodes of the network is 2 (Fig. 7.7) and the series combination of elementary impedances  $Z_{i,j}$  becomes dominant in the network structure. In other terms, changes in the shape of the Nyquist plot are only detected near to the sequential limit. Of course, the value of  $\text{Re}[Z(\omega = 0)]$  depends on both  $R_a$  and  $\rho$ . Therefore, impedance spectroscopy measurements

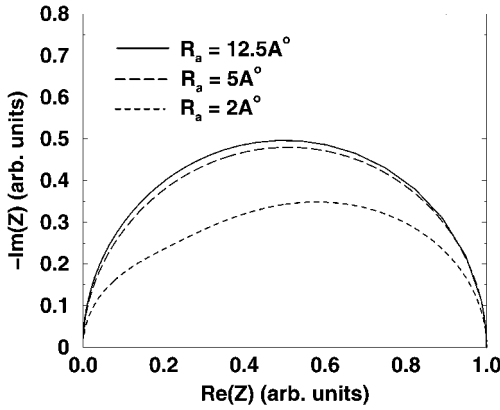


**Figure 7.10.** Nyquist plot of the network impedance: the short-dashed curve corresponds to an interaction radius equal to 2 Å, the long-dashed curve to a radius of 5 Å and the solid curve to a radius of 12.5 Å. The real and the imaginary parts of the impedance are

normalized to the static value of the real part, which is 302 GΩ, 11.2 GΩ, and 1.67 MΩ, respectively, when  $R_a$  is 2, 5 and 12.5 Å. All curves correspond to the basic state of rhodopsin and are obtained by taking a resistivity of 1 GΩm.

could be a method which allows the identification of the values of the parameters to be used in the modelization of the receptor.

Figure 7.11 displays a comparison between the Nyquist plot corresponding to the rhodopsin interaction network and that corresponding to the activated state metarhodopsin II. Precisely, the solid curve is obtained for rhodopsin while the

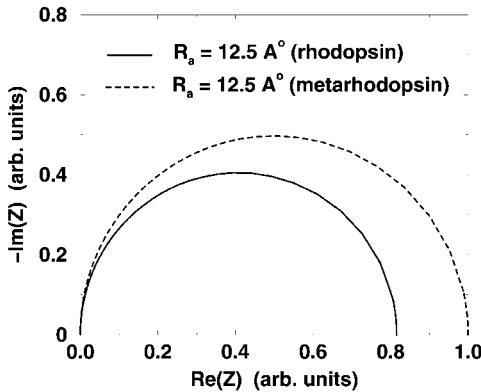


**Figure 7.11.** Nyquist plot of the network impedance: the solid curve is obtained for rhodopsin by taking the interaction radius equal to 12.5 Å and a resistivity of 1 GΩm, the dot-dashed curve is obtained for metarhodopsin by taking the same values of the

parameters. The real and the imaginary parts of the impedance are normalized to the static value of the real part of the network impedance in the metarhodopsin state which takes the value of 2.04 MΩ.

dot-dashed curve for metarhodopsin II. In both cases we have taken  $R_a = 12.5 \text{ \AA}$ ,  $\rho = 10^9 \text{ } \Omega\text{m}$  and  $V_0 = 1 \text{ V}$ . The real and the imaginary parts of the impedance are normalized to the static value of the real part of the impedance in the metarhodopsin state:  $\text{Re}[Z(\omega = 0)] = 2.04 \text{ M}\Omega$ . Figure 7.11 shows that the conformational change of the receptor due to the detection of a photon implies a significant variation in the Nyquist curve, in principle detectable by impedance spectroscopy measurements. This result is of particular relevance also in view of the application of the model to other GPCRs.

## 7.6 Equilibrium Fluctuations

The above results have been obtained by considering an ideally frozen protein, in which no fluctuation occurs and all the atomic positions are fixed at the equilibrium values. However, as discussed in a previous section, proteins are not rigid, but they sample a variety of conformations in the neighborhood of the equilibrium conformation [46, 50, 51, 80]. These fluctuations of the atomic positions result in an intrinsic impedance noise which is present during an electrical measurement performed on such a nanodevice. The level of this noise turns out to be crucial to the actual detection of the ligand capture by the GPCR when compared with the impedance variation due to the conformational transition and with the electrode/amplifier noise.

Therefore, we have extended the previous model by relaxing the frozen protein approximation and by studying the effect of the fluctuations of the atomic positions on the electrical response to an AC field [17, 43–45]. For this purpose, we allow the nodes of the network to fluctuate around their equilibrium positions with an amplitude depending on the temperature [43, 44]. For the sake of simplicity and to get a first qualitative estimation, we describe the system of fluctuating nodes as a set of independent, isotropic, harmonic quantum oscillators, with common values of the force constant  $\gamma$  and of the proper frequency,  $\omega_0$ . The oscillators are assumed to be in contact with a thermal bath at temperature  $T$ . We denote with  $\vec{r}_{n,\text{eq}}$  and  $\delta\vec{r}_n = \vec{r}_n - \vec{r}_{n,\text{eq}}$ , respectively, the equilibrium position and the displacement from the equilibrium at the time  $t$  of the  $n$ th oscillator, and with  $\langle(\delta\vec{r})^2\rangle$  its mean square displacement. It can be easily seen that  $\langle(\delta\vec{r})^2\rangle$  is given by:

$$\langle(\delta\vec{r})^2\rangle = \frac{3}{2} \cdot \frac{k_B\theta}{\gamma} + \frac{k_B\theta}{\gamma} \cdot \frac{1}{\exp[\theta/T] - 1} \quad (4)$$

where  $\theta = \hbar\omega_0/k_B$ . Thus, when  $T \gg \theta$ , Eq. (4) simplifies as:

$$\langle(\delta\vec{r})^2\rangle \approx k_B T / \gamma \quad (5)$$

At an arbitrary temperature the wave function of the oscillator is a superposition of several excited states and its probability density cannot be expressed in a simple

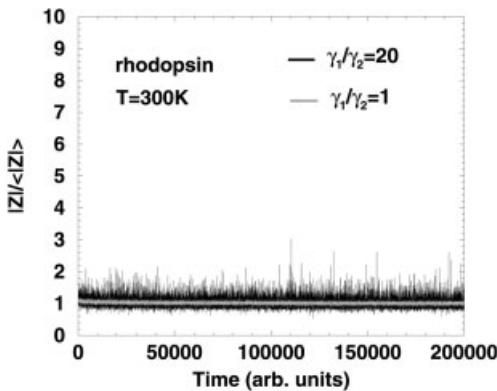
form. Again, for simplicity, we take the following expression for the probability density of presence of the  $n$ th oscillator around its equilibrium position:

$$P(\delta\vec{r}_n) = \frac{3^{3/2}}{[2\pi\langle(\delta\vec{r})^2\rangle]^{3/2}} \cdot \exp\left[-\frac{3}{2} \cdot \frac{(\delta\vec{r}_n)^2}{\langle(\delta\vec{r})^2\rangle}\right] \quad (6)$$

where  $\langle(\delta\vec{r})^2\rangle = 3\langle(\delta x)^2\rangle$  and  $\langle(\delta x)^2\rangle = \langle(\delta y)^2\rangle = \langle(\delta z)^2\rangle$ . The fluctuations of the network impedance have been calculated by a Monte Carlo simulation which generates the position of all the nodes at each step according to the space probability given by Eq. (6). The calculations have been performed by choosing the value  $\gamma = 2.5 \text{ kJ mol}^{-1} \text{ \AA}^{-2}$  for the oscillator force constant, according to the literature [46, 50, 51]. This choice of  $\gamma$  provides  $\theta = 12 \text{ K}$ . Thus, the condition  $T \gg \theta$  is well satisfied at room temperature. The choice of a unique force constant for all the amino acids of the protein is a frequently adopted assumption [46, 50, 51], as in the previously mentioned Gaussian Network Models [46, 50].

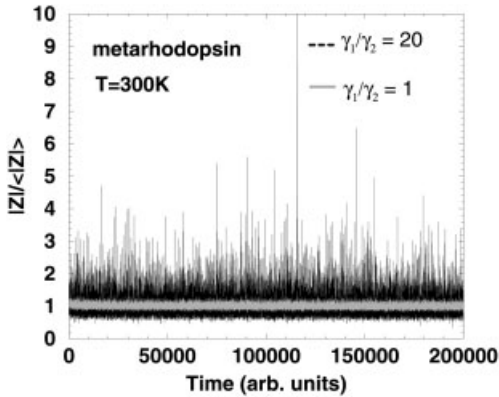
However, it is also well known that  $\alpha$ -helices are much more stable under thermal fluctuations than loops and termini [1–4]. For this reason, we have also calculated the impedance noise by assuming two different force constants,  $\gamma_1/\gamma_2$  and  $\gamma_2 < \gamma_1$  for  $\alpha$ -helices and loops/termini, respectively [44]. The values of  $\gamma_1$  and  $\gamma_2$  have been chosen by taking the mean value of the force constant  $\bar{\gamma} = 2.5 \text{ kJ mol}^{-1} \text{ \AA}^{-2}$  and then by considering different values of the ratio  $\gamma_1/\gamma_2$ . The greater the value of this ratio, the more flexible the loops and termini are with respect to helices.

Figure 7.12 displays the values of the impedance modulus calculated as a function of the time for the case of rhodopsin. Similar data obtained for metarhodopsin



**Figure 7.12.** Calculated values of the impedance modulus versus time for rhodopsin. The impedance modulus has been normalized to its average value and the time is expressed in simulation steps. The grey and the black curves are calculated by taking the ratio  $\gamma_1/\gamma_2 = 1$  and 20, respectively.





**Figure 7.13.** Calculated values of the impedance modulus versus time for metarhodopsin. The impedance modulus has been normalized to its average value and the time is expressed in simulation steps. The grey and the black curves have the same meanings as in Fig. 7.12.

II are reported in Fig. 7.13. All the data in Figs. 7.12 and 7.13 have been normalized to their respective average values and refer to simulations performed at room temperature. In Figs. 7.12 and 7.13, the curves corresponding to  $\gamma_1/\gamma_2 = 1$  and 20 are reported, respectively, in grey and black. The comparison of the data shows that the metarhodopsin state is characterized by impedance fluctuations significantly wider than those in the rhodopsin state. This is particularly true when the force constant of the  $\alpha$ -helices is 20 times greater than the force constant of loops/termini. This result reflects the minor thermal stability of metarhodopsin with respect to rhodopsin, probably due to an expansion of the entire structure consequent to the conformational transition [35].

This conclusion is supported also by Figs. 7.14 and 7.15, which report the probability distribution function,  $\phi$ , of the impedance fluctuations for rhodopsin and metarhodopsin calculated at room temperature by taking the ratio  $\gamma_1/\gamma_2 = 1$  (open diamonds) and 20 (full circles). The probability densities have been obtained by analyzing  $Z(t)$  signals made of about  $5 \times 10^5$  data. Here,  $\sigma$  is the root mean square deviation from the average value of the impedance modulus  $\langle |Z| \rangle$ . This normalized representation has been adopted for convenience because it makes the distribution independent of its first and second moments [88]. In particular, Fig. 7.15 shows that for metarhodopsin the impedance fluctuations are non-Gaussian even when  $\gamma_1/\gamma_2 = 1$  (in contrast, in the case of rhodopsin the fluctuations are Gaussian). Moreover, strong non-Gaussian tails are present when  $\gamma_1/\gamma_2 = 20$  and, in particular, for metarhodopsin. This strong non-Gaussianity at room temperature for  $\gamma_1 \gg \gamma_2$  (and, in particular, for metarhodopsin) is due to the presence of big spikes corresponding to the loss of links that are crucial to ensure the connectivity of the network [48, 88].

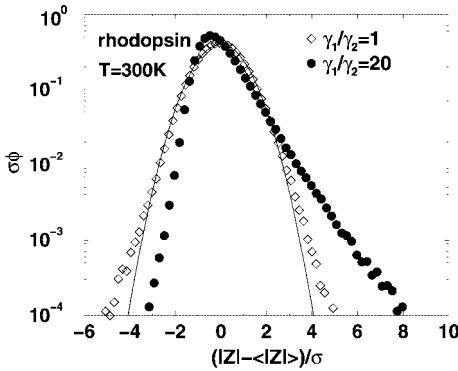


**Figure 7.14.** Normalized PDF of impedance modulus fluctuations at  $T = 300\text{ K}$  for rhodopsin. Diamonds and full circles correspond to simulations performed by taking the ratio  $\gamma_1/\gamma_2 = 1$  and  $20$ , respectively;  $\sigma$  is the root mean square deviation from the average modulus. The solid curve represents the Gaussian distribution.

Finally, Fig. 7.16 reports the values of the relative root mean square fluctuation of the impedance modulus,  $\sigma/\langle|Z|\rangle$ , as a function of the temperature. We can see that once the higher flexibility of loops and termini is accounted for by taking two different values for the force constants  $\gamma_1$  and  $\gamma_2$ , the relative fluctuation of the impedance becomes strongly sensitive to the temperature. In particular, for  $\gamma_1/\gamma_2 = 20$ , the relative root mean square fluctuation of the impedance modulus for rhodopsin is about 15%, while for metarhodopsin it is about 35%. Such high levels of noise would make it problematic to detect the conformational change in terms of variation of the impedance of the nanodevice, being this variation roughly

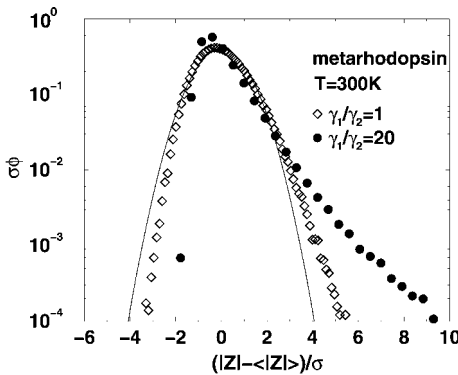


**Figure 7.15.** Normalized PDF of impedance modulus fluctuations at  $T = 300\text{ K}$  for metarhodopsin. The solid curve, the diamonds and full circles have the same meanings as in Fig. 7.14.  $\sigma$  is the root mean square deviation from the average modulus.

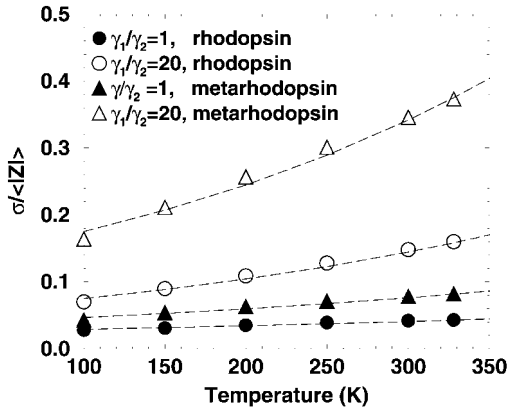


**Figure 7.16.** Relative root mean square deviation of the impedance modulus as a function of temperature for rhodopsin and metarhodopsin. The data shown by full and open symbols are calculated by taking the ratio  $\gamma_1/\gamma_2 = 1$  and 20, respectively. The dashed lines represent the best fit of the data with an exponential law. The temperature is expressed in Kelvin.

of the same order [17]. However, the increase of the impedance noise itself in the rhodopsin  $\rightarrow$  metarhodopsin transition (more than a factor of 2 at room temperature) could in principle provide a way to detect this transition.

## 7.7

### Conclusions

We have considered the possibility of realizing nanobiosensors based on GPRCs. First, we discussed some of the main difficulties to be faced in developing such chip-based sensors, i.e. (a) the preparation and the immobilization of the GPCRs on functionalized surfaces in a manner suitable to preserve their function (to enable the conformational transition associated with the capture of the ligands) and (b) the signal techniques. In this regard, the problem consists of developing experimental and theoretical tools allowing a sensitive and reliable monitoring of the ligand capture and/or of the conformational transition by an analysis of the optical or the electrical response of the nanodevice. Focusing on this last approach, we discussed the EIS technique, which is emerging as a very effective technique for the detection of biosensing events at the electrodes [38–42]. Then, the largest part of this chapter was devoted to illustrating a theoretical model recently proposed for the study of the current response to an external AC voltage of a single-protein device. In particular, we have considered, as a prototype, a two-terminal device consisting of a GPCR (rhodopsin or rat OR-17) embedded in a lipid bilayer and contacted by two ohmic electrodes. A coarse-grain approach has been developed for the description of the electrical properties of the receptor which is modeled as a network of elementary impedances. The conformational changes of the receptor

induced by the capture of the ligand (photon or odorant molecule) are then translated into a variation of the network impedance. The role played by the different model parameters on the network structure and on the impedance spectral properties was analyzed. Furthermore, the study of the impedance noise associated with the equilibrium fluctuations of the protein showed that the conformational transition is followed by a significant increase of the impedance noise level, which, by itself, would offers an interesting possibility to detect the transition. Thus, the results obtained look promising for the practical realization of a GPCR-based nanobiosensor able to perform its sensing functions based on a change of its electrical properties.

### Acknowledgments

This work has been performed within the SPOT-NOSED project IST-2001-38899 of the EC (<http://www.nanobiolab.pcb.ub.es/projectes/Spotnosed/>). Partial support from the cofin-03 project “Modelli e misure di rumore in nanostrutture” financed by Italian MIUR is also gratefully acknowledged.

### References

- LEFKOWITZ R. J. The superfamily of heptahelical receptors, *Nat. Cell Biol.* **2002**, *2*, E133–E136.
- LAMEH J., CONE R. I., MAEDA S., PHILIP M., CORBANI M., NADASDI L., RAMACHANDRAN J., SMITH G. M., SADÈE W. Structure and function of G protein coupled receptors, *Pharmac. Res.* **1990**, *7*, 1213–1221.
- VAIDEHI N., FLORIANO W. B., TRABANINO R., HALL S. E., FREDDOLINO P., CHOI E. J., ZAMANAKOS G., GODDARD W. A. Prediction of structure and function of G protein coupled receptors, *Proc. Natl Acad. Sci. USA* **2002**, *99*, 12622–12627.
- GETHER U., KOBILKA B. K. G protein-coupled receptors, *J. Biol. Chem.* **1998**, *273*, 17979–17982.
- MINIC J., SAUTEL M., SALESSE R., PAJOT-AUGY E. Yeast system as a screening tool for pharmacological assessment of G-protein-coupled receptors, *Curr. Med. Chem.* **2005**, *12*, 961–969.
- BOCKAERT J., PIN J. P. Molecular tinkering of G protein-coupled receptors: an evolutionary success, *EMBO J.* **1999**, *18*, 1723–1729.
- FIRESTEIN S. How the olfactory system makes sense of scents, *Nature* **2001**, *413*, 211–218.
- CRASTO C., SINGER M. S., SHEPHERD G. M. The olfactory receptor family album, *Genome Biol.* **2001**, *2*, 10271–4.
- BAYLEY H., CREMER P. S. Stochastic sensors inspired by biology, *Nature* **2001**, *413*, 226–230.
- WU T. Z. A piezoelectric biosensor as an olfactory receptor for odour detection: electronic nose, *Biosens. Bioelectron.* **1999**, *14*, 9–18.
- JOACHIM C., GIMZEWSKI J. K., AVIRAM A. Electronics using hybrid-molecular and mono-molecular devices, *Nature* **2000**, *408*, 541–548.
- ALFONTA L., BARDEA A., KHERSONSKY O., KATZ E., WILLNER I. Chronopotentiometry and faradaic impedance spectroscopy as signal transduction methods for the biocatalytic precipitation of an insoluble product on electrode supports: routes for enzyme sensors, immunosensors and DNA

- sensors, *Biosens. Bioelectron.* **2001**, *16*, 675–687.
- 13 BOOZER C., YU Q., CHEN S., LEE C., HOMOLA J., YEE S. S., JIANG S. Surface functionalization for self-referencing surface plasmon resonance (SPR) biosensors by multistep self-assembly, *Sens. Actuat. B* **2003**, *90*, 22–30.
  - 14 CUI X., PEI R., WANG Z., YANG F., MA Y., DONG S., YANG X. Layer-by-layer assembly of multilayer films composed of avidin and biotin-labeled antibody for immunosensing. *Biosens. Bioelectron.* **2003**, *18*, 59–67.
  - 15 KARLSSON O. P., LOFAS S. Flow-mediated on-surface reconstitution of G-protein coupled receptors for applications in surface plasmon resonance biosensors, *Anal. Biochem.* **2002**, *300*, 132–138.
  - 16 PATOLSKY F., ZHENG G., HAYDEN O., LAKADAMYALI M., ZHUANG X., LIEBER C. M. Electrical detection of single viruses, *Proc. Natl Acad. Sci. USA* **2004**, *101*, 14017–14022.
  - 17 PENNETTA C., AKIMOV V., ALFINITO E., REGGIANI L., GOMILA G. Fluctuations of complex networks: electrical properties of single protein nano-devices, *Proc. SPIE* **2004**, *5472*, 172–182.
  - 18 MINIC J., GROSCLAUDE J., AIOUN J., PERSUY M. A., GOROJANKINA T., SALESSE R., PAJOT-AUGY E., HOU Y., HELALI S., JAFFREZIC-RENAULT N., BESSUEILLE F., ERRACHID A., GOMILA G., RUIZ O., SAMITIER, J. Immobilization of native membrane-bound rhodopsin on biosensor surfaces, *Biochem. Biophys. Acta* **2005**, *3*, 324–332.
  - 19 OKADA T., ERNST O. P., PALCZEWSKI K., HOFMAN K. P. Activation of rhodopsin: new insights from structural and biochemical studies, *Trends Biochem. Sci.* **2001**, *26*, 318–324.
  - 20 SCARAMELLINI C., LEFF P. A three-state receptor model: predictions of multiple agonist pharmacology for the same receptor type, *Ann. NY Acad. Sci.* **1998**, *861*, 97–103.
  - 21 KENAKIN T. Ligand-selective receptor conformations revisited: the promise and the problem, *Trends Pharmacol. Sci.* **2003**, *24*, 346–354.
  - 22 SWAMINATH G., XIANG Y., LEE T. W., STEENHUIS J., PARNOT C., KOBILKA B. Sequential binding of agonists to the beta2-adrenoceptor, *J. Biol. Chem.* **2004**, *279*, 686–691.
  - 23 ROCHEVILLE M., LANGE D. C., KUMAR U., PATEL S. C., PATEL R. C., PATEL Y. C. Receptors for dopamine and somatostatin: formation of hetero-oligomers with enhanced functional activity, *Science* **2000**, *288*, 154–157.
  - 24 BISSANTZ C., BERNANRD P., HIBERT M., ROGNAN D. Protein-based virtual screening of chemical databases. II. Are homology models of G-protein coupled receptors suitable targets?, *Proteins* **2003**, *50*, 5–15.
  - 25 EVERS A., GOHLKE H., KLEBE G. Ligand-supported homology modelling of protein binding-sites using knowledge-based potentials, *J. Mol. Biol.* **2003**, *334*, 327–345.
  - 26 BLEICHER K. H., GREEN L. G., MARTIN R. E., ROGERS-EVANS M. Ligand identification for G-protein-coupled receptors: a lead generation perspective, *Curr. Opin. Chem. Biol.* **2004**, *8*, 287–296.
  - 27 BERMAN H. M., WESTBROOK J., FENG Z., GILLILAND G., BHAT T. N., WEISSING H., SHINDYALOV I. N., BOURNE P. E. Protein Data Bank, *Nucleic Acids Res.* **2000**, *28*, 235–242.
  - 28 PALCZEWSKI K., HORI T., BEHNKE C. A., MOTOSHIMA H., FOX B. A., LE TRONG I., TELLER D. C., OKADA T., STENKAMP R. E., YAMAMOTO M., MIYANO M. Crystal structure of rhodopsin: a G protein-coupled receptor, *Science* **2000**, *289*, 739–745.
  - 29 TELLER D. C., OKADA T., BEHNKE C. A., PALCZEWSKI K., STENKAMP R. E. Advances in determination of a high-resolution three-dimensional structure of rhodopsin, a model of G-protein-coupled receptors (GPCRs), *Biochemistry* **2001**, *40*, 7761–7772.
  - 30 LI J., EDWARDS P. C., BURGHAMMER M., VILLA C., SCHERTLER G. F. Structure of bovine rhodopsin in a trigonal crystal form, *J. Mol. Biol.* **2004**, *343*, 1409–1438.
  - 31 CHOI G., LANDIN J., GALAN J. F., BIRGE R. R., ALBERT A. D., YEAGLE

- P. L. Structural studies on meta-rhodopsin II, the activated form of the G protein-coupled receptor rhodopsin, *Biochemistry* **2002**, *41*, 7318–7324.
- 32 YEAGLE P. L., CHOI G., ALBERT A. D. Studies on the structure of G protein-coupled receptor rhodopsin including the putative G protein binding site in unactivated and activated forms, *Biochemistry* **2001**, *40*, 11932–11937.
- 33 SAKMAR T. P., MENON S. T., MARIN E. P., AWAD E. S. Rhodopsin: insights from recent structural studies, *Ann. Biomol. Struct.* **2002**, *31*, 443–482.
- 34 YAN E. C., KAZMI M. A., GANIM Z., HOU J. M., PAN D., CHANG B. S., SAKMAR T. P., MATHIES R. A. Retinal counterion switch in the photoactivation of the G protein-coupled receptor rhodopsin, *Proc. Natl Acad. Sci. USA* **2003**, *100*, 9262–9267.
- 35 MENON S. T., HAN M., SAKMAR T. P. Rhodopsin: structural basis of molecular physiology, *Physiol. Rev.* **2001**, *81*, 1659–1688.
- 36 BALLESTEROS J. A., SHI L., JAVITCH J. A. Structural mimicry in G protein coupled receptors: implications of the high-resolution structure of rhodopsin for structure–function analysis of rhodopsin-like receptors, *Mol. Pharmacol.* **2001**, *60*, 1–19.
- 37 MENG E. C., BOURNE H. R. Receptor activation: what does the rhodopsin structure tell us?, *Trends Biochem. Sci.* **2001**, *22*, 587–593.
- 38 GUAN J., MIAO Y., ZHANG Q. Impedimetric biosensors, *J. Biosci. Bioeng.* **2004**, *97*, 219–226.
- 39 KATZ E., WILLNER I. Probing biomolecular interaction at conductive and semiconductive surfaces by impedance spectroscopy: routes to impedimetric immunosensors, DNA-sensors, and enzyme biosensors, *Electroanalysis* **2003**, *15*, 913–947.
- 40 PEI R., CHENG Z., WANG E., YANG X. Amplification of antigen-antibody interactions based on biotin labeled protein–streptavidin network complex using impedance spectroscopy, *Biosens. Bioelectron.* **2001**, *16*, 355–361.
- 41 RICKERT J., GÖPEL W., BECK W., JUNG G., HEIDUSCHKA P. A “mixed” self-assembled monolayer for an impedimetric immunosensor, *Biosens. Bioelectron.* **1996**, *11*, 757–768.
- 42 HOU Y., HELALI S., ZHANG A., JAFFREZIC-RENAULT N., MARTELET C., MINIC J., GOROJANKINA T., PERSUY M. A., PAJOT-AUGY E., SALESSE R., BESSUEILLE F., SAMITIER J., ERRACHID A., AKIMOV V., REGGIANI L., PENNETTA C., ALFINITO E. Immobilization of rhodopsin on a self-assembled multilayer and its detection by electrochemical impedance spectroscopy, *Biosens. Bioelectron.* **2006**, *21*, 1393–1402.
- 43 PENNETTA C., AKIMOV V., ALFINITO E., REGGIANI L., GOMILA G., FERRARI G., FUMAGALLI L., SAMPIETRO M. Modelization of thermal fluctuations in G protein-coupled receptors, in: *Proceedings of the 18th ICFN Conference*, Salamanca, **2005**, pp. 611–614.
- 44 ALFINITO E., AKIMOV V., PENNETTA C., REGGIANI L., GOMILA G. Thermal fluctuations of a GPCR: a two force constant model, in: *Proceedings of the 4th UPoN Conference*, Gallipoli, **2005**, pp. 381–387.
- 45 AKIMOV V., ALFINITO E., PENNETTA C., REGGIANI L., MINIC J., GOROJANKINA T., PAJOT-AUGY E., SALESSE R. An impedance network model for the electrical properties of a single protein nanodevice, in: *Proceedings of the 14th HCIS Conference*, Chicago, IL, **2005**, in press.
- 46 ATILGAN A. R., DURELL S. R., JERNIGAN R. L., DEMIREL M. C., KESKIN O., BAHAR I. Anisotropy of fluctuation dynamics of proteins with an elastic network model, *Biophys. J.* **2001**, *80*, 505–515.
- 47 LATTANZI G., MARITAN A. Force dependent transition rates in chemical kinetics models for motor proteins, *J. Chem. Phys.* **2002**, *117*, 10339–10349.
- 48 ALBERT R., BARABASI A. L. Statistical mechanics of complex networks, *Rev. Mod. Phys.* **2002**, *74*, 47–97.
- 49 HALL S. E., FLORIANO W. B., VAIDEHI N., GODDARD W. A. III. Predicted 3-D structures for mouse I7 and rat I7 olfactory receptors and comparison of predicted odor recognition profiles

- with experiment, *Chem. Sens.* **2004**, *29*, 595–616.
- 50 TIRION M. M. Large amplitude elastic motions in proteins from a single-parameter atomic analysis, *Phys. Rev. Lett.* **1996**, *77*, 1905–1908.
  - 51 BAHAR I., ATILGAN A. R., ERMAN B. Direct evaluations of thermal fluctuations in proteins using a single parameter harmonic potential, *Fold. Des.* **1997**, *2*, 173–181.
  - 52 REBOIS R. V., SCHUCK P., NORTHPUR J. K. Elucidating kinetic and thermodynamic constants for interaction of G protein subunits and receptors by surface plasmon resonance spectroscopy, *Methods Enzymol.* **2002**, *344*, 15–42.
  - 53 ALVES I. D., SALGADO G. F., SALAMON Z., BROWN M. F., TOLLIN G., HRUBY V. J. Phosphatidylethanolamine enhances rhodopsin photoactivation and transducin binding in a solid supported lipid bilayer as determined using plasmon-waveguide resonance spectroscopy, *Biophys. J.* **2005**, *88*, 198–210.
  - 54 BIERI C., ERNST O. P., HEYSE S., HOFMANN K. P., VOGEL H. Micro-patterned immobilization of a G protein-coupled receptor and direct detection of G protein activation, *Nat. Biotechnol.* **1999**, *17*, 1105–1108.
  - 55 GIBSON N. J., BROWN M. F. Lipid headgroup and acyl chain composition modulate the M1–MII equilibrium of rhodopsin in recombinant membranes, *Biochemistry* **1993**, *32*, 2438–2454.
  - 56 LAGANE B., GAIBELET G., MEILHOC E., MASSON J. M., CEZANNE L., LOPEZ A. Role of sterols in modulating the human mu-opioid receptor function in *Saccharomyces cerevisiae*, *J. Biol. Chem.* **2000**, *275*, 33197–33200.
  - 57 HEYSE S., ERNST O. P., DIENES Z., HOFMANN K. P., VOGEL H. Incorporation of rhodopsin in laterally structured supported membranes: observation of transducin activation with spatially and time-resolved surface plasmon resonance, *Biochemistry* **1998**, *37*, 507–522.
  - 58 NEUMANN L., WOHLAND T., WHELAN R. J., ZARE R. N., KOBILKA B. Functional immobilization of a ligand-activated G-protein-coupled receptor, *Chem. Biochem.* **2002**, *3*, 993–998.
  - 59 DEVANATHAN S., YAO Z., SALAMON Z., KOBILKA B., TOLLIN G. Plasmon waveguide resonance studies of ligand binding to the human beta 2-adrenergic receptor, *Biochemistry* **2004**, *43*, 3280–3288.
  - 60 ALVES I. D., CIANO K. A., BOGUSLAVSKI V., VARGA E., SALAMON Z., YAMAMURA H. I., HRUBY V. J., TOLLIN G. Selectivity, cooperativity, and reciprocity in the interactions between the delta-opioid receptor, its ligands, and G-proteins, *J. Biol. Chem.* **2004**, *279*, 44673–44682.
  - 61 ALVES I. D., COWELL S. M., SALAMON Z., DEVANATHAN S., TOLLIN G., HRUBY V. J. Different structural states of the proteolipid membrane are produced by ligand binding to the human delta-opioid receptor as shown by plasmon-waveguide resonance spectroscopy, *Mol. Pharmacol.* **2004**, *65*, 1248–1257.
  - 62 NUZZO R. G., ALLARA D. L. Adsorption of bifunctional organic disulfides on gold surfaces, *J. Am. Chem. Soc.* **1983**, *105*, 4481–4483.
  - 63 ULMAN A. Formation and structure of self-assembled monolayers. *Chem. Rev.* **1996**, *96*, 1533–1554.
  - 64 WINK T., ZUILEN S. J. V., BULT A., BENNEKOM W. P. V. Self-assembled monolayers for biosensors, *Analyst* **1997**, *122*, 43R–50R.
  - 65 FERRETTI S., PAYNTER S., RUSSELL D. A., SAPSFORD K. E. Self-assembled monolayers: a versatile tool for the formulation of bio-surfaces, *Trends Anal. Chem.* **2000**, *19*, 530–540.
  - 66 GOODING J. J., HIBBERT D. B. The application of alkanethiol self-assembled monolayers to enzyme electrodes, *Trends Anal. Chem.* **1999**, *18*, 525–533.
  - 67 SPINKE J., LILEY M., GUDER H. J., ANGERMAIER L., KNOLL W. Molecular recognition at self-assembled monolayers: the construction of multi-component multilayers, *Langmuir* **1993**, *9*, 1821–1825.
  - 68 LADD J., BOOZER C., YU Q., CHEN S.,

- HOMOLA J., JIANG S. DNA-directed protein immobilization on mixed self-assembled monolayers via a streptavidin bridge, *Langmuir* **2004**, *20*, 8090–8095.
- 69 STORRI S., SANTONI T., MINUNNI M., MASCHINI M. Surface modifications for the development of piezoimmunosensors, *Biosens. Bioelectron.* **1998**, *13*, 347–357.
- 70 LIDKE D. S., NAGY P., HEINTZMANN R., ARNDT-JOVIN D. J., POST J. N., GRECCO H. E., JARES-ERIJMAN E. A., JOVIN T. M. Quantum dots ligands provide new insights into erbB/HER receptor-mediated signal transduction, *Nat. Biotechnol.* **2004**, *22*, 198–203.
- 71 POMPA P. P., BIASCO A., FRASCERRA V., CALABI F., CINGOLANI R., RINALDI R., VERBEET M. P., DE WAAL E., CANTERS G. W. Solid state protein monolayers: morphological, conformational and functional properties, *J. Chem. Phys.* **2004**, *121*, 10325–10328.
- 72 WALLRABE H., ELANGOVAN M., BURCHARD A. FRET microscopy reveals clustered distribution of co-internalized receptor–ligand complexes in the apical recycling endosome of polarized epithelial MDCK cells, *Proc. SPIE* **2002**, *4620*, 64–72.
- 73 WALLRABE H., PERIASAMY A. Imaging protein molecules using FRET and FLIM microscopy, *Curr. Opin. Biotechnol.* **2005**, *16*, 19–27.
- 74 FOTIADIS D., SCHEURING S., MÜLLER S. A., ENGEL A., MÜLLER D. J. Imaging and manipulation of biological structures with the AFM, *Micron* **2002**, *33*, 385–397.
- 75 BIASCO A., MARUCCIO G., VISCONTI P., BRAMANTI A., CALOGIURI P., CINGOLANI R., RINALDI R. Self-chemisorption of azurin on functionalized oxide surfaces for the implementation of biomolecular devices, *Mater. Sci. Eng. C* **2004**, *24*, 563–567.
- 76 WANG M., WANG L., WANG G., JI X., BAI Y., LI T., GONG S., LI J. Application of impedance spectroscopy for monitoring colloid Au-enhanced antibody immobilization and antibody–antigen reactions, *Biosens. Bioelectron.* **2004**, *19*, 575–582.
- 77 KOBILKA B., GETHER U., SEIFERT M., LIN S., GHANOUNI P. Characterization of ligand-induced conformational states in the beta 2 adrenergic receptor, *J. Receptor Signal Transduct. Res.* **1999**, *19*, 293–300.
- 78 YANG H., LUO G., KARNCHANAPHANURACH P., LOUIE T. M., RECH I., COVA S., XUN L., XIE X. S. Protein conformational dynamics probed by single-molecule electron transfer, *Science* **2003**, *302*, 262–266.
- 79 HELMREICH, E. J. M., HOFMANN, K. P. Structure and function of proteins in G-protein-coupled signal transfer, *Biochim. Biophys. Acta* **1996**, *1286*, 285.
- 80 PARAK F. G. Physical aspects of protein dynamics, *Rep. Prog. Phys.* **2003**, *66*, 103–129.
- 81 BUDA F., DE GROOT H. J. M., BIFONE A. Charge localization and dynamics in rhodopsin, *Phys. Rev. Lett.* **1996**, *77*, 4474–4477.
- 82 FRAUENFELDER H., SLIGAR S. G., WOLYNES P. G. The energy landscapes and motions of proteins, *Science* **1991**, *254*, 1598–1603.
- 83 CARLONI P., ANDREONI W., PARRINELLO M. Self-assembled peptide nanotubes from first principles, *Phys. Rev. Lett.* **1997**, *79*, 761–764.
- 84 CARLONI P., ROTHLISBERGER U., PARRINELLO M. The role and perspective of ab initio molecular dynamics in the study of biological systems, *Acc. Chem. Res.* **2002**, *35*, 455.
- 85 KITAO A., GO N. Investigating protein dynamics in collective coordinate space, *Curr. Opin. Struct. Biol.* **1999**, *9*, 164–169.
- 86 XIE Q., ARCHONTIS G., SKOURTIS S. S. Protein electron transfer: a numerical study of tunneling through fluctuating bridges, *Chem. Phys. Lett.* **1999**, *312*, 237–246.
- 87 SONG X. An inhomogeneous model of protein dielectric properties: intrinsic polarizabilities of amino acids, *J. Chem. Phys.* **2002**, *116*, 9359–9383.
- 88 PENNETTA C., ALFINITO E., REGGIANI L., RUFFO S. Non-Gaussian resistance noise near breakdown, in granular materials, *Physica A* **2004**, *340*, 380–387.



## 8

# Protein-based Nanotechnology: Kinesin–Microtubule-driven Systems for Bioanalytical Applications

*William O. Hancock*

### 8.1 Introduction

Protein machines carry out tasks critical to cell function, including DNA replication, intracellular transport, ion pumping and cell motility. They have evolved incredible diversity, specificity, efficiency and precision, and a considerable proportion of research in modern biology aims to uncover the fundamental mechanisms underlying their function [1]. The cytoskeletal motors, kinesins, dyneins and myosins, constitute a subset of these protein machines and are notable in being able to convert chemical energy directly to mechanical work. In cells, these motors generate the force that drives muscle contraction, they transport intracellular cargo throughout cells and they drive the critical movements that underlie cell division.

With the ability to engineer devices and systems at the micron and submicron scales, and to synthesize nanoparticles with novel and powerful functionalities, there is a growing need to transport and organize material at submicron dimensions. Because cytoskeletal motors have evolved specifically to transport and organize material at these size scales, there is a current effort to integrate these molecular motors and their cytoskeletal tracks into engineered devices [2–10]. This interdisciplinary research, which involves biologists, bioengineers, chemists, materials scientists, electrical engineers and others, is part of a larger effort to integrate proteins with highly evolved functions into nanoscale engineered systems. For instance, proteins and peptides are also being used as tools to drive self-assembly of inorganic materials such as semiconductors into functional materials [11, 12]. Another example of protein-based nanotechnology is the push to create electronic devices based on proteins or ion channels [13].

Compared to pressure-driven microfluidic flow, active transport by molecular motors in microfluidic channels offers a number of advantages as components of bioanalytical systems or biosensors. First, because of the small size of the motors and cytoskeletal filaments, the channels can be scaled down to dimensions below 100 nm. Second, motor-driven transport can occur up concentration gradients and against fluid flows. Third, because energy for transport (in the form of ATP) is delivered and consumed directly at the site of transport, dense arrays of multiplexed

channels can be created without need for complex electrical connections. However, before biomolecular motors can be integrated into hybrid microscale and nanoscale engineered systems, there are a number of experimental hurdles that must be tackled. First, interfaces between the proteins and material surfaces must be optimized to attach proteins while maintaining their biochemical function. Second, the design of these microsystems needs to be optimized to best capitalize on the unique transport properties of these motors. Finally, to make analytical devices based on biomotors a reality, it is crucial to develop methods for attaching designated cargo to these proteins and to increase the stability of these proteins.

This chapter focuses on the integration of kinesin molecular motors and their microtubule tracks into microdevices for bioanalytical applications. A number of insightful reviews have been written on the molecular mechanism of motor proteins, in general [14, 15], and kinesin motors, in particular [16, 17]. There are also reviews on applications of biomolecular motors in nanotechnology [18, 19] and on applications of kinesin motors in microscale transport [4]. Finally, there is a parallel effort underway using actin and myosin for transport in microscale and nanoscale transport applications, [20–23], but that work is not discussed here.

This chapter is organized as follows. In Section 8.2, the relevant cell biology and biophysics of the kinesin–microtubule system is presented, including a description of the *in vitro* assays that have been developed to study kinesin function. Section 8.3 explores theoretical aspects of motor-driven microscale transport; in particular, the relationship between transport speeds and diffusion times for particles of various sizes. This analysis helps to frame applications in which kinesin-driven transport is best utilized. Section 8.4 discusses experimental approaches to interfacing motor proteins and microtubules with engineered surfaces. Section 8.5 reviews approaches that have been taken to control the direction of kinesin and microtubule movements. These studies provide the core work that needs to be accomplished towards integrating motor proteins into functional microscale devices. To create bioanalytical systems or biosensors driven by the kinesin–microtubule system, it is also crucial to develop strategies for attaching molecular or cellular cargo to microtubules or motors; these strategies are discussed in Section 8.6. Finally, Section 8.7 discusses higher-level design considerations for motor-driven devices, including ways to maximize the lifetime of motors and microtubules, and approaches for introducing minute samples into these devices and detecting low levels of analyte in microfluidic channels.

## 8.2 Kinesin and Microtubule Cell Biology and Biophysics

In eukaryotic cells, organelles, vesicles, chromosomes and protein complexes are actively transported throughout the cell by molecular motors moving along cytoskeletal filaments. This transport system consists of both kinesin and dynein motors moving along microtubule filaments, as well as myosin motors moving along

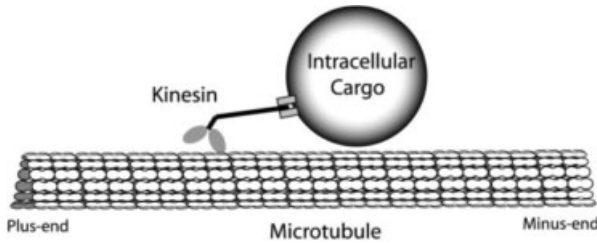


**Figure 8.1.** Structure and function of conventional kinesin. The two heads hydrolyze ATP and walk towards the “plus” end of microtubules. The kinesin tail binds to intracellular cargo. Microtubules, made from tubulin subunits, are 25 nm in diameter and tens of microns long.

actin filaments, but members of the kinesin family carry out the bulk of intracellular transport. Conventional kinesin, the founding member of the kinesin family, serves as a model protein for understanding the molecular basis of intracellular transport and for applications of molecular motors in nanotechnology. Conventional kinesin is a dimeric protein that contains three domains: the head or motor domain, the coiled-coil stalk that holds the two chains together and the tail that, along with two associated light chains, is responsible for binding cargo (Fig. 8.1) [24, 25]. Each motor domain contains both an ATP and a microtubule-binding site, and movement is achieved by a cycle in which each head alternately binds to the microtubule, undergoes a conformational change and releases from the track [16, 26–28]. Following the discovery of conventional kinesin [29], other members of the kinesin family were discovered based on sequence similarity in the motor head domain. The kinesin family can be divided into 14 classes based on sequence similarity and functional properties [30], and in the human genome there are 44 kinesin genes [31]. While almost all of the application work with kinesin motors has utilized conventional kinesin, because other kinesins have different motor properties, they may become useful in future applications.

Microtubules are cylindrical polymers of the protein tubulin that are 25 nm in diameter and up to tens of microns long. Tubulin dimers 8-nm long associate in a head-to-tail manner to make protofilaments, these protofilaments associate laterally to make sheets and the sheets close to make hollow cylinders that normally contain 14 protofilaments [32]. Because the subunits are asymmetric, microtubules have a structural polarity – the “minus” or slow-growing end is anchored near the center of the cell and the fast-growing “plus” ends extend to the perimeter of the cell. Experimentally, tubulin is normally isolated from cow or pig brains [33], which are large, inexpensive and rich in tubulin due to the neurons that require long-distance intracellular transport. Microtubules can be polymerized *in vitro* from purified tubulin, covalently modified with fluorophores or other functional groups and stabilized in polymer form with the drug taxol, making them stable for up to 1 week in normal buffers at room temperature [34].

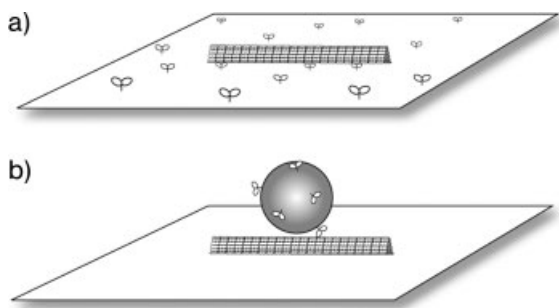


**Figure 8.2.** Assays for studying kinesin motor function. (A) Schematic of the microtubule gliding assay, in which motors are adsorbed to the surface and microtubules are transported across the surface. (B) In the bead assay, in which microtubules are immobilized on the surface, motors are adsorbed to micron-scale beads and the beads are transported along the immobilized microtubules.

### 8.2.1

#### Kinesin Motility Assays

Nearly two decades of biochemical and biophysical experiments on conventional kinesin have resulted in a solid quantitative characterization of this molecular motor. Conventional kinesin motors walk along microtubules at speeds of nearly  $1 \mu\text{m s}^{-1}$ , taking 8-nm steps and hydrolyzing one ATP per step [27, 35, 36]. The motor speed decreases approximately linearly with applied load up to a single motor stall force of 5–7 pN [37, 38]. Kinesin movement *in vitro* is studied predominantly using two different assays – the microtubule gliding assay and the bead assay (Fig. 8.2) [39, 40]. In the microtubule gliding assay, motors are adsorbed to glass surfaces that have been treated with the blocking protein casein, and microtubules are observed landing on and moving over the motors, analogous to a rock star being passed over the hands of an eager crowd. Typically, these assays are performed in 20- $\mu\text{l}$  flow cells constructed from a microscope slide, two pieces of double-sided tape and a cover glass, which enables facile solution exchange by simply pipetting solution in one side and wicking out the other side using filter paper or tissue [41]. Using this geometry, the motor concentration on the surface can be varied and different solutions can be introduced to optimize movement characteristics [42]. Microtubule movements are visualized by covalently labeling the microtubules with a fluorescent dye, observing them under a fluorescent microscope coupled to a sensitive CCD camera and recording the movements on videotape or computer [41]. As the assay is relatively easy to perform and the filaments are transported long distances along the surface, this geometry has generated the most attention for microscale transport applications of the kinesin–microtubule system.

In the other commonly used assay, the bead assay, microtubules are immobilized on glass surfaces, motors are adsorbed to micron-scale beads and the beads

are transported along the microtubules. This system is analogous to the geometry found in cells, and one advantage is that optical tweezers can be used to grab the beads and measure displacements and forces generated by the motors to nanometer and piconewton precision [43]. For transport applications, the bead can in principle be replaced by functional nanoparticles or biomolecules like proteins or nucleotides. As the tail domain of kinesin motors can be deleted or significantly altered with no effect on the motor function [44], in theory antibody fragments, receptors, DNA-binding domains or other protein motifs can be fused to the motor tail and these motor–cargo complexes transported along microtubules.

Motor directionality is a key consideration for applications using either the gliding assay or the bead assay. In the gliding assay, microtubules diffuse out of solution and land on the motors, and the direction of microtubule transport is defined by the orientation of the filament (Fig. 8.3). Because the motors, which are immobilized, move to the microtubule “plus” end, the filaments move with their “minus” ends leading. The coiled-coil of conventional kinesin has a region of random coil that is thought to act like a swivel, enabling the heads to rotate freely and bind to filaments only in the proper stereospecific orientation [45]. As discussed below, a large portion of the work done to harness microtubule transport for nanoscale applications has involved finding ways to control the direction of microtubule transport. The bead geometry has its own directionality problems – the transport direction is determined by the orientation of the immobilized microtubules (Fig. 8.3). In theory, if a dense bundle of oriented microtubules could be immobilized on the surface, they would serve as ideal tracks to direct kinesin transport. However, as described in Section 8.5, achieving these oriented and aligned bundles has proven difficult [9, 46].

For applications using kinesin motors and microtubules, it is important to obtain sufficient amounts of protein and keep the proteins stable over time. As discussed above, tubulin can be purified from native sources following established protocols [33] or it can be bought from commercial sources (Cytoskeleton, Denver, CO). Conventional kinesin is generally bacterially expressed and purified [36, 44, 47], but it too can be purchased. One of the hurdles to using other motors in the kinesin family is that not all of them can be bacterially expressed [48, 49] and they can be more prone to denaturation or precipitation over time. Methods for extending the lifetime of kinesins and microtubules in engineered devices will be discussed below in Section 8.7. For more information and detailed protocols for kinesin and microtubule purification, and *in vitro* motility experiments, readers can consult the book *Kinesin Protocols* edited by Isabelle Vernos [50] or the Kinesin Home Page (<http://www.proweb.org/kinesin/>).

### 8.3 Theoretical Transport Issues for Device Integration

One of the main application goals for molecular motors to date has been active transport of analytes in microfluidic systems. There currently exist a number of ap-

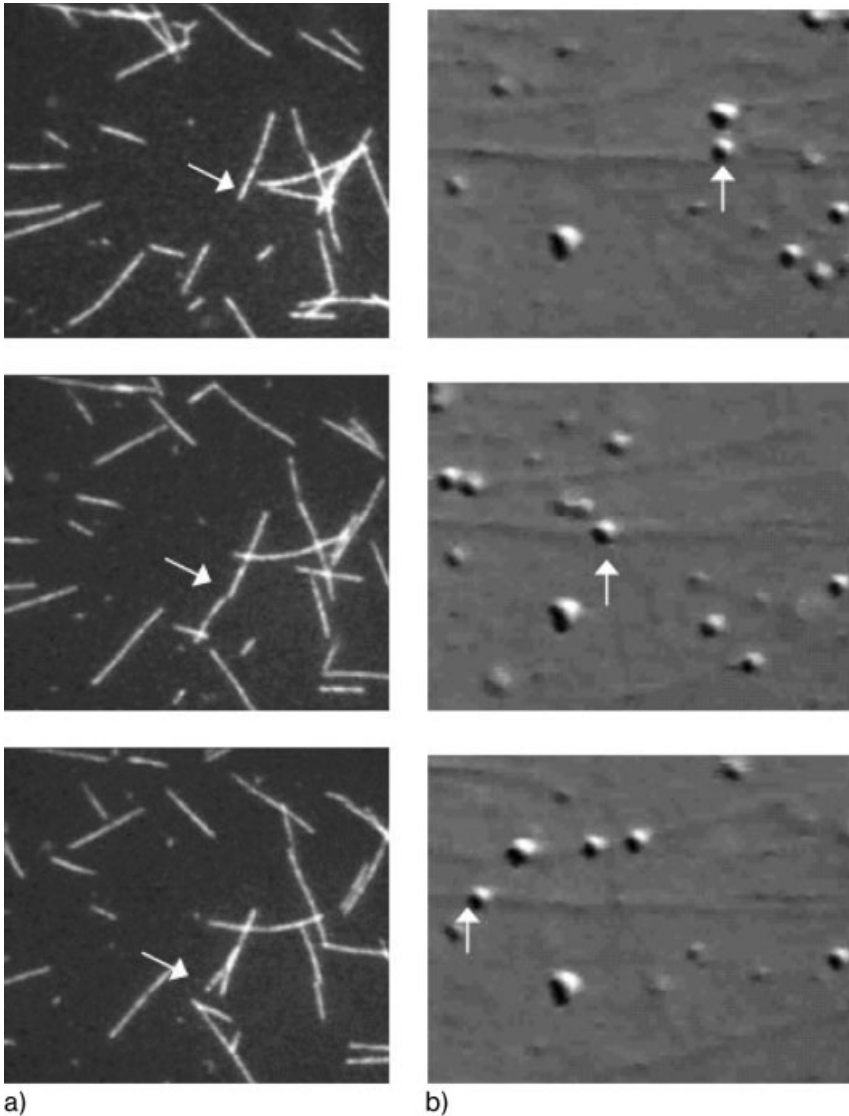


**Figure 8.3.** Kinesin–microtubule *in vitro* motility assays. (A) Microtubule gliding assay, showing fluorescent microtubules moving over immobilized kinesin motors. Screens are 22  $\mu\text{m}$  wide and images are 2 s apart. As can be seen, many microtubules move over the surface and their directions are determined by their orientation when they land on the surface. (B) Bead assay in which 0.2- $\mu\text{m}$  diameter glass beads, to

which many kinesin motors are adsorbed, are transported along surface-immobilized microtubules. Screens are 10  $\mu\text{m}$  wide and images are 4 s apart. The direction of bead movement is determined by the orientation of the immobilized microtubules. Images in (A) are fluorescence and images in (B) are differential interference contrast microscopy.

proaches for moving fluids, analytes and particles through microscale geometries, such as pressure-driven convective flow, electrophoresis, dielectrophoresis and electro-osmotic flow. Rather than supplanting these methods, biomotor-driven transport should be thought of as a new approach that expands the toolbox. The best choice depends on the nature of the problem, and the hope is that in the future biomotor-driven transport will be combined with these other transport and separation approaches to make highly functional microscale devices.

It is informative to investigate from a theoretical perspective the range of particle sizes and transport distances where biomotor-driven transport is the most useful. Specifically, it is important consider the relative roles of diffusion (Brownian motion) versus motor-driven active transport. Small analytes (proteins and nucleotides) in aqueous solutions diffuse rapidly and any transport must overcome this diffusional mixing. For instance, as discussed below, an average protein can diffuse 1  $\mu\text{m}$  in 5 ms and even for distances of 100  $\mu\text{m}$  the average diffusion time is faster than the time it takes a kinesin motor moving at 1  $\mu\text{m s}^{-1}$  to get there. It should be remembered that active transport is unidirectional, while diffusion is random, but the quantitative comparison serves as a useful guide.

### 8.3.1

#### Diffusion versus Transport Times

In Tab. 8.1, diffusion times and motor-driven transport times are compared for a range of potential analytes from proteins up to eukaryotic cells. The Einstein rela-

**Tab. 8.1.** Theoretical diffusional and transport properties for a range of biological analytes

Particle	Diameter	$D$ ( $\mu\text{m}^2 \text{s}^{-1}$ )	1 $\mu\text{m}$		100 $\mu\text{m}$		Transition distance ( $\mu\text{m}$ )
			$t_{\text{Diffusion}}$ (s)	$t_{\text{Transport}}$ (s)	$t_{\text{Diffusion}}$ (s)	$t_{\text{Transport}}$ (s)	
Protein	5 nm	100	0.005	1	50	100	200
Nanoparticle	20 nm	25	0.02	1	200	100	50
Virus	100 nm	5	0.1	1	1,000	100	10
Bacteria	1 $\mu\text{m}$	0.5	1	1	10,000	100	1
Cell	20 $\mu\text{m}$	0.02	20	1	$2 \times 10^5$	100	0.05

Notes:

$$D = k_B T / 6\pi\eta r.$$

$$k_B T = 4.1 \times 10^{-21} \text{ Nm at } 25^\circ \text{C}.$$

$$\text{Viscosity } \eta = 0.89 \text{ cP at } 25^\circ \text{C} = 0.89 \times 10^{-3} \text{ Ns m}^{-2}.$$

$$t_{\text{Diffusion}} = x^2 / 2D \text{ (one-dimensional).}$$

$$t_{\text{Transport}} = x/v, \text{ where } v = 1 \mu\text{m s}^{-1} \text{ for kinesin.}$$

$$\text{Transition distance (when } t_{\text{Transport}} < t_{\text{Diffusion}}) = 2D/v.$$

tion is used to derive the diffusion constant,  $D$  based on the drag coefficient of the particle  $\gamma$ :

$$D = k_B T / \gamma \quad (1)$$

Where  $k_B T$  is Boltzman's constant ( $1.38 \times 10^{-23}$  Nm) multiplied by the absolute temperature [51]. From Stokes' law, the drag coefficient of a spherical particle in low Reynold's number flow is defined as:

$$\gamma = 6\pi\eta r \quad (2)$$

where  $\eta$  is the solution viscosity ( $0.89 \times 10^{-3}$  Ns m<sup>-2</sup> for water at 25 °C) and  $r$  is the radius of the particle [51, 52]. Combining these equations, we get the equation for the diffusion constant for spherical objects:

$$D = k_B T / 6\pi\eta r \quad (3)$$

For the particles in Tab. 8.1, approximate diameters are given and diffusion constants in aqueous buffers at 25 °C are calculated.

Using the diffusion constant, the average time it takes to diffuse a distance  $x$  in one dimension is defined as:

$$t_{\text{Diffusion}} = x^2 / 2D \quad (4)$$

and the time required for kinesin-driven transport is defined as

$$t_{\text{Transport}} = x/v \quad (5)$$

where  $v = 1 \mu\text{m s}^{-1}$  for conventional kinesin [36, 52]. In Tab. 8.1 these times are calculated for the different particles for distances of both 1 and 100  $\mu\text{m}$ . As can be seen, small particles diffuse rapidly and motor-driven transport outpaces diffusion only for distances over a few hundred microns, while large particles like bacteria and eukaryotic cells diffuse very slowly and motor transport is much faster for all distances. A helpful way to understand the utility of kinesins in microscale transport applications is to ask: at what transition distance does motor-driven transport outpace diffusion ( $t_{\text{Transport}} < t_{\text{Diffusion}}$ )? This distance, which gives a rough value for where motor-driven transport becomes useful, is calculated in the final column of Tab. 8.1. The important result is that for proteins and small particles like nanoparticles in the range of tens of nanometers, diffusional mixing is sufficient to get particles where they need to go for distances less than a few hundred microns. However, for larger particles like bacteria and cells, diffusion is inadequate at virtually all length scales. Hence, there is significant potential for these nanoscale motors to drive and control movement of micron-scale biological objects. As discussed in Section 8.6, drag forces for these relatively large objects are negligible compared to the forces kinesin motors can exert.



While it is insightful to compare diffusion and transport times, it is important to appreciate that while diffusion occurs in all directions, motor-driven transport is directional. Hence, even for short distances this transport can establish and maintain concentration gradients provided the transport flux is sufficiently high. Second, because binding these small cargo pulls the particles out of solution and eliminates their random diffusional movement, it reduces the number of degrees of freedom and achieves a significant level of positional control. Furthermore, increasing the solution viscosity either by adding solutes or by creating permeable hydrogels should be able to significantly slow diffusion rates without necessarily slowing motor transport. Finally, as the channels and sorters are fabricated using versatile photolithography techniques [2, 6, 53], there is ample opportunity for optimizing the design of these systems to maximize the utility of motor-based transport and minimize diffusional mixing.

## 8.4

### Interaction of Motor Proteins and Filaments with Synthetic Surfaces

A recurring technical hurdle in integrating functional proteins into engineered devices is the problem of interfacing synthetic materials with biological molecules. The problem of understanding and controlling protein–biomaterial interactions has been a major focus of the biomaterials field for decades [54, 55]. For instance, in the case of implanted biomaterials, the predominant approaches to maximizing biocompatibility are either to create surfaces that completely resist protein adsorption or surfaces to which proteins can adsorb, but not change their activities or otherwise produce an immune response. Due of the importance of this problem, there is a body of work on protein adsorption to biomaterials. However, there are no sure-fire techniques for (a) creating surfaces that bind proteins, but do not affect their function, or (b) creating surfaces that completely resist protein adsorption.

To harness the utility of motor proteins and their cytoskeletal tracks for nanotechnology and microscale transport applications, it is crucial to control the specific adsorption of these proteins to surfaces. Here, techniques for immobilizing motor proteins and cytoskeletal filaments are reviewed.

#### 8.4.1

##### Motor Adsorption

It can be argued that the discovery of conventional kinesin's motor activity [29] was a result of this motor's ability to bind to glass surfaces and retain its function. With proper surface passivation to reduce motor denaturation, conventional kinesin binds functionally to many types of glass as well as various oxides and other hydrophilic surfaces [7, 41, 56, 57]. The most reliable surface passivation is pretreatment of surfaces with casein, a protein found in milk. In solution, casein forms heterogeneous aggregates with diameters of the order of 10–300 nm [58].

The aggregation state of unproteolyzed casein is heterogeneous and depends on the  $\text{Ca}^{2+}$  concentration, pH, degree of phosphorylation and other factors [59]. For kinesin experiments, commercially bought casein is dissolved in buffer and passed through a submicron filter and/or centrifuged to remove aggregates [41].

It is clear that pretreatment of glass surfaces with casein greatly increases the activity of kinesin motors adsorbed to the surface, but the precise mechanism of action is not clear [41]. The working model is that casein aggregates tens of nanometers in diameter pack on the surface, the tail domains of the kinesin motors bind between the casein particles, and the motor heads stick into solution and interact with microtubules. It cannot be ruled out that the kinesin motors bind directly to the surface-adsorbed casein, but the fact that a great excess of casein in the motor solution does not compete with the surface-adsorbed casein (there is no reduction in the concentration of functional motors on the surface) argues against this. Also, it has been reported that casein has a chaperone-like function in stabilizing proteins against denaturation [60]. It cannot be ruled out that part of the enhancement of kinesin function by casein is due to stabilizing the motor protein structure.

One of the problems with the casein pretreatment described above is that it does not work for every motor protein. Apart from conventional kinesin, there are many other kinesin motor proteins (44 total in the human genome) that vary both in their motor properties and in their intracellular cargo [31]. These different motor characteristics – direction of movement along the microtubule, affinity for the microtubule and speed of movement – provide a rich toolbox for engineering hybrid devices based on these motors. However, while there is considerable structural consistency in the head domain, there is great divergence structurally and functionally in the tail domains [31, 61–63]. The result of this diversity is that techniques for attaching one motor to a surface do not necessarily work for other motors. To date, three generalizable approaches have shown promise. The first is to adsorb antibodies to the surface and immobilize the motors through these antibodies [64]. This approach has the advantage that antibodies complementary to virtually any motor can be made or, by attaching a universal protein tag (such as a hexahistidine tag) to recombinant motors, one reliable antibody to be used for a range of motors. A second approach for hexahistidine tagged motors is to functionalize the surface with a surfactant terminated with nitrilotriacetic acid (NTA), which chelates nickel ion. His-tagged proteins bind tightly to the surface through the immobilized Ni-NTA and the motors remain functional on these surfaces [65]. A third method is to attach motors to surfaces through biotin–avidin chemistry [66]. Streptavidin (or its equivalents avidin or neutravidin) can be directly adsorbed to surfaces or specifically bound to biotin-functionalized surfaces and biotinylated motors can be attached to this immobilized streptavidin. Motors attached by this means have been shown to be completely functional and the bond strong enough to not be pulled off by motor forces [67–69].

While a range of hydrophilic surfaces support kinesin-driven microtubule movements, hydrophobic surfaces do not. When glass surfaces are treated with the hydrophobic silane octadecyl trichlorethylsilane or other hydrophobic surface treat-

ments (with contact angles above  $60^\circ$ ) prior to casein and kinesin treatment, no microtubule binding or movement is observed [57, 70]. The interpretation is that motors denature on these hydrophobic surfaces and even casein pretreatment cannot prevent this motor denaturation. This property of surface chemistry-dependent motor function has been used to define where on microfabricated surfaces microtubules will be transported and where they will not (discussed further in Section 8.5).

#### 8.4.2

##### **Microtubule Immobilization**

For applications where microtubules are immobilized on surfaces and cargo-functionalized kinesins move along these filaments, a number of strategies have been developed for immobilizing microtubules. Microtubules will bind to clean glass or quartz microscope slides [71] and this immobilization is sufficient for some investigations into motor function. However, for transport applications, a more robust immobilization is generally required. One of the most common immobilization approaches is to functionalize glass surfaces with an amino silane compound (3-aminopropyltriethoxysilane) that confers a positive charge to the surface [39, 72]. Microtubules, which have a net negative charge at physiological pH, bind tightly to these surfaces and high microtubule densities can be achieved. By lithographically patterning silanes on silicon wafers, this approach has been used to pattern immobilized microtubules at microscale dimensions [73]. Polylysine-treated glass is another approach that uses electrostatic interactions to bind microtubules to surfaces [74].

Two other microtubule immobilization strategies have also been shown to work well. Microtubules can be biotinylated and attached to surfaces through streptavidin, either by adsorbing streptavidin directly to the surface or immobilizing another biotinylated protein (like biotinylated bovine serum albumin), and then using streptavidin as a glue between that protein and the biotinylated microtubule [37, 75]. In principle, self-assembled monolayers (SAMs) in which a portion of the groups are terminated with biotin could be patterned, and streptavidin and microtubules patterned by the underlying biotin. Other techniques for patterning biotin or streptavidin at micron or nanoscale dimensions that have been developed for DNA microarrays or nanoscale two-dimensional protein patterns could be applied to patterning biotinylated microtubules. The final immobilization strategy, in the “turning lemons into lemonade” category, involves using dysfunctional kinesin motors to immobilize microtubules [76, 77]. If kinesin protein is mishandled, e.g. stored at room temperature for days, or when problems arise during expression and purification of functional motors, the motors inactivate in such a way that they bind to microtubules, but do not move along them. When these “dead-heads” are adsorbed to surfaces, they act as an excellent adhesive to immobilize microtubules.

While the optimum immobilization approach depends upon the specific application, there are some general considerations that apply to all microtubule immobili-

zation techniques. First, approaches that permit patterning microtubules on the micron or submicron scale are helpful only if filament orientation can be controlled. For instance, even with narrow strips of adhesive, microtubules can simply lay across the lines, negating the pattern. Finally, from experiences in our laboratory and others, it is clear that from the perspective of kinesins, not all microtubule immobilization strategies are created equal. For instance, when microtubules are immobilized through aminosilanes on glass, motors rarely interact with microtubules that are tightly adsorbed to the surface through their entire length, while they interact much more frequently with microtubules that are more loosely tacked down and have regions that are not directly attached to the surface. Whether these problems are due to deformation of the microtubules when they are tightly adsorbed or to unfavorable motor–surface interactions is not clear, but these observations emphasize that the success of any immobilization strategy must include an analysis of motor function as well.

## 8.5

### Controlling the Direction and Distance of Microscale Transport

The key to harnessing the transport capabilities of molecular motors is controlling the direction of motion. For applications in microscale transport, it is this ability to direct the transport of a particle or analyte independent of fluid flows or concentration gradients that has generated the most interest in the field to date. Redirecting microtubule movements in the microtubule gliding assay has received the most attention because the filaments move long distances (detachment is not a concern), the filaments can be easily visualized by fluorescence microscopy and they can be functionalized to transport cargo. In this section, transport applications utilizing the filament gliding is covered first, followed by the opposite geometry, i.e. cargo-loaded motors moving along immobilized filaments.

#### 8.5.1

##### Directing Kinesin-driven Microtubules

Building on the standard microtubule gliding assay, the first directed transport investigations showed that micron-scale grooves deposited on glass surfaces either by shearing polytetrafluoroethylene (PTFE) or by microfabrication guide microtubule motions parallel to the grooves [2, 4, 7, 78, 79]. This redirection arises from the nature of microtubule movements along surfaces – the front of the filament searches out new motors to bind to as it is propelled along the surface and physical barriers that reorient this free end act to reorient the direction of filament movement (Figs. 8.4 and 8.5). Building on these initial demonstrations, a number of studies using more sophisticated fabrication approaches have amply showed that microtubules can be guided and redirected using surface features. A key advance, first shown by Hiratsuka and coworkers [6], was the demonstration that microtubules moving in microfabricated channels can be redirected by arrowhead-shaped “rectifiers” built into the channels that pass filaments traveling one direction, and buckle and

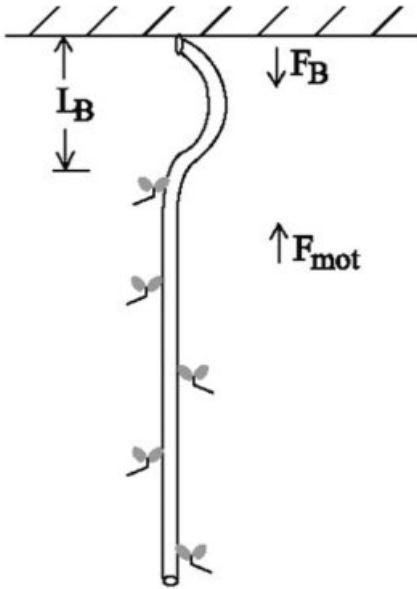
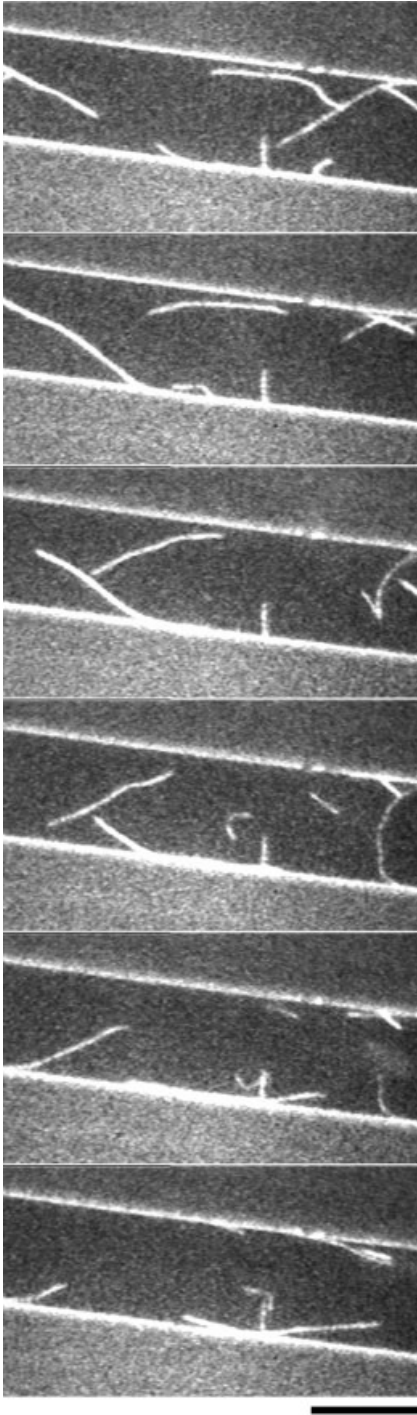


**Figure 8.4.** Physical model of a microtubule, propelled by immobilized kinesins, colliding with a wall and buckling. The length of filament that can buckle,  $L_B$ , is defined as the distance between the last motor and the wall. For the microtubule to buckle, the cumulative motor

forces must be greater than the minimum buckling force for approach normal to the surface, but can be less than that if the incident angle is less than  $90^\circ$ . (Reprinted with permission from Ref. [2] © 2003 American Chemical Society.)

redirect filaments traveling in the opposite direction. Later investigations extended this result using different fabrication approaches and a range of rectifier shapes (Fig. 8.6) [53, 80]. An important advance in this study was to identify photoresist materials that prevent adsorption of functional kinesin motors, such that when the photoresist is patterned on glass, functional motors are only found on the glass surfaces in the bottom of the channel. In both the work by Hiratsuka and co-workers and in a related study by Moorjani and coworkers [2], the key to containing the movement in the channels was not preventing protein adsorption to the walls, but rather the fact that motors that adsorbed to the photoresist denatured or otherwise inactivated. When the photoresist walls were treated to enable functional motor adsorption, the microtubules simply crawled over the walls [2].

One goal in achieving useful transport by this approach is minimizing the number of filaments lost due to detachment from and diffusion away from the surface. If filaments are transported along the surface by a population of motors that each cyclically attach and detach from the filament, there is a low probability that all of the motors are detached at the same time and so long transport distances can be achieved. However, when filaments are redirected by walls or crawl over walls of the channels, there can be significant filament loss if the channels are not enclosed on all sides [2, 79, 81]. This filament loss can be minimized by undercutting the walls of the channels to create overhangs that tend to trap the filaments in the



channels [3]. Also, by designing rectifying shapes and patterning gold on the bottom of the channel to maximize motor adsorption, and silanes on the sides of the channels to resist motor adsorption, high efficiencies of filament rectification have been achieved [80]. Experiments using this “open-top” configuration where motors are adsorbed to patterned and textured surfaces, and the top of the channels are left open to solution, have been instrumental in understanding the optimal channel design and surface chemistry for redirecting microtubule movements in microchannels. However, the best method for eliminating filament loss is to enclose these microchannels on all sides. For practical devices to emerge from this area of research, it is clear that enclosed microchannels will be required, together with apparatus for sample inputs and downstream detectors. As described below, there has been some initial progress toward these goals.

### 8.5.2

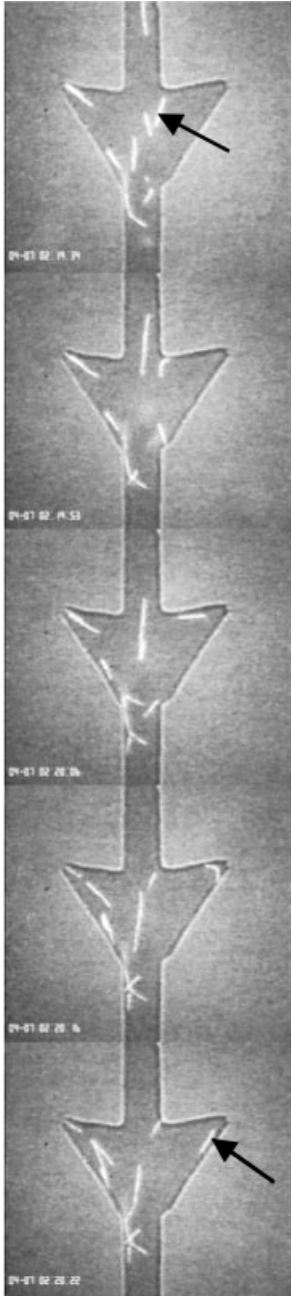
#### Movement in Enclosed Microchannels

Achieving directed movement in enclosed channels entails different design constraints than movement along topographically patterned surfaces. For instance, because microtubules are surrounded on four sides, detachment from the surface is less of a problem because subsequent rebinding is quite rapid. Furthermore, whereas guiding microtubules with open-top channels generally requires that the side walls are not populated with functional motors, in enclosed channels it is fine for microtubules to move along all four walls so long as they are moving down the channel in the desired direction. However, there are some important design constraints for creating enclosed channels for microtubule transport. First, because fluorescence microscopy is generally used to visualize microtubule movements in the channels, at least one side must be transparent and materials that autofluoresce (which includes many photoresists) need to be avoided. Second, as described in Section 8.7 below, polydimethylsiloxane (PDMS), which is regularly used in microfluidics work, can generally not be used because of its high oxygen permeability. Third, because the channels are initially filled and motor-functionalized by pressure-driven flow, the bond between the channels and the top enclosure must be sufficiently strong. Finally, the channel design must include fluidic connections for injecting motor and microtubule solutions into the channels.

Huang and coworkers recently succeeded in achieving kinesin-driven microtubule movements in enclosed microfabricated channels [57]. A number of channel designs were investigated, and a key breakthrough was creating hierarchical channels of decreasing dimensions such that solutions could be exchanged into small

←

**Figure 8.5.** A microtubule being redirected by a microfabricated channel wall. The channel is glass and the walls are 1.5- $\mu\text{m}$  high SU-8 photoresist. The microtubule moves from left to right in the channel, bumps into the photoresist wall and is redirected back into the channel. The scale bar at right is 10  $\mu\text{m}$ ; images are 12 s apart. (Reprinted with permission from Ref. [2] © 2003 American Chemical Society.)



10 μm



channels 15  $\mu\text{m}$  wide and 5  $\mu\text{m}$  deep without large dead volumes. The channels were constructed in SU-8 photoresist patterned on glass, covered with dry film photoresist and topped with a silicon wafer or glass slide for mechanical stability. Microtubules moved long distances in the channels, indicating that the ATP fuel was not limiting in these enclosed volumes. Furthermore, the microtubules could move upstream in convective fluid flows, which means biomotor-driven transport can move against microfluidic transport [57]. Current work in this area aims to simplify fabrication processes and optimize the channel geometries to achieve ideal microtubule transport, concentration and redirection.

### 8.5.3

#### Immobilized Microtubule Arrays

While most studies investigating transport applications of kinesins have utilized the microtubule gliding configuration, there has also been progress on immobilizing aligned microtubules and transporting motor-functionalized cargo along these filaments. Conceptually, binding motors to analytes and transporting this cargo along immobilized filaments is the simpler geometry and because of the ease with which motors can be engineered to contain diverse cargo binding domains in place of their tail, it has significant potential. However, the key hurdle to making this geometry work is immobilizing parallel and *uniformly oriented* filaments on surfaces. While filaments can be aligned in fluid flows, they are of mixed orientation and hence are of little use in transport applications. Current progress in obtaining arrays of uniformly oriented immobilized filaments is described below.

Brown and Hancock created an array of uniformly oriented microtubules by immobilizing short microtubule seeds at defined locations, growing filaments selectively off of the “plus” ends of these seeds, aligning the newly polymerized filaments by fluid flow and then immobilizing them on a surface (Fig. 8.7A) [46]. This process created aligned filaments, but the arrays were not the density needed for useful transport and the method is difficult to adapt to microscale environments. Limberis and coworkers used an elegant technique to bind and align microtubules [82]. Antibodies to the  $\alpha$ -tubulin subunit, which is exposed only at the “minus” ends of microtubules and not the “plus” ends, were immobilized on a surface and microtubules flowed in and allowed to bind end-on (Fig. 8.7B). Fluid flow was then used to push the filaments over and, although they were not immobilized in this study, a final immobilization step should not be difficult. A third technique, which may have the most potential, was demonstrated by Prots and coworkers,



**Figure 8.6.** Arrowhead-shaped structures in photoresist rectify microtubule movements. In this example, 1.5- $\mu\text{m}$  high SU-8 photoresist walls on glass create a rectifier with inlet and outlet channels. A microtubule can be seen moving upward inside the arrowhead, bumping into the photoresist wall and being redirected

back into the channel. Rhodamine-labeled microtubules and SU-8 channel walls were imaged using simultaneous fluorescence and differential interference contrast microscopy. (Reprinted from Ref. [53], with kind permission of Springer Science and Business Media.)

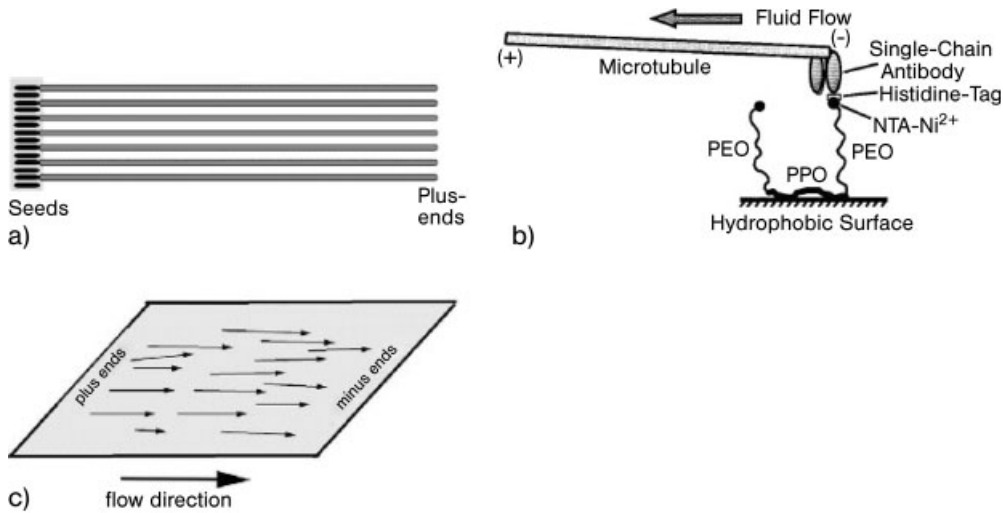


**Figure 8.7.** Three methods to create an array of uniformly oriented microtubules on a surface. (A) Brown and Hancock immobilized short microtubule seeds on an adhesive region, grew microtubules exclusively from the “plus” ends of these filaments, and then aligned and immobilized them. (B) Limberis and coworkers bound antibodies for  $\alpha$ -tubulin

to the surface, captured microtubule “minus” ends and then aligned the microtubules by fluid flow. (C) Prots and coworkers used fluid flow to align kinesin-driven microtubules and then immobilized these filaments on the surface. (Reprinted with permission from Refs. [46, 82, 83] © 2002 and 2001 American Chemical Society and 2003 Elsevier, respectively.)

who started with a field of microtubules moving over immobilized motors, aligned their direction of movement using fluid flow (over time all filaments move parallel and downstream to the flow) and then crosslinked the filaments to the motors using glutaraldehyde (Fig. 8.7C) [83]. Other experiments have shown that glutaraldehyde treatment does inhibit subsequent interactions of the microtubules with motors [84] and the authors showed that kinesin-functionalized beads move unidirectionally along these filament arrays [10].

One of the downsides of using kinesins moving over immobilized microtubules is that the transport distances are generally shorter than distances achieved by many immobilized motors moving long microtubules across surfaces. Single-molecule experiments have shown that during each encounter, conventional kinesin moves approximately 1  $\mu\text{m}$  along a filament before detaching [39, 85]. These motors can then reattach and move further; however, for long distance transport, longer run lengths are desired. Somewhat longer transport distances can be achieved by modifying the motors to increase the amount of positive charge in the “neck” region adjacent to the head [86] or by binding multiple motors to the desired cargo such that dissociation of one motor does not lead to dissociation of the entire cargo. These dissociation problems highlight the fact that if immobilized microtubules are used, they not only need to be uniformly aligned, but they need to be immobilized at high densities to maximize the rate of motor reattachment. To make this geometry feasible for analyte transport applications, more work needs

to be done to develop facile methods to create high density, uniformly oriented microtubule arrays.

## 8.6 Cargo Attachment

Another important hurdle for achieving useful transport from the kinesin–microtubule system is developing methods for selective and reversible attachment of cargo to the microtubules and/or motors. For microtubules moving in microchannels, the long-term vision is that the microtubules will pick up their cargo at one site and be transported along a channel, and the cargo will be deposited in a collection or analysis chamber. The question is: how is cargo attached to microtubules? Successful approaches and future ideas are reviewed here.

One problem with attaching cargo to microtubules is that, in contrast to motors, it is difficult to use the tools of molecular biology to modify tubulin sequences. Generally, tubulin for these applications is purified from cow or pig brain and it is currently prohibitively expensive to produce genetically engineered large animals for this purpose. *In vitro* expression of recombinant tubulin has been achieved [87], but it is technically demanding and yields are low. Hence, the primary route to modifying microtubules to enable cargo attachment has been to covalently link functional cargo attachment groups to the microtubules. By attaching reactive *N*-hydroxysuccinimidyl (NHS) groups to exposed amine residues on tubulin, microtubules have been covalently labeled with a number of fluorescent dyes and biotin [34]. Biotinylated microtubules have by far been the most widely used. Avidin (or its relatives streptavidin and neutravidin) contains four high-affinity biotin binding sites, enabling sandwich configurations where biotin-functionalized cargo can be attached to biotinylated microtubules [88, 89].

Proteins, single-stranded (ss) DNA or RNA molecules and cells represent three potential types of cargo that can be transported, separated and/or concentrated by the kinesin–microtubule system (Fig. 8.8). To date, all three types of cargo have been attached to microtubules through biotin–avidin chemistry. Biotinylated antibodies can be purchased from commercial sources or antibodies of interest can be biotinylated using amine-reactive biotin sold by Molecular Probes (Invitrogen,

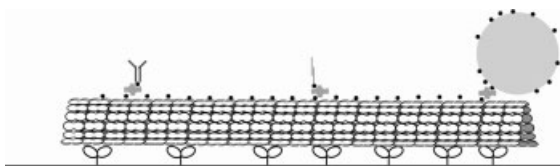


**Figure 8.8.** Attaching cargo to a microtubule through biotin–avidin chemistry. Biotin molecules (black dots) that are covalently linked to tubulin subunits bind streptavidin protein (which has four biotin binding sites).

Biotin-functionalized antibodies (left), DNA oligonucleotides (center) or particles (right) can be linked through the streptavidin and transported by the immobilized kinesin motors.

Carlsbad, CA). These biotinylated antibodies can be attached to microtubules by incubating biotinylated microtubules first with neutravidin and then with the biotinylated antibody, but care must be taken not to overload the microtubule [89]. As the neutravidin binds to the same microtubule surface that the kinesin motors bind to, a portion of the tubulin subunits must remain unlabeled to enable motor binding. By attaching anti-GFP (green fluorescent protein) antibody to microtubules, we showed that microtubules can pick up and transport protein cargo along kinesin-functionalized surfaces [90]. This important proof of principle implies that microtubules could be modified to transport any protein for which a suitable antibody exists.

A second important cargo is nucleic acids. A possible application for a kinesin-based analytical device would be RNA analysis for examining gene expression in a small tissue sample or for detecting viruses. DNA microarrays are now widely used for expression profiling – determining what mRNA species are being expressed in a cell or tissue under certain conditions. However, if the sensitivity could be increased, smaller sample volumes could be used, ideally to the point where mRNA levels from individual cells could be analyzed. As this enhancement would remove any signal loss due to heterogeneity between different cells in a tissue biopsy, this is an active area of research. A kinesin-based transport device would be very valuable if it could bind selected mRNA from a cell lysate, transport these analytes down microscale channels, detect their presence and concentrate them in a collection chamber for later analysis such as sequencing or polymerase chain reaction (PCR) amplification (Fig. 8.9). To demonstrate the feasibility of nucleotide trans-

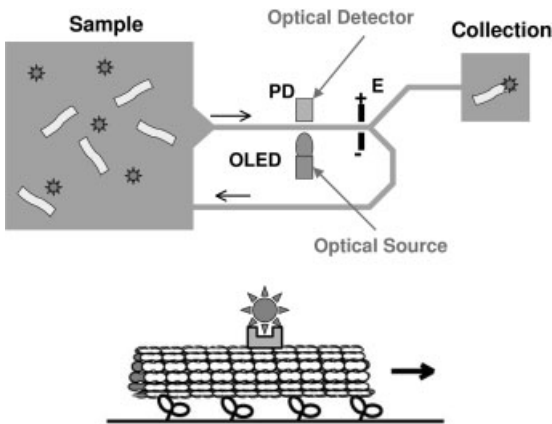


**Figure 8.9.** Diagram of a motor-based detection and purification scheme. Top panel shows an integrated system including a sample chamber containing microtubules and analyte, kinesin-functionalized microchannels through which cargo is transported, a LED excitation source and photodiode (PD) detector inte-

grated into the channels, and electrodes (E) to direct cargo-laden microtubules to the collection chamber. Bottom panel shows that kinesin-based transport that will drive the system. (Reprinted from Ref. [53], with kind permission of Springer Science and Business Media.)

port by microtubules, Muthukrishnan and coworkers bound ssDNA oligonucleotides to microtubules through biotin–avidin chemistry and then bound fluorescently labeled complementary DNA oligonucleotides to these microtubules. Like the protein cargo-functionalized microtubules, these DNA cargo-functionalized microtubules were faithfully transported across kinesin functionalized surfaces [88]. Diez and coworkers showed that kinesins can also be used to transport and stretch large pieces of DNA.  $\lambda$ -phage DNA attached to microtubules through biotin–avidin chemistry was transported along surfaces by immobilized motors and, when bound at one end to the surface or another microtubule, could be stretched by the motor forces up to its maximum contour length [91].

Another cargo attachment strategy that has been investigated is using cyclodextrins attached to microtubules [92]. These versatile molecules are cyclic oligosaccharides that contain a hydrophobic cavity that can be engineered to bind small molecules and proteins [93]. As they can be biotinylated, they can be attached to biotinylated microtubules through a streptavidin crosslinker and transported by surface-immobilized kinesins. Kato and coworkers reported that cyclodextrin-functionalized microtubules moved more than 10-fold slower than normal microtubules, indicating the attachment unfavorably altered the surface of the microtubule [92]. Hence, work needs to be done to improve this strategy, but it has the potential to be of significant utility. Other cargo-binding approaches can be envisaged such as designing RNA aptamers through directed evolution [94], and attaching these to microtubules through biotinylated bases, but no work has been published to date in this area.

### 8.6.1

#### Maximum Cargo Size

An important question for kinesin-based transport is: what is the size limit for cargo transported by kinesins and microtubules? To investigate the potential utility of kinesins in microscale devices, Limberis and Stewart attached kinesins to  $10 \times 10 \times 5\text{-}\mu\text{m}^3$  silicon microchips and found the chips moved at normal motor speeds along immobilized microtubules [56]. Similarly, Jia and coworkers attached clumps of gold nanowires  $6\ \mu\text{m}$  long to microtubules and found that they were transported at normal speeds along motor functionalized surfaces [53]. The fact that the viscous drag forces did not affect the motor transport speeds suggests that even larger objects can be transported. The theoretical maximum size of an object that can be attached to a microtubule and transported by kinesins is calculated below.

The theoretical size limit for spherical objects that can be attached to microtubules and transported by molecular motors can be calculated by comparing motor forces to viscous drag forces for a sphere in aqueous buffer. Individual motors can exert 5–8 pN of force [37, 38, 95]. Kinesin motors can be adsorbed on surfaces to densities of 1000 motors  $\mu\text{m}^{-2}$  or more, so it is reasonable to expect a long microtubule to be able to interact with hundreds of motors [42]. If motor forces sum (which has not been definitively shown, but is consistent with a number of experi-

mental observations), then it is possible that motor forces pushing a microtubule could approach 1 nN. The drag force on a particle moving in aqueous solution is equal to

$$F = \gamma v \quad (6)$$

where  $\gamma$  is the drag coefficient and  $v$  is the velocity [52]. For a microtubule moving cargo at  $1 \mu\text{m s}^{-1}$ , the drag coefficient,  $\gamma$ , that results in 100 pN of force, which would start to slow the microtubule, is  $10^{-4} \text{Ns m}^{-1}$ . The drag coefficient of a spherical object can be calculated from Stokes' law, given in Eq. (2) above. Solving for the diameter of a sphere that would start to slow down the microtubule – the result is 1 cm! Hence, the range of objects that can in principle be transported by this system has only begun to be explored.

## 8.7

### System Design Consideration

The development of biomotor-driven microscale devices has evolved in three phases: (a) recapitulating intracellular motility in *in vitro* experiments, (b) controlling microtubule transport using microfabrication, surface processing and other techniques, and (c) creating integrated functional devices. The first phase was completed by the early 1990s. The second phase has been the focus of considerable effort over the last five years and, although it will continue to advance, the progress will likely slow somewhat. It is now that researchers are turning to the third phase, i.e. device development. There are a number of issues that need to be resolved for this work to move forward, such as protein lifetimes, sample introduction, and analyte detection and processing. Progress to date in these directions and future efforts towards these goals are reviewed here.

#### 8.7.1

##### Protein Stability and Lifetime

As a tool in nanotechnology, there is a trade-off between the exquisite functionality of biomolecular motors and their robustness. For their small size, kinesins are able to achieve long-range transport of microtubules at appreciable speeds and generate significant forces. Due to their small size, they have the potential to be integrated into very microscale and nanoscale device geometries, enabling redundancy, multiplexing, minute sample analysis and minimal reagent costs. However, because they are proteins, they are much more fragile than most nanoscale materials. To assess their potential utility when integrated into analytical devices, and to investigate alternate design approaches, it is necessary to determine the lifetime of kinesin motors and microtubules under normal operating conditions, and then to find conditions that extend these lifetimes.

Under normal laboratory conditions, taxol-stabilized microtubules are stable at room temperature for roughly 1 week [96, 97], and kinesin motors are stable on the order of hours to days depending on their concentration, storage buffer, temperature and other variables. For experiments on motor fundamentals, as long as the motors are stable for a working day, there is no need to put the work in to extend their lifetime because each morning a new aliquot of protein can be thawed from the  $-80^{\circ}\text{C}$  freezer. Hence, it has been the interest in device integration that has driven experiments to uncover the mechanisms that limit the working lifetimes of kinesin and microtubules, and to extend these lifetimes.

In the kinesin–microtubule field, the most convenient technique for observing motor function is fluorescence microscopy. Microtubules can be visualized by differential interference microscopy, but for applications where motors and/or cargo are to be observed fluorescence is much more versatile. In the microfluidics field, a standard approach for creating channels has been PDMS molding and bonding to glass [98] and in a perfect world these two approaches could be combined. However, workers studying fluorescent microtubule movements in PDMS channels quickly ran into problems with photodamage [99]. In the standard microtubule gliding assay, the microtubule cocktail includes buffering salts, ATP to drive motility, and an antifade consisting of an oxygen-scavenging system and reducing agent [41, 45]. In the absence of antifade, exposure of the fluorescent microtubules to the high-intensity mercury arc lamp used for fluorescence excitation results in rapid photobleaching, loss of movement and microtubule depolymerization due to oxygen free radical damage. With antifade, the movement of rhodamine-labeled microtubules can be visualized for roughly 10 min under continual high intensity illumination. Without illumination or by shuttering the light, microtubule movement lasts for around 10 h or longer [100]. However, when the flow cell is enclosed with PDMS instead of glass, illumination leads to inhibition of motion and microtubule breakage or depolymerization after approximately 1 min [99, 100]. The cause of failure was traced to the high oxygen permeability of this silicone polymer, which overwhelms the antifade's ability to remove all of the soluble oxygen. PMMA enclosures also showed this same property. While these results do not rule out these materials as device components, if they are to be used they must be combined with another barrier to oxygen diffusion, increasing the complexity of fabrication.

A central concern in the feasibility of kinesin–microtubule powered devices is long-term storage: if hybrid biological/synthetic devices are manufactured, how long can they be preserved before use? Interestingly, this is a similar concern in the field of tissue engineering, where products like artificial skin that include live cells integrated into a polymer scaffold must be made at a manufacturing site, stored and shipped, and then unpacked and used by a doctor. The obvious first approach is freezing; kinesin motors, tubulin and even taxol-stabilized microtubules can be frozen on liquid nitrogen and stored at  $-80^{\circ}\text{C}$  for years with little loss in functionality. In theory, hybrid devices could be simply dunked in liquid nitrogen and thawed before use, but there are a number of possible problems with this approach, including mechanical problems due to unequal expansion coeffi-

cients of the various materials and the requirement for a deep freeze at every point of use.

There has been some recent work on novel methods for extending kinesin and microtubule lifetimes that has yielded interesting results. With the goal of identifying material-processing approaches that could be used to create hybrid devices, Verma and coworkers tested the stability of casein, kinesin motors and microtubules when exposed to various solvents and strippers used in materials processing and nanofabrication. Interestingly, kinesin motors survived when exposed to either pure isopropyl alcohol or acetone – two solvents commonly used to remove photoresist [101]. Microtubules were less robust than motors, but they did survive exposure to 1:4 dilutions of these chemicals in aqueous buffer and these diluted solvents retained their ability to strip photoresist. While not directly impacting device lifetime, these studies provide new approaches for device manufacture and they suggest that these proteins are more stable than may be indicated by their lifetimes in buffer at room temperature. In other work, it was found that drying immobilized kinesins by wicking the solution out of flow cells and storing them under different conditions resulted in longer kinesin lifetimes [102]. Hence, it is possible that instead of freezing hybrid devices, simply desiccating them and then reconstituting them may provide a simple alternative. These findings should lessen the constraints to hybrid device design.

### 8.7.2

#### **Sample Introduction and Detection**

Two future hurdles to creating kinesin-driven analytical devices are sample introduction and analyte detection. To date there is scant work in this area, but because these requirements are universal to virtually all sensor systems, ideas and modules will undoubtedly be borrowed from other disciplines. With respect to sample introduction, one design constraint is that these biomotors work in aqueous environments. As discussed above, kinesins can survive being dried or exposed to solvents, but for their proper function they must remain in proper buffer solutions. Hence, to detect airborne particles (e.g. viruses or bacteria), the samples would need to be concentrated (i.e. filtered) from the atmosphere and then transferred to the aqueous state. While not impossible, there are clearly a number of engineering problems to be solved for this application to become feasible.

An area where the strengths of kinesin-powered devices are maximized is the detection of proteins, RNA or small molecules in minute aqueous samples. As discussed above, detection of specific molecules from single cells is a holy grail of sorts for bioanalytical detection. Delivering the contents of single cells to kinesin-powered transport and detection machinery is a task in itself. Both convective flows and dielectrophoresis have been used to transport cells in microfluidic systems [103, 104]. Additionally, both optical and electrical methods have been developed to rapidly lyse cells, enabling their intracellular contents to be delivered to the microanalysis machinery [105, 106].



### 8.7.3

#### Analyte Detection and Collection

As in all analytical systems, analyte detection will be a key component to future kinesin-powered hybrid devices. The first choice for analyte detection is fluorescence, because it is sensitive and is the standard technique for observing microtubules moving in channels. Building on work guiding microtubule transport in microfluidic channels, analyte detection could be achieved by binding the analyte to the microtubule and observing the change in fluorescence. If the analyte (cell, protein or nucleotide) is fluorescent and has a different emission peak than the fluorophore labeling the microtubule, analytes could be detected by observing the microtubule fluorescence at one wavelength and measuring the analyte fluorescence at a second wavelength. In this case, the microtubule acts to both concentrate and to localize the analyte.

While this detection could be achieved using epifluorescence microscopy, there is potential for achieving much more utility and sensitivity by integrating the optical components into the microfluidic chips containing the motors and analyte. For instance, if an LED and photodiode are integrated into the microchannel containing the microtubule and bound analyte, the detector could be within microns of the sample (Fig. 8.9). This placement should maximize photon capture and reduce background signal due to extraneous signal. One advantage of using the kinesin–microtubule transport system for analyte detection is that the movement speed is stereotyped, so for low signal levels the time average of fluorescence as the analyte moves across the detector could be used to increase the signal-to-noise ratio.

## 8.8

### Conclusion

Due to the highly evolved properties of protein machines, there is incredible potential in integrating them into hybrid biological/synthetic devices. Their nanometer-size scales match well with emerging nanofabrication capabilities and novel functional nanoscale materials. A continuing struggle in nanotechnology is finding techniques to manipulate and organize molecules and nanoparticles in cases where self-assembly is not energetically favorable. As biomolecular motors have evolved to transport and organize biological materials on the nanoscale and microscale in cells, they have the potential to solve a number of these general problems in nanotechnology. This chapter reviewed the *in vitro* transport capabilities of kinesin motors, with an eye toward creating microfluidic devices for analyte detection. This application is one of the first envisaged for these particular protein machines and it is anticipated that as new approaches are developed for to gain ever more control over the kinesin–microtubule system, these biological machines will be applied to other nanoscale systems.

## Acknowledgments

The author wishes to thank members of his laboratory, especially Maruti Uppalapati, Gayatri Muthukrishnan, Zach Donhauser and Samira Moorjani, as well as collaborators and their students, particularly Tom Jackson, Lili Jia, Ying-Ming Huang, Jeff Catchmark and Vivek Verma. The author's research in this area is supported by the NSF and NIH/NIBIB, and by the Penn State Center for Nanoscale Science (NSF MRSEC DMR0213623).

## References

- 1 ALBERTS, B. The cell as a collection of protein machines: preparing the next generation of molecular biologists. *Cell* **1998**, *92*, 291–294.
- 2 MOORJANI, S. G., JIA, L., JACKSON, T. N., HANCOCK, W. O. Lithographically patterned channels spatially segregate kinesin motor activity and effectively guide microtubule movements. *Nano Lett.* **2003**, *3*, 633–637.
- 3 HESS, H., MATZKE, C. M., DOOT, R. K., CLEMMENS, J., BACHAND, G. D., BUNKER, B. C., VOGEL, V. Molecular shuttles operating undercover: a new photolithographic approach for the fabrication of structured surfaces supporting directed motility. *Nano Lett.* **2003**, *3*, 1651–1655.
- 4 HESS, H., BACHAND, G. D., VOGEL, V. Powering nanodevices with biomolecular motors. *Chemistry* **2004**, *10*, 2110–2116.
- 5 HESS, H., VOGEL, V. Molecular shuttles based on motor proteins: active transport in synthetic environments. *J. Biotechnol.* **2001**, *82*, 67–85.
- 6 HIRATSUKA, Y., TADA, T., OIWA, K., KANAYAMA, T., UYEDA, T. Q. Controlling the direction of kinesin-driven microtubule movements along micro-lithographic tracks. *Biophys. J.* **2001**, *81*, 1555–1561.
- 7 STRACKE, R., BOHM, K. J., BURGOLD, J., SCHACHT, H.-J., UNGER, E. Physical and technical parameters determining the functioning of a kinesin-based cell-free motor system. *Nanotechnology* **2000**, *11*, 52–56.
- 8 STRACKE, R., BOHM, K. J., WOLLWEBER, L., TUSZYNSKI, J. A., UNGER, E. Analysis of the migration behaviour of single microtubules in electric fields. *Biochem. Biophys. Res. Commun.* **2002**, *293*, 602–609.
- 9 BOHM, K. J., STRACKE, R., UNGER, E. Motor proteins and kinesin-based nanoactuatoric devices. *Tsitol. Genet.* **2003**, *37*, 11–21.
- 10 BÖHM, K. J., BEEG, J., MEYER ZUR HÖRSTE, G., STRACKE, R., UNGER, E., Kinesin-driven sorting machines on large scale microtubule arrays. *IEEE Adv. Packaging* **2005**, *28*, 571–576.
- 11 WHALEY, S. R., ENGLISH, D. S., HU, E. L., BARBARA, P. F., BELCHER, A. M. Selection of peptides with semiconductor binding specificity for directed nanocrystal assembly. *Nature* **2000**, *405*, 665–668.
- 12 SEEMAN, N. C., BELCHER, A. M. Emulating biology: building nanostructures from the bottom up. *Proc. Natl Acad. Sci. USA* **2002**, *99* (Suppl. 2), 6451–6455.
- 13 ANRATHER, D., SMETAZKO, M., SABA, M., ALGUEL, Y., SCHALKHAMMER, T. Supported membrane nanodevices. *J. Nanosci. Nanotechnol.* **2004**, *4*, 1–22.
- 14 HOWARD, J. Molecular motors: structural adaptations to cellular functions. *Nature* **1997**, *389*, 561–567.
- 15 MAVROIDIS, C., DUBEY, A., YARMUSH, M. L. Molecular machines. *Annu. Rev. Biomed. Eng.* **2004**, *6*, 363–395.
- 16 VALE, R. D., MILLIGAN, R. A. The way things move: looking under the hood of molecular motor proteins. *Science* **2000**, *288*, 88–95.

- 17 HANCOCK, W. O., HOWARD, J. Kinesin: processivity and chemomechanical coupling. In: *Molecular Motors*, SCHLIWA, M. (Ed.). Wiley-VCH, Weinheim, 2003, pp. 243–269.
- 18 KNOBLAUCH, M., PETERS, W. S. Biomimetic actuators: where technology and cell biology merge. *Cell. Mol. Life Sci.* 2004, 61, 2497–2509.
- 19 KINBARA, K., AIDA, T. Toward intelligent molecular machines: directed motions of biological and artificial molecules and assemblies. *Chem. Rev.* 2005, 105, 1377–400.
- 20 NICOLAU, D. V., SUZUKI, H., MASHIKO, S., TAGUCHI, T., YOSHIKAWA, S. Actin motion on microlithographically functionalized myosin surfaces and tracks. *Biophys. J.* 1999, 77, 1126–1134.
- 21 ASOKAN, S. B., JAWERTH, L., CARROLL, R. L., CHENEY, R. E., WASHBURN, S., SUPERFINE, R. Two-dimensional manipulation and orientation of actin-myosin systems with dielectrophoresis. *Nano Letters.* 3, 431–437.
- 22 PATOLSKY, F., WEIZMANN, Y., WILLNER, I. Actin-based metallic nanowires as bio-nanotransporters. *Nat. Mater.* 2004, 3, 692–695.
- 23 MARTINEZ-NEIRA, R. K. M., NICOLAU, D., DOS REMEDIOS, C. G. A novel biosensor for mercuric ions based on motor proteins. *Biosens. Bioelectron.* 2005, 20, 1428–1432.
- 24 HIROKAWA, N., PFISTER, K. K., YORIFUJI, H., WAGNER, M. C., BRADY, S. T., BLOOM, G. S. Submolecular domains of bovine brain kinesin identified by electron microscopy and monoclonal antibody decoration. *Cell* 1989, 56, 867–878.
- 25 YANG, J. T., LAYMON, R. A., GOLDSTEIN, L. S. A three-domain structure of kinesin heavy chain revealed by DNA sequence and microtubule binding analyses. *Cell* 1989, 56, 879–889.
- 26 HACKNEY, D. D. Evidence for alternating head catalysis by kinesin during microtubule-stimulated ATP hydrolysis. *Proc. Natl Acad. Sci. USA* 1994, 91, 6865–6869.
- 27 HOWARD, J. The movement of kinesin along microtubules. *Annu. Rev. Physiol.* 1996, 58, 703–729.
- 28 SCHIEF, W. R., HOWARD, J. Conformational changes during kinesin motility. *Curr. Opin. Cell Biol.* 2001, 13, 19–28.
- 29 VALE, R. D., REESE, T. S., SHEETZ, M. P. Identification of a novel force-generating protein, kinesin, involved in microtubule-based motility. *Cell* 1985, 42, 39–50.
- 30 LAWRENCE, C. J., DAWE, R. K., CHRISTIE, K. R., CLEVELAND, D. W., DAWSON, S. C., ENDOW, S. A., GOLDSTEIN, L. S., GOODSON, H. V., HIROKAWA, N., HOWARD, J., MALMBERG, R. L., MCINTOSH, J. R., MIKI, H., MITCHISON, T. J., OKADA, Y., REDDY, A. S., SAXTON, W. M., SCHLIWA, M., SCHOLEY, J. M., VALE, R. D., WALCZAK, C. E., WORDEMAN, L. A standardized kinesin nomenclature. *J. Cell Biol.* 2004, 167, 19–22.
- 31 MIKI, H., SETOU, M., KANESHIRO, K., HIROKAWA, N. All kinesin superfamily protein, KIF, genes in mouse and human. *Proc. Natl Acad. Sci. USA* 2001, 98, 7004–7011.
- 32 DESAI, A., MITCHISON, T. J. Microtubule polymerization dynamics. *Annu. Rev. Cell Dev. Biol.* 1997, 13, 83–117.
- 33 WILLIAMS, R. C., JR., LEE, J. C. Preparation of tubulin from brain. *Methods Enzymol.* 1982, 85(B), 376–385.
- 34 HYMAN, A., DRECHSEL, D., KELLOGG, D., SALSER, S., SAWIN, K., STEFFEN, P., WORDEMAN, L., MITCHISON, T. Preparation of modified tubulins. *Methods Enzymol.* 1991, 196, 478–485.
- 35 SVOBODA, K., SCHMIDT, C. F., SCHNAPP, B. J., BLOCK, S. M. Direct observation of kinesin stepping by optical trapping interferometry. *Nature* 1993, 365, 721–727.
- 36 COY, D. L., WAGENBACH, M., HOWARD, J. Kinesin takes one 8-nm step for each ATP that it hydrolyzes. *J. Biol. Chem.* 1999, 274, 3667–3671.
- 37 MEYHOFER, E., HOWARD, J. The force generated by a single kinesin molecule against an elastic load. *Proc. Natl Acad. Sci. USA* 1995, 92, 574–578.

- 38 SVOBODA, K., BLOCK, S. M. Force and velocity measured for single kinesin molecules. *Cell* **1994**, *77*, 773–784.
- 39 BLOCK, S. M., GOLDSTEIN, L. S., SCHNAPP, B. J. Bead movement by single kinesin molecules studied with optical tweezers. *Nature* **1990**, *348*, 348–352.
- 40 HOWARD, J., HUDSPETH, A. J., VALE, R. D. Movement of microtubules by single kinesin molecules. *Nature* **1989**, *342*, 154–158.
- 41 HOWARD, J., HUNT, A. J., BAEK, S. Assay of microtubule movement driven by single kinesin molecules. *Methods Cell Biol.* **1993**, *39*, 137–147.
- 42 HANCOCK, W. O., HOWARD, J. Processivity of the motor protein kinesin requires two heads. *J. Cell Biol.* **1998**, *140*, 1395–1405.
- 43 BLOCK, S. M. Making light work with optical tweezers. *Nature* **1992**, *360*, 493–495.
- 44 YANG, J. T., SAXTON, W. M., STEWART, R. J., RAFF, E. C., GOLDSTEIN, L. S. Evidence that the head of kinesin is sufficient for force generation and motility *in vitro*. *Science* **1990**, *249*, 42–47.
- 45 HUNT, A. J., HOWARD, J. Kinesin swivels to permit microtubule movement in any direction. *Proc. Natl Acad. Sci. USA* **1993**, *90*, 11653–11657.
- 46 BROWN, T. B., HANCOCK, W. O. A polarized microtubule array for kinesin-powered nanoscale assembly and force generation. *Nano Lett.* **2002**, *2*, 1131–1135.
- 47 HUANG, T. G., SUHAN, J., HACKNEY, D. D. *Drosophila* kinesin motor domain extending to amino acid position 392 is dimeric when expressed in *Escherichia coli*. *J. Biol. Chem.* **1994**, *269*, 16502–16507.
- 48 YAMAZAKI, H., NAKATA, T., OKADA, Y., HIROKAWA, N. KIF3A/B: a heterodimeric kinesin superfamily protein that works as a microtubule plus end-directed motor for membrane organelle transport. *J. Cell Biol.* **1995**, *130*, 1387–1399.
- 49 HUNTER, A. W., CAPLOW, M., COY, D. L., HANCOCK, W. O., DIEZ, S., WORDEMAN, L., HOWARD, J. The kinesin-related protein MCAK is a microtubule depolymerase that forms an ATP-hydrolyzing complex at microtubule ends. *Mol. Cell* **2003**, *11*, 445–457.
- 50 VERNOS, I. *Kinesin Protocols*. Humana Press, Totowa, NJ, **2000**.
- 51 HOWARD, J. *Mechanics of Motor Proteins and the Cytoskeleton*. Sinauer, Sunderland, MA, **2001**, pp. 58–61.
- 52 BERG, H. C. *Random Walks in Biology*. Princeton University Press, Princeton, NJ, **1993**, pp. 6–11, 53–58.
- 53 JIA, L., MOORJANI, S. G., JACKSON, T. N., HANCOCK, W. O. Microscale transport and sorting by kinesin molecular motors. *Biomed. Micro-devices* **2004**, *6*, 67–74.
- 54 MRKSICH, M., WHITESIDES, G. M. Using self-assembled monolayers to understand the interactions of man-made surfaces with proteins and cells. *Annu. Rev. Biophys. Biomol. Struct.* **1996**, *25*, 55–78.
- 55 RATNER, B. D., BRYANT, S. J. Biomaterials: where we have been and where we are going. *Annu. Rev. Biomed. Eng.* **2004**, *6*, 41–75.
- 56 LIMBERIS, L., STEWART, R. J. Toward kinesin-powered microdevices. *Nanotechnology* **2000**, *11*, 47–51.
- 57 HUANG, Y. M., UPPALAPATI, M., HANCOCK, W. O., JACKSON, T. N. Microfabricated capped channels for biomolecular motor-based transport. *IEEE Adv. Packaging* **2005**, *28*, 564–570.
- 58 UDABAGE, P., MCKINNON, I. R., AUGUSTIN, M. A. The use of sedimentation field flow fractionation and photon correlation spectroscopy in the characterization of casein micelles. *J. Dairy Res.* **2003**, *70*, 453–459.
- 59 WAUGH, D. F. *Milk Proteins: Chemistry and Molecular Biology*. Academic Press, New York, **1971**, pp. 10–12.
- 60 BHATTACHARYYA, J., DAS, K. P. Molecular chaperone-like properties of an unfolded protein, alpha(s)-casein. *J. Biol. Chem.* **1999**, *274*, 15505–15509.
- 61 KULL, F. J., SABLIN, E. P., LAU, R., FLETTERICK, R. J., VALE, R. D. Crystal structure of the kinesin motor domain

- reveals a structural similarity to myosin. *Nature* **1996**, *380*, 550–555.
- 62 SABLIN, E. P., KULL, F. J., COOKE, R., VALE, R. D., FLETTERICK, R. J. Crystal structure of the motor domain of the kinesin-related motor ncd. *Nature* **1996**, *380*, 555–559.
- 63 HIROKAWA, N. Kinesin and dynein superfamily proteins and the mechanism of organelle transport. *Science* **1998**, *279*, 519–526.
- 64 ZHANG, Y., HANCOCK, W. O. The two motor domains of KIF3A/B coordinate for processive motility and move at different speeds. *Biophys. J.* **2004**, *87*, 1795–1804.
- 65 DECASTRO, M. J., HO, C. H., STEWART, R. J. Motility of dimeric ncd on a metal-chelating surfactant: evidence that ncd is not processive. *Biochemistry* **1999**, *38*, 5076–5081.
- 66 BERLINER, E., MAHTANI, H. K., KARKI, S., CHU, L. F., CRONAN, J. E., JR., GELLES, J. Microtubule movement by a biotinylated kinesin bound to streptavidin-coated surface. *J. Biol. Chem.* **1994**, *269*, 8610–8615.
- 67 HUA, W., YOUNG, E. C., FLEMING, M. L., GELLES, J. Coupling of kinesin steps to ATP hydrolysis. *Nature* **1997**, *388*, 390–393.
- 68 GELLES, J., BERLINER, E., YOUNG, E. C., MAHTANI, H. K., PEREZ-RAMIREZ, B., ANDERSON, K. Structural and functional features of one- and two-headed biotinylated kinesin derivatives. *Biophys. J.* **1995**, *68*, 276S–281S; discussion 282S.
- 69 BERLINER, E., YOUNG, E. C., ANDERSON, K., MAHTANI, H. K., GELLES, J. Failure of a single-headed kinesin to track parallel to microtubule protofilaments. *Nature* **1995**, *373*, 718–721.
- 70 CHENG, L. J., KAO, M. T., MEYHÖFER, E., GUO, J. Highly efficient guiding of microtubule transport with imprinted CYTOP nanotracks. *Small* **2005**, *1*, 409–414.
- 71 LAKAMPER, S., KALLIPOLITOU, A., WOHLKE, G., SCHLIWA, M., MEYHOFER, E. Single fungal kinesin motor molecules move processively along microtubules. *Biophys. J.* **2003**, *84*, 1833–1843.
- 72 HANCOCK, W. O., HOWARD, J. Kinesin's processivity results from mechanical and chemical coordination between the ATP hydrolysis cycles of the two motor domains. *Proc. Natl Acad. Sci. USA* **1999**, *96*, 13147–13152.
- 73 TURNER, D. C., CHANG, C., FANG, K., BRANDOW, S. L., MURPHY, D. B. Selective adhesion of functional microtubules to patterned silane surfaces. *Biophys. J.* **1995**, *69*, 2782–2789.
- 74 MALLIK, R., CARTER, B. C., LEX, S. A., KING, S. J., GROSS, S. P. Cytoplasmic dynein functions as a gear in response to load. *Nature* **2004**, *427*, 649–652.
- 75 BROUHARD, G. J., HUNT, A. J. Microtubule movements on the arms of mitotic chromosomes: polar ejection forces quantified *in vitro*. *Proc. Natl Acad. Sci. USA* **2005**, *102*, 13903–13908.
- 76 DESAI, A., VERMA, S., MITCHISON, T. J., WALCZAK, C. E. Kin I kinesins are microtubule-destabilizing enzymes. *Cell* **1999**, *96*, 69–78.
- 77 DESAI, A., WALCZAK, C. E. Assays for microtubule-destabilizing kinesins. *Methods Mol. Biol.* **2001**, *164*, 109–121.
- 78 DENNIS, J. R., HOWARD, J., VOGEL, V. Molecular shuttles: directed motion of microtubules along nanoscale kinesin tracks. *Nanotechnology* **1999**, *10*, 232–236.
- 79 HESS, H., CLEMMENS, J., QIN, D., HOWARD, J., VOGEL, V. Light-controlled molecular shuttles made from motor proteins carrying cargo on engineered surfaces. *Nano Lett.* **2001**, *1*, 235–239.
- 80 VAN DEN HEUVEL, M. G. L., BUTCHER, C. T., SMEETS, R. M. M., DIEZ, S., DEKKER, C. High rectifying efficiencies of microtubule motility on kinesin-coated gold nanostructures. *Nano Lett.* **2005**, *5*, 1117–1122.
- 81 CLEMMENS, J., HESS, H., HOWARD, J., VOGEL, V. Analysis of microtubule guidance in open microfabricated channels coated with the motor protein kinesin. *Langmuir* **2003**, *19*, 1738–1744.
- 82 LIMBERIS, L., MAGDA, J. J., STEWART,

- R. J. Polarized alignment and surface immobilization of microtubules for kinesin-powered nanodevices. *Nano Lett.* **2001**, *1*, 277–280.
- 83 PROTS, I., STRACKE, R., UNGER, E., BOHM, K. J. Isopolar microtubule arrays as a tool to determine motor protein directionality. *Cell Biol. Int.* **2003**, *27*, 251–253.
- 84 TURNER, D., CHANG, C., FANG, K., CUOMO, P., MURPHY, D. Kinesin movement on glutaraldehyde-fixed microtubules. *Anal. Biochem.* **1996**, *242*, 20–25.
- 85 VALE, R. D., FUNATSU, T., PIERCE, D. W., ROMBERG, L., HARADA, Y., YANAGIDA, T. Direct observation of single kinesin molecules moving along microtubules. *Nature* **1996**, *380*, 451–453.
- 86 THORN, K. S., UBERSAX, J. A., VALE, R. D. Engineering the processive run length of the kinesin motor. *J. Cell Biol.* **2000**, *151*, 1093–1100.
- 87 SHAH, C., XU, C. Z., VICKERS, J., WILLIAMS, R. Properties of microtubules assembled from mammalian tubulin synthesized in *Escherichia coli*. *Biochemistry* **2001**, *40*, 4844–4852.
- 88 MUTHUKRISHNAN, G., ROBERTS, C. A., CHEN, Y.-C., ZAHN, J. D., HANCOCK, W. O. Patterning surface-bound microtubules through reversible DNA hybridization. *Nano Lett.* **2004**, *4*, 2127–2132.
- 89 BACHAND, G. D., RIVERA, S. B., BOAL, A. K., GAUDIOSO, J., LIU, J., BUNKER, B. C. Assembly and transport of nanocrystal CdSe quantum dot nanocomposites using microtubules and kinesin motor proteins. *Nano Lett.* **2004**, *4*, 817–821.
- 90 BASKAR, D., HANCOCK, W. O. Unpublished observations.
- 91 DIEZ, S., REUTHER, C., DINU, C., SEIDEL, R., MERTIG, M., POMPE, W., HOWARD, J. Stretching and transporting DNA molecules using motor proteins. *Nano Lett.* **2003**, *3*, 1251–1254.
- 92 KATO, K., GOTO, R., KATOH, K., SHIBAKAMI, M. Microtubule–cyclodextrin conjugate: functionalization of motile filament with molecular inclusion ability. *Biosci. Biotechnol. Biochem.* **2005**, *69*, 646–648.
- 93 AACHMANN, F. L., OTZEN, D. E., LARSEN, K. L., WIMMER, R., Structural background of cyclodextrin–protein interactions. *Protein Eng.* **2003**, *16*, 905–912.
- 94 CLARK, S. L., REMCHO, V. T. Aptamers as analytical reagents. *Electrophoresis* **2002**, *23*, 1335–1340.
- 95 KOJIMA, H., MUTO, E., HIGUCHI, H., YANAGIDA, T. Mechanics of single kinesin molecules measured by optical trapping nanometry. *Biophys. J.* **1997**, *73*, 2012–2022.
- 96 HANCOCK, W. O. Unpublished observations.
- 97 YOKOKAWA, R., YOSHIDA, Y., TAKEUCHI, S., KON, T., SUTOH, K., FUJITA, H. Evaluation of cryopreserved microtubules immobilized in microfluidic channels for bead-assay-based transportation system. *IEEE Adv. Packaging* **2005**, *28*, 577–583.
- 98 McDONALD, J. C., DUFFY, D. C., ANDERSON, J. R., CHIU, D. T., WU, H., SCHUELLER, O. J., WHITESIDES, G. M. Fabrication of microfluidic systems in poly(dimethylsiloxane). *Electrophoresis* **2000**, *21*, 27–40.
- 99 KIM, T. S., NANJUNDASWAMY, H. K., LIN, C.-T., LAKAMPER, S., CHENG, L. J., HOFF, D., HASSELBRINK, E. F., GUO, L. J., KURABAYASHI, K., HUNT, A. J., MEYHÖFER, E. Biomolecular motors as novel prime movers for microTAS: microfabrication and materials issues. In: *Proceedings of the 7th International Conference on Micro Total Analysis Systems*, NORTHROP, M. A., JENSEN, K. F., HARRISON, D. J. (Eds.), Transducers Research Foundation, Squaw Valley, CA, **2003**, vol. 2, pp. 33–36.
- 100 BRUNNER, C., ERNST, K. H., HESS, H., VOGEL, V. Lifetime of biomolecules in polymer-based hybrid nanodevices. *Nanotechnology* **2004**, *15*, S540–S548.
- 101 VERMA, V., HANCOCK, W. O., CATCHMARK, J. M. Micro- and nanofabrication processes for hybrid synthetic and biological system fabrication. *IEEE Adv. Packaging* **2005**, *28*, 584–593.

- 102 UPPALAPATI, M., HUANG, Y. M., JACKSON, T. N., HANCOCK, W. O. unpublished observations.
- 103 McCLAIN, M. A., CULBERTSON, C. T., JACOBSON, S. C., ALLBRITTON, N. L., SIMS, C. E., RAMSEY, J. M. Microfluidic devices for the high-throughput chemical analysis of cells. *Anal. Chem.* **2003**, *75*, 5646–5655.
- 104 TONER, M., IRIMIA, D. Blood-on-a-chip. *Annu. Rev. Biomed. Eng.* **2005**, *7*, 77–103.
- 105 HAN, F., WANG, Y., SIMS, C. E., BACHMAN, M., CHANG, R., LI, G. P., ALLBRITTON, N. L. Fast electrical lysis of cells for capillary electrophoresis. *Anal. Chem.* **2003**, *75*, 3688–3696.
- 106 IRIMIA, D., TOMPKINS, R. G., TONER, M. Single-cell chemical lysis in picoliter-scale closed volumes using a microfabricated device. *Anal. Chem.* **2004**, *76*, 6137–6143.

## 9

# Self-assembly and Bio-directed Approaches for Carbon Nanotubes: Towards Device Fabrication

*Arianna Filoramo*

### 9.1

#### Introduction

Silicon-CMOS technology is the base of present hardware technology for information processing. Until now, its evolution has been governed by Moore's law (from the 1970s), stating that microprocessor performance (defined as the number of transistors on a chip) doubles every 18 months. However, the International Technology Roadmap for Semiconductors (ITRS) [1] predicts that the present CMOS technology will reach its fundamental limits in terms of miniaturization by 2010–2015, concurrently with a dramatic increase in the cost of the production units.

This prompts us to study and develop alternative nanofabrication technologies that will enable the production and manipulation of well-defined structures at the nanoscale level. Indeed, it is well accepted that conventional technologies based on the “top-down” approach are foreseen to experience experimental difficulties. This is due to the existence of various physical effects that do not down-scale properly and, most importantly, to the fabrication cost issues at the nanoscale dimension. At this scale, as also stressed in the IST Technology Roadmap for Nanoelectronics [2], self-assembly and, more generally, “bottom-up” approaches appear to be a more reasonable way to assemble nano-objects into circuits with a two- and/or three-dimensional layout. In particular, self-assembly is also identified as the most promising way to significantly reduce the fabrication costs compared to what is expected for standard top-down silicon-based devices. Indeed, the basic idea of self-assembly is to use a process involving the spontaneous self-ordering of substructures into superstructures. This spontaneous self-ordering is due to specific chemical or physical properties of matter and relies on the natural tendency of the system to search for a stable configuration. This chapter is not meant to be an exhaustive review of self-assembly techniques, but rather a focused discussion on the application of this concept to a particular nano-object – the carbon nanotube (CNT). At present there are several materials with potential for the fabrication of new-generation nanodevices. They vary from conventional semiconductors to conjugated molecules, but among them CNTs are one of the most interesting. This is



due to the wide range of physical properties they can show as a function of their shape and geometry.

CNTs have already been used to fabricate nanodevices, like field-effect transistors (FETs), with very interesting performance characteristics. In this chapter we describe their fabrication techniques, as well as their principal characteristics. The chapter also contains a more general discussion about these unique materials and their nano-applications. In this sense, we provide a discussion on the relevance of using CNTs as active elements in future nanoelectronic devices. We also critically consider the existing techniques that, by self-assembly, enable us to selectively place the nanotubes at specific locations on a substrate in a circuit configuration.

The self-assembly methods we will consider in this chapter are: *in situ* chemical vapor deposition (CVD) growth, the self-assembled monolayer (SAM) technique and the DNA-directed approach. We present their advantages, drawbacks and perspectives. In particular, we discuss in detail the DNA-directed approach. This bio-directed method constitutes a genuine and complete molecular-scale bottom-up method, since it relies on recognition properties inherent to biological entities and can be employed without using any standard lithography technique (a fingerprint of the top-down strategy). As well as the economically very appealing interest of a self-assembly technique is generated by the perspectives of important reductions in fabrication costs, DNA-directed self-assembly could in addition bring truly new technological perspectives by introducing a disruptive strategy and by stimulating the development of novel architecture paradigms, which could include concepts like self-repairing features, reconfigurability, three-dimensional design and massive parallel processing.

The chapter is organized as follows. Section 9.2 presents a brief review of the basic physical features of CNTs, their synthesis methods and the different families of CNT applications reported in the literature. Section 9.3 is devoted to the discussion of the techniques of fabrication of CNT transistors. Here, the interest in self-assembly is highlighted. The first self-assembly method to be detailed is *in situ* CVD in Section 9.4, whereas two post-growth approaches are extensively discussed in the following two sections: in Section 9.5 we review the SAM method and in Section 9.6 we discuss the different aspects of the DNA-directed self-assembly technique for nanotube electronic applications. Finally, we draw our conclusions in Section 9.7.

The scope of the chapter is to provide an introduction and an overview of the current state of the fabrication of devices made of CNTs by using self-assembly. Nonetheless the degree of maturity of the presented nanofabrication methods is variable; we provide a critical comparison of their perspectives and an analysis of the issues to be solved before they could be integrated to real-world applications. This aims to give to the reader the elements to think about the strategies to be conceived for the future developments of the different nanofabrication techniques. The focus of the chapter is more on the fabrication of devices by self-assembly methods than on the details of their functioning, which are left to the appropriate cited references. This chapter, with the help of the included references, will give

the reader the necessary tools to acclimate, evaluate and enter into this interesting field of research.

## 9.2

### CNTs: Basic Features, Synthesis and Device Applications

Since their discovery in the early 1990s by Sumio Ijima [3], CNTs have been a privileged subject of fundamental and applicative research due to their extraordinary physical properties [4]. For instance, their excellent resilience, tensile strength and thermal stability can be used for resistant car bodies, earthquake-resistant buildings or microscopic robots. More generally, the wide range of potential applications in vastly different domains is a result of the numerous and varied aspects of their physical, chemical, mechanical and electronics properties. Long-term exploitation of these unique properties is expected to allow the elaboration of a whole new family of valuable devices.

#### 9.2.1

##### Basic Features

CNTs can be divided in two classes: single-wall CNTs (SWNTs) and multiwall CNTs (MWNTs). A SWNT is basically a rolled-up shell of graphene sheet made of hexagonal carbon rings with half-fullerenes capping the shell ends. MWNTs were discovered first and are a stack of SWNTs of different diameters disposed in a concentric geometry (like Russian dolls). These two kinds of CNTs are schematically presented in Fig. 9.1.

Figure 9.2(a) shows a small part of the graphene lattice, with carbon atoms labeled according to the Dresselhaus notation [4]. The nomenclature  $(n, m)$ , with  $n > m$ , used to identify SWNT refers to integer indices of two graphene unit lattice vectors corresponding to a nanotube's wrapping index known as the *chiral vector*.

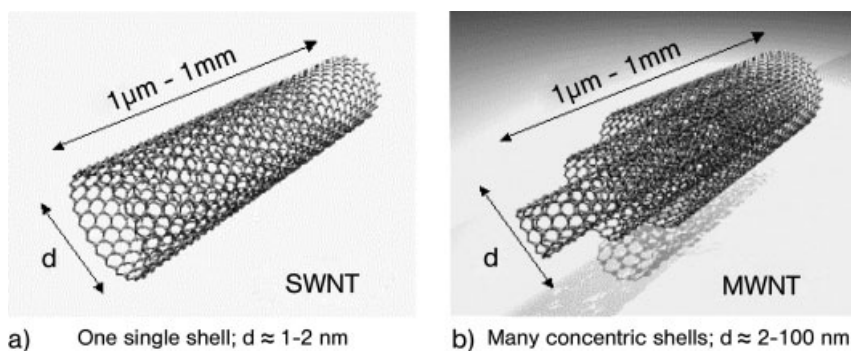
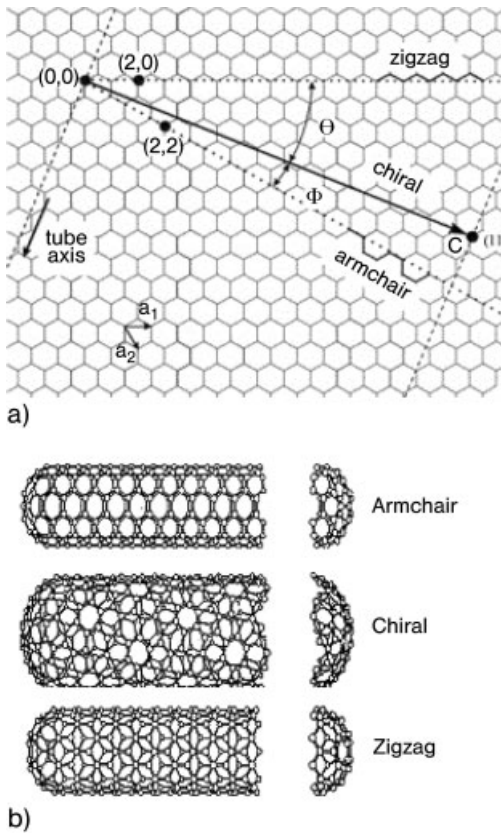


Figure 9.1. Schematic representations of a SWNT (a) and a MWNT (b).



**Figure 9.2.** The graphene sheet is a planar hexagonal lattice of carbon atoms (a). We can recognize the unrolled honeycomb lattice of a nanotube. SWNTs with different chiralities are

obtained by rolling-up parts of the graphene sheet along different axes: an arm-chair, a chiral and a zigzag (from top to bottom in b).

The chiral vector determines the direction along which the graphene sheet is rolled to form the nanotube. It is, by definition, perpendicular to the tube axis vector. The tubes of type  $(n, n)$  are commonly called armchair nanotubes because of their shape ( $\backslash \ / \ / \ \backslash$ ) perpendicular to the tube axis. They make a chiral angle of  $30^\circ$ . The tubes of type  $(n, 0)$  are called zigzag nanotubes due to their shape ( $\backslash \ \backslash \ \backslash$ ) perpendicular to the tube axis. They make a chiral angle of  $0^\circ$ . All the remaining tubes are called chiral nanotubes and have a chiral angle  $\theta$  with  $0 < \theta < 30^\circ$  (see Fig. 9.2b).

CNTs thus possess both nanometric (related to their radius) and microscopic (related to their typical length) characteristic. Correspondingly, most of their original physical properties result from this hybrid nature. For electronic purposes we are principally concerned with the transport properties of CNTs.

In this context, single-wall nanotubes are particularly interesting because of the

following singular physical property: a SWNT can show either metallic or semi-conducting behavior, depending on its chiral vector  $(n, m)$ . The general rule is that if the difference  $n - m$  is an integer multiple of 3 then the nanotube is metallic, whereas in all the other cases the nanotube is a semiconductor. As a consequence, if all chiralities are equiprobable, the metallic:semiconductor abundance ratio for SWNTs should be 1:3. Most importantly, one can envisage the realization of structures with specific transport properties by combining CNTs of different nature into the same device. For instance, nanotubes with different chiralities can be connected to obtain heterojunctions. Applications of SWNTs as electronic devices are discussed in a later section. Concerning MWNTs, the stacking of nanotubes with different chiralities can bring more unexpected results, as suggested by first-principles calculations. Indeed, the outcomes of such model calculations show that the interlayer coupling, which in most cases has little effect on the electronics properties of the individual tubes, can, under specific conditions of the relative positions of one tube shell with respect to the other, strongly modify their individual properties [5].

Finally, it is also important to recall that nanotubes have good elastomechanical properties and that they are thermally very stable. This is related to the fact that the two-dimensional arrangement of carbon atoms in a graphene lattice allows large out-of-plane distortions while the strength of carbon-carbon in-plane bonds keeps the graphene sheets exceptionally strong against distortions [6–8]. Experimental observations of distortions induced to a nanotube demonstrate this high elasticity and point towards its possible use as lightweight, highly elastic material [9–12]. Therefore, CNTs provide one-dimensional wires that enable the fabrication of different complete families of electronic devices.

### 9.2.2

#### **Synthesis of Nanotubes**

There are mainly three methods for the synthesis of nanotubes: arc-discharge [13–18], laser ablation [19–21] and CVD [22–26]. The first two are evaporation methods that employ solid-state carbon precursors as carbon sources for nanotube growth and involve carbon vaporization at high temperatures (in an oven at 1100–1200 °C) assisted, respectively, by an arc-discharge or laser ablation. In order to achieve nanotube growth some metal catalysts are added in the solid graphite source. The third method utilizes hydrocarbon gases as sources for carbon atoms. It also employs metal catalyst particles as “seeds” for nanotube growth, but the process takes place at relatively lower temperatures (500–1000 °C). More details about the CVD method are given in Section 9.4. These three methods have not been equally used in the literature.

Currently, the majority of the work published on the synthesis of CNTs (MWNTs and SWNTs) deals with different types of production by using the CVD route. A large variety of successful production approaches based on this method have been reported in recent years. Indeed, CVD processes are expected to be the solution for the mass production of CNTs.

The state-of-the-art synthesis achievements using CVD methods are: (a) production of centimeter-long CNTs [27, 28], (b) synthesis of CNTs along the direction of an applied electric field [29] and (c) very regular ordering of CNTs grown on templates [30]. The major problems of CVD-based approaches for SWNTs synthesis are: (a) the difficulty of producing CVD-SWNTs with a narrow diameter distribution and (b) the tubes produced generally have more defects. It is worth pointing out that although the best-quality SWNTs so far are produced by evaporation-related methods, the difference with CVD ones is becoming less and less significant.

It should be stressed that an important issue in the growth of SWNTs is the control of the tube diameter and of the chirality distributions. These two parameters are of prime importance in transport studies, since (a) as mentioned in Section 9.2.1, the chirality of a SWNT determines its intrinsic metallic or semiconducting properties and (b) the current of a nanotube transistor in its off-state is strongly dependent upon the nanotube bandgap, which is inversely proportional to the tube diameter  $d$  (the bandgap of a semiconducting SWNT  $\propto 1/d$ ). Despite the importance of having a good control of these distribution parameters, none of the three synthesis methods has yielded bulk materials with homogeneous diameters and chiralities. So far, evaporation techniques remain the best for the selective synthesis of SWNTs with a narrow diameter distribution [31, 32]. With respect to the chirality issue, two interesting reports should be mentioned: the first achievement concerns a preferential CVD growth of semiconducting SWNTs (with a yield of 90%) [33], while the second one concerns a postsynthesis method to separate metallic from semiconducting nanotubes [34].

### 9.2.3

#### Device Applications

A large number of studies on CNT applications have been reported in the literature [35]. They span from field emission electron sources [36–41], supercapacitors [42–44], artificial muscles [45–47], nanoelectromechanical systems [48–53], photoactuators [54], controlled drug delivery/release [55, 56], reinforcement of materials [12, 57–61], composite printable conductors [62], optical components [63, 64], nanoelectronic components [65], scanning probe tips [66–68], etc.

Here, we consider nanoelectronic device applications. In particular, we focus on transistors made of nanotubes and only briefly discuss their nanosensor applications. Indeed, it has been experimentally demonstrated that an individual semiconducting SWNT can be used as the channel of a CNTFET [69, 70]. In 2001, different achievements were accomplished: the demonstration of a room temperature single-electron transistor (SET) [71] and of nanotube transistors showing gain above unity [72], as well as the realization of logical gates mimicking CMOS ones (but with a lateral channel extension reduced to 1 nm) [72, 73]. Recent experimental [74–79] and theoretical [79–82] studies on CNTFETs showed that most of them work as Schottky barrier transistors. Their switching characteristics are limited by the Schottky barriers at the metal/nanotube junction that brings to the fore the

crucial role of interfaces in such a transistor. By optimizing the nanotube/electrode interface [74, 78, 83] and the gate coupling, the device characteristics can be improved both in the “on” and “off” states. Some CNTFETs [84, 85] already exhibit a level of performance comparable to state-of-the-art silicon MOSFETs (at comparable geometry).

It is worth pointing out that SWNTs are also an ideal material for nanosensor fabrication – their one-dimensional structure and their high specific area make the conductance of semiconducting SWNTs highly sensitive to very small amounts of molecules [86].

More precisely, in the context of sensor applications, the exceptional properties of nanotubes are exploited mainly in two ways. The first approach is based on the changes in electrical characteristic of a device constituted by an individual (or very few) SWNT in a transistor configuration. In this case the current in the device is modified by the interaction of the molecules with the semiconducting SWNT channel and/or with the electrodes of the transistor. In some cases the SWNT can be appropriately functionalized in order to enhance its interaction with and its sensitivity to the molecules to be detected. We can quote sensors of gaseous molecules [52, 87], proteins [88, 89], pH/glucose [90], aromatic compounds [91], humidity [92] and DNA hybridization with high sensitivity (concentrations as low as 6.8 fM solution) [93].

In the second approach, the CNTs are used as electrode materials in electrochemical cells [94]. Since their first application for the oxidation of dopamine [95], an increasing number of studies have been devoted to the CNT electrocatalytic behavior towards the oxidation of biomolecules. We can quote studies on dopamine [96–98], ascorbic acid [96], epinephrine [96, 98], 3,4-dihydroxyphenylacetic acid [99], homocysteine [100], thyroxine [101], glucose [102, 103], total cholesterol in blood [104] and DNA hybridization sensors [105–107]. The advantages presented by the CNT electrodes with respect to traditional carbon electrodes are better conducting characteristics, higher chemical stability, increased reaction rates, improved detection limit and reversibility. However, it should be noted that in most of these applications the nanotubes were utilized as a bulk material and not as an individual nano-objects. The nanotubes are generally dispersed in solution by chemical treatments, then incorporated in a matrix and deposited as (or onto) the electrodes. In some more recent reports the nanotubes are directly grown on the electrodes by CVD methods. A recent overview of this type of biosensors can be found in Ref. [108].

### 9.3

#### **Fabrication of CNT Transistors and Self-assembly Approaches**

The majority of the works reported on CNT transistors concern the study of their fundamental properties and performance. In this framework, the techniques that have been developed for the fabrication of such devices do not take into account yield/cost issue and are mainly based on random deposition methods.

Generally, the nanotubes are produced by an evaporation technique (laser ablation or arc-discharge) and, after a purification step, are dispersed in solution (typically in 1,2-dichloroethane). Then, they are deposited on an oxidized silicon substrate [69–78]. The result of this deposition is a completely spatially random distribution of the nanotubes on the substrate. Indeed, in this condition it is only possible to control the nanotube density on the surface by varying their concentration in the solution and not their positioning.

To connect some of these randomly dispersed nanotubes, they are first localized by atomic force microscopy (AFM) imaging with respect to some location marks fabricated on the substrate. Then, the best candidates (in terms of position) are chosen and a set of dedicated electrodes is fabricated. In some cases, a set of pre-patterned electrodes is already present on the substrate before the nanotube deposition and it is a matter of “luck” if the deposited nanotubes are correctly positioned on them. This is normally checked by AFM images of the sample. The same idea is followed if the nanotubes are randomly grown on the substrate by CVD. Indeed, after the growth, the nanotubes are imaged and the best candidates are electrically connected. Finally, it is also worth noting that each nanotube transistor does not always have its own gate electrode and that generally the conductive reverse side of the silicon substrate is used as a back-gate.

However, the possible use of CNTs as active elements in future nanoelectronics is closely related to the question of legacy/compatibility with present information technology. Indeed, it is quite unlikely that a system based on a new technology consisting of architecture with completely random disposition of such devices could be introduced and accepted. Therefore, to take full advantage of the unique electrical properties of SWNTs in device/circuit applications, it is desirable to be able to selectively place them at specific locations on a substrate with a low-cost, high-yield self-assembly-based technique.

Nowadays, the state-of-the-art of self-assembly of CNTs devices can be divided in two different classes of self-assembly methods: (a) *in situ* CVD growth, where the localization arises from the catalyst controlled positioning, and (b) post-growth localized deposition on a substrate. In the latter case, the nanotubes are first grown, handled in solution and only subsequently positioned on the substrate. Obviously, the technique chosen for selective placement of the nanotubes must not degrade the electrical characteristics of the devices and must leave open to all the possibilities of such interesting nano-objects.

The advantage of a post-growth deposition method is that, before deposition, CNTs can be purified and chemically treated in order to separate them by diameter [109–111], length [112] or chirality [34, 113, 114]. Moreover, in this predeposition step the nanotubes can also be chemically functionalized to add to their exceptional features other interesting chemical or physical properties [115, 116]. As discussed previously, the drawback to overcome in this case is mainly related to the deposition issue since it is generally random on the substrate. To solve this SWNT random deposition issue, two post-synthesis methods can be used.

The first one is to achieve a selective placement of SWNTs on regions of the substrate that are predefined by surface treatments. This post-growth selective place-

ment approach is based on the use of SAMs to modify the surface properties of certain regions of a substrate. This, in turn, affects the interactions between the sidewalls of a CNT and the surface, and the CNTs are preferentially attracted there.

The second approach could solve the deposition challenge using biological scaffolds, as DNA molecules, to realize site-controlled implementation of nanocomponents. Indeed, the unique intra- and intermolecular recognition properties of DNA have already been used to build-up scaffold structures and position nanoparticles [117–121].

These two post-synthesis methods are discussed Sections 9.5 and 9.6, while the *in situ* CVD approach is discussed in the next section.

## 9.4

### *In situ* CVD Growth

The *in situ* CVD method is based on the selective growth of CNTs on specified locations on the substrate. We now present the main aspects of this technique.

As previously mentioned, the first step of the CVD is the energy-activated decomposition of some hydrocarbon gas. The energy source can be either a plasma or a resistively heated coil and its function is to “crack” the gaseous molecules to provide reactive carbon atoms. Such carbon atoms diffuse towards the substrate, which is heated and coated with a transition metal catalyst. Then, the carbon atoms are fixed on the substrate and, if the appropriate conditions are fulfilled, CNT growth takes place.

The most commonly used gaseous carbon sources are methane, carbon monoxide and acetylene. Acetylene is widely used as a carbon precursor for the growth of MWNTs, which occurs at temperatures typically in the 600–800 °C range. Carbon monoxide or methane have proven to be more effective for the growth of SWNTs, since the temperature required is usually higher (800–1000 °C) and acetylene is not stable at these temperatures.

It should be noted that the CVD method has undergone dramatic and important developments over the past few years. The yield and average diameter of SWNTs were optimized by controlling the process parameters [122], and, although the diameter distribution is not as narrow as for laser ablation synthesis, impressive progress has been made in the optimization of this growth technique. For instance, as already quoted in Section 9.2.2, some reports have been found to move from the standard yield of 70% for semiconductor nanotube species [30] to a more interesting 90% [33].

Concerning the fabrication of CNT devices, the basic idea is to achieve the *in situ* localized growth of nanotubes by controlling the localization of the metal catalyst. Indeed, CVD CNT synthesis is essentially a two-step process consisting of an initial catalyst preparation step followed by the actual growth of the nanotubes, which starts at the places where the catalysts are present. Following this strategy, the first example of localized growth of SWNTs was realized in 1998 [86]. The authors produced individual SWNTs on silicon wafers patterned with micrometric islands of



catalytic material. Their synthesis procedure begins with the patterning of catalytic islands on silicon substrates by electron beam lithography (EBL). More precisely, they first use EBL to define micrometric square islands in a poly(methyl methacrylate) (PMMA) resist. Then, they deposit a liquid phase of the metal catalysts  $[\text{Fe}(\text{NO}_3)_3 \cdot 9\text{H}_2\text{O}, \text{MoO}_2(\text{acac})_2]$  mixed with alumina nanoparticles. Finally, they obtain the catalyst islands by lift-off of the nonexposed PMMA resist. For nanotube growth, they used methane as carbon precursors and a temperature of about 1000 °C. Moreover, they limited the formation of amorphous carbon by limiting the CVD synthesis to short times (maximum 10 min). They found that all the grown nanotubes were rooted in the islands and that some of them bridged two metallic islands. Following this pioneering work, much activity on *in situ* CVD for CNT devices fabrication has taken place and transistor arrays have been fabricated [30].

However, there is an important issue to be solved before integrating such a CVD method with current CMOS technology. Indeed, for the direct growth by CVD of CNTs on silicon, the temperature regime for the growth of SWNTs and MWNTs must be compatible with CMOS integration. In this sense, substantial progress has been recently achieved by the use of a plasma-enhanced CVD (PECVD) method [33]. In this work, nanotube growth was carried out at 600 °C on  $\text{SiO}_2/\text{Si}$  wafers on which some discrete ferritin particles were randomly adsorbed to act as catalysts. The idea is that the plasma-assisted dissociation of  $\text{CH}_4$  into more reactive higher hydrocarbons and more reactive radicals must be favorable for efficient SWNT growth at lower temperatures. Moreover, the method uses a low-density plasma that propagates down and reaches the sample placed 40 cm from the plasma coil, thus preventing any local heating of the substrate. It should be noted that another advantage of lowering the CVD growth temperature is related to the diameter distribution and chirality issue. Indeed, it is likely that the size and shape of the catalytic nanoparticles should be more stable at lower temperatures, leading to a better control of the size and potential chirality of nanotubes.

In order to fully overcome the growth temperature issue and ensure compatibility with CMOS technology, a very interesting (but fundamentally different) solution can be envisaged. Indeed, these kinds of limitations can be completely avoided by preparing the nanotubes *ex situ*, functionalizing them and then selectively depositing the nanotubes into the CMOS circuit. This is the philosophy of the post-growth strategies, as discussed in the following sections.

## 9.5

### Selective Deposition of CNTs by SAM-assisted Techniques

The technique of localized deposition assisted by SAMs is nowadays the subject of large interest. It started with the pioneering works of the groups of Liu [123], Muster [124] and Choi [125]. It relies either on a local chemical functionalization of the surface [123] or on an electrostatic anchoring of surfactant-covered SWNTs on amino-silane functionalized surfaces [124, 125]. The basic idea beyond these pro-

cesses is the same, but the use of amino-silane surfaces has allowed the control of both deposition density and selective placement in predefined areas of the substrate of isolated SWNTs. Due to its great importance in the selective deposition of SWNTs, the SAM-assisted technique is discussed in detail in the following subsection.

### 9.5.1

#### Methodology and Key Parameters

This process can be summarized as follows [126–128]: the patterns (regions for future selective placement) are defined by performing EBL on a PMMA resist deposited on the  $\text{SiO}_2$  surface of a silicon substrate. After a cleaning step [reactive ion etching (RIE)], a monolayer of aminopropyltriethoxysilane (APTS) is deposited by CVD [129–131] to form a “sticky patch” in the regions opened in the resist (see schematic representation in Fig. 9.3).

Exposure to ethylenediamine (EDA) is used to increase both the surface concentration and the orientation of APTS [132], and consequently to improve interactions with SWNTs. It is likely that this EDA molecule plays the role of a catalyst during the chemical anchoring of APTS on Si-OH. Indeed, it blocks the hydrogen bond formation between the amino group and Si-OH [133]. As a consequence, at the end of the chemical reaction, each amino group is well oriented on the top of the monolayer and their density increases by around 50%. Gas deposition is chosen instead of silanization from an aqueous solution, since it yields a much better control of layer thickness [125]. Once the sticky patch has been formed, it is expected that the adhesion of SWNTs would be enhanced in the functionalized

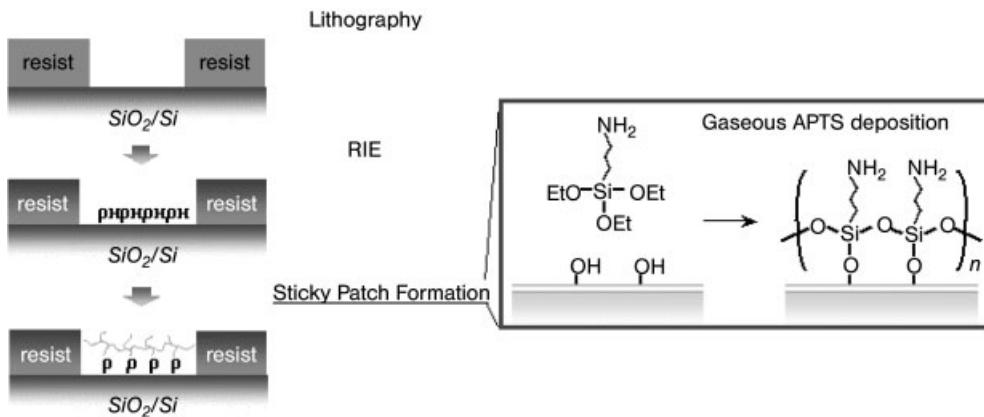


**Figure 9.3.** Schematic vision of the fabrication of the APTS patterns on the substrate surface. The patterns are defined in a PMMA resist by standard electronic lithography. Then, the motifs are developed and, after a cleaning step (RIE), the sticky patches of APTS are deposited in vapor phase.

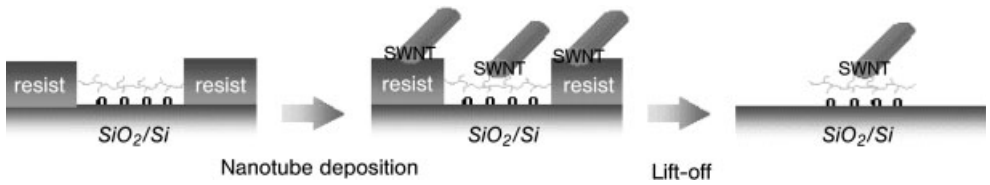


**Figure 9.4.** The sticky patches of APTS are exposed to the nanotube solution. In this case, to enhance placement selectivity, the residual PMMA resist is lifted off after nanotube deposition.

regions with the APTS “sticky patch”. Essentially, two ways can be chosen to selectively place SWNT.

The first method consists of working with an aqueous solution, where sodium dodecylsulfate (SDS) surfactant is used to disperse SWNTs. In this case, the sample is exposed to the SWNT suspension and then the resist is lifted off to enhance selectivity by removing any nanotubes that would have been adsorbed on the PMMA (see schematic representation in Fig. 9.4).

However, in this case, the following bottleneck has to be faced: the density of adsorbed tubes on the surface is too low for the realization of integrated circuits. It turns out that increasing the concentration of SWNTs in the solution leads mainly to the deposition of bundles on the surface. The two problems to be solved within this approach are (a) to improve the dispersion of SWNTs in the solution, and (b) avoid the competition, in the electrostatic anchoring on the amino-silane surface, between the SDS micelles present in the solution and the SDS-covered tubes.

In order to avoid these two drawbacks, a second approach has been developed [126, 127]. The main point is that nanotubes are dispersed not in an aqueous solvent, but in *N*-methyl pyrrolidone (NMP). It has been observed [134] that this solvent allows dispersing nanotubes without any kind of surfactant. Therefore, it can solve point (a) and eliminates point (b). However, due to NMP interaction with the PMMA resist, it has been necessary to modify the process as shown in Fig. 9.5.

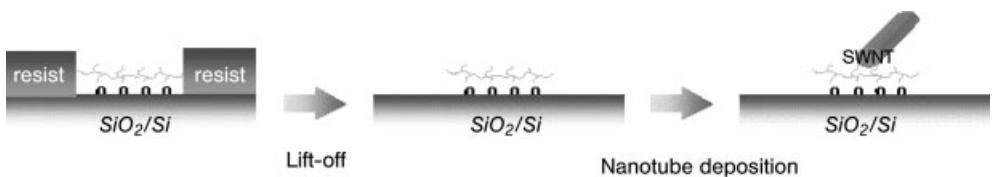


**Figure 9.5.** After the formation of the APTS patterns, the residual PMMA resist is lifted off. Then the sample is exposed to the nanotube solution. In this case, the selectivity is ensured only by the different affinity of nanotubes with different (APTS/SiO<sub>2</sub>) surfaces.

The main difference with respect to the previous sequence (Fig. 9.4) is the reversed order of the last two steps. Thus, in the present case, the resist is removed before exposure to the nanotube solution. *A priori*, one would think that the selectivity of the placement would be partially lost; however, this is not the case, as shown in Refs. [126, 127].

The detailed studies reported in Refs. [126–128] have shown that each of the different steps in Figs. 9.3 and 9.5 play an important role in the selective placement, and that various parameters critically contribute to the success of the deposition process. Since these points are of particular importance in mastering the selective placement technique, we reconsider below the whole deposition process in much more detail. The discussion will follow Refs. [127, 128].

The nanotubes used in Refs. [127, 128] were obtained by the laser ablation technique [135]. The pristine SWNT samples first underwent a purification stage as described in Ref. [136]. Then, they were dispersed in NMP solvent. The solution was sonicated [137] and centrifugation was performed [126]. The SWNT concentration in NMP was varied from 0.1 to 0.005 mg mL<sup>-1</sup> and the variation of the density of deposited SWNTs was recorded. The substrates for that study consisted of 200-nm thick thermally grown SiO<sub>2</sub> on silicon, covered with a monolayer of APTS. The SWNTs in NMP solution were deposited on the surface for 1 min. Finally, the density of deposited SWNTs was quantified by AFM experiments. The main results of this study are presented below.

Before discussing the results concerning the selective placement, it is worth stressing the excellent deposition yield of the NMP-based approach. For the sake of comparison, Fig. 9.6 presents AFM images of APTS-treated substrates after exposure to either an aqueous SDS solution at 1.2 CMC (Fig. 9.6a) or to a NMP solution (Fig. 9.6b) for the same SWNT concentration and exposure time. Contrary to aqueous solvents, for the NMP solution the adsorption process on APTS seems to be independent of any charge effect (though they cannot be completely excluded [138]). Indeed, in the case of NMP, the NH<sub>2</sub> conversion of the silane group to NH<sub>3</sub><sup>+</sup> by exposure to HCl vapor does not seem to be relevant for the deposition yield. The adsorption is likely due to an interaction between the amine group of the APTS and the nanotube, as shown by Kong and Dai [139].

At a concentration of 0.1 mg mL<sup>-1</sup>, the density is 150 SWNTs on a 4-μm<sup>2</sup> area. This result is comparable to that of Liu and coworkers [123], with 240 CNTs on a 6.25-μm<sup>2</sup> area. Between 60 and 70% of the nanotubes on the recorded AFM images are less than 1.6 nm high, indicating individual SWNTs or small bundles. Therefore, the bundling problem observed with surfactants in aqueous solvents [point (a) above] seems to be much less significant in NMP.

The influences of several parameters on the deposition have been analyzed [126, 128], such as the deposition time, centrifugation speed, sonication time and SWNT concentration. The distribution of the nanotube diameter appeared similar for all concentrations (below 0.1 mg mL<sup>-1</sup>), indicating that there is no significant reduction of the bundles in diluted solutions. Concerning the centrifugation, the SWNT solutions were centrifuged for 10 min at different speeds up to 28 000 r.p.m. Unlike the case of SWNTs in aqueous solvents, the rotation speed seems to have no

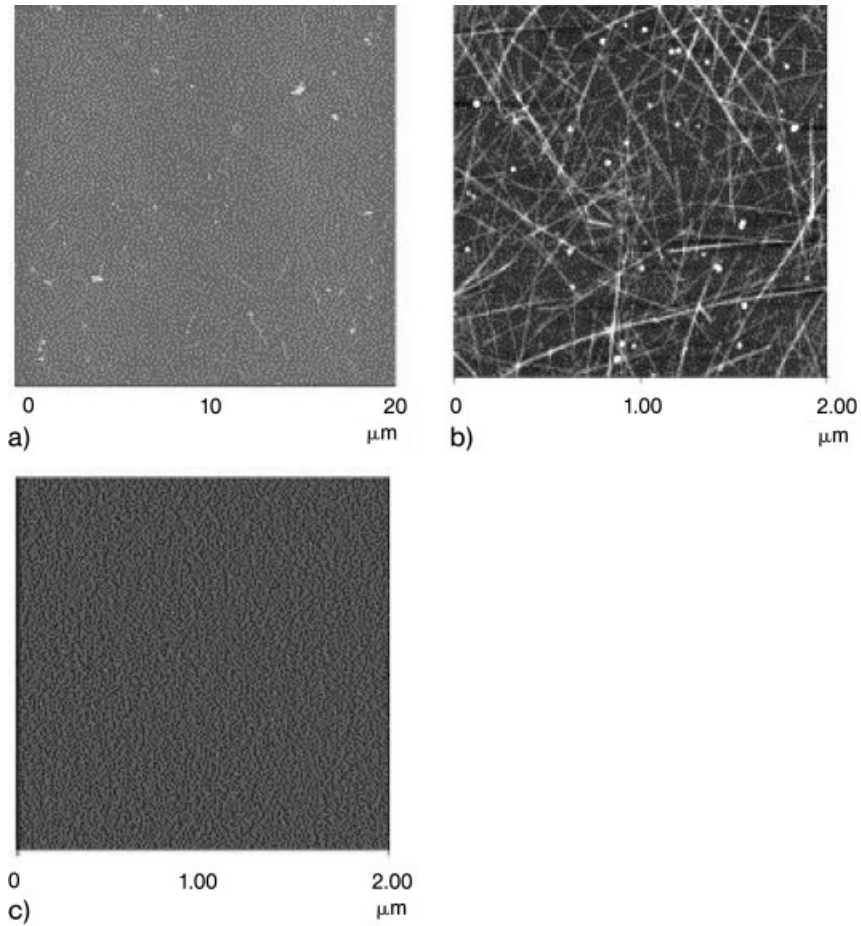


**Figure 9.6.** AFM images of APTS-treated substrates after exposure to two kinds of nanotube solutions. (a) The substrate was exposed to an aqueous solution with SDS surfactant, while in (b) it was exposed to a

NMP solution. (c) A bare  $\text{SiO}_2$  substrate was exposed to the same NMP solution as in (b), note that in this latter case no nanotubes deposition is observed.

significant effect on the dispersion of nanotubes. Concerning the sonication, after 24 h the tubes were up to 1–2 μm long, but they were severely shortened to less than 400 nm length if sonicated for 36 h. Finally, as expected, by increasing the deposition time we observed, accordingly, an increase of the density of SWNTs deposited.

The principal aim of the study reported in Refs. [127, 128] was to achieve selective placement of CNTs. For that, the experiments were repeated on patterned substrates. As already mentioned, the resist was removed before SWNT deposition (Fig. 9.5). In this case, the selectivity is ensured only by the different behavior of

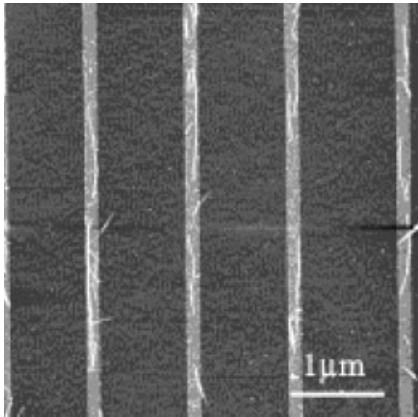


**Figure 9.7.** AFM image of a sample with a series of continuous APTS stripes 100 nm wide and spaced 1  $\mu\text{m}$  from each other. The stripes are defined by lithographic patterning of PMMA, then silanized and finally exposed to the CNTs in NMP solution.

the APTS-treated regions with respect to the nontreated regions. This point was checked by a preliminary experiment where a nonsilanized and a silanized substrate were exposed to the same nanotube solution. The results are reported in Fig. 9.6 [b (APTS-treated substrate) and c (nontreated substrate)]. It is clear from these figures that no deposition is observed for the nonsilanized sample.

An important parameter for the quality of the selective deposition is the geometry of the pattern. For the simple stripes geometry, the key parameter is the width of the stripes. Continuous stripes 500, 200 and 100 nm wide were patterned in PMMA, then silanized and exposed to the SWNTs in NMP solutions. Figure 9.7 shows the selective deposition obtained for the sample with 100-nm trenches. Suitable densities can be achieved for any width by varying the deposition time and/or the SWNT concentration in the solution within reasonable limits. For the same experimental conditions, the SWNT density increases roughly by a factor of 2 when the stripe width is increased from 100 to 200 nm. Moreover, was seen in this study that longer tubes (length  $\gg 1 \mu\text{m}$ ) are better aligned than shorter ones and that the quality of alignment is improved for narrower stripes, as already observed for aqueous solutions [125]. Finally, the use of 100-nm wide stripes represents the best way to limit the number of aligned SWNTs to one, which is crucial for the reliable study of electrical transport in individual SWNTs [127, 128].

Furthermore, in order to reliably control the fabrication of a large number of SWNT transistors on the same wafer, it is necessary not only to anticipate the statistics of deposition on a given pattern, but also the existence of any “proximity” effect, i.e. any effect on the deposition yield due to a possible combined interaction of patterned areas when they are in close vicinity to each other. SWNT deposition has been checked on groups of stripes 100 nm wide and 2  $\mu\text{m}$  long spaced by 1, 3

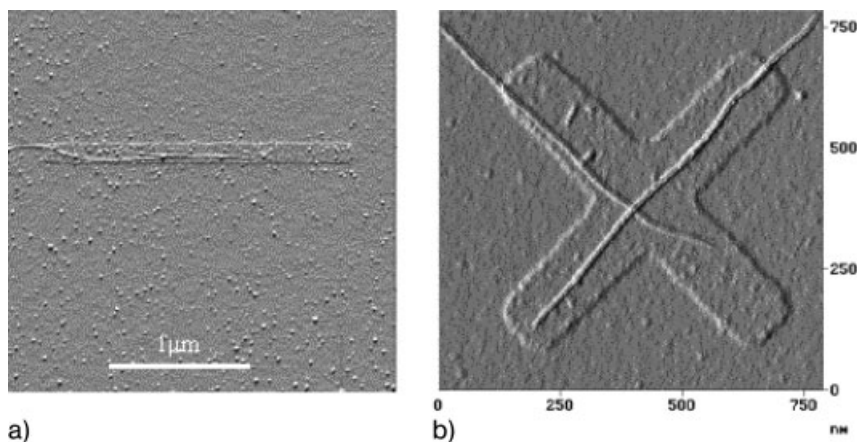


**Figure 9.8.** AFM images of two samples with APTS pre-patterned areas of different geometries, after exposure to a SWNT solution. (a) A single finite APTS stripe with one aligned nanotube. (b) A cross APTS pattern with two nanotubes aligned in each direction of the cross. No combing technique was applied during the nanotube deposition.

and 20  $\mu\text{m}$  on the same substrate. AFM observation showed a placement yield superior to 85% in all groups. The constant density of deposition obtained for all groups clearly indicated that no “proximity” effects were involved in the placement process. An additional test was performed with the realization of a crossed SWNT configuration. Finite size crosses 100 nm wide and typically with 750-nm long arms were submitted to SWNT deposition. Typical results for the deposition of SWNT on striped and crossed APTS motifs are reported in Fig. 9.8.

It should be stressed that this kind of result (in terms of yield and selective deposition) critically depends on the quality of deposited APTS, and can be obtained only if the monolayer is perfectly uniform, homogeneous and well ordered.

In conclusion, for SAM-assisted selective placement, the NMP-based method provides an excellent deposition yield for both unpatterned surfaces and substrates patterned with different geometries (single and groups of stripes, and arrays of crosses), and the feasibility of deposition of a limited number of aligned nanotubes per stripe (ideally one) has already been demonstrated.

The last step in the fabrication of SWNT transistors is the realization of contacts. The choice of depositing SWNTs by a selective placement approach considerably simplifies the subsequent contacting process. Indeed, since we define the deposition areas by EBL, the patterning of electrodes on top of precisely localized SWNTs is simple. No specific and tedious AFM imaging is required to locate SWNTs, as is the case for randomly deposited SWNTs. The transistor is fabricated by first selectively depositing the tubes on a silane pattern prepared on a substrate fitted with position markers. After nanotube deposition, the contact electrodes are patterned and made using standard lithographic techniques (see Fig. 9.9 for electrodes in the crossed and striped geometries).

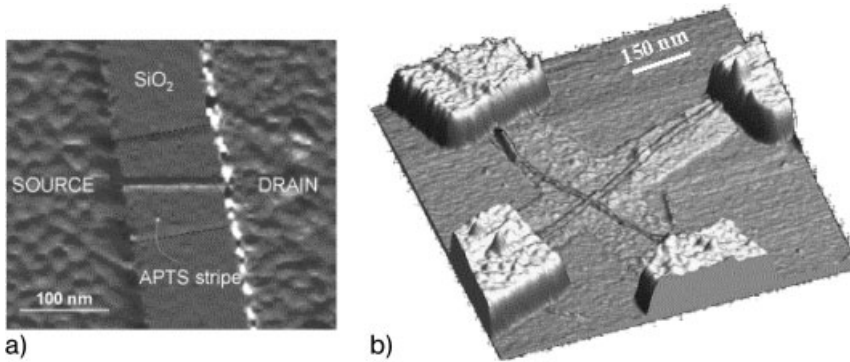


**Figure 9.9.** AFM images of two connected samples with APTS areas of different geometries. (a) A single finite APTS stripe with one aligned nanotube connected by two electrodes (source and drain). (b) A 3-D view of a connected crossed device.

Altogether, these results obviously open the way for the controlled fabrication of a large number of SWNT devices by SAM self-assembly.

#### 9.5.2

##### **Performance of CNTFETs Fabricated by the SAM Method**

CNTFETs obtained by random deposition of nanotubes were introduced in Section 9.2.3. The present subsection is devoted to a comparison of the characteristics of transistors obtained by random and self-assembled depositions.

As already mentioned in Section 9.2.3, CNTFETs have been demonstrated to be Schottky barrier transistors. As a consequence, their transport characteristics can depend on the choice of the metal for electrode fabrication. One can check this point, e.g. by comparing the performance of devices obtained with the same tubes, but with different types of electrodes; this has actually been done for both randomly deposited [74] and self-assembled [83, 127] CNTFETs.

Figure 9.10 reports the characteristics of self-assembled CNTFETs in two configurations: (a) a “standard” configuration with 0.2-nm titanium/40-nm gold electrodes (Fig. 9.10a), and (b) an optimized configuration, hereafter called “TiC” (Fig. 9.10b), with deposition of 20-nm titanium/20-nm platinum electrodes and application of rapid thermal annealing (RTA). This RTA process took place at temperatures in the range 650–850 °C in inert ambient gas to convert the electrode contacts to titanium carbide (as in Ref. [74]). As the electrodes were fabricated on top of SWNTs deposited on 200-nm SiO<sub>2</sub> film grown on a silicon wafer, the wafer itself was used as the gate electrode (“back-gate” configuration). Electrical measurements were performed in vacuum.

“Standard” CNT field effect transistors behaved as p-type FETs, i.e. the dominant carriers are holes. As shown in Fig. 9.10(a), the transconductance ( $dI_D/dV_G$ ) for



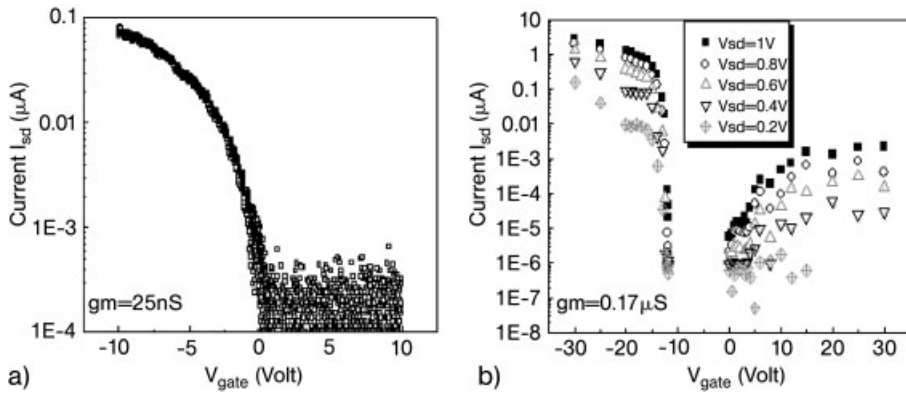


**Figure 9.10.** Transport characteristics of the “standard” (a) and “TiC” (b) devices. (a) Transfer characteristics at room temperature with source to drain voltage  $V_{SD} = 200$  mV;  $dI_D/dV_G = 25$  nA  $V^{-1}$ . The on/off current ratio

is  $10^4$ . (b) Transfer characteristics with source to drain voltage  $V_{SD} = [0.2 \text{ V}:1 \text{ V}]$ ;  $dI_D/dV_G = 0.17 \mu\text{A} V^{-1}$ . The on/off current ratio is  $10^7$ . (Adapted from Ref. [127].)

this kind of device is in the  $10^{-9}$  A  $V^{-1}$  range and the current modulation occurs through 4 orders of magnitude. “TiC” CNTFETs exhibited a drastic improvement of performance. According to several authors, “TiC” decreases the contact resistance for the injection of both p- and n-type carriers [74]. Indeed, the “TiC” CNTFETs in Fig. 9.10 are ambipolar, i.e. they carry a strong current at both negative and positive values of  $V_G$ .  $dI_D/dV_G$  increases by 2 orders of magnitude and results in the  $10^{-7}$  A  $V^{-1}$ , range while the current modulation occurs through 6–7 orders of magnitude, which is also 2 orders of magnitude better than “classical” devices.

The characteristic values of the self-assembled “TiC” devices are close to those obtained on similar back-gated devices fabricated by random deposition directly on  $\text{SiO}_2$  (e.g. as evidenced by the comparison of the results in Fig. 9.10 with those reported in Ref. [74] for a p-type device). Moreover, it has been shown that the transport characteristics of “TiC” CNTFETs obtained with both random and self-assembly techniques are strongly dependent upon the temperature of the annealing process, with an optimum around 800 – 850 K [74, 127].

The results clearly indicate that the electrical performance of self-assembled CNTFETs is mainly determined by the nanotube/metal contact interfaces and by their response to the applied electric fields. This obviously suggests that after RTA, the use of a SAM technique to direct the assembly of the nanotube does not perturb the transport characteristics of such fabricated CNTFETs. It is worth noticing the importance of this result, which validates the self-assembly approaches for large-scale production of nanotube-based electronics. Moreover, it should also be noted that the SAM-based process discussed above is fully compatible with the realization of top-gate devices [140] and/or low thickness and high effective dielectric constant oxide films [141]. In conclusion, this self-assembly technique allows con-

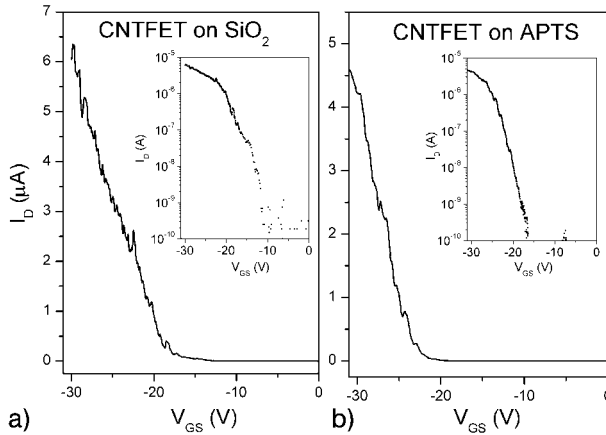


**Figure 9.11.** Transfer characteristics  $I_D(V_{GS})$  at  $V_{DS} = -1$  V of two CNTFETs with a gate oxide thickness of 200 nm. (a) CNTFET made by random deposition on  $\text{SiO}_2$ . (b) CNTFET made by the self-assembly technique. Insets show the same data in log-scale. (From Ref. [83].)

trolled and systematic fabrication of CNTFETs with performances reaching the actual state-of-the-art of CNTFETs as obtained by other techniques.

It should be also mentioned that the APTS monolayers are destroyed in the annealing process. Thus, it is still pertinent to question the role of the APTS monolayer on device characteristics when the RTA step is not performed, as it is the case of standard Ti/Au or Cr/Au electrodes. In order to elucidate this point, it is necessary to compare the performances of devices made by the APTS self-assembly technique (called CNTFETs on APTS) with those of CNTFETs made by random deposition (called CNTFETs on  $\text{SiO}_2$ ). A comparison is presented in Fig. 9.11, which shows the  $I_D(V_{GS})$  characteristics for the two kinds of devices. The measurements were performed at room temperature, in air, with the gate bias swept from the on- to the off-state [83]. We notice that their performances are very similar: on-state current up to around 5  $\mu\text{A}$ , on:off ratio of 4 orders of magnitude, transconductance of 0.4 – 0.5  $\mu\text{S}$  and subthreshold slope  $S = 2000 \pm 300$   $\text{mV dec}^{-1}$ . This means that, under typical atmospheric conditions, the performances are set by the quality of the contacts and the gate efficiency (set by the oxide thickness), independently of the placement technique. Note, finally, that the performances of the devices used in the comparative study shown in Fig. 9.11 are similar to the best performances of CNTFETs of comparable geometry reported in the literature and thus representative of the state-of-the-art of CNTFETs.

In conclusion, the chemical functionalization of  $\text{SiO}_2$  substrates by an APTS monolayer brings a relevant solution to the problems of (a) systematic placement of nanotubes in a transistor geometry and (ii) their subsequent connection to electrodes. Moreover, the use of the SAM deposition process not only does not deteriorate the device characteristics (as one may think), but it is also fully compatible

with the production of high-quality, state-of-the-art CNTFETs. Finally, more recent works have shown that it is possible to take even further advantage of the APTS monolayer to perform chemical optimization of CNTFETs [142]. Indeed, when compared to a CNTFET on SiO<sub>2</sub>, a CNTFET on APTS includes an additional, tunable, chemical interface (nanotube/APTS) to act onto.

In Sections 9.4 and 9.5 we have considered two approaches (CVD and SAMs) to perform selective placement of SWNTs. An important motivation was the development of a bottom-up technology for the implementation of nanodevices. However, standard top-down lithography techniques are still necessary in both two approaches. Indeed, even if the random deposition of nanotubes is avoided and large-scale fabrication can be envisaged, the patterns for the catalyst or for the APTS monolayer, as well as the electrodes, are realized by standard lithographic techniques. A real technological breakthrough in self-assembly would be to develop a complete molecular-scale bottom-up method. In this context, in the following section we discuss a promising technique based on the use of a DNA scaffold to realize nanoscale site-controlled implementation of nanocomponents.

## 9.6

### DNA-directed Self-assembly

Among the new methodologies based on bottom-up approaches for future nanotechnology, the exploration of bio-directed assembly for organizing nano-objects is one of the most promising. Indeed, the nanoscale is the natural scale on which biological systems build up their structural elements, and biological molecules have already shown great potential in the fabrication and construction of nanostructures and devices.

In this context, the DNA molecule is of particular interest, as highlighted by the increasing number of recent works devoted to the study of its physical properties and implementation in nanoelectronics. Indeed, the DNA molecule has already been successfully used to build up nanostructures [117, 143] or scaffolds for nanoparticle assembly [118–121]. Moreover, one can envisage its use for the assembly of devices. The key advantage in using DNA as a scaffold for these constructions is that its intra- and inter-molecular interactions are the most readily known, engineered and reliably predicted. The information contained in DNA sequences can be envisioned to code:

- The assembly of the scaffold.
- Its selective attachment on the surface microscale electrodes.
- The positioning of nano-objects or nanodevices on the scaffold.
- The realization of electrical connections and circuitry.

This idealized pathway to assemble circuit in two (or three)-dimensional geometry is very appealing, and, as we discuss in the following, some of the necessary steps have already been realized and reported in the literature, as well as a first mono-

device demonstrator [144]. In the following we discuss separately these four aspects of the use of DNA molecules for the realization of bio-assembled nanodevices and nanocircuits.

### 9.6.1

#### The Assembly of the Scaffold

In recent years, an increasing number of works have been devoted to the realization of nanostructured scaffolds with DNA molecules. The pioneering experiments concerned the assembly of sticky-ended linear DNA molecules [145]. Since then, a long way has been covered to evolve towards the vision, developed by Seeman and coworkers, of a construction with “smart bricks” made of DNA molecules. The main idea is based on the following simple scheme: the sticky ends of the envisaged DNA “smart bricks” would have the property to recognize each other and act as nanovelcro to realize the required assembly [146]. Obviously, such “smart bricks” must be more complex than linear DNA in order to realize a nanostructured two (or three)-dimensional scaffold. Therefore, in order to implement this scheme, synthetic molecules have been designed to produce branched motifs, taking inspiration from the natural phenomenon of reciprocal exchange crossover between DNA molecules [147]. Indeed, it is well known that natural DNA is not always in the linear configuration, but it passes, during its metabolism, through the configuration of an *unstable* branched molecule. The main idea of the method is to synthesize single-strand (ss) DNA molecules that self-assemble into *stable* macromolecular branched building blocks (called DNA tiles or “smart bricks”). Thus, the tip is to prepare synthetic oligonucleotides that break the homologous sequence symmetry of the natural branched molecules, avoiding in this way the instability due to the isomerization via branch migration [148]. Following this prin-

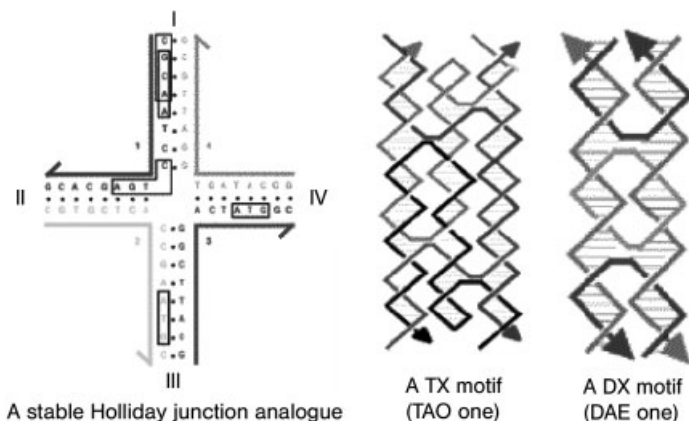


**Figure 9.12.** Schematic representations of various motifs constructed with DNA tiles: Holliday junction analogues, and DX and TX molecules. (From Ref. [148].)

ciple, various motifs have been fabricated, like Holliday junction analogues, double (DX) and triple (TX) crossover molecules, knots, and parallelograms (see Fig. 9.12).

The most interesting motifs in terms of scaffolds for nanotechnology purposes are those leading to a defined geometrical arrangement. In fact, simple branched junctions do not automatically lead to geometrical control [149, 150], essentially due to their lack of rigidity. The famous lattices reported by Seeman and coworkers rely on stiffer motifs, like the DX [151] or TX [152] tiles. More recent studies report the construction by biological recognition properties of a DNA-based nanostructure made of four four-arm junctions ( $4 \times 4$  tile, see Fig. 9.13) [153].

This programmed self-assembly gives rise to two distinct lattice morphologies: uniform-width nanoribbons and two-dimensional nanogrids that have been used to template protein and/or silver nanowires [153].

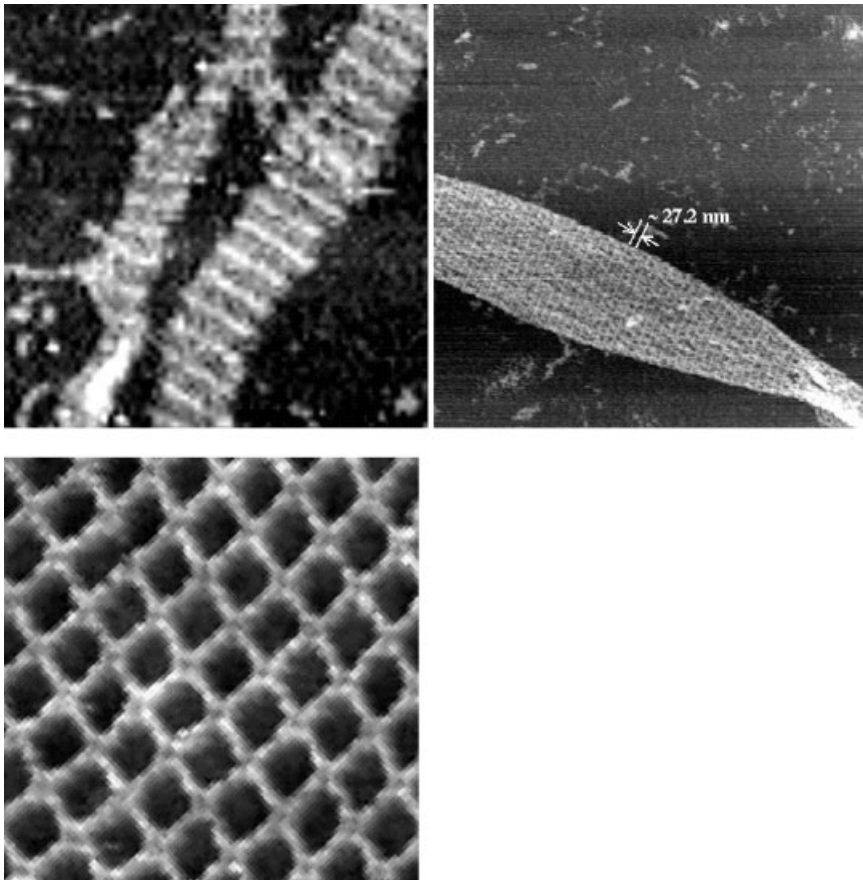


**Figure 9.13.** SEM and AFM images of different lattices constructed with DNA tiles. From left to right: (SEM image of) a DX, (SEM image of) TX and (AFM image of)  $4 \times 4$  lattices. (Adapted from Ref. [146].)

Another interesting approach has been developed by Bergstrom and coworkers, who used rigid tetrahedral linkers with arylethynylaryl spacers to direct the assembly of attached oligonucleotide linker arms into novel DNA macrocycles [154]. The main originality of this method consists in the use of rigid tetrahedral organic vertices and in the fact that a variable number of oligonucleotide arms serve as connectors for the design of more complex architectures.

### 9.6.2

#### Selective Attachment of the DNA Scaffold on the Surface Microscale Electrodes

Another important step in the pathway for the use of DNA-directed assembly of nanocircuits is the fixation/linkage of the DNA scaffolds on the substrate and its connection to external microelectrodes. The issue is to have some anchoring sticky-end points on the electrodes (or substrate) to selectively deposit the scaffold. In this context, the biochip community has made very strong efforts and different methods have been developed for DNA probe technology. The goal to achieve is to fix a specific sequence on each electrode of the chip. In present-day technology, the DNA probes are nearly always attached to inorganic substrates (silicon and glass are the most widely used) [155–157], while the presence of the electrodes is not always required. Nevertheless, the majority of the most advanced techniques proposed in the literature can be transposed to our electrode-specific linkage problem. The solutions that have been found are essentially of two types. The first is to label the surface with defined oligonucleotides sequences, by means of either (a) addressing by micro-nanospotting or (b) addressing assisted by an applied electric field. The second type of specific labeling is more exactly an *in situ* localized synthesis of the desired oligonucleotide sequence. These different techniques are briefly described below.

Historically, the micro-spotting technique was the first method developed. In this case, the immobilization is achieved passively either by covalent bonding or adsorption [158–161]. Nowadays, it is possible to find different variations of the same principle, like the robotic deposition on a prepared substrate [162] or the use of an ink-jet printer [161]. The more recent evolution of this technique is “dip-pen” nanolithography (DPN), which allows a lateral resolution of the order of 50 nm [163]. This technique is based on scanning probe technology, as described in the following. First, an AFM tip is “inked” with a solution of the material to be transferred to the surface. Then the AFM tip “writes” the desired pattern on the surface. However, although advances have been made by the introduction of parallel multipen approaches (by multicantilever AFM), this technique is still fundamentally slow and its throughput cannot compete with standard printing process.

Electrical addressing has also been intensively developed. As one example, Nanogen recently developed an electric-field-assisted DNA immobilization process [164], designed to give pixel-by-pixel selectivity. The Nanogen DNA chip (NanoChip™) uses affinity-based immobilization (noncovalent bonding of the capture probes to the surface). This technology uses the electrophoresis principle of migration of

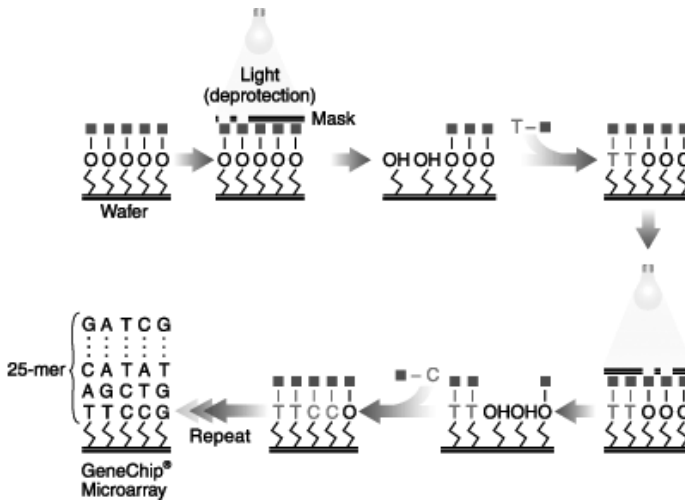


**Figure 9.14.** Schematic representation of the *in situ* oligonucleotides synthesis process using a light-directed method. Adapted from Ref. [167].

the negatively charged DNA molecule: "... when a biotinylated sample solution is introduced onto the array, the negatively charged sample moves to the selected positive electrode, where it is concentrated and bounds to the streptavidin in the permeation layer. The array is then washed and another sample can be added. In this way, site by site, an array of [oligonucleotides] samples is assembled on the [electrodes] array" [165]. A more advanced method of selective attachment of DNA strands to an electrode, also based on electrical addressing, consists of the successive (electrochemically addressed) copolymerization of 5' pyrrole-labeled oligonucleotide and pyrrole. By this method, each electrode is covered by a conducting polymer (polypyrrole) grafted by an oligonucleotide [166].

The second solution concerns the *in situ* synthesis of the oligonucleotide sequence on the electrodes, using a light-directed method. Affymetrix commercializes this kind of array and the fabrication process can be schematized as follows (see Fig. 9.14) [167, 168]. A solid support is derivatized with a covalent linker molecule terminated with a photolabile protecting group. Light is then directed through a mask to de-protect and activate selected sites, and protected nucleotides couple to the activated sites. The process is repeated, activating different sets of sites and coupling different bases, allowing arbitrary DNA probes to be constructed at each site.

### 9.6.3

#### Positioning of Nano-objects or Nanodevices on the Scaffold

In order to position nano-objects on the scaffold, it is necessary to master their linkage to a DNA strand and then use the DNA recognition properties to insert

them on the scaffold. The approach can differ depending on whether the nano-object is inserted during the construction of the scaffold or linked to it successively. In any case, the linkage of the nano-object to the DNA strand is a key step of the process. Many works have been reported aiming to develop methods for functionalizing small inorganic building blocks with DNA and then direct their assembly into extended structures by using the molecular recognition properties associated with DNA. So far, DNA has already been used to functionalize gold nanoparticles [120, 169–172], semiconductor quantum dots [173] and CNTs.

Concerning the chemical derivatization of CNTs, end chemistry of oxidatively etched nanotubes has been largely investigated [174–177]. This functionalization method was mostly used to improve nanotube solubility by reacting the nanotubes with hydrophilic dendra, alkyl chains or polymers. Nonetheless, it is still not clear if this strategy leads uniquely to functionalization of the defect sites of the oxidized ends of the nanotubes or also their side-wall surface. Indeed, the oxidation step performed during the usual purification process of the SWNTs produces such defects in relatively low amounts (estimated to about 2–3%) [178, 179], but they are not specifically localized only at the nanotube ends.

Currently, most of the work performed on nanotube functionalization is based on side-wall chemistry. Both covalent and noncovalent routes have been developed. A series of covalent side-wall functionalizations has been reported recently, including the reaction of nanotubes with nitrene, carbene and radical compounds. These methods should open routes to a wide variety of new nanotubes derivative [180–182]. In contrast, noncovalent routes have been mainly used to wrap nanotubes with polymer to enhance solubility and form composite materials [183–188]. An interesting study about solubilization of SWNTs by means of noncovalent chemistry (peptide wrapping) has been recently reported. In this work the authors first solubilize the nanotubes in aqueous solution by peptide wrapping [189] and then they increase the stability of such solution by crosslinking the wrapped peptides to each other [190].

Most results reported on CNT–DNA linkage also deal with covalent chemistry based on carboxylic acid defect groups present on SWNTs [191–195]. In 2002, a work reported the covalent coupling of peptide nucleic acid (PNA) rather than DNA [195]. The authors chose PNA as an intermediate for the covalent chemistry before hybridizing it with a DNA strand. The reason of this choice was the higher robustness of PNA to environmental conditions, as compared to other oligonucleotides. Nevertheless, in this report, as in each of the other described methods for covalent grafting of DNA onto nanotubes, an additional aggressive oxidation was performed in order to increase the defect density [192–195] and no indication was given on the yield of DNA–SWNT linkages. Moreover, the effect of introducing a large number of defects along the nanotubes is still not clearly known, but is believed to strongly affect their original (mainly  $sp^2$ ) structure and electronic properties. Recently, the same type of covalent chemistry between ssDNA and nanotubes (MWNTs and SWNTs) has been exploited to form multicomponent structures including 150-nm gold nanoparticles [196]. Finally, there is an interesting report about the binding of DNA to nanotubes by photochemistry [197]. In this work,



the covalent linkage is not performed on a carboxylic defect, but by using acid photochemistry and *in situ* DNA synthesis.

Different works have also been reported on the association of biological molecules (DNA and/or proteins) with nanotubes by means of noncovalent chemistry. A strong interaction of DNA with the nanotube surface has been suggested for MWNTs [198] and more recently a demonstration of wrapping of SWNTs by well-defined ssDNA molecules has been published [34]. The great advantage of a noncovalent method is its independence of the presence of the carboxylic groups, so that the DNA binding can also be successfully achieved for completely defect-free nanotubes.

In terms of noncovalent methods, the attachment of streptavidin protein [199] to the nanotube is of particular interest, as we will discuss below. Streptavidin is a relatively small protein (60 000 Da) composed of four identical subunits. The mechanism that binds streptavidin to a  $sp^2$  nanotube surface is probably related to hydrophobic interactions [199]. Indeed, this molecule is known to bind to hydrophobic surfaces [200]. The streptavidin protein is particularly well studied for its various biochemical applications because of its high affinity to biotin. Indeed, each of the streptavidin subunits has an active binding site for biotin molecules and the streptavidin–biotin system has one of the largest free energies of association yet observed for noncovalent binding of a protein and small ligand in aqueous solution ( $K_{\text{assoc}} = 10^{14} \text{ M}^{-1}$ ). Moreover, these complexes are also extremely stable over a wide range of temperature and pH. Correspondingly, the simple idea that has been followed for the DNA–nanotube attachment process is to react a biotinylated DNA strand with a streptavidin-coated nanotube (see scheme in Fig. 9.15). In other words, this technique uses noncovalent chemistry through a biological recognition complex (streptavidin–biotin) in order to link DNA and nanotubes [201, 202].

One great advantage of this method is related to the yield and the robustness of the reaction, while its main inconvenience is its lack of site specificity. However, it is worth pointing out that none of the methods reported above, particularly those based on covalent binding, is genuinely site specific. In fact, it would be extremely naïve to think that the carboxylic defects are present only at the ends of the nanotubes. On the contrary, it is more likely to think that the chemistry on a side-wall defect will be extremely favored with respect to a reaction at the ends, due to the nanotube's particular cylindrical shape and geometry factor (diameter versus length). In order to avoid this unspecific site chemistry and ensure the effective-

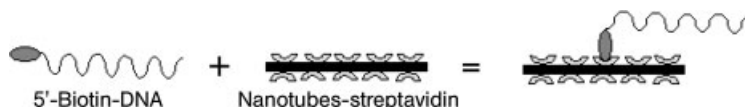


**Figure 9.15.** Schematic representation of the linking process between a biotinylated DNA strand with a streptavidin-coated nanotube.

ness of a covalent reaction on carboxylic defects only at the ends, Willner and co-workers [203] developed a method to mask the nanotube side-walls by a wrapping. In this work the authors succeeded in performing real end chemistry and they were able to link covalently the flavin adenine dinucleotide cofactor only to the nanotube ends. It is thought likely that such a method could be extended/adapted to perform covalent end chemistry between nanotubes and DNA strands in solution.

#### 9.6.4

#### **Realization of Electrical Connections and Circuitry**

So far we have discussed methods to construct and position nanotubes on a DNA scaffold opportunely linked on the substrate microelectrodes. However, an essential step for electronic purposes is the electrical connection of such nanotubes. This latter relies on the transport properties of DNA molecules and has recently generated heated debate among scientists, as evidence both for and against the hypothesis of DNA as a conducting wire has piled up. While no full consensus has been reached, we feel that the extensive transport measurements carried out on single DNA molecules and DNA bundles strongly suggests that DNA in the dry state deposited on a substrate is a good insulator and thus not useful as a conducting element. We believe that in spite of its somewhat negative sense, such a conclusive statement is of great importance in defining strategies for implementing DNA-based technology. Indeed, it now becomes clear that to achieve an electrical connection using DNA strands, it is necessary to proceed to their metallization. During the past 10 years we have seen the development of numerous methods to metalize DNA scaffolds and a recent review of these metalization processes can be found in Ref. [204]. In the following we summarize the main aspects and results concerning this topic.

The feasibility of this biotemplating approach was first shown by Braun and co-workers [205]. The authors first immobilized a DNA strand between two electrodes. Then, they treated it with silver ions in order to perform an  $\text{Ag}^+/\text{Na}^+$  ion exchange and replace the natural sodium counterions of the DNA backbone with silver ones. Successively, these silver ions were subjected to a chemical reduction process by the reducing agent hydroquinone to form small silver aggregates. Finally, the silver nanoclusters fixed on the DNA strand were autocatalytically grown (using an acidic solution of hydroquinone and silver ions) to give a granular (100 nm width) nanowire contacting the two electrodes. The majority of DNA metalization processes follow the same principle and can be decoupled in terms of successive steps, as schematically shown in Fig. 9.16 and discussed below.

The first step consists of biomolecule activation – the metal ions or metal complexes bind to DNA, creating reactive metal sites (Fig. 9.16a). The activation can take place by an ion-exchange mechanism (as discussed above for silver [205]) on the DNA backbone or by insertion of the metal complexes between the DNA bases (like platinum or palladium complexes [206]).

In the second step, the bound seeds are usually treated with a reducing agent

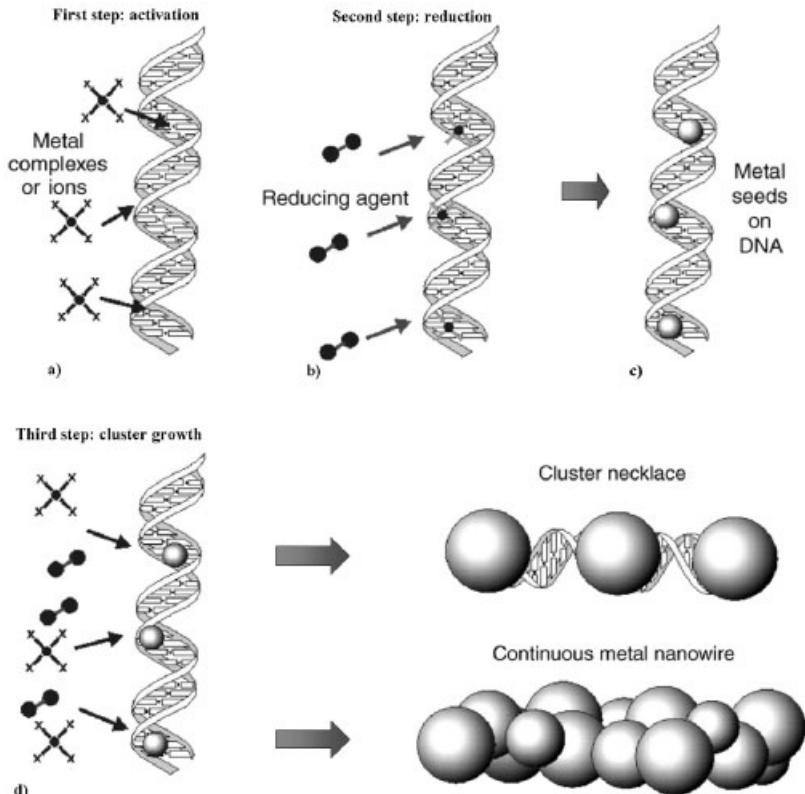


**Figure 9.16.** Schematic representation of the different steps involved in the DNA metallization process. (Adapted from Ref. [204].)

(Fig. 9.16b). This converts the metal ions or metal complexes in metal nanoclusters fixed on the DNA strand. The more often used reducing agents are dimethylaminoborane [207, 208], hydroquinone [205] and sodium borohydride [209]. An interesting variant has been proposed by Keren and coworkers [210, 211], who fixed the reducing agent (glutaraldehyde) directly to the DNA strand in order to enhance specificity and reduce parasitic unwanted background metalization. At the end of these two steps, the DNA strand has some small metal nanoclusters fixed on it (as represented in Fig. 9.16c), which will successively act as “seeds” for the metalization of the DNA molecules.

The third step of the metalization process consists of autocatalytic growth of the fixed metal seeds on the DNA strand (Fig. 9.16d) by the addition of new metal ions (or metal complexes solution) and new reducing agent solution. The idea of this autocatalytic process is that metal complexes or ions from solution are preferably reduced on already reduced metal nanoclusters (the seeds) fixed on the DNA strands. It should be noted that this autocatalytic cluster growth can be generalized

to metal nanoclusters fixed on DNA strands by any other method. Indeed, effective metalization has been reported on *ex situ* prepared gold nanoclusters fixed on the DNA strand by appropriate chemical functionalization [212], by DNA construction [213] or simply by electrostatic interactions [214].

As mentioned above, different metals have been used in the metalization process. For the ion-exchange mechanisms on the DNA backbone we can quote silver [153, 205] or copper [215]. The results are quite convincing for the silver process, where a silver wire is formed consisting of a chain of contiguous 30- to 50-nm silver grains along the DNA backbone. However, the electrical measurements performed on the obtained silver necklace wire were not completely satisfactory. In a following work, the same group improved the process by replacing the silver clusters growth with an electroless gold coating of the silver-loaded DNA molecules [210]. In this way, using silver ions as catalysts, conductive gold DNA-templated wires with widths ranging from 50 to 100 nm were obtained. This procedure can be generalized and the final metal coating does not necessarily have to use the same metal as the seeding one [209, 210, 216].

Concerning the intercalation mechanism of metal complexes between the DNA bases, palladium or platinum complexes have been the more extensively studied. Indeed, the binding process of Pt(II) complexes to DNA is well investigated in the case of cisplatin (*cis*-[Pt(NH<sub>3</sub>)<sub>2</sub>Cl<sub>2</sub>]), which is widely used as an anticancer drug [217]. It follows from these studies that when DNA is incubated with Pt(II) complexes such as cisplatin, the Pt(II) atom binds to one or two stacked DNA bases, forming monofunctional and bifunctional DNA–Pt(II) adducts, respectively. The most favorable binding site for cisplatin to the DNA is the N<sub>7</sub> position of guanine, followed by the N<sub>7</sub> position of adenine [217, 218]. Indeed, the bases A, G and C have exocyclic amine groups as well as ring amines, but it is the ring amines that act as Lewis bases. The Lewis base acidities differ from base to base, with the N<sub>7</sub> position of guanosine being the most basic. Other Lewis bases found in the nucleobases are N<sub>7</sub> of adenosine, N<sub>3</sub> of cytosine and the deprotonated N<sub>3</sub> of thymidine or uridine. The amines are all soft ligands and as such preferably complex to soft metals such as Pt(II), Pd(II) or Ru(II). When the DNA is in double-strand configuration, the arrangement of the basis is controlled by  $\pi$  stacking and then the Lewis base sites available for coordination to the metal (Pd, Pt, etc.) are limited to the exposed portion of the nucleobases found in the major groove (the N<sub>7</sub> position of guanosine and adenosine). It is commonly thought that, of these two sites, the N<sub>7</sub> of guanosine is the preferred one [219]. After these sites are occupied, the binding reaction proceeds more slowly and indiscriminately with other metal-binding sites of all bases [218–221]. Using this intercalation mechanism, palladium and platinum DNA-coated nanowires have been obtained. Generally speaking, these metalization processes of the DNA strands have been performed either (a) in solution and then the metalized DNA molecule is deposited on substrate for the characterization purpose or (b) on the DNA previously deposited on the substrate. The first case concerns the works reported by Ford and coworkers [209] and Mertig and coworkers [222], who showed the formation of tiny platinum nanocluster necklaces consisting of well-separated clusters of 3 – 5 nm diameter with a spacing from

one to several nanometers. On the contrary, Richter and coworkers [223], Deng and coworkers [224], Dupraz and coworkers [216] and Ongaro and coworkers [214] have metalized DNA strands already deposited on the substrate. In more detail, Richter and coworkers fabricated continuous palladium nanowires with average diameters of 60 – 100 nm on DNA strands aligned on interdigitated gold electrodes and obtained interesting transport properties. On the contrary, Deng and coworkers reported very granular 30-nm palladium nanowires without any data about their conduction properties [224]. Actually, both Dupraz and coworkers [216] and Ongaro and coworkers [214] started the metalization process in solution (seeds fixation), and successively stretched the metal-loaded DNA on the substrate. Then they completed the metalization process. They used, respectively, platinum and gold nanoparticles as catalytic seeds, but they both finished by a gold electroless plating process. They both obtained DNA-templated gold nanowires (average diameters about 20 – 50 nm) with estimated resistivities of between  $10^{-5}$  and  $10^{-4}$   $\Omega\text{m}$ .

However, among all the methods discussed above, only a few are really promising in nanocircuit applications. First, the more interesting procedure is the one where the DNA metalization occurs as one of the last steps. Indeed, after the metalization process all the recognition properties of the DNA molecule are completely lost, and the circuit architecture must be necessarily fixed and deposited on the substrate. Moreover, another important point is that some parts of the DNA scaffold must not be metalized to avoid shorts and preserve the device characteristics. In this sense, three convincing studies have been reported [210, 211, 213]. They are all based on the RecA protein properties. *In vivo*, the RecA protein is a central component in recombinational DNA repair pathways and homologous genetic recombination (in *Escherichia coli*). *In vitro*, RecA protein promotes the pairing and exchange of complementary DNA strands in reactions. The mechanism is as follows: RecA catalyzes the pairing of ssDNA with complementary regions of double-stranded (ds) DNA. The RecA monomers first polymerize to form a helical filament around ssDNA (Fig. 9.17a). Duplex DNA is then bound to the polymer (see Fig. 9.17b).

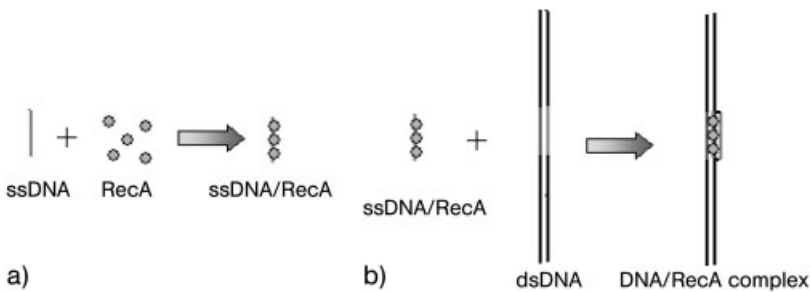


**Figure 9.17.** Schematic representation of the homologous recombination process that leads to binding of the ssDNA–RecA nucleoprotein filament at the complementary address on the dsDNA.

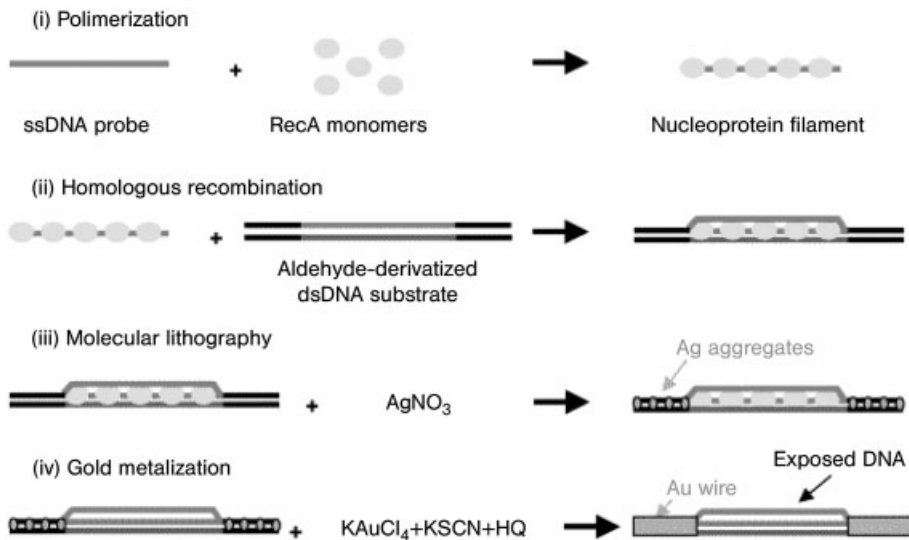


**Figure 9.18.** Mechanism of the sequence-selective metallization process. Thanks to the homologous recombination, the RecA protein acts as a sequence-specific resists for the creation of the silver seeds and successive gold metallization. (From Ref. [210].)

This particular feature has been used to differentiate a part of the sequence of the DNA strand in the metallization process. Indeed, it is clear that the targeted sequence is perfectly identified by the RecA polymerized ssDNA. The idea exploited is that the creation of the complex between the RecA–ssDNA polymer and the complementary regions of dsDNA acts as a mask for the metallization process. In the first report on sequence-specific metallization [210] it is shown that this complex avoids the Ag<sup>+</sup>/Na<sup>+</sup> ion exchange. This blocks the formation of the silver seeds on the targeted sequence of the DNA molecule and, consequently, the successive gold metallization (see Fig. 9.18).

In a successive work [211], the same team showed that sequence-specific lithography can also be achieved by sequence-specific patterning of the local reducing agent (glutaraldehyde). This patterning was performed both by hybridization between aldehyde-derivatized and underivatized DNA molecules and by sequence-specific protection against aldehyde derivatization using homologous recombination processes by the RecA protein. Then, the sequence-specific patterning of the reducing agent is reflected by the sequence-specific creation of silver metallization seeds and successive gold metallization.

The more recent report on selective metallization also uses the homologous recombination properties of the RecA protein and its originality is to employ a modified RecA to act as a “linking factor” for sequence-specific fixation of gold nanoparticles [213]. Then, these gold nanoparticles are used as “seeds” for the

metalization process. To be more specific, the authors use a genetically engineered cysteine derivative RecA protein (Cys-RecA) and, thanks to this derivatization, the gold nanoparticles can be fixed to the Cys-RecA–DNA filament. However, the gold nanoparticles are not fixed on unmodified RecA filament. Therefore, the strategy they developed to achieve selective metalization is to use separately cysteine derivatized RecA and unmodified wild-type RecA (RecA) to complex different sequences of the DNA strand. Then, the fixation of the gold nanoparticles respects the targeted sequences Cys-RecA–DNA and RecA–DNA, and the successive metalization presents a sequence specific gap corresponding to the unmodified RecA–DNA complex.

### 9.6.5

#### Fabrication of DNA-directed CNT Devices

Among the studies that use DNA to fabricate CNT devices [144, 225–227], the most impressive one is the report on the DNA templating of a CNTFET [144]. Indeed, in this work some of the crucial ingredients of the vision discussed in Section 9.6 were tackled and demonstrated, even if in a simple linear back-gate geometry. The authors employed (a) a selective placement of the nanotube on the DNA scaffold and (b) a sequence-selective metalization of the DNA strands. In this way, they were able to realize the electrical connection between the standard (lithographically defined) electrodes and the nanotube device. In both tasks (a) and (b) they exploited the sequence-specific homologous recombination of the RecA protein. They first anchored the SWNT in the desired part of the DNA scaffold and then, after deposition on a substrate, proceeded to the selective metalization process. The SWNT–DNA linkage was performed in buffered solution by the molecular recognition of a streptavidin-functionalized SWNT towards biotin and by the antibodies properties to link the biotin to the RecA–DNA filament, as schematized in Fig. 9.19.

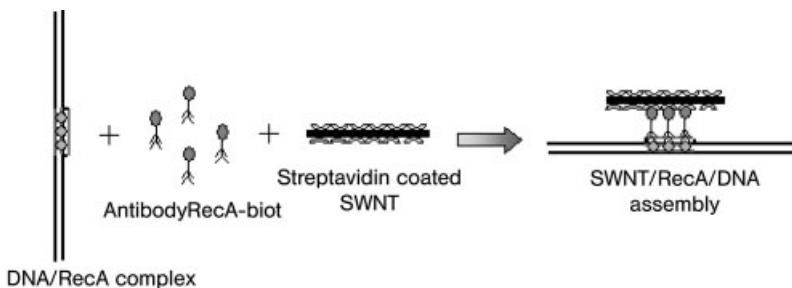


**Figure 9.19.** Schematic representation of the sequence-specific binding of a streptavidin-coated SWNT. The homologous recombination process of RecA is used to target the binding site. The streptavidin-coated nanotube is fixed

to the DNA-bound RecA by using a complex antibodyRecA–biotin (a primary antibody to RecA and a biotin-conjugated secondary antibody).

Then, to fabricate the nanotube device, they stretched the SWNT–RecA–DNA assembly on a silicon substrate and performed the selective Ag/Au metalization process as described in Ref. [210]. One of the interesting features of this experiment is that, even in this more complicated configuration (i.e. presence of the SWNT, streptavidin, biotin and antibodies species), the masking properties of the RecA are preserved and the “protected” segment of the DNA strand is not metalized. Finally, the DNA-templated gold wires were connected by fabricating standard lithography electrodes and the device characteristics were recorded.

However, even if all the steps for DNA-directed self-assembly of a CNT device have been demonstrated and reported in literature, it should be noted that it is still missing a study where all these steps are combined. Indeed, in the work of Keren and coworkers [144] there is no selective attachment to the microscale electrodes. This implies that in order to fabricate these electrodes, the deposited SWNT–RecA–DNA strand must be localized by imaging, as for nanotube devices obtained by random deposition. On the contrary, in the report of Hazani and coworkers [226, 227], the SWNT–DNA complex is fixed to the electrodes by DNA hybridization, but no selective metalization is performed. In this case, it is likely that the contact between the nanotube and the electrodes is ensured by the fact that the DNA strands used are very short and the nanotube touches the metal anyway.

In conclusion, the demonstration of a completely DNA-directed self-assembled CNT device is, at the time of writing, still to be shown, as well as the realization of a more structured scaffold hosting more than one nanotube device in a circuit configuration. The knowledge and mastery of the different steps needed for the implementation of such a demonstrator have already been reported in literature, and it is now a matter of multidisciplinary will and teams to accomplish the task. Finally, for such a still open and exploratory research domain, new findings are expected to further enlarge the present vision and generate novel strategies for the short- to medium-term development of nanoelectronics.

## 9.7

### Conclusion

In this chapter we have presented a review on the self-assembly techniques for fabrication of CNT devices. First, we discussed their main physical features and sketched a few reasons why CNTs benefit from their present status as a serious potential candidate for future nanoelectronic applications. Then, we focused our attention on three methods to manipulate them by self-assembly. Indeed, this promising material could be envisaged to take part in the future nanoelectronic framework only if a cheap, massive parallel technology for fabricating nanotube devices is developed. The timing of this kind of research is particularly appropriate, as it results from an estimation of the ITRS roadmap [1]. From the analysis of this document it appears that, even if the scaling of CMOS device structures is a well-explored science, its limits will be reached in the near future due to various physical effects that do not scale properly, including quantum mechanical tunneling, the



discreteness of dopants, voltage-related effects such as subthreshold swing, fabrication costs and reliability related to very small size variation, built-in voltage and minimum logic voltage swing, and application-dependent power-dissipation limits. Self-assembly of new and interesting materials could bring some answers to these limitations. Indeed, it is extremely naïve to think that a non-CMOS device (based on nanotubes, molecules or other) that simply mimics a CMOS device can solve this scaling limit only because of its reduced size. Among the various issues that CMOS technology is facing, the power dissipation effect is the most serious one and it can actually apply also for any non-CMOS device. Based on this assumption, the study and implementation of non-CMOS devices cannot be motivated only by the scaling issue, but must present other kind of advantages like (a) performing a particular functionality not well covered by standard CMOS technology, (b) be economically very appealing with important reductions of fabrication costs, (c) really introduce a disruptive technology by presenting new physical effects or (d) be prone to the development of new architecture paradigms, which could include concepts like three-dimensional design, defect/fault tolerances, reconfigurability, self-repairing features and massive parallel processing. This is a strong reason to increase the investments in time and resources in studying alternative strategies like self-assembly and, in particular, bio-inspired technologies.

## References

- 1 The Internet Technology Roadmap for Semiconductors (ITRS) is available at <http://public.itrs.net.http://www.itrs.net>.
- 2 European Commission IST Programme Future and Emerging Technologies – Microelectronics Advanced Research Initiative – MELARI NANO. *Technology Roadmap for Nanoelectronics*, 1999. Available at <ftp://ftp.cordis.lu/pub/esprit/docs/melnarm.pdf>.
- 3 IIJIMA S. Helical microtubules of graphitic carbon, *Nature* **1991**, 354, 56–58.
- 4 SAITO R., DRESSELHAUS G., DRESSELHAUS M. S. *Physical Properties of Carbon Nanotubes*. Imperial College Press, London, 1998.
- 5 SAITO R., DRESSELHAUS G., DRESSELHAUS M. S. Electronic structure of double-layer graphene tubules, *J. Appl. Phys.* **1993**, 73, 494–500.
- 6 REICH S., THOMSEN C., ORDEJON P. Elastic properties of carbon nanotubes under hydrostatic pressure, *Phys. Rev. B* **2002**, 65, 153407.
- 7 NATSUKI T., TANTRAKARN K., ENDO M. Prediction of elastic properties for single-walled carbon nanotubes, *Carbon* **2004**, 42, 39–45.
- 8 LU J. P. Elastic properties of carbon nanotubes and nanoropes, *Phys. Rev. Lett.* **1997**, 79, 1297–1300.
- 9 TREACY M. M. J., EBBESEN T. W., GIBSON J. M. Exceptionally high Young's modulus observed for individual carbon nanotubes, *Nature* **1996**, 381, 678–680.
- 10 KRISHNAN A., DUJARDIN E., EBBESEN T. W., YANILOS P. N., TREACY M. M. J. Young's modulus of single-walled nanotubes, *Phys. Rev. B* **1998**, 58, 14013–14019.
- 11 DEMCZYK B. G., WANG Y. M., CUMINGS J., HETMAN M., HAN W., ZETTL A., RITCHIE R. O. Direct mechanical measurement of the tensile strength and elastic modulus of multiwalled carbon nanotubes, *Mater. Sci. Eng.* **2002**, A334, 173–178.

- 12 CADEK M., COLEMAN J. N., BARRON V., HEDICKE K., BLAU W. J. Morphological and mechanical properties of carbon-nanotube-reinforced semicrystalline and amorphous polymer composites, *Appl. Phys. Lett.* **2002**, *81*, 5123–5125.
- 13 EBBESEN T. W., AJAYAN P. M. Large-scale synthesis of carbon nanotubes, *Nature* **1992**, *358*, 220–222.
- 14 IJIMA S., ICHIHASHI T. Single-shell carbon nanotubes of 1-nm diameter, *Nature* **1993**, *363*, 603–605.
- 15 BETHUNE D. S., KIANG C. H., DE VRIES M. S., GORMAN G., SAVOY R., VASQUEZ J., BEYERS R. Cobalt-catalysed growth of carbon nanotubes with single-atomic-layer walls, *Nature* **1993**, *363*, 605–607.
- 16 KIANG C. H., GODDARD III W. A., BEYERS R., BETHUNE D. S. Carbon nanotubes with single-layer walls, *Carbon* **1995**, *33*, 903–914.
- 17 MASER W. K., LAMBERT J. M., AJAYAN P. M., STEPHAN O., BERNIER P. Role of Y-Ni-B mixtures in the formation of carbon nanotubes and encapsulation into carbon clusters, *Synthetic Metals* **1996**, *77*, 243–247.
- 18 JOURNET C., BERNIER P. Production of carbon nanotubes, *Appl. Phys. A* **1998**, *67*, 1–9.
- 19 THESS A., LEE R., NIKOLAEV P., DAI H. J., PETIT P., ROBERT J., XU C. H., LEE Y. H., KIM S. G., RINZLER A. G., COLBERT D. T., SCUSERIA G. E., TOMANEK D., FISHER J. E., SMALLEY R. E. Crystalline ropes of metallic carbon nanotubes, *Science* **1996**, *273*, 483–487.
- 20 GUO T., NIKOLAEV P., THESS A., COLBERT D. T., SMALLEY R. E. Catalytic growth of single-walled nanotubes by laser vaporization, *Chem. Phys. Lett.* **1995**, *243*, 49–54.
- 21 MASER W. K., BENITO A. M., MARTINEZ M. T., DE LA FUENTE G. F., MANIETTE Y., ANGLARET E., SAUVAJOL J. L. Production of high-density single-walled nanotube material by a simple laser-ablation method, *Chem. Phys. Lett.* **1998**, *292*, 587–593.
- 22 JOSÉ-YACAMAN M., YOSHIDA M. M., RENDON L., SANTIESTEBAN J. G. Catalytic growth of carbon microtubules with fullerene structure, *Appl. Phys. Lett.* **1993**, *62*, 657–659.
- 23 ENDO M., TAKEUCHI K., IGARASHI S., KOBORI K., SHIRAISHI M., KROTO H. W. The production and structure of pyrolytic carbon nanotubes (PCNTs), *J. Phys. Chem. Solids* **1993**, *1841*–1848.
- 24 IVANOV V., NAGY J. B., LAMBIN P., ZHANG X. B., ZHANG X. F., BERNAERTS D., VANTENDELOO G., AMELINCKX S., VANLANDUYT J. The study of carbon nanotubules produced by catalytic method, *Chem. Phys. Lett.* **1994**, *223*, 329–335.
- 25 FONSECA A., HERNARDI K., PIEDIGROSSO P., COLOMER J. F., MUKHOPADHYAY K., DOOME R., LAZARESCU S., BIRO L. P., LAMBIN P., THIRY P. A., BERNAERTS D., NAGY J. B. Synthesis of single- and multi-wall carbon nanotubes over supported catalysts, *Appl. Phys. A* **1998**, *67*, 11–22.
- 26 KONG J., CASSEL A. M., DAI H. Chemical vapor deposition of methane for single-walled carbon nanotubes, *Chem. Phys. Lett.* **1998**, *292*, 567–574.
- 27 ZHU H. W., XU C. L., WU D. H., WEI B. Q., VAJTAI R., AJAYAN P. M. Direct synthesis of long single-walled carbon nanotube strands, *Science* **2002**, *296*, 884–886.
- 28 ZHENG L., O'CONNEL M., DOORN S., LIAO X., ZHAO Y., AKHADOV E., HOFFBAUER M., ROOP B., JIA Q., DYE R., PETERSON D., HUANG S., LIU J., ZHU Y. Ultralong single-wall carbon nanotubes, *Nat. Mater.* **2004**, *3*, 673–676.
- 29 URAL A., LI Y., DAI H. Electric-field-aligned growth of single-walled carbon nanotubes on surfaces, *Appl. Phys. Lett.* **2002**, *81*, 3464–3466.
- 30 JAVEY A., WANG Q., URAL A., LI Y., DAI H. Carbon nanotube transistor arrays for multistage complementary logic and ring oscillators, *Nano Lett.* **2002**, *2*, 929–932.
- 31 JOST O., GORBUNOV A. A., MÖLLER J., POMPE W., LIU X., GEORGI P., DUNSCH L., GOLDEN M. S., FINK J. Rate-limiting processes in the forma-

- tion of single-wall carbon nanotubes: pointing the way to the nanotube formation mechanism, *J. Phys. Chem. B* **2002**, *106*, 2875–2883.
- 32 JOST O., GORBUNOV A., LIU X. J., POMPE W., FINK J. Single-walled carbon nanotube diameter, *J. Nanosci. Nanotechnol.* **2004**, *4*, 433–440.
  - 33 LI Y., MANN D., ROLANDI M., KIM W., URAL A., HUNG S., JAVEY A., CAO J., WANG D., YENILMEZ E., WANG Q., GIBBONS J. F., NISHI Y., DAI H. Preferential growth of semiconducting single-walled carbon nanotubes by a plasma enhanced CVD method, *Nano Lett.* **2004**, *4*, 317–321.
  - 34 ZHENG M., JAGOTA A., SEMKE E. D., DINER B. A., MCLEAN R. S., LUSTIG S. R., RICHARDSON R. E., TASSI N. G. DNA-assisted dispersion and separation of carbon nanotubes, *Nat. Mater.* **2003**, *2*, 338–342.
  - 35 BAUGHMAN R. H., ZAKHIDOV A. A., DE HEER W. A. Carbon nanotubes – the route toward applications, *Science* **2002**, *297*, 787–792.
  - 36 DEHEER W. A., CHATELAIN A., UGARTE D. A carbon nanotube field-emission electron source, *Science* **1995**, *270*, 1179–1180.
  - 37 DE JONGE N., BONARD J. M. Carbon nanotube electron sources and applications, *Philos. Trans. Royal Soc. London A* **2004**, *362*, 2239–2266.
  - 38 BONARD J. M., CROCI M., KLINKE C., KURT R., NOURY O., WEISS N. Carbon nanotube films as electron field emitters, *Carbon* **2002**, *40*, 1715–1728.
  - 39 MILNE W. I., TEO K. B. K., AMARATUNGA G. A. J., LEGAGNEUX P., GANGLOFF L., SCHNELL J. P., SEMET V., BINH V. T., GROENING O. Carbon nanotubes as field emission sources, *J. Mater. Chem.* **2004**, *14*, 933–943.
  - 40 BONARD J. M., STOCKLI T., NOURY O., CHATELAIN A. Field emission from cylindrical carbon nanotube cathodes: possibilities for luminescent tubes, *Appl. Phys. Lett.* **2001**, *78*, 2775–2777.
  - 41 CHOI Y. S., CHO Y. S., KANG J. H., KIM Y. J., KIM I. H., PARK S. H., LEE H. W., HWANG S. Y., LEE S. J., LEE C. G., OH T. S., CHOI J. S., KANG S. K., KIM J. M. A field-emission display with a self-focus cathode electrode, *Appl. Phys. Lett.* **2003**, *82*, 3565–3567.
  - 42 KIM I. H., KIM J. H., KIM K. B. Electrochemical characterization of electrochemically prepared ruthenium oxide/carbon nanotube electrode for supercapacitor application, *Electrochem. Solid State Lett.* **2005**, *8*, A369–A372.
  - 43 LEE C. Y., TSAI H. M., CHUANG H. J., LI S. Y., LIN P., TSENG T. Y. Characteristics and electrochemical performances of supercapacitors with manganese oxide–carbon nanotube nanocomposites electrodes, *J. Electrochem. Soc.* **2005**, *152*, A716–A720.
  - 44 SNOW E. S., PERKINS F. K., HOUSER E. J., BADESCU S. C., REINECKE T. L. Chemical detection with a single-walled carbon nanotube capacitor, *Science* **2005**, *307*, 1942–1945.
  - 45 BAUGHMAN R. H., CUI C., ZAKHIDOV A. A., IQBAL Z., BARISCI J. N., SPINKS G. M., WALLACE G. G., MAZZOLDI A., DE ROSSI D., RINZLER A. G., JASCHINSKI O., ROTH S., KERTESZ M. Carbon nanotube actuators, *Science* **1999**, *284*, 1340–1344.
  - 46 VOHRER U., KOLARIC I., HAQUE M. H., ROTH S., DETLAFF-WEGLIKOWSKA U. Carbon nanotube sheets for the use as artificial muscles, *Carbon* **2004**, *42*, 1159–1164.
  - 47 LANDI B. J., RAFFAELLE R. P., HEBEN M. J., ALLEMAN J. L., VANDERVEER W., GENNETT T. Single wall carbon nanotube–Nafion composite actuators, *Nano Lett.* **2002**, *2*, 1329–1332.
  - 48 CAO J., WANG Q., DAI H. Electro-mechanical properties of metallic, quasimetallic, and semiconducting carbon nanotubes under stretching, *Phys. Rev. Lett.* **2003**, *90*, 157601.
  - 49 SAPMAZ S., BLANTER Y. M., GUREVICH L., VAN DER ZANT H. S. J. Carbon nanotubes as nanoelectromechanical systems, *Phys. Rev. B* **2003**, *67*, 235414.
  - 50 BOURLON B., GIATTLI D. C., MIKO C., FORRO L., BACHTOLD A. Carbon nanotube based bearing for rotational motions, *Nano Lett.* **2004**, *4*, 709–712.

- 51 LI C., CHOU T.-W. Single-walled carbon nanotubes as ultrahigh frequency nanomechanical resonators, *Phys. Rev. B* **2003**, *68*, 073405.
- 52 LEE S. W., LEE D. S., MORJAN R. E., JHANG S. H., SVENINGSSON M., NERUSHEV O. A., PARK Y. W., CAMPBELL E. E. B. A three-terminal carbon nanorelay, *Nano Lett.* **2004**, *4*, 2027–2030.
- 53 CHA S. N., JANG J. E., CHOI Y., AMARATUNGA G. A. J., KANG D.-J., HASKO D. G., JUNG J. E., KIM J. M. Fabrication of a nanoelectromechanical switch using a suspended carbon nanotube, *Appl. Phys. Lett.* **2005**, *86*, 083105.
- 54 AHIR S. V., TERENTJEV E. M. Photo-mechanical actuation in polymer–nanotube composites, *Nat. Mater.* **2005**, *4*, 491–495.
- 55 PANTAROTTO D., BRIAND J. P., PRATO M., BIANCO A. Translocation of bioactive peptides across cell membranes by carbon nanotubes, *Chem. Commun.* **2004**, 16–17.
- 56 KOSTARELOS K., LACERDA L., PARTIDOS C. D., PRATO M., BIANCO A. Carbon nanotube-mediated delivery of peptides and genes to the cells: translating nanobiotechnology to therapeutics, *J. Drug Deliv. Sci. Technol.* **2005**, *15*, 41–47.
- 57 SALVETAT J. P., BRIGGS G. A. D., BONARD J. M., BACSA R. R., KULIK A. J., STOCKLI T., BURNHAM N. A., FORRO L. Elastic and shear moduli of single-walled carbon nanotube ropes, *Phys. Rev. Lett.* **1999**, *82*, 944–947.
- 58 DALTON A. B., COLLINS S., MUNOZ E., RAZAL J. M., EBRON V. H., FERRARIS J. P., COLEMAN J. N., KIM B. G., BAUGHMAN R. H. Super-tough carbon-nanotube fibres – these extraordinary composite fibres can be woven into electronic textiles, *Nature* **2003**, *423*, 703–703.
- 59 LI X. D., GAO H. S., SCRIVENS W. A., FEI D. L., XU X. Y., SUTTON M. A., REYNOLDS A. P., MYRICK M. L. Nanomechanical characterization of single-walled carbon nanotube reinforced epoxy composites, *Nanotechnology* **2004**, *15*, 1416–1423.
- 60 CHA S. I., KIM K. T., ARSHAD S. N., MO C. B., HONG S. H. Extraordinary strengthening effect of carbon nanotubes in metal–matrix nanocomposites processed by molecular-level mixing, *Adv. Mater.* **2005**, *17*, 1377–1381.
- 61 QIAN D., DICKEY E. C., ANDREWS R., RANTELL T. Load transfer and deformation mechanisms in carbon nanotube–polystyrene composites, *Appl. Phys. Lett.* **2000**, *76*, 2868–2870.
- 62 BLANCHET G. B., SUBRAMONEY S., BAILEY R. K., JAYCOX G. D., NUCKOLLS C. Self-assembled three-dimensional conducting network of single-wall carbon nanotubes, *Appl. Phys. Lett.* **2004**, *85*, 828–830.
- 63 WU Z. C., CHEN Z. H., DU X., LOGAN J. M., SIPPEL J., NIKOLOU M., KAMARAS K., REYNOLDS J. R., TANNER D. B., HEBARD A. F., RINZLER A. G. Transparent, conductive carbon nanotube films, *Science* **2004**, *305*, 1273–1276.
- 64 SAKAKIBARA Y., ROZHIN A. G., KATAURA H., ACHIBA Y., TOKUMOTO M. Carbon nanotube–poly(vinylalcohol) nanocomposite film devices: applications for femtosecond fiber laser mode lockers and optical amplifier noise suppressors, *Jpn. J. Appl. Phys. 1* **2005**, *44*, 1621–1625.
- 65 AVOURIS Ph., APPENZELLER J., MARTEL R., WIND S. J. Carbon nanotube electronics, *Proc. IEEE* **2003**, *91*, 1772–1784.
- 66 LEE H. W., KIM S. H., KWAK Y. K., HAN C. S. Nanoscale fabrication of a single multiwalled carbon nanotube attached atomic force microscope tip using an electric field, *Rev. Sci. Instrum.* **2005**, *76*, 046108.
- 67 CHEN L. W., CHEUNG C. L., ASHBY P. D., LIEBER C. M. Single-walled carbon nanotube AFM probes: optimal imaging resolution of nanoclusters and biomolecules in ambient and fluid environments, *Nano Lett.* **2004**, *4*, 1725–1731.
- 68 NGUYEN C. V., CHAO K. J., STEVENS R. M. D., DELZEIT L., CASSELL A., HAN J., MEYAPPAN M. Carbon nanotube tip probes: stability and lateral resolu-

- tion in scanning probe microscopy and application to surface science in semiconductors, *Nanotechnology* **2001**, *12*, 363–367.
- 69 TANS S. J., VERSCHUEREN A. R. M., DEKKER C. Room-temperature transistor based on a single carbon nanotube, *Nature* **1998**, *393*, 49–52.
- 70 MARTEL R., SCHMIDT T., SHEA H. R., HERTEL T., AVOURIS Ph. Single- and multi-wall carbon nanotube field-effect transistors, *Appl. Phys. Lett.* **1998**, *73*, 2447–2449.
- 71 POSTMA H. W. Ch., TEEPEN T., YAO Z., GRIFONI M., DEKKER C. Carbon nanotube single-electron transistors at room temperature, *Science* **2001**, *293*, 76–79.
- 72 BACHTOLD A., HADLEY P., NAKANISHI T., DEKKER C. Logic circuits with carbon nanotube transistors, *Science* **2001**, *294*, 1317–1320.
- 73 DERYCKE V., MARTEL R., APPENZELLER J., AVOURIS Ph. Carbon nanotube inter- and intramolecular logic gates, *Nano Lett.* **2001**, *1*, 453–456.
- 74 MARTEL R., DERYCKE V., LAVOIE C., APPENZELLER J., CHAN K. K., TERSOFF J., AVOURIS Ph. Ambipolar electrical transport in semiconducting single-wall carbon nanotubes, *Phys. Rev. Lett.* **2001**, *87*, 256805.
- 75 FREITAG M., RADOSAVLJEVIC M., ZHOU Y., JOHNSON A. T., SMITH W. F. Controlled creation of a carbon nanotube diode by a scanned gate, *Appl. Phys. Lett.* **2001**, *79*, 3326–3328.
- 76 DERYCKE V., MARTEL R., APPENZELLER J., AVOURIS Ph. Controlling doping and carrier injection in carbon nanotube transistors, *Appl. Phys. Lett.* **2002**, *80*, 2773–2775.
- 77 APPENZELLER J., KNOCK J., DERYCKE V., MARTEL R., WIND S. J., AVOURIS Ph. Field-modulated carrier transport in carbon nanotube transistors, *Phys. Rev. Lett.* **2002**, *89*, 126801.
- 78 CUI X., FREITAG M., MARTEL R., BRUS L., AVOURIS Ph. Controlling energy-level alignments at carbon nanotube/Au contacts, *Nano Lett.* **2003**, *3*, 783–787.
- 79 APPENZELLER J., RADOSAVLJEVIC M., KNOCK J., AVOURIS Ph. Tunneling versus thermionic emission in one-dimensional semiconductors, *Phys. Rev. Lett.* **2004**, *92*, 048301.
- 80 HEINZE S., TERSOFF J., MARTEL R., DERYCKE V., APPENZELLER J., AVOURIS Ph. Carbon nanotubes as schottky barrier transistors, *Phys. Rev. Lett.* **2002**, *89*, 106801.
- 81 NAKANISHI T., BACHTOLD A., DEKKER C. Transport through the interface between a semiconducting carbon nanotube and a metal electrode, *Phys. Rev. B* **2002**, *66*, 073307.
- 82 GUO J., DAITA S., LUNDSTROM M. A numerical study of scaling issues for Schottky-barrier carbon nanotube transistors, *IEEE Trans. Electron. Devices* **2004**, *51*, 172–177.
- 83 AUVRAY S., BORGHETTI J., GOFFMAN M. F., FILORAMO A., DERYCKE V., BOURGOIN J. P., JOST O. Carbon nanotube transistor optimization by chemical control of the nanotube–metal interface, *Appl. Phys. Lett.* **2004**, *84*, 5106–5108.
- 84 JAVEY A., GUO J., WANG Q., LUNDSTROM M., DAI H. J. Ballistic carbon nanotube field-effect transistors, *Nature* **2003**, *424*, 654–657.
- 85 JAVEY A., GUO J., FARMER D. B., WANG Q., WANG D. W., GORDON R. G., LUNDSTROM M., DAI H. J. Carbon nanotube field-effect transistors with integrated ohmic contacts and high- $\kappa$  gate dielectrics, *Nano Lett.* **2004**, *4*, 447–450.
- 86 KONG J., FRANKLIN N. R., ZHOU C. W., CHAPLINE M. G., PENG S., CHO K. J., DAI H. J. Nanotube molecular wires as chemical sensors, *Science* **2000**, *287*, 622–625.
- 87 ADU C. K. W., SUMANASEKERA G. U., PRADHAN B. K., ROMERO H. E., EKLUND P. C. Carbon nanotubes: a thermoelectric nano-nose, *Chem. Phys. Lett.* **2001**, *337*, 31–35.
- 88 KOJIMA A., HYON C. K., KANIMURA T., MAEDA M., MATSUMOTO K. Protein sensor using carbon nanotube field effect transistor, *Jpn. J. Appl. Phys. Part 1* **2005**, *44*, 1596–1598.
- 89 STAR A., GABRIEL J. C. P., BRADLEY K., GRUNNER G. Electronic detection of specific protein binding using nano-

- tube FET devices, *Nano Lett.* **2003**, *3*, 459–463.
- 90 BESTEMAN K., LEE J.-O., WIERTZ F. G. M., HEERING H. A., DEKKER C. Enzyme-coated carbon nanotubes as single-molecule biosensors, *Nano Lett.* **2003**, *3*, 727–770.
- 91 STAR A., HAN T. R., GABRIEL J. C. P., BRADLEY K., GRUNNER G. Interaction of aromatic compounds with carbon nanotubes: correlation to the hammett parameter of the substituent and measured carbon nanotube FET response, *Nano Lett.* **2003**, *3*, 1421–1423.
- 92 STAR A., HAN T. R., JOSHI V., STETTER J. R. Sensing with nafion coated carbon nanotube field effect transistors, *Electroanalysis* **2004**, *16*, 108–112.
- 93 MAHASHI K., MATSUMOTO K., KERMAN K., TAKAMURA Y., TAMIYA E. Ultrasensitive detection of DNA hybridization using carbon nanotube field-effect transistors, *Jpn. J. Appl. Phys.* **2004**, *43*, L1558–L1560.
- 94 CABELL J. K., SUN L., CROOKS R. M. Electrochemistry using single wall nanotubes, *J. Am. Chem. Soc.* **1999**, *121*, 3779–3780.
- 95 BRITTO P. J., SANTHANAM K. S. V., AJAYAN P. M. Carbon nanotube electrode for oxidation of dopamine, *Bioelectrochem. Bioenerg.* **1996**, *41*, 121–125.
- 96 LUO H., SHI Z., LI N., GU Z., ZHUANG Q. Investigation of the electrochemical and electrocatalytic behavior of single-wall carbon nanotube film on a glassy carbon electrode, *Anal. Chem.* **2001**, *73*, 915–920.
- 97 WANG J., DEO R. P., POULIN P., MANGY M. Carbon nanotube fiber microelectrodes, *J. Am. Chem. Soc.* **2003**, *125*, 14706–14707.
- 98 CHEN R.-S., HUANG W.-H., TONG H., WANG Z.-L., CHENG J.-K. Carbon fiber nanoelectrodes modified by single-walled carbon nanotubes, *Anal. Chem.* **2003**, *75*, 6341–6345.
- 99 WANG J., LI M., SHI Z., LI N., GU Z. Electrocatalytic oxidation of 3,4-dihydroxyphenylacetic acid at a glassy carbon electrode modified with single-wall carbon nanotubes, *Electrochim. Acta* **2001**, *47*, 651–657.
- 100 GONG K. P., DONG Y., XIONG S. X., CHEN Y., MAO L. Q. Novel electrochemical method for sensitive determination of homocysteine with carbon nanotube-based electrodes, *Biosens. Bioelectron.* **2004**, *20*, 253–259.
- 101 WU K., JI X., FEI J., HU S. The fabrication of a carbon nanotube film on a glassy carbon electrode and its application to determining thyroxine, *Nanotechnology* **2004**, *15*, 287–291.
- 102 LIN Y., LU F., REN Z. Glucose biosensors based on carbon nanotube nanoelectrode ensembles, *Nano Lett.* **2004**, *4*, 191–195.
- 103 WANG J., MUSAMEH M. Carbon-nanotubes doped polypyrrole glucose biosensor, *Anal. Chim. Acta* **2005**, *539*, 209–213.
- 104 LI G., LIAO J. M., HU G. Q., MA N. Z., WU P. J. Study of carbon nanotube modified biosensor for monitoring total cholesterol in blood, *Biosens. Bioelectron.* **2005**, *20*, 2140–2144.
- 105 CAI H., CAO X., JIANG Y., HE P., FANG Y. Carbon nanotube-enhanced electrochemical DNA biosensor for DNA hybridization detection, *Anal. Bioanal. Chem.* **2003**, *375*, 287–293.
- 106 KERMAN K., MORITA Y., TAKAMURA Y., OZSOZ M., TAMIYA E. DNA-directed attachment of carbon nanotubes for enhanced label-free electrochemical detection of DNA hybridization, *Electroanalysis* **2004**, *16*, 1667–1672.
- 107 WANG S. G., WANG R., SELLIN P. J., ZHANG Q. DNA biosensors based on self-assembled carbon nanotubes, *Biochem. Biophys. Res. Commun.* **2004**, *325*, 1433–1437.
- 108 KATZ E., WILLNER I. Biomolecule-functionalized carbon nanotubes: applications in nanobioelectronics, *ChemPhysChem* **2004**, *4*, 1084–1104.
- 109 MENNA E., DELLA NEGRA F., DALLA FONTANA M., MENEGHETTI M. Selectivity of chemical oxidation attack of single-wall carbon nanotubes in solution, *Phys. Rev. B* **2003**, *68*, 193412.
- 110 KAVAN L., DUNSCH L. Diameter-selective electrochemical doping of

- hipco single-walled carbon nanotubes, *Nano Lett.* **2003**, *3*, 969–972.
- 111 WILTSHIRE J. G., KHLOBYSTOV A. N., LI L. J., LYAPIN S. G., BRIGGS G. A. D., NICHOLAS R. J. Comparative studies on acid and thermal based selective purification of HiPCO produced single-walled carbon nanotubes, *Chem. Phys. Lett.* **2004**, *386*, 239–243.
- 112 DUESBERG G. S., MUSTER J., BYRNE H. J., ROTH S., BURGHARD M. Towards processing of carbon nanotubes for technical application, *Appl. Phys. A* **1999**, *69*, 269–274.
- 113 STRANO M. S. Probing chiral selective reactions using a revised kataura plot for the interpretation of single-walled carbon nanotube spectroscopy, *J. Am. Chem. Soc.* **2003**, *125*, 16148–16153.
- 114 CHEN Z., DU X., DU M.-H., RANCKEN C. D., CHENG H.-P., RINZLER A. G. Bulk separative enrichment in metallic or semiconducting single-walled carbon nanotubes, *Nano Lett.* **2003**, *3*, 1245–1249.
- 115 BALASUBRAMANIAN K., BURGHARD M. Chemically functionalized carbon nanotubes, *Small* **2005**, *1*, 180–192.
- 116 SUN Y. P., FU K., LIN Y., HUANG W. Functionalized carbon nanotubes: properties and applications, *Acc. Chem. Res.* **2002**, *35*, 1096–1104.
- 117 SEEMAN N. C. DNA in a material world, *Nature* **2003**, *421*, 427–431.
- 118 ALIVISATOS A. P., JOHNSON K. P., PENG X. G., WILSON T. E., LOWETH C. J., BRUCHEZ M. P., SCHULTZ P. G. Organization of “nanocrystal molecules” using DNA, *Nature* **1996**, *382*, 609–611.
- 119 NIEMEYER C., CEYHAN B. DNA-directed functionalization of colloidal gold with proteins, *Angew. Chem. Int. Ed. Engl.* **2001**, *40*, 3685–3688.
- 120 MIRKIN C. A. Programming the assembly of two- and three-dimensional architectures with DNA and nanoscale inorganic building blocks, *Inorg. Chem.* **2000**, *39*, 2258–2272.
- 121 LI H., PARK S. A., REIF J. H., LABEAN T. H., YAN H. DNA-templated self-assembly of protein and nanoparticle linear arrays, *J. Am. Chem. Soc.* **2004**, *126*, 418–419.
- 122 NIKOLAEV P., BRONIKOSWSKI M. J., BRADELEY K., ROHMUND F., COLBERT D. T., SMITH K. A., SMALLLEY R. E. Gas-phase catalytic growth of single-walled carbon nanotubes from carbon monoxide, *Chem. Phys. Lett.* **1999**, *313*, 91–97.
- 123 LIU J., CASAVANT M. J., COX M., WALTERS D. A., BOUL P., LU W., RIMBERG A. J., SMITH K. A., COLBERT D. T., SMALLLEY R. E. Controlled deposition of individual single-walled carbon nanotubes on chemically functionalized templates, *Chem. Phys. Lett.* **1999**, *303*, 125–129.
- 124 MUSTER J., BURGHARD M., ROTH S., DUESBERG G. S., HERNANDEZ E., RUBIO A. Scanning force microscopy characterization of individual carbon nanotubes on electrode arrays, *J. Vac. Sci. Technol. B* **1998**, *16*, 2796–2801.
- 125 CHOI K. H., BOURGOIN J. P., AUVRAY S., ESTEVE D., DUESBERG G. S., ROTH S., BURGHARD M. Controlled deposition of carbon nanotubes on a patterned substrate, *Surf. Sci.* **2000**, *462*, 195–202.
- 126 VALENTIN E., AUVRAY S., GOETHALS J., LEWENSTEIN J., CAPES L., FILORAMO A., RIBAYROL A., TSUI R., BOURGOIN J. P., PATILLON J. N. High density selective placement methods for carbon nanotubes, *Microelectron. Eng.* **2002**, *61*, 491–496.
- 127 VALENTIN E., AUVRAY S., FILORAMO A., RIBAYROL A., GOFFMAN M. F., CAPES L., BOURGOIN J. P., PATILLON J. N. Self-assembly fabrication of high performance carbon nanotubes based FETs, *Mater. Res. Soc. Symp. Proc.* **2003**, *772*, 201–206.
- 128 VALENTIN E., AUVRAY S., FILORAMO A., RIBAYROL A., GOFFMAN M., GOETHALS J., CAPES L., BOURGOIN J. Ph., PATILLON J. N. Fabrication by self-assembly of carbon nanotubes field effect transistors, in: *NATO Science Series II: Molecular Nanowires and other Quantum Objects*, ALEXANDROV S., DEMSAR J., YANSON I. (Eds.). Kluwer, Dordrecht, **2004**, pp. 57–66.
- 129 HALLER I. Covalently attached organic

- monolayers on semiconductor surfaces, *J. Am. Chem. Soc.* **1978**, *100*, 8050–8055.
- 130** PETRI D. F. S., WENZ G., SCHUNK P., SCHIMMEL T. An improved method for the assembly of amino-terminated monolayers on SiO<sub>2</sub> and the vapor deposition of gold layers, *Langmuir* **1999**, *15*, 4520–4523.
- 131** TSUKRUK V. V., BLIZNYUK V. N. Adhesive and friction forces between chemically modified silicon and silicon nitride surfaces, *Langmuir* **1998**, *14*, 446–455.
- 132** KANAN S. M., TZE W. T. Y., TRIPP C. P. Method to double the surface concentration and control the orientation of adsorbed (3-aminopropyl)dimethylethoxysilane on silica powders and glass slides, *Langmuir* **2002**, *18*, 6623–6627.
- 133** JEHOULET G. I. PhD Thesis, University of Grenoble, **1996**.
- 134** AUSMAN K. D., PINER R., LOURIE O., RUOFF R. S., KOROBV M. Organic solvent dispersions of single-walled carbon nanotubes: toward solutions of pristine nanotubes, *J. Phys. Chem. B* **2000**, *104*, 8911–8915.
- 135** GORBUNOV A. A., FRIEDLEIN R., JOST O., GOLDEN M. S., FINK J., POMPE W. Gas-dynamic consideration of the laser evaporation synthesis of single-wall carbon nanotubes, *Appl. Phys. A* **1999**, *69*, S593–S596.
- 136** CAPES L., VALENTIN E., ESNOUF S., RIBAYROL A., JOST O., FILORAMO A., PATILLON J.-N. High yield non destructive purification of single wall carbon nanotubes monitored by EPR measurements, in: *Proceedings of the 2nd IEEE Conference on Nanotechnology*, Washington, DC, USA, **2002**, pp. 439–442.
- 137** Typically about 12 h at 24 W in a 40-kHz Fisherbrand US bath 2.8 l.
- 138** DIEHL M. R., YALIRAKI S. N., BECKMAN R. A., BARAHONA M., HEATH J. R. Self-assembled, deterministic carbon nanotube wiring networks, *Angew. Chem. Int. Ed. Engl.* **2002**, *41*, 353–356.
- 139** KONG J., DAI H. Full and modulated chemical gating of individual carbon nanotubes by organic amine compounds, *J. Phys. Chem. B* **2001**, *105*, 2890–2893.
- 140** WIND S. J., APPENZELLER J., MARTEL R., DERYCKE V., AVOURIS Ph. Vertical scaling of carbon nanotube field-effect transistors using top gate electrodes, *Appl. Phys. Lett.* **2002**, *80*, 3817–3819.
- 141** JAVEY A., KIM H., BRINK M., WANG Q., URAL A., GUO J., MCINTYRE P., MCEUEN P., LUNDSTROM M., DAI H. High-kappa dielectrics for advanced carbon-nanotube transistors and logic gates, *Nat. Mater.* **2002**, *1*, 241–246.
- 142** AUVRAY S., DERYCKE V., GOFFMAN M., FILORAMO A., JOST O., BOURGOIN J. P. Chemical optimization of self-assembled carbon nanotube transistors, *Nano Lett.* **2005**, *5*, 451–455.
- 143** SEEMAN N. C. The use of branched DNA for nanoscale fabrication, *Nanotechnology* **1991**, *2*, 149–159.
- 144** KEREN K., BERMAN R. S., BUCHSTAB E., SIVAN U., BRAUN E. DNA-templated carbon nanotube field-effect transistor, *Science* **2003**, *302*, 1380–1382.
- 145** COHEN S. N., CHANG A. C., BOYER H. W., HELLING R. B. Construction of biologically functional bacterial plasmids *in vitro*, *Proc. Natl Acad. Sci. USA* **1973**, *70*, 3240–3244.
- 146** <http://scai.snu.ac.kr/cec2001/selfassemble.talk.pdf>.
- 147** SEEMAN N. DNA nicks and nodes and nanotechnology, *Nano Lett.* **2001**, *1*, 22–26.
- 148** SEEMAN N. Biochemistry and structural DNA nanotechnology: an evolving symbiotic relationship, *Biochemistry* **2003**, *42*, 7259–7269.
- 149** MA R.-I., KALLENBACH N. R., SHEARDY R. D., PETRILLO M. L., SEEMAN N. C. Three-arm nucleic acid junctions are flexible, *Nucleic Acids Res.* **1986**, *14*, 9745–9753.
- 150** PETRILLO M. L., NEWTON C. J., CUNNINGHAM R. P., MA R.-I., KALLENBACH N. R., SEEMAN N. C. The ligation and flexibility of four-arm DNA junctions, *Biopolymers* **1998**, *27*, 1337–1352.
- 151** WINFREE E., LIU F., WENZLER L. A., SEEMAN N. C. Design and self-



- assembly of two-dimensional DNA crystals, *Nature* **1998**, *394*, 539–544.
- 152 LABEAN T. H., YAN H., KOPATSCH J., LIU F., WINFREE E., REIF J. H., SEEMAN N. C. Construction, analysis, ligation, and self-assembly of DNA triple crossover complexes, *J. Am. Chem. Soc.* **2000**, *122*, 1848–1860.
- 153 YAN H., PARK S. H., FINKELSTEIN G., REIF J. H., LABEAN T. H. DNA-templated self-assembly of protein arrays and highly conductive nanowires, *Science* **2003**, *301*, 1882–1884.
- 154 SHI J., BERGSTROM D. E. Assembly of novel DNA cycles with rigid tetrahedral linkers, *Angew. Chem. Int. Ed. Engl.* **1997**, *36*, 111–113.
- 155 LENIGK R., CARLES M., IP N. Y., SUCHER N. J. Surface characterization of a silicon-chip-based DNA microarray, *Langmuir* **2000**, *17*, 2497–2501.
- 156 JOOS B., KUSTER H., CONE R. Covalent attachment of hybridizable oligonucleotides to glass supports, *Anal. Biochem.* **1997**, *247*, 96–101.
- 157 ROGERS Y., BAUCOM P. J., HUANG Z. J., BOGDANOV V., ANDERSON S., JACINO M. T. Immobilization of oligonucleotides onto a glass support via disulfide bonds: a method for preparation of DNA microarrays, *Anal. Biochem.* **1999**, *266*, 23–30.
- 158 STROTHER T., CAI W., ZHAO X., HAMERS R. J., SMITH L. M. Synthesis and characterization of DNA-modified silicon (111) surfaces, *J. Am. Chem. Soc.* **2000**, *122*, 1205–1209.
- 159 CHRISEY L. A., O'FERRAL C. E., SPARGO B. J., DULCEY C. S., CALVERT J. M. Fabrication of patterned DNA surfaces, *Nucleic Acids Res.* **1996**, *15*, 3040–3047.
- 160 CHRISEY L. A., LEE G. U., O'FERRAL C. E. Covalent attachment of synthetic DNA self-assembled monolayer films, *Nucleic Acids Res.* **1996**, *15*, 3031–3039.
- 161 OKAMOTO T., SUZUKI T., YAMAMOTO N. Microarray fabrication with covalent attachment of DNA using bubble jet technology, *Nat. Biotechnol.* **2000**, *18*, 438–441.
- 162 CHEUNG V. G., MORLEY M., AGUILAR F., MASSIMI A., KUCHERLAPATI R., CHILDS G. Making and reading microarrays, *Nat. Genet.* **1999**, *21* (Suppl.), 15–19.
- 163 DEMERS L. M., GINGERS D. S., PARK S.-J., LI Z., CHUNG S.-W., MIRKIN C. A. Direct patterning of modified oligonucleotides on metals and insulators by dip-pen nanolithography, *Science* **2002**, *296*, 1836–1838.
- 164 EDMAN C. F., RAYMOND D. E., WU D. J., TU E., SOSNOWSKI R. G., BUTLER W. F., NERENBERG M., HELLER M. J. Electric field directed nucleic acid hybridization on microchips, *Nucleic Acids Res.* **1997**, *25*, 4907–4914.
- 165 <http://www.nanogen.com/technologies/microarray/>.
- 166 LIVACHE T., FOUQUE B., ROGET A., MARCHAND J., BIDAN G., TEOULE R., MATHIS G. Polypyrrole DNA chip on a silicon device: example of hepatitis C virus genotyping, *Anal. Biochem.* **1998**, *255*, 188–194.
- 167 <http://www.affymetrix.com/technology/manufacturing/index.affx>.
- 168 LIPSHUTZ R. J., FODOR S. P. A., GINGERAS T. R., LOCKHART D. J. High density synthetic oligonucleotide arrays, *Nat. Genet.* **1999**, *21* (Suppl.), 20–24.
- 169 STORHOFF J. J., MIRKIN C. A. Programmed materials synthesis with DNA, *Chem. Rev.* **1999**, *99*, 1849–1862.
- 170 NIEMEYER C. M., CEYHAN B., NOYONG M., SIMON U. Bifunctional DNA–gold nanoparticle conjugates as building blocks for the self-assembly of cross-linked particle layers, *Biochem. Biophys. Res. Commun.* **2003**, *311*, 995–999.
- 171 TATON T. A., MUCIC R. M., MIRKIN C. A., LETSINGER R. L. The DNA-mediated formation of supramolecular mono- and multilayered nanoparticle structures, *J. Am. Chem. Soc.* **122**, 6305–6306.
- 172 CSAKI A., MAUBACH G., BORN D., REICHERT J., FRITZCHE W. DNA-based molecular nanotechnology, *Single Molecules* **2002**, *3*, 275–280.
- 173 FU A., MICHEEL C. M., CHA J., CHANG H., YANG H., ALIVISATOS A. P. Discrete nanostructures of quantum

- dots/Au with DNA, *J. Am. Chem. Soc.* **2004**, *126*, 10832–10833.
- 174** CHEN J., HAMON M. A., HU H., CHEN Y., RAO A. M., EKLUND P. C., HADDON R. C. Solution properties of single-walled carbon nanotubes, *Science* **1998**, *282*, 95–98.
- 175** FU K., HUANG W., RIDDLE L. A., CARROLL D. L., SUN Y.-P. Defunctionalization of functionalized carbon nanotubes, *Nano Lett.* **2001**, *1*, 439–441.
- 176** CHEN J., RAO A. M., LYUKSYUTOV S., ITKIS M. E., HAMON M. A., HU H., COHN R. W., EKLUND P. C., COLBERT D. T., SMALLEY R. E., HADDON R. C. Dissolution of full-length single-walled carbon nanotubes, *J. Phys. Chem. B* **2001**, *105*, 2525–2528.
- 177** CZERW R., GUO Z., AJAYAN P. M., CAROLL D. L., SUN Y.-P. Identification of electron donor states in n-doped carbon nanotubes, *Nano Lett.* **2001**, *1*, 457–460.
- 178** RINZLER A. G., LIU J., DAI H., NIKOLAEV P., HUFFMAN C. B., RODRÍGUEZ-MEYÁS F. J., BOUL P. J., LU A. H., HEYMANN D., COLBERT D. T., LEE R. S., FISHER J. E., RAO A. M., EKLUND P. C., SMALLEY R. E. Large-scale purification of single-wall carbon nanotubes: process, product, and characterization, *Appl. Phys. A* **1996**, *67*, 29–37.
- 179** HU H., BHOWMIK P., ZHAO B., HAMON M. A., ITKIS M. E., HADDON R. C. Determination of the acidic sites of purified single wall carbon nanotubes by acid–base titration, *Chem. Phys. Lett.* **2001**, *345*, 25–28.
- 180** BANERJEE S., WONG S. S. Synthesis and characterization of carbon nanotube-nanocrystal heterostructures, *Nano Lett.* **2002**, *2*, 49–54.
- 181** BAHR J. L., YANG J., KOSYNKIN D. V., BRONIKOWSKI M. J., SMALLEY R. E., TOUR J. M. Functionalization of carbon nanotubes by electrochemical reduction of aryl diazonium salts: a bucky paper electrode, *J. Am. Chem. Soc.* **2001**, *123*, 6536–6542.
- 182** BAHR J. L., TOUR J. M. Highly functionalized carbon nanotubes using in situ generated diazonium compounds, *Chem. Mater.* **2001**, *13*, 3823–3824.
- 183** TANG B. Z., XU H. Preparation, alignment, and optical properties of soluble poly(phenylacetylene)-wrapped carbon nanotubes, *Macromolecules* **1999**, *32*, 2569–2576.
- 184** CHEN G. Z., SHAFFER M. S. P., COLEBY D., DIXON G., ZHOU W., FRAY J., WINDLE A. H. Carbon nanotube and polypyrrole composites: coating and doping, *Adv. Mater.* **2000**, *12*, 522–526.
- 185** O'CONNELL M. J., BOUL P., ERICSON L. M., HUFFMAN C., WANG Y., HAROZ E., KUPER C., TOUR J., AUSMAN K. D., SMALLEY R. E. Reversible water-solubilization of single-walled carbon nanotubes by polymer wrapping, *Chem. Phys. Lett.* **2001**, *342*, 265–271.
- 186** STAR A., STODDART J. F., STEUERMAN D., DIEHL M., BOUKAI A., WONG E. W., YANG X., CHOI S. W., HEATH J. R. Preparation and properties of polymer-wrapped single-walled carbon nanotubes, *Angew. Chem. Int. Ed. Engl.* **2001**, *113*, 1721–1725.
- 187** MC CARTHY B., COLEMAN J. N., CZERW R., DALTON A. B., CAROLL D. L., BLAU W. J. Microscopy studies of nanotube-conjugated polymer interactions, *Synthetic Metals* **2001**, *121*, 1225–1226.
- 188** DALTON A. B., BLAU W. J., CHAMBERS G., COLEMAN J. N., HENDERSON K., LEFRANT S., MC CARTHY B., STEPHAN C., BYRNE H. J. A functional conjugated polymer to process, purify and selectively interact with single wall carbon nanotubes, *Synthetic Metals* **2001**, *121*, 1217–1218.
- 189** ZORBAS V., ORTIZ-ACEVEDO A., DALTON A. B., YOSHIDA M. M., DIECKMANN G. R., DRAPER R. K., BAUGHMAN R. H., JOSE-YACAMAN M., MUSSELMAN I. H. Preparation and characterization of individual peptide-wrapped single-walled carbon nanotubes, *J. Am. Chem. Soc.* **2004**, *126*, 7222–7227.
- 190** XIE H., ORTIZ-ACEVEDO A., ZORBAS V., BAUGHMAN R., DRAPER R. K., MUSSELMAN I. H., DALTON A. B., DIECKMANN G. R. Peptide cross-linking modulated stability and

- assembly of peptide-wrapped single-walled carbon nanotubes, *J. Mater. Chem.* **2005**, *15*, 1734–1741.
- 191 HAZANI M., NAAMAN R., HENNRICH F., KAPPES M. M. Confocal fluorescence imaging of DNA-functionalized carbon nanotubes, *Nano Lett.* **2003**, *3*, 153–155.
- 192 DWYER C., GUTHOLD M., FAIYO M., WASHBURN S., SUPERFINE R., ERIE D. DNA-functionalized single-walled carbon nanotubes, *Nanotechnology* **2002**, *13*, 601–604.
- 193 BAKER S. E., CAI W., LASSETER T. L., WEIDKAMP K. P., HAMERS R. J. Covalently bonded adducts of deoxyribonucleic acid (DNA) oligonucleotides with single-wall carbon nanotubes: synthesis and hybridization, *Nano Lett.* **2002**, *2*, 1413–1417.
- 194 NGUYEN V. C., DELZEIT L., CASSELL A. M., LI J., HAN J., MEYAPPAN M. Preparation of nucleic acid functionalized carbon nanotube arrays, *Nano Lett.* **2002**, *2*, 1079–1081.
- 195 WILLIAMS K. A., VEENHUIZEN P. T. M., DE LA TORRE B. G., ERITJA R., DEKKER C. Nanotechnology – carbon nanotubes with DNA recognition, *Nature* **2002**, *420*, 761–761.
- 196 LI S., HE P., DONG J., GUO Z., DAI L. DNA-directed self-assembly of carbon nanotubes, *J. Am. Chem. Soc.* **2005**, *127*, 14–15.
- 197 MOGHADDAM M. J., TAYLOR S., GAO M., HUANG S., DAI L., MCCALL M. J. Highly efficient binding of DNA on the sidewalls and tips of carbon nanotubes using photochemistry, *Nano Lett.* **2004**, *4*, 89–93.
- 198 GUO Z., SADLER P. J., TSANG S. C. Immobilization and visualization of DNA and proteins on carbon nanotubes, *Adv. Mater.* **1998**, *10*, 701–703.
- 199 BALAVOINE F., SCHULTZ P., RICHARD C., MALLOUH V., EBSESEN T. W., MIOSKOWSKI C. Helical crystallization of proteins on carbon nanotubes: a first step towards the development of new biosensors, *Angew. Chem. Int. Ed. Engl.* **1999**, *38*, 1912–1915.
- 200 FURUNO T., SASABE H. Two-dimensional crystallization of streptavidin by nonspecific binding to a surface film: study with a scanning electron microscope, *Biophys. J.* **1993**, *65*, 1714–1717.
- 201 FILORAMO A., DEKKER C., SIVAN U., SCHONENBEGGER C., MICHEL-BEYERLE M. E. Highligh from DNA-based electronic project, *Phantoms Newslett.* **2003**, *10/11*, 4–6.
- 202 GOUX-CAPES L., FILORAMO A., COTE D., VALENTIN E., BOURGOIN J. P., PATILLON J. N. Non-covalent binding of DNA to carbon nanotubes controlled by biological recognition complex, *AIP Conf. Proc.* **2004**, *725* (1), 17–24.
- 203 PATOLSKY F., WEIZMANN Y., WILLNER I. Long-range electrical contacting of redox enzymes by SWCNT connectors, *Angew. Chem. Int. Ed. Engl.* **2004**, *43*, 2113–2117.
- 204 RICHTER J. Metallization of DNA, *Physica E* **2003**, *16*, 157–173.
- 205 BRAUN E., EICHEN Y., SIVAN U., BEN-JOSEPH G. DNA-templated assembly and electrode attachment of a conducting silver wire, *Nature* **1998**, *391*, 775–778.
- 206 SEIDEL R., COLOMBI CIACCHI L., WEIGEL M., POMPE W., MERTIG M. Synthesis of platinum cluster chains on DNA templates: conditions for a template-controlled cluster growth, *J. Phys. Chem. B* **2004**, *108*, 10801–10811.
- 207 RICHTER J., SEIDEL R., KIRSCH R., MERTIG M., POMPE W., PLASCHKE J., SCHACKERT H. K. Nanoscale palladium metallization of DNA, *Adv. Mater.* **2000**, *12*, 507–510.
- 208 SEIDEL R., MERTIG M., POMPE W. Scanning force microscopy of DNA metallization, *Surf. Interface Anal.* **2002**, *33*, 151–154.
- 209 FORD W. E., HARNACK O., YASUDA A., WESSELS J. M. Platinated DNA as precursors to templated chains of metal nanoparticles, *Adv. Mater.* **2001**, *13*, 1793–1797.
- 210 KEREN K., KRUEGER M., GILAD R., BEN-JOSEPH G., SIVAN U., BRAUN E. Sequence-specific molecular lithography on single DNA molecules, *Science* **2002**, *297*, 72–75.

- 211 KEREN K., BERMAN R., BRAUN E. Patterned DNA metallization by sequence-specific localization of a reducing agent, *Nano Lett.* **2004**, *4*, 323–326.
- 212 HARNACK O., FORD W. E., YASUDA A., WESSELS J. Tris(hydroxymethyl)-phosphine-capped gold particles templated by DNA as nanowire precursors, *Nano Lett.* **2002**, *2*, 919–923.
- 213 NISHINAKA T., TAKANO A., DOI Y., HASHIMOTO M., NAKAMURA A., MATSUSHITA Y., KUMAKI J., YASHIMA E. Conductive metal nanowires templated by the nucleoprotein filaments, complex of DNA and RecA protein, *J. Am. Chem. Soc.* **2005**, *127*, 8120–8125.
- 214 ONGARO A., GRIFFIN F., BEECHER P., NAGLE L., IACOPINO D., QUINN A., REDMOND G., FITZMAURICE D. DNA-templated assembly of conducting gold nanowires between gold electrodes on a silicon oxide substrate, *Chem. Mater.* **2005**, *17*, 1959–1964.
- 215 MONSOON C. F., WOOLLEY A. T. DNA-templated construction of copper nanowires, *Nano Lett.* **2003**, *3*, 359–363.
- 216 DUPRAZ C. J.-F., NICKELS P., BEIERLEIN U., HUYNH W. U., SIMMEL F. C. Towards molecular-scale electronics and biomolecular self-assembly, *Superlattices and Microstructures* **2003**, *33*, 369–379.
- 217 LIPPERT B. (Ed.). *Cisplatin: Chemistry and Biochemistry of a Leading Anti-cancer Drug*. Wiley-VCH, Weinheim, **1999**.
- 218 MACQUET J. P., THEOPHANIDES T. Specificity of the interaction of DNA–platinum, amount of platinum, and pH measurement, *Biopolymers* **1975**, *14*, 781–799.
- 219 COLOMBI CIACCHI L., MERTIG M., SEIDEL R., POMPE W., DE VITA A. Nucleation of platinum clusters on biopolymers: a first principles study of the molecular mechanisms, *Nanotechnology* **2003**, *14*, 840–848.
- 220 MACQUET J. P., THEOPHANIDES T. DNA–platinum interactions. Characterization of solid DNA–K<sub>2</sub>[PtCl<sub>4</sub>] complexes, *Inorg. Chim. Acta* **1976**, *18*, 189–194.
- 221 MACQUET J. P., BUTOUR J. L. A circular dichroism study of DNA–platinum complexes. Differentiation between monofunctional, *cis*-bidentate and *trans*-bidentate platinum fixation on a series of DNAs, *Eur. J. Biochem.* **1978**, *83*, 375–385.
- 222 MERTIG M., COLOMBI CIACCHI L., SEIDEL R., POMPE W., DE VITA A. DNA as a selective metallization template, *Nano Lett.* **2002**, *2*, 841–844.
- 223 RICHTER J., MERTIG M., POMPE W., MONCH I., SCHACKERT H. K. Construction of highly conductive nanowires on a DNA template, *Appl. Phys. Lett.* **2001**, *78*, 536–538.
- 224 DENG Z., MAO C. DNA-templated fabrication of 1D parallel and 2D crossed metallic nanowire arrays, *Nano Lett.* **2003**, *3*, 1545–1548.
- 225 BRAUN E., KEREN K. From DNA to transistors, *Adv. Phys.* **2004**, *53*, 441–496.
- 226 HAZANI M., SHVARTS D., PELED D., SIDOROV V., NAAMAN R. Self-assembled carbon-nanotube-based field-effect transistors, *Appl. Phys. Lett.* **2004**, *85*, 5025–5027.
- 227 HAZANI M., HENNRICH F., KAPPES M., NAAMAN R., PELED D., SIDOROV V., SHVARTS D. DNA-mediated self-assembly of carbon nanotube-based electronic devices, *Chem. Phys. Lett.* **2004**, *391*, 389–392.

## 10 Nanodevices for Biosensing: Design, Fabrication and Applications

*Laura M. Lechuga, Kirill Zinoviev, Laura G. Carrascosa,  
and Miguel Moreno*

### 10.1

#### Introduction

There is increasing interest in obtaining biosensor devices based on nanotechnology developments which can detect, in a fast and selective way, any type of substance in air and liquid samples at very low concentrations – ideally at the single-molecule level [1]. Clinical diagnosis, genomics and proteomics are some of the fields where new laboratory analysis methods (faster, direct, more accurate, more selective, having a high throughput and cheaper than conventional methods) are in high demand. Due to their small size, ultra-sensitive transduction and the possibility of integration in “lab-on-a-chip” microsystems, biosensing devices fabricated with nanotechnologies are potential candidates for fulfilling all the above requirements.

In recent years several interesting nano-developments have been proposed as highly sensitive transducers for biosensing [as nanoparticles, carbon nanotubes (CNTs), photonic crystals, micro- and nanocatilevers, etc.], but few biomolecular interactions using such developments have been demonstrated. Many of those developments are still in their infancy, and further research and technological development is needed before real functional biosensing devices will be available. One of the main problems is the implementation. The path to connect such nano-developments to operations in real-world environments has not been paved, and large and complicated laboratory setups are still needed for signal acquisition and processing.

However, micro/nanobiosensor devices based on microelectromechanical systems (MEMS) and related (BIO)MEMS and (bio)nanoelectromechanical systems [BIO(NEMS)] technologies could provide a technological solution to achieve label-free devices which could be operated in stand-alone fashion outside from laboratory environment. For that reason, in this chapter we focus mainly on two important branches of nanodevices for biosensing: (a) nanodevices based on nanophotonics/optoelectronics and (b) nanodevices based on nanomechanics. Nanobiosensors based on optoelectronics and nanomechanics platforms are excellent examples of devices developed with microelectronics technologies, and constitute the platforms with more possibilities for being used in real applications in the near future.

The chapter covers the design, fabrication and testing of both types of biosensor nanodevices. Further integration of nanosensors, microfluidics, optical and electronic functions on a single sensing circuit could lead to a complete “lab-on-a-chip” technological solution which could be used in field applications and *in situ* analysis. Examples of fabrication, characterization and real applications of the devices will be discussed as well as the way of their integration. Although there are a number of reviews covering some aspects of the devices described here, this is the first summary and critical discussion of the developments based on the fields of photonics and nanomechanics, and the development of a new (nano)device combining both fields.

The chapter is organized as follows:

- An overview of the reasons for using nanobiosensors instead of the classical biosensor approaches.
- A brief overview of the immobilization techniques which could be employed for immobilization of the biological receptors in the transducers.
- A complete description of nanophotonic biosensors, starting from a general overview and showing one example, based in integrated optics, of the latest developments in this field.
- A complete description of nanomechanical biosensors, with an extensive overview of these devices, and showing some examples of design, fabrication and testing. One of the last developments in this field, combining nanomechanics and integrated optics, is presented for the first time.
- Finally, the future trends of this exciting nanobiosensor field are discussed.

## 10.2

### From Biosensor to Nanobiosensor Devices

#### 10.2.1

##### Overview

In addition to the excellent results obtained with existing biosensor technologies [2], there is still a need for devices able to detect, in a direct way, very low levels (picomolar to femtomolar and ideally at the single-molecule level) of a great number of chemical and biochemical substances in the areas of environmental monitoring, industrial and food processes, health care, biomedical technology, clinical analysis, etc. In addition to an extreme sensitivity, if we want to apply biosensor technology to real situations, we would need a high selectivity, short time analysis, and must be reversible, stable, simple to operate, robust, low cost and capable of multianalyte determination [2].

To achieve the above characteristics, the application of recent progress in micro- and nanotechnologies seem to be the most appealing alternative [3]. These technologies are already improving both the miniaturization and the sensitivity of the biosensor devices by using nanomaterials for their construction, allowing the intro-

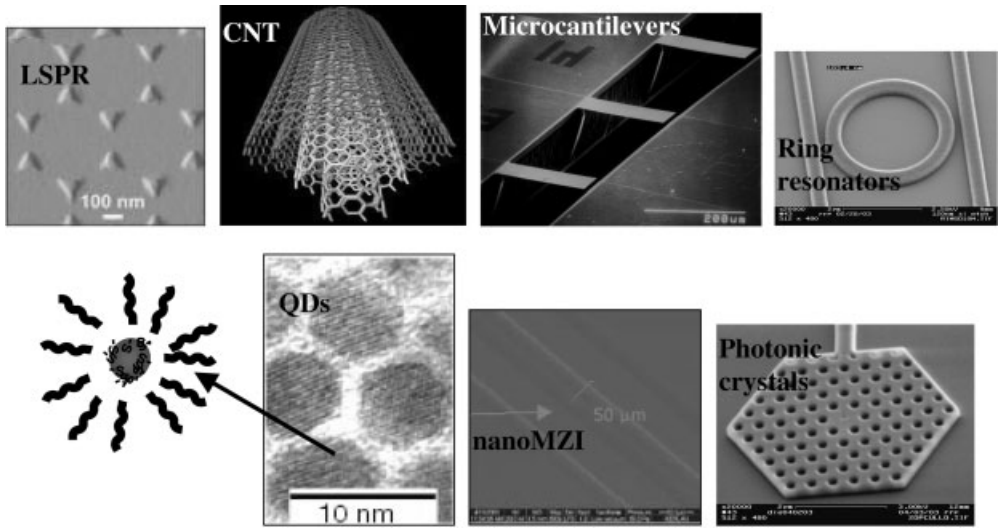


**Figure 10.1.** Schemes and photographs of some nanodevices proposed for biosensing. (Reprinted with permission.)

duction of new signal transduction technologies. Due to their submicron dimensions, nanosensors, nanoprobes and other nanosystems allow simple and rapid analyses *in vivo*. We are assisting to the birth of new biosensor devices at the nanoscale which could be easily integrated in portable “lab-on-chip” platforms to perform “point-of-care” analysis and which in the future could even work inside the human body to detect, at the very early stages, the presence of cancer cells or infectious agents.

Several interesting biosensing developments based on nanotechnology have appeared in the literature during recent years, such as the use of semiconductor, metal or magnetic nanoparticles [4], localized surface plasmon resonance sensors (LSPR) [5], different types of CNT biosensors [6], probes encapsulated by biologically localized embedding (PEBBLE) [7] and many others [8] (Fig. 10.1). Although all of these developments are interesting from a scientific point of view, the real implementation of much of them will be hampered by several factors. Firstly, most of them still require using labels to detect the biomolecular interaction, which is undesirable for real applications (direct reading is much more precise). Secondly, the path to connect such nano-developments to the operation in a real-world environment has not been paved, and large and complicated laboratory set-ups are needed for signal acquisition and processing.

In contrast, micro/nanobiosensor devices based on microelectronics and related (BIO)MEMS/NEMS technologies could provide a technological solution for achieving label-free devices which could be operated in a stand-alone fashion outside of a

laboratory environment [9]. This fabrication approach allows the flexible development of miniaturized compact sensing devices, microfluidics delivery systems and the possibility of fabricating multiple sensors on one chip, opening the way for high-throughput screening. Additional advantages are the robustness, reliability, potential for mass production with consequent reduction of production costs, low energy consumption and simplicity in the alignment of the individual elements [9].

Such nanobiosensors based on optoelectronics and nanomechanics platforms are excellent examples of devices developed with such technologies, and these platforms offer more possibilities for being used in real applications in the near future.

### 10.2.2

#### **Biological Functionalization of Nanobiosensors**

For biosensing purposes, a layer of receptor molecules (proteins, DNA, etc.) capable of selectively binding the substances to be analyzed has to be previously immobilized on the biosensor surface. We must not forget that the immobilization of the receptor molecule on the nanosensor surface is a key step towards the final performance of any biosensor device as it affects to the reproducibility, selectivity and resolution of the device.

The immobilization procedure employed must be stable and reproducible, and must retain the stability and activity of the receptors. Even though the nanodevice that we develop would be the most sensitive one, if the immobilization fails, then the performance of the device will be poor and the theoretical extreme sensitivity of the nanodevice will never be achieved. For handling such diminutive areas, immobilization can be performed with *ex situ* techniques as ink-jet, dip-pen or micro/nanospotting [3] or by *in-situ* techniques through dedicate microfluidics and nanofluidics.

Generally, direct adsorption is not adequate, giving significant losses in biological activity and random orientation of the receptors. Two immobilization strategies are the most employed at the biosensor field: (a) covalent coupling and (b) affinity noncovalent interactions. Covalent coupling gives a stable immobilization as the receptors do not dissociate from the surface or exchange with other receptors in solution. In affinity bonding, a high-affinity capture ligand is nonreversibly immobilized on the sensor surface. The most employed method is the immobilization on gold-coated surfaces using thiol self-assembled monolayers (SAMs) [10]. For example, a widespread method is functionalization of single-stranded (ss) DNA (or proteins) with an alkane chain terminating in a thiol (-SH) or disulfide group (-SS) as sulfurs form a strong bond with gold. This can also be applied for silicon surfaces, using silane monolayers covalently attach to silicon, SiO<sub>2</sub> or Si<sub>3</sub>N<sub>4</sub> sensor surfaces [11]. Several aspects must be taken into account in the development of the immobilization procedures, such as how to avoid nonspecific interactions, getting an optimized surface density of the receptor in order to prevent steric hindrance phenomenon or regenerating the receptor for continuous measurements.

Further details about this subject can be found in the specific literature [12, 13];



it is beyond the scope of this chapter to discuss in detail the immobilization procedures which can be used for (nano)biosensing.

## 10.3

### Nanophotonic Biosensors

#### 10.3.1

##### Overview

Photonic biosensors are providing an increasingly important analytical technology for the detection of biological and chemical species [2, 14]. Most optical biosensors make use of optical waveguides as the basic element of their structure for light propagation and are based on the same operation principle – evanescent field sensing (EFS). With the emergence of nanotechnology, new photonic structures have been suggested as possible highly sensitive transducers for biosensing, such as photonic crystals [15], ring resonators [16] or hollow waveguides [17], but almost no biosensing demonstrations have appeared in the literature using such structures.

Evanescence wave detection combined with nanophotonics structures is proving to be one of the most highly sensitive biosensors. In evanescent wave detection, a receptor layer is immobilized onto the waveguide and the exposure of such a surface to the partner analyte molecules produces a biochemical interaction, which induces a change in its optical properties. This change is detected by the evanescent wave. The extent of the optical change will depend on the concentration of the analyte and on the affinity constant of the interaction, in this way obtaining a quantitative sensor of the interaction. The evanescent wave decays exponentially as it penetrates the outer medium and, therefore, only detects changes taking place on the surface of the waveguide since the intensity of the evanescent field is much higher in this particular region. For that reason, it is not necessary to carry out *a priori* separation of nonspecific components (as in conventional analysis) because any change in the bulk solution will hardly affect the sensor response. In this way, evanescent wave sensors are selective and sensitive devices for the detection of very low levels of chemicals and biological substances, and for the measurement of molecular interactions *in situ* and in real-time [18].

The advantages of optical sensing are significantly improved when the above approach is used within an integrated optics context [19]. Integrated optics technology allows the integration of passive and active optical components (including fibers, emitters, detectors, waveguides and related devices) onto the same substrate, permitting the flexible development of miniaturized compact sensing devices, with the additional possibility to fabricate multiple sensors on a single chip. The integration offers some additional advantages to the optical sensing systems, such as miniaturization, robustness, reliability, potential for mass production with consequent reduction of production costs, low energy consumption and simplicity in the alignment of the individual optical elements [19].

## 10.3.2

**Integrated Mach–Zehnder Interferometer (MZI) Nanodevice**

One of the most sensitive direct biosensor is the MZI. This device fabricated at the micro/nanoscale has shown sensitivity levels close to  $10^{-3}$  nm in adsorbed molecular layers, which means a sensitivity in the picomolar range for biomolecular interactions in a direct assay (without labels) [20].

In a MZI device [18] the light from a laser beam is divided into two identical beams that travel through the MZI arms (sensor and reference areas) and are recombined again into a monomode channel waveguide, giving a signal which is dependent on the phase difference between the sensing and the reference branches. Any change in the sensor area (in the region of the evanescent field) produces a phase difference (and therein a change of the effective refractive index of the waveguide) between the reference and the sensor beam, and thus in the intensity of the outcoupled light. A schematic diagram of this sensor is shown in Fig. 10.2.

When a chemical or biochemical reaction takes place in the sensor area, only the light that travels through this arm will experience a change in its effective refractive index. At the sensor output, the intensity ( $I$ ) of the light coming from both arms will interfere, showing a sinusoidal variation that depends on the difference of the effective refractive indexes of the sensor ( $N_{\text{eff},s}$ ) and reference arms ( $N_{\text{eff},r}$ ) and on the interaction length ( $L$ ):

$$I = \frac{1}{2} I_0 \left[ 1 + \cos \left( \frac{2\pi}{\lambda} (N_{\text{eff},s} - N_{\text{eff},r}) L \right) \right] \quad (1)$$

where  $\lambda$  is the wavelength. This sinusoidal variation can be directly related to the concentration of the analyte to be measured.

For evaluation of specific biosensing interactions, the receptor is covalently attached to the sensor arm surface, while the complementary molecule binds to the receptor from free solution. The recognition of the complementary molecule by the receptor causes a change in the refractive index and the sensor monitors that change. After the molecular interaction, the surface can be regenerated using a

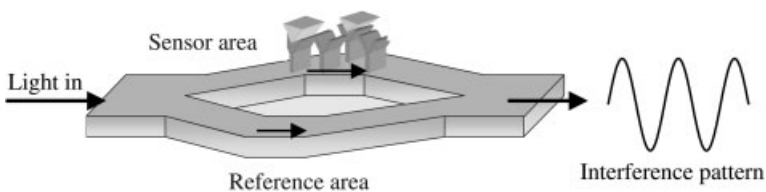


**Figure 10.2.** Scheme of the MZI nanodevice configuration and its working principle. The biomolecular interaction in the sensing area, where the receptors are attached, induces a

phase change of the light traveling through that area as compared to the light traveling through the reference area.

suitable reagent in order to remove the bound analyte without denaturing the immobilized receptor.

The interferometric sensor platform is highly sensitive, and is the only one that provides an internal reference for compensation of refractive index fluctuations and unspecific adsorption. Interferometric sensors have a broader dynamic range than most other types of sensors and show higher sensitivity as compared with other integrated optical biosensors [18, 21]. Due to the high sensitivity of the interferometer sensor, direct detection of small molecules (e.g. environmental pollutants where concentrations down to  $0.1 \text{ ng mL}^{-1}$  must be detected) would be possible with this device.

The detection limit is generally limited by electronic, chemical and mechanical noise, thermal drift, and light source instabilities. However, the intrinsic reference channel of the interferometric devices offers the possibility of reducing common mode effects like temperature drifts and nonspecific adsorptions. A detection limit of  $10^{-7}$  (or better) in the refractive index can be achieved with this device [20], which opens the possibility of the development of highly sensitive devices for *in situ* chemical and biologically harmful agent detection, for example.

### 10.3.2.1 Design and Fabrication

For biosensing applications, the waveguides of the MZI device must be designed to work in the monomode regime and to have a very high surface sensitivity at the sensor arm towards biochemical interactions. If several modes were propagated through the structure, each of them would detect the variations in the characteristics of the outer medium and the information carried by all the modes would interfere between them. The design of the optical waveguide satisfying the above requirements and the dimensions of the Mach-Zehnder structure is achieved by using modeling programs such as the finite difference methods in a nonuniform mesh, the effective index method and the beam-propagation method. Parameters such as propagation constants, attenuation and radiation losses, evanescent field profile, modal properties, and field evolution must be calculated [22]. In order to quantify and optimize the surface sensitivity, the variation of the effective refractive index of the guided modes must be calculated when the thickness of a homogeneous biological layer ( $d_1$ ) changes:

$$n_{\text{sup}} = \partial N / \partial d_1 \quad (2)$$

In Fig. 10.3(b) the surface sensitivity is represented as a function of the core thickness, assuming that the refractive index of this layer is  $n_b = 1.45$ , the external medium is water ( $n_e = 1.33$ ) and the light wavelength is 632 nm.

If we want to use total internal reflection (TIR) waveguides for the sensors, we must come to an agreement between single-mode behavior, low attenuation losses for the fundamental mode and high surface sensitivity. For those reasons, the structure that has been finally chosen [20], for an operating wavelength of  $0.633 \mu\text{m}$ , has the configuration shown in Fig. 10.3(b). In this configuration, the monomode behavior is obtained for core thickness below 200 nm and rib depths

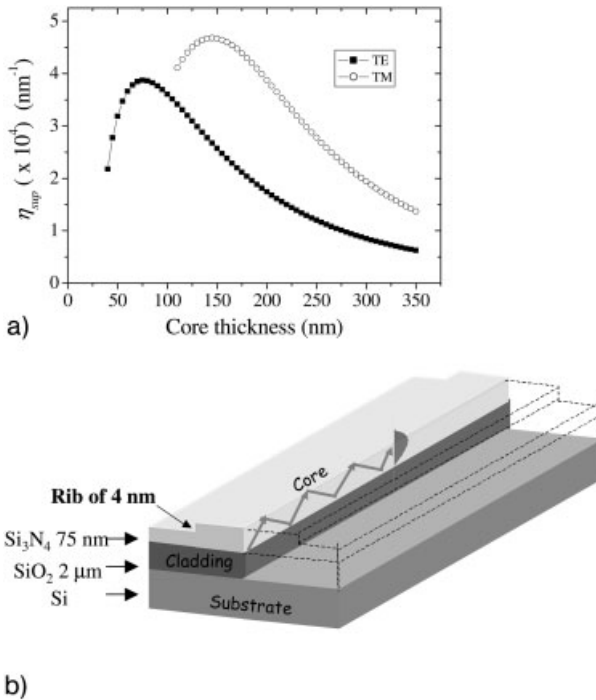


**Figure 10.3.** Cross-section of the optical monomode waveguides used in the Mach–Zehnder device. Note that a rib of only 4 nm is needed for monomode and high-biomolecular sensitivity characteristics.

below 4 nm when the rib width is 4  $\mu\text{m}$ . The small dimensions of this device imply some drawbacks: the reduced core dimensions for monomode behavior (thickness of less than hundreds nanometers and rib depths of a few nanometers) introduces a technological disadvantage for mass production and large insertion losses when coupling light with single-mode optical fibers (with a core thickness of several micrometers). However, the high surface sensitivity for biosensing applications justifies the development of these devices.

The fabrication is done through the following geometry: (a) a conducting silicon wafer of 500  $\mu\text{m}$  thickness, (b) a 2- $\mu\text{m}$  thick thermal  $\text{SiO}_2$  layer on top with a refractive index of 1.46, and (iii) a low-pressure chemical vapor deposition (LPCVD)  $\text{Si}_3\text{N}_4$  layer of 75 nm thickness and a refractive index of 2.00, which is used as a guiding layer. To achieve monomode behavior we needed to define a rib structure, with a depth of only 4 nm, on the  $\text{Si}_3\text{N}_4$  layer by a lithographic step. This rib structure is performed by reactive ion etching (RIE) and is the most critical step in the microfabrication of the device. Finally, a  $\text{SiO}_2$  protective layer is deposited by LPCVD over the structure with a 2  $\mu\text{m}$  thickness and a refractive index of 1.46,

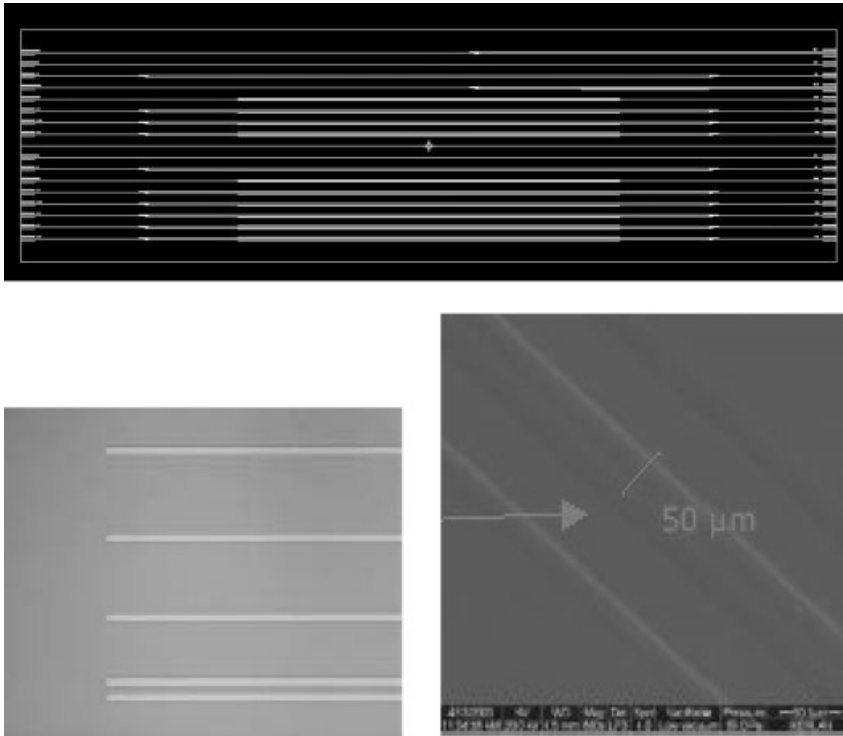


**Figure 10.4.** Photographs of the mask used for MZI fabrication and some of the fabricated devices. The details of the marks alignments and the reference/sensor areas of a device can

be observed. Note that the MZI waveguide cannot be observed due to its dimensions, but is underneath the reference and sensor area.

which is patterned and etched by RIE to define the sensing and reference arms of the interferometer. The final devices (within all the fabrication processes) are CMOS compatible. The MZI configuration is designed to be symmetric with a circular Y-junction (radii of 80 nm). Separation between the sensor and reference arms is of 50  $\mu\text{m}$  to avoid coupling between modes traveling through both branches. Finally, the sensors must be cut in individual pieces and polished for light coupling by the end faces.

In Fig. 10.4, the mask designed for the fabrication of such devices is shown as well some details of the alignment marks and the reference/sensor areas of one fabricated device. Due to the nanometric rib dimension, the device can only be observed by AFM as shown in Fig. 10.5.

### 10.3.2.2 Characterization and Applications

The devices must be implemented with a microfluidics unit, electronics, data acquisition and software for optical and biochemical testing. For the experimental

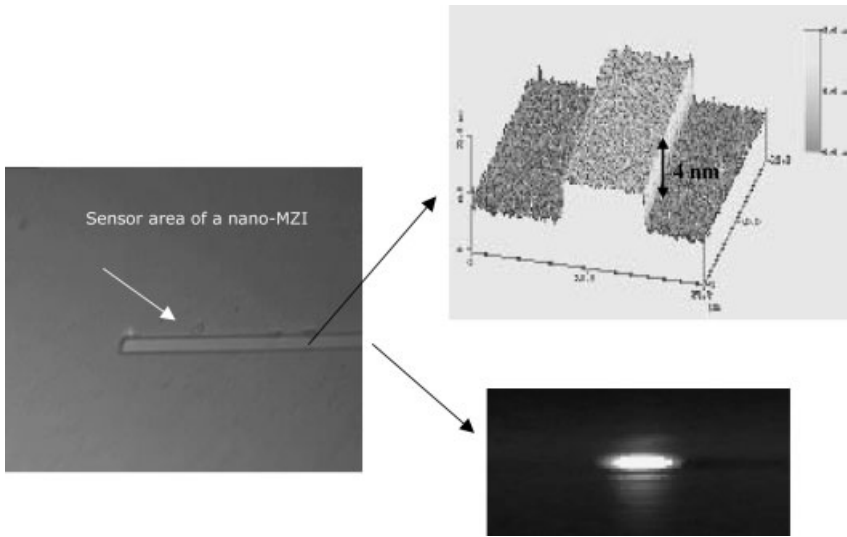


**Figure 10.5.** Image of the sensing area of a nano-MZI device. The AFM photograph of the rib of the waveguide clearly shows the 4-nm step achieved during fabrication. The monomode behavior can be observed at the output light collected from the device.

characterization, the light coming from a connected laser diode at a wavelength of 632 nm is end-fire coupled into the interferometers by a single-mode optical fiber. The light coming out of the interferometer is collected by another single-mode fiber, which is connected to a photodiode. The photodiode signal is amplified, digitalized and processed. The different dissolutions used in the characterizations are controlled by a peristaltic pump and a polymeric flow cell.

The evaluation of the sensitivity is done by flowing dissolutions of varying refractive index and measuring the output signal of the MZI in real-time. With these measurements, a calibration curve is constructed where the phase response of the sensor is plotted versus the variation in the refractive index as depicted in Fig. 10.6.

The lower detection limit measured is  $\Delta n_{o, \min} = 2.5 \times 10^{-6}$ , corresponding to an effective refractive index change of  $\Delta N = 1.4 \times 10^{-7}$ . It can be estimated that the lowest phase shift measurable would be around  $0.03 \times 2\pi$ . The detection limit value corresponds to a very high surface sensitivity around  $2 \times 10^{-4} \text{ nm}^{-1}$ , which means that picomolar detection of a biomolecular interaction in a direct way is feasible using this nanodevice.

As a proof of the utility of MZI technology towards biosensing detection, the application of MZI nanobiosensors for the direct detection of DNA is described. The first step is the immobilization of the biomolecular receptors in the sensor area. This immobilization must be strong and stable to perform the sensitivity measure-

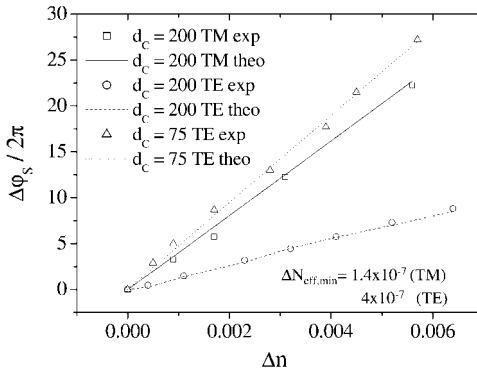
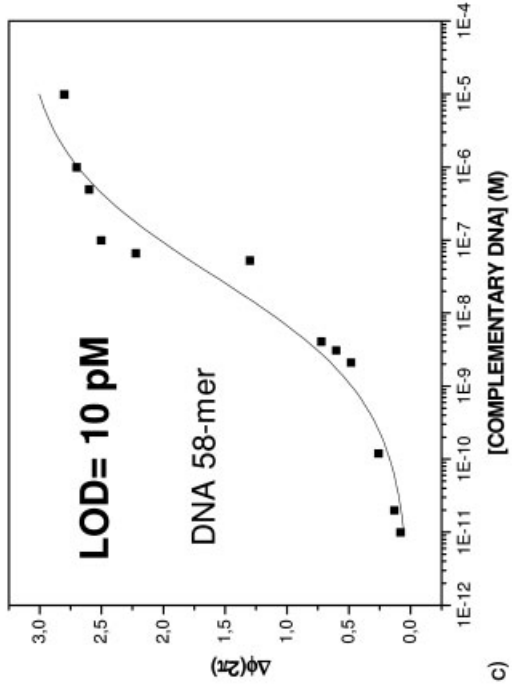
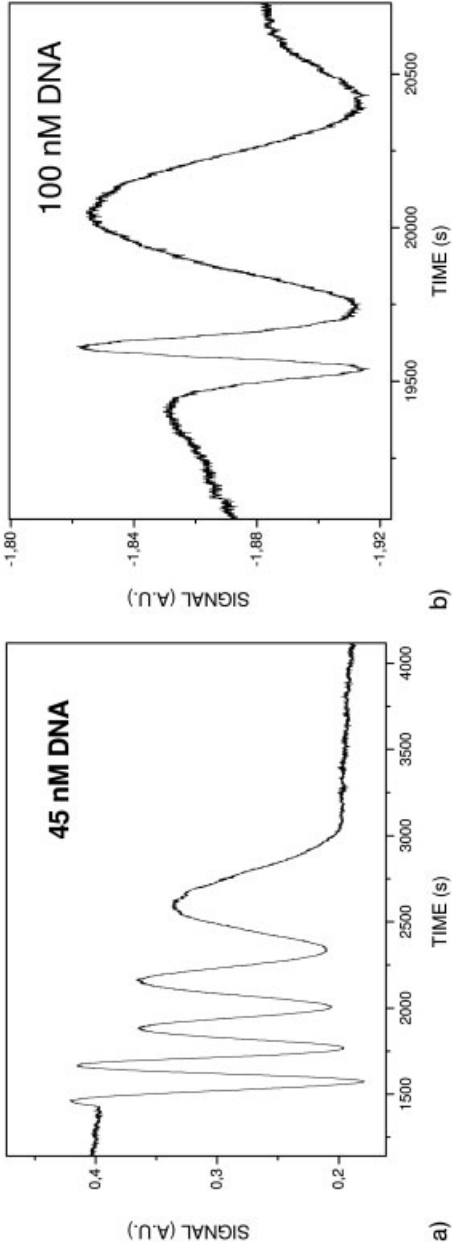


**Figure 10.6.** Experimental and theoretical evaluation of the sensitivity to changes of refractive index for MZI sensors with  $\text{Si}_3\text{N}_4$  core layers of 75 and 200 nm, and for the TE and TM polarizations. In the case of the sensor with a 75-nm core layer, the TM mode is not guided.

ments of the device and for reusability. For that reason, a covalent immobilization protocol through SAMs using silane chemistry is employed.

First, the  $\text{Si}_3\text{N}_4$  surface is cleaned with oxygen plasma and 10% nitric acid in distilled water to oxidize the surface. Second, the  $\text{Si}_3\text{N}_4$  layer is immersed in 10% 3-mercaptopropyltrimethoxysilane (MPTMS) in toluene at room temperature for 12 h. The MPTMS functionalizes the sensor surface with a thiol group, allowing the thioled DNA to be covalently immobilized on the silanized  $\text{Si}_3\text{N}_4$  surface by a disulfide bond. A ssDNA probe (28 nucleotides) with the thiol linker group [SH-( $\text{CH}_2$ )<sub>6</sub>] at the 5' is used. The 15-T tail is employed as a vertical spacer chain to increase the accessibility to the complementary DNA. For the immobilization, a 45-nM solution of the ssDNA probe in phosphate-buffered (PB) solution (pH 7) is used. Figure 10.7(a) shows the real-time detection of the covalent immobilization of the DNA probes by means of a phase change of  $\Delta\phi_S = 7.75 \text{ } 2\pi$  rad.

The hybridization with the complementary ssDNA strand is detected using a 58-nucleotide strand and flowing a 100-nM solution in the same PB buffer. Figure 10.7(b) shows the real-time detection of the hybridization between the complementary sequences inducing a total phase change  $\Delta\phi_S = 2.5 \text{ } 2\pi$  rad. In order to test the specificity of the DNA hybridization, 100 nM dissolutions of a noncomplementary DNA sequence flow after the regeneration of the surface with 10 mM NaOH. This measurement shows a null response of the sensors, ensuring the specificity of the DNA binding. A calibration curve has been obtained by using different DNA concentrations. The lower experimental limit of detection is 10 pM, as can be observed in Fig. 10.7(c). This result clearly demonstrated the high sensitivity which can be obtained for the direct detection of biomolecular interactions by using this nanophotonic concept for a biosensor.





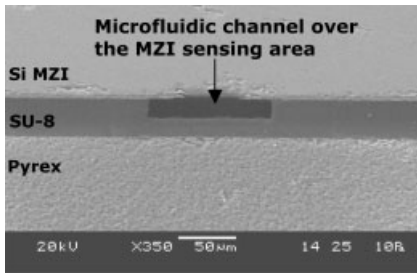


**Figure 10.8.** Scanning electron microscopy image of the cross-section of the polymer microfluidic channels over the sensor area of the photonic MZI device.

### 10.3.3

#### Integration in Microsystems

The integration of optical transducers is a key issue in the further development of “lab-on-a-chip” microsystems [23]. The main advantage of the Mach–Zehnder devices fabricated with standard microelectronics technology comes from the possibility to develop a complete “lab-on-a-chip” by optoelectronic integration of the light source, photodetectors and sensor waveguides on a single semiconductor package together with the flow system and the CMOS electronics [19]. There are many advantages to shrinking down these devices and integrating them for use in high-throughput microsystem applications such as single-molecule detection and DNA sequencing. A complete system fabricated with integrated optics will offer low complexity, robustness, a standardized device and, what is more important, portability. Devices for on-site analysis or point-of-care operations for biological and chemical detection are geared for portability, ease of use and low cost. In this sense, integrated optical devices have a compact structure and could allow fabricating optical sensor arrays on a single substrate for simultaneous detection of multiple analytes. Mass production of sensors will be also possible with the fabrication of miniaturized devices by using standard microelectronics technology.

For the development of a complete MZI microsystem, several units must be incorporated on the same platform: (a) the micro/nanodevices, (b) the flow cells and the flow delivery system, (c) a modulation or compensation system for translating the interferometric signals into direct ones, (d) integration of the light sources and the photodetectors, and (e) CMOS processing electronics. As an example, Fig. 10.8 shows the integration of a nano-MZI device with a microfluidic sys-



**Figure 10.7.** (a) Detection of the covalent immobilization of ssDNA receptor probes from a 45-nM solution by a MZI sensor. (b) Detection of the hybridization with the complementary ssDNA strand (100 nM). (c) Calibration curve for DNA hybridization. A lower detection limit of 10 pM can be achieved.

tem. The microflow cells are specifically designed and fabricated using a novel fabrication method of three-dimensionally embedded microchannels using the polymer SU-8 as structural material [24]. Integration of sources will be achieved by connection with optical fibers or using embedded diffraction gratings.

## 10.4

### Nanomechanical Biosensors

#### 10.4.1

##### Overview

Over recent years, biosensors based on microcantilevers have arisen as interesting devices for measuring biomolecular interactions in a direct way with very high sensitivity [25]. These sensors derive from the microfabricated cantilevers used in AFM and are based on the bending induced in the cantilever when a biomolecular interaction takes place on one of its surfaces. Microcantilevers transduce the molecular recognition of biomolecules into a nanomechanical motion [26] (from a few to hundreds of nanometers), which is commonly detected by an optical or piezoresistive readout system [27–29]. Research in this new type of sensors grew exponentially after the landmark paper of Fritz and coworkers in 2000, where the ability of microcantilever sensors for discerning single-base variations in DNA strands without using fluorescent labels was demonstrated [26]. This paper made a deep impact on the biotechnology area and marked the beginning of a major research effort on this field. Shortly after, microcantilever sensors were used in other works like DNA hybridization [30, 31], detection of proteins involved in cancer [32] and other diseases [33, 34] with increased accuracy, as well as in applications in environmental sciences [35]. Cantilever sensors have also been used for the detection of such chemical molecules as volatile compounds, warfare pathogens, explosives, glucose and even ionic species [25].

Microcantilevers are fabricated by using standard microelectronics technology in arrays of tens to thousands of microcantilevers. For that reason they are a promising alternative to current DNA and protein chips because they could permit the parallel, fast and real-time monitoring of thousands of analytes (proteins, pathogens, DNA strands, etc.) without the need for labeling. When fabricated at the nanoscale (*nanocantilevers*) the sensitivity increases and expected limits of detection are in the femto–atto regime with the astonishing possibility of detection at the single-molecule level in real-time [29].

#### 10.4.2

##### Working Principle

The physical working principle is based on the bending of the cantilever when a biomolecular interaction takes place. The bending arises as consequence of a sur-

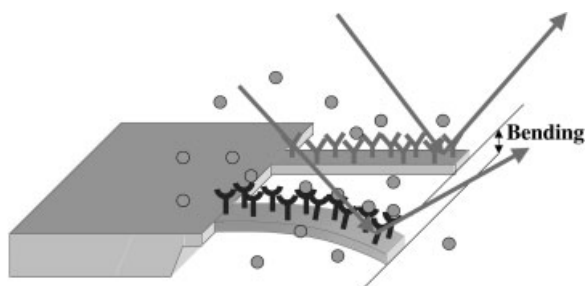


**Figure 10.9.** Scheme of cantilever bending due to a biomolecular interaction between an immobilized receptor and its complementary target. Only the specific recognition causes a change on the surface stress driving the bending of the cantilever.

face stress change induced by the molecular recognition when this phenomena happens just on one of its sides (with regard to the other). Hence, immobilization has to be selectively performed only on one side of the cantilever, allowing the target molecule to react onto the functionalized side (see Fig. 10.9 for details). Detection based on cantilever bending is known as *static mode* detection.

At the same time, the cantilever resonance frequency also varies due to mass loading. This type of detection is known as *dynamic mode* detection. Resonance frequency changes can be detected by measuring the thermal cantilever noise. However, to achieve high-sensitivity resolution, especially when working in liquids, it is necessary to produce a previous excitation of the cantilevers by using alternated electric, magnetic or acoustic fields.

Both static and dynamic modes have proven to be very sensitive when working in air. However, when operated in liquids, the resonance peak and the quality value shift toward much lower values than in air due to the damping effect of the liquid. This factor dramatically affects measurements based on the dynamic mode, making this method less suitable to monitor biochemical process in aqueous environments than when using the static mode. For this reason, as biological reactions take place in liquids, microcantilever sensors operating in the static mode are especially suitable as a platform for performing nanomechanical biomolecular assays. In fact, there are only a few demonstrations of biomolecular interaction detection by using the resonant frequency method [36].

Factors and phenomena responsible for the surface stress response during molecular recognition remain unclear. Several factors are considered to be involved, but a great controversy already exists in the scientific community [30, 37, 38]. Electrostatic interaction between neighboring adsorbates, changes in surface hydrophobicity and conformational changes of the adsorbed molecules can all induce stresses which may contrast with each other and make the change in stress not directly related to the receptor–ligand binding energy. This is particularly the case for biological adsorption due to the complexity of the interactions involved.

## 10.4.3

**Detection Systems**

The readout signal is critical to the real-time measurement, accuracy and possibility of integration of microcantilever biosensors. Therefore, a crucial area is the implementation a readout system capable of monitoring changes with subnanometer accuracy. The bending or/and the resonant frequency changes can be monitored by several techniques including optical beam deflection, piezoresistivity, piezoelectricity, interferometry, capacitance and electron tunneling amongst the most important [27]. In addition, under real conditions, sensors have to be stable long-term, selective and sensitive to the target molecule with no crosstalk reactions. Nonspecific binding of molecules and noise sources such as vibrations and temperature changes have to be avoided. These problems can be overcome by using differential measurements using cantilever array platforms in which a passivated cantilever is used as a reference. Optical and piezoresistive readouts are the most popular, and are compatible with array formats.

For the optical readout, the displacement of the free end of the cantilever is measured using the optical deflection of an incident laser beam on a position-sensitive photodetector which allows us to calculate the absolute value of the cantilever displacement [Fig. 10.10(a)]. This method provides sub-angstrom resolution and can be easily implemented for one cantilever; however, implementation for readout of arrays is technologically challenging, as it requires an array of laser sources with the same number of elements as the cantilever array. This technique is employed

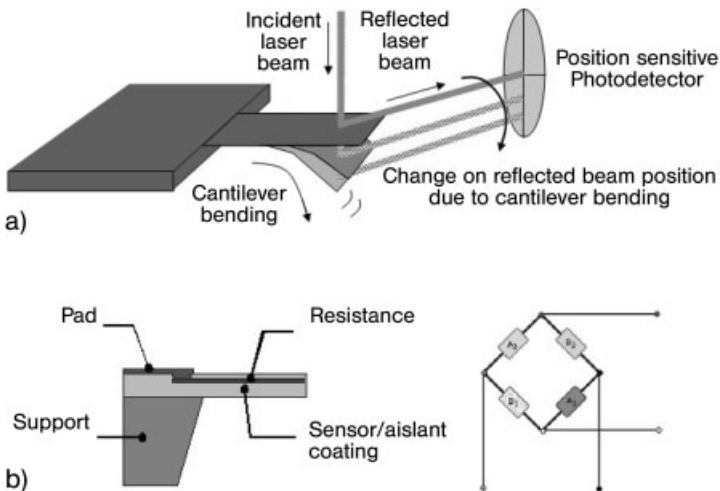


**Figure 10.10.** (a) Scheme of the optical readout method for cantilever bending evaluation. (b) Scheme of the piezoresistive readout and the Wheatstone bridge configuration.

in optically based commercialized array platforms, but sequential switching on and off of each laser source is necessary to avoid overlapping of the reflected beams on the photodetector. This problem can be elegantly solved by using a scanning laser source, where the laser beam is scanned along the array in order to sequentially illuminate the free ends of each microcantilever [39].

Recently, Zinoviev and coworkers introduced a new type of optical waveguide cantilever [40, 41], where the cantilever act as a waveguide for the light. Light going out from the cantilever can be collected by other waveguides or by a photodetector. This new device has shown good performance and offers an interesting approach for further integration in “lab-on-a-chip” microsystems. The design and fabrication of this device is covered in Section 10.4.3.2.

Piezoresistive readout is based on the changes observed in the resistivity of the material of the cantilever as a consequence of a surface stress change [42, 43]. To measure the change on the resistance, silicon cantilevers must be included into a DC-biased Wheatstone bridge (Fig. 10.10b). This configuration is very suitable for further integration using arrays of cantilevers [44]. However, the main disadvantage is the intrinsic high noise level that directly affects to the resolution and the sensitivity when compared to optically detected cantilevers [45], although the reduction of the thickness of piezoresistive cantilevers could increase the sensitivity. However, the cross-sectional structure of piezoresistive cantilevers is complex, with the consequent technological limits in fabricating thin and highly sensitive cantilevers. Moreover, the piezoelectric readout requires electrical connections to the cantilever and their isolation from the solution. For all those reasons, the optical method is the one most employed. In addition, the best detection limits found in the literature are achieved with the optical method [30, 32].

#### 10.4.4

##### **Design of a Standard Microcantilever Sensor**

Microcantilevers are typically made on silicon/ $\text{Si}_3\text{N}_4$  or polymer materials, displaying dimensions ranging from tens to hundred of micrometers long, some tens of micrometers wide and hundreds of nanometers thick. Silicon,  $\text{Si}_3\text{N}_4$  and  $\text{SiO}_2$  cantilevers are available commercially with different shapes and sizes in analogy to AFM cantilevers, with typical lengths between 10 and 500  $\mu\text{m}$ , and ultra-thin cantilevers up to 12 nm thick. However, for specific applications (as in highly sensitive biosensors) cantilevers must be designed and fabricated to satisfy such requirements.

Previous modeling is needed in order to know the ranges of thickness, length and width which could give the highest sensitivity. Several factors must be taken into account. Reducing the thickness and increasing the length results in an increase of sensitivity of the device, but also leads to complex fabrication technology. The width of cantilevers is rather important when cantilevers are used in dynamic mode. A reduction in the width of the beam, in a certain range, results in an increase of the damping and subsequently in a decrease in the quality factor [27]. The effect of the frame and the material must be also taken into account. Cantile-

ver sensitivity depends critically on their spring constant. The lower the constant, the higher the sensitivity for measurements in liquids based on the static method. A key factor that dramatically affects the spring constant of a cantilever is the Young modulus, which is directly related to the characteristics of the cantilever material. Cantilevers are normally made of silicon or related materials that have a high Young's modulus. A cantilever made of a softer material would be more sensitive for static deflection measurements. For that reason, polymers with a much lower Young's modulus than that of silicon have been used as a substitute material for fabricating cantilevers [46]. Among polymers, SU-8 has been shown to be very sensitive, exhibiting a Young's modulus about 40 times lower than for silicon. In addition, the cantilever fabrication process is relatively inexpensive, fast and reliable. It also provides a convenient way to realize arrays of multiple sensors and to integrate them into a miniaturized biochemical analysis system. However, there is still no proof of biosensing testing using polymer cantilever sensors, mainly due to the difficulty in achieving a stable immobilization of the receptor layer.

Modifications of cantilever shape and dimensions could also improve the cantilever spring constant – longer and thinner [47, 48] cantilevers can address very small spring constants. Microfabrication technologies allow fabricating micrometer-sized cantilevers with a high length:thickness ratio in a reproducible and inexpensive way. However, thermal motion of the cantilever severely limits the extent to which the spring constant of the cantilever can be reduced [29]. Modeling can be done by using, finite element programs (ANSYS), for example.

#### 10.4.4.1 Fabrication of a Standard Microcantilever Sensor

Cantilevers are batch fabricated using well-established thin-film-processing technologies which provide low cost, high yield and good reproducibility. Such fabrication techniques include thin-layer deposition, photolithographic patterning and etching, and surface and bulk micromachining. Usually, a sacrificial layer is first deposited on a pre-patterned substrate before the deposition of the cantilever structural material. This structural layer must be free of stress gradients, otherwise problems with the initial bending of cantilevers will appear. The thickness of the layer must be uniform enough around the wafer to make sure that all the beams will be identical. It is possible to fabricate arrays of thousands of identical cantilevers on one wafer.

The cantilevers might be fabricated extended over the border of the chip or they might be located in individual cavities inside the chip. This depends on the type of flow cells to be employed – a common one or a discrete one with independent inlets and outlets for each cantilever. For the chip with cantilevers in a common window, the immobilization of the receptor can be conducted on each cantilever individually using, for example, ink-jet and nanojet printing. The individual cavity design is more complicated from a technological point of view, but allows the immobilization of different receptors in each cantilever *in situ* by using the discrete flow cell and also allows parallel screening of different substances.

As an example, the technology for the fabrication of arrays composed of 20 silicon cantilevers is described. Both types of chips with discrete and common win-

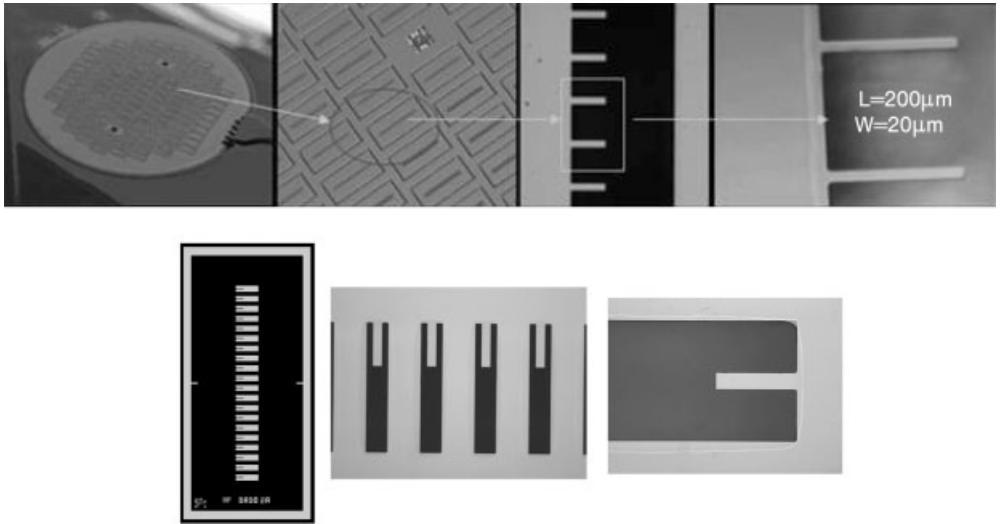


**Figure 10.11.** Photographs of nanomechanical sensors based on microcantilever arrays fabricated at the author's Clean Room facilities. Two different arrays of microcantilevers can be observed, with common and discrete windows (see text for explanation).

dows were fabricated. The cantilevers in the array were separated by a distance of  $250\ \mu\text{m}$ . Photographs of the fabricated devices with common and discrete windows are shown in the Fig. 10.11. The chips were  $3 \times 7\ \text{mm}^2$  in size. The dimensions were chosen small enough to fabricate as many as possible devices on one wafer and large enough to be conveniently handled for measurements.

SOI wafers were chosen as a starting material. The structural silicon layer was free of intrinsic stress gradients and any superficial defects. In this way, it is possible to fabricate arrays of thousands of identical cantilevers on one wafer. To fabricate the cantilevers, the most simple approach is to use bulk micromachining using anisotropic etching of silicon, but this method does not allow us to form a gap between the cavities due to lateral etching. For that reason, deep RIE (DRIE) must be employed to obtain windows with vertical walls.

The sequence of the technological steps is shown in Fig. 10.12. The front side contains a structural silicon layer (1) and a sacrificial  $\text{SiO}_2$  layer (2). The reverse side of the silicon substrate (3) has a  $\text{SiO}_2$  layer (4). As a first step, the reverse side was covered with an aluminum layer (5), the most adequate mask material for the following DRIE. The initial multilayer structure used for the fabrication of the cantilevers is shown in Fig. 10.12(a). Cantilevers on the front side were defined by dry etching of silicon through the pattern obtained by previous photolithography. The aluminum mask was deposited on the reverse side and the  $\text{SiO}_2$  was removed from the areas where the silicon substrate must be etched. Before the next step, the components side was covered with a photoresist layer (6) (Fig. 10.12b).

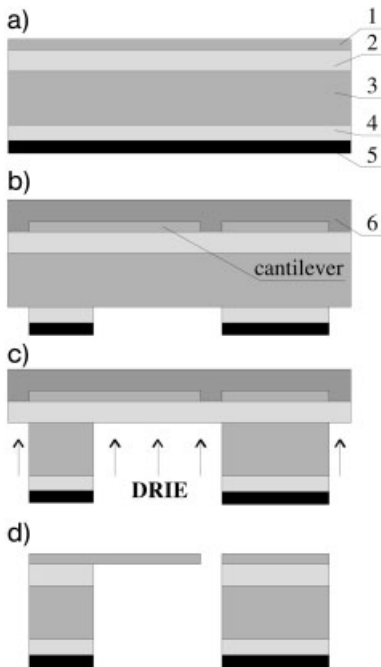


**Figure 10.12.** Fabrication steps for microcantilever arrays (see text for details).

The etching with DRIE of the silicon substrate resulted in almost vertical walls in the cavities with a small (about  $20\ \mu\text{m}$ ) lateral undercut at the top. At this stage, clean  $\text{SiO}_2$  membranes with cantilevers and a photoresist layer on top were obtained (Fig. 10.12c). The photoresist layer (6) prevented the membranes cracking. To release the cantilevers, the membranes were etched in vapors of HF (49%). Afterwards, the wafers were briefly rinsed with deionized water. The photoresist film was removed by oxygen plasma etching.

The next step was dicing the wafers. Common sawing could not be employed as it would break the cantilevers by the cooling water flow and might leave residuals on the sensor surface. As a solution, a DRIE step was applied to have wafers “preliminary diced”. As the cavities under the cantilevers were etched, a groove around every chip was etched to make the array of cantilevers joined to the wafer by two thin hinges, which could be broken manually. With this technology a 100% yield for the cantilever fabrication (2500 cantilevers per wafer) was obtained [49]. All cantilevers were identical and the initial bending was almost negligible. Typical profiles of the fabricated cantilevers are shown in Fig. 10.13. The dispersion did not exceed  $0.6\ \mu\text{m}$ , which corresponded to  $0.005\ \text{rad}$  dispersion of angular deflection. Even cantilevers with an extreme low spring constant ( $k = 0.000061\ \text{N m}^{-1}$ ) can be obtained following this fabrication procedure (cantilever dimensions  $800 \times 20 \times 0.334\ \mu\text{m}^3$ ).



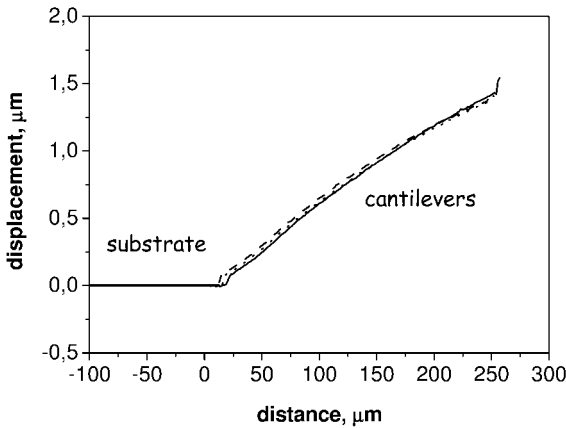


**Figure 10.13.** Typical cantilever profiles after fabrication. Cantilevers are 200  $\mu\text{m}$  long, 40  $\mu\text{m}$  wide and 0.334  $\mu\text{m}$  thick.

Table 10.1 shows the main parameters experimentally evaluated for the fabricated devices and the comparison with the values for the commercial ones, demonstrating the feasibility of the designed and fabricated devices for higher sensitivity than the commercial devices.

#### 10.4.4.2 Optical Waveguide Microcantilever: Design and Fabrication

The optical method is normally employed for microcantilever sensors readout, but has several disadvantages – the major one being the difficulties experienced while performing parallel monitoring of several cantilevers at the same time. In order to achieve further integration, a new optical cantilever sensor has been recently proposed [40, 41]. The detection method is based on monitoring the light exiting a

**Table 10.1.** Main mechanical parameters of fabricated microcantilevers, and comparison with commercial and polymer microcantilevers.

Length $\times$ width $\times$ thickness	$K$ ( $\text{N m}^{-1}$ )	Frequency (kHz)	$Q$
$500 \times 20 \times 0.3$	$9.1 \times 10^{-3}$	1.5	1.8
$200 \times 20 \times 0.3$	$7.4 \times 10^{-3}$	9.9	6.3
$100 \times 20 \times 0.3$	$6.1 \times 10^{-3}$	34.9	13.6
$50 \times 40 \times 0.3$	$7.9 \times 10^{-3}$	86.5	20.7
$200 \times 20 \times 1.5$ (polymer)	$2.5 \times 10^{-3}$	17	15
$550 \times 40 \times 0.8$ (silicon commercial)	$11 \times 10^{-3}$	23.9	34.7

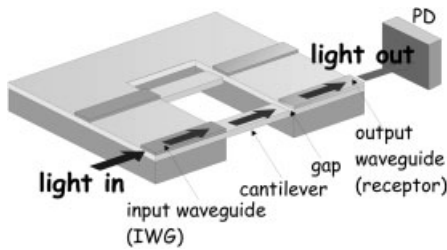
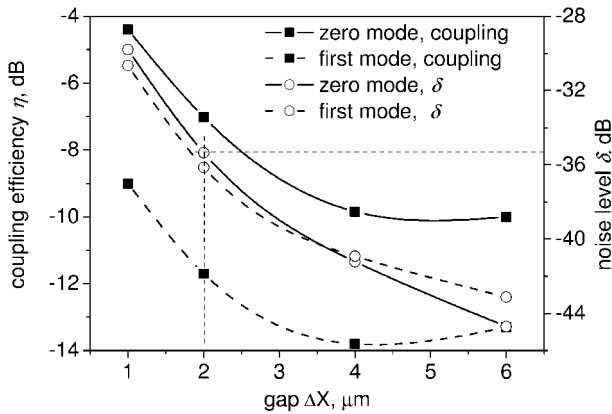


Figure 10.14. Scheme of the novel optical waveguide microcantilever device.

waveguide microcantilever (see Fig. 10.14 for details). This integrated waveguide cantilever sensor can be fabricated as an array of independent waveguide channels designed for monitoring bio-specific reactions. The sensor can work in static or dynamic modes, either by monitoring the deflection or by monitoring the changes in the resonance frequency of the cantilever. The advantage of the device is that the transducer is integrated with the receptor on one chip and the external photodetector is only used for optical power readout. No preliminary alignment or adjustment is needed, except for light coupling into the chip, which does not seriously affect the performance of the device if the coupler is well designed. The sensitivity of the device is comparable to standard microcantilever sensors discussed above.

**10.4.4.2.1 Principle of Operation and Theoretical Analysis** The principle of operation is based on monitoring the coupling efficiency between two butt-coupled waveguides. The energy transfer between the waveguides is very sensitive to their misalignment with respect to each other. In this device the transducer is an optically transparent cantilever beam of submicron thickness. It is located in a cavity and acts as a symmetrical optical waveguide. Light from the cantilever is injected through a short gap into an output waveguide, called a receptor. After exiting the cantilever, light diverges very quickly in the transversal direction and after a few microns its intensity distribution is much larger compared to the distribution of the receptor waveguide modes. Thus, the near field of the cantilever is probed by the receptor, which is a single-mode asymmetrical waveguide. The changes in the power of light exiting the output waveguide, which are attributed to the cantilever bending caused either by the surface stress and/or by vibration of the cantilever, are monitored by a conventional photodetector [41].

The simulations of the coupling efficiency and the sensitivity of the waveguides to their misalignment with respect to each other can be done using overlap integrals [50]. The simulations are performed separately for the fundamental and for the first propagating modes of the cantilever. Two electric field distributions have been overlapped. The first one was the distribution of light exiting the cantilever after propagation through the gap. It was obtained using finite difference beam propagation method (FDBPM) [51]. The second distribution was the fundamental mode of the output waveguide. It was built using the solution of Maxwell equations with appropriate boundary conditions [50]. Waveguide parameters close to



**Figure 10.15.** Modeling of the coupling efficiency and the noise level permitted in the acquisition system for the detection of a 1-nm optical cantilever displacement versus the gap width.

those of the fabricated device were used for the simulations. The cantilever and the receptor were made of  $\text{SiO}_2$  and  $\text{Si}_3\text{N}_4$  materials, respectively.

The sensitivity of the device is defined as the relative change in the output signal per unit cantilever free end displacement. It was calculated as the change in the output power required for the detection of 1-nm cantilever displacement with respect to the power of light exiting the cantilever. This accuracy is equivalent to the noise level allowed in the system. This parameter, further called the noise level, is expressed in relative units. The results of simulations are shown in Fig. 10.15. The noise level demonstrates similar behavior for both modes. The coupling efficiency for the zero mode is higher than that for the first mode. The curves of Fig. 10.15 were produced assuming the cantilever is biased to the most sensitive point which depends on the gap width as well. In general, the width of the gap is a trade-off since a small gap allows for high sensitivity and efficiency, whereas a wide gap makes fabrication tolerances less strict.

**10.4.4.2.2 Fabrication and Characterization** The most difficult step in fabrication of the device is the fabrication of the cantilevers aligned with the output waveguides, implying that the cantilevers should be very flat. A thermally grown  $\text{SiO}_2$  layer was used for the fabrication. The film demonstrated no stress gradient if the bottom layer of a few hundred nanometers was previously eliminated. This allows us to fabricate straight cantilever beams 200  $\mu\text{m}$  long, 40  $\mu\text{m}$  wide and 600 nm thick. The gap between the cantilever and the receptor waveguide was fixed to 3  $\mu\text{m}$ . As the refractive index of  $\text{SiO}_2$  is low, it is not possible to conform a total internal reflection waveguide over the silicon substrate, unlike a  $\text{SiO}_2$  cantilever in air. Therefore, light was launched over the substrate to the cantilever by using a  $\text{Si}_3\text{N}_4$  waveguide, called an input waveguide (IWG). At the cantilever anchoring area, the IWG deposited over the silica buffer forms a junction with the cantilever beam, which is

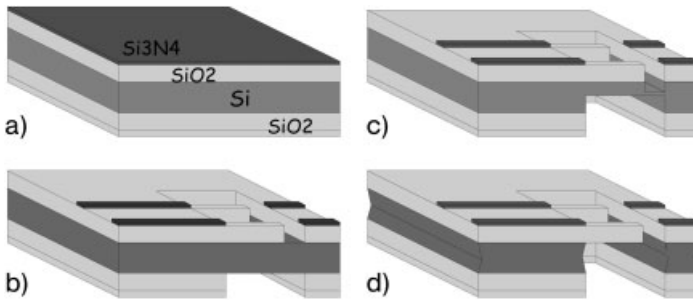


**Figure 10.16.** Technology for the fabrication of the optical waveguide cantilevers.

an extension of the buffer (Fig. 10.14). Light coupling into the cantilever was carried out by means of the evanescent field of the fundamental mode of the IWG. The efficiency of coupling is inversely proportional to the square root of the thickness of the IWG. It can reach 75% if the thickness is close to the value defined by the cut-off condition for the fundamental mode. The silica buffer thickness was  $1.0\ \mu\text{m}$  – enough to avoid leakage of energy into the substrate assuming the thickness of the input and output waveguides was  $140\ \text{nm}$ .

The device was fabricated using standard silicon technologies (Fig. 10.16). First, a  $\text{SiO}_2$  layer was thermally grown by wet oxidation on both sides of a silicon wafer. Then, a high-temperature LPCVD  $\text{Si}_3\text{N}_4$  layer was deposited on the front side and a PECVD  $\text{SiO}_2$  on the reverse side. Standard photolithography and RIE were applied to define the waveguides on the  $\text{Si}_3\text{N}_4$  layer and the cantilevers on the  $\text{SiO}_2$  layer. The same processes were used to obtain the mask for DRIE on the reverse side of the wafer. DRIE was applied to both sides in order to define the cavities under and around the cantilevers. Finally, the cantilevers were released by etching the rests of silicon using TMAH solution. A yield close to 100% was achieved, which means more than 2500 cantilevers per wafer. Figure 10.17 shows some photographs of a fabricated array of waveguide cantilevers. The cantilevers on the chip are located in a common cavity, which is a reach-through chip hole located in the center.

For characterization, the chip was located on a piezoelectric actuator connected to a sine waveform synthesizer. Light from a He–Ne laser ( $632.8\ \text{nm}$ ,  $7.5\ \text{mW}$ ) was coupled into the chip using direct focusing through an objective lens at the exiting light collected by another objective and then directed to a silicon photodetector. The coupling efficiency into the IWG was about 5%. Near 40% of light was transmitted from the IWG into the cantilever. The power of light exiting the output waveguide was  $0.015\ \text{mW}$ . Total losses were  $-27\ \text{dB}$  with respect to the laser output power. The mechanical resonance of the cantilevers was close to  $13.1\ \text{kHz}$ . The spectrum of the output signal measured with AC ( $11.1\ \text{kHz}$ ) voltage of  $50\ \text{mV}$  supplied to the piezoactuator is shown in Fig. 10.18. At this frequency, a small modulation of the output signal was observed, attributed to the modulation of coupling efficiency at the input. AC voltage ( $50\ \text{mV}$ ) applied to the piezoactuator

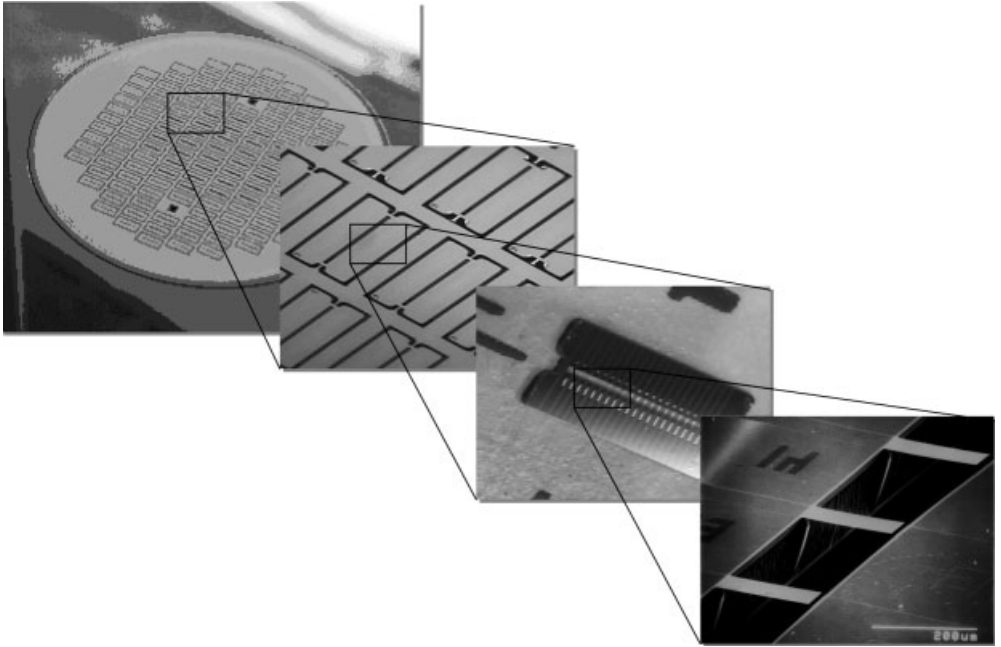


Figure 10.17. Photographs of the fabricated waveguide cantilevers.

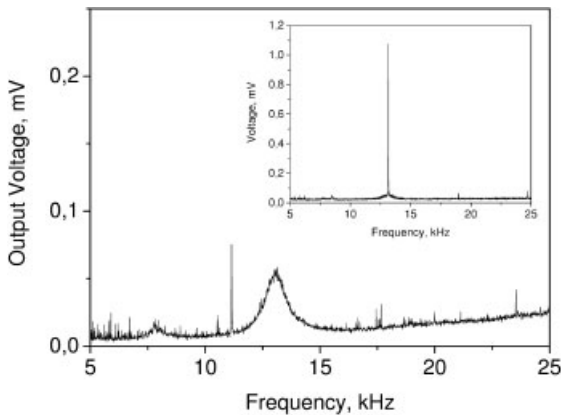


Figure 10.18. Spectrum of the output signal of a waveguide cantilever. The peak at 13.1 kHz corresponds to the cantilever vibration at resonance frequency induced by a piezoelectric actuator. The excitation voltage of the piezoactuator was 50 mV. The cantilever oscillation amplitude was about 1.7 nm at this frequency.

produced a periodic change in the output signal. At a frequency of 13.1 kHz, the cantilever was subject to resonance vibration with an amplitude of about 1.7 nm. The sensitivity, calculated as fractional change ( $\Delta U_{\text{out}} = 1.0$  mV after amplification by factor 100 and subtracting the modulation at the input, see the inset in Fig. 10.18) in the output voltage ( $U_{\text{out}} = 60$  mV) per unit cantilever displacement was  $10^{-4} \text{ nm}^{-1}$ . The signal to noise ratio, which was about 40 at these frequencies, would allow us to register a 0.05-nm cantilever free end displacement. This shows the potential for using this novel structure as a nanomechanical sensor for biomolecular interaction detection with high sensitivity and with a much more integrated approach than that for standard microcantilever sensors.

#### 10.4.5

#### Biosensing Applications of Nanomechanical Sensors

One of the first applications of nanomechanical sensors was in the field of genomics. Fritz and coworkers [26] demonstrated the detection of a single-base mismatch with a detection limit of 10 nM using an array of two cantilevers. One of the cantilevers was functionalized with a control (noncomplementary) oligonucleotide and the DNA probe (complementary) was immobilized in the other. They achieved hybridization deflection signals as small as 10 and 16 nm for 12 and 16mer DNA targets, respectively, within a deflection noise of 0.5 nm. More recently, McKendry and coworker reached a detection of 75 nM for target oligonucleotides in an array of eight microcantilevers [30]. Both results include the specific immobilization by microcapillarity with a 40- $\mu\text{M}$  solution of the thiolated DNA probe. Figure 10.19 shows the cantilever response for a DNA immobilization step. The discrimination of single-nucleotide polymorphisms has been also reported by Thundat and coworkers [31], although with a single cantilever. Other DNA detection schemes have been reported, e.g. the one which used a capture oligonucleotide combined with a DNA probe attached to a gold nanoparticle. This method can detect at least 0.05 nM and is able to discriminate single mismatch measured by resonance [52].

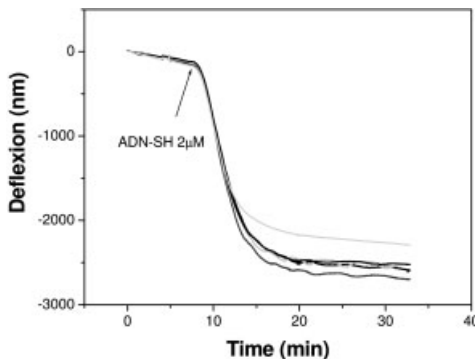


**Figure 10.19.** Simultaneous 2  $\mu\text{M}$  thiolated DNA (27mer) immobilization detection using the cantilever array platform showed in Fig. 10.11.

Proteins have also caught the attention of nanomechanics applications, mainly motivated by the possibility of achieving protein microarrays based on arrays of cantilevers with lower-cost fabrication methods, no labeling of the target protein and improved sensitivity. Recently, Wee and coworkers [53] reported the detection of prostate-specific antigen (PSA), a useful marker for earlier detection of prostate cancer, and C-reactive protein (CRP), a specific marker of cardiac disease, by an electromechanical biosensor using self-sensing piezoresistive microcantilevers. Majumdar and coworkers [32] reported the detection of two isoforms of PSA with an excellent range of discrimination and a detection limit of  $6 \text{ ng mL}^{-1}$  (deflection signal of 20 nm) in a background of  $1 \text{ mg mL}^{-1}$  of BSA protein. In addition, a novel development for early osteosarcoma detection has been described, sensing the interactions between vimentin antibodies and antigens with a single-cantilever-based biosensor [54]. Other clinical applications included the detection of different pathogens like *Salmonella enterica* by Weeks and coworkers [55], vaccinia virus by Gunter and coworkers [56] or fungal spores from *Aspergillus niger* by Nugaeva and coworkers [57]. The use of aptamers as the bioreceptor element has also been widely probed on a number of microcantilever biosensing platforms [58–61].

Biosensing with microcantilevers also extends to applications in environmental sciences. Alvarez and coworkers [35] used this nanodevice for the detection of the organochlorine insecticide compound dichlorodiphenyltrichloroethane (DDT). A competitive assay was performed, in which the cantilever was exposed to a mixed solution of the monoclonal antibody and DDT, and direct detection was proven. With this detection strategy DDT concentrations as low as 10 nM were detected involving deflection signals in the range of 50 nm (Fig. 10.20). Many other applica-

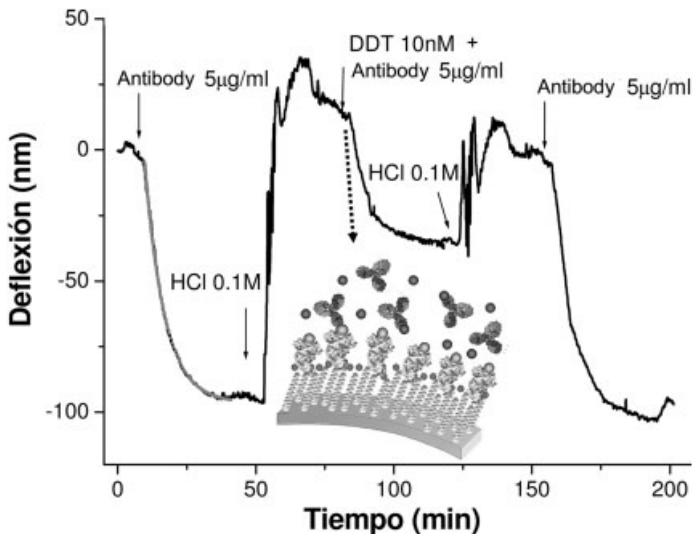


**Figure 10.20.** DDT pesticide detection using a single microcantilever sensor in a real-time competitive immunoassay. The cantilever surface was regenerated with 100 mM HCl.

tions have been described for the detection of pesticides and avidin–streptavidin [28].

Nowadays, there are several commercial platforms based on cantilever array sensors available that demonstrate the potential of nanomechanical biosensors as a reliable sensing tool for biochemical applications [62–65].

## 10.5

### Conclusions and Future Goals

This chapter has provided an overview of most of the technical aspects related to two important branches of nanodevices for biosensing (nanomechanical and nanophotonic biosensors), including design, fabrication and applications of some specific devices. Nanomechanical and nanophotonic biosensors constitute a promising technology as a suitable solution for an important number of problems in the biosensor field. The improvement of the reproducibility and sensitivity along with the integration of microfluidics and detections systems is the main aim of the present research.

Nanobiosensors are still undergoing considerable diversification with respect to technologies, but those fabricated by using standard microelectronics and related MEMS/NEMS approaches could allow the development of portable microsystems platforms which could be employed outside the laboratory. However, limitations in the technology, problems in the integration of all the components in one microsystem and the connection of such tiny devices with the “real” world must be appropriately solved. There is no doubt that such limitations will be overcome in the near future, opening up immense possibilities for early, personalized diagnosis and high-throughput screening.

### Acknowledgments

The authors would like to acknowledge financial support from European and national projects, and thank their colleagues working within the Biosensors Group for their contribution. The authors thank F. J. Blanco and K. Mayora (Ikerlan Corp., Spain) for the microfluidics image.

### References

- 1 JAIN, K. K. Nanotechnology in clinical laboratory diagnostics. *Clin. Chim. Acta* **2005**, 358, 37–54.
- 2 LECHUGA, L. M. Optical biosensors. In: *Biosensors and Modern Biospecific Analytical Techniques, Comprehensive Analytical Chemistry Series XLIV*, GORTON, L. (Ed.). Elsevier, Amsterdam, **2005**.
- 3 NIEMEYER, C. M., MIRKIN, C. A. (Eds.). *Nanobiotechnology. Concepts, Applications and Perspectives*. Wiley-VCH, Weinheim, **2004**.
- 4 GAO, X., CHAN, W. C. W., NIE, S.,



- Quantum-dot nanocrystals for ultrasensitive biological labeling and multicolor optical encoding. *J. Biomed. Opt.* **2002**, *7*, 532–537.
- 5 HAES, A. J., ZOU, S., SCHATZ, G. C., VAN DUYN, R. P. A Nanoscale optical biosensor: the long range distance dependence of the localized surface plasmon resonance of noble metal nanoparticles. *J. Phys. Chem. B* **2004**, *108*, 109–116.
  - 6 WANG, J., LIU, G. D., JAN, M. R., Ultrasensitive electrical biosensing of proteins and DNA: carbon-nanotube derived amplification of the recognition and transduction events. *J. Am. Chem. Soc.* **2004**, *126*, 3010–3011.
  - 7 SUMNER, J. P., AYLOTT, J. W., MONSON, E., KOPELMAN, R. A fluorescent PEBBLE nanosensor for intracellular free zinc. *Analyst* **2002**, *127*, 11–16.
  - 8 FORTINA, P., KRICKA, L. J., SURREY, S., GRODZINSKI, P. Nanobiotechnology: the promise and reality of new approaches to molecular recognition. *Trends Biotechnol.* **2005**, *23*, 168–173.
  - 9 MEDEA+ Program (<http://www.medeas.org>).
  - 10 KASEMO, B. Biological surface science. *Surf. Sci.* **2002**, *500*, 656–677.
  - 11 MANNELLI, I., MINUNNI, I., TOMBELLI, S., WANG, R., SPIRITI, M. M., MASCINI, M., Direct immobilization of DNA probes for the development of affinity biosensors. *Bioelectrochemistry* **2005**, *66*, 129–138.
  - 12 FERRETTI, S., PAYNTER, S., RUSSELL, D. A., SAPSFORD, K. E., RICHARDSON, D. J. Self-assembled monolayers: a versatile tool for the formulation of bio-surfaces. *Trends Anal. Chem.* **2000**, *19*, 530–540.
  - 13 GOODING, J. J., HBBERT, D. B. The application of alkanethiol self-assembled monolayers to enzyme electrodes. *Trends Anal. Chem.* **1999**, *18*, 525–533.
  - 14 LIEGLER, F. S., TAITT, C. R. (Eds.). *Optical Biosensor: Present and Future*. Elsevier, Amsterdam, **2002**.
  - 15 BURR, G. W., CHOW, E., MIRKARIMI, L. W., SIGALAS, M., GROT, A. Photonic crystals microcavities as ultracompact film-thickness monitors for bio-sensing. *Nanophotonics for Information Systems*, paper NPIS-ThC4.
  - 16 BOYD, R. W., HEEBNER, J. E. Sensitive disk resonator photonic biosensor. *Appl. Optics* **2001**, *40*, 5742–5747.
  - 17 YIN, D., BARBER, J. P., HAWKINS, A. R., SCHMIDT, H. Low-loss integrated optical sensors based on hollow-core ARROW waveguide. *Proc. SPIE* **2005**, *5730*, 218–225.
  - 18 LECHUGA, L. M., PRIETO, F., SEPÚLVEDA, B. Interferometric biosensors for environmental pollution detection. In: *Optical Sensors for Industrial E (Springer Series on Chemical Sensors and Biosensors)*, NARAYANASWAMY, R., WOLFBEIS, O. S. (Eds.). Springer, Berlin, **2003**, pp. 227–250.
  - 19 DOMÍNGUEZ, C., LECHUGA, L. M., RODRÍGUEZ, J. A. Integrated optical chemo- and Biosensors. In: *Integrated Analytical Systems*, ALEGRET, S. (Ed.). Elsevier, Amsterdam, **2003**, pp. 541–586.
  - 20 PRIETO, F., SEPÚLVEDA, B., CALLE, A., LLOBERA, A., DOMÍNGUEZ, C., ABAD, A., MONTOYA, A., LECHUGA, L. M. An integrated optical interferometric nanodevice based on silicon technology for biosensor applications. *Nanotechnology* **2003**, *14*, 907–912.
  - 21 CAMPBELL, D. P., MCCLOSKEY, J. Interferometric biosensor. In: *Optical Biosensors: Present and Future*. LIEGLER, F., ROWE, C. (Eds.). Elsevier, Amsterdam, **2002**, pp. 277–304.
  - 22 PRIETO, F., LLOBERA, A., CALLE, A., DOMÍNGUEZ, C., LECHUGA, L. M. Design and analysis of silicon antiresonant reflecting optical waveguides for highly sensitive sensors. *J. Lightwave Technol.* **2000**, *18*, 966–972.
  - 23 THRUSH, E., LEVI, O., COOK, L. J., DEICH, J., KURTZ, A., SMITH, S. J., MOERNER, W. E., HARRIS, J. S. Monolithically integrated semiconductor fluorescence sensor for microfluidic applications. *Sens. Actuators B* **2005**, *105*, 393–399.
  - 24 BLANCO, F. J., AGIRREGABIRIA, M., GARCIA, J., BERGANZO, J., TIJERO, M.,

- ARROYO, M. T., RUANO, J. M., ARAMBURU, I., MAYORA, K. Novel three-dimensional embedded SU-8 microchannels fabricated using a low temperature full wafer adhesive bonding. *J. Micromech. Microeng.* **2004**, *14*, 1047–1056.
- 25 CARRASCOSA, L. G., MORENO, M., ALVAREZ, M., LECHUGA, L. M. Nanomechanical biosensors: a new sensing tool. *Trends Anal. Chem.* **2006**, *25*(3), 196–206.
- 26 FRITZ, J., BALLER, M. K., LANG, H. P., ROTHUIZEN, H., VETTER, P., MEYER, E., GÜNTHERODT, H. J., GERBER, Ch., GIMZEWSKI, J. W. Translating biomolecular interactions into nanomechanics. *Science* **2000**, *88*, 316–318.
- 27 LAVRIK, N., SEPANIAK, M., DATSKOS, P. Cantilever transducers as a platform for chemical and biological sensors. *Rev. Sci. Instrum.* **2004**, *75*, 2229–2253.
- 28 RAITERI, R., GRATAROLA, M., BUTT, H.-J., SKLÁDAL, P. Micromechanical cantilever-based biosensors. *Sens. Actuators B* **2001**, *79*, 115–126.
- 29 DATSKOS, P. G., THUNDAT, T., LAVRIK, N. V. Micro and nanocantilever sensors. In: *Encyclopedia of Nanoscience and Nanotechnology*. NALWA, H. S. (Eds.), American Scientific Publishers, Stevenson Ranch, CA, **2004**, vol. X, pp. 1–10.
- 30 MCKENDRY, R., ZHANG, J., ARNTZ, Y., STRUNZ, T., HEGNER, M., LANG, H. P., BALLER, M. K., CERTA, U., MEYER, E., GÜNTHERODT, H.-J., GERBER, Ch. Multiple label-free biodetection and quantitative DNA-binding on a nanomechanical cantilever array. *Proc. Natl Acad. Sci. USA* **2002**, *99*, 9783–9788.
- 31 HANSEN, K. M., JI, H.-F., WU, G., DATAR, R., COTE, R., MAJUMDAR, A. THUNDAT, T., Cantilever-based optical deflection assay for discrimination of DNA single-nucleotide mismatches. *Anal. Chem.* **2001**, *73*, 1567–1571.
- 32 WU, G., DATAR, H., HANSEN, K. M., THUNDAT, T., COTE, R. J., MAJUMDAR, A. Bioassay of prostate-specific antigen (PSA) using microcantilevers. *Nat. Biotechnol.* **2001**, *19*, 856–860.
- 33 ARNTZ, Y., SEELIG, J., LANG, H., ZHANG, J., HUNZIKER, P., RAMSEYER, J., MEYER, E., HEGNER, M., GERBER, C., Label-free protein assay based on a nanomechanical cantilever array. *Nanotechnology* **2003**, *14*, 86–90.
- 34 SAVRAN, C., KNUDSEN, S., ELLINGTON, A., MANALIS, S., Micromechanical detection of proteins using aptamer-based receptor molecules. *Anal. Chem.* **2004**, *76*, 3194–3198.
- 35 ALVAREZ, M., CALLE, A., TAMAYO, J., ABAD, A., MONTOYA, A., LECHUGA, L. M. Development of nanomechanical biosensors for detection of the pesticide DDT. *Biosens. Bioelectron.* **2003**, *18*, 649–653.
- 36 GHATKESAR, M. K., BARWICH, V., BRAUN, T., BREDEKAMP, A. H., DRECHSLER, U., DESPONT, M., LANG, H. P., HEGNER, M., GERBER, C., Real-time mass sensing by nanomechanical resonators in fluid. *IEEE Sensors* **2004**, *2004*, 1060–1063.
- 37 ALVAREZ, M., CARRASCOSA, L. G., MORENO, M., CALLE, A., ZABALLOS, A., LECHUGA, L. M., MARTÍNEZ-A, C., TAMAYO, J. Nanomechanics on the formation of DNA self-assembled monolayers and hybridization on microcantilevers. *Langmuir* **2004**, *20*, 9663–9676.
- 38 WU, G., JI, H., HANSEN, K., THUNDAT, T., DATAR, R., COTE, R., HAGAN, M. F., CHAKRABORTY, A. K., MAJUMDAR, A. Origin of nanomechanical cantilever motion generated from biomolecular interactions. *Proc. Natl Acad. Sci. USA* **2001**, *98*, 1560–1564.
- 39 TAMAYO, J., ALVAREZ, M., LECHUGA, L. M. System and method for detecting the displacement of a plurality of micro- and nanomechanical elements, such as microcantilevers. *European Patent PCT/EP-05/002356*, **2004**.
- 40 ZINOVIEV, K., DOMÍNGUEZ, C., LECHUGA, L. M., PLAZA, J. A., CADARSO, V. Cantilever-based detector device and method of manufacturing such a device. *European Patent PCT/EP-05/380137*, **2005**.
- 41 ZINOVIEV, K., DOMÍNGUEZ, C., PLAZA, J. A., LECHUGA, L. M. Light coupling into an optical microcantilever by an embedded diffraction grating. *Appl. Optics* **2005**, *45*(2), 229–234.

- 42 LINNEMANN, R., GOTSZALK, T., HADJIISKI, L., RANGELOW, I. W., Characterization of a cantilever with an integrated deflection sensor. *Thin Solid Films* **1995**, *264*, 159–164.
- 43 MINNE, S. C., MANALIS, S. R., QUATE, C. F. Parallel atomic force microscopy using cantilevers with integrated piezoresistive sensors and integrated piezoelectric actuators. *Appl. Phys. Lett.* **1995**, *67*, 3918–3920.
- 44 VETTIGER, P., DESPONT, M., DRECHSLER, U., DURIG, U. T., HABERLE, W., LUTWYCHE, M., ROTHUIZEN, H., STUTZ, R., WIDMER, R., BINNIG, G. K. The “Millipede” – more than one thousand tips for future AFM data storage. *IBM J. Res. Dev.* **2000**, *44*, 323–340.
- 45 YU, X., THAYSEN, J., HANSEN, O., BOISEN, A., Optimization of sensitivity and noise in piezoresistive cantilevers. *J. Appl. Phys.* **2002**, *92*, 6296–6307.
- 46 THAYSEN, J., YALVINKAYA, A. D., VETTIGER, P., MENON, A., Polymer-based stress sensor with integrated readout. *J. Phys. D* **2002**, *35*, 2698–2703.
- 47 HARLEY, J. A., KENNY, T. W. High-sensitivity piezoresistive cantilevers under 1000 Å thick. *Appl. Phys. Lett.* **1999**, *75*, 289–291.
- 48 STOWE, T. D., YASUMURA, K., KENNY, T. W. Attonewton force detection using ultrathin silicon cantilevers. *Appl. Phys. Lett.* **1997**, *71*, 288–230.
- 49 Optonanogen project, <http://eprints.ecs.soton.ac.uk/view/projects/optonanogen.html>.
- 50 KIM, C. M., RAMASWAMY, R. V. Modeling of graded-index channel waveguides using non-uniform finite difference method. *J. Lightwave Technol.* **1989**, *7*, 1581–1589.
- 51 ANEMOGIANNIS, E., GLYTSIS, E. N. Multilayer waveguides: efficient numerical analysis of general structures. *J. Lightwave Technol.* **1992**, *10*, 1344–1351.
- 52 SU, M., LI, S., DRAVID, V. P. Microcantilever resonance-based DNA detection with nanoparticle probes. *Appl. Phys. Lett.* **2003**, *82*, 3562–3564.
- 53 WEE, K. W., KANG, G. Y., PARK, J., KANG, J. Y., YOON, D. S., PARK, J. H., KIM, T. S., Novel electrical detection of label-free disease marker proteins using piezoresistive self-sensing micro-cantilevers. *Biosens. Bioelectron.* **2005**, *20*, 1932–1938.
- 54 MILBURN, C., ZHOU, J., BRAVO, O., KUMAR, C., SOBOYEJO, W. O., Sensing interactions between vimentin antibodies and antigens for early cancer detection. *J. Biomed. Nanotechnol.* **2005**, *1*, 30–38.
- 55 WEEKS, B. L., CAMARERO, J., NOY, A., MILLER, A. E., STANKER L., DE YOREO, J. J. A microcantilever-based pathogen detector. *Scanning* **2003**, *25*, 297–299.
- 56 GUNTER, R. L., DELINGER, W. G., MANYGOATS, K., KOOSER, A., PORTER, T. L., Viral detection using an embedded piezoresistive microcantilever sensor. *Sens. Actuators A* **2003**, *107*, 219–224.
- 57 NUGAEVA, N., GFELLER, K., BACKMANN, N., GÜNTHERODT, H.-J., HEGNER, M., Micromechanical cantilever array sensors for selective fungal immobilization and fast growth detection. *Biosens. & Bioelect.* **2005**, *21*(6), 849–856.
- 58 GOKULRANGAN, G., UNRUH, J. R., HOLUB, D. F., INGRAM, B., JOHNSON, C. K., WILSON, Q. S., DNA aptamer-based bioanalysis of IgE by fluorescence anisotropy. *Anal. Chem.* **2005**, *77*, 1963–1970.
- 59 IKEBUKURO, K., KIYOHARA, C., SODE, K. Novel electrochemical sensor system for protein using the aptamers in sandwich manner. *Biosens. Bioelectron.* **2005**, *20*, 2168–2172.
- 60 POTYRAILO, R., CONRAD, R., ELLINGTON, A., HIEFTJE, G., Adapting selected nucleic acid ligands (aptamers) to biosensors. *Anal. Chem.* **1998**, *703*, 419–3425.
- 61 ZIEGLER, C. Cantilever-based biosensors. *Anal. Bioanal. Chem.* **2004**, *379*, 946–959.
- 62 <http://www.concentris.ch>.
- 63 <http://www.cantion.com>.
- 64 <http://www.veeco.com>.
- 65 <http://www.protiveris.com>.

## 11 Fullerene-based Devices for Biological Applications

Ginka H. Sarova, Tatiana Da Ros, and Dirk M. Guldi

### 11.1 Introduction

The great excitement commencing with the advent of fullerenes and their large-scale production was the inception of a wealth of scientific projects focused on two major disciplines – material chemistry and biomedical applications. Research and development of biomedical applications was, however, penalized by the necessity to work with soluble and biocompatible materials. Still, the outstanding physicochemical features of fullerenes, in general, and [60]fullerene, in particular, together with their unique shape, renders this class of carbon nanostructures as a candidate *par excellence* for biological applications. The ability, for example, to uptake electrons causes fullerenes to act as a very appropriate radical sponge, which is unequivocally reflected in their neuroprotective action. Photoexcitation of fullerenes, however, produces selectively reactive oxygen species (ROS) that are known to be cytotoxic. In this chapter we report on the solubility, toxicity and major biological applications of C<sub>60</sub>, considering both milestone achievements and the most recent advances in these intriguing areas.

### 11.2 Solubility

Considering the unique and hydrophobic structure of fullerenes, it is not surprising that C<sub>60</sub> renders absolutely insoluble in polar solvent. This aspect is, however, detrimental for developing biological and medical applications, and it consequently slowed down research activities in this intriguing field. To overcome this limitation, different approaches have been used – suspension in co-solvents, encapsulation into water-soluble hosts and chemical functionalization were mainly pursued as potent alternatives. In a number of instances the last two methods have been combined through the preparation, for example, of covalently linked cyclodextrins (CDs), which play a double role, i.e. providing solubilizing features and also physically entrapping the carbon cage.

Suspensions of fullerenes are achieved by dissolving them first in a nonpolar organic solvent, such as benzene, adding medium polar tetrahydrofuran (THF) and then acetone. In the last steps, the addition of water to the mixture and the subsequent evaporation of the organic solvents are performed to produce yellow stable suspensions [1, 2]. Notably, such suspensions are composed of fullerene aggregates of variable sizes.

The encapsulation and/or the association of fullerenes into CDs or calixarenes eventually led to the solubilization of fullerenes in aqueous media [3–12]. In this context, the complex formation, for example, between sulfonated thiocalix[4]arene and calix[6]arene and fullerene has been reported [13]. In this case, the stoichiometry between  $C_{60}$  and complexing molecules depends mainly on the dimension of the latter, and it is 1:1 in the case of calix[6]arene and 1:2 for calix[4]arene.

Poly(vinyl pyrrolidone) (PVP), dimethyldioctadecylammonium bromide, Triton X-100, dihexadecyl hydrogen phosphate and lecithin also gave interesting results, leading to rather concentrated solutions of pristine fullerenes with concentrations as high as  $10^{-5}$  M [14].

The covalent functionalization of fullerenes with hydrophilic groups is, however, by far the most powerful strategy to obtain water-soluble derivatives. Different functionalities, including ethylene glycol chains [15, 16], hydroxyl groups [17], carboxylic acids [18], ammonium groups [19] and CDs (Fig. 11.1) [7, 20–22], have been introduced onto the carbon cage in recent years with good results.

In the same manner, preparation of monosaccharide and oligosaccharide fullerene derivatives has been recently re-proposed [23–26]. Similarly, fullerene amino acids and fulleropeptides emerged as other important classes of soluble fullerene compounds that are abundantly reported [27]. Functionalization of the carbon cage has been performed by either direct attachment of amino acids [28] or by tra-

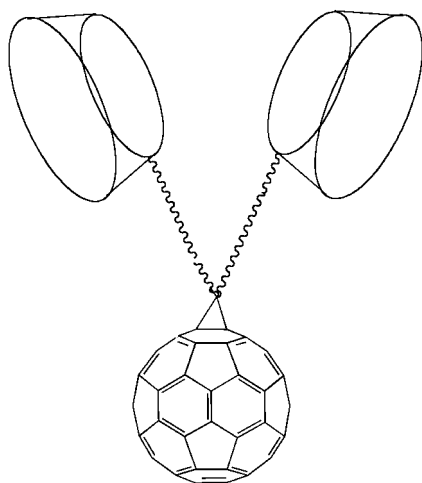
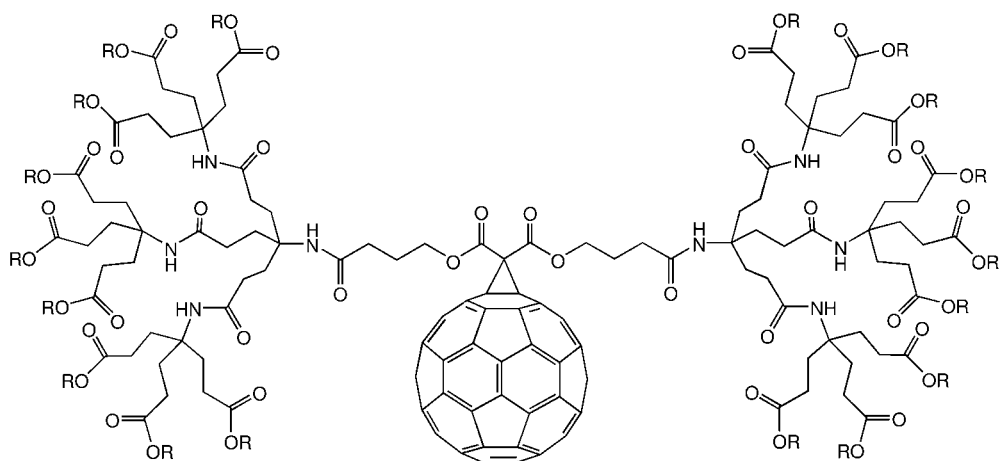


Figure 11.1. Example of covalent functionalization of fullerene with CDs.

ditional cycloaddition reactions that are followed by subsequent modification of the appendage [29–31].

A parallel development involves the synthesis of polyadducts to increase fullerene solubility. Nevertheless, the best results are currently achieved through the monofunctionalization of fullerenes – in the form of dendrofullerene **1** – that reaches water solubilities of the order of 34 or 254 mg mL<sup>-1</sup> at pH 7.4 or 10, respectively [32].



1

### 11.3 Toxicity

The wide-ranging appeal of fullerenes has triggered concern about their potential toxicity. If they are employed widely, it is important that the toxicity of fullerenes be measured and counteracted, if possible. Of key consideration is fullerene solubility in water. Although they are inherently hydrophobic, their water solubility is essential for many emerging biomedical technologies.

Early work focused on studying the effects of unfunctionalized C<sub>60</sub>, raw soot and fullerene black on bovine alveolar macrophage cells and macrophage-like cells. Raw soot and fullerene black are often the intermediaries and byproducts created during the bulk production of fullerenes in the laboratory. Enzyme tests for lysosomal damage and generation of ROS were undertaken as indicators for toxicity. Such tests demonstrate that C<sub>60</sub> and the raw soot did induce a slight cytotoxic effect on alveolar and HL-60 cells after 48 h of incubation [33].

Functionalization of normally hydrophobic fullerenes is primarily done to render them hydrophilic. Cells, tissues and living systems all operate in a hydrophilic environment, and functionalization aids in the interaction between the fullerene and the biological system of interest. Their toxicity, both in tissue culture and *in vivo*, is

an important characteristic for defining and constraining these applications. In fact, there have been a few papers on the influence of  $C_{60}$  and its derivatives on cell growth as well [1]. Surprisingly, no toxic effects of unfunctionalized  $C_{60}$  on biological samples were noted in these early assays.

Some water-soluble fullerene derivatives were found to cross the cellular membrane and localize in the mitochondria of HS 68 human fibroblast and COS-7 monkey kidney cells, but no toxicity studies of this derivative have been performed [34]. Carboxylic acid  $C_{60}$  derivatives inhibited excitotoxic cell death of mouse cortical neurons *in vitro*, and delayed the death and functional deterioration of a transgenic mouse containing the human superoxide dismutase (SOD) gene responsible for the neurodegenerative disease called familial amyotrophic lateral sclerosis (ALS; also known as Lou Gehrig's disease) [35].

When  $C_{60}$  was solubilized with PVP in water and the aqueous solution was applied to a mouse midbrain cell differentiation system, both cell differentiation and proliferation were potently inhibited [36, 37]. However, water-soluble fullerene carboxylic acids derived from  $C_{60}$  and  $C_{70}$ , which were examined for photocytotoxicity toward Raji cells (B lymphocytes), did not show any photocytotoxic effect even at 50  $\mu\text{M}$  [38].

In some cases, the phototoxicity of fullerene molecules has been identified as a feature useful for therapeutics [39, 40]. Other work has sought to minimize the toxicity of water-soluble fullerenes so as to permit their use in drug-delivery applications.

Recent attention has been drawn to the environmental effects of nanoscale aggregates of  $C_{60}$ . This form results when pristine  $C_{60}$ , from either the solid state or organic solution, is placed into contact with neutral water [41]. Rather than completely precipitating, some  $C_{60}$  will form suspended and water-stable aggregates up to 100-p.p.m. concentrations. The environmental and biological significance of fullerenes in water was examined by comparing the cytotoxicity of several important types of water-soluble fullerenes using human liver carcinoma cells and dermal fibroblasts. It has been shown that nanoscale aggregates of  $C_{60}$  are cytotoxic to HDF and HepG2 cells at the 20-p.p.b. level [42].

In conclusion, fullerenes are toxic to human cells as well, but surface modifications can significantly reduce the effect. Fullerenes are toxic because they have a high affinity for electrons and in the presence of oxygen they can generate radical species that damage cell walls. Some studies even postulate that blockage of the cell cycle might be a mechanism of this activity [43]. The low-energy, unoccupied molecular orbitals that make it easy for fullerenes to accept electrons also make them electrically conductive. Such results could help pave the way for the general use of fullerenes.

## 11.4 DNA Photocleavage

DNA cleaving and lipid peroxidation activities of fullerenes have attracted considerable attention [44–46]. Importantly,  $C_{60}$ , if exposed to light, can either make singlet

oxygen (type II energy transfer pathway) or be an electron donor to make superoxide radicals. For example, photoirradiation of  $C_{60}$  results in the formation of the singlet excited state  $^1C_{60}^*$ , which undergoes efficient intersystem crossing to give the triplet excited state  $^3C_{60}^*$ .  $^3C_{60}^*$  reacts with nearly diffusion-controlled rate constants with molecular oxygen to yield singlet oxygen [47]. In principle,  $^1O_2$  would then cleave DNA [48].

Possible involvement of  $^1O_2$  was examined in some detail by comparing the reactivity of a fullerene–oligonucleotide linked system with a similarly linked eosin–oligonucleotide [49]. Fullerene–oligonucleotides that either bind single- or double-stranded DNA cleave the strand(s) proximal to the fullerene moiety upon exposure to light and oxygen. DNA damage occurs predominantly at guanine bases, without revealing a significant specificity between the various G sites [44]. Only when  $C_{60}$  was conjugated to an oligonucleotide was a good selectivity observed [50]. A key observation was that addition of a singlet oxygen quencher, sodium azide, largely inhibits the eosin–oligonucleotide cleavage, while no discernable effect was noted for the fullerene–oligonucleotide cleavage. A likely rationale suggests that the fullerene–oligonucleotide cleavage does not involve the singlet oxygen mechanism, but rather an alternative mechanism must be involved.

The alternative mechanism implies an electron transfer scenario – the type I electron transfer pathway. More precisely, the triplet excited state  $^3C_{60}^*$  is subject to reactions with reductants to afford the radical anion of  $C_{60}$ . In this case, the rate constant for electron transfer quenching as a function of donor oxidation potential typically follows the Weller relationship [51]. Evidence for this pathway comes from early work by Foote and coworkers, who reported that  $^3C_{60}^*$  directly oxidizes guanine in a DNA stack, because the oxidation potential of a guanosine derivative is located at 1.26 V, which is close to the reduction potential of  $^3C_{60}^*$  (1.14 V). Conceptually similar is the sequence of reacting the radical anion of  $C_{60}$  with molecular oxygen to generate superoxide radicals and then indirectly cleaving DNA through reductive electron transfer. Such a reductive activation of molecular oxygen by photoexcited fullerenes was shown to be highly feasible under physiological conditions.

However, the poor solubility of fullerenes in water precluded in most instances the detailed mechanistic studies of  $C_{60}$  photosensitized DNA damage. However, of course, the binding to and recognition of DNA by synthetic organic compounds – fullerenes – is important.

Photoinduced DNA cleavage occurs efficiently by  $C_{60}$  in  $O_2$  saturated solutions containing NADH – the most important redox coenzyme acting as the source of electrons in the living system – through superoxide radicals. In fact, spectroscopic and kinetic studies using a laser flash photolysis technique enabled the detection of superoxide ( $O_2^-$ ) through the use of a radical scavenger – 5-diethoxyphosphoryl-5-methyl-1-pyrroline *N*-oxide (DEPMPO) [52, 53].

Highly efficient DNA cleavage by small amounts of water-soluble poly(fullerocyclodextrin)s under visible light conditions and the photocleavage of DNA by pristine fullerene in mixed organic solvent system have also been observed [54]. The cleaving is followed by a strong interaction between cleaved DNA fragments and  $C_{60}$  leading to DNA– $C_{60}$  conjugates in high yields. Similarly, water soluble  $C_{60}$ –



homooxacalix[3]arene complexes and lipid-membrane-incorporated C<sub>60</sub> acted as efficient DNA photocleavage reagents [11, 55].

Several concepts were followed to enhance the fullerene DNA interactions. A promising strategy involves fullerene derivatives that bear DNA minor groove binders, such as triple-helix-forming oligonucleotides. The rational design of this synthesis is based on a reinforced effect due to the simultaneous presence of two different agents able to confer sequence selectivity [56]. This, for example, is expected to assist in targeting the fullerene moiety to a desired DNA sequence. Although the triplex formation was demonstrated, the presence of fullerene moieties gives rise to a high degree of instability. In this context, the approach to introduce nucleic acid-specific agents such as acridine [57] or netropsin [45] to understand the mechanism of action of these classes of conjugates and to increase both cytotoxicity and sequence selectivity was unsuccessful.

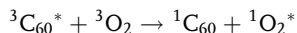
An alternative concept implies that DNA can be used as a framework for the assembly of fullerene materials – bearing cationic functionalities – through electrostatic interactions with the phosphate groups along the DNA backbone [58, 59]. This concept was driven by the finding that a simple carboxylic acid derivative does not bind to DNA and hence it is unlikely that DNA undergoes direct chemical reaction with the fullerene derivative. However, some mediating function – most likely due to the involvement of superoxide radical anions – helped in cleaving DNA fragments at guanine residues upon exposure to light [60].

#### 11.4.1

#### Photodynamic Therapy (PDT)

Photosensitizers that are typically employed in PDT are aromatic molecules, able to efficiently form long-lived triplet excited states. The latter display the potential to generate ROS with high quantum yields. In addition, these compounds should possess low energy absorptions, low toxicity *in vivo* and high selectivity towards biological target in order to avoid side-effects.

Due to the small singlet-triplet energy gap and to the forbidden nature of the radiative S<sub>1</sub> → S<sub>0</sub> transition, the dominant deactivation pathway of the fullerene photoexcited singlet state is S<sub>1</sub> → T<sub>1</sub> intersystem crossing. The quantum yield of triplet formation is close to unity for both C<sub>60</sub> and C<sub>70</sub> [61, 62]. The triplet excited state with lifetimes in the range of hundreds of microseconds is photoactive and gives rise to the formation of cytotoxic species such as O<sub>2</sub><sup>•-</sup>, <sup>•</sup>OH and H<sup>•</sup>. For instance, quenching of the fullerene triplet by oxygen through triplet-triplet annihilation is close to diffusion control:



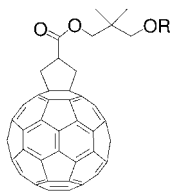
The fact that the reverse process, i.e. quenching of the singlet oxygen by ground state fullerene, proceeds at a rate much lower than diffusion control, together with the low fluorescence quantum yield of fullerenes, makes this class of compounds good photosensitizers with a great potential in PDT [61].

The main drawback for the application of fullerenes as photosensitizers *in vivo* is

the lack of significant absorption at longer wavelengths. However, this disadvantage can be overcome when functional groups are appended that act as a “light harvesting” antenna. Indeed, this pathway was considered and reported first by Cheng and coworkers [63] and later by other authors [64].

To characterize fullerenes  $C_{60}$  and  $C_{70}$  as photosensitizers in biological systems, the generation of active oxygen species through energy and electron transfer was studied *in vitro* [60]. It was found that  $^1O_2^*$  is generated effectively in nonpolar solvents, such as benzene, whereas in water,  $O_2^{\cdot-}$  and  $\cdot OH$  were produced instead, especially in the presence of a physiological concentration of reductants including NADH. These redox active species were shown to contribute to the photoinduced DNA cleavage under physiological conditions.

The effect of the fullerene core substitution on singlet oxygen formation has revealed interesting trends [65]. The efficiency of singlet oxygen production from a series of fullerene derivatives – epoxides and diethylmalonate derivatives – was evaluated by measuring the near-IR emission at 1268 nm, which corresponds to the  $O_2(^1\Delta_g) \rightarrow O_2(^3\Sigma_g^-)$  transition. Overall, it was shown that functionalization of the fullerene core reduced the photodynamic activity. Fascinatingly, the effect was independent of the nature of the addend, but dependent on the number of addends. Higher degrees of functionalization, for example, lead to decreasing efficiencies of singlet oxygen production with greater effects imposed by adjacent addends compared to more remotely placed addends. Complementary studies showed that even multifunctionalized fullerene compounds, such as fullerol  $C_{60}(OH)_n$  ( $n > 18$ ) and fullerene-core star-like polymer,  $C_{60}[>N-CH_2CH_2(OCH_2CH_2OCH_3)]_6$ , are efficient  $^1\Delta_g$  generators *in vitro* [66]. Although the photophysical capabilities of fullerols have been shown to be reduced by hydroxylation, when compared to pristine  $C_{60}$ , sufficient photoactivity remains to trigger sizeable effects on aqueous systems [67]. Indeed, fullerol  $C_{60}(OH)_{24}$  has been shown to produce a mixture of singlet oxygen and superoxide under both visible and UV irradiation.



2

**R = CO(CH<sub>2</sub>)<sub>2</sub>CO<sub>2</sub>H (a)**

**R = H (b)**

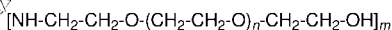
**R = CO(CH<sub>2</sub>)<sub>2</sub>CO<sub>2</sub>H.NEt<sub>3</sub> (c)**

Fullerenes **2a** and **2c**, incubated with HeLa S3 cells, were shown to be cytotoxic upon irradiation [44]. Cells in the presence of fullerenes were not affected when not exposed to light. Compound **2b** was found to be noncytotoxic even when irra-

diated, possibly due to its lower water solubility compared to **2a** and **2c**. A reference compound lacking the fullerene moiety was inactive when incubated with cells and exposed to light. These interesting results were explained by the formation of singlet oxygen through fullerenes.

Li and coworkers reported a 2-fold proliferation of human cervix cancer cells incubated with liposome-encapsulated  $C_{60}$  and irradiated for a short period of time relative to unirradiated cells [68]. The authors concluded that the cancer cells were likely to be killed only if the laser power was above a certain threshold during the irradiation time, otherwise it would have promoted cell growth.

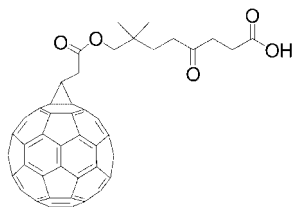
$C_{60}$  derivatives bearing poly(ethylene glycol) (PEG) chains were found to be cytotoxic to L929 cells, but only when photoirradiated with visible light – measurements in the dark disclosed no appreciable impact [69]. The authors considered the generation of singlet oxygen as the critical step. Moreover, cytochrome *c* was reduced when irradiated in the presence of the fullerene derivative and addition of SOD suppressed the cytochrome *c* reduction. However, when SOD, cytochrome *c* and the  $C_{60}$  derivative were administered all together to the cells, no change in cytotoxicity was noted that would have been caused by adding SOD.



**3**

PEG-modified  $C_{60}$  fullerene **3** was shown to accumulate in tumor tissues to a greater extent than in normal tissues upon intravenous injection into tumor-bearing mice, exhibiting prolonged  $C_{60}$  retention at the tumor tissue [70, 71]. Light irradiation that was applied after the injection of **3** significantly suppressed the volume increase of the tumor. The compound was basically released from the mice within 1 week.

Derivative **4** was not active at all up to concentrations of 50  $\mu\text{M}$ , whereas at higher concentrations the cell growth was inhibited – even in the absence of light [38]. The light-triggered oxidative properties of singlet oxygen were considered responsible for a series of biological activities exhibited by fullerene solutions.

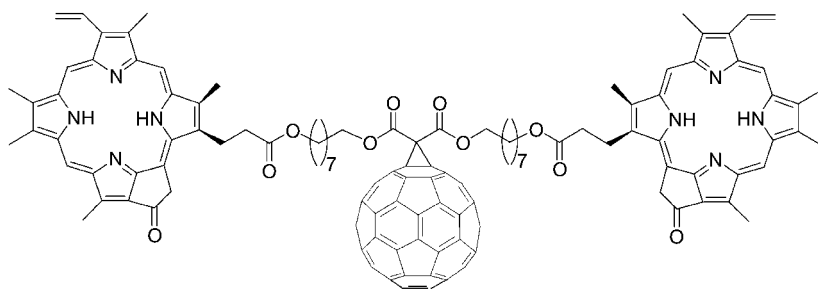


**4**

In the search of new photosensitizers for PDT, the attachment of sugar moieties to the fullerene chromophores attracted considerable attention, since carbohydrates

play, in general, an important role in cell–cell interactions [72, 73]. Sugar-pendant monofunctionalized and bisfunctionalized fullerene derivatives were recently synthesized starting with carbohydrate-linked azides, and their photocytotoxicity against HeLa cells was studied [74]. The photosensitizing ability of the sugar-pendant derivatives to produce singlet oxygen in dimethylsulfoxide solution was demonstrated by the direct observation of the emission due to the  $O_2 (^1\Delta_g) \rightarrow O_2 (^3\Sigma_g^-)$  transition at 1268 nm. In agreement with the established trend that functionalization of fullerenes reduces the efficiency of singlet oxygen production [65], mono-adducts were shown to produce singlet oxygen with higher efficiencies than the corresponding bis-adducts. The cells were incubated for 12 h prior to the addition of photosensitizer and further incubated for an additional 6 h. After washing and irradiating with  $10 \text{ J cm}^{-2}$  of laser energy, cells were further incubated for 24 h before the numbers of living cells were counted by the MTT [3-(4,5-dimethylthiazol-2-yl)-2,5-diphenyltetrazolium bromide] assay. Overall, the dark cytotoxicity of all investigated compounds was found to be quite small, while significant phototoxicities were observed for D-glucose, D-mannose and D-galactose derivatives bearing a single carbohydrate unit. However, D-xylose and maltose derivatives were less toxic despite the fact that comparable amounts of singlet oxygen were produced *in vitro*. Also, under the chosen experimental conditions the bis-adducts failed to display any meaningful phototoxicity, since they gave rise to poorer performance in terms of generating singlet oxygen than the analogous mono-adducts.

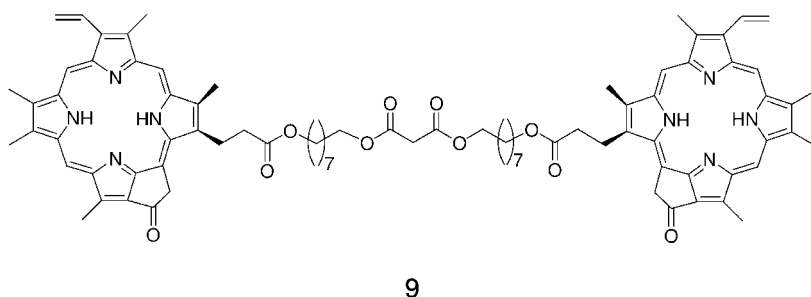
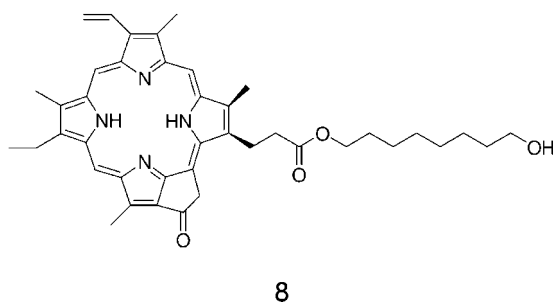
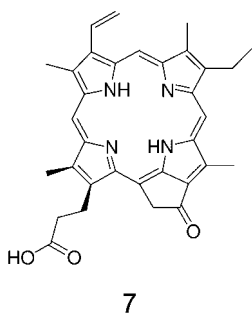
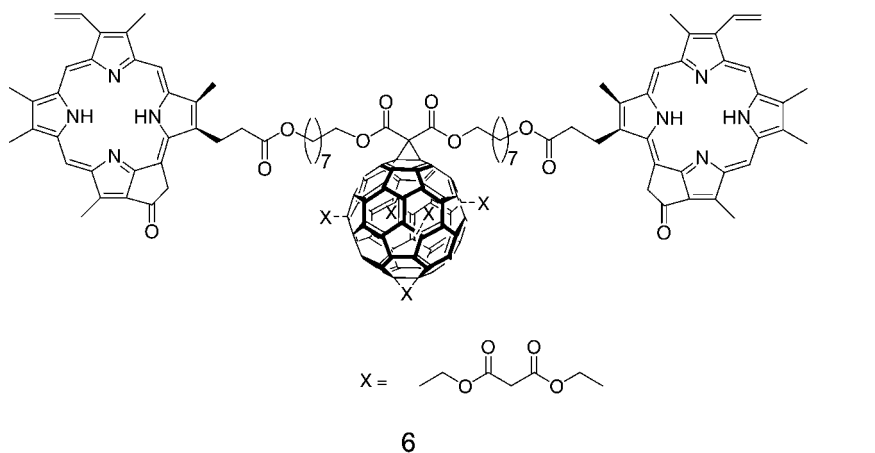
Recently, two new fullerene-bis-pyrophephorbide *a* derivatives, i.e. a mono-adduct **5** and a hexakis-adduct **6**, were synthesized and tested *in vitro* with regard to their intracellular uptake and photosensitizing activity towards human leukemia T lymphocytes (Jurkat cells) [75, 76].



5

The uptake of **5**, **6** and the reference compounds **7–9** by Jurkat cells was investigated with confocal laser scanning microscopy and by measuring the fluorescence intensity of cell extracts at the emission wavelength of pyrophephorbide *a*. The intracellular concentrations of fullerene complexes and **9** were 27 times lower than that of the free sensitizers after 24 h of incubation. They also showed slower

accumulation in cells. The authors rationalized these results on the basis of different uptake mechanisms – lipophilic molecules with molecular weights lower than 100 Da normally diffuse through the membranes, while bigger molecules, such as fullerene–sensitizer complexes **5** and **6**, and **9** can be taken up only by endocytosis or pinocytosis, which have slower kinetics than passive diffusion through cell membranes.



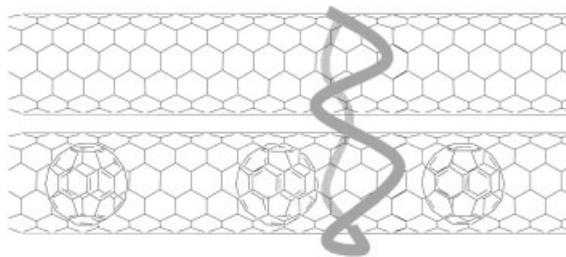


**Figure 11.2.** Hybrid nanotube rope controlling protein activity *in vivo* by near-IR radiation.

The phototoxicity of fullerene–sensitizer complexes was tested in comparison with the fullerene-free sensitizers. The rates of necrotic and apoptotic cells were determined 24 h after irradiation with a laser diode (688 nm,  $2.12 \text{ mW cm}^{-2}$ ). The fullerene complexes were found to be less phototoxic compared to the fullerene-free sensitizers **7** and **8**. This is mainly due to the high molecular weight of the fullerene complexes, leading to lower intracellular concentration.

The hexakis-adduct **6** showed significant phototoxic activity (58% dead cells after a dose of  $400 \text{ mJ cm}^{-2}$ , 688 nm), while the mono-adduct **5** showed very low toxicity even at higher doses of irradiation. The latter was attributed to a low intracellular uptake for **5** and to an efficient electron transfer process from the pyropheophorbide singlet state to the fullerene moiety, resulting in low yield of the intersystem crossing (ISC) and low quantum yield of singlet oxygen formation.

No dark cytotoxicity was found towards Jurkat cells after 24 and 48 h of incubation with all studied sensitizers.

Recently, it has been demonstrated that chemical reactions of importance for PDT could be directly activated by a hybrid carbon nanotube (CNT) rope consisting of two adjacent metallic CNTs, where one is filled, i.e. the peapod, and the other is empty [77]. Under electric bias, a substantial charge transfer from the entrapped metal ion to the fullerene cage in metallofullerenes occurs. In the CNT rope this process also involves the peapod and the twin (empty) CNT, thus the two CNTs become oppositely charged. This process can be partly inverted at elevated temperatures, since the metallofullerenes have levels close to the Fermi levels. In this way, by heating with near-IR excitation, recharging of the CNTs is expected that would result in a change of the local electric field and further to a deformation of proteins selectively attached to the CNT (Fig. 11.2).

#### 11.4.2

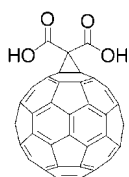
##### **Fullerene-mediated Electron Transfer Across Membranes**

Both  $C_{60}$  and  $C_{70}$  embedded within a lipid bilayer act as efficient electron acceptors at interfaces [78, 79]. Moreover, fullerenes can efficiently transport negative charges across membranes [80]. Mauzerall and coworkers have observed that transmembrane electron transfer takes place via electronic conduction mediated by fullerene aggregates [81]. The possible role of small fullerene aggregates, which act as an an-

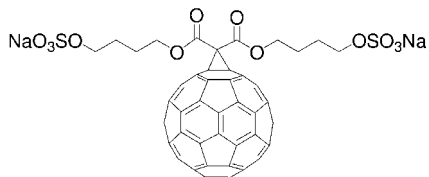
tenna for collecting photons, in the presence of monomers was also discussed by Seta and coworkers [82]. In a study of the photoconductivity of ultra-thin bilayer lipid membranes doped with  $C_{60}$ , the authors suggested that since the extinction coefficient of the aggregated form is higher than that of the monomeric form, the absorption spectrum is dominated by the contribution of the aggregates. Thus, the energy absorbed by the aggregates is transferred to the monomers via singlet-singlet energy transfer and the excited monomers are then reduced by the donor species at the membrane interface. The reduction can take place either in the singlet excited state or in the triplet excited state of the fullerene. An alternative mechanism could be exciton-induced charge injection at the interface of the  $C_{60}$  aggregates with the bilayer membrane.

Photoinduced charge transfer across membranes has also been achieved in the composite assembly of  $C_{60}$  and CdS nanoparticles prepared by the Langmuir-Blodgett technique [83]. The CdS nanoparticles exciton emission was quenched due to efficient electron transfer from CdS nanoparticles to  $C_{60}$  across a lipid layer (2–3 nm). The fatty layer between  $C_{60}$  and CdS played an important role in preventing charge recombination in the composite assembly.

Amino acid derivatives of  $C_{60}$  were shown to penetrate through the lipid bilayer of liposomes without destroying the membrane integrity [84]. The L-isomer was able to diffuse through the phospholipid membrane into the liposome interior, whereas the D-isomer localized in the region of the outer membrane surface. These derivatives were also able to carry bivalent metal ions through phospholipid bilayers as a result of the formation of complexes. The study of the effects of the two stereoisomers on lipid peroxidation in mitochondria of rat cortex brain showed that  $C_{60}$ -L-Arg exhibits a prolonged inhibition in the malonaldehyde accumulation, whereas  $C_{60}$ -D-Arg led to no discernable effects on malonaldehyde accumulation. This data showed that amino acid derivatives of  $C_{60}$  affect membrane-bound enzymes. In particular, the L-isomer stimulates the catalytic activity of monoamine oxidase A (MAO) A, while the main action of the D-isomer is an increase in the catalytic activity of MAO B. It is worth pointing out that MAO is a known redox enzyme. This led to the postulate that the observed effect of the amino acid derivatives of  $C_{60}$  on the catalytic activity of MAO A and MAO B is due to an intra-protein electron transfer process.



10



11

Recently, fullerene derivatives **10** and **11** were studied as counteranions in the activation of oligo/polyarginine-anion complexes in living cells, and, thus, to modulate cellular uptake and anion carrier activity of oligo/polyarginines [85, 86]. The fact that cell-penetrating peptides (CPPs) are anion carriers and that bilayer pene-

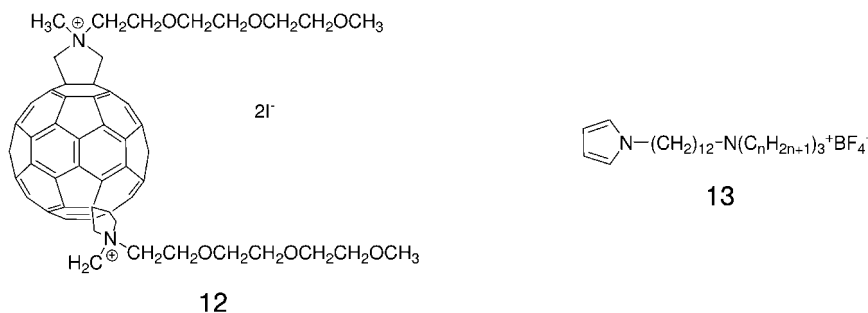
tration is regulated by amphiphilic anions suggested that the carrier activity of oligo/polyarginines occurs via counterion exchange, which facilitates the reversible adaptation of their solubility to a changing environment. An efficient counteranion activator should, therefore, have one or more negative charges for ion pairing with guanidinium cations of the oligo/polyarginine. In addition, an amphiphilic character with large hydrophobic domains and an aromatic surface is expected to favor interactions with bilayer membranes. R-rich CPPs usually exist as complexes  $R_n(X)_m$  ( $X$  = hydrophilic counteranion) to minimize intramolecular charge repulsion and the exchange of the scavenged  $X^-$  with an activator  $Y^-$  yields the active complex  $R_n(X)_m'(Y)_m''$  at the membrane water interface. This active complex can then shuttle across the bilayer. In this respect, the activator  $Y$  should have also the ability to form stable, but labile, guanidinium anion complexes.

The key finding in the aforementioned study was that the efficiency of counteranion activators significantly depends on activator membrane and activator carrier interactions. Specifically, the activator efficiency was found to increase with increasing aromatic surface of the activator, decreasing size of the transported anion, increasing carrier concentration as well as increasing membrane fluidity. Fullerenes **10** and **11** were the most efficient counteranions in egg yolk phosphatidylcholine, where compound **10** showed an extraordinary  $EC_{50}$  value. Below the binding of one activator per carrier, fullerene activators acted at catalytic concentrations [86]. At high concentrations, fullerenes **10** and **11** became inhibitors of CPP uptake. However, in sol-phase dipalmitoyl phosphatidylcholine (DPPC) and in gel-phase DPPC, as well as in HeLa cells, the efficiency of the planar activators (pyrene and coronene) exceeded that of spherical activators (fullerenes and calixarenes). These results showed that spherical activators, particularly fullerene **10**, may specifically mediate CPP uptake.

The transmembrane extraction of fullerenes  $C_{60}$  and  $C_{70}$  across a membrane having  $\gamma$ -CDs as molecular recognition sites attached to a poly(vinyl alcohol) matrix was achieved [87].  $C_{60}$  molecules were transported from a feed aqueous phase, in which fullerene was rendered water soluble in the form of  $\gamma$ -CD: $C_{60}$  complexes, to a stripping organic phase such as toluene, xylene or tetralin. The high affinity of the fullerene  $C_{60}$  towards  $\gamma$ -CD allows their interfacial exchange and penetration into the membrane core. The loading of the membrane was confirmed by the observed color change of the membrane to magenta. During the first 20 h of the experiment the flux of permanent  $C_{60}$  rapidly reached a constant value. However, the membrane was far from saturation as the majority of the  $\gamma$ -CD cavities were unoccupied. It was suggested that steric hindrance due to crosslinking prevents the formation of the inclusion complex and the occurrence of a complex involving more than two  $\gamma$ -CDs due to the high local concentration of these moieties is possible. Moreover, small aggregates of fullerenes, which are surrounded by several CD cavities, were observed in the membrane. In this way the membrane acted as a reservoir of  $C_{60}$  molecules that were afterwards slowly released into the receiving solution. The rate-limiting step of the membrane transport was demonstrated to be governed by the dissociation of the inclusion complex at the stripping interface. This led to a low overall membrane transport flux.

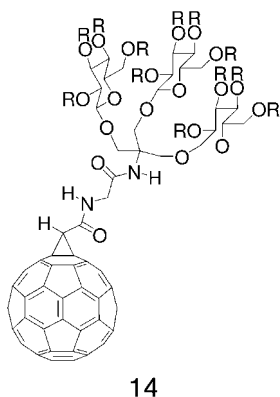


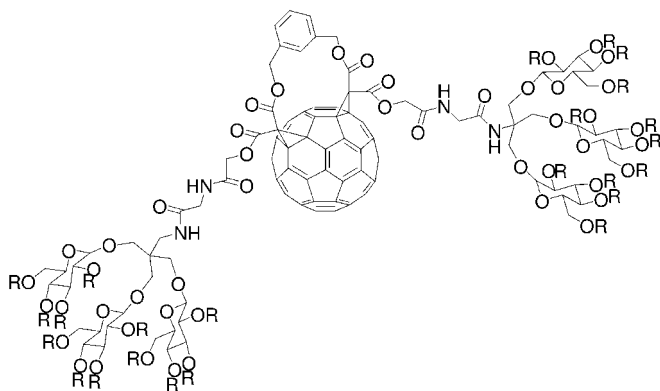
The good electron acceptor properties of fullerenes stimulated studies on their possible applications as biosensors. A novel biosensor for the amperometric detection of glutathione was obtained by co-immobilizing a redox enzyme with a redox mediator (fullerene derivative **12**) realized at the glassy carbon electrode by the use of an amphiphilic pyrrole derivative **13** ( $n = 2$ ) [88]. The reversible reduction of **12**, which is entrapped within the poly-**13** film, was deduced from the coefficient of variation curves and the electron transfer was likely to occur via a vectorial charge-hopping mechanism involving neighboring fullerene molecules that are coupled to the diffusion of the counterions. The poly-**13**/**12**/GR film was investigated for its electrocatalytic properties. The biosensor showed a fast and reproducible response to glutathione.



A C<sub>60</sub>-containing lipid bilayer membrane was shown to function as a light-sensitive diode and to be useful for electrochemical biosensor electronic device developments [89].

The potential of glycosylated fullerene layers as biosensors for glycoproteins was reported [90]. The amphiphilic C<sub>60</sub> dendrimer conjugates **14** and **15** with one or two glucodendrion headgroups form stable, ordered monomolecular Langmuir layers at the air/water interface, which were further transferred onto quartz slides as X-type Langmuir–Blodgett films. The bulky glucodendrion headgroups were very effective in suppressing fullerene aggregation.





15

## 11.4.3

**Neuroprotective Activity via Radical Scavenging**

Excess production of superoxide and/or nitric oxide radicals, as well as nonradical  $\text{H}_2\text{O}_2$  and hypochloric acid, is considered as one of the primary initiators of neurodegenerative diseases. Endogenous cellular antioxidants, vitamin E analogs and SOD enzymes, have evolved in organisms – from bacteria to mammals – to inactivate low levels of free radicals produced under regular metabolic conditions. However, their antioxidant defense may be overwhelmed by ROS in the cells that are generated in the pathogenesis of a number of neuronal injuries and, as a result, they are no longer able to achieve meaningful therapeutic results.

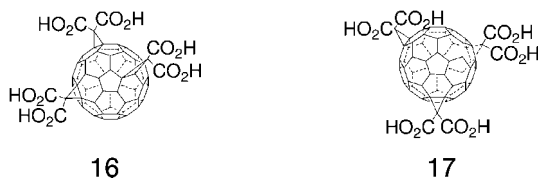
In this respect, compounds that act as free radical scavengers were shown to reduce neuronal death. Fullerenes and related derivatives reveal promising antioxidant properties, i.e. their ability to react with multiple radical species at diffusion-controlled rates [91]. To this end, several  $\text{C}_{60}$  derivatives, including carboxyfullerenes [18, 35, 92–112], polyhydroxyfullerenes [113–116] and a limited number of other derivatives [19, 107, 117–120] have been investigated as neuroprotective agents.

In particular, two different tris-adducts,  $\text{C}_3$  (16) and  $\text{D}_3$  (17), of  $\text{C}_{60} \cdot [\text{C}(\text{COOH})_2]_3$ , have been confirmed to be the most promising compounds for preventing neuronal damage [35, 92]. The presence of six carboxylic functional groups improves the solubility in biological media and avoids the fullerene aggregation that is commonly encountered in polar solvents. As a result of an improved intercalation into biological membranes, the  $\text{C}_3$  isomer has been studied in more detail. These studies demonstrated that the  $\text{C}_3$  isomer is an excellent radical scavenger, which reacts both with hydroxyl radicals,  $\cdot\text{OH}$ , and  $\text{H}_2\text{O}_2$  at micromolar concentrations [35, 93].

Dugan and coworkers also evaluated the ability of  $\text{C}_3$  to eliminate superoxide generation in intact cells [94]. Using confocal microscopy and a superoxide-sensitive fluorescent compound, dihydroethidium, they determined that this iso-

mer can reduce basal mitochondria production of superoxide in cortical astrocytes and neurons. In addition,  $C_3$  blocks iron-induced lipid peroxidation *in vitro* [92] and *in vivo* [95]. The free radical nitric oxide, produced by three different synthase isoforms and responsible for the generation of citrulline, is also an important effector molecule in immune and cardiovascular system.

Although Dugan and coworkers have found that  $C_3$  is unreactive with  $NO\cdot$  itself, in another study [96] carboxyfullerenes **16** and **17** were shown to exert some inhibition on the three synthases. This work also substantiated a reduction in the level of nitric oxide production and the rate of citrulline formation. However, this effect was attributed to interactions of the fullerene molecules with the enzyme and not to their properties as radical scavengers. The same authors also reported that these compounds inhibit the Arg-independent nicotinamide adenine dinucleotide phosphate (NADPH) oxidase activity of one of the synthase isoforms without affecting its catalyzed cytochrome *c* reductive activity.



To explore the neuroprotective and cytoprotective properties of the malonic acid tris-adducts, Dugan and coworkers prepared neocortical cell cultures from fetal (E15) Swiss-Webster mice (Simonson). These were subjected to tests with different antioxidants after carrying out a brief exposure to *N*-methyl-D-aspartate (NMDA) [97]. Both the  $C_3$  and  $D_3$  isomers produced a dose-dependent decrease of the excitotoxic death of cultured cortical neurons.  $C_3$  fully blocked NMDA receptor-mediated toxicity at 100  $\mu$ M concentration, showing greater protection and efficacy against acute toxicity initiated by brief (10 min) exposure to high-dose NMDA. This isomer also provided protection against AMPA ( $\alpha$ -amino-3-hydroxy-5-methyl-4-isoxazolepropionic acid) receptor-mediated injury in neurons [35] and oligodendroglia [98], the cell type responsible for central myelin formation. The authors stressed that the observed behavior not only reflects the antioxidant properties of the compound, but other features of the molecule, e.g. its amphiphilic nature.

Moreover, the carboxyfullerene **16** limited apoptotic neuronal death produced by several insults, including serum deprivation and exposure to the Alzheimer's peptide  $A\beta_{1-42}$  [18], and has shown robust neuroprotection in a number of other cell culture models of neurological disease including Parkinson's disease [35].

In a study of neurotoxin-mediated death of dopamine neurons, the same authors have pursued the concept that carboxyfullerene derivatives could block the toxic effect of the neurotoxins 6-OHDA (6-hydroxydopamine) and  $MPP^+$  (1-methyl-4-phenylpyridinium). 6-OHDA and  $MPP^+$  are widely used to generate animal models of Parkinson's disease, since after administering *in vivo* they cause Parkinsonian conditions. Parkinsonian conditions are marked by decreased dopamine

levels and tyrosine hydroxylase activity, impaired dopamine uptake, and an ensuing loss of dopaminergic neurons. With regard to oxidative injuries, the  $C_3$  isomer dramatically rescued dopaminergic neurons from 6-OHDA-induced cell death in a dose-dependent manner (92% recovery at the highest dose), whereas it quickly plateaued in the case of MPP<sup>+</sup> (37.5% recovery). Concentrations of  $C_3$  in excess of 100  $\mu$ M were found to be cytotoxic [99]. The  $D_3$  isomer was also found to be protective against 6-OHDA injury and MPP<sup>+</sup>-mediated death, but to a lesser extent than the  $C_3$  isomer. The  $C_3$  isomer proved more effective than the dopaminergic neuroprotectant glial cell line-derived neurotrophic factor (GDNF) in rescuing dopamine neurons from 6-OHDA- or MPP<sup>+</sup>-mediated cell death.

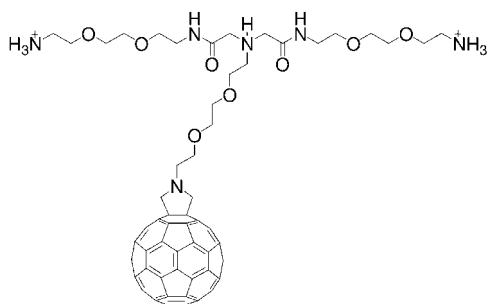
A parallel assay that focused on utilizing the two isomers,  $C_3$  and  $D_3$ , of tris-adducts, among other antioxidant agents, showed that these fullerene derivatives inhibited apoptosis of human hepatoma HEP-3B cells, induced by transforming growth factor (TGF)- $\beta$  [100]. The mechanism of action is supposed to be indirect, because all other actions induced by TGF- $\beta$  remained, surprisingly, unaltered.

The same carboxyfullerenes have been demonstrated to protect human keratinocytes from apoptosis induced both by UV-B irradiation and exposure to deoxy-D-ribose [101]. However, **16** and **17** failed in preventing the downregulation by UV-B light of the Bcl-2 levels. This suggested that these compounds protect human keratinocytes from UV-B damage via generation of ROS from depolarized mitochondria without the possible involvement of Bcl-2.

The same group of authors reported the protective activity of carboxyfullerenes against oxidative stress-induced apoptosis in human peripheral blood mononuclear cells [102]. Two models of apoptosis were used – one, induced by 2-deoxy-D-ribose, a reducing sugar capable to induce oxidative stress and glutathione depletion, and second, induced by tumor necrosis factor (TNF)- $\alpha$  plus cycloheximide. In both models, the studied fullerene derivatives were able to inhibit apoptosis, likely acting as an antioxidant drug and partially preventing the depolarization of mitochondrial membrane potential as in the case of keratinocyte cells [101].

In another study, the  $C_3$  isomer was shown to inhibit lymphotoxin- $\beta$  receptor-mediated apoptosis signal-regulating kinase 1 activation in Hep3BT2 cells treated with LIGHT-R228E [103].

In recent work, Prato and coworkers synthesized and investigated a water-soluble fullerene derivative **18** that bears three ethylene glycol chains and three ammonium groups for increasing the water solubility as a potential neuroprotecting agent [19]. This compound was designed as a monofunctionalized derivative in order to resemble the free radical scavenging ability of pristine  $C_{60}$ , as it is known that higher numbers of addends on the fullerene moiety decreases its radical scavenging features [91]. As observed by UV-vis spectroscopy, this mono-adduct showed aggregation at concentrations higher than  $10^{-5}$  M not only in water, but also in water/ethanol and water/dimethylformamide mixtures. In a series of spectrophotometric assays employing the xanthine/xanthine oxidase system for the generation of superoxide radicals and ferricytochrome *c* reduction for measuring superoxide concentration, this new fulleropyrrolidine derivative did not show a significant re-



18

action with  $O_2^{\cdot-}$ . In a neuroprotection model, in cerebral cortical cell death induced by glutamate, the compound was not only found to be ineffective, but also showed a significant concentration-dependent toxicity. The authors explained this undesirable toxicity by the lipophilic character of the derivative, which coupled with its hydrophilic part confers surfactant properties favoring its interaction with cell membranes, with their possible disruption and subsequent cell death. An important conclusion from this work is that the neuroprotective activity of  $C_{60}$  derivatives correlates more with the number of substitutions than with their nature. Increased number of polar groups on  $C_{60}$  probably prevents its interaction with the cell membrane and, consequently, effects its disruption.

Although *in vivo* studies bear great importance for understanding how well the neuroprotective activity of novel antioxidant agents – observed in cell cultures – translates to an intact organism, only a limited number of *in vivo* studies have been published in this field so far [35, 92, 94–95, 109]. Continuous intraperitoneal infusion of **16** into a transgenic mouse model of ALS, carrying the human mutant (G93A) SOD gene responsible for a form of familial ALS, delayed both death and functional deterioration [35]. The initial *in vivo* studies of two models of Parkinson's disease have shown that **16** when co-injected with iron, intrastrially injected to produce striatal injury, reduced dopamine depletion [95]. A first proposed rationale prompts the ability of **16** – once injected – to reduce injury, reflecting its interaction either directly with iron or direct involvement in lipid peroxidation. A second model, in which **16** was delivered systemically for 1 month to rats intrastrially injected with 6-OHDA to provoke Parkinsonian conditions, indicated that dopaminergic terminals and behavior were significantly improved by  $C_3$  treatment [94]. Due to their antioxidizing action,  $C_3$  tris-adducts also prevent iron-induced stress in rat brain, and lipid peroxidation induced by superoxide and hydroxyl radicals [95, 109].

Towards the goal of reducing the oxidative stress in brain damage, the neuroprotective effect of carboxyfullerenes on transient focal ischemia reperfusion injury was recently studied in rat brains [95, 104]. Carboxyfullerene was administered either intravenously or intracerebroventricularly to chloral hydrate-anesthetized Sprague-Dawley rats 30 min prior to transient ischemia reperfusion. The data

showed that intravenous injection did not inhibit the reperfusion injury. This is likely due to the limited permeability of this compound to the blood–brain barrier. In contrast, pre-treatment with local carboxyfullerene-attenuated cortical infarction prevented both elevated lipid peroxidation and depleted glutathione (GHS) levels in the infarcted cortex induced by transient ischemia reperfusion. Adverse behavior changes were simultaneously observed in rats receiving intracerebroventricular infusion of carboxyfullerene, including writhing accompanied by trunk stretching and even death.

Intravenous administration of hexasulfobutylated  $C_{60}$  (FC4S) has been found to reduce the total volume of infarction produced by transient ischemia reperfusion in rat brain [117].

The redox properties of carboxyfullerenes correlate with another interesting activity exhibited by this class of compounds – they were shown to inhibit bacterial meningitis [105, 106]. The effect of the  $C_3$  isomer on the regulation of brain inflammatory responses after intracerebral injection of *Escherichia coli* in B6 mice that induced TNF- $\alpha$  and interleukin (IL)-1 $\beta$  production and recruited neutrophil infiltration at 6–9 h post-injection was studied [106]. Pre-treatment of each mouse with  $C_3$  protected 40% of mice in a dose-dependent manner. Fullerene-treated showed less TNF- $\alpha$  and IL-1 $\beta$  production compared with the levels of production for non-treated mice. TNF- $\alpha$  and IL-1 $\beta$  production is typically detected in the cerebrospinal fluid of patients infected with bacterial meningitis and in experimental animals. The authors conclude their work by ascribing the inhibition of *E. coli*-induced meningitis not due to direct antimicrobial activity, since  $C_3$  did not exhibit the growth of *E. coli* in LB broth culture. Moreover, the *E. coli* cells were cleared from the brain after 24 h in fullerene-treated mice. At the same time they were found to replicate significantly in untreated mice. This leads to the suggestion that  $C_3$  might have enhanced the natural antibacterial defense in the brain. A series of similar fullerene mono- and bis-adducts was also able to suppress *E. coli* growth [105, 107].

Some cationic fullerene derivatives were found to exhibit bacteriostatic effects [118, 107].  $C_{60}$ -bis(*N,N*-dimethylpyrrolidinium iodide), for example, in low concentrations inhibits *E. coli* growth and dioxygen uptake caused by *E. coli* and glucose [119], whereas at high concentrations dioxygen was consumed and converted to  $H_2O_2$ .

Derivative **16** was tested *in vitro* against apoptotic neuronal death in rat cerebellar granule cells [108]. Cerebellar granule cells represent one of the best *in vitro* models of neuronal apoptosis, both for the mitochondria and the nucleus, which is strictly related to the generation of ROS.

Dugan and coworkers studied the effect of polyhydroxy fullerols  $C_{60}(OH)_n$  ( $n = 6–15, 24$ ) on apoptotic death of culture neurons and found that these compounds reduced excitotoxic and apoptotic death of cultured neurons by 80% following NMDA treatment [113].

Polyhydroxylated fullerols also display excellent efficiency in quenching superoxide radicals ( $O_2^{\cdot-}$ ) generated by xanthine/xanthine oxidase [114]. The same fullerols  $C_{60}(OH)_n$  ( $n = 6–15$ ) were shown to attenuate bronchoconstriction induced

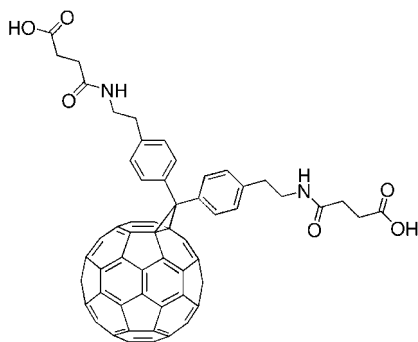
by the xanthine/xanthine oxidase system in guinea pigs [115]. The intratracheal instillation of xanthine/xanthine oxidase caused a marked decrease in dynamic respiratory compliance, which was significantly reduced by these fullerenes [116].

Whereas carboxyfullerenes were indicated as effective neuroprotection against excitotoxic cell death, apoptosis initiated by several different types of triggers and metabolic insults in cultured cells, the molecular mechanism behind the antioxidant reactions of  $C_{60}$  compounds, particularly the mechanism of  $O_2^{\cdot-}$  removal by malonic acid  $C_{60}$  derivative, remains controversial. Krusic and coworkers first suggested that direct reactions between radical species and the highly conjugated double-bond system of  $C_{60}$  were responsible for the antioxidant action of carboxyfullerenes and attributed this property to their delocalized  $\pi$  system [91]. The spherical structure of  $C_{60}$  was also believed to increase the reactivity towards free radicals compare to that of the planar aromatic and polyene compounds. The study by Bensasson and coworkers [110], however, failed to detect a  $C_{60}$  radical intermediate in the reaction of  $C_3$  and several other malonic acid derivatives with  $O_2^{\cdot-}$ . In addition, no correlation was found between the  $IC_{50}$  values and the reduction potentials of various carboxyfullerenes [111]. A recent study of SOD mimetic properties of **16** has made a step forward showing that the reaction between **16** and the superoxide is not via stoichiometric scavenging, where  $O_2^{\cdot-}$  donates an electron to  $C_{60}$ , but through catalytic dismutation of superoxide [112]. The catalytic mechanism was indicated by the time invariability of the concentration and structure of **16** during the exposure to a continuous flux of  $O_2^{\cdot-}$ , produced by xanthine/hypoxanthine metabolism, regeneration of oxygen, production of hydrogen peroxide, as well as absence of paramagnetic intermediate products, detectable by electron paramagnetic resonance (EPR) spectroscopy. In particular, a mechanism has been proposed in which electron-deficient areas on the  $C_{60}$  sphere work in concert with the malonyl addends to electrostatically guide and stabilize superoxide, promoting dismutation. The latter process occurs at a rate of  $2 \times 10^6 \text{ M}^{-1} \text{ s}^{-1}$ , approximately 100-fold slower than what is known for SOD, but within the range of several biologically effective, metal-containing SOD mimetics. To determine whether **16** is capable of acting as a SOD mimetic *in vivo*, the authors tested its efficacy in *Sod2*<sup>+/-</sup> mice, which lack expression of mitochondrial manganese SOD (MnSOD) and found that treatment with this compound increased the lifespan of mice by 300%. These data, coupled with the evidence that **16** localizes to mitochondria [34], suggested that the  $C_3$  isomer functionally replaces MnSOD, acting as a biologically effective SOD mimetic.

#### 11.4.4

#### Enzyme Inhibition and Antiviral Activity

The inhibition of enzymes by fullerene derivatives became one of the most important fields of biological application of fullerene since the publication of milestone works in 1993 [44, 121]. Tokuyama and coworkers reported the inhibition of papain, cathepsin, trypsin, plasmin and thrombin by derivative **3**, while Wudl's group described the inhibition of HIV protease (HIV-P) by compound **19**.



19

The HIV-P is one of the key enzymes in HIV replication. This protease bears a hydrophobic cavity, whose diameter is about 10 Å, in which two catalytic aspartic acid residues are present. Considering the dimensions of C<sub>60</sub>, this fullerene is a perfect match for the cavity size of HIV-P. Furthermore, the presence of C<sub>60</sub> might prevent interactions between the catalytic portions of HIV-P and any virus substrates. The inhibition constant ( $K_i$ ) of compound **19** is 5.3 μM *in vitro*, but fullerene derivatives with positive charges, able to interact with the aspartic negative residues, are expected to raise the binding constant up to 1000 times and consequently dramatically decrease the  $K_i$  [121].

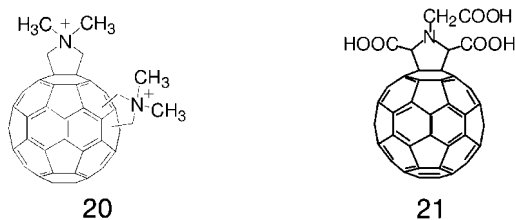
Although current therapy against HIV infection utilizes HIV-P inhibitors active at nanomolar and subnanomolar concentrations, the potential use of fullerene derivatives can be taken into account considering the common problem of resistance versus the used drugs – a phenomenon partially caused by the tendency of the virus to present frequent genetic mutation.

A selection of fullerene derivatives was studied by Schuster and coworkers as potential inhibitors of HIV on human peripheral blood mononuclear cells infected with HIV-1 and three of these compounds presented an EC<sub>50</sub> in the range of 0.9–2.9 μM [122]. In the same way, a peptidic fullerene bearing the C-terminal sequence of peptide T, which is able to activate chemotaxis of human monocytes through CD4/T4 antigen and to inhibit HIV-P activity, was prepared by Toniolo and coworkers [123].

Better results were achieved with compound **1** [124] and the *trans-2* isomer of **20** [125]. In both cases the EC<sub>50</sub> was 0.2 μM. Is it interesting to note that, in the cases of bis-adducts, the regioisomers are not equally active, with the *trans-2* regioisomers presenting the highest activity among the studied compounds [125, 126].

Recently, the same salts (**20**) have been used, together with fulleropyrrolidine **21**, to study the inhibition of HIV reverse transcriptase – yet another enzyme that plays a determinant role in the HIV replication. The results obtained are outstanding. In fact, the IC<sub>50</sub> of derivative **21**, bearing three carboxylic functions, is 100 times lower than nevirapine. Interesting results have also been obtained on hepatitis C virus RNA-dependent RNA polymerase when assaying the same derivative [127].





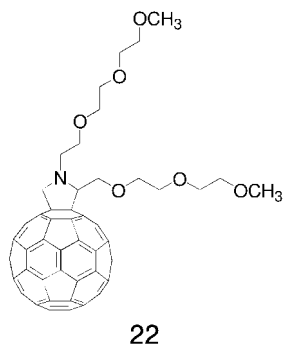
Other important biological enzymatic targets blocked by fullerene derivatives are glutathione-S-transferase, P450-cytochrome-dependent monooxygenases, plasmatic reticulum enzymes of hepatic cells and mitochondrial ATPase in the process of oxidative phosphorylation [128, 129].

The inhibition of all the three forms of nitric oxide synthase (NOS), i.e. neuronal, epithelial and inducible, has been found by trimalonic tris-adducts of C<sub>60</sub>, mainly C<sub>3</sub> (16) and D<sub>3</sub> (17) [96]. The same compounds have been reported as potential inhibitors of  $\beta$ -lactamase [130].

#### 11.4.5

##### Antibacterial Activity

One of the first experiments developed to study the effect of fullerene derivatives on bacteria was performed in 1996 [16]. Derivative 22 was tested on *Candida albicans* (eukaryote), *Bacillus subtilis* (Gram-positive bacterium), *E. coli* (Gram-negative enteric bacterium) and a clinical isolate strain 261/6 of *Mycobacterium avium* (acid-fast, emerging pathogen resistant to most antimicrobial drugs) with promising results. No particular reaction mechanism was demonstrated for this action, but the disruption of the cell wall was hypothesized.



Further studies on the antibacterial activity of fulleropyrrolidinium salts have been reported [118]. Lately, however, attention has been re-focused on bis-adduct mixtures (Fig. 11.3), which demonstrate bacteriostatic effects on *E. coli* and the inhibition of oxygen uptake. In this context, blocking the energy metabolism seems to be the mechanism of action [107]. Additional studies on antimicrobial PDT have

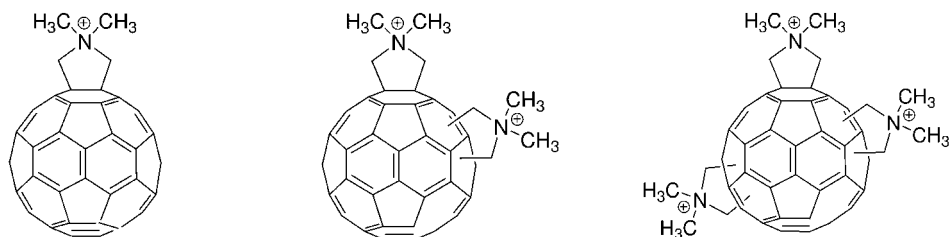


Figure 11.3. Mono-, bis- and tris-*N,N*-dimethylfulleropyrrolidinium salts.

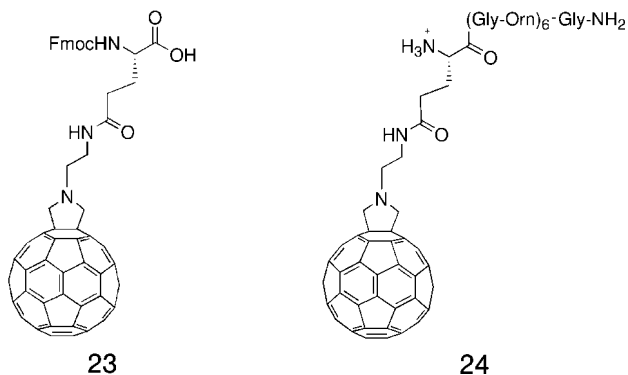
been performed, testing the same mixture of cationic bis-adducts, cationic fullerene and a combination of tris-adducts/parent mono-adduct (Fig. 11.3). In this particular case a very interesting selectivity for microbes (*Staphylococcus aureus* and *E. coli*) over mammalian cells was demonstrated [131]. At present, the question remains if the reaction mechanism involves the formation of singlet oxygen or the generation of hydroxyl and superoxide radicals.

The *trans*-2 and *trans*-4 *N,N*-dimethyl-bisfulleropyrrolidinium salts exhibit their antibacterial action by inhibition of the respiratory chain, with a biphasic effect on oxygen uptake [132]. A fullerene derivative concentration up to 5  $\mu\text{M}$  decreases the oxygen uptake, while at higher concentrations of  $\text{C}_{60}$  salts, an increase of oxygen uptake is found and oxygen is converted to  $\text{H}_2\text{O}_2$  correspondingly. Fascinatingly, irradiation with light did not affect the results at all. In terms of mechanistic aspects this observation indicates that the electron transfer from the respiratory chain to  $\text{C}_{60}$  is independent of light.

Another water-soluble derivative, i.e. one that bears six sulfo-butyl chains, inhibits environmental bacteria. In contrast to the preceding studies, the noted effects have been ascribed to singlet oxygen – produced by photoexcitation. Apparently, in this case, the multifunctionalization does not seem to alter the yield of singlet oxygen formation with respect to comparable mono-adducts. Its incorporation into coated polymers and their subsequent irradiation with fluorescent visible light leads to germicidal effects on *E. coli* [133].

Very recently, the utilization of  $\text{C}_{60}$  water suspension, also called nano- $\text{C}_{60}$ , was reported in studies on cell association and toxicity versus *E. coli* and *B. subtilis* [2]. For the first bacterium, the minimum inhibitory concentration (MIC) was 0.5–1  $\text{mg L}^{-1}$ , while for the bacillus it is slightly higher (1.5–3.0  $\text{mg L}^{-1}$ ). The presence of this nano- $\text{C}_{60}$  inhibits bacterial growth independent of the presence of light, both in aerobic and anaerobic conditions [134]. Notably, higher concentrations of fullerenes were detrimental to the antimicrobial action because of aggregating nanoparticles, followed by subsequent precipitation that consequently causes the reduction or loss of activity [2].

A different group of fullerene derivatives with good potential antibacterial activity is represented by fulleropeptides. Amino acid  $\text{C}_{60}$  derivative **23** has been utilized in solid-phase synthesis for the preparation of derivative **24**. It was tested on *S. aureus* and *E. coli*, with MICs of 8 and 64  $\text{mM}$ , respectively [135, 136].



#### 11.4.6

#### Fullerenes as Nanodevices in Monoclonal Immunology

Recent studies with antibodies of the IgG isotype focused specifically on  $C_{60}$  derivatives conjugated to bovine thyroglobulin [137–139]. Such work pointed towards the potential of fullerenes in the development of nanodevices applicable in monoclonal immunology. However, only a limited number of reports on the use of fullerenes in this field have appeared so far.

To produce an antibody with specificity to fullerenes, Chen and coworkers [137] successfully linked water-soluble fullerene derivatives to large foreign proteins – including bovine thyroglobulin, and bovine and rabbit serum albumin. Immunization of mice with these  $C_{60}$ –protein conjugates produced a polyclonal immune response comprised of IgG antibodies specific for  $C_{60}$  fullerene and a subpopulation that crossreacted with a  $C_{70}$  derivative. This study showed for the first time that the immune system could recognize and process fullerenes as protein conjugates, and display the processed peptides for recognition by T cells to yield IgG antibodies. Later [138], the sequences of light and heavy chains of this IgG antibody were determined. Using X-ray crystallography of its Fab' fragment, it was found that the binding cavity was formed by the clustering of hydrophobic amino acids, several of which participate in stacking interactions with the fullerene core. Alternatively, weak hydrogen bond interactions between the fullerenes and the antibodies are considered to contribute to the  $C_{60}$ –antibody complex stability. Molecular dynamics simulation studies revealed that the fullerene molecule in the corresponding  $C_{60}$ –antibody complex is readily accommodated in the suggested binding site of the antibody [139]. In particular, an eminent trend towards predominant surroundings by hydrophobic amino acid side-chains, which are involved in  $\pi$ -stacking interactions with the fullerene molecule, evolves. Moreover, fullerenes inside the binding site undergo a small relative translational motion and a much larger rotation motion. However, no favored axis of rotation was found to exist. About 17% of the surface is exposed to the solvent that might potentially be used for functional derivatization.

The discovery that the mouse immune repertoire is diverse enough to recognize and produce antibodies specific for fullerenes has allowed the indirect determination of the distribution of fullerenes within a cellular environment. For the first time, Foley and coworkers reported that the water-soluble fullerene derivative  $C_{61}(CO_2H)_2$  is able to cross the cell membrane and to bind preferentially to the mitochondria [34]. The finding that fullerenes locate close to this organelle indicates the protective effects of fullerenes, in general, with respect to ROS [35].

Furthermore, the selective binding of proteins to carbon nanostructures has been extended from fullerenes to CNTs [140–142]. For example, particular antigens have been attached to the CNT walls, while retaining their conformation and thereby inducing an antibody response with the right specificity [143].

Erlanger, Chen and coworkers have shown that the monoclonal IgG  $C_{60}$ -specific antibody recognizes and specifically binds to aqueous suspensions of single-wall CNT (SWNT) bundles [144]. The authors considered these findings to have practical application. For example, the antibody-coated SWNTs can be used as probes of cell or membrane function. The antifullerene antibody on the surfaces of CNTs can be covalently decorated with probes of cell function, e.g. redox or luminescent probes, and after insertion, the probe molecule can be optically excited or electrically addressed via the conducting SWNT wire.

Using a polymer coating that is receptive to selected proteins, while rejecting others, is an elegant way to render nanotubes capable of interacting selectively with biomolecules. A variety of polymer coatings and self-assembled monolayers (SAMs) have been used to prevent nonspecific binding of proteins on surfaces for biosensor and biomedical device applications [145]. Among the coating materials, PEG is one of the most effective and widely used polymer materials that irreversibly adsorbs onto SWNTs. In this context, it has been shown that the protein streptavidin adsorbs spontaneously onto multiwalled CNTs (MWNTs) via hydrophobic interactions and thereby forms close packs. On the contrary, in the case of SWNTs that are coated with a surfactant and PEG, the protein nonspecific binding is prevented. A feasible way to circumvent this problem and to achieve selective binding involves the co-functionalization of SWNTs with PEG and biotin [146]. Surfactants, such as Triton X-100 or Triton X-405, that are prior adsorbed onto the surface of SWNTs as a wetting layer, significantly enhance the PEG adsorption and, thus, lead to high resistance of CNTs to the nonspecific binding of streptavidin. In the final step biotin was added through the covalently linkage of amine-terminated PEG chains and amine-reactive biotin reagents – biotinamidocaproic acid 3-sulfo-*N*-hydroxysuccinimide ester. For CNTs that are coated with Triton/PEG–biotin, selective binding of streptavidin was revealed by the high density of adsorbed proteins along the CNTs after exposure to a streptavidin solution. No appreciable adsorption was seen when CNTs functionalized in the same manner were exposed to streptavidin plugged with four equivalents of free biotin. These results demonstrate that functionalization of CNTs is one way to achieve specific protein recognition, while eliminating or minimizing nonspecific protein binding, and, thus, this has important implications for the biocompatibility of CNTs and specifically for the development of potential bioelectronic devices that integrate CNTs [147].

The design of selective piezoelectric crystal immunosensors that assist in the detection of IgG and hemoglobin in aqueous media utilizing water-soluble immobilized C<sub>60</sub>-antibodies as coating material has recently been demonstrated successfully [148]. The piezoelectric biosensors were prepared by coating C<sub>60</sub> fullerene from a toluene solution of poly(vinyl chloride) and C<sub>60</sub>, using spin coating at 10 cycles s<sup>-1</sup> (Hz) and subsequent adsorption of the antibodies.

The prepared biosensors exhibited linear frequency responses to the concentration of human IgG and hemoglobin with sensitivities of  $1.25 \times 10^2$  and  $1.56 \times 10^4$  Hz (mg mL)<sup>-1</sup> and reveal detection limits of 10<sup>-4</sup> mg mL<sup>-1</sup>. The optimal conditions for the IgG sensor were found at pH 6.7 and 30 °C. Important implications from the findings are that species such as urea, uric acid, cysteine, tyrosine and ascorbic acid imposed no interference on the biosensor activities. This corroborates the high selectivity.

#### 11.4.7

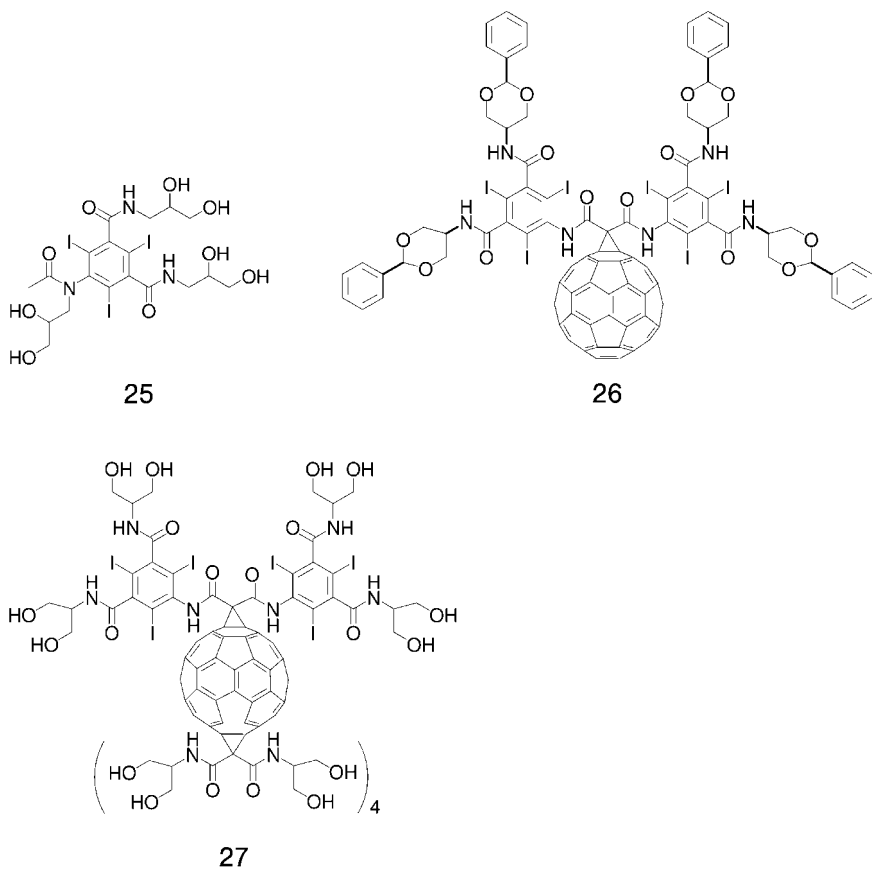
##### Fullerenes as Radiotracers

Encapsulating metal atoms inside the fullerene interior bears promising prospects for biomedical applications that might lead ultimately to nanodevices for diagnostic and therapeutic nuclear medicine. The rigid structure of the fullerene cage protects the encapsulated metal ion from external chemical attack and toxic metal ion release *in vivo*. Wilson and coworkers have, for example, demonstrated the feasibility of metallofullerenes as *in vivo* radiotracers [149]. Biodistribution studies of <sup>166</sup>Ho<sub>x</sub>@C<sub>82</sub>(OH)<sub>y</sub> in mice over a 48-h period showed selective localization of the tracer in the liver, but with continued slow excretion as well as retainment in the bone.

The same group has explored the concept of utilizing the nontoxic scaffold of C<sub>60</sub> for the development of new X-ray contrast agents [150, 151]. Like other contemporary contrast agents (25), the C<sub>60</sub>-based agents use iodine active X-ray attenuating vehicles. However, these compounds take advantage of the unique structure of fullerene. For instance, in contrast to the disk-like shape of contemporary contrast agents, the inherited globular shape of the fullerene-based contrast agent reduces viscosity in clinical formulations, which allows rapid intravenous injection of the agent. The fullerene core may also block one side of the tri-iodinated phenyl rings in 26 and 27 from having hydrophobic interactions with blood plasma proteins, and, thus, would lead to decreased protein binding and increased *in vivo* tolerability. Additionally, the existence of more than three iodine atoms will allow lower concentrations of contrast agents to be used.

Gadolinium-containing metallofullerenes have recently emerged as a new generation of magnetic resonance imaging (MRI) contrast agents. This development is driven, largely, by the high proton relaxivities of these metallofullerenes and the complete lack of Gd<sup>3+</sup> release under metabolic conditions. The most extensive study on the potential of gadofullerenes has been carried out by Wilson's group. Recently, they reported the synthesis and *in vivo* biodistribution study of the first water-soluble Gd@C<sub>60</sub> derivative [152–154]. The respective malonate derivative

$\text{Gd@C}_{60}[\text{C}(\text{COOH})_2]_{10}$  was found to possess a relaxivity ( $4.6 \text{ mM}^{-1} \text{ s}^{-1}$  at 20 MHz and  $40^\circ \text{C}$ ) comparable to that of commercially available Gd(III) chelate-based MRI agents. Moreover, an *in vivo* MRI biodistribution study revealed that  $\text{Gd@C}_{60}[\text{C}(\text{COOH})_2]_{10}$  is the first-water soluble endohedral metallofullerene with decreased uptake by the reticuloendothelial system (RES) and facile excretion via the urinary tract, consistent with its lack of intermolecular aggregation in solution.



Other polyhydroxyl derivatives of gadolinium-containing metallofullerenes and endohedral fullerenes with a series of lanthanide metal ions for  $\text{M@C}_{82}(\text{OH})_n$  ( $\text{M} = \text{La}, \text{Ce}, \text{Dy}, \text{Er}$ ) [155] have also been proposed as potential MRI agents, with  $\text{Gd@C}_{82}(\text{OH})_2$  being the most efficient relaxing agent [156, 157].

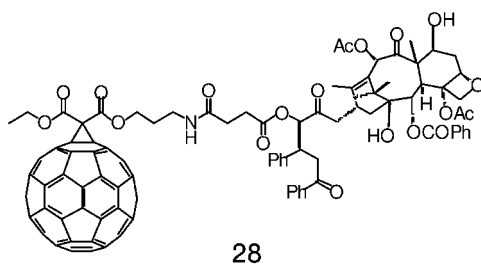
Studies by Dorn and coworkers are currently focusing on the development of trimetallic nitride templated endohedral metallofullerenes as a powerful, new generation of imaging contrast agents and radiotracers. These endohedral fullerenes are designed at the nanoscale level with improved contrast features as well as multi-

modal imaging potential (X-ray, MRI). Recent milestones in the development of tri-metallic nitride templated endohedral metallofullerenes involve the synthesis of a lutetium-based series of mixed metal species of gadolinium/lutetium and holmium/lutetium  $\text{Lu}_{3-x}\text{A}_x\text{N}@C_{80}$  ( $x = 0-2$ ) endohedral metallofullerenes [158], and the subsequent functionalization of both diamagnetic  $\text{Sc}_3\text{N}@C_{80}$  and paramagnetic  $\text{Er}_3\text{N}@C_{80}$  [159].

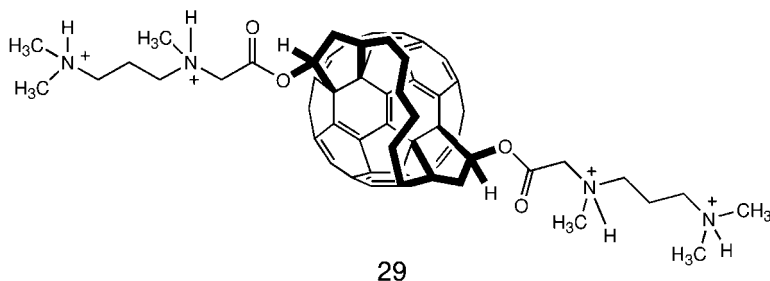
#### 11.4.8

##### Fullerenes as Vectors

Finally, biological use of fullerenes should be discussed that finds frequent mention over the years, but has only been scarcely pursued, i.e. the application of  $C_{60}$  as a drug vector. In particular, the hydrophobic nature of fullerenes should expedite membrane crossing. The paclitaxel fullerene derivative **28** has been prepared by Wilson and coworkers, who design a  $C_{60}$ -based slow release system of paclitaxel for a liposome aerosol delivery system in lung cancer treatment [160].



This initial work shows the first attempts to use fullerenes in pro-drug design and synthesis, while derivative **29** was the first compound – and up to now the only one – utilized to transfect DNA materials into cells [161]. The presence of four positive charges is particularly promising in light of facilitating DNA binding through electrostatic interactions with the phosphate groups of the oligonucleotide, but without specific recognition of the bases. The cells take up the complex through phagocytosis, triggering the release of duplex DNA in the cells.



## Acknowledgments

This work was carried out with partial support from the EU (RTN network "CASSIUS CLAYS"), SFB 583, DFG (GU 517/4-1), FCI and the Office of Basic Energy Sciences of the US Department of Energy.

## References

- 1 W. A. SCRIVENS, J. M. TOUR, K. E. CREEK, L. PIRISI. Synthesis of  $^{14}\text{C}$ -labeled  $\text{C}_{60}$ , its suspension in water, and its uptake by human keratinocytes. *J. Am. Chem. Soc.* **1994**, *116*, 4517–4518.
- 2 D. Y. LYON, J. D. FORTNER, C. M. SAYES, V. L. COLVIN, J. B. HUGHES. Bacterial cell association and antimicrobial activity of a  $\text{C}_{60}$  water suspension. *Environ. Toxicol. Chem.* **2005**, *24*, 2757–2762.
- 3 Y. LIU, H. WANG, P. LIANG, H.-Y. ZHANG. Water-soluble supramolecular fullerene assembly mediated by metallobridged beta-cyclodextrins. *Angew. Chem. Int. Ed. Engl.* **2004**, *43*, 2690–2694.
- 4 S. SAMAL, K. E. GECKELER. Cyclodextrin–fullerenes: a new class of water-soluble fullerenes. *J. Chem. Soc. Chem. Commun.* **2000**, 1101–1102.
- 5 T. BRAUN. Water soluble fullerene–cyclodextrin supramolecular assemblies – preparation, structure, properties. *Fullerene Sci. Technol.* **1997**, *5*, 615–626.
- 6 T. ANDERSSON, K. NILSSON, M. SUNDAHL, G. WESTMAN, O. WENNERSTRÖM.  $\text{C}_{60}$  embedded in gamma-cyclodextrin: a water-soluble fullerene. *J. Chem. Soc. Chem. Commun.* **1992**, 604–606.
- 7 S. D. M. ISLAM, M. FUJITSUKA, O. ITO, A. IKEDA, T. HATANO, S. SHINKAI. Photoexcited state properties of  $\text{C}_{60}$  encapsulated in a water-soluble calixarene. *Chem. Lett.* **2000**, *1*, 78–79.
- 8 A. IKEDA, Y. SUZUKI, M. YOSHIMURA, S. SHINKAI. On the prerequisites for the formation of solution complexes from [60]fullerene and calix[ $n$ ]arenes: a novel allosteric effect between [60]fullerene and metal cations in calix[ $n$ ]aryl ester complexes. *Tetrahedron* **1998**, *54*, 2497–2508.
- 9 A. IKEDA, S. NOBUKUNI, H. UDZU, Z. ZHONG, S. SHINKAI. A novel [60]fullerene-calixarene conjugate which facilitates self-inclusion of the [60]fullerene moiety into the homooxalix[3]arene cavity. *Eur. J. Org. Chem.* **2000**, 3287–3293.
- 10 S. SHINKAI, A. IKEDA. Calixarene–fullerene conjugates: marriage of the third generations of inclusion compounds and carbon clusters. *Gazz. Chim. It.* **1997**, *127*, 657–662.
- 11 A. IKEDA, T. HATANO, M. KAWAGUCHI, H. SUENAGA, S. SHINKAI. Water-soluble [60]fullerene–cationic homooxalix[3]arene complex which is applicable to the photocleavage of DNA. *J. Chem. Soc. Chem. Commun.* **1999**, 1403–1404.
- 12 J. L. ATWOOD, G. A. KOUTSANTONIS, C. L. RASTON. Purification of  $\text{C}_{60}$  and  $\text{C}_{70}$  by selective complexation with calixarenes. *Nature* **1994**, *368*, 229–231.
- 13 S. KUNSÁGI-MÁTÉ, K. SZABÓ, I. BITTER, G. NAGY, L. KOLLAR. Complex formation between water-soluble sulfonated calixarenes and  $\text{C}_{60}$  fullerene. *Tetrahedron Lett.* **2004**, *45*, 1387–1390.
- 14 Y. N. YAMAKOSHI, T. YAGAMI, K. FUKUHARA, S. SUEYOSHI, N. MIYATA. Solubilization of fullerenes into water with polyvinylpyrrolidone applicable to biological tests. *J. Chem. Soc. Chem. Commun.* **1994**, 517–518.
- 15 Y. TABATA, Y. MURAKAMI, Y. IKADA. Antitumor effect of poly(ethylene glycol)modified fullerene. *Fullerene Sci. Technol.* **1997**, *5*, 989–1007.



- 16 T. DA ROS, M. PRATO, F. NOVELLO, M. MAGGINI, E. BANFI. Easy access to water-soluble fullerene derivatives via 1,3-dipolar cycloadditions of azomethine ylides to C<sub>60</sub>. *J. Org. Chem.* **1996**, *61*, 9070–9072.
- 17 L. Y. CHIANG, J. B. BHONSLE, L. WANG, S. F. SHU, T. M. CHANG, J. R. HWU. Efficient one-flask synthesis of water-soluble [60]fullerenols. *Tetrahedron* **1996**, *52*, 4963–4972.
- 18 I. LAMPARTH, A. HIRSCH. Water-soluble malonic acid derivatives of C<sub>60</sub> with a defined three-dimensional structure. *J. Chem. Soc. Chem. Commun.* **1994**, 1727–1728.
- 19 C. CUSAN, T. DA ROS, G. SPALLUTO, S. FOLEY, J.-M. JANOT, P. SETA, C. LARROQUE, M. C. TOMASINI, T. ANTONELLI, L. FERRARO, M. PRATO. A new multi-charged C<sub>60</sub> derivative: synthesis and biological properties. *Eur. J. Org. Chem.* **2002**, 2928–2934.
- 20 S. FILIPPONE, F. HEIMANN, A. RASSAT. A highly water-soluble 2:1 beta-cyclodextrin–fullerene conjugate. *J. Chem. Soc. Chem. Commun.* **2002**, 1508–1509.
- 21 J. YANG, Y. WANG, A. RASSAT, Y. ZHANG, P. SINAÏ. Synthesis of novel highly water-soluble 2:1 cyclodextrin/fullerene conjugates involving the secondary rim of beta-cyclodextrin. *Tetrahedron* **2004**, *60*, 12163–12168.
- 22 Y. LIU, Y.-L. ZHAO, Y. CHEN, P. LIANG, L. LI. A water-soluble beta-cyclodextrin derivative possessing a fullerene tether as an efficient photodriven DNA-cleavage reagent. *Tetrahedron Lett.* **2005**, *46*, 2507–2511.
- 23 A. VASELLA, F. UHLMANN, C. A. WALDRAFF, F. DIEDERICH, C. THILGEN. Fullerene sugars: preparation of enantiomerically pure, spiro-linked C-glycosides of C<sub>60</sub>. *Angew. Chem. Int. Ed. Engl.* **1992**, *31*, 1388–1390.
- 24 H. KATO, A. YASHIRO, A. MIZUNO, Y. NISHIDA, K. KOBAYASHI, H. SHINOHARA. Syntheses and biological evaluations of alpha-D-mannosyl [60]fullerenols. *Bioorg. Med. Chem. Lett.* **2001**, *11*, 2935–2939.
- 25 Y. NISHIDA, A. MIZUNO, H. KATO, A. YASHIRO, T. OHTAKE, K. KOBAYASHI. Stereo- and biochemical profiles of the 5–6- and 6–6-junction isomers of alpha-D-mannopyranosyl [60]fullerenes. *Chem. Biodivers.* **2004**, *1*, 1452–1564.
- 26 S. ABE, H. MORIYAMA, K. NIJKURA, F. FENG, K. MONDE, S.-I. NISHIMURA. Versatile synthesis of oligosaccharide-containing fullerenes. *Tetrahedron Asymm.* **2005**, *16*, 15–19.
- 27 D. PANTAROTTO, N. TAGMATARCHIS, A. BIANCO, M. PRATO. Synthesis and biological properties of fullerene-containing amino acids and peptides. *Mini-Rev. Med. Chem.* **2004**, *4*, 805–814.
- 28 G. N. BOGDANOV, R. A. KOTELNIKOVA, E. S. FROG, V. N. SHTOLKO, V. S. ROMANOVA, YU. N. BUBNOV. Enantiomers of the amino acid derivatives of fullerene C<sub>60</sub> possess stereospecific membranotropic properties. *Doklady Biochem. Biophys.* **2004**, *396*, 165–167.
- 29 J. YANG, A. R. BARRON. A new route to fullerene substituted phenylalanine derivatives. *J. Chem. Soc. Chem. Commun.* **2004**, 2884–2885.
- 30 L. WATANABE, M. BHUIYAN, B. JOSE, T. KATO, N. NISHINO. Synthesis of novel fullerene amino acids and their mult fullerene peptides. *Tetrahedron Lett.* **2004**, *45*, 7137–7140.
- 31 A. BIANCO. Efficient solid-phase synthesis of fullerene-peptides using Merrifield strategy. *J. Chem. Soc. Chem. Commun.* **2005**, 3174–3175.
- 32 M. BREITREICH, A. HIRSCH. A highly water-soluble dendro[60]fullerene. *Tetrahedron Lett.* **1998**, *39*, 2731–2740.
- 33 T. BAIERL, E. DROSSELMAYER, A. SEIDEL, S. HIPPELI. Comparison of immunological effects of fullerene C<sub>60</sub> and raw soot from fullerene production on alveolar macrophages and macrophage like cells *in vitro*. *Exp. Toxicol. Pathol.* **1996**, *48*, 508–511.
- 34 S. FOLEY, C. CROWLEY, M. SMAIHI, C. BONFILS, B. F. ERLANGER, P. SETA, C. LARROQUE. Cellular localization of a water-soluble fullerene derivative. *Biochem. Biophys. Res. Commun.* **2002**, *294*, 116–119.

- 35 L. L. DUGAN, D. M. TURETSKY, C. DU, D. LOBNER, M. WHEELER, C. R. ALMLI, C. K. F. SHEN, T. Y. LUH, D. W. CHOI, T. S. LIN. Carboxyfullerenes as neuroprotective agents. *Proc. Natl. Acad. Sci. USA* **1997**, *94*, 9434–9439.
- 36 T. TSUCHIYA, I. OGURI, Y. N. YAMAKOSHI, N. MIYATA. Novel harmful effects of [60]fullerene on mouse embryos *in vitro* and *in vivo*. *FEBS Lett.* **1996**, *393*, 139–145.
- 37 T. TSUCHIYA, Y. N. YAMAKOSHI, N. MIYATA. A novel promoting action of fullerene C<sub>60</sub> on the chondrogenesis in rat embryonic limb bud cell-culture system. *Biochem. Biophys. Res. Commun.* **1995**, *206*, 885–894.
- 38 K. IRIE, Y. NAKAMURA, H. OHIGASHI, H. TOKUYAMA, S. YAMAGO, E. NAKAMURA. Photocytotoxicity of water-soluble fullerene derivatives *Biosci. Biotechnol.* **1996**, *60*, 1359–1361.
- 39 S. YAMAGO, H. TOKUYAMA, E. NAKAMURA, K. KIKUCHI, S. KANANISHI, K. SUEKI, H. NAKAHARA, S. ENOMOTO, F. AMBE. *In-vivo* behavior of a water-soluble fullerene – C14 labeling, absorption, distribution, excretion and acute toxicity. *Chem. Biol.* **1995**, *2*, 385–389.
- 40 A. YANG, D. L. CARDONA, F. A. BARILE. *In vitro* cytotoxicity testing with fluorescence-based assays in cultured human lung and dermal cells. *Cell Biol. Toxicol.* **2002**, *18*, 97–108.
- 41 J. P. SIMONIN. Solvent effects on osmotic second virial coefficient studied using analytic molecular models. Application to solutions of C<sub>60</sub> fullerene. *J. Phys. Chem. B* **2001**, *105*, 5262–5270.
- 42 C. M. SAYES, J. D. FORTNER, W. GUO, D. LYON, A. M. BOYD, K. D. AUSMAN, Y. J. TAO, B. SITHARAMAN, L. J. WILSON, J. B. HUGHES, J. L. WEST, V. L. COLVIN. The differential cytotoxicity of water-soluble fullerenes. *Nano Lett.* **2004**, *4*, 1881–1887.
- 43 X. YANG, C. FAN, H. S. ZHU. Photo-induced cytotoxicity of malonic acid [C<sub>60</sub>]fullerene derivatives and its mechanism. *Toxicol. In Vitro* **2002**, *16*, 41–46.
- 44 H. TOKUYAMA, S. YAMAGO, E. NAKAMURA, T. SHIRAKI, Y. SUGIURA. Photoinduced biochemical activity of fullerene carboxylic acid. *J. Am. Chem. Soc.* **1993**, *115*, 7918–7919.
- 45 E. NAKAMURA, H. TOKUYAMA, S. YAMAGO, T. SHIRAKI, Y. SUGIURA. Biological activity of water-soluble fullerenes. Structural dependence of DNA cleavage, cytotoxicity, and enzyme inhibitory activities including HIV-protease inhibition. *Bull. Chem. Soc. Jpn.* **1996**, *69*, 2143–2151.
- 46 A. S. BOUTORINE, H. TOKUYAMA, M. TAKASUGI, H. ISOBE, E. NAKAMURA, C. HÉLÈNE. Fullerene–oligonucleotide conjugates – photoinduced sequence-specific DNA cleavage. *Angew. Chem. Int. Ed. Engl.* **1995**, *33*, 2462–2465.
- 47 D. M. GULDI, M. PRATO. Excited-state properties of C<sub>60</sub> fullerene derivatives. *Acc. Chem. Res.* **2000**, *33*, 695–703.
- 48 J. L. ANDERSON, Y.-Z. AN, Y. RUBIN, C. S. FOOTE. Photophysical characterization and singlet oxygen yield of a dihydrofullerene. *J. Am. Chem. Soc.* **1994**, *116*, 9763.
- 49 R. BERNSTEIN, F. PRAT, C. S. FOOTE. On the mechanism of DNA cleavage by fullerenes investigated in model systems: electron transfer from guanosine and 8-oxo-guanosine derivatives to C<sub>60</sub>. *J. Am. Chem. Soc.* **1999**, *121*, 464–465.
- 50 E. NAKAMURA, H. ISOBE. Functionalized fullerenes in water. The first 10 years of their chemistry, biology, and nanoscience. *Acc. Chem. Res.* **2003**, *36*, 807–815.
- 51 J. W. ARBOGAST, C. S. FOOTE, M. KAO. Electron transfer to triplet C<sub>60</sub>. *J. Am. Chem. Soc.* **1992**, *114*, 2277–2278.
- 52 Y. YAMAKOSHI, S. SUEYOSHI, K. FUKUHARA, N. MIYATA. ·OH and O<sub>2</sub><sup>·-</sup> generation in aqueous C<sub>60</sub> and C<sub>70</sub> solutions by photoirradiation: an EPR study. *J. Am. Chem. Soc.* **1998**, *120*, 12363–12364.
- 53 I. NAKANISHI, S. FUKUZUMI, T. KONISHI, K. OHKUBO, M. FUJITSUKA, O. ITO, N. MIYATA. DNA cleavage via superoxide anion formed in photoinduced electron transfer from

- NADH to gamma-cyclodextrin-bicapped C<sub>60</sub> in an oxygen-saturated aqueous solution. *J. Phys. Chem. B.* **2002**, *106*, 2372–2380.
- 54 S. SAMAL, K. E. GECKELER. DNA-cleavage by fullerene-based synzymes. *Macromol. Biosci.* **2001**, *1*, 329–331.
  - 55 A. IKEDA, T. SATO, K. KITAMURA, K. NISHIGUCHI, Y. SASAKI, J. KIKUCHI, T. OGAWA, K. YOGO, T. TAKEY. Efficient photocleavage of DNA utilizing water-soluble lipid membrane-incorporated [60]fullerenes prepared using a [60]fullerene exchange method. *Org. Biomol. Chem.* **2005**, *3*, 2907–2909.
  - 56 T. DA ROS, M. BERGAMIN, E. VÁZQUEZ, G. SPALLUTO, B. BAITI, S. MORO, A. BOUTORINE, M. PRATO. Synthesis and molecular modeling studies of fullerene-5,6,7-trimethoxyindole-oligonucleotide conjugates as possible probes for study of photochemical reactions in DNA triple helices. *Eur. J. Org. Chem.* **2002**, 405–413.
  - 57 Y. N. YAMAKOSHI, T. YAGAMI, S. SUEYOSHI, N. MIYATA. Acridine adduct of [60]fullerene with enhanced DNA-cleaving activity. *J. Org. Chem.* **1996**, *61*, 7236–7237.
  - 58 A. M. CASSELL, W. A. SCRIVENS, J. M. TOUR. Assembly of DNA/fullerene hybrid materials. *Angew. Chem. Int. Ed. Engl.* **1998**, *37*, 1528–1531.
  - 59 Q. YING, J. ZHANG, D. LIANG, W. NAKANISHI, H. ISOBE, E. NAKAMURA, B. CHU. Fractal behavior of functionalized fullerene aggregates. I. Aggregation of two-handed tetraaminofullerene with DNA. *Langmuir* **2005**, *21*, 9824–9831.
  - 60 Y. YAMAKOSHI, N. UMEZAWA, A. RYU, K. ARAKANE, N. MIYATA, Y. GODA, T. MASUMIZU, T. NAGANO. Active oxygen species generated from photoexcited fullerene (C<sub>60</sub>) as potential medicines: O<sub>2</sub><sup>•-</sup> versus <sup>1</sup>O<sub>2</sub>. *J. Am. Chem. Soc.* **2003**, *125*, 12803–12809.
  - 61 J. W. ARBOGAST, A. O. DARMANNYAN, C. S. FOOTE, F. N. DIEDERICH, R. L. WHETTEN, Y. RUBIN, M. M. ALVAREZ, S. J. ANZ. Photophysical properties of sixty atom carbon molecule (C<sub>60</sub>). *J. Phys. Chem.* **1991**, *95*, 11–12.
  - 62 J. W. ARBOGAST, C. S. FOOTE. Photophysical properties of C<sub>70</sub>. *J. Am. Chem. Soc.* **1991**, *113*, 8886–8889.
  - 63 P. CHENG, S. R. WILSON, D. I. SCHUSTER. A novel parachute-shaped C<sub>60</sub>-porphyrin dyad. *Chem. Commun.* **1999**, 89–90.
  - 64 M. D. MEIJER, G. P. M. VAN KLINK, G. VAN KOTEN. Metal-chelating capacities attached to fullerenes. *Coord. Chem. Rev.* **2002**, *230*, 141–163.
  - 65 T. HAMANO, K. OKUDA, T. MASHINO, M. HIROBE, K. ARAKANE, A. RYU, S. MASHIKO, T. NAGANO. Singlet oxygen production from fullerene derivatives: effect of sequential functionalization of the fullerene core. *J. Chem. Soc. Chem. Commun.* **1997**, 21–22.
  - 66 B. VILENO, A. SIENKIEWICZ, M. LEKKA, A. J. KULIK, L. FORRÓ. *In vitro* assay of singlet oxygen generation in the presence of water-soluble derivatives of C<sub>60</sub>. *Carbon* **2004**, *42*, 1195–1198.
  - 67 K. D. PICKERING, M. R. WIESNER. Fullerol-sensitized production of reactive oxygen species in aqueous solution. *Environ. Sci. Technol.* **2005**, *39*, 1359–1365.
  - 68 W. LI, K. QIAN, W. HUANG, X. ZHANG, W. CHEN. Water-soluble C<sub>60</sub>-liposome and the biological effect of C<sub>60</sub> to human cervix cancer cells. *Chin. Phys. Lett.* **1994**, *11*, 207–210.
  - 69 N. NAKAJIMA, C. NISHI, F.-M. LI, Y. IKADA. Photo-induced cytotoxicity of water-soluble fullerene. *Fullerene Sci. Technol.* **1996**, *4*, 1–19.
  - 70 Y. TABATA, Y. MURAKAMI, Y. IKADA. Antitumor effect of poly(ethylene glycol)-modified fullerene. *Fullerene Sci. Technol.* **1997**, *5*, 989–1007.
  - 71 Y. TABATA, Y. MURAKAMI, Y. IKADA. Photodynamic effect of polyethylene glycol-modified fullerene on tumor. *Jpn. Cancer Res.* **1997**, *88*, 1108–1116.
  - 72 A. HAMAZAWA, I. KINOSHITA, B. BREEDLOVE, K. ISOBE, M. SHIBATA, Y. BABA, T. KAKUCHI, S. HIROHARA, M. OBATA, Y. MIKATA, S. YANO. Meso-tetraphenylporphyrin having hexamaltosyl and decyl chain as an amphiphilic photosensitizer toward photodynamic therapy. *Chem. Lett.* **2002**, *3*, 388–389.

- 73 G. ZHENG, A. GRAHAM, M. SHIBATA, J. R. MISSERT, A. R. OSEROFF, T. J. DOUGHERTY, R. K. PANDEY. Synthesis of beta-galactose-conjugated chlorins derived by enyne metathesis as galectin-specific photosensitizers for photodynamic therapy. *J. Org. Chem.* **2001**, *66*, 8709–8716.
- 74 Y. MIKATA, S. TAKAGI, M. TANAHASHI, S. ISHII, M. OBATA, Y. MIYAMOTO, K. WAKITA, T. NISHISAKA, T. HIRANO, T. ITO, M. HOSHINO, C. OHTSUKI, M. TANIHARA, S. YANO. Detection of 1270 nm emission from singlet oxygen and photocytotoxic property of sugar-pendant [60]fullerenes. *Bioorg. Medicinal Chem. Lett.* **2003**, *13*, 3289–3292.
- 75 S. A. OMARI, E. A. ERMILOV, M. HELMREICH, N. JUX, A. HIRSCH, B. RÖDER. Transient absorption spectroscopy of a monofullerene C-60-bis-(pyropheophorbide *a*) molecular system in polar and nonpolar environments. *Appl. Phys. B* **2004**, *79*, 617–622.
- 76 F. RANCAN, M. HELMREICH, A. MOELICH, N. JUX, A. HIRSCH, B. RÖDER, C. WITT, F. BOEHM. Fullerene-pyropheophorbide *a* complexes as sensitizer for photodynamic therapy: uptake and photo-induced cytotoxicity on Jurkat cells. *J. Photochem. Photobiol. B* **2005**, *80*, 1–7.
- 77 P. KRÁL. Control of catalytic activity of proteins *in vivo* by nanotube ropes excited with infrared light. *Chem. Phys. Lett.* **2003**, *382*, 399–403.
- 78 K. C. HWANG, D. MAUZERALL. Vectorial electron transfer from an interfacial photoexcited porphyrin to ground state fullerene C<sub>60</sub> and C<sub>70</sub> and from ascorbate to triplet C<sub>60</sub> and C<sub>70</sub> in a lipid bilayer. *J. Am. Chem. Soc.* **1992**, *114*, 9705–9706.
- 79 R. V. BENSASSON, J. L. GERAUD, S. LEACH, G. MIQUEL, P. SETA. Transmembrane electron transport mediated by photoexcited fullerenes. *Chem. Phys. Lett.* **1993**, *210*, 141.
- 80 K. C. HWANG, D. MAUZERALL. Photoinduced electron transport across a lipid bilayer mediated by C<sub>70</sub>. *Nature* **1993**, *361*, 138–140.
- 81 S. NIU, D. MAUZERALL. Fast and efficient charge transport across a lipid bilayer is electronically mediated by C<sub>70</sub> fullerene aggregates. *J. Am. Chem. Soc.* **1996**, *118*, 5791–5795.
- 82 J. M. JANOT, P. SETA, R. V. BENSASSON, S. LEACH. Involvement of C-60 fullerene monomers and aggregates in the photoconductivity of ultrathin bilayer lipid membranes. *Synthetic Metals* **1996**, *77*, 103–106.
- 83 L. WANG, X. ZHANG, Z. DU, Y. BAI, T. LI. The photo-electronic transfer across membrane between C<sub>60</sub> and CdS nanoparticles. *Chem. Phys. Lett.* **2003**, *372*, 331–335.
- 84 R. A. KOTELNIKOVA, G. N. BOGDANOV, E. C. FROG, A. I. KOTELNIKOV, V. N. SHTOLOKO, V. S. ROMANOVA, S. M. ANDREEV, A. A. KUSHCH, N. E. FEDOROVA, A. A. MEDZHIDOVA, G. G. MILLER. Nanobionics of pharmacologically active derivatives of fullerene C<sub>60</sub>. *J. Nanoparticle Res.* **2003**, *5*, 561–566.
- 85 M. NISHIHARA, F. PERRET, T. TAKEUCHI, S. FUTAKI, A. N. LAZAR, A. W. COLEMAN, N. SAKAI, S. MATILE. Arginine magic with new counterions up the sleeve. *Org. Biomol. Chem.* **2005**, *3*, 1659–1669.
- 86 F. PERRET, M. NISHIHARA, T. TAKEUCHI, S. FUTAKI, A. N. LAZAR, A. W. COLEMAN, N. SAKAI, S. MATILE. Anionic fullerenes, calixarenes, coronenes, and pyrenes as activators of oligo/polyarginines in model membranes and live cells. *J. Am. Chem. Soc.* **2005**, *127*, 1114–1115.
- 87 H. EDDAUDI, A. DERATANI, S. TINGRY, F. SINAN, P. SETA. Fullerene membrane transport mediated by  $\gamma$ -cyclodextrin immobilized in poly(vinyl alcohol) films. *Polym. Int.* **2003**, *52*, 1390–1395.
- 88 M. CARANO, S. COSNIER, K. KORDATOS, M. MARCACCIO, M. MARGOTTI, F. PAOLUCCI, M. PRATO, S. ROFFIA. A glutathione amperometric biosensor based on an amphiphilic fullerene redox mediator immobilized within an amphiphilic polypyrrole film. *J. Mater. Chem.* **2002**, *12*, 1996–2000.

- 89 H. T. TIEN, L.-G. WANG, X. WANG, A. L. OTTOVA. Electronic processes in supported bilayer lipid membranes (s-BLMs) containing a geodesic form of carbon (fullerene C<sub>60</sub>). *Bioelectrochem. Bioenerg.* **1997**, *42*, 161–167.
- 90 F. CARDULLO, F. DIEDERICH, L. ECHEGOYEN, T. HABICHER, N. JAYARAMAN, R. M. LEBLANC, J. F. STODDART, S. WANG. Stable Langmuir and Langmuir–Blodgett films of fullerene–glycodendron conjugates. *Langmuir* **1998**, *14*, 1955–1959.
- 91 P. J. KRUSIC, E. WASSERMAN, P. N. KEIZER, J. R. MORTON, K. F. PRESTON. Radical reactions of C<sub>60</sub>. *Science* **1991**, *254*, 1183–1185.
- 92 L. L. DUGAN, E. LOVETT, S. CUDDIHY, B.-W. MA, T.-S. LIN, D. W. CHOI. Carboxyfullerenes as neuroprotective antioxidants. In: *Handbook of Fullerenes*, K. KADISH, R. RUOFF, (Eds.). Wiley, New York, **2000**, pp. 467–479.
- 93 K. L. QUICK, J. I. HARDT, L. L. DUGAN. Rapid microplate assay for superoxide scavenging efficiency. *J. Neurosci. Methods* **2000**, *97*, 139–144.
- 94 L. L. DUGAN, E. G. LOVETT, K. L. QUICK, J. LOTHARIUS, T. T. LIN, K. L. O'MALLEY. Fullerene-based antioxidants and neurodegenerative disorders. *Parkinsonism Rel. Disord.* **2001**, *7*, 243–246.
- 95 A. M. LIN, B. Y. CHYI, S. D. WANG, H. H. YU, P. P. KANAKAMMA, T. Y. LUH, C. K. CHOI, L. T. HO. Carboxyfullerene prevents iron-induced oxidative stress in rat brain. *J. Neurochem.* **1999**, *72*, 1634–1640.
- 96 D. J. WOLF, A. D. PAPOIU, K. MIALKOWSKI, C. F. RICHARDSON, D. I. SCHUSTER, S. R. WILSON. Inhibition of nitric oxide synthase isoforms by tris-malonyl-C<sub>60</sub>-fullerene adducts. *Arch. Biochem. Biophys.* **2000**, *378*, 216–223.
- 97 L. L. DUGAN, V. M. G. BRUNO, S. M. AMAGASU, R. G. GIFFARD. GLIA modulate the response of murine cortical-neurons to excitotoxicity – GLIA exacerbate AMPA neurotoxicity. *J. Neurosci.* **1995**, *15*, 4545–4555.
- 98 M. P. GOLDBERG, S. P. ALTHOMSONS, T. CHAPMAN, D. W. CHOI, L. L. DUGAN. Carboxyfullerene free radical scavengers reduce hypoxic and excitotoxic oligodendrocyte death *in vitro*. *Neurology* **1998**, *50*, A370 (S59002 Suppl. 4).
- 99 J. LOTHARIUS, L. L. DUGAN, K. L. O'MALLEY. Distinct mechanisms underlie neurotoxin-mediated cell death in cultured dopaminergic. *J. Neurosci.* **1999**, *19*, 1284–1293.
- 100 Y. L. HUANG, C. K. SHEN, T. Y. LUH, H. C. YANG, K. C. HWANG, C. K. CHOU. Blockage of apoptotic signaling of transforming growth factor-beta in human hepatoma cells by carboxyfullerene. *Eur. J. Biochem.* **1998**, *254*, 38–43.
- 101 C. FUMELLI, A. MARCONI, S. SALVIOLI, E. STRAFACE, W. MALORNI, A. M. OFFIDANI, R. PELLICCIARI, G. SCHETTINI, A. GIANNETTI, D. MONTI, C. FRANCESCHI, C. PINCELLI. Carboxyfullerenes protect human keratinocytes from ultraviolet-B-induced apoptosis. *J. Invest. Dermatol.* **2000**, *115*, 835–841.
- 102 D. MONTI, L. MORETTI, S. SALVIOLI, E. STRAFACE, W. MALORNI, R. PELLICCIARI, G. SCHETTINI, M. BISAGLIA, C. PINCELLI, C. FUMELLI, M. BONAFÉ, C. FRANCESCHI. C<sub>60</sub> carboxyfullerene exerts a protective activity against oxidative stress-induced apoptosis in human peripheral blood mononuclear cells. *Biochem. Biophys. Res. Commun.* **2000**, *277*, 711–717.
- 103 M.-C. CHEN, M.-J. HWANG, Y.-C. CHOU, W.-H. CHEN, G. CHENG, H. NAKANO, T.-Y. LUH, S.-C. MAI, S.-L. HSIEH. The role of apoptosis signal-regulating kinase 1 in lymphotoxin-β-receptor-mediated cell death. *J. Biol. Chem.* **2003**, *278*, 16073–16081.
- 104 A. M.-Y. LIN, S.-F. FANG, S.-Z. LIN, C.-K. CHOU, T.-Y. LUH, L.-T. HO. Local carboxyfullerene protects cortical infarction in rat brain. *Neurosci. Res.* **2002**, *43*, 317–321.
- 105 K. OKUDA, M. HIROBE, M. MOCHIZUKI, T. MASHINO. Effects of fullerene derivatives on active oxygen toxicity in *E. coli*. *Proc. Electrochem. Soc.* **1997**, *97*, 337–338.

- 106 N. TSAO, P. P. KANAKAMMA, T.-Y. LUH, C.-K. CHOU, H.-Y. LEI. Inhibition of *Escherichia coli*-induced meningitis by carboxyfullerene. *Antimicrob. Agents Chemother.* **1999**, *43*, 2273–2277.
- 107 T. MASHINO, K. OKUDA, T. HIROTA, M. HIROBE, T. NAGANO, M. MOCHIZUCHI. Inhibition of *E. coli* growth by fullerene derivatives and inhibition mechanism. *Bioorg. Med. Chem. Lett.* **1999**, *9*, 2959–2962.
- 108 M. BISAGLIA, B. NATALINI, R. PELLICCIARI, E. STRAFACE, W. MALORNI, D. MONTI, C. FRANCESCHI, G. SCHETTINI. C<sub>3</sub>-fullero-tris-methanodicarboxylic acid protects cerebellar granule cells from apoptosis. *J. Neurochem.* **2000**, *74*, 1197–1204.
- 109 I. C. WANG, L. TAI, D. LEE, P. KANAKAMMA, C. F. SHEN, T. Y. LUH, C. CHENG, K. HWANG. C<sub>60</sub> and water-soluble fullerene derivatives as antioxidants against radical-initiated lipid peroxidation. *J. Med. Chem.* **1999**, *42*, 4614–4620.
- 110 R. V. BENSASSON, M. BRETTREICH, J. FREDRIKSEN, H. GOTTINGER, A. HIRSCH, E. J. LAND, S. LEACH, D. J. MCGARVEY, H. SCHONBERGER. Reactions of e<sup>-</sup><sub>aq</sub>, CO<sub>2</sub><sup>-</sup>, HO<sup>-</sup>, O<sub>2</sub><sup>-</sup> and O<sub>2</sub>(<sup>1</sup>D<sub>g</sub>) with a dendro[60]fullerene and C<sub>60</sub>[C(COOH)<sub>2</sub>]<sub>n</sub> (n = 2–6). *Free Radic. Biol. Med.* **2000**, *20*, 26–33.
- 111 K. OKUDA, T. HIROTA, M. HIROBE, T. NAGANO, M. MOCHIZUKI, T. MASHINO. Synthesis of various water-soluble C<sub>60</sub> derivatives and their superoxide-quenching activity. *Fullerene Sci. Technol.* **2000**, *8*, 89–104.
- 112 S. S. ALI, J. I. HARDT, K. L. QUICK, J. S. KIM-HAN, B. F. ERLANGER, T.-T. HUANG, C. J. EPSTEIN, L. L. DUGAN. A biologically effective fullerene (C<sub>60</sub>) derivative with superoxide dismutase mimetic properties. *Free Radic. Biol. Med.* **2004**, *37*, 1191–1202.
- 113 L. L. DUGAN, J. K. GABRIELSON, S. P. YU, T.-S. LIN, D. W. CHOI. Buckminsterfullerenol free radical scavengers reduce excitotoxic and apoptotic death of cultured cortical neurons. *Neurobiol. Dis.* **1996**, *3*, 129–135.
- 114 L. Y. CHIANG, F.-J. LU, J.-T. LIN. Free-radical scavenging activity of water-soluble fullerenols. *J. Chem. Soc. Chem. Commun.* **1995**, 1283–1284.
- 115 Y.-L. LAI, L. Y. CHIANG. Water-soluble fullerene derivatives attenuate exsanguination-induced bronchoconstriction of guinea-pigs. *J. Auton. Pharmacol.* **1997**, *17*, 229–235.
- 116 Y.-L. LAI, W.-Y. CHIOU, L. Y. CHIANG. Fullerene derivatives attenuate bronchoconstriction induced by xanthine–xanthine oxidase. *Fullerene Sci. Technol.* **1997**, *5*, 1337–1345.
- 117 H. C. C. CHEN, Y. T. HUANG, V. F. PAUG, S. C. LIANG, L. Y. CHIANG. Water-soluble C<sub>60</sub> and macrophages: morphologic features of FC4S-treated peritoneal macrophages *in vitro* and *in vivo* – a preliminary report. *Fullerene Sci Technol.* **1999**, *7*, 505–517.
- 118 S. BOSI, T. DA ROS, S. CASTELLANO, E. BANFI, M. PRATO. Antimycobacterial activity of ionic fullerene derivatives. *Bioorg. Med. Chem. Lett.* **2000**, *10*, 1043–1045.
- 119 T. MASHINO, N. USUI, K. OKUDA, T. HIROTA, M. MOCHIZUKI. Respiratory chain inhibition by fullerene derivatives: Hydrogen peroxide production caused by fullerene derivatives and a respiratory chain system. *Bioorg. Med. Chem.* **2003**, *11*, 1433–1438.
- 120 Y. I. PUKHOVA, G. N. CHURILOV, V. G. ISAKOVA, A. YA. KORETS, Y. N. TITARENKO. Biological activity of water-soluble fullerene complexes. *Doklady Akad. Nauk.* **1997**, *355*, 269.
- 121 R. SIJBESMA, G. SRDANOV, F. WUDL, J. A. CASTORO, C. WILKINS, S. H. FRIEDMAN, D. L. DECAMP, G. L. KENYON. Synthesis of a fullerene derivative for the inhibition of HIV enzymes. *J. Am. Chem. Soc.* **1993**, *115*, 6510–6512.
- 122 D. I. SCHUSTER, S. R. WILSON, R. F. SCHINAZI. Anti-human immunodeficiency virus activity and cytotoxicity of derivatized buckminsterfullerenes. *Bioorg. Med. Chem. Lett.* **1996**, *6*, 1253–1256.
- 123 C. TONIOLO, A. BIANCO, M. MAGGINI, G. SCORRANO, M. PRATO, M. MARASTONI, R. TOMATIS, S. SPISANI, G. PALÙ, E. D. BLAIR. A bioactive

- fullerene peptide. *J. Med. Chem.* **1994**, *37*, 4558–4562.
- 124** D. I. SCHUSTER, L. WILSON, A. N. KIRSCHNER, R. F. SCHINAZI, S. SCHLUETER-WIRTZ, P. THARNISH, T. BARNETT, J. ERMOLIEFF, J. TANG, M. BRETTREICH, A. HIRSCH. Evaluation of the anti-HIV potency of a water-soluble dendrimeric fullerene. In: *Fullerene 2000 – Functionalized Fullerenes. Proceedings of the 197th Meeting of the Electrochemical Society*. The Electrochemical Society, Pennington, NJ, **2000**, vol. 9, p. 267.
- 125** S. MARCHESAN, T. DA ROS, G. SPALLUTO, J. BALZARINI, M. PRATO. Anti-HIV properties of cationic fullerene derivatives. *Bioorg. Med. Chem. Lett.* **2005**, *15*, 3615–3618.
- 126** S. BOSI, T. DA ROS, G. SPALLUTO, J. BALZARINI, M. PRATO. Synthesis and anti-HIV properties of new water-soluble bis-functionalized [60]fullerene derivatives. *Bioorg. Med. Chem. Lett.* **2003**, *13*, 4437–4440.
- 127** T. MASHINO, K. SHIMOTOHNO, N. IKEGAMI, D. NISHIKAWA, K. OKUDA, K. TAKAHASHI, S. NAKAMURA, M. MOCHIZUKI. Human immunodeficiency virus-reverse transcriptase inhibition and hepatitis C virus RNA-dependent RNA polymerase inhibition activities of fullerene derivatives. *Bioorg. Med. Chem. Lett.* **2005**, *15*, 1107–1109.
- 128** N. IWATA, T. MUKAI, Y. YAMAKOSHI, S. HARA, T. YANASE, M. SHOJI, T. ENDO, N. MIYATA. Effects of C<sub>60</sub>, a fullerene, on the activities of glutathione S-transferase and glutathione-related enzymes in rodent and human livers. *Fullerene Sci. Technol.* **1998**, *6*, 213–226.
- 129** T. H. UENG, J. J. KANG, H. W. WANG, Y. W. CHENG, L. Y. CHIANG. Suppression of microsomal cytochrome P450-dependent monooxygenases and mitochondrial oxidative phosphorylation by fullereneol, a polyhydroxylated fullerene C<sub>60</sub>. *Toxicol. Lett.* **1997**, *93*, 29–37.
- 130** S. L. MCGOVERN, E. CASELLI, N. GRIGORIEFF, B. K. SHOICHET. A common mechanism underlying promiscuous inhibitors from virtual and high-throughput screening. *J. Med. Chem.* **2002**, *45*, 1712–1722.
- 131** G. P. TEGOS, T. N. DEMIDOVA, D. ARCILA-LOPEZ, H. LEE, T. WHARTON, H. GALI, M. R. HAMBLIN. Cationic fullerenes are effective and selective antimicrobial photosensitizers. *Chem. Biol.* **2005**, *12*, 1127–1135.
- 132** T. MASHINO, D. NISHIKAWA, K. TAKAHASHI, N. USUI, T. YAMORI, M. SEKI, T. ENDO, M. MOCHIZUKIA. Antibacterial and antiproliferative activity of cationic fullerene derivatives. *Bioorgan. Med. Chem. Lett.* **2003**, *13*, 4395–4397.
- 133** C. YU, T. CANTEENWALA, L. Y. CHIANG, B. WILSON, K. PRITZKER. Photodynamic effect of hydrophilic C<sub>60</sub>-derived nanostructures for catalytic antitumoral antibacterial applications. *Synthetic Metals* **2005**, *153*, 37–40.
- 134** J. D. FORTNER, D. Y. LYON, C. M. SAYES, A. M. BOYD, J. C. FALKNER, E. M. HOTZE, L. B. ALEMANY, Y. J. TAO, W. GUO, K. D. ASMUS, V. L. COLVIN, J. B. HUGHES. C<sub>60</sub> in water: nanocrystal formation and microbial response. *Environ. Sci Technol.* **2005**, *39*, 4307–4316.
- 135** F. PELLARINI, D. PANTAROTTO, T. DA ROS, A. GIANGASPERO, A. TOSSI, M. PRATO. A novel [60]fullerene amino acid for use in solid-phase peptide synthesis. *Org. Lett.* **2001**, *3*, 1845–1848.
- 136** D. PANTAROTTO, A. BIANCO, F. PELLARINI, A. TOSSI, A. GIANGASPERO, I. ZELEZETSKY, J.-P. BRIAND, M. PRATO. Solid-phase synthesis of fullerene-peptides. *J. Am. Chem. Soc.* **2002**, *124*, 12543–12549.
- 137** B.-X. CHEN, R. S. WILSON, M. DAS, D. J. COUGHLIN, B. F. ERLANGER. Antigenicity of fullerenes: antibodies specific for fullerenes and their characteristics. *Proc. Natl Acad. Sci. USA* **1998**, *95*, 10809–10813.
- 138** B. C. BRADEN, F. A. GOLDBAUM, B.-X. CHEN, A. N. KIRSCHNER, S. R. WILSON, B. F. ERLANGER. X-ray crystal structure of an anti-Buckminsterfullerene antibody Fab fragment: biomolecular recognition of

- C<sub>60</sub>. *Proc. Natl Acad. Sci. USA* **2000**, *97*, 12193–12197.
- 139 W. H. NOON, Y. KONG, J. MA. Molecular dynamic analysis of a buckyball-antibody complex. *Proc. Natl Acad. Sci. USA* **2002**, *99*, 6466–6470.
- 140 D. PANTAROTTO, C. D. PARTIDOS, R. GRAFF, J. HOEBEKE, J.-P. BRIAND, M. PRATO, A. BIANCO. Synthesis, structural characterization, and immunological properties of carbon nanotubes functionalized with peptides. *J. Am. Chem. Soc.* **2003**, *125*, 6160–6164.
- 141 G. R. DIECKMANN, A. B. DALTON, P. A. JOHNSON, J. M. RAZAL, J. CHEN, G. M. GIORDANO, E. MUNOZ, I. H. MUSSELMAN, R. H. BAUGHMAN, R. DRAPER. Controlled assembly of carbon nanotubes by designed amphiphilic peptide helices. *J. Am. Chem. Soc.* **2003**, *125*, 1770–1777.
- 142 S. Q. WANG, E. S. HUMPHREYS, S.-Y. CHUNG, D. F. DELDUCCO, S. R. LUSTIG, H. WANG, K. PARKER, N. W. RIZZO, S. SUBRAMONEY, Y.-M. CHIANG. Peptides with selective affinity for carbon nanotubes. *Nat. Mater.* **2003**, *2*, 196–200.
- 143 D. PANTAROTTO, C. D. PARTIDOS, J. HOEBEKE, F. BROWN, E. KRAMER, J.-P. BRIAND, S. MULLER, M. PRATO, A. BIANCO. Immunization with peptide-functionalized carbon nanotubes enhances virus-specific neutralizing antibody responses. *Chem. Biol.*, **2003**, *10*, 961–966.
- 144 B. F. ERLANGER, B.-X. CHEN, M. ZHU, L. BRUS. Binding of an anti-fullerene IgG monoclonal antibody to single wall carbon nanotubes. *Nano Lett.* **2001**, *1*, 465–467.
- 145 E. OSTUNI, R. G. CHAPMAN, R. E. HOLMLIN, S. TAKAYAMA, G. M. WHITESIDES. A survey of structure–property relationships of surfaces that resist the adsorption of protein. *Langmuir* **2001**, *17*, 5605–5620 and references therein.
- 146 M. SHIM, N. W. S. KAM, R. J. CHEN, Y. LI, H. DAI. Functionalization of carbon nanotubes for biocompatibility and biomolecular recognition. *Nano Lett.* **2002**, *2*, 285–288.
- 147 M. P. MATTSO, R. C. HADDON, A. M. RAO. Molecular functionalization of carbon nanotubes and use as substrates for neuronal growth. *J. Mol. Neurosci.* **2000**, *14*, 175–182.
- 148 N.-Y. PAN, J.-S. SHIH. Piezoelectric crystal immunosensors based on immobilized fullerene C<sub>60</sub>-antibodies. *Sens. Actuators B* **2004**, *98*, 180–187.
- 149 D. W. CAGLE, S. J. KENNEL, S. MIRZADEH, J. M. ALFORD, L. J. WILSON. *In vivo* studies of fullerene-based materials using endohedral metallofullerene radiotracers. *Proc. Natl Acad. Sci. USA* **1999**, *96*, 5182–5187.
- 150 T. WHARTON, L. J. WILSON. Highly-iodinated fullerenes as a contrast agent for X-ray imaging. *Bioorg. Med. Chem.* **2002**, *10*, 3545–3554.
- 151 T. WHARTON, L. J. WILSON. Towards fullerene-based X-ray contrast agents: design and synthesis of non-ionic, highly-iodinated derivatives of C<sub>60</sub>. *Tetrahedron Lett.* **2002**, *43*, 651–654.
- 152 R. D. BOLSKAR, A. F. BENEDETTO, L. O. HUSEBO, R. E. PRICE, E. F. JACKSON, S. WALLACE, L. J. WILSON, J. M. ALFORD. First soluble M@C<sub>60</sub> derivatives provide enhanced access to metallofullerenes and permit *in vivo* evaluation of Gd@C<sub>60</sub>[C(COOH)<sub>2</sub>]<sub>10</sub>. *J. Am. Chem. Soc.* **2003**, *125*, 5471–5478.
- 153 S. LAUS, B. SITHARAMAN, É. TÓTH, R. D. BOLSKAR, L. HELM, S. ASOKAN, M. S. WONG, L. J. WILSON, A. E. MERBACH. Destroying gadofullerene aggregates by salt addition in aqueous solution of Gd@C<sub>60</sub>(OH)<sub>x</sub> and Gd@C<sub>60</sub>[C(COOH)<sub>2</sub>]<sub>10</sub>. *J. Am. Chem. Soc.* **2005**, *127*, 9368–9369.
- 154 É. TÓTH, R. D. BOLSKAR, A. BOREL, G. GONZÁLEZ, L. HELM, A. E. MERBACH, B. SITHARAMAN, L. J. WILSON. Water-soluble gadofullerenes: towards high-relaxivity, pH-responsive MRI contrast agents. *J. Am. Chem. Soc.* **2005**, *127*, 799–805.
- 155 H. KATO, Y. KANAZAWA, M. OKUMURA, A. TANINAKA, T. YOKAWA, H. SHINOHARA. Lanthanoid endohedral metallofullerenols for MRI contrast agents. *J. Am. Chem. Soc.* **2003**, *125*, 4391–4397.



- 156 M. MIKAWA, H. KATO, M. OKUMURA, M. NARAZAKI, Y. KANAZAWA, N. MIWA, H. SHINOHARA. Paramagnetic water-soluble metallofullerenes having the highest relaxivity for MRI contrast agents. *Bioconjugate Chem.* **2001**, *12*, 510–514.
- 157 H. SHINOHARA, K. YAGI, J. NAKAMURA. *Japanese Patent 94-285395*.
- 158 E. B. IEZZI, J. C. DUCHAMP, K. R. FLETCHER, T. E. GLASS, H. C. DORN. Lutetium-based trimetallic nitride endohedral metallofullerenes: new contrast agents. *Nano Lett.* **2002**, *2*, 1187–1190.
- 159 T. CAI, Z. GE, E. B. IEZZI, T. E. GLASS, K. HARICH, H. W. GIBSON, H. C. DORN. Synthesis and characterization of the first trimetallic nitride templated pyrrolidino endohedral metallofullerenes. *J. Chem. Soc. Chem. Commun.* **2005**, 3594–3596.
- 160 T. Y. ZAKHARIAN, A. SERYSHEV, B. SITHARAMAN, B. E. GILBERT, V. KNIGHT, L. J. WILSON. A fullerene–paclitaxel chemotherapeutic: synthesis, characterization, and study of biological activity in tissue culture. *J. Am. Chem. Soc.* **2005**, *127*, 12508–12509.
- 161 E. NAKAMURA, H. ISOBE, N. TOMITA, M. SAWAMURA, S. JINNO, H. OKAYAMA. Functionalized fullerene as an artificial vector for transfection. *Angew. Chem. Int. Ed. Engl.* **2000**, *39*, 4254–4257.

## 12 Nanotechnology for Biomedical Devices

*Lars Montelius*

### 12.1 Introduction

The pace of employment of advanced microfabrication technology for realizing biomedical devices has been accelerated with the development of a seemingly never-ending increased packing density of functionalities in semiconductor chips [1] as a consequence of the downscaling of device dimensions in such chips [2]. This area of microelectronic development has been one of the major drivers in the development of our modern, technological society. However, this success has not only been brought to us by simple dimensional downscaling, but also by impressive developments in the fields of material sciences that have led to several new basic material discoveries [3–5]. Such inventions have, in turn, been brought into the engineering sciences, realizing these devices into everyday life. One can especially think about the invention of the concept of hetero-structures, making it possible to fabricate semiconductor lasers and optical detectors – the key to modern fiber optic-based communication [4–7]. In the area of biomedical devices, the development in material sciences has brought diagnostic tools such as computer-based imaging systems relying on the interplay between tissue and X-rays, magnetic radiation and ultrasound, etc. [8–10]. We have also witnessed various electronic devices being developed for enhancing impaired senses such as hearing aids, etc. Several devices have made life easier for those suffering from glucose-related diseases, for example [11, 12]. Handheld devices have been developed allowing individuals to monitor the sugar content of their blood in their own environment and, hence, also permitting the use of insulin delivery when needed.

With the introduction of nanotechnology for fabrication of significantly down-scaled materials, we are now facing another even more rapid development. These materials do not only occupy an immensely small volume, but they also possess certain functions being created just due to the reduction in size [4–7, 13–15]. A conservative and often heard definition of nanodevices is that at least one of the scalar dimensions is below 100 nm and that the functionality of the device itself is changed due to its nanometer size.

The development of microfabrication methods and technologies in the nanometer domain is considered by many people not only to be a simple evolutionary step, but also to have a more revolutionary aspect [13, 15]. Basically, this is achieved through the downscaling that led not only to an added packing density of functions, which means higher modality, but also to objects with certain unique properties. Such evolution has not yet been experienced by mankind on any large scale and right now we are in the middle of it. Although we have developed a lot of new tools for fabrication, characterization, imaging and manipulation of matter at the nanoscale [15–25], we must still consider ourselves to be in a time rather similar to the “hammer and sledge” stage in the stone-age. Nevertheless, we have already experienced an enormous impact in many of today’s consumer products, e.g. recently a new cellular phone was announced having silver particles on its surface, killing bacteria and germs [26]. During the 5 last years we have also seen the introduction of various kinds of garments making the fabric more or less impossible to stain [27]. Recently, nanotechnology-based methods have been implemented to spin fibers, creating possibilities for enhanced fabrics having built-in intelligent functions [28]. Today we can buy self-cleaning windows that use a catalytic process to break down inorganic dirt that will eventually be washed off the window during next rain fall [29]. We can tailor-make surfaces with certain hydrophilic properties so that they can serve either as a surface that a liquid just wets or that a liquid will form droplets on. Such droplets may encapsulate drugs or reagents for future fluidic “factory-on-a-chip” applications, and can be manipulated by their surface tension [28] and/or by electro-wetting, making it possible to move droplets of liquids at will on a two-dimensional (2-D) surface [30]. In the area of biomedical devices, there are many devices that rely on absolute modern microfabrication standards; however, when talking about real nanotechnology-based devices (in the concept of the definition given above), such devices are much less numerous.

In this chapter, I introduce the reader to various forms of nanotechnologies and try to explain why some of these methods are more likely, and more suitable, than others to be employed in the biomedical field. I try to describe how modern nanotechnology may impact the fields of biomedical engineering by giving some examples of nanotechnologies applied in the domain of life sciences. Of course, it is impossible to cover fully the fields of nanobiological and nanomedical research and development, and there are various journals and other publications that cover these areas of nanotechnology. What I present here is solely an attempt to give some representative and, hopefully, interesting examples that may bring the interest and excitement in this field to the reader.

I have divided this chapter into various main parts, each part being divided in subsections. In the first part, I describe various forms of nanotechnologies and nanotools, mainly coming from the field of inorganic nanotechnology. After an overall introductory discussion, some technologies are described in more detail in various subsections. In the second part, I give an overview of various forms of applications having a relation to biomedical devices and technology. In further subsections, I describe a couple of such applications in more depth. The final part presents a discussion and a short speculation of what the future may bring.

## 12.2

### Nanotechnologies

#### 12.2.1

##### Overview of Nanotechnologies and Nanotools

In order to create nanostructures, one is bound to follow two approaches – either top-down or bottom-up. The former is considered to be the driving force for nanotechnology development, while the latter can often be described as a molecular nanotechnology approach [13]. However, these two approaches are more and more blending together, and one is often obliged to make use of both methods in order to fabricate functional devices. Hence, both technologies are just as important for the development of the field. In the top-down approach, one usually relies on a lithographic technology where one can pattern a surface into a relief structure by using some kind of a polymer layer that is put on top of a hard material, e.g. a piece of silicon. The lithographic tools necessary for making nanostructures are based on either electromagnetic [31–37] interactions with the polymer chains or mechanical deformation of it [20, 38–41]. Table 12.1 presents a summarized compilation showing some of the important characteristics. For the electromagnetic lithographies, one often uses optical illumination [31–34]. This is the method used by most semiconductor companies. However, the smallest dimensions using these methods are around 50 nm and if one needs smaller size definition, one is bound to utilize other technologies. Here, electron beam lithography (EBL) dominates [34–36], either using a vectorial or a circular exposure strategy depending on the application [42]. In all cases, the energized electrons either break or make molecular junctions in the polymer layer, making it either harder or softer for the subsequent solvent to develop the latent pattern, i.e. one can obtain both a positive and negative contrast [34–36]. With this method, one can obtain resolutions down to a few nanometers. After the exposure and development of the resist, one usually employs an etching method to induce a surface relief in the underlying substrate material [34]. One can also utilize lift-off methods [43] in order to make a metal pattern on the surface or a combination of both, possibly repeated time after time, thereby creating a complex pattern on a surface. Alternate technologies, also based on radiation, rely on the use of X-rays [35]. Most often the X-rays are produced as a consequence of Bremsstrahlung in synchrotron rings [44] or due to laser-induced emission [45].

Another more recent approach is to employ various forms of mechanical deformations of the polymer layer, e.g. nanoimprint lithography (NIL). This technology was pioneered by Chou, presently at Princeton [19, 37–41]. The method resembles, in some sense, the way compact discs (CDs and DVDs) are fabricated. The difference is that for CDs one uses an embossing tool to make an all-plastic structure, while in NIL (Fig. 12.1) one makes a mechanical indentation into a polymer layer, having been spun onto a solid support, usually a silicon wafer [46]. It is also fair, in this connection, to mention the close resemblance of NIL to microcontact printing [41, 47–49]. Classically that denotes a technology that transfers a molecular layer

**Table 12.1.** Compilation of top-down lithographies. In the table is shown some key data of the major top-down lithographies. The numbers are not absolute but more given as indicative numbers to define in which “ball-park” the various lithographies presently belong. Interesting to note is that the various printing technologies show an overall good performance making them to be the possible preferred choices in a future perspective. For more discussions and references, see text.

Technologies	Generation of pattern	Exposure field per “exposure”	Possible feature resolution	Type of interaction	Throughput 10–12 inch diameter Wafer/hour
UV-lithographies	Mask	Chip (Dize)	$\geq 50$ nm	Electro magnetic	>50
X-ray	Mask	Chip	$\geq 100$ nm	Electro magnetic	$\approx 10$ –30
Focussed Ion beam lithography	Serial	Chip	$\geq 50$ nm	Electro magnetic	1
E-beam lith	Serial	Chip	$\geq 5$ nm	Electro magnetic	0.1
SPM lithography	Serial	Chip	$\geq 10$ nm	Electro magnetic	<0.1
SPM manipulation	Serial	Chip	Individual atoms	Mechanical	<0.01
Micro-contact printing	Stamp	Wafers, $\approx 6$ inch	$\geq 20$ nm	Mechanical	>20
Nanoimprint lithographies	Stamp	Wafer scale $\approx 8$ –10 inch	$\geq 5$ nm	Mechanical	>50
Injection moulding	Stamp	Wafer scale 130 mm	$\geq 50$ nm	Mechanical	$\geq$ several 100

by soft contacting of a stamp, made of a soft polymer inked with a layer of molecules, to the substrate. Thereby transferring the inked layer from the protruding features of the stamp. After this “fabrication” step, one may continue with etching or metal deposition, or by building another molecular layer on top of the first layer, sometimes utilizing covalent binding chemistry. It is also fair to mention the so-called step and flash technology [39, 41, 50–53], being heavily pushed as a NIL, although the process is a bit different. In this concept (Fig. 12.2) one utilizes a floating resist and a stamp that deforms the floating resist so that a relief structure is obtained (still in a liquid phase). By applying a UV exposure through the transparent mask/stamp, one can UV-harden the resist so that it is possible to remove the stamp leaving a UV-cured, structured polymer on the surface. These different “mechanical deformation” technologies can be denoted as a family of technologies, but one could also place the step and flash technology, for example, in the category of

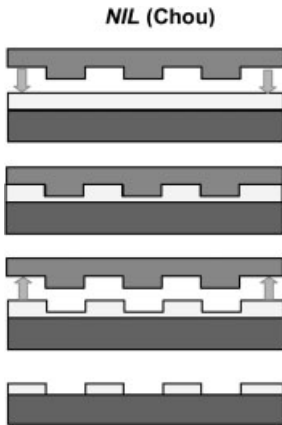


**Figure 12.1.** The process flow of NIL. (From Ref. [41].)

optical lithography. Nowadays, there is often a blending of technologies and one has come up with a hybrid technology, based on ideas borrowed from both areas. Here, one uses a hard stamp and spun on resist, but the actual hardening of the resist is not by temperature as in classical NIL, but by illumination. This technology, often denoted UV-NIL [41, 53–58], is maybe one of the most promising technologies for future high-volume manufacturing (HVM) of nanostructures. I will continue a bit longer on nanoimprint-related methods, since they offer an opportunity for fabrication of biomedical devices [59]. Using this technology, one can fabricate many samples having nanostructures in a very economical way [60]. This has previously been the limiting factor for not introducing nanotechnology in the biomedical field. There is a need in biomedical research to be able to make many structures in order to be able to build significance in the observations. This is in-

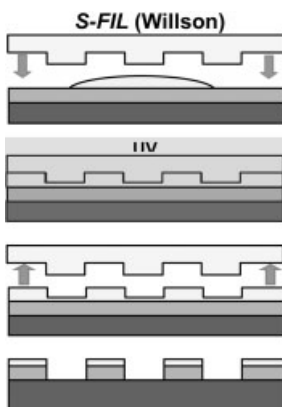


**Figure 12.2.** The process flow of step and flash NIL. (From Ref. [41].)

deed different from in physics, where one observable “always” will behave in a similar fashion from measurement to measurement. In biology, there is a natural spread due to the biological variability between species, etc., which necessitates that many samples need to be analyzed in order to obtain statistically significant results. Due to the importance that NIL may have in the future [61–63], I spend more time describing it in more depth in a separate subsection below.

The invention of scanning tunneling microscopy [64] and related atomic force microscopy (AFM) [18] has brought tools to nanoscience with which it is possible to image, characterize and manipulate individual atoms, molecules and structures [16–19, 21–25]. It is even possible to image a few magnetic spins of a few atoms below a sharp magnetic tip [66]. Also, as we see later, it has been instrumental for another class of sensor structures [65] as well as inspiring some of the nanotechnologies described above. Hence, it is fair to conclude that this technology has probably been the single most important one for the development of the nanotechnology field as we know it today. Scanning probe technology is discussed further in a separate subsection.

Lately, there has been considerable interest for making and exploring nanowires, e.g. carbon nanotubes (CNTs) and epitaxial wires [67–74], being made by a bottom-up approach (Figs. 12.3 and 12.4). This is a new class of materials with large pos-

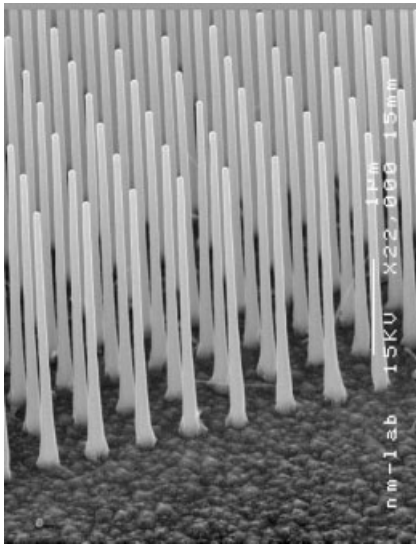


**Figure 12.3.** Epitaxial nanowires of, in this case, InP as defined by a bottom-up approach. The lateral position is governed by catalytic metal particles (Au) deposited by a lift-off procedure before growth has taken place. The shape and length can be controlled in the

process, while the diameter is determined by the size of the catalytic metal particle. The wires can be branched by putting additional metal particles on the sides, making an additional growth run and thereby creating a 3-D network. (From Ref. [68].)

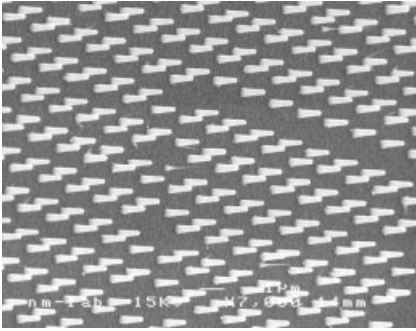


**Figure 12.4.** Epitaxial nanowires patterned by using NIL allowing exact control of the wire positions over a large surface area. (From Ref. [70].)

sibilities for future applications in many different areas of science. They offer extremely small sizes with extremely large aspect ratios. They are not made by top-down lithography; hence, their electronic properties have not been damaged or affected by the processing. Their smallness offers mechanical properties that may be explored for various nanomechanical applications. Some of the foreseeable biomedical applications of nanowires are described below in more detail. The nanomechanics of small objects [74–77] also offer several opportunities for applications as sensors in the biomedical area. Coupled with the increased efforts in nanotechnology is the possibility to utilize nanoparticles for various applications. These particles can be solid, semipermeable, hollow or core–shell particles. They have immediate medical applications, such as magnetic nanoparticles [78–79] that may be used as mobile reporters in magnetic imaging, allowing 3-D capabilities.

There are a lot of other research areas of great importance for handling molecular materials and cells at the nanoscale, e.g. the employment of biomimetic ideas, which is a field on its own. Modifying surfaces using biomaterials can be very important for the development of methods allowing construction of model biological structures for studies of various bio-reactions and for sensor applications, etc. For instance, lipid bilayer membranes supported on surfaces can be very valuable since they may offer possibilities to investigate membranes and membrane proteins in an artificial environment [80–86].

Presently, there is an increased interest for using optical techniques based on surface enhanced Raman scattering (SERS) and surface plasmon resonance (SPR) as mediators for biomolecular interactions [87]. There is also an increased interest in the use of light-emitting point sensors [88] as passive reporters for various chemical and biological reactions/processes. However, due to space limitations, these techniques will not be further explored in this chapter. The interested reader is instead referred to other articles/reports (e.g. Ref. [88]).



### 12.2.1.1 NIL

The process of NIL (Fig. 12.1) is essentially a rather simple process based on pressing a pre-patterned substrate into a layer of polymer spun onto a hard support, the substrate, usually a silicon wafer. The stamp must be pre-processed containing the relief structure that is going to be printed into the polymer layer. For stamp fabrication, one usually employs EBL in combination with etching [89]. In order to be able to press the tool into the polymer layer one usually heats up the sandwiched tool–substrate to a process temperature, where the polymer layer has become fluid, i.e. one heats everything above the glass transition temperature ( $T_g$ ) of the polymer. We have investigated several polymers [90] and found, as a rule of thumb, that the process temperature should be slightly above the  $T_g$  [91]. After applying a pressure high enough for the stamp to be pressed into the polymer layer, one cools down the sandwich, whilst relieving the pressure. Then one can separate the stamp and substrate from each other. This last separation is easier if one has put an anti-sticking layer onto the stamp [92–95]. There are several problem areas associated with such a process. If the stamp and substrate are made of different materials, heating may cause large problems due to the different thermal expansion coefficients, making the materials move laterally with respect to each other. Hence, one has been trying to come up with new polymers enabling patterning at lower temperatures [96]. Also, for HVM, one considers possibilities such as keeping the process temperature constant and pressing/removing at process temperature, thereby also minimizing the problem of any lateral mismatch between expansions of the stamp and substrate, respectively. An outstanding problem with NIL is the necessity of being able to align subsequent stamps to previous structures on a substrate [97]. A lot of activity is presently being pursued in order to solve this problem, [97–100]. Nevertheless, this technology is promising and it can fabricate nanostructures on a wafer scale [40, 46, 101, 102], and the imprint time can be less than seconds [103]. Hence, it is a very powerful technology for future nanoscale materials that may be employed in a variety of application fields.

### 12.2.1.2 Other Lithography Techniques

Just as NIL is a very good alternative as one of the next-generation technologies (NGL) [1, 13, 61, 62] of importance for the information technology sector, other printing techniques, such as microcontact printing [41, 51–53, 104], offer similar advantages. The method (to be more precise, the family of microcontact printing technologies) offers additional benefits as compared to NIL, since the process is simpler, it is a room temperature process, does not require a high pressure (although that problem can be circumvented by using soft NIL [41, 55–57]), has limited stamp–substrate sticking problems, etc. The major drawback is the flexible stamp commonly used that limits the resolution to the order of 100 nm and its use for wafer-scale single printing with high resolution. However, there is presently a tremendous development in nanoimprinting, microcontact and other printing technologies, so we will certainly soon experience an even larger variety of such technologies [105]. For instance, a method based on “printing” was reported recently by Yuand coworkers where they used DNA as a template in a repli-

cation “printing” process, making it possible to replicate DNA assemblies in a hybridization–contact–dehybridization process, which they denoted as “supramolecular nanostamping” [106]. In a similar way, high-density metal lateral nanowires were reported to be transferred from a template to a silicon surface through a contact mechanism. The authors employed “stamps”, fabricated from a superlattice of III–V materials, combined with cleaving and selective etching and metalization. Using such an approach, it is possible to make very high-density and ordered lines that would be very difficult to make using other top-down approaches [107, 108].

A candidate for NGL has for many years been X-ray lithography [1, 35, 44, 45] and with the continuous push from the microelectronic industry for using UV lithographies there has been a merge of the two into the concept of extreme (E)-UV lithography where one utilizes light with wavelengths in the 10-nm regime (for a compilation of papers on E-UV lithography, see Ref. [109]). Usually, such light is generated from plasma sources [2, 45, 109]. The positive aspect of this technology is that the main processing infrastructure technology is rather similar that already employed in the big fabrication facilities. The drawback of E-UV, however, is the enormous costs required in order to put it into a working technology. The costs will not stop it, but it will effectively limit the number of facilities that can afford the investment. Hence, its importance for the biomedical field as a technology for making small series of chips is limited, since the initial cost for such a small series will be high. Another type of lithography technology is based on scanning probe microscopy (SPM) [110]. It will probably have a limited impact on wafer-scale processing. However, it is still one of the most important since it will allow small series of samples to be made in a rather inexpensive way. The needed development, which is making steady progress, is the increase of scanning speed, allowing both imaging and lithography to be made fast enough. However, the limitation of the method, even when it has gained real-time speeds of scanning, is the same as for EBL, i.e. the serial nature of pixel-by-pixel exposure. However, in contrast to several attempts made over the years for making an array of small electron-beam-based exposure sources that could expose a wafer in parallel, the use of an array of scanning probes might just overcome this problem (see also Sections 12.2.3 and 12.3.8). Dip-pen lithography [111, 112] has also been introduced, presenting us with another possibility to fabricate “molecular” lines or patterns without the need for going through the cumbersome pattern transferring method that is needed for other lithographies. Here, one has a tool that makes it possible to write only on those parts of a surface that one needs in a direct way, using the fountain pen principle. It is, to some extent at least, principally a scanning probe lithography method, based on the fact that there is always a water layer on a surface in air. If two surfaces are in contact with each other, the content of the water layer may, depending on the respective hydrophobicity of the two surfaces in contact with each other, be transferred from the tip to the surface and the water layer on the tip may not be consumed if it is connected to a reservoir of liquid or if it is dipped (inked) into a reservoir repeatedly. This is a method that naturally has a large potential for writ-

ing various forms of important molecular patterns for use in protein chip applications, etc. Some examples are given in the next section. In a further extension of the technique, one can fabricate a hollow cantilever tip with a small opening at its end allowing molecules to be transferred from the hollow tips to surfaces [113]. Using concepts from the old days, when one used shadow mask evaporation masks for making electrical (metal) contacts to semiconductors, one has refined the shadow mask technology into stencil mask nanolithography, enabling us to draw metal lines arbitrarily on surfaces in a vacuum [114, 115]. The technique allows a fine pattern to be made by moving the stencil (the shadow mask) while metal (or molecules or something else that can be evaporated) is flowing through the apertures of the stencil. This is a nice method that may have its specific areas application. It can easily be parallelized by having an array of such nanostencil masks moving in unison, allowing large areas to be covered in a short time. The drawback is the clogging of the nanoscale aperture that has to be overcome in order to find a real industrial use for it. The possibilities to develop the tools being described above have been enabled by the development of nanotechnologies in a pull–push fashion. One nanofabrication method that has been instrumental in this aspect, and actually is just in its initial phase of development at the moment, is the use of focused ion beams [116], allowing extremely nice structures to be fabricated in a true 3-D space. The method is often combined with scanning electron microscopy (SEM), allowing observation of the structures being made (although it is also possible to use the ions for scanning and imaging purposes). The principle is to make local and directed deposition or etching of materials due to the energetic ions impinging onto the surface. The method has the same limitations as EBL systems – it is a serial method. Still, it is not at all a mature technology at this stage and I guess that we will experience a tremendous development in other technologies, since it is such a generic technology.

### 12.2.1.3 Scanning Probes

Scanning probes offer many other possibilities in addition to imaging capabilities. For instance they have been utilized to make a new kind of memory device, the Millipede [117], which in principle is an array of cantilevers (Fig. 12.5) that can be controlled individually, allowing the possibility to melt a plastic material and press the tip into it, thereby cause cooling. Hence, it is possible to write information on the nanoscale. Such information, consisting of local deformations, can easily be read out with the cantilevers in imaging mode. Using the technology behind AFM [65], basically a cantilever beam that can be moved in the  $xyz$  directions with a sharp tip mounted at the end, one can make an analysis tool that will be able to detect interactions on the cantilever surface being observed through induced bending as a function of, for example, heat, or stress as a function of molecular adhesion to one of the surfaces, thereby creating a bimetal-like switching behavior [118] (Fig. 12.6). Such cantilever-based sensing, transforming molecular recognition into a mechanical displacement [119], has been used for many aspects, e.g. detection of antigen–antibody reactions [118]. These results are discussed further below. AFM

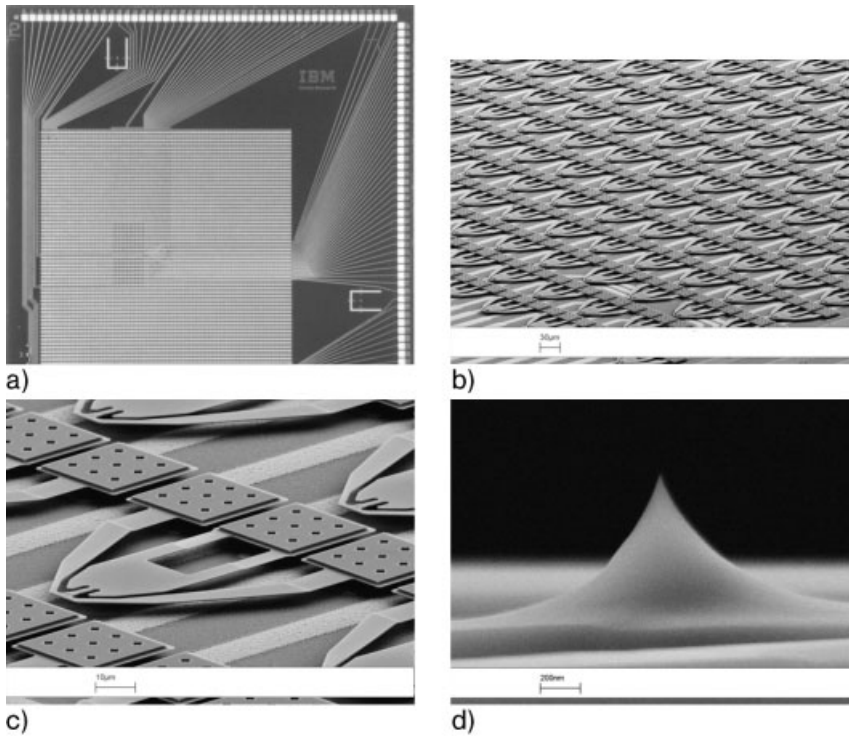


**Figure 12.5.** The Millipede chip: optical micrograph of a  $64 \times 64$  cantilever array chip (A), and SEM images of the center of the array (B), one cantilever (C) and a tip apex (D). Data can be written at extremely high densities (greater than  $1 \text{ TB in}^{-1}$ ). The cantilevers have separate

heaters for reading and writing, and utilize electrostatic actuation for the z-direction. The cantilevers are around  $70 \mu\text{m}$  long, with a  $500\text{--}700 \text{ nm}$  tip integrated directly above the write heater. (Reprinted with permission from IBM.)

has been utilized for force detection, allowing a detailed understanding of binding forces between molecules. One could denote this as “molecular fishing”. It is based on coating the tip with a certain type of molecule and having another molecule that will bind to it on the substrate. When the tip is lowered into the molecules at the surface, a mechanical bond may be formed and, by subsequent retraction of the AFM tip from the surface, one can follow the sequence when breaking the chemical bonds. This provides valuable information about bond strengths and other molecular properties. This technology has been advanced to the level where it is possible to identify single molecular binding events [120]. Such detailed knowledge will be of great value in the biological area, e.g. in order to increase the understanding of cell signaling mechanisms and protein folding [121]. To fully use SPM for enhancing our understanding in biology, we must continue the development of probes so that they can obtain information from both time and space simultaneously, i.e. allow the possibility to capture images revealing important biological processes in real-time.

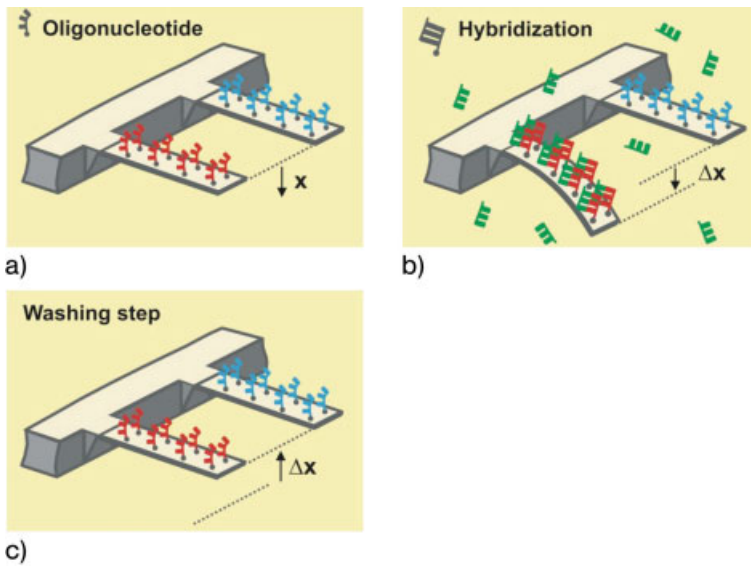


**Figure 12.6.** Operating modes of cantilevers employed as sensors: (A) static deflection mode, (B) dynamic resonance mode and (C) bimetallic heat mode. (From Ref. [118].)

## 12.3 Applications

### 12.3.1 Introduction

Here, I explore various directions of nanotechnology in the life sciences sector paving its way into the biomedical sector. However, so far, very few examples of real employment of nanotechnology in the biomedical sector can be found. Nanotechnology offers many chances for applications, but hitherto the development has been mainly focused on being used as sensors. In the following section, I show how passive and active nanostructures surfaces can be explored, how nanotechnology can affect the area of proteomics, and how nanowires and nanomechanics may be employed as sensors for molecular detection.

### 12.3.2 Biomedical Applications based on Nanostructured Passive Surfaces

For many life sciences applications, one might need to detect only a few substances dispersed into a solution and blended with other substances. One needs to have a functionality of the substances, giving them a kind of a handle. This can be solved by utilizing different kinds of chemistry, often in conjunction with attaching cer-

tain dyes in order to be able to detect various reactions. However, what one really would like to have is a system providing identification without the use of a marker, i.e. a label-free diagnostic method. The reason is 2-fold – a marker may change the biological function of the substance and there is a probability that markers may not attach with 100% fidelity. In order to find a species at low concentration, it would be advantageous to increase the concentration. Many of these aspects can be dealt with using nanotechnology and passive surfaces. By passive we mean a surface that may or should have a function, but we cannot influence that function from the outside during a measurement, observation or reaction.

#### 12.3.2.1 Separation, Concentration and Enriching Structures

Separation can be achieved by employing nanotechnology in various ways. One form is to use a system of nanoscaled posts (functioning as bumpers) in an array format, together with time-alternating electric fields, making it possible to separate various molecules according to the entropic force they experience in the confined region, which in turn limits the natural conformation possibilities that they have [122, 123] (Figs. 12.7 and 12.8). Since the entropy of a molecule depends on its length, these confined space structures act as a sorter of molecules with various lengths, e.g. lengths of sequences of DNA. Such a molecular sorter at the nano-scale has been fabricated by EBL. Similar confinement-related devices, but instead of posts, using nanochannels in an array format have been proposed and realized utilizing NIL [41, 124, 125]. Here, NIL was employed (Figs. 12.9 and 12.10) creating ultra-narrow channels, forcing fluorescently labeled DNA to stretch out while passing through the narrow channel [124]. The vision for these kinds of structures is to be able to integrate light emitters along the channel and to determine the DNA code down to individual bases by reading them as they pass the emitters using near-field excitation/detection mechanisms. The first steps have been realized (Fig. 12.11), allowing the detection of a marker attached to the DNA at a certain position, using excitation through narrow slits positioned perpendicular to the channels [125, 126].

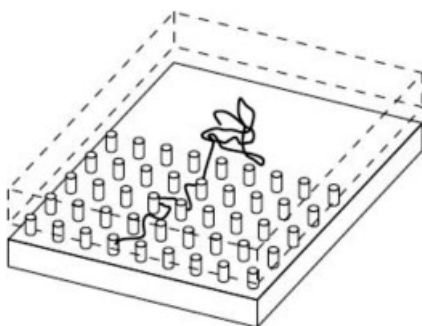


**Figure 12.7.** A fluidic device consisting of an array of nanopillars in between a roof and a floor. (From Ref. [122].)

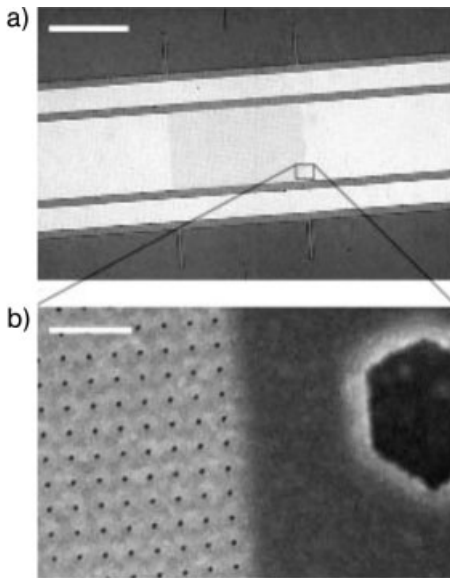


**Figure 12.8.** (A) An optical micrograph of the fabricated device. (B) A close-up showing the 35-nm pillars with a center-to-center distance of 160 nm. (From Ref. [122].)

It is especially interesting to note the use of another polymer, Topaz, with important benefits when it comes to biocompatibility and nanofluidicity in combination with optical spectroscopy [127]. The properties are such that it is an ideal candidate for integration of a waveguide directly in the polymer (Figs. 12.12 and 12.13). Furthermore, it would be possible to insert dye molecules acting as local emitters for locally addressing, for example, a DNA chain being swept in a channel close to the emitter. The full utilization of these concepts has not yet been reported. Similar kinds of nanofluidic structures have been employed to create a cell-based assay

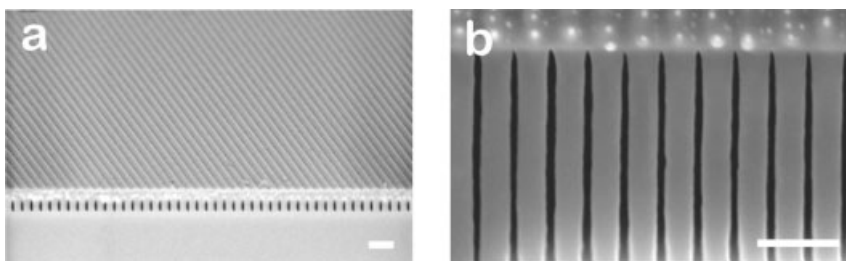


**Figure 12.9.** SEM images showing (a) the cross-section of the NIL-fabricated nanochannels and (b) the top view displaying the channels. (From Ref. [124].)

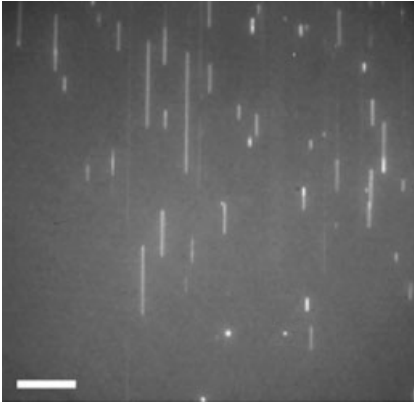


**Figure 12.10.** CCD image showing DNA stretched out in the nanochannels. Scale bar is 30  $\mu\text{m}$ . (From Ref. [124].)

[128], and in a recent paper a nanofluidic transistor (Fig. 12.14) was reported enabling control of ion and molecular flow in a channel [129].

#### 12.3.2.2 Molecular Motors Transported in Nanometer Channels

Other kinds of nanoscaled channel structures have been reported in the field of molecular motors (Figs. 12.15 and 12.16). This work, using nanoscaled structures, has been pioneered in a collaborative effort by the author and Mansson at Kalmar University [130–135]. Several other groups have reported micrometer-sized channels [136, 137], showing a performance similar to that obtained by us. However, we have, in contrast to the others, a precision in the motor guidance at the nanometer level [132, 135]. We have further refined the concepts and have built a com-

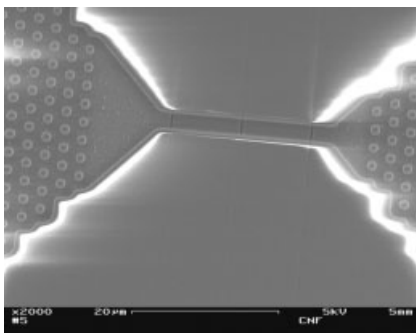


**Figure 12.11.** SEM image of a device with 100-nm wide slits for optical detection of DNA molecules as they pass by in the 5- $\mu\text{m}$  wide channel. At the outer ends are nanopillars for stretching the DNA filaments before entry into the channel region. (From Ref. [125].)



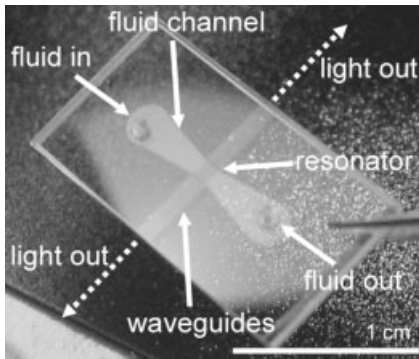


**Figure 12.12.** A photo of the microfluidic device made from Topaz with incorporated laser resonator. (From Ref. [127].)

plete toolbox system (Fig. 12.17) around this activity, where we can direct motion by fabrication of rectifiers, roundabouts, injectors, etc. [135]. Basically, we have combined nanolithography and surface functionalization (Figs. 12.18 and 12.19) using silane procedures, resulting in a very robust structure permitting detailed studies of the actomyosin system [134–136]. Such a system may be explored as a “lab-on-a-chip” system for use in drug development. For instance, one can imagine using a circular pattern into which individual motors are directed and, by counting the rotation speed of the motors in these circles as a function of the added drug, for instance, one may be able to investigate the effect of various formulas or concentrations of added drugs. If so, maybe such a system can work favorable as a pre-screening system for drug development.

### 12.3.2.3 Topographical Structures, Cells and Guidance of Neurons

Another class of passive structures is topographical patterns in conjunction with cell survival, growth and adhesion, with important implications for medical im-

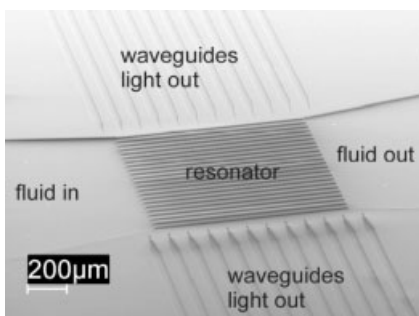


**Figure 12.13.** A SEM image showing the laser resonator structure located in the flow region. (From Ref. [127].)

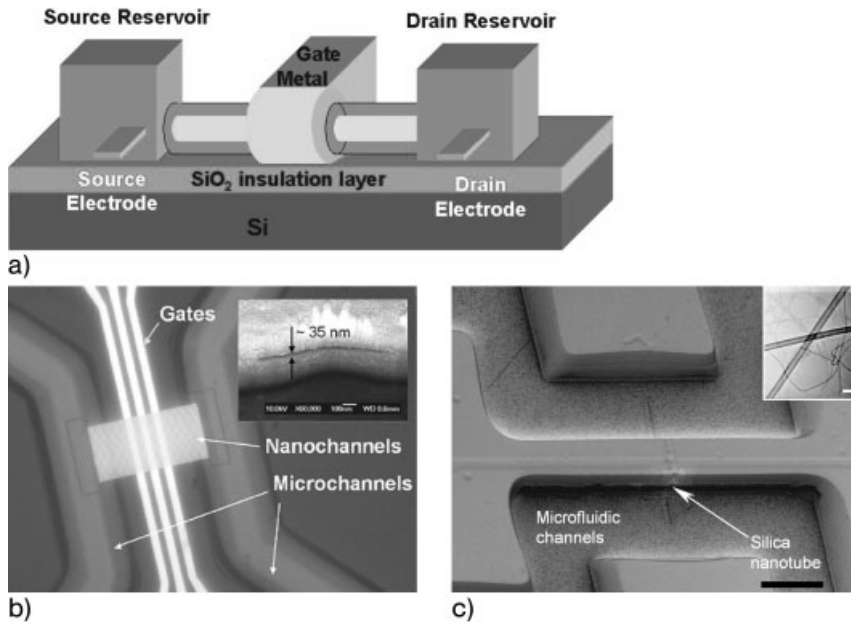


**Figure 12.14.** A nanofluidic transistor. (A) Schematic representation of the device. (B) Micrograph showing the 35 nanochannels running from left to right and the three electrode lines perpendicular to the nanochannels. (From Ref. [129].)

plants and prosthetic devices. Several investigations have been performed showing the positive effects of micrometer structures with respect to individual cell attachments, but results employing real nanometer-sized structures are sparse [138]. For the single-cell case and microstructures, grooved topography especially has been found to interact [139] and cells have been reported to change their shape in order to follow the grooves (and ridges) [140]. It has also been observed that cell regulation and transcription may be affected [141]. For nanostructures, macrophages, endothelial and fibroblast cells have been reported to interact in one way or another way [142–144]. We have recently performed a pilot study in which we have utilized nerve cells and studied the possibility of aligning nerve cells during growth [145]. Using NIL we made a large number of nanostructured surfaces containing grooves in the commonly employed polymer poly(methyl methacrylate) (PMMA). We made both positive and negative structures in  $200\ \mu\text{m} \times 200\ \mu\text{m}$  squares, containing lines with dimensions varying between 100 and 400 nm, while the distance in between the lines varied from 200 to 1200 nm. Ganglia, both sympathetic and sensory, were dissected from an adult female NMRI mouse and mounted on the chip surfaces, about 1 mm from 17 nanostructured squares, as described above. After 5–7 days in culture media, we found that most axons had regenerated along all of the lines with an apparent preference to grow along the line peripheries (Figs. 12.20–12.22) [145]. The aim of the study was to investigate if we could separate

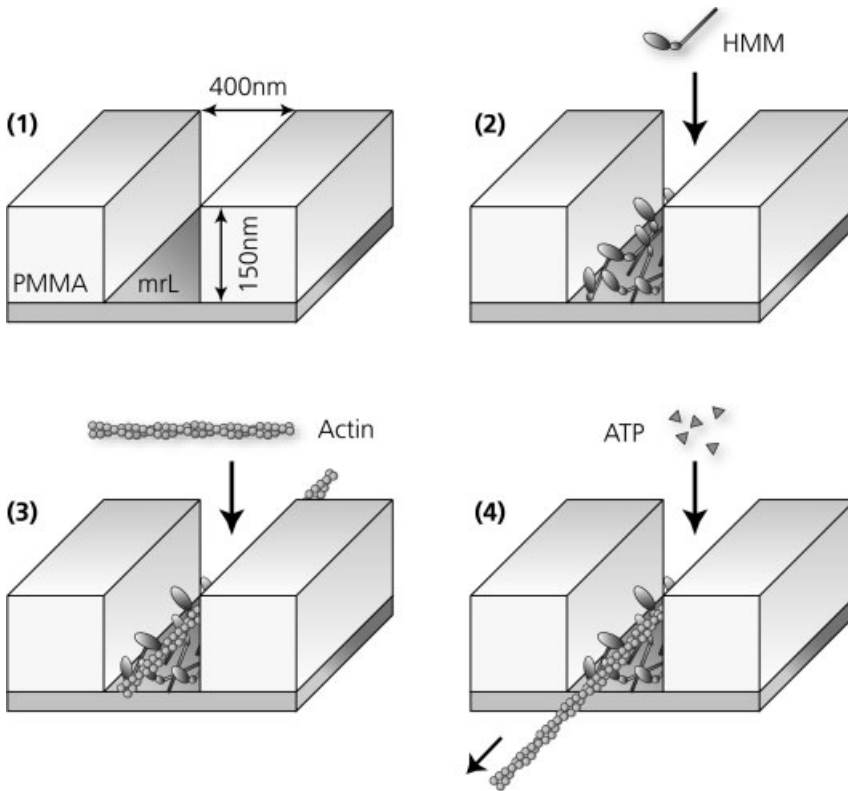


**Figure 12.15.** Schematic presentation of the nanochannels defined by a lithographic method followed by immobilization of myosin heads to the patterned surface, and addition of fluorescently labeled actin filament and ATP. The actin filaments will, with the proper choice of material for the lines, be effectively transported through the channels. (From Ref. [130].)

a large number of axons on a small area and, indeed, we showed that possibility. Such spatial separation and the possibility to organize axons have important consequences for the possible ability to make electronic connections to the nervous system [146]. State-of-the-art implanted electronic devices found in practical use today

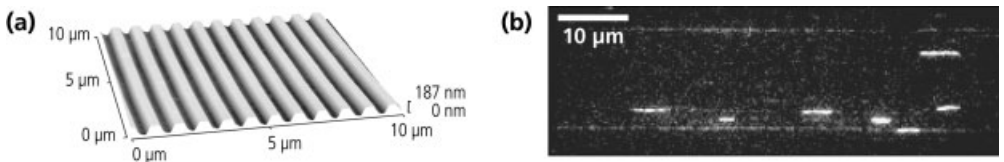


**Figure 12.16.** Similar nanochannels defined by NIL (a) and a snapshot of fluorescently labeled actin filaments (white colored) being transported in the lines (b). (From Ref. [131].)

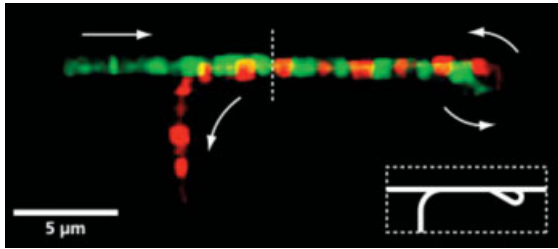


**Figure 12.17.** Three nanotools, rectifiers, roundabouts and directional couplers, put together to transport actin filaments (fluorescently labeled) first in a rectified way from left to right (green colored), and then in a roundabout structure being forced to make a 360° turn and go back into the same channel

as before, moving in the opposite direction (red colored) and then halfway back it will follow a route downwards (directional coupler) and out to a reservoir. Note that the filament cannot enter into this downward branch on its move from left to right. (From Ref. [135].)

are the cortical implant BrainGate [147] and the very well-known cochlear implant. These devices have only a hundred electrodes on a 1-mm<sup>2</sup> area and such a density is not sufficient for making a functional brain-machine interface (BMI). Our results above show that it may be possible, using NIL, to increase the spatial resolution considerably; we found hundreds of axons on an area of 0.4-mm<sup>2</sup> [148]. Our

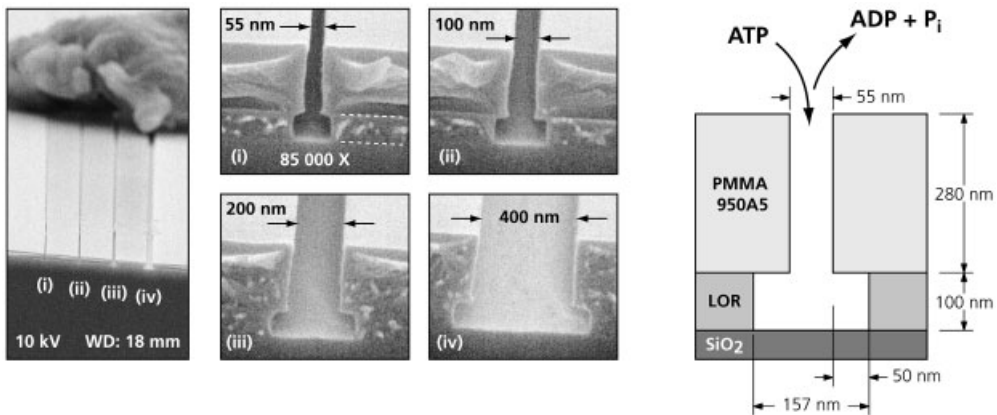


**Figure 12.18.** Cross-section of the double layer of resists combined with selective silanization of the channels employed to achieve the nanometer control of the movement of actin filaments. It consists of a LOR layer and on top of a PMMA layer. By proper patterning and processing, an undercut as shown in the cross-section picture, can be obtained. As illustrated, the slit along the wire (opening) serves an

important role – through this opening ATP can be inferred and products such as ADP can be removed. If we employed sealed nanochannels we would eventually get clogging and we would also be limited by diffusion of ATP, leading to unstable conditions. The bottom layer is functionalized through a vapor-phase silanization procedure to enhance motility. (From Ref. [132].)

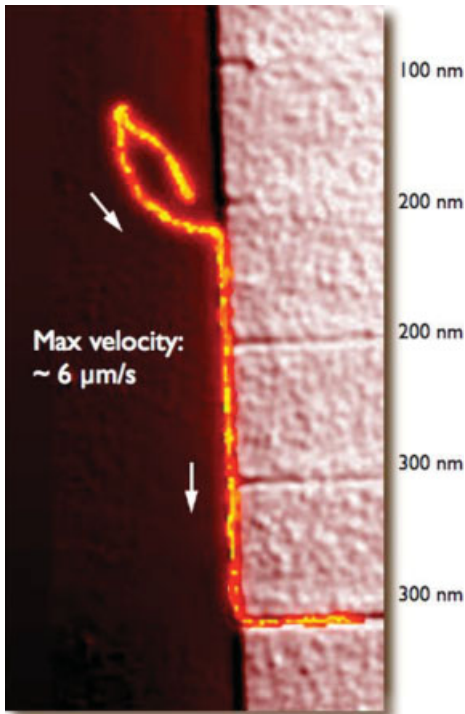


**Figure 12.19.** A top view of the pattern showing the loading zone to the left and nanochannels going to the right in the picture. An actin filament (fluorescently labeled) is

shown to have followed the edge of the loading zone (under the undercut) until a suitable nanochannel made the filament turn right and follow the nanochannel. (From Ref. [132].)

simple, nonoptimized study shows the possibility to concentrate and separate nerve cells on a small area of a surface. Furthermore, the topographical structures are highly stable and NIL, as a method, is scaleable, providing additional support for possible future BMI applications based on nanostructured surfaces. Recently, we have also employed epitaxial nanowires as a support surface showing excellent guidance of neuronal outgrowth (Fig. 12.23). Further details are reported elsewhere [149]. The review by Melechko and coworkers [69] showed various life sciences applications of carbon nanowires. Large sets of interconnected CNTs with cell membranes were recently reported, showing that the biological properties of the membrane were retained and that they could perform electrical measurements [150].

### 12.3.3

#### **Biomedical Applications utilizing Active Nanostructured Surfaces**

In contrast to the previous topics, active nanostructured surfaces can be activated from the outside world in order to investigate the interaction of various forms of

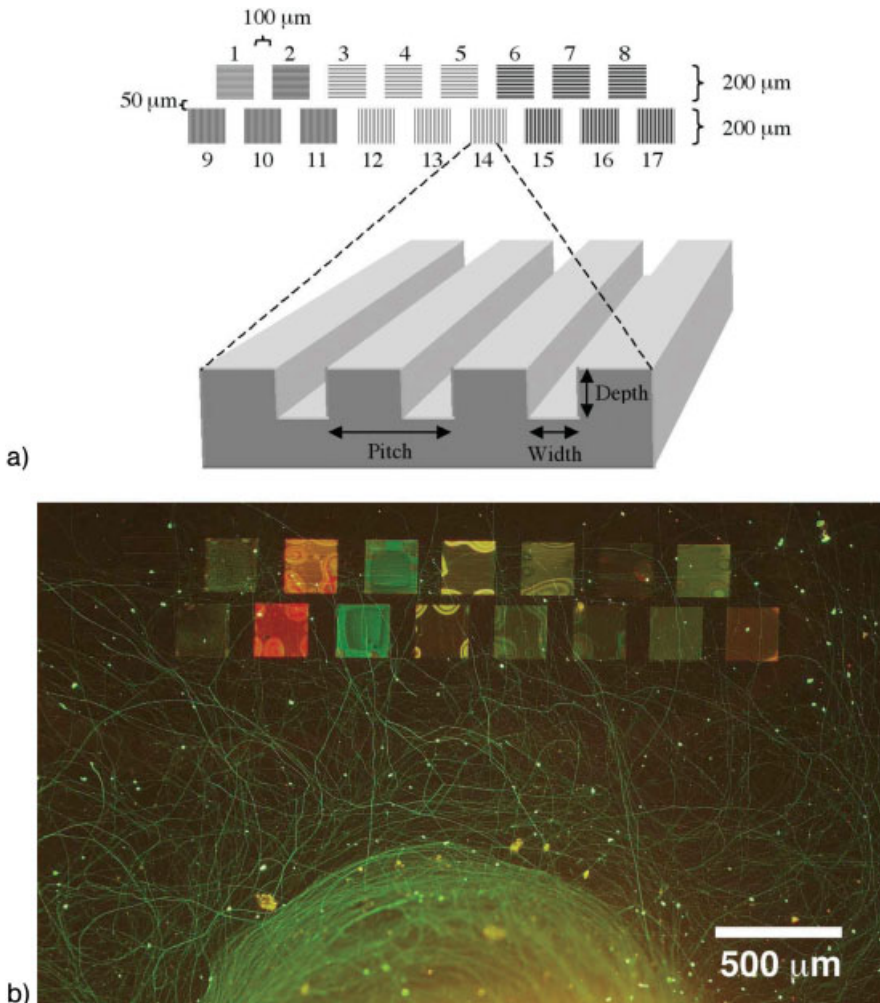


**Figure 12.20.** A number of NIL-patterned squares ( $200\ \mu\text{m} \times 200\ \mu\text{m}$ ) containing grooves oriented horizontally (the two at the bottom) and vertically (the two top ones) having different widths and pitches. As can be

seen, the axonal outgrowth (mouse cervical ganglion) follows the orientation of the grooves in the squares and changes growth direction when the grooves turn  $90^\circ$ . (From Ref. [145].)

biomolecules that such activation may invoke. A paper by Hamad-Schifferly reported remote inductive control of local DNA hybridization events by the use of a nanocrystal serving as an antenna covalently linked to DNA [151]. Another such class of structures that are made at the nanoscale is the so-called interdigitated array (IDA) of electrodes (Fig. 12.24). Although several groups have been able to fabricate such devices [152–155], few have been able to report any useful information

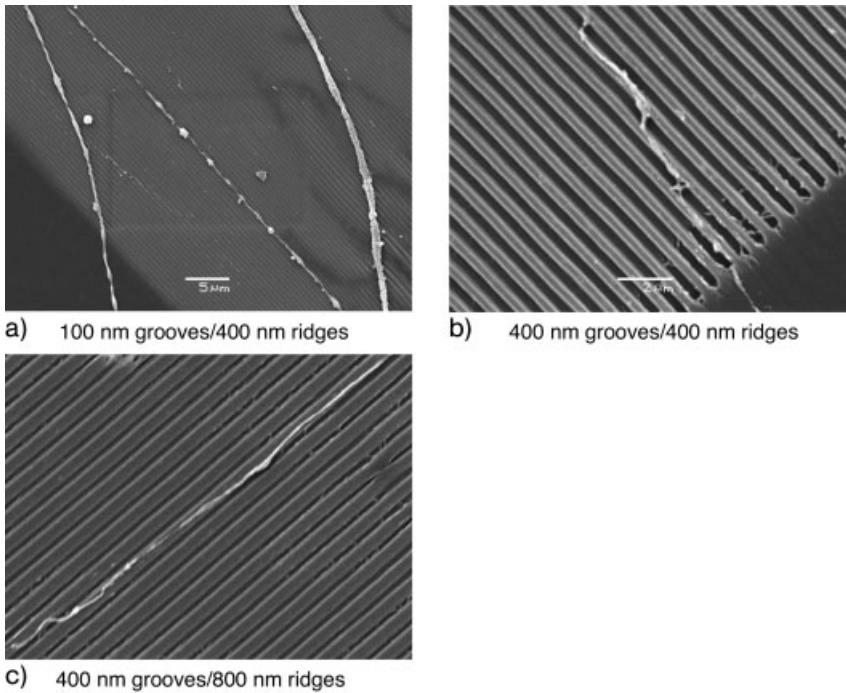


**Figure 12.21.** SEM images showing axons growing on a positive pattern. The ridges are 400 nm on the (A) and (B), and 800 nm wide on (C). The linewidths are 100, 400 and 400 nm, respectively (A–C). The ridges are all

100 nm high. Note especially that all axons seem to grow on top of the ridges and not in the grooves between the ridges. (From Ref. [145].)

having the IDA in the nanometer regime. One of the common obstacles is the noisy environments for all kind of electrical measurements. However, in a set of publications, we have been able to follow some results as a consequence of using nanosized interdigitated electrodes. Choi and coworkers [155] report the possibility to detect DNA binding events by monitoring the impedance (Figs. 12.25 and 12.26). In the paper they report, using NIL in combination with certain nanoprocessing steps, that an array of electrodes having nanogaps of the order of 50 nm provided a way to make label-free detection of DNA hybridization events. Figure 12.25 shows a SEM image of the fabricated structure and the schematics for detection, and Fig. 12.26 displays the frequency-dependent capacitance. Clearly, the hybridized structure of T–A base pairs is detected by the capacitance increase at lower frequencies, in contrast to the nonconjugated base pair reference measurement. The explanation given is that the single- and double-stranded DNAs have different geometrical structures, and hence a different induced counterion profile. In another report [156] using IDA, the authors have investigated the relative increase in signal due to the nanoscale of various scaled IDAs (Fig. 12.27).



**Figure 12.22.** Neurons supported on a surface consisting of randomly located epitaxial GaP nanowires on GaP substrate, revealing a healthy appearance. Note that some wires are bent and in some cases wires are inserted into the neuronal cells and processes. (From Ref. [149].)

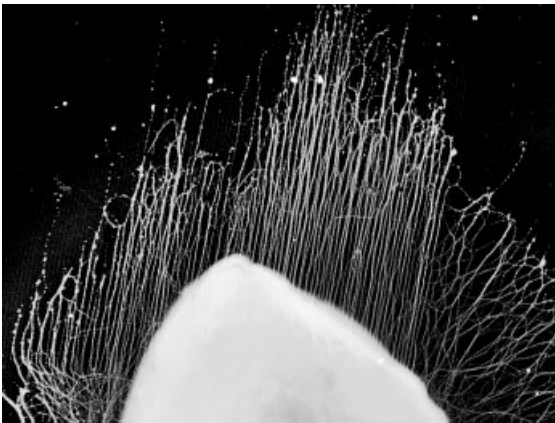


**Figure 12.23.** Nanowires were placed in rows with varying pitch and wire diameters. As can be seen, the neurons align to the wires and follow them in a very nice way, allowing governance of the growth direction to be engineered by the sample morphology. (From Ref. [149].)



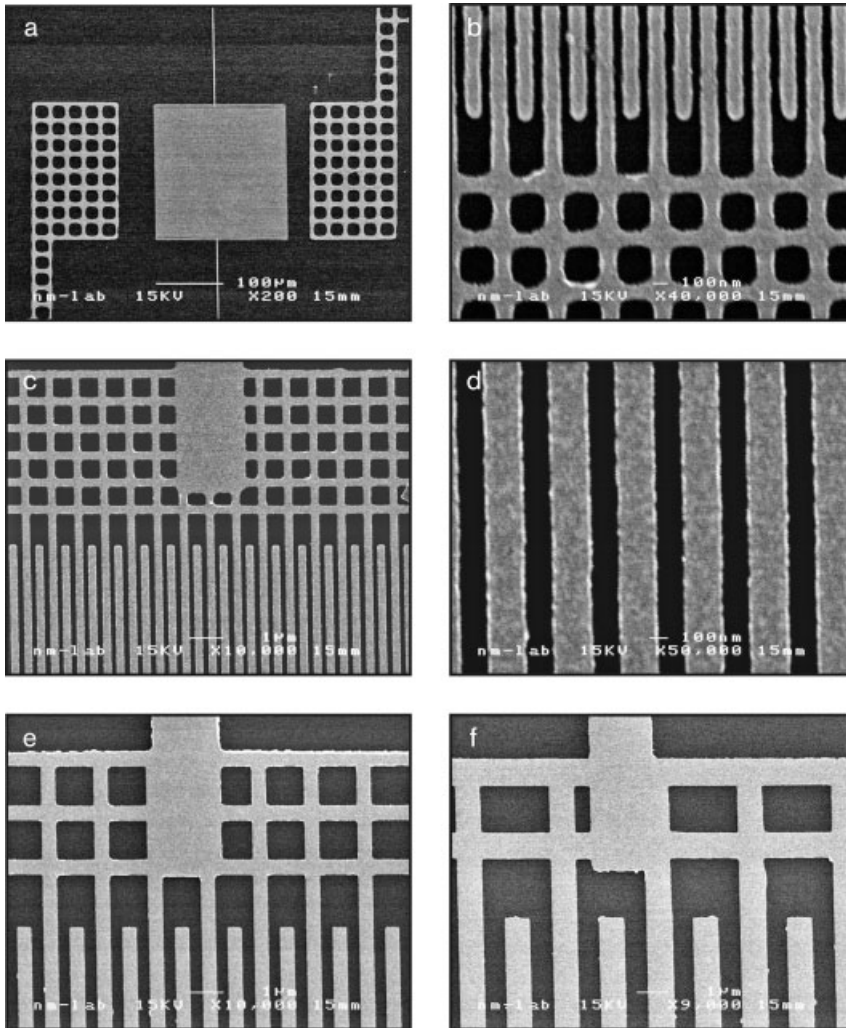


**Figure 12.24.** An example of an IDA of nanolines as defined by NIL, metallization and lift-off. SEM micrographs from the 2-in. wafer with several IDA electrodes after NIL processing and gold lift-off. (a) One single  $3.5 \times 3.5 \text{ mm}^2$  transducer chip, (b) overview of the central

part of the transducer chip, (c) area of a 100-nm IDA and (d) part of a 200-nm IDA electrode. Note the contact areas with holes making it possible to print both nanometer lines and micrometer-sized regions in one printing step. (From Ref. [153].)

#### 12.3.4

#### Protein Chips

Protein-binding detection devices are an important class of devices that may have a large impact on drug screening in conjunction with drug development. They may

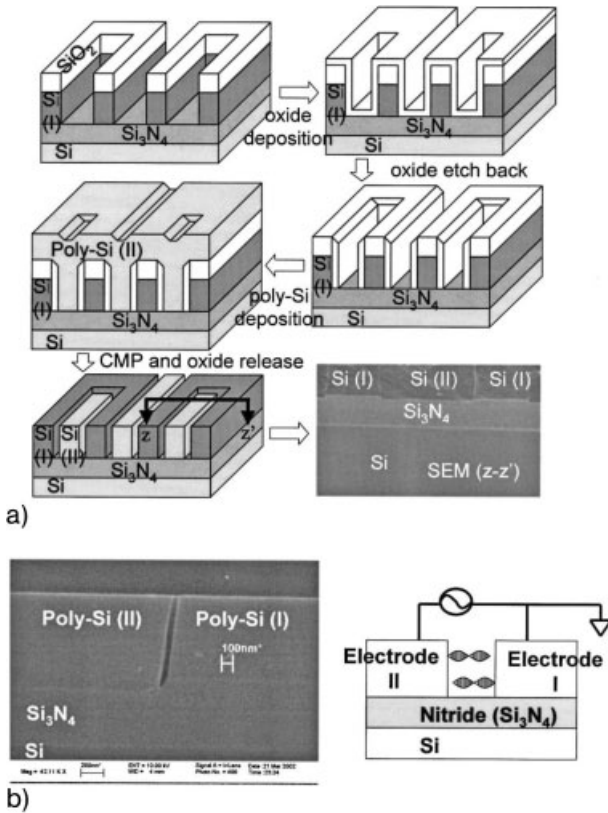


**Figure 12.25.** (a) The process flow for the creation of the nanogaps and a SEM image. (b) A schematic cross-section showing the measurement principle. The nanogap can be controlled by the deposited oxide film thickness. (From Ref. [155].)

also have a potential to be developed into small and portable handheld devices for point-of-care analysis or even as home-doctor kits. For this, the main direction is to utilize antibody–antigen detection [157, 158]. Hence, what it boils down to is an ability to detect whether molecular binding between an antibody and an antigen has taken place. Of course, one usually makes measurements of large arrays of antibodies distributed on a surface using some kind of spotting procedure. Then, by spotting a liquid containing an unknown blend of antigens, one will detect which reactions take place and hence a fingerprint will be obtained. By comparing this individual fingerprint with a set of control fingerprints, it is possible by using various decision mechanisms to tell which antigens were present in the liquid and what disease that set of antigens is a representation of. In order to fully understand the various expressions as a consequence of a certain disease, one would like to make the antibody library extensive [159]. Present-day arrays contain hundreds of

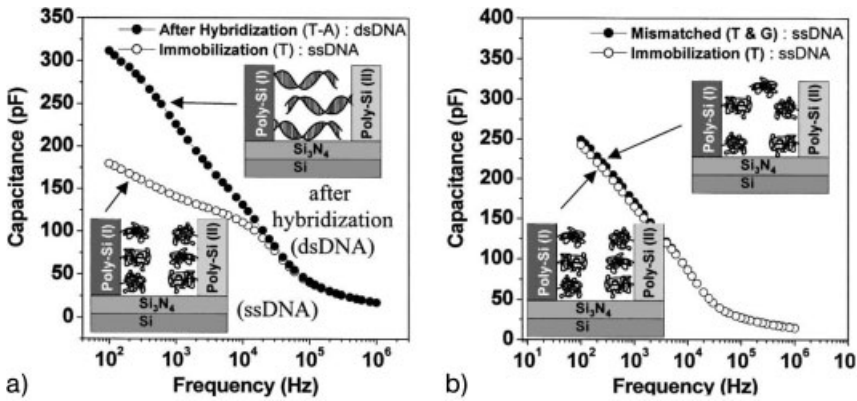


**Figure 12.26.** Measured capacitance versus input frequency after immobilization and hybridization. Capacitance increases as the frequency decreases for the conjugated pairs, whereas there is no significant effect of the capacitance for the nonconjugated base pairs. (From Ref. [155].)

antibodies, but using nanotechnology it is foreseeable that one could make arrays containing millions of antibodies, if one could confine (pattern) the antibodies onto a small surface spot [159–161]. In a prototype study we have fabricated such structures using EBL [162]. They are fabricated by making nanocontainers in the

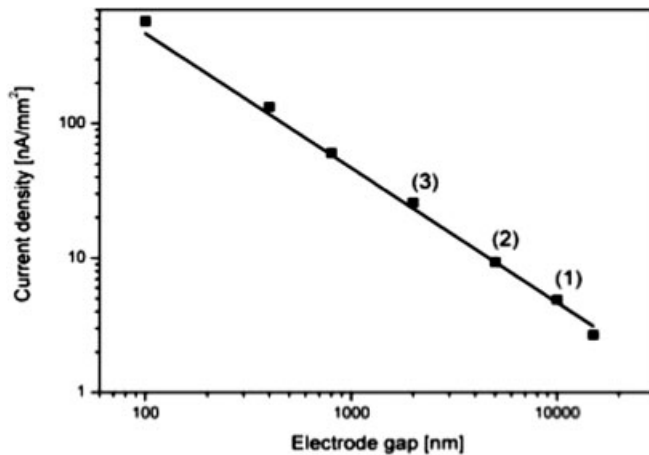


**Figure 12.27.** Normalized signal strength for redox current as a function of nanogap width showing the increased signal as the gap size is reduced. The increase of current is an effect of more effective redox cycling when the electrodes are closer to each other. (From Ref. [156].)

form of small holes (down to 50 nm in diameter) in a PMMA layer on top of a solid substrate with a waveguide as a surface layer. This means that antibodies can be immobilized inside the nanowells and by excitation through the evanescent field created by establishing a standing wave in the waveguide, one will excite only those molecules situated at the bottom of the well directly on top of the waveguide layer. The other molecules found on top of the polymer around the nanowells will not be excited due to the fast decaying electromagnetic field as a result of the near-field excitation mechanism. This approach has allowed us to study specific antibody–antigen interactions of biological interest [162]. Similar ideas using nanotechnology have been published, but they did not confine the antibodies to the surface effectively, leading to a larger analyzing droplet, or alternatively they employed larger nanowells [160, 161].

### 12.3.5

#### **Protein Interactions**

The field of protein patterning is not only limited to protein chip applications, but also used in other kinds of applications. The reason is that proteins are essential for so many life functions – force production in molecular motors, intra- and extracellular transport, mechanical stability, sensing and signaling, etc. What they all have in common is the procedure to make a surface functionalized in one way or another. Usually, functionalization is based on (covalent) coupling of the primary molecule to a certain surface structure. An example of a popular covalent coupling is thiol coupling to gold surfaces. If the surface is a silicon wafer, then one can utilize the large variety of well-established silanization procedures commonly found in conjunction with separation columns based on silica particles.

An often employed silanization procedure is to covalently bond chlorosilanes to a hydroxylated  $\text{SiO}_2$  surface layer, expelling  $\text{HCl}$  as a result of the binding [163]. The chlorosilanes can then have functional amine, carboxyl or hydroxyl (or fluorine if one likes to have a repelling surface, compare this with NIL stamp fabrication [92–95]) groups at the other end. These functional groups may interact with a second molecular group that one intends to attach to the surface, e.g. enzymes. Hence, many approaches to make patterns in various silane layers on the nanoscale can be found [41, 164–166]. After patterning, one must retain the function of the functional groups and nanoprocessing, in general, is rather harsh to many of these molecular layers. Other approaches found in the literature are results obtained by nanoscale patterning of protein layers (compare also the functional protein layers in the tracks for the motor proteins as described above and in Refs. [130–135]). Several such reports have been made, usually employing some kind of model protein–protein reaction as the probe of success. Most often one employs streptavidin–biotin reactions to show proof of the patterning. In the report by Falconnet and coworkers [166], they combined standard NIL with a lift-off procedure of a biotin functionalized poly(ethylene glycol)–poly(L-lysine) (PEG–PLL) copolymer (Fig. 12.28). After lift-off, a backfilled layer of a non-biotin-

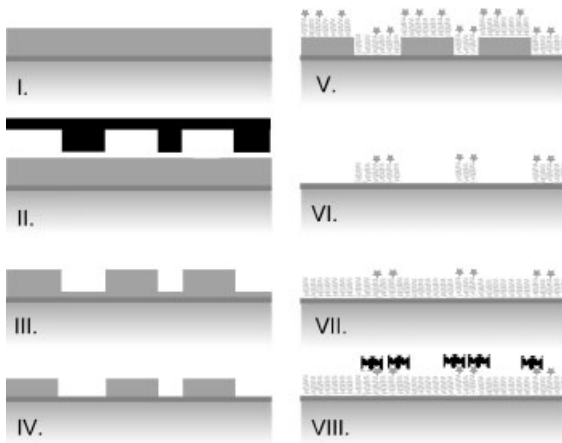


**Figure 12.28.** The NIL and protein patterning process. (I) Spin coating the PMMA layer and pre-bake. (II) Imprinting of the PMMA layer with the quartz stamp. (III) De-molding of stamp from substrate. (IV) Etching of the residual layer of PMMA opening the niobium oxide surface. (V) Dipping into solution of

biotinylated PEG-PLL-mixture. (VI) Lift-off of the remaining PMMA layer leaving a patterned layer of biotinylated PEG-PLL on the surface. (VII) Filling of the background with non-biotinylated PEG-PLL. (VIII) Selective binding of streptavidin to the biotinylated layer. (From Ref. [166].)

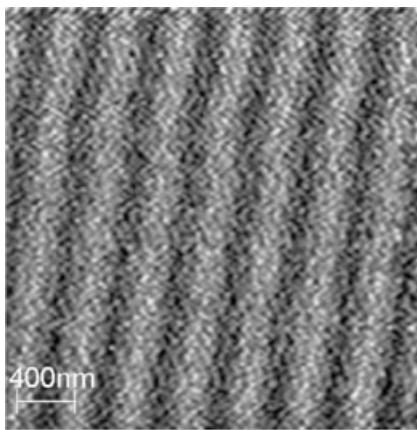


**Figure 12.29.** Scanning near-field micrograph of 100-nm wide biotinylated PEG-PLL lines with Alexa-conjugated streptavidin in a background of nonbiotinylated PEG-PLL showing the successful selective lateral patterning of active protein binding lines. (From Ref. [166].)

functionalized PEG–PLL copolymer was established. In this way, they managed to produce patterned biotin-functionalized lines surrounded by PEG. They then successfully managed to selectively bind streptavidin to the 100-nm wide biotin lines (Fig. 12.29), showing that the biotin properties remained after a common nanoprocessing lift-off procedure. They also discuss the versatility of the process since the PEG copolymer can be functionalized in many different ways. In previous reports by Hoff and coworkers [167] and Gou [41], successful NIL-based protein patterning was displayed. Hoff and coworkers performed NIL and fluorine passivation of the naked silicon surface after reactive ion etching (RIE) exposure, but before removal of the unpatterned resist. A covalent immobilization step of an aminosilane monolayer was performed in combination with a series of subsequent covalent binding events of biotin, streptavidin and, finally, a biotinylated fluorescently labeled protein layer, respectively (Fig. 12.30), creating a sandwich structure. Using epifluorescence, the resulting structures were observed, proving the success of a very uniform sub-100 nm patterning and biofunctional NIL-based process (Figs. 12.31 and 12.32).

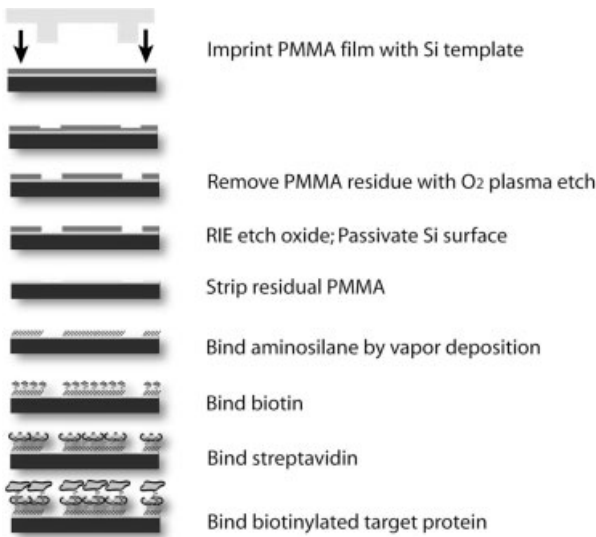


**Figure 12.30.** Process flow diagram of substrate-selective lateral patterning and subsequent protein immobilization. Spin-coated PMMA polymer is patterned by NIL. Exposed SiO<sub>2</sub> regions are etched and passivated by a RIE-deposited CF-based monolayer. The remaining PMMA is lifted off and an

aminosilane is covalently attached to the exposed SiO<sub>2</sub> through a gas-phase deposition procedure. A layer of biotin is covalently linked to the amino layer followed by streptavidin attachment and then, finally, a biotinylated protein is linked to the streptavidin. (From Ref. [167].)

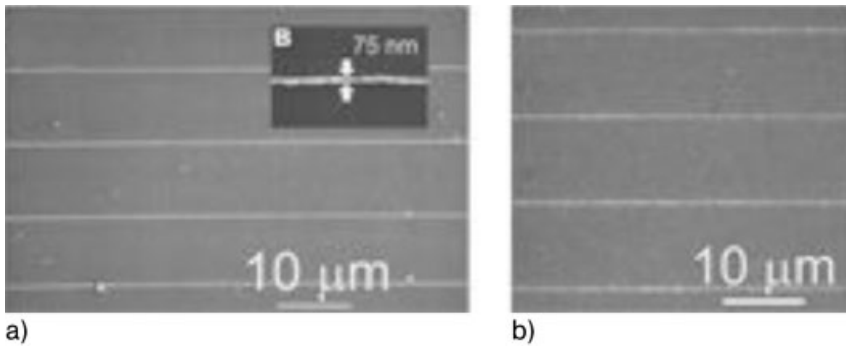


**Figure 12.31.** Proteins patterned onto sub-100 nm patterns. (A) SEM image showing the nanolines after NIL, oxidation and passivation. The inset shows that the linewidth is less than

100 nm. (B) Fluorescence micrograph of the lines after linking rhodamine-labeled streptavidin to the biotin-modified aminosilane-functionalized lines. (From Ref. [167].)

### 12.3.6

#### Biomedical Applications using Nanowires

Nanowires having diameters of the order of tens of nanometers have been employed as extremely sensitive charge sensors. This is based on the fact that if one employs contacts at the two ends of the wire, there will be a possibility (depending on the wire conductivity) for the formation of a narrow 1-D current path along (inside) the wire. If a charge is exposed to the outer surface, this path will be quenched (or opened) (Fig. 12.33) in a way very similar to how a modern CMOS gate functions. By proper functionalization of the wire surface, one may use it as a sensor able to detect specific binding to the wire surface. Wang and coworkers have re-

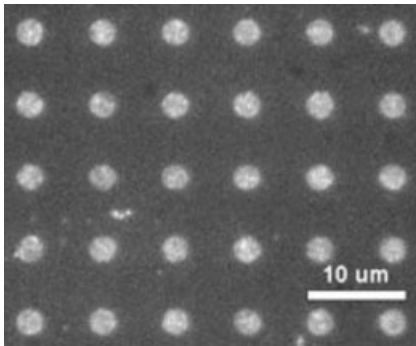


**Figure 12.32.** Epifluorescence image showing bioactivity on NIL-patterned surfaces. The contrast arises from rhodamine-labeled catalase bound to the antibody anticatalase patterned in 2-μm dots using the process described in Fig. 12.31. (From Ref. [167].)

ported label-free detection of molecular binding to silicon nanowires [168], and Chen and coworkers [169] discussed non-covalent functionalization of such CNTs and biosensor applications. Other reports have been made dealing with virus detection [170]. Hahm and coworkers [171] showed label-free DNA detection by first attaching streptavidin, then biotin with a linker to peptide nucleic acid, which in turn contained a specific sequence of base pairs that enabled specific binding to DNA. They reported a 2-fold increase of wire conductance attributed to increased negative charge on the nanowires. In the near future, such structures may become very important as direct label-free detectors for clinical use. In a paper by Zhao [172], nanowires consisting of nanotube–metal clusters are discussed, providing proof-of-principle for a novel high-specificity molecular sensor utilizing the possibility to bind various kinds of molecular receptors to metal clusters. Further uses of nanowires are exploited in recent reviews [69, 173].

### 12.3.7

#### **Biomedical Applications using Nanoparticles**

Nanoparticles are excellent transducing components with the ability to report on interactions of biomedical relevance in various ways. The reporting mechanisms are often based on the fact that the magnetic, electronic, mechanical, chemical and optical properties of small objects differ from bulk materials, and small changes in size and shape can often be more easily monitored, since the effects are large. One such class of small objects is the “semiconducting quantum dot” that may change its luminescence (or fluorescence) properties as a function of surface coverage [174–176]. Generally speaking, also for this class of devices, one needs a handshaking procedure in order to utilize them as sensors, for example. This means that different surface functionalization procedures are also highly relevant for these kinds of structures. For instance, a magnetic particle having a certain molecule chemically linked to it can be manipulated using magnetic fields. In a paper by Nam and coworkers [177], such a use was discussed for the detection of proteins; specifically, they showed detection of prostate-specific antigen with a sensitivity 6 orders of magnitude higher than standard clinical assays.

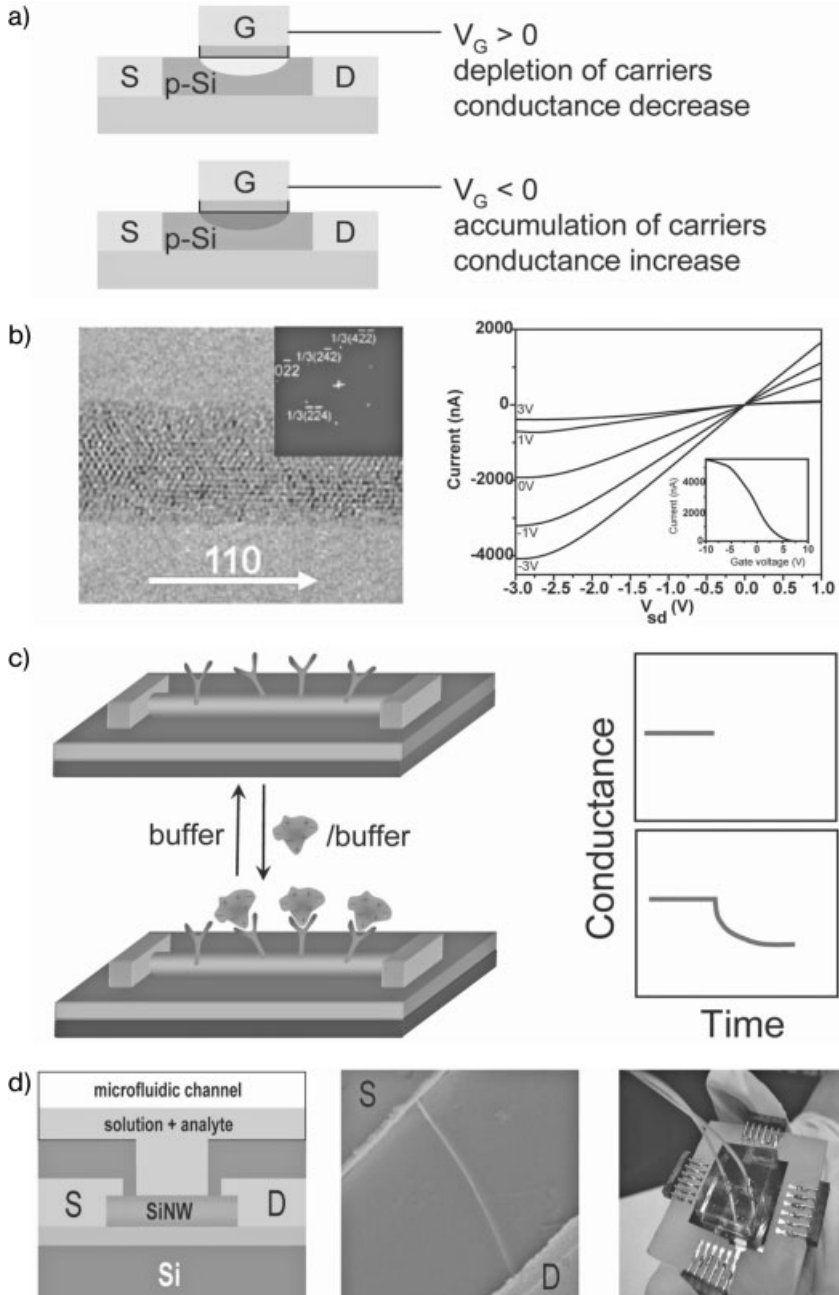
The preparation and use of magnetic particles is a whole scientific field on its own, and interested readers are referred to additional publications [172–181]. Other classes of nanoparticles of great relevance for the biomedical community are soft core–shell nanoparticles and capsules [182–184] with a pharmaceutical content. For example, the core is envisaged to be able to locate a tumor and then by an enzymatic process the core is opened, allowing directed drug delivery to the tumor. Here, readers are also referred to other publications [182–184].

### 12.3.8

#### **Biomedical Applications using SPM Technology**

Here we can distinguish between investigations performed in microscopy mode, chemical force detection and as a sensor structure giving a multitude of possibilities.





### 12.3.8.1 Imaging of Biomolecules using SPM

AFM is often employed for high-resolution microscopy aiming at molecular resolution of soft material, such as tissues, etc. AFM, in contrast to many of the other relatives in the large family of scanning probes, can be used in a liquid environment without losing much of its resolving power [185, 186]. To image soft and delicate materials it is mainly used in one of the noncontact modes or the intermittent-contact mode equipped with super-sharp tips. For this purpose, nanowires have been integrated in various ways with the usually pre-formed tip on the cantilever in order to serve as the sharp tip. A review in this subject area has been published by Hansma [187]. Recently, AFM has been taken to new dimensions, and a publication by Imer and coworkers describes how a minute AFM may be placed inside the body [188] in order to be able to report to an external source about how a knee joint surface develops after a surgical procedure.

### 12.3.8.2 Force Detection of Single Molecular Events

In force detection mode, using a chemically modified tip that will bind to a single molecule on a surface when lowered towards the surface, it is possible to study conformation changes and the mechanics of individual molecules. Such investigations have led to detailed knowledge about DNA recoiling, forces involved in antigen–antibody binding and receptor–ligand interactions, as well as cell–cell adhesion due to discrete adhesion proteins [118–121, 189]. An excellent review of this field is given by Gimzewski and Joachim [190] and many details can be found in the papers by Gaub, who is one of the key drivers in Europe in this field [120, 191]. Gaub's group have, for instance, recently published measurements revealing single base pair mismatches [192].

### 12.3.8.3 Cantilever-based Detection of Molecular Events

The remaining class of scanning probe activities with biomedical relevance utilize the mechanical movement or properties of a cantilever when a chemical interaction has taken place on the cantilever arm [118, 119, 193]. Here, one can distinguish between two classes – a static displacement of the cantilever or a shift of the dynamic motion of the cantilever, e.g. a shift in resonance frequency. For these investigations one can utilize an AFM set-up and a standard AFM cantilever with a tip, but the tip in itself does not play any role since the instrument *per se* is not go-

---

**Figure 12.33.** Nanowire FET sensor. (A) Schematic view of a normal p-type FET device where a positive (negative) voltage applied to the gate (G) led to depletion (or enhancement) of the current path between the source (S) and drain (D) contacts. (B) Transmission electron microscopy image and diffraction pattern of a 4.5-nm diameter silicon single-crystal nanowire and typical electrical characteristics for a p-type nanowire. (C) Schematics of a p-type nanowire employed as a sensor with antibodies and positively charged protein that upon binding quench the conductance of the wire (similar to the positive bias situation in A). (D) Schematics of the nanowire sensor configuration and SEM image showing the nanowire between the two contacts and a photo of the complete biochip with integrated fluidic sample delivery. (From Ref. [172].)

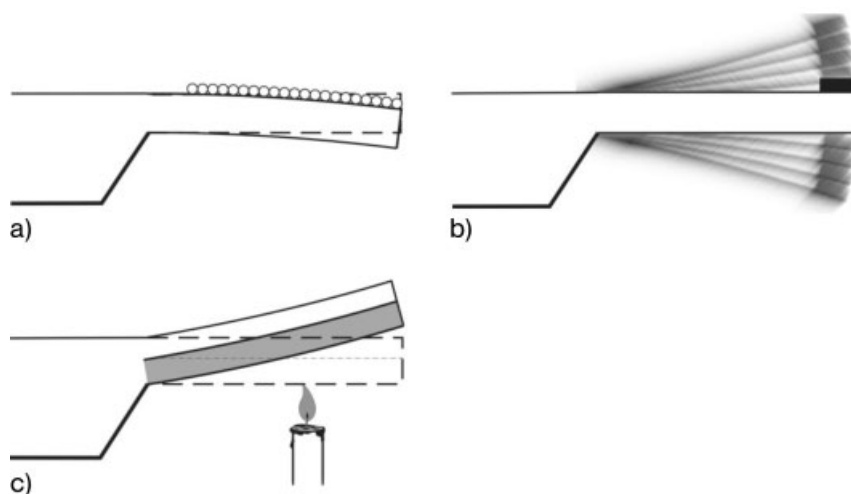


**Figure 12.34.** Schematic of a cantilever array-based hybridization sensor. (A) Each cantilever is functionalized with different self-assembled monolayers (SAMs) of thiolated oligonucleotides. (B) Upon injection of complimentary sequences to the oligonucleotides on the

various cantilevers, recognition and binding occurs to one of the cantilevers, and the cantilever bends down due to the stress. (C) After rinsing, the cantilevers are ready to detect again. (From Ref. [118].)

ing to give any images. There is usually no need to have a scanner able to sweep the cantilever in the lateral directions. In order to achieve a static deflection, one often employs a scheme like a bimetal switch, i.e. when one side of the cantilever is influenced by chemical interactions, such that a strain or compression is experienced, the cantilever will bend. Typical levels of stress are of the order of  $10^{-3}$   $\text{N m}^{-1}$ , causing deflections to be around 10 nm or so; the bending will of course depend on the cantilever employed. Therefore, one usually coats one side of the cantilever with a metal that interacts with the molecules of interest, possibly by having a coating on the metal surface permitting only one kind of molecule to bind onto that surface (Fig. 12.34 and 12.35). Using this principle, it has been possible to follow chemical interaction and DNA hybridization, detect explosives, determine pH, detect of bacteria, detect of various vapors, etc. [118]. For dynamic detection, instead of monitoring surface strain or stress, one actually measures the mass being adsorbed on the cantilever surfaces [194]. The basic equation for a cantilever in resonance ( $df/dm \sim f/m$ ) involves the mass, and hence a measurement of the change of the resonance frequency directly measures the added mass (or removed mass if one performs such an experiment). This method resembles quartz crystal mass (QCM) technology, although the QCM crystal is macroscopically large. Nevertheless, the use of QCM, and especially the dissipative mode of QCM, is frequently used for studying various biological processes and reactions to surfaces [195, 196]. The drawback of QCM is the sensitive surface area, which cannot be

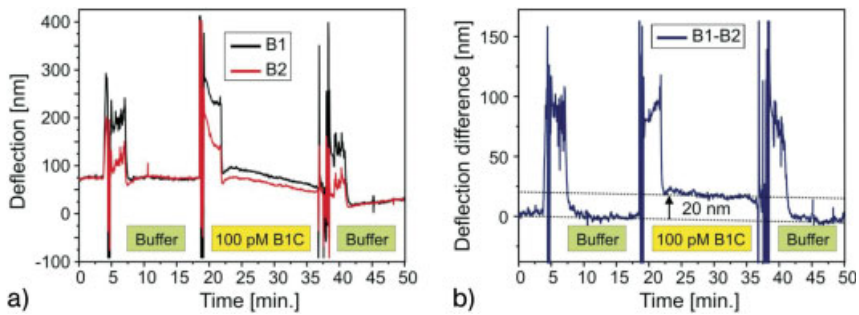


**Figure 12.35.** (A) Deflection traces of two differently oligonucleotide-functionalized cantilevers upon injection of the complement entity to one of the cantilevers. (B) Differential signal between the two deflection curves. Buffer = rinsing. (From Ref. [118].)

miniaturized in order to study processes happening on a small lateral scale. In order to detect very small masses, interest in the cantilever detection community is, at this stage, directed towards the development of small cantilevers. This is due to the increased mass detection ability that follows if the eigenmass is low and the unloaded resonance frequency is high. However, most of the cantilevers reported in this field have micrometer dimensions. The reason being that there are plenty of opportunities for good research and technology development using these more conventional cantilevers [197–199]. In particular, the coating of functionalized layers with the resulting exclusive binding is still not yet at a fully mature level. There is a necessity to make real systems with arrays of cantilevers (Fig. 12.36) hav-

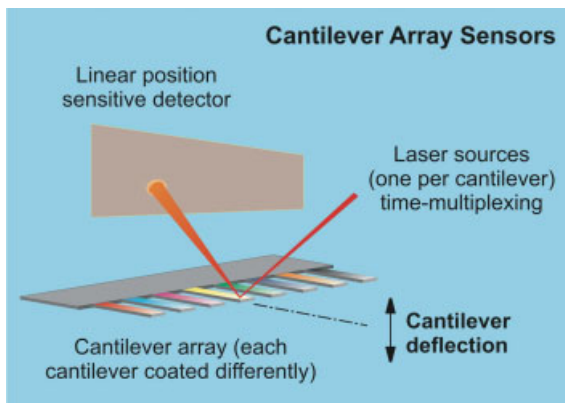


**Figure 12.36.** Schematic view of the array format used together with cantilever sensors. Each cantilever has a different coating. (From Ref. [118].)

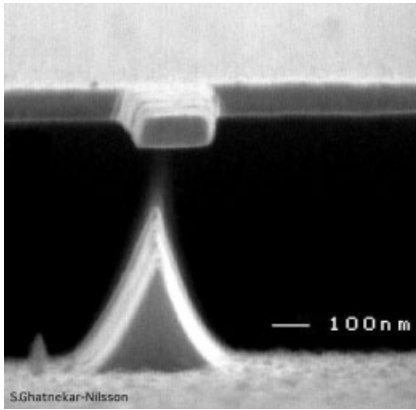


**Figure 12.37.** Cantilever cross-section view of a true nanosized metal cantilever having a width of 200 nm and a thickness of 50 nm. When the mechanical properties were investi-

gated on this and similar metal cantilevers, it was found that they appear to be softer than one could predict from classical mechanics. (From Ref. [201].)

ing different kinds of coatings in order to detect and discriminate various contents in, for example, an unknown liquid [118, 200]. (Compare with Sections 12.3.4 and 12.3.5.) However, a few papers have recently reported [201, 202] cantilevers in the true nanometer regime, with thicknesses well below 100 nm (Fig. 12.37). In these papers, the nanomechanical properties of solid metal cantilevers were investigated as a function of length and thickness. It was found that the properties of thin cantilevers shift as compared to bulk material, making the cantilevers increasingly softer than expected as they get thinner. The cantilever-based nanomechanical concept is nice, since it allows investigations to be performed in a liquid, e.g. in body fluid or whole blood (serum). For static measurements, this is rather straightforward [203–205], although care has to be exercised when making a flow system, allowing the actual detection to work. For the dynamic case, the situation is more tricky – the main reason being the drastic decrease of the  $Q$ -value of such dynamic systems when operated in liquid. During the many years of investigations, very few papers have yet been published. Just recently, two such papers have appeared, one from Professors Gerber's group in Basel and one from the author's group [206, 207]. In the paper by Braun and coworkers they have, in a model experiment, investigated binding of streptavidin-coated latex beads onto biotinylated cantilevers, while in the paper by Nilsson and coworkers [207] they have addressed the challenge to combine detection of adsorption of lipid vesicles onto cantilevers (Fig. 12.38). In that report, it was shown that the lipid vesicles formed a close-packed layer keeping their spherical shape and the mass resolution obtained was of the order of  $3 \text{ fg Hz}^{-1}$ . This low value is promising when compared with similar measurements of mass performed in vacuum [208], where a mass sensitivity of  $0.2 \text{ fg Hz}^{-1}$  was reported. Using an oscillating cantilever of poly-silicon,  $1 \text{ }\mu\text{m}$  long,

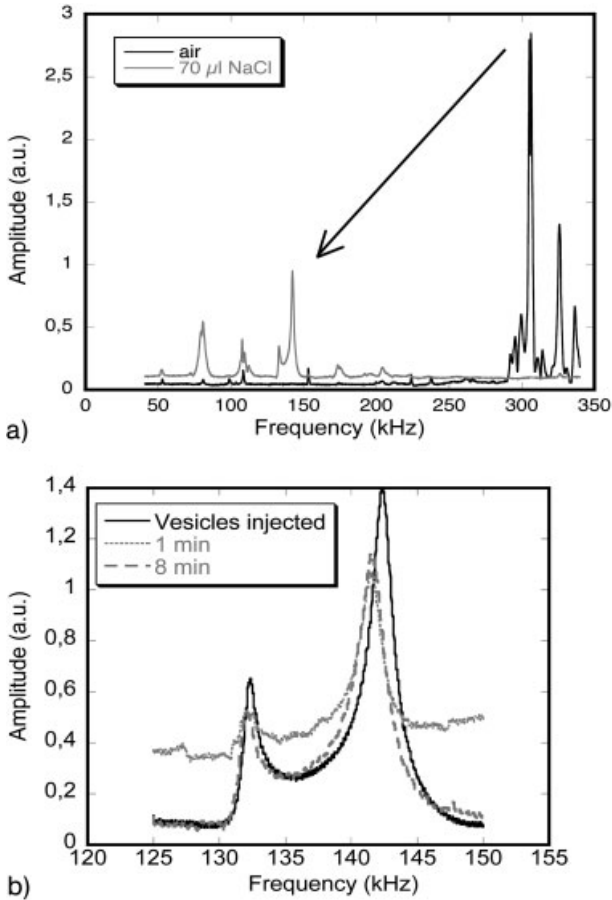


**Figure 12.38.** (A) The cantilever resonance spectra before and after being immersed in NaCl buffer liquid. (B) The shift of frequency due to immobilization of phospholipid vesicles onto the cantilever. The nonoptimized mass detection sensitivity was found to be  $3 \text{ fg Hz}^{-1}$ . (From Ref. [207].)

500 nm wide and 150 nm thick with an integrated  $1\text{-}\mu\text{m}^2$  paddle, functionalized with antigen, specific virus detection has been reported with a detection sensitivity of single viruses [209]. The detection of ultra-low masses leads us into another important class of nanotechnologies – nanomechanical systems. Using nanomechanics, it has been possible to make wonderful devices that can elucidate mechanical motion close to the quantum limits. A recent review on this subject can be found in *Physics Today* [210] and in Ref. [211]. Here, the authors, in a fascinating way, describe the development of the nanoelectromechanical systems (NEMS) field and how it interacts with quantum physics. This development leads the way to

be able to construct measurement apparatus that may be able to discriminate and analyze individual macromolecules with atomic-level detection in 3-D. Recently, Roukes and coworkers have shown exceptional weighing measurements down to a few molecules, the sensitivity reported to be 7 zg [212]. The sensitivity of MEMS and NEMS devices, as already mentioned in the Introduction, has also enabled measurements of single electron spins [66] and individual nuclear spins may soon be distinguished.

## 12.4

### Discussion and Outlook

In this chapter, we have seen how modern nanotechnology is increasingly accepted and employed in the biomedical field, and especially in the field of sensors, genomics and proteomics [213–214]. Most of the issues dealt with here and in other similar overviews [215] are of great importance for the development of nanobio research, i.e. controlled surface functionalization, high-resolution imaging, fluidic governance, sensor principles, nanomechanics, etc. In order for nanotechnology to increase its impact on the biomedical field, we have to continue to develop basic technologies, as well as trying to utilize them in the biomedical area in a “play and see” fashion; by doing so one may find uses of the technologies in fields and areas of sciences that one could not otherwise envisage. The Nobel Laureate Herbert Kroemer has formulated a lemma [63] stating that any sufficiently new and innovative technology will find its own principal application created by that technology.

As is obvious from this chapter, most nanotechnologies so far have been employed for sensor purposes or as passive surfaces for molecular interactions. The main reason for this is that nanotechnology offers several orders of magnitude higher sensitivity than present technology. The step for nanoscientists, most often coming from the hard inorganic (top-down) nanotechnology scientific field, is smaller to take, as they can apply well-known concepts in order to study some biological processes, together with the fact that most nanotechnology efforts are presently driven from that field into the medical or biological field, in contrast to the reverse mechanisms. The day when scientists from very different fields start to collaborate in a more mutual way may also witness fundamentally new uses of nanotechnology in the biomedical sector. In this context, it is foreseeable that new nanoscience educational programs that presently are starting all over the world will be instrumental for this interdisciplinary development.

The area of using nanomechanics for biomedical applications and for probing cellular, intracellular as well as intercellular, events and interactions will probably entertain us in the coming years. Surely the class of epitaxial nanowires will be of specific instrumental importance, providing functional tools that, for example, may give full 3-D information when employed as large arrays of point detectors. Another area that will have a large influence on our understanding of biology and biological processes is the development of techniques for achieving fast imaging,

using SPM. Such possibilities to gather both nanometer-scale space and millisecond time information will open new avenues for life sciences research. The further development and utilization of printing-like methods, based on nanoimprint and nanoprinting methods, and similar printing nanotechnologies, to create large arrays of nanostructured surfaces of one or another kind will surely be of great future importance, both for high- and low-volume applications. Such printing methods are already able to create small series of nanostructured surfaces economically enough to be used in research applications in the life sciences domain. The development of mega-dense protein chips and DNA sensors may, in combination with hand-held devices, provide us with efficient point-of-care analysis or home-doctor kits that will fundamentally change our way of living. Within the next 10 years the mortality rate in the USA from various cancer forms is predicted to be close to zero due to increased early detection principles with significantly higher sensitivities than at present [215]. We will probably also witness the use of nanotechnology for various forms of prosthetic devices giving freedom back to impaired persons. In this context, however, stem cell research may be of even larger future importance, providing natural means to connect new functional nerve cells to the impaired nervous system, maybe in combination with nanotechnology. Increased abilities in the form of enhanced functions, such as IR vision for use during darkness when driving, may soon be within reach. Research and development activities for increased abilities for learning, enhanced memory and cognitive functions, as well as personalized medical treatments, etc., are presently also being pursued, often under the term “converging technologies” [216].

Most importantly, we should not forget that the tools being developed to handle nanomaterials are still very young, actually being in their caring or nursing stage; typical development time scales are of the order of 10–15 years before a real impact can be judged.

It is my hope that this overview will have inspired the reader to engage in this vigorous research field with so many possibilities open for exploration, where maybe the only limitations are governed by the individuals own ingenuities.

### **Acknowledgments**

This chapter would not have been possible without the collaboration, support, friendship and sharing of knowledge from all my Lund University colleges within the Nanometer Consortium, Division of Solid State Physics, and at the Departments of Physics, ElectroScience, Electrical Measurements Technology, Chemistry, Analytical Chemistry Immunotechnology, Cell & Organism Biology, Neurophysiology, Hand Surgery and Philosophy, as well as all international friends and collaborators in various EU programs (Charge, Nanotech, Chanil, Nanomass, Nano2Life, NaPa, Bionel, Parnass, etc.), and of course also my previous and present graduate students supplying a constant flow of joy and enthusiasm. Last, but not least, the support from my loving daughters Caroline and Cecilia is of great and very special importance for me.



## References

- 1 See for instance: The Internet Technology Roadmap for Semiconductors (ITRS), <http://public.itrs.net>.
- 2 See for instance: Moores law, <http://www.intel.com/technology/magazine/silicon/moores-law-0405.htm>.
- 3 <http://nobelprize.org/physics/laureates/1987/bednorz-lecture.html>.
- 4 <http://nobelprize.org/physics/laureates/2000/kroemer-lecture.html>.
- 5 <http://nobelprize.org/physics/laureates/2000/alferov-lecture.html>.
- 6 <http://nobelprize.org/physics/laureates/1973/esaki-lecture.html>.
- 7 J. SINGH, *Physics of Semiconductors and Their Heterostructures*. McGraw-Hill, New York, 1993.
- 8 <http://nobelprize.org/physics/laureates/1901/rontgen-bio.html>.
- 9 <http://nobelprize.org/chemistry/laureates/1991/ernst-lecture.html>.
- 10 <http://www.ob-ultrasound.net/ingehertz.html>.
- 11 P. U. ABEL, T. VON WOEDTKE, Biosensors for *in vivo* glucose measurement: can we cross the experimental stage, *Biosens. Bioelectron.* 17, 1059, 2002.
- 12 [http://www7.nationalacademies.org/keck/Keck\\_Futures\\_Nano\\_Conferences\\_Glucose\\_Sensor\\_Description.html](http://www7.nationalacademies.org/keck/Keck_Futures_Nano_Conferences_Glucose_Sensor_Description.html).
- 13 See for instance: <http://www.nano.gov>.
- 14 D. C. RALPH, C. T. BLACK, M. TINKHAM, Spectroscopic measurements of discrete electronic states in single metal particles, *Phys. Rev. Lett.* 74, 3241, 1995.
- 15 C. ZANDONELLA, The Tiny Toolkit news feature, *Nature* 423, 10, 2003.
- 16 A. GUSTAFSSON, M.-E. PISTOL, L. MONTELIUS, L. SAMUELSON, Local probe techniques for luminescence studies of low-dimensional semiconductor structures, *J. Appl. Phys.* 84, 1715, 1998.
- 17 G. BINNIG, H. ROHRER, Scanning tunneling microscopy, *Helv. Phys. Acta* 55, 6, 1982.
- 18 G. BINNIG, C. F. QUATE, Ch. GERBER, Atomic force microscope, *Phys. Rev. Lett.* 56, 930, 1986.
- 19 R. WIESENDANGER, Contributions of scanning probe microscopy and spectroscopy to the investigation and fabrication of nanometer-scale structures, *J. Vac. Sci. Technol. B* 12, 515, 1994.
- 20 S. Y. CHOU, P. R. KRAUSS, P. J. RENSTROM, Imprint of sub-25 nm vias and trenches in polymers, *Appl. Phys. Lett.* 67, 14, 1995.
- 21 J. K. STROSCIO, D. M. EIGLER, Atomic and molecular manipulation with the scanning tunneling microscope, *Science* 254, 1319, 1991.
- 22 Ph. AVOURIS, Manipulation of matter at the atomic and molecular levels, *Acc. Chem. Res.* 28, 95, 1995.
- 23 G. MEYER, J. REPP, S. ZÖPHEL, K.-F. BRAUN, S. W. HLA, S. FÖLSCH, L. BARTELS, F. MORESCO, K. H. RIEDER, Controlled manipulation of atoms and small molecules with a low temperature scanning tunneling microscope, *Single Molecules* 1, 79, 2000.
- 24 S.-B. CARLSSON, K. DEPPERT, T. JUNNO, M. H. MAGNUSSON, L. MONTELIUS, L. SAMUELSON, Ångström-level, real time control of the formation of quantum devices, *Semicond. Sci. Technol.* 13, A119, 1998; T. JUNNO, S.-B. CARLSSON, H. XU, L. MONTELIUS, L. SAMUELSON, Fabrication of quantum devices by Ångström-level manipulation of nanoparticles with an atomic force microscope, *Appl. Phys. Lett.* 72, 548, 1998.
- 25 T. JUNNO, M. H. MAGNUSSON, S.-B. CARLSSON, K. DEPPERT, J.-O. MALM, L. MONTELIUS, L. SAMUELSON, Single-electron devices via controlled assembly of designed nano-particles, *Microelectron. Eng.* 47, 179, 1999.
- 26 <http://www.samsung.com>.
- 27 <http://www.nano-tex.com>.
- 28 S.-W. LEE, A. M. BELCHER, Virus-based fabrication of micro- and nanofibers using electrospinning, *Nano Lett.* 4, 387, 2004.
- 29 <http://www.pilkington.com>.
- 30 A. TORKKELI, Droplet microfluidics on

- a planar surface, *PhD Thesis*, VTT, Espoo, 2003.
- 31 G. Y. JUNG, S. GANAPATHIAPPAN, X. LI, D. A. A. OHLBERG, D. L. LLYNICK, Y. CHEN, W. M. TONG, R. S. WILLIAMS, Fabrication of molecular-electronic circuits by nanoimprint lithography at low temperatures and pressures, *Appl. Phys. A* 78, 1169, 2004.
  - 32 T. TADA, T. KANAYAMA, A. P. G. ROBINSIN, R. E. PLAMER, M. T. ALLEN, J. A. PREECE, K. D. M. HARRIS, A triphenylene derivative as a novel negative/positive tone resist of 10 nanometer resolution, *Microelectron. Eng.* 53, 425, 2000; see also: G. O'SULLIVAN, *EUVL Source Workshop*, Antwerp, 2003, <http://www.sematech.org>.
  - 33 A. K. BATES, M. ROTHSCHILD, T. M. BLOOMSTEIN, T. H. FEDYNYSHYN, R. R. KUNZ, V. LIBERMANAND, M. SWITKES, Review of technology for 157-nm lithography, *IBM J Res. Dev.* 45, 605, 2001.
  - 34 S. M. SZE, *Semiconductor Devices: Physics and Technology*, 2nd edn. Wiley, New York, 2001.
  - 35 H. I. SMITH, M. L. SCHATTENBURG, X-ray lithography from 500 to 30 nm: X-ray nanolithography, *IBM J. Res. Dev.* 37, 319, 1993.
  - 36 A. N. BROERS, Resolution limits for electron-beam lithography, *IBM J Res. Dev.* 32, 502, 1988.
  - 37 J. GIERAK, C. VIEU, M. SCHNEIDER, H. LAUNOIS, G. B. ASSAYAG, A. SEPTIER, Optimization of experimental operating parameters for very high resolution focused ion beam applications, *J. Vac. Sci. Technol. B* 15, 2373, 1997.
  - 38 B. HEIDARI, A. BOGDANOV, M. KEIL, L. MONTELIUS, Imprint lithography for mass production, in: *Digest of Papers of Microprocesses and Nanotechnology 2001. (2001 International Microprocesses and Nanotechnology Conference)*, Matsue-shi, p. 9, 2001.
  - 39 T. BAILEY, B. J. CHOI, M. COLBURN, M. MEISSL, S. SHAYA, J. G. EKERDT, S. V. SREENIVASAN, C. G. WILLSON, Step and flash imprint lithography: template surface treatment and defect analysis, *J. Vac. Sci. Technol. B* 18, 3572, 2000.
  - 40 B. HEIDARI, I. MAXIMOV, E.-L. SARWE, L. MONTELIUS, Large scale nanolithography using nanoimprint lithography, *J. Vac. Sci. Technol. B* 17, 2961, 1999.
  - 41 L. J. GOU, Recent progress in nanoimprint technology and its applications, *J. Phys. D* 37, R123, 2004.
  - 42 A. L. BOGDANOV, T. HOLMQVIST, P. JEDRASIK, B. NILSSON, Dual pass electron beam writing of bit arrays with sub-100 nm bits on imprint lithography masters for patterned media production, *Microelectron. Eng.* 67/68, 381, 2003.
  - 43 W. M. MOREAU, *Semiconductor Lithography*, Plenum, New York, 1998.
  - 44 KHAN, L. MOHAMMAD, J. XIAO, L. OCOLA, F. CERRINA, Updated system model for x-ray lithography, *J. Vac. Sci. Technol. B* 12, 3930, 1994.
  - 45 L. MALMQVIST, A. BOGDANOV, L. MONTELIUS, H. M. HERTZ, Nanometer table-top proximity x-ray lithography with liquid-target laser-plasma source, *J. Vac. Sci. Technol. B* 15, 814, 1997.
  - 46 B. HEIDARI, I. MAXIMOV, E.-L. SARWE, L. MONTELIUS, Nanoimprint lithography at the 6-inch wafer scale, *J. Vac. Sci. Technol. B* 18, 3557, 2000.
  - 47 A. KUMAR, G. M. WHITESIDES, Features of gold having micrometer to centimeter dimensions can be formed through a combination of stamping with an elastomeric stamp and an alkanethiol "ink" followed by chemical etching, *Appl. Phys. Lett.* 63, 2002, 1993.
  - 48 K. E. PAUL, T. L. BREEN, J. AIZENBERG, G. M. WHITESIDES, Maskless photolithography: embossed photoresist as its own optical element, *Appl. Phys. Lett.* 73, 2893, 1998.
  - 49 J. A. ROGERS, K.-E. PAUL, R. J. JACKMAN, G. M. WHITESIDES, Using an elastomeric phase mask for sub-100 nm photolithography in the optical near field, *Appl. Phys. Lett.* 70, 2658, 1997.
  - 50 M. COBURN, M. STEWART, J. SEAWALL, T. MICHAELSON, S. V. SREENIVASAN, C. G. WILLSON, Step and flash imprint

- lithography: a novel approach to imprint lithography, in: *Proceedings of the SPIE 24th International Symposium on Microlithography: Emerging Lithographic Technologies III*, Santa Clara, CA, p. 379, 1999, p. 379.
- 51 T. BAILEY, B. J. CHOI, M. COLBURN, M. MEISSL, S. SHAYA, J. G. EKERDT, S. V. SREENIVASAN, C. G. WILLSON, Step and flash imprint lithography: template surface treatment and defect analysis, *J. Vac. Sci. Technol. B* 18, 3572, 2000.
  - 52 M. D. STEWART, S. C. JOHNSON, S. V. SREENIVASAN, D. J. RESNICK, C. G. WILLSON, Nanofabrication with step and flash imprint lithography, *J. Microlithogr.* 4, 11002, 2005.
  - 53 K. E. PAUL, T. L. BREEN, J. AIZENBERG, G. M. WHITESIDES, Maskless photolithography: embossed photoresist as its own optical element, *Appl. Phys. Lett.* 73, 2893, 1998.
  - 54 M. KOMURO, J. TANIGUCHI, S. INOUE, N. KIMURA, Y. TOKANO, H. HORISHIMA, S. MATSUI, Imprint characteristics by photo-induced solidification of liquid polymer, *Jpn. J. Appl. Phys.* 39, 7075, 2000.
  - 55 B. VRATZOV, A. FUCHS, M. LEMME, W. HENSCHL, H. KURZ, Large scale ultraviolet-based nanoimprint lithography, *J. Vac. Sci. Technol. B* 21, 2760, 2003.
  - 56 M. OTTO, M. BENDER, F. RICHTER, B. HADAM, T. KLIEM, R. JEDE, B. SPANGENBERG, H. KURZ, Reproducibility and homogeneity in step and repeat UV-nanoimprint lithography, *Microelectron. Eng.* 73/74, 152, 2004.
  - 57 U. PLCHETKA, M. BENDER, A. FUCHS, B. VRATZOV, T. GLINSNER, F. LINDNER, H. KURZ, Wafer scale patterning by soft UV-nanoimprint lithography, *Microelectron. Eng.* 73/74, 167, 2004.
  - 58 J. JEONG, Y. SIM, H. SOHN, E. LEE, *Proc. SPIE* 5751, 227, 2005.
  - 59 B. HEIDARI, I. MAXIMOV, E.-L. SARWE, L. MONTELIUS, Nanoimprint lithography at the 6-inch wafer scale, *J. Vac. Sci. Technol. B* 17, 2961, 1999.
  - 60 L. MONTELIUS, B. HEIDARI, M. GRACZYK, I. MAXIMOV, E.-L. SARWE, T. G. I. LING, Nanoimprint- and UV-lithography: mix and match process for fabrication of interdigitated nanobiosensors, *Microelectron. Eng.* 53, 521, 2000.
  - 61 Nanoimprint lithography was included in the ITRS roadmap 2002 (see Ref. [1]).
  - 62 MIT: Emerging Technologies, 2003. MIT news: 10 emerging technologies, March 2003, <http://web.mit.edu>
  - 63 H. KROEMER, Speculations about future directions, *J. Crystal Growth* 251, 17, 2003.
  - 64 G. BINNIG, H. ROHRER, C. H. GERBER, E. WEIBEL, Surface studies by scanning tunneling microscopy, *Phys. Rev. Lett.* 49, 57, 1982.
  - 65 G. BINNIG, C. F. QUATE, C. H. GERBER, Atomic force microscope, *Phys. Rev. Lett.* 56, 930, 1986.
  - 66 D. RUGAR, R. BUDAKIAN, H. J. MAMIN, B. W. CHUI, Single spin detection by magnetic resonance force microscopy, *Nature* 430, 329, 2004.
  - 67 A. M. MORALES, C. M. LIEBER, A laser ablation method for the synthesis of crystalline semiconductor nanowires, *Science* 279, 208, 1998.
  - 68 B. J. OHLSSON, M. T. BJÖRK, A. I. PERSSON, C. THELANDER, L. R. WALLENBERG, M. H. MAGNUSSON, K. DEPERT, L. SAMUELSON, Growth and characterization of GaAs and InAs nano-whiskers and InAs/GaAs heterostructures, *Physica E*, 13, 1126, 2002; L. SAMUELSON, C. THELANDER, M. T. BJÖRK, M. BORGSTRÖM, K. DEPERT, K. A. DICK, A. E. HANSEN, T. MÅRTENSSON, N. PANEV, A. I. PERSSON, W. SEIFERT, N. SKÖLD, M. W. LARSSON, L. R. WALLENBERG, Semiconductor nanowires for 0D and 1D physics and applications, *Physica E*, 25, 313, 2004 and references therein.
  - 69 A. V. MELECHKO, V. I. MERKULOV, T. E. MCKNIGHT, M. A. GUILLORN, K. L. KLEIN, D. H. LOWNDES, M. L. SIMPSON, Vertically aligned carbon nanofibers and related structures: controlled synthesis and directed assembly, *J. Appl. Phys.* 97, 041301-1, 2005.
  - 70 T. MÅRTENSSON, P. CARLBERG, M. BORGSTRÖM, L. MONTELIUS,

- W. SEIFERT, L. SAMUELSON, Nanowire arrays defined by nanoimprint lithography, *Nano Lett.* 4, 699, 2004.
- 71 K. A. DICK, K. DEPPERT, M. W. LARSSON, T. MÄRTENSSON, W. SEIFERT, L. R. WALLENBERG, L. SAMUELSON, Synthesis of branched “nanotrees” by controlled seeding of multiple branching events, *Nat. Mater.* 3, 380, 2004.
- 72 C. E. FLYNN, S.-W. LEE, B. R. PELLE, A. M. BELCHER, Viruses as vehicles for growth, organization and assembly of materials, *Acta Mater.* 51, 5867, 2003.
- 73 C. MAO, D. J. SOLIS, B. D. REISS, S. T. KOTTMANN, R. Y. SWEENEY, A. HAYHURST, G. GEORGIU, B. IVERSON, A. M. BELCHER, Virus-based toolkit for the directed synthesis of magnetic and semiconducting nanowires, *Science* 303, 213, 2004.
- 74 A. M. FENNINMORE, T. D. YUZVINSKY, W.-Q. HAN, M. S. FUHRER, J. CUMINGS, A. ZETTI, Rotational actuators based on carbon nanotubes, *Nature* 424, 408, 2003.
- 75 M. L. ROUKES, Nanoelectromechanical systems face the future, *Phys. World* 14, 25, 2001.
- 76 A. N. CLEVELAND, M. L. ROUKES, Fabrication of high frequency nanometer scale mechanical resonators from bulk Si crystals, *Appl. Phys. Lett.* 69, 2653, 1996.
- 77 X. M. H. HUANG, C. ZORMAN, M. MEHREGANY, M. L. ROUKES, Nanodevice motion at microwave frequencies, *Nature* 421, 496, 2003.
- 78 Q. A. PANKHURST, J. CONNOLLY, S. K. JONES, J. DOBSON, Applications of magnetic nanoparticles in biomedicine, *J. Phys. D* 36, R167, 2003.
- 79 L. LACONTE, N. NITIN, G. BAO, Magnetic nanoparticle probes, *Mater. Today* 8, 32, 2005.
- 80 E. SACKMAN, Supported membranes: scientific and practical applications, *Science* 271, 43, 1996.
- 81 H. M. MCCONNELL, T. H. WATTS, R. M. WEISS, A. A. BRIAN, Supported planar membranes in studies of cell-cell recognition in the immune-system, *Biochim. Biophys. Acta* 864, 95, 1986.
- 82 C. A. KELLER, B. KASEMO, Surface specific kinetics of lipid vesicle adsorption measured with a quartz crystal microbalance, *Biophys. J.* 75, 1397, 1998.
- 83 F. F. ROSETTI, I. REVIKINE, G. CSÜCS, F. ASSI, J. VÖRÖS, M. TEXTOR, Interaction of poly(L-lysine)-g-poly(ethylene glycol) with supported phospholipid bilayers, *Biophys. J.* 87, 1711, 2004.
- 84 E. REIMHULT, F. HÖÖK, B. KASEMO, Intact vesicle adsorption and supported biomembrane formation from vesicles in solution: influence of surface chemistry, vesicle size, temperature, and osmotic pressure, *Langmuir* 19, 1681, 2003.
- 85 A. DAHLIN, M. ZACH, T. RINDZEVICIUS, M. KALL, D. S. SUTHERLAND, F. HOOK, Localized surface plasmon resonance sensing of lipid-membrane-mediated biorecognition events, *J. Am. Chem. Soc.* 127, 5043, 2005.
- 86 S. SVEDHEM, D. DAHLBORG, J. EKEROTH, J. KELLY, F. HÖÖK, J. GOLD, *In situ* peptide-modified supported lipid bilayers for controlled cell attachment, *Langmuir* 19, 6730, 2003.
- 87 I. H. EL-SAYED, X. HUANG, M. EL-SAYED, Surface plasmon resonance scattering and absorption of anti-EGFR antibody conjugated gold nanoparticles in cancer diagnostics: applications in oral cancer, *Nano Lett.* 5, 829, 2005 and references therein; E. REIMHULT, C. LARSSON, B. KASEMO, F. HÖÖK, Simultaneous surface plasmon resonance and quartz crystal microbalance with dissipation monitoring measurements of biomolecular adsorption events involving structural transformations and variations in coupled water, *Anal. Chem.* 76, 7211, 2004.
- 88 Chemical and biological point sensors for homeland defense, *Proc. SPIE* 5585, 2004.
- 89 I. MAXIMOV, E.-L. SARWE, M. BECK, K. DEPPERT, M. GRACZYK, M. H. MAGNUSSON, L. MONTELIUS, Fabrication of Si-based nanoimprint stamps with sub-20 nm features, *Microelectron. Eng.* 61/62, 449, 2002.

- 90 K. PFEIFFER, F. REUTHER, M. FINK, G. GRUETZNER, P. CARLBERG, I. MAXIMOV, L. MONTELIUS, J. SEEKAMP, S. ZANKOVYCH, C. M. SOTOMAYOR TORRES, H. SCHULZ, H.-C. SCHEER, A comparison of thermally and photochemically cross-linked polymers for nanoimprinting, *Microelectron. Eng.* 67/68, 266, 2003.
- 91 K. PFEIFFER, M. FINK, G. AHRENS, G. GRUETZNER, F. REUTHER, J. SEEKAMP, S. ZANKOVYCH, C. M. SOTOMAYOR TORRES, I. MAXIMOV, M. BECK, M. GRACZYK, L. MONTELIUS, H. SCHULZ, H.-C. SCHEER, F. STEINGRUEBER, Polymer stamps for nanoimprinting, *Microelectron. Eng.* 61/62, 393, 2002.
- 92 M. BECK, M. GRACZYK, I. MAXIMOV, E.-L. SARWE, T. G. I. LING, M. KEIL, L. MONTELIUS, Improving stamps for 10 nm level wafer scale nanoimprint lithography, *Microelectron. Eng.* 61/62, 441, 2002.
- 93 J.-K. CHEN, F.-H. KO, K.-F. HSIEH, C.-T. CHOU, F.-C. CHANG, Effect of fluoroalkyl substituents on the reactions of alkylchlorosilanes with mold surfaces for nanoimprint lithography, *J. Vac. Sci. Technol. B* 22, 3233, 2004.
- 94 M. KEIL, M. BECK, T. G. I. LING, M. GRACZYK, L. MONTELIUS, B. HEIDARI, Development and characterization of silane antisticking layers on nickel-based stamps designed for nanoimprint lithography, *J. Vac. Sci. Technol. B* 23, 575, 2005.
- 95 M. KEIL, M. BECK, G. FRENNESSON, E. THEANDER, E. BOLMSJÖ, L. MONTELIUS, B. HEIDARI, Process development and characterization of antisticking layers on nickel-based stamps designed for nanoimprint lithography, *J. Vac. Sci. Technol. B* 22, 3283, 2004.
- 96 F. REUTHER, P. CARLBERG, M. FINK, G. GRUETZNER, L. MONTELIUS, Reactive polymers: a route to nanoimprint lithography at low temperatures, *Proc. SPIE* 5037, 203, 2003.
- 97 W. ZHANG, S. Y. CHOU, Multilevel nanoimprint lithography with submicron alignment over 4 in. Si wafers, *Appl. Phys. Lett.*, 79, 845, 2001.
- 98 A. FUCHS, B. VRATZOV, T. WAHLBRINK, Y. GEORGIEV, H. KURZ, Interferometric in situ alignment for UV-based nanoimprint, *J. Vac. Sci. Technol. B* 22, 3242, 2004.
- 99 R. HUANG, X. FAN, Z. LU, L. WANG, Progress of machining technology, in: *Proceedings of the 7th International Conference on Progress of Machining Technology*, Suzhou, p. 197, 2004.
- 100 C. PICCIOTTO, J. GAO, E. HOARAU, W. WU, Image displacement sensing (NDSE) for achieving overlay alignment, *Appl. Phys. A* 80, 1287, 2005.
- 101 L. MONTELIUS, B. HEIDARI, M. GRACZYK, T. G. I. LING, I. MAXIMOV, E.-L. SARWE, Large-area nanoimprint fabrication of sub-100-nm interdigitated metal arrays, *Proc. SPIE* 3997, 442, 2000.
- 102 C. PERRET, C. GOURGON, F. LAZZARINO, J. TALLAL, S. LANDIS, R. PELZER, Characterization of 8-in. wafers printed by nanoimprint lithography, *Microelectron. Eng.* 73/74, 172, 2004.
- 103 Q. XIA, C. KEIMEL, H. GE, Z. YU, W. WU, S. Y. CHOU, Ultrafast patterning of nanostructures in polymers using laser assisted nanoimprint lithography, *Appl. Phys. Lett.*, 83, 24, 2003.
- 104 B. MICHEL, A. BERNARD, A. BIETSCH, E. DELAMARCHE, M. GEISSLER, D. JUNCKER, H. KIND, J.-P. RENAULT, H. ROTHUIZEN, H. SCHMID, P. SCHMIDT-WINKEL, R. STUTZ, H. WOLF, Printing meets lithography: soft approaches to high-resolution patterning, *IBM J Res. Dev.* 45, 697, 2001.
- 105 See the conference series *NNT: Nanoimprint, Nanoprinting and Related Technologies*, <http://www.nnt.org>.
- 106 A. A. YU, T. A. SAVAS, G. S. TAYLOR, A. GUISEPPE-ELIE, H. I. SMITH, F. STELLACI, Supramolecular nanostamping: using DNA as movable type, *Nano Lett.* 5, 1061, 2005.
- 107 N. A. MELOSH, A. BOUKAI, F. DIANA, B. GERARDOT, A. BADOLATO, P. M. PETROFF, J. R. HEATH,

- Ultrahigh-density nanowire lattices and circuits, *Science* 300, 112, 2003.
- 108 R. A. BECKMAN, E. JOHNSTON-HALPERIN, N. A. MELOSH, Y. LUO, J. E. GREEN, J. R. HEATH, Fabrication of conducting Si nanowire arrays, *J. Appl. Phys. Lett.* 96, 5921, 2004.
- 109 G. D. KUBIAK, D. R. KANIA (Eds.), *OSA Trends in Optics and Photonics Vol. 4: Extreme Ultraviolet Lithography*, Optical Society of America, Washington, DC, 1996.
- 110 A. A. TSENG, A. NOTARGIACOMO, T. P. CHEN, Nanofabrication by scanning probe microscope lithography: a review, *J. Vac. Sci. Technol. B* 23, 877, 2005.
- 111 S. HONG, J. ZHU, C. A. MIRKIN, Multiple ink nanolithography: toward a multiple-pen nano-plotter, *Science* 286, 523, 1999.
- 112 D. S. GINGER, H. ZHANG, C. A. MIRKIN, The evolution of dip-pen nanolithography, *Angew. Chem. Int. Ed. Engl.* 43, 30, 2004.
- 113 A. MEISTER, M. LILEY, J. BRUGGER, R. PUGIN, H. HEINZELMANN, Nanodispenser for attoliter volume deposition using atomic force microscopy probes modified by focused-ion-beam milling, *Appl. Phys. Lett.* 85, 6260, 2004.
- 114 R. LÜTHI, R. R. SCHLITTLER, J. BRUGGER, P. VETTIGER, M. E. WELLAND, J. K. GIMZEWSKI, Parallel nanodevice fabrication using a combination of shadow mask and scanning probe methods, *Appl. Phys. Lett.* 75, 1314, 1999.
- 115 J. BRUGGER, J. W. BERENSCHOT, S. KUIPER, W. NIJDAM, B. OTTER, M. ELWENSPOEK, Resistless patterning of sub-micron structures by evaporation through nanostencils, *Microelectron. Eng.* 53, 403, 2000.
- 116 H. W. LI, D.-J. KANG, M. G. BLAMIRE, W. T. S. HUCK, Focused ion beam fabrication of silicon print masters, *Nanotechnology* 14, 220, 2003.
- 117 P. VETTIGER, M. DESPONT, U. DRECHSLER, U. DÜRIG, W. HÄBERLE, M. I. LUTWYCHE, H. E. ROTHUIZEN, R. STUTZ, R. WIDMER, G. K. BINNIG, The “Millipede” – more than thousand tips for future AFM storage, *IBM J. Res. Dev.* 44, 323, 2000; P. VETTIGER, J. BRUGGER, M. DESPONT, U. DRECHSLER, U. DÜRIG, W. HÄBERLE, M. LUTWYCHE, H. ROTHUIZEN, R. STUTZ, R. WIDMER, G. BINNIG, Ultrahigh density, high-data-rate NEMS-based AFM data storage system, *Microelectron. Eng.* 46, 11, 1999.
- 118 H. P. LANG, M. HEGNER, C. GERBER, Cantilever array sensors, *Mater. Today April issue*, 30, 2005.
- 119 J. FRITZ, M. K. BALLER, H. P. LANG, H. ROTHUIZEN, P. VETTIGER, E. MEYER, H.-J. GÜNTHERODT, Ch. GERBER, J. K. GIMZEWSKI, Translating biomolecular recognition into nanomechanics, *Science* 288, 316, 2000.
- 120 M. RIEF, M. GAUTEL, F. OSTERHELT, J. M. FERNANDEZ, H. E. GAUB, Reversible unfolding of individual titin immunoglobulin domains by AFM, *Science* 276, 1109, 1997.
- 121 J. M. FERNANDEZ, H. B. LI, Force-clamp spectroscopy monitors the folding trajectory of a single protein, *Science* 303, 1674, 2004.
- 122 S. W. P. TURNER, M. CABODI, H. G. CRAIGHEAD, Confinement-induced entropic recoil of single DNA molecules in a nanofluidic structure, *Phys. Rev. Lett.* 88, 128103, 2002.
- 123 J. HAN, H. G. CRAIGHEAD, Entropic trapping and sieving of long DNA molecules in a nanofluidic channel, *J. Vac. Sci. Technol. A* 17, 2142, 1999.
- 124 H. CAO, Z. YU, J. WANG, J. O. TEGENFELDT, R. H. AUSTIN, E. CHEN, W. WU, S. Y. CHOU, Fabrication of 10 nm enclosed nanofluidic channels, *Appl. Phys. Lett.* 81, 174, 2002.
- 125 R. H. AUSTIN, J. O. TEGENFELDT, H. CAO, S. Y. CHOU, E. C. COX, Scanning the controls: genomics and nanotechnology, *IEEE Trans. Nanotechnol.* 1, 12, 2002; L. J. GOU, X. CHENG, C.-F. CHOU, Fabrication of size-controllable nanofluidic channels by nanoimprinting and its application for DNA stretching, *Nano Lett.* 4, 69, 2004.

- 126 J. O. TEGENFELDT, O. BAJAKIN, C.-F. CHOU, S. CHAN, R. AUSTIN, W. PANN, L. LIOU, E. CHAN, T. DUKE, T. COX, Near-field scanner for moving molecules, *Phys. Rev. Lett.* 86, 1378, 2001.
- 127 T. NIELSEN, D. NILSSON, F. BUNDGAARD, P. SHI, P. SZABO, O. GESCHKE, A. KRISTENSEN, Nanoimprint lithography in the cyclic olefin copolymer, Topas, a highly ultraviolet-transparent and chemically resistant thermoplast, *J. Vac. Sci. Technol. B* 22, 1770, 2004; D. NILSSON, S. BALSLEV, A. KRISTENSEN, A microfluidic dye laser fabricated by nanoimprint lithography in a highly transparent and chemically resistant cyclo-olefin copolymer (COC), *J. Micromech. Microeng.* 15, 296, 2005.
- 128 K.-S. YUN, E. YOON, Micro/nanofluidic device for single-cell-based assay, *Biomed. Microdevices* 7, 35, 2005.
- 129 R. KARNIK, R. FAN, M. YUE, D. LI, P. YANG, A. MAJUMDAR, Electrostatic control of ions and molecules in nanofluidic transistors, *Nano Lett.* 5, 943, 2005.
- 130 R. BUNK, J. KLINTH, L. MONTELIUS, I. A. NICHOLLS, P. OMLING, S. TÅGERUD, A. MÅNSSON, Actomyosin motility on nanostructured surfaces, *Biochem. Biophys. Res. Commun.* 301, 783, 2003.
- 131 R. BUNK, A. MÅNSSON, I. A. NICHOLLS, P. OMLING, M. SUNDBERG, S. TÅGERUD, P. CARLBERG, L. MONTELIUS, Guiding molecular motors with nano-imprinted structures, *Jpn. J. Appl. Phys.* 44, 3337, 2005.
- 132 M. SUNDBERG, J. P. ROSENGREN, R. BUNK, J. LINDAHL, I. A. NICHOLLS, S. TÅGERUD, P. OMLING, L. MONTELIUS, A. MÅNSSON, Silanized surfaces for *in vitro* studies of actomyosin function and nanotechnology applications, *Anal. Biochem.* 323, 127, 2003.
- 133 R. BUNK, J. KLINTH, L. MONTELIUS, I. A. NICHOLLS, P. OMLING, S. TÅGERUD, A. MÅNSSON, Actomyosin motility on nanostructured surfaces, *Biochem. Biophys. Res. Commun.* 301, 783, 2003.
- 134 R. BUNK, M. SUNDBERG, A. MÅNSSON, I. A. NICHOLLS, P. OMLING, S. TÅGERUD, L. MONTELIUS, Guiding motor-propelled molecules with nanoscale precision through silanized bi-channel structures, *Nanotechnology* 16, 710, 2005.
- 135 R. BUNK, Creation of a nanometer-scale toolbox for molecular transport-circuits, *PhD Thesis*, Lund University, 2005.
- 136 H. SUZUKI, A. YAMADA, K. OIWA, H. NAKAYAMA, S. MASHIKO, Control of actin moving trajectory by patterned poly(methylmethacrylate) tracks, *Biophys. J.* 72, 1997, 1997.
- 137 H. HESS, C. M. MATZKE, R. K. DOOT, J. CLEMMENS, G. D. BACHAND, B. C. BUNKER, V. VOGEL, Molecular shuttles operating undercover: a new photolithographic approach for the fabrication of structured surfaces supporting directed motility, *Nano Lett.* 3, 1651, 2003.
- 138 A. I. TEIXERA, G. A. ABRAMS, C. J. MURPHY, P. F. NEALEY, Cell behavior on lithographically defined nanostructured substrates, *J. Vac. Sci. Technol. B* 21, 683, 2003; M. J. DALBY, N. GADEGAARD, M. O. RIEHLE, C. D. W. WILKINSON, A. S. G. CURTIS, Investigating filopodia sensing using arrays of defined nano-pits down to 35 nm diameter in size, *J. Biochem. Cell Biol.* 36, 2005, 2004.
- 139 A. S. G. CURTIS, C. D. W. WILKINSON CDW, Topographical control of cells, *Biomaterials* 18, 1573, 1997.
- 140 A. S. G. CURTIS, Small is beautiful but smaller is the aim: review of a life of research, *Eur. Cells Mater.* 8, 27, 2004.
- 141 M. J. DALBY, M. O. RIEHLE, S. J. YARWOOD, C. D. W. WILKINSON, A. S. G. CURTIS, Nucleus alignment and cell signaling in fibroblasts: response to a micro-grooved topography, *Exp. Cell Res.* 284, 274, 2003.
- 142 B. WOJCIAK-STOTHARD, A. S. G. CURTIS, W. MONAGHAN, K. MACDONALD, C. D. W. WILKINSON, Guidance and activation of murine macrophages by nanometric scale topography, *Exp. Cell Res.* 223, 426, 1996.

- 143 M. J. DALBY, M. O. RIEHLE, H. JOHNSTONE, S. AFFROSSMAN, A. S. G. CURTIS, *In vitro* reaction of endothelial cells to polymer demixed nanotopography, *Biomaterials* 23, 2945, 2002.
- 144 M. J. DALBY, M. O. RIEHLE, H. JOHNSTONE, S. AFFROSSMAN, A. S. G. CURTIS, Investigating the limits of filopodial sensing: a brief report using SEM to image the interaction between 10 nm high nanotopography and fibroblast filopodia, *Cell Biol. Int.* 28, 229, 2004.
- 145 F. JOHANSSON, P. CARLBERG, N. DANIELSEN, L. MONTELIUS, M. KANJE, Axonal outgrowth on nanoimprinted patterns, *Biomaterials* 27(8), 1251–1258, 2006.
- 146 P. FROMHERZ, Electrical interfacing of nerve cells and semiconductor chips, *Chem. Phys. Chem.* 3, 276, 2002.
- 147 <http://www.cyberkineticsinc.com>.
- 148 P. CARLBERG, F. JOHANSSON, T. MARTENSSON, R. BUNK, M. BECK, F. PERSSON, M. BORGSTROM, S. GHATNEKAR-NILSSON, B. HEIDARI, M. GRAZCYK, I. MAXIMOV, E.-L. SARWE, T. G. I. LING, A. MANSSON, M. KANJE, W. SEIFERT, L. SAMUELSON, L. MONTELIUS, Nanoimprint – a tool for realizing nano-bio research, in: *Proceedings of the 4th IEEE Conference on Nanotechnology*, Munich, p. 199, 2004.
- 149 W. HÄLLSTRÖM, T. MÅRTENSSON, M. KANJE, L. MONTELIUS, L. SAMUELSSON, Neurons cultured on gallium phosphide nanowires adherence, survival and interactions, in preparation, 2005; C. PRINZ, W. HÄLLSTRÖM, T. MÅRTENSSON, L. SAMUELSON, M. KANJE, L. MONTELIUS, Aligning neurons, in preparation, 2005.
- 150 K. BRADLEY, A. DAVIS, J.-C. P. GABRIEL, G. GRÜNNER, Integration of cell membranes and nanotube transistors, *Nano Lett.* 5, 841, 2005.
- 151 K. HAMAD-SCHIFFERLI, J. J. SCHWARTZ, A. T. SANTOS, S. ZHANG, J. M. JACOBSON, Remote electronic control of DNA hybridization through inductive coupling to an attached metal nanocrystal antenna, *Nature* 415, 152, 2002.
- 152 L. MONTELIUS, J. O. TEGENFELDT, T. G. I. LING, Fabrication and characterization of a nanosensor for admittance spectroscopy of biomolecules, *J. Vac. Sci. Technol. A* 13, 1755, 1995.
- 153 M. BECK, F. PERSSON, P. CARLBERG, M. GRAZCYK, I. MAXIMOV, T. G. I. LING, L. MONTELIUS, Nanoelectrochemical transducers for (bio-)chemical sensor applications fabricated by nanoimprint lithography, *Microelectron. Eng.* 73/74, 837, 2004.
- 154 H. WHITLOW, Ng. MAY LING, V. AUZELYTE, I. MAXIMOV, L. MONTELIUS, J. VAN KAN, A. A. BETTIOL, F. WATT, Lithography of high spatial density biosensor structures with sub-100 nm spacing by MeV proton beam writing with minimal proximity effect, *Nanotechnology* 15, 223, 2004.
- 155 Y.-K. CHOI, J. S. LEE, J. ZHU, G. A. SOMORJAI, L. P. LEE, J. BOKOR, Sublithographic nanofabrication technology for nanocatalysts and DNA chips, *J. Vac. Sci. Technol. B* 21, 2951, 2003.
- 156 F. PERSSON, M. BECK, P. CARLBERG, T. G. I. LING, L. MONTELIUS, Redox cycling in nanometer sized interdigitated sensor structures: a case for nanoimprint lithography, *Appl. Nanotechnol.* 1, 2003.
- 157 C. A. K. BORREBAECK, Antibodies in diagnostics – from immunoassays to protein chips, *Immunol. Today* 21, 379, 2000.
- 158 C. WINGREN, J. INGVARSSON, M. LINDSTEDT, C. A. K. BORREBAECK, Recombinant antibody microarrays – a viable option?, *Nat. Biotechnol.* 21, 223, 2003.
- 159 C. WINGREN, L. MONTELIUS, C. A. K. BORREBAECK, Mega-dense nano-arrays – the challenge of novel antibody array formats, in: *Protein Microarrays*, M. SCHENA, S. WEAVER (Eds.). Jones & Bartlett, Sudbury, MA, 2004.



- 160 M. LYNCH, C. MOSHER, J. HUFF, S. NETTIKADAN, J. JOHNSON, E. HENDERSON, Functional protein nanoarrays for biomarker profiling, *Proteomics* 4, 1695, 2004.
- 161 A. BRUCKBAUER, D. ZHOU, D.-J. KANG, Y. E. KORCHEV, C. ABELL, D. KLENERMAN, An addressable antibody nanoarray produced on a nanostructured surface, *J. Am. Chem. Soc.* 126, 6508, 2004.
- 162 S. NILSSON, L. DEXLIN, C. WINGREN, C. A. K. BORREBAECK, L. MONTELIUS, in preparation.
- 163 T. G. I. LING, M. BECK, R. BUNK, E. FORSEN, J. O. TEGENFELDT, A. A. ZAKHAROV, L. MONTELIUS, Fabrication and characterization of a molecular adhesive layer for micro- and nanofabricated electrochemical electrodes, *Microelectron. Eng.* 67/68, 887, 2003.
- 164 A. PALLANDRE, K. GLINEL, A. M. JONAS, B. NYSTEN, Binary nano-patterned surfaces prepared from silane monolayers, *Nano Lett.* 4, 365, 2004.
- 165 C. K. HARNETT, K. M. SATYALAKSHMI, H. G. CRAIGHEAD, Low-energy electron-beam patterning of amine-functionalized self-assembled monolayers, *Appl. Phys. Lett.* 76, 2466, 2000.
- 166 D. FALCONETT, D. PASQUI, S. PARK, R. ECKERT, H. SCHIFT, J. GOBRECHT, R. BARBUCCI, M. TEXTOR, A novel approach to produce protein nanopatterns by combining nanoimprint lithography and molecular self-assembly, *Nano Lett.* 4, 1909, 2004.
- 167 J. D. HOFF, L.-J. CHENG, E. MEYHÖFER, L. J. GOU, A. J. HUNT, Nanoscale protein patterning by imprint lithography, *Nano Lett.* 4, 853, 2004.
- 168 W. U. WANG, C. CHEN, K. LIN, Y. FANG, C. M. LIEBER, Label-free detection of small-molecule-protein interactions by using nanowire nanosensors, *Proc. Natl Acad. Sci. USA* 102, 3208, 2005.
- 169 W. CHEN, C. H. TZANG, J. TANG, M. YANG, S. T. LEE, Covalently linked deoxyribonucleic acid with multiwall carbon nanotubes: synthesis and characterization, *Appl. Phys. Lett.* 86, 103114, 2005.
- 170 F. PATOLSKY, G. ZHENG, O. HAYDEN, M. LAKADAMYALI, X. ZHUANG, C. M. LIEBER, Electrical detection of single viruses, *Proc. Natl Acad. Sci. USA* 101, 14017, 2004.
- 171 J. HAHM, C. M. LIEBER, Direct ultrasensitive electrical detection of DNA and DNA sequence variations using nanowire nanosensors, *Nano Lett.* 4, 51, 2004.
- 172 F. PATOLSKY, C. M. LIEBER, Nanowire nanosensors, *Mater. Today*, April, 20, 2005.
- 173 Q. ZHAO, M. BUONGIORNO NARDELLI, W. LU, J. BERNHOLC, Carbon nanotube-metal cluster composites: a new road to chemical sensors, *Nano Lett.* 5, 847, 2005.
- 174 X. MICHALET, F. PINAUD, T. D. LACOSTE, M. DAHAN, M. P. BRUCHEZ, A. P. ALIVISATOS, S. WEISS, Properties of fluorescent semiconductor nanocrystals and their application to biological labeling, *Single Molecules* 2, 261, 2001.
- 175 A. P. ALIVISATOS, *Nat. Biotechnol.* 22, 47, 2004; M. BRUCHEZ, M. MORONNE, P. GIN, S. WEISS, A. P. ALIVISATOS, Semiconductor nanocrystals as fluorescent biological labels, *Science* 281, 2013, 1998.
- 176 News Feature, Biologists join the dots, *Nature* 413, 450, 2001.
- 177 J.-M. NAM, C. S. THAXTON, C. A. MIRKIN, Nanoparticle-based bio-bar codes for the ultrasensitive detection of proteins, *Science* 301, 1884, 2003.
- 178 U. HAFELI, W. SCHUFT, J. TELLER, M. ZBOROWSKI (Eds.), *Scientific and Clinical use of Magnetic Carriers*, Plenum Press, New York, 1997.
- 179 H. NISHIBIRAKI, C. S. KURODA, M. MAEDA, N. MATSUSHITA, M. ABE, Preparation of medical magnetic nanobeads with ferrite particles encapsulated in a polyglycidyl methacrylate (GMA) for bioscreening, *J. Appl. Phys.* 97, 10Q919-1, 2005.
- 180 L. SHAO, D. CARUNTU, J. F. CHEN, C. J. O'CONNOR, W. L. ZHOU,

- Fabrication of magnetic hollow silica nanospheres for bioapplications, *J. Appl. Phys.* 97, 10Q908-1, 2005.
- 181 D. K. KIM, D. KAN, T. VERES, F. MORMADIN, J. K. LIAO, H. H. KIM, S.-H. LEE, M. ZAHN, M. MUHAMMED, *J. Appl. Phys.* 97, 10Q918-1, 2005.
- 182 M. A. N. COELHO, A. GLIOZZI, H. MOHWALD, E. PEREZ, U. SLEYTR, H. VOGEL, M. WINTERHALTER, nanocapsules with functionalized surfaces and walls, *IEEE Trans. Nanobiosci.* 3, 3, 2004.
- 183 C. LOO, A. LIN, L. HIRSCH, M. H. LEE, J. BARTON, N. HALAS, J. WEST, R. DREZEK, Nanoshell-enabled photonics-based imaging and therapy of cancer, *Cancer Res. Treat.* 3, 33, 2004.
- 184 H. MOEHWALD, From Langmuir monolayers to nanocapsules, *Colloids Surf. A* 171, 25, 2000.
- 185 T. ANDO, N. KODERA, Y. NAITO, T. KINOSHITA, K. FURUTA, Y. Y. TOYOSHIMA, A high-speed atomic force microscope for studying biological macromolecules in action, *Chem. Phys. Chem.* 4, 1196, 2003.
- 186 M. B. VIANI, T. E. SCHAFFER, G. T. PALOZZI, L. I. PIETRASANTA, B. L. SMITH, J. B. THOMPSON, M. RICHTER, M. RIEF, H. E. GAUB, K. W. PLAXCO, A. N. CLELAND, H. G. HANSMA, P. K. HANSMA, Fast imaging and fast force spectroscopy of single biopolymers with a new atomic force microscope designed for small cantilevers, *Rev. Sci. Instrum.* 70, 4300, 1999; T. FUKUMA, K. KOBAYASHI, K. MATSUSHIGE, H. YAMADA, True atomic resolution in liquid by frequency-modulation atomic force microscopy, *Appl. Phys. Lett.* 87, 0314101, 2005.
- 187 P. HANSMA, Surface biology of DNA by atomic force microscopy, *Annu. Rev. Phys. Chem.* 52, 71, 2001.
- 188 R. IMER, T. AKIYAMA, N. F. DE ROOIJ, M. STOLZ, U. AEBI, N. F. FRIEDERICH, D. WIRZ, A. U. DANIELS, U. STAUFER, in: *Proceedings of the 13th International Conference on Scanning Tunneling Microscopy/Spectroscopy and Related Techniques*, Sapporo, see also STOLZ, R. RAITERI, A. U. DANIELS, M. R. VAN LANDINGHAM, W. BASCHOMG, U. AEBI, Dynamic elastic modulus of porcine articular cartilage determined at two different levels of tissue organization by indentation-type atomic force microscopy, *Biophys. J.* 86, 3269, 2004.
- 189 M. BENOIT, D. GABRIEL, G. GERISCH, H. E. GAUB, Discrete interactions in cell adhesion measured by single-molecule force spectroscopy, *Nat. Cell Biol.* 2, 313, 2000.
- 190 J. K. GIMZEWSKI, C. JOACHIM, Nano-scale science of single molecules using local probes, *Science* 283, 1683, 1999.
- 191 Gaub homepage: <http://www.biophysik.physik.uni-muenchen.de>.
- 192 C. FRIEDSAM, A. K. WEHLE, F. KÜHNER, H. E. GAUB, Dynamic single-molecule force spectroscopy: bond rupture analysis with variable spacer length, *J. Phys. Condens. Matt.* 15, S1709, 2003.
- 193 H. P. LANG, M. HEGNER, Ch. GERBER, Nanomechanics – the link to biology and chemistry, *Chimia* 56, 515, 2002.
- 194 S. GHATNEKAR-NILSSON, Nano-mechanical studies and applications of cantilever sensors, *PhD Thesis*, Lund University, 2005.
- 195 F. HÖÖK, M. RODAHL, C. KELLER, K. GLASMÄSTAR, C. FREDRIKSSON, P. DAHLQVST, B. KASEMO, The dissipative QCM D-technique: interfacial phenomena and sensor applications for proteins, biomembranes, living cells and polymers, *Proc. IEEE*, 966, 1999.
- 196 E. REIMHULT, C. LARSSON, B. KASEMO, F. HÖÖK, Simultaneous surface plasmon resonance and quartz crystal microbalance with dissipation monitoring measurements of biomolecular adsorption events involving structural transformations and variations in coupled water, *Anal. Chem.* 76, 7211, 2004.
- 197 E. FORSÉN, S. G. NILSSON, P. CARLBERG, G. ABADAL, F. PÉREZ-MURANO, J. ESTEVE, J. MONTSERRAT, E. FIGUERAS, F. CAMPABADAL, J. VERD, L. MONTELIUS, N. BARNIOL, A. BOISEN, Fabrication of cantilever based mass sensors integrated with CMOS

- using direct write laser lithography on resist, *Nanotechnology* 15, S628, 2004.
- 198 S. G. NILSSON, E. FORSÉN, G. ABADAL, J. VERD, F. CAMPABADAL, F. PÉREZ-MURANO, J. ESTEVE, N. BARIOL, A. A. BOISEN, L. MONTELIUS, Resonators with integrated CMOS circuitry for mass sensing applications, fabricated by electron beam lithography, *Nanotechnology* 16, 98, 2004; E. FORSEN, G. ABADAL, S. GHATNEKAR-NILSSON, J. TEVA, J. VERD, R. SANDBERG, W. SVENDSEN, F. PEREZ-MURANO, J. ESTEVE, E. FIGUERAS, F. CAMPABADAL, L. MONTELIUS, N. BARNIOL, A. BOISEN, Ultrasensitive mass sensor fully integrated with complimentary metal-oxide-semiconductor circuitry, *Appl. Phys. Lett.* 87, 034507, 2005.
- 199 Gerber homepage: <http://www.nccr-nano.org/nccr> and <http://www.zurich.ibm.com/st/nanoscience/cantilever.html>.
- 200 A. BIETSCH, J. ZHANG, M. HEGNER, H. P. LANG, C. GERBER, Rapid functionalization of cantilever array sensors by inkjet printing, *Nanotechnology* 15, 873, 2004.
- 201 S. G. NILSSON, X. BORRISÉ, L. MONTELIUS, Size effect on Young's modulus of thin chromium cantilevers, *Appl. Phys. Lett.* 85, 3555, 2004.
- 202 S. G. NILSSON, E.-L. SARWE, L. MONTELIUS, Fabrication and mechanical characterization of ultrashort nanocantilevers, *Appl. Phys. Lett.* 83, 990, 2003.
- 203 H. P. LANG, M. HEGNER, E. MEYER, Ch. GERBER, Tutorial: Nanomechanics from atomic resolution to molecular recognition based on atomic force microscopy technology, *Nanotechnology* 13, R29, 2002.
- 204 J. FRITZ, M. K. BALLER, H. P. LANG, T. STRUNZ, E. MEYER, H.-J. GÜNTHERODT, E. DELAMARCHE, Ch. GERBER, J. K. GIMZEWSKI, Stress at the solid-liquid interface of self-assembled monolayers on gold investigated with a nanomechanical sensor, *Langmuir* 16, 9694, 2000.
- 205 J. SADER, T. UCHIHASHI, M. J. HIGGINS, A. FARRELL, Y. NAKAYAMA, S. P. JARVIS, Quantitative force measurements using frequency modulation atomic force microscopy – theoretical foundations, *Nanotechnology* 16, S94, 2005.
- 206 T. BRAUN, V. BARWICH, M. K. GHATSEKAR, A. H. BREDEKAMP, C. GERBER, M. HEGNER, H. P. LANG, Micromechanical mass sensors for biomolecular detection in a physiological environment, *Phys. Rev. E* 72, 03907, 2005.
- 207 S. GHATNEKAR-NILSSON, J. LINDAHL, A. DAHLIN, T. STJERNHOLM, S. JEPPESEN, F. HÖÖK, L. MONTELIUS, Phospholipid vesicle adsorption measured *in situ* with resonating cantilevers in a liquid cell, *Nanotechnology* 16, 1512, 2005.
- 208 B. ILIC, D. CZAPLEWSKI, H. G. CRAIGHEAD, P. NEUZIL, C. CAMPAGNOLO, C. BATT, Mechanical resonant immunospecific biological detector, *Appl. Phys. Lett.* 77, 450, 2000.
- 209 B. ILIC, Y. YANG, H. G. CRAIGHEAD, Virus detection using nanoelectromechanical devices, *Appl. Phys. Lett.* 85, 2604, 2004.
- 210 K. C. SCHWAB, M. L. ROUKES, Putting mechanics into quantum mechanics, *Phys. Today* 58, 36, 2005.
- 211 K. L. EKINCI, M. L. ROUKES, Nanoelectromechanical systems, *Rev. Sci. Instrum.* 76, 061101, 2005.
- 212 M. L. ROUKES, Zeptogram mass detection: weighing molecules, *Phys. News Update* 725, April, 2005.
- 213 C.-F. CHOU, J. GU, Q. WEI, J. LIU, R. GUPTA, T. NISHIO, F. ZERNHAUSERN, Nanopatterned structures for biomolecular analysis towards genomic and proteomic applications, *Proc. SPIE* 5592, 2004.
- 214 H. G. CRAIGHEAD, Nanostructure science and technology: impact and prospects for biology, *J. Vac. Sci. Technol. A* 21, S216, 2003.
- 215 M. ROCHO, Statement by at: *Global Nanotechnology Conference*, Saarbrücken, 2005.
- 216 To get an overview of these activities, visit the *Conference Series NanoBioInfoCogno (NBIC)*.

## 13 Nanodevices in Nature

*Alexander G. Volkov and Courtney L. Brown*

### 13.1 Introduction

Living organisms are intricately designed with systems of “checks and balances” which regulate biological processes and minimize malfunctions. Biological nanodevices are largely responsible for the nearly flawless function of various organisms. The use of biological organisms as model systems for the engineering of new technologies is a form of applied case-based reasoning. The wealth of information generated from the study of biological systems creates a database that can be utilized to find solutions to various problems.

In this chapter, we discuss the role of various nanodevices in a wide variety of biological processes. Furthermore, we focus specifically on nanoreactors in multi-electron reactions, the biological function of cytochrome oxidase, nanodevices in photosynthesis and phototropism, membrane transport, molecular motors, and electroreceptors. There are many publications that focus on isolated nanodevices within very specific model systems; however, this approach allows us to analyze the role and significance of nanodevices in a variety of life forms, including plants, animals and bacteria. The study of nanodevices has limitless applications in bioelectronics, biology, chemistry, genetics, biophysics, bioengineering, technology and other fields of scientific study.

Nanodevices are molecules or molecular complexes that have clear and specific functions, and are a few nanometers in size. Millions of nanodevices exist in nature and in this chapter we discuss a few examples. Natural nanodevices include photochemical, electrochemical and synthetic nanoreactors. Photosystem (PS) I and PS II, enzymes, enzymatic systems in the citric acid cycle, and carbon fixation in the reductive carboxylic acid cycle are also common nanodevices in nature. Molecular motors such as ATP synthase, myosin, kinesin, DNA helicases, DNA topoisomerase, DNA helixase, RNA polymerase and bacterial rotary motors are vital nanodevices that serve to regulate biological processes. Molecules in electron transfer chains act as nanorectifiers and nanoswitches. Biological applications for nanodevices include information transfer, molecular computing, mechanosensors, elec-

troreceptors, magnetoreceptors, magnetosomes, neuronal networks, light sensors and ion channels.

## 13.2

### Multielectron Processes in Bioelectrochemical Nanoreactors

Vectorial charge transfer and molecular recognition at the interface between two dielectric media are important stages in many bioelectrochemical processes such as those mediated by energy-transducing membranes [1–5]. Many biochemical redox reactions take place at aqueous medium/membrane interfaces and some of these reactions are multielectron processes. About 90% of the oxygen consumed on Earth is reduced in a four-electron reaction catalyzed by cytochrome *c* oxidase. Multielectron reactions take place during photosynthesis, which is one of the most important processes on Earth.

Synchronous multielectron reactions may proceed without the formation of intermediate radicals. These radicals are highly reactive, and can readily enter a side-reaction of hydroxylation and destruction of the catalytic complex. Since multielectron reactions do not pollute the environment with toxic intermediates and are ecologically safe, they are used by nature for biochemical energy conversion during respiration and photosynthesis. In the multielectron reaction that takes place in a series of consecutive single-electron stages, the Gibbs energy necessary for single-electron transfer cannot be completely and uniformly distributed over the stages. The energy demand for various stages is varied and the excess energy in the simpler stages is converted into heat. In a synchronous multielectron reaction, the energy is used very economically [6–9].

An important parameter in the quantum theory of charge transfer in polar media is the medium reorganization energy,  $E_s$ , that determines activation energy. The energy of medium reorganization in systems with complicated charge distribution was calculated by Kharkats [10]. Reagents and products can be represented by a set of  $N$  spherical centers arbitrarily distributed in a polar medium. The charges of each of the reaction centers in the initial and final state are  $z^i$  and  $z^f$  respectively. Taking  $R_k$  to represent coordinates of the centers and  $\epsilon_i$  for dielectric constants of the reagents, it follows that:

$$E_s = 0.8 \left( \frac{1}{\epsilon_{\text{opt}}} - \frac{1}{\epsilon_{\text{st}}} \right) \times \left\{ \sum_{p=1}^N \left[ \frac{(\delta z_k)^2}{2a_p} + \sum_{\substack{k=1 \\ k \neq p}}^N \frac{(\delta z_p)(\delta z_k)}{2R_{pk}} + \sum_{\substack{k=1 \\ k \neq p}}^N \sum_{\substack{l=1 \\ l \neq p}}^N \frac{(\delta z_p)(\delta z_l) a_p^3 (\vec{R}_{pk} \vec{R}_{pl})}{R_{pk}^3 R_{pl}^3} \left( \frac{3\epsilon_{\text{st}}^2}{(2\epsilon_{\text{st}} + \epsilon_i)^2} - \frac{1}{2} \right) \right] \right\} \quad (1)$$

where  $(\delta z_k) = z_k^f - z_k^i$ ,  $R_{pk} = R_p - R_k$ , and  $z_k^f$  and  $z_k^i$  are charge numbers of particle  $k$  in the initial and final states, respectively. The term  $a_p$  is the radius of

particle  $p$ ,  $R_k$  is the coordinate of  $k$ -particle center and  $\epsilon_i$  is the dielectric constant of reactant. Reactions with synchronous transfer of several charges present a particular case of Eq. (1).

It follows from Eq. (1) that  $E_s$  is proportional to the square of the number of charges transferred. Homogeneous multielectron processes are unlikely, due to the high activation energy resulting from a distinct rise in the energy of solvent reorganization. For multielectron reactions, the exchange currents of  $n$ -electron processes are small compared to those of single-electron multistep processes, which makes the stage-by-stage reaction mechanism more advantageous. Therefore, multielectron processes can proceed only if the formation of an intermediate is energetically disadvantageous. However, conditions can be chosen which reduce  $E_s$  during transfer of several charges to the level of the reorganization energy of ordinary single-electron reactions. These conditions require systems with a low dielectric constant and large reagent radii. Furthermore, the substrate must be included in the coordination sphere of the charge acceptor with several charge donors or acceptors bound into a multicenter complex. Recent papers have presented theoretical studies on the kinetics of heterogeneous multielectron reactions at water/oil interfaces, which proved to be capable of catalyzing multielectron reactions and sharply reducing the activation energy.

The most effective coupling of ion and electron transport can be obtained if the activation energy of the coupled process is lower than that of the charge transfer in the electron transport chain. It is obvious from Eq. (1) that this requires a simultaneous transfer of opposite charges, so that the second and the third terms of Eq. (1) are negative. An optimal geometry between the centers of charges of donors and acceptors must also be chosen.

To illustrate this point, we can consider two instances of multielectron reactions: simultaneous transfer of  $n$  charges from one donor to an acceptor and simultaneous transfer of several charges (one from each of the centers) to  $m$  acceptors ( $m \leq n$ ). In the former case,  $E_s$  is proportional to  $n^2$ , while in the latter it may be significantly lower (depending on the sign of the charge being transferred and the reciprocal positions of reagents). The concerted multicenter mechanism of multielectron reactions markedly reduces  $E_s$  and, hence the activation energy, compared to a two-center multielectron process. With the appropriate arrangement of the reactants, the activation energy associated with electron transfer in a heterogeneous multielectron reaction may be lower than the energy of reorganization of the media.

### 13.3

#### Cytochrome Oxidase: A Nanodevice for Respiration

The function of the enzymes of the mitochondrial respiratory chain is to transform the energy of redox reactions into an electrochemical proton gradient across the hydrophobic barrier of a coupling membrane.

Cytochrome oxidase (EC 1.9.3.1, PDB 2OCC) is the terminal electron acceptor of

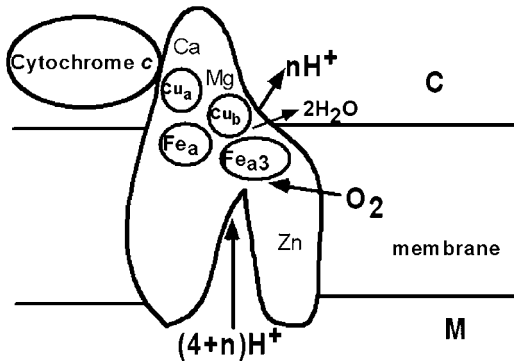


**Figure 13.1.** Scheme of the structural organization of cytochrome *c* and cytochrome *c* oxidase monomer in the inner mitochondrial membrane.

the mitochondrial respiratory chain. Its main function is to catalyze the reaction of oxygen reduction to water using electrons from ferrocycytochrome *c*:



Reaction (2) is exothermic and this energy can be used to transport protons across the mitochondrial membrane (Fig. 13.1). Mitochondrial cytochrome *c* oxidase is a dimer; each monomer is composed of 13 subunits. The enzyme contains cytochromes *a* and *a*<sub>3</sub>, one binuclear copper complex Cu<sub>a</sub>, one mononuclear copper site Cu<sub>b</sub>, and one bound Mg<sup>2+</sup> per monomer. It has a molecular weight ranging from 180 000 to 200 000 kDa for the most active form [11–13]. Cytochrome oxidases can transport a maximum of eight protons across the membrane per oxygen molecule reduction [14, 15]. Four of the protons bind to the reaction complex during the reduction of oxygen to water and up to four other protons are transported across the membrane. The resulting chemiosmotic proton gradient is used in ATP synthesis.

There are two types of respiration in photosynthetic organisms – dark respiration and photorespiration. Dark respiration includes O<sub>2</sub> reduction and the oxidation of NADH and FADH<sub>2</sub> in mitochondrial membranes, glycolysis, the Krebs cycle, and the oxidative pentose phosphate pathway. Respiration is commonly subdivided into two functional components – growth respiration and maintenance respiration. Growth respiration supplies energy for the production of new biomass; however, maintenance respiration provides the energy needed to maintain the integrity of existing structures and their turnover.

The respiratory chain of mitochondria is an integral part of the inner mitochondrial membrane. It is composed of four electron-transporting protein complexes (NADH dehydrogenase complex I, succinate dehydrogenase complex II, cytochrome reductase complex III and cytochrome *c* oxidase complex IV), ATP synthase (complex V), and mobile electron carriers ubiquinone and cytochrome *c*.

Plant mitochondria have additional enzymes not found in mitochondria of animals – the cyanide-insensitive alternative oxidase, an internal rotenone-insensitive NADPH dehydrogenase and an externally located NADPH dehydrogenase, which does not conserve energy. The alternative oxidase catalyzes the oxidation of ubiquinol to ubiquinone and the reduction of oxygen to water. It is inhibited by salicylhydroxamic acid.

Kharkats and Volkov were the first to present proof that cytochrome *c* oxidase reduces molecular oxygen by synchronous multielectron mechanism without the formation of an  $O_2^-$  intermediate [7–9, 14, 15]. The calculations predicted that the first step in oxygen reduction by cytochrome *c* oxidase should be a concerted multielectron process. As the field progresses, it became clear that the first step of oxygen reduction is a two-electron concerted process. The possible concerted molecular 2:1:1-electron and 2:2 proton pump mechanism of cytochrome *c* oxidase function is discussed in this chapter.

The 1:1:1:1-electron mechanisms of oxygen reduction by cytochrome oxidase were most frequently discussed in biochemistry. The reaction implies that the Gibbs free energy of the first electron transfer from cytochrome oxidase to  $O_2$  is positive (Fig. 13.2). As a result, this route should be abandoned or the reaction rate should be extremely low. Since the Gibbs free energy of  $O_2$  binding in the catalytic site of cytochrome oxidase is  $-21 \text{ kJ mol}^{-1}$  [16], cytochrome *c* redox potential is 0.25 V. The Gibbs free energy of the first electron donation to oxygen at pH 7 is  $+33 \text{ kJ mol}^{-1}$ . The Gibbs free energy of the reaction



in a cytochrome oxidase catalytic site is equal to  $+79 \text{ kJ mol}^{-1}$ . Activation energy for  $O_2$  reduction by fully reduced cytochrome oxidase is equal to  $16 \text{ kJ mol}^{-1}$  [17].

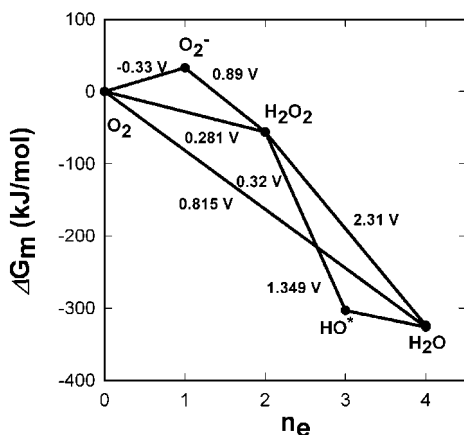


**Figure 13.2.** Energy diagrams for possible routes of the reaction  $O_2 + 4H^+ \leftrightarrow 2H_2O$ .  $G_m$  is the reaction midpoint Gibbs free energy at pH 7.



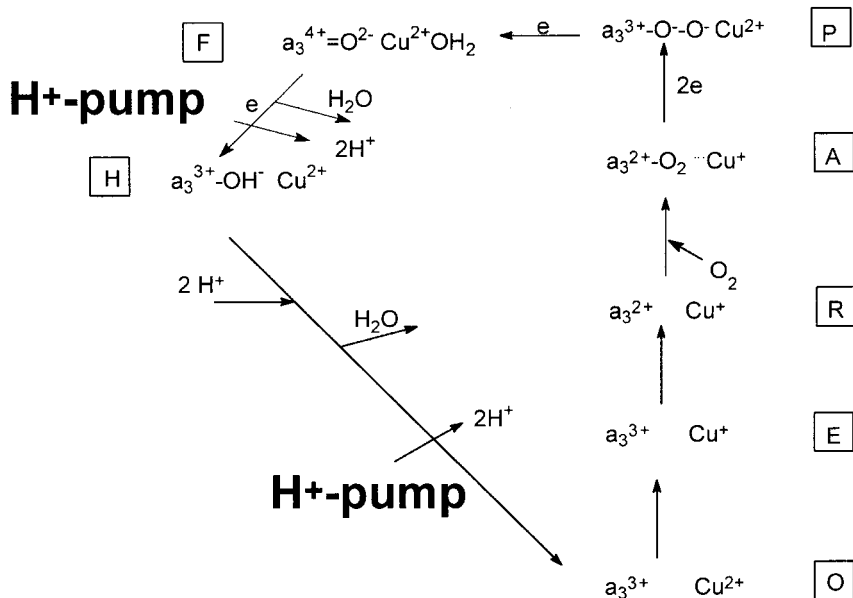


**Figure 13.3.** Scheme of the 2:1:1-electron reduction mechanism at the cytochrome *c* oxidase active site and its coupling to proton pumping. Starting from the oxidized form (O), the one-electron reduced form (E) and the doubly reduced form (R) are generated. Upon

binding, compound (A) is observed. Next the peroxy-intermediate (P) is formed. The oxoferryl state (F) and a hydroxyl state (H) are formed after protonation of the iron-bound oxygen atom. After water formation and release, the O state is regenerated.

Since the Gibbs free energy of the endothermic reaction (3) is 5 times the measured activation energy for  $\text{O}_2$  reduction by cytochrome oxidase, the single-electron mechanisms 1:1:1:1, 1:2:1, 1:1:2 and 1:3 at room temperature are unlikely. These reaction mechanisms are favorable when the binding energy of the single-electron intermediate is less than  $-52 \text{ kJ mol}^{-1}$  in magnitude. The significant covalent bonding energy allows this intermediate to be experimentally detected. However, it has not been detected thus far.

The fact that the first electron addition to  $\text{O}_2$  is endothermic accounts for the relative chemical inertness of oxygen in nature and it permits the existence of life on Earth.

A possible mechanism of oxygen reduction by cytochrome *c* oxidase is outlined in Fig. 13.3, and is to be considered in detail after the discussion of the thermodynamic and kinetic aspects of the problem.

### 13.3.1

#### Nanodevice Architectonics

Equation (1) sets the conditions for the structure of cytochrome *c* oxidase catalytic site necessary for oxygen reduction to occur by the concerted  $n$ -electron mecha-

nism. In order to reduce the reorganization energy of the medium, and thus the activation energy, several conditions must be met.

- The dielectric constant of the medium where oxygen reduction takes place should be low. Simply stated, the catalytic site should be immersed in a hydrophobic phase of the membrane (protein).
- There should be  $n$  spatially separated electron donors. For the proposed mechanism, heme and protein–copper complexes satisfy this condition.
- Cation, preferably a proton, transport should accompany electron transport via cytochrome  $c$  oxidase. Based on Eq. (1), when opposing charges are simultaneously transferred in close directions, the reorganization energy of the medium may be reduced due to a dependence on the third and fourth terms in Eq. (1). It implies that the coupling of the electron and proton pumps in cytochrome oxidase can be attained if the simultaneous transfer of opposing charges in close directions neutralizes medium reorganization. If electron transfer via cytochrome oxidase is coupled with proton transport across the mitochondrial membrane, then the energy liberated in the second reaction is consumed as opposed to being converted to heat.
- The radii of electron donors should be sufficiently large. This condition is achieved by utilizing the metal ion components of organic complexes (e.g. hemes and cysteines), the systems of conjugated bonds and ligands capable of undergoing redox reactions.

### 13.3.2

#### Activation Energy and Mechanism of Oxygen Reduction

The dependence of oxygen reduction rate on temperature reveals that cytochrome oxidase exists in two conformations – “hot” (h) and “cold” (c). The respective activation energies  $E_a^h$  and  $E_a^c$  are  $16 \text{ kJ mol}^{-1}$  (at  $23\text{--}35 \text{ }^\circ\text{C}$ ) and  $60 \text{ kJ mol}^{-1}$  (below  $20 \text{ }^\circ\text{C}$ ) [18]. A phase transition accompanied by conformational changes and absorption spectrum takes place between  $18$  and  $23 \text{ }^\circ\text{C}$ . The temperature  $T^c$  depends on the surrounding lipid composition. The low  $E_a^h$  value suggests that the single-electron mechanisms 1:1:1:1, 1:2:1, 1:3 and 1:1:2 are unlikely at temperatures above  $T^c$  since the enthalpy for the transfer of first electron from the reduced cytochrome oxidase to oxygen is 5 times more than the measured activation energy.

For the multielectron reaction 2:1:1, according to Eq. (1),  $E_s$  for two-electron reactions between  $\text{O}_2$ ,  $a_3$  and  $\text{Cu}_b$  strongly depend on geometry and distances in a catalytic site. Only the 2:1:1 mechanism of oxygen reduction by cytochrome oxidase can be realized *in vivo* in both “hot” and “cold” conformations.

Consider the molecular mechanism of oxygen reduction outlined in Fig. 13.3 in more detail [9, 14, 15].

The oxidized catalytic site of cytochrome oxidase is composed of cytochrome  $a_3$  and  $\text{Cu}_b$ . It is reduced via the bridge mechanism by two electrons supplied from the electron reservoir of the respiratory chain. This reduced complex then binds an oxygen molecule. The reaction center is oxidized to the initial state in a double-

electron reaction with the formation of a peroxide bridge between  $a_3$  and  $\text{Cu}_b$ . The partially reduced (to peroxide) oxygen molecule must be bound in the reaction center since cytochrome oxidase is known to reduce oxygen to water without the release of any intermediates from the membrane. Next, the catalytic complex accepts two electrons from the electron reservoir  $\text{Fe}(c) \rightarrow a_3$ . In the next step, the peroxide bridge undergoes 1:1-electron reduction and protonation to water.

### 13.3.3

#### Proton Pump

Water molecules released in the course of oxygen reduction are transferred from the hydrophobic catalytic site to the aqueous phase. The continuous movement of the product away from the reaction center causes the equilibrium of the second reaction to shift to the right. Energy liberated in the exothermic reaction (2) is sufficient for transporting 8  $\text{H}^+$  ions across the membrane. Four of the  $\text{H}^+$  ions couple with  $\text{O}_2$  to form two  $\text{H}_2\text{O}$  molecules. The remaining  $\text{H}^+$  ions can be transported across the hydrophobic zone of the membrane and used for ATP synthesis in ATP synthase complex. As follows from thermodynamics (Fig. 13.2), the energy needed for the function of the  $\text{H}^+$  pump is liberated only at the last steps of water formation on the addition of third and fourth electrons independently of the reaction route [9, 14]. The functioning of protons pump after formation of ferryl intermediate is possible only if the difference between Gibbs energy of ferryl and peroxy intermediates binding is less than  $-35 \text{ kJ mol}^{-1}$ .

The binding energy of the ferryl intermediate is negative. This energy supports the proton pump function not only during the addition of the fourth electron, but also after the formation of the three-electron oxygen intermediate. The stoichiometry of proton pumping by cytochrome oxidase can be 0:2:2 [14].

As it follows from Eq. (1), media reorganization energy corresponding to simultaneous electron and proton transfer is minimized when the transfer directions are close.

Alternative cytochrome oxidase in green plants can reduce  $\text{O}_2$  without concomitant proton transfer. In such a case, the enzymes work like machines converting the energy of electron transfer to heat.

## 13.4

### Photosynthetic Electrochemical Nanoreactors, Nanorectifiers, Nanoswitches and Biologically Closed Electrically Circuits

Life on Earth has been supported by the continuous flow of solar energy over billions of years. The power of this flux is extremely high:  $4.14 \times 10^{15} \text{ kWh day}^{-1}$  or  $1.5 \times 10^{18} \text{ kWh year}^{-1}$ . These values are extremely vast and difficult to imagine. According to Einstein's equation  $E = mc^2$ , the energy equivalent of 1 kg of mass is approximately  $2.5 \times 10^{10} \text{ kWh}$ . The net daily energy flux incident upon Earth can thus be expressed as 165 tons and the thus net annual flux is 60 000 tons. By

comparison, the annual production of electric energy in United States corresponds to an equivalent mass of about 100 kg and the total use of all kinds of energy corresponds to about 800 kg. At present, the annual consumption of energy by mankind is  $4 \times 10^{17}$  kJ, rising rapidly and doubling every 20 years. The known reserves of fossil fuels are limited to an estimated energy equivalent of  $5 \times 10^{19}$  kJ, so new sources of energy are of fundamental importance. One obvious possibility is solar energy. The amount of solar energy incident on the Earth is about  $5 \times 10^{21}$  kJ year<sup>-1</sup>, of which  $3 \times 10^{18}$  kJ is converted into chemical energy by photosynthesis in plants and microorganisms [5].

The vast majority of the pigments in a photosynthetic organism is not chemically active, but functions primarily as an antenna. The photosynthetic antenna system is a nanodevice that collects and delivers the excited state energy by means of excitation transfer to the reaction center complexes where photochemistry takes place. The antenna system increases the effective cross-section of photon absorption by increasing the number of pigments associated with each photochemical complex. The intensity of sunlight is sufficiently dilute so that any given chlorophyll molecule only absorbs at most a few photons per second.

By incorporating many pigments into a single unit, the reaction centers and electron transport chain can be used to maximum efficiency. A remarkable variety of antenna complexes have been identified from various classes of photosynthetic organisms. Excitation transfer must be fast enough to deliver excitations to the photochemical reaction center and have them trapped in a short amount of time compared to the excited state lifetime in the absence of trapping. Excited state lifetimes of isolated antenna complexes, where the reaction centers have been removed, are typically in the range of 1–5 ns. Observed excited state lifetimes of systems where antennas are connected to reaction centers are generally on the order of a few tens of picoseconds, which is sufficiently fast so that under physiological conditions almost all the energy is trapped by photochemistry.

In water-oxidizing photosynthesis two membrane-integrated protein complexes PS II and PS I are operating in series (Fig. 13.4). The electron transfer starts in both photosystems vectorially across the membrane. Light energy is harvested by photosynthetic pigment systems in which the electronic structure of excited-state chlorophyll donates an electron to a primary acceptor pheophytin, the first component of an electron transport chain. The electron is fortified with it the energy of the original photon of light it absorbed. In the process of electron transport, the energy is captured in two ways. The first involves the coupling a proton pump mechanism to the sequential redox reactions in the electron transport chain, so that a proton gradient is established across the thylakoid membrane. The electrochemical energy of the proton gradient is then used to drive ATP synthesis by the ATP synthase enzymes embedded in the membrane. The second energy capture occurs when an acceptor molecule such as  $\text{NADP}^+$  is reduced to NADPH, which in turn is used to reduce carbon dioxide in the Calvin cycle. Systems modeling photosynthesis should have the capability of carrying out relatively simple versions of these fundamental reactions.

The redox map of photosynthesis in green plants can be described in terms of

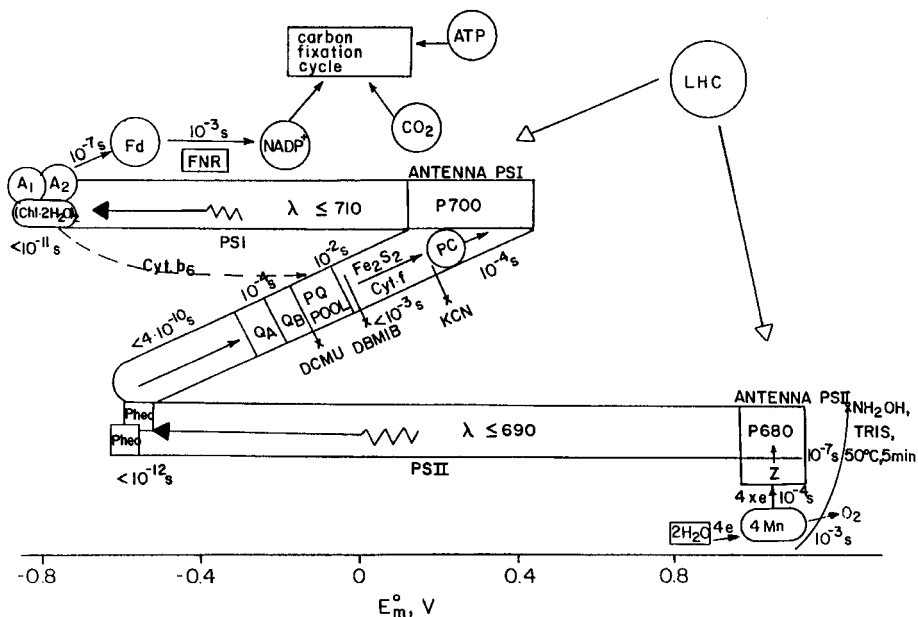


**Figure 13.4.** Scheme of electron transfer in photosynthesis in higher plants.  $E_m^o$  on the abscissa stands for midpoint redox potential at pH 7.0. Light quanta ( $h\nu$ ) are absorbed in two sets of antenna chlorophyll molecules, the excitation energy is transferred to the reaction

center chlorophyll a molecules of PS II (P680) and PS I (P700) forming (P680)\* and (P700)\*, and the latter two initiate electron transport. (Reproduced from Ref. [21] with permission from Elsevier Science.)

the well-known Z-scheme proposed by Hill and Bendall [19]. The molecular organization of a thylakoid membrane is shown in Fig. 13.5. The spectral characteristics of PS II indicate that the primary electron donor is the dimer of chlorophyll P680 with absorption maxima near 680 and 430 nm. Water can be oxidized by an oxygen-evolving center (OEC) composed of several chlorophyll molecules, two molecules of pheophytin, plastoquinol, several plastoquinone (PQ) molecules and a manganese-protein complex containing four manganese ions. The OEC is a highly ordered structure in which a number of polypeptides interact to provide the appropriate environment for cofactors such as manganese, chloride and calcium, as well as for electron transfer within the complex. Figure 13.6 shows the electronic equivalent circuit of PS I and PS II.

Manganese-binding centers were first revealed in thylakoid membranes by electron paramagnetic resonance (EPR) methods and it is now understood that four manganese ions are necessary for oxygen evolution during water photooxidation. PQ acts as a transmembrane carrier of electrons and protons between reaction centers of two photosystems in the case of noncyclic electron transfer. It may also serve as a molecular "tumbler" that switches between one- and two-electron reactions. Pheophytin is an intermediate acceptor in PS II. Direct formation of P680

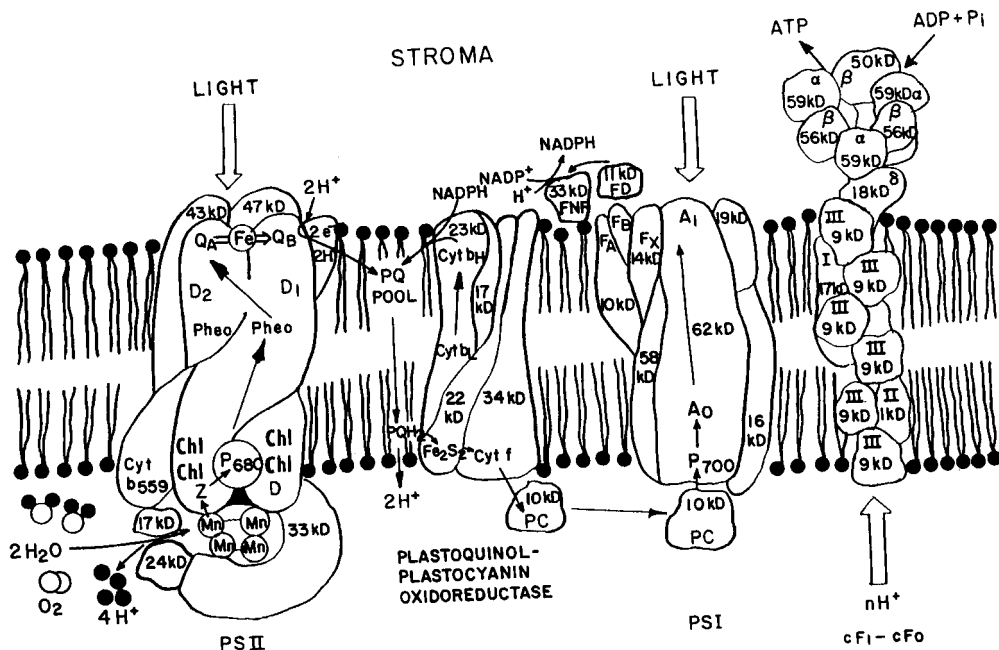
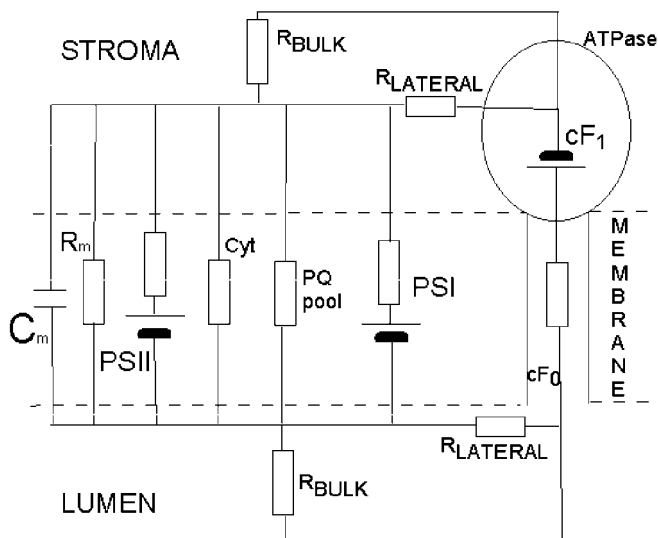


Figure 13.5. A stylized model of the electron transport chain with most of the light-harvesting pigment–protein complexes omitted. (Reproduced from Ref. [21] with permission from Elsevier Science.)

pheophytin ion radical pairs was revealed by experiments on magnetic interactions between pheophytin and PQ as reflected in the EPR spectra.

The photocatalytic oxidation of two molecules of water to oxygen cannot be a single-quantum process since the total energy expenditure of a catalytic cycle cannot be less than  $476 \text{ kJ mol}^{-1}$ . However, there is no fundamental reason why one quantum process should not induce the transfer of several electrons. For instance, a two-quantum process would require light with a wavelength less than 504 nm, while a four-quantum process would involve a sequential mechanism in which each light quantum is used to transfer one electron from photocatalyst to an electron acceptor. The threshold wavelength for the oxidation of water in this case is 1008 nm. The eight-quantum scheme which is actually used in photosynthesis can be explained by the need to compensate for energy losses in a long electron-transfer chain of redox reactions.

Water oxidation to molecular oxygen is a multielectron process that proceeds with surprisingly high quantum efficiency. The water oxidation reaction can proceed upon illumination at 680 nm – a wavelength of light that excludes one-electron mechanisms using hydroxyl and oxygen radicals. For a three-electron reaction an oxidant stronger than the cation-radical  $\text{P680}^+$  is needed. A synchronous two-by-two electron pathway of the reaction is thermodynamically possible if the standard



**Figure 13.6.** The equivalent electrical circuit of thylakoid membrane. C, capacity; R, resistance;  $cF_1$ , coupling factor; cyt, cytochrome.

free energy of binding of the two-electron intermediate is about  $-40 \text{ kJ mol}^{-1}$ . This value corresponds to the energy of formation for two hydrogen bonds between  $\text{H}_2\text{O}_2$  and the catalytic center. For this case a molecular mechanism was proposed [20, 21] and is discussed below (Fig. 13.7).

Membrane-bound P680 enters an excited state upon illumination. In dimers and other aggregated forms of chlorophyll, the quantum efficiency of triplet states is

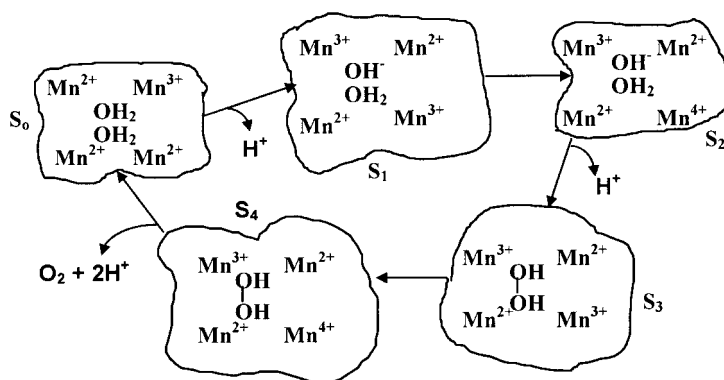


**Figure 13.7.** Possible 2:2-electron mechanism of water photooxidation by a manganese nanodevice in PS II.

low. It is the singlet excited state that undergoes photochemical transformations. In several picoseconds, an electron is first transferred to pheophytin, then to PQA, and from PQA to polypeptide-bound PQB in thylakoid membranes (Fig. 13.4), resulting in an oxidized pigment and a reduced acceptor. The cation radical  $P680^+$  successively oxidizes four manganese ions, which in turn drives the production of molecular oxygen. Formation of a cation radical of chlorophyll or oxidation of manganese ions is accompanied by dissociation of water bound to the reaction center and ejection of protons. A synchronous multielectron process that describes all four oxidizing states of the OEC was proposed earlier. The transfer of electrons in a 1:1:1:1 series from a manganese cluster to the electron transport chain is accompanied by the ejection of 1:0:1:2 protons and the evolution of molecular oxygen [20, 21].

### 13.5

#### **Phototropic Nanodevices in Green Plants: Sensing the Direction of Light**

Plants continually gather information about their environment. Environmental changes elicit various biological responses. The cells, tissues and organs of plants possess the ability to become excited under the influence of environmental factors, referred to as irritants [22–25].

Nerve cells in animals and phloem cells in plants share one fundamental property – they possess excitable membranes through which electrical excitations, in the form of action potentials, can propagate. Plants generate bioelectrochemical signals that resemble nerve impulses and these are present in plants at all evolutionary levels [26].

The conduction of bioelectrochemical excitation is a rapid method of long-distance signal transmission between plant tissues and organs. Plants quickly respond to changes in luminous intensity, osmotic pressure, temperature, cutting, mechanical stimulation, water availability, wounding, and chemical compounds such as herbicides, plant growth stimulants, salts and water [27–30]. Once initiated, electrical impulses can propagate to adjacent excitable cells. The change in transmembrane potential creates a wave of depolarization or action potential, which affects the adjoining resting membrane.

The phloem is a sophisticated tissue in the vascular system of higher plants. Representing a continuum of plasma membranes, the phloem is a potential pathway for transmission of electrical signals. It consists of two types of conducting cells – the characteristic sieve-tube elements and the companion cells. Sieve-tube elements are elongated cells that have end walls perforated by numerous minute pores through which dissolved materials can pass. Sieve-tube elements are connected in a vertical series known as sieve tubes. Sieve-tube elements are alive at maturity; however, before the element begins its conductive function, their nuclei dissipate. The smaller companion cells have nuclei at maturity and are living. They are adjacent to the sieve-tube elements. It is hypothesized that they control the process of conduction in the sieve tubes. Thus, when the phloem is stimulated at any



point, the action potential is propagated over the entire length of the cell membrane and along the phloem with a constant voltage.

Electrical potentials have been measured at the tissue and whole-plant level. At the cellular level, electrical potentials exist across membranes, and thus between cellular and specific compartments. Electrolytic species such as  $K^+$ ,  $Ca^{2+}$ ,  $H^+$  and  $Cl^-$  are actively involved in the establishment and modulation of electrical potentials [31–35]. The highly selective ion channels serve as natural nanodevices [25]. Voltage-gated ion channels, as nanopotentiostats, regulate the flow of electrolytic species and determine the membrane potential [25].

Light is an essential source of energy on which many of the biological functions of plants depend. The sun's radiant energy optimizes germination, photosynthesis, flowering and other processes needed to maintain homeostasis. Plants contain specific photoreceptors that perceive light ranging from UV to far-red light. Natural radiation concurrently excites multiple photoreceptors in higher plants. Specific receptors initiate distinct signaling pathways leading to wavelength-specific light responses. Photoreceptors, phototropins, cryptochromes and phytochromes have been identified at the molecular level [36–42].

Phototropins, such as PHOT1 and PHOT2, are the flavoprotein photoreceptor that responds to light with a wavelength of 360–500 nm (blue light). It regulates phototropism and intracellular chloroplast movements. PHOT1 contains two 12-kDa flavin mononucleotide (FMN)-binding domains. LOV1 (light, oxygen and voltage) and LOV2 are located within its N-terminal region and a C-terminal serine/threonine protein kinase domain. Phototropin, when activated by light, undergoes a conformational change. PHOT1 and PHOT2 bind FMN, and undergo light-dependent autophosphorylation. PHOT2 is localized in the plasma membrane. Cryptochromes and phototropin have different transduction pathways, but similar traits.

Phototropism is one of the best-known plant tropic responses. A positive phototropic response is characterized by a bending or turning toward the source of light. When plants bend or turn away from the source of light, the phototropic response is considered negative. A phototropic response is a sequence of the four following processes: reception of the directional light signal, signal transduction, transformation of the signal to a physiological response and the production of directional growth response.

After 1–2 min of irradiation, a change in the direction of irradiation generates action potentials in soybean (Fig. 13.8) depending on the wavelength of light irradiation. Irradiation at wavelengths 400–500 nm induces fast action potentials in soybean with duration time of about 0.5 ms; conversely, the irradiation of soybean at wavelengths between 500 and 600 nm fails to generate action potentials. Irradiation between 500 and 600 nm does not induce phototropism. Irradiation of soybean by blue light induces positive phototropism.

The sensitive membranes in phloem cells facilitate the passage of electrical excitations in the form of action potentials. The action potential has a stereotyped form and an essentially fixed amplitude – an “all or none” response to a stimulus. Each impulse is followed by the absolute refractory period [43, 44]. The fiber cannot

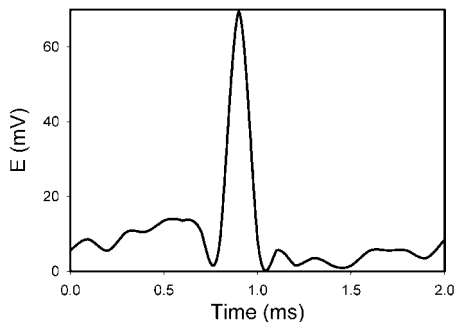


**Figure 13.8.** Action potentials in soybean induced by irradiation at 450 nm 2 min after changing the direction of irradiation. Irradiance was  $10 \mu\text{E} (\text{m}^2\text{s})^{-1}$ . Distance between electrodes was 5 cm. The soil was preliminary treated by water every day. Volume of soil was 0.5 L. Frequency of scanning was 50 000 samples  $\text{s}^{-1}$ .

transmit a second impulse during the refractory period. The integral organism of a plant can be maintained and developed in a continuously varying environment only if all cells, tissues and organs function in concordance.

These propagating excitations are theoretically modeled as traveling wave solutions of certain parameter-dependant nonlinear reaction–diffusion equations coupled with some nonlinear ordinary differential equations. These traveling wave solutions can be classified as single- and multiple-loop pulses, fronts and backs waves or periodic waves of different wave speed. This classification is matched by the classification of the electrochemical responses observed in plants. The experimental observations also show that under the influence of various pathogens, the shapes and speeds of the electrochemical responses undergo changes. From the theoretical perspective, the changes in the shapes and wave speeds of the traveling waves can be accounted by appropriate changes in parameters in the corresponding nonlinear differential equations.

Hodgkin and Huxley's membrane model [45] accounts for  $\text{K}^+$ ,  $\text{Na}^+$  and ion leakage channels in squid giant axons (Fig. 13.9A). The membrane resting potential for each ion species is treated like a battery and a variable resistor models the degree to which the channel is open. In an axon there is the  $\text{K}^+$  and  $\text{Na}^+$  transmembrane transport; conversely, in phloem cells the  $\text{K}^+$ ,  $\text{Ca}^+$  and, more than likely,  $\text{H}^+$  channels are involved in this process (Fig. 13.9B).

Some voltage-gated ion channels work as plasma membrane nanopotentiostats. Blockers of ion channels such as tetraethylammonium chloride and  $\text{ZnCl}_2$  stopped the propagation of action potentials in soybean plants induced by blue light and inhibited phototropism. Voltage-gated ionic channels control the plasma membrane potential and the movement of ions across membranes, thereby regulating various biological functions. These biological nanodevices play vital roles in signal transduction in higher plants.

All processes of life have been found to generate electric fields in every organism that has been examined with suitable and sufficiently sensitive measuring tech-

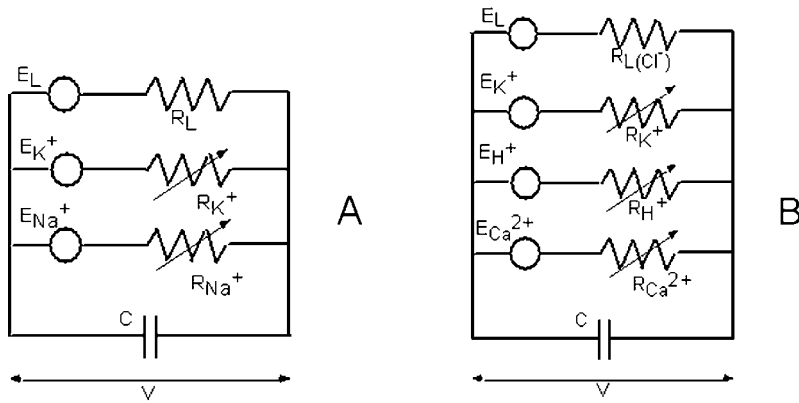


**Figure 13.9.** The Hodgkin–Huxley (HH) equivalent circuit for an axon (A) and the modified HH circuit for sieve tubes in phloem (B).

niques. The conduction of electrochemical excitation is regarded as one of the most universal properties of living organisms. It arose in connection with a need for the transmission of a signal in response to an external influence from one part of a biological system to another. The nature of regulatory relations of the plant organism with the environment is a basic bioelectrochemical problem, one that has a direct bearing on tasks of controlling the growth and development of plants.

### 13.6 Membrane Transport and Ion Channels

Membrane transport is vital to cell survival. Two major mechanisms used to transport ions and solutes across biological membranes are ion pumps and ion channels [1, 5, 46–48]. Ion transport is essential to the generation of membrane potentials, signal transduction and other biological processes. A membrane potential is a difference in electrical potential between intercellular and extracellular aqueous solutions. The membrane potential is influenced by the unequal distribution of electrolytic species inside and outside of the cell. Many intercellular proteins are negatively charged and remain inside the cell. The leakage of  $K^+$  and  $H^+$  ions is largely responsible for the generation of membrane potentials. The open  $K^+$  ion channel facilitates the outward diffusion of  $K^+$  ions without hydrolyzing ATP.

Ion channels are integral proteins that quickly facilitate the movement of specific ions across a biological membrane down their electrochemical gradient. Ion channels can facilitate the movement of approximately  $10^6$ – $10^8$  ions  $s^{-1}$  [49]. These channels are classified as mechanically gated, non-gated, voltage gated or ligand gated. Non-gated channels remain permeable to specific ions. Voltage-gated chan-

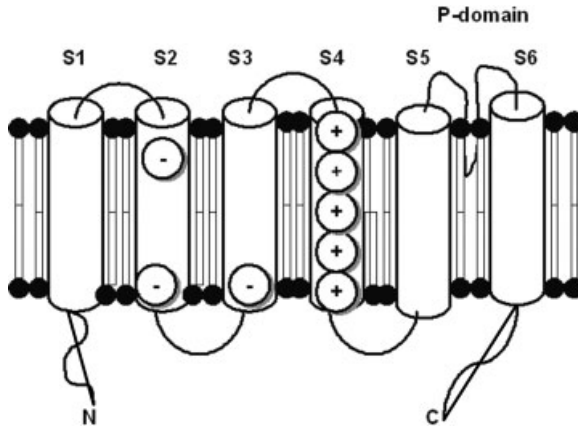


**Figure 13.10.** General architecture of the voltage-gated inward rectifying  $K^+$  channel AKT1.

nels become permeable when the membrane voltage is modulated above its threshold. Ligand-gated channels become permeable when the bound ligand is removed. Ion pumps employ a different mechanism. Ion pumps undergo conformational changes and they require energy to move specific ions against the electrochemical gradient. Ion pumps can facilitate the movement of approximately  $10\text{--}100$  ions  $s^{-1}$ . Ion channels are highly specific filters, allowing only desired ions through the cell membrane. Ion channels are devices in the engineering sense – they have signal inputs, power supplies and signal outputs. They use their complex structure to convert input signals to output signals [50, 51].

Voltage-gated channels open or close depending on the transmembrane potential. Examples include the sodium and potassium voltage-gated channels of nerve and muscle cells that are involved in the propagation of action potentials, and voltage-gated calcium channels that control neurotransmitter release in presynaptic endings. Voltage-gated channels are found in neurons, muscle cells and plant cells. Voltage-gated ion channels are membrane proteins that conduct ions at high rates regulated by the membrane potential [52–54]. Voltage-gated channels consist of three major parts – the gate, the voltage sensor and the ion-selective conducting channel (Fig. 13.10). The voltage sensor is a region of protein-bearing charged amino acids that relocate upon changes in the membrane potential. The movement of the sensor initiates a conformational change in the gate of the conductive pathway thus controlling the flow of ions. The voltage-gated  $K^+$ ,  $Na^+$  and  $Ca^{2+}$  channels have a common domain of six helical transmembrane segments S1–S6. The fourth segment, S4, is the voltage sensor of the channel and has a symmetrical arrangement of charged residues, with each third residue being arginine or lysine. A voltage-sensing domain consists of membrane segments S1–S4 and controls the conformation of gates located in the pore domain S5–S6.

Ligand-gated channels open in response to a specific ligand molecule on the external face of the membrane in which the channel resides. Examples include the

“nicotinic” acetylcholine receptor, AMPA receptor and other neurotransmitter-gated channels. Cyclic nucleotide-gated channels, Calcium-activated channels and others open in response to internal solutes, and they mediate cellular responses to second messengers. Stretch-activated channels open or close in response to mechanical forces that arise from local stretching or compression of the membrane around them. Such channels are believed to underlie touch sensation and the transduction of acoustic vibrations into the sensation of sound. G-protein-gated channels open in response to G-protein activation via its receptor. Inward-rectifier K channels allow potassium to flow into the cell in an inwardly rectifying manner, e.g. potassium flows into the cell, but not out of the cell. They are involved in important physiological processes such as the pacemaker activity in the heart, insulin release, and potassium uptake in glial cells. Light-gated channels like channelrhodopsin 1 and channelrhodopsin 2 are directly opened by the action of light [55]. Resting channels remain open at all times.

### 13.7 Molecular Motors

A molecular motor is a protein that uses energy from ATP hydrolysis or the gradient of electrochemical potentials of protons or cations to generate directed movement along filamentous track, or rotation [56–59]. There are three different classes of motor proteins that move along either actin or microtubule tracks – myosin moves along actin filaments; the kinesins and dyneins move along microtubules. Protein motors are used in nature for force generation and motion. Motor proteins convert chemical energy into mechanical force via conformational changes. One important difference between molecular motors and macroscopic motors is that molecular motors operate in an environment where thermal noise is significant relative to the motor’s energy consumption.

Myosins contain common motor domains that are responsible for muscle contraction. Myosin, like other molecular motors, uses energy obtained from ATP to travel along the action filament. Normally, myosin is bound to ADP. In the process of muscle contraction, the ADP molecule is freed when the myosin head binds to actin. An ATP molecule replaces ADP and induces a conformational change. Once changed into a ready state, the ATP is hydrolyzed. This process influences the protein to migrate from the negative end to the positive end. This migration, in addition to other processes, compels the muscle fibers to contract.

Dynein is another type of motor protein that also transforms energy from ATP hydrolysis into a form of energy that may be used to do mechanical work. This motor protein complex is composed of multiple heavy chains, intermediate chains and light chains. The heavy chain weighs approximately 530 kDa, and has four ATP-binding sites and a microtubule-binding site. The intermediate chains range from 53 to 79 kDa. The larger of the intermediate chains binds the protein to the cargo site. This binding equips the dynein with the ability to move the cargo to the negative end of a microtubule. Additional motor proteins known as kinesins move the cargo in the opposite direction to the positive end.

DNA helicases are classified as nanodevices, because they are molecular motors. One of their functions is to detach conjoined strands of DNA during genetic processes. Another function of DNA helicases is to transform the chemical energy produced from ATP into a form that may be used to perform mechanical work. A hexamer is a common type of helicase found in many organisms. Traditionally, this motor protein utilizes its multimeric structure to provide numerous DNA-binding sites.

Rotary motor proteins present in flagella are another class of motor proteins and, thus, nanodevices. The electrochemical energy is provided from the  $H^+$  or  $Na^+$  transmembrane gradient (Fig. 13.11). *Escherichia coli* and other bacteria employ rotary proteins in conjunction with the flagella to propel them in aqueous solutions. This small, yet powerful, protein complex has the capacity to rotate at a speed of approximately 20 000 r.p.m. and it is extremely energy efficient. These

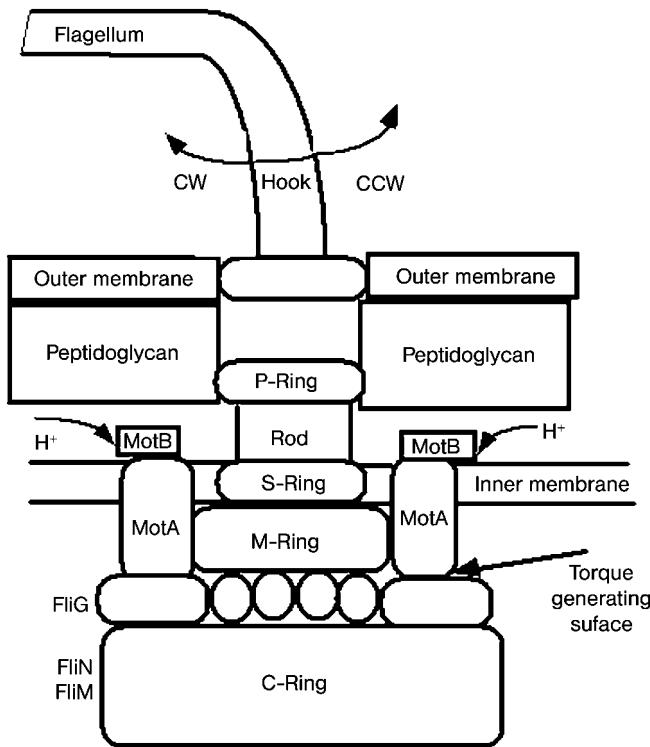


**Figure 13.11.** The bacterium flagellar motor is a rotary motor that sits in the cell envelope of bacteria. It is driven by the flow of ions ( $H^+$  or  $Na^+$ ) across the cytoplasmic membrane, and its purpose is to rotate long helical filaments that protrude from the cell and propel

swimming bacteria. The diagram depicts a Gram-negative envelope. Torque is generated by the flow of ions across the inner membrane via ion channels MotA–MotB and by interactions between MotA (stator) and FliG (rotor).

proteins reverse their rotation patterns by inducing conformational changes in the filament and the uncoupling of the associated flagellar complex, to influence the traveling direction of the bacteria. *E. coli* flagellar motors have the ability to oscillate between counterclockwise and clockwise motions, while bacteria like *Rhodobacter sphaeroides* employ clockwise motions and then pause.

### 13.8

#### Nanodevices for Electroreception and Electric Organ Discharges

Living organisms have the ability to gather, translate and respond to information regarding their environment. Electroreceptors are also classified as nanodevices; they play a crucial role in the sensory systems of various categories of animals. Sensory systems that rely on electroreception mechanisms are sophisticated in certain families of fish [60–63]. However, this sensory system is significantly more primitive in small families of amphibians and mammals. In its passive form, the electroreceptors are used to filter and map electric fields present in their surroundings. This mechanism aids in an organism's awareness of other organisms and objects within close proximity. The more active form of electroreceptor-based sensory involves the production of currents that work in harmony with sensory organs to distinguish the organism's electric field from that of any objects in the surrounding area. Once the perceived electric fields are distinguished, they are analyzed with respect to spatial and temporal structure.

Species such as the *Torpedo*, commonly referred to as the electric ray, and *Electrophorus*, also known as the electric eel, have well-developed electric organs which aid in the visualization of their present venue. The electric sensory organs dedicated to the production of high and low currents arise from altered muscle cells and nerve endings; yet the primary mechanism for the sustained electromotive force is the ion pump – a well-known nanodevice.

An electric discharge is generated when one side of the electromotor cell is stimulated, causing a potential difference to develop across the faces of the cell. The continuum of charged membranes within the electric organ is able to discharge an electric current into the environment.

The arrangements of the nerve endings in the electric organ determine the discharge patterns. In the case of the electric eel, the stimulated face discharges while the other face is at rest. Shortly following the discharge, the resting face is stimulated and then discharges. This alternating sequence allows for a series of currents to be released. Other aquatic organisms send low and irregular currents. Species employing this tactic are referred to as “pulse fish”. However, some fish expel currents at regular time intervals and are known as “wave fish.” This sensory mechanism allows for a continuous exchange of information between the organism and the environment in real-time. Lateral line nerves innervate the electric organ. Ampullary receptors are unable to perceive stimuli above 20 Hz. Conversely, tuberous receptors are unable to perceive stimuli below 30 Hz. Various species increase the rate of impulses or shorten their response times.

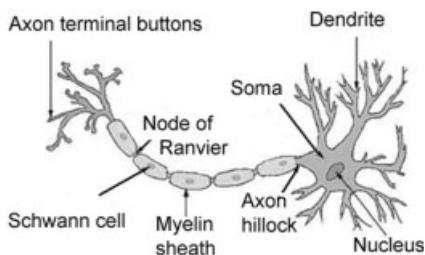


Figure 13.12. Morphology of a neuron.

### 13.9

#### Neurons

The human body is made up of approximately  $10^{13}$  cells and roughly  $10^{11}$  of them are neurons [64]. The brain is the major component of the central nervous system; it is a highly sophisticated network of neurons. There are three standard classes of neurons – afferent, efferent and interneurons. Afferent networks channel information from the surroundings to the central nervous system and efferent networks channel information away from the central nervous system to the peripheral nervous system.

Neurons are classified as microdevices, which include many nanodevices such as ion channels, enzymatic systems and different proteins. The average neuronal cell has a body, axon and dendrites (Fig. 13.12). Often referred to as the soma, the body houses the nucleus and is not extremely active in the conduction of impulses. The axons are slender projections of the soma that allow signals to travel away from the soma. In most neurons, the axon is protected by a myelin sheath. Glial cells are the main components of the sheath. Not only does the sheath serve as a protective covering, it also facilitates the rapid propagation of action potentials. The dendrites are small branches at the ends of the neuron. They are intricately connected to other dendrites forming a plexus or dendritic tree. Primarily, dendrites are responsible for receiving information. Gaps between dendrites are known as synaptic gaps and they serve as avenues for neurotransmitters to travel.

Neurons have the capability to become excited in response to various internal and external stimuli. The excitations induced are characterized as action potentials. These characteristic responses can be induced by stimuli such as applied pressure, chemical substances, thermal stimuli, electrical stimuli and mechanical stimuli.

#### References

- 1 VOLKOV, A. G., DEAMER, D., TANELIAN, D., MARKIN, V. S. *Liquid Interfaces in Chemistry and Biology*. Wiley, New York, 1998.
- 2 VOLKOV, A. G., DEAMER, D. (Eds.). *Liquid-Liquid Interfaces: Theory and Methods*. CRC Press, Boca Raton, FL, 1996.



- 3 VOLKOV, A. G. (Ed.). *Liquid Interfaces in Chemical, Biological, and Pharmaceutical Applications*. Dekker, New York, 2001.
- 4 VOLKOV, A. G. (Ed.). *Interfacial Catalysis*. Dekker, New York, 2003.
- 5 KSENZHEK, O. S., VOLKOV, A. G. *Plant Energetics*. Academic Press, New York, 1998.
- 6 VOLKOV, A. G. Molecular mechanism of the photooxidation of water during photosynthesis: cluster catalysis of synchronous multielectron reactions, *Mol. Biol.* **1986**, *20*, 728–736.
- 7 KHARKATS, YU. I., VOLKOV, A. G. Interfacial catalysis: multielectron reactions at liquid/liquid interface, *J. Electroanal. Chem.* **1985**, *184*, 435–439.
- 8 KHARKATS, YU. I., VOLKOV, A. G. Membrane catalysis: synchronous multielectron reactions at the liquid–liquid interface. Bioenergetical mechanisms, *Biochim. Biophys. Acta* **1987**, *891*, 56–67.
- 9 KHARKATS, YU. I., VOLKOV, A. G. Cytochrome oxidase: the molecular mechanism of functioning, *Bioelectrochem. Bioenerg.* **1989**, *22*, 91–103.
- 10 KHARKATS, YU. I. The calculation of the solvent energy reorganization of reactions with complex distribution of charges in reactants, *Sov. Electrochem.* **1978**, *14*, 1721–1724.
- 11 EINARSDOTTIR, O. Fast reactions of cytochrome oxidase, *Biochim. Biophys. Acta* **1995**, *1229*, 129–147.
- 12 TSUKIHARA, T., AOYAMA, H., YAMASHITA, E., TOMIZAKI, T., YAMAGUCHI, H., SHINZAWA-LTOH, K., NAKASHIMA, R., YAONO, R., YOSHIKAWA, S. The whole structure of the 13-subunit oxidized cytochrome *c* oxidase at 2.5 Å, *Science* **1996**, *272*, 1136–1144.
- 13 SUCHETA, A., GEORGIADIS, K. E., EINARSDOTTIR, O. Mechanism of cytochrome *c* oxidase-catalysed reduction of dioxygen to water: evidence for peroxy and ferryl intermediates at room temperature, *Biochemistry* **1997**, *36*, 554–565.
- 14 KHARKATS, YU. I., VOLKOV, A. G. 2:1:1 Molecular mechanism of cytochrome oxidase functioning, in: *Charge and Field Effects in Biosystems 4*, ALLEN, M. J., CLEARY, S. F., SOWERS, A. E. (Eds.). World Scientific, Hackensack, NJ, **1994**, pp. 70–77.
- 15 KHARKATS, YU. I., VOLKOV, A. G. Cytochrome oxidase at the membrane/water interface: mechanism of functioning and molecular recognition, *Anal. Sci.* **1998**, *14*, 27–30.
- 16 CHANCE, B., SARONIO, C., LEIGH, I. S. Functional intermediates in the reaction of membrane-bound cytochrome oxidase with oxygen, *J. Biol. Chem.* **1975**, *250*, 9226–9237.
- 17 ERECINSKA, M., CHANCE, B. Studies on the electron transport chain at subzero temperatures: electron transport at site III, *Arch. Biochem. Biophys.* **1972**, *151*, 304–315.
- 18 ORI, Y. M., MANABE, M., YONEDA, M. Molecular architecture of cytochrome oxidase and its transition on treatment with alkali or sodium dodecyl sulfate, *J. Biochem.* **1977**, *81*, 505–517.
- 19 HILL, R., BENDAL, P. Function of the two cytochrome components in chloroplasts: a working hypothesis, *Nature* **1960**, *186*, 136–137.
- 20 VOLKOV, A. G. Thylakoid membrane: electrochemical mechanisms of photosynthesis. The mechanism of oxygen evolution in the reaction center of photosystem II of green plants, *Biol. Membr.* **1987**, *4*, 984–993.
- 21 VOLKOV, A. G. Oxygen evolution in the course of photosynthesis, *Bioelectrochem. Bioenerg.* **1989**, *21*, 3–24.
- 22 VOLKOV, A. G. Green plants: electrochemical interfaces, *J. Electroanal. Chem.* **2000**, *483*, 150–156.
- 23 VOLKOV, A. G., MWESIGWA, J. Interfacial electrical phenomena in green plants: action potentials, in: *Liquid Interfaces in Chemical, Biological, and Pharmaceutical Applications*, VOLKOV, A. G. (Ed.). Dekker, New York, **2001**, pp. 649–681.
- 24 VOLKOV, A. G. Electrophysiology and phototropism, in: *Communication in Plants. Neuronal Aspects of Plant Life*, BALUSHKA, F., MANUSCO, S., VOLKMAN, D. (Eds.). Springer, Berlin, **2006**, pp. 351–367.

- 25 VOLKOV, A. G., DUNKLEY, T., LABADY, A., BROWN, C. Phototropism and electrified interfaces in green plants, *Electrochim. Acta* **2005**, *50*, 4241–4247.
- 26 GOLDSWORTHY, A. The evolution of plant action potentials, *J. Theor. Biol.* **1983**, *103*, 645–648.
- 27 MWESIGWA, J., COLLINS, D. J., VOLKOV, A. G. Electrochemical signaling in green plants: Effects of 2,4-dinitrophenol on resting and action potentials in soybean, *Bioelectrochemistry* **2000**, *51*, 201–205.
- 28 VOLKOV, A. G., DUNKLEY, T. C., MORGAN, S. A., RUFF II, D., BOYCE, Y., LABADY, A. J. Bioelectrochemical signaling in green plants induced by photosensory systems, *Bioelectrochemistry* **2004**, *63*, 91–94.
- 29 VOLKOV, A. G., HAACK, R. A. Insect induces bioelectrochemical signals in potato plants, *Bioelectrochem. Bioenerg.* **1995**, *35*, 55–60.
- 30 VOLKOV, A. G. (Ed.). *Plant Electrophysiology*. Springer, Berlin, **2006**.
- 31 VOLKOV, A. G., DUNKLEY, T. C., LABADY, A. J., RUFF, D., MORGAN, S. A. Electrochemical signaling in green plants induced by photosensory systems: molecular recognition of the direction of light, in: *Chemical Sensors VI: Chemical and Biological Sensors and Analytical Methods*, BRUCKNER-LEA, C., HUNTER, G., MIURA, K., VANYSEK, P., EGASHIRA, M., MIZUTANI, F. (Eds.). The Electrochemical Society, Pennington, NJ, **2004**, pp. 344–353.
- 32 SHVETSOVA, T., MWESIGWA, J., VOLKOV, A. G. Plant electrophysiology: FCCP induces fast electrical signaling in soybean, *Plant Sci.* **2001**, *161*, 901–909.
- 33 VOLKOV, A. G., MWESIGWA, J., LABADY, A., KELLY, S., THOMAS, D'J., LEWIS, K., SHVETSOVA, T. Soybean electrophysiology: effects of acid rain, *Plant Sci.* **2002**, *162*, 723–731.
- 34 LABADY, A., THOMAS, D'J., SHVETSOVA, T., VOLKOV, A. G. Plant electrophysiology: excitation waves and effects of CCCP on electrical signaling in soybean, *Bioelectrochemistry* **2002**, *57*, 47–53.
- 35 SINUKHIN, A. M., BRITIKOV, E. A. Action potentials in the reproductive system of plant, *Nature* **1967**, *215*, 1278–1280.
- 36 CASAL, J. J. Phytochromes, cryptochromes, phototropin: photoreceptor interactions in plants, *Photochem. Photobiol.* **2000**, *71*, 1–11.
- 37 QUAIL, P. H. An emerging molecular map of the phytochromes, *Plant Cell Environ.* **1997**, *20*, 657–665.
- 38 SHORT, T. W., BRIGGS, W. R. The transduction of blue light signals in higher plants, *Annu. Rev. Plant Physiol. Plant Mol. Biol.* **1994**, *45*, 143–171.
- 39 AHMAD, M., JARILLO, J. A., SMIRNOVA, O., CASHMORE, A. R. Cryptochrome blue-light photoreceptors implicated in phototropism, *Nature* **1998**, *392*, 720–723.
- 40 CASHMORE, A. R., JARILLO, J. A., WU, Y. J., LIU, D. Cryptochromes: blue light receptors for plants and animals, *Science* **1999**, *284*, 760–765.
- 41 FRECHILLA, S., TALBOTT, L. D., BOGOMOLNI, R. A., ZEIGER, E. Reversal of blue light-stimulated stomatal opening by green light, *Plant Physiol.* **2000**, *122*, 99–106.
- 42 SWARTZ, T. E., CORCHNOY, S. B., CHRISTIE, J. M., LEWIS, J. W., SZUNDI, I., BRIGGS, W. R., BOGOMOLNI, R. A. The photocycle of a flavin-binding domain of the blue light photoreceptor phototropin, *J. Biol. Chem.* **2001**, *276*, 36493–36500.
- 43 FROMM, J., BAUER, T. Action potentials in maize sieve tubes change phloem translocation, *J. Exp. Botany* **1994**, *45*, 463–469.
- 44 VOLKOV, A. G., SHVETSOVA, T., MARKIN, V. S. Waves of excitation and action potentials in green plants, *Biophys. J.* **2002**, *82*, 218a–218a.
- 45 HODGKIN, A. L., HUXLEY, A. F. A quantitative description of membrane current and its application to conduction and excitation in nerve, *J. Physiol. London* **1952**, *117*, 500–544.
- 46 HILLE, B. *Ion Channels of Excitable Membranes*. Sinauer, Sunderland, MA, **2001**.
- 47 DECOURSEY, T. E. Voltage-gated proton channels and other proton transfer pathways, *Physiol. Rev.* **2003**, *83*, 475–550.

- 48 MACKINNON, R. Potassium channels, *FEBS Lett.* **2003**, 555, 62–65.
- 49 JORDAN, P. C., MILOSHEVSKY, G. V., PARTENSKII, M. B. Energetics and gating of narrow ionic channels: the influence of channel architecture and lipid–channel interactions, in: *Interfacial Catalysis*, VOLKOV, A. G. (Ed.). Dekker, New York, **2003**, pp. 493–534.
- 50 OTTOVA, A. L., TIEN, H. Ti supported planar BLM (lipid bilayers): formation, methods of study, and applications, in: *Interfacial Catalysis*, VOLKOV, A. G. (Ed.). Dekker, New York, **2003**, pp. 421–459.
- 51 EISENBERG, B. Ionic channels as natural nanodevices, *J. Comput. Electron.* **2002**, 1, 331–333.
- 52 ARHEM, P. Voltage sensing in ion channels: a 50-year-old mystery resolved? *Lancet* **2004**, 363, 1221–1223.
- 53 GANDHI, C. S., CLARK, E., LOOTS, E., PRALLE, A., ISACOFF, E. Y. The orientation and molecular movement of a K<sup>+</sup> channel voltage-sensing domain, *Neuron* **2003**, 40, 515–525.
- 54 BEZANILLA, F. Voltage gated ion channels, *IEEE Trans. Nanobiosci.* **2005**, 4, 34–48.
- 55 NAGEL, G., SZELLAS, T., HUHN, W., KATERIYA, S., ADEISHVILI, N., BERTHOLD, P., OLLIG, D., HEGEMANN, P., BAMBERG, E. Channelrhodopsin-2, a directly light-gated cation-selective membrane channel, *Proc. Natl Acad. Sci. USA* **2003**, 100, 13940–13945.
- 56 TITUS, M. A., GILBERT, S. P. The diversity of molecular motors: an overview, *Cell. Mol. Life Sci.* **1999**, 56, 181–183.
- 57 SCHMITT, R. Helix rotation model of the flagellar rotary motor, *Biophys. J.* **2003**, 85, 843–852.
- 58 DEROSIER, D. J. The turn of the screw: the bacterial flagellar motor, *Cell* **1998**, 93, 17–20.
- 59 BERRY, R. M., BERG, H. C. Torque generated by the flagellar motor of *Escherichia coli* while driven backward, *Biophys. J.* **1999**, 76, 580–587.
- 60 BULLOCK, T. H., HOPKINS, C. D., POPPER, A. N., FAY R. R. (Eds.). *Electroreception*. Springer, New York, **2005**.
- 61 KALMIJN, A. J. Electric and magnetic field detection in elasmobranch fishes, *Science* **1982**, 218, 916–918.
- 62 HOPKINS, C. D. Lightning as background noise for communication among electric fish, *Nature* **1973**, 242, 268–270.
- 63 LISSMANN, H. W., MACHIN, K. E. Electric receptors in a non-electric fish (*Clarias*), *Nature* **1963**, 199, 88–89.
- 64 SHEPHERD, G. M. *Neurobiology*. Oxford University Press, New York, **1994**.

## Index

- a**
- activated hopping conductor, DNA conductivity 163–169
  - adsorption
    - of motor proteins 253–255
    - protein immobilization 71–74
  - AFM *see* atomic force microscopy
  - aldehyde-terminated SAMs, nanopatterns 95
  - alkanethiols
    - electrostatic immobilization 70
    - microcantilever 110
    - SAM chemistry 74–75
  - alkylsilane
    - electrostatic immobilization 70
    - SAM chemistry 76
  - aluminum mask, diamond probes 124
  - aminopropyltriethoxysilane (APTS), monolayer 286–292
  - analyte capture, kinetics 19–24
  - analyte detection, fluorescence microscopy 269
  - analyte–receptor binding 19–20
  - Anderson and Chaplain's model 40–45
  - anisotropic wet etching 118
  - antiangiogenic drugs, chemotherapy model 57
  - antibody capture domains, virus patterning 143
  - apertured pyramidal tips, nanofluidic systems 126–128
  - APTS *see* aminopropyltriethoxysilane
  - arrays
    - BSA 93
    - cantilever 8–11, 97–101
    - DPN probe 118
    - fluid-coupled 16
    - microcantilever sensor 112–115, 118–121
    - microneedle 136–137
    - microtubule 261–263
    - millipede 100
    - protein dot 81
  - assays
    - development 94
    - immuno- 142
    - kinesin 248–249
    - surface 69–76
  - associative memories, holographic 180
  - atomic force microscopy (AFM) 2, 67
    - cantilever arrays 98–99
    - diamond probes 123
  - Au(111)-surfaces, SAM chemistry 75
  - avidin–fluorescein isothiocyanate (FITC) 81
  - azurin, protein devices 182
- b**
- B–Z device 197–198
  - background noise, cantilever 4
  - bacteriorhodopsin (BR), protein devices 179
  - bandgap behavior, DNA conductivity 169–170
  - base pair, DNA electron transfer 162
  - bead assay, kinesin 248
  - Bell's deterministic model, receptor–ligand-mediated binding 49–52
  - bias-induced electrochemistry, DPN 91
  - bias-induced lithography 78, 81
  - biased-induced SPL 81
  - bifurcation, flow simulations 45
  - binding
    - analyte–receptor 19–21
    - electrostatic-mediated 70
    - receptor–ligand 47–54
  - binding affinity, analyte capture 21
  - bio-building blocks, fundamentals 153–155
  - bio-self-assembly 150
  - bioanalysis, kinesin–microtubule-driven systems 245–269
  - bioassays development 94

- biochip technology development 96
  - biofunctionalized nanoelectromechanical systems (BIONEMS) 1–28
  - biological scales 1
  - biomolecules, immobilization 69–76
  - biomotor-driven transport 249–253
  - BIONEMS *see* biofunctionalized nanoelectromechanical systems
  - biosensors 221–240
    - microcantilever 337–346
    - nanodevices 321–348
    - nanomechanical 334–348
    - nanophotonic 325–333
    - protein binding detection 94
    - SAMs 224–225
    - single-molecule 7
  - biotin–avidin chemistry, cargo attachment 263–264
  - biotin–streptavidin, ligand–receptor binding 20
  - blood cells, flow simulations 45
  - BOE *see* buffered oxide etching
  - bond formation, Bell's deterministic model 51
  - bonds distribution, stochastic model 52
  - boron-doped silicon, microcantilever sensor array 117
  - bovine serum albumin (BSA) 71
    - latex particle lithography 93
  - BR *see* bacteriorhodopsin
  - branched photocycle 3-D optical memories 180
  - Brownian noise, cantilever 4
  - BSA *see* bovine serum albumin
  - buckling, immobilized microtubules 257
  - buffered oxide etching (BOE) solution, NFP 140
- C**
- cancer cells, folate-targeting 48
  - cancer employing liposomes 29
  - cancer treatment 30
  - cantilever arrays 8–11
    - development 97–101
  - cantilever bending, nanomechanical biosensors 335
    - *see also* microcantilever sensors
  - cantilever microspotter
    - microfabrication process 129
    - open-channel 128–133
  - cantilever probes
    - microfabrication process 127
    - nanopatterning 116–121
  - cantilever tip, noise detection 24
  - cantilevered nanopipettes 133–136
  - cantilevers 126–141
    - autocorrelation function 17–18
    - cross-correlation function 17–18
    - doped silicon 81
    - fabrication process 123–124
    - fluid-coupled array 16
    - functionalization 19
    - models 11–16
    - nanofabrication 84
    - oscillating 2
    - passive 3
    - quill-type 130
    - spring constant 15
    - stochastic oscillations 5
  - carbon nanotube field-effect transistors (CNTFETs) 281–282
    - DNA electronics 176
    - performance 292–295
  - carbon nanotubes (CNTs) 2
    - basic features 278–280
    - device applications 281–282
    - DNA linkage 299–302
    - DNA-directed self-assembly 295–308
    - in situ CVD growth 284–285
    - SAMs 285–295
    - self-assembly and bio-directed approaches 276–308
    - synthesis 280–281
  - cargo attachment, microtubules 263–266
  - cations, conformational DNA changes 197–200
  - cell chips, cantilevered microspotters 128
  - cell diffusion, Anderson and Chaplain's model 41
  - cell flow, blood 45
  - cell kill, chemotherapy model 55
  - cellular drug kinetics 54–61
  - charge transfer, DNA 161–163
  - charge transport, proteins 155
  - chemical interactions, time scales 2
  - chemical vapor deposition (CVD), CNT growth 284–285
  - chemotherapy model
    - refinement 57–61
    - two-dimensional 55–57
  - cisplatin, compartment model 57, 59
  - clathrin, receptor–ligand-mediated binding 49
  - closed-channel cantilevered nanopipettes 133–136
  - CNT transistors 281–282
    - fabrication 282–284

- CNTFETs *see* carbon nanotube field-effect transistors
- CNTs *see* carbon nanotubes
- collision-coupling rate constant, ligand-receptor binding 22
- compartment model 57–59
- conductance, DNA, temperature dependence 168
- conductive diamond probes 122–126
- conformation fluctuations, equilibrium 235–239
- conformational changes, DNA 197–200
- contact-mode topograph, nanografting 82
- continuum, fluids 5
- correlated noise, cantilever 4
- covalent immobilization 70–71
- cowpea mosaic virus (CPMV), DPN 89
- CPMV *see* cowpea mosaic virus
- critical force
- Bell's deterministic model 51
  - stochastic model 52
- CVD *see* chemical vapor deposition (CVD)
- Cy3 fluorescent dye, nanofluidic systems 127
- Cy3-streptavidin sample, cantilevered microspotters 132
- d**
- damping, cantilever dynamics 12–13
- delivering molecules 157–159
- delivery systems 29
- density of states (DOS), DNA conductivity 169
- deterministic model, Bell 49–52
- deterministic response, cantilever dynamics 10
- device implementation, bio-building blocks 155–159
- dG(C<sub>10</sub>)<sub>2</sub>, self-assembly 177
- diamond film 123
- diamond probes 122–126
- diffusion, kinesin-microtubule-driven systems 251–253
- dip-pen nanolithography (DPN) 88–91
- diamond probes 125
  - microcantilevers 110, 118
  - molecular delivery 158
  - NFP 139
  - silicon nitride 141
- dispensing tip, NFP 138
- displacement fluctuations, cantilever dynamics 13
- DNA
- autonomous behavior 213–216
  - bio-building blocks 153–154
  - microtubule cargos 264–265
  - DNA bases 159–178
    - energy levels 163
  - DNA-bound drug, chemotherapy model 60
  - DNA chips 177–178
  - DNA-CNT linkage 299–302
  - DNA conductivity 163–178
  - DNA-directed self-assembly, CNT fabrication 295–308
  - DNA electronics 175–176
  - DNA immobilization detection, nanomechanical biosensors 346
  - DNA nanodevices 193–216
    - simple 197–202
  - DNA patterning 141–142
  - DNA-protein interaction 206–209
  - DNA repair 160
  - DNA scaffolds
    - CNTs 296–302
    - metalization 302–307
  - DNA tiles 296–297
  - DNA tweezers 200–201
  - DNA walkers 203–206
  - DNA/RNA chimera 213
  - doped films, diamond probes 123
  - doped silicon, cantilevers 81
  - DOS *see* density of states
  - double crossover (DX) molecules, DNA tiles 296–297
    - doxorubicin, compartment model 59
  - DPN *see* dip-pen nanolithography
  - DRAM half-pitch, nanobioelectronics 151
  - drug delivery
    - chemotherapy model 57
    - nanodevices 29–66
  - drug flow simulation, Anderson and Chaplain's model 42–44
  - drug kinetics 54–61
  - DTT pesticide detection, nanomechanical biosensors 347
  - DX *see* double crossover
  - dynamic mode detection, nanomechanical biosensors 335
- e**
- EBL *see* electron beam lithography
- EDP *see* ethylene-diamine pyrocatechol
- EIS *see* electrochemical impedance spectroscopy
- elasticity theory, cantilever dynamics 11
- elastomeric AFM probes 121–122
- elastomeric tips 122
- electrical addressing, DNA scaffolds 298
- electrical connections, CNTs 302–307

- electrical property measurements, single protein devices 222  
 electrochemical impedance spectroscopy (EIS) 223, 226  
 electron beam lithography (EBL), miniaturization 152  
 electron transfer rate, DNA 161–163  
 electronic conductors, DNA bases 160  
 electrophoresis, microneedle arrays 137  
 electrostatic immobilization, protein linking 70  
 electrostatic interactions, DPN 88  
 electrostatic molecule trapping, interconnecting molecules 157  
 encounter complex, Bell's deterministic model 50  
 endocytosis, folate-targeting 48  
 endothelial cell density, Anderson and Chaplain's model 41  
 energy levels, DNA bases 163  
 environmental scanning electron microscopy (SEM) 117  
 equation of motion, cantilever dynamics 12  
 equilibrium fluctuations 9  
 – protein conformation 235–239  
 etching  
 – anisotropic 118  
 – microcantilever sensor array 115  
 ethylene-diamine pyrocatechol (EDP), microcantilever sensor array 118  
 evaporation, molecular delivery 158
- f**
- FETs *see* field-effect transistors  
 FIB *see* focused ion beam  
 fibronectin, Anderson and Chaplain's model 40  
 field-effect transistors (FETs)  
 – carbon nanotube 281–282  
 – DNA applications 173  
 – DNA-templated 181  
 – guanosine-based 174  
 filaments, interaction with synthetic surfaces 253–256  
 films, nitrogen-doped 123  
 FITC *see* avidin–fluorescein isothiocyanate  
 flow simulations, Anderson and Chaplain's model 40–45  
 fluctuating force, cantilever dynamics 13  
 fluctuation–dissipation theorem, cantilever dynamics 8  
 fluctuations  
 – autocorrelation 10  
 – displacement 14
- fluid dynamics  
 – cantilevers 8–11  
 – small scale 4–19  
 fluorescence microscopy, cantilevered microspotters 132  
 – kinesin–microtubule-driven systems 267–269  
 fluorescent detection, protein binding 94  
 focused ion beam (FIB) 126  
 folate-targeting, liposomes 47–48  
 folic acid, receptor–ligand-mediated binding 47  
 force constant, microcantilevers 112, 117  
 force-induced nanolithography 82–88  
 force magnitudes, biologically relevant 1  
 forces, modeling 35  
 free energies, PEO chain 35  
 functional groups, covalent immobilization 71  
 functionalized surfaces, GPCRs 224–225
- g**
- G-protein-coupled receptors (GPCRs) 221–240  
 – electrical response 226  
 – on functionalized surfaces 224–225  
 G quartets, DNA 202  
 genetic control, DNA nanodevices 214–216  
 GFP *see* green fluorescent protein  
 Gillespie approach, analyte capture 23  
 GIXD *see* grazing incidence X-ray diffraction  
 gliding assay, kinesin 248  
 glioblastoma, chemotherapy model 55  
 gold surfaces, microcantilever 110  
 gold thin films, SAM chemistry 75  
 GPCR *see* G-protein-coupled receptor  
 grazing incidence X-ray diffraction (GIXD) 75  
 green fluorescent protein (GFP), protein devices 179  
 growth processes, invasion percolation model 38  
 guanosine-based FET 174
- h**
- haptotaxis, Anderson and Chaplain's model 41  
 helical structure, DNA 154  
 hemodynamics 35–47  
 – invasion percolation model 37–40  
 high-density DNA chips, cantilevered microspotters 128  
 high-throughput screening (HTS) 221

- highest occupied molecular orbital (HOMO), DNA conductivity 169
- HIV-1 *see* human immunodeficiency virus type 1
- Holliday junction analogues, DNA tiles 296
- holographic associative memories, protein devices 180
- HOMO *see* highest occupied molecular orbital
- hopping conductor, activated 163–169
- HTS *see* high-throughput screening
- human immunodeficiency virus type 1 (HIV-1)
- protein binding detection 95
  - protein patterning 142
- humidity, protein patterns 91
- hybrid biodevices, processing steps 156
- hybrid materials, DNA 211–212
- hybrid transistor, protein devices 182
- hybridization-driven devices 200–202
- hydrophobic attraction, free energy 36
- hypodermic needle arrays, micromachined 136
- i**
- IBL *see* ion-beam lithography
- IgG *see* immunoglobulin G
- immobilization
- biomolecules 69–76
  - covalent 70–71
  - DNA 346
  - electrostatic 70
  - IgG 85
  - lysozyme 88
  - microtubule 255–256
  - microtubule arrays 261–263
  - protein 69, 71–74
- immunoglobulin G (IgG)
- immobilization 85
  - surface assays 69
- impedance fluctuations, rhodopsin 235–239
- impedance network model, nanobiosensors 228–235
- in-plane microneedles 136
- in situ CVD growth, CNTs 284–285
- information processing, DNA 210–211
- insulating behavior, DNA conductivity 170
- integrated fluids, cantilevers 126–141
- integrated Mach–Zehnder interferometer (MZI) 326–334
- interconnecting molecules 156–157
- interconnection, bio-building blocks 155–159
- intratumoral drug kinetics 54–61
- invasion percolation model 37–40
- ion-beam lithography (IBL), miniaturization 152
- j**
- juxtaposed (JX2) configuration, DNA 201, 203
- k**
- kinesin
- cell biology and biophysics 246–249
  - motility assays 248–249
  - stability and lifetime 266–268
- kinesin–microtubule-driven systems 245–269
- directing 256–259
  - fluorescence microscopy 267–269
  - transport properties 249–253
- kinetic equation, analyte–receptor binding 20
- kinetic rate constants, Bell's deterministic model 50
- Knudsen number, fluid dynamics 5
- KOH *see* potassium hydroxide
- l**
- lab-on-a-chip microsystems 321, 333
- Langmuir–Blodgett techniques, molecular delivery 158
- latex particle lithography 91–94
- LEEPS *see* low-energy electron point source
- life sciences, microcantilevers 111
- ligand–receptor binding 19–21
- surface-enhanced 22
- light-directed method, DNA scaffolds 299
- liposomal delivery systems 29
- liposomes, folate-targeting 47
- liquid flow, nanofluidic systems 126
- lithography
- bias-induced 78
  - force-induced 82, 85
  - latex particle 91–94
  - surface engineering 67
- low-energy electron point source (LEEPS) microscopy, interconnecting molecules 157
- low-pressure chemical vapor deposition (LPVCD) 118
- lowest unoccupied molecular orbital (LUMO), DNA conductivity 169
- low-temperature silicon oxide (LTO), cantilevered microspotters 129
- LPCVD *see* low-pressure chemical vapor deposition
- LTO *see* low-temperature silicon oxide



- LUMO *see* lowest unoccupied molecular orbital
- lysozyme immobilization, DPN 88
- m**
- Mach-Zehnder interferometer (MZI), nanodevice 326–334
- Markus theory, quantum mechanical tunneling 161
- M-DNA 174
- memory devices 180
- protein 179
- MEMS *see* microelectromechanical systems
- meniscus, NFP 138
- 16-mercaptohexadecanoic acid (MHDA)
- DPN 88
  - HIV-1 immunoassay 142
  - microcantilever sensor array 118
  - SAMs 225
- 11-mercaptoundecanoic acid (11-MUA), nanografting 82–83
- metal complexes, DNA 304
- metal–insulator–metal nanojunction 183
- metal surfaces, SAM chemistry 74
- metalization, DNA scaffolds 302–307
- metarhodopsin, impedance modulus 237–239
- MHA *see* 16-mercaptohexadecanoic acid
- MHDA *see* 16-mercaptohexadecanoic acid
- micro-spotting technique, DNA scaffolds 298
- microcantilever sensors 113, 337–346
- microcantilevers 110–149
- parallelization 110
- microchannels
- microneedle arrays 136
  - microtubule movement 259–261
  - PDMS 267
- microelectromechanical systems (MEMS) 321–323
- microfabrication 112–116
- microfluidic dispensing probes, NFP 137
- microfluidic systems
- cantilevers 126–141
  - transport properties 249–253
- micromachined hypodermic needle arrays 136
- micromolding 114
- microneedle arrays 136
- fabrication steps 137
- micropipette pullers, nanopipettes 134
- microspotters, cantilevered 128–133
- microtubule arrays, immobilization 261–263
- microtubule gliding assay 248
- microtubule immobilization 255–256
- microtubules
- cargo attachment 263–266
  - cell biology and biophysics 246–249
  - microchannel movement 259–261
  - oriented 256–263
- microwave plasma CVD (MPCVD) 123
- millipede array, cantilever development 100
- miniaturization, fundamental limits 151
- modeling, nanodevices 29–66
- molding-pit cantilevers, fabrication 114
- molecular delivery 157–159
- molecular electronics
- DNA applications 173–178
  - miniaturization 152
- molecular lithography 181
- molecular motors 245–247
- molecular orbital gap, DNA conductivity 169
- molecular photodiode, protein devices 180
- molecular recognition
- nanografting 86
  - protein immobilization 71
- molecules, interconnecting 156–157
- monolayers
- APTS 286–292
  - self-assembled *see* self-assembled monolayers (SAMs)
- monolithically fabricated conductive diamond probes 122–126
- Moore's Law, nanobioelectronics 150–151
- MOSFET behavior, protein devices 184
- motor proteins, interaction with synthetic surfaces 253–256
- MPCVD *see* microwave plasma CVD
- 11-MUA *see* 11-mercaptoundecanoic acid
- multidrug resistance effect, receptor–ligand-mediated binding 49
- multiple-cantilever SPT, microfabrication process 132–133
- multiply charged cations, conformational DNA changes 197–200
- multiwall CNTs (MWCNTs) 278–280
- MWNTs *see* multiwall CNTs
- MZI *see* Mach-Zehnder interferometer
- n**
- NanoArrayer, cantilevered microspotters 132
- nanobioelectronics 150–192
- nanobiosensors 221–240, 321–348
- impedance network model 228–235
  - signal techniques 225–226
  - *see also* biosensors
- nanocircuit applications, CNTs 302–307
- nanodevices
- biosensors *see* biosensors

- DNA 193–216
  - drug delivery 29–66
  - fabrication 276–308
  - microcantilever-based 110–149
  - nanoelectromechanical systems (NEMS) 126, 321–323
  - biofunctionalized 1–28
  - nanoelectronic device applications, CNTs 281–282
  - nanofabrication
    - AFM-based 77
    - surface components 81
  - nanofluidic systems, cantilevers 126–141
  - nanofountain probe (NFP) 126, 137–141
    - chip fabrication 139
    - second generation 140
  - nanografting 82–88
  - nanojunction, metal–insulator–metal 183
  - nanolithography 67–108
    - bias-induced 78
    - force-induced 82–88
    - protein 76–94
  - nanomechanical biosensors 334–348
  - nanoparticle chemotherapy, model 56, 58
  - nanoparticle delivery systems 29
  - nanopatterning 116–121
    - methods 79
    - molecular delivery 159
  - nanophotonic biosensors 325–333
  - nanopipettes, cantilevered 133–136
  - nanoscale detection 96–97
  - nanostructured scaffolds, DNA 296–302
  - nanotube transistors 281–282
    - *see also* CNT transistors
  - nanovector performance, critical phases 30, 61
  - nanovector surface coverage, statistical model 31–34
  - Navier–Stokes equations 5
  - near-edge X-ray absorption fine structure (NEXAFS) 75
  - near-field scanning optical microscopy (NSOM), microcantilever 110
  - near-ohmic behavior, DNA conductivity 163–169
  - needle arrays, hypodermic 136
  - NEMS *see* nanoelectromechanical systems
  - network growth processes, invasion
    - percolation model 38
  - network model, impedance 228–235
  - NEXAFS *see* near-edge X-ray absorption fine structure
  - NFP *see* nanofountain probe (NFP)
  - nitrogen-doped films, diamond probes 123
  - n-methyl pyrrolidone (NMP) 287–290
  - noise
    - cantilever 4, 16
    - detection 24–25
  - NSOM *see* near-field scanning optical microscopy
  - nucleic acids
    - biophysical and biochemical properties 194–197
    - microtubule cargos 264–265
  - Nyquist plot, network impedance 234
- o**
- octadecanethiol (ODT)
    - microcantilever sensor array 118
    - surface topography 75
  - open-channel cantilevered microspotters 128–133
  - opsonization, prevention 31
  - optical memories, branched photocycle 3-D 180
  - OR-I7
    - activated state 227
    - interaction network 231–232
  - order/disorder transition (ODT) 83
  - organic conductors, DNA 154
  - oscillator
    - stochastic dynamics 4–19
    - target analyte capture 19–24
  - oxidation, bias-induced 78
- p**
- palladium layer, microneedle arrays 136
  - parallelization, microcantilever 110
  - paranemic crossover (PX) conformation, DNA 201, 203
  - particle dynamics, tumoral vasculature 45–47
  - particle flow distribution 46
  - particle lithography 78, 91–94
  - patterning
    - nano- *see* nanopatterning
    - of DNA 141–142
    - of proteins *see* protein patterning
    - of viruses 143
  - PDMS *see* poly(dimethylsiloxane)
  - Peclet number, analyte capture 22–23
  - PEG *see* poly(ethylene glycol)
  - peptides, synthetic 88
  - percolation model 37–40
  - pharmacodynamics 54–61
  - phase space, microscopic 9
  - photodiode, molecular 180

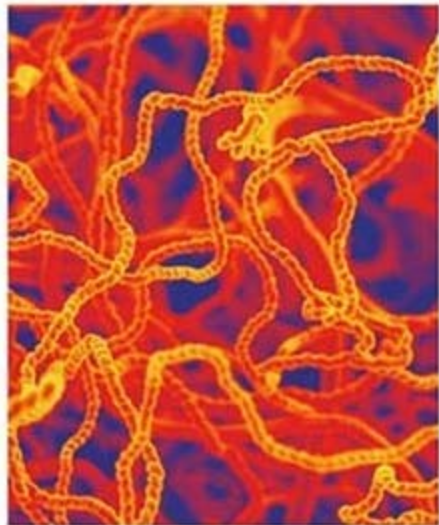
- photolithography, interconnecting molecules 157  
 piezoelectric actuator, microcantilever sensor array 113  
 piezoresistivity, nanomechanical biosensors 335  
 PLA *see* poly(lactic acid)  
 PMMA *see* poly(methyl methacrylate)  
 poly(dA)–poly(dT), near-ohmic behavior 166  
 poly(dG)–poly(dC)  
   – insulating behavior 170  
   – near-ohmic behavior 166  
 poly(dimethylsiloxane) (PDMS)  
   – microcantilever sensor array 121  
   – microchannels 267  
 poly(ethylene glycol) (PEG),  
   reticuloendothelial system 31  
 poly(lactic acid) (PLA), reticuloendothelial system 31  
 poly(methyl methacrylate) (PMMA) 81  
   – APTS monolayers 286–287  
 polymer chain, modeling 32  
 potassium hydroxide (KOH), microcantilever sensor array 112–115  
 printheads, cantilevered microspotters 128  
 probability distribution, polymer chain 32  
 protein adsorption, SAM chemistry 76  
 protein binding  
   – detection 94–96  
   – forces 35  
   – nanografting 86  
   – nanovector surface coverage 31  
 protein chips, cantilevered microspotters 128  
 protein conformation, equilibrium fluctuations 235–239  
 protein devices 178–186  
 protein dot arrays, bias-induced  
   nanolithography 81  
 protein immobilization  
   – strategies 72–73  
   – surface assays 69  
 protein interaction, DNA 206–209  
 protein machines 245–269  
 protein monolayer 183  
 protein nanolithography 76–94  
 protein nanostructures, particle lithography 92  
 protein patterning 67  
   – bias-induced lithography 81  
   – cantilevers 142  
   – DPN 89  
   – force-induced SPL 87  
 protein solutions, nanopipettes 134  
 proteins  
   – bio-building blocks 154–155  
   – DPN 88–91  
   – latex particle lithography 91–94  
   – microtubule cargos 263–264  
   – receptor 221–240  
   – stability and lifetime 266–268  
 protons, conformational DNA changes 198–199  
 PX conformation, DNA *see* paranemic crossover conformation  
 pyramidal tips, apertured 126–128
- q**  
 QMT *see* quantum mechanical tunneling  
 quantum mechanical tunneling (QMT), DNA 161  
 quartz capillary tubes, nanopipettes 134  
 quill-type cantilever 130
- r**  
 real-time AFM images, nanofabrication 84  
 RecA nucleoprotein, DNA metalization 305–307  
 receptor–ligand binding 30, 47–54  
 receptors, G-protein-coupled 221–240  
 repair rate, chemotherapy model 60  
 RES *see* reticuloendothelial system  
 reticuloendothelial system (RES) 30  
 Reynolds number 6  
 rhodopsin  
   – activated state 227  
   – impedance modulus 236–239  
   – interaction network 231–232  
 RNA, microtubule cargos 264–265
- s**  
 SAMs *see* self-assembled monolayers  
 scales, biological 1  
 scanning ion conductance microscopy (SICM),  
   nanopipettes 135  
 scanning probe lithography (SPL) 67  
   – biased-induced 81  
 scanning probe microscopy (SPM) 67  
   – microcantilever 110  
   – protein binding detection 94  
 scanning tunneling microscopy (STM),  
   microcantilever 110  
 SDS *see* sodium dodecylsulfate  
 self-assembled monolayers (SAMs) 19, 110  
   – biosensors 224–225  
   – chemistry 74–76  
   – CNT fabrication 285–295  
   – DNA-directed 295–308

- DPN 88–91
  - nanografting 82
  - nanolithography 78, 82–88
  - surface engineering 68
  - self-assembly
    - bio-building blocks 155–159
    - molecular electronics 152
  - SEM *see* scanning electron microscopy
  - semiconducting behavior, DNA conductivity 169–170
  - sensitivity, cantilever 25
  - sensor array, microcantilever 113
  - sensor performance evaluation 21
  - sensors *see* biosensors
    - *see also* nanobiosensors
  - SICM *see* scanning ion conductance microscopy
  - signal-processing, noise detection 24–25
  - signal-to-noise ratio (SNR), cantilever tip 25
  - silicon nitride DPN tips 141
  - silicon nitride layer, microcantilever sensor array 115
  - silicon-on-insulator (SOI), cantilevered microspotters 129
  - single-molecule biosensor 7
  - single protein devices, electrical property measurements 222
  - single-wall CNTs (SWNTs) 177, 278–280
    - SAM technique 285–295
  - smart bricks, DNA scaffolds 296–297
  - SNR *see* signal-to-noise ratio
  - sodium dodecylsulfate (SDS) 287
  - SOI *see* silicon-on-insulator
  - spatial distribution, polymer chain 33
  - specific interaction, protein immobilization 71
  - spectroscopy, electrochemical impedance *see* electrochemical impedance spectroscopy
  - spin-coating, molecular delivery 158
  - SPL *see* scanning probe lithography
  - SPM *see* scanning probe microscopy
  - spot size, cantilevered microspotters 130
  - spring constant, microcantilever sensor array 113
  - SPT cantilevers, microfabrication process 131
  - static mode detection, nanomechanical biosensors 335
  - step force, cantilever dynamics 9
  - steric repulsion, protein binding 35–36
  - STM *see* scanning tunneling microscopy
  - stochastic dynamics, cantilever arrays 8–11
  - stochastic model, receptor–ligand-mediated binding 52–54
  - Stokes equations 7
  - streptavidin, ligand–receptor binding 20
  - surface adsorption, protein immobilization 71–74
  - surface assays 69–76
  - surface components, nanofabrication 81
  - surface coverage
    - liposomes 34
    - nanovector 31–34
  - surface-enhanced ligand–receptor binding 22
  - surface topography, SAM chemistry 75
  - surfaces
    - engineering 67–69
    - metal 74
    - protein linking 69–74
  - switchable networks, DNA 211–212
  - SWNTs *see* single-wall CNTs
  - synthetic peptides, DPN 88
  - synthetic surfaces, interaction with motor proteins 253–256
- t**
- TAF *see* tumor angiogenic factor (TAF)
  - target analyte capture 19
  - targets, tumor cells 47
  - TDSA *see* thermodynamically driven self-assembly
  - tetrathiafulvalene-tetracyano-*p*-quinodimethane (TTF-TCNQ) 154
  - TFT *see* thin-film transistor
  - thermal hopping, charge transfer 161
  - thermodynamic equilibrium, cantilever dynamics 8
  - thermodynamically driven self-assembly (TDSA), molecular delivery 158
  - thin-film transistor (TFT) 185
  - thin films
    - microcantilevers 111
    - SAM chemistry 75
  - thin oxide film, microcantilever sensor array 118
  - thiol endgroups
    - SAM chemistry 74
    - nanografting 82
  - tip
    - coating 116–117
    - elastomeric 122
    - pyramidal 126–128
    - radii 110
    - sharpness 114
    - silicon nitride 141
  - tip integration, fabrication methods 116
  - tip surface, functionalization 141

- topology, tumoral vasculature 37
  - Torchilin's model 32
  - transfer rate, chemotherapy model 60
  - transistors, nanotube *see also* CNT
    - transistors, 281–282
  - transport, biomotor-driven 249–253
  - transport characterization techniques 157
  - transport process, analyte capture 23
  - transport properties, DNA conductivity 172
  - triple crossover (TX) molecules, DNA tiles 296–297
  - TTF-TCNQ *see* tetrathiafulvalene-tetracyano-*p*-quinodimethane
  - tumor angiogenic factor (TAF) 40
  - tumoral tissue, invasion percolation model 39
  - tumoral vasculature 35–47
    - particle dynamics 45–47
  - TX *see* triple crossover
  - type-1 probe array 119
  - type-2 probe array 120
- u**
- ultra-nanocrystalline diamond (UNCD) 123–125
- v**
- vascular topology, chemotherapy model 55
  - vasculature, tumoral 35–47
  - vasculogenesis, invasion percolation model 37–40
  - vector
    - ligand-conjugated 54
    - nanoscale 31–34
  - vessel bifurcation 45
  - vessel occupancy, invasion percolation model 37
  - ViriChip, cantilevers 143
  - virus patterning 143
  - viscosity, fluid dynamics 6
- w**
- walker systems, DNA 203–206
  - water meniscus, nanopatterning 117
  - wear characteristics, diamond probes 122
  - Weibull model, pharmacodynamics 54
  - wet etching
    - anisotropic 118
    - elastomeric AFM probes 121
- Y**
- Young's modulus, cantilever dynamics 11



# Nanomaterials – Toxicity, Health and Environmental Issues



## Contents

	<b>Preface</b>	<i>XII</i>
	<b>List of Authors</b>	<i>XVI</i>
<b>I</b>	<b>Toxicity</b>	<i>1</i>
<b>1</b>	<b>Biotoxicity of Metal Oxide Nanoparticles</b>	<i>3</i>
	<i>Amanda M. Fond and Gerald J. Meyer</i>	
1.1	Introduction	<i>3</i>
1.2	Nanoparticles in the Environment	<i>5</i>
1.3	How Nanoparticles are Introduced into Mammalian Systems	<i>7</i>
1.4	Health Threats	<i>8</i>
1.5	Nanomaterials and Biotoxicity	<i>9</i>
1.5.1	Iron Oxide	<i>9</i>
1.5.2	Titanium Dioxide	<i>13</i>
1.5.2.1	Dark Studies	<i>14</i>
1.5.2.2	UV Irradiation Studies	<i>18</i>
1.5.3	Other Metal Oxides	<i>25</i>
1.6	Conclusions	<i>28</i>
	Acknowledgment	<i>29</i>
	References	<i>29</i>
<b>2</b>	<b>Ecotoxicity of Engineered Nanomaterials</b>	<i>35</i>
	<i>Eva Oberdörster, Patricia McClellan-Green, and Mary Haasch</i>	
2.1	Introduction	<i>35</i>
2.2	Water	<i>38</i>
2.3	Air	<i>42</i>
2.4	Soils	<i>42</i>
2.5	Weathering	<i>43</i>
2.6	Biomarkers	<i>44</i>
2.7	Conclusions	<i>46</i>
	References	<i>47</i>



II	<b>Health</b>	51
3	<b>Possible Health Impact of Nanomaterials</b>	53
	<i>Peter H. M. Hoet, Irene Bröske-Hohfeld, and Oleg V. Salata</i>	
3.1	Introduction	53
3.2	Sources of Nanoparticles	53
3.3	Epidemiological Evidence	54
3.4	Entry Routes into the Human Body	56
3.4.1	Lung	57
3.4.1.1	Inhalation, Deposition and Pulmonary Clearing of Insoluble Solids	57
3.4.1.2	Biopersistence of Inhaled Solid Material	59
3.4.1.3	Systemic Translocation of Inhaled Particles	60
3.4.2	Intestinal Tract	61
3.4.2.1	Deposition and Translocation	61
3.4.2.2	Intestinal Translocation and Disease	62
3.4.3	Skin	62
3.4.3.1	Deposition and Penetration through the Skin	62
3.4.3.2	Irritation of Skin	64
3.5	What Makes Nanoparticles Dangerous?	64
3.5.1	Particle Size – Surface and Body Distribution	65
3.5.1.1	Effect of Size	65
3.5.1.2	Effect of Surface Charges	65
3.5.2	Nanoparticles, Thrombosis and Lung Inflammation	67
3.5.2.1	Prothrombotic Effect	67
3.5.2.2	Oxidative Stress, Inflammation and Endotoxins	68
3.5.3	Nanoparticles and Cellular Uptake	69
3.5.4	Nanoparticles and the Blood–Brain Barrier	69
3.6	Summary and Discussion	69
3.7	What Can be Done?	71
	References	72
4	<b>Dosimetry, Epidemiology and Toxicology of Nanoparticles</b>	81
	<i>Wolfgang G. Kreyling, Manuela Semmler-Behnke, and Winfried Möller</i>	
4.1	Introduction	81
4.1.1	Overview	81
4.1.2	General Background	81
4.1.3	Epidemiological Evidence for Health Effect Associations with Ambient Particulate Matter	83
4.1.4	Toxicological Evidence for Ambient Particulate Matter Induced Adverse Health Effects	84
4.2	Inhaled Nanoparticle Dosimetry	85
4.2.1	Particle Measures	85
4.2.2	Deposition of Ultrafine Particles in the Respiratory System	86
4.2.3	Fate of Particles in the Lungs	87
4.2.3.1	Soluble Particle Compounds	87

4.2.3.2	Slowly Dissolving and Insoluble Particles Deposited on the Airway Wall	87
4.2.3.3	Slowly Dissolving and Insoluble Particles Deposited in the Alveolar Region	87
4.2.3.4	Macrophage-mediated Particle Transport	88
4.2.4	Translocation of Ultrafine Particles into Systemic Circulation	88
4.2.4.1	Studies of Systemic Particle Translocation in Humans	88
4.2.4.2	Studies of Systemic Particle Translocation in Animals	89
4.3	Toxicological Plausibility of Health Effects Caused by Nanoparticles	93
4.3.1	Pulmonary Inflammation Induced by Ultrafine Particles	94
4.3.2	Systemic Inflammation and other Responses	95
4.3.3	Relevant Parameters in Nanoparticle Toxicology	96
4.3.3.1	Number Concentration and Surface Area	96
4.3.3.2	Particle Shape (Fibers and Nanotubes)	97
4.3.3.3	Transition Metals	98
4.3.3.4	Organic Compounds	99
4.3.3.5	Extrapolation of Health Effects Observed in Animals towards Human	100
4.4	Integrated Concept of Risk Assessment of Nanoparticles	101
	References	103
<b>5</b>	<b>Impact of Ceramic and Metallic Nano-scaled Particles on Endothelial Cell Functions <i>in Vitro</i></b>	<b>108</b>
	<i>Kirsten Peters, Ronald E. Unger, Antonietta M. Gatti, Enrico Sabbioni, Andrea Gambarelli, and C. James Kirkpatrick</i>	
5.1	Introduction	108
5.1.1	Origin of Particles in the Human Environment	108
5.1.1.1	Evidence for Size-dependent Toxicity of Particles	109
5.1.1.2	Dissemination and Interferences of Nanoparticles within the Body	109
5.1.1.3	Endothelial Cells and Nanoparticle Exposure	110
5.1.1.4	Testing of Nanoparticle-induced Effects on Human Endothelial Cells <i>In Vitro</i>	110
5.2	Materials and Methods	111
5.2.1	Cell Culture	111
5.2.2	Particles	111
5.2.3	Transmission Electron Microscopy (TEM)	111
5.2.4	Cytotoxicity Assay	111
5.2.5	Detection of Ki67 Expression	112
5.2.6	Quantification of IL-8 Release in Cell Culture Supernatant	112
5.2.7	Quantification of E-selectin Cell Surface Protein Expression	112
5.2.8	Fluorescence Staining	113
5.2.9	Statistical Analysis	113
5.3	Results	113
5.4	Discussion	120
5.4.1	Particle Internalization	121

VIII | Contents

5.4.2	Particle Cytotoxicity	122
5.4.3	Pro-inflammatory Activation	123
5.4.4	Conclusions and Consideration of the Risk of Nanoparticles to Human Health	124
	Acknowledgments	125
	References	125
<b>6</b>	<b>Toxicity of Carbon Nanotubes and its Implications for Occupational and Environmental Health</b>	<b>130</b>
	<i>Chiu-wing Lam, John T. James, Richard McCluskey, Andrij Holian, and Robert L. Hunter</i>	
6.1	Introduction	130
6.1.1	Overview	130
6.1.2	General Background	131
6.2	Carbon Nanotubes and Nanotechnology	131
6.3	Manufactured Carbon Nanotubes: Their Synthesis, Properties, and Potential Applications	132
6.3.1	Discovery and Synthesis	132
6.3.2	Physical and Chemical Properties	133
6.3.3	Applications	134
6.4	Occurrence of Carbon Nanotubes in the Environment	134
6.4.1	Potential Occupational Exposures and Environmental Impact of Manufactured Carbon Nanotubes	134
6.4.2	Combustion-generated Carbon Nanotubes in the Environment	136
6.4.2.1	MWCNT Formation from Natural Gas Combustion Indoors	137
6.4.2.2	MWCNTs in Metropolitan Outdoor Air	137
6.4.2.3	MWCNTs in Ancient Ice	137
6.4.2.4	Concern about Combustion-generated MWCNTs in the Environment	138
6.4.3	Comparison of the Physical Structures of Manufactured and Non-manufactured Carbon Nanotubes	139
6.5	Toxicological Studies and Toxicity of Manufactured CNTs	139
6.5.1	Study of SWCNTs in Guinea Pigs by Huczko et al. of Warsaw University	142
6.5.2	Study of SWCNTs in Mice by Lam et al. of NASA-JSC Toxicology Laboratory	142
6.5.3	Study of SWCNTs in Rats by Warheit et al. of DuPont Company	143
6.5.4	Study of SWCNTs in Mice by Shvedova et al. of NIOSH	145
6.5.5	Study of MWCNTs by Muller et al. of Belgium	146
6.6	Health Risk Implications	146
6.6.1	Toxicity Summary of CNTs and Occupational Exposure Risk	146
6.6.2	Impact of SWCNTs on Environmental Health	147
6.6.3	Toxicity of MWCNTs and Impact on Environmental Health	147
	Acknowledgment	148
	References	149

<b>7</b>	<b>Toxicity of Nanomaterials – New Carbon Conformations and Metal Oxides</b>	<b>153</b>
	<i>Harald F. Krug, Katrin Kern, Jörg M. Wörle-Knirsch, and Silvia Diabaté</i>	
7.1	Introduction	153
7.1.1	Nanoscale Materials and Adverse Health Effects: Precautionary Measures	155
7.1.2	Hazard Identification and Exposure Estimation	156
7.2	Production and Use of “New Carbon Modifications” and Metal Oxides	157
7.2.1	Health Aspects	159
7.2.2	Uptake and Possible Transport, Depots, and Accumulation in Living Organisms	160
7.2.3	Biological Effects on Cellular Mechanisms	164
7.2.3.1	Metal Oxides	165
7.2.3.2	New Carbon Modifications	169
7.2.4	Possible Hazards – Toxicological Impacts	175
7.3	Risk Characterization – A Conclusion	176
7.3.1	Opportunities and Risks of Nanomaterials	177
7.3.2	New Materials without Risks?	177
	References	179
<b>III</b>	<b>Environment</b>	<b>187</b>
<b>8</b>	<b>Nanomaterials for Environmental Remediation</b>	<b>189</b>
	<i>Glen E. Fryxell and Shas V. Mattigod</i>	
8.1	Introduction	189
8.2	Nanoparticle-based Remediation Materials	190
8.2.1	Acid–Base Chemistry	191
8.2.2	Redox Chemistry	194
8.2.3	Field Deployments of ZVI	195
8.2.4	Absorption Chemistry	196
8.3	Hybrid Nanostructured Remediation Materials	196
8.3.1	Nanostructured Metal Phosphonates	196
8.3.1.1	Iminodiacetic Acids and Related Chelating Ligands	198
8.3.1.2	Macrocyclic Metal Phosphonates	199
8.3.2	Self-assembled Monolayers on Mesoporous Supports (SAMMS)	200
8.3.2.1	Thiol SAMMS Performance with Actual Waste	200
8.3.2.2	Thiol SAMMS Performance on Contaminated Oil	202
8.3.2.3	Anion SAMMS	203
8.3.2.4	Actinide SAMMS	204
8.3.3	Functional CNTs	204
8.4	Conclusions	205
	References	206

<b>9</b>	<b>Nanomaterials for Water Treatment</b>	<b>211</b>
	<i>Peter Majewski</i>	
9.1	Introduction	211
9.2	Iron Nanoparticles	214
9.3	Inorganic Photocatalysts	217
9.4	Functionalized Self-assembled Monolayers	221
9.5	Other Materials	225
9.6	Magnetic Iron Exchange Resin (MIEX)	226
	References	227
<b>10</b>	<b>Nanoparticles for the Photocatalytic Removal of Endocrine-disrupting Chemicals in Water</b>	<b>234</b>
	<i>Heather M. Coleman</i>	
10.1	Introduction	234
10.2	Background to Oestrogens in the Environment	235
10.2.1	Advanced Oxidation Techniques (AOTs)	237
10.2.2	Ultraviolet Photolysis	238
10.3	Nanoparticles for Water Treatment Applications	238
10.3.1	Titanium Dioxide Photocatalysis	239
10.3.1.1	The Principle	239
10.3.1.2	Titanium Dioxide Nanoparticles as a Photocatalyst	240
10.3.1.3	Mechanism of TiO <sub>2</sub> Photocatalysis	241
10.4	Photocatalytic Degradation of 17 $\beta$ -Oestradiol in Water over an Immobilized TiO <sub>2</sub> Catalyst	243
10.5	Rapid Loss of Oestrogenicity of Natural and Synthetic Oestrogens in Water by Photocatalysis and UVA Photolysis Monitored using a Yeast Screen Bioassay	245
10.6	Photocatalytic Degradation of 17 $\beta$ -Oestradiol, Oestriol and 17 $\alpha$ -Ethinylestradiol in a Quartz Coil Reactor Monitored using Fluorescence Spectroscopy	251
10.7	Comparison of Photocatalysis with UVA and UVC Radiation for the Degradation of Natural and Synthetic Oestrogens in Water	259
10.8	Overall Conclusions and Identification of Research Needs	262
	References	265
<b>11</b>	<b>Nanosensors for Environmental Applications</b>	<b>271</b>
	<i>Wan Y. Shih and Wei-Heng Shih</i>	
11.1	Introduction	271
11.1.1	Overview	271
11.1.2	Sensor	271
11.1.3	Piezoelectric Cantilever Sensors (PECS)	273
11.2	Theory of PECS	273
11.2.1	Unimorph	274
11.2.2	PECS with a Nonpiezoelectric Extension	275
11.3	Examples of Detections	278

11.3.1	Immobilization and In-solution Quantification of Yeast Cells	278
11.3.2	Detection of Binding of Biotinylated Polystyrene Spheres to Immobilized Avidin	280
11.3.3	Detection of Avidin Immobilization at the Cantilever Tip	281
11.3.4	<i>Salmonella typhimurium</i> Detection	281
11.3.5	Nerve Gas Simulant Detection	286
11.4	Piezoelectric Cantilever Miniaturization	287
11.4.1	PMN-PT/Cu Microcantilevers and PZT/SiO <sub>2</sub> -Si <sub>3</sub> N <sub>4</sub> Nanocantilevers	288
11.4.2	PZT/SiO <sub>2</sub> Microcantilevers	289
11.5	Conclusions	290
	Acknowledgment	291
	References	291
<b>12</b>	<b>Toxicology of Nanoparticles in Environmental Air Pollution</b>	<b>294</b>
	<i>Ken Donaldson, Nicholas Mills, David E. Newby, William MacNee, and Vicki Stone</i>	
12.1	Introduction	294
12.2	History of Air Pollution	294
12.3	Introduction to Air Pollution Particles	296
12.4	Adverse Effects of PM in Epidemiological Studies	296
12.5	Nanoparticles are an Important Component of PM	298
12.6	Role of Nanoparticles in Mediating the Adverse Pulmonary Effects of PM	300
12.7	Effects of Nanoparticles on the Cardiovascular System	302
12.8	Inflammation, Atherosclerosis and Plaque Rupture	303
12.9	Nanoparticle Translocation and Direct Vascular Effects	304
12.10	Endothelial Dysfunction and Endogenous Fibrinolysis	305
12.11	Coagulation and Thrombosis	307
12.12	Cardiac Autonomic Dysfunction	308
12.13	Effects of Nanoparticles on the Liver and Gastrointestinal Tract	308
12.14	Effects of NP on the Nervous System	310
12.15	Summary	310
	References	310
	<b>Index</b>	<b>319</b>

## Preface

It is my pleasure to welcome the readers back to *Nanotechnologies for the Life Sciences* with the first volume published in 2006. I am presenting to you, on behalf of yet another dedicated team of contributors and supporters, the fifth volume, *Nanomaterials – Toxicity, Health and Environmental Issues*, of the ten volume series. We are bringing the fifth volume while the fourth is still in print for a number of reasons. The most important being the fact that a potential \$1 trillion nanotechnology market hinges on understanding the toxic effects of nanomaterials on our health and environment. With continuous world-wide increase in both government and private funding in nanoscience and nanotechnology touching close to \$35 billion, the stakes are even higher. With increase in stakes, there is a worldwide awakening to understand the toxic effect of nanomaterials and the scholarly chapters presented in this book are testimony to the efforts of several research groups to understand these effects. While the current knowledge base is small compared to what needs to be understood, it certainly provides a scaffold for this knowledge base to take definite shape.

Some of the critical risk assessment issues that are currently being investigated by the health & environmental nano researchers are toxicology, exposure assessment, environmental and biological fate, transport, persistence, transformation, recyclables and overall sustainability of manufactured nanomaterials. I am aware that the scientific data generated so far is very scanty and requires more worldwide concerted effort in this direction. Nevertheless, the amount of information presented by the authors covers almost everything of what is currently available in the literature. The book is divided into three distinct sections in an attempt to emphasize the three major issues related to nanomaterials, which are toxicology, health and environment. The boundaries are only artificial and have been created for the sake of clarity. I am aware that the three issues are interrelated, yet unique in their own way. I am also aware the field is very nascent and hence there could be some amount of overlap in terms of information that is presented in the chapters. However, the USP of the book is that all the chapters provide very unique and intellectually stimulating perspectives on the most important topics in the field of nanoscience and nanotechnology.

The first section of the book deals, in general, with issues around the toxicity of nanomaterials and begins with a scholarly report on the toxic effects of metal oxide

nanoparticles which are by far, commercially, the most significant materials as they find applications in cosmetics, sunscreens, fillers in dental materials, water filtration processes, catalysis, glare-reducing coating for glasses, and so on. Amanda M. Fond and Gerald J. Meyer from the Department of Chemistry, Johns Hopkins University, USA have reviewed the literature, in addition to capturing their own findings, on biotoxicity of metal oxide nanoparticles keeping the emphasis more on *in vitro* rather than *in vivo* studies. In this chapter entitled, *Biotoxicity of Metal Oxide Nanoparticles*, their critical analysis provides to the reader possible mechanisms by which the metal oxide nanoparticles enter the environment and the body, and the potential health impacts that might be expected. Eva Oberdörster from Southern Methodist University, Patricia McClellan-Green from NC State University and Mary Haasch from University of Mississippi have collaborated to present their critical evaluation in the second chapter, *Ecotoxicity of Engineered Nanomaterials*, impact of nanomaterials on the environment, and more specifically on air, water and soil. In addition, readers will find very useful the authors' insight into how the activity of nanomaterials is effected by extraneous factors such as abiotic factors, microbial degradation/activation and identification of biomarkers associated with nanoparticle exposure.

In the second section of the book, illuminating perspectives on the effect of nanomaterials on health are presented. Relative to the increased use of nanomaterials in a variety of industrial applications, the amount of information regarding their health effects is limited. Peter Hoet from Katholieke Universiteit Leuven, Belgium, Irene Brüske-Hohlfeld from GSF-Forschungszentrum für Umwelt und Gesundheit, Germany, and Oleg V. Salata from Sir William Dunn School of Pathology, University of Oxford, UK, teamed up in order to review the epidemiological studies of the technogenic nanoparticles and to highlight the apparent health effects associated with the inhalation of ultrafine particulate matter. The third chapter by them, aptly entitled *Possible Health Impact of Nanomaterials*, provides information on likely pathways for nanoparticulates in general and nanofibers in particular inside the body, the effects associated with their interactions on the cellular level, and analysis of the origins of bioactivity of nanomaterials. Continuing on the same theme, chapter number four, *Dosimetry, Epidemiology and Toxicology of Nanoparticles*, describes the dosimetry, epidemiology and toxicology of nanoparticles with reference to generally well established principles and paradigms. The chapter is contributed by Wolfgang G. Kreyling, Manuela Semmler and Winfried Möller from GSF-National Research Centre for Environment & Health, Institute for Inhalation Biology, Focus-Network Aerosols and Health, and Clinical Research Group 'Inflammatory Lung Diseases' respectively, from Germany. The highlight of the chapter, in my view, is described best by the authors themselves: "extrapolating findings and principles observed in particle inhalation toxicology into recommendations for an integrated concept of risk assessment of nanoparticles for a broad range of use in science, technology and medicine." Focusing more specifically on ceramic and metallic nanoparticles, the team lead by Kirsten Peters from Institute of Pathology, Johannes Gutenberg University, Germany, discusses in chapter five their effects on primary human endothelial cells which are highly relevant for



nanoparticle transmigration from the blood into tissues. The chapter, *Impact of Ceramic and Metallic Nano-Scaled Particles on Endothelial Cell Functions in vitro*, clearly helps readers to understand, with an example of pro-inflammatory stimulation of endothelial cells by nanoparticles, that even though it is clear that the nanoparticles exert effects that are relevant in vivo, these cannot be easily interpreted and may not be of relevance in vivo. The sixth chapter, *Toxicity of Carbon Nanotubes and its Implications for Occupational and Environmental Health*, written by the team lead by Chiu-Wing Lam from the Division of Space Life Sciences, NASA Johnson Space Center, and Wyle Laboratories, Houston, USA, is a comprehensive review on the toxicological risk of carbon nanotubes (CNT) and the impurities present in them due to inhalation exposures using both rodent and in vitro cell culture studies. In addition, the authors discuss the mechanisms of CNT pathogenesis in the lung and other toxicological manifestations. In view of the growing expectations that CNTs will find extraordinary applications in the field of not only life sciences but also in electronics, computer, and aerospace industries, the chapter is timely and will be a single source of information for the readers. The final chapter in this section is the seventh chapter, wherein the authors review the latest results from various studies on the biological effects of nanoparticles that may be the basis for adverse effects, especially in humans. The chapter, *Toxicity of Nanomaterials – New Carbon Conformations and Metal Oxides*, provides a comparative study on two most important classes of nanomaterials, viz carbon and metal oxide based nanomaterials, with respect to their cellular uptake and possible influence on important cellular mechanisms in vitro. The chapter is a testimony to the intensive analysis on the topic carried out by the authors Harald F. Krug, Katrin Kern, Jörg M. Wörle-Knirsch, and Silvia Diabate from the Institute of Toxicology and Genetics at Forschungszentrum Karlsruhe, Germany.

The final section and the most important one, in my view, is dedicated to the investigations related to impact of nanomaterials on environment. While the chapters 1–7 in the previous sections dealt with possible negative effects of nanomaterials, this section portrays the positive aspects of nanomaterials. The first chapter in this section (8th in the book) is contributed by Glen E. Fryxell and Shas V. Matigod of Materials Chemistry and Surface Research Group, Pacific Northwest National Laboratory, USA. In this chapter, *Nanomaterials for Environmental Remediation*, the authors address one of the key global political and economic issues of the 21<sup>st</sup> century – how does one ensure that the majority of the world population has clean environment in general and air & water in particular in future? An analysis of nanoparticle-based remediation technologies for air and water treatment including field tests on actual waste streams is presented. Moving into the ninth chapter, readers will find more specific information regarding the variety of approaches being utilized for treatment of water with nanomaterials. In this chapter, entitled *Nanomaterials for Water Treatment*, Peter Majewski of Ian Wark Research Institute, University of South Australia, Australia, is upbeat about various technologies currently under development and more specifically about the approach using magnetic iron exchange resin (MIEX) which is already commercially applied in water treatment. It is heartening to read the next chapter, chapter ten, wherein

Heather Coleman from the Centre for Particle and Catalyst Technologies of the University of New South Wales, Sydney, Australia, elaborates on how nanotechnologies are proving to be playing a major role in alleviating the concerns about the release into the aquatic environment of natural and synthetic oestrogens and compounds that have the ability to mimic oestrogens. In this chapter, *Nanoparticles for the Photocatalytic Removal of Endocrine Disrupting Chemicals in Water*, the author describes nanoscale titanium dioxide photocatalysis for the degradation of the natural and synthetic oestrogens in water. Chapter eleven by Wan Y. Shih and Wei-Heng Shih, Department of Materials Science and Engineering, Drexel University, Philadelphia, USA, is very unique in the sense that the authors describe their own investigations into the development of piezoelectric microcantilever sensors of different sizes and types that can perform rapid, in-situ, in-water pathogen detection with sensitivities well above that of the current techniques. The chapter describes both theoretical and experimental studies that were carried out to characterize the sensors. While the information provided in the chapter, *Nanosensors for Environmental Applications*, clearly demonstrates that we have a long way to go before realizing the dream of fabricating truly nanosize sensors, it is hoped that the chapter will form a strong basis for readers in designing their own nanosensors for environmental applications. The final chapter, *Toxicology of Nanoparticles in Environmental Air Pollution* by Ken Donaldson and his collaborators, puts forward the evidence that nano-sized air pollutants play adverse role on our health. I confess that this chapter could have been included in the previous section. However, since the chapter describes nanosized particulate matter present in the natural environment, I have decided to include it in this section. As a final chapter, I also wanted the reader to take home the message that while certainly nanomaterials can be utilized to clean up our environment and treat variety of diseases, one needs to be aware of the deleterious effects of nano-sized particulate matter in the environment.

In the end, I would like to state that I am indeed very grateful to all the authors for their contribution of quality manuscripts on time. I am thankful to my employer, family, friends and Wiley-VCH publishers for making this book a reality. I am always indebted to you, the reader, who is an integral part of this journey into brining nanotechnologies to life sciences and life sciences into nanotechnologies. I am eagerly waiting to receive your comments, suggestions and constructive criticism to make this journey even more enjoyable and a learning experience for all.

March 2006, Baton Rouge

Challa S. S. R. Kumar

I  
Toxicity



## 1

## Biototoxicity of Metal Oxide Nanoparticles

*Amanda M. Fond and Gerald J. Meyer*

## 1.1

### Introduction

Nanotechnology is a relatively new and evolving field. Although the uses and technological advances in nanotechnology are endless, very little is known about its future consequences or impacts. This leaves some a little skeptical about current research and advances. Concerns range from the health and economic impacts that the once popular material asbestos had on society [1] to nanotechnology careening out of control [2]. However, even though nanotechnology is a fairly new field, nanomaterials are not. Some nanomaterials stem back to the 10<sup>th</sup> century, such as nanometer-diameter particles of gold and silver, which were used in stained glass and ceramics to generate different hues [3]. In addition, Egyptians were thought to have consumed colloidal gold, believing that it would raise vitality [4]. Nowadays, nanoparticles are frequently found in such commercial products as cosmetics and sunscreens (TiO<sub>2</sub>, Fe<sub>2</sub>O<sub>3</sub>, and ZnO), fillers in dental fillings (SiO<sub>2</sub>), water filtration processes, catalysis, and glare-reducing coating for glasses. In addition, they are currently being used in the development of stain and wrinkle-free fabrics and to make longer-lasting tennis balls [5].

Metal oxide nanoparticles have a rich history with applications in food, materials, and chemical and biological studies. The thermodynamically stable form of most metals are their oxides. In many cases metal oxides, e.g., SiO<sub>2</sub>, TiO<sub>2</sub>, ZnO, have been approved by the Food and Drug Administration for decades [6]. It is, therefore, tempting to assume that metal oxide nanoparticles will also be non-toxic. However, as this chapter demonstrates, and asbestos toxicity has taught us, the shape, size and morphology can also play a significant role in biotoxicity [5].

For such a rapidly growing field, surprisingly little is known about either nanotoxicology or the toxicity of nanoparticles. Funding for nanotoxicology is necessary because nanomaterials often behave differently than their bulk counterparts. At the nanoscale, the surface area of particles greatly increases and can result in a higher reactivity of the material, since the surface atoms now dominate the particle's physical and chemical properties. The material's electrical, optical and thermal properties change and quantum effects become significant [1]. For example, gold

particles are inert when in bulk material; however, gold nanoparticles are highly reactive and are used in catalysis.

Donaldson et al. concluded that ultrafine particles cause more inflammation than larger respirable particles of the same material when delivered at the same mass dose. Although the exact role of ultrafine particle toxicity remains unknown, experimental evidence showed that ultrafine particles inhibit phagocytosis more than fine particles of the same mass. In addition, even when composed of low toxicity materials, ultrafine particles caused inflammation in the lungs. Many believe it is because of the large surface area of ultrafine nanoparticles [7, 8].

Both *in vivo* and *in vitro* studies are currently underway around the world to evaluate the biotoxicity of metal oxide nanoparticles. However, difficulty arises in marrying these two sets of experiments. Hart states that the main reason *in vivo* and *in vitro* studies are not complementary is due to biopersistence, which relies on particle dissolution rate and the capability of the particles to be translocated out of the lung [9]. In addition, *in vitro* studies are used to measure more short-term toxicity effects and fail to look at how a specific cell type will interact when incorporated with other cell types within an animal. However, *in vivo* studies can prove to be very time consuming and costly.

This chapter will only review *in vitro* biotoxicity literature reports with metal oxide nanoparticles, and broadly overviews mechanisms by which they enter mammalian systems. *In vitro* studies help in the understanding of toxicity mechanisms at a molecular level, information that is difficult if not impossible to gain from *in vivo* studies. In addition, *in vitro* studies make it possible to determine a relationship between toxicity and particle characteristics [9]. Therefore, this chapter will cover literature studies of metal oxide nanoparticles with cells, bacteria and biopolymers, and will not cover the vast breadth of animal studies found in the literature. Additionally, studies on sulfides, selenides, noble metals or organic coatings are not included. However, notably, these particles may prove to have biotoxic effects as well.

First, it is worth defining “nanomaterial” as descriptions in the literature often vary. The National Nanotechnology Initiative defines nanotechnology as: (1) Research and technology development involving structures with at least one dimension on the 1–100 nm range. (2) Creating/using structures, devices, systems that have novel properties and functions because of their nanometer scale dimensions. (3) The ability to control or manipulate on the atomic scale [5]. Here, we have adopted a broader definition and have included all studies of metal oxide materials with length scales less than 1000 nm, as a result of the size relationships of ultrafine particles and cellular structures described by Donaldson (Fig. 1.1) [8].

In the remainder of this chapter we discuss the mechanisms by which nanoparticles enter the environment and the body, and the potential health impacts that might be expected. We then review literature including biotoxicity studies of cells with metal oxide nanoparticles. The literature in this area is conveniently divided into areas based on materials: (a) iron oxide; (b) titanium dioxide; and (c) other oxides. In addition to reviewing the published literature, some background on the materials is also included.

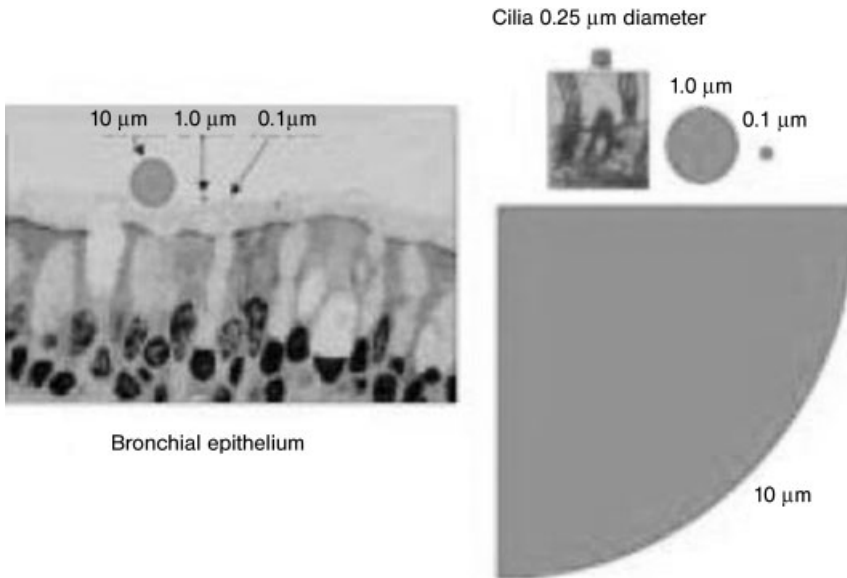


**Fig. 1.1.** Left-hand side: relationship between ultrafine particles and cellular structures of the lung. Right-hand side: same three particles relative to cilia. (Figure taken from Donaldson [8] with permission from the BMJ Publishing Group.)

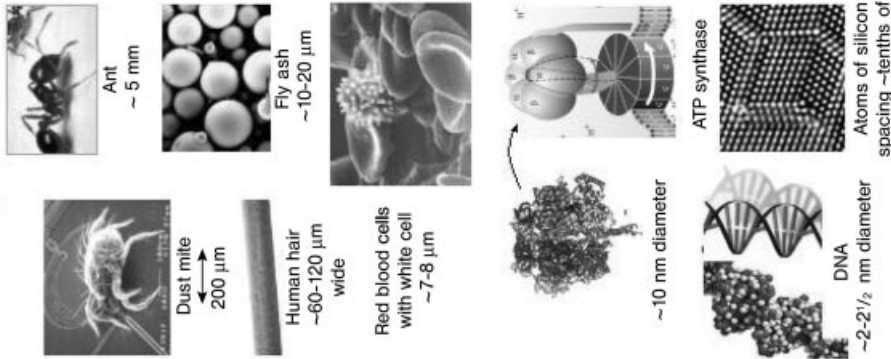
## 1.2 Nanoparticles in the Environment

According to the U.S. Department of Labor, in the U.S. alone, 2 million people work with nanometer-diameter particles regularly in development, production, and use of nanomaterials and products [10]. The National Institute for Occupational Safety and Health (NIOSH) claimed that between 1997 and 2005 the U.S. government investment went from \$432 million to \$1240 million per year [5], and by 2015 global investment is expected to be \$1 trillion [11]. If growth continues as expected, an additional 2 million workers will be required worldwide [5].

Nature has also utilized “nanotechnology.” Nanoparticles are found everywhere in the environment. Natural materials such as proteins and colloids, like milk, are composed of nanoparticles. Indeed, most subcellular structures are “nanomaterials.” The left-hand side of Fig. 1.2 shows additional examples [12]. Man-made particles produced as a by-product of industry are also a source of nanoparticles in the environment (Fig. 1.2) [12]. However, the lack of information on the environmental impact of nanoparticles has society concerned. Some of these concerns have been brought to the attention of the Department of Health and Human Services. As a result, the National Toxicology Program is assessing the health effects associated with nanoscale materials, such as size and composition dependent biological

# The scale of things - nanometers and more

## Things natural



## Things manmade

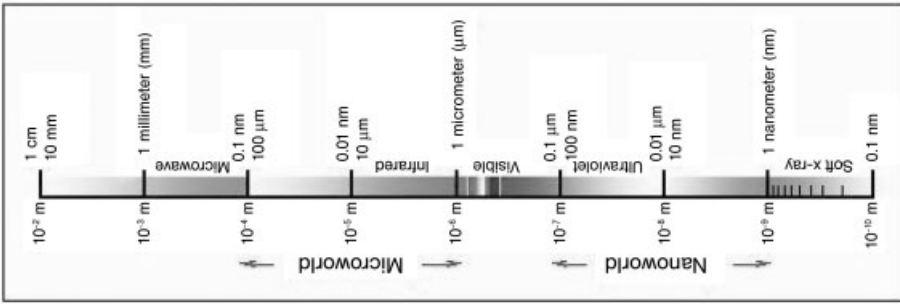
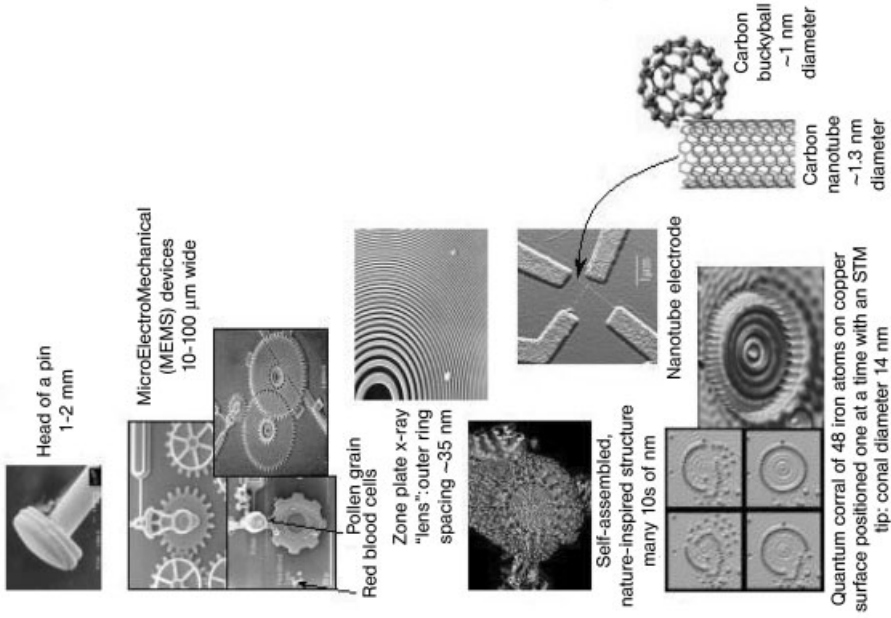
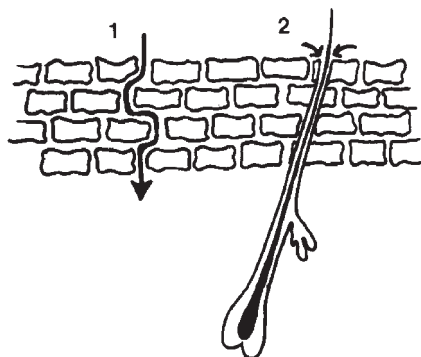


Fig. 1.2. Examples of natural and synthetic nanometer-sized materials. (Figure adapted from [www.nano.gov](http://www.nano.gov) [12].)





**Fig. 1.3.** Penetration routes of nanoparticles into human skin. Path 1 shows an intercellular route and path 2 a route through a hair follicle. (Figure taken from Bennat [15] with permission from Blackwell Publishing.)

disposition of fluorescent semiconductor nanomaterials and the phototoxicity of metal oxide nanoparticles [13].

### 1.3

#### How Nanoparticles are Introduced into Mammalian Systems

Currently, there is a vague understanding of a nanoparticles' path of entry into one's system, cell uptake, distribution, and health effects. Three main routes of nanoparticle exposure are penetration through the skin, ingestion, and exposure by inhalation – from which the particles may then be able to translocate from the respiratory system to other organs [14].

There can be two routes of entry into the skin, transepidermal intercellular or penetration via pores and hair follicles (Fig. 1.3). Bennat et al. believe that  $\text{TiO}_2$  nanoparticles penetrate the skin through the lipids of hair follicles. They found that the more hair follicles in the skin, the deeper the  $\text{TiO}_2$  nanoparticle penetration. Furthermore,  $\text{TiO}_2$  particles from an oily dispersion penetrated deeper than those from an aqueous solution, possibly because the palmitic acid component of the skin lipids was acting as a penetration enhancer [15]. In contrast, a separate study using pig skin samples showed that the stratum corneum layer of the skin effectively prevented dermal uptake of an oil-in-water emulsion of  $\text{TiO}_2$  particles (20–50 nm) [16]. Animal studies, quantified by autoradiography, in which emitted radiation is measured from a tissue specimen that has been treated with a radioactively labeled isotope, have indicated that  $\text{ZnO}$  nanoparticles pass through rat and rabbit skin [17–19]. Therefore, some reports raise the idea that it may be possible for  $\text{ZnO}$  and  $\text{TiO}_2$  nanoparticles to pass through human skin. For example, particles of 10–50 nm in diameter would be able to penetrate skin because the intracellular space in the stratum corneum is around 100 nm [20, 21], and the gap in

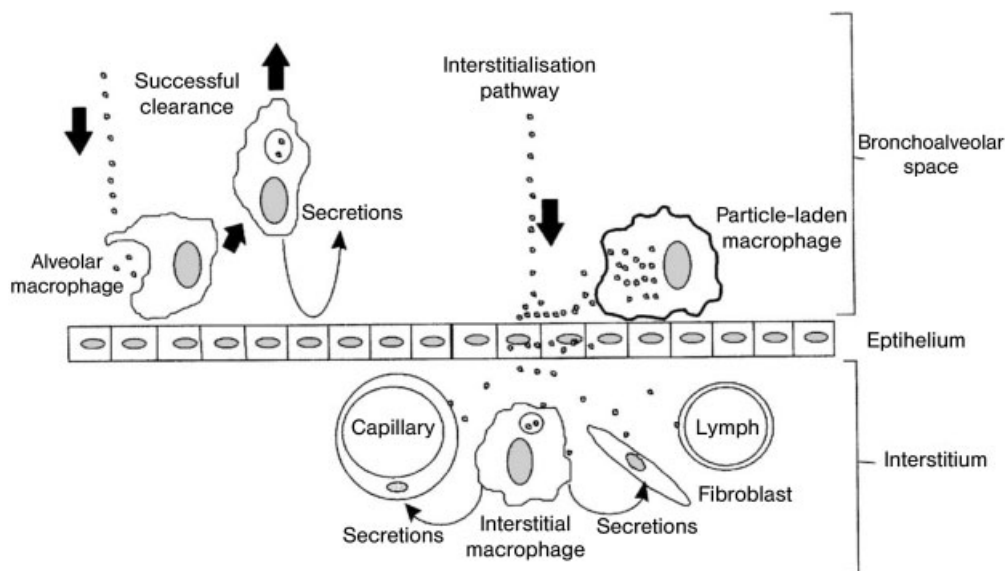


**Fig. 1.4.** Potential pathways for nanoparticles once they enter the lung; see text for additional details. (Figure taken from Donaldson [25] with permission from Elsevier.)

the lamellar bilayer is 0.5–1 nm. When filled with topically applied materials, the gap has the ability to enlarge [21–23]. Currently, human skin models, such as Skin<sup>2</sup>™, are being used for *in vitro* penetration studies of UV-irradiated particles [24].

Once inhaled, particles enter the deep lung region where they are engulfed by macrophages and removed before damage to the epithelium occurs. However, with nanoparticles, the burden becomes too large for the macrophages to remove all of the particles. The particles can then interact with the epithelium and cause inflammatory effects, enter the interstitium where they promote chronic effects on cells, or transfer to lymph nodes (Fig. 1.4) [25].

#### 1.4 Health Threats

Some believe that human exposure to most nanoparticles is not large enough to cause significant health effects in healthy individuals [1, 8]. TiO<sub>2</sub> is reported to be harmless when swallowed by man [26]. However, occupational health risks may be significant due to exposure of nanoparticles at levels higher than ambient conditions. In addition, man-made nanomaterials may have novel sizes, and physical and chemical properties, which can lead to biocompatibility problems when intro-

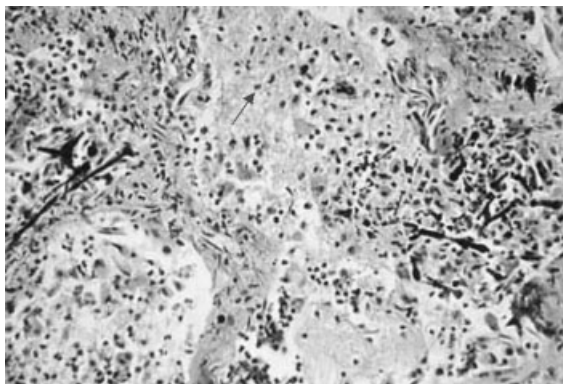


**Fig. 1.5.** Asbestos fiber surrounded by macrophages in the lung. (Figure taken from [www.cdc.gov](http://www.cdc.gov) [5].)

duced into one's system [1, 5, 11, 12]. NIOSH concluded, on the basis of thousands of studies, that it was the shape of the asbestos fibers that caused its high toxicity, not its elemental composition. Indeed, asbestos is a general term used to describe a broad class of alumina silicate minerals (Fig. 1.5). For example, the long, thin dimensions of asbestos fibers enable them to reach the gas-exchanging part of lung when inhaled; however, they are not easily removed by macrophages in the lung, thus leading to inflammation and scarring [1]. Long-term exposure may even lead to cancer. Additional health effects of particulate materials include increased attacks of asthma in asthma patients, silicosis, asbestosis, and “black lung” [1, 8, 27].

## 1.5 Nanomaterials and Biotoxicity

### 1.5.1 Iron Oxide

Iron oxide nanoparticles have been used extensively for biological applications and as pigments [28, 29]. The common oxidation states of iron found in the environment are +2 (ferrous) and +3 (ferric). Nanoparticles with a wide degree of morphologies and crystal structures exist. According to Schwertmann, there are fifteen known polymorphs of ferric oxide [28, 29]. Ferric oxide nanoparticles are in fact one of the few classes of nanomaterials approved by the FDA for prenatal (IV) administration to humans [30, 31].

The magnetic properties of mixed valent  $\text{Fe(II)}$ ,  $\text{Fe(III)}$  oxides are finding increased applications for imaging, drug delivery, and separations [32, 33]. The toxicity of these mixed valent materials is far less clear. The ability of many microorgan-

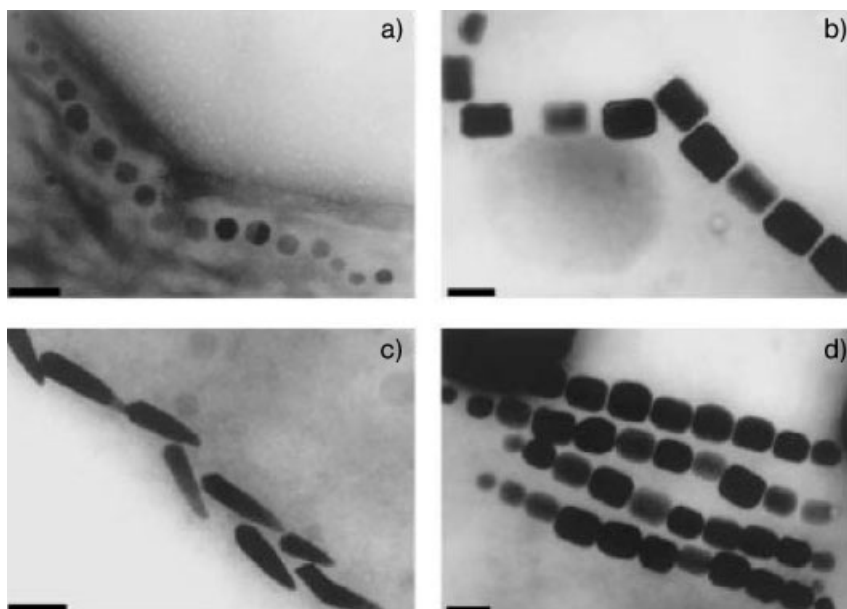


**Fig. 1.6.** Electron micrographs of magnetosomes found in magnetotactic bacteria. Scale bar: 100 nm. (Figure taken with permission from Safarik [34].)

isms (i.e., magnetosomes), fish and mammals to produce and/or utilize magnetite,  $\text{Fe}_3\text{O}_4$ , demonstrates that they are not toxic under all conditions. Figure 1.6 shows a transmission electron micrograph of  $\text{Fe}_3\text{O}_4$  particles synthesized by a microorganism [34]. Magnetic nanoparticles are also thought to be exploited by more advanced organisms such as trout, migrating birds, and whales. Conversely, the well-known Fenton reaction of  $\text{Fe(II)}$  yields hydroxyl radicals that damage DNA and can oxidize a wide variety of organic and biological reagents [35].

Below we review recent cellular studies of magnetic iron oxide nanoparticles. The vast majority of these studies are focused on superparamagnetic  $\text{Fe}_3\text{O}_4$  particles that respond rapidly to magnetic fields but retain no residual magnetism when the field is removed. Such materials have long been commercially available as micron-sized magnetic beads, in which the superparamagnetic particles are encapsulated within an organic sphere [36]. The use of nanometer-sized materials presents new opportunities for separations and imaging technologies, where possible biototoxicity is a critical concern.

Goetze et al. prepared biocompatible superparamagnetic nanoparticles of 2–30 nm diameter. The particles were coated with citric acid or carboxymethyl dextran (CMD) [37]. Lacava et al. had previously studied the biological effects of ionic and

citrate based magnetic fluids composed of  $\text{MnFe}_2\text{O}_4$  on mice. The citrate and ionic nanoparticles caused diarrhea and ultimately animal death. While citrate alone did not cause toxicity, it was not clear whether the manganese or the iron were responsible for death [38].

Mikhaylova et al. have studied the effects of biocompatible coating layers on superparamagnetic iron nanoparticles. Bovine serum albumin (BSA), poly(L,L-lactic acid), or poly( $\epsilon$ -caprolactone) were coated on 8 nm particles. FTIR spectroscopy was used to characterize the nanoparticles and confirm the presence of the coatings. For uncoated or gold-coated nanoparticles, superparamagnetic behavior was observed. However, Mössbauer and magnetic susceptibility studies indicated significant cluster formation in the case of BSA modified particles, and chain-like structures for the lactic acid and caprolactone modified nanoparticles [39].

Gupta and Gupta reported a cytotoxicity decrease and internalization increase for pullulan-coated superparamagnetic nanoparticles with human fibroblasts. Uncoated, 20 nm iron oxide particles were toxic to human dermal fibroblasts. Internalization of these particles resulted in disruption of the cell cytoskeleton. Pullulan coated particles were non-toxic and had a different effect on the cytoskeleton. TEM data indicated that the internalization mechanisms were different for the two particles – behavior that was attributed to the hydrophilic nature of the pullulan coating [40].

Petri-Fink et al. studied the effects of surface-coated superparamagnetic iron oxide nanoparticles with human cancer cells. Nine-nm iron oxide nanoparticles were coated with poly(vinyl alcohol) (PVA) or PVA with carboxylate, amine or thiol functional groups. The PVA and the carboxyl and thiol functionalized PVA nanoparticles were non-toxic to the melanoma cells. Some cytotoxicity was observed for the amine functionalized PVA nanoparticles, particularly when the polymer concentrations were high. The amine groups increased cellular uptake of the nanoparticles [41].

Stroh et al. reported on studies of rat macrophages incubated with citrate coated iron oxide nanoparticles (9 nm). Atomic absorption and NMR studies showed a large uptake of the nanoparticles that could be easily visualized by confocal microscopy (Fig. 1.7). Rhodamine green-labeled iron oxide nanoparticles were incubated with the cells for 90 min at 37 °C. The cells were then centrifuged, washed with PBS buffer, resuspended in medium, and seeded in six-well plates. The next day the adherent cells were incubated with the lipophilic fluorescent dye ANEPPS, which is a common stain for outer and intracellular membrane structures including vesicles. After 45 min incubation, the cells were washed and studied by confocal microscopy. With 488 nm laser excitation, both the rhodamine green emission and the ANEPPS red emission were simultaneously monitored. Control experiments without the iron oxide nanoparticles are also shown [42].

The confocal results clearly indicate that the iron oxide nanoparticles were taken up by the cells. Even though some cell autofluorescence was seen in the control data, it was much weaker in intensity. The high fluorescence intensity from

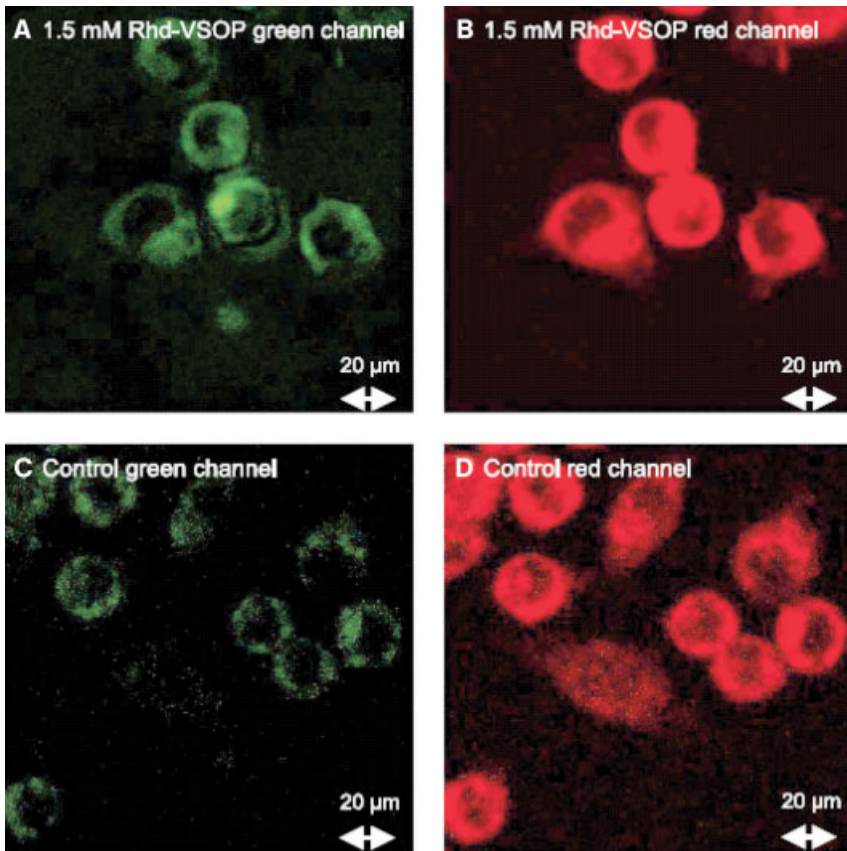


**Fig. 1.7.** Cell internalization quantified by confocal microscopy; see text for details. (Figure taken from Stroh [42] with permission from Elsevier.)

ANEPPS in the same region as the nanoparticles led the authors to suggest that the iron oxide nanoparticles form intracellular aggregates in membrane coated vesicles [42].

The cells were lysed at various times after nanoparticle exposure and the levels of malonydialdehyde (MDA) and protein carbonyls were measured. At short incubation times, a significant increase in protein oxidation and MDA was observed. Interestingly, the yields diminished with time and by 24 h there was no evidence for oxidative stress. Therefore, the oxidative stress was transient and the cells remained viable and useful for magnetic imaging applications. Iron chelators and spin traps caused a reduction in the concentrations of MDA and oxidized proteins, leading the authors to conclude that free iron present during the incubation procedure caused the transient oxidative stress [42].

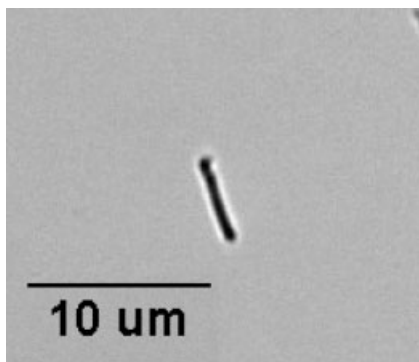


Fig. 1.8. Optical image of a high-aspect ratio  $\text{TiO}_2$  nanoparticle or nanowire.

### 1.5.2

#### Titanium Dioxide

Titanium dioxide is commonly found in three crystalline forms: rutile, anatase and brookite [43]. In all three crystalline forms,  $\text{Ti(IV)}$  is in an octahedral coordination environment.

For bulk  $\text{TiO}_2$ , rutile is the thermodynamically stable form, while for nanoparticles ( $<14$  nm) the anatase form is most stable [44–46]. Therefore, most synthetic routes for the preparation of  $\text{TiO}_2$  nanoparticles yield anatase, and rutile is far less common [47–49]. Some preparations yield a mixture of the three phases. The commercially available DeGussa P25 consists of  $\sim 25$  nm particles of about 80% anatase and 20% rutile. Because of the large effective mass of electrons in  $\text{TiO}_2$ , quantum size effects, which are well known for other semiconductors, are not observed until the particle size is less than 1 nm [50]. While spherical particles are by far the most common, it is possible to synthesize high-aspect ratio particles like those shown in Fig. 1.8.

Titanium dioxide is classified as a wide band-gap semiconductor, the anatase form having a band gap of 3.2 eV (Fig. 1.9) [43]. Much of the biotoxicity of  $\text{TiO}_2$  is attributed to photoeffects wherein the material is illuminated with ultraviolet light. Band gap illumination produces an electron–hole pair excited state that is a much stronger oxidant and reductant than is the ground state. Under standard conditions the excited electron has a reduction potential of about 0.0 V vs. NHE while the hole has an oxidizing power of about +3.2 V [51].

Under many conditions, the initially formed electron–hole pairs trap at specific sites to yield radicals. The nature of these radicals has been the subject of many investigations, particularly because of their possible relevance in splitting water into hydrogen and dioxygen [52]. It is now widely accepted that the electrons trap at localized  $\text{Ti(IV)}$  sites. Titanium<sub>(III)</sub> is a reductant that reduces dioxygen to form superoxide ions [53]. Superoxide has long been thought to abstract hydrogen atoms from various biological substrates [53].

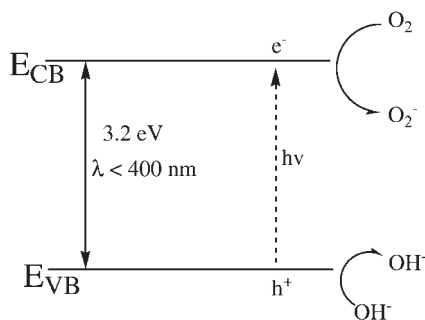


**Fig. 1.9.** Simplified band structure for anatase  $\text{TiO}_2$ . Band gap light excitation produces an electron in the conduction band and a hole in the valence band. The electron reduces dioxygen to superoxide, a reactive oxygen species that can abstract hydrogen atoms from organic biomolecules. The valence band hole

can oxidize water to dioxygen, and can also produce hydroxyl radicals – potent reactive oxygen species that oxidize most organic compounds. Not shown is the trapping of the photogenerated carriers. See text for additional details.

The fate of the photogenerated hole in  $\text{TiO}_2$  is less certain. Electron pair repulsion spectroscopic measurements indicate that the hole is initially trapped at an oxygen bridged between two  $\text{Ti(IV)}$  sites [54]. This “hole” is very reactive and is thought to ultimately yield a hydroxyl radical under ambient aqueous conditions. Much of the environmental photocatalysis of  $\text{TiO}_2$  is best understood by invoking the presence of hydroxyl radicals. Hydroxyl radicals are highly reactive and generally react with the first substrate they encounter [53].

Titanium dioxide nanoparticles are of considerable industrial interest. The high refractive index (2.7) makes it an ideal material for light scattering and it has historically been used in paints, polymers, enamels, and coatings. It is also an ingredient in some suntan lotions and used as a colorant in foods. Growing applications in solar energy conversion and environmental remediation have been envisioned.

The body of literature for  $\text{TiO}_2$  nanoparticle biotoxicity was by far the largest. We have organized the literature descriptions based on whether the nanoparticles were illuminated or kept in the dark.

#### 1.5.2.1 Dark Studies

Donaldson et al. have examined the cytotoxic effects of  $\text{TiO}_2$  by measuring the DNA strand breakage on a supercoiled DNA band caused by free radical activity. A DNA plasmid (290 ng  $\phi$  X174 RF) was incubated with either  $\text{TiO}_2$  (0.5  $\mu\text{m}$ ) or ultrafine  $\text{TiO}_2$  (0.02  $\mu\text{m}$ ) particles. The plasmid was separated into the three possible forms, super-coiled, relaxed coil or linear by electrophoresis and quantified by scanning laser densitometry. Findings showed that  $\text{TiO}_2$  particles had little effect on DNA strand breakage, whereas the ultrafine particles caused complete destruc-



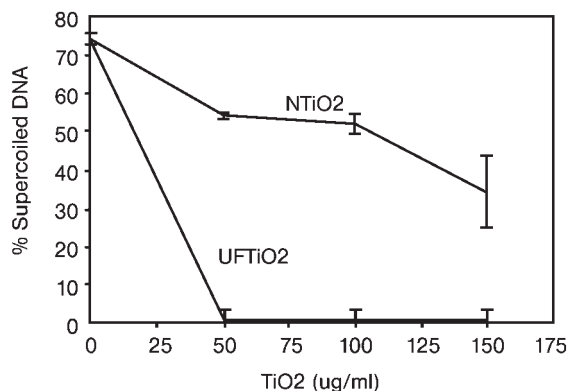


**Fig. 1.10.** Relationship between TiO<sub>2</sub> (NTiO<sub>2</sub>) and ultrafine TiO<sub>2</sub> (UFTiO<sub>2</sub>) particles and DNA strand breakage. (Figure taken from Donaldson [55] with permission from Elsevier.)

tion of the super-coiled DNA plasmid at concentrations greater than 50  $\mu\text{g mL}^{-1}$  (Fig. 1.10). In addition, crocidolite and amosite asbestos caused supercoiled DNA depletion. At lower ultrafine TiO<sub>2</sub> concentrations (5  $\mu\text{g mL}^{-1}$ ) and in both asbestos samples the amount of DNA damage was improved by the addition of a radical scavenger, such as mannitol, indicating the role of free radical activity at the surface of the particles. The researchers also suggested that the surface of the particles can react with reductants generated by inflammatory cells and physiological chelators to generate more free radicals to assist in the destruction of DNA [55].

Tan et al. studied human subjects whom applied sunscreen to skin for 2–6 weeks until up to 2 days before excision of the skin lesion. Studies were performed by removing the stratum corneum by using cyanoacrylate ester and elastic plaster and a tissue sample was obtained. The samples were digested by microwave extraction and analyzed using mass spectrometry. The results showed that the levels of TiO<sub>2</sub> in the dermis were higher, yet not statistically different from, the control samples (post mortem cadavers). However, if the outlier in the control samples was excluded, the TiO<sub>2</sub> concentrations were significantly higher than the control. No correlation was found between the concentration of TiO<sub>2</sub> in the samples and the duration of application. A small test group, and concentrations of TiO<sub>2</sub> close to the detection limits, made it difficult to compare the concentrations of TiO<sub>2</sub> in the dermis samples with the control [21].

In a study by Hart et al., CHO-K1 cells were incubated for 2–5 days with dusts: chrysotile (1.4  $\times$  0.1  $\mu\text{m}$ ), crocidolite (1.8  $\times$  0.2  $\mu\text{m}$ ), and TiO<sub>2</sub> (0.6  $\mu\text{m}$ ). Viability was determined by an esterase activity viability assay, where cells are treated with 5(6)-carboxyfluorescein diacetate, which is a non-fluorescing ester conjugate. When internalized by cells, carboxyfluorescein is cleaved by cytoplasmic esterases and becomes polar and fluorescent. If the cell is not viable, the ester conjugate would not be retained by the cell. In all samples the loss of cell viability was not significant.

However, micronuclei and polynuclei tests with acridine orange staining expressed nuclear abnormalities. Chrysotile was the most cytotoxic sample, while  $\text{TiO}_2$  was the least, indicating a particle size dependence on toxicity. Since viability remained high and only nuclear abnormalities resulted from particle interactions, the proposed mechanism of toxicity involved the interference of the internalized particles with mitosis, which causes a distortion in nuclear morphology and cytostasis, cessation of cell division [9].

In another study by Hart et al., Chinese hamster ovary (CHO) cells were exposed to particles for 3 days and then counted using a Coulter counter. For all fibers tested, ranging from glass, ceramics, and slag wool to asbestos, similar toxic effects were observed. Cultures showed little loss in viability ( $\sim 90\%$ ); however, cell proliferation was almost completely inhibited and a concentration-dependent increase in morphological changes was observed. Unexposed samples retained a viability of 99% and showed a 20-fold increase in cell population [56].

Size comparisons indicated that thinner fibers were more toxic than thicker ones of similar lengths when concentration was a function of fiber mass per unit area. However, when concentration was expressed as a function of number of fibers per unit area, the difference in effects was non-existent [56].

The researchers concluded that cytotoxicity and genotoxicity correlate with fiber length and the mechanism of toxicity was by cytostasis, or the disruption of cell division. Possible explanations include longer fibers being more easily entangled in migrating chromosomes or spindle apparatus, which leads to the formation of micronuclei [56, 57]. In addition, long fibers are more biocompatible because they support cell growth *in vitro* by providing a substratum for attachment and proliferation of fibroblast cell lines [56, 58, 59].

Peters et al. have analyzed the effects of  $\text{TiO}_2$  (14 nm) and  $\text{SiO}_2$  (70 nm) particles on human dermal microvascular endothelial cells. Viability tests along with Ki67, a protein expressed in the nucleus of proliferating cells, and the cytokine interleukin-8 (IL-8) measurements were performed to determine the cytotoxic effects of the metal oxide particles on cells [60]. The CellTiter AQ<sub>ueous</sub> non-radioactive assay was used to determine cell viability by measuring the conversion of an enzymatic tetrazolium salt (MTS) via mitochondrial dehydrogenase [61]. Results showed no significant difference in cell viability; however, an increase in IL-8 production for both the  $\text{SiO}_2$  and  $\text{TiO}_2$  particle ( $50 \mu\text{g mL}^{-1}$ ) treated samples was taken as evidence for pro-inflammatory effects (Fig. 1.11) [60]. The only sample that induced a decrease in Ki67 expression was  $\text{SiO}_2$  ( $50 \mu\text{g mL}^{-1}$ ), indicating a decrease in the number of cells participating in the active part of the cell cycle. Since biocompatible  $\text{TiO}_2$  showed some inflammatory effects, the authors concluded that particles can possess different features when in the nano versus bulk scale [60].

Shanbhag et al. have studied the effects of  $\text{TiO}_2$  particles on P388D<sub>1</sub> macrophages. Viability was measured as a function of  $^3\text{H}$ -thymidine ( $^3\text{H}$ -TdR). Cells were incubated with particles for 8 h followed by the addition of  $^3\text{H}$ -TdR for 16 h.  $^3\text{H}$ -TdR suppresses DNA synthesis and is used as a way to measure DNA fragmentation. The results showed that  $\text{TiO}_2$  decreased  $^3\text{H}$ -TdR levels in macrophages in a size- and concentration-dependent manner [62].

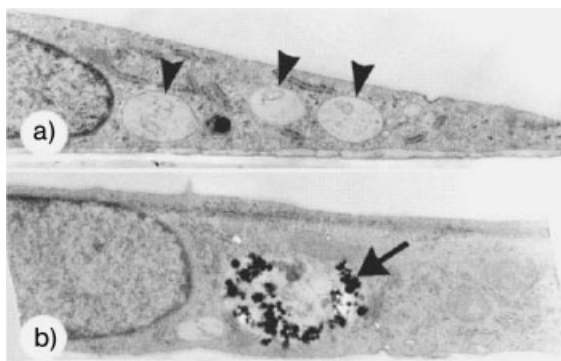


**Fig. 1.11.** A human dermal microvascular endothelial cell exposed to (a) no particles and (b)  $\text{TiO}_2$  particles. (Figure adapted from Peters [60] with kind permission of Springer Science and Business Media.)

Stearns et al. have investigated the effects of  $\text{TiO}_2$  particles (50 nm) on a human epithelium cell line (A549). In as little as 1–2 h, minimal internalization of the particles was observed by energy-filter TEM. Short exposure times to  $\text{TiO}_2$  yielded particles found in the vacuoles; however, longer incubation times showed  $\text{TiO}_2$  in the lamellar bodies. Addition of the inhibitor cytochalasin D (cyto D), which is known to affect actin polymerization and particle internalization, to cells before they were introduced to  $\text{TiO}_2$  neither inhibited phagocytosis of the nanoparticles nor decreased cell viability. However, a change in cell morphology was observed in the presence of cyto D and more particles were internalized in membrane-bound vacuoles rather than the lamellar bodies [63].

Westmoreland et al. have used  $\text{TiO}_2$  as a reference compound because it is known as a “nuisance dust.” In the study,  $\text{TiO}_2$  particles were introduced into an epithelial cell line (16HBE14o-) for 24 h [64]. However, after 24 h, there was no toxicity induced as measured by the MTT reduction assay [65], neutral red uptake assay or transepithelial resistance.

Kilgour et al. have modeled inhalation exposure *in vitro* by exposing olfactory and respiratory turbinates of rats to  $\text{TiO}_2$  ( $<1 \mu\text{m}$ ) for short and long durations. They found that  $\text{TiO}_2$  exposure had no effect on adenosine triphosphate (ATP) or potassium concentrations in olfactory epithelium for any of the times studied. Conversely, when exposed to respiratory epithelium, a minimal decrease in ATP and potassium concentration was observed for the 4 h particle incubation and 20 h fresh media incubation. An observed decrease in potassium concentration at the 24 h exposure time was attributed to mechanical damage arising from  $\text{TiO}_2$  particle precipitation. These studies concluded that  $\text{TiO}_2$  is not acutely toxic to the nasal cavity [66].

Miller et al. found  $\text{TiO}_2$  to have no effect on CHO cells with or without metabolic activation, which is potentially a result of  $\text{TiO}_2$  nanoparticle insolubility. The effect

of the particles was analyzed by micronucleus testing of cells that were incubated with TiO<sub>2</sub> particles for 48 h [67].

The Scientific Committee on Cosmetics and Non Food Products intended for consumers (SCCNFP) has evaluated the acute toxicity, mucous membrane irritation, phototoxicity, genotoxicity, carcinogenicity and percutaneous absorption of TiO<sub>2</sub> and deduced that TiO<sub>2</sub> is safe to use at maximum concentration of 25% w/w in cosmetics. Furthermore, this includes crystalline TiO<sub>2</sub> particles irrespective of particle size and requires no further restrictions or conditions for use in cosmetic products [68].

#### 1.5.2.2 UV Irradiation Studies

In addition to the dark studies mentioned above, it is notable that in the following reports of UV-irradiated nanoparticles, the control groups, often consisting of nanoparticles reacted with cells in the absence of UV light, also showed no evidence of cytotoxicity. Dunford et al. set out to determine the potential ill effects that metal oxide nanoparticles (TiO<sub>2</sub> and ZnO) found in over-the-counter sunscreens can have on DNA. Titanium dioxide (2%w/v – 0.02 µg µL<sup>-1</sup>) and zinc oxide (0.4% w/v) nanoparticles (20–50 nm) were extracted from sunscreens and added to plasmid DNA (50:50 – 25 µL). The samples were then irradiated with UVA (365 nm) light from a 1000-W Hg/Xe lamp for 0–60 min increments. Strand breaks in the DNA were assayed on agarose gels by the transformation of a supercoiled plasmid into the relaxed or linear form. The damage of the photoactive nanoparticles was independent of crystal type, with the most active sample containing as much as 1.95% ZnO. DNA damage was suppressed by hydroxyl radical quenchers, dimethyl sulfoxide (DMSO) and mannitol, and proteins, catalase and bovine serum albumin, but not superoxide dismutase, which provided evidence that the hydroxyl radical rather than superoxide was the source of DNA damage [19].

Uchino et al. probed the effect of TiO<sub>2</sub> crystal form and size on cytotoxicity as well as the relationship between the amount of radicals produced from UV-irradiated TiO<sub>2</sub> particles and cytotoxicity. The effect of the irradiated particles on cell viability was determined by the addition of varying concentrations of Degussa P-25 TiO<sub>2</sub> particles in cultures of a Chinese hamster ovary (CHO) cell line. After incubation for 48 h with TiO<sub>2</sub> particles, the samples were irradiated with UV light for 24 h [69]. Cell viability was determined using the 3-(4,5-dimethylthiazol-2-yl)-2,5-diphenyltetrazolium bromide (MTT) assay. Upon reduction by living cells, MTT is converted into a purple formazan. The amount of MTT formazan produced can be quantified by using a microplate reader to measure absorbancies at a test and a reference wavelength [65]. The viability of CHO cells with internalized TiO<sub>2</sub> particles decreased significantly after UV irradiation. Although the intensity of the UV light did not influence cytotoxicity, the anatase fraction in the TiO<sub>2</sub> particles had a significant effect on cytotoxicity. In addition, cell viability was proportional to the DMPO-OH radical adduct formed. This was accomplished by electron spin resonance (ESR). The compound 5,5-dimethyl-1-pyrroline *N*-oxide (DMPO) was used to spin trap the OH<sup>•</sup> radical. The ESR results confirmed the presence of a DMPO-OH radical adduct, consistent with the formation of an OH<sup>•</sup>

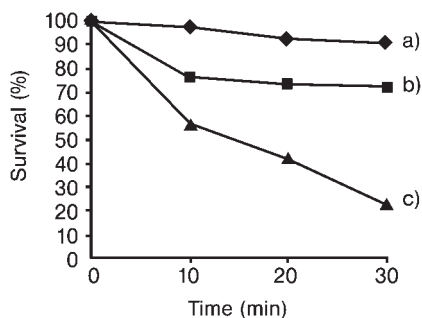


**Fig. 1.12.** Effects of UV irradiation and TiO<sub>2</sub> particles on Ls-174-t cells. (a) TiO<sub>2</sub> particles in the dark, (b) UV irradiation with no TiO<sub>2</sub>, (c) TiO<sub>2</sub> and UV irradiation. (Figure taken from Zhang [70] with permission from Elsevier.)

radical. The optimum crystal size for OH<sup>•</sup> radical formation was 30 nm for anatase and 90 nm for rutile. The results also demonstrated a dependence of cytotoxicity on hydroxyl radical formation and crystal form and size; however, these variables were independent of each other. For example, hydroxyl radical formation differed with crystal form and size. Most anatase samples produced more hydroxyl radicals than rutile or amorphous TiO<sub>2</sub>. The percentage of anatase in these samples had no effect on the amount of radical generated; however, the viability of the cells was dependent on the amount of DMPO-OH radical formed. This indicated that when anatase forms of TiO<sub>2</sub> are irradiated with UV light, hydroxyl radicals form that have cytotoxic effects. This was not the case for rutile and amorphous samples, indicating the need for further investigation of a different mechanism for radical formation. In addition, ESR data showed no relation between the formation of a DMPO-OH radical adduct and UV absorbance; therefore, radical formation is due to another factor besides UV absorbance [69].

Zhang et al. found that Ls-174-t cells, a human colon carcinoma cell line, had over 90% viability when reacted with TiO<sub>2</sub> nanoparticles alone. However, when the TiO<sub>2</sub>-cell samples were irradiated with UV light, viability fell to a meager 20% when TiO<sub>2</sub> concentration was >200 μg mL<sup>-1</sup> (Fig. 1.12). The effects of TiO<sub>2</sub> concentration on cell viability were investigated using the MTT assay. Cell viability decreased as the concentration of UV-irradiated TiO<sub>2</sub> nanoparticles internalized in the cells increased. Furthermore, the cell morphology changed with increasing nanoparticle concentration, giving rise to shrinkage and fragmentation of the cell. These observations led the researchers to believe that the mechanism of cell death by photoexcited TiO<sub>2</sub> nanoparticles was through reactive oxygen species. The means by which the nanoparticles damage the cells was theorized to occur in two stages. The first stage being oxidative damage by the photoexcited TiO<sub>2</sub> nanoparticle surface as it comes in contact with the cell membrane. This resulted in permeabilization of the cell membrane and did not produce a significant decrease in cell

viability. The decrease in cell viability, and eventually cell death, occurred as a result of intracellular components leaking out of the permeable membrane and additional TiO<sub>2</sub> nanoparticles trafficking into the damaged cells and directly attacking the nucleus and other intracellular components [70].

Cai et al. observed that HeLa cells incubated with TiO<sub>2</sub> particles without UV irradiation had 90% survival, as did cells irradiated with UV light for less than 19 min. However, cultures exposed to both TiO<sub>2</sub> particles and UV light showed a dramatic fall in survival rate that decreased with increasing TiO<sub>2</sub> concentration. Irradiation of HeLa–TiO<sub>2</sub> adducts with visible light did not cause any photodynamic effects, and simply raised the temperature of the culture to around 36 °C. Since this is less than the culture temperature of the cells, thermal death is not very likely and the observed behavior with UV light was attributed to photochemistry, not thermal effects. Irradiation with wavelengths greater than 440 nm produced cell survival of 90%, but when the sample was irradiated with a slightly lower wavelength (300–400 nm), for an equal amount of time, all cells in the culture were killed. This same irradiation wavelength range on cells without TiO<sub>2</sub> yielded an 85% survival rate [71].

Cell death was proposed to take place by two possible mechanisms. In the first, cells were oxidized by photogenerated holes in the valence band. In the second, the holes reacted with water to produce OH<sup>•</sup> radicals that can attack the cell membrane and intracellular components [71]. Cai et al. and Sakai et al. deduced that the viability of T-24 cells decreased with both variations in UV irradiation intensity and TiO<sub>2</sub> particle concentration [72, 73].

Saito et al. have investigated the photocatalytic bactericidal effects of TiO<sub>2</sub> particles (21 nm) on three strains of bacteria (*Streptococcus mutans*, *S. rattus*, and *S. cricetus*). TiO<sub>2</sub> particles were introduced to the specimen, irradiated with UV light and incubated for two days. The bactericidal action of TiO<sub>2</sub> increased with TiO<sub>2</sub> particle concentration. In addition, potassium leakage, measured by flame photometry, paralleled the loss of cell viability. In bacteria, a cell wall of peptidoglycan is formed around the cell membrane. When observed by TEM, the TiO<sub>2</sub> particles took over 30 min to reach the cell membrane of the bacteria, yet leakage of intracellular protein and cell death occurred in less than 1 min. Cell death was rapid and the cell wall was not destroyed until after 60–120 min; therefore, the TiO<sub>2</sub> particles could not have been able to attach to the cell membrane directly to cause any damage. Rather, cell death was assumed to result from membrane damage caused by the superoxide and perhydroxy radicals produced from TiO<sub>2</sub> photocatalysis [26].

Nakagawa et al. studied the effects of four sizes of UV irradiated TiO<sub>2</sub> particles on a mouse lymphoma cell line. DNA tail length was measured by means of a SCG assay. The results showed that UV-irradiated Degussa P-25 (anatase, 21 nm), TP-3 (rutile, 420 nm) and WA (anatase, 255 nm) samples all elicited increased DNA damage and a decrease in cell survival (Fig. 1.13) [74, 75, 76].

Warmer et al. determined whether nucleic acids were targets for photooxidative damage caused by UV-irradiated TiO<sub>2</sub> by investigating the effects of UV-irradiated TiO<sub>2</sub> on calf thymus DNA and human skin fibroblasts. A suspension of TiO<sub>2</sub> particles was added to samples of calf thymus DNA and fibroblasts and exposed to

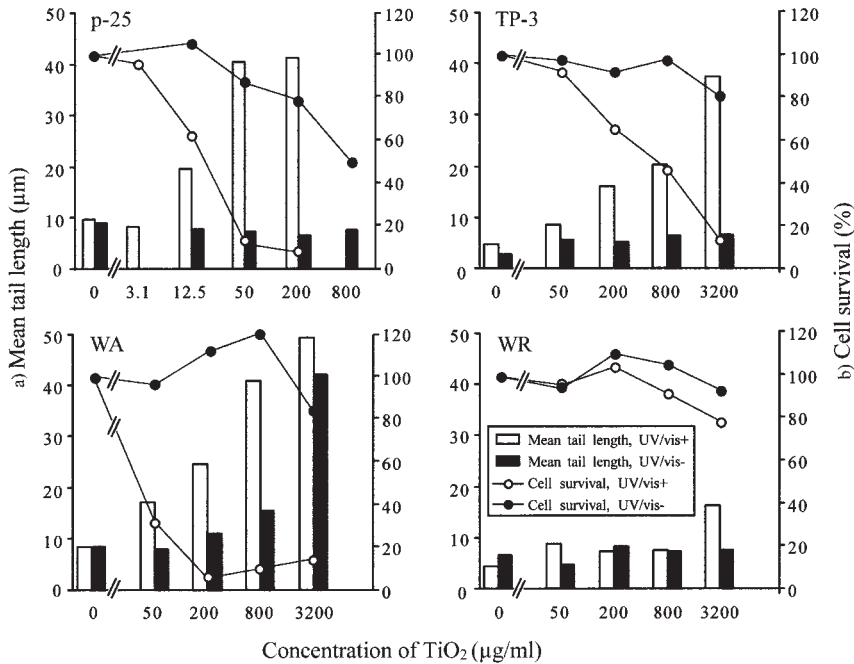


**Fig. 1.13.** Effects of TiO<sub>2</sub> on DNA tail length and cell survival. Abbreviations: p-25, anatase 21 nm; WA, anatase 255 nm; WR, rutile 255 nm; TP-3, rutile 420 nm. (Figure taken from Nakagawa [74] with permission from Elsevier.)

UVA light for 1 h. The calf thymus DNA and cellular DNA samples were then enzymatically hydrolyzed and analyzed using reversed-phase high-performance liquid chromatography (HPLC). HPLC was used to measure the hydroxylation of guanine bases (forms 8-oxodG) and indicated whether any nucleic acids were oxidatively damaged [75].

Results with calf thymus DNA showed that levels of 8-oxodG increased directly with the addition of TiO<sub>2</sub> and fluence of UV irradiation, when they were both present in calf thymus DNA experiment. Furthermore, the fibroblast samples showed that both TiO<sub>2</sub> particulates and UV light must be present to induce oxidative damage, in which case cytotoxicity was 85%. The phototoxicity was UV fluence dependent. Although oxidative damage did not occur in cellular DNA, there was a 3-fold increase in 8-oxoG in the presence of TiO<sub>2</sub> and UV irradiation, indicating the oxidative damage of the guanine bases in cellular RNA. This gave evidence that oxidative stress caused by irradiated TiO<sub>2</sub> particles was occurring in the cytoplasmic and nuclear compartments of the cell. The photocytotoxicity of TiO<sub>2</sub> is a result of intracellular damage induced by reactive oxygen species. However, the relative importance of the reactive oxygen species formed by photoexcited TiO<sub>2</sub> is still unknown.

ESR studies to measure the formation of a DMPO-OH radical adduct were also performed. The formation of adduct increased with time and then leveled off [77]. Since there is evidence of reactive oxygen species, the hydrolysis of guanine in calf thymus DNA can be due to any of the following: hydroxyl radical formation, decomposition of hydrogen peroxide from UV irradiation, or the Fenton reaction [78–80].

Kubota et al. incubated T-24 human bladder cancer cells with TiO<sub>2</sub> particles, cultured them for 24 h and observed the effects. The TiO<sub>2</sub> particles were contained mainly in the cytoplasm and cell membrane of the T-24 cells, as found by transmission electron microscopy (TEM). There was a 90% survival rate amongst cells introduced with up to 300 µg mL<sup>-1</sup> of TiO<sub>2</sub>. However, when exposed to UV light for as little as 5 min there was as much as a 20% decrease in the survival rate even with TiO<sub>2</sub> concentrations as low as 10 µg mL<sup>-1</sup>. They also found that cell killing was more effective in phosphate buffered saline (PBS) than in F-12 media. This is possibly due to either the absorptive abilities of F-12 or the fact that it contains radical scavengers such as mannitol and tryptophan. These researchers also investigated the role that radical scavengers play in irradiated TiO<sub>2</sub> cytotoxicity. Molecular scavengers of both hydrogen peroxide and hydroxyl radicals, catalase and L-cysteine, respectively, effectively diminished cell death when added to the cell samples. This provided evidence of the role of hydroxyl radicals and hydrogen peroxide in cell death [81].

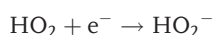
In addition, they investigated the mechanism of photoexcited TiO<sub>2</sub> biototoxicity by depositing TiO<sub>2</sub> nanoparticles onto conductive tin oxide glass. The cells were subsequently cultured on the conductive glass. In the dark, when a potential was applied to the TiO<sub>2</sub> electrode, the cells remained viable. However, in the presence of UV light, cells were killed when the electrode potential was more positive than -0.5 V. The percent of cells surviving was proportional to the photoinduced current. Due to the strong photocurrent, at anodic potentials, the researchers concluded that photogenerated TiO<sub>2</sub> holes were responsible for cell death [81].

An *in vitro* experiment using T-24 cells was also carried out by the same group. TiO<sub>2</sub> particles (0.03–10 nm) were added to cell cultures and irradiated with a 500-W Hg lamp. The cells were cultured for another 10 days before fixing and staining with Giemsa in order to count. With either TiO<sub>2</sub> or UV light alone, survival was >90%, indicating no cytotoxic effects. However, in the presence of both TiO<sub>2</sub> and UV light a cytotoxic effect was observed that increased with increasing TiO<sub>2</sub> concentrations. Scavenger experiments were conducted to determine the mechanism of cell death. In the presence of the hydrogen peroxide scavenger, catalase, and hydroxyl radical quencher, L-cysteine, cell death of the photoexcited TiO<sub>2</sub> samples decreased, pointing to the participation of H<sub>2</sub>O<sub>2</sub> and OH<sup>•</sup> radical in cell death [81].

Cai et al. set out to determine the mechanism behind the photodamaging of cells with TiO<sub>2</sub>. To investigate the mechanism by which TiO<sub>2</sub> can photokill HeLa cells, superoxide dismutase (SOD), which converts the superoxide anion (O<sub>2</sub><sup>-</sup>) into H<sub>2</sub>O<sub>2</sub>, was added to a TiO<sub>2</sub> infused cell culture. The TiO<sub>2</sub> nanoparticles were incubated in cultured HeLa cells for 24 h, while SOD was added to the cell culture for the final hours of incubation. After a short irradiation with UV light, the cells were



counted to determine viability. Cell survival in the absence of SOD was a meager 55%, which indicated that cell death may be due to  $\text{H}_2\text{O}_2$  and  $\text{OH}^\cdot$  radical formed by the irradiation of  $\text{TiO}_2$ . The addition of SOD caused a decrease in survival rate, which increased with SOD concentration when irradiated for the same amount of time. Controls showed that samples containing SOD in the absence of  $\text{TiO}_2$  had no effect on survival rate, therefore indicating that the decrease in cell survival was due to the conversion of  $\text{O}_2^-$  into  $\text{H}_2\text{O}_2$  by SOD [82]. Further evidence of the production of  $\text{H}_2\text{O}_2$  was given by the addition of the fluorophore scopoletin (6-methoxy-7-hydroxy-1,2-benzopyrone), whose fluorescence is quenched by  $\text{H}_2\text{O}_2$  [83]. A much higher concentration of  $\text{H}_2\text{O}_2$  was produced in irradiated HeLa- $\text{TiO}_2$  samples that contained SOD than in samples without SOD. With the addition of catalase (EC 1.11.1.6), which converts hydrogen peroxide into water and molecular oxygen, to the  $\text{TiO}_2$ -SOD sample, the surviving fraction of cells increased, further confirming the production of  $\text{H}_2\text{O}_2$ . In addition, the presence of catalase increased survival even in the absence of SOD, indicating that  $\text{H}_2\text{O}_2$  can be produced by another method:



However,  $\text{O}_2^-$  must also be converted into some other reactive oxygen species because cell death still occurred in the presence of catalase and the absence of SOD [82].

Jang et al. have studied bacterial death by photocatalyzed  $\text{TiO}_2$ . The  $\text{TiO}_2$  was added to cultures of either *Escherichia coli* (*E. coli*) or *Pseudomonas aeruginosa* and were then irradiated with UV light. Smaller particles of  $\text{TiO}_2$  had a larger effect on the degree of decomposition of the bacteria, while increased anatase mass fraction caused an increase in decomposition (Fig. 1.14) [84].

Sakai et al. have investigated the cytotoxicity of  $\text{TiO}_2$  particles (30 nm) on a T-24 human malignant cell line. Cells were incubated with  $\text{TiO}_2$  particles for 24 h and irradiated with UV light. Cell viability was determined by a colony forming assay, and the change in  $\text{Ca}^{2+}$  concentration was monitored by ethidium bromide staining [73]. The  $\text{Ca}^{2+}$  ions play a role in differentiation, intracellular transport, secretion and metabolism [73, 85]. A change in  $\text{Ca}^{2+}$  concentration is linked to cytotoxicity [73, 86–91]. The addition of  $\text{TiO}_2$  particles to T24 cells yielded a 90% survival rate of the cells. Conversely, when the samples were irradiated with UV light, the  $\text{Ca}^{2+}$  concentration increased as determined by ratiometric imaging. With increased  $\text{TiO}_2$  concentration, less irradiation is required to cause an increase in  $\text{Ca}^{2+}$  concentration. However, since the stepwise increase in  $\text{Ca}^{2+}$  concentration remained constant it was concluded that there is a minimum amount of reactive oxygen species needed to trigger their uptake.

The processes for  $\text{Ca}^{2+}$  mobilization include influx through the plasma membrane and release from  $\text{Ca}^{2+}$  storage in the endoplasmic reticulum. The change

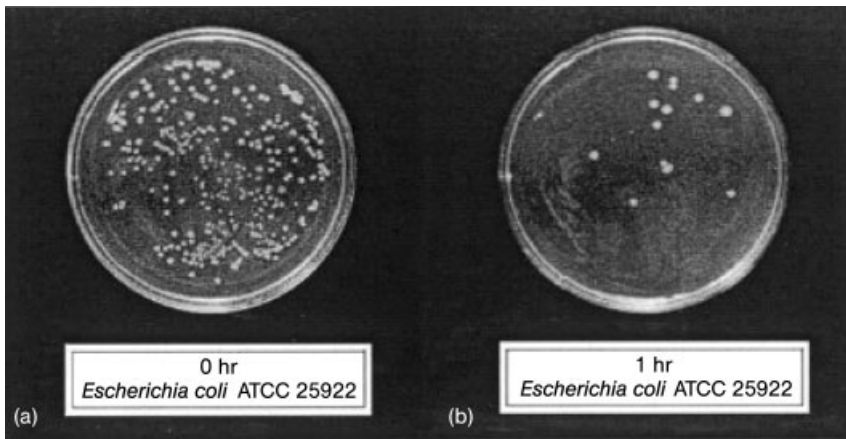


**Fig. 1.14.** *Escherichia coli* in (a) absence and (b) presence of  $\text{TiO}_2$  nanoparticles. (Figure taken with permission from Jang [82].)

in  $\text{Ca}^{2+}$  distribution was monitored to determine the mechanism taking place. When the concentration of  $\text{Ca}^{2+}$  was monitored with UV and  $\text{TiO}_2$  present in cell culture, the concentration was greatest near the cell membrane. However, without the addition of  $\text{TiO}_2$  particles, the concentration was low and evenly distributed. The increase was attributed to an increase in cell membrane permeability, but no loss in cell viability, and the  $\text{Ca}^{2+}$  was from the buffer. However, in later stages the cell dies.  $\text{Ca}^{2+}$  cannot directly be responsible for cell death because in buffer without  $\text{Ca}^{2+}$  there is still loss in cell viability. There is a simply an increase in  $\text{Ca}^{2+}$  caused by a change in permeability associated with cell death. Instead, the hydroxyl radical and hydrogen peroxide promote cell death [73].

Cai et al. showed that HeLa cells were effectively killed in the presence of photo-excited  $\text{TiO}_2$  particles. The cytotoxic effects were suppressed in the presence of L-tryptophan and catalase, which quench hydroxyl radicals and scavenge hydrogen peroxide, respectively. This suggests that cell death resulted from the production of reactive oxygen species on the particle surface [72].

Linnainmaa et al. found no effect upon the addition to rat liver epithelial cells of three particle types, uncoated anatase, rutile coated with aluminum hydroxide and stearic acid, and P25 Degussa  $\text{TiO}_2$ . The inhibition of cell growth was measured by the multinuclei assay, in which the addition of cytochalasin B prevents cell division but not division of the nucleus. Cytotoxicity was measured by the increase in the amount of cells that contained only one nucleus after treatment. The micronucleus test assessed the chromosomal damage of cells caused by the addition of  $\text{TiO}_2$ . After 1 h incubation with  $\text{TiO}_2$  particles, the cells were irradiated with UV light for 5 min. The results indicated no inhibition of cell growth or cytotoxic effects with any of the  $\text{TiO}_2$  samples. Small cytotoxic effects were seen in the irradiated samples, but they were not of statistical significance [92].

Donaldson et al. have stated that TiO<sub>2</sub> particles are cleared from the lung by phagocytosis of alveolar macrophages. They studied the impact of ultrafine (20 nm) versus fine (200 nm) particles of TiO<sub>2</sub> and carbon black on a macrophage cell line. Fluorescent latex beads were then added to the cell line to indicate phagocytic uptake. The results indicated that the ultrafine particles inhibited phagocytosis by the macrophages when compared to the fine particles, which may lend one possible explanation for their adverse effects. The mechanism is a result of the increased surface area and increased number of ultrafine particles present, due to inhibited phagocytosis, that interact with the epithelium and lead to oxidative stress and thus inflammation [8].

Wilson et al. have stated that the surface of particles may be a source of reactive oxygen species. Ultrafine and fine particles were incubated with a compound that undergoes activation to a fluorescent state when oxidized. Fluorescence intensity measurements revealed that ultrafine particles yielded a dose-dependent increase in fluorescence, whereas fine particles did not. This result is likely a consequence of the high surface area of the particles yielding more reactive oxygen species [93].

Maness et al. set out to determine the mechanism by which photocatalytic TiO<sub>2</sub> kills bacteria. They studied the effects of Degussa P25 TiO<sub>2</sub> particles (surface area 50 m<sup>2</sup> g<sup>-1</sup>) on a strain of *E. coli* in the presence of UV light. Membrane damage was determined by measuring the production of malondialdehyde (MDA), a product of lipid peroxidation, by the colored adduct it forms with thiobarbituric acid. More MDA is produced when TiO<sub>2</sub> was present than without. Reactive oxygen species are proposed to play a role because they attack the polyunsaturated phospholipids in *E. coli*, causing deterioration of the cell membrane and loss of functions within the cell [94].

### 1.5.3

#### Other Metal Oxides

Our literature searches revealed a handful of biototoxicity studies with other metal oxide nanomaterials. These studies are described below.

Yamamoto et al. have looked at the cytotoxic effects of metal oxide particles on murine fibroblasts and murine monocyte macrophages. The particles were added to cells and the relative plating efficiency was obtained after 6–8 days, depending on the cell type. The results showed that the cytotoxicity of Al<sub>2</sub>O<sub>3</sub> and ZrO<sub>2</sub> particles ( $d = 500\text{--}700$  nm) were enhanced relative to TiO<sub>2</sub> particles ( $d = 130\text{--}180$  nm). TiO<sub>2</sub> particles and Al<sub>2</sub>O<sub>3</sub>-coated TiO<sub>2</sub> particles both demonstrated similar cytotoxic effects, and showed larger particles to be more toxic than the smaller ones. Shape-dependent cytotoxicity was also determined, and dendritic TiO<sub>2</sub> proved to have the highest cytotoxicity when calculated as a function of number, volume and surface area. When cytotoxicity was determined as a function of volume, the particles ranked as dendritic > spindle > spheric. But when particle toxicity was ranked as a function of surface area the cytotoxic effects changed: dendritic > spheric > spindle. The overall conclusion on cytotoxicity ranked the dendritic particles as the most cytotoxic, followed by spindle and spheric particles. The number

of particle edges is important when determining cytotoxicity – the more edges the more of a cytotoxic effect [95]. Cytotoxicity was then compared to that of the parent metal ions. It was concluded that toxicity results because of two processes: chemical toxicity of released metal ions or other soluble components [95–97] or mechanical stimulation caused by sizes and shapes [95].

Cytotoxicity of metal ions and other chemicals differs among cell lines. Larger particles (only if phagocytosed) tended to have higher cytotoxicity than smaller particles. For example, larger  $\text{TiO}_2$  particles caused a higher inhibition of  $^3\text{H}$ -thymidine incorporation of human monocyte macrophages. However, if the particle is too large to be phagocytosed by the cells, then there is no cytotoxic effect. The authors concluded that the cytotoxicity of insoluble particles does not depend on chemical composition. In addition, cytotoxicity was not dependent on chemical species but on particle size and phagocytic properties [95].

Hanawa et al. have studied the toxicity of metal oxide nanoparticles ranging from 500 to 3000 nm in diameter. The particles were incubated in human fibroblasts for 24 h and stained with haematotoxylin and eosin to determine the magnitude of toxicity. With this assay, cells that adhered to the coverglass would stain, while dead cells would detach from the glass during staining. A digitizer was used to assess the area that was stained. The area stained was considered to be proportional to the magnitude of cytotoxicity of the metal oxide particles. Cells incubated with  $\text{Al}_2\text{O}_3$ ,  $\text{TiO}_2$ ,  $\text{Fe}_2\text{O}_3$ ,  $\text{Fe}_3\text{O}_4$ ,  $\text{Co}_2\text{O}_3$ ,  $\text{NiO}$ ,  $\text{Ga}_2\text{O}_3$ ,  $\text{SnO}$ ,  $\text{SnO}_2$ ,  $\text{HgO}$  showed no cytotoxic effects. A difference in formal oxidation state of some of these metals yielded different effects, e.g.,  $\text{CoO}$ ,  $\text{Co}_3\text{O}_4$ , and  $\text{Ni}_2\text{O}_3$  appeared to be toxic. In addition,  $\text{Cr}_2\text{O}_3$ ,  $\text{Cu}_2\text{O}$ ,  $\text{CuO}$ ,  $\text{ZnO}$ , and  $\text{Ag}_2\text{O}$  proved to be cytotoxic. A potential problem would be that the study was based on particles dissolving into elements/ions, which have a cytotoxic response. Therefore, larger areas of affected cells indicated a more cytotoxic effect, which does not necessarily correlate with the components of the particles being more effective at killing cells. Larger cytotoxic effects could have been a result of a higher particle concentration in the medium [98].

Lison et al. have studied the surface area effects of  $\text{MnO}_2$  particles (Fig. 1.15). Mouse peritoneal macrophages were incubated with  $\text{MnO}_2$  particles of varying sur-

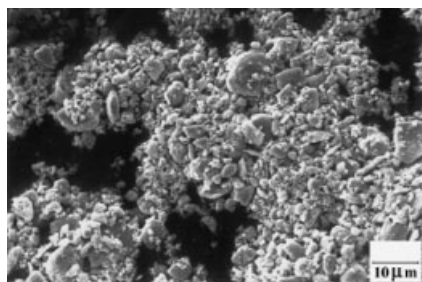


**Fig. 1.15.** Scanning electron micrograph of  $\text{MnO}_2$  particles. (Figure taken from Lison [99] with kind permission of Springer Science and Business Media.)

face areas (0.5, 17, and 62 m<sup>2</sup> g<sup>-1</sup>) for 6 h. Lactate dehydrogenase (LDH) release was measured to indicate the degree of membrane damage. At the same particle concentrations, the particle with the highest surface induced the greatest amount of cytotoxic activity. However, freshly ground particles (5 m<sup>2</sup> g<sup>-1</sup>) from the 0.5 m<sup>2</sup> g<sup>-1</sup> sample showed the highest toxicity of all. The researchers concluded that the toxicity of MnO<sub>2</sub> particles is surface dependent, indicating the possible effect of surface chemistry on cytotoxicity [99]. Lehnert et al. have claimed that cytotoxic effects are a result of intracellular dissolution of the nanoparticles in the phagolysosomes [100]. Therefore, since dissolution is a function of specific surface area, toxicity should increase with increasing surface area, which is consistent with the results of Lison. The increased toxicity of the freshly ground particle is attributed to additional reactive sites present on the surface [99].

Keceli et al. have studied the cytotoxicity of various metal oxides. Titanium, tantalum, and niobium are biocompatible due to the native oxide layer formed on the surface. Toxicity studies with these particles were performed with African green monkey kidney cells (Vero fibroblasts). Glass plates were spin-coated with a metal oxide layer (>100 nm) from a sol-gel solution. Cells were then cultured on the metal oxide for 7 days before they were counted. At the end of 7 days, no visible morphology change or apoptosis was observed, indicating that the samples were not cytotoxic. However, there was an effect on cell proliferation, which indicated an effect on biocompatibility. Al<sub>2</sub>O<sub>3</sub> and Nb<sub>2</sub>O<sub>5</sub> showed a 30% decrease in cell proliferation, while Ta<sub>2</sub>O<sub>5</sub> and ZrO<sub>2</sub> showed a 45% and 58% decrease, respectively. The TiO<sub>2</sub> sample did not differ from the control. The observed decrease in proliferation was consistent with the dielectric constants of the metal oxides, showing that metal oxides with a higher dielectric constant have more isolating effects and, as a result, are more biocompatible [101].

Chiu et al. have treated CHO cells with GeO<sub>2</sub> particles of varying concentrations for 12 h to determine their impact on cytotoxicity. Cytochalasin B, a proliferation inhibitor, was then added and an additional 24 h incubation applied. The cells were stained with Giemsa solution and counted to determine the number of binuclear cells. The number of binuclear cells decreased with the addition of GeO<sub>2</sub> particles, indicating that the particles induce G2/M block [102]. G2/M block is indicative of the cells not entering the mitosis stage of the cell cycle (Fig. 1.16). The G<sub>2</sub>, or Gap 2, phase is an intermittent stage that occurs after the synthesis of DNA, but before nuclear and cytoplasmic division of the cell. Prolonged periods in the G<sub>2</sub> phase inhibit cell proliferation (M phase) without inhibiting the formation of daughter cells (S phase), thus yielding binuclear cells [103].

Viability was determined by the sulforhodamine B viability assay [31] in which cells are fixed and stained with sulforhodamine B followed by dye extraction and analysis with an ELISA plate reader at 540 nm. Cell survival decreased with an increase in GeO<sub>2</sub> particle concentration. However, with the clonogenic survival assay, in which cells were cultured for an additional 7 days after treatment with the GeO<sub>2</sub> particles before they were assayed, survival rates were above 80%. This discrepancy is possibly due to delayed cell growth after treatment. Studies were also conducted to determine the phase of the cell cycle that the cells were in after treatment with GeO<sub>2</sub> particles. Treated samples showed a dose-dependent increase in the number

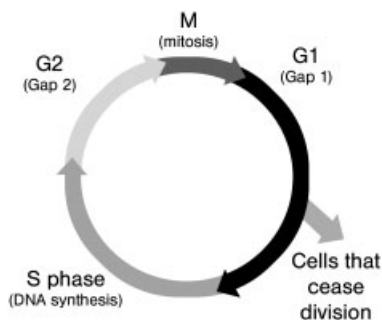


Fig. 1.16. Cell cycle; see text for details. (Figure taken from Ref. [101].)

of cells in the G2/M phase of the cell cycle. Therefore,  $\text{GeO}_2$  particles slow cell proliferation, but do not play a major role in cytotoxicity [102].

Gaudenzi et al. have demonstrated the effects of CdO on a lymphocyte cell line (Jurkat cells). Cells were treated with CdO particles and a survival index, the ratio of the average number of viable cells in the treated and control samples, was calculated. The CdO particles induced a decrease in the survival index of Jurkat cells over time until 24 h when a zero factor was obtained. The mechanism of cell death was probed by FT-IR studies, which showed a decrease in intensity of the amide bands, suggesting a decrease in H-bonding energy and protein degradation. In addition, evidence of additional carbonyl groups was present, which is indicative of protein oxidation [104].

Pigott et al. have found that amorphous  $\text{SiO}_2$  (100 nm) has a biphasic response when exposed to Chinese hamster lung cells. At a dosage of less than  $30 \mu\text{g mL}^{-1}$ , there were little or no cytotoxic effects, based on cloning efficiency; however, there was a progressive increase in cytotoxicity at higher concentrations [105]. Amorphous  $\text{SiO}_2$  was also found to be cytotoxic in other studies, and disrupts cell membrane functions when studied in cell culture [106–108]. However, this should not be of great concern for exposure of airborne amounts of  $\text{SiO}_2$  by inhalation.

## 1.6

### Conclusions

Currently, the National Institute of Occupational Safety and Health (NIOSH) is trying to answer the questions: In what ways might employees be exposed to nanomaterials in manufacture and use? How do nanoparticles enter the body? Once in the body, where would they travel? How would they interact physiologically and chemically with the body's systems [5]? The cellular and subcellular studies described herein provide some clues that address these questions.

In general, the reviewed studies showed that ferric oxide and titanium dioxide nanomaterials are not biotoxic in the dark and that  $\text{TiO}_2$  illuminated with ultraviolet light has a high cytotoxicity to both bacteria and mammalian cells. The toxicity

of ferric oxides under illumination has not been previously studied to our knowledge. There is an environmental photochemistry of ferric oxides with environmental pollutants [28], the products of which often include ferrous ions that could undergo Fenton-like chemistry and produce reactive hydroxyl radicals. Additional studies are warranted in this area.

However, there exist some important exceptions to the generalized statement above. For example, Linnainmaa et al. found no cytotoxicity with illuminated TiO<sub>2</sub> toward rat liver epithelial cells. Since the experimental conditions of light source, TiO<sub>2</sub> materials, and cell lines were different, it is difficult to pinpoint why this study differs. Likewise, Donaldson reported conditions where 20 nm TiO<sub>2</sub> particles linearized plasmid DNA, while 50 nm particles did not. These exceptions underscore some of the difficulties associated with answering NIOSH's questions. When "the body" is replaced by "a single mammalian cell," the answers remain unknown, even for a well-studied nanomaterial like TiO<sub>2</sub>. Additional studies are required before biotoxicity relationships can be understood in more complex human systems at the molecular level.

### Acknowledgment

The authors acknowledge equipment support from the NSF MRSEC Grant number DMR00-80031. The authors also acknowledge support from DARPA/AFOSR Grant F49620-02-1-0307 and from the David and Lucille Packard Foundation Grant #2001-17715. We thank the National Science Foundation (CRAEMS) for support of the environmental chemistry aspects of this work.

### References

- 1 DOWLING, A., Development of nanotechnologies. *Nanotoday*. **2004**, 30–35.
- 2 JOY, B., Why the future doesn't need us. *Wired*. **2000**, 8.04, 37.
- 3 ERHARDT, D., Materials conservation: Not-so-new technology. *Nat. Mater.* **2003**, 2, 509–510.
- 4 www.visionminerals.com.
- 5 www.cdc.gov.
- 6 www.fda.gov.
- 7 DONALDSON, K., STONE, V., Current hypothesis on the mechanisms of toxicity of ultrafine particles. *Ann. 1<sup>st</sup> Super Sanita*. **2003**, 39, 405–410.
- 8 DONALDSON, K., STONE, V., CLOUTER, A., RENWICK, L., MACNEE, W., Ultrafine particles. *Occup. Environ. Med.* **2001**, 58, 211–218.
- 9 HART, G., HESTERBERG, T., In vitro toxicity of respirable-size particles of diatomaceous earth and crystalline silica compared with asbestos and titanium dioxide. *J. Occup. Environ. Med.* **1998**, 40, 29–42.
- 10 U.S. Department of Labor, Bureau of Labor Statistics www.bls.gov.
- 11 ROCO, M., Broader societal issues of nanotechnology. *J. Nanopart. Res.* **2003**, 5, 181–189.
- 12 www.nano.gov.
- 13 *Federal Register*, **2003**, 68, 42 068–42 071.
- 14 SLIVKA, S., LANDEEN, L., ZEIGLER, F., ZIMMER, M., BARTEL, R., Characterization, barrier function, and drug metabolism of an in vitro skin model. *J. Invest. Dermatol.* **1993**, 100, 40–46.
- 15 BENNAT, C., MÜLLER-GOYMAN, C., Skin penetration and stabilization of formulations containing microfine

- titanium dioxide as physical UV filter. *Inter. J. Cos. Sci.* **2000**, *22*, 271–283.
- 16 PFLÜCKER, F., HOHENBERG, H., HÖLZLE, E., WILL, T., PFEIFFER, S., WEPF, R., DIEMBECK, W., WENCK, H., GERS-BARLAG, H., The outermost stratum corneum layer is an effective barrier against dermal uptake of topically applied micronized titanium dioxide. *Inter. J. Cos. Sci.* **1999**, *21*, 399–411.
  - 17 HALLMANS, G., LIDEN, S., Penetration of <sup>65</sup>Zn through the skin of rats. *Acta Dermatol. Venereol.* **1979**, *59*, 105–112.
  - 18 KAPUR, S., BHUSSRY, B., RAO, S., HORMOUTH-HOENE, E. Percutaneous uptake on zinc in rabbit skin. *Proc. Soc. Exp. Biol. Med.* **1974**, *145*, 932–937.
  - 19 DUNFORD, R., SALINARO, A., CAI, L., SERPONE, N., HORIKOSHI, S., HIDAKA, H., KNOWLAND, J., Chemical oxidation and DNA damage catalysed by inorganic sunscreen ingredients. *FEBS Lett.* **1997**, *418*, 87–90.
  - 20 JACKSON, S., ELIAS, P., Skin as an organ of protection. In FITZPATRICK, T., EISEN, A., WOLFF, K., FREEDBERG, I., AUSTEN, K., eds. *Dermatol. Gen. Med.* **1993**, *1*, 241–243.
  - 21 TAN, M., COMMENS, C., BURNETT, L., SNITCH, P., A pilot study on the percutaneous absorption of microfine titanium dioxide from sunscreens. *Austral. J. Dermatol.* **1996**, *37*, 185–187.
  - 22 GHADIALLY, R., HALKIER-SORENSEN, L., ELIASS, P., Effects of petrolatum on stratum corneum structure and function. *J. Am. Acad. Dermatol.* **1992**, *26*, 387–396.
  - 23 NEMANIC, M., ELIAS, P., In situ precipitation: A novel cytochemical technique for visualization of permeability pathways in mammalian stratum corneum. *J. Histochem. Cytochem.* **1980**, *28*, 573–578.
  - 24 EDWARDS, S., DONNELLY, T., SAYRE, R., RHEINS, L. Quantitative in vitro assessment of phototoxicity using a human skin model, Skin<sup>2TM</sup>. *Photodermatol. Photoimmunol. Photomed.* **1994**, *10*, 111–117.
  - 25 DONALDSON, K., LI, X., MACNEE, W., Ultrafine (nanometer) particle mediated lung injury. *J. Aerosol. Sci.* **1998**, *29*, 553–560.
  - 26 SAITO, T., IWASE, T., HORIE, J., MORIOKA, T., Mode of photocatalytic bactericidal action of powdered semiconductor TiO<sub>2</sub> on mutants streptococci. *J. Photochem. Photobiol. B: Biol.* **1992**, *14*, 369–379.
  - 27 WHITESIDES, G., Nanoscience, nanotechnology, and chemistry. *Small.* **2005**, *1*, 172–179.
  - 28 SCHWERTMANN, U., CORNELL, R.M. *The Iron Oxides*, VCH Publishers, Weinheim, **1996**.
  - 29 SCHWERTMANN, U., CORNELL, R.M. *Iron Oxides in the Laboratory: Preparation and Characterization*, VCH Publishers, Weinheim, **1991**.
  - 30 LAWRENCE, R. Development and comparison of iron dextran products. *PDA J. Pharm. Sci. Technol.* **1998**, *52*, 190–198.
  - 31 BAILIE, G.R., JOHNSON, C.A., MASON, N.A. Parenteral iron use in the management of anemia in end-stage renal disease patients. *Am. J. Kidney Dis.* **2000**, *35*, 1–12.
  - 32 ANDRÁ, W., NOWAK, H. *Magnetism in Medicine: A Handbook*, Wiley-VCH, Berlin, **1998**.
  - 33 HÄFELI, U., SCHÜTT, W., TELLER, J., ZBOROWSKI, M. *Scientific and Clinical Applications of Magnetic Microspheres*. Plenum Press, New York, **1997**.
  - 34 SAFARIK, I., SAFARIKOVA, M. Magnetic nanoparticles in biosciences. *Mont. FurChem.* **2002**, *133*, 737–759.
  - 35 KOPPENOL, W.H. The centennial of the Fenton reaction. *Free Rad. Biol. Med.* **1993**, *15*, 645–651.
  - 36 www.polysciences.com.
  - 37 GOETZE, T., GANSAU, C., BUSKE, N., ROERDER, M., GORNERT, P., BAHT, M. Biocompatible magnetic core/shell nanoparticles. *J. Magn. Mater.* **2002**, *252*, 399–402.
  - 38 LACAVA, Z.G.M., AZEVEDO, R.B., MARTINS, E.V., LACAVA, L.M., FREITAS, M.L.L., GARCIA, V.A.P., REBULA, C.A., LEMOS, A.P.C., SOUSA, M.H., TOURINHO, F.A., DA SILVA, M.F., MORAIS, P.C. *J. Magn. Mater.* **1999**, *201*, 431–434.



- 39 MIKHAYLOVA, M., JO, Y.S., KIM, D.K., BOBRYsheVA, N., ANDERSSON, Y., ERIKSSON, T., OSOLOWSKY, M., SEMENOV, V., MUHAMMED, M. The effect of biocompatible coating layers on magnetic properties of superparamagnetic iron oxide nanoparticles. *Hyperfine Int.* **2004**, 156/157, 257–263.
- 40 GUPTA, A.K., GUPTA, M. Cytotoxicity suppression and cellular uptake enhancement of surface modified magnetic nanoparticles. *Biomaterials* **2005**, 26, 1565–1573.
- 41 PETRI-FINK, A., CHASTELLAIN, M., JUILLERAT-JENNERET, L., FERRARI, A., HOFMANN, H. Development of functionalized superparamagnetic iron oxide nanoparticles for interaction with human cancer cells. *Biomaterials* **2005**, 26, 2685–2694.
- 42 STROH, A., ZIMMER, C., GUTZEIT, C., JAKSTADT, M., MARSCHINKE, F., JUNG, T., PILGRIMM, H., GRUNE, T. Iron oxide particles for molecular magnetic resonance imaging cause transient oxidative stress in rat macrophages. *Free Rad. Biol. Med.* **2004**, 36, 976–984.
- 43 FINKLEA, H.O. *Semiconductor Electrodes*, Chapter 2: TiO<sub>2</sub>, Elsevier, New York **1988**.
- 44 LI, G., LI, L., BOERIO-GOATES, J., WOODFIELD, B.F. High purity anatase TiO<sub>2</sub> nanocrystals: near room temperature synthesis, grain growth kinetics, and surface hydration chemistry. *J. Am. Chem. Soc.* **2005**, 127, 8659–8666.
- 45 ZHANG, H., BANFIELD, J.F. Thermodynamic analysis of phase stability of nanocrystalline titania. *J. Mater. Chem.* **1998**, 8, 2073–2076.
- 46 ZHANG, H., BANFIELD, J.F. Understanding polymorphic phase transformation behavior during growth of nanocrystalline aggregates: Insights from TiO<sub>2</sub>. *J. Phys. Chem. B* **2000**, 104, 3481–3487.
- 47 MATIJEVIC, E., BUDNIK, M., MEITES, L. Preparation and mechanism of formation of titanium dioxide hydrosols of narrow size distribution. *J. Colloid Interf. Sci.* **1977**, 61, 302–311.
- 48 WANG, C.-C., YING, J.Y. Sol-gel synthesis and hydrothermal processing of anatase and rutile titania nanocrystals. *Chem. Mater.* **1999**, 11, 3113–3120.
- 49 FU, G., VARY, P.S., LIN, C.-T. Anatase TiO<sub>2</sub> nanocomposites for antimicrobial coatings. *J. Phys. Chem. B* **2000**, 104, 8889–8898.
- 50 NIRMAL, M., BRUS, L.E. Luminescence photophysics in semiconductor nanocrystals. *Acc. Chem. Res.* **1999**, 32, 407–414.
- 51 KAVA, L., GRATZEL, M., GILBERT, S.E., KLEMENZ, C., SCHEEL, H.J. Electrochemical and photoelectrochemical investigations of single-crystal anatase. *J. Am. Chem. Soc.* **1996**, 118, 6716–6723.
- 52 FUJISHIMA, A., HONDA, K. Electrochemical photolysis of water at a semiconductor electrode. *Nature* **1972**, 238, 37–38.
- 53 KHAN, A.U., WILSON, T. Reactive oxygen species as cellular messengers. *Curr. Biol.* **1995**, 2, 437–445.
- 54 MICIC, O., ZHANG, Y., CROMACK, K.R., TRIFUNAC, A., THURNAUER, D.M. Photoinduced hole transfer from titanium dioxide to methanol aqueous solution studied by electron paramagnetic resonance. *J. Phys. Chem.* **1993**, 97, 13 284–13 288.
- 55 DONALDSON, K., BESWICK, P., GILMOUR, P., Free radical activity associated with the surface of particles: a unifying factor in determining biological activity? *Toxicol. Lett.* **1996**, 88, 293–298.
- 56 HART, G., KATHMAN, L., HESTERBERG, T., In vitro cytotoxicity of asbestos and man-made vitreous fibers: roles of fiber length, diameter and composition. *Carcinogen* **1994**, 15, 971–977.
- 57 HESTERBERG, T., BARRETT, J., Induction by asbestos fibers of anaphase abnormalities: Mechanism for aneuploidy induction and possible carcinogenesis. *Carcinogen* **1985**, 6, 473–475.
- 58 WOODWORTH, C., MOSSMAN, B., CRAIGHEAD, J., Induction of squamous metaplasia in organic cultures of hamster trachea by

- naturally occurring and synthetic fibers. *Cancer Res.* **1983**, 43, 4906–4912.
- 59 MAROUDAS, N., O'NEILL, C., STANTON, M., Fibroblast anchorage in carcinogenesis by fibres. *Lancet*, **1973**, I, 807–809.
- 60 PETERS, K., UNGER, R., KIRKPATRICK, J., GATTI, A., MONARI, E., Effects of nano-scaled particles on endothelial cell function in vitro: Studies on viability, proliferation and inflammation. *J. Mater. Sci.: Mater. Med.* **2004**, 15, 321–325.
- 61 www.promega.com.
- 62 SHANBHAG, A., JACOBS, J., BLACK, J., GALANTE, J., GLANT, T., Macrophage/particle interactions: Effect of size, composition and surface area. *J. Biomed. Mater. Res.* **1994**, 28, 81–90.
- 63 STEARNS, R., PAULASKIS, J., GODLESKI, J., Endocytosis of ultrafine particles by A549 cells. *Am. J. Respir. Cell Mol. Biol.* **2001**, 24, 108–115.
- 64 WESTMORELAND, C., WALKER, T., MATTHEWS, J., MURDOCK, J., Preliminary investigations into the use of a human bronchial cell line (16HBE14o-) to screen for respiratory toxins in vitro. *Toxicol. in Vitro.* **1999**, 13, 761–764.
- 65 ABE, K., SAITO, H., Both oxidative stress-dependent and independent effects of amyloid  $\beta$  protein are detected by 3-(4,5-dimethylthiazol-2-yl)-2,5-diphenyltetrazolium bromide (MTT) reduction assay. *Brain Res.* **1999**, 830, 146–154.
- 66 KILGOUR, J., SIMPSON, S., ALEXANDER, D., REED, C., A rat nasal epithelial model for predicting upper respiratory tract toxicity: in vivo-in vitro correlations. *Toxicology.* **2000**, 145, 39–49.
- 67 MILLER, B., PUJADAS, E., GOCKE, E., Evaluation of the micronucleus test in vitro using Chinese hamster cells: Results of four chemicals weakly positive in the in vivo micronucleus test. *Environ. Mol. Muta.* **1995**, 26, 240–247.
- 68 Opinion concerning titanium dioxide, Colipa n° S75 adopted by the SCCNFP during the 14<sup>th</sup> plenary meeting of 24 October 2000. [www.europa.eu.int/comm/health/ph\\_risk/committees/sccp](http://www.europa.eu.int/comm/health/ph_risk/committees/sccp).
- 69 UCHINO, T., TOKUNAGA, H., ANDO, M., UTSUMI, H., Quantitative determination of OH radical generation and its cytotoxicity induced by TiO<sub>2</sub>-UVA treatment. *Toxicol. in Vitro.* **2002**, 16, 629–635.
- 70 ZHANG, A., SUN, Y., Photocatalytic killing effect of TiO<sub>2</sub> nanoparticles on Ls-174-t human colon carcinoma cells. *World J. Gastroenterol.* **2004**, 10, 3191–3193.
- 71 CAI, R., HASHIMOTO, K., ITOH, K., KUBOTA, Y., FUJISHIMA, A., Photokilling of malignant cells with ultrafine TiO<sub>2</sub> powder. *Bull. Chem. Soc. Jpn.* **1991**, 64, 1268–1273.
- 72 CAI, R., KUBOTA, Y., SHUIN, T., SAKAI, H., HASHIMOTO, K., FUJISHIMA, A., Induction of cytotoxicity by photoexcited TiO<sub>2</sub> particles. *Cancer Res.* **1992**, 52, 2346–2348.
- 73 SAKAI, H., ITO, E., CAI, R., YOSHIOKA, T., KUBOTA, Y., HASHIMOTO, K., FUJISHIMA, A., Intracellular Ca<sup>2+</sup> concentration change of T24 cell under irradiation in the presence of TiO<sub>2</sub> ultrafine particles. *Biochim. Biophys. Acta.* **1994**, 1201, 259–265.
- 74 NAKAGAWA, Y., WAKURI, S., SAKAMOTO, K., TANAKA, N., The photogenotoxicity of titanium dioxide particles. *Mut. Res.* **1997**, 394, 125–132.
- 75 SINGH, N. P., MCCOY, M. T., TICE, R. R., SCHNEIDER, E. L., A simple technique for quantation of low levels of DNA damage in individual cells, *Exp. Cell Res.* **1988**, 175, 184–191.
- 76 HARTMANN, A., SPEIT, G., Comparative investigations of the genotoxic effects of metals in the single cell gel (SCG) assay and sister chromatid exchange (SCE) test, *Envir. Mol. Mutagen.* **1994**, 23, 299–305.
- 77 WARMER, W., YIN, J., WEI, R., Oxidative damage to nucleic acids photosensitized by TiO<sub>2</sub>. *Free Rad. Biol. Med.* **1997**, 23, 851–858.
- 78 DIZDAROGLU, M., Formation of an 8-hydroxyguanine moiety in deoxyribonucleic acid on  $\gamma$  irradiation

- in aqueous solution. *Biochemistry* **1985**, *24*, 4476–4481.
- 79 FLOYD, R., WEST, M., ENEFF, K., HOGSETT, W., TINGEY, D., Hydroxyl free radical mediated formation of 8-hydroxyguanine in isolated DNA. *Arch. Biochem. Biophys.* **1988**, *262*, 266–272.
- 80 BLAKELY, W., FUCIARELLI, A., WEGHER, B., DIZDAROGLU, M., Hydrogen peroxide-induced base damage in deoxyribonucleic acid. *Radiat. Res.* **1990**, *121*, 338–343.
- 81 KUBOTA, Y., SHUIN, T., KAWASAKI, C., HOSAKA, M., KITAMURA, H., CAI, R., SAKAI, H., HASHIMOTO, K., FUJISHIMA, A., Photokilling of T-24 human bladder cancer cells with TiO<sub>2</sub>. *Br. J. Cancer* **1994**, *70*, 1107–1111.
- 82 CAI, R., HASHIMOTO, K., KUBOTA, Y., FUJISHIMA, A., Increment of photocatalytic killing of cancer cells using TiO<sub>2</sub> with the aid of superoxide dismutase. *Chem. Lett.* **1992**, 427–430.
- 83 CAI, R., HASHIMOTO, K., FUJISHIMA, A., KUBOTA, Y., Conversion of photogenerated superoxide anion into hydrogen peroxide in TiO<sub>2</sub> suspension system. *J. Electroanal. Chem.* **1992**, *326*, 345–350.
- 84 JANG, H., KIM, S., Effect of particle size and phase composition of titanium dioxide nanoparticles on the photocatalytic properties. *J. Nanopart. Res.* **2001**, *3*, 141–147.
- 85 CARAFOLI, E., Intracellular calcium homeostatis. *Annu. Rev. Biochem.* **1987**, *56*, 395–433.
- 86 FARBER, J., The role of calcium in cell death. *Life Sci.* **1981**, *29*, 1289–1295.
- 87 ORRENIUS, S., MCCONKEY, D., BELLOMO, G., NICOTERA, P., Role of Ca<sup>2+</sup> in toxic cell killing. *Trends Pharmacol. Sci.* **1989**, *10*, 281–285.
- 88 KOMULAINEN, H., BONDY, S., Increased free intracellular Ca<sup>2+</sup> by toxic agents: an index of potential neurotoxicity? *Trends Pharmacol. Sci.* **1988**, *8*, 154–156.
- 89 NICOTERA, P., HARTZELL, P., BALDI, C., SVENSSON, S., BELLOMO, G., ORRENIUS, S., Cystamine induces toxicity in hepatocytes through the elevation of cytosolic Ca<sup>2+</sup> and the stimulation of a nonlysosomal proteolytic system. *J. Biol. Chem.* **1986**, *261*, 14628–14635.
- 90 KANE, A., STANTON, R., RAYMOND, E., DOBSON, E., KNAFELC, E., FARBER, J., Dissociation of intracellular lysosomal rupture from the cell death caused by silica. *J. Cell Biol.* **1980**, *87*, 643–651.
- 91 LEMASTERS, J., DIGUISEPPI, J., NIEMINEN, A., HERMAN, B., Blebbing, free calcium and mitochondrial membrane preceding cell death in heptaocytes. *Nature.* **1987**, *325*, 78–81.
- 92 LINNAINMAA, K., KIVIPENSAS, P., VAINIO, H., Toxicity and cytogenetic studies of ultrafine titanium dioxide in cultured rat liver epithelial cells. *Toxicol. in Vitro.* **1997**, *11*, 329–335.
- 93 ULLAH KHAN, A., WILSON, T. Reactive oxygen species as cellular messengers. *Chem. Biol.* **1995**, *2*, 437–445.
- 94 MANESS, P., SMOLINSKI, S., BLAKE, D., HUANG, Z., WOLFRUM, E., JACOBY, W., Bactericidal activity of photocatalytic TiO<sub>2</sub> reaction: toward an understanding of its killing mechanism. *Appl. Environ. Microbiol.* **1999**, *65*, 4094–4098.
- 95 YAMAMOTO, A., HONMA, R., SUMITA, M., HANAWA, T., Cytotoxicity evaluation of ceramic particles of different sizes and shapes. *J. Biomed. Mater. Res.* **2004**, *68A*, 244–256.
- 96 RAE, T., A study on the effects of particulate metals of orthopaedic interest on murine macrophages in vitro. *J. Bone Joint Surg.* **1975**, *57-B*, 444–450.
- 97 RAE, T., The toxicity of metals used in orthopaedic prostheses. *J. Bone Joint Surg.* **1981**, *63-B*, 435–440.
- 98 HANAWA, T., KAGA, M., ITOH, Y., ECHIZENYA, T., OGUCHI, H., OTA, M., Cytotoxicities of oxides, phosphates and sulphides of metals. *Biomaterials* **1992**, *13*, 20–24.
- 99 LISON, D., LARDOT, C., HUAUX, F., ZANETTI, G., FUBINI, B., Influence of particle surface area on the toxicity of insoluble manganese dioxide dusts. *Arch. Toxicol.* **1997**, *71*, 725–729.
- 100 LEHNERT, B., Defense mechanisms against inhaled particles and associated particle-cell interactions.,

- In: GUTHRIE, G., MOSSMAN, B., *Review in Mineralogy, Health Effects in Mineral Dusts*, Mineralogical Society of America, Washington, DC, 1993, p. 28.
- 101 KECELI, S., ALANYALI, H., A study on the evaluation of the cytotoxicity of  $\text{Al}_2\text{O}_3$ ,  $\text{Nb}_2\text{O}_5$ ,  $\text{Ta}_2\text{O}_5$ ,  $\text{TiO}_2$ , and  $\text{ZrO}_2$ . *Turk. J. Eng. Environ. Sci.* 2004, 28, 49–54.
- 102 CHIU, S., LEE, M., CHEN, H., CHOU, W., LIN, L., Germanium oxide inhibits the transition from G2 to M phase of CHO cells. *Chem. Biol. Interact.* 2002, 141, 211–228.
- 103 [http://www.biology.arizona.edu/cell\\_bio/tutorials/cell\\_cycle/cells2.html](http://www.biology.arizona.edu/cell_bio/tutorials/cell_cycle/cells2.html).
- 104 GAUDENZI, S., FURFARO, M., POZZI, D., SILVESTRI, I., CASTELLANO, A., Cell-metal interaction studied by cytotoxic and FT-IR spectroscopic methods. *Environ. Toxicol. Pharmacol.* 2003, 14, 51–59.
- 105 PIGOTT, G., PINTO, P., Effects of nonfibrous minerals in the V79-4 cytotoxicity test. *Environ. Health Perspect.* 1983, 51, 173–179.
- 106 TIMBRELL, V., GILSON, J., WEBSTER, I., UICC standard reference samples of asbestos. *Int. J. Cancer.* 1968, 3, 406–408.
- 107 DAVIES, R., The effect of ducts on enzyme release from macrophages. In: *The In Vitro Effects of Mineral Dusts*. Academic Press, London 1980, 67–74.
- 108 PIGOTT, G., JUDGE, P., The effects of mineral dusts “in vitro”: a comparison of the response of rat peritoneal macrophages and the P388D1 cell line. In: *The In Vitro Effects of Mineral Dusts*. Academic Press, London 1980, 53–57.

## 2

# Ecotoxicity of Engineered Nanomaterials

*Eva Oberdörster, Patricia McClellan-Green, and Mary Haasch*

### 2.1

#### Introduction

To date there has only been one thorough review of the nanotoxicology literature from a biological viewpoint [1], and that review through necessity was based on related work done primarily on the toxicology of ultrafine particulate matter in mammalian models. In this chapter we will not repeat the previous report, but will instead focus on new investigations of engineered nanomaterials in environmentally relevant species and models. Initial “eco-nano” considerations were focused on using nanomaterials in the environment for remediation, in the development of more accurate and sensitive biosensors, and for green energy production, for example (Table 2.1). With these initial efforts there was little concern for engineered nanomaterials functioning as toxicants themselves, and the focus was on technology development. Only since 2004 has the issues of nano-ecotoxicology of highly reactive, lipophilic engineered nanomaterials come to the front. The numerous benefits to society from the development of NP should not be minimized. Decreasing our dependence on highly toxic fossil fuels, remediating superfund sites, creating new and better drug delivery systems and green manufacturing are all processes whose benefits portend great promise. We should not approach these technologies wearing blinders, but rather be cognizant of the big picture. In other words: Be aware of the benefits and the costs.

One issue that immediately confronts any scientist in the area of nanoparticle toxicology is terminology. Standardized terminology is not yet in use, although efforts are underway by Rice University’s CBEN to move forward on this front. In this chapter, we will use engineered nanoparticles (NP) to designate any man-made nanomaterial (one dimension < 100 nm) with specific chemical, size, and shape characteristics, including materials such as fullerenes (C<sub>60</sub>, C<sub>70</sub>), single-walled carbon nanotubes (SWNT), quantum dots, nano-wires-films, -textiles, and so forth. The more general term, nanosized particle (NSP), will include both the NP and naturally occurring particles that are less than 100 nm in one dimension, such as the ultrafine particles (UFP) in air pollution, and small bacteria and viruses. This chapter will focus on engineered nanoparticles (NP).

**Tab. 2.1.** Some recent funding by the US EPA to develop applications of NP for use in the environment [38].

Type of NP used	Potential use	Lead PIs and Institutions
	<i>Remediation</i>	
NanoTiO <sub>2</sub>	Photocatalysis of organic contaminants	D.D. Dionysiou Miami University-Oxford, OH; University of Cincinnati, OH
Carbon nanostructures	Sorption of organics	M.B. Tomson Rice University
Nano-metal oxides	Control NO <sub>x</sub> production	S. Senkan UCLA
Nano-iron	Degradation of PAH-based contaminants	G.V. Lowry, S.A. Majetich, K. Matyjaszewski, R.D. Tilton Carnegie Mellon University
Nano-biopolymers	Control of heavy metals	W. Chen, M. Matsumoto, A. Mulchandani UC Riverside
Bi-metallic nano-Fe/Pd	Remediation of inorganics and organics	W.X. Zhang Lehigh University
Nano-crystalline zeolite	NO <sub>x</sub> , photocatalytic oxidation of organics	S.C. Larsen, V.H. Grassian University of Iowa
Nano-magnetite	Groundwater contamination	M. Hull Luna Innovations, Inc.
	<i>Filtration</i>	
Ferromagnetic particles	Using nanocomposites to monitor and filter (smart particles)	W.M. Sigmund, D. Mazyck, C.Y. Wu University of Florida
Nano-crystalline catalysts	Disinfection by-product control in drinking water	S.J. Masten, M.J. Baumann Michigan State University
Nanostructured electrodes	Perchlorate from drinking water	S.M. Jaffe Material Methods LLC
	<i>Sensors</i>	
Carbon nanoparticle based microchip	Analytical chemistry of environmentally relevant endpoints	J. Wang New Mexico State University

Tab. 2.1 (continued)

Type of NP used	Potential use	Lead PIs and Institutions
Nanocrystalline metallic conductors	Gas sensor	V. Subramanian UC Berkeley
Colloidal-metal nanoparticles	Monitoring heavy metals	O. Sadik, J. Wang New Mexico State University
Polystyrene beads coated with peptides	Detection of aquatic toxins	R.E. Gawley University of Miami
Fullerene	Tracers for water pollution	J.B. Callegary University of Arizona
	<i>Green energy/manufacturing</i>	
Nano-clay	Substitute petroleum-based products for nano-composites	L.T. Drzal, M. Misra, A.K. Mohanty Michigan Sate University
Nano-micelles	Replacing VOCs with nano-structured microemulsions	D.A. Sabatini, J.H. Harwell University of Oklahoma
Nano-plastic fibrils and crystals	Alternative to petroleum-based composites	W.T. Winter SUNY College of Environmental Science and Forestry
Nano-TiO <sub>2</sub>	Photocatalyst for solar cells	G. Chumanov Clemson University
Semi-conducting nanoparticles	Catalyst fuel cells	N.Y. Dolney University of Michigan-Ann Arbor

When “nano” first became the hot new technology, immediate environmental applications were sought using these reactive materials. Numerous funding agencies encouraged development of NP use in the environment (applications, Table 2.1) and initially very little consideration was given to the unintended consequences or implications of nanomaterial production or use in the environment. The new technologies developed include a wide array of materials designed for remediation activities (some of which are in commercial use), the development of biosensors for chemicals or biological agents, the development of environmental filtration processes, and green manufacturing. Although one could argue that both applications and implications are important areas of research, the implica-

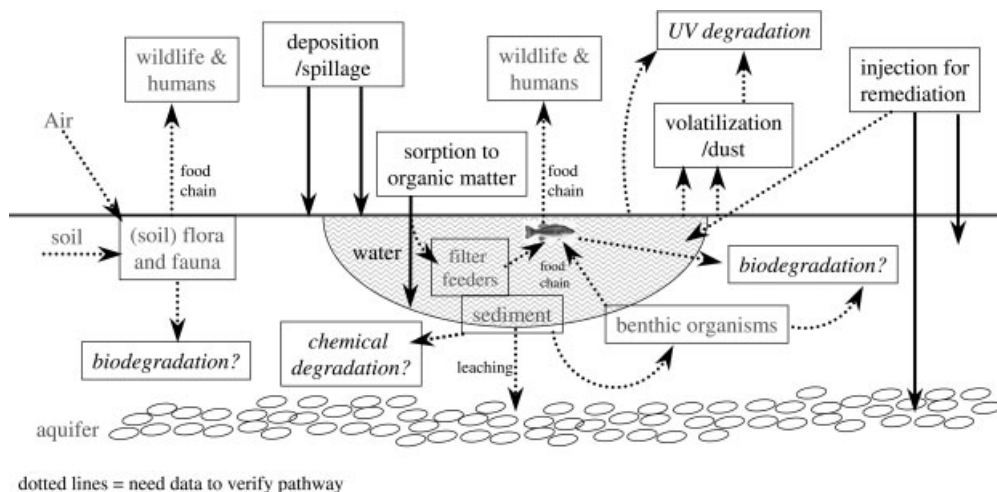


**Fig. 2.1.** Model of NP movement through the environment. Dotted lines indicate pathways not yet verified, while solid arrows indicate verified pathways. (From Oberdörster et al. [1].)

tions research of NPs has lagged behind. In this chapter, we focus on some of the recent environmental implications of NPs as toxicants, and will discuss issues that need to be addressed through future research.

The complexity of NP in ecotoxicology can be seen in Fig. 2.1. Particle movement through water, air and soils has been poorly studied, and biological uptake and food chain transport have not been considered. Biotransformation and chemical and UV breakdown have been given scant consideration and in-depth chemical analysis or other characterizations, including electron microscopic imaging of NP before and after environmental ageing, have not been conducted. In the following sections, we review these issues along with suggested areas of future research.

## 2.2

### Water

Many NP are poorly soluble in water (e.g., SWNT,  $C_{60}$ ). However, if coated with an appropriate molecule, such as peptides or proteins [2, 3], poly(ethylene glycol) (PEG), or other surfactants, even non-water-soluble NP can be rendered miscible with water, including water-containing humic acids and salts [4]. Another effective method to render lipophilic NP (such as  $C_{60}$ ) water-soluble is to allow the particle powders (clumps of NP) to stir in water for a few days or up to several weeks (longer agitation times equal more dissolution). This slow procedure is a more environmentally relevant method of introducing NP into solution. Recent data shows that using organic solvents as an intermediary to render NP water-soluble leaves



traces of the organic solvent in centers of fullerene clusters. For example, Andrievsky et al. [5], Brant et al. [6], and Fortner et al. [4] have demonstrated that using tetrahydrofuran (THF), a common organic solvent, to solubilize  $C_{60}$  in water resulted in formation of  $nC_{60}$  aggregates that contained residual amounts of THF. This residual THF is of biological concern and toxicologically relevant. In daphnia we have found that the 48-hour  $LC_{50}$  is orders of magnitude different between THF-solubilized  $nC_{60}$  (0.8 ppm) and stirred  $nC_{60}$  (>30 ppm, which was the highest concentration tested). (For a review of solubility levels of NP in various solvents please refer to Nakamura and Isobe [7].) Thus, when performing ecotoxicity tests, it is crucial to determine not only a valid range of concentrations for testing (will we really see ppm levels?), but also to use realistic methods of water-solubilization of NP.

There are several target areas of concern when discussing ecotoxicology of NP. Engineered NP will tend to agglomerate to each other or to larger particles in the environment, and will tend to sorb onto or associate with sediments. These sediments can then be ingested by benthos, creating a food-chain through which these NP can move (Fig. 2.1). In preliminary studies with the suspension-feeding worm *C. elegans*, we have shown that FITC-labeled SWNT (which can be easily tracked through the exposure dishes and inside the worms) move through the digestive tract (DG) and are not absorbed into the animal (unpublished data, laboratory of Eva Oberdörster in collaboration with Jim Waddell, Southern Methodist University and Ya-Ping Sun, Clemson University). This type of tracking has not been done for other NP, but is a crucial step in determining uptake into biota. Even if NP remain solely in the DG tract and do not bioaccumulate, they are still likely to move up the food chain as worms and other organisms are consumed by benthivores (Fig. 2.1). This scenario seems even more likely with a detritivore benthic organism like *Hyalalella azteca* in which the  $nC_{60}$   $LC_{50}$  is greater than 7 ppm. In fact, no toxic effects are observed in *Hyalalella* even when the  $nC_{60}$  is mixed in the food [8].

In contrast to the *C. elegans* study, we have shown that filter-feeding crustaceans (*Daphnia magna*) can accumulate NP when exposed via the water column (Figs. 2.2 and 2.3). Nano-iron used in remediation is ingested by daphnia and can coat their carapace, including filtering apparatus and appendages (Fig. 2.3). Even though the daphnids were coated with nano-iron, they were able to survive in the laboratory test and were able to feed and reproduce. The toxicity of nano-iron was the same as that for bulk iron, approximately 55 ppm (Fig. 2.3). The daphnids containing nano-iron in the gut and on the carapace are much darker in coloration than daphnids without the nano-iron. Since many daphnid predators (fish) are visual feeders, it would be interesting to determine whether the darker daphnids are more likely to be preyed upon than lighter daphnids, similar to what has been shown with melanized (darker) vs. lighter-colored daphnids [9].

Daphnids are generalist filter feeders specializing in larger-sized phytoplankton [9]. However, numerous species are specialized filter feeders, including many rotifers that specialize in nanosized prey, such as Archaea and other small bacteria. The differential impact of NP on filter feeders that are generalists vs. specialists still needs to be determined. A study by Conova [10] has shown that some filter-

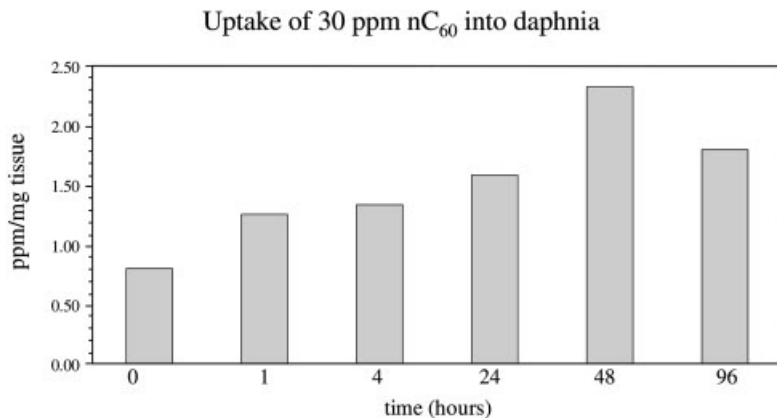
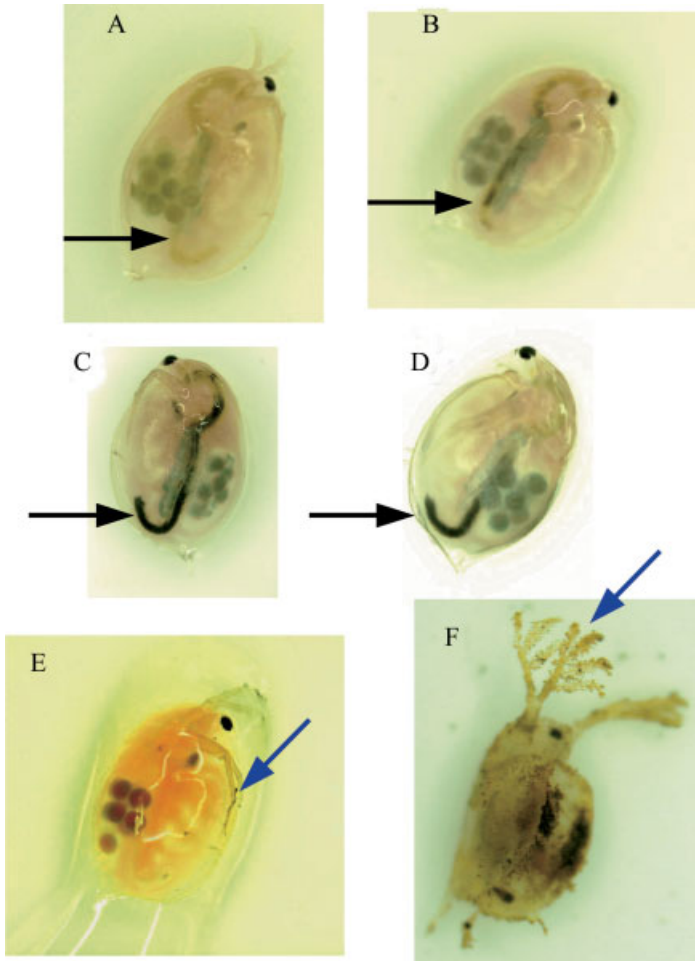


**Fig. 2.2.** Uptake of  $nC_{60}$  into *Daphnia magna*. Approximately 15 daphnids were collected at each time point, and were rinsed 5× with reconstituted hard water during 1 h. Water was removed by blotting, and a wet-weight was taken. The  $nC_{60}$  was oxidized, using 1 mL bleach, and extracted overnight into toluene. Absorbance was read at 332 nm and compared to a standard curve.

feeders select their prey by surface chemistry, not necessarily size. Therefore, coating NP to make them more “biocompatible” may make them easier for certain species to selectively filter. In addition, many aquatic and marine organisms, especially crustaceans, carry out their feeding and reproductive behaviors through the use of chemosensory organs. Adherence of NP to the surface of the chemosensory structures such as seen in Fig. 2.3 could disrupt their growth, development or reproduction by interfering both physically or physiologically with these structures. These are not minor considerations given that zooplankton is the basis of aquatic food chains. Specific impacts on zooplankton can significantly alter predator/prey balance and lead to shifts in ecosystem health.

Vertebrates would be exposed not only via the food chain (either by ingesting sediments directly or by ingesting NP-contaminated prey) but also through gill and skin. Observations by Tjälve [11, 12] and Oberdörster [13] have shown that translocation of toxicants, including NP, via the olfactory neuron into the brain is likely in several species of fish. Although most NP will tend to sorb to sediments or onto phytoplankton, NP will likely move up the food chain due to benthos and filter-feeding invertebrates. These types of studies – systematic bioaccumulation/biodistribution – have not been done to date. Considering the current restrictions on fish consumption for humans due to PCBs and methyl mercury [14], it is not only an ecosystem health issue, but also a human-health issue.

Although movement of NP through the food chain is likely, recent studies by Le-coanet [15] have shown that NP are of very low mobility in aquifers. Even though NP are currently injected into aquifers and ground-water for remediation, it has been hypothesized that they will not move far from the injection point. However, the rate of movement of NP in real-life applications has not been tested. The size,



*Daphnia magna* 48 hour mortality after exposure to nano-iron

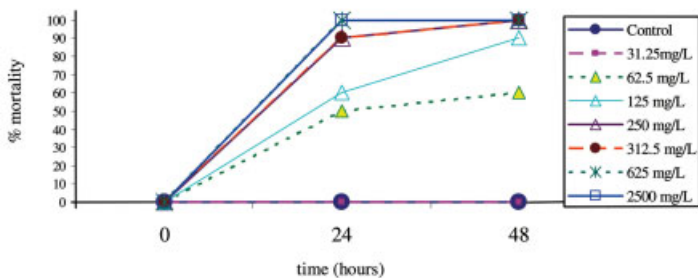


**Fig. 2.3.** *Daphnia magna* exposed to various concentrations of nano-iron used in remediation. A = control; B = 3; C = 7.5; D = 15; E = 30; F = 125 mg L<sup>-1</sup> (dead daphnid). All daphnids shown are 21-days-old and eggs are visible in their brood pouches (green circles).

Note the darkening of the digestive tract from A (normal greenish color) to D with increased ingestion of nano-iron particles (black arrows). Antennae become clogged with nano-iron in E and F (blue arrows). The 24 and 48 h mortality curves are also shown.

shape and surface chemistry of NPs that make them so attractive in various technologies will also influence their behavior in the environment. Pharmaceutical NPs that have been coated to make them more soluble or to improve the solubility of attached drugs or compounds will surely enter the waste-water stream, similar to what has been observed with other drugs and medicines [16]. Once there, NP will be transported, broken down or accumulated based on their physicochemical properties. For example, polyhydroxylated  $C_{60}$  (fullerenols) or surfactant modified nanotubes are specifically engineered to increase their solubility in water, and could therefore remain in the aqueous phase. But these modifications also increase NP movement through porous media [17]. Movement of specific NPs in environmental media has not been thoroughly investigated, although researchers at Rice University are beginning to address this issue.

### 2.3

#### Air

Most research on airborne NSP has been on ultrafine particles (UFP) of various chemical and size compositions, and of NP in the workplace [1]. NSP can either agglomerate to each other or to other particles in the air, depending on particle number density and time. Particle sizes of less than 5 nm in diameter will behave more like gases, while larger sized NSP behave more like bulk particles; for a review see Ref. [1]. NSP are produced from combustion by-products, and can deposit as dust particles, and can also be re-suspended by wind (Fig. 2.1). Global movement of NSP through atmospheric deposition and re-suspension is likely, similar to what has been found in other gaseous and particle pollutants, such as CFCs. Biswas and Wu have recently reviewed the NP/NSP literature [18]; please refer to that reference and to Chapters 4 and 7 of this text for more details on airborne NSP effects, especially as they relate to workplace exposure.

### 2.4

#### Soils

Soils are a complex mixture of organic and inorganic compounds, and microbial and other living organisms. Soils are so complex that standard “soils” are used in ecotoxicology testing. To date, no studies have been performed using these standard soil protocols, but one recent study shows that at relatively high doses (ppm) microbial growth (*E. coli* and *B. subtilis*) was reduced with nano- $TiO_2$  and  $nC_{60}$  [4]. Since these are relatively high levels of nanomaterials, modeling exercises are needed to determine relevant doses before being able to decide whether there are risks involved in release of NP into soils.

Another source of NP in the environment (especially soils and sediments) are NP-containing matrices that function as slow-release agents for various biocides [19]. These matrices can be applied to various surfaces to inhibit biological growth

(e.g., of fungi), but as the matrices weather or wear off, NP will be released into the environment. What happens to these matrices (how fast do they break down? are NP released from them as they break down?) is unknown.

Toxic NSP can be inadvertently created in soils, as bacteria absorb toxicants, creating “biological” toxic NSP. Pollmann et al. [20] have demonstrated that the outer layer of some bacterial species function as selective matrices for the binding of toxic metals. They demonstrated the S-layer of *Bacillus sphaericus* JG-A12, through its hydrophobic construction and the presence of phosphorylated proteins, possesses an extremely high and reversible binding capacity for toxic metals such as uranium and palladium. This binding creates NSP that can be removed from the environment. But what happens to the inadvertently created NSP? Where do they go? And how does sorption of toxicants, including NP, affect microbial communities?

In addition to effects on microbial communities, it is likely that plants can take-up and bioaccumulate NP. Some interesting solar-cell applications have been developed using synthetic chlorophyll and fullerene [21], but it has not yet been determined whether fullerene can interfere with or enhance natural photosynthesis by bypassing the usual electron transport chain. Given that solar-power research is focused on using nanomaterials, it is critical to determine whether natural solar-power (i.e., photosynthesis) can be disrupted or enhanced by NP. Preliminary studies in our laboratory indicate that  $nC_{60}$  may influence (enhance) the growth rates of blue-green algae (*Anabaena* sp.) (unpublished observation, B. Craig and P. McClellan-Green). The mechanism behind the change in growth is unknown. The  $nC_{60}$  might act as a nutrient source, facilitate uptake of media nutrients, or possibly interact with photosynthesis to accelerate the process. Although it is difficult to predict the types of challenges that could arise due to NP in soils, another area of concern is that these NP could interfere with cell signaling, such as with root nodulation of nitrogen-fixing bacteria. Such interference has been shown with pesticides [22], and could lead to unintended agricultural consequences.

Movement of NP through soil food chains is likely. Owing to the tendency to sorb to particles, NP will likely be ingested or absorbed by soil organisms (bacteria, worms, insects, plants, fungi, etc.) and could move up the food chain (Fig. 2.1). No studies have been performed on soil-food chain transport, but this will likely be an important future area of research given the human manipulation of environmental NP and NSP, and cycling between air deposition and re-suspension in air and water by dust and debris (Fig. 2.1).

## 2.5 Weathering

Currently, studies on NP and ecologically-relevant endpoints have been carried out under laboratory conditions without allowing for action by abiotic factors, such as UV, other chemicals, and dissolved oxygen levels/anoxia. Few studies have been carried out on UV interactions with NP that are either coated or covalently linked to molecules that render the NP less toxic. These studies have shown that even a

short exposure to UV light can un-coat and/or cleave the covalent linkage to produce the more toxic parent NP [23, 24]. Therefore, studies using standard laboratory procedures are an important first step; however, environmentally realistic exposures need to include UV exposures. This is similar to what has been shown with PAHs, where UV light exposure photoactivates and increases the toxicity of PAHs. In addition to UV, chemical activation of NP must be considered. Molecules such as fullerenes, which are redox active due to their chemistry, may interact with toxicants present or entering the environment. The question of whether other redox active toxicants will enhance or suppress fullerene toxicity has not been addressed. Can fullerenes donate or accept electrons from environmental compounds in such a manner that will create more or less toxic elements? In addition, the level of anoxia, which can increase the oxidative stress response in affected organisms may or may not influence fullerene toxicity. These types of questions, i.e., mixtures studies, studies including UV as co-factors, and varying levels of oxygenation have not been addressed as yet but will be valuable in determining realistic environmental hazards.

Aside from the abiotic factors, microbial degradation/activation may also affect the activity of NPs in the environment. Several studies have shown that bacterial and microsomal P450s can metabolize NP [25–28]. Microbes could, possibly, weather both covalent modifications and coatings from NP, altering their toxicity. Model P450s produce oxidation products of fullerene, including sequential epoxidation products [25]. The introduction of hydroxy groups (as is common with P450 metabolism) makes at least some NP less toxic [4, 29], and therefore microbial weathering may help reduce the environmental impact of NP. Fortner et al. [4] recently found a hormetic effect in *B. subtilis* bacteria exposed to hydroxylated-fullerene – the highly hydroxylated fullerene ( $C_{60}(OH)_{24}$ ) enhanced microbial growth as compared to control and non-hydroxylated  $nC_{60}$ . Could upregulation of key enzymes (e.g., cytochrome P450s) be responsible for this hormetic effect? It is too early to make such determinations, but research is being conducted in this area to develop a database from which to draw better mechanistic conclusions.

## 2.6

### Biomarkers

Given that microbial P450s metabolize NP *in vitro* [25–28, 30], it is possible that this class of enzymes may be useful as biomarkers of NP exposure. Previously, Ueng et al. [27] demonstrated that exposure of mice to fullerenol-1 decreased monooxygenase activities towards the compounds benzo[*a*]pyrene, 7-ethoxycoumarin, aniline and erythromycin. They also demonstrated an inhibition of ADP-induced uncoupling and mitochondrial  $Mg^{2+}$  ATPase activity. In our laboratory, we have found that the CYP2 family of enzymes are upregulated in two species of fish following exposure to SWNT at both the protein and mRNA levels (Fig. 2.4) [31, 32]. Although preliminary, it would be interesting if specific biomarkers of exposure could be developed for NP. To this end, an effort is currently underway in

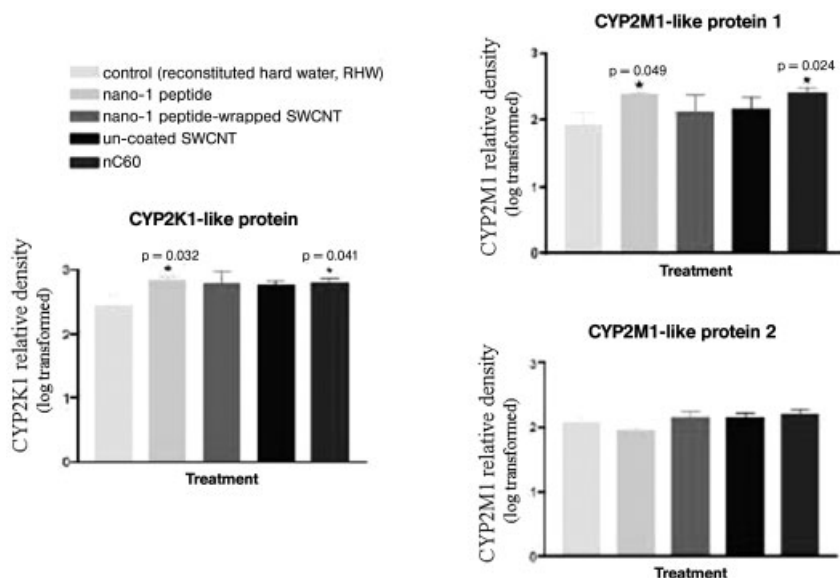


**Fig. 2.4.** Upregulation of cytochrome P450 isozymes in male fathead minnow exposed for 48 h to 0.2 ppm synthetic nano-1 peptide, 0.2 ppm SWNT or 1 ppm water-soluble fullerene ( $nC_{60}$ ) (Oberdörster et al. [31]). It appears that both  $nC_{60}$  and the synthetic peptide used to make SWNT biocompatible induce CYP2-family proteins.

conjunction with the Woodrow Wilson Center for International Scholars, interested NP-producing Industries, and academia to create a “nano-chip” (microarray) that could serve as a basis for both laboratory screening and field-testing to determine exposures to NP [33]. Endpoints of interest would not only include the P450-family of enzymes, but also enzymes related to oxidative stress management, and proteins involved in the inflammatory response. Several studies have shown that NP can cause oxidative stress both *in vivo* and *in vitro* [13, 23, 24, 29, 34–37], and that NP can also cause inflammation; for a review see Ref. [1].

To develop a systematic approach to detecting and validating biomarkers of exposure, it is necessary to adapt current standard toxicity tests for NP. The biggest challenge will be to use uniform NP, both chemically uniform and using a standardized preparation method. Fortner et al. [4] have shown that the preparation method can alter the ultimate end-product of NP, and anecdotal evidence suggests differences between stirring vs. bath sonication vs. probe sonication. As mentioned earlier, we have shown that, in daphnia, the 48-hour  $LC_{50}$  is orders of magnitude different between THF-solubilized  $nC_{60}$  (0.8 ppm) and stirred  $nC_{60}$  (>30 ppm). In addition, the many compounds that are attached to NPs will influence their bioaccumulation, breakdown and toxicity, especially if the attached compounds are removed within different compartments in the environment.

As well as standardized testing, environmentally relevant doses need to be used. Using only high concentrations and looking only for mortality does not give in-

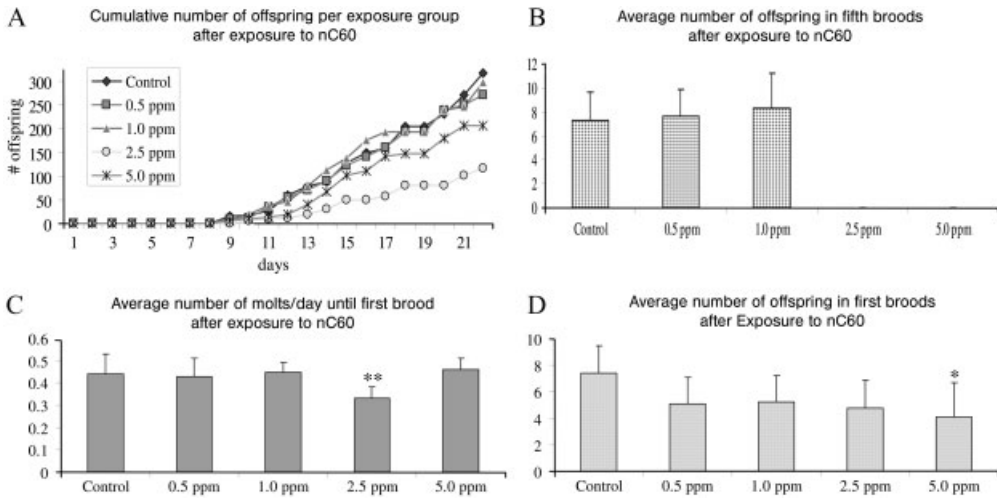


**Fig. 2.5.** Exposure of *Daphnia magna* to sub-lethal levels of  $nC_{60}$  delays reproduction (A), results in one fewer brood (no fifth brood) over 21 days (B), slows molting (C), and reduces the number of offspring in the first brood (D); \*  $p < 0.05$ , \*\*  $p < 0.01$ . Therefore, sub-lethal

endpoints need to be investigated when studying NP effects in environmentally relevant species.  $nC_{60}$  used in this study was prepared by stirring. No organic solvents were used to solubilize the  $nC_{60}$ .

sights into mechanisms of action. For example, in daphnia we have found that sub-LC<sub>50</sub> doses of  $nC_{60}$  can inhibit reproduction by delaying brood production and brood size (Fig. 2.5). Gene chips can also give insights into sub-lethal effects and mechanisms of action. Clearly, a combination of population-level data (such as reproductive output) and protein and gene expression can give a clearer picture of environmental risks posed by NP. To date this information is not available, although several researchers are addressing these issues.

## 2.7

### Conclusions

NP are already in the environment, used either for remediation, or from normal use and wear of products containing NP (tires, clothing, sporting equipment, cosmetics, etc.). As there is almost no data on the toxicity of NP to environmentally relevant species, it is difficult to predict ecosystem risks. Although steps are being taken to remedy this lack of knowledge, several key research areas will need to be addressed. These include, but are not limited to:

1. How far can NP move through air, water and soil? How do size, shape, surface chemistry and agglomeration state affect this movement?



2. What are the most likely routes of exposure for environmentally relevant species (ingestion, dermal, inhalation, root uptake)?
3. Can NP interfere with photosynthesis, with microbial communities, or with inter-species communication (such as root nodulation)?
4. Can NP bioaccumulate?
5. Can NP be metabolized to more or less toxic forms?
6. What biomarkers are relevant for measuring NP exposure levels?
7. What end-points are significant for determining risk of NP?
8. What are the mechanisms of toxicity of NP in environmentally relevant systems?
9. Does the presence of NP in the environment affect the toxicity of other compounds and vice versa?

Many of these questions are currently being addressed by scientists around the world. We may well be able to come to a better consensus on eco-risks of NP once these basic questions are answered. Until then, the numerous benefits of NP should not be underestimated! Decreasing our dependence on highly toxic fossil fuels, remediating superfund sites, creating new and better drug delivery systems and green manufacturing are all processes whose benefits need to be considered alongside any toxic effects of NP.

## References

- 1 OBERDÖRSTER, G., E. OBERDÖRSTER, J. OBERDÖRSTER, Nanotoxicology: An emerging discipline evolving from studies of ultrafine particles. *Environ. Health Persp.*, **2005**. 113(7), 823–839.
- 2 OBERDÖRSTER, E., A. ORTIZ-ACEVEDO, H. XIE, P. PANTANO, R.H. BAUGHMAN, G.R. DIECKMANN, I.H. MUSSELMAN, R.K. DRAPER, Exposure of fathead minnow to fullerene and single-walled carbon nanotubes. *The toxicologist CD*, An official Journal of the Society of Toxicology, **2005**. 84(S1), 325.
- 3 DIECKMANN, G., A. DALTON, P. JOHNSON, J. RAZAL, J. CHEN, G. GIORDANO, E. MUNOZ, I. MUSSELMAN, R. BAUGHMAN, R. DRAPER, Controlled assembly of carbon nanotubes by designed amphiphilic peptide helices. *J. Am. Chem. Soc.*, **2003**. 125(7), 1770–1777.
- 4 FORTNER, J.L., LYON, D.Y., C.M. SAYES, A.M. BOYD, J. FALKNER, E. HOTZE, L. ALEMANY, Y. TAO, K. AUSMAN, V. COLVIN, J. HUGHES, C<sub>60</sub> in water: Nanocrystal formation and microbial response. *Environ. Sci. Technol.*, **2005**. 39(11), 4307–4316.
- 5 ANDRIEVSKY, G., V. KLOCHKOV, A. BORDYUH, G. DOVBESHKO, Comparative analysis of two aqueous-colloidal solutions of C<sub>60</sub> fullerene with help of FTIR reflectance and UV-vis spectroscopy. *Chem. Phys. Lett.*, **2002**. 364, 8–17.
- 6 BRANT, J., H. LECOANET, M. HOTZE, M. WIESNER, Comparison of electrokinetic properties of colloidal fullerenes (nC<sub>60</sub>) formed using two procedures. *Environ. Sci. Technol.*, **2005**. 39(17): 6343–6351.
- 7 NAKAMURA, E., H. ISOBE, Functionalized fullerenes in water. The first 10 years of their chemistry, biology, and nanoscience. *Acc. Chem. Res.*, **2003**. 36(11), 807–815.
- 8 OBERDÖRSTER, E., S. ZHU, T.M. BLICKLEY, P. MCCLELLAN-GREEN, M.L. HAASCH, Ecotoxicology of carbon-

- based engineered nanoparticles: Effects of fullerene (C<sub>60</sub>) on aquatic organisms. *Carbon*, **2005**, in press, available on-line December 22, 2005 (but no issue or page numbers) doi:10.1016/j.carbon.2005.11.008.
- 9 DODSON, S., *Introduction to Limnology*. 1st edn, **2004**. McGraw-Hill, New York, NY, USA.
  - 10 CONOVA, S., Role of particle wettability in capture by suspension-feeding crab (*Emerita talpoida*). *Marine Biol.*, **1999**, 133, 419–428.
  - 11 TJÄLVE, H., J. HENRIKSSON, Uptake of metals in the brain via olfactory pathways. *Neurotoxicology*, **1999**, 20(2–3), 181–196.
  - 12 TJÄLVE, H., C. MEJARE, K. BÖRGNECZAK, Uptake and transport of manganese in primary and secondary olfactory neurones in pike. *Pharmacol. Toxicol.*, **1995**, 77(1), 23–31.
  - 13 OBERDÖRSTER, E., Manufactured nanomaterials (fullerenes, C<sub>60</sub>) induce oxidative stress in brain of juvenile largemouth bass. *Environ. Health Persp.*, **2004**, 112(10), 1058–1062.
  - 14 US EPA, *Fish Advisories*, **2005**. <http://www.epa.gov/ost/fish/>, accessed July 24, 2005.
  - 15 LECOANET, H., J. BOTTERO, M. WIESNER, Laboratory assessment of the mobility of nanomaterials in porous media. *Environ. Sci. Technol.*, **2004**, 38, 5164–5169.
  - 16 KOLPIN, D., E. FURLONG, M. MEYER, E. THURMAN, S. ZAUGG, L. BARBER, H. BUXTON, Pharmaceuticals, hormones, and other organic wastewater contaminants in US streams, 1999–2000: A national reconnaissance. *Environ. Sci. Technol.*, **2002**, 36, 1202–1211.
  - 17 LECOANET, H., M. WIESNER, Velocity effects on fullerene and oxide nanoparticle deposition in porous media. *Environ. Sci. Technol.*, **2004**, 38(16), 4377–4382.
  - 18 BISWAS, P., C.-Y. WU, Nanoparticles and the environment. *J. Air Waste Manage. Assoc.*, **2005**, 55, 708–746.
  - 19 CIOFFI, N., L. TORSI, N. DITARANTO, L. SABBATINI, P.G. ZAMBONIN, G. TANTILLO, L. GHIBELLI, M. D'ALESSIO, T. BLEVE-ZACHEO, E. TRAVERSA, Antifungal activity of polymer-based copper nanocomposite coatings. *Appl. Phys. Lett.*, **2004**, 85(12), 2417–2419.
  - 20 POLLMANN, K., J. RAFF, M. MERROUN, K. FAHMY, S. SELENSKA-POBELL, Metal binding by bacteria from uranium mining waste piles and its technological applications. *Biotechnol Adv.*, **2006**, 24(1) 58–68.
  - 21 KUREISHI, Y., H. TAMIAMI, H. SHIRAIISHI, K. MARUYAMA, Photoinduced electron transfer from synthetic chlorophyll analogue to fullerene C<sub>60</sub> on carbon paste electrode. Preparation of a novel solar cell. *Bioelectrochem. Bioenerg.*, **1999**, 48(1), 95–100.
  - 22 FOX, J., M. STARCEVIC, P. JONES, M. BURROW, J. MCLACHLAN, Phytoestrogen signaling and symbiotic gene activation are disrupted by endocrine-disrupting chemicals. *Environ. Health Persp.*, **2004**, 112(6), 672–677.
  - 23 KAMAT, J., T. DEVASAGAYAM, K. PRIYADARSINI, H. MOHAN, J. MITTAL, Oxidative damage induced by the fullerene C<sub>60</sub> on photosensitization in rat liver microsomes. *Chem. Biol. Interact.*, **1998**, 114(3), 145–159.
  - 24 RANCAN, F., S. ROSAN, F. BOEHM, A. CANTRELL, M. BRELLREICH, H. SCHOENBERGER, A. HIRSCH, F. MOUSSA, Cytotoxicity and photocytotoxicity of a dendritic (C<sub>60</sub>) mono-adduct and a malonic acid (C<sub>60</sub>) tris-adduct on Jurkat cells. *J. Photochem. Photobiol. B*, **2002**, 67(3), 157–162.
  - 25 HAMANO, T., T. MASHINO, M. HIROBE, Oxidation of [C<sub>60</sub>] fullerene by cytochrome P450 chemical models. *Chem. Commun.*, **1995**, 1537–1538.
  - 26 SANTOS, L. The effects of fullerenes compounds on the microsomal cytochrome P450-monoxygenase system present in human liver microsomes. In *223rd American Chemical Society National Meeting*. **2005**. Orlando, FL, American Chemical Society, Washington, DC, 389.

- 27 UENG, T., J. KANG, H. WANG, Y. CHENG, L. CHIANG, Suppression of microsomal cytochrome P450-dependent monooxygenases and mitochondrial oxidative phosphorylation by fullereneol, a polyhydroxylated fullerene C<sub>60</sub>. *Toxicol. Lett.*, **1997**. 93(1), 29–37.
- 28 WANG, H., L. CHIANG, Inhibition of drug-metabolizing enzymes in mouse liver by a water soluble fullerene C<sub>60</sub>. *Fullerene Sci. Technol.*, **1999**. 7(4), 681–694.
- 29 SAYES, C., J. FORTNER, W. GUO, D. LYON, A. BOYD, K. AUSMAN, Y. TAO, B. SITHARAMAN, L. WILSON, J. HUGHES, J. WEST, V. COLVIN, The differential cytotoxicity of water-soluble fullerenes. *Nano Lett.*, **2004**. 4(10), 1881–1887.
- 30 FISCHER, A., R. HOCH, D. MOY, M. LU, M. MARTIN, C. NIU, N. OGATA, H. TENNENT, F. JAMEISON, P. LIANG, D. SIMPSON, et al. SWNT can be functionalized by P450s. US. Patent Office, Hyperion Catalysis International, Inc: USA. Kramer Levin Naftalis & Frankel, LLP, Attorneys & Agents. **2004**. International Patent #D01F 009/12; C07C 063/333.
- 31 ZHU, S., E. OBERDÖRSTER, M. HAASCH, Toxicity of an engineered nanoparticle (fullerene, C<sub>60</sub>) in two aquatic species, *Daphnia* and fathead minnow. *Marine Environ. Res.*, **2006**. in press.
- 32 HAASCH, M. L., P. MCCLELLAN-GREEN, E. OBERDÖRSTER, Consideration of the toxicity of manufactured nanoparticles. In XIX International Winterschool/Euroconference on Electronic Properties of Novel Materials. American Institute of Physics (AIP), Kirchberg, Tirol, Austria. H. Kuzmany, J. Fink, M. Mehring, S. Roth, eds. **2005**. 786, 586–589.
- 33 OBERDÖRSTER, E., Informal information on the toxicity of engineered nanomaterials. **2005**. [www.nanotox.info](http://www.nanotox.info). accessed 9/25/05.
- 34 KAMAT, J., T. DEVASAGAYAM, K. PRIYADARSINI, H. MOHAN, Reactive oxygen species mediated membrane damage induced by fullerene derivatives and its possible biological implications. *Toxicology*, **2000**. 155(1–3), 55–61.
- 35 NAKAJIMA, N., C. NISHI, F. LI, Y. KADA, Photo-induced cytotoxicity of water-soluble fullerene. *Fullerene Sci. Technol.*, **1996**. 4, 1–19.
- 36 YAMAKOSHI, Y., N. UMEZAWA, A. RYU, K. ARAKANE, N. MIYATA, Y. GODA, T. MASUMIZU, T. NAGANO, Active oxygen species generated from photoexcited fullerene (C<sub>60</sub>) as potential medicines: O<sub>2</sub><sup>•-</sup> versus 1O<sub>2</sub>. *J. Am. Chem. Soc.*, **2003**. 125(42), 12 803–12 809.
- 37 ZHANG, T., P. LU, F. WANG, G. WANG, Reaction of [60] fullerene with free radicals generated from active methylene compounds by manganese(III) acetate dihydrate. *Org. Biomol. Chem.*, **2003**. 1(24), 4403–4407.
- 38 US EPA, NCER STAR grants related to nanotechnology. **2005**. [http://cfpub.epa.gov/ncer\\_abstracts/index.cfm/fuseaction/searchControlled.main?RequestTimeout=180&records\\_per\\_page=ALL&abstyperesearch=on&abstypelifellowship=on&abstyperegrants=on&abstypesmallBiz=on&identifier=on&institute=on&annual=on&pubcount=on&principal=on&EPAREp=on&grantamt=on&proposedstart=on&addRptOption=on&hiliteOption=on&refreshPage=True&txtSearch=nanotechnology](http://cfpub.epa.gov/ncer_abstracts/index.cfm/fuseaction/searchControlled.main?RequestTimeout=180&records_per_page=ALL&abstyperesearch=on&abstypelifellowship=on&abstyperegrants=on&abstypesmallBiz=on&identifier=on&institute=on&annual=on&pubcount=on&principal=on&EPAREp=on&grantamt=on&proposedstart=on&addRptOption=on&hiliteOption=on&refreshPage=True&txtSearch=nanotechnology). Accessed 9/26/05.



## **II**

### **Health**



### 3

## Possible Health Impact of Nanomaterials

*Peter H. M. Hoet, Irene Brüske-Hohlfeld, and Oleg V. Salata*

### 3.1

#### Introduction

Nanotechnology is often portrayed as a force that will help to materialize ultimate solutions to today's technological problems. Nanomaterials are the first nanotechnological products hitting the markets. Widespread use of nanomaterials in the consumer and industrial products is also causing some health concerns [1, 2]. Proponents of nanotechnology [3] as well as its opponents find it hard to argue their case due to the limited information available.

How much do we know? To try to answer this question, we start this chapter by looking at the scale and current sources of nanomaterials engineered by men. Next, we use the relative wealth of research data available from the epidemiological studies of the technogenic nanoparticles to highlight the apparent health effects associated with the inhalation of ultrafine particulate matter. The inhalation of ultrafine particles is a well established entry route; hence we discuss the potential entry points of nanoparticles into the human body via airways, and also alternative paths through the skin and gastrointestinal tract. Then, we explore their likely pathways inside the body, the effects associated with nanoparticle interactions on the cellular level, and analyze the origins of the bioactivity of nanomaterials. Nanofibers, a special case of nanomaterials that are known to be hazardous in the micron domain because of their shape, are given some thought. In addition, recent observations on nanoparticle penetration through the blood–brain barrier are evaluated. Finally, the implications of our findings for the field of nanotechnology are discussed. This chapter is one of the very first attempts to overview a rapidly developing field of nanotoxicology, and to sum up and reflect upon recent experimental findings in this field.

### 3.2

#### Sources of Nanoparticles

Nanoparticles can be classified into three groups: natural, anthropogenic and man-made (or artificial). The natural kind is produced, for example, during forest fires

or volcanic eruptions; anthropogenic particles are quite often a by-product of industrial activities like welding or polishing. Diesel exhaust particles are also placed in this group. The last group includes engineered nanomaterials deliberately produced because of their technologically beneficial properties caused by the reduction in particle size. These novel properties of common materials observable only at nano-scale dimensions already have commercial applications [4]. For example, nanomaterials can be found in sunscreens, toothpastes, sanitary ware coatings and even food. The production volumes of man-made nanoparticles range from the multi-ton for carbon black and fumed silica used in plastic fillers and car tires to the microgram quantities of fluorescent quantum dots used as markers in biological imaging.

Following massive investments [5, 6], efforts to exploit the unique properties of everyday materials at the sub-micrometer scale are truly world-wide [7, 8] and consumer products relying on nanotechnology will experience a steady growth [9].

### 3.3 Epidemiological Evidence

Man-made nanoparticles are a relatively recent phenomena. As no data are available yet to evaluate the long-term risks of engineered nanoparticles, the epidemiological evidence on adverse health effects of ultrafine particles will be overviewed as a surrogate source of information.

Environmental air pollution consists of a complex mixture of compounds in gaseous, liquid and solid phases, the latter usually referred to as particulate matter (PM). In general, ambient levels of particulate matter are characterized as total suspended matter (TSP), and particulate matter with an effective aerodynamic diameter of less than 10  $\mu\text{m}$  ( $\text{PM}_{10}$ ) or 2.5  $\mu\text{m}$  ( $\text{PM}_{2.5}$ ). Particles in the sub-micrometer ranges, particularly in the range  $< 100$  nm, are labeled as ultrafine particles in epidemiological studies. Ultrafine particles in ambient air vary in chemical composition and size, as do technically produced nanoparticles. The number concentration of these small particles exceeds by far that of larger ones in urban area, but their contribution to the total mass concentration is relatively low. Therefore, it is standard to measure  $\text{PM}_{10}$  and  $\text{PM}_{2.5}$  in mass concentration ( $\mu\text{g m}^{-3}$ ). For ultrafine particles, the number concentration ( $\text{cm}^{-3}$ ) or surface area concentration ( $\mu^2 \text{m}^{-3}$ ) or particle length concentration ( $\text{mm cm}^{-3}$ ) is more relevant. Particles in ambient air are generated by numerous sources: motor vehicles, power plants, wind blown dust, photochemical processes, cigarette smoking, nearby quarry operation, etc. Some particles are introduced from the source into the air in solid or liquid form, while others are formed in the air by gas into particle conversion.

In the United States, the Environmental Protection Agency set National Ambient Air Quality Standards for particulate matter. According to the 1987 standard of  $\text{PM}_{10}$ , the maximal allowable 24-hour concentration was set at  $150 \mu\text{g m}^{-3}$  and the maximal annual mean was set at  $50 \mu\text{g m}^{-3}$ . From 1988 to 1993, the averages of the annual mean  $\text{PM}_{10}$  concentrations at 799 sites monitored by the US EPA



declined by 20%. Despite these improvements in air quality, Samet and coworkers [10] reported associations between particle concentrations and the number of deaths per day in 20 of the largest cities and metropolitan areas in the United States from 1987 to 1994 with mean 24-hour  $PM_{10}$  concentrations well below the standard. Analysis of the daily number of deaths occurring within an urban region has shown that  $10 \mu\text{g m}^{-3}$   $PM_{10}$  were associated with an increase of 0.2%. The result is based on a recent reevaluation of the National Mortality Morbidity Air Pollution Study (NMMAPS) that included 90 urban areas of United States in these analyses [11]. In 29 European cities, an increase of 0.6% in daily mortality was observed in association with an increase of  $10 \mu\text{g m}^{-3}$  in the study by the Air Pollution and Health Effect Association (APHEA) [12]. Studies on particles mass concentration indicate that there is a linear relationship between  $PM_{10}$  and  $PM_{2.5}$  and various health indicators (like cough, symptom exacerbation, bronchodilator use, hospital admissions and mortality [13]) for concentration levels between 0 and  $200 \mu\text{g m}^{-3}$ , and no threshold in particle concentrations below which health would not be jeopardized.

Within most established monitoring networks, ambient particulate matter is measured as either  $PM_{10}$  or  $PM_{2.5}$ . The epidemiological research has therefore focused on the links between these mass characteristics of ambient particles and adverse health effects. However, with reductions in particulate emissions from industry and power stations, the relevance of the number concentrations of ultrafine particles increased (mainly from traffic emissions). Not much was known about their impact on health. Panel morbidity studies with asthmatic subjects indicated that both fine and ultrafine particles were negatively associated with the respiratory health of the exposed population [14]. A decrease of respiratory functions, e.g., peak expiratory flow [15], and an increase in symptoms and medication use [16], was associated with elevated particle concentrations of ultrafine particles, independently from fine particles. Inflammatory events in the lungs took several days to develop. It was considered as likely that a lag time existed between exposure to ultrafine particles and the acute respiratory health effects of the exposed population. Cumulative effects over 5 days seemed to be stronger than same-day effects. There was an indication that the acute effects of the number of ultrafine particles on respiratory health were stronger than those of the mass of the fine particles [17, 18].

To improve our knowledge on human exposure to particulate matter of different sizes and of different chemical composition in Europe, and to develop standards for air quality in Europe, the ULTRA project was initiated. Specifically, the project aimed to improve exposure assessment to fine particles by assessing the size distributions, including ultrafine particles, and elemental compositions of fine particles in ambient air in three European cities with different sources of particulate air pollution. Three panel studies were carried out, in Amsterdam, the Netherlands, Erfurt, Germany, and Helsinki, Finland, during winter and spring 1998–1999 [19–21]. In all three cities, about 50 elderly persons with coronary heart disease were followed up for six months with bi-weekly intensive examinations, which included measurements of the function of the heart and lungs, blood pressure and of bio-

markers for lung damage from urine. The subjects also kept daily symptom diaries. These studies were limited to the investigation of the acute health effects of short-term exposure by evaluating the impact of day-to-day variation in ambient pollution on health through correlating mortality and morbidity with daily pollution levels. There is an association between exposure to ultrafine particles and cardiovascular morbidity in the population with chronic heart diseases. In Helsinki [22] independent associations between both fine and ultrafine particles and the risk of ST-segment depression in their ECG were observed among subjects with coronary heart disease. ST-segment depression is regarded as an indicator of myocardial ischemia. The study reported increased odds ratios for 45 subjects, ranging from 1.03 to 3.29, with 95% confidence intervals ranging from 0.54 to 6.32. Several plausible mechanistic pathways have been described, including enhanced coagulation/thrombosis, a propensity for arrhythmias, acute arterial vasoconstriction, systemic inflammatory responses, and the chronic promotion of atherosclerosis [23].

A study conducted in Erfurt, Germany, on daily mortality showed comparable and independent increases in mortality in association with fine and ultrafine particles [24]. All particles had a strong seasonal dependency, with maximal concentrations in winter. The concentrations of ultrafine particles showed a pronounced day of the week effect with concentrations during the weekend 40% lower than during the week. This and a clear increase of the ultrafine particles concentrations during the rush hours suggest that the main source for ultrafine particles was automobile traffic. Associations between health effects and particle number and particle mass concentrations have been observed in different size classes, and both immediate effects (lags 0 or 1 days) and delayed effects (lags 4 or 5 days) were found. The effects could be found for total mortality and also for respiratory and cardiovascular causes. There was a tendency for more immediate effects on respiratory causes and more delayed effects for cardiovascular causes. Mortality increased in association with ambient particles after adjustment for season, influenza epidemics, day of week and meteorology, and sensitivity analyses showed the results to be stable.

In summary, both fine and ultrafine particles are associated with respiratory and cardiovascular morbidity and mortality and appear to be so independently of each other. There is also epidemiological evidence of similar responses to fine and ultrafine particles, although the size of the effects is often larger for ultrafine than for fine particles (at least on a per mass basis). One can expect that similar effects can be induced due to the presence of man-made nanoparticles.

### 3.4

#### **Entry Routes into the Human Body**

The above-mentioned health effects result from the inhalation of ultrafine particles. In general, compounds or materials can enter the body via three “natural” portals: skin, intestinal tract and respiratory tract (nose, airways and alveoli), or via intentional delivery through injection, intravenous (i.v.), intraperitoneal (i.p.) or

intramuscular (i.m.). Although our knowledge in this field is partly built on studies concerning drug delivery (pharmaceutical research) and toxicology (xenobiotics) of an intentional dose, in this chapter we will mainly concentrate on the health effects of nanomaterials entering the body via one of the natural portals.

The skin acts as a strict barrier between the body and the environment; no essential elements are taken up through the skin (except solar radiation necessary to build up vitamin D).

The respiratory tract and the intestinal tract allow transport (passive and/or active) of various substances like water, nutrients and gasses. The lungs exchange oxygen and carbon dioxide with the environment, and some water escapes with the warm exhaled air. The intestinal tract is in close contact with all the materials taken up orally; here all nutrients (except gasses) are exchanged between the body and the environment. The anatomy and histology of the three organs in contact with the environment differ significantly.

The skin of an adult human is roughly  $1.5 \text{ m}^2$  in area, and is at most places covered with a relatively thick first barrier ( $10 \text{ }\mu\text{m}$ ) built of strongly keratinized dead cells. This first barrier is difficult to pass for ionic compounds as well as water-soluble molecules.

The respiratory tract consists of three different parts: nose, airways (transporting the air in and out the lungs) and alveoli (gas exchange areas). The nose and the airways are a relatively robust barrier, built of an active epithelium protected with a viscous layer of mucus. In the gas exchange area, the barrier between the alveolar wall and the capillaries is very thin. The air in the lumen of the alveoli is only  $0.5 \text{ }\mu\text{m}$  ( $500 \text{ nm}$ ) away from the blood flow. The large surface area of the alveoli,  $140 \text{ m}^2$  in adults, and the intense air–blood contact in this region make the alveoli less well protected than the airways against environmental damage.

The intestinal tract is a more complex barrier – exchange side, it is the portal for macromolecules to enter the body. From the stomach, only small molecules can diffuse through the epithelium. The epithelium of the small and large intestines, in close contact with ingested material, allows and controls the uptake of nutrients such as disaccharides, peptides, fatty acids, and monoglycerides generated by digestion. The overall surface available to exchange nutrients is about  $200 \text{ m}^2$  in adults.

In the following sub-sections, interactions of the three portals with nanomaterials are briefly discussed. Two critical aspects, from the health effect point of view, will be discussed for each. First, how can nanomaterials have a local effect in each of these organs and, second, can nanomaterials move from the portal into the body.

### 3.4.1

#### Lung

##### 3.4.1.1 Inhalation, Deposition and Pulmonary Clearing of Insoluble Solids

**Inhalation and Deposition** The deposition of solid material in the respiratory tract depends on the physical characteristics of the material, such as particle size and

shape, relative weight, and on the anatomy of the respiratory tract, such as diameter of the airways, air speed, branching angle etc. [25–27].

Spherical solid material can be inhaled when its aerodynamic diameter is less than 10  $\mu\text{m}$ . The smaller the particulates the deeper they can travel into the lung – particles < 2.5  $\mu\text{m}$  will even reach the alveoli. Ultrafine particles (nanoparticles with an aerodynamic diameter of less than 100 nm) are deposited mainly in the alveolar region, largely by diffusion (Brownian movement). Models have shown that the deposition efficiency at the three pulmonary regions is not linear with size: particles of between 5 and 50 nm are deposited mainly in the alveoli, smaller and larger ones are more efficiently deposited in the higher regions [25, 28].

Fibers are defined, in pulmonary sciences, as solid materials with a length-to-diameter ratio of at least 3:1. Their aerodynamic diameter can be used to judge their penetration into the lungs. Fibers with a small diameter will penetrate deeper into the lungs, while very long fibers ( $\gg 20 \mu\text{m}$ ) are easily stuck in the higher airways, although some long fibers can enter the alveolar space [29–34].

**Clearance** The removal of solid material from the lungs is carried out by two distinct mechanisms. The mucociliary escalator dominates the clearance from the airways and the nose; in the alveolar region the clearance takes predominantly place by macrophage phagocytosis.

The mucociliary escalator, driven by the cilia of airway epithelium, is an efficient transport system, pushing the mucus, which covers the airways, together with the trapped solid materials towards the mouth.

The phagocytosis of particles and fibers results in activation of macrophages and induces the release of chemokines, cytokines, reactive oxygen species, and other mediators; this can lead to sustained inflammation and eventually fibrotic changes [35, 36]. The phagocytosis efficiency can be affected by the (physical-chemical) characteristics of the solid material [37] (see below); moreover, fibers too long to be phagocytized (fibers longer than the diameter of the alveolar macrophage, depending on the species studied) will not (or very slowly) be cleared [32, 38–40].

Laboratory exposure studies have shown that if the inhaled concentrations are low, such that the deposition rate of the inhaled particles is less than the clearance rate, then the retention half-time is about 70 days. For fine and nanoparticulates, the alveolar macrophage-mediated clearance is the limiting factor. If the deposition rate of the inhaled particles exceeds this clearance rate, the retention half-time is significantly increased, reflecting an impaired or prolonged alveolar macrophage-mediated clearance function with continued accumulation of lung burden (overload) [41–43].

Clearance from the lung depends not only on the total mass of particles inhaled but also on the particle size and, by implication, on particle surface, as shown in the following studies. A sub-chronic 3 months inhalation exposure of rats to ultrafine ( $\sim 20 \text{ nm}$ ) and fine ( $\sim 200 \text{ nm}$ ) titanium dioxide ( $\text{TiO}_2$ ) particles demonstrated that the ultrafine particles cleared significantly slower and showed more translocation to interstitial sites and to regional lymph nodes than the fine  $\text{TiO}_2$  particles [25].

To summarize, most nanosized spherical solid materials are likely to enter the lungs and reach the alveoli. These particles can be cleared from the lungs, as long as the clearance mechanisms are not affected by the particles themselves or by any other cause. Nanosized particles are more likely to hamper the clearance, resulting in a higher burden [44], possibly amplifying any related chronic effects caused by these particles. Notably, specific particle surface area is probably a better indication for maximum tolerated exposure level than total mass [28, 45], suggesting that the biological effects are linked to surface reactivity.

#### 3.4.1.2 Biopersistence of Inhaled Solid Material

The main determinants of biopersistence are species-specific physiological clearance and material specific bio-durability (physical-chemical processes).

In the alveoli, the rate at which fibers are cleared depends on the ability of alveolar macrophages to phagocytose them. Macrophages containing fibers longer than their own diameter (in humans longer than 20  $\mu\text{m}$ ) may not be mobile and will be unable to clear the fibers from the lung [39].

The bio-durability of a fiber depends on its dissolution and leaching as well as mechanical breaking and splitting [46, 47]. Biopersistent fibers such as amosite asbestos (brown asbestos) [39, 48], where breakage occurs longitudinally, result in more fibers of the same length but smaller diameter. Other types of fibers (e.g., amorphous) break perpendicular to their long axis, resulting in fibers that can be engulfed by the macrophages [49].

Self-evidently, the slower the fibers are cleared (high biopersistence), the higher is the tissue burden and the longer the fibers reside in a tissue the higher is the probability of an adverse response [29]. Despite the crucial role played by the length of the fibers (Stanton hypothesis) [50], it does not strictly indicate that all fibers longer than the lower threshold are equally active or that shorter fibers are not. Although fibers less than 5  $\mu\text{m}$  long did not appear to contribute to lung cancer risk in exposed rats [39], fibers more than 40  $\mu\text{m}$  long impose the highest risk (recent review by Schins [38]).

Inhaled fibers, which are persistent in the alveoli, can further interact with the pulmonary epithelial cells or even penetrate the alveolar wall and enter the lung tissue. These fibers are often described as being in the “interstitial” because they may lie between or within the cells making up the alveolar walls. Biopersistent solid materials, certainly those containing mutagenic potency and which remain for years in the lungs, increase the risk of developing cancer [32, 33].

Not much is known on the long-term health effects of fibrous purpose-made nanomaterials. There are no indications that the bio-durability of fibers with a diameter < 100 nm will differ from larger inhalable fibers. Therefore, great caution must be taken in the case of contact with nanofibers; bio-durability tests must be performed before releasing any products containing them.

Technologically, carbon nanotubes are an important group of nanofibers. Recently, they have been reported to show signs of toxicity in the lung of laboratory animals [51]. This is confirmed in two independent publications, by Warheit et al. [52] and Lam et al. [53], which demonstrated the pulmonary effects of single-

walled carbon nanotubes *in vivo* after intratracheal instillation, in both rats and mice. Both groups reported granuloma formation, and some interstitial inflammation. Warheit et al. [52] concluded that these findings (multifocal granulomas) may not have physiological relevance, and may be related to the instillation of a bolus of agglomerated nanotubes. The other group [53] suggested that if carbon nanotubes reach the lungs they are much more toxic than carbon black and can be more toxic than quartz. These studies have to be read with some caution because a study by the National Institute for Occupational Safety and Health (NIOSH) showed that none or only a small fraction of the nanotubes present in the air can be inhaled [54] (see short review of Donaldson and Tran [55]).

As noted above, at similar lung burdens, spherical TiO<sub>2</sub> ultrafine particles cleared significantly more slowly from the alveoli and showed more translocation to interstitial sites and to regional lymph nodes than did fine particles. Thus, besides the greater biological effects (see below) of ultrafine particles, the difference in toxicokinetics in the lung results in a higher burden [44].

#### 3.4.1.3 Systemic Translocation of Inhaled Particles

The impact of inhaled particles on other organs has been reported in several epidemiological studies. Most research has concentrated on the possible consequences of particle related malfunction of the cardiovascular system, such as arrhythmia, coagulation [56] etc. However, the autonomic nervous system [57, 58] as well as the olfactory nerves may be a target for inhaled particulates [28].

Until recently, the possible passage of xenobiotic particles has not attracted much attention, although the concept is now gaining acceptance in pharmacology for the administration of macromolecular drugs by inhalation [59].

In evaluating the health effects of inhaled nanoparticles, translocation to the systemic circulation is an important issue. Several para- and trans-cellular mechanisms have been described in the pulmonary epithelium, but it is unclear which one allows the translocation of nanoparticulates. Conhaim and coworkers [60] found that the lung epithelial barrier was best fitted by a three-pore-sized model, including a small number (2%) of large-sized pores (pore radius 400 nm), an intermediate number (30%) of medium-sized pores (40-nm pore radius), and a very large number (68%) of small-sized pores (1.3-nm pore radius). The exact anatomical location of this structure, however, remains to be established (see the review by Hermans and Bernard [61]). Possible endocytic pathways have been reviewed by Rejman et al. [62]. Of all endocytic pathways caveolae seem (the most) important portals for large molecules to enter cells or to cross the epithelial border [63–65]. Caveolae allow internalization of particles as large as 500 nm in diameter, though it depends on the surface coating.

In humans, translocation of inhaled ultrafine technetium (<sup>99m</sup>Tc) labeled carbon particles into the blood circulation has been studied independently by Nemmar et al. [66] and Kawakami et al. [67]. However, the translocation mechanism is still unclear. Nemmar et al. demonstrated that technetium (<sup>99m</sup>Tc) labeled carbon particles, which are very similar to the ultrafine fraction of actual pollutant particles, diffused rapidly – within 5 min – into the systemic circulation [66]. The authors

concluded, therefore, that it was unlikely that phagocytosis by macrophages and/or endocytosis by epithelial and endothelial cells are solely responsible for particle translocation to the blood, but that a paracellular mechanism probably also plays a role. More recently, Kato et al. [68] showed, morphologically, that inhaled polystyrene particles are transported into the pulmonary capillary space, presumably by transcytosis.

Aerosolized insulin gives a rapid therapeutic effect [69], although the pathways for this translocation are still unclear [70]. In addition to human studies, extra-pulmonary translocation of ultrafine particles after intratracheal instillation or inhalation has been reported in experimental animal studies [66, 71–73]. However, the amount of ultrafine particles that translocate into blood and extra-pulmonary organs was different. Following intranasal delivery, polystyrene microparticles (1.1  $\mu\text{m}$ ) can translocate to tissues in the systemic compartment [74].

Oberdörster et al. have explored another alley of translocation from the respiratory tract towards other organs [31]. In inhalation experiments with rats, using  $^{13}\text{C}$ -labeled particles, they found that nanosized particles (25 nm) were present in several organs 24 hours after exposure. The most extraordinary finding was the discovery of particles in the central nervous system (CNS). The authors examined this phenomenon further and found that particles, after being taken up by the nerve cells, can be transported via nerves (in this experiment via the olfactory nerves) at  $2.5 \text{ mm h}^{-1}$  [72].

Passage of solid material from the pulmonary epithelium to the circulation seems not to be restricted to nanoparticles, as shown by Kato et al. [68], and depends on the surface characteristics of the material. The issue of particle translocation still needs to be clarified: both the trans-epithelial transport in the alveoli and the transport via nerve cells. Thus, the role of factors governing particle translocation, such as the way of exposure, dose, size, surface chemistry and time course, should be investigated. For instance, it would be very important to know how and to what extent the extra-pulmonary translocation of particles is modulated by the lung inflammation.

### 3.4.2

#### **Intestinal Tract**

##### **3.4.2.1 Deposition and Translocation**

Already in 1926, Kumagai recognized that particles could translocate from the lumen of the intestinal tract via aggregations of intestinal lymphatic tissue (PP) containing M-cells (specialized phagocytic enterocytes). Particulate uptake happens not only via the M-cells in the PP and the isolated follicles of the gut-associated lymphoid tissue but also via the normal intestinal enterocytes. There have been several excellent reviews on the intestinal uptake of particles [75, 76]. Uptake of inert particles occurs trans-cellularly through normal enterocytes and in PP via M-cells, and, to a lesser extent, across paracellular pathways [77]. Initially it was assumed that the PP did not discriminate strongly in the type and size of the absorbed particles. Subsequently, it has been shown that modifying characteristics, such as particle

size [78] the surface charge of particles [79, 80], attachment of ligands [81, 82] or coating with surfactants [83], offers possibilities of site-specific targeting to different regions of the gastrointestinal tract (GIT), including the PP [84].

The kinetics of particle translocation in the intestine depends on diffusion and accessibility through mucus, initial contact with enterocyte or M-cell, cellular trafficking, and post-translocation events. Charged particles, such as carboxylated polystyrene nanoparticles [80] or those composed of positively charged polymers, exhibit poor oral bioavailability [85].

Specific studies on nanomaterials are rather scarce; in general, they show that most of them simply pass through the GIT and are rapidly eliminated. In one study [79], the body distribution after translocation of polystyrene particles was examined in some detail. Polystyrene spheres (ranging from 50 nm to 3  $\mu\text{m}$ ) were fed by gavage to female Sprague–Dawley rats daily for 10 days at a dose of 1.25 mg kg<sup>-1</sup>. As much as 34% and 26% of the 50 and 100 nm particles, respectively, were absorbed. Those larger than 300 nm were absent from blood. No particles were detected in heart or lung tissue. In another study, the oral uptake of radio-labeled functionalized C<sub>60</sub> fullerenes (water solubilized using albumin and PEG) in rats resulted in a 98% clearance (faeces) within 48 h, and the rest was eliminated via the urine, which is an indication for systemic uptake [86]. Kreyling et al. [71], using ultrafine <sup>192</sup>Ir, did not find any significant nanoparticle uptake in the GI tract.

#### 3.4.2.2 Intestinal Translocation and Disease

Crohn's disease is characterized by transmural inflammation of the gastrointestinal tract. It is of unknown aetiology, but it is suggested that a combination of genetic predisposition and environmental factors play a role. Particles (0.1–1.0  $\mu\text{m}$ ) are associated with the disease [87] and indicated as potent adjuvants in model antigen-mediated immune responses. A double-blind randomized study showed that a diet low in calcium and exogenous microparticles alleviates the symptoms of Crohn's disease [88].

Other studies found that material uptake (endocytosis) capacity of M cells is induced under various immunological conditions, e.g., a greater uptake of particles (0.1, 1 and 10  $\mu\text{m}$  diameter) has been demonstrated in the inflamed colonic mucosa of rats compared to non-ulcerated tissue [89, 90] and inflamed esophagus [91].

Clearly, from the literature cited above, engineered nanoparticles can be taken up via the intestinal tract. In general, the intestinal uptake of particles is better understood and studied in more detail than pulmonary and skin uptake. Because of this advantage, it may be possible, with caution, to predict the behavior of some particles in the intestines.

### 3.4.3

#### Skin

##### 3.4.3.1 Deposition and Penetration through the Skin

Skin is an important barrier, protecting against insult from the environment. The skin is structured in three layers: the epidermis, the dermis and the subcutaneous



layer. The outer layer of the epidermis, the stratum corneum (SC), covers the entire outside of the body. In the SC we find only dead cells, which are strongly keratinized. For most chemicals, the SC is the rate-limiting barrier to percutaneous absorption (penetration). The skin of most mammalian species is covered with hair on most parts of the body.

At the sites where hair follicles grow, the barrier capacity of the skin differs slightly from the “normal” stratified squamous epidermis [92]. Most studies concerning penetration of materials into the skin have focused on whether drugs penetrate through the skin using different formulations containing chemicals and/or particulate materials as a vehicle [93]. The main types of particulate materials commonly used are liposomes, solid poorly soluble materials such as TiO<sub>2</sub>, polymer particulates, and submicron emulsion particles, such as solid lipid nanoparticles. The penetration of these particulate carriers has not been studied in detail.

TiO<sub>2</sub> particles are often used in sunscreens to absorb UV light and therefore to protect skin against sunburn or genetic damage. Lademann et al. have reported [94] that micrometer-sized particles of TiO<sub>2</sub> get through the human stratum corneum and even into some hair follicles, including their deeper parts.

Tinkle et al. have demonstrated that 0.5 and 1.0 μm particles, in conjunction with motion, penetrate the stratum corneum of human skin and reach the epidermis and, occasionally, the dermis [95]. It has been hypothesized that the lipid layers within the cells of the stratum corneum form a pathway by which the particles can move [96] into the skin and be phagocytized by the Langerhan’s cells. In this study, the penetration of particles was limited to a particle diameter of 1 μm or less. Nevertheless, other studies reported penetration through the skin to the dermis using particles with diameters of 3–8 μm [92, 94, 97] but only limited penetration was found, often clustered at the hair follicle (see above). This can lead to an interaction with the immune system [93].

Penetration of non-metallic solid materials such as biodegradable poly(D,L-lactic-co-glycolic acid) (PLGA) microparticles, 1 to 10 μm with a mean diameter of  $4.61 \pm 0.8$  μm, has been studied after application on porcine skin. The number of microparticles in the skin decreased with depth (measured from the airside towards the subcutaneous layer). At 120 μm depth (where viable dermis is present) a relatively high number of particles was found, at 400 μm (dermis) some microparticles were still seen. At a depth of 500 μm no microparticles were found [98]. In the skin of individuals who had an impaired lymphatic drainage of the lower legs, soil microparticles, frequently 0.4–0.5 μm, were found, and particles as large as 25 μm in diameter were seen in the dermis of the foot of a patient with endemic elephantiasis. The particles are seen to be in the phagosomes of macrophages or in the cytoplasm of other cells. The failure to conduct lymph to the node produces a permanent deposit of silica in the dermal tissues (a parallel is drawn with similar deposits in the lung in pneumoconiosis). This indicates that soil particles penetrate through (damaged) skin, most probably in every individual, and normally are removed via the lymphatic system [99, 100].

According to Hostynek [101] the uptake of metals through the skin is complex. Both exogenous (e.g., dose, vehicle, protein reactivity, and valence) and endogenous factors (e.g., age of skin, anatomical site, and homeostatic control) are in-

volved. Attempts to define rules governing skin penetration to give predictive quantitative structure–diffusion relationships for metallic elements for risk assessment purposes have been unsuccessful, and penetration of the skin still needs to be determined separately for each metal species, either by *in vitro* or *in vivo* assays.

From the limited literature on nanoparticles penetrating the skin some conclusions can be drawn. Firstly, penetration of the skin barrier is size dependent – nanosized particles are more likely to enter more deeply into the skin than larger ones. Secondly, different types of particles are found in the deeper layers of the skin and, at present, it is impossible to predict the behavior of a particle in the skin. Thirdly, materials that can dissolve or leach from a particle (e.g., metals) can possibly enter the systemic circulation.

#### 3.4.3.2 Irritation of Skin

Glass fibers and Rockwool fibers are widely used man-made mineral fibers, mainly as thermal insulation materials, which have become important as a replacement for asbestos fibers. While in contact with the skin, these fibers can induce dermatitis simply resulting from mechanical irritation. Why these fibers are such a strong irritant has not been examined in detail. In occlusion irritant patch tests in humans, Rockwool fibers with a diameter of  $4.20 \pm 1.96 \mu\text{m}$  were found to be more irritating than those with a mean diameter of  $3.20 \pm 1.50 \mu\text{m}$  [102].

Some recent experimental work that exposed human epidermal keratinocytes (HEK) to carbon nanotubes (CNT) indicates that caution should be taken in handling these materials [103, 104]. Single-wall (SW) CNT induce apoptosis and decrease cellular adhesion ability, in a dose and time dependent manner [104]. Multi-wall (MW) CNT are taken up by the HEK, in vacuoles present within the cytoplasm, but no CNT were found in the nuclei of the cells [103]. In the same study the release, into the culture medium, of IL-8, a marker of irritation in human skin, was found to be dose dependent.

### 3.5

#### What Makes Nanoparticles Dangerous?

Several mechanisms have been proposed to explain the adverse health effects of nanomaterials. In “nanotoxicology”, probably two distinct characteristics would play a role: on the one hand, the material-specific and intrinsic toxicity and, on the other hand, more general but specific nanoparticle-induced responses [1, 45].

Material-specific responses can often be understood and/or explained by material-specific toxic responses, local stimulation of irritant receptors, covalent modification of key enzyme receptors, etc. More general nanoparticle dependent responses, certainly in lung and liver, can often be categorized as inflammatory responses concurrent with cytokine and chemokine release, production of white blood cells, free-radical production, etc. [28, 40]. Certainly, it would be incorrect to separate these two responses too much as, most often, after exposure to a nanomaterial multiple responses can be observed that can influence each other.

Another aspect, which has not been studied in any detail in respect to nanomaterials, is the deposition of nanomaterials at any specific sink in the body [71, 72]. In kidney toxicity, the precipitation of chemicals and formation of crystals, certainly in chronic exposure, can lead to tissue damage [105].

The next section discusses some material characteristics and toxic mechanisms important in the adverse health effects of nanomaterials.

### 3.5.1

#### Particle Size – Surface and Body Distribution

Reports on the surface properties of nanoparticles, both physical and chemical, stress that nanoparticles differ from bulk materials. The biological effects do not just depend on the intrinsic toxicity of the material itself but on the size and surface area the nanoparticles made out of this material. Nanoparticles are not merely small crystals but an intermediate state of matter placed between bulk and molecular material. Independently of the particle size, two other parameters play dominant roles: the charges carried by the particle in contact with the cell membranes and the chemical reactivity of the particle [28, 45, 106–108].

##### 3.5.1.1 Effect of Size

Two samples of carbon black, which can be considered as a relatively inert material, of similar size and composition but with significantly different specific surface areas (300 versus  $37 \text{ m}^2 \text{ g}^{-1}$ ) showed biological effects (inflammation, genotoxicity, and histology) that depend on the specific surface area and not on particle mass. Similar findings were reported in earlier studies on tumorigenic effects of inhaled particles. In the lung, tumor incidence of chronically inhaled  $\text{TiO}_2$  of nanosized particles (20 nm diameter) at low exposure ( $10 \text{ mg m}^{-3}$ ) was significantly higher than for high exposure ( $250 \text{ mg m}^{-3}$ ) of 300 nm particles [109]. Tumor incidence correlates better with specific surface area than with particle mass [25, 110]. *In vivo* and *in vitro*, nanosized particles inhibit phagocytosis when compared to fine particles [111] and can change the chemotactic behavior of macrophages significantly [112].

Size is also a critical parameter in the distribution of particles in the body.

Oral uptake (gavage) of polystyrene spheres of different sizes (50 nm to  $3 \mu\text{m}$ ) in female Sprague–Dawley rats (for 10 days at a dose of  $1.25 \text{ mg kg}^{-1} \text{ day}^{-1}$ ) resulted in systemic distribution of the nanoparticles. About 7% (50 nm) and 4% (100 nm) was found in the liver, spleen, blood and bone marrow. Particles larger than 100 nm did not reach the bone marrow and those larger than 300 nm were absent from blood. No particles were detected in heart or lung tissue [80].

##### 3.5.1.2 Effect of Surface Charges

Beside particle size, surface characteristics play a dominant role in the distribution of material in the body.

Coating poly(methyl methacrylate) nanoparticles with different types and concentrations of surfactants significantly changes their body distribution [113]. Coat-

ing these nanoparticles with  $\geq 0.1\%$  poloxamine 908, a non-ionic surfactant, reduces their liver concentration significantly (from 75% to 13% of total amount of particles administrated) 30 min after i.v. injection. Another surfactant, polysorbate 80, was effective above 0.5%. A different report showed that modification of the nanoparticle surface with a cationic compound, didodecyldimethylammonium bromide (DMAB), facilitates the arterial uptake 7–10-fold [114]. The authors noted that the DMAB surface-modified nanoparticles had a mean zeta potential of +22.1 mV, which is significantly different from the original  $-27.8 \pm 0.5$  mV (mean  $\pm$  sem,  $n = 5$ ). The mechanism for the altered biological behavior is unclear, but surface modifications have possible applications for intra-arterial drug delivery.

Polycationic macromolecules show a strong interaction with cell membranes *in vitro*. The Acramin F textile paint system is a good example. Three polycationic paint components exhibited considerable cytotoxicity ( $LC_{50}$  generally below 100 mg mL<sup>-1</sup> for an incubation of 20–24 h) in diverse cell cultures, such as primary cultures of rat and human type II pneumocytes, and alveolar macrophages and human erythrocytes. The multiple positive charges play, speculatively, an important role in the toxic mechanism [115, 116].

A study of the biocompatibility (cytotoxicity) of polycationic materials [117] as a function of molecular weight found that with increasing molecular weight some macromolecules, such as DEAE-dextran and poly-l-lysine (PLL) [118, 119], dendrimers [120] and polyethylenimine (PEI) [121], become more toxic. The toxic mechanism is not fully understood but membrane integrity plays a role.

Dekie et al. [122] concluded that a primary amine group on poly(L-glutamic acid) derivatives has a significant toxic effect on red blood cells, causing them to agglutinate. Not only the type of amino function but also the charge density resulting from the number and special arrangement of the cationic residues is important for cytotoxicity. Ryser [123] has suggested that a three-point attachment is necessary to elicit a biological response on cell membranes, and speculated that the activity of a polymer will decrease when the space between reactive amine groups is increased. The arrangement of cationic charges depends on the three-dimensional structure and flexibility of the macromolecules and determines the accessibility of their charges to the cell surface.

Branched molecules are more efficient in neutralizing the cell surface charge than polymers with linear or globular structure; the latter are more rigid and so have more difficulty attaching to the membranes [124]. Therefore, high cationic charge densities and highly flexible polymers should cause higher cytotoxic effects than those with low cationic charge densities. Globular polycationic polymer structures [cationised Human Serum Albumin (cHSA), ethylenediamine-core poly(amidoamine) dendrimers (PAMAM)] exhibit good biocompatibility (low cytotoxicity) whereas polymers with a more linear or branched and flexible structure [poly(dialyldimethylammonium chloride) (DADMAC), PLL, PEI] showed higher cell-damaging effects.

The serum half-life and body distribution of CdSe quantum dots with different surface characteristics, coatings with short-chain or long-chain PEG, have been

studied by Ballou et al. [125]. The mPEG-750 coated quantum dots were, 24 h after dosage, found in lymph nodes and the spleen. The long-chain (PEG-5000) coated quantum dots were less apparent in lymph nodes but more in the liver, spleen, and bone marrow. This type of coating allowed a slow clearance from the body and the particles were still observed after 133 days.

Regardless of uptake route, the body distribution of particles is most dependent on the surface characteristics and size of the particles. This is important in drug design in order to help to deliver medication to the right target.

### 3.5.2

#### **Nanoparticles, Thrombosis and Lung Inflammation**

##### **3.5.2.1 Prothrombotic Effect**

Epidemiological studies have reported a close association between particulate air pollution and cardiovascular adverse effects [126] such as myocardial infarction [127]. The latter results from rupture of an atherosclerotic plaque in the coronary artery, followed by rapid thrombus growth caused by exposure of highly reactive sub-endothelial structures to circulating blood, thus leading to additional or complete obstruction of the blood vessel [127].

Nemmar et al. have studied the possible effects of particles on haemostasis, focusing on thrombus formation as a relevant endpoint [128–130]. Polystyrene particles 60 nm in diameter (surface modifications: neutral, negatively or positively charged) had a direct effect on haemostasis after intravenous injection. Positively charged amine-particles led to a marked increase in prothrombotic tendency, resulting from platelet activation. These observations have been confirmed recently by Silva et al. [131] in a comparable model.

A similar effect could be obtained after the intratracheal administration of these positively charged polystyrene particles, which also caused lung inflammation [132]. Importantly, the pulmonary instillation of larger (400 nm) positive particles caused a definite pulmonary inflammation (of similar intensity to 60 nm particles), but they did not lead to a peripheral thrombosis within the first hour of exposure. This lack of effect of the larger particles on thrombosis, despite their marked effect on pulmonary inflammation, suggests that pulmonary inflammation by itself was insufficient to influence peripheral thrombosis. Consequently, the effect found with the smaller, ultrafine particles is most probably due, at least in part, to their systemic translocation from the lung into the blood.

Using pollutant particles, namely diesel exhaust particles (DEP), it was shown that, within an hour after their deposition in the lungs, DEP cause a marked pulmonary inflammation. Moreover, intratracheal instillation of DEP promotes femoral venous and arterial thrombosis in a dose-dependent manner, already starting at a dose of 5  $\mu\text{g}$  per hamster (ca. 50  $\mu\text{g kg}^{-1}$ ). Subsequent experiments showed that prothrombotic effects persisted at 6 and 24 h after instillation (50  $\mu\text{g}$  per animal) and confirmed that peripheral thrombosis and pulmonary inflammation are not always associated [129, 133].

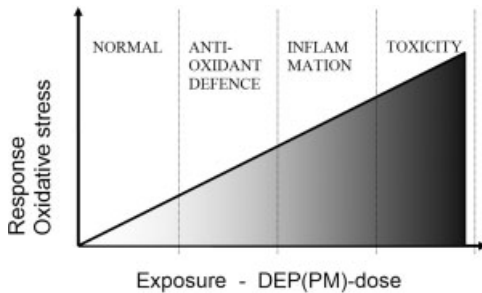


**Fig. 3.1.** Hierarchic oxidative stress model (Bernstein et al. [137] and Li et al. [134]). At low concentrations of PM a small change in oxidative stress can be observed without the induction of changes at cellular or tissue level. At a higher level of exposure, anti-oxidant

defense mechanisms are triggered. With increasing concentrations, an inflammatory response is induced. Finally, at the highest concentration, toxicity and cellular and/or tissue damage can be observed.

### 3.5.2.2 Oxidative Stress, Inflammation and Endotoxins

Particle-induced pulmonary inflammation can induce protective and adverse cellular responses in a dose-dependent manner. Li et al. have proposed a “hierarchical oxidative stress model” in response to DEP exposure (Fig. 3.1) [134]. This model suggests that at a lower oxidative stress level (tier 1) PM induces cytoprotective responses, e.g., through the activation of antioxidant response elements, inducing the expression of several antioxidant and phase II drug metabolizing enzymes (e.g., heme oxygenase 1 and glutathione-S-transferase). If this level of protection fails, the oxidative stress (tier 2) will lead to mitogen-activated protein kinase/nuclear factor  $\kappa$ B activation and pro-inflammatory effects. Further escalation (tier 3), will trigger disturbance of the mitochondrial function, resulting in cellular apoptosis or necrosis. A weakened antioxidant defense can increase the susceptibility toward PM-induced airway inflammation, to infection, and maybe to asthma; it can explain the existence of susceptible human subsets. Xioa et al. showed that the hierarchical oxidative stress model can be applied in a macrophage cell line [135]. The authors demonstrated that in the dose range  $10\text{--}100\text{ g mL}^{-1}$  organic DEP extracts induce a progressive decline in the cellular GSH/GSSG ratio. In parallel, it causes a linear increase in newly expressed proteins, including antioxidant enzymes (e.g., heme oxygenase-1 and catalase), pro-inflammatory components (e.g., 38 MAPK and Rel A), and products of intermediary metabolism that are regulated by oxidative stress.

*In vivo* in rats, Arimoto et al. showed that exposure to DEP and Lipopolysaccharides (LPS) (intratracheal co-instillation) resulted in synergistic enhancement of free radical generation in the lungs, paralleled by a synergistic increase in total protein and by infiltration of neutrophils in the bronchoalveolar lavage fluid of the lungs [136]. The free radicals result from activated macrophages; more specifically, because of enhanced xanthine xanthine-oxidase activity.

### 3.5.3

#### **Nanoparticles and Cellular Uptake**

Reviewing the literature, there are several reports on cellular uptake of micro- and nanosized particles and CNT. Reports on particle uptake by endothelial cells [137, 138], pulmonary epithelium [68, 139, 140], intestinal epithelium [75, 91] alveolar macrophages [41, 73, 111, 141–143], other macrophages [88, 99, 144, 145], nerve cells [146, 147] and other cells [71, 148] are available. This is an expected phenomenon for phagocytic cells (macrophages) and cells that function as a barrier and/or transport for (large) compounds. Except for macrophages, the health effects of cellular uptake of nanoparticles have not been studied in depth.

In designing quantum dots specifically to enter cells, endocytosis is highly size-dependent, and an optimal size of around 50 nm has been suggested [149]. Besides the size, the surface plays a role: quantum dots with amine-modified coating were more efficiently internalized into the various human cells examined [150].

### 3.5.4

#### **Nanoparticles and the Blood–Brain Barrier**

One of the promising avenues of nanotechnology is organ- or cell-specific drug delivery mediated by nanoparticles [151–153]. Transport of nanoparticles across the blood–brain barrier (BBB) is expected to be possible by either passive diffusion or by carrier-mediated endocytosis. Coating of particles with polysorbates (e.g., polysorbate-80) results in anchoring of apolipoprotein E (apo E) or other blood components. Surface-modified particles seem to mimic Low Density Lipoproteins (LDL) particles and can interact with the LDL receptor, leading to uptake by endothelial cells. Hereafter, the drug (which was loaded in the particle) may be released in these cells and diffuse into the brain interior or the particles may be trans-cytosed.

Also, other processes such as tight junction modulation or P-glycoprotein (Pgp) inhibition may occur [154]. The translocation of inhaled nanoparticles via the olfactory nerves to the brain has been reported by Oberdörster et al. [72] and Fechter et al. [155].

## 3.6

### **Summary and Discussion**

In general, in the search for potential adverse effects of a new product, toxicologists initially look into basic mechanisms such as acute toxicity (cytotoxicity), uptake and distribution and excretion of the material in organisms (pharmaco- or toxicokinetics). In a somewhat later phase, the mode of action at the target organs, tissues, and cells is studied.

Reviewing the knowledge collected concerning health effects of nanomaterials we have to conclude that it is still premature to draw final conclusions, simply because too little has been investigated.

A first important remark is that current knowledge is mainly based on epidemiological and experimental work concerning environmental particle pollution, most often referred to as coarse (10–2.5  $\mu\text{m}$ ), fine (2.5–0.1  $\mu\text{m}$ ) and ultrafine particulates (UFP) (<0.1  $\mu\text{m}$ ). We can certainly learn from this research, but it has to be taken into account that exposure to man-made nanomaterials differs from exposure to environmental particles in several ways. UFP, often arising from combustion, have a complex composition, have no uniform size and some compounds are soluble in biological systems, while man-made nanoparticles often have a uniform (crystalline) structure and size, and are often not soluble. Beside these differences it has to be remembered that some effects of particulate matter will be more generic, not discriminating between the nature (chemical composition) of the materials, e.g., activation (or inhibition) of phagocytosis, cellular uptake or other cellular interactions. Also, with decreasing particle diameter their surface area increases significantly, resulting in increased surface activity; health effects can often be better correlated with the total surface area of the material in the exposure rather than with its total mass.

*In conclusion*, some important observations are summarized below:

- Of the three exposure routes, inhalation of nanomaterials is easily the most troublesome for two reasons: (1) the lung itself is a target organ because the inhaled particulates can easily induce inflammation and oxidative stress locally, and the particulates are not always efficiently cleared from the alveoli and (2) the lung is, as far as investigated, a portal to enter the systemic circulation.
- Exposure to skin will not, as far as we know, lead to systemic uptake but penetration into the dermis can induce immunological effects.
- Oral exposure can result in systemic penetration – a feature that can be used in medicine, but unintended penetration from the intestinal tract, given the current state of knowledge, is not a worrying issue.
- Penetration, independent of portal, and the subsequent distribution are related to the size and surface properties of the particles.

From previous studies, using environmental particles, we know that oxidative mechanisms, local inflammation, thrombotic effects, and, only recently reported, uptake into sensory nerves are the important issues. Some of the reported effects will be specific for the complex DEP or Urban Particulate Matter (UPM), but new previously unobserved effects can be expected for man-made nanomaterials, therefore research focused on novel effects due to the specific nanomaterials will certainly be required.

Besides the expected and predictable risks, nanomaterials can induce a biologic response in a way we are not familiar with from previous studies of known compounds. For example, it has recently been observed that green-light-emitting quantum dots are more toxic *in vitro* than red-light-emitting dots, simply because of the difference in DNA damage by the emitted light [156].

Moreover, nanomaterials are often defined as materials with a dimension smaller than 100 nm. The definition proposed by the European Academy at Bad Neuenahr,





Fig. 3.2. “From exposure to decease” flowchart.

Germany is probably more appropriate: “Nanotechnology is dealing with functional systems based on the use of subunits with specific size-dependent properties of the individual sub-units or of a system of those” [157]. This definition takes into account size-dependent activity and/or effect rather than a certain size; following this it is expected that for many materials the border between “bulk” and “nano” will be mainly situated at a size range smaller than 20 nm, thus defining the size window more strictly.

Finally, although nanotoxicology will discover some new or specific toxicological mechanisms, the general concepts describing the process from exposure to disease, shown in Fig. 3.2, will not change. This paradigm can be used for any compound and it stresses the most important steps in exposure related diseases.

Without exposure, no health effects can develop, even not from very harmful compounds. From the portal of exposure, the compound must have the capability to enter the body, and then be distributed to the target tissue(s). In contact with the target tissue the compound can induce malfunction, most often subtle at first, but resulting in irreversible changes after chronic exposure.

This scheme can easily be adopted for nanomaterials; the challenge will be to find those (few) nanomaterials out of the large pool of newly produced materials, with specific sizes, composition and coating, that would induce significant health effects.

### 3.7

#### What Can be Done?

Although few direct reports are available on the health implications of exposure to man-made nanoparticles, the indirect evidence assembled here from epidemiological sources, drug delivery studies, as well as some *in vivo* and *in vitro* results, suggests that potential health risks can not be neglected. With growing volumes of production and their incorporation into more and more products, the chances of exposure of the general public to the engineered nanoparticles are likely to grow. Seemingly safe bulk materials, when reduced to nanoparticles, can drastically change their chemical, biological and catalytic activities, and become toxic. Moreover, their minute dimensions often help to overcome the existing biological barriers and body defense mechanisms. The whole issue is complicated by the difficulties associated with the detection and monitoring of nanoparticles.

On the bright side, most nanomaterials are currently used as additives or property enhancers that are highly diluted in a matrix material. The nanomaterials are

bound to the matrix and unlikely to be released in serious quantities. In addition, most material manufacturers prefer to use liquid dispersions of nanomaterials (as opposed to dry powders) as these are much easier to handle. Unfortunately, some nanomaterials can only be produced in either a dry atmosphere or under vacuum. This raises a series of questions on their safe collection, handling, dispersion, cleaning, disposal, recycling, and environmental protection. At the time of writing, the issue of potential health risks that might be associated with nanomaterials is getting both an adequate press coverage and reasonable attention from the regulatory bodies and governments.

University laboratories are often at the forefront of nanomaterial research. Their laboratory procedures and practices should perhaps be critically re-evaluated in light of the material presented in this chapter. Both small and big manufacturers who state on the MSDS forms that nanomaterials are “safe because the bulk material is considered safe” should, perhaps, reconsider and try to get some proof. Finally, the public should be learning about the benefits and risks of nanotechnology not from scandal-driven tabloids but from the scientific community directly engaged in nanotechnology.

## References

- 1 HOET, P.H., BRUSKE-HOHLFELD, I., SALATA, O.V. Nanoparticles – known and unknown health risks. *J. Nanobiotechnol.* **2004**, 2, 12.
- 2 UK Royal Society and Royal Academy of Engineering, Nanoscience and nanotechnologies: Opportunities and uncertainties. Final Report **2004** [<http://www.nanotec.org.uk/finalReport.htm>].
- 3 Anonymous. Nanotech is not so scary. *Nature* **2003**, 421, 299.
- 4 SALATA, O. Applications of nanoparticles in biology and medicine. *J. Nanobiotechnol.* **2004**, 2, 3.
- 5 MAZZOLA, L. Commercializing nanotechnology. *Nat. Biotechnol.* **2003**, 21, 1137–1143.
- 6 PAULL, R., WOLFE, J., HEBERT, P., SINKULA, M. Investing in nanotechnology. *Nat. Biotechnol.* **2003**, 21, 1144–1147.
- 7 FEYNMAN, R.P. There's Plenty of Room at the Bottom, *Science* **1991**, 254, 1300–1301.
- 8 BALL, P. Roll-up for the revolution. *Nature* **2001**, 414, 142–144.
- 9 NanoBusiness Alliance. **2003**. [www.nanobusiness.org](http://www.nanobusiness.org).
- 10 SAMET, J.M., DOMINICI, F., CURRIERO, F.C., COURSAK, I., ZEGER, S.L. Fine particulate air pollution and mortality in 20 U.S. cities, 1987–1994. *N. Engl. J. Med.* **2000**, 343, 1742–1749.
- 11 DOMINICI, F., McDERMOTT, A., DANIELS, M., ZEGER, S.L., AND SAMET, J.M. Revised Analysis of the National Morbidity, Mortality, and Air Pollution Study (NMMAPS), Part II: Mortality Among Residents of 90 Cities. In: Revised Analyses of Time-series Studies of Air Pollution and Health, Anon, Boston: Health Effects Institute, **2003**, p. 9–24.
- 12 KATSOYANNI, K., TOULOUMI, G., SAMOLI, E., GRYPARIS, A., LE TERTRE, A., MONOPOLIS, Y., ROSSI, G., ZMIROU, D., BALLESTER, F., BOUMGHAR, A., ANDERSON, H.R., WOJTYNIAK, B., PALDY, A., BRAUNSTEIN, R., PEKKANEN, J., SCHINDLER, C., SCHWARTZ, J. Confounding and effect modification in the short-term effects of ambient particles on total mortality: Results from 29 European cities within the APHEA2 project. *Epidemiology* **2001**, 12, 521–531.

- 13 WHO *Air Quality Guidelines for Europe*. 2nd edn 2000. WHO, Regional Office for Europe, Copenhagen.
- 14 PETERS, A., WICHMANN, H.E., TUCH, T., HEINRICH, J., HEYDER, J. Respiratory effects are associated with the number of ultrafine particles. *Am. J. Respir. Crit. Care Med.* **1997**, 155, 1376–1383.
- 15 PEKKANEN, J., TIMONEN, K.L., RUUSKANEN, J., REPONEN, A., MIRME, A. Effects of ultrafine and fine particles in urban air on peak expiratory flow among children with asthmatic symptoms. *Environ. Res.* **1997**, 74, 24–33.
- 16 VON KLOT, S., WOLKE, G., TUCH, T., HEINRICH, J., DOCKERY, D.W., SCHWARTZ, J., KREYLING, W.G., WICHMANN, H.E., PETERS, A. Increased asthma medication use in association with ambient fine and ultrafine particles. *Eur. Respir. J.* **2002**, 20, 691–702.
- 17 PENTTINEN, P., TIMONEN, K.L., TIITTANEN, P., MIRME, A., RUUSKANEN, J., PEKKANEN, J. Number concentration and size of particles in urban air: Effects on spirometric lung function in adult asthmatic subjects. *Environ. Health Perspect.* **2001**, 109, 319–323.
- 18 PENTTINEN, P., TIMONEN, K.L., TIITTANEN, P., MIRME, A., RUUSKANEN, J., PEKKANEN, J. Ultrafine particles in urban air and respiratory health among adult asthmatics. *Eur. Respir. J.* **2001**, 17, 428–435.
- 19 IBALD-MULLI, A., TIMONEN, K.L., PETERS, A., HEINRICH, J., WOLKE, G., LANKI, T., BUZORIUS, G., KREYLING, W.G., DE HARTOG, J., HOEK, G., TEN BRINK, H.M., PEKKANEN, J. Effects of particulate air pollution on blood pressure and heart rate in subjects with cardiovascular disease: A multicenter approach. *Environ. Health Perspect.* **2004**, 112, 369–377.
- 20 DE HARTOG, J.J., HOEK, G., PETERS, A., TIMONEN, K.L., IBALD-MULLI, A., BRUNEKREEF, B., HEINRICH, J., TIITTANEN, P., VAN WIJNEN, J.H., KREYLING, W., KULMALA, M., PEKKANEN, J. Effects of fine and ultrafine particles on cardiorespiratory symptoms in elderly subjects with coronary heart disease: The ULTRA study. *Am. J. Epidemiol.* **2003**, 157, 613–623.
- 21 RUUSKANEN, J., TUCH, T., TEN BRINK, H.M., PETERS, A., KHLYSTOV, A., MIRME, A., KOS, G.P., BRUNEKREEF, B., WICHMANN, H.E., BUZORIUS, G., VALLIUS, M., PEKKANEN, J. Concentrations of ultrafine, fine and PM2.5 particles in three European cities. *Atmos. Environ.* **2001**, 35, 3729–3738.
- 22 PEKKANEN, J., PETERS, A., HOEK, G., TIITTANEN, P., BRUNEKREEF, B., DE HARTOG, J., HEINRICH, J., IBALD-MULLI, A., KREYLING, W.G., LANKI, T., TIMONEN, K.L., VANNINEN, E. Particulate air pollution and risk of ST-segment depression during repeated submaximal exercise tests among subjects with coronary heart disease: The Exposure and Risk Assessment for Fine and Ultrafine Particles in Ambient Air (ULTRA) study. *Circulation* **2002**, 106, 933–938.
- 23 BROOK, R.D., FRANKLIN, B., CASCIO, W., HONG, Y., HOWARD, G., LIPSETT, M., LUEPKER, R., MITTLEMAN, M., SAMET, J., SMITH, S.C., JR., TAGER, I. Air pollution and cardiovascular disease: A statement for healthcare professionals from the Expert Panel on Population and Prevention Science of the American Heart Association. *Circulation* **2004**, 109, 2655–2671.
- 24 WICHMANN, H.E., SPIX, C., TUCH, T., WOLKE, G., PETERS, A., HEINRICH, J., KREYLING, W.G., HEYDER, J. Daily mortality and fine and ultrafine particles in Erfurt, Germany part I: Role of particle number and particle mass. *Res. Rep. Health Eff. Inst.* **2000**, 5–86.
- 25 OBERDÖRSTER, G., FERIN, J., LEHNERT, B.E. Correlation between particle size, in vivo particle persistence, and lung injury. *Environ. Health Perspect.* **1994**, 102(Suppl 5), 173–179.
- 26 BORM, P.J. Particle toxicology: From coal mining to nanotechnology. *Inhal. Toxicol.* **2002**, 14, 311–324.

- 27 SANFELD, A., STEINCHEN, A. Does the size of small objects influence chemical reactivity in living systems? *C. R. Biol.* **2003**, 326, 141–147.
- 28 OBERDÖRSTER, G., OBERDÖRSTER, E., OBERDÖRSTER, J. Nanotoxicology: An emerging discipline evolving from studies of ultrafine particles. *Environ. Health Perspect.* **2005**, 113, 823–839.
- 29 LIPPMANN, M. Effects of fiber characteristics on lung deposition, retention, and disease. *Environ. Health Perspect.* **1990**, 88, 311–317.
- 30 MOORE, M.A., BROWN, R.C., PIGOTT, G. Material properties of MMVFs and their time-dependent failure in lung environments. *Inhal. Toxicol.* **2001**, 13, 1117–1149.
- 31 OBERDÖRSTER, G. Pulmonary effects of inhaled ultrafine particles. *Int. Arch. Occup. Environ. Health* **2001**, 74, 1–8.
- 32 OBERDÖRSTER, G. Toxicokinetics and effects of fibrous and nonfibrous particles. *Inhal. Toxicol.* **2002**, 14, 29–56.
- 33 OBERDÖRSTER, G. Determinants of the pathogenicity of man-made vitreous fibers (MMVF). *Int. Arch. Occup. Environ. Health* **2000**, 73 Suppl, S60–S68.
- 34 WARHEIT, D.B., HART, G.A., HESTERBERG, T.W., COLLINS, J.J., DYER, W.M., SWAEN, G.M., CASTRANOVA, V., SOIEFFER, A.I., KENNEDY, G.L., JR. Potential pulmonary effects of man-made organic fiber (MMOV) dusts. *Crit. Rev. Toxicol.* **2001**, 31, 697–736.
- 35 DONALDSON, K., TRAN, C.L. Inflammation caused by particles and fibers. *Inhal. Toxicol.* **2002**, 14, 5–27.
- 36 SEATON, A., MACNEE, W., DONALDSON, K., GODDEN, D. Particulate air pollution and acute health effects. *Lancet* **1995**, 345, 176–178.
- 37 BROWN, D.M., WILSON, M.R., MACNEE, W., STONE, V., DONALDSON, K. Size-dependent proinflammatory effects of ultrafine polystyrene particles: A role for surface area and oxidative stress in the enhanced activity of ultrafines. *Toxicol. Appl. Pharmacol.* **2001**, 175, 191–199.
- 38 SCHINS, R.P. Mechanisms of genotoxicity of particles and fibers. *Inhal. Toxicol.* **2002**, 14, 57–78.
- 39 BERMAN, D.W., CRUMP, K.S., CHATFIELD, E.J., DAVIS, J.M., JONES, A.D. The sizes, shapes, and mineralogy of asbestos structures that induce lung tumors or mesothelioma in AF/HAN rats following inhalation. *Risk Anal.* **1995**, 15, 181–195.
- 40 KREYLING, W.G., SEMMLER, M., MOLLER, W. Dosimetry and toxicology of ultrafine particles. *J. Aerosol Med.* **2004**, 17, 140–152.
- 41 OBERDÖRSTER, G. Lung particle overload: Implications for occupational exposures to particles. *Regul. Toxicol. Pharmacol.* **1995**, 21, 123–135.
- 42 MUHLE, H., MANGELSDORF, I. Inhalation toxicity of mineral particles: Critical appraisal of endpoints and study design. *Toxicol. Lett.* **2003**, 140–141, 223–228.
- 43 MOSSMAN, B.T. Mechanisms of action of poorly soluble particulates in overload-related lung pathology. *Inhal. Toxicol.* **2000**, 12, 141–148.
- 44 MOOLGAVKAR, S.H., BROWN, R.C., TURIM, J. Biopersistence, fiber length, and cancer risk assessment for inhaled fibers. *Inhal. Toxicol.* **2001**, 13, 755–772.
- 45 DONALDSON, K., STONE, V. Current hypotheses on the mechanisms of toxicity of ultrafine particles. *Ann. Ist. Super. Sanita* **2003**, 39, 405–410.
- 46 HESTERBERG, T.W., CHASE, G., AXTEN, C., MILLER, W.C., MUSSELMAN, R.P., KAMSTRUP, O., HADLEY, J., MORSCHIEDT, C., BERNSTEIN, D.M., THEVENAZ, P. Biopersistence of synthetic vitreous fibers and amosite asbestos in the rat lung following inhalation. *Toxicol. Appl. Pharmacol.* **1998**, 151, 262–275.
- 47 WARHEIT, D.B., REED, K.L., WEBB, T.R. Man-made respirable-sized organic fibers: What do we know about their toxicological profiles? *Ind. Health* **2001**, 39, 119–125.
- 48 WYLIE, A.G., SKINNER, H.C., MARSH, J., SNYDER, H., GARZIONE, C., HODKINSON, D., WINTERS, R., MOSSMAN, B.T. Mineralogical features associated with cytotoxic and

- proliferative effects of fibrous talc and asbestos on rodent tracheal epithelial and pleural mesothelial cells. *Toxicol. Appl. Pharmacol.* **1997**, *147*, 143–150.
- 49 SEARL, A. A comparative study of the clearance of respirable para-aramid, chrysotile and glass fibres from rat lungs. *Ann. Occup. Hyg.* **1997**, *41*, 217–233.
- 50 STANTON, M.F., WRENCH, C. Mechanisms of mesothelioma induction with asbestos and fibrous glass. *J. Natl. Cancer Inst.* **1972**, *48*, 797–821.
- 51 SERVICE, R.F. American Chemical Society meeting. Nanomaterials show signs of toxicity. *Science* **2003**, *300*, 243.
- 52 WARHEIT, D.B., LAURENCE, B.R., REED, K.L., ROACH, D.H., REYNOLDS, G.A., WEBB, T.R. Comparative pulmonary toxicity assessment of single wall carbon nanotubes in rats. *Toxicol. Sci.* **2003**, *77*, 117–125.
- 53 LAM, C.W., JAMES, J.T., MCCCLUSKEY, R., HUNTER, R.L. Pulmonary toxicity of single-wall carbon nanotubes in mice 7 and 90 days after intratracheal instillation. *Toxicol. Sci.* **2003**, *77*, 126–134.
- 54 MAYNARD, A.D., BARON, P.A., FOLEY, M., SHVEDOVA, A.A., KISIN, E.R., CASTRANOVA, V. Exposure to carbon nanotube material: Aerosol release during the handling of unrefined single-walled carbon nanotube material. *J. Toxicol. Environ. Health A* **2004**, *67*, 87–107.
- 55 DONALDSON, K., TRAN, C.L. An introduction to the short-term toxicology of respirable industrial fibres. *Mutat. Res.* **2004**, *553*, 5–9.
- 56 YEATES, D.B., MAUDERLY, J.L. Inhaled environmental/occupational irritants and allergens: Mechanisms of cardiovascular and systemic responses. Introduction. *Environ. Health Perspect.* **2001**, *109*(Suppl 4), 479–481.
- 57 GOLD, D.R., LITONJUA, A., SCHWARTZ, J., LOVETT, E., LARSON, A., NEARING, B., ALLEN, G., VERRIER, M., CHERRY, R., VERRIER, R. Ambient pollution and heart rate variability. *Circulation* **2000**, *101*, 1267–1273.
- 58 LIAO, D., CREASON, J., SHY, C., WILLIAMS, R., WATTS, R., ZWEIDINGER, R. Daily variation of particulate air pollution and poor cardiac autonomic control in the elderly. *Environ. Health Perspect.* **1999**, *107*, 521–525.
- 59 BROWN, J.S., ZEMAN, K.L., BENNETT, W.D. Ultrafine particle deposition and clearance in the healthy and obstructed lung. *Am. J. Respir. Crit. Care Med.* **2002**, *166*, 1240–1247.
- 60 CONHAIM, R.L., EATON, A., STAUB, N.C., HEATH, T.D. Equivalent pore estimate for the alveolar-airway barrier in isolated dog lung. *J. Appl. Physiol.* **1988**, *64*, 1134–1142.
- 61 HERMANS, C., KNOOPS, B., WIEDIG, M., ARSALANE, K., TOUBEAU, G., FALMAGNE, P., BERNARD, A. Clara cell protein as a marker of Clara cell damage and bronchoalveolar blood barrier permeability. *Eur. Respir. J.* **1999**, *13*, 1014–1021.
- 62 REJMAN, J., OBERLE, V., ZUHORN, I.S., HOEKSTRA, D. Size-dependent internalization of particles via the pathways of clathrin- and caveolae-mediated endocytosis. *Biochem. J.* **2004**, *377*, 159–169.
- 63 ELJAMAL, M., NAGARAJAN, S., PATTON, J.S. In situ and in vivo methods for pulmonary delivery. *Pharm. Biotechnol.* **1996**, *8*, 361–374.
- 64 PATTON, J.S. Mechanisms of macromolecule absorption by the lungs. *Adv. Drug Deliv. Rev.* **1996**, *19*, 3–36.
- 65 SMITH, A.E., HELENIUS, A. How viruses enter animal cells. *Science* **2004**, *304*, 237–242.
- 66 NEMMAR, A., VANBILLOEN, H., HOYLAERTS, M.F., HOET, P.H., VERBRUGGEN, A., NEMERY, B. Passage of intratracheally instilled ultrafine particles from the lung into the systemic circulation in hamster. *Am. J. Respir. Crit. Care Med.* **2001**, *164*, 1665–1668.
- 67 KAWAKAMI, K., IWAMURA, A., GOTO, E., MORI, Y., ABE, T., HIRASAWA, Y., ISHIDA, H., SHIMADA, T., TOMINAGA, G. Kinetics and clinical application of <sup>99m</sup>Tc-technegas. *Kaku Igaku* **1990**, *27*, 725–733.

- 68 KATO, T., YASHIRO, T., MURATA, Y., HERBERT, D.C., OSHIKAWA, K., BANDO, M., OHNO, S., SUGIYAMA, Y. Evidence that exogenous substances can be phagocytized by alveolar epithelial cells and transported into blood capillaries. *Acc. Chem. Res.* **2003**, 311, 47–51.
- 69 STEINER, S., PFUTZNER, A., WILSON, B.R., HARZER, O., HEINEMANN, L., RAVE, K. Technosphere/Insulin – proof of concept study with a new insulin formulation for pulmonary delivery. *Exp. Clin. Endocrinol. Diabetes* **2002**, 110, 17–21.
- 70 PATTON, J.S., BUKAR, J.G., ELDON, M.A. Clinical pharmacokinetics and pharmacodynamics of inhaled insulin. *Clin. Pharmacokinet.* **2004**, 43, 781–801.
- 71 KREYLING, W., SEMMLER, M., ERBE, F., MAYER, P., SCHULZ, H., OBERDÖRSTER, G., ZIESENIS, A. Translocation of ultrafine insoluble iridium particles from lung epithelium to extrapulmonary organs is size dependent but very low. *J. Toxicol. Environ. Health A* **2002**, 65, 1513–1530.
- 72 OBERDÖRSTER, G., SHARP, Z., ATUDOREI, V., ELDER, A., GELEIN, R., LUNTS, A., KREYLING, W., COX, C. Extrapulmonary translocation of ultrafine carbon particle following whole-body inhalation exposure of rats. *J. Toxicol. Environ. Health A* **2002**, 65, 1531–1543.
- 73 TAKENAKA, S., KARG, E., ROTH, C., SCHULZ, H., ZIESENIS, A., HEINZMANN, U., SCHRAMMEL, P., HEYDER, J. Pulmonary and systemic distribution of inhaled ultrafine silver particles in rats. *Environ. Health Perspect.* **2001**, 109(Suppl 4), 547–551.
- 74 EYLES, J.E., BRAMWELL, V.W., WILLIAMSSON, E.D., ALPAR, H.O. Microsphere translocation and immunopotentiality in systemic tissues following intranasal administration. *Vaccine* **2001**, 19, 4732–4742.
- 75 FLORENCE, A.T., HUSSAIN, N. Transcytosis of nanoparticle and dendrimer delivery systems: Evolving vistas. *Adv. Drug Deliv. Rev.* **2001**, 50(Suppl 1), S69–S89.
- 76 HUSSAIN, N., JAITLEY, V., FLORENCE, A.T. Recent advances in the understanding of uptake of microparticulates across the gastrointestinal lymphatics. *Adv. Drug Deliv. Rev.* **2001**, 50, 107–142.
- 77 APRAHAMIAN, M., MICHEL, C., HUMBERT, W., DEVISSAGUET, J.P., DAMGE, C. Transmucosal passage of polyalkylcyanoacrylate nanocapsules as a new drug carrier in the small intestine. *Biol. Cell* **1987**, 61, 69–76.
- 78 HILLYER, J.F., ALBRECHT, R.M. Gastrointestinal persorption and tissue distribution of differently sized colloidal gold nanoparticles. *J. Pharm. Sci.* **2001**, 90, 1927–1936.
- 79 JANI, P., HALBERT, G.W., LANGRIDGE, J., FLORENCE, A.T. Nanoparticle uptake by the rat gastrointestinal mucosa: Quantitation and particle size dependency. *J. Pharm. Pharmacol.* **1990**, 42, 821–826.
- 80 JANI, P., HALBERT, G.W., LANGRIDGE, J., FLORENCE, A.T. The uptake and translocation of latex nanospheres and microspheres after oral administration to rats. *J. Pharm. Pharmacol.* **1989**, 41, 809–812.
- 81 HUSSAIN, N., FLORENCE, A.T. Utilizing bacterial mechanisms of epithelial cell entry: Invasin-induced oral uptake of latex nanoparticles. *Pharm. Res.* **1998**, 15, 153–156.
- 82 HUSSAIN, N., JANI, P.U., FLORENCE, A.T. Enhanced oral uptake of tomato lectin-conjugated nanoparticles in the rat. *Pharm. Res.* **1997**, 14, 613–618.
- 83 HILLERY, A.M., JANI, P.U., FLORENCE, A.T. Comparative, quantitative study of lymphoid and non-lymphoid uptake of 60 nm polystyrene particles. *J. Drug Target* **1994**, 2, 151–156.
- 84 WOODLEY, J.F. Lectins for gastrointestinal targeting – 15 years on. *J. Drug Target* **2000**, 7, 325–333.
- 85 SZENTKUTI, L. Light microscopical observations on luminally administered dyes, dextrans, nanospheres and microspheres in the pre-epithelial mucus gel layer of the rat distal colon. *J. Control. Release* **1997**, 46, 233–242.
- 86 YAMAGO, S., TOKUYAMA, H.,

- NAKAMURA, E., KIKUCHI, K., KANANISHI, S., SUEKI, K., NAKAHARA, H., ENOMOTO, S., AMBE, F. In vivo biological behavior of a water-miscible fullerene: <sup>14</sup>C labeling, absorption, distribution, excretion and acute toxicity. *Chem. Biol.* **1995**, *2*, 385–389.
- 87 GATTI, A.M. Biocompatibility of micro- and nano-particles in the colon. Part II. *Biomaterials* **2004**, *25*, 385–392.
- 88 LOMER, M.C., THOMPSON, R.P., POWELL, J.J. Fine and ultrafine particles of the diet: Influence on the mucosal immune response and association with Crohn's disease. *Proc. Nutr. Soc.* **2002**, *61*, 123–130.
- 89 POWELL, J.J., HARVEY, R.S., ASHWOOD, P., WOLSTENCROFT, R., GERSHWIN, M.E., THOMPSON, R.P. Immune potentiation of ultrafine dietary particles in normal subjects and patients with inflammatory bowel disease. *J. Autoimmun.* **2000**, *14*, 99–105.
- 90 KUCHARZIK, T., LUGERING, A., LUGERING, N., RAUTENBERG, K., LINNEPE, M., CICHON, C., REICHEL, R., STOLL, R., SCHMIDT, M.A., DOMSCHKE, W. Characterization of M cell development during indomethacin-induced ileitis in rats. *Aliment. Pharmacol. Ther.* **2000**, *14*, 247–256.
- 91 HOPWOOD, D., SPIERS, E.M., ROSS, P.E., ANDERSON, J.T., MCCULLOUGH, J.B., MURRAY, F.E. Endocytosis of fluorescent microspheres by human oesophageal epithelial cells: Comparison between normal and inflamed tissue. *Gut* **1995**, *37*, 598–602.
- 92 LADEMANN, J., OTBERG, N., RICHTER, H., WEIGMANN, H.J., LINDEMANN, U., SCHAEFER, H., STERRY, W. Investigation of follicular penetration of topically applied substances. *Skin Pharmacol. Appl. Skin Physiol.* **2001**, *14*, 17–22.
- 93 KREILGAARD, M. Influence of microemulsions on cutaneous drug delivery. *Adv. Drug Deliv. Rev.* **2002**, *54*(Suppl 1), S77–S98.
- 94 LADEMANN, J., WEIGMANN, H., RICKMEYER, C., BARTHELMES, H., SCHAEFER, H., MUELLER, G., STERRY, W. Penetration of titanium dioxide microparticles in a sunscreen formulation into the horny layer and the follicular orifice. *Skin Pharmacol. Appl. Skin Physiol.* **1999**, *12*, 247–256.
- 95 TINKLE, S.S., ANTONINI, J.M., RICH, B.A., ROBERTS, J.R., SALMEN, R., DEPREE, K., ADKINS, E.J. Skin as a route of exposure and sensitization in chronic beryllium disease. *Environ. Health Perspect.* **2003**, *111*, 1202–1208.
- 96 MENON, G.K., ELIAS, P.M. Morphologic basis for a pore-pathway in mammalian stratum corneum. *Skin Pharmacol.* **1997**, *10*, 235–246.
- 97 ANDERSSON, K.G., FOGH, C.L., BYRNE, M.A., ROED, J., GODDARD, A.J., HOTCHKISS, S.A. Radiation dose implications of airborne contaminant deposition to humans. *Health Phys.* **2002**, *82*, 226–232.
- 98 DE JALON, E.G., BLANCO-PRieto, M.J., YGARTUA, P., SANTOYO, S. PLGA microparticles: Possible vehicles for topical drug delivery. *Int. J. Pharm.* **2001**, *226*, 181–184.
- 99 BLUNDELL, G., HENDERSON, W.J., PRICE, E.W. Soil particles in the tissues of the foot in endemic elephantiasis of the lower legs. *Ann. Trop. Med. Parasitol.* **1989**, *83*, 381–385.
- 100 CORACHAN, M. Endemic non-filarial elephantiasis of lower-limbs – Podoconiosis. *Med. Clin.* **1988**, *91*, 97–100.
- 101 HOSTYNEK, J.J. Factors determining percutaneous metal absorption. *Food Chem. Toxicol.* **2003**, *41*, 327–345.
- 102 EUN, H.C., LEE, H.G., PAIK, N.W. Patch test responses to rockwool of different diameters evaluated by cutaneous blood flow measurement. *Contact Dermatitis* **1991**, *24*, 270–273.
- 103 MONTEIRO-RIVIERE, N.A., NEMANICH, R.J., INMAN, A.O., WANG, Y.Y., RIVIERE, J.E. Multi-walled carbon nanotube interactions with human epidermal keratinocytes. *Toxicol. Lett.* **2005**, *155*, 377–384.
- 104 SHVEDOVA, A.A., CASTRANOVA, V., KISIN, E.R., SCHWEGLER-BERRY, D., MURRAY, A.R., GANDELSMAN, V.Z.,

- MAYNARD, A., BARON, P. Exposure to carbon nanotube material: Assessment of nanotube cytotoxicity using human keratinocyte cells. *J. Toxicol. Environ. Health* **2003**, 66, 1909–1926.
- 105 MARKOWITZ, G.S., PERAZELLA, M.A. Drug-induced renal failure: A focus on tubulointerstitial disease. *Clin. Chim. Acta* **2005**, 351, 31–47.
- 106 SCHINS, R.P., DUFFIN, R., HOHR, D., KNAAPEN, A.M., SHI, T., WEISHAUPT, C., STONE, V., DONALDSON, K., BORM, P.J. Surface modification of quartz inhibits toxicity, particle uptake, and oxidative DNA damage in human lung epithelial cells. *Chem. Res. Toxicol.* **2002**, 15, 1166–1173.
- 107 HOET, P.H., NEMMAR, A., NEMERY, B. Health impact of nanomaterials? *Nat. Biotechnol.* **2004**, 22, 19.
- 108 BECKETT, W.S., CHALUPA, D.F., PAULY-BROWN, A., SPEERS, D.M., STEWART, J.C., FRAMPTON, M.W., UTELL, M.J., HUANG, L.S., COX, C., ZAREBA, W., OBERDÖRSTER, G. Comparing inhaled ultrafine versus fine zinc oxide particles in healthy adults: A human inhalation study. *Am. J. Respir. Crit. Care Med.* **2005**, 171, 1129–1135.
- 109 LEE, K.P., KELLY, D.P., SCHNEIDER, P.W., TROCHIMOWICZ, H.J. Inhalation toxicity study on rats exposed to titanium tetrachloride atmospheric hydrolysis products for two years. *Toxicol. Appl. Pharmacol.* **1986**, 83, 30–45.
- 110 DRISCOLL, K.E., DEYO, L.C., CARTER, J.M., HOWARD, B.W., HASSENBEIN, D.G., BERTRAM, T.A. Effects of particle exposure and particle-elicited inflammatory cells on mutation in rat alveolar epithelial cells. *Carcinogenesis* **1997**, 18, 423–430.
- 111 RENWICK, L.C., DONALDSON, K., CLOUTER, A. Impairment of alveolar macrophage phagocytosis by ultrafine particles. *Toxicol. Appl. Pharmacol.* **2001**, 172, 119–127.
- 112 RENWICK, L.C., BROWN, D., CLOUTER, A., DONALDSON, K. Increased inflammation and altered macrophage chemotactic responses caused by two ultrafine particle types. *Occup. Environ. Med.* **2004**, 61, 442–447.
- 113 ARAUJO, L., LOBENBERG, R., KREUTER, J. Influence of the surfactant concentration on the body distribution of nanoparticles. *J. Drug Target* **1999**, 6, 373–385.
- 114 LABHASETWAR, V., SONG, C., HUMPHREY, W., SHEBUSKI, R., LEVY, R.J. Arterial uptake of biodegradable nanoparticles: Effect of surface modifications. *J. Pharm. Sci.* **1998**, 87, 1229–1234.
- 115 HOET, P.H., GILISSEN, L., NEMERY, B. Polyanions protect against the in vitro pulmonary toxicity of polycationic paint components associated with the Ardystil syndrome. *Toxicol. Appl. Pharmacol.* **2001**, 175, 184–190.
- 116 HOET, P.H., GILISSEN, L.P., LEYVA, M., NEMERY, B. In vitro cytotoxicity of textile paint components linked to the “Ardystil syndrome”. *Toxicol. Sci.* **1999**, 52, 209–216.
- 117 FISCHER, D., LI, Y., AHLEMEYER, B., KRIEGLSTEIN, J., KISSEL, T. In vitro cytotoxicity testing of polycations: Influence of polymer structure on cell viability and hemolysis. *Biomaterials* **2003**, 24, 1121–1131.
- 118 MORGAN, D.M., LARVIN, V.L., PEARSON, J.D. Biochemical characterisation of polycation-induced cytotoxicity to human vascular endothelial cells. *J. Cell Sci.* **1989**, 94(Pt 3), 553–559.
- 119 MORGAN, D.M., CLOVER, J., PEARSON, J.D. Effects of synthetic polycations on leucine incorporation, lactate dehydrogenase release, and morphology of human umbilical vein endothelial cells. *J. Cell Sci.* **1988**, 91(Pt 2), 231–238.
- 120 HAENSLE, J., SZOKA, F.C., JR. Polyamidoamine cascade polymers mediate efficient transfection of cells in culture. *Bioconj. Chem.* **1993**, 4, 372–379.
- 121 FISCHER, D., BIEBER, T., LI, Y., ELSASSER, H.P., KISSEL, T. A novel non-viral vector for DNA delivery based on low molecular weight, branched polyethylenimine: Effect of molecular weight on transfection efficiency and cytotoxicity. *Pharm. Res.* **1999**, 16, 1273–1279.



- 122 DEKIE, L., TONCHEVA, V., DUBRUEL, P., SCHACHT, E.H., BARRETT, L., SEYMOUR, L.W. Poly-L-glutamic acid derivatives as vectors for gene therapy. *J. Control. Release* **2000**, 65, 187–202.
- 123 RYSER, H.J. A membrane effect of basic polymers dependent on molecular size. *Nature* **1967**, 215, 934–936.
- 124 SINGH, A.K., KASINATH, B.S., LEWIS, E.J. Interaction of polycations with cell-surface negative charges of epithelial cells. *Biochim. Biophys. Acta* **1992**, 1120, 337–342.
- 125 BALLOU, B., LAGERHOLM, B.C., ERNST, L.A., BRUCHEZ, M.P., WAGGONER, A.S. Noninvasive imaging of quantum dots in mice. *Bioconjug. Chem.* **2004**, 15, 79–86.
- 126 SCHULZ, H., HARDER, V., IBALD-MULLI, A., KHANDOGA, A., KOENIG, W., KROMBACH, F., RADYKEWICZ, R., STAMPFL, A., THORAND, B., PETERS, A. Cardiovascular effects of fine and ultrafine particles. *J. Aerosol Med.* **2005**, 18, 1–22.
- 127 PETERS, A., DOCKERY, D.W., MULLER, J.E., MITTLEMAN, M.A. Increased particulate air pollution and the triggering of myocardial infarction. *Circulation* **2001**, 103, 2810–2815.
- 128 NEMMAR, A., HOYLAERTS, M.F., HOET, P.H., NEMERY, B. Possible mechanisms of the cardiovascular effects of inhaled particles: Systemic translocation and prothrombotic effects. *Toxicol. Lett.* **2004**, 149, 243–253.
- 129 NEMMAR, A., HOET, P.H., DINSDALE, D., VERMYLEN, J., HOYLAERTS, M.F., NEMERY, B. Diesel exhaust particles in lung acutely enhance experimental peripheral thrombosis. *Circulation* **2003**, 107, 1202–1208.
- 130 NEMMAR, A., HOYLAERTS, M.F., HOET, P.H., DINSDALE, D., SMITH, T., XU, H., VERMYLEN, J., NEMERY, B. Ultrafine particles affect experimental thrombosis in an in vivo hamster model. *Am. J. Respir. Crit. Care Med.* **2002**, 166, 998–1004.
- 131 SILVA, V.M., CORSON, N., ELDER, A., OBERDÖRSTER, G. The rat ear vein model for investigating in vivo thrombogenicity of ultrafine particles (UFP). *Toxicol. Sci.* **2005**, 85, 983–989.
- 132 NEMMAR, A., HOYLAERTS, M.F., HOET, P.H., VERMYLEN, J., NEMERY, B. Size effect of intratracheally instilled particles on pulmonary inflammation and vascular thrombosis. *Toxicol. Appl. Pharmacol.* **2003**, 186, 38–45.
- 133 NEMMAR, A., HOET, P.H., VERMYLEN, J., NEMERY, B., HOYLAERTS, M.F. Pharmacological stabilization of mast cells abrogates late thrombotic events induced by diesel exhaust particles in hamsters. *Circulation* **2004**, 110, 1670–1677.
- 134 LI, N., HAO, M., PHALEN, R.F., HINDS, W.C., NEL, A.E. Particulate air pollutants and asthma. A paradigm for the role of oxidative stress in PM-induced adverse health effects. *Clin. Immunol.* **2003**, 109, 250–265.
- 135 XIAO, G.G., WANG, M., LI, N., LOO, J.A., NEL, A.E. Use of proteomics to demonstrate a hierarchical oxidative stress response to diesel exhaust particle chemicals in a macrophage cell line. *J. Biol. Chem.* **2003**, 278, 50781–50790.
- 136 ARIMOTO, T., KADIISKA, M.B., SATO, K., CORBETT, J., MASON, R.P. Synergistic production of lung free radicals by diesel exhaust particles and endotoxin. *Am. J. Respir. Crit. Care Med.* **2005**, 171, 379–387.
- 137 BERNSTEIN, J.A., ALEXIS, N., BARNES, C., BERNSTEIN, I.L., BERNSTEIN, J.A., NEL, A., PEDEN, D., DIAZ-SANCHEZ, D., TARLO, S.M., WILLIAMS, P.B. Health effects of air pollution. *J. Allergy Clin. Immunol.* **2004**, 114, 1116–1123.
- 138 AKERMAN, M.E., CHAN, W.C., LAAKKONEN, P., BHATIA, S.N., RUOSLAHTI, E. Nanocrystal targeting in vivo. *Proc. Natl. Acad. Sci. U.S.A.* **2002**, 99, 12617–12621.
- 139 JUVIN, P., FOURNIER, T., BOLAND, S., SOLER, P., MARANO, F., DESMONTS, J.M., AUBIER, M. Diesel particles are taken up by alveolar type II tumor cells and alter cytokines secretion. *Arch. Environ. Health* **2002**, 57, 53–60.
- 140 BOLAND, S., BAEZA-SQUIBAN, A., FOURNIER, T., HOUCINE, O., GENDRON, M.C., CHEVRIER, M.,

- JOUVENOT, G., COSTE, A., AUBIER, M., MARANO, F. Diesel exhaust particles are taken up by human airway epithelial cells in vitro and alter cytokine production. *Am. J. Physiol.* **1999**, 276, L604–L613.
- 141 HOET, P.H., NEMERY, B. Stimulation of phagocytosis by ultrafine particles. *Toxicol. Appl. Pharmacol.* **2001**, 176, 203.
- 142 LUNDBORG, M., JOHARD, U., LASTBOM, L., GERDE, P., CAMNER, P. Human alveolar macrophage phagocytic function is impaired by aggregates of ultrafine carbon particles. *Environ. Res.* **2001**, 86, 244–253.
- 143 MOSSMAN, B.T., SESKO, A.M. In vitro assays to predict the pathogenicity of mineral fibers. *Toxicology* **1990**, 60, 53–61.
- 144 POWELL, J.J., AINLEY, C.C., HARVEY, R.S., MASON, I.M., KENDALL, M.D., SANKEY, E.A., DHILLON, A.P., THOMPSON, R.P. Characterisation of inorganic microparticles in pigment cells of human gut associated lymphoid tissue. *Gut* **1996**, 38, 390–395.
- 145 FERNANDEZ-URRUSUNO, R., FATTAL, E., FEGER, J., COUVREUR, P., THEROND, P. Evaluation of hepatic antioxidant systems after intravenous administration of polymeric nanoparticles. *Biomaterials* **1997**, 18, 511–517.
- 146 OBERDÖRSTER, G., SHARP, Z., ATUDOREI, V., ELDER, A., GELEIN, R., KREYLING, W., COX, C. Translocation of inhaled ultrafine particles to the brain. *Inhal. Toxicol.* **2004**, 16, 437–445.
- 147 OBERDÖRSTER, G., SHARP, Z., ATUDOREI, V., ELDER, A., GELEIN, R., LUNTS, A., KREYLING, W., COX, C. Extrapulmonary translocation of ultrafine carbon particles following whole-body inhalation exposure of rats. *J. Toxicol. Environ. Health A* **2002**, 65, 1531–1543.
- 148 PRATTEN, M.K., LLOYD, J.B. Uptake of microparticles by rat visceral yolk sac. *Placenta* **1997**, 18, 547–552.
- 149 OSAKI, F., KANAMORI, T., SANDO, S., SERA, T., AOYAMA, Y. A quantum dot conjugated sugar ball and its cellular uptake. On the size effects of endocytosis in the subviral region. *J. Am. Chem. Soc.* **2004**, 126, 6520–6521.
- 150 HASEGAWA, U., NOMURA, S.M., KAUL, S.C., HIRANO, T., AKIYOSHI, K. Nanogel-quantum dot hybrid nanoparticles for live cell imaging. *Biochem. Biophys. Res. Commun.* **2005**, 331, 917–921.
- 151 ALYAUDTIN, R.N., REICHEL, A., LOBENBERG, R., RAMGE, P., KREUTER, J., BEGLEY, D.J. Interaction of poly(butylcyanoacrylate) nanoparticles with the blood-brain barrier in vivo and in vitro. *J. Drug Target* **2001**, 9, 209–221.
- 152 PULFER, S.K., CICCOTTO, S.L., GALLO, J.M. Distribution of small magnetic particles in brain tumor-bearing rats. *J. Neurooncol.* **1999**, 41, 99–105.
- 153 SCHROEDER, U., SOMMERFELD, P., ULRICH, S., SABEL, B.A. Nanoparticle technology for delivery of drugs across the blood-brain barrier. *J. Pharm. Sci.* **1998**, 87, 1305–1307.
- 154 KREUTER, J. Nanoparticulate systems for brain delivery of drugs. *Adv. Drug Deliv. Rev.* **2001**, 47, 65–81.
- 155 FECHTER, L.D., JOHNSON, D.L., LYNCH, R.A. The relationship of particle size to olfactory nerve uptake of a non-soluble form of manganese into brain. *Neurotoxicology* **2002**, 23, 177–183.
- 156 LOVRIC, J., BAZZI, H.S., CUITE, Y., FORTIN, G.R., WINNIK, F.M., MAYSINGER, D. Differences in subcellular distribution and toxicity of green and red emitting CdTe quantum dots. *J. Mol. Med.* **2005**, 83, 377–385.
- 157 SCHMID, G., DECKER, M., ERNST, H., FUCHS, H., GRÜNWARD, W., GRUNWALD, A., HOFMANN, H., MAYOR, M., RATHGEBER, W., SIMON, U., WYRWA, D. Small dimensions and material properties. A definition of nanotechnology. *Gaue Reihe* **2003**, 35, 1–134.

## 4

# Dosimetry, Epidemiology and Toxicology of Nanoparticles<sup>1</sup>

Wolfgang G. Kreyling, Manuela Semmler-Behnke, and Winfried Möller

### 4.1

#### Introduction

##### 4.1.1

#### Overview

Nanoparticles are increasingly used in a wide range of applications in science, technology and medicine. Since they are produced for specific purposes that cannot be met by larger particles and bulk material they are likely to be highly reactive, in particular with biological systems. However, a large body of know-how in environmental sciences is available from toxicological effects of ultrafine particles after inhalation. Since nanoparticles feature similar reactivity to ultrafine particles a sustainable development of new emerging nanoparticles is required. This chapter briefly reviews the dosimetry of nanoparticles, including deposition in the various regions of the respiratory tract and systemic translocation and uptake in secondary target organs, epidemiologic associations with health effects and toxicology of inhaled nanoparticles. General principles and current paradigms to explain the specific behavior of nanoparticles in toxicology are discussed. Since the evidence for health risks of ultrafine and nanoparticles after inhalation has been increasing over the last decade, this chapter attempts to extrapolate these findings and principles observed in particle inhalation toxicology into recommendations for an integrated concept of risk assessment of nanoparticles for a broad range of use in science, technology and medicine.

##### 4.1.2

#### General Background

Definition: Since the term “nanoparticle” is used heterogeneously in current discussion we want to define that they are shorter than 100 nm at least in one dimen-

<sup>1</sup> This chapter is based on a recently published article: Kreyling, W.G., Semmler-Behnke, M., Moeller, W., Health implications of nanoparticles. *J. Nanoparticle Res.* DOI 10.1007/s11051-005-9068-z.

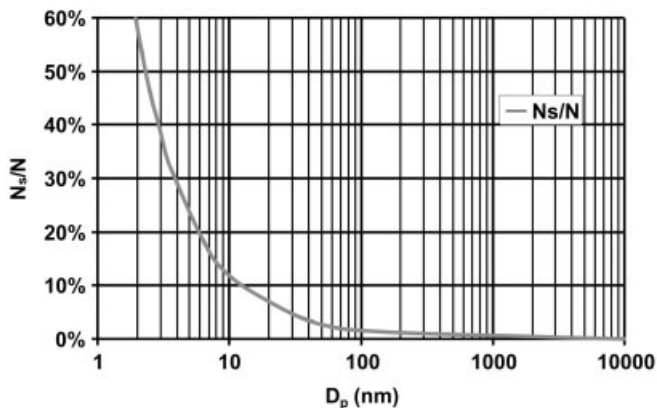


Fig. 4.1. Dependence of the percentage of surface molecules, relative to total number of molecules, of spherical nanoparticles on the diameter of the particles. Note: below 100 nm this ratio increases steeply. (From Ref. [7].)

sion, according to a recent suggested definition within the European Union [1]. In addition, nanoparticles are so-called “intended” particles, intentionally produced for specific use in science, technology, medicine, industries and many day-to-day applications. Therefore, they have a well-defined composition and are structured to fit the anticipated properties. As a result they differ from ultrafine particles (UP), a term frequently used in environmental sciences for ambient or occupational particles that are less than 100 nm in size in each dimension and which are unintended particles, originating often from combustion processes, of diverse sources and gas–particle interactions in their environment. Therefore, ultrafine ambient particles are often composed of a multitude of compounds, which may be structured in a highly complex manner. This is an additional basic difference between well-defined intended nanoparticles and unintended ultrafine particles.

Particles in the nanometer size range have two particular properties: (a) anything smaller than about 50 nm is no longer subject to the laws of classical physics but of quantum physics. This means that nanoparticles can exhibit optical, magnetic or electrical capabilities that distinguish them clearly from larger particles or bulk material; (b) with decreasing size the ratio between mass and surface area increases rapidly, i.e., the ratio of atoms or molecules at the surface to the total number of atoms or molecules rises steeply with decreasing particle size (Fig. 4.1). According to their very large specific surface area (surface area per mass), nanoparticles exert a stronger effect on their environment, i.e., with any adjacent materials. In other words, nanoparticles can catalyze chemical reactions at the surface; a given mass of material in nanoparticulate form will be much more reactive than the same mass of material made up of larger particles. For instance, crystalline nanoparticles have abundant atoms on their surface that are less strongly bonded than those in the interior of the particle. Given their unstable situation in the curvature of the surface, the atoms will try to change their binding: they are reactive towards their

environment. This may well be desirable and is usually the purpose of their generation; however, exposure to such particles, for instance by inhalation or ingestion, may have harmful consequences [2–9].

Although the economic and societal health benefits of the introduction of nanomaterials have been welcomed, concerns have been expressed that properties that are being exploited by researchers and industry might have negative health effects and environmental impacts and, particularly, those might result in greater toxicity. Hence, the rapid development of a multitude of nanoparticle applications needs to be complemented by assessing possible implications, assuring a safe and sustainable handling of those nanoparticles. The challenge of an integrated application development and implication assessment is pro-active collaboration at the earliest stage to optimize functionality of the nanoparticle and to minimize its side effects without losses in terms of costs and time because of one-sided mismanagement or unfocused or delayed initiation of risk assessment.

To understand the potential risks to humans from nanoparticles, it is necessary to understand the dosimetry and to consider the body's defenses against particles in general and the properties that particles require to overcome these defenses, as discussed in Chapter 4.2. Throughout much of their evolutionary history, humans have been exposed to small particles, often in very high concentrations, and the mechanisms evolved for defense against microorganisms are also used to defend the body against such particles. Generally, access to the human body can occur through the lungs, the skin or the gastrointestinal tract. Each organ presents a barrier to penetration by microorganisms or particles.

Chapter 4.3 discusses toxicological data that show a specific toxicological response of ultrafine particles, *in vitro* and *in vivo*, that is not found using fine particles of the same composition.

The general approach to assessing and controlling risk, as discussed in Chapter 4.4, involves identification of hazards (the potential of a nanoparticle or parts of it to cause harm) and then a structured approach to determining the probability of exposure to the hazard and the associated consequences. As in any new technology, foresight of possible risks depends on a consideration of the entire life cycle of a new nanoparticle being produced. This involves understanding the processes and materials used in manufacture, the likely interactions between the product and individuals or the environment during its manufacture and useful life, and the methods used in its eventual disposal.

#### 4.1.3

##### **Epidemiological Evidence for Health Effect Associations with Ambient Particulate Matter**

Since safety issues are not yet very well developed in the field of science and technology of nanoparticles, this young rapidly developing interdisciplinary field may make use of existing knowledge. In fact, for over a decade, environmental risk assessment has continuously investigated potential health effects that may be associated with exposure to ultrafine particles in the environment [10, 11]. The need for those toxicological studies came from epidemiological investigations that had

shown consistent associations between exposure to particulate air pollution in urban areas and acute increases in morbidity and mortality rates, especially for persons with obstructive lung and cardiovascular diseases [12]. The relative risk is surprisingly similar in many of these studies although the studies have been performed at very different global locations – predominantly in North America and Western Europe. These data have recently been collected and summarized by the US-EPA in a review of the Air Quality Criteria Document on Particulate Matter in 2004 [13].

Interestingly, epidemiological studies on health effects of ultrafine particles provided the first evidence that this particle fraction may induce adverse health effects independent of those of larger fine particles ( $<2.5\ \mu\text{m}$  aerodynamic diameter) and other air toxics, as reviewed by Wichmann and Peters [10]. Furthermore, none of these single compounds are present at sufficiently high concentrations in the environmental aerosol that they may be considered toxicologically relevant based on occupational hygiene. Therefore, it appeared reasonable to investigate the interactions of complex mixtures of compounds with biological systems. Although the risks from these mixtures of compounds may be low to an individual, the large number of persons at risk can make these compounds an important public health threat. Frequently, health effects are only manifested in specific risk groups, i.e., persons predisposed by genetic susceptibility, age, and/or disease. Translating these insights to the use of nanoparticles, the more widespread the use by the general population the fewer implications are allowed. In particular, particulate nanomedicines specifically generated for treatment of patients – i.e., subjects predisposed by their disease – require extremely high safety standards, taking the specific physicochemical properties of all components on the scale of nanoparticles into account.

#### 4.1.4

#### **Toxicological Evidence for Ambient Particulate Matter Induced Adverse Health Effects**

The adverse health effects shown in epidemiological studies have inspired scientists to use various techniques to study the toxicological mechanisms that form the biological background for adverse health effects associated with gaseous and particulate pollutants. At the beginning of the last decade, classical attempts like lung function tests, etc. were chosen in toxicological studies. This has changed substantially in recent years. An early key study demonstrated that ultrafine  $\text{TiO}_2$  nanoparticles caused more inflammation in rat lungs than exposure to the same airborne mass concentration of larger, so-called “fine”  $\text{TiO}_2$  [14]. Before this study,  $\text{TiO}_2$  had been considered as a non-toxic dust and indeed had served as an innocuous control dust in many studies on the toxicology of particles. Therefore, this report was highly influential in highlighting that a material with low toxicity in the form of fine particles could be toxic in the form of ultrafine particles.

Although many questions are not yet fully answered, it is reasonable to apply this acquired knowledge to nanoparticles. With ambitious expectations of the widespread introduction, use and application of nanoparticles into nearly *everything*, it

cannot be emphasized enough that accompanying safety measures must be devised early enough in their development. A major accident or a development similar to that of, for example, asbestos fibers related to health effects may turn public perception negative with the disastrous result that the promising potential of nanosciences and nanotechnology may be jeopardized in part, or even largely, by emotional arguments of the public that are not based on rational cost–benefit calculations.

This chapter summarizes key issues of risk assessment based on studies on the interaction of inhaled ultrafine particles found in urban atmospheres as well as on some nanoparticles that had been considered innocuous since their larger counterparts had not shown any toxic effect. We outline current understanding of modes of actions and underlying mechanisms involved in the pathogenesis of adverse health effects that eventually lead to disease. Therefore, we only consider the use of nanoparticles as long as they have access to the environment. There is no reason to consider firmly fixed nanoparticles in macroscopic entities that are unlikely to cause any harm. Inhalative exposure needs to distinguish between that of healthy adult workers during their work shift at the workplace in science, technology and industry and rather uncontrolled, eventually continuous, exposure of the entire public, including susceptible individuals such as infants, children, and the elderly, as well as diseased and genetically predisposed subjects.

## 4.2

### Inhaled Nanoparticle Dosimetry

#### 4.2.1

##### Particle Measures

In the past, particle mass concentration was by far the most common metric used. Daily averages range nowadays from 20 to 50  $\mu\text{g m}^{-3}$  in most cities of industrialized countries. Taking the size range of particulate matter (PM) over more than four decades (1 nm–30  $\mu\text{m}$ ) into account, mass concentration overestimates large PM in the coarse fraction and basically neglects ultrafine particles < 100 nm in size. The limitation of this metric is illustrated by the fact that the water solubility of ambient PM may vary from 20 to 80% of PM mass and yet the toxicity of soluble compounds is unlikely to be similar to that of the insoluble fraction. With clearer insights into particle–lung interactions, other measures such as the particle number concentration and/or surface area need to be taken into account, depending on whether ultrafine or larger particles are to be considered. However, exposure measures may be inadequate, since it may be the number of deposited particles per unit surface area of airways and bifurcations and of alveoli, or dose to a specific cell such as macrophages or epithelial cells, that determines the response of specific regions. Therefore, the use of a metric depends on specific questions posed, requiring specifically defined measures.

## 4.2.2

**Deposition of Ultrafine Particles in the Respiratory System**

Particle deposition of ultrafine particles in the respiratory tract is determined predominantly by diffusional motion (thermal motion of air molecules) distorting particles from their stream lines of the inhaled and exhaled air towards the airway walls, where they deposit once they have touched the walls. The diffusion mechanism affects particle deposition through three important components of aerosol properties and respiratory tract physiology during breathing: (a) particle dynamics, including size and shape, and possible dynamic change during breathing; (b) geometry of the branching airways and the alveolar structures; and (c) breathing pattern, which determines the airflow velocity and the residence time in the respiratory tract, and includes nose versus mouth breathing [15].

Regarding regional particle deposition in the respiratory tract, the tract can be considered as a series of filters (Fig. 4.2), starting with the nose or mouth via the various diameters of airways to the alveoli [16, 17]. Figure 4.2 displays the deposition probability of particles of different sizes in the larger and smaller airways, as well as the alveolar region. This means that the toxicity of particles of different sizes can have different effects in different parts of the lungs. This may be particularly important in children with developing lungs or with asthma, which mainly affects the larger airways, or with COPD, which affects both large and small airways and alveoli. These diseases may also cause an up to several-fold increase in deposition of PM in diseased parts of the lungs, which may deteriorate their functions [18].

The ultrafine particle density per airway surface area may, notably, often exceed that of the gas exchange region because the alveolar surface area (adult lungs ~

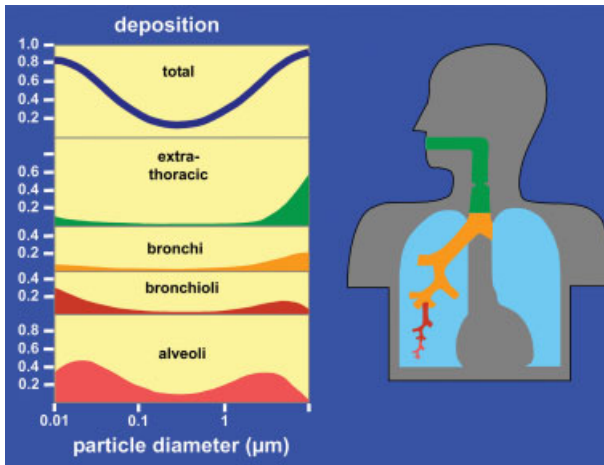


**Fig. 4.2.** Regional deposition of particles in the human respiratory tract during mouth-breathing at rest. (According to Ref. [16].)



140 m<sup>2</sup>) is 100-fold larger than that of airways. In general, ultrafine particles are very capable of reaching the fragile structures of alveoli; their deposition in the alveoli increases with decreasing diameter until 20 nm. Particles < 20 nm deposit less in alveoli since their high diffusivity leads to their deposition in the airways.

#### 4.2.3

##### **Fate of Particles in the Lungs**

On the walls of the respiratory tract (epithelium) particles contact first the mucous or serous lining fluid and its surfactant layer on top. Therefore, the fate of particle compounds soluble in this lining fluid need to be distinguished from slowly dissolving or even insoluble compounds.

##### **4.2.3.1 Soluble Particle Compounds**

Soluble particle compounds may either be lipid soluble or water soluble. They will be dissolved and rapidly diluted while spreading in the mucous layer or in the serous lining fluid or in the cellular sol. According to their chemical properties solutes and soluble components can undergo absorption and diffusion or binding to proteins and membranous or subcellular structures. Solute and their metabolic products will eventually be transferred to the blood and lymphatic circulation, undergoing further metabolism, with a potential to reach any organ and to produce toxic effects, far from their site of entry in the lungs [19, 20].

##### **4.2.3.2 Slowly Dissolving and Insoluble Particles Deposited on the Airway Wall**

Slowly dissolving and insoluble particles deposited on the airway wall will be mostly moved by mucociliary transport or by cough within 1–2 days to the throat (larynx), where they are swallowed and taken up by the gastrointestinal tract for further metabolism or excretion. While this clearance mechanism removes basically all particles larger than 5 μm, the fraction of long-term retained particles in the airways increases with decreasing particle size such that the uncleared fraction of ultrafine particles is ~80% of those deposited in the airways [21].

##### **4.2.3.3 Slowly Dissolving and Insoluble Particles Deposited in the Alveolar Region**

Slowly dissolving and insoluble particles deposited in the alveolar region will be taken up and digested by specialized defense cells in the alveoli called macrophages within a few hours after deposition – at least under physiological conditions in healthy lungs. Therefore, alveolar macrophages will determine the fate of these particles. While alveolar macrophages are well suited to recognize and phagocytize particles > 200 nm within several hours after deposition, mechanisms of recognition are increasingly less effective for ultrafine particles with decreasing size [21].

Note, cells and solutes of body fluids, like proteins interacting with an insoluble particle, will not recognize what is inside the particle but only react with the molecules according to their structure at the particle surface. In other words, the vast amount of a reactive molecular species attached to the surface of insoluble particles

and of an insoluble particle core (remaining after dissolution of the soluble components) may be the ultimate metric that determines adverse responses, although this species may add only a small fraction to PM mass.

#### 4.2.3.4 Macrophage-mediated Particle Transport

Macrophage-mediated particle transport: we list below the major pathways and actions of macrophages from the human alveolar epithelium and indicate fractions of deposited insoluble particles undergoing these pathways, as reviewed earlier [21]. Particularly, the fractions differ consistently from those observed in rodents as the most common experimental animal models. Macrophage-mediated particle transport is directed:

1. Towards ciliated airways on the epithelium for further removal by ciliary action, passage through the gut and excretion (about a third of deposited insoluble particles).
2. To storage on the epithelium or uptake into the lining cells [together with (3) more than half of deposited insoluble particles].
3. Across the epithelial lining cells towards the spaces between underlying cells.
4. Across the epithelial lining cells towards the lymphatic drainage system (1–10% of deposited insoluble particles).
5. Into and across the epithelial lining cells and eventually into the blood vessels towards secondary target organs. There is evidence for the uptake of ultrafine particles into the blood circulation, depending on the physical structure and chemical composition of their surface. Fractions and rates of uptake are currently under debate. Identified secondary target organs are liver, spleen, kidneys, vasculature and heart, the immune system and the central nervous system.

Ultrafine particles are less effectively taken up by macrophages but interact to a greater extent with epithelial lining cells than large particles. Due to their vast numbers, they provide a very large surface area, which is the interface by which they interact with biological systems. Generally, depending on their molecular surface composition, nanoparticles may have a greater capacity to induce or mediate more adverse effects than larger particles.

#### 4.2.4

#### Translocation of Ultrafine Particles into Systemic Circulation

While a growing number of reports confirms that there is translocation of ultrafine particles into blood circulation and subsequent uptake in secondary target organs, the size of the translocated fraction, the transport mechanisms and the rate-determining parameters are under debate.

##### 4.2.4.1 Studies of Systemic Particle Translocation in Humans

Conflicting translocation data are reported in human studies. Nemmar et al. [22] have demonstrated a rapid 3–5% uptake of radiolabeled carbonaceous ultrafine

particles into the bloodstream within minutes after exposure and subsequent uptake in the liver. In this study, leaching of the radiolabel from the particles was not considered. In contrast, also using radiolabeled carbonaceous ultrafine particles, Brown et al. [18] could not find any detectable particulates (<2% of inhaled ultrafine particles, limit of detection) beyond the lungs when the data were corrected for leaching of the radiolabel off the particles. In another study on healthy subjects as well as mild asthmatics and smokers we found no significant clearance from the lungs of 100 nm carbonaceous particles, for which we carefully controlled radiolabel leaching off the particles to be <2% within 24 h [23]. Due to the limit of detection used in this study systemic translocation and subsequent uptake in organs like the liver was below 1% of the deposited particles.

#### 4.2.4.2 Studies of Systemic Particle Translocation in Animals

Oberdörster and coworkers have observed rapid translocation towards the liver of more than 50% of  $^{13}\text{C}$  labeled ultrafine carbonaceous particles (26 nm size) within 24 h in a rat model [24]. Takenaka et al. [25] showed about 5–10% ultrafine silver particle translocation to the liver. Kreyling et al. [26], however, observed only minute (<1%) translocation of iridium ultrafine particles (15–20 nm and 80 nm in size) into the blood of rats. However, these test particles did not only accumulate in the liver, but also in spleen, kidneys, brain and heart to similar fractions. Uptake of the 15–20 nm particles in secondary target organs was about a factor of 2–3 higher than for 80 nm particles. In this study we challenged the question of particle dissolution and were able to show that these ultrafine particles dissolved to a very small extent, for which the particle data were corrected. Interestingly, in a long-term retention study Semmler et al. [27] have shown that ultrafine iridium particle contents in each of these secondary target organs did not increase with increasing retention time after a single 1-h exposure but peaked after one week at about 0.5% in each secondary organ. Thereafter, fractions declined again and remained detectable but below 0.1% of the initial deposit throughout the six-months-period of observation, indicating clearance mechanisms in these organs.

However, even though the mass fractions of iridium particles were rather low in secondary target organs the number of particles is impressively high. Data at one week and six months after the single inhalation are shown for lungs and all secondary target organs – liver, spleen, heart, brain and kidneys – in Table 4.1 (data taken from Refs. [26, 27]). More than one billion particles were found in each of the secondary target organs one week after a single 1-h exposure; and more than 100 million particles were still determined six months after the inhalation.

Importantly, particle uptake in the brain was not via the neural pathway from the olfactory epithelium in the nose, since extrathoracic airways of the rats were bypassed when ventilated through an endotracheal tube during exposure. Therefore, two principal pathways from the lung epithelium towards the brain are possible: (1) along neural axons and synapses [28–30], as reviewed by Oberdörster et al. [7] or (2) via systemic circulation. While the second route, via blood circulation, intuitively seems likely by analogy to uptake in other secondary organs the neural route should be kept in mind when designing the next generation of investigations. For

**Tab. 4.1.** Retained mass fractions as well as the corresponding numbers of insoluble iridium particles in the lungs and in secondary target organs one week and six months after single 1 h inhalation of 15 nm-sized iridium particles by WKY rats [26, 27]. The corresponding surface area of the retained particles is also calculated, based on the BET surface area of  $123 \text{ m}^2 \text{ g}^{-1}$  or  $1500 \text{ m}^2 \text{ cm}^{-3}$  (per mass or per volume of particles, respectively).

Organs	Retained mass fraction		Retained particles number		Particle surface area ( $\text{cm}^2$ )	
	One week	Six months	One week	Six months	One week	Six months
Lungs	0.6	0.06	$7.00 \times 10^{11}$	$7.00 \times 10^{10}$	$1.26 \times 10^2$	12.6
Liver	0.006	0.0005	$7.00 \times 10^9$	$5.83 \times 10^8$	1.26	0.105
Spleen	0.004	0.0003	$4.66 \times 10^9$	$3.50 \times 10^8$	0.842	$6.32 \times 10^{-2}$
Heart	0.004	0.0005	$4.66 \times 10^9$	$5.83 \times 10^8$	0.842	0.105
Brain	0.003	0.0005	$3.50 \times 10^9$	$5.83 \times 10^8$	0.632	0.105
Kidney	0.006	0.0001	$7.00 \times 10^9$	$1.17 \times 10^8$	1.26	$2.11 \times 10^{-2}$

instance, Hunter and Undem [31] have demonstrated the transport of fluorescent 40 nm polystyrene nanoparticles from the nerve endings in the tracheal epithelium along their neurons to their cell body in the ganglion nodosum and jugular ganglia in the neck of guinea pigs along neurons innervating the trachea. Furthermore, translocation along olfactory nerves from the olfactory epithelium to the olfactory bulb was first reported by Howe and Bodian [32] for 0.03- $\mu\text{m}$  polio virus in monkeys, and was later described for nasally deposited colloidal 0.05- $\mu\text{m}$  gold particles, moving into the olfactory bulb of squirrel monkeys [29]. Carbonaceous ultrafine particles were reported to translocate also along the same pathway to the central nervous system (CNS), based on their presence in the olfactory bulb of rats after inhalation [30, 33].

In addition, the surface area of the retained iridium particles was calculated based on the BET specific surface area of  $123 \text{ m}^2 \text{ g}^{-1}$  or  $1500 \text{ m}^{-2} \text{ cm}^{-3}$  per mass or volume of particles [34]; (BET surface area was determined by nitrogen absorption measurements). Since there is now evidence that the iridium particles are covered with iridium oxide [35], the density of iridium oxide ( $11.7 \text{ g cm}^{-3}$ ) and not that of iridium ( $22.4 \text{ g cm}^{-3}$ ) was used for calculations. One week after inhalation the total surface area of the retained iridium particles is close to  $1 \text{ cm}^2$  and after six months data are still a tenth of the one-week data. Compared to 1- $\mu\text{m}$ -sized particles this retained surface area of the 15 nm particles in secondary target organs is five orders of magnitude larger because of their very large specific surface area. It remains to be investigated what impact that may have, and whether the large number of retained particles and the accordingly large particle surface area may

have any adverse effects on the surrounding biological microstructures, like proteins, extracellular fluids, cells and their multiple functional and structural compartments as well as whole tissue of organs that usually are not considered to be exposed to such foreign bodies.

Recent studies of Nemmar and coworkers have shed light on possible prothrombotic effects in the systemic circulation as a result of activation of platelets [36, 37]. In their hamster model of experimentally induced thrombus formation they observed thrombotic clots in peripheral veins and arteries after intravenous and intratracheal administration of positively charged 60 nm polystyrene nanoparticles. They emphasized the importance of size and surface charge of test particles. In fact, the induced thrombus formation was not detectable after administration of negatively charged or neutral 60 nm as well as 400 nm sized positively charged polystyrene test particles; astonishingly, they observed similar thrombus formation after application of diesel exhaust particles via both routes [36]. These observations were confirmed by another group using a slightly modified approach [38]. From the fact that they observed peripheral thrombus formation even after intratracheal nanoparticle instillation into the lungs they concluded particle translocation from the lung epithelium to circulation. Whether particle translocation really occurred or whether thrombus formation was indirectly triggered by mediators released in the presence of the particles in the lungs needs to be proven in the next generation of studies. Nevertheless, the presence of these ultrafine particles with specific properties obviously was able to trigger biological responses that may initiate adverse health effects.

The fact that surface properties and possibly the particle matrix may play an important role in systemic translocation was demonstrated in a previous study [39, 40] in which ultrafine titanium dioxide ( $\text{TiO}_2$ ) particles were produced basically by the same method as the iridium particles, yielding primary particles of about 5 nm, very similar to those of iridium. Figure 4.3 shows the aggregation of both particle agglomerates of about 20 nm size.  $\text{TiO}_2$  agglomerates were inhaled by endotracheally intubated and ventilated WKY rats and the lungs were morphometrically studied in great detail immediately after the 1-h inhalation and 24 h later to determine the location of the retained  $\text{TiO}_2$  particles within the various lung compartments. Interestingly, a substantial fraction was already found at each time point in the vascular compartment, including the endothelium and the vascular lumen, indicating a rapid systemic translocation, which was obviously not the case after the inhalation of iridium particles. There are hints that these  $\text{TiO}_2$  show a positive zeta potential similar to commercially available  $\text{TiO}_2$  nanoparticles and as opposed to the negative zeta potential of iridium particles.

In studies using radioactively labeled ultrafine particles, the observed translocated fractions always appeared to be higher when less care was taken to minimize particle dissolution and/or the leaching of the radiolabel from the particles. Likewise, analysis of the stable  $^{13}\text{C}$  isotope-label is hampered by the fact that natural  $^{13}\text{C}$  occurs in all biological tissues at the level of 1% of the other stable isotope  $^{12}\text{C}$ , and ultrafine particle deposition in the lungs of the exposed rats made up only about a tenth of the natural  $^{13}\text{C}$  in the lungs; therefore, slight variability of the

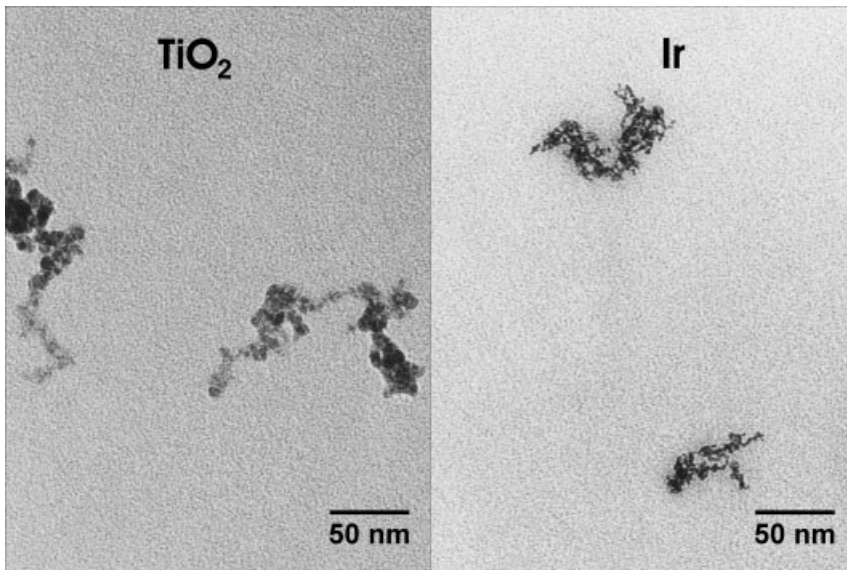


**Fig. 4.3.** Agglomerates of primary titanium dioxide particles (left) and iridium particles (right); primary particles are in the size range of 5 nm.

abundant natural  $^{13}\text{C}$  or uncertainties of the estimate of total carbon content in a given organ or tissue may lead to erroneous estimates.

Although the first data on susceptible humans – asthmatics and adults – did not alter the translocation pathway, a recent mechanistic study on excised blocks of heart and lungs of rats indicated increased translocation rates when either or both was compromised experimentally by induced epithelial inflammation or histamine activated endothelium [41].

Recently, more attention has been paid to surface characteristics and charges that could influence this process, as is well known in drug delivery [42]. Studies of drug delivery across the blood–brain barrier further confirmed the importance of surface properties, showing that particle surface components may bind to the ApoE-receptor of endothelial cells, which mediates crossing of this otherwise very tight barrier [43]. In addition, current discussion focuses on other transport pathways: clathrin-mediated endocytosis and non-clathrin-mediated endocytosis, the latter including internalization via caveolae [44–46]. Vesicular caveolae migrate from the luminal to the mucosal side of epithelial and endothelial cells [47]. After internalization caveolae are involved in endocytosis, transcytosis, and pinocytosis. In a recent study Rejman and coworkers showed that both pathways are clearly size-dependent for ligand-devoid polystyrene particles [48]. Using non-phagocytic cells, internalization of microspheres with a diameter  $< 200$  nm involved clathrin-coated pits. With increasing size, a shift to a mechanism that relied on caveolae-

mediated internalization became apparent, which became the predominant pathway of entry for particles of 500 nm in size. Under these conditions, delivery to the lysosomes was no longer apparent. The data indicate that the size itself of (ligand devoid) particles can determine the pathway of entry. The clathrin-mediated pathway of endocytosis shows an upper size limit for internalization of approx. 200 nm, and kinetic parameters may determine the almost exclusive internalization of such particles along this pathway rather than via caveolae. These studies on non-phagocytic melanoma cells B16 are supported by others using primary oral or esophageal epithelial cells [49, 50]. Likewise, endothelial cells are known to have bottle-shape-like caveolar invaginations of the plasma membrane [46]. Interestingly, studies aiming for cell transfection and gene delivery are focusing on these transport pathways [44–46].

Besides transcellular pathways para- or intercellular pathways are other routes by which nanoparticles can penetrate membranous cell barriers. Recently, Heckel and coworkers have shown in an inflammatory rabbit model induced by infused lipopolysaccharide (LPS) that intravenously administered 8 nm gold particles coated with autologous albumin were found on their way between endothelial as well as epithelial cells of the alveolar air–blood barrier [51]. The control rabbits showed the same pathway at a lower extent reflecting the transfer of albumin from the vascular to the luminal side of the air–blood barrier also under physiological conditions. Besides this paracellular pathway they also found albumin-coated gold particles in intracellular caveolae vesicles, indicative of transcellular pathways in both the control and the inflammatory model. At the same time it shows that nanoparticles coated with the appropriate serum protein can rapidly be translocated across a membrane, particularly when there is a protein gradient between the two sides of the barrier. It remains open whether these albumin-modulated para- and transcellular pathways are important in human lungs in the reverse direction, when an inhaled particle deposited on the alveolar epithelium is translocated into blood circulation.

### 4.3

#### Toxicological Plausibility of Health Effects Caused by Nanoparticles

Toxicological experiments can be categorized into *in vivo* and *in vitro* experiments. *In vivo* experiments investigate effects in living organisms such as experimental animals or healthy subjects and patients in clinical studies, whereas *in vitro* experiments are conducted in organs, tissues, cells or biomolecules isolated from the living organism. In general, toxicology studies on air pollutants are shorter-term experimental approaches that tend, for ethical reasons, not to study people but experimental animals. They often analyze the early events rather than waiting for final disease. In addition, in those studies high doses are required to detect significant effects; and they may use cells and biochemical systems rather than whole animals. To compensate for such shortcomings, models of susceptibility are an important experimental approach in which the biological system is predisposed prior

to treatment with air pollutants. Predisposition of the system acts already like a change of the homeostatic balance; such systems may respond more vigorously than the normal system. If, in addition, the predisposition reflects or resembles human diseases or human predisposition, such a model may be a powerful analytical tool, providing insights on how air pollutants may change responses of the susceptible system.

While human clinical studies provide closer insight in nanoparticle related modes of action, they usually are limited in yielding firm dose-response-relationships because of ethical reasons. Such relationships, however, can be provided by toxicological studies on susceptible animal models as well as cell systems. Hence, animal studies are supposed to provide biological explanations and plausibility and create hypotheses that may then be proven in human clinical studies.

#### 4.3.1

##### **Pulmonary Inflammation Induced by Ultrafine Particles**

Many of the effects that occur rapidly after ultrafine particles deposit on the respiratory epithelium are not fully understood. Cells in contact with ultrafine particles like macrophages, epithelial cells and neutrophilic granulocytes are activated and may synthesize compounds referred to as *reactive oxygen or nitrogen species* (including free radicals, hydrogen peroxide, and superoxide) that try to inactivate and eliminate the invading foreign material [52]. Within hours, cytokines and chemokines are synthesized and secreted into the affected area. These molecules are mediators that interact with specific receptors on the surfaces of many cell types and thereby activate cells in the surrounding environment as well as in the blood and other tissues. As a result, cells leave the bloodstream and enter the fluid filled interstitial spaces, where they can attack the foreign material. Consequently, particle-induced cell activation events in the airways frequently result in an *inflammatory response*. This response includes both the activation of cells of the epithelium (including the production of “pro-inflammatory” and reactive oxygen molecules described above) and the activation and migration of cells (particularly, neutrophilic granulocytes and eosinophilic granulocytes in the case of a specific immunological response) from the blood into the airways. While the inflammatory response may occur after interaction of both fine and ultrafine particles with respiratory tissues, the enhanced surface area of ultrafine and nanoparticles compared to fine particles (as the acting interface) suggests a more prominent reaction.

Airway nerve cells may also contribute to inflammation in the airways by synthesizing neurotransmitters [53]. In this *neurogenic inflammation*, the neurotransmitters can affect many types of white blood cells in the lung, as well as epithelial and smooth muscle cells. Inflammatory cytokines synthesized by white blood cells may also affect the nerve cells. The inflammatory response may damage the epithelial cell layer at the surface of the tissue and other cells in the airway (such as macrophages), which results in the loss of integrity of the tissue’s defenses. One potential consequence may be increased exposure to and reduced capacity to defend against microorganisms.



Thus, particle deposition on the respiratory epithelium can trigger a cascade of events in many different cells, potentially resulting in changes in tissues and organs at sites progressively further from the initial stimulus. These defense mechanisms are normal responses in healthy individuals, but they may lead to deleterious changes in the host. Such changes may be rapid and temporary and may resolve quickly but, depending on the level and pattern of exposure and the agent to which the host is exposed to, they may last longer. It is not clear whether or how such modulations are relevant to the development of particle-induced adverse health effects at low levels of exposure. Yet, these changes are thought to have a greater impact on individuals whose respiratory, cardiac, or vascular tissues have been previously altered or damaged.

One possible consequence of damage to the airways is that the individual may become more susceptible to respiratory infections if exposed to viruses or bacteria, as discussed in Ref. [54]. A second possible consequence is that it may further decrease respiratory function in a person whose airways are already damaged by diseases such as bronchitis or asthma. As a result, symptoms of asthma, for example, may be exacerbated [55].

#### 4.3.2

#### **Systemic Inflammation and other Responses**

Recent studies have suggested that exposure to particles results in systemic inflammatory effects within hours [56]. Pathways are discussed as either via direct particle translocation into circulation or via mediators released in the respiratory tract. In particular, the former pathway supports the concept of enhanced cardiovascular responses after ultrafine or nanoparticles exposure due to the higher likelihood of ultrafine particle translocation into circulation when compared with larger particles. Recently, a panel of cardiologists has reviewed the existing literature and compiled a statement in which possible pathways of interference of particulate matter are summarized [57]. They have developed a schematic (Fig. 4.4), which has been adopted in this chapter.

The panel link particle exposure with cardiovascular disease via four major routes: pulmonary inflammation, pulmonary reflexes and systemic translocation to circulation and to the heart. It is currently unclear whether the systemic response is a consequence of an inflammatory response in the respiratory tract, because some studies on systemic inflammation have detected little or no inflammatory lung response after exposure to PM. As described above, there are studies that indicate that either particles per se (ultrafine and nanoparticles in particular) or components that may detach or dissolve from particles may move rapidly into the circulation, triggering either oxidative stress or pro-thrombotic or acute-phase or other responses of the cardiovascular system [22, 56, 58]. Therefore, a direct systemic inflammatory response is possible via particle translocation into the circulation. This pathway of systemic inflammation is thought to be capable of triggering a cascade of responses, leading eventually to atherosclerotic plaque rupture and/or thrombosis as precursors of myocardial infarction. The other two pathways

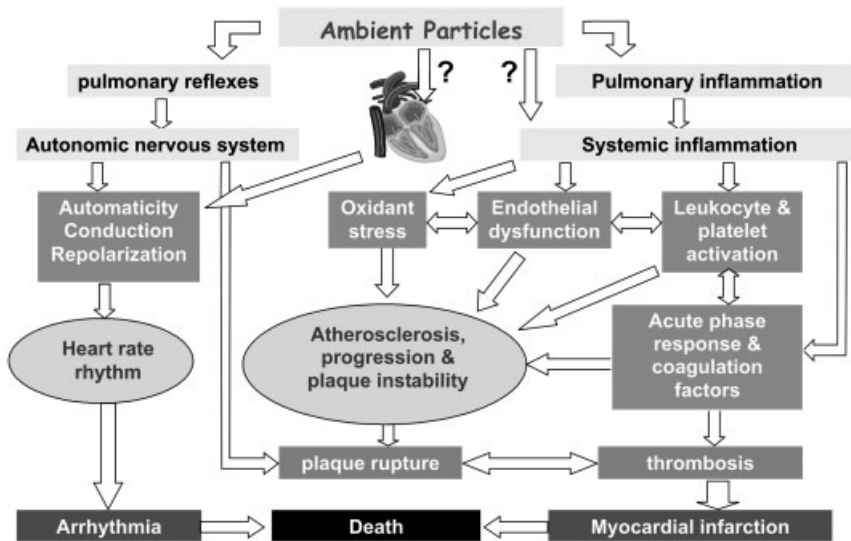


Fig. 4.4. Mechanisms involved in the link between cardiovascular disease and PM exposure. (After Ref. [57].)

of pulmonary reflexes and direct particle action on the heart are thought to interfere with heart rate functions, leading to arrhythmia. Both myocardial infarctions and arrhythmia are severe diseases with a substantial mortality rate.

#### 4.3.3

##### Relevant Parameters in Nanoparticle Toxicology

Biologically, it appears unmeaningful to presume that low solubility ultrafine or nanoparticles are hazards per se, since adverse reactions result from the interaction between the ultrafine particle and biological tissues. Currently, certain parameters of ultrafine particles are considered to trigger or mediate a cascade of reactions, starting with the formation of free radicals, which lead to oxidative stress in extracellular matrix and cells with the subsequent onset of pro-inflammatory processes (outlined in Fig. 4.5) [2, 11, 59]. These particle parameters are now discussed below.

##### 4.3.3.1 Number Concentration and Surface Area

Considering health effects initiated by the exposure to ultrafine and nanoparticles requires a change of the paradigm that effects are correlated with the mass of noxae accumulated during exposure. In ambient air the mass concentration of ultrafine particles is usually less than 10% of the mass concentration of  $PM_{2.5}$ . However, the number concentration of ultrafine particles dominates the number concentra-

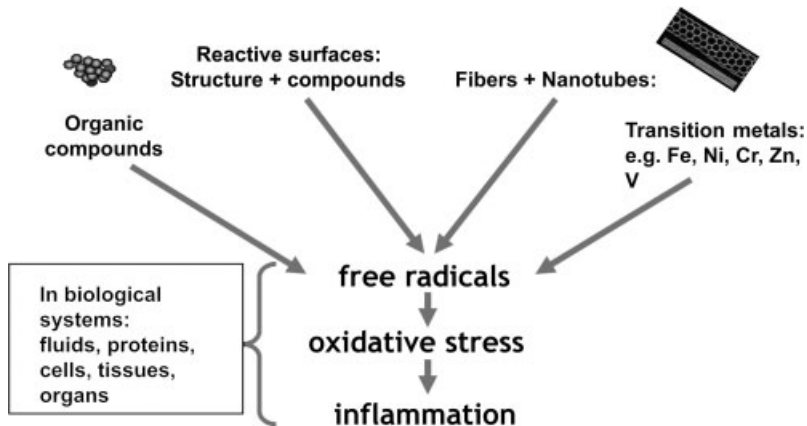


Fig. 4.5. Parameters of ultrafine particles considered to be involved in the initiation of oxidative stress and inflammatory processes. (Adapted from [3].)

tion of fine particles by >90% [60]. Therefore, surface area and number concentration appear to be the more reasonable metrics of ultrafine and nanoparticle exposure than mass concentration. Furthermore, exposure metrics may be inadequate since it may be the number of deposited particles per unit surface area or dose to a specific cell (e.g., alveolar macrophage) that determines response for specific regions. Therefore, the use of a metric depends on specific questions posed, requiring specifically defined metrics.

Oberdörster and co-workers have tested the relation between surface area of particles and inflammatory response [61]. Ultrafine TiO<sub>2</sub> with an average particle size of 20 nm and pigment grade (fine) TiO<sub>2</sub> with an average particle size of about 250 nm were used. Doses ranging from 30 to 2000 µg of TiO<sub>2</sub> were intratracheally instilled into rats and mice. When the deposited TiO<sub>2</sub> dose was expressed as particle surface area, there was a unique relationship to the inflammatory responses of these two different sizes of TiO<sub>2</sub> particles. The importance of particle surface area for eliciting inflammatory responses in the lung has been confirmed [62, 63]. This concept of particle surface area as the appropriate dose metric has been recognized as an important principle in particulate matter toxicology [11, 64, 65].

#### 4.3.3.2 Particle Shape (Fibers and Nanotubes)

Newer materials or those under development, such as synthetic organic fibers and carbon nanotubes, may have different toxicology paradigms [3]. The existing paradigm for silicate fibers suggests that respirable fiber types vary in their ability to cause lung disease and that this can be understood on the basis of the length of the fibers and their biopersistence in the lungs. Because fibers are regulated on a fiber number basis and the hazard is understood on the basis of the number of

long fibers, in fiber testing the dose should always be expressed as fiber number (not mass), and the length and diameter distribution also need to be known. Carbon nanotubes are long thin structures that can have diameters of a few nanometers but be many thousands of nanometers long. These could have very unusual toxicological properties, in that they share shape characteristics of both fibers and nanoparticles; such limited toxicology as presently exists supports the contention that these may be harmful to the lungs [3, 66]. Thus, the physiological relevance of these findings needs ultimately be determined by conducting inhalation toxicity studies.

#### 4.3.3.3 Transition Metals

For more than 10 years transition metals have been suspected and proved to cause health effects. Convincing evidence has been provided by a combination of epidemiologic and subsequent toxicological studies. An epidemiological study showed reduced effects of several morbidity endpoints as well as mortality in the population of Utah Valley, Utah, during a one-year period when a steel mill had been shut down, resulting in considerable reduction of transition metals in ambient fine particles, while symptoms and metal-containing air pollution were high in the year prior and after the closure of the steel mill [67–69]. Dust sampled from each period was applied in a human clinical study [70] as well as in a mechanistic study demonstrating pulmonary injury, neutrophilic inflammation and increased airway responsiveness of the metal-rich samples using a sensitive animal model [71]. Hence, the clinical and toxicological animal study provided a better understanding of the modes of actions of the ambient particles that had been found to be associated with adverse health effects within the population of Utah Valley.

Similar combined studies are being applied to air pollution in the city of Hettstedt, in former Eastern Germany, which has a history of several centuries of non-ferrous metal mining and smelting in comparison with the city of Zerbst, serving as a control in a nearby agricultural area. High  $PM_{2.5}$  levels were shown to be associated with significant decline of lung function and with significant increase of prevalence for bronchitis, otitis media, frequent colds, and febrile infections in three surveys on children over a decade in the 1990s. At the same time, high levels of the transition metals zinc, lead, copper, and cadmium were associated with allergic responses [55, 72, 73]. Dusts from Hettstedt and Zerbst were studied in an allergic mouse model, showing increased allergic responses and increased allergic sensitization [74]. This dust also had the capacity to form radical species [75] and further clinical human studies demonstrated that dust obtained from Hettstedt induced distinct airway inflammation in healthy subjects with a selective influx of monocytes and increased generation of oxidant radicals [76].

Both series of combinatory “epi-tox” studies provide comprehensive evidence for the association of adverse health effects in susceptible population groups and modes of actions of these ambient particles in either clinical and animal models studies or in *in vitro* studies. Importantly,  $PM_{2.5}$  is the basic dose metric in these studies and not ultrafine particle parameters. Note that in the second series of epidemiological studies ultrafine particle number concentration was measured in addition and do-

minated the number concentration of the fine particle fraction by 90% [77]. Therefore, additional research is required to demonstrate whether the ultrafine particle fraction plays a role in the observed effects and modes of actions and whether they may even drive the effects because of the very peculiar properties of the ultrafine particle fraction.

#### 4.3.3.4 Organic Compounds

Organic chemicals associated with ultrafine particles play a role in the pro-inflammatory effects of diesel exhaust particles (DEP), as demonstrated in several *in vitro* studies. For example, DEP caused modest stimulation of interleukin-8 (IL-8), granulocyte macrophage colony-stimulating factor (GM-CSF) and RANTES production by epithelial cells, and this activity was lost on extraction of the organic matter [78]; the benzene extracts contained most of the stimulatory activity seen in the whole DEP. Benzene extracts contained almost 90% of the benzo[*a*]pyrene, B(a)P, content and the authors concluded that poly aromatic hydrocarbons (PAHs) such as B(a)P were likely responsible for the stimulation of cytokine production by the epithelial cells. Boland et al. have demonstrated that DEP stimulated IL-8, GM-CSF, and IL-1 $\beta$  release from the bronchial epithelial cell-line 16HBE [79]. Furthermore, they contended, this was related to the amount of adsorbed organic compounds, because carbon black with virtually no adsorbed organic matter did not cause cytokine release. In support of this, exhaust gas post-treatments that diminished the adsorbed organic compounds also reduced the DEP-induced increase in GM-CSF release. Further studies with the organic extracts confirmed that most of the stimulating activity was in the organic fraction [80]. In another study, PAH extracted from DEP induced expression of IL-8 and RANTES in peripheral blood mononuclear cells [81], demonstrating that both macrophages and epithelial cells could be important in the pro-inflammatory effect induced by DEP in the lungs. Chin and coworkers [82] demonstrated that carbon-black treatment of the RAW264.7 mouse macrophage cell line had no effect on TNF $\alpha$  release but that the addition of B(a)P to the particles caused them to become stimulatory for TNF $\alpha$ .

More recently, investigators started to find evidence that amongst the large variety of organic compounds, particularly in the particulate fraction of ambient air originating from combustion processes, there are biologically highly reactive compounds like redox cycling quinones – oxidized and nitrated polyaromatic hydrocarbons, which can catalyze release of reactive oxygen species (ROS), leading to the induction of oxidative stress and inflammation. PM from the Los Angeles basin as well as organic extracts obtained from DEP induce a stratified oxidative stress response leading to Heme-oxygenase-1 expression, followed by activation of Jun kinase and pro-inflammatory interleukin-8 production, and culminated in cellular apoptosis in parallel with a sharp decline of antioxidant levels. These effects were more prominent in the fine particle fraction than the coarse, and they were positively correlated with higher contents of organic carbon and polyaromatic hydrocarbons [83]. Admittedly, the ultrafine particle fraction was not analyzed explicitly; however, the organic carbon load is highly associated with the ultrafine particle

fraction since this fraction predominantly originates from combustion processes. Pro-inflammatory effects in the respiratory tract are related to the particle content of redox cycling chemicals and are involved in the adjuvant effect of DEP in atopic sensitization [84]. Cytotoxicity in epithelial cells and macrophages is the result of mitochondrial damage, which manifests as ultramicroscopic changes in organelle morphology, a decrease in the mitochondrial membrane potential, superoxide production, and ATP depletion.

#### 4.3.3.5 Extrapolation of Health Effects Observed in Animals towards Human

Comparison between rodents and humans is rather difficult due to anatomical and physiological differences, which can result in considerably lower concentrations to sensitive regions of the respiratory tract of animals compared to similar regions in humans.

Laboratory animals used in toxicological studies are genetically very similar within specific strains, whereas human populations are heterogeneous. Thus, extrapolating results from animals to humans must not only take strain and species differences into account, but must also consider inter-individual variation among humans.

With animal studies, the presumed susceptible part of the human population is mimicked by inducing specific cardiopulmonary diseases or focusing on senescent animals. For instance, animal research has been done in the laboratory using a model of asthma, increased blood pressure in lung arteries, lung inflammation and general high blood pressure. An advantage of these models is that hypotheses on the mechanisms of action and biological plausibility can be examined. Using DEP, residual oil fly ash or ambient particles, it has been demonstrated in models for respiratory infection and allergy that symptoms can exacerbate. A drawback with these disease models in animals is that they are not completely equivalent to the human disease counterpart. Yet the development of susceptible animal models is a prerequisite to the search for biological plausibility of the higher vulnerability of susceptible and diseased individuals. A second issue is a certain degree of uncertainty as to whether the laboratory animal used is representative of the reactions of a human being, or whether the endpoints examined are sensitive enough and representative for human endpoints. An additional consideration is whether the timing of exposure and observation has been correctly chosen in the animal studies. However, studies in animals continue to be the main methodology on which to predict adverse health outcomes in humans and to clarify the relationship between exposure dose and toxic effects.

Since the development of ambient particle related health effects is a multifactorial process that may start with genetic predisposition and is propagated by life-long exposure to air pollution and a history of diseases, acute effect studies in animal models seem not to be likely to mimic this progression, which would require long-term exposure studies to carefully controlled fractions of air pollutants. Whether long-term exposures to nanoparticles will occur and whether such precautions are required will depend on the use of future nanoparticles.

#### 4.4

#### **Integrated Concept of Risk Assessment of Nanoparticles**

Nanoparticles are expected to be used in a wide range of new technologies. To highlight the importance of sustainable risk assessment, let us consider the use of nanoparticles in medicine: in this field nanoparticles are designed for therapeutic drug delivery and/or imaging techniques in diagnostics to be administered directly to the patient as multifunctional drug nanocarriers. This may require targeting across several membranes while the drug is sufficiently bound to the nanocarrier, and specific and controlled release of the drug at the target site, allowing for increased efficiency of the drug in target organs or cells, while side effects are minimized in sensitive but not-targeted organs and tissues [9]. This also includes non-toxic effects of the carrier nanoparticles. Although these may be future visions, nanomedicines are likely to represent the most challenging nanoparticles in terms of their safe and sustained application since patients predisposed by their disease are likely to be more susceptible to any such treatments, responding eventually more sensitively than healthy subjects. Hence, the rapid development of a multitude of nanoparticle applications needs to be complemented by assessing possible implications, assuring safe and sustainable handling of those nanoparticles. The challenge of an integrated application development and implication assessment is pro-active collaboration at the earliest stage to optimize functionality of the nanoparticle and to minimize its side effects without losses in terms of costs and time because of one-sided mismanagement or unfocussed or delayed initiation of risk assessment. While most other nanoparticles are not aimed for specific administration in human subjects, possible exposure scenarios still need to be considered.

Hence we propose an integrated conception to estimate the health hazards of newly generated nanoparticles during their development. For this risk analysis the whole life-cycle of the newly developed nanoparticle has to be considered, including its scientific or industrial generation, its storage and distribution, its anticipated application and possible abuse, and finally its disposal. That means potential human incorporation may vary at different stages of the life cycle of nanoparticles and different groups of the population may be exposed. During generation an occupational group of healthy adult workers may be exposed to nanoparticles, while its anticipated application may possibly lead to exposure of the whole population, including susceptible people, like infants, children, elderly and diseased individuals. The challenge is to produce a reasonable estimate that takes into account the widespread use of mass-wise produced nanoparticles versus those produced in small quantities.

As a result, possible incorporation pathways can be foreseen for the respective usage of a given nanoparticle, which will include organs of uptake, organs involved in the distribution and secondary target organs. In all these organs the nanoparticles or their metabolic products eventually accumulate in different ways. Within these organs, interaction of the nanoparticles will take place at the level of proteins of body fluids and on the cell surface and within cells; this will eventually be the

beginning of a cascade of reactions, mediating or initiating adverse health effects, leading to disease, as outlined above. Therefore, only those proteins and cells need to be examined that interact with the nanoparticle. Nevertheless, these may be more than those within the organ of predominant uptake and anticipated target organs or tissues.

To assess the interaction between nanoparticles and biological materials, a strategic concept is necessary that (a) classifies nanoparticles according to their chemical compounds, physical structure and, particularly, such properties at their surface; (b) takes into account possible exposures in different phases of the nanoparticle's life cycle; (c) estimates delivered doses to the various biological systems; and (d) stratifies toxicological assessment from simple high-throughput screening methods towards more complex *in vivo* studies only when required and based on previous findings at a lower level of analysis. Initially, simple acellular tests may evaluate free radical formation, oxidative stress, antigen–antibody reactions, etc. followed by genetic (regulation of cytokines and mediators, nucleus-signaling) and proteomic (structural and functional modification of proteins) high-throughput methods. Actually, these methods, which aim to understand the underlying mechanisms, will predominantly make use of modern nanotechnology, such as gene and protein-array chip technology specifically designed to screen nanoparticle–gene and –protein interactions. This genetic and proteomic information will provide guidance to the next step of assessment. As a result a second series of biologically and toxicologically more relevant tests aimed toward specific reactions may become necessary – first on cells, followed by multicell models and *in vivo* animal models, which finally may require clinical phase trials in the case of medicinal nanoparticles. Figure 4.6 shows a schematic of this integrated concept.

From this structured approach, life-cycle-specific recommendations for regulation will be derived for each nanoparticle. Such an approach would even allow the use of a nanoparticle that may have an elevated risk at some stage of its life as an

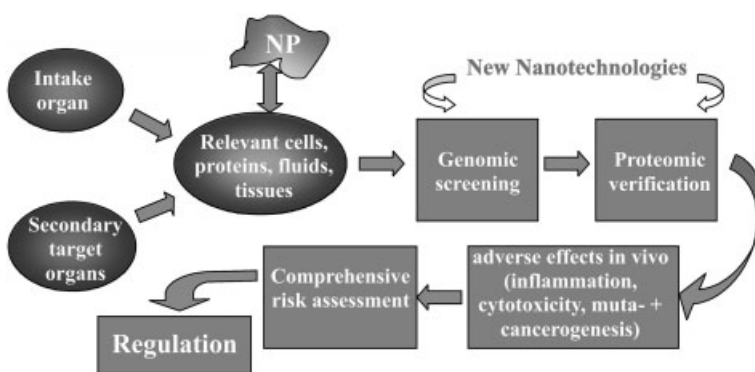


**Fig. 4.6.** Integrated concept for sustained toxicological risk assessment in relation to newly developed ultrafine particles and nanoparticles.



overall risk–benefit analysis may still be in support of its use while including specific prevention measures when they become necessary – e.g., in the application of nanoparticles in medicine. In fact, controlled application of new emerging nanoparticles will require knowledge-based development, production and application, including sustainable risk assessment prior to their widespread use.

Public perception is an important factor for the future development of nanosciences and nanotechnologies. Efforts need to be undertaken to convince the public of the beneficial potential of nanosciences and nanotechnologies. It would be a tragedy if a major accident jeopardized in part, or even largely, the development of this future technology with its splendid prognoses.

## References

- 1 BSI-PAS71, British Standard Institution (BSI), 2005, [www.bsi-global.com/nano](http://www.bsi-global.com/nano).
- 2 BORM, P. J., KREYLING, W., Toxicological hazards of inhaled nanoparticles – potential implications for drug delivery. *J. Nanosci. Nanotechnol.* 2004, 4, 521–531.
- 3 DONALDSON, K., TRAN, C. L., An introduction to the short-term toxicology of respirable industrial fibres. *Mutat. Res.* 2004, 553, 5–9.
- 4 KREYLING, W. G., SEMMLER, M., MÖLLER, W., Dosimetry and toxicology of ultrafine particles. *J. Aerosol Med.* 2004, 17, 140–152.
- 5 The Royal Society (2004). Nanosciences and nanotechnologies: opportunities and uncertainties. The Royal Society and The Royal Academy of Engineering, London, UK. <http://www.ost.gov.uk/policy/issues/introduction.htm>.
- 6 SCHULZ, H., HARDER, V., IBALD-MULLI, A., KHANDOGA, A., KOENIG, W., KROMBACH, F., RADYKEWICZ, R., STAMPFL, A., THORAND, B., PETERS, A., Cardiovascular effects of fine and ultrafine particles. *J. Aerosol Med.* 2005, 18, 1–22.
- 7 OBERDÖRSTER, G., OBERDÖRSTER, E., OBERDÖRSTER, J., Nanotoxicology: An emerging discipline evolving from studies of ultrafine particles. *Environ. Health Perspect.* 2005, 113, 823–839.
- 8 SEATON, A., DONALDSON, K., Nanoscience, nanotoxicology, and the need to think small. *Lancet* 2005, 365, 923–924.
- 9 ESF, European Science Foundation Policy Briefings., 2005, <http://www.esf.org/newsrelease/83/SPB23Nanomedicine.pdf>.
- 10 WICHMANN, H. E., PETERS, A., Epidemiological evidence of the effects of ultrafine particle exposure. *Philos. Trans. Roy. Soc. A* 2000, 358, 2751–2769.
- 11 DONALDSON, K., STONE, V., BORM, P. J., JIMENEZ, L. A., GILMOUR, P. S., SCHINS, R. P., KNAAPEN, A. M., RAHMAN, I., FAUX, S. P., BROWN, D. M., MACNEE, W., Oxidative stress and calcium signaling in the adverse effects of environmental particles (PM10). *Free Radic. Biol. Med.* 2003, 34, 1369–1382.
- 12 POPE, C. A., III, Epidemiology of fine particulate air pollution and human health: biologic mechanisms and who's at risk? *Environ. Health Perspect.* 2000, 108(Suppl. 4), 713–723.
- 13 US Environmental Protection Agency (EPA). Air quality criteria for particulate matter. EPA/600/p-99/022aD and bD. 2004. Research Triangle Park, NC, USEPA, National Center for Environmental Assessment.
- 14 OBERDÖRSTER, G., FERIN, J., LEHNERT, B. E., Correlation between particle size, in vivo particle persistence, and lung injury. *Environ. Health Perspect.* 1994, 102(Suppl 5), 173–179.

- 15 SCHULZ, H., BRAND, P., HEYDER, J., Particle deposition in the respiratory tract. In *Particle-Lung Interactions* (ed., P. GEHR, J. HEYDER), Marcel Dekker Inc., New York, Basel, 2000, pp. 229–290.
- 16 ICRP Publication 66, Human respiratory tract model for radiological protection. A report of a Task Group of the International Commission on Radiological Protection. *Ann. ICRP* 1994, 24, 1–482.
- 17 ASGHARIAN, B., HOFMANN, W., BERGMANN, R., Particle deposition in a multiple-path model of the human lung. *Aerosol Sci. Technol.* 2001, 34, 332–339.
- 18 BROWN, J. S., ZEMAN, K. L., BENNETT, W. D., Ultrafine particle deposition and clearance in the healthy and obstructed lung. *Am. J. Respir. Crit. Care Med.* 2002, 166, 1240–1247.
- 19 OBERDÖRSTER, G., Lung clearance of inhaled insoluble and soluble particles. *J. Aerosol Med.* 1988, 1, 289–330.
- 20 OBERDÖRSTER, G., Lung dosimetry: pulmonary clearance of inhaled particles. *Aerosol Sci. Technol.* 1993, 18, 279–289.
- 21 KREYLING, W. G., SCHEUCH, G., Clearance of particles deposited in the lungs. In *Particle-Lung Interactions* (ed. P. GEHR, J. HEYDER), Marcel Dekker Inc., New York, Basel, 2000, pp. 323–376.
- 22 NEMMAR, A., HOET, P. H., VANQUICKENBORNE, B., DINSDALE, D., THOMEER, M., HOYLAERTS, M. F., VANBILLOEN, H., MORTELMANS, L., NEMERY, B., Passage of inhaled particles into the blood circulation in humans. *Circulation* 2002, 105, 411–414.
- 23 WIEBERT, P., SANCHEZ-CRESPO, A., SEITZ, J., FALK, R., PHILIPSON, K., KREYLING, W. G., MÖLLER, W., SOMMERER, K., LARSSON, S., SVARTENGREN, M., High retention of 100 nm <sup>99m</sup>Tc-labeled carbonaceous particles in healthy and affected human lungs. *Eur. Respir. J.* 2006, submitted.
- 24 OBERDÖRSTER, G., SHARP, Z., ATUDOREI, V., ELDER, A., GELEIN, R., LUNTS, A., KREYLING, W. G., COX, C., Extrapulmonary translocation of ultrafine carbon particles following whole-body inhalation exposure of rats. *J. Toxicol. Environ. Health A* 2002, 65, 1531–1543.
- 25 TAKENAKA, S., KARG, E., ROTH, C., SCHULZ, H., ZIESENIS, A., HEINZMANN, U., SCHRAMEL, P., HEYDER, J., Pulmonary and systemic distribution of inhaled ultrafine silver particles in rats. *Environ. Health Perspect.* 2001, 109, 547–551.
- 26 KREYLING, W. G., SEMMLER, M., ERBE, F., MAYER, P., TAKENAKA, S., SCHULZ, H., OBERDÖRSTER, G., ZIESENIS, A., Translocation of ultrafine insoluble iridium particles from lung epithelium to extrapulmonary organs is size dependent but very low. *J. Toxicol. Environ. Health A* 2002, 65, 1513–1530.
- 27 SEMMLER, M., SEITZ, J., ERBE, F., MAYER, P., HEYDER, J., OBERDÖRSTER, G., KREYLING, W. G., Long-term clearance kinetics of inhaled ultrafine insoluble iridium particles from the rat lung, including transient translocation into secondary organs. *Inhal. Toxicol.* 2004, 16, 453–459.
- 28 BODIAN, D., HOWE, H. A., The rate of progression of poliomyelitis virus in nerves. *Bull. Johns Hopkins Hospital* 1941, 69, 79–85.
- 29 DE LORENZO, A. J. D., DARIN, J., The olfactory neuron and the blood-brain barrier. In *Taste and Smell in Vertebrates* (ed. G. E. W. WOLSTENHOLME, J. KNIGHT), Churchill, London, 1970, pp. 151–176.
- 30 OBERDÖRSTER, G., SHARP, Z., ATUDOREI, V., ELDER, A., GELEIN, R., KREYLING, W., COX, C., Translocation of inhaled ultrafine particles to the brain. *Inhal. Toxicol.* 2004, 16, 437–445.
- 31 HUNTER, D. D., UNDEM, B. J., Identification and substance P content of vagal afferent neurons innervating the epithelium of the guinea pig trachea. *Am. J. Respir. Crit. Care Med.* 1999, 159, 1943–1948.
- 32 HOWE, H. A., BODIAN, D., Poliomyelitis in the chimpanzee: A clinical–pathological study. *Proc. Soc. Exp. Biol. Med.* 1940, 43, 718–721.

- 33 OBERDÖRSTER, G., UTELL, M. J., Ultrafine particles in the urban air: to the respiratory tract – and beyond? *Environ. Health Perspect.* **2002**, *110*, A440–441.
- 34 ROTH, C., FERRON, G. A., KARG, E., LENTNER, B., SCHUMANN, G., TAKENAKA, S., HEYDER, J., Generation of ultrafine particles by spark discharging. *Aerosol Sci. Technol.* **2004**, *38*, 228–235.
- 35 SZYMCAK, W., KREYLING, W. G., SEITZ, J., WITTMACK, K., Mass spectrometric characterisation of pure and mixed ultrafine particles of iridium and carbon. *J. Aerosol Sci.* **2004**, *35*, 37–38.
- 36 NEMMAR, A., HOYLAERTS, M. F., HOET, P. H., DINSDALE, D., SMITH, T., XU, H., VERMYLEN, J., NEMERY, B., Ultrafine particles affect experimental thrombosis in an in vivo hamster model. *Am. J. Respir. Crit. Care Med.* **2002**, *166*, 998–1004.
- 37 NEMMAR, A., HOET, P. H., DINSDALE, D., VERMYLEN, J., HOYLAERTS, M. F., NEMERY, B., Diesel exhaust particles in lung acutely enhance experimental peripheral thrombosis. *Circulation* **2003**, *107*, 1202–1208.
- 38 SILVA, V. M., CORSON, N., ELDER, A., OBERDÖRSTER, G., The rat ear vein model for investigating in vivo thrombogenicity of ultrafine particles (UFP). *Toxicol. Sci.* **2005**, *85*, 983–989.
- 39 KAPP, N., KREYLING, W., SCHULZ, H., IM HOF, V., GEHR, P., SEMMLER, M., GEISER, M., Electron energy loss spectroscopy for analysis of inhaled ultrafine particles in rat lungs. *Microsc. Res. Technol.* **2004**, *63*, 298–305.
- 40 GEISER, M., ROTHEN-RUTISHAUSER, B., KAPP, N., SCHÜRCH, S., KREYLING, W. G., SCHULZ, H., SEMMLER, M., IM HOF, V., HEYDER, J., GEHR, P., Ultrafine particles cross cellular membranes by non-phagocytic mechanisms in lungs and in cultured cells. *Environ. Health Perspect.* **2005**, *113*, 1555–60.
- 41 MEIRING, J. J., BORM, P. J., BAGATE, K., SEMMLER, M., SEITZ, J., TAKENAKA, S., KREYLING, W. G., The influence of hydrogen peroxide and histamine on lung permeability and translocation of iridium nanoparticles in the isolated perfused rat lung. *Part. Fibre Toxicol.* **2005**, *2*, 3.
- 42 BROOKING, J., DAVIS, S. S., ILLUM, L., Transport of nanoparticles across the rat nasal mucosa. *J. Drug Target.* **2001**, *9*, 267–279.
- 43 KREUTER, J., SHAMENKOV, D., PETROV, V., RAMGE, P., CYCHUTEK, K., KOCH-BRANDT, C., ALYAUTDIN, R., Apolipoprotein-mediated transport of nanoparticle-bound drugs across the blood-brain barrier. *J. Drug Target.* **2002**, *10*, 317–325.
- 44 NICHOLS, B., Caveosomes and endocytosis of lipid rafts. *J. Cell Sci.* **2003**, *116*, 4707–4714.
- 45 PARTON, R. G., RICHARDS, A. A., Lipid rafts and caveolae as portals for endocytosis: new insights and common mechanisms. *Traffic* **2003**, *4*, 724–738.
- 46 BATHORI, G., CERVENAK, L., KARADI, I., Caveolae – an alternative endocytotic pathway for targeted drug delivery. *Crit. Rev. Ther. Drug Carrier Syst.* **2004**, *21*, 67–95.
- 47 GUMBLETON, M., Caveolae as potential macromolecule trafficking compartments within alveolar epithelium. *Adv. Drug Deliv. Rev.* **2001**, *49*, 281–300.
- 48 REJMAN, J., OBERLE, V., ZUHORN, I. S., HOEKSTRA, D., Size-dependent internalization of particles via the pathways of clathrin- and caveolae-mediated endocytosis. *Biochem. J.* **2004**, *377*, 159–169.
- 49 HOPWOOD, D., SPIERS, E. M., ROSS, P. E., ANDERSON, J. T., MCCULLOUGH, J. B., MURRAY, F. E., Endocytosis of fluorescent microspheres by human oesophageal epithelial cells: comparison between normal and inflamed tissue. *Gut* **1995**, *37*, 598–602.
- 50 INNES, N. P., OGDEN, G. R., A technique for the study of endocytosis in human oral epithelial cells. *Arch. Oral Biol.* **1999**, *44*, 519–523.
- 51 HECKEL, K., KIEFMANN, R., DORGER, M., STOECKELHUBER, M., GOETZ, A. E., Colloidal gold particles as a new in vivo marker of early acute lung injury.

- Am. J. Physiol. Lung Cell Mol. Physiol.* **2004**, 287, L867–L878.
- 52 NEL, A. E., DIAZ-SANCHEZ, D., LI, N., The role of particulate pollutants in pulmonary inflammation and asthma: evidence for the involvement of organic chemicals and oxidative stress. *Curr. Opin. Pulm. Med.* **2001**, 7, 20–26.
- 53 BARNES, P. J., Neurogenic inflammation in the airways. *Respir. Physiol.* **2001**, 125, 145–154.
- 54 GILMOUR, P. S., RAHMAN, I., HAYASHI, S., HOGG, J. C., DONALDSON, K., MACNEE, W., Adenoviral E1A primes alveolar epithelial cells to PM(10)-induced transcription of interleukin-8. *Am. J. Physiol. Lung Cell Mol. Physiol.* **2001**, 281, L598–606.
- 55 HEINRICH, J., HOELSCHER, B., FRYE, C., MEYER, I., WJST, M., WICHMANN, H. E., Trends in prevalence of atopic diseases and allergic sensitization in children in Eastern Germany. *Eur. Respir. J.* **2002**, 19, 1040–1046.
- 56 DONALDSON, K., STONE, V., SEATON, A., MACNEE, W., Ambient particle inhalation and the cardiovascular system: potential mechanisms. *Environ. Health Perspect.* **2001**, 109, 523–527.
- 57 BROOK, R. D., FRANKLIN, B., CASCIO, W., HONG, Y., HOWARD, G., LIPSETT, M., LUEPKER, R., MITTLEMAN, M., SAMET, J., SMITH, S. C., JR., TAGER, I., Air pollution and cardiovascular disease: a statement for healthcare professionals from the Expert Panel on Population and Prevention Science of the American Heart Association. *Circulation* **2004**, 109, 2655–2671.
- 58 NEMMAR, A., VANBILLOEN, H., HOYLAERTS, M. F., HOET, P. H., VERBRUGGEN, A., NEMERY, B., Passage of intratracheally instilled ultrafine particles from the lung into the systemic circulation in hamster. *Am. J. Respir. Crit. Care Med.* **2001**, 164, 1665–1668.
- 59 DONALDSON, K., The biological effects of coarse and fine particulate matter. *Occup. Environ. Med.* **2003**, 60, 313–314.
- 60 KREYLING, W. G., TUCH, T., PETERS, A., PITZ, M., HEINRICH, J., STÖLZEL, M., CYRYS, J., HEYDER, J., WICHMANN, H. E., Diverging long-term trends in ambient urban particle mass and number concentrations associated with emission changes caused by the German unification. *Atmos. Environ.* **2003**, 37, 3841–3848.
- 61 OBERDÖRSTER, G., Toxicology of ultrafine particles: in vivo studies. *Philos. Trans. Roy. Soc. A* **2000**, 358, 2719–2739.
- 62 LI, X. Y., GILMOUR, P. S., DONALDSON, K., MACNEE, W., Free radical activity and pro-inflammatory effects of particulate air pollution (PM10) in vivo and in vitro. *Thorax* **1996**, 51, 1216–1222.
- 63 FAUX, S. P., TRAN, C. L., MILLER, B. G., JONES, A. D., MONTEILLER, C., AND DONALDSON, K. (2003). In vitro determinants of particulate toxicity: The dose-metric for poorly soluble dusts. Health and Safety Executive, Crown, Norwich, UK.
- 64 OBERDÖRSTER, G., Significance of particle parameters in the evaluation of exposure-dose-response relationships of inhaled particles. *Inhal. Toxicol.* **1996**, 8, 73–89.
- 65 DONALDSON, K., LI, X. Y., MACNEE, W., Ultrafine (nanometre) particle mediated lung injury. *J. Aerosol Sci.* **1998**, 29, 553–560.
- 66 WARHEIT, D. B., LAURENCE, B. R., REED, K. L., ROACH, D. H., REYNOLDS, G. A., WEBB, T. R., Comparative pulmonary toxicity assessment of single-wall carbon nanotubes in rats. *Toxicol. Sci.* **2004**, 77, 117–125.
- 67 POPE, C. A., III, Respiratory disease associated with community air pollution and a steel mill, Utah Valley. *Am. J. Public Health* **1989**, 79, 623–628.
- 68 RANSOM, M. R., POPE, C. A., III, Elementary school absences and PM10 pollution in Utah Valley. *Environ. Res.* **1992**, 58, 204–219.
- 69 POPE, C. A., III, SCHWARTZ, J., RANSOM, M. R., Daily mortality and PM10 pollution in Utah Valley. *Arch. Environ. Health* **1992**, 47, 211–217.
- 70 GHIO, A. J., DEVLIN, R. B., Inflammatory lung injury after

- bronchial instillation of air pollution particles. *Am. J. Respir. Crit. Care Med.* **2001**, 164, 704–708.
- 71 DYE, J. A., LEHMANN, J. R., MCGEE, J. K., WINSETT, D. W., LEDBETTER, A. D., EVERITT, J. I., GHIO, A. J., COSTA, D. L., Acute pulmonary toxicity of particulate matter filter extracts in rats: coherence with epidemiologic studies in Utah Valley residents. *Environ. Health Perspect.* **2001**, 109, 395–403.
- 72 HEINRICH, J., HOELSCHER, B., WICHMANN, H. E., Decline of ambient air pollution and respiratory symptoms in children. *Am. J. Respir. Crit. Care Med.* **2000**, 161, 1930–1936.
- 73 HEINRICH, J., HOELSCHER, B., FRYE, C., MEYER, I., PITZ, M., CYRYS, J., WJST, M., NEAS, L., WICHMANN, H. E., Improved air quality in reunified Germany and decreases in respiratory symptoms. *Epidemiology* **2002**, 13, 394–401.
- 74 GAVETT, S. H., BISHOP, L. R., HAYKAL-COATES, N., HEINRICH, J., GILMOUR, M. I., Effects of particles from two German cities on allergic responses in mice. *Am. J. Respir. Crit. Care Med.* **2001**, 163, A50.
- 75 SHI, T., SCHINS, R. P., KNAAPEN, A. M., KUHNBUSCH, T. A. J., PITZ, M., HEINRICH, J., BORM, P. J. A., Hydroxyl radical generation by electron paramagnetic resonance as a new method to monitor ambient particulate matter composition. *J. Environ. Monitor.* **2003**, 5, 550–556.
- 76 SCHAUMANN, F., BORM, P. J., HERBRICH, A., KNOCH, J., PITZ, M., SCHINS, R. P., LUETTIG, B., HOHLFELD, J. M., HEINRICH, J., KRUG, N., Metal-rich ambient particles (particulate matter 2.5) cause airway inflammation in healthy subjects. *Am. J. Respir. Crit. Care Med.* **2004**, 170, 898–903.
- 77 PITZ, M., KREYLING, W. G., HOELSCHER, B., CYRYS, J., WICHMANN, H. E., HEINRICH, J., Change of the ambient particle size distribution in East Germany between 1993 and 1999. *Atmos. Environ.* **2001**, 35, 4357–4366.
- 78 KAWASAKI, S., TAKIZAWA, H., TAKAMI, K., DESAKI, M., OKAZAKI, H., KASAMA, T., KOBAYASHI, K., YAMAMOTO, K., NAKAHARA, K., TANAKA, M., SAGAI, M., OHTOSHI, T., Benzene-extracted components are important for the major activity of diesel exhaust particles: effect on interleukin-8 gene expression in human bronchial epithelial cells. *Am. J. Respir. Cell Mol. Biol.* **2001**, 24, 419–426.
- 79 BOLAND, S., BAEZA-SQUIBAN, A., FOURNIER, T., HOUCINE, O., GENDRON, M. C., CHÉVRIER, M., JOUVENOT, G., COSTE, A., AUBIER, M., MARANO, F., Diesel exhaust particles are taken up by human airway epithelial cells in vitro and alter cytokine production. *Am. J. Physiol.* **1999**, 276, L604–613.
- 80 BOLAND, S., BONVALLOT, V., FOURNIER, T., BAEZA-SQUIBAN, A., AUBIER, M., MARANO, F., Mechanisms of GM-CSF increase by diesel exhaust particles in human airway epithelial cells. *Am. J. Physiol.* **2000**, 278, L25–32.
- 81 FAHY, O., TSICHOPOULOS, A., HAMMAD, H., PESTEL, J., TONNEL, A. B., WALLAERT, B., Effects of diesel organic extracts on chemokine production by peripheral blood mononuclear cells. *J. Allergy Clin. Immunol.* **1999**, 103, 1115–1124.
- 82 CHIN, B. Y., CHOI, M. E., BURDICK, M. D., STRIETER, R. M., RISBY, T. H., CHOI, A. M., Induction of apoptosis by particulate matter: role of TNF-alpha and MAPK. *Am. J. Physiol.* **1998**, 275, L942–949.
- 83 LI, N., KIM, S., WANG, M., FROINES, J., SIOUTAS, C., NEL, A., Use of a stratified oxidative stress model to study the biological effects of ambient concentrated and diesel exhaust particulate matter. *Inhal. Toxicol.* **2002**, 14, 459–486.
- 84 LI, N., WANG, M., OBERLEY, T. D., SEMPFF, J. M., NEL, A. E., Comparison of the pro-oxidative and proinflammatory effects of organic diesel exhaust particle chemicals in bronchial epithelial cells and macrophages. *J. Immunol.* **2002**, 169, 4531–4541.

## 5

# Impact of Ceramic and Metallic Nano-scaled Particles on Endothelial Cell Functions *in Vitro*

*Kirsten Peters, Ronald E. Unger, Antonietta M. Gatti, Enrico Sabbioni, Andrea Gambarelli, and C. James Kirkpatrick*

### 5.1

#### Introduction

##### 5.1.1

#### Origin of Particles in the Human Environment

The term “particles” is defined as “very small pieces of solid or liquid matter, light enough to be suspended in the air”. The human body is exposed to many types of particles during its lifetime. These particles can be of natural origin or they can develop as (by-)products of industrial processes, and technical or pharmaceutical engineering. Thus, these particles vary largely in composition, size, shape, surface property and habitat. Dependent on these characteristics, the internalization of particles and their dissemination within the body is variable and may take place by ingestion (by polluted food or food additives) [1], inhalation (smoking, diesel soot, medical aerosols), via the skin (e.g., cosmetics, pharmaceuticals), implantation (e.g., wear from implants), and also injection (e.g., drug delivery and cancer therapy) [2]. Particulate air pollution is associated with enhanced mortality from respiratory and cardiovascular diseases [3]. The World Health Organisation (WHO) estimates that inhalation of particulate matter is responsible for at least 500 000 deaths each year worldwide [4].

Particles can be divided into those that are internalized accidentally (e.g., by air or food pollution) and those that are administered intentionally (e.g., for drug delivery, diagnostic agents). Among the naturally occurring particles in the air are pollen grains and their fragments and other vegetable particles, such as starch granules, which might, for example, carry mold spores with high allergenic potential. Furthermore, particles from volcanic eruptions occur naturally in the atmosphere. Particles evolved by pollution are from industry, motor vehicles, and other sources of thermodegradation. Furthermore, man-made/engineered particles have become relevant in recent years, e.g., due to the enormous progress in industrial use (e.g., in automotive, electronic, textile, household, and chemical industries)

and in pharmaceutical development of nanometer-scaled particles for drug delivery in asthma or cancer diagnosis and therapy [2, 5]. However, this rapid technical development has led to concerns about unknown risks of engineered nanometer-scaled materials [6].

#### 5.1.1.1 Evidence for Size-dependent Toxicity of Particles

Among the most abundant air pollutants in urban areas is particulate matter with a mean diameter of  $\leq 10 \mu\text{m}$  (also called  $\text{PM}_{10}$ , defined as particulate matter  $10 \mu\text{m}$  in diameter and smaller, by environmental toxicologists). Over the years it has become clear that particles with very low sizes (especially those below  $100 \text{ nm}$ ) are more noteworthy than larger particles since they induce more severe effects [7, 8]. There are different reasons for this phenomenon:

1. Particle size as a limiting factor of accessibility to the body's organs and tissues.  
For example, intact pollen grains,  $>10 \mu\text{m}$  in diameter, are too large to enter the lower airways. They are eliminated by mucociliary clearance. However, the naturally occurring break-up of pollen grains (e.g., by osmotic shock) produces smaller pollen fragments that can reach the lower parts of the airways and exert asthma-inducing effects in sensitized patients [9, 10].
2. Particle size as a limiting factor of accessibility to cells and cell compartments.  
Recent studies indicate that particle size alone can strongly affect the efficiency of cellular uptake [11].
3. The surface/size-ratio increases exponentially with decreasing particle sizes, leading to increased surface reactivity. This increased surface reactivity might lead to greater biological activity per given mass compared to larger particles, which in turn might have effects on, for example, particle internalization into tissues, cells and organelles, toxicity, or the induction of oxidative stress [2, 12].

This leads to the question: Are materials that are generally recognized as safe as bulk materials by the accredited standard tests also safe as (nano-scaled) particles? To date no standards exist for testing the safety of nanoparticles.

As mentioned above, particles with sizes below  $100 \text{ nm}$  are especially problematic. By definition, particles smaller than  $100 \text{ nm}$  are called nanoparticles or ultra-fine particles. Nanoparticles are at least 100-fold smaller than mammalian cells and are mostly smaller than viruses. Since the diameter of DNA molecules is  $2 \text{ nm}$  and atoms have diameters between  $0.1$  and  $0.4 \text{ nm}$ , concern about the interference of small nanoparticles with cellular structures at the molecular level is legitimate.

#### 5.1.1.2 Dissemination and Interferences of Nanoparticles within the Body

Owing to the minute size of nanoparticles, internalization into the body's tissues appears to be extremely easy. This has been shown by experiments in human volunteers with radioactive-labeled carbon nanoparticles (i.e., "Technegas") that passed rapidly into the systemic circulation after inhalation. Radioactivity could already be detected in blood after  $1 \text{ min}$  of inhalation [13]. Furthermore, animal studies re-

vealed that inhaled nanoparticles were translocated into the liver [14] and into the brain [15]. Thus, nanoparticles seem to be able to circumvent the tight blood–brain barrier; the movement of nanoparticles across the blood–placenta barrier has also been discussed [16, 17].

The incidence of higher asthma frequency during severe air pollution episodes has long been known [18]. Recent studies indicate that the ultrafine particles in air pollution are especially important in the course of asthma and chronic obstructive pulmonary disease (COPD) [19, 20]. Furthermore, other tissues in addition to the lung seem to be affected by nanoparticle exposure: In mice exposed to nanoparticles in ambient air the levels of pro-inflammatory cytokines were increased in brain tissue so that a coherency between inhaled particulate matter and the development of neurodegenerative diseases was suggested [21]. Moreover, nanoparticles are suggested to be involved in thrombus formation in the blood [22, 23]. There is evidence that fine and ultrafine particles are involved in the pathogenesis of Crohn's disease, a transmural inflammation of the gastrointestinal tract [24].

#### 5.1.1.3 Endothelial Cells and Nanoparticle Exposure

As the sources of internalized nanoparticles (food, air, etc.) and the location of particle detection are generally far apart, a distribution via the blood stream must have occurred. Thus, endothelial cells, which line the inner surface of blood vessels, will have direct contact with the particles. Endothelial cells are important in inflammation and wound healing. Upon pro-inflammatory stimulation of the endothelium, adhesion molecules are expressed on the cell surface, thus mediating leukocyte attachment (e.g., E-selectin and intercellular adhesion molecule-1/ICAM-1). Furthermore, endothelial cells are able to release cytokines, such as interleukin-8 (IL-8, a key factor in neutrophil chemotaxis). Thus, these features contribute to the pro-inflammatory endothelial phenotype that permits the transmigration of leukocytes from the blood into the perivascular space [25]. Activation of IL-8, E-selectin and ICAM-1 is regulated by the same transcription factors, NF- $\kappa$ B (nuclear factor- $\kappa$ B) and AP-1 (activator protein-1) [26–28].

#### 5.1.1.4 Testing of Nanoparticle-induced Effects on Human Endothelial Cells *In Vitro*

Little is known about the effects of nanoparticles on endothelial cell functions. Therefore, their effects on human endothelial cells have been studied *in vitro* and are reported here. Ceramic nanoparticles of TiO<sub>2</sub> and SiO<sub>2</sub> and metallic nanoparticles of Co and Ni were examined with respect to cellular internalization and their influence on cell viability, proliferative activity, and the pro-inflammatory endothelial phenotype. Moreover, due to the effects of the metallic nanoparticles they were compared with metal ion treatment. Endothelial cells *in vitro* were able to internalize many particles and reacted differentially in response to the internalization, dependent on the composition of the different nanoparticles. Furthermore, divergent effects of metallic nanoparticles vs. metal ions were observed. The link between these results and the possible risk of nanoparticles to human health is also discussed.



## 5.2

### Materials and Methods

All chemicals were obtained from Sigma if not otherwise indicated.

#### 5.2.1

##### Cell Culture

Human dermal microvascular endothelial cells (HDMEC) were isolated from juvenile foreskin as described before [29] and cultured in Endothelial Cell Basal Medium MV (PromoCell) supplemented with 15% fetal calf serum (Invitrogen), basic fibroblast growth factor (bFGF,  $2.5 \text{ ng mL}^{-1}$ ), sodium heparin ( $10 \text{ } \mu\text{g mL}^{-1}$ ), penicillin/streptomycin (10 000 units penicillin per mL, 10 000  $\mu\text{g}$  streptomycin sulfate per mL, Invitrogen), cultivated in a humidified atmosphere at  $37 \text{ }^\circ\text{C}$  (5%  $\text{CO}_2$ ) and used in passage 4.

#### 5.2.2

##### Particles

$\text{SiO}_2$  and  $\text{TiO}_2$  particles were produced by flame spray pyrolysis (TAL Materials Inc.). The size spectrum of  $\text{SiO}_2$  particles was between 4 and 40 nm with 14 nm mean particle size. The  $\text{TiO}_2$  particles were between 20 and 160 nm with 70 nm mean particle size. The mean size of Co particles was 28 nm (Nanoamor) and the Ni particles had a mean size of 62 nm (Nanoamor). Particles were added to the cell culture medium and tested at three different concentrations (0.5, 5, and 50  $\mu\text{g}$  per mL of culture medium).

Particles were analyzed by means of an Environmental Scanning Electron Microscope (ESEM-Quanta, FEI-Company). This instrument is called "Environmental" by the Manufacturer, as it can analyze samples in many different modes: at high and medium vacuum, and also at environmental conditions. It can also accept wet or oily samples, which is ideal for biological specimens.

#### 5.2.3

##### Transmission Electron Microscopy (TEM)

Cells were seeded onto fibronectin-coated Thermanox coverslips (Nunc). Exposure to particles was performed two days after seeding (50  $\mu\text{g}$  particles per mL medium). After 48 h incubation cells were fixed in cacodylate-buffered glutaraldehyde (2.5%) and embedded in Agar100 (Plano). Ultrathin sections were made with an Ultracut E microtome (Leica). TEM was performed with a Phillips 410 EM (Phillips).

#### 5.2.4

##### Cytotoxicity Assay

To evaluate cytotoxicity the CellTiter 96® AQueous non-radioactive assay (Promega) was performed according to the manufacturer's instructions. This assay gives

a measure of the enzymatic conversion of a tetrazolium salt (MTS reagent) by mitochondrial dehydrogenase and thus presents indirect evidence for cell viability.

#### 5.2.5

##### **Detection of Ki67 Expression**

Cells were seeded onto fibronectin-coated 96-well microtiter plates (6500 cells per well) and grown to subconfluence. Afterwards, cells were exposed to particles (0.5, 5, and 50  $\mu\text{g mL}^{-1}$  culture medium) and cultivated for an additional 24 h. The cells were fixed with methanol:ethanol (2:1, 15 min, room temperature) and permeabilized with buffered 0.1% Triton X-100 (5 min, room temperature).

Ki67, a protein expressed in the nucleus of proliferating cells, was detected with mouse-anti human Ki67-antibody (Dako). The secondary antibody was a peroxidase-conjugated rabbit-anti mouse-antibody (Dako). The staining reaction was performed by addition of the peroxidase substrate (*o*-phenylenediamine dihydrochloride) for 15 min at 37 °C. The staining reaction was stopped with 3 M HCl. Light extinction was determined with a microtiter plate photometer (ThermoLab Systems) at 492 nm.

#### 5.2.6

##### **Quantification of IL-8 Release in Cell Culture Supernatant**

Cells were seeded onto fibronectin-coated microtiter plates (13 500 cells per well), grown for 24 h and exposed to particles (0.5, 5, and 50  $\mu\text{g}$  per mL of culture medium for different samples) and  $\text{TNF}\alpha$  (300 U  $\text{mL}^{-1}$ ; inflammatory control). Cell culture supernatants were collected 24 h after substance or particle exposure. The IL-8 content in supernatants was assayed using human IL-8 immunoassay/ELISA (Hiss Diagnostics) according to the manufacturer's instructions.

#### 5.2.7

##### **Quantification of E-selectin Cell Surface Protein Expression**

This cell surface antigen is generally only expressed in inflammatory-stimulated endothelial cells and can be detected by using an enzyme-linked immunoassay based on a peroxidase staining reaction and subsequent dye quantification by a microplate reader. Therefore, cells were seeded onto fibronectin-coated 96-well microtiter plates (13 500 cells per well) and grown to confluence. Cells were then subjected to specific cell culture conditions (different particles and  $\text{TNF}\alpha$  as a positive control, 300 U  $\text{mL}^{-1}$ ) and cultivated for an additional 4 h. The cells were fixed with methanol:ethanol (2:1, 15 min, room temperature).

E-selectin was detected with mouse-anti human E-selectin-antibody (Bender MedSystems). The secondary antibody was a biotinylated goat-anti mouse-antibody (Amersham). Afterwards, the streptavidin–horseradish peroxidase conjugate was added (Amersham). The staining reaction was performed by addition of the perox-

idase substrate (*o*-phenylenediamine dihydrochloride) for 15 min at 37 °C. The staining reaction was stopped with 3 M HCl. Light extinction was determined with a microtiter plate spectrophotometer (ThermoLab Systems) at 492 nm.

### 5.2.8

#### Fluorescence Staining

HDMEC were seeded onto fibronectin-coated glass chamber-slides (Nunc). After 48 h, cells were exposed to particles (50  $\mu\text{g mL}^{-1}$ ) or  $\text{CoCl}_2$  (0.7 mM), incubated for an additional 24 h and fixed with buffered 3.7% paraformaldehyde (15 min, room temperature). Staining for Hypoxia-inducible factor-1 $\alpha$  (HIF-1 $\alpha$ ) was performed with the HIF-1 $\alpha$ -antibody (IgG1, BD Transduction Laboratories). Nuclear staining was performed with Hoechst 33342. Fluorescence-labeled cells were covered with GelMount (Biomed/Natutec).

### 5.2.9

#### Statistical Analysis

All results are shown as means  $\pm$  standard deviations (SD). Statistical analysis was carried out with Microsoft Excel software. According to the results of variance ratio analysis (F-test  $p < 0.05$ ) an unpaired t-test for either homoscedastic or heteroscedastic variances was performed ( $p < 0.05$  or  $p < 0.001$  as indicated in the figures).

## 5.3

### Results

Analysis of the different nanoparticles acquired by Environmental Scanning Electron Microscopy (ESEM) revealed a relative homogenous particle size for the ceramic nanoparticles ( $\text{TiO}_2$ , Fig. 5.1a;  $\text{SiO}_2$ , Fig. 5.1b). According to the manufacturer's specification the size spectrum of  $\text{TiO}_2$  particles was between 20 and 160 nm with 70 nm mean particle size and that of  $\text{SiO}_2$  particles between 4 and 40 nm with 14 nm mean particle size. In contrast, the metallic nanoparticles of Co and Ni were more inhomogeneous (Co, Fig. 5.1c; Ni, Fig. 5.1d). Both particle types possess nanoparticle character since the specified mean sizes of Co and Ni particles were 28 and 62 nm, respectively.

Ultrastructural studies (TEM) from perpendicular sections of endothelial cell monolayers demonstrated a flattened cell phenotype. Cytoplasm of the untreated control cells contained numerous organelles and vacuoles (Fig. 5.2a, arrowhead: vacuole with autophagic function containing cellular debris). When HDMEC were exposed to the different particles, internalization of the nanoparticles occurred that was independent of particle composition. The particles were localized within cytoplasmic vacuoles, partially containing cellular debris. Both the  $\text{TiO}_2$  and  $\text{SiO}_2$  particles were partially detectable as large aggregations and partially as smaller particulate matter. However, striking ultrastructural changes were not observed (Fig.

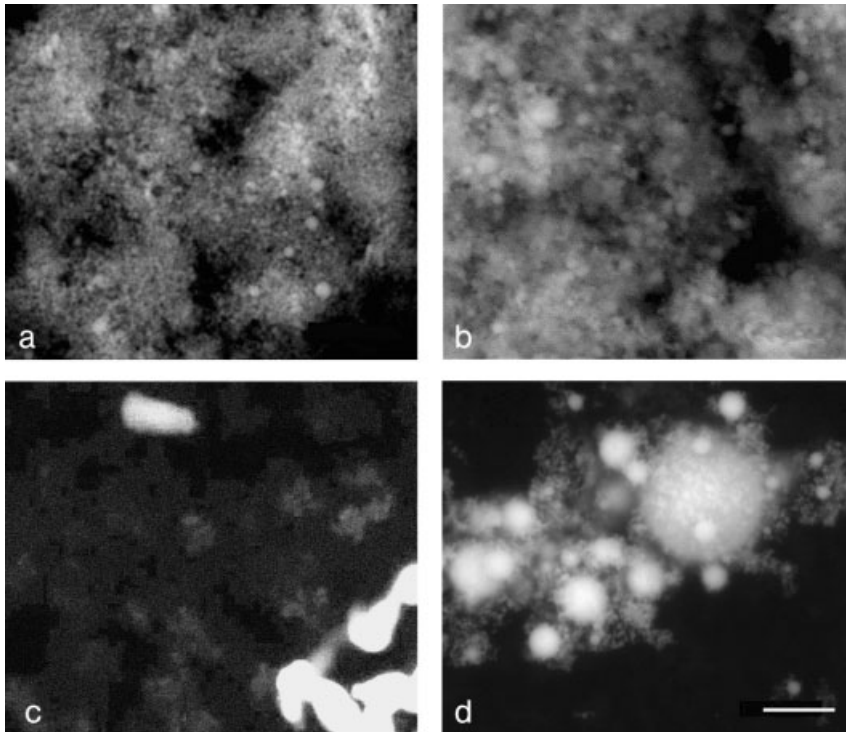


**Fig. 5.1.** ESEM images of the different nanoparticles used in this study. (a)  $\text{TiO}_2$ , (b)  $\text{SiO}_2$ , (c) Co, (d) Ni (scale bar:  $2\ \mu\text{m}$ ).

5.2b/c). The exposure to Co (Fig. 5.2d) and Ni (Fig. 5.2e) particles led to the enlargement of vacuoles; simultaneously, the number of vacuoles appeared to decrease. The Co- and Ni-particle-induced vacuoles partially filled the complete height of the cells (Fig. 5.2d/e). Interestingly, Co-particle exposure induced some annular-shaped, electron-dense material within the vacuoles (Fig. 5.2d, asterisk). Beside this electron-dense material the vacuoles of the Co-particle exposed cells contained a large amount of cellular debris.

Exposure of  $\text{TiO}_2$  particles to HDMEC did not induce an effect on cell number within 24 h (Fig. 5.3a; detected by a DNA staining with crystal violet; 0.5, 5 and  $50\ \mu\text{g mL}^{-1}$  were each tested). Also, the staining for the proliferation marker Ki67 after 24 h (Fig. 5.3b) and metabolic activity after 72 h (shown by the MTS conversion assay, Fig. 5.3c) did not show significant changes after exposure to  $\text{TiO}_2$  particles. High amounts of  $\text{SiO}_2$  particles ( $50\ \mu\text{g mL}^{-1}$ ) induced a slight decrease in cell number after 24 h (Fig. 5.3a). This  $\text{SiO}_2$ -particle-induced decrease is also reflected by a slight decrease of Ki67 protein expression after 24 h (Fig. 5.3b). However, the MTS conversion assay showed no significant reduction after 72 h (Fig.

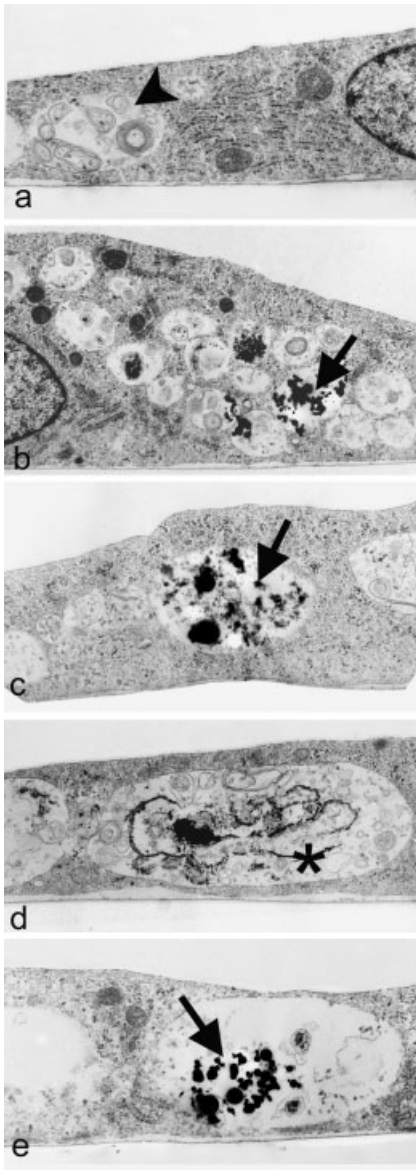


**Fig. 5.2.** Perpendicular sections of HDMEC monolayers: (a) Nontreated HDMEC (control) and HDMEC exposed to particles of (b)  $\text{TiO}_2$ , (c)  $\text{SiO}_2$ , (d) Co and (e) Ni (TEM, magnification 26 000 $\times$ ).

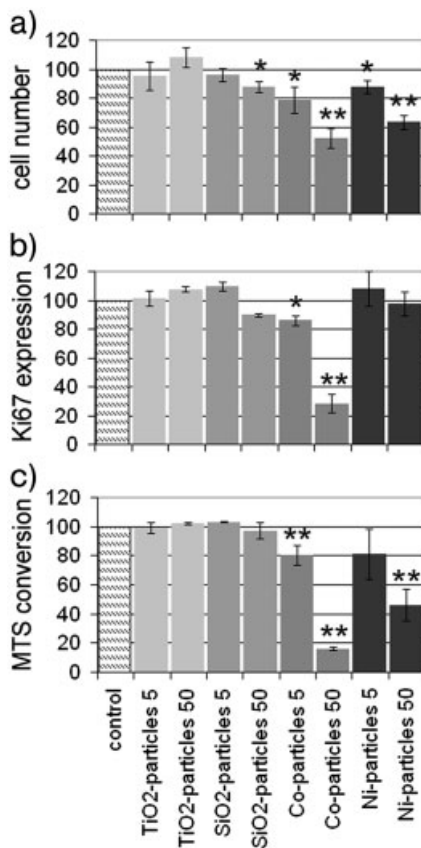


**Fig. 5.3.** Cytotoxicity of different nanoparticles. Tests were for (a) cell number after exposure of 24 h (crystal violet staining), (b) proliferation after 24 h particle exposure (Ki67 detection), and (c) metabolic activity

after 72 h (MTS conversion). Particle amounts are in  $\mu\text{g mL}^{-1}$ , untreated control set as 100%;  $n = 4$ , means  $\pm$  SDs, significantly different from normoxia: \* $p < 0.05$ , \*\* $p < 0.001$ .

5.3c). Co and Ni particles induced a significant, concentration-dependent decrease in cell number after 24 h (Fig. 5.3a). Also, the reduction of Ki67 expression and MTS conversion in Co-particle treated cells was significantly reduced after Co-particle exposure (Fig. 5.3b/c). Interestingly, the Ni particles, which also induce a concentration-dependent decrease in cell number, showed no significant deviations in protein expression of Ki67 (Fig. 5.3b). Nickel particles led to a significant, concentration-dependent reduction of MTS conversion after 72 h (Fig. 5.3c). Thus, protein expression of the proliferation marker Ki67 was not reduced after Ni particle exposure, although cell number and metabolic activity were decreased.

Four hours after exposure of the different particles the cells did not show

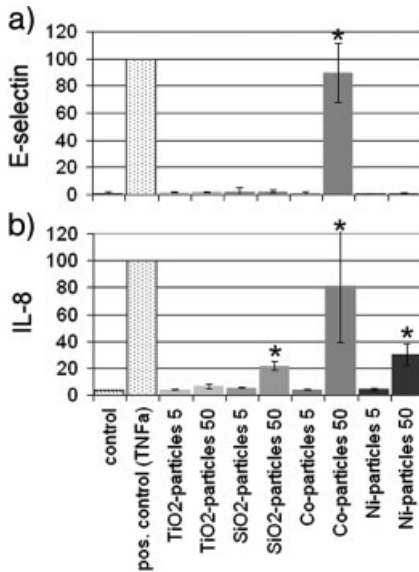


**Fig. 5.4.** Detection of pro-inflammatory effects induced by particle exposure. Detection of (a) E-selectin after 4 h and (b) IL-8 after 24 h particle exposure; TNF $\alpha$ -stimulated cells serve as positive control and set as 100%,  $n = 4$ , means  $\pm$  SDs, significantly different from the untreated control: \* $p < 0.05$ .

E-selectin protein expression except for high Co particle amounts, which induced a significant increase in E-selectin protein expression (Fig. 5.4a, TNF $\alpha$ -stimulated cells served as the positive control and were set as 100%). In addition, ICAM-1 cell surface protein expression after 24 h was induced by high Co-particle amounts only; whereas all other particles did not induce an increase (data not shown). IL-8 release in the cell culture supernatant was stimulated by high amounts of SiO<sub>2</sub>, Co and Ni particles. High amounts of TiO<sub>2</sub> particles induced only a minor, non-significant increase (Fig. 5.4b).

An important protein in cell signaling is the hypoxia-inducible factor HIF-1 $\alpha$ . This protein is not detectable in normoxic cells (controls, Fig. 5.5a/b). Under oxygen deficiency (hypoxia) the protein is stabilized within the cells by complex mechanisms and transported into the nuclei. In this context it was important that divalent cobalt and nickel ions (Co<sup>2+</sup> and Ni<sup>2+</sup>) were able to stabilize and induce a translocation of the protein into the nuclei comparable to hypoxia conditions (results for Co<sup>2+</sup>-treatment shown in Fig. 5.5c/d). Comparable with the effects of Co<sup>2+</sup>, the exposure of Co particles induced the stabilization and translocation of HIF-1 $\alpha$  protein into the nuclei of endothelial cells *in vitro* (Fig. 5.5e/f). These HIF-1 $\alpha$  effects also occurred upon exposure to Ni-ions and -particles (data not shown).

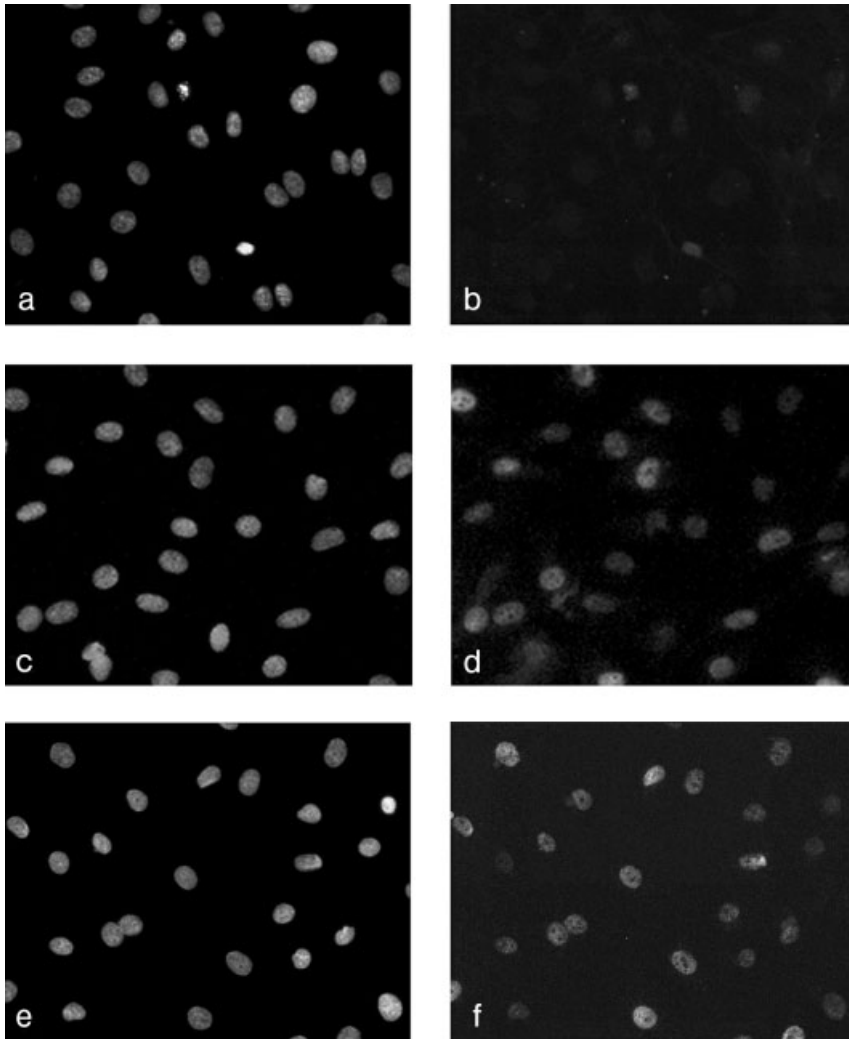


**Fig. 5.5.** Nuclear- and HIF-1 $\alpha$ -staining in HDMEC. (a/b) Control: (a) nuclear and (b) HIF-1 $\alpha$  staining images the same section; (c/d) Co<sup>2+</sup>-treated HDMEC; 24 h, 0.7 mM, (c) nuclear and (d) HIF-1 $\alpha$  staining; (e/f) Co-particle-treated HDMEC; 24 h, 50  $\mu\text{g mL}^{-1}$ , (e) nuclear and (f) HIF-1 $\alpha$  staining.

The major changes after particle exposure, induced by the metallic nanoparticles and the Co<sup>2+</sup>-induced comparable stabilization of HIF-1 $\alpha$  induced after Co particle exposure, suggested that these effects were triggered by the release of metal ions from the particles. Therefore we compared the effects of the respective ions in con-



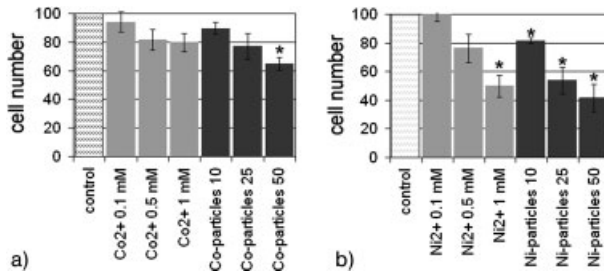


**Fig. 5.6.** Analysis of HDMEC number after exposure to Co and Ni ions and Co and Ni particles: (a) Co-ions and -particles, (b) Ni-ions and -particles; untreated control set as 100%,  $n = 4$ , means  $\pm$  SDs, significantly different from normoxia: \* $p < 0.01$ , crystal violet staining after 24 h exposure.

centrations that were equivalent to the molarity of the utilized particles (e.g., 50  $\mu\text{g}$  Co-particles per mL corresponds to 0.85 mM cobalt, 25  $\mu\text{g mL}^{-1}$  corresponds to 0.42 mM, and 10  $\mu\text{g mL}^{-1}$  to 0.17 mM; the calculations depend on the assumption that pure Co- and Ni-particles were present and are, therefore, only an approximation).

The cell number was concentration-dependently decreased by Co-/Ni-ions and -particles after 24 h of exposure (Fig. 5.6a/b). Nickel showed more pronounced effects than cobalt (for both ions and particles). Interestingly, both types of particles induced a stronger reduction of cell number than the ions, indicating a higher cytotoxicity of particles than the respective ions: 1 mM of  $\text{CoCl}_2$  induced a 20% decrease in cell number, whereas 50  $\mu\text{g mL}^{-1}$  ( $\sim 0.85$  mM) of cobalt particles induced a nearly 40% decrease (Fig. 5.6a), 1 mM of  $\text{NiCl}_2$  induced a nearly 50% reduction of cell number whereas 50  $\mu\text{g mL}^{-1}$  of Ni particles (also  $\sim 0.85$  mM) induced a 60% reduction (Fig. 5.6b).

We also compared the pro-inflammatory capacity of the Co and Ni ions with the respective particles. Cobalt ions and particles were effective in inducing the cell surface protein expression of E-selectin (Fig. 5.7a, effect after 4 h). Interestingly, only Ni ions showed a concentration-dependent increase in E-selectin expression, whereas the Ni particles failed to induce E-selectin cell surface expression (Fig. 5.7b). The same effect was detectable in the expression of ICAM-1 after 24 h; again Co-particles and -ions induced ICAM-1 protein expression on the cell surface, whereas only Ni ions were able to induce ICAM-1 expression, with the Ni particles eliciting no change (data not shown). Moreover, an increase in IL-8 release after 24 h was effectively induced by Co-ions and -particles (Fig. 5.7c). Nickel ions were also able to induce IL-8 release. Contrary to the absence of pro-inflammatory stimulation of Ni particles in the expression of the cell surface adhesion molecules E-selectin and ICAM-1, release of the pro-inflammatory chemokine IL-8 was induced by Ni particles (Fig. 5.7d).

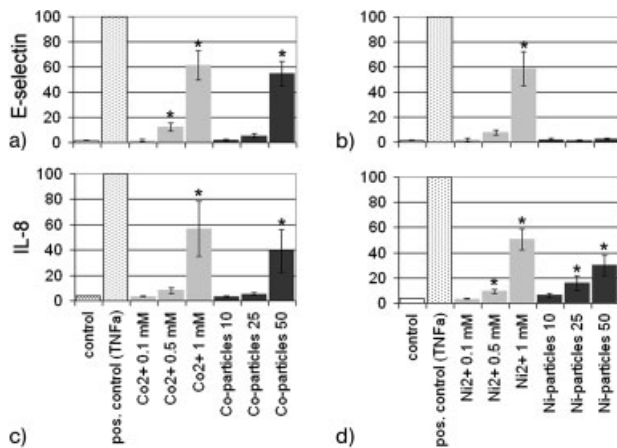


**Fig. 5.7.** Detection of pro-inflammatory stimulation of HDMEC after exposure to Co and Ni ions and Co and Ni particles: (a) E-selectin protein expression after Co-ion and -particle exposure (4 h), (b) E-selectin expression after Ni-ion and -particle exposure

(4 h), (c) IL-8 release after Co-ion and -particle exposure (24 h), and (d) IL-8 release after Ni-ion and -particle exposure (24 h, TNF $\alpha$ -treated cells serve as positive control and set as 100%,  $n = 4$ , means  $\pm$  SDs, significantly different from normoxia: \* $p < 0.01$ ).

## 5.4

### Discussion

The role of particulate matter of nano-scaled size has received increasing attention in recent years. As mentioned before, this attention evolved due to the accidental internalization of particles with (partially) described effects on human health and also due to the intended administration of pharmaceutical, therapeutic, and diagnostic agents in nano-scaled sizes, which today is an important research field [30, 31]. Independent of the pathway of nanoparticle internalization, the distribution of nanoparticles within the body must occur in large part via the blood stream. Therefore, the endothelium will have contact with the nanoparticles during their passage throughout the body. The endothelium is an important cell population in the development of a multitude of diseases (e.g., tumor growth, atherosclerosis, and inflammatory diseases). Therefore, we focused on the effects of nanoparticles on viability and inflammatory status in human endothelial cells *in vitro*.

Endothelial cells *in vitro* maintain several features that their originals *in vivo* express under physiological situations. Furthermore, endothelial cells *in vitro* can be induced by pro-inflammatory compounds to synthesize and release factors that play an important role in the development of diseases. Thus, endothelial cells *in vitro* are a model system suitable for the examination of physiological and pathophysiological situations. Due to the availability of different recombinant growth factors and highly defined cell culture media several types of human endothelial

cell types can be more or less easily propagated *in vitro* (e.g., macrovascular endothelial cells from arteries or veins and microvascular cells derived from the capillaries of different tissues) [32, 33].

#### 5.4.1

##### Particle Internalization

Our study has shown that human endothelial cells possess a large capacity for the internalization of nanoparticles. All nanoparticles tested were taken up by the endothelial cells and to a major extent into vacuoles. Endothelial cells are able to internalize particles by different mechanisms. A large portion of the endothelial cell population possesses a prominent vesicular system that is called the vesiculo-vacuolar organelle (VVO) that other cells do not have with this specificity. The VVO is, together with specific plasma membrane compartments, the caveolae (invaginations of the plasma membrane), involved in the regulated transendothelial cell passage of macromolecules and particles [34]. Since, primarily, endothelial cells possess such a distinct vacuole system this way of particle internalization might be specific for a part of the endothelial cell population. There is also evidence for other means of particle internalization: In endothelial cells, particle internalization is also suggested to occur via specific receptors (e.g., low-density lipoprotein/LDL-receptor, platelet-derived growth factor/PDGF-receptor, albumin-receptor) since nanoparticles covered with LDL [35], PDGF [36], and bovine serum albumin [37] were shown to be internalized via coated pits/vesicles. It is not yet known if both pathways work independently in endothelial cells or if there is a mechanistic link.

There is evidence that a particle's size also affects the pathway of internalization, e.g., beads of 200 nm diameter were internalized into murine melanoma cells (cell line B16-F10) via clathrin-coated pits, whereas 500 nm beads enter the cells by a clathrin-independent pathway [11]. Whether endothelial cells show these size-dependent differences in internalization mechanisms is not yet known and a particle internalization pathway for the endothelial cells used in this study cannot be defined.

Nanoparticles of the biodegradable compound *D,L*-lactide-*co*-glycolide with a mean size of about 300 nm (larger than the particles used in this study, with mean sizes between 14 and 120 nm) are rapidly internalized by endothelial cells *in vitro* (as early as at 30 min) [38]. Moreover, *in vivo* experiments showed rapid particle internalization by endothelial cells; carbon nanoparticles (~50 nm) injected intravenously into tumor-bearing guinea pigs were detected in vacuoles and in the sub-endothelial space of tumor blood vessels 60 min after administration. However, the endothelial cells of non-tumorous blood vessels did not show carbon particle internalization in this animal model [34].

In our *in vitro* model, particles were detectable within vacuoles. The occurrence of vacuoles containing cellular debris together with the internalized particles was partially detectable. This co-localization of cellular debris and particles indicates an overlap between endocytosis and autophagocytosis [39, 40]. Interestingly, these

“mixed content” vacuoles (called amphisomes [41]) appeared very distinct in the case of the Co and Ni particle treatment, whereas TiO<sub>2</sub> and SiO<sub>2</sub> particle filled vacuoles were mostly free of cellular debris. The vacuole enlargement after Co and Ni particle treatment might be connected directly with the possible endocytotic/autophagocytic overlap and may be regulated by different mechanisms depending on the type of vacuole that evolves. The sizes of autophagic vacuoles can be regulated by vacuole fusion or enlargement of the vacuole [42]. The regulation of amphisomal sizes is unknown. We have suggested a connection between the release of divalent metal ions from metallic nanoparticles and the development of amphisomes in endothelial cells. This is supported by the fact that HIF-1 $\alpha$  was stabilized after Co- and Ni-particle exposure, as described for Co- and Ni-ion exposure [43, 44].

#### 5.4.2

##### **Particle Cytotoxicity**

Whereas the ceramic particles of TiO<sub>2</sub> and SiO<sub>2</sub> showed no significant cytotoxic effects, the nanoparticles of Co and Ni induced a significant, concentration dependent impairment of cellular viability. This impairment is obvious at different levels of cellular function (i.e., decrease of cell number, protein expression of the proliferation marker Ki67, and the metabolic activity).

Due to the stabilization of HIF-1 $\alpha$  (see above) it appeared that the observed metal particle cytotoxicity was induced by the release of divalent metal ions from the particles. Therefore we compared the effects of the nanoparticles with those of the metal ions Co<sup>2+</sup> and Ni<sup>2+</sup> (as chloride salts) in concentrations similar to the solid matter utilized. The particles exerted a higher cytotoxicity than the corresponding ions (e.g., 1 mM Co<sup>2+</sup> and ca. 0.85 mM Co particles induced a reduction in cell number after 24 h of ca. 20% and ca. 35%, respectively). These findings are in agreement with the results of a study on the cytotoxicity of Co nanoparticles and Co<sup>2+</sup> ions in mouse fibroblast Balb/3T3 cells [45].

At this point we can only speculate about the higher cytotoxicity of transition metal nanoparticles compared to the corresponding metal ions. The presence of metal-ion-specific transporters is one possible explanation: Transition metal ions like Co<sup>2+</sup> and Ni<sup>2+</sup> (which are essential trace elements and also toxic when present in excess) are transported into cells against concentration gradients with ion selectivity. Furthermore, mammalian cells have intracellular mechanisms to deliver the metal ions to specialized proteins [46]. This specified delivery system is necessary due to the toxicity of metal ions such as Co<sup>2+</sup> and Ni<sup>2+</sup> [47, 48]. The vacuolar system of eukaryotic cells is important in metal ion homeostasis because it provides several organelles for storage of metal ions and also provides the proper amounts of transporters in the various cellular membranes through the secretory pathway. Thus, the concentration of metal ions is regulated [46]. Therefore, it might be suggested that an excess of metal ions can be regulated via specific transporters or that an excess of metal ions is transferred into cellular organelles possessing mechanisms to avoid damage of sensitive cellular compartments. This would, however,

imply that metal nanoparticles are translocated to regions of the cell that are more sensitive to the release of metal ions than the regions that are attained via the specific metal ion transporters.

Severe problems may not only be a result of ion release but also due to the development of free radicals or reactive oxygen species (ROS) that occur from both transition metal ions [49, 50] and (nano-)particles [51–53]. Furthermore, it has been shown that nanosized particulate matter together with transition metals induces ROS production that exhibits a higher response than the single compounds (tested were carbon black particles with a mean size of 14 nm plus exposure of different iron and cupric salts). This increased ROS production suggested a synergistic effect of nanoparticles together with transition metals [54]. The metal particles used in this study, which are made of transition metals, contained a combination of both of these characteristics, i.e., nano-scaled particles and transition metals. Interestingly, Co particles might produce ROS by mechanisms different from ROS production by  $\text{Co}^{2+}$  ions [55, 56]. In addition, the binding of metal ions to extracellular and intracellular proteins such as transferrin and albumin, which are also known to bind  $\text{Co}^{2+}$  and  $\text{Ni}^{2+}$  efficiently [57–59], might influence the cytotoxicity of metal ions. A recent *in vitro* biokinetic study on simultaneous exposure of mouse fibroblast Balb/3T3 cells to Co particles and  $\text{Co}^{2+}$  ions showed different abilities of the two Co compounds to penetrate cells and cellular organelles. In addition, the study confirmed that serum components, particularly albumin and histidine, play a crucial role in determining the eventual toxic effects [60].

Interestingly, Ni particles did not show a reduction of Ki67 protein although the cell number and the metabolic activity were significantly decreased. In contrast, Co particles showed a very distinct down-regulation of Ki67 protein expression, in accordance with the reduced cell number and metabolic activity. Since we have previously shown that Co ions induced apoptosis whereas Ni ions induced cell death that was most likely due to necrosis (no signs of apoptosis were detectable) [48], we suggest that the absence of down-regulation of Ki67 expression after Ni particle exposure indicates a missing regulation of proliferative activity in the course of cell death. This is absent in necrotic cell death [61].

### 5.4.3

#### **Pro-inflammatory Activation**

A pro-inflammatory effect in HDMEC occurred after exposure to  $\text{SiO}_2$ , Co, and Ni particles and was apparent by an enhanced release of IL-8. Only higher particle concentrations (25 and  $50 \mu\text{g mL}^{-1}$ ) induced this increase in IL-8 release. E-selectin protein expression was enhanced by high amounts of Co particles, whereas Ni particles induced no protein expression of E-selectin. In contrast to the particles, divalent Co and Ni ions induced the expression of all pro-inflammatory markers tested (i.e., IL-8, E-selectin, ICAM-1).

The enhancement of IL-8 release in response to high amounts of  $\text{SiO}_2$  particles indicated a pro-inflammatory state. Since  $\text{SiO}_2$  particles can cause chronic inflammatory lung disease by inhalation [62] a comparable effect might be present in

nanoparticle-induced pro-inflammatory activation of endothelial cells *in vitro*. The SiO<sub>2</sub>-induced inflammation is mediated by the activation of the transcription factors NF- $\kappa$ B and AP-1, which are both involved in the regulation of inflammation. This transcription factor activation appears to be triggered by adverse biologic reactions such as the generation of ROS [63]. Moreover, SiO<sub>2</sub>-induced AP-1 activation plays an important role in neoplastic transformation and tumor promotion [64].

The observed pro-inflammatory activation after Co-particle exposure may be attributed to a release of divalent Co-ions by the particles, since the exposure of endothelial cells with these ions leads to impaired endothelial viability and pro-inflammatory stimulation [65]. In addition, with Co-ions the concerted activation of the above-mentioned transcription factors NF- $\kappa$ B and AP-1 has been demonstrated [66, 67] and the Co particles used in this study induced pro-inflammatory activation with Co-ion comparable dimensions.

This contrasts with the effects of the Ni particles. Here, the suggestion of a Ni ion release by the particles, resulting in an induced pro-inflammatory stimulation, is not congruent with the pro-inflammatory effects induced by the respective ions, since Ni-ions induced both an increase in the release of IL-8 and the protein expression of endothelial cell adhesion molecules (i.e., E-selectin and ICAM-1), whereas Ni-particles induced only an increased IL-8 release and the expression of adhesion molecules was not initiated. This indicates an activation mechanism for the Ni particles that deviates from the Ni-ion-induced activation shown to occur via a cooperation of the above-mentioned transcription factors NF- $\kappa$ B and AP-1 [66, 67]. Such differential activation of IL-8 and ICAM-1 was also shown by the treatment of endothelial and epithelial cells with H<sub>2</sub>O<sub>2</sub> [68, 69]: Whereas H<sub>2</sub>O<sub>2</sub> induced an IL-8 expression in epithelial cells lines without the expression of ICAM-1, endothelial cells expressed ICAM-1 after H<sub>2</sub>O<sub>2</sub> treatment without the expression of IL-8. There is evidence that this cell-type-specific differential induction of IL-8 gene expression by H<sub>2</sub>O<sub>2</sub> (and thus oxidative stress) is by a differential binding of NF- $\kappa$ B and AP-1 to the IL-8 promoter [68]. Since oxidative stress is also a relevant aspect in the mechanisms of (Ni-) particulate-matter-induced effects [52] this mechanism of differential activation of pro-inflammatory gene promoters might play a role. Thus, it can be suggested that Ni-ion release by the nanoparticles remains under the critical limit for pro-inflammatory activation but further Ni-nanoparticle-induced effects (possibly oxidative stress) are responsible for the enhanced IL-8 release. However, this hypothesis requires further examination and is the subject of a separate study.

#### 5.4.4

### Conclusions and Consideration of the Risk of Nanoparticles to Human Health

This study has shown that nanoparticles exert effects that deviate from the effects of bulk materials and also from possible corrosion products. The experiments were performed with a cell type highly relevant for nanoparticle transmigration from the blood into tissues, i.e., primary human endothelial cells. Whether the described effects shown *in vitro* are of relevance *in vivo* remains unanswered. However, nano-

particles clearly exert effects that are not easily interpreted. If a pro-inflammatory stimulation of endothelial cells by nanoparticles occurs *in vivo*, chronic inflammation (such as granulomatosis) could be a possible consequence.

Although much progress has been made in recent years to understand the effects of nano-scaled particulate matter, knowledge about its risk in humans is clearly limited. This lack of knowledge is due to the complexity of the chemical and physical characteristics of nanoparticles combined with the difficulty of predicting reactivity in biological systems. Furthermore, nanoparticles possess an impressively high accessibility to different types of tissues and cells, which large-scaled particulate matter usually does not have (reviewed in Ref. [2]). Thus, two different risk aspects are combined in nanoparticles: The ability of foreign materials to enter biological compartments that are usually not easily accessible and the potential for the exertion of effects on these locations, which are difficult to control.

The above-mentioned characteristic behavior of nanoparticles could be useful for medical applications such as in diagnostic and therapeutic devices. The endothelium is an important target for therapy due to its role in several physiological and pathological conditions. Also, the penetration of physiological barriers with endothelial participation such as, for example, the blood–brain barrier is of interest. Therefore, several diagnostic and therapeutic approaches that involve nanoparticulate compounds are under consideration (reviewed in Refs. [5, 70]). However, the utilization of nanoparticle-formulated drugs appears to be afflicted by a similar complexity described above, e.g., the chemotherapeutic agent paclitaxel showed different rates of clearance and different tissue distributions when formulated as nanoparticles compared to the conventional formulation as emulsion [71]. Thus, both accidental and intended exposure of humans to nanoparticles is connected to a certain risk that could be influenced by the type of particle and the state of health of the affected person. Therefore, detailed toxicological research should be carried out to improve the scientific basis of the risk assessment at all stages of the life cycle of nanotechnology [72].

## Acknowledgments

This work was supported by the Deutsche Forschungsgemeinschaft (Priority Programme Biosystem 322 1100) and the European Commission (QOL-2002-147).

The authors thank Susanne Barth, Marianne Müller, and Karin Molter for their excellent technical assistance.

## References

- 1 LOMER, M. C., THOMPSON, R. P., COMMISSO, J., KEEN, C. L., POWELL, J. J., Determination of titanium dioxide in foods using inductively coupled plasma optical emission spectrometry. *Analyst* **2000**, 125, 2339–2343.
- 2 OBERDORSTER, G., OBERDORSTER, E.,

- OBERDORSTER, J., Nanotoxicology: An emerging discipline evolving from studies of ultrafine particles. *Environ. Health Perspect.* **2005**, 113, 823–839.
- 3 POPE, C. A., III, Epidemiology of fine particulate air pollution and human health: Biologic mechanisms and who's at risk?, *Environ. Health Perspect.* **2000**, 108(Suppl 4), 713–723.
  - 4 Anonymous, Air pollution in the world's megacities. *Environment* **1994**, 36, 4–37.
  - 5 BRIGGER, I., DUBERNET, C., COUVREUR, P., Nanoparticles in cancer therapy and diagnosis. *Adv. Drug Deliv. Rev.* **2002**, 54, 631–651.
  - 6 COLVIN, V. L., The potential environmental impact of engineered nanomaterials. *Nat. Biotechnol.* **2003**, 21, 1166–1170.
  - 7 DONALDSON, K., STONE, V., Current hypotheses on the mechanisms of toxicity of ultrafine particles. *Ann. Ist Super Sanita* **2003**, 39, 405–410.
  - 8 OBERDORSTER, G., Pulmonary effects of inhaled ultrafine particles. *Int. Arch. Occup. Environ. Health* **2001**, 74, 1–8.
  - 9 SUPHIOGLU, C., Thunderstorm asthma due to grass pollen. *Int. Arch. Allergy Immunol.* **1998**, 116, 253–260.
  - 10 SALVAGGIO, J. E., Inhaled particles and respiratory disease. *J. Allergy Clin. Immunol.* **1994**, 94, 304–309.
  - 11 REJMAN, J., OBERLE, V., ZUHORN, I. S., HOEKSTRA, D., Size-dependent internalization of particles via the pathways of clathrin- and caveolae-mediated endocytosis. *Biochem. J.* **2004**, 377, 159–169.
  - 12 DUFFIN, R., CLOUTER, A., BROWN, D. M., TRAN, C. L., MACNEE, W., STONE, V., DONALDSON, K., The importance of surface area and specific reactivity in the acute pulmonary inflammatory response to particles. *Ann. Occup. Hyg.* **2002**, 46, 242–245.
  - 13 NEMMAR, A., HOET, P. H., VANQUICKENBORNE, B., DINSDALE, D., THOMEER, M., HOYLAERTS, M. F., VANBILLOEN, H., MORTELMANS, L., NEMERY, B., Passage of inhaled particles into the blood circulation in humans. *Circulation* **2002**, 105, 411–414.
  - 14 OBERDORSTER, G., SHARP, Z., ATUDOREI, V., ELDER, A., GELEIN, R., LUNTS, A., KREYLING, W., COX, C., Extrapulmonary translocation of ultrafine carbon particles following whole-body inhalation exposure of rats. *J. Toxicol. Environ. Health A* **2002**, 65, 1531–1543.
  - 15 OBERDORSTER, G., SHARP, Z., ATUDOREI, V., ELDER, A., GELEIN, R., KREYLING, W., COX, C., Translocation of inhaled ultrafine particles to the brain. *Inhal. Toxicol.* **2004**, 16, 437–445.
  - 16 REICHRTOVA, E., DOROCIAC, F., PALKOVICOVA, L., Sites of lead and nickel accumulation in the placental tissue. *Hum. Exp. Toxicol.* **1998**, 17, 176–181.
  - 17 KAIGLOVA, A., REICHRTOVA, E., ADAMCAKOVA, A., WSOLOVA, L., Lactate dehydrogenase activity in human placenta following exposure to environmental pollutants. *Physiol. Res.* **2001**, 50, 525–528.
  - 18 LEVY, D., GENT, M., NEWHOUSE, M. T., Relationship between acute respiratory illness and air pollution levels in an industrial city. *Am. Rev. Respir. Dis.* **1977**, 116, 167–173.
  - 19 FRAMPTON, M. W., UTELL, M. J., ZAREBA, W., OBERDORSTER, G., COX, C., HUANG, L. S., MORROW, P. E., LEE, F. E., CHALUPA, D., FRASIER, L. M., SPEERS, D. M., STEWART, J., Effects of exposure to ultrafine carbon particles in healthy subjects and subjects with asthma. *Res. Rep. Health Eff. Inst.* **2004**, 1–47; discussion 49–63.
  - 20 MACNEE, W., DONALDSON, K., Mechanism of lung injury caused by PM10 and ultrafine particles with special reference to COPD. *Eur. Respir. J.* **2003**, 40(Suppl.), 47s–51s.
  - 21 CAMPBELL, A., OLDHAM, M., BECARIA, A., BONDY, S. C., MEACHER, D., SIOUTAS, C., MISRA, C., MENDEZ, L. B., KLEINMAN, M., Particulate matter in polluted air may increase biomarkers of inflammation in mouse brain. *Neurotoxicology* **2005**, 26, 133–140.
  - 22 NEMMAR, A., HOYLAERTS, M. F., HOET, P. H., DINSDALE, D., SMITH, T., XU, H., VERMYLEN, J., NEMERY, B.,



- Ultrafine particles affect experimental thrombosis in an *in vivo* hamster model. *Am. J. Respir. Crit. Care Med.* **2002**, 166, 998–1004.
- 23 GATTI, A. M., MONTANARI, S., MONARI, E., GAMBARELLI, A., CAPITANI, F., PARISINI, B., Detection of micro- and nano-sized biocompatible particles in the blood. *J. Mater. Sci. Mater. Med.* **2004**, 15, 469–472.
- 24 LOMER, M. C., THOMPSON, R. P., POWELL, J. J., Fine and ultrafine particles of the diet: Influence on the mucosal immune response and association with Crohn's disease. *Proc. Nutr. Soc.* **2002**, 61, 123–130.
- 25 COOK-MILLS, J. M., DEEM, T. L., Active participation of endothelial cells in inflammation. *J. Leukoc. Biol.* **2005**, 77, 487–495.
- 26 MONTGOMERY, K. F., OSBORN, L., HESSION, C., TIZARD, R., GOFF, D., VASSALLO, C., TARR, P. I., BOMSZTYK, K., LOBB, R., HARLAN, J. M., et al., Activation of endothelial-leukocyte adhesion molecule 1 (ELAM-1) gene transcription. *Proc. Natl. Acad. Sci. U.S.A.* **1991**, 88, 6523–6527.
- 27 ROEBUCK, K. A., RAHMAN, A., LAKSHMINARAYANAN, V., JANAKIDEVI, K., MALIK, A. B., H<sub>2</sub>O<sub>2</sub> and tumor necrosis factor- $\alpha$  activate intercellular adhesion molecule 1 (ICAM-1) gene transcription through distinct cis-regulatory elements within the ICAM-1 promoter. *J. Biol. Chem.* **1995**, 270, 18966–18974.
- 28 MUKAIDA, N., OKAMOTO, S., ISHIKAWA, Y., MATSUSHIMA, K., Molecular mechanism of interleukin-8 gene expression. *J. Leukoc. Biol.* **1994**, 56, 554–558.
- 29 PETERS, K., SCHMIDT, H., UNGER, R. E., OTTO, M., KAMP, G., KIRKPATRICK, C. J., Software-supported image quantification of angiogenesis in an *in vitro* culture system: Application to studies of biocompatibility. *Biomaterials* **2002**, 23, 3413–3419.
- 30 KUBIK, T., BOGUNIA-KUBIK, K., SUGISAKA, M., Nanotechnology on duty in medical applications. *Curr. Pharm. Biotechnol.* **2005**, 6, 17–33.
- 31 REYNOLDS, A. R., MOEIN MOGHIMI, S., HODIVALA-DILKE, K., Nanoparticle-mediated gene delivery to tumor neovasculature. *Trends Mol. Med.* **2003**, 9, 2–4.
- 32 KIRKPATRICK, C. J., UNGER, R. E., KRUMP-KONVALINKOVA, V., PETERS, K., SCHMIDT, H., KAMP, G., Experimental approaches to study vascularization in tissue engineering and biomaterial applications. *J. Mater. Sci. Mater. Med.* **2003**, 14, 677–681.
- 33 KIRKPATRICK, C. J., KRUMP-KONVALINKOVA, V., UNGER, R. E., BITTINGER, F., OTTO, M., PETERS, K., Tissue response and biomaterial integration: The efficacy of *in vitro* methods. *Biomol. Eng.* **2002**, 19, 211–217.
- 34 FENG, D., NAGY, J. A., DVORAK, H. F., DVORAK, A. M., Ultrastructural studies define soluble macromolecular, particulate, and cellular trans-endothelial cell pathways in venules, lymphatic vessels, and tumor-associated microvessels in man and animals. *Microsc. Res. Technol.* **2002**, 57, 289–326.
- 35 HANDLEY, D. A., ARBEENY, C. M., CHIEN, S., Sinusoidal endothelial endocytosis of low density lipoprotein-gold conjugates in perfused livers of ethynyl-estradiol treated rats. *Eur. J. Cell Biol.* **1983**, 30, 266–271.
- 36 ROSENFELD, M. E., BOWEN-POPE, D. F., ROSS, R., Platelet-derived growth factor: Morphologic and biochemical studies of binding, internalization, and degradation. *J. Cell Physiol.* **1984**, 121, 263–274.
- 37 GEOFFROY, J. S., BECKER, R. P., Endocytosis by endothelial phagocytes: Uptake of bovine serum albumin-gold conjugates in bone marrow. *J. Ultrastruct. Res.* **1984**, 89, 223–239.
- 38 DAVDA, J., LABHASETWAR, V., Characterization of nanoparticle uptake by endothelial cells. *Int. J. Pharm.* **2002**, 233, 51–59.
- 39 LIOU, W., GEUZE, H. J., GEELLEN, M. J., SLOT, J. W., The autophagic and endocytic pathways converge at the nascent autophagic vacuoles. *J. Cell Biol.* **1997**, 136, 61–70.
- 40 GORDON, P. B., HOYVIK, H., SEGLEN,

- P. O., Prelysosomal and lysosomal connections between autophagy and endocytosis. *Biochem. J.* **1992**, 283 (Pt 2), 361–369.
- 41 BERG, T. O., FENGSRUD, M., STROMHAUG, P. E., BERG, T., SEGLEN, P. O., Isolation and characterization of rat liver amphisomes. Evidence for fusion of autophagosomes with both early and late endosomes. *J. Biol. Chem.* **1998**, 273, 21 883–21 892.
- 42 DUNN, W. A., JR., Studies on the mechanisms of autophagy: Maturation of the autophagic vacuole. *J. Cell Biol.* **1990**, 110, 1935–1945.
- 43 HIRSILA, M., KOIVUNEN, P., XU, L., SEELEY, T., KIVIRIKKO, K. I., MYLLYHARJU, J., Effect of desferrioxamine and metals on the hydroxylases in the oxygen sensing pathway. *FASEB J.* **2005**.
- 44 PETERS, K., SCHMIDT, H., UNGER, R. E., KAMP, G., PROLS, F., BERGER, B. J., KIRKPATRICK, C. J., Paradoxical effects of hypoxia-mimicking divalent cobalt ions in human endothelial cells in vitro. *Mol. Cell Biochem.* **2005**, 270, 157–166.
- 45 SABBIONI, E., GATTI, A. M., HARTUNG, T., Pathology of new diseases induced by nanomaterials and in vitro toxicology research. *Pathol. Int.* **2004**, 54, S141–148.
- 46 NELSON, N., Metal ion transporters and homeostasis. *EMBO J.* **1999**, 18, 4361–4371.
- 47 ERMOLLI, M., MENNE, C., POZZI, G., SERRA, M. A., CLERICI, L. A., Nickel, cobalt and chromium-induced cytotoxicity and intracellular accumulation in human haec keratinocytes. *Toxicology* **2001**, 159, 23–31.
- 48 PETERS, K., UNGER, R. E., BARTH, S., GERDES, T., KIRKPATRICK, C. J., Induction of apoptosis in human microvascular endothelial cells by divalent cobalt ions. Evidence for integrin-mediated signaling via the cytoskeleton. *J. Mater. Sci. Mater. Med.* **2001**, 12, 955–958.
- 49 STOHS, S. J., BAGCHI, D., Oxidative mechanisms in the toxicity of metal ions. *Free Radic. Biol. Med.* **1995**, 18, 321–336.
- 50 GINSBURG, I., SADOVNIC, M., VARANI, J., TIROSH, O., KOHEN, R., Hemolysis of human red blood cells induced by the combination of diethylldithiocarbamate (DDC) and divalent metals: Modulation by anaerobiosis, certain antioxidants and oxidants. *Free Radic. Res.* **1999**, 31, 79–91.
- 51 PETTIT, A., MWALE, F., TKACZYK, C., ANTONIOU, J., ZUKOR, D. J., HUK, O. L., Induction of protein oxidation by cobalt and chromium ions in human U937 macrophages. *Biomaterials* **2005**, 26, 4416–4422.
- 52 DICK, C. A., BROWN, D. M., DONALDSON, K., STONE, V., The role of free radicals in the toxic and inflammatory effects of four different ultrafine particle types. *Inhal. Toxicol.* **2003**, 15, 39–52.
- 53 DONALDSON, K., BESWICK, P. H., GILMOUR, P. S., Free radical activity associated with the surface of particles: A unifying factor in determining biological activity?, *Toxicol. Lett.* **1996**, 88, 293–298.
- 54 WILSON, M. R., LIGHTBODY, J. H., DONALDSON, K., SALES, J., STONE, V., Interactions between ultrafine particles and transition metals in vivo and in vitro. *Toxicol. Appl. Pharmacol.* **2002**, 184, 172–179.
- 55 LISON, D., CARBONNELLE, P., MOLLO, L., LAUWERYS, R., FUBINI, B., Physicochemical mechanism of the interaction between cobalt metal and carbide particles to generate toxic activated oxygen species. *Chem. Res. Toxicol.* **1995**, 8, 600–606.
- 56 LISON, D., DE BOECK, M., VEROUGSTRAETE, V., KIRSCH-VOLDERS, M., Update on the genotoxicity and carcinogenicity of cobalt compounds. *Occup. Environ. Med.* **2001**, 58, 619–625.
- 57 AISEN, P., AASA, R., REDFIELD, A. G., The chromium, manganese, and cobalt complexes of transferrin. *J. Biol. Chem.* **1969**, 244, 4628–4633.
- 58 BAR-OR, D., CURTIS, G., RAO, N., BAMPOS, N., LAU, E., Characterization of the Co(2+) and Ni(2+) binding amino-acid residues of the N-terminus of human albumin. An insight into

- the mechanism of a new assay for myocardial ischemia. *Eur. J. Biochem.* **2001**, 268, 42–47.
- 59 SADLER, P. J., TUCKER, A., VILES, J. H., Involvement of a lysine residue in the N-terminal Ni<sup>2+</sup> and Cu<sup>2+</sup> binding site of serum albumins. Comparison with Co<sup>2+</sup>, Cd<sup>2+</sup> and Al<sup>3+</sup>. *Eur. J. Biochem.* **1994**, 220, 193–200.
- 60 DEL TORCHIO, R. (2005). Nanotossicologia in vitro mediante tecniche analitiche avanzate. Uno studio di Co nanoparticelle in fibroblasti di topo (Balb/3T3). MSc thesis, University of Milan, Milan.
- 61 CORCORAN, G. B., FIX, L., JONES, D. P., MOSLEN, M. T., NICOTERA, P., OBERHAMMER, F. A., BUTTYAN, R., Apoptosis: Molecular control point in toxicity. *Toxicol. Appl. Pharmacol.* **1994**, 128, 169–181.
- 62 McDONALD, J. C. (1996). Silica and lung cancer. In *Silica and Silica-induced Lung Diseases* (ed. V. CASTRANOVA, V. VALLYATHAN, W. E. WALLACE), CRC Press, Boca Raton, FL.
- 63 CASTRANOVA, V., Signaling pathways controlling the production of inflammatory mediators in response to crystalline silica exposure: Role of reactive oxygen/nitrogen species. *Free Radic. Biol. Med.* **2004**, 37, 916–925.
- 64 DING, M., CHEN, F., SHI, X., YUCESAY, B., MOSSMAN, B., VALLYATHAN, V., Diseases caused by silica: Mechanisms of injury and disease development. *Int. Immunopharmacol.* **2002**, 2, 173–182.
- 65 KIRKPATRICK, C. J., BARTH, S., GERDES, T., KRUMP-KONVALINKOVA, V., PETERS, K., [Pathomechanisms of impaired wound healing by metallic corrosion products]. *Mund Kiefer Gesichtschir* **2002**, 6, 183–190.
- 66 WAGNER, M., KLEIN, C. L., VAN KOOTEN, T. G., KIRKPATRICK, C. J., Mechanisms of cell activation by heavy metal ions. *J. Biomed. Mater. Res.* **1998**, 42, 443–452.
- 67 WAGNER, M., KLEIN, C. L., KLEINERT, H., EUCHENHOFER, C., FORSTERMANN, U., KIRKPATRICK, C. J., Heavy metal ion induction of adhesion molecules and cytokines in human endothelial cells: The role of NF-kappaB, I kappaB-alpha and AP-1. *Pathobiology* **1997**, 65, 241–252.
- 68 LAKSHMINARAYANAN, V., DRAB-WEISS, E. A., ROEBUCK, K. A., H<sub>2</sub>O<sub>2</sub> and tumor necrosis factor-alpha induce differential binding of the redox-responsive transcription factors AP-1 and NF-kappaB to the interleukin-8 promoter in endothelial and epithelial cells. *J. Biol. Chem.* **1998**, 273, 32 670–32 678.
- 69 LAKSHMINARAYANAN, V., BENO, D. W., COSTA, R. H., ROEBUCK, K. A., Differential regulation of interleukin-8 and intercellular adhesion molecule-1 by H<sub>2</sub>O<sub>2</sub> and tumor necrosis factor-alpha in endothelial and epithelial cells. *J. Biol. Chem.* **1997**, 272, 32 910–32 918.
- 70 EMERICH, D. F., THANOS, C. G., Nanotechnology and medicine. *Expert Opin. Biol. Ther.* **2003**, 3, 655–663.
- 71 YEH, T. K., LU, Z., WIJENTJES, M. G., AU, J. L., Formulating paclitaxel in nanoparticles alters its disposition. *Pharm. Res.* **2005**, 22, 867–874.
- 72 European Commission (2004). Towards a European strategy for nanotechnology, <http://www.cordis.lu/nanotechnology>

## 6 Toxicity of Carbon Nanotubes and its Implications for Occupational and Environmental Health

*Chiu-wing Lam, John T. James, Richard McCluskey, Andrij Holian,  
and Robert L. Hunter*

### 6.1 Introduction

#### 6.1.1 Overview

Manufactured carbon nanotubes (CNTs) exist in two forms, single-wall (SWCNTs) and multiwall (MWCNTs). Structurally, a SWCNT is a rolled-up, single-layer graphene sheet with a diameter of  $\sim 1$  nm and a length of several micrometers or longer, whereas a MWCNT contains two or more concentric layers with various diameters and lengths. CNTs are thermally generated from carbon atoms in carbon-bearing sources by electrical arc, laser, or chemical vapor deposition processes; the yield of SWCNTs is increased by the presence of catalytic metals. Because of their unique electrical, mechanical, and thermal properties, manufactured CNTs could have many applications in the electronics, computer, and aerospace industries. These widespread applications would require CNTs to be produced on a large scale. Unprocessed CNTs are very light, and if they entered the environment as suspended particulates of respirable sizes, they would reach the lungs. Concerned about the potential toxicity of these novel materials, several groups have conducted rodent studies to assess pulmonary toxicity of SWCNTs or MWCNTs. The test materials were made by different methods and contained different types and amounts of residual metals. Aqueous suspensions of test dusts were administered to the lungs of animals by intratracheal instillation or by pharyngeal aspiration. The results of these studies collectively showed that CNTs themselves, no matter how they were synthesized or what metals they contained, could produce inflammation, granulomas, fibrosis, and biochemical toxicological changes in the lungs. Results of comparative toxicity studies in animals given equal weights of CNTs, carbon black, and quartz showed that if CNTs reach the lungs they are much more toxic than carbon black. They can also be more toxic than quartz, which is considered a serious occupational health hazard if it is chronically inhaled. MWCNTs have been identified in fine particulate matter (PM) collected from combustion streams of

methane and natural-gas flames of typical kitchen ranges and from indoor and outdoor air. Exposure to fine PM has been shown to be associated with pollution-induced cardiopulmonary diseases. Because manufactured CNTs produce deleterious effects in animals, it is speculated that combustion-generated MWCNTs may play a significant role in pathogenesis of pollutant-induced diseases. Therefore, CNTs from manufactured and combustion sources in the environment could have adverse effects on human health.

### 6.1.2

#### General Background

The growing field of nanotechnology promises to bring a host of innovations that will profoundly affect modern societies. CNTs have helped to lay the foundation of this new technology. MWCNTs have recently been found to be generated in fuel combustion processes and to be present in indoor and outdoor environments. As nanotechnology finds new applications, manufactured CNTs will also become widespread. Although combustion-generated CNTs have probably existed in the Earth's environment for thousands of years, little is known about their effects on health. Several laboratories have studied the toxicity of manufactured CNTs, and their results indicate that precautions should be taken to minimize inhalation exposures to CNTs.

This chapter has five further sections. Section 6.2 describes the promotion of nanotechnology and its expected economic impact. Section 6.3 describes manufactured CNTs in three subsections: their discovery and synthesis, their properties, and the scope of their possible applications. Section 6.4 reviews findings demonstrating the current and past occurrence of CNTs in the environment. Section 6.5 describes methods used to assess the toxicity of respirable dust in the lung and reviews several studies assessing pulmonary toxicity of manufactured CNTs in guinea pigs, mice, and rats. Section 6.6, a discussion of health risk implications of CNTs, summarizes the toxicity of CNTs and addresses the potential occupational exposure risk for manufactured CNTs and the likely impact of manufactured and combustion-generated CNTs on environmental health. This chapter contains more emphasis on environmental implications of CNTs and less detail about the risk of occupational exposures than does a recent toxicological review and risk assessment of CNTs published in *Critical Review in Toxicology* [1].

## 6.2

### Carbon Nanotubes and Nanotechnology

The discovery of C<sub>60</sub> (Buckminsterfullerene) and CNTs has propelled nanotechnology to the forefront of science and engineering research in the last decade. Several government agencies, under the leadership of the National Science and Technology Council, jointly established the Interagency Working Group on Nanotechnology, shortly after the discovery of CNTs and the awarding of the Nobel Prize in

1996 for the discovery of fullerene. In 2000, this federal effort was raised by President Clinton to the level of a federal initiative, which was known as the National Nanotechnology Initiative (NNI) [2]. The NNI is promoting nanotechnology research and development to lead the United States to the next industrial revolution [3]. The National Science Foundation [4] predicted that nanotechnology will drive prodigious nanoscience research and engineering development efforts in materials science, physics, chemistry, biology, medicine, and biotechnology, and will generate, in 10 to 15 years' time, an annual business and economic impact of close to \$1 trillion. One of the major objectives of the NNI is "developing materials that are 10 times stronger than steel, but a fraction of the weight for making all kinds of land, sea, air and space vehicles lighter and more fuel efficient." The materials implicated in the initiative are CNTs.

### 6.3

#### **Manufactured Carbon Nanotubes: Their Synthesis, Properties, and Potential Applications**

##### 6.3.1

##### **Discovery and Synthesis**

CNTs are the most important and most-studied nanomaterials. They are a new allotropic form of carbon similar to fullerene (Fig. 6.1). Buckminsterfullerene was first synthesized in 1985 by a laser ablation process developed by Richard Smalley, a Nobel Prize laureate at Rice University (Houston, TX), and his colleagues [5]. CNTs were discovered in 1991 by Sumio Iijima during his investigation of fullerene formation from atomized carbon dissociated from heated graphite in an arc-discharge process [6, 7]. This Japanese electron microscopist observed CNTs, predominately multiwalled (Fig. 6.1), and other nanoparticles deposited at the graphite cathode. Ebbesen and Ajayan of Iijima's laboratory showed that CNTs could be produced in bulk quantities by varying the arc-evaporation conditions [8]. Iijima found that the synthetic yield of single-wall carbon nanotubes (SWCNTs; Fig. 6.1) could be increased by incorporating cobalt or other catalytic transition metals with the graphite source in the arc vaporization process [9]. Smalley's group at Rice University also succeeded in synthesizing SWCNTs, by adapting the laser ablation process used to make C<sub>60</sub> [10, 11]. In the arc vaporization and laser ablation processes, solid or powdered graphite is used as the carbon source, but in the chemical vapor deposition method, carbon-bearing gaseous compounds such as methane, acetylene, or other hydrocarbons are the source [12, 13]. Using carbon monoxide as a feedstock, Nikolaev in Smalley's laboratory developed a gas-phase catalytic growth of SWCNTs from carbon atoms generated from a stream of continuous-flow high-pressure carbon monoxide [14]. This patented synthesis method is referred to by Smalley's group as the HiPco™ process.

All these synthetic processes involve formation of nanotubes from carbon atoms thermally generated from the carbon-bearing sources. CNT synthesis is generally carried out in an argon or other inert atmosphere at 600–1200 °C [15]. Typically,

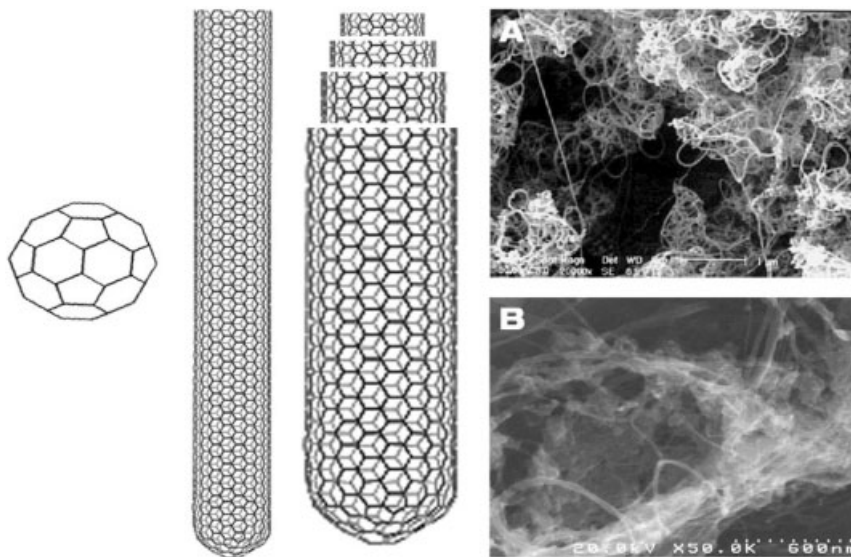


**Fig. 6.1.** Drawings of a  $C_{60}$  fullerene, a single-wall carbon nanotube (SWCNT), and a multiwall carbon nanotube (MWCNT); also shown are scanning electron micrographs of SWCNT ropes (A) and MWCNT ropes (B). ((B) is courtesy of Jordi Rodriguez of University of Barcelona, Spain.)

the carbon atoms are formed on the surface of the catalytic metal; they then dissolve in molten metal nanoparticles. From the molten metal, CNTs grow [15]; when they reach a certain length, they drop off from the metal particles. At the temperature of synthesis, the metal(s) needs to be catalytically active and remain in the molten state, allowing dissolution of carbon atoms in the metal(s); these requirements limit the metals that can be used, of which cobalt, nickel, iron, and molybdenum are the most common. All unprocessed SWCNT or MWCNT products contain residual metal(s). Generally metal(s) accounts for up to 30% of a raw SWCNT product; the metal content in a MWCNT product is much less (Table 6.1 below). The metal impurities are undesirable; some products on the market are sold in purified form after removal of metal. CNT products may contain other impurities that consist of non-nanotube carbon. Product purity depends on both manufacturing processes and post-manufacturing treatments.

### 6.3.2

#### Physical and Chemical Properties

Structurally, a SWCNT is a rolled-up sheet of graphene or graphite with its carbon atoms arranged in hexagonal and pentagonal patterns. It is about 1 nm in diameter and several micrometers long. MWCNTs contain multiple concentric layers

with various diameters and lengths. Immense efforts have been devoted to making CNTs longer for practical uses. Because MWCNTs are more heterogeneous, characterization of CNT physicochemical properties has been carried out predominately on SWCNTs.

Theoretical calculations and experimental results have shown that SWCNTs have highly desirable mechanical, thermal, photochemical, and electrical properties. SWCNTs are both strong and stiff, yet flexible; in fact, they are the strongest of all synthetic fibers [16]. According to Smalley, "... calculations show [they] should be somewhere between 30 and 100 times stronger than steel." [17, 18]. The van der Waals force attraction of SWCNTs causes the tubes to bundle into microscopic ropes, which in turn aggregate to form loose clumps. SWCNTs are among the best electrical conductors and can conduct electricity twice as well as copper [19]. SWCNTs have unique electron-transport properties; they may be either metallic or semiconducting, determined by the chiral vector of the tubes [20]. In a typical batch of synthesized material, one-third of the SWCNTs are metal conductors and two-thirds are semiconductors [21, 22]. MWCNTs are made up of concentrically rolled-up graphene sheets. Each rolled-up sheet is like a SWCNT, and MWCNTs probably have many physicochemical properties similar to those of SWCNTs.

### 6.3.3

#### **Applications**

Both SWCNTs and MWCNTs are very light; they are very strong and stiff and yet flexible [16]. These very desirable mechanical properties make them ideal materials, by themselves or in composites, for potential wide applications in engineering structures. Even composite materials containing CNTs may be strong enough for building such things as spacecraft structures, space elevators, artificial muscles, combat jackets, and land and sea vehicles [23]. Commenting on the SWCNTs that have metal-like properties, Smalley stated [24], "... they will conduct electricity better than copper. Membranes made from arrays of these nanotubes are expected to have a revolutionary impact on the technology of rechargeable batteries and fuel cells, perhaps giving us all-electric vehicles within the next 10–20 years." Smalley [24] further predicted that, several decades from now, CNT-based nanoelectronics having vastly greater performance and scope will supplant our current silicon-based microelectronics. CNTs also have many other potential applications.

## 6.4

### **Occurrence of Carbon Nanotubes in the Environment**

#### 6.4.1

#### **Potential Occupational Exposures and Environmental Impact of Manufactured Carbon Nanotubes**

Unprocessed CNTs are very light and can become airborne (Fig. 6.2), and if they entered the environment as fine suspended particulates they could reach the lungs



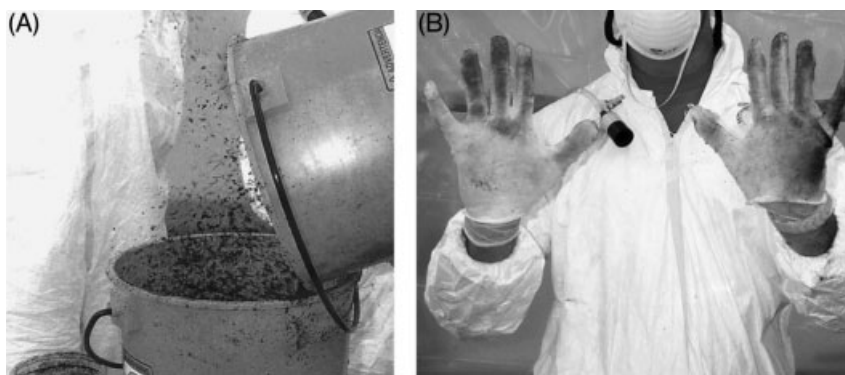


**Fig. 6.2.** (A) SWCNT particles became airborne when the raw material (HiPco CNTs) was poured between containers. (B) Contaminated gloves showing SCWNT particles appearing like black soot. (Courtesy of Dr. Andrew Maynard of NIOSH [27].)

of exposed workers. If CNTs exist in nanosize fibers, they might penetrate unprotected skin (Fig. 6.2). The CNT manufacturing industry is still in its infancy and the products remain expensive. In an interview conducted in 2003 [25], Smalley stated that the price of SWCNTs was hundreds of thousands of dollars per pound. Currently (2005), raw SWCNTs and MWCNTs are sold by BuckyUSA (Houston) at  $> \$100$  per gram (or  $> \$50\,000\text{ lb}^{-1}$ ) [26]. In 2003, Baron et al. [27], of the aerosol group of the National Institute of Occupational Safety and Health (NIOSH) visited CNT synthesis laboratories at Rice University and NASA's Johnson Space Center and the CNT manufacturing facility at Carbon Nanotechnologies Incorporated (Houston) where SWCNT are produced by the HiPco and laser processes. They observed the recovery of CNTs from synthetic ovens and reported that handling of the collected samples was gentle, and losses of this expensive material were minimized. Occupational exposure in the facilities that make these expensive materials is expected to be minimal, with very little CNT industrial waste contaminating the environment.

Smalley [28] predicted, however, that "... in time, millions of tonnes of nanotubes will be produced worldwide every year." The Department of Energy's 2010 target goal for the price of CNTs is  $\$8\text{ kg}^{-1}$  (or  $< \$20\text{ lb}^{-1}$ ). The extent of industrial and commercial applications would depend on the price of CNT products. If millions of tons of CNTs could be produced annually and if the CNT industry achieves the goal of "a couple dollars a pound," [25] occupational exposures to airborne dusts of these lightweight materials during synthesis, processing, and product manufacturing would be very substantial. Because of the potential for rapid merging or incorporation of CNTs into fabrics, plastic, lubricants, composite materials, and household commodities that are used worldwide, concerns have arisen about the adverse impact of CNTs on human health and the environment (Fig. 6.3). If

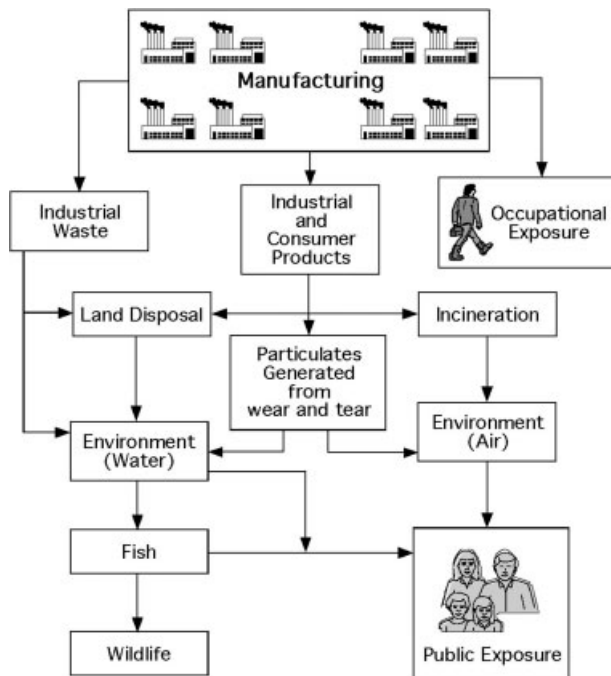


**Fig. 6.3.** Potential environmental impact and health concern when the production volume of carbon nanotubes becomes very large.

they are incorporated into materials such as plastic and composite structures, the CNT materials will need to be pulverized; working with pulverized CNTs would pose an inhalation exposure risk. In the U.S. we have also witnessed the use of asbestos in automotive brake shoes until it was found that asbestos particles generated from abrasion contribute to environmental pollution, leading the U.S. Environmental Protection Agency to ban the use of this carcinogenic material in automobiles [29]. CNTs are light and strong, and if the price of CNTs drops to a few dollars a pound, a potential exists for finding this type of application for CNTs and for them to contribute to environmental pollution. It is important that the chronic toxicity of CNT dusts be known before CNTs become more widespread.

#### 6.4.2

#### **Combustion-generated Carbon Nanotubes in the Environment**

The fact that thermal processes are used to synthesize fullerenes and MWCNTs from atomized carbon generated from heated graphite [5, 9] and the finding that carbon nanotubes can be produced by chemical vapor deposition methods involv-

ing thermally dissociated methane, acetylene, and other hydrocarbons [30] have triggered interest in looking for these carbon allotropes in the environment.

#### 6.4.2.1 MWCNT Formation from Natural Gas Combustion Indoors

Samples of airborne particulate material (PM) collected from combustion streams of methane, propane, or natural gas (containing 96% methane) of typical kitchen gas-ranges were found to contain aggregates of MWCNTs and other carbonaceous nanoforms [31–33]. The aggregates, which had aerodynamic diameters of about 0.4 to 2  $\mu\text{m}$ , were essentially pure carbon or graphene. They contained several hundred to several thousand individual MWCNTs and other carbon nanocrystals of about 20 nm diameter; individual MWCNTs were ca. 3 to 30 nm in diameter [34]. The authors [34] concluded that CNTs and fullerene nanoparticles are ubiquitous in homes with gas cooking ranges. Their findings suggest that MWCNTs and other carbonaceous nanoparticles may also be produced by water heaters, furnaces, and other appliances that use natural gas.

#### 6.4.2.2 MWCNTs in Metropolitan Outdoor Air

Outdoor airborne PM collected in El Paso (TX) by Murr et al. and analyzed using a transmission electron microscope showed the presence of MWCNTs aggregated with other forms of carbon nanocrystals (shells, spheres, and other structures) (Fig. 6.4a and b) [34]. The structure of these aggregates collected outdoors was similar to that of MWCNTs collected indoors, except that the outdoor PM included agglomerates of other mineral nanocrystals, such as silica, that are common in the atmosphere [34]. The carbon nanocrystals, largely MWCNTs, accounted for 15% of the weight of the dust. Diesel-related aggregates accounted for 5% of the dust collected. According to Murr et al., their laboratory had collected hundreds of samples in El Paso over several years and had previously characterized dusts as silica or other nanocrystals with carbonaceous materials [35]; reexamination of these samples indicated that 90% of them contained MWCNTs and other carbon nanocrystals [33]. Environmental samples collected recently from areas close to a heavy-traffic road in Houston were also shown to contain complex aggregates of MWCNTs and other carbon nanocrystals intermixed with silica nanocrystals (Fig. 6.4c and d) [34]. Murr et al. concluded that MWCNTs and carbonaceous nanoparticles are ubiquitous in the environment, and they speculated that MWCNTs make up a significant portion of airborne PM both indoors and outdoors [32].

#### 6.4.2.3 MWCNTs in Ancient Ice

Nanoparticulates were found in an ice sample from a core drilled into a Greenland ice cap to a depth of 1646 feet and dated at roughly 10 000 years old [36]. MWCNTs, fullerene-like nanocrystal forms, and silica nanoparticles were observed in complex mixtures of nanoaggregates in this sample. The aggregates were less than 1  $\mu\text{m}$  in diameter. The authors reported that the particulate pattern was similar to that they observed in samples collected from metropolitan air. These findings showed that MWCNTs and other carbonaceous nanoparticles were present in respirable particles in the air in prehistoric times.

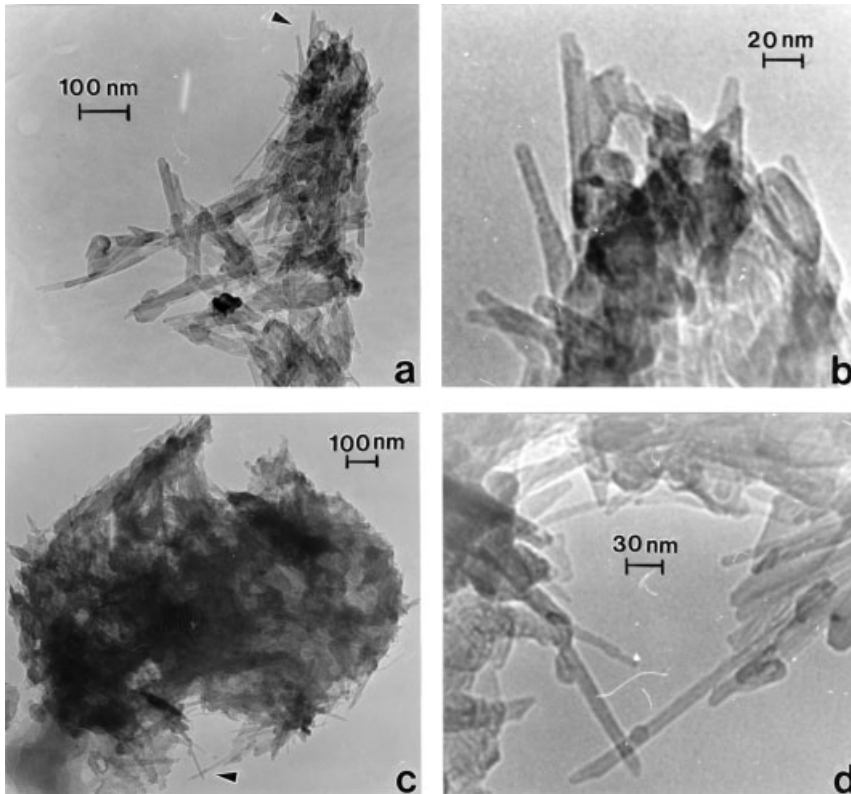


**Fig. 6.4.** Transmission electron microscope images of environmental particulate matter collected from El Paso, TX (a, b) and from Houston, TX (c, d), showing the presence of

multi-wall carbon nanotubes [33] (Courtesy of Dr. L. Murr of University of Texas at El Paso, TX, and with permission to print from Springer Publishing Company, New York, NY).

#### 6.4.2.4 Concern about Combustion-generated MWCNTs in the Environment

MWCNTs are components of airborne particulate aggregates smaller than  $2.5\ \mu\text{m}$  in diameter ( $\text{PM}_{2.5}$ ) [32, 33]. Natural gas is considered an environmentally clean fuel. Combustion of natural gas produces only 7 pounds of PM per billion BTU compared with 84 pounds for oil and 2774 pounds for coal combustion [37]. The numbers may be underestimated if nanosize particulates were not captured. Even though natural gas produces a relatively small amount of PM, global fuel-gas consumption is very large, making the contribution of MWCNTs to air pollution very substantial. In 1999, 22 096 billion BTU of natural gas was consumed in the U.S. [38]; this was 27% of the global consumption. The consumption of natural gas, especially in indoor activities, is expected to increase, and this can be expected to increase the contribution of MWCNTs to air pollution.

Other well-established sources of  $PM_{2.5}$  include products of fuel combustion by automobiles, power plants, wood burning, industrial processes, and diesel-powered vehicles such as buses and trucks [39]. Combustion processes typically generate very fine particles of from 0.01 to 2.5  $\mu m$  [40]; combustion of fossil fuels is the major contributor of fine particulates [41]. The PM contains elemental carbon, organic carbon, trace elements, and common ions [42]. Commenting on CNTs and fullerenes, Richard Smalley stated [23, 43], “They’re also made in every candle flame and in forest fires.” If CNTs are formed in such mundane places as candle flames and forest fires, MWCNTs are likely to be produced by combustion of other fuels in addition to natural gas. Because airborne MWCNTs are ubiquitous and are present in substantial amounts in the environment, all people are exposed to this newly identified environmental pollutant.

#### 6.4.3

#### **Comparison of Physical Structures of Manufactured and Non-manufactured Carbon Nanotubes**

Manufactured CNTs are produced in ovens that allow them to form bundles, ropes, and clumps. Under optimal conditions, long fibers of high purity are preferably produced for practical applications such as spinning into threads or ropes. Most of the particles produced by CNT manufacture (such as by the HiPco and laser processes) are probably larger than respirable sizes [27]. In the environment outside the laboratory, where fuels are heterogeneous, combustion conditions are various, the reactions are not confined, and metal catalysts are generally not present, combustion-generated CNTs, which are exclusively multi-walled, are expected to be highly irregular in size and quality [34]. This probably decreases the effectiveness of van der Waals forces; MWCNTs thus produced are less orderly, shorter in length, and fewer in number than manufactured CNTs, and are intermingled with other nanoparticles (Fig. 6.4). This may explain why manufactured CNTs generally exist in larger dust aggregates whereas aggregates containing MWCNTs in the environment are often found in particles of respirable size [34].

### 6.5

#### **Toxicological Studies and Toxicity of Manufactured CNTs**

Toxicological studies on CNTs were conducted primarily to investigate the potential toxicity of manufactured CNTs in the lungs for occupational risk assessment. The first study of SWCNT toxicity, in which lung histopathology in exposed mice was examined, was triggered by NASA’s concern that workers in occupational settings could be exposed to the airborne dust of this light material of unknown toxicity [44]. The study was also supported by the Center of Nanoscale Science and Technology of Rice University; both organizations have facilities that make SWCNTs. Particle characterization of the HiPco and laser CNTs by NIOSH aerosol scientists showed that respirable particles can be generated, albeit with difficulty, from bulk

SWCNT materials [27]. Inhalation would be the primary route of occupational exposure. Parallel to the NASA study [44], Warheit et al. [45] of Du Pont Company (Wilmington, DE) conducted a toxicity study in rats of a SWCNT product made by their company. Although the two studies yielded some similar histopathological findings, the two groups reached different conclusions about the toxicity of SWCNTs, which have been a subject of wide debate. Shvedova et al. [46] of NIOSH conducted a very comprehensive study in mice “to resolve this conflict...” The toxicity of MWCNTs had drawn little attention until very recently a Belgian group led by Muller et al. [47] published their study. All these toxicological studies are outlined in Table 6.1 and are the subjects of this chapter.

The portion of dust that could reach the pulmonary region (where air exchange takes place) of the respiratory system is termed the respirable fraction (or dust). For humans, a dust particle of respirable size is generally 10  $\mu\text{m}$  or less, depending on its density and geometry; for rodents, the diameter of a respirable dust particle is a few micrometers less. The extent (fraction) of deposition of respirable dust in different locations in the respiratory system depends on the particle size, density, and geometry. To assess the toxicity of a dust in the lung, the respirable fraction is generally isolated or prepared from the bulk material.

The action of the van der Waals force causes CNTs to have a great tendency to bundle to form ropes, each containing a few hundred parallel tubes [48]. These secondary structures, in turn, aggregate into loose clumps. As shown by the NIOSH aerosol scientists for the HiPco and laser products [27], it would be difficult to isolate and collect enough fine CNT particles or clumps of respirable sizes from the bulk materials to use in an inhalation study, which would require a large amount of fine dust of this expensive material. A controlled CNT concentration would have to be generated in a chamber, and particle sizes and the actual exposure level would have to be monitored. This is difficult even with more workable dusts or powders of other compounds. Because it is technically difficult and costly to conduct inhalation toxicity experiments, investigators often assess the effects of dusts and aerosols in the lungs by intratracheal instillation (ITI) [49–51].

A dust is administered by the ITI route by injecting a suspension of a fine dust into the trachea of a small animal and allowing the dust to be pulled deeper into the lung during breathing. Dust administered by inhalation is inhaled continuously; when dust is administered by ITI it is generally instilled into the trachea as a bolus dose. Administration by the ITI route does not allow investigators to assess the effects of a test dust in the upper respiratory tract, and the distribution of dust in the lung is unnatural and less even than with administration by inhalation. In an ITI study, dust aggregates suspended in an aqueous solution usually need to be dissociated or broken down to respirable sizes by ultrasonication with or without a non-toxic dispersion agent. A dose of dust particles administered by ITI can swamp the respiratory system's dust clearance mechanisms, and ITI results are often exaggerated. However, an ITI study does allow investigators to determine the relative toxicity of the test material by giving reference compounds of known inhalation toxicities to control groups of animals [52, 53]. The ITI administration

**Tab. 6.1.** Pulmonary toxicity studies of SWCNTs in animals and characteristics of these materials.

Test materials and characteristics	Maker of test materials	Synthetic process	Metal content (%) <sup>a</sup>	Animal species	Ref.
Soot containing CNTs	Toyo Tanso Co. Ltd., Japan	Electric arc	Co/Ni No info on %	Guinea pig	Huczko et al., 2001 [54]
SWCNTs	Rice University, Houston, TX	Laser <sup>b</sup>	Ni: 10 <sup>c</sup>	Mouse	Lam et al., 2000 (unpublished report)
SWCNTs	Rice University, Houston, TX	HiPco <sup>b</sup>	Fe: 26.9 Mo: 0.95 Ni: 0.8	Mouse	Lam et al., 2004 [44]
SWCNTs, purified	Rice University, Houston, TX	HiPco <sup>b</sup>	Fe: 2.1	Mouse	Lam et al., 2004 [44]
SWCNTs	CarboLex Inc., Lexington, KY	Electric arc	Ni: 26.0 Y: 5.0 Fe: 0.5	Mouse	Lam et al., 2004 [44]
SWCNTs	DuPont Co., Wilmington, DE	Laser <sup>b</sup>	Ni: 5 Co: 5	Rat	Warheit et al., 2004 [45]
SWCNTs, purified <sup>d</sup>	Carbon Nano-Technologies, Inc. Houston, TX	HiPco <sup>b</sup>	Fe: 0.23	Mouse	Shvedova et al., 2005 [46]
SWCNTs	Facultés Universitaires Notre-Dame de la Paix in Namur, Belgium	CVD	Co: 0.95 Fe: ~1	Rat	Muller et al., 2005 [47]

<sup>a</sup>Percent by weight in final products.

<sup>b</sup>Process developed by Rice University or originally developed by Rice University.

<sup>c</sup>Information provided by Smalley's group at Rice University.

<sup>d</sup>Purified by NASA Johnson Space Center Nanotechnology Laboratory.

route is acceptable for screening dusts for pulmonary toxicity, if the investigators or risk assessors recognize the limitations of this technique [51].

#### 6.5.1

##### **Study of SWCNTs in Guinea Pigs by Huczko et al. of Warsaw University**

Huczko et al. conducted the first animal study on the toxicity of CNTs [54]. They intratracheally instilled two groups of five guinea pigs each with a bolus dose of 0 or 25 mg of CNT-containing soot in saline solution. They found no difference between the two groups in tidal volume, breathing frequency, or pulmonary resistance. Analysis of bronchoalveolar lavage fluid (BALF) obtained from the CNT-treated and control animals indicated that treatment with CNTs had no effect on cell differentials or total protein concentration. The authors concluded that “the soot with a high content of CNTs does not induce any abnormalities of pulmonary function or measurable inflammation in guinea pigs treated with carbon nanotubes.” However, examination of lung pathology, which is the most critical toxicological endpoint of any pulmonary toxicity study with dust, was not included in the study. Lung pathology was examined in the other studies reviewed in this section.

#### 6.5.2

##### **Study of SWCNTs in Mice by Lam et al. of NASA-JSC Toxicology Laboratory**

Lam et al. conducted a pilot 7-day ITI study to determine pulmonary toxicity of an early experimental SWCNT sample made at Rice University by the laser evaporation process and containing nickel. The ITI method used was a modified version of a method previously used in our laboratory [54]. Granulomas were observed in mice (C57/BL/6J) treated with 1 mg SWCNT per mouse. Because the test sample contained 10% (by weight) residual nickel, the lung lesions could not be attributed to the effect of CNTs.

A “core” study was conducted to assess the intrinsic toxicity of CNTs and the influence of the residual metals in the toxicological manifestation of the test compounds. The three types of CNTs we studied had been manufactured by different processes and contained different types and/or amounts of residual metals (Table 6.1) [44]. These materials were (1) unprocessed iron-containing SWCNTs made by the HiPco process, (2) a purified HiPco product that had been vigorously treated with concentrated acid to remove metal residues [56], and (3) a CarboLex SWCNT sample, made by an arc-discharge process, that contained nickel and yttrium. The core study included two standard reference materials: carbon black (Printex 90<sup>®</sup>, a dust with relatively low toxicity) and quartz (Min-U-Sil 5<sup>®</sup>, a fibrogenic dust). Groups of B6C3F<sub>1</sub> mice (4 mice per group for 7 d, 5 mice per group for 90 d) were intratracheally instilled with a suspension of the test dust (0, 0.1, or 0.5 mg 50  $\mu\text{L}^{-1}$  per mouse, equal to about 0, 3.3, or 16.5 mg  $\text{kg}^{-1}$ , respectively). Mice were euthanized 7 or 90 d after the single treatment, and their lungs were excised, fixed, and stained for histopathological study [44].

Lung histopathology results showed that CNTs induced lesions, chiefly intersti-



tial granulomas (Fig. 6.5), in the lungs of the 7-d and 90-d groups of mice [44]. These microscopic nodules, located beneath the bronchial epithelium, were present throughout most of the microscopic fields of lung tissue. The lesions were similar to the ones we saw in the pilot study. The granulomas contained macrophages that had engulfed CNTs, but they contained very few inflammatory cells. The severity of lesions was dose-dependent. Prominent granulomas were found in the lungs of all the mice that received 0.5 mg CNTs per mouse. Granulomas were less prominent but were still observed in the mice each treated with 0.1 mg of HiPco-synthesized CNTs. The lung lesions in the 90-d high-dose groups were generally more pronounced than those in the 7-d high-dose groups. The lungs of some animals in the 90-d groups showed peribronchial and interstitial inflammation, fibrosis, and necrosis that had extended into the alveolar septa. Mice in the group treated with carbon black had black particles in alveolar regions, but tissue reactions were minimal (Fig. 6.5a). The lungs of mice treated with the high dose of quartz had mild to moderate inflammation. The lesions induced by quartz were considered much less severe than those produced by CNTs. Similar results were obtained for all three types of SWCNTs. The lungs of mice in the serum control groups were normal. Lam et al. concluded that SWCNTs are intrinsically toxic to the lungs; these authors advise caution in allowing exposure to the dust and advocate implementation of strategies to minimize human exposures [44].

### 6.5.3

#### **Study of SWCNTs in Rats by Warheit et al. of DuPont Company**

Warheit et al. also presented evidence that CNTs produce granulomas in the lungs of treated animals [45]. These authors instilled a suspension containing a laser-synthesized SWCNT product (containing nickel and cobalt) into the trachea of Sprague–Dawley (CrI:CD(SD)IGS BR) rats. In addition to examining lung histopathology, Warheit's group assessed biomarkers of toxicity in bronchoalveolar lavage fluid (BALF) obtained from the treated rats. The animals were given the CNTs (suspended in saline containing 1% Tween 80) at 0, 1, or 5 mg kg<sup>-1</sup> (0, 0.25, or 1.25 mg per rat) and were euthanized at 1, 7, 30, or 90 d after the single treatment. The high dose in this rat study was comparable to the low dose in the NASA mouse study. Histopathological results revealed multifocal granulomas, which became evident 1 month after the treatment (Fig. 6.6). The authors found that instillation of CNT dust produced granulomatous lesions in the lungs of treated rats, and the lesions were non-dose-dependent, non-uniform, and non-progressive. Quartz was given as a positive control, and was observed to produce cytotoxicity, inflammation, and fibrosis in a dose-dependent manner. Study of the BALF showed that SWCNTs induced only a transient increase in the concentration of lactate dehydrogenase (LDH; marker of cytotoxicity) in the 1-d group. Quartz at a high dose produced increases in LDH and protein concentrations at all time points. Unable to find a dose-dependent and time-dependent granulomatous response, or prolonged inflammation in the lungs, coupled with the observations

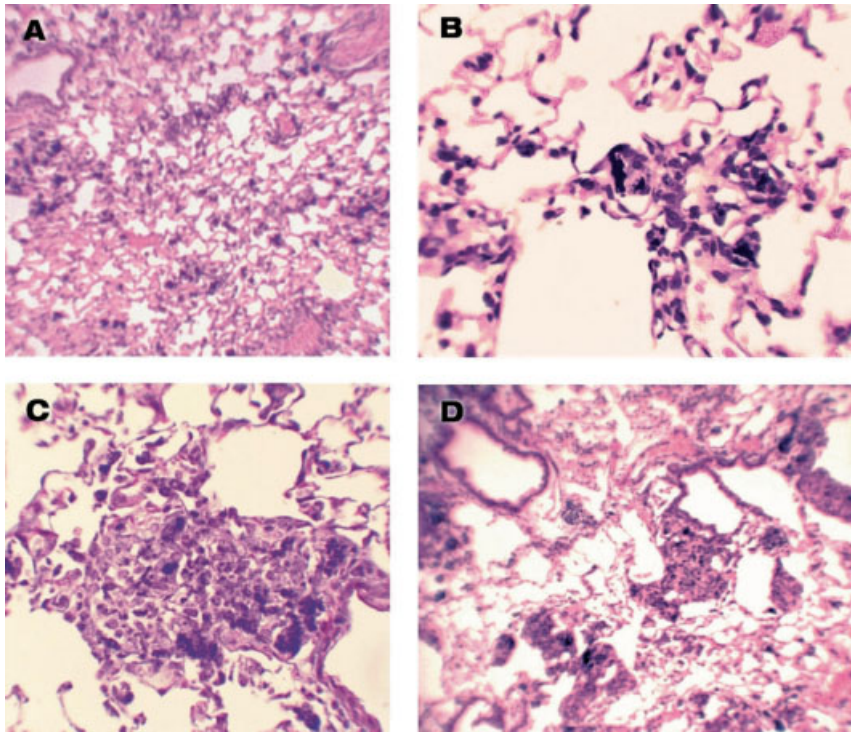


**Fig. 6.5.** Lung tissues from mice intratracheally instilled with 0.1 or 0.5 mg per mouse of a test material and euthanized 7 or 90 days (d) after the single treatment. (A) Carbon black, 0.5 mg, 90 d. Particles were scattered in alveoli, and no tissue reaction was observed. (B) Purified HiPco CNTs, 0.1 mg, 7

d. The figure shows a low-grade granuloma. (C) CarboLex arc-produced CNTs, 0.5 mg, 7 d. A well-defined granuloma is shown. (D) Unprocessed HiPco CNTs, 0.5 mg, 90 d. Granulomas, alveolar wall thickening, and some fibrotic tissue are shown. Magnifications 40–200 $\times$ .

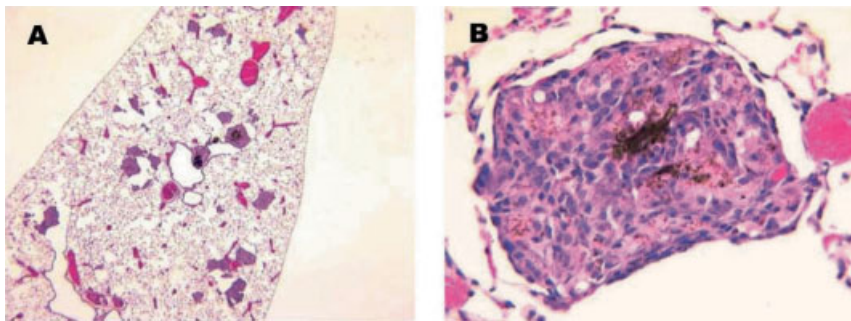


**Fig. 6.6.** Granulomas in lung tissues from rats 1 month after they were intratracheally instilled with 1 mg kg<sup>-1</sup> of laser-synthesized CNTs. (Courtesy of Dr. David Warheit.)

that CNTs have a great tendency to aggregate, Warheit et al. concluded that the granulomatous reaction was a nonspecific response to instilled aggregates of SWCNTs and the results may not be relevant to human exposures [45]. Warheit showed that some instilled CNTs stuck in the major airway and the mechanical blockage suffocated 15% of the high-dose group. The proportion of the dose that clogged the airway must have been substantial. The inability of the dose to reach the alveolar region, where CNT-induced granulomas could occur, may partially explain why the results were both non-dose- and non-time-dependent.

#### 6.5.4

##### **Study of SWCNTs in Mice by Shvedova et al. of NIOSH**

As pointed out above, to address the differences in conclusions about the potential hazard of exposures to SWCNTs drawn by Lam et al. and Warheit et al., Shvedova et al. [46] carried out a comprehensive pulmonary toxicity study in mice (C57CL/6), testing a purified HiPco CNT product (>99% SWCNTs) that was exhaustively subjected to purification to remove metals (final iron content 0.23% by weight). The animals were given a single treatment of CNTs, carbon black, or quartz at a dose of 0, 10, 20, or 40  $\mu\text{g}$  per mouse (about 0, 0.5, 1, or 2  $\text{mg kg}^{-1}$ , respectively). Aqueous suspensions of test dusts were aspirated at the pharyngeal area of mice, allowing droplets to be pulled into the lung during inspiration. The mice were then killed 1, 3, 7, 28, or 60 d after treatment. Histopathological examination of the lungs showed an acute inflammation, early onset of formation of granulomas, and progressive fibrosis. The histopathology was characterized by SWCNT-induced granulomas mainly associated with hypertrophied epithelial cells surrounding the dust aggregates, and diffusive interstitial fibrosis and alveolar wall thickening likely associated with dispersed SWCNTs. The total mass of granulomas in the lungs of mice in the 60-d group increased with an increase in the CNT dose. In general, lung lesions were dose-dependent and progressive, like those reported by Lam et al. [44]. Pulmonary function tests showed increases in functional respiratory deficiencies with increased concentrations of CNTs, a finding consistent with fibrosis. Compared with saline-treated controls, CNT-treated mice showed slower bacterial clearance assessed 7 days after bacterial inoculation. The test doses of quartz and carbon black did not induce granulomas or fibrosis.

Like Warheit et al., Shvedova et al. [46] examined the biomarkers of toxicity in BALF from CNT-treated animals. The results showed increases in total protein concentration, cell counts, concentration of transforming growth factor beta (TGF- $\beta$ ), and LDH and  $\gamma$ -glutamyltranspeptidase activities; these biomarkers of inflammation or cytotoxicity in the lungs were dose-dependent. Shvedova et al. concluded that crystalline silica caused less cytotoxicity than CNTs (compared on an equal-weight basis) and recruited fewer polymorphonuclear leucocytes into the lungs. These biomarker results from mice treated with quartz and SWCNTs differ from those of a similar study in rats reported by Warheit et al. and discussed above [45]. Like Lam et al. [44], Shvedova et al. demonstrated that CNTs were intrinsically

toxic and cautioned that exposures of workers to high concentrations of respirable SWCNT particles may pose a risk of developing some lung lesions.

#### 6.5.5

##### **Study of MWCNTs by Muller et al. of Belgium**

MWCNTs have been shown to produce lung lesions similar to those observed in studies with SWCNTs. Muller et al. tested two forms of MWCNTs, unprocessed (unground) MWCNTs and MWCNTs that had been ground [47]. They reported that 60 days after rats (Sprague–Dawley) were each given a single ITI dose of 0.5, 2, or 5 mg MWCNTs (sonicated and suspended in a normal saline solution containing a dispersing agent, Tween 80) their lungs showed inflammation, granulomas, and fibrosis. The unground CNTs remained in the bronchial lumen and produced collagen-rich granulomas. The bronchial lumen was partially or completely blocked, as in the study by Warheit et al. [45]; very few CNT particles were seen in the parenchymal (alveolar) region. The ground CNTs were “better dispersed” in the parenchyma and in the interstitium induced granulomas consisting of macrophages laden with particles, multinuclear giant cells, and some inflammatory cells, like those reported by Lam et al. [44]. Muller et al. [47] also showed that hydroxyproline and soluble collagen, two biomarkers of fibrosis, increased in the lung tissues in a dose-dependent fashion. BALF obtained from rats 3 days after the CNT treatment showed dose-dependent increases in LDH activity, total protein concentration, and neutrophil number. Muller et al. also concluded that CNTs are potentially toxic and advocated strict industrial hygiene [47].

## 6.6

### **Health Risk Implications**

#### 6.6.1

##### **Toxicity Summary of CNTs and Occupational Exposure Risk**

The results of four histopathology studies reported previously in the literature and reviewed here collectively showed that SWCNTs and MWCNTs themselves were capable of inducing granulomas and other lesions in the lungs, regardless of the process by which they were synthesized and the types and amounts of metals they contained. The metal residues and other impurities played only a small role in the formation of these pulmonary lesions (see Lam et al. [1] for detailed discussion). Dust of respiratory size is difficult to separate from bulk materials because CNT bundles or ropes tend to stick to each other. Moreover, all four studies were conducted similarly by ITI to expose a rat or mouse to a fine-particle suspension of a CNT dust ultrasonicated in an aqueous system containing a dispersing agent, or by pharyngeal aspiration of a CNT suspension obtained by boiling and sonicating CNTs. These instillation or aspiration studies, involving CNT particles mechanically dispersed in an aqueous system containing a dispersion agent, are considered

screening assays of CNTs for potential pulmonary toxicity [44, 45]. However, even though these studies do not answer the important health risk question of whether airborne CNT particles can reach the lungs, they do reveal the intrinsic toxicity of CNTs. The findings convey the important message that if a CNT product contains a substantial amount of respirable dust that reaches the lung at a high enough concentration it is likely to produce the types of serious lung lesions seen in rodents. Certainly, it would be very important to conduct inhalation studies to confirm these pathology findings; data from inhalation studies are also needed for setting occupational exposure limits. Because it is difficult to conduct an inhalation study on CNTs, inhalation toxicity data will not be available for some time.

Lam et al. [44] and Shvedova et al. [46], who used carbon black and quartz as references in their comparative toxicity studies, concluded that if CNTs reach the lungs, under the test conditions described here and on an equal-weight basis they are much more toxic than carbon black and can be more toxic than quartz, chronic inhalation of which is considered a serious occupational health hazard. Study with MWCNTs led Muller et al. [47] to reach the same conclusion, i.e., that CNTs are intrinsically toxic. Therefore, it is prudent to assume that if significant amounts of airborne fine CNT particles were present in a workplace, occupational exposures to CNTs could produce substantial injury in the lungs and potentially the upper respiratory tract (see Lam et al. [1] for a detailed risk assessment of occupational exposures). If CNT dust is present in a work environment, strategies to minimize human exposure to it should be implemented.

### 6.6.2

#### **Impact of SWCNTs on Environmental Health**

The manufacture of CNTs is still on a small scale and the products remain expensive; the current impact of manufactured CNTs on environmental health is nonexistent or very minimal. However, if millions of tons of CNTs are produced annually some day, as predicted by Richard Smalley [28], and if the CNT industry achieves the goal of charging “a couple dollars a pound” for CNTs [25], then CNTs will likely be incorporated or formulated into fabric, plastic, composite materials, and household commodities that will touch all aspects of human life. Then CNT-containing industrial wastes and degraded CNT-containing materials will probably appear in the environment (Fig. 6.2). Will CNTs bioaccumulate in the environment? Will ingested SWCNTs in the alimentary canal reach internal organs to produce toxicity? Studies will need to address these environmental health issues.

### 6.6.3

#### **Toxicity of MWCNTs and Impact on Environmental Health**

Murr and colleagues found MWCNTs in fine particulate matter generated from combustion of natural gas in typical kitchen ranges [31–33]. Finding MWCNTs in PM collected indoors and outdoors, they concluded [32] that MWCNTs and carbonaceous nanoparticles are ubiquitous in the environment. They further speculated

that MWCNTs are a major component of indoor and outdoor airborne PM. Because MWCNTs are ubiquitously present in fine airborne particulate aggregates in our environments [34], it is reasonable to postulate that all humans are exposed to low levels of MWCNTs.

Dockery et al. found a positive correlation between fine particulate air pollution and excess mortality in six U.S. cities [56]. In a large-scale epidemiological study with 1.2 million adults, Pope et al. [57, 58] found that fine PM in ambient air is a risk factor associated with cardiopulmonary mortality and cardiovascular and pulmonary diseases. The underlying mechanisms by which exposure to fine PM might play a role in the pathogenesis of cardiopulmonary diseases are not known [59]. Pollutants may produce oxidative lung damage and inflammation [60]. Seaton et al. have proposed that fine particles deposited in the lung provoke alveolar inflammation, which causes potentially harmful cytokines to be released [61].

The pulmonary toxicity of SWCNTs and MWCNTs are similar; collectively, CNTs can produce lung lesions and biomarkers of toxicity, such as inflammation, fibrosis, granulomas, harmful cytokine release, and oxidative biochemical toxicological changes. Shvedova et al. also showed that SWCNTs impaired pulmonary functions and bacterial clearance. In a cell culture study, Monteiro-Riviere et al. have found that MWCNTs caused release of the proinflammatory cytokine interleukin 8 [62].

Gauderman et al. have found that adverse effects on the growth of lung functions in teenagers were associated with exposures to NO<sub>2</sub>, acid vapor, fine PM, and elemental carbon, which had the highest correlation ( $p = 0.007$ ) [63]. Fine PM, derived primarily from combustion, contains elemental carbon; MWCNTs, which are also produced by combustion, were found in fine PM collected in outdoor air in El Paso and Houston. The results of the four studies reviewed here showed that manufactured MWCNTs and SWCNTs were much more toxic than ultrafine carbon black (used as a negative control by Muller et al. [47] and Shvedova et al. [46]) and graphite (used in the study by Warheit et al. [45]). It is probably true that environmental MWCNTs are a minor component in fine PM, but the unique toxicity of CNTs, which has not been seen with other elemental forms of carbon, raises a concern about these combustion-generated fibrous MWCNTs. Very possibly, they play a significant role in the pathogenesis of pollution-related cardiopulmonary diseases. Confirmation of this postulation requires results from toxicity studies on this newly-identified environmental pollutant.

### Acknowledgment

The authors thank Dr. J. Krauhs for technical editing and Dr. D. Warheit of DuPont Company, Dr. A. Maynard of NIOSH, Dr. L. Murr of University of Texas at El Paso, TX, Dr. J. Rodriguez of University of Barcelona, Spain, and Springer Publishing Company, New York, NY, for granting permission to use their figures.

## References

- 1 C.-w. LAM, J. T. JAMES, R. MCCLUSKEY, S. AREPALI, R. L. HUNTER, A review of carbon nanotube toxicity and assessment of potential occupational and human health, *Crit. Rev. Toxicol.* **2006**, in press.
- 2 White House Press Secretary, National Nanotechnology Initiative: Leading to the next industrial revolution. Press release January 21, 2000, in *What's New at the White House*, U. S. Government, Washington, DC, **2000**, [http://clinton4.nara.gov/textonly/WH/New/html/20000121\\_4.html](http://clinton4.nara.gov/textonly/WH/New/html/20000121_4.html), accessed May 25, 2005.
- 3 National Science and Technology Council, *National Nanotechnology Initiative: Research and Development Supporting the Next Industrial Revolution. Supplement to the President's FY 2004 Budget*, National Science and Technology Council, Washington, DC, **2003**, <http://nano.gov/html/res/fy04-pdf/fy04-main.html>, accessed May 25, 2005.
- 4 M. Roco, Government nanotechnology funding: An international outlook, *J. Minerals, Metals Mater. Soc.* **2002**, *54*, 22–23.
- 5 H. W. KROTO, J. R. HEATH, S. C. O'BRIEN, R. F. CURL, R. E. SMALLEY, C<sub>60</sub>: Buckminsterfullerene, *Nature* **1985**, *318*, 162–163.
- 6 S. IIJIMA, Helical microtubules of graphitic carbon, *Nature* **1991**, *354*, 56–58, <http://www.nature.com/nature/journal/v354/n6348/abs/354056a0.html>, accessed May 25, 2005.
- 7 S. IIJIMA, Carbon nanotube, NEC Laboratories, **2004**, <http://www.labs.nec.co.jp/Eng/innovative/E1/top.html>, accessed June 10, 2005.
- 8 T. W. EBBESEN, P. M. AJAYAN, Large-scale synthesis of carbon nanotubes, *Nature* **1992**, *358*, 220–222.
- 9 S. IIJIMA, T. ICHIHASHI, Single-shell carbon nanotubes of 1-nm diameter, *Nature* **1993**, *363*, 603.
- 10 T. GUO, P. NIKOLAEV, A. THESS, D. T. COLBERT, R. E. SMALLEY, Catalytic growth of single-walled nanotubes by laser vaporization, *Chem. Phys. Lett.* **1995**, *243*, 49–54.
- 11 A. THESS, R. LEE, P. NIKOLAEV, H. J. DAI, P. PETIT, J. ROBERT, C. H. XU, Y. H. LEE, S. G. KIM, A. G. RINZLER, D. T. COLBERT, G. E. SCUSERIA, D. TOMANEK, J. E. FISCHER, R. E. SMALLEY, Crystalline ropes of metallic carbon nanotubes, *Science* **1996**, *273*, 483–487, <http://www.sciencemag.org/cgi/content/abstract/273/5274/483>, accessed May 25, 2005.
- 12 J. KONG, A. M. CASSELL, H. DAI, Chemical vapor deposition of methane for single-walled carbon nanotubes, *Chem. Phys. Lett.* **1998**, *292*, 567–574.
- 13 Z. F. REN, Z. P. HUANG, J. W. XU, J. H. WANG, P. BUSH, M. P. SIEGAL, P. N. PROVENCIO, Synthesis of large arrays of well-aligned carbon nanotubes on glass, *Science* **1998**, *282*, 1105–1107.
- 14 P. NIKOLAEV, M. J. BRONIKOWSKI, R. K. BRADLEY, F. ROHMUND, D. T. COLBERT, K. A. SMITH, R. E. SMALLEY, Gas-phase catalytic growth of single-walled carbon nanotubes from carbon monoxide, *Chem. Phys. Lett.* **1999**, *313*, 91–97.
- 15 A. MOISALA, A. G. NASIBULIN, E. I. KAUPPINEN, The role of metal nanoparticles in the catalytic production of single-walled carbon nanotubes – a review, *J. Phys.: Condensed Matter* **2003**, *15*, S3011–S3035.
- 16 P. BALL, Focus carbon nanotubes, *Nat. Scienceupdate* **1999**, <http://www.nature.com/nsu/991202/991202-1.html>, accessed May 25, 2005.
- 17 S. AREPALI, P. NIKOLAEV, W. HOLMES, B. S. FILES, Production and measurements of individual single-wall nanotubes and small ropes of carbon, *Appl. Phys. Lett.* **2001**, *78*, 1610–1612.
- 18 P. BALL, Roll up for the revolution, *Nature* **2001**, *414*, 142–144, <http://www.phys.washington.edu/~cobden/>

- P600/Philip\_Ball\_tube\_news.pdf, accessed May 25, 2005.
- 19 Rice University, Small is big @ Rice! The world's largest nanotube model, in *blogs@Rice*, Rice University, 2005, [http://blogs.rice.edu/blog/templates/blog\\_274/nanotube/files/nano-program.pdf](http://blogs.rice.edu/blog/templates/blog_274/nanotube/files/nano-program.pdf), accessed June 13, 2005.
  - 20 A. JENSEN, J. R. HAUPTMANN, J. NYGÅRD, J. SADOWSKI, P. E. LINDELOF, Hybrid devices from single wall carbon nanotubes epitaxially grown into a semiconductor heterostructure, *Nano Lett.* 2004, 4, 349–352, <http://pubs.acs.org/cgi-bin/jcen?nalefd/4/i02/html/nl0350027.html>, accessed June 14, 2005.
  - 21 H. STAHL, *Electronic Transport in Ropes of Single Wall Carbon Nanotubes* (Doctoral Thesis Dissertation), Aachen University of Technology, 2000, [http://sylvester.bth.rwth-aachen.de/dissertationen/2000/28/00\\_28.pdf](http://sylvester.bth.rwth-aachen.de/dissertationen/2000/28/00_28.pdf), accessed September 7, 2005.
  - 22 P. C. P. WATTS, W. K. HSU, D. P. RANDALL, H. W. KROTO, D. R. M. WALTON, Non-linear current-voltage characteristics of electrically conducting carbon nanotube-polystyrene composites, *Phys. Chem. Chem. Phys.* 2002, 4, 5655–5662.
  - 23 Wikipedia, Carbon nanotube, 2005, [http://en.wikipedia.org/wiki/Carbon\\_nanotube](http://en.wikipedia.org/wiki/Carbon_nanotube), accessed August 30, 2005.
  - 24 R. E. SMALLEY, Nanotechnology. Prepared written statement and supplemental material of R. E. SMALLEY, Rice University, June 22, 1999, in *U.S. House of Representatives Committee on Science, Basic Research Subcommittee Hearings*, U. S. Government, Washington, DC, 1999, pp. 1–17, [http://www.house.gov/science/smalley\\_062299.htm](http://www.house.gov/science/smalley_062299.htm), accessed September 7, 2005.
  - 25 T. BEARDEN, Interview: Nobel Prize Winner Dr. Richard Smalley, in *Online NewsHour*, Public Broadcasting System, 2003, <http://www.pbs.org/newshour/science/hydrogen/smalley.html>, accessed June 10.
  - 26 BuckyUSA, BuckyUSA – price list, 2005, <http://home.flash.net/~buckyusa/page17.html>, accessed October 6, 2005.
  - 27 P. A. BARON, A. D. MAYNARD, M. FOLEY, *Evaluation of Aerosol Release during the Handling of Unrefined Single Walled Carbon Nanotube Material*, Tech. Report No. NIOSH DART-02-191, National Institute of Occupational Safety and Health, Cincinnati, OH, 2003.
  - 28 G. TAUBES, Nanotechnology. An interview with Dr. RICHARD SMALLEY, *ISI Essential Sci. Indicators Special Top.* 2002, <http://www.esi-topics.com/nano/interviews/Richard-Smalley.html>, accessed May 25, 2005.
  - 29 Anonymous, 40 CFR Part 763, *Fed. Regist.* 1989, 54.
  - 30 B. O. BOSKOVIC, V. STOLOJAN, R. U. A. KHAN, S. HAQ, S. R. P. SILVA, Large-area synthesis of carbon nanofibres at room temperature, *Nat. Mater.* 2002, 1, 165–168.
  - 31 W. MERCHAN-MERCHAN, A. V. SAVELIEV, L. A. KENNEDY, Carbon nanostructures in opposed-flow methane oxy-flames, *Combust. Sci. Technol.* 2003, 175, 2217–2236.
  - 32 J. J. BANG, P. A. GUERRERO, D. A. LOPEZ, L. E. MURR, E. V. ESQUIVEL, Carbon nanotubes and other fullerene nanocrystals in domestic propane and natural gas combustion streams, *J. Nanosci. Nanotechnol.* 2004, 4, 716–718.
  - 33 L. E. MURR, J. J. BANG, D. A. LOPEZ, P. A. GUERRERO, E. V. ESQUIVEL, A. R. CHOUDHURI, M. SUBRAMANYA, M. MORANDI, A. HOLIAN, Carbon nanotubes and nanocrystals in methane combustion and the environmental implications, *J. Mater. Sci.* 2004, 39, 2199–2204.
  - 34 L. E. MURR, J. J. BANG, E. V. ESQUIVEL, P. A. GUERRERO, D. A. LOPEZ, Carbon nanotubes, nanocrystal forms and complex nanoparticle aggregates in common fuel-gas combustion source and ambient air, *J. Nanoparticle Res.* 2004, 5, 1–11.
  - 35 J. J. BANG, L. E. MURR, Collecting and characterizing atmospheric nanoparticles, *J. Minerals, Metals Mater. Soc.* 2002, 54, 28–30.



- 36 E. V. ESQUIVEL, L. E. MURR, A TEM analysis of nanoparticulates in a polar ice core, *Mater. Characterization* **2004**, *52*, 15–25.
- 37 Natural Gas Supply Association, Natural gas and the environment, **2004**, <http://www.naturalgas.org/environment/naturalgas.asp>, accessed August 30, 2005.
- 38 National Energy Foundation, Fuel consumption stats, **2002**, <http://www.nef1.org/ea/eastats.html>, accessed September 8, 2005.
- 39 U.S. Environmental Protection Agency, PM2.5. Objectives and history, in *Laboratory and Field Operations – PM 2.5. Ambient Air Quality Monitoring Program*, U.S. Environmental Protection Agency, Washington, DC, **2003**, <http://www.epa.gov/region4/sesd/pm25/p2.htm>, accessed September 9, 2005.
- 40 F. E. HUGGINS, G. P. HUFFMAN, W. P. LINAK, C. A. MILLER, Quantifying hazardous species in particulate matter derived from fossil-fuel combustion, *Environ. Sci. Technol.* **2004**, *38*, 1836–1842.
- 41 J. SCHWARTZ, G. NORRIS, T. LARSON, L. SHEPPARD, C. CLAIBORNE, J. KOENIG, Episodes of high coarse particle concentrations are not associated with increased mortality, *Environ. Health Perspect.* **1999**, *107*, 339–342, <http://ehp.niehs.nih.gov/members/1999/107p339-342schwartz/schwartz-full.html>, accessed September 12, 2005.
- 42 U.S. Environmental Protection Agency, Research opportunities: Epidemiologic research on health effects of long-term exposure to ambient particulate matter and other air pollutants, **2003**, [http://es.epa.gov/ncer/rfa/current/2003\\_pm\\_epi.html](http://es.epa.gov/ncer/rfa/current/2003_pm_epi.html), accessed September 7, 2005.
- 43 I. AMATO, The soot that could change the world, *Fortune Mag.* **2001**, *June 25*, <http://www.nano-lab.com/fortune.html>, accessed August 30, 2005.
- 44 C.-W. LAM, J. T. JAMES, R. McCLUSKEY, R. L. HUNTER, Pulmonary toxicity of single-wall carbon nanotubes in mice 7 and 90 days after intratracheal instillation, *Toxicol. Sci.* **2004**, *77*, 126–134.
- 45 D. B. WARHEIT, B. R. LAURENCE, K. L. REED, D. H. ROACH, G. A. M. REYNOLDS, T. R. WEBB, Comparative pulmonary toxicity assessment of single-wall carbon nanotubes in rats, *Toxicol. Sci.* **2004**, *77*, 117–125.
- 46 A. A. SHVEDOVA, E. R. KISIN, R. MERCER, A. R. MURRAY, V. J. JOHNSON, A. I. POTAPOVICH, Y. Y. TYURINA, O. GORELIK, S. AREPALLI, D. SCHWEGLER-BERRY, A. F. HUBBS, J. ANTONINI, D. E. EVANS, B. K. KU, D. RAMSEY, A. MAYNARD, V. E. KAGAN, V. CASTRANOVA, P. BARON, Unusual inflammatory and fibrogenic pulmonary responses to single walled carbon nanotubes in mice, *Am. J. Physiol. Lung Cell. Mol. Physiol.* **2005**, *289*, L698–L708.
- 47 J. MULLER, F. HUAUX, N. MOREAU, P. MISSON, J. F. HEILLIER, M. DELOS, M. ARRAS, A. FONSECA, J. B. NAGY, D. LISON, Respiratory toxicity of multi-wall carbon nanotubes, *Toxicol. Appl. Pharmacol.* **2005**, *207*, 221–231.
- 48 J.-P. SALVETAT, J.-M. BONARD, N. THOMSON, A. KULIK, L. FORRÓ, Mechanical properties of carbon nanotubes, *Appl. Phys. A* **1999**, *69*, 255–260.
- 49 C. P. SABAITIS, B. K. LEONG, D. A. ROP, C. S. AARON, Validation of intratracheal instillation as an alternative for aerosol inhalation toxicity testing, *J. Appl. Toxicol.* **1999**, *19*, 133–140.
- 50 B. K. LEONG, J. K. COOMBS, C. P. SABAITIS, D. A. ROP, C. S. AARON, Quantitative morphometric analysis of pulmonary deposition of aerosol particles inhaled via intratracheal nebulization, intratracheal instillation or nose-only inhalation in rats, *J. Appl. Toxicol.* **1998**, *18*, 149–160.
- 51 K. E. DRISCOLL, D. L. COSTA, G. HATCH, R. HENDERSON, G. OBERDORSTER, H. SALEM, R. B. SCHLESINGER, Intratracheal instillation as an exposure technique for the evaluation of respiratory tract toxicity: Uses and limitations, *Toxicol. Sci.* **2000**, *55*, 24–35.

- 52 C.-W. LAM, J. T. JAMES, J. N. LATCH, R. F. HAMILTON, A. HOLIAN, Pulmonary toxicity of simulated lunar and Martian dusts in mice. II. Biomarkers of acute responses after intratracheal instillation, *Inhal. Toxicol.* **2002**, *14*, 917–928.
- 53 C.-W. LAM, J. T. JAMES, R. MCCLUSKEY, S. COWPER, C. MURO-CACHO, Pulmonary toxicity of simulated lunar and Martian dusts in mice. I. Histopathology 7 and 90 days after intratracheal instillation, *Inhal. Toxicol.* **2002**, *14*, 901–916.
- 54 A. HUCZKO, H. LANGE, E. CAŁKO, H. GRUBEK-JAWORSKA, P. DROSZCZ, Physiological test of carbon nanotubes: Are they asbestos-like? *Fullerenes, Nanotubes, Carbon Nanostruct.* **2001**, *9*, 251–254.
- 55 A. G. RINZLER, J. LIU, H. DAI, P. NIKOLAEV, C. B. HUFFMAN, F. J. RODRIGUEZ-MACIAS, P. J. BOUL, A. H. LU, D. HEYMANN, D. T. COLBERT, R. S. LEE, J. E. FISCHER, A. M. RAO, P. C. EKLUND, R. E. SMALLEY, Large-scale purification of single-wall carbon nanotubes: Process, product, and characterization, *Appl. Phys. A* **1998**, *67*, 29–37.
- 56 D. W. DOCKERY, C. A. POPE, 3rd, X. XU, J. D. SPENGLER, J. H. WARE, M. E. FAY, B. G. FERRIS, JR, F. E. SPEIZER, An association between air pollution and mortality in six U.S. cities, *N. Engl. J. Med.* **1993**, *329*, 1753–1759.
- 57 C. A. POPE, R. T. BURNETT, M. J. THUN, E. E. CALLE, D. KREWSKI, K. ITO, G. D. THURSTON, Lung cancer, Cardiopulmonary mortality, and long-term exposure to fine particulate air pollution, *JAMA* **2002**, *287*, 1132–1141.
- 58 C. A. POPE, 3rd, R. T. BURNETT, G. D. THURSTON, M. J. THUN, E. E. CALLE, D. KREWSKI, J. J. GODLESKI, Cardiovascular mortality and long-term exposure to particulate air pollution: Epidemiological evidence of general pathophysiological pathways of disease, *Circulation* **2004**, *109*, 71–77.
- 59 C. A. POPE, Epidemiology of fine particulate air pollution and human health: Biologic mechanisms and who's at risk? *Environ. Health Perspect.* **2000**, *108*(Suppl. 4), 713–723.
- 60 C. A. POPE, D. W. DOCKERY, R. E. KANNER, G. M. VILLEGAS, J. SCHWARTZ, Oxygen saturation, pulse rate, and particulate air pollution: A daily time-series panel study, *Am. J. Respir. Crit. Care Med.* **1999**, *159*, 354–356.
- 61 A. SEATON, W. MACNEE, K. DONALDSON, D. GODDEN, Particulate air pollution and acute health effects, *Lancet* **1995**, *345*, 176–178.
- 62 N. A. MONTEIRO-RIVIERE, R. J. NEMANICH, A. O. INMAN, Y. Y. WANG, J. E. RIVIERE, Multi-walled carbon nanotube interactions with human epidermal keratinocytes, *Toxicol. Lett.* **2005**, *155*, 377–384.
- 63 W. J. GAUDERMAN, E. AVOL, F. GILLILAND, H. VORA, D. THOMAS, K. BERHANE, R. MCCONNELL, N. KUENZLI, F. LURMANN, E. RAPPAPORT, H. MARGOLIS, D. BATES, J. PETERS, The effect of air pollution on lung development from 10 to 18 years of age, *N. Engl. J. Med.* **2004**, *351*, 1057–1067.

## 7

## Toxicity of Nanomaterials – New Carbon Conformations and Metal Oxides

Harald F. Krug, Katrin Kern, Jörg M. Wörle-Knirsch,  
and Silvia Diabaté

## 7.1

### Introduction

Nanomaterials are on the same scale as most elements of living cells, including proteins, nucleic acids, lipids and even cellular organelles. When considering nanoparticles it must be asked how man-made nanostructures can interact with or influence biological systems. On the one hand, nanosystems are specifically engineered to interact with biological systems for particular medical or biological applications. On the other hand, the large-scale production of nanoparticles for either non-medical applications or as side-product of combustion processes may affect a wide range of organisms throughout the environment. Since the 1970s, an increasing number of investigations concerning the use of nanoscale structures, e.g., liposomes, for drug transport and comparable applications have been undertaken [1–9]. In addition to liposomes, nanoparticles produced from other materials came into the focus of physicians for various treatments of diseases [10–16]. This work aims to design inert auxiliary accompanying materials and to use body-friendly and biodegradable excipients. However, dependent on their target organ and functionality, not all of these materials are degradable and some stay in the body for long periods. In light of this, side effects and foreign body reactions may be detectable and a good local and systemic tolerance during and after medication should be a condition *sine qua non*.

Nanostructured materials come into contact with biological systems not only through their use in drug delivery systems or for gene transfer. They are also produced for food and cosmetic chemistry and many other technical applications (Tab. 7.1). The increasing production, particularly of metal oxide nanoparticles and new carbon materials, will enhance the possible exposure at work places, packing stations and during application of the products [17]. In addition, waste treatment and containment at the end of a products life cycle must be considered. For all these reasons, it is of great interest to determine how these materials, when coming in contact with living organisms, are taken up, transported in or through cell layers, and affect biological functions. To cover these questions we review the latest

**Tab. 7.1.** Examples of metal oxides and carbon modifications manufactured as nanomaterials of commercial interest.

Type	Examples for use
Metal oxides <ul style="list-style-type: none"> <li>• Silica (SiO<sub>2</sub>)</li> <li>• Titania (TiO<sub>2</sub>)</li> <li>• Alumina (Al<sub>2</sub>O<sub>3</sub>)</li> <li>• Iron oxide (Fe<sub>3</sub>O<sub>4</sub>, Fe<sub>2</sub>O<sub>3</sub>)</li> <li>• Zirconia (ZrO<sub>2</sub>)</li> <li>• Zinc dioxide (ZnO<sub>2</sub>)</li> </ul>	<ul style="list-style-type: none"> <li>• Additives for polymer composites</li> <li>• UV-A protection</li> <li>• Solar cells</li> <li>• Pharmacy/medicine</li> <li>• Additives for scratch resistance coatings</li> </ul>
Carbon modifications <ul style="list-style-type: none"> <li>• Carbon black</li> </ul>	<ul style="list-style-type: none"> <li>• Tires, printer, copier</li> </ul>
Fullerenes <ul style="list-style-type: none"> <li>• Buckminsterfullerene (C<sub>60</sub>)</li> </ul>	<ul style="list-style-type: none"> <li>• Mechanical and tribological applications/additives to grease</li> </ul>
Carbon nanotubes <ul style="list-style-type: none"> <li>• Single-wall carbon nanotubes</li> <li>• Multi-wall carbon nanotubes</li> </ul>	<ul style="list-style-type: none"> <li>• Additives for polymer composites</li> <li>• Electronic field emitters</li> <li>Batteries</li> <li>Fuel cells</li> </ul>
Carbon nanofibers <ul style="list-style-type: none"> <li>• Various conformations</li> </ul>	<ul style="list-style-type: none"> <li>• Mechanical and tribological applications</li> <li>Carrier for catalysts</li> <li>Additives for polymer composites</li> <li>Elastic foams</li> </ul>

results from various studies on the biological effects of nanoparticles that may be the basis for adverse effects, especially in humans. Because metal oxides are the most prominent produced variants of nanoparticles and new carbon modifications are the most promising ones we focus on these two types with respect to their cellular uptake and possible influence on important cellular mechanisms *in vitro*. The effects of ambient particulate matter or particulate emissions from combustion devices such as diesel engines or oil burners are not reviewed. These particles, produced unintentionally with a complex chemical composition, are released into the environment and affect the general population. Although these particles stimulated much concern over their health effects, this chapter concentrates on the effects of intentionally produced nanoparticles of low solubility with well-known chemical composition, form and size to provide condensed information for a possible occupational exposure. Our short overview on biological hazards ends with a more general aspect of the risks connected with the production and use of nano-

materials and, on the other hand, the opportunities that are an important component in all long-term considerations.

### 7.1.1

#### **Nanoscale Materials and Adverse Health Effects: Precautionary Measures**

Although nanoparticles have been used in various products for several decades, the expected increase of production and use of newly developed materials makes the question of their safety to life and the environment increasingly important. However, classical risk regulation is not adequate because the risk can not be quantified. At this early stage, where most of the materials are under development and produced only in small amounts for research laboratories, precautionary measures can be taken to keep exposure below particular thresholds and avoid possible adverse effects by employing the “as low as reasonably achievable – ALARA” principle. As soon as the conditions required for the risk management approach are no longer fulfilled, controversies and ambivalent situations result. This is especially the case if fundamental knowledge concerning the toxicity of these materials is missing, controversial, or based on not sufficiently validated experimental models. In past cases, severe adverse effects resulting from the implementation of new materials or technologies were not been detected at an early stage (e.g., asbestos) and the resulting health, environmental, and economic damage has spurred calls for stronger regulatory measures. These debates resulted in the implementation of the precautionary principle in the European Union that reached wide international agreement during the Earth Summit (United Nations Conference on Environment and Development, UNCED) in Rio de Janeiro 1992 and became part of Agenda 21. Based on this, several demands have to be made for nanotechnology and its products:

1. Without knowledge of possible adverse effects, nanoparticle exposure should be avoided at work places as well as in the population and the environment.
2. Multiple studies are necessary to clarify the biological effects of nanoparticles, with the caveat that different materials, sizes and surface characteristics often behave differently.
3. As with normal chemicals, extrapolation from *in vitro* system and/or animal experiments with regards to a specific nanoparticle is reasonable for judging human exposure to the nanoparticle in question, but can not be the base for a fundamental evaluation or assessment of nanoparticles in general.

As past experience has illustrated, precautionary measures are needed for nanotechnological developments, new materials, and nanoparticles [18, 19]. However, the call for a moratorium on nanotechnology is unrealistic because a moratorium for the chemical, physical and pharmaceutical industries (new substances and new techniques are possible new hazards and risks) would logically follow. From the point of view of toxicologists, the database of biological effects of nanoparticles must be increased by intensifying research on adverse health effects of these new

## Risk Assessment

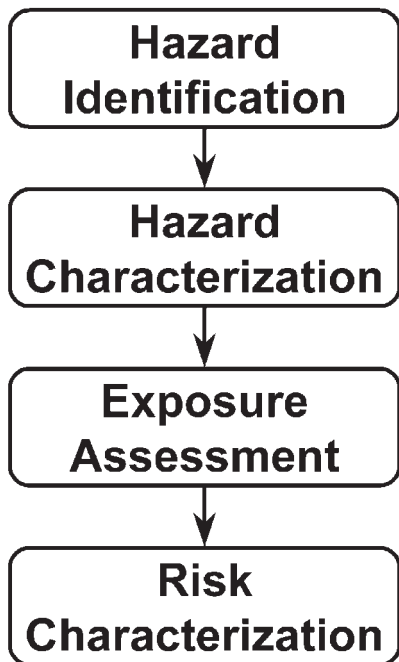


Fig. 7.1. Sequence of events leading to risk assessment.

materials. Most of the presented data in this chapter on nanosized metal oxides and carbonaceous materials are either preliminary or poorly confirmed by other research groups. So far, few nanomaterials have been investigated intensely. These two nanomaterial categories are in production for commercial applications and, therefore, several studies on their health effects have already been performed, whereas information on the impact of nanomaterials on the environment is rare and hence considered marginally.

### 7.1.2

#### **Hazard Identification and Exposure Estimation**

The health and safety issues related to metal oxides and carbon nanomaterials are in a very early phase. Hence, it seems premature to draw far-ranging conclusions regarding the potential hazards related to exposures to these materials. Since the toxicology database for inhalation or dermal exposure to these nanomaterials is rather sparse, efforts to obtain this information must be intensified. Most important is the development of methodologies and protocols concomitant with the implementation of hazard/toxicity studies, as well as workplace exposure assess-

ments, to better ascertain the impact of nanomaterials on human health. For a valid risk assessment both parts of the following equation must be taken into account:

$$\text{Risk} = \text{Exposure} \times \text{Hazard}$$

Within the risk assessment procedure, hazard identification is the first step (Fig. 7.1). Because of the lack of knowledge, it is an open question as to whether established mechanisms of risk analysis and risk regulation may be applied to nanotechnology. Regardless, both hazard characterization and exposure assessment are fundamental pre-requisites, leading to risk characterization.

## 7.2

### Production and Use of “New Carbon Modifications” and Metal Oxides

Nanoscaled insoluble metal oxides are used in applications in almost all fields of technology and industry (Tab. 7.1). They are used as additives in sun screens and textiles to block UV light ( $\text{TiO}_2$ ), to clear apple juice and beer ( $\text{SiO}_2$ ) as well as to degrade toxic chemical waste very efficiently ( $\text{MgO}$ ). While only poor data is available on the toxicity of most synthesized nanoparticles, most investigations on these new materials have been done with titania and silica. At present the assessment of nanoscaled metal oxide toxicity is focused on free and primary particles. As nanoparticles are sintered and agglomerated to larger structures, they lose most of the vast toxic potential to human health that appears in primary particles.

Carbonaceous particles are generated by pyrolysis of gaseous or liquid hydrocarbons, or by spark generation between two graphite electrodes. The most common product is *carbon black*, consisting of amorphous, variably sized colloidal particles of elemental carbon (Fig. 7.2). In contrast to soot, which results from incom-

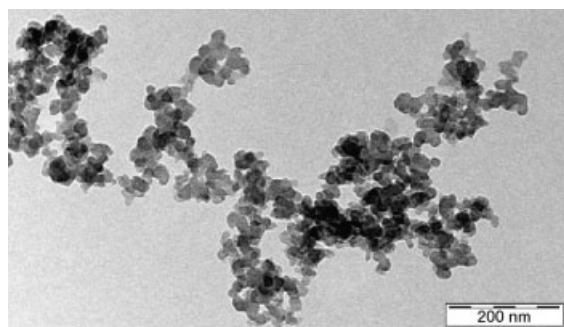


**Fig. 7.2.** Transmission electron micrograph of carbon black (Printex 90), showing aggregates of primary particles with an average diameter of 14 nm. (T. Detzel, ITG.)

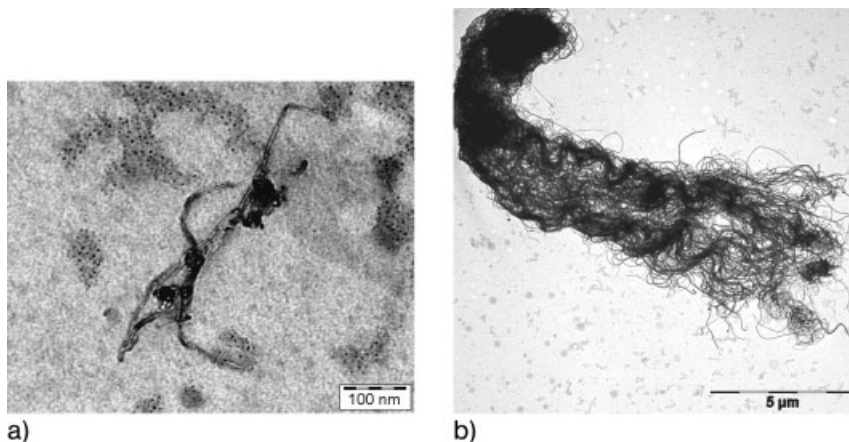


**Fig. 7.3.** Transmission electron micrograph of (a) single SWCNT and (b) MWCNTs forming a bundle. (T. Detzel, ITG.)

plete combustion of carbon-containing material, carbon black contains only low amounts of solvent-extractable organic matter. The material is used as an additive in the rubber of automobile tires, in inks, batteries and protective coatings.

Buckyballs (also known as fullerenes) are cage-like molecules, e.g. the spherical buckminsterfullerene, which consists of 60 carbon atoms ( $C_{60}$ ) and was discovered in the 1980s [20]. They can be generated in the arc between two graphite electrodes in a helium atmosphere. The heat vaporizes the graphite, and fullerenes form as the gaseous carbon cools.

Carbon fibers consisting of amorphous carbon with a diameter of 7–10  $\mu\text{m}$  have been produced by similar methods since the 1980s. The fibers are embedded in resin or plastic to produce composite materials used in aerospace, automotive, sports goods, and prosthetic industries. By modification of the production method, long tube-like *carbon nanotubes* are formed [21]. Single-walled carbon nanotubes (SWCNTs) have a diameter of 1–2 nm and are up to 100  $\mu\text{m}$  long. Multi-walled carbon nanotubes (MWCNTs) consist of several layers of carbon cylinders, which increases the diameter to 10–30 nm (Fig. 7.3). This new material has high potential for new commercial products because it exhibits very interesting properties such as great tensile strength, high conductivity, or unique electronic features. Therefore, it is predicted that tons of carbon nanotubes will be produced worldwide every year in the near future [22].

Recently, carbon fibers with nanometer dimensions have been synthesized [23]. The diameters range from 60 to 200 nm and, unlike carbon nanotubes, they do not possess a helical carbon arrangement (Fig. 7.4). There is evidence that when carbon nanofibers are used as an orthopedic or dental material some of the common problems associated with implant material such as insufficient cytocompatibility may be avoided.



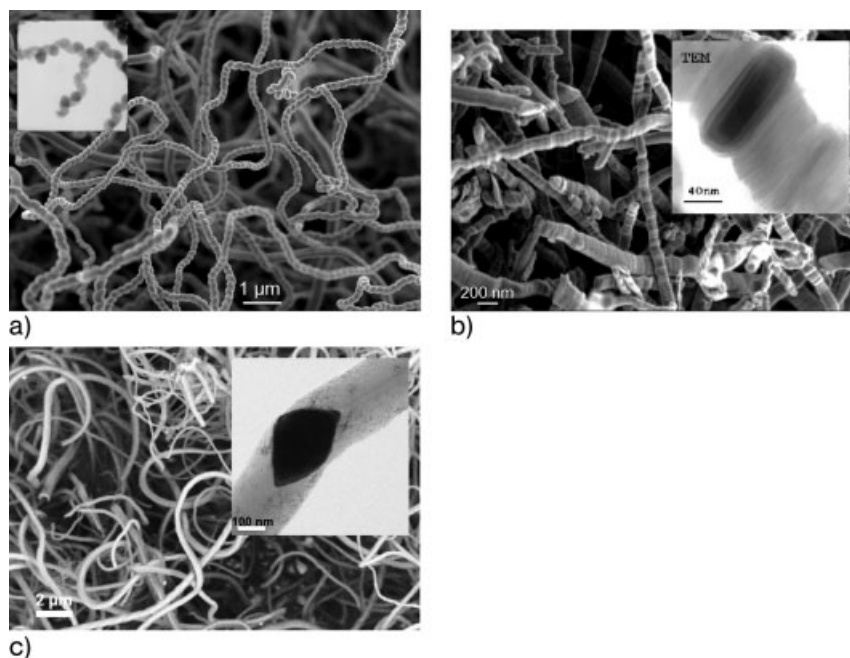


**Fig. 7.4.** Carbon nanofibers of different size and properties. (a) Screws (CNF-SC) are 50 to 200 nm in diameter and 1 to 10 µm long (upper left). (b) Platelets (CNF-PL) are between 150 and 250 nm in diameter and 5–50 µm long. (c) Herringbones (CNF-HB) are

the thickest and shortest fibers, with a diameter of 200–600 nm and a length of 0.5 to 5 µm. These fibers are used as catalysts, part of composite materials, different polymers etc. (Reprinted with permission of FutureCarbon GmbH, Bayreuth.)

### 7.2.1

#### Health Aspects

It is of increasing concern to the public as well as toxicologists and occupational physicians that nanotechnology may create contaminants whose tiny size makes them ultra-hazardous. A further complication is that these very small materials may bind or react with other contaminants in the air or water that are harmful and facilitate their transport into living organisms, thus leading to additional adverse effects.

Most knowledge of the adverse health effects of very small particles comes from recent studies on ambient ultrafine particles (UFP) unintentionally released into the atmosphere. Epidemiological studies have shown that increased levels of UFP (<0.1 µm in aerodynamic diameter) are associated with increased respiratory and cardiovascular mortality and morbidity as well as worsening of asthma. These effects were observed in particular in susceptible persons such as the very young and old, and those with compromised respiratory and cardiovascular systems [24–

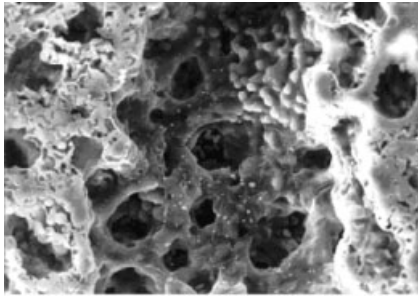


**Fig. 7.5.** Scanning electron micrograph demonstrating deposition of inhaled iron carbonyl particles at the alveolar duct bifurcations in the distal lung of a rat. (Reprinted from Ref. [31], with permission from Elsevier.)

26]. The composition of ambient UFP includes organic and elemental carbon, metals, chloride, nitrate and sulfate. Since the core typically consists of elemental carbon [27], it was obvious to study the biological effects using ultrafine carbonaceous particles as model particles.

#### 7.2.2

#### **Uptake and Possible Transport, Depots, and Accumulation in Living Organisms**

Most studies on the uptake and transport of nanoparticles as well as the formation of depots and their accumulation have been performed *in vivo* (Fig. 7.5). The laboratory of Günter Oberdörster carried out fundamental studies during the last decade that delivered basic data on distribution, uptake and retention of titanium nanoparticles in lungs of rats or mice. It was demonstrated that after instillation or inhalation in rats, equivalent masses of 20 nm  $\text{TiO}_2$  were deposited in the alveoli and accessed the pulmonary interstitium to a significantly larger extent than 250 nm  $\text{TiO}_2$  particles [28, 29]. This resulted in a prolonged retention of the smaller particles in the lung. But these studies in rat also indicate that there is a difference between inhalation and instillation of nanoscaled  $\text{TiO}_2$ . As measured by bronchovascular lavage parameters, animals receiving particles via inhalation showed a decreased pulmonary response, in both severity and persistence, compared with animals receiving particles via instillation [30].

Dose–response curves are incompatible when the instilled mass of ultrafine and fine  $\text{TiO}_2$  particles are used as parameters for the measured neutrophil infiltration. Alternatively, when using the particle surface area of the instilled dose, it became obvious that the inflammatory response in the lung for both ultrafine and fine  $\text{TiO}_2$  fitted the same dose–response curve [32]. These results strongly suggest that for particles of the same surface material/chemistry, such as  $\text{TiO}_2$ , particle surface area is a more important dosimetric parameter than particle mass (or particle number). The same authors demonstrated a perfect correlation of the inflamma-

tory response in both experimental animals by fitting the particle surface dose with the lung weights of mice and rats. This assumption to use surface area as a relevant dosimetric parameter to express toxicity data is confirmed by several studies but has to be validated in more detail (for further literature see Ref. [33]).

During the last decade several studies have shown that the response to instillation or inhalation of nanoscaled  $\text{TiO}_2$  in various species such as hamster, rat, or mouse differs. Under conditions of equivalent lung burden with nanoscaled  $\text{TiO}_2$ , rats developed more severe inflammatory responses than mice, while the clearance of particles from the lungs was markedly impaired in both species [34]. In contrast, the clearance rate of hamsters is totally unaffected at all applied particle concentrations. The difference in clearance rates seems to be caused by a translocation of the particles into the lymph nodes of rats and mice. This was not seen in hamsters and thus the retention time in hamsters is shorter. Another variation within the three species was described by histopathological methods. After instillation or inhalation of nanoparticles an accumulation of particle-loaded macrophages surrounded by normal alveolar structures has been observed in hamster, whereas in rats the particle-loaded macrophages accumulate intra-alveolar. Moreover, interstitial fibrosis and alveolar metaplasia of lining epithelium has been demonstrated in rats and were not noted in either mice or hamsters. In contrast, no macrophage accumulation could be detected in hamsters [35]. A further study showed that, compared with mice or hamsters, rats were hypersensitive to a high lung burden of insoluble dust [34].

For ultrafine cadmium oxide particles, *in vivo* studies in rats were performed and showed that the inhaled particles cause an increasing cadmium content in lung, liver, kidney and blood. However, systemic translocation of the particles only appeared if the animals were exposed to high particle concentrations, which generated lung injury. J774 macrophages treated with CdO were swollen with poorly preserved cell membranes, cytoplasmic structures and nuclear morphology [36].

Few studies have been performed within *in vitro* systems dealing with the transport and uptake of nanoparticulate metal oxides and a direct comparison of these studies is not feasible because different cell types and particles differing in size and material were used. Fundamentally, metal oxide and carbonaceous nanoparticles can be taken up by cells by very different mechanisms (Fig. 7.6). In several human cell lines nanoscaled material, such as  $\text{TiO}_2$ ,  $\text{SiO}_2$  and  $\text{ZrO}_2$ , was taken up into the cells [37]. The incorporated particles were detected in autophagic vacuoles, which also contained amorphous cellular material and membranes [38], as well as within the cytoplasm (Fig. 7.7).

Nanoscaled  $\text{TiO}_2$  significantly impaired macrophage phagocytosis at a lower dose than its fine counterpart [39]. Thus, the slower clearance of ultrafine particles from the lung can be in part attributed to a particle-mediated impairment of macrophage phagocytosis. Nanoscaled  $\text{TiO}_2$  caused cytoskeletal dysfunction as decreased phagosome transport and increased cytoskeletal stiffness could be observed in concentrations of  $100 \mu\text{g mL}^{-1}$  per  $10^6$  cells and above in macrophages [40].

A more recent study demonstrated that particle size and particle composition, respectively, were responsible for the observed biological effects by using hematite

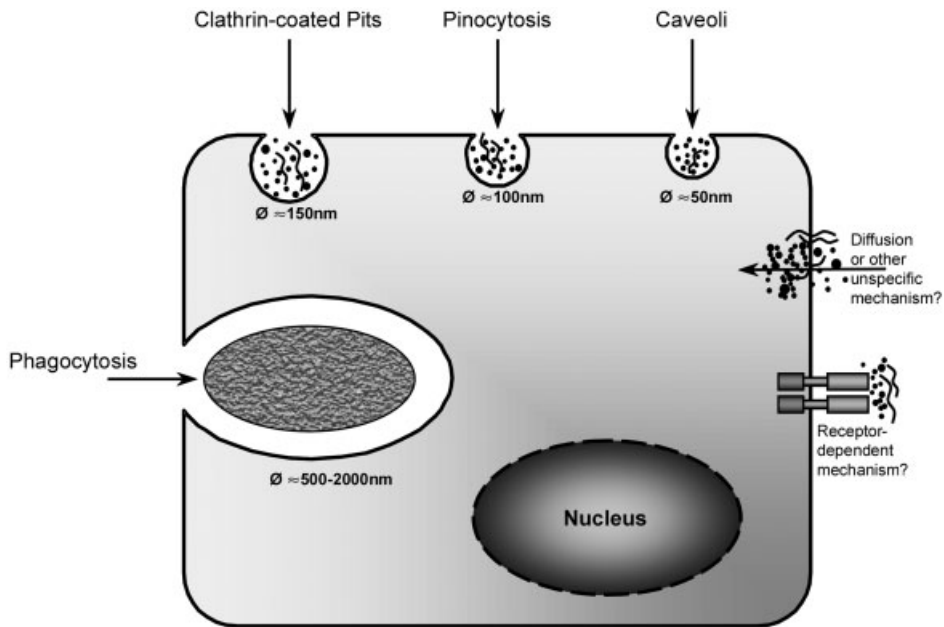


Fig. 7.6. Possible cellular uptake pathways for particles of different sizes.

(70 nm) and amorphous  $\text{SiO}_2$  between 40 and 300 nm in diameter. Furthermore, co-culture systems of lung epithelial cells and macrophages showed an increased sensitivity to particle exposure concerning the cytokine release in comparison to the monocultures of each cell type [41].

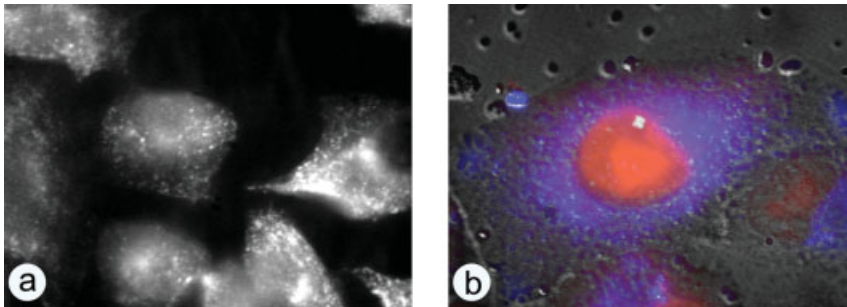
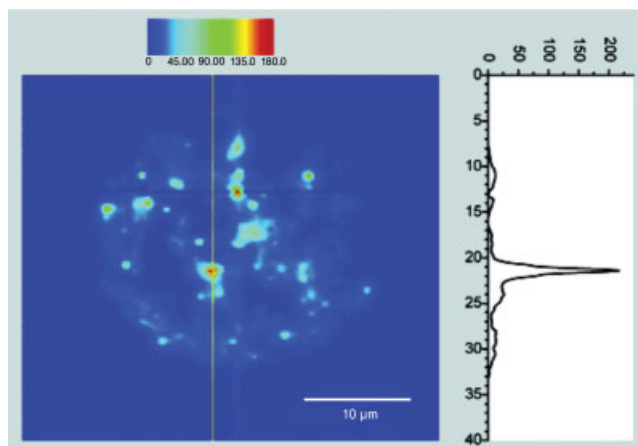


Fig. 7.7. Fluorescence micrographs of human lung epithelial cells (A549). (a) Caveolin detected with Cy3 coupled antibody, demonstrating the overall appearance of caveoli within these cells. (b) A549 cells after exposure to  $\text{ZrO}_2$  (5 nm in diameter) coated

with Coumarin 307 (blue fluorescence). The particles are equally distributed in the cytoplasm of the cells whereas none could be detected within the nuclei (counterstained with ethidium bromide – red fluorescence). Magnification: 630-fold. (K. Kern, ITG.)

The deposition and fate of inhaled ultrafine carbon particles generated by spark discharge (26 nm) was studied with the stable isotope  $^{13}\text{C}$  [42]. In the rat model, more than 50% of the  $^{13}\text{C}$  particles was rapidly translocated to the liver within 24 h while no significant increase in  $^{13}\text{C}$  was detected in the other organs. In contrast, another study with insoluble ultrafine  $^{192}\text{Ir}$  particles (15–20 nm) detected less than 1% translocation into the extracellular organs. The particles not only accumulated in the liver, but also in spleen, kidneys, brain and heart [43]. Interestingly, in this study a much lesser fraction of ultrafine particles could be removed by bronchoalveolar lavage compared with inhalation studies with larger particles. It was suggested that the ultrafine particles penetrate the epithelium or the interstitium where they are retained. A human study observed an uptake of 3–5% of radiolabeled carbonaceous ultrafine particles into the blood and translocation into the liver [44]. These results differ from those of Brown and colleagues [45] who could not find any particles outside the lungs and the cleared fractions after inhalation of an ultrafine technetium-99m-labeled carbon aerosol in their human study.

Newer studies indicate that inhaled ultrafine  $^{13}\text{C}$  particles translocate into the brain of rats. The particles are suggested to deposit on the olfactory mucosa of the nasopharyngeal region and translocate via the olfactory nerve to the brain [46]. Despite conflicting results, it can be summarized that inhaled ultrafine particles are able to translocate to extrapulmonary organs via the blood; however, this fraction is very low.



**Fig. 7.8.** Near-infrared fluorescence image of one macrophage-like cell incubated with SWCNTs, showing emission detected from 1125 to 1600 nm with excitation at 660 nm. Intensities are coded with false color, and the image was obtained from a z-axis series by

deconvolution processing. Intensity along the yellow vertical line is plotted in the graph on the right, showing high image contrast and localized emission sources. (Adapted with permission from Ref. [50].)

Despite recent investigations in systemic transport, none of the published data strongly illustrate that a substantial amount of the inhaled dose is indeed translocated systemically [43, 47–49]. Carbonaceous particles are particularly difficult to detect in cells and tissues by electron microscopy because of low contrast and small diameters. Recently, near-IR fluorescence was applied to detect SWCNTs after phagocytosis in mouse macrophages (Fig. 7.8).

The image clearly shows the nanotubes inside the cell [50]. Because of their photostability, which is comparable to quantum dots, carbon nanotubes might be applied as fluorescent markers and contrast agents with low toxic potential for cell biology research and medical diagnosis. Diabaté et al. also demonstrated by transmission electron imaging that carbon nanotubes are taken up by macrophages and epithelial cells as bundles [51]. These large agglomerates of carbon nanotubes as well as single nanotubes separated from these bundles can be clearly detected within the cells by this method (Fig. 7.9).

There exist several studies on the uptake and distribution of nanoparticles within cells. In nearly all these experiments the investigated cells have ingested the applied nanoparticles. Only two examples demonstrate the fact that nanoscaled metal oxide particles are found in cellular systems *in vitro* (Fig. 7.10) as well as after inhalation *in vivo* (Fig. 7.11). Transmission electron microscopy is fundamentally a useful and necessary tool. It appears that nanoscaled materials can be found either enclosed within organelles like phagosomes, lysosomes, or endosomes, or are freely distributed within the cytosol [38, 41, 52].

The same is true for carbonaceous nanomaterial that has been found in various cell types after treatment *in vitro* (Figs. 7.8 and 7.9) as well as in exposed mice or rats after instillation [53, 54].

### 7.2.3

#### **Biological Effects on Cellular Mechanisms**

Nanoparticles produced from different materials, such as metal oxides or carbon, have enhanced properties not found in bulk materials. Unsurprisingly, therefore, the enhancement of material properties could also occur when the particles encounter biological components. With the ability to manipulate atoms and molecules, we now can create predefined nanostructures with unprecedented precision and selective affectivity. An improved understanding of the biological effects of nanoscaled materials, as described in this book, also deserves attention. Several investigations of biological interactions with nanometer-scale materials demonstrate the possible impacts on living systems (Fig. 7.12):

1. Cell membrane proteins/adhesion molecules; integrins and extracellular matrix (ECM), receptor molecules, transporters [12, 55–61];
2. phospholipid turnover and lipid mediator release [62–64];
3. ion channels [65];
4. endolysosomes [66–68];

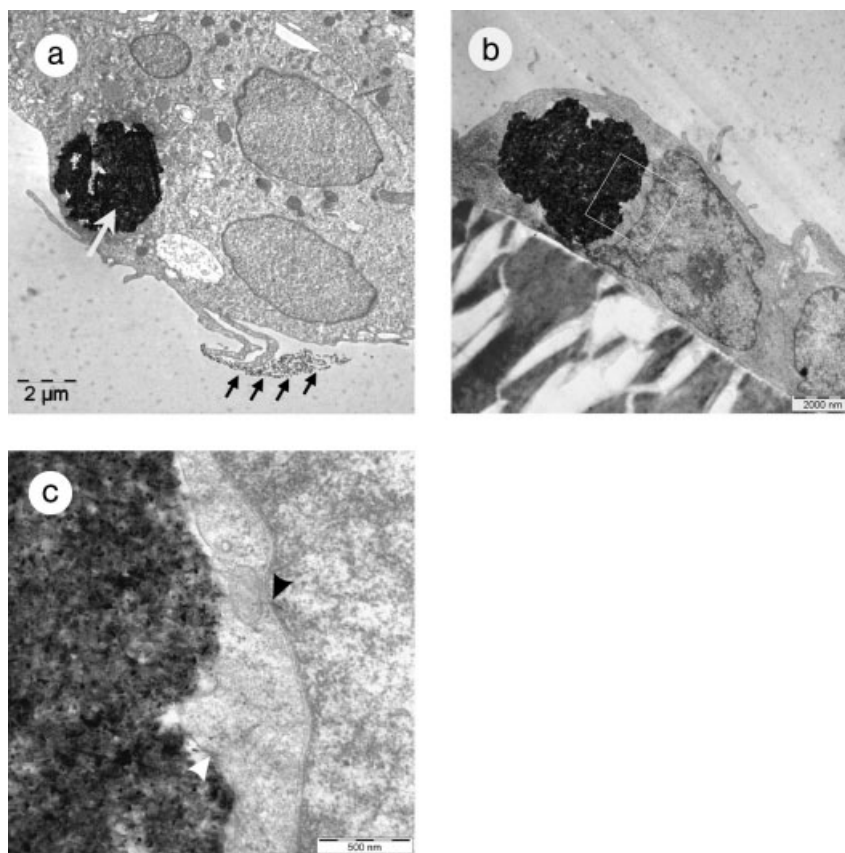


**Fig. 7.9.** Transmission electron micrographs of rat alveolar macrophages (NR8383) and human lung epithelial cells (BEAS2B) ingesting bundles of primary SWCNTs. (a) NR8383 cell ingested a bundle of carbon nanotubes (white arrow) and contacted another one (black arrows); (b) BEAS2B cells ingested a SWCNT-

bundle of similar size, the white square is shown in higher magnification in (c), where single carbon nanotubes can be found next to the bundle in the cytosol (white arrowhead) and at the nuclear envelope (black arrowhead). (T. Detzel, ITG.)

5. mitochondria [69–71];
6. nucleus and DNA [72, 73].

### 7.2.3.1 Metal Oxides

Nanosized materials are easily taken up into cells and are either stored in several compartments or freely located within the cytosol (Section 7.2.2). Metal oxides interfere with membranes, proteins or other structures of the cells (see above). Incorporation takes place via caveoli, clathrin-coated pits or endocytosis (Fig. 7.6),

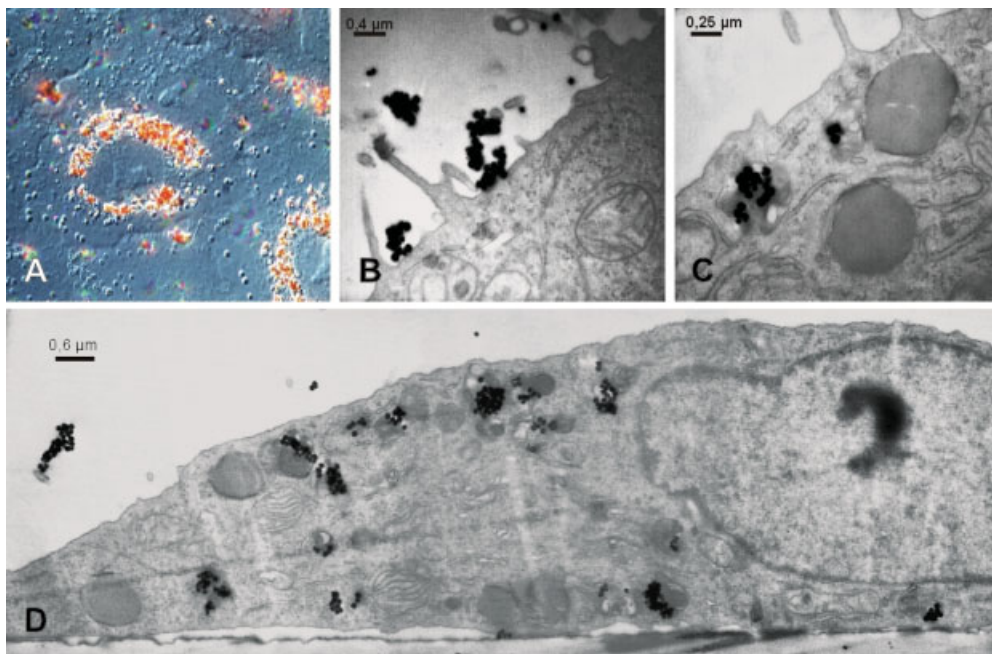


**Fig. 7.10.** Hematite particles are taken up into the cytosol of alveolar epithelial cells (A549). Light microscopic image of A549 cells (DIC, 630 $\times$ ; A) after 24 h of hematite exposure (100  $\mu\text{g mL}^{-1}$  or 32  $\mu\text{g cm}^{-2}$ ). Transmission electron micrographs of A549 cells after 3 h (20000 $\times$ ; B), 6 h (30000 $\times$ ; C), and 16 h of exposure to hematite particles (50  $\mu\text{g mL}^{-1}$  or 16  $\mu\text{g cm}^{-2}$ ) (12000 $\times$ ; D). (Reprinted from Ref. [41], with permission from Elsevier.)

leaving these nanosized metal oxides in lysosomes [38, 41]. A distinct mechanism for nanoparticle uptake has not been described yet, but it appears to be a dependency on primary particle and agglomerate size. The possible cellular mechanism for the recognition and initiation of the uptake process has recently been suggested to be a member of the Toll-like receptor family [74].

**Size Dependency** Recently, ultrafine (20 nm) preparations of  $\text{TiO}_2$  have been shown to cause a significant loss in viability compared to fine (220 nm) particles [40], similar to results for ultrafine and fine nickel [75]. Additionally, an increase in fibrogenic mediators like procollagen can be observed that appear to be stronger for ultrafine preparations [76]. Proliferation of macrophages is impaired in these samples as well, and to a greater extent than in fine particle treated controls [40]. Inhalation studies revealed a higher pulmonary deposition in rats with ultrafine CdO (40 nm) aerosol than was measured with fine CdO particles [36]. Bermudez and his colleagues have suggested particle clearance in mice and rats is retarded



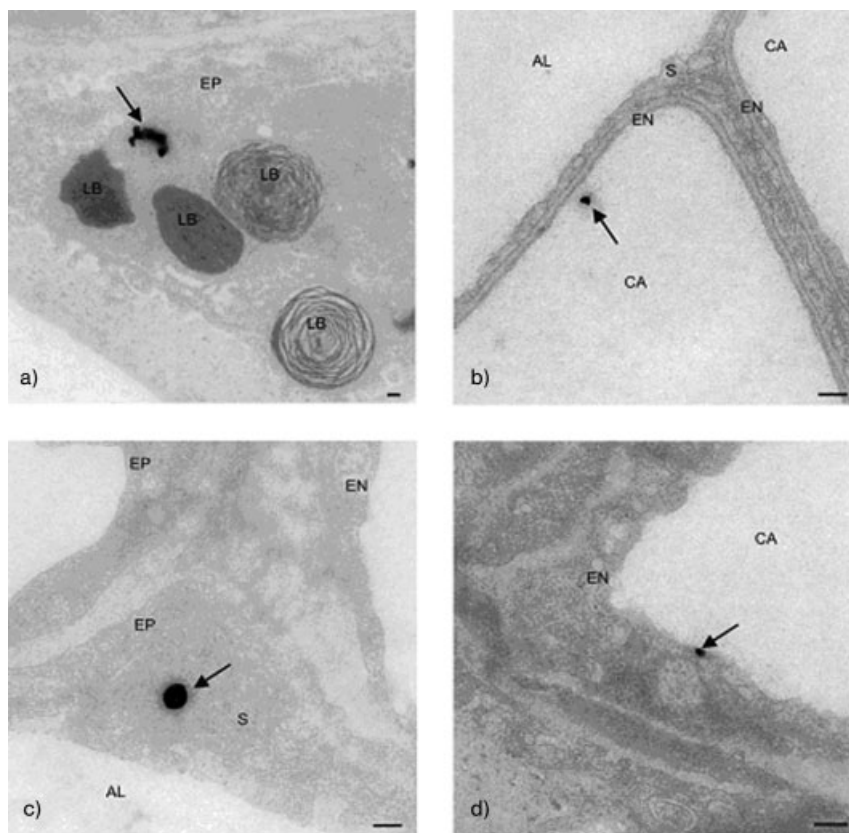


**Fig. 7.11.** EFTEM (energy filtering transmission electron microscopy) images taken at 0 eV of particles (arrows) on ultrathin sections of the lung parenchyma of exposed rats. (a) Type II cell (EP) close to lamellar bodies (LB). (b) A capillary (CA), near the alveolar endothelium (EN). (c) Surfactant

material (S) accumulated within the surface lining layer in the corner of an alveolus, close to the epithelium (EP), alveolar lumen (AL). (d) Cytoplasm of an endothelial cell (EN). Scale bars = 100 nm. (Adapted with permission from Ref. [52].)

because of pulmonary particle overload in animals treated with high dosages of nanoscale titania [35].

Koper and his coworkers have described another size-dependent finding [77]. Nanoscale powders of MgO or CaO that tend to be nontoxic as large scale particles were doped with halogens and found to have a very strong degrading effect on certain bacteria and fungi. It was suggested that the activated nanoparticles directly interfere with proteins and nucleotides. If these formulations kill more than 90% of contacted bacteria within minutes, why should these particles (4 nm) not be

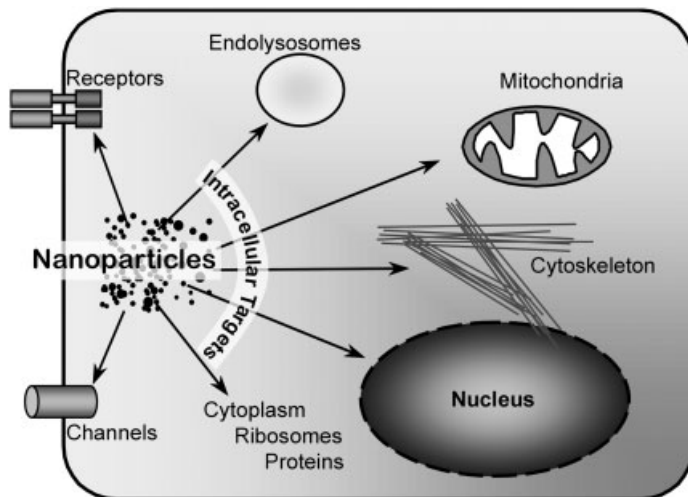


Fig. 7.12. Possible intracellular targets of nanoparticles.

harmful to human health? The key to these observations lays obviously in the large surface area of nanoparticles, which can be as high as  $430 \text{ m}^2 \text{ g}^{-1}$  and therefore be very reactive. Klabunde and coworkers suggest a surface reaction of these nanomaterials with P–O and P–F bonds that breaks important chemical compounds, leading to a disruption of the cellular homeostasis [78].

**Inflammation** Several studies have shown that incorporated metal oxide nanoparticles can lead to inflammatory responses. These include the release of pro-inflammatory cytokines like IL-1, IL-6, IL-8 and TNF- $\alpha$ . In addition, fibrogenic factors (PDGF-A and PDGF-B) can be released upon treatment with fine and ultrafine particles in rat tracheal explants [76]. Toll-like receptors (TLR) may be also involved in a nanomaterial specific manner and appeared to be induced after application of different nanoparticles, such as TiO<sub>2</sub>, ZrO<sub>2</sub> and SiO<sub>2</sub>, to human myelomonocytic U-937 cells [74]. These studies observed an increase in IL-1 $\beta$ , TNF- $\alpha$  and IL-1RA release in this macrophage cell line. A change in the cytological profile has been noted recently in inhalation experiments in mice, rats, and hamsters [35]. The mice had significantly elevated numbers of macrophages, lymphocytes and neutrophils in bronchoalveolar lavage fluids even 52 weeks after the end of exposure.

**Acute Toxicity** Several assays have been used and developed to determine the acute toxicity of nanomaterials. By measuring the metabolic activity of mitochondria, many laboratories have determined the viability of various cell cultures after treatment with metal oxides or carbon nanoparticles [38, 41, 74, 79, 80]. Other

studies use bacterial systems by giving the number of colony forming units as a marker for acute toxicity [77]. Consistent across different methods or biological systems, nanoscaled metal oxide particles exhibit a strong decrease in viability.

**Genotoxicity** To overcome severe effects on DNA such as was demonstrated for asbestos, it is very important to increase our knowledge of direct DNA damaging effects or indirect genotoxic mechanisms via oxidative stress by nanoscaled metal oxides.

TiO<sub>2</sub> nanoparticles caused lung tumors in rats at the end of lifetime exposure [81]. Thus, it can be speculated that metal oxide nanoparticles in general exhibit a strong reactivity to induce oxidation or electron transfer reactions because the number of metal atoms on their surface compared to those hidden within the particles is very high. Moreover, it might be assumed that these materials can induce DNA damage, enhancing the risk for tumor development (Section 7.2.3.2). Here, a broad basis of data is missing and knowledge of the retention, biological half-life and accumulation within specific target organs has to be increased.

**Cytoskeletal Organization** Hydroxyapatite, a major building block in bones, is used as a nanomaterial to improve adhesion of human osteoblast-like cells (HOB) to inorganic materials. Upon treatment with a high dosage of 200 particles per cell ( $1 \times 10^8$  per 500 000 cells) of nHA (nanosized, rod-like hydroxyapatite) HOB cells released lactate dehydrogenase into the surrounding media, indicating a loss in cell viability [79]. Surfaces coated with nHA increase the quality of focal contacts in HOB cells and support growth *in vitro* if used in lower concentrations (Fig. 7.13). However, ultrafine particles made of titania (20 nm TiO<sub>2</sub>) cause retarded relaxation and stiffness of the cytoskeleton in macrophages that can not be observed for micronized titania (220 nm) [40]. Moreover, the alveolar ability for clearance is slowed due to reduced macrophage phagocytosis and mobility [39], as has been demonstrated by measuring the uptake of control beads. Recognition of nanoscale metal oxides may take place via a Toll-like receptor (TLR) mediated uptake process that has been described for bacteria and viruses, as suggested by Lucarelli et al. [74]. They observed changes in mRNA expression levels (TLR1-10, MD2 and CD14) upon metal oxide treatment of human differentiated myelomonocytic U-937 cells.

#### 7.2.3.2 New Carbon Modifications

Induction of intracellular oxidative stress seems to be a key biological response to combustion generated [82] and manufactured particles, as well as organic components associated with particles. Furthermore, there is evidence for additive or synergistic interactions between ultrafine carbon black particles and soluble transition metals in causing oxidative stress and inflammation [83]. The oxidative potential of particles can be observed in cell-free systems, e.g., by electron spin resonance (ESR) spectroscopy [84].

If particles with oxidative potential find their way inside cells, that same ability may convert oxygen and other molecules into highly reactive radicals that can in-

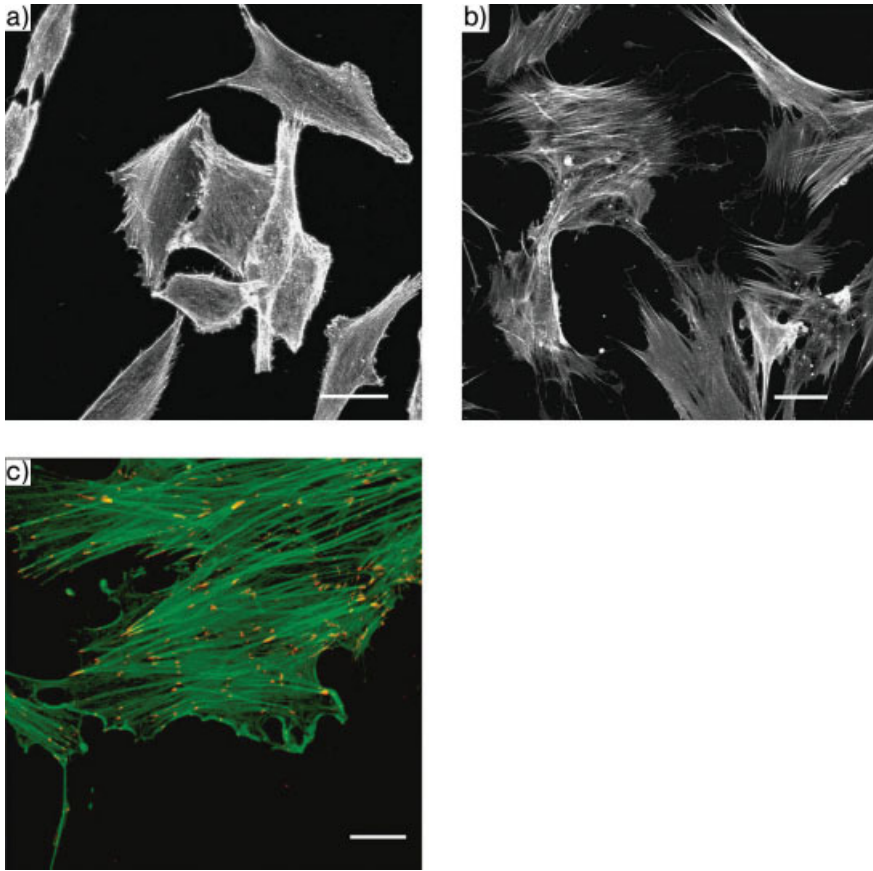


**Fig. 7.13.** CLSM images of actin cytoskeleton (green) and vinculin (red), as in (b) after two days culture. Scale bar = 20  $\mu\text{m}$ . (Reprinted from Ref. [79], with permission from Kluwer Academic Publishers.) Scale bar = 40  $\mu\text{m}$ . (c) CLSM image of actin

duce intracellular signaling pathways as a defense mechanism or even damage cellular components, leading to cell death.

Figure 7.14 shows the possible sequence of events occurring after contact of particles with living cells. If particles make contact with proteins located at the outer plasma membrane, they may induce changes in the molecular conformation of these proteins. Many of these proteins are receptors that transmit external signals into the cell, and a conformational change of the receptor may activate it, leading to the onset of a cellular response. Once inside the cell, particles may induce intracellular oxidative stress by disturbing the balance between oxidant and antioxidant processes, e.g., the glutathione system. The oxidative stress may also stimulate an

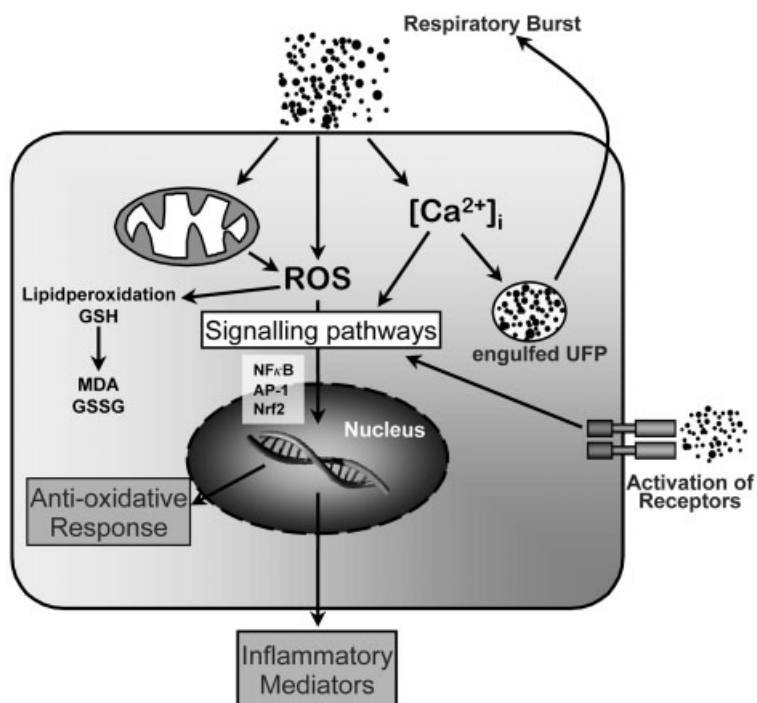


**Fig. 7.14.** Possible events after interaction of particles with cells. Particles may interact with receptors or may cause oxidative stress that induces an increase in intracellular calcium concentration, decrease intracellular GSH and/

or activate transcription factors via different signaling cascades. Activated transcription factors translocate into the nucleus, leading to gene activation, synthesis of antioxidant enzymes and/or inflammatory mediators.

increase of the cytosolic calcium concentration, possibly via interaction with calcium channels on the plasma membrane or on the endoplasmic reticulum, leading to influx of  $Ca^{2+}$  from the extracellular environment or to release of  $Ca^{2+}$  from intracellular stores [85]. The intracellular calcium concentration strongly regulates signaling pathways via interaction with several proteins such as calmodulin and protein kinases. These changes cause the activation of redox-sensitive transcription factors, such as NF- $\kappa$ B, AP-1 or Nrf2, which translocate to the nucleus and bind to the promoter regions of the genes regulated by these transcription factors. For NF- $\kappa$ B these genes include TNF- $\alpha$ , IL-6, IL-8, ICAM-1, iNOS and others, which are highly pro-inflammatory [86]. Exceeding oxidative stress may also modify proteins, lipids (lipid peroxidation) and nucleic acids, which further stimulates the antioxidant defense system or even leads to cell death.

Experiments with rats have demonstrated that inhalation of particles consisting of elemental carbon may cause considerable injury to the lung and that the toxic potential increases with decreasing particle size and increasing particle surface

area [81, 87]. Freshly prepared ultrafine carbon particles generated from pure graphite electrodes in an electric spark discharge generator [88] induce an increase in heart rate and a decrease in heart-rate variability after 24 h inhalation by healthy rats [89]. These studies indicate a systemic effect of the inhaled carbon particles (38 nm,  $180 \mu\text{g m}^{-3}$ ) without evidence of an inflammation-mediated mechanism. The authors suggest the responses may have induced an alteration of the cardiac autonomic balance mediated by a pulmonary receptor activation.

Frampton and colleagues have conducted a large clinical inhalation study of the effects of laboratory-generated ultrafine carbon particles [90]. Healthy people and people with asthma inhaled 10 or  $25 \mu\text{g m}^{-3}$  of ultrafine carbon particles (average diameter 25 nm) for 2 h. This dose was 10 to  $100\times$  higher than average concentrations of ultrafine particles of this size class reported in urban air. They did not detect changes in any airway inflammatory endpoint in both groups although it was calculated that about 50% more particles deposited in lungs of asthmatic people than in healthy people and over  $4\times$  as many particles were deposited in the lungs of exercising as in the lungs of resting participants. Electrocardiogram analysis after exposure showed a transient reduction of the heart rate variability and a reduced repolarization interval in healthy people and in people with asthma.

**Inflammation** *In vitro* studies with different cell systems also demonstrated that small carbon black particles (14 nm) induced more oxidative stress and pro-inflammatory cytokines than primary particle sizes of 250 nm [84]. These effects could not be explained by adhering transition metals since leaching of the particles with different buffers and complexing iron with desferrioxamin did not reduce the carbon-black-induced effects [91].

Freshly prepared spark discharge-generated ultrafine carbon particles have a higher oxidative potential than both aged particles and larger particles with less surface area [84]. However, the particle-induced release of arachidonic acid and derived lipid mediators in canine alveolar macrophages was independent of their oxidative potential but dependent on their ability to activate cytosolic and secretory phospholipases  $A_2$  (PLA<sub>2</sub>). PLA<sub>2</sub> hydrolyzes membrane phospholipids to release arachidonic acid, which is further metabolized to prostaglandins and leukotrienes. The particle-induced effects were also observed in human alveolar macrophages.

In normal human bronchial epithelial cells, these types of particles induced the expression of the pro-inflammatory cytokine (IL-8), possibly controlled by the p38 mitogen-activated protein kinase (MAPK) signaling pathway. Activation of the transcription factor NF- $\kappa$ B, however, seems not to play a role [92]. IL-8 is a potential chemoattractant for neutrophils. An elevated level of IL-8 in the lung is a characteristic of respiratory diseases such as cystic fibrosis, asthma, chronic bronchitis and acute respiratory distress symptom.

**Genotoxicity** Inhalation of carbon black by rats induced the formation of 8-oxo-7,8-dihydro-2'-deoxyguanosin (8-oxo-dG) in the lungs [73]. 8-Oxo-dG, a modified nucleotide, is a well-known and commonly used biomarker of free radical-induced oxidative DNA damage. This DNA modification may induce point mutations,

which are widely observed in mutated oncogenes and tumor suppressor genes, and is therefore associated with many diseases such as cancer and neurodegenerative diseases. Interestingly, studies with rats showed that particles without organics ( $\text{TiO}_2$ ) or with very low amounts of organics (carbon black) resulted in a similar induction of tumors compared with diesel particles, which contain considerably higher amounts of organics [81]. Therefore, tumor development is suggested to be caused by secondary genotoxic events due to particle-induced persistent inflammation and increased cell proliferation due to lung particle overload rather than by direct genotoxic effects.

While the toxic effects of carbon black or spark discharge-generated particles of elemental carbon have been studied very intensely, few studies with toxicological background exist on fullerenes and carbon nanotubes. Adelman et al. [93] studied the effects of fullerenes in primary bovine alveolar macrophages and HL-60 macrophages using particles generated in the arc between two graphite electrodes in a helium atmosphere. The fullerenes reduced the viability of the cells and induced increased levels of the pro-inflammatory cytokines  $\text{TNF-}\alpha$ , IL-6 und IL-8. The effects were comparable with those of graphite. Another *in vitro* study with  $\text{C}_{60}$  demonstrated low cytotoxicity compared to quartz, a moderate increase of  $\text{TNF-}\alpha$  and IL-8 release, and no oxidative potential compared to zymosan in macrophages [94, 95].

E. Oberdörster has studied the effects of  $\text{C}_{60}$  fullerenes after exposure of fish (juvenile largemouth bass) as a model for the impact of nanoparticles produced in bulk with the potential to be released into the environment [64]. She demonstrated that a 48 h treatment with fullerenes significantly increased the lipid peroxidation in the brain and depleted the glutathione content in the gill. Both parameters are indicators of increased oxidative stress.

For carbon nanotubes, it is uncertain if there are analogous mechanisms to those of other fibrous particles such as asbestos and synthetic vitreous fibers (SVFs), which penetrate into the lung and may persist in the tissue. Large epidemiological studies of SVF manufacturing workers provided very little evidence of harmful effects in humans [96]. However, it is widely assumed that all biopersistent fibers may be harmful if inhaled in large enough doses. Long insoluble fibers are difficult to clear by phagocytic cells. The macrophages die after a long process of trying to engulf the fibers and release inflammatory cytokines into the lung. This may trigger the complex cellular response mechanisms that cause cancer after exposure to asbestos [97]. Nevertheless, a study at the University of Warsaw sought to determine if carbon nanotubes may behave like asbestos [98]. The experiments with guinea pigs revealed that carbon nanotubes do not exhibit effects similar to asbestos and it is suggested that working with soot containing carbon nanotubes is unlikely to be associated with health risks.

Two more studies from the same group in Warsaw have dealt with the dermatological and inhalation effects of fullerenes and carbon nanotubes. In the study on dermatological effects, rabbits were treated and the researchers "did not *find* any signs of health hazards related to skin irritation and allergic risks." This group recommended no special precautions with respect to both fullerenes and carbon

nanotubes in the working environment; in fact, the articles were titled “Fullerenes: Null Risk of Skin Irritation and Allergy” and “Carbon Nanotubes: Null Risk of Skin Irritation and Allergy” [99, 100]. However, these studies may not have been sensitive enough because recently published experimental data suggest a variety of effects in rat, mouse or human cellular systems (see below). Moreover, one has to take into account that carbon nanotubes are always contaminated with catalytic metals used during their production.

For most production processes, predominantly Fe and Ni are used as metal catalysts. They are normally removed from the raw product, but part of the metal is encased in the tubes and cannot be removed completely. Manufacturing of carbon nanotubes leads to bundles of nanotubes forming clumps and aggregates. If they are inhaled or come into contact with the skin during handling, the potential hazard will strongly depend on the metal content and on the size of the aggregates. The hazard of exposure to carbon nanotubes at occupational settings has been investigated by only a few studies. Maynard and his coworkers measured the aerosol mass and number concentration in three laboratories where SWCNTs were generated by different processes and handled manually [17]. They observed concentrations of 0.70 to 53  $\mu\text{g m}^{-3}$  of nanotubes in the atmosphere and considerable masses on gloves during handling.

Because of reports that carbon fibers induced dermal irritation such as contact dermatitis in humans after occupational exposure of the skin to carbon fibers [101], some *in vitro* studies have investigated the effects of carbon particles in immortalized keratinocyte cultures. In a companion article to Maynard et al. [17], the biological effects of SWCNTs before catalyst removal (containing 30% Fe by mass) was studied in human keratinocytes [102]. An observed dose-dependent decrease in cell viability and glutathione (GSH) levels was dramatically reversed by the metal chelator desferrioxamin. This indicates a significant role of iron in the biological effects of the SWCNTs. This study further confirmed oxidative stress in SWCNT-treated cells by the formation of free radical species, increased lipid peroxidation and decrease of the antioxidant reserve. The effects of MWCNTs in human dermal keratinocytes were also studied by Monteiro-Riviere et al. [103]. They demonstrated by transmission electron microscopy that MWCNTs were present in cytoplasmic vacuoles.

Two independent studies with rats [53] and mice [54] reported the appearance of granulomas, interstitial inflammation, and obstruction of the airways after instillation of high doses of aggregated carbon nanotubes. Granulomas are a combination of dead and live tissue surrounding the foreign material. Warheit and his coworkers [53] concluded that the acute effects are normal responses to persistent particulate material and are not specific for carbon nanotubes. Lam et al. [54] observed that the SWCNTs were more toxic than carbon black and quartz particles after instillation in mice and that nanotubes treated to remove the metals were nearly as toxic as raw nanotubes (see Chapter 6). Histological tests showed that all particles reached the alveoli and remained there even after 90 days. The biopersistence of SWCNTs and the induction of granulomatous lesions are important evi-



dences for adverse health effects. Because of strong aggregation on the nanotubes it is necessary to study the effects either by inhalation or by *in vitro* experiments.

*In vitro* experiments with alveolar epithelial cells and macrophages showed that SWCNTs and MWCNTs induced oxidative stress, inflammatory responses, and cell death in a dose-dependent manner [51]. The authors found that the toxic potential of SWCNTs was similar to ultrafine carbon black (Printex 90) and higher than MWCNTs and quartz.

Recently, SWCNTs, MWCNTs and C<sub>60</sub> fullerenes were tested in comparison to quartz in primary alveolar macrophages isolated from guinea pigs [104]. A sequence order of the cytotoxic potential of SWCNTs > MWCNTs > quartz > C<sub>60</sub> fullerenes was found. The C<sub>60</sub> fullerenes were shown to be non-toxic in the MTT test even at the highest concentration of 226 μg cm<sup>-2</sup> while the SWCNTs reduced the viability by 20% at 1.4 μg cm<sup>-2</sup>. These observations are compatible with results obtained with mice where carbon nanotubes are more toxic to the lung than quartz [54]. The carbon nanotubes were ~90% pure; impurities included mainly amorphous carbon and only trace amounts of the catalysts Fe, Y and Ni. The particles also reduced the phagocytic ability of the alveolar macrophages, as seen by microscopic and flow cytometry analysis. Phagocytosis of carbon nanotubes was accompanied by ultrastructural alterations, as demonstrated by transmission electron imaging, indicating the onset of apoptotic processes.

Besides the mechanical and electrical characteristics, carbon nanotubes can be functionalized with different molecules to achieve improved properties and functions such as biocompatibility and biomolecular recognition capabilities. This would enable applications in biomedical engineering and drug delivery. Amino acids and peptides coupled to SWCNTs yield SWCNT derivatives with higher water solubility that can translocate across cell membranes [105]. Furthermore, plasmid DNA associates with ammonium-functionalized CNTs, and these complexes were taken up by mammalian cells. The CNT-mediated DNA delivery to cells was very effective, resulting in a 10× higher gene expression than achieved with DNA alone [105]. These studies indicate that CNTs have a high potential in delivery systems in the molecular therapy of diseases.

#### 7.2.4

#### Possible Hazards – Toxicological Impacts

We tried in the above-described toxicological issues to point to important mechanisms and studies that gave hints where the hazards of nanoparticles could be detected. Obviously, dependent on the material nanoparticles are produced from, their biological effects can be very different. Above all, metal oxides are strongly expected to be harmful because the toxicity of metals and their compounds is well described. The question is do they behave differently as nanosized particles than as dissolved ionic forms or organic compounds? Therefore, it is of interest to know if these materials are soluble in biological fluids, and how long they persist in their target tissues. Such criteria may directly influence the use of metal oxide nano-

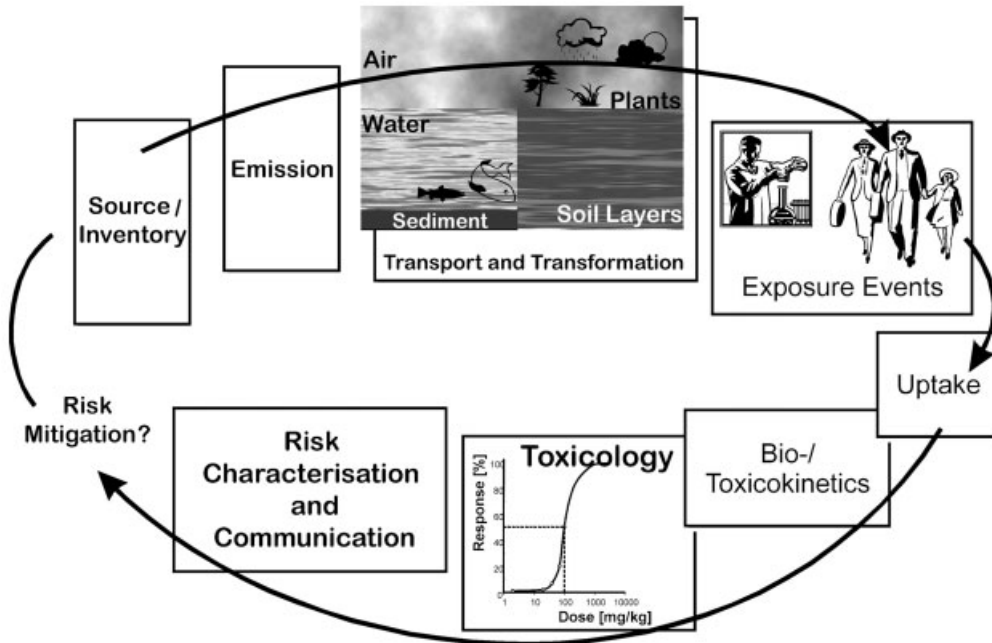


Fig. 7.15. Schematic presentation of life-cycle assessment of nanomaterials. From source to dose, an evaluation loop to the reduction of emission of nanomaterials.

particles in technical, cosmetic, and medical products with which an exposure is obvious. Carbonaceous material, though, has been less intensively investigated and long-term effects are mostly speculative. First results, from studies with animals and cellular systems, point to oxidative mechanisms that might have the potency to kill cells or could be discussed in connection to DNA damage. Regarding these effects, further investigations are needed to clarify such fundamental biological mechanisms before these materials, like fullerenes or carbon nanotubes, are produced in very high amounts and possibly released into the environment. Thus, it is important to include the entire life-cycle of nanomaterials (Fig. 7.15).

### 7.3

#### Risk Characterization – A Conclusion

As stated in Section 7.1.2 risk characterization stands at the end of the sequence of hazard and exposure identification and assessment (Fig. 7.1). To fulfill the criteria of risk assessment, besides the toxicological and pharmacological studies, exposure situations have to be recognized. Therefore, one has to keep in mind that bioaccumulation processes can lead to an enrichment in organisms or organs over several

orders of magnitude. Thus, a minimum catalogue of action has to be set up to reduce the risk at working places and within the environment.

Generally, in a recent report from the Institute of Occupational Medicine in Great Britain [106], it has been postulated to consider:

- the existence of potential routes for human exposure;
- possible industrial sources of occupational exposure;
- the levels of exposure;
- means of, and effectiveness of control measures;
- potential numbers of humans exposed;
- trends in the (potential) use of nanotechnology;
- views as to the likely impact of the implementation of the change from research use to full-scale industrial use.

### 7.3.1

#### **Opportunities and Risks of Nanomaterials**

All the above-described mechanisms of uptake, transport and distribution of nanoparticles in cells of different species and organs are important for their implications and applications. During discussion of the adverse effects of nanoparticles it is always important to consider the positive applications within the environment as well as in biological systems. Only a few are listed here:

- tools in imaging and microscopy;
- diagnostics and analysis (research and therapy);
- production of bioactive compounds and materials (Lab-on-a-Chip);
- targeting and dosing of drugs;
- intervention in biological processes (cell growth);
- nutrition (bioavailability, stability, optics);
- cosmetics (UV-filter, liposomal formulations);
- sensors and detectors;
- biomolecules for information and communication technology (ICT; DNA computing).

### 7.3.2

#### **New Materials without Risks?**

Nanotechnological products are developed with regard to the future: for a presumed need, to solve foreseeable problems, and for a future market. Besides intended effects (the use and functions of nanomaterials), unintended effects (the “side effects”, which also include misappropriation and misuse) might occur and might influence the overall balance of opportunities and risks. Technological risks belong to unintended and undesirable side effects.

Not only environmental or health risks are subject to a risk assessment but also economic risks and potential social problems like technology conflicts as well as

risks for sustainable development in a general sense. Classical types of technical or technologically-initiated risks are [107]:

- *Accidents in technical facilities:* These are disruptions of normal operation. Release of high amounts of material in such cases can enhance public distrust of new technology (e.g., poisonous gas catastrophes in Seveso and Bophal).
- *Consequences for human health:* New materials or completely new emissions can affect human health, e.g., in the production or use of technology. To these belong the known risks and side effects of medicines (e.g., diethylstilbestrol – DES), but also the dramatic history of asbestos. Entire chapters of modern regulations for handling hazardous substances are reactions to actual health problems. Special problems of risk assessment arise in the case of low dose exposures.
- *Consequences for the natural environment:* Air pollution, the ozone hole, chemical residues in ground water and in the soil are well-known, unintended consequences of the use of technology. Other than in the case of accidents in technical facilities alluded to above, these are often *gradual* processes. They are not always readily recognizable, and there is dissent on the question of tolerance limits or “cut-off-” or “threshold values”, from which point on protective or remedial measures would have to be taken.
- *Social and cultural effects of technology:* Social risks connected with technology are, for instance, the loss of many jobs through rationalization and automation, especially as far as less highly qualified work is concerned. Ethical “slippery slopes” in biomedical questions are also felt by segments of the population to be “cultural” risks (e.g., positive eugenics).

Such technological risks show certain characteristics that influence the approaches to their anticipative investigation and evaluation through risk research and technology assessment. Among these, in particular, are:

- local and global effects (atmospheric emissions and the global water cycle);
- enlargement of number of people affected by hazards (even in future);
- the problem of delayed effects: Perceptible damage appears decades after its cause (e.g., ozone hole, asbestos case);
- complexity of cause-relationship connections (e.g., the mad cow disease BSE);
- inability to perceive risks (e.g., radioactivity) with human sensory organs;
- irreversibility of hazards (e.g., persistent pollutants can not be completely retrieved from the environment).

In summary, it has turned out in past decades that side effects can interfere with or even counteract the goals pursued by means of technology. This ambivalence of technology, the greater discrepancy between the intended and the (then) actually realized effects constitutes a *conditio humana* of technological civilization. Two positions are futile: the demand for absolute safe and risk-free technology (“zero risk”) and the disregard or denial of the “dark side” of technology. The challenge consists much rather in addressing, analyzing, and evaluating the risks, comparing

them with the expected benefits, and then taking the results of these deliberations into consideration in decision-making processes [107].

## References

- 1 AGRAWAL, A. K., SINGHAL, A., GUPTA, C. M. Functional drug targeting to erythrocytes in vivo using antibody bearing liposomes as drug vehicles. *Biochem. Biophys. Res. Commun.* **1987**, 148, 357–361.
- 2 CLARK, A. P. Liposomes as drug delivery systems. *Cancer Pract.* **1998**, 6, 251–253.
- 3 DESMUKH, D. S., BEAR, W. D., WISNIEWSKI, H. M., BROCKERHOFF, H. Long-living liposomes as potential drug carriers. *Biochem. Biophys. Res. Commun.* **1978**, 82, 328–334.
- 4 FENDLER, J. H., ROMERO, A. Liposomes as drug carriers. *Life Sci.* **1977**, 20, 1109–1120.
- 5 GABIZON, A. Liposomes as a drug delivery system in cancer chemotherapy. *Horiz. Biochem. Biophys.* **1989**, 9, 185–211.
- 6 GREGORIADIS, G. Drug entrapment in liposomes. *FEBS Lett.* **1973**, 36, 292–296.
- 7 GREGORIADIS, G., WILLS, E. J., SWAIN, C. P., TAVILL, A. S. Drug-carrier potential of liposomes in cancer chemotherapy. *Lancet* **1974**, 1, 1313–1316.
- 8 KSHIRSAGAR, N. A., GOKHALE, P. C., PANDYA, S. K. Liposomes as drug delivery system in leishmaniasis. *J. Assoc. Physicians India* **1995**, 43, 46–48.
- 9 SPEISER, P. P. Nanoparticles and liposomes: A state of the art. *Methods Find. Exp. Clin. Pharmacol.* **1991**, 13, 337–342.
- 10 ALLEN, T. M., CULLIS, P. R. Drug delivery systems: Entering the mainstream. *Science* **2004**, 303, 1818–1822.
- 11 CHEN, Y., XUE, Z., ZHENG, D., XIA, K., ZHAO, Y., LIU, T., LONG, Z., XIA, J. Sodium chloride modified silica nanoparticles as a non-viral vector with a high efficiency of DNA transfer into cells. *Curr. Gene Ther.* **2003**, 3, 273–279.
- 12 GUPTA, A. K., CURTIS, A. S. Lactoferrin and ceruloplasmin derivatized superparamagnetic iron oxide nanoparticles for targeting cell surface receptors. *Biomaterials* **2004**, 25, 3029–3040.
- 13 JORDAN, A., WUST, P., SCHOLZ, R., TESCHE, B., FAHLING, H., MITROVIC, T., VOGL, T., CERVOS-NAVARRO, J., FELIX, R. Cellular uptake of magnetic fluid particles and their effects on human adenocarcinoma cells exposed to AC magnetic fields in vitro. *Int. J. Hyperthermia* **1996**, 12, 705–722.
- 14 LI, K. C., GUCCIONE, S., BEDNARSKI, M. D. Combined vascular targeted imaging and therapy: A paradigm for personalized treatment. *J. Cell Biochem.* **2002**, 39(Suppl.), 65–71.
- 15 SHI KAM, N. W., JESSOP, T. C., WENDER, P. A., DAI, H. Nanotube molecular transporters: Internalization of carbon nanotube-protein conjugates into Mammalian cells. *J. Am. Chem. Soc.* **2004**, 126, 6850–6851.
- 16 OTSUKA, H., NAGASAKI, Y., KATAOKA, K. PEGylated nanoparticles for biological and pharmaceutical applications. *Adv. Drug Deliv. Rev.* **2003**, 55, 403–419.
- 17 MAYNARD, A. D., BARON, P. A., FOLEY, M., SHVEDOVA, A. A., KISIN, E. R., CASTRANOVA, V. Exposure to carbon nanotube material: Aerosol release during the handling of unrefined single-walled carbon nanotube material. *J. Toxicol. Environ. Health A* **2004**, 67, 87–107.
- 18 KRUG, H. F., KERN, K., DIABATÉ, S. Toxikologische Aspekte der Nanotechnologie. Versuch einer Abwägung. *Technikfolgenabsch.: Theorie Praxis* **2004**, 13, 58–64.
- 19 KRUG, H. F., KERN, K., WÖRLE-KNIRSCH J. M., DIABATÉ, S. Ultrafine

- particles. Health risk and possible applications. *Internist. prax.* **2004**, 45, 443–455.
- 20 KROTO, H. W., HEATH, J. R., O'BRIEN, S. C., CURL, R. F., SMALLEY, R. E. C-60 – Buckminsterfullerene. *Nature* **1985**, 318, 162–163.
- 21 IIJIMA, S., AJAYAN, P. M., ICHIHASHI, T. Growth model for carbon nanotubes. *Phys. Rev. Lett.* **1992**, 69, 3100–3103.
- 22 BALL, P. Roll up for the revolution. *Nature* **2001**, 414, 142–144.
- 23 PRICE, R. L., ELLISON, K., HABERSTROH, K. M., WEBSTER, T. J. Nanometer surface roughness increases select osteoblast adhesion on carbon nanofiber compacts. *J. Biomed. Mater. Res. A* **2004**, 70, 129–138.
- 24 IBALD-MULLI, A., WICHMANN, H. E., KREYLING, W. G., PETERS, A. Epidemiological evidence on health effects of ultrafine particles. *J. Aerosol Med.* **2002**, 15, 189–201.
- 25 WICHMANN, H. E., SPIX, C., TUCH, T., WOLKE, G., PETERS, A., HEINRICH, J., KREYLING, W. G., HEYDER, J. Daily mortality and fine and ultrafine particles in Erfurt, Germany part I: Role of particle number and particle mass. *Res. Rep. Health Eff. Inst.* **2000**, 98, 5–86.
- 26 SAMET, J. M., DOMINICI, F., CURRIERO, F. C., COURSAK, I., ZEGER, S. L. Fine particulate air pollution and mortality in 20 U.S. cities, 1987–1994. *N. Engl. J. Med.* **2000**, 343, 1742–1749.
- 27 HUGHES, L. S., CASS, G. R., GONE, J., AMES, M., OLMEZ, I. Physical and chemical characterization of atmospheric ultrafine particles in the Los Angeles area. *Environ. Sci. Technol.* **1998**, 32, 1153–1161.
- 28 BAGGS, R. B., FERIN, J., OBERDÖRSTER, G. Regression of pulmonary lesions produced by inhaled titanium dioxide in rats. *Vet. Pathol.* **1997**, 34, 592–597.
- 29 FERIN, J., OBERDÖRSTER, G., PENNEY, D. P. Pulmonary retention of ultrafine and fine particles in rats. *Am. J. Respir. Cell Mol. Biol.* **1992**, 6, 535–542.
- 30 OBERDÖRSTER, G., COX, C., GELEIN, R. Intratracheal instillation versus intratracheal-inhalation of tracer particles for measuring lung clearance function. *Exp. Lung Res.* **1997**, 23, 17–34.
- 31 WARHEIT, D. B. Nanoparticles: Health impacts? *Mater. Today* **2004**, 7, 32–35.
- 32 OBERDÖRSTER, G. Toxicology of ultrafine particles: In vivo studies. *Philos. Trans. R. Soc. Lond. Ser. A – Math. Phys. Eng. Sci.* **2000**, 358, 2719–2739.
- 33 OBERDÖRSTER, G., OBERDÖRSTER, E., OBERDÖRSTER, J. Nanotoxicology: An emerging discipline evolving from studies of ultrafine particles. *Environ. Health Perspect.* **2005**, 113, 823–839.
- 34 HEXT, P. M., TOMENSON, J. A., THOMPSON, P. Titanium dioxide: Inhalation toxicology and epidemiology. *Ann. Occup. Hyg.* **2005**, 49, 461–472.
- 35 BERMUDEZ, E., MANGUM, J. B., WONG, B. A., ASGHARIAN, B., HEXT, P. M., WARHEIT, D. B., EVERITT, J. I. Pulmonary responses of mice, rats, and hamsters to subchronic inhalation of ultrafine titanium dioxide particles. *Toxicol. Sci.* **2004**, 77, 347–357.
- 36 TAKENAKA, S., KARG, E., KREYLING, W. G., LENTNER, B., SCHULZ, H., ZIESENIS, A., SCHRAMEL, P., HEYDER, J. Fate and toxic effects of inhaled ultrafine cadmium oxide particles in the rat lung. *Inhal. Toxicol.* **2004**, 16(Suppl 1), 83–92.
- 37 KERN, K., WÖRLE-KNIRSCH, J. M., KRUG, H. F. Nanonoxes: Nanoparticle uptake, transport and toxicity. *Signal Transduct.* **2004**, 3–4, 149.
- 38 PETERS, K., UNGER, R. E., KIRKPATRICK, C. J., GATTI, A. M., MONARI, E. Effects of nano-scaled particles on endothelial cell function in vitro: Studies on viability, proliferation and inflammation. *J. Mater. Sci. Mater. Med.* **2004**, 15, 321–325.
- 39 RENWICK, L. C., DONALDSON, K., CLOUTER, A. Impairment of alveolar macrophage phagocytosis by ultrafine particles. *Toxicol. Appl. Pharmacol.* **2001**, 172, 119–127.
- 40 MÖLLER, W., HOFER, T., ZIESENIS, A., KARG, E., HEYDER, J. Ultrafine

- particles cause cytoskeletal dysfunctions in macrophages. *Toxicol. Appl. Pharmacol.* **2002**, *182*, 197–207.
- 41 WOTTRICH, R., DIABATÉ, S., KRUG, H. F. Biological effects of ultrafine model particles in human macrophages and epithelial cells in mono- and co-culture. *Int. J. Hyg. Environ. Health* **2004**, *207*, 353–361.
- 42 OBERDÖRSTER, G., SHARP, Z., ATUDOREI, V., ELDER, A., GELEIN, R., LUNTS, A., KREYLING, W. G., COX, C. Extrapulmonary translocation of ultrafine carbon particles following whole-body inhalation exposure of rats. *J. Toxicol. Environ. Health A* **2002**, *65*, 1531–1543.
- 43 KREYLING, W. G., SEMMLER, M., ERBE, F., MAYER, P., TAKENAKA, S., SCHULZ, H., OBERDÖRSTER, G., ZIESENIS, A. Translocation of ultrafine insoluble iridium particles from lung epithelium to extrapulmonary organs is size dependent but very low. *J. Toxicol. Environ. Health A* **2002**, *65*, 1513–1530.
- 44 NEMMAR, A., HOET, P. H., VANQUICKENBORNE, B., DINSDALE, D., THOMEER, M., HOYLAERTS, M. F., VANBILLOEN, H., MORTELMANS, L., NEMERY, B. Passage of inhaled particles into the blood circulation in humans. *Circulation* **2002**, *105*, 411–414.
- 45 BROWN, J. S., ZEMAN, K. L., BENNETT, W. D. Ultrafine particle deposition and clearance in the healthy and obstructed lung. *Am. J. Respir. Crit. Care Med.* **2002**, *166*, 1240–1247.
- 46 OBERDÖRSTER, G., SHARP, Z., ATUDOREI, V., ELDER, A., GELEIN, R., KREYLING, W. G., COX, C. Translocation of inhaled ultrafine particles to the brain. *Inhal. Toxicol.* **2004**, *16*, 437–445.
- 47 KHANDOGA, A., STAMPFL, A., TAKENAKA, S., SCHULZ, H., RADYKEWICZ, R., KREYLING, W. G., KROMBACH, F. Ultrafine particles exert prothrombotic but not inflammatory effects on the hepatic microcirculation in healthy mice in vivo. *Circulation* **2004**, *109*, 1320–1325.
- 48 NEMMAR, A., HOYLAERTS, M. F., HOET, P. H., NEMERY, B. Possible mechanisms of the cardiovascular effects of inhaled particles: Systemic translocation and prothrombotic effects. *Toxicol. Lett.* **2004**, *149*, 243–253.
- 49 SEMMLER, M., SEITZ, J., ERBE, F., MAYER, P., HEYDER, J., OBERDÖRSTER, G., KREYLING, W. G. Long-term clearance kinetics of inhaled ultrafine insoluble iridium particles from the rat lung, including transient translocation into secondary organs. *Inhal. Toxicol.* **2004**, *16*, 453–459.
- 50 CHERUKURI, P., BACHILO, S. M., LITOVSKY, S. H., WEISMAN, R. B. Near-infrared fluorescence microscopy of single-walled carbon nanotubes in phagocytic cells. *J. Am. Chem. Soc.* **2004**, *126*, 15 638–15 639.
- 51 DIABATÉ, S., PULSKAMP, K., KRUG, H. F. Carbon nanotubes induce oxidative stress, inflammatory responses and cell death in pulmonary epithelial cells and macrophages. *Signal Transduct.* **2004**, 3–4, 116.
- 52 KAPP, N., KREYLING, W. G., SCHULZ, H., IM HOF, V., GEHR, P., SEMMLER, M., GEISER, M. Electron energy loss spectroscopy for analysis of inhaled ultrafine particles in rat lungs. *Microsc. Res. Technol.* **2004**, *63*, 298–305.
- 53 WARHEIT, D. B., LAURENCE, B. R., REED, K. L., ROACH, D. H., REYNOLDS, G. A., WEBB, T. R. Comparative pulmonary toxicity assessment of single-wall carbon nanotubes in rats. *Toxicol. Sci.* **2004**, *77*, 117–125.
- 54 LAM, C. W., JAMES, J. T., MCCUSKEY, R., HUNTER, R. L. Pulmonary toxicity of single-wall carbon nanotubes in mice 7 and 90 days after intratracheal instillation. *Toxicol. Sci.* **2004**, *77*, 126–134.
- 55 BERRY, C. C., WELLS, S., CHARLES, S., AITCHISON, G., CURTIS, A. S. Cell response to dextran-derivatised iron oxide nanoparticles post internalisation. *Biomaterials* **2004**, *25*, 5405–5413.
- 56 DE CAMPOS, A. M., DIEBOLD, Y., CARVALHO, E. L., SANCHEZ, A., ALONSO, M. J. Chitosan nanoparticles

- as new ocular drug delivery systems: In vitro stability, in vivo fate, and cellular toxicity. *Pharm. Res.* **2004**, *21*, 803–810.
- 57 GUALBERT, J., SHAHGALDIAN, P., COLEMAN, A. W. Interactions of amphiphilic calix[4]arene-based solid lipid nanoparticles with bovine serum albumin. *Int. J. Pharm.* **2003**, *257*, 69–73.
- 58 KRISTL, J., VOLK, B., AHLIN, P., GOMBAC, K., SENTJURC, M. Interactions of solid lipid nanoparticles with model membranes and leukocytes studied by EPR. *Int. J. Pharm.* **2003**, *256*, 133–140.
- 59 LIDKE, D. S., NAGY, P., HEINTZMANN, R., ARNDT-JOVIN, D. J., POST, J. N., GRECCO, H. E., JARES-ERIJMAN, E. A., JOVIN, T. M. Quantum dot ligands provide new insights into erbB/HER receptor-mediated signal transduction. *Nat. Biotechnol.* **2004**, *22*, 198–203.
- 60 MAYE, I., DE FRAISSINETTE, A., CRUZ-ORIVE, L. M., VONDERSCHER, J., RICHTER, F., GEHR, P. Comparison of the rate of phagocytosis of orthorhombic cyclosporine A (CsA) and latex particles by alveolar macrophages from hamsters. *Cell Mol. Life Sci.* **1997**, *53*, 689–696.
- 61 PRYHUBER, G. S., HUYCK, H. L., BAGGS, R., OBERDÖRSTER, G., FINKELSTEIN, J. N. Induction of chemokines by low-dose intratracheal silica is reduced in TNFR I (p55) null mice. *Toxicol. Sci.* **2003**, *72*, 150–157.
- 62 BECK-SPEIER, I., DAYAL, N., KARG, E., MAIER, K. L., ROTH, C., ZIESENIS, A., HEYDER, J. Agglomerates of ultrafine particles of elemental carbon and TiO<sub>2</sub> induce generation of lipid mediators in alveolar macrophages. *Environ. Health Perspect.* **2001**, *109*(Suppl 4), 613–618.
- 63 BECK-SPEIER, I., DAYAL, N., KARG, E., MAIER, K. L., SCHULZ, H., SCHUMANN, G., ZIESENIS, A., HEYDER, J. Formation of prostaglandin E<sub>2</sub>, leukotriene B<sub>4</sub> and 8-isoprostane in alveolar macrophages by ultrafine particles of elemental carbon. *Adv. Exp. Med. Biol.* **2003**, *525*, 117–120.
- 64 OBERDÖRSTER, E. Manufactured nanomaterials (fullerenes, C<sub>60</sub>) induce oxidative stress in the brain of juvenile largemouth bass. *Environ. Health Perspect.* **2004**, *112*, 1058–1062.
- 65 PARK, K. H., CHHOWALLA, M., IQBAL, Z., SESTI, F. Single-walled carbon nanotubes are a new class of ion channel blockers. *J. Biol. Chem.* **2003**, *278*, 50 212–50 216.
- 66 KREYLING, W. G. Intracellular particle dissolution in alveolar macrophages. *Environ. Health Perspect.* **1992**, *97*, 121–126.
- 67 LUNDBORG, M., JOHARD, U., JOHANSSON, A., EKLUND, A., FALK, R., KREYLING, W. G., CAMNER, P. Phagolysosomal morphology and dissolution of cobalt oxide particles by human and rabbit alveolar macrophages. *Exp. Lung Res.* **1995**, *21*, 51–66.
- 68 PANYAM, J., ZHOU, W. Z., PRABHA, S., SAHOO, S. K., LABHASETWAR, V. Rapid endo-lysosomal escape of poly(DL-lactide-co-glycolide) nanoparticles: Implications for drug and gene delivery. *FASEB J.* **2002**, *16*, 1217–1226.
- 69 CRUZ, T., GASPAR, R., DONATO, A., LOPES, C. Interaction between polyalkylcyanoacrylate nanoparticles and peritoneal macrophages: MTT metabolism, NBT reduction, and NO production. *Pharm. Res.* **1997**, *14*, 73–79.
- 70 KNAAPEN, A. M., BORM, P. J., ALBRECHT, C., SCHINS, R. P. Inhaled particles and lung cancer. Part A: Mechanisms. *Int. J. Cancer* **2004**, *109*, 799–809.
- 71 THIBODEAU, M., GIARDINA, C., HUBBARD, A. K. Silica-induced caspase activation in mouse alveolar macrophages is dependent upon mitochondrial integrity and aspartic proteolysis. *Toxicol. Sci.* **2003**, *76*, 91–101.
- 72 CARLISLE, R. C., BETTINGER, T., OGRIS, M., HALE, S., MAUTNER, V., SEYMOUR, L. W. Adenovirus hexon protein enhances nuclear delivery and increases transgene expression of polyethylenimine/plasmid DNA vectors. *Mol. Ther.* **2001**, *4*, 473–483.



- 73 GALLAGHER, J., SAMS, R., INMON, J., GELEIN, R., ELDER, A., OBERDÖRSTER, G., PRAHALAD, A. K. Formation of 8-oxo-7,8-dihydro-2'-deoxyguanosine in rat lung DNA following subchronic inhalation of carbon black. *Toxicol. Appl. Pharmacol.* **2003**, 190, 224–231.
- 74 LUCARELLI, M., GATTI, A. M., SAVARINO, G., QUATTRONI, P., MARTINELLI, L., MONARI, E., BORASCHI, D. Innate defence functions of macrophages can be biased by nano-sized ceramic and metallic particles. *Eur. Cytokine Netw.* **2004**, 15, 339–346.
- 75 ZHANG, Q., KUSAKA, Y., ZHU, X., SATO, K., MO, Y., KLIZ, T., DONALDSON, K. Comparative toxicity of standard nickel and ultrafine nickel in lung after intratracheal instillation. *J. Occup. Health* **2003**, 45, 23–30.
- 76 CHURG, A., GILKS, B., DAI, J. Induction of fibrogenic mediators by fine and ultrafine titanium dioxide in rat tracheal explants. *Am. J. Physiol.* **1999**, 277, L975–L982.
- 77 KOPER, O. B., KLABUNDE, J. S., MARCHIN, G. L., KLABUNDE, K. J., STOIMENOV, P., BOHRA, L. Nanoscale powders and formulations with biocidal activity toward spores and vegetative cells of bacillus species, viruses, and toxins. *Curr. Microbiol.* **2002**, 44, 49–55.
- 78 RAJAGOPALAN, S., KOPER, O., DECKER, S., KLABUNDE, K. J. Nanocrystalline metal oxides as destructive adsorbents for organophosphorus compounds at ambient temperatures. *Chemistry* **2002**, 8, 2602–2607.
- 79 HUANG, J., BEST, S. M., BONFIELD, W., BROOKS, R. A., RUSHTON, N., JAYASINGHE, S. N., EDIRISINGHE, M. J. In vitro assessment of the biological response to nano-sized hydroxyapatite. *J. Mater. Sci. Mater. Med.* **2004**, 15, 441–445.
- 80 OKESON, C. D., RILEY, M. R., RILEY-SAXTON, E. In vitro alveolar cytotoxicity of soluble components of airborne particulate matter: Effects of serum on toxicity of transition metals. *Toxicol. In Vitro* **2004**, 18, 673–680.
- 81 HEINRICH, U., FUHST, R., RITTINGHAUSEN, S., CREUTZENBERG, O., BELLMANN, B., KOCH, W., LEVSEN, K. Chronic inhalation exposure of Wistar rats and 2 different strains of mice to diesel-engine exhaust, carbon-black, and titanium-dioxide. *Inhal. Toxicol.* **1995**, 7, 533–556.
- 82 VÖLKE, K., KRUG, H. F., DIABATÉ, S. Formation of reactive oxygen species in rat epithelial cells upon stimulation with fly ash. *J. Biosci.* **2003**, 28, 51–55.
- 83 WILSON, M. R., LIGHTBODY, J. H., DONALDSON, K., SALES, J., STONE, V. Interactions between ultrafine particles and transition metals in vivo and in vitro. *Toxicol. Appl. Pharmacol.* **2002**, 184, 172–179.
- 84 BECK-SPEIER, I., DAYAL, N., KARG, E., MAIER, K. L., SCHUMANN, G., SCHULZ, H., SEMMLER, M., TAKENAKA, S., STETTMAIER, K., BORS, W., GHIO, A., SAMET, J. M., HEYDER, J. Oxidative stress and lipid mediators induced in alveolar macrophages by ultrafine particles. *Free Radic. Biol. Med.* **2005**, 38, 1080–1092.
- 85 BROWN, D. M., DONALDSON, K., BORM, P. J., SCHINS, R. P., DEHNHARDT, M., GILMOUR, P., JIMENEZ, L. A., STONE, V. Calcium and ROS-mediated activation of transcription factors and TNF-alpha cytokine gene expression in macrophages exposed to ultrafine particles. *Am. J. Physiol Lung Cell Mol. Physiol.* **2004**, 286, L344–L353.
- 86 CASTRANOVA, V. Signaling pathways controlling the production of inflammatory mediators in response to crystalline silica exposure: Role of reactive oxygen/nitrogen species. *Free Radic. Biol. Med.* **2004**, 37, 916–925.
- 87 DRISCOLL, K. E., CARTER, J. M., HOWARD, B. W., HASENBEIN, D. G., PEPELKO, W., BAGGS, R. B., OBERDÖRSTER, G. Pulmonary inflammatory, chemokine, and mutagenic responses in rats after subchronic inhalation of carbon black. *Toxicol. Appl. Pharmacol.* **1996**, 136, 372–380.
- 88 ROTH, C., FERRON, G. A., KARG, E., LENTNER, B., SCHUMANN, G., TAKENAKA, S., HEYDER, J. Generation of ultrafine particles by spark

- discharging. *Aerosol Sci. Technol.* **2004**, *38*, 228–235.
- 89 HARDER, V., GILMOUR, P., LENTNER, B., KARG, E., TAKENAKA, S., ZIESENIS, A., STAMPFL, A., KODAVANTI, U., HEYDER, J., SCHULZ, H. Cardiovascular responses in unrestrained WKY rats to inhaled ultrafine carbon particles. *Inhal. Toxicol.* **2005**, *17*, 29–42.
- 90 FRAMPTON, M. W., UTELL, M. J., ZAREBA, W., OBERDORSTER, G., COX, C., HUANG, L. S., MORROW, P. E., LEE, F. E., CHALUPA, D., FRASIER, L. M., SPEERS, D. M., STEWART, J. Effects of exposure to ultrafine carbon particles in healthy subjects and subjects with asthma. *Res. Rep. Health Eff. Inst.* **2004**, 1–47.
- 91 BROWN, D. M., STONE, V., FINDLAY, P., MACNEE, W., DONALDSON, K. Increased inflammation and intracellular calcium caused by ultrafine carbon black is independent of transition metals or other soluble components. *Occup. Environ. Med.* **2000**, *57*, 685–691.
- 92 KIM, Y. M., REED, W., LENZ, A. G., JASPERS, I., SILBAJORIS, R., NICK, H. S., SAMET, J. M. Ultrafine carbon particles induce interleukin-8 gene transcription and p38 MAPK activation in normal human bronchial epithelial cells. *Am. J. Physiol Lung Cell Mol. Physiol.* **2005**, *288*, L432–L441.
- 93 ADELMANN, P., BAIERL, T., DROSSELMAYER, E., POLITIS, C., POIZER, G., SEIDEL, A., SCHWEGLER-BERRY, D., STEINLEITNER, C. Effects of fullerenes on alveolar macrophages in vitro. In: *Toxic and Carcinogenic effects of Solid Particles in the Respiratory Tract* (ed. MOHR, U., DUNGWORTH, D. L., MAULDERLY, J., OBERDÖRSTER, G.), ILSI Press, Washington DC, **1994**.
- 94 BAIERL, T., DROSSELMAYER, E., SEIDEL, A., HIPPELI, S. Comparison of immunological effects of fullerene C60 and raw soot from fullerene production on alveolar macrophages and macrophage like cells in vitro. *Exp. Toxicol. Pathol.* **1996**, *48*, 508–511.
- 95 BAIERL, T., SEIDEL, A. In vitro effects of fullerene C-60 and fullerene black on immunofunctions of macrophages. *Fullerene Sci. Technol.* **1996**, *4*, 1073–1085.
- 96 HESTERBERG, T. W., HART, G. A. Synthetic vitreous fibers: A review of toxicology research and its impact on hazard classification. *Crit. Rev. Toxicol.* **2001**, *31*, 1–53.
- 97 GODLESKI, J. J. Role of asbestos in etiology of malignant pleural mesothelioma. *Thorac. Surg. Clin.* **2004**, *14*, 479–487.
- 98 HUCZKO, A., LANGE, H., CALKO, E., GRUBEK-JAWORSKA, H., DROSZCZ, P. Physiological testing of carbon nanotubes: Are they asbestos-like? *Fullerene Sci. Technol.* **2001**, *9*, 251–254.
- 99 HUCZKO, A., LANGE, H., CALKO, E. Fullerenes: Experimental evidence for a null risk of skin irritation and allergy. *Fullerene Sci. Technol.* **1999**, *7*, 935–939.
- 100 HUCZKO, A., LANGE, H. Carbon nanotubes: Experimental evidence for a null risk of skin irritation and allergy. *Fullerene Sci. Technol.* **2001**, *9*, 247–250.
- 101 EEDY, D. J. Carbon-fibre-induced airborne irritant contact dermatitis. *Contact Dermatitis* **1996**, *35*, 362–363.
- 102 SHVEDOVA, A. A., CASTRANOVA, V., KISIN, E. R., SCHWEGLER-BERRY, D., MURRAY, A. R., GANDELSMAN, V. Z., MAYNARD, A., BARON, P. Exposure to carbon nanotube material: Assessment of nanotube cytotoxicity using human keratinocyte cells. *J. Toxicol. Environ. Health A* **2003**, *66*, 1909–1926.
- 103 MONTEIRO-RIVIERE, N. A., NEMANICH, R. J., INMAN, A. O., WANG, Y. Y., RIVIERE, J. E. Multi-walled carbon nanotube interactions with human epidermal keratinocytes. *Toxicol. Lett.* **2005**, *155*, 377–384.
- 104 JIA, G., WANG, H., YAN, L., WANG, X., PEI, R., YAN, T., ZHAO, Y., GUO, X. Cytotoxicity of carbon nanomaterials: Single-wall nanotube, multi-wall nanotube, and fullerene. *Environ. Sci. Technol.* **2005**, *39*, 1378–1383.
- 105 PANTAROTTO, D., BRIAND, J. P., PRATO, M., BIANCO, A. Translocation of bioactive peptides across cell

- membranes by carbon nanotubes. *Chem. Commun.* **2004**, 16–17.
- 106** AITKEN, R. J., CREELY, K. S., TRAN, C. L. Nanoparticles: An occupational hygiene review. HSE Books, Inst. of Occupational Medicine, Edinburgh, UK, **2004**, Vol. 274.
- 107** KRUG, H. F., GRUNWALD, A. Risk assessment and risk management. In: *Assessment and Perspectives of Nanotechnology* (ed. BRUNE, H., ERNST, H., GRUNWALD, A., GRÜNWARD, W., HOFMANN, H., JANICH, P., KRUG, H. F., MAYOR, M., SCHMID, G., SIMON, U., VOGEL, V., GETHMANN, C. F.), Springer, Berlin, **2005**.



### **III Environment**



## 8

# Nanomaterials for Environmental Remediation

Glen E. Fryxell and Shas V. Mattigod

### 8.1

#### Introduction

Over the last 10–15 years there has been an explosion of activity in the design and synthesis of nanomaterials built around a wide variety of basic architectures. More recently, a portion of this effort has focused on the environmental impacts and environmental applications of these nanomaterials. Why all this interest in nanomaterials? What advantages might these tiny structures provide to environmental remediation efforts? This chapter overviews research in this area, and outlines some of the advantages that these materials provide to environmental clean-up efforts.

The most obvious advantage that nanostructured materials provide for environmental remediation is that they offer very high specific surface areas (measured in square meters per gram). Thus, for a base material of a given density, nanostructured materials can concentrate large amounts of surface area into a very small volume. When the goal is to selectively remove a toxic contaminant from a large volume feed stream (industrial effluent, contaminated groundwater, polluted river, etc.), the ability to selectively treat (sorb or react) a specific contaminant with a small amount of material has clear advantages, both in terms of efficacy and cost. Nanomaterials can do exactly this.

For certain remediation applications, especially those dealing with dilute or trace level contamination, mass-transfer issues can dominate the kinetics of the treatment process. An *in situ* treatment process can address some of this by sending the treatment out after the contaminant in a hunter–seeker sense. The facile dispersion of nanomaterials, especially nanoparticulate materials, facilitates the efficiency of this treatment strategy, particularly in highly channeled flow systems with high tortuosity (e.g., soil matrices).

Another advantage provided by nanomaterials is that the bulk of the reagent is not buried deep beneath the surface, inaccessible to solution-borne contaminants. Whether the intent is sorption or chemical modification of the contaminant, for the treatment method to be effective the contaminant species must be able to access an active reaction/binding site. Anything buried deep beneath the surface is wasted. Because of the high surface area to mass ratios of nanomaterials, most of the material is at, or adjacent to, an accessible surface.

For macroparticulate porous materials, portions of the material in the core of the particle may be kinetically inaccessible if the diffusion path-length from free solution is too long. By tailoring the particle size (or macroporosity), to provide adequate access to the nanoporosity, this limitation can be overcome. Synthetic methods have been actively investigated to develop hierarchical pore structures to address these issues.

The revolution in nanomaterials synthesis started with researchers exploring what shapes and structural motifs could be made (spherical nanoparticles, hexagonal pores, cylindrical nanorods, etc.). This was followed by an exploration of chemical compositions ( $\text{SiO}_2$ ,  $\text{ZrO}_2$ ,  $\text{CdS}$ , etc.). More recently there has been a great deal of interest in making *functional* nanomaterials, either using self-assembly, surface modification chemistry, or by tuning the chemical composition of the material itself for the job at hand. The results of these efforts are a wide variety of functional nanomaterials that have been tailored to address the environmental remediation of several chemical contaminants, including dense non-aqueous phase liquids (DNAPLs), organophosphonate pesticides, polycyclic aromatic hydrocarbons (PAHs), heavy metals, radionuclides, oxometallate anions,  $\text{CO}_2$  management, and more. These functional nanomaterials are aimed at ensuring that we have clean air to breathe and clean water to drink. Clean water, and access to clean water, is emerging as one of the key global political/economic issues of the 21<sup>st</sup> century. Nanomaterials are being designed and synthesized to address these needs. This chapter summarizes nanoparticle-based remediation technologies that use acid–base chemistry, redox chemistry and absorption to remove specifically targeted contaminants. Also included are hybrid nanoporous materials that contain chemically selective ligand fields, based on metal phosphonate chemistry and organosilane self-assembly. Examples of field tests on actual waste streams for reactive nanoparticle and hybrid nanoporous sorbents are also summarized.

## 8.2

### Nanoparticle-based Remediation Materials

The simplest, geometrically, entry into the class of nanomaterials is the spherical nanoparticle. These have been made by imposing either kinetic or thermodynamic controls on the production processes, and by confining chemical reactions and/or nucleation and growth in confined spaces [1]. Nanoparticle synthetic methods result in nanoparticles that range in size from a just a few nanometers in diameter (e.g., the reverse micelle templated synthesis of gold nanoparticles), to methods that produce nanoparticles a couple of hundred nanometers in diameter (e.g., Stöber sphere synthesis).

Nanoparticles tend to be more reactive than the corresponding bulk material because of the increased chemical potential resulting from the high degree of curvature of the interface [2]. This property can make nanoparticle-based remediation methods particularly effective since they are easily dispersed and undergo the targeted chemical reaction more readily.



## 8.2.1

**Acid–Base Chemistry**

An example of the unusual reactivity of nanomaterials and how it has been exploited for the benefit of the environment is found in the work of Klabunde's group [3–6]. For the last 10 years, this group has systematically studied the destruction of halogenated hydrocarbons by nanoparticulate metal oxide aerogels (e.g., CaO). In this work nanoparticulate CaO aerogels were prepared using the “autoclave method” (hydrolysis of calcium methoxide, followed by heating under vacuum to 500 °C for 6 hours). These aerogels typically have surface areas of the order of 120 m<sup>2</sup> g<sup>-1</sup>, and are composed of aggregates of spherical 25 nm nanoparticles. They were found to effectively destroy various chlorocarbon solvents, including CCl<sub>4</sub>, CHCl<sub>3</sub>, trichloroethylene and tetrachloroethylene. Generally, the reaction products are CaCl<sub>2</sub> and CO<sub>2</sub> (or CO) [Eq. (1)]. With the less reactive tetrachloroethylene, higher temperatures were required, and this led to the partial formation of CaCO<sub>3</sub> by reaction of the CO<sub>2</sub> product with CaO starting material.



Similar studies were carried out with aerogel MgO [7]. In this case the autoclave method resulted in material with a surface area of 364 m<sup>2</sup> g<sup>-1</sup>, a crystallite size of 4.7 nm and average pore diameter of 98.7 Å. Compressing these materials with loads of up to 20 000 lbs did not significantly change the surface area of the MgO aerogel; however, the pore volume and average pore diameter could be systematically reduced with increasing compression, introducing an interesting method of nanostructural control. A slight reduction in crystallite size was also noted. These MgO aerogels, of varying pore diameters, were evaluated for their abilities to sorb alcohols of different chain lengths; some size discrimination was noted.

Nanoparticulate aerogel MgO also reacts with 1-chlorobutane at elevated temperatures [8]. Here, the products are a mixture of butanes and MgCl<sub>2</sub>. At 200 °C the reaction stops when a monolayer of MgCl<sub>2</sub> is formed, but at higher temperatures the rate and degree of conversion are enhanced considerably. Coordination of organic molecules onto the surface of these materials has been modeled to gain a better understanding of their reactivity [9].

The “autoclave method” was improved to include a supercritical drying procedure [3]. This resulted in dry Mg(OH)<sub>2</sub> powders with surface areas as high as 1100 m<sup>2</sup> g<sup>-1</sup>, more than twice those observed previously. Solvent effects in this hydrolysis and crystallization were carried out, and increasing the amount of toluene in the alkoxide hydrolysis reaction mixture resulted in faster gelation and higher surface areas in the final product [10]. Subsequent mechanistic studies revealed that solvation of the alkoxide/alcohol mixtures is important to the gelation process and the structure of the subsequently formed dry gel [11]. This was rationalized with a partial charge model, and was found to be purely a solvent effect, and not the result of the high-temperature supercritical procedure.

An interesting manifestation of the unusual reactivity of nanoparticle interfaces is the unusual biocidal activity of aerogel MgO [12]. While aerogel MgO nanoparticles exhibited several properties that made them desirable as a potential disinfectant, when doped with a small amount of Cl<sub>2</sub> (or Br<sub>2</sub>) they displayed effective biocidal action against Gram positive bacteria, Gram negative bacteria and spore cells. This was explained by the fact that many of these small particles could very effectively coat the bacterium, and deliver a localized high concentration of active halogen to the cell membrane. ζ-Potential measurements have shown that the aerogel MgO nanoparticles have a positively charged surface, and thus will experience a Coulombic attraction with the negatively charged cell membrane, helping to drive this targeted delivery process. These chlorinated nanoparticulate metal oxides are also selective catalysts for the chlorination of alkanes [13].

Aerogel MgO nanoparticles have also been coated with various surfactants to improve their dispersability in non-polar media [14]. This is important for the destruction of pesticides (which tend to be applied in non-polar solvents) or chemical warfare agents in the event of a leak or spill. In all cases, the surfactant-coated aerogel MgO nanoparticles dispersed more readily in organic solvents after they were treated with surfactants. The surfactant-coated MgO nanoparticles effectively destroyed Paraoxon (a pesticide); however, there was some variation in efficacy from one surfactant to another. A similar trend was observed for reaction with 2-chloroethyl ethyl sulfide (a “mustard” derivative). The surfactant coating decreased the reactivity of the MgO nanomaterials in all cases, presumably by sterically blocking surface reaction sites.

Similarly, these aerogel MgO nanomaterials have been subjected to CVD carbon treatment to increase their hydrophobicity [15]. These materials have surface areas in the range of 409 to 467 m<sup>2</sup> g<sup>-1</sup>, and pore volumes of 0.39 to 0.48 cm<sup>3</sup> g<sup>-1</sup>. The carbon formed “nanoislands” on the particles, which were estimated to be 1 or 2 graphite layers thick. Partial carbon coating of these nanoparticles has a beneficial effect on their ability to destroy hazardous materials [16]. Detailed characterization of these materials has shown that carbon is first deposited inside the pores of the aerogel aggregates, and the outer surfaces are covered with carbon only after the pores are filled.

One of the many benefits provided by alkaline earth metal oxide nanomaterials is the ability to treat a wide variety of hazardous materials. In addition to those already touched upon (chlorinated solvents, microbes, pesticides and “mustards”), these materials are effective at removing hydrogen sulfide, which is very toxic, corrosive and odiferous, from gas streams. At lower temperatures (e.g., ≤100 °C), ZnO nanoparticles destroyed H<sub>2</sub>S more effectively than CaO or MgO nanoparticles [Eq. (2)], which is consistent with the superior thermodynamic driving force for the Zn sulfidation [17]. However, at higher temperatures (e.g., >250 °C), the CaO nanoparticles were the better choice, due to sintering of the ZnO nanocrystals. ZnO nanocrystals also effectively destroy chlorinated solvents, SO<sub>2</sub>, and Paraoxon [18].



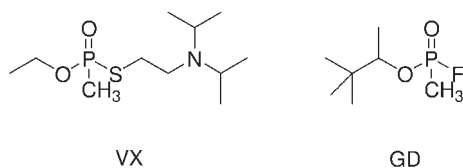


Fig. 8.1. Structures of the chemical warfare agents VX and GD.

These materials have also shown clear efficacy in the destruction of chemical warfare agents. For example, reaction of aerogel MgO nanoparticles with 2-chloroethyl ethyl sulfide [a mimic for bis(2-chloroethyl)sulfide, a.k.a. “HD”, “distilled mustard” or “mustard gas”] in pentane solution destroyed between 25% and 65% of the mustard derivative in 4 h [19]. Addition of trace amounts of water to the mixture slightly enhanced the reaction rate, while larger amounts of water reduced both reaction rate and degree of conversion. When the reaction was performed in tetrahydrofuran (THF), the rate was slower than in pentane. Reaction in methanol resulted in solvolysis. These materials have also been applied against organophosphonate chemical warfare agents, like VX and GD (a.k.a. “Soman”) (Fig. 8.1) [20]. The aerogel MgO nanomaterials were highly reactive towards GD, VX and HD. The rate was a function of surface tension and vapor pressure (these studies were carried out neat, in the absence of carrier or solvent). Similar results were obtained with CaO nanomaterials [21]. In this case, trace levels of water appear to induce an autocatalytic reaction. These chemical warfare agents were also destroyed at room temperature using nanosized  $\text{Al}_2\text{O}_3$  [22]. Here, the reactions proceed to the particle core, resulting in extremely large reaction capacities for these nerve agents.

Similar enhanced reactivities towards halogenated solvents,  $\text{SO}_2$  and Paraoxon were seen for nanocrystalline CuO and NiO [23].

Bimetallic nanocrystalline analogs to these materials have also been made and studied. For example, a mixed  $\text{Al}_2\text{O}_3/\text{MgO}$  phase was prepared and found to have a high surface area ( $559\text{--}834\text{ m}^2\text{ g}^{-1}$ ), to display remarkably high thermal stability (minimal sintering at  $700\text{ }^\circ\text{C}$ ), and to be effective in the destruction of  $\text{CCl}_4$ , Paraoxon and  $\text{SO}_2$  [24]. In a variation on this theme, the alumina may be replaced with ferric oxide; the alkaline earth oxide serves as the support for the second metal oxide. A small amount of  $\text{Fe}_2\text{O}_3$  was layered on top of the CaO support, resulting in sub-monolayer coverage, and no visible island formation [25]. This layered mixed metal oxide system effectively destroyed chlorinated solvents, organophosphonates, carbon disulfide and carbonyl sulfide. The small overlayer of  $\text{Fe}_2\text{O}_3$  induced a remarkable enhancement in reactivity.

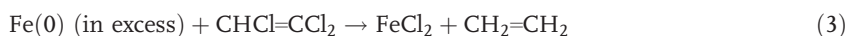
A similar layered bimetallic nanomaterial was prepared using an  $\text{Fe}_2\text{O}_3$  overlayer atop of SrO nanoparticles [26]. This system was chosen since its K-edge energy absorption was a better fit for EXAFS analysis. These studies revealed that the  $\text{Fe}_2\text{O}_3$  overlayer enhanced the reactivity of the SrO inner layers, indicating that this is not a surface-limited reaction in these bimetallic nanomaterials.

## 8.2.2

**Redox Chemistry**

Environmental remediation reactions are not limited to the acid–base reactions described above, in which electrophilic hazardous materials are converted into benign species by reaction with a nucleophilic oxide. Another area that has received much attention in recent years is the use of zero-valent metal nanoparticles to reduce certain highly oxidized species that are of environmental concern. Common targets in this area are the DNAPLs that contaminate certain groundwater supplies. As an early example, high surface area (“cryo prepared”) Zn and Sn particles were found to be more effective at reducing chlorinated solvents (e.g., CCl<sub>4</sub>, CHCl<sub>3</sub>, etc.) than their bulk counterparts [27]. Magnesium is a more electropositive metal than either Zn or Sn, and hence might be expected to more efficiently reduce the chlorinated hydrocarbons. However, Mg reacted preferentially with water, emphasizing the need to balance the reactivity of these species for successful *in situ* remediation.

Zhang and coworkers extended this work to use zero-valent iron (ZVI) nanoparticles, and demonstrated their use for *in situ* remediation of chlorocarbon contaminated groundwaters [28]. In this work, the ZVI nanoparticles (made by NaBH<sub>4</sub> reduction of FeCl<sub>3</sub> in water) were more effective than either commercial iron powders or palladized iron powders (Pd enhances reactivity in these reductions) for the dechlorination of trichloroethylene (TCE) [Eq. (3)]. The dechlorination process was complete in approximately 15 min (initial concentration was 20 ppm). Palladized nanoparticle ZVI was even more rapid and more effective than bare nanoparticle ZVI. PCBs were completely dechlorinated in 17 h at ambient temperature with the Fe/Pd nanoparticles, while bare Fe nanoparticles induced less than 25% conversion under the same conditions. These Fe nanoparticles were 1–200 nm in diameter (with most between 100 and 200 nm) and had a bulk surface area of 33.5 m<sup>2</sup> g<sup>-1</sup>.



The mechanistic role of the Pd islands has been studied in detail [29]. Chemisorption of tetrachloroethylene onto the Pd surface was studied by high-resolution XPS, revealing that dissociation of C<sub>2</sub>Cl<sub>4</sub> was complete at temperatures above 291 K. Systematic laboratory testing on all the chlorinated ethenes has shown that these ZVI nanoparticles are tens to hundreds of times faster than commercially available iron powders [30].

Similar reductions were performed using Fe/Ag nanoparticles in the dechlorination of chlorinated benzenes [31]. These materials were noticeably slower than the Fe/Pd nanoparticles reported earlier. Other bimetals (e.g., Cu/Al) have also shown promise for dehalogenating chloromethanes [32].

ZVI has also shown promise for the immobilization/fixation of As(III) in groundwater, both *in situ* and *ex situ* [33].

Mallouk and coworkers have actively studied the synthesis and application of

bimetallic nanoparticles for environmental remediation of DNAPLs and toxic heavy metals. For example, they have shown that ZVI nanoparticles (10–30 nm in diameter) supported on a PolyFlo resin (the authors refer to this adduct as a “Ferragel”) is a very effective reductive sorbent for Cr(VI) or Pb(II) contamination, and suggest that it could be useful as an *in situ* remediation strategy [34]. The surface chemistry and electrochemistry of these Ferragels have been studied in detail [35]. In addition, the Mallouk group has also looked at the synthesis and chemistry of zero-valent Ni-Fe nanoparticles [36]. Previous work had shown the value of incorporating catalytic islands onto the ZVI nanoparticle surface, and in this work they replaced the Pd with the more affordable Ni. These materials were found to have crystallite sizes of 3–5 nm, particle diameters of 10–30 nm and surface areas of 59 m<sup>2</sup> g<sup>-1</sup>. The NaBH<sub>4</sub> reduction resulted in residual boron content within these nanoparticles (~5%). These Ni/Fe nanoparticles dehalogenated all of the TCE in approximately 2 h (initial concentration 23.4 ppm). This is considerably faster than commercial Fe powders, or Fe/Ni powders, but not quite as fast as the Fe/Pd nanoparticles; this difference was attributed to the better ability of Pd to catalyze the hydrogenation reaction. These Fe and Ni/Fe nanoparticles have also been coated with “hydrophilic carbon” (i.e., carbon rendered hydrophilic by reaction with the diazonium salt of sulfanilic acid). Similar materials were coated with poly(acrylic acid). These coatings tend to lower the aggregation tendencies and sticking coefficients of these ZVI nanoparticles, thereby enhancing their transport and delivery to the contamination site. This strategy was effective in some soil types, but not all. These coated materials were also effective at dehalogenating TCE.

### 8.2.3

#### Field Deployments of ZVI

An actual field assessment of the Fe/Pd nanoparticle remediation technology was undertaken to evaluate how effectively these materials could treat a known industrial contamination site [37]. Gravity injection of nanoparticle suspensions into well holes was used to deliver the nanoparticles to the contaminated plume. TCE concentrations declined rapidly after nanoparticle injection (as much as 96.5%), with significant variability from monitoring site to monitoring site (this pattern was consistent with known colloid transport and chemistry in porous media). Details of how these materials react with contaminants in soil and water over extended periods, and *in situ* reactions of the nanoparticles in sub-surface environments, have also been summarized [38].

Quinn and coworkers have reported detailed study of an actual field deployment of *emulsified* ZVI [39]. The thinking behind this strategy is that emulsification of the nanoparticles enhances dechlorination by increasing the contact between the DNAPL and the ZVI, as well as providing vegetable oil, which is hypothesized to increase biological activity (thought to be important to certain stages of the overall reduction process). Significant reductions in TCE levels were observed at nearly all monitoring sites (commonly > 80%).

## 8.2.4

**Absorption Chemistry**

Nanoparticles do not have to chemically alter the target species to effectively remove it from the environment. Lion and coworkers have devised an interesting strategy for removing polynuclear aromatic hydrocarbons (PAHs) from contaminated soils using amphiphilic polyurethane (APU) nanoparticles [40]. These are made by emulsifying and crosslinking certain precursor polymer chains in water, and result in APU particles 17–97 nm in diameter [41]. Several variations on the basic formulation were evaluated for sorption and transport, and it was found that by increasing the size of the hydrophobic backbone it was possible to enhance the APU particle's affinity for the PAH. Increasing the number of ionic groups reduced the APU particle aggregation, and replacing carboxylates with PEG [poly(ethylene glycol)] chains prevented particle aggregation while greatly enhancing particle stability and mobility in the soils.

Similar PEG-modified urethane acrylate (PMUA) nanoparticles enhance bioremediation of PAH contaminants by increasing their bioavailability [42]. PAHs commonly sorb to soil particles and non-aqueous phase liquids (NAPLs), which limits their bioavailability. The PMUA nanoparticles released the sorbed PAHs, thereby increasing their availability to bacteria, suggesting that this might be an effective strategy for *in situ* bioremediation.

## 8.3

**Hybrid Nanostructured Remediation Materials**

Hybrid organic/inorganic materials allow for the incorporation of complex ligands into the nanomaterial structure, thereby empowering a high degree of chemical selectivity or molecular recognition. Work in this area is typified by two slightly different strategies: The first incorporates the organic ligand into the fundamental building block of the nanomaterial before construction of the scaffold, and the second entails construction of the scaffold first, followed by decoration with the organic ligand. Each approach has its advantages, and both allow for the incorporation of complex ligands and various structural backbones.

## 8.3.1

**Nanostructured Metal Phosphonates**

Abe Clearfield and coworkers have studied in great depth the synthesis and chemistry of nanostructured transition metal phosphonates. Portions of this elegant body of work have been reviewed [43, 44]. Part of the motivation behind this work is to use these nanostructured hybrid materials as ion exchangers [45]. The basic strategy is to build a scaffold based on the strong metal–phosphonate interactions to form the backbone of the material, and to tether an organic ligand to the phosphonic acid. This ligand may participate in dictating the final structure of the ma-

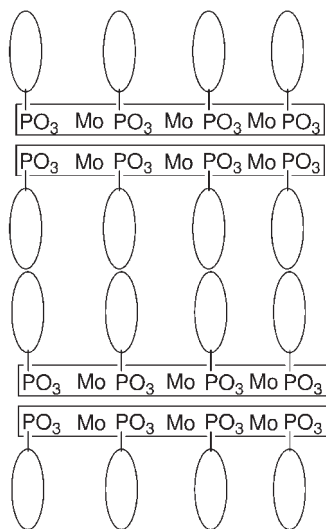


**Fig. 8.2.** Simplified schematic showing the structure of  $\text{MoO}_2(\text{O}_3\text{PC}_6\text{H}_5) \cdot \text{H}_2\text{O}$ .

terial, or it may simply be a spectator. The advantages of this synthetic strategy are that, in general, it is procedurally simple and the products are generally robust and not subject to hydrolysis or other modes of degradation.

It is useful to introduce this class of hybrid materials with the phenylphosphonic acid derivatives to showcase some basic structural features. For example, molybdenyl phenylphosphonate forms double-stranded chains, with the molybdenyl chains held together with hydrogen bonds [46]. This leaves the phenyl rings oriented roughly perpendicular to the double stranded chain, creating a hydrophobic pocket between the polar molybdenyl backbones (Fig. 8.2). Molybdenyl phenylphosphonate was found to intercalate short-chain alkyl amines, but not short-chain alcohols. Zinc phenylphosphonate, however, forms a pleated sheet, in which the zinc–phosphonate interactions form the backbone of the sheet, and the pendant phenyl rings form hydrophobic pockets between the sheets [47]. The zinc materials were also intercalated alkylamines, in this case in a 1:1 stoichiometry. Detailed characterization of the intercalation process revealed that the N atom is coordinated to the Zn center, disrupting a portion of the structure of the zinc phosphonate sheet (opening holes), but the layered sheet structure remained intact. This intercalation can be reversed by washing the adduct with dilute HCl.

A unique structural motif may be created by tying the metal-phosphonate layers together with a diphosphonic acid to create a pillared layer nanostructure. For example, Cu and Zn complexes of short-chain ( $\text{C}_2$  and  $\text{C}_3$ ) diphosphonic acids form such pillared layered structures [48]. In general, these complexes appear to be densely packed, with no open spaces for molecular intercalation. An exception

is the Cu(II) complex of propylenebis(phosphonate), in which the organic groups are about 6.8 Å apart. This is due to the presence of water molecules in the Cu-phosphonate lattice. Longer tethers might allow for increased interlayer spacing, providing more room for molecular intercalation.

Zinc biphenylenebis(phosphonate) is an interesting material [49]. When produced at pH 1.6, it forms a linear chain compound since only two of the three phosphonate oxygen atoms are ionized. When made at pH 4.5, all of the oxygen atoms are ionized and the pillared layer structure is once again obtained. To increase the microporosity (and ion-exchange capacity) of these materials, analogs were made in which a portion of the bis(phosphonate) pillars was replaced with phosphate groups. These mixed systems have notably higher surface areas than the pure pillared structures (35–136, vs. 20–28 m<sup>2</sup> g<sup>-1</sup>), and these phosphate groups were chemically accessible, as shown by acid–base titration.

The structurally similar Zr(IV) biphenylenebis(phosphonate), and the terphenylene analog, were also prepared under acidic conditions [50]. If the HF/Zr ratio was 20 or less, these materials have remarkable surface areas of ~400 m<sup>2</sup> g<sup>-1</sup> and pore diameters on the order of 10–20 Å. These pillared aromatics were also able to be sulfonated by either fuming sulfuric acid or gaseous SO<sub>3</sub>. Acid–base titration revealed an impressive acid functional density of 3.2 mmol g<sup>-1</sup>. These sulfonic acids proved to be effective acid catalysts for several reactions, and would clearly also make fine ion-exchange materials.

#### 8.3.1.1 Iminodiacetic Acids and Related Chelating Ligands

Layered metal phosphonate structures have also been prepared using tethered iminodiacetic acid (IDAA) moieties (the functional subunit of EDTA) [51, 52]. These materials have alternating Zr-phosphonate layers, and iminodiacetic acid layers. The Zr-phosphonate layers provide the structural backbone, while the pendant iminodiacetic acids can serve for molecular recognition and ion-exchange materials (Fig. 8.3). These compounds were found to be effective intercalation hosts for various alkylamines, which packed into the structures in well-ordered bilayers [52]. The complex in which the Zr center was fully substituted (i.e., there were four IDAA phosphonate ligands per metal center, resulting in only IDAA ligands in the interstitial layers) exhibited a surprisingly low affinity for transition metals and lanthanide cations at pH 2 ( $K_{ds} < 100$  mL g<sup>-1</sup> in all cases), presumably due to steric congestion. However, in compounds where a fraction of the IDAA-phosphonates were substituted with phosphate (resulting in vacancies in the interstitial layer), much higher affinities for transition metals resulted, particularly for the lanthanides. In some cases,  $K_{ds}$  as high as 25 000 were measured. Presumably, this is due to a combination of steric relief in the interstitial layer, as well as the ion-exchange capacity of the exposed phosphate hydroxyls in these vacancies.

Analogously, nitrilotris(methylenephosphonic acid) (NTP) has also been used to create functional nanostructured host materials [53]. These ligands undergo a unique self-assembly process when allowed to react with various aromatic amines (e.g., 1,10-phenanthroline, quinoline, acridine, etc.). The products are three-dimensional networks that are extensively stabilized by short, symmetrical hydro-



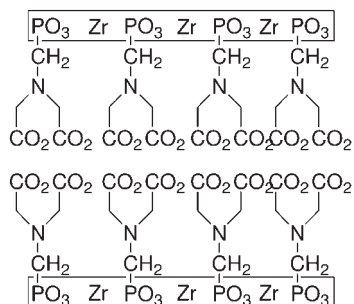


Fig. 8.3. Simplified schematic showing the structure of Zr N-(phosphonomethyl)iminodiacetic acid.

gen bonds, forming complex open porous structures. Some of these supramolecular structures (e.g., that formed between NTP and 1,7-phenanthroline) have unique chromophoric properties, forming charge-transfer complexes when protonated, suggesting that perhaps these materials might be useful in sensing/detection applications. Metal complexes of NTP have also been prepared [54]. Once again, open, highly hydrogen-bonded structures were obtained. These materials have the potential to be excellent ion-exchange materials, as well as molecular hosts.

#### 8.3.1.2 Macrocyclic Metal Phosphonates

The Clearfield group has achieved an elegant level of molecular sophistication with their design and synthesis of layered metal phosphonates containing pendant macrocyclic ligands, such as crown ethers and azamacrocycles [55]. Once again, in these compounds the metal phosphonate/phosphate forms the structural backbone of the material, while the phosphate hydroxyls and macrocyclic ligands fill the interstitial layers (Fig. 8.4). The presence of an acidic, exchangeable phosphate proton in the immediate proximity of a chemoselective macrocyclic ligand is of obvious value for ion-exchange applications. Bridging diposphonic acid crown ether complexes have also been prepared, and shown to have anion exchange capability (these azacrowns were protonated and could serve as anion hosts) [56]. Changing the metal from Zr to Cu(II) has a profound impact on the structure of these complexes [57], with the Cu(II) ion chelated within the macrocycle, and wrapped up by the phosphonate “arms”. The units were then arrayed in a linear fashion, held together by hydrogen bonds between the phosphonate units. Cadmium(II) was also chelated, in this case to form a dinuclear complex (one in the ring and one between the phosphonates); the bent geometry of this dinuclear complex ultimately gave rise to a convoluted cyclic arrangement of hydrogen-bonded complexes. For optimal exploitation of chemical selectivity of the macrocyclic ligand, it appears that Zr is the preferred metal for making these nanostructured crown ether complexes.

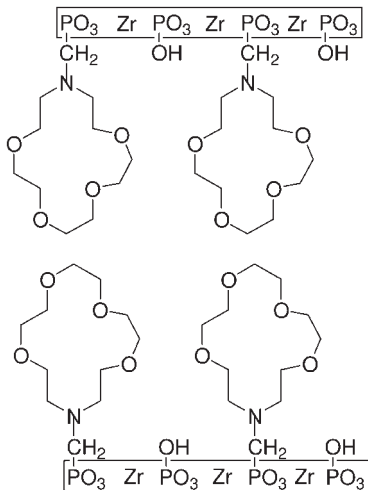


Fig. 8.4. Schematic showing the structure of Zr 1-aza-15-crown-5 phosphonate/phosphate.

### 8.3.2

#### Self-assembled Monolayers on Mesoporous Supports (SAMMS)

The surfactant-templated synthesis of mesoporous ceramic oxides has provided an excellent foundation for environmental sorbent and sensor materials [58, 59]. This foundation provides for the ability to install a wide variety of chemically selective ligand fields with which to bind the target analyte. The first work in this area addressed the need to remove mercury from groundwater [60–62]. This was accomplished by anchoring an organosilane monolayer terminated with a thiol group inside the pore surfaces of these mesoporous materials. The resulting product is called self-assembled monolayers on mesoporous supports (SAMMS) (Fig. 8.5). These hierarchical materials have unprecedented capacity and kinetics for sequestering mercury [63–65]. In addition, the mercury laden sorbent passed the EPA TCLP leachate test, revealing that the Hg is indeed very tightly bound within the mesoporous matrix. By trapping the Hg inside the nanoporous matrix, it is inaccessible to microbial attack and subsequent methylation and release (a limitation of polymer-based ion-exchange resins). Other “soft” heavy metals, like Cd, Au and Ag can also be bound by thiol-terminated SAMMS [63]. Other groups have also attached thiol-terminated monolayers inside similar mesoporous materials [66–68]. Jaroniec has tackled Hg by attaching some related sulfur-based ligand systems inside mesoporous silica phases [69]. Jaroniec’s materials have excellent Hg binding capacity, but can only be partially regenerated.

##### 8.3.2.1 Thiol SAMMS Performance with Actual Waste

Bench-scale treatability tests were carried out at Pacific Northwest National Laboratory (PNNL) on actual waste to evaluate the mercury adsorption performance of

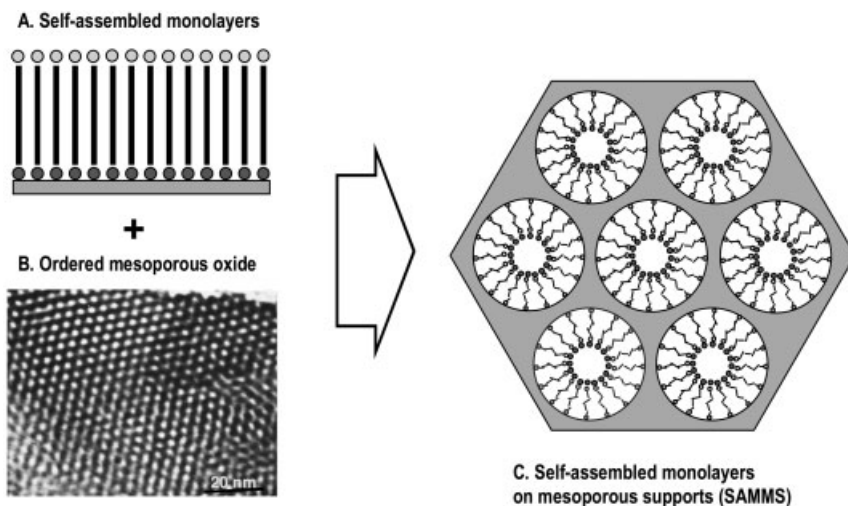


Fig. 8.5. Schematic showing the structure of self-assembled monolayers on mesoporous supports (SAMMS).

thiol-SAMMS from a real-world waste stream, originating from a pilot-scale waste glass melter operation. The principal dissolved components in this alkaline waste stream (pH 8.5) consisted mainly of sodium borate ( $\sim 30$  mM) and sodium fluoride ( $\sim 9$  mM), with minor concentrations of sodium chloride ( $\sim 3$  mM), sodium nitrite ( $\sim 0.9$  mM), sodium sulfate ( $\sim 0.8$  mM), sodium nitrate ( $\sim 0.6$  mM) and sodium iodide ( $\sim 0.2$  mM). The mercury concentration in solution was measured to be  $4.64$  mg L<sup>-1</sup>. Iodide ion is a strong mercury complexing ligand and the speciation calculations for this mixture indicated that all the soluble mercury existed as iodide complexes ( $\text{HgI}_2^0$ ,  $\sim 52\%$ ;  $\text{HgI}_3^-$ ,  $\sim 47\%$ ; and  $\text{HgI}_4^{2-}$ ,  $\sim 1\%$ ). Other dissolved components such as Al, Ba, Ca, Cd, Co, Cr, Cu, Fe, Mo, Ni,  $\text{PO}_4$ , Pb and Zn were present in trace concentrations ( $< 2$  mg L<sup>-1</sup>). To test the effectiveness of thiol-SAMMS in adsorbing mercury from this complexing matrix, a 50 mL aliquot of the filtered solution was treated with 40 mg of thiol-SAMMS (solution to solid ratio 1250 mL g<sup>-1</sup>) and after 8 h of equilibration the residual mercury concentration was determined.

The results (Table 8.1) indicate that thiol-SAMMS effectively removes mercury to meet the U.S. Environmental Protection Agency's (EPA) regulatory level of  $0.15$  mg L<sup>-1</sup> from both filtered and unfiltered samples of waste solution. However, filtering prior to thiol-SAMMS treatment was more effective than treating unfiltered waste solution. By filtering the solution prior to thiol-SAMMS treatment, we can remove  $\sim 99\%$  of mercury in the waste stream, leaving a residual concentration of only  $0.05$  mg L<sup>-1</sup>. Notably, the residual mercury concentration resulting from the first experiment is about an order of magnitude less than the EPA regulatory limit [70]. These results confirmed previous observations that thiol-SAMMS can effectively remove iodide-complexed mercury from solutions [65].

**Tab. 8.1.** Thiol-SAMMS mercury removal data for melter condensate waste solution.

Tr #	Waste solution	Conc (mg L <sup>-1</sup> )	Removal (%)	pH
0	Untreated	4.640	–	8.5
1	Filtered – treated <sup>[a]</sup>	0.052	98.9	8.0
1A	Unfiltered – treated <sup>[b]</sup>	0.179	96.1	8.0
2A	Unfiltered – treated <sup>[c]</sup>	0.148	96.8	8.0

EPA discharge limit for Hg in treated effluent is 0.15 mg L<sup>-1</sup>.

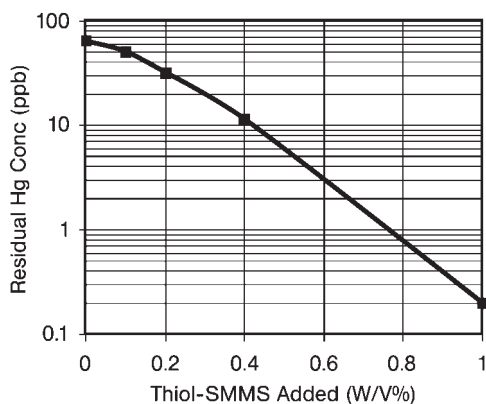
<sup>a</sup> 50 mL of waste solution filtered (0.45 μm) and treated with 40 mg of 35/thiol-SAMMS.

<sup>b</sup> 50 mL unfiltered waste solution treated with 60 mg of 35/thiol-SAMMS.

<sup>c</sup> 50 mL unfiltered waste solution treated with 40 mg of 65/thiol-SAMMS.

### 8.3.2.2 Thiol SAMMS Performance on Contaminated Oil

Not all chemical separation needs to involve aqueous media, and sorbent materials that are effective in aqueous systems are not always effective in hydrophobic media. Previous testing at the Oak Ridge National Laboratory demonstrated that thiol-SAMMS is effective at removing Hg from contaminated vacuum pump oil [71]. These batch tests consisted of equilibrating 50 mL aliquots of oil containing about 650 ppb mercury with thiol-SAMMS (w/v 0.1–1%) for 24 h. Following equilibration, the residual mercury concentration in the treated oil was measured. The data (Fig. 8.6) showed that the residual concentration of mercury decreased logarithmically as a function of thiol-SAMMS added to the solution (w/v). Thus, these

**Fig. 8.6.** Mercury adsorption by thiol-SAMMS from vacuum pump oil.

tests demonstrated that thiol-SAMMS could also effectively remove mercury from viscous, hydrophobic media, such as contaminated vacuum pump oil.

### 8.3.2.3 Anion SAMMS

Anion exchange technologies are not as mature as cation exchange methods, and anion exchange materials tend to be built around quaternary ammonium salt functionalities. While this approach works, it doesn't generally provide a direct anion–cation interaction, and therefore selectivity is dictated by indirect properties, such as anion hydration energies, adduct solubilities, etc. SAMMS have been made in which the pore surfaces have been lined with cationic transition metal complexes, thereby allowing a cationic “docking station” for the target anion [72–75]. With a metal-tris(ethylenediamine) complex (Cu-EDA), the complex contains a trifurcate cleft on the upper surface, with three exofacial protons, creating a stereospecific binding site that is ideally structured for binding tetrahedral oxometallate anions, like arsenate and chromate [72]. By selecting the metal and oxidation state appropriately, it is possible to install a metal cation such that, while forced into an octahedral coordination geometry by the chelating diamines, the cation is electronically predisposed to undergo Jahn–Teller distortion to alleviate orbital degeneracy. This provides a driving force for departing from an octahedral coordination environment and facilitates a direct bond between the anion and the metal center. Indeed, detailed EXAFS studies have revealed that Cu-EDA SAMMS loses two of the primary amine nitrogen ligands and adopts a trigonal bipyramidal coordination environment when binding oxometallate anions (Fig. 8.7) [73]. Sulfate is a ubiquitous tetrahedral anion, commonly encountered in many groundwaters, and while it is indeed bound by Cu-EDA SAMMS, the binding is reversible and it can be displaced by more problematic anions like arsenate and chromate [72]. Binding kinetics are fast, with equilibrium achieved in minutes.

This sort of anion binding can also be used as a synthetic strategy to install more complex interfacial functionality. For example, Cu-EDA SAMMS treated with ferrocyanide anion affords the corresponding Cu-EDA ferrocyanide adduct (Fig. 8.8), which has excellent affinity for binding cesium [76]. Cesium binding capacity is

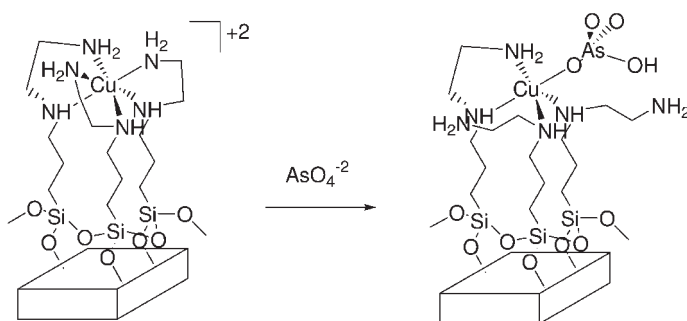


Fig. 8.7. Schematic showing Cu-EDA SAMMS binding an arsenate anion.

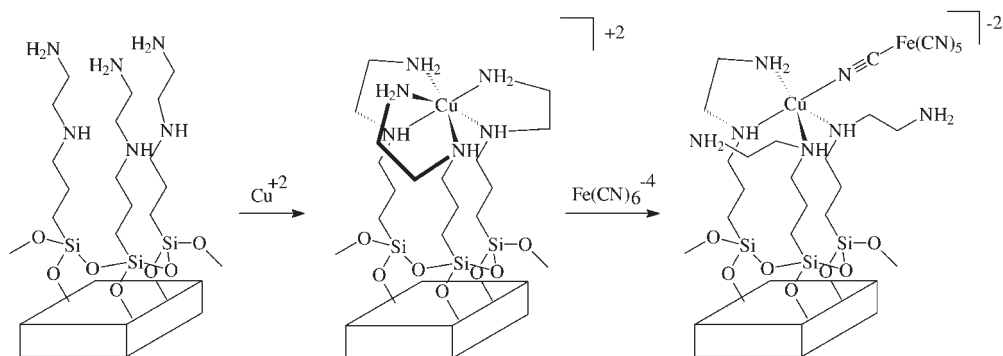


Fig. 8.8. Schematic showing the synthesis of ferrocyanide Cu-EDA SAMMS.

good and binding kinetics are moderately fast, with equilibrium achieved in less than half an hour.

Metallation can also be used as a synthetic strategy to create new classes of SAMMS. For example, thiol-SAMMS used to bind Hg or Ag have an excellent affinity for radioiodide [77].

#### 8.3.2.4 Actinide SAMMS

More sophisticated ligand fields have also been incorporated into mesoporous materials to create highly selective sorbent materials for radioactive actinides [78–81]. In this case, CMPO-inspired [78, 79], or HOPO classes [80, 81] of ligand were installed inside a mesoporous silica matrix and found to have exceptional selectivity and affinity for binding lanthanide and actinide species from complex mixtures. For example, the acetamide-phosphonate (a.k.a. “Ac-Phos”) ligand can be employed in either the ester or acid form, making it well-suited for either hydrophobic (e.g., contaminated cutting oils) or hydrophilic waste streams, respectively. The phosphonate-based ligands exhibited very good affinities for all actinides studied (except  $\text{NpO}_2^+$ ), down to pHs as low as 0.5. The actinide-binding affinities of similar carboxylate-based ligand systems drop off at lower pHs [78, 79]. The HOPO class of ligands is the result of 20+ years of ligand design and development by Ken Raymond’s group at Berkeley, and these ligands are superb actinide binders [82–84]. Incorporation of the HOPO ligands into the SAMMS superstructure has resulted in a superior class of actinide sorbent material [80, 81]. In this case the 3,2-HOPO ligand was the most effective actinide ligand, capable of even binding the hard-to-grab  $\text{NpO}_2^+$  cation very effectively, with  $K_{\text{d}}$ s in excess of 150 000 (Fig. 8.9).

#### 8.3.3

##### Functional CNTs

Self-assembly is not limited to organosilanes on metal oxide surfaces. Chen et al. have reported an interesting variation on this theme [85]. Using this approach, Fif

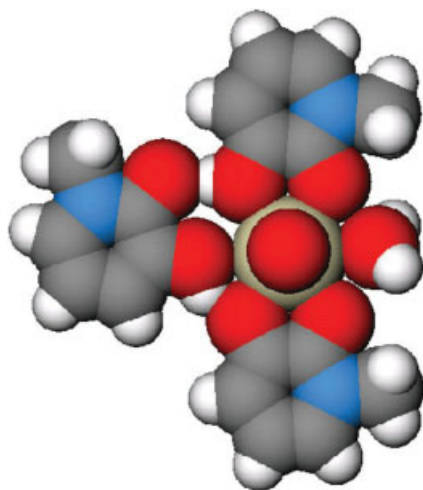


**Fig. 8.9.** Hexagonal bipyramidal geometry of the complex formed between 3,2-HOPO and the  $\text{NpO}_2$  cation (looking down the  $\text{O}=\text{Np}=\text{O}$  bond). The brown atom in the center is Np, and the red atoms surrounding it are O atoms.

The pair of bidentate 3,2-HOPO ligands (top and bottom) are strongly hydrogen bound to the monodentate 3,2-HOPO ligand (left). The remaining equatorial coordination site is filled by a water molecule (on the right).

field and coworkers have successfully modified carbon nanotubes for selective binding of catalysts, radionuclides and  $\text{CO}_2$  [86]. Here, supercritical  $\text{CO}_2$  was an advantageous reaction medium for the self-assembly process, as it can dissolve the modified pyrenes used as anchors, but provides poor solvent shielding, so that the pyrene/CNT  $\pi$ -stacking interaction is allowed to predominate, thereby facilitating self-assembly. These selectively functionalized CNT's are envisioned to be very useful in environmental sensing and detection applications.

## 8.4

### Conclusions

Nanomaterials offer many useful properties for environmental remediation: high surface area, enhanced interfacial reactivity, easy dispersability, and facile sorption kinetics. Nanoparticle-based strategies have been built around alkaline earth oxide materials, zero-valent metals and crosslinked polymers. These different classes of materials offer widely differing chemistries that can be tailored to address differing remediation needs, from DNAPLs to chemical warfare agents to PAHs. Hybrid nanostructured materials are also finding application in environmental chemistry. The elegant work of Clearfield and coworkers has shown that layered metal phosphonates can be made in which the interstitial layers are composed of a wide variety of ligand structures, including crown ethers, amino acids and arylsulfonates. Surfactant templated synthesis of mesoporous ceramic oxides has provided a versatile foundation upon which a wide range of environmental sorbents can be made,

tailored to sequester “soft” heavy metals, oxometallate anions, cesium and the actinides. Similar self-assembly routes are currently being explored as ways to chemically modify carbon nanotubes. Functional nanomaterials constitute a versatile, and powerful, toolbox for environmental remediation. The future is indeed bright for environmental nanomaterials.

## References

- 1 CAO, G. *Nanostructures and Nanomaterials: Synthesis Properties and Applications*, Imperial College Press, London, 2004, pp. 51–104.
- 2 CAO, G. *Nanostructures and Nanomaterials: Synthesis Properties and Applications*, Imperial College Press, London, 2004, pp. 26–31.
- 3 KOPER, O. B., LAGADIC, I., VOLODIN, A., KLABUNDE, K. J., Alkaline-earth oxide nanoparticles obtained by aerogel methods. Characterization and rational for unexpectedly high surface chemical reactivities, *Chem. Mater.* **1997**, 9, 2468–2480.
- 4 KOPER, O. B., WOVCHKO, E. A., GLASS, J. A. JR., YATES, J. T. JR., KLABUNDE, K. J., Decomposition of  $\text{CCl}_4$  on  $\text{CaO}$ , *Langmuir* **1995**, 11, 2054–2059.
- 5 KOPER, O. B., LAGADIC, I., KLABUNDE, K. J., Destructive adsorption of chlorinated hydrocarbons on ultrafine (nanoscale) particles of calcium oxide. 2, *Chem. Mater.* **1997**, 9, 838–848.
- 6 KOPER, O. B., KLABUNDE, K. J., Destructive adsorption of chlorinated hydrocarbons on ultrafine (nanoscale) particles of calcium oxide. 3. Chloroform, trichloroethene, and tetrachloroethene, *Chem. Mater.* **1997**, 9, 2481–2485.
- 7 RICHARDS, R., LI, W., DECKER, S., DAVIDSON, C., KOPER, O., ZAIKOVSKI, V., VOLODIN, A., RIEKER, T., KLABUNDE, K. J., Consolidation of metal oxide nanocrystals. Reactive pellets with controllable pore structure that represent a new family of porous inorganic materials, *J. Am. Chem. Soc.* **2000**, 122, 4921–4925.
- 8 FENELONOV, V. B., MEL'GUNOV, M. S., MISHAKOV, I. V., RICHARDS, R. M., CHESNOKOV, V. V., VOLODIN, A. M., KLABUNDE, K. J., Changes in texture and catalytic activity of nanocrystalline  $\text{MgO}$  during its transformation to  $\text{MgCl}_2$  in the reaction with 1-chlorobutane, *J. Phys. Chem. B* **2001**, 105, 3937–3941.
- 9 KAKKAR, R., KAPOOR, P. N., KLABUNDE, K. J., Theoretical study of the adsorption of formaldehyde on magnesium oxide nanosurfaces: Size effects and the role of low-coordinated and defect sites, *J. Phys. Chem. B* **2004**, 108, 18 140–18 148.
- 10 DIAO, Y., WALAWENDER, W. P., SORENSEN, C. M., KLABUNDE, K. J., RICKER, T., Hydrolysis of magnesium methoxide. Effects of toluene on gel structure and gel chemistry, *Chem. Mater.* **2002**, 14, 362–368.
- 11 RANJIT, K. T., KLABUNDE, K. J., Solvent effects in the hydrolysis of magnesium methoxide, and the production of nanocrystalline magnesium hydroxide. An aid in understanding the formation of porous inorganic materials, *Chem. Mater.* **2005**, 17, 65–73.
- 12 STOIMENOV, P. K., KLINGER, R. L., MARCHIN, G. L., KLABUNDE, K. J., Metal oxide nanoparticles as bactericidal agents, *Langmuir* **2002**, 18, 6679–6686.
- 13 SUN, N., KLABUNDE, K. J., Nanocrystal metal oxide-chlorine adducts: Selective catalysts for chlorination of alkanes, *J. Am. Chem. Soc.* **1999**, 121, 5587–5588.
- 14 JEEVANANDAM, P., KLABUNDE, K. J., Redispersion and reactivity studies on surfactant-coated magnesium oxide nanoparticles, *Langmuir* **2003**, 19, 5491–5495.
- 15 MEL'GUNOV, M. S., MEL'GUNOV, E. A., ZAIKOVSKI, V. I., FENELONOV, V. B., BEDILO, A. F., KLABUNDE, K. J.,



- Carbon dispersion and morphology in carbon-coated nanocrystalline MgO, *Langmuir* **2003**, *19*, 10426–10433.
- 16 BEDILO, A. F., SIGEL, M. J., KOPER, O. B., MEL'GUNOV, M. S., KLABUNDE, K. J., Synthesis of carbon-coated MgO nanoparticles, *J. Mater. Chem.* **2002**, *12*, 3599–3604.
- 17 CARNES, C. L., KLABUNDE, K. J., Unique chemical reactivities of nanocrystalline metal oxides towards hydrogen sulfide, *Chem. Mater.* **2002**, *14*, 1806–1811.
- 18 CARNES, C. L., KLABUNDE, K. J., Synthesis, isolation, and chemical reactivity studies of nanocrystalline zinc oxide, *Langmuir* **2000**, *16*, 3764–3772.
- 19 NARSKE, R. M., KLABUNDE, K. J., FULTZ, S., Solvent effects on the heterogeneous adsorption and reactions of (2-chloroethyl)ethyl sulfide on nanocrystalline magnesium oxide, *Langmuir* **2002**, *18*, 4819–4825.
- 20 WAGNER, G. W., BARTRAM, P. W., KOPER, O., KLABUNDE, K. J., Reactions of VX, GD, and HD with nanosize MgO, *J. Phys. Chem. B* **1999**, *103*, 3225–3228.
- 21 WAGNER, G. W., KOPER, O., LUCAS, E., DECKER, S., KLABUNDE, K. J., Reactions of VX, GD, and HD with nanosize CaO: Autocatalytic dehydrohalogenation of HD, *J. Phys. Chem. B* **2000**, *104*, 5118–5123.
- 22 WAGNER, G. W., PROCELL, L. R., O'CONNOR, R. J., MUNAVALLI, S., CARNES, C. L., KAPOOR, P. N., KLABUNDE, K. J., Reactions of VX, GD, and HD with nanosize Al<sub>2</sub>O<sub>3</sub>: Formation of aluminophosphates, *J. Am. Chem. Soc.* **2001**, *123*, 1636–1644.
- 23 CARNES, C. L., STIPP, J., KLABUNDE, K. J., Synthesis, characterization, and adsorption studies of nanocrystalline copper oxide and nickel oxide, *Langmuir* **2002**, *18*, 1352–1359.
- 24 CARNES, C. L., KAPOOR, P. N., KLABUNDE, K. J., Synthesis, characterization, and adsorption studies of nanocrystalline aluminum oxide and a bimetallic nanocrystalline aluminum oxide/magnesium oxide, *Chem. Mater.* **2002**, *14*, 2922–2929.
- 25 DECKER, S. P., KLABUNDE, J. S., KHALEEL, A., KLABUNDE, K. J., Catalyzed destructive adsorption of environmental toxins with nanocrystalline metal oxides. Fluoro-, chloro-, bromocarbons, sulfur, and organophosphorous compounds, *Environ. Sci. Technol.* **2002**, *36*, 762–768.
- 26 DECKER, S., LAGADIC, I., KLABUNDE, K. J., EXAFS observation of the Sr and Fe site structural environment in SrO and Fe<sub>2</sub>O<sub>3</sub>-coated SrO nanoparticles used as carbon tetrachloride destructive adsorbents, *Chem. Mater.* **1998**, *10*, 674–678.
- 27 BORONINA, T., KLABUNDE, K. J., Destruction of organohalides in water using metal particles: Carbon tetrachloride/water reactions with magnesium, tin, and zinc, *Environ. Sci. Technol.* **1995**, *29*, 1511–1517.
- 28 WANG, C. B., ZHANG, W. X., Synthesizing nanoscale iron particles for rapid and complete dechlorination of TCE and PCBs, *Environ. Sci. Technol.* **1997**, *31*, 2154–2156.
- 29 PARK, K. T., KLIER, K., WANG, C. B., ZHANG, W. X., Interaction of tetrachloroethylene with Pd(100) studied by high-resolution x-ray photoemission spectroscopy, *J. Phys. Chem. B* **1997**, *101*, 5420–5428.
- 30 LIEN, H. L., ZHANG, W. X., Nanoscale iron particles for complete reduction of chlorinated ethenes, *Colloids Surf. A: Physicochem. Eng. Aspects* **2001**, *191*, 97–105.
- 31 XU, Y., ZHANG, W. X., Subcolloidal Fe/Ag particles for reductive dehalogenation of chlorinated benzenes., *Ind. Eng. Chem. Res.* **2000**, *39*, 2238–2244.
- 32 LIEN, H. L., ZHANG, W. X., Enhanced dehalogenation of halogenated methanes by bimetallic Cu/Al, *Chemosphere* **2002**, *49*, 371–378.
- 33 KANEL, S. R., MANNING, B., CHARLET, L., CHOI, H., Removal of arsenic(III) from groundwater by nanoscale zero-valent iron, *Environ. Sci. Technol.* **2005**, *39*, 1291–1298.
- 34 PONDER, S. M., DARAB, J. G., MALLOUK, T. E., Remediation of Cr(VI) and Pb(II) aqueous solutions using supported, nanoscale zero-valent

- iron, *Environ. Sci. Technol.* **2000**, *34*, 2564–2569.
- 35 PONDER, S. M., DARAB, J. G., BUCHER, J., CAULDER, D., CRAIG, I., DAVIS, L., EDELSTEIN, N., LUKENS, W., NITSCHKE, H., RAO, L., SHUH, D. K., MALLOW, T. E., Surface chemistry and electrochemistry of supported zerovalent iron nanoparticles in the remediation of aqueous metal contaminants, *Chem. Mater.* **2001**, *13*, 479–486.
- 36 SCHRICK, B., BLOUGH, J. L., JONES, A. D., MALLOW, T. E., Hydrodechlorination of trichloroethylene to hydrocarbons using bimetallic nickel-iron nanoparticles, *Chem. Mater.* **2002**, *14*, 5140–5147.
- 37 ELLIOTT, D. W., ZHANG, W. X., Field assessment of nanoscale bimetallic particles for groundwater treatment, *Environ. Sci. Technol.* **2001**, *35*, 4922–4926.
- 38 ZHANG, W. X., Nanoscale iron particles for environmental remediation: An overview, *J. Nanoparticle Res.* **2003**, *5*, 323–332.
- 39 QUINN, J., GEIGER, C., CLAUSEN, C., BROOKS, K., COON, C., O'HARA, S., KRUG, T., MAJOR, D., YOON, W. S., GAVASCAR, A., HOLDSWORTH, T., Field demonstration of DNAPL dehalogenation using emulsified zerovalent iron, *Environ. Sci. Technol.* **2005**, *39*, 1309–1318.
- 40 KIM, J. Y., COHEN, C., SCHULER, M. L., LION, L. W., Use of amphiphilic polymer particles for in situ extraction of sorbed phenanthrene from a contaminated aquifer material, *Environ. Sci. Technol.* **2000**, *34*, 4133–4139.
- 41 TUNGITTIPLAKORN, W., LION, L. W., COHEN, C., KIM, J. Y., Engineered polymeric nanoparticles for soil remediation, *Environ. Sci. Technol.* **2004**, *38*, 1605–1610.
- 42 TUNGITTIPLAKORN, W., COHEN, C., LION, L. W., Engineered polymeric nanoparticles for bioremediation of hydrophobic contaminants, *Environ. Sci. Technol.* **2005**, *39*, 1354–1358.
- 43 CLEARFIELD, A., KRISHNAMOHAN SHARMA, C. V., ZHANG, B. P., Crystal engineered supramolecular metal phosphonates: Crown ethers and iminodiacetates, *Chem. Mater.* **2001**, *13*, 3099–3112.
- 44 CLEARFIELD, A., Organically pillared micro- and mesoporous materials, *Chem. Mater.* **1998**, *10*, 2801–2810.
- 45 CLEARFIELD, A., Inorganic ion exchangers: A technology ripe for development, *Ind. Eng. Chem. Res.* **1995**, *34*, 2865–2872.
- 46 POOJARY, D. M., ZHANG, Y., ZHANG, B., CLEARFIELD, A., Synthesis, x-ray powder structure, and intercalation behavior of molybdenyl phenylphosphonate,  $\text{MoO}_2(\text{O}_3\text{PC}_6\text{H}_5)_2 \cdot \text{H}_2\text{O}$ , *Chem. Mater.* **1995**, *7*, 822–827.
- 47 POOJARY, D. M., CLEARFIELD, A., Coordinative intercalation of alkylamines into layered zinc phenylphosphonate. Crystal structures from x-ray powder diffraction data, *J. Am. Chem. Soc.* **1995**, *117*, 11 278–11 284.
- 48 POOJARY, D. M., ZHANG, B., CLEARFIELD, A., Pillared layered metal phosphonates. Synthesis and x-ray powder structures of copper and zinc alkylenebis(phosphonates), *J. Am. Chem. Soc.* **1997**, *119*, 12 550–12 559.
- 49 ZHANG, B., POOJARY, D. M., CLEARFIELD, A., Synthesis and characterization of layered zinc biphenylenebis(phosphonate) and three mixed-component arylenebisphosphonate/phosphates, *Inorg. Chem.* **1998**, *37*, 1844–1852.
- 50 WANG, Z., HEISING, J. M., CLEARFIELD, A., Sulfonated microporous organic-inorganic hybrids as strong Bronsted acids, *J. Am. Chem. Soc.* **2003**, *125*, 10 375–10 383.
- 51 ZHANG, B., POOJARY, D. M., CLEARFIELD, A., Synthesis, characterization, and amine intercalation behavior of zirconium N-(phosphonomethyl)iminodiacetic acid layered compounds, *Chem. Mater.* **1996**, *8*, 1333–1340.
- 52 ZHANG, B., POOJARY, D. M., CLEARFIELD, A., Synthesis and crystal structure of the linear chain zirconium organophosphonate  $(\text{NH}_4)\text{Zr}[\text{F}_2][\text{H}_3\{\text{O}_3\text{PCH}_2\text{NH}(\text{CH}_2\text{CO}_2)_2\}_2] \cdot 3\text{H}_2\text{O} \cdot \text{NH}_4\text{Cl}$ , *Inorg. Chem.* **1998**, *37*, 249–254.
- 53 KRISHNAMOHAN SHARMA, C. V.,

- CLEARFIELD, A., Three-dimensional hexagonal structures from a novel self-complementary molecular building block, *J. Am. Chem. Soc.* **2000**, *122*, 4394–4402.
- 54 CABEZA, A., OUYANG, X., KRISHNAMOHAN SHARMA, C. V., ARANDA, M. A. G., BRUQUE, S., CLEARFIELD, A., Complexes formed between nitriлотris(methylenephosphonic acid) and  $M^{2+}$  transition metals: Isostructural organic-inorganic hybrids, *Inorg. Chem.* **2002**, *41*, 2325–2333.
- 55 ZHANG, B., CLEARFIELD, A., Crown ether pillared and functionalized layered zirconium phosphonates: A selective new strategy to synthesize novel ion selective materials, *J. Am. Chem. Soc.* **1997**, *119*, 2751–2752.
- 56 CLEARFIELD, A., POOJARY, D. M., ZHANG, B., ZHAO, B., DERESKEI-KOVACS, A., Azacrown ether pillared layered zirconium phosphonates and the crystal structure of  $N,N'$ -bis(phosphonomethyl)-1,10-diaza-18-crown-6, *Chem. Mater.* **2000**, *12*, 2745–2752.
- 57 MAO, J. G., WANG, Z., CLEARFIELD, A., Synthesis, characterization, and crystal structures of two new divalent metal complexes of  $N,N'$ -bis(phosphonomethyl)-1,10-diaza-18-crown-6: A hydrogen bonded 1D array and a 3D network with a large channel, *Inorg. Chem.* **2002**, *41*, 3713–3720.
- 58 FRYXELL, G. E., ADDLEMAN, R. S., MATTIGOD, S. V., LIN, Y., ZEMANIAN, T. S., WU, H., BIRNBAUM, J. C., LIU, J., FENG, X., Environmental and sensing applications of molecular self-assembly, in *Encyclopedia of Nanoscience and Nanotechnology*, Marcel-Dekker, **2004**, pp. 1135–1145.
- 59 LIN, Y., YANTASEE, W., FRYXELL, G. E., Electrochemical sensors based on functionalized nanoporous silica, in *Encyclopedia of Nanoscience and Nanotechnology*, Marcel-Dekker, **2004**, pp. 1051–1061.
- 60 FENG, X., FRYXELL, G. E., WANG, L. Q., KIM, A. Y., LIU, J., Organic monolayers on ordered mesoporous supports, *Science* **1997**, *276*, 923–926.
- 61 LIU, J., FENG, X., FRYXELL, G. E., WANG, L. Q., KIM, A. Y., GONG, M., Hybrid mesoporous materials with functionalized monolayers, *Adv. Mater.* **1998**, *10*, 161–165.
- 62 MERCIER, L., PINNAVAIA, T. J., Heavy metal ion adsorbents formed by the grafting of a thiol functionality to mesoporous silica molecular sieves: Factors affecting Hg(II) uptake, *Chem. Mater.* **1997**, *9*, 2491–2498.
- 63 MATTIGOD, S. V., FRYXELL, G. E., FENG, X., LIU, J., Self-assembled monolayers on mesoporous supports for metal separation, in *Metal Separation Technologies Beyond 2000: Integrating Novel Chemistry with Processing*, ed. K. C. LIDDELL, D. J. CHAIKO, The Minerals, Metals and Materials Society, Warrendale, PA, USA, **1999**, pp. 71–79.
- 64 KEMNER, K. M., FENG, X., LIU, J., FRYXELL, G. E., WANG, L.-Q., KIM, A. Y., GONG, M., MATTIGOD, S. V., Investigation of the local chemical interactions between Hg and self assembled monolayers on mesoporous supports, *J. Synchrotron Rad.* **1999**, *6*, 633–635.
- 65 MATTIGOD, S. V., FENG, X., FRYXELL, G. E., LIU, J., GONG, M., Separation of complexed mercury from aqueous wastes using self-assembled mercaptan on mesoporous silica, *Sep. Sci. Technol.* **1999**, *34*, 2329–2345.
- 66 KIM, Y., LEE, B., YI, J., Effect of framework and textural porosities of functionalized mesoporous silica on metal ion adsorption capacities, *Sep. Sci. Technol.* **2004**, *39*, 1427–1442.
- 67 WALCARIUS, A., ETIENNE, M., LEBEAU, B., Rate of access to the binding sites in organically modified silicates. 2. Ordered mesoporous silicas grafted with amine or thiol groups, *Chem. Mater.* **2003**, *15*, 2161–2173.
- 68 KANG, T., PARK, Y., YI, J., Highly selective adsorption of  $Pt^{2+}$  and  $Pd^{2+}$  using thiol-functionalized mesoporous silica, *Ind. Eng. Chem. Res.* **2004**, *43*, 1478–1484.
- 69 ANTOCHSHUK, V., OLKHOVYK, O., JARONIEC, M., PARK, I.-S., RYOO, R., Benzoylthiourea-modified mesoporous silica for mercury(II) removal, *Langmuir* **2003**, *19*, 3031–3034.

- 70 *Universal Treatment Standards 40CFR* § 268.38, United States Environmental Protection Agency, Washington, D.C., USA.
- 71 KLASSON, K. T., *Treatment of Mercury Contaminated Oil from the Mound site. Topical Report.* Oak Ridge National Laboratory, Oak Ridge, TN 37831, **2000**.
- 72 FRYXELL, G. E., LIU, J., GONG, M., HAUSER, T. A., NIE, Z., HALLEN, R. T., QIAN, M., FERRIS, K. F., Design and synthesis of selective mesoporous anion traps, *Chem. Mater.* **1999**, *11*, 2148–2154.
- 73 KELLY, S., KEMNER, K. M., FRYXELL, G. E., LIU, J., MATTIGOD, S. V., FERRIS, K. F., An X-ray absorption fine structure spectroscopy study of the interactions between contaminant tetrahedral anions to self-assembled monolayers on mesoporous supports, *J. Phys. Chem. B* **2001**, *105*, 6337–6346.
- 74 YOSHITAKE, H., YOKOI, T., TATSUMI, T., Adsorption of chromate and arsenate by amino-functionalized MCM-41 and SBA-1, *Chem. Mater.* **2002**, *14*, 4603–4610.
- 75 YOSHITAKE, H., YOKOI, T., TATSUMI, T., Adsorption behavior of arsenate at transition metal cations captured by amino-functionalized mesoporous silicas, *Chem. Mater.* **2003**, *15*, 1713–1721.
- 76 LIN, Y., FRYXELL, G. E., WU, H., ENGLEHARD, M., Selective sorption of cesium using self-assembled monolayers on mesoporous supports (SAMMS), *Environ. Sci. Technol.* **2001**, *35*, 3962–3966.
- 77 MATTIGOD, S. V., FRYXELL, G. E., SERNE, R. J., PARKER, K. E., MANN, F. M., Evaluation of novel getters for adsorption of radioiodine from groundwater and waste glass leachates, *Radiochim. Acta* **2003**, *91*, 539–545.
- 78 FRYXELL, G. E., WU, H., LIN, Y., SHAW, W. J., BIRNBAUM, J. C., LINEHAN, J. C., NIE, Z., KEMNER, K. M., KELLY, S., Lanthanide selective sorbents: Self-assembled monolayers on mesoporous supports (SAMMS), *J. Mater. Chem.* **2004**, *14*, 3356–3363.
- 79 FRYXELL, G. E., LIN, Y., FISKUM, S., BIRNBAUM, J. C., WU, H., KEMNER, K. M., KELLY, S., Actinide sequestration using self-assembled monolayers on mesoporous supports (SAMMS), *Environ. Sci. Technol.* **2005**, *39*, 1324–1331.
- 80 LIN, Y., FISKUM, S. K., YANTASEE, W., WU, H., MATTIGOD, S. V., FRYXELL, G. E., RAYMOND, K. N., XU, J., Incorporation of hydroxypyridinone (HOPO) ligands into self-assembled monolayers on mesoporous supports (SAMMS) for selective actinide sequestration., *Environ. Sci. Technol.* **2005**, *39*, 1332–1337.
- 81 YANTASEE, W., FRYXELL, G. E., LIN, Y., WU, H., RAYMOND, K. N., XU, J., Hydroxypyridinone (HOPO) functionalized self-assembled monolayers on mesoporous supports (SAMMS) for sequestering rare earth cations, *J. Nanosci. Nanotechnol.* **2005**, *5*(9), 1537–1540.
- 82 GORDEN, A. E. V., XU, J., RAYMOND, K. N., DURBIN, P. W., Rational design of sequestering agents for plutonium and other actinides, *Chem. Rev.* **2003**, *103*, 4207–4282.
- 83 XU, J., WHISENHUNT, D. W. JR., VEECK, A. C., UHLIR, L. C., RAYMOND, K. N., Thorium(IV) complexes of bidentate hydroxypyridinonates, *Inorg. Chem.* **2003**, *42*, 2665–2674.
- 84 XU, J., DURBIN, P. W., KULLGREN, B., EBBE, S. N., UHLIR, L. C., RAYMOND, K. N., Synthesis and initial evaluation for in vivo chelation of Pu(IV) of a mixed octadentate spermine-based ligand containing 4-carbamoyl-3-hydroxy-1-methyl-2(1H)-pyridinone and 6-carbamoyl-1-hydroxy-2(1H)-pyridinone, *J. Med. Chem.* **2002**, *45*, 3963–3971.
- 85 CHEN, R. J., ZHANG, Y., WANG, D., DAI, H., Noncovalent sidewall functionalization of single-walled carbon nanotubes for protein immobilization, *J. Am. Chem. Soc.* **2001**, *123*, 3838.
- 86 FIFIELD, L. S., DALTON, L. R., ADDLEMAN, R. S., GALHOTRA, R. A., ENGLEHARD, M. H., FRYXELL, G. E., AARDAHL, C. L., Noncovalent functionalization of carbon nanotubes with molecular anchors using supercritical fluids, *J. Phys. Chem. B* **2004**, *108*, 8737–8741.

## 9

# Nanomaterials for Water Treatment

*Peter Majewski*

### 9.1

#### Introduction

Water is one of the most valuable substances in the world and its availability in the form of potable and drinking water is of great importance for any society. However, the conversion of water from various sources into potable and good quality drinking water can be very demanding.

The recent report entitled “Water for People – Water for Life” of the World Water Assessment Program of UNESCO [1] emphasizes that the availability of potable and drinking water is of major socio-economic importance worldwide. It also clearly states the importance of foreseeing water economy in terms of use, availability, quality, and technologies. The report also emphasizes that organic pollutants in water are the main reason for water-related diseases, such as diarrhea, worm infections, and infectious diseases, and more than 6000 people die every day due to water-related diseases.

Water use is increasing everywhere. The world's six billion inhabitants are already appropriating 54% of all the accessible freshwater contained in rivers, lakes and underground aquifers. By 2025 humankind's share will be 70%. This estimate reflects the impact of population growth alone. If per capita consumption of water resources continues to rise at its current rate, humankind could be using over 90% of all available freshwater within 25 years, leaving just 10% for all other living beings. Currently, on a global basis, 69% of all water withdrawn for human use on an annual basis is soaked up by agriculture (mostly as irrigation); industry accounts for 23% and domestic use (household, drinking water, sanitation) accounts for about 8%. These global averages vary a great deal between regions. In Africa, for instance, agriculture consumes 88% of all water withdrawn for human use, while domestic use accounts for 7% and industry for 5%. In Europe, most water is used in industry (54%), while agriculture and domestic use take 33% and 13% respectively [1].

Shrinking fresh water resources, increasing salinity of bore water, especially in arid areas of the world, and increasing demand for potable, drinking, and irriga-

tion water requires the utilization of sea, brackish, and saline bore water for fresh water supply. The conventional industrial way to desalinate water is reverse osmosis (RO), which is widely used, especially in arid costal areas, such as Arabia, the USA, especially Florida, Australia, and on ships. Although RO has proven to be a robust desalination method, its major drawback is its high demand in electric energy and the related high costs as well as biofouling of the membranes [2]. This fact requires either a relevant infrastructure of electric energy or additional equipment for local supply of electric energy, both of which are not always provided, especially in remote and/or underdeveloped areas as well as disaster and combat areas. Therefore, a simple “coffee filter”-like desalination method without the need of electric energy is highly desired and would significantly facilitate the utilization of sea, brackish, and saline bore water for the supply of potable, drinking, and irrigation water. Another important aspect, especially for underdeveloped and disaster areas, of such a “low-tech” method would be that the actual desalination treatment could be performed by a non-trained person.

Natural organic matter (NOM) is one of the key water quality parameters that affects treatment processes. NOM reduces the effectiveness of water treatment by interfering with the flocculation process, makes treatment with activated carbon and membrane filtration less efficient and is a precursor to the formation of disinfectant by-products (DBP). Furthermore, NOM acts as a food source for microorganisms, resulting in bacterial regrowth in distribution systems. These concerns have resulted in removal of NOM from raw water being of prime concern for water authorities. This has been acknowledged by the United States in the Disinfectant and Disinfection By-product Rule. This rule requires removal of NOM, as measured by total organic carbon (TOC), to minimize the formation of DBP. Enhanced coagulation has been designated as the best available technology for TOC reduction, with the required removal determined by influent TOC concentration and alkalinity. TOC of less than  $2 \text{ mg L}^{-1}$  prior to disinfection requires no treatment while TOC levels above this require removal of between 20 to 50%, with the higher removal required at higher TOC and lower alkalinity.

NOM is also well-known in drinking water. It is a complex matrix of heterogeneous organic material, consisting of particulate and dissolved fractions, harmless and harmful pollutants like pyrogens, such as endotoxins, proteins, and bacteria, as well as colored and non-colored components [3, 4]. Therefore, the ability to remove NOM is a key factor in determining the efficiency of novel methods for water treatment.

DBPs consist of various organic compounds, the best known of which are trihalomethanes (THMs). The presence of chloroform and other THMs in finished drinking water was first associated with the chlorination of drinking water in 1974. It was discovered that, in addition to killing microorganisms, disinfectants react with organic and inorganic substances naturally present in the water to produce various DBPs, which include THMs. DBPs associated with chlorination are THMs, haloacetic acids, haloacetonitriles and halopicrins. Chlorite and chlorate are by-products of chlorine dioxide disinfection, while ozonation may result in bro-

mate formation. Nitrosodimethylamine (NDMA) is a by-product of chlorination and chloramination.

Certain DBPs have been shown to be detrimental to health in laboratory animal studies. As a result the Environmental Protection Agency (EPA) regulated the most prevalent DBPs, the THMs, in 1979, setting the limit at  $100 \text{ mg L}^{-1}$ . With the promulgation of the Stage 1 Disinfectants and Disinfection By-product Rule in December 1998, the trihalomethane limit has since been reduced to  $80 \text{ } \mu\text{g L}^{-1}$  and limits of  $60 \text{ } \mu\text{g L}^{-1}$  for haloacetic acid,  $1.0 \text{ mg L}^{-1}$  for chlorite and  $10 \text{ } \mu\text{g L}^{-1}$  for bromate have been introduced. While haloacetoneitriles, halopicrins, chlorate and NDMA have been identified as health hazards, further research needs to be conducted before identifying appropriate regulatory levels. It is important to achieve a balance between reducing exposure to DBPs and maintaining control of waterborne diseases through regulatory efforts (see also: U.S. Environmental Protection Agency, <http://yosemite.epa.gov/water/>).

Conventional treatment process, i.e., coagulation/flocculation – sedimentation – filtration, is one of the most widely used treatment methods in drinking water treatment. However, especially organic matter with high molecular weight ( $\gg 10 \text{ kDa}$ ), such as pyrogens, are often not or not completely removed by coagulation and flocculation, with major consequences for peoples' health. Consequently, water has to be disinfected, mainly by chlorination and chloramination. However, as mentioned above, DBPs are a health risk and some are known carcinogens. Therefore, a reduction of disinfection of water is highly desired.

Even artificial organic matter such as pesticides, herbicides, and fungicides, drugs like antibiotics, detergents like alkyl aryl sulfonates and laureth sulfonates, organic solvents, such as trichloroethylene (TCE), and also organics from the food processing industry are often not, or not completely, removable from potable water because of their chemical stability against disinfectants. In addition, organic residues are the most frequent pollutants in wastewater of major industry, such as pulp and paper, textiles and leather, iron and steel, and petrochemicals and refineries.

Novel nanomaterials for water treatment and remediation, which in some cases are close to industrial applications, could provide some new innovative concepts to match the above outlined demands. In some cases they also represent more efficient alternatives to conventional treatment technologies, such as coagulation and flocculation, and provide novel concepts for desalination. However, in most cases there is still a long way to go before large-scale applications, i.e., the treatment of giga liters per year by nanomaterials, are commercially and technically feasible. However, the first important steps have already been carried out.

The present chapter provides a comprehensive overview of the most promising approaches to applying nanomaterials for water treatment and remediation. The nanomaterials will be introduced and their synthesis, physical properties, and operating issues reviewed. In addition, as far as the existing literature provides sufficient data about operational issues of the material, their possible application will be assessed.

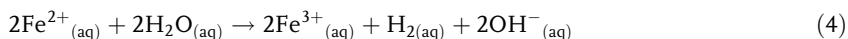
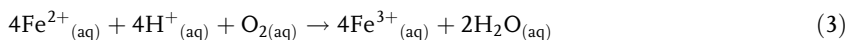
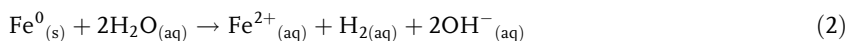
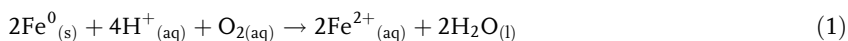
## 9.2

## Iron Nanoparticles

Iron nanoparticles represent a new generation of materials for water treatment and environmental remediation, which could provide a cost-effective alternative for the solution of some pollution problems [5–13]. Owing to several factors, iron nanoparticles are an extremely versatile tool for water treatment. One important reason for this is their minute particle sizes, ranging from 1 to 100 nm, which is significantly smaller than a typical bacterial cell, which is of the order of 1000 nm. Due to the small size, the surface to volume ratio is huge. This is important because the degradation of pollutants is controlled by their interaction with the surface of the particles. In addition, nanoparticles of iron in water create a highly reducing environment through the rapid consumption of oxygen at the surface of the particles. In field trials, the addition of nanoparticles of iron reduced the oxidation–reduction potential, which favors the growth of anaerobic bacteria, which further enhances biodegradation [5–13].

Unfortunately, free-floating nanoparticles are often not stable and form tight agglomerates, which often exhibit more minor properties than the single nanoparticle. In addition, it is very difficult to separate nanoparticles from the fluid medium, which, however, is crucial with respect to health related issues when nanoparticles are applied, especially in the treatment of drinking and potable water. But nanoparticles can be anchored onto a solid matrix, such as solid substrates of metals, metal oxides, and minerals like zeolite, for the treatment of drinking and potable water, wastewater, and process water.

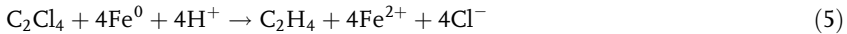
Metallic or zero-valent iron, as well as FeO, is a moderate reducing reagent, which can react with dissolved oxygen (DO) and to some extent with water, following Eqs. (1)–(4).



Equations (1)–(4) are the classic reactions of electrochemical corrosion, where iron is oxidized due to the exposure to oxygen and water [14, 15]. Like in corrosion chemistry, the function of water and molecular oxygen is typically that of the electron acceptors in aqueous environments. Iron acts as the electron donor, whereas relatively oxidized compounds serve as the electron acceptors and will be reduced. Over the past decade, several detailed studies have demonstrated that diverse well-known environmental contaminants, both organic and inorganic, can be reduced by iron oxidation so that these contaminants are transformed into less toxic or even benign end products [14–19]. For example, contaminants such as tetrachloro-

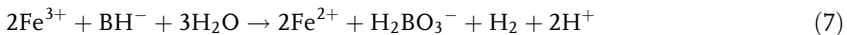
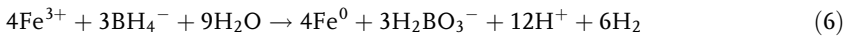


ethene (TCS,  $C_2Cl_4$ ), a common solvent, can readily accept the electrons from iron oxidation and, in the case of TCS, be reduced to ethene in accordance with Eq. (5).



Corrosion reactions can be accelerated or inhibited by manipulating the solution chemistry and/or solid (metal) composition. Since the early 1990s, the iron corrosion chemistry has been put into productive use in the treatment of hazardous and toxic chemicals [14, 16, 20]. The environmental chemistry of metallic iron has been extensively documented [21].

Nanoparticles of FeO and metallic iron can be prepared by using sodium borohydride as the key reductant to form FeO and Fe nanoparticles from solutions, which contain  $Fe^{3+}$  cations. For example,  $NaBH_4$  (0.2 M) is added into  $FeCl_3 \cdot xH_2O$  (0.05 M) solution with a volume ratio of 1:1.  $Fe^{3+}$  cations are reduced by the borohydride according to Eqs. (6) and (7) [22].



Reduction resulting in the formation of metallic iron nanoparticles has to be performed in an oxygen-free atmosphere. An excess of borohydride is needed to accelerate the synthesis reaction and provide a uniform growth of nanoparticles.

Iron is oxidized more rapidly when it is attached to a noble metal such as palladium and gold. The degradation of pollutants can significantly be enhanced by coupling iron to a noble metal [22–28]. A composite material consisting of iron nanoparticles and patches of a noble metal onto the surface of the particle creates numerous galvanic cells on the surface. Iron represents the anode and becomes preferably oxidized, whereas the noble metal represents the cathode and remains unchanged. Studies also suggest that noble metals such as palladium can promote dechlorination through catalytic functions such as hydrogenation [29, 30].

Palladized Fe particles can be prepared by soaking the freshly prepared iron nanoparticles with an ethanol solution containing 1 wt% of palladium acetate ( $[Pd(C_2H_3O_2)_2]_3$ ). This provides the reduction and subsequent deposition of Pd onto the surface of the particle, following Eq. (8) [22].



Similar methods have been employed successfully to prepare Fe/Pt, Fe/Ag, Fe/Ni, Fe/Co, and Fe/Cu bimetallic particles [25].

Metallic iron has been successfully applied in environmental field tests and is a promising novel technology for wastewater treatment, largely due to the low costs and absence of any known toxicity induced by its use [21, 30–36].

**Tab. 9.1.** Common environmental contaminants that can be transformed by nanoscale iron particles [5].

Chlorinated methanes	Trihalomethanes
Carbon tetrachloride (CCl <sub>4</sub> )	Bromoform (CHBr <sub>3</sub> )
Chloroform (CHCl <sub>3</sub> )	Dibromochloromethane (CHBr <sub>2</sub> Cl)
Dichloromethane (CH <sub>2</sub> Cl <sub>2</sub> )	Dichlorobromomethane (CHBrCl <sub>2</sub> )
Chloromethane (CH <sub>3</sub> Cl)	<i>Chlorinated ethenes</i>
<i>Chlorinated benzenes</i>	Tetrachloroethene (C <sub>2</sub> Cl <sub>4</sub> )
Hexachlorobenzene (C <sub>6</sub> Cl <sub>6</sub> )	Trichloroethene (C <sub>2</sub> HCl <sub>3</sub> )
Pentachlorobenzene (C <sub>6</sub> HCl <sub>5</sub> )	<i>cis</i> -Dichloroethene (C <sub>2</sub> H <sub>2</sub> Cl <sub>2</sub> )
Tetrachlorobenzenes (C <sub>6</sub> H <sub>2</sub> Cl <sub>4</sub> )	<i>trans</i> -Dichloroethene (C <sub>2</sub> H <sub>2</sub> Cl <sub>2</sub> )
Trichlorobenzenes (C <sub>6</sub> H <sub>3</sub> Cl <sub>3</sub> )	1,1-Dichloroethene (C <sub>2</sub> H <sub>2</sub> Cl <sub>2</sub> )
Dichlorobenzenes (C <sub>6</sub> HCl <sub>2</sub> )	Vinyl chloride (C <sub>2</sub> H <sub>3</sub> Cl)
Chlorobenzene (C <sub>6</sub> H <sub>5</sub> Cl)	<i>Other polychlorinated hydrocarbons</i>
<i>Pesticides</i>	PCBs
DDT (C <sub>14</sub> H <sub>9</sub> Cl <sub>5</sub> )	Dioxins
Lindane (C <sub>6</sub> H <sub>6</sub> Cl <sub>6</sub> )	Pentachlorophenol (C <sub>6</sub> HCl <sub>5</sub> O)
<i>Organic dyes</i>	<i>Other organic contaminants</i>
Orange II (C <sub>16</sub> H <sub>11</sub> N <sub>2</sub> NaO <sub>4</sub> S)	N-Nitrosodimethylamine (C <sub>4</sub> H <sub>10</sub> N <sub>2</sub> O)
Chrysoidine (C <sub>12</sub> H <sub>13</sub> N <sub>4</sub> Cl)	TNT (C <sub>7</sub> H <sub>5</sub> N <sub>3</sub> O <sub>6</sub> )
Tropaeolin O (C <sub>12</sub> H <sub>9</sub> N <sub>2</sub> NaO <sub>5</sub> S)	<i>Inorganic anions</i>
Acid Orange	Dichromate (Cr <sub>2</sub> O <sub>7</sub> <sup>2-</sup> )
Acid Red	Arsenic (AsO <sub>4</sub> <sup>3-</sup> )
<i>Heavy metal ions</i>	Perchlorate (ClO <sub>4</sub> <sup>-</sup> )
Mercury (Hg <sup>2+</sup> )	Nitrate (NO <sub>3</sub> <sup>-</sup> )
Nickel (Ni <sup>2+</sup> )	
Silver (Ag <sup>+</sup> )	
Cadmium (Cd <sup>2+</sup> )	

Table 9.1 lists several pollutants in water that have been successfully degraded by iron nanoparticles [5]. Figure 9.1 shows the effect of the addition of iron nanoparticles on water contaminated with TCE. After only a few days the concentration of TCE has been reduced significantly at the well, but also at some distance from the well.

Equations (1) and (2) clearly show that adding iron nanoparticles to water should produce a characteristic increase in pH and decline in the redox potential ( $E_H$ ) of the solution. A highly reducing environment ( $E_H \ll 0$ ) is created due to the rapid consumption of oxygen and other potential oxidants as well as production of hydrogen. Figure 9.2 shows that the oxidation–reduction potential (ORP) decreases after the addition of the nanoscale iron particles into a solution. Typically, in a closed batch reactor, a pH increase of 2–3 units was reported while ORP reduction was in the range 500–900 mV [5, 31].

In poorly buffered water, the increase in pH can be significant. However, most

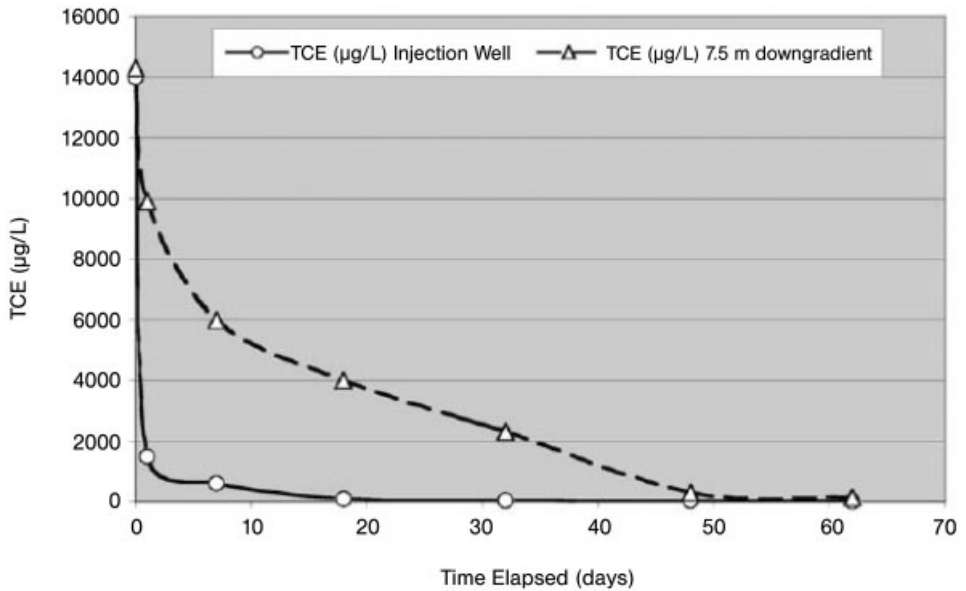


**Fig. 9.1.** Effect of the addition of iron nanoparticles on water contaminated with TCE. After only a few days the TCE concentration has been reduced significantly at the well, and also at some distance from the well [5].

often, natural water reservoirs contain some buffering capacity and, therefore, the anticipated increase in pH would be less pronounced.

Nanoparticles of iron and FeO surely provide an innovative, simple and cheap alternative to conventional methods. However, crucially, wide range applications, especially for drinking and potable water, require removal of the particles or the resulting iron cations from the water, which will be one of the major challenges facing a future application of the method.

### 9.3

#### Inorganic Photocatalysts

Increased public concern over environmental pollutants as well as waterborne pyrogens has prompted the need to develop novel treatment methods, with photocatalysis attracting a lot of attention concerning the degradation of pollutants [37, 38]. Much of the natural purification of aqueous system lagoons, ponds, streams, rivers and lakes is caused by sunlight initiating the breakdown of organic molecules into simpler molecules and ultimately into carbon dioxide and other mineral products [39].

Photocatalytic detoxification of wastewater combines heterogeneous catalysis with solar technologies [40]. Semiconductor photocatalysis, with a primary focus on  $\text{TiO}_2$ , has been applied to various problems of environmental interest in addition

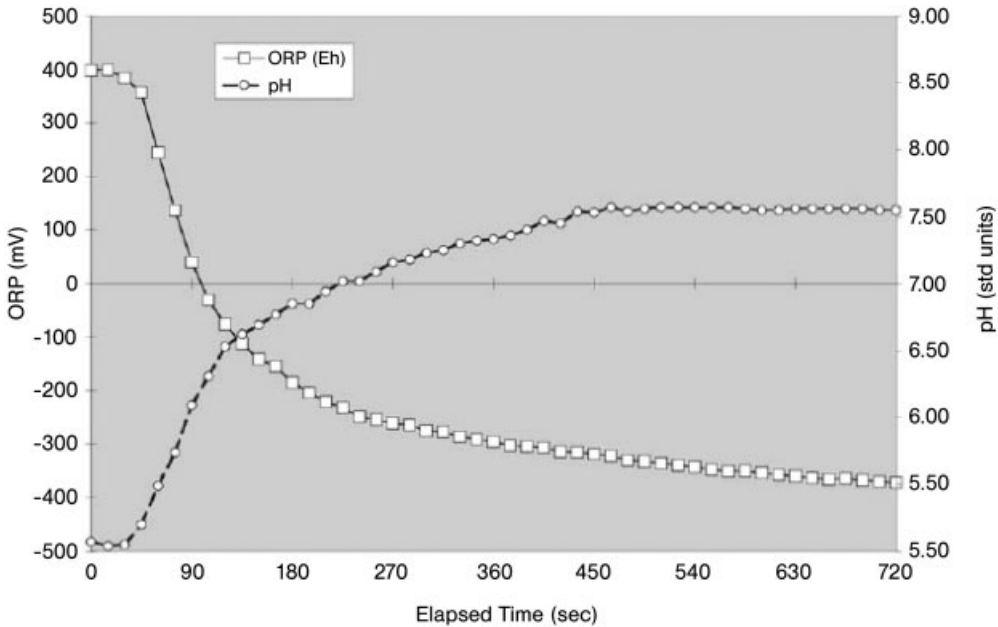


**Fig. 9.2.** Water chemistry of nanoscale iron particles. Rapid pH and oxidation–reduction potential (ORP) changes were observed after the addition of  $0.11 \text{ g L}^{-1}$  of Pd/Fe nanoparticles in water. A very low ORP can be established in 200 s [5].

to water and air purification. The application of illuminated semiconductors for degrading undesirable organics dissolved in air or water is well documented and has been successful for a wide variety of compounds [41].

Organic compounds such as alcohols, carboxylic acids, amines, herbicides and aldehydes have been degraded via photocatalysis in both laboratory and field studies. The photocatalytic process can mineralize the hazardous organic molecules into carbon dioxide, water and simple mineral acids [42]. Thus, a major advantage of the photocatalytic process over existing technologies is that it provides an almost complete degradation of the organic toxins, whereas other methods, such as conventional coagulation and flocculation, most often only concentrates the toxins, which then have to be separated from the water by filtering or sedimentation of the flocculant. Compared to other advanced oxidation technologies, especially those using oxidants such as hydrogen peroxide and ozone, additional oxidizing chemicals are not required when applying photocatalysis, because ambient oxygen is the oxidant [38].

The photocatalytic process can also be applied to destroy nuisance odors, taste and odor compounds, and naturally occurring organic matter, which contains the precursors to trihalomethanes formed during the chlorine disinfection step in drinking water treatment [43].

Tab. 9.2. Band gap energy of various photocatalysts [44].

Photocatalyst	Band gap energy (eV)	Photocatalyst	Band gap energy (eV)
Si	1.1	ZnO	3.2
TiO <sub>2</sub> (rutile)	3.0	TiO <sub>2</sub> (anatase)	3.2
WO <sub>3</sub>	2.7	CdS	2.4
ZnS	3.7	SrTiO <sub>3</sub>	3.4
SnO <sub>2</sub>	3.5	WSe <sub>2</sub>	1.2
Fe <sub>2</sub> O <sub>3</sub>	2.2	X-Fe <sub>2</sub> O <sub>3</sub>	3.1

During photocatalysis, illumination of a semiconductor photocatalyst with ultraviolet (UV) radiation activates the catalyst, establishing a redox environment in the aqueous solution [40]. The physical and chemical fundamentals underlying this phenomenon are comprehensively described by Bhatkhande et al. [38] and Beydoun et al. [44].

An ideal photocatalyst should be stable, inexpensive, non-toxic and, of course, highly photoactive. Another primary criteria for the degradation of organic compounds is that the redox potential of the H<sub>2</sub>O/·OH couple (OH<sup>-</sup> + ·OH + e<sup>-</sup>;  $E^0 = -2.8$  V) lies within the bandgap of the semiconductor [41]. Several semiconductors have bandgap energies sufficient for catalyzing a wide range of chemical reactions. These include TiO<sub>2</sub>, WO<sub>3</sub>, SrTiO<sub>2</sub>,  $\alpha$ -Fe<sub>2</sub>O<sub>3</sub>, ZnO and ZnS (Table 9.2). Of these materials, TiO<sub>2</sub> seems to be the most promising for photocatalytic destruction of organic pollutants [45–63]. This semiconductor provides the best compromise between catalytic performance and stability in aqueous media [64]. The anatase phase of titanium dioxide is the material with the highest photocatalytic detoxification properties [65]. Binary metal sulfide semiconductors such as CdS, CdSe or PbS are insufficiently stable for catalysis, at least in aqueous media, because they undergo photoanodic corrosion [45, 66], and, more important with respect to drinking water treatment, these materials are also toxic. The iron oxides are not suitable semiconductors as they are quickly subjected to photocathodic corrosion to FeOOH and other iron hydroxide species. The band gap of ZnO (3.2 eV) is equal to that of anatase. However, ZnO is also not stable in water and forms Zn(OH)<sub>2</sub> on the surface of the ZnO particles, resulting in deactivation of the catalyst [45].

Nanocrystalline photocatalysts are of increasing interest due to their unique photophysical and photocatalytic properties [44, 65, 67]. Several review articles deal with the photophysical properties of nanocrystalline semiconductors and various studies have demonstrated that some properties of nanocrystalline semiconductor particles differ from those of bulk materials [37, 65, 68–71]; for a comprehensive review see Ref. [44].

Nanosized particles, with diameters ranging between 1 and 10 nm, possess properties that represent a transition between the molecular and bulk phases [65]. In bulk material, the electron excited by light absorption finds a high density of states in the conduction band, where it can exist with different kinetic energies [67]. However, the size of a nanoparticle can be the same as or even smaller than the size of the first excited state. Thus, the electron and hole generated by illumination cannot fit into such a particle unless a state of higher kinetic energy is created [72].

Hence, as the size of the semiconductor particle is reduced below a critical diameter, the spatial confinement of the charge carriers within a potential well causes them to behave quantum mechanically [41, 73, 74]. In solid-state terminology this means that the bands split into discrete electronic states representing quantized levels in the valence and conduction bands [72] and the nanoparticle behaves like a giant atom [67]. Nanosized semiconductor particles that exhibit size-dependent optical and electronic properties are called quantized particles or quantum dots [75]. Quantum-size effects occur when the semiconductor particles become smaller than the Bohr radius of the first excitation state [74]. This has also been stated by other authors when the particle size of a colloidal particle becomes comparable to the DeBroglie wavelength of the charge carriers [72, 76].

The excitation radius of TiO<sub>2</sub> nanoparticles has been reported to be between 0.3 and 2 nm [73, 77, 78]. Quantization effects of TiO<sub>2</sub> nanoparticles have been observed at particles sizes at and below about 10 nm [45, 72, 77–81].

One important advantage of the application of quantum-sized particles is the increase in bandgap energy with decreasing particle size. At the critical radius and below, the charge carriers begin to behave quantum mechanically and the confinement of the charge results in a series of discrete electronic states, prompting an increase in the effective band gap and a shift of the band edges. Thus, by varying the size of the semiconductor particles, it is possible to enhance the redox potential of the valence-band holes and the conduction band electrons [82], which results in an increase in the rate constants for charge transfer at the surface [41, 81]. Consequently, the use of quantum-sized semiconductor particles may result in increased photoactivity for systems in which the rate-limiting step is interfacial charge transfer [81]. Hence, semiconductor nanoparticles of sufficient size can possess enhanced photoredox chemistry that might not otherwise exist in bulk materials [73, 79, 81, 83–87].

Another factor that could be advantageous is the fact that a very large fraction of atoms are located at the surface of a nanoparticle [67]. Quantum-sized particles also have high surface area to volume ratios, which further enhances their catalytic activity [82]. One disadvantage of nanosized particles is the need for light with a shorter wavelength for photocatalyst activation – a smaller percentage of a polychromatic light source will be useful for photocatalysis.

The maximum efficiency of photocatalysis of TiO<sub>2</sub> has been observed at a particles size of about 10 nm. However, even a slight decrease or increase of particle size results in a decrease in efficiency [77, 79, 86, 88, 89].

Nanoparticles of titania can be synthesized by flame synthesis [90], chemical vapor deposition [91], wet chemical methods, such as chloride method using TiCl<sub>4</sub>

solutions [92], hydrothermal processing [93], and the alkoxide method [94, 95]. The alkoxide method, better known as the sol–gel method, which is widely used in the synthesis of ceramic materials, has the advantage that it is capable of producing photocatalysts of better homogeneity as well as high purity, involves lower processing temperatures, and can be tailored to control the materials properties [96].

Although photocatalysis exhibits various significant advantages over conventional methods such as flocculation and coagulation, its major disadvantage is that it needs illumination, preferably by UV light. However, with respect to operational aspects of the treatment of drinking, potable, waste, and process water, solar illumination is not always possible or, if provided by UV lamps, causes considerable costs. Thus, even if photocatalysts represent a very efficient, reliable, and innovative alternative to conventional treatment or other oxidizing treatments, such as ozone or H<sub>2</sub>O<sub>2</sub> treatment, operational issues and often the costs will be the main criteria when considering their application.

## 9.4

### Functionalized Self-assembled Monolayers

Another nanomaterial for water treatment consists of a particular silica (quartz sand) or silicate material with a nanometer-sized coating, a so-called functionalized self-assembled monolayer (SAM). SAMs for water treatment have been deposited onto solid  $\mu\text{m}$ -sized silicate particles as well as on so-called mesoporous silicates. Mesoporous silicates are silicate particles that contain a nanometer-sized open porosity. This porosity provides an enormous increase of the effective surface area available for interactions between the SAM and pollutants. A few grams of mesoporous silicate provide a surface area the size of three football fields [97].

Although applications of silane-based self-assembled monolayers have been elaborated for surface modification in terms of controlling its hydrophobicity, introducing and controlling the surface chemistry, and the synthesis of crystalline oxide thin films via self-assembled monolayers, the removal of pollutants from water via SAMs has not been considered widely.

A SAM is a close packed, highly ordered array of chained hydrocarbon molecules containing 3–17 CH<sub>2</sub> units (Fig. 9.3). Especially, long-chain molecules (17 CH<sub>2</sub>-units, e.g., octadecyltrichlorosilane) form a highly ordered array of surfactant molecules due to stabilizing van der Waals forces between the molecules, whereas short-chain molecules (three CH<sub>2</sub>-units, e.g., aminopropyltrimethoxysilane) are less perfectly arrayed. Hence, the length of the hydrocarbon molecules and the related thickness of the SAM varies between about 0.6 nm (three CH<sub>2</sub>-units) and about 2.5 nm (17 CH<sub>2</sub>-units) [98].

The SAM is simply described as a hydrocarbon with the general formula X-(CH<sub>2</sub>)<sub>n</sub>-Y. Y represents the “bonding group”, such as trichlorosilyl (–SiCl<sub>3</sub>), trimethoxysilane [Si(OCH<sub>3</sub>)<sub>3</sub>] etc., forming tightly covalent Si–O–Si bonds to the surface atoms of silicon and silica [99, 100]. X denotes the “head group”, chosen from

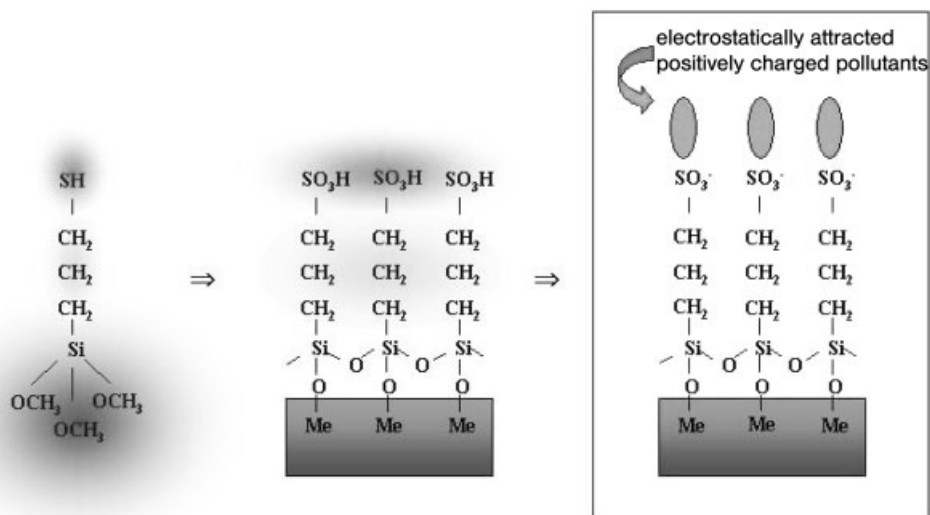


**Fig. 9.3.** The surfactant 3-mercaptopropyltrimethoxysilane (left) and the resulting sulfonate SAM on a substrate (middle) and immersed into contaminated water (right).

among several possible species, such as  $\text{NH}_2$ ,  $\text{NHNH}_2$ ,  $\text{NH}_3\text{Cl}$ ,  $\text{SH}$ ,  $\text{SO}_3\text{H}$ ,  $\text{COOH}$ ,  $\text{PO}_4\text{H}_2$  etc. When immersed into aqueous solutions, the head groups deprotonate and form negatively surfaces or capture protons at low pH and form positively charged surfaces. Therefore, by carefully choosing the self-assembled monolayer and pH of the aqueous solution in which the SAM is immersed, negatively as well as positively charged surfaces can be obtained [101, 102]. Removal of charged pollutants is due either to electrostatic attraction between the SAM and the counter-charged pollutant or to chemisorption of the pollutants by the functional group of the SAM.

Surfaces are coated with SAMs by simply immersing the substrate material into an organic solution, such as toluene, that contains surfactant molecules, such as 3-mercaptopropyltrimethoxysilane [101–105]. After thoroughly washing with ethanol and water, the SAMs-coated powder is ready for application.

SAMs for water treatment are mainly employed on silica and silicate particles, which are dispersed in the water during treatment, and subsequently filtered. Mesoporous silicates coated with SAMs containing a thiol-functionality ( $\text{SH}$  functionality), so-called thiol-SAMMS (self-assembled monolayers on mesoporous supports), have been developed specifically for the removal of mercury from liquid media [106–118]. They have the unique ability to bind cationic, organic, metallic, and complexed forms of mercury. Because of the high surface area, extensive binding sites, and tailored functional group, results of tests with mercury demonstrate the high loadings (up to 635 mg Hg per gram of SAMMS), high affinity (distribution coefficient, or  $K_d$ ,  $\sim 1 \times 10^8$ ) and rapid kinetics (minutes) possible through the



Tab. 9.3. Binding affinity of thiol-SAMMS for selected metal species [97].

Metal	Initial concentration ( $\mu\text{g L}^{-1}$ )	Final concentration ( $\mu\text{g L}^{-1}$ )	Metal loading ( $\text{mg g}^{-1}$ )	Distribution coefficient ( $K_d$ ) ( $\text{mL g}^{-1}$ )
Ag(I)	90	1	0.0089	8900
Ca(II)	2070	2070	0	0
Cd(II)	4670	32	0.4638	14 467
Co(II)	2810	2670	0.0140	5
Cu(II)	2240	<5	>0.2235	>44 700
Eu(III)	9010	1220	0.7790	639
Hg(II)	487	0	1.0146	$1 \times 10^8$
Mg(II)	1580	1580	0	0
Pb(II)	3040	300	0.2740	913
Zn(II)	2790	2410	0.0380	16

use of these molecularly-engineered materials. The efficiency of SAMMS in a non-aqueous system (oil) has also been demonstrated with mercury with excellent results.

Selectivity, isotherm, kinetic, stability, and regeneration data on thiol-SAMMS are available for multiple metals. Table 9.3 summarizes the binding affinity of thiol-SAMMS for selected metal species. Results show that thiol-SAMMS can selectively adsorb, in addition to mercury, other soft acid cations: silver, cadmium, copper, and lead. In all cases, thiol-SAMMS show minimal interference from alkali and alkali earth metals, such as  $\text{Na}^+$ ,  $\text{Mg}^{2+}$ , and  $\text{Ca}^{2+}$ . Kinetic experiments exploring the adsorption of mercury in 10 and 500 ppm mercury solutions have demonstrated the rapid binding kinetics of thiol-SAMMS. The SAMMS rapidly reduced the mercury concentration from 500 to 0.5 ppb within 5 min. At a mercury concentration of 10 ppm, a reduction down to 3.1 ppb was observed within 5 min, which is significantly faster than the kinetics of commercial mercury absorbers.

In addition, the use of metal-chelated ligands immobilized on mesoporous silica as novel anion-binding materials for toxic anions such as chromate, arsenate, perchlorate, and selenite has also been demonstrated. Novel chemical interfaces with chelate-SAMMS have shown selective removal of toxic metal oxoanions by a ligand exchange mechanism. This approach allows the construction of binding sites that satisfy the stereoelectronic requirements of tetrahedral anions. This SAMMS form can remove chromate and arsenate to low levels, even with competing sulfate ion present.

Nearly complete removal of arsenate and chromate has been reported in the presence of interfering anions for solutions containing up to 100 ppm toxic metal anions under various conditions. The material remains effective for even higher concentration solutions (in excess of 1000 ppm anions). Anion loading of more

than  $130 \text{ mg g}^{-1}$  ( $1.12 \text{ mmol g}^{-1}$ ) of SAMMS and distribution coefficients of  $>100\,000$  have been observed.

Anion removal tests have been performed in water containing 1, 10, and 100 ppm arsenate and chromate with a solution-to-silica (SAMMS) ratio of 100. In all tests, essentially 100% of the chromate was removed in a single treatment. The addition of 150-ppm-sulfate-competing anions had little effect on the adsorption behavior. At the same solution-to-silica ratio ( $100 \text{ mL g}^{-1}$ ), chromate concentrations  $> 1000$  ppm began to produce saturation of the binding sites. The maximum adsorbing capacity is about  $130 \text{ mg g}^{-1}$  or  $1.12 \text{ mmol g}^{-1}$ . For a much higher solution-to-silica ratio ( $500 \text{ mL g}^{-1}$ ), almost 100% removal of the chromate is observed for chromate concentrations up to 100 ppm. Higher concentrations of chromate under these conditions result in saturation of the binding sites.

Similar results were also obtained for arsenate removal. The maximum loading capacity is  $140 \text{ mg g}^{-1}$  or  $1.0 \text{ mmol g}^{-1}$ . Under the same conditions, the residual concentrations of arsenate are all slightly higher than chromate at low anion concentrations. This suggests the binding chemistry has higher affinity for chromate than arsenate.

Bulk chemical analysis of treated water samples of various sources clearly indicates the capability of SAMs to remove metal cations from water. The amount of powder per liter of water and the treatment time have been identified as important factors in increasing the efficiency of the method. However, the concentration of the contaminant appears to be less crucial, as metal cations of very high as well as very low concentrations could be removed with almost the same efficiency. Recent experiments with seawater show that this method has considerable potential for desalination [119, 120]. The concentration of all analyzed metals could be significantly reduced by the treatment, whereas that of chloride was only reduced by about 20%. However, it may only be a matter of further optimization before the desalination of water by SAMs is technically possible.

These recent studies have also shown that organic matter can be removed by functionalized SAMs [119, 120]. Figure 9.4 shows the absorbance of organic matter of the Myponga Valley reservoir near Adelaide, Australia, at a wavelength of 260 nm versus the molecular weight of the molecules. Clearly, after only a few hours of treatment with a few grams of SAMs-coated silica particles per liter, organic matter with a molecular weight of more than 1 kDa has been almost completely removed. Organic matter with a molecular weight between 300 and 1000 Da has been removed very efficiently ( $>90\%$ ), whereas compounds with a molecular weight below 300 Da are almost untouched. The fact that especially organic matter with high molecular weight, such as pyrogens, could significantly be reduced indicates that the amount of disinfection of the water, such as by chlorination and chloramination, could be decreased significantly when SAMs are applied to water treatment.

Besides natural organic matter, contaminants like sodium alkyl aryl sulfonate and sodium laureth sulfonate based detergents and drugs could also be removed from water. In all cases, the contaminants were removed almost completely after a treatment of about 30 min, as indicated by measuring the UV absorbance of the water

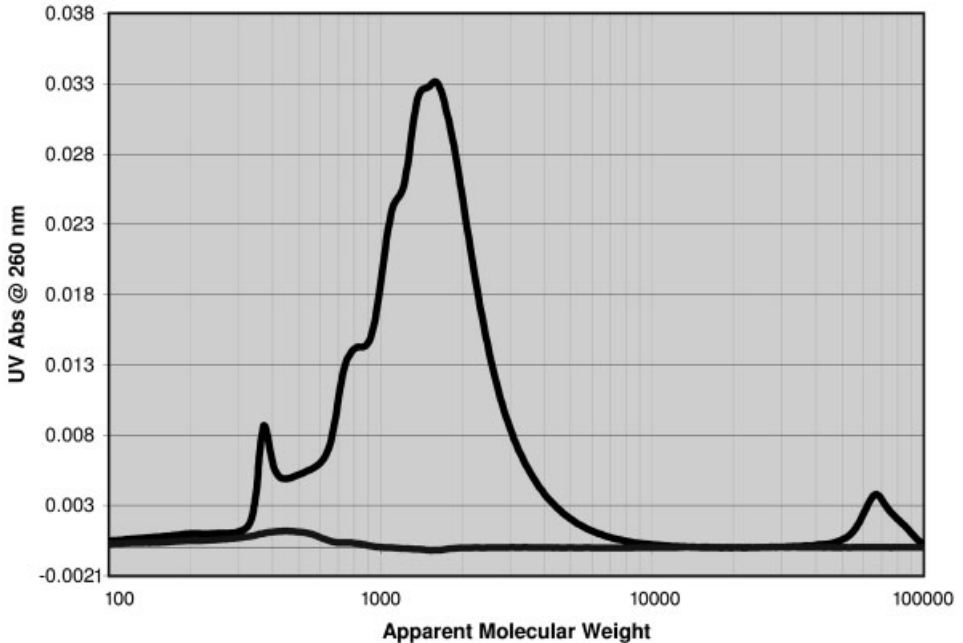


**Fig. 9.4.** UV absorbance at 260 nm of Myponga raw water (black) and treated water (lighter, almost horizontal line) [120].

samples [119, 120]. Although these results are very promising, further detailed studies are necessary to optimize the efficiency of the removal of organic detergents.

Although SAMs for water treatment have great potential, the technology is still at the beginning. For a technical application, SAMs will have to show that they can be recycled, are stable under physical conditions during treatment, and do not contaminate the water due to release of the SAM layers from the substrate during treatment. However, the main innovative aspect of the method is the fact that the actual treatment can be performed without the need of electric or thermal power as well as illumination, which may be a significant advantage over conventional methods such as reverse osmosis for desalination and microfiltration for the removal of pathogens [121].

## 9.5 Other Materials

Some other nanomaterials as well as nanocomposites have been studied for water treatment and remediation [122, 123]. Because these studies are very recent, it is yet not possible to assess whether these approaches offer significant advantages

over conventional methods or more established nanomaterials as described in Chapters 2–4. However, some of the approaches are very promising and further research will clarify their potential.

Paknikar et al. [124] have studied iron sulfide nanoparticles for the degradation of lindane. Lindane is an organochlorine pesticide and a persistent organic pollutant. Lindane residues have been detected in drinking water sources as well as beverages and the development of viable methods for their removal is highly desirable. Iron nanoparticles have already been shown to transform effectively chlorinated organic compounds. However, their use in the treatment of drinking water and beverages has toxicity concerns. This study employed FeS nanoparticles, which were synthesized by a standard wet chemical method and were stabilized by novel polymers of microbial origin. The authors could show that the stabilized FeS nanoparticles dechlorinate lindane rapidly with very high efficiency. Dechlorinated compounds and the stabilized polymers could be completely degraded in a subsequent microbiological treatment, which facilitated precipitation of bulk iron. This novel integrated nano-biotechnological method may offer a safe, viable, and cost-effective solution to the removal of pollutants from various drinking water sources.

Peng et al. [125] have developed a novel adsorbent, consisting of nanoparticles of ceria supported on carbon nanotubes (CeO<sub>2</sub>-CNTs), for the removal of arsenate from water. Their experiments showed that CeO<sub>2</sub>-CNTs are an effective adsorbent for arsenate, and that the adsorption depends on the pH of the water. Cations of Ca and Mg significantly enhance the adsorption capacity, suggesting that this material may be a promising adsorbent for drinking water purification. The loaded adsorbent could be efficiently regenerated by dilute NaOH; a regeneration efficiency of some 90% was achieved. However, the mechanism of adsorption is not yet clear.

## 9.6 Magnetic Iron Exchange Resin (MIEX)

MIEX is, so far, the only approach employing a nanomaterial that is already commercially applied in water treatment [126–130]. MIEX, which is licensed by Orica Australia Pty. Ltd, is used as an alternative material for flocculation and coagulation. It has a very rapid reactivity and high capacity for the removal of NOM and forms the basis of a novel process for NOM removal. MIEX consists of nanoparticles (10–100 nm) of Fe<sub>2</sub>O<sub>3</sub>, which has weak permanent magnetic properties, bounded in a granular resin. Individual particles of the resin have average grain sizes of about 150 μm and, under moderate agitation, will completely separate from one another, giving a high surface area and rapid reaction rates. As soon as agitation is reduced, the particles behave like individual magnets and clump together in an open structure, which has high settling rate. The resin can easily be regenerated and recycled. To provide optimum magnetic properties of the individual granules it is crucial to have the nanoparticulate Fe<sub>2</sub>O<sub>3</sub> homogeneously distributed within the MIEX granules, requiring some expertise in the organic synthesis of the material [130].

## References

- 1 *Water for People – Water for Life*, World Water Assessment Program, UNESCO, [www.unesco.org/water/wwap](http://www.unesco.org/water/wwap).
- 2 Summary Report *Introduction to Desalination Technologies in Australia*, National Dryland Salinity Program, Department of Agriculture, Fisheries and Forestry – Australia, July 2002.
- 3 D. M. OWEN, G. L. AMY, Z. K. CHOWDHURY, R. PAODE, G. MCCOY, K. VISCOIL, NOM characterisation and treatability, *J. Australian Water & Wastewater Assoc.* 1995, 87, 46–63.
- 4 C. W. K. CHOW, J. A. VAN LEEUWEN, M. DRIKAS, R. FABRIS, K. M. SPARK, D. W. PAGE, The impact of the character of natural organic matter in conventional treatment, *Water Sci. Technol.* 1999, 40, 97–104.
- 5 W.-X. ZHANG, Nanoscale iron particles for environmental remediation: An overview, *J. Nanoparticle Res.*, 2003, 5, 323–332.
- 6 C. R. O'MELIA, *Aquatic Chemistry: Interfacial and Interspecies Processes*, ed. C. HUANG, C. R. O'MELIA, J. MORGAN, American Chemical Society: Washington, DC, 1995, ACS Advances in Chemistry Series 244, pp. 315–337.
- 7 W. STUMM, J. J. MORGAN, *Aquatic Chemistry*, 3rd edn., John Wiley & Sons, New York, 1996, Ch. 14.
- 8 J. CLEASBY, *Water Quality and Treatment, a Handbook of Community Water Supply*, 4th edn., American Water Works Association, McGraw-Hill, New York, 1990, Ch. 8.
- 9 C. R. O'MELIA, C. L. TILLER, Natural organic matter and colloidal stability: Models and measurements, in *Environmental Particles*, ed. J. BUFFLE, H. VAN LEEUWEN, Lewis Publishers, Chelsea, MI, 1993, Ch. 8, pp. 353–386.
- 10 M. ELIMELECH, J. GREGORY, X. JIA, R. A. WILLIAMS, *Particle Deposition and Aggregation: Measurement, Modeling, and Simulation*, Butterworth-Heinemann, Oxford, 1995.
- 11 K.-M. YAO, M. T. HABIBIAN, C. R. O'MELIA, *Environ. Sci. Technol.* 1970, 5, 1105–1112.
- 12 R. RAJAGOPALAN, C. TIEN, *Am. Inst. Chem. Eng. J.* 1976, 22, 523–533.
- 13 J. E. TOBIASON, *Physical Aspects of Particle Deposition in Porous Media*, Doctoral Dissertation, The Johns Hopkins University, Baltimore, MD, 1987, p. 280.
- 14 R. W. GILLHAM, S. F. O'HANNESIN, Enhanced degradation of halogenated aliphatics by zero-valent iron, *Ground Water* 1994, 32, 958–967.
- 15 P. G. TRATNYEK, Correlation analysis of the environmental reactivity of organic substances, in *Perspectives in Environmental Chemistry*, ed. D. L. MACALADY, Oxford University Press, New York, 1998, pp. 167–194.
- 16 W. S. ORTH, R. W. GILLHAM, Dechlorination of trichloroethene in aqueous solution using Fe(0), *Environ. Sci. Technol.* 1996, 30, 66–71.
- 17 R. W. PULS, C. J. PAUL, R. W. POWELL, The application of in situ permeable reactive (zero-valent iron) barrier technology for the remediation of chromate-contaminated groundwater: A field test, *Appl. Geochem.* 1999, 14, 989–1000.
- 18 S. NAM, P. G. TRATNYEK, Reduction of azo dyes with zero-valent iron, *Water Res.*, 2000, 34, 1837–1845.
- 19 D. P. SIANTAR, C. G. SCHREIER, C.-S. CHOU, M. REINHARDT, Treatment of 1,2-dibromo-3-chloropropane and nitrate-contaminated water with zero-valent iron or hydrogen/palladium catalysts, *Water Res.* 1996, 30, 215–232.
- 20 S. F. O'HANNESIN, R. W. GILLHAM, Long-term performance of an in situ “ironwall” for remediation of VOCs, *Ground Water* 1998, 36, 164–170.
- 21 EPA (US Environmental Protection Agency), 2003c. Databases of innovative technologies. <http://www.epa.gov/tio/databases/>.
- 22 C. WANG, W. ZHANG, Nanoscale metal particles for dechlorination of PCE and PCBs, *Environ. Sci. Technol.* 1997, 31(7), 2154–2156.

- 23 W. ZHANG, C. WANG, H. LIEN, Catalytic reduction of chlorinated hydrocarbons by bimetallic particles, *Catal. Today* **1998**, *40*, 387–395.
- 24 H. LIEN, W. J. ZHANG, Reactions of chlorinated methanes with nanoscale metal particles, *Environ. Eng.* **1999**, *125*, 1042–1047.
- 25 Y. XU, W. ZHANG, Subcolloidal Fe/Ag particles for reductive dehalogenation of chlorinated benzenes, *Ind. Eng. Chem. Res.* **2000**, *39*, 2238–2244.
- 26 H. LIEN, W. ZHANG, Enhanced dehalogenation by bimetallic Cu/Al, *Chemosphere* **2002**, *49*, 371–378.
- 27 C. GRITINI, M. MALCOMSON, Q. FERNANDO, N. KORTE, Rapid dechlorination of polychlorinated biphenyls on the surface of a Pd/Fe bimetallic system, *Environ. Sci. Technol.* **1995**, *29*, 2898–2900.
- 28 R. MUFTIKIAN, Q. FERNANDO, N. KORTE, A method for the rapid dechlorination of low molecular weight chlorinated hydrocarbons in water, *Water Res.* **1995**, *29*, 2434–2439.
- 29 Z. KARPINSKI, K. EARLY, J. J. D'ITRI, Catalytic hydrodechlorination of 1,1-dichlorotetrafluoroethane by Pd/Al<sub>2</sub>O<sub>3</sub>, *J. Catal.* **1996**, *164*, 378–386.
- 30 K. PARK, K. KLIER, C. WANG, W. J. ZHANG, Interaction of tetrachloroethylene (PCE) with Pd (100) Studied by high resolution X-ray emission spectroscopy (HRXPS), *J. Phys. Chem. B* **1997**, *101*, 5420–5428.
- 31 D. W. ELLIOTT, W.-X. ZHANG, Field assessment of nanoscale bimetallic particles for groundwater treatment, *Environ. Sci. Technol.* **2001**, *35*, 4922–4926.
- 32 T. MASCIANGIOLI, W. ZHANG, Environmental technology at the nanoscale, *Environ. Sci. Technol.* **2003**, *37*, 102A–108A.
- 33 R. GLAZIER, R. VENKATAKRISHNAN, F. GHEORGHIU, L. WALATA, R. NASH, W. ZHANG, Nanotechnology takes root. *Civil Eng.* **2003**, *73*, 64–69.
- 34 H. LIEN, W. ZHANG, Complete dechlorination of chlorinated ethenes with nanoparticles, *Colloids Surf. A* **2001**, *191*, 97–105.
- 35 W. ZHANG, Iron awe – nanoparticles for mine site remediation, *Mater. World* **2004**, 33–34.
- 36 National Research Council, *Natural Attenuation for Groundwater Remediation*, National Academy Press, Washington, DC, **2000**.
- 37 W. A. ZELTNER, M. A. ANDERSON, The use of nanoparticles in environmental applications, in *Fine Particles Science and Technology*, ed. E. PELIZZETTI, Kluwer Academic Publishers, Boston, MA, USA, **1996**, pp. 643–656.
- 38 D. S. BHATKHANDI, V. G. PANGARKAR, A. A. C. M. BEENACKERS, Photocatalytic degradation for environmental applications—a review, *J. Chem. Technol. Biotechnol.* **2001**, *77*, 102–116.
- 39 R. MATTHEWS, Photocatalysis in water purification: Possibilities, problems and prospects, in *Photocatalytic Purification and Treatment of Water and Air*, ed. D. F. OLLIS, H. AL-EKABI, Elsevier Science Publishers, Oxford, UK, **1993**, 121–139.
- 40 Y. ZHANG, J. C. CRITTENDEN, D. W. HAND, D. L. PERRAM, Fixed-bed photocatalysis for solar decontamination of water, *Environ. Sci. Technol.* **1994**, *28*, 435–442.
- 41 M. R. HOFFMANN, S. T. MARTIN, W. CHOI, D. BAHNEMANN, Environmental applications of semiconductor photocatalysis, *Chem. Rev.* **1995**, *95*, 69–96.
- 42 S. AHMED, D. F. OLLIS, Solar assisted catalytic decomposition of the chlorinated hydrocarbons trichloroethylene and trichloromethane, *Solar Energy* **1984**, *32*(5), 597–601.
- 43 Y. ZHANG, J. C. CRITTENDEN, D. W. HAND, The solar photocatalytic decontamination of water, *Chem. Ind.* **1994**, 714–717.
- 44 D. BEYDOUN, R. AMAL, G. LOW, S. McEVoy, Role of nanoparticles in photocatalysis, *J. Nanoparticle Res.* **1999**, *1*, 439–458.
- 45 R. F. HOWE, Recent developments in photocatalysis, *Dev. Chem. Eng. Mineral Process* **1998**, *6*(1), 55–84.
- 46 W. A. ZELTNER, C. G. HILL, JR., M. A. ANDERSON, Supported titania for

- photodegradation, *Chemtech* **1993**, *23*, 21–28.
- 47 K. HOFSTADLER, R. BAUER, S. NOVALIC, G. HEISER, New reactor design for photocatalytic wastewater treatment with TiO<sub>2</sub> immobilized on fused-silica glass fibers: Photomineralization of 4-chlorophenol, *Environ. Sci. Technol.* **1994**, *28*, 670–674.
  - 48 M. TOMKIEWICZ, G. DAGAN, Z. ZHU, Morphology and photocatalytic activity of TiO<sub>2</sub> aerogels, *Res. Chem. Intermed.* **1994**, *20*, 701–710.
  - 49 N. XU, S. ZAIFENG, Y. FAN, J. DONG, J. SHI, M. Z. U. HU, Effects of particle size of TiO<sub>2</sub> on photocatalytic degradation of methylene blue in aqueous suspensions, *Ind. Eng. Chem. Res.* **1999**, *38*, 373–379.
  - 50 H. HIDAHA, Photodegradation of surfactants with TiO<sub>2</sub> semiconductor for the environmental wastewater treatment, *Proc. Indian Acad. Sci.* **1998**, *110*, 215–228.
  - 51 I. MAZZARINO, P. PICCININI, Photocatalytic oxidation of organic acids in aqueous media by supported catalyst, *Chem. Eng. Sci.* **1999**, *54*, 3107–3111.
  - 52 J. F. TANGUAY, S. L. SUIT, R. W. COUGHLIN, Dichloromethane photodegradation using titanium dioxide, *J. Catal.* **1989**, *117*, 335–347.
  - 53 D. F. OLLIS, C. Y. HSIAO, L. BUDIMAN, L. L. CHUNG, Heterogeneous photoassisted catalysis: conversions of perchloroethylene, dichloroethylene, chloroacetic acids and chlorobenzene, *J. Catal.* **1984**, *88*, 89–96.
  - 54 R. D. BARRETO, K. A. GRAY, K. ANDERS, Photocatalytic degradation of methyl-tert-butyl ether in TiO<sub>2</sub> slurries: A proposed reaction scheme, *Water Res.* **1995**, *29*, 1243–1248.
  - 55 R. W. MATTHEWS, S. R. McEVOY, Destruction of phenol in water with sun sand and photocatalysis, *Solar Energy* **1992**, *49*, 507–513.
  - 56 V. AUGUGLIARO, F. INGLESE, L. PALMISANO, M. SCHIAVELLO, Annular flow photoreactor for phenol degradation in aqueous titanium dioxide dispersion, *Chem. Biochem. Eng. Q.* **1992**, *6*, 63–70.
  - 57 W. F. JARDIM, S. G. MORAES, M. M. K. TAKIYAMA, Photocatalytic degradation of aromatic chlorinated compounds using TiO<sub>2</sub>: Toxicity of intermediates, *Water Res.* **1997**, *31*, 1728–1732.
  - 58 C. MINERO, V. MAURINO, E. PELIZZETTI, Photocatalytic degradation of free and chemically bound silicones on irradiated titanium dioxide, *Langmuir* **1995**, *11*, 4440–4444.
  - 59 R. W. MATTHEWS, Photooxidative degradation of coloured organics in water using supported catalysts. TiO<sub>2</sub> on sand, *Water Res.* **1991**, *25*, 1169–1176.
  - 60 A. TOPALOV, D. M. GABOR, J. CSANAD, Photocatalytic oxidation of the fungicide metalaxyl dissolved in water over TiO<sub>2</sub>, *Water Res.* **1999**, *33*, 1371–1376.
  - 61 J. CHEN, D. F. OLLIS, W. H. RULKENS, H. BRUNING, Photocatalyzed oxidation of alcohols and organochlorides in the presence of native TiO<sub>2</sub> and metallized TiO<sub>2</sub> suspensions. Part (I): Photocatalytic activity and pH influence, *Water Res.* **1999**, *33*, 661–668.
  - 62 M. M. KONDO, W. F. JARDIM, Photodegradation of chloroform and urea using Ag-loaded titanium dioxide as catalyst, *Water Res.* **1991**, *25*, 823–827.
  - 63 R. M. ALBERICI, W. F. JARDIM, Photocatalytic degradation of phenol and chlorophenols using Ag-TiO<sub>2</sub> in a slurry reactor, *Water Res.* **1994**, *28*, 1845–1849.
  - 64 S. T. ARUNA, K. C. PATIL, Synthesis and properties of nanosized titania, *J. Mater. Synthesis Process.* **1996**, *4*(3), 175–179.
  - 65 D. W. BAHNEMANN, Ultrasmall metal oxide particles. Preparation, photophysical characterisation, and photocatalytic properties, *Isr. J. Chem.* **1993**, *33*, 115–136.
  - 66 Ch.-H. FISCHER, J. LILLIE, H. WELLER, L. KATSIKAS, A. HENGLEIN, Photochemistry of colloidal semiconductors. 29. Fractionation of CdS sols of small particles by exclusion chromatography, *Ber. Bunsenges, Phys. Chem.* **1989**, *93*, 61–64.
  - 67 A. HENGLEIN, Nanoclusters of

- semiconductors and metals – colloidal nanoparticles of semiconductors and metals: Electronic structure and process, *Ber. Bunsen-Gesellsch. Phys. Chem.* **1997**, 101(11), 1562–1572.
- 68 A. HENGLEIN, Mechanism of reactions on colloidal microelectrodes and size quantization effects, *Top. Curr. Chem.* **1988**, 143, 113–180.
- 69 A. HENGLEIN, Small particle research. Physicochemical properties of extremely small colloidal metal and semiconductor particles, *Chem. Rev.* **1989**, 89, 1861–1873.
- 70 Y. WANG, N. HERRON, Nanometer-sized semiconductor clusters. Materials synthesis, quantum size effects, and photophysical properties, *J. Phys. Chem.* **1991**, 95, 525–532.
- 71 B. LEVY, Photochemistry of nanostructured materials for energy applications. *J. Electroceram. I* **1997**, (3), 239–272.
- 72 H. WELLER, A. EYCHMULLER, Photochemistry and photo electrochemistry of quantized matter: Properties of semiconductor nanoparticles in solution and thin-film electrodes, in *Advances in Photochemistry*, ed. C. DOUGLAS, NECKERS, H. D. VOLMAN, G. VON BUNAU, John Wiley and Sons, New York, NY, USA **1995**, Vol. 20.
- 73 N. SERPONE, D. LAWLESS, E. PELIZZETTI, Subnanosecond characteristics and photophysics of nanosized TiO<sub>2</sub> particulates from Rp, " = 10A to 34A: Meaning for heterogeneous photocatalysis, in *Fine Particles Science and Technology*, ed. E. PELIZZETTI, Kluwer Academic Publishers, Boston, MA, USA **1996**, pp. 657–673.
- 74 A. HAGFELDT, M. GRATZEL, Light-induced redox reactions in nanocrystalline systems, *Chem. Rev.* **1995**, 95, 49–68.
- 75 P. V. KAMAT, B. PATRICK, Photo-physics and photochemistry of quantized ZnO colloids, *J. Phys. Chem.* **1992**, 96, 6829–6834.
- 76 A. HENGLEIN, Q-particles: Size quantization effects in colloidal semiconductors, *Progr. Colloid Polym. Sci.* **1987**, 73, 1–4.
- 77 C. KORMANN, D. W. BAHNEMANN, M. HOFTMANN, Preparation and characterisation of quantum-size titanium dioxide, *J. Phys. Chem.* **1988**, 92, 5196–5201.
- 78 M. GRATZEL, *Heterogeneous Photochemical Electron Transfer*, CRC Press, Boca Raton, FL, **1989**.
- 79 M. ANPO, T. SHIMA, S. KODAMA, Y. KUBOKAWA, Photocatalytic hydrogenation of CHCCH with H<sub>2</sub>O on small particle TiO<sub>2</sub>. Size quantization effects and reaction intermediates, *J. Phys. Chem.* **1987**, 91, 4305–4310.
- 80 L. KAVAN, T. STOTO, M. GRATZEL, D. FITZMAURICE, V. SHKLOVER, Quantum size effects in nanocrystalline semiconducting TiO<sub>2</sub> layers prepared by anodic oxidative hydrolysis of TiCl<sub>3</sub>, *J. Phys. Chem.* **1993**, 97, 9493–9498.
- 81 S. MARTIN, H. HERRMANN, W. CHOI, M. HOFFMANN, Photochemical destruction of chemical contaminants on quantum-sized semiconductor particles, *J. Sol. Energ.-T. ASME*, **1995**, 409–413.
- 82 A. J. HOFFMANN, G. MILLS, H. YEE, M. R. HOFFMANN, Q-sized CdS: Synthesis, characterisation, and efficiency of photoinitiation of polymerisation of several vinylic monomers, *J. Phys. Chem.* **1992**, 96, 5546–5552.
- 83 J. M. NEDELJKOVIC, M. T. NENODOVIC, O. I. MICIC, A. J. NOZIK, Enhanced photoredox chemistry in quantized semiconductor colloids, *J. Phys. Chem.* **1986**, 90, 12–13.
- 84 A. J. HOFFMANN, E. R. CARRAWAY, M. R. HOFFMANN, Photocatalytic production of H<sub>2</sub>O<sub>2</sub> and organic peroxides on quantum-sized semiconductor colloids, *Environ. Sci. Technol.* **1994**, 28, 776–785.
- 85 Y. NOSAKA, N. OHTA, H. MIYAMA, Photochemical kinetics of ultrasmall semiconductor particles in solution: Effect of size on the quantum yield of electron transfer, *J. Phys. Chem.* **1990**, 94, 3752–3755.
- 86 G. P. LEPORE, C. H. LANGFORD, J. VICHOVA, A. VLCEK, Photochemistry



- and picosecond absorption spectra of aqueous suspensions of a polycrystalline titanium dioxide optically transparent in the visible spectrum, *J. Photochem. Photobiol. A, Chem.* **1993**, *75*, 67–75.
- 87 A. J. HOFFMANN, H. YEE, G. MILLS, M. R. HOFFMANN, Photoinitiated polymerisation of methyl methacrylate using Q-sized ZnO colloids, *J. Phys. Chem.* **1992**, *96*, 5540–5546.
- 88 C. WANG, C. Z. ZHANG, J. Y. YING, Photocatalytic decomposition of halogenated organics over nanocrystalline titania, *Nanostructured Mater.* **1997**, *9*, 583–586.
- 89 Z. ZHANG, C.-C. WANG, R. ZAKARIA, J. Y. YING, Role of particle size in nanocrystalline TiO<sub>2</sub>-based photocatalysts, *J. Phys. Chem. B* **1998**, *102*, 10871–10878.
- 90 S. E. PRATSINIS, *J. Aerosol Sci.* **1996**, *27*, 153–154.
- 91 Z. X. DING, P. L. HU, G. Q. YUE, P. F. GREENFIELD, *Catal. Today* **2001**, *68*, 173–182.
- 92 B. XIA, W. LI, B. ZHANG, X. YOUCHANG, *J. Mater. Sci.* **1999**, *34*, 3505–3511.
- 93 R. R. BACSA, M. GRATZEL, *J. Am. Ceram. Soc.* **1996**, *79*, 2185–2188.
- 94 C. ANDERSON, A. J. BARD, *J. Phys. Chem.* **1995**, *99*, 9882–9885.
- 95 S. WATSON, D. BEYDOUN, J. SCOTT, R. AMAL, Preparation of nanosized crystalline TiO<sub>2</sub> particles at low temperature for photocatalysis, *J. Nanoparticle Res.* **2004**, *6*, 193–207.
- 96 S. T. ARUNA, K. C. PATIL, Synthesis and properties of nanosized titania, *J. Mater. Synth. Process.* **1996**, *4*, 175–179.
- 97 <http://samms.pnl.gov/index.stm>
- 98 F. SCHREIBER, Structure and growth of self-assembling monolayers, *Science* **2000**, *65*, 151–156.
- 99 M. R. DE GUIRE, T. NIESEN, S. SUPOTHINA, J. WOLFF, J. BILL, C. N. SUKENIK, F. ALDINGER, A. H. HEUER, M. RUEHLE, Synthesis of Oxide and Non-Oxide Inorganic Materials at Organic Surfaces, *Z. Metallkunde*, **1998**, *89*, 758–766.
- 100 J. BILL, R. C. HOFFMANN, T. M. FUCHS, F. ALDINGER, Deposition of Ceramic Materials from Aqueous Solution Induced by Organic Templates, *Z. Metallkunde*, **2002**, *93*, 478–490.
- 101 P. MAJEWSKI, T. FUCHS, S. PRAKASH, Synthesis and properties of silane-based self-assembled-monolayers onto silica particles, *Mater. Forum* **2005**, *29*, 489–493.
- 102 P. MAJEWSKI, T. FUCHS, S. PRAKASH, L. TRIBALAT, Synthesis of manganese oxide onto silica particles coated with self-assembled-monolayers, *J. Mater. Sci. Technol.* **2005**, *21*, 29–32.
- 103 N. BALACHANDER, C. N. SUKENIK, Monolayer transformation by nucleophilic substitution: Applications to the creation of new monolayer assemblies, *Langmuir* **1990**, *6*, 1622–1627.
- 104 R. J. COLLINS, C. N. SUKENIK, Sulfonate-functionalized, siloxane-anchored, self-assembled monolayers, *Langmuir* **1995**, *11*, 2322–2324.
- 105 H. PIZEM, C. N. SUKENIK, U. SAMPATHKUMARAN, A. K. MCLIWAIN, M. R. DE GUIRE, Effects of substrate surface functionality on solution-deposited titania films, *Chem. Mater.* **2002**, *13*, 2476–2485.
- 106 G. E. FRYXELL, J. LIU, Designing surface chemistry in mesoporous silica, in *Adsorption at Silica Surfaces*, ed. E. PAPIRER, Marcel Dekker, New York, NY, USA, **2000**, pp. 665–688.
- 107 J. LIU, Y. SHIN, Z. NIE, J. H. CHANG, LI-Q. WANG, G. E. FRYXELL, W. D. SAMUELS, J. GREGORY, Exarhos, Molecular assembly in ordered mesoporosity: A new class of highly functional nanoscale materials, *J. Phys. Chem. A* **2000**, *104*, 8328–8339.
- 108 J. LIU, G. E. FRYXELL, M. QIAN, LI-Q. WANG, Y. WANG, Interfacial chemistry in self-assembled nanoscale materials with structural ordering, *Pure Appl. Chem.*, **2000**, *72*, 269–279.
- 109 (a) W. YANTASEE, Y. LIN, E. G. FRYXELL, B. BUSCHE, J. C. BIRNBAUM, Removal of heavy metals from aqueous solution using novel nanoengineered sorbents: Self-

- assembled carbamoylphosphonic acids on mesoporous silica, *Sep. Sci. & Technol.*, **2003**, 38, 3809–3825; (b) G. E. FRYXELL, Y. LIN, S. FISKUM, J. C. BIRNBAUM, H. WU, K. KEMNER, S. KELLEY, Actinide sequestration using self-assembled monolayers on mesoporous supports, *Environ. Sci. Technol.*, **2005**, 39, 1324–1331; (c) G. E. FRYXELL, H. WU, Y. LIN, W. J. SHAW, J. C. BIRNBAUM, J. C. LINEHAN, Z. NIE, K. KEMNER, S. KELLY, Lanthanide selective sorbents: Self-assembled monolayers on mesoporous supports (SAMMS), *J. Mater. Chem.*, **2004**, 14, 3356–3363.
- 110 S. V. MATTIGOD, G. E. FRYXELL, R. J. SERNE, K. E. PARKER, F. M. MANN, Evaluation of novel getters for adsorption of radioiodine from groundwater and waste glass leachates, *Radiochim. Acta*, **2003**, 91, 539–545.
- 111 W. YANTASEE, Y. LIN, G. E. FRYXELL, B. J. BUSCHE, J. C. BIRNBAUM, Removal of heavy metals from aqueous solution using novel nanoengineered sorbents: self-assembled carbamoylphosphonic acids on mesoporous silica. *Sep. Sci. Technol.*, **2003**, 38(15), 3809–3825.
- 112 G. E. FRYXELL, Y. LIN, H. WU, K. M. KEMNER, Environmental applications of self-assembled monolayers on mesoporous supports (SAMMS), in *Studies in Surface Science and Catalysis*, Vol. 141, ed. A. SAYARI, M. JARONIEC, Elsevier, Oxford, UK, **2003**, pp. 583–590.
- 113 Y. LIN, G. E. FRYXELL, H. WU, M. ENGLEHARD, Selective sorption of cesium using self-assembled monolayers on mesoporous supports (SAMMS) *Environ. Sci. Technol.*, **2001**, 35, 3962–3966.
- 114 G. E. FRYXELL, J. LIU, S. V. MATTIGOD, L. Q. WANG, M. GONG, T. A. HAUSER, Y. LIN, K. F. FERRIS, X. FENG, Environmental applications of interfacially modified mesoporous ceramics, in *Environmental Issues and Waste Management Technologies in the Ceramic and Nuclear Industries*, ed. G. T. CHANDLER, X. FENG, **2000**, Ceramics Transactions, American Ceramic Society, Westerville, OH, USA, Vol. 107, pp. 29–37.
- 115 G. E. FRYXELL, J. LIU, S. MATTIGOD, Environmental applications of self-assembled monolayers on mesoporous supports (SAMMS), *Mater. Technol.*, **1999**, 14, 188–191.
- 116 S. V. MATTIGOD, X. FENG, G. E. FRYXELL, J. LIU, M. GONG, Separation of complexed mercury from aqueous wastes using self-assembled mercaptan on mesoporous silica, *Sep. Sci. Technol.*, **1999**, 34, 2329–2345.
- 117 S. MATTIGOD, G. E. FRYXELL, X. FENG, J. LIU, Self-assembled monolayers on mesoporous supports for metal separation, in *Metal Separation Technologies Beyond 2000: Integrating Novel Chemistry with Processing*, ed. K. C. LIDDELL, D. J. CHAIKO, The Minerals, Metals and Materials Society, Warrendale, PA, USA, **1999**, pp. 71–79.
- 118 X. FENG, L. RAO, T. R. MOHS, J. XU, Y. XIA, G. E. FRYXELL, J. LIU, K. N. RAYMOND, Self-assembled monolayers on mesoporous silica, a super sponge for actinides, in *Environmental Issues and Waste Management Technologies IV*, ed. J. C. MARA, G. T. CHANDLER, **1999**, Ceramic Transactions, American Ceramic Society, Westerville, OH, USA, Vol. 93, pp. 35–42.
- 119 P. MAJEWSKI, Interaction of Functionalized Self-Assembled Monolayers with Pathogens in Water, *The Nano and Bio-Newsletter*, II, Ian Wark Research Inst., Adelaide, Australia, 2006.
- 120 P. MAJEWSKI, *Water Treatment based on Functionalised Organic Self-Assembled Monolayers*, Annual Report **2004**, Ian Wark Research Institute, University of South Australia, [www.unisa.edu.au/iwri](http://www.unisa.edu.au/iwri).
- 121 B. BRENNAN, Waterworks, *Sci. & Technol.*, **2001**, 79, 32–38.
- 122 S. O. OBARE, G. J. MEYER, Nanostructured materials for environmental remediation of organic contaminants in water, *J. Environ. Sci. Health, Part A: Toxic/Hazardous Substances Environ. Eng.*, **2004**, A39(10), 2549–2582.

- 123 C. H. COOPER, A. G. CUMMINGS, M. Y. STAROSTIN, C. P. HONSINGER, Purification of fluids with nanomaterials containing defective carbon nanotubes, *PCT Int. Appl. WO 2004080578* (2004), 106 pp. CODEN: PIXXD2.
- 124 K. M. PAKNIKAR, V. NAGPAL, A. V. PETHKAR, J. M. RAJWADE, Degradation of lindane from aqueous solutions using iron sulfide nanoparticles stabilized by polymers, *Sci. Technol. Adv. Mater.*, **2005**, 6, 370–374.
- 125 X. PENG, Z. LUAN, J. DING, Z. DI, Y. LI, BINGHUI, Ceria nanoparticles supported on carbon nanotubes for the removal of arsenate from water, *Mater. Lett.*, 59(4), 399–403.
- 126 J. Y. MORAN, D. B. BURSILL, M. DRIKAS, H. NGUYEN, A new technique for the removal of natural organic matter, Proceedings of the Australian Water & Wastewater Assoc., Water TECH Conference 1996, Australian Water & Wastewater Assoc., Sydney, Australia, pp. 428–432.
- 127 J. Y. MORRAN, M. DRIKAS, D. COOK, D. B. BURSILL, Comparison of MIEX<sup>®</sup> treatment and coagulation on NOM character, *Water Sci. Technol.: Water Supply*, **2004**, 4(4), 129–137.
- 128 M. DRIKAS, J. Y. MORRAN, C. PELEKANI, C. HEPPLEWHITE, D. B. BURSILL, Removal of natural organic matter – a fresh approach, *Water Sci. Technol.: Water Supply*, **2002**, 2(1), 71–79.
- 129 M. DRIKAS, J. Y. MORRAN, D. COOK, D. B. BURSILL, Operating the MIEX<sup>®</sup> process with microfiltration or coagulation, Proceedings of the WQTC 2003, American Water Works Assoc., Denver, CO, USA, pp. 1–11.
- 130 H. VAN NGUYEN, D. BRUCE BURSILL, J. YOUNG MORRAN, M. DRIKAS, V. L. PEARCE, *US Patent No. 6669849*, **2003**.

## 10

# Nanoparticles for the Photocatalytic Removal of Endocrine-disrupting Chemicals in Water

*Heather M. Coleman*

### 10.1 Introduction

There is currently much concern about the release into the aquatic environment of natural and synthetic oestrogens and compounds that can mimic oestrogens. Since the turn of the last century, new testing methods have allowed scientists to detect traces of at least 500 new synthetic chemicals in our bodies. Some of these chemicals are persistent; others that we are regularly exposed to are short-lived. The long-term effects of most of these chemicals are unknown but evidence is mounting that some of these substances, known as endocrine disrupters, could be wreaking havoc with human and animal hormones, reducing the chances of successful reproduction by lowering sperm counts and contributing to an increased incidence of several rare cancers and birth defects [1]. The range of substances reported to cause endocrine-disrupting effects is diverse, and continues to expand as the number of studies increases. Some are likely to be distributed widely in the environment, are long-lived, and can accumulate in the tissues of plants and animals. The term “Environmental oestrogens” includes all oestrogens that may affect the endocrine system (the communication system of glands, hormones and cellular receptors that control the body’s internal functions) [2] and includes the natural oestrogens, synthetic oestrogens, xenoestrogens (oestrogen mimics) and phytoestrogens (plant oestrogens). However, the main compounds of concern are the natural and synthetic oestrogens that have been detected at significant biological levels in sewage effluent [3]. New methods for water treatment, as well as improvements to existing processes, are required because of more severe regulations resulting from increasing awareness of the urgent need to protect our environment. Concerning the new oxidation methods under development (usually termed “advanced oxidation technologies or processes”, AOTs or AOPs), heterogeneous titanium dioxide photocatalysis appears very promising in terms of destroying organic micro-pollutants, leaving them in very low concentrations. The degradation of organic pollutants present in wastewaters using irradiated dispersions of TiO<sub>2</sub> nanoparticles is a fast growing field in basic and applied research.

This chapter describes the use of titanium dioxide photocatalysis for the degrada-

tion of natural and synthetic oestrogens in water. The background to oestrogens in the environment is described in Section 10.2 and titanium dioxide ( $\text{TiO}_2$ ) photocatalysis is discussed along with the main aim and objectives of the work in Section 10.3. Each objective is then addressed in the sections that follow (Sections 10.4–10.7) and conclusions are made and research needs identified (Section 10.8).

## 10.2

### Background to Oestrogens in the Environment

The main substances of concern are the natural oestrogens  $17\beta$ -oestradiol, oestrone and oestriol and the synthetic oestrogen  $17\alpha$ -ethinyloestradiol. This chapter involves the photocatalytic degradation of all of the oestrogens and particularly deals with  $17\beta$ -oestradiol, the principal, natural and most potent oestrogen. Natural oestrogens are steroid hormones made primarily in the female ovaries and the male testes in humans and other animals. Known as the female hormones, oestrogens are found in greater amounts in females than males. These essential molecules influence growth, development and behavior (puberty), regulate reproductive cycles (menstruation, pregnancy) and affect many other body parts (bones, skin, arteries, the brain, etc.) [2]. Oestradiol is the principal, natural and most potent oestrogen, followed by oestrone and finally oestriol (Fig. 10.1).

$17\beta$ -Oestradiol is a potent endogenous oestrogen responsible for the development of female secondary sex characteristics and reproduction [4]. As illustrated in Fig. 10.1,  $17\beta$ -oestradiol and its derivatives oestrone and oestriol are 18-carbon steroids with a phenolic ring. The phenolic A ring is the structural component responsible for high affinity binding to the oestrogen receptor [4].

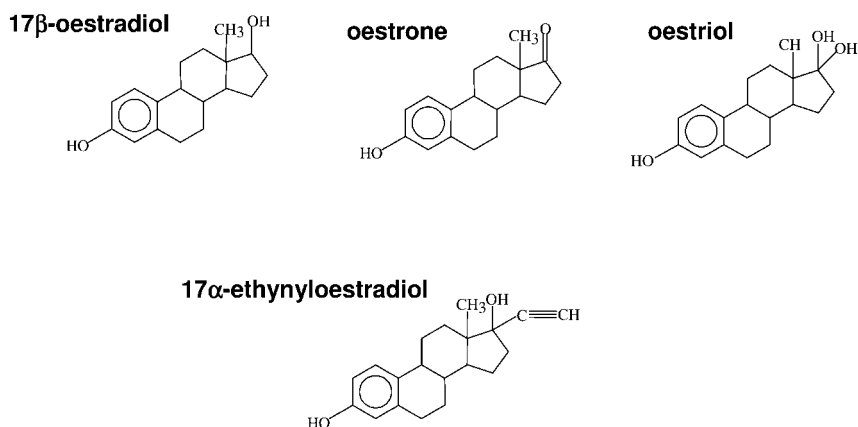


**Fig. 10.1.** Structures of the natural oestrogens ( $17\beta$ -oestradiol, oestrone and oestriol) and the synthetic oestrogen  $17\alpha$ -ethinyloestradiol.

17 $\alpha$ -Ethinylloestradiol is a synthetic oestrogen used extensively in oral contraceptive formulations. It is structurally similar to 17 $\beta$ -oestradiol, with the exception of an ethynyl substitution at carbon-17 and has a higher affinity for the oestrogen receptor than 17 $\beta$ -oestradiol [4] (Fig. 10.1). Introducing an ethynyl group at the 17 $\alpha$ -position of the oestradiol molecule produces a more stable compound. 17 $\alpha$ -Ethinylloestradiol is the most frequently used oestrogen component in the contraceptive pill. The ethynyl group makes the D ring much more resistant to oxidation. Consequently, ethinylloestradiol is excreted up to 80% unchanged [5]. Oestrogen pharmaceutical products are used in both human and veterinary medicine [6], e.g., oral contraceptives, hormone replacement therapy and livestock yield improvement [4].

Exposure to endocrine-disrupting chemicals (EDCs) in the environment has been associated with abnormal thyroid function in birds and fish; decreased fertility in birds, fish, shellfish and mammals; decreased hatching success in fish, birds and turtles; demasculinization and feminization of male fish, birds and mammals; defeminization and masculinization of female fish, gastropods and birds; and alteration of immune function in birds and mammals [7]. Human illnesses linked to endocrine disruption include breast, prostate and testicular cancer, reproductive abnormalities such as declining sperm counts and malformed male genitals, learning and behavioral problems and immune system deficiencies.

The presence of low concentrations of natural and synthetic steroid oestrogens in the aquatic environment has been reported over the last 30 years [8–10], but only relatively recently was it realized that steroid oestrogens constitute the main oestrogenic component in domestic sewage treatment work (STW) effluents [9]. The major oestrogenic components of STW effluent include the natural oestrogens, 17 $\beta$ -oestradiol and oestrone, and the synthetic steroid oestrogen 17 $\alpha$ -ethinylloestradiol [9]. These steroid oestrogens have been widely reported in sewage effluents [9, 11], rivers [12, 13] and spring water [14]. Steroid oestrogens are eliminated from the body mainly as biologically inactive forms, following their conjugation to water-soluble glucuronide and/or sulfate ester groups [15]. However, a large proportion of these steroid conjugates in wastewater are probably deconjugated before reaching the STW by faecal bacteria (such as *Escherichia coli*), which synthesize large quantities of the enzyme  $\beta$ -glucuronidase [16]. STWs typically remove in excess of 80% of the steroid content (or oestrogenic activity) present within the influent [17–20]. However, due to their extremely high biological potency, even trace amounts of steroid remaining in the effluent are capable of exerting biological effects on fish [21] and other aquatic organisms. The time needed for conventional biological methods to remove total organic carbon, combined with the relatively short hydraulic residency times of many STWs, means that many wastewater discharges still contain environmentally relevant levels of steroid oestrogens and their biotransformation products (Table 10.1). The need to reduce the output of steroid oestrogens in STW effluents is critical in countries with limited water resources, where effluent can become a major component of river flow in the summer months [22]. Therefore, there is a need to consider alternative strategies for the removal of trace amounts of steroid and steroid-like compounds pres-

Tab. 10.1. Oestrogen levels in STWs around the world [9, 23–25].

Location	Concentration (ng L <sup>-1</sup> )	
	17 $\beta$ -Oestradiol	17 $\alpha$ -Ethinylestradiol
United Kingdom (1998)	1–50	0–7
France, Paris (2003)	4.5–8.6	3.1–4.5
Netherlands (1999)	<0.6–12	<0.2–7.5
Germany (1999)	3	15
Canada (1999)	64	42
Sweden (1999)	1.1	4.5
Japan, Tokyo (2003)	15	9

ent in STW effluents before their discharge into rivers. There are also increasing regulatory pressures to reduce environmental levels of many EDCs.

### 10.2.1

#### Advanced Oxidation Techniques (AOTs)

In view of the growing medical use of synthetic steroids and the increasing use of birth-control pills, the synthetic ovulation-inhibiting hormones are expected to increase in concentration in wastewaters. While the concentrations in wastewater are bound to be extremely low at present, their high physiological activity at extremely low concentrations and their relatively greater stability in aqueous media than that of natural urinary hormones deserve consideration as possible contaminants of water to be processed for drinking. Consideration, therefore, needs to be given to the management strategies available in the light of such oestrogenic contamination, as the removal of these substances by current conventional water treatment methods is ineffective. A possible alternative treatment for the purification of water is titanium dioxide semiconductor photocatalysis, which is an advanced oxidation technology and a rapidly growing area of interest to both research workers and water purification companies [26]. Almost all these studies have been directed towards the oxidative degradation of organic pollutants in water [27]. While water purification techniques such as UV, ozonation or activated charcoal could significantly remove these microorganic contaminants, the high costs involved suggest that research into treatment optimization should receive more attention [3].

The common characteristic of all AOTs is the generation of very reactive free-radicals that oxidize pollutants. AOTs include thermal processes, H<sub>2</sub>O<sub>2</sub> or ozone, and light-induced reactions such as homogeneous photolysis, UV/H<sub>2</sub>O<sub>2</sub> photolysis, UV/ozone photolysis, heterogeneous photolysis and radiolysis [28]. Chemical oxidation technologies are useful in the oxidative degradation or transformation of a

wide range of pollutants for the treatment of drinking water, groundwater, wastewater and contaminated soils. Chemical oxidation methods are especially applicable for: the treatment of hazardous organics present at low concentrations, such as in contaminated groundwaters; use as a pre-treatment step before biological treatment of low-volume, high strength wastewaters; treatment of wastewaters with constituents that are resistant to biodegradation methods or upset biological treatment reactors, such as cyanides and complex metals; and use as a post-treatment step following biological treatment to reduce aquatic toxicity. Chemical oxidation methods can also be combined with other treatment technologies to achieve optimum and cost-effective treatment technologies [29]. However, approaches for controlling the release of steroid oestrogens, or other compounds that are natural by-products of our very existence, is a unique challenge.

### 10.2.2

#### **Ultraviolet Photolysis**

Treatment by UV radiation alone was also investigated in this study as a comparison to photocatalysis. Direct ultraviolet photolysis was the first photochemical method used for pollutant degradation. Although several authors have proposed direct photooxidation with ultraviolet light for water treatment [30], there are several limitations to its general applicability. Direct photochemical degradation can be achieved only when the incident light [vacuum ultraviolet (VUV) light:  $\lambda < 200$  nm or UV-light:  $\lambda > 200$  nm] is absorbed by the pollutant. There are numerous reports of UV degradation of organics present in water, including fluorinated or chlorinated aliphatics, chlorinated hydrocarbons, trihalomethanes, dinitrotoluene, chlorophenols, pesticides, PCBs, chlorinated and nitrated aromatics, phenols, halogenated aliphatics, and other hazardous wastes [31]. Direct photolysis procedures are generally of low efficiency than procedures involving hydroxyl radical generation. However, photolysis of pollutants may be important in cases where hydroxyl radical reactions are very slow [30]. UVC disinfection is currently being used in some treatment facilities around the world (e.g., Orange County Water District, California, USA; Sydney Water, Australia; Essex and Suffolk Water, UK).

### 10.3

#### **Nanoparticles for Water Treatment Applications**

Chemists have known for decades that several semiconductor metal oxides are light-sensitive and can initiate redox reactions of adsorbates [32]. In 1972, Fujishima and Honda discovered the photocatalytic splitting of water on titanium dioxide electrodes [33]. This event marked the beginning of a new era in heterogeneous photocatalysis, stimulating a worldwide effort to characterize the physical features that control efficiency in these interfacial reactions [31]. Since then, research efforts in understanding the fundamental processes and in enhancing the photocatalytic efficiency of TiO<sub>2</sub> nanoparticles have come from extensive research performed



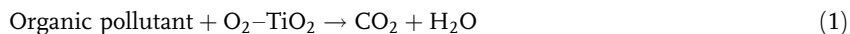
by chemists, physicists and chemical engineers. In recent years, applications to environmental clean-up have been one of the most active areas in heterogeneous photocatalysis. This has been inspired by the potential application of TiO<sub>2</sub>-based photocatalysts for the total destruction of organic compounds in polluted air and wastewaters [31]. The degradation of organic pollutants present in wastewaters using irradiated dispersions of TiO<sub>2</sub> is a fast growing field in basic and applied research. The development of this process to achieve complete mineralization of organic pollutants has been widely tested for a large variety of chemicals [31]. Carey et al. first reported, in 1976, the photocatalytic degradation of biphenyl and chlorophenyls in the presence of TiO<sub>2</sub> [34]. Since then, many applications using the TiO<sub>2</sub>/UV process have been investigated. Other semiconductor dispersions have also been used for the photocatalytic degradation of pollutants [31]. There is an exhaustive amount of literature on titanium dioxide photocatalysis. Mills and Le Hunte published an excellent review in 1997 and estimated that over 2000 papers had been published since 1981 [35]. Over the years, reviews have been published [31, 36–39] and books written on the subject [40–43]. Commercial applications of titanium dioxide photocatalysis have been reviewed by Mills et al. [44].

### 10.3.1

#### Titanium Dioxide Photocatalysis

##### 10.3.1.1 The Principle

Photocatalysis, as the name suggests, involves light and a catalyst to bring about a chemical reaction. Mills and Le Hunte define photocatalysis as the “acceleration of a photoreaction by the presence of a catalyst” [35]. In photocatalysis the catalyst is activated by the absorption of photons of light whose energy is used to overcome the activation energy. In this case the catalyst is a semiconductor and it provides a low energy activation pathway for the passage of electronic charge. The charge is effectively transferred from the reactant through the semiconductor (activated by a photon of light) to the product (a redox reaction) [41]. In TiO<sub>2</sub> photocatalysis for water purification the pollutants are usually organic compounds and, therefore, the overall process can be summarized by reaction Eq. (1) [27].



$$h\nu, \lambda \leq 400 \text{ nm}$$

The advantages of TiO<sub>2</sub> over other semiconductors, for photocatalytic treatment of water, are that it is an inexpensive readily available material, and it is non-toxic, insoluble and photostable. In addition, solar illumination is a possibility, organic compounds are completely oxidized, no expensive chemicals need be added and a wide spectrum of pollutants can be degraded [27]. The process can also be turned on and off at the flick of a switch. TiO<sub>2</sub> photocatalysis has potential application in the treatment of both waste and drinking water [45].

### 10.3.1.2 Titanium Dioxide Nanoparticles as a Photocatalyst

The initial process for heterogeneous photocatalysis of organic and inorganic compounds by semiconductors is the generation of electron–hole pairs in the semiconductor particles [31]. Several semiconductors have been evaluated as photocatalysts, including metal oxides ( $\text{TiO}_2$ ,  $\text{ZnO}$ ,  $\text{SnO}_2$  and  $\text{WO}_3$ ) and chalcogenides ( $\text{ZnS}$ ,  $\text{CdS}$ ). For oxidation reactions, the most useful and widely employed is titanium dioxide.  $\text{TiO}_2$  is an intrinsic n-type semiconductor (due to an intrinsic oxygen deficiency, like  $\text{ZnO}$ ). It is ionic and has a wider band gap ( $>3$  eV) than non-ionic semiconductors. To promote an electron from the valence band to the conduction band, light of wavelength less than 400 nm is necessary to supply the required energy to cross the band gap [27].  $\text{TiO}_2$  nanoparticles have long been used in such applications as paint pigments and scratch-resistant optical coatings but can also display high activity for photocatalysis, which chemists and chemical engineers are beginning to exploit [46].  $\text{TiO}_2$  exhibits three different crystal forms: brookite, rutile and anatase. Rutile and anatase are the most stable and most common forms and their unit cells are shown in Fig. 10.2 [37]. They consist of chains of slightly distorted octahedrons of oxygen atoms around a titanium atom. Differences in the distortion of each octahedron by the assembly pattern of the octahedral chains cause differences in the mass densities and electronic band structure. For instance, the band gap for anatase is larger than that for rutile (3.23 and 3.02 eV respectively). The metastable anatase form transforms into the rutile form at high temperatures [37].

Many researchers have evaluated the photocatalytic activity of rutile and anatase

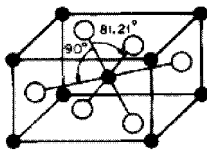
#### Rutile

$$d_{\text{Ti-O}}^{\text{eH}} = 1.949 \text{ \AA}$$

$$d_{\text{Ti-O}}^{\text{AP}} = 1.980 \text{ \AA}$$

$$a = 4.593 \text{ \AA}$$

$$c = 2.959 \text{ \AA}$$



$$E_g = 3.1 \text{ eV}$$

$$\rho = 4.250 \text{ g/cm}^3$$

$$\Delta G_f^\circ = -212.6 \text{ kcal/mole}$$

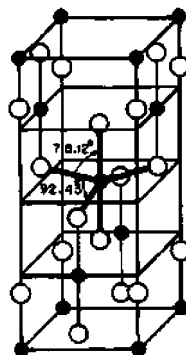
#### Anatase

$$d_{\text{Ti-O}}^{\text{eH}} = 1.934 \text{ \AA}$$

$$d_{\text{Ti-O}}^{\text{AP}} = 1.980 \text{ \AA}$$

$$a = 3.784 \text{ \AA}$$

$$c = 9.515 \text{ \AA}$$



$$E_g = 3.3 \text{ eV}$$

$$\rho = 3.894 \text{ g/cm}^3$$

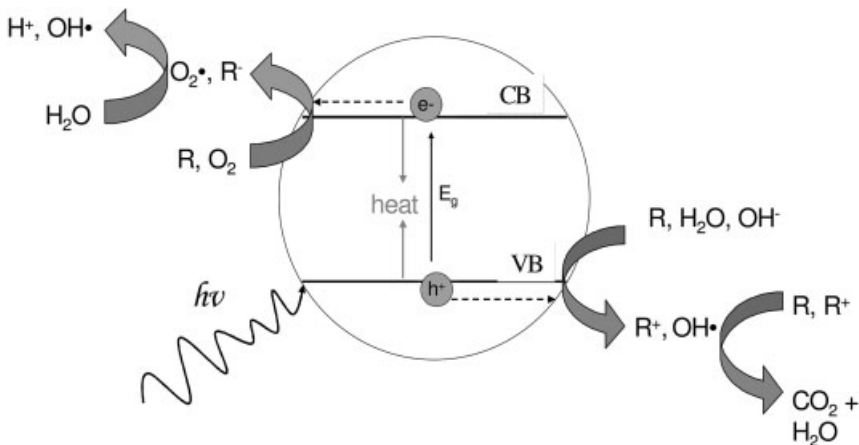
$$\Delta G_f^\circ = -211.4 \text{ kcal/mole}$$

Fig. 10.2. Structure of rutile and anatase [37].

and, in general, rutile is claimed to be less active than anatase or even inactive [27, 47]. This is because anatase has a much larger surface area than rutile. Anatase requires photons having energies greater than 3.2 eV ( $\lambda \sim 380$  nm) to excite an electron from the valence band to the conduction band. The separated electron–hole pairs can then be made available for oxidation–reduction reactions. The reduction potential for  $\cdot\text{OH}$  has been assigned a value of +2.85 V. It is, therefore, thermodynamically favorable for the hole site formed in the valence band of  $\text{TiO}_2$  to oxidize water to  $\cdot\text{OH}$  and for the separated electron promoted to the conduction band to reduce oxygen at  $-0.13$  V. The production of an OH radical from water, and the reduction of oxygen, requires a semiconductor with a band gap above 3 eV. Hence, anatase is an ideal photocatalyst for use in aqueous solutions [27, 35]. The most widely used form of  $\text{TiO}_2$ , which was used in this research, with high activity, is actually a mixture of the anatase and rutile forms (ca. 70–80% anatase). It is produced in particulate form (30 nm diameter crystalline size, aggregated together into 0.1  $\mu\text{m}$  macroscopic particle sizes) by the Degussa Corporation and is called Degussa P25. Its high activity is suggested to be because the conduction band of anatase is more positive than that of rutile, and the light-promoted electrons may pass from rutile to anatase, enhancing the separation of holes and electrons [48, 49].

### 10.3.1.3 Mechanism of $\text{TiO}_2$ Photocatalysis

Figure 10.3 shows a schematic of a  $\text{TiO}_2$  particle, illustrating the mechanism of  $\text{TiO}_2$  photocatalysis. When a photon of light of sufficient energy ( $E \geq E_{\text{bg}}$ ) strikes a  $\text{TiO}_2$  particle the energy of the photon is absorbed and used to promote an electron ( $e^-$ ) from the valence band to the conduction band. This movement of an electron leaves a hole ( $h^+$ ) in the valence band. These species ( $h^+$  and  $e^-$ ) produced by the absorption of light can either recombine or migrate to the surface of the  $\text{TiO}_2$



**Fig. 10.3.** Schematic of a titanium dioxide particle, illustrating the mechanism of titanium dioxide photocatalysis (VB = valence band, CB = conduction band,  $E_g$  = band gap energy,  $e^-$  = electron,  $h^+$  = hole, R = organic).

particle where they can react with other species at the interface. The holes can directly oxidize organic species adsorbed onto the  $\text{TiO}_2$  particle or can give rise to hydroxyl radicals ( $\cdot\text{OH}$ ) by reacting with water or  $\text{OH}^-$ . These highly reactive hydroxyl radicals then attack organic compounds present at or near the surface [27]. Electrons promoted to the conduction band must be removed rapidly from the  $\text{TiO}_2$  to prevent recombination with the holes and allow the mechanism to continue. Usually the electrons are passed on to molecular oxygen at the interface [31].

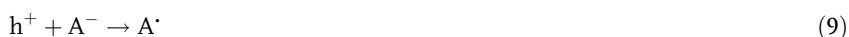
The source of  $\text{OH}^-$  may be related to the nature of the surface-bound water associated with anatase. The hydroxyl radical can oxidize organic contaminants. This process finally affords carbon dioxide and water if the reaction proceeds to completion [45]. The strong oxidizing power of the photogenerated holes, together with the chemical inertness and non-toxicity of  $\text{TiO}_2$ , has made it an attractive photocatalyst [46]. Photocatalysis has seen explosive growth, particularly during the past ten years. The general mechanism of photocatalysis on the  $\text{TiO}_2$  surface involves the oxidation of surface hydroxyl groups, which participate in the photocatalytic oxidation process. Although direct oxidation of substrates by photo-generated holes is possible, the involvement of  $\cdot\text{OH}$  in the oxidation process has gained much experimental support. To drive the photocatalytic reaction and maintain charge neutrality, oxygen undergoes reduction in aerated aqueous media, yielding  $\text{O}_2^-$  and  $\text{H}_2\text{O}_2$ , which in turn participate in further oxidation processes [46]. The band-gap model has proven very useful in explaining the mechanism of semiconductor-catalyzed oxidative degradation of organic material in aqueous systems [36, 37, 50]. The first event in the photocatalytic process is absorption of a photon of ultraband gap energy to produce the electron-hole pair on a particle [Eq. (2)].

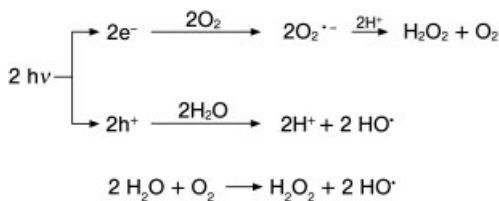


The electron in the conduction band can be transferred to adsorbed  $\text{H}^+$ ,  $\text{O}_2$  or a chlorinated pollutant (RX) [Eqs. (3)–(6)], initiating various reactions [30].



The hole ( $h^+$ ) in the valence band can react with surface-bound water, hydroxide groups, and anions ( $\text{A}^-$ ) to give the  $\text{HO}\cdot$  (or  $\text{A}\cdot$ ) radical, and with organic substrate (RH) to give radical cations ( $\text{RH}^+$ ) [Eqs. (7)–(10)] [30, 31].





Scheme 10.1.

Once formed, oxidative intermediates, mainly hydroxyl radicals, can react with the organic contaminant to initiate a sequence of reactions that lead to complete oxidative mineralization. Scheme 10.1 summarizes the material balance of H<sub>2</sub>O<sub>2</sub> and HO<sup>•</sup> formation [31].

The main aim of this work was to investigate the degradation of the natural oestrogens 17 $\beta$ -oestradiol, oestrone and oestriol and the synthetic oestrogen 17 $\alpha$ -ethnyloestradiol in water, using titanium dioxide photocatalysis.

The main objectives were:

- To determine if oestrogens in water can be degraded by titanium dioxide photocatalysis and UV radiation.
- To determine if all oestrogenic activity is removed after treatment with photocatalysis and UV radiation.
- To investigate the effect of varying reaction conditions on the photocatalytic reaction, i.e., initial concentration of pollutant and light intensity.
- To compare photocatalysis with UVA and UVC radiation.

These objectives were investigated and are discussed in Sections 10.4–10.7.

## 10.4

### Photocatalytic Degradation of 17 $\beta$ -Oestradiol in Water over an Immobilized TiO<sub>2</sub> Catalyst

Initial work involved investigating the degradation of the principal most potent natural oestrogen 17 $\beta$ -oestradiol in water by photocatalysis monitored using high-performance liquid chromatography (HPLC) with fluorescence detection in a quartz water-jacketed reactor [51].

Given its low solubility in water, 17 $\beta$ -oestradiol (Sigma > 98%) was initially dissolved in acetonitrile (Labscan) and then diluted with water to the desired concentration. TiO<sub>2</sub> (Degussa P25) was immobilized on Ti-6Al-4V alloy by an electrophoretic method described previously [52]. A 1 cm<sup>2</sup> area of support was coated with a catalyst loading of 1.5 mg cm<sup>-2</sup>. The photocatalytic reactor was a water-jacketed quartz cell that held 8 mL of solution [52]. The supported TiO<sub>2</sub> film was submerged in the reactant solution and irradiated through the wall of the quartz

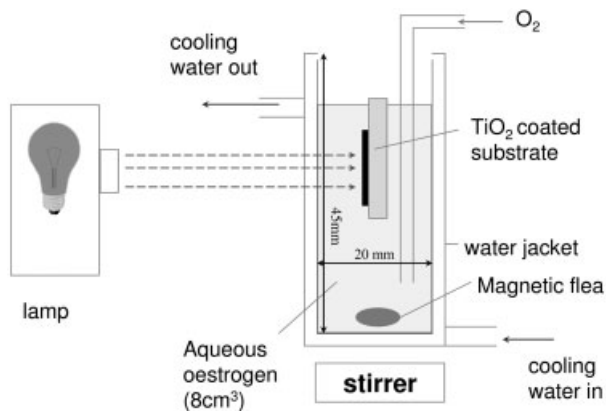


Fig. 10.4. Quartz water-jacketed reactor [52].

reactor using a 150-W xenon lamp (Sage Analytical) with stabilized power supply (Applied Photophysics) (Fig. 10.4). The incident light was passed through a borosilicate glass filter prior to the reactor to remove  $\lambda < 300$  nm. The solution was purged with oxygen (BOC) before and during illumination and the reactor was thermostatted at  $20 \pm 2$  °C. The photonic flux entering the reactor ( $\lambda = 300\text{--}400$  nm) was determined to be  $8 \times 10^{-8}$  Einsteins  $\text{s}^{-1} \text{cm}^{-2}$  by ferrioxalate actinometry [53] with a 300–400 nm band pass filter (Speirs Robertson).  $17\beta$ -Oestradiol degradation was monitored using HPLC with fluorescence detection. The HPLC conditions were: 25 cm ODS column (Hypersil), P2000 solvent delivery pump (Thermo-separation Products), mobile phase 40:60% acetonitrile:water, flow rate of  $1 \text{ mL min}^{-1}$ . The fluorescence detector (Perkin Elmer LS30) was linked to an  $x - y$  plotter. Excitation and emission wavelengths used were  $\lambda_{\text{ex}} = 280$  nm and  $\lambda_{\text{em}} = 315$  nm.

In the presence of the illuminated TiO<sub>2</sub> film,  $3 \mu\text{mol dm}^{-3}$  ( $0.8 \text{ mg L}^{-1}$ )  $17\beta$ -oestradiol was 50% degraded in 40 min and 98% degraded in 3.5 hours. When the samples were illuminated in the absence of titanium dioxide, there was about 11% degradation in 40 min, and 44% in 3.5 h, showing that some direct photolysis takes place. A semi-log plot of initial concentration versus irradiation time was linear, indicating overall pseudo-first order kinetics. The experiment was repeated with a range of initial concentrations from 0.05 to  $3 \mu\text{mol dm}^{-3}$ . The initial rates for each concentration were determined from the pseudo-first-order rate constants and initial concentrations. The data were then fitted to the Langmuir–Hinshelwood kinetic rate model, which has been applied to the initial rates of photocatalytic destruction of many organic compounds [36]. The rate law is shown in Eq. (11), where  $R_i$  is the initial rate of disappearance of substrate and  $C_i$  is the initial concentration,  $k$  is the reaction rate constant and  $K$  is the Langmuir adsorption constant.

$$R_i = -dC_i/dt = kKC_i/(1 + KC_i) \quad (11)$$

From a plot of  $1/R_i$  versus  $1/C_i$ , with the slope equal to  $1/kK$  and intercept equal to  $1/k$ ,  $k$  and  $K$  were determined as  $4.4 \times 10^{-2} \mu\text{mol dm}^{-3} \text{min}^{-1}$  and  $3.47 \times 10^{-1} \text{dm}^3 \mu\text{mol}^{-1}$ , respectively.

This initial study showed that the principal natural oestrogen  $17\beta$ -oestradiol is readily degraded by semiconductor photocatalysis under oxygen on immobilized  $\text{TiO}_2$  powder and that photocatalysis was much more effective than UV light alone. The initial rate kinetics fit the Langmuir–Hinshelwood model. Micromolar concentrations of aqueous  $17\beta$ -oestradiol were 98% degraded in 3.5 h by photocatalysis over the titanium dioxide powder immobilized on Ti-6Al-4V alloy. The degradation kinetics were fitted to a Langmuir–Hinshelwood model with  $k = 0.044 \mu\text{mol dm}^{-3} \text{min}^{-1}$  and  $K = 0.347 \text{dm}^3 \mu\text{mol}^{-1}$ . The pseudo-first order rate constant was  $0.016 \text{min}^{-1}$ . It is very important to determine if all oestrogenic activity is removed from water samples after treatment with photocatalysis since this is the main concern. This was, therefore, investigated in the same quartz water-jacketed reactor and monitored using a yeast screen bioassay as a test for oestrogenicity (Section 10.5).

## 10.5

### Rapid Loss of Oestrogenicity of Natural and Synthetic Oestrogens in Water by Photocatalysis and UVA Photolysis Monitored using a Yeast Screen Bioassay

The presence of low levels of natural and synthetic steroid oestrogens in the aquatic environment, and their biological and oestrogenic effects on aquatic organisms, are presently issues of concern. In this study, we investigated the temporal removal of oestrogenic activity of the potent and environmentally relevant steroid oestrogens by photocatalysis over an immobilized titanium dioxide catalyst. We used a recombinant yeast assay to measure oestrogenic activity. Application of photocatalysis to remove steroid compounds and their oestrogenic activity within STW effluent released into the aquatic environment is discussed.

Stock solutions of  $17\beta$ -oestradiol, oestriol, oestrone and  $17\alpha$ -ethynylestradiol ( $100 \text{mg L}^{-1}$ ) (>98%; Sigma-Aldrich) were prepared in ethanol and then diluted 10 000-fold to a working stock concentration of  $10 \mu\text{g L}^{-1}$  using sterile double-distilled water (0.01% ethanol final concentration). These working stocks were prepared shortly before the experiments, and were added directly to the reactor. The working stock concentration was chosen on the basis that a  $10\text{-}\mu\text{L}$  aliquot would produce a maximal response in the yeast screen (concentration of  $500 \text{ng-steroid L}^{-1}$  in the assay) without the need for further sample manipulation. Moreover, any removal of steroid during the reactions would result in a readily detectable loss in the assay response, as the steroid concentrations would fall within the linear part of the dose–response curve of the assay.

The quartz water-jacketed reactor with titanium dioxide immobilized on titanium alloy (Fig. 10.4) was used with a 125-W Philips high-pressure mercury lamp placed 3 cm from the reactor. Some 8 mL of freshly prepared steroid ( $10 \mu\text{g L}^{-1}$ ) in

sterile water was transferred to the reactor and allowed to equilibrate for 1 h before irradiation with or without the TiO<sub>2</sub> catalyst (photocatalysis and photolysis, respectively). Duplicate samples (10 µL) were removed at intervals starting at time 0 (before UV light exposure), and then regularly throughout the experiments. The 10 µL aliquots were assayed directly in the recombinant yeast oestrogen assay. Details of the oestrogen-inducible expression system in yeast (validation) and preparation of the medium components have been described previously [54]. In brief, this yeast expresses the human oestrogen receptor (hER $\alpha$ ) and contains expression plasmids containing oestrogen-responsive sequences that control expression of the reporter gene Lac-Z (coding for the enzyme  $\beta$ -galactosidase). In the presence of oestrogens,  $\beta$ -galactosidase is produced and is secreted into the medium, where it breaks down the yellow chromogenic substrate chlorophenol red- $\beta$ -D-galactopyranoside (CPRG) into a red product that can be measured by absorbance at 540 nm. Duplicate water samples (10 µL) from each run were transferred to a 96-well optically flat microtiter plate (Linbro/Titertek, ICN FLOW, Bucks UK) at frequent time intervals throughout the experiments. Seeded yeast medium (190 µL) containing CPRG was then added to the microtiter plate and the plates were then sealed with autoclave tape, shaken vigorously for 2 min on a titer plate shaker, and incubated for 72 h at 32 °C. Each plate contained duplicate rows of samples at each time point, a row of blanks (200 µL assay medium only), a row containing sterile water (solvent control) and a row containing a serial dilution of the appropriate steroid substrate (positive control). After incubation, the plates were shaken and allowed to settle for 1 h, after which the absorbance was read at 540 nm (for color) and at 620 nm (for turbidity) using a Titertek Multiscan MCC/340 plate reader. To correct the oestrogenic response of each test chemical for turbidity ( $A_{\text{corr}}$ ), the correction shown in Eq. (12) was applied to the data in each well.

$$A_{\text{corr}} \text{ Chem} = A_{540} \text{ Chem} - (A_{620} \text{ Chem} - A_{620} \text{ Blank}) \quad (12)$$

Nominal steroid concentrations in the reactor were derived from the appropriate steroid standard curve, using the mean corrected absorbance values from each duplicate sample.

17 $\beta$ -Oestradiol, oestrone and 17 $\alpha$ -ethinyloestradiol were found to be oestrogenic *in vitro*, and their relative potencies agreed with previous findings [54]. Limits of detection for the measurement of oestrogenic activity within the reactor were 53 ng L<sup>-1</sup> for 17 $\beta$ -oestradiol and 17 $\alpha$ -ethinyloestradiol, and 100 ng L<sup>-1</sup> for oestrone. Oestriol did not produce an oestrogenic response in the yeast screen bioassay, indicating that it has insufficient oestrogenic activity to be detected at this level.

Results from the water control experiments were negative, indicating that both the reactor and the sterile water were free of oestrogenic contamination before commencing the experiments (data not shown). Similarly, in control experiments (8.5 h duration) with steroids in the absence of UV light the level of oestrogenic activity was unchanged over that time (data not shown). Therefore, no discernable adsorption of oestrogenic substrate on to the surface of the reactor, immobilized titanium dioxide or magnetic flea had occurred. There was also no difference in activity between standards prepared in ethanol and those prepared in sterile water.



**Tab. 10.2.** Time (minutes) taken for 50%, 90% and 100% removal of oestrogenic activity by photocatalysis and UVA photolysis.

Steroid oestrogen	Photocatalysis			UV radiation		
	50%	90%	100%	50%	90%	100%
17 $\beta$ -oestradiol	10	24	55	195	248	485
Oestrone	7	18	60	68	195	360
17 $\alpha$ -Ethinyl-oestradiol	8	27.5	50	23	72	120

Photocatalysis was the most effective method of inactivating all three steroid oestrogens, with virtually all oestrogenic activity being removed within 55 min. In contrast, UVA photolysis took 9 $\times$  longer for oestradiol, 6 $\times$  longer for oestrone and 2.4 $\times$  longer for ethinyl-oestradiol. For all three oestrogens, 50% of their oestrogenic activity was removed by photocatalysis within 10 min, and 100% within 1 h (Table 10.2 and Figs. 10.5–10.7). The decay rates (measured as loss of oestrogenic activity)

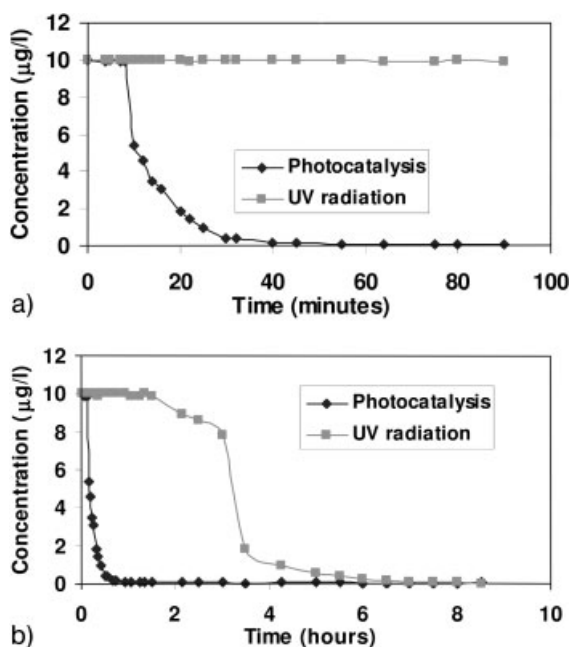


**Fig. 10.5.** Photocatalysis and UVA photolysis of 17 $\beta$ -oestradiol monitored using the yeast screen bioassay. Temporal removal of oestrogenic activity is shown over 90 min (a) and 8.5 h (b) reaction time.

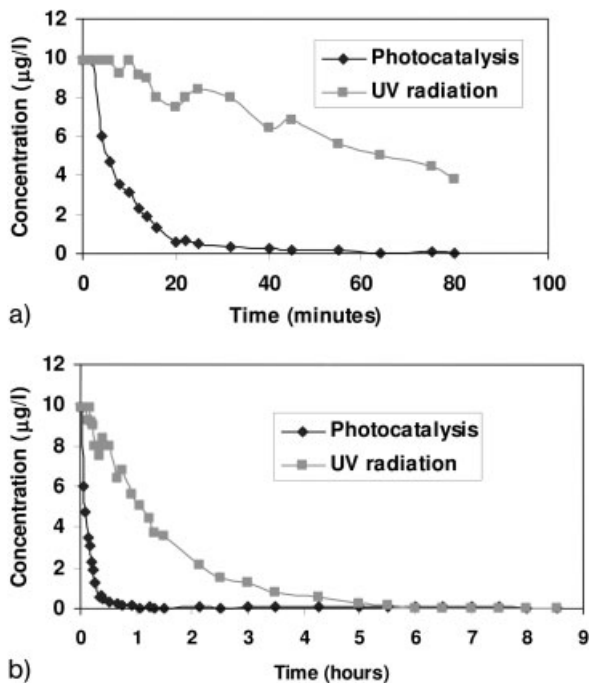
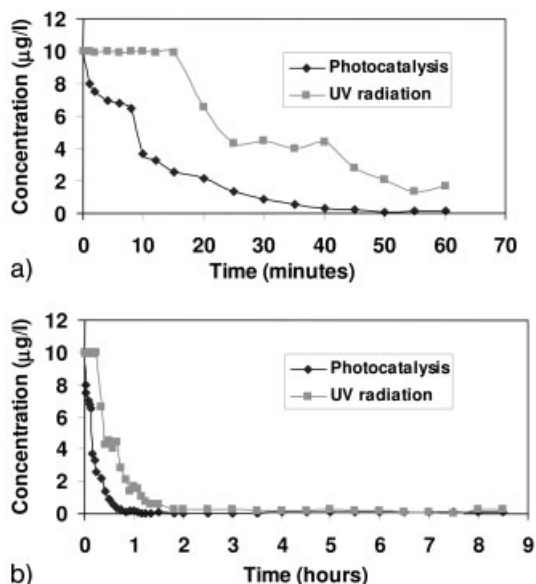


Fig. 10.6. Photocatalysis and UVA photolysis of oestrone monitored using the yeast screen bioassay. Temporal removal of oestrogenic activity is shown over 80 min (a) and 8.5 h (b) reaction time.

were similar for all three oestrogens (Table 10.3). In contrast, there were substantial differences in decay rates of the three steroids by UVA photolysis (no  $\text{TiO}_2$  catalyst), with  $17\alpha$ -ethynylestradiol decaying considerably faster than either of the two other steroids (Table 10.3).

We have directly compared temporal changes in the oestrogenic activity of aqueous solutions (initially  $10 \mu\text{g L}^{-1}$ ) of  $17\beta$ -oestradiol, oestrone and  $17\alpha$ -ethynylestradiol following both UVA photolysis and  $\text{TiO}_2$  photocatalytic degradation. A recombinant oestrogen assay based on yeast was used to measure the biological activity of the reaction mixtures. This yeast screen assay was previously shown to be highly specific for a range of steroid oestrogens and their metabolites, and the relative potencies of the steroids used in this study were found to be consistent with previous findings [54]. The yeast oestrogen screen detects both the parent compounds and any intermediate degradation products that bind to, and activate, the oestrogen receptor, regardless of their identity. Thus, this approach provides a real indication of the ability of the various treatments to affect the biological activity of the reaction mixture over time; information that cannot be obtained by analytical chemistry alone. This is particularly important given the rela-



**Fig. 10.7.** Photocatalysis and UVA photolysis of 17 $\alpha$ -ethinyloestradiol monitored using the yeast screen bioassay. Temporal removal of oestrogenic activity is shown over 60 min (a) and 8.5 h (b) reaction time.

tively persistent and poorly characterized nature of the intermediate products of endocrine disrupters generated during photocatalytic degradation [55, 56].

We have demonstrated that the oestrogenic activity of 17 $\beta$ -oestradiol, oestrone and 17 $\alpha$ -ethinyloestradiol was eliminated at the same rate during photocatalysis, whereas variable (and much slower) removal rates of oestrogenic activity occurred by UVA photolysis, with the order 17 $\alpha$ -ethinyloestradiol > oestrone > 17 $\beta$ -oestradiol. This compares favorably with our work in a quartz coil reactor monitored using fluorescence detection (Section 10.6) [57]. The ability of UVA to

**Tab. 10.3.** Kinetic data for photocatalysis and UVA photolysis of oestrogens.

Steroid	Photocatalysis pseudo-first order rate constant ( $\text{min}^{-1}$ )	UVA photolysis pseudo-first order rate constant ( $\text{min}^{-1}$ )
17 $\beta$ -Oestradiol	0.106	0.011
Oestrone	0.086	0.012
17 $\alpha$ -Ethinyloestradiol	0.086	0.035

remove all three steroids is important given that surface water systems are exposed to natural sunlight, and this may provide a mechanism for the removal of oestrogenic effects. Also, some water treatment plants employ UVC radiation to disinfect potable water, which may help eliminate oestrogenic compounds. The effect of UVC disinfection on degrading oestrogens in water is discussed further in Section 10.7. Although  $17\alpha$ -ethynyoestradiol appears to be more susceptible to UVA degradation than the natural oestrogens  $17\beta$ -oestradiol and oestrone, the ethynyl group of  $17\alpha$ -ethynyoestradiol also increases its resistance to bacterial oxidation, and therefore its persistence during STW aerobic digestion [5]. The similarity in removal rates of oestrogenic activity during  $\text{TiO}_2$  photocatalysis supports a similar mechanism of degradation for the steroid compounds. This may occur via extraction of the benzylic hydrogen to form the  $\cdot\text{CH}$  radical, which combines with oxygen, or via attack of the hydroxyl group to form the quinone. Indeed, Ohko and colleagues previously reported that photocatalysis of  $17\beta$ -oestradiol starts via oxidation of the phenol moiety [58], which is critical for receptor binding and for conferral of oestrogenicity to all steroid oestrogens [59].

Given that most known xenoestrogens are phenolic chemicals, and benzene rings are rapidly photodegraded by preferential hydroxyl radical attack [55, 58], it is likely that photocatalysis may quickly remove the capacity of these chemicals to bind to, and activate, the oestrogen receptor. The measurement of total organic carbon (TOC) may therefore underestimate the true capacity of photocatalysis to inactivate endocrine-disrupting chemicals (EDCs), where early reaction stages are key. However, the production of intermediate products with different types of biological activity must be considered. For example, testosterone-like species were identified by GC/MS during the photocatalysis of  $17\beta$ -oestradiol [58], although any putative androgenic activity of these degradation products was not investigated.

Oestrone is a major and relatively persistent biotransformation product of oestradiol during aerobic digestion [11]. The fact that photocatalysis was able to eliminate oestrone as quickly as  $17\beta$ -oestradiol is therefore encouraging, given that oestrone is only around 2-fold less oestrogenic than  $17\beta$ -oestradiol. However,  $17\alpha$ -ethynyoestradiol is probably the most important steroid pollutant, given that it is biologically active in fish at concentrations as low as  $0.1 \text{ ng L}^{-1}$  [60, 61]. The greater potency of  $17\alpha$ -ethynyoestradiol *in vivo* depends on the 17-ethynyl group, which increases its longevity in the body by reducing the rate of metabolism at C-16 and C-17 compared with endogenous steroids [62]. As photocatalysis was able to eliminate all three steroid oestrogens at a similar rate, it may be a valuable process for reducing the impact of this persistent and highly active group of compounds in the aquatic environment. The initial concentrations of steroids used in our reactor were three to four orders of magnitude greater than reported environmental levels, while the limits of detection for the steroids within the reactor approached levels reported for oestradiol and oestrone measured in influents to STWs [3].

In summary, we have demonstrated rapid temporal removal of the biological activity in aqueous solutions of oestrone,  $17\beta$ -oestradiol and  $17\alpha$ -ethynyoestradiol by photocatalysis over an immobilized  $\text{TiO}_2$  catalyst. Photocatalysis was much

more efficient than UV light alone. Similar rates of removal for all these oestrogens support an identical mechanism of action that is likely to involve oxidation of the phenol moiety of the steroids. Photocatalytic treatment of wastewaters could therefore serve to further decrease the oestrogenic steroid load entering the aquatic environment. In a more detailed study on photocatalysis of the natural and synthetic oestrogens in water we employed fluorescence detection, and also investigated the effects of initial pollutant concentration and light intensity (Section 10.6).

## 10.6

### Photocatalytic Degradation of 17 $\beta$ -Oestradiol, Oestriol and 17 $\alpha$ -Ethinylestradiol in a Quartz Coil Reactor Monitored using Fluorescence Spectroscopy

Photocatalytic degradation of the natural oestrogens 17 $\beta$ -oestradiol and oestriol and the synthetic oestrogen 17 $\alpha$ -ethinylestradiol in water were investigated. Reactions were carried out in a quartz coil reactor coated internally with titanium dioxide (Degussa P25). Degradation by UV light alone was also investigated. Fluorescence spectroscopy was used to monitor the reactions. The effect of both initial concentration and light intensity on photocatalysis and photolysis of 17 $\beta$ -oestradiol in water were also investigated.

A quartz coil reactor and a Hanovia 125-W medium pressure mercury lamp blanketed in nitrogen were used [57]. Coils were prepared from a 1 m length of 2 mm ID quartz tubing with TiO<sub>2</sub> immobilized onto the quartz coil as follows. The coil was first cleaned with chromic acid, rinsed thoroughly and dried. It was then filled with a 20% solution of hydrofluoric acid and allowed to stand for about 30 min, after which it was washed thoroughly with distilled water. The coil was filled with TiO<sub>2</sub> suspension (1% suspension of Degussa P25 TiO<sub>2</sub> powder, sonicated for 20 min) and allowed to stand for a few minutes, drained and then dried by passing warm air through it. A thin white film of TiO<sub>2</sub> was formed on the inside surface of the coil. This procedure was repeated 2–3 times to ensure that the inside surface of the coil is completely covered. After the final drying, distilled water was continuously pumped through the coil to wash away any loose powder [63]. The wavelength of light emitted from the Hanovia lamp also includes the UVB and UVC regions of the spectrum. Experiments with TiO<sub>2</sub> are therefore photolysis as well as photocatalysis. A solution (3  $\mu\text{mol dm}^{-3}$ ;  $\sim 0.8 \text{ mg L}^{-1}$ ) of the oestrogen under study was made up in MilliQ water from a stock solution in acetonitrile. The oestrogen solution was passed through the quartz coil reactor at different flow rates, giving different retention times, and a sample was collected and analyzed by fluorescence detection,  $\lambda_{\text{ex}}$  230 nm,  $\lambda_{\text{em}}$  310 nm. This experiment was repeated using an identical quartz coil without TiO<sub>2</sub>, i.e., photolysis of the oestrogen solution. This procedure was carried out at least twice for each oestrogen. The effect of initial concentration on the reaction with 17 $\beta$ -oestradiol was investigated by repeating the procedure at varying concentrations (3, 2, 1, 0.5, 0.25, and 0.1  $\mu\text{mol dm}^{-3}$ ) (0.8–0.03  $\text{mg L}^{-1}$ ). The effect of light intensity on photocatalysis and photolysis of 17 $\beta$ -oestradiol was investigated by placing the reactor at different distances from the

**Tab. 10.4.** Average values for rate constant,  $k$ , initial rate and half-life for photocatalysis and photolysis of  $17\beta$ -oestradiol, oestriol and  $17\alpha$ -ethynyloestradiol.

	$k$ ( $\text{min}^{-1}$ )	Initial rate ( $\mu\text{mol dm}^{-3}$ $\text{min}^{-1}$ )	Half-life (min)	$R^2$
<i>17<math>\beta</math>-Oestradiol</i>				
Photocatalysis	0.174	0.522	2.095	0.934
Standard error	0.016		0.282	0.005
Photolysis	0.134	0.402	3.45	0.920
Standard error	0.004		0.259	0.018
<i>Oestriol</i>				
Photocatalysis	0.156	0.468	3.775	0.972
Standard error	0.001		0.018	0.003
Photolysis	0.093	0.280	6.65	0.966
Standard error	0.006		0.318	0.010
<i>17<math>\alpha</math>-Ethynyloestradiol</i>				
Photocatalysis	0.231	0.694	1.55	0.907
Standard error	0.006		0.106	0.001
Photolysis	0.195	0.585	1.775	0.926
Standard error	0.011		0.018	0.007

lamp (3.25, 5, 7.5 and 10 cm, corresponding to light intensities of 2509, 1060, 470 and 265 mW, respectively).

Table 10.4 gives average values obtained for the rate constant,  $k$ , the initial rate and the half-life for photocatalysis and photolysis of  $17\beta$ -oestradiol, oestriol and  $17\alpha$ -ethynyloestradiol.

The fact that the lamp used in this work (125-W Hanovia medium-pressure mercury) emits radiation in the UVA, UVB and UVC region of the spectrum some photolysis as well as photocatalysis takes place. The results show that both photocatalysis and photolysis are effective in degrading all three oestrogens in water. Plots of time against  $\ln(C/C_0)$  for the photocatalysis and photolysis of  $17\beta$ -oestradiol confirm our earlier work [51, 64] (Sections 10.4 and 10.5) that photocatalytic and photolysis of  $17\beta$ -oestradiol and  $17\alpha$ -ethynyloestradiol follow pseudo-first order reactions. More recently, other workers [58, 65–67] have reported similar findings. This work shows that oestriol follows similar behavior to the other natural oestrogens and the synthetic oestrogen. The sets of results are consistent with each other, with a good correlation in each case. This is confirmed by the low standard errors of the average values for the rate constant,  $k$ , initial rate and correlation coefficient ( $R^2$ ) (Table 10.4). The average rate constants for photocatalysis and photolysis show that the photocatalytic degradation of  $17\beta$ -oestradiol and oestriol is almost

1.5 $\times$  faster than degradation by UV light alone. However, photocatalysis and photolysis of 17 $\alpha$ -ethinyloestradiol occur at almost the same rate (Table 10.4).

Table 10.4 also shows that 17 $\alpha$ -ethinyloestradiol has the fastest rate for photocatalysis, followed by 17 $\beta$ -oestradiol and finally oestriol (1.5 $\times$  slower than 17 $\alpha$ -ethinyloestradiol). 17 $\alpha$ -Ethinylloestradiol also degrades the fastest by photolysis, at almost the same rate as photocatalysis, degrading 1.5 $\times$  faster than 17 $\beta$ -oestradiol and over twice as fast as oestriol. '17 $\alpha$ -ethinyloestradiol seems to be a less stable molecule than 17 $\beta$ -oestradiol and oestriol under photocatalytic and photolytic conditions. The addition of the ethynyl group possibly causes the molecule to be less stable and degrade more rapidly under these conditions due to the triple bond of the ethynyl group which would absorb UV light more easily. Oestriol seems to be the most stable molecule of the three oestrogens, degrading at the slowest rate. The addition of the OH group may stabilise the phenolic ring and help resist breakdown by photocatalysis and UV light. The mechanism of degradation of the oestrogens may occur via extraction of the benzylic hydrogen to form the CH $\cdot$  radical which combines with oxygen, or via attack of the hydroxyl group to form the quinone (as outlined in section 5). Ohko *et al.* previously reported that the photocatalysis reaction with 17 $\beta$ -oestradiol starts via the phenol moiety and also confirmed that 17 $\beta$ -oestradiol in water is completely mineralised as a result of the photocatalytic reactions and suggested a mechanism for the reaction, identifying 10 $\epsilon$ -17 $\beta$ -dihydroxy-1,4-estradien-3-one and testosterone-like species as intermediate products [58].

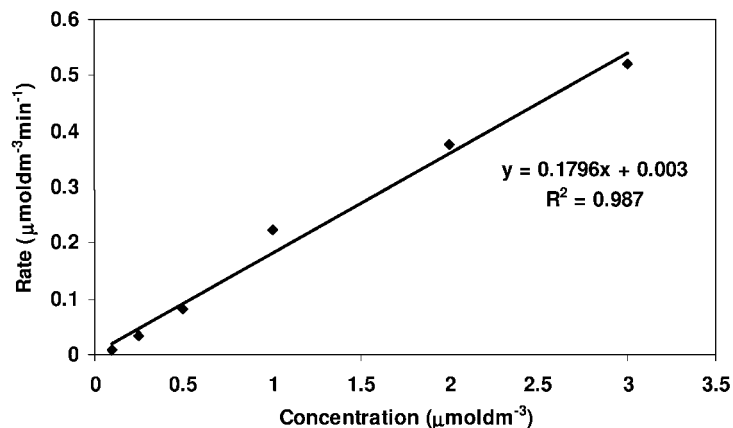
Initial work on photocatalysis of 17 $\beta$ -oestradiol [51] in a batch reactor with TiO $_2$  immobilized on Ti alloy gave a first-order rate constant of 0.016 min $^{-1}$  (Section 10.4). This is much lower than the rate constant obtained in this work (0.174 min $^{-1}$ ), indicating that the quartz coil reactor is a much more efficient system, owing to the increased surface area. The trend obtained here for photocatalysis compares favorably with work [64] detailed in Section 10.5 where photocatalytic degradation of 17 $\beta$ -oestradiol, 17 $\alpha$ -ethinyloestradiol and oestrone were monitored using a yeast screen bioassay as a test for oestrogenicity. The oestrogenic activity of 17 $\beta$ -oestradiol, oestrone and 17 $\alpha$ -ethinyloestradiol was eliminated at the same rate during photocatalysis whereas variable (and much slower) removal rates occurred by UVA photolysis, with the order 17 $\alpha$ -ethinyloestradiol > oestrone > 17 $\beta$ -oestradiol (0.086–0.106 min $^{-1}$ ). The rates of photolysis in this work (0.134 min $^{-1}$  for 17 $\beta$ -oestradiol and 0.195 min $^{-1}$  for 17 $\alpha$ -ethinyloestradiol) are much higher than for this previous work (0.011 and 0.035 min $^{-1}$ , respectively) due to the different lamps used. The lamp used in this work (125-W Hanovia medium-pressure mercury) emits radiation in UVA, UVB and UVC region of the spectrum, indicating that some photolysis is taking place as well as photocatalysis. The increase may also be due to the increased area for reaction in the coil reactor.

Table 10.5 gives the average values for the rate constant,  $k$ , initial rate and half-life calculated for each concentration.

Initial concentration against rate was plotted for the results obtained above for both photocatalysis and photolysis of 17 $\beta$ -oestradiol (Figs. 10.8 and 10.9, respectively).

**Tab. 10.5.** Average values of rate constant,  $k$ , initial rate and half-life for photocatalysis and photolysis of  $17\beta$ -oestradiol at different initial concentrations.

Concentration ( $\mu\text{mol dm}^{-3}$ )	$k$ ( $\text{min}^{-1}$ )	Initial rate ( $\mu\text{mol dm}^{-3}$ $\text{min}^{-1}$ )	Half-life (min)	$R^2$
<i>Photocatalysis</i>				
0.1	0.086	0.009	7.4	0.925
0.25	0.141	0.036	4.062	0.944
0.5	0.164	0.082	3.188	0.953
1	0.224	0.224	2.062	0.942
2	0.188	0.376	2.125	0.898
3	0.174	0.522	2.095	0.934
<i>Photolysis</i>				
0.1	0.125	0.012	2.7	0.785
0.25	0.137	0.034	2.55	0.844
0.5	0.187	0.094	1.44	0.862
1	0.200	0.200	2.0	0.944
2	0.138	0.276	2.812	0.898
3	0.134	0.402	3.45	0.920



**Fig. 10.8.** Initial concentration against rate for photocatalysis of  $17\beta$ -oestradiol monitored using fluorescence.



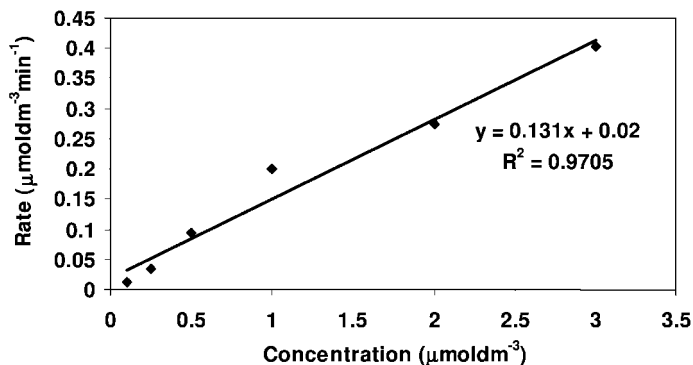


Fig. 10.9. Initial concentration against rate for photolysis of 17 $\beta$ -oestradiol monitored using fluorescence.

The results are consistent with each concentration with good correlation (Table 10.5). The slope of the best-fit line is 0.180 for photocatalysis and 0.131 for photolysis (Figs. 10.8 and 10.9, respectively). The results demonstrate that, as the initial concentration of 17 $\beta$ -oestradiol increases, the reaction rate increases proportionally for both photocatalysis and photolysis, confirming that the reactions are first order [51, 57]. The slope of the graph for photocatalysis is 1.5 $\times$  that of photolysis, indicating that photocatalysis coupled with photolysis occurs at 1.5 $\times$  the rate of photolysis alone.

Interestingly, the effect of initial concentration on photocatalysis follows a different pattern than shown previously [51] where the Langmuir–Hinshelwood model applied for the same concentration range. In this model, adsorption of the reactant on the surface of the catalyst is considered. The rate increases with initial concentration of 17 $\beta$ -oestradiol and then levels off at higher concentrations. This is because, at higher concentrations, the surface of the TiO<sub>2</sub> becomes saturated with oestradiol molecules and the reaction rate reaches a maximum. In this work, photolysis occurs at a rate comparable to that of photocatalysis. This competing reaction also consumes 17 $\beta$ -oestradiol, reducing the number of molecules available for saturation of the titanium dioxide surface. This observation may be important in industrial applications of the photocatalytic breakdown of organic pollutants in water. Photocatalysis and photolysis could be applied together to increase rates of reaction at high concentrations of pollutants.

Table 10.6 summarizes results obtained for the effect of light intensity on both photocatalysis and photolysis of 17 $\beta$ -oestradiol. Good correlation was obtained for all the results.

Light intensity ( $I$ ) is an important parameter to consider in photocatalysis ( $R \propto I$ ), especially for industrial applications in terms of cost. Increasing the light intensity affects the rate of the reaction by increasing the number of charge carriers generated in the semiconductor. Most researchers have found different effects at different levels of light intensity [68].

**Tab. 10.6.** Average values for  $k$ , initial rate, half-life and  $R^2$  for effect of light intensity on photocatalysis and photolysis of 17 $\beta$ -oestradiol.

Distance (cm)	Light intensity (mW)	$k$ ( $\text{min}^{-1}$ )	Initial rate ( $\mu\text{mol dm}^{-3} \text{min}^{-1}$ )	Half-life (min)	$R^2$
<i>Photocatalysis</i>					
3.25	2509	0.500	1.501	0.362	0.926
5	1060	0.324	0.972	1.25	0.939
7.5	470	0.236	0.708	1.625	0.882
10	265	0.174	0.522	2.095	0.934
<i>Photolysis</i>					
3.25	2509	0.400	1.200	0.1	0.876
5	1060	0.364	1.092	0.875	0.973
7.5	470	0.229	0.687	1.7	0.918
10	265	0.134	0.402	3.45	0.920

- At low light intensities, the rate increases in proportion to the light intensity, i.e.,  $R \propto I$ ,  $n = 1$ .
- At intermediate light intensities the rate only varies with the square root of intensity [69, 70], i.e.,  $R \propto I^{1/2}$ ,  $n = 1/2$ .
- At high light intensities the rate of photodegradation is independent of light intensity, i.e.,  $R \propto I^0$ ,  $n = 0$ .

For photocatalysis, as light intensity increases the rate increases due to the increased number of oxidizing species produced. The rate increases with light intensity to a power  $n$  (the gradient of a linear log–log plot, [Eq. (14)]). At low light intensities the rate of initial degradation increases directly in proportion to light intensity (gradient  $\sim 1$ ), suggesting that few oxidizing species are lost through recombination processes. At high light intensities the rate of initial degradation increases in proportion to  $I$  to the power of 0, i.e., the rate becomes independent of light intensity and the expected rate-limiting factor is mass transfer. At intermediate light intensities the rate only varies with the square root of intensity [69, 70] and hence efficiency suffers. This was attributed by Egerton and King [71] to energy wasting recombination reactions between electrons and holes and by Kormann [72] to bimolecular combination of hydroxyl radicals.

Increased intensity always results in an increase in the volumetric reaction rate until the mass transfer limit is encountered. However, once intermediate light intensities are reached any increase in  $I$  will not lead to a proportional increase in rate and industrially may not be worth the extra cost. The  $I^1$  to  $I^{0.5}$  rate transition is

**Tab. 10.7.** Dependency of rate of photocatalysis on light intensity for various organic substrates.

Substrate	$n$	Ref.
Phenol	0.6	74
Phenol	0.5	69
4-Chlorophenol	0.7	47
Formaldehyde	0.4	75
Methyl orange	0.2	76
Dichlorophenoxyacetic acid	0.5	77
Phenoxyacetic acid	0.5	78
2,4-Dichlorophenol	0.5	79
Cyanide	0.5	80
Salicyclic acid	0.6	81

said to depend on the catalyst material [73]. The relationship between rate and light intensity can therefore be represented by Eq. (13).

$$\text{Rate} = k_1 I^n \quad (13)$$

The rate constant  $k$  will include terms for the extent of recombination, substrate concentration, etc. This constant will be different for different transition regions. The linear form of this equation is:

$$\ln(\text{rate}) = \ln k + n \ln(I) \quad (14)$$

A plot of  $\ln(\text{rate})$  against  $\ln(\text{light intensity})$  will yield a straight line for each transition region, with a slope equal to  $n$ . For the photocatalysis of 17 $\beta$ -oestradiol, such a plot gave a best fit line with a slope,  $n$ , of 0.461, which is approximately 0.5, indicating intermediate light intensities. Other workers found similar results when investigating light intensities for other substrates. Table 10.7 shows the literature values of  $n$  for different organic compounds.

Dionysiou et al. have reported the photocatalytic degradation of 4-chlorobenzoic acid as a function of light intensity, using a rotating disk photocatalytic reactor [82]. They found that the rate of degradation followed a linear dependency with incident light intensity and attributed it to the existence of low local values of incident light intensity on the illuminated disk. Ohko et al. have investigated the effect of light intensity on the degradation of propan-2-ol and the effect of concentration [83]. They suggested that for small concentrations of contaminant it is more beneficial to operate the process at low light intensities and at the range where the rates are not mass-transport controlled. At high contaminant concentration, the reaction

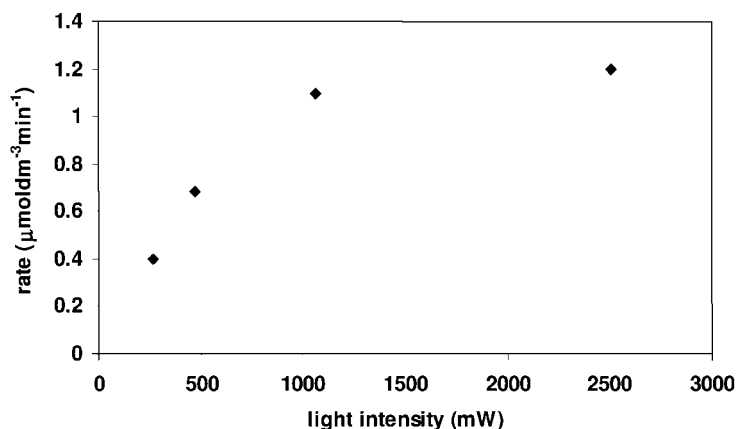


**Fig. 10.10.** Rate against light intensity for photolysis of  $17\beta$ -oestradiol monitored using fluorescence.

may be light-limited but light utilization efficiency will be higher. This was also reported by Minero [84], who recommended that, in solar photocatalytic applications, concentration of the solar light is unnecessary. Industrially, these are important points to consider if photocatalysis were applied for the treatment of real environmental water samples where oestrogens and other EDCs are present in very low concentrations and also in situations where solar illumination is used as the UV source. Figure 10.10 shows the plot of rate against light intensity for the photolysis of  $17\beta$ -oestradiol.

The relationship is linear at low light intensities up to a certain point (intermediate light intensity) where the rate starts to level off (high light intensities). This suggests that the rate is proportional to light intensity up to a certain point, where it then becomes independent of light intensity. This could be interesting from an industrial viewpoint, where a combination of photocatalysis and UV radiation could be used to increase the rate of reaction instead of increasing the UV light alone, where the rate levels off at high light intensities.

Photocatalysis and photolysis are effective for the degradation of the three oestrogens  $17\beta$ -oestradiol, oestriol and  $17\alpha$ -ethnyloestradiol in water. Photocatalysis coupled with photolysis is much more effective in degrading the oestrogens than photolysis alone. The reactions follow pseudo-first order kinetics.  $17\alpha$ -Ethnyloestradiol degrades the fastest for both photocatalysis and photolysis followed by  $17\beta$ -oestradiol and then oestriol. This was attributed to the triple bond of the ethynyl group, which absorbs UV light more easily. The rate varies linearly with initial concentration both for photocatalysis combined with photolysis and for photolysis of  $17\beta$ -oestradiol in water. Photocatalysis degrades  $17\beta$ -oestradiol at twice the rate of photolysis. The rate was proportional to the square root of light intensity for photocatalysis of  $17\beta$ -oestradiol. The relationship between light intensity and degradation rate by photolysis is linear up to a point, when it then starts to

level off. The ability of UV light to remove all steroids is important given that surface water systems are exposed to natural sunlight, and this may provide a mechanism for the removal of oestrogenic effects. Also, some water treatment plants employ UVC radiation to disinfect potable water, which would help to eliminate oestrogenic compounds in the water. An investigation into the efficiency of UVC disinfection for the removal of the natural and synthetic oestrogen in water was made and compared with photocatalysis and UVA light alone. This work is outlined in section 7 below.

## 10.7

### Comparison of Photocatalysis with UVA and UVC Radiation for the Degradation of Natural and Synthetic Oestrogens in Water

Our previous studies have shown that  $\text{TiO}_2$  photocatalysis is effective for the degradation of natural and synthetic oestrogens in water and that it is more effective than UV light alone. Some water treatment companies currently use UVC disinfection to remove trace organics as a final stage in the water treatment process. UVC radiation uses high intensity light at 253 nm, which is energy intensive and therefore very expensive. In this work we study the effect of UVC disinfection for the removal of the natural and synthetic oestrogens in water and compare it with photocatalysis and UVA light alone.

Photocatalysis experiments were carried out in a spiral Pyrex reactor (85 mL volume), with  $\text{TiO}_2$  immobilized onto the inside wall, with a black light blue fluorescent lamp (NEC, 15 W, maximum emission at  $\sim 350$  nm, emission range 300–400 nm) fitted through the centre of the coil.  $\text{TiO}_2$  was immobilized onto the reactor walls as described previously [57] (Section 10.6). Experiments with UVA light alone were carried out in the same reactor free from  $\text{TiO}_2$ . A similar set-up was used for the UVC radiation experiments except the spiral reactor (85 mL volume) was made from quartz and free from  $\text{TiO}_2$  and was used with a slim line germicidal lamp (UV Air Pty Ltd, emission  $\lambda = 253$  nm). The reactors were connected to a peristaltic pump (Masterflex<sup>®</sup> Quick-Load, Cole-Palmer Instrument Co.) by Masterflex flexible tubing to enable solution circulation through the reactor at  $150 \text{ mL min}^{-1}$  and to an on-line fluorescence spectrometer (Perkin Elmer LS-45 with FLWinLab software), which monitored degradation of the oestrogens at  $\lambda_{\text{ex}} = 230$  nm and  $\lambda_{\text{em}} = 310$  nm.

A standard solution of  $3 \mu\text{mol dm}^{-3}$  of oestrogen (i.e.,  $0.82 \text{ mg L}^{-1}$   $17\beta$ -oestradiol,  $0.86 \text{ mg L}^{-1}$  oestriol and  $0.89 \text{ mg L}^{-1}$   $17\alpha$ -ethinyloestradiol) was made up in MilliQ water from stock solutions in acetonitrile (final pH 5.5). Oestrogen (120 mL) was then pumped through the reactor set-up at  $150 \text{ mL min}^{-1}$  for approximately 5 min to allow the solution to equilibrate before the experiment was started. The UV lamp was then turned on and the “timedrive” method (FLWinLab software), which measured fluorescence intensity over time, was started where measurements were taken every second. This procedure was carried out for each oestrogen in duplicate for  $\text{TiO}_2$  photocatalysis, UVA radiation and UVC radiation.

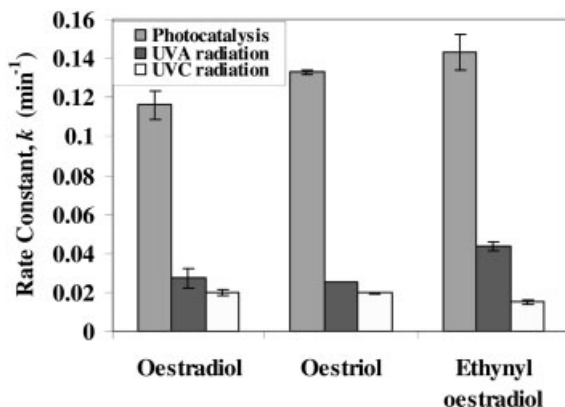


Fig. 10.11. Degradation by photocatalysis, UVA and UVC radiation of natural and synthetic oestrogens in water in a spiral reactor monitored using fluorescence spectroscopy.

Figure 10.11 shows a histogram of the rate constants for photocatalysis of the natural and synthetic oestrogens over  $\text{TiO}_2/\text{UVA}$  compared to UVA and UVC radiation alone. Table 10.8 presents the first-order rate constants for each reaction with standard errors.

Clearly, from Fig. 10.11 and Table 10.8, photocatalysis is much more effective than UVA or UVC radiation for all of the oestrogens. The rates are up to 5× greater for photocatalysis than for UVA light alone and up to 9× faster (17 $\alpha$ -ethynyl-oestradiol) than with UVC disinfection. Photocatalytic rates are quite comparable for all three oestrogens when standard errors are taken into account, although rates for 17 $\alpha$ -ethynyl-oestradiol and oestriol are slightly higher than for 17 $\beta$ -oestradiol. UVA radiation rates for the natural oestrogens 17 $\beta$ -oestradiol and oestriol are comparable. However, UVA radiation for the synthetic oestrogen 17 $\alpha$ -ethynyl-oestradiol is significantly higher. This agrees with previous work in a

Tab. 10.8. Kinetic data for photocatalysis, UVA photolysis and UVC photolysis of oestrogens in water.

Steroid	First order rate constants, $k$ (min <sup>-1</sup> )		
	Photocatalysis	UVA photolysis	UVC photolysis
17 $\beta$ -Oestradiol	0.116 ± 0.007	0.028 ± 0.005	0.0201 ± 0.002
Oestriol	0.133 ± 0.001	0.025	0.196
17 $\alpha$ -Ethynyl-oestradiol	0.143 ± 0.009	0.044 ± 0.002	0.0151 ± 0.001

stirred-tank batch reactor with a 125-W high-pressure mercury lamp (Section 10.5) [64] and a photocatalytic quartz coil reactor and 125-W medium-pressure mercury lamp (Section 10.6) [57] and, as mentioned earlier, may be because the triple bond of the ethynyl group present would absorb UV light more easily. Rates for UVA and UVC radiation are comparable for  $17\beta$ -oestradiol and oestriol. However, UVA and UVC radiation rates for  $17\alpha$ -ethynyloestradiol differ significantly, with UVA radiation being almost  $3\times$  faster than UVC radiation.  $17\alpha$ -Ethynyloestradiol may absorb better in the UVA region of the spectrum than in the UVC region. The blue-black lamp (UVA radiation) covers a broader spectrum ( $\lambda = 300\text{--}400$  nm with maximum emission at  $\lambda = 350$  nm), and so also covers part of the visible and the UVB spectrum, whereas the UVC lamp emits radiation only at  $\lambda = 253$  nm. The UV spectra of  $17\beta$ -oestradiol, oestriol and  $17\alpha$ -ethynyloestradiol show that they absorb at  $\lambda = 230$  nm and  $\lambda = 280$  nm and that absorption is much more intense at  $\lambda = 230$  nm. Both peaks are broad and there may be some absorption at  $\lambda = 300$  nm for the  $\lambda = 280$  nm peak. The rate of photons absorbed per reactor volume for each lamp was calculated using ferrioxalate actinometry [85]. Table 10.9 shows the results.

Table 10.9 shows that the UVC lamp is much more intense than the UVA lamp. However, UVA is sufficient to breakdown the oestrogens in water. This is encouraging from an industrial viewpoint since UVC disinfection requires much more energy and is therefore more costly. Photocatalysis, however, is still much more efficient than UV light alone, with rates up to  $9\times$  faster.

Our initial work on the photocatalysis of  $17\beta$ -oestradiol [51] (Section 10.4) in a batch reactor with  $\text{TiO}_2$  immobilized on Ti alloy gave a first-order rate constant of  $0.016 \text{ min}^{-1}$ . This is much lower than the rate constant obtained in this work ( $0.116 \text{ min}^{-1}$ ), which is comparable with more recent work in a quartz coil reactor ( $0.174 \text{ min}^{-1}$ ) (Section 10.6) [57], indicating that a coil reactor is a much more efficient system due to the increased surface area. The trend obtained here for photocatalysis compares favorably with previous work (Sections 10.5 and 10.6) [57, 64] where  $17\beta$ -oestradiol and  $17\alpha$ -ethynyloestradiol were degraded at the same rate during photocatalysis whereas variable and slower degradation rates occurred by UV radiation, with the order  $17\alpha$ -ethynyloestradiol  $>$   $17\beta$ -oestradiol ( $0.086\text{--}0.106 \text{ min}^{-1}$ ). Nakashima et al. [86] reported rate constants of  $0.033$  and  $0.050 \text{ min}^{-1}$

**Tab. 10.9.** Photons absorbed per reactor volume for each of the lamps measured using ferrioxalate actinometry ( $\mu\text{Einsteins s}^{-1} \text{ L}^{-1} \pm$  standard error).

Lamp	Photons absorbed ( $\mu\text{Einsteins s}^{-1} \text{ L}^{-1}$ )
UVC lamp ( $\lambda = 253$ nm)	$74 \pm 3$
UVA lamp ( $\lambda = 350$ nm)	$57 \pm 1$

for  $17\beta$ -oestradiol in two different types of reactors with  $\text{TiO}_2$  immobilized on PTFE mesh sheets, and, in more recent work [87],  $0.15$  and  $0.12 \text{ min}^{-1}$  for  $17\beta$ -oestradiol and oestrone, respectively.

Titanium dioxide photocatalysis is an effective method for the degradation of the natural oestrogens  $17\beta$ -oestradiol and oestriol and the synthetic oestrogen  $17\alpha$ -ethinyloestradiol in water in an immobilized  $\text{TiO}_2$  spiral coil reactor. It is much more efficient than UVA or UVC radiation alone (up to  $9\times$  faster). Industrially, this is very important as costs and energy requirements can be drastically reduced. Particle-mediated photocatalytic techniques can improve the performance of water treatment systems employing UV by reducing the energy requirements for the UV stage. The successful and efficient degradation of these compounds will potentially provide cheaper and cleaner means of removing them from groundwater, wastewaters and drinking water. Because the only energy source is near-UV light, the technology should, ultimately, be able to function on sunlight alone.

## 10.8

### Overall Conclusions and Identification of Research Needs

The main aim of this work was to investigate the degradation of natural oestrogens ( $17\beta$ -oestradiol, oestrone and oestriol) and a synthetic oestrogen ( $17\alpha$ -ethinyloestradiol) in water using titanium dioxide photocatalysis. This was carried out using different chemical and biological analytical techniques.

The first objective was to determine if oestrogens could be degraded by photocatalysis and UV radiation. Initial studies in a batch reactor monitored using HPLC and fluorescence detection showed that  $17\beta$ -oestradiol in water could be degraded by photocatalysis and was much more effective than UV light alone. The reaction followed first-order reaction kinetics and Langmuir–Hinshelwood behavior was observed.

The second objective was to determine if oestrogenic activity is removed from the oestrogenic water samples after treatment with photocatalysis and UV radiation since the oestrogenic activity of these substances is the main concern. This was carried out using a yeast screen bioassay. It was found that photocatalysis and UV radiation can remove all oestrogenic activity from water samples containing the natural oestrogens  $17\beta$ -oestradiol and oestrone and the synthetic oestrogen  $17\alpha$ -ethinyloestradiol. Again, photocatalysis is much more efficient than UV light alone. The rates of reaction for the three oestrogens studied were very similar for photocatalysis. For UV radiation,  $17\alpha$ -ethinyloestradiol degraded the fastest followed by oestrone and  $17\beta$ -oestradiol.

The work with fluorescence spectroscopy also fulfilled the first objective, showing that all the natural and synthetic oestrogens in water could be degraded by photocatalysis. The results demonstrated that  $17\alpha$ -ethinyloestradiol degraded the fastest followed by  $17\beta$ -oestradiol and oestriol for both photocatalysis and UV radiation combined and for UV light alone. Direct photolysis reactions are generally of low efficiency compared with procedures involving hydroxyl radical generation.



However, here there was no major difference in the rates for photocatalysis and UV light alone. This was due to the lamp used, which emitted in the UVA, UVB and UVC range of the spectrum. The reactions also follow pseudo-first order kinetics.  $17\alpha$ -Ethinylloestradiol degrades the fastest for both photocatalysis and photolysis followed by  $17\beta$ -oestradiol and oestriol. This was attributed to the triple bond of the ethynyl group in  $17\alpha$ -Ethinylloestradiol, which absorbs UV light more easily.

The third objective was to investigate the effect of varying reaction conditions on the photocatalytic reaction, i.e., initial concentration and light intensity. The relationship between initial concentration and rate is linear for both photocatalysis combined with photolysis and for photolysis of  $17\beta$ -oestradiol in water. Photocatalysis degrades  $17\beta$ -oestradiol at twice the rate of photolysis. The rate was proportional to the square root of light intensity for photocatalysis of  $17\beta$ -oestradiol. The relationship between light intensity and the rate of degradation by photolysis is linear up to a point; it then starts to level off.

The final objective was to compare photocatalysis with UVA and UVC disinfection. Here, photocatalysis was found to be much more efficient than UV light alone. Titanium dioxide photocatalysis is an effective method for the degradation of the natural oestrogens  $17\beta$ -oestradiol and oestriol and the synthetic oestrogen  $17\alpha$ -ethinylloestradiol in water in an immobilized  $\text{TiO}_2$  spiral coil reactor. The spiral reactor was much more efficient than a batch reactor with  $\text{TiO}_2$  immobilized on Ti alloy due to the increased surface area of the former. Photocatalysis was much more efficient than UVA or UVC radiation alone (up to  $9\times$  faster). This is very important industrially, where costs and energy requirements can be drastically reduced. Particle-mediated photocatalytic techniques can improve the performance of water treatment systems employing UV by reducing the energy requirements for the UV stage. The fact that solar illumination can be used in these systems is an added advantage for applications in countries with a hot and sunny climate. As the importance of water reuse and water recycling increases, an effective technique is needed to remove trace organics in our water supply.  $\text{TiO}_2$  photocatalysis can be used to develop a safe, cost-efficient water treatment process.

Based on the work presented in this chapter, several research areas and needs can be proposed:

1. Improvements in chemical and biological analysis for the detection of steroid oestrogens at  $\text{ng L}^{-1}$  levels and for real water sample analysis.
2. Investigations into the application of photocatalysis for the removal of steroid oestrogens in real water samples, e.g., treated sewage effluent samples where other substances are present.
3. Improvement in the engineering design of photocatalytic reactor systems with a view to incorporating the photocatalytic treatment stage into existing water treatment systems.

In summary, the challenge is for water treatment scientists to design and apply titanium dioxide nanoparticles for the photocatalytic breakdown of micropollutants such as steroid oestrogens in real water samples.

The principles of organic photoelectrochemistry elaborated over the past decade clearly show that interfacial electron transfer to surface adsorbates can result in oxidative degradation, often leading to complete mineralization of organic pollutants. The wide band gap and high chemical stability of TiO<sub>2</sub> nanoparticles gives them an extremely broad reactivity range. Irradiated TiO<sub>2</sub> nanoparticles efficiently degrade nearly every significant functional group, including the most environmentally hazardous and persistent substances. Since our first report of the use of photocatalysis for the degradation of oestrogens in water [51], its potential use as a method for reducing discharges of EDCs into the aquatic environment has been of increasing interest [57, 64–66, 86–92]. Indeed, the degradation of nonylphenol polyethoxylate surfactants [90] and their biotransformation products [65, 66, 88], Bisphenol-A [83, 86, 89, 92–94], phthalates [93], atrazine [95], resorcinol [96] and amitrole [97] using TiO<sub>2</sub> photocatalysts have been reported. However, the significant proportion of the overall oestrogenic activity of many effluent discharges [9] is due to the steroid oestrogens. Photocatalytic degradation of 17β-oestradiol [51, 57, 64, 83, 86–88, 91, 98, 99], oestrone [51, 57, 64, 98, 99] and 17α-ethynylestradiol [51, 57, 64, 87, 88, 91, 98, 99] has been shown. Solar photocatalytic degradation has also been investigated for the degradation of bisphenol A [100]. TiO<sub>2</sub> nanoparticles are the most widely used for the removal of EDCs in water. However, there is one report of the use of a visible-light-driven BiVO<sub>4</sub> photocatalyst for the degradation of nonylphenols in water by solar radiation [101]. However, titanium dioxide nanoparticles have been shown to be the most effective photocatalyst for water treatment applications. TiO<sub>2</sub> as a suspension, coating, or immobilized catalyst exhibits promising potential for environmental amelioration, particularly as continuing research into the engineering optimization of photocatalyst dispersal builds on the framework of earlier investigations [32]. Few studies have evaluated the efficacy of TiO<sub>2</sub>-assisted photodegradation in the treatment of mixtures of contaminants and actual wastewaters. The process is unlikely to be used in the treatment of high-strength industrial wastewaters or for the large-scale direct clean-up of contaminated soils. Loss of efficiency due to competing substrates in the case of mixtures, interference by dissolved anions and cations, which cause significant reductions in rates of photodegradation, and light interference by high concentrations of soils are likely problems in industrial wastewaters and soils [29]. The literature indicates that oestrogens play an important role in the development of reproductive abnormalities and other health problems. Hopefully, growing awareness that reproductive function may be at risk will stimulate both the basic and clinical research within this field that have received relatively little attention [102]. Biologists, chemists and engineers should continue to work in this area to fully understand the environmental implications of these compounds and in the disposal, monitoring and removal of them. There is a need for the development of an effective technique for the removal of these compounds and other trace organic contaminants in our water supply. Titanium dioxide nanoparticles and UV light to produce the photocatalytic process could be a solution to the problem of EDCs and other micropollutants in the aquatic environment.

## References

- 1 CARMICHAEL, H., Sex offenders, *Chem. Br.* **1998**, 34(10), 25–28.
- 2 *Environmental Estrogens and other Hormones*, Center for Bioenvironmental Research of Tulane and Xavier Universities, New Orleans, L.A., website; <http://www.tmc.tulane.edu/ecme/eehome/>.
- 3 JOHNSON, A.C., SUMPTER, J.P., Removal of endocrine-disrupting chemicals in activated sludge treatment works, *Environ. Sci. Technol.* **2001**, 35(24), 4697–4703.
- 4 ARCAND-HOY, L.D., NIMROD, A.C., BENSON, W.H., Endocrine-modulating substances in the environment: estrogenic effects of pharmaceutical products, *Int. J. Toxicol.* **1998**, 17, 139–158.
- 5 TURAN, A., Excretion of natural and synthetic estrogens and their metabolites: Occurrence and behaviour in water, in *Expert Round Endocrinologically Active Chemicals in the Environment*, ed. A. GILES Umweltbundesamt, Berlin, **1996**, pp. 15–20.
- 6 BITMAN, J., CECIL, H.C., Estrogenic activity of DDT analogs and polychlorinated biphenyls. *J. Agric. Food Chem.* **1970**, 18(6), 1108–1112.
- 7 COLBURN, T., VOM SAAL, F.S., SOTO, A.M., Developmental effects of endocrine-disrupting chemicals in wildlife and humans, *Environ. Health Perspect.* **1993**, 101(5), 378–384.
- 8 BARONTI, C., CURINI, R., D'ASCENZO, G., DI CORCIA, A., GENTILI, A., SAMPERI, R., Monitoring natural and synthetic estrogens at activated sludge sewage treatment plants and in a receiving river water, *Environ. Sci. Technol.* **2000**, 34, 5059–5066.
- 9 DESBROW, C., ROUTLEDGE, E.J., BRIGHTY, G.C., SUMPTER, J.P., WALDOCK, M., Identification of estrogenic chemicals in STW effluent. I. Chemical fractionation and in vitro biological screening, *Environ. Sci. Technol.* **1998**, 32, 1549–1558.
- 10 TABAK, H.H., BLOOMHUFF, R.N., BUNCH, R.L., Steroid hormones as water pollutants. II. Studies on the persistence and stability of natural and synthetic ovulation-inhibiting hormones in untreated and treated wastewaters, *Develop. Ind. Microbiol.* **1970**, 11, 497–519.
- 11 TERNES, T.A., STUMPF, M., MUELLER, J., HABERER, K., WILKEN, R.-D., SERVOS, M., Behaviour and occurrence of estrogens in municipal sewage treatment plants – I. Investigations in Germany, Canada and Brazil, *Sci. Total Environ.* **1999**, 225, 81–90.
- 12 STUMPF, M., TERNES, T.A., HABERER, K., BAUMANN, W., Determination of natural and synthetic estrogens in sewage plants and river water, *Vom Wasser* **1996**, 87, 251–261.
- 13 ISOBE, T., SHIRAIISHI, H., YASUDA, M., SHINODA, A., SUZUKI, H., MORITA, M., Determination of estrogens and their conjugates in water using solid-phase extraction followed by liquid chromatography-tandem mass spectrometry, *J. Chromatogr. A* **2003**, 984, 195–202.
- 14 RURAINSKI, R.D., THEISS, H.J., ZIMMERMANN, W., The occurrence of natural and synthetic oestrogens in drinking water, *Das Gas-und Wasserfach wasser/abwasser* **1977**, 118, 288–291.
- 15 ADLERCREUTZ, H., FOSTIS, T., BANNEWART, C., HÄMÄLÄINEN, E., BLOIGU, S., OLLUS, A., Urinary estrogen profile determination in young Finnish vegetarian and omnivorous women, *J. Steroid Biochem.* **1986**, 24, 289–296.
- 16 DRAY, J., TILLIER, F., DRAY, F., ULLMANN, A., Etude de l'hydrolyse des métabolites urinaires de différentes hormones stéroïdes par la  $\beta$ -glucuronidase de *Escherichia coli*, *Ann. l'Institut Pasteur* **1972**, 123, 853–857.
- 17 KIRK, L.A., TYLER, C.R., LYE, C.M., SUMPTER, J.P., Changes in estrogenic and androgenic activities at different stages of treatment in wastewater

- treatment works, *Environ. Toxicol. Chem.* **2002**, 21(9), 72–79.
- 18 JOHNSON, A.C., BELFROID, A., DI CORCIA, A., Estimating steroid oestrogen inputs into activated sludge treatment works and observations on their removal from the effluent, *Sci. Total Environ.* **2000**, 256, 163–173.
  - 19 KORNER, W., BOLZ, U., SUSSMUTH, W., HILLER, G., SCHULLER, W., HANF, V., HAGENMAIER, H., Input/output balance of estrogenic active compounds in a major municipal sewage plant in Germany, *Chemosphere* **2000**, 40, 1131–1142.
  - 20 SHORE, L.S., GUREVITZ, M., SHEMES, M., Estrogen as an environmental pollutant, *Bull. Environ. Contam. Toxicol.*, **1993**, 51, 361–366.
  - 21 ROUTLEDGE, E.J., SHEAHAN, D., DESBROW, C., BRIGHTY, G.C., WALDOCK, M., SUMPTER, J.P., Identification of estrogenic chemicals in STW effluent. 2. *In vivo* responses in trout and roach, *Environ. Sci. Technol.* **1998**, 32, 1559–1565.
  - 22 WILLIAMS, R.J., JURGENS, M.D., JOHNSON, A.C., Initial predictions of the concentrations and distribution of 17(R)-oestradiol, oestrone and ethinyloestradiol in 3 English rivers, *Water Res.* **1999**, 33, 1663–1671.
  - 23 LARSSON, D.G.J., ADOLFSSON-ERICI, M., PARKKONEN, J., PETTERSON, M., BERG, A.H., OLSSON, P.-E., FORLIN, L., Ethinyloestradiol – an undesired fish contraceptive?, *Aquatic Toxicol.* **1999**, 42, 91–97.
  - 24 EC, *European Workshop on the Impact of Endocrine Disrupters on Human Health and Wildlife: Report of the Proceedings*, Weybridge, UK, European Commission, **1997**.
  - 25 SVENSON, A., ALLARD, A.S., EK, M., Removal of estrogenicity in Swedish municipal sewage treatment plants, *Water Res.* **2003**, 37, 4433–4443.
  - 26 LITCHEN, N.N., DONG, J., VIJAYAKUMAR, K.M., Photopromoted TiO<sub>2</sub>-catalyzed oxidative decomposition of organic pollutants in water and in the vapor phase, *Water Pollut. Res. J., Can.* **1992**, 27, 203–210.
  - 27 MILLS, A., DAVIES, R.H., WORSLEY, D., Purification of water by semiconductor photocatalysis, *Chem. Soc. Rev.* **1993**, 22(6), 417–425.
  - 28 LITTER, M.I., Heterogeneous photocatalysis. Transition metal ions in photocatalytic systems, *Appl. Catal. B: Environ.* **1999**, 23, 89–114.
  - 29 VENKATADRI, R., PETERS, R.W., Chemical oxidation technologies: Ultraviolet light/hydrogen peroxide, Fenton's reagent, and titanium dioxide-assisted photocatalysis, *Hazardous Waste Hazardous Mater.* **1993**, 10(2), 107–149.
  - 30 PROUSEK, J., Advanced oxidation processes for water treatment, *Chem. Listy* **1996**, 90, 307–315.
  - 31 LEGRINI, O., OLIVEROS, E., BRAUN, A.M., Photochemical processes for water treatment, *Chem. Rev.* **1993**, 93, 671–698.
  - 32 FOX, M.A., Photocatalysis: Decontamination with sunlight, *Chemtech* **1992**, 11, 680–685.
  - 33 FUJISHIMA, A., HONDA, K., Electrochemical photolysis of water at a semiconductor electrode, *Nature*, **1972**, 238, 37–38.
  - 34 CAREY, J.H., LAWRENCE, J., TOSINE, H.M., Photodechlorination of PCB's in the presence of titanium dioxide in aqueous suspensions, *Bull. Environ. Contam. Toxicol.* **1976**, 16(6), 697–701.
  - 35 MILLS, A., LE HUNTE, S., An overview of semiconductor photocatalysis, *J. Photochem. Photobiol. A, Chem.* **1997**, 108, 1–35.
  - 36 HOFFMANN, M.R., MARTIN, S.T., CHOI, W., BAHNEMANN, D.W., Environmental applications of semiconductor photocatalysis, *Chem. Rev.* **1995**, 95, 69–96.
  - 37 LINSEBIGLER, A.L., LU, G., YATES, J.T., JR., Photocatalysis on TiO<sub>2</sub> surfaces: Principles, mechanisms, and selected results, *Chem. Rev.* **1995**, 95, 735–758.
  - 38 FUJISHIMA, A., RAO, T.N., TRYK, D.A., Titanium dioxide photocatalysis, *J. Photochem. Photobiol. C: Photochem. Rev.* **2000**, 1, 1–21.
  - 39 CARP, O., HUISMAN, C.L., RELLER, A., Photoinduced reactivity of titanium dioxide, *Progr. Solid State Chem.* **2004**, 32, 33–177.

- 40 SCHIAVELLO, M. (ed.), *Heterogeneous Photocatalysis*, John Wiley and Sons Chichester, UK, 1997.
- 41 OLLIS, D.F., AL-EKABI, H., *Photocatalytic Purification and Treatment of Water and Air*, Elsevier Amsterdam, The Netherlands, 1993.
- 42 SERPONE, N., PELIZZETTI, E., *Photocatalysis: Fundamentals and Applications*, John Wiley and Sons, New York, 1989.
- 43 PELIZZETTI, E., SCHIAVELLO, M., *Photochemical Conversion and Storage of Energy, Proceedings of the Eighth International Conference on Photochemical Conversion and Storage of Solar Energy*, IPS-8, held July 15–20, 1990, Palermo, Italy, Kluwer Academic Publishers, Dordrecht, 1991.
- 44 MILLS, A., LEE, S.K., A web-based overview of semiconductor photochemistry-based current commercial applications, *J. Photochem. Photobiol. A: Chem.* **2002**, 152, 233–247.
- 45 WOLD, A., Photocatalytic properties of TiO<sub>2</sub>, *Chem. Mater.* **1993**, 5, 280–283.
- 46 FUJISHIMA, A., RAO, T.N., Recent advances in heterogeneous TiO<sub>2</sub> photocatalysis, *Proc. Indian Acad. Sci. (Chem. Sci.)* **1997**, 109(6), 471–486.
- 47 MILLS, A., MORRIS, S., DAVIES, R.J., Photomineralisation of 4-chlorophenol sensitised by titanium dioxide: A study of the intermediates, *J. Photochem. Photobiol. A: Chem.* **1993**, 70(2), 183–191.
- 48 SCHINDLER, K.-M., KUNST, M., Charge-carrier dynamics in titania powders, *J. Phys. Chem.* **1990**, 94, 8222–8226.
- 49 BICKLEY, R.I., GONZALEZ-CARRENO, T., LEES, J.S., PALMISANO, L., TILLEY, R.D., A structural investigation of titanium dioxide photocatalysts, *J. Solid State Chem.* **1991**, 92, 178.
- 50 KAMAT, P.V., Photochemistry on non-reactive and reactive (semiconductor) surfaces, *Chem. Rev.* **1993**, 93, 267.
- 51 COLEMAN, H.M., EGGINS, B.R., BYRNE, J.A., PALMER, F.L., KING, E., Photocatalytic degradation of 17 $\beta$ -oestradiol on immobilised TiO<sub>2</sub>, *Appl. Catal. B: Environ.* **2000**, 24(1), 1–5.
- 52 BYRNE, J.A., EGGINS, B.R., BROWN, N.M.D., MCKINNEY, B., ROUSE, M., Immobilisation of TiO<sub>2</sub> powder for the treatment of polluted water, *Appl. Catal. B: Environ.* **1998**, 17, 25–36.
- 53 CALVERT, J.G., PITTS, J.N., *Photochemistry*, Wiley, New York, 1973.
- 54 ROUTLEDGE, E.J., SUMPTER, J.P., Estrogenic activity of surfactants and some of their degradation products assessed using a recombinants yeast screen, *Environ. Toxicol. Chem.* **1996**, 15(3), 242–248.
- 55 OHKO, Y., ANDO, I., NIWA, C., TATSUMA, T., YAMAHURA, T., NAKASHIMA, T., KUBOTA, Y., FUJISHIMA, A., Degradation of Bisphenol A in water by TiO<sub>2</sub> photocatalyst, *Environ. Sci. Technol.* **2001**, 35, 2365–2368.
- 56 HORIKOSHI, S., HIDAKA, H., Non-degradable triazine substrates of atrazine and cyanuric acid hydrothermally and in supercritical water under the UV-illuminated photocatalytic cooperation, *Chemosphere* **2003**, 51(2), 139–142.
- 57 COLEMAN, H.M., ABDULLAH, M., EGGINS, B.R., PALMER, F.L., Photocatalytic degradation of 17 $\beta$ -oestradiol, oestriol and 17 $\alpha$ -ethinyloestradiol in water monitored using fluorescence spectroscopy, *Appl. Catal. B: Environ.* **2005**, 55(1), 23–30.
- 58 OHKO, Y., IUCHI, K.-I., NIWA, C., TATSUMA, T., NAKASHIMA, T., IGUCHI, T., KUBOTA, Y., FUJISHIMA, A., 17 $\beta$ -Estradiol degradation by TiO<sub>2</sub> photocatalysis as a means of reducing estrogenic activity, *Environ. Sci. Technol.* **2002**, 36, 4175–4181.
- 59 BRZozowski, A., PIKE, A.C.W., DAUTER, Z., HUBBARD, R.E., BONN, T., ENGSTROM, O., OHMAN, L., GREENE, G.L., GUSTAFSSON, J.-A., CARLQUIST, M., Molecular basis of agonism and antagonism in the oestrogen receptor, *Nature* **1997**, 389(16), 753–758.
- 60 PURDOM, C.E., HARDIMAN, P.A., BYE, V.J., ENO, N.C., TYLER, C.R., SUMPTER, J.P., Estrogenic effects of effluent from sewage treatment works, *Chem. Ecol.* **1994**, 8, 275–285.
- 61 THORPE, K.L., CUMMINGS, R.I.,

- HUTCHINSON, T.H., SCHOLZE, M., BRIGHTY, G., SUMPTER, J.P., TYLER, C.R., Relative potencies and combination effects of steroidal estrogens in fish, *Environ. Sci. Technol.* **2003**, 37, 1142–1149.
- 62 GUENGERICH, F.P., Minireview: Metabolism of 17 $\alpha$ -ethynylestradiol in humans, *Life Sci.* **1990**, 47, 1981–1988.
- 63 ABDULLAH, M.I., EEK, E., Automatic photocatalytic method for the determination of dissolved organic carbon (DOC) in natural waters, *Water Res.* **1996**, 30(8), 1813–1822.
- 64 COLEMAN, H.M., ROUTLEDGE, E.J., SUMPTER, J.P., EGGINS, B.R., BYRNE, J.A., Rapid loss of estrogenicity of steroid estrogens by UVA photolysis and photocatalysis over an immobilised titanium dioxide catalyst, *Water Res.* **2004**, 38(14–15), 3233–3240.
- 65 IKE, M., ASANO, M., BELKADA, F.D., TSUNOI, S., TANAKA, M., FUJITA, M., Degradation of biotransformation products of nonylphenol ethoxylates by ozonation and UV/TiO<sub>2</sub> treatment, *Water Sci. Technol.* **2002**, 46, 127–132.
- 66 KOHTANI, S., MAKINO, S., KUDO, A., TOKUMURA, K., ISHIGAKI, Y., MATSUNGA, T., NIKAIKIDO, O., HAYAKAWA, K., NAKAGAKI, R., Photocatalytic degradation of 4-n-nonylphenol under irradiation from solar simulator: Comparison between BiVO<sub>4</sub> and TiO<sub>2</sub> photocatalysts, *Chem. Lett.* **2002**, 7, 660–661.
- 67 LIU, B., LIU, X., Direct photolysis of estrogens in aqueous solutions, *Sci. Total Environ.* **2004**, 320(2–3), 269–274.
- 68 OLLIS, D.F., *Photochemical Conversion and Storage of Solar Energy*, ed. PELIZETTI, E., SCHIAVELLO, E., Kluwer Academic Publishers, Dordrecht, **1991**, p. 593.
- 69 OKAMOTO, K., YAMAMOTO, Y., TANAKA, H., TANAKA, M., ITAYA, A., Heterogeneous photocatalytic decomposition of phenol over anatase powder, *Bull. Chem. Soc. Jpn.* **1985**, 58, 2015.
- 70 KORMANN, C., BAHNEMANN, D.W., HOFFMANN, M.R., Photolysis of chloroform and other organic molecules in aqueous titanium dioxide suspensions, *Environ. Sci. Technol.* **1991**, 25, 494–500.
- 71 EGERTON, T.A., KING, C.J., The influence of light intensity on photoactivity in titanium dioxide pigmented systems, *J. Oil Colour Chem. Assoc.* **1979**, 62(10), 386–391.
- 72 KORMANN, C., Ph.D. thesis, California Institute of Technology, Pasadena CA, **1989**.
- 73 MATTHEWS, R.W., ABDULLAH, M., LOW, G.K.-C., Photocatalytic oxidation for total organic carbon analysis, *Anal. Chim. Acta* **1990**, 233(2), 171–179.
- 74 WEI, T.-Y., WAN, C.-C., Kinetics of photocatalytic oxidation of phenol on titanium oxide (TiO<sub>2</sub>) surface, *J. Photochem. Photobiol. A: Chem.* **1992**, 69(2), 241–249.
- 75 SHIN, E.-M., SENTHURCHELVAN, R., MUNOZ, J., BASAK, S., RAJESHWAR, K., Photolytic and photocatalytic destruction of formaldehyde in aqueous media, *J. Electrochem. Soc.* **1996**, 143(5), 1562–1570.
- 76 CHEN, L.C., CHOU, T.C., Kinetics of photodecolorization of methyl orange using titanium dioxide as catalyst, *Ind. Eng. Chem. Res.* **1993**, 32, 1520–1527.
- 77 TRILLAS, M., PERAL, J., DOMENECH, X., Redox photodegradation of 2,4-dichlorophenoxyacetic acid over TiO<sub>2</sub>, *Appl. Catal. B: Environ.* **1995**, 5, 377–387.
- 78 TRILLAS, M., PERAL, J., DOMENECH, X., Photo-oxidation of phenoxyacetic acid by TiO<sub>2</sub>-illuminated catalyst, *Appl. Catal. B: Environ.* **1993**, 3(1), 45–53.
- 79 SERRA, F., TRILLAS, M., GARCIA, J., DOMENECH, X., Titanium dioxide-photocatalyzed oxidation of 2,4-dichlorophenol, *J. Environ. Sci. Health, Part A: Environ. Sci. Eng.* **1994**, 29(7), 1409–1421.
- 80 AUGUGLIARO, V., LODDO, V., MARCI, G., PALMISANO, L., LOPEZ-MUNOZ, M.J., Photocatalytic oxidation of cyanides in aqueous titanium dioxide suspensions, *J. Catal.* **1997**, 166(2), 272–283.
- 81 MILLS, A., HOLLAND, C.E., DAVIES, R.H., WORSLEY, D., Photomineralization of salicylic acid: A kinetic study,

- J. Photochem. Photobiol. A: Chem.* **1994**, 83(3), 257–263.
- 82** DIONYSIOU, D.D., SUIDAN, M.T., BAUDIN, I., LAINE, J.-M., Oxidation of organic contaminants in a rotating disk photocatalytic reactor: Reaction kinetics in the liquid phase and the role of mass transfer based on the dimensionless Damköhler number, *Appl. Catal. B: Environ.* **2002**, 38(1), 1–16.
- 83** OHKO, Y., IKEDA, K., RAO, T.N., HASIMOTO, K., FUJISHIMA, A., Photocatalytic reaction kinetics on TiO<sub>2</sub> thin films under light-limited and mass transport-limited conditions, *Z. Physik. Chem. (Muenchen)* **1999**, 213, 33–42.
- 84** MINERO, C., Kinetic analysis of photoinduced reactions at the water semiconductor interface, *Catal. Today* **1999**, 54(2–3), 205–216.
- 85** HATCHARD, C.G., PARKER, C.A., A new sensitive chemical actinometer. II. Potassium ferrioxalate as a standard chemical actinometer, *Proc. Royal Soc. (London)* **1956**, A235, 518–536.
- 86** NAKASHIMA, T., OHKO, Y., TRYK, D.A., FUJISHIMA, A., Decomposition of endocrine-disrupting chemicals in water by use of TiO<sub>2</sub> photocatalysts immobilized on polytetrafluoroethylene mesh sheets, *J. Photochem. Photobiol. A: Chem.* **2002**, 151, 207–212.
- 87** NAKASHIMA, T., OHKO, Y., KUBOTA, Y., FUJISHIMA, A., Photocatalytic decomposition of estrogens in aquatic environment by reciprocating immersion of TiO<sub>2</sub>-modified polytetrafluoroethylene mesh, *J. Photochem. Photobiol. A: Chem.* **2003**, 160, 115–120.
- 88** TANIZAKI, T., KADOKAMI, K., SHINOHARA, R., Catalytic photodegradation of endocrine disrupting chemicals using titanium dioxide photoconductor thin films, *Bull. Environ. Contam. Toxicol.*, **2002**, 68, 5, 732–739.
- 89** FUKAHORI, S., ICHIURA, H., KITAOKA, T., TANAKA, H., Photocatalytic decomposition of bisphenol A in water using composite TiO<sub>2</sub>-zeolite sheets prepared by a papermaking technique, *Environ. Sci. Technol.*, **2003**, 37(5), 1048–1051.
- 90** HORIKOSHI, S., WATANABE, N., ONISHI, H., HIDAKA, H., SERPONE, N., Photodecomposition of a nonylphenol polyethoxylate surfactant in a cylindrical photoreactor with TiO<sub>2</sub> immobilized fiberglass cloth, *Appl. Catal. B: Environ.*, **2002**, 37(2), 117–129.
- 91** ONARI, Y., YOSHIOKA, O., IWASAKI, S., TAKAHASHI, M., Decompositions of endocrine disrupting chemicals by advanced oxidations such as oxidation with ozone, photo-catalysis and ultraviolet light irradiation, *Mie-ken Kagaku Gijutsu Shinko Senta Hoken Kankyo Kenkyubu Nenpo*, **2002**, 4, 98–101 (in Japanese).
- 92** WATANABE, N., HORIKOSHI, S., KAWABE, H., SUGIE, Y., ZHAO, J., HIDAKA, H., Photodegradation mechanism for bisphenol A at the TiO<sub>2</sub>/H<sub>2</sub>O interfaces, *Chemosphere* **2003**, 52, 851–859.
- 93** OOKA, C., YOSHIDA, H., HORIO, M., SUZUKI, K., HATTORI, T., Adsorptive and photocatalytic performance of TiO<sub>2</sub> pillared montmorillonite in degradation of endocrine disruptors having different hydrophobicity, *Appl. Catal. B: Environ.* **2003**, 41, 313–321.
- 94** LEE, J.-M., KIM, M.-S., KIM, B.-W., Photodegradation of bisphenol-A with TiO<sub>2</sub> immobilized on the glass tubes including the UV light lamps, *Water Res.* **2004**, 38, 3605–3613.
- 95** HORIKOSHI, S., HIDAKA, H., Non-degradable triazine substrates of atrazine and cyanuric acid hydrothermally and in supercritical water under the UV-illuminated photocatalytic cooperation, *Chemosphere* **2003**, 51, 139–142.
- 96** LAM, S.W., CHIANG, K., LIM, T.M., AMAL, R., Low, G.K.-C., Effect of charge trapping species of cupric ions on the photocatalytic oxidation of resorcinol, *Appl. Catal. B: Environ.* **2005**, 55, 123–132.
- 97** WATANABE, N., HORIKOSHI, S., KAWASAKI, A., HIDAKA, H., Formation of refractory ring-expanded triazine

- intermediates during the photocatalyzed mineralization of the endocrine disruptor mintrole and related trazole derivatives at UV-irradiated TiO<sub>2</sub>/H<sub>2</sub>O interfaces, *Environ. Sci. Technol.* **2005**, 39, 2320–2326.
- 98 MITAMURA, K., NARUKAWA, H., MIZUGUCHI, T., SHIMADA, K., Degradation of estrogen conjugates using titanium dioxide as a photocatalyst, *Anal. Sci.* **2004**, 20, 3–4.
- 99 COLEMAN, H.M., HON, H., AMAL, R., LESLIE, G., WEHNER, M., FITZSIMMONS, S., Removal of oestrogenic and carcinogenic substances from water using alternative water treatment methods, Proceedings of the *Australian Water Association Speciality Conference on Contaminants of Concern*, Rydges Lakeside Hotel, Canberra, Australia, 22–23 June **2005**.
- 100 KANECO, S., RAHMAN, M.A., SUZUKI, T., KATSUMATA, H., OHTA, K., Optimization of solar photocatalytic degradation conditions of bisphenol A in water using titanium dioxide, *J. Photochem. Photobiol. A: Chem.* **2004**, 163, 419–424.
- 101 KOHTANI, S., KOSHIKO, M., KUDO, A., TOKUMURA, K., ISHIGAKI, Y., TORIBA, A., HAYAKAWA, K., NAKAGAKI, R., Photodegradation of 4-alkylphenols using BiVO<sub>4</sub> photocatalyst under radiation with visible light from a solar simulator, *Appl. Catal. B: Environ.* **2003**, 46, 573–586.
- 102 CARLSEN, E., GIWERCMAN, A., KEIDING, N., SKAKKEBAEK, N.E., Declining semen quality and increasing incidence of testicular cancer: Is there a common cause?, *Environ. Health Perspect.* **1995**, 103(7), 137–139.



## 11

# Nanosensors for Environmental Applications

Wan Y. Shih and Wei-Heng Shih

### 11.1

#### Introduction

##### 11.1.1

###### Overview

Current water-borne pathogen sensor development relies on colony growth or fluorescent-based techniques, which are not *in situ*, rapid, or sensitive. In our laboratory, we have developed piezoelectric microcantilever sensors that can perform rapid, *in situ*, in-water pathogen detection with sensitivities well above that of current techniques. We have shown that using PZT/glass cantilevers of sub-millimeter length with a 2 mm glass tip, which exhibited  $5 \times 10^{-11}$  g Hz<sup>-1</sup> mass detection sensitivity, *in situ* quantification of *Salmonella typhimurium* was achieved with a concentration limit of  $10^3$  cells mL<sup>-1</sup>; this is lower than the infectious dosage,  $10^5$  cells mL<sup>-1</sup>, which is also the concentration limit of commercial ELISA, QCM, and nanowire-based sensors. Furthermore, we have developed two types of miniaturized piezoelectric cantilevers for even better sensitivity. With 500 μm long PMN-PT/Cu microcantilevers, fabricated from freestanding PMN-PT films, that exhibited  $3 \times 10^{-13}$  g Hz<sup>-1</sup> detection sensitivity we achieved a better than 50 spores mL<sup>-1</sup> detection limit in 1 mL of *Bacillus anthracis* suspension. With PZT/SiO<sub>2</sub> microcantilevers less than 50 μm long, fabricated by silicon-based microfabrication techniques, the detection sensitivity is expected to reach better than  $10^{-16}$  g Hz<sup>-1</sup> and further lower the concentration limit. In addition to ultrasensitive, rapid, *in situ* detection, piezoelectric microcantilevers use simple electrical measurements, which is ideal for portable simultaneous array sensing in environmental applications.

##### 11.1.2

###### Sensor

Current sensing technologies rely on fluorescence [1, 2], laser [3] or fiber-optics-based methods [4], quartz crystal microbalance [5], electrochemical enzyme immu-

noassays [6], amplification schemes such as polymerase chain reaction (PCR) [7–9], and binding to nanometer-size metal particles [10]. Most of the techniques are neither direct nor quantitative and are slow. They do not lend themselves to multiplexing and high throughput. Development of direct sensing technologies relies heavily on silicon-based microcantilevers [11–15] due to their availability and ease of integration with existing silicon-based methodologies. Binding of target antigens to the antibody on the cantilever surface is directly detected by monitoring the cantilever's resonance frequency shift due to the mass of the adsorbed target antigens. Silicon-based microcantilevers offer high detection sensitivity,  $\Delta m/\Delta f \sim 10^{-12}$  g Hz<sup>-1</sup> [16, 17], where  $\Delta m$  and  $\Delta f$  denote, respectively, the mass change and corresponding resonance frequency change due to the binding of target molecules. However, all silicon-based microcantilevers rely on complex external optical components for deflection detection and an external driver for actuation generation. Moreover, immersing silicon-based microcantilevers in water reduces the  $Q$  factor (ratio of the resonance peak frequency relative to the resonance peak width at half peak height) to about one, prohibiting silicon-based microcantilevers from in-water detection [18]. Silicon-based microcantilevers cannot have high resonance peaks in water because they are not piezoelectric. They rely on a vibration driver located at the cantilever base to generate deflections at the cantilever tip, which is ineffective. In comparison, piezoelectric sensors use electrical means for detection and do not have the bulkiness and complexity of silicon-based sensors. However, current piezoelectric biosensors are based on quartz crystal microbalances (QCM) [19], which are disk devices with a mass detection sensitivity of  $10^{-8}$  g Hz<sup>-1</sup>, about  $10\,000\times$  less sensitive than the silicon-based microcantilevers. A QCM is about 1–3 cm in size, and silicon microcantilevers require laser alignment. Both are unfit for high-throughput array environmental applications.

In this chapter, we describe a new type of biosensor: array piezoelectric microcantilever sensors (PEMS) that can simultaneously detect multiple antigens *in situ* both in water and in-air with high sensitivity for water-borne pathogen applications. Section 11.1.3 provides an introduction to piezoelectric cantilever sensors (PECS). Section 11.2 gives a brief theoretical description of PECS without (Section 11.2.1) and with (Section 11.2.2) a nonpiezoelectric tip. Section 11.3 gives various examples of *in situ*, in-water biodetection as well as in-air nerve-gas simulant detection. Section 11.4 describes the miniaturization approaches of piezoelectric cantilever and the detection sensitivity enhancement with a reducing sensor size.

Current commercial enzyme-linked immunosorbent assays (ELISA), which use optical means for detection, offer a concentration limit of  $10^5$  cells mL<sup>-1</sup> for *Salmonella typhimurium*, about the same as the infection dosage. Other nanobiosensors such as nanowire-based sensors that also use electrical measurements for detection offer a concentration sensitivity of about  $10^5$  cells mL<sup>-1</sup> in *Escherichia coli* detection [20]. In comparison, current 400  $\mu\text{m}$  long piezoelectric lead magnesium niobate–lead titanate/copper (PMN-PT/Cu) microcantilevers have already achieved 50 spores mL<sup>-1</sup> concentration sensitivity in a 1 mL *Bacillus anthracis* (which is about the same size as *E. coli* and *S. typhimurium*) suspension, far exceeding the concentration limit of ELISA and that of nanowire sensors. Although silicon-based nano-

cantilevers offer similar detection sensitivity as piezoelectric microcantilevers they require optical measurements in air [17] or in vacuum [21], which prohibits their use for portable, *in situ*, multiplexed detection. As we have demonstrated, in addition to their high sensitivities, piezoelectric microcantilevers offer the advantages of *in situ*, real-time, multiplexed detection, and are thus more suitable for environmental applications.

### 11.1.3

#### Piezoelectric Cantilever Sensors (PECS)

Piezoelectric cantilever sensors (PECS) are a new type of mass sensors we have developed that uses electrical means for detection and can be miniaturized for better mass detection sensitivity [22]. By monitoring the resonance frequency shifts we have demonstrated PECS for rapid, label-free, *in situ* quantitative detection of pathogens with simple all-electrical measurements. We have shown that millimeter size PECS could detect *S. typhimurium* at concentrations below 5000 cells mL<sup>-1</sup> without flow or concentration, which is lower than the infection dosage level (10<sup>5</sup> cells mL<sup>-1</sup>) and more sensitive than enzyme-linked immunosorbent assays (ELISA) and array biosensors [23]. Piezoelectric sensors have the advantage of both driving and sensing the mechanical resonance electrically. Receptors are coated on the piezoelectric device surface to bind the molecules of interest [24, 25]. The change in mass due to the binding of the target molecules shifts the mechanical resonance frequency of the device.

## 11.2

### Theory of PECS

A piezoelectric cantilever is a flexural transducer that consists of a piezoelectric layer, e.g., lead zirconate titanate (PZT) bonded to a nonpiezoelectric layer, e.g., stainless steel. Figure 11.1(a) and (b) show, respectively, a schematic of a piezoelectric cantilever of a uniform thickness (unimorph) and a piezoelectric cantilever with a nonpiezoelectric extension. The nonpiezoelectric extension may also be narrower than the piezoelectric section [26]. Bending vibrations can be generated by applying a small alternating-current (ac) voltage (<1 V) across the thickness of the piezoelectric layer. The stress generated by the bending vibration in the piezoelectric layer in turn induces a measurable piezoelectric voltage in phase with the applied voltage. A piezoelectric cantilever's mechanical resonance frequency and resonance strength can be measured by monitoring the maximum of the real part or the phase angle of the complex electrical impedance. Monitoring a cantilever's resonance frequency has many useful applications. In mass detection, a piezoelectric cantilever's resonance frequency shift is measured to quantify the small mass attached to the cantilever surface [27]. In liquid property characterization, both the resonance peak frequency and the resonance peak width of PECS inserted in the liquid are measured to simultaneously determine the liquid's viscosity and density

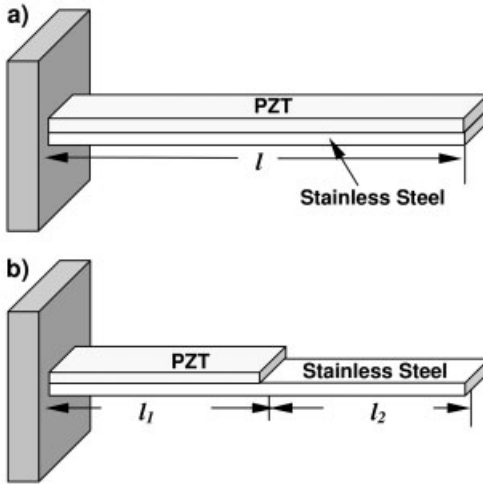


**Fig. 11.1.** Schematic of a piezoelectric cantilever of (a) uniform thickness (unimorph) and (b) with a nonpiezoelectric extension.

[28]. In liquid–solid transition detection, an abrupt resonance frequency shift with respect to temperature is measured to identify the transition [29]. A piezoelectric cantilever has the advantage of having a built-in piezoelectric layer to generate strong vibrations that can better withstand damping in water. The ability to withstand damping in water makes piezoelectric cantilevers excellent biosensors for direct and label-free detection. To this end, recent experiments have demonstrated real-time, in-water, direct detection of cells where the mass of the attached cells and the cell concentration in the solution were deduced from the cantilever resonance frequency shift and the resonance frequency shift with time, respectively.

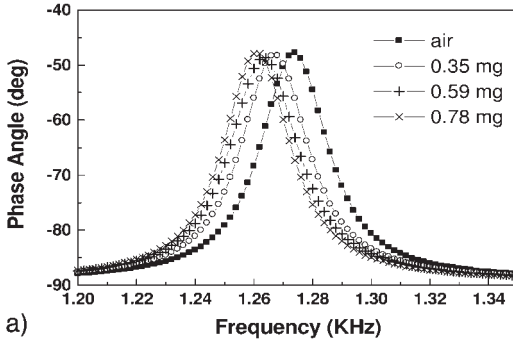
### 11.2.1

#### Unimorph

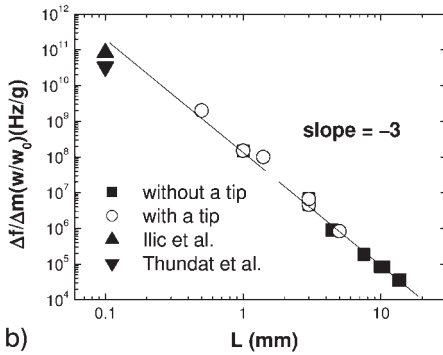
When an ac voltage is applied to a unimorph cantilever, vibration occurs. The  $n$ th-mode flexural resonance frequency is related to the bending modulus per unit width, the length, and the mass per unit area,  $m$ , of the cantilever as

$$f'_n = \frac{v_n^2}{2\pi} \sqrt{\frac{K}{M_e + \Delta m}} \quad (1)$$

where  $v_n^2$  is the dimensionless  $n$ th-mode eigen value,  $K$  and  $M_e$  the effective spring constant and the effective mass of the cantilever, respectively. For an added mass  $\Delta m \ll M_e$ , the resonance frequency shift,  $\Delta f'_n$ , due to the added mass,  $\Delta m$ , is given by Eq. (2).



a)



b)

**Fig. 11.2.** (a) Phase-angle versus frequency spectrum of a 12 mm long piezoelectric cantilever with a 8 mm long stainless steel extension. As the mass of aluminum foil on the cantilever increases, the resonance frequency shifts to lower values. (b) Resonance

frequency shift per unit mass,  $\Delta f/\Delta m$ , with a normalized width versus cantilever length. Open circles and filled squares denote cantilevers with and without a stainless steel tip, respectively.

$$\Delta f_n = f'_n - f_n \cong -\frac{1}{2} f_n \frac{\Delta m}{M_e} \quad (2)$$

The resonance frequency shift per unit loaded mass is therefore

$$\frac{\Delta f_n}{\Delta m} \cong -\frac{1}{2} \frac{f_n}{M_e} = -\frac{1}{2} \left( \frac{v_n^2}{2\pi\sqrt{12}} \frac{h}{L^2} \sqrt{\frac{\bar{E}}{\bar{\rho}}} \right) \frac{1}{0.236Lwh\bar{\rho}} = -\frac{v_n^2}{4\pi} \frac{1}{L^3w} \left( \frac{1}{0.236\sqrt{12}\bar{\rho}} \sqrt{\frac{\bar{E}}{\bar{\rho}}} \right) \quad (3)$$

where  $h$ ,  $L$ ,  $w$ ,  $\bar{E}$ ,  $\bar{\rho}$ , are the total thickness, length, width, effective Young's modulus, and effective density of the cantilever, respectively. To verify Eq. (3), measurements were carried out with cantilevers of 0.4 and 0.2 cm in width with a PZT layer 0.25 mm thick bonded to a stainless steel 0.1 mm thick. The length of the cantilevers was varied from 1.37 cm to 0.44 cm by changing the clamp position. These

resonant frequencies were identified and monitored by measuring the electrical impedance spectrum with an impedance analyzer (Agilent 4294A, Agilent, Palo Alto, CA). Figure 11.2 shows the experimental results. Note that off resonance the cantilever was a capacitor, exhibiting a phase angle around  $-90^\circ$ . At resonance, the flexural motion gave rise to a peak in the real part of the impedance, and hence a peak in the phase angle due to the direct piezoelectric effect. As an example, Fig. 11.2(a) shows the first-mode resonance frequency spectrum, i.e., phase angle versus frequency, of a cantilever of  $L = 1.37$  cm and  $w = 0.4$  cm without loading (■), loaded with an aluminum foil of  $3.5 \times 10^{-4}$  g (○),  $5.9 \times 10^{-4}$  g (+), and  $7.8 \times 10^{-4}$  g (×) at the cantilever tip. Clearly, the resonance peak shifted to a lower frequency as the mass of the aluminum foil increased. Presently, a 1 cm long cantilever has a  $\Delta f/\Delta m = 3.2 \times 10^5$  Hz  $g^{-1}$ . To compare with Eq. (3), the normalized  $\Delta f/\Delta m(w/w_0)$  versus cantilever length,  $L$ , is plotted in Fig. 11.2(b), where  $w_0$  was 2 mm. Clearly, the log–log plot of the normalized  $\Delta f/\Delta m(w/w_0)$  yielded a slope of  $-3$ , validating Eq. (3). Also plotted in Fig. 11.2(a) are data points obtained with PZT cantilevers with a nonpiezoelectric tip described below. Extrapolating from Fig. 11.2(b), for a cantilever 10  $\mu\text{m}$  long, its  $\Delta f/\Delta m$  will approach  $10^{17}$  Hz  $g^{-1}$ . A more detailed description of the application of a piezoelectric cantilever as a mass sensor and how the sensitivity changes with the length, width, and height of the cantilever can be found in Yi et al. [27].

### 11.2.2

#### PECS with a Nonpiezoelectric Extension

A piezoelectric cantilever of uniform thickness (Fig. 11.1a) exhibits the strongest peak intensity in the first mode and the intensity of higher-order resonance peaks decreases with an increasing order [30, 31]. The ratio of the  $n$ th resonance frequency to the first resonance frequency is also predicted by the solution of the vibration wave equation of a uniform beam. Surprisingly, a piezoelectric cantilever with a nonpiezoelectric extension (Fig. 11.1b) could exhibit a higher second-mode peak intensity than the first-mode one and the ratio of the  $n$ th-mode resonance frequency to the first-mode one could be quite different from that of a uniform beam.

Theoretically, we considered a piezoelectric cantilever with a nonpiezoelectric extension as two distinctive sections, (1) the piezoelectric section and (2) the nonpiezoelectric extension section, with each section possessing a different thickness, elastic modulus and mass density distribution in the thickness direction. We solved the cantilever's flexural vibration equation analytically to derive a transcendental equation that could be solved numerically to obtain the cantilever's flexural vibration wave forms and its resonance spectrum.

Examples of spectra in region I where the first peak was always higher than the second peak are shown in Fig. 11.3(a) with cantilevers of a 8 mm and 9.2 mm PZT section and a 4 mm nonpiezoelectric extension length ( $l_1/l_2 = 2.0$  and 2.3, respectively). Figure 11.3(b) shows examples of spectra in region II with cantilevers of a 2, 4, 6, 8 and 10 mm PZT section and an 8 mm nonpiezoelectric extension length

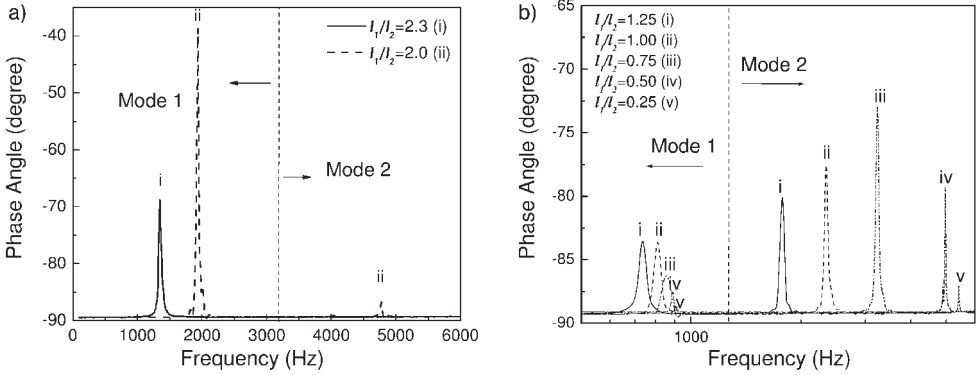


**Fig. 11.3.** Phase-angle versus frequency of cantilevers with (a)  $l_1/l_2 \geq 1.5$  [ $l_2 = 4$  mm and  $l_1 = 8$  (dashed line) and 9.2 mm (solid line)] and (b)  $l_1/l_2 \leq 1.5$  [ $l_2 = 8$  mm and  $l_1 = 10$  (i), 8 (ii), 6 (iii), 4 (iv), and 2 mm (v)].

( $l_1/l_2$  ranging from 0.25 to 1.25). Clearly, the ratio  $l_1/l_2$  played an important role in determining the resonance peak intensity ratio. This came about because the resonance electrical impedance signals were solely determined by the vibration amplitude within the piezoelectric layer. How the peak height of a higher-mode resonance compared to the peak height of the first-mode depended mainly on how the higher-mode vibration amplitude within piezoelectric layer compared to that of the first mode, which could be strongly affected by the ratio of the length of the piezoelectric section to that of the nonpiezoelectric extension,  $l_1/l_2$ . To illustrate this point, calculated  $h_1(x)$  and  $h_2(x)$  versus  $x$  are plotted in Fig. 11.4(a) for the cantilever with  $l_1 = 9.2$  mm and  $l_2 = 4$  mm ( $l_1/l_2 = 2.3$ ) whose spectrum

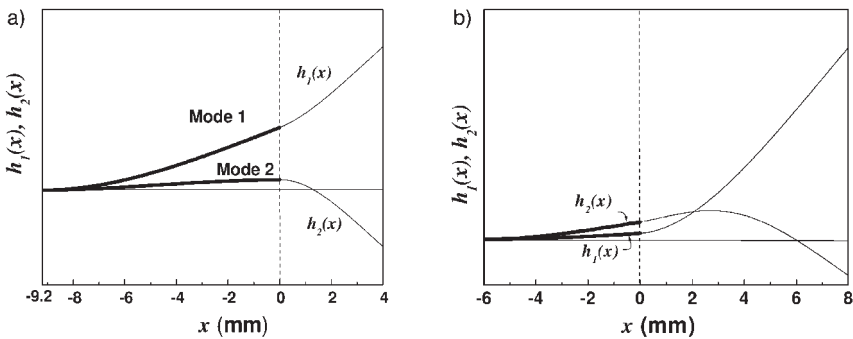


**Fig. 11.4.** Calculated amplitudes,  $h_1(x)$  and  $h_2(x)$ , versus  $x$  for a cantilever with (a)  $l_1 = 9.2$  mm and  $l_2 = 4$  mm ( $l_1/l_2 = 2.3$ ) and (b)  $l_1 = 6$  mm and  $l_2 = 8$  mm ( $l_1/l_2 = 0.75$ ).

was shown as the solid line in Fig. 11.3(a), and in Fig. 11.4(b) for the cantilever with  $l_1 = 6$  mm and  $l_2 = 8$  mm ( $l_1/l_2 = 0.75$ ) whose spectrum is labeled (iii) in Fig. 11.3(b). Figure 11.3(a) shows that the second-mode vibration amplitude,  $h_2(x)$ , exhibited a nodal point near  $x = l_1$ . Note that the second peak of this cantilever was absent in Fig. 11.3(a), as is consistent with the presence of the nodal point at  $x = l_1$  shown in Fig. 11.4(a), which indicated that there was little bending stress and therefore little induced piezoelectric voltage near  $x = l_1$ . In contrast, for  $l_1/l_2 = 0.75$ , the second-mode vibration amplitude within the piezoelectric section ( $x \leq l_1$ ) was higher than that of the first mode, indicating a higher stress and hence a higher piezoelectric response, although the first-mode vibration amplitude was higher than the second mode towards the free end ( $x = l_1 + l_2$ ) of the nonpiezoelectric extension section.

### 11.3

#### Examples of Detections

##### 11.3.1

#### Immobilization and In-solution Quantification of Yeast Cells

A PZT/stainless steel cantilever with a 3 mm long, 4 mm wide, and 0.3 mm thick PZT layer bonded to a 0.1 mm thick stainless steel with a 4 mm long stainless steel tip thinly coated with a poly-L-lysine (Sigma P8920, 0.1% w/v) layer was used for yeast detection. Poly-L-lysine is positively charged, to which negatively charged yeast is attracted and immobilized. The stainless steel tip was immersed in yeast suspensions of 1 and 2 g L<sup>-1</sup> with a 3 mm dipping depth. The in-water resonance peak intensity of this cantilever is similar to its resonance peak intensity in air (Fig. 11.5a) with a  $Q$  factor about 30, making the in-water measurements as accurate and reliable as the in-air ones. Figure 11.6(a) shows the optical micrographs of yeast cells on the stainless steel tip after 60 min of immersion in the yeast suspension. A scanning electron microscopic (SEM) micrograph provided a close-up of the immobilized yeast cells (Fig. 11.6b). Adsorption of the yeast cells indeed caused a shift in the cantilever resonance frequency. Figure 11.5(b) shows a plot of the resonance frequency shift versus time. Note that the resonance frequency changed more slowly in 1 than in 2 g L<sup>-1</sup>, eventually reaching the same saturated  $\Delta f$  in both concentrations. The resonance frequency change with time was used to characterize the cell concentration. The adsorption of cells was limited by the diffusion of cells to the cantilever surface. At short times, e.g.,  $t < 10$  min for 2 g L<sup>-1</sup> and  $t < 40$  min for 1 g L<sup>-1</sup> (Fig. 11.5b), the adsorbed amount and hence the resonance frequency shift should be proportional to  $t^{1/2}$  and the slope of  $\Delta f$  versus  $t^{1/2}$  should be proportional to concentration [3]. For 1 g L<sup>-1</sup> (2 g L<sup>-1</sup>), at  $t < 40$  min ( $t < 10$  min),  $\Delta f$  is linear with  $t^{1/2}$  and the slope for 2 g L<sup>-1</sup> is indeed twice that for 1 g L<sup>-1</sup>, indicating that one can use  $\Delta f$  versus  $t$  to quantify the concentration. More detailed results on yeast detection are presented in a recent paper by Yi et al. [32].



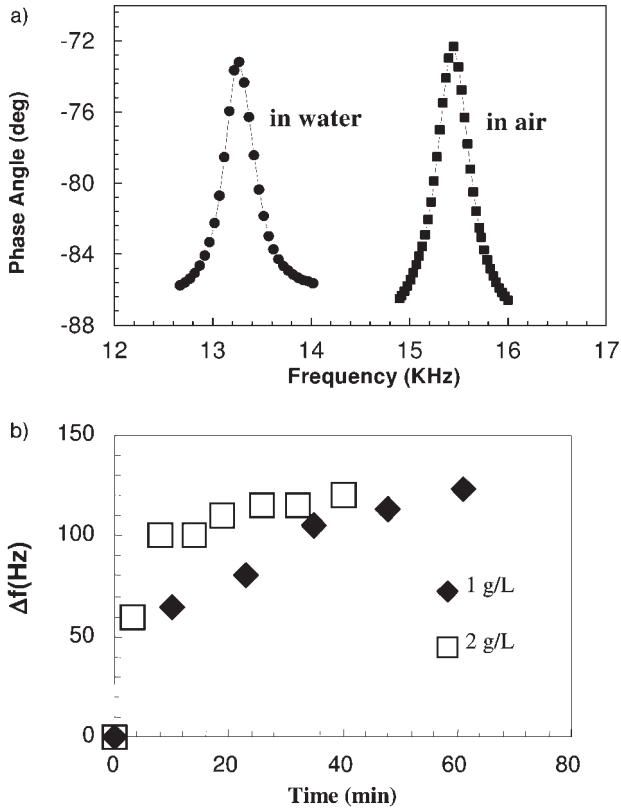


**Fig. 11.5.** (a) First-mode resonance frequency spectra of the yeast-detecting cantilever; (b) resonance frequency shift versus time after the cantilever was immersed in the  $1 \text{ g L}^{-1}$  (filled diamonds) and  $2 \text{ g L}^{-1}$  (open squares) suspension.

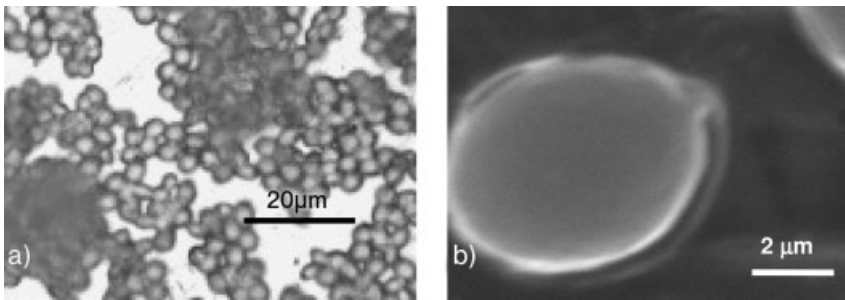


**Fig. 11.6.** (a) Optical micrograph of yeast cells immobilized on the poly-L-lysine layer coated on the cantilever stainless steel tip surface after 60 min and (b) SEM micrograph of immobilized yeast cells.

## 11.3.2

**Detection of Binding of Biotinylated Polystyrene Spheres to Immobilized Avidin**

We have demonstrated that a piezoelectric cantilever could detect the binding of a target protein (biotin) to an immobilized protein (avidin) at the cantilever tip. We used a PZT/stainless steel cantilever, 1.3 mm long, 2 mm wide and with a 0.127 mm thick PZT layer bonded to a 0.05 mm thick stainless steel foil, and a 2.87 mm long stainless steel tip coated with a gold layer by sputtering. The cantilever was rigidly set in an epoxy-filled glass tube that served as the clamp [insert (a) Fig. 11.7]. Avidin was immobilized on the gold surface via 3-mercaptopropionic acid (MPA). The carboxyl groups of MPA bind to avidin covalently while the sulfur binds to the gold surface chemically [33–35]. The avidin-coated tip was then vertically immersed in a 0.125 wt% suspension of biotin-coated polystyrene microspheres of 2  $\mu\text{m}$  diameter (Polysciences, Warrington, PA) with a 2.2 mm dipping depth. The resonance frequency of the cantilever decreased with time and the resonance frequency shift with time is shown in Fig. 11.7. The resonance frequency shift increased with time and reached about 240 Hz shift at  $t = 40$  min. An optical micrograph of the immobilized biotinylated microspheres on the avidin-coated stainless steel cantilever tip taken at 20 min is given in insert (b) of Fig. 11.7, which shows about 10% surface coverage and corresponds to about  $1 \times 10^{-6}$  g microspheres adsorbed on the cantilever tip, indicating that the cantilever has a mass detection sensitivity,  $\Delta m/\Delta f$ , of about  $4 \times 10^{-9}$  g  $\text{Hz}^{-1}$ .

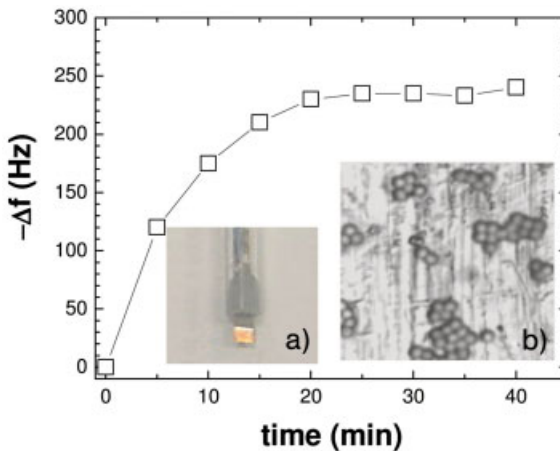


**Fig. 11.7.** Resonance frequency shift with time of a PZT/stainless steel cantilever in a biotinylated polystyrene suspension. Inserts: (a) photograph of the cantilever. The PZT layer was 1.3 mm long, 3.35 mm wide. The 2.87 mm long gold-coated stainless steel tip was coated with avidin. (b) Optical micrograph of immobilized biotinylated spheres after 20 min.

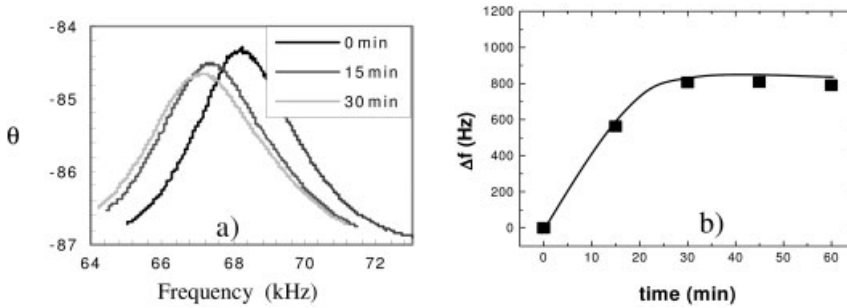


**Fig. 11.8.** (a) Resonance spectra at different times due to the immobilization of avidin on the stainless steel tip and (b) the resultant resonance frequency shift versus time.

### 11.3.3

#### Detection of Avidin Immobilization at the Cantilever Tip

To detect the immobilization of avidin we used an even *shorter* cantilever that had a PZT layer *0.7 mm long*, 2.27 mm wide, and 0.127 mm thick bonded to a 0.05 mm thick stainless steel foil. The cantilever has a 2 mm long gold-coated stainless steel tip. The freshly sputtered gold surface was first coated with MPA as described above and then immersed in a  $0.1 \text{ mg mL}^{-1}$  avidin solution. The dipping depth was 1.3 mm. Immobilization of avidin on the cantilever tip was detected by monitoring the resonance frequency shift of the cantilever at around 68 kHz. Figure 11.8(a) shows the resonance spectrum at different times and Fig. 11.8(b) shows the frequency shift with time after the cantilever tip was immersed in the avidin solution. The saturated adsorption amount of avidin was known to be about  $3 \text{ ng mm}^{-2}$  [36, 37]. This indicated that the mass detection sensitivity of this 0.7 mm long cantilever was  $\Delta m/\Delta f \sim 1 \times 10^{-10} \text{ g Hz}^{-1}$ . The saturated adsorption amount of avidin yields a resonance frequency change of 40 Hz with a conventional 5 MHz QCM. The present piezoelectric cantilever's 800 Hz resonance frequency change is already  $20\times$  better than that of a 5 MHz QCM.

### 11.3.4

#### *Salmonella typhimurium* Detection

*Salmonella* is a water-borne/food-borne pathogen that causes more than 500 deaths each year [38]. It is also a category B bioterrorism agent that can seriously contaminate water resources. There is no device at present that can actually monitor a space and perform an analysis of the air or water within that space in real-time. However, such a device would dramatically decrease the “lag time between release of an agent and its detection,” and thus enable more prompt treatment of those

individuals possibly exposed to a particular bioterrorism agent in addition to reducing the total number of individuals affected [39].

A piezoelectric microcantilever was fabricated by bonding a layer of lead zirconate titanate (PZT) 0.127 mm thick, 2 mm long, and 1.5 mm wide to a titanium foil 0.127 mm thick with a titanium tip 3 mm long (Fig. 11.1b). The PZT layer had a piezoelectric coefficient  $d_{31}$  of  $-320 \text{ pm V}^{-1}$  and a Young's modulus  $Y_{11}$  of 62.5 GPa. The titanium foil has a Young's modulus of 103 GPa. The salmonella strain was *Salmonella typhimurium* and the antibody used was an antibody to Salmonella Common Structural Antigens (CSA-1) (both from Krikegaard & Perry Laboratories, Inc., Gaithersburg, Maryland). This antibody is specifically designed to recognize several species of bacteria in the *Salmonella* genera, including our *typhimurium* species. The CSA-1 antibody was immobilized on the tip of a PZT-Ti microcantilever by means of a linking molecule. Titanium was chosen as the non-piezoelectric layer as a result of its good mechanical properties as well as its outstanding biocompatibility [40]. This biocompatibility is demonstrated by its widespread use as a material for implants in the human body.

Though common methods of immobilization on surfaces rely on MPA or 3-aminopropyltriethoxysilane (APS) followed by activation with 1-ethyl-3-(3-dimethylaminopropyl)carbodiimide (EDC) and *N*-hydroxysulfosuccinimide (NHS) [41], we used a much simpler method adapted from silica-silane chemistry. Since a passivated titanium surface exhibits similar surface chemistry to that of silica [42], a bifunctional linker, glycidoxypropyltrimethoxysilane (GOPTS), was used as the linking molecule [43, 44]. GOPTS presents, on one end, a trialkyloxysilane group, like APS, which allows its incorporation on activated silica or silica-like surfaces. Once GOPTS is deposited on a surface, it exposes epoxy moieties that are unstable and therefore very reactive toward nucleophilic groups such as amines, thiols, and alcohols. These groups will promptly react, causing opening of the bond angle strained epoxide ring. The main advantage of GOPTS over other bifunctional linkers is that it does not require an activation step, whereas activation with EDC/NHS is required for standard carboxylic functionalities. In our work, the trimethoxysilane end of GOPTS was bound to the titanium surface of the microcantilever and CSA-1 antibody was subsequently immobilized on the sensor under basic conditions, through addition of its amine groups to epoxide rings exposed on the surface.

Following functionalization of the microcantilever with antibody, several detections of the *S. typhimurium* cells were performed by lowering the cantilever tip into a vial containing the cell suspension by means of a micropositioner, such that approximately two-thirds of the tip was submerged. This allowed the resonance frequency shift to be monitored with time as described above.

In the present detection set-up, the titanium tip was only partially immersed in the solution to avoid wetting of the PZT layer by the solution. As a result, there was an upward background resonance shift due to a receding water level along with the resonance frequency shift due to cell binding. Consequently, a typical cell-detection resonance frequency shift versus time plot exhibited an initial decrease, reaching a minimum that was followed by an almost linear rise (solid curve

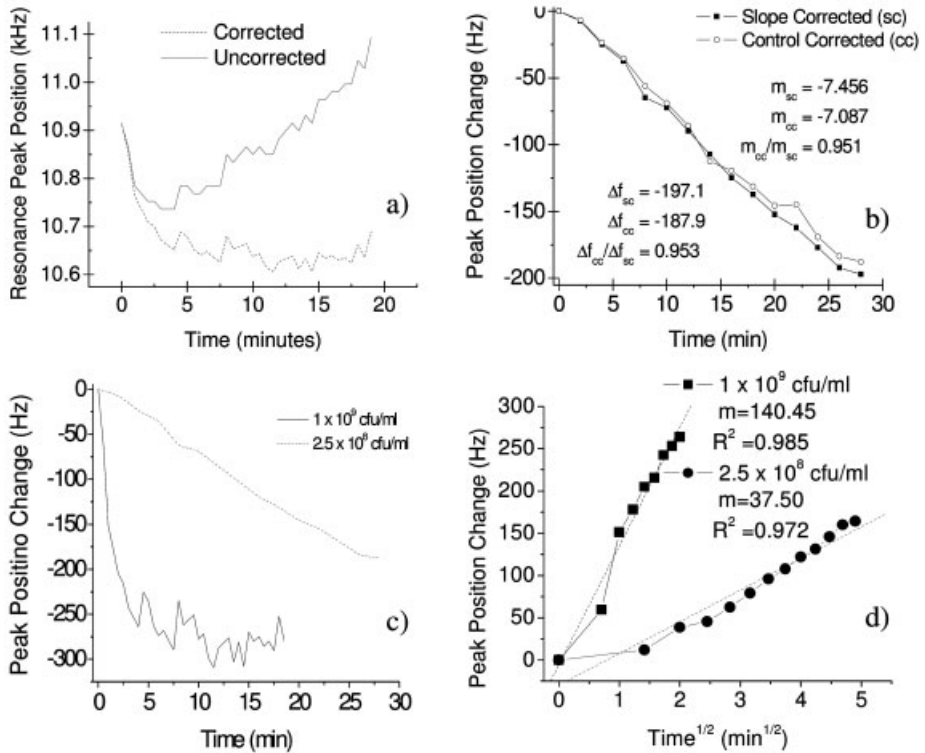


**Fig. 11.9.** (a) Uncorrected salmonella detection data with the corresponding corrected data. (b) Comparison of slope corrected vs. control corrected detection. (c) Detection of  $1 \times 10^9$  and  $2.5 \times 10^8$  cells  $\text{mL}^{-1}$  *Salmonella typhimurium* suspensions. (d) Kinetic analysis of *S. typhimurium* binding.

in Fig. 11.9a). To address the issue of background resonance frequency shift, we carried out three different checks. The first was to obtain the rate of upward background shift in water prior to the detection experiment. The second was to obtain the rate of upward background shift using the later stage of the resonance frequency shift that showed an almost linear increase. The third check was to use a two-cantilever array to perform the detection. One cantilever was treated with the GOPTS as detailed above, while the other cantilever was left passivated but untreated with GOPTS. Then, both cantilevers were simultaneously subjected to the same series of steps associated with a detection process: (a) exposure to the antibody, (b) rinse in phosphate-buffered saline (PBS) and (c) dipping in the cell suspension. We found that the first two corrections were practically the same, indicating that the upward shift in the later stages of detection was indeed a manifest of receding water level. In Fig. 11.9(a), the corrected resonance frequency shift due to

cell binding is shown as the dashed line after subtracting the background upshift from the initial data (solid line). Figure 11.9(b) shows two curves from the same detection of a  $2.5 \times 10^8$  cells  $\text{mL}^{-1}$  *S. typhimurium* suspension. The *control corrected* data represent subtraction of the upward drift based on the control cantilever that was not coated with the GOPTS (and thus was not functionalized with the CSA-1 antibody). The *slope corrected* data represent the removal of the linear drift simply by taking a linear regression of the detection data after cell adhesion on the sensor tip had ceased. As can be seen in the figure, the ratio of the two slopes is nearly unity, as is the ratio of the total resonant frequency shifts. Furthermore, as mentioned above, the cantilever used in Fig. 11.9(a) was also monitored in water alone and the same linear up-drift was obtained, thus providing further substantiation of the post-cell adhesion up-drift subtraction method. Based on these findings, all subsequent cell detection experiments used only the post-cell adhesion linear drift data to correct for the upward drift. This greatly simplified the experiments and thus allowed for more efficient data collection.

Meanwhile, PZT/gold-coated glass cantilever sensors with a 0.127 mm thick, 0.5 mm long and 2 mm wide PZT layer bonded to a gold coated glass layer of 0.150 mm in thickness that had a 2 mm long gold-coated glass tip were also tested in *S. typhimurium* detection. The gold-coated glass surface was coated with MPA, which was treated in a solution of 5 mg  $\text{mL}^{-1}$  EDC and 5 mg  $\text{mL}^{-1}$  NHS in distilled water for 30 min followed by dipping in 1  $\mu\text{L}$  of a 0.1 mg  $\text{mL}^{-1}$  solution of CSA-1 in a phosphate-buffered saline (PBS) solution at pH 7.4 for 30 min. The antibody-coated cantilevers were then used to detect *S. typhimurium* at various concentrations for up to 30 min. Figure 11.10 gives the resultant  $\Delta f$  versus time plots from the PZT/gold-coated cantilevers at various *S. typhimurium* concentrations. As can be seen,  $\Delta f$  decreases sharply initially and reached a plateau after 10 min. The detections were quite repeatable as each curve was the average of 3–4 independent measurements. The standard deviations of  $\Delta f$  were about 10–20%. Table 11.1 lists

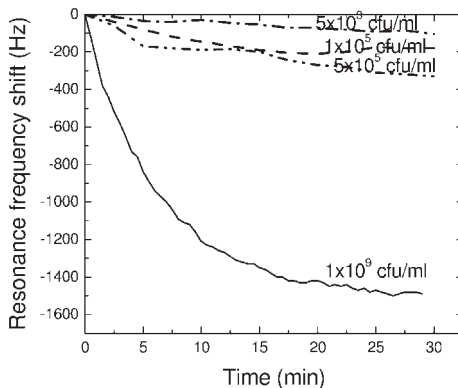


**Fig. 11.10.** Resonance frequency shift versus time of the PZT/gold-coated glass cantilever in various *Salmonella typhimurium* concentrations.

**Table 11.1.** Resonance frequency shift of a PZT/Au-coated glass cantilever with  $5 \times 10^{-11}$  g/Hz sensitivity in various concentrations of *Salmonella t.*

Salmonella concentration (cells/ml)	$\Delta f$ (PZT/Au-coated glass)
$10^9$	1500
$5 \times 10^5$	330
$1 \times 10^5$	180
$5 \times 10^3$	90

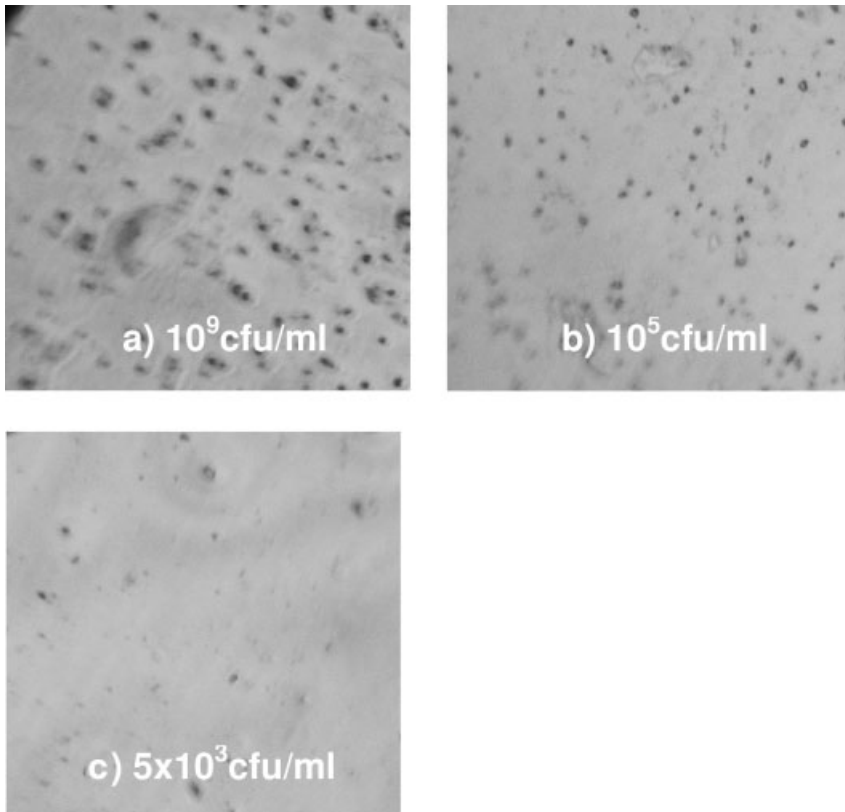


**Fig. 11.11.** Optical micrographs of a PZT/gold-coated cantilever surface after 30 min detection in a)  $1 \times 10^9$  (b)  $1 \times 10^5$  and (c)  $5 \times 10^3$  cells  $\text{mL}^{-1}$  *Salmonella typhimurium* suspensions.

the average  $\Delta f$  at  $t = 30$  min for various *Salmonella* concentrations, as obtained from the PZT/gold coated glass cantilever. As can be seen, at  $5 \times 10^3$  cells  $\text{mL}^{-1}$ , the  $\Delta f$  obtained by the PZT/gold coated glass cantilevers at  $t = 30$  min was 90 Hz, well above the standard deviation of 20 Hz, and at  $1 \times 10^3$  cells  $\text{mL}^{-1}$  the obtained  $\Delta f$  was no longer meaningful compared to the standard deviation. This puts the detection limit of the current PZT/gold-coated glass cantilever at about the  $1 \times 10^3$  cells  $\text{mL}^{-1}$  range.

To validate the results shown in Fig. 11.10, the PZT/gold-coated glass cantilever surface was examined by optical microscopy after 30 min of detection. Figure 11(a)–(c) shows SEM micrographs of captured *Salmonella* cells on the PZT/gold-coated glass cantilever surface at  $t = 30$  min from  $1 \times 10^9$ ,  $1 \times 10^5$ , and  $5 \times 10^3$  cells  $\text{mL}^{-1}$  suspensions, respectively. With the mass of each cell being  $2 \times 10^{-12}$  g and by counting the number of cells in the micrographs, the mass of the captured cells on the cantilever surface was estimated to be  $5 \times 10^{-8}$ ,  $3 \times 10^{-9}$ , and  $1 \times 10^{-9}$  g for  $1 \times 10^9$ ,  $1 \times 10^5$ , and  $5 \times 10^3$  cells  $\text{mL}^{-1}$  suspensions, respectively. With  $\Delta f$  at 30 min being 970, 300 and 100 Hz for the  $1 \times 10^9$ ,  $1 \times 10^5$ , and  $5 \times 10^3$  cells  $\text{mL}^{-1}$  suspensions, respectively,  $\Delta m/\Delta f$  was  $5 \times 10^{-11}$  g  $\text{Hz}^{-1}$ , which is consistent with the  $5 \times 10^{-11}$  g  $\text{Hz}^{-1}$  as calibrated with a quartz crystal microbalance (QCM) in the antibody immobilization.

### 11.3.5

#### Nerve Gas Simulant Detection

The piezoelectric cantilever sensors we have developed are quantitative and suitable for use in air. As an example of detecting chemical agents, we studied the de-

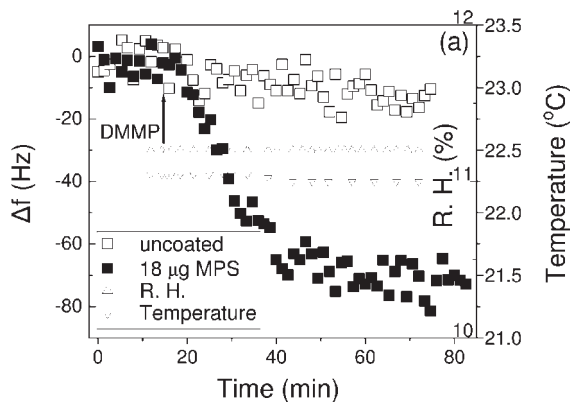


**Fig. 11.12.** Resonance frequency shift versus time of the uncoated (open squares) and  $18 \mu\text{g}$  (filled squares) microporous silica (MPS)-coated cantilever after spraying 10 mL liquid DMMP in a 66 L chamber. Also shown are

relative humidity (open triangles) and temperature (inverted open triangles) in the chamber during the test. The arrow indicates the injection of DMMP.



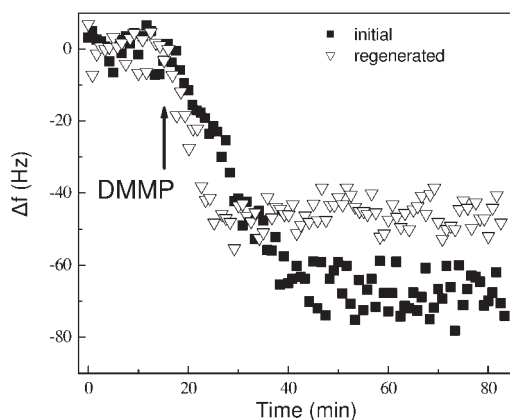


**Fig. 11.13.** Resonance frequency shift versus time during the initial DMMP test (filled squares) and after regeneration (inverted open triangles).

tection of the nerve gas simulant dimethyl dimethyl phosphonate (DMMP) using a PZT cantilever that had a PZT layer 1 mm long, 2.1 mm wide, and 0.127 mm thick bonded to a 0.05 mm thick stainless steel foil. The cantilever had a stainless steel tip 2.4 mm long and 0.05 mm thick coated with ultrahigh surface area ( $800 \text{ m}^2 \text{ g}^{-1}$  and pore size  $10 \text{ \AA}$ ) microporous  $\text{SiO}_2$ . The coated cantilever had a lower resonance frequency ( $\sim 80 \text{ Hz}$  shift) due to the mass of the microporous  $\text{SiO}_2$  coating. The  $\text{SiO}_2$ -coated cantilever was placed in a closed chamber with a constant humidity of 11.2% and a constant temperature of  $22.2 \text{ }^\circ\text{C}$ , as shown in Fig. 11.12 for DMMP tests. When 5 mL of DMMP was injected and sprayed into the chamber, the cantilever resonance frequency decreased with time and saturated at about 70 Hz change (■ in Fig. 11.12). Note that without the silica coating, the resonance frequency was stable (□), indicating that silica-coated cantilevers can indeed be sensitive DMMP sensors.

After the initial test, the cantilever was regenerated in air for 5 days. In the second DMMP test, the resonance frequency of the regenerated cantilever decreased at a similar rate as in the initial test, except that the resonance frequency shift saturated at 50 Hz instead of 70 Hz (Fig. 11.13). The smaller saturated resonance frequency shift for the regenerated cantilever was probably due to incomplete removal of DMMP. A clear advantage of oxide adsorbent is that it is readily reusable due to the physical nature of the adsorption.

#### 11.4 Piezoelectric Cantilever Miniaturization

As shown in Fig. 11.2(b), miniaturized cantilevers can achieve higher mass detection sensitivity. We have developed two types of piezoelectric microcantilevers: one

is fabricated from freestanding lead magnesium niobate-lead titanate (PMN-PT) films developed in our laboratory, exhibiting up to  $2 \times 10^{-14}$  g Hz<sup>-1</sup> sensitivity; the other is fabricated using silicon microfabrication techniques with lead zirconate titanate thin films on silicon wafers that can be as small as 50  $\mu$ m long, offering better than  $10^{-16}$  g Hz<sup>-1</sup> sensitivity.

#### 11.4.1

##### PMN-PT/Cu Microcantilevers

The PMN-PT/Cu microcantilevers consisted of a highly piezoelectric layer fabricated from freestanding lead magnesium niobate-lead titanate (PMN-PT) films bonded to a copper layer by electroplating. The microcantilever shape was achieved by wire-saw cutting. As an example, the top-view optical micrograph, cross-section scanning electron microscopy (SEM) micrograph, and a typical resonance spectrum of 500  $\mu$ m long, 700  $\mu$ m wide PMN-PT/Cu microcantilevers made of 22  $\mu$ m thick PMN-PT and 5  $\mu$ m thick copper are shown in Fig. 11.14(a)–(c) respectively. The spectrum shown in Fig. 11.14(c) exhibits multiple resonance peaks with

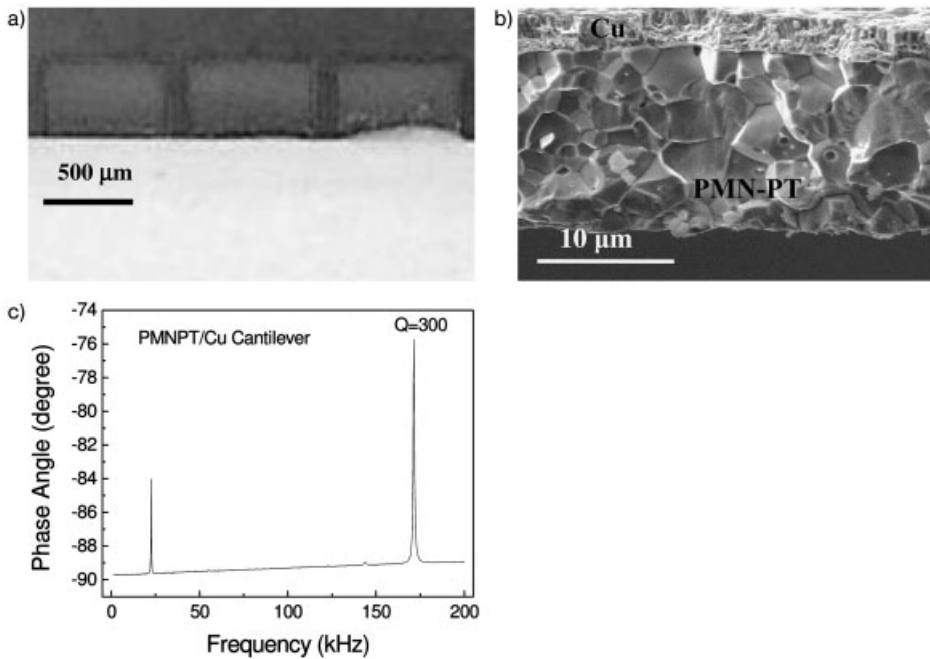


**Fig. 11.14.** (a) Optical micrograph and (b) SEM cross-section micrograph of 500  $\mu$ m long, 700  $\mu$ m wide PMN-PT/Cu microcantilevers with 22  $\mu$ m thick PMN-PT and 5  $\mu$ m thick Cu on a glass substrate, and (c) a typical resonance spectrum. Note that because of the

highly piezoelectric PMN-PT layer we were able to retain the higher-mode resonance peaks with  $Q > 300$  for better detection sensitivities. This PMN-PT PEMS exhibited femtogram mass detection sensitivity,  $\Delta m/\Delta f = 3 \times 10^{-13}$  g Hz<sup>-1</sup>.

**Tab. 11.2.** Resonance frequency shift of a PMN-PT/Cu microcantilever with  $3 \times 10^{-13}$  g Hz<sup>-1</sup> sensitivity compared with a PZT/Au-coated glass cantilever with  $5 \times 10^{-11}$  g Hz<sup>-1</sup> sensitivity. Note: the PMN-PT/Cu microcantilever lowered the BA concentration limit by two orders of magnitude.

BA concentration (cells mL <sup>-1</sup> )	$\Delta f$ (PMN-PT/Au-Cu) <sup>[a]</sup>	$\Delta f$ (PZT/Au-coated glass)
10 <sup>5</sup>		1200
2 × 10 <sup>4</sup>		600
5 × 10 <sup>3</sup>	6800	110
2 × 10 <sup>3</sup>		50
500	5700	
50	100	

<sup>a</sup> PMN-PT/Cu microcantilever had copper on one side and was cold coated on the other side for antibody immobilization.

$Q > 300$  ( $Q$  is the ratio of the resonance frequency to the resonance peak width at half the peak height). The mass detection sensitivity of this PMN-PT/Cu microcantilever was determined to be  $3 \times 10^{-13}$  g Hz<sup>-1</sup>, with the second resonance peak at 170 kHz, as calibrated by QCM. The PMN-PT/Cu microcantilever was gold coated on both sides for antibody immobilization using the MPA self-assembly monolayer approach (Section 11.3.4). Because the PMN-PT/Cu microcantilevers were about two orders of magnitude more sensitive than the PZT PECS described in Sections 11.3.3–11.3.5, they realized an even lower concentration limit. For example, Table 11.2 lists the resonance frequency shifts of PMN-PT microcantilevers at various *Bacillus anthracis* (BA) concentrations in BA spores detection. Also listed are the resonance frequency shifts of a PZT/Au-coated glass cantilever with a sensitivity of  $5 \times 10^{-11}$  g Hz<sup>-1</sup> (similar to that used in *S. typhimurium* detection in Section 11.3.4). Clearly, the more sensitive PMN-PT/Cu microcantilevers lowered the detection concentration limit to 50 cells mL<sup>-1</sup> – two orders of magnitude lower than that of the PZT/Au-coated glass cantilevers.

#### 11.4.2

##### PZT/SiO<sub>2</sub> Microcantilevers and PZT/SiO<sub>2</sub>-Si<sub>3</sub>N<sub>4</sub> Nanocantilevers

Alternatively, we have successfully fabricated PZT/SiO<sub>2</sub> microcantilevers by depositing 1.6 μm thick PZT films on a Pt/TiO<sub>2</sub>/SiO<sub>2</sub>/Si substrate with a novel sol-gel process and repeated spin coating. The Pt/TiO<sub>2</sub>/SiO<sub>2</sub> substrate was necessary to prevent unwanted interfacial reactions and diffusions. The precursor solution contained 50% excess lead to compensate for lead loss during repeated heat treatment. Figure 11.15(a) shows a SEM micrograph of a 1.6 μm thick PZT film. The film was further made into piezoelectric microcantilevers by integrating the piezoelectric films with the microfabrication process. Examples of a 50 μm long PZT/SiO<sub>2</sub> mi-

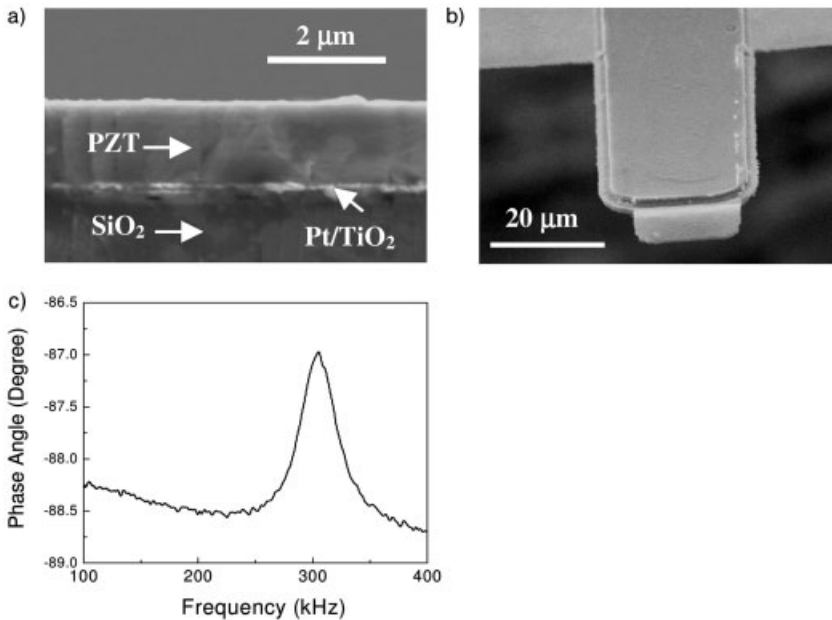


**Fig. 11.15.** SEM cross-section of (a) a 1.6  $\mu\text{m}$  thick PZT film and (b) a 50  $\mu\text{m}$  long, 20  $\mu\text{m}$  wide PZT/SiO<sub>2</sub> microcantilever with a 10  $\mu\text{m}$  long SiO<sub>2</sub> tip. (c) Resonance frequency spectrum of the PZT/SiO<sub>2</sub> microcantilever in (b).

crocantilever and its resonance frequency spectrum are shown in Fig. 11.15(b) and 11.15(c), respectively. From our earlier experimental and theoretical work, we expect such piezoelectric microcantilevers to have better than  $10^{-16}$  g Hz<sup>-1</sup> sensitivity. Furthermore, in the making are PZT/SiO<sub>2</sub>-Si<sub>3</sub>N<sub>4</sub> piezoelectric nanocantilever sensors (PENS) with a 20  $\mu\text{m}$  long PZT/SiO<sub>2</sub>-Si<sub>3</sub>N<sub>4</sub> section and a nano-size SiO<sub>2</sub>-Si<sub>3</sub>N<sub>4</sub> tip that is less than 300 nm in width and less than 1  $\mu\text{m}$  in length. Theoretical calculation indicates that such PZT/SiO<sub>2</sub>-Si<sub>3</sub>N<sub>4</sub> PENS will exhibit better than  $10^{-18}$  g Hz<sup>-1</sup> sensitivity (the mass of a single protein or DNA).

## 11.5

### Conclusions

We have developed piezoelectric microcantilever sensors of different sizes and types that can perform rapid, *in situ*, in-water pathogen detection with sensitivities well above that of current techniques. Both theoretical and experimental studies were carried out to characterize the sensors. We showed that using PZT/glass cantilevers of sub-millimeter length with a 2 mm glass tip that exhibited  $5 \times 10^{-11}$  g Hz<sup>-1</sup> mass detection sensitivity, *in situ* quantification of *S. typhimurium* was achieved

with a concentration limit of  $10^3$  cells  $\text{mL}^{-1}$ , lower than the infectious dosage,  $10^5$  cells  $\text{mL}^{-1}$ , which is also the concentration limit of ELISA and QCM. Furthermore, using 500  $\mu\text{m}$  long miniaturized PMN-PT/Cu microcantilevers that exhibited  $3 \times 10^{-13}$  g  $\text{Hz}^{-1}$  detection sensitivity, we showed that in a liquid volume of less than 1 mL the detection concentration limit was lowered to below 50 cells  $\text{mL}^{-1}$ . With PZT/SiO<sub>2</sub> microcantilevers less than 50  $\mu\text{m}$  long and PZT/SiO<sub>2</sub>-Si<sub>3</sub>N<sub>4</sub> PENS less than 20  $\mu\text{m}$  long with a SiO<sub>2</sub>-Si<sub>3</sub>N<sub>4</sub> less than 300 nm wide and less than 1  $\mu\text{m}$  long, we expect the detection sensitivity to reach better than  $10^{-16}$  g  $\text{Hz}^{-1}$  and  $10^{-18}$  g  $\text{Hz}^{-1}$ , respectively and the detection concentration to be further lowered.

## Acknowledgment

This work is supported in part by the National Aeronautics and Space Administration (NASA) under Grant No. NAG2-1475, the National Institute of Health (NIH) under Grant No. 1 R01 EB000720, and the Environmental Protection Agency (EPA) under Grant No. R82960401.

## References

- 1 S. NIE, R. N. ZARE, Optical detection of single molecules, *Annu. Rev. Biophys. Biomol. Struct.*, 26, 567–596 (1997).
- 2 S.-K. KRAEFT, A. LADANYI, K. GALIGER, A. HERLITZ, A. C. SHER, D. E. BERGSRUD, G. EVEN, S. BRUNELLE, L. HARRIS, R. SALGIA, T. DAHL, J. KESTERSON, L. B. CHEN, Reliable and sensitive identification of occult tumor cells using the improved rare event imaging system, *Clin. Cancer Res.*, 10, 3020 (2004).
- 3 <http://optics.org/articles/news/8/3/27/1>.
- 4 R. T. KRIVACIC, A. LADANYI, D. N. CURRY, H. B. HSIEH, P. KUHN, D. E. BERGSRUD, J. F. KEPROS, T. BARBERA, M. Y. HO, L. B. CHEN, R. A. LERNER, R. H. BRUCE, A rare-cell detector for cancer, *Proc. Natl. Acad. Sci. U.S.A.*, 101(29), 10501–10504 (2004).
- 5 M. MINUNNI, M. MASCINI, G. G. GUILBAULT, B. HOCK, The quartz crystal microbalance as biosensor, a status report on its future, *Anal. Lett.*, 28, 749–764 (1995).
- 6 A. G. GEHRING, D. L. PATTERSON, S.-I. TU, Use of a light-addressable potentiometric sensor for the detection of Escherichia coli O157:H7, *Anal. Biochem.*, 258, 293–298 (1998).
- 7 A. K. BEJ, M. H. MAHBUBANI, M. J. BOYCE, R. M. ATLAS, Detection of Salmonella sp. in oysters by PCR, *Appl. Environ. Microbiol.*, 60, 368–373 (1994).
- 8 B. A. ABACK, S. J. O'DAY, D. S. B. HOON, Quantification of circulating DNA in the plasma and serum of cancer patients, *Ann. New York Acad. Sci.*, 1022, 17 (2004).
- 9 F. OSHITA, A. SEKIYAMA, R. SUZUKI, M. IKEHARA, K. YAMADA, H. SAITO, K. NODA, Y. MIYAGI, Detection of occult tumor cells in peripheral blood from patients small cell lung cancer by promoter methylation and silencing of retinoic acid receptor-beta, *Oncol. Rep.* 10, 105 (2003).
- 10 S.-J. PARK, T. A. TATON, C. A. MIRKIN, Array-based electrical detection of DNA with nanoparticle probes, *Science*, 295, 1503–1506 (2002).
- 11 J. FRITZ, M. K. BALLER, H. P. LANG, H. ROTHUIZEN, P. VETTIGER, E. MEYER, H.-J. GUNTHERODT, Ch. GERBER, J. K. GIMZEWSKI, Translating biomolecular

- recognition into nanomechanics, *Science*, 288, 316–318 (2000).
- 12 A. SCHEMMELE, H. E. GAUB, Single molecule force spectrometer with magnetic force control and inductive detection, *Rev. Sci. Instrum.* 70(2), 1313–1317 (1999).
  - 13 D. R. BASELT, G. U. LEE, R. J. COLTON, Biosensor based on force microscope technology, *J. Vac. Sci. Technol.* B14(2), 798–793 (1996).
  - 14 G. U. LEE, D. A. KIDWELL, R. J. COLTON, *U. S. Pat. Appl.* 38 (1996). NTIS Order No. PAT-APPL-8-505 547.
  - 15 W. HAN, S. M. LINDSAY, T. JING, A magnetically driven oscillating probe microscope for operation in liquids, *Appl. Phys. Lett.* 69(26), 4111–4113 (1996).
  - 16 T. THUNDAT, E. A. WACHTER, S. L. SHARP, R. J. WARMACK, Detection of mercury vapor using resonating microcantilevers, *Appl. Phys. Lett.*, 66, 1695 (1995).
  - 17 B. ILIC, D. CZAPLEWSKI, H. G. CRAIGHEAD, P. NEUZIL, C. CAMPAGNOLO, C. BATT, Mechanical resonant immunospecific biological detector, *Appl. Phys. Lett.*, 77, 450 (2000).
  - 18 P. I. ODEN, G. Y. CHEN, R. A. STEELE, R. J. WARMACK, T. THUNDAT, Viscous drag measurements utilizing microfabricated cantilevers, *Appl. Phys. Lett.*, 68, 3814 (1996).
  - 19 Z. LIN, C. M. YIP, I. S. JOSHEPH, M. D. WARD, Operation of an ultrasensitive 30-MHz quartz crystal microbalance in liquids, *Anal. Chem.*, 65, 1546–1551 (1993).
  - 20 M. BASU, S. SEGGERSON, J. HENSHAW, J. JIANG, R. DEL A CORDONAL, C. LEFAVE, P. J. BOYLE, A. MILLER, M. PUGIA, S. BASU, Nano-biosensor development for bacterial detection during human kidney infection: Use of glycoconjugate-specific antibody-bound gold nanowire arrays (GNWA), *J. Glycoconj.*, 21, 487–496 (2004).
  - 21 B. ILIC, Y. YANG, K. AUBIN, R. REICHENBACH, S. KRYLOV, H. G. CRAIGHEAD, Enumeration of DNA molecules bound to a nanomechanical oscillator, *Nano Lett.*, 5(5), 925 (2005).
  - 22 W. Y. SHIH, W.-H. SHIH, Z. SHEN, Piezoelectric cantilever sensor, US Patent Application No. PCT/US2004/036705, filed October 27, 2004.
  - 23 C. A. ROWE, L. M. TENDER, M. J. FELDSTEIN, J. P. GOLDEN, S. B. SCRUGGS, B. D. MACCRAITH, J. J. CRAS, F. S. LIGLER, Array biosensor for simultaneous identification of bacterial, viral, and protein analytes, *Anal. Chem.* 71, 3846–3852 (1999).
  - 24 S. P. SAKTI, S. RÖSLER, R. LUCKIUM, P. HAUPTMANN, F. BÜHLING, S. ANSORGE, Thick polystyrene-coated quartz crystal microbalance as a basis of a cost effective immunosensor, *Sens. Actuators A*, 76, 98 (1999).
  - 25 M. D. WARD, D. A. BUTTRY, In situ interfacial mass detection with piezoelectric transducers, *Science*, 249, 1000–1007 (1990).
  - 26 T. G. THUNDAT, J. ADAMS, The 2004 Scientific American 50 Award: Research Leaders, *Sci. Am.*, 291(6), 47 (2004).
  - 27 J. W. YI, W. Y. SHIH, W.-H. SHIH, Effect of length, width, and mode on the mass detection sensitivity of piezoelectric unimorph cantilevers, *J. Appl. Phys.*, 91(3), 1680 (2002).
  - 28 W. Y. SHIH, X. LI, H. GU, W.-H. SHIH, I. A. AKSAY, Simultaneous liquid viscosity and density determination with piezoelectric unimorph cantilevers, *J. Appl. Phys.*, 89(2), 1497 (2001).
  - 29 W. Y. SHIH, X. LI, J. VARTULI, D. L. MILIUS, R. PRUD'HOMME, I. A. AKSAY, W.-H. SHIH, Detection of water-ice transition using a lead zirconate titanate brass transducer, *J. Appl. Phys.* 92(1), 106 (2002).
  - 30 J. MERHAUT, *Theory of Electroacoustics*, McGraw-Hill, New York, 1981.
  - 31 C. DE SILVA, *Vibration, Fundamentals and Practice*, CRC Press, New York, 2000, p. 302.
  - 32 J. W. YI, WAN Y. SHIH, R. MUTHARASAN, WEI-HENG SHIH, In situ cell detection using piezoelectric PZT-stainless steel cantilevers, *J. Appl. Phys.*, 93, 619 (2003).
  - 33 R. G. NUZZO, F. A. FUSCO, D. L. ALLARA, *J. Am. Chem. Soc.*, 109, 2358 (1987).

- 34 R. G. NUZZO, F. A. FUSCO, D. L. ALLARA, *J. Am. Chem. Soc.*, **109**, 733 (1987).
- 35 C. STEINEM, A. JANSHOFF, H.-J. GALLA, M. SIEBER, *Bioelectrochem. Bioenerg.* **42**, 213 (1997).
- 36 D. CLERC, W. LUKOSZ, Real-time analysis of avidin adsorption with an integrated-optical grating coupler: Adsorption kinetics and optical anisotropy of adsorbed monomolecular layers, *Biosensors Bioelectron.*, **12**(3), 185–194 (1997).
- 37 B. L. FREY, C. E. GORDAN, S. JORNGUTH, R. M. CORN, Control of the specific adsorption of proteins onto gold surfaces, *Anal. Chem.*, **67**(24), 4452–4457 (1995).
- 38 Centers for Disease Control and Prevention, Division of Bacterial and Mycotic Diseases, Disease Information. [http://www.cdc.gov/ncidod/dbmd/diseaseinfo/salmonellosis\\_t.htm](http://www.cdc.gov/ncidod/dbmd/diseaseinfo/salmonellosis_t.htm). Accessed, 6 December 2004.
- 39 P. J. MEEHAN, N. E. ROSENSTEIN, M. LILLEN, R. F. MEYER, M. J. KIEFER, S. DEITCHMAN, R. E. BESSER, R. L. EHRENBURG, K. M. EDWARDS, K. F. MARTINEZ, Responding to detection of aerosolized *Bacillus anthracis* by autonomous detection systems in the workplace, *Morbidity Mortality Weekly Rep.*, **2004**, 30 Apr (53, early release), 1–11.
- 40 B. D. RATNER, A. S. HOFFMAN, F. J. SCHOEN, J. E. LEMONS, *Biomaterials Science: An Introduction to Materials in Medicine*, Academic Press, San Diego, **1996**, p. 263.
- 41 V. FAUST, Biofunctionalized biocompatible titania coatings for implants, *Euro. Ceramics, Key. Eng. Mat.*, **VII**, part 1–3, 206-2, 1547–1550 (2002).
- 42 B. ARKLES, Tailoring surfaces with silanes, *Chemtech*, **7**, 766–778 (1997).
- 43 J. YAKOVLEVA, R. DAVIDSSON, A. LOBANOVA, M. BENGTSSON, S. EREMIN, T. LAURELL, J. EMNEUS, Microfluidic enzyme immunoassay using silicon microchip with immobilized antibodies and chemiluminescence detection, *Anal. Chem.*, **74**(13), 2994–3004 (2002).
- 44 J. PIEHLER, A. BRECHT, R. VALIOKAS, B. LIEBERG, G. GAUGLITZ, A high-density poly(ethylene glycol) polymer brush for immobilization on glass-type surfaces, *Biosens. Bioelectron.*, **15**(9–10), 473–481 (2000).

## 12 Toxicology of Nanoparticles in Environmental Air Pollution

*Ken Donaldson, Nicholas Mills, David E. Newby, William MacNee,  
and Vicki Stone*

### 12.1 Introduction

The toxicology of engineered nanoparticles is a topic of increasing interest. However the existing toxicology database on nanoparticles rests almost entirely on combustion-derived nanoparticle in environmental air. This research reached a peak in the mid to late 1990s, focused around the ‘ultrafine hypothesis’<sup>1,2</sup>. This suggested that the combustion-derived nanoparticle component of PM was a key component of PM in causing adverse health effects, by virtue of its ability to cause oxidative stress and inflammation and translocate from the site of deposition<sup>3</sup>. This review puts forward the evidence that nanoparticles do play a role on the adverse health effects of environmental particles and what the mechanism may be, in the belief that this may illuminate the toxicology of engineered nanoparticles.

### 12.2 History of Air Pollution

The adverse health effects of air pollution have been recognized for centuries. In the UK, the burning of fossil fuels in towns and cities combined with periods of cold weather, where there is little mixing of air, have been associated with the generation of smogs. Due to the sulfurous nature of the coal, these smogs consisted mainly of sulfur dioxide and particles, the latter measured historically as “black smoke” (Table 12.1). The famous smog that occurred in London in December 1952 saw midday London appear more like midnight, with theatres closed due to the inability of the audience to see the stage! Interestingly, for the underlying theme of this article, analysis of the particles in the lungs of people dying during such episodes showed there to be a large proportion of carbon-centered combustion-derived nanoparticles [1], presumably from domestic coal combustion. The 1952 London smog episode, which was associated with thousands of deaths, had particle levels estimated at up to 4000  $\mu\text{g m}^{-3}$  as compared to average current



**Tab. 12.1.** Size fractions and description of the main size fractions of PM that are usually measured.

Size fraction	Unit	Description
Total suspended particulate (TSP)	$\mu\text{g m}^{-3}$	A TSP monitor measures by mass the atmospheric particulate smaller than about $40\ \mu\text{m}$ in diameter
Black smoke	$\mu\text{g m}^{-3}$	This system was used in the UK and in other countries until the end of the 1980s. Air was drawn through a size-selective filter onto a white paper and the blackness of the “smudge” was measured; this method obviously is biased towards black, i.e., carbon-based, particles; there is a variable relationship between particles as measured by black smoke and $\text{PM}_{10}$
$\text{PM}_{10}$	$\mu\text{g m}^{-3}$	This size-selective sampling convention measures the mass per unit volume air of particles of aerodynamic diameter $10\ \mu\text{m}$ with 50% efficiency; it roughly corresponds to the thoracic fraction of particles as defined by the International Standards Association (ISO) [3]
$\text{PM}_{2.5}$	$\mu\text{g m}^{-3}$	A size-selective sampling convention that measures the mass per unit volume air of particles of aerodynamic diameter $2.5\ \mu\text{m}$ with 50% efficiency; it roughly corresponds to the respirable fraction of particles as defined by ISO [3]
$\text{PM}_{0.1}$ /nanoparticles	$\mu\text{g m}^{-3}$	Also called ultrafine particles, these particles correspond to $\text{PM}_{0.1}$ and have a diameter of $<0.1\ \mu\text{m}$ (i.e., $<100\ \text{nm}$ ).

London pollution levels of about  $40\ \mu\text{g m}^{-3}$ . As a result of such smogs, succeeding Governments introduced the Clean Air Acts that resulted in a steady decline in air pollution, leading to the present relatively clean air in UK cities.

However, in UK cities today there remains an air pollution problem, if lesser in magnitude than was seen in the past. The modern UK pollution environment is dominated by effluent from transport sources due to the increased number of cars on our roads and increased numbers of car journeys. In some cities, such as Los Angeles and Athens, air pollution is much worse than in the UK because of higher traffic density and the action of sunlight combining to produce “photo-

chemical smog”, which is qualitatively different, with ozone and particles as the dominant pollutants.

### 12.3

#### Introduction to Air Pollution Particles

Particles or particulate matter (PM) represent a part of the air pollution cocktail present in ambient air, which also consists of gases such as ozone, nitrogen dioxide etc. Particles have a special problem of nomenclature because they are measured by sampling conventions that collect only some fraction of the particulate material suspended in the air. These size fractions, including nanoparticles, are described in Table 12.1. Particles have received special attention because they are the most potent component of the air pollution mix in causing ill-health in the great majority of epidemiological studies. The adverse health effects of PM are seen at the levels that pertain in UK and other cities today and there is often no threshold. In other words, there is a background of ill-health caused by PM that increases when the ambient particle cloud increases in concentration and goes down when the amount of particles in the air decreases [2].

### 12.4

#### Adverse Effects of PM in Epidemiological Studies

The adverse effects of air pollution have been measured in thousands of studies. The levels of PM in any city vary both temporally – as a fluctuating hourly/daily level – and spatially, dependent on levels or traffic in an area or local industrial sources. The temporal and spatial variations in air pollution underlie the two main approaches to detecting and quantifying the adverse effects of PM (and indeed any air pollutant) in human populations. Time series studies utilize the temporal dimension and seek to relate the moving average of PM level to the moving average of a defined end-point, e.g., mortality [4]. Various lag-times are used to detect the relation between level of PM and the endpoint, e.g., 1 day. Environmental epidemiological studies seek to compare an endpoint such as the death rate in cities or suburbs characterized by high air pollution with the death rate in a city or suburb with lower air pollution [5]. Panel studies form a third category where small, well-characterized populations are followed for a defined endpoint that can be related to PM levels measured by personal or fixed point samplers [6].

When these different approaches are taken together and examined over hundreds of such studies there is good coherence between the acute effects, seen in time series and panel studies, and the chronic effects seen in environmental studies. More importantly, many of these studies show no evidence of a threshold, i.e., these adverse effects are occurring at the levels of PM that pertain in our cities today. Table 12.2 summarizes these adverse effects; the quantitative extent of mortality effects of PM in European studies is shown in Fig. 12.1.

**Tab. 12.2.** Adverse health effects due to PM.

---

Mortality from cardiovascular and respiratory causes  
 Admission to hospital for cardiovascular causes

Exacerbations of asthma in pre-existing asthmatics  
 Symptoms and use of asthma medication in asthmatics

Exacerbations of Chronic Obstructive Pulmonary Disease  
 Lung function decrease

Lung cancer

---

Within a short-lag time of one or two days following an increase in PM there are increases in the following (summarized in Ref. [8]) – (1) all-cause mortality; (2) attacks of asthma and increased usage of asthma medication; (3) deaths in COPD patients; (4) exacerbations of COPD; (5) deaths and hospitalizations for cardiovascular disease. The adverse cardiovascular effects associated with increases in PM are well-documented. Panel studies have documented associations between elevated levels of particles and

1. onset of myocardial infarction [6];
2. increased heart rate [9];
3. decreased heart rate variability [10].

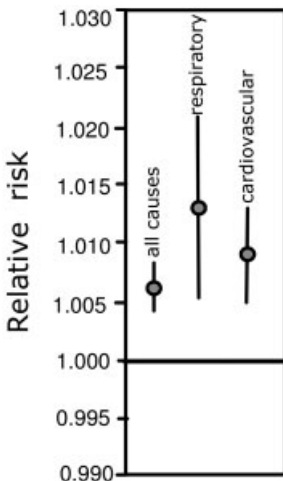


**Fig. 12.1.** Relative risk for mortality endpoints related to a 10  $\mu\text{g m}^{-3}$  increase in  $\text{PM}_{10}$ , summarized from European studies [7].

Chamber studies with concentrated airborne particles (CAPs) have also shown increased lung inflammation [11] and altered brachial artery diameter in relation to increased exposure [12]. A recent epidemiological study of carotid intima-media thickness (CIMT), a measure of atherosclerosis, demonstrated evidence of an association between atherosclerosis and ambient air pollution level. Living in an area with a  $10 \mu\text{g m}^{-3}$  higher level of  $\text{PM}_{2.5}$  was associated with a CIMT increase of 5.9% (95% confidence interval, 1–11%); an even larger effect, 15.7%, was seen in older women.

## 12.5

### Nanoparticles are an Important Component of PM

Urban PM is a complex mixture of particle types that depend on season, time of day, siting of sampler etc. Clearly, however, combustion-derived nanoparticles represent a major toxicologically important component (see below). Table 12.3 shows the common components of PM.

Whilst levels of PM, along with other pollutants, have gone down markedly over the last 35 years, the traffic-derived portion has gone up as the numbers of vehicles on the road has increased [13]. Release of nanoparticles from vehicle tailpipes during diesel and petrol combustion is the predominant source of nanoparticles (Fig. 12.2) although there are other sources, such as energy production (power stations) and industry [14]. The medians of ultrafine (NP) particle number concentrations across three European cities were recently (2005) found to range from 15 000 to 18 000 particles per  $\text{cm}^3$  [15]. However, locally much higher exposures can be experienced. Using a nanoScanning Mobility Particle Sizer, multiple samples were

**Tab. 12.3.** Common components of PM and comments on their origin, nature and likely toxic potency.

<b>PM<sub>10</sub> component</b>	<b>Comment</b>	<b>Toxic potency</b>
Combustion-derived nanoparticles	Nanoparticles containing metals and organic volatiles; derived from combustion, e.g., vehicle exhaust particles	High
Sodium/magnesium compounds	Derived from sea spray	Low
Sulfate	Predominantly ammonium sulfate	Low
Nitrate	Predominantly ammonium nitrate	Low
Calcium/potassium compounds and insoluble minerals	Derived from the Earth's crust, e.g., clay	Low
Biologically-derived materials	For example, endotoxin	High

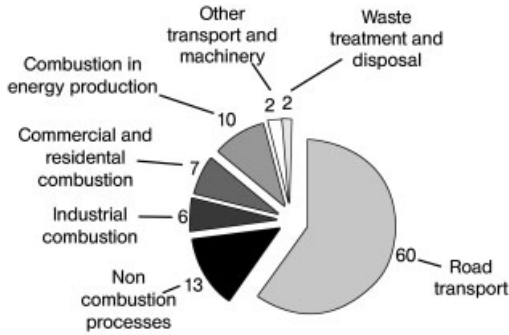


Fig. 12.2. Pie chart illustrating the source of PM<sub>0.1</sub> emissions in the UK in 1996 [21].

taken in Marylebone Road, a busy London street [16]. These showed that approximately 10 000 to 50 000 particles per cm<sup>3</sup> in the size range 30–100 nm were present. The daily pattern showed a typical one for traffic-derived nanoparticles [16]. A study on US highways suggested that the likely exposure in a vehicle traveling in busy traffic could be 200 to 560 × 10<sup>3</sup> particles (predominantly nanoparticles) per cm<sup>3</sup> [17, 18]. Indoors, there are also sources of nanoparticles such as cooking, vacuuming and burning wax candles [19]. Nanoparticles arise from combustion of domestic gas and in one study three gas rings produced a peak approaching 50 000 particles per cm<sup>3</sup> that underwent rapid aggregation, with increases in particle size and decrease in apparent number within a few minutes [20] (Fig. 12.3). Other sources of combustion, primarily industry, make a contribution to the nanoparticle cloud (Fig. 12.2). Secondary nanoparticles may also arise from environmental

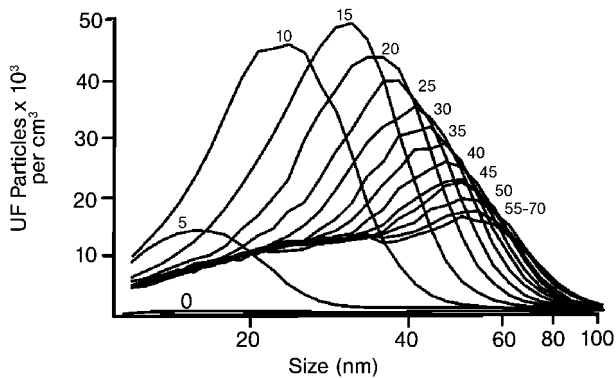


Fig. 12.3. Nanoparticle size distribution arising from burning of domestic gas in cooker rings. The family of curves shows the particle size distribution 5, 10, 15, 20 min etc. after lighting the rings. Note the decrease in number and increase in size with time, indicative of particle aggregation [20].

chemistry, e.g., nitrates, but these are unlikely to be as toxicologically potent as combustion-derived nanoparticles (see below).

## 12.6

### Role of Nanoparticles in Mediating the Adverse Pulmonary Effects of PM

Epidemiological studies do not readily allow associations of adverse effects with sub-components of PM such as the nanoparticles, dependent as they usually are on a simple mass measure such as PM<sub>10</sub> or PM<sub>2.5</sub>. However, a few epidemiological studies have been able to identify combustion-derived particles as an important component in driving adverse effects of PM [22–24].

Toxicology can more readily address the relative toxic potency of the components of PM. Examining the components of PM toxicologically allows them to be divided into those with a high toxic potency and those with low toxic potency (Table 12.3). Combustion-derived nanoparticles (CDNP) stand out as common components of PM with high potency and several such nanoparticles have been utilized in toxicological studies, including carbon black and welding fume. As the predominant CDNP in PM, diesel soot has been specially studied.

Diesel fuel is a distillate of petroleum that contains paraffins, alkenes and aromatics [25]. On combustion in automobile engines it is transformed into low solubility carbon-centered nanoparticles of complex chemical and physical structure. Sulfates and organics, consisting of unburnt fuel, lube oil and polycyclic aromatic hydrocarbons (PAHs), also condense on the particles [25, 26]. Single diesel nanoparticles are 60 to 100 nm but these readily form complex chains and aggregates [27]. Diesel exhaust particles (DEP) are usually the most common CDNP in urban environmental air and in environmental particulate air pollution (PM<sub>10</sub>) in conurbations generally. In the general environment the concentration of DEP in PM<sub>10</sub> is likely to range from 5 to 30  $\mu\text{g m}^{-3}$ .

Exposure to DEP is also highly inflammatory in rats and mice in non-overload conditions [28–30] and induces pro-inflammatory effects on cells *in vitro* [31–33]. The well-documented link between inflammation and lung cancer [34–36] supports the idea that diesel exhaust may indeed be carcinogenic via an inflammatory pathway. The inflammatory effects of DEP appear to be driven by the particulate component, i.e., the surface area effect [37]. However, the organic [38] and metal components [39] also appear to play a role in pro-inflammatory effects and thereby affect pathogenicity.

CDNP, such as carbon black and diesel soot, show several pro-inflammatory effects that are relevant to pulmonary inflammation (summarized in Table 12.4). Inflammation caused by CDNP in PM could be important in mediating the observed adverse effects (Fig. 12.4).

Studies with several CDNP suggest that various different ones are a hazard to the lungs through the pathways of oxidative stress and inflammation [45] (Fig. 12.5). Heterogeneity in composition and solubility means that the key initiating

Tab. 12.4. Some pro-inflammatory effects of combustion-derived nanoparticles.

Pulmonary-related effects of combustion-derived nanoparticles	Ref.
Generate oxidative stress in cell-free systems	40
Cause oxidative stress and activation of oxidative stress-responsive signaling pathways in epithelial cells	41, 42
Cause synthesis and release of pro-inflammatory cytokines	43
Causes pulmonary inflammation in laboratory animals	44

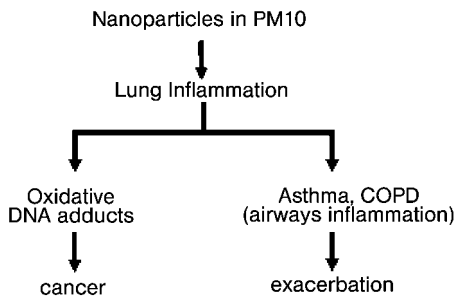


Fig. 12.4. Role of inflammation in the pulmonary effects of combustion-derived nanoparticles (CDNP).

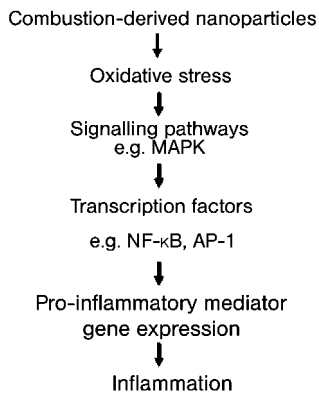


Fig. 12.5. Mechanism of the pro-inflammatory effects of combustion-derived nanoparticles (CDNP).

event of oxidative stress may originate from different components such as surfaces, metals or organics. These may even interact to produce oxidative stress as in the case of metals and organics interacting in the redox-cycling of quinoids [46] or nanoparticle surfaces and transition metals interacting additively in their ability to cause inflammation [47]. Inside the lung cells, oxidative stress can trigger inflammation through well-documented oxidative stress–response signaling pathways, including the MAPK and NF- $\kappa$ B. This culminates in the expression of genes that are involved in the recruitment and activation of leukocytes that are characteristic of inflammation. In addition, CDNP may exert genotoxic effects via well-documented pathways, including both oxidative stress adducts, such as 8-hydroxydeoxyguanosine, and bulky PAH-type adducts.

Lifetime animal exposure studies generally demonstrate that exposures to DEP and other nanoparticulate forms of carbon are carcinogenic [37] but these findings are complicated by the issue of rat lung overload [48]. Rat lung overload is a condition when very high lung surface area burden [49] of low toxicity, low soluble particles leads to failure of clearance. This leads to rapid accumulation of dose with concomitant inflammation and proliferation, which culminates in fibrosis and cancer [50]. Humans are unlikely to experience overload levels of diesel soot, even in occupational settings, and there is a question over whether overload can occur at all in humans. It is, therefore, unlikely that cancer associated with DEP exposure in humans results from a mechanism similar to rat lung overload.

## 12.7

### Effects of Nanoparticles on the Cardiovascular System

Adverse cardiovascular effects associated with increases in PM are well-documented and have been reviewed extensively [51]. Exposure to particulate matter is associated with increases in mortality from ischemic heart disease and hospital admissions with acute myocardial infarction, heart failure and arrhythmia in time-series studies and population studies. Cohort studies have provided insight into the likely mechanisms responsible for these clinical events, and have documented associations between elevated levels of particles and heart rate, heart rate variability, blood pressure, myocardial ischemia and sub-clinical atherosclerosis.

Epidemiological studies cannot prove a causative biological effect of particulate exposure. Systems designed to deliver controlled amounts of ambient and combustion derived particulate now exist to allow a mechanistic approach to determining the effect of inhaled PM. Several plausible interlinking mechanisms have been proposed to explain these observations, and multiple pathways are likely to be involved (Fig. 12.6). These putative biological mechanisms involve direct effects of particles on the cardiovascular system following translocation across the alveolar-epithelial barrier, and indirect effects mediated by pulmonary oxidative stress and inflammation.



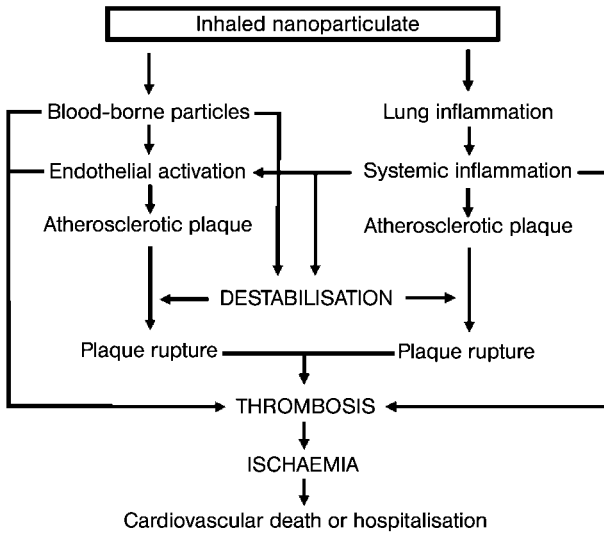


**Fig. 12.6.** Hypothetical pathways for the impact of inhaled nanoparticles on cardiovascular endpoints.

## 12.8 Inflammation, Atherosclerosis and Plaque Rupture

Markers of systemic inflammation are elevated in patients with cardiovascular disease [52]. In previously healthy individuals, elevated plasma concentrations of the acute phase reactant C-reactive protein have been shown to predict the development of ischemic heart disease [53], and in particular the risk of a first myocardial or cerebral infarction, independent of other risk factors [54].

Atherosclerosis is widely recognized to be an inflammatory process that is initiated through an injury to the vascular endothelium [55]. The resulting endothelial dysfunction leads to increased expression of leukocyte adhesion proteins, reduced anticoagulant activity and the release of growth factors, inflammatory mediators and cytokines. Continued inflammation results in leukocyte and monocyte recruitment, induction of atheroma formation and further arterial damage. Cycles of further damage cause plaque expansion and disruption that can lead to angina, crescendo angina and acute coronary syndromes, including myocardial infarction.

Inhalation of PM induces changes that are indicative of systemic inflammation such as increases in white blood cells and platelets [56], rises in C-reactive protein [57] and fibrinogen [58]. Experimental exposures mirror these clinical findings [59] and demonstrate evidence of combined systemic inflammation and endothelial dysfunction [60]. Repeated exposure to PM<sub>10</sub> may, therefore, induce or exacerbate the vascular inflammation of atherosclerosis and promote plaque expansion or

rupture. Indeed, using a Watanabe hereditary hyper-lipidemic rabbit model, Suwa and coworkers [61] have described plaque progression and destabilization following instillation of high doses of PM<sub>10</sub>.

## 12.9

### Nanoparticle Translocation and Direct Vascular Effects

It has been proposed that environmental nanoparticulate may translocate from the lung into the circulation and exert a direct effect on the vasculature. Once circulating, particles could interact with the vascular endothelium, or have direct effects on atherosclerotic plaque. Local inflammation could destabilize a coronary plaque, resulting in rupture, thrombosis, and an acute coronary syndrome.

Several factors influence the likelihood of particle translocation, including the properties of the particles themselves, size, affinity for water, rate of aggregation, surface charge, and the integrity or permeability of the alveolar-blood barrier. Inhaled nanoparticles deposit in the nasopharyngeal, tracheobronchial or alveolar regions by diffusion as discussed previously. Particles can evade phagocytosis by the alveolar macrophage and gain access to the interstitium whereupon they may be cleared directly into the circulation or by the lymphatic system. Environmental nanoparticulate may, possibly, gain access to the interstitium through pores in the blood-alveolar barrier. A three-pore model has been proposed to explain the ability of macromolecules to cross the alveolar-airway barrier, where the alveolar epithelial barrier contains many pores of 1 nm (68%) and 40 nm (30%) diameter and a few larger, 400 nm (2%), ones [62]. Alternatively, the mechanism may be analogous to the receptor-mediated transcytosis used by virus particles to enter and transfer between epithelial cells.

The first description of nanoparticulate translocation across the alveolar epithelium identified 30 nm gold particles in pulmonary capillary platelets following intra-tracheal instillation [63]. As well as identifying a novel pathway for the clearance of inhaled particulate, platelet uptake of particulate could result in aggregation and predispose to thrombus formation and atherothrombosis. Since then several studies have used radiolabeling to track the distribution of inhaled particles. Following intra-tracheal instillation of <sup>99m</sup>-technetium-labeled albumin nanocolloid (particles < 80 nm diameter) radioactivity was detected in the blood stream within 5 min, suggesting that particles underwent rapid translocation rather than being phagocytosed [64]. The mass of activity instilled did not alter the proportion of blood-borne radioactivity, suggesting the translocation is passive. Quantification of this process is hampered by methodological difficulties such as leaching of radiolabel and partial solubility of some particles. However, rats inhaling elemental carbon (<sup>13</sup>C; particles 20–29 nm diameter) showed a substantial accumulation of <sup>13</sup>C in the liver 24 h after exposure [65]. The lung is not the only portal where airborne nanoparticles may enter the body and low levels of pulmonary deposition of <sup>13</sup>C suggested that ingestion or up-take through the skin could also be important.

Evidence that inhaled nanoparticulate can translocate in humans is less well es-

established and the only two published studies to date are contradictory. In Nemmar et al. inhaled  $^{99\text{m}}\text{Tc}$ -labeled ultrafine carbon particles (5 nm diameter) were detected almost immediately in whole blood by thin-layer chromatography and accumulated in the liver and other extra-pulmonary organs [66]. In the study by Brown et al. using the same radiolabeled particles no such accumulation of activity out-with the lungs was reported [67]. Leaching of soluble radiolabel from the particles prevents any form of quantification of the extent of particle translocation using these methods. Further studies are required to determine whether alveolar translocation of nanoparticulate is an important pathway for the clearance of inhaled nanoparticles in man, and whether it can potentially explain the extra-pulmonary effects of particulate air pollution.

Oxidative stress increases the permeability of lung epithelium [68], potentially allowing particles, and macrophage laden with particles, to pass into the pulmonary interstitium and enter the circulation. Transfer of particles into the blood stream may be a more important pathway in patients with reduced antioxidant defenses, such as cigarette smokers or patients with underlying lung disease. In support of this, in an *ex vivo* lung perfusion model histamine and hydrogen peroxide perfusion increased alveolar permeability and the proportion of instilled iridium particles detected in the pulmonary venous effluent [69]. Likewise, increased epithelial permeability may encourage molecules produced in the lungs response to particles, e.g., IL-6 or oxidized LDL, to enter the interstitium and diffuse into the circulation.

Once circulating, nanoparticles could incorporate into sites of arterial injury and contribute to the development and progression of arterial atherosclerotic plaque formation. Oxidized LDL particles are typically around 200 nm in diameter and incorporation of these particles into the arterial wall is the central pathological process in the formation of atheroma. There is evidence that non-biological nanoparticles can be incorporated into the arterial wall. Following the infusion of ultrasmall paramagnetic iron oxide particles (USPIOs, 18 nm mean diameter) into hyperlipidaemic rabbits, the particles are phagocytosed by macrophages in atherosclerotic plaques of the aortic wall in quantities sufficient to be detectable by MRI [70]. Fluorescent-labeled nanoparticles, infused intra-luminally after balloon injury to the carotid artery in an animal model, successfully penetrated into the vessel wall and persisted for up to 14 days [71]. In humans, infusion of USPIOs before elective carotid endarterectomy revealed uptake of particles in 75% of ruptured, 54% of rupture-prone and only 7% of stable atheromatous plaques, suggesting that nanoparticles may incorporate into unstable plaques preferentially and potentially precipitate clinical events [72].

## 12.10

### Endothelial Dysfunction and Endogenous Fibrinolysis

The endothelium plays a vital role in the control of blood flow, coagulation, fibrinolysis and inflammation. Following the seminal work of Furchgott and Zawadzki

[73], it is widely recognized that an array of mediators, including cigarette smoking, can influence vascular tone through endothelium-dependent actions, and there is now extensive evidence of abnormal endothelium-dependent vasomotion in patients with atherosclerosis [74–76]. Endothelial dysfunction is one of the earliest pathological processes in atherosclerosis and can predict the likelihood of future cardiovascular events and death in both healthy individuals [77] and those with coronary artery disease [78].

Endothelial dysfunction has been described in both the peripheral and coronary circulation of cigarette smokers [76, 79]. As combustion products and particulate matter are common to both air pollution and cigarette smoke, it is likely that air pollution is likely to have similar detrimental vascular effects. The tar phase of cigarette smoke and combustion-derived particulate may contribute to the oxidative burden and generate equivalent numbers of oxidative radicals. *In vitro* studies provide support for a mechanism of oxidative stress induced vascular dysfunction, with Ikeda et al. demonstrating that the incubation of aortic ring preparations with diesel exhaust particles results in a dose-dependent inhibition of acetylcholine-mediated relaxation, an effect abolished by co-incubation with superoxide dismutase [80].

Whilst endothelium-dependent vasomotion is important, it may not be representative of other aspects of endothelial function, such as the regulation of fibrinolysis. The fibrinolytic factor tissue plasminogen activator (t-PA) regulates the degradation of intravascular fibrin and is released from the endothelium through the translocation of a dynamic intracellular storage pool. Acute endogenous t-PA release from the endothelium regulates the dissolution of intravascular thrombosis and is a critical determinant of cardiovascular outcome. This is exemplified by the clinical observation that in approximately 30% of patients with acute myocardial infarction, spontaneous reperfusion occurs within 12 h of vessel occlusion. Culture of human umbilical vein endothelial cells with particulate matter for 6 h inhibits both the synthesis and release of t-PA in a dose-dependent manner [81].

Direct adverse effects of particulates on the vascular endothelium are important only if sufficient quantities of inhaled particulate reach the circulation. Alternatively, it is possible that the local pulmonary inflammatory response to particulate is sufficient to release inflammatory cells and cytokines into the circulation and induce a mild systemic inflammation. Healthy adults exposed to dilute diesel exhaust for one hour had a mild systemic inflammatory response with increased blood neutrophil levels [82], and mild systemic inflammation also causes a profound, but temporary, suppression of endothelium-dependent vasodilatation [83].

Our group has recently shown that these pathways are adversely affected *in vivo* following controlled human exposures to dilute diesel exhaust [84]. Exposures to particulate at levels encountered in the urban environment for one hour markedly impaired the regulation of vascular tone and endogenous fibrinolysis. This study confirms *in vitro* findings and provides a plausible mechanism linking air pollution to the pathogenesis of atherothrombosis.

The acute effects of exposure to particulate are consistent with recent epidemiological studies that report a significant increase in risk of acute myocardial infarc-

tion as little as two hours after exposure to road traffic [85] or an increase in  $PM_{2.5}$  [6]. Our studies add to those of Brook et al. who demonstrated a reduction in brachial artery diameter immediately after exposure to a mixture of concentrated ambient particles and ozone [12]. In contrast, they found no effect on endothelium-dependent or -independent vasodilatation using flow-mediated and nitro-glycerine induced dilatation. This may reflect differences in the potency of the pollution models used or the technique used to assess vascular function. Exposures to concentrated ambient particulate are inherently variable in magnitude and composition, whereas in our study each volunteer received a standard exposure to combustion-derived particulate of known toxicity. Alternatively, the vascular effects of particulate matter are, possibly, mediated primarily in the resistance vessels assessed by plethysmography rather than in the conduit arteries assessed by ultrasound of the brachial artery.

## 12.11

### Coagulation and Thrombosis

Atherothrombosis is characterized by disruption of an atherosclerotic plaque with thrombus formation and is the major cause of acute coronary syndromes and cardiovascular death worldwide. To explain the association between environmental air pollution and acute cardiovascular events we proposed a hypothetical mechanism whereby particles reaching the alveolar epithelium could influence blood coagulability, resulting in a prothrombotic state and potentially triggering acute thrombus formation in susceptible individuals [86]. Over the last 10 years, experimental evidence has provided support for this mechanism.

Exposure to particulate matter increases the levels of blood fibrinogen, a key component in coagulation cascade and determinant of blood viscosity [11]. Fibrinogen levels are associated with increased blood thrombogenicity, and can independently predict outcome in patients with existing cardiovascular disease [87]. Blood viscosity also increased in association with levels of ambient particulate during a prolonged air pollution episode [88]. In human challenge studies, exposure to diesel exhaust increases the number of circulating platelets [56], and in animal studies exposure to diesel exhaust and ultrafine particles rapidly activates blood platelets and enhances venous thrombosis in a model of endothelial injury [89, 90]. In a subsequent study, the pro-thrombotic effect of diesel exhaust particles was abrogated by intra-peritoneal dexamethasone, suggesting this effect is mediated by either local or systemic inflammation [91].

PM can induce various prothrombotic effects, including enhanced tissue factor expression on endothelial cells [92]. Tissue factor is the main stimulus for thrombin generation, initiates the extrinsic coagulation pathway, and circulating levels are present in patients with coronary artery disease. In an *in vivo* perfusion study, intra-arterial carbon ultrafine particles enhanced endothelial von-Willebrand factor expression and accumulation of fibrin and platelets on the endothelial surface [93]. In addition to altering the properties of endothelial cells and platelets to promote

thrombus formation, nanoparticles may themselves act as a focus for thrombus formation. Scanning electron micrographic evaluation of thrombus on the surface of explanted temporary vena cava filters revealed the presence of foreign nanoparticles within thrombus [94]. These findings taken together support the notion that particulate matter causes inflammation, endothelial activation and can acutely increase the risk of thrombosis, thus predisposing to acute cardiovascular events.

## 12.12

### Cardiac Autonomic Dysfunction

There is an important relationship between autonomic regulation of the cardiac cycle and cardiovascular mortality [95]. Variation in the interval between consecutive heart beats or heart rate variability (HRV) is controlled by the contrasting effects of the sympathetic and parasympathetic nervous systems. Reduction in HRV reflects either an increase in sympathetic drive or a decrease in vagal parasympathetic tone. Reduced HRV increases the risk of cardiovascular morbidity and mortality in both healthy individuals [96] and patients following myocardial infarction [97].

Several panel studies have reported a consistent association between reduced HRV and high ambient PM [98, 99]. The finding of altered HRV in an elderly cohort exposed to concentrated ambient particles (CAPs) provides direct evidence of the effects of PM on autonomic activity [10]. The importance of this effect in the presence of cardiovascular pathology was demonstrated in a canine model of myocardial infarction, where exposure to residual oil fly ash (ROFA) reduced HRV and increased cardiac arrhythmia following infarction [100]. Furthermore, in patients with implanted cardiac defibrillators there appears to be a relationship between ambient PM and the incidence of ventricular fibrillation [101].

The influence of PM on the autonomic nervous system may result in hospitalization or cardiac death by triggering tachyarrhythmia or altering coronary vascular tone. How inhaled PM interacts with the nervous system is unclear. The effects could be mediated by interstitialized particles directly irritating the nerve endings or through the local release of inflammatory cytokines in response to the particles.

## 12.13

### Effects of Nanoparticles on the Liver and Gastrointestinal Tract

As described previously, particles depositing in the lung may gain access to the blood, allowing them to be transported around the body. For many years it has been recognized that the reticulo-endothelial system, a concentration of phagocytic cells in organs such as the liver and spleen, quickly accumulate particles injected into the blood [102]. For example, in 1970 Stuart reported that colloidal carbon injected into the tail vein accumulates in the liver and spleen [103]. NP designed as drug carriers are also sequestered by these phagocytic cells, with negatively

charged carboxylated polystyrene nanoparticles being taken up into the liver via scavenger receptors [104]. The effects of interaction between such cells and nanoparticles is as yet unclear, but some studies suggest that polystyrene nanoparticles can induce mild oxidative stress in the liver via activation of the macrophage phagocytic burst [105]. *In vitro*, both nanoparticles [106, 107] and PM<sub>10</sub> [108] stimulate calcium signaling via oxidative stress, leading to the production of pro-inflammatory cytokines such as tumor necrosis factor alpha. On the whole this work has been discussed in relation to the effects of PM and NP on the lung, but it is also feasible that NP translocated into the blood could initiate an inflammatory reaction in other organs such as the liver via their effects on macrophages.

There have been very few studies on the potentially adverse effects of NP directly on hepatocytes. Ref. [109] investigated the effects of various nanoparticles, differing in size and chemical composition, on hepatocyte viability as assessed by standard assays, including a measure of mitochondrial function (MTT assay) and enzyme leak through dysfunctional membranes (LDH assay). The silver particles studied (10–50 µg mL<sup>-1</sup>) were found to be highly toxic via oxidative stress (glutathione depletion), whereas molybdenum, aluminum, iron oxide and titanium dioxide only exhibited mild toxicity at doses greater than 100 µg mL<sup>-1</sup>. Further studies are required to establish how nanoparticles interact with liver cells and to elucidate the consequences.

The main route of particle clearance from the lung is via the mucociliary escalator, some of which is cleared via the nose, but most of which is swallowed [110]. This means that a significant proportion of the particle dose enters the gastrointestinal system. In relation to drug delivery, translocation of particulate matter across the gastrointestinal tract is now well documented [111]. There is histological, radiological and chemical evidence that 50–100 nm polystyrene nanoparticles cross the gastrointestinal tract and pass via the mesentery lymph supply and lymph nodes to the liver and spleen [112]. In addition, gastrointestinal uptake of particles of 100 nm diameter is 15–250-fold higher than for larger microparticles [113].

Furthermore, the uptake efficiency of the particles was dependent upon the tissue type, with Peyer's patches exhibiting a 2–200-fold higher uptake than non-patch tissue. The 100 nm particles were diffuse throughout the submucosal layers of the gastrointestinal tract while the larger particles were predominantly localized in the epithelium. In fact, histological studies have revealed a build-up of pigment particles accumulated from the diet in Peyer's patches of humans [114]. The ability of NP to cross the gut wall suggests that they would enter the body by the hepatic portal vein that drains the intestine, delivering blood directly to the liver. Hence, this would suggest that the liver would be exposed to particles translocated into the blood from both the lungs and the gastrointestinal tract.

The impact of nanoparticles on the gastrointestinal tract is relatively unknown. Some studies have suggested that exposure to nano- and microparticles in our diet could be associated with worsening of conditions such as Crohn's disease [115] through their ability to act as adjuvants in antigen-mediated immune responses, in tissues such as the Peyer's patches [116]. More work is required to verify these results and to elucidate the mechanisms involved.

### 12.14

#### Effects of NP on the Nervous System

In the past, in relation to the pulmonary toxicology of inhaled particles, most emphasis has been placed on the particles (<2.5 µm diameter) that gain access to the respiratory regions of the lung. This is because those particles depositing in the upper airways are easily cleared via the mucociliary escalator, whereas those depositing in the deeper lung depend upon the phagocytic activity of macrophages to minimize exposure and hence toxicity. However, more recently, Oberdörster et al. have demonstrated the ability of <sup>13</sup>C nanoparticles depositing on the nasal epithelium to gain access to the brain via the olfactory nerve [117]. They pointed out that neurophysiologists have long recognized that polio virus particles can be transported along nerve axons.

### 12.15

#### Summary

We have reviewed the literature pertaining to the role of nanoparticles in the adverse health effects of air pollution particles. Nanoparticles from combustion processes, predominantly automobile engines, are ubiquitous in ambient air and are strongly suspected of driving inflammatory and oxidative stress responses in the lungs. This is a factor in the exacerbations of airways disease seen in association with increases in PM. In addition to effects in the lungs, marked effects are seen in patients with cardiovascular disease. These may be explained by the ability of nanoparticles to gain access to the blood or indirectly through pro-inflammatory effects in the lungs, causing activation and destabilization of atheromatous plaques and leading to atherothrombosis and its associated morbidity and mortality. Nanoparticles may also gain access to the blood and directly affect the endothelium and the coagulation system. Nanoparticles in blood could affect the liver and potentially cross the brain barrier although nanoparticles could also enter the brain via olfactory neurones after deposition in the nose. Nanoparticles in the air are cleared to the gut via the mucociliary escalator and so their potential effects on the gut were considered. Once combustion-derived nanoparticles are resident in tissue they can deliver oxidative stress and affect inflammatory pathways and have genotoxic effects. Combustion-derived nanoparticles are a main driver of pulmonary and cardiovascular mortality and morbidity and, because of their potential to translocate around the body, have the potential to affect a number of extra-pulmonary target organs and systems.

#### References

- 1 HUNT, A., J. L. ABRAHAM, B. JUDSON, C. L. BERRY. 2003. Toxicologic and epidemiologic clues from the characterization of the 1952 London



- smog fine particulate matter in archival autopsy lung tissues. *Environ. Health Perspect.* 111, 1209–1214.
- 2 BRUNEKREEF, B., S. T. HOLGATE. 2002. Air pollution and health. *Lancet* 360, 1233–1242.
  - 3 International Standards Organisation. 1994. *Air Quality: Particle Size Fraction definitions for Health-related Sampling*. IS 7708, ISO, Geneva.
  - 4 SCHWARTZ, J., D. W. DOCKERY, L. M. NEAS. 1996. Is daily mortality associated specifically with fine particles? *J. Air Waste Manage. Assoc.* 46, 927–939.
  - 5 DOCKERY, D. W., C. A. POPE, X. P. XU, J. D. SPENGLER, J. H. WARE, M. E. FAY, B. G. FERRIS, F. E. SPEIZER. 1993. An association between air-pollution and mortality in 6 United-States cities. *N. Eng. J. Med.* 329, 1753–1759.
  - 6 PETERS, A., D. W. DOCKERY, J. E. MULLER, M. A. MITTLEMAN. 2001. Increased particulate air pollution and the triggering of myocardial infarction. *Circulation* 103, 2810–2815.
  - 7 World Health Organization Europe. 2004. *Health Aspects of Air Pollution*. World Health Organization Copenhagen, Denmark.
  - 8 POPE, C. A., D. W. DOCKERY. 1999. Epidemiology of particle effects, in *Air Pollution and Health*. ed. HOLGATE S. T., SAMET J. M., KOREN H. S., MAYNARD R. L., Academic Press, San Diego, pp. 673–705.
  - 9 GONG, H., JR., W. S. LINN, S. L. TERRELL, K. W. CLARK, M. D. GELLER, K. R. ANDERSON, W. E. CASCIO, C. SIOUTAS. 2004. Altered heart-rate variability in asthmatic and healthy volunteers exposed to concentrated ambient coarse particles. *Inhal. Toxicol.* 16, 335–343.
  - 10 DEVLIN, R. B., A. J. GHIO, H. KEHRL, G. SANDERS, W. CASCIO. 2003. Elderly humans exposed to concentrated air pollution particles have decreased heart rate variability. *Eur. Respir. J. Suppl.* 40, 76s–80s.
  - 11 GHIO, A. J., C. KIM, R. B. DEVLIN. 2000. Concentrated ambient air particles induce mild pulmonary inflammation in healthy human volunteers. *Am. J. Respir. Crit Care Med.* 162, 981–988.
  - 12 BROOK, R. D., J. R. BROOK, B. URCH, R. VINCENT, S. RAJAGOPALAN, F. SILVERMAN. 2002. Inhalation of fine particulate air pollution and ozone causes acute arterial vasoconstriction in healthy adults. *Circulation* 105, 1534–1536.
  - 13 Airborne Particles Expert Group. 1999. *Source Apportionment of Airborne Particulate Matter in the United Kingdom*. Prepared on behalf of the Department of Environment, Transport and the Regions, the Welsh Office, the Scottish Office and the Department of the Environment (Northern Ireland), Crown copyright 158 pp.
  - 14 WICHMANN, H. E. 2004. 20 years after the winter smog episode 1985 – the particle problem then and today. *Int. J. Hyg. Environ. Health* 207, 489–491.
  - 15 DE HARTOG, J. J., G. HOEK, A. MIRME, T. TUCH, G. P. KOS, H. M. TEN BRINK, B. BRUNEKREEF, J. CYRYS, J. HEINRICH, M. PITZ, T. LANKI, M. VALLIUS, J. PEKKANEN, W. G. KREYLING. 2005. Relationship between different size classes of particulate matter and meteorology in three European cities. *J. Environ. Monit.* 7, 302–310.
  - 16 Air Quality Expert Group. 2005. *Particulate Matter in the United Kingdom*. Department of Environment, Food and Rural Affairs, London.
  - 17 ELDER, A., R. GELEIN, J. FINKELSTEIN, R. PHIPPS, M. FRAMPTON, M. UTELL, D. B. KITTELSON, W. F. WATTS, P. HOPKE, C. H. JEONG, E. KIM, W. LIU, W. ZHAO, L. ZHUO, R. VINCENT, P. KUMARATHASAN, G. OBERDÖRSTER. 2004. On-road exposure to highway aerosols. 2. Exposures of aged, compromised rats. *Inhal. Toxicol.* 16(Suppl. 1), 41–53.
  - 18 KITTELSON, D. B., W. F. WATTS, J. P. JOHNSON, M. L. REMEROWKI, E. E. ISCHE, G. OBERDÖRSTER, R. M. GELEIN, A. ELDER, P. K. HOPKE, E. KIM, W. ZHAO, L. ZHOU, C. H. JEONG. 2004. On-road exposure to highway aerosols. 1. Aerosol and gas

- measurements. *Inhal. Toxicol.* 16(Suppl. 1), 31–39.
- 19 AFSHARI, A., U. MATSON, L. E. EKBERG. 2005. Characterization of indoor sources of fine and ultrafine particles: A study conducted in a full-scale chamber. *Indoor Air* 15, 141–150.
- 20 DENNEKAMP, M., S. HOWARTH, C. A. DICK, J. W. CHERRIE, K. DONALDSON, A. SEATON. 2001. Ultrafine particles and nitrogen oxides generated by gas and electric cooking. *Occup. Environ. Med.* 58, 511–516.
- 21 HARRISON, R. M., J. P. SHI, S. XI, A. KHAN, D. MARK, R. KINNERSLEY, J. YIN. 2000. Measurement of number, mass and size distribution of particles in the atmosphere. *Phil. Trans. R. Soc. London A* 358, 2567–2580.
- 22 POPE, C. A., III, R. W. HILL, G. M. VILLEGAS. 1999. Particulate air pollution and daily mortality on Utah's wasatch front. *Environ. Health Perspect.* 107, 567–573.
- 23 LADEN, F., L. M. NEAS, D. W. DOCKERY, J. SCHWARTZ. 2000. Association of fine particulate matter from different sources with daily mortality in six U.S. cities. *Environ. Health Perspect.* 108, 941–947.
- 24 SCHWARTZ, J. 1994. What are people dying of on high air-pollution days. *Environ. Res.* 64, 26–35.
- 25 HEI. 1995. *Diesel Exhaust: A Critical Analysis of Emissions, Exposure and Health Effects. A Special Report of the Insititute's Diesel Working Group.* HEI Research Report, HEI Cambridge, MA, USA.
- 26 TOBIAS, H. J., D. E. BEVING, P. J. ZIEMANN, H. SAKURAI, M. ZUK, P. H. McMURRY, D. ZARLING, R. WAYTULONIS, D. B. KITTELSON. 2001. Chemical analysis of diesel engine nanoparticles using a nano-DMA/thermal desorption particle beam mass spectrometer. *Environ. Sci. Technol.* 35, 2233–2243.
- 27 KITTELSON, DB. 1998. Engines and nanoparticles: A review. *J. Aerosol Sci.* 29, 575–588.
- 28 ISHIHARA, Y., J. KAGAWA. 2003. Chronic diesel exhaust exposures of rats demonstrate concentration and time-dependent effects on pulmonary inflammation. *Inhal. Toxicol.* 15, 473–492.
- 29 MAUDERLY, J. L., M. B. SNIPES, E. B. BARR, S. A. BELINSKY, J. A. BOND, A. L. BROOKS, I. Y. CHANG, Y. S. CHENG, N. A. GILLETT, W. C. GRIFFITH. 1994. Pulmonary toxicity of inhaled diesel exhaust and carbon black in chronically exposed rats. Part I: Neoplastic and nonneoplastic lung lesions. *Res. Rep. Health Eff. Inst.*, 1–75.
- 30 MIYABARA, Y., R. YANAGISAWA, N. SHIMOJO, H. TAKANO, H. B. LIM, T. ICHINOSE, M. SAGAI. 1998. Murine strain differences in airway inflammation caused by diesel exhaust particles. *Eur. Respir. J.* 11, 291–298.
- 31 ABE, S., H. TAKIZAWA, I. SUGAWARA, S. KUDOH. 2000. Diesel exhaust (DE)-induced cytokine expression in human bronchial epithelial cells: A study with a new cell exposure system to freshly generated DE in vitro. *Am. J. Respir. Cell Mol. Biol.* 22, 296–303.
- 32 BONVALLOT, V., A. BAEZA-SQUIBAN, A. BAULIG, S. BRULANT, S. BOLAND, F. MUZEAU, R. BAROUKI, F. MARANO. 2001. Organic compounds from diesel exhaust particles elicit a proinflammatory response in human airway epithelial cells and induce cytochrome p450 1A1 expression. *Am. J. Respir. Cell Mol. Biol.* 25, 515–521.
- 33 HENDERSON, R. F., H. W. LEUNG, A. G. HARMSSEN, R. O. MCCLELLAN. 1988. Species differences in release of arachidonate metabolites in response to inhaled diluted diesel exhaust. *Toxicol. Lett.* 42, 325–332.
- 34 KNAAPEN, A. M., F. SEILER, P. A. SCHILDERMAN, P. NEHLS, J. BRUCH, R. P. SCHINS, P. J. BORM. 1999. Neutrophils cause oxidative DNA damage in alveolar epithelial cells. *Free Radic. Biol. Med.* 27, 234–240.
- 35 PARKE, D. V., A. L. PARKE. 1996. Chemical-induced inflammation and inflammatory diseases. (Review; 24 refs). *Int. J. Occup. Med. Environ. Health* 9, 211–217.
- 36 SCHINS, R. P. 2002. Mechanisms of genotoxicity of particles and fibers. *Inhal. Toxicol.* 14, 57–78.

- 37 HEINRICH, U., R. FUHST, S. RITTINGHAUSEN, O. CREUTZENBERG, B. BELLMANN, W. KOCH, K. LEVSEN. 1995. Chronic inhalation exposure of Wistar rats and 2 different strains of mice to diesel-engine exhaust, carbon-black, and titanium-dioxide. *Inhal. Toxicol.* 7, 533–556.
- 38 BAEZA-SQUIBAN, A., V. BONVALLOT, S. BOLAND, F. MARANO. 1999. Airborne particles evoke an inflammatory response in human airway epithelium. Activation of transcription factors. *Cell Biol. Toxicol.* 15, 375–380.
- 39 BALL, J. C., A. M. STRACCIA, W. C. YOUNG, A. E. AUST. 2000. The formation of reactive oxygen species catalyzed by neutral, aqueous extracts of NIST ambient particulate matter and diesel engine particles. *J. Air Waste Manag. Assoc.* 50, 1897–1903.
- 40 DONALDSON, M., J. H. LIGHTBODY, K. DONALDSON, V. STONE. 2002. Interactions between ultrafine particles and metals *in vitro* and *in vivo*. *Toxicol. Appl. Pharmacol.* 184, 172–179.
- 41 BECK-SPEIER, I., N. DAYAL, E. KARG, K. L. MAIER, G. SCHUMANN, H. SCHULZ, M. SEMMLER, S. TAKENAKA, K. STETTMAIER, W. BORS, A. GHIO, J. M. SAMET, J. HEYDER. 2005. Oxidative stress and lipid mediators induced in alveolar macrophages by ultrafine particles. *Free Radic. Biol. Med.* 38, 1080–1092.
- 42 TAMAOKI, J., K. ISONO, K. TAKEYAMA, E. TAGAYA, J. NAKATA, A. NAGAI. 2004. Ultrafine carbon black particles stimulate proliferation of human airway epithelium via EGF receptor-mediated signaling pathway. *Am. J. Physiol. Lung Cell Mol. Physiol.* 287, L1127–L1133.
- 43 BROWN, D. M., K. DONALDSON, P. J. BORM, R. P. SCHINS, M. DEHNHARDT, P. GILMOUR, L. A. JIMENEZ, V. STONE. 2004. Calcium and ROS-mediated activation of transcription factors and TNF-alpha cytokine gene expression in macrophages exposed to ultrafine particles. *Am. J. Physiol. Lung Cell Mol. Physiol.* 286, L344–L353.
- 44 GILMOUR, P. S., A. ZIESENIS, E. R. MORRISON, M. A. VICKERS, E. M. DROST, I. FORD, E. KARG, C. MOSSA, A. SCHROEPEL, G. A. FERRON, J. HEYDER, M. GREAVES, W. MACNEE, K. DONALDSON. 2004. Pulmonary and systemic effects of short-term inhalation exposure to ultrafine carbon black particles. *Toxicol. Appl. Pharmacol.* 195, 35–44.
- 45 DONALDSON, K., C. L. TRAN, L. A. JIMENEZ, R. DUFFIN, D. E. NEWBY, N. MILLS, W. MACNEE, V. STONE. 2005. Combustion-derived nanoparticles: A review of their toxicology following inhalation exposure. *Particle Fibre Toxicol.* 2, 10.
- 46 SQUADRITO, G. L., R. CUETO, B. DELLINGER, W. A. PRYOR. 2001. Quinoid redox cycling as a mechanism for sustained free radical generation by inhaled airborne particulate matter. *Free Radic. Biol. Med.* 31, 1132–1138.
- 47 WILSON, M., J. H. LIGHTBODY, K. DONALDSON, J. H. SALES, V. STONE. 2001. Oxidative Interactions between ultrafine particles and transition metals *in vivo* and *in vitro*. *Toxicol. Appl. Pharmacol.* 163, A495.
- 48 ILSI Workshop. 2000. The relevance of the rat lung response to particle overload for human risk assessment. *Inhal. Toxicol.* 12, 1–148.
- 49 TRAN, C. L., D. BUCHANAN, R. T. CULLEN, A. SEARL, A. D. JONES, K. DONALDSON. 2000. Inhalation of poorly soluble particles. II. Influence of particle surface area on inflammation and clearance. *Inhal. Toxicol.* 12, 1113–1126.
- 50 MAUDERLY, J. L. 1997. Relevance of particle-induced rat lung tumors for assessing lung carcinogenic hazard and human lung cancer risk. *Environ. Health Perspect.* 105, 1337–1346.
- 51 BROOK, R. D., B. FRANKLIN, W. CASCIO, Y. HONG, G. HOWARD, M. LIPSETT, R. LUEPKER, M. MITTLEMAN, J. SAMET, S. C. SMITH, JR., I. TAGER. 2004. Air pollution and cardiovascular disease: A statement for healthcare professionals from the Expert Panel on Population and Prevention Science of the American Heart Association. *Circulation* 109, 2655–2671.

- 52 LIUZZO, G., L. M. BIASUCCI, J. R. GALLIMORE, R. L. GRILLO, A. G. REBUZZI, M. B. PEPYS, A. MASERI. 1994. The prognostic value of C-reactive protein and serum amyloid a protein in severe unstable angina. *N. Engl. J. Med.* 331, 417–424.
- 53 RIDKER, P. M., P. HAUGHIE. 1998. Prospective studies of C-reactive protein as a risk factor for cardiovascular disease. *J. Investig. Med.* 46, 391–395.
- 54 RIDKER, P. M., M. CUSHMAN, M. J. STAMPFER, R. P. TRACY, C. H. HENNEKENS. 1997. Inflammation, aspirin, and the risk of cardiovascular disease in apparently healthy men. *N. Engl. J. Med.* 336, 973–979.
- 55 LIBBY, P., P. M. RIDKER, A. MASERI. 2002. Inflammation and atherosclerosis. *Circulation* 105, 1135–1143.
- 56 SALVI, S., A. BLOMBERG, B. RÜDELL, F. KELLY, T. SANDSTROM, S. T. HOLGATE, A. FREW. 1999. Acute inflammatory responses in the airways and peripheral blood after short-term exposure to diesel exhaust in healthy human volunteers. *Am. J. Respir. Crit. Care Med.* 159, 702–709.
- 57 POPE, C. A., III. 2001. Particulate air pollution, C-reactive protein, and cardiac risk. *Eur. Heart J.* 22, 1149–1150.
- 58 PEKKANEN, J., E. J. BRUNNER, H. R. ANDERSON, P. TIITANEN, R. W. ATKINSON. 2000. Daily concentrations of air pollution and plasma fibrinogen in London. *Occup. Environ. Med.* 57, 818–822.
- 59 VAN EEDEN, S. F., W. C. TAN, T. SUWA, H. MUKAE, T. TERASHIMA, T. FUJII, D. QUI, R. VINCENT, J. C. HOGG. 2001. Cytokines involved in the systemic inflammatory response induced by exposure to particulate matter air pollutants (pm(10)). *Am. J. Respir. Crit. Care Med.* 164, 826–830.
- 60 VINCENT, R., P. KUMARATHASAN, P. GEOGAN, S. G. BJARNASON, J. GUENETTE, D. BERUBE, I. Y. ADAMSON, S. DESJARDINS, R. BURNETT, F. J. MILLER, B. BATTISTINI. 2001. Inhalation toxicology of urban ambient particulate matter: Acute cardiovascular effects in rats. *Health Effects Res. Rep.* No 104.
- 61 SUWA, T., J. C. HOGG, K. B. QUINLAN, A. OHGAMI, R. VINCENT, S. F. VAN EEDEN. 2002. Particulate air pollution induces progression of atherosclerosis. *J. Am. Coll. Cardiol.* 39, 935–942.
- 62 CONHAIM, R. L., A. EATON, N. C. STAUB, T. D. HEATH. 1988. Equivalent pore estimate for the alveolar-airway barrier in isolated dog lung. *J. Appl. Physiol.* 64, 1134–1142.
- 63 BERRY, J. P., B. ARNOUX, G. STANISLAS, P. GALLE, J. CHRETIEN. 1977. A microanalytic study of particles transport across the alveoli: Role of blood platelets 25. *Biomedicine.* 27, 354–357.
- 64 NEMMAR, A., H. VANBILLOEN, M. F. HOYLAERTS, P. H. HOET, A. VERBRUGGEN, B. NEMERY. 2001. Passage of intratracheally instilled ultrafine particles from the lung into the systemic circulation in hamster. *Am. J. Respir. Crit. Care Med.* 164, 1665–1668.
- 65 OBERDÖRSTER, G., Z. SHARP, V. ATUDOREI, A. P. ELDER, R. GELEIN, A. K. LUNTS, W. KREYLING, C. COX. 2002. Extrapulmonary translocation of ultrafine carbon particles following inhalation exposure. *J. Toxicol. Environ. Health.* 65, 1531–1545.
- 66 NEMMAR, A., P. H. HOET, B. VANQUICKENBORNE, D. DINSDALE, M. THOMEER, M. F. HOYLAERTS, H. VANBILLOEN, L. MORTELMANS, B. NEMERY. 2002. Passage of inhaled particles into the blood circulation in humans. *Circulation* 105, 411–414.
- 67 BROWN, J. S., K. L. ZEMAN, W. D. BENNETT. 2002. Ultrafine particle deposition and clearance in the healthy and obstructed lung. *Am. J. Respir. Crit. Care Med.* 166, 1240–1247.
- 68 LI, X. Y., K. DONALDSON, I. RAHMAN, W. MACNEE. 1994. An investigation of the role of glutathione in increased epithelial permeability induced by cigarette smoke in vivo and in vitro. *Am. J. Respir. Crit. Care Med.* 149, 1518–1525.

- 69 MEIRING, J. J., P. J. BORM, K. BAGATE, M. SEMMLER, J. SEITZ, S. TAKENAKA, W. G. KREYLING. 2005. The influence of hydrogen peroxide and histamine on lung permeability and translocation of iridium nanoparticles in the isolated perfused rat lung 2. *Part Fibre Toxicol.* 2, 3.
- 70 RUEHM, S. G., M. GOYEN, J. BARKHAUSEN, K. KROGER, S. BOSK, M. E. LADD, J. F. DEBATIN. 2001. Rapid magnetic resonance angiography for detection of atherosclerosis. *Lancet* 357, 1086–1091.
- 71 GUZMAN, L. A., V. LABHASETWAR, C. SONG, Y. JANG, A. M. LINCOFF, R. LEVY, E. J. TOPOL. 1996. Local intraluminal infusion of biodegradable polymeric nanoparticles. A novel approach for prolonged drug delivery after balloon angioplasty. *Circulation* 94, 1441–1448.
- 72 KOOI, M. E., V. C. CAPPENDIJK, K. B. CLEUTJENS, A. G. KESSELS, P. J. KITSLAAR, M. BORGERS, P. M. FREDERIK, M. J. DAEMEN, J. M. VAN ENGELSHOVEN. 2003. Accumulation of ultrasmall superparamagnetic particles of iron oxide in human atherosclerotic plaques can be detected by in vivo magnetic resonance imaging. *Circulation* 107, 2453–2458.
- 73 FURCHGOTT, R. F., J. V. ZAWADZKI. 1980. The obligatory role of endothelial cells in the relaxation of arterial smooth muscle by acetylcholine. *Nature* 288, 373–376.
- 74 LUDMER, P. L., A. P. SELWYN, T. L. SHOOK, R. R. WAYNE, G. H. MUDGE, R. W. ALEXANDER, P. GANZ. 1986. Paradoxical vasoconstriction induced by acetylcholine in atherosclerotic coronary arteries. *N. Engl. J. Med.* 315, 1046–1051.
- 75 CELERMAJER, D. S., M. R. ADAMS, P. CLARKSON, J. ROBINSON, R. MCCREDIE, A. DONALD, J. E. DEANFIELD. 1996. Passive smoking and impaired endothelium-dependent arterial dilatation in healthy young adults. *N. Engl. J. Med.* 334, 150–154.
- 76 NEWBY, D. E., A. L. MCLEOD, N. G. UREN, L. FLINT, C. A. LUDLAM, D. J. WEBB, K. A. FOX, N. A. BOON. 2001. Impaired coronary tissue plasminogen activator release is associated with coronary atherosclerosis and cigarette smoking: Direct link between endothelial dysfunction and atherothrombosis. *Circulation* 103, 1936–1941.
- 77 HALCOX, J. P., W. H. SCHENKE, G. ZALOS, R. MINCEMOYER, A. PRASAD, M. A. WACLAWIW, K. R. NOUR, A. A. QUYYUMI. 2002. Prognostic value of coronary vascular endothelial dysfunction. *Circulation* 106, 653–658.
- 78 HEITZER, T., T. SCHLINZIG, K. KROHN, T. MEINERTZ, T. MUNZEL. 2001. Endothelial dysfunction, oxidative stress, and risk of cardiovascular events in patients with coronary artery disease. *Circulation* 104, 2673–2678.
- 79 NEWBY, D. E., R. A. WRIGHT, C. LABINJOH, C. A. LUDLAM, K. A. FOX, N. A. BOON, D. J. WEBB. 1999. Endothelial dysfunction, impaired endogenous fibrinolysis, and cigarette smoking: A mechanism for arterial thrombosis and myocardial infarction. *Circulation* 99, 1411–1415.
- 80 IKEDA, M., M. SHITASHIGE, H. YAMASAKI, M. SAGAI, T. TOMITA. 1995. Oxidative modification of low density lipoprotein by diesel exhaust particles. *Biol. Pharm. Bull.* 18, 866–871.
- 81 GILMOUR, P. S., E. R. MORRISON, M. A. VICKERS, I. FORD, C. A. LUDLAM, M. GREAVES, K. DONALDSON, W. MACNEE. 2005. The procoagulant potential of environmental particles (PM10). *Occup. Environ. Med.* 62, 164–171.
- 82 SALVI, S., A. BLOMBERG, B. RUDELL, F. KELLY, T. SANDSTROM, S. T. HOLGATE, A. FREW. 1999. Acute inflammatory responses in the airways and peripheral blood after short-term exposure to diesel exhaust in healthy human volunteers. *Am. J. Respir. Crit. Care Med.* 159, 702–709.
- 83 HINGORANI, A. D., J. CROSS, R. K. KHARBANDA, M. J. MULLEN, K. BHAGAT, M. TAYLOR, A. E. DONALD, M. PALACIOS, G. E. GRIFFIN, J. E. DEANFIELD, R. J. MACALLISTER, P.

- VALLANCE. 2000. Acute systemic inflammation impairs endothelium-dependent dilatation in humans. *Circulation* 102, 994–999.
- 84 MILLS, N., S. TORNQUIST, S. ROBINSON, K. DARNLEY, N. A. BOON, W. MACNEE, K. DONALDSON, A. BLOMBERG, T. SANDSTROM, D. NEWBY. 2005. Diesel exhaust inhalation causes vascular dysfunction and impaired endogenous fibrinolysis. *Circulation* 112, 3930–3936.
- 85 PETERS, A., K. S. VON M. HEIER, I. TRENTINAGLIA, A. HORMANN, H. E. WICHMANN, H. LOWEL. 2004. Exposure to traffic and the onset of myocardial infarction. *N. Engl. J. Med.* 351, 1721–1730.
- 86 SEATON, A., W. MACNEE, K. DONALDSON, D. GODDEN. 1995. Particulate air-pollution and acute health-effects. *Lancet* 345, 176–178.
- 87 THOMPSON, S. G., J. KIENAST, S. D. PYKE, F. HAVERKATE, J. C. VAN DE LOO. 1995. Hemostatic factors and the risk of myocardial infarction or sudden death in patients with angina pectoris. European Concerted Action on Thrombosis and Disabilities Angina Pectoris Study Group. *N. Engl. J. Med.* 332, 635–641.
- 88 PETERS, A., A. DORING, H. E. WICHMANN, W. KOENIG. 1997. Increased plasma viscosity during an air pollution episode: A link to mortality? *Lancet* 349, 1582–1587.
- 89 NEMMAR, A., P. H. HOET, D. DINSDALE, J. VERMYLEN, M. F. HOYLAERTS, B. NEMERY. 2003. Diesel exhaust particles in lung acutely enhance experimental peripheral thrombosis. *Circulation* 107, 1202–1208.
- 90 NEMMAR, A., M. F. HOYLAERTS, P. H. HOET, J. VERMYLEN, B. NEMERY. 2003. Size effect of intratracheally instilled particles on pulmonary inflammation and vascular thrombosis. *Toxicol. Appl. Pharmacol.* 186, 38–45.
- 91 NEMMAR, A., M. F. HOYLAERTS, P. H. HOET, B. NEMERY. 2004. Possible mechanisms of the cardiovascular effects of inhaled particles: Systemic translocation and prothrombotic effects. *Toxicol. Lett.* 149, 243–253.
- 92 GILMOUR, P. S., E. R. MORRISON, M. A. VICKERS, I. FORD, C. A. LUDLAM, M. GREAVES, K. DONALDSON, W. MACNEE. 2005. The procoagulant potential of environmental particles (PM10). *Occup. Environ. Med.* 62, 164–171.
- 93 KHANDOGA, A., A. STAMPFL, S. TAKENAKA, H. SCHULZ, R. RADYKEWICZ, W. KREYLING, F. KROMBACH. 2004. Ultrafine particles exert prothrombotic but not inflammatory effects on the hepatic microcirculation in healthy mice in vivo. *Circulation* 109, 1320–1325.
- 94 GATTI, A. M., S. MONTANARI, E. MONARI, A. GAMBARELLI, F. CAPITANI, B. PARISINI. 2004. Detection of micro- and nano-sized biocompatible particles in the blood. *J. Mater. Sci. Mater. Med.* 15, 469–472.
- 95 BECKETT, W. S., D. F. CHALUPA, A. PAULY-BROWN, D. M. SPEERS, J. C. STEWART, M. W. FRAMPTON, M. J. UTELL, L. S. HUANG, C. COX, W. ZAREBA, G. OBERDÖRSTER. 2005. Comparing inhaled ultrafine versus fine zinc oxide particles in healthy adults: A human inhalation study. *Am. J. Respir. Crit. Care Med.* 171, 1129–1135.
- 96 TSUJI, H., F. J. VENDITTI, JR., E. S. MANDERS, J. C. EVANS, M. G. LARSON, C. L. FELDMAN, D. LEVY. 1994. Reduced heart rate variability and mortality risk in an elderly cohort. The Framingham Heart Study. *Circulation* 90, 878–883.
- 97 KLEIGER, R. E., P. K. STEIN, J. T. BIGGER, JR. 2005. Heart rate variability: Measurement and clinical utility. *Ann. Noninvasive. Electrocardiol.* 10, 88–101.
- 98 POPE, C. A., III, D. J. EATOUGH, D. R. GOLD, Y. PANG, K. R. NIELSEN, P. NATH, R. L. VERRIER, R. E. KANNER. 2001. Acute exposure to environmental tobacco smoke and heart rate variability. *Environ. Health Perspect.* 109, 711–716.
- 99 MAGARI, S. R., J. SCHWARTZ, P. L.

- WILLIAMS, R. HAUSER, T. J. SMITH, D. C. CHRISTIANI. 2002. The association between personal measurements of environmental exposure to particulates and heart rate variability. *Epidemiology* 13, 305–310.
- 100 WELLENIUS, G. A., P. H. SALDIVA, J. R. BATALHA, G. G. KRISHNA MURTHY, B. A. COULL, R. L. VERRIER, J. J. GODLESKI. 2002. Electrocardiographic changes during exposure to residual oil fly ash (ROFA) particles in a rat model of myocardial infarction. *Toxicol. Sci.* 66, 327–335.
- 101 DOCKERY, D. W., H. LUTTMANN-GIBSON, D. Q. RICH, M. S. LINK, M. A. MITTLEMAN, D. R. GOLD, P. KOUTRAKIS, J. D. SCHWARTZ, R. L. VERRIER. 2005. Association of air pollution with increased incidence of ventricular tachyarrhythmias recorded by implanted cardioverter defibrillators. *Environ. Health Perspect.* 113, 670–674.
- 102 MOGHIMI, S. M., A. E. HAWLEY, N. M. CHRISTY, T. GRAY, L. ILLUM, S. S. DAVIS. 1994. Surface engineered nanospheres with enhanced drainage into lymphatics and uptake by macrophages of the regional lymph nodes. *FEBS Lett.* 344, 25–30.
- 103 STUART, A. E. 1970. *The Reticulo-endothelial System*. E and S Livingstone, Edinburgh.
- 104 FURUMOTO, K., S. NAGAYAMA, K. OGAWARA, Y. TAKAKURA, M. HASHIDA, K. HIGAKI, T. KIMURA. 2004. Hepatic uptake of negatively charged particles in rats: Possible involvement of serum proteins in recognition by scavenger receptor. *J. Controlled Release* 97, 133–141.
- 105 FERNANDEZ-URRUSUNO, R., E. FATTAL, J. FEGER, P. COUVREUR, P. THEROND. 1997. Evaluation of hepatic antioxidant systems after intravenous administration of polymeric nanoparticles. *Biomaterials* 18, 511–517.
- 106 BROWN, D. M., K. DONALDSON, P. J. BORM, R. P. SCHINS, M. DEHNHARDT, P. GILMOUR, L. A. JIMENEZ, V. STONE. 2004. Calcium and ROS-mediated activation of transcription factors and TNF-alpha cytokine gene expression in macrophages exposed to ultrafine particles. *Am. J. Physiol. Lung Cell Mol. Physiol.* 286, L344–L353.
- 107 STONE, V., M. TUINMAN, J. E. VAMVAKOPOULOS, J. SHAW, D. BROWN, S. PETERSON, S. P. FAUX, P. BORM, W. MACNEE, F. MICHAELANGELI, K. DONALDSON. 2000. Increased calcium influx in a monocytic cell line on exposure to ultrafine carbon black. *Eur. Respir. J.* 15, 297–303.
- 108 BROWN, D. M., K. DONALDSON, V. STONE. 2004. Effects of PM10 in human peripheral blood monocytes and J774 macrophages. *Respir. Res.* 5, 29.
- 109 HUSSAIN, S. M., K. L. HESS, J. M. GEARHART, K. T. GEISS, J. J. SCHLAGER. 2005. In vitro toxicity of nanoparticles in BRL 3A rat liver cells. *Toxicol. in Vitro.* 19, 975–983.
- 110 DONALDSON, K., D. BROWN, A. CLOUTER, R. DUFFIN, W. MACNEE, L. RENWICK, L. TRAN, V. STONE. 2002. The pulmonary toxicology of ultrafine particles. *J. Aerosol Med.* 15, 213–220.
- 111 FLORENCE, A. T., N. HUSSAIN. 2001. Transcytosis of nanoparticle and dendrimer delivery systems: Evolving vistas. *Adv. Drug Deliv. Rev.* 50(Suppl. 1), S69–S89.
- 112 JANI, P., G. W. HALBERT, J. LANGRIDGE, A. T. FLORENCE. 1990. Nanoparticle uptake by the rat gastrointestinal mucosa: Quantitation and particle size dependency. *J. Pharm. Pharmacol.* 42, 821–826.
- 113 DESAI, M. P., V. LABHASETWAR, G. L. AMIDON, R. J. LEVY. 1996. Gastrointestinal uptake of biodegradable microparticles: Effect of particle size. *Pharm. Res.* 13, 1838–1845.
- 114 POWELL, J. J., C. C. AINLEY, R. S. HARVEY, I. M. MASON, M. D. KENDALL, E. A. SANKEY, A. P. DHILLON, R. P. THOMPSON. 1996. Characterisation of inorganic microparticles in pigment cells of human gut associated lymphoid tissue. *Gut* 38, 390–395.
- 115 POWELL, J. J., R. S. HARVEY, P. ASHWOOD, R. WOLSTENCROFT, M. E. GERSHWIN, R. P. THOMPSON. 2000.

- Immune potentiation of ultrafine dietary particles in normal subjects and patients with inflammatory bowel disease. *J. Autoimmun.* 14, 99–105.
- 116 LOMER, M. C., R. P. THOMPSON, J. J. POWELL. 2002. Fine and ultrafine particles of the diet: Influence on the mucosal immune response and association with Crohn's disease. *Proc. Nutr. Soc.* 61, 123–130.
- 117 OBERDÖRSTER, G., Z. SHARP, V. ATUDOREI, A. ELDER, R. GELEIN, W. KREYLING, C. COX. 2004. Translocation of inhaled ultrafine particles to the brain. *Inhal. Toxicol.* 16, 437–445.



## Index

### a

- acid cation absorption 223
- actinide SAMMS 204
- activation
  - microbial 44
  - pro-inflammatory 123–124
- advanced oxidation techniques (AOT) 237
- adverse health effects 155–156
  - air pollution 296–298, 300–302
  - matter induced 84–85
  - ultrafine particles (UFP) 159
- aerogels 191–193
- aggregates
  - acid-base chemistry 191
  - aerogel 192
  - airborne 138
  - CNT formation 39, 137
  - CNT toxicity 140
  - diesel 137, 300
  - dust 139
  - MWCNT 145
  - new carbon modifications 174
- air pollution 294–318
  - adverse health effects 296–298, 300–302
  - alveolar epithelium 304
  - asthma 297
  - atherosclerosis 303–304
  - atherothrombosis 307
  - black smoke 294
  - blood fibrinogen levels 307
  - cardiac autonomic dysfunction 308
  - cardiovascular disease 297, 302–303
  - CDNP 300–301
  - CNT toxicity 148
  - coagulation 307–308
  - diesel fuel 300
  - direct vascular effects 304–306
  - endogenous fibrinolysis 306–307
  - endothelial dysfunction 306–307
  - epidemiological studies 296–298
  - gastrointestinal tract 308–309
  - health effects 300–302
  - heart rate variability 308
  - history 294
  - inflammations 301, 303–304
  - liver 308–309
  - lymphatic system 304
  - mortality risk 297
  - MWCNT 137–138
  - nanoparticles 54, 299, 304–306
  - nervous system 309
  - oxidative stress 305
  - particles 296–298
  - phagocytosis 304
  - photochemical smog 295
  - plaque rupture 303–304
  - PM 296
  - rat lung overload 302
  - smog 294
  - SWCNT particles 135
  - thrombosis 307–308
  - transition metals 98
  - translocation 304–306
- airway wall, particle deposition 86–87
- ALARA principle 155
- alveolar duct bifurcations 160
- alveolar epithelium 304
- alveolar macrophages 165
- alveolar region, slowly dissolving particles 87–88
- anatase 13–24
  - band structure 14
  - photocatalytic removal 240
  - *see also* rutile, titanium dioxide
- ancient ice, MWCNT 137
- animals
  - health effects 100
  - iridium particles 89

- animals (*cont.*)
  - lung toxicity studies 59, 130
  - particle translocation 89–93
  - particle uptake 160
  - pulmonary toxicity studies 141–142
- anthropogenic nanoparticles (NP) 53
- AOT *see* advanced oxidation techniques
- arc vaporization process, carbon nanotubes 132
- arsenate removal 224
- artificial nanoparticles (NP) 71
  - health impact 54
- artificial organic matter, water treatment 213
- asbestos fibers
  - biotoxicity 9
  - CNTcomparison 173
  - inhaled 59, 64
- asthma
  - air pollution 297
  - frequency 109
  - nanoparticles 55
- atherosclerosis 303–304
- atherothrombosis 307
- avidin, nanosensors 280–286
  
- b**
- Bacillus anthracis*
  - nanosensors 271–272
  - PMN-PT/Cu microcantilevers 289
- Bacillus sphaericus*, toxic metals 43
- band gap energy, photocatalysts 219
- band gap model, photocatalytic removal 242
- BBB *see* blood-brain barrier
- bimetallic nanocrystalline analogs 193
- binuclear cells 27
- bioassay, yeast 245–251
- biocides 42
- biomarkers 44–46
  - CNT toxicity 145–146
- biotoxicity 3–34
  - anatase 13
  - asbestos fibers 9
  - binuclear cells 27
  - biocompatible coating layers 11
  - cell cycle 28
  - cell proliferation 27
  - coated nanoparticles 11
  - Cytochalasin B 27
  - free radical activity 15
  - GeO<sub>2</sub> particles 27–28
  - hair follicles penetration 7
  - hydroxyl radical formation 19
  - iron oxide 9–13
  - magnetosomes 10
  - metal oxides 3–34
  - MnO<sub>2</sub> 26
  - murine fibroblasts 25
  - nanomaterials 6, 9
  - particle size 26
  - pathways 8
  - proliferation inhibitor 27
  - rutile 13
  - superparamagnetic particles 10
  - synthetic nanoparticles 6
  - titanium dioxide 13–26
  - transepidermal intercellular penetration 7
  - ultrafine particles (UFP) 4
- black smoke, air pollution 294
- blood fibrinogen levels 307
- blood-brain barrier (BBB)
  - drug delivery 92
  - nanoparticles uptake 69
  - penetration 125
- brain
  - particle uptake 40, 89, 163, 310
- branched molecules 66
- bronchial lumen, MWCNTs 146
- brookite
  - titanium dioxide 13
  - *see also* anatase, rutile
- Buckyballs *see* fullerenes
  
- c**
- C. elegans* 39
- C<sub>60</sub> *see* fullerenes
- cadmium oxide particles 161
- cancer cells, coated nanoparticles 11
- cantilever tip 281–286
- cantilevers
  - miniaturization 287–290
  - resonance frequency 278
  - unimorph 274–278
- CaO aerogels 191
- carbon black 157
- carbon conformations 153–185
- carbon fibers, nanomaterial toxicity 158
- carbon nanoparticles
  - acute toxicity 168
  - internalization 121
  - radioactive-labeled 109
  - *see also* fullerenes, nanoparticles
- carbon nanotubes (CNTs)
  - arc vaporization process 132
  - combustion-generated 136–139
  - exposure risk 146
  - functional 204
  - health effects 97–98, 130–152
  - intrinsic toxicity 142

- laser ablation process 132
  - lung 59
  - manufactured *see* manufactured carbon nanotubes
  - non-manufactured 139
  - occupational exposure risk 146
  - occupational exposures 134–136
  - occupational health 130–152
  - physical structures 139
  - skin 64
  - synthesis 132
  - toxicity 130–152
  - *see also* fullerenes, SWCNTs, MWCNTs, CNT formation
  - cardiac autonomic dysfunction 308
  - cardiovascular disease
    - air pollution 297, 302–303
    - ultrafine particles (UFP) 95–96
  - catalysts 239
    - carbon nanofibers 154, 159
    - immobilized TiO<sub>2</sub> 243–245, 261–261
    - metal *see* metal catalysts
    - photo- *see* photocatalysts
  - caveolae
    - endocytic pathways 60
    - internalization 92
  - CDNP *see* combustion-derived nanoparticles
  - cell cycle 28
  - cell death, UV irradiation studies 20
  - cell membrane proteins 164
  - cell proliferation 27–28
    - tumor development 173
  - cell survival, superoxide dismutase 23
  - cellular structures, ultrafine particles (UFP) 5
  - cellular uptake 69, 162
  - ceramic nanoparticles 108–129
  - ceria nanoparticles 226
  - chelating ligands 198–199
  - chemistry
    - absorption 196
    - acid-base 191–193
    - redox 194–195
  - chlorinated benzenes, dechlorination 194
  - chlorophenol red- $\beta$ -D-galactopyranoside (CPRG), photocatalytic degradation 246
  - cigarette smokers, endothelial dysfunction 306
  - cilia, ultrafine particles (UFP) 5
  - CNT formation, aggregates 39, 137
  - CNT toxicity 140, 144–148
    - air pollution 148
  - CNTs *see* carbon nanotubes
  - coagulation 56, 60, 307–308
  - coated nanoparticles 11–12
  - coating 69
    - biocompatible 11
    - PEG 66–67
  - colloids, natural materials 5
  - combustion-generated carbon nanotubes (CDNP) 136–139
  - contaminated oil 200
  - contamination
    - groundwater 36
    - oestrogenic 237, 246
    - traces 189
    - ZVI nanoparticles 195
  - coronary heart disease 55–56
  - CPRG *see* chlorophenol red- $\beta$ -D-galactopyranoside
  - Crohn's disease 62, 309
    - pathogenesis 110
  - Cytochalasin B, cell growth 24, 27
  - cytokines
    - inflammatory 94
    - production 99
  - cytoskeletal organization, dysfunction 161, 169
  - cytotoxicity
    - *Escherichia coli* 23
    - *Pseudomonas aeruginosa* 23
    - assay 111
    - dermal microvascular endothelial cell 16–17
    - different nanoparticles 116
    - particles 122–123
    - phagocytosis 25
    - plasmid 14
    - PSB 22
    - shape-dependent 25
    - UV irradiation studies 18–26
- d**
- Daphnia magna* 39–41
    - biomarkers 46
  - dechlorination, chlorinated benzenes 194
  - degradation
    - microbial 44
    - oestrogens in water 259–262
    - photocatalytic 243–245
  - dense non-aqueous phase liquids (DNAPLs), dense non-aqueous phase (DNAPLs) 190, 194–195, 205
  - DEP *see* diesel exhaust particles
  - deposition *see* particle deposition
  - depots, particles 160
  - dermal irritation, new carbon modifications 174

- dermal microvascular endothelial cell, cytotoxicity 16–17
  - didodecyldimethylammonium bromide (DMAB) 66
  - diesel engines, particulate emissions 154
  - diesel exhaust particles (DEP) 54, 99
    - adverse pulmonary effects 300
    - inhalation 108
    - lung 67
    - oxidative stress 68
    - thrombosis 91, 307
    - tumors 173
  - diesel fuel, air pollution 137, 300
  - dimethyl dimethyl phosphonate (DMMP), nanosensors 287
  - 3-(4,5-dimethylthiazol-2-yl)-2,5-diphenyl-tetrazolium bromide (MTT) 17–18, 175, 309
    - *see also* methylthiazol-2-yl)-diphenyl-tetrazolium bromide
  - disease 71
    - cardiovascular 95–96, 297, 302–303
    - coronary heart 55–56
    - Crohn's 62, 110, 309
    - intestinal tract 62
    - molecular therapy 175
    - neurodegenerative 110
    - risk assessment 101
  - DMAB *see* didodecyldimethylammonium bromide
  - DMMP *see* dimethyl dimethyl phosphonate
  - DNA
    - carbon nanotubes 175–177
    - dark studies 14–15
    - nanomaterial toxicity 165
    - tail length 21
    - UV irradiation studies 17–22
  - DNAPLs *see* dense non-aqueous phase liquids
  - dosimetry 81–107
    - *see* nanoparticle dosimetry
  - dust particles 42
  - dysfunction, endothelial 306–307
- e**
- ecotoxicity 35–50
  - EDC *see* endocrine-disrupting chemicals
  - ELISA *see* enzyme-linked immunosorbent assays
  - endocrine-disrupting chemicals (EDC), photocatalytic removal 234–270
  - endogenous fibrinolysis 306–307
  - endothelial cell functions *in vitro*, ceramic nanoparticles 108–129
  - endothelial cells 69
    - *see* human dermal microvascular endothelial cells
  - endothelial dysfunction, air pollution 306–307
  - endotoxins 68
  - engineered nanomaterials 35
  - entry routes, nanoparticles 56
  - environment 187–318
    - background to oestrogens 235–238
    - carbon nanotubes 134–139
    - nanoparticles 5–8
    - particle origin 108–110
  - environmental air pollution 294–318
  - environmental contaminants 216
  - environmental health, carbon nanotubes 130–152
  - environmental particulate matter 138
  - environmental remediation 189–210
    - absorption chemistry 196
    - actual waste 201–202
    - aerogels 191–193
    - anion SAMMS 200–203
    - chelating ligands 198–199
    - chemical warfare agents 192
    - contaminants 189–190
    - contaminated oil 200
    - dechlorination 194
    - dense non-aqueous phase liquids (DNAPLs) 190
    - field deployments 195–196
    - functional CNTs 204
    - functional nanomaterials 190
    - iminodiacetic acid 198
    - macrocycle metal phosphonates 199–200
    - redox chemistry 194
    - spherical particles 190
    - zinc biphenylenebis(phosphonate) 198
    - Zr N-(phosphonomethyl)iminodiacetic acid 199
    - ZVI nanoparticles 194–195
  - enzyme upregulation, biomarkers 44
  - enzyme-linked immunoassay 112
  - enzyme-linked immunosorbent assays (ELISA), nanosensors 272–273
  - epidemiological evidence 54–56
    - particulate matter 83–84
  - epidemiological studies
    - air pollution 296–298
    - ultrafine particles (UFP) 84
  - epidemiology 81–107
  - epithelial barrier, lung 60
  - epithelial cells, lung 162, 165–166
  - epithelial lining, particle deposition 88

- Escherichia coli*  
 – cytotoxicity 23  
 – environmental oestrogens 236  
 – nanosensors 272  
 E-selectin  
 – endothelial cell functions *in vitro* 112–113  
 – protein expression 119, 123  
 ethical limitations 94  
 17  $\alpha$ -ethynylloestradiol  
 – photocatalytic degradation 251–259  
 – photocatalytic removal 236  
 excess mortality, carbon nanotubes 148  
 exposure risk, CNTs 146  
 exposure routes 70
- f**  
 ferrocyanide Cu-EDA SAMMS, synthesis 204, 204  
 fibers  
 – asbestos 9, 85  
 – biopersistence 59  
 – biotoxicity 16  
 – carbon 158  
 – CNTs 139  
 – health effects 97–98  
 – lung 58  
 – nanomaterial toxicity 158  
 – skin 64  
 – SWCNTs 134  
 fibrinolysis, endogenous 306–307  
 fibroblasts  
 – coated nanoparticles 11  
 – murine 25  
 filter feeders, Daphnids 39  
 fluorescence spectroscopy 251–260  
 fluorescence staining, endothelial cell functions *in vitro* 113–120  
 food chain 38–40, 43  
 free radicals  
 – dark studies 14–15  
 – lungs 68  
 – SWCNTs 174  
 – tests 102  
 fresh water resources, shrinking 211  
 fuel combustion, MWCNT 139  
 fullerenes 133  
 – biological effects 173–176  
 – nanomaterial toxicity 158  
 – *see also* carbon nanoparticles, carbon nanotubes, CNTs, SWCNTs, MWCNTs
- g**  
 gas combustion, MWCNT formation 136–137  
 gastrointestinal tract 308–309  
 – inflammation 62  
 genotoxicity  
 – metal oxides 169  
 – nanoparticles (general) 16  
 – new carbon modifications 172  
 GeO<sub>2</sub> particles, biotoxicity 27–28  
 glass cantilever sensors, gold-coated 284–286  
 glycidoxypropyltrimethoxysilane (GOPTS), *Salmonella typhimurium* detection 282–284  
 gold-coated glass cantilever sensors, *Salmonella typhimurium* detection 284–286  
 GOPTS *see* glycidoxypropyltrimethoxysilane  
 granulomas  
 – CNT toxicity 144  
 – new carbon modifications 174
- h**  
 hair follicles, entry routes 7, 63  
 hazards 175  
 – nanoparticles 83  
 – risk assessment 156–157, 175–179  
 HDMEC *see* human dermal microvascular endothelial cells  
 health effects 83–84, 93–100  
 – adverse *see* adverse health effects  
 – air pollution 296–298, 300–302  
 – ambient particulate matter 83–84  
 – animals 100  
 – carbon nanotubes 130–152  
 – cytokine production 99  
 – DEP 99  
 – environmental 130–152  
 – fibers 97–98  
 – inhaled iron carbonyl particles 160  
 – insoluble solids 57–59  
 – matter induced 84–85  
 – MWCNTs 147–148  
 – nanomaterial toxicity 100, 155–156, 159–160  
 – nanotubes 97–98  
 – occupational 130–152  
 – organic compounds 99–100  
 – PAH 99  
 – particle shape 97–98  
 – particulate matter 83–84  
 – SWCNTs 147  
 – toxicological plausibility 93–100  
 – transition metals 98  
 – ultrafine particles (UFP) 159  
 health impact 51–186  
 health risks 146–148  
 health threats, nanoparticles 8–9

- heart rate, effects due to PM 96, 297
    - ultrafine carbon particles 172
  - heart rate variability, air pollution 308
  - HEK *see* human epidermal keratinocytes
  - hematite particles, biological effects 166
  - hierarchical oxidative stress model 68
  - HIF-1 $\alpha$  *see* hypoxia-inducible factor1 $\alpha$
  - human dermal microvascular endothelial cells (HDMEC) 16–17
    - *in vitro* cell functions 111, 114
    - HIF-1 $\alpha$ -staining 118
    - monolayers 115
    - nanoparticle-induced effects 110
    - pro-inflammatory stimulation 120
  - human environment, particle origin 108–110
  - human epidermal keratinocytes, skin 64
  - human lung epithelial cells, nanomaterial toxicity 162
  - human oestrogen receptor, photocatalytic degradation 246
  - human osteoblast-like cells, metal oxide nanoparticles 170
  - humans
    - health effects extrapolation 100
    - health risk 124–125
    - particle translocation 88
  - hybrid nanostructured remediation materials 196–205
  - hydroxyl radicals
    - formation 19, 22
    - photocatalytic removal 242–243
  - hypoxia-inducible factor1 $\alpha$  (HIF-1 $\alpha$ ) 117
- i**
- ice sample, MWCNT 137
  - IL-8 release
    - endothelial cell functions *in vitro* 112
    - pro-inflammatory activation 123
  - iminodiacetic acid 198
  - immobilization, nanosensors 278–281
  - immunoassay, enzyme-linked 112
  - incorporation pathways, risk assessment 101
  - inflammation
    - air pollution 301, 303–304
    - biomarkers 45
    - diesel exhaust particles 300
    - epithelial 92
    - insoluble solids 58
    - lung 67–68, 298
    - metal oxide nanoparticles 168
    - new carbon modifications 172
    - pulmonary 300
    - transition metals 172, 302
    - ultrafine particles (UFP) 4, 94–95
  - inhalation
    - CNT toxicity 140
    - diesel exhaust particles 108
    - dust 140
    - insoluble solids 57–59
    - iron carbonyl particles 160
    - ultrafine particles (UFP) 163
  - inhaled nanoparticles, dosimetry 85–93
  - inorganic photocatalysts 217–221
  - insoluble particles
    - alveolar region 87–88
  - insoluble solids, health impact 57–59
  - in-solution quantification, nanosensors 278–279
  - insulin, aerosolized 61
  - internalization
    - carbon nanoparticles 121
    - caveolae 92
    - coated nanoparticles 12
    - nano-scaled particles 108
  - intestinal tract
    - entry routes 57, 61–62
  - intracellular calcium concentration, new carbon modifications 171
  - intracellular targets, nanoparticles 168
  - intrinsic toxicity, CNT 142
  - iridium particles
    - agglomerates 92
    - animals 89
  - iron carbonyl particles, inhaled 160
  - iron exchange resin (MIEX), magnetic 226
  - iron nanoparticles 214–218
    - palladized *see* palladized iron particles
  - iron oxide particles 9–13, 219, 305
  - iron sulfide nanoparticles 226
- k**
- key research areas, NP 46
  - Ki67 protein 16
    - detection 114–116
    - endothelial cell functions *in vitro* 112
    - particle internalization 122–123
- l**
- lactate dehydrogenase (LDH) 27, 143, 169
  - D,L-lactide-co-glycolide, particle internalization 121
  - Langmuir-Hinshelwood kinetic rate model, photocatalytic degradation 244
  - laser ablation process, carbon nanotubes 132
  - laser synthesized CNTs, lung tissues 144
  - layers
    - biocompatible coating 11
    - mono- *see* monolayers

- poly-L-lysine 279
  - LDH *see* lactate dehydrogenase
  - LDL *see* low density lipoproteins
  - lead magnesium niobate-lead titanate (PMT-PT), microcantilevers 288–289
  - lead zirconate titanate (PZT)
    - *Salmonella typhimurium* detection 282
    - microcantilevers 289
    - nanosensors 273
    - thick film 290
  - life-cycle assessment 176
  - ligands, chelating 198–199
  - light intensity
    - 17 $\beta$ -oestradiol 258
    - photocatalytic degradation 255–256
  - lipid mediator release 164
  - liquids *see* dense non-aqueous phase liquids (DNAPLs)
  - liver 64–67
    - air pollution 308–309
    - particle translocation 88–89, 163
  - living organisms, nanomaterial toxicity 160
  - low density lipoproteins (LDL)
    - oxidized 305
    - receptor 69, 121
  - lung
    - aerosolized insulin 61
    - asbestos fiber 9
    - carbon nanotubes 59
    - diesel exhaust particles 67
    - entry routes 57–61
    - epithelial barrier 60
    - epithelial cells 162, 165–166
    - epithelium, permeability 305
    - fibers 58
    - free radicals 68
    - histopathology 143
    - inflammation 67–68, 298
    - laser synthesized CNTs 144
    - particle deposition 57–59, 87–88, 160–161, 166
    - tissues 144
    - ultrafine particles (UFP) 5
  - lymphatic system, air pollution 304
  - lymphatic tissue (PP), intestinal 61
- m**
- macrophages
    - coated nanoparticles 11
    - nanomaterial toxicity 165
    - particle transport 88
    - phagocytosis 161
  - magnetic iron exchange resin (MIEX) 226
  - magnetosomes, biotoxicity 10
  - man-made nanoparticles (NP) *see* artificial nanoparticles, nanoparticles
  - manufactured carbon nanotubes 132, 139–146
    - potential occupational exposures 134–136
    - *see also* carbonnanoparticles, CNTs, fullerenes, SWCNTs, MWCNTs
  - MAPK *see* mitogen-activated protein kinase
  - matter induced adverse health effects 84–85
  - 3-mercaptopropyltrimethoxysilane, water treatment 222
  - mercury
    - adsorption 200
    - pressure lamp 251–253
    - removal 202, 222–223
  - mesoporous silicates, water treatment 222
  - mesoporous supports 200–205
  - metal catalysts 139, 174, 264
  - metal oxides
    - acute toxicity 168
    - biological effects 165–170
    - biotoxicity 3–34
    - cytoskeletal organization 161, 169
    - human osteoblast-like cells 170
    - inflammation 168
    - osteoblast-like cells 170
    - production 157–159
    - surface area effects 26
    - toxicity (general) 153–185
  - metal particle cytotoxicity 122
  - metal phosphonates, nanostructured 196–200
  - metallic nanoparticles 108–129
    - endothelial cell functions *in vitro* 110
    - particle size 113
    - pro-inflammatory capacity 119, 123–124
  - 3-(4,5-dimethylthiazol-2-yl)-2,5-diphenyl-tetrazolium bromide (MTT) *see also* dimethyl-thiazol-2-yl)-diphenyltetrazolium bromide
  - MgO aerogel 191
  - mice, SWCNTs 142–143, 145–146
  - microbial growth, soils 42
  - microbial P450s, biomarkers 44
  - microcantilevers
    - piezoelectric 271–272
    - PMN-PT/Cu 288–289
    - PZT/SiO<sub>2</sub> 289
    - silicon-based 272
  - microscopy, transmission electron *see* transmission electron microscopy
  - MIEX *see* magnetic iron exchange resin
  - miniaturization, piezoelectric cantilevers 287–290

- mitochondria
  - damage 100
  - enzymatic conversion 16, 112
  - metabolic activity 168
  - MTTassay 309
  - nanomaterial toxicity 165
- mitogen-activated protein kinase (MAPK) 172
- MnO<sub>2</sub> particles 26–27
- monolayers
  - acid-base chemistry 191
  - endothelial cells 113
  - HDMEC 115
  - microcantilevers 289
  - self assembled 200–205, 221–226
- mortality
  - *Daphnia magna* 41
  - cardiovascular 159, 302, 308
  - excess 148
  - nanoparticles 55–56
  - risk 297
- MTT *see* 3-(4,5-dimethylthiazol-2-yl)-2,5-diphenyltetrazolium bromide
- mucociliary escalator 58
- multi-wall CNTs (MWCNTs) 133
  - aggregates 145
  - air pollution 137–138
  - bronchial lumen 146
  - diesel-related aggregates 137
  - environmental concerns 138–139, 147–148
  - formation *see* MWCNT formation
  - fuel combustion 139
  - health effects 147–148
  - ice sample 137
  - metropolitan outdoor air 137
  - skin 64
  - toxicity 130, 146–148, 158
- murine fibroblasts, biotoxicity 25
- MWCNT formation 131, 136–140
- MWCNTs *see* multi-wall CNTs
  
- n**
- nanocomposites, water treatment 225
- nanocrystalline photocatalysts, water treatment 219
- nano-iron, ecotoxicity 39, 41
- nanomaterial toxicity 153–185
  - accumulation 160
  - aggregates 157
  - cadmium oxide particles 161
  - carbon black 157
  - carbon fibers 158
  - cellular mechanisms 164–175
  - DNA 165
  - endolysosomes 164
  - exposure estimation 156–157
  - ion channels 164
  - precautionary measures 155–156
  - primary particle aggregates 157
  - SWCNTs 158
- nanomaterials
  - biotoxicity 6, 9
  - commercial 154
  - definition 4
  - endothelial cell functions *in vitro* 111–120
  - engineered 35
  - environmental remediation 189–210
  - health impact 53–80
  - risks 177–179
  - synthesis 189–190
  - transport 160–164
  - water treatment 211–233
- nanoparticle dosimetry 81–107
  - brain 89
  - caveolae 92
  - drug delivery 92
  - inhaled nanoparticles 85–93
  - PM exposure 96
  - predisposition 94
  - prothrombotic effects 91
- nanoparticle exposure, endothelial cells 110
- nanoparticle movement
  - ecotoxicity 38
  - soils 43
- nanoparticle toxicology 67–68, 81–107, 294–318
  - dosimetry 96–100
  - number concentration 96–97
  - size effects 65–67, 109
- nanoparticle-based remediation materials 190–196
- nanoparticle-induced effects, endothelial cell functions *in vitro* 110
- nanoparticles (NP)
  - air pollution 54, 304–306
  - alveolar region 87
  - anthropogenic 53
  - artificial 54, 71
  - asthma 55
  - carbon *see* carbon nanoparticles
  - cell culture 111
  - cell internalization 12
  - ceramic 108–129
  - ceria 226
  - coated 11, 38
  - coronary heart disease 55



- Crohn's disease 62, 309
- cytotoxicity 14, 16, 116, 122, *see also* cytotoxicity
- diesel exhaust particles 54
- disease 71
- dissemination 109
- drug delivery 92
- endothelial cells 108–129
- entry routes 56–57
- environmental aspects (general) 5–8, 36
- environmental remediation 192
- epidemiology 54–56, 81–107
- exposure routes 70
- genotoxicity *see* genotoxicity
- hazards 83
- health effects 8–9, 83–84, 93–100, 124
- human endothelial cells *see* human dermal microvascular endothelial cells (HDMEC)
- inhaled 85–93
- interferences 109
- intestinal tract 57
- intestinal translocation 62
- intracellular targets 168
- iron 214–218
- iron sulfide 226
- LDL particles 69
- man-made *see* artificial nanoparticles
- metal oxide *see* metal oxide nanoparticles
- metallic *see* metallic nanoparticles
- mortality risk 56
- natural *see* natural nanoparticles
- osteoblast-like cells 170
- penetration routes 7, 62–64
- photocatalytic removal 234–270
- PM 298–300
- pro-inflammatory effects 117
- quantum effects 82–83
- reactivity 191
- respiratory tract 57
- risk assessment 101–102
- safety issues 83
- size distribution 82, 299
- skin 57
- sources 53–54
- spherical 190
- standard toxicity tests 45
- surface area 82, 90, 96–97, 189–195
- synthetic 6
- titanium dioxide *see* titanium dioxide
- toxic 44
- toxicity 109
- toxicology *see* nanoparticle toxicology
- ULTRA project 55
- uptake 69
- UV irradiation studies 19
- water treatment applications 238–243
- zero-valent iron *see* zero-valent iron nanoparticles
- nanoparticulate aerogel, environmental remediation 191
- nanoscale iron particles, water chemistry 218
- nanoscale materials, toxicity 155–156
- nanoscale powders, nontoxic 167
- nanoscaled particles *see* nanoparticles
- nanoscaled TiO<sub>2</sub>, toxicity 161
- nanosensors 271–293
  - cantilever miniaturization 287–290
  - cantilever resonance frequency 278
  - PECS 273–278
  - PEMS 271–272
  - polystyrene spheres 280–281
  - target antigens 272
- nanosized particles (NSPs)
  - ecotoxicity 35, 43
  - *see also* nanoparticles
- nanostructured metal phosphonates 196
- nanostructured remediation materials, hybrid 196–205
- nanotechnology, health 131–132
- nanotoxicology 64
  - branched molecules 66
  - endotoxins 68
  - *see also* nanomaterial toxicity
- nanotubes
  - carbon *see* carbon nanotubes
  - health effects 97–98
  - manufactured *see* manufactured carbon nanotubes
  - toxicity 164
  - *see* fullerenes
- natural gas combustion
  - environmental health 147
  - MWCNT formation 137
- natural nanoparticles
  - biotoxicity 6
  - health impact 54
- natural oestrogens
  - photocatalytic degradation 245–251, 259–262
  - photocatalytic removal 235
- natural organic matter (NOM) 212
- nerve gas simulants detection, nanosensors 286–287
- nervous system, air pollution 309
- neurogenic inflammation, ultrafine particles (UFP) 94

- new carbon modifications
  - biological effects 164–175
  - calcium concentration 171
  - production 157–159
- new materials, risks 177–179
- NOM *see* natural organic matter
- non-manufactured carbon nanotubes 139
- non-metallic solid materials, skin 63
- nonpiezoelectric extension, nanosensors 276
- nontoxic nanoscale powders, biological effects 167
- NP *see* nanoparticles
- NSP *see* nanosized particles
- nucleic acids
  - photooxidative damage 20
  - *see also* DNA
- number concentration, nanoparticle toxicology 96–97
- o**
- occupational health, carbon nanotubes 130–152
- 17 $\beta$ -oestradiol
  - photocatalysis 254
  - photocatalytic degradation 243–245, 251–259
  - photocatalytic removal 235
  - photolysis 247, 255, 258
- oestriol, photocatalytic degradation 251–259
- oestrogen levels, photocatalytic removal 237
- oestrogenic activity, photocatalytic degradation 249, 253
- oestrogenic contamination 237, 246
- oestrogenicity, rapid loss 245–251
- oestrogens
  - *Escherichia coli* 236
  - environment 235–238
  - natural *see* natural oestrogens
  - photocatalytic degradation 245–251, 259–262
  - photocatalytic removal 235–238
  - recombinant assay 248
  - steroid 236
  - synthetic *see* synthetic oestrogens
- oestrone, UVA photolysis 248
- oil, contaminated 200
- organic compounds, health effects 99–100
- organic photoelectrochemistry 264
- organic pollutants, endocrine-disrupting chemicals 239
- organic solvents, nanoparticles 38
- organophosphonate pesticides, environmental remediation 190
- osmosis, reverse 212
- osteoblast-like cells, metal oxide nanoparticles 170
- oxidative stress
  - air pollution 305
  - hierarchic model 68
  - ultrafine particles (UFP) 97
- 8-oxo-7,8-dihydro-20-deoxyguanosin (8-oxo-dG), carbon black 172
- p**
- P450s, biomarker 44
- PAH *see* poly aromatic hydrocarbons
- palladized iron particles
  - environmental remediation 194
  - water treatment 215
- particle deposition
  - airway wall 86–87
  - ciliated airways 88
  - diffusion mechanism 86
  - intestinal tract 61–62
  - lung 57–59, 160, 166
  - respiratory system 86–87
  - skin 62, 304
- particle internalization 121–122
- particle measures, dosimetry 85
- particle origin, endothelial cell functions *in vitro* 108–110
- particle shape, health effects 97–98
- particle size
  - biotoxicity 26
  - metallic nanoparticles 113
  - nanotoxicology 65–67
- particle translocation
  - animals 89–93
  - humans 88
  - liver 88–89, 163
  - vascular effects 304–306
- particle transport, macrophage-mediated 88
- particle–cell interactions 171
  - biological effects 171
- particles
  - air pollution 296–298
  - endothelial cell functions *in vitro* 111
  - *see* nanoparticles, *see* slowly dissolving particles
- particulate matter (PM)
  - air pollution 296
  - environmental 138
  - epidemiological studies 296–298
  - health effects 83–84
  - nanoparticle dosimetry 96
  - nanoparticles 298–300
  - toxic potency 298
  - toxicology 84–85

- urban *see* urban particulate matter
- PECS *see* piezoelectric cantilever sensors
- PEG *see* poly(ethylene glycol)
- PEMS *see* piezoelectric microcantilever sensors
- penetration routes, nanoparticles 7, 62–64
- phagocytosis
  - air pollution 304
  - cytotoxicity 25
- phenylphosphonic acid, environmental remediation 197
- phosphate buffered saline (PSB), cytotoxicity 22
- phospholipases A<sub>2</sub> (PLA<sub>2</sub>), new carbon modifications 172
- phosphonates, nanostructured 196–200
- photocatalysis 245–251
  - 17 $\beta$ -oestradiol 254
  - endocrine-disrupting chemicals 237
  - oestrogen degradation 259–262
  - reaction conditions 263
  - titanium dioxide 234, 239–243, 261
- photocatalysts
  - band gap energy 219
  - inorganic 217–221
  - metal 264
  - titanium dioxide nanoparticles 240
- photocatalytic degradation 243–245
  - 17 $\alpha$ -ethinyloestradiol 251–259
  - 17 $\beta$ -oestradiol 243–245, 251–259
  - chlorophenol red- $\beta$ -D-galactopyranoside 246
  - fluorescence spectroscopy 251–259
  - Langmuir-Hinshelwood kinetic rate model 244
  - light intensity 255–256
  - oestriol 251–259
  - oestrogens 245–251, 253, 259–262
  - quartz coil reactor 251–259
  - quartz water-jacketed reactor 244
  - spiral reactor 259–260
  - TiO<sub>2</sub> catalyst 243–245, 261
  - UV radiation 245–251, 259–262
  - volumetric reaction rate 256
  - xenoestrogens 250
  - yeast bioassay 245–251
- photocatalytic detoxification
  - wastewater 217
  - water treatment 217
- photocatalytic removal 234–270
  - 17 $\alpha$ -ethinyloestradiol 236
  - 17 $\beta$ -oestradiol 235
  - anatase 240
  - band gap model 242
  - chalcogenides 240
  - endocrine-disrupting chemicals 234–270
  - hydroxyl radicals 242
  - oestrogens 235–238
  - rutile 240
- photochemical smog, air pollution 295
- photoelectrochemistry, organic 264
- photolysis, UVA 238, 245–251
- photosynthesis, ecotoxicity 43
- phototoxicity, UV irradiation studies 21
- photooxidative damage, nucleic acids 20
- piezoelectric cantilever sensors (PECS) 273–278
- piezoelectric cantilevers, miniaturization 287–290
- piezoelectric microcantilever sensors (PEMS) 271–272
- PLA<sub>2</sub> *see* phospholipases A<sub>2</sub>
- plaque rupture, air pollution 303–304
- plasmids, titanium dioxide cytotoxicity 14
- PLGA *see* poly(D,L-lactic-co-glycolic acid)
- PM *see* particulate matter
- PMN-PT *see* lead magnesium niobate-lead titanate
- poly(D,L-lactic-co-glycolic acid) (PLGA) 63
- poly-L-lysine layer, nanosensors 279
- polyaromatic hydrocarbons (PAH) 99
  - environmental remediation 190
- polycatalytic bactericidal effects, titanium oxide 20
- polycationic macromolecules, nanotoxicology 66
- poly(ethylene glycol) (PEG)
  - aggregation 196
  - coatings 66–67
  - nanoparticles solubility 38
- polystyrene spheres 280–281
  - intestinal tract 62
  - nanotoxicology 67
- PP *see* lymphatic tissue
- pro-inflammatory activation, metallic nanoparticles 123–124
- pro-inflammatory capacity, metal nanoparticles 119
- pro-inflammatory effects, nanoparticles 117
- pro-inflammatory stimulation, HDMEC 120
- proliferation inhibitor, biotoxicity 27
- protein expression, endothelial cell functions *in vitro* 112
- proteins
  - cell membrane 164
  - cytotoxicity 122–123
  - E-selectin 119
  - inflammation 45, 68

- proteins (*cont.*)
  - lipo- *see* lipoproteins
  - natural materials 5
  - NP coating 38
  - NP contact 170–171
  - oxidized 12
  - risk assessment 101–102
  - soil 43
  - soluble particle binding 87
  - target 280
  - UV radiation 18
- prothrombotic effects
  - nanoparticle dosimetry 91
  - nanotoxicology 67–68
- PSB *see* phosphate buffered saline
- Pseudomonas aeruginosa*, cytotoxicity 23
- pulmonary clearing, insoluble solids 57–59
- pulmonary effects, combustion-derived nanoparticles 300–301
- pulmonary inflammation, ultrafine particles (UFP) 94–95
- pulmonary toxicity studies, animals 141
- PZT *see* lead zirconate titanate
  
- q**
- quantum dots, nanotoxicology 69–70
- quantum effects, nanoparticles 82–83
- quartz, exposure risk 147
- quartz coil reactor, photocatalytic degradation 251–259
- quartz water-jacketed reactor, photocatalytic degradation 244
  
- r**
- radiation effects, photocatalytic degradation 259–262
- rat alveolar macrophages, nanomaterial toxicity 165
- rat lung overload, air pollution 302
- rats, SWCNTs 143–145
- recombinant oestrogen assay, photocatalytic degradation 248
- recombinant yeast assay, photocatalytic degradation 245
- remediation, environmental *see* environmental remediation
- remediation materials
  - hybrid nanostructured 196–205
  - nanoparticle-based 190–196
- removal
  - arsenate 224
  - photocatalytic *see* photocatalytic removal
- resin, magnetic iron exchange 226
- resonance frequency, nanosensors 275, 278
- respiratory epithelium, ultrafine particles (UFP) 95
- respiratory system
  - deposition 86–87
  - dosimetry 86–87
- respiratory tract
  - insoluble solids 57
  - nanoparticles entry routes 57
- reverse osmosis (RO), water treatment 212
- risk assessment 101–102
  - hazard 176–179
  - incorporation pathways 101
  - nanomaterial toxicity 156
- risk characterization
  - nanomaterials 176–179
- risks
  - CNTs 146–148
  - health *see* health risk
  - mortality *see* mortality
  - technologically-initiated 177–179
- RO *see* reverse osmosis
- rutile 13–24
  - photocatalytic removal 240
  - *see also* anatase, titanium dioxide
  
- s**
- safety issues, nanoparticles 83
- Salmonella typhimurium*, nanosensors 271–272, 281–286
- SAM *see* self-assembled monolayer
- SAMMS *see* self-assembled monolayers on mesoporous supports
- SC *see* stratum corneum
- self-assembled monolayer (SAM) 200–200, 221–226
  - *see also* monolayers
- self-assembled monolayers on mesoporous supports (SAMMS) 200–205
  - binding 223
  - thiol *see* thiol-SAMMS
- semiconductor particles, water treatment 220
- semiconductor photocatalysis, endocrine-disrupting chemicals 237
- sensors 271–273
  - glass cantilever 284–286
  - piezoelectric 271–278
  - *see also* nanosensors
- silicate material 221
  - mesoporous 222
- single-wall CNTs (SWCNTs) 133
  - air pollution 135
  - fibers 134
  - free radicals 174
  - guinea pigs 142

- health effects 147
  - mice 142–143, 145–146
  - nanomaterial toxicity 158
  - physical properties 133
  - rats 143–145
  - skin 64
  - toxicity 130
  - size effects 167
    - nanoparticle toxicology 65–67, 109
  - skin
    - irritation by fibers 64
    - irritation by nanotubes 174
    - nanoparticle deposition 304
    - nanoparticle entry routes 57
    - nanoparticle penetration 62–64
  - slowly dissolving particles, lung 87
  - smog, air pollution 294
  - SOD *see* superoxide dismutase
  - soils 42–43
    - contaminated 196, 238
  - soluble particle compounds, particle deposition 87
  - spherical particles, environmental remediation 190
  - spiral reactor, photocatalytic degradation 259–260
  - standard toxicity tests 45
  - steroid oestrogens 236
    - *see also* oestrogens
  - stratum corneum (SC), entry routes 63
  - superoxide dismutase (SOD), cell survival 23
  - superparamagnetic particles 10–11
  - surface area
    - metal oxides 26
    - *see* nanoparticles, surface area
  - surface charges, particle size 65–67
  - surfactants
    - nanotoxicology 66
    - SAM 221
    - SAMMS 200
    - water treatment 222
  - SWCNTs *see* single-wall CNTs
  - synthesis
    - ferrocyanide Cu-EDA SAMMS 204
    - manufactured carbon nanotubes 132
    - nanomaterial 189–190
  - synthetic oestrogens, photocatalysis 235, 245–251, 259–262
    - *see also* oestrogens
  - systemic circulation 60
    - radioactivity 109
    - ultrafine particles (UFP) 88–93
  - systemic inflammation, ultrafine particles (UFP) 95–96
  - systemic particle translocation *see* particle translocation
- t**
- target antigens, binding 272
  - target protein, binding 280
  - TCE *see* trichloroethylene
  - Technegas, endothelial cell functions *in vitro* 109
  - TEM *see* transmission electron microscopy
  - terminology, toxicology 35
  - testing, nanoparticle-induced effects 110
  - tetrahydrofuran (THF) 39
  - THF *see* tetrahydrofuran
  - thiol-functionality, water treatment 222
  - thiol-SAMMS
    - binding affinity 223
    - performance 200–202
  - THM *see* trihalomethanes
  - thrombosis
    - air pollution 307–308
    - diesel exhaust particles 91, 307
    - nanotoxicology 67–68
  - thyroid function, abnormal 236
  - TiO<sub>2</sub> *see* titanium dioxide
  - titanium dioxide
    - agglomerates 92
    - biotoxicity 13–26
    - crystallographic forms 13
    - dark studies 14–18
    - endocrine-disrupting chemicals 240–241
    - immobilized 243–245
    - photocatalysis 234, 239–243, 261
    - polycatalytic bactericidal effects 20
    - skin 63
    - transmission electron microscopy 22
    - UV irradiation studies 19
  - titanium oxide, DNA tail length 21
  - TOC *see* total organic carbon
  - total organic carbon (TOC) 212, 236, 250
  - toxic metals, binding 43
  - toxic potency, PM components 298
  - toxicity 1–50
    - acute 168
    - adverse health effects 155–156
    - aggregates 140, 157
    - air 42
    - air pollution 148
    - ALARA principle 155
    - alveolar duct bifurcations 160
    - alveolar macrophages 165
    - anatase 13
    - animals 59, 130, 141–142
    - asbestos fibers 9

- toxicity (*cont.*)
  - binuclear cells 27
  - biocompatible coating layers 11
  - biomarkers 44–46, 143, 145, 148
  - carbon conformations 153–185
  - carbon fibers 158
  - carbon nanotubes 130–152, 164
  - CNTs 139–148
  - metal oxides 153–185
  - MWCNTs 130, 146–148
  - risk assessment 156
  - size-dependent 109
  - standard tests 45
  - SWCNT 130
  - SWCNTs 158
- toxicological impacts 175–176
- toxicological plausibility, health effects 93–100
- toxicological studies, carbon nanotubes 139–146
- toxicology 81–107
  - environmental air pollution 294–318
  - nanoparticles *see* nanoparticle toxicology
  - terminology 35
- transepidermal penetration, entry routes 7
- transition metals 122–123
  - health effects 98
  - inflammation 172, 302
- translocation
  - direct vascular effects 304–306
  - intestinal tract 61–62
  - lung 60–61
  - systemic circulation 88–93
- transmission electron microscopy (TEM)
  - endothelial cell functions *in vitro* 111
  - metal oxide particles 164
  - TiO<sub>2</sub> 22
- trichloroethylene (TCE)
  - contamination 216–217
  - dechlorination 194
- trihalomethanes (THM), water treatment 212, 218
- tumors
  - diesel exhaust particles 173
  - TiO<sub>2</sub> 169
- u**
  - UFP *see* ultrafine particles
  - ULTRA project, nanoparticles health impact 55
  - ultrafine particles (UFP) 35
    - adverse health effects 159
    - air 42
    - cardiovascular disease 95
    - cilia 5
    - deposition 86–87
    - entry route 53
    - epidemiological studies 84
    - health effects 159
    - inflammation 94–95
    - inhalation 163
    - oxidative stress 97
    - radioactively labeled 91
    - respiratory epithelium 95
    - respiratory system 86–87
    - systemic circulation 88–93
    - systemic inflammation 95–96
    - titanium oxide 15
  - ultraviolet photolysis 238, 245–251
  - UPM *see* urban particulate matter (UPM)
  - upregulation, enzymes 44–45
  - uptake, cellular 69, 162
  - urban particulate matter (UPM) 70, 298
  - UV irradiation studies 18–26
  - UVA photolysis 238, 245–251
  - UVA radiation, photocatalytic degradation 259–262
  - UVC radiation
    - photocatalytic degradation 259–262
    - water treatment 250
- v**
  - vacuoles
    - CNTs 64
    - endothelial cell functions *in vitro* 114
    - particle internalization 121–122
  - vascular effects, particle translocation 304–306
  - vesiculovacuolar organelle (VVO), particle internalization 121
  - vibration, nanosensors 274
  - vibration amplitude, nanosensors 277
  - volumetric reaction rate, photocatalytic degradation 256
  - VVO *see* vesiculovacuolar organelle
- w**
  - waste, thiol SAMMS performance 201–202
  - wastewater 236–239, 264
    - photocatalytic detoxification 217
  - water 38–42
    - oestrogen degradation 259–262
    - quality parameters 212
  - water chemistry, nanoscale iron particles 218
  - water treatment
    - 3-mercaptopropyltrimethoxysilane 222
    - anion removal 224
    - applications 238–243

- arsenate removal 224
  - ceria nanoparticles 226
  - coagulation 212–213
  - contaminants 214, 216
  - corrosion 214–215
  - detoxification 217
  - functionalized SAMs 221–226
  - inorganic photocatalysts 217–221
  - mesoporous silicates 222
  - nanocomposites 225
  - nanocrystalline photocatalysts 219
  - nanomaterials 211–233
  - semiconductor particles 220
  - sodium alkyl aryl sulfonate 224
  - surfactants 222
  - trihalomethanes (THM) 212, 218
  - UVC radiation 250
  - zero-valent iron (ZVI) nanoparticles 214
  - weathering 43–44
- x**
- xenoestrogens, photocatalytic degradation 250
- y**
- yeast
    - bioassay 245–251
    - nanosensors 278–279
- z**
- zero-valent iron (ZVI) nanoparticles
    - contaminations 194–196
    - water treatment 214
  - zinc biphenylenebis(phosphonate) 198
  - Zr N-(phosphonomethyl)iminodiacetic acid 199
  - ZrO<sub>2</sub> 162
  - ZVI nanoparticles *see* zero-valent iron nanoparticles





Nanotechnologies for the Life Sciences

Edited by Challa Kumar

WILEY-VCH

# Nanomaterials for Cancer Therapy



**NtLS** 

## Contents

Preface XIII

List of Contributors XVII

<b>1</b>	<b>Conventional Chemotherapeutic Drug Nanoparticles for Cancer Treatment</b>	<b>1</b>
	<i>Loredana Serpe</i>	
1.1	Introduction	1
1.2	Cancer as Drug Delivery Target	2
1.3	Nanoparticles as Anticancer Drug Delivery System	4
1.3.1	Conventional Nanoparticles	5
1.3.2	Sterically Stabilized Nanoparticles	6
1.3.3	Actively Targetable Nanoparticles	8
1.3.4	Routes of Drug Nanoparticles Administration	10
1.4	Anticancer Drug Nanoparticles	12
1.4.1	Anthracyclines	12
1.4.1.1	Reverse of P-glycoprotein Mediated Multidrug Resistance of Cancer Cells to Doxorubicin	17
1.4.2	Antiestrogens	19
1.4.3	Anti-metabolites	20
1.4.4	Camptothecins	20
1.4.5	Cisplatin	21
1.4.6	Paclitaxel	21
1.4.7	Miscellaneous Agents	26
1.4.7.1	Arsenic Trioxide	26
1.4.7.2	Butyric Acid	26
1.4.7.3	Cystatins	26
1.4.7.4	Diethylenetriaminepentaacetic Acid	26
1.4.7.5	Mitoxantrone	27
1.4.8	Gene Therapy	27
	References	30

<b>2</b>	<b>Nanoparticles for Photodynamic Therapy of Cancer</b>	<b>40</b>
	<i>Magali Zeisser-Labouèbe, Angelica Vargas, and Florence Delie</i>	
2.1	Introduction	40
2.2	Concept and Basis of Photodynamic Therapy and Photodetection	41
2.2.1	Mechanisms of Photodynamic Therapy and Photodiagnosis	41
2.2.2	Selective Tumor Uptake of Photosensitizers	43
2.2.3	Photosensitizers	45
2.2.3.1	Conventional Photosensitizers	45
2.2.3.2	New Entities	47
2.2.4	Photodynamic Therapy: Advantages and Limitations	51
2.2.5	Photosensitizer Formulations	53
2.3	Non-biodegradable Nanoparticles for Photodynamic Therapy	54
2.3.1	Metallic Nanoparticles	54
2.3.2	Ceramic Nanoparticles	55
2.3.3	Nanoparticles Made of Non-biodegradable Polymers	56
2.4	Biodegradable Polymeric Nanoparticles for Photodynamic Therapy	57
2.4.1	Preparation of Biodegradable Polymeric Nanoparticles	58
2.4.1.1	<i>In situ</i> Polymerization	58
2.4.1.2	Dispersion of a Preformed Polymer	59
2.4.1.3	“Stealth” Particles	60
2.4.1.4	Targeted Nanoparticles	60
2.4.2	<i>In Vitro</i> Relevance of Polymeric Nanoparticles in PDT on Cell Models	61
2.4.2.1	Photodynamic Activity of PS-loaded Nanoparticles	61
2.4.2.2	Uptake and Trafficking of Photosensitizers	66
2.4.3	<i>In Vivo</i> Relevance of Polymeric Nanoparticles in PDT	70
2.4.3.1	Biodistribution and Pharmacokinetics of Photosensitizers Coupled to Nanoparticles	70
2.4.3.2	Vascular Effects	71
2.4.3.3	<i>In Vivo</i> Efficacy on Tumor: Tumor Suppression Effects	73
2.4.3.4	Adverse Effects	74
2.5	Conclusions	75
	Acknowledgments	75
	Abbreviations	76
	References	77
<b>3</b>	<b>Nanoparticles for Neutron Capture Therapy of Cancer</b>	<b>87</b>
	<i>Hideki Ichikawa, Hiroyuki Tokumitsu, Masahito Miyamoto, and Yoshinobu Fukumori</i>	
3.1	Introduction	87
3.2	Principle of Neutron Capture Therapy of Cancer	88
3.3	Boron Neutron Capture Therapy	89
3.3.1	Boron Compounds	89
3.3.2	Delivery of Boron Using Nanoparticles	90
3.4	Approaches to GdNCT	93

3.4.1	Typical Research on GdNCT	94
3.4.2	Delivery of Gadolinium using Lipid Emulsion (Gd-nanoLE)	95
3.4.2.1	Preparation of Gd-nanoLE	95
3.4.2.2	Biodistribution of Gadolinium after Intraperitoneal Administration of Gd-nanoLE	98
3.4.2.3	Biodistribution of Gadolinium after Intravenous Administration of Gd-nanoLE	101
3.4.3	Delivery of Gadolinium using Chitosan Nanoparticles (Gd-nanoCPs)	104
3.4.3.1	Preparation of Gd-nanoCPs	105
3.4.3.2	Gd-DTPA Release Property of Gd-nanoCPs	107
3.4.3.3	Gd-DTPA Retention in Tumor Tissue after Intratumoral Injection	107
3.4.3.4	<i>In vivo</i> Growth Suppression of Experimental Melanoma Solid Tumor	108
3.4.3.5	Bioadhesion and Uptake of Gd-nanoCP in Three Different Cell Lines	109
3.5	Conclusions	113
	References	114
<b>4</b>	<b>Nanovehicles and High Molecular Weight Delivery Agents for Boron Neutron Capture Therapy</b>	<b>122</b>
	<i>Gong Wu, Rolf F. Barth, Weilian Yang, Robert Lee, Werner Tjarks, Marina V. Backer, and Joseph M. Backer</i>	
4.1	Introduction	122
4.1.1	Overview	122
4.1.2	General Background	123
4.2	General Requirements for Boron Delivery Agents	124
4.3	Low Molecular Weight Delivery Agents	124
4.4	High Molecular Weight Boron Delivery Agents	125
4.5	Dendrimer-related Delivery Agents	125
4.5.1	Properties of Dendrimers	125
4.5.2	Boronated Dendrimers Linked to Monoclonal Antibodies	126
4.5.2.1	Boron Clusters Directly Linked to mAb	126
4.5.2.2	Attachment of Boronated Dendrimers to mAb	129
4.5.3	Boronated Dendrimers Delivered by Receptor Ligands	127
4.5.3.1	Epidermal Growth Factors (EGF)	127
4.5.3.2	Folate Receptor Targeting Agents	129
4.5.3.3	Vascular Endothelial Growth Factor (VEGF)	129
4.5.4	Other Boronated Dendrimers	130
4.6	Liposomes as Boron Delivery Agents	130
4.6.1	Overview of Liposomes	130
4.6.2	Liposomal Encapsulation of Sodium Borocaptate and Boronophenylalanine	133
4.6.2.1	Boron Delivery by Non-targeted Liposomes	133
4.6.2.2	Liposomal Encapsulation of other Boranes and Carboranes	134

VIII | Contents

4.6.3	Boron Delivery by Targeted Liposomes	137
4.6.3.1	Immunoliposomes	137
4.6.3.2	Folate Receptor-targeted Liposomes	138
4.6.3.3	EGFR Targeted Liposomes	138
4.7	Boron Delivery by Dextrans	139
4.8	Other Macromolecules used for Delivering Boron Compounds	141
4.9	Delivery of Boron-containing Macromolecules to Brain Tumors	142
4.9.1	General Considerations	142
4.9.2	Drug-transport Vectors	142
4.9.3	Direct Intracerebral Delivery	142
4.9.4	Convection-enhanced Delivery (CED)	143
4.10	Clinical Considerations and Conclusions	144
	Acknowledgments	145
	References	145

**5 Local Cancer Therapy with Magnetic Drug Targeting using Magnetic Nanoparticles 156**

*Christoph Alexiou and Roland Jurgons*

5.1	Introduction	156
5.2	Local Chemotherapy	156
5.3	Magnetic Drug Delivery	158
5.3.1	<i>In Vitro</i> Applications	158
5.3.2	<i>In Vivo</i> Applications	159
	References	163

**6 Nanomaterials for Controlled Release of Anticancer Agents 168**

*Do Kyung Kim, Yun Suk Jo, Jon Dobson, Alicia El Haj, and Mamoun Muhammed*

6.1	Introduction	168
6.2	Nanoparticles for Biomedical Applications	170
6.2.1	First Generation Nanoparticles	171
6.2.2	Second Generation Nanoparticles	171
6.2.3	Advanced Generation Nanoparticles	172
6.3	Polymer Materials for Drug Delivery Systems	174
6.4	Design of Drug Delivery Vectors and Their Prerequisites	175
6.4.1	Polymeric Nanoparticles	175
6.4.2	Inorganic Nanoparticles	180
6.4.3	Metallic Nanoparticles	181
6.5	Kinetics of the Controlled Release of Anticancer Agents	181
6.5.1	Diffusion Model	182
6.5.2	Dissolution Model	183
6.5.3	Kinetics of the Indomethacin (IMC, 1-[ <i>p</i> -chlorobenzoyl]-2-methyl-5-methoxy-3-indoleacetic acid) Release	183
6.6	Controlled Release of Anticancer Agents	186

6.6.1	Alkylating Agents	186
6.6.1.1	Chlorambucil	187
6.6.1.2	Cyclophosphamide	187
6.6.1.3	Carmustine	188
6.6.2	Antimetabolic Agent	188
6.6.2.1	Cytarabine	188
6.6.2.2	Fluorouracil (FU)	189
6.6.2.3	Methotrexate	189
6.6.3	Anticancer Antibiotics	190
6.6.3.1	Actinomycin D	190
6.6.3.2	Bleomycin	190
6.6.3.3	Daunorubicin	191
6.7	Future Directions	191
	References	192
<b>7</b>	<b>Critical Analysis of Cancer Therapy using Nanomaterials</b>	<b>199</b>
	<i>Lucienne Juillerat-Jeanneret</i>	
7.1	Introduction	199
7.2	Anticancer Therapies	200
7.3	Characteristics of Nanoparticles for Cancer Therapy	202
7.3.1	Nanovectors	203
7.3.2	Biological Issues	205
7.3.3	Nanoparticle Targeting: Passive or Active	206
7.4	Nanovectors in Biomedical Applications: Drug Delivery Systems (DDS) for Cancer	207
7.4.1	Physicochemical Drug Delivery	208
7.4.2	Biological Drug Delivery	208
7.4.3	Chemical Drug Delivery	208
7.4.4	Nanoparticles for Anticancer Drug Delivery	209
7.4.4.1	Existing Systems	209
7.4.4.2	Systems under Development and Challenges	210
7.4.5	Nanoparticles for Drug Delivery in Clinical Use or under Clinical Evaluation	211
7.4.5.1	Doxorubicin Family	211
7.4.5.2	Paclitaxel (Taxol)	212
7.4.5.3	5-Fluorouracil	213
7.4.5.4	Tamoxifen	213
7.4.5.5	Cisplatin	213
7.4.5.6	Camptothecins	214
7.4.5.7	Methotrexate	214
7.4.6	New Experimental Drugs and Therapies	214
7.4.6.1	Proteins, Peptides, their Inhibitors and Antagonists	214
7.4.6.2	New Drugs	215
7.4.6.3	New Therapeutic Approaches: Photodynamic Therapy (PDT)	215

7.4.7	Gene Therapy	215
7.4.7.1	Nanoparticle for Gene Delivery: Non-chitosan and Chitosan-type Polymers	216
7.4.8	New Approaches	216
7.4.8.1	Improvement of Biological Characteristics	217
7.4.8.2	New Technological Approaches	219
7.4.9	Superparamagnetic Iron Oxide Nanoparticles (SPIONs) as Magnetic Drug Nanovectors	219
7.5	Targeting	220
7.5.1	Passive Targeting	222
7.5.2	Active Targeting	223
7.5.2.1	Targeting Cancer-associated Cells	223
7.5.2.2	Targeting Cancer Markers	224
7.5.3	Intracellular Drug Delivery	225
7.5.4	Development of the Necessary Chemistry: Synthetic Routes and Linkers for Conjugation	226
7.6	Overcoming the Mechanisms of Resistance to Therapy of Cancers	227
7.7	Toxicity Issues	229
7.8	Conclusions	231
7.8.1	Opportunities and Challenges of Nanomedicine in Cancer	231
	References	232
<b>8</b>	<b>Nanoparticles for Thermotherapy</b>	<b>242</b>
	<i>Andreas Jordan, Klaus Maier-Hauff, Peter Wust, and Manfred Johannsen</i>	
8.1	Introduction	242
8.2	Thermotherapy following Intratumoral Administration of Magnetic Nanoparticles	244
8.3	Ferromagnetic Embolization Hyperthermia	248
8.4	First Clinical Experiences with Thermotherapy using Magnetic Nanoparticles: MagForce Nanotherapy	249
8.4.1	Feasibility Study on Thermotherapy using Magnetic Nanoparticles in Recurrent Glioblastoma Multiforme	250
8.4.2	Feasibility Study on Thermotherapy using Magnetic Nanoparticles in Recurrent and Residual Tumors	251
8.4.3	Feasibility Study on Thermotherapy using Magnetic Nanoparticles in Recurrent Prostate Carcinoma	253
	References	254
<b>9</b>	<b>Ferromagnetic Filled Carbon Nanotubes as Novel and Potential Containers for Anticancer Treatment Strategies</b>	<b>259</b>
	<i>Ingolf Moench, Axel Meye, and Albrecht Leonhardt</i>	
9.1	Introduction	259
9.2	Prostate Cancer	260
9.2.1	Incidence, Risk Factors and Diagnostic Criteria	260
9.2.2	Treatment Options, Outcome and Limits	261

9.2.3	MWCNT Model	263
9.3	Carbon Nanotubes	264
9.3.1	General Remarks	264
9.3.2	Preparation and Structure of Filled Multi-walled Carbon Nanotubes	266
9.3.2.1	Synthesis of Ferromagnetic Filled Multi-walled Carbon Nanotubes	266
9.3.2.2	Crystallographic Structure of Core Material in Filled Multi-walled Carbon Nanotubes	269
9.3.2.3	Growth Mechanism of Multi-walled Carbon Nanotubes	271
9.3.3	Post-treatment: Opening, Filling and Closing of MWCNTs	275
9.4	Magnetism in Nano-sized Materials	277
9.4.1	General Remarks	277
9.4.2	Magnetization in Nano-sized Materials	278
9.4.3	Influence of the Dimensions on the Magnetization Distribution	279
9.4.4	Anisotropy and Interaction	283
9.4.5	Magnetic Reversal	284
9.4.6	Magnetic Properties of Filled Multi-walled Carbon Nanotubes	285
9.5	Heat Generation	290
9.5.1	General Remarks	290
9.5.2	Requirements for the Development of Materials for Hyperthermia and Magnetism	296
9.5.3	Specific Absorption Rate (SAR)	300
9.6	Study Results for <i>In Vitro</i> and <i>In Vivo</i> Applications of ff-MWCNTs	309
9.6.1	Efficient Endocytosis <i>In Vitro</i> , Lipid-mediated Could Enhance the Internalization Rate and Efficiency	309
9.6.2	Production of Two Types of ff-MWCNTs for <i>In Vivo</i> Application	312
9.6.3	Outlook/Next Steps in Evaluation of these fff-MWCNTs	313
	Acknowledgments	324
	Abbreviations	324
	References	325
<b>10</b>	<b>Liposomes, Dendrimers and other Polymeric Nanoparticles for Targeted Delivery of Anticancer Agents – A Comparative Study</b>	<b>338</b>
	<i>Yong Zhang and Dev K. Chatterjee</i>	
10.1	Introduction	338
10.2	Cancer Chemotherapy: so Far, but not so Good	339
10.3	Nanoparticles and Drug Delivery in Cancer: a new Road	341
10.3.1	Importance of Nanoparticles in Cancer Therapy	341
10.3.2	An Overview of Targeting Methods	343
10.4	Means to the End: Methods for Targeting	343
10.4.1	Passive Targeting	343
10.4.2	Magnetic Targeting of Nanoparticles	345
10.4.3	Ligands for Active Targeting	346
10.4.3.1	Monoclonal Antibodies against Tumor-specific Antigens	347
10.4.3.2	Targeting the Angiogenic Process	349



XII | Contents

10.4.3.3	Folic Acid and Cancer Targeting	350
10.4.3.4	Transferrin as a Targeting Ligand	354
10.4.3.5	Other Targeting Ligands	354
10.5	Targeting with Different Types of Nanoparticles	355
10.5.1	Liposomes in Cancer Targeting	355
10.5.1.1	Beyond Immunoliposomes	357
10.5.2	Dendrimers	357
10.5.3	Other Polymeric Nanoparticles	359
10.6	Conclusion	362
	References	364
<b>11</b>	<b>Colloidal Systems for the Delivery of Anticancer Agents in Breast Cancer and Multiple Myeloma</b>	<b>371</b>
	<i>Sébastien Maillard, Elias Fattal, Véronique Marsaud, Brigitte Sola, and Jack-Michel Renoir</i>	
11.1	Introduction	371
11.2	Hormone Therapy in Breast Cancers	374
11.2.1	Molecular Mechanisms of Estrogen Action in Breast Cancers	375
11.2.1.1	Classical ER-ligand and ERE-dependent Mechanism	375
11.2.1.2	ERE-independent Pathway	377
11.2.1.3	ER-ligand-independent Pathway	377
11.2.1.4	“Non-genomic” Pathway	378
11.2.2	Differential Activity of Antiestrogens	378
11.2.3	The Need to Encapsulate Antiestrogens	379
11.3	Multiple Myeloma	380
11.3.1	Current Treatments	380
11.3.2	New Biological Therapies for MM Treatment	380
11.3.3	Incidence of Estrogens and Antiestrogens on Multiple Myeloma	381
11.4	Colloidal Systems for Antiestrogen Delivery	381
11.4.1	Nanoparticles Charged with AEs in Breast Cancer	381
11.4.2	Liposomes Charged with RU 58668 in MM	386
11.4.3	Tumor-targeted Drug-loaded Colloidal Systems	387
11.5	Conclusions and Perspectives	390
	Acknowledgments	391
	References	391
	<b>Index</b>	<b>404</b>

## Preface

Even five years into the new millennium, cancer continues to torment humanity as the second leading cause of death with 10.9 million newly diagnosed cases worldwide in the year 2005 alone. Despite new discoveries of drugs and treatment combinations as evidenced by reports of close to 200,000 experimental studies on mice, two million scientific publications and an annual spending of around 15 billion US dollars world wide, the mortality rate due to cancer did not change in the past five to six decades. Therefore, there is still a strong need for a paradigm shift in the approach to cancer diagnosis and therapy. The advent of nanotechnological revolution offers an opportunity to achieve this paradigm shift. Since the biological processes in general and those that lead to cancer in particular occur at the nanoscale, there is a great opportunity for nanotechnologists to treat cancer at an as early stage as possible. Several innovative nanoscale constructs have been demonstrated to radically change cancer therapy with capabilities to deliver large doses of chemotherapeutic agents or therapeutic genes into malignant cells while sparing healthy cells. They have also shown great promise in enabling rapid and sensitive detection of single cancer cells and cancer-related molecules. Reports of these investigations are being published in a very broad range of journals spanning several traditional disciplines. It is becoming difficult for researchers to gather all the available information on 'Cancer Nanotechnology'. I am, therefore, pleased to share with you, again on behalf of dedicated team of researchers in cancer nanotechnology, two volumes of the ten volume series on nanotechnologies for the life sciences specifically dedicated to cancer. The first of these two volumes, sixth in the series, that is being presented to you here is dedicated to cancer therapy and is aptly titled as "*Nanomaterials for Cancer Therapy*."

The book is divided into eleven chapters encompassing a number of therapeutic approaches in cancer treatment through use of a variety of nanomaterials. It begins with a chapter reviewing the progress that has been made to date in utilization of conventional chemotherapeutic drug nanoparticles for cancer treatment. The chapter *Conventional Chemotherapeutic Drug Nanoparticles for Cancer Treatment* contributed by Loredanna Serpa from the University of Turin, Italy, is an up to date review of literature on advances being made in cancer treatment through use of nanoparticle formulations containing conventional chemotherapeutic drugs such as doxorubicin, cisplatin, paclitaxel and other drugs. Moving from conventional anticancer

drugs to conventional therapies that are being affected by nanotechnological tools, the second chapter starts with fundamental aspects of Photo Dynamic Therapy (PDT) that has been found to be promising in selectively treating tumors as well as metastasis without affecting the surrounding healthy tissue. The chapter *Nanoparticles for Photodynamic Therapy of Cancer*, written by Florence Delie and her team from the Laboratory of Pharmaceutical Technology and Biopharmaceutics, University of Geneva, Switzerland, provides an in-depth analysis of how nanoparticles, with special emphasis on polymeric biodegradable ones, are being developed to improve the conventional approaches to PDT. Continuing on a similar theme of improving conventional therapies, Yoshinobu Fukumori and co-workers from Kobe Gakuin University in Japan provide a general background on neutron capture therapy (NCT), a new radiotherapy that differs from the conventional radiotherapies, in the third chapter. This is followed by the authors reviewing more specifically both gadolinium neutron capture therapy (GdNCT) and boron neutron capture therapy (BNCT) with reference to use of nanomaterials. The remainder of the chapter *Nanoparticles for Neutron Capture Therapy of Cancer* provides a detailed account of the authors' experiences in developing Gd-containing lipid nanoemulsions and chitosan nanoparticles to demonstrate the usefulness of nanoparticle technology in NCT. Addressing a different facet of NCT, the fourth chapter entitled *Nanovehicles and High Molecular Weight Delivery Agents for Boron Neutron Capture Therapy* focuses on various high molecular weight (HMW) agents consisting of macromolecules and nanovehicles such as monoclonal antibodies, dendrimers, liposomes, dextrans, polylysine, avidin and folic acid, epidermal and vascular endothelial growth factors (EGF and VEGF) as delivery vehicles for introducing boron atoms. In it, Gong Wu, Rolf F. Barth, Weilian Yang, Robert Lee, Werner Tjarks, Marina V. Backer and Joseph M. Backer from the Department of Pathology at Ohio State University in Columbus, USA, have done a remarkable job in describing procedures for introducing boron atoms into HMW agents in addition to providing information on their chemical properties, bio-distribution based on in vivo studies, delivery across the blood brain barrier and various routes of their administration. Overall, the work reported in chapters three & four is very valuable and exciting not only from the scientific point of view, but also from the commercial point of view as recently clinical BNCT trials mainly for brain tumors were carried out in Japan.

Switching gears from earlier parts of the book where applications of nanotechnology to already well established treatments for cancer are presented, the rest of the chapters describe 'non-traditional' and innovative approaches completely based on nanotechnology that are being investigated for cancer therapy. Christoph Alexiou and Roland Jurgons from the Policlinic for otorhinolaryngological Illnesses of Friedrich-Alexander University, Erlangen-Nuremberg, Germany, contributed the fifth chapter, *Local Cancer Therapy with Magnetic Drug Targeting using Magnetic Nanoparticles*, in which they review current literature on the use of magnetic nanoparticles in biomedicine in general and local chemotherapies, focusing especially on regional cancer therapy, in particular. In the sixth chapter, *Nanomaterials for Controlled Release of Anticancer Agents*, the team lead by Do Kyung Kim at the

Massachusetts Institute of Technology, Cambridge, USA, has done a remarkable job in capturing nuances of nanotechnologies, particularly those based on polymeric nanomaterials, being developed for controlled release of anticancer agents. In this chapter, the authors discuss various design aspects, theoretical models and kinetics of controlled release of anticancer drugs. The seventh chapter on the other hand provides a much broader perspective to cancer therapy using nanomaterials by providing a critical analysis of various approaches. While the chapter starts with a description of the tools of nanoparticle technology that can be used to treat cancer, it goes a step further in critically reviewing and discussing the advantages and drawbacks of nanoparticles for the targeted delivery of anticancer agents to defined cells of human cancers. The chapter entitled *Critical Analysis of Cancer Therapy using Nanomaterials* contributed by Lucienne Juillerat-Jeanneret from the University Institute of Pathology in Lausanne, Switzerland, concludes the section with a final section that describes the author's own design of how an ideal nanoparticulate system should be for the targeted treatment of human cancers.

Treating cancer using heat has been known for a long time as cells are known to undergo apoptosis when exposed to temperatures around 40 °C. Thermotherapy, as it is called, as performed using conventional approaches has several drawbacks. In the eighth chapter, *Nanoparticles for Thermotherapy*, a team of cancer specialists lead by Andreas Jordan describe, based on their own experience, how some of these drawbacks are being overcome using magnetic nanoparticles. The chapter is particularly valuable as the team from the Center of Biomedical Nanotechnology (CBN), Berlin, Germany, share their experience in conducting the first ever clinical trials with thermotherapy using magnetic nanoparticles. Moving conceptually to a more elegant approach, the ninth chapter entitled *Ferromagnetic Filled Carbon Nanotubes as Novel and Potential Containers for Anticancer Treatment Strategies* explores the feasibility of different applications using magnetic multi-walled CNTs (MWCNTs) more specifically as heat mediators for hyperthermia of solid tumors. While authors Ingolf Mönch et al. from the Leibniz Institute for Solid State and Materials Research in Dresden, Germany, are upbeat about potential opportunities in the use of different types of functionalized MWCNTs, they restrict their review to only those that are novel and those that have benefits specifically in the treatment of prostate cancer.

Several types of nanomaterials are currently being investigated for targeted delivery of anticancer agents and there is a need for understanding the pros and cons of using these different types of nanomaterials. Chapter ten written by Yong Zhang and Dev K. Chatterjee from the Division of Bioengineering at the National University of Singapore provides a platform for comparing the efficacy of different types of nanomaterials for targeted delivery. The chapter, *Liposomes, Dendrimers and other Polymeric Nanoparticles for Targeted Delivery of Anticancer Agents – A Comparative Study*, provides a unique perspective on different types of nanomaterials in general and three major types in particular that are gaining importance in this field. The chapter is a must for those interested in learning about background information on mechanisms and methods of targeting cancer cells. At this point of time, liposomes seem to have an edge over the other types of nanomaterials and in the au-

thor's own words, "the most exciting news is the performance of Epeius Biotechnologies Corporation's liposomal based active targeting system that delivers genetic material to treat several cancers, including pancreatic head carcinoma, which has one of the worst prognoses among all neoplasms." In the eleventh and final chapter of the book, the team lead by Jack-Michel Renoir from University of Paris-Sud in Châtenay-Malabry, France, focuses on the benefits of encapsulating a class of anticancer drugs known as antiestrogens (AEs) to improve antitumoral activities in vivo. In addition, the authors discuss in this chapter, *Colloidal Systems for the Delivery of Anticancer Agents in Breast Cancer and Multiple Myeloma*, the use of passive targeting through long-circulating drug delivery systems in different types of xenografts. They strongly believe that the approach using colloidal systems is promising not only for the administration of antiestrogens in estrogen-dependent breast cancers and multiple myeloma (MM), but also for the delivery of much more toxic anticancer agents such as taxol, thalidomide, bortezomib, VEGF inhibitors, farnesyltransferase inhibitors, histone transferase inhibitors and hsp90 inhibitors.

I am pleased by the broad range of useful information gathered by the dedicated contributors working in the area of cancer nanotechnology, and I am hoping that the book will be a guide for all those who wish to be associated with the growing field of 'Nanomaterials for Cancer Therapy'. I am indebted to all the authors for their extraordinary efforts and as always grateful to my employer, family, friends and Wiley VCH publishers for making this book a reality. I am thankful to you, the reader, who has taken time to join the journey with fellow cancer nanotechnologists. It will be my pleasure to hear back from you and I look forward to receiving your comments, suggestions and constructive criticism in order to make further improvements in the next editions of the book.

April 2006, Baton Rouge

*Challa S. S. R. Kumar*

# 1

## Conventional Chemotherapeutic Drug Nanoparticles for Cancer Treatment

*Loredana Serpe*

### 1.1 Introduction

Chemotherapy is a major therapeutic approach for the treatment of localized and metastasized cancers. The selective increase in tumor tissue uptake of anticancer agents would be of great interest in cancer chemotherapy since anticancer drugs are not specific to cancer cells. Routes of administration, biodistribution and elimination of available chemotherapeutic agents can be modified by drug delivery systems to optimize drug therapy.

This chapter focuses on progress in targeted treatment of cancer through the delivery of conventional anticancer agents via microparticulate drug carriers as nanoparticles. Briefly, nanoparticles may be defined as submicronic colloidal systems that are generally made of polymers and, according to the preparation process used, nanospheres (matrix systems) or nanocapsules (reservoir systems) can be obtained. The drug can either be directly incorporated during polymerization or by adsorption onto preformed nanoparticles [1].

The first part of this chapter pays particular attention to cancer as a drug delivery target and to the development of different types of nanoparticles as drug delivery device. The interaction of drug carrier systems with the biological environment is an important basis for designing strategies; these systems should be independent in the environment and selective at the pharmacological site. If designed appropriately, nanoparticles may act as a drug vehicle able to target tumor tissues or cells, protecting the drug from inactivation during its transport. The formulation of nanoparticles and physicochemical parameters such as pH, monomer concentration, added stabilizer and ionic strength as well as surface charge, particle size and molecular weight are important for drug delivery.

For instance, poly(acrylamide) nanocapsules, due to their polymeric nature, are stable in biological fluids and during storage, and can entrap various agents in a stable and reproducible way but, since they are not lysed by lysosomal enzymes, their clinical application is restricted [2]. The development of biodegradable polymers by the polymerization of various alkyl cyanoacrylate monomers and the association of anticancer agents with these poly(alkyl cyanoacrylate) polymers has

afforded further improvement. These colloidal drug carriers are biodegradable and can associate with various drugs in a non-specific manner. The binding capacity of these nanoparticles to dactinomycin (90%), vinblastin (36–85%) and methotrexate (15–40%) exceeds that of these drugs incorporated in liposomes [1].

Furthermore, certain types of nanoparticles are able to reverse multidrug resistance – a major problem in chemotherapy – and selectivity in drug targeting can be achieved by the attachment of certain forms of homing devices, such as a monoclonal antibody or lecithin [3].

Finally, the last part of the chapter reports some of the most significant and recently developed nanoparticle formulations for the delivery of specific anticancer agents.

## 1.2

### Cancer as Drug Delivery Target

Tumor blood vessels have several abnormalities compared with physiological vessels, such as a relatively high proportion of proliferating endothelial cells, an increased tortuosity and an aberrant basement membrane formation. The rapidly expanding tumor vasculature often has a discontinuous endothelium, with gaps between the cells that may be several hundred nanometers large [4, 5].

Macromolecular transport pathways across tumor vessels occur via open gaps (interendothelial junctions and transendothelial channels), vesicular vacuolar organelles and fenestrations. However, it remains controversial which pathways are predominantly responsible for tumor hyperpermeability and macromolecular transvascular transport [6].

Tumor interstitium is also characterized by a high interstitial pressure, leading to an outward convective interstitial fluid flow, as well as the absence of an anatomically well-defined functioning lymphatic network. Hence, the transport of an anticancer drug in the interstitium will be governed by the physiological (i.e., pressure) and physicochemical (i.e., composition, structure) properties of the interstitium and by the physicochemical properties of the molecule itself (i.e., size, configuration, charge, hydrophobicity). Physiological barriers at the tumor level (i.e., poorly vascularized tumor regions, acidic environment, high interstitial pressure and low microvascular pressure) as well as at the cellular level (i.e., altered activity of specific enzyme systems, altered apoptosis regulation and transport based mechanisms) and in the body (i.e., distribution, biotransformation and clearance of anticancer agent) must be overcome to deliver anticancer agents to tumor cells *in vivo* [1].

Colloidal nanoparticles incorporating anticancer agents can overcome such resistances to drug action, increasing the selectivity of drugs towards cancer cells and reducing their toxicity towards normal cells.

The accumulation mechanism of intravenously injected nanoparticles in cancer tissues relies on a passive diffusion or convection across the hyperpermeable tumor vasculature. Additional retention of the colloidal particles in the tumor inter-

stitium is due to the compromised clearance via lymphatics. This so-called “enhanced permeability and retention effect” results in an important intratumoral drug accumulation that is even higher than that observed in plasma and other tissues [7]. Controlled release of the drug content inside the tumoral interstitium may be achieved by controlling the nanoparticulate structure, the polymer used and the way by which the drug is associated with the carrier (adsorption or encapsulation).

However, anticancer drugs, even if they are located in the tumoral interstitium, can have limited efficacy against numerous tumor types because cancer cells are able to develop mechanisms of resistance. Simultaneous cellular resistance to multiple lipophilic drugs is one of the most important problems in chemotherapy. This drug resistance may appear clinically either as a lack of tumor size reduction or as the occurrence of clinical relapse after an initial positive response to antitumor treatment. Multidrug resistance is mainly due to overexpression of the plasma membrane P-glycoprotein, which is capable of extruding various generally positively charged xenobiotics, including some anticancer drugs, out of the cell. Multidrug resistance is always multifactorial when other mechanisms can be associated with this drug efflux pump in cancer cells, such as enzymatic function modification (topoisomerase, glutathione S-transferase) or altered intracellular drug distribution due to increased drug sequestration into cytoplasmic acidic vesicles [8]. P-glycoprotein probably recognizes the drug to be effluxed out of the cancer cell only when the drug is present in the plasma membrane, and not when it is located in the cytoplasm of lysosomes, after endocytosis. Many cancer cell types can develop resistance to doxorubicin, which is a P-glycoprotein substrate, therefore incorporation of this compound into nanoparticles to reverse multidrug resistance P-glycoprotein mediated has been extensively investigated [9]. Certain types of nanoparticles are able to overcome multidrug resistance mediated by the P-glycoprotein, such as poly(alkyl cyanoacrylate) nanoparticles [10].

The delivery of anticancer agents to a highly perfused tumoral lesion and the tumor cells response have been described through the development of a two-dimensional tumor simulator with the capability of showing tumoral lesion progression through the stages of diffusion-limited dormancy, neo-vascularization and subsequent rapid growth and tissue invasion. Two-dimensional simulations based on a self-consistent parameter estimation demonstrated fundamental convective and diffusive transport limitations in delivering anticancer drug into tumors via intravenous free drug administration or via 100 nm nanoparticles injected into the bloodstream, able to extravasate and release the drug into the tumoral tissue, or via 1–10 nm nanoparticles, able to diffuse directly and target the individual tumor cell. Even with constant drug release from the nanoparticles, homogenous drug-sensitive tumor cell type, targeted nanoparticle delivery and model parameters calibrated to ensure sufficient drug or nanoparticle blood concentration to kill all cells *in vitro*, analysis shows that fundamental transport limitations are severe and that drug levels inside the tumor are far less than *in vitro*. This leaves large parts of the tumor with inadequate drug concentration. Comparison of cell death rates predicted by simulations reveals that the *in vivo* rate of tumor reduction is



several orders of magnitude less than *in vitro* for equal chemotherapeutic carrier concentrations in the blood. Small nanoparticles equipped with active transport mechanisms would overcome the predicted limitations and result in improved tumor response [11].

### 1.3

#### Nanoparticles as Anticancer Drug Delivery System

The fate of a drug after administration *in vivo* is determined by a combination of several processes, such as distribution, metabolism and elimination when given intravenously or absorption, distribution, metabolism and elimination when an extravascular route is used. The result depends mainly on the physicochemical properties of the drug and therefore on its chemical structure. In recent decades, much work has been directed towards developing delivery systems to control the fate of drugs by modifying these processes, in particular the drug distribution within the organism. Nanoparticles loaded with anticancer agents can successfully increase drug concentration in cancer tissues and also act at cellular levels, enhancing anti-tumor efficacy. They can be endocytosed/phagocytosed by cells, with resulting cell internalization of the encapsulated drug. Nanoparticles may consist of either a polymeric matrix (nanospheres) or of a reservoir system in which an oily or aqueous core is surrounded by a thin polymeric wall (nanocapsules). Suitable polymers for nanoparticles include poly(alkyl cyanoacrylates), poly(methylidene malonate) and polyesters such as poly(lactic acid), poly(glycolic acid), poly( $\epsilon$ -caprolactone) and their copolymers [3].

Nanoparticles of biodegradable polymers can provide controlled and targeted delivery of the drug with better efficacy and fewer side-effects. Lipophilic drugs, which have some solubility either in the polymer matrix or in the oily core of nanocapsules, are more readily incorporated than hydrophilic compounds, although the latter may be adsorbed onto the particle surface. Nanospheres can also be formed from natural macromolecules such as proteins and polysaccharides, from non polar lipids, and from inorganic materials such as metal oxides and silica [3].

As cancer chemotherapeutic agents are often administered systemically, numerous biological factors, associated with the tumor, influence the delivery of the drugs to the tumors. Consequently, drug delivery systems to solid tumors have been redesigned and, subsequently, injectable delivery systems (i.e., solid lipid nanoparticles) have been developed as an alternative to polymeric nanoparticles for adequate drug delivery to solid tumors [12].

The introduction of synthetic material into the body always affects different body systems, including the defense system. Synthetic polymers are usually thymus-independent antigens with only a limited ability to elicit antibody formation or to induce a cellular immune response against them. However, they influence, or can be used to influence, the immune system of the host in many other ways. Low-immunogenic water-soluble synthetic polymers sometimes exhibit significant immunomodulating activity, mainly concerning the activation/suppression of NK

cells, LAK cells and macrophages. Some of them, such as poly(ethylene glycol) and poly[N-(2-hydroxypropyl)methacrylamide], can be used as effective protein carriers, as they can reduce the immunogenicity of conjugated proteins and/or reduce non-specific uptake of nanoparticle-entrapped drugs and other therapeutic agents [13].

### 1.3.1

#### Conventional Nanoparticles

Association of a cytostatic drug to colloidal carriers modifies the drug biodistribution profile, as it is mainly delivered to the mononuclear phagocytes system (liver, spleen, lungs and bone marrow). Once in the bloodstream, surface non-modified nanoparticles, (conventional nanoparticles), are rapidly opsonized and massively cleared by the fixed macrophages of the mononuclear phagocytes system organs.

The size of the colloidal carriers as well as their surface characteristics greatly influence the drug distribution pattern in the reticuloendothelial organs, since these parameters can prevent their uptake by macrophages. The exact underlying mechanism was not fully understood, but it was rapid and compatible with endocytosis. A high curvature (resulting in size < 100 nm) and/or a hydrophilic surface (as opposed to the hydrophobic surface of conventional nanoparticles) are needed to reduce opsonization reactions and subsequent clearance by macrophages [14]. Since conventional nanoparticles are naturally concentrated within macrophages, they can be used to deliver drugs to these cells. The muramyl dipeptide, a low-molecular-weight, soluble, synthetic compound based on the structure of peptidoglycan from mucobacteria, stimulates the antitumoral activity of macrophages. Although it acts on intracellular receptors, it penetrates poorly into macrophages. Furthermore, it is eliminated rapidly after intravenous administration. These problems can be overcome by encapsulation within nanocapsules, and lipophilic derivatives such as muramyl tripeptide-cholesterol have been developed to increase encapsulation efficiency. *In vitro* studies have shown increased intracellular penetration of muramyl peptides into macrophages when they are associated with nanoparticles, increasing macrophage effector functions (i.e., nitric oxide, cytokine and prostaglandin production) and cytostatic activity against tumor cells [3].

The contribution of conventional nanoparticles to enhance anticancer drugs efficacy is limited to targeting tumors at the organs of the mononuclear phagocytes system organ. Owing to their very short circulation time (the mean half-life of conventional nanoparticles is 3–5 min after intravenous administration) addressing anticancer drug-loaded nanoparticles to other tumoral tissues is not reasonable. Moreover, penetration of such a carrier system across the tumoral endothelium would be minimum, leading to subtherapeutic concentrations of the drug near the cancer cells. This biodistribution can be of benefit for the chemotherapeutic treatment of mononuclear phagocytes system localized tumors (i.e., hepatocarcinoma, hepatic metastasis, bronchopulmonary tumors, myeloma and leukemia). Activity against hepatic metastases has been observed in mouse models, although this treatment is only therapeutic when the tumor load is low [15].

Both the polymeric composition of the nanoparticles and the associated drug greatly influence the drug distribution pattern in the mononuclear phagocytic system. Conventional nanoparticles, likely, have a better safety profile than free anticancer agents when acting on normal tissue. For example, a reduction of the cardiac accumulation of drugs [16] and of the genotoxicity of mitomycin [17] have been reported. Moreover, encapsulation of doxorubicin within nanoparticles reduces its cardiotoxicity by reducing the amount of drug that reaches the myocardium with a significant increase of drug concentrations in the liver. In one study this was not associated with any overall toxicity [18] while another study, using unloaded nanoparticles, observed a reversible decline in the phagocytic capacity of the liver after prolonged dosing, as well as a slight inflammatory response [19]. Accumulation of drug nanoparticles in the liver may also influence its elimination, since this organ is the site of metabolism and biliary excretion. Biliary clearance of indomethacin was increased three-fold by inclusion in nanocapsules [20]. Nanoparticle-associated doxorubicin accumulated in bone marrow and led to a myelosuppressive effect in one study [21]. Thus, altered distribution may generate new types of toxicity. When conventional nanoparticles are used as carriers in chemotherapy, some cytotoxicity against the Kupffer cells or other targeted macrophages can be expected, as the class of drugs being used is able to induce apoptosis in these cells. Treatments featuring frequent administrations (with intervals shorter than two weeks – the restoration period of Kupffer cells) could result in a deficiency of Kupffer cells, which in turn could lead to decreased liver uptake and a subsequent decreased therapeutic efficacy for hepatic tumors. In addition, a risk for bacteremia can not to be excluded [22]. Moreover, conventional carriers also target the bone marrow, hence chemotherapy with such carriers may increase myelosuppressive effects. However, this tropism of carriers can also be used to deliver myelostimulating compounds such as granulocyte-colony-stimulating factor [23].

Certain types of nanoparticles were also found to be able to overcome multidrug resistance mediated by the P-glycoprotein efflux system localized at the cancerous cell membrane. This simultaneous cellular resistance to multiple lipophilic drugs represents a major problem in cancer chemotherapy. Such drug resistance may appear clinically either as a lack of tumor size reduction or as the occurrence of clinical relapse after an initial positive response to antitumor treatment. The resistance mechanism can have different origins, either directly linked to specific mechanisms developed by the tumor tissue or connected to the more general problem of distribution of a drug towards its targeted tissue. Poly(alkyl cyanoacrylate) nanoparticles have been developed to overcome multidrug resistance [10]. Despite encouraging results with conventional carrier systems, much research has been dedicated to designing carriers with modified distribution and new therapeutic applications.

### 1.3.2

#### **Sterically Stabilized Nanoparticles**

Since the usefulness of conventional nanoparticles is limited by their massive capture by the macrophages of the mononuclear phagocytes system after intravenous

administration, systems with modified surface properties to reduce the disposition of plasma proteins and the recognition by phagocytes have been developed [14]. These are known as sterically stabilized carriers or “stealth carriers” and may remain in the blood compartment for a considerable time. The hydrophilic polymers poly(ethylene glycol), poloxamines, poloxamers, polysaccharides have been used to coat efficiently conventional nanoparticles’ surface [24]. These coating provide a dynamic cloud of hydrophilic and neutral chains at the particle surface that keep away plasma proteins [25]. Poly(ethylene glycol) (PEG) has been introduced at the surface either by adsorption of surfactants [24] or by using block or branched copolymers, usually with poly(lactide) [26, 27]. These Stealth™ nanoparticles are characterized by a prolonged half-life in the blood compartment and by extravasation into sites where the endothelium is more permeable, such as solid tumors, regions of inflammation and infection. Consequently, such long-circulating nanoparticles are supposed to be able to target directly most tumors located outside the mononuclear phagocytes system [22]. A higher tumor uptake, thanks to the small size and the hydrophilicity of the carrier device, as well as a sustained release of the drug could improve the efficacy of anticancer chemotherapy. The complement-rejecting properties of nanocapsules are superior to those of nanospheres at equivalent surface area [28].

Coating conventional nanoparticles with surfactants to obtain a long-circulating carrier, the first strategy used to direct tumor targeting *in vivo*, has been demonstrated using photosensitizers like phthalocyanines in PEG-coated nanoparticles [29] and *meta*-tetra(hydroxyphenyl)chlorin in poly(lactide)-PEG nanocapsules [30].

PEG chains have been attached covalently to poly(alkyl cyanoacrylate) polymers by two chemical strategies; both types of particle have shown long-circulating properties *in vivo* [31]. Such particles have been loaded with tamoxifen with a view to their use in treating hormone-dependent tumors [32]. Poly(alkyl cyanoacrylate) nanoparticles allow the delivery of several drugs, including doxorubicin, across the blood–brain barrier after coating with surfactants. However, only the surfactants polysorbate (Tween 20, 40, 60 and 80) and some poloxamers (Pluronic F68) can induce this uptake. A therapeutic effect with this sterically stabilized carrier system has been noted in rats bearing intracranial glioblastoma [33]. The delivery mechanism across the blood–brain barrier is most likely endocytosis via the LDL receptor by the endothelial cells lining the brain blood capillaries after injection of the nanoparticles into the blood stream. This endocytotic uptake seems to be mediated by the adsorption of apolipoprotein B and/or E adsorption from the blood. The drug, then, may be released either within these cells followed by passive diffusion into the brain or be transported into the brain by transcytosis [34]. Long-circulating nanoparticles have also been used in tumor targeting followed by irradiation of tumor site in the case of photodynamic therapy. To improve anticancer efficacy and avoid systemic phototoxicity this combination was evaluated in a EMT-6 tumor-bearing mice model. Unfortunately, poly(lactic acid) nanospheres covered by PEG did not allow a higher intratumoral accumulation of its incorporated photosensitizer (hexadecafluoro zinc phthalocyanine). The fragility of the adsorbed coating and the large size (>900 nm) could be responsible for this failure. How-

ever, formulation of the photosensitizer in the biodegradable nanospheres improved photodynamic therapy response, probably by influencing the intratumoral distribution pattern of the photosensitizer [35]. The biodistribution of non-biodegradable poly(methyl methacrylate) nanospheres coated or not with different surfactants (Polysorbate 80, Poloxamer 407 and Polaxamine 908) have been investigated in several mice bearing tumor models, including a murine B16-melanoma (inoculated intramuscularly), a human breast cancer MaTu (engrafted subcutaneously) and an U-373 glioblastoma (implanted intracerebrally). The coated poly(methyl methacrylate) nanospheres in circulation showed a prolonged half-life, especially with the Poloxamer 407 and Poloxamine 908 coatings. Moreover, an accumulation and retention of the coated nanospheres in the B-16 and MaTu tumors were observed, depending on the particle surface hydrophilicity and the specific growth difference of the tumor [36].

Although interesting results have been obtained with adsorbed surfactant, a covalent linkage of amphiphilic copolymers is generally preferred to obtain a protective hydrophilic cloud on nanoparticles that avoids the possibility of rapid coating desorption upon either dilution or after contact with blood components. This approach has been employed with poly(lactic acid), poly(caprolactone) and poly(cyanoacrylate) polymers, which were chemically coupled to PEG [27, 31, 37].

The surface characteristics of nanospheres prepared from poly(lactide-co-glycolide) copolymers have been optimized to reduce their interactions with plasma proteins and to increase their circulating half-life [26, 27, 38]. Biodegradable nanospheres prepared from poly(lactide-co-glycolide) coated with poly(lactide)-PEG diblock copolymers showed a significant increase in blood circulation time and reduced liver uptake in a rat model compared with non-coated poly(lactide-co-glycolide) nanospheres [39]. Nanocapsules containing poly(lactide)-PEG showed reduced association with a macrophage-like cell line (J774 A1) irrespective of dilution and incubation time up to 24 h [40]. This formulation, which showed a lower capture by macrophages *in vitro*, also gave good results *in vivo*, yielding a plasma area under the curve 15-fold higher than that obtained with nanocapsules stabilized by adsorbed Poloxamer F68. Persistence in the blood compartment was accompanied by delayed liver and spleen uptake [41].

### 1.3.3

#### **Actively Targetable Nanoparticles**

Nanoparticles can be targeted to the particulate region of capillary endothelium, to concentrate the drug within a particular organ and allow it to diffuse from the carrier to the target tissue. The folate receptor is overexpressed on many tumor cells. Folic acid has some advantages over transferrin or antibodies as a ligand for long-circulating carriers because it is a much smaller molecule that is unlikely to interact with opsonines and can be coupled easily to a poly(ethylene glycol) (PEG) chain without loss of receptor-binding activity. This targeting strategy has also been applied to long-circulating nanoparticles prepared from a cyanoacrylate-based polymer. Folate grafted to PEG cyanoacrylate nanoparticles has a ten-fold higher appar-

ent affinity for the folate-binding protein than the free folate. Indeed, the particles represent a multivalent form of the ligand folic acid and folate receptors are often disposed in clusters. Thus conjugated nanoparticles could display a stronger interaction with the surface of malignant cells [42]. Bovine serum albumin nanoparticles have been reacted with the activated folic acid to conjugate folate via amino groups of the nanoparticle to improve their intracellular uptake to target cells. The nanoparticles were taken up to SKOV3 cells (human ovarian cancer cell line) and levels of binding and uptake were increased with the time of incubation until 4 h. The levels of folate-conjugated bovine serum albumin nanoparticles were higher than those of non-conjugated nanoparticles and saturable. Association of folate conjugated bovine serum albumin nanoparticles to SKOV3 cells was inhibited by an excess amount of folic acid, suggestive of binding and/or uptake mediated by the folate receptor [43].

Folate-linked microemulsions of the antitumor antibiotic aclacinomycin have been developed and investigated both *in vitro* and *in vivo*. Three kinds of folate-linked microemulsions with different PEG chain lengths loading aclacinomycin were formulated. *In vitro* studies were performed in a human nasopharyngeal cell line, KB, which overexpresses the folate receptor and in a human hepatoblastoma cell line, folate receptor (-), HepG2. *In vivo* experiments were carried out in a KB xenograft by systemic administration of folate-linked microemulsions loading aclacinomycin. This afforded selective folate receptor mediated cytotoxicity in KB but not in HepG2 cells. Association of the folate-PEG 5000 linked and folate-PEG 2000 linked microemulsions with the cells was 200- and 4-fold higher, respectively, whereas their cytotoxicity was 90- and 3.5-fold higher than those of non-folate microemulsion. The folate-PEG 5000 linked microemulsions showed a 2.6-fold higher accumulation in solid tumors 24 h after intravenous injection and greater tumor growth inhibition than free aclacinomycin. This study showed how folate modification with a sufficiently long PEG-chain on emulsions can be an effective way of targeting emulsion to tumor cells [44].

Transferrin is another well-studied ligand for tumor targeting due to upregulation of transferrin receptors in numerous cancer cell types. A transferrin-modified, cyclodextrin polymer-based gene delivery system has been developed. The nanoparticle is surface-modified to display PEG for increasing stability in biological fluids and transferrin for targeting of cancer cells that express transferrin receptor. At low transferrin modification, the particles remain stable in physiologic salt concentrations and transfect K562 leukemia cells with increased efficiency over untargeted particles. The transferrin-modified nanoparticles are appropriate for use in the systemic delivery of nucleic acid therapeutics for metastatic cancer applications [45].

Nanoparticles conjugated with an antibody against a specific tumor antigen have been developed to obtain selective drug delivery systems for the treatment of tumors expressing a specific tumor antigen. For instance, biodegradable nanoparticles based on gelatin and human serum albumin have been developed. The surface of the nanoparticles was modified by covalent attachment of the biotin-binding protein NeutrAvidin, enabling the binding of biotinylated drug targeting ligands by

avidin–biotin complex formation. Using the HER2 receptor specific antibody trastuzumab (Herceptin) conjugated to the surface of these nanoparticles, a specific targeting to HER2-overexpressing cells could be shown. Confocal laser scanning microscopy demonstrated an effective internalization of the nanoparticles by HER2-overexpressing cells via receptor-mediated endocytosis [46].

There is a tremendous effort to develop and test gene delivery vectors that are efficient, non-immunogenic, and applicable for cancer gene systemic therapy. Since internalization of colloidal carriers usually leads to the lysosomal compartment, in which hydrolytic enzymes will degrade both the carrier and its content, the intracellular distribution of the carrier must be modified when the encapsulated drug is a nucleic acid. Thus, systems have been developed that either fuse with the plasma membrane or have a pH-sensitive configuration that changes conformation in the lysosomes and allows the encapsulated material to escape into the cytoplasm [3]. Rapid endo-lysosomal escape of biodegradable nanoparticles formulated from the copolymers of poly(D,L-lactide-co-glycolide) has been reported. This occurred by selective reversal of the surface charge of nanoparticles (from anionic to cationic) in the acidic endo-lysosomal compartment, which causes the nanoparticles to interact with the endo-lysosomal membrane and escape into the cytosol. These nanoparticles can deliver various therapeutic agents, including macromolecules such as DNA at a slow rate, resulting in a sustained therapeutic effect. Thermo-responsive, pH-responsive and biodegradable nanoparticles have been developed by grafting biodegradable poly(D,L-lactide) onto N-isopropyl acrylamide and methacrylic acid. It may be sufficient for a carrier system to concentrate the drug in the tissue of interest. However, for hydrophilic molecules such as nucleic acid, which cross the plasma membrane with difficulty, intracellular delivery is required. Clinical trials for deadly pancreatic cancer have recently begun on two continents. The aim is to evaluate the safety and efficacy of engineered nanoparticles guided by a targeted delivery system to overcome dilution, filtration and inactivation encountered in the human circulatory system to deliver a killing designer gene to metastatic tumors that are refractory to conventional chemotherapy. The first patients receiving multiple intravenous infusions of the targeted delivery system-encapsulated genetic bullets have all responded favorably [47].

#### 1.3.4

#### **Routes of Drug Nanoparticles Administration**

The most convenient route of drug administration is the oral one but this presents several barriers to the use of colloidal carrier owing to conditions within the gastrointestinal tract. Duodenal enzymes and bile salts destroy the lipid bilayers of most types of liposome, releasing the drug. Polymeric nanoparticles are more stable, although there is some evidence that polyesters can be degraded by pancreatic lipases [48]. They may be able to improve bioavailability, particularly for highly insoluble drugs, by increasing the surface area for dissolution and as a result of bioadhesion. However, nanoparticles can be used to protect a labile drug from degradation in the gastrointestinal tract or to protect it from toxicity due to the drug.

Polymeric nanoparticles, due to their bioadhesive properties, may be immobilized within the mucus or, when in contact with the epithelial cells, show a slower clearance from the gastrointestinal tract [49]. Nanoparticles of biodegradable polymers containing alpha-tocopheryl PEG 1000 succinate (vitamin E TPGS) have been proposed to replace the current method of clinical administration and to provide an innovative solution for oral chemotherapy. Vitamin E TPGS could be a novel surfactant as well as a matrix material when blended with other biodegradable polymers – it has great advantages for the manufacture of polymeric nanoparticles for controlled release of paclitaxel and other anticancer drugs [50].

Potential applications of colloidal drug carriers by the intravenous route can be summarized as concentrating drugs in accessible sites, rerouting drugs away from sites of toxicity and increasing the circulation time of labile or rapidly eliminated drugs.

After subcutaneous or intraperitoneal administration, nanoparticles are taken up by regional lymph nodes [51].

Subcutaneously or locally injected (in the peri-tumoral region) nanoparticles can be used for lymphatic targeting as a tool for chemotherapy against lymphatic tumors or metastases since they penetrate the interstitial space around the injection site and are gradually absorbed by the lymphatic capillaries into the lymphatic system. Aclarubicin adsorbed onto activated carbon particles has been tested after subcutaneous injection in mice, against a murine model (P288 leukemia cells) of lymph node metastases [52]. The same system has also been used as a locoregional chemotherapy adjuvant for breast cancer in patients after intratumoral and peritumoral injections [53]. In both cases, this carrier system distributed selectively high levels of free aclarubicin to the regional lymphatic system and low levels to the rest of the body. However, this carrier system is not biodegradable and it is rather big (>100 nm), impeding drainage from the injection site. In addition, the drug is associated to the particles by adsorption, leading to a rapid release with possible systemic absorption. Biodegradable systems coated by adsorption of the surfactant Poloxamine 904 or poly(isobutyl cyanoacrylate) nanocapsules [51, 54] have been developed to improve lymphatic targeting. Poloxamine 904 caused an increased sequestration of the particles in lymph nodes, reducing the systemic absorption of any encapsulated drug [54]. Poly(isobutyl cyanoacrylate) nanocapsules were also able to retain the lipophilic indicator 12-(9-anthroxy)stearic acid in the regional lymph nodes for 168 h after intramuscular administration [51]. A study combining intratumoral administration of gadolinium-loaded chitosan nanoparticles and neutron-capture therapy has been performed on the B16F10 melanoma model subcutaneously implanted in mice. Gadolinium retention in tumor tissue increased when it was encapsulated with respect to the free drug. Tumor irradiation 8 h after the last intratumoral injection of gadolinium nanoparticles prevented further tumor growth in the animals treated, thereby increasing their life expectancy [55].

Retention of carriers instilled into the eye also occurs, leading to important therapeutic potential in this area. As well as a bioadhesive effect, some evidence has been presented to show that nanoparticles can penetrate through the corneal epithelium [56].



## 1.4

### Anticancer Drug Nanoparticles

#### 1.4.1

##### Anthracyclines

One of the most powerful and widely used anticancer drugs is doxorubicin, an anthracyclenic antibiotic that inhibits the synthesis of nucleic acids. This drug has a very narrow therapeutic index as its clinical use is hampered by several undesirable side-effects like cardiotoxicity and myelosuppression [57]. Thus, much effort has been made to target doxorubicin to cancer tissues, improving its efficacy and safety.

Poly(isohexyl cyanoacrylate) nanospheres incorporating doxorubicin have been developed. On an hepatic metastases model in mice (M5076 reticulum cell sarcoma) such doxorubicin nanospheres afforded a greater reduction in the number of metastases than when free doxorubicin was used and it appeared to increase the life span of the metastasis-bearing mice [58]. Another study found higher concentrations of doxorubicin in mice liver, spleen and lungs with doxorubicin incorporated into poly(isohexyl cyanoacrylate) than in mice treated with free doxorubicin. At the same time, the concentration of doxorubicin in heart and kidneys of the mice were lower than when free doxorubicin was used [18]. Tissue pharmacokinetic studies showed that the underlying mechanism responsible for the increased therapeutic efficacy of the nanoparticle formulation was a transfer of doxorubicin from the healthy hepatic tissue, acting as a drug reservoir, to the malignant cells. Kupffer cells, after a massive uptake of nanoparticles by phagocytosis, were able to induce the release of doxorubicin, leading to a gradient concentration, favorable for a prolonged diffusion of the free and still active drug towards the neighboring metastatic cells [59]. Thus, this biodistribution profile can be of benefit for chemotherapeutic treatment of tumors localized in the mononuclear phagocytic system.

Clinical pharmacokinetics after a single intravenous administration of doxorubicin adsorbed onto poly(methacrylate) nanospheres has been investigated in hepatoma patients. This type of conventional carrier, although of limited use *in vivo* because not biodegradable, allowed a reduction in both the volume of distribution and the elimination half-life of doxorubicin [60]. Another phase I clinical investigation has been carried out on 21 cancer patients with doxorubicin associated to biodegradable poly(isohexyl cyanoacrylate) nanospheres. Pharmacokinetic studies conducted in 3/21 patients revealed important interindividual variation for doxorubicin (encapsulated or not) plasma levels. Clinical toxicity of encapsulated doxorubicin consisted of dose-dependent myelosuppression of different grades in all patients, in pseudo-allergic reactions in 3/21 patients and in diffuse bone pain in 3/21 patients. However, neither cardiac toxicity nor hepatotoxicity were encountered among 18 patients treated with the nanoparticles formulation. According to WHO criteria, there were only 2/21 stable diseases lasting 4–6 months. All the other patients had progressive disease after the first course of doxorubicin-loaded poly(isohexyl cyanoacrylate) nanospheres. This could be due to tumor localization, as

they were rarely located at sites of the mononuclear phagocytic system, resulting in subtherapeutic anticancer drug concentration exposure [61].

As doxorubicin-loaded poly(isobutyl cyanoacrylate) nanoparticles are more efficient than free drug in mice bearing hepatic metastasis of the M5076 tumor, and Kupffer cells could have acted as a drug reservoir after nanoparticle phagocytosis, the role of macrophages in mediating the cytotoxicity of doxorubicin-loaded nanoparticles on M5076 cells was studied. After direct contact, free doxorubicin and doxorubicin-loaded nanoparticles had the same efficacy against M5076 cell growth. Co-culture experiments with macrophages J774.A1 led to a five-fold increase in the IC<sub>50</sub> for both doxorubicin and doxorubicin-loaded nanoparticles. The activation of macrophages by IFN- $\gamma$  in co-culture significantly decreased the IC<sub>50</sub>s. After phagocytosis of doxorubicin-loaded nanoparticles, J774.A1 cells were able to release active drug, allowing it to exert its cytotoxicity against M5076 cells. Drug efficacy was potentiated by the activation of macrophages releasing cytotoxic factors such as NO, which resulted in increased tumor cell death [62]. Similarly, the use in a murine tumor model (implanted subcutaneously J774.A1 macrophages) of a dextran-doxorubicin conjugate incorporated into small chitosan nanospheres was reported to outperform the free conjugate, especially in relation to life expectancy [63].

The body distribution of nanoparticle incorporating doxorubicin injected into the hepatic artery of hepatoma bearing rats was investigated. The nanoparticle formulation and free doxorubicin were injected into the hepatic artery of Walker-256 hepatoma bearing rats on the seventh day after tumor implantation. Survival time, tumor enlargement ratio and tumor necrosis degree were compared. Nanoparticles containing doxorubicin substantially increased the drug concentrations in liver, spleen, and tumor of rats compared to free drug, whereas the concentrations in plasma, heart and lungs were significantly decreased. The nanoparticulate formulation brought on a more significant tumor inhibition and more extensive tumor necrosis. The prolonged life span ratio was 109.22% as compared with rats that accepted normal saline [64, 65].

The nanoparticle modified biodistribution may generate new types of toxicity, as has been observed with doxorubicin incorporated in poly(isobutyl cyanoacrylate) and poly(isohexyl cyanoacrylate) nanospheres, whose hematopoietic toxicity was generally more pronounced and long-lasting than that of free doxorubicin [21]. Acute renal toxicity was another murine-reported doxorubicin toxicity, which was amplified by the association of the drug to poly(isobutyl cyanoacrylate) nanospheres. Proteinuria was probably the result of a modified biodistribution of the associated drug, which resulted in glomerular damage [66]. In another instance, doxorubicin was incorporated into gelatin nanospheres by a covalent bond on its amino group via glutaraldehyde [67]. Unfortunately, no or only marginal antitumor activity against a C26 tumor (mouse colon adenocarcinoma) *in vivo* was showed, and in certain cases there was even an increased doxorubicin cardiotoxicity. Once again this lack of antitumor activity may due to slow dissociation of the complex due to the covalent linkage or to the slow diffusion of the complex across the cellular membrane.

Polysorbate 80-coated poly(isobutyl cyanoacrylate) nanospheres provided no ma-

for changes in doxorubicin biodistribution and pharmacokinetic parameters in rats when compared to those of conventional poly(isobutyl cyanoacrylate) nanospheres. However, the coated nanospheres did transport a significant amount of incorporated doxorubicin to the brain of healthy rats, reaching the highest drug levels in this organ 2–4 h after intravenous administration. Consequently, an active transport from the blood to the brain was suspected since cerebral accumulation occurred against a concentration gradient. A mechanism involving an endocytosis by brain endothelial cells was hypothesized, as the brain uptake was inhibited at 4 °C and after a pretreatment with cytochalasin B [68]. Then, polysorbate 80-coated poly(isobutyl cyanoacrylate) nanoparticles were shown to enable the transport of doxorubicin across the blood–brain barrier to the brain after intravenous administration and to considerably reduce the growth of brain tumors in rats. The acute toxicity of doxorubicin associated with polysorbate 80-coated nanoparticles in healthy rats was studied and a therapeutic dose range for this formulation in rats with intracranially implanted 101/8 glioblastoma was established. Single intravenous administration of empty poly(isobutyl cyanoacrylate) nanoparticles in the dose range 100–400 mg kg<sup>-1</sup> did not cause mortality within the period of observation. Association of doxorubicin with poly(isobutyl cyanoacrylate) nanoparticles did not produce significant changes of quantitative parameters of acute toxicity of the antitumor agent. Likewise, the presence of polysorbate 80 in the formulations was not associated with changes in toxicity compared with free or nanoparticulate drug. The results in tumor-bearing rats were similar to those in healthy rats. The toxicity of doxorubicin bound to nanoparticles was similar or even lower than that of free doxorubicin [69]. As doxorubicin bound to polysorbate-coated nanoparticles crossed the intact blood–brain barrier, reaching therapeutic concentrations in the brain, the therapeutic potential of this formulation *in vivo* was studied using an animal model created by implantation of 101/8 glioblastoma tumor in rat brains. Rats treated with doxorubicin bound to polysorbate-coated nanoparticles had significantly higher survival times than with free doxorubicin; over 20% of the animals showed a long-term remission (Fig. 1.1). All animals treated with polysorbate-containing formulation also had a slight inflammatory reaction to the tumor. There was no indication of neurotoxicity [70].

Doxorubicin has also been conjugated chemically to a terminal end group of poly(D,L-lactic-co-glycolic acid) by an ester linkage and then formulated into nanoparticles. The conjugated doxorubicin nanoparticles showed increased uptake within a HepG2 cell line. They exhibited a slightly lower IC<sub>50</sub> against the HepG2 cell line than did free doxorubicin. An *in vivo* antitumor activity assay also showed that a single injection of the nanoparticles had comparable activity to that of free doxorubicin administered by daily injection [71]. Doxorubicin-loaded poly(butyl cyanoacrylate) nanoparticles have been used to enhance the delivery of the drug to Dalton's lymphoma solid tumor. <sup>99m</sup>Tc-labeled complexes of doxorubicin and doxorubicin-loaded poly(butyl cyanoacrylate) nanoparticles were administered subcutaneously below the Dalton's lymphoma tumor. The distribution of doxorubicin-loaded poly(butyl cyanoacrylate) nanoparticles to the blood, heart and organs of the

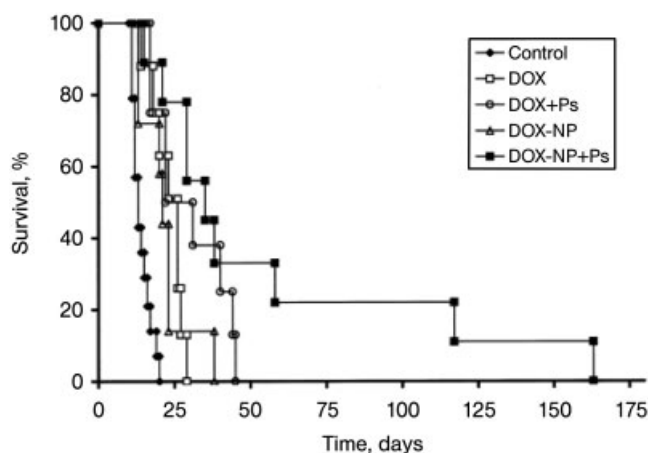


**Fig. 1.1.** Kaplan–Meier survival curves. Percentage of survival of the rats with intracranially transplanted glioblastoma after intravenous injection of  $2.5 \text{ mg kg}^{-1}$  doxorubicin each on day 2, 5 and 8 using one of the following formulations: DOX, doxorubicin in saline; DOX+Ps, doxorubicin

in saline plus polysorbate 80; DOX-NP, doxorubicin bound to poly(butyl cyanoacrylate) nanoparticles; DOX-NP+Ps, doxorubicin bound to poly(butyl cyanoacrylate) nanoparticles coated with polysorbate 80. (Reproduced with permission from Ref. [70].)

reticuloendothelial system was biphasic with a rapid initial distribution, followed by a significant decrease later at 6 h post-injection. The distribution of doxorubicin to tissues was very low initially and increased significantly at 6 h post-injection, indicating its accumulation at the injection site for a longer time. The concentration of doxorubicin-loaded poly(butyl cyanoacrylate) nanoparticles was also high in tissues at 6 h post-injection, indicating their accumulation at the subcutaneous site and consequent disposition to tissues with time. A significantly high tumor uptake of doxorubicin-loaded poly(butyl cyanoacrylate) nanoparticles (approx. 13-fold higher at 48 h post-injection) was found compared to free doxorubicin. Tumor concentrations of both doxorubicin and doxorubicin-loaded poly(butyl cyanoacrylate) nanoparticles increased with time, indicating their slow penetration from the injection site into tumor [72].

Poly(ethylene glycol)-coated poly(hexadecyl cyanoacrylate) nanospheres also displayed a significant accumulation within an orthotopic 9L gliosarcoma model, after intravenous administration to rats. Hence, in the same model, the pre-clinical efficacy of this carrier when loaded with doxorubicin was evaluated. The cumulative maximum tolerated dose of nanoparticulate doxorubicin was 1.5-fold higher than that of free doxorubicin. Nevertheless, encapsulated doxorubicin was unable to elicit a better therapeutic response in the 9L gliosarcoma. A biodistribution study revealed that the doxorubicin-loaded nanospheres accumulated to a 2.5-fold lesser extent in the 9L tumor than did the unloaded nanospheres and that they were mainly

localized in the lungs and the spleen. Such a typical profile indicated aggregation with plasma proteins as a consequence of the positive surface charge of these loaded particles; this ionic interaction resulting from drug encapsulation was mainly responsible for 9L treatment failure [73].

The ability of doxorubicin-loaded solid lipid nanoparticles to achieve prolonged drug plasma levels was also investigated. One study observed a low uptake of solid lipid nanoparticles by the liver and spleen macrophages. This might be explained by a low surface hydrophobicity of the nanoparticles avoiding the adsorption of any blood proteins mediating the uptake by liver and spleen macrophages [74]. Moreover, uptake of the solid lipid nanoparticles (SLNs) by the brain might be explained by adsorption of a blood protein mediating adherence to the endothelial cells of the blood–brain barrier [75]. Pharmacokinetic studies of doxorubicin incorporated into SLNs showed higher blood levels in comparison to a commercial drug solution after intravenous injection in rats. Concerning the body distribution, doxorubicin-loaded SLNs caused higher drug concentrations in lung, spleen and brain, while the solution led to a distribution more into liver and kidneys [76]. Furthermore, incorporation of doxorubicin into SLNs strongly enhanced its cytotoxicity in several cell lines [77, 78]. In particular, in the human colorectal cancer cell line HT-29, the intracellular doxorubicin content was double after 24 h exposure to loaded SLNs versus the conventional drug formulation [78]. Pharmacokinetics and tissue distribution of doxorubicin incorporated in non-sterically stabilized SLNs and in sterically stabilized SLNs at increasing concentration of stearic acid-PEG 2000 as stabilizing agent after intravenous administration to rabbits have been studied. The doxorubicin area under the concentration–time curve increased as a function of the amount of sterically stabilizing agent present in the SLNs. Doxorubicin was present in the brain only after doxorubicin-loaded SLNs administration and the increase in the stabilizing agent affected the doxorubicin transported into the brain. There was always less doxorubicin in the liver, lungs, spleen, heart and kidneys after injection of any of the types of SLNs than after the doxorubicin solution. In particular, all SLNs formulations significantly decreased heart and liver concentrations of doxorubicin [79]. Interestingly, both non-coated and coated SLNs showed a similar low uptake by liver and spleen macrophages [80]. The bioavailability of idarubicin can be also improved by administering idarubicin-loaded SLNs duodenally to rats. The pharmacokinetic parameters of idarubicin found after duodenal administration of idarubicin solution and idarubicin-loaded SLNs were different. The area under the concentration–time curve and the elimination half-life were 2- and 30-fold higher after administration of idarubicin-loaded SLNs than after solution administration, respectively. Tissue distribution also differed: idarubicin and its main metabolite idarubicinol concentrations were lower in heart, lung, spleen and kidneys after idarubicin-loaded SLNs administration than after solution administration. Furthermore, the drug and its metabolite were detected in the brain only after idarubicin-loaded SLNs administration, indicating that SLNs were able to cross the blood–brain barrier. After intravenous idarubicin-loaded SLNs administration, the area under the time–concentration curve of idarubicin was lower than after duodenal administration of the same formulation [81].

#### 1.4.1.1 Reverse of P-glycoprotein Mediated Multidrug Resistance of Cancer Cells to Doxorubicin

Different types of nanoparticles have been developed to reverse the P-glycoprotein mediated multidrug resistance of cancer cells to doxorubicin, an important problem in its clinical use.

Conventional poly(cyanoacrylate) nanoparticles allow doxorubicin P-glycoprotein mediated multidrug resistance to be overcome *in vitro* only when the nanoparticles and the resistant cancer cell line are in close contact [82]. The nanoparticle-associated drug accumulated within the cells and appeared to avoid P-glycoprotein dependent efflux. This reversal was only observed with poly(alkyl cyanoacrylate) nanoparticles and was not due to particle endocytosis. The formation of a complex between positively charged doxorubicin and negatively charged polymer degradation products seemed to favor diffusion across the plasma membrane [82].

When doxorubicin was coupled via an ionic interaction to non-biodegradable poly(methacrylate) nanospheres, the P-glycoprotein mediated multidrug resistance reversal differed from that of doxorubicin incorporated into biodegradable poly(cyanoacrylate) nanoparticles.

When adsorbed onto the surface of poly(methacrylate) nanospheres, doxorubicin was demonstrated to be cell internalized by an endocytic process in cultured rat hepatocytes and in a human monocyte-like cancer cell line expressing P-glycoprotein (U-937). Once internalized, poly(methacrylate) nanospheres generated an intracellular sustained release of doxorubicin in U-937 cells. A higher intracellular accumulation, related to a more important cytotoxicity on U-937 cells, was noted for encapsulated doxorubicin than for free doxorubicin. However, such a carrier, despite its ability to mask the positive charge of doxorubicin, is of limited use *in vivo* since it is not biodegradable [83].

When doxorubicin was incorporated into rapidly biodegraded poly(isobutyl cyanoacrylate) nanospheres and tested in a resistant murine leukemia sub-line over-expressing P-glycoprotein (P388/ADR), a higher cellular uptake was observed. Furthermore, the cell uptake kinetics of doxorubicin nanoparticles were unchanged in the presence of cytochalasin B, an endocytosis inhibitor. Efflux studies showed a similar profile for doxorubicin in nanoparticulate or free form. This suggests that poly(isobutyl cyanoacrylate) nanospheres did not enter the cells. In an *in vitro* model of doxorubicin-resistant rat glioblastoma (C6 cells sub-lines), doxorubicin incorporated into poly(isobutyl cyanoacrylate) nanospheres was always more cytotoxic, and also had a lower intracellular concentration, than the free drug. The polymer constituting the nanospheres did not inhibit the P-glycoprotein by direct interaction with the protein. It was also observed that on C6 cell sub-lines with different expression of P-glycoprotein that doxorubicin nanospheres were only efficient on pure P-glycoprotein mediated multidrug resistance phenotype cells and not on the additional mechanisms of resistance to doxorubicin [84]. Thus, the mechanism of P-gp reversion by nanoparticles could only be explained by a local delivery of the drug in high concentration close to the cell membrane, after degradation of the polymeric carrier. Such local microconcentration of doxorubicin was supposed to be able to saturate P-glycoprotein [85]. P-glycoprotein mediated multidrug resis-

tance is overcome with poly(isobutyl cyanoacrylate) and poly(isobutyl cyanoacrylate) doxorubicin-loaded nanospheres not only due to the adsorption of nanoparticles to the cell surface but also due to an increased diffusion of doxorubicin across the plasma membrane, thanks to the formation of an ion pair between negatively charged cyanoacrylic acid (a nanoparticle degradation product) and the positively charged doxorubicin. Such ion-pair formation has been evidenced by Raman spectroscopy and by ion-pair reversed-phase HPLC [86]. Masking the positive charge of the amino sugar of doxorubicin appears to be key to overcoming P-gp mediated multidrug resistance. At the same time, the cytotoxic activity of doxorubicin was only slowly compromised after chemical modifications of the amino sugar. Consequently, some studies focused on developing systems featuring covalent linkage between the polymers and the amino sugar of doxorubicin [87]. Such a complex mechanism for overcoming P-glycoprotein mediated multidrug resistance was only observed with cyanoacrylate nanoparticles.

The failure to overcome P-glycoprotein mediated multidrug resistance with nanoparticles designed with other polymers could be explained by an appropriate release mechanism of drug (diffusion could lead to the release of the active compound without the polymeric counter ion), by degradation kinetics of the polymer that are too slow, or by the size of the polymeric counter ion, which could be the limiting factor for diffusion across the cell membrane.

Interestingly, the association of doxorubicin with poly(alkyl cyanoacrylate) nanoparticles also reversed the resistance to doxorubicin in numerous multidrug-resistant cell lines [88].

Furthermore, doxorubicin encapsulated in poly(isohexyl cyanoacrylate) nanospheres can circumvent P-glycoprotein mediated multidrug resistance. K562 and MCF7 cell lines were more resistant to free doxorubicin than to doxorubicin poly(isohexyl cyanoacrylate) nanospheres. The MCF7 sub-lines selected with doxorubicin poly(isohexyl cyanoacrylate) nanospheres exhibited a higher level of resistance to both doxorubicin formulations than those selected with free doxorubicin. Different levels of overexpression of several genes involved in drug resistance occurred in the resistant variants. MDR1 gene overexpression was consistently higher in free doxorubicin selected cells than in doxorubicin poly(isohexyl cyanoacrylate) nanosphere selected cells, while this was the reverse for the BCRP gene. Overexpression of the MRP1 and TOP2 alpha genes was also observed in the selected variants. Thus, drug encapsulation markedly alters or delays the several mechanisms involved in the acquisition of drug resistance [89].

Other strategies to bypass doxorubicin multidrug resistance, such as the use of Stealth™ poly(cyanoacrylate) nanoparticles, could be considered, as well as the co-administration of doxorubicin with chemo-sensitizing agents, generally acting as P-glycoprotein inhibitors. Co-encapsulation of the reversing agent cyclosporin and doxorubicin into poly(isobutyl cyanoacrylate) nanospheres was investigated to reduce the side-effects of both drugs while enhancing their efficacy. This formulation, compared to incubation of cyclosporin and doxorubicin, or doxorubicin nanoparticles and cyclosporin, elicited the most effective growth rate inhibition on

P388/ADR cells. Such a high efficacy was supposed to result from the synergistic effect of the rapid release of both doxorubicin and cyclosporin at the surface of cancer cells, allowing a better internalization of doxorubicin, while inhibiting its efflux by blocking the P-gp with the cyclosporin [90].

#### 1.4.2

##### **Antiestrogens**

Nanospheres and nanocapsules made of biodegradable copolymers and coated with poly(ethylene glycol) (PEG) chains have been developed as parenteral delivery system for the administration of the anti-estrogen 4-hydroxytamoxifen RU 58668 (RU). Coating with PEG chains lengthened the anti-estrogen activity of RU, with prolonged antiuterotrophic activity of the encapsulated drug into PEG-poly(D,L-lactic acid) nanospheres as compared with non-coated nanospheres. In mice bearing MCF-7 estrogen-dependent tumors, free RU injected by the intravenous route slightly decreased estradiol-promoted tumor growth while RU-loaded PEG-poly(D,L-lactic acid) nanospheres injected at the same dose strongly reduced it. The antitumoral activity of RU encapsulated within PEGylated nanocapsules was stronger than that of RU entrapped with PEGylated nanospheres loaded at an equivalent dose. The PEGylated nanocapsules decreased the tumor size in nude mice transplanted with estrogen receptor-positive but estrogen-independent MCF-7/Ras breast cancer cells at a concentration 2.5-fold lower than that of the PEGylated nanospheres [91, 92].

To increase the local concentration of tamoxifen in estrogen receptor-positive breast cancer cells poly( $\epsilon$ -caprolactone) nanoparticle formulation has been developed. Poly( $\epsilon$ -caprolactone) nanoparticles labeled with rhodamine123 were incubated with MCF-7 estrogen receptor-positive breast cancer cells. A significant fraction of the administered rhodamine123-loaded poly( $\epsilon$ -caprolactone) nanoparticles was found in the perinuclear region of the MCF-7 cells, where estrogen receptors are also localized, after 1 h of incubation. These nanoparticles were rapidly internalized in MCF-7 cells and intracellular tamoxifen concentrations followed a saturable process [93]. In another study, the biodistribution profile of tamoxifen encapsulated in polymeric nanoparticulate formulations after intravenous administration was evaluated, with or without surface-stabilizing agents. *In vivo* biodistribution studies of tamoxifen-loaded poly(ethylene oxide)-modified poly( $\epsilon$ -caprolactone) nanoparticles were carried out in Nu/Nu athymic mice bearing a human breast carcinoma xenograft, MDA-MB-231, using tritiated [ $^3\text{H}$ ]tamoxifen as radio-marker for quantification. After intravenous administration the drug-loaded nanoparticles accumulated primarily in the liver, though up to 26% of the total activity could be recovered in tumor at 6 h post-injection for poly(ethylene oxide)-modified poly( $\epsilon$ -caprolactone) nanoparticles. In comparison with free drug and uncoated nanoparticles, the modified nanoparticles exhibited a significantly increased level of accumulation of the drug within the tumor with time as well as prolonged drug presence in the systemic circulation [94].



## 1.4.3

**Anti-metabolites**

Poly(amidoamine) dendritic polymers coated with poly(ethylene glycol) have been developed to deliver 5-fluorouracil. In rats after intravenous administration this nanoparticle formulation showed a lower drug clearance than after the free drug administration [95]. In addition, poly(D,L-lactide)-*g*-poly(*N*-isopropyl acrylamide-co-methacrylic acid) nanoparticles have been studied as drug carrier for intracellular delivery of 5-fluorouracil [96].

Methotrexate has been incorporated in modified poly(amidoamine) dendritic polymers conjugated to folic acid as a targeting agent. These conjugates were injected intravenously into immunodeficient mice bearing human KB tumors that overexpress the folic acid receptor. Targeting methotrexate increased its antitumor activity and markedly decreased its toxicity, allowing therapeutic responses not possible with the free drug [97].

## 1.4.4

**Camptothecins**

Solid lipid nanoparticles (SLNs) are a promising sustained release system for camptothecin after oral administration. The pharmacokinetics and body distribution of camptothecin after intravenous injection in mice have been studied. Two plasma peaks were observed after administration of camptothecin-loaded SLNs. The first was attributed to the presence of free drug, the second peak can be attributed to controlled release or potential gut uptake of the SLNs. In comparison to the drug solution, SLNs lead to a much higher area under the concentration–time curve/dose and mean residence times, especially in brain, heart and organs containing reticuloendothelial cells. The highest area under the concentration time curve ratio of SLNs to drug solution among the tested organs was found in the brain. Incorporation of camptothecin into SLNs also prevented its hydrolysis [98].

The *in vitro* and *in vivo* antitumor characteristics of methoxy poly(ethylene glycol)-poly(D,L-lactic acid) nanoparticles containing camptothecin have been examined. After intravenous administration in rats, camptothecin-loaded nanoparticles showed a longer plasma retention than camptothecin solution and high and long tumor localization. In both single and double administration to mice bearing sarcoma 180 solid tumor, camptothecin-loaded nanoparticles were much more effective than camptothecin solution, in particular the tumor disappeared completely in three of the four mice after double administration of camptothecin-loaded nanoparticles [99].

Irinotecan-containing nanoparticles have been prepared by co-precipitation with addition of water to an acetone solution of poly(D,L-lactic acid), PEG-*block*-poly(propylene glycol)-*block*-PEG and irinotecan. When the antitumor effect was examined using mice bearing sarcoma 180 subcutaneously, only nanoparticles suppressed tumor growth significantly. After intravenous injection in rats, nanopar-

ticles maintained irinotecan plasma concentration longer than irinotecan aqueous solution [100].

Lipid based nanoparticles incorporating the irinotecan analog SN-38 have been developed and studied *in vitro* and *in vivo*. Interestingly, incorporation of SN-38 into nanoparticles improved the stability of the active drug, the lactone form, in serum-containing medium. Furthermore, studies in nude mice showed a prolonged half-life of the active drug in whole blood and increased efficacy compared to irinotecan in a mouse xenograft tumor model [101].

#### 1.4.5

##### **Cisplatin**

Nanoparticles prepared from poly(lactide-co-glycolide) copolymers increase the circulating half-life of cisplatin [102]. A system for the local delivery of chemotherapy to malignant solid tumors has been developed based on calcium phosphate nanoparticles containing cisplatin. Cytotoxicity was investigated in a K8 clonal murine osteosarcoma cell line. Drug activity was retained after adsorption onto the apatite crystals and the apatite/cisplatin formulation exhibited cytotoxic effects with a dose-dependent decrease of cell viability [103].

#### 1.4.6

##### **Paclitaxel**

Paclitaxel, a microtubule-stabilizing agent that promotes polymerization of tubulin causing cell death by disrupting the dynamics necessary for cell division, is effective against a wide spectrum of cancers, including ovarian cancer, breast cancer, small and non-small cell lung cancer, colon cancer, head and neck cancer, multiple myeloma, melanoma and Kaposi's sarcoma. In clinical practice high incidences of adverse reactions of the drug such as neurotoxicity, myelosuppression and allergic reactions have been reported. Since its clinical administration is hampered by its poor solubility in water, excipients such as Cremophor EL (polyethoxylated castor oil) and ethanol are used in the pharmaceutical drug formulation of the current clinical administration [104].

Cremophor EL and polysorbate 80 (Tween 80) are widely used as drug formulation vehicles for the taxane anticancer agents paclitaxel and docetaxel. Both solubilizers are biologically and pharmacologically active compounds, and their use as drug formulation vehicles has been implicated in clinically important adverse effects, including acute hypersensitivity reactions and peripheral neuropathy. Cremophor EL and Tween 80 have also been demonstrated to influence the disposition of solubilized drugs that are administered intravenously. The overall resulting effect is a highly increased systemic drug exposure and a simultaneously decreased clearance, leading to alteration in the pharmacodynamic characteristics of the solubilized drug. Kinetic experiments revealed that this effect is caused primarily by reduced cellular uptake of the drug from large spherical micellar-like structures with a highly hydrophobic interior, which act as the principal carrier of circulating drug.

The existence of Cremophor EL and Tween 80 in blood as large polar micelles has also raised additional complexities in the case of combination chemotherapy regimens with taxanes, such that the disposition of several co-administered drugs, including anthracyclines and epipodophyllotoxins, is significantly altered. In contrast to the enhancing effects of Tween 80, addition of Cremophor EL to the formulation of oral drug preparations seems to result in significantly diminished drug uptake and reduced circulating concentrations [105]. Nanoparticles of biodegradable polymers can provide an ideal solution to such an adjuvant problem and realize a controlled and targeted delivery of paclitaxel with better efficacy and less side-effects. With further development, such as particle size optimization and surface coating, nanoparticle formulation of paclitaxel can promote full paclitaxel efficacy, thereby improving the quality of life of the patients.

Paclitaxel incorporated into poly(vinylpyrrolidone) nanospheres has been assayed on a B16F10 murine melanoma transplanted subcutaneously in C57B1/6 mice. Mice treated with repeated intravenous injections of paclitaxel-loaded nanospheres showed a significant tumor regression and higher survival rates than mice treated with free paclitaxel [106]. Sterically stabilized SLNs were also prepared to prolong the blood circulation time following intravenous administration [107]. Incorporation of paclitaxel into SLNs enhanced paclitaxel cytotoxicity on the human breast adenocarcinoma cell line MCF-7, but not on the human promyelocytic leukemia cell line HL-60 [77].

In a phase I study, ABI-007 – a novel formulation prepared by high-pressure homogenization of paclitaxel in the presence of human serum albumin, which results in a nanoparticle colloidal suspension – was found to offer several clinical advantages, including a rapid infusion rate and a high maximum tolerated dose. Furthermore, the absence of Cremophor EL allowed ABI-007 to be administered to patients without a need for premedication that is routinely used to prevent the hypersensitivity reactions associated with the conventional formulation of paclitaxel. Hematologic toxicities were mild throughout treatment, while most non-hematologic toxicities were grade 1 or 2 [108].

The feasibility, maximum tolerated dose, and toxicities of intraarterial administration of ABI-007 were studied in patients with advanced head and neck and recurrent anal canal squamous cell carcinoma in 43 patients (31 with advanced head and neck and 12 with recurrent anal canal squamous cell carcinoma). Patients were treated intraarterially with paclitaxel-albumin nanoparticles every four weeks for three cycles. Paclitaxel albumin nanoparticles were compared preliminarily with paclitaxel for *in vitro* cytostatic activity. Significantly, pharmacokinetic profiles after intraarterial administration were obtained (Fig. 1.2). The dose-limiting toxicity of the nanoparticles formulation was myelosuppression consisting of neutropenia in three patients. Non-hematologic toxicities included total alopecia, gastrointestinal toxicity, skin toxicity, neurologic toxicity, ocular toxicity, flu-like. The maximum tolerated dose in a single administration was  $270 \text{ mg m}^{-2}$ . Most dose levels showed considerable antitumor activity (80.9% complete response and partial response) [109].

The effectiveness of intraarterial infusion of paclitaxel incorporated into human

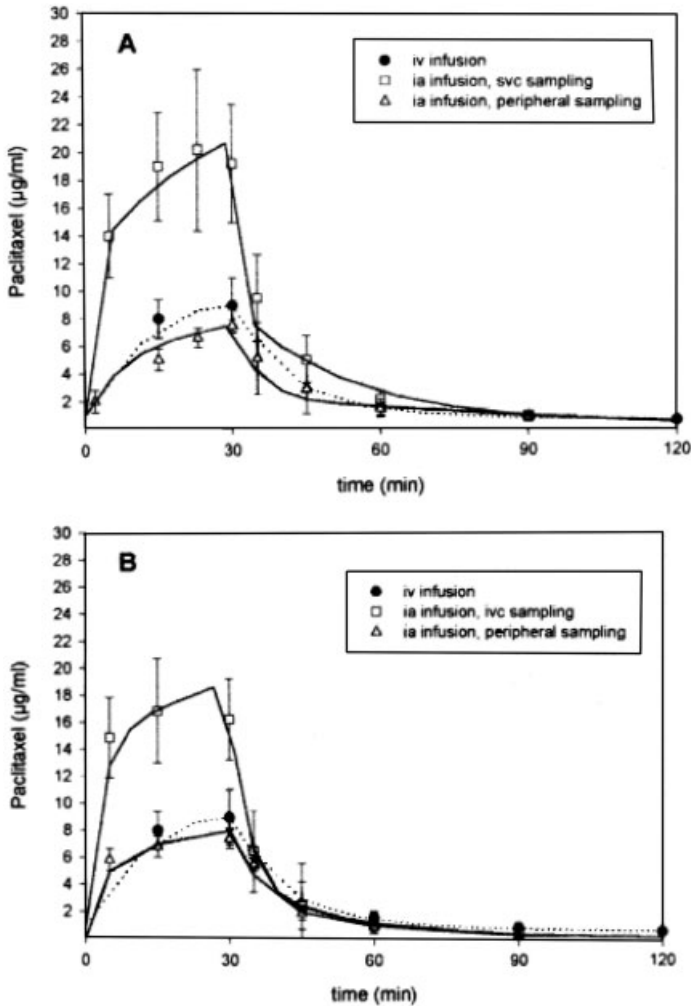


**Fig. 1.2.** Concentration–time curves. Mean paclitaxel concentration versus time profiles in patients with head and neck (A) or anal canal (B) carcinomas during and after 30 min

constant infusion of ABI-007 ( $250 \text{ mg m}^{-2}$  of paclitaxel); iv, intravenous; ia, intraarterial; svc, superior vena cava; ivc, inferior vena cava. (Reproduced with permission from Ref. [109].)

albumin nanoparticles for use as induction chemotherapy before definitive treatment of advanced squamous cell carcinoma of the tongue was also evaluated on 23 untreated patients who had carcinoma of the tongue. Each patient received two to four infusions, with a three-week interval between infusions. Sixteen patients underwent surgery, and of the remaining seven patients one received chemotherapy alone, four received radiotherapy alone, one received chemotherapy plus radio-

therapy and one refused any further treatment. Eighteen patients (78%) had a clinical and radiologic objective response (complete, 26%; partial, 52%). Three patients (13%) showed stable disease and two (9%) showed disease progression. The toxicities encountered were hematologic in two patients (8.6%) and neurologic in two patients (8.6%) [110].

Furthermore, a recent phase III trial in patients with metastatic breast cancer compared ABI-007 with paclitaxel. ABI-007 resulted in significantly higher response rates and time to tumor progression than paclitaxel. Toxicity data showed that ABI-007 resulted in less grade 4 neutropenia than paclitaxel, and although the incidence of grade 3 sensory neuropathy was higher with ABI-007, the time until the neuropathy decreased to grade 2 was significantly less with ABI-007 compared with paclitaxel [111].

A cholesterol-rich microemulsion or nanoparticle termed LDE has been developed and its cytotoxicity, pharmacokinetics, toxicity to animals and therapeutic action has been compared with those of the commercial paclitaxel. The cytostatic activity of the drug in the complex was diminished compared with commercial paclitaxel due to the cytotoxicity of the vehicle Cremophor EL used in the commercial formulation. Competition experiments in neoplastic cultured cells showed that paclitaxel oleate and LDE were internalized together by the LDL receptor pathway. LDE-paclitaxel oleate arrested the G<sub>2</sub>/M phase of cell cycle, similarly to commercial paclitaxel. Tolerability to mice was remarkable, such that the lethal dose (LD<sub>50</sub>) was nine-fold greater than that of the commercial formulation. Furthermore, LDE concentrated paclitaxel oleate in the tumor four-fold relative to the normal adjacent tissues. At equimolar doses, the association of paclitaxel oleate with LDE resulted in remarkable changes in the drug pharmacokinetic parameters when compared to commercial paclitaxel, with increasing half-life, area under the time–concentration curve and diminishing clearance [112].

The *in vitro* antitumoral activity of a developed poly(lactic-co-glycolic acid) nanoparticle formulation incorporating paclitaxel-loaded has been assessed on a human small cell lung cancer cell line (NCI-H69 SCLC) and compared to the *in vitro* antitumoral activity of the commercial formulation. The release behavior of paclitaxel from the nanoparticles exhibited a biphasic pattern characterized by an initial fast release during the first 24 h, followed by a slower and continuous release. Incorporation of paclitaxel in these nanoparticles strongly enhanced the cytotoxic effect of the drug as compared to free drug, this effect being more relevant for prolonged incubation times [113]. In addition, nanoparticles of poly(lactic-co-glycolic acid) have been developed by a modified solvent extraction/evaporation technique, in which natural emulsifiers, such as phospholipids, cholesterol and vitamin E TPGS were applied. These natural emulsifiers showed great advantages for nanoparticle formulation of paclitaxel over the traditional macromolecular emulsifiers such as poly(vinyl alcohol). In the human adenocarcinoma cell line HT-29 the cytotoxicity caused by the drug administered after 24 h incubation was 13-fold higher than that caused by the free drug [114].

To improve paclitaxel use in intravesical therapy of superficial bladder cancer, paclitaxel-loaded gelatine nanoparticles have been developed. The excipient Cremo-

phor EL contained in the commercial formulation of paclitaxel forms micelles that entrap the drug, reducing its partition across the urothelium. The paclitaxel-loaded nanoparticles were active against human RT4 bladder transitional cancer cells with  $IC_{50}$ s nearly identical to those of the commercial solution of paclitaxel. In dogs given an intravesical dose of paclitaxel-loaded particles, drug concentrations in the urothelium and lamina propria tissue layers, where Ta and T1 tumors would be located, were 2.6-fold greater than those reported for dogs treated with the Cremophor EL formulation [115].

The *in vitro* cytotoxicity, *in vivo* antitumor activity, pharmacokinetics, pharmacodynamics, and neurotoxicity of a micellar nanoparticle formulation of paclitaxel, NK105, has been compared with those of free paclitaxel. NK105 showed significantly potent antitumor activity on a human colorectal cancer cell line (HT-29) xenograft as compared with paclitaxel. The area under the time–concentration curve was approximately 90-fold higher for NK105 than for free paclitaxel. Leakage of paclitaxel from normal blood vessels was minimal and its capture by the reticulo-endothelial system minimized. Thus, the tumor area under the time–concentration curve was 25-fold higher for NK105 than for free paclitaxel. Neurotoxicity was significantly weaker with NK105 than with free paclitaxel [116].

Paclitaxel-loaded biodegradable nanoparticles following conjugation to transferrin ligand have been developed to enhance the therapeutic efficacy of the encapsulated drug in the treatment of prostate cancer. The antiproliferative activity of nanoparticles was determined in a human prostate cancer cell line (PC3) and the effect on tumor inhibition in a murine model of prostate cancer. The  $IC_{50}$  of the drug with transferrin ligand conjugated nanoparticles was about five-fold lower than that with unconjugated nanoparticles or drug in solution. Animals that received an intratumoral injection of paclitaxel loaded transferrin ligand conjugated nanoparticles demonstrated complete tumor regression and greater survival rate than those that received either unconjugated nanoparticles or paclitaxel Cremophor EL formulation [117].

Poly(ethylene glycol)-coated biodegradable poly(cyanoacrylate) nanoparticles were also conjugated to transferrin for paclitaxel delivery. This nanoparticle formulation exhibited a markedly delayed blood clearance in mice and the paclitaxel level remained much higher at 24 h compared with that of free drug after paclitaxel intravenous injection. In S-180 solid tumor-bearing mice, tumor regression was significant with the actively targetable nanoparticles, and complete tumor regression occurred for five out of nine mice. In addition, the life span of tumor-bearing mice was significantly increased when they were treated with the nanoparticle formulation [118].

Paclitaxel is active against gliomas and various brain metastases, though its use in treating brain tumors is limited due to low blood–brain barrier permeability. The lack of paclitaxel brain uptake is thought to be associated with the P-glycoprotein efflux transporter. To improve paclitaxel brain uptake, paclitaxel was entrapped in ethyl alcohol/polysorbate nanoparticles. The paclitaxel nanoparticles cytotoxicity profile was monitored in two different cell lines, U-118 and HCT-15. Brain uptake of paclitaxel nanoparticles was evaluated using an *in situ* rat brain

perfusion model. The results suggest that entrapment of paclitaxel in nanoparticles significantly increases the drug brain uptake and its toxicity toward P-glycoprotein-expressing tumor cells. It was hypothesized that paclitaxel nanoparticles could mask paclitaxel characteristics and thus limit its binding to P-glycoprotein, which consequently would lead to higher brain and tumor cell uptake of the otherwise effluxed drug [119].

#### 1.4.7

#### Miscellaneous Agents

##### 1.4.7.1 Arsenic Trioxide

Arsenic trioxide was considered as a novel antitumor agent. However, it also showed a severe toxicity effect on normal tissue. To improve its therapeutic efficacy and decrease its toxicity, arsenic trioxide-loaded albuminates immuno-nanospheres targeted with monoclonal antibody (McAb) BDI-1 have been developed and its specific killing effect against bladder cancer cells (BIU-87) investigated. The albuminates immuno-nanospheres were tightly junctioned with the BIU-87 cells and specific killing activity of bladder tumor cells was observed [120].

##### 1.4.7.2 Butyric Acid

Butyric acid, a short-chain fatty acid naturally present in the human colon, regulates cell proliferation. It specifically modulates the expression of oncogenes such as c-myc, c-fos and H-ras, and various genes involved in the activation of apoptosis like p53 and bcl-2. The clinical applicability of the sodium salt of butyric acid is limited because of its short half-life of approximately 5 min. To improve its efficacy the pro-drug cholesterylbutyrate has been used as a lipid matrix to develop SLNs. The *in vitro* antiproliferative effect of cholesterylbutyrate SLNs was stronger than that of sodium butyrate in several human cell lines [121–123].

##### 1.4.7.3 Cystatins

Cystatins can inhibit the tumor-associated activity of intracellular cysteine proteases cathepsins B and L and have been suggested as potential anticancer drugs. Chicken cystatin, a model protein inhibitor of cysteine proteases, in poly(lactide-co-glycolide) nanoparticles has been developed to improve its bioavailability and delivery into tumor cells. Poly(lactide-co-glycolide) nanoparticles and cystatin-loaded poly(lactic-co-glycolic acid) (PLGA) nanoparticles were cytotoxic towards mammary MCF-10A neoT cells, but free cystatin at the same concentrations was not. Poly(lactide-co-glycolide) nanoparticles were rapidly internalized into MCF-10A neoT cells, whereas the uptake of free cystatin was very slow. These nanoparticles are a useful carrier system. Delivery of the protein inhibitor into tumor cells was rapid and useful to inhibit intracellular proteolysis [124].

##### 1.4.7.4 Diethylenetriaminepentaacetic Acid

Since chelating agents exhibit anticancer effects, the cytotoxicity of the extracellular chelator diethylenetriaminepentaacetic acid (DTPA) has been evaluated in breast

cancer cells, MCF-7, and neuroblastoma cells, UKF-NB-3. DTPA inhibited cancer cell growth in three-fold lower concentrations compared to human foreskin fibroblasts. The anticancer activity of chelating agents is caused by intracellular complexation of metal ions. DTPA was covalently coupled to human serum albumin nanoparticles and gelatin type B (GelB) nanoparticles to increase its cellular uptake. Coupling of DTPA to this drug carrier system increased its cytotoxic activity by five-fold [125].

#### 1.4.7.5 Mitoxantrone

Mitoxantrone-loaded poly(butyl cyanoacrylate) nanoparticles have been tested in leukemia- or melanoma-bearing mice after intravenous injection. Efficacy and toxicity of mitoxantrone nanoparticles were compared with a drug solution and with a mitoxantrone-liposome formulation. The poly(butyl cyanoacrylate) nanoparticles and liposomes influenced the efficacy of mitoxantrone in cancer therapy in different ways. Liposomes prolonged survival time in P388 leukemia, whereas nanoparticles led to a significant tumor volume reduction in B16 melanoma. Neither nanoparticles nor liposomes were able to reduce the toxic side-effects caused by mitoxantrone, specifically leucocytopenia [126].

In a different study, mitoxantrone adsorbed onto poly(isobutyl cyanoacrylate) nanospheres, coated or not with poloxamine 1508, was administered by intravenous injection in B16 melanoma-bearing mice. In both cases, the observed tumor concentrations of mitoxantrone were high. However, the influence of the hydrophilic coating of the nanoparticles on the biodistribution and pharmacokinetics was minor. Moreover, the non-adsorbed drug was not removed from the nanoparticle preparation and the hydrophilic coating was rapidly desorbed *in vivo* [127].

#### 1.4.8

#### Gene Therapy

Delivery systems are necessary for molecules such as antisense oligonucleotides since they are susceptible to nuclease-mediated degradation in the circulation and penetrate poorly through the membranes. They are also susceptible to nuclease attack within the lysosomes and their site of action is either in the cytoplasm in the case of an antisense strategy or in the nucleus for gene replacement or antigene therapy.

Antisense oligonucleotides are molecules that can inhibit gene expression being potentially active for the treatment of cancer. Short nucleic acid sequences specific to oncogene targets such as bcl-2, bcr-abl and c-myc have been shown to exhibit specific anticancer activity *in vitro* through antigene or antisense activity. However, their negative charge seriously hinders the intracellular penetration of these short fragments of nucleic acid. Efficient *in vivo* delivery of oligonucleotides remains a major limitation for their therapeutic application.

To prevent the degradation of oligonucleotides and improve their intracellular capture, it was proposed to associate them with nanoparticles. Oligonucleotides associated to nanoparticles were shown to be protected against degradation and to



penetrate more easily into different types of cells. Poly(alkyl cyanoacrylate) nanoparticles mainly release their drug content by biodegradation, thus rendering the release profile of an entrapped compound independent of its physicochemical characteristics. After intratumoral injection, the bioavailability of oligonucleotides is seriously reduced due to their fast degradation by ubiquitous exo- and endonucleases [128].

For instance, a carrier system consisting of a cationic hydrophobic detergent (cetyltrimethylammonium bromide, CTAB), which interacted with the oligonucleotides by ion-pairing, was developed. *In vivo*, HBL100ras1 cells implanted in nude mice were treated intratumorally with several formulations of oligonucleotides targeted against Has-ras oncogene. Tumor growth inhibition was achieved at concentrations 100-fold lower than those needed with free oligonucleotides, when the oligonucleotides-CTAB complex was adsorbed onto the surface of the poly(isohexyl cyanoacrylate) nanospheres. Interestingly, the oligonucleotides-CTAB complex alone exerted no effect on HBL100ras1 cell proliferation. Analysis of the amount of intact intracellular oligonucleotides, in cell culture experiments, revealed concentrations 100-fold higher in cells treated with oligonucleotides-CTAB adsorbed onto nanospheres [129].

The nanospheres were able to enhance oligonucleotides cell internalization and to protect oligonucleotides from both rapid cell internalization and rapid intracellular breakdown, which led to a considerably higher intracellular concentration of intact oligonucleotides and to a more efficient antisense activity. However, the oligonucleotides release was followed by the release of the detergent CTAB, which, at high intracellular concentrations, could induce cell toxicity.

Cholesterol-modified oligonucleotides, capable of direct adsorption onto poly(alkyl cyanoacrylate) nanospheres without the need for potentially toxic intermediates, have also been tested, but they proved less able to inhibit T24 human bladder carcinoma cells proliferation in culture than the system previously described [130].

To circumvent CTAB toxicity while maintaining an efficient biological activity, another approach was developed. Functional nanospheres were obtained by free radical emulsion polymerization of methyl methacrylate using the quaternary ammonium salt of 2-(dimethylamino)ethyl methacrylate as the reactive emulsifier [131].

The cationic dextran derivative diethylaminoethyl-dextran, by formation of an ion pair at the oligonucleotides surface, was developed to replace CTAB and was associated with poly(isohexyl cyanoacrylate) nanospheres. Poly(isohexyl cyanoacrylate) nanoparticles, with an aqueous core containing oligonucleotides, were prepared by interfacial polymerization of isobutyl cyanoacrylate in water/oil emulsion. Further studies also demonstrated that nanoencapsulation was able to protect oligonucleotides against degradation by serum nucleases contained in the cell culture medium [132].

For *in vivo* studies, phosphorothioate oligonucleotides against EWS Fli-1 chimeric RNA were encapsulated into cyanoacrylate nanocapsules and their efficacy was tested on experimental Ewing sarcoma, after intratumoral administration. Oligo-

nucleotides nanocapsules led to more efficient tumor growth inhibition. The encapsulation of oligonucleotides provided enhanced protection against *in vivo* degradation, resulting in a higher number of oligonucleotides available. Cyanoacrylate nanocapsules yielded a higher ratio of oligonucleotides targeting the tumor cells [133].

*In vivo*, poly(alkyl cyanoacrylate) nanoparticles were able to efficiently distribute the oligonucleotides to the liver and to improve, in mice, the treatment of RAS cells expressing the point mutated Ha-ras gene. As all the oligonucleotides studied had a specific therapeutic efficacy, this means that the oligonucleotides delivered by nanoparticles escape from the lysosome compartment before degradation [134].

Preclinical studies have shown that DOTAP:cholesterol nanoparticles are effective systemic gene delivery vectors that efficiently deliver tumor suppressor genes to disseminated lung tumors. A phase-I trial for systemic treatment of lung cancer using a novel tumor suppressor gene, FUS1, has been initiated. Although DOTAP:cholesterol nanoparticles complexed to DNA are efficient vectors for systemic therapy, induction of an inflammatory response in a dose-dependent manner has also been observed, thus limiting its use. Systemic administration of DNA nanoparticles induced multiple signaling molecules both *in vitro* and *in vivo* that are associated with inflammation. Use of small molecule inhibitors against the signaling molecules resulted in their suppression and thereby reduced inflammation without affecting transgene expression [135]. Nanoparticles coated with ligands such as transferrin and epidermal growth factor (EGF) have also been developed in gene delivery to target selectively the tumor cells [136]. Complexes for DNA delivery composed of polyethylenimine (polyplexes) linked to poly(ethylene glycol) and coated with transferrin or EGF were prepared with fixed nanoparticle diameters. Intravenous injection of the transferrin-coated polyplexes resulted in gene transfer to subcutaneous neuroblastoma tumors in syngenic mice, and intravenous injection of the EGF-coated polyplexes targeted human hepatocellular carcinoma xenografts in SCID mice. In these models, luciferase marker gene expression levels in tumor tissues were 10- to 100-fold higher than in other organ tissues. Repeated systemic application of the transferrin polyplexes encoding tumor necrosis factor alpha (TNF- $\alpha$ ) into tumor-bearing mice induced tumor necrosis and inhibition of tumor growth in different murine tumor models [137].

Transferrin-modified nanoparticles containing DNazymes (short catalytic single-stranded DNA molecules) for tumor targeting have been developed. Linear,  $\beta$ -cyclodextrin-based polymers were complexed with DNazyme molecules to form sub-50 nm particles termed "polyplexes". Adamantane forms inclusion complexes with the surface cyclodextrins of the polyplexes, allowing a sterically stabilizing layer of poly(ethylene glycol) to be added. The stabilized polyplexes were also modified with transferrin to increase the targeting to tumor cells expressing transferrin receptors. Administration by intraperitoneal bolus, infusion, intravenous bolus and subcutaneous injection were studied in tumor-bearing nude mice. DNazymes packaged in polyplex formulations were concentrated and retained in tumor tissue and other organs, whereas unformulated DNazyme was eliminated from the body

within 24 h post-injection. Tumor cell uptake was observed with intravenous bolus injection only and intracellular delivery requires transferrin targeting [138].

Potent sequence selective gene inhibition by siRNA is also hindered by poor intracellular uptake, limited blood stability and non-specific immune stimulation. Thus, ligand-targeted, sterically stabilized nanoparticles have been developed for siRNA. Self-assembling nanoparticles with siRNA were constructed with poly(ethyleneimine) that is PEGylated with an Arg-Gly-Asp peptide ligand, as a means to target tumor neovasculature expressing integrins, and used to deliver siRNA inhibiting vascular endothelial growth factor receptor-2 (VEGF R2) expression and thereby tumor angiogenesis. Intravenous administration into tumor-bearing mice gave selective tumor uptake, siRNA sequence-specific inhibition of protein expression within the tumor and inhibition of both tumor angiogenesis and growth rate [139].

## References

- 1 I. BRIGGER, C. DUBERNET, P. COUVREUR, Nanoparticles in cancer therapy and diagnosis, *Adv. Drug Deliv. Rev.* **2002**, 54, 631–651.
- 2 R.K.Y. ZEE-CHENG, C.C. CHENG, Delivery of anticancer agents, *Meth. Find. Exp. Clin. Pharmacol.* **1989**, 11, 439–529.
- 3 G. BARRATT, Colloidal drug carriers: Achievements and perspectives, *Cell. Mol. Life Sci.* **2003**, 60, 21–37.
- 4 R.K. JAIN, Transport of molecules in the tumor interstitium: A review, *Cancer Res.* **1987**, 47, 3039–3051.
- 5 D. BABAN, L.W. SEYMOUR, Control of tumor vascular permeability, *Adv. Drug Deliv. Rev.* **1998**, 34, 109–119.
- 6 S.K. HOBBS, W.L. MONSKY, F. YUAN, W.G. ROBERTS, L. GRIFFITH, V.P. TORCHILIN, R.K. JAIN, Regulation of transport pathway in tumor vessels: Role of tumor type and microenvironment, *Proc. Natl. Acad. Sci. U.S.A.* **1998**, 95, 4607–4612.
- 7 H. MAEDA, The enhanced permeability and retention (EPR) effect in tumor vasculature: The key role of tumor-selective macromolecular drug targeting, *Adv. Enzyme Regul.* **2001**, 41, 189–207.
- 8 R. KRISHNA, L.D. MAYER, Multidrug resistance (MDR) in cancer—mechanisms, reversal using modulators of MDR and the role of MDR modulators in influencing the pharmacokinetics of anticancer drugs, *Eur. J. Cancer Sci.* **2000**, 11, 265–283.
- 9 A.K. LARSEN, A.E. ESCARGUEIL, A. SKLADANOWSKI, Resistance mechanisms associated with altered intracellular distribution of anticancer agents, *Pharmacol. Ther.* **2000**, 88, 217–229.
- 10 C. VAUTHIER, C. DUBERNET, C. CHAUVIERRE, I. BRIGGER, P. COUVREUR, Drug delivery to resistant tumors: The potential of poly(alkyl cyanoacrylate) nanoparticles, *J. Control. Release* **2003**, 93, 151–160.
- 11 J. SINEK, H. FRIEBOES, X. ZHENG, V. CRISTINI, Two-dimensional chemotherapy simulations demonstrate fundamental transport and tumor response limitations involving nanoparticles, *Biomed. Microdevices* **2004**, 6, 297–309.
- 12 V.S. SHENOY, I.K. VIJAY, R.S. MURTHY, Tumour targeting: Biological factors and formulation advances in injectable lipid nanoparticles, *J. Pharm. Pharmacol.* **2005**, 57, 411–422.
- 13 B. RIHOVA, Immunomodulating activities of soluble synthetic polymer-

- bound drugs, *Adv. Drug Deliv. Rev.* **2002**, *54*, 653–674.
- 14 G. STORM, S.O. BELLLOT, T. DAEMEN, D.D. LASIC, Surface modification of nanoparticles to oppose uptake by the mononuclear phagocyte system, *Adv. Drug Deliv. Rev.* **1995**, *17*, 31–48.
  - 15 G.M. BARRAT, F. PUISIEUX, W.P. YU, C. FOUCHER, H. FESSI, J.P. DEVISSAGUET, Anti-metastatic activity of MDP-L-alanyl-cholesterol incorporated into various types of nanocapsules, *Int. J. Immunopharm.* **1994**, 457–461.
  - 16 P. COUVREUR, B. KANTE, L. GRISLAIN, M. ROLAND, P. SPEISER, Toxicity of polyalkylcyanoacrylate nanoparticles II: Doxorubicin-loaded nanoparticles, *J. Pharm. Sci.* **1982**, *71*, 790–792.
  - 17 P.M. BLAGOEVA, R.M. BALANSKY, T.J. MIRCHEVA, M.I. SIMEONOVA, Diminished genotoxicity of mitomycin C and farmorubicin included in polybutylcyanoacrylate nanoparticles, *Mut. Res.* **1992**, *268*, 77–82.
  - 18 C. VERDUN, F. BRASSEUR, H. VRANCKX, P. COUVREUR, M. ROLAND, Tissue distribution of doxorubicin associated with polyisohexylcyanoacrylate nanoparticles, *Cancer Chemother. Pharmacol.* **1990**, *26*, 13–18.
  - 19 R. FERNANDEZ-URRUSUNO, E. FATTAL, J.M. RODRIGUES, J. FÉGER, P. BEDOSSA, P. COUVREUR, Effect of polymeric nanoparticle administration on the clearance activity of the mononuclear phagocyte system in mice, *J. Biomed. Mater. Res.* **1996**, *31*, 401–408.
  - 20 F. FAWAZ, F. BONINI, M. GUYOT, A.M. LAGUENY, H. FESSI, J.P. DEVISSAGUET, Influence of poly(DL-lactide) nanocapsules on the biliary clearance and enterohepatic circulation of indomethacin in the rabbit, *Pharm. Res.* **1993**, *10*, 750–766.
  - 21 S. GIBAUD, J.P. ANDREUX, C. WEINGARTEN, M. RENARD, P. COUVREUR, Increased bone marrow toxicity of doxorubicin bound to nanoparticles, *Eur. J. Cancer* **1994**, *30A*, 820–826.
  - 22 S.M. MOGHIMI, A.C. HUNTER, J.C. MURRAY, Long-circulating and target-specific nanoparticles: Theory to practice, *Pharmacol. Rev.* **2001**, *53*, 283–318.
  - 23 S. GIBAUD, C. ROUSSEAU, C. WEINGARTEN, R. FAVIER, L. DOUAY, J.P. ANDREUX, P. COUVREUR, Polyalkylcyanoacrylate nanoparticles as carriers for granulocyte colony stimulating factor (G-CSF), *J. Control. Release* **1998**, *52*, 131–139.
  - 24 L. ILLUM, L.O. JACOBSEN, R.H. MÜLLER, R. MAK, S.S. DAVIS, Surface characteristics and the interaction of colloidal particles with mouse peritoneal macrophages, *Biomaterials* **1987**, *8*, 113–117.
  - 25 S.I. JEON, J.H. LEE, J.D. ANDRADE, P.G. DE GENNES, Protein-surface interactions in the presence of polyethylene oxide: Simplified theory, *J. Colloid. Interface Sci.* **1991**, *142*, 149–158.
  - 26 R. GREF, A. DOMB, P. QUELLEC, T. BLUNK, R.H. MÜLLER, J.M. VERBAVATZ, R. LANGER, The controlled intravenous delivery of drugs using PEG-coated sterically stabilized nanospheres, *Adv. Drug Deliv. Rev.* **1995**, *16*, 215–233.
  - 27 D. BAZILE, C. PRUD'HOMME, M.T. BASSOULTET, M. MARLARD, G. SPENLEHAUER, M. VEILLARD, Stealth Me.PEG-PLA nanoparticles avoid uptake by the mononuclear phagocyte system, *J. Pharm. Sci.* **1995**, *84*, 493–498.
  - 28 V.C.F. MOSQUEIRA, P. LEGRAND, A. GULIK, O. BOURDON, R. GREF, D. LABARRE, G. BARRATT, Relationship between complement activation, cellular uptake and surface physicochemical aspects of novel PEG-modified nanocapsules, *Biomaterials* **2001**, *22*, 2967–2979.
  - 29 V. LENAERTS, A. LABIB, F. CHOINARD, J. ROUSSEAU, H. ALI, J. VAN LIER, Nanocapsules with a reduced liver uptake: Targeting of phthalocyanines to EMT-6 mouse mammary tumor *in vivo*, *Eur. J. Pharm. Biopharm.* **1995**, *41*, 38–43.
  - 30 O. BOURDON, V. MOSQUEIRA, P. LEGRAND, J. BLAIS, A comparative study of the cellular uptake,

- localization and phototoxicity of meta-tetra(hydroxyphenyl) chlorin encapsulated in surface-modified submicronic oil/water carriers in HT29 tumor cells, *J. Photochem. Photobiol. B* **2000**, 55, 164–171.
- 31 M.T. PERACCHIA, C. VAUTHIER, F. PUISIEUX, P. COUVREUR, Development of sterically stabilized poly(isobutyl 2-cyanoacrylate) nanoparticles by chemical coupling of poly(ethylene glycol), *J. Biomed. Mater. Res.* **1997**, 34, 317–326.
- 32 I. BRIGGER, P. CHAMINADE, V. MARSAUD, M. APPEL, M. BESNARD, R. GURNY, M. RENOIR, P. COUVREUR, Tamoxifen encapsulation within polyethylen glycol-coated nanospheres: A new antiestrogen formulation, *Int. J. Pharm.* **2001**, 214, 37–42.
- 33 S.E. GHELPERINA, Z.S. SMIRNOVA, A.S. KHALANSKIY, I.N. SKIDAN, A.I. BOBRUSKIN, J. KREUTER, Chemotherapy of brain tumours using doxorubicin bound to polysorbate 80-coated nanoparticles, *Proceedings of 3<sup>rd</sup> World Meeting APV/APGI*, Berlin, Germany **2000**, 441–442.
- 34 J. KREUTER, Influence of the surface properties on nanoparticle-mediated transport of drugs to the brain, *J. Nanosci. Nanotechnol.* **2004**, 4, 484–488.
- 35 E. ALLÉMANN, J. ROUSSEAU, N. BRASSEUR, S.V. KUDREVICH, K. LEWIS, J.E. VAN LIER, Photodynamic therapy of tumours with hexadecafluoro zinc phthalocyanine formulated in PEG-coated poly(lactic acid) nanoparticles, *Int. J. Cancer* **1996**, 66, 821–824.
- 36 J. LODE, I. FICHTNER, J. KREUTER, A. BERNDT, J.E. DIEDERICHS, R. RESZKA, Influence of surface-modifying surfactants on the pharmacokinetic behaviour of <sup>14</sup>C-poly(methylmethacrylate) nanoparticles in experimental tumor models, *Pharm. Res.* **2001**, 18, 1613–1619.
- 37 M.T. PERACCHIA, C. VAUTHIER, D. DESMAËLE, A. GULIK, J.C. DEDIEU, M. DEMOY, J. D'ANGELO, P. COUVREUR, Pegylated nanoparticles from a novel methoxypolyethylene glycol cyanoacrylate-hexadecyl cyanoacrylate amphiphilic copolymer, *Pharm. Res.* **1998**, 15, 550–556.
- 38 S.E. DUNN, A.G.A. COOMBES, M.C. GARNETT, S.S. DAVIS, M.C. DAVIES, L. ILLUM, *In vitro* interaction and *in vivo* biodistribution of poly(lactide-glycolide) nanospheres surface modified by poloxamer and poloxamine copolymers, *J. Control. Release* **1997**, 44, 65–76.
- 39 S. STOLNIK, S.E. DUNN, M.C. GARNETT, M.C. DAVIES, A.G.A. COOMBES, D.C. TAYLOR, M.P. IRVING, S.C. PURKISS, T.F. TADROS, S.S. DAVIS, Surface modification of poly(lactide-co-glycolide) nanospheres by biodegradable poly(lactide)-poly(ethylene glycol) copolymers, *Pharm. Res.* **1994**, 11, 1800–1808.
- 40 V.C.F. MOSQUEIRA, P. LEGRAND, R. GREF, B. HEURTAULT, M. APPEL, G. BARRATT, Interactions between a macrophage cell line (J774A1) and surface-modified poly(D,L-lactide) nanocapsules bearing poly(ethylene glycol), *J. Drug Target.* **1999**, 7, 65–78.
- 41 V.C.F. MOSQUEIRA, P. LEGRAND, A. GULIK, O. BOURDON, R. GREF, D. LABARRE, G. BARRATT, Biodistribution of novel long circulating PEG-grafted nanocapsules in mice: Effects of PEG chain length and density, *Pharm. Res.* **2001**, 18, 1411–1419.
- 42 B. STELLA, S. ARPICCO, M.T. PERACCHIA, D. DESMAËLE, J. HOEBENE, M. RENOIR, J. D'ANGELO, L. CATTEL, P. COUVREUR, Design of folic acid-conjugated nanoparticles for drug targeting, *J. Pharm. Sci.* **2000**, 89, 1452–1464.
- 43 L. ZHANG, S. HOU, S. MAO, D. WEI, X. SONG, Y. LU, L. ZHANG, S. HOU, S. MAO, D. WEI, X. SONG, Y. LU, Uptake of folate-conjugated albumin nanoparticles to the SKOV3 cells, *Int. J. Pharm.* **2004**, 287, 155–162.
- 44 T. SHIOKAWA, Y. HATTORI, K. KAWANO, Y. OHGUCHI, H. KAWAKAMI, K. TOMA, Y. MAITANI, Effect of polyethylene glycol linker chain length of folate-linked microemulsions loading aclacinomycin A on targeting ability and antitumor effect *in vitro*

- and *in vivo*, *Clin. Cancer Res.* **2005**, *11*, 2018–2025.
- 45 N.C. BELLOCQ, S.H. PUN, G.S. JENSEN, M.E. DAVIS, Transferrin-containing, cyclodextrin polymer-based particles for tumor-targeted gene delivery, *Bioconj. Chem.* **2003**, *14*, 1122–1132.
  - 46 H. WARTLICK, K. MICHAELIS, S. BALTHASAR, K. STREBHARDT, J. KREUTER, K. LANGER, Highly specific HER2-mediated cellular uptake of antibody-modified nanoparticles in tumour cells, *J. Drug Target.* **2004**, *12*, 461–471.
  - 47 E.M. GORDON, F.L. HALL, Nanotechnology blooms, at last, *Oncol. Rep.* **2005**, *13*, 1003–1007.
  - 48 F.B. LANDRY, D.V. BAZILE, G. SPENLEHAUER, M. VEILLARD, J. KREUTER, Peroral administration of 14C-poly-(D,L-lactic acid) nanoparticles coated with human serum albumin or polyvinyl alcohol to guinea pigs, *J. Drug Target* **1998**, *6*, 293–307.
  - 49 G. PONCHEL, J.M. IRACHE, Specific and non-specific bioadhesive particulate systems for oral delivery to the gastrointestinal tract, *Adv. Drug Deliv. Rev.* **1998**, *34*, 191–219.
  - 50 L. MU, S.S. FENG, A novel controlled release formulation for the anticancer drug paclitaxel (Taxol): PLGA nanoparticles containing vitamin E TPGS, *J. Control. Release* **2003**, *86*, 33–48.
  - 51 Y. NISHIOKA, H. YOSHINO, Lymphatic targeting with nanoparticulate system, *Adv. Drug Deliv. Rev.* **2001**, *47*, 55–64.
  - 52 C. SAKAKURA, T. TAKAHASHI, K. SAWAI, A. HAGIWARA, M. ITO, S. SHOBAYASHI, S. SASAKI, K. OZAKI, M. SHIRASU, Enhancement of therapeutic efficacy of aclarubicin against lymph node metastases using a new dosage form: Aclarubicin adsorbed on activated carbon particles, *Anti-Cancer Drugs* **1992**, *3*, 233–236.
  - 53 A. HAGIWARA, T. TAKAHASHI, K. SAWAI, C. SAKAKURA, M. SHIRASU, M. OHGAKI, T. IMANASHI, J. YAMASAKI, Y. TAKEMOTO, N. KAGEYAMA, Selective drug delivery to peri-tumoral region and regional lymphatics by local injection of aclarubicin adsorbed on activated carbon particles in patients with breast cancer – a pilot study. *Anti-Cancer Drugs* **1997**, *8*, 666–670.
  - 54 A.E. HAWLEY, S.S. DAVIS, L. ILLUM, Targeting of colloids to lymph nodes: Influence of lymphatic physiology and colloidal characteristics, *Adv. Drug Deliv. Rev.* **1995**, *17*, 129–148.
  - 55 H. TOKUMITSU, J. HIRATSUKA, Y. SKURAI, T. KOBAYASHI, H. ICHIKAWA, Y. FUKUMORI, Gadolinium neutron-capture therapy using novel gadopentetic acid-chitosan complex nanoparticles: *In vivo* growth suppression of experimental melanoma solid tumor, *Cancer Lett.* **2000**, *150*, 177–182.
  - 56 P. CALVO, J.L. VILA-JATO, M.J. ALONSO, Evaluation of cationic polymer-coated nanocapsules as ocular drug carriers, *Int. J. Pharm.* **1997**, *153*, 41–50.
  - 57 G. MINOTTI, P. MENNA, E. SALVATORELLI, G. CAIRO, L. GIANNI, Anthracyclines: Molecular advances and pharmacological developments in antitumor activity and cardiotoxicity. *Pharmacol. Rev.* **2004**, *56*, 185–229.
  - 58 N. CHIANNILKULCHAI, Z. DRIOUCHE, J.P. BENOIT, A.L. PARODI, P. COUVREUR, Doxorubicin-loaded nanoparticles: Increased efficiency in murine hepatic metastasis, *Sel. Cancer Ther.* **1989**, *5*, 1–11.
  - 59 N. CHIANNILKULCHAI, N. AMMOURY, B. CAILLOU, J.Ph. DEVISSAGUET, P. COUVREUR, Hepatic tissue distribution of doxorubicin-loaded particles after i.v. administration in reticulosarcoma M 5076 metastasis-bearing mice, *Cancer Chemother. Pharmacol.* **1990**, *26*, 122–126.
  - 60 A. ROLLAND, Clinical pharmacokinetics of doxorubicin in hepatoma patients after a single intravenous injection of free or nanoparticle-bound anthracycline, *Int. J. Pharm.* **1989**, *54*, 113–121.
  - 61 J. KATTAN, J.P. DROZ, P. COUVREUR, J.P. MARINO, A. BOUTAN-LAROZE, P. ROUGIER, P. BRAULT, H. VRANCKX, J.M. GROGNET, X. MORGE, H. SANCHO-GARNIER, Phase I clinical trial and pharmacokinetics evaluation of doxorubicin carried by poly-

- isohexylcyanoacrylate nanoparticles, *Invest. New Drugs* **1992**, *10*, 191–199.
- 62 C.E. SOMA, C. DUBERNET, G. BARRATT, S. BENITA, P. COUVREUR, Investigation of the role of macrophages on the cytotoxicity of doxorubicin and doxorubicin-loaded nanoparticles on M5076 cells *in vitro*, *J. Control. Release* **2000**, *68*, 283–289.
- 63 S. MITRA, U. GAUR, P.C. GOSH, A.N. MAITRA, Tumor targeted delivery of encapsulated dextran-doxorubicin conjugate using chitosan nanoparticles as carrier, *J. Control. Release* **2001**, *74*, 317–323.
- 64 J.H. CHEN, R. LING, Q. YAO, L. WANG, Z. MA, Y. LI, Z. WANG, H. XU, Enhanced antitumor efficacy on hepatoma-bearing rats with adriamycin-loaded nanoparticles administered into hepatic artery. *World J. Gastroenterol.* **2004**, *10*(13), 1989–1991.
- 65 J.H. CHEN, L. WANG, R. LING, Y. LI, Z. WANG, Q. YAO, Z. MA, Body distribution of nanoparticle-containing adriamycin injected into the hepatic artery of hepatoma-bearing rats, *Dig. Dis. Sci.* **2004**, *49*, 1170–1173.
- 66 L. MANIL, P. COUVREUR, P. MAHIEU, Acute renal toxicity of doxorubicin (adriamycin)-loaded cyanoacrylate nanoparticles, *Pharm. Res.* **1995**, *12*, 85–87.
- 67 E. LEO, R. ARLETTI, F. FORNI, R. CAMERONI, General and cardiac toxicity of doxorubicin-loaded gelatin nanoparticles, *Il Farmaco* **1997**, *52*, 385–388.
- 68 J. KREUTER, Nanoparticulate systems for brain delivery of drugs, *Adv. Drug Deliv. Res.* **2000**, *47*, 65–81.
- 69 S.E. GELPERINA, A.S. KHALANSKY, I.N. SKIDAN, Z.S. SMIRNOVA, A.I. BOBRUSKIN, S.E. SEVERIN, B. TUROWSKI, F.E. ZANELLA, J. KREUTER, Toxicological studies of doxorubicin bound to polysorbate 80-coated poly(butyl cyanoacrylate) nanoparticles in healthy rats and rats with intracranial glioblastoma, *Toxicol. Lett.* **2002**, *126*, 131–141.
- 70 S.C. STEINIGER, J. KREUTER, A.S. KHALANSKY, I.N. SKIDAN, A.I. BOBRUSKIN, Z.S. SMIRNOVA, S.E. SEVERIN, R. UHL, M. KOCK, K.D. GEIGER, S.E. GELPERINA, Chemotherapy of glioblastoma in rats using doxorubicin-loaded nanoparticles, *Int. J. Cancer* **2004**, *109*, 759–767.
- 71 H.S. YOO, K.H. LEE, J.E. OH, T.G. PARK, *In vitro* and *in vivo* anti-tumor activities of nanoparticles based on doxorubicin-PLGA conjugates, *J. Control. Release* **2000**, *68*, 419–431.
- 72 L.H. REDDY, R.K. SHARMA, R.S. MURTHY, Enhanced tumour uptake of doxorubicin loaded poly(butyl cyanoacrylate) nanoparticles in mice bearing Dalton's lymphoma tumour, *J. Drug Target* **2004**, *12*, 443–451.
- 73 I. BRIGGER, J. MORIZET, L. LAUDANI, G. AUBERT, M. APPEL, V. VELASCO, M.J. TERRIER-LACOMBE, D. DESMAELE, J. D'ANGELO, P. COUVREUR, G. VASSAL, Negative preclinical results with stealth nanospheres-encapsulated doxorubicin in an orthotopic murine brain tumor model, *J. Control. Release* **2004**, *100*, 29–40.
- 74 R.H. MÜLLER, K. MÄDER, S. GOHLA, Solid lipid nanoparticles (SLN) for controlled drug delivery – a review of the state of the art, *Eur. J. Pharm. Biopharm.* **2000**, *50*, 161–177.
- 75 R.N. ALYAUTDIN, V.E. PETROV, K. LANGER, A. BERTHOLD, D.A. KHARKEVICH, J. KREUTER, Delivery of loperamide across the blood-brain barrier with Polysorbate 80-coated polybutylcyanoacrylate nanoparticles, *Pharm. Res.* **1997**, *14*, 325–328.
- 76 G.P. ZARA, R. CAVALLI, A. FUNDARÒ, A. BARGONI, O. CAPUTO, M.R. GASCO, Pharmacokinetics of doxorubicin incorporated in solid lipid nanospheres (SLN), *Pharm. Res.* **1999**, *44*, 281–286.
- 77 A. MIGLIETTA, R. CAVALLI, C. BOCCA, L. GABRIEL, M.R. GASCO, Cellular uptake and cytotoxicity of solid lipid nanospheres (SLN) incorporating doxorubicin or paclitaxel, *Int. J. Pharm.* **2000**, *210*, 61–67.
- 78 L. SERPE, M.G. CATALANO, R. CAVALLI, E. UGAZIO, O. BOSCO, R. CANAPARO, E. MUNTONI, R. FRAIRIA, M.R. GASCO, M. EANDI, G.P. ZARA, Cytotoxicity of

- anticancer drugs incorporated in solid lipid nanoparticles on HT-29 colorectal cancer cell line, *Eur. J. Pharm. Biopharm.* **2004**, *58*, 673–680.
- 79** G.P. ZARA, R. CAVALLI, A. BARGONI, A. FUNDARÒ, D. VIGHETTO, M.R. GASCO, Intravenous administration to rabbits of non stealth and stealth doxorubicin-loaded solid lipid nanoparticles at increasing concentrations of stealth agent: Pharmacokinetics and distribution of doxorubicin in brain and other tissues, *J. Drug Target* **2002**, *10*, 327–335.
- 80** A. FUNDARÒ, R. CAVALLI, A. BARGONI, D. VIGHETTO, G.P. ZARA, M.R. GASCO, Non-stealth and stealth solid lipid nanoparticles (SLN) carrying doxorubicin: Pharmacokinetics and tissue distribution after i.v. administration to rats, *Pharm. Res.* **2000**, *42*, 337–343.
- 81** G.P. ZARA, A. BARGONI, R. CAVALLI, A. FUNDARÒ, D. VIGHETTO, M.R. GASCO, Pharmacokinetics and tissue distribution of idarubicin-loaded solid lipid nanoparticles after duodenal administration to rats, *J. Pharm. Sci.* **2002**, *91*, 1324–1333.
- 82** A.C. DE VERDIÈRE, C. DUBERNET, F. NÉMATI, E. SOMA, M. APPEL, J. FERTÉ, S. BERNARD, F. PUISIEUX, P. COUVREUR, Reversion of multidrug resistance with polyalkylcyanoacrylate nanoparticles: Towards a mechanism of action, *Br. J. Cancer* **1997**, *76*, 198–205.
- 83** A. ASTIER, B. DOAT, M.J. FERRER, G. BENOIT, J. FLEURY, A. ROLLAND, R. LEVERGE, Enhancement of adriamycin antitumor activity by its binding with an intracellular sustained-release form, polymethacrylate nanospheres, in U-937 cells, *Cancer Res.* **1988**, *48*, 1835–1841.
- 84** S. BENNIS, C. CHAPEY, P. COUVREUR, J. ROBERT, Enhanced cytotoxicity of doxorubicin encapsulated in polyisohexylcyanoacrylate nanospheres against multi-drug-resistant tumour cells in culture, *Eur. J. Cancer* **1994**, *30A*, 889–893.
- 85** A.C. DE VERDIÈRE, C. DUBERNET, F. NÉMATI, M.F. POUPON, F. PUISIEUX, P. COUVREUR, Uptake of doxorubicin from loaded nanoparticles in multidrug-resistant leukemic murine cells, *Cancer Chemother. Pharmacol.* **1994**, *33*, 504–508.
- 86** X. PÉPIN, L. ATTALI, C. DOMRAULT, S. GALLET, J.M. METREAU, Y. REAULT, P.J. CARDOT, M. IMALALEN, C. DUBERNET, E. SOMA, P. COUVREUR, On the use of ion-pair chromatography to elucidate doxorubicin release mechanism from polyalkylcyanoacrylate nanoparticles at the cellular level, *J. Chromatogr. B* **1997**, *702*, 181–187.
- 87** J. NAFZIGER, G. AVERLAND, E. BERTOUNESQUE, G. GAUDEL, C. MONNERET, Synthesis and antiproliferative effects of a 4'-morpholino-9-methyl anthracycline, *J. Antibiot.* **1995**, *48*, 1185–1187.
- 88** C.E. SOMA, C. DUBERNET, G. BARRATT, F. NEMATI, M. APPEL, S. BENITA, P. COUVREUR, Ability of doxorubicin-loaded nanoparticles to overcome multidrug resistance of tumor cells after their capture by macrophages, *Pharm. Res.* **1999**, *16*, 1710–1716.
- 89** A. LAURAND, A. LAROCHE-CLARY, A. LARRUE, S. HUET, E. SOMA, J. BONNET, J. ROBERT, Quantification of the expression of multidrug resistance-related genes in human tumour cell lines grown with free doxorubicin or doxorubicin encapsulated in polyisohexylcyanoacrylate nanospheres, *Anticancer Res.* **2004**, *24*, 3781–3788.
- 90** C.E. SOMA, C. DUBERNET, D. BENTOLILLA, S. BENITA, P. COUVREUR, Reversion of multidrug resistance by co-encapsulation of doxorubicin and cyclosporin A in polyalkylcyanoacrylate nanoparticles, *Biomaterials* **2000**, *21*, 1–7.
- 91** T. AMELLER, V. MARSAUD, P. LEGRAND, R. GREF, J.M. RENOIR, *In vitro* and *in vivo* biologic evaluation of long-circulating biodegradable drug carriers loaded with the pure antiestrogen RU 58668, *Int. J. Cancer* **2003**, *106*, 446–454.
- 92** S. MAILLARD, T. AMELLER, J. GAUDUCHON, A. GOUGELET, F. GOUILLEUX, P. LEGRAND, V. MARSAUD, E. FATTAL, B. SOLA, J.M. RENOIR,



- Innovative drug delivery nanosystems improve the anti-tumor activity *in vitro* and *in vivo* of anti-estrogens in human breast cancer and multiple myeloma, *J. Steroid Biochem. Mol. Biol.* **2005**, *94*, 111–121.
- 93 J.S. CHAWLA, M.M. AMIJI, Cellular uptake and concentrations of tamoxifen upon administration in poly(epsilon-caprolactone) nanoparticles, *AAPS Pharm. Sci.* **2003**, *5*, E3.
- 94 D.B. SHENOY, M.M. AMIJI, Poly(ethylene oxide)-modified poly(epsilon-caprolactone) nanoparticles for targeted delivery of tamoxifen in breast cancer, *Int. J. Pharm.* **2005**, *293*, 261–270.
- 95 D. BHADRA, S. BHADRA, S. JAIN, N.K. JAIN, A PEGylated dendritic nanoparticulate carrier of fluorouracil, *Int. J. Pharm.* **2003**, *257*, 111–124.
- 96 C.L. LO, K.M. LIN, G.H. HSIUE, Preparation and characterization of intelligent core-shell nanoparticles based on poly(D,L-lactide)-g-poly(N-isopropyl acrylamide-co-methacrylic acid), *J. Control. Release* **2005**, *104*, 477–488.
- 97 J.F. KUKOWSKA-LATALLO, K.A. CANDIDO, Z. CAO, S.S. NIGAVEKAR, I.J. MAJOROS, T.P. THOMAS, L.P. BALOGH, M.K. KHAN, J.R. JR BAKER, Nanoparticle targeting of anticancer drug improves therapeutic response in animal model of human epithelial cancer, *Cancer Res.* **2005**, *65*, 5317–5324.
- 98 S. YANG, J. ZHU, B. LU, B. LIANG, C. YANG, Body distribution of camptothecin solid lipid nanoparticles after oral administration, *Pharm. Res.* **1999**, *16*, 751–757.
- 99 H. MIURA, H. ONISHI, M. SASATSU, Y. MACHIDA, Antitumor characteristics of methoxypolyethylene glycol-poly(DL-lactic acid) nanoparticles containing camptothecin, *J. Control. Release* **2004**, *97*, 101–113.
- 100 H. ONISHI, Y. MACHIDA, Y. MACHIDA, Antitumor properties of irinotecan-containing nanoparticles prepared using poly(DL-lactic acid) and poly(ethylene glycol)-block-poly(propylene glycol)-block-poly(ethylene glycol), *Biol. Pharm. Bull.* **2003**, *26*, 116–119.
- 101 J. WILLIAMS, R. LANSDOWN, R. SWEITZER, M. ROMANOWSKI, R. LABELL, R. RAMASWAMI, E. UNGER, Nanoparticle drug delivery system for intravenous delivery of topoisomerase inhibitors, *J. Control. Release* **2003**, *91*, 167–172.
- 102 K. AVGOUSTAKIS, A. BELETSI, Z. PANAGI, P. KLEPETSANIS, A.G. KARYDAS, D.S. ITHAKISSIOS, PLGA-mPEG nanoparticles of cisplatin: *In vitro* nanoparticle degradation, *in vitro* drug release and *in vivo* drug residence in blood properties, *J. Control. Release* **2002**, *79*, 123–135.
- 103 A. BARROUG, L.T. KUHN, L.C. GERSTENFELD, M.J. GLIMCHER, Interactions of cisplatin with calcium phosphate nanoparticles: *In vitro* controlled adsorption and release, *J. Orthop. Res.* **2004**, *22*, 703–708.
- 104 A.K. SINGLA, A. GARG, D. AGGARWAL, Paclitaxel and its formulations, *Int. J. Pharm.* **2002**, *235*, 179–192.
- 105 A.J. TEN TIJE, J. VERWEIJ, W.J. LOOS, A. SPAREBOOM, Pharmacological effects of formulation vehicles: Implications for cancer chemotherapy, *Clin. Pharmacokin.* **2003**, *42*, 665–685.
- 106 D. SHARMA, T.P. CHELVI, J. KAUR, K. CHAKRAVORTY, T.K. DE, A. MAITRA, R. RALHAN, Novel Taxol formulation: Polyvinylpyrrolidone nanoparticle-encapsulated Taxol for drug delivery in cancer therapy, *Oncol. Res.* **1996**, *8*, 281–286.
- 107 R. CAVALLI, O. CAPUTO, M.R. GASCO, Preparation and characterization of solid lipid nanoparticles incorporating paclitaxel, *Eur. J. Pharm. Sci.* **2000**, *10*, 305–309.
- 108 N.K. IBRAHIM, N. DESAI, S. LEGHA, P. SOON-SHIONG, R.L. THERIAULT, E. RIVERA, B. ESMALI, S.E. RING, A. BEDIKIAN, G.N. HORTOBAGYI, J.A. ELLERHORST, Phase I and pharmacokinetic study of ABI-007, a cremophor-free, protein-stabilized, nanoparticle formulation of paclitaxel, *Clin. Cancer Res.* **2002**, *8*, 1038–1044.

- 109 B. DAMASCELLI, G. CANTU, F. MATTAVELLI, P. TAMPLENIZZA, P. BIDOLI, E. LEO, F. DOSIO, A.M. CERROTTA, G. DI TOLLA, L.F. FRIGERIO, F. GARBAGNATI, R. LANOCITA, A. MARCHIANO, G. PATELLI, C. SPREAFICO, V. TICHA, V. VESPRO, F. ZUNINO, Intraarterial chemotherapy with polyoxyethylated castor oil free paclitaxel, incorporated in albumin nanoparticles (ABI-007): Phase II study of patients with squamous cell carcinoma of the head and neck and anal canal: Preliminary evidence of clinical activity, *Cancer* **2001**, 92, 2592–2602.
- 110 B. DAMASCELLI, G.L. PATELLI, R. LANOCITA, G. DI TOLLA, L.F. FRIGERIO, A. MARCHIANO, F. GARBAGNATI, C. SPREAFICO, V. TICHA, C.R. GLADIN, M. PALAZZI, F. CRIPPA, C. OLDINI, S. CALO, A. BONACCORSI, F. MATTAVELLI, L. COSTA, L. MARIANI, G. CANTU, A novel intraarterial chemotherapy using paclitaxel in albumin nanoparticles to treat advanced squamous cell carcinoma of the tongue: Preliminary findings, *Am. J. Roentgenol.* **2003**, 181, 253–260.
- 111 W.J. GRADISHAR, The future of breast cancer: The role of prognostic factors, *Breast Cancer Res. Treat.* **2005**, 89, 17–26.
- 112 D.G. RODRIGUES, D.A. MARIA, D.C. FERNANDES, C.J. VALDUGA, R.D. COUTO, O.C. IBANEZ, R.C. MARANHAO, Improvement of paclitaxel therapeutic index by derivatization and association to a cholesterol-rich microemulsion: *in vitro* and *in vivo* studies, *Cancer Chemother. Pharmacol.* **2005**, 55, 565–576.
- 113 C. FONSECA, S. SIMOES, R. GASPAR, Paclitaxel-loaded PLGA nanoparticles: Preparation, physicochemical characterization and *in vitro* antitumoral activity, *J. Control. Release* **2002**, 83, 273–286.
- 114 S.S. FENG, L. MU, K.Y. WIN, G. HUANG, Nanoparticles of biodegradable polymers for clinical administration of paclitaxel, *Curr. Med. Chem.* **2004**, 11, 413–424.
- 115 Z. LU, T.K. YEH, M. TSAI, J.L. AU, M.G. WIENTJES, Paclitaxel-loaded gelatin nanoparticles for intravesical bladder cancer therapy, *Clin. Cancer Res.* **2004**, 10, 7677–7684.
- 116 T. HAMAGUCHI, Y. MATSUMURA, M. SUZUKI, K. SHIMIZU, R. GODA, I. NAKAMURA, I. NAKATOMI, M. YOKOYAMA, K. KATAOKA, T. KAKIZOE, NK105, a paclitaxel-incorporating micellar nanoparticle formulation, can extend *in vivo* antitumour activity and reduce the neurotoxicity of paclitaxel, *Br. J. Cancer* **2005**, 92, 1240–1246.
- 117 S.K. SAHOO, W. MA, V. LABHASETWAR, Efficacy of transferrin-conjugated paclitaxel-loaded nanoparticles in a murine model of prostate cancer, *Int. J. Cancer* **2004**, 112, 335–340.
- 118 Z. XU, W. GU, J. HUANG, H. SUI, Z. ZHOU, Y. YANG, Z. YAN, Y. LI, *In vitro* and *in vivo* evaluation of actively targetable nanoparticles for paclitaxel delivery, *Int. J. Pharm.* **2005**, 288, 361–368.
- 119 J.M. KOZIARA, P.R. LOCKMAN, D.D. ALLEN, R.J. MUMPER, Paclitaxel nanoparticles for the potential treatment of brain tumors, *J. Control. Release* **2004**, 99, 259–269.
- 120 J. ZHOU, F.Q. ZENG, C. LI, Q.S. TONG, X. GAO, S.S. XIE, L.Z. YU, Preparation of arsenic trioxide-loaded albumin immunonanospheres and its specific killing effect on bladder cancer cell *in vitro*, *Chin. Med. J.* **2005**, 118, 50–55.
- 121 C. PELLIZZARO, D. CORADINI, S. MOREL, E. UGAZIO, M.R. GASCO, M.G. DAIDONE, Cholesteryl butyrate in solid lipid nanoparticles as an alternative approach for butyric acid delivery, *Anticancer Res.* **1999**, 15, 3921–3926.
- 122 B. SALOMONE, R. PONTI, M.R. GASCO, E. UGAZIO, P. QUAGLINO, S. OSELLA-ABATE, M.G. BERNENGO, *In vitro* effects of cholesteryl butyrate solid lipid nanoparticles as a butyric acid pro-drug on melanoma cells: Evaluation of antiproliferative activity and apoptosis induction, *Clin. Exp. Metastasis* **2001**, 18, 663–673.
- 123 L. SERPE, S. LAURORA, S. PIZZIMENTI, E. UGAZIO, R. PONTI, R. CANAPARO, F. BRIATORE, G. BARRERA, M.R.

- GASCO, M.G. BERNENGO, M. EANDI, G.P. ZARA, Cholesteryl butyrate solid lipid nanoparticles as a butyric acid pro-drug: Effects on cell proliferation, cell-cycle distribution and c-myc expression in human leukemic cells, *Anticancer Drugs* **2004**, 15, 525–536.
- 124** M. CEGNAR, A. PREMZL, V. ZAVASNIK-BERGANT, J. KRISTL, J. KOS, Poly(lactide-co-glycolide) nanoparticles as a carrier system for delivering cysteine protease inhibitor cystatin into tumor cells, *Exp. Cell Res.* **2004**, 301, 223–231.
- 125** M. MICHAELIS, K. LANGER, S. ARNOLD, H.W. DOERR, J. KREUTER, J. JR. CINATL, Pharmacological activity of DTPA linked to protein-based drug carrier systems, *Biochem. Biophys Res. Commun.* **2004**, 323, 1236–1240.
- 126** P. BECK, J. KREUTER, R. RESZKA, I. FICHTNER, Influence of polybutylcyanoacrylate nanoparticles and liposomes on the efficacy and toxicity of the anticancer drug mitoxantrone in murine tumour models, *J. Microencapsul.* **1993**, 10, 101–114.
- 127** R. RESZKA, P. BECK, I. FICHTNER, M. HENTSCHEL, L. RICHTER, J. KREUTER, Body distribution of free, liposomal and nanoparticle-associated mitoxantrone in B16-melanoma-bearing mice, *J. Pharm. Exp. Ther.* **1997**, 280, 232–237.
- 128** R.L. JULIANO, S. ALAHARI, H. YOO, R. KOLE, M. CHO, Antisense pharmacodynamics: Critical issues in the transport and delivery of antisense oligonucleotides, *Pharm. Res.* **1999**, 16, 494–502.
- 129** G. SCHWAB, C. CHAVANY, I. DUROUX, G. GOUBIN, J. LEBEAU, C. HÉLÈNE, T. SAISON-BEHMOARAS, Antisense oligonucleotides adsorbed to polyalkylcyanoacrylate nanoparticles specifically inhibit mutated Ha-ras-mediated cell proliferation and tumorigenicity in nude mice, *Proc. Natl. Acad. Sci. U.S.A.* **1994**, 91, 10460–10464.
- 130** G. GODARD, A.S. BOUTORINE, E. SAISON-BEHMOARAS, C. HÉLÈN, Antisense effect of cholesterol-oligodeoxynucleotide conjugates associated with poly(alkylcyanoacrylate) nanoparticles, *Eur. J. Biochem.* **1995**, 232, 404–410.
- 131** L. TONDELLI, A. RICCA, M. LAUS, M. LELLI, G. CITRO, Highly efficient cellular uptake of c-myc antisense oligonucleotides through specifically designed polymeric nanospheres, *Nucleic Acids Res.* **1998**, 26, 5425–5431.
- 132** G. LAMBERT, E. FATTAL, H. PINTO-ALPHANDARY, A. GULIK, P. COUVREUR, Polyisobutylcyanoacrylate nanocapsules containing an aqueous core as a novel colloidal carrier for the delivery of oligonucleotides, *Pharm. Res.* **2000**, 17, 707–714.
- 133** G. LAMBERT, J.R. BERTRAND, E. FATTAL, F. SUBRA, H. PINTO-ALPHANDARY, C. MALVY, C. AUCLAIR, P. COUVREUR, EWS Fli-1 antisense nanocapsules inhibits Ewing sarcoma-related tumor in mice, *Biochem. Biophys. Res. Commun.* **2000**, 279, 401–406.
- 134** G. LAMBERT, E. FATTAL, P. COUVREUR, Nanoparticulate systems for the delivery of antisense oligonucleotides, *Adv. Drug Deliv. Rev.* **2001**, 47, 99–112.
- 135** B. GOPALAN, I. ITO, C.D. BRANCH, C. STEPHENS, J.A. ROTH, R. RAMESH, Nanoparticle based systemic gene therapy for lung cancer: Molecular mechanisms and strategies to suppress nanoparticle-mediated inflammatory response, *Technol. Cancer Res. Treat.* **2004**, 3, 647–657.
- 136** L. BRANNON-PEPPAS, J.O. BLANCHETTE, Nanoparticle and targeted systems for cancer therapy, *Adv. Drug Deliv. Rev.* **2004**, 56, 1649–1659.
- 137** M. OGRIS, G. WALKER, T. BLESSING, R. KIRCHEIS, M. WOLSHEK, E. WAGNER, Tumor-targeted gene-therapy: Strategies for the preparation of ligand-polyethylene glycol-polyethyleneimine/DNA complexes, *J. Control. Release* **2003**, 91, 173–181.
- 138** S.H. PUN, F. TACK, N.C. BELLOCQ, J. CHENG, B.H. GRUBBS, G.S. JENSEN, M.E. DAVIS, M. BREWSTER, M. JANICOT, B. JANSSENS, W. FLOREN, A. BAKKER, Targeted delivery of RNA-

- cleaving DNA enzyme (DNAzyme) to tumor tissue by transferrin-modified, cyclodextrin-based particles, *Cancer Biol. Ther.* **2004**, *3*, 641–650.
- 139 R.M. SCHIFFELERS, A. ANSARI, J. XU, Q. ZHOU, Q. TANG, G. STORM, G. MOLEMA, P.Y. LU, P.V. SCARIA, M.C. WOODLE, Cancer siRNA therapy by tumor selective delivery with ligand-targeted sterically stabilized nanoparticle, *Nucleic Acids Res.* **2004**, *32*, 149.

## 2 Nanoparticles for Photodynamic Therapy of Cancer

*Magali Zeisser-Labouèbe, Angelica Vargas, and Florence Delie*

### 2.1 Introduction

Currently, the limiting factor in cancer chemotherapy is still the lack of selectivity of anticancer drugs towards neoplastic cells. Photosensitizers (PS), the active compounds used for photodynamic therapy (PDT), have the intrinsic advantage of distributing primarily in highly regenerative tissues after intravenous or topical administration. Therefore, they will accumulate preferentially in tumor tissue when present. In addition, these molecules are inactive as such; indeed, the anticancer effect is only attained after irradiation with light at the right wavelength. Compared to other current cancer therapies such as surgery, radiotherapy or chemotherapy, PDT is an effective and selective means of suppressing diseased tissues without altering the surrounding healthy tissue. It also offers a unique opportunity to reach unseen metastasis. As fluorescent molecules, PS may also be used as a tool, namely photodetection (PD), to reveal tumor tissues that remain unseen by other conventional methods.

Interestingly, PD and PDT are mutually beneficial. Ideally, a PS could be used to detect tumors and then to treat them. Quantification of PS fluorescence allows us to follow PS uptake and pharmacokinetics [1–3]. Finally, after treatment, the tissue can be examined by PD to evaluate disease control or possible recurrence [4, 5].

The first compound on the market was Photofrin<sup>®</sup>, a synthetic haematoporphyrin derivative characterized by a pronounced skin photosensitivity. Second-generation PS have since been designed with less pronounced adverse effects. There are, currently, about ten molecules marketed worldwide. The most potent PS currently under development are hydrophobic molecules with a high tendency to localize in cancer tissue. However, water-insoluble products are difficult to administer to patients, especially when the intravenous route is considered. Therefore several strategies have developed, among which polymeric nanoparticles offer multiple advantages.

This chapter briefly presents the basis of PDT and the most used PS and then reviews the interest in developing nanoparticles (NPs) to improve current PDT, with special interest on polymeric biodegradable NPs. First, the main preparation

methods used to load nanoparticles with PS will be introduced. The major achievements obtained both *in vitro* and *in vivo* with encapsulated PS are then critically appraised, especially with regards to methodologies. The primary outcomes are discussed, highlighting the interest in polymeric nanoparticles as delivery systems for PS. To our knowledge, this is the first published review on the use of polymeric nanoparticles for the delivery of PS in the framework of cancer therapy or detection.

## 2.2

### Concept and Basis of Photodynamic Therapy and Photodetection

Photodynamic therapy, an innovative alternative to conventional therapies, is based on the systemic or topical administration of a photosensitizing drug, also known as a photosensitizer. After biodistribution of the drug, the diseased tissue is illuminated with light at an appropriate wavelength. Light will activate the PS and, in the presence of molecular oxygen, will generate cytotoxic species. In turn, those highly oxidizing species will damage cellular constituents, leading to tumor destruction. Fluorescence PD of cancer is also based on the administration of a PS, and takes advantage of the fluorescence emission of these substances. Cancer diagnosis is of major importance, as early detection of malignancies and metastasis can improve the chance of success for anticancer therapies. In addition, PD is a valuable tool to help guide biopsy and resection to minimize the removal of non-cancerous tissue. Although PS are usually administered systemically, the therapeutic effect of PDT is local rather than systemic. The selectivity of the treatment is not only due to the preferential biodistribution of the PS in cancer tissues but also to the precise activation of the drug by a light beam, usually from a laser source directed to the target tissue.

#### 2.2.1

##### Mechanisms of Photodynamic Therapy and Photodiagnosis

The phototoxic effects on which PDT is based and the fluorescence used for PD are both initiated by the absorption of light by a PS, leading to its excitation from the ground state to the singlet state (Fig. 2.1). The singlet state lifetime, which is on the nanosecond time scale, is too short to allow significant interaction with surrounding molecules [6]. The singlet state can be deactivated via three pathways. The first, fluorescence, results in the emission of photons of a wavelength longer than the excitation light (Fig. 2.1A), and thus allows fluorescence photodetection. The use of highly sensitive imaging devices in PD permits visualization of diseased tissues over normal tissues due to the preferential accumulation of PS in the former [7]. The singlet state can also be deactivated by the release of heat (Fig. 2.1B) or by undergoing intersystem crossing to generate the triplet state (Fig. 2.1C). Since the lifetime of the triplet state is in the micro- to millisecond range, the transfer energy to surrounding molecules is possible [6]. The triplet state is the

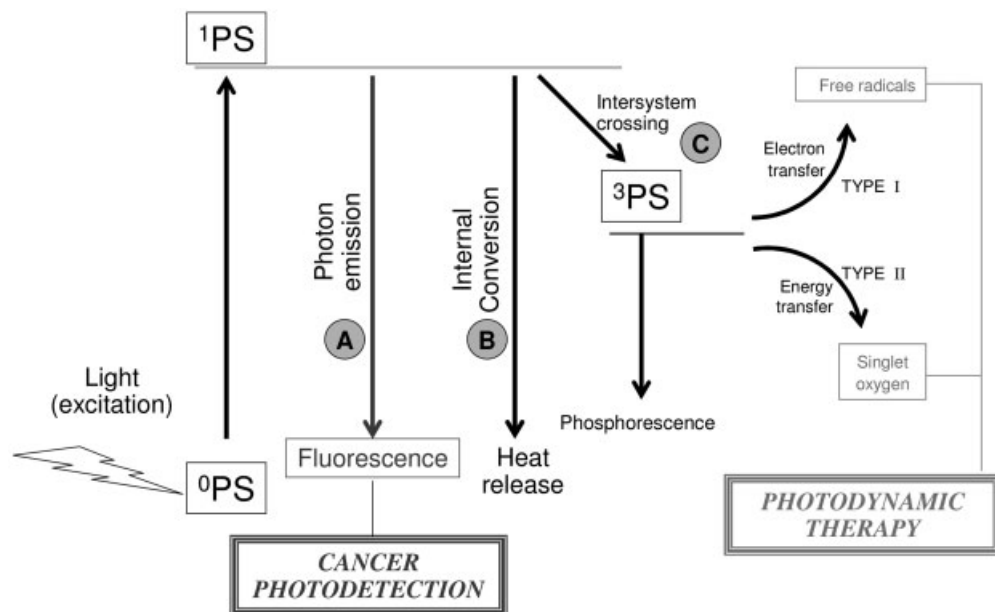


**Fig. 2.1.** Schematic representation of the photophysical and photochemical mechanisms associated with photodiagnosis and photodynamic therapy. After light irradiation, photosensitizer in its ground state ( $^0\text{PS}$ ) is excited to the singlet state ( $^1\text{PS}$ ). This state can be deactivated by (A) emitting fluorescence, (B) releasing heat or (C)

undergoing intersystem crossing, which results in the generation of PS in its triplet state ( $^3\text{PS}$ ). The PS triplet state induces phototoxicity via type I and type II reactions, generating free radical species and singlet oxygen, respectively. These entities are toxic in biological systems, inducing cellular death and vascular occlusion.

key to initiating the photochemical process that induces phototoxicity, and it occurs via two main mechanisms [8, 9]. The type I mechanism involves hydrogen-atom abstraction or electron-transfer between the triplet state and neighboring molecules, generating free radicals. These radicals react with oxygen and generate a mixture of highly reactive oxygen intermediates, such as  $\cdot\text{O}_2^-$ ,  $\text{H}_2\text{O}_2$  and  $\cdot\text{OH}$ , which are highly oxidizing [10, 11]. In the type II mechanism, energy is transferred from the PS in its triplet state to molecular oxygen to form highly reactive singlet oxygen ( $^1\text{O}_2$ ), which is presumed to be the most reactive species in PDT. Reactive intermediate oxygen species, including both radicals and non-radicals, are called reactive oxygen species (ROS). Type I and type II pathways are not mutually exclusive and both ultimately lead to the formation of oxidized products and radical chain reactions, which can trigger cascades of biochemical, immunological, and physiological reactions, finally resulting in the destruction of the irradiated tissue [7, 12–14].

At a cellular level, PDT induces cytotoxic effects through photodamage to subcellular organelles and biomolecules. Various cellular components can react with sin-

glet oxygen, such as amino acid residues (especially cysteine, methionine, tyrosine, histidine and tryptophan), nucleosides (mainly guanine) and unsaturated lipids [12]. PS can localize in lysosomes, mitochondria, plasma membrane, Golgi apparatus and endoplasmic reticulum of tumor cells, as well as in tumor vasculature. Interestingly, most PS do not accumulate in cell nuclei; thus PDT has a low potential for causing DNA damage, mutation and carcinogenesis [15]. Two distinct types of cell death may be induced by PDT. First, PDT can trigger apoptosis, a form of programmed cell death that involves the activity of proteolytic caspases, whose action dismantles the cell and results in cell death. Apoptosis begins internally with condensation and subsequent fragmentation of the cell nucleus while the plasma membrane remains intact. Afterwards, apoptotic cells are ultimately fragmented into multiple membrane-enclosed spherical vesicles, which are scavenged by phagocytes [16, 17]. The second mode of cell death induced by PDT is necrosis, characterized by cytoplasm swelling, destruction of organelles and disruption of plasma membrane, leading to the release of intracellular content and inflammatory factors. The cell type, PS subcellular localization and applied light dose determine the type of cell death. PS with tropism for mitochondria are more likely to induce apoptosis, whereas PS localized in the plasma membrane are expected to cause necrosis [15].

There are three main mechanisms for suppressing malignant tissue when using PDT:

1. Direct cellular damage by necrotic and/or apoptotic mechanisms [16, 17].
2. Alteration of tumor vascularization such as occlusion, stasis and/or increase in vascular permeability, thereby depriving cancer tissue of oxygen and nutrients [18–20].
3. Stimulation of inflammatory and immune responses against the tumor [21–23].

The impact of these pathways in the therapeutic effects of PDT depends on the PS and its formulation, the route of administration, and the time interval between administration and light irradiation.

### 2.2.2

#### **Selective Tumor Uptake of Photosensitizers**

One of the key aspects of PDT is the preferential accumulation of PS into tissues with a high rate of regeneration such as cancer tissue and neovasculature [15, 24, 25]. Although the exact underlying mechanisms that drive this tropism have not been completely elucidated, the abnormal physiology of tumors is the main contributor to the selectivity of PS. The affinity of PS for tumors and their surrounding stroma has been related to some of the unique characteristics of hyperproliferative tissues listed in Table 2.1. Of great importance is the increased vascular permeability of tumors, which facilitates the crossing of PS, or their carriers to the interstitial space. This effect, called the enhanced permeability and retention (EPR) effect, is potentiated by an impaired lymphatic drainage reducing macromolecule clearance



**Tab. 2.1.** Characteristics of tumor tissues.

- 
- Decreased pH of interstitial fluid, due to an increased glycolysis and a decreased supply of oxygen.
  - Increased number of low-density lipoprotein receptors at the cell surface.
  - Abundance of macrophages.
  - Abnormal stromal composition, due to the newly formed collagen.
  - Leaky vasculature.
  - High rate of angiogenesis (neovasculature development).
  - Poor lymphatic drainage.
- 

from the tumors [26]. Indeed, macromolecules can be entrapped and retained in solid tumors at high concentration for an extended period (>100 h) whereas low-molecular weight substances return to circulating blood by diffusion. Consequently, entrapping PS in macromolecular drug carriers, such as nanoparticles, is thought to increase PS concentration within tumors.

The physicochemical characteristics of PS molecules, such as molecular weight, hydrophile–lipophile balance value [1, 27–29], ionic charge [30], and protein binding characteristics, also influence their biodistribution. In a literature review, Boyle and Dolphin have attempted to correlate PS structure with its biodistribution and pharmacokinetics [31]. Evaluation of this relationship was, however, made impossible by the disparity between delivery vehicles, animals and tumor types used in the different studies. The PS hydrophile–lipophile balance value appears to be a key factor that is able to regulate pharmacokinetic profiles. Indeed, hydrophobic PS induce preferential damage to tumor cells, whereas hydrophilic PS mainly cause damage to the tumor vasculature. This selectivity will be determined by the nature of the binding between the PS and plasma proteins. Hydrophobic PS are bound to the lipid moiety of lipoproteins [32–36] whereas hydrophilic PS are bound to albumin and globulins [37]. Hydrophobic PS bound to low-density lipoproteins (LDL) can be endocytosed via LDL receptors [34, 38], which are over-expressed in tumor cells. Thus, they accumulate in the lipophilic compartment of tumor cells, including plasma, mitochondrial, endoplasmic reticulum, nuclear and lysosomal membranes. In this case, photodamage of tumor cells occurs preferentially. Conversely, hydrophilic PS will be preferentially localized within the interstitial space and the vascular stroma of the tumor tissue. Owing to their hydrophilic character, diffusion across the plasma membrane into the cytoplasm is limited. Subsequently, these PS cause extensive impairment of the vascular system, promoting tumor ischemia and hypoxia [15, 39].

Since ROS have a short life-time and act close to their site of generation, the sites of initial cell and tissue damage induced by PDT are closely related to both the lo-

calization of the PS within cells and the site of illumination. As a strategy to improve photosensitizer efficiency regardless of the properties of the PS itself, several pharmaceutical formulations have emerged. Indeed, PS delivery systems influence the pharmacokinetic profiles and tissue distribution of PS [40–45].

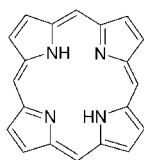
### 2.2.3

#### Photosensitizers

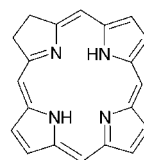
A photosensitizer is defined as a chemical entity that, upon absorption of light, induces a chemical or physical alteration of another chemical entity [14]. Photosensitizers used against cancer must be able to absorb light and then to transfer the absorbed energy to molecular oxygen in order to cause biological effects. Several publications have described the characteristics of the ideal PS [7, 12, 14, 46, 47]. Since the triplet state of the PS initiates the photochemical process, a good PS requires a long-lived triplet state with a high quantum yield to allow enough time to interact with neighboring target molecules [8]. Ideally, a PS should absorb photons efficiently in the red part of the spectrum because light with long wavelengths have an increased penetration depth in tissues. High chemical purity, good solubility in pharmaceutical acceptable formulations and low aggregation tendency are also mandatory. PS used for photodetection should be photostable, have a high fluorescence quantum yield with low interference with tissue autofluorescence and induce minimal photodamage. Allison et al. have reviewed the clinically relevant properties of PS intended for PDT of cancer [48]. PS should not induce dark toxicity, which is defined as toxicity in the absence of light. Furthermore, PS should have a preferential biodistribution in the tumor as selectively as possible and be eliminated quickly enough to avoid generalized skin photosensitization and systemic toxicity.

##### 2.2.3.1 Conventional Photosensitizers

Originally, PDT was based on the topical application of dyes such as eosin, methylene blue (MB) and rose bengal with remarkable success [46]. Most compounds able to reach triplet states and to produce ROS have either tricyclic, heterocyclic or porphyrin-like ring structures with conjugated double bonds ( $\pi$ -electron system) [14]. Figure 2.2 shows examples of these structures. PS used in clinics have been classified as first, second and third-generation PS. Haematoporphyrin derivative (HpD) or Photofrin<sup>®</sup>, a first-generation PS, is a very complex mixture of monomers and oligomers. It was the first PS approved by the U.S. Food and Drug Administration (FDA), in 1995. Photofrin<sup>®</sup> has been used widely in clinics to treat esophageal, papillary bladder and endobronchial cancers. It is also indicated for ablation of high-grade dysplasia associated with Barrett's esophagus, which is a precancerous condition, thus reducing the risk of progression to esophageal cancer [49]. However, HpD and its analogues not only have poor tumor selectivity, resulting in long-lasting skin photosensitivity [50, 51], but also lack strong absorption bands in the red region of the spectrum [52]. Furthermore, they are complex mixtures and their synthesis and biological activity are difficult to reproduce [12, 48,

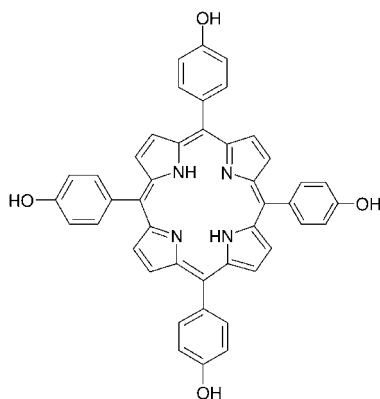
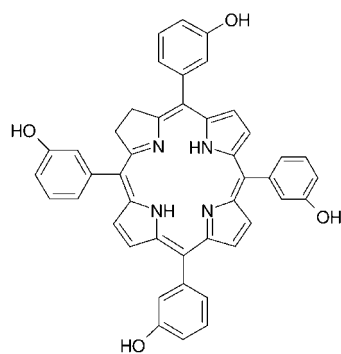
CORE  
STRUCTURE

Porphin



Chlorin

## EXAMPLE

Meso-tetra(p-hydroxyphenyl)  
porphyrin or pTHPPMeta-tetra(m-hydroxyphenyl)  
chlorin or mTHPC

**Fig. 2.2.** Structure of some photosensitizers. Porphins consist of four pyrrole subunits linked together by four methylene bridges. Derivatives of porphin are named porphyrins. Reduction of one of the pyrrole units on the porphin ring leads to a class of porphyrin derivatives called chlorins.

53]. Therefore, considerable effort has been devoted to developing new second-generation photosensitizers, characterized by greater selectivity for tumor tissue, rapid excretion from the body, and improved purity, stability, solubility and photophysical properties. Owing to the high oxygen quantum yield of the porphyrin skeleton, most second-generation PS belong to this family. The porphyrin structure provides 12 positions that can potentially be substituted. Furthermore, the porphyrin cycle can be oxidized, extended and/or a central ion may be introduced to modulate the pharmacological, as well as the photophysical, properties of the molecule [7, 52]. Porphyrins, chlorins, texaphyrins, purpurins and phthalocyanines have been most actively investigated [24, 47].

Recently, considerable interest in the use of 5-aminolevulinic acid (5-ALA) in PDT has risen. 5-ALA itself is not a photosensitizer, but it can induce the formation of protoporphyrin IX (PpIX), a potent PS. 5-ALA is a substrate in the biosynthetic pathway of heme, the iron(II) complex of PpIX. In contrast to heme, PpIX is

a fluorescent molecule and a potent PS. When 5-ALA is administered, its biosynthesis leads to the selective transient accumulation of PpIX in neoplastic cells [7, 54]. If tissues containing the 5-ALA-induced PpIX are irradiated, photochemical processes are triggered, resulting in tissue destruction. Although the underlying mechanisms of the preferential accumulation of 5-ALA-induced PpIX in tumors and other proliferating tissues are not fully understood, the 5-ALA approach is one of the most selective modalities currently available in anticancer therapy. Collaud et al. have recently reviewed the mechanisms of the selective formation of PpIX in neoplastic tissue after 5-ALA administration [55]. Topical administration (e.g., skin and bladder) of 5-ALA and 5-ALA ester derivatives induced no skin photosensitivity and had short half-life in the treated area [56–59]. 5-ALA and its derivatives can also be used for photodiagnosis [60–62], because PpIX emits red fluorescence upon irradiation with blue light.

Recently, the third generation of PS has emerged. These are second-generation photosensitizers with fine tuned properties that allow selective delivery to tumor tissue. Different strategies have been proposed, such as conjugation to biomolecules like monoclonal antibodies [63].

Although the clinical potential of PDT has been recognized for over 25 years, it is only now starting to be used clinically [24]. Table 2.2 summarizes clinically relevant PS for PDT and the PD of cancer. There are few PS intended for PD, only 5-ALA-hexyl ester has been recently approved for detection of bladder cancer in Europe and has been submitted to the FDA ([www.photocure.com](http://www.photocure.com)). Local administration of hypericin has also shown promising results for the PD of bladder carcinoma [64]. Other PS evaluated for PD such as haematoporphyrin derivative and meta-tetra(hydroxyphenyl)chlorin induced prolonged skin and eye photosensitivity [50, 51, 65, 66] and are not yet approved for photodiagnosis.

### 2.2.3.2 New Entities

New systems such as semiconductors, fullerenes and transition metal complexes are promising photosensitizers, as shown by several studies measuring singlet oxygen production and *in vitro* phototoxicity against tumor cells. However, since little is known about their biocompatibility, their use in clinical PDT of cancer is still unexplored.

Semiconductors, such as titanium dioxide ( $\text{TiO}_2$ ), can sensitize the photogeneration of ROS, thus inducing damage similar to that found in traditional PDT [67]. Particles of  $\text{TiO}_2$  have shown phototoxicity against HeLa cells *in vitro* and were not toxic when administered orally or parenterally to nude mice. After UV irradiation,  $\text{TiO}_2$  particles significantly suppressed the growth of HeLa [68] and T-24 cells [69] implanted in nude mice. However, this approach is limited because UV light, used to irradiate  $\text{TiO}_2$  particles, does not penetrate deep in the skin [70].

When the size of a semiconductor particle is decreased to the nanometric scale, these materials are called quantum dots (QDs). QDs are single crystals of semiconductor material, a few nanometers in diameter. Their size and shape can be controlled precisely [71]. A quantum dot can have anything from a single electron to a collection of several thousands. Therefore, light absorption of QDs can be precisely

Tab. 2.2. Relevant photosensitizers under clinical trials or approved for PDT and PD of cancer [5, 15, 24, 48, 163, 164].

Photosensitizer/ Generic name	Commercial name	Formulation/ Administration	Approved oncological indications	Clinical trials for different types of cancer	Drug-light interval <sup>[a]</sup>	Skin photosensitivity <sup>[b]</sup>
Haematoporphyrin derivative (HpD)/ Porfimer sodium	Photofrin <sup>®</sup>	Powder for solution/ i.v. or topical	Esophageal adenocarcinoma and high-grade dysplasia in Barrett's esophagus. Cervical, superficial gastric, bronchial, bladder, and advanced and early lung cancer	Intraperitoneal, hilar bile-duct, head and neck, intestinal, lung, larynx, skin, bladder and metastatic breast	40–50 h	1–3 months
Meta- tetra(hydroxyphenyl) chlorin (mTHPC)/ Temoporfin	Foscan <sup>®</sup>	Solution in ethanol and propylene glycol/i.v.	Palliative advanced head and neck cancer. Squamous cell carcinoma	Brain, gastric, prostate and oral cavity, Mesothelioma	24–96 h	Up to 6 weeks
5-Aminolevulinic acid (5-ALA) <sup>[c]</sup>	Levulan <sup>®</sup>	Powder for solution/ Topical. Oral and i.v. have been also evaluated	Actinic keratosis	Basal-cell carcinoma, esophageal, gastrointestinal and non-melanoma skin	2 h	1–2 days
5-ALA-methyl ester <sup>[c]</sup>	Metvix <sup>®</sup>	Cream/Topical	Actinic keratosis, superficial basal-cell carcinoma and basal cell-carcinoma. Bowen's disease		3 h	Uncommon

5-ALA-hexyl ester <sup>c</sup>	Hexix <sup>®</sup>	Powder for solution/ Intravesical injection	Bladder cancer diagnosis. Surgeons can easily define bladder lesions and ablate them	1–2 h	Uncommon
Benzoporphyrin- derivative monoacid ring A (BPD-MA)/ Verteporfin	Visudyne <sup>®</sup>	Liposomes/i.v.	None. It is approved for choroidal neovascularization associated to age-related macular degeneration (CNV-AMD), a non- malignant disease	30–150 min	3–5 days
Tin-ethyl etiopurpurin (SnET2)	Purlytin <sup>™</sup>	Lipid emulsion		24 h	2–3 weeks
Lutetium texaphyrin/Lutex	Lutrin <sup>™</sup>	Powder for solution			1–2 days

<sup>a</sup> Interval between drug administration and light irradiation.

<sup>b</sup> Skin photosensitivity reactions include erythema, edema, blistering, hyperpigmentation and sunburn. Ultraviolet sunscreens provide no protection. Patients must avoid exposure of eyes and skin to direct sunlight and wear protective clothing and dark sunglasses when outdoors.

<sup>c</sup> Prodrug of protoporphyrin IX.

tuned from the UV to the infrared (IR) region of the spectrum by changing their size and composition. At the same time, QDs have narrow emission spectra that can be tuned to emit in the near-IR region, in contrast to the visible emission of most conventional PS [72–74]. QDs are highly resistant to degradation and their fluorescence is remarkably stable. Most work on semiconductor QDs has focused on fluorescence imaging and diagnosis applications [71, 74–76]. However, they are seen as suitable candidates for PDT because of their capacity to generate ROS after light irradiation [72, 73, 77]. Interestingly, QDs can enhance the effect of conventional photosensitizers if light-mediated energy transfer between both molecules is possible. Consequently, in addition to their intrinsic efficacy as photosensitizers, QDs have been used to potentiate conventional PS. Semiconductor QDs of cadmium selenide (CdSe) conjugated to anti-CD90 antibodies potentiate the activity of the PS trifluoperazine against leukemia cells [77]. Moreover, CdSe QDs linked to silicon phthalocyanine have enabled the use of an excitation wavelength where the PS alone does not absorb [72]. Unwanted potential toxicity of QDs is a key issue inhibiting their development as a therapeutic tool. Since the primary site of acute injury within the body after exposure to Cd is the liver, the cytotoxicity of CdSe QDs was investigated *in vitro* on primary hepatocytes isolated from rats [78]. QDs were cytotoxic due to the slow release of Cd. Surface oxidation of QDs after air and UV light exposure leads to the formation of reduced Cd on the QDs surfaces. Surface coating of QDs with either zinc sulfide or bovine serum albumin decreased the oxidation and consequently the cytotoxicity of the nanoparticles [78]. However, even when QDs are coated, there is still the risk of Cd release into the body after *in vivo* oxidation of these particles.

Before considering the use of QDs in clinics, some concerns regarding the propensity of QDs to aggregate, their toxicity profile and potential to release heavy metals should be addressed.

Fullerenes are a class of spherically-shaped molecules made exclusively of carbon atoms. Fullerene C<sub>60</sub> and C<sub>70</sub> efficiently generate singlet oxygen when irradiated with light. However, fullerenes are practically insoluble in both aqueous and most polar media – not to mention their poor absorption in the red region of the visible spectrum [79, 80]. These properties hamper the development of fullerene-based agents for PDT. Furthermore, the mechanism of action of photoexcited fullerenes in biological systems is not at all understood [81]. Nevertheless, intense research has been devoted to evaluate the potential applications of fullerenes in medicine and biology [79, 80].

Some inorganic complexes are also efficient photosensitizers, among them transition metal complexes of ruthenium(II), osmium(II), iridium(III), chromium(III), platinum(II) and palladium(II) have been investigated [46].

As described above, the selectivity of PDT can be increased using a PS that preferentially accumulates in cancer tissues. The affinity of PS for neoplastic cells is in part governed by the lipoprotein transport of PS and subsequent cellular uptake of these protein-PS complexes [34, 38]. However, little is known about the interaction of semiconductors, fullerenes and transition metal complexes with serum proteins. Besides the ability of such PS to photogenerate singlet oxygen, their toxicity, bio-

distribution and selectivity towards cancer tissues should be addressed before clinical application.

#### 2.2.4

#### **Photodynamic Therapy: Advantages and Limitations**

PDT is effective, minimally invasive and offers several advantages over other cancer therapies, such as surgery, radiation therapy and chemotherapy. Generation of cytotoxic species after PDT is only due to the combination of PS, light and oxygen; therefore, great selectivity towards diseased tissues is achieved. Indeed, singlet oxygen has a short lifetime in the biological environment ( $<40$  ns) [82] and cannot diffuse far from its point of origin (radius of action  $\leq 70$  nm) [83]. Differences in PS clearance between tissues enable optimization of the interval between PS administration and light irradiation, which should be performed when the drug has reached the maximum concentration in the tumor. Additionally, the ability of cells to recover from photodynamic damage also contributes to the selectivity of PDT. Indeed, healthy tissues are able to recover better than tumor tissues after PDT. For example, in the treatment of skin cancers, even if healthy tissue is damaged during PDT, the cosmetic results are usually excellent with little or no scarring, as has been demonstrated with topically applied 5-ALA [59] and intravenously administered verteporfin (benzoporphyrin derivative monoacid ring A) [84]. Additionally, PDT is a photochemical process without tissue heating, thus connective tissues such as collagen and elastin stay largely unaffected [53]. PDT can be repeated if necessary, and performed after surgery, chemotherapy or radiotherapy. Last but not least, PDT can be used to treat different types of cancers, including tumor resistant to other treatments [85].

Even though PS are expected to be retained preferentially by neoplastic tissues and their activity is triggered by light activation at a specific wavelength, the drug is still distributed throughout the whole body [53]. Therefore, PS administration can induce side effects in tissues exposed to daylight such as skin and eyes. Skin photosensitivity reactions are characterized by erythema, edema, blistering, hyperpigmentation and sunburn. Some precautions are strongly recommended during the period in which the PDT patient remains photosensitive. Physical barriers, particularly protective clothing and sun glasses, provide some protection against UV and visible light, but by far the optimum safety for these patients is complete sun avoidance. The period during which these safety measures have to be applied depends specifically on the nature of the photosensitizer [86]. Depending on the molecule, it ranges from a few days to up to three months. PDT can induce also occasional systemic and metabolic disturbances, and excessive tissue destruction at the treated site [12]. Adverse effects of PDT depend mainly on the nature of the PS, the route of administration and the type and localization of the malignancy. Table 2.3 summarizes the main adverse effects induced by PS used in PDT and PD of cancer. Intravenously administered PS, such as temoporfin (Foscan<sup>®</sup>) and HpD (Photofrin<sup>®</sup>), induce prolonged skin and eye photosensitivity [50, 51, 65, 66]. Conversely, 5-ALA (Levulan<sup>®</sup>) and 5-ALA-hexyl ester (Hexvix<sup>®</sup>), which are topically ap-



Tab. 2.3. Adverse effects induced by commonly used PS in clinical oncology [5, 48, 49].

Generic and commercial name/route of administration	Manufacturer and website/ PS approval date	Adverse effects <sup>(a)</sup> General	Specific to the pathology to be treated
Porfimer sodium Photofrin <sup>®</sup> /i.v.	Axcan Pharma, Inc www.axcan.com/FDA (1995)	Skin and eye photosensitivity. Local swelling and inflammation in and around the treated area. Pain in the chest, back, or abdomen. Breathing difficulties. Nausea and constipation	(S) <i>Papillary bladder cancer</i> . Urination alterations (frequency, haematuria, dysuria and nocturia), genital edema, suprapubic pain and urinary tract infection. (S) <i>Partially-obstructing esophageal cancer</i> . Pleural effusion, respiratory insufficiency, fever and anemia. (S) <i>Endobronchial cancer</i> . Respiratory disorders (dyspnoea, coughing, pneumonia, bronchitis, increased sputum, chest pain and respiratory insufficiency), and fever [50, 51]. (S) <i>High-grade dysplasia associated with Barrett's esophagus</i> . Abdominal problems (esophageal narrowing, vomiting, upper or lower abdominal pain, dysphagia, diarrhea), pain chest, dyspnoea, fever and headache (S) <i>Advanced head and neck cancer</i> . Pain, hemorrhage, pain in face, scar, mouth necrosis, dysphagia, and face edema [65, 66]
Temoporfin Foscan <sup>®</sup> /i.v	Biolitec Pharma, Ltd www.biolitecpharma.com/ European Union, Norway and Iceland (2001)	Skin and eye photosensitivity, injection site pain, constipation, and vomiting	(M) <i>Actinic keratosis</i> . Only in the treated region of the skin: scaling, crusting, itching and hypo- or hyperpigmentation [57, 59, 165]
5-ALA Levulan <sup>®</sup> /Topical (skin)	DUSA Pharmaceuticals, Inc. www.dusapharma.com/ FDA (1999)	Pain during treatment. Photosensitivity is only reported in skin under treatment. No adverse effects are reported in the body system [59].	(M) <i>Bladder cancer photodiagnosis</i> . Bladder spasm and pain, dysuria, headache, nausea and vomiting [56, 58]
5-ALA-hexyl ester Hexix <sup>®</sup> /Intravesical	PhotoCure ASA www.photocure.com/ European Union (2005)		

<sup>(a)</sup>(S) = severe and (M) = mild to moderate adverse effects.

plied on either skin or bladder, induce no skin photosensitivity and have a short residence time at the application site [56–59].

The therapeutic outcome of PDT is limited by the penetration of light in tissues. Light is either scattered or absorbed when it enters tissues and the extent of both processes depends on the tissue type and the light wavelength. Between 600 and 1000 nm, however, light is scattered to a relatively small extent and is poorly absorbed by important endogenous chromophores such as melanin and hemoglobin [87]. As a consequence, red light possesses a high penetration power into human tissues. Ochsner has compared the penetration of light as a function of the wavelength. At an equal incident light intensity, the penetration depth in human skin is of 6.8 mm at 800 nm, whereas it is only 0.4 mm at 400 nm [88]. The deeper penetration of longer wavelengths is a major incentive for the development of PS absorbing at these wavelengths. Additionally, to improve the outcome of PDT, new light delivery devices have been developed for this particular application. The traditional argon-dye and copper-dye lasers can be replaced by diode lasers, which are cheaper, very stable, reliable and easily transportable [89]. However, they are not tunable and may only be used at fixed wavelengths [90]. Optical fibers can be used to deliver light to the target tissue. They facilitate the illumination in various directions using either cylindrical or spherical diffusers. Furthermore, the versatility of optical fibers enables illumination of the skin or inside a body cavity [91]. PDT is usually performed with external illumination of the target site; however, deeply localized tumors should be treated with special light delivery devices that are inserted percutaneously. This technique, namely interstitial PDT, uses multiple laser fibers that are inserted directly into tumors through needles positioned under image guidance. Therefore, it is possible to use PDT for the treatment of internal tumors [92, 93].

The dependence of PDT on the oxygenation of the irradiated tissue represents a limitation of this treatment. Indeed, the efficacy of PDT depends on the amount of singlet oxygen produced within the tumor, which in turn depends on the concentration of oxygen in the tissue [94, 95]. Consequently, hypoxic tumor cells are generally more resistant to PDT, and may contribute to treatment failures.

Finally, most PS are hydrophobic, which is a key factor contributing to their selectivity for cancer tissues. However, PS lipophilicity makes formulation difficult due to the lack of physiologically acceptable solvents, especially when intravenous administration is considered. Furthermore, hydrophobic PS can aggregate in aqueous media, leading to quenching; thus in their aggregated form PS are less efficient than in their monomeric form [96–98]. Additionally, some PS lack selectivity for accumulating in cancerous tissues. Therefore, the design of adequate PS delivery systems is critical to improving the outcome and acceptability of PDT and PD in a clinical context.

### 2.2.5

#### **Photosensitizer Formulations**

Different formulation approaches have been proposed, such as the incorporation of PS into liposomes, micelles, polymeric particles, and LDL, as well as the develop-

ment of hydrophilic polymer–drug complexes, as reviewed by Konan et al. [99]. The delivery carrier can influence the PS biodistribution and hence the mechanisms and kinetics of PS transport to tissues, as well as PS subcellular distribution [15]. Among the different approaches, nanoparticles (NPs) offer numerous advantages, including high drug loading, controlled release, and a large variety of carrier materials and manufacturing processes. Nanoparticles are defined as particles in the nanometer scale, typically  $<1 \mu\text{m}$ . NPs appear to be suitable delivery systems for PS because encapsulation of PS into NPs would make it possible to disperse hydrophobic PS in aqueous media. Moreover, NPs have large surface areas, and their surface can be modified with functional groups to modulate their biochemical and physicochemical properties. Owing to their size, direct targeting of tumor tissues is also possible by taking advantage of the tumor vasculature enhanced permeability [100, 101]. Biodegradable and non-biodegradable materials can be used to produce NPs. The use of biodegradable materials enables the controlled release of the encapsulated drug. Conversely, non-biodegradable materials offer the advantage of enhancing the direct interaction of PS with molecular oxygen, either within the nanoparticles or at their surface. The use of non-biodegradable NPs made of metals, ceramics and non-biodegradable polymers are discussed in the next section. The final section is devoted to biodegradable polymeric NPs used for photodynamic activity. The biodegradability and biocompatibility of polymeric NPs bring them closer to clinical application than non-biodegradable carriers.

## 2.3

### Non-biodegradable Nanoparticles for Photodynamic Therapy

#### 2.3.1

##### Metallic Nanoparticles

This approach involves the coating of metallic nanoparticles, mainly made of gold or magnetic materials, with photosensitizers. The design of PS-coated metallic NPs for PDT has been primarily developed in two directions. First, the adhesion of hydrophobic PS to gold NPs enables an aqueous PS suspension, where the PS photophysical properties are enhanced. This concept has been demonstrated with phthalocyanine derivative-coated NPs that were able to generate singlet oxygen with higher quantum yield than the free PS [102]. In the second approach, the development of magnetic nanoparticles coated with PS allowed either the targeting of the pathological tissue by directing the NPs by an external magnetic field or cancer diagnosis by using the NPs as magnetic resonance (MR) contrast agents. For instance, magnetic NPs made of  $\text{Fe}_3\text{O}_4$  have been coated with haematoporphyrin [103]. Likewise, pheophorbide-a has been complexed to  $\text{Fe}_3\text{O}_4$  NPs and the spectroscopic and photophysical properties of this complex characterized [104]. The authors hypothesized that these NPs might be used to combine the action of hyperthermia therapy (HT) and PDT synergistically. Similarly, Gu et al. have conjugated porphyrin to  $\text{Fe}_3\text{O}_4$  NPs for the same combination of anticancer therapies [105]. The conjugation of porphyrin to the NPs induced a blue-shift in the fluorescence

emission spectrum of the PS. No dark toxicity on HeLa cells was seen 5 h after incubation with NPs at 37 °C. Fluorescence microscopy observations showed that NPs were taken up and localized intracellularly. Irradiation of HeLa cells, incubated with the PS-conjugated NPs for 10 min, induced changes in cell morphology. Although the authors interpreted this data as a qualitative sign of phototoxicity, further experiments should be performed to assess the potential of such NPs.

So far, the efficacy of metallic nanoparticles in photodynamic experiments with cancer animal models has not been yet evaluated, although the biocompatibility of metallic nanoparticles has been tested. Neither gold nor magnetic nanoparticles made of iron oxides were toxic *in vivo*. Indeed, 2-nm-gold NPs were administered intravenously to Balb/C mice (2.7 g-Au kg<sup>-1</sup>) and no lethality was observed [106]. It was also shown that gold NPs were largely cleared from the body through the kidneys. Furthermore, blood analysis two weeks after injection from mice treated with 0.8 g-Au kg<sup>-1</sup> demonstrated no signs of toxicity as far as haematocrits and plasmatic enzymes are concerned. Similarly, iron oxides particles seem to be generally well tolerated [107, 108] and are intended for several medical applications, as recently reviewed by Ito et al. [109]. The safety of colloidal dispersions of magnetic nanoparticles made of iron oxides has been also demonstrated [110, 111]. In fact, magnetic resonance agents, such as Feridex I.V.<sup>TM</sup> (Advanced Magnetic, Cambridge, MA, USA) and Resovist<sup>®</sup> (Schering, AG, Germany), have already been approved for the detection of focal hepatic lesions by MR imaging.

### 2.3.2

#### Ceramic Nanoparticles

Ceramic NPs made of silica have been developed as an alternative to polymeric NPs. Ceramic NPs are resistant to microbial attack [112] and their particle size, shape, and porosity can be easily controlled during the preparation process [113]. Ceramic NPs do not release encapsulated compounds even at extreme pH conditions and temperature [114]. This feature represents a limitation for the delivery of common drugs, but can be suitably used in PDT. Since ceramic matrices are generally porous, molecular oxygen can diffuse through the pores and interact with the PS entrapped within the NPs [115]. The photogenerated singlet oxygen can diffuse out of the particle to generate the cytotoxic effect. This approach has been evaluated by entrapping 2-devinyl-2-(1-hexyloxyethyl) pyropheophorbide (HPPH) into 30 nm silica NPs; unfortunately, the percentage of PS loaded into the NPs was not reported. *In vitro* studies with HeLa and UCI-107 cells demonstrated that HPPH-loaded silica NPs were taken up by tumor cells and induced significant cell death, similarly to Tween-80 micelles, which were used as a control [113]. *m*-tetra(Hydroxyphenyl)chlorin (mTHPC) has been embedded in amine-functionalized silica NPs of 180 nm to deliver singlet oxygen instead of releasing PS molecules [116]. The results showed that singlet oxygen production from mTHPC embedded in silica NPs exceeds that of free mTHPC. However, the tests were run in a mixture of water and ethanol in which mTHPC is soluble. Thus, it is possible that mTHPC could be released from the core of the NPs during oxygen

sensitization. As a result, more molecules of mTHPC would be soluble and the amount of singlet oxygen would be higher than if mTHPC would have been a solid dispersion inside the NP core. Ideally, singlet oxygen production should be evaluated in aqueous media simulating biological environments. These experiments are far from physiological conditions and may not reflect what would be observed in the cellular environment. Methylene blue, a water-soluble PS of low molecular weight, was encapsulated into three types of sub-200 nm NPs, achieving different MB loadings: polyacrylamide (20–30 nm; loading 0.1%), sol–gel silica (190 nm; loading 3.0%) and organically modified silicate (160 nm; loading 0.4%) [117]. Polyacrylamide NPs were, *in vitro*, the most efficient delivery of singlet oxygen per MB molecule. Moreover, these particles gave the most stable aqueous suspension and therefore were used for *in vitro* photodynamic experiments on rat C6 glioma tumor cells. MB-loaded polyacrylamide NPs were more active than free MB. Notably, concerning silica NPs, the potential toxicity of ceramic nanoparticles is controversial. Toxicological data from studies investigating silica NPs as DNA delivery systems suggest that these carriers have little toxicity [118]. Likewise, organically modified silica NPs have been used for *in vivo* gene delivery in mice and no toxicity was reported up to four weeks after transfection [119]. Conversely, Chen and von Mikecz showed that the uptake of silica NPs (40–70 nm) by the cell nucleus of HEp-2 and RPMI 2650 cells induced nuclear damages close to those seen in neurodegenerative disorders [120]. The nuclear architecture was altered, probably as a result of the formation of nucleoplasmic protein aggregates. Furthermore, silica NPs (4–40 nm) induced inflammatory reactions in cultured human endothelial cells, as shown by the overexpression of interleukin-8 [121].

### 2.3.3

#### **Nanoparticles Made of Non-biodegradable Polymers**

Polyacrylamide (PAA) and amine-functionalized PAA have been used to encapsulate the disulfonated PS 4,7-diphenyl-1,10-phenanthroline ruthenium into nanoparticles of 40–50 nm [122]. Incorporation of the PS into the polyacrylamide matrix did not affect the singlet oxygen production, allowing it to be released into the aqueous media in which the NPs were suspended. PS delivery from amine-functionalized PAA was slower than from PAA NPs. Furthermore, less singlet oxygen was produced than with both free PS and PAA nanoparticles [122]. Recently, the same group developed polyacrylamide NPs to perform simultaneously magnetic resonance imaging and PDT of a rat brain cancer model, providing a real-time tumor death measurement [123]. In this approach, Photofrin<sup>®</sup> and a magnetic resonance contrast agent were encapsulated together within a polyacrylamide core, resulting in 30–60 nm NPs. The NPs were surface-coated with poly(ethylene glycol) (PEG) to increase the plasma half-life of the carrier. Singlet oxygen production and *in vitro* photoactivity against 9L rat gliosarcoma cells were evaluated. Although the PS was not released from the NPs, as demonstrated by *in vitro* degradation studies in phosphate buffer at 37 °C, the photoactivity of the encapsulated PS was retained. The photoactivity and magnetic resonance contrast ability of this formulation have

been evaluated after intravenous administration in intracerebral 9L tumor bearing rats, but the dose of Photofrin<sup>®</sup> is not mentioned. The activity of the free compound was not tested; however, rats receiving no treatment and treated only with laser were used as controls. The evolution of tumor volume was followed by magnetic resonance imaging. Photofrin<sup>®</sup>-loaded NPs induced tumor shrinkage, whereas tumors not treated or treated only with laser continued to grow. However, tumor re-growth was observed 12 days post-PDT treatment with Photofrin<sup>®</sup>-loaded NPs. Polyacrylamide NPs showed no toxicity, in terms of alterations in histopathology or clinical chemistry values, after administration of doses up to 500 mg of NPs per kg over four weeks. The authors suggest that these NPs, namely a multifunctional nanoparticle platform, might enable simultaneous cancer detection, therapy and monitoring. Additionally, particles coated with an integrin ligand for the recognition of the tumor neovasculature were prepared. The specific binding of these NPs was demonstrated *in vitro* with MDA 435 cells expressing integrins. The authors hypothesized that these multifunctional nanoparticles stay in the extracellular compartment and do not release the PS; only singlet oxygen would be delivered after light irradiation [123]. However, the intracellular localization of these NPs after *in vivo* administration should be further studied to confirm the advantages of such a system.

Most research on non-biodegradable materials for the administration of PS has focused on the development of carriers delivering singlet oxygen without releasing the PS. Additionally, non-biodegradable NPs are thought to protect the entrapped PS from the biological environment. The internalization of such NPs into target cells is thought to be unnecessary. In this context, only the external contact of NPs with the cell membrane is required. However, none of these systems have undoubtedly demonstrated the absence of internalization of such NPs. Despite the promising results encountered with these materials, their use in PS delivery has not yet been fully explored, probably due to toxicity concerns in the administration of non-biodegradable materials, particularly if chronic or repeated administrations are needed. Degradation is desired to prevent accumulation of extraneous material and possible subsequent toxicity. Indeed, recent histopathological studies of human biopsies indicate that the development of kidney and liver pathologies, such as chronic inflammation and granulomas, was associated with the presence of non-biodegradable micro- and nanoparticles in these organs [124]. These particles probably originated from debris of implants and prostheses. Certainly, studies of the long-term toxicity non-biodegradable nanoparticles should be undertaken before clinical investigations can be launched.

## 2.4

### Biodegradable Polymeric Nanoparticles for Photodynamic Therapy

Polymeric nanoparticles, as drug delivery systems, have been investigated for over three decades. Several polymers and preparation methods have been developed and the choice of both depends on the physicochemical nature of the drug, as well as

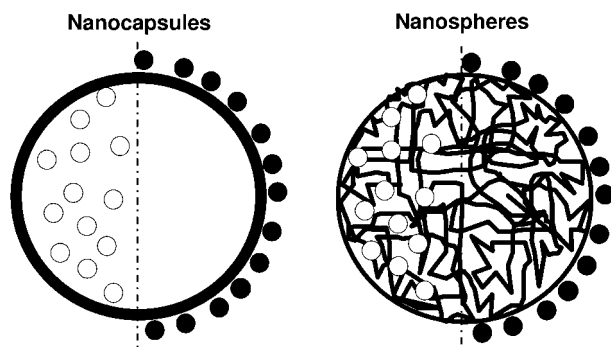


**Fig. 2.3.** Different types of drug-loaded nanoparticles: drugs may be either adsorbed at the surface of the polymer (●) or encapsulated within the particle (○).

on the type of controlled release kinetic being sought, and the desired target site. Polymeric nanoparticles used for drug delivery are defined as submicron (<1000 nm) colloidal systems made of solid polymers that may be classified according to their preparation processes and internal structure (Fig. 2.3). Nanocapsules (NCs) are composed of a polymeric wall containing a liquid inner core, while nanospheres (NS) are made of a polymeric matrix in which the drug can be dispersed. Active substances may be either adsorbed at the surface of the polymer or encapsulated in the particle. After administration, the drug is released by diffusion from the particles to the surrounding medium or after particle erosion resulting from polymer degradation. Ester or amide functions can be hydrolyzed, and the rate of this process depends on the nature of the polymer (chemical composition and molecular weight), and is triggered by water or the presence of enzymes.

#### 2.4.1

##### **Preparation of Biodegradable Polymeric Nanoparticles**

Particles may be produced by polymerization of synthetic monomers, or dispersion of synthetic polymers or natural macromolecules. The preparation methods have been extensively reviewed in the literature [125–127] and will be described only briefly here.

Nanoencapsulation of PS has been considered primarily for hydrophobic molecules that are difficult to formulate in aqueous media, which are mostly used for parenteral administration. The development of a solid suspension offers an interesting alternative. Owing to their hydrophobicity, organosoluble polymers have been mainly used as encapsulating material.

##### **2.4.1.1 *In situ* Polymerization**

*In situ* polymerization of monomers has been used mainly with poly(alkyl cyanoacrylates) (PACA) to prepare either nanoparticles or nanocapsules. The different

methods of preparation as well as medical application of these polymers have been reviewed recently [128].

The preparation of nanoparticles is based on an emulsion-polymerization process in which the cyanoacrylic monomer is dissolved in an organic solvent and dispersed in an aqueous phase containing a surfactant. Anionic polymerization is then induced by hydroxide ions present in water. The polymerization rate is mainly determined by the surrounding pH or the presence of inhibitors. PS can be encapsulated directly during the reaction [129, 130] or adsorbed on the particle surface by incubation with the nanoparticles after neutralization of the aqueous medium [131, 132]. For PACA, the major degradation pathway is based on enzymatic hydrolysis, the rate of degradation being governed by the length of the side chain.

Nanocapsules are usually prepared by interfacial polymerization, where an organic phase containing the monomer and the PS is emulsified in an aqueous phase [129, 130]. Concomitantly, solvent diffusion and anionic polymerization will occur, creating a polymeric wall around the oil core. These particles are especially well adapted for the encapsulation of lipophilic material.

One of the critical concerns with these techniques is the purification step to remove all the residual monomers and the surfactant which may induce undesirable effects.

#### 2.4.1.2 Dispersion of a Preformed Polymer

To reduce toxicity related to the presence of monomer residues or traces of polymerization initiators, preparation methods based on the use of preformed polymers have been developed. These are based on the formation of an emulsion in which the polymer is solubilized in an organic solvent immiscible with the external phase. Polymer precipitation is initiated by the removal of the organic solvent. Another approach, called nanoprecipitation, is based on direct precipitation of the solubilized polymer when in contact with a non-solvent. However, to our knowledge, this method has not been yet reported in the literature for PS.

Polymers used for nanoparticle preparation may be of natural origin. For instance, Zhao et al. have used gelatine to encapsulate hypocrellin B [133]. Particles were made by a modified salting-out coagulation process. An organic solution of the photosensitizer is added to an aqueous solution of the polymer and a surfactant. After nanoparticle formation, glutaraldehyde, a crosslinking agent, is added to the NP suspension. The suspension is then dialyzed to eliminate the glutaraldehyde. However, for hydrophobic photosensitizers, using water-soluble polymers might not be the best choice for their encapsulation. Indeed, no encapsulation rate was reported; therefore, it is not possible to assess how much drug was actually entrapped in the particles. The fluorescence quantum yields decreased as compared to the free drug, but this may also be the result of quenching due to the high number of molecules in the particles. Furthermore, the use of gelatine is warranted due to the potential allergenic reactions induced by this protein; thus, biocompatibility may be a concern at least with certain patients prone to allergies.

To promote entrapment of hydrophobic compounds into polymeric particles, synthetic hydrophobic polymers are frequently used. Polyesters such as poly(lactic



acid) (PLA) and copolymers such as poly(lactic-co-glycolic acid) (PLGA) are widely used due to their good biocompatibility and because they are accepted by the authorities (FDA) as suture threads. Several methods have been described for PLA and PLGA particle preparation. They are based on the formation of an emulsion of an organic solvent containing the polymer (and the drug) solubilized in an aqueous phase containing a surfactant. The solvent is then removed to induce polymer precipitation and particle formation. The size of the particles is governed by the size of the emulsion and the rate of solvent removal. Several methods have been developed to eliminate the solvent, including evaporation, diffusion [134–138] and dilution after salting-out [138–141]. These methods allow high encapsulation rates since usually more than 80% of the compound is entrapped in the polymeric matrix.

Encapsulation of sensitizers has also been reported in PLA nanocapsules [142, 143]; they were obtained by a solvent-displacement process. The polymer was dissolved in acetone while the hydrophobic photosensitizer was dissolved in Miglyol® (caprylic/capric diglyceryl myristate) and added to the polymer solution. The organic solution was then poured into a water solution containing surfactants. Solvent removal leads to precipitation of the polymer around the oil core containing the active compound.

The emulsion-diffusion method has also been used to prepare particles from a complex made of poly(sebacic anhydride) and phthalocyanine, where the drug was conjugated with the polymer before particle formation [144]. Different complexes were made with various amounts of phthalocyanine, and were characterized by UV/visible spectra. Depending on the degree of aggregation of the photosensitizer in the copolymers, different spectra were found.

Complexation of a photosensitizer and a polymer has been further studied by associating poly( $\epsilon$ -caprolactone) and silicon phthalocyanine [145]. Particles 30–90 nm in diameter were prepared by an emulsion-diffusion process.

#### 2.4.1.3 “Stealth” Particles

When administered *in vivo*, polymeric nanoparticles are rapidly taken up by the reticuloendothelial system (RES) due to the adsorption of proteins at their surface [146–148]. Thus, the biodistribution of particles is mainly directed towards liver and spleen where they are sequestered and made unavailable to other target tissues. This propensity to localize in RES has been related to the hydrophobicity of the particle surface. Therefore, “stealth” particles have been designed to limit this drawback. The principle is based on “hydrophilization” of the surface. The first approach reported was the coating of the particles with polymers such as poloxamer [130, 142] or PEG [139, 142]. Another approach is to use a directly modified polymer such PLA-PEG [142, 143] or PLGA-PEG.

#### 2.4.1.4 Targeted Nanoparticles

Even though biodistribution of PS is characterized by a preferential accumulation into target tissues such as cancer cells and neovasculature, their distribution in normal tissues induces adverse side effects. Therefore, a more specific distribution

may be sought by using active targeting. One way to increase the biodistribution of colloidal carriers to the target site is to covalently bind a recognition molecule to their surface that will drive the carrier to the target site. This approach was used by Kopelman et al. with non-biodegradable particles [123], but to our knowledge it has not yet been developed with PS-loaded biodegradable nanoparticles. Several methods are available to covalently bind ligands to the surface of colloidal systems [149] and numerous recognition molecules are available to target either cancer cells or neovasculature surrounding tumor sites. This aspect of active targeting strategies will be further developed in chapter 10.

#### 2.4.2

#### ***In Vitro* Relevance of Polymeric Nanoparticles in PDT on Cell Models**

*In vitro* studies with cultured cells are usually an easy way to evaluate the efficacy of new drug delivery systems. Two main issues are evaluated with *in vitro* studies: either the activity of the drug-loaded carriers on cancer cells or the cellular uptake and trafficking of the photosensitizers encapsulated into nanoparticles.

##### 2.4.2.1 Photodynamic Activity of PS-loaded Nanoparticles

First, the potential activity of encapsulated photosensitizers has to be verified on the targeted cancer cells. For this purpose, several *in vitro* models are used, corresponding to different cancer cell lines, but the principle is generally similar. The activity of PS formulations is evaluated by measuring the inhibition of cell growth. Cells are incubated with either the free drug or the drug-loaded carriers, PDT is applied to the cells by illumination at the right wavelength, and the damage, namely cell death, is evaluated by a simple viability test, such as the colorimetric 3-(4,5-dimethylthiazol-2-yl)-2,5-diphenyltetrazolium bromide (MTT) assay (Fig. 2.4).

Nanoencapsulation does not affect the activity of photosensitizers. Indeed, the phototoxicity of loaded nanoparticles, when compared to free drug under the same experimental conditions, was similar or even better.

The effect of mTHPC in different formulations: in solution, PLA NCs, poloxamer-coated NCs, PEG-grafted PLA (PLA-PEG) NCs, and oil/water nanoemulsion (NE) has been compared by Bourdon et al. [142]. HT29 human adenocarcinoma cells were treated with increasing concentrations of PS (0.125 to 1.25  $\mu\text{g mL}^{-1}$ ). A long incubation time (300 min) and high light dose (25  $\text{J cm}^{-2}$ ) were used, as fluences of 5 or 10  $\text{J cm}^{-2}$  seemed to be inefficient. Phototoxicity increased when PS concentrations increased, regardless of formulation. In their experimental setting, all formulations showed similar photoactivity, except PLA-PEG NCs, which yielded a lower phototoxicity.

The activity of loaded nanocarriers was demonstrated with mTHPC on HT29 tumor cells, but the same concentration-dependent profile was obtained for other nanocarriers or photosensitizers such as meso-tetra(*p*-hydroxyphenyl)porphyrin (pTHPP) used by Konan et al. [136]. In this case, the influence of drug concentration on cellular toxicity with pTHPP-loaded nanoparticles (PLA or PLGA) was compared to free pTHPP. For this purpose, EMT-6 mammary tumor cells were used

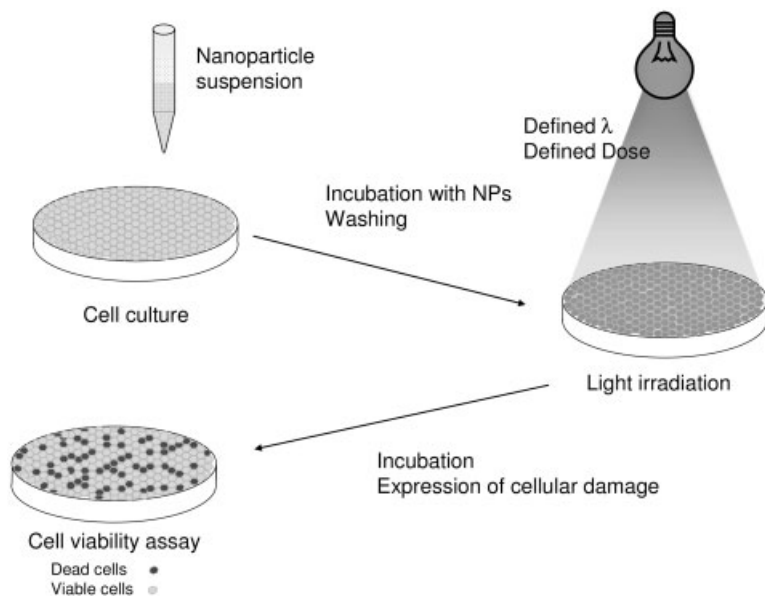


**Fig. 2.4.** Schematic representation of *in vitro* efficacy assay on cell culture. Cells are incubated with NPs; after washing, the plate is irradiated with light at the right wavelength.

The light dose depends on the power of the light and time of exposure. Photodamage is assessed by cell viability assay after incubation in fresh medium.

under the following conditions: 1 h of incubation with increasing concentrations of PS (3 to 10  $\mu\text{g mL}^{-1}$ ) and a light exposure of 6  $\text{J cm}^{-2}$ . For all delivery systems tested, the phototoxicity increased with PS concentration. The most important difference between formulations was observed at 3  $\mu\text{g mL}^{-1}$ , where loaded NPs exhibited a two-fold higher activity than free pTHPP. In contrast, at 6  $\mu\text{g mL}^{-1}$  all formulations reached a plateau of cell death (90% dead cells). Thus, encapsulation of a photosensitizer is an advantage, as the same photodynamic effect could be obtained with a lower concentration, thereby minimizing possible side effects.

Before analyzing the phototoxicity of photosensitizers, the following controls have to be performed: dark toxicity of photosensitizers, effect of irradiation on untreated cells and finally toxicity of unloaded nanoparticles. With this intention, Bourdon et al. [142] related no dark toxicity with mTHPC-loaded NCs in human colorectal adenocarcinoma (HT29) cells after incubation times of up to 18 h. Light or photosensitizer alone did not lead to a significant decrease in survival fraction according to Konan et al. [136] on EMT-6 mammary tumor cells. Moreover, unloaded nanoparticles, after a 24 h-incubation and an irradiation at 9  $\text{J cm}^{-2}$ , induced no phototoxicity in concentrations up to 20  $\mu\text{g mL}^{-1}$ . Thus, the observed phototoxic effects were only triggered by the combination of a specific photosensitizer and its activation by light.

The research by Bourdon et al. and Konan et al. have validated the proof of con-

cept of using polymeric NPs for PDT [136, 142]. It is, however, difficult to compare the ability of two different photosensitizers when the carriers and the experimental conditions are different. Indeed, several parameters can influence the photoactivity of a drug: experimental conditions (incubation time, light dose), nature of drugs and delivery systems (free or encapsulated), size of carriers, mechanisms of uptake (diffusion, endocytosis), subcellular localization and mechanism of cells destruction.

**Influence of Experimental Settings** The survival rate is determined by a viability assay, which is generally done one day after irradiation. Konan et al. have studied the influence of the time delay between irradiation and viability assay [136]. For this purpose, the cell viability was determined either immediately or 18 h after irradiation. The effect of the photosensitizer (pTHPP) was undervalued when the MTT assay was carried out immediately after irradiation: in this case the drug dose needed to kill 50% of cells ( $IC_{50}$ ) was doubled. Cell damage resulting from photochemical reactions may not be immediately lethal. Indeed, cell death implicates several cascades of reactions such as activation of enzymatic processes. Therefore, cell death can not be observed immediately after illumination. This study on the time delay is the only one in the literature on PDT with loaded-nanoparticles. However, a study carried out on 5-ALA in solution by Betz et al. [150], evaluating cell viability 18 or 24 h after irradiation, seemed to be reasonable to compare different carriers or experimental conditions. It is, however, difficult to deduce a general trend from these results as the needed post-irradiation incubation will depend at least on the PS and the cell line.

The incubation time of the PS with cells and irradiation parameters also have an effect on the phototoxicity of photosensitizers on cancer cells. Indeed, phototoxicity generally increases with incubation time and this correlation is intensified at higher drug concentrations. For example, for pTHPP-nanoparticles, cell viability began to show a decrease after 30 min incubation at  $3 \mu\text{g mL}^{-1}$ ; however, this was reduced to 15 min when using 6 and  $8 \mu\text{g mL}^{-1}$  [136]. At higher concentrations, more NPs are available, so cellular uptake may be improved and then the time required for a good efficiency is reduced.

If the incubation time is long enough, an increase in light dose can also play a considerable role on phototoxicity. PDT is performed at a fixed wavelength, where the photosensitizer absorbs photons, from a laser source [142] or from white light passing through an aqueous filter (e.g., rhodamine) [136]. The fluence rate is determined using a photometer and the irradiation times are adjusted accordingly to the desired light doses. The homogeneity of the light delivered to cells is very important to allow comparison between different treatments. Moreover, the temperature during irradiation has to be controlled to avoid thermal effects on cell viability. Therefore, irradiation times should not be too long. For PLA-nanoparticles, an increase from 6 to  $9 \text{ J cm}^{-2}$  triggered a decrease in cell viability from 85 to 18% after 15 min incubation [136]. Such a fall in viability was observed for all polymeric systems, whereas the influence of light dose with free drug was quite low, 100 to 73%, respectively, for the same dose. Perhaps the free drug needs more time to penetrate

the cells, and thus 15 min is not long enough to obtain a reasonable phototoxicity. Moreover, encapsulation may change the intracellular distribution into the different compartments of the cell, bringing the PS closer to the targets.

**Influence of Incubation Medium** Photoactivity of loaded NPs is generally affected by the presence of serum proteins. When cells are incubated with a photosensitizer in the presence of proteins from fetal calf serum (FCS) or fetal bovine serum (FBS), phototoxicity is improved [135, 141]. This trend was observed for all nanoparticle formulations, whereas free drug did not seem to be influenced by serum. For example, pTHPP-loaded nanoparticles [135] were two-fold more efficient in the presence of 10% FBS regardless of the polymer (PLA, 50:50 and 75:25 PLGA). The serum may enhance the intracellular accumulation of photosensitizer but also favor the monomeric form of the photosensitizer. Indeed, as hydrophobic entities, photosensitizer molecules tend to aggregate in aqueous solution or within the nanoparticles. In this aggregated state, the photosensitizer exhibits a low photodynamic activity and has to be first dispersed to become efficient [151]. Proteins could enhance this dispersion process mainly by lipoprotein association with PS. Improvements in phototoxicity were observed according to the formulations by Konan et al. with pTHPP and verteporfin [135, 141] and Bourdon et al. with mTHPC [142]. Indeed, when compared to nanoparticle formulations, free drug and drug formulated in oil/water NE were not affected by the presence of proteins. The association of PS molecules and proteins can be studied by fluorescence. When aggregated, PS emits very little fluorescence, so the state of dispersion can be observed by following the increase in fluorescence after adding serum. A rapid transfer of verteporfin seems to occur from the nanoparticles to the serum proteins, as Konan-Kouakou et al. observed a rapid increase in fluorescence immediately after the injection of 5% FBS in the suspension medium [141]. In contrast, verteporfin was slightly transferred from DMSO/PBS formulation, which correlates well with the results observed for *in vitro* phototoxicity.

**Influence of Carrier Characteristics** Different types of polymers are available for NP manufacture. The characteristics of the surface can also be changed either by using block copolymers or by coating particles with different excipients. Finally, managing the preparation processes parameters allows control of NP size. It is therefore possible to design customized particles that exhibit very different characteristics in terms of physicochemical properties as well as delivery features. Several studies have evaluated the influence of these parameters.

**Polymer and Surface Modifications** The carrier nature can modulate the photoactivity. The nature of the polymer influences the phototoxicity of drug-loaded nanoparticles. Nanoparticles having the same characteristics (size, drug loading and polymer molecular weight) can exhibit different *in vitro* toxicities that depend on the polymer they are made of. Konan et al. have shown that PLGA-nanoparticles are more efficient than PLA-nanoparticles [136]. Even the lactic/glycolic ratio played a role, since 50:50 PLGA induced a drop in viability at lower doses than 75:25

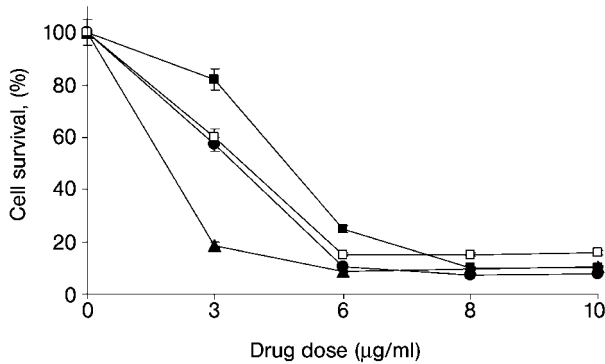


**Fig. 2.5.** Influence of drug concentration on photocytotoxicity of free pTHPP (■) or pTHPP-loaded nanoparticles (▲, 50:50 PLGA; □, 75:25 PLGA; ●, PLA). The EMT-6 tumor cells were incubated for 1 h, at equivalent drug concentrations, ranging from 3 to 10  $\mu\text{g mL}^{-1}$ , for 1 h and irradiated at a light dose of 6  $\text{J cm}^{-2}$  (655 nm). The MTT assay was performed 18 h after light exposure. Each data point represents the mean ( $\pm$ S.D.) of six values. (Redrawn from [136].)

PLGA (Fig. 2.5). Thus, with the same photosensitizer, *in vitro* activity can be affected by the polymer hydrophile–lipophile balance value, degradation rate and drug release profile. The hydrolysis-labile ester linkages are more accessible to water in PLGA than PLA. In the same way, the higher the content of glycolide in the polymer, the more accessible it would be to water, resulting in a faster hydrolysis. Thus, a faster intracellular release of drug is expected from 50:50 PLGA nanoparticles, which explains their higher efficiency.

By coating nanoparticles with poloxamer or using PEG-grafted polymers, different efficacies can also be obtained with the same polymer (PLA). Naked PLA NCs or poloxamer NCs exhibited quite similar toxicities as determined by Bourdon et al. [142]. However, PLA-PEG NCs induced a slight decrease in phototoxicity.

**Particle Size** The influence of particle size is a key factor regarding cellular internalization [141, 152, 153]. Usually, smaller particles tend to be more readily internalized, and thus higher activity is expected. This parameter has not been yet extensively studied for PDT. The efficiency of a photosensitizer seems to be improved by encapsulating it into small nanoparticles rather than larger nanoparticles. Konan-Kouakou et al. have compared three formulations of verteporfin on EMT-6 mammary tumor cells [141]. Free verteporfin and verteporfin-loaded nanoparticles with different mean sizes (167 and 370 nm) resulted in different survival rates after 1 h-incubation when irradiated at 6  $\text{J cm}^{-2}$ . Treatment with 70  $\text{ng mL}^{-1}$  of free or entrapped verteporfin into large nanoparticles yielded only 11 and 29% cell death, respectively. At the same concentration, almost 69% of cells were killed by small nanoparticles. The small size can increase the particles capacity to be taken up by cells and allow a faster drug release into cells. Furthermore, the distri-

bution of photosensitizer in the nanoparticles can also be affected by their size. With small NPs, the PS could be absorbed on the particle's surface rather than being incorporated into the polymeric matrix. The PS is then more exposed to the external medium and available at its site of action. This influence of size has also been reported recently *in vivo* by Vargas et al. [154].

**Influence of Photosensitizer** Depending on their nature, photosensitizers could enter the cells by different mechanisms and/or rates. In solution, free PS are generally taken up by diffusion, leading to a low intracellular concentration. In contrast, nanoparticles seem to be taken up by endocytosis, leading to higher accumulation and delivery of drug.

In the same chemical family of PS, different derivatives can exhibit different phototoxic activities but these differences can be minimized by encapsulation. The free photosensitizers, depending on their physicochemical properties and, especially, on their hydrophile–lipophile balance value, can penetrate the cell membrane to different extents. However, when encapsulated, all PS derivatives could lead to similar photoactivities. For example, for free zinc-phthalocyanine derivatives, photodynamic activity increased when the degree of sulfonation decreased, according to Lenaerts et al. [130]. In V-79 Chinese hamster cells, the free disulfonated derivative ( $\text{ZnPcS}_2$ ) yielded an  $\text{IC}_{90}$  of 0.19 versus 7.5  $\mu\text{M}$  for the tetrasulfonated derivative ( $\text{ZnPcS}_4$ ). However, after encapsulation into poly(isohexyl cyanoacrylate) (PIHCA) NCs, both PS exhibited similar  $\text{IC}_{90}$  (0.19 and 0.28  $\mu\text{M}$ , respectively). One possible explanation is that amphiphilic molecules, such as  $\text{ZnPcS}_2$ , are readily taken up by cells in their free forms, and thus they are not more active after encapsulation. In contrast, hydrophilic drugs, when incorporated into carriers, can be delivered more readily to the cells and thus be more active. This hypothesis should be verified by internalization experiments and *in vivo* assays. Indeed, in contrast with these conclusions, Pegaz et al. have demonstrated on the chick chorioallantoic membrane (CAM) model that the photodynamic activity of PS is strongly influenced by their hydrophile–lipophile balance [138]. Once entrapped into NPs, the most hydrophobic PS exhibited a higher photoactivity.

Lenaerts et al. [130] have also suggested that encapsulation would reduce the degree of aggregation of the drug, aggregation that is detrimental to PS activity. This point is considered to be of key importance for the success of PDT because the susceptibility of highly hydrophobic PS to undergo aggregation in aqueous environments has a deleterious effect on the photoinduced oxidative process [151]. Indeed, due to the lack of physiological acceptable solvents for hydrophobic PS, encapsulation allows one to overcome formulation problems, especially when intravenous administration is needed.

#### 2.4.2.2 Uptake and Trafficking of Photosensitizers

PS, depending on their properties (hydrophile–lipophile balance value, charge, etc.), enter cells through different mechanisms, thereby determining their subcellular localization and ultimately their photodynamic efficacy. PS may penetrate into the cell by passive diffusion or by endocytosis [12].

Interest in using polymeric nanoparticles for PDT was first demonstrated by studies from Bachor et al. who conjugated the porphyrin derivative chlorine  $e_6$  ( $Ce_6$ ) on 1000 nm polystyrene particles [155]. Association of PS to the particles increased the cellular uptake of the drug while the free drug stayed in the membrane of MGH-U1 cells (human bladder carcinoma cell line). The intracellular concentration was  $20\times$  higher in cells treated with  $Ce_6$ -microspheres than in cells treated with unconjugated  $Ce_6$ . As a consequence, after irradiation at 659 nm, encapsulated  $Ce_6$  ( $0.43 \mu M$ ) induced total growth inhibition at a light dose of  $5 J cm^{-2}$ , whereas treatment with unconjugated  $Ce_6$  did produced no effect.

PS, free or entrapped, enters the cells in a concentration- and time-dependent manner [135, 142]. However, different uptake rates could be obtained depending on the PS or on the nature of the carrier. mTHPC has been entrapped in plain, or surface modified with PLA-PEG, NCs [142]. The cellular uptake, evaluated by the total fluorescence intensity of cells, showed that encapsulation decreased the intracellular uptake of the drug. Indeed, a higher internalization rate was obtained when the drug was solubilized in an ethanol/PEG/water (20/30/50 by volume) solution than with the encapsulated drug. Plain PLA NCs were less internalized than either poloxamer-coated nanocapsules or PLA-PEG NCs (Fig. 2.6). Nevertheless, quite similar phototoxic activity was observed for all treated groups. This strongly suggests that the PS does not follow the same cellular uptake pathway depending

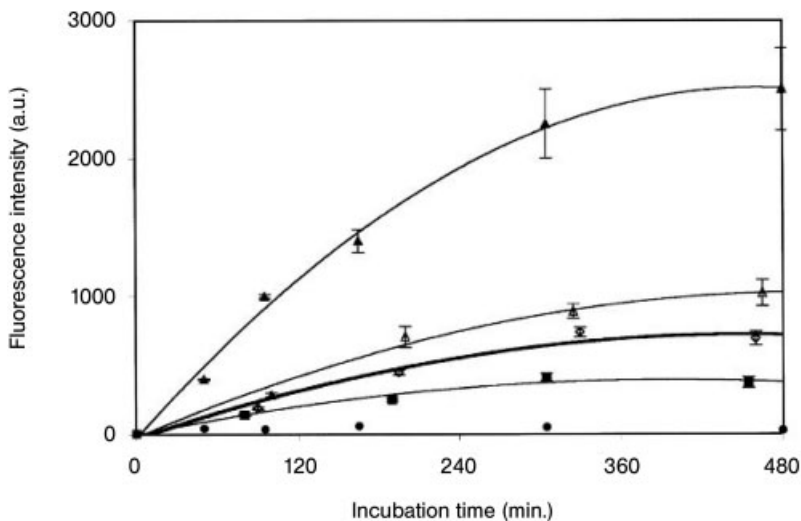


**Fig. 2.6.** Uptake of mTHPC ( $0.25 \mu g mL^{-1}$ ) by HT29 cells as determined by microspectrofluorimetry. mTHPC formulations: solution ( $\blacktriangle$ ), nanoemulsion ( $\triangle$ ), poloxamer-coated PLA NCs ( $\circ$ ), PLA-PEG NCs ( $\blacksquare$ ) and PLA NCs ( $\bullet$ ). Cellular fluorescence intensities were measured at 654 nm. For each experiment, data have been averaged from intensity values determined on 30 individual living cells. Experiments were carried out in triplicate (bars represent S.E.). (Reprinted from Ref. [142] with permission.)



on whether it is encapsulated or free. This was further demonstrated in a recent publication where the degree of internalization of pTHPP-loaded nanoparticles sharply dropped when incubation was performed at +4 °C whereas no effect on the uptake of the free drug was observed [135]. Thus, an energy-dependent process is involved in the uptake of loaded-nanoparticles. Endocytosis of NPs leads to higher intracellular concentration whereas free pTHPP, owing to its hydrophobic nature, tends to diffuse passively into the cell membrane, where it is less active. Therefore, encapsulation favors the PS internalization; however, PLA nanoparticles were less likely to be taken up than PLGA NP. In this case, pTHPP is a PS able to cross the membrane by diffusion; however, other PS, which are less hydrophobic or too polar to diffuse through the plasma membrane, are taken up, similar to the NPs, by endocytosis.

ROS have a short life-time, and their activity is limited to sites close to ROS generation; thus, PS uptake by cancer cells is crucial for effective PDT. To a certain degree, the type of damage that occurs in cells depends on the subcellular localization of the PS. The localization of PS in cancer cells, studied by fluorescence microscopy, seems to be formulation-dependent. The intracellular localization of PS might differ between free PS and loaded-carriers, permitting induction of different photochemical lesions in irradiated cells. A specific subcellular localization could determine the mechanism of cell death. For example, localization in mitochondria has been associated with the tendency of PS to produce apoptosis [12].

Precise PS localization can be determined by confocal laser scanning microscopy and by using co-staining of cellular organelles using fluorescent markers or indirect immunofluorescence. Bachor et al. first showed that microspheres loaded with Ce<sub>6</sub> can be visualized in the cytoplasm and more precisely in phagolysosomes [155]. In contrast, unconjugated PS, due to their lipophilicity, seemed to stay in cellular membranes, including plasma, nuclear and mitochondrial membranes. The cellular distribution within HT29 cells reported by Bourdon et al. was also affected by encapsulation [142]. Cells treated with free drug showed a diffused distribution throughout the cytoplasm, with a non-fluorescent nuclear area. As for NCs, even if the nuclear area is still non-fluorescent, PS was localized in the Golgi system.

In contrast to these studies reporting different localization for free and encapsulated PS, Konan et al. observed, in EMT-6 cells, similar localization in early and late lysosomes for free and encapsulated pTHPP [135]. However, this discrepancy might be related to the use of different cell lines and experimental parameters. Indeed, as far as uptake is concerned, a specific behavior of EMT-6 cells has been reported compared to other cell lines [156].

The photochemical reactions induced by irradiation may damage membrane integrity and therefore cause the release of PS from their primary site of localization. The efflux of pTHPP from EMT-6 cells was studied in a comparative manner after treatment with PLGA loaded-nanoparticles and free drug at 6 µg mL<sup>-1</sup> for 15 min incubation [135]. After irradiation at 6 J cm<sup>-2</sup>, the rate of the pTHPP escape was evaluated by loss of fluorescence as a function of time. Indeed, free or loaded drug gradually escaped from cells as a function of time. This trend was faster for a treatment with NPs. This may be due to a higher uptake and thus to more severe pho-

tochemical damage, including important membrane disruption. Before total efflux from cells, redistribution inside the cells could be observed, e.g., from lysosomes to cytoplasm or nuclei [157]. This phenomenon has been demonstrated with PS, such as porphyrins or phthalocyanines derivatives [158, 159], but not yet with PS-loaded nanoparticles.

One of the limitations of nanocarriers is their rapid uptake by the reticuloendothelial system (RES), which results from the adsorption of opsonins (plasma proteins) on these carriers. Then, they are taken up by the cells of the immune system located mainly in the liver and the spleen. Thus, a strategy has been developed to avoid the adsorption of opsonins. Bourdon et al. have studied this phenomenon with macrophage-like cells (J774) [142]. For this purpose they compared different mTHPC formulations with the aim of evaluating the capability of surface-modified NCs to reduce phagocytosis. Compared with naked PLA NCs, drug uptake by macrophages is indeed decreased by poloxamer coating of particles, or by using PEGylated polymers (Fig. 2.7). This reduction in uptake is better achieved with PLA-PEG NCs. These results are a positive indication that RES clearance *in vivo* could be limited with such PEGylated carriers (as discussed below). Interaction between carriers and opsonins is of van der Waals type, and coating nanoparticles with a hydrophilic chain of poloxamer or PEG could increase the circulating time in the body.

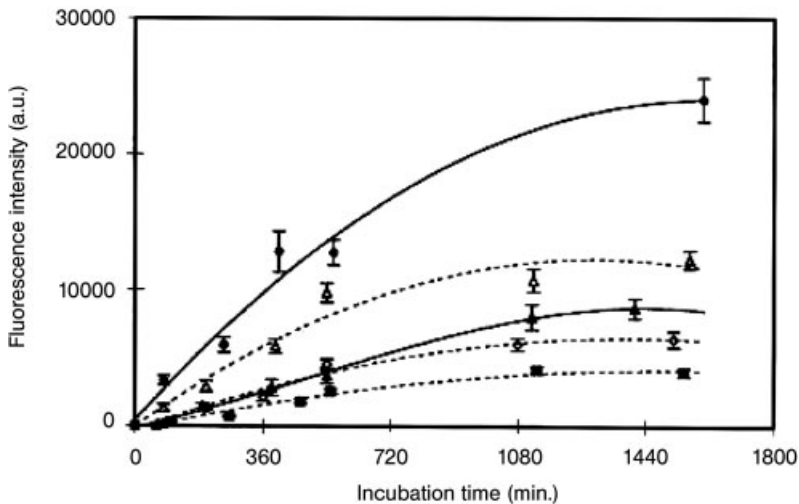


**Fig. 2.7.** Uptake of mTHPC ( $0.25 \mu\text{g mL}^{-1}$ ) by macrophage-like J774 cells as determined by microspectrofluorimetry. mTHPP formulations: PLA NCs (●), nanoemulsion (△), solution (▲), poloxamer-coated PLA NCs (○) and PLA-PEG NCs (●). Cellular fluorescence intensities were measured at 654 nm. For each experiment, data have been averaged from intensity values determined on 30 individual living cells. Experiments were carried out in triplicate (bars represent S.E.). (Reprinted from Ref. [142] with permission.)

## 2.4.3

**In Vivo Relevance of Polymeric Nanoparticles in PDT**

Encapsulation may lead to a different intracellular localization of the hydrophobic photosensitizers, favoring light activated phototoxicity. One must, however, be very careful in extrapolating previous data to an *in vivo* situation. Indeed, *in vitro* experiments are obtained on cell monolayers directly in contact with light and PS, conditions rarely encountered *in vivo*. These studies are a proof of concept as they document the ability of the NP approach to improve PDT efficacy. Encapsulation would allow one not only to reduce the PS dose administered to the patients but also to use a lower light dose, thus reducing potential collateral damage to neighboring tissues. To demonstrate these advantages of NPs, *in vivo* studies have to be carried out with several goals: first, to compare the body biodistribution of PS according to their formulations, to assess the efficacy of PS-loaded nanocarriers as far as vascular or tumor suppression effects are concerned, and finally to investigate possible side effects, such as skin photosensitization.

**2.4.3.1 Biodistribution and Pharmacokinetics of Photosensitizers Coupled to Nanoparticles**

As with therapies against cancer, one of the main challenges in photodynamic therapy is enhancement of the PS concentration ratio between tumor and other organs [7]. However, the localization of NP in specific tissues may depend on the intrinsic characteristics of the carrier (e.g., nature of the polymer, size, and surface properties). The tissue distribution and pharmacokinetics of a PS can be influenced by its incorporation into nanoparticles. Generally, following *i.v.* administration, nanoparticles are rapidly and extensively taken up by the RES [125]. Accordingly, as soon as a few minutes after intravenous injection of nanoparticles, the PS mainly accumulates in the liver and spleen. Thereafter, the RES drug level gradually decreases over several days, depending on the biodegradability of the polymer and on the drug release kinetics.

Although few *in vivo* studies have been carried out, the advantages of surface modification to decrease the accumulation of the photosensitizer in the liver have been demonstrated. The body distribution of poloxamer-coated-PIHCA NCs containing radiolabeled tetraiodinated zinc-phthalocyanine ( $\text{ZnPcI}_4$ ) were studied in healthy Balb-C mice and mice bearing the EMT-6 mammary tumor [130]. The accumulation of PS in the liver was significantly lower with poloxamer-coated NCs than with free  $\text{ZnPcI}_4$  in solution. As a consequence, the main fraction of PS was present in blood when NCs are used as a carrier. The experiments in tumor-bearing mice confirmed not only the reduced liver uptake with NCs but also showed a higher uptake by the tumor. Photodynamic therapy should be performed when PS concentrations have a maximum value in the tumor, thus, in this study, tumor-to-blood ratios  $> 200$  were obtained as early as 12 h post-injection. This high tumor selectivity achieved by surface modification of nanocarriers confirmed that NPs could be an efficient drug delivery system for cancer treatment.

PLA biodegradable nanoparticles coated with PEG-20 000 have also been suggested to enhance tumor uptake of the encapsulated compound [139]. Coating PLA NPs with PEG-20 000 substantially enhanced the blood circulation time of the photosensitizer hexadecafluoro zinc phthalocyanine (ZnPcF<sub>16</sub>), as compared to plain particles. After 24 and 168 h, the cumulated uptake of the compound in the liver and spleen represented 61% and 44% for plain NPs versus 50% and 29% for PEG-coated NPs, respectively. The reduction of the uptake of the NPs by the RES and the resulting longer blood circulation time were associated with a three-fold increase of the compound concentration in the tumor after 24 h. Such coated NPs yielded advantageous tumor-to-skin and tumor-to-muscle ratios, which is important in predicting the risk of damage to adjacent tissues during PDT.

Similar results were also observed by fluorescence with poloxamer-coated nanocapsules and PEG-grafted PLA nanocapsules loaded with mTHPC [143]. A decrease in liver distribution was observed with coated particles and was more pronounced for PLA-PEG NCs. Tumor distribution was also affected, and PLA-PEG particles seemed to better accumulate in the tumor tissue. Nonetheless, the influence of surface modification on particle biodistribution is difficult to compare between studies because results are frequently presented in arbitrary units of fluorescence, and the relative fluorescence of each formulation is not given.

#### 2.4.3.2 Vascular Effects

Vascular damage and blood flow stasis are consequences of PDT on solid tumors. The irreversible destruction of the tumor vasculature, with the subsequent ischemia, is primarily responsible for an effective PDT of solid tumors and contributes to the long-term tumor control [18, 160]. Vascular events observed after PDT include release of vasoactive molecules, enhanced leakage and platelet aggregation, followed by occlusion of the blood vessels. Apart from oncological applications, the vascular occlusion induced by PDT has been used to treat the wet form of age-related macular degeneration, characterized by choroidal neovascularization. The mechanisms underlying the vascular effects of PDT differ greatly according to the nature of the PS and have been studied in different animal models [25]. However, the effect of incorporating photosensitizers in nanoparticles on the PDT-induced vascular occlusion is still unexplored and has only been studied *in vivo* using the chick chorioallantoic (CAM) model. The chorioallantoic membrane is a highly vascularized organ of the chick embryo, which allows the evaluation of vascular occlusion induced by PDT [161]. The pharmacokinetics of intravenously injected PS in the CAM is followed by measurement of the fluorescence of the vascularized and non-vascularized tissues. The photodynamic activity of the PS can be assessed by evaluation of the vascular occlusion achieved after irradiation of the CAM. Vargas et al. have compared the vascular effects of pTHPP, either in solution or encapsulated in 120 nm PLGA NPs, on the CAM vessels [137]. Vascular occlusion was greatly enhanced by the incorporation of pTHPP into NPs (Fig. 2.8), probably because of the reduced diffusion of NPs out of vessels during irradiation. Indeed, non-encapsulated PS quickly leaked out of the vasculature, whereas PS-

## a. Evaluation of PDT induced damage on CAM vessels

Damage Scale	Criterion
0	No damage
1	Partial closure of capillaries of diameter < 10 $\mu\text{m}$
2	Closure of capillary system, partial closure of blood vessels of diameter < 30 $\mu\text{m}$ and size reduction of larger blood vessels
3	Closure of vessels of diameter < 30 $\mu\text{m}$ and partial closure of higher order vessels
4	Total closure of vessels of diameter < 70 $\mu\text{m}$ and partial closure of larger vessels
5	Total occlusion of vessels in the irradiated area

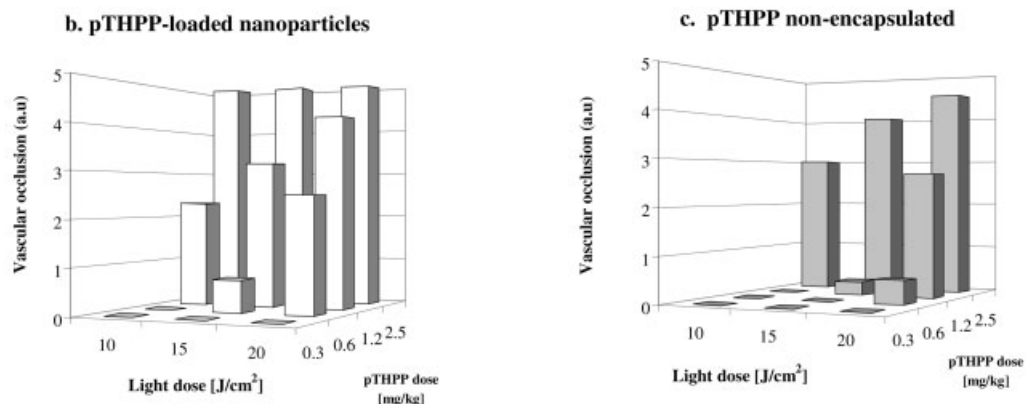


**Fig. 2.8.** Top. (a) Evaluation criteria of vascular occlusion induced in CAM vessels. Bottom: Comparison of the vascular damage induced by (b) pTHPP-loaded nanoparticles

and (c) pTHPP dissolved in a mixture of ethanol, poly(ethylene glycol) and water. CAM was irradiated with various light doses. Mean ( $n = 3$ ). (Adapted from [137].)

loaded NPs remained longer intravascularly during the 25 min observation time. Using the CAM model, Pegaz et al. have evaluated the influence of the encapsulation of PS with different degrees of lipophilicity on the vascular effects of PDT [138]. Porphyrin derivatives, such as meso-tetraphenylporphyrin (TPP) and meso-tetra(4-carboxyphenyl)porphyrin (TCPP), and chlorin derivatives, such as pheophorbide-a (phéo-a) and  $\text{Ce}_6$ , were encapsulated in PLA nanoparticles of around 200 nm. The PS loading increased with the lipophilicity of the encapsulated PS, ranging from 0.5% for  $\text{Ce}_6$  to 4.6% for TPP. The more hydrophobic PS, TPP for porphyrins and phéo-a for chlorins, extravasated to a lesser extent than the more hydrophilic derivatives. At 1 mg per kg of chick embryo body weight, the extent of vascular occlusion induced by the NPs decreased with decreasing lipophilicity of the PS: TPP > TCPP > phéo-a >  $\text{Ce}_6$ . The authors suggest that the hydrophile-

lipophile balance value of the PS plays an important role in the release of porphyrins and chlorins from these NPs. However, NPs with different drug loadings were compared in this study, and the loading rate may also influence the phototoxicity of NPs. Furthermore, controls using the PS in solution were not performed. Recently, the effect of the NP size on the extent of vascular occlusion has been investigated in the same model. pTHPP was incorporated into PLGA NPs of about 100, 300 and 600 nm [154]. Although the nanoparticles had similar porphyrin loading, the phototoxic effects and the pharmacokinetic profile of the drug were influenced by the size of the nanocarrier. Vascular occlusion decreased as the NPs size rose. Although *in vivo* cancer models should be used to further evaluate the vascular effects of photosensitizers loaded in NPs, observations on the CAM model suggest that the pharmacokinetic profile and the vascular effects induced by PS can be enhanced and modulated by their incorporation into NPs.

#### 2.4.3.3 *In Vivo* Efficacy on Tumor: Tumor Suppression Effects

Encapsulation of ZnPcF<sub>16</sub> into PEG-coated PLA NPs greatly improved its photodynamic activity against EMT-6 mouse mammary tumor implanted in Balb/c mice [140]. Light irradiation was performed 24, 48 and 72 h after intravenous injection of ZnPcF<sub>16</sub> in PEG-coated NPs or Cremophor® [polyoxethylated castor oil (CRM)] based emulsion. At a concentration of 1  $\mu\text{mol kg}^{-1}$ , the best tumor response was obtained when irradiation was carried out 24 h post-injection. Indeed, 63% of Balb/c mice showed no macroscopic sign of tumor progression one week after PDT, and they were completely cured three-weeks post-treatment. In contrast, treatment with CRM formulation led to only 14% tumor regression. Thus, uptake is not the only important parameter as the two formulations were taken up by tumor at a similar rate at this time point (24 h), but the distribution inside the tumor might be different, depending on the formulation. To improve early tumor response, Allémann et al. [140] increased the PS doses (2 and 5  $\mu\text{mol kg}^{-1}$ ). For both doses, early tumor response, in terms of edema, was observed for all treated mice. At 2  $\mu\text{mol kg}^{-1}$ , no effect of the time delay between NP injection and irradiation was observed. In this case, three-weeks post-PDT, 40% of the mice showed complete healing when PDT was performed either at 24, 48 or 72 h post-injection. At 5  $\mu\text{mol kg}^{-1}$ , the treatment with NPs is even more efficient as all mice were cured as compared to only 60% when treated with CRM. Unfortunately, no comparison with uncoated NPs was performed. Nonetheless, uncoated NPs appear to be efficient as well, since Konan-Kouakou et al. have shown the ability of verteporfin-loaded PLGA NPs to control rhabdomyosarcoma (M1) tumor growth implanted in DBA/2 mice [141]. At 1.4  $\mu\text{mol kg}^{-1}$ , tumor suppression was obtained with irradiation as early as 15 and 30 min after injection, with 66 and 75% tumor-free animals, respectively, on day 20. However, irradiation performed 60 min post-injection led to only 33% tumor-free animals. This suggests rapid *in vivo* clearance of the PS when administered in NPs. Moreover, the size of NPs might influence their efficacy *in vivo*, as demonstrated *in vitro* [141]. Indeed, small NPs could reach the target sites and thus be active more rapidly than large NPs. But in this part of the study, Konan-Kouakou et al. showed no control formulations, such

as free PS in solution or emulsion in order to compare the possible differences in efficacy *in vivo* [141].

#### 2.4.3.4 Adverse Effects

Despite promising results in the treatment of cancer, the use of photosensitizers is associated with undesirable side effects, such as prolonged cutaneous photosensitivity that persists for a long time (up to several months). New sensitizers have thus been developed to combine acceptably low rates of skin phototoxicity and clinically useful tumor tissue specificity.

Konan-Kouakou et al. have evaluated the skin photosensitivity caused by verteporfin when administered in NPs to SKH1 hairless mice [141]. Mice were exposed to  $60 \text{ J cm}^{-2}$  of light 15 or 60 min after PS injection. Photosensitivity was assessed 1 and 3 days later using a scoring system for erythema/eschar and edema formation (Table 2.4). The total skin photosensitivity score was calculated as the sum of scores from injury observations. The highest skin photosensitivity scores were observed one day after light exposure when mice were exposed to light 15 min after injection. The average score was then  $1.7 \pm 0.6$ , and 3 days after exposure the value came back to the normal. No skin photosensitivity was observed when mice were irradiated 60 min after injection. Thus, the animals are photosensitive for only a short period, which is very important in limiting the risk of adverse side effects. However, this might be limited to verteporfin, for which a rapid clearance has been described [162]. Although NPs appear to prevent adverse effects, this aspect has only been evaluated in one report – confirmation requires more experimental data.

**Tab. 2.4.** Skin photosensitivity scoring system<sup>[a]</sup>.

---

#### Erythema plus eschar

- 0 No observable reaction
- 1 Minimally detectable erythema
- 2 Slightly visible pale pink erythema, no vessels broken, no red spots
- 3 Blanching, few broken vessels, no eschar formation
- 4 Definite erythema, more broken vessels leading to yellow eschar formation
- 5 Severe reaction, many broken vessels, eschar formation – but less than 50% of site
- 6 Very severe rosette, eschar formation on more than 50% of site

#### Edema

- 0 No observable reaction
  - 1 Slight edema within exposure site
  - 2 Mild edema within exposure site (skin fold measurement < 1 mm)
  - 3 Moderate edema (skin fold measurement 1–2 mm thick)
  - 4 Severe edema extending beyond exposure site (skin fold measurement > 2 mm thick)
- 

<sup>a</sup>Total skin photosensitivity score is the sum of scores from erythema plus eschar and edema observations (minimum = 0, maximum = 10).

## 2.5

### Conclusions

Photodynamic therapy and photodetection are innovative and newly developed approaches for the treatment and detection of cancer. It implies the photoactivation of photosensitizers to induce cellular damage in the target tissue. This approach to cancer chemotherapy, due to the nature of the drug itself, is characterized by better targeting of the treatment, thus limiting side effects usually encountered with conventional therapies. The development of this therapy is somehow limited by the fact that the more potent molecules are hydrophobic, thus requiring potentially harmful solvents to have injectable formulations. The use of biodegradable or non-biodegradable particles as a photosensitizer formulation allows injectable suspensions to be obtained. Encapsulation of different types of photosensitizers does not reduce their photoactivity and in most cases leads to a better activity than shown by the free compounds.

Promising results have been found with non-biodegradable materials. However, non-biodegradable nanoparticles do not offer the possibility of drug release patterns achieved with biodegradable polymers. Further, toxicological aspects have not been yet fully addressed.

*In vivo* and *in vitro* literature data have reported interest in the encapsulation of PS into polymeric nanoparticles, a system offering long-term stable shelf life. The main strength of polymeric nanoparticles for PS delivery is that they are well tolerated both *in vivo* and *in vitro*. Furthermore, encapsulation of PS preserves their pharmacological activity and may decrease the occurrence of adverse effects. Currently, the mechanistic approach behind pharmacological efficiency has not yet been explored and it would be interesting to better understand how photosensitizers can be still active when incorporated into a polymeric shell. Indeed, is the release of the PS necessary for the PDT effect to happen? Since PDT is a two-step process with, first, drug administration and, second, light activation, release kinetics from the polymeric matrix may have a determining influence on treatment dose and schedule. Another unevaluated aspect is the possibility of using particles to actively target cancer or neovascularized tissues. Active targeting with nanoparticles is still at an early stage and its development in the field of PDT will increase tremendously the interest in this type of carrier.

Photodetection with PS loaded NPs has not yet been evaluated. However, there are many opportunities to develop delivery systems explicitly for PD. For instance, PD is mostly used to detect superficial cancers, but the detection of deeper localized tumor, using optic fibers, could take advantage of the tumor localizing properties of NPs.

### Acknowledgments

The authors are very grateful to Dr. Marino Campo for interesting discussions and for critical reading of the manuscript.



**Abbreviations**

5-ALA	5-Aminolevulinic acid
BPD-MA	Benzoporphyrin derivative monoacid ring A
CAM	Chick chorioallantoic membrane
Ce <sub>6</sub>	Chlorine e <sub>6</sub>
CNV-AMD	Choroidal neovascularization associated with age-related macular degeneration
CRM	Cremophor <sup>®</sup>
DMSO	Dimethyl sulfoxide
EPR	Enhanced permeability and retention
FBS	Fetal bovine serum
FCS	Fetal calf serum
FDA	U.S. food and drug administration
HpD	Haematoporphyrin derivative
HPPH	2-Devinyl-2-(1-hexyloxyethyl)pyrophephorbide
HT	Hyperthermia therapy
IC <sub>x</sub>	Inhibitory concentration (drug dose needed to kill x% of cells)
i.v.	Intravenous
IR	Infrared
LDL	Low-density lipoproteins
MB	Methylene blue
MR	Magnetic resonance
mTHPC	meta-tetra(Hydroxyphenyl)chlorin
MTT	3-(4,5-Dimethylthiazol-2-yl)-2,5-diphenyltetrazolium bromide
NC(s)	Nanocapsule(s)
NE	Nanoemulsion
NP(s)	Nanoparticle(s)
NS	Nanosphere
PAA	Polyacrylamide
PACA	Poly(alkyl cyanoacrylate)
PD	Photodetection
PDT	Photodynamic therapy
PEG	Poly(ethylene glycol)
pheo-a	Pheophorbide-a
PIHCA	Poly(isohexyl cyanoacrylate)
PLA	Poly(lactic acid)
PLGA	Poly(lactic-co-glycolic acid)
PpIX	Protoporphyrin IX
PS	Photosensitizer
pTHPP	meso-tetra( <i>p</i> -Hydroxyphenyl)porphyrin
QD(s)	Quantum dot(s)
RES	Reticuloendothelial system
ROS	Reactive oxygen species
SnET2	Tin-ethyl etiopurpurin

TCPP	meso-tetra(4-Carboxyphenyl)porphyrin
TPP	meso-Tetraphenylporphyrin
UV	Ultraviolet
ZnPcF <sub>16</sub>	Hexadecafluoro zinc phthalocyanine
ZnPcI <sub>4</sub>	Tetraiodinated zinc phthalocyanine
ZnPcS <sub>2</sub>	Disulfonated zinc phthalocyanine
ZnPcS <sub>4</sub>	Tetrasulfonated zinc phthalocyanine

## References

- 1 A. RUCK, G. BECK, R. BACHOR, N. AKGUN, M. H. GSCHWEND, R. STEINER, Dynamic fluorescence changes during photodynamic therapy in vivo and in vitro of hydrophilic Al(III) phthalocyanine tetrasulphonate and lipophilic Zn(II) phthalocyanine administered in liposomes, *J. Photochem. Photobiol. B*, **1996**, *36*, 127–133.
- 2 L. MORLET, V. VONARX-COINSMANN, P. LENZ, M. T. FOULTIER, L. X. DE BRITO, C. STEWART, T. PATRICE, Correlation between meta(tetrahydroxyphenyl)chlorin (m-THPC) biodistribution and photodynamic effects in mice, *J. Photochem. Photobiol. B*, **1995**, *28*, 25–22.
- 3 T. GLANZMANN, M. FORRER, S. A. BLANT, A. WOODTLI, P. GROSJEAN, D. BRAICHOTTE, H. VAN DEN BERGH, P. MONNIER, G. WAGNIERES, Pharmacokinetics and pharmacodynamics of tetra(m-hydroxyphenyl)chlorin in the hamster cheek pouch tumor model: Comparison with clinical measurements, *J. Photochem. Photobiol. B*, **2000**, *57*, 22–32.
- 4 G. A. WAGNIERES, W. M. STAR, B. C. WILSON, In vivo fluorescence spectroscopy and imaging for oncological applications, *Photochem. Photobiol.*, **1998**, *68*, 603–632.
- 5 R. R. ALLISON, H. C. MOTA, C. H. SIBATA, Clinical PD/PDT in North America: An historical review, *Photodiagn. Photodyn. Therap.*, **2004**, *1*, 263–277.
- 6 J. E. VAN LIER, Photosensitization: Reaction pathways, in D. P. VALENZENO, R. H. POTTIER, P. MATHIS, R. H. DOUGLAS (eds.), *Photobiological Techniques*, Plenum Press, New York, **1991**, ch. 7.
- 7 N. LANGE, Controlled drug delivery in photodynamic therapy and fluorescence-based diagnosis of cancer, in M.-A. MYCEK, B. W. POGUE (eds.), *Handbook of Biomedical Fluorescence*, Marcel Dekker, Inc., New York, **2003**, ch. 16.
- 8 C. S. FOOTE, Mechanisms of photosensitized oxidation, *Science*, **1968**, *162*, 963–970.
- 9 C. S. FOOTE, Definition of type I and type II photosensitized oxidation, *Photochem. Photobiol.*, **1991**, *54*, 659.
- 10 C. HADJUR, G. WAGNIERES, F. IHRINGER, P. MONNIER, H. VAN DEN BERGH, Production of the free radicals O<sub>2</sub><sup>-</sup> and OH by irradiation of the photosensitizer zinc(II) phthalocyanine, *J. Photochem. Photobiol. B*, **1997**, *38*, 196–202.
- 11 T. SHUTOVA, T. KRISKA, A. NÉMETH, V. AGABEKOV, D. GÀL, Physicochemical modeling of the role of free radicals in photodynamic therapy, *Biochem. Biophys. Res. Commun.*, **2000**, *270*, 125–130.
- 12 A. P. CASTANO, T. N. DEMIDOVA, M. R. HAMBLIN, Mechanisms in photodynamic therapy: Part one – photosensitizers, photochemistry and cellular localization, *Photodiagn. Photodyn. Ther.*, **2004**, *1*, 279–293.
- 13 H. M. CHEN, C. T. CHEN, H. YANG, M. Y. KUO, Y. S. KUO, W. H. LAN, Y. P. WANG, T. TSAI, C. P. CHIANG,

- Successful treatment of oral verrucous hyperplasia with topical 5-aminolevulinic acid-mediated photodynamic therapy, *Oral Oncol.*, **2004**, 40, 630–637.
- 14 K. BERG, P. K. SELBO, A. WEYERANG, A. DIETZE, L. PRASMICKAITE, A. BONSTED, B. O. ENGESAETER, E. ANGELL-PETERSEN, T. WARLOE, N. FRANSEN, A. HOGSET, Porphyrin-related photosensitizers for cancer imaging and therapeutic applications, *J. Microsc.*, **2005**, 218, 133–147.
  - 15 T. J. DOUGHERTY, C. J. GOMER, B. W. HENDERSON, G. JORI, D. KESSEL, M. KORBELIK, J. MOAN, Q. PENG, Photodynamic therapy, *J. Natl. Cancer Inst.*, **1998**, 90, 889–905.
  - 16 N. OLEINICK, R. MORRIS, I. BELICHENKO, The role of apoptosis in response to photodynamic therapy: What, where, why, and how, *Photochem. Photobiol. Sci.*, **2002**, 1, 1–21.
  - 17 A. P. CASTANO, T. N. DEMIDOVA, M. R. HAMBLIN, Mechanisms in photodynamic therapy: Part two – Cellular signaling, cell metabolism and modes of cell death, *Photodiagn. Photodyn. Ther.*, **2005**, 2, 1–23.
  - 18 V. H. FINGAR, Vascular effects of photodynamic therapy, *J. Clin. Laser Med. Surg.*, **1996**, 14, 323–328.
  - 19 J. V. MOORE, C. M. L. WEST, C. WHITEHURST, The biology of photodynamic therapy, *Phys. Med. Biol.*, **1997**, 42, 913–935.
  - 20 B. KRAMMER, Vascular effects of photodynamic therapy, *Anticancer Res.*, **2001**, 21, 4271–4277.
  - 21 J. KRUTMANN, Therapeutic photoimmunology: Photoimmunological mechanisms in photo(chemo) therapy, *J. Photochem. Photobiol. B*, **1998**, 44, 159–164.
  - 22 M. KORBELIK, G. J. DOUGHERTY, Photodynamic therapy-mediated immune response against subcutaneous mouse tumors, *Cancer Res.*, **1999**, 59, 1941–1946.
  - 23 G. CANTI, A. DE SIMONE, M. KORBELIK, Photodynamic therapy and the immune system in experimental oncology, *Photochem. Photobiol. Sci.*, **2002**, 1, 79–80.
  - 24 S. B. BROWN, E. A. BROWN, I. WALKER, The present and future role of photodynamic therapy in cancer treatment, *Lancet Oncol.*, **2004**, 5, 497–508.
  - 25 A. P. CASTANO, T. N. DEMIDOVA, M. R. HAMBLIN, Mechanisms in photodynamic therapy: Part three – Photosensitizer pharmacokinetics, biodistribution, tumor localization and modes of tumor destruction, *Photodiagn. Photodyn. Ther.*, **2005**, 2, 91–106.
  - 26 H. MAEDA, J. WU, Y. SAWA, Y. MATSUMURA, K. HORI, Tumor vascular permeability and the EPR effect in macromolecular therapeutics: A review, *J. Controlled Release*, **2000**, 65, 271–284.
  - 27 J. P. ROVERS, A. E. SAARNAK, M. DE JODE, H. J. C. M. STERENBORG, O. T. TERPSTRA, M. F. GRAHN, Biodistribution and bioactivity of tetra-pegylated meta-tetra(hydroxyphenyl)chlorin compared to native meta-tetra(hydroxyphenyl)chlorin in a rat liver tumor model, *Photochem. Photobiol.*, **2000**, 71, 210–217.
  - 28 T. REUTHER, A. C. KUBLER, U. ZILLMANN, C. FLECHTENMACHER, H. SINN, Comparison of the in vivo efficiency of photofrin II-, mTHPC-, mTHPC-PEG- and mTHPCnPEG-mediated PDT in a human xenografted head and neck carcinoma, *Lasers Surg. Med.*, **2001**, 29, 314–322.
  - 29 F. RANCAN, A. WIEHE, M. NOBEL, M. O. SENGE, S. A. OMARI, F. BOHM, M. JOHN, B. RÖDER, Influence of substitutions on asymmetric dihydroxychlorins with regard to intracellular uptake, subcellular localization and photosensitization of Jurkat cells, *J. Photochem. Photobiol. B*, **2005**, 78, 17–28.
  - 30 D. J. BALL, S. R. WOOD, D. I. VERNON, J. GRIFFITHS, T. M. DUBBELMAN, S. B. BROWN, The characterisation of three substituted zinc phthalocyanines of differing charge for use in photodynamic therapy. A comparative study of their aggregation and photosensitising ability in relation to mTHPC and polyhaematoporphyrin,

- J. Photochem. Photobiol. B*, **1998**, *45*, 28–35.
- 31 R. W. BOYLE, D. DOLPHIN, Structure and biodistribution relationships of photodynamic sensitizers, *Photochem. Photobiol.*, **1996**, *64*, 469–485.
  - 32 M. KONGSHAUG, J. MOAN, S. B. BROWN, The distribution of porphyrins with different tumour localising ability among human plasma proteins, *Br. J. Cancer*, **1989**, *59*, 184–188.
  - 33 J. C. MAZIERE, P. MORLIERE, R. SANTUS, New trends in photobiology: The role of the low density lipoprotein receptor pathway in the delivery of lipophilic photosensitizers in the photodynamic therapy of tumours, *J. Photochem. Photobiol. B*, **1991**, *8*, 351–360.
  - 34 B. A. ALLISON, P. H. PRITCHARD, J. G. LEVY, Evidence for low-density lipoprotein receptor-mediated uptake of benzoporphyrin derivative, *Br. J. Cancer*, **1994**, *69*, 833–839.
  - 35 A. S. SOBOLEV, D. A. JANS, A. A. ROSENKRANZ, Targeted intracellular delivery of photosensitizers, *Prog. Biophys. Mol. Biol.*, **2000**, *73*, 51–90.
  - 36 A. K. HAYLETT, J. V. MOORE, Comparative analysis of foetal calf and human low density lipoprotein: Relevance for pharmacodynamics of photosensitizers, *J. Photochem. Photobiol. B*, **2002**, *66*, 171–178.
  - 37 G. JORI, In vivo transport and pharmacokinetic behavior of tumour photosensitizers, *Ciba Found. Symp.*, **1989**, *146*, 78–86.
  - 38 L. POLO, G. VALDUGA, G. JORI, E. REDDI, Low-density lipoprotein receptors in the uptake of tumour photosensitizers by human and rat transformed fibroblasts, *Int. J. Biochem. Cell Biol.*, **2002**, *34*, 10–23.
  - 39 M. OCHSNER, Photophysical and photobiological processes in the photodynamic therapy of tumours, *J. Photochem. Photobiol. B*, **1997**, *39*, 1–18.
  - 40 K. WOODBURN, C. K. CHANG, S. LEE, B. HENDERSON, D. KESSEL, Biodistribution and PDT efficacy of a ketochlorin photosensitizer as a function of the delivery vehicle, *Photochem. Photobiol.*, **1994**, *60*, 154–159.
  - 41 M. M. ZUK, B. D. RIHTER, M. E. KENNEY, M. A. J. RODGERS, Effect of delivery system on the pharmacokinetics and tissue distribution of bis(Di-isobutyl octadecylsiloxy)silicon 2,3-naphthalocyanine (isoBOSINC), a photosensitizer for tumor therapy, *Photochem. Photobiol.*, **1996**, *63*, 132–140.
  - 42 E. REDDI, Role of delivery vehicles for photosensitizers in the photodynamic therapy of tumours, *J. Photochem. Photobiol. B*, **1997**, *37*, 189–195.
  - 43 Z.-J. WANG, Y.-Y. HE, C.-G. HUANG, J.-S. HUANG, Y.-C. HUANG, J.-Y. AN, Y. GU, L.-J. JIANG, Pharmacokinetics, tissue distribution and photodynamic therapy efficacy of liposomal-delivered hypocrellin A, a potential photosensitizer for tumor therapy, *Photochem. Photobiol.*, **1999**, *70*, 773–780.
  - 44 D. WÖRLE, S. MULLER, M. SHOPOVA, V. MANTAREVA, G. SPASSOVA, F. VIETRI, F. RICCHELLI, G. JORI, Effect of delivery system on the pharmacokinetic and phototherapeutic properties of bis(methyloxyethyleneoxy)silicon-phthalocyanine in tumor-bearing mice, *J. Photochem. Photobiol. B*, **1999**, *50*, 124–128.
  - 45 A. CASAS, H. FUKUDA, G. DI VENOSA, A. M. BATLLE, The influence of the vehicle on the synthesis of porphyrins after topical application of 5-aminolaevulinic acid. Implications in cutaneous photodynamic sensitization, *Br. J. Dermatol.*, **2000**, *143*, 564–572.
  - 46 M. C. DEROSA, R. J. CRUTCHLEY, Photosensitized singlet oxygen and its applications, *Coord. Chem. Rev.*, **2002**, *233–234*, 351–371.
  - 47 E. S. NYMAN, P. H. HYNINEN, Research advances in the use of tetrapyrrolic photosensitizers for photodynamic therapy, *J. Photochem. Photobiol. B*, **2004**, *73*, 1–28.
  - 48 R. R. ALLISON, G. H. DOWNIE, R. CUENCA, X. H. HU, C. J. H. CHILDS, C. H. SIBATA, Photosensitizers in

- clinical PDT, *Photodiagn. Photodyn. Ther.*, **2004**, 1, 27–42.
- 49 S.-J. TANG, N. E. MARCON, Photodynamic therapy in the esophagus, *Photodiagn. Photodyn. Ther.*, **2004**, 1, 65–74.
- 50 S. LAM, E. C. KOSTASHUK, E. P. COY, E. LAUKKANEN, J. C. LERICHE, H. A. MUELLER, I. J. SZASZ, A randomized comparative study of the safety and efficacy of photodynamic therapy using Photofrin II combined with palliative radiotherapy versus palliative radiotherapy alone in patients with inoperable obstructive non-small cell bronchogenic carcinoma, *Photochem. Photobiol.*, **1987**, 46, 893–897.
- 51 K. MOGHISSI, K. DIXON, J. A. C. THORPE, C. OXTOBY, M. R. STRINGER, Photodynamic therapy (PDT) for lung cancer: the Yorkshire Laser Centre experience, *Photodiagn. Photodyn. Ther.*, **2004**, 1, 253–262.
- 52 G. JORI, Tumor photosensitizers: Approaches to enhance the selectivity and efficiency of photodynamic therapy, *J. Photochem. Photobiol. B*, **1996**, 36, 87–93.
- 53 C. HOPPER, Photodynamic therapy: A clinical reality in the treatment of cancer, *Lancet Oncol.*, **2000**, 1, 212–219.
- 54 P. UEHLINGER, M. ZELLWEGER, G. WAGNIERES, L. JUILLERAT-JEANNERET, H. VAN DEN BERGH, N. LANGE, 5-Aminolevulinic acid and its derivatives: Physical chemical properties and protoporphyrin IX formation in cultured cells, *J. Photochem. Photobiol. B*, **2000**, 54, 72–80.
- 55 S. COLLAUD, A. JUZENIENE, J. MOAN, N. LANGE, On the selectivity of 5-aminolevulinic acid-induced protoporphyrin IX formation, *Curr. Med. Chem. Anti-Canc. Agents*, **2004**, 4, 301–316.
- 56 P. JICHLINSKI, Hexyl aminolevulinic fluorescence cystoscopy: A new diagnostic tool for photodiagnosis of superficial bladder cancer – a multicenter study, *J. Urol.*, **2003**, 170, 226–229.
- 57 V. MATZI, A. MAIER, O. SANKIN, J. LINDENMANN, P. REHAK, F. M. SMOLLE-JUTTNER, 5-Aminolevulinic acid compared to polyhematoporphyrin photosensitization for photodynamic therapy of malignant bronchial and esophageal stenosis: Clinical experience, *Photodiagn. Photodyn. Ther.*, **2004**, 1, 137–143.
- 58 J. SCHMIDBAUER, Improved detection of urothelial carcinoma in situ with hexaminolevulinic fluorescence cystoscopy, *J. Urol.*, **2004**, 171, 135–138.
- 59 A. SIERON, A. KAWCZYK-KRUPKA, M. A. W. CEBULA, M. SZYGULA, W. ZIELEZNIK, M. GRUK, B. SUWALA-JURCZYK, Photodynamic therapy (PDT) using topically applied [delta]-aminolevulinic acid (ALA) for the treatment of malignant skin tumors, *Photodiagn. Photodyn. Ther.*, **2004**, 1, 311–317.
- 60 C. FRITSCH, K. LANG, W. NEUSE, T. RUZICKA, P. LEHMANN, Photodynamic diagnosis and therapy in dermatology, *Skin Pharmacol. Appl. Skin Physiol.*, **1998**, 11, 358–373.
- 61 C. J. KELTY, N. J. BROWN, M. W. REED, R. ACKROYD, The use of 5-aminolevulinic acid as a photosensitizer in photodynamic therapy and photodiagnosis, *Photochem. Photobiol. Sci.*, **2002**, 1, 158–168.
- 62 S. JAIN, R. C. KOCKELBERGH, The role of photodynamic diagnosis in the contemporary management of superficial bladder cancer, *BJU Int.*, **2005**, 96, 17–21.
- 63 G. A. M. S. VAN DONGEN, G. W. M. VISSER, M. B. VROUENRAETS, Photosensitizer-antibody conjugates for detection and therapy of cancer, *Adv. Drug Deliv. Rev.*, **2004**, 56, 31–52.
- 64 M. A. D'HALLEWIN, A. R. KAMUHABWA, T. ROSKAMS, P. A. M. DE WITTE, L. BAERT, Hypericin-based fluorescence diagnosis of bladder carcinoma, *BJU Int.*, **2002**, 89, 760–763.
- 65 A. K. D'CRUZ, M. H. ROBINSON, M. A. BIEL, mTHPC-mediated photodynamic therapy in patients with advanced, incurable head and neck cancer: A multicenter study of 128

- patients, *Head Neck*, **2004**, *26*, 232–240.
- 66 C. HOPPER, A. KUBLER, H. LEWIS, I. B. TAN, G. PUTNAM, mTHPC-mediated photodynamic therapy for early oral squamous cell carcinoma, *Int. J. Cancer*, **2004**, *111*, 138–146.
- 67 A. MILLS, S. LE HUNTE, An overview of semiconductor photocatalysis, *J. Photochem. Photobiol. A*, **1997**, *108*, 35.
- 68 R. CAI, Y. KUBOTA, T. SHUIN, H. SAKAI, K. HASHIMOTO, A. FUJISHIMA, Induction of cytotoxicity by photoexcited TiO<sub>2</sub> particles, *Cancer Res.*, **1992**, *52*, 2346–2348.
- 69 Y. KUBOTA, T. SHUIN, C. KAWASAKI, M. HOSAKA, H. KITAMURA, R. CAI, H. SAKAI, K. HASHIMOTO, A. FUJISHIMA, Photokilling of T-24 human bladder cancer cells with titanium dioxide, *Br. J. Cancer*, **1994**, *70*, 1107–1111.
- 70 K. HOFFMANN, K. KASPAR, P. ALTMAYER, T. GAMBICHLER, UV transmission measurements of small skin specimens with special quartz cuvettes, *Dermatology*, **2000**, *201*, 307–311.
- 71 X. MICHALET, F. F. PINAUD, L. A. BENTOLILA, J. M. TSAY, S. DOOSE, J. J. LI, G. SUNDARESAN, A. M. WU, S. S. GAMBHIR, S. WEISS, Quantum dots for live cells, in vivo imaging, and diagnostics, *Science*, **2005**, *307*, 538–544.
- 72 A. C. S. SAMIA, X. CHEN, C. BURDA, Semiconductor quantum dots for photodynamic therapy, *J. Am. Chem. Soc.*, **2003**, *125*, 15736–15737.
- 73 R. BAKALOVA, H. OHBA, Z. ZHELEV, M. ISHIKAWA, Y. BABA, Quantum dots as photosensitizers?, *Nat. Biotechnol.*, **2004**, *22*, 1360–1361.
- 74 M. OZKAN, Quantum dots and other nanoparticles: What can they offer to drug discovery?, *Drug Discov. Today*, **2004**, *9*, 1065–1071.
- 75 X. GAO, Y. CUI, R. M. LEVENSON, L. W. K. CHUNG, S. NIE, In vivo cancer targeting and imaging with semiconductor quantum dots, *Nat. Biotechnol.*, **2004**, *22*, 969–976.
- 76 K. K. JAIN, Nanotechnology in clinical laboratory diagnostics, *Clin. Chim. Acta*, **2005**, *358*, 37–54.
- 77 R. BAKALOVA, H. OHBA, Z. ZHELEV, M. ISHIKAWA, Y. BABA, Quantum dot anti-CD conjugates: Are they potential photosensitizers or potentiators of classical photosensitizing agents in photodynamic therapy of cancer?, *Nano Lett.*, **2004**, *4*, 1567–1573.
- 78 A. M. DERFUS, W. C. W. CHAN, S. N. BHATIA, Probing the cytotoxicity of semiconductor quantum dots, *Nano Lett.*, **2004**, *4*, 11–18.
- 79 A. W. JENSEN, S. R. WILSON, D. I. SCHUSTER, Biological applications of fullerenes, *Bioorg. Med. Chem.*, **1996**, *4*, 767–779.
- 80 T. DA ROS, M. PRATO, Medicinal chemistry with fullerenes and fullerene derivatives, *Chem. Commun.*, **1999**, 663–669.
- 81 Y. YAMAKOSHI, N. UMEZAWA, A. RYU, K. ARAKANE, N. MIYATA, Y. GODA, T. MASUMIZU, T. NAGANO, Active oxygen species generated from photoexcited fullerene (C60) as potential medicines: O<sub>2</sub><sup>•-</sup> versus <sup>1</sup>O<sub>2</sub>, *J. Am. Chem. Soc.*, **2003**, *125*, 12803–12809.
- 82 J. MOAN, K. BERG, The photodegradation of porphyrins in cells can be used to estimate the lifetime of singlet oxygen, *Photochem. Photobiol.*, **1991**, *53*, 549–553.
- 83 J. MOAN, On the diffusion length of singlet oxygen in cells and tissues, *J. Photochem. Photobiol. B*, **1990**, *6*, 343–344.
- 84 H. LUI, L. HOBBS, W. D. TOPE, P. K. LEE, C. ELMETS, N. PROVOST, A. CHAN, H. NEYENDORFF, X. Y. SU, H. JAIN, I. HAMZAVI, D. MCLEAN, R. BISSENETTE, Photodynamic therapy of multiple nonmelanoma skin cancers with verteporfin and red light-emitting diodes: Two-year results evaluating tumor response and cosmetic outcomes, *Arch. Dermatol.*, **2004**, *140*, 26–32.
- 85 M. A. CAPELLA, L. S. CAPELLA, A light in multidrug resistance: Photodynamic treatment of multidrug-resistant tumors, *J. Biomed. Sci.*, **2003**, *10*, 361–366.
- 86 M. TREHAN, C. R. TAYLOR, Cutaneous photosensitivity and photoprotection for photodynamic therapy patients, in

- B. V. Calzavara-Pinton, R.-M. SZEIMIES, B. ORTEL (eds.), *Photodynamic Therapy and Fluorescence Diagnosis in Dermatology*, Elsevier, Amsterdam, The Netherlands, 2001, ch. 6.
- 87 G. JORI, Far-red-absorbing photosensitizers: Their use in the photodynamic therapy of tumours, *J. Photochem. Photobiol. A*, 1992, 62, 371–378.
- 88 M. OCHSNER, Light scattering of human skin: A comparison between zinc(II)-phthalocyanine and photofrin II(R), *J. Photochem. Photobiol. B*, 1996, 32, 3–9.
- 89 M. J. HAMMER-WILSON, C. H. SUN, M. GHAHRAMANLOU, M. W. BERNIS, In vitro and in vivo comparison of argon-pumped and diode lasers for photodynamic therapy using second-generation photosensitizers, *Lasers Surg. Med.*, 1998, 23, 274–280.
- 90 C. H. SIBATA, V. C. COLUSSI, N. L. OLEINICK, T. J. KINSELLA, Photodynamic therapy: A new concept in medical treatment, *Braz. J. Med. Biol. Res.*, 2000, 33, 869–880.
- 91 F. STEWART, P. BAAS, W. STAR, What does photodynamic therapy have to offer radiation oncologists (or their cancer patients)?, *Radiother. Oncol.*, 1998, 48, 233–248.
- 92 P. J. LOU, H. R. JAGER, L. JONES, T. THEODOSSY, S. G. BOWN, C. HOPPER, Interstitial photodynamic therapy as salvage treatment for recurrent head and neck cancer, *Br. J. Cancer*, 2004, 91, 441–446.
- 93 T. J. VOGL, K. EICHLER, M. G. MACK, S. ZANGOS, C. HERZOG, A. THALHAMMER, K. ENGELMANN, Interstitial photodynamic laser therapy in interventional oncology, *Eur. Radiol.*, 2004, 14, 1063–1073.
- 94 J. D. CHAPMAN, C. C. STOBBE, M. R. ARNFELD, R. SANTUS, J. LEE, M. S. MCPHEE, Oxygen dependency of tumor cell killing in vitro by light-activated Photofrin II, *Radiat. Res.*, 1991, 126, 73–79.
- 95 B. W. HENDERSON, V. H. FINGAR, Relationship of tumor hypoxia and response to photodynamic treatment in an experimental mouse tumor, *Cancer Res.*, 1987, 47, 3110–3114.
- 96 U. ISELE, K. SCHIEWECK, R. KESSLER, P. VAN HOOGVEST, H. G. CAPRARO, Pharmacokinetics and body distribution of liposomal zinc phthalocyanine in tumor-bearing mice: Influence of aggregation state, particle size, and composition, *J. Pharm. Sci.*, 1994, 84, 166–173.
- 97 F. RICCHELLI, Photophysical properties of porphyrins in biological membranes, *J. Photochem. Photobiol. B*, 1995, 29, 109–118.
- 98 R. BONNETT, B. D. DJELAL, A. NGUYEN, Physical and chemical studies related to the development of m-THPC (FOSCAN®) for the photodynamic therapy (PDT) of tumors, *J. Porphyrins Phthalocyanines*, 2001, 5, 652–661.
- 99 Y. N. KONAN, R. GURNY, E. ALLÉMAN, State of the art in the delivery of photosensitizers for photodynamic therapy, *J. Photochem. Photobiol. B*, 2002, 66, 89–106.
- 100 I. BRIGGER, C. DUBERNET, P. COUVREUR, Nanoparticles in cancer therapy and diagnosis, *Adv. Drug Deliv. Rev.*, 2002, 54, 631–651.
- 101 L. BRANNON-PEPPAS, J. O. BLANCHETTE, Nanoparticle and targeted systems for cancer therapy, *Adv. Drug Deliv. Rev.*, 2004, 56, 1649–1659.
- 102 D. C. HONE, P. I. WALKER, R. EVANS-GOWING, S. FITZGERALD, A. BEEBY, I. CHAMBRIER, M. J. COOK, D. A. RUSSEL, Generation of cytotoxic singlet oxygen via phthalocyanine-stabilized gold nanoparticles: A potential delivery vehicle for photodynamic therapy, *Langmuir*, 2002, 18, 2985–2987.
- 103 J. H. KIM, S. D. KWON, C. O. KIM, Adhesion of photosensitizer to ferrofluids for use in photodynamic therapy, *Nanotechnology*, 2002, 13, 610–614.
- 104 P. P. MACAROFF, D. M. OLIVEIRA, Z. G. M. LACAVA, E. C. D. LIMA, P. C. MORAIS, A. C. TEDESCO, Investigation of pheophorbide/magnetic fluid complex as a promising system for early cancer detection and treatment, *J. Appl. Phys.*, 2005, 97, 10Q906-1-3.

- 105 H. GU, K. XU, Z. YANG, C. K. CHANG, B. XU, Synthesis and cellular uptake of porphyrin decorated iron oxide nanoparticles-a potential candidate for bimodal anticancer therapy, *Chem. Commun.*, **2005**, 4270–4272.
- 106 J. F. HAINFELD, D. N. SLATKIN, H. M. SMILOWITZ, The use of gold nanoparticles to enhance radiotherapy in mice, *Phys. Med. Biol.*, **2004**, *49*, N309–N315.
- 107 Y. ZHANG, N. KOHLER, M. ZHANG, Surface modification of superparamagnetic magnetite nanoparticles and their intracellular uptake, *Biomaterials*, **2002**, *23*, 1553–1561.
- 108 O. BOMATI-MIGUEL, M. P. MORALES, P. TARTAJ, J. RUIZ-CABELLO, P. BONVILLE, M. SANTOS, X. ZHAO, S. VEINTEMILLAS-VERDAGUER, Fe-based nanoparticulate metallic alloys as contrast agents for magnetic resonance imaging, *Biomaterials*, **2005**, *26*, 5695–5703.
- 109 A. ITO, M. SHINKAI, H. HONDA, T. KOBAYASHI, Medical application of functionalized magnetic nanoparticles, *J. Biosci. Bioeng.*, **2005**, *100*, 1–11.
- 110 P. REIMER, T. BALZER, Ferucarbotran (Resovist): A new clinically approved RES-specific contrast agent for contrast-enhanced MRI of the liver: Properties, clinical development, and applications, *Eur. Radiol.*, **2003**, *13*, 1266–1276.
- 111 A. F. KOPP, M. LANIADO, F. DAMMANN, W. STERN, E. GRONEWALLER, T. BALZER, C. SCHIMPFKY, C. D. CLAUSSEN, MR imaging of the liver with Resovist: Safety, efficacy, and pharmacodynamic properties, *Radiology*, **1997**, *204*, 749–756.
- 112 H. H. WEETALL, Storage stability of water-insoluble enzymes covalently coupled to organic and inorganic carriers, *Biochim. Biophys. Acta*, **1970**, *212*, 1–7.
- 113 I. ROY, T. Y. OHULCHANSKY, H. E. PUDAVAR, E. J. BERGEY, A. R. OSEROFF, J. MORGAN, T. J. DOUGHERTY, P. N. PRASAD, Ceramic-based nanoparticles entrapping water-insoluble photosensitizing anticancer drugs: A novel drug-carrier system for photodynamic therapy, *J. Am. Chem. Soc.*, **2003**, *125*, 7860–7865.
- 114 T. K. JAIN, I. ROY, T. K. DE, A. MAITRA, Nanometer silica particles encapsulating active compounds: A novel ceramic drug carrier, *J. Am. Chem. Soc.*, **1998**, *120*, 11 092–11 095.
- 115 S. WANG, R. GAO, F. ZHOU, M. SELKE, Nanomaterials and singlet oxygen photosensitizers: Potential applications in photodynamic therapy, *J. Mater. Chem.*, **2004**, *14*, 487–493.
- 116 F. YAN, R. KOPELMAN, The embedding of meta-tetra(hydroxyphenyl)-chlorin into silica nanoparticle platforms for photodynamic therapy and their singlet oxygen production and pH-dependent optical properties, *Photochem. Photobiol.*, **2003**, *78*, 587–591.
- 117 W. TANG, H. XU, R. KOPELMAN, M. A. PHILBERT, Photodynamic characterization and in vitro application of methylene blue-containing nanoparticle platforms paragraph sign, *Photochem. Photobiol.*, **2005**, *81*, 242–249.
- 118 D. LUO, E. HAN, N. BELCHEVA, W. M. SALTZMAN, A self-assembled, modular DNA delivery system mediated by silica nanoparticles, *J. Controlled Release*, **2004**, *95*, 333–341.
- 119 D. J. BHARALI, I. KLEJBOR, E. K. STACHOWIAK, P. DUTTA, I. ROY, N. KAUR, E. J. BERGEY, P. N. PRASAD, M. K. STACHOWIAK, Organically modified silica nanoparticles: A nonviral vector for in vivo gene delivery and expression in the brain, *Proc. Natl. Acad. Sci. U.S.A.*, **2005**, *102*, 11 539–11 544.
- 120 M. CHEN, A. VON MIKECZ, Formation of nucleoplasmic protein aggregates impairs nuclear function in response to SiO<sub>2</sub> nanoparticles, *Exp. Cell Res.*, **2005**, *305*, 51–62.
- 121 K. PETERS, R. E. UNGER, C. J. KIRKPATRICK, A. M. GATTI, E. MONARI, Effects of nano-scaled particles on endothelial cell function in vitro: Studies on viability, proliferation and inflammation, *J. Mater. Sci. Mater. Med.*, **2004**, *15*, 321–325.
- 122 M. J. MORENO, E. MONSON, R. G.



- REDDY, A. REHEMTULLA, B. D. ROSS, M. PHILBERT, R. J. SCHNEIDER, R. KOPELMAN, Production of singlet oxygen by Ru(dpp(SO<sub>3</sub>)<sub>2</sub>)<sub>3</sub> incorporated in polyacrylamide PEBBLES, *Sens. Actuators, B*, **2003**, 90, 82–89.
- 123 R. KOPELMAN, Y. E. L. KOO, M. PHILBERT, B. A. MOFFAT, G. R. REDDY, P. MCCONVILLE, D. E. HALL, T. L. CHENEVERT, M. S. BHOJANI, S. M. BUCK, A. REHEMTULLA, B. D. ROSS, Multifunctional nanoparticle platforms for in vivo MRI enhancement and photodynamic therapy of a rat brain cancer, *J. Magn. Magn. Mater.*, **2005**, 293, 404–410.
- 124 A. M. GATTI, F. RIVASI, Biocompatibility of micro- and nanoparticles. Part I: In liver and kidney, *Biomaterials*, **2002**, 23, 2381–2387.
- 125 E. ALLÉMANN, R. GURNY, E. DOELKER, Drug-loaded nanoparticles – Preparation methods and drug targeting issues, *Eur. J. Pharm. Biopharm.*, **1993**, 39, 173–191.
- 126 P. COUVREUR, C. DUBERNET, F. PUISIEUX, Controlled drug-delivery with nanoparticles – Current possibilities and future-trends, *Eur. J. Pharm. Biopharm.*, **1995**, 41, 2–13.
- 127 M. J. ALONSO, Nanoparticulate drug carrier technology, *Drugs Pharm. Sci.*, **1996**, 77, 203–242.
- 128 C. VAUTHIER, C. DUBERNET, E. FATTAL, H. PINTO-ALPHANDARY, P. COUVREUR, Poly(alkylcyanoacrylates) as biodegradable materials for biomedical applications, *Adv. Drug Deliv. Rev.*, **2003**, 55, 519–548.
- 129 A. LABIB, V. LENAERTS, F. CHOUINARD, J. C. LEROUX, R. OUELLET, J. E. VAN LIER, Biodegradable nanospheres containing phthalocyanines and naphthalocyanines for targeted photodynamic tumor therapy, *Pharm. Res.*, **1991**, 8, 1027–1031.
- 130 V. LENAERTS, A. LABIB, F. CHOUINARD, J. ROUSSEAU, H. ALI, J. VAN LIER, J. E. VAN LIER, Nanocapsules with a reduced liver uptake: Targeting of phthalocyanines to EMT-6 mouse mammary tumour in vivo, *Eur. J. Pharm. Biopharm.*, **1995**, 41, 38–43.
- 131 N. BRASSEUR, D. BRAULT, P. COUVREUR, Adsorption of hemato-porphyrin onto polyalkylcyanoacrylate nanoparticles: Carrier capacity and drug release, *Int. J. Pharm.*, **1991**, 70, 129–135.
- 132 S. STEINIGER, S. E. GELPERINA, I. N. SKIDAN, A. I. BOBRUSKIN, S. E. SEVERIN, J. KREUTER, Optimization of photosensitizer pharmacokinetics with biodegradable nanoparticles, *Proceedings – 28th International Symposium on Controlled Release of Bioactive Materials and 4th Consumer & Diversified Products, San Diego, CA, United States, Controlled Release Society, Minneapolis*, **2001**.
- 133 B. ZHAO, J. XIE, J. ZHAO, A novel water-soluble nanoparticles of hypocrellin B and their interaction with a model protein: C-phycoyanin, *Biochim. Biophys. Acta*, **2004**, 1670, 113–120.
- 134 Y. N. KONAN, R. CERNY, J. FAVET, M. BERTON, R. GURNY, E. ALLÉMANN, Preparation and characterization of sterile sub-200 nm meso-tetra(4-hydroxyphenyl)porphyrin-loaded nanoparticles for photodynamic therapy, *Eur. J. Pharm. Biopharm.*, **2003**, 55, 115–124.
- 135 Y. N. KONAN, J. CHEVALLIER, R. GURNY, E. ALLÉMANN, Encapsulation of p-THPP into nanoparticles: Cellular uptake, subcellular localization and effect of serum on photodynamic activity, *Photochem. Photobiol.*, **2003**, 77, 638–644.
- 136 Y. N. KONAN, M. BERTON, R. GURNY, E. ALLÉMANN, Enhanced photodynamic activity of meso-tetra(4-hydroxyphenyl)porphyrin by incorporation into sub-200 nm nanoparticles, *Eur. J. Pharm. Sci.*, **2003**, 18, 241–249.
- 137 A. VARGAS, B. PEGAZ, E. DEBEFVE, Y. N. KONAN-KOUAKOU, N. LANGE, J. P. BALLINI, H. VAN DEN BERGH, R. GURNY, F. DELIE, Improved photodynamic activity of porphyrin loaded into nanoparticles: An in vivo evaluation using chick embryos, *Int. J. Pharm.*, **2004**, 286, 131–145.
- 138 B. PEGAZ, E. DEBEFVE, F. BORLE, J. P.

- BALLINI, H. VAN DEN BERGH, Y. N. KOUAKOU-KONAN, Encapsulation of porphyrins and chlorins in biodegradable nanoparticles: The effect of dye lipophilicity on the extravasation and the photothrombic activity. A comparative study, *J. Photochem. Photobiol. B*, **2005**, *80*, 19–27.
- 139 E. ALLÉMANN, N. BRASSEUR, O. BENREZZAK, J. ROUSSEAU, S. V. KUDREVICH, R. W. BOYLE, J. C. LEROUX, R. GURNY, J. E. VAN LIER, PEG-coated poly(lactic acid) nanoparticles for the delivery of hexadecafluoro zinc phthalocyanine to EMT-6 mouse mammary tumours, *J. Pharm. Pharmacol.*, **1995**, *47*, 382–387.
- 140 E. ALLÉMANN, J. ROUSSEAU, N. BRASSEUR, S. V. KUDREVICH, K. LEWIS, J. E. VAN LIER, Photodynamic therapy of tumours with hexadecafluoro zinc phthalocyanine formulated in PEG-coated poly(lactic acid) nanoparticles, *Int. J. Cancer*, **1996**, *66*, 821–824.
- 141 Y. N. KONAN-KOUAKOU, R. BOCH, R. GURNY, E. ALLÉMANN, In vitro and in vivo activities of verteporfin-loaded nanoparticles, *J. Controlled Release*, **2005**, *103*, 83–91.
- 142 O. BOURDON, V. MOSQUEIRA, P. LEGRAND, J. BLAIS, A comparative study of the cellular uptake, localization and phototoxicity of meta-tetra(hydroxyphenyl) chlorin encapsulated in surface-modified submicronic oil/water carriers in HT29 tumor cells, *J. Photochem. Photobiol. B*, **2000**, *55*, 164–171.
- 143 O. BOURDON, I. LAVILLE, D. CARREZ, A. CROISY, Ph. FEDEL, A. KASSELORI, P. PROGNON, P. LEGRAND, J. BLAIS, Biodistribution of meta-tetra(hydroxyphenyl)chlorin incorporated into surface-modified nanocapsules in tumor-bearing mice, *Photochem. Photobiol. Sci.*, **2002**, *1*, 709–714.
- 144 J. FU, X. Y. LI, D. K. P. NG, C. WU, Encapsulation of phthalocyanines in biodegradable poly(sebacic anhydride) nanoparticles, *Langmuir*, **2002**, *18*, 3843–3847.
- 145 P. P. S. LEE, T. NGAI, J.-D. HUANG, C. WU, W.-P. FONG, D. K. P. NG, Synthesis, characterization, biodegradation, and in vitro photodynamic activities of silicon(IV) phthalocyanines conjugated axially with poly( $\epsilon$ -caprolactone), *Macromolecules*, **2003**, *36*, 7527–7533.
- 146 R. H. MÜLLER, K. H. WALLIS, S. D. TRÖSTER, J. KREUTER, In vitro characterization of poly(methylmethacrylate) nanoparticles and correlation to their in vivo fate, *J. Controlled Release*, **1992**, *20*, 237–246.
- 147 G. BORCHARD, J. KREUTER, Interaction of serum components with poly(methyl methacrylate) nanoparticles and the resulting body distribution after intravenous injection in rats, *J. Drug Target.*, **1993**, *1*, 15–19.
- 148 J. C. LEROUX, P. GRAVEL, L. BALANT, B. VOLET, B. M. ANNER, E. ALLÉMANN, E. DOELKER, R. GURNY, Internalization of poly(D,L-lactic acid) nanoparticles by isolated human leukocytes and analysis of plasma proteins adsorbed onto the particles, *J. Biomed. Mater. Res.*, **1994**, *28*, 471–481.
- 149 L. NOBS, F. BUCHEGER, R. GURNY, E. ALLÉMANN, Current methods for attaching targeting ligands to liposomes and nanoparticles, *J. Pharm. Sci.*, **2004**, *93*, 1980–1992.
- 150 C. S. BETZ, J. P. LAI, W. XIANG, P. JANDA, P. HEINRICH, H. STEPP, R. BAUMGARTNER, A. LEUNIG, In vitro photodynamic therapy of nasopharyngeal carcinoma using 5-aminolevulinic acid, *Photochem. Photobiol. Sci.*, **2002**, *1*, 315–319.
- 151 B. M. AVELINE, T. HASAN, R. W. REDMOND, The effects of aggregation, protein binding and cellular incorporation on the photophysical properties of benzoporphyrin derivative monoacid ring A (BPDMA), *J. Photochem. Photobiol. B*, **1995**, *30*, 161–169.
- 152 R. RAGHUVANSHI, Y. KATARE, K. LALWANI, M. ALI, O. SINGH, A. PANDA, Improved immune response from biodegradable polymer particles entrapping tetanus toxoid by use of different immunization protocol and

- adjuvants 585, *Int. J. Pharm.*, **2002**, 245, 109.
- 153 P. JANI, G. W. HALBERT, J. LANGRIDGE, A. T. FLORENCE, Nanoparticle uptake by the rat gastrointestinal mucosa: Quantitation and particle size dependency, *J. Pharm. Pharmacol.*, **1990**, 42, 821–826.
- 154 A. VARGAS, R. GURNY, F. DELIE, Photosensitizer-loaded nanoparticles: A strategy to enhance the vascular occlusion in response to photodynamic therapy, *Proceedings – 32nd Annual Meeting & Exposition of the Controlled Release Society, Miami Beach, FL, United States*, **2005**.
- 155 R. BACHOR, C. R. SHEA, R. GILLES, T. HASAN, Photosensitized destruction of human bladder carcinoma cells treated with chlorin  $e_6$ -conjugated microspheres, *Proc. Natl. Acad. Sci. U.S.A.*, **1991**, 88, 1580–1584.
- 156 K. BERG, J. C. MAZIERE, M. GEZE, R. SANTUS, Verapamil enhances the uptake and the photocytotoxic effect of PII, but not that of tetra(4-sulfonatophenyl)porphine, *Biochim. Biophys. Acta*, **1998**, 1370, 317–324.
- 157 A. A. ROSENKRANZ, D. A. JANS, A. S. SOBOLEV, Targeted intracellular delivery of photosensitizers to enhance photodynamic efficiency, *Immunol. Cell Biol.*, **2000**, 78, 452–464.
- 158 K. BERG, K. MADSLIEN, J. C. BOMMER, R. OFTEBRO, J. W. WINKELMAN, J. MOAN, Light induced relocalization of sulfonated meso-tetraphenylporphines in NHIK 3025 cells and effects of dose fractionation, *Photochem. Photobiol.*, **1991**, 53, 203–210.
- 159 S. R. WOOD, J. A. HOLROYD, S. B. BROWN, The subcellular localization of Zn(II) phthalocyanines and their redistribution on exposure to light, *Photochem. Photobiol.*, **1997**, 65, 397–402.
- 160 C. ABELS, Targeting of the vascular system of solid tumours by photodynamic therapy (PDT), *Photochem. Photobiol. Sci.*, **2004**, 3, 765–771.
- 161 N. LANGE, J. P. BALLINI, G. WAGNIERES, H. VAN DEN BERGH, A new drug-screening procedure for photosensitizing agents used in photodynamic therapy for CNV, *Invest. Ophthalmol. Vis. Sci.*, **2001**, 42, 38–46.
- 162 A. M. RICHTER, S. YIP, E. WATERFIELD, P. M. LOGAN, Mouse skin photosensitization with benzoporphyrin derivative and photofrin: Macroscopic and microscopic evaluation, *Photochem. Photobiol.*, **1991**, 53, 281–286.
- 163 W. M. SHARMAN, C. M. ALLEN, J. E. VAN LIER, Photodynamic therapeutics: Basic principles and clinical applications, *Drug Discov. Today*, **1999**, 4, 507–517.
- 164 T. J. DOUGHERTY, An update on photodynamic therapy applications, *J. Clin. Laser Med. Surg.*, **2002**, 20, 3–7.
- 165 C. A. MORTON, S. B. BROWN, S. COLLINS, S. IBBOTSON, H. JENKINSON, H. KURWA, K. LANGMACK, K. MCKENNA, H. MOSELEY, A. D. PEARSE, M. STRINGER, D. K. TAYLOR, G. WONG, L. E. RHODES, Guidelines for topical photodynamic therapy: Report of a workshop of the British Photodermatology Group, *Br. J. Dermatol.*, **2002**, 146, 552–567.

### 3

## Nanoparticles for Neutron Capture Therapy of Cancer

*Hideki Ichikawa, Hiroyuki Tokumitsu, Masahito Miyamoto, and Yoshinobu Fukumori*

### 3.1

#### Introduction

Conventional radiotherapy using X-rays or  $\gamma$ -rays has been applied to cancer treatment due to its non-invasive methodology. However, some types of tumor are radioresistive; even if radiosensitive, the radiation dose that can be delivered to the tumor is limited by the tolerance of surrounding normal tissues within the treatment volume. In addition, some special techniques are required to treat tumors in deeper parts of the body or in organs because the radiation dose is in general highest on the surface of the body. In particle radiotherapy using beams of accelerated protons or carbon nuclei, the dose has the Brag peak, i.e., becomes maximal at the depth depending on the energy of the particles. Despite this benefit of particle radiotherapy, the dose is also limited by the tolerance of surrounding normal tissues within the treatment volume. Targeting radiotherapy uses radioactive isotopes that can be selectively targeted to tumor after injection, but special attention has to be paid to handling of the radioactive isotopes.

This chapter describes neutron capture therapy (NCT), a new radiotherapy that differs from the conventional radiotherapies described above. Coderre and Morris have reviewed the radiation biology of boron neutron capture therapy (BNCT), including the biodistribution of currently used boron compounds, in detail, but they limited the coverage to BNCT [1]. Consequently, the present chapter also covers gadolinium neutron capture therapy (GdNCT), and drug delivery issues in BNCT and GdNCT are discussed with special focus on the roles of nanoparticle technology. Section 3.2 explains the principle of NCT, and Section 3.3 reviews the present status of BNCT, including two boron compounds clinically used at present and past investigations on their nanoparticulate delivery systems. Section 3.4 deals with the approaches to GdNCT carried out so far, including a detailed account of the present authors' experiences in developing Gd-containing lipid nanoemulsions and chitosan nanoparticles to demonstrate the usefulness of nanoparticle technology in NCT.

**Tab. 3.1.** Neutron capture cross section of typical atoms.

Atom	Cross section (barn)	Reaction
$^{16}\text{O}$	0.00019	
$^{12}\text{C}$	0.0035	
$^1\text{H}$	0.333	$^1\text{H}(\text{n}, \gamma)^2\text{H}$
$^{14}\text{N}$	1.83	$^{14}\text{N}(\text{n}, \text{p})^{14}\text{C}$
$^{10}\text{B}$	3840	$^{10}\text{B}(\text{n}, \alpha)^7\text{Li}$
$^{157}\text{Gd}$	254000	$^{157}\text{Gd}(\text{n}, \gamma)^{158}\text{Gd}$

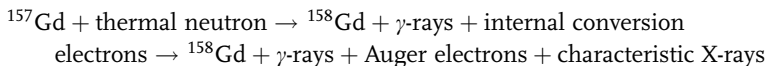
### 3.2

#### Principle of Neutron Capture Therapy of Cancer

NCT is a cancer therapy that utilizes the radiations emitted *in vivo* as a result of the nuclear neutron capture reaction (NCR) between radiation-producing agents administered in the body and thermal or epithermal neutrons irradiated from outside of the body. NCT is a binary treatment system, consisting of dosing the radiation-producing agents and neutrons. Neutrons have in general been classified according to their energies,  $E$ , as thermal neutrons ( $E < 0.4$  eV), epithermal neutrons ( $0.4$  eV  $< E < 10$  keV), and fast neutrons ( $E > 10$  keV) [1]. Table 3.1 shows the NCRs and neutron capture cross sections of typical elements [1]. Commonly existing O, C, H and N in the body or tissues have small cross sections, but boron ( $^{10}\text{B}$ ) and gadolinium ( $^{157}\text{Gd}$ ) have extremely large cross sections.

The most common radiation-producing element for NCT is  $^{10}\text{B}$  at present [2]. In clinical experiences, NCT with  $^{10}\text{B}$  (BNCT) has achieved encouraging results using the mercaptoundecahydro-*closo*-dodecaborate dianion ( $[\text{B}(12)\text{H}(11)\text{SH}]^{2-}$ , BSH) in patients with grades III–IV glioma and using the boronophenylalanine (BPA) in patients with malignant melanoma (Fig. 3.1). In BNCT, the  $^{10}\text{B}$  compounds administered have to be delivered to tumor intracellularly to obtain an antitumor effect, because  $^{10}\text{B}$  emits  $\alpha$ -particles whose range is nearly equal (9  $\mu\text{m}$ ) to a cell diameter or shorter [3]: success in clinical BNCT trials depends on the selective accumulation of  $^{10}\text{B}$  compounds into individual tumor cells.

$^{157}\text{Gd}$  causes the following neutron capture reaction by thermal neutron irradiation [4]:



$^{157}\text{Gd}$  NCR (Gd-NCR) results in emission of long-range prompt  $\gamma$ -rays, internal conversion electrons, X-rays and Auger electrons with a large total kinetic energy (7.94 MeV) [4]. The  $\gamma$ -rays and the electrons thus generated provide a tumor-killing

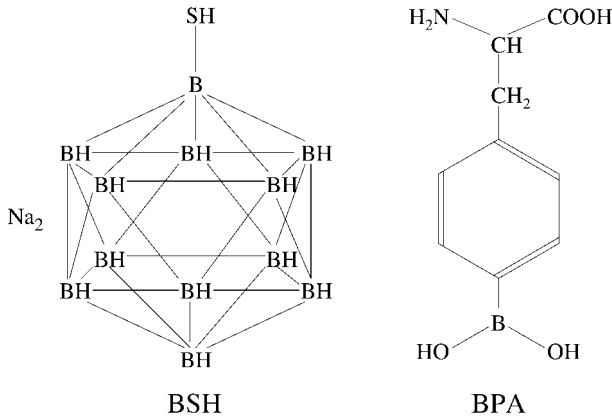


Fig. 3.1. Compounds in clinical use for BNCT.

effect [5, 6]. GdNCT has the following theoretical and possible advantages over typical BNCT: (a)  $^{157}\text{Gd}$  has the highest thermal neutron capture cross section (254 000 barns) among naturally occurring isotopes,  $66\times$  larger than that of  $^{10}\text{B}$  [7]; (b) the  $\gamma$ -rays released by Gd-NCR have a long range ( $>100\ \mu\text{m}$ ) in contrast with the  $\alpha$ -particles, so that they may extensively affect tumors even if Gd exists extracellularly in tumor tissue [8]; (c) Auger electrons with a short-range and high linear energy transfer may lead to a local and intensive execution of DNA in neoplastic cells [9]; (d) since Gd has been used as a magnetic resonance imaging (MRI) diagnostic agent [10, 11], it will be possible in future to integrate GdNCT with MRI diagnosis by using Gd-loaded dosage forms.

NCT has certain advantages over traditional cancer chemotherapy. Unlike chemotherapy that uses antitumor drugs, NCT does not need to use pharmacologically active substances in a traditional sense, since it is the neutron capture element itself that contributes to tumor inactivation. Therefore, a large amount of the radiosensitizer can be administered, provided the elements are modified so as to be non-toxic compounds. Thus, severe side effects, which are often experienced in cancer chemotherapy, are not a major concern in NCT.

### 3.3

#### Boron Neutron Capture Therapy

##### 3.3.1

##### Boron Compounds

NCT was first postulated by Locher in 1936 [12]. The earliest clinical treatments of malignant glioma were carried out at the Brookhaven National Laboratory in 1951–1961, and the Massachusetts Institute of Technology in 1959–1961, but no success-

ful result could be obtained, possibly because of the poor tumor-selectivity of the compounds used. Thereafter, many boron compounds have been synthesized for this purpose and their potential to accumulate boron in tumors has been evaluated. However, most compounds could not be used clinically due to chemical instability and toxicity even if they would exhibit a high tumor accumulation. Nonetheless, two compounds, i.e., BSH and BPA (Fig. 3.1), were found to be applicable to clinical treatment.

Hatanaka et al. at Teikyo University, Japan, started clinical trials on brain tumors by using BSH in 1968 [13–15]. They reported one case where a brain tumor seemed to be completely treated. Thereafter, they have employed BNCT for over 200 patients to date. In 1987 Mishima et al. at Kobe University, Japan, also began BNCT of malignant melanoma, subsequently reporting 18 excellent, almost completely treated, results in the treatment of 22 patients [16, 17].

BSH and BPA are the only boron compounds that can be applied to clinical trials at present. They are intravenously (i.v.) administered only as solutions; however, the selectivity in tumor accumulation has to be increased to gain a more efficient treatment outcome. Consequently, new compounds having a high potential for selective tumor-accumulation are still actively sought [18].

BNCT of melanoma has been carried out clinically as follows. Fukuda et al. in Mishima's group have analyzed the neutron dose in 22 melanoma patients with primary or metastatic melanomas who received BPA and subsequently underwent BNCT [19]. The blood concentration in nine patients receiving  $179.7 \pm 14.9$  mg-BPA per kg body weight (BW) increased with time during i.v. infusion, peaked at the end of administration and decreased thereafter. The peak values at the end of administration were  $9.4 \pm 2.6$   $\mu\text{g}^{-10}\text{B}$  per gram of blood, and half-lives for the initial and second components of the blood clearance were 2.8 and 9.2 h, respectively. Skin concentrations in ten patients varied from case to case; however, skin-to-blood (Sk/B) ratios were relatively constant at  $1.31 \pm 0.22$  during the 6 h after the end of administration. Boron concentrations in the tumors resected from the seven patients who were operated on decreased in parallel with the blood values, the tumor-to-blood (T/B) ratio being relatively constant at  $3.40 \pm 0.83$ . Based on these analytical data of BPA pharmacokinetics, they optimized the timing of irradiation and the setting of the neutron flux large enough for tumor eradication but still tolerable for normal skin.

### 3.3.2

#### **Delivery of Boron Using Nanoparticles**

Drug delivery system (DDS) is most often associated with fine particulate carriers, such as emulsion, liposomes and nanoparticles, which are designed to localize drugs in the target site. They have actively been studied as injectable devices that may enhance therapeutic potency and reduce side effects. From a clinical viewpoint, they might have to be biodegradable and/or highly biocompatible. In addition, high drug content is desirable, because in many cases actual drug-loading efficiency is often too low to secure an effective dose at the target site. Biodegradable

liposomes have received considerable attention as potent vehicles for targeting a site and controlled release of a drug.

The successful treatment of cancer by BNCT requires the selective, very high concentration of  $^{10}\text{B}$  within malignant tumors. To achieve this, many approaches relating to the liposomal delivery of boron have been carried out [20–51]. The results from typical studies are described in the following.

Shelly et al. [40] have carried out model studies on  $^{10}\text{B}$  delivery to murine tumors with small unilamellar liposomes of 70 nm or less in tumor-bearing mice. The liposomes were composed of a pure synthetic phospholipid (distearoyl phosphatidylcholine) and cholesterol, encapsulating high concentrations of water-soluble ionic boron-rich compounds, with hydrolytically stable borane anions such as  $[\text{B}(20)\text{H}(18)]^{2-}$ . Unlike the boron compounds themselves, which exhibited no affinity for tumors and are normally rapidly cleared, liposomes selectively delivered the borane anions to tumors. The highest tumor concentrations after i.v. injection of the two isomers of  $[\text{B}(20)\text{H}(18)]^{2-}$  reached the therapeutic range ( $>15\ \mu\text{g-B}$  per g tumor) while maintaining high T/B ratios ( $>3$ ). The authors suggested that these boron compounds might have the capability to react with intracellular components after they had been deposited within tumor cells by the liposome, thereby preventing the borane ion from being released into blood.

Feakes et al. [41] in the same group have investigated the newly synthesized  $[\text{B}(20)\text{H}(17)\text{NH}(3)]^{3-}$  as a water-soluble boron-delivery agent. The  $[\text{ae-B}(20)\text{H}(17)\text{NH}(3)]^{3-}$  anion was encapsulated in liposomes prepared with 5% poly(ethylene glycol) (PEG)-2000–distearoyl phosphatidylethanolamine in the liposome membrane. As expected, these liposomes exhibited a longer circulation lifetime in the biodistribution experiment, resulting in the continued accumulation of boron in the tumor over the entire 48 h experiment, reaching a maximum of 47  $\mu\text{g-B}$  per g tumor.

Subsequently, these authors have synthesized the acylated nido-carborane species  $\text{K}[\text{nido-7-CH}_3(\text{CH}_2)_{15}\text{-7,8-C2B(9)H(11)}]$  for use as an addend for the bilayer membrane of liposomes [42]. Low injected doses of approximately 5–10 mg-B per kg BW afforded a peak tumor boron concentration of approximately 35  $\mu\text{g-B}$  per g tumor and a T/B boron ratio of approximately 8. These values are sufficiently high for the successful application of BNCT. Further, the incorporation of both hydrophilic and hydrophobic species within the same liposomes demonstrated significantly enhanced biodistribution characteristics, as exemplified by the maximum tumor boron concentration of approximately 50  $\mu\text{g-B}$  per g tumor and a T/B ratio of approximately 6. The same authors have also synthesized the thiol derivative [43]. At low i.v. injected doses, the tumor boron concentration increased throughout the time-course experiment, resulting in a maximum observed boron concentration of 46.7  $\mu\text{g-B}$  per g tumor at 48 h and a T/B boron ratio of 7.7. They also reported that the most favorable results were obtained with the polyhedral borane  $\text{Na}_3[\text{a2-B}(20)\text{H}(17)\text{NH}_2\text{CH}_2\text{CH}_2\text{NH}_2]$  [44]. Liposomes encapsulating this species produced a tumor boron concentration of 45  $\mu\text{g-B}$  per g tumor at 30 h post-injection, at which time the T/B ratio was 9.3.

Watson-Clark et al. have reported model studies directed toward the application



of BNCT to rheumatoid arthritis using the above liposomes incorporating K[nido-7-CH<sub>3</sub>(CH<sub>2</sub>)<sub>15-7,8</sub>-C<sub>2</sub>B(9)H(11)] as an addend in the lipid bilayer and encapsulated Na<sub>3</sub>[a<sub>2</sub>-B(20)H(17)NH<sub>2</sub>CH<sub>2</sub>CH<sub>2</sub>NH<sub>2</sub>] in the aqueous core [45]. With low i.v. injected doses of 13–18 mg-B per kg BW, the peak boron concentration observed in arthritic synovium was 29 µg-B per g tumor. The highest synovium/B ratio observed was 3.0, when the synovial boron concentration was 22 µg-B per g tumor.

Yanagie et al. have reported BNCT using <sup>10</sup>B entrapped anti-CEA (carcinoembryonic antigen) immunoliposome. A new murine monoclonal antibody (2C-8) was prepared by immunizing mice i.p. with a CEA-producing human pancreatic cancer cell line, AsPC-1 [46]. This anti-CEA monoclonal antibody was conjugated with large multilamellar liposomes incorporating BSH. AsPC-1 cells were incubated with the <sup>10</sup>B-Lip-MoAb (CEA) for 8 h. After irradiation with thermal neutrons (10<sup>11</sup>–10<sup>13</sup> neutrons cm<sup>-2</sup>), AsPC-1 cells showed decreasing uptake of <sup>3</sup>H-TdR compared with control group, indicating that the immunoliposomes could exert cytotoxic effect by thermal neutrons. Further, the boronated anti-CEA immunoliposome was applied to tumor cell growth inhibition in an *in vitro* BNCT model [47]. The liposomes were shown to bind selectively to cells bearing CEA on their surface. The immunoliposomes attached to tumor cells suppressed growth *in vitro* upon thermal neutron irradiation, and suppression was dependent upon the concentration of the <sup>10</sup>B compound in the liposomes and on the density of antibody conjugated to the liposomes. The cytotoxic effects of locally injected <sup>10</sup>B compound, multilamellar liposomes containing <sup>10</sup>B compound or <sup>10</sup>B immunoliposomes (anti-CEA) on human pancreatic carcinoma xenografts in nude mice have been evaluated with thermal neutron irradiation [48]. Injection of <sup>10</sup>B immunoliposomes caused the greatest tumor suppression with thermal neutron irradiation *in vivo*. Histopathologically, hyalinization and necrosis were found in boron-treated tumors, while tumor tissue injected with saline or saline-containing immunoliposomes showed neither destruction nor necrosis, suggesting that BNCT with intratumoral (i.t.) injection of immunoliposomes was able to destroy malignant cells in the marginal portion between normal tissues and cancer tissues.

Yanagie et al. have also extended the use of BNCT assisted by liposomal boron delivery to breast cancer [49]. In addition, they have employed neutron capture autoradiography (NCAR) of the sliced whole-body samples of tumor-bearing mice [50]. They obtained NCAR images for mice i.v. injected by <sup>10</sup>B-PEG liposome, <sup>10</sup>B-transferrin (TF)-PEG liposome, or <sup>10</sup>B-bare liposome. This study demonstrated the increased accumulation of <sup>10</sup>B atoms in the tumor tissues by binding PEG-chains to the surface of liposome, which increased retention in the blood flow and escaped phagocytosis by the reticuloendothelial system (RES).

Maruyama et al. have prepared unilamellar TF-PEG liposomes less than 200 nm in diameter for intracellular targeting of BSH to solid tumors [51]. When TF-PEG liposomes were injected at 35 mg-<sup>10</sup>B per kg BW, a prolonged residence time in the circulation and a low uptake by RES in Colon 26 tumor-bearing mice were observed. TF-PEG liposomes maintained a high <sup>10</sup>B level in the tumor with concentrations above 30 µg g<sup>-1</sup> for at least 72 h after injection, indicating that binding and

concomitant cellular uptake of the extravasated TF-PEG liposomes occurred by TF receptor and receptor-mediated endocytosis, respectively. On the other hand, the plasma level of  $^{10}\text{B}$  decreased, resulting in a tumor/plasma ratio of 6.0 at 72 h after injection. Administration of BSH encapsulated in TF-PEG liposomes at a dose of 5 or 20 mg- $^{10}\text{B}$  per kg BW and irradiation with  $2 \times 10^{12}$  neutrons  $\text{cm}^{-2}$  produced tumor growth suppression and improved long-term survival compared with controls. Thus, intravenous injection of TF-PEG liposomes could increase the tumor retention of  $^{10}\text{B}$  atoms, which were introduced by receptor-mediated endocytosis of liposomes after binding, causing tumor growth suppression *in vivo* upon thermal neutron irradiation.

Koning et al. have tried to target  $^{10}\text{B}$  to the tumor vasculature for NCT [24]. Alpha ( $\nu$ )-integrin specific RGD-peptides were coupled to liposomes that encapsulated BSH. These RGD-liposomes strongly associated with human umbilical vein endothelial cells (HUVEC) expressing this integrin and were internalized. Irradiation of RGD- $^{10}\text{B}$ -liposome-incubated HUVEC with neutrons strongly inhibited endothelial cell viability.

Low-density lipoproteins (LDLs) are internalized by the cell through receptor-mediated mechanisms. A boronated analogue of LDL has been synthesized for possible application in BNCT by Laster et al. [52]. The analogue was tested in cell culture for uptake and biological efficacy in the thermal neutron beam. The boron concentration found was  $10\times$  higher than that required in tumors for BNCT, 240  $\mu\text{g}\text{-}^{10}\text{B}$  per gram of cells.

### 3.4

#### Approaches to GdNCT

Therapeutic potential in GdNCT has been explored theoretically and experimentally [53–69]. Magnevist<sup>®</sup> (gadopentetate dimeglumine aqueous solution), an MRI contrast agent, has been most used as gadolinium source in GdNCT studies. Because of the lack of its targeting ability, however, an adequate amount of gadolinium required for an efficient therapeutic index could not be delivered through the i.v. route. In addition, even i.t. injection did not give rise to significantly prolonged retention of gadolinium in tumor tissues. Thus, a key for success in current GdNCT trails is the use of a device by which gadolinium can be delivered efficiently and retained in a high level inside tumor tissues and/or cells during thermal neutron irradiation. In addition, this may extend NCT to wider types of tumors. From these perspectives, the present authors have prepared delayed-release type ethyl cellulose-coated microcapsules containing gadopentetate dimeglumine for preliminary GdNCT trials [61]. GdNCT using the microcapsules demonstrated a significant effectiveness in survival time of the murine Ehrlich ascites tumor model [62]. This result, which first demonstrated the potential of GdNCT *in vivo*, led us develop a more elaborate gadolinium-loaded particulate system and to establish its potential application to GdNCT, as described below.

## 3.4.1

**Typical Research on GdNCT**

Hofmann et al. have reported GdNCT of melanoma cells and solid tumors with a neutral macrocyclic gadolinium complex (Gadobutrol), a magnetic resonance imaging contrast agent [53]. In mice, i.t. administration of 1.2 mmol-Gd per kg BW of the Gd complex, corresponding to about 23 000  $\mu\text{g-Gd}$  per mL of tumor, before neutron irradiation ( $3.6 \times 10^{12}$  neutrons  $\text{cm}^{-2}$ ) resulted in a significant delay in tumor growth with respect to control groups.

Kobayashi et al. have developed avidin-dendrimer-(1B4M-Gd)(254) (Av-G6Gd) as a tumor-targeting therapeutic agent for GdNCT of intraperitoneal disseminated tumor that can be monitored by MRI in order to deliver large quantities of Gd atoms into tumor cells [63]. An *in vitro* internalization study showed that Av-G6Gd accumulated and was internalized into SHIN3 cells, a human ovarian cancer, 50- and 3.5-fold greater than gadolinium diethylenetriaminepentaacetic acid (Gd-DTPA, Magnevist<sup>®</sup>) and G6Gd. The accumulation of Gd in the cells was also detected by the increased signal on T1-weighted MRI. Av-G6Gd showed specific accumulation in the SHIN3 tumor 366- and 3.4-fold greater than Gd-DTPA and G6Gd one day after intraperitoneal (i.p.) injection. Thus, a sufficient amount of Av-G6Gd (162 ppm of Gd) was accumulated and internalized into the SHIN3 cells *in vivo*.

De Stasio et al. have observed directly the microdistribution of Gd in cultured human glioblastoma cells exposed at 1–25 mg of Gd-DTPA per mL, corresponding to 300–7100  $\mu\text{g-Gd mL}^{-1}$  [64]. They demonstrated that Gd-DTPA penetrated the plasma membrane, and observed no deleterious effect on cell survival and a higher Gd accumulation in cell nuclei compared with cytoplasm. They also exposed Gd-containing cells to thermal neutrons ( $3.6 \times 10^{12}$  neutrons  $\text{cm}^{-2}$ ) and demonstrated the effectiveness of Gd-NCR in inducing cell death. However, the efficacy of Gd-DTPA and Gd-DOTA as GdNCT agents *in vivo* was predicted to be low due to the insufficient number of tumor cell nuclei incorporating Gd [65]. The authors then suggested that although multiple administration schedules *in vivo* might induce Gd penetration into more tumor cell nuclei, a search for new Gd compounds with higher nuclear affinity would be warranted before planning GdNCT in animal models or clinical trials.

Oyewumi and Mumper have used microemulsions (oil-in-water) as templates to engineer stable emulsifying wax or Brij 72 (polyoxyl 2 stearyl ether) nanoparticles [66]. The technique was simple, reproducible, and amenable to large-scale production of stable nanoparticles having diameters below 100 nm. The emulsifying wax and Brij 72 nanoparticles ( $2 \text{ mg mL}^{-1}$ ) made together with polyoxyl-20 stearyl ether and polysorbate 80, respectively, were the most stable based on retention of nanoparticle size over time. Gadolinium acetylacetonate (GdAcAc), a potential anti-cancer agent for NCT, was entrapped in the nanoparticles. Challenges of these cured nanoparticles in biologically relevant media at 37 °C for 60 min demonstrated that these nanoparticles were stable. The results showed the ease of preparation of these very small, stable nanoparticles and the ability to entrap lipophilic drugs such as GdAcAc with high efficiency.

Oyewumi's group further synthesized gadolinium hexanedione (GdH) by complexation of  $Gd^{3+}$  with hexane-2,4-dione as NCT agent, and a folate ligand by chemically linking folic acid to distearoylphosphatidylethanolamine (DSPE) through a PEG (MW 3350) spacer [67]. To obtain folate-coated nanoparticles, the folate ligand (0.75 to 15% w/w) was added either to the microemulsion templates at 60 °C or to nanoparticle suspensions at 25 °C. Cell uptake studies were carried out in KB cells (human nasopharyngeal epidermal carcinoma cell line), which are known to overexpress folate receptors. The uptake of folate-coated nanoparticles was about ten-fold higher than uncoated nanoparticles after 30 min at 37 °C. The uptake of folate-coated nanoparticles at 4 °C was 20-fold lower than the uptake at 37 °C and comparable to that of uncoated nanoparticles at 37 °C. Folate-mediated endocytosis was further verified by the inhibition of the uptake of folate-coated nanoparticles by free folic acid. Folate-coated nanoparticle uptake decreased to approximately 2% of its initial value with the co-incubation of 0.001 mM of free folic acid. The authors suggested that these tumor-targeted nanoparticles containing high concentrations of Gd may have potential for NCT. Thiamine was also effective as a tumor-specific ligand for gadolinium nanoparticles in a methotrexate-resistant breast cancer cell line, MTX(R)ZR75, transfected with thiamine transporter genes (THTR1 and THTR2) [68].

Using the folate-coated and PEG-coated gadolinium (Gd) nanoparticles, Oyewumi et al. carried out *in vivo* studies in KB tumor-bearing athymic mice [69]. Gd nanoparticles did not aggregate platelets or activate neutrophils. The retention of nanoparticles in the blood 8, 16 and 24 h post-injection of nanoparticles (1.6 mg-Gd per kg BW) was 60, 13 and 11% of the injected dose (ID), respectively. The maximum Gd tumor localization was  $33 \pm 7 \mu\text{g-Gd g}^{-1}$ . Both folate-coated and PEG-coated nanoparticles had comparable tumor accumulation. However, the cell uptake and tumor retention of folate-coated nanoparticles was significantly enhanced over PEG-coated nanoparticles. Thus, the folate-ligand coating shows beneficial facilitation of tumor cell internalization and retention of Gd-nanoparticles in the tumor tissue.

### 3.4.2

#### Delivery of Gadolinium using Lipid Emulsion (Gd-nanoLE)

##### 3.4.2.1 Preparation of Gd-nanoLE

Oil-in-water (o/w) emulsions stabilized with emulsifiers such as phospholipids have attracted much attention as drug carriers because they are biodegradable and biocompatible and, unlike liposomes, they can be prepared on an industrial scale and are relatively stable below 25 °C for long periods [70]. One problem with using emulsion particles as drug carriers is how they can leave the vascular space and reach their site of action. The extravascular transfer of particulate carriers largely depends on their size. A diameter of approximately 100 nm is the cut-off value for drug carriers able to pass through the discontinuous capillary endothelium of tumors [71]. In addition, drug carriers <100 nm are expected to more easily avoid uptake by RES and to circulate for longer periods in blood, as estimated from the

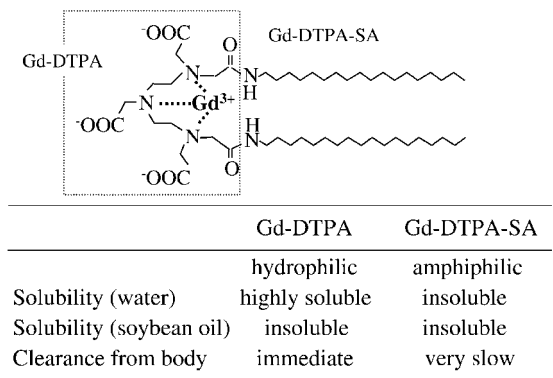


Fig. 3.2. Chemical structure and properties of Gd-DTPA-SA.

finding that small unilamellar liposomes of about 70–100 nm are cleared more slowly from the circulation than larger ones of the same composition [72].

The authors' first study on developing nanoparticulate systems for GdNCT was to prepare Gd-containing emulsions with reduced particle size, surface properties exhibiting prolonged blood retention, and a high gadolinium content [73]. As a Gd-source, a water-insoluble and oil-insoluble Gd-DTPA derivative, distearylamine (Gd-DTPA-SA) (Fig. 3.2), was synthesized. Gd-DTPA-SA has two hydrophobic tails (side-chains) consisting of stearyl amines that are connected to the Gd-DTPA moiety through amide linkages. It can be incorporated into the membrane of liposomal vesicles as a component of the liposomal lamella [74].

The particle structure is schematically shown in Fig. 3.3. Emulsions containing soybean oil, water, Gd-DTPA-SA, as an amphiphilic drug, and hydrogenated egg yolk phosphatidylcholine (HEPC), as an emulsifier, in a weight ratio of 7.36:92:1:2 were prepared by the thin-layer hydration method using a bath-type sonicator (Table 3.2). The mean particle size of the emulsions was 250 nm.

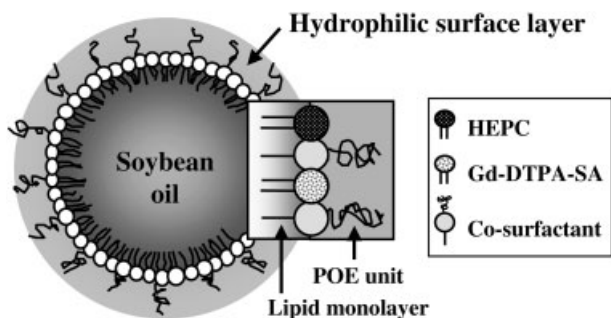


Fig. 3.3. Structure of Gd-nanoLP.

**Tab. 3.2.** Formulation, Gd content and particle size of the standard- and high-Gd-nanoLE.

	Formulation		
	Standard-Gd-nanoLE		High-Gd-nanoLE
	Plain	With co-surfactant	
HEPC <sup>[a]</sup> (mg)	500	500	250
Gd-DTPA-SA (mg)	250	250	500
Soybean oil (mL)	2	2	2
Co-surfactant <sup>[b]</sup> (mg)	–	750	750
Water (mL)	23	23	23
Gd-content <sup>[c]</sup> (mg mL <sup>-1</sup> )	–	1.5	3.0
Particle size (nm)	250	78	84

<sup>a</sup>L-Phosphatidylcholine hydrogenated from egg yolk.

<sup>b</sup>HCO-60.

<sup>c</sup>Theoretical Gd content.

To prepare o/w emulsions, oils other than the commonly used soybean oil have been employed. The particle size of triolein-emulsion (240 nm) was almost the same as that of soybean oil-emulsion. Lipiodol Ultra-Fluide<sup>®</sup> (Guerbert Laboratories, France) produced a mean droplet size of 195 nm. When castor oil (448 mPa s/25 °C; 262 mPa s/37 °C [75a]) with a higher viscosity was selected as an oil component, no emulsion could be prepared by the procedure used here, while stable emulsions could be prepared using oils with a lower viscosity such as soybean oil (49 mPa s/25 °C, 29 mPa s/37 °C [75a]), Lipiodol (37 mPa s/25 °C, 25 mPa s/37 °C [75a]) and ethyl oleate (4 mPa s/37 °C [75b]). The mean particle size of the emulsions seemed to be closely correlated to the viscosity of the oils: the particle size of the emulsions fell on reducing the viscosity of the oil. This indicated that oil viscosity is an important factor, influencing the particle size of the Gd-DTPA-SA emulsions. Despite this, soybean oil was used in this study because of its widespread application. To make the droplet size of the emulsions smaller than 100 nm, as well as to modify the emulsion surfaces, a co-surfactant, Tween<sup>®</sup> 80, HCO<sup>®</sup>-60, Pluronic<sup>®</sup> F68, polyoxyethylene alkyl ether (Brij<sup>®</sup>) or polyoxyethylene alkyl ester (Myrj<sup>®</sup>), was introduced into the standard system. Figure 3.4 shows the chemical structures of typical co-surfactants. Tween 80, HCO-60, Brij 76, 78 and 700 were effective in reducing the particle size to below 100 nm when the co-surfactant weight ratio (CWR), defined as co-surfactant/(HEPC+Gd-DTPA-SA) (w/w), was larger than 0.67. The particle size with Tween 80 and HCO-60 was reduced to 53 and 78 nm, respectively, at a CWR of 1.0 (w/w) (Table 3.2). To increase the gadoli-

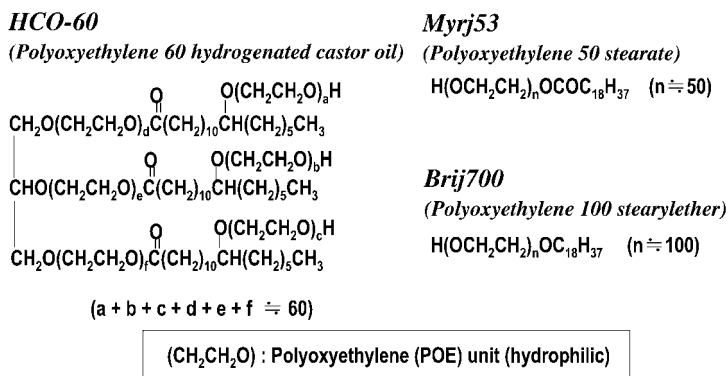


Fig. 3.4. Chemical structure of co-surfactants.

nium content, the weight ratio of Gd-DTPA-SA to HEPC was increased from 1:2 of the standard-Gd formulation to 2:1 of the high-Gd formulation (Table 3.2). The measured particle size of the HCO-60 high-Gd emulsions was 84 nm when the CWR was 1.0 (w/w). In this case, the calculated gadolinium content reached 3.0 mg-Gd mL<sup>-1</sup>. These results indicate that HCO-60 is an effective co-surfactant not only in terms of particle size reduction but also with respect to gadolinium enrichment.

#### 3.4.2.2 Biodistribution of Gadolinium after Intraperitoneal Administration of Gd-nanoLE

Tokuuye et al. have reported the effect of <sup>157</sup>Gd concentration on tumor inactivation in GdNCT [76]. The neutron fluence required for 10% survival of the Chinese hamster cells (V79) decreased rapidly between 0 and 100 μg-<sup>157</sup>Gd mL<sup>-1</sup>, but leveled off above that. This result indicates that the optimal tumor inactivation effect would be achieved around 100 μg-<sup>157</sup>Gd mL<sup>-1</sup>. To achieve this level *in vivo*, Gd-nanoLEs were i.p. administrated in Greene's melanotic melanoma (D<sub>1</sub>-179)-bearing hamsters as a model system and the biodistribution of gadolinium was investigated [77].

The inferior surface of the diaphragm is very rich in lymphatic capillaries. The lymphatic lumen is separated from the abdominal cavity by its own endothelium, a fenestrated basement membrane and the peritoneal mesothelium. Hirano and Hunt have reported that, at least in rats, most compounds of molecular weight smaller than 20 000 were exclusively absorbed via splenic or intestinal blood capillaries into the portal vein [78]. In contrast, the lymphatic system was a major absorption route for compounds with a molecular weight larger than 70 000 that were impermeable to blood capillary membranes. Klein et al. have reported that even particles administered through the abdominal cavity were transported through pores in the diaphragm directly to lymphatic and then to the venous system [79]. Thus, lymphatic capillaries could accommodate and transport large materials such

as erythrocytes of about 10  $\mu\text{m}$  in diameter [80] and particles with a diameter of up to 22  $\mu\text{m}$  [81]. Hirano and Hunt also reported that the use of liposomes 50–720 nm in diameter gave no size effect on absorption from the abdominal cavity [78]. These results suggested that almost all the emulsion particles so-prepared might have the potential to be absorbed through the lymphatic system.

For our *in vivo* experiments, a Greene's melanotic melanoma (D<sub>1</sub>-179) [82] fragment ( $2 \times 2 \times 2$  mm) was subcutaneously inoculated on the left thigh of Syrian hamster. The experiments were performed at 10 d after inoculation, when the diameter of the tumor mass became about 10 mm ( $0.81 \pm 0.60$  g) and the body weight was  $99.7 \pm 10.6$  g. Gd-DTPA derivative-containing lipid emulsion (Table 3.2) was i.p. injected at a dose of 2.0 mL per hamster (30 mg-Gd/kg BW for the standard-Gd formulation and 60 mg-Gd/kg BW for the high-Gd formulation). Tissue concentration was measured by inductively coupled plasma atomic emission spectroscopy (ICP-AES) at 355.047 nm.

**Effect of Co-surfactant** In addition to HCO-60, polyoxyethylene (POE) stearyl ether (Brij, C18POEm) and POE stearyl ester (Myrj, C18POEm') were also selected as co-surfactant to build up the steric hindrance on the emulsion particle surface. Figure 3.5 shows time-courses of gadolinium levels in blood and tumor after i.p. injection of Gd-DTPA-SA-containing plain, HCO-60, Myrj 53 (C18POE50) and Brij 700 (C18POE100) emulsions prepared in the standard-Gd formulation (Table 3.2). The Gd levels in blood (Fig. 3.5A) with the co-surfactant-containing emulsions were significantly higher than those with the plain emulsion. The gadolinium level in blood with the Brij 700 emulsion was prolonged during 12–48 h at the highest level. The high blood gadolinium level with Brij 700 emulsion is related to the stable nature of its ether linkage, in contrast to the ester linkage of the Myrj family (Fig. 3.4).

The Gd concentration in tumor with all emulsions leveled off 24 h after i.p. injection (Fig. 3.5B). Although the gadolinium level in tumor with the Myrj 53 emul-

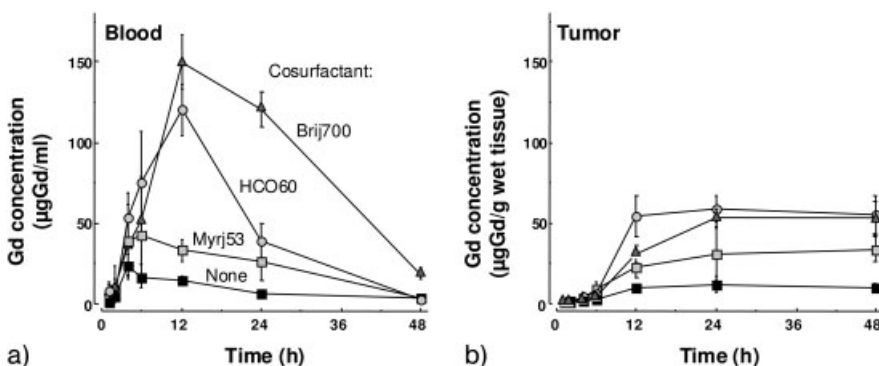


Fig. 3.5. Effect of co-surfactant on Gd distribution after i.p. injection of the standard Gd-nanoLE at 3 mg/2 mL. Data are represented as the mean  $\pm$  SD ( $n = 3-9$ ).



sion was 31  $\mu\text{g-Gd}$  per g tumor (wet) at 24 h, those with the HCO-60 and Brij 700 emulsions were 59  $\mu\text{g-Gd}$  per g tumor (wet) and 53  $\mu\text{g-Gd}$  per g tumor (wet) at 24 h, respectively. Although gadolinium retention in blood with the Brij 700 emulsion was prolonged at a higher level (Fig. 3.5A), the gadolinium level in tumor increased more slowly, and the final level was not higher than that with the HCO-60 emulsion (Fig. 3.5B). HCO-60 was the most effective co-surfactant for gadolinium accumulation in tumor.

The T/B ratio at 48 h was  $>2.8$  in every emulsion, reaching 21.4 with the HCO-60 emulsion. T/B with the Brij 700 emulsion was as low as that with the plain emulsion. This was related to the prolonged and higher blood gadolinium level. The T/Sk values with the Brij 700 and HCO-60 emulsions were larger than 6.0. Conversely, the Sk/B ratios at 24 h were low (0.05–0.5).

In NCT, thermal neutrons are irradiated from outside the body. As a result, the T/Sk ratio, T/B ratio and/or Sk/B ratio of radiation sensitizer (gadolinium or boron) concentration are important factors influencing in the therapeutic effects. For BNCT, Mishima [83a] and Honda et al. [83b] have reported that when  $^{10}\text{B}$ -BPA fructose complex was administered by the drip infusion method, the average T/B ratio of  $^{10}\text{B}$  concentration was 3–4, T/Sk was 3–6 and Sk/B was around 1.2 [19]. The T/B ratio at 48 h in the present study using the high-Gd-DTPA-SA was far higher (13.2), with the sensitizer concentration in tumor being kept very high (Fig. 3.5), whereas the T/Sk and Sk/B ratios were comparable with the corresponding values in BNCT. These results indicate that the methodology developed here can be used efficiently when a high and long retention of sensitizer in tumor and a high T/B ratio are required.

**Effect of Gadolinium Content in Emulsion and Derivative Type** The Gd content in the HCO-60 emulsion could be increased while the particle size was kept small (Table 3.2). Gadolinium levels in tumor, blood, liver and spleen with the high-Gd emulsion were almost twice as high as those with the standard-Gd emulsion. At 48 h after i.p. injection, the Gd level in tumor with the high-Gd-DTPA-SA HCO-60 emulsion reached 107  $\mu\text{g-Gd}$  per g tumor (wet).

The amide linkages of Gd-DTPA-SA were not expected to degrade *in vivo*. Thus, the stearyl ester derivative of Gd-DTPA (Gd-DTPA-SE) was synthesized. The Gd levels in tumor and blood with the high-Gd-DTPA-SE HCO-60 emulsion were far lower than those with the high-Gd-DTPA-SA HCO-60 emulsion. Conversely, gadolinium levels in liver and spleen in the early period (2–6 h) with the high-Gd-DTPA-SE HCO-60 emulsion were higher than those with the high-Gd-DTPA-SA HCO-60 emulsion. However, both liver and spleen gadolinium levels decreased to levels lower than those with the high-Gd-DTPA-SA HCO-60 emulsion thereafter. Gd-DTPA-SA was very stable in serum: no transfer to serum proteins and no metabolism to small-molecular-weight compounds occurred up to 24 h at 37 °C [74b, 84]. However, the Gd-DTPA-SE complex was not stable, showing both the transfer and metabolism in a time-dependent manner [74b, 84]. The more rapid elimination of gadolinium from liver and spleen with the Gd-DTPA-SE emulsion could be well explained by the faster degradation of Gd-DTPA-SE.

The pharmacokinetic parameters of MRT, Vdss and Cltot with the standard- and the high-Gd-DTPA-SA HCO-60 emulsion were similar. In addition, the AUC with the high-Gd-DTPA-SA HCO-60 emulsion was twice that with the standard-Gd-DTPA-SA HCO-60 emulsion. Since the gadolinium content in the high-Gd-DTPA-SA HCO-60 emulsion was just twice that with the standard-Gd-DTPA-SA HCO-60 emulsion (Table 3.2), these results indicated that particles of both types of emulsion, with different gadolinium content, behaved similarly *in vivo*. This led to the high level in tumor reaching 107  $\mu\text{g-Gd}$  per g tumor (wet) at 48 h, which was the level reported by Tokuyue et al. [76] as an optimal level for tumor inactivation when  $^{157}\text{Gd}$  would be used.

#### 3.4.2.3 Biodistribution of Gadolinium after Intravenous Administration of Gd-nanoLE

The administration route is one of the most important factors in the biodistribution and pharmacokinetics of drug carriers such as liposomes and lipid-emulsions. Previously, the i.p. route was adopted as an administration route of Gd-nanoLE because it allows the injection of a relatively large amount and, consequently, delivers a large amount of Gd to the tumor via the systemic circulation [85]; as a result, the Gd concentration in the tumor reached 107  $\mu\text{g-Gd}$  per g wet tumor at a dose of 60 mg-Gd per kg BW (2 mL as an administration volume of the Gd-nanoLE). However, even with i.p. injection, many factors affect the biodistribution and pharmacokinetics of the drug carriers, including the absorption of these carriers from the abdominal cavity and their localization in the lymph nodes, making estimation of the *in vivo* fate of the drug carriers difficult. In contrast, i.v. injection delivers drugs more simply and, therefore, has been widely employed instead of i.p. injection in clinical treatments. Consequently, our next study aimed to evaluate i.v. as an alternative to i.p. injection with respect to tumor accumulation of Gd incorporated in Gd-nanoLE.

**Comparison of I.V. with I.P. Injection of Gd-nanoLE** The biodistribution of Gd after i.v. or i.p. injection of the standard-Gd-nanoLE with HCO-60 (particle size, 78 nm) was determined at a dose of 15 mg-Gd/kg BW, half that of the previous case [85]. Table 3.3 summarizes the calculated pharmacokinetic parameters. The Gd concentration in the blood after i.v. injection of the Gd-nanoLE consistently decreased from the initial high concentration of 136  $\mu\text{g-Gd}$  per mL blood at the first sampling time, whereas i.p. injection showed a peak concentration of 50  $\mu\text{g-Gd}$  per mL blood at 4 h after administration (Table 3.3).

The AUC of Gd after i.p. injection was only 57% of that after i.v. injection (Table 3.3). It was reported earlier that the blood concentration of a marker incorporated into liposomes containing sphingomyelin and cholesterol after i.p. injection peaked at several hours after administration and subsequently declined [86]. In addition, some reports have shown that the absorption route of the conventional liposomes from the peritoneal cavity to the bloodstream is mediated by the lymphatic system [87, 88], and part of the i.p. injected liposomes are localized in the lymphatic system over 24 h [88]. These findings can probably be extended to interpret the behavior of the lipid-nanoemulsions in the peritoneal cavity. Accordingly, the

**Tab. 3.3.** Pharmacokinetic parameters after i.p. or i.v. administration of the standard-Gd-nanoLE with HCO-60 at a dose of 1.5 mg Gd in 1 mL.

Route	$C_{\max}^{[a]}$ ( $\mu\text{g mL}^{-1}$ )	$T_{\max}^{[a]}$ (h)	AUC <sup>[b]</sup> ( $\mu\text{g h mL}^{-1}$ )	MRI <sup>[b]</sup> (h)
i.p.	50.0	4.0	612	9.2
i.v.	(135.9)	(0.5)	1071	6.3

<sup>a</sup>The maximum blood concentration,  $C_{\max}$ , and the time of maximum blood concentration,  $T_{\max}$ , were derived directly from the mean blood concentration–time curve.

<sup>b</sup>Area under the blood concentration time curve. Each value was calculated from the mean values of blood concentration up to infinite time ( $n = 3-5$ ).

delayed increase of Gd concentration in the blood after i.p. injection might be ascribed to the transport time of the Gd-nanoLE from the peritoneal cavity to the bloodstream through the lymphatic system. In addition, the lower AUC of Gd after i.p. injection, compared with i.v. injection might be explained by the partial localization of Gd-nanoLE in the lymphatic system, since the Gd-nanoLE remaining in the peritoneal cavity, as determined by visual observation, was negligible at 12 h after administration.

In terms of the tumor accumulation of Gd, i.v. injection of the Gd-nanoLE had an advantage over i.p. injection, namely, faster accumulation. The Gd concentration in the tumor after i.v. injection rapidly increased for 6 h after administration, and thereafter it almost leveled off. In contrast, the Gd concentration after i.p. injection remained at a low level for the first 6 h. The maximum Gd tumor concentrations after i.v. and i.p. injections of the Gd-nanoLE were 30  $\mu\text{g-Gd per g wet tumor}$  at 24 h and 22  $\mu\text{g-Gd per g wet tumor}$  at 12 h, respectively.

**Effect of Repeated Dosing and Gd Content of Gd-nanoLE** To achieve a higher Gd accumulation in the tumor, two i.v. injections at a 24 h interval were made at a dose of 15 and 30 mg-Gd/kg BW per injection by using the standard- and high-Gd-nanoLE, respectively. Biodistribution was determined at 12 h after administration, because the tumor accumulation almost leveled off thereafter with Gd-nanoLEs prepared with HCO-60 (Fig. 3.5) [77]. Two i.v. injections of the standard-Gd-nanoLE made the Gd concentration in the tumor higher, reaching a level of 50  $\mu\text{g-Gd per g wet tumor}$  at 12 h after the second injection. Unfortunately, Gd concentrations in the liver and spleen concurrently increased to almost twice those observed after a single i.v. injection.

In certain cases of the repeated administration of liposomes, an accelerated blood clearance and altered biodistribution of the liposomes were observed at the second or later administration for a certain period after the administration, resulting from the induction of an immunoreaction [89]. Oussoren and Storm, though,

**Tab. 3.4.** Effect of dosing frequency and Gd content of the Gd-nanoLE with HCO-60 on blood and tumor concentrations of Gd ( $\mu\text{g}$ -Gd wet tissue) at 12 h after the final i.v. administration at a dose of 1.5 mg Gd per injection for the standard- or 3.0 mg Gd per injection for the high-Gd formulation.

Tissue	Standard-Gd-nanoLE		High-Gd-nanoLE
	Single (1.5) <sup>[a]</sup>	Double (3.0) <sup>[a]</sup>	Double (6.0) <sup>[a]</sup>
Blood	29.7 $\pm$ 2.8	25.3 $\pm$ 5.7	45.1 $\pm$ 11.4*
Tumor	26.9 $\pm$ 1.4	49.7 $\pm$ 30.9	100.7 $\pm$ 35.9**

<sup>a</sup> Values in parentheses are total dose of Gd (mg). Each value represents the mean  $\pm$  S.D. ( $n = 3-5$ ). \* $p < 0.05$  and \*\* $p < 0.01$ , significantly different from the Gd concentration of the standard-Gd-nanoLE injected twice.

demonstrated that the kinetic profiles of the first and second injections of the PEG-liposomes with a 24 h interval were virtually identical [90]. In our case, the Gd concentrations in tissues after two administrations of the standard-Gd-nanoLE seemed to be almost twice as high as those after a single administration (Table 3.4). This implied that, by employing the same schedule as Oussoren and Storm, the repeated administration had no significant effect on the biodistribution mechanisms of the Gd-nanoLE.

With the administration of two i.v. injections of the high-Gd-nanoLE, the Gd concentration in the tumor reached 101  $\mu\text{g}$  per g wet tissue (Table 3.4). This was comparable to the level achieved by a single i.p. injection of 2 mL of the high-Gd-nanoLE at a dose of 60 mg-Gd per kg body weight per injection [85]. These results indicated that even i.v. injection of the Gd-nanoLE whose tolerable volume was only 1 mL could result in the accumulation of Gd in the tumor at a high concentration when an appropriate dosing schedule was employed.

Many researchers have demonstrated that the charge and fluidity of the liposomal membrane affect the biodistribution even in conventional liposomes [91, 92]. For instance, Nagayasu et al. [92] reported that the tumor-to-bone marrow accumulation ratio of the HEPC-containing liposomes increased remarkably with a decrease in cholesterol content. In the present study, it was anticipated that the membrane property of the high-Gd-nanoLE would differ from that of the standard-Gd-nanoLE. However, the biodistribution of Gd-nanoLE after i.v. injection of each formulation was likely to be almost identical, as it had been after i.p. injection [85]. Thus, the biodistribution of the Gd-nanoLE was hardly affected by the membrane property. In concurrence, it was also observed that the Gd tumor concentration was proportional to the Gd content of the lipid particles in the Gd-nanoLE. According to this finding, a higher Gd tumor concentration could be

achieved by loading a highly lipophilic Gd compound into the core component, though the further introduction of the Gd-DTPA-SA into the membrane of the Gd-nanoLE led to instability of the emulsion.

### 3.4.3

#### Delivery of Gadolinium using Chitosan Nanoparticles (Gd-nanoCPs)

A major problem with previous GdNCT trials using an MRI contrast agent such as Magnevist<sup>®</sup> was that a sufficient quantity of gadolinium could not be retained in the tumor tissue during neutron irradiation [53, 54]. The commercially available gadolinium agent does not exhibit such a selective accumulation in the tumor after i.v. injection as BPA in BNCT [17] and is eliminated rapidly from the tumor tissue after i.t. injection. Therefore, gadolinium compounds that can be efficiently accumulated in the tumor have been sought [93]. We have developed novel Gd-nanoCPs in order to retain gadolinium in the tumor tissue during a GdNCT trial.

As is well-known, chitosan (poly[ $\beta$ -(1  $\rightarrow$  4)-2-amino-2-deoxy-D-glucopyranose]) is a hydrophilic, cationic polysaccharide derived by the deacetylation of chitin (Fig. 3.6), which is the second most abundant polysaccharide, next to cellulose, in the world and a promising resource, originating from crustaceans shells and insects [94]. Chitosan has some interesting properties such as bioadhesive (cationic), biocompatible (nontoxic) and biodegradable (bioerodible) capabilities. Therefore, it has been investigated in depth and used in various industrial and medical applications [95]. Furthermore, these interesting properties make it one of the most promising biopolymers for drug delivery [96–107]. Indeed, chitosan has been studied as a drug carrier in various forms, such as tablets, beads, granules, microparticles and nanoparticles. In particular, micro- and nano-particles are being most widely studied as a drug carrier for the purpose of protein, peptide, vaccine and DNA delivery. A wide variety of preparation methods of chitosan particles have been investigated, such as solvent evaporation techniques, multiple emulsion methods, spray drying methods, electrostatic complex-formation with anionic materials (ionotropic gelation) and block copolymerization. These methods often require a crosslinking agent, such as glutaraldehyde. While such crosslinking agents afford hardened par-

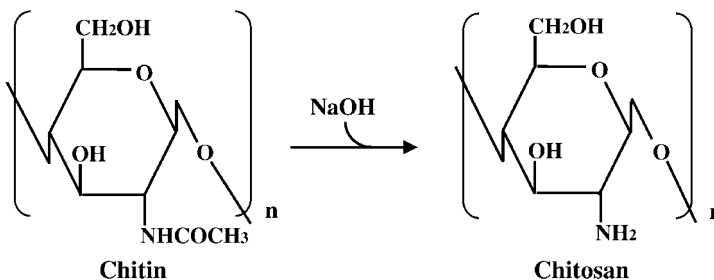


Fig. 3.6. Chemical structures of chitin and chitosan (100% deacetylated).

ticles as well as the possibility of controlling the drug-release rate through the degree of crosslinking, the toxicity of the crosslinking agent would become a major concern. In addition, it leads to low loading of anionic drugs because amino groups in chitosan responsible for electrostatic interaction with anionic drugs become unavailable due to the crosslinking reaction between the amino groups in chitosan and aldehyde groups in crosslinking agents. As an alternative approach, a novel emulsion-droplet coalescence technique has been developed in our laboratory to prepare non-crosslinked chitosan nanoparticles. In fact, this technique offered a useful methodology for the preparation of Gd-nanoCPs specially designed for GdNCT as an i.t. injectable device.

#### 3.4.3.1 Preparation of Gd-nanoCPs

Figure 3.7 shows the preparation of Gd-nanoCPs [108, 109]. Chitosan (2.5% w/v) was dissolved in a Gd-DTPA aqueous solution (5–15% w/v) and an aliquot (1 mL) was added to 10 mL of liquid paraffin containing 5% v/v sorbitan sesquioleate (Arlacel C). The mixture was then stirred to form a water-in-oil (w/o) emulsion A using a high-speed homogenizer. Similarly, a w/o emulsion B was prepared by adding 3 M sodium hydroxide solution (1.5 mL) to liquid paraffin (10 mL) containing 5% v/v Arlacel C. As emulsion B was added to emulsion A, they were mixed and stirred vigorously. As a result of coalescence of droplets, chitosan was deposited as nanoparticles. Gd-nanoCPs in the mixed emulsion were washed and separated by centrifugation at 3000 rpm for 60 min using toluene, ethanol and water

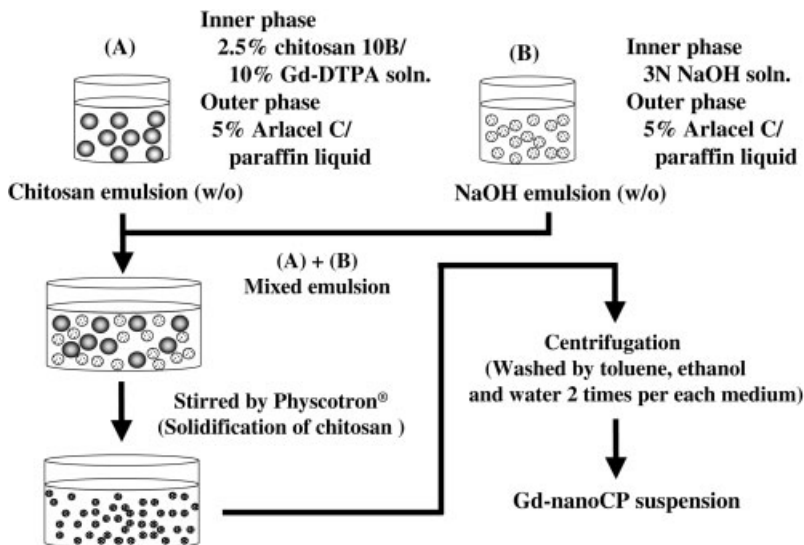


Fig. 3.7. Preparation process of Gd-nanoCPs using an emulsion droplet coalescence technique.

**Tab. 3.5.** Mean particle size and Gd content of Gd-nanoCP.

	No. of batch	Mean particle size (nm) <sup>[a]</sup>	Gd content (% w/w) <sup>[a]</sup> [Gd-DTPA content (%)]
Chitosan 10B			
5% Gd-DTPA soln	3	461 ± 15	7.7 ± 1.7 [26.9 ± 5.9]
10% Gd-DTPA soln	6	426 ± 28	9.3 ± 3.2 [32.4 ± 11.0]
15% Gd-DTPA soln	3	452 ± 25	13.0 ± 1.8 [45.3 ± 6.2]
Chitosan 9B			
10% Gd-DTPA soln	3	594 ± 96	4.1 ± 1.0 [14.2 ± 3.4]
Chitosan 8B			
10% Gd-DTPA soln	3	750 ± 77	3.3 ± 0.8 [11.6 ± 2.7]

<sup>a</sup> Value shows average ± S.D. of 3–6 batches.

successively. Finally, the Gd-nanoCPs were obtained as water suspensions or powders lyophilized after suspending in isotonic mannitol solution.

This technique utilized the fact that, when two emulsions of the same type with the same continuous phase are mixed and stirred vigorously, droplets of each emulsion collide at random, coalesce and split, and all of the droplets finally become uniform in content. Thus, Gd-nanoCP generation was triggered by neutralization of the acidic chitosan-dissolving droplets of emulsion A with sodium hydroxide in the droplets of emulsion B. Nanoparticle generation consequently occurred within the emulsion droplets. The size of nanoparticles did not reflect the droplet size.

Chitosans of grade 10B (100% deacetylated), 9B (91.4% deacetylated) and 8B (84.9% deacetylated) (Katokichi Bio, Japan) were used. Table 3.5 shows the mean particle diameter and gadolinium content in Gd-nanoCPs for each chitosan grade. When chitosan 9B and 8B were used, the mean particle diameters were 594 and 750 nm, respectively, and the gadolinium contents were 4.1% and 3.3% (corresponding to 14.2% and 11.6% as Gd-DTPA), respectively. Namely, as the deacetylation degree of chitosan decreased, the particle size increased gradually and, in contrast, the Gd content decreased markedly. With chitosan 10B, Gd-nanoCPs prepared using 5% and 15% Gd-DTPA solution had mean particle diameters of 461 and 452 nm, respectively, and the gadolinium contents were 7.7% and 13.0% (corresponding to 27% and 45% as Gd-DTPA), respectively. Thus, as the Gd-DTPA concentration in the solution of chitosan 10B increased, the gadolinium content increased, but the particle size was not significantly influenced.

The crosslinking [110–115] and electrostatic interaction by anionic materials such as alginate [116, 117] have been generally used to prepare solid chitosan particles, since it is difficult to form microparticles using only chitosan and drug. In addition, the precipitation technique [118, 119] and block copolymerization [119] have been studied to produce chitosan nanoparticulate carriers in recent years. A major problem with the clinical application of nanoparticles is that the drug load is too low to deliver an effective dose; the performance of the above chitosan particles in past studies was also unexceptional. In the present emulsion-droplet coalescence technique, the Gd-DTPA appears to strongly interact electrostatically with the amino groups of chitosan in the deposition of Gd-nanoCPs. This would contribute to the extraordinarily high Gd-DTPA content (45.3%) and their small particle size, which was reduced to i.t. injectable size (452 nm), in Gd-nanoCPs prepared using chitosan 10B and 15% Gd-DTPA solution.

#### 3.4.3.2 Gd-DTPA Release Property of Gd-nanoCPs

Gd-DTPA release from Gd-nanoCPs that were prepared using chitosan 10B and 10% Gd-DTPA solution has been examined *in vitro* [109]. As test media, an isotonic phosphate-buffered saline solution (PBS) of pH 7.4 and human plasma, as a biological medium, were used, and the method was based on a dynamic dialysis. The gadolinium release behavior was significantly different between Gd-nanoCPs in PBS and those in the human plasma. Gd-nanoCPs released only 1.8% up to 7 d in PBS, whereas 67.9 and 91.5% of gadolinium were eluted from Gd-nanoCPs in human plasma for 6 and 24 h, respectively. This again suggested strong complex formation of Gd-DTPA with chitosan in a simple aqueous medium, because highly water-soluble Gd-DTPA was hardly eluted for a long time in PBS. This releasing property might be advantageous to GdNCT trial by i.t. injection into a solid tumor. The mechanism of fast release of gadolinium from Gd-nanoCPs in human plasma was not clear.

#### 3.4.3.3 Gd-DTPA Retention in Tumor Tissue after Intratumoral Injection

The quantity of gadolinium in the melanoma tissue on mice after i.t. injection of each Gd-DTPA dosage form containing 1200  $\mu\text{g}$  as gadolinium has been determined [109]. In an *in vivo* experiment, the B16F10 malignant melanoma cell suspension (0.1 mL) in an isotonic PBS containing  $3 \times 10^6$  cells was carefully inoculated subcutaneously (s.c.) into the posterior flank of a six-week-old C57BL/6 mouse. At 10 d after tumor implantation by the above procedure, 200  $\mu\text{L}$  of the Gd-nanoCP (prepared with chitosan 10B and 10% Gd-DTPA solution) suspension in isotonic mannitol solution (Gd 6000 ppm) was injected gently into a block of grown tumor that was about 10 mm in diameter (Gd dose, 1200  $\mu\text{g}$  per mouse). In parallel, the dilute Magnevist<sup>®</sup> solution (Gd 6000 ppm) was injected in the same manner. At 5 min or 24 h after i.t. injection, mice were sacrificed and tumoral blocks were excised. The amount of gadolinium in the tumor tissue was analyzed by ICP-AES after incineration.

When a dilute solution of Magnevist<sup>®</sup> was administered, the quantities of gadolinium in a tumor block were 452  $\mu\text{g}$  (37.6% of dose) and 5.3  $\mu\text{g}$  (0.4%) 5 min and



24 h after injection, respectively. In contrast, 892  $\mu\text{g}$  (74.3% of dose) and 821  $\mu\text{g}$  (68.4%) of gadolinium remained in the tumor block 5 min and 24 h after administration of Gd-nanoCP suspension, respectively. Thus, since the gadolinium hardly leaked to the surrounding normal tissues, in particular to the subcutaneous space on tumor tissue, over 24 h, damage beyond the tumor part by GdNCT would be kept to a minimum. No Gd-DTPA release from Gd-nanoCPs in the aqueous medium might contribute to prolonged retention in the tumor tissue. This extended retention was thought to lead to greater enhancement of the antitumor effect as compared with past GdNCT trials using Magnevist<sup>®</sup> [52].

#### 3.4.3.4 *In vivo* Growth Suppression of Experimental Melanoma Solid Tumor

A GdNCT trial has been carried out *in vivo* by i.t. injection using Gd-nanoCPs prepared with chitosan 10B and 10% Gd-DTPA solution [120]. The Gd-nanoCPs were 430 nm in mean particle diameter and the content of the natural form of gadolinium was 9.3 w/w %. Therefore, the content of <sup>157</sup>Gd, 15.6% of the natural form, corresponded to 1.45 w/w %. The radioresistive B16F10 malignant melanoma was selected as tumor model [121, 122] to demonstrate a potential for GdNCT.

When the s.c. B16F10 melanoma tumor in the five-week-old male C57BL/6 mice (body weight, 21–27 g) grew to about 10 mm in diameter 10 d after tumor implantation by the above procedure, i.t. administration of the Gd-nanoCP suspension in isotonic mannitol solution or Magnevist<sup>®</sup> solution as a control was started. Each gadolinium dosage form (corresponding to natural Gd 6000  $\mu\text{g mL}$ ), 200  $\mu\text{L}$ , was injected twice into the block of tumor, 24 and 8 h before neutron irradiation (total natural Gd dose, 2400  $\mu\text{g}$  per mouse). The source of the thermal neutron beams was obtained from the Kyoto University Research Reactor Institute, Japan (the Heavy Water Facility; operating power, 5 MW; irradiation time, 60 min; operating mode, OO-0011-F) [123, 124]. The measured average fluence on the tumor surface was  $6.32 \times 10^{12}$  neutrons  $\text{cm}^{-2}$ . Neutron irradiation was performed only once.

In the gadolinium-loaded nanoparticle-administered and neutron-irradiated (Gd-P, N+) group, the tumor growth was significantly suppressed despite the radioresistance of melanoma model [121, 122] and the long interval (8 h) until neutron irradiation after second gadolinium administration. Its mean tumor volume was less than 15%, compared with that in the non-gadolinium-administered and neutron-irradiated (Gd–, N+) group, 14 d after neutron irradiation. The mean time taken to reach a tumor volume ratio of 10 in the [Gd-P, N+] group was prolonged to 23.2 d, which was 227% and 374% of that in the [Gd–, N+] group and the non-gadolinium-administered and non-neutron-irradiated (Gd–, N–) group, respectively. In addition, the survival time of mice in the [Gd-P, N+] group was also significantly prolonged, to 22.2 d as the mean time. Three of the six mice in the [Gd-P, N+] group were alive at 28 d after neutron irradiation, while all mice in the other groups were dead by 21 d.

Conversely, no GdNCT effect was observed in the Magnevist<sup>®</sup> solution-administered and neutron-irradiated (Gd-S, N+) group, since the change in the tumor volume ratio and the survival time of mice did not differ from those in the [Gd–, N+] group. When the gadolinium nanoparticle or solution was adminis-

tered and there was no neutron irradiation (Gd-P or Gd-S, N-), tumor growth was not inhibited at all: the mean time to reaching a tumor volume ratio of 10 was about 6–7 d, which is no different from that in the [Gd-, N-] group.

The content of gadolinium in the tumor just at the starting point of neutron irradiation was estimated to explain the GdNCT effect enhanced by Gd-nanoCPs. When Gd-nanoCPs were administered in the same manner as that in the GdNCT trial, the gadolinium content in melanoma tissue in mice was  $1766 \pm 96 \mu\text{g}$ , corresponding to 74% of dose. However, following the administration of Magnevist<sup>®</sup> solution, the gadolinium content in the tumoral block was  $16 \pm 7 \mu\text{g}$ , corresponding to only 0.7% of dose. Clearly, the strong suppression of tumor growth observed in the present GdNCT trial with Gd-nanoCPs resulted from the excellent Gd-DTPA retention in the tumor tissue of chitosan nanoparticles after i.t. injection.

No skin damage over the tumor was apparent in [Gd-, N+] and [Gd-S, N+] groups. However, the skin over the tumor in the [Gd-P, N+] group became red for a few days after neutron irradiation and, later, ulcer formation was observed. This severe side effect demonstrated that the photons and/or electrons emitted by the frequent Gd-NCR would have a sufficient destructive effect for the tumor if selective gadolinium distribution in the tumor tissue and neutron fluence were controlled as optimally as possible in GdNCT.

In one report on a GdNCT trial, a neutral macrocyclic gadolinium complex (Gadobutrol, Gadovist<sup>®</sup>) was used as the gadolinium source and excellent results were obtained by i.t. injection [53]. The biological half-life of the wash-out from the tumor tissue after i.t. injection of Gadobutrol was estimated to be 50–151 min (average, 115 min) and might contribute to the assured antitumor effect, because it was longer than that of Magnevist<sup>®</sup> [53, 54]. In the present study, the outstanding gadolinium retention in the tumor tissue following i.t. injection of Gd-nanoCPs clearly led to the potent GdNCT effect even though the tumors were irradiated at an exceptionally longer interval after gadolinium administration compared with the usual GdNCTs with Magnevist<sup>®</sup> and Gadovist<sup>®</sup>. This property will also contribute to flexible adaptation in duration and frequency of neutron irradiation in future GdNCT trials.

In the present GdNCT trial, the dose of natural gadolinium per a tumor block with the nanoparticle formulation (2400  $\mu\text{g-Gd}$  per tumor) was considerably smaller than that in past trials [53, 54]. This gadolinium dose indicated that if gadolinium enriched to 100% of <sup>157</sup>Gd was used the corresponding level of growth inhibition could be gained by about 16% of gadolinium dose (460  $\mu\text{g}$ ) against B16F10 melanoma block about 10 mm in diameter [53].

#### 3.4.3.5 Bioadhesion and Uptake of Gd-nanoCP in Three Different Cell Lines

The extracellular matrix is composed of sulfated glycosaminoglycans and polysaccharide acids, which form hydrophilic, negatively charged gels over the cell membrane. Membrane glycoproteins, most often bearing sialic acid residues, also contribute to the negative charge of the cell surface. Chitosan, however, has the characteristics of a cationic polyelectrolyte, thereby providing a strong electrostatic interaction with negatively charged cell surfaces. Therefore, the use of cationic

polymers, such as chitosan, in preparing particulate carriers would give rise to higher drug retention in cells and tissues because of the electrostatic interaction between particle surfaces and cell surfaces. Indeed, many workers have reported that the bioadhesive properties of chitosan originate from electrostatic interaction between positively charged amino groups in chitosan and negatively charged sialic acid residues on the cell surface [125–127]. In addition, Chatelet et al. have demonstrated the role of deacetylation degree of chitosan on bioadhesive properties using chitosan film [128]. They showed that the adhesion of chitosan on fibroblasts isolated from foreskins of children was increased as the deacetylation degree of chitosan was increased. Therefore, the use of 100% deacetylated chitosan in the present Gd-nanoCPs was expected to lead to such a bioadhesive property.

L929 mouse fibroblast cells, B16F10 melanoma cells and SCC-VII squamous cell carcinoma were employed to evaluate the bioadhesion and uptake of Gd-nanoCPs in cultured cells in order to clarify the mechanism of high tumor-killing effects observed in our GdNCT trials [129]. Gd-DTPA incorporated in Gd-nanoCPs was hardly released in culture medium during the experiments.

**Transmission Electron Microscopy** Using a transmission electron microscope (TEM), L929 cells after exposure to Gd-nanoCPs were observed. Following exposure to the autoclaved Gd-nanoCP suspension in the culture medium at 37 °C for 12 h, L929 cells were washed with phosphate-buffered saline solution (PBS) to remove the free Gd-nanoCPs not adhered on and not endocytosed into the cells. The cells were then fixed with formaldehyde solution and epoxy resin, thinly sliced with a microtome, and observed by TEM.

Transmission electron micrographs of L929 cells incubated with Gd-nanoCPs for 12 h at 37 °C indicated that Gd-nanoCPs were not so stably dispersed in the culture medium because they loosely aggregated (Fig. 3.8). However, a considerable number of Gd-nanoCPs adhered to L929 cells and some of these were being endocytosed or incorporated in the cells in the form of particles.

**Effect of Gd Concentration, Incubation Time and Temperature** The amount of Gd in and on the cells after 12 h incubation was increased with increasing feed concentration of Gd (ranging from 0 to 20 ppm). At 20 ppm of applied Gd concentration, the amount of Gd reached 18  $\mu\text{g-Gd per } 10^6$  cells and this value was unchanged up to 40 ppm. However, it was experimentally confirmed that no further increase in cellular uptake and adhesion was observed beyond 40 ppm. Cationic macromolecules such as polylysine affect, in general, cell viability [130]. However, the cytotoxicity of Gd-nanoCPs against L929 cells was negligible in the range 20–40 ppm. Therefore, the following studies were performed at a Gd feed concentration of 40 ppm.

The Gd accumulation in L929 cells, B16F10 melanoma cells and SCC-VII squamous cell carcinoma incubated with Gd-nanoCPs at 37 and 4 °C was determined as a function of incubation time. The accumulation at 37 °C seemed to level off after 12 h. When incubated with Gd-nanoCPs for 12 h at 37 °C, the total Gd amounts were 18, 27 and 60  $\mu\text{g Gd per } 10^6$  cells with L929 fibroblast cells,

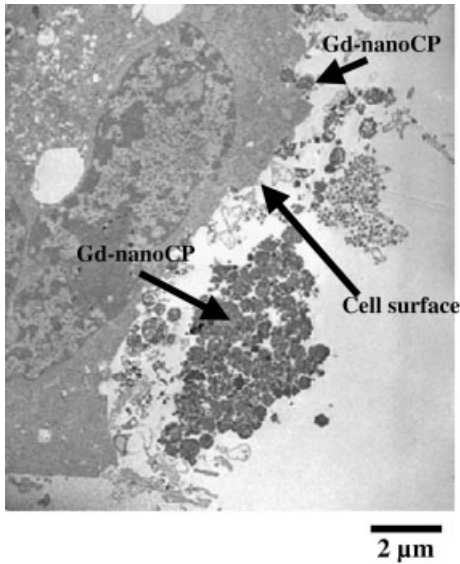


**Fig. 3.8.** Transmission electron micrograph of L929 fibroblast cells after exposure to Gd-nanoCPs for 12 h.

B16F10 cells and SCC-VII cells, respectively (Fig. 3.9). In contrast, the Gd accumulation at 4 °C where endocytic activity would not exist rapidly leveled off and was far lower, about 5 or less  $\mu\text{g Gd}$  per  $10^6$  cells in all three cell lines. Thus, this significantly higher cellular-accumulation at 37 °C, which would be attributed to endocytosis that was active at 37 °C but suppressed at 4 °C, indicated that endocytic

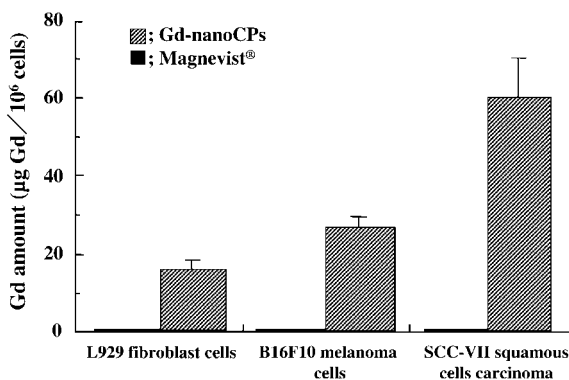


**Fig. 3.9.** Uptake and adhesion of Gd-nanoCPs or Magnevist at Gd-dose of 40 ppm in three different cell lines 12 h after exposure to the cells under a 5% CO<sub>2</sub> atmosphere at 37 °C.

uptake of Gd-nanoCPs made a major contribution to the total accumulation. The notably varied accumulation behavior of Gd in these three cell lines is attributed to their differing endocytic activity.

The size and bioadhesive property of Gd-nanoCPs is related to the endocytic uptake by the cells. Indeed, Green et al. have examined the particle size dependence of endocytosis of polyethylene particles in C3H murine peritoneal macrophages [131]. They found that polyethylene particles in the range 0.3–10  $\mu\text{m}$  in diameter were endocytosable. The size of the present Gd-nanoCPs, 430 nm, is included in this range. In addition, Lee et al. have demonstrated that a high level uptake of liposomes in J774 cells, a murine macrophage-like cell line, could be obtained by altering the lipid formulation to provide an adhesive property on their surfaces, as might be achieved by the present Gd-nanoCPs [132]. These results support the idea that the adhesion of optimally sized Gd-nanoCPs on the cell surface might be an important step in the subsequent uptake by endocytosis.

The cellular accumulation behavior observed *in vitro* may also be related to the tumor-killing effects *in vivo*. B16F10 cell-bearing mice were employed in our GdNCT trials *in vivo* as described earlier [120]. The tumor-killing effects observed in SCC-VII cell-bearing mice [133] were nearly identical to those achieved with B16F10 cell-bearing mice [120] at the same i.t. Gd dose of 2400  $\mu\text{g}$  per tumor even though the thermal neutron fluence in the GdNCT trials using SCC-VII cell-bearing mice ( $3.31 \times 10^{12}$  neutrons  $\text{cm}^{-2}$ ) was only a half of that in the cases of B16F10 cell-bearing mice ( $6.32 \times 10^{12}$  neutrons  $\text{cm}^{-2}$ ). From these results, at least one reason for the relatively higher tumor-killing effects obtained with SCC-VII cell-bearing mice *in vivo* would be their higher endocytic activity. Further, since the accumulation was almost saturated at 40 ppm of Gd in the *in vitro* studies described here, which was far lower than the Gd level in the previous GdNCT trials at a dose of 2400  $\mu\text{g}$  per tumor, it was suggested that most of Gd i.t. administered as Gd-nanoCPs might exist in tumor tissue extracellularly, as might be estimated from the TEM photograph given in Fig. 3.8, which shows the presence of agglomerates in the cultured cells.

**Comparative Studies with Magnevist<sup>®</sup>** In a comparative study using the solution system, the most important point to be emphasized again was that Gd accumulation in all cell lines utilized in the present study was mostly achieved in the form of particles by cell-surface adhesion and endocytosis of Gd-nanoCPs, though the activity more or less varied. In fact, Magnevist<sup>®</sup> solution scarcely showed intra- and extracellular Gd accumulation in any of the cell lines (Fig. 3.9). The Gd amount detected in the Magnevist<sup>®</sup> group after 12 h at 37 °C was less than 1% of that in Gd-nanoCP group (Fig. 3.9), which is probably related to the well-known fact that Magnevist<sup>®</sup> was eliminated from the tumor tissue immediately after i.t. injection [120]. Conversely, bioadhesion, endocytosis and strong Gd-DTPA-binding of optimally sized Gd-nanoCPs would significantly extend the elimination half-life of Gd i.t. administered [120]. The present results evidenced that Gd-nanoCPs have great potential to accumulate Gd into tumor tissue and/or cells, consequently leading to improved therapeutic efficiency in our GdNCT trials [120].

A major concern in past GdNCT trials using cultured cells and solution systems had been the necessity of a large amount of Gd for cell-growth suppression. Akine et al. reported that 10% survival level of the cultured Chinese hamster cells was obtained with a fluence of  $1.55 \times 10^{12}$  neutrons  $\text{cm}^{-2}$  in the presence of Gd of 5000 ppm [58]. Tokuyue et al. have evaluated the effect of radiation released during neutron capture reaction by  $^{157}\text{Gd}$  of 800 ppm,  $^{10}\text{B}$  of 51 ppm or their combination, using Magnevist<sup>®</sup> and BSH, on cell survival [134] – fluences of 1.13, 1.69 and  $0.95 \times 10^{12}$  neutrons  $\text{cm}^{-2}$  were required for 10% survival levels, respectively. Further, Hofmann et al. have demonstrated, using the Gadovist<sup>®</sup>, that at a fluence of  $3.6 \times 10^{12}$  neutrons  $\text{cm}^{-2}$  a Gd concentration of 10 mmol-Gd  $\text{L}^{-1}$ , equivalent to 1570 ppm, was required to obtain about a 52% survival level of Sk-Mel-28 cells, a melanoma cell line of human origin [53]. A possible problem of these studies was that they had to apply high Gd concentrations, because only Gd-agents that show no affinity to the tumor cells, possibly including Gadovist<sup>®</sup>, were available. As a result, cells were unable to suffer sufficient neutron-irradiation because of obstruction by the presence of excess neutron capture elements in the medium. Unlike such a solution-based formulation, Gd would be concentrated on and in cells when using the present Gd-nanoCPs. This situation is clearly favorable for obtaining effective cell-growth suppression.

It has been believed that a contact between the cells and Gd is not always necessary for the tumor cell inactivation in GdNCT, because of the long-range  $\gamma$ -rays emitted as a result of Gd-NCR. Akine and coworkers, however, have proposed that the electrons might also play an important role in the tumor-killing effect in GdNCT [58]. Therefore, the presence of Gd in the intracellular space may be rather desirable for GdNCT, since the electrons, especially Auger electrons, have a short-range and a high linear energy transfer. As shown in the present study, Gd-nanoCPs could bind to the cell surfaces, owing to their cationic nature, and subsequently be endocytosed. These intra- and extracellular accumulation behaviors would provide a compatible way to accomplish the high suppression of tumor growth in GdNCT.

### 3.5

#### Conclusions

Recently, clinical BNCT trials have often been carried out, mainly for brain tumors in Japan. It is hopeful that BNCT has been extended to other types of cancer such as head-neck and tongue cancers, with excellent treatment results being reported. In the near future, lung cancer and hepatoma are to be treated by BNCT. Proton accelerators as a source of neutron beams are also going to become a reality, instead of the nuclear reactors currently used. Success in NCT, essentially, depends on the selective tumor-accumulation of boron or gadolinium. Only BPA and BSH are now used clinically as solutions, but their selectivity in the accumulation is not necessarily high. We believe that applications of nanoparticulate “atom” delivery technologies can contribute to NCT.

## References

- 1 CODERRE J. A., MORRIS G. M., The radiation biology of boron neutron capture therapy, *Radiat. Res.*, **1999**, 151, 1–18.
- 2 BARTH R. F., SOLOWAY A. H., Boron neutron capture therapy of primary and metastatic brain tumors, *Mol. Chem. Neuropathol.*, **1994**, 21, 139–154.
- 3 BARTH R. F., SOLOWAY A. H., FAIRCHILD R. G., Boron neutron capture therapy of cancer, *Cancer Res.*, **1990**, 50, 1061–1070.
- 4 GREENWOOD R. C., REICH C. W., BAADER H. A., KOCH H. R., BREITIG D., SCHULT O. W. B., FOGELBERG B., BÄCKLIN A., MAMPE W., VON EGIDY T., SCHRECKENBACH K., Collective and two-quasiparticle states in  $^{158}\text{Gd}$  observed through study of radiative neutron capture in  $^{157}\text{Gd}$ , *Nucl. Phys.*, **1978**, A304, 327–428.
- 5 BRUGGER R. M., SHIH J. A., Evaluation of gadolinium-157 as a neutron capture therapy agent, *Strahlenther. Onkol.*, **1989**, 165, 153–156.
- 6 ALLEN B. J., MCGREGOR B. J., MARTIN R. F., Neutron capture therapy with gadolinium-157, *Strahlenther. Onkol.*, **1989**, 165, 156–157.
- 7 GARBER D. I., KINSEY R. R., in *Neutron Cross Sections Report*, BNL-325, 3rd edn., Brookhaven National Laboratory, New York, **1976**.
- 8 SHIH J. A., BRUGGER R., Gadolinium as a neutron capture therapy agent, *Med. Phys.*, **1992**, 19, 733–744.
- 9 MARTIN R. F., D’CUNHA G., PARDEE M., ALLEN B. J., Induction of double-strand breaks following neutron capture by DNA-bound  $^{157}\text{Gd}$ , *Int. J. Radiat. Biol.*, **1988**, 54, 205–208.
- 10 WEINMANN H. J., BRASCH R. C., PRESS W. R., WESBEY G. E., Characteristics of gadolinium-DTPA complex: A potential NMR contrast agent, *Am. J. Rad.*, **1984**, 142, 619–624.
- 11 GOLDSTEIN H. A., KASHANIAN F. K., BLUMETTI R. F., HOLYOAK W. L., HUGO F. P., BLUMENFIELD D. M., Safety assessment of gadopentetate dimeglumine in U.S. clinical trials, *Radiology*, **1990**, 174, 17–23.
- 12 LOCHER G. L., Biological effects and therapeutic possibilities of neutron, *Am. J. Roentgenol. Radium Ther.*, **1936**, 36, 1–13.
- 13 HATANAKA H., Boron neutron capture therapy for tumors, in *Boron Neutron Capture Therapy for Tumors* (H. HATANAKA, ed.), Nishimura, Niigata, **1986**, pp. 1–28.
- 14 HATANAKA H., NAKAGAWA Y., Clinical results of long-surviving brain tumor patients who underwent boron neutron capture therapy, *Int. J. Radiat. Oncol. Biol. Phys.*, **1994**, 28, 1061–1066.
- 15 NAKAGAWA Y., HATANAKA H., Boron neutron capture therapy: Clinical brain tumor studies, *J. Neuro-Oncol.*, **1997**, 33, 105–115.
- 16 MISHIMA Y., ICHIHASHI M., NAKANISHI T., TSUJI M., UEDA M., NAKAGAWA T., SUZUKI T., Cure of malignant melanoma by single thermal neutron capture treatment using melanoma seeking compounds:  $^{10}\text{B}$ /melanogenesis interaction to in vitro/in vivo radiobiological analysis to preclinical studies, in *Neutron Capture Therapy* (FAIRCHILD R. G., BROWNELL G., eds.), Brookhaven National Laboratory, Upton, NY, **1983**, pp. 355–364.
- 17 MISHIMA Y., ICHIHASHI M., HATTA S., HONDA C., YAMAMURA K., NAKAGAWA T., New thermal neutron capture therapy for malignant melanoma: Melanogenesis-seeking  $^{10}\text{B}$  molecule-melanoma cell interaction from in vitro to first clinical trial, *Pigment Cell Res.*, **1989**, 2, 226–234.
- 18 SOLOWAY A. H., TJARKS W., BARNUM B. A., RONG F. G., BARTH R. F., CODOGNI I. M., WILSON J. G., The chemistry of neutron capture therapy, *Chem. Rev.*, **1998**, 98, 1515–1562.
- 19 FUKUDA H., HONDA C., WADABAYASHI N., KOBAYASHI T., YOSHINO K., HIRATSUKA J., TAKAHASHI J.,

- AKAIZAWA T., ABE Y., ICHIHASHI M., MISHIMA Y., Pharmacokinetics of 10B-p-boronophenylalanine in tumours, skin and blood of melanoma patients: A study of boron neutron capture therapy for malignant melanoma, *Melanoma Res.*, **1999**, 9(1), 75–83.
- 20 ROSSI S., SCHINAZI R. F., MARTINI G., ESR as a valuable tool for the investigation of the dynamics of EPC and EPC/cholesterol liposomes containing a carboranyl-nucleoside intended for BNCT, *Biochim. Biophys. Acta*, **2005**, 1712(1), 81–91.
- 21 RISTORI S., OBERDISSE J., GRILLO I., DONATI A., SPALLA O., Structural characterization of cationic liposomes loaded with sugar-based carboranes, *Biophys. J.*, **2005**, 88(1), 535–547.
- 22 MARTINI S., RISTORI S., PUCCI A., BONECHI C., BECCIOLINI A., MARTINI G., ROSSI C., Boronophenylalanine insertion in cationic liposomes for Boron Neutron Capture Therapy, *Biophys. Chem.*, **2004**, 111(1), 27–34.
- 23 NAKAMURA H., MIYAJIMA Y., TAKEI T., KASAOKA S., MARUYAMA K., Synthesis and vesicle formation of a nido-carborane cluster lipid for boron neutron capture therapy, *Chem. Commun.*, **2004**, (17), 1910–1911.
- 24 KONING G. A., FRETZ M. M., WORONIECKA U., STORM G., KRIJGER G. C., Targeting liposomes to tumor endothelial cells for neutron capture therapy, *Appl. Radiat. Isot.*, **2004**, 61(5), 963–967.
- 25 MORANDI S., RISTORI S., BERTI D., PANZA L., BECCIOLINI A., MARTINI G., Association of sugar-based carboranes with cationic liposomes: An electron spin resonance and light scattering study, *Biochim. Biophys. Acta*, **2004**, 1664(1), 53–63.
- 26 WEI Q., KULLBERG E. B., GEDDA L., Trastuzumab-conjugated boron-containing liposomes for tumor-cell targeting: development and cellular studies, *Int. J. Oncol.*, **2003**, 23(4), 1159–1165.
- 27 STEPHENSON S. M., YANG W., STEVENS P. J., TJARKS W., BARTH R. F., LEE R. J., Folate receptor-targeted liposomes as possible delivery vehicles for boron neutron capture therapy, *Anticancer Res.*, **2003**, 23(4), 3341–3345.
- 28 KULLBERG E. B., CARLSSON J., EDWARDS K., CAPALA J., SJOBERG S., GEDDA L., Introductory experiments on ligand liposomes as delivery agents for boron neutron capture therapy, *Int. J. Oncol.*, **2003**, 23(2), 461–467.
- 29 CARLSSON J., KULLBERG E. B., CAPALA J., SJOBERG S., EDWARDS K., GEDDA L., Ligand liposomes and boron neutron capture therapy, *J. Neurooncol.*, **2003**, 62(1–2), 47–59.
- 30 KULLBERG E. B., NESTOR M., GEDDA L., Tumor-cell targeted epidermal growth factor liposomes loaded with boronated acridine: Uptake and processing, *Pharm. Res.*, **2003**, 20(2), 229–236.
- 31 PEACOCK G. F., JI B., WANG C. K., LU D. R., Cell culture studies of a carborane cholesteryl ester with conventional and PEG liposomes, *Drug. Deliv.*, **2003**, 10(1), 29–34.
- 32 SUDIMACK J. J., ADAMS D., ROTARU J., SHUKLA S., YAN J., SEKIDO M., BARTH R. F., TJARKS W., LEE R. J., Folate receptor-mediated liposomal delivery of a lipophilic boron agent to tumor cells in vitro for neutron capture therapy, *Pharm. Res.*, **2002**, 19(10), 1502–1508.
- 33 PAN X. Q., WANG H., LEE R. J., Boron delivery to a murine lung carcinoma using folate receptor-targeted liposomes, *Anticancer Res.*, **2002**, 22(3), 1629–1633.
- 34 KULLBERG E. B., BERGSTRAND N., CARLSSON J., EDWARDS K., JOHNSON M., SJOBERG S., GEDDA L., Development of EGF-conjugated liposomes for targeted delivery of boronated DNA-binding agents, *Bioconj. Chem.*, **2002**, 13(4), 737–743.
- 35 PAN X. Q., WANG H., SHUKLA S., SEKIDO M., ADAMS D. M., TJARKS W., BARTH R. F., LEE R. J., Boron-containing folate receptor-targeted liposomes as potential delivery agents for neutron capture therapy, *Bioconj. Chem.*, **2002**, 13(3), 435–442.
- 36 JI B., CHEN W., LU D. R., HALPERN D. S., Cell culture and animal studies



- for intracerebral delivery of borocaptate in liposomal formulation, *2001, Drug Deliv.*, 8(1), 13–17.
- 37 PAVANETTO F., PERUGINI P., GENTA I., MINOIA C., RONCHI A., PRATI U., ROVEDA L., NANO R., Boron-loaded liposomes in the treatment of hepatic metastases: Preliminary investigation by autoradiography analysis, *Drug Deliv.*, **2000**, 7(2), 97–103.
- 38 MORAES A. M., SANTANA M. H., CARBONELL R. G., Preparation and characterization of liposomal systems entrapping the boronated compound o-carboranylpropylamine, *J. Microencapsul.*, **1999**, 16(5), 647–664.
- 39 ZHOU R., BALASUBRAMANIAN S. V., KAHL S. B., STRAUBINGER R. M., Biopharmaceutics of boronated radiosensitizers: Liposomal formulation of MnBOPP (manganese chelate of 2,4-(alpha, beta-dihydroxyethyl) deuterioporphyrin IX) and comparative toxicity in mice, *J. Pharm. Sci.*, **1999**, 88(9), 912–917.
- 40 SHELLY K., FEAKES D. A., HAWTHORNE M. F., SCHMIDT P. G., KRISCH T. A., BAUER W. F., Model studies directed toward the boron neutron-capture therapy of cancer: Boron delivery to murine tumors with liposomes, *Proc. Natl. Acad. Sci. U.S.A.*, **1992**, 89, 9039–9043.
- 41 FEAKES D. A., SHELLY K., KNOBLER C. B., HAWTHORNE M. F., Na<sub>3</sub>[B<sub>20</sub>H<sub>17</sub>NH<sub>3</sub>]: Synthesis and liposomal delivery to murine tumors, *Proc. Natl. Acad. Sci. U.S.A.*, **1994**, 91, 3029–3033.
- 42 FEAKES D. A., SHELLY K., HAWTHORNE M. F., Selective boron delivery to murine tumors by lipophilic species incorporated in the membranes of unilamellar liposomes, *Proc. Natl. Acad. Sci. U.S.A.*, **1995**, 92, 1367–1370.
- 43 FEAKES D. A., WALLER R. C., HATHAWAY D. K., MORTON V. S., Synthesis and in vivo murine evaluation of Na<sub>4</sub>[1-(1<sup>\*</sup>-B<sub>10</sub>H<sub>9</sub>)-6-SHB<sub>10</sub>H<sub>8</sub>] as a potential agent for boron neutron capture therapy, *Proc. Natl. Acad. Sci. U.S.A.*, **1999**, 96, 6406–6410.
- 44 HAWTHORNE M. F., SHELLY K., Liposomes as drug delivery vehicles for boron agents, *J. Neurooncol.*, **1997**, 33(1–2), 53–58.
- 45 WATSON-CLARK R. A., BANQUERIGO M. L., SHELLY K., HAWTHORNE M. F., BRAHN E., Model studies directed toward the application of boron neutron capture therapy to rheumatoid arthritis: Boron delivery by liposomes in rat collagen-induced arthritis, *Proc. Natl. Acad. Sci. U.S.A.*, **1998**, 95, 2531–2534.
- 46 YANAGIE H., FUJII Y., TAKAHASHI T., TOMITA T., FUKANO Y., HASUMI K., NARIUCHI H., YASUDA T., SEKIGUCHI M., UCHIDA H., Boron neutron capture therapy using 10B entrapped anti-CEA immunoliposome, *Hum. Cell*, **1989**, 2(3), 290–296.
- 47 YANAGIE H., TOMITA T., KOBAYASHI H., FUJII Y., TAKAHASHI T., HASUMI K., NARIUCHI H., SEKIGUCHI M., Application of boronated anti-CEA immunoliposome to tumour cell growth inhibition in in vitro boron neutron capture therapy model, *Br. J. Cancer*, **1991**, 63(4), 522–526.
- 48 YANAGIE H., TOMITA T., KOBAYASHI H., FUJII Y., NONAKA Y., SAEGUSA Y., HASUMI K., ERIGUCHI M., KOBAYASHI T., ONO K., Inhibition of human pancreatic cancer growth in nude mice by boron neutron capture therapy, *Br. J. Cancer*, **1997**, 75(5), 660–665.
- 49 YANAGIE H., KOBAYASHI H., TAKEDA Y., YOSHIZAKI I., NONAKA Y., NAKA S., NOJIRI A., SHINNKAWA H., FURUYA Y., NIWA H., ARIKI K., YASUHARA H., ERIGUCHI M., Inhibition of growth of human breast cancer cells in culture by neutron capture using liposomes containing 10B, *Biomed. Pharmacother.*, **2002**, 56(2), 93–99.
- 50 YANAGIE H., OGURA K., TAKAGI K., MARUYAMA K., MATSUMOTO T., SAKURAI Y., SKVARC J., ILLIC R., KUHNE G., HISA T., YOSHIZAKI I., KONO K., FURUYA Y., SUGIYAMA H., KOBAYASHI H., ONO K., NAKAGAWA K., ERIGUCHI M., Accumulation of boron compounds to tumor with polyethylene-glycol binding liposome by using neutron capture

- autoradiography, *Appl. Radiat. Isot.*, **2004**, 61(4), 639–646.
- 51 MARUYAMA K., ISHIDA O., KASAOKA S., TAKIZAWA T., UTOGUCHI N., SHINOHARA A., CHIBA M., KOBAYASHI H., ERIGUCHI M., YANAGIE H., Intracellular targeting of sodium mercaptoundecahydrododecaborate (BSH) to solid tumors by transferrin-PEG liposomes for boron neutron-capture therapy (BNCT), *J. Controlled Release*, **2004**, 98(2), 195–207.
- 52 LASTER B. H., KAHL S. B., POPENOE E. A., PATE D. W., FAIRCHILD R. G., Biological efficacy of boronated low-density lipoprotein for boron neutron capture therapy as measured in cell culture, *Cancer Res.*, **1991**, 51(17), 4588–4593.
- 53 HOFMANN B., FISCHER C. O., LAWACZEK R., PLATZKE J., SEMMLER W., Gadolinium neutron capture therapy (GdNCT) of melanoma cells and solid tumors with the magnetic resonance imaging contrast agent Gadobutrol, *Invest. Radiol.*, **1999**, 34, 126–133.
- 54 KHOKHLOV V. F., YASHKIN P. N., SILIN D. I., DJOROVA E. S., LAWACZEK R., Neutron capture therapy with Gd-DTPA in tumor-bearing rats, in *Cancer Neutron Capture Therapy* (Y. MISHIMA, ed.), Plenum Press, New York, **1996**, pp. 865–869.
- 55 LAWACZEK R., FISCHER C. O., KRÜGER U., LEUTHER W., MENRAD J., Gadolinium neutron capture therapy (GdNCT) with MRI contrast media. In vitro study, in *Cancer Neutron Capture Therapy* (Y. MISHIMA, ed.), Plenum Press, New York, **1996**, pp. 859–864.
- 56 AKINE Y., TOKITA N., TOKUUYE K., SATOH M., CHUREI H., PECHOUX C. L., KOBAYASHI T., KANDA K., Suppression of rabbit VX-2 subcutaneous tumor growth by gadolinium neutron capture therapy, *Jpn. J. Cancer Res.*, **1993**, 84, 841–843.
- 57 AKINE Y., TOKITA N., TOKUUYE K., SATOH M., KOBAYASHI T., KANDA K., Electron-equivalent dose for the effect of gadolinium neutron capture therapy on the growth of subcutaneously-inoculated Ehrlich tumor cells in mice, *Jpn. J. Clin. Oncol.*, **1993**, 23, 145–148.
- 58 AKINE Y., TOKITA N., MATSUMOTO T., OYAMA H., EGAWA S., AIZAWA O., Radiation effect of gadolinium-neutron capture reactions on survival of Chinese hamster cells, *Strahlenther. Onkol.*, **1990**, 166, 831–833.
- 59 TAKAGAKI M., ODA T., MIYATAKE S., KIKUCHI H., KOBAYASHI T., KANDA K., UJENO Y., Killing effects of gadolinium neutron capture reactions on brain tumors, in *Progress in Neutron Capture Therapy for Cancer* (ALLEN B. J. et al. eds.), Plenum Press, New York, **1992**, pp. 407–410.
- 60 MATSUMOTO T., Transport calculations of depth-dose distributions for gadolinium neutron capture therapy, *Phys. Med. Biol.*, **1992**, 37, 155–162.
- 61 FUKUMORI Y., ICHIKAWA H., TOKUMITSU H., MIYAMOTO M., JONO K., KANAMORI R., AKINE Y., TOKITA N., Design and preparation of ethyl cellulose microcapsules of gadopentetate dimeglumine for neutron-capture therapy using the Wurster process, *Chem. Pharm. Bull.*, **1993**, 41, 1144–1148.
- 62 AKINE Y., TOKITA N., TOKUUYE K., SATOH M., FUKUMORI Y., TOKUMITSU H., KANAMORI R., KOBAYASHI T., KANDA K., Neutron-capture therapy of murine ascites tumor with gadolinium-containing microcapsules, *J. Cancer Res. Clin. Oncol.*, **1992**, 119, 71–73.
- 63 KOBAYASHI H., KAWAMOTO S., SAGA T., SATO N., ISHIMORI T., KONISHI J., ONO K., TOGASHI K., BRECHBIEL M. W., Avidin-dendrimer-1B4M-Gd(254): A tumor-targeting therapeutic agent for gadolinium neutron capture therapy of intraperitoneal disseminated tumor which can be monitored by MRI, *Bioconj. Chem.*, **2001**, 12, 587–593.
- 64 DE STASIO G., CASALBONE P., PALLINI R., GILBERT B., SANITA F., CIOTTI M. T., ROSI G., FESTINESI A., LAROCCHA L. M., RINELLI A., PERRET D., MOGK D. W., PERFETTI P., MEHTA M. P., MERCANTI D., Gadolinium in human glioblastoma cells for gadolinium

- neutron capture therapy, *Cancer Res.*, **2001**, *61*, 4272–4277.
- 65 DE STASIO G., RAJESH D., CASALBORE P., DANIELS M. J., ERHARDT R. J., FRAZER B. H., WIESE L. M., RICHTER K. L., SONDEREGGER B. R., GILBERT B., SCHAUB S., CANNARA R. J., CRAWFORD J. F., GILLES M. K., TYLISZCZAK T., FOWLER J. F., LAROCCA L. M., HOWARD S. P., MERCANTI D., MEHTA M. P., PALLINI R., Are gadolinium contrast agents suitable for gadolinium neutron capture therapy? *Neurol. Res.*, **2005**, *27*(4), 387–398.
- 66 OYEWUMI M. O., MUMPER R. J., Gadolinium-loaded nanoparticles engineered from microemulsion templates, *Drug Dev. Ind. Pharm.*, **2002**, *28*(3), 317–328.
- 67 OYEWUMI M. O., MUMPER R. J., Engineering tumor-targeted gadolinium hexanedione nanoparticles for potential application in neutron capture therapy, *Bioconj. Chem.*, **2002**, *13*(6), 1328–1335.
- 68 OYEWUMI M. O., LIU S., MOSCOW J. A., MUMPER R. J., Specific association of thiamine-coated gadolinium nanoparticles with human breast cancer cells expressing thiamine transporters, *Bioconj. Chem.*, **2003**, *14*(2), 404–411.
- 69 OYEWUMI M. O., YOKEL R. A., JAY M., COAKLEY T., MUMPER R. J., Comparison of cell uptake, biodistribution and tumor retention of folate-coated and PEG-coated gadolinium nanoparticles in tumor-bearing mice, *J. Controlled Release*, **2004**, *95*(3), 613–626.
- 70 HANSRANI P. K., DAVIS S. S., GROVES M. J., *J. Parenteral Sci. Technol.*, **1983**, *37*, 145–150.
- 71 WISSE E. J., *Ultrstruct. Res.*, **1970**, *31*, 125–150.
- 72 (a) ALLEN T. M., EVEREST J. M., *J. Pharmacol. Exp. Ther.*, **1983**, *226*, 539–544; (b) SENIOR J. H., *Crit. Rev. Ther. Drug Carrier Syst.*, **1987**, *3*, 123–193; (c) SATO Y., KIWADA H., KATO Y., *Chem. Pharm. Bull.*, **1986**, *34*, 4244–4252; (d) WOODLE M. C., LASIC D. D., *Biochim. Biophys. Acta*, **1992**, *1113*, 171–199.
- 73 MIYAMOTO M., HIRANO K., ICHIKAWA H., FUKUMORI Y., AKINE Y., TOKUUYE K., *Chem. Pharm. Bull.*, **1999**, *47*, 203–208.
- 74 (a) HNATOWICH D. J., FRIEDMAN B., CLANCY B., NOVAK M., *J. Nucl. Med.*, **1981**, *22*, 810–814; (b) KABALKA G. W., DAVIS M. A., MOSS T. H., BUONOCORE E., HUBNER K., HOLMBERG E., MARUYAMA K., HUANG L., *Magn. Reson. Med.*, **1991**, *19*, 406–415.
- 75 (a) YANAI S., OKADA H., SAITO K., KUGE Y., OGAWA Y., TOGUCHI H., *Int. J. Pharm.*, **1995**, *123*, 237–245; (b) NATSUME H., IMAMIZU M., SUGIBAYASHI K., SHIBATA T., MIYAGAWA A., MORIMOTO Y., *Chem. Pharm. Bull.*, **1992**, *40*, 1545–1552.
- 76 TOKUUYE K., TOKITA N., AKINE Y., KOBAYASHI T., KANDA K., in *Advances in Neutron Capture Therapy* (SOLOWAY A. H., BARTH R. F., CARPENTER D. E., eds.), Plenum Press, New York, **1993**, pp. 245–248.
- 77 MIYAMOTO M., HIRANO K., ICHIKAWA H., FUKUMORI Y., AKINE Y., TOKUUYE K., Biodistribution of gadolinium incorporated in lipid-emulsions intraperitoneally administered for neutron-capture therapy with tumor-bearing hamsters, *Biol. Pharm. Bull.*, **1999**, *22*, 1331–1340.
- 78 HIRANO K., HUNT C. A., *J. Pharm. Sci.*, **1985**, *74*, 915–921.
- 79 KLEIN M. D., CORAN A. G., DRONGOWSKI R. A., WESLEY J. R., *J. Pediatr. Surg.*, **1985**, *20*, 765–771.
- 80 COURTICE F. C., HARDING J., STEINBECK A. W., *Aust. J. Exp. Biol.*, **1953**, *31*, 215–226.
- 81 ALLEN L., *Anat. Rec.*, **1956**, *124*, 639–657.
- 82 GREENE H. S. N., *Cancer Res.*, **1958**, *18*, 422–425.
- 83 *Cancer Neutron Capture Therapy* (MISHIMA Y., ed.), Plenum Press, New York, **1996**, (a) MISHIMA Y., pp. 1–26; (b) HONDA C., WADABAYASHI N., YOSHINO K., HIRATSUKA J., KARASHIMA H., KOBAYASHI T., FUKUDA H., ICHIHASHI M., MISHIMA Y., pp. 679–684.
- 84 (a) ECKELMAN W. C., KARESH S. M., REBA R. C., *J. Pharm. Sci.*, **1975**, *64*,

- 704–706; (b) KABALKA G. W., BUONOCORE E., HUBNER K., DAVIS M., HUANG L., *Magn. Reson. Med.*, **1988**, *8*, 89–95.
- 85 WATANABE T., ICHIKAWA H., FUKUMORI Y., Tumor accumulation of gadolinium in lipid-nanoparticles intravenously injected for neutron-capture therapy of cancer, *Eur. J. Pharm. Biopharm.*, **2002**, *54*, 119–124.
- 86 ELLENS H., MORSELT H., SCHERPHOF G., In vivo fate of large unilamellar sphingomyelin-cholesterol liposomes after intraperitoneal and intravenous injection into rats, *Biochim. Biophys. Acta*, **1981**, *674*, 10–18.
- 87 HIRANO K., HUNT A., Lymphatic transport of liposome-encapsulated agents: Effects of liposome size following intraperitoneal administration, *J. Pharm. Sci.*, **1985**, *74*, 915–921.
- 88 PARKER R. J., PRIESTER E. R., SIEBER S. M., Comparison of lymphatic uptake, metabolism, excretion, and biodistribution of free and liposome-entrapped [<sup>14</sup>C]cytosine β-D-arabinofuranoside following intraperitoneal administration to rats, *Drug Metab. Dispos.*, **1982**, *10*, 40–46.
- 89 DAMS E. T. M., LAVERMAN P., OYEN W. J. G., STORM G., SCHERPHOF G. L., VAN DER MEER J. W. M., CORSTENS F. H. M., BOERMAN O. C., Accelerated blood clearance and altered biodistribution of repeated injections of sterically stabilized liposomes, *J. Pharmacol. Exp. Ther.*, **2000**, *292*, 1071–1079.
- 90 OUSSOREN C., STORM G., Effect of repeated intravenous administration on the circulation kinetics of poly(ethyleneglycol)-liposomes in rats, *J. Liposome Res.*, **1999**, *9*, 349–355.
- 91 JONAH M. M., CERNY E. A., RAHMAN Y. E., Tissue distribution of EDTA encapsulated within liposomes of varying surface properties, *Biochim. Biophys. Acta*, **1975**, *401*, 336–348.
- 92 NAGAYASU A., UCHIYAMA K., NISHIDA T., YAMAGIWA Y., KAWAI Y., KIWADA H., Is control of distribution of liposomes between tumors and bone marrow possible? *Biochim. Biophys. Acta*, **1996**, *1278*, 29–34.
- 93 MATSUMURA A., SHIBATA Y., YAMAMOTO T., NAKAGAWA K., YASUDA S., NAKAJIMA S., SAKATA I., YOSHIZAWA T., NOSE T., Mn-metalloporphyrin conjugated with Gd-DTPA (Gd-ATN10): Tumor enhancement agent for magnetic resonance imaging, *Neurol. Med. Chir. (Tokyo)*, **1997**, *37*, 327–331.
- 94 KAS H. S., *J. Microencapsulat.*, **1997**, *14*(6), 689–711.
- 95 PAUL W., SHARMA C. P., *S.T.P. Pharma. Sci.*, **2000**, *10*(1), 5–22.
- 96 REGE P. R., SHUKLA D. J., BLOCK L. H., *Int. J. Pharm.*, **1999**, *181*, 49–60.
- 97 SHU X. Z., ZHU K. J., *Int. J. Pharm.*, **2000**, *201*, 51–58.
- 98 KAWASHIMA Y., HANDA T., KASAI A., TAKENAKA H., LIN S. Y., ANDO Y., *J. Pharm. Sci.*, **1985**, *74*(3), 264–268.
- 99 MI F. L., SYU S. S., CHEN C. T., SCHOUNG J. Y., *Biomaterials*, **1999**, *20*, 1603–1612.
- 100 CALVO P., REMUÑÁN-LÓPEZ C., VILA-IATO J. L., ALONSO M. J., *J. Appl. Polym. Sci.*, **1997**, *63*, 125–132.
- 101 ILLUM L., FARRAJ N., DAVIS S. S., *Pharm. Res.*, **1994**, *11*(8), 1186–1189.
- 102 CALVO P., REMUÑÁN-LÓPEZ C., VILA-IATO J. L., ALONSO M. J., *Pharm. Res.*, **1997**, *14*(10), 1431–1436.
- 103 ERBACHER P., ZOU S., BETTINGER T., STEFFAN A. M., REMY J. S., *Pharm. Res.*, **1998**, *15*(9), 1332–1339.
- 104 HASSAN E. E., PARISH R. C., GALLO J. M., *Pharm. Res.*, **1992**, *9*(3), 390–397.
- 105 PAVANETTO F., PERUGINI P., CONTI B., MODENA T., GENTA I., *J. Microencapsulat.*, **1996**, *13*(6), 679–688.
- 106 GANZA-GONZÁLEZ ANGUIANO-IGEA S., OTEO-ESPINAR F. J., MÉNDEZ J. B., *Eur. J. Pharm. Biopharm.*, **1999**, *48*, 149–155.
- 107 HUNG R. G., SCHWARTZ J. B., OFNER III C. M., *Pharm. Dev. Technol.*, **1999**, *4*(1), 107–115.
- 108 TOKUMITSU H., ICHIKAWA H., FUKUMORI Y., BLOCK L. H., Preparation of gadopentetic acid-loaded chitosan microparticles for gadolinium neutron-capture therapy of

- cancer by a novel emulsion-droplet coalescence technique, *Chem. Pharm. Bull.*, **1999**, *47*, 838–842.
- 109 TOKUMITSU H., ICHIKAWA H., FUKUMORI Y., Chitosan-gadopentetic acid complex nanoparticles for gadolinium neutron-capture therapy of cancer: Preparation by novel emulsion-coalescence technique and characterization, *Pharm. Res.*, **1999**, *16*, 1830–1835.
- 110 NISHIOKA Y., KYOTANI S., OKAMURA M., MIYAZAKI M., OKAZAKI K., OHNISHI S., YAMAMOTO Y., ITO K., Release characteristics of cisplatin chitosan microspheres and effect of containing chitin, *Chem. Pharm. Bull.*, **1990**, *38*, 2871–2873.
- 111 OHYA Y., TAKEI T., KOBAYASHI H., OUCHI T., Release behavior of 5-fluorouracil from chitosan-gel microspheres immobilizing 5-fluorouracil derivative coated with polysaccharides and their cell specific recognition, *J. Microencapsulat.*, **1993**, *10*, 1–9.
- 112 AKBUGA J., DURMAZ G., Preparation and evaluation of crosslinked chitosan microspheres containing furosemide, *Int. J. Pharm.*, **1994**, *111*, 217–222.
- 113 HASSAN E. E., PARISH R. C., GALLO J. M., Optimized formulation of magnetic chitosan microspheres containing the anticancer agent, oxantrazole, *Pharm. Res.*, **1992**, *9*, 390–397.
- 114 THANOO B. C., SUNNY M. C., JAYAKRISHNAN A., Cross-linked chitosan microspheres: Preparation and evaluation as a matrix for the controlled release of pharmaceuticals, *J. Pharm. Pharmacol.*, **1992**, *44*, 283–286.
- 115 JAMEELA S. R., JAYAKRISHNAN A., Glutaraldehyde cross-linked chitosan microspheres as a long acting biodegradable drug delivery vehicle: Studies on the in vitro release of mitoxantrone and in vivo degradation of microspheres in rat muscle, *Biomaterials*, **1995**, *16*, 769–775.
- 116 POLK A., AMSDEN B., DE YAO K., PENG T., GOOSEN M. F. A., Controlled release of albumin from chitosan-alginate microcapsules, *J. Pharm. Sci.*, **1994**, *83*, 178–185.
- 117 LIU L. S., LIU S. Q., NG S. Y., FROIX M., OHNO T., HELLER J., Controlled release of interleukin-2 for tumour immunotherapy using alginate/chitosan porous microspheres, *J. Controlled Release*, **1997**, *43*, 65–74.
- 118 BERTHOLD A., CREMER K., KREUTER J., Preparation and characterization of chitosan microspheres as drug carrier for prednisolone sodium phosphate as model for anti-inflammatory drugs, *J. Controlled Release*, **1996**, *39*, 17–25.
- 119 CALVO P., REMUÑAN-LÓPEZ C., VILAJATO J. L., ALONSO M. J., Chitosan and chitosan/ethylene oxide-propylene oxide block copolymer nanoparticles as novel carriers for proteins and vaccines, *Pharm. Res.*, **1997**, *14*, 1431–1436.
- 120 TOKUMITSU H., HIRATSUKA J., SAKURAI Y., KOBAYASHI T., ICHIKAWA H., FUKUMORI Y., Gadolinium neutron capture therapy using novel gadopentetic acid chitosan complex nanoparticles: In vivo growth suppression of experimental melanoma solid tumor, *Cancer Lett.*, **1999**, *150*, 177–182.
- 121 ICHIHASHI M., SASASE A., HIRAMOTO T., FUNASAKA Y., HAITA S., MISHIMA Y., KOBAYASHI T., FUKUDA H., YOSHINO K., Relative biological effectiveness (RBE) of thermal neutron capture therapy of cultured B-16 melanoma cells preincubated with 10B-paraboronophenylalanine, *Pigment Cell Res.*, **1989**, *2*, 325–329.
- 122 FUKUDA H., KOBAYASHI T., MATSUZAWA T., KANDA K., ICHIHASHI M., MISHIMA Y., RBE of a thermal neutron beam and the 10B (n, $\alpha$ ) 7Li reaction on cultured B-16 melanoma cells, *Int. J. Radiat. Biol.*, **1987**, *51*, 167–175.
- 123 HIRATSUKA J., FUKUDA H., KOBAYASHI T., KARASHIMA H., YOSHINO K., IMAJO Y., MISHIMA Y., The relative biological effectiveness of 10B-neutron capture therapy for early skin reaction in the hamster, *Radiat. Res.*, **1991**, *128*, 186–191.
- 124 KOBAYASHI T., KANDA K., FUJITA Y.,

- SAKURAI Y., ONO K., The upgrade of the heavy water facility of the Kyoto University Reactor for neutron capture therapy, in *Advances in Neutron Capture Therapy* (LARSSON B. et al. eds.), Elsevier Science, Amsterdam, 1997, vol. I, pp. 321–325.
- 125 HE P., DAVIS S. S., ILLUN L., *Int. J. Pharm.*, 1998, 166, 75–88.
- 126 LUEBEN H. L., LEEUW B. J. D., LANGEMEYER M. W. E., BOER A. G., VERHOEF J. C., JUNGINGER H. E., *Pharm. Res.*, 1996, 13(11), 1668–1672.
- 127 DESAI M. P., LABHASETWAR V., WALTER E., LEVY R. J., AMIDON G. L., *Pharm. Res.*, 1997, 14(11), 1568–1573.
- 128 CHATELET C., DAMOUR O., DOMARD A., *Biomaterials*, 2001, 22(3), 261–268.
- 129 SHIKATA F., TOKUMITSU H., ICHIKAWA H., FUKUMORI Y., In vitro cellular accumulation of gadolinium incorporated into chitosan nanoparticles designed for neutron-capture therapy of cancer, *Eur. J. Pharm. Biopharm.*, 2002, 53, 57–63.
- 130 CHOKSAKULNIMITR S., MASUDA S., TOKUDA H., TAKAKURA Y., HASHIDA M., *J. Controlled Release*, 1995, 34(3), 233–241.
- 131 GREEN T. R., FISHER J., STONE M., WROBLEWSKI B. M., INGHAM E., *Biomaterials*, 1998, 19, 2297–2302.
- 132 LEE K. D., HONG K., PAPAHAJIOPOULOS D., *Biochem. Biophys. Acta*, 1992, 1103, 185–197.
- 133 TOKUMITSU H., HIRATSUKA J., SAKURAI Y., SHIKATA F., ICHIKAWA H., FUKUMORI Y., KOBAYASHI T., Gadolinium neutron-capture therapy trial using gadopentetic acid-chitosan complex nanoparticles: Effect of gadolinium dose on tumor growth suppression in vivo, *Kyoto University Research Reactor Progress Report, Section I*, 1998, p. 179.
- 134 TOKUUYE K., TOKITA N., AKINE Y., NAKAYAMA H., SAKURAI Y., KOBAYASHI T., KANDA K., Comparison of radiation effects of gadolinium and boron neutron capture reactions, *Strahlenther. Onkol.* 2000, 176, 81–83.

## 4

## Nanovehicles and High Molecular Weight Delivery Agents for Boron Neutron Capture Therapy<sup>1)</sup>

Gong Wu, Rolf F. Barth, Weilian Yang, Robert Lee, Werner Tjarks, Marina V. Backer, and Joseph M. Backer

## 4.1

### Introduction

## 4.1.1

#### Overview

Boron neutron capture therapy (BNCT) is based on the nuclear capture and fission reactions that occur when non-radioactive boron-10 is irradiated with low energy thermal neutrons to yield high linear energy transfer (LET) alpha particles ( $^4\text{He}$ ) and recoiling lithium-7 ( $^7\text{Li}$ ) nuclei. For BNCT to be successful, a sufficient number of  $^{10}\text{B}$  atoms ( $\sim 10^9$  atoms per cell) must be selectively delivered to the tumor and enough thermal neutrons must be absorbed by them to sustain a lethal  $^{10}\text{B}(n, \alpha) ^7\text{Li}$  capture reaction. BNCT primarily has been used to treat patients with brain tumors, and more recently those with head and neck cancer. Two low molecular weight (LMW) boron delivery agents are currently used clinically, sodium borocaptate and boronophenylalanine. However, various high molecular weight (HMW) agents consisting of macromolecules and nanovehicles have been developed. This chapter focuses on the latter, which include monoclonal antibodies, dendrimers, liposomes, dextrans, polylysine, folate receptor targeting agents, epidermal and vascular endothelial growth factors (EGF and VEGF). Procedures for introducing boron atoms into these HMW agents and their chemical properties will be discussed. *In vivo* studies on their biodistribution will be described, and the efficacy of a subset of them, which have been used for BNCT of tumors in experimental animals, will be discussed. Since brain tumors currently are the primary candidates for treatment by BNCT, delivery of these HMW agents across the blood-brain barrier presents a special challenge. Various routes of administration will be discussed, including receptor-facilitated transcytosis following intravenous admin-

1) We thank Bentham Science Publishers, Ltd for granting copyright release to republish the text and figures of this article.

istration, direct intratumoral injection and convection-enhanced delivery by which a pump is used to apply a pressure gradient to establish bulk flow of the HMW agent during interstitial infusion. Finally, we conclude with a discussion relating to issues that must be addressed if these HMW agents are to be used clinically.

#### 4.1.2

### General Background

After decades of intensive research, high grade gliomas, and specifically glioblastoma multiforme (GBM), are still extremely resistant to all current forms of therapy, including surgery, chemotherapy, radiotherapy, immunotherapy and gene therapy [1–5]. The five-year survival rate of patients diagnosed with GBM in the United States is less than a few percent [6, 7] despite aggressive treatment using combinations of therapeutic modalities. This is due to the infiltration of malignant cells beyond the margins of resection and their spread into both gray and white matter by the time of surgical resection [8, 9]. High grade gliomas are histologically complex and heterogeneous in their cellular composition. Recent molecular genetic studies of gliomas have shown how complex the development of these tumors is [10]. Glioma cells and their neoplastic precursors have biologic properties that allow them to evade a tumor-associated host immune response [11], and biochemical properties that allow them to invade the unique extracellular environment of the brain [12, 13]. Consequently, high grade supratentorial gliomas must be regarded as a whole brain disease [14]. The inability of chemo- and radiotherapy to cure patients with high grade gliomas is due to their failure to eradicate micro-invasive tumor cells within the brain. To successfully treat these tumors, therefore, strategies must be developed that can selectively target malignant cells with little or no effect on normal cells and tissues adjacent to the tumor.

BNCT is based on nuclear capture and fission reactions that occur when non-radioactive  $^{10}\text{B}$  is irradiated with low energy thermal neutrons to yield high LET alpha particles ( $^4\text{He}$ ) and recoiling  $^7\text{Li}$  nuclei. In order to be successful BNCT, sufficient  $^{10}\text{B}$  atoms ( $\sim 10^9$  atoms per cell) must be delivered selectively to the tumor and enough thermal neutrons must be absorbed by them to sustain a lethal  $^{10}\text{B}(n,\alpha)^7\text{Li}$  capture reaction. The destructive effects of these high-energy particles are limited to boron-containing cells. BNCT primarily has been used to treat high grade gliomas [15, 16], and either cutaneous primaries [17] or cerebral metastases of melanoma [18]. More recently, it also has been used to treat patients with head and neck [19, 20] and metastatic liver cancer [21, 22]. BNCT is a biologically rather than physically targeted type of radiation treatment. If sufficient amounts of  $^{10}\text{B}$  and thermal neutrons can be delivered to the target volume, the potential exists to destroy tumor cells dispersed in the normal tissue parenchyma. Readers interested in more in-depth coverage of other topics related to BNCT are referred to several recent reviews and monographs [15, 23–25]. The present chapter focuses on boron-containing macromolecules and nanovehicles as boron delivery agents.



## 4.2

## General Requirements for Boron Delivery Agents

A successful boron delivery agent should have (1) no or minimal systemic toxicity with rapid clearance from blood and normal tissues; (2) high tumor ( $\sim 20 \mu\text{g}^{-10}\text{B g}^{-1}$ ) and low normal tissue uptake; (3) high tumor:brain (T:Br) and tumor:blood (T:Bl) concentration ratios ( $>3\text{--}4:1$ ); and (4) persistence in the tumor for a sufficient period of time to carry out BNCT. At this time *no* single boron delivery agent fulfills all these criteria. However, as a result of new synthetic techniques and increased knowledge of the biological and biochemical requirements for an effective agent, several promising new boron agents have emerged, and these are described in a special issue of *Anti-Cancer Agents in Medicinal Chemistry* (6, 2, 2006). The major challenge in their development has been the requirement for specific tumor targeting to achieve boron concentrations sufficient to deliver therapeutic doses of radiation to the tumor with minimal normal tissue toxicity. The selective destruction of GBM cells in the presence of normal cells represents an even greater challenge than malignancies at other anatomic sites.

## 4.3

## Low Molecular Weight Delivery Agents

In the 1950s and early 1960s clinical trials of BNCT were carried out using boric acid and some of its derivatives as delivery agents. These simple chemical compounds had poor tumor retention, attained low T:Br ratios and were non-selective [26, 27]. Among the hundreds of low-molecular weight boron-containing compounds that were synthesized, two appeared to be promising. One, based on aryl-boronic acids [28], was L-4-dihydroxyborylphenylalanine, referred to as boronophenylalanine or BPA (Fig. 4.1, 1). The second, a polyhedral borane anion, was

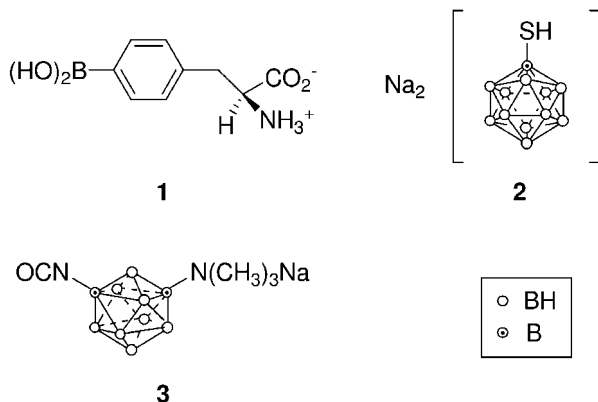


**Fig. 4.1.** Structure of two compounds used clinically for BNCT, dihydroxyborylphenylalanine or boronophenylalanine (BPA, 1) and disodium borocaptate (BSH, 2), and the isocyanato polyhedral borane (3), which has been used to heavily boronate dendrimers.

sodium mercaptoundecahydro-*closo*-dodecaborate [29], more commonly known as sodium borocaptate or BSH (2). These two compounds persisted longer in animal tumors than did related molecules, attained T:Br and T:Bi boron ratios > 1 and had low toxicity.  $^{10}\text{B}$ -enriched BPA, complexed with fructose to improve its water solubility, and BSH have been used clinically for BNCT of brain, as well as extracranial tumors. Although their selective accumulation in tumors is not ideal, the safety of these two drugs following i.v. administration has been well established [30, 31].

#### 4.4

#### High Molecular Weight Boron Delivery Agents

High molecular weight (HMW) delivery agents usually contain a stable boron group or cluster linked via a hydrolytically stable bond to a tumor-targeting moiety, such as monoclonal antibodies (mAbs) or low molecular weight receptor targeting ligands. Examples of these include epidermal growth factor (EGF) or the mAb cetuximab (IMC-C225) to target the EGF receptor or its mutant isoform EGFRvIII, which are overexpressed in various malignant tumors, including gliomas and squamous cell carcinomas of the head and neck [32]. Agents that are to be administered systemically should be water soluble, but lipophilicity is important in order to cross the blood–brain barrier (BBB) and diffuse within the brain and the tumor. There should be a favorable differential in boron concentrations between tumor and normal brain, thereby enhancing their tumor specificity. Their amphiphilic character is not as crucial for LMW agents that target specific biological transport systems and/or are incorporated into nanovehicles such as liposomes. Molecular weight also is an important factor, since it determines the rate of diffusion both within the brain and the tumor. Detailed reviews of the state-of-the-art of compound development for BNCT have been published [33, 34]. The present chapter focuses on boron-containing macromolecules and liposomes as delivery agents for BNCT, and how they can be most effectively administered.

#### 4.5

#### Dendrimer-related Delivery Agents

##### 4.5.1

##### Properties of Dendrimers

Dendrimers are synthetic polymers with a well-defined globular structure. They are composed of a core molecule, repeat units that have three or more functionalities, and reactive surface groups (Fig. 4.2) [35, 36]. Two techniques have been used to synthesize these macromolecules: divergent growth outwards from the core [37], or convergent growth from the terminal groups inwards towards the core [36, 38]. Regular and repeated branching at each monomer group gives rise to a symmetric structure and pattern to the entire globular dendrimer. Dendrimers are an attrac-

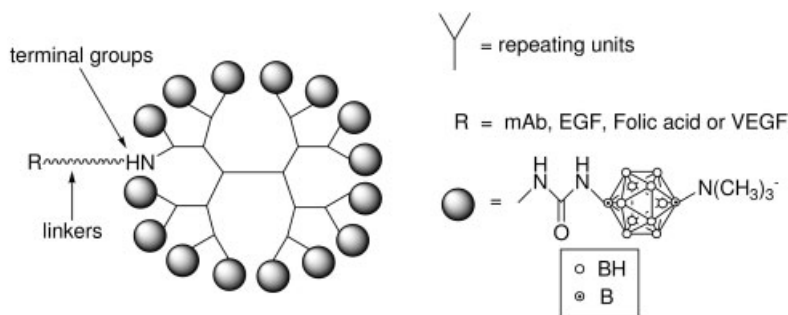


**Fig. 4.2.** Structure of a boronated PAMAM dendrimer that has been linked to targeting moieties. PAMAM dendrimers consist of a core, repeating polyamido amino units, and reactive terminal groups. Each successfully higher generation of PAMAM dendrimer has a

geometrically incremental number of terminal groups. Dendrimers have been boronated by reaction with water-soluble isocyanato polyhedral boranes and subsequently attached to targeting moieties by means of heterobifunctional linkers.

tive platform for macromolecular imaging and gene delivery because of their low cytotoxicity and their multiple types of reactive terminal groups [36, 39–44].

#### 4.5.2

#### Boronated Dendrimers Linked to Monoclonal Antibodies

##### 4.5.2.1 Boron Clusters Directly Linked to mAb

Monoclonal antibodies have been attractive targeting agents for delivering radio-nuclides [45], drugs [46–50], toxins [51] and boron to tumors [52–55]. Before the introduction of dendrimers as boron carriers, boron compounds were directly attached to mAbs [53, 54]. Approximately  $\sim 10^9$   $^{10}\text{B}$  atoms per cell ( $\sim 20 \mu\text{g g}^{-1}$  tumor) must be delivered to kill tumor cells [55, 56]. Based on the assumption of  $10^6$  antigenic receptor sites per cell,  $\sim 50$ – $100$  boron cage structures of carboranes, or polyhedral borane anions and their derivatives must be linked to each mAb molecule to deliver the required amount of boron for NCT. The attachment of such a large number of boron cages to a mAb may result in precipitation of the bioconjugate or a loss of its immunological activity. Solubility can be improved by inserting a water-soluble gluconamide group into the protein-binding boron cage compounds, thereby enhancing their water solubility [57]. This modification makes it possible to incorporate up to 1100 boron atoms into a human gamma globulin (HGG) molecule without any precipitation. Other approaches to enhance solubility include the use of negatively charged carboranes [58] or polyhedral borane anions [59], as well as the insertion of carbohydrate groups [60, 61]. A major limitation of using an agent containing a single boron cage is that many sites must be modified to deliver  $10^3$  boron atoms per molecule of antibody and this can reduce its immunoreactivity activity. Alam et al. have shown that attachment of an average of

1300 boron atoms to mAb 17-1A, which is directed against human colorectal carcinoma cells, resulted in a 90% loss of immunoreactivity [62].

#### 4.5.2.2 Attachment of Boronated Dendrimers to mAb

Dendrimers are one of the most attractive polymers that have been used as boron carriers due to their well-defined structure and multiple reactive terminal groups. Depending on the antigen site density, ~1000 boron atoms need to be attached per molecule of dendrimer and subsequently linked to the mAb. In our first study, second- and fourth-generation polyamido amino (PAMAM or “starburst”) dendrimers, which have 12 and 48 reactive terminal amino groups, respectively, were reacted with the water-soluble isocyanato polyhedral borane [Na(CH<sub>3</sub>)<sub>3</sub>NB<sub>10</sub>H<sub>8</sub>NCO] (3, Fig. 4.1) [63, 64]. The boronated dendrimer then was linked to the mAb IB16-6, which is directed against the murine B16 melanoma, by means of two heterobifunctional linkers, *m*-maleimidobenzoyl-*N*-hydroxysulfosuccinimide ester (sulfo-MBS) and *N*-succinimidyl 3-(2-pyridyldithio)propionate (SPDP) [63, 65]. However, following intravenous (i.v.) administration, large amounts of the bioconjugate accumulated in the liver and spleen and it was concluded that random conjugation of boronated dendrimers to a mAb could alter its binding affinity and biodistribution. To minimize the loss of mAb reactivity, a 5<sup>th</sup> generation PAMAM dendrimer was boronated with the same polyhedral borane anion, and more recently it was site-specifically linked to the anti-EGFR mAb cetuximab (or IMC-C225) or the EGFRvIII specific mAb L8A4 (Fig. 4.3). Cetuximab was linked via glycosidic moieties in the Fc region by means of two heterobifunctional reagents, SPDP and *N*-( $\kappa$ -maleimidoundecanoic acid) hydrazide (KMUH) [66, 67]. The resulting bioconjugate, designated C225-G5-B<sub>1100</sub>, contained ~1100 boron atoms per molecule of cetuximab and retained its aqueous solubility in 10% DMSO and its *in vitro* and *in vivo* immunoreactivity. As determined by a competitive binding assay, there was a <1 log unit decrease in affinity for EGFR(+) glioma cell line F98<sub>EGFR</sub>, compared to that of unmodified cetuximab [66]. *In vivo* biodistribution studies, carried out 24 h after intratumoral (i.t.) administration of the bioconjugate, demonstrated that 92.3  $\mu\text{g g}^{-1}$  of boron was retained in rats bearing F98<sub>EGFR</sub> gliomas compared to 36.5  $\mu\text{g g}^{-1}$  in EGFR(-) F98 parental tumors and 6.7  $\mu\text{g g}^{-1}$  in normal brain [67] thereby indicating specific molecular targeting of the receptor.

### 4.5.3

#### Boronated Dendrimers Delivered by Receptor Ligands

##### 4.5.3.1 Epidermal Growth Factors (EGF)

Due to its increased expression in various human tumors, including high grade gliomas, and its low or undetectable expression in normal brain, EGFR is an attractive target for cancer therapy [68–70]. As described above, targeting of EGFR has been carried out using either mAbs or alternatively, as described in this section, EGF, which is a single-chain, 53-mer heat- and acid-stable polypeptide. It binds to a transmembrane glycoprotein with tyrosine kinase activity, which triggers dimeri-

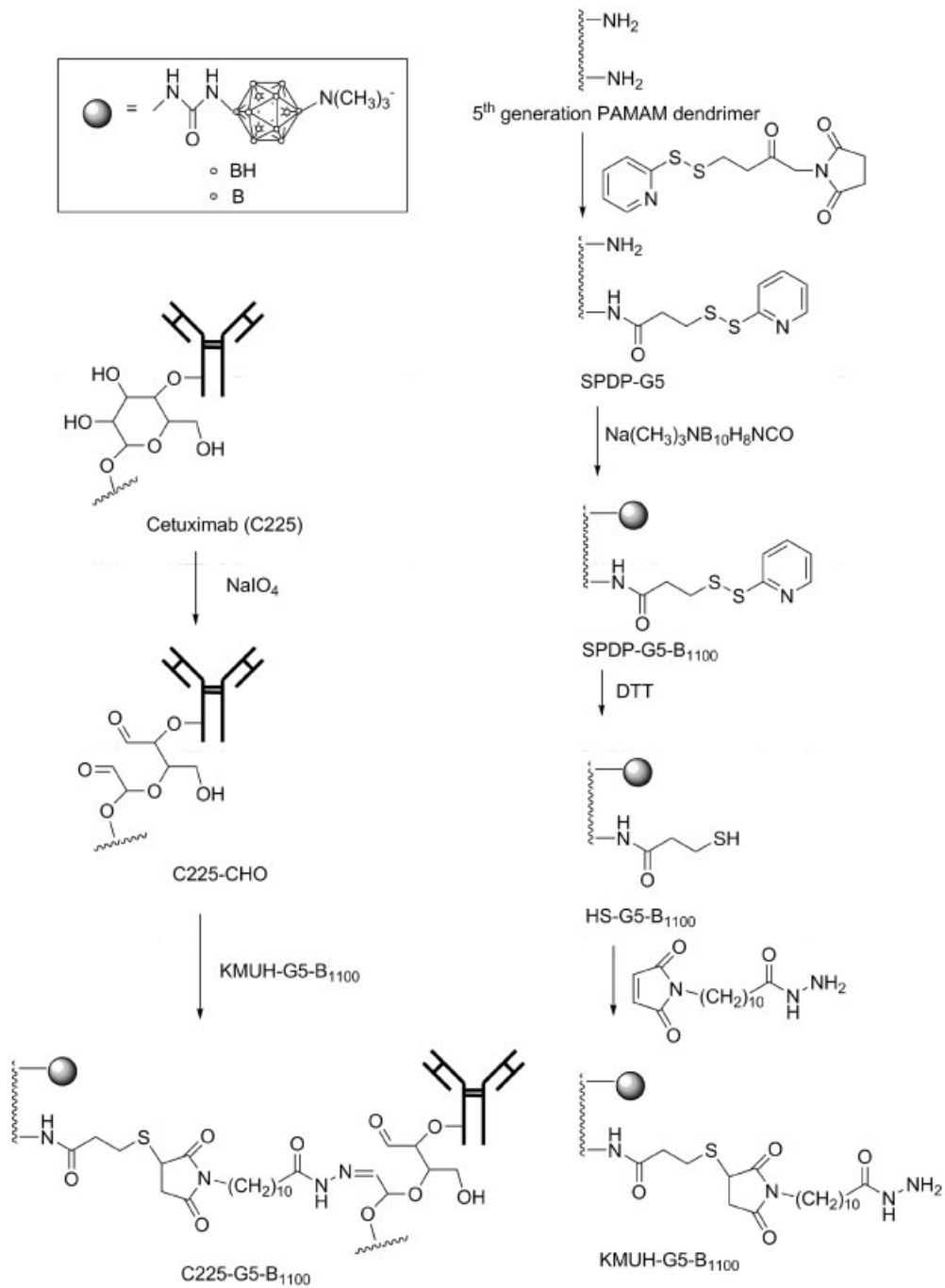


**Fig. 4.3.** Conjugation scheme for linking a boron-containing dendrimer to the monoclonal antibody C225 (cetuximab), which is directed against EGFR [66, 69].

zation and internalization [71, 72]. Since the EGF boron bioconjugates have a much smaller MW than mAb conjugates, they should be capable of more rapid and effective tumor targeting than mAbs [69, 73].

The procedure used to conjugate EGF to a boronated dendrimer was slightly different from that used to boronate mAbs. A fourth-generation PAMAM dendrimer was reacted with the isocyanato polyhedral borane  $\text{Na}(\text{CH}_3)_3\text{NB}_{10}\text{H}_8\text{NCO}$ . Next, reactive thiol groups were introduced into the boronated dendrimer using SPDP, and EGF was derivatized with *m*-maleimidobenzoyl-*N*-hydroxysulfosuccinimide ester (MBS). Reaction of the thiol groups of the derivatized, boronated dendrimer with maleimide groups produced stable BSD-EGF bioconjugates, which contained ~960 atoms of boron per molecule of EGF [74]. The BSD-EGF initially was bound to the cell surface membrane and then was endocytosed, which resulted in accumulation of boron in lysosomes [74]. Subsequently, *in vitro* and *in vivo* studies were carried out to evaluate the potential efficacy of the bioconjugate as a boron delivery agent for BNCT [73]. As will be described in more detail later below (Section 4.9.3), therapy studies demonstrated that F98<sub>EGFR</sub> glioma bearing rats that received either boronated EGF or mAb by either direct i.t. injection or convection-enhanced delivery into the brain had a longer mean survival time than animals bearing F98 parental tumors following BNCT [75–77].

#### 4.5.3.2 Folate Receptor Targeting Agents

Folate receptor (FR) is overexpressed on various human cancers, including those originating in ovary, lung, breast, endometrium and kidney [78–80]. Folic acid (FA) is a vitamin that is transported into cells via FR-mediated endocytosis. The attachment of FA via its  $\gamma$ -carboxylic function to other molecules does not alter its endocytosis by FR-expressing cells [81]. FR targeting has been used successfully to deliver protein toxins, chemotherapeutic, radio-imaging, therapeutic and MRI contrast agents [82], liposomes [83], gene transfer vectors [84], antisense oligonucleotides [85], ribozymes and immunotherapeutic agents to FR-positive cancers [86]. To deliver boron compounds, FA was conjugated to heavily boronated 3<sup>rd</sup> generation PAMAM dendrimers containing poly(ethylene glycol) (PEG) [87]. PEG was introduced into the bioconjugate to reduce its uptake by the reticuloendothelial system (RES) and, more specifically, the liver and spleen. Folate linked to 3<sup>rd</sup> generation PAMAM dendrimers containing 12–15 decaborate clusters and 1–1.5 PEG<sub>2000</sub> units had the lowest hepatic uptake in C57Bl/6 mice (7.2–7.7% injected dose [ID] per gram of liver). *In vitro* studies using FR (+) KB cells have demonstrated receptor-dependent uptake of the bioconjugate. Biodistribution studies with this conjugate, carried out in C57Bl/6 mice bearing subcutaneous (s.c.) implants of the FR (+) murine sarcoma 24JK-FBP, demonstrated selective tumor uptake (6.0% ID per g tumor), but there was high hepatic (38.8% ID per g) and renal (62.8% ID per g) uptake [87].

#### 4.5.3.3 Vascular Endothelial Growth Factor (VEGF)

There is preclinical and clinical evidence indicating that angiogenesis plays a major role in the growth and dissemination of malignant tumors [88, 89]. Inhibition of angiogenesis has yielded promising results in several experimental animal tumor

models [90, 91]. The most important molecular targets have been vascular endothelial growth factor (VEGF) and its receptor (VEGFR) [92, 93]. We recently have constructed a targeting vehicle consisting of a human VEGF<sub>121</sub> isoform fused to a novel 15-aa cysteine-containing tag designed for site-specific conjugation of therapeutic and diagnostic agents [94] (Fig. 4.4). A boronated 5<sup>th</sup> generation PAMAM dendrimer (BD), tagged with a near-infrared (IR) fluorescent dye Cy5, was conjugated using the heterobifunctional reagent sulfo-LC-SPDP to BD/Cy5 via reactive SH-groups, which was generated in the VEGF fusion protein by mild dithiothreitol (DTT) treatment. The bioconjugate, designated VEGF-BD/Cy5, contained 1050–1100 boron atoms per dimeric VEGF molecule. VEGF-BD/Cy5 retained the *in vitro* functional activity of VEGF<sub>121</sub>, which was similar to that of native VEGF. Tagging the bioconjugate with Cy5 dye permitted near-IR fluorescence imaging of its *in vitro* and *in vivo* uptake. *In vitro* uptake was determined by incubating VEGF-BD/Cy5 with VEGFR-2 overexpressing PAE/KDR cells and *in vivo* uptake was evaluated in mice bearing s.c. tumor implants. *In vitro*, the bioconjugate localized in the perinuclear region and *in vivo* it primarily localized in regions of active angiogenesis. Furthermore, depletion of VEGFR-2 overexpressing cells from the tumor vasculature with VEGF-toxin fusion protein significantly decreased bioconjugate uptake, indicating that these cells were the primary targets of VEGF-BD/Cy5. These studies demonstrated that VEGF-BD/Cy5 potentially could be used as a diagnostic agent [94]. Further studies are planned to evaluate its therapeutic efficacy using the F98 rat glioma model, which we have used extensively to evaluate both low and high MW boron delivery agents [95].

#### 4.5.4

##### Other Boronated Dendrimers

An alternative method to deliver boron compounds by means of dendrimers is to incorporate carborane cages within the dendrimer (Fig. 4.5). Parrott et al. have reported that 4, 8 or 16 carboranes could be inserted into an aliphatic polyester dendrimer by means of a highly effective synthon, a bifunctional carborane derivative with an acid group and a benzyl ether protected alcohol [96]. The procedure employed a divergent synthesis with high yield. The resulting polyhydroxylated dendrimer was water soluble with a minimum ratio of eight hydroxyl groups per carborane cage. Carborane-containing dendrimers potentially could be used as boron delivery agents for BNCT, since it is possible to control the number of carborane moieties and overall solubility.

#### 4.6

##### Liposomes as Boron Delivery Agents

#### 4.6.1

##### Overview of Liposomes

Liposomes are biodegradable, non-toxic vesicles that have been used to deliver both hydrophilic and hydrophobic agents (Fig. 4.6) [97]. Both classical and PEGylated

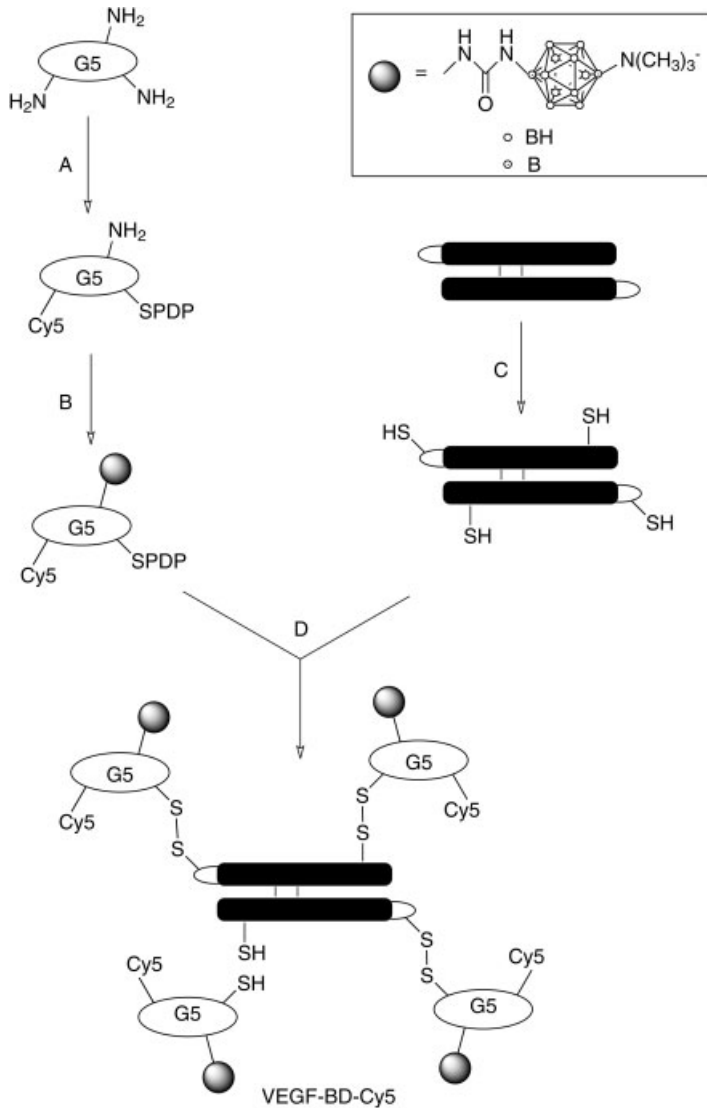


**Fig. 4.4.** Preparation of a vascular endothelial growth factor (VEGF) receptor targeting nanovehicle (VEGF-BD/Cy5). (A) A fifth-generation (G5) PAMAM dendrimer is initially reacted with SPDP and the near-infrared dye Cy5-NHS dissolved in a dimethylformamide-methanol mixture for 1 h. (B) Reaction with the polyisocyanato polyhedral borane  $\text{Na}(\text{CH}_3)_3\text{-NB}_{10}\text{H}_8\text{NCO}$  in a carbonate buffer

(pH 9.0)/9% acetone mixture for 24 h. (C) A 1.5-fold molar excess of DTT is added to the VEGF monomer in a solution containing  $20 \text{ mmol L}^{-1}$  NaOAc (pH 6.5),  $0.5 \text{ mol L}^{-1}$  urea and  $0.5 \text{ mol L}^{-1}$  NDSB-221 and incubated at  $4^\circ\text{C}$  for 16 h. (D) The boronated dendrimer is incubated with the targeting vehicle for 15 min to produce the VEGF-BD/Cy5 [94].



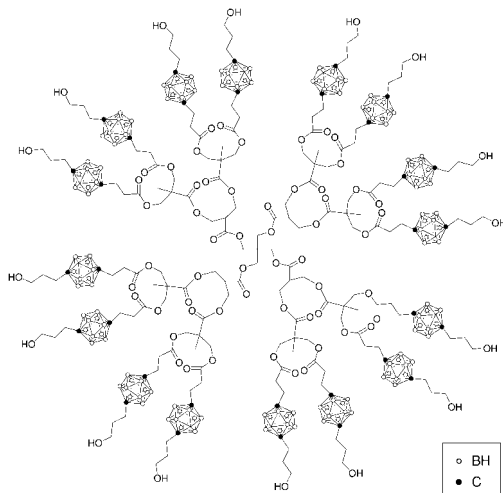


**Fig. 4.5.** Structure of a carborane-containing aliphatic polyester dendrimer. Carborane cages were incorporated into the interior of the dendrimer structure and the peripheral hydrophilic groups improved water solubility and were available for modification.

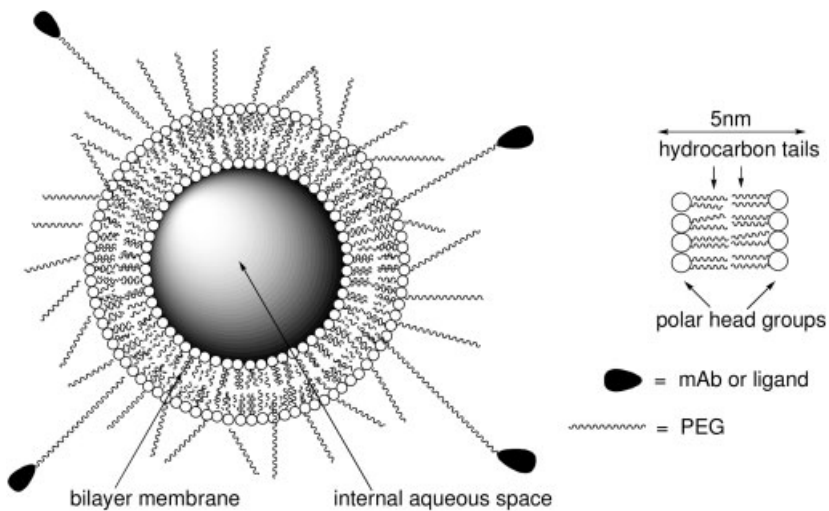


**Fig. 4.6.** Schematic structure of a liposome that has an aqueous core and a lipid bilayer membrane. The latter is composed of polar head groups with hydrocarbon tails. The

liposomal surface can be modified by PEGylation to prolong its circulation time and can be linked to either a mAb or a ligand for targeting.

(“stealth”) liposomes can increase the amounts of anticancer drugs that can be delivered to solid tumors by passive targeting. Rapidly growing solid tumors have increased permeability to nanoparticles due to increased capillary pore size. These can range from 100 to 800 nm compared to 60–80 nm for those in normal tissues, which are impermeable to liposomes. In addition, tumors lack efficient lymphatic drainage, and, consequently, clearance of extravasated liposomes is slow [98]. Modification of the liposomal surface by PEGylation or attachment of antibodies or receptor ligands will improve their selective targeting and increase their circulation time [98].

#### 4.6.2

### Liposomal Encapsulation of Sodium Borocaptate and Boronophenylalanine

#### 4.6.2.1 Boron Delivery by Non-targeted Liposomes

Liposomes have been extensively evaluated as nanovehicles for the delivery of boron compounds for NCT [99, 100]. *In vitro* and *in vivo* studies have demonstrated that they can effectively and selectively deliver large quantities of boron to tumors and that the compounds delivered by liposomes have a longer tumor retention time. BPA is an amino acid analogue that is preferentially taken up by cells with increased metabolic activity, such as tumor cells of varying histopathologic types, including melanomas [31, 101], gliomas [102] and squamous cell carcinomas [103, 104]. Because of its low aqueous solubility, BPA has been used as a fructose complex, which has permitted it to be administered i.v. rather than orally [105, 106]. Following i.v. administration of BPA, which had been incorporated into conventional liposomes, there was rapid elimination by the reticuloendothelial system (RES) with very low blood and liver boron concentrations at 3 h. In contrast, if BPA was incorporated into liposomes composed of DSPE-PEG, therapeutically useful tumor boron concentrations ( $>20 \mu\text{g g}^{-1}$ ) were seen at 3 and at 6 h, indicating that PEG-liposomes had evaded the RES [107]. In addition, BPA has been incorporated into the lipid bilayer of liposomes, composed of either the positively charged lipid 1,2-dioleoyl-3-trimethylammonium propane (DOTAP) or the zwitterionic lipid, 1,2-dioleoyl-*sn*-glycerol-3-phosphoethanolamine (DOPE) [108]. Cationic liposomes have been widely used as carriers of biomolecules that specifically target the cell nucleus [109], which would be advantageous for BNCT. Another clinically used drug, sodium borocaptate (BSH), has been incorporated into liposomes composed of DPPC/Chol in a 1:1 molar ratio with or without PEG stabilization [110]. The average diameter of liposomes containing BSH was in the range 100–110 nm. Both types of liposomes resulted in a significant improvement in their circulation time compared with that of free BSH. At 24 h following i.v. injection of PEG-liposomes, 19% of the injected dose of boron was in the blood compared with 7% following formulation of BSH in conventional liposomes. The mean percent uptake by the liver and spleen was not significantly different for the two types of liposomes. However, the blood:RES ratios were higher for PEG-liposomes at all time points, indicating that a higher fraction of the injected dose of BSH was still in the blood. Ji et al. have reported that there were no significant differences in the *in vitro* up-

take by 9L gliosarcoma cells of free BSH versus a liposomal formulation after 16 h incubation. However, cellular persistence was increased at 12 and 24 h for BSH-loaded liposomes [111]. BSH has also been incorporated into transferrin (TF) conjugated PEG liposomes (TF-PEG liposomes) [112], which then were taken up by cells via transferrin receptor-mediated endocytosis. Intravenous administration of this formulation increased boron retention at the tumor site compared with PEG liposomes, bare liposomes or free BSH, and suppressed tumor growth following BNCT. These results suggest that TF-targeted liposomes might be a useful intracellular targeting vehicle.

#### 4.6.2.2 Liposomal Encapsulation of other Boranes and Carboranes

Polyhedral boranes [34] and carboranes [113, 114] are another class of boron compounds that have been used for NCT. They contain multiple boron atoms per molecule, are resistant to metabolic degradation, and are lipophilic, thereby permitting easier penetration of the tumor cell membrane [113]. In addition to BSH, carboranylpropylamine (CPA, Fig. 4.7, 4) [115] has been incorporated into conventional and PEGylated liposomes by active loading, using a transmembrane pH gradient [115, 116]. Although as many as 13 000 molecules of CPA were loaded into liposomes having a mean average diameter of 100 nm, there was *in vitro* toxicity to both the glioblastoma cell line SK-MG-1 and normal human peripheral blood lymphocytes. Borane anions, such as  $B_{10}H_{10}^{2-}$ ,  $B_{12}H_{11}SH^{2-}$ ,  $B_{20}H_{17}OH^{4-}$  and  $B_{20}H_{19}^{3-}$ , and the normal form and photoisomer of  $B_{20}H_{18}^{2-}$ , also have been encapsulated into small unilamellar vesicles with mean diameters of 70 nm or less [117–120]. These were composed of the pure synthetic phospholipids, distearoyl phosphatidylcholine and cholesterol [117]. Although encapsulation efficiencies were only 2–3%, following *i.v.* injection these liposomes were selectively delivered to tumors in mice bearing the EMT6 mammary carcinoma and had attained boron concentrations of  $>15 \mu\text{g-B g}^{-1}$ , with a T:Bl ratio of  $>3$ . Two isomers of  $B_{20}H_{18}^{2-}$  attained boron concentrations of 13.6 and  $13.9 \mu\text{g g}^{-1}$  with T:Bl ratios of 3.3 and 12, respectively, at 48 h following administration. The high boron retention and prolongation of their circulation time was due to interaction with intracellular components after it had been released from liposomes within tumor cells [117].

To examine the effect of charge and substitution on the retention of boranes the two isomers  $[B_{20}H_{17}NH_3]^{3-}$  and  $[1-(2'-B_{10}H_9)-2-NH_3B_{10}H_8]^{3-}$  (5) have been prepared from the polyhedral borane anion  $[n-B_{20}H_{18}]^{2-}$  (6) [118, 119]. The sodium salts of these two isomers had been encapsulated within small unilamellar liposomes, composed of distearoyl phosphatidylcholine/cholesterol at a 1:1 ratio. Both isomers of  $[B_{20}H_{17}NH_3]^{3-}$  had excellent tumor uptake and selectivity in EMT 6 tumor bearing mice, even at very low injected doses, and this resulted in peak tumor boron concentrations of  $30\text{--}40 \mu\text{g-B g}^{-1}$  and a T:Bl ratio of  $\sim 5$ . Owing to low boron retention of liposomal  $Na_3[B_{20}H_{19}]$  and  $Na_4[e^2-B_{20}H_{17}OH]$  and rapid clearance of liposomal  $[2-NH_3B_{10}H_9]^-$ , the enhanced retention of liposomal  $Na_3[ae-B_{20}H_{17}NH_3]$  was not due to the anionic charge or substitution in the borane cage. Rather, it could be attributed to facile intracellular oxidation to an extremely re-

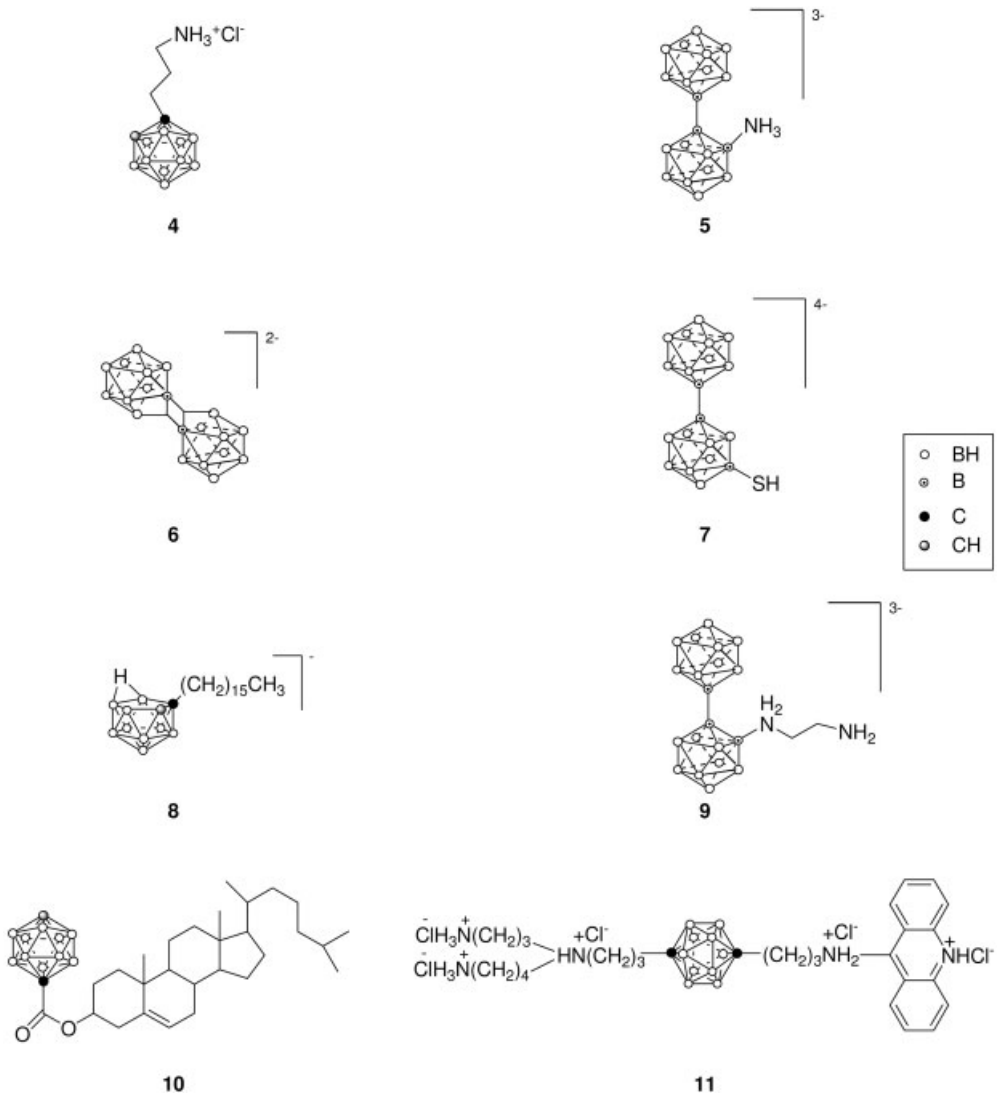


**Fig. 4.7.** Structures of hydrophilic and lipophilic boron-containing compounds incorporated into liposomes. Carboranylpropylamine (CPA, **4**), [1-(2'-B<sub>10</sub>H<sub>9</sub>)-2-NH<sub>3</sub>B<sub>10</sub>H<sub>8</sub>]<sup>3-</sup> (**5**), [n-B<sub>20</sub>H<sub>18</sub>]<sup>2-</sup> (**6**), [B<sub>20</sub>H<sub>17</sub>SH]<sup>4-</sup> (**7**), Na<sub>3</sub>[α2-B<sub>20</sub>H<sub>17</sub>NH<sub>2</sub>CH<sub>2</sub>CH<sub>2</sub>NH<sub>2</sub>] (**9**) and boronated

water-soluble acridine (WSA, **11**) have been encapsulated into the aqueous core. K[nido-7-CH<sub>3</sub>(CH<sub>2</sub>)<sub>15</sub>-7,8-C<sub>2</sub>B<sub>9</sub>H<sub>11</sub>] (**8**) and cholesteryl 1,12-dicarba-*closo*-dodecaborane-1-carboxylate (**10**) have been incorporated into the lipid bilayer of liposomes.

active  $\text{NH}_3^{3-}$  substituted  $[\text{n-B}_{20}\text{H}_{18}]^{2-}$  electrophilic anion,  $[\text{B}_{20}\text{H}_{17}\text{NH}_3]^-$ . Another anion,  $[\text{ae-B}_{20}\text{H}_{17}\text{NH}_3]^{3-}$ , also was encapsulated into liposomes prepared with 5% PEG-2000-distearoyl phosphatidylethanolamine as a constituent of the membrane. These liposomes had longer *in vivo* circulation times, which resulted in continued accumulation of boron in the tumor over the entire 48 h, and reached a maximum concentration of 47  $\mu\text{g-B}$  per g tumor.

$[\text{B}_{20}\text{H}_{17}\text{SH}]^{4-}$  (7), a thiol derivative of  $[\text{B}_{20}\text{H}_{18}]^{4-}$ , possesses a reactive thiol substituent that can be oxidized to give the more reactive  $[\text{B}_{20}\text{H}_{17}\text{S}]^{2-}$  anion. Both species were considered to be essential for high tumor boron retention [120] and they have been encapsulated into small, unilamellar liposomes. Biodistribution was determined after i.v. injection into BALB/c mice bearing EMT6 tumors. At low injected doses, tumor boron concentrations increased throughout the experiment, resulting in a maximum concentration of 47  $\mu\text{g-B}$  per g tumor at 48 h, which corresponded to 22.2% ID  $\text{g}^{-1}$  and a T:Bl ratio of 7.7. This was the most promising of the polyhedral borane anions that had been investigated for liposomal delivery. Although they were able to deliver adequate amounts of boron to tumor cells, their application to BNCT has been limited due to their low incorporation efficiency ( $\sim 3\%$ ).

Lipophilic boron compounds incorporated into the lipid bilayer would be an alternative approach. Small unilamellar vesicles composed of a 3:3:1 ratio of distearoylphosphatidylcholine, cholesterol and  $\text{K}[\text{nido-7-CH}_3(\text{CH}_2)_{15}\text{-7,8-C}_2\text{B}_9\text{H}_{11}]$  (8) in the lipid bilayer and  $\text{Na}_3[\text{a2-B}_{20}\text{H}_{17}\text{NH}_2\text{CH}_2\text{CH}_2\text{NH}_2]$  (9) in the aqueous core were produced as a delivery agents for NCT-mediated synovectomy [121]. Biodistribution studies were carried out in Louvain rats that had a collagen-induced arthritis. The maximum synovial boron concentration was 29  $\mu\text{g}$  per gram of tissue at 30 h and this had only decreased to 22  $\mu\text{g g}^{-1}$  at 96 h following i.v. administration. The prolonged retention by synovium provided sufficient time for extensive clearance of boron from other tissues so that at 96 h the synovium: blood (Syn:Bl) ratio was 3.0. To accelerate blood clearance, serum stability of the liposomes was lowered by increasing the proportion of compound 8 embedded in the lipid bilayer. Liposomes were formulated with a 3:3:2 ratio DSPE:Ch:8 in the lipid bilayer and 9 was encapsulated in the aqueous core. The boron concentration in the synovium reached a maximum of 26  $\mu\text{g g}^{-1}$  at 48 h with a Syn:Bl ratio of 2, following which it slowly decreased to 14  $\mu\text{g g}^{-1}$  at 96 h, at which time the Syn:Bl ratio was 7.5 [121].

Another method to deliver hydrophilic boron-containing compounds would be to incorporate them into cholesterol to target tumor cells expressing amplified low density lipoprotein (LDL) receptors [122–124]. Glioma cells, which absorb more cholesterol, have been reported to take up more LDL than the corresponding normal tissue cells [125–127]. The cellular uptake of liposomal cholesteryl 1,12-dicarba-*closo*-dodecaborane-1-carboxylate (10) by two fast-growing human glioma cell lines, SF-763 and SF-767, was mediated via the LDL receptor and was much higher than that of human neurons. The cellular boron concentration was  $\sim 10\text{--}11\times$  greater than that required for BNCT [128].

## 4.6.3

**Boron Delivery by Targeted Liposomes**

To improve the specificity of liposomally encapsulated drugs and to increase the amount of boron delivered, targeting moieties have been attached to the surface of liposomes. These could be any molecules that selectively recognized and bound to target antigens or receptors that were overexpressed on neoplastic cells or tumor-associated neovasculature. These have included either intact mAb molecules or fragments, and low molecular weight, naturally occurring or synthetic ligands such as peptides or receptor-binding ligands such as EGF. To date, liposomes linked to mAbs or their fragments [129], EGF [130], folate [131] and transferrin [112] have been the most extensively studied as targeting moieties (Fig. 4.8).

**4.6.3.1 Immunoliposomes**

The murine anti-carcinoembryonic antigen (CEA) mAb 2C-8 has been conjugated to large multilamellar liposomes containing  $^{10}\text{B}$  compounds [132, 133]. The maximum number of  $^{10}\text{B}$  atoms attached per molecule of mAb was  $\sim 1.2 \times 10^4$ . These immunoliposomes bound selectively to the human pancreatic carcinoma cell line, AsPC-1, that overexpressed CEA. Incubating the immunoliposomes with either MRKnu/nu-1 or AsPC-1 tumor cells suppressed *in vitro* tumor cell growth follow-

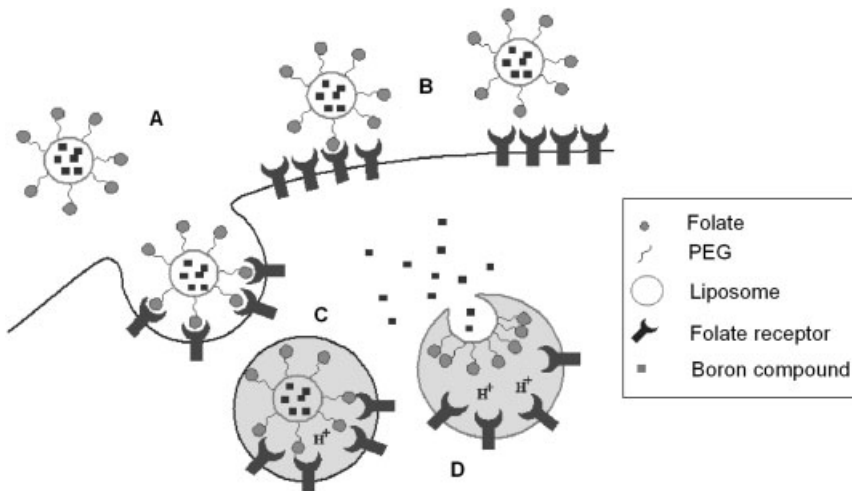


**Fig. 4.8.** Proposed mechanism of intracellular boron delivery based on receptor-mediated tumor cell targeting. Liposomes loaded with a boron compound (A) are conjugated to a targeting ligand (e.g., folate, transferrin, or anti-EGFR antibody). These bind to receptors on the cell surface (B), and are then

internalized by receptor-mediated endocytosis (C) into the acidified endosomal/lysosomal compartment. The boron compound is then released (D) into the cytosol by liposomal degradation, endosome/lysosome disruption or liposome-endosome/lysosome membrane fusion.

ing thermal neutron irradiation [134]. This was dependent upon the liposomal concentration of the  $^{10}\text{B}$ -compound and on the number of molecules of mAb conjugated to the liposomes. Immunoliposomes containing either  $(\text{Et}_4\text{N})_2\text{B}_{10}\text{H}_{10}$  and linked to the mAb MAb 2, directed against human gastric cancer [135, 136] or water-soluble boronated acridine (WSA, 11; Fig. 4.7) linked to trastuzumab, directed against HER-2, have been prepared and evaluated *in vitro* [129]. There was specific binding and high uptake of these immunoliposomes, which delivered a sufficient amount of  $^{10}\text{B}$  to produce a tumoricidal effect following thermal neutron irradiation.

#### 4.6.3.2 Folate Receptor-targeted Liposomes

A highly ionized boron compound,  $\text{Na}_3\text{B}_{20}\text{H}_{17}\text{NH}_3$ , has been incorporated into liposomes by passive loading [131, 137, 138]. This showed high *in vitro* uptake by the FR-expressing human cell line KB (American Type Culture Collection CCL 17), which originally was thought to be derived from a squamous cell carcinoma of the mouth, and subsequently was shown to be identical to HeLa cells, as determined by isoenzyme markers, DNA fingerprinting and karyotypic analysis. KB-tumor-bearing mice that received either FR-targeted or non-targeted control liposomes had equivalent tumor boron values ( $\sim 85 \mu\text{g g}^{-1}$ ), which attained a maximum at 24 h, while the T:Bl ratio reached a maximum at 72 h. Additional studies were carried out with the lipophilic boron compound  $\text{K}[\text{nido-7-CH}_3(\text{CH}_2)_{15}\text{-7,8-C}_2\text{B}_9\text{H}_{11}]$  (8). This was incorporated into large unilamellar vesicles,  $\sim 200$  nm in diameter, composed of egg PC/chol/8 in a 2:2:1 mol/mol ratio, and an additional 0.5 mol% of folate-PEG-DSPE or PEG-DSPE for the FR-targeted or non-targeted liposomal formulations [139]. Boron uptake by FR-overexpressing KB cells, treated with these targeted liposomes, was  $\sim 10\times$  greater compared with those treated with control liposomes. In addition, BSH and five weakly basic boronated polyamines were evaluated (Fig. 4.9). Two of these were the spermidine derivatives  $N^5$ -(4-carboranylbutyl)spermidine  $\cdot 3\text{HCl}$  (12) and  $N^5$ -[4-(2-aminoethyl-*o*-carboranyl)butyl]spermidine  $\cdot 4\text{HCl}$  (13). Three were the spermine derivatives  $N^5$ -(4-*o*-carboranylbutyl)spermine  $\cdot 4\text{HCl}$  (14),  $N^5$ -[4-(2-aminoethyl-*o*-carboranyl)butyl]spermine  $\cdot 5\text{HCl}$  (15), and  $N^5, N^{10}$ -bis(4-*o*-carboranylbutyl)spermine  $\cdot 4\text{HCl}$  (16). These were incorporated into liposomes by a pH-gradient-driven remote-loading method with varying loading efficiencies, which were influenced by the specific trapping agent and the structure of the boron compound. Greater loading efficiencies were obtained with lower molecular weight boron derivatives, using ammonium sulfate as the trapping agent, compared with those obtained with sodium citrate.

#### 4.6.3.3 EGFR Targeted Liposomes

Acridine is a water-soluble (WS) DNA-intercalator. Its boronated derivative WSA has been incorporated into liposomes composed of EGF-conjugated lipids. Their surface contained  $\sim 5$  mol% PEG and 10–15 molecules of EGF, and  $10^4$ – $10^5$  of the WSA molecules were encapsulated. These liposomes had EGFR-specific cellular binding to cultured human glioma cells [130, 140] and were internalized following specific binding to the receptor. Following internalization, WSA, primarily, was

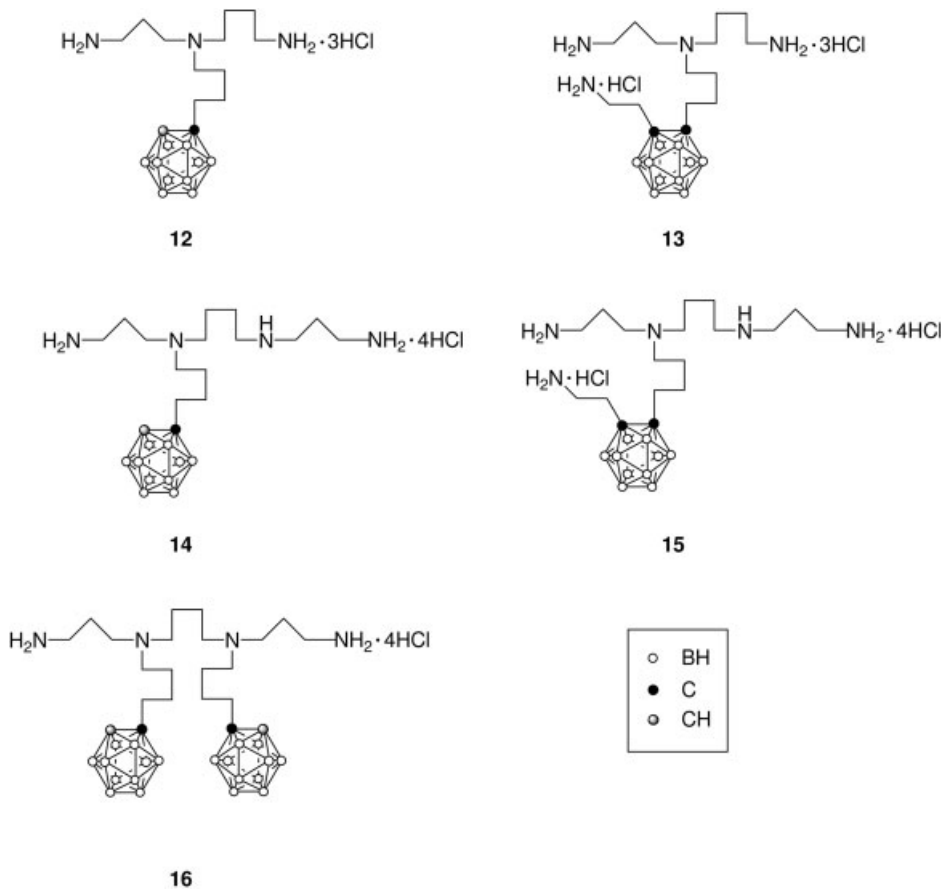


**Fig. 4.9.** Structures of five weakly basic boronated polyamines encapsulated in FR targeting liposomes. The two spermidine (**12**, **13**) and three spermine derivatives (**14**–**16**), which contain hydrophilic amine groups and lipophilic carboranyl cages, had DNA-binding properties.

localized in the cytoplasm, and had high cellular retention, with 80% of the boron remaining cell-associated after 48 h [141].

#### 4.7 Boron Delivery by Dextrans

Dextrans are glucose polymers that consist mainly of a linear  $\alpha$ -1,6-glucosidic linkage with some degree of branching via a 1,3-linkage [142, 143]. Dextrans have been



used extensively as drug and protein carriers to increase drug circulation time [144, 145]. In addition, native or chemically-modified dextrans have been used for passive targeting to tumors, the RES or active receptor-specific cellular targeting. To link boron compounds to dextrans [146],  $\beta$ -decachloro-*o*-carborane derivatives, in which one of the carbon atoms is substituted by  $-\text{CH}_2\text{CHOHCH}_2\text{-O-CH}_2\text{CH=CH}_2$ , have been epoxidized and subsequently bound to dextran, with a resulting boron content of 4.3% (w/w) [147]. The modified dextran could then be attached to tumor-specific antibodies [147–150]. BSH has been covalently coupled to dextran derivatives by two methods [151]. In the first, dextran was activated with 1-cyano-4-(dimethylamino)pyridine (CDAP) and subsequently coupled with 2-aminoethyl pyridyl disulfide. Then, thiolated dextran was linked to BSH in a disulfide exchange reaction. A total of 10–20 boron cages were attached to each dextran chain. In the second method, dextran was derivatized to a multiallyl derivative (Fig. 4.10, 17), which was reacted with BSH in a free-radical-initiated addition reaction. Using this method, 100–125 boron cages could be attached per dextran chain, suggesting

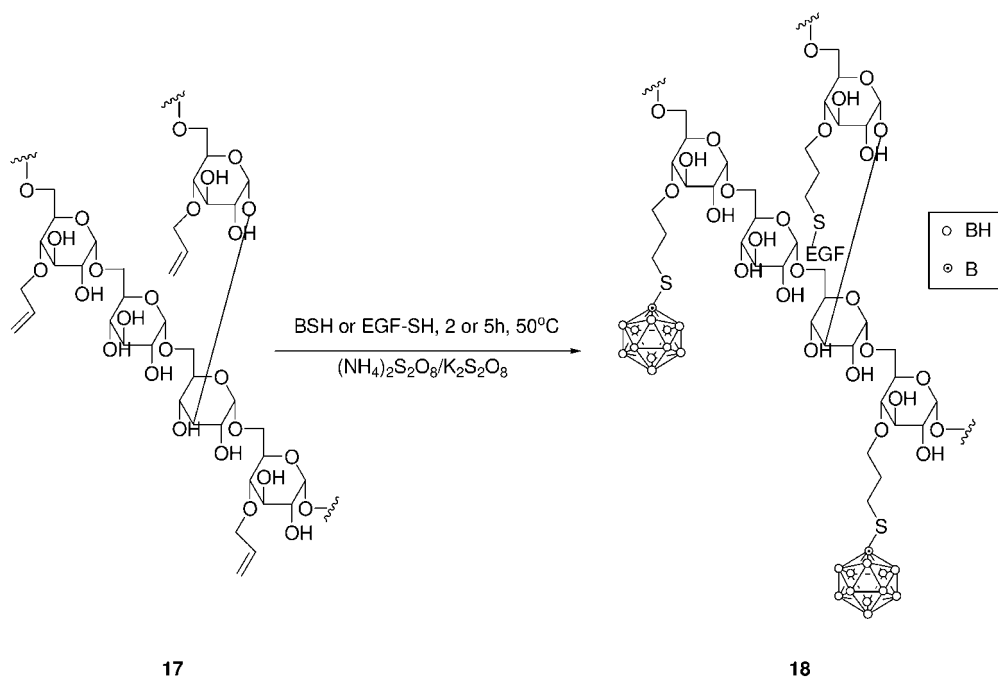


**Fig. 4.10.** Preparation of EGF-targeted, boronated dextrans. The bioconjugate was prepared by a free-radical-initiated addition reaction between multiallyl dextran derivatives and BSH or thiolated EGF at 50 °C using  $\text{K}_2\text{S}_2\text{O}_8$  as an initiator.

that this derivative might be a promising template for the development of other HMW delivery agents. By the second method, designed to target EGFR over-expressing cells, EGF and BSH have been covalently linked to a 70 kDa dextran (18) [152–154]. Bioconjugates having a few BSH molecules attained maximum *in vitro* binding at 4 h with the human glioma cell line U-343 MGaC12:6. In contrast, there was a slow increase of binding over 24 h for those having many BSH molecules. Although most of the bioconjugates were internalized, *in vitro* retention was low, as was *in vivo* uptake following i.v. injection into nude mice bearing s.c. implants of Chinese hamster ovary (CHO) cells transfected with the human gene encoding EGFR (designated CHO-EGFR). However, following i.t. injection, boron uptake was higher with CHO-EGFR(+) tumors compared to wild-type EGFR(–) CHO tumors [155].

#### 4.8

#### Other Macromolecules used for Delivering Boron Compounds

Polylysine is another polymer having multiple reactive amino groups that has been used as a platform for the delivery of boron compounds [53, 156]. The protein-binding polyhedral boron derivative isocyanatoundecahydro-*closo*-dodecaborate ( $B_{12}H_{11}NCO^{2-}$ ) has been linked to polylysine and subsequently to the anti-B16 melanoma mAb IB16-6 using two heterobifunctional linkers, SPDP and sulfo-MBS. The bioconjugate had an average of 2700 boron atoms per molecule and retained 58% of the immunoreactivity of the native antibody, as determined by a semiquantitative immunofluorescent assay or by ELISA. Other bioconjugates prepared by this method had >1000 boron atoms per molecule of antibody and retained 40–90% of the immunoreactivity of the native antibody [53]. Using another approach, site-specific linkage of boronated polylysine to the carbohydrate moieties of anti-TSH antibody resulted in a bioconjugate that had  $\sim 6 \times 10^3$  boron atoms with retention of its immunoreactivity [156].

A streptavidin–biotin system has also been developed to specifically deliver boron to tumors. Biotin was linked to a mAb and streptavidin was attached to the boron-containing moiety. The indirect linking of boron to the mAb minimized loss of its immunoreactivity. BSH was attached to poly-(D-glutamate D-lysine) (poly-GL) via a heterobifunctional agent [157]. This boronated poly-GL then was activated by a carbodiimide reagent and in turn reacted with streptavidin. Another approach employed a streptavidin mutant that had 20 cysteine residues per molecule. BSH was conjugated via sulfhydryl-specific bifunctional reagents to incorporate  $\sim 230$  boron atoms per molecule [158]. A closomer species with an icosahedral dodecaborate core and twelve pendant anionic *nido*-7,8-carborane groups has been developed as a new class of unimolecular nanovehicles for evaluation as a delivery agent for BNCT [159].

## 4.9

### Delivery of Boron-containing Macromolecules to Brain Tumors

#### 4.9.1

##### General Considerations

Drug delivery to brain tumors is dependent upon (1) the plasma concentration profile of the drug, which depends upon the amount and route of administration, (2) the ability of the agent to traverse the blood brain barrier (BBB), (3) blood flow within the tumor, and (4) the lipophilicity of the drug. In general, a high steady-state blood concentration will maximize brain uptake, while rapid clearance will reduce it, except in the case of intra-arterial (i.a.) drug administration. Although the i.v. route is currently being used clinically to administer both BSH and BPA, this may not be ideal for boron-containing macromolecules, and other strategies must be employed to improve their delivery.

#### 4.9.2

##### Drug-transport Vectors

One approach to improve brain tumor uptake of boron compounds has been to conjugate them to a drug-transport vector by means of receptor-specific transport systems [160, 161]. Proteins such as insulin, insulin-like growth factor (IGF), transferrin (TF) [162], and leptin can traverse the BBB. BSH encapsulated in TF-PEG-liposomes had a prolonged residence time in the circulation and low RES uptake in tumor-bearing mice, resulting in enhanced extravasation of the liposomes into the tumor and concomitant internalization by receptor-mediated endocytosis [163, 164]. Mice that received BSH-containing TF-liposomes followed by BNCT had significantly longer survival times than those that received PEG-liposomes, bare liposomes and free BSH, thereby establishing *proof-of-principle* for transcytosis of a boron-containing nanovehicle [112].

#### 4.9.3

##### Direct Intracerebral Delivery

Studies carried out by us have clearly demonstrated that the i.v. route of administration is not suitable for delivery of boronated EGF or mAbs to glioma bearing rats [75, 165]. Intravenous injection of technetium-99m labeled EGF to rats bearing intracerebral implants of the C6 rat glioma, which had been genetically engineered to express the human EGFR gene, resulted in 0.14% ID localizing in the tumor. Intracarotid (i.c.) injection with or without BBB disruption increased the tumor uptake to 0.34 to 0.45% ID  $g^{-1}$ , but based even on the most optimistic assumptions the amount of boron that could be delivered to the tumor by i.v. injection would be inadequate for BNCT [165]. Direct i.t. injection of boronated EGF (BSD-EGF), however, resulted in tumor boron concentrations of 22  $\mu g g^{-1}$  compared to 0.01  $\mu g g^{-1}$  following i.v. injection and almost identical boron uptake values were ob-

tained using the F98<sub>EGFR</sub> glioma model [77]. This was produced by transfecting F98 glioma cells with the gene encoding human EGFR. Based on our biodistribution results, therapy studies were initiated with the F98<sub>EGFR</sub> glioma in syngeneic Fischer rats. F98<sub>EGFR</sub> glioma bearing rats that received BSD-EGF i.t. had a mean survival time (MST) of  $45 \pm 1$  d compared to  $33 \pm 2$  d in animals that had EGFR(-) wild-type F98 gliomas. Since it is unlikely that any single boron delivery agent will be able to target all tumor cells, the combination of i.t. administration of BSD-EGF with i.v. injection of BPA was evaluated. This furthered increased the MST to  $57 \pm 8$  d compared to  $39 \pm 2$  d for i.v. BPA alone [73]. These data provide *proof-of-principle* for the idea of using a combination of low and HMW boron delivery agents.

#### 4.9.4

#### Convection-enhanced Delivery (CED)

CED, by which therapeutic agents are directly infused into the brain, is an innovative method to increase their uptake and distribution [166–168]. Under normal physiological conditions, interstitial fluids move through the brain by both convection and diffusion. Diffusion of a drug in tissue depends upon its molecular weight, ionic charge and its concentration gradient within normal tissue and the tumor. The higher the molecular weight of the drug and the more positively charged the ionic species, the lower its concentration, then the slower its diffusion. For example, diffusion of antibody into a tumor requires three days to diffuse 1 mm from the point of origin. Unlike diffusion, however, convection or “bulk” flow results from a pressure gradient that is independent of the molecular weight of the substance. CED, potentially, can improve the targeting of both low and HMW molecules, as well as liposomes, to the CNS by applying a pressure gradient to establish bulk flow during interstitial infusion. The volume of distribution ( $V_d$ ) is a linear function of the volume of the infusate ( $V_i$ ). CED has been used to efficiently deliver drugs and HMW agents such as mAbs and toxin fusion proteins to brain tumors [168–170]. CED can provide a more homogenous dispersion of the agent and at higher concentrations than otherwise would be attainable by i.v. injection [165]. For example, in our own studies, CED of <sup>125</sup>I-labeled EGF to F98<sub>EGFR</sub> glioma bearing rats resulted in 47% ID  $g^{-1}$  of the bioconjugate localizing in the tumor compared to 10% ID  $g^{-1}$  in normal brain at 24 h following administration. The corresponding boron values were 22 and 2.9–4.9  $\mu g g^{-1}$ , respectively [76]. Based on these results, therapy studies were initiated. F98<sub>EGFR</sub>-glioma-bearing rats that received BD-EGF by CED had a MST of  $53 \pm 13$  d compared to  $40 \pm 5$  d for animals that received BPA i.v. [73]. Similar studies have been carried out using either boronated cetuximab (IMC-C225) or the mAb L8A4 [171, 172], which is specifically directed against the tumor-specific mutant isoform EGFRvIII; comparable results were obtained [173]. Direct intracerebral administration of these and other HMW agents by CED has opened up the possibility that they actually could be used clinically, since CED is being used to administer radiolabeled antibodies, toxin fusion proteins and gene vectors to patients with GBM [168–170, 175–179].

It is only a matter of time before this approach is also used to deliver both low and HMW boron-containing agents for NCT.

#### 4.10

#### Clinical Considerations and Conclusions

In this chapter we have focused on HMW boron delivery agents and nanovehicles that potentially could be used clinically for targeting intra- and extracranial tumors. Animal studies, carried out in glioma-bearing rats, have demonstrated that boronated EGF and the mAb cetuximab, both of which bind to EGFR, selectively target receptor (+) tumors following direct i.c. delivery. Furthermore, following BNCT, a significant increase in MST was observed, and this was further enhanced if BPA was administered in combination with the HMW agents. These studies provide *proof-of-principle* first for the potential utility of HMW agents and, second, the therapeutic gain associated with combining them with LMW boron delivery agents. A major question is whether any of these agents will ever be used clinically? There are several critical issues that must be addressed if BNCT is to ever become a useful modality for the treatment of cancer. *First*, large clinical trials, preferably randomized, must be carried out to convincingly demonstrate the efficacy of the two drugs that currently are being used, BPA and BSH. Once this has been established, studies with HMW EGFR targeting agents could move forward. Both direct i.t. injection [174, 175] and CED [170, 176–179] have been used clinically to deliver mAbs and toxin fusion proteins to patients who have had surgical resection of their brain tumors. These studies provide a strong clinical rationale for the direct intracerebral delivery of HMW agents. Initially, the primary focus should be on determining the safety of administering them to patients prior to surgical resection of their brain tumors. Once this has been established, then biodistribution studies could be carried out in patients who were going to have surgical resection of their brain tumors. Tumor and normal tissues would be analyzed for their boron content, and if there was evidence of preferential tumor localization with boron concentrations in the range 10–20  $\mu\text{g g}^{-1}$  and normal brain concentrations of  $<5 \mu\text{g g}^{-1}$  then therapy studies could be undertaken. Since there is considerable variability in EGFR expression in gliomas, it is highly unlikely that any single agent will be able to deliver the requisite amount of boron to all tumor cells, and they would be used in combination with BPA/BSH. This general plan would also be applicable to the other HMW delivery agents and nanovehicles that have been discussed here. The joining together of chemistry and nanotechnology [180, 181] represents a major step towards the development of effective boron delivery agents for NCT. Nanovehicles offer the possibility of tumor targeting with enhanced boron payloads. Potentially, this could solve the central problem of how to selectively deliver a large number of boron atoms to individual cancer cells.

The preceding discussion shows that the development of HMW boron delivery agents must proceed in step with strategies to optimize their delivery and an appre-

ciation as to how they would be used clinically. Intracerebral delivery has been used in clinically advanced settings, but nuclear reactors, which currently are the only source of neutrons for BNCT, would not be conducive to this. Therefore, the development of accelerator neutron sources [24], which could be easily sited in hospitals, is especially important. This would also facilitate the initiation of large-scale clinical trials at selected centers that treat large numbers of patients with brain tumors and would permit evaluation of new boron delivery agents. In conclusion, as should be apparent from this review, a plethora of HMW boron delivery agents have been designed and synthesized. The challenge is to move from experimental animal studies to clinical biodistribution studies, a step that has yet to be taken.

### Acknowledgments

We thank Dr. Achintya Bandyopadhyaya for suggestions on figures and Mrs. Beth Kahl for secretarial assistance. Experimental studies described in this report were supported by N.I.H. grants 1 R01 CA098945 (R.F. Barth), 1 R01 CA79758 (W. Tjarks), and Department of Energy grants DE-FG02-98ER62595 (R.F. Barth) and DE-FG-2-02FR83520 (J.M. Backer).

### References

- 1 BERGER M. S., Malignant astrocytomas: Surgical aspects, *Semin. Oncol.*, **1994**, *21*, 172–185.
- 2 GUTIN P. H., POSNER J. B., Neuro-oncology: Diagnosis and management of cerebral gliomas – past, present, and future, *Neurosurgery*, **2000**, *47*, 1–8.
- 3 PARNEY I. F., CHANG S. M., Current chemotherapy for glioblastoma, *Cancer J.*, **2003**, *9*, 149–156.
- 4 PAUL D. B., KRUSE C. A., Immunologic approaches to therapy for brain tumors, *Curr. Neurol. Neurosci. Rep.*, **2001**, *1*, 238–244.
- 5 RAINOV N. G., REN H., Gene therapy for human malignant brain tumors, *Cancer J.*, **2003**, *9*, 180–188.
- 6 CURRAN W. J., JR., SCOTT C. B., HORTON J., NELSON J. S. et al., Recursive partitioning analysis of prognostic factors in three Radiation Therapy Oncology Group malignant glioma trials, *J. Natl. Cancer Inst.*, **1993**, *85*, 704–710.
- 7 LACROIX M., ABI-SAID D., FOURNEY D. R., GOKASLAN Z. L. et al., A multivariate analysis of 416 patients with glioblastoma multiforme: Prognosis, extent of resection, and survival, *J. Neurosurg.*, **2001**, *95*, 190–198.
- 8 HENTSCHEL S. J., LANG F. F., Current surgical management of glioblastoma, *Cancer J.*, **2003**, *9*, 113–125.
- 9 LAWS E. R., JR., SHAFFREY M. E., The inherent invasiveness of cerebral gliomas: Implications for clinical management, *Int. J. Dev. Neurosci.*, **1999**, *17*, 413–420.
- 10 WARE M. L., BERGER M. S., BINDER D. K., Molecular biology of glioma tumorigenesis, *Histol. Histopathol.*, **2003**, *18*, 207–216.
- 11 PARNEY I. F., HAO C., PETRUK K. C., Glioma immunology and

- immunotherapy, *Neurosurgery*, **2000**, 46, 778–792.
- 12 KACZAREK E., ZAPF S., BOUTERFA H., TONN J. C. et al., Dissecting glioma invasion: Interrelation of adhesion, migration and intercellular contacts determine the invasive phenotype, *Int. J. Dev. Neurosci.*, **1999**, 17, 625–641.
  - 13 NUTT C. L., MATTHEWS R. T., HOCKFIELD S., Glial tumor invasion: A role for the upregulation and cleavage of BEHAB/brevican, *Neuroscientist*, **2001**, 7, 113–122.
  - 14 HALPERIN E. C., BURGER P. C., BULLARD D. E., The fallacy of the localized supratentorial malignant glioma, *Int. J. Radiat. Oncol. Biol. Phys.*, **1988**, 15, 505–509.
  - 15 BARTH R. F., A critical assessment of boron neutron capture therapy: An overview, *J. Neurooncol.*, **2003**, 62, 1–5.
  - 16 NAKAGAWA Y., POOH K., KOBAYASHI T., KAGEJI T. et al., Clinical review of the Japanese experience with boron neutron capture therapy and a proposed strategy using epithermal neutron beams, *J. Neurooncol.*, **2003**, 62, 87–99.
  - 17 WADABAYASHI N., HONDA C., MISHIMA Y., ICHIHASHI M., Selective boron accumulation in human ocular melanoma vs surrounding eye components after <sup>10</sup>B1-p-boronophenylalanine administration. Prerequisite for clinical trial of neutron-capture therapy, *Melanoma Res.*, **1994**, 4, 185–190.
  - 18 BUSSE P. M., HARLING O. K., PALMER M. R., KIGER W. S. 3rd et al., A critical examination of the results from the Harvard-MIT NCT program phase I clinical trial of neutron capture therapy for intracranial disease, *J. Neurooncol.*, **2003**, 62, 111–121.
  - 19 KATO I., ONO K., SAKURAI Y., OHMAE M. et al., Effectiveness of BNCT for recurrent head and neck malignancies, *Appl. Radiat. Isot.*, **2004**, 61, 1069–1073.
  - 20 RAO M., TRIVILLIN V. A., HEBER E. M., CANTARELLI MDE L. et al., BNCT of 3 cases of spontaneous head and neck cancer in feline patients, *Appl. Radiat. Isot.*, **2004**, 61, 947–952.
  - 21 KOIVUNORO H., BLEUEL D. L., NASTASI U., LOU T. P. et al., BNCT dose distribution in liver with epithermal D-D and D-T fusion-based neutron beams, *Appl. Radiat. Isot.*, **2004**, 61, 853–859.
  - 22 PINELLI T., ZONTA A., ALTIERI S. et al., TAO<sub>r</sub>MINA: From the first idea to the application to the human liver, in *Research and Development in Neutron Capture Therapy, Proceedings of the International Congress on Neutron Capture Therapy*, SAUERWEIN M. W., MOSS R., WITTIG A. eds., Monduzzi Editore, Bologna, Italy, **2002**, pp. 1065–1072.
  - 23 CODERRE J. A., TURCOTTE J. C., RILEY K. J., BINNS P. J. et al., Boron neutron capture therapy: Cellular targeting of high linear energy transfer radiation, *Technol. Cancer Res. Treat.*, **2003**, 2, 355–375.
  - 24 BARTH R. F., CODERRE J. A., VICENTE M. G., BLUE T. E., Boron neutron capture therapy of cancer: Current status and future prospects, *Clin. Cancer Res.*, **2005**, 11, 3987–4002.
  - 25 ZAMENHOF R. G., CODERRE J. A., RIVARD M. J., PATEL H., Eleventh world congress on neutron capture therapy, *Appl. Radiat. Isot.*, **2004**, 61, 731–1130.
  - 26 FARR L. E., SWEET W. H., ROBERTSON J. S., FOSTER C. G. et al., Neutron capture therapy with boron in the treatment of glioblastoma multiforme, *Am. J. Roentgenol. Radium Ther. Nucl. Med.*, **1954**, 71, 279–293.
  - 27 GOODWIN J. T., FARR L. E., SWEET W. H., ROBERTSON J. S., Pathological study of eight patients with glioblastoma multiforme treated by neutron-capture therapy using boron <sup>10</sup>, *Cancer*, **1955**, 8, 601–615.
  - 28 SNYDER H. R., REEDY A. J., LENNARZ W. J., Synthesis of aromatic boronic acids. Aldehyde boronic acids and a boronic acid analog of tyrosine, *J. Am. Chem. Soc.*, **1958**, 80, 835–838.
  - 29 SOLOWAY A. H., HATANAKA H., DAVIS M. A., Penetration of brain and brain tumor. VII. Tumor-binding sulfhydryl boron compounds, *J. Med. Chem.*, **1967**, 10, 714–717.

- 30 HATANAKA H., NAKAGAWA, Y., Clinical results of long-surviving brain tumor patients who underwent boron neutron capture therapy, *Int. J. Radiat. Oncol. Biol. Phys.*, **1994**, *28*, 1061–1066.
- 31 MISHIMA Y., Selective thermal neutron capture therapy of cancer cells using their specific metabolic activities – melanoma as prototype, in *Cancer Neutron Capture Therapy*, Y. MISHIMA, ed., Plenum Press, New York, **1996**, pp. 1–26.
- 32 ANG K. K., BERKEY B. A., TU X., ZHANG H. Z. et al., Impact of epidermal growth factor receptor expression on survival and pattern of relapse in patients with advanced head and neck carcinoma, *Cancer Res.*, **2002**, *62*, 7350–7356.
- 33 HAWTHORNE M. F., LEE M. W., A critical assessment of boron target compounds for boron neutron capture therapy, *J. Neurooncol.*, **2003**, *62*, 33–45.
- 34 SOLOWAY A. H., TJARKS W., BARNUM B. A., RONG F. G. et al., The chemistry of neutron capture therapy, *Chem. Rev.*, **1998**, *98*, 1515–1562.
- 35 GILLIES E. R., FRECHET J. M. J., Dendrimers and dendritic polymers in drug delivery, *Drug. Discovery Today*, **2005**, *10*, 35–43.
- 36 ESFAND R., TOMALIA D. A., Poly(amidoamine) (PAMAM) dendrimers: From biomimicry to drug delivery and biomedical applications, *Drug. Discov Today*, **2001**, *6*, 427–436.
- 37 TOMALIA D. A., NAYLOR A. M., GODDARD W. A. III, Starburst dendrimers: Control of size, shape, surface chemistry, topology and flexibility in the conversion of atoms to macroscopic materials, *Angew. Chem.*, **1990**, *102*, 119–157.
- 38 VERHEYDE B., MAES W., DEHAEN W., The use of 1,3,5-triazines in dendrimer synthesis, *Mater. Sci. Eng., C: Biomim. Supramol. Systems*, **2001**, *C18*, 243–245.
- 39 MCCARTHY T. D., KARELLAS P., HENDERSON S. A., GIANNIS M. et al., Dendrimers as drugs: Discovery and preclinical and clinical development of dendrimer-based microbicides for HIV and STI prevention, *Mol. Pharm.*, **2005**, *2*, 312–318.
- 40 VENDITTO V. J., REGINO C. A., BRECHBIEL M. W., PAMAM dendrimer based macromolecules as improved contrast agents, *Mol. Pharm.*, **2005**, *2*, 302–311.
- 41 AMBADE A. V., SAVARIAR E. N., THAYUMANAVAN S., Dendrimeric micelles for controlled drug release and targeted delivery, *Mol. Pharm.*, **2005**, *2*, 264–272.
- 42 MAJOROS I. J., THOMAS T. P., MEHTA C. B., BAKER, JR., J. R., Poly(amidoamine) dendrimer-based multifunctional engineered nanodevice for cancer therapy, *J. Med. Chem.*, **2005**, *48*, 5892–5899.
- 43 BOAS U., HEEGAARD P. M., Dendrimers in drug research, *Chem. Soc. Rev.*, **2004**, *33*, 43–63.
- 44 KLAJNERT B., BRYZIEWSKA M., Dendrimers: Properties and applications, *Acta Biochim. Pol.*, **2001**, *48*, 199–208.
- 45 SHARKEY R. M., GOLDENBERG D. M., Perspectives on cancer therapy with radiolabeled monoclonal antibodies, *J. Nucl. Med.*, **2005**, *46*(Suppl 1), 115S–127S.
- 46 JARACZ S., CHEN J., KUZNETSOVA L. V., OJIMA I., Recent advances in tumor-targeting anticancer drug conjugates, *Bioorg. Med. Chem.*, **2005**, *13*, 5043–5054.
- 47 GARNETT M. C., Targeted drug conjugates: Principles and progress, *Adv. Drug Deliv. Rev.*, **2001**, *53*, 171–216.
- 48 CHARI R. V., Targeted delivery of chemotherapeutics: Tumor-activated prodrug therapy, *Adv. Drug Deliv. Rev.*, **1998**, *31*, 89–104.
- 49 HAMBLETT K. J., SENTER P. D., CHACE D. F., SUN M. M. et al., Effects of drug loading on the antitumor activity of a monoclonal antibody drug conjugate, *Clin. Cancer Res.*, **2004**, *10*, 7063–7070.
- 50 TRAIL P. A., KING H. D., DUBOWCHIK G. M., Monoclonal antibody drug immunoconjugates for targeted



- treatment of cancer, *Cancer Immunol. Immunother.*, **2003**, 52, 328–337.
- 53 FRACASSO G., BELLISOLA G., CASTELLETTI D., TRIDENTE G., COLOMBATTI M., Immunotoxins and other conjugates: Preparation and general characteristics, *Mini Rev. Med. Chem.*, **2004**, 4, 545–562.
  - 54 LIU L., BARTH R. F., ADAMS D. M., SOLOWAY A. H., REISFELD R. A., Bispecific antibodies as targeting agents for boron neutron capture therapy of brain tumors, *J. Hematother.*, **1995**, 4, 477–483.
  - 55 ALAM F., SOLOWAY A. H., BARTH R. F., MAFUNE N. et al., Boron neutron capture therapy: Linkage of a boronated macromolecule to monoclonal antibodies directed against tumor-associated antigens, *J. Med. Chem.*, **1989**, 32, 2326–2330.
  - 56 BARTH R. F., JOHNSON C. W., WEI W. Z., CAREY W. E. et al., Neutron capture using boronated monoclonal antibody directed against tumor-associated antigens, *Cancer Detect. Prev.*, **1982**, 5, 315–323.
  - 57 ALAM F., BARTH R. F., SOLOWAY A. H., Boron containing immunconjugates for neutron capture therapy of cancer and for immunocytochemistry, *Antibody, Immunconjugates, and Radiopharmaceuticals*, **1989**, 2, 145–163.
  - 58 TOLPIN E. I., WELLMUM G. R., DOHAN F. C. JR., KORNB�ITH P. L., ZAMENHOF R. G., Boron neutron capture therapy of cerebral gliomas. II. Utilization of the blood-brain barrier and tumor-specific antigens for the selective concentration of boron in gliomas, *Oncology*, **1975**, 32, 223–246.
  - 59 SNEATH R. L. JR., WRIGHT J. E., SOLOWAY A. H., O'KEEFE S. M. et al., Protein-binding polyhedral boranes, *J. Med. Chem.*, **1976**, 19, 1290–1294.
  - 60 VARADARAJAN A., SHARKEY R. M., GOLDENBERG D. M., HAWTHORNE M. F., Conjugation of phenyl isothiocyanate derivatives of carborane to antitumor antibody and in vivo localization of conjugates in nude mice, *Bioconj. Chem.*, **1991**, 2, 102–110.
  - 61 TAKAHASHI T., FUJII Y., FUJII G., NARIUCHI H., Preliminary study for application of anti-alpha-fetoprotein monoclonal antibody to boron-neutron capture therapy, *Jpn. J. Exp. Med.*, **1987**, 57, 83–91.
  - 62 COMPOSTELLA F., MONTI D., PANZA L., POLETTI L., PROSPERI D., Synthesis of glycosyl carboranes with different linkers between the sugar and the boron cage moieties, *Research and Development in Neutron Capture Therapy, Proceedings of the International Congress on Neutron Capture Therapy*, SAUERWEIN M.W., MOSS R., WITTIG A. eds., Monduzzi Editore, Bologna, Italy, **2002**, 81–84.
  - 63 GIOVENZANA G. B., LAY L., MONTI D., PALMISANO G., PANZA L., Synthesis of carboranyl derivatives of alkynyl glycosides as potential BNCT agents, *Tetrahedron*, **1999**, 55, 14 123–14 136.
  - 64 ALAM F., SOLOWAY A. H., MCGUIRE J. E., BARTH R. F. et al., Dicesium N-succinimidyl 3-(undecahydro-closo-dodecaboranyldithio)propionate, a novel heterobifunctional boronating agent, *J. Med. Chem.*, **1985**, 28, 522–525.
  - 65 BARTH R. F., ADAMS D. M., SOLOWAY A. H., ALAM F., DARBY M. V., Boronated starburst dendrimer-monoclonal antibody immunconjugates: Evaluation as a potential delivery system for neutron capture therapy, *Bioconj. Chem.*, **1994**, 5, 58–66.
  - 66 LIU L., BARTH R. F., ADAMS D. M., SOLOWAY A. H., REISFELD R. A., Critical evaluation of bispecific antibodies as targeting agents for boron neutron capture therapy of brain tumors, *Anticancer Res.*, **1996**, 16, 2581–2588.
  - 67 BARTH R. F., ADAMS D. M., SOLOWAY A. H., DARBY M. V., In vivo distribution of boronated monoclonal antibodies and starburst dendrimers, *Adv. Neutron Capture Ther., [Proc. 5th Int. Symp.]*, **1993**, 351–355.
  - 68 WU G., BARTH R. F., YANG W., CHATTERJEE M. et al., Site-specific conjugation of boron-containing dendrimers to anti-EGF receptor

- monoclonal antibody cetuximab (IMC-C225) and its evaluation as a potential delivery agent for neutron capture therapy, *Bioconj. Chem.*, **2004**, *15*, 185–194.
- 67 ARTEAGA C. L., Overview of epidermal growth factor receptor biology and its role as a therapeutic target in human neoplasia, *Semin. Oncol.*, **2002**, *29*, 3–9.
- 68 MENDELSON J., Targeting the epidermal growth factor receptor for cancer therapy, *J. Clin. Oncol.*, **2002**, *20*, 1S–13S.
- 69 BARTH R. F., WU G., YANG W., BINNS P. J. et al., Neutron capture therapy of epidermal growth factor (+) gliomas using boronated cetuximab (IMC-C225) as a delivery agent, *Appl. Radiat. Isot.*, **2004**, *61*, 899–903.
- 70 PAL S. K., PEGRAM M., Epidermal growth factor receptor and signal transduction: Potential targets for anti-cancer therapy, *Anticancer Drugs*, **2005**, *16*, 483–494.
- 71 NORMANNO N., BIANCO C., STRIZZI L., MANCINO M. et al., The ErbB receptors and their ligands in cancer: An overview, *Curr. Drug Targets*, **2005**, *6*, 243–257.
- 72 JORISSEN R. N., WALKER F., POULIOT N., GARRETT T. P. et al., Epidermal growth factor receptor: Mechanisms of activation and signalling, *Exp. Cell Res.*, **2003**, *284*, 31–53.
- 73 YANG W., BARTH R. F., WU G., BANDYOPADHYAYA, A. K. et al., Boronated epidermal growth factor as a delivery agent for neutron capture therapy of EGF receptor positive gliomas, *Appl. Radiat. Isot.*, **2004**, *61*, 981–985.
- 74 CAPALA J., BARTH R. F., BENDAYAN M., LAUZON M. et al., Boronated epidermal growth factor as a potential targeting agent for boron neutron capture therapy of brain tumors, *Bioconj. Chem.*, **1996**, *7*, 7–15.
- 75 YANG W., BARTH R. F., ADAMS D. M., SOLOWAY A. H., Intratumoral delivery of boronated epidermal growth factor for neutron capture therapy of brain tumors, *Cancer Res.*, **1997**, *57*, 4333–4339.
- 76 YANG W., BARTH R. F., ADAMS D. M., CIESIELSKI M. J. et al., Convection-enhanced delivery of boronated epidermal growth factor for molecular targeting of EGF receptor-positive gliomas, *Cancer Res.*, **2002**, *62*, 6552–6558.
- 77 BARTH R. F., YANG W., ADAMS D. M., ROTARU J. H. et al., Molecular targeting of the epidermal growth factor receptor for neutron capture therapy of gliomas, *Cancer Res.*, **2002**, *62*, 3159–3166.
- 78 REDDY J. A., ALLAGADDA V. M., LEAMON C. P., Targeting therapeutic and imaging agents to folate receptor positive tumors, *Curr. Pharm. Biotechnol.*, **2005**, *6*, 131–150.
- 79 LEAMON C. P., REDDY J. A., Folate-targeted chemotherapy, *Adv. Drug Deliv. Rev.*, **2004**, *56*, 1127–1141.
- 80 SUDIMACK J., LEE R. J., Targeted drug delivery via the folate receptor, *Adv. Drug Deliv. Rev.*, **2000**, *41*, 147–162.
- 81 PAULOS C. M., REDDY J. A., LEAMON C. P., TURK M. J., LOW P. S., Ligand binding and kinetics of folate receptor recycling in vivo: Impact on receptor-mediated drug delivery, *Mol. Pharmacol.*, **2004**, *66*, 1406–1414.
- 82 REDDY J. A., LOW P. S., Folate-mediated targeting of therapeutic and imaging agents to cancers, *Crit. Rev. Ther. Drug Carrier Syst.*, **1998**, *15*, 587–627.
- 83 STEPHENSON S. M., YANG W., STEVENS P. J., TJARKS W. et al., Folate receptor-targeted liposomes as possible delivery vehicles for boron neutron capture therapy, *Anticancer Res.*, **2003**, *23*, 3341–3345.
- 84 WARD C. M., Folate-targeted non-viral DNA vectors for cancer gene therapy, *Curr. Opin. Mol. Ther.*, **2000**, *2*, 182–187.
- 85 GOTTSCHALK S., CRISTIANO R. J., SMITH L. C., WOO S. L., Folate receptor mediated DNA delivery into tumor cells: Protosomal disruption results in enhanced gene expression, *Gene Ther.*, **1994**, *1*, 185–191.
- 86 HILGENBRINK A. R., LOW P. S., Folate receptor-mediated drug targeting:

- From therapeutics to diagnostics, *J. Pharm. Sci.*, **2005**, 94, 2135–2146.
- 87 SHUKLA S., WU G., CHATTERJEE M., YANG W. et al., Synthesis and biological evaluation of folate receptor-targeted boronated PAMAM dendrimers as potential agents for neutron capture therapy, *Bioconj. Chem.*, **2003**, 14, 158–167.
- 88 BENOUGHAN M., COLOMBO B. M., Anti-angiogenic strategies for cancer therapy (Review), *Int. J. Oncol.*, **2005**, 27, 563–571.
- 89 TORTORA G., MELISI D., CIARDIELLO F., Angiogenesis: A target for cancer therapy, *Curr. Pharm. Des.*, **2004**, 10, 11–26.
- 90 BREKKEN R. A., LI C., KUMAR S., Strategies for vascular targeting in tumors, *Int. J. Cancer*, **2002**, 100, 123–130.
- 91 GAYA A. M., RUSTIN G. J., Vascular disrupting agents: A new class of drug in cancer therapy, *Clin. Oncol. (R. Coll. Radiol.)*, **2005**, 17, 277–290.
- 92 BERGSLAND E. K., Vascular endothelial growth factor as a therapeutic target in cancer, *Am. J. Health Syst. Pharm.*, **2004**, 61, S4–11.
- 93 HICKLIN D. J., ELLIS L. M., Role of the vascular endothelial growth factor pathway in tumor growth and angiogenesis, *J. Clin. Oncol.*, **2005**, 23, 1011–1027.
- 94 BACKER M. V., GAYNUTDINOV T. I., PATEL V., BANDYOPADHYAYA A. K. et al., Vascular endothelial growth factor selectively targets boronated dendrimers to tumor vasculature, *Mol. Cancer Ther.*, **2005**, 4, 1423–1429.
- 95 BARTH R. F., YANG W., CODERRE J. A., Rat brain tumor models to assess the efficacy of boron neutron capture therapy: A critical evaluation, *J. Neurooncol.*, **2003**, 62, 61–74.
- 96 PARROTT M. C., MARCHINGTON E. B., VALLIANT J. F., ADRONOV, A., Synthesis and properties of carborane-functionalized aliphatic polyester dendrimers, *J. Am. Chem. Soc.*, **2005**, 127, 12 081–12 089.
- 97 PARK J. W., BENZ C. C., MARTIN F. J., Future directions of liposome- and immunoliposome-based cancer therapeutics, *Semin. Oncol.*, **2004**, 31, 196–205.
- 98 SAPRA P., ALLEN T. M., Ligand-targeted liposomal anticancer drugs, *Prog. Lipid Res.*, **2003**, 42, 439–462.
- 99 CARLSSON J., KULLBERG E. B., CAPALA J., SJOBERG S. et al., Ligand liposomes and boron neutron capture therapy, *J. Neurooncol.*, **2003**, 62, 47–59.
- 100 HAWTHORNE M. F., SHELLY K., Liposomes as drug delivery vehicles for boron agents, *J. Neurooncol.*, **1997**, 33, 53–58.
- 101 MISHIMA Y., HONDA C., ICHIHASHI M., OBARA H. et al., Treatment of malignant melanoma by single thermal neutron capture therapy with melanoma-seeking <sup>10</sup>B-compound, *Lancet*, **1989**, 2, 388–389.
- 102 CODERRE J. A., GLASS J. D., FAIRCHILD R. G., MICCA P. L. et al., Selective delivery of boron by the melanin precursor analogue p-boronophenylalanine to tumors other than melanoma, *Cancer Res.*, **1990**, 50, 138–141.
- 103 ONO K., MASUNAGA S., SUZUKI M., KINASHI Y. et al., The combined effect of boronophenylalanine and borocaptate in boron neutron capture therapy for SCCVII tumors in mice, *Int. J. Radiat. Oncol. Biol. Phys.*, **1999**, 43, 431–436.
- 104 OBAYASHI S., KATO I., ONO K., MASUNAGA S. et al., Delivery of (<sup>10</sup>)boron to oral squamous cell carcinoma using boronophenylalanine and borocaptate sodium for boron neutron capture therapy, *Oral Oncol.*, **2004**, 40, 474–482.
- 105 YOSHINO K., SUZUKI A., MORI Y., KAKIHANA H. et al., Improvement of solubility of p-boronophenylalanine by complex formation with monosaccharides, *Strahlenther Onkol.*, **1989**, 165, 127–129.
- 106 RYNNANEN P. M., KORTESNIEMI M., CODERRE J. A., DIAZ A. Z. et al., Models for estimation of the <sup>10</sup>B concentration after BPA-fructose complex infusion in patients during epithelial neutron irradiation in BNCT, *Int. J. Radiat. Oncol. Biol. Phys.*, **2000**, 48, 1145–1154.

- 107 PAVANETTO F., PERUGINI P., GENTA I., MINOIA C. et al., Boron-loaded liposomes in the treatment of hepatic metastases: Preliminary investigation by autoradiography analysis, *Drug Deliv.*, **2000**, 7, 97–103.
- 108 MARTINI S., RISTORI S., PUCCI A., BONECHI C. et al., Borophenylalanine insertion in cationic liposomes for Boron Neutron Capture Therapy, *Biophys. Chem.*, **2004**, 111, 27–34.
- 109 SMYTH TEMPLETON N., Cationic liposomes as in vivo delivery vehicles, *Curr. Med. Chem.*, **2003**, 10, 1279–1287.
- 110 MEHTA S. C., LAI J. C., LU D. R., Liposomal formulations containing sodium mercaptoundecahydro-dodecaborate (BSH) for boron neutron capture therapy, *J. Microencapsul.*, **1996**, 13, 269–279.
- 111 JI B., CHEN W., LU D. R., HALPERN D. S., Cell culture and animal studies for intracerebral delivery of borocaptate in liposomal formulation, *Drug Deliv.*, **2001**, 8, 13–17.
- 112 MARUYAMA K., ISHIDA O., KASAOKA S., TAKIZAWA T. et al., Intracellular targeting of sodium mercaptoundecahydrododecaborate (BSH) to solid tumors by transferrin-PEG liposomes, for boron neutron-capture therapy (BNCT), *J. Controlled Release*, **2004**, 98, 195–207.
- 113 VALLIANT J. F., GUENTHER K. J., KING A. S., MOREL P. et al., The medicinal chemistry of carboranes, *Coord. Chem. Rev.*, **2002**, 232, 173–230.
- 114 HAWTHORNE M. F., The role of chemistry in the development of cancer therapy by the boron-neutron capture reaction, *Angew. Chem.*, **1993**, 105, 997–1033 (See also *Angew. Chem., Int. Ed. Engl.*, 1993, 950–984).
- 115 MORAES A. M., SANTANA M. H. A., CARBONELL R. G., Preparation and characterization of liposomal systems entrapping the boronated compound o-carboranylpropylamine, *J. Microencapsulat.*, **1999**, 16, 647–664.
- 116 MORAES A. M., SANTANA M. H. A., CARBONELL R. G., Characterization of liposomal systems entrapping boron-containing compounds in response to pH gradients, *Biofunctional Membranes, Proceedings of the International Conference on Biofunctional Membranes*, BUTTERFIELD D. A. ed., Plenum Press, New York, **1996**, 259–275.
- 117 SHELLY K., FEAKES D. A., HAWTHORNE M. F., SCHMIDT P. G. et al., Model studies directed toward the boron neutron-capture therapy of cancer: Boron delivery to murine tumors with liposomes, *Proc. Natl. Acad. Sci. U.S.A.*, **1992**, 89, 9039–9043.
- 118 FEAKES D. A., SHELLY K., KNOBLER C. B., HAWTHORNE M. F., Na<sub>3</sub>[B<sub>20</sub>H<sub>17</sub>NH<sub>3</sub>]: Synthesis and liposomal delivery to murine tumors, *Proc. Natl. Acad. Sci. U.S.A.*, **1994**, 91, 3029–3033.
- 119 HAWTHORNE M. F., SHELLY K., LI F., The versatile chemistry of the [B<sub>20</sub>H<sub>18</sub>]<sup>2-</sup> ions: Novel reactions and structural motifs, *Chem. Commun. (Camb)*, **2002**, 547–554.
- 120 FEAKES D. A., WALLER R. C., HATHAWAY D. K., MORTON V. S., Synthesis and in vivo murine evaluation of Na<sub>4</sub>[1-(1'-B<sub>10</sub>H<sub>9</sub>)-6-SHB<sub>10</sub>H<sub>8</sub>] as a potential agent for boron neutron capture therapy, *Proc. Natl. Acad. Sci. U.S.A.*, **1999**, 96, 6406–6410.
- 121 WATSON-CLARK R. A., BANQUERIGO M. L., SHELLY K., HAWTHORNE M. F., BRAHN E., Model studies directed toward the application of boron neutron capture therapy to rheumatoid arthritis: Boron delivery by liposomes in rat collagen-induced arthritis, *Proc. Natl. Acad. Sci. U.S.A.*, **1998**, 95, 2531–2534.
- 122 FEAKES D. A., SPINLER J. K., HARRIS F. R., Synthesis of boron-containing cholesterol derivatives for incorporation into unilamellar liposomes and evaluation as potential agents for BNCT, *Tetrahedron*, **1999**, 55, 11 177–11 186.
- 123 JI B., PEACOCK G., LU D. R., Synthesis of cholesterol-carborane conjugate for targeted drug delivery, *Bioorg. Med. Chem. Lett.*, **2002**, 12, 2455–2458.
- 124 PAN G., OIE S., LU D. R., Uptake of

- the carborane derivative of cholesteryl ester by glioma cancer cells is mediated through LDL receptors, *Pharm. Res.*, **2004**, *21*, 1257–1262.
- 125** MALETINSKA L., BLAKELY E. A., BJORNSTAD K. A., DEEN D. F. et al., Human glioblastoma cell lines: Levels of low-density lipoprotein receptor and low-density lipoprotein receptor-related protein, *Cancer Res.*, **2000**, *60*, 2300–2303.
- 126** NYGREN C., VON HOLST H., MANSSON J. E., FREDMAN P., Increased levels of cholesterol esters in glioma tissue and surrounding areas of human brain, *Br. J. Neurosurg.*, **1997**, *11*, 216–220.
- 127** LEPPALA J., KALLIO M., NIKULA T., NIKKINEN P. et al., Accumulation of <sup>99m</sup>Tc-low-density lipoprotein in human malignant glioma, *Br. J. Cancer*, **1995**, *71*, 383–387.
- 128** PEACOCK G., SIDWELL R., PAN G., OLE S., LU D. R., In vitro uptake of a new cholesteryl carborane ester compound by human glioma cell lines, *J. Pharm. Sci.*, **2004**, *93*, 13–19.
- 129** WEI Q., KULLBERG E. B., GEDDA L., Trastuzumab-conjugated boron-containing liposomes for tumor-cell targeting, development and cellular studies, *Int. J. Oncol.*, **2003**, *23*, 1159–1165.
- 130** BOHL KULLBERG E., BERGSTRAND N., CARLSSON J., EDWARDS K. et al., Development of EGF-conjugated liposomes for targeted delivery of boronated DNA-binding agents, *Bioconj. Chem.*, **2002**, *13*, 737–743.
- 131** STEPHENSON S. M., YANG W., STEVENS P. J., TJARKS W. et al., Folate receptor-targeted liposomes as possible delivery vehicles for boron neutron capture therapy, *Anticancer Res.*, **2003**, *23*, 3341–3345.
- 132** YANAGIE H., FUJII Y., TAKAHASHI T., TOMITA T. et al., Boron neutron capture therapy using <sup>10</sup>B entrapped anti-CEA immunoliposome, *Hum. Cell*, **1989**, *2*, 290–296.
- 133** YANAGIE H., TOMITA T., KOBAYASHI H., FUJII Y. et al., Application of boronated anti-CEA immunoliposome to tumour cell growth inhibition in vitro boron neutron capture therapy model, *Br. J. Cancer*, **1991**, *63*, 522–526.
- 134** YANAGIE H., KOBAYASHI H., TAKEDA Y., YOSHIZAKI I. et al., Inhibition of growth of human breast cancer cells in culture by neutron capture using liposomes containing <sup>10</sup>B, *Biomed. Pharmacother.*, **2002**, *56*, 93–99.
- 135** XU L., Boron neutron capture therapy of human gastric cancer by boron-containing immunoliposomes under thermal neutron irradiation (in Chinese), *Zhonghua Yi Xue Za Zhi*, **1991**, *71*, 568–571.
- 136** XU L., ZHANG X. Y., ZHANG S. Y., In vitro and in vivo targeting therapy of immunoliposomes against human gastric cancer (in Chinese), *Zhonghua Yi Xue Za Zhi*, **1994**, *74*, 83–86, 126.
- 137** PAN X. Q., WANG H., LEE R. J., Boron delivery to a murine lung carcinoma using folate receptor-targeted liposomes, *Anticancer Res.*, **2002**, *22*, 1629–1633.
- 138** PAN X. Q., WANG H., SHUKLA S., SEKIDO M. et al., Boron-containing folate receptor-targeted liposomes as potential delivery agents for neutron capture therapy, *Bioconj. Chem.*, **2002**, *13*, 435–442.
- 139** SUDIMACK J. J., ADAMS D., ROTARU J., SHUKLA S. et al., Folate receptor-mediated liposomal delivery of a lipophilic boron agent to tumor cells in vitro for neutron capture therapy, *Pharm. Res.*, **2002**, *19*, 1502–1508.
- 140** BOHL KULLBERG E., CARLSSON J., EDWARDS K., CAPALA J. et al., Introductory experiments on ligand liposomes as delivery agents for boron neutron capture therapy, *Int. J. Oncol.*, **2003**, *23*, 461–467.
- 141** KULLBERG E. B., NESTOR M., GEDDA L., Tumor-cell targeted epidermal growth factor liposomes loaded with boronated acridine: Uptake and processing, *Pharm. Res.*, **2003**, *20*, 229–236.
- 142** MEHVAR R., Dextrans for targeted and sustained delivery of therapeutic and imaging agents, *J. Controlled Release*, **2000**, *69*, 1–25.

- 143 MEHVAR, R., Recent trends in the use of polysaccharides for improved delivery of therapeutic agents: Pharmacokinetic and pharmacodynamic perspectives, *Curr. Pharm. Biotechnol.*, **2003**, 4, 283–302.
- 144 CHAU Y., TAN F. E., LANGER R., Synthesis and characterization of dextran-peptide-methotrexate conjugates for tumor targeting via mediation by matrix metalloproteinase II and matrix metalloproteinase IX, *Bioconj. Chem.*, **2004**, 15, 931–941.
- 145 ZHANG X., MEHVAR R., Dextran-methylprednisolone succinate as a prodrug of methylprednisolone: Plasma and tissue disposition, *J. Pharm. Sci.*, **2001**, 90, 2078–2087.
- 146 LARSSON B., GABEL D., BORNER H. G., Boron-loaded macromolecules in experimental physiology: Tracing by neutron capture radiography, *Phys. Med. Biol.*, **1984**, 29, 361–370.
- 147 GABEL D., WALCZYNA R., B-Decachloro-o-carborane derivatives suitable for the preparation of boron-labeled biological macromolecules, *Z. Naturforsch. Teil C*, **1982**, 37, 1038–1039.
- 148 PETTERSSON M. L., COUREL M. N., GIRARD N., GABEL D., DELPECH B., In vitro immunological activity of a dextran-boronated monoclonal antibody, *Strahlenther Onkol.*, **1989**, 165, 151–152.
- 149 UJENO Y., AKABOSHI M., MAKI H., KAWAI K. et al., The enhancement of thermal-neutron induced cell death by 10-boron dextran, *Strahlenther Onkol.*, **1989**, 165, 201–203.
- 150 PETTERSSON M. L., COUREL M. N., GIRARD N., ABRAHAM R. et al., Immunoreactivity of boronated antibodies, *J. Immunol. Methods*, **1990**, 126, 95–102.
- 151 HOLMBERG A., MEURLING L., Preparation of sulfhydrylborane-dextran conjugates for boron neutron capture therapy, *Bioconj. Chem.*, **1993**, 4, 570–573.
- 152 CARLSSON J., GEDDA L., GRONVIK C., HARTMAN T. et al., Strategy for boron neutron capture therapy against tumor cells with over-expression of the epidermal growth factor-receptor, *Int. J. Radiat. Oncol. Biol. Phys.*, **1994**, 30, 105–115.
- 153 GEDDA L., OLSSON P., PONTEN J., CARLSSON J., Development and in vitro studies of epidermal growth factor-dextran conjugates for boron neutron capture therapy, *Bioconj. Chem.*, **1996**, 7, 584–591.
- 154 MEHTA S. C., LU D. R., Targeted drug delivery for boron neutron capture therapy, *Pharm. Res.*, **1996**, 13, 344–351.
- 155 OLSSON P., GEDDA L., GOIKE H., LIU L. et al., Uptake of a boronated epidermal growth factor-dextran conjugate in CHO xenografts with and without human EGF-receptor expression, *Anticancer Drug Des.*, **1998**, 13, 279–289.
- 156 NOVICK S., QUASTEL M. R., MARCUS S., CHIPMAN D. et al., Linkage of boronated polylysine to glycoside moieties of polyclonal antibody; boronated antibodies as potential delivery agents for neutron capture therapy, *Nucl. Med. Biol.*, **2002**, 29, 159–167.
- 157 FERRO V. A., MORRIS J. H., STIMSON W. H., A novel method for boronating antibodies without loss of immunoreactivity, for use in neutron capture therapy, *Drug Des. Discov.*, **1995**, 13, 13–25.
- 158 SANO T., Boron-enriched streptavidin potentially useful as a component of boron carriers for neutron capture therapy of cancer, *Bioconj. Chem.*, **1999**, 10, 905–911.
- 159 THOMAS J., HAWTHORNE M. F., Dodeca(carboranyl)-substituted closomers: Toward unimolecular nanoparticles as delivery vehicles for BNCT, *Chem. Commun. (Camb)*, **2001**, 1884–1885.
- 160 PARDRIDGE W. M., Vector-mediated drug delivery to the brain, *Adv. Drug Deliv. Rev.*, **1999**, 36, 299–321.
- 161 PARDRIDGE W. M., Blood-brain barrier biology and methodology, *J. Neurovirool.*, **1999**, 5, 556–569.

- 162 HATAKEYAMA H., AKITA H., MARUYAMA K., SUHARA T., HARASHIMA H., Factors governing the in vivo tissue uptake of transferrin-coupled polyethylene glycol liposomes in vivo, *Int. J. Pharm.*, **2004**, 281, 25–33.
- 163 YANAGIE H., OGURA K., TAKAGI K., MARUYAMA K. et al., Accumulation of boron compounds to tumor with polyethylene-glycol binding liposome by using neutron capture autoradiography, *Appl. Radiat. Isot.*, **2004**, 61, 639–646.
- 164 MARUYAMA K., TAKIZAWA T., YUDA T., KENNEL S. J. et al., Targetability of novel immunoliposomes modified with amphipathic poly(ethylene glycol)s conjugated at their distal terminals to monoclonal antibodies, *Biochim. Biophys. Acta*, **1995**, 1234, 74–80.
- 165 YANG W., BARTH R. F., LEVEILLE R., ADAMS D. M. et al., Evaluation of systemically administered radiolabeled epidermal growth factor as a brain tumor targeting agent, *J. Neurooncol.*, **2001**, 55, 19–28.
- 166 BOBO R. H., LASKE D. W., AKBASAK A., MORRISON P. F. et al., Convection-enhanced delivery of macromolecules in the brain, *Proc. Natl. Acad. Sci. U.S.A.*, **1994**, 91, 2076–2080.
- 167 GROOTHUIS D. R., The blood-brain and blood-tumor barriers: A review of strategies for increasing drug delivery, *Neurooncol.*, **2000**, 2, 45–59.
- 168 VOGELBAUM M. A., Convection enhanced delivery for the treatment of malignant gliomas: Symposium review, *J. Neurooncol.*, **2005**, 73, 57–69.
- 169 HUSAIN S. R., PURI R. K., Interleukin-13 receptor-directed cytotoxin for malignant glioma therapy: From bench to bedside, *J. Neurooncol.*, **2003**, 65, 37–48.
- 170 KUNWAR S., Convection enhanced delivery of IL13-PE38QQR for treatment of recurrent malignant glioma: Presentation of interim findings from ongoing phase 1 studies, *Acta Neurochir. Suppl.*, **2003**, 88, 105–111.
- 171 WIKSTRAND C. J., HALE L. P., BATRA S. K., HILL M. L. et al., Monoclonal antibodies against EGFRvIII are tumor specific and react with breast and lung carcinomas and malignant gliomas, *Cancer Res.*, **1995**, 55, 3140–3148.
- 172 WIKSTRAND C. J., MCLENDON R. E., FRIEDMAN A. H., BIGNER D. D., Cell surface localization and density of the tumor-associated variant of the epidermal growth factor receptor, EGFRvIII, *Cancer Res.*, **1997**, 57, 4130–4140.
- 173 YANG W., BARTH R. F., WU G., CIESIELSKI M. J. et al., Development of a syngeneic rat brain tumor model expressing EGFRvIII and its use for molecular targeting studies with monoclonal antibody L8A4, *Clin. Cancer Res.*, **2005**, 11, 341–350.
- 174 COKGOR I., AKABANI G., KUAN C. T., FRIEDMAN H. S. et al., Phase I trial results of iodine-131-labeled antitenascin monoclonal antibody 81C6 treatment of patients with newly diagnosed malignant gliomas, *J. Clin. Oncol.*, **2000**, 18, 3862–3872.
- 175 AKABANI G., REARDON D. A., COLEMAN R. E., WONG T. Z. et al., Dosimetry and radiographic analysis of 131I-labeled anti-tenascin 81C6 murine monoclonal antibody in newly diagnosed patients with malignant gliomas: A phase II study, *J. Nucl. Med.*, **2005**, 46, 1042–1051.
- 176 LASKE D. W., YOULE R. J., OLDFIELD E. H., Tumor regression with regional distribution of the targeted toxin TF-CRM107 in patients with malignant brain tumors, *Nat. Med.*, **1997**, 3, 1362–1368.
- 177 SAMPSON J. H., AKABANI G., ARCHER G. E., BIGNER D. D. et al., Progress report of a Phase I study of the intracerebral microinfusion of a recombinant chimeric protein composed of transforming growth factor (TGF)-alpha and a mutated form of the Pseudomonas exotoxin termed PE-38 (TP-38) for the treatment of malignant brain tumors, *J. Neurooncol.*, **2003**, 65, 27–35.
- 178 WEBER F., ASHER A., BUCHOLZ R., BERGER M. et al., Safety, tolerability,

- and tumor response of IL4-Pseudomonas exotoxin (NBI-3001) in patients with recurrent malignant glioma, *J. Neurooncol.*, **2003**, *64*, 125–137.
- 179** WEBER F. W., FLOETH F., ASHER A., BUCHOLZ R. et al., Local convection enhanced delivery of IL4-Pseudomonas exotoxin (NBI-3001) for treatment of patients with recurrent malignant glioma, *Acta Neurochir. Suppl.*, **2003**, *88*, 93–103.
- 180** FERRARI M., Nanovector therapeutics, *Curr. Opin. Chem. Biol.*, **2005**, *9*, 343–346.
- 181** FERRARI M., Cancer nanotechnology: Opportunities and challenges, *Nat. Rev. Cancer*, **2005**, *5*, 161–171.



## 5

# Local Cancer Therapy with Magnetic Drug Targeting using Magnetic Nanoparticles

*Christoph Alexiou and Roland Jurgons*

### 5.1

#### Introduction

A continual problem in cancer therapy is the fact that applied drugs do not have a selective site of action. To achieve a therapeutic concentration in the region of interest using systemic administration it is necessary to administer high doses of drugs. Frequently, the dose of therapeutic agents is limited by their body distribution and subsequently their negative side effects and toxicity. During the last three decades many approaches and techniques have been developed in medicine for diagnosis and therapy both *in vivo* and *in vitro* to obtain a more site-specific transport of therapeutic agents, especially anticancer drugs in *local chemotherapy*, so as to increase the agent's local concentration in specific body compartments without harming healthy tissue [1–5]. Targeted drug delivery systems for accumulating pharmaceuticals in specific areas can be passive, based on specific properties of pathological tissues or specific characteristics of targeted organs [6], or active, often magnetically directed as *magnetic targeting* or *magnetic drug delivery*, based on various carrier systems [7]. Inflamed tissues or tumors, for example, differ from healthy tissue concerning pH, temperature or permeability of the vascular endothelium [8]. This enables the use of drug loaded pH-sensitive or thermosensitive liposomes to achieve a high amount of the therapeutic agent in the respective tissue [9–11]. Among liposomes, various substances such as peptides or proteins can be used for targeted drug delivery. Drug-containing monoclonal antibodies can be used for thrombolysis [12] or tumor-specific antibodies can be employed in cancer treatment [13, 14]. In addition to reviewing magnetic nanoparticles in biomedicine, this chapter overviews local chemotherapies, focusing especially on regional cancer therapy with magnetic nanoparticles.

### 5.2

#### Local Chemotherapy

The therapeutic effectiveness of drugs, especially of chemotherapeutic agents, is connected with their cell toxic properties [15]. This cell toxicity can cause a cell-

**Tab. 5.1.** Application techniques of local chemotherapy.

- 
1. Intratumoral (intralesional) therapy
  2. Intracavitary therapy
  3. Intra-arterial infusion
  4. Intraportal infusion
  5. Regional perfusion of extremities
  6. Chemoembolization
- 

depression of bone marrow or the gastrointestinal tract. Furthermore, it may have serious consequences such as mutagenic, teratogenic or cancerogenic effects. The occurrence of secondary tumors induced by chemotherapy is evaluated at about 3% [16]. Targeted drug delivery may increase the therapeutic effects, reduce the costs of therapies and, especially for patients, would mean less negative side effects.

The easiest way of drug targeting involves local injection directly in the region of interest, which in cancer therapy is the tumor region (Table 5.1) [17, 18].

Another possibility of local chemotherapy is the intracavitary application of cytostatics. After systemic administration, chemotherapeutic agents reach the tumor by the vascular system; given intracavitally the site of action is penetration of the tumor tissue. The effectiveness of such local chemotherapy depends on a high plasma clearance and a small cavital clearance of the chemotherapeutic agent [19], on a good penetration of the tumor tissue and on the tumor size. With tumors larger than 2 cm in diameter, penetration is less and there is no advantage over systemic administration [20]. Application can be performed intraperitoneally [21], intrapleurally [22] or intravesically [23].

Secondary liver tumors can be treated by the injection of cytostatics in the portal vein [24] or in most cases in the hepatic artery [25].

Actually, regional perfusion with chemotherapeutic agents in an isolated circulation is used in treating liver tumors. Furthermore, isolated perfusion is performed in malignant melanoma of extremities [26].

A very effective palliative treatment of non-resectable hepatocellular carcinomas is chemoembolization. The combination of embolization and application of chemotherapeutics induces a high accumulation and a long residence time of the drug in the tumor [27].

Intraarterial infusion of chemotherapeutics bypasses a possible so-called first-pass-effect through liver and spleen before reaching the tumor. This results in a higher concentration of the drug compared with systemic administration. This effect can be increased by diminishing the arterial flow rate, which can be accomplished by the use of balloon-catheters [28], by administration of vasoconstrictive drugs [29, 30] or embolization [31, 32].

### 5.3

#### Magnetic Drug Delivery

Drug targeting with magnetic carrier systems enables an active transport of drugs into the respective region. Therefore, therapeutic agents such as drugs [33, 34] or radioisotopes [35] bound to a magnetic carrier will be injected in the vascular system. Under the influence of an external magnetic field this compound will be held in the targeted area and concentrated in the region of interest. Magnetic particles have been used in medicine for about 40 years and different sophisticated biomedical applications have been developed. Magnetic particles are frequently used *in vitro* and *in vivo*, depending on their size, surface and coating.

##### 5.3.1

#### *In Vitro* Applications

For *in vitro* applications several biotechnological approaches have been developed. A molecular-biological diagnostic procedure that has become increasingly important is biomagnetic separation. Magnetic nanoparticles are bound to a ligand (i.e., antibodies) that can be used to target cells, DNA or bacteria. After binding of the ligands to the targets they can be separated by the use of an external magnetic field. Magnetic cell separation is a medical approach of this biomagnetic separation technique that has become standard for *in vitro* diagnosis in cancer patients [36, 37]. By the use of superparamagnetic nanospheres (Fig. 5.1) and an automated magnetic cell separation (MACS®, Miltenyi Biotech®) this system allows the detection of disseminated tumor cells in the peripheral blood of cancer patients.

Another approach for *in vitro* application of magnetic nanoparticles is Magnetofection™. Gene vectors bound to starch-coated magnetic nanoparticles are attracted by an external magnetic field and used to transfect cells *in vitro*. The respective cells show greater transfection than without the influence of an external magnetic field [38].

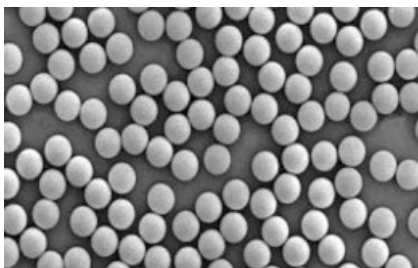


**Fig. 5.1.** Magnetic particles with homogenous size for the magnetic cell separation system (Dynabeads®).

## 5.3.2

**In Vivo Applications**

For *in vivo* applications the magnetic particles have to be biocompatible. They can be incorporated in, or coated with, different biological materials. Therefore, different carriers have been used, such as magnetic microparticles, magnetoliposomes or magnetic iron oxide nanoparticles and also ferromagnetic substances. Alksne et al. (1966) have used carbonated iron and the influence of an external magnetic field to occlude intracranial aneurysms [39].

McNeil et al. (1995) have described a magnetic guidance system for a promising use in neurosurgery. Six external electromagnetic coils are able to guide magnetic neodymium-iron-bor capsules in the brain [40].

Another drug delivery system that can target chemotherapeutic agents is magnetic microspheres [41, 42]. Widder et al. have used magnetic albumin microspheres to increase the concentration of drugs in the tumor-region after applying an external magnetic field to this region [43–46]. Tumor remissions in rats could be shown [45]. These particles were about 1–7  $\mu\text{m}$  in size. Because of enzymatic breakdown of the albumin, a controlled release of the incorporated drug could not be achieved.

Another approach is the use of activated carbonated iron [47, 48]. Allen et al. (1997) have formulated Magnetically Targetable Carriers (MTC<sup>TM</sup>) made of iron and activated carbon bound to the chemotherapeutic agent paclitaxel for targeted drug delivery [49].

A magnetically targeted carrier bound to doxorubicin (MTC-Dox, FerX<sup>®</sup>, CA, USA) has been used to treat hepatocellular carcinomas. In human patients, MTC-Dox was administered in the hepatic artery while an external magnetic field was focused to the tumor region. In one case, reduction of tumor size could be shown [50]. However, another study has described a necrosis of the liver corresponding to embolization after treatment with these particles [51]. Recently, a global multicenter phase II/III study using MTC-Dox in human patients had to be stopped because “the clinical endpoints of the trial could not be met with statistical significance with the product as currently manufactured” (FerX<sup>®</sup>, San Diego, April 30, 2004).

Magnetoliposomes are also used for magnetically targeted drug delivery. These colloidal particles are composed of a lipid layer and qualified as drug carriers [52]. The chemotherapeutic agent Methotrexat encapsulated in thermosensitive liposomes can be accumulated in the tumor region after intravenous administration and local hyperthermia [53]. The use of magnetic thermosensitive liposomes and the influence of an external magnetic field placed over the tumor-region may increase the concentration of the encapsulated drug [54]. Furthermore, thermosensitive magnetoliposomes can also be used for local hyperthermia in cancer treatment [55]. Whole body hyperthermia in combination with chemotherapy is a very common approach in cancer treatment. A possibility to achieve local hyperthermia with magnetic particles is the use of magnetic iron oxide particles, which can be heated to over 40 °C by an alternating magnetic field after intralesional injection [56].

The size of albumin-microspheres or magnetoliposomes is in the range of  $\mu\text{m}$ s. As a consequence there is a risk of embolization in the capillary system because of these particles. Also useful for magnetically targeted drug delivery and smaller in size are magnetic nanoparticles. On nanoparticles, the surface-to-volume ratio is much higher than on larger particles. Therefore, nanomaterials show completely new characteristics and can be used for various new approaches. After application in an organism, different components such as material, size, charge and coating of the nanoparticles and the bound chemotherapeutic agent have an influence on biocompatibility and the biodistribution as well as the applied magnetic field and the respective gradient [57–68]. Nanoparticles have to be small enough not to occlude the capillary system and cause embolization, but they have to be large enough to be attractable by an external magnetic field. Furthermore, nanoparticles over 100 nm in diameter are more readily cleared by cells of the MPS (mononuclear phagocyte system) than smaller particles [57]. Research on biocompatible magnetic nanoparticles has focused on superparamagnetic iron oxide nanoparticles ( $\text{Fe}_3\text{O}_4$ ). These particles have been used as a contrast agent in magnetic resonance imaging for lymphography [69] (Fig. 5.2).

A first clinical trial with superparamagnetic iron oxide nanoparticles bound to a chemotherapeutic agent was performed in 1996 by Lübke et al. [33]. For experimental studies on rats and in a clinical trial on 14 human patients they used

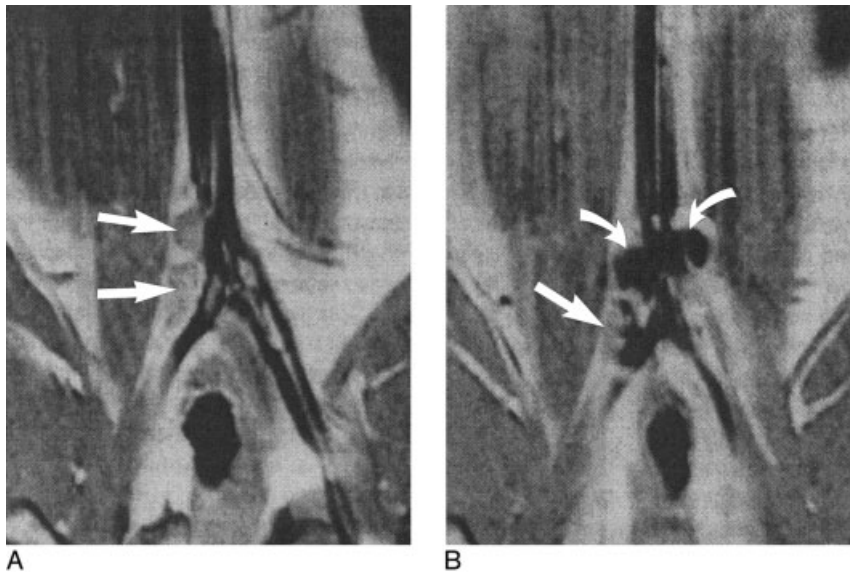


**Fig. 5.2.** MR-Imaging of iliac lymph nodes in tumor-bearing rabbits. MRI before (A) and after (B) administration of superparamagnetic iron oxide particles. There is a homogeneous signal in healthy lymph nodes (curved arrows) and an inhomogeneous signal in metastatic lymph nodes [69].

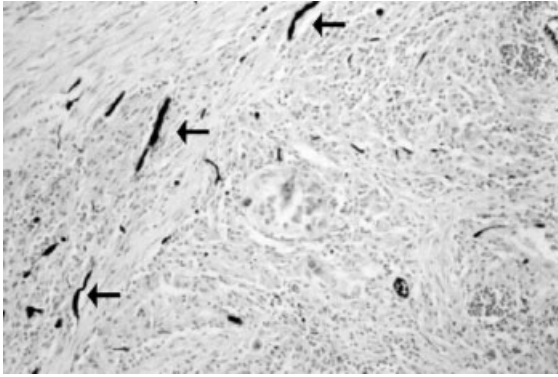


**Fig. 5.3.** Histological cross section of a rabbit's VX2-squamous cell carcinoma after treatment with intraarterial magnetic drug targeting (MDT). Arrows show the ferrofluids in tumor vessels. Staining: Prussian blue; magnification: 200× [72].

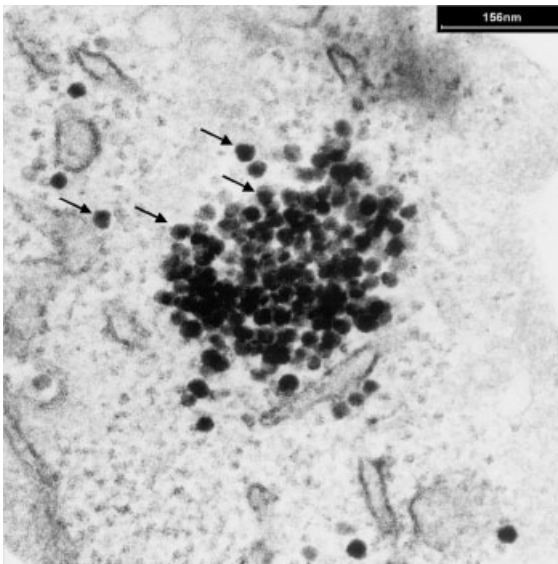


**Fig. 5.4.** Typical multidomain-particle in the intracellular space of tumor cells. Single particles (marked with arrows) are surrounded by starch polymers (not visible in the electron-microscopic picture) [73].

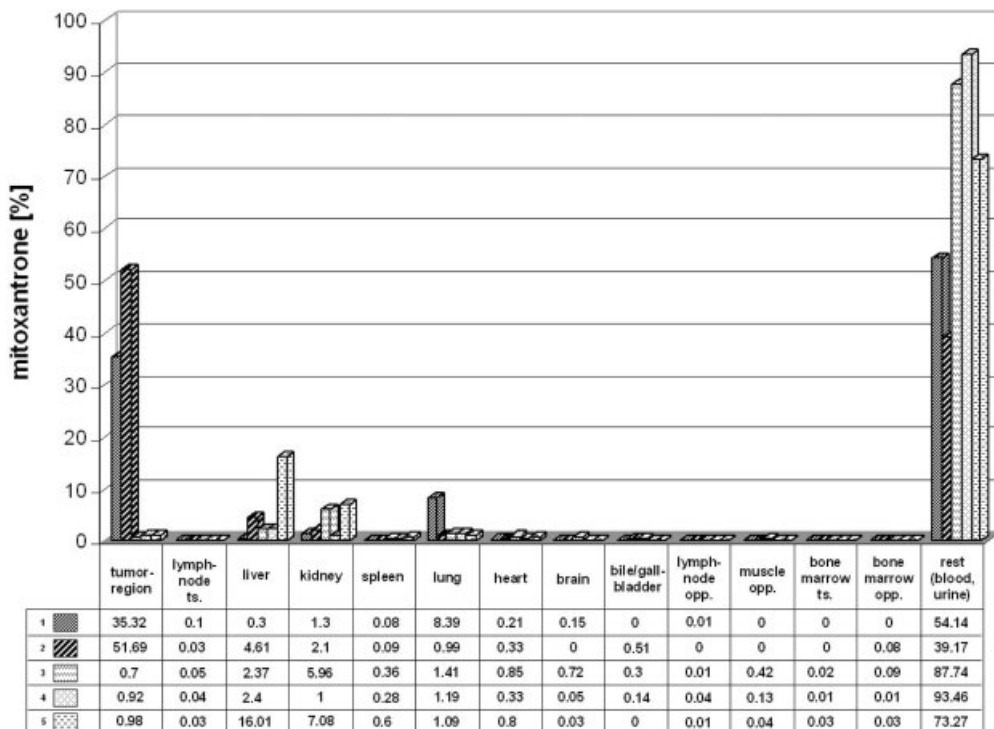


**Fig. 5.5.** Concentration of mitoxantrone in different body compartments 60 min after the respective injection in percent of the applied dose. Experiments were performed on tumor-bearing rabbits (i.a. = intraarterial, i.v. = intravenous).

1 ■ i.a. application of  $5 \text{ mg m}^{-2}$  ferrofluid-bound mitoxantrone with an external magnetic field [ $n = 1$ , magnetic drug targeting (MDT)].  
 2 ▨ i.a. application of  $2 \text{ mg m}^{-2}$  ferrofluid-bound mitoxantrone with an external magnetic field ( $n = 1$ , MDT).

3 ▩ i.v. application of  $10 \text{ mg m}^{-2}$  mitoxantrone without an external magnetic field ( $n = 1$ , application of the regular systemic dose).

4 ▤ i.a. application of  $5 \text{ mg m}^{-2}$  ferrofluid-bound mitoxantrone without an external magnetic field ( $n = 1$ ).

5 ▥ i.a. application of  $10 \text{ mg m}^{-2}$  mitoxantrone without an external magnetic field ( $n = 1$ ).

ts. = tumor side; opp. = opposite; tumor region = tumor and surrounding area (<1 cm) [72].

starch-coated magnetic nanoparticles ionically bound to epidoxorubicin. It could be demonstrated that these particles are biocompatible. In another preclinical study, intraarterial Magnetic Drug Targeting (MDT) on tumor-bearing rabbits was performed using a powerful external magnetic field (1.7 Tesla) placed over the tumor region. Starch-coated superparamagnetic iron oxide nanoparticles (about 100–150 nm in diameter) ionically bound to the chemotherapeutic agent mitoxantrone were injected in the tumor supplying artery.

Through this intraarterial MDT, complete tumor remissions could be shown only by the use of 50% and 20% of the regular systemic chemotherapeutic dose

without any negative side effects [34, 70, 71]. It could be demonstrated histologically that the nanoparticles were enriched in the tumor tissue (Figs. 5.3 and 5.4). Radioactive  $^{59}\text{Fe}$ -nanoparticles showed  $114\times$  more activity in the tumor region after MDT than the control without magnetic field [72]. Furthermore, with this system a high and specific enrichment of the bound chemotherapeutic agent in a desired body compartment (i.e. the tumor) is possible. HPLC-analysis of the chemotherapeutic agent after MDT revealed a  $75\times$  higher concentration of the administered chemotherapeutic agent in the tumor region compared with the regular systemic administration (Fig. 5.5) [72, 73]. These encouraging data will lead to further studies on cancer patients.

## References

- 1 COLLINS, J.M., Pharmacological rationale for regional drug delivery, *J. Clin. Oncol.* **1984**, *2*, 498–505.
- 2 GUPTA, P.K., HUNG, C.T., Comparative disposition of adriamycin delivered via magnetic albumin microspheres in presence and absence of magnetic fields in rats, *Life Sci.* **1990**, *46*, 471–484.
- 3 GUPTA, P.K., HUNG, C.T., Targeted delivery of low dose doxorubicin hydrochloride administered via magnetic albumin microspheres in rats, *J. Microencap.* **1990**, *7*, 85–92.
- 4 GUPTA, P.K., Drug targeting in chemotherapy: A clinical perspective, *J. Pharm. Sci.*, **1990**, *79*, 949–962.
- 5 TORCHILIN, V.P., Drug targeting, *Eur. J. Pharm. Sci.*, **2000**, *11*, 81–91.
- 6 ARAP, W., HAEDICKE, W., BERNASCONIE, M., KAIN, R., RAJOTTE, D., KRAJEWSKI, S., ELLERBY, H.M., BREDESEN, D.E., PASQUALINI, R., RUOSLATHI, E., Targeting the prostate for destruction through a vascular address, *Proc. Natl. Acad. Sci. U.S.A.*, **2002**, *99*, 1527–1531.
- 7 ZACHARSKI, L.R., ORNSTEIN, D.L., GABAZZA, E.C., D'ALESSANDRO-GABAZZA, C.N., BRUGAROLAS, A., SCHNEIDER, J., Treatment of malignancy by activation of the plasminogen system, *Semin. Thromb. Hemost.*, **2002**, *28*, 5–18.
- 8 GERLOWSKI, L.E., JAIN, R.K., Microvascular permeability of normal and neoplastic tissues, *Microvasc. Res.*, **1986**, *31*, 288–299.
- 9 TORCHILIN, V.P., ZHOU, F., HUANG, L., pH-sensitive liposomes, *Liposome Res.*, **1993**, *3*, 201–205.
- 10 YATVIN, M.B., KREUTZ, W., HORWITZ, B.A., SHINITZKY, M., pH-sensitive liposomes: Possible clinical implications, *Science* **1980**, *210*, 1253–1255.
- 11 SULLIVAN, S.M., HUANG, L., Preparation and characterization of heat-sensitive immunoliposomes, *Biochem. Biophys. Acta*, **1985**, *812*, 116–126.
- 12 HABER, E., Antibody targeting as a strategy in thrombolysis, in KAW, B.A., NARULA, J., STRAUSS, H.W. (eds.), *Monoclonal Antibodies in Cardiovascular Diseases*, Lea and Febiger, Malvern, PA, U.S.A., **1994**, pp. 187–197.
- 13 SACHDEVA, M.S., Drug targeting systems for cancer therapy, *Expert Opin. Investig. Drugs*, **1998**, *7*, 1849–1864.
- 14 LEVEUGLE, B., MANN, D., MADIYALKAN, R., NOUJAIM, A.A., Therapeutic antibodies for prostate cancer, *IDrugs*, **2000**, *3*(10), 1191–1198.
- 15 POSTE, G., KIRSH, R., Site specific (targeted) drug delivery in cancer therapy, *Biotechnology*, **1983**, *10*, 869–885.
- 16 NEGLIA, J.P., FRIEDMANN, D.L., YASUI, Y., Second malignant neoplasms in five-year survivors of childhood cancer:



- Childhood cancer survivor study, *J. Natl. Cancer Inst.*, **2001**, 93, 618.
- 17 WALTER, K.A., TAMARGO, R.J., OLIVI, A., BURGER, P.C., BREM, H., Intratumoral chemotherapy, *Neurosurgery* **1995**, 37, 1128–1145.
  - 18 WERNER, J.A., KEHRL, W., PLUZANSKA, A., ARNDT, O., LAVERY, K.M., GLAHOLM, J., DIETZ, A., DYCKHOFF, A., MAUNE, S., STEWART, M.E., ORENBERG, E.K., LEAVITT, R.D., A phase III placebo-controlled study in advanced head and neck cancer using intratumoural cisplatin/epinephrine gel, *Br. J. Cancer*, **2002**, 87, 938–944.
  - 19 PREIS, J., LINK, K.H., SCHMOLL, E., Regionale chemotherapie, in SCHMOLL, H.J., HÖFFKEN, K., POSSINGER, K. (eds.), *Kompendium Internistische Onkologie*, Teil 1, Springer Verlag, Berlin, Heidelberg, New York, **1999**, pp. 1755–1763.
  - 20 KEMENY, N.E., Is hepatic infusion of chemotherapy effective treatment for liver metastases? Yes. In, DeVITA, V.T. JR., HELLMAN, S., ROSENBERG, S.A. (eds.), *Important Advances in Oncology*, Lippincott, Philadelphia, **1992**, pp. 207–227.
  - 21 DUFOUR, P., BERGERAT, J.P., BARATS, J.C., GIRON, C., DUCLOS, B., DELLENBACH, P., RITTER, J., RENAUD, R., AUDHUY, B., OBERLING, F., Intraperitoneal mitoxantrone as consolidation treatment of patients with ovarian carcinoma in pathologic complete remission, *Cancer*, **1994**, 73, 1865–1869.
  - 22 KIKUMORI, T., HAYASHI, H., SHIBATA, A., SEKIYA, M., ITOH, T., MASE, T., OIWA, M., IMAI, T., FUNAHASHI, H., Administration of docetaxel in cases of recurrent breast carcinoma with malignant pleural effusion controlled by intrapleural administration of OK-432, *Gan To Kagaku Ryoho.*, **1999**, 26, 2091–2094.
  - 23 RASSWEILER, J., Neoadjuvant chemotherapy of invasive bladder cancer, *Urologe A*, **1994**, 33, 576–581.
  - 24 LORENZ, M., ROSSION, I., Adjuvante und palliative regionale therapie von lebermetastasen kolorektaler tumoren, *Dtsch. Med. Wschr.*, **1995**, 120, 690–697.
  - 25 OETTL, H., KRATSCHMER, B., LÖFFEL, J., VOGL, T.J., RIESS, H., Regionale chemotherapie von lebermetastasen bei kolorektalen karzinomen, *Onkologe*, **1998**, 4, 67–78.
  - 26 SCOTT, R.N., KERR, D.J., BLACKIE, R., HUGHES, J., BURNSIDE, G., MACKIE, R.M., BYRNE, D.S., MCKAY, A.J., The pharmacokinetic advantages of isolated limb perfusion with melphalan for malignant melanoma, *Br. J. Cancer*, **1992**, 66, 159–166.
  - 27 BERGER, H., BAETHGE, I., RUDOLPHI, A., BOOS, K., STÄBLER, A., REISER, M., SEIDEL, D., Transcatheter chemo-embolisation of hepatocellular carcinoma: A study of the pharmacokinetics of epirubicin with Lipiodol® or starch microspheres as embolizing agent, *Reg. Cancer Treat.*, **1996**, 9, 181–185.
  - 28 BENGMARK, S., Regional chemotherapy of liver and hepatic artery occlusion, in BERGER, H.G., BÜCHLER, M., REISFELD, R.A., SCHULZ, G. (eds.), *Cancer Therapy Monoclonal Antibodies, Lymphokines, New Development in Surgical Oncology and Chemo- and Hormonal Therapy*, Springer, Berlin, Heidelberg, New York, **1989**, pp. 201–215.
  - 29 HEMINGWAY, D.M., ANDERSON, W.J., ANDERSON, J.H., GOLDBERG, J.A., MCARDLE, C.S., COOKE, T.G., Monitoring blood flow to colorectal liver metastases using laser Doppler flowmetry: The effect of angiotensin II, *Br. J. Cancer*, **1992**, 66, 958–960.
  - 30 NOGUCHI, S., MIYAUCHI, K., NISHIZAWA, Y., SASAKI, Y., IMAOKA, S., IWANAGA, T., KOYAMA, H., TERASAWA, T., Augmentation of anticancer effect with angiotensin II in intraarterial infusion chemotherapy for breast cancer, *Cancer*, **1988**, 62, 467–473.
  - 31 LEYLAND-JONES, B., Targeted drug delivery, *Semin. Oncol.*, **1993**, 20, 12–17.
  - 32 SCHULTHEIS, K.H., PLIES, M., GENTSCH, H.H., Chemoembolization of liver tumors, in BERGER, H.G., BÜCHLER, M., REISFELD, R.A., SCHULZ,

- G. (eds.), *Cancer Therapy With Monoclonal Antibodies, Lymphokines, New Development in Surgical Oncology and Chemo- and Hormonal Therapy*, Springer, Heidelberg, New York, Tokyo, 1989, pp. 201–215.
- 33 LÜBBE, A.S., BERGEMANN, Ch., RIESS, H., SCHRIEVER, F., REICHARDT, P., POSSINGER, K., MATTHIAS, M., DORKEN, B., HERRMANN, F., GÜRTLER, R., HOHENBERGER, P., HAAS, N., SOHR, R., SANDER, B., LEMKE, A.J., OHLENDORF, D., HUHNT, W., HUHNT, D., Clinical experiences with magnetic drug targeting: A phase I study with 4'-epidoxorubicin in 14 patients with advanced solid tumors, *Cancer Res.*, 1996, 56, 4686–4693.
- 34 ALEXIOU, Ch., ARNOLD, W., KLEIN, R., PARAK, F., HULIN, P., BERGEMANN, C., ERHARDT, W., WAGENPFEIL, S., LÜBBE, A.S., Locoregional cancer treatment with magnetic drug targeting, *Cancer Res.*, 2000, 60, 6641–6648.
- 35 HÄFELI, U.O., Magneto- and radio-pharmaceuticals, radioactive magnetic microspheres, in ARSHADY, R. (ed.), *Microspheres, Microcapsules Liposomes*, 2001, 3, 559–584.
- 36 BILKENROTH, U., TAUBERT, H., RIEMANN, D., REBMANN, U., HEYNEMANN, H., MEYE, A., Detection and enrichment of disseminated renal carcinoma cells from peripheral blood by immunomagnetic cell separation., *Int. J. Cancer*, 2001, 92, 577–582.
- 37 TRELEAVEN, J.G., GIBSON, F.M., UGELSTAD, J., REMBAUM, A., PHILIP, T., CAINE, G.D., KEMSHEAD, J.T., Removal of neuroblastoma cells from bone marrow with monoclonal antibodies conjugated to magnetic microspheres, *The Lancet*, 1984, 70–73.
- 38 SCHERER, F., ANTON, M., SCHILLINGER, U., HENKE, J., BERGEMANN, C., KRUGER, A., GÄNSBACHER, B., PLANK, C., Magnetofection enhancing and targeting gene delivery by magnetic force in vitro and in vivo, *Gene Ther.*, 2002, 9, 102–109.
- 39 ALKSNE, J.F., FINGERHUT, A., RAND, R., Magnetically controlled metallic thrombosis of intracranial aneurysms, *Surgery*, 1966, 60, 212–218.
- 40 MCNEIL, R.G., RITTER, R.C., WANG, B., LAWSON, M.A., GILLIES, G.T., WIKI, K.G., QUATE, E.G., HOWARD, M.A., GRADY, M.S., Functional design features and initial performance characteristics of a magnetic-implant guidance system for stereotactic neurosurgery, *IEEE Trans. Biomed. Eng.*, 1995, 42, 793–801.
- 41 DEVINENI, D., BLANTON, C.D., GALLO, J.M., Preparation and in vitro evaluation of magnetic microsphere-methotrexate conjugate drug delivery systems, *Bioconj. Chem.*, 1995, 6, 203–210.
- 42 DRISCOLL, C.F., MORRIS, R.M., SENYEI, A.E., WIDDER, K.J., HELLER, G.S., Magnetic targeting of microspheres in blood flow, *Microvascular Res.*, 1984, 27, 353–369.
- 43 WIDDER, K.J., SENYEI, A.E., SCARPELLI, D.G., Magnetic microspheres: A model system for site specific drug delivery in vivo, *Proc. Soc. Exp. Biol. Med.*, 1978, 158, 141–146.
- 44 WIDDER, K.J., SENYEI, A.E., RANNEY, D.F., Magnetically responsive microspheres and other carriers for the biophysical targeting of antitumor agents, in GAVATTINI, S., GOLDIN, A., HOWKING, F., KOPIN, I.J., SCHNITZER, R.J. (eds.), *Advances in Pharmacology and Chemotherapy*, Academic Press, New York, 1979, pp. 213–239.
- 45 WIDDER, K.J., MORRIS, R.M., POORE, G.A., HOWARD, D.P., SENYEI, A.E., Selective targeting of magnetic albumin microspheres containing low-dose doxorubicin: Total remission in yoshida sarcoma bearing rats, *Eur. Cancer Clin. Oncol.*, 1983, 19, 135–199.
- 46 WIDDER, K.J., MANRINO, P.A., MORRIS, R.M., HOWARD, D.P., POORE, G.A., SENYEI, A.E., Selective targeting of magnetic albumin microspheres to the yoshida sarcoma: Ultrastructural evaluation of microsphere distribution, *Eur. J. Cancer. Clin. Oncol.*, 1993, 19, 141–147.
- 47 LEAKAKOS, T., JI, C., LAWSON, G., PETERSON, C., GOODWIN, S., Intravesical administration of

- doxorubicin to swine bladder using magnetically target carriers, *Cancer Chemother. Pharmacol.*, **1996**, *51*, 445–450.
- 48 RUDGE, S., PETERSON, C., VESSELY, C., KODA, J., STEVENS, S., CATTERALL, L., Adsorption and desorption of chemotherapeutic drugs from a magnetically targeted carrier (MTC), *J. Controlled Release*, **2001**, *74*, 335–340.
- 49 ALLEN, L.M., KENT, J., WOLFE, C., FICCO, C., JOHNSON, J., MTC<sup>TM</sup>: A magnetically targetable drug carrier for paclitaxel, in HÄFELI, U., SCHÜTT, W., TELLER, J., ZBOROWSKI, M. (eds.), *Scientific and Clinical Applications of Magnetic Carriers*, Plenum Press, New York and London, **1997**, pp. 481–494.
- 50 WILSON, M.W., KERLAN, R.K., FIDELMAN, N.A., VENOOK, A.P., LA BERGE, J.M., KODA, J., GORDON, R.L., Hepatocellular carcinoma: Regional therapy with a magnetic targeted carrier bound to doxorubicin in a dual MR-imaging/conventional angiography suite – initial experience with four patients, *Radiology*, **2004**, *230*, 287–293.
- 51 GOODWIN, S.C., BITTNER, C.A., PETERSON, C.L., WONG, G., Single dose toxicity study of hepatic intra-arterial infusion of doxorubicin coupled to a novel magnetically targeted drug carrier, *Toxicol. Sci.*, **2001**, *60*, 177–183.
- 52 KUBO, T., SUGITA, T., SHIMOSE, S., NITTA, Y., IKUTA, Y., MURAKAMI, T., Targeted delivery of anticancer drugs with intravenously administered magnetic liposomes in osteosarcoma-bearing hamsters, *Int. J. Oncol.*, **2000**, *17*, 309–315.
- 53 WEINSTEIN, J.N., MAGIN, R.L., YATVIN, M.B., ZAHARKO, D.S., Liposomes and local hyperthermia: Selective delivery of methotrexate to heated tumors, *Science*, **1979**, *13*, 188–191.
- 54 VIROONCHATAPAN, E., SATO, H., UENO, M., ADACHI, I., TAZAWA, K., HORKOSHI, I., Magnetic targeting of thermosensitive magnetoliposomes to mouse livers in an in situ on-line perfusion system, *Life Sci.*, **1996**, *58*, 2251–2261.
- 55 SHINKAI, M., SUZUKI, M., IIJIMA, S., KOBAYASHI, T., Antibody-conjugated magnetoliposomes for targeting cancer cells and their application in hyperthermia, *Biotechnol. Appl. Biochem.*, **1994**, *21*, 125–137.
- 56 HILGER, I., HIERGEIST, R., HERGT, R., WINNEFELD, K., SCHUBERT, H., KAISER, W.A., Thermal ablation of tumors using magnetic nanoparticles: An in vivo feasibility study, *Invest. Radiol.*, **2002**, *37*, 580–586.
- 57 STORM, G., BELLIOU, S.O., DAEMEN, T., LASIC, D.D., Surface modification of nanoparticles to oppose uptake by the mononuclear phagocyte system, *Adv. Drug Deliv. Rev.*, **1995**, *17*, 31–48.
- 58 TORCHILIN, V.P., TRUBETSKOY, V.S., Which polymer can make nanoparticulated drug carriers long circulating?, *Adv. Drug Deliv. Rev.*, **1995**, *16*, 141–155.
- 59 ZHAO, A., YAO, P., KANG, C., YUAN, X., CHANG, J., PU, P., Synthesis and characterization of tat-mediated O-CMC magnetic nanoparticles having anticancer function, *J. Magn. Magn. Mater.*, **2005**, *295*, 37–43.
- 60 MYKHAYLYK, O., DUDCHENKO, N., DUDCHENKO, A., Doxorubicin magnetic conjugate targeting upon intravenous injection into mice: High gradient magnetic field inhibits the clearance of nanoparticles from the blood, *J. Magn. Magn. Mater.*, **2005**, *293*, 473–482.
- 61 NEUBERGER, T., SCHÖPF, B., HOFMANN, H., HOFMANN, M., VON RECHENBERG, B., Superparamagnetic nanoparticles for biomedical applications: Possibilities and limitations of a new drug delivery system, *J. Magn. Magn. Mater.*, **2005**, *293*, 483–496.
- 62 XU, H., SONG, T., BAO, X., HU, L., Site-directed research of magnetic nanoparticles in magnetic drug targeting, *J. Magn. Magn. Mater.*, **2005**, *293*, 514–519.
- 63 ASMATULU, R., ZALICH, M.A., CLAUS, R.O., RIFFLE, J.S., Synthesis, characterization and targeting of

- biodegradable magnetic nanocomposite particles by external magnetic fields, *J. Magn. Magn. Mater.*, **2005**, 292, 108–119.
- 64 ITO, A., KUGA, Y., HONDA, H., KIKKAWA, H., HORIUCHI, A., WATANABE, Y., KOBAYASHI, T., Magnetite nanoparticle-loaded anti-HER2 immunoliposomes for combination of antibody therapy with hyperthermia, *Cancer Lett.*, **2004**, 212, 167–175.
- 65 SON, S.J., REICHEL, J., HE, B., SCHUCHMAN, M., LEE, S.B., Magnetic nanotubes for magnetic-field-assisted bioseparation, biointeraction, and drug delivery, *J. Am. Chem. Soc.*, **2005**, 127, 7316–7317.
- 66 JAIN, T.K., MORALES, M.A., SAHOO, S.K., LESLIE-PELECKY, D.L., LABHASETWAR, V., Iron oxide nanoparticles for sustained delivery of anticancer agents, *Mol. Pharm.*, **2005**, 2, 194–205.
- 67 KOHLER, N., SUN, C., WANG, J., ZHANG, M., Methotrexate-modified superparamagnetic nanoparticles and their intracellular uptake into human cancer cells, *Langmuir*, **2005**, 21, 8858–8864.
- 68 VEISEH, O., SUN, C., GUNN, J., KOHLER, N., GABIKIAN, P., LEE, D., BHATTARAI, N., ELLENBOGEN, R., SZE, R., HALLAHAN, A., OLSON, J., ZHANG, M., Optical and MRI multifunctional nanoprobe for targeting gliomas, *Nano Lett.*, **2005**, 5, 1003–1008.
- 69 TAUPITZ, M., WAGNER, S., HAMM, B., DIENEMANN, D., LAWACZECK, R., WOLF, K.J., MR Lymphography using iron oxide particles. Detection of lymph node metastases in the VX2 rabbit tumor model, *Acta Radiol.*, **1993**, 34, 10–15.
- 70 ALEXIOU, Ch., ARNOLD, W., HULIN, P., KLEIN, R.J., RENZ, H., PARAK, F.G., BERGEMANN, Ch., LÜBBE, A.S., Magnetic mitoxantrone nanoparticle detection by histology, x-ray and MRI after magnetic drug targeting, *J. Magn. Magn. Mater.*, **2001**, 225, 187–193.
- 71 ALEXIOU, Ch., SCHMIDT, A., HULIN, P., KLEIN, R.J., BERGEMANN, Ch., ARNOLD, W., Magnetic drug targeting: Biodistribution and dependency on magnetic field strength, *J. Magn. Magn. Mater.*, **2002**, 252, 363–366.
- 72 ALEXIOU, Ch., JURGONS, R., SCHMID, R.J., BERGEMANN, Ch., HENKE, J., ERHARDT, W., HUENGES, E., PARAK, F.G., Magnetic drug targeting-biodistribution of the magnetic carrier and the chemotherapeutic agent Mitoxantron after locoregional cancer treatment, *J. Drug Targeting*, **2003**, 11, 139–149.
- 73 ALEXIOU, Ch., JURGONS, R., SCHMID, R.J., HILPERT, A., BERGEMANN, Ch., PARAK, F.G., IRO, H., In vitro and in vivo investigations of targeted chemotherapy with magnetic nanoparticles, *J. Magn. Magn. Mater.*, **2005**, 293, 389–393.

## 6 Nanomaterials for Controlled Release of Anticancer Agents

*Do Kyung Kim, Yun Suk Jo, Jon Dobson, Alicia El Haj, and  
Mamoun Muhammed*

### 6.1 Introduction

The enormous advances made in basic cancer research have not been paralleled by similar improvements in treatment results. Metastatic breast cancer, late-stage colon cancer, malignant melanoma and other forms of cancer are still essentially incurable in most cases. Enormous efforts have been made in recent years to develop “smart drugs” that are directed to tumor cell-specific enzymes and surface receptors. Almost without exception, these drugs have encountered problems in clinical trials. Today’s cancer treatment is therefore primarily based on the use of conventional cytotoxic drugs that have adverse side effects and only limited effectiveness. The gains in health that would be achieved by efficient tumor treatment with fewer side effects (owing to specific targeting to tumor tissue) are therefore enormous. Cancer is a group of diseases characterized by uncontrolled growth and spread of abnormal cells. If the growth and spread of cancer cells is not controlled, the disease is fatal. Though in many cases the specific cause of cancer is unknown, in general it can be caused by several external factors (tobacco, chemicals, radiation, and infectious organisms) and internal factors (inherited mutations, hormones, immune conditions and mutations that occur from metabolism). These factors may act together or in sequence to initiate or promote carcinogenesis. Generally, cancer is treated by surgery, radiation, chemotherapy, hormones and immunotherapy [1]. Cancer therapy can be successful in treating solid tumors/cancers in lesions that can be removed by surgery or treated by radiotherapy/chemotherapy, the major treatment modalities for primary cancer/tumor and metastases. Each of these cancer treatments has advantages and disadvantages, thus the combination with other treatments is recommended to achieve the optimum outcome.

Chemotherapy for cancer is a whole body treatment that is administered either orally or intravenously. This results in systemic distribution of cytotoxic chemotherapeutic compounds that can be more effective for the treatment of micro-

metastases. However, the systemic distribution of cytotoxic compounds results in more severe side effects (some of which can be life-threatening) compared to surgery or radiotherapy. The major goal of targeted therapies is to reduce the side effects of cytotoxic drugs, resulting in more effective control of cell growth or tumor angiogenesis.

Presently, numerous anticancer agents are available in the clinic. These anticancer agent/drugs have an elimination half-life that results in a decrease of therapeutic potential and side effects such as bone marrow depression and gastrointestinal damage [2]. For example, poly(alkyl cyanoacrylate) nanoparticles as drug delivery systems (DDSs) play an important role in the incorporation of anticancer drugs as they can enhance the drug's concentration in the tumor and reduce drug levels in the heart, thus avoiding some side effects [3]. Targeting toxic therapeutics to tumors through binding to receptors overexpressed on the surface of cancer cells can also reduce systemic toxicity and increase the effectiveness of the targeted compounds. Small molecule-targeted therapeutics have several advantages over toxic immunoconjugates, including better tumor penetration, lack of neutralizing host immune response and superior flexibility in the selection of drug components with optimal specificity, potency and stability in circulation [4].

Novel strategies have been developed to decrease the toxicity of active molecules by targeting the specific tumor site, where the drug can selectively bind to the targeted tissue at cellular and/or sub-cellular level to influence its therapeutic effects. The chemotherapeutic activity can be enhanced by using macromolecules as a vector to control the release rate of anticancer agents. The use of polymeric nanoparticles is mainly focused on controlling the loaded anticancer agent/drug at the targeted lesion. Polymeric nanoparticles are a form of core-shell structure/nanocapsule that can be loaded with therapeutic agents. Several kinds of inorganic or metallic nanoparticles can be used due to their intrinsic physical properties even without a core-shell structure. Superparamagnetic iron oxide nanoparticles (SPION) in particular can be used as a transducer for active targeting by responding to both external ac and dc magnetic fields [5].

Despite major advances in the development of small-scale devices, however, most DDSs still use small molecules administered orally, transdermally, parenterally, or through the nose or lung. The emergence of novel, biologically targeted anticancer agents such as gefitinib ("Iressa", ZD1839) has raised the question of how the dose for later-stage clinical development and clinical use is best determined. For cytotoxic drugs, because toxic effects and antitumor activity often fall within the same dose range and are dose dependent, the clinically used dose will depend on the therapeutic window [6]. Cytostatic drug handling in hospitals is not unproblematic. Large doses are given of compounds that are highly mutagenic. Administration of the drugs and also disposal of patient urine etc. is therefore potentially hazardous. Target-oriented, controlled drug delivery will lead to decreases in the quantities of drugs used and will, therefore, help to reduce these problems. The development of novel smart biomaterials is already having an enormous effect on nanomedicine [7].

## 6.2 Nanoparticles for Biomedical Applications

Modern technological realizations are concerned with the development of advanced, multifunctional, and even more “smart” materials for specific applications in highly integrated biomedical approaches (Table 6.1). These novel interdisciplinary concepts are recently emerging at the intersection of material science and molecular biotechnology. They are closely associated with surface chemistry and the physical properties of inorganic nanoparticles, the topics of bioorganic and bioinorganic chemistry, and various aspects of molecular biology, recombinant DNA technology and protein expression, and immunology.

**Tab. 6.1.** Examples of nano-sized inorganic components in biomedical applications.

Particle composition	Particle size (nm)	Applications	Ref.
Metals			
Au	2–150	Drug and gene delivery	8
Ag	1–80	Antibody tagged marker	9
Pt	1–20	Sensors and electrodes	10
Co	1–50	Magnetic separation, drug targeting	11
Semiconductors			
CdX (X = S, Se, Te)	1–20	Fluorescent labeling	12
ZnX (X = S, Se, Te)	1–20	Fluorescent labeling	13
PbS	2–18	Photoluminescence	14
TiO <sub>2</sub>	3–50	Biomedical devices for nerve tissue monitoring	15
ZnO	1–30	Photoluminescence	16
CaAs, InP	1–15	Nonlinear optics	17
Ge	6–30	Photoluminescence	18
Magnetic			
Fe-O	6–40	MR contrast agent, drug delivery	[19]
Fe-Pt	2–10	MR contrast agent, drug delivery	[20]

### 6.2.1

#### First Generation Nanoparticles

First generation nanoparticles have been available for several years. Colloids are representative of nanoparticles stabilized in solution to prevent uncontrolled growth, aggregation, and flocculation of the nanoparticles. Utilization of colloidal processing leads to attractive new concepts for the fabrication of advanced nanostructured materials. For this reason, many investigations have focused on colloidal processing of inorganic materials through chemical methods.

### 6.2.2

#### Second Generation Nanoparticles

As a result of an increasing degree of complexity and sophistication needed for the engineering of nanostructures for advanced applications, second generation nanoparticles have emerged. A key aspect here is the need for multifunctionality of these materials in which several properties are combined to achieve a specific function. For example, certain properties could be achieved through the reduction of building blocks to the nanometer regime, e.g., magnetite ( $\text{Fe}_3\text{O}_4$ )/maghemite ( $\gamma\text{Fe}_2\text{O}_3$ ) nanoparticles become superparamagnetic at sizes below about 30 nm. Ferrofluids – which have the fluid properties of a liquid but are strongly magnetized in applied fields – can be produced by suspending these sub-30 nm nanoparticles in a suitable media. Ferrofluids are useful as active components for enhancing the performance of many devices, e.g., mechanical (seals, bearings and dampers) or electromechanical (loudspeakers, stepper motors and sensors, etc.). However, by combining the superparamagnetic properties of ferrofluids with functional chemical groups on the particles' surface there are opportunities for advanced applications in magnetically targeted drug delivery.

For second generation nanoparticles, the surface layer (a few or several monolayers) is distinctly different from that of the core material (composition or structure). Again, such particles are categorized as core-shell structures. The surface layer may be thin or thick, depending on the functionality required. Figure 6.1 shows a schematic representation of different types of second generation nanoparticles with surface modifications and nanoparticles with a core-shell structure. Broadly speaking, these particles can also be considered as composite nanoparticles. However, the term nanocomposite generally refers to materials consisting of a dispersion of nanoparticles within a suitable matrix. The most common example of nanocomposites is the precipitation of inorganic (often metal) nanoparticles within a nanoporous polymer structure. Interestingly, the fundamental properties of the polymeric materials can be dramatically altered as a result of the dispersion of few percent of inorganic nanoparticles – particularly with the addition of magnetic iron oxides.



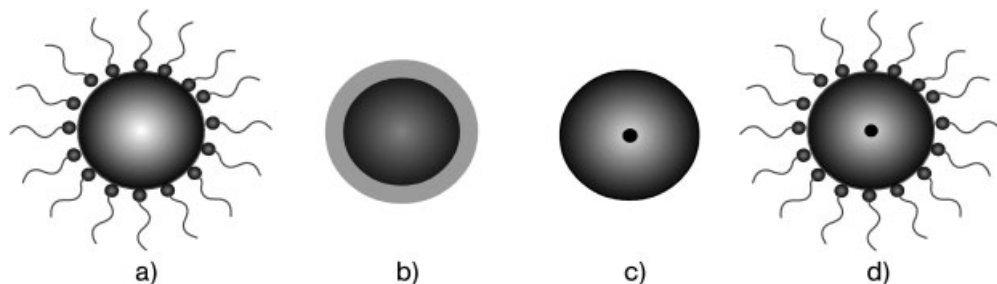


**Fig. 6.1.** Evolution of second generation nanoparticles: (a) Nanoparticle coated with surfactant to form a stable suspension, (b) nanoparticle coated with a thin metallic layer,

(c) small nanoparticle coated with a porous ceramic layer and (d) dispersion of core-shell combination of (a) and (c) for stable suspension.

### 6.2.3

#### Advanced Generation Nanoparticles

Recently, advanced generation nanoparticles have emerged to meet the need for the fabrication of more complex nanoparticles. Further to the core-shell structure, nanoparticles with structures similar to nanocomposites have been fabricated (nanobeads). In these nanobeads, a single bead consists of a nanocomposite core, where one or more smaller nanoparticles are dispersed into the matrix. Several possible combinations of organic and inorganic particles can be dispersed within the matrix of the core structure. Each dispersed component can be selected to achieve a specific function or properties of the particle. The surface layer can combine both physical (e.g., diffusion control) and chemical (e.g., allowing certain conjugation chemistries) functionality to the particles. In this way, it is possible to “program” the nanobeads with multiple functionalities, suitable for performing certain tasks, that can be triggered under specific conditions. For example, it is possible to fabricate such nanobeads that can be magnetically moved or localized for controlled drug release. The release of the drug can be controlled by diffusion control of the matrix of the bead or through the control of the porosity of a suitable shell layer on the surface of the bead. Nanobeads can be programmed to be responsive to the environment, e.g., small variations in temperature or pH. Fabrication of these advanced generation nanoparticles requires the use of comprehensive and detailed procedures.

The design and fabrication of biochemically functionalized superparamagnetic iron oxide nanoparticles and near-infrared light absorbing nanoparticles is of particular interest for cancer targeting and therapy applications. Figure 6.2 illustrates a strategy to construct magnetic drug carriers in combination with thermosensitive polymeric materials. Target-oriented release of drugs encapsulated in polymeric nanocapsules is presently the most active research area in this field. Processing of

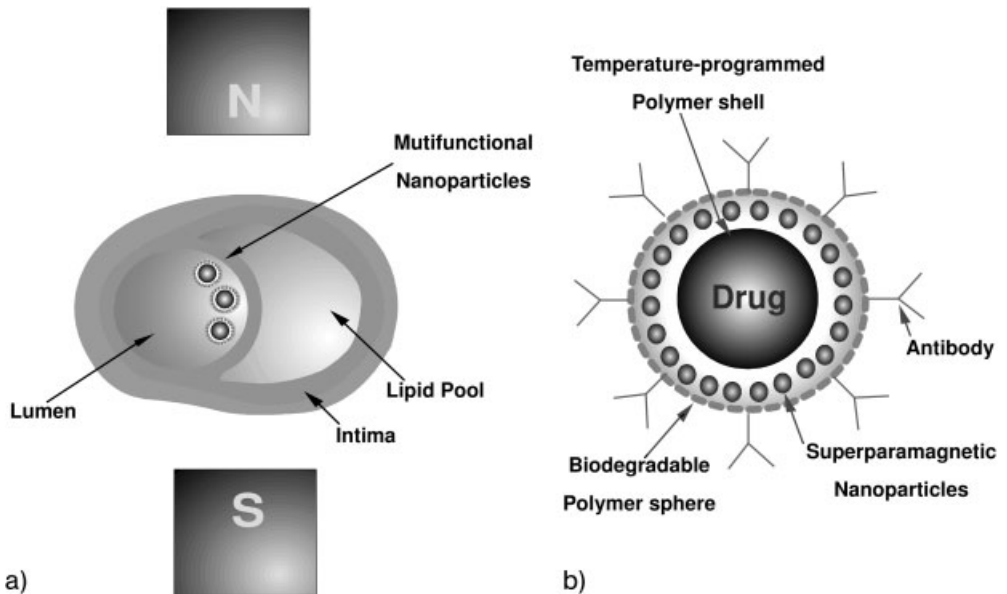


**Fig. 6.2.** Functional nanoparticles: (A) Coronary plaque removal by nanofluid of magnetic nanoparticles under RF magnetic field and (b) multipurpose nanovectors for target oriented controlled drug release.

nanoparticles with controlled properties, such as chemical properties (composition of the bulk, interaction between the particles, and surface charge) and structural properties (crystalline or amorphous structure, size, and morphology), is the main feature in designing the nanoprecursors (nanoparticles/nanotube/nanolayer). The development of supramolecular, biomolecular, and dendrimer chemistries for engineering substances of ångström and nanoscale dimensions has been encouraged for requirements in nanotechnology. The emerging disciplines of nanoengineering, nanoelectronics, and nanobioelectronics require suitably sized and functional building blocks to construct their architecture and devices [21].

Nanoparticles are in the solid phase and may be either amorphous or crystalline. They can be constructed to absorb, conjugate and encapsulate therapeutic agents inside or outside. Several parameters of colloidal systems developed have been considered, such as the temperature, osmolality and pH of the polymerization medium, that could influence the characteristics (morphology and morphometry, drug content, melting point transition or the enthalpy of transition) and stability of nanospheres. On the other hand, based on their unique mesoscopic physical, chemical, thermal and mechanical properties, nanoparticles offer great potential for many biomedical applications, including bioanalysis and biosepara-

tion, tissue-specific drug therapeutic applications, gene and radionuclide delivery [5, 22].

To be used effectively in fighting disease, the specific surface chemistry of the nanoparticles must be tailored for the desired biomedical applications. Magnetic nanoparticles are also of particular interest as inhomogeneous external magnetic fields exert a force on them, and thus they can be manipulated or transported to a specific diseased tissue by a magnetic field gradient. They also have controllable sizes, so that their dimensions can match either that of a virus (20–500 nm), a protein (5–50 nm) or a gene (2 nm wide and 10–100 nm long). In addition, superparamagnetic particles are of interest because they do not retain any magnetism after removal of the magnetic field.

### 6.3

#### Polymer Materials for Drug Delivery Systems

The past few decades has seen considerable interest in developing biodegradable nanoparticles as effective drug delivery devices [23]. Biodegradable polymers are polymers that can be degraded and/or catabolized, eventually to carbon dioxide and water, by microorganisms (bacteria, fungi, etc.) under natural environments [24]. However, due to the development of a wide variety of synthetic biocompatible polymers, the definition has been altered to include many artificially synthesized polymeric materials. Needless to say, degraded components of the polymers should not be toxic and should not promote the generation of harmful substances. Biodegradable polymers can be classified into three major categories:

1. Polyesters produced by microorganisms.
2. Natural polysaccharides (i.e., chitosan [25–29], dextran [30]).
3. Artificially synthesized polymers, especially aliphatic polyesters, {i.e., polylactide (PLA) [31, 32], poly(lactide-*r*-glycolide) (PLGA) [33], and poly(*ε*-caprolactone) (PCL) [34]}, polyamide (i.e., poly L-lysine [35]), and others such as poly(methyl methacrylate) (PMMA) [36] and poly(ethyl-2-cyanoacrylate) (PECA) [37], which have also been developed as nanoparticles for the same purpose.

Biodegradable polymers are not only limited to medical devices and wound dressing, but are also used for the fabrication of scaffolds in tissue engineering [38], and as DDSs for controlled release of 5-fluorouracil [39], cisplatin [40], lidocaine [41–43], indomethacin [32, 34], taxol [44], 4-nitroanisole [45], dexamethasone [46], radioactive compound [47], peptides [48], and proteins [49–54] at characteristic rates and specific target sites. For DDS, interest has focused on the use of particle formations prepared from aliphatic polyesters due to their biocompatibility and resorbability. In terms of these required characteristics, numerous workers use polyesters produced from glycolic acid and lactic acid polymers, which are approved by the FDA. These polymers do not require surgical removal after the completion of drug release [55].

## 6.4

### Design of Drug Delivery Vectors and Their Prerequisites

The development of micro/nanospheres for novel drug delivery systems has become an important area of research as such systems enable the controlled release of toxic drugs into the target organs. They also make it possible to deliver useful drugs into sites of inflammation or tumor cells. One of the most important characteristics required by these materials to be suitable for biomedical applications is their biocompatibility, especially with respect to their surface chemistry.

Biocompatibility of nanospheres can be further improved by modifying the terminal groups located on the polymer surface as well as its structure. Obviously, it is important to stabilize the nanospheres sterically by a coating process or chemical modification so as to minimize recognition by phagocytic cells in the reticuloendothelial system (RES). The most promising materials for this purpose are polymeric drug carriers. In general, a polymer that tends to lose mass over time within a living organism is called an absorbable, resorbable, or bioabsorbable, as well as a biodegradable polymer. In comparison with the strict definition, biodegradable polymers require enzymes of microorganisms for natural hydrolytic or oxidative degradation. Regardless of its degradation behavior, this terminology applies to both enzymatic and non-enzymatic hydrolysis.

The physiochemical properties of the materials should be considered to develop nanoparticles as vectors for controlled DDS. Toxins must be removed from the drugs in the patient's body as quickly as possible. Engineered nanoparticles are strong candidates for drug detoxification because the particle size is the key to preventing further damage to the patient's healthy organs [33].

#### 6.4.1

##### Polymeric Nanoparticles

Numerous factors should be considered when designing a DDS. The first generation of polymeric vectors is simple core-shell structures/capsules within which the therapeutic agents are loaded. The second generation of polymeric vectors aims to enhance degradation rates by synthesizing block copolymers with more than two different species and by varying the molecular weight of the polymer components. Obviously, the release time of the therapeutic agents can be effectively improved in this way by understanding the physiochemical properties of the human body. Even though the drugs are effectively incorporated into the vectors, the nanoparticles can be easily agglomerated after dosing via various routes of administration (i.e., oral, intravenous, intramuscular, subcutaneous, etc.).

A particular consideration to take into account when designing nanoparticles for these applications is that the body's fluids are composed of quite complex compositions such as water, hormones, plasma (e.g., erythrocytes, leukocytes, platelets), fats, protein (e.g., albumin, globulin, fibrinogen), and numerous ions etc. For example, stable colloidal suspensions of DDS can be prepared simply in water-based solvent. However, the nanoparticles, once administrated into the blood stream, typ-

ically create a serious blockage of blood flow due to their agglomeration and particle growth through interactions with compounds in the blood. Moreover, many kinds of biological substances are hydrophilic and water soluble, and cannot therefore pass through the hydrophobic lipid bilayer membranes. For example, MPEG has uncharged hydrophilic residues and a very high surface mobility, leading to high steric exclusion. Therefore, it is expected to effectively improve the biocompatibility of nanoparticles and to possibly avoid accumulation in the RES or the mononuclear phagocyte system. Obviously, it is important to stabilize the nanospheres sterically by a coating process or chemical modification so as to minimize recognition by phagocyte cells in the RES.

The most advanced generation of polymeric DDSs has been developed to resolve the above-mentioned problems for multifunctional applications. This can be achieved via the use of nano-biotechnology to fabricate nanovectors with a higher degree of complexity based on the design and fabrication of bio-active and biocompatible, functionalized nanofluids using nanoparticles with several chemistries relevant to specific biological/medical activities.

Surface functionalization of nanovectors is designed to perform the following tasks:

1. Carrier for certain functional compound, e.g., drug(s) and other materials.
2. Formation of stable suspension in physiologically compatible solutions.
3. Controlled targeting to an organ or tissue within the body of a living animal or human subject.
4. Keeping the particles in a given location for a desired period.
5. Controlled release of drugs or chemicals through the pores of the shell according to defined conditions.

As one of the stimuli-sensitive polymers (SSPs), PNIPAAm is well known as a thermosensitive polymer due to its distinct phase transition at a specific lower critical solution temperature (LCST) of 32 °C in water [56–60]. PNIPAAm is hydrophilic below the LCST but becomes hydrophobic when it is heated up above the LCST. PNIPAAm has been consistently investigated as it has “smart” characteristics and is being developed for biomedical applications in the form of micelles [56], tablets [59], and hydrogels.

A new class of temperature-programmed “shell-in-shell” structures with two different copolymers synthesized by a modified-double-emulsion method (MDEM) has been reported as an advanced generation nanovector [31]. In this approach, thermosensitive inner shells composed of poly(N-isopropylacrylamide-co-D,L-lactide) (PNIPAAm-PDLA) with a lower critical solution temperature (LCST) can be fabricated. This novel concept can effectively load any hydrophilic proteins into a polymeric DDS and construct an adequate vector together with the programmable release rate. The release rates are governed by several key parameters, which only involve the PLLA-PEG outer shell, such as the volumetric ratio between the organic phase and aqueous phase, the interaction parameter between the therapeutic agents and the core domain, tacticity of the copolymer, the encapsulation efficiency, etc. Figure 6.3 shows a schematic representation of “shell-in-shell”

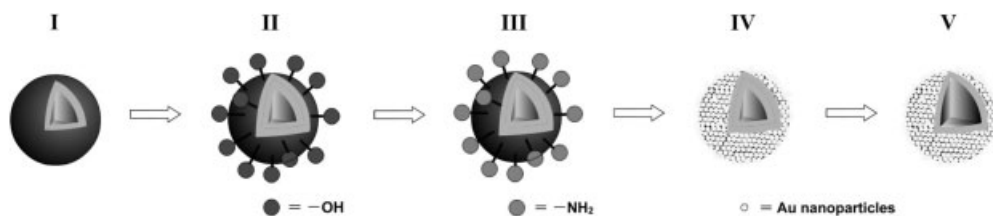


**Fig. 6.3.** Schematic of the fabrication of Au@PLLA-PEG@PNIPAAm-PDLA: (I) Formation of the hydrophilic protein-loaded PNIPAAm-PDLA sphere; (II) construction of PLLA-PEG@PNIPAAm-PDLA dual-shell structure via a MDEM; (III) functionalization of PLLA-PEG@PNIPAAm-PDLA dual-shell structure with 3-aminopropyltrimethoxysilane (APTMS); (IV) *in situ* reduction of Au<sup>3+</sup> for the self-assembly of Au nanoparticles on the surface of PLLA-PEG@PNIPAAm-PDLA; (V) completion to load a protein in Au@PLLA-PEG@PNIPAAm-PDLA by elimination of the PNIPAAm-PDLA inner shell.

structures produced by a MDEM. Generally, a hydrophilic protein such as bovine serum albumin (BSA) can be encapsulated in the polymeric spheres using a double-emulsion method (DEM), a so-called “water-in-oil-in-water” (w/o/w) emulsion method [51, 60, 61]. However, the DEM has a disadvantage with respect to the stability of amphiphilic polymer spheres because both the inner shells and the outer shells are composed of the same species of copolymer. Instead, as for the MDEM, two different kinds of copolymers are sequentially incorporated in the organic phase to promote enhanced stability of the spheres. In this way, the inner shells can be prepared with PNIPAAm-PDLA diblock copolymers and the outer shells can be prepared with PLLA-PEG diblock copolymers.

For another class of thermosensitive nanocarriers, poly[(NIPAAm-*r*-AAm)-co-lactic acid] (PNAL) has been reported [62]. As schematically illustrated in Fig. 6.4(b), Au nanoparticles can be directly self-assembled on the surface of PNAL nanospheres by virtue of primary amino groups coming from acrylamide (AAm) molecules of the PNAL diblock terpolymer. The primary amino groups can be strongly bound to noble metals such as gold or silver. Therefore, the “shell” domain of Au@PNAL becomes an affinity site for biomolecules to be conjugated. Furthermore, the LCST of poly(*N*-isopropylacrylamide-*r*-acrylamide) (PNA) was modulated from 32 up to approximately 36 °C through the manipulation of the ratio between *N*-isopropylacrylamide (NIPAAm) and AAm units. This nanostructure is expected to serve as a synchronous delivery system by virtue of its Au-modified surface and hydrophobic inner core site (Fig. 6.4).

Figure 6.5 shows TEM images of the “shell-in-shell” spherical structures of PLLA-PEG@PNIPAAm-PDLA (parts a and b) and Au@PLLA-PEG@PNIPAAm-PDLA (c and d). The well-defined PLLA-PEG@PNIPAAm-PDLA can be prepared by MDEM and the Au nanoparticles are further deposited by self-assembly, resulting in hybrid nanosphere, i.e., Au@PLLA-PEG@PNIPAAm-PDLA. The bright contrast in the TEM images shown in Fig. 6.5(b) can be identified by a distinct difference in gray scale, which infers the “shell-in-shell” structures are properly fabricated. By increasing the temperature above the LCST, the inner shell of

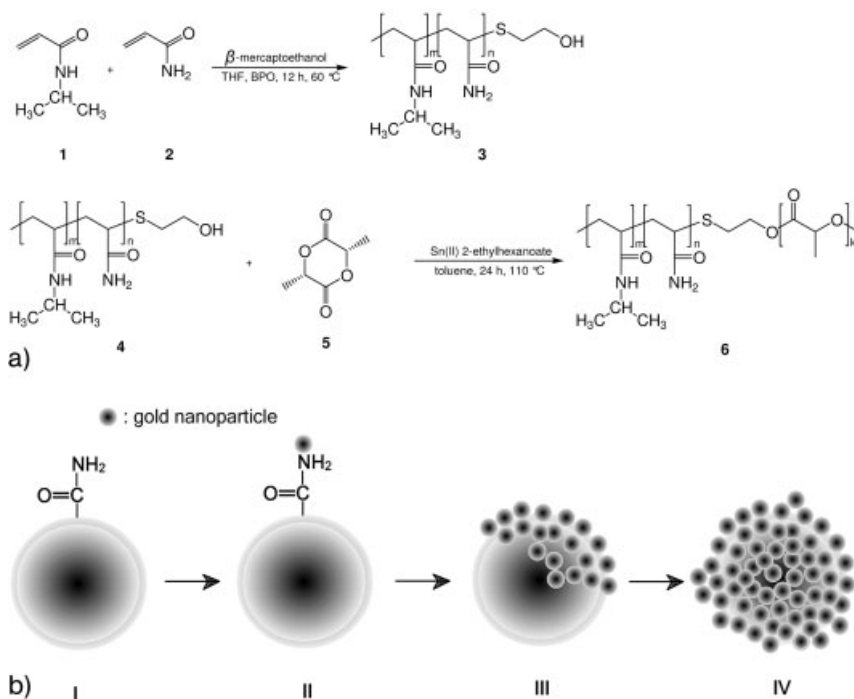


**Fig. 6.4.** Strategy to fabricate Au@PNAL spheres: (a) Synthetic pathway to PNAL diblock terpolymer: (1) NIPAAm; (2) AAm; (3) PNA; (4) hydroxyl-terminated PNA; (5) L,L-lactide; (6) PNAL. (b) Schematic of direct self-assembly of Au nanoparticles on PNAL

nanospheres: step (I) PNAL nanospheres; (II) direct self-assembly of Au nanoparticles to the primary amide groups of AAm; (III and IV) completion of the self-assembly of Au nanoparticles.

PLLA-PEG@PNIPAAm-PDLA undergoes the phase transition, resulting in elimination of the inner shell. Finally, PLLA-PEG@PNIPAAm-PDLA dual-shell structures are changed to the simple core-shell structure.

Hydrolyzable diblock copolymers of poly(ethylene glycol)-poly(L-lactic acid) (PEG-PLA) or poly(ethylene glycol)-poly(caprolactone) (PEG-PCL) have been prepared and loaded with doxorubicin for controlled release of the anticancer agent. The release rates of doxorubicin from the hydrolyzable vector can be modulated by increasing the amount of PEG in the polymeric systems, and also increased linearly with the molar ratio of degradable copolymer blended into the non-degradable membranes. In both nano- (100 nm) and micro-size vectors, the average release time reflects a highly quantized process in which any given vector is either intact or retains its encapsulant. Poration occurs as the hydrophobic PLA or PCL block is hydrolytically scissioned, progressively generating an increasing number of pore-preferring copolymers in the membrane. The kinetics of this evolving detergent mechanism underlies the phase behavior of amphiphiles, with transitions from membranes to micelles allowing controlled release [63].

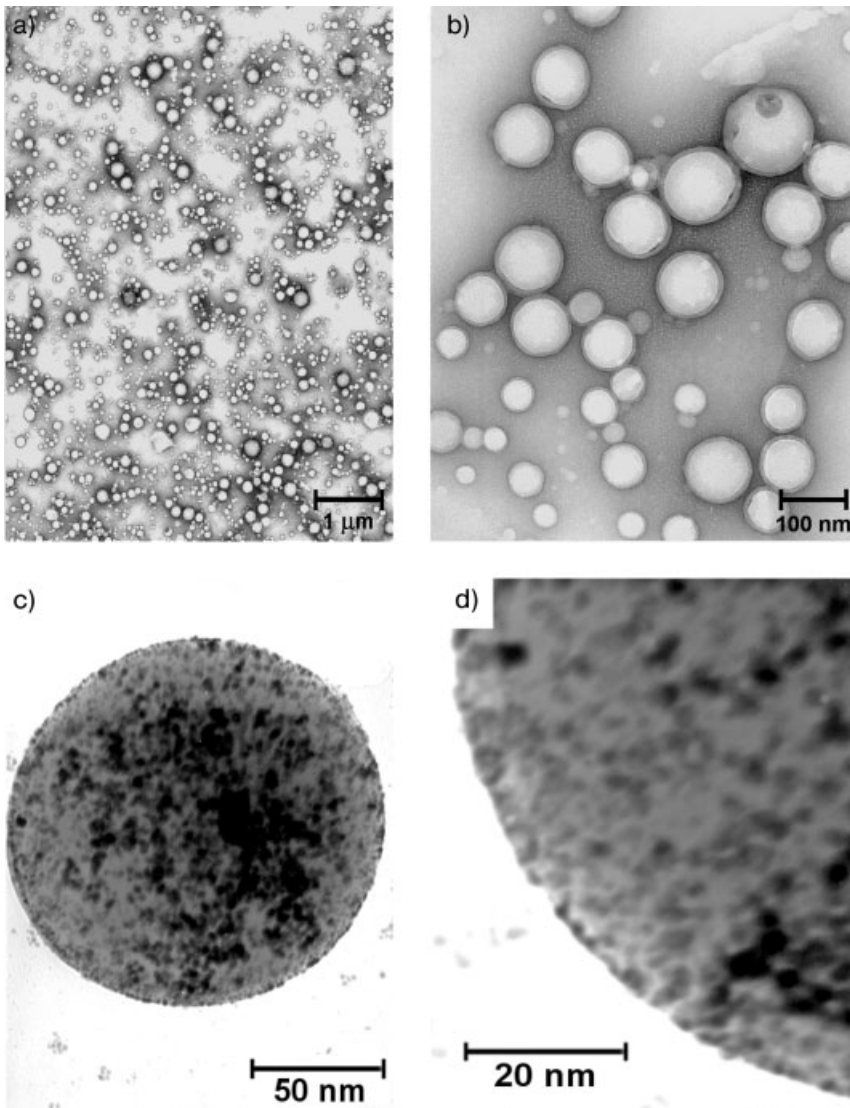


**Fig. 6.5.** TEM images of PLLA-PEG@PNIPAAm-PDLA (negatively stained with 2 wt.% ammonium molybdate aqueous solution for 2 min) (a and b) and Au@PLLA-PEG@PNIPAAm-PDLA (without staining) (c and d).

Chitosan is a polysaccharide obtained by alkaline deacetylation of the naturally occurring abundant polysaccharide chitin. It is biodegradable, biocompatible, non-immunogenic, and non-carcinogenic, making it suitable for pharmaceutical applications [64]. Chitosan tripolyphosphate (TPP) microspheres have been prepared by spray-drying methods using acetaminophen as a model drug substance. Such



ionically crosslinked chitosan-TPP microspheres afforded slower release rates. The vectors can be prepared using a higher concentration of chitosan, higher volume of TPP solution, a higher molecular weight chitosan and/or higher drug loading. In this study, acetaminophen release rates were mainly controlled by the chitosan-TPP matrix density and by the degree of swelling of the hydrogel matrix. The overall release trend of acetaminophen from spray-dried chitosan-TPP microspheres is a two-step biphasic process, with an initial burst followed by subsequent slower release [65]. A complex composite of proteins glycoproteins and proteoglycans has provided an important model for the design of biomaterials [66, 67]. Recent progress in the development of methods for incorporating non-natural amino acids into recombinant proteins using DNA technology points the way to an alternative strategy for preparing new types of drug deliver systems (DDS).

#### 6.4.2

##### **Inorganic Nanoparticles**

Inorganic porous materials are emerging as novel host systems. Owing to some interesting features, such as their biological stability and their drug-releasing properties, there is a significant and increasing interest in these potential vectors. Several porous materials have been used, including synthetic zeolites and silica xerogel materials. MCM 41 is typical mesoporous, templated silica that has been widely investigated. This material presents nanosized pores that allow the incorporation of therapeutic agents. The release properties of ibuprofen-loaded MCM 41 show the feasibility of such systems as vectors for DDS [68].

Porous calcium hydroxyapatite is also used as a vector for anticancer drugs (cis-platinum). The slow release of cis-platinum from the inorganic vector has been confirmed by *in vitro* experiments [69]. When the drug-loaded vector was implanted into normal back muscle, or the tibia, sustained release of cis-platinum was observed during the subsequent 12 weeks. The diffusion rate of cis-platinum into the blood and other organs (liver, kidney, brain) was <10% of that at the implanted site. The vector administered into tumors of mice also showed a steady release of cis-platinum for more than three months. Inhibition of tumor growth was more obvious after local implantation of the cis-platinum-loaded inorganic vector than after intraperitoneal administration of cis-platinum. Based on these results, this novel mesoporous vector shows great potential as controlled DDS of anticancer agents. It is more attractive in bone tumors because the mechanical strength of calcium hydroxyapatite permits partial surgical excision and replacement of the bone defect at the same time.

Porous CuX zeolite has been synthesized as an inorganic vector to incorporate cyclophosphamide (CP). Biochemical and anatomopathological evaluations of antitumoral effects by oral administration of the CP-loaded CuX zeolite show that the intensity of the antitumoral effects is similar to that with normal administration of CP. An advantage of the CP-loaded CuX zeolite is the maintenance of a CP concentration ranging between 100 and 1000 ng per mL of plasma in the blood [70].

### 6.4.3

#### Metallic Nanoparticles

Recently, the immobilization of biomolecules, ligands and therapeutic agents onto the surface of metallic nanoparticles has been the focus of intense activity in biological engineering and biotechnology [71–77]. Especially, amine groups and cysteine residues in the proteins can be bound onto the surface of Au nanoparticles and can be stabilized electrostatically [71, 75]. In parallel with this work, several groups have focused on the fabrication of Au nanoparticles-organic/inorganic hybrid structures with polyurethane (PU) [71], silica [78–80], polystyrene (PS) [81], and stimuli-sensitive polymers (SSPs) [31, 62, 82].

Colloidal Au can be used as a vector for therapeutic agents as well as an indicator for immunodiagnosics. However, the use of these Au nanoparticles for *in vivo* DDS was not well established. A colloidal gold (cAu) nanoparticle vector has been used to target the delivery of tumor necrosis factor (TNF) to a solid tumor growing in mice [83]. The optimal vector, designated PT-cAu-TNF, consists of molecules of thiol-derivatized PEG (PT) and recombinant human TNF that can be directly bound onto the surface of the Au nanoparticles. Following intravenous administration, PT-cAu-TNF rapidly accumulates in MC-38 colon carcinoma tumors and shows little to no accumulation in the liver, spleen (i.e., the RES) or other healthy organs of animals. PT-cAu-TNF was less toxic and more effective in reducing tumor burden than native TNF since maximal antitumor responses were achieved at lower drug doses. Svarovsky et al. have described the synthesis of Au nanoshells encapsulated with up to 90 units of the Thomsen-Friedenreich (TF) tumor-associated carbohydrate antigen (TACA) disaccharide (Galbeta1-3GalNAc-alpha-O-Ser/Thr) as well as the assembly of a suitably linked designer glycopeptide as a precursor to similar multivalent presentations on Au. The TF-coated Au nanoparticles are highly stable, water soluble, and easily handled. Improvements in the linker technology used to attach the disaccharide to the Au nanoparticles led to a robust multivalent platform. The antigen retains all recognition characteristics while displayed on this template, as shown by several *in vitro* assays. This approach can be used to develop novel therapeutic agents that inhibit protein–carbohydrate interactions [84].

## 6.5

### Kinetics of the Controlled Release of Anticancer Agents

*In vivo* treatment requires the release of therapeutic agents into the body; this is followed by absorption, metabolism, distribution, and elimination of the therapeutic agents that are administered, and subsequent target organ effects, both therapeutic and toxic. The process of release followed by absorption, distribution, metabolism, and elimination is referred to as “pharmacokinetics” – a process commonly represented by a mathematical description of the behavior of a drug, and possibly its metabolites, in the system. Pharmacokinetics are frequently

described as what the body does to the drug. A major goal of clinical pharmacology is to integrate pharmacokinetics and pharmacodynamics so that their relationships can be understood, and so that drug treatment can be optimized based upon such an understanding [85].

The release rate of DDS predicted by the diffusion- and the dissolution-based release systems can be applicable for the controlled-release of drugs during circulation in the blood stream or localization at the target site. Diffusion models are defined literally as a mass transfer process of the individual substance, brought about by random molecular motion and associated with a concentration gradient. In monolithic devices, the drug is uniformly mixed within a polymeric matrix and is present either in a dissolved or dispersed structure.

Generally, the release model of the devices where the drug is dissolved follows Fickian kinetics. When the drug is dispersed in a polymeric matrix, the rate of release follows the square root of time kinetics until the concentration of the drug decreases below the saturation value. In addition, the preferred release profiles of the drug in bulk degrading systems can be manipulated by adjusting the molecular weight of the polymer, copolymer composition, crystallinity, loading amounts of the drug, and interactions between polymer and drug, etc. Generally, drug release may be diffusion controlled or dissolution controlled, depending on parameters such as the permeability of the polymer to water, the solubility of the drug in the polymer and in the water phase, the molecular weight of the drug, etc. With methotrexate-loaded gelatin nanoparticles, the drug release follows a diffusion-controlled mechanism [86].

Polakovič et al. have made a significant contribution to the investigation of the release profiles of model drugs for spherical shapes of DDS [42]. They suggested that two main models, consisting of the diffusion and the dissolution, should be considered to determine the release rate of the drug from polymeric spheres. Generally, drug release mechanisms from micro/nanoparticles should be assumed based on (a) surface desorption, (b) diffusion through particle pores, (c) diffusion through intact polymers, (d) diffusion through water swollen polymers and (e) surface or bulk erosion of polymeric matrix [87]. The last phenomenon partly represents a mechanism of drug-release. However, other factors will change the morphologies of the platforms, resulting in changes to the rate of diffusion for drug release [42].

### 6.5.1

#### Diffusion Model

The release of a drug from a polymeric matrix generally follows Fick's second law. The concentration gradient of the spherical particles follows the form given by Eq. (1).

$$\frac{\partial c}{\partial t} = D \left( \frac{\partial^2 c}{\partial r^2} + \frac{2}{r} \frac{\partial c}{\partial r} \right) \quad (1)$$

where  $c$  is the local drug concentration at time  $t$  and the distance  $r$  from the center

of the particle and  $D$  is the diffusion coefficient of the drug in the polymeric matrix.

Therefore,

$$\frac{c_1}{c_{1\infty}} = 1 - \sum_{n=1}^{\infty} \frac{6(\alpha + 1)\alpha}{(9 + 3\alpha + q_n^2\alpha^2)} e^{-(q_n^2/R^2)Dt} \quad (2)$$

$\alpha = V/(V_s K_p)$ , where  $V$  is the bulk liquid volume of the surrounding medium,  $V_s$  is the total volume of the particles  $q_n = \lambda R$  where  $\lambda$  is eigen value and  $R$  is radius of particles.

### 6.5.2

#### Dissolution Model

The dissolution model can be expected when a solid drug is dissolved in media. The dissolution rate of a drug can often be the rate-determining step when the absorption rates are faster than the dissolution rates (e.g., as with steroids). If the drugs are not dissolved before they are removed from the intestinal absorption site, the proper effects can not be expected due to a limited residence time at the absorption site. Therefore, the rate of the dissolution should be considered rather than the diffusion model for drugs that are poorly soluble. For this reason, the dissolution rate of drugs in solid dosage forms is an important parameter in the design of proper DDSs.

Drug release by the dissolution model can be defined by Eq. (3).

$$r_d = -\frac{dc}{dt} = k(c - K_p c_1) \quad (3)$$

where  $r_d$  is the rate of drug dissolution and  $k$  is the dissolution coefficient. The drug concentration is eliminated after introducing the mass balance and its derivative in Eq. (3). Integration of the rearranged equation provides the relationship of  $c_1$  with time given in Eq. (4).

$$c_1 = \frac{c_0}{K_p(\alpha + 1)} \left[ 1 - \exp\left(-\frac{\alpha + 1}{\alpha} kt\right) \right] \quad (4)$$

$K_p = c_{\infty}/c_{1\infty}$  is the partition coefficient characterized by the concentration ratio of the concentration inside the particles to the bulk liquid drug concentration in thermodynamic equilibrium.

### 6.5.3

#### Kinetics of the Indomethacin (IMC, 1-[*p*-chlorobenzoyl]-2-methyl-5-methoxy-3-indoleacetic acid) Release

The release kinetics of IMC as a model drug have been examined with parameters obtained by comparing the diffusion and dissolution kinetic models. Table 6.2

Tab. 6.2. Different series of IMC-loaded PLA-PEO spheres.

Code	Ratio (o/w)	Ratio (drug/ polymer)	Water phase (mL)	Organic phase	
				PLA soln (mL)	IMC soln (mL)
LL <sub>1</sub>	0.11	1	3	0.165	0.165
LL <sub>2</sub>	0.22	1	3	0.330	0.330
LL <sub>3</sub>	0.33	1	3	0.660	0.660
DL <sub>1</sub>	0.11	1	3	0.165	0.165

summarizes the codes of IMC-loaded PLA-PEO spheres for *in vitro* experiments on the controlled-release of IMC. Figure 6.6(a–d), representing LL<sub>1</sub>, LL<sub>2</sub>, LL<sub>3</sub>, and DL<sub>1</sub> respectively, shows four different kinetic behaviors. The results of LL<sub>1</sub> and DL<sub>1</sub> are in a good agreement with the diffusion model only. However, the release profiles gradually shift from the diffusion model towards the dissolution model as  $c_{1\infty} V_r/c_0$  decreases. Figure 6.6(b) shows the release profile of LL<sub>2</sub>, which is more dissolution-dependent than that of LL<sub>1</sub>.

A similar phenomenon can be observed in LL<sub>3</sub>, which shows the greatest dissolution-dependent characteristics with the lowest  $c_{1\infty} V_r/c_0$ . Consequently, LL<sub>2</sub> has intermediate behavior between the two different models, showing that the *in vitro* release profile is located between the diffusion and the dissolution profiles. This demonstrates that the kinetic models are strongly dependent upon  $c_{1\infty} V_r/c_0$ . A high  $c_{1\infty} V_r/c_0$  can directly affect the diffusion kinetics. Therefore, a high apparent efficiency ( $\zeta$ ) can result in an intermediate characteristic between the diffusion- and dissolution-dependent mechanisms. In addition to the parameters mentioned above, other parameters should be considered during the fabrication of nanospheres for DDS. Yang et al. have reported a correlation between the release behavior and surface porosity of microspheres [61]. They also reported that the organic phase used for the fabrication of the nanospheres by emulsion/evaporation techniques plays a critical role in determining the overall release characteristics of the drugs. The fabrication temperature also becomes a critical factor because the shell of the nanospheres is vulnerable to evaporating solvents with a low-boiling point such as chlorine-based solvents (i.e., methylene chloride and/or chloroform). The release rate is increased owing to a larger pore size on the surface of the spheres when the DDS has a lower  $V_r$ . The release profiles of LL<sub>1</sub> and DL<sub>1</sub> show initial fast release rates. In contrast, the initial “bursting” behaviors of LL<sub>2</sub> and LL<sub>3</sub> are less pronounced. This phenomenon explains that  $V_r$  can affect the release rates at the initial stage, especially within a short period, i.e., as soon as exposed to the surrounding medium. From the mathematical modeling and *in vitro* experiments, we should not use only one model to predict the release behavior of therapeutic agents because the releasing environments are usually more complicated than ex-

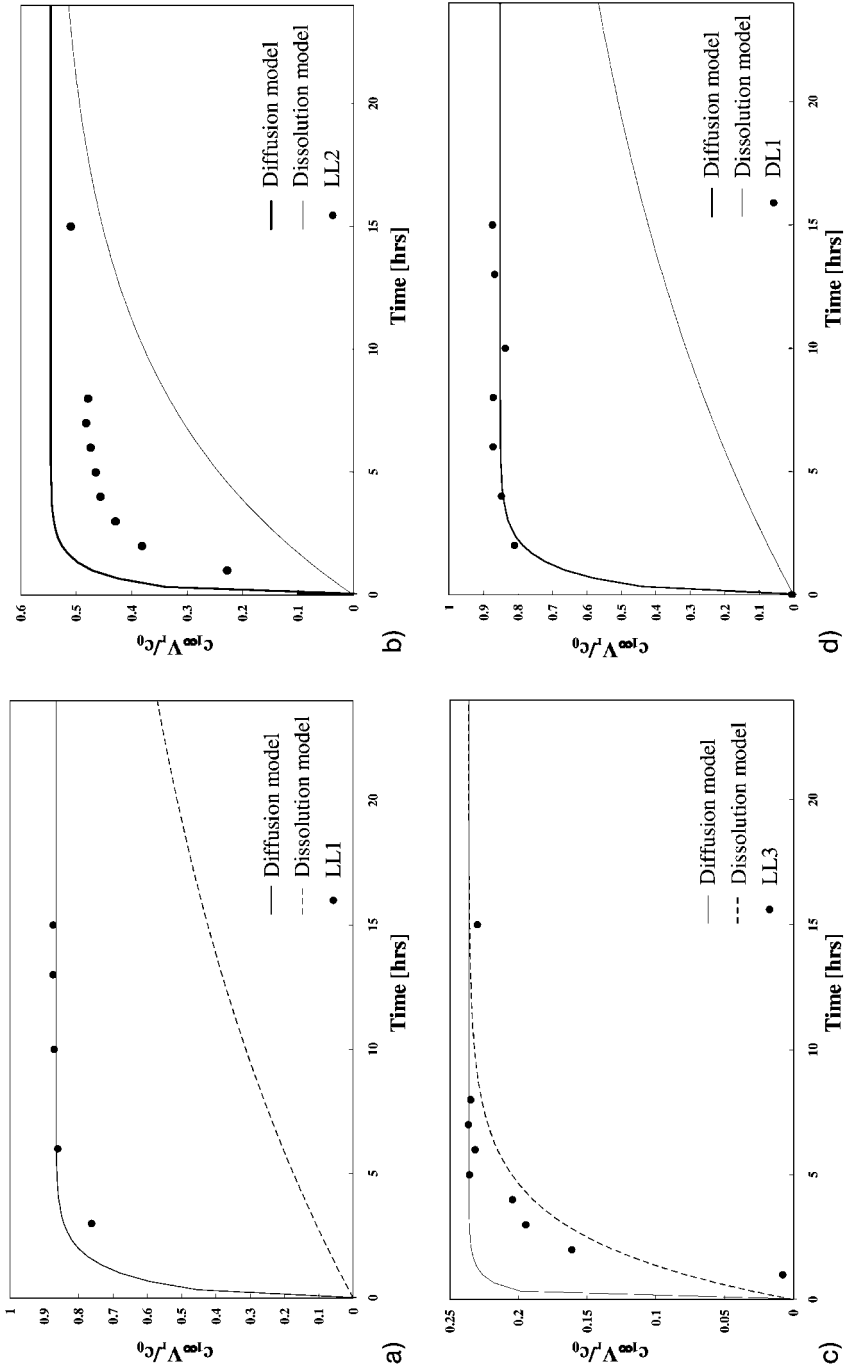


Fig. 6.6. Drug-releasing profiles in comparison with diffusion and dissolution models: (a) LL<sub>1</sub>, (b) LL<sub>2</sub>, (c) LL<sub>3</sub>, and (d) DL<sub>1</sub>.

pected. Thus, proper assumptions and possible variables should be considered for both theoretical and practical applications.

## 6.6

### Controlled Release of Anticancer Agents

Although biomaterials (biologically derived components) are useful for new medical treatments, critical problems in biocompatibility, mechanical properties, degradation and numerous other issues remain. Stealth properties and responsiveness to factors such as pH, temperature, specificity and other critical problems have to be resolved. The possibility of delivering cytotoxic agents directly into tumor cells has several advantages: drug losses in the bloodstream and upon liposome–cell interaction are minimized and the preparation of drug-loaded nanoparticles becomes simpler. To be effective, a material must possess several attributes, including the ability to condense therapeutic molecules to a size of less than 150 nm so that it can be taken up by receptor-mediated endocytosis, the ability to be taken up by endosomes in the cell and to allow therapeutic molecules to be released in active form, and to enable it to travel to cell's nucleus. Moreover, gene therapy is gaining in popularity as a medical treatment for cancer, tumors, Alzheimer's diseases, diabetes etc.; however, the clinical efficacy is lower than expected due to the detergent effect. When administered directly into the blood vessel or lesion, the therapeutic molecules are taken up by other healthy organs/cells and the residual time in biological systems is less than 2 h, and thus the pharmacological action is diminished. In addition, it has been reported that therapeutic molecules taken up by healthy organs/cells undergo mutation and may cause other, more serious diseases, including cancer. Also, most antitumor agents are hydrophilic compounds and, therefore, cannot be retained within the membrane. Thus, the use of prodrug forms of anticancer agents to alter the phase behavior of the chemicals is becoming more popular.

#### 6.6.1

##### Alkylating Agents

Alkylating reagents are chemical reagents that have an alkyl group such as propyl in place of a nucleophilic group. They include several cytotoxic drugs, some of which react specifically with N7 of the purine ring, resulting in depurination of DNA. These alkylating drugs interact with DNA and prevent the division of the cells.

The alkylation of DNA bases can disrupt the replication mechanism of the cell. The nitrogen bases in DNA molecules are nucleophilic and can be easily alkylated. If the N–H groups are replaced by N–R groups then the DNA base pairing is disrupted and can lead to cellular dysfunction. This should have an effect on the replication of cancerous cells, thus leading to a slow-down or stoppage of growth of the cancer.

### 6.6.1.1 Chlorambucil

Chlorambucil (pronounced “klor-AM-byoo-sil”) is a well-known anticancer agent for blood cancers and acts to reduce the number of blood cells. It is also used to treat other cancers such as lymphomas. Chlorambucil is an aromatic derivative of mechlorethamine and is closely related in structure to melphalan. The therapeutic effects are the slowest acting and generally least toxic among the alkylating agents. Alkylation of DNA results in breaks in the DNA molecule as well as crosslinking of the twin strands, thus interfering with DNA replication and transcription of RNA. Like other alkylators, chlorambucil is cell cycle phase-nonspecific [88, 89].

Leroux et al. have demonstrated that polymeric nanoparticles can be loaded with chlorambucil (8.52% m/m) with an entrapment efficiency of 60%. Polymeric nanospheres have been prepared by emulsification of a benzyl alcohol solution of a polymer in a hydrocolloid-stabilized aqueous solution followed by dilution of the emulsion with water. Nanoparticles as small as 70 nm in diameter can be produced by increasing the percentage of poly(vinyl alcohol) to 27.5% in the external phase. The particle size can be controlled by using gelatin instead of poly(vinyl alcohol) and the smallest nanoparticles, with an average size of 70 nm, can be obtained [90].

Chitin-based biodegradable microspheres have also been investigated for their ability to encapsulate chlorambucil as a model drug. The polymer sphere can be prepared by directly blending chitin with different contents of poly(D,L-lactide-co-glycolide 50:50) (PLGA 50/50) in dimethylacetamide–lithium chloride solution, followed by coagulating in water via wet phase inversion. Chlorambucil-loaded chitin/PLGA (50/50) has a two-step release mechanism. In the initial stage, the drug release rate increases with increased chitin content due to hydration and surface erosion of the hydrophilic chitin phase; however, the subsequent slow release is sustained for several days, mainly due to bulk hydrolysis of the hydrophobic PLGA phase [91].

### 6.6.1.2 Cyclophosphamide

Cyclophosphamide is a cyclic phosphamide ester of mechlorethamine. It is transformed via hepatic and intracellular enzymes into active alkylating metabolites, acrolein and phosphoramidate mustard. Cyclophosphamide prevents cell division primarily by crosslinking DNA strands. This anticancer agent is applicable to breast cancer, lung cancer, multiple myeloma, mycosis fungoides, neuroblastoma and retinoblastoma etc. It must be handled carefully as it is considered to be highly carcinogenic in humans. Cyclophosphamide-loaded poly(butyl cyanoacrylate) nanospheres have been investigated to obtain a suitable and tolerated ocular delivery device for therapeutic applications, involving treatment of severe ocular inflammatory processes that localize in the anterior chamber of the eye [92, 93].

Local delivery of 4-hydroperoxycyclophosphamide (4HC derived from cyclophosphamide) has been carried out via a controlled-release biodegradable polymer to determine whether the use of a polymer vector can enhance efficacy. Ninety Fischer 344 rats implanted with 9L or F98 gliomas were treated with an intracranial polymer implant containing 0–50% loaded 4HC in the polymer. The 20%



4HC-loaded polymers caused minimum local brain toxicity and maximum survival. These polymers were then used to compare the *in vivo* efficacy of 4HC to BCNU in rats implanted with 9L glioma. Animals with brain tumors treated with 4HC had a median survival of 77 days compared to that of 21 days in BCNU-treated animals and 14 days in untreated animals. Long-term survival for more than 80 days was 40% in the 4HC-treated rats versus 30% in the BCNU-treated rats.

In conclusion, 4HC-impregnated polymers provide an effective, safe local treatment for rat glioma [94].

### 6.6.1.3 Carmustine

Carmustine [BCNU, 1,3-bis(2-chloroethyl)-1-nitrosourea] is a highly lipophilic nitrosourea compound that undergoes hydrolysis *in vivo* to form reactive metabolites. These metabolites cause alkylation and crosslinking of DNA. Nitrosoureas generally lack cross-resistance with other alkylating agents [88, 89]. The US Food and Drug Administration (FDA) approval of Gliadel® in 1996 represented the first new treatment approved for brain tumors in over 20 years. It has also been approved by numerous regulatory agencies worldwide.

Gliadel® is a polymer–drug combination that delivers the chemotherapeutic agent carmustine directly to the site of a brain tumor via controlled release from a biodegradable matrix [95]. To compare the effectiveness of lipid microspheres with Gliadel®, Takenaga has incorporated a BCNU into lipid microspheres by homogenizing a soybean oil solution of BCNU with egg yolk lecithin. Compared with the corresponding conventional dose of BCNU, the lipid microsphere-encapsulated BCNU significantly enhanced antitumor activity with reduced toxicity in mice with L1210 leukemia. Lipid nanospheres with an average size of 50 nm also showed a similar level of *in vivo* antitumor activity. In this report, [<sup>14</sup>C]triolein uptake by L1210 leukemia cells was increased by incorporation into microspheres. The nanospheres showed a longer *in vivo* half-life due to the avoidance of cellular uptake by the RES, resulting in higher accumulation at the tumor sites [96].

## 6.6.2

### Antimetabolic Agent

#### 6.6.2.1 Cytarabine

Cytarabine is metabolized intracellularly into its active triphosphate form (cytosine arabinoside triphosphate). This metabolite then damages DNA by multiple mechanisms, including the inhibition of  $\alpha$ -DNA polymerase, inhibition of DNA repair through an effect on  $\beta$ -DNA polymerase, and incorporation into the DNA. The latter mechanism is probably the most important. Cytotoxicity is highly specific for the S phase of the cell cycle [88, 89]. Ellena et al. have investigated the distribution of phospholipid and triglyceride molecules in the membranes forming the nonconcentric vesicular network within a multivesicular lipid particle (MLP). MLP formulations exhibited controlled release of encapsulated pharmaceuticals on time scales of a few days to a few weeks. The MLP can be synthesized by a double emul-

sification process with a neutral lipid such as a triglyceride. MLP formulations with the antineoplastic agent cytarabine encapsulated in the aqueous compartments have been prepared that further contained [ $^{13}\text{C}$ ]carbonyl-enriched triolein. This rational approach can be used to develop MLP formulations with variable rates of sustained release, modulated by changes in the distribution of various phospholipids and triglycerides [97].

#### 6.6.2.2 Fluorouracil (FU)

Fluorouracil was developed in 1957 based on the observation that tumor cells utilized the base pair uracil for DNA synthesis more efficiently than did normal cells of the intestinal mucosa. It is a fluorinated pyrimidine that is metabolized intracellularly to its active form, fluorodeoxyuridine monophosphate (FdUMP). The active form inhibits DNA synthesis by inhibiting the normal production of thymidine. Fluorouracil is cell cycle phase-specific (S phase) [88]. 5-Fluorouracil (5-FU)-loaded poly(L-lactide) (PLLA) or its carbonate copolymer microspheres have been prepared by a modified oil-in-oil (o/o) emulsion solvent evaporation technique. The dispersed phase was a solvent mixture of *N,N*-dimethylformamide (DMF) and acetonitrile, and the continuous phase was liquid paraffin containing 1–10% (w/v) Span 80(R). Using this modified process, microspheres with various particle sizes can be prepared with high 5-FU entrapment efficiency (~80%). *In vitro* drug release experiments showed a burst release of 5-FU from PLLA microspheres, followed by a sustained release over 50 days. With other vectors, poly(L-lactide-co-1,3-trimethylene carbonate) (PLTMC) and poly(L-lactide-co-2,2-dimethyl-1,3-trimethylene carbonate) (PLDTMC), the drug release rate can be prolonged to over 60 days [98].

Roullin et al. have developed 5-FU-loaded poly(L-lactide-co-glycolide) (PLGA) microspheres to deliver therapeutic agents into the CNS for stereotactic intracerebral implantation [39]. *In vivo* experiments with C6 glioma-bearing rats showed promising results – the median survival time was doubled [99]. A phase I–II pilot study was conducted on eight patients with high-grade glioma who underwent surgical removal before 5-FU-loaded microspheres were implanted. After 18 months the patients' survival rate and welfare was improved [100]. Microsphere fate and the 5-FU diffusion area from these particles in the brain was also investigated, depending on the inserted locations of the drug-loaded microspheres. [ $^3\text{H}$ ]5-FU microspheres were used to evaluate diffusion areas from the implantation site [39].

Another approach for controlled DDSs into the brain has also been developed using implantable, biodegradable microspheres. The strategy was evaluated initially to provide localized and sustained delivery of the radiosensitizer 5-FU after patients underwent surgical resection of malignant glioma [101].

#### 6.6.2.3 Methotrexate

Methotrexate and its active metabolites compete for folate-binding sites of the enzyme dihydrofolate reductase. Folic acid must be reduced to tetrahydrofolic acid by this enzyme for DNA synthesis and cellular replication to occur. Competitive inhibition of the enzyme leads to blockage of tetrahydrofolate synthesis, depletion of

nucleotide precursors, and inhibition of DNA, RNA and protein synthesis. Methotrexate is cell cycle phase-specific (S phase) [88, 102]. Methotrexate can be widely employed for breast cancer, bladder cancer and head and neck cancer, etc.

ABA-type triblock copolymers of poly(trimethylene carbonate)-poly(ethylene glycol)-poly(trimethylene carbonate) were synthesized by ring-opening polymerization. The anticancer drug methotrexate was loaded into a core-shell structure of polymeric nanoparticles 50–160 nm in diameter. Generally, the release rate of methotrexate from the nanoparticles was comparatively faster than that of microsphere systems due the higher surface area and smaller particle size [103].

Hydrophilic gelatin nanoparticles have also been prepared that incorporated the methotrexate by solvent evaporation techniques based on a single water-in-oil (w/o) emulsion with glutaraldehyde as a crosslinking agent. The mean diameter of the methotrexate-loaded gelatin particles was 100–200 nm [86].

### 6.6.3

#### Anticancer Antibiotics

##### 6.6.3.1 Actinomycin D

At low concentrations actinomycin D inhibits DNA-directed RNA synthesis and at higher concentrations DNA synthesis is also inhibited. All types of RNA are affected, but ribosomal RNA is more sensitive. Actinomycin D binds to double-stranded DNA, permitting RNA chain initiation but blocking chain elongation. Binding to the DNA depends on the presence of guanine. It is applicable to the treatment of testicular, ovarian, and germ cell cancers. Isobutyl cyanoacrylate nanoparticles loaded with actinomycin D were shown to concentrate preferentially in rat mesangial cells and to increase the drug's uptake in these cells *in vitro* and *in vivo*, as compared to the free drug. Drug targeting by nanoparticles to renal cells and macrophages may be possible, resulting in a lowering of the critical level of drug dosage in tubular cells and a reduction of tubular toxicity [104].

The effects of actinomycin D-loaded poly(methyl cyanoacrylate) nanoparticles on the growth of a transplantable soft tissue sarcoma has also been investigated in a rat model. Actinomycin D-loaded poly(methyl cyanoacrylate) nanoparticles showed a greater inhibitory action than the free drug on the growth of the S250 sarcoma but the nanoparticles alone did not demonstrate any significant antitumor effect [105]. This study demonstrated that, 24 h after injection, adsorbed actinomycin D is 5.6-, 44- and 64-fold more concentrated than the free drug in muscle, spleen and liver, respectively [106].

##### 6.6.3.2 Bleomycin

Bleomycin is an antineoplastic antibiotic. It is used to treat several types of cancer, including cervical and uterine cancer, head and neck cancer, testicular and penile cancer, and certain types of lymphoma. Bleomycin causes DNA strand scission through formation of an intermediate metal complex requiring a metal ion cofactor such as copper or iron. This action results in inhibition of DNA synthesis and, to a lesser degree, in inhibition of RNA and protein synthesis. The drug is cell

cycle-specific for G phase, M-phase and S phase [107]. Manipulation of the physicochemistry of water-soluble polymers such as glycolchitosan can be used to create hybrid materials for drug delivery and gene delivery with biocompatibility. Glycolchitosan modified by the attachment of a strategic number of fatty acid pendant groups (11–16 mol%) assembles into unilamellar, polymeric vesicles in the presence of cholesterol. An ammonium sulfate gradient bleomycin (MW 1400), for example, can be efficiently loaded onto these polymeric vesicles to yield a bleomycin-to-polymer ratio of 0.5 units  $\text{mg}^{-1}$  [108].

Bleomycin has been conjugated to carbon nanoparticles as a new DDS for the treatment of digestive cancer. In this way, higher levels of anticancer drug can be localized to the regional lymph nodes and at the injection site compared with distribution of the drug in aqueous solution. In 12 patients with histologically proven carcinoma, bleomycin-conjugated carbon nanoparticles were injected endoscopically into the primary lesions. Endoscopic injection of this dosage formulation shows that it can control these digestive cancers in patients in whom operation is contraindicated [109].

Formulations of ultra-deformable liposomes containing bleomycin (Bleosome™) also have been reported and proposed for topical treatment of skin cancer [110]. Bleosome™ exerted a lethal effect on human keratinocytes cell lines and a cell line derived from a primary carcinoma *in vitro* when loaded with sufficient bleomycin. The cell line, derived from squamous cell carcinoma, seemed to be more susceptible to Bleosome™ than HPV-immortalized keratinocytes (NEB-1) [111].

#### 6.6.3.3 Daunorubicin

Daunorubicin is an anthracycline antibiotic that damages DNA by intercalating between base pairs, resulting in uncoiling of the helix, ultimately inhibiting DNA synthesis and DNA-dependent RNA synthesis [112]. DaunoXome®, a tumor-targeting daunorubicin liposome, is commercially available and its beneficial effects are well reported. It is a formulation of daunorubicin in small unilamellar vesicles (SUVs) composed of highly pure distearoylphosphatidylcholine (DSPC) and cholesterol in a 2:1 mole ratio. Several countries have approved DaunoXome® for use in for treating Kaposi's sarcoma (KS) in HIV-positive patients. Preclinical investigations indicate that DaunoXome® increases *in vivo* daunorubicin tumor delivery by about ten-fold over conventional drugs, yielding a comparable increase in therapeutic efficacy [113].

## 6.7

### Future Directions

Although many trials on different types of DDS have been reported, these laboratory experiments still remain far from clinical application due to matters of their reproducibility and production. New strategies for the design of DDS vectors should be developed to move these systems into the clinic by decreasing the toxicity of anticancer agents and targeting them to malignant tissues. Furthermore,

novel techniques for the effective loading of active molecules and surface activation (i.e., antibodies and functional groups) for active targeting are essential to improve the therapeutic effectiveness by reducing both the dose and the side effects. Several functions should be considered, such as effective targeting, maximum uptake and retention at the target sites, and rapid clearance after finishing the mission. For this reason, the generation of intelligent smart biomaterials (ISB) based on nanotechnology is being intensively investigated for controlled DDS of anticancer agents and is already having an enormous effect on nanomedicine as a new research field.

While many of nanoparticle synthesis techniques have focused on the empirical basis for controlled release of anticancer agents, increasing demand for multifunctional vectors represents a major fabrication challenge. These vectors should be designed to integrate several aspects: (a) theoretical and practical considerations of the evolution of novel phenomena coming from their composition and size, (b) design of complex or composite structures with given morphology required for multifunctionality, (c) generation and assembly of new molecular and macromolecular structures using suitable processing routes, (d) incorporation of drugs to be delivered to the target cells, and (e) modification of the nanoparticulate surfaces and interfaces, rendering them suitable for interaction with the target.

To develop artificial synthetic biomaterials based on nanotechnology for cancer-oriented drug delivery systems (CoDDS), we should consider the extracellular matrix biology, cell receptors and immunology, and how the body responds to specific materials. These novel vectors should incorporate hydrophobic/hydrophilic drugs with active surface modifications by the attachment of active functional ligands for passive targeting at specific target organs, receptors, etc.

Moreover, novel concepts of ISB for CoDDS can be developed based on core-shell, mesoporous nanotechnology. These vectors can be programmed to respond to external environmental conditions, e.g., pH, ionic strength, temperature, ultrasound, radiation, magnetic fields, UV-light, etc. The development of suitable nanostructures, methodologies for drug incorporation, methodologies for controlling releasing rates, and acceptable biological activity should be considered in the design process.

Targeting is also an important concept for CoDDS. Passive and active targeting to specific lesions, degradation/release rates, and surface activation/functionalization should be considered for optimization of these systems. Toxicology and pharmacological evaluation are also important factors. Thus, the therapeutic compounds, loading methods, quantity and efficacy, etc. should all be carefully considered during the design proper vectors.

## References

- 1 American Cancer Society, <http://www.cancer.org>.
- 2 F. L. MI, S. S. SHYU, C. Y. KUAN, S. T. LEE, K. T. LU, S. F. JANG, Chitosan-polyelectrolyte complexation for the preparation of gel beads and con-

- trolled release of anticancer drug. I. Effect of phosphorous polyelectrolyte complex and enzymatic hydrolysis of polymer, *J. Appl. Polym. Sci.* **1999**, *74*, 1868–1879.
- 3 S. GOLUBOVIC, B. Z. RADMANOVIC, Increase of corneal graft-survival by use of topically immunosuppressive agents in rabbits, *Graefes Arch. Clin. Exp. Ophthalmol.* **1988**, *226*, 288–290.
  - 4 M. DYBA, N. I. TARASOVA, C. J. MICHEJDA, Small molecule toxins targeting tumor receptors, *Curr. Pharm. Des.* **2004**, *10*, 2311–2334.
  - 5 Q. A. PANKHURST, J. CONNOLLY, S. K. JONES, J. DOBSON, Applications of magnetic nanoparticles in biomedicine, *J. Phys. D: Appl. Phys.* **2003**, *36*, R167–R181.
  - 6 M. WOLF, H. SWAISLAND, S. AVERBUCH, Development of the novel biologically targeted anticancer agent gefitinib: Determining the optimum dose for clinical efficacy, *Clin. Cancer Res.* **2004**, *10*, 4607–4613.
  - 7 M. P. LUTOLF, J. A. HUBBELL, Synthetic biomaterials as instructive extracellular microenvironments for morphogenesis in tissue engineering, *Nat. Biotechnol.* **2005**, *23*, 47–55.
  - 8 L. REN, G. M. CHOW, Synthesis of nir-sensitive Au-Au<sub>2</sub>S nanocolloids for drug delivery, *Mater. Sci. Eng., C* **2003**, *23*, 113–116.
  - 9 M. MORAWSKI, T. REINERT, C. MEINECKE, T. ARENDT, T. BUTZ, Antibody meets the microbeam – Or how to find neurofibrillary tangles, *Nucl. Instrum. Methods Phys. Res., Sect. B* **2005**, *231*, 229–233.
  - 10 K. SIVAKUMAR, B. PANCHAPAKESAN, Electric field-assisted deposition of nanowires on carbon nanotubes for nanoelectronics and sensor applications, *J. Nanosci. Nanotechnol.* **2005**, *5*, 313–318.
  - 11 J. CONNOLLY, T. G. ST PIERRE, M. RUTNAKORNPIITUK, J. S. RIFFLE, Cobalt nanoparticles formed in polysiloxane copolymer micelles: Effect of production methods on magnetic properties, *J. Phys. D: Appl. Phys.* **2004**, *37*, 2475–2482.
  - 12 C. BARGLIK-CHORY, D. BUCHOLD, M. SCHMITT, W. KIEFER, C. HESKE, C. KUMPF, O. FUCHS, L. WEINHARDT, A. STAHL, E. UMBACH, M. LENTZE, J. GEURTS, G. MULLER, Synthesis, structure and spectroscopic characterization of water-soluble CdS nanoparticles, *Chem. Phys. Lett.* **2003**, *379*, 443–451.
  - 13 L. MENG, Z. X. SONG, Applications of quantum dots to biological medicine, *Prog. Biochem. Biophys.* **2004**, *31*, 185–187.
  - 14 A. MARTUCCI, J. FICK, S. E. LEBLANC, M. LOCASCIO, A. HACHE, Optical properties of PbS quantum dot doped sol-gel films, *J. Non-Cryst. Solids* **2004**, *345–346*, 639–642.
  - 15 D. S. KOKTYSH, X. R. LIANG, B. G. YUN, I. PASTORIZA-SANTOS, R. L. MATTS, M. GIERSIG, C. SERRA-RODRIGUEZ, L. M. LIZ-MARZAN, N. A. KOTOV, Biomaterials by design: Layer-by-layer assembled ion-selective and biocompatible films of TiO<sub>2</sub> nanoshells for neurochemical monitoring, *Adv. Funct. Mater.* **2002**, *12*, 255–265.
  - 16 T. HIRAI, Y. ASADA, Preparation of ZnO nanoparticles in a reverse micellar system and their photoluminescence properties, *J. Colloid Interface Sci.* **2005**, *284*, 184–189.
  - 17 R. A. GANEEV, M. BABA, A. I. RYASNYANSKY, M. SUZUKI, H. KURODA, Laser ablation of GaAs in liquids: Structural, optical, and nonlinear optical characteristics of colloidal solutions, *Appl. Phys. B* **2005**, *80*, 595–601.
  - 18 H. YANG, R. YANG, X. WAN, W. WAN, Structure and photoluminescence of Ge nanoparticles with different sizes embedded in SiO<sub>2</sub> glasses fabricated by a sol-gel method, *J. Cryst. Growth* **2004**, *261*, 549–556.
  - 19 M. MIKHAYLOVA, D. K. KIM, N. BOBRYsheva, M. OSMOLOWSKY, V. SEMENOV, T. TSAKALAKOS, M. MUHAMMED, Superparamagnetism of magnetite nanoparticles: Dependence on surface modification, *Langmuir* **2004**, *20*, 2472–2477.
  - 20 D. K. KIM, D. KAN, T. VERES, F. NORMADIN, J. K. LIAO, H. H. KIM, S.-H. LEE, M. ZAHN, M. MUHAMMED,

- Monodispersed Fe–Pt nanoparticles for biomedical applications, *J. Appl. Phys.* **2005**, *97*, 10Q918.
- 21 A. S. EDELSTEIN, R. C. CAMMARATA, *Nanomaterials: Synthesis, Properties and Applications*, Institute of Physics Publishing, London, **1998**.
  - 22 A. K. GUPTA, M. GUPTA, Synthesis and surface engineering of iron oxide nanoparticles for biomedical applications, *Biomaterials* **2005**, *26*, 3995–4021.
  - 23 K. S. SOPPIMATH, T. M. AMINABHAVI, A. R. KULKARNI, W. E. RUDZINSKI, Biodegradable polymeric nanoparticles as drug delivery devices, *J. Controlled Release* **2001**, *70*, 1–20.
  - 24 M. OKADA, Chemical syntheses of biodegradable polymers, *Prog. Polym. Sci.* **2002**, *27*, 87–133.
  - 25 Z. S. MA, H. H. YEOH, L. Y. LIM, Formulation pH modulates the interaction of insulin with chitosan nanoparticles, *J. Pharm. Sci.* **2002**, *91*, 1396–1404.
  - 26 E. RUEL-GARIEPY, A. CHENITE, C. CHAPUT, S. GUIRGUIS, J. C. LEROUX, Characterization of thermosensitive chitosan gels for the sustained delivery of drugs, *Int. J. Pharm.* **2000**, *203*, 89–98.
  - 27 K. A. JANES, M. P. FRESNEAU, A. MARAZUELA, A. FABRA, M. J. ALONSO, Chitosan nanoparticles as delivery systems for doxorubicin, *J. Controlled Release* **2001**, *73*, 255–267.
  - 28 A. M. DE CAMPOS, A. SANCHEZ, M. J. ALONSO, Chitosan nanoparticles: A new vehicle for the improvement of the delivery of drugs to the ocular surface. Application to cyclosporin A, *Int. J. Pharm.* **2001**, *224*, 159–168.
  - 29 Y. HU, X. Q. JIANG, Y. DING, H. X. GE, Y. Y. YUAN, C. Z. YANG, Synthesis and characterization of chitosan-poly(acrylic acid) nanoparticles, *Biomaterials* **2002**, *23*, 3193–3201.
  - 30 S. MITRA, U. GAUR, P. C. GHOSH, A. N. MAITRA, Tumour targeted delivery of encapsulated dextran-doxorubicin conjugate using chitosan nanoparticles as carrier, *J. Controlled Release* **2001**, *74*, 317–323.
  - 31 Y. S. JO, D. K. KIM, Y. K. JEONG, K. J. KIM, M. MUHAMMED, Encapsulation of bovine serum albumin in temperature-programmed “shell-in-shell” structures, *Macromol. Rapid Commun.* **2003**, *24*, 957–962.
  - 32 S. Y. KIM, I. G. SHIN, Y. M. LEE, Preparation and characterization of biodegradable nanospheres composed of methoxy poly(ethylene glycol) and DL-lactide block copolymer as novel drug carriers, *J. Controlled Release* **1998**, *56*, 197–208.
  - 33 D. KIM, H. EL-SHALL, D. DENNIS, T. MOREY, Interaction of PLGA nanoparticles with human blood constituents, *Colloids Surf., B* **2005**, *40*, 83–91.
  - 34 S. Y. KIM, I. L. G. SHIN, Y. M. LEE, C. S. CHO, Y. K. SUNG, Methoxy poly(ethylene glycol) and epsilon-caprolactone amphiphilic block copolymeric micelle containing indomethacin. II. Micelle formation and drug release behaviours, *J. Controlled Release* **1998**, *51*, 13–22.
  - 35 P. CALVO, J. L. VILAJO, M. J. ALONSO, Evaluation of cationic polymer-coated nanocapsules as ocular drug carriers, *Int. J. Pharm.* **1997**, *153*, 41–50.
  - 36 P. AHLIN, J. KRISTL, A. KRISTL, F. VREGER, Investigation of polymeric nanoparticles as carriers of enalaprilat for oral administration, *Int. J. Pharm.* **2002**, *239*, 113–120.
  - 37 J. L. ARIAS, V. GALLARDO, S. A. GOMEZ-LOPERA, R. C. PLAZA, A. V. DELGADO, Synthesis and characterization of poly(ethyl-2-cyanoacrylate) nanoparticles with a magnetic core, *J. Controlled Release* **2001**, *77*, 309–321.
  - 38 N. KUMAR, M. N. V. RAVIKUMAR, A. J. DOMB, Biodegradable block copolymers, *Adv. Drug Deliv. Rev.* **2001**, *53*, 23–44.
  - 39 V. G. ROULLIN, J. R. DEVERRE, L. LEMAIRE, F. HINDRE, M. C. VENIER-JULIENNE, R. VIENET, J. P. BENOIT, Anti-cancer drug diffusion within living rat brain tissue: An experimental study using [H-3](6)-5-fluorouracil-loaded PLGA microspheres, *Eur. J. Pharm. Biopharm.* **2002**, *53*, 293–299.

- 40 K. AVGOUSTAKIS, A. BELETSI, Z. PANAGI, P. KLEPETSANIS, A. G. KARYDAS, D. S. ITHAKISSIOS, PLGA-mPEG nanoparticles of cisplatin: In vitro nanoparticle degradation, in vitro drug release and in vivo drug residence in blood properties, *J. Controlled Release* **2002**, *79*, 123–135.
- 41 T. GORNER, R. GREF, D. MICHENOT, F. SOMMER, M. N. TRAN, E. DELLACHERIE, Lidocaine-loaded biodegradable nanospheres. I. Optimization of the drug incorporation into the polymer matrix, *J. Controlled Release* **1999**, *57*, 259–268.
- 42 M. POLAKOVIC, T. GORNER, R. GREF, E. DELLACHERIE, Lidocaine loaded biodegradable nanospheres. II. Modelling of drug release, *J. Controlled Release* **1999**, *60*, 169–177.
- 43 M. T. PERACCHIA, R. GREF, Y. MINAMITAKE, A. DOMB, N. LOTAN, R. LANGER, PEG-coated nanospheres from amphiphilic diblock and multiblock copolymers: Investigation of their drug encapsulation and release characteristics, *J. Controlled Release* **1997**, *46*, 223–231.
- 44 L. MU, S. S. FENG, A novel controlled release formulation for the anticancer drug paclitaxel (Taxol (R)): PLGA nanoparticles containing vitamin E TPGS, *J. Controlled Release* **2003**, *86*, 33–48.
- 45 M. S. ROMERO-CANO, B. VINCENT, Controlled release of 4-nitroanisole from poly(lactic acid) nanoparticles, *J. Controlled Release* **2002**, *82*, 127–135.
- 46 S. GHASSABIAN, T. EHTEZAZI, S. M. FORUTAN, S. A. MORTAZAVI, Dexamethasone-loaded magnetic albumin microspheres: Preparation and in vitro release, *Int. J. Pharm.* **1996**, *130*, 49–55.
- 47 J. F. W. NIJSEN, M. J. VAN STEENBERGERN, H. KOIJMAN, H. TALSMA, L. M. J. KROON-BATENBURG, M. VAN DE WEERT, P. P. VAN RIJK, A. DE WITTE, A. D. V. SCHIP, Characterization of poly(L-lactic acid) microspheres loaded with holmium acetylacetonate, *Biomaterials* **2001**, *22*, 3073–3081.
- 48 W. I. LI, K. W. ANDERSON, P. P. DELUCA, Kinetic and thermodynamic modeling of the formation of polymeric microspheres using solvent extraction/evaporation method, *J. Controlled Release* **1995**, *37*, 187–198.
- 49 J. C. GAYET, G. FORTIER, High water content BSA-PEG hydrogel for controlled release device: Evaluation of the drug release properties, *J. Controlled Release* **1996**, *38*, 177–184.
- 50 T. VERRECCHIA, G. SPENLEHAUER, D. V. BAZILE, A. MURRYBRELIER, Y. ARCHIMBAUD, M. VEILLARD, Non-stealth (poly(lactic acid albumin)) and stealth (poly(lactic acid-polyethylene glycol)) nanoparticles as injectable drug carriers, *J. Controlled Release* **1995**, *36*, 49–61.
- 51 P. QUELLEC, R. GREF, L. PERRIN, E. DELLACHERIE, F. SOMMER, J. M. VERBAVATZ, M. J. ALONSO, Protein encapsulation within polyethylene glycol-coated nanospheres. I. Physicochemical characterization, *J. Biomed. Mater. Res.* **1998**, *42*, 45–54.
- 52 J. SLAGER, A. J. DOMB, Biopolymer stereocomplexes, *Adv. Drug Deliv. Rev.* **2003**, *55*, 549–583.
- 53 J. M. BEZEMER, R. RADERSMA, D. W. GRIJPMMA, P. J. DIJKSTRA, C. A. VAN BLITTERSWIJK, J. FEIJEN, Microspheres for protein delivery prepared from amphiphilic multiblock copolymers 1. Influence of preparation techniques on particle characteristics and protein delivery, *J. Controlled Release* **2000**, *67*, 233–248.
- 54 T. MORITA, Y. HORIKIRI, T. SUZUKI, H. YOSHINO, Applicability of various amphiphilic polymers to the modification of protein release kinetics from biodegradable reservoir-type microspheres, *Eur. J. Pharm. Biopharm.* **2001**, *51*, 45–53.
- 55 H. Y. KWON, J. Y. LEE, S. W. CHOI, Y. S. JANG, J. H. KIM, Preparation of PLGA nanoparticles containing estrogen by emulsification-diffusion method, *Colloids Surf., A* **2001**, *182*, 123–130.
- 56 S. H. YUK, S. H. CHO, S. H. LEE, pH/temperature-responsive polymer composed of poly((N,N-dimethylamino)ethyl methacrylate-co-



- ethylacrylamide), *Macromolecules* **1997**, *30*, 6856–6859.
- 57 S. R. SERSHEN, S. L. WESTCOTT, N. J. HALAS, J. L. WEST, Temperature-sensitive polymer-nanoshell composites for photothermally modulated drug delivery, *J. Biomed. Mater. Res.* **2000**, *51*, 293–298.
- 58 F. EECKMAN, A. J. MOES, K. AMIGHI, Surfactant induced drug delivery based on the use of thermosensitive polymers, *J. Controlled Release* **2003**, *88*, 105–116.
- 59 J. E. CHUNG, M. YOKOYAMA, K. SUZUKI, T. AOYAGI, Y. SAKURAI, T. OKANO, Reversibly thermo-responsive alkyl-terminated poly(N-isopropylacrylamide) core-shell micellar structures, *Colloids Surf., B* **1997**, *9*, 37–48.
- 60 S. B. ZHOU, X. M. DENG, H. YANG, Biodegradable poly(epsilon-caprolactone)-poly(ethylene glycol) block copolymers: Characterization and their use as drug carriers for a controlled delivery system, *Biomaterials* **2003**, *24*, 3563–3570.
- 61 Y. Y. YANG, T. S. CHUNG, X. L. BAI, W. K. CHAN, Effect of preparation conditions on morphology and release profiles of biodegradable polymeric microspheres containing protein fabricated by double-emulsion method, *Chem. Eng. Sci.* **2000**, *55*, 2223–2236.
- 62 Y. S. JO, D. K. KIM, M. MUHAMMED, Synchronous delivery systems composed of Au nanoparticles and stimuli-sensitive diblock terpolymer, *J. Mater. Sci.: Mater. Med.* **2004**, *15*, 1291–1295.
- 63 F. AHMED, D. E. DISCHER, Self-porating polymersomes of PEG-PLA and PEG-PCL: Hydrolysis-triggered controlled release vesicles, *J. Controlled Release* **2004**, *96*, 37–53.
- 64 R. HEJAZI, M. AMIJI, Chitosan-based gastrointestinal delivery systems, *J. Controlled Release* **2003**, *89*, 151–165.
- 65 K. G. H. DESAI, H. J. PARK, Preparation and characterization of drug-loaded chitosan-tripolyphosphate microspheres by spray drying, *Drug Dev. Res.* **2005**, *64*, 114–128.
- 66 R. LANGER, Drug delivery and targeting, *Nature* **1998**, *392*, 5–10.
- 67 D. G. ANDERSON, J. A. BURDICK, R. LANGER, Materials science – Smart biomaterials, *Science* **2004**, *305*, 1923–1924.
- 68 C. CHARNAY, S. BEGU, C. TOURNEPETEILH, L. NICOLE, D. A. LERNER, J. M. DEVOISSELLE, Inclusion of ibuprofen in mesoporous templated silica: Drug loading and release property, *Eur. J. Pharm. Biopharm.* **2004**, *57*, 533–540.
- 69 A. UCHIDA, Y. SHINTO, N. ARAKI, K. ONO, Slow release of anticancer drugs from porous calcium hydroxyapatite ceramic, *J. Orthop. Res.* **1992**, *10*, 440–445.
- 70 C. V. UGLEA, I. ALBU, A. VATAJANU, M. CROITORU, S. ANTONIU, L. PANAITESCU, R. M. OTTENBRITE, Drug-delivery systems based on inorganic materials. 1. Synthesis and characterization of a zeolite-cyclophosphamide system, *J. Biomater. Sci. Polym. Ed.* **1994**, *6*, 633–637.
- 71 S. PHADTARE, A. KUMAR, V. P. VINOD, C. DASH, D. V. PALASKAR, M. RAO, P. G. SHUKLA, S. SIVARAM, M. SASTRY, Direct assembly of gold nanoparticle “shells” on polyurethane microsphere “cores” and their application as enzyme immobilization templates, *Chem. Mater.* **2003**, *15*, 1944–1949.
- 72 A. GOLE, C. DASH, V. RAMAKRISHNAN, S. R. SAINKAR, A. B. MANDALE, M. RAO, M. SASTRY, Pepsin-gold colloid conjugates: Preparation, characterization, and enzymatic activity, *Langmuir* **2001**, *17*, 1674–1679.
- 73 A. GOLE, C. DASH, C. SOMAN, S. R. SAINKAR, M. RAO, M. SASTRY, On the preparation, characterization, and enzymatic activity of fungal protease-gold colloid bioconjugates, *Bioconjug. Chem.* **2001**, *12*, 684–690.
- 74 A. GOLE, S. VYAS, S. PHADTARE, A. LACHKE, M. SASTRY, Studies on the formation of bioconjugates of endoglucanase with colloidal gold, *Colloids Surf., B* **2002**, *25*, 129–138.
- 75 A. CSAKI, G. MAUBACH, D. BORN, J. REICHERT, W. FRITZSCHE, DNA-based

- molecular nanotechnology, *Single Mol.* **2002**, 3, 275–280.
- 76 A. SCHROEDTER, H. WELLER, Ligand design and bioconjugation of colloidal gold nanoparticles, *Angew. Chem. Int. Ed.* **2002**, 41, 3218–3221.
- 77 R. C. MUCIC, J. J. STORHOFF, C. A. MIRKIN, R. L. LETSINGER, DNA-directed synthesis of binary nanoparticle network materials, *J. Am. Chem. Soc.* **1998**, 120, 12674–12675.
- 78 V. G. POL, A. GEDANKEN, J. CALDERON-MORENO, Deposition of gold nanoparticles on silica spheres: A sonochemical approach, *Chem. Mater.* **2003**, 15, 1111–1118.
- 79 M. S. FLEMING, D. R. WALT, Stability and exchange studies of alkanethiol monolayers on gold-nanoparticle-coated silica microspheres, *Langmuir* **2001**, 17, 4836–4843.
- 80 K. S. MAYYA, B. SCHOELER, F. CARUSO, Preparation and organization of nanoscale polyelectrolyte-coated gold nanoparticles, *Adv. Funct. Mater.* **2003**, 13, 183–188.
- 81 Z. J. LIANG, A. SUSHA, F. CARUSO, Gold nanoparticle-based core-shell and hollow spheres and ordered assemblies thereof, *Chem. Mater.* **2003**, 15, 3176–3183.
- 82 N. NATH, A. CHILKOTI, Creating “smart” surfaces using stimuli responsive polymers, *Adv. Mater.* **2002**, 14, 1243–1247.
- 83 G. F. PACIOTTI, L. MYER, D. WEINREICH, D. GOIA, N. PAVEL, R. E. McLAUGHLIN, L. TAMARKIN, Colloidal gold: A novel nanoparticle vector for tumor directed drug delivery, *Drug Deliv.* **2004**, 11, 169–183.
- 84 S. A. SVAROVSKY, Z. SZEKELY, J. J. BARCHI, Synthesis of gold nanoparticles bearing the Thomsen-Friedenreich disaccharide: A new multivalent presentation of an important tumor antigen, *Tetrahedron: Asymmetry* **2005**, 16, 587–598.
- 85 M. J. EGORIN, Overview of recent topics in clinical pharmacology of anticancer agents, *Cancer Chemother. Pharmacol.* **1998**, 42, S22–S30.
- 86 M. G. CASONE, L. LAZZERI, C. CARMIGNANI, Z. H. ZHU, Gelatin nanoparticles produced by a simple W/O emulsion as delivery system for methotrexate, *J. Mater. Sci.: Mater. Med.* **2002**, 13, 523–526.
- 87 R. JALLI, J. R. NIXON, Biodegradable poly(lactic acid) and poly(lactide-co-glycolide) microcapsules – Problems associated with preparative techniques and release properties, *J. Microencapsul.* **1990**, 7, 297–325.
- 88 C. M. HASKELL, *Cancer Treatment*, WB Saunders Co., Philadelphia, **1990**.
- 89 B. A. CHABNER, C. E. MYERS, *Cancer: Principles and Practice of Oncology, Clinical Pharmacology of Cancer Chemotherapy*, JB Lippincott Co, Philadelphia, **1989**.
- 90 J. C. LEROUX, E. ALLEMANN, E. DOELKER, R. GURNY, New approach for the preparation of nanoparticles by an emulsification-diffusion method, *Eur. J. Pharm. Biopharm.* **1995**, 41, 14–18.
- 91 F. L. MI, Y. M. LIN, Y. B. WU, S. S. SHYU, Y. H. TSAI, Chitin/PLGA blend microspheres as a biodegradable drug-delivery system: Phase-separation, degradation and release behavior, *Biomaterials* **2002**, 23, 3257–3267.
- 92 A. SALGUEIRO, F. GAMISANS, M. ESPINA, X. ALCOBER, M. L. GARCIA, M. A. EGEA, Cyclophosphamide-loaded nanospheres: Analysis of the matrix structure by thermal and spectroscopic methods, *J. Microencapsul.* **2002**, 19, 305–310.
- 93 A. SALGUEIRO, M. A. EGEA, M. ESPINA, O. VALLS, M. L. GARCIA, Stability and ocular tolerance of cyclophosphamide-loaded nanospheres, *J. Microencapsul.* **2004**, 21, 213–223.
- 94 K. D. JUDY, A. OLIVI, K. G. BUAHIN, A. DOMB, J. I. EPSTEIN, O. M. COLVIN, H. BREM, Effectiveness of controlled-release of a cyclophosphamide derivative with polymers against rat gliomas, *J. Neurosurg.* **1995**, 82, 481–486.
- 95 C. GUERIN, A. OLIVI, J. D. WEINGART, H. C. LAWSON, H. BREM, Recent advances in brain tumor therapy: Local intracerebral drug delivery by polymers, *Invest. New Drugs* **2004**, 22, 27–37.

- 96 M. TAKENAGA, Application of lipid microspheres for the treatment of cancer, *Adv. Drug Deliv. Rev.* **1996**, *20*, 209–219.
- 97 J. F. ELLENA, M. LE, D. S. CAFISO, R. M. SOLIS, M. LANGSTON, M. B. SANKARAM, Distribution of phospholipids and triglycerides in multivesicular lipid particles, *Drug Deliv.* **1999**, *6*, 97–106.
- 98 K. J. ZHU, J. X. ZHANG, C. WANG, H. YASUDA, A. ICHIMARU, K. YAMAMOTO, Preparation and in vitro release behaviour of 5-fluorouracil-loaded microspheres based on poly(L-lactide) and its carbonate copolymers, *J. Microencapsul.* **2003**, *20*, 731–743.
- 99 P. MENEI, M. BOISDRONCELLE, A. CROUE, G. GUY, J. P. BENOIT, Effect of stereotactic implantation of biodegradable 5-fluorouracil-loaded microspheres in healthy and C6 glioma-bearing rats, *Neurosurgery* **1996**, *39*, 117–123.
- 100 P. MENEI, M. C. VENIER, E. GAMELIN, J. P. SAINT-ANDRE, G. HAYEK, E. JADAUD, D. FOURNIER, P. MERCIER, G. GUY, J. P. BENOIT, Local and sustained delivery of 5-fluorouracil from biodegradable microspheres for the radiosensitization of glioblastoma – A pilot study, *Cancer* **1999**, *86*, 325–330.
- 101 P. MENEI, E. JADAUD, N. FAISANT, M. BOISDRON-CELLE, S. MICHALAK, D. FOURNIER, M. DELHAYE, J. P. BENOIT, Stereotaxic implantation of 5-fluorouracil-releasing microspheres in malignant glioma – A phase I study, *Cancer* **2004**, *100*, 405–410.
- 102 D. S. FISCHER, M. T. KNOBF, H. J. DURIVAGE, N. BEAULIEU, *The Cancer Chemotherapy Handbook*, Mosby-Year Book, Inc., New York, **2003**.
- 103 Y. ZHANG, R. X. ZHUO, Synthesis and drug release behavior of poly(trimethylene carbonate)-poly(ethylene glycol)-poly(trimethylene carbonate) nanoparticles, *Biomaterials* **2005**, *26*, 2089–2094.
- 104 L. MANIL, J. C. DAVIN, C. DUCHENNE, C. KUBIAK, J. FOIDART, P. COUVREUR, P. MAHIEU, Uptake of nanoparticles by rat glomerular mesangial cells in vivo and in-vitro, *Pharm. Res.* **1994**, *11*, 1160–1165.
- 105 F. BRASSEUR, P. COUVREUR, B. KANTE, L. DECKERSPASSAU, M. ROLAND, C. DECKERS, P. SPEISER, Actinomycin-D adsorbed on polymethylcyanoacrylate nanoparticles – Increased efficiency against an experimental tumor, *Eur. J. Cancer* **1980**, *16*, 1441–1445.
- 106 B. KANTE, P. COUVREUR, V. LENAERTS, P. GUIOT, M. ROLAND, P. BAUDHUIIN, P. SPEISER, Tissue distribution of [actinomycin]-H-3 D adsorbed on polybutylcyanoacrylate nanoparticles, *Int. J. Pharm.* **1980**, *7*, 45–53.
- 107 R. H. BLUM, S. K. CARTER, K. AGRE, Clinical review of bleomycin – New antineoplastic agent, *Cancer* **1973**, *31*, 903–914.
- 108 I. F. UCHEGBU, A. G. SCHATZLEIN, L. TETLEY, A. I. GRAY, J. SLUDDEN, S. STDDIQUE, E. MOSHA, Polymeric chitosan-based vesicles for drug delivery, *J. Pharm. Pharmacol.* **1998**, *50*, 453–458.
- 109 A. HAGIWARA, T. TAKAHASHI, O. KOJIMA, K. KITAMURA, C. SAKAKURA, S. SHOUBAYASHI, K. OSAKI, A. IWAMOTO, M. LEE, K. FUJITA, Endoscopic local injection of a new drug-delivery format of peplomycin for superficial esophageal cancer – A pilot-study, *Gastroenterology* **1993**, *104*, 1037–1043.
- 110 K. G. LAU, S. CHOPRA, Y. MAITANI, Entrapment of bleomycin in ultra-deformable liposomes, *Stp Pharma Sci.* **2003**, *13*, 237–239.
- 111 K. G. LAU, Y. HAITTORI, S. CHOPRA, E. A. O'TOOLE, A. STOREY, T. NAGAI, Y. MAITANI, Ultra-deformable liposomes containing bleomycin: In vitro stability and toxicity on human cutaneous keratinocyte cell lines, *Int. J. Pharm.* **2005**, *300*, 4–12.
- 112 R. S. BENJAMIN, Clinical-pharmacology of daunorubicin, *Cancer Treat. Rep.* **1981**, *65*, 109–110.
- 113 E. A. FORSSEN, The design and development of DaunoXome(R) for solid tumor targeting in vivo, *Adv. Drug Deliv. Rev.* **1997**, *24*, 133–150.

## 7

# Critical Analysis of Cancer Therapy using Nanomaterials

*Lucienne Juillerat-Jeanneret*

### 7.1

#### Introduction

The treatment of diseases such as cancer is challenging because these pathologies involve dysregulation of endogenous and often essential cellular processes. Cancer cells replicate faster than most non-tumoral cells, and the vast majority of presently used therapies capitalize on these differences. More selective therapies, such as anti-angiogenic therapies, are under development and/or clinical evaluation, whereas a few targeted therapies are in clinical use, such as antiestrogen therapies in estrogen receptor-positive breast cancer. With targeted approaches, not only patient survival will increase due to improved treatment efficiency, but also the quality of life of patients will improve by decreasing side effects to normal cells. Most solid tumors possess unique features, such as extensive angiogenesis, defective vascular architecture, increased vascular permeability, impaired lymphatic drainage, which can also be used as therapeutic targets. Nanoparticles can take advantage of these features and act as a vehicle to selectively and specifically deliver anti-cancer drugs to tumors, either by using passive mechanisms such as increased vascular permeability or acting as drug reservoir in a defined location, or by using active targeting. These combined approaches would result not only in increased efficacy but also in decreased collateral side effects. However, targeting strategies and chemical synthesis routes need to be improved, and the mechanisms of interactions of these functionalized nanostructures with living materials need to be better understood.

This chapter describes not only the tools of nanoparticle technology that can be used to treat cancer, as many excellent reviews (indicated below the section headings) have been published, but rather critically reviews and discusses the advantages and drawbacks of nanoparticles for the *targeted* delivery of anticancer agents to defined cells of human cancers. Approaches that have been developed or are under development to achieve improved cancer therapy using nanoparticles as targeting delivery agents for anticancer drugs are reviewed, and the problems and issues that need to be answered to validate these approaches are summarized. Section 7.2 reviews the characteristics of human tumors that can be used to develop anticancer

treatments. Section 7.3 covers the characteristics of already developed nanoparticles, considering the chemical, biophysical and biological demands of such devices. Information from the previous two sections is combined in Section 7.4 to review the characteristics of already developed, or under development, nanoparticles for anticancer treatments using drugs employed in clinics or under development, photodynamic and gene therapy approaches, or magnetically controlled delivery. Section 7.5 describes the defects and characteristics of human tumors that can be used to develop targeted anticancer treatments using nanoparticles, via cancer-associated cells, cancer cell molecules, or by achieving intracellular delivery, and also describes the chemical challenges involved in preparing these nanovectors. Section 7.6 hypothesizes how nanoparticles may result in the delivery of anticancer drugs in drug-resistant human cancers. Issues not yet resolved issues concerning the potential toxicity of nanoparticulate vectors to patients and the general population are covered in Section 7.7. Finally, Section 7.8 describes what might be the ideal nanoparticle in the context of targeted treatment of human cancer using nanodevices.

## 7.2

### Anticancer Therapies

For a more extensive review see Ref. [1] and references herein. Effective therapies of cancer capitalize on differences between diseased and healthy tissues that can be targeted with drugs. Cancer drugs used in patients target the cell cycle, DNA replication, and cytoskeletal assembly. The general toxicity to the whole body of current anticancer chemotherapeutic treatments, resulting in important side effects such as sterility, loss of digestive capacities and appetite, loss of hair, defects in immune functions, etc., is a challenge facing the development of new modalities of cancer treatment. In addition, combination therapies or scheduled therapies improved patient response to chemotherapy regimen. One of the main challenges in cancer treatment is no longer the development of efficient drugs but the improvement of drug selectivity. More recently, the targeting of growth receptors and cellular signaling pathways, “targeted therapeutics”, has become a new approach in cancer treatment. However, even targeted and combined therapies suffer from side effects that result from imperfect selectivity for diseased tissue. The availability of novel molecular targets and drug delivery systems that distinguish diseased from healthy cells could vastly amplify therapeutic opportunities. The identification of new disease-associated changes in cellular biology, and the development of associated tools, that may be used to improve selectivity in diagnosis, treatment and evaluation of response to treatment will be the next challenges in cancer therapy. Most cancer-related deaths occur as a consequence of metastasis, and the major problem facing oncologists treating cancer is metastatic disease. Metastasis of tumor cells to organs distant from the original primary tumor site involves about half of all cancers and is generally detected only at an advanced stage of metastatic disease. Successful eradication of metastatic lesions still depends on the early detection of

metastases, which only rarely happens. Therefore, devising new means to detect metastatic tumor lesions at the earliest possible stage, and at the same time to be able to treat them, would be an important breakthrough in cancer treatment. Magnetic nanoparticles can be used for this purpose. Therefore, one goal in the field of cancer is to develop chemically derivatized nanoparticles able to target tumor cells and tumor-associated stromal cells via specific recognition mechanisms, and dual cancer detection such as magnetic resonance imaging and cancer therapy using cell-directed drugs.

Neoplastic tissue can be divided into three compartments, vascular, interstitial and cellular, and cancers are constituted of several cell types:

- Endothelial cells and pericytes, either overnumbered or undernumbered;
- immune/inflammatory cells, including macrophages and lymphocytes, and fibroblasts and myofibroblasts;
- normal cells and tumor cells derived from these normal cells;
- and by the absence of a well-defined lymphatic network.

Tumor vasculature is highly abnormal, proliferating, activated, tortuous, and presenting increased permeability and gaps, with pores between 350 and 800 nm, and a cutoff around 400 nm. Tumor vascularization is generally poorly perfused. Tumor interstitium is predominantly constituted of a protein network, including collagens, elastin, proteoglycans and glycoproteins, forming a hydrophilic gel and producing high interstitial osmotic pressure, leading to an outward convective fluid flow. The tumor environment is oxidative and acidic, and thus ionization of basic drugs may decrease their interstitial transport and oxidation destroy their anti-cancer properties. The transport of drugs in the interstitium will thus be governed by interstitial osmotic pressure and the relative chemical composition and characteristics of drugs and the interstitium.

Therefore, the delivery of a therapeutic agent to tumor must:

1. Resist hydrostatic, hydrophilic/hydrophobic and biophysical/biochemical barriers;
2. resist cellular resistance to treatment;
3. resist biotransformation, degradation and clearance mechanisms;
4. reach its treatment target: extracellular or intracellular compartments, tumor cells or vascular cells, etc.;
5. achieve distribution in all tumor areas even with low vascularization, or poor perfusion;
6. and be active in tumors at efficient concentrations, without unacceptable side effects to non-tumoral cells.

Both tissue- and cell-distribution of anticancer drugs can be controlled and improved by their entrapment in colloidal nanoparticles, increasing anti-tumor efficacy, reversing resistance mechanisms and decreasing side effects. Active tumor targeting with long-circulating nanoparticles decorated with targeting agents is the

main development required to achieve these goals. The association of drugs with colloidal nanoparticles may be a way to overcome many of these resistance mechanisms of tumors to treatment and increase selectivity. In this context, nanoparticles are defined as submicroscopic colloidal systems, which may act as a drug vehicle either as nanospheres (a matrix system in which the drug is dispersed) or nanocapsules, which are reservoirs in which the drug is confined in a hydrophobic or hydrophilic core surrounded by a single polymeric membrane. The structure of the polymer and the method of trapping the drugs in the nanoparticles will define the drug release kinetics and characteristics. The necessary characteristics to be useful in cancer treatment, and the drug–nanoparticle systems that have reached clinical use, are under clinical evaluation or are under development will be reviewed.

### 7.3

#### Characteristics of Nanoparticles for Cancer Therapy

For more extensive reviews see Refs. [2–6] and references herein. The treatment of cancer is limited by the inability to deliver therapeutic agents in such a way that most drug molecules will selectively reach the desired targets, with only marginal collateral damage. To achieve such efficient treatments, two main goals must be met:

- Increasing targeting selectivity for defined organ, tissue or cells.
- Devising a therapeutic formulation able to overcome the biological barriers that prevent drugs efficiently reaching their targets.

However, the realization of such a system faces formidable challenges, which include:

- Identification of neoplastic biomarkers as biological targets, and their evolution over time.
- Development of biotechnologies to develop biomarker-targeted delivery of multiple therapeutic agents, coupled to the possibility to avoid biological barriers and various resistance mechanisms.

Nanoparticles are interesting for medical application since they present a large surface for functionalization with drugs compared to larger particles made of the same materials, and hopefully achieve targeted drug delivery. They can pass epithelial and vascular barriers. Thus, nanoparticles have the potential to provide opportunities to meet the challenges of cancer therapy, and also of therapeutic approaches for other disorders.

The dawning era of polymer therapeutics started with improved knowledge of polymer characteristics and the development of polymer chemistry (reviewed in Ref. [3]). Initially, polymer–drugs, polymer–proteins, and, in particular, PEGylated derivatives and HPMA [*N*-(hydroxypropyl)-methacrylamide] copolymers have been

used in the context of anticancer therapy [7], and are the precursors of nanoparticulate systems. Self-assembling block-copolymers were then evaluated to deliver drugs to cancer. A pluronic block copolymer-doxorubicin was able to circumvent Pgp [8, 9], and PEG-polyAsp-doxorubicin accumulated preferentially in tumors due to vascular leakage [10, 11], while the increased size prevented back-diffusion and renal clearance when evaluated in clinical trials. These approaches opened the way to nanotechnology for drug delivery.

### 7.3.1

#### Nanovectors

Nanotechnology implies that the drug delivery device is man-made, and of dimensions in the nm range (sub-cellular size), which includes nanovectors such as liposomes or monomeric or block copolymeric nanoparticles for the (targeted) delivery of anticancer drugs, imaging contrast agents such as gadolinium or iron-oxide nanosized magnetic resonance imaging contrast agents (cf., for example, Chapters 3 and 5), or quantum dots. First, basic definitions for the various nanoparticulate systems in the context of cancer are given as they will be developed in this chapter. Nanoparticles are non-viral solid nanovectors made of one or several different materials, including water-soluble polymers, whose upper size limit is  $<1 \mu\text{m}$ , generally  $<100 \text{ nm}$ . These nanostructures have unique properties, such as modification of the properties, spacing and arrangement of surface atoms, and physics and chemistry compared to larger particles of the same material, and they also have a large surface area to volume ratio. Nanoparticles may be built of polymeric drugs (nanosuspensions), polymer–drug conjugates, polymer–protein conjugates, polymeric drug-micelles, etc. Micelles are self-assembling colloidal aggregates of amphipathic molecules–polymeric block copolymers to give polymeric micelles, which occurs when the concentration reaches the crucial micelle concentration (c.m.c.). Polyplexes are polyelectrolyte complexes formed by a polycation and an anionic molecule, generally an oligonucleotide. Dendrimers are macromolecule that contain symmetrically arranged branches arising from a multifunctional core, to which a precise number of terminal groups are added stepwise. Drug nanosuspensions are insoluble nanocrystals of drugs, generally coated with a surfactant.

Rational approaches in design and surface engineering for site-specific delivery of drugs, genetic material and diagnostic agents, to tissues, cells and intracellular cell compartments, after intravascular, parenteral, intraperitoneal, etc., administration, include:

- Liposomes: closed vesicles formed by hydration of phospholipids above their transition temperature. Nanoliposomes are bilayer structures of less than 100 nm, surrounding the drug entrapped in the aqueous space. Drugs can also be contained in the lipid space between bilayers. Surface modification is possible, and nucleic acids are adsorbed on cationic liposomes by ion-pairing. These structures have been the first to reach clinical use.
- Micelles: amphiphilic aggregates,  $<50 \text{ nm}$ , made of hydrophilic (A) and hydro-



phobic (B) block copolymers (AB or ABA), in which hydrophobic or hydrophilic drugs are physically trapped or covalently bound. Drugs may include nucleic acids for transfection and gene therapy.

- Nanospheres: made of polymer (synthetic or natural) aggregates (tens to hundreds nm size) in which the drug is either dissolved, entrapped, encapsulated or covalently attached. Surface modification is possible.
- Superparamagnetic iron oxide crystals: made of an iron oxide core (5–10 nm) obtained by coprecipitation of  $\text{Fe}^{2+}$  and  $\text{Fe}^{3+}$ , and coated with a polymer [dextran, poly(ethylene glycol), poly(vinyl alcohol), etc.]. Surface modification is possible by covalent links or adsorption (drug, antibodies, nucleic acid, targeting agents). These nanostructures have mainly been used for cancer detection, and are now developed to couple detection with drug delivery.
- Carbohydrates-ceramic nanoparticles: core composed of calcium phosphate or ceramic, surrounded by a polyhydroxyl oligomeric film, on which drugs are adsorbed.
- Dendrimers: highly branched three-dimensional macromolecules that grow by outward-controlled polymerization; drugs are covalently bound at the surface.

Therapeutic agents (chemically synthesized therapeutic small or large drugs, therapeutic peptides or proteins, nucleic acids for gene therapy) can be entrapped, encapsulated, adsorbed, covalently bound either to the surface or at the interior of biodegradable polymeric nanoparticles (Table 7.1). These approaches can improve drug solubility, and also achieve better drug selectivity. Drugs can be made to form small aggregates, surrounded by a water- and bio-compatible, biodegradable poly-

**Tab. 7.1.** Biological characteristics of the polymers.

Polymer	Efficient for
PEG	Increases biocompatibility, increases circulating time, decreases uptake by macrophages
Dextrans	Increases circulating time, decreases aggregation and opsonization, decreases uptake by macrophages
Poly(vinylpyrrolidone)	Increases circulating time, decreases aggregation and opsonization, decreases uptake by macrophages
PVA	Decreased aggregation/coagulation
Polyacrylates	Biostabilization, biocompatibility, increases bioadhesion
Polypeptides	Targeting
Poly(DL-lactide)	Increases biocompatibility, decreases cytotoxicity
Chitosan	Increases biocompatibility, increases hydrophilicity

meric thin layer, improving the biodistribution and bioavailability of drugs. Surface or polymers functionalization with appropriate ligands can allow the targeting of these nanostructures to defined cells, tissues or body locations, depending on the chosen specificity and selectivity of the ligand, improving the therapeutic effectiveness and decreasing side effects of drugs. Finally, the polymer properties may also be defined to respond to changes in pH or redox state, chemical environment, heat (either internal or external), or an external physical stimulus, therefore allowing choice for the rate and location of drug release, e.g., acidic intracellular organelles such as the lysosomes.

The development of nanovectors has given birth to what has been called “nanomedicine”: the applications of nanotechnology for the rational delivery and targeting of pharmaceuticals, therapeutics and diagnostic agents. The next challenges include:

- Identification of precise targets for selective delivery.
- Choice of appropriate nano-carriers.
- Avoidance of mononuclear phagocytes and the reticuloendothelial system, to selectively target either angiogenic cancer-associated endothelial cells or cancer cells, which are key targets in cancer.

### 7.3.2

#### **Biological Issues**

Injection in the blood and lymphatic vessels, but also inhalation or intraperitoneal injection, etc., are possible routes of administration for the delivery of therapeutic nanoparticles. The stability, extracellular or cellular distribution of nanoparticles depend on their surface properties, chemical composition, morphology and size. The main challenges for intravenously injected nanoparticles are rapid opsonization and clearance by the reticuloendothelial system (RES) of the liver and the spleen or excretion by the kidneys (Fig. 7.1). Opsonization by complement proteins, vitronectin, fibronectin, immunoglobulins, lipoproteins, etc. renders nanoparticles recognizable by the major defense systems of the body, the RES and the mononuclear phagocyte system, depending on the surface properties of nanoparticles, their size (< or >200 nm) and surface characteristics. Nanoparticles with a largely hydrophobic surface are efficiently coated with plasma components, trapped in the liver and rapidly removed from circulation, while smaller particles can stay in circulation. More hydrophilic nanoparticles can resist coating process to a variable extent and are more slowly cleared from the blood stream [2]. Therefore, clearance kinetics depend on the chemical and physical properties of the nanoparticles: surface charges and charge density, lipophilic/hydrophilic area ratio, presence of functional and chemically reactive groups. Consequently, successful drug delivery requires careful control of the physicochemical properties (size and surface) of nanovectors. Suppression of opsonization will increase the retention of nanoparticles in locations other than macrophages and so afford a longer circulatory time. In addition, macrophages are heterogeneous, in different tissues and within a tis-

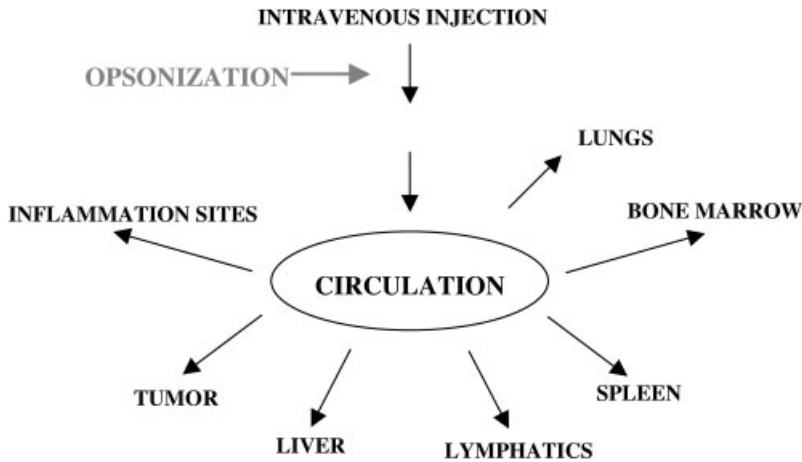


**Fig. 7.1.** Fate and distribution in the body of intravenously injected nanoparticles – their uptake by different organs, according to the particles' size and surface.

sue. PEGylation [the coating of the surface by poly(ethylene glycols)] of nanoparticles has been the main approach up to now to solve opsonization problems and short circulation times. PEG coating decreases liver, spleen, lung, or kidney clearance. A large surface area is also an issue in the aggregation of nanoparticles in a biological environment, determining the effective clearance rates and mechanisms.

### 7.3.3

#### **Nanoparticle Targeting: Passive or Active**

Long circulation times are efficient in both treating circulatory disorders and vascular imaging. Passive targeting depends on vascular leakage and passive diffusion [enhanced permeability and retention (EPR) effect] of nanovectors to achieve drug delivery. Nanoparticles escape from the vasculature compared with virus behavior and is restricted to endothelial fenestration (between 150 and 300 nm) of leaky areas in inflammation or tumors, or splenic filtration for non-deformable nanoparticles (200–250 nm). Initially, targeting was passively achieved at the organ/tissue level by virtue of particle size, 50–200 nm carriers restricting the distribution volume to the blood compartment.

Active (ligand-targeting, cationic lipids or polymers cytotoxic and low circulating times) delivery using selective recognition mechanisms can be achieved with more recent nanoparticles, and is presently under development and evaluation. Therefore, the surface engineering of nanoparticles is a crucial determinant of their biological behavior, and much effort is presently undertaken to improve these modifications (see below). A thorough understanding of the elaborate cell transport ma-

chinery as well as an understanding and the finding of targets to achieve selective delivery will be necessary to fulfill the potential of nanobiotechnologies in cancer.

Many drugs are agonists and antagonists of chemicals inappropriately produced by diseased cells. Intelligent systems should respond to differences in concentration of these chemicals or changes in external biological conditions, e.g., by modification of the polymer lattices, allowing increased or decreased release of drugs, dependent on a biosensor to achieve “intelligent therapeutics”. Delivery of therapeutic agents precisely where and when they are needed in the human body is becoming realistic due to rapid, tremendous progress in physiology, nanoparticle and nanobiotechnology. Nanoparticles can improve the targeting of cytotoxic drugs to cancer only if they can be directed to cancer areas and maintained there for long time periods with their drug cargo for selective and local release of drugs such as alkylating agents, 5-fluorouracyl, platinum derivatives, taxol derivatives, and more selective kinase inhibitors. Chemical bonding, ionic or hydrophobic adsorption or embedding of drugs into nanoparticles have been devised to be sensitive to cancer tissue properties, including high proteolytic or glycolytic activity, high metabolism, low pH, and high oxidative environments in tumors, to further ensure selective release of the drug in the tumor area. The discovery and design of intelligent material will be the next drug-delivery system generation for chronic diseases. These approaches will now be reviewed.

#### 7.4

#### **Nanovectors in Biomedical Applications: Drug Delivery Systems (DDS) for Cancer**

For general reviews see Refs. [6, 12] and references herein. Present treatments for cancer include various unique or combined approaches, encompassing total or partial surgical excision of tumor tissue, chemotherapy and radiotherapy. Anticancer chemotherapeutic drugs are generally administered intravenously, leading to general systemic distribution. As drugs used in cancer chemotherapy are mostly non-selective for tumor or tumor-associated cells, important and deleterious side effects result from their use [2, 13, 14]. These secondary effects in patients result in loss of quality of life and necessitate drugs to alleviate them. Therefore, means are needed to deliver drugs to specific areas of the body, maximizing drug action (exclusively in diseased cells), together with minimizing side effects, and consequently increasing treatment efficiency. Selective or targeted DDS, and in particular nanoparticles, have the potential to achieve the goals of drug-targeted delivery:

- Delivery to a particular organ;
- to a specific cell type (differentiation from tumor and normal cells);
- to a structure within a cell (such as the nucleus in gene therapy, where targeting to the nucleus is a prerequisite of gene expression).

They use (a) physicochemical, (b) biological or (c) chemical methods to control the distribution of drugs to improve the outcome of chemotherapy.

## 7.4.1

**Physicochemical Drug Delivery**

Polymers and colloidal nanocarriers (nanoparticles) can be used for passive or active drug delivery. Passive targeting implies a physiological uptake mechanism (filtration or macrophage sequestration), while active methods involve the use of a recognition ligand.

## 7.4.2

**Biological Drug Delivery**

With biological targeting a specific marker (a target) is selectively expressed on diseased cells and not, or at a much lower level, in normal cells. The targeting agent, such as antibodies, a ligand for a receptor or a lectin, is covalently conjugated via an appropriate spacer to the nanoparticle. It can be directed towards an antigen or receptor residing on or within the target tissue.

## 7.4.3

**Chemical Drug Delivery**

Chemical methods involve the use of modified forms of active drugs, e.g., prodrugs, by exploiting differences in pathophysiological conditions within target tissues (e.g., pH, redox state, enzyme content) and normal tissues.

The efficiency of drug delivery depends strongly on the nanovector size and surface characteristics, controlling the fate of a drug in the organism, and the selective delivery of drugs. The size, zeta potential (surface charge, coating), release characteristics (polymers and linkers), biodegradability and cytotoxicity and encapsulation efficiency are the main factors determining efficient drug delivery. Expression at the surface of nanovectors of cell-specific ligands can further increase selectivity. Control of the release of a drug, in a defined localization in an organism, organ, tissue, at the cell surface or intracellularly, and the kinetics of drug release must also be characterized. Finally, the stability, cytotoxicity, mechanisms of cell uptake and the biodegradation of the nanovectors are also important. Passive (EPR effect) versus active (ligand-targeting, cationic lipids or polymer cytotoxicity and poor circulating times) delivery is also a choice to consider for efficient delivery, and must be dictated by the characteristics of the cancer to be treated, whether a marked angiogenesis is present or not.

Various nanovectors are available to achieve drug delivery, such as liposomes, micro/nanospheres, nanoemulsions and micro/nanocapsules. They can be used to deliver hydrophilic drugs, hydrophobic drugs, proteins, nucleic acids, vaccines, biological macromolecules, etc. Nanovectors, such as liposomes, protect drugs from degradation and biological metabolism; however, liposomes have a low encapsulation efficiency, poor storage stability, and rapid leakage of water-soluble drugs in the blood. As such, their ability to control the release of many drugs is not optimal. Nanoparticles made of colloidal suspensions and biodegradable poly-

mers offer better stability than liposomes and allow controlled release. Finally, the efficiency of drug delivery is increased by using magnetic vectors, which can be targeted with an external gradient magnetic field; such vectors also have the potential to record the drug delivery sites as contrast agents in magnetic resonance imaging (MRI) for diagnostics (see below). The characteristics, composition, etc. of nanoparticles (which are in clinical use, in clinical trials or under development) necessary to achieve targeted delivery of anticancer agents to treat human cancers will be reviewed as a function of their physicochemical properties and the chemical and biological properties of the drug, or the cancer type characteristics. However, this chapter is not an extensive review of all the published information available.

#### 7.4.4

#### **Nanoparticles for Anticancer Drug Delivery**

For more extensive reviews see Refs. [6, 12, 15]. What has been attempted and what are the next challenges of the nanoparticulate approach to drug delivery in cancer?

##### 7.4.4.1 Existing Systems

**Colloidal Delivery Systems** Encapsulation of therapeutic agents in colloidal carriers, including liposomes, emulsion, solid lipid nanoparticles, polymeric particle and polymeric micelles, form colloidal delivery systems.

**Liposome Nanoparticles** These nanoparticles are biodegradable and flexible, have an aqueous core containing the drug, and are bilayer amphipathic lipids. Drugs encapsulated in liposomes under evaluation or in clinics include paclitaxel, lurtotecan, platinum derivatives, vincristine, doxorubicin (see below).

**Emulsion/Solid Lipid Nanoparticles** Here an oily core, either liquid or solid lipids at body temperature, or a monolayer of amphipathic lipids contains the drug. Drugs under evaluation include protoporphyrin IX, for photodynamic therapy, and taxol (see below).

**Polymeric Nanospheres** Polymers [such as poly(lactide-co-glycolide), poly(vinylpyrrolidone), poly( $\epsilon$ -caprolactone)] and entrapped drugs allow controlled drug release from the polymer.

**Polymeric Micelles** Biodegradable polymeric micelles with the drug in the core have been prepared from di-block copolymers (one core-forming segment, one shell-forming segment).

**Drug-conjugated Delivery Systems** In these systems drugs are covalently bound to the polymer and are either active when coupled to the polymer or after release (acid-sensitive, enzyme-sensitive bonds) or polymer degradation.

Lipid-based or polymer–drug conjugate-based nanoparticles (<200 nm) can im-

prove the pharmacological properties, pharmacokinetics and biodistribution, and sustained release of free drugs. But they also present new challenges and issues [12] that need to be taken into account for the DDS to reach clinical use, including potency (the fewer the carrier can carry, the more potent the drug must be), the stability of the drug carrier (either shelf or biological stability), solubility of the drug, size of the carrier and the cargo (e.g., proteins and small carriers), charge, carrier biocompatibility, cytotoxicity, degradation products, drug survival to chemical procedures and coupling routes, rates and efficacy of drug release in the tumor space (e.g., for schedule-dependent anticancer drug therapies drugs must stay above minimal efficacy levels for several hours or days, for schedule-independent drugs a large burst is more important than constant release), hypersensitivity reaction to the carrier–drug conjugates. A drug linked to a carrier may have the same activity as the free drug or, alternatively, its pharmacological properties may be modified, e.g., the toxicity of liposomal vincristine is similar to that of the free drug, but its potency is augmented, liposomal topotecan is protected from biodegradation, and doxorubicin-linked *N*-2-hydroxypropyl methacrylamide copolymer displays a slow release and an increased maximal tolerated dose.

#### 7.4.4.2 Systems under Development and Challenges

**Targeted Drug Delivery Nanoparticulate Systems** These are the most recent development, presently only at the initial stages. Drugs are conjugated to ligands/antibodies or incorporated in carriers bearing ligands/antibodies for recognition by cell surface receptors expressed by target cells, e.g., doxorubicin-nanoparticles targeting HerB2/neu for breast cancer. Major obstacles for the delivery of anti-cancer drugs include the definition of selective cell-specific targets and physiological barriers, in particular the epithelial and blood–brain barriers. For example, approaches using LDL-mimic nanoparticles targeting the LDL receptors on brain endothelial cells [16] or galactose-HPMA copolymer bearing doxorubicin for the asialoglycoprotein receptors in liver tumors, which is under clinical trial [17], have been attempted. One major problem in these approaches is to identify relevant targeting entities in cancers compared with normal cells of the whole body. A few have been identified and evaluated in preliminary trials, e.g., folate receptors and PSA-doxorubicin conjugates for PSA-positive prostate cancer.

**Intracellular Delivery** For maximal efficacy, cancer drugs must reach their appropriate targets, in the appropriate location within cells, which are mainly located either in the cytosol, the nucleus, and more recently in cell organelles such as mitochondria. Therefore, either drug-loaded carriers must be transported intact inside cells, then carriers must release their cargo, or carriers must release their cargo at the targeted-cell surface, and free drug must be transported inside cells. Colloids and nanoparticles are mostly taken up by endocytosis in cancer cells, via the endosome/lysosome pathway. Therefore, the drug must be released intact from the lysosomal compartment. Most approaches have used the acidic characteristics of this compartment to dissociate the drug from its carrier, e.g., HPMA copolymer,

liposomes, polymeric micelles, cationic lipids and photosensitizers [18–22], and release into the cytosol; more recently, the presence of lysosomal enzymes have been used to release covalently bound drug from a carrier system. Nuclear delivery is also necessary for many drugs, mainly nucleic acid or protein drugs. In this case tagging with a nuclear location signal is necessary.

**Avoiding Drug Resistance Mechanisms** Resistance of tumor cells to chemotherapeutic agents is a major cause of treatment failure in cancer therapy, mainly mediated by families of energy-dependent ATP-driven efflux pumps (MDR, Pgp). Liposomes, polymer conjugates, polymeric micelles have the potential to overcome resistance mechanisms, and positive results in this direction have been obtained (reviewed in Ref. [23], and see below).

Methods of delivery and tumor targeting are key areas for the future of nanotechnology in anticancer therapy. For this, innovative nanotechnological methodologies have been initiated, are under active development and will be further improved, to achieve better, more efficient and less aggressive therapies of cancer for the whole organism.

#### 7.4.5

#### **Nanoparticles for Drug Delivery in Clinical Use or under Clinical Evaluation**

More extensive reviews are given in Refs. [6, 12, 24]. Several polymer–drug conjugates are in clinical use or under clinical evaluation as anticancer agents (Table 7.2).

Hydrophilic drugs can be easily entrapped with high efficiency in the aqueous core of liposomes whereas hydrophobic weak bases, such as doxorubicin or vincristine, are loaded by pH and chemical gradients across the liposome bilayer. Consequently, as many of the agents active against cancer are hydrophobic molecules, most presently used DDSs in clinics are liposomes, and many have been decorated with PEG to increase their bioavailability (decreased opsonization, decreased clearance by the RES, increased circulation time), e.g., PEGylated doxorubicin-liposomes.

##### 7.4.5.1 **Doxorubicin Family**

Liposomes encapsulating doxorubicin are the archetypal, simplest and first form of nanoparticles used for cancer therapy. Doxorubicin-liposomes were the first to be used clinically and ameliorated versions, such as PEGylated doxorubicin liposomes, have been in clinical use for breast and other cancers for several years.

Doxorubicin belongs to the anthracyclines and is used to treat breast, ovarian, bronchial cancers by inhibiting the synthesis of nucleic acids in cancer cells, but at the price of cardiotoxicity and myelosuppression and a very narrow therapeutic index. Doxorubicin-liposomes of phosphatidylcholinum-carbamoyl-cholesterol coated (glycosylated) with methoxypoly(ethylene glycol) (MPEG) (100 nm particles) to form an hydrophilic layer that protects against phagocytosis by macrophages and increases the circulation half-life, extravasation via defective tumor vessels and release of doxorubicin chlorhydrate selectively in tumor vicinity are in clinical use.



**Tab. 7.2.** Some nanoparticulate drugs under clinical use or evaluation. (Adapted from Ref. [12] with modifications.)

Nanoparticulate drug	Clinical use or evaluation
Doxorubicin-liposome/PEG	Breast and ovarian carcinoma
Zinostatin-styrene	Hepatocellular carcinoma
Liposomal-vincristine	non-Hodgkin's lymphoma
Liposomal all-trans-retinoic acid	non-Hodgkin's lymphoma
Polyglutamate-paclitaxel	non-Small cell lung carcinoma
Liposomal paclitaxel	Advanced solid tumors
Liposomal oxaliplatin	Colorectal cancer
Liposomal lurtotecan or irinotecan	Solid tumors, ovarian, small cell lung cancer
N-(2-Hydroxypropyl)methacrylamide copolymer doxorubicin	Breast, colon, lung cancer
N-(2-Hydroxypropyl)methacrylamide copolymer doxorubicin-galactosamine	Liver cancer

Conjugates of doxorubicin and dextran have been encapsulated with chitosan (100 nm size particles) or conjugated to PLGA, PCAA or poly( $\gamma$ -benzyl-L-glutamate)/poly(ethylene oxide) nanoparticles (200–250 nm), resulting in long-term *in vitro* release of the drug [25] and *in vivo* suppression of tumor growth in *in vivo* experimental models [26], proving efficacy. Efficacy was also suggested to be macrophage-mediated [27]. Brain delivery of doxorubicin has also been obtained by biodegradable poly(butyl cyanoacrylate)-polysorbate 80-coated nanoparticles [28]. Recent developments of nanoparticles for doxorubicin include the development of lecithin lipid core-drug/pluronic [poly(ethylene oxide)-poly(propylene oxide)-poly(ethylene oxide) triblock copolymer]-shell nanoparticles, obtained by a freeze-drying procedure [29]. In addition, solid lipid nanoparticles of cholesteryl butyrate of doxorubicine with paclitaxel, which had additive effects [30], and nanoparticles of poly(isohexyl cyanoacrylate) able to overcome MDR and increase sensitivity to doxorubicin [31], have also been developed recently.

#### 7.4.5.2 Paclitaxel (Taxol)

Paclitaxel (taxol) is a microtubule-stabilizing agent that causes polymerization of tubulin and cell death. Paclitaxel is used in ovarian, breast, colon, non-small cell lung carcinomas. Paclitaxel is poorly aqueous soluble, but soluble in organic solvents, and is presently formulated in Cremophor EL (polyoxyethyleneglycerol triiricinoleate 35) or polysorbate (Tween) 80 (polyoxyethylenene-sorbitan-20-monooleate), which have important side effects and drawbacks. Strategies have

been developed to formulate taxanes in Cremophor and Tween 80 based on pharmaceuticals such as albumin nanoparticles, emulsions, liposomes, polyglutamates, and prodrugs strategies [32]. New formulations that have been developed include biodegradable nanoparticle formulations (140 nm mean diameter) using poly(lactic-co-glycolic) and nanoprecipitation in acetone, showing efficiency and high incorporation loading [33, 34], poly(ethylene glycol)-poly(lactide) (PLGA) nanoparticles (<100 nm) [35–38] and d- $\alpha$ -tocopheryl PEG as an emulsifier. In addition, the use of methoxy poly(ethylene glycol)-poly(lactide) (MPEG-PLA) results in a slow and long-lasting release after an initial burst [39]. More recently, entrapment of paclitaxel by hydrophobic forces in micelles of block copolymers (NK105) led to increased blood stability, bioavailability and anticancer drug efficacy, extended *in vivo* antitumor activity and reduced the neurotoxicity of paclitaxel [40].

#### 7.4.5.3 5-Fluorouracil

5-Fluorouracil is used in the treatment of rectum, colon, breast, stomach, pancreas, liver, uterus, ovarian and bladder cancers. Intravenous injection of an aqueous solution of 5-fluorouracil inhibits cell growth by blocking thymine (5-methyluracile) formation, and DNA synthesis, and the formation of aberrant RNA; however, the drug is very short-lived under this route of application. For clinical formulation, 5-fluorouracil has been incorporated in dendrimers of poly(amidoamine) modified with mPEG-500 by simple incubation due to the hydrophilicity of the drug, achieving longer-lasting release than the free drug. The *in vivo* half-life of 5-fluorouracil, a clinical problem necessitating continuous infusion for several hours, has been increased by drug formulation by a diafiltration procedure in biodegradable amphiphilic PEG-poly( $\gamma$ -benzyl-L-Glu) micelles (180–250 nm) and an hydrophilic shell of 30 nm [41].

#### 7.4.5.4 Tamoxifen

Tamoxifen is a non-steroid inhibitor of estrogen receptors mainly used to treat breast cancer. For clinical use, tamoxifen is encapsulated within PEG-coated nanospheres and located at the nanosphere surface, resulting in immediate drug release [23]. More recently, tamoxifen was encapsulated in poly(ethylene oxide)-modified poly( $\epsilon$ -caprolactone) nanoparticles of an average diameter of 150–250 nm, for targeted delivery of tamoxifen to breast cancer. The primary site of accumulation *in vivo* was the liver; however, 26% of the total drug-loaded nanoparticles were recovered in the tumor at 6 h post-injection, increasing further with time. Extended presence in the circulation was also observed. Therefore, these nanoparticles achieved preferential tumor-targeting and a circulating drug reservoir [42]. Anti-estrogens were also incorporated at high amounts in nanocapsules [polymers with an oily core and coupling with PEG] displaying enhanced anti-tumoral activity toward breast cancer cells [43].

#### 7.4.5.5 Cisplatin

Platinum derivatives (cisplatin and carboplatin) are inorganic metallic complexes of the Pt<sup>2+</sup> cation and pairs of chloride and amino ligands in the cis position for

cisplatin. Their mechanism of action resembles that of alkylating agents active on DNA, independently of the cell cycle. Cisplatin, alone or in combination with other drugs, is used to treat testicular, ovarian, bladder, prostate, respiratory carcinomas, and lymphoma, sarcomas and melanoma. Platinum derivatives have a short half-life in the biological environment and are frequently associated with drug resistance in many cancers and, therefore, their entrapment in liposomes has been attempted to enhance efficacy – these formulations are presently under clinical evaluation [44–47].

#### 7.4.5.6 Camptothecins

Camptothecins (irinotecan and topotecan) are cytostatic drugs that act as specific inhibitors of DNA topoisomerase I, active in S phase and on P-glycoprotein (MDR)-positive cells, with activity that depends on exposure time; they induce single-strand lesions in DNA and inhibition of replication. They are in clinical use mainly for advanced colorectal cancer in conjunction with 5-fluorouracil, but are extremely hydrophobic. Lipid-based nanoparticles (100–375 nm) of irinotecan have been prepared and their activity was size-dependent: 375 nm irinotecan-nanoparticles > irinotecan > 100 nm irinotecan-nanoparticles > no treatment [24].

#### 7.4.5.7 Methotrexate

Methotrexate is a cytotoxic antagonist (antimetabolite) of folic acid during the S phase of the cell cycle of actively proliferating cells, acting by competitive inhibition of dihydrofolate reductase and blocking the reduction of dihydrofolic acid (FH<sub>2</sub>) into tetrahydrofolic acid (FH<sub>4</sub>), and hence the synthesis of pyrimidine and purine bases and amino acids, and of DNA, RNA and protein synthesis. Methotrexate has been entrapped in triblock poly(trimethylene carbonate)-PEG-poly(trimethylene carbonate) copolymer core-shell type nanoparticles (50–160 nm) by ring-opening polymerization [48]. Very recently, in a very elegant approach, polyamidoamine (PAMAM) dendrimers (<5 nm size), conjugated to folic acid for tumor targeting and methotrexate as anticancer agent for tumor treatment, injected i.v. into folate receptor-positive human KB tumor-bearing immunodeficient mice displayed increased anti-tumor activity of methotrexate and markedly decreased toxicity, allowing a tumor drug dosage not possible with the free drug [49].

### 7.4.6

#### New Experimental Drugs and Therapies

##### 7.4.6.1 Proteins, Peptides, their Inhibitors and Antagonists

- The cysteine protease cathepsin B inhibitor cystatin, potentially active as an anticancer drug, has been incorporated in poly(lactide-co-glycolide) nanoparticles (300–350 nm size), preserving its cathepsin B inhibitory activity; it was internalized and was cytotoxic for tumor cells whereas free cystatin was not [50, 51].
- Conjugation of an anti-EGF receptor monoclonal antibody to colloidal gold nano-

particles increased their selectivity toward cancer cells versus non-cancer cells, suggesting their utility in both detection and targeted delivery [52].

- Magnetic nanoparticle-loaded anti-Her2 immunoliposomes have been developed for a combination of antibody therapy with hyperthermia [53].
- Increased transmembrane transport has been observed using positively charged, membrane translocation-inducing poly-D-Arg and Tat-peptide crosslinked to dextran nanoparticles (30 nm) [54].

#### 7.4.6.2 New Drugs

- All-trans retinoic acid incorporated in solid lipid nanoparticle powder displayed increased stability, decreased hemolytic toxicity, and efficacy was maintained against human cell lines [55].
- Clinical application of cucurbitacin in poly(lactic acid) nanoparticles (85 nm diameter), as anticancer targeting against metastasis foci of cervical lymph nodes in patients with oral carcinoma, displayed enhanced efficacy, decreased side effects and a long-lasting high concentration of the drug in lymph nodes [56].

#### 7.4.6.3 New Therapeutic Approaches: Photodynamic Therapy (PDT)

Ceramic-based nanoparticles entrapping water-insoluble photosensitizing anti-cancer drugs have been developed as a novel drug-carrier system for the PDT of tumor cells [57]. Methylene blue, as a photosensitizer and a source of singlet oxygen in PDT, has been encapsulated in polyacrylamide, sol-gel silica or organically modified silicate sub-200 nm nanoparticles. Of these three matrices, polyacrylamide was the most efficient delivery system but its content in methylene blue was low, whereas the opposite was true for the sol-gel nanoparticles. PDT treatment of cells was demonstrated to be efficient [58]. PDT protocols have also been developed using photosensitizers incorporated in PLA-PEG nanospheres and tumor irradiation (EMT-6 cells). However, the large (>900 nm) particle size did not allow high enough intra-tumoral accumulation [59]. Therefore, the nanoplatform represents a functional system for decreasing the side effects in detection and therapy of cancer in PDT protocols.

#### 7.4.7

#### Gene Therapy

Viral vectors are very efficient but present the inherent risk that the inactivated virus reverts to wild-type and that viruses induce immunogenic reaction. Therefore, attempts have been made to replace viruses by synthetic vectors with improved safety, greater flexibility and easier manufacturing. Synthetic polymers (mainly cyclodextrin-modified, branched polyethyleneimine) are generally cationic molecules to which negatively charged DNA or RNA molecules electrostatically bind, forming polyplexes of a few tens to hundreds of nm in diameter, but with excess cationic charges maintained to favor cell uptake. Serum stability, aggregation, and clearance of polyplexes depend on the packaging polymer and surface

modification. Surface modification with a hydrophilic polymer, such as PEG, N-2(hydroxypropyl)methacrylamide, oligosaccharides and sugars or proteins, can increase serum compatibility and provides a basis for chemically grafting target addresses, which include membrane receptors, lectins, transferrin, antibodies, lectins. Targeting efficacy depends on the conjugation chemistry, the length and chemical composition of the spacer between the polyplex and the ligand, the kinetics characteristics and the number of interactions between the ligand and receptor. Intracellular trafficking and endosomal escape are also important factors for targeting approaches.

Polymers used for gene delivery include polylysine, branched polyethyleneimine, poly(amidoamine) dendrimers, membrane-disrupting pH-responsive or pH-degradable acrylate-based polymers, allowing lysosomal escape, peptides, cyclodextrins and non-cytotoxic biodegradable polymers of L-glycolic acid (for a discussion of the advantages/disadvantages of the various polymers see the reviews in Refs. [60–62]). However, whereas substantial progress has been made *in vitro*, their utilization in clinics remains to be evaluated. Moreover, the much lower efficacy of all synthetic vectors than that of viruses makes them generally considered as unacceptable for clinical applications.

#### 7.4.7.1 Nanoparticle for Gene Delivery: Non-chitosan and Chitosan-type Polymers

Progress in gene therapy has relied on the emergence of polymeric and non-polymeric nanoparticles that have been investigated for their ability to deliver genes, mainly encompassing two families: chitosan-related and chitosan-unrelated materials.

##### Non-chitosan Polymers

- Polyethyleneimine-DNA complexes (39–1200 nm) linked to PEG coated with transferrin or EGF have achieved 10–100× higher tumor selectivity over other organs in mice [24].
- Dextran-SPION plasmid as a model for gene carrier (59 nm effective diameter) has achieved efficient transfer in a human bladder cancer cells line [63].
- Positively charged calcium phosphate nanoparticles (30 nm) were able to transfer foreign DNA with high transfection efficiency and were less cytotoxic than DNA liposomes [64].

**Chitosan-type Polymers** The inclusion of poly(propyl acrylic acid), which disrupts lipid bilayer membranes at defined pH incorporated in chitosan-DNA plasmid, increased delivery from the endosomal to cytoplasmic compartment for non-viral gene delivery [65].

#### 7.4.8

##### New Approaches

Recent, new and innovative approaches have been aimed mainly at (a) improving existing systems, by enhancing biocompatibility, biodegradability and biological

characteristics of existing systems, and (b) developing novel nanotechnological approaches for drug–nanoparticle preparation as anticancer agents (for more detailed reviews see Refs. [6, 23]).

#### 7.4.8.1 Improvement of Biological Characteristics

**Conventional Drug-loaded Nanoparticles** These nanoparticles are rapidly opsonized in the circulation and cleared by the RES, mainly macrophages, in the liver, spleen, lungs, bone marrow where drug accumulates. Conventional nanoparticles induce some cytotoxic effects against phagocytes, and drugs accumulate in bone marrow and result in myelosuppression, an unfavorable event. Nephrotoxicity has also been observed. However, the drug–nanoparticle toxicity profile is more favorable than the free drug toxicity profile, in particular for the cardiotoxicity of doxorubicin. The accumulation of nanoparticle–doxorubicin in the lysosomes of Kupffer cells in the liver, but not in tumor cells, acts as a long-term active drug delivery system [66]. For example, in mice treated with doxorubicin–poly(isohexyl cyanoacrylate) (PIHCA) nanospheres [67] the drug accumulates in the liver, spleen and lungs, but a reduction of hepatic metastasis and a longer life span were also observed [68] compared with free doxorubicin. The same was seen for actinomycin D adsorbed on poly(methyl cyanoacrylate) (PMCA) and lung accumulation [69], and for actinomycin D adsorbed on the more slowly degradable poly(ethyl cyanoacrylate) (PECA) and small intestine accumulation [70] or vinblastine incorporated into PECA and accumulation in the spleen [70]. Therefore, as both the polymer composition and the drug chemical characteristics, as well as the location in the nanoparticle (adsorbed or incorporated), are important for tissue localization these factors have been modified.

An ideal drug carrier should be a system that can reside *in vivo* for long periods, targeting particular cell types, compartmentalizing a large set of molecules and releasing them in the appropriate environment at the appropriate rate and dose. Creating a toolbox of molecules that hierarchically assemble in ordered structures, spatially and chemically controlled, is requisite to making them attractive and efficient for encapsulating and delivering drugs. The chemistry used to achieve biomimetic assemblies, which consist of the polymer, a linker and a bioactive molecule, has been reviewed [71]. Di- or tri-block copolymers with low polydispersity can be obtained via anionic polymerization. Subsequent manipulation involves self-assembly at concentrations favoring spherical micelles, controlled crosslinking using radical chemistry to obtain a hydrogel shell and polymer micelle architecture, followed by conjugation with a biological molecule to achieve targeting, such as peptides via a carboxyl end group on the polymer. The most commonly incorporated polymer is PEG [poly(ethylene glycol)], a flexible water-soluble molecule that can be end-functionalized to obtain aldehyde, methacryloyl, hydroxyl, primary amine, acetal, mercapto groups, and copolymerization with other polymers [72–74]. The chemical procedures available have been outlined [71].

Factors controlling the rate of drug release are not well understood but depend on the assembly morphology, drug molecular weight, chemical composition, etc. These factors have also been addressed. Biodegradable polymers are preferred for

controlled drug delivery systems, and are made of natural or synthetic polymers, which have the advantage over natural polymers in that they can be tailored to obtain defined properties. They must match the mechanical properties and degradation rates required for the application. Commonly used biodegradable polymers for biomedical applications include polyglycolic acid, L-, D-, DL-poly(lactic acid), poly( $\epsilon$ -caprolactone), poly(DL-lactide-co-glycolide), and poly(vinyl alcohol). These polymers have features such as controllable mechanical properties, controllable degradation rates, minimal toxicity and immune responses [75].

**Long-circulating Biocompatible and Biodegradable Drug-loaded Nanoparticles** To escape the RES, stealth nanoparticles that are “invisible” to macrophages, and which are long-lasting in the blood compartment, need to be designed. For this, modification of the surface (hydrophilic/hydrophobic) and a small size (<100 nm) of the colloidal carrier are essential [23]. The hydrophilicity of the carrier and sustained drug release are also important. A previous breakthrough was the use of PEG or polysaccharides to coat the nanoparticle surface and, thereby, repel plasma proteins. Hydrophilic polymers are either adsorbed at the surface of nanoparticles or are block copolymers. Finally, covalent linkage of amphiphilic copolymers is the preferred way to obtain a protective hydrophilic coat, using poly(lactic) (PLA), poly( $\epsilon$ -caprolactone), or poly(cyanoacrylate) copolymers chemically coupled to PEG. Controlled drug-delivery systems are generally based on either diffusion or degradation of the polymer. The choice of polymer depends on potential interactions with the drugs, surface characteristics, the hydrophilic–hydrophobic balance, surface charges, and the biological properties of the target. Novel approaches to solve the drug release problems have been addressed.

The preparation and characterization of biodegradable/bioerodible polymers for the controlled targeted release of proteic drugs (interferon or growth factors for tissue engineering) have been described. *Bioerodible polymeric matrices* are hemiesters of alternating copolymers of maleic anhydride with alkyl vinyl ethers of oligo(ethylene glycol). Hydrophilic shell coating to minimize opsonization was achieved with grafted  $\beta$ -cyclodextrins. Coprecipitation was used for formulation, based on dropwise addition of synthetic polymer in water-miscible organic solvent to aqueous protein solution under stirring, followed by the addition of the glycolipid. Particles 130–150 nm diameter were obtained, with  $\beta$ -galactose residues exposed at the surface. *Biodegradable polymer matrices* solve the issue of removal of the device after drug delivery. Among them, poly(malolactonates) are biocompatible, degrading to malic acid, and contain reactive side-chain carboxyl groups that can be esterified [76] for adjustment of the hydrophilic–hydrophobic balance [76–81]. The starting components are commercially available and nanoparticles of 100–150 nm can be obtained by coprecipitation (reviewed in Ref. [82]).

The effects of the following surface modifications have also been evaluated:

- Poly(lactic-co-glycolic acid) nanoparticles coated with vitamin E TPGS [82, 83], or polysaccharide-decorated nanoparticles [84].
- Poly(alkyl cyanoacrylate) nanoparticles [85].
- Amphiphilic poly(lactic)-pluronic block copolymers, which can release either hy-

drophobic anthracene and hydrophilic procaine drugs due to slow hydrolytic degradation of poly(lactic acid) [86].

- Poly(ethylene oxide)- $\beta$ -poly(N-isopropylacrylamide) nanoparticles with crosslinked cores as hydrophobic drug carriers [87].

#### 7.4.8.2 New Technological Approaches

**Local Administration and Long-time Delivery** Small particles injected locally in the tumor vicinity infiltrate gradually the lymphatics, representing a tool for lymph node metastases, and locoregional adjuvant therapy, for breast cancer for example. In this model the size and choice of the carrier are of fundamental importance to avoid clogging of small lymphatic vessels. For this purpose magnetic systems would be a good choice (see below).

Polymer gels have been designed for controlled release and as systems for modulated delivery. The hydrophobic–hydrophilic balance of a gel carrier can be modulated to provide useful diffusion characteristics for periods up to months. Current polymer network drug delivery systems incorporate the pharmaceutical agent by imbibition, equilibrium partitioning after the network is formed, before or after polymerization depending on the drug stability to UV light. Reference [88] gives a more extensive review of the features of these devices.

**New Materials Evaluated as Carriers: Thermoresponsive or Oxidation-sensitive Materials** The preparation and characterization of “intelligent” core–shell nanoparticles has been described. Thermoresponsive, pH-responsive and biodegradable nanoparticles of poly(D,L-lactide)-*graft*-poly(N-isopropyl acrylamide-*co*-methacrylic acid) have been developed as a core–shell type nanoparticle with high drug loading capacity. A hydrophilic outer shell and a hydrophobic inner core, with a phase transition above 37 °C, have been prepared. Heating above the phase transition temperature or pH modification caused leakage of the drugs, demonstrating the potential of these nanoparticles as drug carriers for intracellular delivery of anticancer drugs [89]. Monodisperse polymeric nanoparticles of polyacrylic/isopropyl acrylamide, prepared by seed-and-feed method, displayed inverse thermogellation at 33 °C. Therefore, drug–polymer mixtures that are liquids at room temperature become a gel at body temperature without chemical reaction, allowing the sustained release of drugs [90]. Oxidation-sensitive polymeric nanoparticles of crosslinked polysulfides have also been developed as oxidation-sensitive vehicles for hydrophilic or hydrophobic drugs able to release drugs in the more oxidative environment of cancer and inflammation [91].

#### 7.4.9

##### Superparamagnetic Iron Oxide Nanoparticles (SPIONs) as Magnetic Drug Nanovectors

Nanovectors able to both detect cancer and deliver drugs have also been developed, mainly using the outstanding superparamagnetic properties of iron-oxide nanoparticles. Superparamagnetic iron oxide nanoparticles (SPIONs) are usually used as



magnetic nanovectors since their superparamagnetic properties, depending on their nanoscale size, make them magnetic in the presence of an external magnetic field, but no magnetic remanence remains after removal of this external field. Magnetic nanoparticles offer additional attractive possibilities in biomedicine since their magnetic properties allow them to be manipulated by an external magnetic field gradient, further improving chemical and biological drug delivery strategies, in addition to magnetic resonance imaging (MRI) contrast enhancement detection of their sites of localization. Previous experiments using this approach have been performed by some groups with magnetic particles or magnetic liposomes, ranging from 10  $\mu\text{m}$  to 100 nm, loaded with chemotherapeutic agents [92–94]. Some positive effects were obtained, in particular a decreased general toxicity, due to lower dosages, of the agents. This approach has the advantage of being non-invasive and efficient.

Biocompatible superparamagnetic nanoparticles have been developed for *in vivo* biomedical application, mainly in magnetic resonance imaging [63, 95, 96], and have been only preclinically evaluated in the tissue-specific release of therapeutic agents [97]. Dextran-SPIONs have been used in gene transfer experiments in a human bladder cancer cell line [98]. SPIONs combined with albumin [99] or as liposomes with antibodies targeting Her2 have been used for combination of antibody therapy with hyperthermia [53]. Surface modification of the PEG film of SPIONs with folic acid decreased their uptake by mouse macrophages and increased their uptake by human cancer cells [100]. Anionic SPIONs, coated with albumin, were taken up by cells [101], and anionic to cationic surface charge in the acidic lysosomal compartment may allow escape from the endo-lysosomal compartment to the cytosol [102]. Dextran-coated SPIONs of 150 nm, but not of 10 nm, were taken up by macrophages involving type I and II scavenger receptor SR-A-mediated endocytosis [103]. For the latter application, the internalization of nanoparticles into specific cells is the critical step, but is limited by non-specific targeting and a low efficiency of internalization of the endocytosed ligands grafted on the nanoparticles [104]. Clearly, this step needs to be improved to enhance efficiency. Few published studies have addressed the uptake by cells or the cell-surface binding of functionalized superparamagnetic nanoparticles [105]. Therefore, a firm theoretical foundation of magnetic drug targeting is still lacking.

Interactions of magnetic nanoparticles with cells may have an impact on cell functions. Macaque T cells labeled with monocrystalline SPIONs following adsorptive pinocytosis or receptor-mediated endocytosis and which localized in the cytoplasm did not cause any measurable effects on T cell functions [106]. Conversely, transferrin magnetic nanoparticles localized to the cell membrane without inducing endocytosis, but this surface localization induced the expression of several genes of the cytoskeleton and cell signaling pathways [107].

## 7.5 Targeting

Detecting and treating cancer by targeted means at the earliest possible stage of cancer will improve the quality of life and the life expectancy of patients. The use of nanoparticles has a bright future towards achieving these goals. Probably the

most promising features of nanovectors are related to the possibility of modifying their properties, mainly their surface, to achieve organ-, tissue- and cell-specific and -selective delivery of anticancer drugs, to increase drug efficacy and decrease side effects, and ultimately improve the quality of life and survival of patients. Technical problems of developing targeting nanoparticles include the increased complexity/size of the nanoparticles, as well as the increased risks of adverse reactions, while advantages include the fact that more drug will reach the target, selectivity is increased, the delivery of multiple agents at the same site will become possible for targeted combination therapies, and the ability to bypass biological barriers.

Cancer targeting using drug-loaded nanovectors may be achieved in three ways:

1. Using the tissue characteristics of cancer, mainly the leaky vessels associated with many human cancers – what has been called passive targeting.
2. Using the characteristics of cancer cells, mainly increased metabolism and active cell proliferation, and *active circumstantial targeting*.
3. Using molecular markers overexpressed by either cancer cells or cancer-associated cells, mainly the neo-angiogenic endothelium of cancer tissue, and *active molecular targeting*.

Active targeting of drugs to cancer is probably the most challenging biotechnological approach. To achieve these goals it will be necessary to:

1. Define valid targets: markers of tumor and tumor-associated cells and vasculature.
2. Develop the necessary chemistry to bind drugs to nanovectors: validate synthetic routes.
3. Release the drugs at the right place and time from the carrier: develop intelligent linkers.
4. Achieve intracellular delivery: define cell penetration means and organelle addresses.

The greatest challenge in designing strategies for targeting is to define the optimal targeting system, able to selective bind to tumor or tumor-associated cells, then to trigger internalization of the drug cargo (for a more extensive review see Ref. [24]). Most studies have used a modification of the nanoparticle surface, e.g.,

- covalently-linked antibodies,
- tumor vascular markers (RGD and integrins, VEGF-R, EGF-R),
- and permeation-enhancing agents.

The endothelium is a very attractive tissue for drug targeting using nanoparticles in cancer. Surface properties of the nanocarrier may provide passive–active targeting to endothelium, e.g., polystyrene nanoparticles arrest in bone marrow endothelium, followed by receptor-mediated endocytosis [108], while polysorbate 80-coated nanoparticles arrest in the blood–brain barrier vasculature [16, 28]. Cationic lipo-

somes are internalized within 1 h in endothelial cells, according to an organ- and vessel-specific manner [109], and these effects are likely mediated by vessel-type specific properties. Recent approaches have also provided information concerning specific molecules expressed by the various endothelia. Issues to consider in targeting tumor vasculature include the fact that tumors are poorly perfused, tumor vasculature destruction is not enough to totally destroy tumors, that high intratumoral osmotic pressure will result from antiangiogenic therapies, and it has to be considered that the destruction of tumor vasculature will also result in the loss of access to the tumors.

### 7.5.1

#### **Passive Targeting**

Passive targeting utilizes tissue features that are characteristics of cancer, mainly the defects of the cancer vascular system, enhanced permeability and retention time of tumor vasculature and tissue [24], avoiding trapping in the RES, or kidney clearance. Heterogeneity of blood flow in a tumor is also a challenge, but the leakiness of tumor vasculature and the poor lymphatic drainage of human cancers may be advantageous, allowing an enhanced permeation and retention (EPR) effect. Following systemic administration, drug delivery devices to solid tumors must be transported through blood vessels, across the vascular wall into the surrounding tissues, and through the interstitial space within a tumor. These processes are determined both by the characteristics of the drug and of the delivery system, and by the biological properties of tumors. Functional and morphological differences exist between normal and tumor-associated blood and lymphatic vasculature, offering therapeutic opportunities and windows for the delivery of therapeutic agents [110, 111].

Tumors smaller than 2–3 mm in diameter receive nutrients, oxygen, etc. from the surrounding host tissue by diffusion and do not develop their own vasculature, and will not be targeted by passive targeting. The growth of tumors results in the development of their own vascularization, which is more heterogeneous and heterogeneously distributed, larger, tortuous and permeable than that of normal tissue, depending on the tumor. In a tumor, defects in tumor vasculature result in increased resistance to flow, lower blood flow and decreased perfusion of tumor tissue. In tumors the lymphatic system, which returns the interstitial fluid to blood circulation, is defective. The lack of lymphatic drainage in solid tumors also results in decreased water clearance and the retention of high molecular weight components (>40 kDa), but at the price of increased interstitial pressure and decreased extravasation from blood vessels. The extravasation of molecules is accompanied by fluid movement across the leaky vessel walls by passive diffusion or convection, dependent on the hydrostatic and osmotic pressure differences between blood and interstitial space. Small molecules mainly diffuse whereas large molecules are transported by convection/pressure differences. In a tumor, convection is directed out of the tumor. Macromolecules, extracellular matrix and cell density are important factors in the repartition of therapeutic agents in the tumors.

Thus, in cancer, blood perfusion is heterogeneous, the vascular wall frequently is collapsed and the intratumoral hydrostatic pressure high; therefore, nanoparticle distribution is unpredictable. Passive diffusion of nanoparticles (20–150 nm) at sites of vascular leakage in cancer is possible. Drug release, near the cancer, by the carrier must follow extravasation and drug therapeutic dosages must be achieved. The release rates depend on both the drug and chemical and biophysical properties of the nanomaterials and on the biological characteristics (pH, redox, etc.) of the tissue where the drugs has to be released and be active. Drug release from the nanocarrier remains an issue – some polymeric materials do not allow drug release at levels and rates that are compatible with those necessary for treatment efficacy.

## 7.5.2

### Active Targeting

Actively targeted treatment of cancer and tumor-specific targets include nanoparticle delivery systems selective either for cells forming tumor angiogenic vessels and stroma or tumor cells.

#### 7.5.2.1 Targeting Cancer-associated Cells

Human cancers are heterogeneous entities, made of several different cell types: the tumor cells, the normal cells from which tumor cells have evolved, the cells forming the normal and the tumor-associated vascular system, fibroblasts and tumor-associated fibroblasts, and immune cells and cancer-associated immune-cells (mainly macrophages and lymphocytes). Theoretically, all these cells may be useful for drug targeting, but presently the cells forming the tumor vasculature have been evaluated in most experimental approaches.

**Targeting Cancer Vasculature** The molecular signature of the endothelial surface is tissue- and disease-specific, allowing one to direct functionalized nanoparticles to selected sites through vascular markers, via appropriate ligands, receptors, and enzymes. Drugs in cancer may be targeted using angiogenesis-associated molecules, such as the receptors for VEGF/VPF, bFGF, PDGF, or proteases associated with invasion, such as the matrix metallo- and serine-proteases. The use of angiogenesis inhibitors as drugs, including IFN $\alpha$ ,  $\beta$ , or  $\gamma$ , thrombospondins, TIMPs, and anti-VEGF antibody (Avastin), has been investigated. The inhibitors approach allows one to combine drug targeting and anti-angiogenic therapy. Gene therapy using liposome and poly(*N*-vinyl-2-pyrrolidone) delivery [112, 113] with the integrin  $\alpha v \beta 3$  and lipid-based cationic nanoparticles to target a mutant of Raf [114] has been shown to be a potential approach only in animal models. A web site exists that lists the clinical trials and molecules under evaluation [24].

**Macrophages** In cancer, macrophages have been used in the detection of lymph node metastasis with SPIONs (see Section 7.4.9). The targeting of tumor-associated macrophages for therapy has been little attempted to date, but might in

the near future become an option since these cells are involved in cancer progression. The lessons gained from knowledge acquired of immune, inflammatory, infectious and vascular disorders may be important.

#### 7.5.2.2 Targeting Cancer Markers

To achieve active targeting and drug delivery to the right cells based on molecular recognition processes, including ligand–receptor and antibody antigen, high expression at the tumor cell-surface of cancer-specific molecules is to be used. However, such molecules are frequently cancer-type specific and not expressed by all cancer cells in human cancers, resulting in resistance mechanisms. Pro-drugs, whose activation depends on specific biological properties of cancer cells, can also be useful in achieving treatment selectivity. Among these approaches, peptidase- or acid-sensitive linkers have been evaluated. For example, adriamycin conjugated to PEG via a linker containing Ala-Val, Ala-Pro, Gly-Pro sequences that can be cleaved by proteolytic enzymes displayed tumor cell selectivity [115]. Liposomes may be destabilized by enzymes, e.g., phospholipases or proteases, which are highly expressed and secreted in many cancers; depending on the lipid composition and structure, pH changes or the high redox potential associated with the cancer environment can also be useful for this purpose.

To achieve these goals, the methods of assembling recognition molecules on the surface of nanoparticles, through adsorption or chemical linkages, must be developed and validated. The surface density, orientation, presentation, spacing, and conformation of ligands on the surface of nanoparticles are crucial for the success of the ligand–receptor binding and, therefore, targeting and drug delivery. Particle stability, aggregation, and degradability may become problematic. If intracellular delivery of therapeutics is the goal, the choice of the ligand–receptor pair is of the utmost importance (phagocytosis, endocytosis, lipid rafts, receptor-mediated, etc.) for efficiency of internalization, the cellular localization of the nanoparticle payload, and the pattern of activation of cell signaling pathways.

These approaches may bypass multidrug resistance systems, but drug release from the carrier in a biological situation is still a major problem.

**Folate and Folate Receptor** One of the most investigated approaches involves the folate receptor, which is expressed at the surface of many cancer cells. Targeting may be obtained with folate linked to PEG to target folate receptors overexpressed on cancer cells, such as ovarian, lung, colorectal cancers, and internalization of the nanocarrier by this receptor [116]. Folate-PEGylated cyanoacrylate nanoparticles have been developed [104] and high affinity was achieved, probably due to increased multivalent interaction of folate-nanoparticles with the clustered folate receptors on the cell surface. As a consequence, increased internalization of encapsulated drug was achieved. Monodisperse (10 nm) magnetite nanoparticles, derivatized with PEG-folate, were more efficiently taken up than PEG or folate nanoparticles by breast cancer cells [117]. Folate-mediated uptake of folate-conjugated albumin nanoparticles (mean diameter 70 nm) prepared by a coacervation method and chemical crosslinking has been demonstrated in ovarian SKOV3 cancer cells

[118]. Polyamidoamine (PAMAM) dendrimers, <5 nm, conjugated to folic acid and methotrexate as anticancer agent were injected i.v. into folate receptor-positive human KB tumor-bearing immunodeficient mice. The folate-derived dendrimers concentrated in the tumor and methotrexate was internalized into tumor cells. The anti-tumor activity of methotrexate was increased and toxicity markedly decreased, allowing a tumor drug dosage not possible with the free drug [49].

**Antibodies** Targeting via monoclonal antibodies (listed in Table 7.1 of [24]) has been attempted, either as direct therapeutic agents or as carriers for drug delivery systems, to exploit differences between the expression of the corresponding antigens in cancer and normal cells [119].

Breast cancers express high levels of estrogen and EGF receptors, and prostate cancers express androgen receptors, which can also be used to achieve targeting. The ERB-2 receptor, a growth factor receptor belonging to the EGF receptor family, is overexpressed in about one-quarter of human breast cancers. An experimental study has used commercial liposomal doxorubicin, incubated with an anti-ErbB2 antibody coupled to modified PEG, to induce faster and greater tumor regression [120]. Chemical conjugation of mitoxantrone-loaded nanospheres and anti-C-erbB-2 monoclonal antibodies to nanospheres (665 nm mean diameter) prepared by an emulsion heating solidification technique displayed selective binding to breast cancer cells [121]. The conjugation of an anti-EGF receptor monoclonal antibody to colloidal gold nanoparticles increased their selectivity toward cancer cells versus non-cancer cells, suggesting their utility in both detection and targeted drug delivery [52]. Interaction of immunotargeted nanoshells, optically active nanoparticles, whose relative dimensions allow either the scattering or absorption light and, therefore, the imaging or photothermal destruction of target tissue, has been demonstrated in Her2-positive breast cancer cells [122].

**Carbohydrates** Liver cells express asialoglycoprotein, a galactose ligand, that has been evaluated as a target for primary or metastatic liver cancers. Nanoparticles based on biotinylated diamine-terminated PEG and using the galactose moiety of lactobionic acid as targeting agent and A11-transretinoic acid as drug have afforded a constant drug release *in vitro* over one month [123, 124].

**Transferrin Receptors** Transferrin receptors are overexpressed at the surface of many tumor cells, and have been used for liposomes or PEGylated liposomes of doxorubicin or cisplatin for intracellular targeting of tumor cells [125].

### 7.5.3

#### **Intracellular Drug Delivery**

Nanoparticles (nanovesicles, nanocontainers, liposomes) are generally internalized into cells via fluid phase endocytosis, receptor-mediated endocytosis or phagocytosis, resulting in the potential delivery of the nanoparticles in different cell compartments [125–128]. Efficient cytoplasmic delivery of drugs is important for drugs

whose action is intracellular, and sustained cytoplasmic delivery of drugs with intracellular receptors can only be envisioned using biodegradable nanoparticles [129].

Nanoparticle made from poly(DL-lactide-co-glycolide) can rapidly (of the order of minutes) escape the endo-lysosomal compartment, in intact form, after internalization, and reach the cytoplasm [102]. This escape mechanism is related to the anionic to cationic surface charge in the acidic environment of endosomes-lysosomes. pH-Sensitive liposomes have been designed using phospholipids/pH-sensitive polymethacrylate [130, 131], which become unstable at the acidic pH of lysosomes. Therefore, to date most approaches have involved pH effects between cellular compartments and surface-functionalized drug-loaded nanoparticles. Chitosan nanoparticles uptake was inhibited by chlorpromazine, suggesting clathrin-mediated endocytosis [132]. Wheat-germ agglutinin-PLGA nanoparticles were taken up by lung carcinoma cells according to a receptor-mediated, caveolae-dependent mechanism [133]. Exocytosis and intracellular retention are also factors that may control the efficacy of cellular delivery. A study using PLGA nanoparticles has shown that uptake is an endocytic, concentration, time and energy-dependent process [134]; however, a large proportion of the endocytosed nanoparticles were excreted from cells by an energy-dependent exocytic process as early as 30 min later [134].

Nanoparticle surface manipulations may be performed to increase cytoplasmic delivery, in particular with protein-transduction domain peptides [54, 135, 136] such as HIV-TAT peptides, or poly-Arg. These effects are related to the interaction of positively charged peptides with negatively charged heparan sulfate proteoglycans and sialic acid-containing glycoproteins, resulting in cell internalization of the complex by lipid-raft pinocytosis [137]; this is receptor independent, and then destabilization of the complex and release into the cytoplasm of the nanoparticle payload arises without fusion with lysosomes. However, cytotoxicity issues of the carrier have been raised.

Gene transfer by carrier destabilization via surface charge modification has also been used. Negatively charged nucleic acid material is adsorbed onto cationic polymeric nanoparticles, such as poly(ethyleneimine), and the complexes then undergo endocytosis. In the low pH of endosomes, the polycation-nucleic acid complexes are then released into the cytoplasm. Virus- or bacterial toxin-mimicking nanoparticles have been also used to achieve membrane disruption or forced-internalization. The viral components are intercalated between the lipid bilayer of 150 nm vesicles, and the structure is destabilized at the acidic pH of lysosomes. Gold particles modified with nuclear localization signal peptides were able to target the nucleus [96].

#### 7.5.4

#### **Development of the Necessary Chemistry: Synthetic Routes and Linkers for Conjugation**

Active targeting requires that selective ligands for defined tumor or tumor-associated cell markers are presented in adequate configuration and concentration

at the surface of nanoparticles. But this means that reactive groups must exist at the surface of nanoparticles for chemical coupling. PEG has been widely used to coat the surface of polyester or poly(alkyl cyanoacrylate), delaying phagocytosis by macrophages, and making them compatible for passive targeting by the increased vascular permeability associated to cancer [126, 138]. Polysaccharide (e.g., chitosan) coating may be a valuable alternative to PEG for this purpose, having the additional advantages of providing targeting by themselves for saccharide cell surface receptors, of being biocompatible and biodegradable [84], and being able to control the interactions with cells:

1. Dextran, pullulan and glycolipid, or sialic acid, decrease macrophage uptake;
2. hyaluronic acid provides bioadhesive properties;
3. functionalized dextran allows vascular targeting;
4. galactose-containing copolymer achieves liver targeting;
5. polysaccharide modified by vitamin H and biotin improved cancer targeting.

Preparation methods include (reviewed in Ref. [84]):

1. Adsorption on preformed nanoparticles. This depends on the relative polysaccharide and nanoparticle surface characteristics and chemical composition: hydrophobic, hydrophilic, covalent photopolymerization.
2. Incorporation during nanoparticle preparation: nano-coprecipitation or emulsion solvent evaporation (water–organic solvent) and stabilization with a surfactant (PVA or modified dextrans), diafiltration and sequential layering.
3. Copolymerization: alkyl cyanoacrylate chain elongation under basic conditions, or radical polymerization. A stabilizing agent (dextran) may be necessary and is important for particle characteristics, drug release.
4. Using preformed copolymer: polysaccharide backbone grafted with preformed polyester chains, and a core–shell structure.

In many situations, drugs have to be linked to the nanocarriers via *linkers*, several of which have been evaluated (Table 7.3).

## 7.6

### Overcoming the Mechanisms of Resistance to Therapy of Cancers

One important mechanism of resistance of tumors to treatment involves the poor distribution of drug into the tumor, high intratumoral osmotic pressure and/or short residence times at the tumor site. Another problem associated with cancer chemotherapy is the concentration of the active compounds to be reached in the tumor tissue at the expense of massive toxicity to the rest of the body, representing an obstacle to effective anti-tumor therapy. Most drugs currently used are active on cells in the process of cell division or proliferation. However, at any given time, a proportion of tumor cells are in a resting state and are, therefore, irresponsive to



Tab. 7.3. Some examples of linkers.

Linker	Ref.
Peptides	
Peptidyl spacers designed for cleavage by the lysosomal thiol-dependent (cysteine) proteases (Gly-Phe-Leu-Gly)	153, 154
Glu-Lys (cleaved with bovine trypsin)	155
Leu, Ala or Leu-Ala	154
Trp-Ser-Gln	156
Valine (less prone to ester hydrolysis)	157
Chemical	
4-Acyl-oxy-3-carboxybenzyloxy moiety (recognized by a specific lipase)	155
C4-Chain spacer tetramethylenediamine (TMDA, MW = 88)	158
Diaminated poly(ethylene glycol) (PEG, MW 3400)	158
Ester linker, formed between a hydroxyl-containing drug and a mercaptoacid	159
Ethylene glycobis(succinimidylsuccinate) (EGS): used to link particles having amino groups with each other via an ester linkage	160
Glutaraldehyde (crosslinker)	161
N-Hydroxysuccinimidyl active ester linker (synthesis with dianhydride)	74
Phenylacetyl derivatives, phenylacetamide moiety	162, 155
Scissile linkers	155
Succinic acid, glutaric acid	163
3-Sulfanylpropionyl	159
4-Sulfanylbutyryl	159
Triazene	164, 165
Dual linker systems	166
Coupling agents for peptide synthesis:	115
1-ethyl-3-(3-dimethylaminopropyl)carbodiimide (EDCI) N-succinimidyl 3-(2-pyridyldithio) propionate (SPDP) N-hydroxysuccinimide N,N'-methylene bis-acrylamide	

the drug. Thus it is necessary to maintain the drugs for a long period at the tumor site. Nanoparticles with long, controlled drug release may thus ameliorate this defect in anticancer treatment.

A second important mechanism of resistance of cancer cells to therapeutic drugs is the simultaneous resistance mechanisms linked to ATP-driven efflux pumps (MDR, Pgp) able to efflux positive drugs (such as doxorubicin) out of cells. Resistance may appear at the onset of therapy, or later during treatment. It is mainly linked to ATP-driven cell membrane efflux pumps on the tumor cells or the tumor-associated vascular cells, or as detoxifying enzymes expressed by these cells. Increased efficacy of PIHCA-doxorubicin was dependent on an increased adsorption of nanoparticles to the cell surface, and to increased diffusion of doxorubicin forming ion pairs between the drug and cyanoacrylic monomer degradation product [139]. This effect was initially observed with cyanoacrylate polymers. Inhibitors of Pgp (verapamil, amiodarone, cyclosporine), or the encapsulation of drugs into colloidal carriers, shield drugs from Pgp, which recognizes drugs associated to the membrane but not in the cytoplasm. Inhibitors for pumps, or for detoxifying enzymes, may be co-administered, or anticancer drugs delivered using nanoparticles able to overcome the resistance of pumps. Since the amino sugar of doxorubicin is a substrate for Pgp, doxorubicin was covalently coupled to PEG-poly(Asp) (MW 14 400 and 3500 kDa, respectively) block copolymer before micelle formation or to gelatin, but without success, probably due to poor diffusion of the drug out of the carrier. Co-encapsulation of the Pgp inhibitor cyclosporin with doxorubicin into PICBA inhibited efficiently growth of doxorubicin-resistant tumor cells, by continuous and simultaneous release of both drugs by polymer biodegradation [140, 141]. Doxorubicin encapsulated in poly(alkyl cyanoacrylate) PIHCA nanoparticles was able to kill Pgp-positive tumor cells, but not PIBCA nanospheres, which are more rapidly degraded and do not enter cells [139, 142–144]. This effect requires direct contact between the carrier and tumor cells and was mediated by poly(alkyl cyanoacrylate) degradation products, which formed ion-pairs with the drug, and the doxorubicin concentration was increased in tumor cells. Pgp remains active. The same effect was obtained by encapsulating doxorubicin in the core and expressing cyclosporin A at the surface of the nanoparticles. Pluronic block copolymer may inhibit the efflux pumps (MDR/P-glycoproteins), and their gene expression, on the endothelial cells forming the blood–brain barrier (BBB) [145, 146] that protects the brain from unwanted chemicals, but which are also involved in the resistance of brain tumors to chemotherapeutic agents. Therefore, they may be of interest in the treatment of brain cancer only if they can be made selective to tumor-associated endothelium.

## 7.7 Toxicity Issues

For more extensive reviews see Refs. [5, 6]. Nanoparticles interact differently with organs, tissues and cells than do larger particles made of the same components.

Therefore, the evaluation of toxicity performed with larger particles cannot be extrapolated to nanoparticles without control. The hazards of inhaled micro- and nanoparticles in air pollution are well established, epidemiological and toxicological studies have coherently demonstrated pro-inflammatory and prothrombotic adverse effects in diverse organs. There is virtually no toxicological data available, for patients, researchers or medical workers concerning the new types of nanoparticles under development for drug delivery. Size and surface modification may modify biocompatibility and biodistribution, and a combination of drugs, devices and biological agents may behave differently than each agent separately – therefore combination approval must be obtained from drug control agencies. The exact mechanisms of interaction of nanovectors and cells have been determined in very few situations. Therefore, coordinated studies will be rapidly needed to address these issues. Nanostructures can minimize solubility and stability problems, and improve the negative impact of drugs to collateral non-tumoral tissues and organs. However, nanomaterials themselves may be cytotoxic [147, 148] or induce and/or potentiate cell death [149, 150] or immunogenic reactions, or nanoparticle aggregates may clog small blood vessels. For example, micelles of cisplatin differently induced gene expression than cisplatin alone [149], and degradation products from poly(L-lactic acid) were cytotoxic for immune cells [150].

Gene therapy with viruses has had poor success and many problems have been linked to immunogenic reaction to the viral vector constituents, and random integration in the genome. Therefore, cationic nanoparticle vectors have been designed to complete viral vectors. Polycations are cytotoxic for cells, inducing mitochondria-mediated necrosis and/or apoptosis or membrane destabilization and pore-formation mediated by interactions of polycations with negatively-charged cell-surface glycoproteins or actin [151]. The interactions of cationic polymers with mitochondria need to be better understood, in particular with the proteins of the bcl-2 family. Hypersensitivity reactions secondary to complement activation and induced by infusion of PEG-modified liposomes [152] may be a potential problem with these materials. Careful design of the polymer formulation and surface functionalization is needed to reduce these side effects. Therefore, nanoparticle design and polymer formulation and functionalization for gene therapy *in vivo* must be carefully optimized before such treatments can be envisioned.

To gain wide acceptance of nanovectors as anticancer delivery agents, the following toxicity issues need to be addressed:

- The ultimate biological fate of nanomaterials, and their degradation products, particularly non-biodegradable nanomaterials such as functionalized poly(ethylene glycol).
- The immunological and pharmacological activities and toxicities.
- Possible interferences with cellular machineries, gene expression, protein processing.
- Short- and long-term consequences of exposure to nanovectors.
- How *in vitro* studies translate to *in vivo* application.

## 7.8

### Conclusions

In summary, medical benefits can be expected within the next 10 years from the branch of nanotechnology named “Nanomedicine”. However, for drug delivery, nanocarriers have to become smarter, and the biophysical, biochemical and biological processes and the mechanisms associated with the interaction of nanoparticles with living tissue, at large, must be understood in detail to design optimized materials for defined therapeutic goals. This includes carrier stability, targeting, extracellular and intracellular drug release mechanisms, overcoming mechanisms of resistance to biological barriers and to anticancer agents, and understanding the immunogenic reaction mechanisms of the nanodevices, and toxicity issues in great detail. The future of nanomedicine will in part depend on the rational design of smart nanoparticles.

#### 7.8.1

##### Opportunities and Challenges of Nanomedicine in Cancer

1. Passive targeting effects can enhance the amounts of drug at tumor sites, but circumstantial or active targeting can be designed to improve the selectivity and specificity of drug delivery; therefore, combining these approaches may greatly increase the quality of cancer treatment.
2. Targeted drug delivery systems can improve the therapeutic index of approved drugs.
3. New drugs that are macromolecules, proteins, peptides, oligonucleotides or plasmids will need such delivery systems to achieve an efficient local concentration.
4. Externally activated (ultrasound, irradiation, magnetic field, photodynamic therapy, etc.) drug delivery of therapeutic agents can be designed to control the timing of drug delivery and administration schedules, without multiple injections.
5. Overcoming of the biological barriers:
  - Including tight junctions (BBB) and epithelial barriers.
  - Using permeation enhancers: tight junction opening agents, osmotic shock.
  - Avoiding the RES: using surface modification of nanoparticles, e.g., by poly(ethylene glycol)s.
  - Controlling sensitization reactions: protein-dendrimers are highly immunogenic.
  - Overpassing intratumoral increased osmotic barriers: limit to the diffusion of nanoparticles and drugs.
6. Challenges also include the control of drug release and bioavailability at the tumor site, enhancing selective targeting, and achieving controlled and efficient intracellular delivery, together with acceptable toxicological hazards.

Therefore, an ideal nanovector should look as shown in Fig. 7.2. One representation of the ideal goal is an injectable nanoparticle for targeted drug delivery, without, or with highly reduced, collateral toxicity, and with a reporter device.

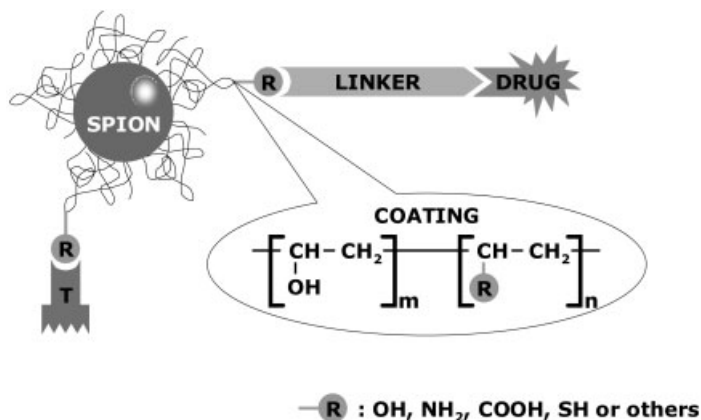


**Fig. 7.2.** Ideal drug delivery nanovector, containing a reporter system (SPION), a targeting agent (T) linked to the polymer, and a drug linked to the polymer via a releasing linker.

## References

- 1 GORDON, E. M., HALL, F. L., Nanotechnology blooms, at last, *Oncol. Rep.*, **2005**, 13, 1003–1007.
- 2 DAVIS, S. S., Biomedical applications of nanotechnology – Implications for drug targeting and gene therapy, *Trends Biotechnol.*, **1997**, 15, 217–224.
- 3 DUNCAN, R., The dawning era of polymer therapeutics, *Nat. Rev. Drug Discov.*, **2003**, 2, 347–360.
- 4 RABINOW, B. E., Nanosuspensions in drug delivery. *Nat. Rev. Drug Discov.*, **2004**, 3, 785–796.
- 5 MOGHIMI, S. M., HUNTER, A. C., MURRAY, J. C., Nanomedicine: Current status and future prospects, *FASEB J.*, **2005**, 19, 311–330.
- 6 FERRARI, M., Cancer nanotechnology: Opportunities and challenges, *Nat. Rev., Cancer*, **2005**, 5, 161–171.
- 7 SATCHI-FAINARO, R., PUDER, M., DAVIES, J. W., TRAN, H. T., SAMPSON, D. A., GREENE, A. K., CORFAS, G., FOLKMAN, J., Targeting angiogenesis with a conjugate of HPMA copolymer and TNP-470, *Nat. Med.*, **2004**, 10, 255–261.
- 8 BATRAKOVA, E. V., DORODNYCH, T. Y., KLINSKII, E. Y., KLIUSHNENKOVA, E. N., SHEMCHUKOVA, O. B., GONCHAROVA, O. N., ARJAKOV, S. A., ALAKHOV, V. Y., KABANOV, A. V., Anthracyclin antibiotics noncovalently incorporated into block copolymer micelles: In vivo evaluation of anticancer activity, *Br. J. Cancer*, **1996**, 74, 1545–1552.
- 9 DANSON, S., FERRY, D., ALAKHOV, V., MARGISON, J., KERR, D., JOWLE, D., BRAMPTON, M., HALBERT, G., RANSON, M., Phase I dose escalation and pharmacokinetic study of pluronic polymer-bound doxorubicin (SP1049C) in patients with advanced cancer, *Br. J. Cancer*, **2004**, 90, 2085–2091.
- 10 YASUGI, K., NAGASAKI, Y., KATO, M., KATAOKA, K., Preparation and characterization of polymer micelles from poly(ethylene glycol)-poly(D, L-lactide) block copolymers as potential drug carrier, *J. Controlled Release*, **1999**, 62, 89–100.
- 11 NAKANISHI, T., FUKUSHIMA, S., OKAMOTO, K., SUZUKI, M., MATSUMURA, Y., YOKOYAMA, M., OKANO, T., SAKURAI, Y., KATAOKA, K., Development of the polymer micelle

- carrier system for doxorubicin, *J. Controlled Release*, **2001**, 74, 295–302.
- 12 ALLEN, T. M., CULLIS, P. R., Drug delivery systems: Entering the mainstream, *Science*, **2004**, 303, 1818–1822.
  - 13 LÜBBE, A. S., ALEXIOU, C., BERGEMANN, C., Clinical applications of magnetic drug targeting, *J. Surg. Res.*, **2001**, 95, 200–206.
  - 14 ULBRICH, K., SUBR, V., Polymeric anticancer drugs with pH-controlled activation, *Adv. Drug Deliv. Rev.*, **2004**, 56, 1023–1050.
  - 15 KIM, C. K., LIM, S. J., Recent progress in drug delivery systems for anticancer agents, *Arch. Pharm. Res.*, **2002**, 25, 229–239.
  - 16 KREUTER, J., Influence of the surface properties on nanoparticle-mediated transport of drugs to the brain, *J. Nanosci. Nanotechnol.*, **2004**, 4, 484–488.
  - 17 JULYAN, P. J., SEYMOUR, L. W., FERRY, D. R., DARYANI, S., BOIVIN, C. M., DORAN, J., DAVID, M., ANDERSON, D., CHRISTODOULOU, C., YOUNG, A. M., HESSLEWOOD, S., KERR, D. J., Preliminary clinical study of the distribution of HPMA copolymers bearing doxorubicin and galactosamine, *J. Controlled Release*, **1999**, 57, 281–290.
  - 18 WYMAN, T. B., NICOL, F., ZELPHATI, O., SCARIA, P. V., PLANK, C., SZOKA, F. C., Design, synthesis and characterization of a cationic peptide that binds to nucleic acids and permeabilize bilayers, *Biochemistry*, **1997**, 36, 3008–3017.
  - 19 ETRYCH, T., JELINKOVA, M., LHOVA, B., ULBRICH, K., New HPMA copolymers containing doxorubicin bound via pH-sensitive linkage: Synthesis and preliminary in vitro and in vivo biological properties, *J. Controlled Release*, **2001**, 73, 89–102.
  - 20 LEROUX, J. C., ROUX, E., LEGARREC, D., HONG, K., DRUMMOND, D. C., N-isopropylacrylamide copolymers for the preparation of pH-sensitive liposomes and polymeric micelles, *J. Controlled Release*, **2001**, 72, 71–84.
  - 21 STRAUBINGER, R. M., pH-sensitive liposomes for delivery of macro-molecules into cytoplasm of culture cells, *Methods Enzymol.*, **1993**, 221, 361–376.
  - 22 PRASMICKAITE, L., HOGSET, A., BERG, K., Evaluation of different photosensitizers for use in photochemical gene transfection, *Photochem. Photobiol.*, **2001**, 73, 388–395.
  - 23 BRIGGER, I., CHAMINADE, P., MARSAUD, V., APPEL, M., BESNARD, M., GURNY, R., RENOIR, M., COUVREUR, P., Tamoxifen encapsulation within polyethylene glycol-coated nanospheres. A new antiestrogen formulation, *Int. J. Pharm.*, **2001**, 214, 37–42.
  - 24 BRANNON-PEPPAS, L., BLANCHETTE, J. O., Nanoparticle and targeted systems for cancer therapy, *Adv. Drug Deliv. Rev.*, **2004**, 56, 1649–1659.
  - 25 OH, I., LEE, K., KWON, H. Y., LEE, Y. B., SHIN, S. C., CHO, C. S., KIM, C. K., Release of adriamycin from poly(gamma-benzyl-L-glutamate)/poly(ethylene oxide) nanoparticles, *Int. J. Pharm.*, **1999**, 181, 107–115.
  - 26 CHEN, J. H., LING, R., YAO, Q., WANG, L., MA, Z., LI, Y., WANG, Z., XU, H., Enhanced antitumor efficacy on hepatoma-bearing rats with adriamycin-loaded nanoparticles administered into hepatic artery, *World J. Gastroenterol.*, **2004**, 10, 1989–1991.
  - 27 SOMA, C. E., DUBERNET, C., BARRATT, G., BENITA, S., COUVREUR, P., Investigation of the role of macrophages on the cytotoxicity of doxorubicin and doxorubicin-loaded nanoparticles on M5076 cells in vitro, *J. Controlled Release*, **2000**, 68, 283–289.
  - 28 GULYAEV, A. E., GELPERINA, S. E., SKIDAN, I. N., ANTROPOV, A. S., KIVMAN, G. Y., KREUTER, J., Significant transport of doxorubicin into the brain with polysorbate 80-coated nanoparticles, *Pharm. Res.*, **1999**, 16, 1564–1569.
  - 29 OH, K. S., LEE, K. E., HAN, S. S., CHO, S. H., KIM, D., YUK, S. H., Formation of core/shell nanoparticles with a lipid core and their application as a drug delivery system, *Biomacromoles*, **2005**, 6, 1062–1067.
  - 30 SERPE, L., CATALANO, M. G., CAVALLI,

- R., UGAZIO, E., BOSCO, O., CANAPARO, R., MUNTONI, E., FRAIRIA, R., GASCO, M. R., EANDI, M., ZARA, G. P., Cytotoxicity of anticancer drugs incorporated in solid lipid nanoparticles on HT-29 colorectal cancer cell line, *Eur. J. Pharm. Biopharm.*, **2004**, 58, 673–680.
- 31 BARRAUD, L., MERLE, P., SOMA, E., LEFRANCOIS, L., GUERRET, S., CHEVALLIER, M., DUBERNET, C., COUVREUR, P., TREPO, C., VITVITSKI, L., Increase of doxorubicin sensitivity by doxorubicin-loading into nanoparticles for hepatocellular carcinoma cells in vitro and in vivo, *J. Hepatol.*, **2005**, 42, 736–743.
- 32 TEN TIJE, A. J., VERWEIJ, J., LOOS, W. J., SPARREBOOM, A., Pharmacological effects of formulation vehicles: Implications for cancer chemotherapy, *Clin. Pharmacokin.*, **2003**, 42, 665–685.
- 33 WANG, Y. M., SATO, H., DACHI, I., HORIKOSHI, I., Preparation and characterization of poly(lactic-co-glycolic acid) microspheres for targeted delivery of novel anticancer agent, taxol, *Chem. Pharm. Bull.*, **1996**, 44, 1935–1940.
- 34 SI-SHEN, F., GUOFENG, H., Effect of emulsifiers on the controlled release of paclitaxel/taxol from nanospheres of biodegradable polymer, *J. Controlled Release*, **2001**, 71, 53–69.
- 35 FONSECA, CM, SIMOES, S., GASPAR, R., Paclitaxel-loaded PLGA nanoparticles: Preparation, physicochemical characterization, and in vitro antitumoral activity, *J. Controlled Release*, **2002**, 83, 273–286.
- 36 MU, L., FENG, S. S., A novel controlled release formulation for the anticancer drug paclitaxel (taxol):PLGA nanoparticles containing vitamin E TPGS, *J. Controlled Release*, **2003**, 86, 33–48.
- 37 CHEN, D. B., YANG, T. Z., LU, W. L., ZHANG, Q., In vitro and in vivo study of two types of long-circulating solid lipid nanoparticles containing paclitaxel, *Chem. Pharm. Bull.*, **2001**, 49, 1444–1447.
- 38 FENG, S. S., MU, L., WIN, K. Y., HUANG, G., Nanoparticles of biodegradable polymers for clinical administration of paclitaxel, *Curr. Med. Chem.*, **2004**, 11, 413–424.
- 39 DONG, Y., FENG, S. S., Methoxy poly(ethylene glycol)-poly(lactide) (MPEG-PLA) nanoparticles for controlled delivery of anticancer drugs, *Biomaterials*, **2004**, 25, 2843–2849.
- 40 HAMAGUCHI, T., MATSUMURA, Y., SUZUKI, M., SHIMIZU, K., GODA, R., NAKAMURA, I., NAKATOMI, I., YOKOYAMA, M., KATAOKA, K., KAKIZOE, T., NK105, a paclitaxel-incorporating micellar nanoparticle formulation, can extend in vivo antitumor activity and reduce the neurotoxicity of paclitaxel, *Br. J. Cancer*, **2005**, 92, 1240–1246.
- 41 LI, S., JIANG, W. Q., WANG, A. X., GUAN, Z. Z., PAN, S. R., Studies on 5-FU/PEG-PBLG nano-micelles: Preparation, characteristics, and drug releasing in vivo, *Aizheng*, **2004**, 23, 381–385.
- 42 SHENOY, D. B., AMIJI, M. M., Poly(ethylene oxide)-modified poly(epsilon-caprolactone) nanoparticles for targeted delivery of tamoxifen in breast cancer, *Int. J. Pharm.*, **2005**, 293, 261–270.
- 43 MAILLARD, S., AMELLER, T., GAUDUCHON, J., GOUGELET, A., GOUILLEUX, F., LEGRAND, P., MARSAUD, V., FATTAL, E., SOLA, B., RENOIR, J. M., Innovative drug delivery nanosystems improve the anti-tumor activity in vitro and in vivo of anti-estrogens in human breast cancer and multiple myeloma, *J. Steroid Biochem. Mol. Biol.*, **2005**, 94, 111–121.
- 44 AVGOUSTAKIS, K., BELETSI, A., PANAGI, Z., KLEPTSANIS, P., KARYDAS, A. G., ITHAKISSIOS, D. S., PLGA-mPEG nanoparticles of cisplatin: In vitro nanoparticles degradation, in vitro drug release and in vivo drug residence in blood properties, *J. Controlled Release*, **2002**, 79, 123–135.
- 45 LU, C., PEREZ-SOLER, R., PIPERDI, B., WALSH, G. L., SWISHER, S. G., SMYTHE, W. R., SHIN, H. J., RO, J. Y., FENG, L., TRUONG, M., YALAMANCHILI, A., LOPEZ-BERESTEIN, G., HONG, W. K., KHOBAR, A. R.,

- SHIN, D. M., Phase II study of a liposome-entrapped cisplatin analog (L-NDDP) administered intrapleurally and pathologic response rates in patients with malignant pleural mesothelioma, *J. Clin. Oncol.*, **2005**, *23*, 3495–3501.
- 46 MARR, A. K., KURZMAN, I. D., VAIL, D. M., Preclinical evaluation of a liposome-encapsulated formulation of cisplatin in clinically normal dogs, *Am. J. Vet. Res.*, **2004**, *65*, 1474–1478.
- 47 HOVING, S., VAN TIEL, S. T., EGGERMONT, A. M., TEN HADEN, T. L., Effect of low-dose tumor necrosis factor- $\alpha$  in combination with STEALTH liposomal cisplatin (SPI-077) on soft-tissue- and osteosarcoma-bearing rats, *Anticancer Res.*, **2005**, *25*, 743–750.
- 48 ZHANG, Y., ZHUO, R. X., Synthesis and drug release behavior of poly(trimethylene carbonate)-poly(ethylene glycol)-poly(trimethylene carbonate) nanoparticles, *Biomaterials*, **2005**, *26*, 2089–2094.
- 49 KUKOWSKA-LATALLO, J. F., CANDIDO, K. A., CAO, Z., NIGAVEKAR, S. S., MAJOROS, I. J., THOMAS, T. P., BALOGH, L. P., KHAN, M. K., BAKER, J. R., Nanoparticles targeting of anticancer drug improves therapeutic response in animal model of human epithelial cancer, *Cancer Res.*, **2005**, *65*, 5317–5324.
- 50 CEGNAR, M., KOS, J., KRISTL, J., Cystatin incorporated in poly(lactide-co-glycolide) nanoparticles: Development and fundamental studies on preservation of its activity, *Eur. J. Pharm. Sci.*, **2004**, *22*, 357–364.
- 51 CEGNAR, M., PREMZL, A., ZAVASNIK-BERGANT, V., KRISTL, J., KOS, J., Poly(lactide-co-glycolide) nanoparticles as a carrier system for delivering cysteine protease inhibitor cystatin into tumor cells, *Exp. Cell Res.*, **2004**, *301*, 223–231.
- 52 EL-SAYED, I. H., HUANG, X., EL-SAYED, M. A., Surface plasmon resonance scattering and absorption of anti-EGFR antibody conjugated gold nanoparticles in cancer diagnostics: Applications in oral cancer, *NanoLetters*, **2005**, *5*, 829–834.
- 53 ITO, A., KUGA, Y., HONDA, H., KIKKAWA, H., HORIUCHI, A., WATANABE, Y., KOBAYASHI, T., Magnetite nanoparticle-loaded anti-HER2 immunoliposomes for combination of antibody therapy with hyperthermia, *Cancer Lett.*, **2004**, *212*, 167–1675.
- 54 KOCH, A. M., REYNOLDS, F., MERKLE, H. P., WEISSLEDER, R., JOSEPHSON, L., Transport of surface-modified nanoparticles through cell monolayers, *Chembiochem*, **2005**, *6*, 337–345.
- 55 LIM, S. J., LEE, M. K., KIM, C. K., Altered chemical and biological activities of all-trans retinoic acid incorporated in solid lipid nanoparticle powders, *J. Controlled Release*, **2004**, *100*, 53–61.
- 56 YANG, K., WEN, Y., WANG, C., Clinical application of anticancer nanoparticles targeting metastasis foci of cervical lymph nodes in patients with oral carcinoma, *Hua Xi Kou Qiang Yi Xue Za Zhi*, **2003**, *21*, 447–450.
- 57 ROY, I., OHULCHANSKY, T. Y., PUDAVAR, H. E., BERGEY, E. J., OSEROFF, A. R., MORGAN, J., DOUGHERTY, T. J., PRASAD, P. N., Ceramic-based nanoparticles entrapping water-insoluble photosensitizing anticancer drugs: A novel drug-carrier system for photodynamic therapy, *J. Am. Chem. Soc.*, **2003**, *125*, 7860–7865.
- 58 TANG, W., XU, H., KOPELMAN, R., PHILBERT, M. A., Photodynamic characterization and in vitro application of methylene blue-containing nanoparticle platforms, *Photochem. Photobiol.*, **2005**, *81*, 242–249.
- 59 ALLEMAN, E., ROUSSEAU, J., BRASSEUR, N., KUDREVICH, S. V., LEWIS, K., VAN LIER, J. E., Photodynamic therapy of tumors with hexadecafluoro zinc phthalocyanine formulated in PEG-coated poly(lactic acid) nanoparticles, *Int. J. Cancer*, **1996**, *66*, 821–824.
- 60 PACK, D. W., HOFFMAN, A. S., PUN, S., STATON, P. S., Design and development of polymers for gene



- therapy, *Nat. Rev. Drug Discov.*, **2005**, *4*, 581–593.
- 61 BRIGGER, I., DUBERNET, C., COUVREUR, P., Nanoparticles in cancer therapy and diagnosis, *Adv. Drug Deliv. Rev.*, **2002**, *54*, 631–651.
- 62 KUMAR, R. M., HELLERMANN, G., LOCKEY, R. F., MOHAPATRA, S. S., Nanoparticle-mediated gene delivery: State of the art, *Expert Opin. Biol. Ther.*, **2004**, *4*, 1213–1224.
- 63 CAO, Z. G., ZHOU, S. W., SUN, K., LU, X. B., LUO, G., LIU, J. H., Preparation and feasibility of superparamagnetic dextran iron oxide nanoparticles as gene carrier, *Aizheng*, **2004**, *23*, 1105–1109.
- 64 LIU, T., TANG, A., ZHANG, G., CHEN, Y., ZHANG, J., PENG, S., CAI, Z., Calcium phosphate nanoparticles as a novel nonviral vector for efficient transfection of DNA in cancer gene therapy, *Cancer Biother. Radiopharm.*, **2005**, *20*, 141–149.
- 65 KIANG, T., BRIGHT, C., CHEUNG, C. Y., STAYTON, P. S., HOFFMAN, A. S., LEONG, K. W., Formulation of chitosan-DNA nanoparticles with poly(propyl acrylic acid) enhances gene expression, *J. Biomater.*, **2004**, *15*, 1405–1421.
- 66 CHIANNIKULCHAI, N., AMMOURY, N., CAILLOU, B., DEVISSAGUET, J. P., COUVREUR, P., Hepatic tissue distribution of doxorubicin-loaded particles after i. v. administration in reticulosarcoma M 5076 metastasis-bearing mice, *Cancer Chemother. Pharmacol.*, **1990**, *26*, 122–126.
- 67 VERDUN, C., BRASSEUR, F., VRANCKS, H., COUVREUR, P., ROLAND, M., Tissue distribution of doxorubicin associated with polyhexylcyanoacrylate nanoparticles, *Cancer Chemother. Pharmacol.*, **1990**, *26*, 13–18.
- 68 CHIANNIKULCHAI, N., DRIOUCH, Z., BENOIT, J. P., PARODI, A. L., COUVREUR, P., Doxorubicin-loaded nanoparticles: Increased efficiency in murine hepatic metastasis, *Sel. Cancer Ther.*, **1989**, *5*, 1–11.
- 69 BRASSEUR, F., COUVREUR, P., KANTE, B., DECKERS-PASSAU, L., ROLAND, M., DECKERS, C., SPEISER, P., Actinomycin D adsorbed on polymethylcyanoacrylate nanoparticles: Increased efficiency against an experimental tumor, *Eur. J. Cancer*, **1980**, *10*, 1441–1445.
- 70 COUVREUR, P., KANTE, B., LENAERTS, V., SCAILTEUR, V., ROLAND, M., SPEISER, P., Tissue distribution of antitumor drugs associated with polyalkylcyanoacrylate nanoparticles, *J. Pharm. Sci.*, **1980**, *69*, 199–202.
- 71 TU, R. S., TIRRELL, M., Bottom-up design of biomimetic assemblies, *Adv. Drug Deliv. Rev.*, **2004**, *56*, 1537–1563.
- 72 NAGASAKI, Y., KUTSUNA, T., IJIMA, M., KATO, M., KATAOKA, K., KITANO, S., KADOMA, Y., Formyl-ended heterobifunctional poly(ethylene oxide) synthesis of poly(ethylene oxide) with a formyl group at one end and a hydroxyl group at the other end, *Bioconj. Chem.*, **1996**, *6*, 231–233.
- 73 LEE, K. B., YOON, K. R., WOO, S. I., CHOI, I. S., Surface modification of poly(glycolic acid) (PGA) for biomedical applications, *J. Pharm. Sci.*, **2003**, *92*, 933–937.
- 74 SHAO, H., ZHANG, Q., GOODNOW, R., CHEN, L., TAM, A new polymer-bound N-hydroxysuccinimidyl active ester linker, *Tetrahedron Lett.*, **2000**, *41*, 4257–4260.
- 75 LU, Y., CHEN, S. C., Micro- and nanofabrication of biodegradable polymers for drug delivery, *Adv. Drug Deliv. Rev.*, **2004**, *56*, 1621–1333.
- 76 MARTINEZ BARBOSA, M. E., CAMMAS, S., APPEL, M., PONCHEL, G., Investigation of the degradation mechanisms of poly(malic acid) esters in vitro and their related cytotoxicities on J774 macrophages, *Biomacromolecules*, **2004**, *5*, 137–143.
- 77 CAMMAS, S., BEAR, M. M., MOINE, L., ESCALUP, R., PONCHEL, G., KATAOKA, K., GUERIN, P., Polymers of malic acid and 3-alkylmalic acid as synthetic PHAs in the design of biocompatible hydrolyzable devices, *Int. J. Biol. Macromol.*, **1999**, *25*, 273–282.
- 78 CAMMAS, S., NAGASAKI, Y., KATAOKA, K., Heterobifunctional poly(ethylene oxide): Synthesis of alpha-methoxy-omega-amino and alpha-hydroxy-omega-amino PEOs with the same

- molecular weights, *Bioconj. Chem.*, **1995**, *6*, 226–230.
- 79** MISSIRLIS, D., TIRELLI, N., HUBBELL, J. A., Amphiphilic hydrogel nanoparticles. Preparation, characterization, and preliminary assessment as new colloidal drug carriers, *Langmuir*, **2005**, *21*, 2605–2613.
- 80** ROSSIGNOL, H., BOUSTA, M., VERT, M., Synthetic poly(beta-hydroxyalkanoates) with carboxylic acid or primary amine pendent groups and their complexes, *Int. J. Biol. Macromol.*, **1999**, *25*, 255–264.
- 81** GRAZIA CASCONI, M., ZHU, Z., BORSSELLI, F., LAZZERI, L., Poly(vinyl alcohol) hydrogels as hydrophilic matrices for the release of lipophilic drugs loaded in PLGA nanoparticles, *J. Mater. Sci. -Mater. Med.*, **2002**, *13*, 29–32.
- 82** SOLARO, R., CHIELLINI, F., SIGNORI, F., FIUMI, C., BIZZARRI, R., CHIELLINI, E., Nanoparticle systems for the targeted release of active principles of proteic nature, *J. Mater. Sci. -Mater. Med.*, **2003**, *14*, 705–711.
- 83** WIN, K. Y., FENG, S. S., Effects of particle size and surface coating on cellular uptake of polymeric nanoparticles for oral delivery of anticancer drugs, *Biomaterials*, **2005**, *26*, 2713–2711.
- 84** LEMARCHAND, C., GREF, R., COUVREUR, P., Polysaccharide-decorated nanoparticles, *Eur. J. Pharm. Biopharm.*, **2004**, *58*, 327–341.
- 85** VAUTHIER, C., DUBERNET, C., CHAUVIERRE, C., BRIGGER, I., COUVREUR, P., Drug delivery to resistant tumors: The potential of poly(alkyl cyanoacrylate) nanoparticles, *J. Controlled Release*, **2003**, *93*, 151–160.
- 86** XIONG, X. Y., TAM, K. C., GAN, L. H., Release kinetics of hydrophobic and hydrophilic model drugs from pluronic F127/poly(lactic acid) nanoparticles, *J. Controlled Release*, **2005**, *103*, 73–82.
- 87** ZENG, Y., PITT, W. G., Poly(ethylene oxide)- $\beta$ -poly(N-isopropylacrylamide) nanoparticles with cross-linked cores as drug carriers, *J. Biomater. Sci. Polymer Ed.*, **2005**, *16*, 371–380.
- 88** HILT, J. Z., BYRNE, M. E., Configurational biomimesis in drug delivery: Molecular imprinting of biologically significant molecules, *Adv. Drug Deliv. Rev.*, **2004**, *56*, 1599–1620.
- 89** LO, C. L., LIN, K. M., HSIUE, G. H., Preparation and characterization of intelligent core-shell nanoparticles based on poly(d, l-lactide)-g-poly(N-isopropyl acrylamide-co-methacrylic acid), *J. Controlled Release*, **2005**, *104*, 477–488.
- 90** XIA, X., HU, Z., MARQUEZ, M., Physically bonded nanoparticle networks: A novel drug delivery system, *J. Controlled Release*, **2005**, *103*, 21–30.
- 91** REHOR, A., HUBBELL, J. A., TIRELLI, N., Oxidation-sensitive polymeric nanoparticles, *Langmuir*, **2005**, *21*, 411–417.
- 92** ALEXIOU, C., ARNOLD, W., KLEIN, R. J., PARAK, F. G., HULIN, P., BERGEMANN, C., ERHARDT, W., WAGENPEIL, S., LÜBBE, A. S., Locoregional cancer treatment with magnetic drug targeting, *Cancer Res.*, **2000**, *60*, 6641–6648.
- 93** RUDGE, S., PETERSON, C., VESSELY, C., KODA, J., STEVENS, S., CATERALL, L., Adsorption and desorption of chemotherapeutic drugs from a magnetically targeted carrier (MTC), *J. Controlled Release*, **2001**, *74*, 335–340.
- 94** JAIN, T. K., MORALES, M. A., SAHOO, S. K., LESLIE-PELECKI, D. L., LABHASETWAR, V., Iron oxide nanoparticles for sustained delivery of anticancer agents, *Mol. Pharm.*, **2005**, *2*, 194–205.
- 95** GUPTA, A. K., GUPTA, M., Synthesis and surface engineering of iron oxide nanoparticles for biomedical applications, *Biomaterials*, **2005**, *26*, 3995–4021.
- 96** TKACHENKO, A. G., XIE, H., COLEMAN, D., GLOMM, W., RYAN, J., ANDERSON, M. F., FRANZEN, S., FELDHEIM, D. L., Multifunctional gold nanoparticle-peptide complexes for nuclear targeting, *J. Am. Chem. Soc.*, **2003**, *125*, 4700–4701.
- 97** LUBBE, A. S., BERGEMANN, C., HUHNT, W., FRICKE, T., RIESS, H.,

- BROCK, J. W., HUHN, D., Preclinical experiences with magnetic drug targeting: Tolerance, and efficacy, *Cancer Res.*, **1996**, *56*, 4694–4701.
- 98 FLYNN, E. R., BRYANT, H. C., A biomagnetic system for in vivo cancer imaging, *Phys. Med. Biol.*, **2005**, *50*, 1273–1293.
- 99 GONG, L. S., ZHANG, Y. D., LIU, S., Target distribution of magnetic albumin nanoparticles containing adriamycin in transplanted rat liver cancer model, *Hepatobil. Pancr. Dis. Int.*, **2004**, *3*, 365–368.
- 100 ZHANG, Y., KOHLER, N., ZHANG, M., Surface modification of superparamagnetic magnetite nanoparticles and their intracellular uptake, *Biomaterials*, **2002**, *23*, 1553–1561.
- 101 WILHELM, C., BILLOTEY, C., ROGER, J., PONS, J. N., BACRI, J. C., GAZEAU, F., Intracellular uptake of anionic superparamagnetic nanoparticles as a function of their surface coating, *Biomaterials*, **2003**, *24*, 1001–1011.
- 102 PANYAM, J., ZHOU, W. Z., PRABHA, S., SAHOO, S. K., LABHASETWAR, V., Rapid endo-lysosomal escape of poly(D, L-lactide-co-glycolide) nanoparticles: Implications for drug and gene delivery, *FASEB J.*, **2002**, *16*, 1217–1226.
- 103 RAYNAL, I., RRIGENT, P., PEYRAMAURE, S., NAJID, A., REBUZZI, C., COROT, C., Macrophage endocytosis of superparamagnetic iron oxide nanoparticles: Mechanisms and comparison of ferumoxides and ferumoxtran-10, *Invest. Rad.*, **2004**, *39*, 56–63.
- 104 STELLA, B., ARPICCO, S., PERACCHIA, M. T., DESMAELE, D., HOEBEKE, J., RENOIR, M., D'ANGELO, J., CATTEL, L., COUVREUR, P., Design of folic acid conjugated nanoparticles for drug targeting, *J. Pharm. Sci.*, **2000**, *89*, 1452–1464.
- 105 PETRI-FINK, A., CHASTELLAIN, M., JUILLERAT-JEANNERET, L., FERRARI, A., HOFMANN, H., Development of functionalized superparamagnetic iron oxide nanoparticles for interaction with human cancer cells, *Biomaterials*, **2005**, *26*, 2685–2694.
- 106 SUNDSTROM, J. B., MAO, H., SANTOIANI, R., VILLINGER, F., LITTLE, D. M., HUYNH, T. T., MAYNE, A. E., HAO, E., ANSARI, A. A., Magnetic resonance imaging of activated proliferating rhesus macaque T cells labeled with superparamagnetic monocrySTALLINE iron oxide nanoparticles, *J. AIDS*, **2004**, *35*, 9–21.
- 107 BERRY, C. C., CHARLSE, S., WELLS, S., DALBY, M. J., CURTIS, A. S., The influence of transferrin stabilised magnetic nanoparticles on human dermal fibroblasts in culture, *Int. J. Pharm.*, **2004**, *269*, 211–225.
- 108 PORTER, C. J. H., MOGHIMI, S. M., ILLUM, L., DAVIS, S. S., The polyoxoethylene/polyoxopropylene block copolymer poloxamer-407 selectively redirects intravenously injected microspheres to sinusoidal endothelial cells of rabbit bone-marrow, *FEBS Lett.*, **1992**, *305*, 62–66.
- 109 McLEAN, J. W., FOX, E. A., BALUK, P., BOLTON, P. B., HASKELL, A., PEARLMAN, R., THURSTON, C., UNEMOTO, E. Y., McDONALD, D. M., Organ-specific endothelial uptake of cationic liposome-DNA complexes in mice, *Am. J. Physiol.*, **1997**, *273*, H387–H404.
- 110 SHENOY, V. S., VIJAY, I. K., MURTHY, R. S., Tumour targeting: Biological factors and formulation advances in injectable lipid nanoparticles, *J. Pharm. Pharmacol.*, **2005**, *57*, 411–422.
- 111 VIDEIRA, M. A., BOTELHO, M. F., SANTOS, A. C., GOUVEIA, L. F., DE LIMA, J. J., ALMEIDA, A. J., Lymphatic uptake of pulmonary delivered radiolabelled solid lipid nanoparticles, *J. Drug Target.*, **2002**, *10*, 607–613.
- 112 CHEN, Q. R., ZHANG, L., GASPER, W., MIXSON, A. J., Targeting tumor angiogenesis with gene therapy, *Mol. Gen. Metab.*, **2001**, *74*, 120–127.
- 113 REYNOLDS, A. R., MOGHIMI, S. M., HODIVALA-DILKE, K., Nanoparticle-mediated gene delivery to tumor vasculature, *Trends Mol. Med.*, **2003**, *9*, 2–4.
- 114 HOOD, J. D., BEDNARSKI, M., FRAUSTO, R., GUCCIONE, S., RESIFELD, R. A., XIANG, R., CHERESH, D. A., Tumor

- regression by targeted gene delivery to the vasculature, *Science*, **2002**, 296, 2404–2407.
- 115 SUZAWA, T., NAGAMURA, S., SAITO, H., OHTA, S., HANAI, N., KANAZAWA, J., OKABE, M., YAMASAKE, M., Enhanced tumor cell selectivity of adriamycin monoclonal antibody conjugate via a poly(ethylene glycol)based cleavable linker, *J. Controlled Release*, **2002**, 79, 229–242.
- 116 MOGHIMI, S. M., HUNTER, A. C., MURRAY, J. C., Long-circulating and target-specific nanoparticles: Theory to practice, *Pharm. Rev.*, **2001**, 53, 283–318.
- 117 ZHANG, Y., ZHANG, J., Surface modification of monodisperse magnetite nanoparticles for improved intracellular uptake to breast cancer cells, *J. Colloid Interf. Sci.*, **2005**, 283, 352–357.
- 118 ZHANG, L., HOU, S., MAO, S., WEI, D., SONG, X., LU, Y., Uptake of folate-conjugated albumin nanoparticles to the SKOV3 cells, *Int. J. Pharm.*, **2004**, 287, 155–162.
- 119 PARK, J. W., BENZ, C. C., MARTIN, F. J., Future directions of liposome- and immunoliposome-based cancer therapeutics, *Semin. Oncol.*, **2004**, 31(Suppl 13), 196–205.
- 120 NIELSEN, U. B., KIRPOTIN, D. B., PICKERING, E. M., HONG, K., PARK, J. W., SHALABY, M. R., SHAO, Y., BENZ, C. C., MARKS, J. D., Therapeutic efficacy of anti-ErbB2 immunoliposomes targeted by a phage antibody selected for cellular endocytosis, *Biochim. Biophys. Acta*, **2002**, 1591, 109–118.
- 121 ZHANG, Z. R., GONG, Y., HUANG, Y., HE, Q., Conjugation of mitoxantrone-loaded nanospheres and anti-C-erbB-2 monoclonal antibodies, *Yao Hsueh Hsueh Pao – Acta Pharm. Sin.*, **2001**, 36, 151–154.
- 122 LOO, C., LOWERY, A., HALAS, N., WEST, J., DREZEK, R., Immunotargeted nanoshells for integrated cancer imaging and therapy, *NanoLetters*, **2005**, 5, 709–711.
- 123 KIM, I. S., KIM, S. H., Development of a polymeric nanoparticulate drug delivery system. In vitro characterization of nanoparticles based on sugar-containing conjugates. *Int. J. Pharm.*, **2002**, 245, 67–73.
- 124 KIM, I. S., KIM, S. H., Development of polymeric nanoparticulate drug delivery systems: Evaluation of nanoparticles based on biotinylated poly(ethylene glycol) with sugar moiety, *Int. J. Pharm.*, **2003**, 257, 195–203.
- 125 IINUMA, H., MARUYAMA, K., OKINAGA, K., SASAKI, K., SEKINE, T., ISHIDA, O., OGIWARA, N., JOHKURA, K., YONEMURA, Y., Intracellular targeting therapy of cisplatin-encapsulated transferrin-polyethylene glycol liposome on peritoneal dissemination of gastric cancer, *Int. J. Cancer*, **2002**, 99, 130–137.
- 126 DUBOWCHIK, G. M., WALKER, M. A., Receptor-mediated and enzyme-dependent targeting of cytotoxic anticancer drugs, *Pharmacol. Ther.*, **1999**, 83, 67–123.
- 127 SAVIC, R., LUO, L., EISENBERG, A., MAYSINGER, D., Micellar nanocontainers distribute to defined cytoplasmic organelles, *Science*, **2003**, 300, 615–618.
- 128 PANYAM, J., LABHASETWAR, V., Sustained cytoplasmic delivery of drugs with intracellular receptors using biodegradable nanoparticles, *Mol. Pharm.*, **2004**, 1, 77–84.
- 129 MOGHIMI, S. M., HUNTER, A. C., MURRAY, J. C., SZEWCHYK, A., Cellular distribution of non-ionic micelles, *Science*, **2004**, 303, 626–627.
- 130 DRUMMOND, D. C., ZIGNANI, M., LEROUX, J. C., Current status of pH-sensitive liposomes in drug delivery, *Prog. Lipid Res.*, **2000**, 39, 409–460.
- 131 HAINING, W. N., ERSON, D. G., LITTLE, S. R., VONBERWELT-BAILDON, M. S., CARDOSO, A. A., ALVES, P., KOSMATOPOULOS, K., NADLER, L. M., LANGER, R., KOHANE, D. S., pH-sensitive microparticles for peptide vaccination, *J. Immunol.*, **2004**, 173, 2578–2585.
- 132 MA, Z., LIM, L. Y., Uptake of chitosan and associated insulin in Caco-2 cell monolayers: A comparison between

- chitosan molecules and chitosan nanoparticles, *Pharm. Res.*, **2003**, *20*, 1812–1819.
- 133 Mo, Y., LIN, L. Y., Mechanistic study of the uptake of wheat germ agglutinin-conjugated nanoparticles by A549 cells, *J. Pharm. Sci.*, **2004**, *93*, 20–28.
- 134 PANYAM, J., LABHSETWAR, V., Dynamics of endocytosis and exocytosis of poly(D, L-lactide-co-glycolide) nanoparticles in vascular smooth muscle cells, *Pharm. Res.*, **2003**, *20*, 212–220.
- 135 CONSOLE, S., MARTY, C., GARCIA-ECHVERRIA, C., SCHWENDENER, R., BALLMER-HOFER, K., Antennapedia and HIV transactivator of transcription (TAT) “protein transduction domains” promote endocytosis of high molecular weight cargo upon binding to cell surface glycosaminoglycans, *J. Biol. Chem.*, **2003**, *278*, 35 109–35 114.
- 136 SILHOL, M., TYAGI, M., GIACCA, M., LEBLEU, B., VIVES, E., Different mechanisms for cellular internalization of the HIV-1 Tat-derived cell penetrating peptide and recombinant proteins fused to Tat, *Eur. J. Biochem.*, **2002**, *269*, 494–501.
- 137 WADIA, J. S., STAN, R. V., DOWDY, S. F., Transducible TAT-HA fusogenic peptide enhances escape of TAT-fusion proteins after lipid raft macropinocytosis, *Nat. Med.*, **2004**, *10*, 310–315.
- 138 TORCHILIN, V. P., Recent advances with liposomes as pharmaceutical carriers, *Nat. Rev. Drug Discov.*, **2005**, *4*, 145–160.
- 139 COLIN DE VERDIÈRE, A., DUBERNET, C., NÉMATI, F., SOMA, M., APPEL, M., FERTÉ, J., BERNARD, S., PUISIEUX, F., COUVREUR, P., Reversion of multidrug resistance with polyalkylcyano acrylate nanoparticles: Toward a mechanism of action, *Br. J. Cancer*, **1997**, *76*, 198–205.
- 140 SOMA, C. E., DUBERNET, C., BENTOLILA, D., BENITA, S., COUVREUR, P., Reversion of multidrug resistance by co-encapsulation of doxorubicin and cyclosporin A in polyalkylcyanoacrylate nanoparticles, *Biomaterials*, **2000**, *21*, 1–7.
- 141 MÜLLER, R. H., LHERM, C., HERBORT, J., COUVREUR, P., In vitro model for the degradation of alkylcyanoacrylate nanoparticles, *Biomaterials*, **1990**, *11*, 590–595.
- 142 TREUPEL, L., POUPON, M. F., COUVREUR, P., PUISIEUX, F., Vectorization of doxorubicin in nanospheres and reversion of pleiotropic resistance of tumor cells, *C. R. Acad. Sci.*, **1991**, *313*, 1–174.
- 143 CUVIER, C., ROBLLOT-TREUPEL, L., MILLOT, J. M., LIZARD, G., CHEVILLARD, S., MANFAIT, M., COUVREUR, P., POUPON, M. F., Doxorubicin-loaded nanospheres bypass tumor cell multidrug resistance, *Biochem. Pharmacol.*, **1992**, *44*, 509–517.
- 144 NEMATI, F., DUBERNET, C., FESSI, H., COLIN DE VERDIÈRE, A., POUPON, M. F., PUISIEUX, F., COUVREUR, P., Reversion of multidrug resistance using nanoparticles in vitro: Influence of the nature of the polymer, *Int. J. Pharm.*, **1996**, *138*, 237–246.
- 145 BATRAKOVA, E. V., LI, S., ALAKHOV, V. Y., MILLER, D. W., KABANOV, A. V., Optimal structure requirements for pluronic acid block copolymers in modifying P-glycoprotein drug efflux transporter activity in bovine brain microvessels endothelial cells, *J. Pharm. Exp. Ther.*, **2003**, *304*, 845–854.
- 146 KABANOV, A. V., BATRAKOVA, E. V., ALAKHOV, V. Y., An essential relationship between ATP depletion and chemosensitizing activity of pluronic acid block copolymers, *J. Controlled Release*, **2003**, *91*, 75–83.
- 147 COLVIN, V. L., The potential environmental impact of engineered nanomaterials, *Nat. Biotechnol.*, **2003**, *21*, 1166–1170.
- 148 HUNTER, A. C., MOGHIMI, S. M., Therapeutic synthetic polymers: A game of Russian roulette? *Drug Discov. Today*, **2002**, *7*, 998–1001.
- 149 NISHIYAMA, N., KIOZUMI, F., OKAZAKI, S., MATSUMURA, Y., NISHIO, K., KATAOKA, K., Differential gene expression profile between PC14 cells treated with free cisplatin and

- cisplatin-incorporated polymeric micelles, *Bioconj. Chem.*, **2003**, *14*, 449–457.
- 150 LAM, K. H., SCHAKENRAAD, J. M., ESSELBRUGGE, H., FEIJEN, J., NIEUWEHUIS, P., The effect of phagocytosis of poly(L-lactic acid) fragments on cellular morphology and viability, *J. Biomed. Mater. Res.*, **1993**, *27*, 1569–1577.
- 151 MURRAY, J. C., MOGHIMI, S. M., HUNTER, A. C., SYMONDS, P., DEBSKA, G., SZEWczyk, A., Lymphocytic death by cationic polymers: A role for mitochondrion and implications in gene therapy, *Br. J. Cancer*, **2004**, *91*, S75.
- 152 SZEbENI, J., Complement activation-related pseudoallergy caused by liposomes, micellar carriers of intravenous drugs, and radiocontrast agents, *Crit. Rev. Ther. Drug Carr. Syst.*, **2001**, *18*, 587–606.
- 153 DUNCAN, R., Polymer conjugates for tumour targeting and intracytoplasmic delivery. The EPR effect as a common gateway? *PSTT*, **1999**, *2*, 441–449.
- 154 LU, Z. R., SHIAH, J. G., SAKUMA, S., KOPECHOVA, P., KOPEcHEK, J., Design of novel bioconjugates for targeted drug delivery, *J. Controlled Release*, **2002**, *78*, 165–173.
- 155 REENTS, R., JEYARAJ, D. A., WALDMANN, H., Enzymatically cleavable linker groups in polymer-supported synthesis, *Drug Discov. Today*, **2002**, *7*, 71–76.
- 156 BRAUN, K., PESCHKLE, P., PIPKORN, R., LAMPEL, S., WACHAMUTH, M., WALDECK, W., FRIEDRICH, E., DUBUS, J., A biological transporter for the delivery of peptide nucleic acids (PNAs) to the nuclear compartment of living cells, *J. Mol. Biol.*, **2002**, *318*, 237–243.
- 157 LU, Y., MILLER, M. J., Syntheses and studies of multiwarhead siderophore-5-fluorouridine conjugates, *Bioorg. Med. Chem.*, **1999**, *7*, 3025–3038.
- 158 MARSCHÜTZ, M. K., VERONESE, F. M., BERNKOP-SCHNURCH, A., Influence of the spacer on the inhibitory effect of different polycarbophil-protease inhibitor conjugates, *Eur. J. Pharm. Biopharm.*, **2001**, *52*, 137–144.
- 159 SCHOENMAKERS, R. G., VAN DE WETERING, P., ELBERT, D. L., HUBBELL, J. A., The effect of the linker on the hydrolysis rate of drug-linked ester bonds, *J. Controlled Release*, **2004**, *95*, 291–300.
- 160 BHAVANE, R., KARATHANASIS, E., ANNAPRAGADA, A. V., Agglomerated vesicle technology: A new class of particles for controlled and modulated pulmonary drug delivery, *J. Controlled Release*, **2003**, *93*, 15–28.
- 161 GANGULY, S., DASH, A. K., A novel in situ gel for sustained drug delivery and targeting, *Int. J. Pharm.*, **2004**, *276*, 83–92.
- 162 BÖHM, G., DOWDENM, J., RICE, D. C., BURGESS, I., PILARD, J. F., GUILBERT, B., HAXTON, A., HUNTER, R. C., TURNER, N. J., FLITSCH, S. L., A novel linker for the attachment of alcohols to solid supports, *Tetrahedron Lett.*, **1998**, *39*, 3819–3822.
- 163 MEHVAR, R., Dextrans for targeted and sustained delivery of therapeutic and imaging agents, *J. Controlled Release*, **2000**, *69*, 1–25.
- 164 LAZNY, R., NODZEWSKA, A., KLOSOWSKI, P., A new strategy for synthesis of polymeric supports with triazene linkers, *Tetrahedron*, **2004**, *60*, 121–130.
- 165 BRÄSE, S., KÖBBERLING, J., ENDERS, D., LAZNY, R., WANG, M., Triazenes as robust and simple linkers for amines in solid-phase organic synthesis, *Tetrahedron Lett.*, **1999**, *40*, 2105–2108.
- 166 KRCHNAK, V., SLOUGH, G. A., Dual linker with a reference cleavage site for information rich analysis of polymer-supported transformations, *Tetrahedron Lett.*, **2004**, *45*, 5237–5241.

## 8

# Nanoparticles for Thermotherapy

*Andreas Jordan, Klaus Maier-Hauff, Peter Wust, and  
Manfred Johannsen*

### 8.1

#### Introduction

The biological effectiveness of heat in treating cancer has been known for decades and many of the corresponding molecular mechanisms are understood. Elevation of tissue temperature to above 40–41 °C is termed hyperthermia. It alters the function of many structural and enzymatic proteins within cells as a function of time and temperature, which in turn alters cell growth and differentiation and can induce apoptosis [1, 2]. Modest temperature rises are particularly effective against cells that tend to be resistant to radiation, cells in the S phase of the cell cycle and nutrient-deprived, low pH hypoxic cells [3]. Hyperthermia inhibits repair of sublethal radiation damage and also induces increasing radiosensitivity due to tumor reoxygenation [4, 5]. Treatments with tissue temperatures above 46 °C are termed thermoablation and have direct cytotoxic effects.

Thermotherapy is a physical therapy with fewer limitations than chemotherapy or radiotherapy and is typically used in combination with both of these therapies [6–8]. This allows a greater number of repeated treatments without accumulation of toxic side effects.

Although successful clinical trials have been conducted, thermotherapy is not yet established in clinical routine. This discrepancy probably derives from technical limitations in achieving effective temperature distributions in the depth of the human body rather than from a general lack of biological effectiveness [9].

Common thermotherapy techniques use different energy sources for generating heat in body tissue: Electromagnetic waves radiated by antennas (radiofrequency- or microwave-hyperthermia) [10, 11], ultrasonic sound [12, 13], magnetically excited thermosteds as well as tubes with hot water [14, 15]. For reviews see Refs. [16, 17].

The major problem with all present conventional thermotherapy systems is achieving a homogenous heat distribution and deep regional therapeutic temperatures in the treated tumor tissue. According to this hypothesis, treatment failure results from an insufficient temperature rise in parts of the tumor, enabling tumor

regrowth. However, excessive intratumoral temperatures might on the other hand induce damage of adjacent structures.

The heating of tissues using magnetic nanoparticles as a new treatment modality for interstitial thermotherapy has the potential to overcome these shortcomings.

When describing the properties of magnetic nanoparticles for thermotherapy, one has to consider that the magnetic properties are influenced to a large extent by the size and shape of the particles. Although there has been much progress regarding nanoparticle synthesis, the control of particle size and shape on the nanoscale level remains a synthetic challenge. Nevertheless, nanoscaled particles have several advantages over larger particles that favor their application in biomedicine. One advantage arises because particles change their magnetic properties when entering the size regime below approximately 20 nm, giving rise to distinct mechanisms of heating in alternating magnetic fields.

The use of magnetic nanoparticles for heating purposes was investigated comprehensively by Jordan et al. in 1993 [18]. Different studies have revealed that the specific absorption rate (SAR) of magnetic nanoparticles depends strongly on the diameter of the particle core [19–22]. In general, the heat production of magnetic nanoparticles in alternating magnetic fields can be attributed to hysteresis and relaxation losses, the latter being more pronounced in particles below 20 nm. Hysteresis losses play a role in larger particles, which consist of more than one magnetic domain and magnetization reversal occurs due to motions of the domain boundaries. In this case, the energy produced is proportional to the coercivity of the particles [19]. Magnetic fluids are dispersions of ultrafine magnetic particles, which are mostly superparamagnetic, meaning that each particle has only a single magnetic domain. For these so-called subdomain particles (SDP), coercivity is zero and magnetization reversal is only possible by relaxation processes. In alternating magnetic fields heat can be produced by two distinct relaxation mechanisms, Brownian and Néel relaxation. The first can be attributed to the rotation of the single-domain particle, which is related to the Brownian motion. The second corresponds to rotation of the magnetization vector in the crystal, if the particle is considered to be immobile [18].

To date, all magnetic nanoparticles intended to be used *in vivo* are composed of magnetic iron oxides. The main reason for this is their low toxicity and the known pathways of metabolism. The only two clinically relevant materials used are magnetite ( $\text{Fe}_3\text{O}_4$ ) and maghemite ( $\gamma\text{-Fe}_2\text{O}_3$ ). The crystal structures of both oxides are based on a cubic dense packing of oxide atoms, but they differ in the distribution of Fe ions in the crystal lattice. Magnetite is the most common ferrite and has an inverse spinel structure,  $\text{Fe}_{(\text{II})}\text{Fe}_{(\text{III})}_2\text{O}_4$ .

Pure iron-oxide nanoparticles have a high tendency to agglomerate and thus to build larger structures even in the absence of a magnetic field, which has a strong influence on the biomedical and magnetic properties of the particles. To prepare magnetic fluids for biomedical applications, the iron-oxide particles have to be coated with a protecting shell that prevents agglomeration. Furthermore, the protecting shell is responsible for the interaction of the particles with its surrounding (e.g., tumor tissue) and can provide functional domains that are useful for the cou-



pling of biomolecules or drugs to the surface. Common shell materials are polymers such as dextran, starch or poly(ethylene glycol).

Most techniques established so far concerning the use of magnetic particles for thermotherapy are basically based on direct instillation of magnetic fluids into the tumor tissue followed by exposure to an externally applied alternating magnetic field.

Ferromagnetic embolization hyperthermia is another technique for the local application of nanoparticles, in which the arterial supply of certain body regions is used as a pathway to carry magnetic particles directly into the tumor area.

## 8.2

### Thermotherapy following Intratumoral Administration of Magnetic Nanoparticles

Magnetic particles suspended in a carrier fluid can be injected directly into tumor tissue and subsequently be heated in an alternating magnetic field.

The history of magnetic particles for selective heating of tumors had already begun in 1957, when Gilchrist et al. used magnetic particles a few micrometers in size for inductive heating of lymph nodes in dogs [23].

In 1979, Gordon et al., for the first time, used magnetic fluids of dextran-coated magnetite-particles (often referred to as “dextran-magnetites”) for hyperthermia of implanted mammary tumors of rats [24]. After systemic application of the nanoparticles with a core size of up to 6 nm and exposition to an alternating magnetic field, the authors demonstrated histological evidence of tumor necrosis after intratumoral temperature increases of 8 °C.

Direct injection of microscaled ferromagnetic particles into renal carcinomas of rabbits and subsequent hysteresis heating in an alternating magnetic field was reported by Rand et al. in 1981 [25]. They measured tumor surface temperatures of 55 °C, leading to destruction of most of the treated tumor tissue within 3 days.

Direct injection of “truly nanoscaled” magnetic particles into tumors was first reported by our group in 1997 [26]. We studied single high dose thermotherapy on intramuscularly implanted mammary carcinoma of mice. Dextran-coated magnetite particles with a core size of approximately 3 nm were injected intratumorally 20–30 min before excitation and trapped by magnetic targeting (50 mT), which yielded a 2.5-fold enhancement of the intratumoral iron concentration. An intratumoral steady state temperature of 47 °C was maintained for 30 min with whole-body alternating magnetic fields of 6–12.5 kA m<sup>-1</sup> at 520 kHz. The study demonstrated that a single high thermal dose was able to induce local tumor control in many of the treated animals within 30 days after therapy. Histological examinations of tumor tissue after thermotherapy showed widespread tumor necrosis. Tumor growth after thermotherapy was heterogeneous; some tumors did not show evidence for regrowth after 50 days whereas others had grown rapidly. This was most probably due to inhomogeneities of the intratumoral particle distribution, which was also confirmed qualitatively by magnetic resonance imaging (MRI).

In 2002 Hilger et al. injected colloidal suspensions of coated nanoparticles with

average total particle sizes of 10 nm and 200 nm into human breast adenocarcinoma implanted into immunodeficient mice (4–18 mg magnetite per 100 mg tumor tissue) [27]. During exposure to an alternating magnetic field temperature increases between 12 and 73 °C in circumscribed areas within the tumor could be induced (termed “magnetic thermal ablation”). Histological examination revealed the presence of early stages of coagulation necrosis in the treated tumor cells.

Ohno et al. have investigated a new type of magnetite for interstitial hyperthermia [28]. They inserted stick-type carboxymethylcellulose-magnetite containing nanoparticles ( $\text{Fe}_3\text{O}_4$ , average particle size approximately 10 nm) stereotactically into gliomas of rats and exposed the animals to an alternating magnetic field. This investigation revealed a characteristic spreading of the magnetite particles through the tumor after three heat treatments and an approximately three-fold prolongation of survival time.

Groups at the University of Nagoya in Japan have developed “magnetic cationic liposomes” (MCLs) with improved adsorption and accumulation properties and demonstrated the efficacy of this approach in several animal tumor models:

Induction of antitumoral immunity to rat glioma by intratumoral hyperthermia using these particles was investigated by Yanase et al. in 1998 [29]. For intratumoral hyperthermia, the cationic liposomes containing magnetite ( $\text{Fe}_3\text{O}_4$  core with approximately 10 nm diameter) were directly injected into glioma tissue transplanted subcutaneously into the thigh of rats. Three subsequent treatments in an alternating magnetic field led to killing of the tumor cells and to the induction of a host immune response, which could be demonstrated by suppressed tumor growth after rechallenge with glioma cells 3 months later. In similar experiments using the same tumor model and the same particles, published one year later [30], complete tumor regression was observed in about 90% of the animals.

Le et al. have described successful tumor control (over two weeks) after hyperthermia of 43 °C using immuno-targeted magnetoliposomes [31].

In 2003, Ito et al. investigated the effect of intratumoral hyperthermia in combination with an immunotherapy of melanoma in mice [32]. After direct injection of MCLs into the tumors, the animals were exposed to an alternating magnetic field that raised the tumor temperature up to 43 °C; 24 h later, in a second treatment, interleukin-2 (IL-2) or granulocyte macrophage-colony stimulating factor (GM-CSF) was injected directly into the melanomas. In 75% (receiving IL-2) and 40% (receiving GM-CSF) of the animals treated by both therapies complete regression of the tumors was observed, while no tumor regression was observed in mice receiving only one of the treatments.

In 2005, Tanaka et al. investigated the therapeutic effects of tumor-specific hyperthermia using MCLs combined with an immunotherapy (intratumorally injected immature dendritic cells) on mouse melanoma [33]. Complete regression of tumors was observed in 60% of the mice and the cured animals rejected a second challenge of melanoma cells.

Kawai et al. have used the same liposomes to heat prostate cancer cells injected subcutaneously into the flank of rats [34]. They reported on tumor regression after generating intratumoral temperatures of 45 °C in an alternating magnetic field.

Carcinoma of the prostate represents an attractive target for minimally invasive, interstitial treatments due to its relatively easy accessibility via the transrectal or transperineal route.

To explore the potential of magnetic nanoparticle thermotherapy in an orthotopic prostate carcinoma, we have carried out experiments using the Dunning R3327 tumor model (MatMyLu-subtype), an established rat model developed to study prostate cancer progression [35]. This model resembles the human prostate with respect to physiological blood supply and local growth and may thus allow a more accurate analysis of the effects of a local hyperthermia treatment than a heterotopic model. In a preliminary *in vivo* evaluation, the feasibility and good overall tolerability of this technique in prostate cancer could be demonstrated [36].

Thermotherapy was carried out using an alternating magnetic field applicator system for small animals, operating at a frequency of 100 kHz and variable field strength of 0–18 kA m<sup>-1</sup>.

Thermoablative temperatures of 50 °C were achieved at a field strength of 15 kA m<sup>-1</sup>. Iron measurements were carried out to determine the percentage of nanoparticles present in the prostate tumors at different time points following intratumoral application. Without thermotherapy, 7 days after injection of magnetic fluid into the rat prostates, 53% of the injected amount of iron oxide was still present in the prostates. At 4 and 13 days after application 79% and 64%, respectively, of the injected amount of iron was still retained in the prostates after two sequential thermotherapy treatments. This difference in iron content between untreated and treated animals was attributed to the so-called “thermal bystander effect”, which describes a hyperthermia-induced spread of coated nanoparticles in the target tissue, where they seem to escape rapid removal by macrophages [26]. This effect could also be demonstrated by means of histopathology. After magnetic fluid application alone, a loose distribution of nanoparticles within the tumor tissue with deposits in capillaries could be seen in sections of rat prostate tumors, whereas homogeneous distribution and co-localization of nanoparticles with necrotic areas could be demonstrated in animals that had undergone thermotherapy.

In a further systematic *in vivo* analysis using a more concentrated magnetic fluid containing approximately 112 mg-iron mL<sup>-1</sup>, as well as a slightly modified aminosilane-based coating, intraprostatic temperatures of 70 °C could be achieved at a maximum magnetic field strength of 18 kA m<sup>-1</sup> in the same tumor model [37]. Up to 0.5 mL of magnetic fluid per mL of tumor volume was injected into the prostate tumors in these experiments. The animals received two thermotherapy treatments carried out 48 h apart to avoid heat shock protein-induced thermoresistance. At a constant field strength of 12.6 kA m<sup>-1</sup>, mean minimal intratumoral temperatures during the first and second thermotherapy sessions were 41.2 and 41.4 °C, respectively, whereas mean maximal temperatures were 54.8 and 54.2 °C (averaged over 12 animals). In this study, animals were sacrificed on day 20 after tumor cell inoculation (10 days following the first thermotherapy treatment) to compare tumor weights in the treatment and control groups and for iron measurements. A significant inhibition of prostate cancer growth of 44–51% over controls

was demonstrated in the thermotherapy group. Mean iron content of the prostates of treated and untreated control animals was 81.6% and 83.7%, respectively, whereas 7.6% and 2.3% of the injected dose of iron was found in the liver. No detectable amount of iron was found in the blood stream. While thermal treatment itself had a significant impact on intratumoral distribution and stable deposition of nanoparticles in the previous pilot study, no such effect was observed using the modified magnetic fluid. In fact, intratumoral deposition of the MFL AS particles was the same with or without thermotherapy treatment. Histological analysis revealed a co-localization of nanoparticles with areas of necrosis, but a rather inconsistent pattern of intratumoral distribution, which appeared less homogeneous than with the previously used magnetic fluid preparation.

Further experimental studies have investigated the effect of combined magnetic nanoparticle thermotherapy and external irradiation in the Dunning tumor model [38].

Mean maximal and minimal intratumoral temperatures obtained in these experiments were 59 (centrally) and 43 °C (peripherally) during the first thermotherapy and 55 and 42 °C, respectively, during the second of two treatment sessions. Combined thermotherapy and radiation with 20 Gy was significantly more effective than radiation with 20 Gy alone and reduced tumor growth by 88% versus controls, achieving an equal tumor growth inhibition as irradiation alone with 60 Gy. As in the previous experiments, sequential heat treatments were possible without repeated injection of magnetic fluid. The mean iron content in the prostates on day 20 was 88% of the injected dose of ferrites, whereas only 2.5% was found in the liver.

In conclusion, thermotherapy using magnetic nanoparticles achieved significant growth inhibition, but not tumor control or eradication in the orthotopic Dunning tumor model of the rat. The results of preclinical evaluation of magnetic nanoparticle thermotherapy suggest that this technique may, in principle, be suitable for both local hyperthermia and thermoablation of prostate carcinoma, since the desired treatment temperatures can be freely selected by modulating the magnetic field strength [39].

However, for complete thermal ablation of the prostate, homogeneous infiltration of the whole prostatic tissue with magnetic nanoparticles would be required and high magnetic field strengths would have to be applied. In view of the synergistic effects of hyperthermia and radiotherapy, a combination of magnetic nanoparticle thermotherapy with irradiation may also be an attractive option for the treatment of prostate cancer.

In a rat model of glioblastoma multiforme we could also demonstrate the high efficacy of our new technique, leading to an up to 4.5-fold prolongation of survival [40]. The animals received two thermotherapy treatments within 48 h after a single stereotactic injection of the magnetic fluid into the tumor. Intratumoral temperatures between 43 and 47 °C correlated well with prolonged survival. As in our prostate tumor model, the application of aminosilane-coated nanoparticles led to the formation of stable deposits in the brain, thus allowing for repeated magnetic field treatments without repeated applications of the particles.

### 8.3

#### Ferromagnetic Embolization Hyperthermia

Another technique of using magnetic nanoparticles for thermotherapy is ferromagnetic embolization hyperthermia, in which a feeding artery is used to carry ferromagnetic particles into a tumor.

The technique seems to be well suited for the treatment of hepatic malignancies due to the differences in blood supply of hepatic tumor cells and normal liver parenchyma. Liver tumors mainly derive their blood supply from the hepatic arterial system, while the normal liver parenchyma receives most of its blood supply from the portal venous system [41]. Hence any substance infused into the arterial system will have the potential to preferentially target liver tumors [42].

Several preclinical studies have reported on arterial embolization hyperthermia of liver cancer.

Moroz et al. have demonstrated successful ferromagnetic embolization hyperthermia of rabbit hepatic carcinomas after arterial infusion of magnetic nanoparticles suspended in lipiodol [43, 44].

In 1994, Mitsumori et al. tested the thermotherapeutical properties of dextran-coated magnetite particles suspended in lipiodol or in degradable starch microspheres [45]. The study reported an increase of over 12 °C after 10 min of heating after embolization of the renal artery and selective heating of the embolized kidney by exposure to an alternating magnetic field. The authors followed up this work with a study in 1996 [46], in which hepatic carcinoma-bearing rabbits were arterially infused with the same sub-domain sized particles (75 nm in diameter with a 7.4 nm magnetite core). Slight tumor temperature increases were recorded *in vivo*.

In a study performed by Minamimura et al. a novel preparation of microspheres incorporating a dextran magnetite complex was used for arterial embolization and inductive hyperthermia of liver tumors in rats [47]. Tumor temperatures of around 43 °C were maintained for 30–40 min and three days after treatment the increase of tumor volume in the treated animals differed significantly from that of the control groups.

Jones et al. have achieved positive temperature differences between tumor and normal liver and consequent therapeutic responses in experimental rabbit liver tumors after arterially infused ferromagnetic microspheres [48]. Heating to over 42 °C for 20 min by exposure to an alternating magnetic field resulted in large areas of tumor necrosis 14 days after treatment.

After arterial infusion of iron-oxide particles suspended in lipiodol into rabbit hepatic carcinoma, Moroz et al. have found that an iron concentration of 2–3 mg per gram of tumor was necessary to produce heating rates up to 11.5× greater than those in adjacent normal liver parenchyma [43]. The authors reported a mean tumor to normal liver iron concentration ratio of 5.3.

Further work by this group employing the same tumor model and infusion regimen has shown that large hepatic tumors are more amenable to thermotherapy after arterial embolization than small tumors [44]. The authors concluded from their data that, for a given tumor iron concentration, larger tumors heat at a

greater rate than small tumors, owing to poorer tissue cooling and better heat conduction in the necrotic regions of large tumors.

In a later study the authors investigated the clearance of ferromagnetic particles from the liver [49]. The normal liver of pigs was arterially embolized with  $\gamma$ - $\text{Fe}_2\text{O}_3$  particles (150 nm) suspended in lipiodol and polymer microspheres (32  $\mu\text{m}$ ) containing ferromagnetic particles suspended in 1% Tween-water. Both types of particles were extensively phagocytosed in the liver and there was no significant reduction in the hepatic iron concentration in either treatment group 28 days after infusion. The suspension of 150 nm ferromagnetic particles in lipiodol was too vaso-occlusive for use in hepatic tissue, while the suspension of 32  $\mu\text{m}$  spheres was safe and well tolerated.

Although few preclinical studies have been described, arterial embolization hyperthermia has demonstrated encouraging results. The technique seems to be particularly well suited for the treatment of hepatic malignancies. Potential advantages are a very selective local heat deposition and a more homogeneous tissue temperature distribution than other hyperthermia techniques.

#### 8.4

#### **First Clinical Experiences with Thermotherapy using Magnetic Nanoparticles: MagForce Nanotherapy**

The pathways developed so far for thermotherapy using magnetic nanoparticles have in common that they deliver the magnetic material directly into or adjacent to the tumor tissue. To facilitate cellular uptake by tumor cells, the particle coatings often were modified with targeting ligands such as antibodies or peptides.

Magnetic fluids can be instilled into tumor tissue percutaneously under CT, ultrasound or fluoroscopy guidance. Owing to inductive excitation of the nanoparticles this technique allows very precise heating of almost every part of the body.

A major advantage of direct intratumoral application of the particles is the good control of deposition, leading to high concentrations of the magnetic material within the tumor while healthy tissue can be spared. The magnetic fluid can be distributed in very small portions and, therefore, almost continuously within the targeted area. Therefore, the requirement of maximal heat deposition within the target area while sparing neighboring healthy tissue can be met.

MagForce Nanotherapy, formerly designated magnetic fluid hyperthermia, has been developed at Charité – University Medicine Berlin over the last 15 years. Our preclinical studies have demonstrated that this innovative approach has the potential to improve heating capabilities with certain cancer types and thus overcome existing prejudices against routine application of heat to treat cancer.

It is the first nanotechnology-based local thermotherapy to enter clinical trials.

Beginning in 2003, we started four different clinical studies to investigate the feasibility of our new thermotherapy approach on different tumor entities.

The magnetic fluid MFL AS used in these studies is manufactured by MagForce Nanotechnologies, Berlin, and consists of superparamagnetic iron-oxide nanopar-



**Fig. 8.1.** Thermotherapy treatment of a glioblastoma multiforme patient in the magnetic field applicator MFH<sup>®</sup> 300F (MagForce Nanotechnologies, AG, Berlin, Germany).

ticles in aqueous solution with an iron concentration of  $2 \text{ mol L}^{-1}$ . The iron oxide core is covered by an aminosilane-type shell and has a diameter of approximately 15 nm. The particles generate heat in an alternating magnetic field by Brownian and Néel relaxation processes.

Thermotherapy is performed in a magnetic field applicator (MFH<sup>®</sup> 300F, MagForce Nanotechnologies, AG, Berlin, Germany), generating an alternating magnetic field (100 kHz) and a variable field strength of  $0\text{--}18 \text{ kA m}^{-1}$  (Fig. 8.1). This applicator meets the safety and practicability criteria for medical use imposed by the respective European authorities. Owing to its universal design, it can be used for treatment of malignancies in every location of the human body. Fixation or anesthesia of the patients during treatment is not necessary.

Minimally invasive measurement of treatment temperatures is carried out by fiber-optic thermometry probes as part of the therapy system.

#### 8.4.1

##### **Feasibility Study on Thermotherapy using Magnetic Nanoparticles in Recurrent Glioblastoma Multiforme**

From March 2003 to June 2004 we performed the world's first phase I trial on tumor thermotherapy using magnetic nanoparticle, with 14 glioblastoma multiforme patients.

Malignant gliomas (anaplastic astrocytoma and glioblastoma multiforme, WHO grades III and IV, respectively) have an incidence of approximately 5 in 100 000 per year and represent approximately 40% of primary brain tumors in adults, with 50% of them belonging to the most malignant phenotype, glioblastoma multiforme. Clinically, they are highly problematic due to their widely invasive nature, which makes complete resection almost impossible. Median overall survival after first-line therapy does not exceed 12–15 months [50, 51] and no significant in-

crease has been achieved over the last decade, despite modern diagnostics and treatments with surgery, radio- and chemotherapy.

All patients of our trial received stereotactic injection of the magnetic fluid into the tumor area. Before starting thermotherapy, the position of the instilled nanoparticles was determined by computed tomography (CT). These data were matched to presurgical MR images using specially designed software (MagForce NanoPlan®, not commercially available), thus allowing calculation of the expected heat distribution within the treatment area in relation to the magnetic field strength [52].

The preoperatively planned and neuro-navigationally guided procedure led to an almost atraumatic instillation of the magnetic fluid and rise of intracranial pressure could be avoided by slow injection of the magnetic fluid.

Patients received 4–10 thermotherapy sessions where intratumoral temperatures of 42–49 °C could be measured; body temperatures increased by 1.0–1.5 °C.

All patients tolerated the instillation of the nanoparticles without complications and side effects such as headache, nausea, vomitus or allergic reactions were not observed. Neurological deficits or infections did not occur.

As documented by CT-scans and thermometry measurements, a high stability of the nanoparticle deposits can be assumed. In fact, reproducible intratumoral temperatures could be achieved during the therapy, even several weeks after administration.

Data of the trial concerning overall survival and time to progression suggest that intracranial thermotherapy using magnetic nanoparticles can be safely applied with therapeutic temperatures and without side effects [53]. A phase II study is in progress to evaluate the efficacy of this treatment approach.

#### 8.4.2

#### **Feasibility Study on Thermotherapy using Magnetic Nanoparticles in Recurrent and Residual Tumors**

Another phase I trial started in February 2004, which enrolled 21 patients suffering from non-resectable and pre-treated local relapses of different tumor entities (e.g., rectum, ovarian, prostate, and cervix carcinoma as well as soft tissue sarcoma). All patients received thermotherapy in combination with radio- or chemotherapy [54].

The objectives of the study were treatment planning, application and subsequent control of magnetic fluid distributions in circumscribed lesions (<4–5 cm) and, furthermore, assessment of safety, quality and feasibility of the heating patterns achieved *in situ*.

Patients with metallic implants <30 cm from the treatment area had to be excluded. Teeth amalgam fillings or gold crowns had to be replaced by ceramics if involved in the treatment field (head and neck, upper thorax). Metallic clips or seeds several millimeters long and <1 mm in diameter were permitted due to their very low power absorption capacities.

Two principally different techniques for the instillation of the magnetic fluid were evaluated.



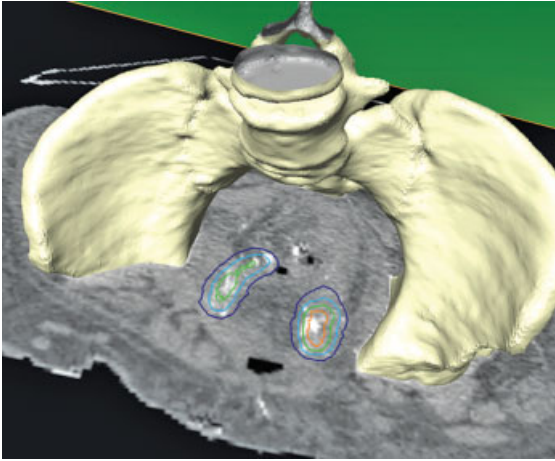


**Fig. 8.2.** Thermotherapy using magnetic nanoparticles of a patient suffering from metastases of a cervical carcinoma. Three-dimensional reconstruction of a pelvis sliced by a CT scan: The calculated temperature

distributions (isotherms) during thermotherapy decrease from orange to blue. White spots within the colored lines show the magnetic nanoparticle deposits.

The first strategy implied a prospective planning of the “ideal” nanofluid distribution on the basis of a three-dimensional CT dataset performed in treatment position. This dataset is then transferred via the radiological information system into a software platform to calculate the temperature distribution during thermotherapy within the treatment area (Fig. 8.2).

The second implantation technique consisted of intraoperative injection under visual control. In this case prospective planning is not possible, because after tumor debulking an individual (non-resectable) tumor rest or an area at risk (R1/2-situation) has to be infiltrated. Cervical cancer recurrences at the pelvic wall (after primary treatment) are typical clinical examples.

Nanofluid concentration in the target area was claimed to be as high as possible. In these patients a retrospective planning based on a post-operative CT dataset was performed.

Direct temperature measurements via implanted catheters were suitable to estimate a mean perfusion and to calculate the temperature distributions in and around the target volume.

Tolerated H-fields were limited by local discomfort to 3–6 kA m<sup>-1</sup> in the pelvic region and up to 7.5 kA m<sup>-1</sup> in the upper thorax.

From our experience with brain tumor patients we know that magnetic fields of 10–14 kA m<sup>-1</sup> are technically achievable and tolerated well. The H-field limitations are related to the periphery of the body where the accompanying electric fields and the current densities are highest. The larger the cross section, the lower the tolerated H field strength (comparing pelvis with head). However, treatment-limiting

hot spots arise from skin folds, where the current path narrows and the current density, therefore, increases.

We also observed relative temperature maxima at tissue boundaries such as the anal sphincter and pelvic floor. These locations were, however, never treatment-limiting during our study, but are a typical problem during RF hyperthermia, where the E-fields are considerably higher.

One particular advantage of MagForce Nanotherapy is the option to plan the magnetic fluid distribution prospectively and to control the heat distribution thereafter to a high degree of reliability, thus increasing the safety of the application significantly.

Another major advantage of the new treatment is that, owing to the stability of the nanoparticle deposits, it can be repeated over weeks without additional injection of the magnetic fluid. This enables multimodal treatment concepts.

The heat treatments were tolerated well with only moderate side effects. The follow-up showed encouraging results for severe oncological diseases. Several strategies are available to further improve the effectiveness of treatment, e.g., to elevate the H-field (after modification of the applicator) or to increase the amount of magnetic fluid in the target.

#### 8.4.3

#### **Feasibility Study on Thermotherapy using Magnetic Nanoparticles in Recurrent Prostate Carcinoma**

Despite much progress in the development of hyperthermia application and treatment planning systems for prostate cancer, clinical hyperthermia of this deep-seated organ is still a challenging problem [55].

Reported mean intraprostatic temperatures obtained with conventional heating methods have been between 40 and 42 °C, rarely reaching or exceeding the critical temperature of 43.0 °C, where a measurable cytotoxic effect is documented for various cell types [56, 57].

The first published report on thermotherapy treatment of human cancer using magnetic nanoparticles describes the preliminary experience with this technique in patients with locally recurrent, radioresistant prostate cancer [58]. In this investigation, treatment planning based on computerized tomography of the prostate preceded intraprostatic application of magnetic fluid. The number and position of magnetic fluid depots required for sufficient heat deposition was calculated according to the anatomy of the prostate and the estimated SAR of magnetic fluids in prostatic tissue. Nanoparticle suspensions were injected transperineally into the prostate under transrectal ultrasound and fluoroscopy guidance and six weekly treatments were delivered in an alternating magnetic field. Temperatures of up to 48.5 °C with a minimum of 40.0 °C were achieved in the prostate during the 1st treatment at a field strength of 4–5 kA m<sup>-1</sup>, whereas during the 6th treatment, intraprostatic temperatures between 42.5 and 39.4 °C were recorded by means of invasive thermometry. Maximum and minimal temperatures, respectively, measured in the urethra were 42.4 and 38.0 °C whereas in the rectum 42.1 and 37.9 °C were

recorded. Treatment was well tolerated without anesthesia. Since the injected magnetic fluid depots appear as signal-intense areas on the CT-scan, it could be documented that nanoparticles are retained in the prostate well beyond the treatment interval of 6 weeks. Thus, further applications of magnetic fluid are unnecessary for effective thermal treatments and at least hyperthermic temperatures can be achieved many weeks following intratumoral injection of nanoparticles.

Further refinement of the technique appears necessary regarding several important aspects. Firstly, the intraprostatic application and homogeneous distribution of nanoparticles appeared suboptimal due to fibrotic changes induced by the previous radiotherapy and may be improved. Most importantly, however, only one-third of the available power was used in these first clinical treatments, since an increase of magnetic field strength beyond  $5 \text{ kA m}^{-1}$  led to substantial patient discomfort in the perineum and the groin. This may be due to accompanying electric fields and current densities, which are highest in skin folds and at areas with the largest cross-sectional volume such as the pelvis. Since SAR increases quadratically with the magnetic field strength, significantly higher treatment temperatures can be achieved in the prostate by applying higher magnetic field strengths. Interposition of devices for focusing of the magnetic field may improve tolerability of treatment in the future. Furthermore, non-invasive temperature calculations based on evaluation of CT data are another area of ongoing research.

A phase I study evaluating feasibility, toxicity and quality of life during hyperthermia using magnetic nanoparticles, involving ten patients with radio-recurrent prostate carcinoma, is nearing completion. Preliminary clinical results suggest that thermotherapy using magnetic nanoparticles may be suitable for thermoablation of the prostate, since intratumoral temperatures well above  $44^\circ\text{C}$  were achieved at low magnetic field strengths. However, further technical developments regarding the magnetic field applicator may be necessary to fully exploit the potential of this technique as a monotherapy. In addition, this treatment modality may also be combined with interstitial or external irradiation in patients with localized prostate cancer.

## References

- 1 SELLINS KS, COHEN JJ, Hyperthermia induces apoptosis in thymocytes, *Radiation Res.*, **1991**, 126, 88–95.
- 2 CHRISTOPHI C, WINKWORTH A, MURALIHARAN V, EVANS P, The treatment of malignancy by hyperthermia, *Surg. Oncol.*, **1999**, 7, 83–90.
- 3 DEWEY WC, FREEMAN ML, RAAPHORST GP, CLARK EP, WONG RSL, HIGHFIELD DP, SPIRO IJ, TOMASOVIC SP, DENMAN DL, COSS RA, Cell biology of hyperthermia and radiation, in MEYN RE, WITHERS HR (eds.), *Radiation Biology in Cancer Research*, Raven Press, New York, **1980**.
- 4 OLESON JR, Eugene Robertson special lecture. Hyperthermia from the clinic to the laboratory: A hypothesis, *Int. J. Hyperthermia*, **1995**, 11, 315–322.
- 5 OVERGAARD J, HORSMAN MR, Modification of hypoxia-induced radioresistance in tumors by the use of oxygen and sensitizers, in TEPPER JE (ed.) *Seminars in Radiation Oncology*, W. B. Saunders Company, Philadelphia, **1996**, pp. 10–19.

- 6 OVERGAARD J, The current and potential role of hyperthermia in radiotherapy, *Int. J. Radiat. Oncol. Biol. Phys.*, **1989**, 16, 535–549.
- 7 ANDERSON RL, KAPP DS, Hyperthermia in cancer therapy: Current status, *Med. J. Aust.*, **1990**, 152, 310–315.
- 8 OVERGAARD J, GONZALEZ D, HULSHOF MC, ARCANGELI G, DAHL O, MELLA O, BENTZEN SM, Randomised trial of hyperthermia as adjuvant to radiotherapy for recurrent or metastatic malignant melanoma. European Society for Hyperthermic Oncology, *Lancet*, **1995**, 345, 540–543.
- 9 WUST P, HILDEBRANDT B, SREENIVASA G, RAU B, GELLERMANN J, RIESS H, FELIX R, SCHLAG PM, Hyperthermia in combined treatment of cancer, *Lancet Oncol.*, **2002**, 3, 487–497.
- 10 STAHL H, WUST P, MAIER-HAUFF K, SEEBASS M, MISCHEL M, GREMLER M, GOLDE G, LOFFEL J, FELIX R, The use of an early postoperative interstitial-hyperthermia combination therapy in malignant gliomas, *Strahlenther Onkol.*, **1995**, 171, 510–524.
- 11 SNEED PK, STAUFFER PR, McDERMOTT MW, DIEDERICH CJ, LAMBORN KR, PRADOS MD, CHANG S, WEAVER KA, SPRY L, MALEC MK, LAMB SA, VOSS B, DAVIS RL, WARA WM, LARSON DA, PHILLIPS TL, GUTIN PH, Survival benefit of hyperthermia in a prospective randomized trial of brachytherapy boost +/- hyperthermia for glioblastoma multiforme, *Int. J. Radiat. Oncol. Biol. Phys.*, **1998**, 40, 287–295.
- 12 CLEMENT GT, HYNYNEN K, A non-invasive method for focusing ultrasound through the human skull, *Phys. Med. Biol.*, **2002**, 47, 1219–1236.
- 13 MITSUMORI M, HIRAOKA M, OKUNO Y, NISHIMURA Y, LI YP, FUJISHIRO S, NAGATA Y, ABE M, KOISHI M, SANO T, MARUME T, TAKAYAMA N, A phase I and II clinical trial of a newly developed ultrasound hyperthermia system with an improved planar transducer, *Int. J. Radiat. Oncol. Biol. Phys.*, **1996**, 36, 1169–1175.
- 14 SCHREIER K, BUDIHNA M, LESNICAR H, HANDI-ZELLER L, HAND JW, PRIOR MV, CLEGG ST, BREZOVICH IA, Preliminary studies of interstitial hyperthermia using hot water, *Int. J. Hyperthermia*, **1990**, 6, 431–444.
- 15 WUST P, SEEBASS M, NADOBNY J, FELIX R, Electromagnetic deep heating technology, in SEEGENSCHMIDT MH, FESSENDEN P, VERNON CC (eds.), *Medical Radiology, Principles and Practice of Thermoradiotherapy and Thermochemotherapy*, Springer Verlag, Berlin, **1995**, pp. 219–251.
- 16 WUST P, RAU B, GREMLER M, SCHLAG P, JORDAN A, LOEFFEL J, RIESS H, FELIX R, Radio-thermotherapy in multimodal surgical treatment concepts, *Onkologie*, **1995**, 18, 110–121.
- 17 VAN DER ZEE J, Heating the patient: A promising approach? *Ann. Oncol.*, **2002**, 13, 1173–1184.
- 18 JORDAN A, WUST P, FAHLING H, JOHN W, HINZ A, FELIX R, Inductive heating of ferrimagnetic particles and magnetic fluids: Physical evaluation of their potential for hyperthermia, *Int. J. Hyperthermia*, **1993**, 9, 51–68.
- 19 MA M, WU Y, ZHOU H, SUN YK, ZHANG Y, GU N, Size dependence of specific power absorption of Fe<sub>3</sub>O<sub>4</sub> particles in AC magnetic field, *J. Magn. Magn. Mater.*, **2004**, 268, 33–39.
- 20 JORDAN A, WUST P, SCHOLZ R, FAEHLING H, KRAUSE J, FELIX R, Magnetic fluid hyperthermia (MFH), in HAEFELI U, SCHUETT W, TELLER J, ZBOROWSKY M (eds.), *Scientific and Clinical Applications of Magnetic Carriers*, Plenum Press, New York, **1997**, pp. 569–595.
- 21 JORDAN A, RHEINLANDER T, WALDOFNER N, SCHOLZ R, Increase of the specific absorption rate (SAR) by magnetic fractionation of magnetic fluids, *J. Nanoparticle Res.*, **2003**, 5, 597–600.
- 22 HERGT R, HIERGEIST R, ZEISBERGER M, GLOCKL G, WEITSCHIES W, RAMIREZ P, HILGER I, KAISER WA, Enhancement of AC-losses of magnetic nanoparticles for heating applications, *J. Magn. Magn. Mater.*, **2004**, 280, 358–368.

- 23 GILCHRIST RK, SHOREY WD, HANSELMAN RC, PARROTT JC, TAYLOR CB, MEDAL R, Selective inductive heating of lymph nodes, *Ann. Surg.* **1957**, 146, 596–606.
- 24 GORDON RT, HINES JR, GORDON D, Intracellular hyperthermia. A biophysical approach to cancer treatment via intracellular temperature and biophysical alterations, *Med. Hypotheses*, **1979**, 5, 83–102.
- 25 RAND RW, SNOW HD, BROWN WJ, Thermomagnetic surgery for cancer, *J. Surg. Res.*, **1981**, 33, 177–183.
- 26 JORDAN A, SCHOLZ R, WUST P, FAHLING H, KRAUSE J, WLODARCZYK W, SANDER B, VOGL T, FELIX R, Effects of magnetic fluid hyperthermia (MFH) on C3H mammary carcinoma in vivo, *Int. J. Hyperthermia*, **1997**, 13, 587–605.
- 27 HILGER I, HIERGEIST R, HERGT R, WINNEFELD K, SCHUBERT H, KAISER WA, Thermal ablation of tumors using magnetic nanoparticles: An in vivo feasibility study, *Invest. Radiol.*, **2002**, 37, 580–586.
- 28 OHNO T, WAKABAYASHI T, TAKEMURA A, YOSHIDA J, ITO A, SHINKAI M, HONDA H, KOBAYASHI T, Effective solitary hyperthermia treatment of malignant glioma using stick type CMC-magnetite. In vivo study, *J. Neurooncol.*, **2002**, 56, 233–239.
- 29 YANASE M, SHINKAI M, HONDA H, WAKABAYASHI T, YOSHIDA J, KOBAYASHI T, Antitumor immunity induction by intracellular hyperthermia using magnetite cationic liposomes, *Jpn. J. Cancer Res.*, **1998**, 89, 775–782.
- 30 SHINKAI M, YANASE M, SUZUKI M, HONDA H, WAKABAYASHI T, YOSHIDA J, KOBAYASHI T, Intracellular hyperthermia for cancer using magnetite cationic liposomes, *J. Magn. Mater.*, **1999**, 194, 176–184.
- 31 LE B, SHINKAI M, KITADE T, HONDA H, YOSHIDA J, WAKABAYASHI T, KOBAYASHI T, Preparation of tumor-specific magnetoliposomes and their application for hyperthermia, *J. Chem. Eng. Jpn.*, **2001**, 34, 66–72.
- 32 ITO A, TANAKA K, KONDO K, SHINKAI M, HONDA H, MATSUMOTO K, SAIDA T, KOBAYASHI T, Tumor regression by combined immunotherapy and hyperthermia using magnetic nanoparticles in an experimental subcutaneous murine melanoma, *Cancer Sci.*, **2003**, 94, 308–313.
- 33 TANAKA K, ITO A, KOBAYASHI T, KAWAMURA T, SHIMADA S, MATSUMOTO K, SAIDA T, HONDA H, Intratumoral injection of immature dendritic cells enhances antitumor effect of hyperthermia using magnetic nanoparticles, *Int. J. Cancer*, **2005**, 116, 624–633.
- 34 KAWAI N, ITO A, NAKAHARA Y, FUTAKUCHI M, SHIRAI T, HONDA H, KOBAYASHI T, KOHRI K, Anticancer effect of hyperthermia on prostate cancer mediated by magnetite cationic liposomes and immune-response induction in transplanted syngeneic rats, *Prostate*, **2005**, 64, 373–381.
- 35 LUCIA MS, BOSTWICK DG, BOSLAND M, COCKETT AT, KNAPP DW, LEAV I, POLLARD M, RINKER-SCHAEFFER C, SHIRAI T, WATKINS BA, Workgroup I: Rodent models of prostate cancer, *Prostate*, **1998**, 36, 49–55.
- 36 JOHANNSEN M, JORDAN A, SCHOLZ R, KOCH M, LEIN M, DEGER S, ROIGAS J, JUNG K, LOENING S, Evaluation of magnetic fluid hyperthermia in a standard rat model of prostate cancer, *J. Endourol.*, **2004**, 18, 495–500.
- 37 JOHANNSEN M, THIESEN B, JORDAN A, TAYMOORIAN K, GNEVECKOW U, WALDOFNER N, SCHOLZ R, KOCH M, LEIN M, JUNG K, LOENING SA, Magnetic fluid hyperthermia (MFH) reduces prostate cancer growth in the orthotopic Dunning R3327 rat model, *Prostate*, **2005**, 64, 283–292.
- 38 JOHANNSEN M, THIESEN B, GNEVECKOW U, TAYMOORIAN K, WALDOFNER N, SCHOLZ R, DEGER S, JUNG K, LOENING S, JORDAN A, Thermotherapy using magnetic nanoparticles combined with external radiation in an orthotopic Dunning rat model of prostate cancer, *Prostate*, **2005**, 66, 97–104.
- 39 DEGER S, TAYMOORIAN K, BOEHMER D, SCHINK T, ROIGAS J, WILLE AH,

- BUDACH V, WERNECKE KD, LOENING SA, Thermoradiotherapy using interstitial self-regulating thermo-seeds: An intermediate analysis of a phase II trial, *Eur. Urol.*, **2004**, 45, 574–579; discussion 580.
- 40 JORDAN A, SCHOLZ R, MAIER-HAUFF K, VAN LANDEGHEM F, WALDOEFNER N, TEICHGRAEBER U, PINKERNELLE J, BRUHN H, NEUMANN F, THIESEN B, VON DEIMLING A, FELIX R, The effect of thermotherapy using magnetic nanoparticles on rat malignant glioma, submitted for publication, **2005**.
- 41 ARCHER SG, GRAY BN, Vascularization of small liver metastases, *Br. J. Surg.*, **1989**, 76, 545–548.
- 42 ARCHER SG, GRAY BN, Comparison of portal vein chemotherapy with hepatic artery chemotherapy in the treatment of liver micrometastases, *Am. J. Surg.*, **1990**, 159, 325–329.
- 43 MOROZ P, JONES SK, WINTER J, GRAY BN, Targeting liver tumors with hyperthermia: Ferromagnetic embolization in a rabbit liver tumor model, *J. Surg. Oncol.*, **2001**, 78, 22–29; discussion 30–31.
- 44 MOROZ P, JONES SK, GRAY BN, The effect of tumour size on ferromagnetic embolization hyperthermia in a rabbit liver tumour model, *Int. J. Hyperthermia*, **2002**, 18, 129–140.
- 45 MITSUMORI M, HIRAOKA M, SHIBATA T, OKUNO Y, MASUNAGA S, KOISHI M, OKAJIMA K, NAGATA Y, NISHIMURA Y, ABE M, et al., Development of intra-arterial hyperthermia using a dextran-magnetite complex, *Int. J. Hyperthermia*, **1994**, 10, 785–793.
- 46 MITSUMORI M, HIRAOKA M, SHIBATA T, OKUNO Y, NAGATA Y, NISHIMURA Y, ABE M, HASEGAWA M, NAGAE H, EBISAWA Y, Targeted hyperthermia using dextran magnetite complex: A new treatment modality for liver tumors, *Hepatogastroenterology*, **1996**, 43, 1431–1437.
- 47 MINAMIMURA T, SATO H, KASAOKA S, SAITO T, ISHIZAWA S, TAKEMORI S, TAZAWA K, TSUKADA K, Tumor regression by inductive hyperthermia combined with hepatic embolization using dextran magnetite-incorporated microspheres in rats, *Int. J. Oncol.*, **2000**, 16, 1153–1158.
- 48 JONES SK, WINTER JG, GRAY BN, Treatment of experimental rabbit liver tumours by selectively targeted hyperthermia, *Int. J. Hyperthermia*, **2002**, 18, 117–128.
- 49 MOROZ P, JONES SK, METCALF C, GRAY BN, Hepatic clearance of arterially infused ferromagnetic particles, *Int. J. Hyperthermia*, **2003**, 19, 23–34.
- 50 FINE HA, DEAR KB, LOEFFLER JS, BLACK PM, CANELLOS GP, Meta-analysis of radiation therapy with and without adjuvant chemotherapy for malignant gliomas in adults, *Cancer*, **1993**, 71, 2585–2597.
- 51 STUPP R, MASON WP, VAN DEN BENT MJ, WELLER M, FISHER B, TAPHOORN MJ, BELANGER K, BRANDES AA, MAROSI C, BOGDHANN U, CURSCHMANN J, JANZER RC, LUDWIN SK, GORLIA T, ALLGEIER A, LACOMBE D, CAIRNCROSS JG, EISENHAEUER E, MIRIMANOFF RO, Radiotherapy plus concomitant and adjuvant temozolomide for glioblastoma, *N. Engl. J. Med.*, **2005**, 352, 987–996.
- 52 GNEVECKOW U, JORDAN A, SCHOLZ R, BRUENS V, WALDOEFNER N, RICKE J, FEUSSNER A, HILDEBRANDT B, RAU B, WUST P, Description and characterization of the novel hyperthermia- and thermoablation-system MFH 300F for clinical magnetic fluid hyperthermia, *Med. Phys.*, **2004**, 31, 1444–1451.
- 53 MAIER-HAUFF K, ROTHE R, SCHOLZ R, GNEVECKOW W, WUST P, THIESEN B, FEUSSNER A, VON DEIMLING A, WALDOEFNER N, FELIX R, JORDAN A, Deep regional thermotherapy using magnetic nanoparticles: Results of a feasibility study with 14 glioblastoma multiforme patients, submitted for publication, **2006**.
- 54 WUST P, GNEVECKOW U, RICKE J, FEUSSNER A, HENKEL T, KAHMANN F, JOHANNSEN M, KÜMMEL S, SEHOULI J, FELIX R, JORDAN A, Magnetic nanoparticles for interstitial thermotherapy – feasibility, tolerance, achieved temperatures, submitted for publication, **2006**.

- 55 TILLY W, GELLERMANN J, GRAF R, HILDEBRANDT B, WEISSBACH L, BUDACH V, FELIX R, WUST P, Regional hyperthermia in conjunction with definitive radiotherapy against recurrent or locally advanced prostate cancer T3 pN0 M0, *Strahlenther Onkol.*, **2005**, 181, 35–41.
- 56 ALGAN O, FOSMIRE H, HYNYNEN K, DALKIN B, CUI H, DRACH G, STEA B, CASSADY JR, External beam radiotherapy and hyperthermia in the treatment of patients with locally advanced prostate carcinoma, *Cancer*, **2000**, 89, 399–403.
- 57 HURWITZ MD, KAPLAN ID, HANSEN JL, PROKOPIOS-DAVOS S, TOPULOS GP, WISHNOW K, MANOLA J, BORNSTEIN BA, HYNYNEN K, Association of rectal toxicity with thermal dose parameters in treatment of locally advanced prostate cancer with radiation and hyperthermia, *Int. J. Radiat. Oncol. Biol. Phys.*, **2002**, 53, 913–918.
- 58 JOHANNSEN M, GNEVECKOW U, ECKELT L, FEUSSNER A, WALDOEFNER N, SCHOLZ R, DEGER S, WUST P, LOENING S, JORDAN A, Clinical hyperthermia of prostate cancer using magnetic nanoparticles: Presentation of a new interstitial technique, *Int. J. Hyperthermia* E-pub, 27th June **2005**.

## 9

## Ferromagnetic Filled Carbon Nanotubes as Novel and Potential Containers for Anticancer Treatment Strategies

*Ingolf Moench, Axel Meyer, and Albrecht Leonhardt*

## 9.1

### Introduction

Especially during recent years, the discovery of various species and modifications of carbon nanotubes (CNTs) have stimulated research on their applications, including in human medicine. The success of these applications depends significantly on the physical, chemical and biological properties of the CNTs and their modifications. For application in the human body, CNTs must be pure and biologically inert.

The development and testing of novel and alternative therapeutic concepts against cancer are needed, especially for advanced tumor types where no curative conservative treatment option is established. Attractive novel and potential tools for anticancer treatment strategies are nanoparticles (e.g., for hyperthermia) and nano-scaled tubes (e.g., for targeted drug release).

Here, we propose novel types of functionalized and ferromagnetic filled multi-walled CNTs (fff-MWCNTs) with various advantages for application in human medicine, especially in anti-tumor therapeutic concepts. These structures represent multifunctional nano-scaled containers for possible use in different medical treatments, including (a) magnetically guided hyperthermia, (b) heat-inducible drug delivery/carrier and stepwise drug release and enhancement systems, (c) internal tracer/drug carrier systems for the detection and/or (d) combinational applications with conservative treatment modalities. Such fff-MWCNT containers are schematically illustrated in Fig. 9.1. These structures combine the advantages of ferromagnetic containers (for hyperthermia or other mechanisms of heat transfer) with those from a broad spectrum for encapsulations and modifications within the carbon tube as well as outside.

Presently, human prostate cancer (PCa) – the most abundant tumor in men – with the well-known limitations of conventional therapies serves as an attractive model object for developing and optimizing treatment concepts based on and/or associated with fff-MWCNTs. First, a short overview and a clinical introduction about this tumor entity are given, followed by the different methods and techniques of synthesis and characterization of the MWCNTs, including novel techniques for their modification and functionalization. The treatment concept pro-



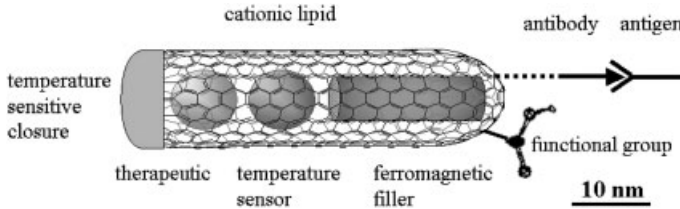


Fig. 9.1. Schematic of a multifunctional nanocontainer. (Modified from Ref. [232].)

posed will be realized by principles of nanotechnology; therefore, the magnetic properties of nano-scaled objects and materials are introduced. Furthermore, we discuss the relevant parameters for and mechanisms of heat transfer as well as of the specific absorption rate.

Recent knowledge of modified MWCNT will be summarized, including our own results for synthesis strategies for fMWCNT, (bio)functionalization for the *in vitro* and *in vivo* transfer into different cellular systems and the accumulation in target cells and tissues. Future steps in the development of these nanocontainers are also discussed. These containers must fulfill numerous criteria, especially basic safety and efficacy requirements, before being used in humans.

For a potential future application *in vivo*, fundamental issues that need to be resolved include the homogeneity (uniformity of the carbon multi-wall sidewall, grade and composition of the ferromagnetic and additional filling materials) and purity of the MWCNT at the various stages of intrinsic and extrinsic functionalization.

This chapter describes the feasibility of different applications using MWCNTs, e.g., as heat mediators for hyperthermia of solid tumors. The extraordinary potential of the proposed MWCNTs is shown by their functionality as multiple containers. These therapies are based on heat dissipation in the ferromagnetic filling material of the MWCNTs. Therefore, the requirements for the heat transfer of the nanocontainer are related to those of the hyperthermia. Thus, the material requirements were derived from the knowledge of hyperthermia but are not limited to this application field. For this reason it is difficult to present a complete and comprehensive overview of all modifications and variants of functionalized MWCNTs, and so for technical and medical reasons the focus here will be on novel types of fff-MWCNTs and the model system of prostate cancer.

## 9.2

### Prostate Cancer

#### 9.2.1

#### Incidence, Risk Factors and Diagnostic Criteria

Prostate cancer (PCa) is the most commonly diagnosed cancer in men of western countries. However, except for the risk factors of age, race, geographic dependence,

and family history of PCa, the etiology of this tumor entity remains poorly understood. PCa is primarily a tumor of older men. The incidence rate for men over the age of 65 is about 20-fold greater than that for men between 50 and 54. Less than 1% of PCa are diagnosed in patients in their first three decades of life. About 2–3% of all male deaths are attributable to PCa.

A familial history of PCa, *per definitionem* an affected father or brother with an association with at least a two-fold increase of disease, remains a consistent and important risk factor. About 40% of PCa cases are estimated to have a genetic component. However, PCa is a outstanding example of a tumor entity characterized by tumorbiological and genetic heterogeneity (reviewed in Ref. [1]). The prostate of a man diagnosed with PCa contains an average of five apparently independent lesions [2], and this multifocality is independent of familial history.

In the general population of the U.S., the risk of PCa is highest in African-American men, being approximately double that of their Caucasian counterparts. Moreover, Caucasians and African-American men in the U.S. have a PCa incidence that is 5–50× greater than that of Japanese men residing in Japan, and the incidence of PCa on Japanese immigrants to the U.S. is four times that of their native Japanese counterparts. This marked racial and cultural disparity indicates that dietary factors might affect PCa onset and growth.

As a serum tumor marker, prostate specific antigen (PSA), a serine protease belonging to the human glandular kallikrein family, has revolutionized the detection and management of PCa like no other marker in the history of oncology. With early identification of PCa using serum PSA, less than 10% of PCa with distant metastases are now diagnosed, a stage with five-year survival of only about one-third.

A patient's serum level of PSA, clinical tumor stage and Gleason grade provide valuable information to clinicians. The Tumor-Node-Metastases (TNM) classification system is used for the staging of PCa, whereas the Gleason score system is used for histologic grading characterizing the aggressiveness of this malignancy. Classification of PCa is based on size, invasion of the prostate capsule, and clinical stage. PCa develops in two different regions of the gland, with about 80% being found in the periphery, whereas the remaining cancers are found in the periurethral region, termed transitional zone (Fig. 9.2).

Primary PCa growth is characterized by an extremely heterogeneous and multifocal pattern. Initially, the tumor growth is an androgen-dependent and mediated by the androgen receptor. Despite an initial sensitivity, PCa become more or less quickly androgen-independent. Then the PCa becomes metastatic and, finally, hormone refractory [3].

The entity of PCa represents a significant public health problem and underscores the need for the development of improved diagnostic markers [4] as well as of treatment modalities.

### 9.2.2

#### Treatment Options, Outcome and Limits

The serum marker PSA improves the detection of clinically important tumors without significantly increasing the detection of unimportant tumors; most PSA-

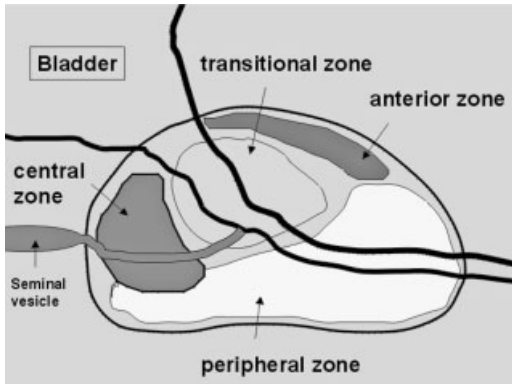


**Fig. 9.2.** Staging modality section of the prostate. The prostate gland with a branched structure can be divided in four distinct regions that reveal a different incidence of PCa: the anterior zone is purely fibro-muscular, the central zone contains the ejaculatory ducts (8% of cancers), the transitional zone (25% of cancers) is characterized by two lateral lobes, together with the periurethral glands, and the peripheral zone gives rise to 67% of cancers.

detected tumors are curable using current techniques, but there is no cure for metastatic disease. Treatment options, mostly radical prostatectomy, external beam radiation and brachytherapy, have become increasingly used to manage localized disease.

Contemporary methods of radical prostatectomy for patients with clinically localized disease are generally associated with excellent outcomes (reviewed in Ref. [5]). The cancer specific survival 10 years after radical perineal prostatectomy for patients with organ confined disease is approximately 90%. Crude survival rates at 10 and 15 years after surgery were similar to those of age-matched men from the general population without PCa. However, about 30–50% of patients thought to have organ-confined PCa at the time of surgery are later found to have disease beyond the prostate based on a careful review of the surgical specimen [5].

Neoadjuvant therapy with hormonal ablation has been evaluated in several studies and resulted in reduced positive surgical margins, and decreased volume of the PCa, equivalent to a pathological down-staging [6].

Virtually all recurrent clinical and metastatic diseases are preceded by a rising PSA, and only a few sporadic cases of recurrence have been reported in the absence of a detectable serum PSA. Biochemical failure is defined as either the persistence of detectable PSA after surgery or the development of detectable PSA in those with previously undetectable postoperative level.

For advanced disease, ablating androgenic hormones is the mainstay of therapy (reviewed in Ref. [7]), and will result in tumor response in about 80% of men.

For men considered to be at high-risk of treatment failure after local therapy alone, multimodal treatment strategies, for instance the combination of radiotherapy followed by hormonal therapy, may result in improved cancer-control out-

comes. The benefit of neoadjuvant or adjuvant hormonal and/or chemotherapy followed by radical prostatectomy in high-risk patients is unclear but is the subject of ongoing or planned Phase III clinical trials. These studies will help to examine the role of multimodal treatment strategies in these high-risk patients.

In summary, alternative therapeutic strategies are needed for the treatment, especially, of locally advanced and metastatic PCa.

### 9.2.3

#### **MWCNT Model**

Figure 9.1 depicts a schematic diagram of a multifunctional nanocontainer that is possibly applicable for future anticancer therapy. The main component is a multi-wall carbon nanotube, filled with a ferromagnetic material, with an external diameter of 20–60 nm and a length of approx. 100–10 000 nm, as required. The case is made up of a pre-defined number of graphene layers (2–20), which guarantee an extremely high chemical stability. The external case is already filled during production. Iron [8–12], nickel [11], cobalt [13, 11], or FeCo [11, 14] may be used as ferromagnetic materials. The deposits can grow without a substrate in powder form [8, 9] or on substrates [10, 12], which is of particular technological advantage. Of these materials, we favor iron as a filling material for future application in antitumor therapy, owing to the possible toxic side effects of Ni, Co or FeCo alloys. Even at this early stage, the ff-MWCNT can be put to practical use as part of a therapy. One particularly notable consideration is magnetic particle hyperthermia. The basic effectiveness of this therapy and the biological compatibility of the material system have been confirmed in animal testing (mice). With regard to superparamagnetic particles (SPM, see Chapter 8) also discussed for these applications – using magnetite and maghemite – the different mechanism for heat generation must be born in mind.

The primary field of application is the single “magnetic particle hyperthermia” (MPH) or in combinations with other treatment modalities. Therapeutic efficacy and the biocompatibility of ff-MWCNTs have been confirmed in cell culture and animal experiments in recent years by our group.

For these applications and in comparison with other nanoparticles, especially superparamagnetic particles containing magnetite or maghemite (see Chapter 8), the function of ff-MWCNTs is based on a completely different mechanism of heat induction.

Apart from the basic functionality (for hyperthermia), the container system proposed allows a broad spectrum of further applications. Since the ferromagnetic filling is often partial and the ff-MWCNTs can be opened after synthesis, a secondary filling with an additional agent and a subsequent defined closing is applicable. The agents could be (a) enhancer substances for hyperthermia, (b) chemotherapeutics with better efficiency at higher temperatures (e.g., cisplatin). Furthermore, minimized sensors can be integrated for contact-free measurement of local temperatures. The inclusion of rare elements for the localization of ff-MWCNT within the body has been suggested.

The opened ff-MWCNT is re-closed by the chemical reconstruction of the carbon tube or by addition of foreign materials such as heat-inducible and biocompatible polymers. Moreover, specific functionalization increases the accumulation within the target tissue and can stimulate the uptake by the target cells [15]. The proposed nanocontainers are suitable (a) alone for hyperthermia, (b) as adjuvant therapeutics or (c) alone or in combination with other nanoparticles (e.g.,  $\gamma\text{-Fe}_2\text{O}_3$  as SPM) for heat-inducible drug-releasing containers.

### 9.3

#### Carbon Nanotubes

##### 9.3.1

##### General Remarks

After detailed systematic studies of very thin carbon filaments in a high-resolution transmission microscope Iijima reported the existence of SWCNT and MWCNT in 1991 [16, 17]. Since then there have been intensive investigations into the synthesis, structure and properties of these new nanostructured materials. Their unique electrical, thermal, optical and mechanical properties have already generated great interest for applications in many different fields. They have shown increasing potential for use as field emission devices, nanoscale transistors, tips for scanning microscopy or components for composite materials [18]. Moreover, CNTs filled with ferromagnetic metals such as Fe, Ni, or Co represent a fascinating new material. Owing to their size and enhanced magnetic coercivities these carbon-covered ferromagnetic nanowires have significant possibilities in different areas too. They can be used in magnetic recording media or, as individually filled ff-CNTs, as sensors for magnetic force microscopy [19]. In addition to pure CNTs, derivative nanotubes with attached chemical or biochemical groups have been prepared that should find applications in biomedicine [20].

Two types of CNTs can be distinguished, single-walled (SWCNTs) and multi-walled (MWCNTs). They can be described as cylindrically shaped molecules made of rolled up single or multilayer sheets of graphitic planes. Typical diameters are approximately 1 nm for a SWCNT and 10–100 nm for a MWCNT and a length reaching up to the centimeter-range (Fig. 9.3). Besides catalytic chemical vapor deposition (cCVD) [21, 22], electric discharge [17, 23] and laser ablation methods [24], various types of plasma-enhanced chemical vapor deposition methods [25–27] are practicable and controllable methods for the preparation of CNTs.

The electrical and electronic properties of carbon nanotubes depend on their geometrical structure and, for SWCNTs, on the so-called chirality. SWCNTs can be either metallic or semiconducting. CNTs are among the strongest and most resilient materials in nature.

The properties of MWCNTs strongly depend on the structure of their shells. Especially, the electrical conductivity varies between nearly metallic and insulator. The quality of shells depends on the synthesis method used.

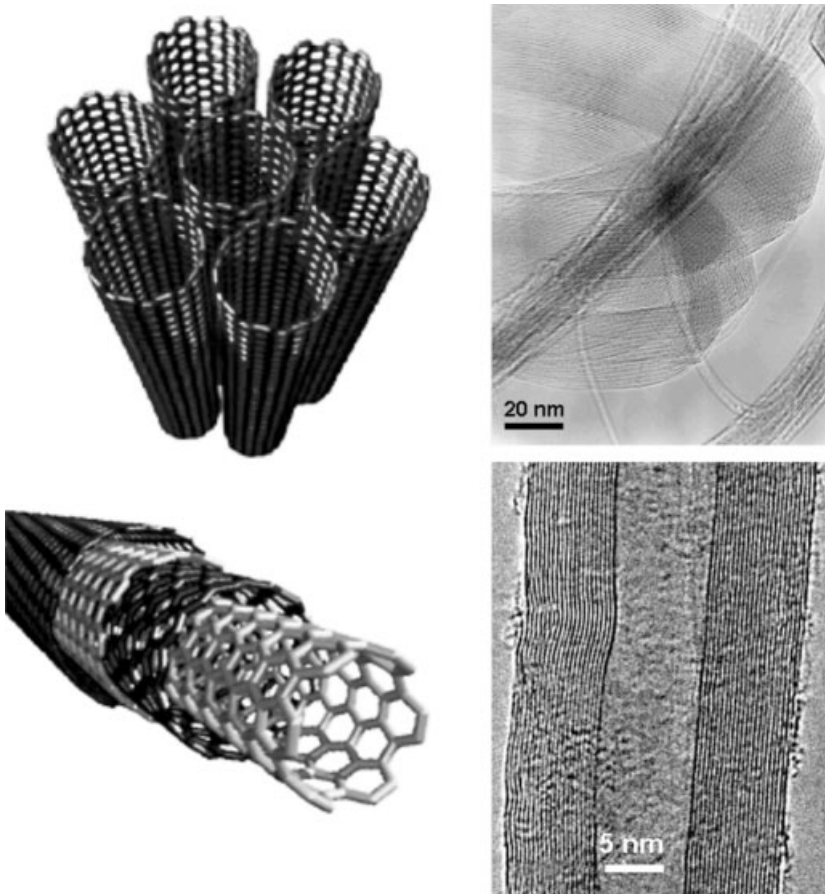


**Fig. 9.3.** Schematic and TEM images of SWCNT (single-walled carbon nanotubes) bundles and MWCNT (multi-walled CNT carbon nanotubes). (Modified from Ref. [233].)

Both SWCNTs and MWCNTs consist of two regions: the first is the sidewall of the tube and the second is the cap of the tube. By using different chemical and physical methods, the end caps can be opened and caps and sidewalls can be derivatized with different functional groups, radicals or molecules. Such manipulable nanotubes are well suited for application in biology and/or medicine. With a special material as filling (e.g., a ferromagnetic metal) CNTs can play an important role as a multifunctional nanocontainer in the diagnosis and therapeutic treatment of different diseases.

The next section describes the synthesis of f-MWCNTs and shows the unusual magnetic properties and possibilities of functionalization and manipulation (open, fill, close).

## 9.3.2

**Preparation and Structure of Filled Multi-walled Carbon Nanotubes****9.3.2.1 Synthesis of Ferromagnetic Filled Multi-walled Carbon Nanotubes**

f-MWCNTs can be synthesized by various methods. We classify two general versions: the first is an “*in situ* method”, in which the formation of the CNTs and their filling with different elements or compounds take place simultaneously. The other method is a “step by step process”: synthesis of empty CNTs – opening the tubes by chemical treatment – depositing and diffusion of filling material using different methods, mostly by wet chemical techniques – and, finally, closing the filled nanotubes by redeposition with a polymer or other carbon-containing phases (post-filling method).

In the following we only deal with “*in situ* techniques” for which there are physical and chemical methods. A physical, promising method is the “arc discharge”. This method delivers long, relatively continuous nanowires of many different elements, e.g., transition metals (Cr, Ni, Re, Au) rare earth metals (Sm, Gd, Dy, Yb) and other elements (S, Ge, Se, Sb) [28, 29]. The alternative, well-established method for synthesizing CNTs filled with metals as Fe, Co or Ni is catalytic chemical vapor deposition (cCVD). Different groups world-wide have used this method in a similar way.

With the suitable precursors, cCVD can deliver well-defined MWCNTs with a relatively high grade of filling and on a large scale, especially with elements of the iron triad. Compounds of the organometallic complex family “metallocenes” are such precursors. They have a “sandwich structure” of two parallel cyclopentadienyl rings and a metal in the center between these rings [ $M(C_5H_5)_2$  with  $M = Fe, Co, Ni$ ]; they are solid at room temperature, readily applicable, soluble in different organic solvents but also show suitable decomposition behavior in the temperature range 600–1150 °C. Pyrolysis of these metallocenes (Fe, Co, Ni) has been analyzed by Dyagileva et al. [30]. They showed that the decomposition is a complex process of homogeneous–heterogeneous nature of a series of consecutive, parallel and catalytic reactions.

Thus, the synthesis process of ff-MWCNTs, based on the decomposition of metallocenes, will also be catalytically determined and, consequently, a support (substrate) covered (completely or partially) with an active catalyst material will promote the formation of filled nanotubes.

In principle, all known methods for manufacturing (Fe,Co,Ni)-filled CNTs have the same basic concept. Figure 9.4 shows a typical synthesis (two-band) reactor, as used by different groups of researchers.

Sen et al. reported the first experimental results for the synthesis of f-MWCNTs [31]. The pyrolysis of metallocenes (ferrocene, cobaltocene, nickelocene) was carried out in a quartz tube located in a two-stage furnace system. In a typical experiment a defined quantity of a metallocene was placed in a quartz boat, placed inside a furnace and a mixture of argon and hydrogen passed through the quartz tube (in some experiments acetylene is used as additional gas-phase component). The furnace temperature was increased to 200 °C, leading to the generation of the met-

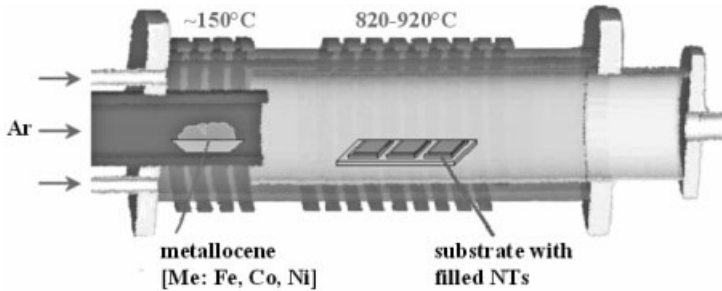


**Fig. 9.4.** Typical two-band furnace for the synthesis of filled carbon nanotubes, based on the decomposition of metallocenes. (Modified from Ref. [12].)

allocene vapor, which was carried by the Ar/H<sub>2</sub>-stream into a quartz tube maintained at 900 °C in a second furnace. Depending on the deposition conditions, partially filled CNTs were unoriented or aligned deposited on the quartz tube walls, and no substrate was positioned in the reactor. Sen et al. have recognized that this method is a real alternative to previously known methods (arc discharge) [31].

Grobert et al. at Cambridge University (Kroto's group) has synthesized iron and Invar (iron/nickel alloy) f-CNTs in an aligned structure by using a mixture of ferrocene and fullerene (C<sub>60</sub>) in the temperature range 900–1050 °C [9]. For the first time, the Cambridge group could also show the enhanced magnetic properties in such iron nanowires inside the CNTs. Later, Grobert used the aerosol-technique for the decomposition of ferrocene [32]. Here, a benzene solution containing ferrocene is nebulized by an aerosol generator in an argon flow and is injected in the reactor through a nozzle directly (Fig. 9.5).

In a further study the same group have prepared aligned, partly filled MWNTs (30–130 μm long) in high yield by using a compressed gas Ar driven atomizer

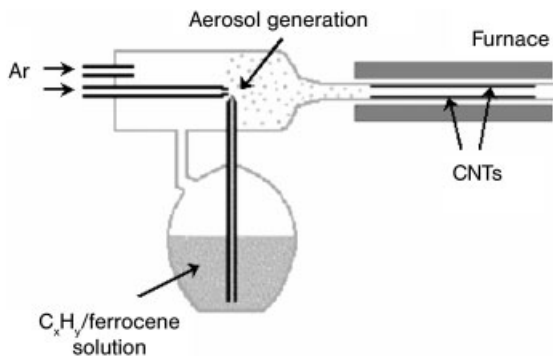


**Fig. 9.5.** Aerosol-technique for the injection of ferrocene in the deposition zone. (Modified from Ref. [32].)



[33]. They demonstrated that the yield of filling is proportional to the ferrocene concentration, but complete filling could be not achieved.

In 2002, Satishkumar et al. from Rao's group observed, besides increased coercivity, Barkhausen jumps with  $5 \text{ emu g}^{-1}$  steps in Fe-filled CNTs [34]. The ff-MWCNTs were prepared by pyrolysis of ferrocene along with acetylene. Selected area diffraction patterns of the nanowires show spots due to (011) planes of an  $\alpha$ -phase, the ferromagnetic modification of iron. Additional X-ray investigations revealed  $\gamma$ -Fe and, as the minor phase, cementite ( $\text{Fe}_3\text{C}$ ).

In our laboratory we have synthesized ff-MWCNTs on precoated substrates [10, 12]. On oxidized Si-wafers, thin layers (few nm) of the iron triad group (the catalyst material) have been deposited by using the sputter technique. Before beginning the deposition process, the pre-coated substrates were annealed at 900–1000 °C, directly in the deposition apparatus for a short time (few minutes). The annealing yielded some nm-sized islands on the substrate surface, which act as a source for nanotube growth. Hence, both iron from the surface in a solid or liquid-like state and the iron from the gas phase (ferrocene pyrolysis) deliver the material for the filling, causing a higher yield of filling than obtained by the groups of Kroto and Rao. With the higher filling yield the magnetic properties were also improved. The aligned-grown nanotubes show a pronounced magnetic anisotropy, with the easy axis perpendicular to the substrate plane and parallel to the axis of the aligned MWCNTs. Coercivity for the magnetic field direction perpendicular to the substrate amounts to  $44.56 \text{ kA m}^{-1}$  ( $\mu_0 H = 56 \text{ mT}$ ) compared with  $19.89 \text{ kA m}^{-1}$  (25 mT) for the direction parallel to the substrate. For comparison, the coercivity of bulk iron amounts to  $0.072 \text{ kA m}^{-1}$  (0.09 mT).

X-Ray diffraction analysis indicated the presence of bcc-Fe ( $\alpha$ -Fe), fcc-Fe ( $\gamma$ -Fe) and, as minor phase,  $\text{Fe}_3\text{C}$  with a relatively strong  $\langle 011 \rangle$  texture. An annealing process below the transition temperature of  $\gamma$ -Fe to  $\alpha$ -Fe led to an increase of the ferromagnetic phase ( $\alpha$ ) and an enhancement of magnetization saturation [35]. Similar results could be realized in the same group for Co- and Co/Fe-filled MWCNTs. In the latter, the filled material enhanced coercivities to about  $103.5 \text{ kA m}^{-1}$  (130 mT) [14, 36].

Recently, our group has explored various means of improving the deposition procedure in regard to increasing the grade of filling and the abundance of ff-MWCNTs. We have also investigated aligned and relatively small, short f-CNTs that are suitable for special applications.

Figure 9.6 illustrates a so-called two-stage reactor. It shows a first conveyor belt system for a constant and reproducible transport of the ferrocene precursor. The ferrocene is dissolved in cyclopentane and dropped on the moving band continuously. In the first part the solvent is vaporized and the ferrocene is transported alone in the reactor at a defined temperature and constant transport velocity. In the deposition reactor a second moving band, populated with Fe-precoated substrates is positioned. In principle, such an apparatus can work continuously [37]. By using this equipment, very strong aligned f-MWCNTs can be synthesized with extremely high magnetic anisotropies and coercivities. The tube lengths are linearly dependent on the concentration of ferrocene in the solvent cyclopentane and

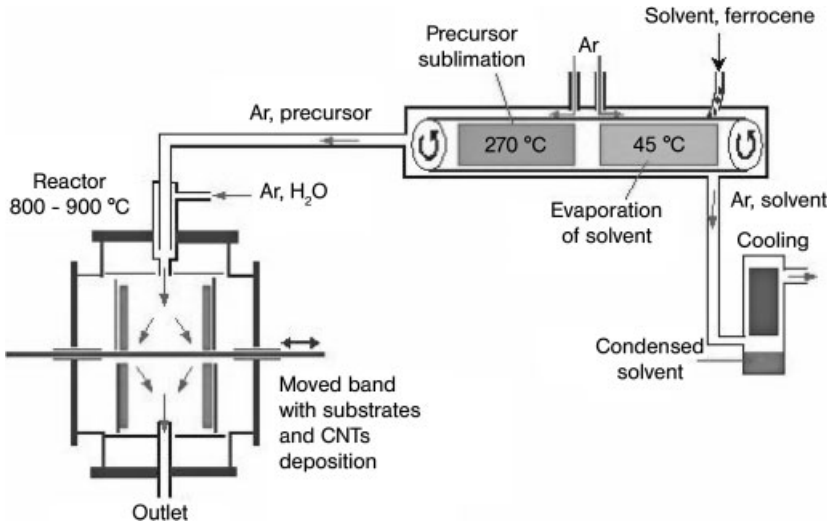


Fig. 9.6. A two-stage reactor for continuous deposition of filled carbon nanotubes. (Modified from Ref. [37].)

range between a few  $\mu\text{m}$  to 40  $\mu\text{m}$ . In contrast, the diameter of filled nanotubes is independent of ferrocene concentration and constantly in the range  $< 10\text{--}50\text{ nm}$  [inner (Fe-wire) diameter] and 20–180 nm (outer tube diameter).

### 9.3.2.2 Crystallographic Structure of Core Material in Filled Multi-walled Carbon Nanotubes

Some research groups have determined the structure of the core material in f-MWCNTs. Detailed results exist about Fe-filled tubes, which we only report on here. Figure 9.7 shows typical TEM images of CNTs with a partial and a complete

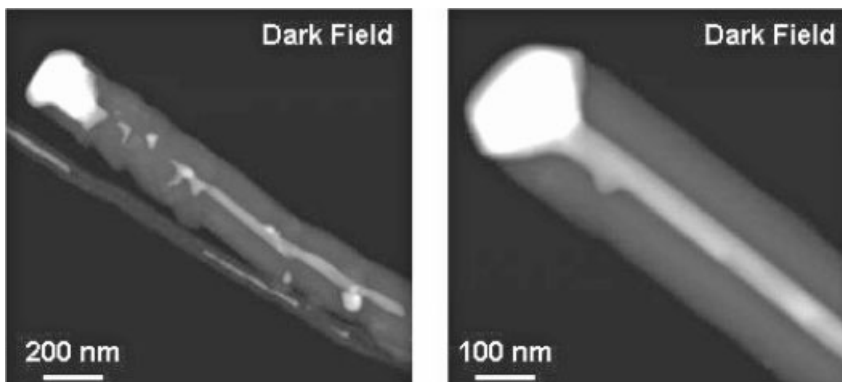


Fig. 9.7. Partly and completely filled multi-walled carbon nanotubes (MWCNT).

iron filling. The core material seems to be homogeneous. But which crystallographic phases does this material consist of? Several studies have investigated the X-ray-diffraction patterns of Fe-filled carbon nanotubes synthesized by cCVD in the temperature range 830–900 °C [33, 38, 39]. In most cases, the body-centered cubic phase of iron ( $\alpha$ -Fe) is the main component of the core material and is  $\langle 100 \rangle$ -textured along the tube axis.

Only Che et al. have reported that the filling material is amorphous if the cooling rate is very high after the synthesis process [40]. A post-annealing leads to crystalline  $\alpha$ -iron. In addition, Pichot et al. have shown that inside their aligned grown MWCNTs face-centered cubic iron ( $\gamma$ -Fe) is the dominant phase, with a  $\langle 110 \rangle$  texture parallel to the tube axis [41]. Finally, if the argon transport gas contains small amounts of oxygen (~1%) it is also possible that the filling consists of iron oxides such as hematite or magnetite [42]. These partly contrary results deserved detailed study. Recently, Kim and Sigmund have examined the crystallographic structures and orientations of iron nanowires inside carbon nanotubes with and without heat treatments at various temperatures [43]. The core material was found to consist of both bcc- and fcc-iron, in general, with their ratio dependent on the post-annealing temperature (without post-annealing and at room temperature the ratio  $\gamma/\alpha$  is  $<1$ ; after post-annealing at 1000 °C the ratio is near 1.0 and at 1400 °C approx. 2.3). Interestingly, the high temperature  $\gamma$ -Fe remains stable in a large quantity at room temperature. The reason why is explained below. The bcc-structure of iron is oriented in the  $\langle 001 \rangle$  or  $\langle 111 \rangle$  directions, while the fcc-structure is aligned only in the  $\langle 110 \rangle$  directions, along the axis of CNTs.

Besides the two modifications of iron a third phase, the thermodynamically unstable iron carbide phase  $\text{Fe}_3\text{C}$ , is often detected as a core material component. This phase plays a decisive role in the growth of empty and filled carbon nanotubes [44, 45]. Both Kim [43] and Shaper [45] have found that the iron carbide is enriched in the tips of the aligned CNT, and Shaper concluded that this iron carbide is an important intermediate in the catalyst-mediated growth of the tubes.

The application of iron-filled CNTs as nanomagnets requires complete filling with ferromagnetic iron, namely the bcc-phase  $\alpha$ -Fe.

As reported, at a synthesis temperature of 850–920 °C the core material consists of  $\alpha$ - and  $\gamma$ -Fe in various ratios, depending on the temperature, and a small amount of  $\text{Fe}_3\text{C}$ . Comparison with the Fe–C phase diagram shows that we do not have a thermodynamically stable state. The  $\gamma$ -Fe and  $\text{Fe}_3\text{C}$  cores are in a “frozen” state. Therefore, for the paramagnetic  $\gamma$ -phase to be transformed into the ferromagnetic  $\alpha$ -phase, a post-annealing process at a temperature below the eutectic line at 723 °C is needed. However, the  $\gamma \rightarrow \alpha$  transformation is connected with a 9% volume dilatation and if the  $\gamma$ -Fe is in a tight contact with the carbon shells it cannot expand and transform into  $\alpha$ -Fe because of the high elastic modulus of CNTs. Nevertheless, such a post-annealing has been realized at 645 °C for 20 h by our laboratory [46]. After this treatment the fcc-phase was completely transformed into the bcc-phase, as proved by X-ray diffraction.

Investigations of the crystallographic structures of core material, especially filled with iron, have led to differing views on the growth mechanism of empty and filled MWCNTs.

### 9.3.2.3 Growth Mechanism of Multi-walled Carbon Nanotubes

The growth mechanism of MWCNTs, especially of filled MWCNTs is still under discussion. However, some experimental facts are certain. First, growth is always carried out by a catalytically determined process, which means that a catalyst material is absolutely necessary. Secondly, tubular MWCNTs grow by a vapor–liquid–solid (VLS) mechanism with the catalyst particle in a liquid-like constitution, in contrast to the bamboo-like structures produced with a solid catalyst particle (VSS growth mechanism, see Fig. 9.8) [47, 48].

When a CNT is grown on a substrate, two types of growth modes are observed: so-called tip growth and the base or root growth mode (Fig. 9.9). The actual mode depends on the contact forces between the particle and the substrate. Strong adhesion promotes the base or root growth mode – it is often observed on plain substrates.

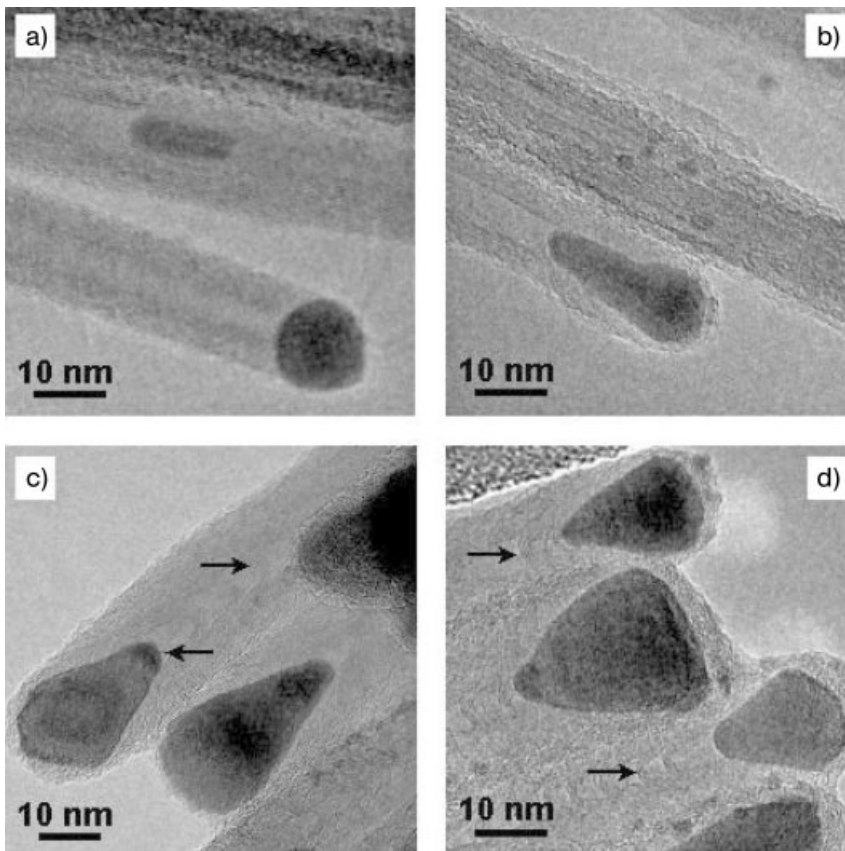


**Fig. 9.8.** Tubular MWCNT with a spherical catalyst (a, b) and a bamboo-like nanotube with a conic-shaped catalyst (c, d). (Modified from Ref. [230].)

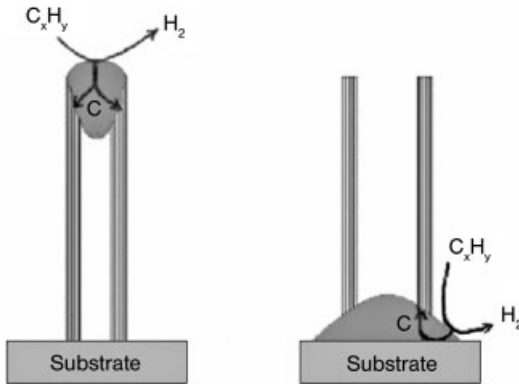


Fig. 9.9. Tip and root growth modes of a CNT (carbon nanotube) on a substrate [231].

The diameter of the growing nanotubes depends on the size of catalyst particle on the substrate and on the size of a stable catalyst particle on the Young contact angle between substrate and particle. Figure 9.10 shows an example.

Catalytic acting metals are mainly the iron triad group, i.e., iron, cobalt and nickel. Thus, metallocenes of these elements are used as precursors for the synthesis of CNTs. An effective, well-known method for the preparation of tubular MWCNTs is the injection method [49, 50] using ferrocene dissolved in a hydrocarbon (e.g., xylene or benzene). This mixture is injected in the hot zone of the reactor chamber. By spontaneous decomposition of both ferrocene and xylene a rapid and aligned growth of MWCNT is performed on the reactor walls or on a used substrate.

Dyagileva et al. have investigated the decomposition behavior of (Fe, Co, Ni)-metallocenes and ascertained that their thermal stability decreases in the order  $Cp_2Fe > Cp_2Co > Cp_2Ni$  [30]. Furthermore, ferrocene decomposes mainly into  $H_2$  and  $CH_4$  above  $500^\circ C$ , in contrast to the Co- and Ni-metallocenes, which mainly decompose to give cyclopentadiene ( $C_5H_6$ ) and less  $H_2$  and  $CH_4$ . This decomposition behavior of ferrocene is advantageous for growth because by hydrogen formation the Cp-complex is completely cleaved and carbon is released for tube shell growth. The hydrogen produced additionally reduces fresh ferrocene in the

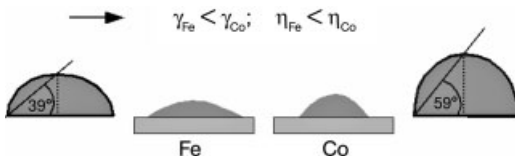
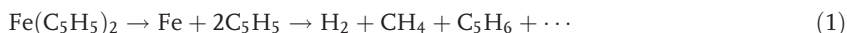


Fig. 9.10. Calculated Young contact angles for Fe and Co on oxidized silicon. Iron has a lower surface energy and a lower viscosity than cobalt. (Modified from Ref. [54].)

gas flux and inhibits oxidation of the iron and carbon. In fact, Dormans has observed the reduction of ferrocene at between 673 and 1173 K in a hydrogen atmosphere, whereas no decomposition was detected up to 1173 K in helium [51].

Consequently, the first step of the CNT growth mechanism is the homogeneous gas-phase decomposition of ferrocene:



As additional carbon feedstock the solvent xylene or benzene is used in the injection method. For the hydrocarbon xylene, a derivative of benzene, Endo et al. have considered two gas-phase and four surface reactions and found very good agreement between experimentally determined and calculated production rates of MWNTs allowing for these six elementary equations [52].

Xylene reacts with the hydrogen formed by ferrocene decomposition to afford toluene which then yields benzene:



These four hydrocarbons (xylene, toluene, benzene, methane) will decompose on the catalyst particle surface, and Eqs. (2) and (3) are named as the second step in the growth mechanism of MWNTs.

Promotion of reactions according to Eqs. (1–3) is always observed on the walls of the reactor chamber or on an inert substrate, positioned in the hot zone of the oven, because a heterogeneous reaction, two-dimensional nuclei formation, is always energetically favored. At relatively low temperatures (820–850 °C) such heterogeneous reactions are exclusively dominant.

It is assumed that the iron particles impinge on the substrate and solve the carbon. The solved carbon diffuses through the particles and precipitates again as tube shells. As mentioned above, a tip or root growth mode can be observed, depending on the adhesion forces on the exclusive substrate material. Wafers composed of oxidized silicon are often as substrates. The tip growth mode is often realized on such materials, where the catalyst material is deposited by a sputter technique on the substrate before nanotube growth is started. Nanometer-sized droplets are subsequently formed by a thermal pre-treatment of these very thin sputtered layers (a few nm thick) in either an argon or hydrogen atmosphere [12, 52]. The subsequent CNT growth is affected by the introduction of a catalyst-free hydrocarbon in the reaction chamber. In contrast, using spray pyrolysis of ferrocene dissolved in a hydrocarbon, spontaneous deposition on the reactor walls leads to base growth [53].

Normally, a grown MWCNT has only one catalyst particle on either the base or tip. The core of tube is hollow and free of inclusions.

By using the ferrocene pyrolysis technique with and without an additional hydrocarbon the synthesized carbon nanotubes show a partial filling with catalyst mate-

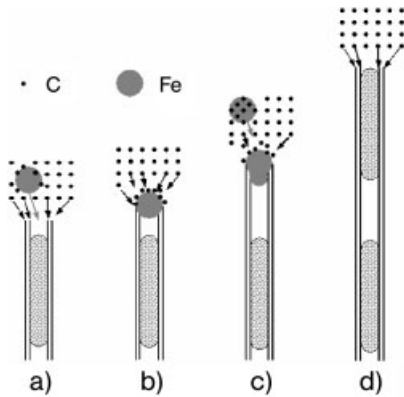


Fig. 9.11. Continued growth of partially filled carbon nanotubes. (Modified from Ref. [234].)

rial; the tubes exhibit multiple particles or wires along the middle of the tube (Fig. 9.11).

Investigations aiming to explain this phenomena have shown that the root or base growth mode is a suitable model for describing the growth of such partially ff-MWCNTs [50, 52, 53]. Figure 9.12 shows the initial state schematically. Short catalyst-containing tubes deposit on the reactor wall or on the substrate. The tubes always show an open tube end (root growth). With continued growth the gas-phase delivered carbon and iron particles can fall into these open tube ends. Simultaneously, carbon dissolves in the particle and graphite precipitation occurs into the wall of the CNT, thereby increasing the tube length. The particle is deformed due to the squeeze of the tip. As the distance between the open tube end and the catalyst particle increases, it becomes harder for carbon to reach this particle. After a defined time, a new iron particle falls on the open end and growth is continued. The model explains not only the growth of partially filled tubes but also the growth of very long tubes.

Is it possible to influence the yield of filling by deposition conditions? Cer-

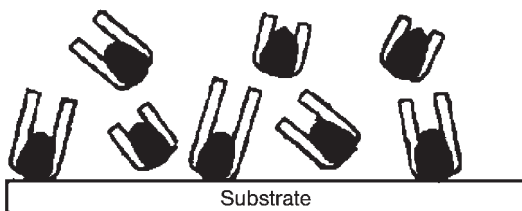


Fig. 9.12. Initial state of growth of partially filled carbon nanotubes when using the spray technique with continuous catalyst addition. (Modified from Ref. [53].)

tainly, the catalyst addition rate plays an important role. This addition rate can be increased by a higher Fe/carbon ratio in the gas phase (ferrocene decomposition without hydrocarbon) or by first and additional catalyst particles on the substrate. Using latter method we have reached a filling yield of nearly 50 vol% [46]. In doing so, we could prove that both the catalyst material from the substrate and from the gas phase participates in the filling of nanotubes. Furthermore, the deposition of filled tubes using cobaltocene as catalyst and a carbon feedstock was realized on an iron pre-coated substrate. The result was a carpet of aligned Fe/Co filled MWCNTs. The iron could be detected in the tips of tubes, meaning that it diffused into the Co filling material that was delivered from the gas phase.

As mentioned above, the open tube end model can explain the rapid growth of super long MWCNTs. Nevertheless, with longer deposition times the growth rate decreases and more Fe particles and no nanotubes are formed [11, 54]. This means that although new catalyst material is supplied again and again the catalytic reaction at a tube material will be ever more deactivated. This effect of catalyst deactivation is well known and is indicated by an overcoating of the iron particles with an amorphous carbon layer. It is caused by a momentary supersaturation of carbon on the surface of the catalyst particle due to too high a carbon supply from the gas phase.

### 9.3.3

#### **Post-treatment: Opening, Filling and Closing of MWCNTs**

The application of ff-MWCNTs as multifunctional nanocontainers (for instance in the medicine) requires the ends of these tubes to be opened, further filled with drugs or agents and, finally, re-closed (cf. Fig. 9.1).

The opening process of both SWCNTs and MWCNTs is relatively well controlled. This procedure is often connected with a necessary purification of the synthesized nanotube material. CNTs are effectively purified and opened by an oxidation process, either by a treatment in an oxidizing atmosphere at increased temperature ( $O_2$  annealing or treatment in a  $O_2$ -containing Ar-plasma [55–57]) or by a wet-chemical post-treatment in an oxygen acid ( $HNO_3$ ) [58, 59].

Tsang et al. first published the method of wet-chemical opening with  $HNO_3$  in 1993 [60, 61] and today this method is used by many research groups. However, all these procedures, which are primarily developed for the purification of CNTs, i.e., as means of eliminating of amorphous carbon and metal particles, are very aggressive. They not only remove the ends of the carbon nanotubes, they also damage parts of the tube walls. Such defects in the tube walls reduce the mechanical properties and limit the application fields. Recently, Raymondo-Pinero have reported on the simultaneous purification and opening of MWCNTs by using of solid NaOH [62]. By such a solid–solid reaction between NaOH and as-grown carbon nanotubes the MWCNTs will be purified and opened without defects in the tube shells (Fig. 9.13).

The next necessary step for the construction of a nanocontainer is to fill the opened carbon with the desired agents, drugs or sensor materials. In principle,



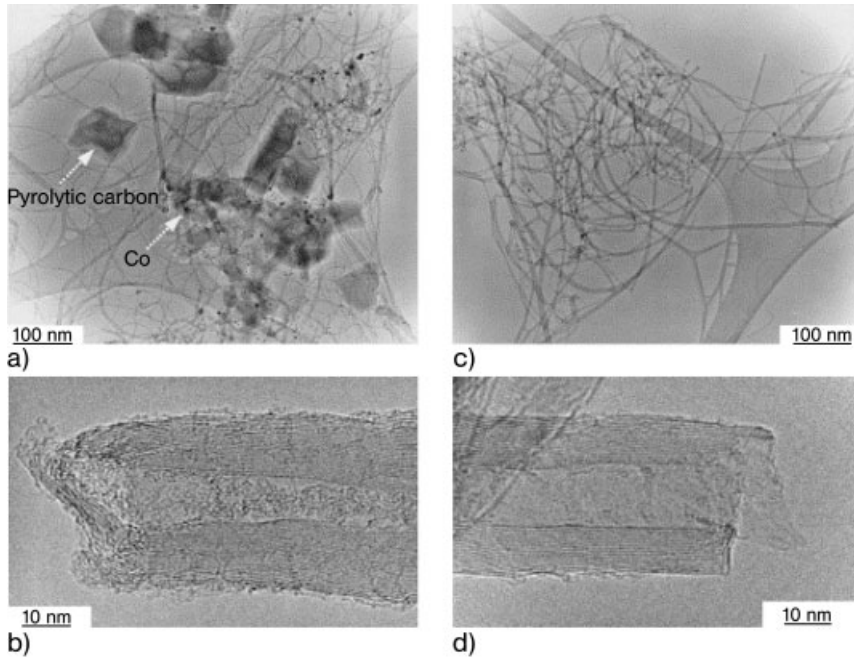


**Fig. 9.13.** TEM images of carbon nanotubes: (a, b) as grown and (c, d) after reaction with NaOH at 800 °C for 1 h. (Modified from Ref. [62].)

this is generally possible because the hollow interior can serve as a nanometer-sized capillary.

Ajayan and Iijima could already show in 1993 that CNTs can be filled with molten material through such a capillary action (Pb and Bi melts) [63]. By using a simple wet chemical method (suspending the CNTs in a nitric acid solution containing nickel nitrate), Tsang et al. have filled the CNTs with Ag [61]. In 1996, Chu et al. described a two-step method for filling CNTs with silver and gold metal with a high grade of filling [64]. Ugarte et al. have studied in detail the wetting and capillarity by metal salts by a similar two-step method [65]. First, nanotubes were opened by oxidation in the air and, subsequently, nanotubes were immersed in molten salt (e.g.,  $\text{AgNO}_3$ ).

Wu et al. have successfully prepared Fe-Ni alloy nanoparticles inside carbon nanotubes by wet chemistry [66a]. Using nitrates of iron and nickel, filling lengths of up to 50 nm were reached. Gao and Bando have developed a special nanothermometer by filling carbon nanotubes with liquid gallium [66]. Gallium has one of the greatest liquid ranges of any metal and has a low vapor pressure and a high thermal expansion coefficient. Such a thermometer can be used over a wide temperature range.

Besides filling with metals or salts, CNTs can be also filled with oxides [67, 68]

and halides [69, 70]. Recently, CNTs have been filled controllably with fluorescent particles by immersion in liquid ethylene glycol, by the complementary action of capillary forces and evaporation of the liquid [71]. In addition, Korneva et al. have described a simple capillary action technique to fill CNTs with paramagnetic iron oxide particles using commercial ferrofluids (particle size  $\sim 10$  nm) [72].

Both of the latter results show important progress and that filling a CNT with solid particles (up to 10 nm diameter!) is generally possible. This is one of the most important requirements for filling CNTs with drugs or agents and thus for possible application as a nanocontainer to transport these drugs to specific locations in the human body.

After the post-filling process it is necessary to re-close the nanotubes. This can be achieved by reaction with different reagents such as ethylene glycol or by treatment with benzene or another hydrocarbon vapor in a reducing atmosphere of argon and hydrogen at increased temperatures [73].

Another possibility is an additional thermal treatment with a biocompatible monomer that will polymerize at higher temperatures.

## 9.4

### Magnetism in Nano-sized Materials

#### 9.4.1

##### General Remarks

The principles suggested here for putting the multifunctional nanocontainer to use can only really become effective when it is produced on a nm scale. Understanding the difference between bulk and nm materials and the changes in properties they cause is the main condition for appreciating how magnetic materials can be used in biomedical applications [74, 75]. To better understand the special uses of ferromagnetic materials, especially those with geometric forms at the nm scale, some fundamental magnetic parameters, and dimension-related changes where necessary, must be briefly elaborated. These relations are, however, highly complex and extensive, meaning that only some selected challenges can be briefly described at this point. For complementary, continuing deliberations, reference should be made to the relevant standard works on magnetism [76–80], and to studies that deal specifically with physical characteristics specific to nanoscale arrays of ferromagnetic materials [81–86]. For an immediate understanding of the problem, we explain briefly some of the parameters necessary for the suggested therapy plan using a nanocontainer to be effective. In particular, these include those that affect heat development by AC heating. Magnetic reorientation is responsible for losses in ferro- or ferrimagnetic materials such as ff-MWCNT. The reorientation depends on the type of demagnetization process. These processes are determined by intrinsic magnetic properties such as magneto crystalline anisotropy and magnetization, on the one hand, and extrinsic properties such as shape, particle size and aspect ratio on the other hand. The size and shape dependence of  $H_c$  are well known.

$H_c$  will be maximized when the size reaches a critical low size (single domain particle). In the same way, it can be enhanced for particles having large aspect ratios [75]. To study these dependences in detail, the challenge of producing uniform nanomagnets must be solved. To prepare nanomagnets, complex technologies are often used, not only based on conventional thin film or CVD technology but also on a combination of wet chemical methods and special technology. One technique that has proved particularly valuable is the electrolytic deposition of ferromagnetic materials in the pores of suitable substrates (e.g.,  $\text{Al}_2\text{O}_3$ ) [82–85, 87, 88].

Another point that needs to be explained is that the preferred ferromagnetic metals (iron, cobalt and nickel) are, for example, susceptible to oxidation [89–92] and that the oxides may have different magnetic characteristics than the pure metal. If the characteristics of nanoparticles with diameters of  $<100$  nm are to be determined and used, the volume/surface ratio detrimental to oxidization must be considered here. The improvement of biocompatibility is often the reason why nanoparticles are coated with paramagnetic materials. For this purpose, Al or  $\text{Al}_2\text{O}_3$  [93–95], Au [96], Si or  $\text{SiO}_2$  [97–99], and other materials are discussed. Several groups suggest the use carbon [92, 100–104]. In the case of the ff-MWCNT, protection from oxidation is guaranteed by the carbon [9]. Even a small number of graphene layers provide excellent protection against chemical changes. The magnetic characteristics do not change over a long time, even in unfavorable conditions [9]. For example, Fe-filled MWCNTs can be stored in acids and brines [105] with no demonstrable reaction and thus no demonstrable change in their magnetic characteristics. This avoidance of oxidation is acquired at the cost of possible limited biodegradability, however. Nonetheless, these external cases/coatings can also indirectly have an (sometimes positive) effect on the magnetic qualities, e.g., by mechanical stresses [106], even if these case materials are paramagnetic by nature. As well as the applications described here, magnets in the desirable single-domain state generally demonstrate a wide range of potential uses in biomedicine [107], if the challenges of production can be solved.

#### 9.4.2

#### Magnetization in Nano-sized Materials

Ferromagnetism is the result of an ordered alignment of the atomic magnetic moments. Fe, Co, Ni and their alloys are the most important substances of this material class. Ferromagnetic materials are materials that can remain magnetized after application of an external magnetic field. This external field is typically applied by another permanent magnet, or by an electromagnet. If the temperature of a ferromagnetic material is raised above a certain point, called the Curie temperature ( $T_c$ ), the ferromagnet loses its long-range magnetic order that establishes the spontaneous magnetization and becomes simply paramagnetic [108].

The magnetic behavior of a ferromagnetic material can be illustrated in a plot of the magnetization ( $M$ ) versus the applied field ( $H$ ). For ferromagnets, which are the focus of this work, the “hysteresis loop” [109] is the most evident distinction. The remnant magnetization ( $M_r$ ), the saturation magnetization ( $M_{\text{sat}}$ ) and the co-

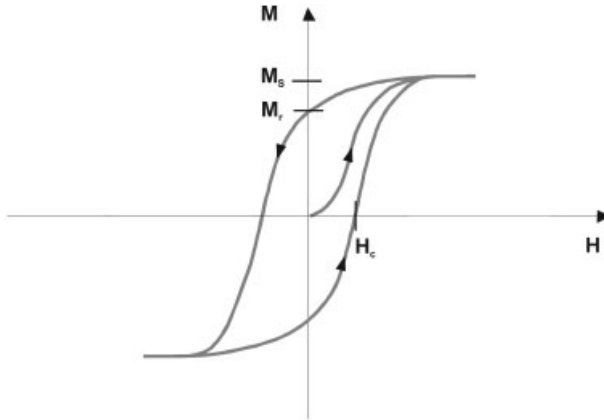


Fig. 9.14. Typical hysteresis loop ( $M$  vs.  $H$ ) for ferromagnetic materials.

ercive field ( $H_c$ ) are important magnetic properties (Fig. 9.14).  $M_r$  is the magnetization of the sample in the absence of an external applied field and is often used in relation with  $M_{\text{sat}}$  (i.e.,  $M_r/M_{\text{sat}}$ ).  $H_c$  is the applied field in the direction opposite to the current magnetization direction, which is necessary to bring the global magnetization to zero [79]. This does not imply that  $M = 0$ , but the magnetization breaks up into domains that are magnetically oriented such that the integration over the entire sample disappears. Table 9.1 shows the values of some magnetic characteristics for bulk Fe, Co and Ni.

In contrast to bulk material, enhanced values of the coercivity have been obtained for ferromagnetic nanoparticles [110, 111] or nanowires encapsulated inside a carbon envelope, where the coercivity reaches tens of millitesla [9]. Generally, the origin of this phenomenon is related to the small size and the single domain nature of the encapsulated metal crystals [9].

#### 9.4.3

#### Influence of the Dimensions on the Magnetization Distribution

Without a magnetic field applied, a piece of a ferromagnet often assumes a state with global magnetization vanishing. Such behavior indicates the presence of domain closures inside the material. The overall magnetization  $M_{\text{overall}}$  of the magnetic object is given by Eq. (4).

$$M_{\text{overall}} = \frac{1}{V_{\text{overall}}} \sum_i M_i V_i \quad (4)$$

where  $M_i$  and  $V_i$  are the magnetization and the volume of the domain, respectively, and  $V_{\text{overall}}$  is the volume of the ferromagnet.

**Tab. 9.1.** Some magnetic characteristics of the ferromagnetic elements Fe, Co and Ni (bulk and nano-sized materials).

		Fe (bcc)	Co (hcp)	Ni (fcc)
Bulk material				
Curie-temperature	$T_c$ ( $^{\circ}\text{C}$ )	770	1131	355
Saturation magnetization	$M_s$ ( $\text{emu cm}^{-3}$ )	1710	1422	484
First anisotropy constant	$K_1$ ( $\text{erg cm}^{-3}$ )	$4.6 \times 10^5$	$45 \times 10^5$	$-0.5 \times 10^5$
Exchange constant	$A$ ( $\text{erg cm}^{-1}$ )	$2.5 \times 10^{-6}$	$1.3 \times 10^{-6}$	$0.86 \times 10^{-6}$
Coercive field (bulk)	$H_c$ ( $\text{A m}^{-1}$ )	71.6	795.8	159.2
Nano-sized material				
Coercive field (nano-sized)	$H_c$ ( $\text{A m}^{-1}$ )	31 830 [96] 127 337 [54] 99 470 [11] 21 200 (par.) [136] 37 900 (perp.) [136] 6446 [110] 49 800 [111] 9700 [166] 24 020 [166] 270 572 [171]	55 900 [111] 47 100 [36]	1190 [172] 1800 [111]
Critical diameter	$D_{cr}$ (nm)	32 ( $l/d \approx 3$ ) [84] 45 ( $l/d \approx 2$ ) [86] 85 ( $l/d \approx 5$ ) [86] 140 ( $l/d = 10$ ) [86]	28 ( $l/d \approx 3$ ) [84] 140 ( $l/d = 10$ ) [86]	64 ( $l/d \approx 3$ ) 600 ( $l/d = 10$ ) [86]

Figure 9.15(a) depicts a ferromagnet consisting of many domains with an overall magnetic moment ( $M_{\text{overall}}$ ) equal to zero. At zero applied fields, a domain circuit or closure is created to approach the lowest energy state and the minimum demagnetizing field [78]. In the following, we consider the changes in domain state that depend on the diameter of the ferromagnetic material ( $D_p$ ) relative to the critical diameter  $D_{cr}$  for a single domain state.

When  $D_p$  of a magnetic nanowire is larger than  $D_{cr}$ , the creation of more magnetic domains or a strong non-uniform magnetization ( $\nabla M \neq 0$ ) allows a more stable lower energy state. When  $D_p$  is less than the critical single domain diameter, the magnetization of the nanowire is almost uniform ( $\nabla M \approx 0$ ) and spreads along the wire axis (Fig. 9.15b). Micromagnetic calculations for magnetic nanowires with an aspect ratio (length/diameter) of  $\approx 3$  have shown the following dependence:

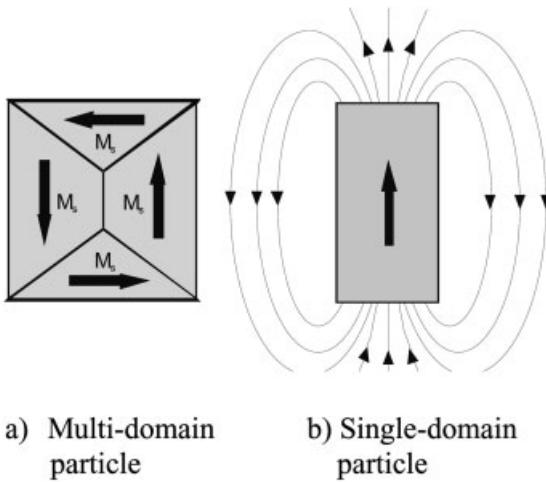


**Fig. 9.15.** Magnetization in magnetic elements: (a) multi- and (b) single-domain particle. (Modified from Ref. [84].)

$$D_{cr} \approx 3.5 \frac{\sqrt{A}}{M_s} \quad (5)$$

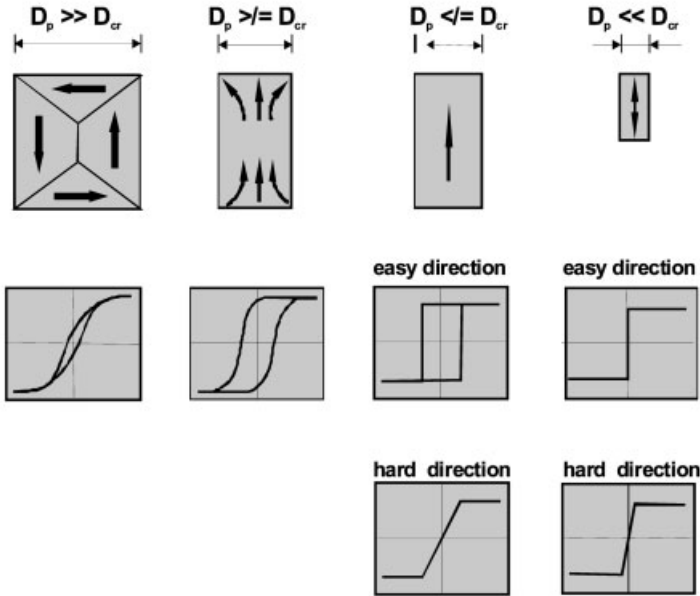
where  $A$  is the exchange constant (Table 9.1). Estimated  $D_{cr}$  for Fe, Co and Ni are 32, 28 and 64 nm, respectively. The critical diameter should also increase with increasing aspect ratio (length/diameter). These dependences for Fe, Co, and Ni have been determined by Sun et al. using micromagnetic calculations [86]. They reported critical diameters (Fe) of  $\approx 45$  nm (aspect ratio = 2),  $\approx 85$  nm (aspect ratio 5) and 140 nm (aspect ratio 10).

Figure 9.16 shows several magnetization configurations and their respective hysteresis curves, which depend on the nanowire diameter. Magnetic nanowires with a diameter significantly larger than  $D_{cr}$  break into domains of uniform magnetization to approach the lowest energy state (Fig. 9.16a). The overall remnant magnetization of this multidomain state is negligible. When the nanowire diameter decreases down to  $D_{cr}$ , the formation of a domain wall will not be energetically favored and no domains are formed. In this case, the magnetization is non-uniform. Such a magnetization configuration is called a “flower” [112] (Fig. 9.16b).

Another configuration observed in this type of magnetic material is the “vortex” structure. There is a flower–vortex transition that depends on the particle size and the aspect ratio. Micromagnetic calculations for Ni nanowires (aspect ratio < 3) made by Ross et al. point to the existence of a “flower-state” magnetization for small diameters [113]. As the diameter increases, a gradual transition to a “vortex” state occurs.

For ff-MWCNTs with filler diameters of 10–70 nm and aspect ratios of 1  $\rightarrow$  100 (Fig. 9.7), from the point of view of magnetism we are in the transitional area from

a) many domains    b) "flower" domain    c) single domain    d) superparamagnetic



**Fig. 9.16.** Schematic magnetization configuration and hysteresis loops of ferromagnetic materials of different sizes. (Modified from Ref. [84].)

single domain to “flower/vortex” structures. For specific applications it seems of advantage, in the long run, to aim for a single domain structure. However, to carry out alternating field heating with this single domain material, taking into consideration the limiting values for magnetic fields in medical applications, a specific alteration is necessary; seen from the point of view of the maximum values attained on the material we synthesized, it is a *reduction* of  $H_c \leq 15 \text{ kA m}^{-1}$  (18.8 mT).

When the nanowire diameter is  $< D_{cr}$ , the magnetization is almost uniform and is oriented along the wire axis (Fig. 9.16c). In this case, the hysteresis loop for the direction along the nanowire axis has the form of a rectangle. As the nanowire size continues to decrease within the single domain range, another critical threshold is reached, at which the remnant magnetization and the coercivity go to zero. When this happens, the material becomes superparamagnetic (Fig. 9.16d). Superparamagnetism occurs when the wire becomes so tiny that random thermal vibrations at room temperature cause them to lose their ability to hold their magnetic orientation, resulting in a spontaneous reversal of the magnetization. The geometric dimensions at which this transition from the ferromagnetic to the superparamagnetic state takes place are known as the superparamagnetic limit (SPL). For

iron [114, 115] and carbon-wrapped Fe wires [116], arranged in an array, these dimensions have been estimated at <10 nm.

#### 9.4.4

#### Anisotropy and Interaction

Magnetic anisotropy is another characteristic evident from the hysteresis. This is described as the tendency of a ferromagnetic material to have a preferential direction, “easy axis”, of magnetization [80]. For Fe, which has a bcc structure, the (100) axis is the easy axis, whereas the (110) and (111) axes correspond to the medium and hard axis, respectively. The anisotropy of magnetic nanowires is usually determined by the form of the ferromagnetic material and its crystal structure. In our experience, the crystal structure of the filler is a given fact. As described above, ff-MWCNT filler consists mainly of monocrystal  $\alpha$ - or  $\gamma$ -Fe. The  $\gamma$ -Fe phase can be transformed into ferromagnetic  $\alpha$ -Fe(110) by subsequent heat treatment.

In addition to the magnetocrystalline anisotropy, the preferential direction of magnetization can be determined by the shape of the material (i.e., a wire prefers the easy axis to be along its large dimensions) – shape anisotropy. The essential anisotropy contribution in thin metal nanowires is the shape anisotropy with the easy axis of magnetization parallel to the wire axis [117]. This anisotropic contribution can be decisively influenced by production technology, by means of the filler diameter and length. The shape anisotropy of a ferromagnetic nanowire is determined by the stray field energy of each nanomagnet, the decisive factor being the stray field vector  $\mathbf{H}_D$ , which determines the easy magnetic direction. According to Eq. (6) the local stray field energy density  $E_D$  is lowest when  $M$  points in the direction of the stray field determined by the nanomagnet.

$$E_D = -\frac{1}{2}|\vec{H}_D| \cdot |\vec{M}| \cdot \cos\beta \quad (6)$$

To estimate the stray field energy, the conventional model of Stoner and Wohlfarth is often drawn upon [118]. This model assumes that the cylinder (ff-MWCNT filler) can be approximately represented by a homogeneously magnetized rotationally symmetric ellipsoid. The aspect ratio of a Stoner–Wohlfarth particle,  $a = l/D_p$ , is decisive for its shape anisotropy energy. With further simplifications, such as presuming an aspect ratio of  $\gg 1$  and the orientation of the magnetic moment along the axis, the effect of the stray field can be described in a simplified manner as an additional anisotropy field  $H_D$  of the shape anisotropy.  $H_D$  is given by Eq. (7).

$$H_D = 2\pi M_{\text{sat}}\{1 + 3/a^2[1 - \ln(2a)]\} \quad (7)$$

This means it is possible to determine the magnetic field necessary to rotate the magnetization in the axis  $180^\circ$ . In the borderline case of infinitely long nanowires,  $H_D$  approaches the value given in Eq. (8).

$$H_{D,\infty} = 2\pi M_{\text{sat}} \quad (8)$$



The model of Stoner and Wohlfarth drawn upon here can only describe a simple estimation, but clearly shows the principal influencing variables.

For  $H_D$  we examined a single nanomagnet. When a collection of several nanowires is involved, they affect each other interactively.

In terms of material production, a distinction must be made here between the conditions of the production of ff-MWCNTs on a substrate and the conditions of ff-MWCNTs in tumor tissues. Whereas magnetic nanowires on a substrate are very closely packed in great numbers, once they are detached and transferred into the tissue they spread out. The magnetostatic interaction of the nanomagnets with the external field is described by the *Zeeman* therm.

$$E_{\text{zee}} = -HM_{\text{sat}}V \cos \Phi \quad (9)$$

In Eq. (9),  $\Phi$  is the angle between the magnetic field and the magnetization. When the magnetic field is realized along the easy axis of the nanomagnet, the hysteresis loop is rectangular. The coercivity  $H_c$  is equal to the anisotropy field ( $H_A$ , Eq. 10).

$$H_A = \frac{2K_u}{M_{\text{sat}}} \quad (10)$$

In evaluating the magnetic properties of nanomagnets like ff-MWCNTs we have to differentiate between the properties of structures arranged on a substrate and disordered in a tissue. Here it is meaningful to appropriate an ensemble of non-interacting and randomly oriented Stoner–Wohlfarth particles. Averaging over all possible spatial direction results in a hysteresis loop characterized by  $M_r = 0.5M_{\text{sat}}$  and  $H_c = 0.48H_{\text{sat}}$ . Hysteresis losses are reduced by a factor of  $\approx 0.25$  in comparison with the aligned situation [119, 120]. These differences mean that the hysteresis loops of a single material can be markedly different on the substrate (after production) and after being transferred to biological systems. For further examination of this problem, reference should be made to the relevant technical literature.

#### 9.4.5

#### Magnetic Reversal

The mechanisms of magnetic reversal are also important for future therapy options using ff-MWCNTs. What is of significance here is the relative size of the nanomagnets expressed by the  $D_p/D_{\text{cr}}$  ratio (as in Fig. 9.16). To turn the magnetization in a nanomagnet around  $180^\circ$ , a reversal field,  $H_{\text{SW}}$ , is necessary. This field depends mainly on the stray fields and the anisotropic contributions. For the magnetic reversal of particles with the dimensions examined here, a homogeneous rotation is mostly discussed [86, 118] or, by Curling's rotation [86, 121], an inhomogeneous rotation. The magnetic bipolar moments remain in parallel alignment in the case of homogeneous rotation during magnetic reversal. They rotate to the new orientation together. This mechanism is often adopted for mesoscopic, single-

domain ferromagnets with a uniaxial anisotropy. The accompanying magnetization curve is rectangular when the external magnetic field  $H_{\text{ex}}$  is parallel to the axis of the nanomagnets; it is a linear function of the external field in the case of a perpendicular field direction. Curling's inhomogeneous rotation is discussed for  $D_p \geq D_{\text{cr}}$ , i.e., for flower structures, for example. At the ends of the ferromagnetic cylinder, vortex structures are expected to form and then spread out across the cylinder as the opposing field increases. In practice, especially when a very high number of nanomagnets are spatially randomly dispersed and interact with one another, magnetic reversal can not be satisfactorily described using a model. It must be assumed that all energy contributions according to Eq. (11) are moving towards a common minimum;  $E_K$  is the magnetocrystalline anisotropic density,  $E_A$  is the exchange energy density,  $E_{\text{zee}}$  is the magnetostatic energy density (*Zeeman* energy), and  $E_D$  the stray field energy density.

$$E_{\text{ges}} = E_K + E_A + E_{\text{zee}} + E_D \quad (11)$$

#### 9.4.6

#### Magnetic Properties of Filled Multi-walled Carbon Nanotubes

The effects described above are crucial for ff-MWCNTs as a material system, which is the central element of the proposed multifunctional nanocontainer. In evaluating the magnetic properties, we must take into account the following aspects:

1. The fillers are mainly produced in a monocrystalline form (Fig. 9.17). They may exist not only as  $\alpha$ -Fe but in some cases also as  $\gamma$ -Fe or  $\text{Fe}_3\text{C}$ . In the present case,  $\alpha$ -Fe is the desired ferromagnetic phase. A transformation of  $\gamma \rightarrow \alpha$  is partly possible using temperature treatment. The higher volume of the  $\alpha$ -phase may in some cases change the mechanical stress state. By this means the shape of the magnetization curve and  $H_c$  could sometimes be influenced.

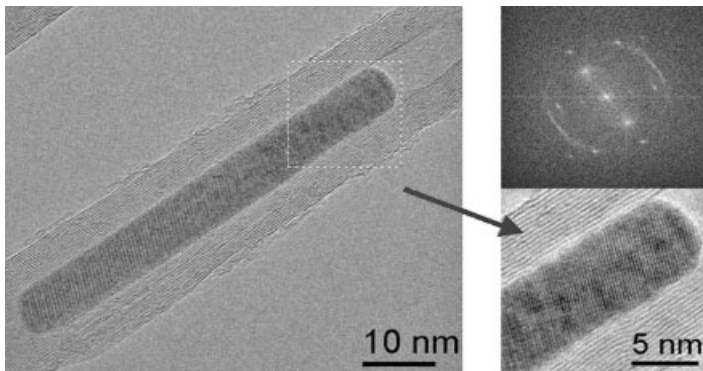


Fig. 9.17. TEM image and SAED pattern of a partly filled Fe-MWCNT.

2. Consideration must be given to variation in the level of filling in general, the filler diameter and the length of the ferromagnetic nanoparticles (aspect ratio  $1 \rightarrow 100$ , see Fig. 9.7). Because of these, both single domain and flower/vortex states may be achieved in nanotubes from one batch.
3. During therapy, the ff-MWCNTs are no longer arranged parallel to one another in the form of up to  $10^9$  tubes per  $\text{cm}^2$ , but face in all directions in a statistically even manner. This affects the way the ff-MWCNTs interact magnetically.
4. The number of carbon shells can vary considerably, which is another reason why the influence of mechanical stresses on magnetic properties can not be ruled out.

These few points suffice to make it clear that many different variables must be considered when evaluating the magnetic properties of ff-MWCNTs. Much fundamental research is still necessary for a complete understanding of these relations. Rising to this fascinating challenge is important not only for the biomedical applications discussed but also for a whole array of other interesting applications.

CNTs filled with most different materials have numerous applications in different areas. These unique nanostructured materials with a nanowire as material inside and the carbon shell around are receiving increasing attention. The closed CNT saves the sensitive core material by their relatively chemically inert carbon shells against oxidation or reduction. Therefore, the material will open up new applications, e.g., in nanoelectronics. ff-MWCNTs have attracted increasing interest. "Saved magnetic wires" are fascinating objects in itself, revealing unusual magnetic properties [122, 123], e.g., they will find application as magnetic electrodes in future molecular spintronic devices or as new material for high-density magnetic recording media [124]. As already mentioned, one very interesting application area is their utilization as magnetic nanoparticles in medicine, as material for hyperthermic therapy of cancer tissues.

The major advantage of filled CNTs is that their catalyst materials, the metals of the iron triad group (Fe, Co, Ni), are ferromagnetic over a wide temperature range. Thus, the catalyst and the necessary ferromagnetic material are identical (Section 9.3.2.1).

All three metals are suitable for hyperthermic application at temperatures up to  $45^\circ\text{C}$  as they are all ferromagnetic in this temperature range.

Nevertheless, the ferromagnetic properties of the filling material are determined by the presence of the ferromagnetic Fe-phase ( $\alpha$ -Fe). Therefore, the synthesis temperature is one of the most important parameters. Conforming with the phase diagram, unsurprisingly, at a synthesis temperature of  $850^\circ\text{C}$  the Fe filling consists of both para- and ferromagnetic iron and, particularly in the presence of carbon, iron carbide too. Complete transformation into the ferromagnetic phase is not possible, because the transformation of paramagnetic (fcc lattice) into the ferromagnetic phase (bcc lattice) is associated with a 10% volume dilatation. Iron tightly embedded in the nanotube would cause a permanent strain on the carbon shells; however, that is not possible due to the high elastic modulus of CNTs. The alternative is, necessarily, destruction of the nanotubes.

Several groups have investigated the magnetic properties of ff-MWCNTs. Figure

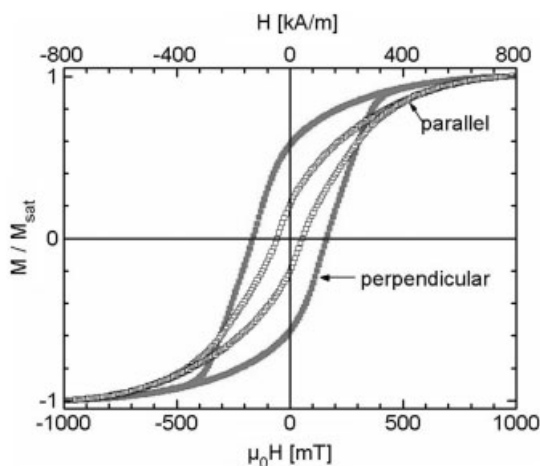


**Fig. 9.18.** Typical hysteresis loops of Fe-MWCNTs grown on a silicon substrate (parallel = magnetic field parallel to the substrate on which the Fe-MWCNTs are in perpendicular positions).

9.18 shows a typical hysteresis loop of an ff-CNT carpet on a silicon substrate. The measurements always reveal a uniaxial magnetic anisotropy with the easy axis along the tube axis. The magnetic characteristics saturation magnetization ( $M_{\text{sat}}$ ) and coercivity ( $H_C$ ) depend not only on the synthesis parameters and the  $\gamma/\alpha$ -Fe ratio, as mentioned above, but also on the alignment level, the diameter and the length of the CNTs on the substrate (Fig. 9.19). For instance, Satishkumar et al. have found that these magnetic properties are significantly dependent on the used hydrocarbon [34] (Table 9.2). This is because of the different diameters, lengths and alignment levels produced as a result of the significantly different growth rates obtained with different hydrocarbons. The higher the growth rate the stronger the alignment. With elongation of the aligned CNTs the magnetic anisotropy increased. This means that the aspect ratio determined the magnetic anisotropy too (so-called shape anisotropy). This phenomenon causes the extremely high coercivities observed in such CNT carpets.

Table 9.3 summarizes experimentally determined coercivities parallel to the tube axis. The values were determined using superconducting quantum interference devices (SQUID), an alternating gradient magnetometer (AGM) and a vibrating-sample magnetometer (VSM). As can be seen, the single values differ greatly, but are always higher at low temperature. In addition, the coercivities are far higher than in bulk material [ $H_{C(\text{Fe-bulk})} = 0.072 \text{ kA m}^{-1}$  (0.09 mT),  $H_{C(\text{Ni-bulk})} = 0.159 \text{ kA m}^{-1}$  (0.2 mT) and  $H_{C(\text{Co-bulk})} = 0.796 \text{ kA m}^{-1}$  (1 mT)]. This is due to the shape anisotropy and to the aligned arrangement of the CNTs on Si substrates.

Figure 9.19 illustrates clearly that at a strong alignment the anisotropy and the  $H_C$  values are very high in contrast to the case of sub-optimal alignment, where the shape anisotropy is weak and the  $H_C$  values are identical. This very interesting behavior is typical for arrangement on a substrate. After removal from the sub-

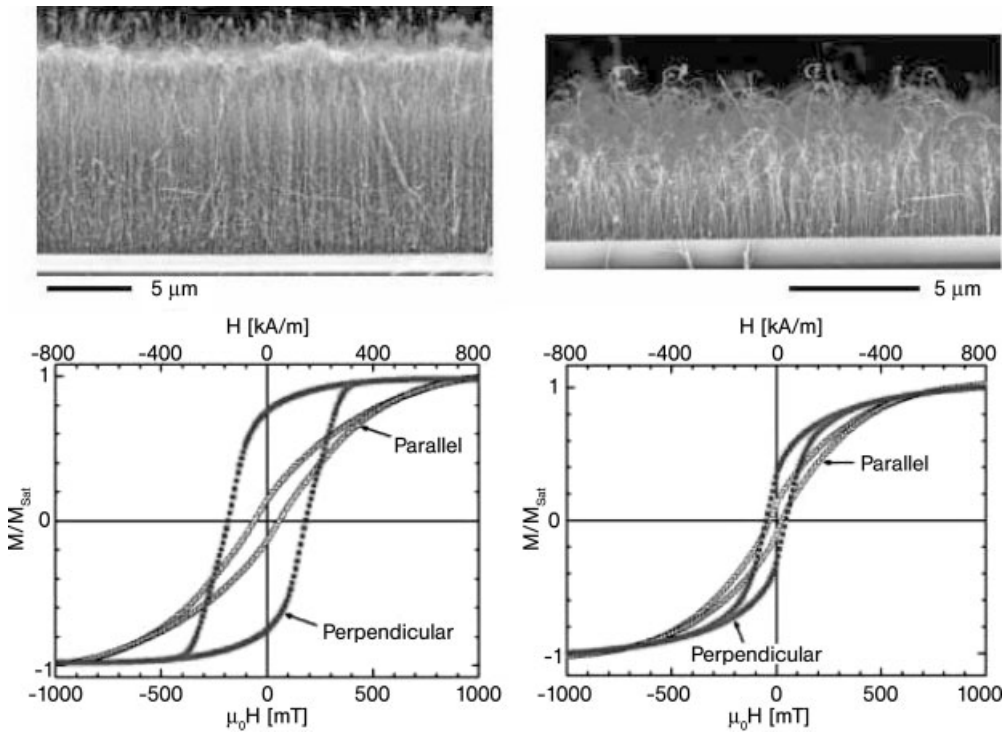


**Fig. 9.19.** Comparison of hysteresis loops of strong and sub-optimal aligned fCNT on Si-substrates. Left: strong, optimal alignment; right: sub-optimal alignment.

strate the ff-MWCNs lose their alignment. To study this effect, the removed nanotubes were transferred into human cancer cells [15] on a sample holder substrate. Figure 9.20 shows a typical hysteresis loop for this situation. The measured curves for magnetic fields in the  $x$ ,  $y$ , and  $z$  directions are almost identical. This is most likely due to the statistical random orientation of the ff-MWCNTs. The  $H_{c_s}$  for the individual directions in  $\text{kA m}^{-1}$  are  $H_{c_x} = 18.35$  (23 mT),

**Tab. 9.2.** Magnetic properties of Fe-filled carbon nanotubes obtained from the pyrolysis of ferrocene–hydrocarbon mixtures.

Hydrocarbon	Ar flow (sccm)	$M_S$ ( $\text{emu g}^{-1}$ )	$H_C$ ( $\text{kA m}^{-1}$ )
Methane (50 sccm)	950	20	40.9
Acetylene (50 sccm)	950	29	45.4
Butane (50 sccm)	950	48	46.2
Acetylene (100 sccm)	900	90	45.4

Tab. 9.3. Coercivities of filled carbon nanotubes.

Filling material	$H_c$ (5 K) ( $\text{kA m}^{-1}$ )	$H_c$ (300 K) ( $\text{kA m}^{-1}$ )	Ref.
Fe	85.2	34.2	9
Fe	74.8	27.7	199
Fe	111.4	63.7	39
Fe		$\leq 79.6$	200
Fe	52.5	24.4	38
Fe	46.2 <sup>[a]</sup>	6.4 <sup>[a]</sup>	136
Fe	87.6	31.8	19
Fe		52.5	34
Fe		42.2 <sup>[a]</sup>	11
Fe		44.6 <sup>[a]</sup>	46
Fe		127.3 <sup>[a]</sup>	54
Fe/Co		100.3 <sup>[a]</sup>	14
Co		47.0 <sup>[a]</sup>	36
Co		26.6	201
Ni		14.6	202
Ni	3.2		203

<sup>a</sup> Aligned ff-MWCNTs on Si-substrates, measured along the tube axis.

$H_{cy} = 18.43$  (23.1 mT) and  $H_{cz} = 18.83$  (23.6 mT). These values give the relation  $H_{c\_perpendicular}/H_{c\_parallel} \approx 1.02$ , which is significantly smaller than for parallel aligned nanotubes on a Si substrate.  $H_{c\_par}/H_{c\_perp}$  for ff-MWCNTs grown on a wafer lies in the range 1.8–6. The magnetic characteristics determined for ferromagnetic filled nanotubes in cells and tissues are much more representative for

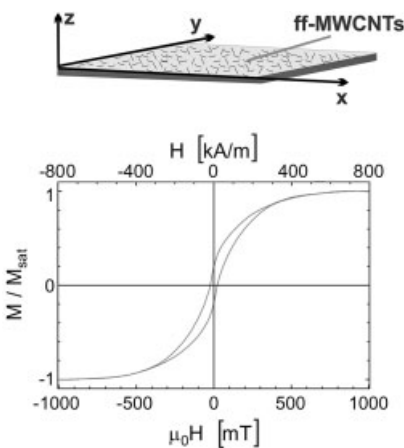
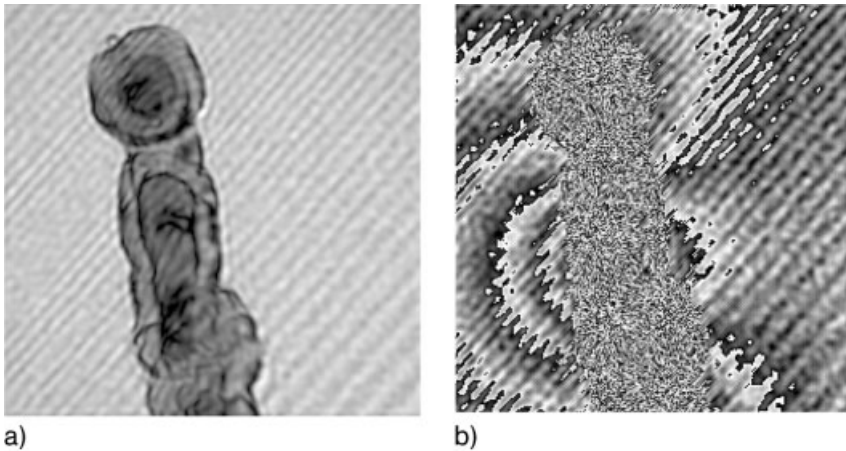


Fig. 9.20. Hysteresis loop of Fe-MWCNTs in cancer cells on a sample holder substrate.



**Fig. 9.21.** Electron holography images of a single Fe-filled MWCNT. (a) Reconstructed intensity distribution and (b) reconstructed phase distribution outside the structure. The phase shift reflects the enclosed magnetic flux line pattern. (Modified from Ref. [122].)

applications in therapy than those obtained for ff-MWCNTs on a substrate. Our data – based on hysteresis loops, holographic experiments (Fig. 9.21) and MFM measurements – strongly suggest that *single* nanotubes can display switching behaviors as single-domain element. Because of the large number of tubes in an issuing batch it is possible to find different filling diameters and different aspect ratios. In the present state of technology, you can produce particles with an aspect ratio in the range  $1 \rightarrow 100$  in one batch (Fig. 9.7). The fraction of single domain and flower/vortex structures is not well-defined. The present state of technological knowledge is insufficient to predetermine the fraction of single domain and flower/vortex structures in one batch. Remarkably, concerning Fe-MWCNTs there is a gap in the evidence regarding the general transferability of results, because either 1 or  $>10^4$  tubes have been evaluated. It is a challenge to transfer the results from one area to another. Study of the intermediate area should be expanded experimentally. Detailed investigations would be important in addressing these issues.

## 9.5

### Heat Generation

#### 9.5.1

##### General Remarks

When exposing materials in alternating magnetic fields, apart from the qualities of the materials, the geometric conditions and the frequency applied, we may in some

cases also have to take into account several heating principles, which differ due to their individual dependency on frequency ( $f$ ) and modulation ( $\hat{B}$ ) [120, 125–127]. The possible heating principles do not generally all occur at the same time in the different applications. What are principally seen are relaxation losses, dielectric losses, hysteresis losses and eddy current losses. In the technical literature, different formulae are sometimes used for the dependencies that apply, according to whether the work is of a magnetic or biomedical nature. Here, we mainly use the formulae that have become established in the biomedical literature. For hyperthermia using superparamagnetic (very small) particles, Rosenszweig has refined a model that was originally developed to describe dielectric dispersion in polar liquids [128].

For small field amplitudes, and assuming minimal interactions between the particles, the response of the magnetization to an AC field can be described in terms of its complex susceptibility  $\chi = \chi' + i\chi''$ . Both parts,  $\chi'$  and  $\chi''$ , are frequency dependent. The out-of-phase  $\chi''$  components result in heat generation, given by Eq. (12) [128].

$$P_{\text{spm}} = \mu_0 \pi \chi'' H^2 \quad (12)$$

This can be interpreted physically as meaning that if  $M$  lags  $H$  there is a positive conversion of magnetic energy into internal energy. This simple theory compares favorably with experimental results, e.g., in predicting a square dependence of  $P_{\text{spm}}$  on  $H$ , and the dependence of  $\chi''$  on the driving frequency.

As this heating principle does not play a decisive part in the ferromagnetic particles we favor, for further considerations and a detailed description of the dependencies reference should be made to Chapter 8 (Jordan et al.) of this book. Another principle considered is that of dielectric losses. These result in Eq. (13).

$$P_{\text{d}} \approx c_1 f^3 \hat{B} \quad (13)$$

For a concrete example of the application of ff-MWCNTs in alternating magnetic fields  $<20 \text{ kA m}^{-1}$  ( $<25.1 \text{ mT}$ ) with frequencies of up to 250 kHz (the operating range we prefer for ferromagnetic filled nanocontainers) the dielectric losses and the energy transfer in the tissue are also not the determining factor. They are only of importance for far higher frequencies [129–134]. In the application suggested here, the heating of ferromagnetic materials (e.g., ff-MWCNTs) with dimensions above the superparamagnetic limit, the determining heating principle is assumed to be that of heating by hysteresis losses. The general view is that the such losses are determined according to Eq. (14).

$$P_{\text{FM}} = \mu_0 f \int H dM \quad (14)$$

Apart from the frequency used, the area under the magnetization curve is also an



especially decisive factor in heat transfer. Equation (14) is sometimes also used in the form of Eq. (15).

$$P_{\text{FM}} \approx c_2 f H_c B_r \quad (15)$$

From this it can be seen that the hysteresis losses of different materials can be compared using the material parameters  $H_c$  and  $B_r$ . To achieve the high heat transfer desirable in the application of hyperthermia, it appears expedient to choose a material with a high  $H_c$  and a high  $B_r$ . However, in this case, notably, the application of very high magnetic fields is not possible for medical reasons (meaning hard magnetic materials can be considered only to a limited extent) and, physiologically, not all possible materials can be used. For example, the elements cobalt and nickel and their alloys, which are often used for magnetic materials, must be considered toxic and therefore questionable [135]. For this reason we prefer to discuss the use of iron as a possible material. The magnetic parameters that characterize iron have been investigated in many studies and determined with great precision. The coercivity of bulk Fe is considered verified at  $0.072 \text{ kA m}^{-1}$  ( $0.09 \text{ mT}$ ). As described above, the dimensionality of the ferromagnetic materials has a significant influence on the parameters examined [9, 19, 136]. In Fe-CNTs synthesized by our group, as the filler mainly consisted of single-domain particles, and because of the shape anisotropy, we were able to verify values from  $103.45 \text{ kA m}^{-1}$  ( $130 \text{ mT}$ ) [11]. This rise by a factor of  $>1300$  compared with the  $H_c$  of the bulk material has a direct influence, according to Eq. (15), on the energy transfer that can be achieved and is therefore of fundamental importance. Pure iron can only be considered as a possible material for hyperthermia when there is a rise of  $H_c$  compared with the bulk material values and in particular when the *shape* of the magnetization curve is specifically modified. Iron with any other magnetic configuration (multi-domain particles) does not allow sufficient energy transfer [137]. Furthermore, the demands on the magnetizing field concerning the field strength needed also depend on the  $H_c$  and  $B_r$  of the material to be re-magnetized. For an isotropic dispersal of magnetically uniaxial particles,  $B_r \approx J_s/2$ , where  $J_s$  is the saturation polarization. The magnetic field amplitude should fulfill the condition of Eq. (16) in order for the material to be nearly entirely re-magnetized (see also Ref. [120]).

$$H_{\text{ext}} > H_c + \frac{1}{3} \mu_0 J_s \quad \text{with } \mu_0 = 4\pi \times 10^{-7} \text{ Vs m}^{-2} \quad (16)$$

The magnetic reversal losses of various hard magnetic materials have been studied [138]. At a diameter of  $30 \mu\text{m}$ , the particle size was such that eddy current losses are no longer negligible. Nonetheless, it was still possible to show that the conditions of Eq. (16) must be fulfilled to achieve high-performance yields. In Ref. [120] this is also confirmed for the use of magnetite.

According to Eq. (15), as well as the aspect that can be technologically influenced (shape of magnetization curve), the energy transfer is linearly dependant on the frequency of the alternating field applied.

As well as the alternating magnetic field losses discussed above, one last sub-

stantial contribution in particular must be considered, namely energy transfer due to eddy current losses that occur. This heating, known technically as inductive heating, occurs when conductive materials – even non-magnetic ones – are subjected to an alternating field. Several important parameters, including conductivity, essentially determine the possible energy transfer. As the human body also possesses an appreciable degree of electrical conductivity it too can be heated according to this principle. Considering these losses is extremely important as they directly determine the boundary conditions of the alternating field heating actually desired. For inductive heating, both the geometric dimensions and electrical conductivity are determining factors. There are great differences between the factors to be considered. While ff-MWCNTs are geometrically very small ( $10^1$  nm) and exhibit very high electrical conductivity, biological tissue displays only low electrical conductivity, but the dimensions of a real patient are significant ( $10^8$  nm). For this reason, both systems reach the limiting values when considered as a whole and both materials connect differently. It therefore seems advisable to examine these cases separately, taking that of ff-MWCNTs first. In the usual technical discussions on inductive heating, the losses that occur are generally described by Eq. (17).

$$P_{\text{eddy}} \approx c_3 f^2 \hat{B}^2 d^2 \sigma_e \quad (17)$$

In Eq. (17),  $f$  is the frequency,  $\hat{B}$  the working induction,  $\sigma$  is the penetration depth, and  $c$  is a parameter that depends on the materials and geometry;  $d$  represents the work-piece diameter.

An essential difference between the heating methods discussed here is the frequency dependency of the energy transfer. Whereas alternating field losses increase linearly with frequency during magnetization reversal processes, the square of the frequency is a determinant of eddy current losses. Figure 9.22 presents these

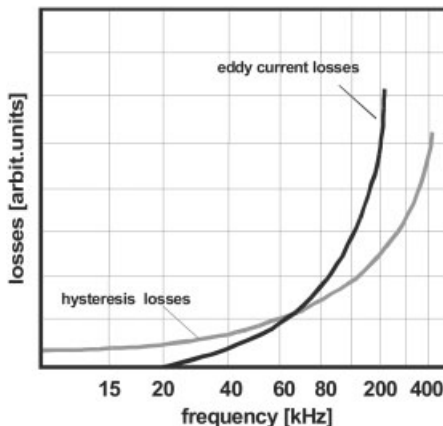


Fig. 9.22. Variation of both hysteresis losses and eddy current losses with frequency. (Modified from Ref. [204].)

**Tab. 9.4.** Dependence of the degree of efficiency on the ratio  $d/\sigma$  ( $d/\sigma = 0.4\text{--}8$ ). (Modified from [204].)

$d/\sigma$	8	6	4	2	1	0.6	0.4	0.0001 (Fe-MWCNTs)
Degree of efficiency (%)	95	85	65	30	10	4	1	$\ll 1^*$

\*  $\ll 1$  is a postulation, but the value could not be determined experimentally.

ratios for iron with large geometric dimensions. Clearly, above approx. 70 kHz – i.e., in the area of interest for a therapy – the eddy current losses very quickly come to dominate in the case of electrical conductivity *and* dimensions on a mm level. A special feature of inductive heating is that energy transfer tends to occur more in the outer areas of the work piece. Because of the skin effect, eddy current flow is mostly on the surface of the material. The depth at which the energy density drops to  $1/e = 0.368$  is known as the current penetration depth. Some 86% of the energy is transformed between the edge of the work piece and  $\sigma$ , and the rest heats lower-lying layers.

The penetration depth itself depends on the electrical conductivity of the material to be heated. For energy transfer to be very effective, the geometric conditions must be optimally adjusted. The most important (influencable) parameters here in particular are the work-piece diameter  $d$  and the construction of the coil system. Once the boundary conditions, which can be technically altered, have been optimized, the ratio work-piece diameter  $d$  to penetration depth  $\sigma$  is of decisive importance for the energy transfer that can be achieved. Table 9.4 illustrates the effect of this parameter on energy transfer. Whereas energy transfer still reaches 10% at a  $d/\sigma$  ratio of 1, at a ratio of 0.4 it already drops to 1%. When Fe-containing ff-MWCNTs are used a  $d/\sigma$  ratio of  $\approx 10^{-4}$  is achieved. Figure 9.23 illustrates these dependencies. The figure 9.23(a) shows a screw with a diameter of 10 mm 10 s after start of AC-heating. The induced increase in temperature was  $>500$  K. Moreover, the so-called “skin” effect is clearly seen. The large temperature difference was mediated by the high electric conductivity and the nearly optimal geometry. Figure 9.23(b) shows a substrate placed at the same site ( $10 \times 10$  mm) with aligned Fe-MWCNTs. In this case and under the same conditions no change in temperature was found. The difference between the two cases is based on the geometry because both consist of the same material (Fe).

Gilchrist et al. have already dealt with this challenge in their fundamental publication describing the initial application of magnetic particle hyperthermia [130]. They were able to show that, in metallic powders, the eddy current loss becomes negligible at a level of  $<5$   $\mu\text{m}$ . With the ff-MWCNTs the diameter of the magnetic particles is not 5  $\mu\text{m}$  but only 0.015  $\mu\text{m}$ . This seems to verify the assumption that eddy current heating does not dominate in nanoparticles of this dimension; an as-

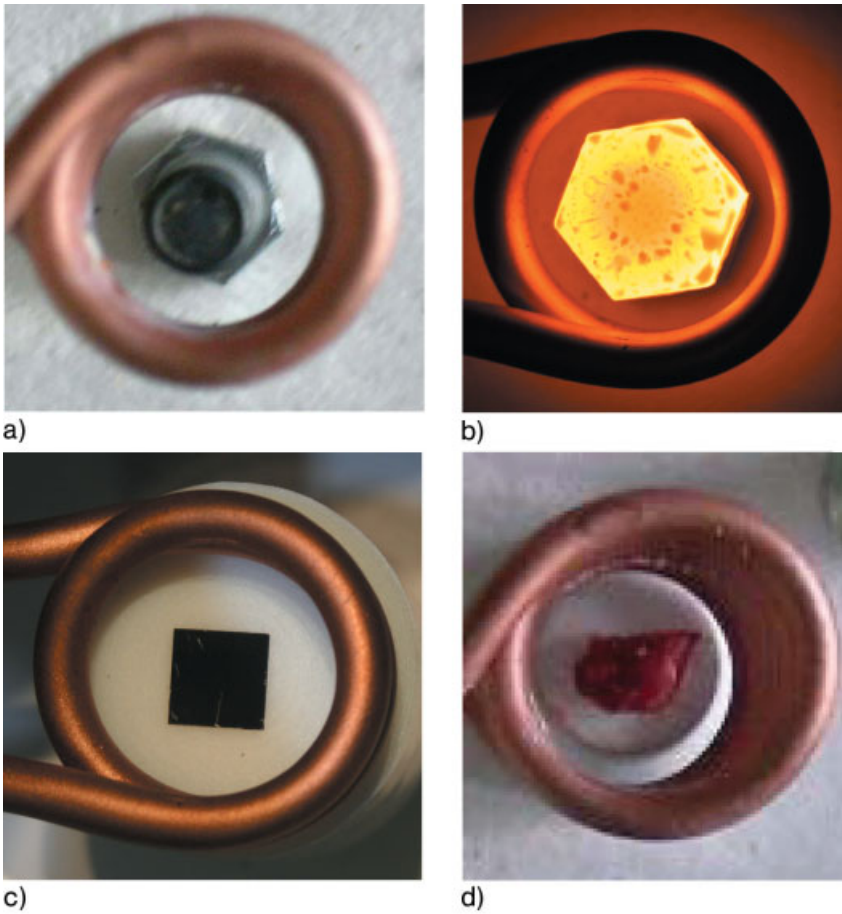


**Fig. 9.23.** Schematic images and photographs of AC-heating experiments using iron in the cm- (a) or nm-range (b).

sumption shared by other authors [120, 125, 128, 139]. Taking these results into consideration, we conclude that for hyperthermia using Fe-containing MWCNTs, eddy current losses are negligible and magnetic alternating field losses can be assumed to dominate.

The other borderline case with eddy current heating is the direct heating of human tissue. In the biomedical literature, the modification of the Eq. (17) written as Eq. (18) has become established [131, 133, 140], where  $\sigma_T$  is the conductivity of tissue and  $r$  is the distance from the central axis of the body.

$$P_{\text{tissue}} = \frac{\pi^2 \mu^2 \mu_0^2 \sigma_T r^2 (f^2 H_0^2)}{2} \quad (18)$$

Equation (18) is valid only for  $H_0 = \text{const}$  and  $\sqrt{(\omega\sigma\mu_0 r_{\text{max}})} \ll 1$  [135]. Biological tissue fulfills this condition because of its low electrical conductivity.

In principle, this heating method can also be used to treat patients. It has not become established as defined localized heating, e.g., in lower-lying tissue, is only possible to a very limited extent. Instead, the objective is to concentrate the heat precisely in the tumor tissue. For thermoseed treatment, Stauffer et al. called for a performance ratio of at least 10:1 [131].

When therapy focuses on magnetization reversal heating it is, therefore, wise to find ways to minimize eddy current heating. According to Eq. (18)  $r$ ,  $f$  and  $H$  are the alterable parameters. As the square of the radius is a determinant of performance rate, an undesirably high level of heating is most likely to occur if the body is surrounded by the coil system at its widest point (the chest cavity). The problem is then lessened if treatment can be carried out in the extremities with far smaller radii. Theoretical calculations and experiments have shown that an  $H \times f$  product of  $\leq 4 \times 10^8 \text{ A m}^{-1} \text{ s}^{-1}$  can be safely applied when treating tumors in the chest cavity. Higher values can be achieved if the radius can be reduced. Hilger et al., for example, specify an  $H \times f$  product of  $1.5 \times 10^9 \text{ A m}^{-1} \text{ s}^{-1}$  when treating breast cancer (coil diameter 150 mm) [141]. For this very important boundary value to be determined with certainty, however, in our opinion too few experimental data are as yet available.

### 9.5.2

#### Requirements for the Development of Materials for Hyperthermia and Magnetism

The use of magnetic nanoparticles in hyperthermia goes back to Gilchrist et al., who treated different tissue samples with particles of  $\gamma\text{-Fe}_2\text{O}_3$  (20–100 nm) in a magnetic field of up to  $20 \text{ kA m}^{-1}$  (25.1 mT) and a frequency of 1200 kHz [130]. Since then, numerous different materials and technical boundary conditions have been proposed.

The concept of locally and contact-free heating in the tumor tissue itself by raising the temperature up to  $>42 \text{ }^\circ\text{C}$  for 30 min to influence apoptosis and/or to destroy the tumor is fascinating, but requires reproducible conditions for particle production as well as reproducible heat dispersal in the tumor. At the same time, the therapeutic effects on humans depends on the actual conditions in the appropriate target tissue and organ. In particular, heat transport in different kinds of tissue and the differing blood supply in the organs mean that only limited theoretical predictions can be made. What is more, the temperature rise required for long-term therapy success has been estimated at varying levels. Hilger et al., for example, have suggested implementing temperatures around  $55 \text{ }^\circ\text{C}$ , the thermoablative level, when treating breast cancer, as when the temperature is limited to  $44 \text{ }^\circ\text{C}$  approx. 50% of the tumors recur [142].

Since the pioneering work of Gilchrist et al. [130] various materials have been suggested for hyperthermia using magnetic nanoparticles. These can be classified conveniently according to their magnetic condition at the temperature of application ( $41\text{--}55 \text{ }^\circ\text{C}$ ). There is a differentiation between:

1. Particles that are in a superparamagnetic state under the application conditions due to their geometric dimensions or their physical properties. These include  $\text{Fe}_3\text{O}_4$  (magnetite) or  $\gamma\text{-Fe}_2\text{O}_3$  particles (maghemite) with *small* dimensions

and

2. Particles that are in a ferri- or ferromagnetic state under the application conditions due to their geometric dimensions or their physical properties, e.g.,  $\gamma\text{-Fe}_2\text{O}_3$  particles (maghemite) of *large* dimensions, multidomain ferrite or ferromagnetic materials.

Several interesting studies have been carried out using materials of these two groups [120, 130, 137, 140–156]. This summary of different studies can not be complete. It reflects the different goals concerning the material and the heating mechanism. Many different materials – such as alloy-based systems – have been used by other groups. Our focus is directed towards pure iron or some iron compounds.

Another interesting alternative option in terms of heat generation, although with geometric dimensions at the  $\mu\text{m}$  or  $\text{mm}$  scale, is:

3. “Self-regulating thermoseeds” with a Curie temperature of  $>42$  to approx.  $57^\circ\text{C}$  [157–160], i.e., above the Curie temperature these materials change their properties and the energy transfer is greatly reduced. This strategy shows that self-regulation mechanisms can be achieved by optimizing material properties – here the Curie temperature – in a targeted manner. If the AC losses of these types of alloys can successfully be raised considerably in moderate fields, then this principle of temperature limiting could also be of interest for magnetic particle hyperthermia.

Materials can only be sorted into categories (1) and (2) above as suggested because the materials of one composition can be placed in either group solely on the basis of their geometric dimensions. For maghemite and magnetite particles, it is not always possible to state unequivocally that the material is in a superparamagnetic state. The division does, however, take into account the fact that the mechanism for heat transfer is fundamentally different [120, 161], meaning that different steps must be taken to selectively develop the material. Based on this division, we now confine this review to particles with ferromagnetic properties. With regard to superparamagnetic nanoparticles, which are very important for hyperthermia, the reader is referred to Chapter 8 by Jordan et al., which describes this point in detail.

As the first, simplest application of ff-MWCNTs – note that this principle only applies here – we begin from a therapeutical point of view by focusing on the treatment of urological carcinomas, including PCa. These are diseases that are, statistically, more likely to occur in later life. It must be taken into account that quite a substantial number of patients may already be fitted with metal implants, e.g., hip prostheses. This means that the use of high frequencies is only possible and/or

practical in a limited way due to the occurrence of eddy current heating [129, 132, 133, 157]. For this reason, within the limits of the admissible  $H \times f$  product [133, 141], we focus our attention on higher fields and not the commonly-implemented higher frequencies. According to the conditions described in Section 9.5.1, high frequencies produce eddy current losses on a mm scale, and thus possibly very high temperatures (Fig. 9.23) that can result in serious health problems.

For the successful therapeutic application of magnetic particle hyperthermia, the key data contained in Table 9.5 must be taken as a starting point. In the last few years, superparamagnetic material (SPM) particles have increasingly been discussed, as they are attributed with better heat generation. This judgment is based on the magnetic values of the materials in a multidomain state [137]. The production, for instance, of Fe nanoparticles that are, magnetically, in the desirable single domain or flower condition constitutes a technological challenge. For example, Fe

Tab. 9.5. SAR values of different materials.

Material	Diameter (nm)	SAR (W g <sup>-1</sup> )	Frequency (kHz)	H (kA m <sup>-1</sup> )	Ref.
Magnetite (Fe <sub>3</sub> O <sub>4</sub> )					
Fe <sub>3</sub> O <sub>4</sub>		7.5	400	6.5	143
Fe <sub>3</sub> O <sub>4</sub>		950	410	10	
Fe <sub>3</sub> O <sub>4</sub>		50–200	410	6.5	161
Fe <sub>3</sub> O <sub>4</sub>		<0.1–45	300	6.5	161
Fe <sub>3</sub> O <sub>4</sub>	10	≤45	300	14	120
Fe <sub>3</sub> O <sub>4</sub>	350	≤75	300	14	120
Maghemite (γ-Fe <sub>2</sub> O <sub>3</sub> )					
γ-Fe <sub>2</sub> O <sub>3</sub>		210	880	7.2	176
γ-Fe <sub>2</sub> O <sub>3</sub>	12	240	880	9.3	177
	240				
γ-Fe <sub>2</sub> O <sub>3</sub>		250–370	1100	6.84	205
γ-Fe <sub>2</sub> O <sub>3</sub>	100–150	42	880	7.2	175
γ-Fe <sub>2</sub> O <sub>3</sub>	6–12	12–240	880	7.2	175
γ-Fe <sub>2</sub> O <sub>3</sub>	20–160	≤400	410	11	206
γ-Fe <sub>2</sub> O <sub>3</sub>	3.3	120	520	13.2	137
	13.1	146			
Pure metals					
Fe	1000–2500	21	880	7.2	175
Fe	20–50	100 <sup>[a,b]</sup>	230	20	188
Fe	20–50	720 <sup>[a,c]</sup>	230	34	188

<sup>a</sup> SAR [W g(x-Fe)<sup>-1</sup>].

<sup>b</sup> Quality: high grade.

<sup>c</sup> Quality: best grade.

as a favored material is susceptible to oxidation [89] and at this particle size a substantial proportion of the volume has been transformed into Fe oxides. Furthermore, iron is pyrophoric [162], meaning that conventional production techniques such as milling, which is often used in industry, can only be used to a limited extent and/or after further technological measures have been taken. Only the much-used wet-chemical, dry-chemical methods or thin film technologies, sometimes with the implementation of extra protective coatings where applicable, have led to any obvious progress [92, 102, 111, 163–171]. Materials with unusual magnetic properties are described in these studies.

These materials have also been rendered interesting for this kind of application by alternative nanotechnology processes. Natural nanostructures, such as magnetotactic bacteria, are not the focus of our interest. Using these particles, a defined influencing of the magnetic properties is hardly possible. Useful magnetic nanostructures can also be obtained by the production of ff-MWCNTs using CVD, affording  $> 1000\times$  higher  $H_c$ s, magnetization properties that are more favorable to this kind of application compared with bulk material, and permanent oxidation protection. However, notably, the characteristics of the nanoparticles are always partly determined by structure and by production-caused contamination, mechanical stresses, etc.

Several parameters play an important role in optimizing a material; some parameters affect, negatively or positively, optimization of the magnetic properties. For example, the nickel nanoparticles encapsulated in graphite by Hwang et al. showed distinctly lower  $H_c$ s than in bulk material [172]. Pirota et al., however, showed from the example of magnetic-phase multilayer microwires at the  $\mu\text{m}$  scale that by adding another coating to the microwires the hysteresis loop could be clearly improved towards single-domain characteristics [106]. Thus, production technology is of decisive importance, and the hysteresis loops can and must be adjusted. On the basis of these methods of influencing magnetic parameters and their effect on heat generation, it must again be underlined that the therapeutic method we suggest using the multifunctional nanocontainer is only made possible when the entire system, or the decisive parameters, is optimized (not maximized).

Taking as a basis an  $H \times f$  product of  $1.5 \times 10^9 \text{ A m}^{-1}\text{s}^{-1}$  [141], the maximum that can be applied during therapy, a magnetic field that can usefully be applied is at most approx.  $20 \text{ kA m}^{-1}$  (25.1 mT). As the hysteresis loop must be modulated to exceed  $H_c$  for heat to develop, seen from this angle it appears pointless to try to achieve  $H_c$ s higher than  $100 \text{ kA m}^{-1}$  (125.3 mT), even though this is possible with the ff-MWCNTs (Table 9.3). The point is much rather to influence the shape of the magnetization curve, as in Fig. 9.24, with an  $H_c$  of approximately  $15 \text{ kA m}^{-1}$  (18.8 mT). To do this, it is advantageous to provide a material in a single domain state. This, again, means that the aim should be a Fe filler diameter of between approx. 10 nm ( $< 10 \text{ nm SPL}$ ) and approx. 32 nm [84] or approximately 45 nm [86] (no single-domain particles). As mentioned above, the higher values depend on the aspect ratio. The given values are representative for  $d/l \leq 3$ . For favorable shape anisotropy, the particles should have a length/diameter ratio of  $\geq 2$ , requiring a



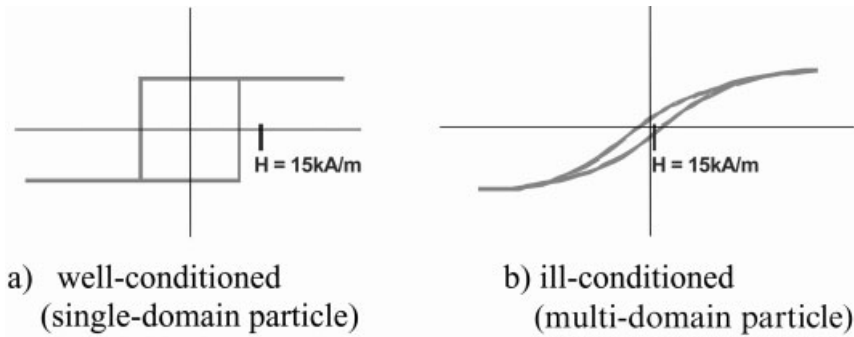


Fig. 9.24. Schematic of well- and ill-conditioned hysteresis loops for medical applications (e.g., hyperthermia).

nanoparticle length of at least 20–60 nm. Furthermore, as high a magnetization as possible should be guaranteed. Based on these benchmark figures, high heat dispersion is possible in the case of single-domain-ff-MWCNT. However, this remains a distant goal.

Our data strongly suggests that *single* ff-MWCNTs can display switching behaviors as a single-domain element. Because of the large number of tubes in an issuing batch the fraction of single domain and flower/vortex structures is not well-defined. The present state of knowledge is insufficient to determine the optimal conditions (single domain, flower/vortex or mixing) for heat generation. To answer this question the conditions of the therapy must be considered.

Single-domain elements can generate a large amount of heat only in magnetic fields  $H_{\text{ext}} > (H_c + \Delta H)$ . From a medical viewpoint, the therapy might need be performed in a low magnetic field. Under this condition the application of another type of ff-MWCNTs could be advantageous. Detailed investigations are important in further answering these questions.

The ff-MWCNTs described at present are, most likely, not yet entirely in a single-domain state. Because of the magnetization behavior and the varying diameters, we must assume that significant proportions of the materials are in a flower/vortex condition. Nonetheless, considerable heat dispersion could be proved.

### 9.5.3

#### Specific Absorption Rate (SAR)

A characteristic parameter is necessary to evaluate the effectiveness of a material system. For hyperthermia two processes must be considered. In principle, we have to evaluate the process of heat generation. It is determined by the loss power or specific heating power of the material. We also have to consider the process of heat absorption by a biological tissue. The specific absorption rate (SAR), the mass-normalized rate of energy absorption by a biological body, in  $\text{W g}^{-1}$ , has become

the most important parameter in characterizing the effectiveness of a material system in hyperthermia. It is determined according to Eq. (19) [140, 173], where  $c$  is the specific heat capacity.

$$\text{SAR} = c \, dT/dt \quad (19)$$

For water,  $c_{\text{water}} = 4.118 \text{ J g}^{-1} \text{ K}^{-1}$ . For better comparability with different magnetic materials, some groups have used a particular SAR that is related to the active magnetic component [174–177]. This SAR of iron is given by Eq. (20), with  $m_{\text{tot}}$  the total mass of the specimen, and  $m_{\text{Fe}}$  the mass of the iron content.

$$\text{SAR}_{\text{Fe}} = \text{SAR}(m_{\text{tot}}/m_{\text{Fe}}) \quad (20)$$

This means the specific absorption rate  $\text{SAR}_{\text{Fe}}$  allows comparison of the efficiencies of different types of magnetic particles. In the description of our own material, we use this type of evaluation too.

With ff-MWCNTs, magnetic reversal losses are assumed to dominate for the mechanism of heat generation. On account of the opinion sometimes raised in the literature that sufficient heat transfer is not possible by this means with compatible magnetic fields [137, 139], it seems expedient to start with a calculated estimate. According to Eq. (21), the amount of heat generation per unit volume can be obtained by the frequency multiplied by the area of the hysteresis loop [75, 139].

$$P_{\text{FM}} = \mu_0 f \int H \, dM \quad (21)$$

Here, the substantiated assumption is made that the magnetization curve in the area examined is not dependent on frequency.

Under these conditions,  $P_{\text{FM}}$  can be readily determined from quasi-static measurements of the hysteresis loop [120, 139, 150] using an AGM, VSM or SQUID. To make these estimates, Fe-MWCNTs were transferred into tumor cells [15] and washed, and 50 000 cells were separated using fluorescence-activated cell sorting (see below). A defined volume of this solution was transferred onto a suitable substrate material. The magnetic properties of samples of this kind were studied by recording hysteresis loops in an alternating gradient magnetometer (AGM, 2900 MicroMag). As well as measuring complete hysteresis loops (major loops) the minor loops, which are decisive for the conditions of application, were also determined. For this purpose, when recording individual minor loops the maximum magnetic fields were limited to  $H_{\text{max}} \text{ (kA m}^{-1}\text{)} = 0.796, 1.591, 9.549, 12.732, 15.915, 39.788, 59.683, 79.577, 119.366, 159.155, 198.943, 397.887, 238.732, 318.310, 477.464, 557.042, 636.620, 716.197, \text{ and } 795.775 \text{ (1 mT–1 T)}$ . Typical magnetization curves are presented in Fig. 9.25. Notably, the curves shown here are not those of Fe-containing ff-MWCNTs in parallel alignment on substrates, but of Fe-containing ff-MWCNTs at a random spatial orientation in tumor cells. Where a parallel magnetic field orientation is mentioned this means, in this case, parallel to the substrate and no longer parallel to the tube axis. Because of the random ori-

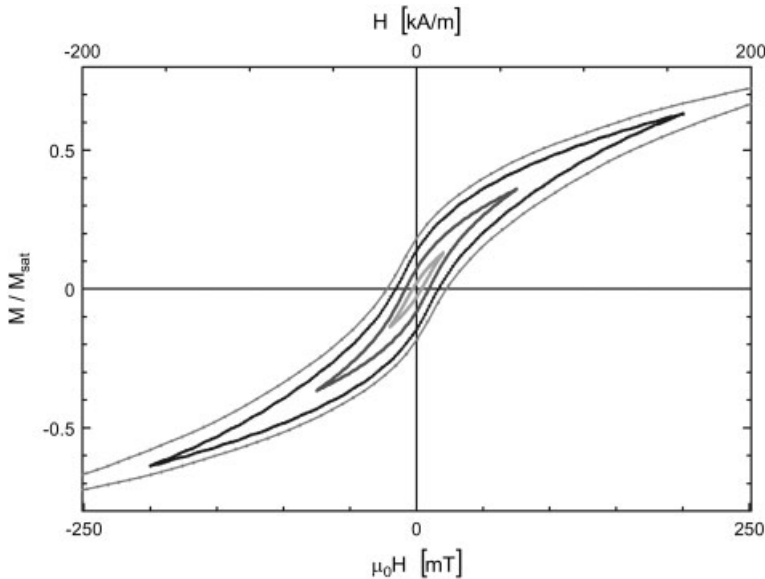


**Fig. 9.25.** Hysteresis loops of Fe-MWCNTs in cancer cells. Outermost line: major loop; inner lines: minor loops.

entation, to some extent an averaging-out of all the spatial axes takes place. This is reflected in the directional dependence of the magnetization curves, which is now only weak. By determining the areas of the magnetization curves and multiplying them with an assumed frequency, the energy dissipation calculated for each magnetic field was estimated at  $0.796\text{--}796 \text{ kA m}^{-1}$  ( $1 \text{ mT}\text{--}1 \text{ T}$ ). For the calculated frequency, we drew upon the limiting frequencies of 50 and 1200 kHz generally accepted in the literature as well as our favored frequency of 250 kHz. Figure 9.26 shows the results obtained. Based upon quasi-stationary measurements, sufficiently high energy losses can already be achieved with magnetic fields of  $10 \text{ kA m}^{-1}$  ( $12.5 \text{ mT}$ ). Energy losses  $> 250 \text{ W (g-}\alpha\text{-Fe)}^{-1}$  are, however, only to be expected for this material from above  $30 \text{ kA m}^{-1}$  ( $37.7 \text{ mT}$ ). Although fields of  $20 \text{ kA m}^{-1}$  ( $25.1 \text{ mT}$ ) at 1200 kHz [130] or  $45 \text{ kA m}^{-1}$  ( $56.4 \text{ mT}$ ) at 53 kHz [153] have been used for hyperthermia treatments, lower magnetic fields are often preferred, in the range of the recommended  $f \times H$  product of  $4.85 \times 10^8$  [133] to  $1.5 \times 10^9 \text{ A (m s)}^{-1}$  [141]. The range of possible combinations of frequency and magnetic field that result from this fit in with the range defined as acceptable for clinical applications by Pankhurst et al. [139],  $f = 50\text{--}1200 \text{ kHz}$  and  $H = 0\text{--}15 \text{ kA m}^{-1}$  ( $0\text{--}18.8 \text{ mT}$ ). Based on these first fundamental assertions on the possible achievement of high energy losses by magnetic reversal, in a further step the SAR was also determined experimentally.

Determination by measurement often takes place using a calorimetric (time-resolved) method, with certain boundary conditions concerning technology and/or

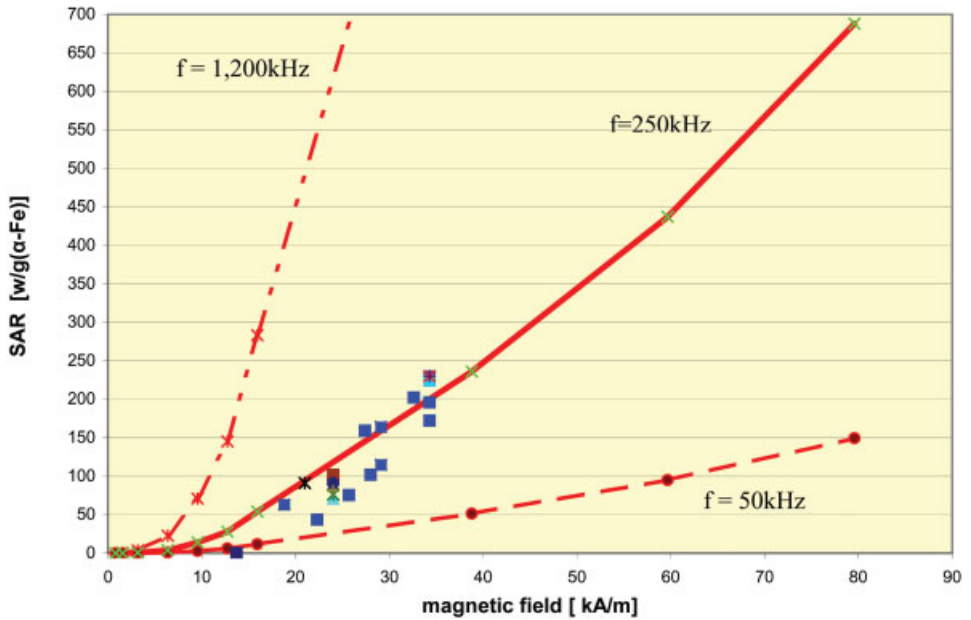


Fig. 9.26. Variation of specific absorption rate ( $SAR_{Fe}$ ) of Fe-MWCNTs with magnetic field (lines: calculated from hysteresis loops; symbols: experimental measurements).

measuring techniques due to the high-frequency alternating fields. As illustrated in Fig. 9.27, the set-up we used consists of a high-frequency generator with an impedance matching network and the magnetic coil system. Water-cooled copper tubes are wound into a coil system (e.g., 4–10 turns, diameter of bore 20–100 mm,  $l = 60$ –120 mm) in which the sample to be examined is placed. The sample must have good heat insulation and the coils must be sufficiently cooled. The sample in the coil system is heated by applying an alternating magnetic field. The temperature change per time unit is determined using an appropriate device. Fiber-optic systems such as the FLUOROPTIK® Thermometer have proven effective for high-frequency magnetic fields: these metal-free systems are not affected by the alternating magnetic field and eddy current effects do not occur. With these systems, the temperature can be measured *in situ*. The output resolution and the accuracy also meet the demands posed, at  $0.001\text{ }^{\circ}\text{C}$  and  $\pm 0.2\text{ }^{\circ}\text{C}$  respectively.

Another notable point is that the magnetic field amplitudes are often determined by measuring the coil current and then calculating  $H$ . This is possible with sufficient precision in the case of coil geometries, which are generally simple. For the simplest case of a single circular conductor loop with radius  $R$  in the  $x$ - $y$  plane (if the origin is the center of the circle) we obtain Eq. (22) for the field components in the  $z$  direction, with  $I$  the current passing through the conductor.

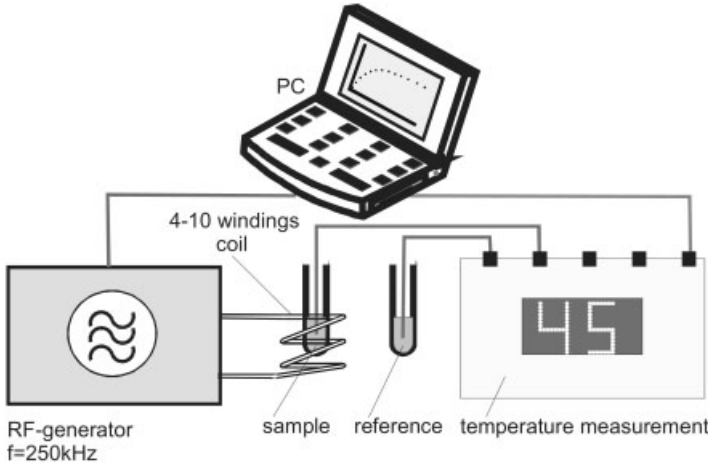


Fig. 9.27. Experimental setup for time-dependent calorimetric measurements.

$$H_z = \frac{1}{2} IR^2 \frac{1}{(R^2 + z^2)^{3/2}} \quad (22)$$

Clearly, for  $z \gg R$  the field decreases at about  $1/z^3$ , and therefore outside the coil there is only slight stress on the tissue during treatment. For therapy the field is of importance within a long coil. It applies to Eq. (23), where  $n$  is the number of turns and  $l$  is the length of the coil.

$$H = \frac{nI}{l} \quad (23)$$

Initial attempts to determine the SAR experimentally used water, physiological salt solution and agarose gel blocks, to each of which was added a defined quantity of ff-MWCNTs. Heat insulation of the sample is extremely important, as mentioned above. When simple glass vessels were used we observed a distinct time dependency of the determined SAR. As shown in Fig. 9.28, the values vary from about  $750 \text{ W (g-}\alpha\text{-Fe)}^{-1}$  (30 s measuring time) up to  $150 \text{ W (g-}\alpha\text{-Fe)}^{-1}$  (900 s measuring time). We ascribe these differences to an unfavorable ratio of sample volume/sample surface at the time and, in particular, to heat conduction from the sample into the sample vessel. After the geometry of the materials used was optimized and heat conduction was minimized, this problem was reduced. It was possible to increase the accuracy and to realize the well-known  $t$ - $T$  characteristics. The initial slope was used to determine the SAR.

Figure 9.26 shows the SAR obtained by experiment under these altered conditions at a frequency of 250 kHz, depending on the magnetic field strength for the mid-quality material used for the quasi-static measurements. The figure also shows the SAR curves calculated for this material. The material used was from

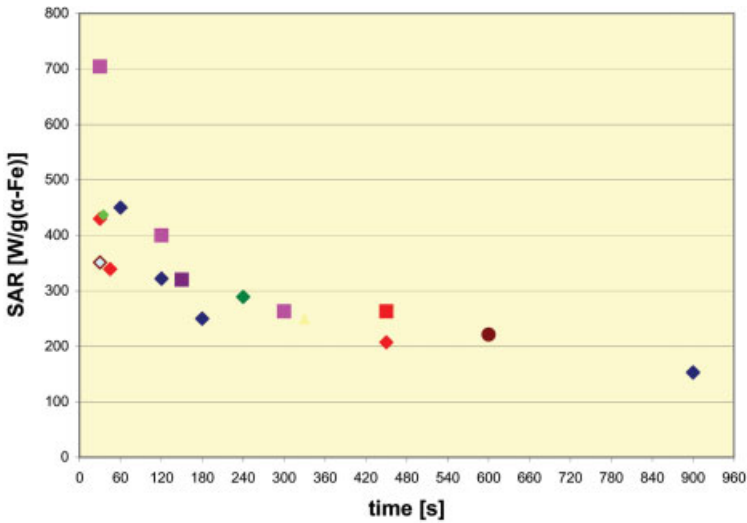


**Fig. 9.28.** Variation of specific absorption rate ( $SAR_{Fe}$ ) of Fe-MWCNTs with time ( $H = 30 \text{ kA m}^{-1}$ ). Different colors represent data points from independent experimental series.

one batch but was not that used for the magnetic measurements. Clearly, the values obtained by experiment in a magnetic field area of up to about  $28 \text{ kA m}^{-1}$  ( $35.1 \text{ mT}$ ) tend to be lower than expected from the quasi-static measurements. What is more, there is distinct scattering of the measured results in all magnetic fields. We ascribe this scattering to instrument-related problems in controlling the HF current, as when the HF transmitter was at full drive, values were determined that could easily be reproduced. The SARs determined by experiment at  $34 \text{ kA m}^{-1}$  ( $42.6 \text{ mT}$ ) came out at 286, 280, 286, 292, 286, and 292  $\text{W (g-}\alpha\text{-Fe)}^{-1}$  in a series of measurements, for example. At the level of magnetic fields  $<12 \text{ kA m}^{-1}$  ( $<15 \text{ mT}$ ) it was not yet possible to obtain any sufficiently firm measured values. One reason could be the switching behavior of single-domain particles. To throw light on the real cause, further equipment-related improvements and basic studies of the switching characteristics of *individual* ff-MWCNTs must be carried out. The results already gathered by experiment, however, tend to confirm the expected course. In the range that can be applied in therapy, up to approximately  $20 \text{ kA m}^{-1}$  ( $25.1 \text{ mT}$ ), we were able to verify SARs of  $\leq 100 \text{ W (g-}\alpha\text{-Fe)}^{-1}$  for this not yet optimized material. However, clearly, far higher values could be obtained in the range  $>30 \text{ kA m}^{-1}$  ( $37.6 \text{ mT}$ ). From this, central questions emerge concerning:

1. The maximum  $H \times f$  product that is possible to use;
2. how these values appear in relation to the superparamagnetic particles;
3. whether the present situation achieved is sufficient for treating urological tumors.

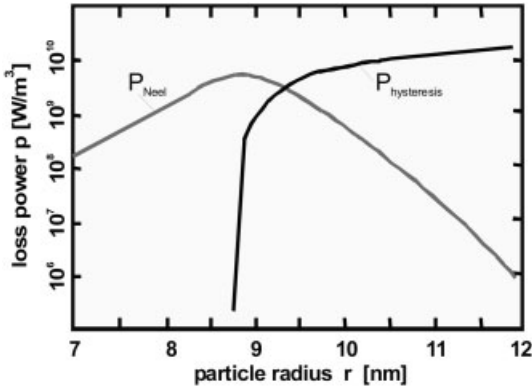


Fig. 9.29. Grain size dependence of the loss power density for small ellipsoidal particles of magnetite ( $H = 6.5 \text{ kA m}^{-1}$ ). (Modified from Ref. [120].)

Table 9.5 lists typical SARs for the most important material systems, magnetite and maghemite, as well as for iron. The differing values for the frequencies and magnetic fields must be taken into account when comparing the results. Even after numerical correction of the SARs to “standard frequencies” and “standard magnetic fields” in accordance with the known dependences given by Eqs. (12) or (15), a great deal of scattering still clearly takes place within each material system. One reason for this can be found in the dependence of the energy loss on particle diameter and working frequency. As shown by Hergt et al. (Figs. 9.29 and 9.30), when using superparamagnetic nanoparticles, a distinct reduction in energy transfer achieved can be expected, even from a deviation of around  $\pm 1 \text{ nm}$  from the op-

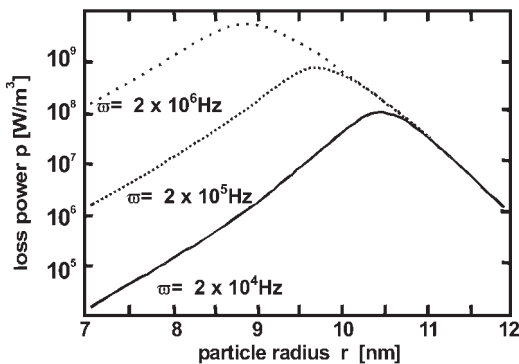


Fig. 9.30. Dependence of magnetic loss power density on particle size for magnetite ( $H = 6.5 \text{ kA m}^{-1}$ ). (Modified from Ref. [120].)

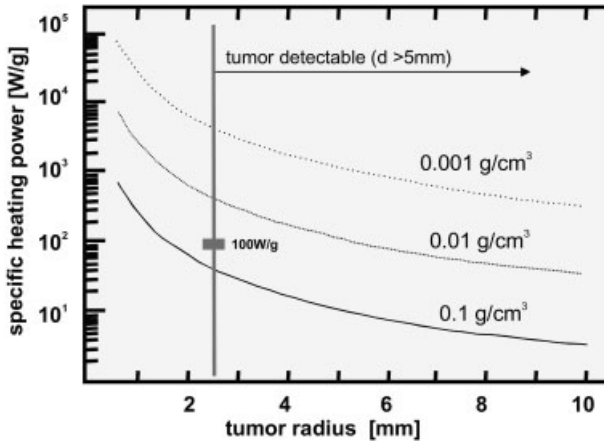


Fig. 9.31. Power requirements of magnetic nanoparticles. (Modified from Ref. [120]; 3 curves.)

timal diameter [120]. With ferromagnetic particles up to the superparamagnetic limit, however, only a relatively minor change occurs depending on the diameter. Here too, the marked influence of technology on the results that can be obtained is apparent. As has already been established, controlling heat conduction in the tumor and the surrounding tissue is of decisive importance in connection with the SAR achieved. The group of Andrä, Hergt and Hilger [141, 143, 178] have stated more precisely results [143] for the range of thermoablation ( $T = 51\text{--}55\text{ }^\circ\text{C}$ ). The calculations imply that the specific heating power needed to achieve the required rise in temperature in the tumor goes up sharply as the diameter of the tumor falls. With thermoablation, the target is a temperature difference of 15 K.

Figure 9.31 shows the specific heating power required for this for three different concentrations of magnetite, depending on the tumor diameter. The low and high concentrations of  $0.001$  and  $0.1\text{ g cm}^{-3}$  are approximately the limiting values that are usefully applicable in practice. From the graphic representation, the required specific heating power clearly varies by several orders of magnitude, depending on the concentration of particles achieved. According to this, for an average particle concentration of  $0.01\text{ g cm}^{-3}$  and  $100\text{ W g}^{-1}$  (Table 9.5), tumors from a diameter of about 1 cm can be treated. By analogy, a higher particle concentration results in a size of 4 mm. These observations apply to the range of thermoablation. For hyperthermia, the proportions are slightly more favorable due to the lower temperature difference required. As only slight differences can be made to the heat conductivity conditions in the tumor tissue, one urgent task for materials development is to raise the performance of the material. The heat condition problem, on the one hand, and the amount of heat generated by a few magnetic nanoparticles inside a biological cell, on the other hand, are the background for the discussion: Is hyperthermia on a cellular level possible [137, 141, 179]?



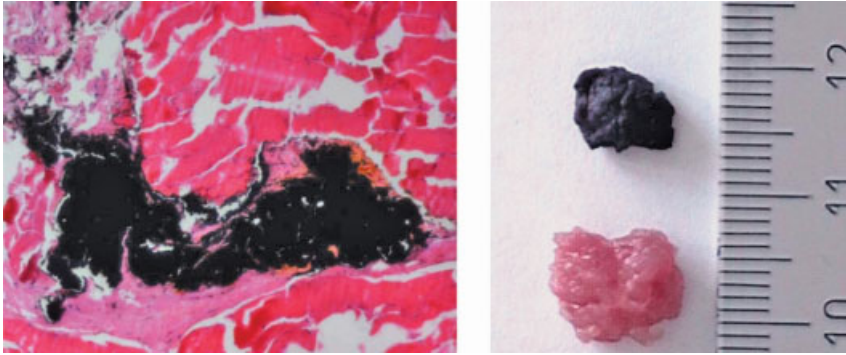


Fig. 9.32. AC-heating using model tissue: (a) Muscle tissue containing Fe-MWCNTs (black), (b) muscle tissue: before and after AC-heating.

Taking as a basis the SARs for Fe-containing ff-MWCNTs at the *level used in therapy* of approx.  $100 \text{ W (g-}\alpha\text{-Fe)}^{-1}$ , the minimum SARs postulated in the literature to achieve the necessary temperature rise in the tissue, it can be concluded that this ferromagnetic material in a single-domain state should be suited for the treatment of a diagnosed PCa with an extension of at least several millimeters. Assuming this to be the case, experiments have been made in heating model systems. Beef was used as a model substance for the first heating experiments (specimen  $7 \times 7 \times 7 \text{ mm}$ ). Fe-MWCNTs were injected into this tissue (see Fig. 9.32a) and the sample was heated (at  $H = 20 \text{ kA m}^{-1}$  and  $f = 250 \text{ kHz}$ ). Figure 9.33 shows the temperature curve within the muscle tissue ( $43 \text{ }^\circ\text{C}$  after 7.5 min AC-heating). By compari-

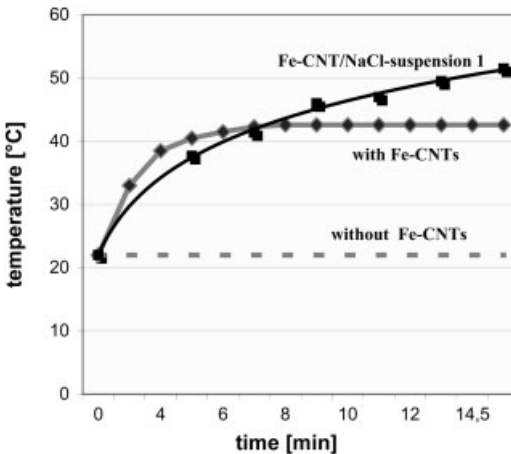


Fig. 9.33. Temperature development during AC-heating.

son, without an injection of Fe-MWCNTs no temperature difference was measured for at least 15 min after the start of magnetic induction. Figure 9.32(b) shows typical photographs of model specimens/tissues before and after AC-heating. Based on these results, further experiments were carried out on cell cultures, tissue and organ samples and animals.

## 9.6

### Study Results for *In Vitro* and *In Vivo* Applications of ff-MWCNTs

#### 9.6.1

#### Efficient Endocytosis *In Vitro*, Lipid-mediated Could Enhance the Internalization Rate and Efficiency

Using different types of ff-MWCNTs we have studied the uptake by different urologic cancer cell lines. In cell culture experiments an efficient delivery into human EJ28 bladder cancer cells after complex formation of the ff-MWCNTs with cationic lipids was detected [15]. Our original conclusion was that the lipid is necessary for efficient uptake of ff-MWCNTs by cancer cells in our settings. However, systematic investigations of several cancer cell lines indicated that the ff-MWCNTs with different sizes (1–10  $\mu\text{m}$  long) were also internalized without lipid addition. Therefore, we hypothesized that lipid addition *in vitro* can stimulate the internalization, probably via endocytosis. Internalization by cancer cells under optimal growth conditions *in vitro* guarantees an efficient transfer in the cytoplasm of most of the cells. Our data implicate a potential direct association between the proliferating capacity of the individual cell type and the rate of internalization, which is in accordance with an active uptake mechanism. Further analyses should clarify this point in more detail because of its potential importance for the development of future therapeutic concepts.

Using TEM we have detected clusters of ff-MWCNTs mainly in the cytoplasm of the PCa model cell line PC-3. This uptake had no influence on the cell viability quantified by WST-1-assay in the first three days after short-term (4 h) treatment with ff-MWCNTs. These data confirm several reports for unfilled SWCNT [180–186] and also indicate that ff-MWCNTs appear non-toxic once internalized into mammalian cells of malignant (PCa and bladder cancer cells) and non-malignant origin, and without adverse effects to cell viability.

Beside the intracellular detection of ff-MWCNTs in the form of clusters or bundles the association with cells was further evaluated by flow cytometry. The results indicate that clusters of ff-MWCNTs are detectable in solution by FSC-SSC scatter flow cytometric analyses (FACS) (Fig. 9.34). They can be discriminated from cancer cells because of their higher granularity and smaller size (cf. Fig. 9.34b). After addition of ff-MWCNTs in serum-free culture medium to the cancer cells for 2 h, FACS analysis revealed a high percentage of cells characterized by a larger granularity, indicating an association between cells and ff-MWCNTs. Cells with internalized ff-MWCNTs and those with ff-MWCNTs at their surface can not be differenti-

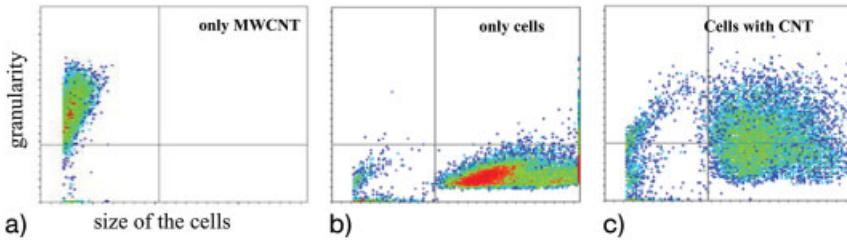


**Fig. 9.34.** Representative results of flow cytometric analyses of human PC3 cells without MWCNT transfection (b). In comparison, 4 h after incubation of cells with Fe-MWCNTs (c) the granularity and size of the cells have increased. Remarkably, bundles of Fe-MWCNTs are also detectable in solution (a).

ated by this technique. However, the detection of a broad spectrum of increasing granularity confirms the TEM studies, showing that cancer cells have internalized different amounts of ff-MWCNTs. Moreover, on repeating the flow cytometry two days later, the same percentages of cells associated with ff-MWCNTs were found. Summarizing these experiments, clearly, by addition to the culture medium an intracellular accumulation of ff-MWCNTs takes place within a few hours, especially as cytoplasmic localized aggregates (Fig. 9.35). In addition, cell-associated and internalized ff-MWCNTs have the same magnetic properties as ff-MWCNTs in solution without cells.

A pilot animal study has checked the distribution of Fe-MWCNTs in mice [187, 188]. Briefly, male mice at 8 weeks of age were narcotized, and different doses of ff-MWCNTs were injected once intraperitoneally (i.p.) or intravenously (i.v.; via the tail vein). The animals were sacrificed 20 h after treatment. Tissue samples of different organs were conserved for TEM and histological analyses. Mice without treatment were used as controls. The remaining but treated animals were observed over a period of 150 days. For several mice of this treatment group, the injections were repeated. All animals survived and showed no abnormalities in their behavior or food consumptions. Remarkably, one mouse with a five-fold injection over a period of 3 months was treated with a total of >1 g ff-MWCNTs per kg of body weight.

In sacrificed animals, large agglomerates of ff-MWCNTs were detected at various organs in the retroperitoneum for the i.p. treatment but not in the i.v. treatment group. This indicates that most of the intraperitoneally administrated ff-MWCNTs is retained within the retroperitoneum over several weeks. Interestingly, the macroscopically visible agglomerates were attached in most cases to the surface of organs and penetrated to the peripheral zone of different organs, including kidney and liver. So, remarkably, magnetic force was transferred to the organs (Fig. 9.36).

The amount of magnetic material required to produce the appropriate temperature for hyperthermia or thermoablation depends to a large extent on the method of *in vivo* administration. Intra- or peritumoral injection or deposit allows for sub-

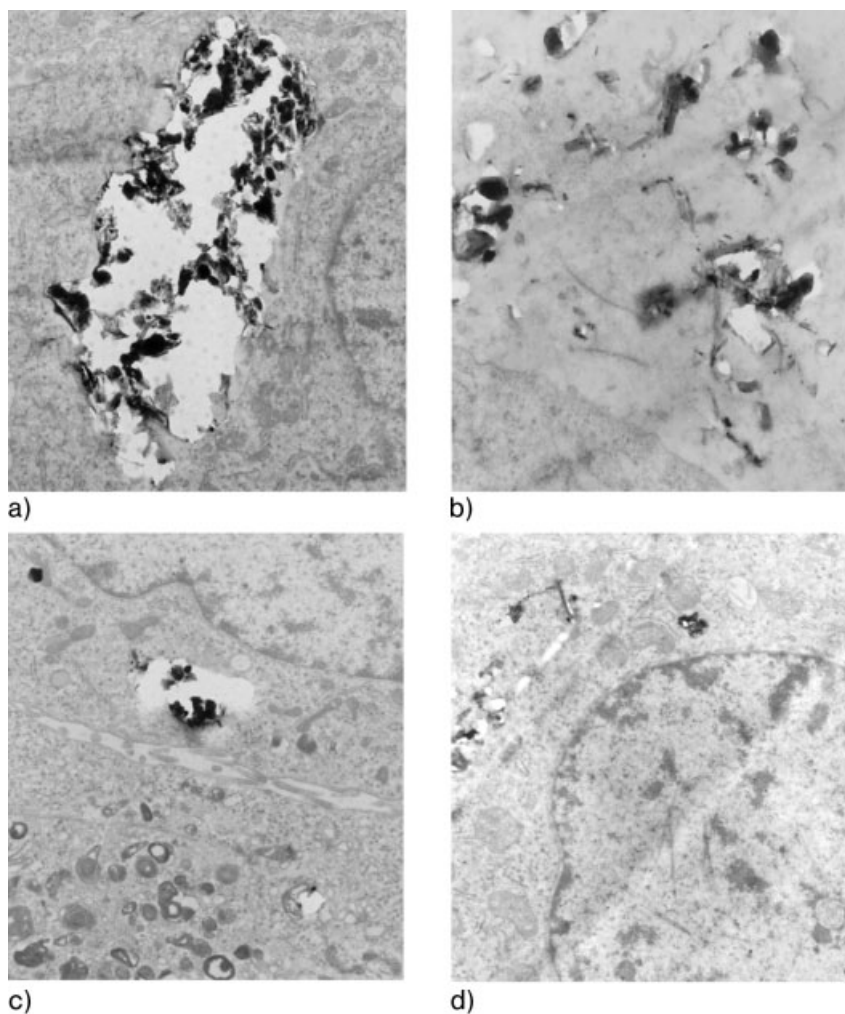


**Fig. 9.35.** Representative TEM photographs showing the internalization of ff-MWCNT by the PCa cell line PC-3. Black structures represent an accumulation of Fe-MWCNTs. (a) One large complex with many single CNTs was detected within the cytoplasm (magnification  $\times 7000$ ); (b) intracytoplasmically localized

CNTs with different grades of ferromagnetic filling (dark) (magnification  $\times 12\,100$ ); (c) different types of complex formation within the cytoplasm of PC-3 cells containing many CNTs (4 h after incubation, magnification each  $\times 7000$ ).

stantially greater amounts of magnetic material to be concentrated in a tumor than do other methods employing intravascular, intradermal or intraperitoneal administration and/or targeting. A general assumption is the concentration of at least 5 mg of the magnetic material within 1 cm<sup>3</sup> of target (tumor) tissue.

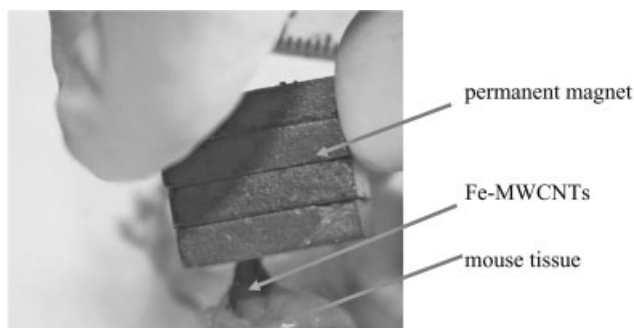


Fig. 9.36. Transfer of magnetic force to tissue.

### 9.6.2

#### Production of Two Types of ff-MWCNTs for *In Vivo* Application

ff-MWCNTs can be synthesized by two different types of CVD. The first, solid source CVD (SSCVD), uses a simple quartz-tube gas flow reactor inside a two-zone furnace system [12]. Ferrocene,  $\text{Fe}(\text{C}_5\text{H}_5)_2$ , is sublimated in the first zone at about 150 °C. Decomposition is then realized in the second, the hot, zone at about 830 °C in an Ar flow on oxidized Si-wafers.

The second CVD system (so-called liquid source CVD, LSCVD) consists of a band evaporator with continuous action and a hot wall reactor with a tape on which the precoated substrates are positioned. This tape can be moved through the hot zone of the reactor. Here the ferrocene is solved in cyclopentane and drops continuously on the moving band evaporator. At 45 °C the solvent evaporates, at 270 °C the ferrocene is completely sublimated and, finally, the vapor is transported into the CVD reactor. At 900 °C the precursor decomposes and ff-MWCNTs are deposited on the precoated substrates directly. The CVD system has been described in detail previously [189].

Therefore, this method has the important advantage of producing filled nanotubes continuously and is, thus, favorable for a large-scale application.

The nanotube material was investigated by scanning (SEM, XL 30, Philips) and transmission electron microscopy (TEM; TECNAI F30 with GiF 200). Thermal gravimetric analysis (TGA, RUBOTHERM) in an Ar/O<sub>2</sub> atmosphere up to 450 °C was used to determine the thermal stability and the filling grade of the nanotubes (oxidation of nanotubes up to the remaining Fe<sub>2</sub>O<sub>3</sub>). Alternating gradient magnetometry (AGM) revealed the ferromagnetic behaviors of the filled nanotube-ensembles on the Si-substrates.

Depending on the deposition conditions, the length, structure, filling grade and the magnetic properties of the CNTs varied. Here, two different batches of ff-MWCNTs were used. One batch was synthesized by SSCVD, affording ff-MWCNTs about 10 μm long (type 1), with a filling yield of 25–30 wt.%. The ff-MWCNTs of

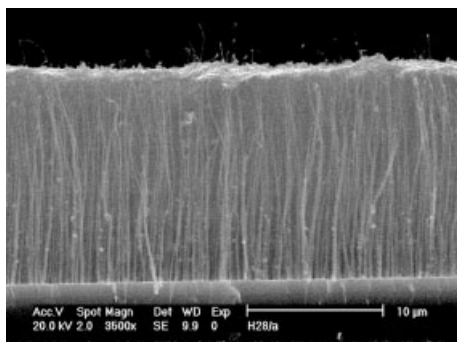


**Fig. 9.37.** SEM image of Type 1 ff-MWCNTs used for administration studies in mice.

the other batch (type 2), produced by LSCVD, were about 15  $\mu\text{m}$  long (Fig. 9.37), with filling yields of 30–35 wt.%. Both types had the same diameter distribution, i.e., 10–30 nm (inner) and 20–130 nm (outer). The number of carbon shells ranged between 20 and 100.

### 9.6.3

#### Outlook/Next Steps in Evaluation of these ff-MWCNTs

The future goal is the design and optimization of biofunctionalized ff-MWCNTs for different anticancer applications (Table 9.6). These multifunctional nanocontainers are finely regulated regarding the site of action, the temperature induced by external magnetic field application, and the step-by-step release of different drugs. In addition to therapeutic applications, nanocontainers could also be functional units for diagnostic and therapeutic monitoring purposes. They fulfill all the criteria for nanoscaled mediators of anticancer treatment with an optional intrinsic sensoric unit. The latter can function both for the detection of small tumor lesions as well as for the control of therapeutic effects. Note that either all of the individual characteristics can be incorporated in a single MWCNT species or a combination of different species with various behaviors can be synthesized, produced on a large scale, and applied under standardized conditions.

In our view, a variable experimental model is needed to test these possibilities. Therefore, we suggest a chamber model for the administration and characterization of *in vitro* and *in vivo* effects using a standardized device (Fig. 9.38).

Potential applications (Tables 9.6 and 9.7) of improved functionalization of ff-MWCNTs include:

1. Selective tumor-targeting by coupling of specific antibodies to the sidewall or the ends of ff-MWCNTs.
2. The formation of complexes with suitable lipids for better internalization of ff-MWCNTs inside target cells and tissues.

**Purposes for the experiments with the model chamber:**

- Objects of analyses: solution with different species of fff-MWCNT, adherente growing normal and cancer cell lines, slices of explanted model tissues (normal & malignant prostate from mouse or rat) including xenografts, organ bathes, or whole animals (mouse, rat)
- Study of the intrinsic magnetic properties of ff-MWCNT and fff-MWCNT in aqueous solution & within tissue slices
- Targeting, selective labeling & detection of tumor cells
- Study and optimization of different treatment modalities (microscopy, measurements within the chamber, external temperature control): intracellular intratumoral hyperthermia, drug release, combinational therapies

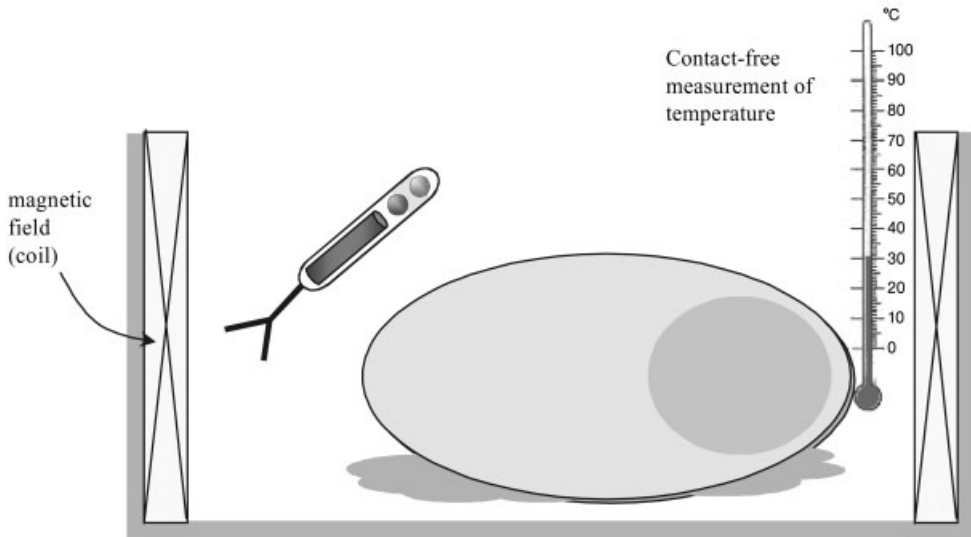


**Fig. 9.38.** Principle of the chamber used to analyze the interaction between ff-MWCNTs and tissues or organs.

3. Conjugation with other nanomaterials (nanoparticles, nanotubes, nanowires) characterized by other intrinsic biological, chemical or physical properties for an enhanced effect in diagnosis and treatment of malignant tumors.
4. Biofunctionalization and/or labeling of the ends of CNTs.
5. Potential as dual container (intrinsic chambers) and cargo system (functionalization, e.g., conjugation at the sidewall and at both ends of ff-MWCNTs).

Kam and coworkers have described recently the overall potential of functionalized CNT for anticancer therapies in general because of the intrinsic advanced physical and biological properties of these nanomaterials [185]. They reported that short ( $\approx 150$  nm long and  $\approx 1.2$  nm in diameter) and unfilled HIPCO-SWCNT solubilized in the aqueous phase by noncovalently and strongly adsorbing either fluorescently labeled 15-mer oligonucleotides (ODN) or phospholipid-PEG-grafted folic

Tab. 9.6. Advantages of CNTs and particles.

Parameter/behavior	CNT	Particles (and SWCNT?)
Functionality	<p>Filling with diagnostics and therapeutics in defined chambers</p> <p>Possibility of different locations of the anti-tumor substances (as intrinsic filling) and the tumor/tissue targeting system (as extrinsic bio-functional units)</p> <p>Minimum of ferromagnetic filling (for necessary magnetic properties and energy transfer)</p> <p>High energy transfer within a target cell and tissue</p> <p>Low(er) immunogenicity and/or toxicity?</p> <p>Relatively inert tissue distribution of deposited long CNT (&gt;1 <math>\mu\text{m}</math> long)</p>	
Morphology	<p>Length–width ratio</p> <p>Intrinsic depot function</p> <p>Compared to the filling volume, a relatively large and single surface area/sidewall for functionalization or coupling to other structures and molecules; f.e. MWCNT offer a higher available surface for interaction with DNA (compared with SWCNT and round beads)</p> <p>Possibility of defined (and temperature-dependent) release of filling substances in two directions</p> <p>Relative flexibility of the tubular structure</p> <p>Inert covering by the carbon multi-wall</p> <p>Relatively large surface area improves functionality as shuttling system/vector (cf. Singh et al. 2005 [196])</p>	Optimal surface area–diameter ratio



**Tab. 9.7.** Reported examples of studies with functionalized CNTs.

Type of functionalization	Methods and results	Ref.
Drug/vaccine delivery Delivery of nucleic acids and proteins	Crossing the cell membrane and cytoplasmic accumulation enhance the immune (ab) response against peptides with no cross-reactivity to CNT, SWCNT as molecular cargoes into cells by noncovalently and non-specifically bound proteins to the nanotube sidewall and intracellular delivery by endocytosis, delivery of plasmid DNA by binding and condensation onto ammonium-functionalized SWCNT and MWCNT and onto lysine-functionalized SWCNT, selective targeting and destruction of tumor cells	180, 182–186, 190–193, 207–212
Usage as new types of biosensors based on DNA or proteins	Examples: CNT functionalized with PNA bind DNA containing a complementary sequence, nanoassembly by DNA–DNA interaction	213–220
Complement activation and protein adsorption	Description only for SWCNT and double-wall CNT	221
Imaging of cells, use in atomic force microscopy	By covalent linkage to visible-wavelength fluorophores or as Pluronic SWCNT fluorophores through near-infrared microscopy	180, 181, 192, 222, 223
Enzyme immobilization, usage as ion channel blockers		224, 225
Molecular electronics	Formation of nanoassemblies useful as molecular switches	226–229

acid were internalized inside folate-overexpressing HeLa cancer cells by simple incubation in cell culture medium at 37 °C (Fig. 9.39). This was in contrast to the results of the same experiment at 4 °C, which indicated that uptake is based on receptor-mediated and energy-dependent endocytosis. The SWCNT were heated by external near-infrared laser pulses, resulting in an intracytoplasmic release of ODN

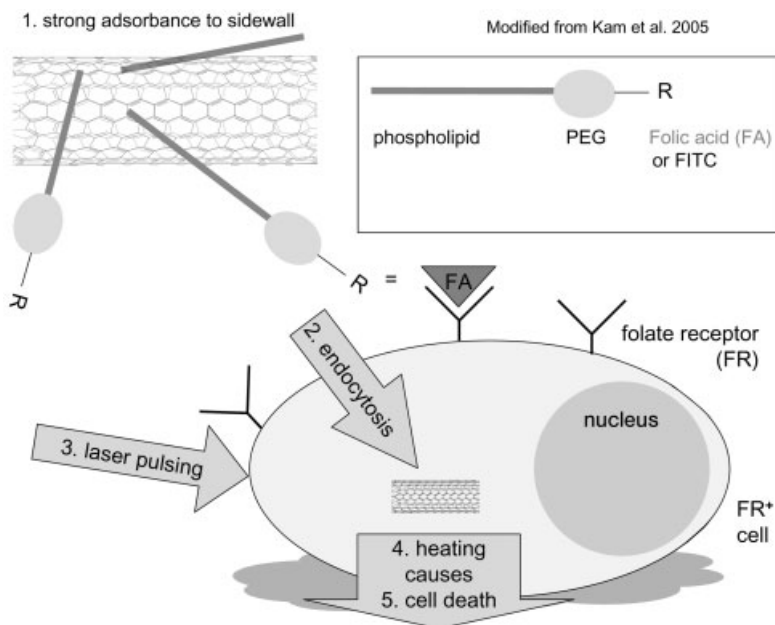


**Fig. 9.39.** Selective targeting and killing of tumor cells using functionalized SWNT. After internalization of modified SWCNT via folate receptor (FR) binding on FR expressing tumor cells laser radiation induces selective tumor cell death. (Modified from Ref. [191].)

from the SWCNT and translocation into the nucleus. Note that radiation of the aqueous SWCNT solution ( $25 \mu\text{g mL}^{-1}$ , without cells) by an 808 nm laser ( $1.4 \text{ W cm}^{-2}$ ) continuously for 2 min caused heating to  $\approx 70^\circ\text{C}$ . The authors suggested that the SWCNTs can act as tiny “heaters” in living cells overexpressing the receptor molecule (folate receptor) targeted by the functionalized SWCNTs. Selective targeting and induction of necrosis of HeLa cells was observed after the same laser pulse treatment, without harming receptor-free normal cells. Dying cells released the ODN cargoes and were mixed with cell debris in black aggregates.

The same properties should be transferred and adapted to our *fff*-MWCNT model because of the intrinsic heating function of the ferromagnetic filling. In general, new PCa-specific antigens recognized by PCa-specific receptors can be applied for a selective *fff*-MWCNT-based hyperthermia in the histologically remarkably heterogeneous PCa tissue containing also receptor-negative stromal and normal prostatic cells.

A major advantage of using *ff*-MWCNTs would be the external control available for localization and intrinsic heating. Note that the finely-regulated, slow and controlled induction of heating should also improve the internalization of *fff*-

MWCNTs by target cells that did not primarily take them up; this implies a possible multiplicity of anticancer therapeutic efficacy once or in multiple treatments: stepwise (a) heating, (b) improvement of uptake within the target tissue, (c) release of drug from the container at a defined temperature, (d) repeating the hyperthermia as secondary local treatment and release of other drug classes by realization of higher temperatures than at the time of primary hyperthermia.

Biocompatibility is a major concern when introducing a therapeutic agent inside the human body. For different, mainly short and pure, species of unfilled SWCNT no adverse or toxic effects have been reported by various groups on testing the cellular viability and the proliferation [180–182, 184–186, 190].

Studies with SWCNTs indicate that simple mixing of oxidized SWCNT with solutions of various types of proteins resulted in covalent and non-covalent bonds to the sidewall [191]. The sidewall was functionalized with oxygen-containing groups by refluxing and sonication of SWCNTs in nitric acid. Interestingly, the adsorption of proteins with a molecular weight of  $\leq 80$  kDa (bovine serum albumine and cytochrome c) on SWCNTs imparts hydrophilicity to the CNTs. The spontaneously formed nanotube–protein conjugates were internalized by different cell types of non-malignant as well as malignant origin. While single proteins were unable to cross the cell membranes by themselves, SWCNTs efficiently traffick protein cargos inside the cells. An energy-dependent endocytosis mechanism for the uptake of the conjugates was proposed [191].

However, other mechanisms as the dominant internalization processes *in vitro* have also been discussed recently in the literature, including uptake of the CNTs by insertion and diffusion through cellular membrane phagocytosis [181, 182, 184, 190, 192]. The detailed uptake mechanisms and efficacy for the different target and non-target cells should be evaluated in various animal models.

Kam et al. have further described the release of internalized conjugates with SWCNTs and proteins from endosomes by adding the membrane-passing base chloroquine to the culture medium [191]. The functionality of adsorbed protein was shown for cytochrome-c because, after release of this protein from the endosomes, cells died by active apoptosis (mediated by the delivered cytochrome c).

Recently, derivatization of unfilled MWCNTs with N-protected amino acids based on a cycloaddition reaction to the external sidewall was described by Georgakilas et al. [193]. The modified MWCNTs had a lower solubilization than functionalized SWCNTs. However,  $12 \text{ mg mL}^{-1}$  of functionalized MWCNTs gave a clear solution in water. The authors conclude that this result represents the basis towards the synthesis of peptide-based CNTs.

Other reports have shown the interactions between SWCNT (HiPco tubes) and nucleic acids. Refs. [194, 195] describe the extremely strong binding of short single stranded DNA (oligonucleotide) by  $\pi$ -stacking. The binding of the oligonucleotide was realized by helical wrapping with right- and left-hand turns or simply by adsorption at the sidewall with linearly extended structures. This DNA coating of bundled SWCNTs was effectively dispersed in water by sonication. Moreover, subsequent functionalization was made by labeling one terminus of the oligonucleotides with biotin.

Ammonium-functionalized SWCNTs and MWCNTs facilitate the delivery of plasmid DNA in different murine [180, 196]. Complexes of DNA and unfilled, ammonium-functionalized MWCNTs formed aggregates  $>4 \mu\text{m}$  and possessed a planar lattice structure, whereas the double-stranded plasmid molecules formed a planar structure with MWCNTs buried within. Compared with SWCNTs, the sidewall of MWCNTs had a higher charge density and an increased surface, resulting in a closer DNA association with the MWCNTs. The authors found  $>96\%$  of plasmid DNA is condensed by ammonium-functionalized MWCNTs at a charge ratio of 1:1.

Future developments in this fascinating application spectrum will depend on whether the specific synthesis methods and, afterwards, the defined functionalization for CNTs of a desired structure can be realized (Tables 11.6 and 11.7). According to the planned therapeutic application of fff-MWCNTs, the focus should be on the stepwise shortening of the length of the sidewall, the definition of a feasible amount of sidewall. In addition, the dependence of chemical reactivity on the detailed MWCNT structure is particularly interesting.

As well as investigation of the general toxicities of ff-MWCNTs, the principal biodistribution has been studied in a mouse model for the i.v. and i.p. administration route. For biological TEM analyses, different organs were fixed immediately after removal from sacrificed mice by fixating them in glutaraldehyde. Ultrathin slices were prepared as described recently by us [187]. Additionally, other samples of the same tissues were also collected, fixed in formaldehyde and embedded in paraffin for routine H&E staining and subsequent histological analyses.

The major goal of these studies was to investigate the short-term accumulation and distribution of the containers within the body. Furthermore, by histopathological investigations potential toxic effects after single or multiple *in vivo* administrations were assessed.

Recent results of both TEM and histological light microscopy studies indicate that aggregated to form clusters, independently of the localization site *in vivo* [187]. The aggregation can be observed even macroscopically after sonication and during injection. Therefore, the ff-MWCNTs can reach different tissues by diffusing through capillaries. The cluster sizes, detected by TEM, ranged from 0.5 to several microns. The structure of these clusters was identical to those found in cell culture incubation experiments. From the calculated sizes each cluster, mainly detected intracellular, may consist of several to hundreds or thousands of individual ff-MWCNTs. Remarkably, the tendency of *in vivo* formation of such large clusters did not influence the health conditions of the animals, and did not reduce survival. All animals ( $n = 14$ ) treated with different dosages of MWCNTs of both subtypes (once or several times) survived 150 days.

In several animals injected once with one of both types of ff-MWCNTs, the CNTs were detected within different cell types of different organs, including lung, heart, liver, colon or accumulated within the tissues (Fig. 9.40). Only in the minority of TEM positive samples were individual ff-MWCNTs found.

Moreover, after i.p.-injection low amounts of bundled ff-MWCNTs were also detected in feces. This observation needs further detailed investigation.

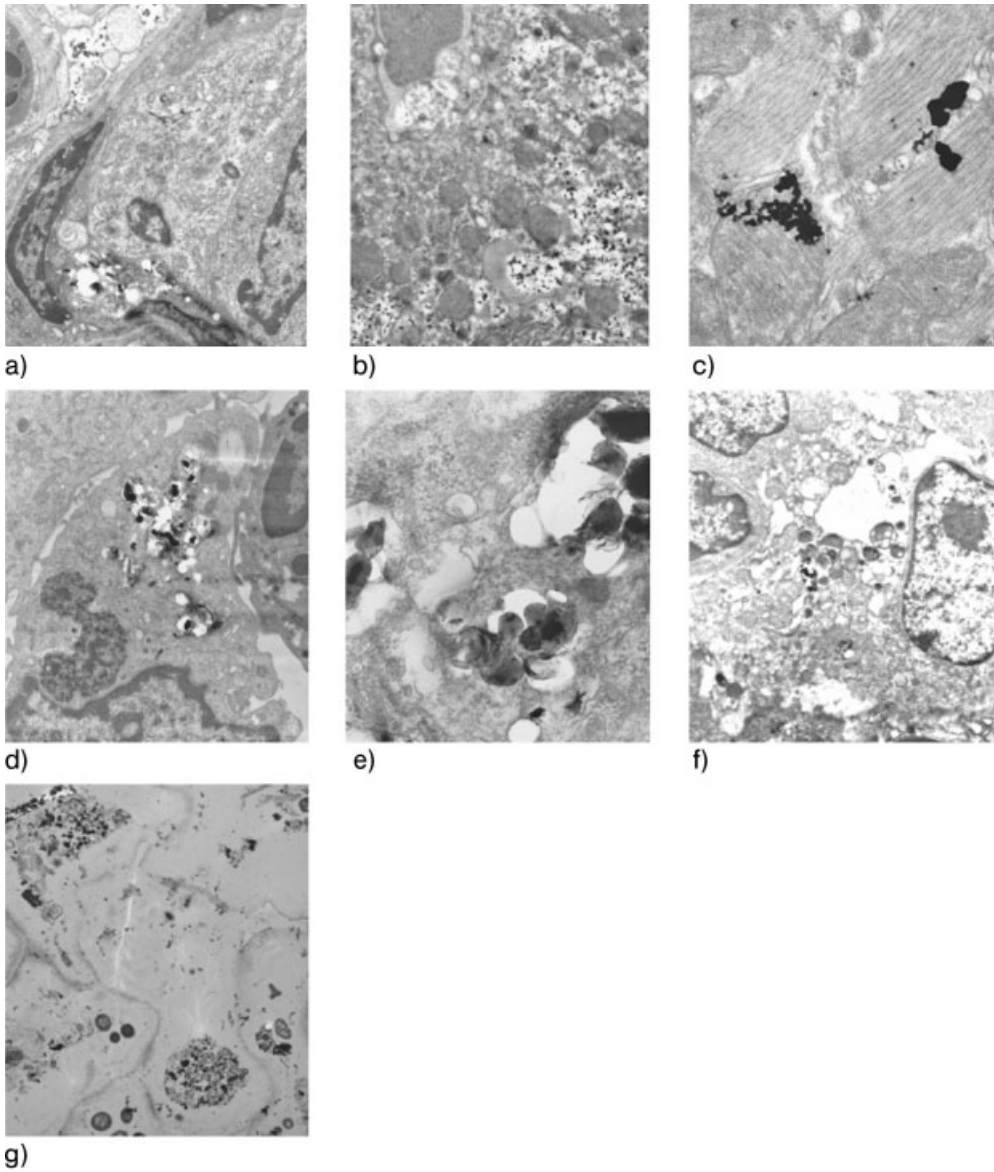


**Fig. 9.40.** Representative results of ff-MWCNTs detected by TEM analysis in different mouse organs 20 h after injections (i.v. or i.p.). (a) Lung section collected 20 h after i.v. injection of type 2 (mouse No 8, 9 weeks of age); magnification  $\times 7000$ . (b) Liver section collected 20 h after i.v. injection of type 1 (mouse No 4, 9 weeks old); magnification  $\times 7000$ . (c) Diaphragm section derived from

the same mouse as (b); magnification  $\times 7000$ . (d) Colon section collected 20 h after i.p. injection of type 1 (mouse No 6, 9 weeks old); magnification  $\times 7000$ . (e) Same as (d) but at magnification  $\times 32\,000$ . (f) Heart section collected 20 h after i.v. injection of type 1 (mouse No 3, 9 weeks old); magnification  $\times 4700$ . (g) Faeces collected 20 h after i.p. injection of type 1 (mouse No 15, 9 weeks old).

Other animals injected once or several times with doses of approximately 100–400  $\mu\text{g}$  ff-MWCNTs per injection survived more than 150 days without any indication of toxic or other adverse events. Analysis of the body weight indicated no influence of the administration of ff-MWCNTs on health condition.

Moreover, for example, several animals were sacrificed 6 weeks after first injections and analyzed by an experienced pathologist for potential alterations caused by the accumulation of ff-MWCNTs. In general, 6 weeks after the first injection ff-MWCNTs were detected cell-associated in most cases. Several microphotographs revealed an association of ff-MWCNTs accumulation with macrophages.

No formation of giant cells or granuloma was detected, indicating the absence of inflammation signs. The unrestricted localization of bundles and clusters of ff-MWCNTs was not associated with encapsulation of the accumulated tubes within the different tissues and organs. Especially in lung tissue specimens, the clusters were found near the alveolae and beside microvessels (Fig. 9.41). Interestingly, after i.p.-administration, in some cases tubes were also detected in the lung but in significantly lower amounts and number than after the i.v. administration.

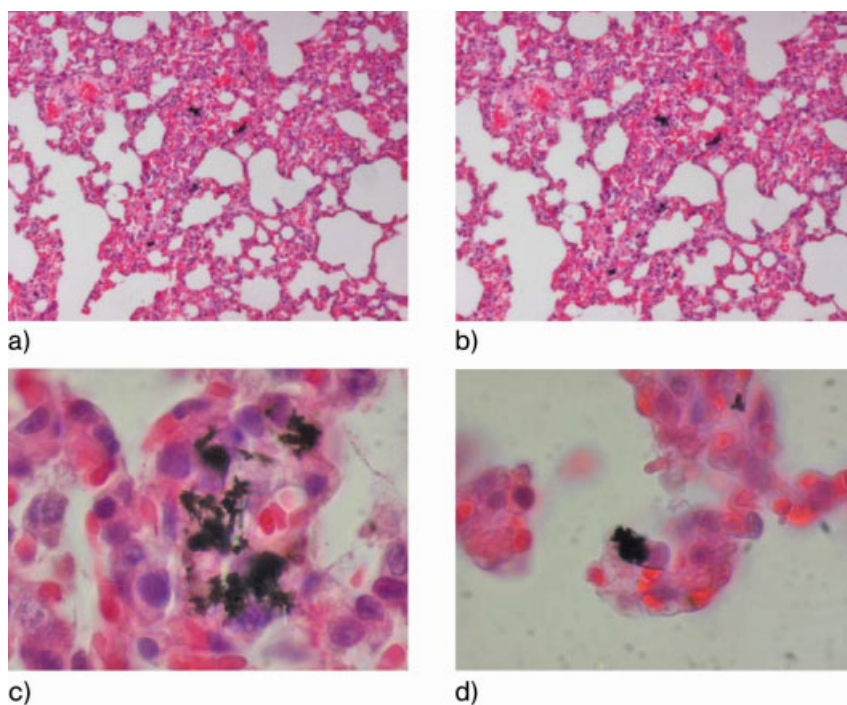


**Fig. 9.41.** Detection of Fe-MWCNTs by H&E-stained histological slices of different mouse tissue 6-weeks after i.v. or i.p. administration. Black structures represent an accumulation of

Fe-MWCNTs. Lung section at a magnification of (a)  $\times 100$ , (b)  $\times 1000$ , (c)  $\times 10000$ , and (d) with accumulation of ff-MWCNTs in the alveole at  $\times 1000$ .

**Tab. 9.8.** Temperature developed during AC-heating in mouse tissue containing Fe-MWCNTs.

Time (min)	Mouse muscle ( $T/^\circ\text{C}$ )	Kidney from mouse ( $T/^\circ\text{C}$ )
0	28.0	29.2
5	40.5	40.0
10	42.6	40.7

The determined long-term accumulation of ff-MWCNTs in different organs and tissue indicated the biocompatibility of this compound over several weeks without dramatic toxicity. The comparable patterns of accumulation between short- and long-term treated animals showed the injected ff-MWCNTs can accumulate within hours and persist in these depot tissues without encapsulation.

Partially needle-like formations of bundles were detected. In the liver, low numbers of clusters of ff-MWCNTs were localized at the sinus.

In an additional experiment series the principle of ff-MWCNTs-mediated hyperthermia was tested using freshly explanted mouse tissue specimens. At seven months of age, one untreated mouse was sacrificed, and one kidney and muscle from the leg ( $5 \times 3 \times 3$  mm) was collected for heating analyses. After injection of approximately 10–20  $\mu\text{L}$  of freshly sonicated 0.9% saline containing type 1 ff-MWCNTs ( $20 \mu\text{g} \mu\text{L}^{-1}$ ) the heating potential was tested immediately using the device described in Section 9.5.3. A magnetic field of  $20 \text{ kA m}^{-1}$  was realized at a frequency of 230 kHz. The explanted tissue specimens were incubated in the magnetic field. The temperature was measured in the centre of the treated specimens at the beginning, after 5 and 10 min (Table 9.8). Remarkably, for both explanted tissues an increase of  $>10$  K was detectable after 10 min of treatment with  $<400 \mu\text{g}$  of ff-MWCNTs. In comparison with control experiments (applying the same magnetic field for equivalent tissue specimens without injections of ff-MWCNTs) the heat injection clearly confirmed our working hypothesis that ff-MWCNTs are useful for hyperthermia purposes. These pilot experiments *ex vivo* clearly showed that doses of lower than the mg range of ff-MWCNTs can mediate an intrinsic temperature shift to  $>40^\circ\text{C}$  after a couple of minutes of treatment.

The traditional approaches to hyperthermia, including radiofrequency, microwave and ultrasound, showed only limited efficacy in clinical studies because of (a) mediating of inhomogeneous temperature conditions, (b) difficulties in focusing in the target tissue, and/or (c) relatively high absorption of the heat by the intratumoral capillaries and connective tissues. The prostate as the target organ for local treatment primary PCa represents an extraordinary example because of the anatomy of the pelvis and the high perfusion of this gland.

Jordan et al. (Magforce GmbH, Berlin) have developed amino-silane-coated iron-oxide superparamagnetic nanoparticles with a mean diameter of 15 nm.

Aqueous ferromagnetic fluid (nanoparticles at a concentration of  $120 \text{ mg mL}^{-1}$ ) were injected directly in the target tissue and subsequently heated by intracellular hyperthermia. The particles were taken up efficiently by endocytosis. The so-called magnetic fluid thermotherapy (MFH) was proposed in principal as suitable for both local hyperthermia and thermoablation of PCa, since the intratumoral temperature conditions can be selected over a broad range by modulating the magnetic field. Moreover, in contrast to E-field dominant systems used for regional hyperthermia, the boundaries of differently conductive tissues do not interfere with power absorption in the MFH treatment.

In a subsequent animal study using orthotopically implanted MatLyLu-cells (Dunning R3327 model), magnetic fluid ( $200\text{--}400 \mu\text{L}$ ) was injected into the prostate tumors ( $0.5 \text{ mL per cm}^3$  of tumor). Immediately after injection, an AC field was applied ( $100 \text{ kHz}$ ,  $0\text{--}18 \text{ kA m}^{-1}$ ; gradually increased field strength from 45% to 70% over a period of 17 min, heat treatment at 70% field strength for 30 min) using the MFH 12-TS (MagForce Nanotechnologies GmbH, Berlin) [197, 198]. By intratumoral temperature control, the authors described mean maximal temperatures of up to  $58 \text{ }^\circ\text{C}$ . The observation that  $>85\%$  of the nanoparticles were retained in the prostate 10 days after injection indicates that repeated thermal treatment is possible. Afterwards, external radiation of  $20 \text{ Gy}$  was applied. Combined thermoradiotherapy resulted in a higher inhibition of tumor growth than radiation with the same dose alone. The combinational treatment was as effective in tumor growth control as radiation therapy alone with a three-times higher dose.

Recent data from a phase I clinical study has been used to evaluate the toxicity and tolerability of MFH using a novel hyperthermia- and thermoablation-system (MFH 300F) [174] in PCa patients [147]. To our knowledge, this is the first report of the clinical application of interstitial hyperthermia using magnetic nanoparticles in the treatment on human carcinomas. A patient with locally progressive growing PCa following a high dose brachytherapy received a total of  $12.5 \text{ mL}$  of magnetic fluid in 24 depots (each of  $0.5 \text{ mL}$ ) in the prostate (intraperineal injection under rectal ultrasound control and fluoroscopy guidance) with an approximate volume of  $35 \text{ mL}$ . Thermotherapy was applied using an initial magnetic field strength of  $2.5 \text{ kA m}^{-1}$ , which was gradually increased to  $5 \text{ kA m}^{-1}$ , and was kept constant for one hour. Five subsequent MFH applications took place at weekly intervals. The maximum intra-prostatic temperatures determined ( $48.5$  and  $42.2 \text{ }^\circ\text{C}$  during the first and second treatment, respectively) achieved were in the thermoablative range.

It was assumed that for sufficient heating of the prostate gland, and ideally a homogenous distribution of the nanoparticles field strength of  $10 \text{ kA m}^{-1}$  toxicity,  $0.2 \text{ mL}$  of the magnetic fluids per  $\text{mL}$  of tissue volume is necessary to guarantee an  $\text{SAR}_{\text{tissue}}$  of  $300 \text{ W kg}^{-1}$ . However, the measured particle distribution within the tumor tissue was sub-optimal and must be improved.

As side effects, the patients experienced local pain several times (especially when the field strength was  $>5 \text{ kA m}^{-1}$ ) and moderate bladder spasms occurred after the first treatment cycle.

Moreover, in this report the authors also described preliminary experiences in



glioblastoma and recurrent soft-tissue sarcomas of the ongoing phase I study. Interestingly, the particles are retained in the PCa tissue for at least several weeks.

The authors conclude that this observation represents an important pre-requisite for the clinical application of MPH in locally advanced PCa.

In comparison, an aqueous solution of ff-MWCNTs *per se* represents a homogeneous population of particles based on the principles of their synthesis. This could be a major advantage over superparamagnetic particles for a cost-effective clinical use as thermal transmitters.

This development of nanoscaled containers, including the proposed fff-MWCNTs, opens a new chapter in the field of anticancer therapeutic concepts based on nanotechnology. Further steps of evaluation and optimization must undergo very different and detailed tests to ensure their therapeutic efficacy and mechanical stability and safety after local implantation or systemic injection. Progress in medical device technology is strongly linked to progress in material science technology, and new combinations of different materials that have been developed for different application in human medicine have influenced the design, and also the structural, chemical and biological properties of CNTs.

### Acknowledgments

The authors thank Brigitte Hamann for TEM and Dr. M. Haase (both from the Institute of Pathology, Technical University Dresden) for histopathological studies, and Dietmar Meiler (IFW Dresden) for expert technical assistance. We thank Dr. Gerd Hammermann (HAMSTEIN-Consult, Dresden, Germany) for helpful cooperation and Systemanix GmbH (Dresden, Germany) for support. Furthermore, we are thankful to Kai Krämer, and to Dr. Vladimir Novotny for participation and support in animal experiments. The ff-MWCNTs were synthesized and characterized by Dr. Manfred Ritschel, Radinka Kozhuharova-Koseva, Dr. Silke Hampel and Christian Müller. The magnetic measurements were performed by Dr. Dieter Elefant. We thank Kai Krämer and Vicky Rutschmann-Will for critical language editing. The project was generously supported by Prof. Dr. M.P. Wirth (Head of the Department of Urology, Technical University Dresden) and by Prof. Dr. B. Büchner (Head of the Institute for Solid State Research; IFW Dresden).

### Abbreviations

AC	Alternating current
CNT	Carbon nanotube
CVD	Chemical vapor deposition
FACS	Fluorescence-activated cell sorting
fff-MWCNT	Functionalized and ferromagnetic filled MWCNT
ff-MWCNT	Ferromagnetic filled MWCNT
f-MWCNT	Filled MWCNT

$H_c$	Coercivity
MFH	Magnetic fluid hyperthermia
MPH	Magnetic particle hyperthermia
$M_r$	Remnant magnetization
$M_{\text{sat}}$	Saturation magnetization
MWCNT	Multi-walled carbon nanotube
PCa	Prostate cancer
$P_{\text{FM}}$	Power loss of ferromagnetic material
PSA	Prostate specific antigen
$P_{\text{SPM}}$	Power loss of superparamagnetic material
$\text{SAR}_{\text{Fe}}$	Specific absorption rate of iron
SAR	Specific absorption rate
SEM	Scanning electron microscope
SWCNT	Single-walled carbon nanotube
TEM	Transmission electron microscope
$T$	Temperature
$t$	Time

## References

- GONZALGO ML, ISAACS WB, Molecular pathways to prostate cancer, *J. Urol.*, **2003**, 170, 2444–2452.
- BASTACKY SI, WOJNO KJ, WALSH PC, CARMICHAEL MJ, EPSTEIN JI, Pathological features of hereditary prostate cancer, *J. Urol.*, **1995**, 153, 987–992.
- FELDMAN BJ, FELDMAN D, The development of androgen-independent prostate cancer, *Nat. Rev. Cancer*, **2001**, 1, 34–45.
- TRICOLI JV, SCHOENFELDT M, CONLEY BA, Detection of prostate cancer and predicting progression: Current and future diagnostic markers, *Clin. Cancer Res.*, **2004**, 10, 3943–3953.
- DOWNS TM, KANE GD, GROSSFELD GD, MENG MV, CAROLL PR, Surgery for prostate cancer: Rational, techniques and outcome, *Cancer Metastasis Rev.*, **2002**, 21, 29–44.
- GOMELLA LG, ZELTSER I, VALICENTI RK, Use of neoadjuvant and adjuvant therapy to prevent or delay recurrence of prostate cancer in patients undergoing surgical treatment for prostate cancer, *Urology*. **2003**, 62(Suppl 1), 46–54.
- MIYAMOTO H, MESSING EM, CHANG C, Androgen deprivation therapy for prostate cancer: Current status and future prospects, *Prostate*, **2004**, 61, 332–353.
- RAO CNR, SEN R, SATISKUMAR BC, GOVINDARAJ A, Large aligned-nanotube bundles from ferrocene pyrolysis, *Chem. Commun.*, **1998**, 1525.
- GROBERT N, HSU WK, ZHU YQ, HARE JP, KROTO HW, WALTON DRM, TERRONES M, TERRONES H, REDLICH P, RUHLE M, ESCUDERO R, MORALES F, Enhanced magnetic coercivities in Fe nanowires, *Appl. Phys. Lett.*, **1999**, 75, 3363–3365.
- KOZHUHAROVA R, RITSCHEL M, ELEFANT D, GRAFF A, LEONHARDT A, MONCH I, MUHL T, SCHNEIDER CM, Synthesis and characterization of aligned Fe-filled carbon nanotubes on silicon substrates, *J. Mater. Sci.-Mater. Electron.*, **2003**, 14, 789–791.
- KOZHUHAROVA R, PhD-thesis: “Preparation and characterization of ferromagnetic filled carbon nanotubes”, in *Fakultät Maschinenwesen*, Technische Universität, Dresden, **2006**.

- 12 LEONHARDT A, RITSCHEL A, KOZHUHAROVA R, GRAFF A, MUHL T, HUHLE R, MONCH I, ELEFANT D, SCHNEIDER CM, Synthesis and properties of filled carbon nanotubes, *Diamond Relat. Mater.*, **2003**, 12, 790–793.
- 13 KOZHUHAROVA R, RITSCHEL M, MONCH I, MUHL T, LEONHARDT A, GRAFF A, SCHNEIDER CM, Selective growth of aligned Co-filled carbon nanotubes on silicon substrates, *Fullerenes Nanotubes Carbon Nanostruct.*, **2005**, 13, 347–353.
- 14 KOZHUHAROVA R, RITSCHEL M, ELEFANT D, GRAFF A, MONCH I, MUHL T, SCHNEIDER CM, LEONHARDT A, (FexCo1-x)-alloy filled vertically aligned carbon nanotubes grown by thermal chemical vapor deposition, *J. Magn. Magn. Mater.*, **2005**, 290–291, 250–253.
- 15 MONCH I, MEYE A, LEONHARDT A, KRAMER K, KOZHUHAROVA R, GEMMING T, WIRTH MP, BÜCHNER B, Ferromagnetic filled carbon nanotubes and nanoparticles: Synthesis and lipid-mediated delivery into human tumor cells, *J. Magn. Magn. Mater.*, **2005**, 290–291, 276–278.
- 16 IJIMA S, Helical microtubules of graphitic carbon, *Nature* **1991**, 354, 56–58.
- 17 IJIMA S, ICHIHASHI T, Single-shell carbon nanotubes of 1-nm diameter, *Nature*, **1993**, 363, 603–605.
- 18 DRESSELHAUS MS, DRESSELHAUS G, AVOURIS P, Carbon nanotubes, synthesis, structure, properties, applications, *Top. Appl. Phys.*, **2001**, 80.
- 19 PRADOS C, CRESPO P, GONZALEZ JM, HERNANDO A, MARCO JF, GANCEDO R, GROBERT N, TERRONES M, WALTON RM, KROTO HW, Hysteresis shift in Fe-filled carbon nanotubes due to gamma-Fe, *Phys. Rev. B (Condensed Matter Mater. Phys.)*, **2002**, 65, 113 404–113 405.
- 20 WONG SHI KAM N, O'CONNELL M, WISDOM JA, DAI H, *Proc. Natl. Acad. Sci. U.S.A.*, **2005**, 102, 11 600.
- 21 CHENG HM, LI F, SUN X, BROWN SDM, PIMENTA MA, MARUCCI A, DRESSELHAUS G, DRESSELHAUS MS, Bulk morphology and diameter distribution of single-walled carbon nanotubes synthesized by catalytic decomposition of hydrocarbons, *Chem. Phys. Lett.*, **1998**, 289, 602–610.
- 22 COLOMER J-F, STEPHAN C, LEFRANT S, VAN TENDELOO G, WILLEMS I, KONYA Z, FONSECA A, LAURENT C, NAGY BJ, Large-scale synthesis of single-wall carbon nanotubes by catalytic chemical vapor deposition (CCVD) method, *Chem. Phys. Lett.*, **2000**, 317, 83–89.
- 23 JOUMET C, MASER WK, BERNIER P, *Nature*, **1997**, 388, 756.
- 24 GUO T, NIKOLAEV P, THESS A, COLBERT DT, SMALLEY RE, Catalytic growth of single-walled nanotubes by laser vaporization, *Chem. Phys. Lett.*, **1995**, 243, 49–54.
- 25 TÄSCHNER C, PACAL F, LEONHARDT A, SPATENKA P, BARTSCH K, GRAFF A, KALTOFEN R, *Surf. Coatings Technol.*, **2003**, 81.
- 26 CHHOWALLA M, TEO KBK, DUCATI C, RUPESINGHE NL, AMARATUNGA GAJ, FERRARI AC, ROY D, ROBERTSON J, MILNE WI, Growth process conditions of vertically aligned carbon nanotubes using plasma enhanced chemical vapor deposition, *J. Appl. Phys.*, **2001**, 90, 5308–5317.
- 27 REN ZF, HUANG ZP, XU JW, WANG JH, BUSH P, SIEGAL MP, PROVENCIO PN, Synthesis of large arrays of well-aligned carbon nanotubes on glass, *Science*, **1998**, 282.
- 28 LOISEAU A, PASCARD H, Synthesis of long carbon nanotubes filled with Se, S, Sb and Ge by the arc method, *Chem. Phys. Lett.*, **1996**, 256, 246–252.
- 29 LOISEAU A, WILLAIME F, Filled and mixed nanotubes: From TEM studies to the growth mechanism within a phase-diagram approach, *Appl. Surf. Sci.*, **2000**, 164, 227–240.
- 30 DYAGILEVA LM, MAR'IN VP, TSYGANOVA EI, RAZUVAEV GA, Reactivity of the first transition row metallocenes in thermal decomposition reaction, *J. Organomet. Chem.*, **1979**, 175, 63–72.
- 31 SEN R, GOVINDARAJ A, RAO CNR,

- Carbon nanotubes by the metallocene route, *Chem. Phys. Lett.*, **1997**, 267, 276–280.
- 32 GROBERT N, MAYNE M, TERRONES M, SLOAN J, DUNIN-BORKOWSKI RE, KAMALAKARAN R, SEEGER T, TERRONES H, RÜHLE M, WALTON DRM, KROTO HW, HUTCHISON JL, *Chem. Commun.*, **2001**, 471.
  - 33 MAYNE M, GROBERT N, TERRONES M, KAMALAKARAN R, RÜHLE M, KROTO HW, WALTON DRM, Pyrolytic production of aligned carbon nanotubes from homogeneously dispersed benzene-based aerosols, *Chem. Phys. Lett.*, **2001**, 338, 101–107.
  - 34 SATISHKUMAR BC, GOVINDARAJ A, VANITHA PV, RAYCHAUDHURI AK, RAO CNR, Barkhausen jumps and related magnetic properties of iron nanowires encapsulated in aligned carbon nanotube bundles, *Chem. Phys. Lett.*, **2002**, 362, 301–306.
  - 35 LEONHARDT A, RITSCHEL A, ELEFANT D, MATTERN N, BIEDERMANN K, HAMPEL S, MÜLLER C, GEMMING T, BÜCHNER B, *J. Appl. Phys.*, **2005**, 98, 074315-1-5.
  - 36 KOZHUHAROVA R, RITSCHEL M, ELEFANT D, GRAFF A, LEONHARDT A, MONCH I, MUHL T, GROUDEVA-ZOTOVA S, SCHNEIDER CM, Well-aligned Co-filled carbon nanotubes: Preparation and magnetic properties, *Appl. Surf. Sci.*, **2004**, 238, 355–359.
  - 37 HAMPEL S, LEONHARDT A, SELBMANN D, BIEDERMANN K, ELEFANT D, BÜCHNER B, Growth and characterization of filled carbon nanotubes with ferromagnetic properties, *Carbon*, accepted for publication, **2006**.
  - 38 KARMAKAR S, SHARMA SM, MUKADAM MD, YUSUF SM, SOOD AK, Magnetic behavior of iron-filled multiwalled carbon nanotubes, *J. Appl. Phys.*, **2005**, 97, 54 305–54 306.
  - 39 MUNOZ-SANDOVAL E, LOPEZ-URIAS F, DIAZ-ORTIZ A, TERRONES M, REYES-REYES M, MORAN-LOPEZ JL, Magnetic and transport properties of Fe nanowires encapsulated in carbon nanotubes, *J. Magn. Magn. Mater.*, **2004**, 272–276, E1255–E1257.
  - 40 CHE R, PENG L-M, CHEN Q, DUAN XF, ZOU BS, GU ZN, Controlled synthesis and phase transformation of ferrous nanowires inside carbon nanotubes, *Chem. Phys. Lett.*, **2003**, 375, 59–64.
  - 41 PICHOT V, LAUNOIS P, PINAULT M, MAYNE-L'HERMITE M, REYNAUD C, Evidence of strong nanotube alignment and for iron preferential growth axis in multiwalled carbon nanotube carpets, *Appl. Phys. Lett.*, **2004**, 85, 473–475.
  - 42 SCHNITZLER MC, OLIVEIRA MM, UGARTE D, ZARBIN AJG, One-step route to iron oxide-filled carbon nanotubes and bucky-onions based on the pyrolysis of organometallic precursors, *Chem. Phys. Lett.*, **2003**, 381, 541–548.
  - 43 KIM H, SIGMUND W, Iron nanoparticles in carbon nanotubes at various temperatures, *J. Crystal Growth*, **2005**, 276, 594–605.
  - 44 KIM H, SIGMUND W, Iron particles in carbon nanotubes, *Carbon*, **2005**, 43, 1743–1748.
  - 45 SHAPER AK, HOU H, GREINER A, PHILLIPP F, *J. Catal.*, **2004**, 222, 250.
  - 46 LEONHARDT A, MÜLLER C, HAMPEL S, SELBMANN D, RITSCHEL A, GEMMING T, BIEDERMANN K, ELEFANT D, BÜCHNER B, *Proc. Electrochem. Soc. Inc., Euro CVD*, **2005**, 15, 372.
  - 47 BARTSCH K, LEONHARDT A, Growth and morphology of aligned carbon nanotube layers, *Thin Solid Films*, **2004**, 469–470, 115–119.
  - 48 BARTSCH K, BIEDERMANN K, GEMMING T, LEONHARDT A, On the diffusion-controlled growth of multiwalled carbon nanotubes, *J. Appl. Phys.*, **2005**, 97, 114 301–114 307.
  - 49 ANDREWS R, JACQUES D, RAO AM, DERBYSHIRE F, QIAN D, FAN X, DICKEY EC, CHEN J, Continuous production of aligned carbon nanotubes: A step closer to commercial realization, *Chem. Phys. Lett.*, **1999**, 303, 467–474.
  - 50 ZHANG X, CAO A, WEI B, LI Y, WEI J, XU C, WU D, Rapid growth of well-aligned carbon nanotube arrays, *Chem. Phys. Lett.*, **2002**, 362, 285–290.
  - 51 DORMANS GJM, OMCVD of transition

- metals and their silicides using metallocenes and (di) silane or silicon tetra-bromide, *J. Crystal Growth*, **1991**, 108, 806–816.
- 52 ENDO H, KUWANA K, SAITO K, QIAN D, ANDREWS R, GRULKE EA, CFD prediction of carbon nanotube production rate in a CVD reactor, *Chem. Phys. Lett.*, **2004**, 387, 307–311.
- 53 DECK CP, VECCHIO K, Prediction of carbon nanotube growth success by the analysis of carbon-catalyst binary phase diagrams, *Carbon*, **2006**, 43, 2608–2617.
- 54 MÜLLER C, HAMPEL S, ELEFANT D, BIEDERMANN K, LEONHARDT A, RITSCHEL A, BÜCHNER B, Iron filled carbon nanotubes grown on substrates with thin metal layers and their magnetic properties, *Carbon*, accepted for publication, **2006**.
- 55 ERLANGER BF, CHEN BX, ZHU M, BRUNS L, *Nano Lett.*, **2001**, 1, 465.
- 56 YU X, CHATTOPADHYAY D, GALESKA I, PAPANIMITRAKOPOULOS F, RUSLING JF, Peroxidase activity of enzymes bound to the ends of single-wall carbon nanotube forest electrodes, *Electrochem. Commun.*, **2003**, 5, 408–411.
- 57 ZHANG L, ZHAO, GC, WIE XW, YANG, ZS, *Chem. Lett.* **2004**, 33, 86.
- 58 DAI H, PETIL A, VAIA RA, in *Molecular Structures, XVII. International Winterschool/Euroconference on Electronic Properties of Novel Materials; AIP Conference Proceedings*, ed. KUZMANY H, MEHRING M, ROTH S, FINK J, Melville, New York, **2003**.
- 59 AHN KS, KIM JS, KIM CO, HONG JP, Non-reactive rf treatment of multiwall carbon nanotube with inert argon plasma for enhanced field emission, *Carbon*, **2003**, 41, 2481–2485.
- 60 TSANG SC, HARRIS PJF, GREEN M, *Nature*, **1993**, 362, 520.
- 61 TSANG SC, CHEN YK, HARRIS PJF, GREEN M, *Nature*, **1994**, 327, 159.
- 62 RAYMONDO-PINERO E, CACCIAGUERRA T, SIMON P, BEGUIN F, A single step process for the simultaneous purification and opening of multiwalled carbon nanotubes, *Chem. Phys. Lett.*, **2005**, 412, 184–189.
- 63 AJAYAN PM, IIJIMA S, *Nature*, **1993**, 361, 333.
- 64 CHU A, COOK J, HEESOM RJR, HUTCHISON JL, GREEN MLH, SLOAN J, *Chem. Mater.*, **1996**, 8, 2751.
- 65 UGARTE D, STÄCKLI T, BONARD JM, CHÂCTELAIN A, DE HEER WA, Filling carbon nanotubes, *Appl. Phys. A, Mater. Sci. & Process.*, **1998**, 67, 101–105.
- 66 GAO Y, BANDO Y, *Nature*, **2002**, 415, 599.
- 66a WU H, WEI X, SHAO M, GU J, QU M, Preparation of Fe-Ni-alloy nanoparticles inside carbon nanotubes via wet chemistry, *J. Mater. Chem.*, **2002**, 12, 1919–1921.
- 67 CORIO P, SANTOS AP, SANTOS PS, TEMPERINI MLA, BRAR VW, PIMENTA MA, DRESSELHAUS MS, Characterization of single wall carbon nanotubes filled with silver and with chromium compounds, *Chem. Phys. Lett.*, **2004**, 383, 475–480.
- 68 MITTAL J, MONTHIOUX M, ALLOUCHE H, STEPHAN O, Room temperature filling of single-wall carbon nanotubes with chromium oxide in open air, *Chem. Phys. Lett.*, **2001**, 339, 311–318.
- 69 SLOAN J, COOK J, CHU A, ZWIEFKASIBLEY M, GREEN MLH, HUTCHINSON J, *J. Solid State Chem.*, **1998**, 140, 83.
- 70 HSU WK, LI WZ, ZHU YQ, GROBERT N, TERRONES M, TERRONES H, YAO N, ZHANG JP, FIRTH S, CLARK RJH, KCl crystallization within the space between carbon nanotube walls, *Chem. Phys. Lett.*, **2000**, 317, 77–82.
- 71 KIM BM, QUIAN S, BAU HH, *Nano Lett.*, **2005**, 5, 873.
- 72 KORNEVA G, YE H, GOGOTSI Y, HALVERSON D, FRIEDMAN G, BRADLEY J-C, KORNEV KG, *Nano Lett.*, **2005**, 5, 879.
- 73 SATISHKUMAR BC, GOVINDARAJ A, MOFOKENG J, SUBBANNA GN, RAO CNR, *J. Phys. B, At. Mol. Opt. Phys.*, **1996**, 29, 4925.
- 74 KODAMA RH, Magnetic nanoparticles, *J. Magn. Magn. Mater.*, **1999**, 200, 359–372.
- 75 BAHADUR D, GIRI J, Biomaterials and magnetism, *Sadhana*, **2003**, 28, 639–656.

- 76 CHIKAZUMI S, *Physics of Magnetism*, John Wiley & Sons, Inc., New York, London, Sydney, 1964.
- 77 AHARONI A, *Introduction to the Theory of Ferromagnetism*, Oxford University Press, Oxford, UK, 1996.
- 78 CULLITY BD, *Introduction to Magnetic Materials*, Addison-Wesley, Boston, MA, U.S.A., 1972.
- 79 YOSHIDA K, *Theory of Magnetism*, Springer, New York, 1996.
- 80 ZIJLSTRA H, *Ferromagnetic Materials 3*, North-Holland Publishing Company, Amsterdam, 1982.
- 81 SELLMYER DJ, ZHENG M, SKOMSKI R, Magnetism of Fe, Co and Ni nanowires in self-assembled arrays, *J. Phys., Condensed Matter*, 2001, R433–R460.
- 82 LI F, REN L, NIU Z, WANG H, WANG T, Magnetic moment orientations in  $\alpha$ -Fe nanowire arrays embedded in anodic aluminum oxide templates, *J. Phys., Condensed Matter*, 2002, 6875–6882.
- 83 NIELSCH K, WEHRSPHON RB, BARTHEL J, KIRSCHNER J, GOSELE U, FISCHER SF, KRONMULLER H, Hexagonally ordered 100 nm period nickel nanowire arrays, *Appl. Phys. Lett.*, 2001, 79, 1360–1362.
- 84 NIELSCH K, PhD-thesis, Hochgeordnete ferromagnetische nanostabensembles: Elektrochemische herstellung und magnetische charakterisierung, in *Mathematisch-Naturwissenschaftlich-Technische fakultät*, Halle (Saale), Martin-Luther-Universität Halle-Wittenberg, 2002.
- 85 ROSS CA, HWANG M, SHIMA M, CHENG JY, FARHOUD M, SAVAS TA, SMITH HI, SCHWARZACHER W, ROSS FM, REDJDAL M, HUMPHREY FB, Micromagnetic behaviour of electrodeposited cylinder arrays, *Phys. Rev. B*, 2002, 65, 144 411–144 418.
- 86 SUN L, HAO Y, CHIEN C-L, SEARSON PC, Tuning the properties of magnetic nanowires, *IBM J. Res. & Dev.*, 2005, 49, 79–102.
- 87 CHENG GS, ZHANG LD, ZHU YQ, FREI GT, LI L, MO CM, MAO YQ, *Appl. Phys. Lett.* 1999, 75, 2455.
- 88 WANG XF, ZHANG LD, SHI HZ, PENG XS, ZHENG MJ, FANG J, CHEN JL, GAO BJ, *J. Phys. D, Appl. Phys.*, 2001, 34, 418.
- 89 MORAS K, SCHAARSCHUCH R, RIEHEMANN W, MORAS K, SCHAARSCHUCH R, RIEHEMANN W, Production of nanoscale fesi and fecr powders for magnetofluide application using laser evaporation. *Magnetohydrodynamics*, 2003, 39, 35–39.
- 90 BAO Y, KRISHNAN KM, Preparation of functionalized and gold-coated cobalt nanocrystals for biomedical applications, *J. Magn. Magn. Mater.*, 2005, 293, 15–19.
- 91 BUTTER K, PHILIPSE AP, VROEGE GJ, Synthesis and properties of iron ferrofluids, *J. Magn. Magn. Mater.*, 2002, 252, 1–3.
- 92 SAITO Y, YOSHIKAWA T, OKUDA M, FUJIMOTO A, YAMAMURO S, WAKOH K, SUMIYAMA K, SUZUKI K, KASUYA A, NISHINA Y, Cobalt particles wrapped in graphitic carbon prepared by an arc discharge method, *J. Appl. Phys.*, 1994, 75, 134–137.
- 93 BÖNNEMANN H, BRIJOUX W, BRINKMANN R, MATOUSSEVITCH N, WALDÖFNER N, *Magnetohydrodynamics*, 2003, 39, 29.
- 94 BÖNNEMANN H, BRAND RA, BRIJOUX W, HOFSTADT H-W, FRERICHS M, KEMPTER V, MAUS-FRIEDRICHS W, MATOUSSEVITCH N, NAGABHUSHANA KS, VOIGTS F, CAPS V, Air stable Fe and Fe–Co magnetic fluids – synthesis and characterization, *Appl. Organomet. Chem.*, 2005, 19, 790–796.
- 95 GIRI J, RAY A, DASGUPTA S, DATTA D, BAHADUR D, Investigations on Tc tuned nano particles of magnetic oxides for hyperthermia applications, *Bio-Med. Mater. Eng.*, 2003, 13, 387–399.
- 96 CARPENTER EE, Iron nanoparticles as potential magnetic carriers, *J. Magn. Magn. Mater.*, 2001, 225, 17–20.
- 97 CONNOLLY J, PIERRE TGS, RUTNAKRNPITUK M, RIFFLE JS, Silica coating of cobalt nanoparticles increase their magnetic and chemical stability for biomedical applications, *Eur. Cells Mater.*, 2002, 3, 106–109.
- 98 HÜLSER T, Strukturelle und

- magnetische eigenschaften von eisenkarbid- und eisenoxid-nanopartikeln, in *Fakultät für Naturwissenschaften der Universität Duisburg-Essen*, Duisburg-Essen, 2003.
- 99 HE YP, WANG SQ, LI CR, MIAO YM, WU ZY, ZOU BS, Synthesis and characterization of functionalized silica-coated Fe<sub>3</sub>O<sub>4</sub> superparamagnetic nanocrystals for biological applications, *J. Phys. D, Appl. Phys.*, 2005, 1342–1350.
- 100 DRAVID VP, HORST JJ, TENG MH, ELLIOTT B, HWANG L, JOHNSON DL, MASON TO, WEERTMAN JR, Controlled-size nanocapsules, *Nature*, 1995, 374, 602–602.
- 101 FU L, DRAVID VP, KLUG K, LIU X, MIRKIN CA, Synthesis and patterning of magnetic nanostructures, *Eur. Cells Mater.*, 2002, 3, 156–157.
- 102 SAITO Y, YOSHIKAWA T, OKUDA M, FUJIMOTO N, SUMIYAMA K, SUZUKI K, KASUYA A, NISHINA Y, Carbon nanocapsules encaging metals and carbides, *J. Phys. Chem. Solids*, 1993, 54, 1849–1860.
- 103 BRUNSMAN EM, SUTTON R, BORTZ E, KIRKPATRICK S, MIDELFORT K, WILLIAMS J, SMITH P, MCHENRY ME, MAJETICH SA, ARTMAN JO, DE GRAEF M, STALEY SW, Magnetic properties of carbon-coated, ferromagnetic nanoparticles produced by a carbon-arc method, in *38th Annual Conference on Magnetism and Magnetic Materials*, AIP, Minneapolis, Minnesota, 1994, vol. 75, pp 5882–5884.
- 104 MCHENRY ME, MAJETICH SA, ARTMAN JO, DEGRAEF M, STALEY SW, Superparamagnetism in carbon-coated Co particles produced by Kratschmer carbon arc process, *Phys. Rev. B*, 1994, 49, 11 358–11 363.
- 105 IVANTCHENKO A, Syntheses, investigations and applications on carbon materials from reactions of graphite oxide, acetylene, metal acetylides, and ferrocene through transition metal catalysts, in *Swiss Federal Institute of Technology Zürich*, Zürich, 2004.
- 106 PIROTA KR, PROVENCIO M, GARCIA KL, ESCOBAR-GALINDO R, MENDOZA ZELIS P, HERNANDEZ-VELEZ M, VAZQUEZ M, Bi-magnetic microwires: A novel family of materials with controlled magnetic behavior, *J. Magn. Mater.*, 2005, 290–291, 68–73.
- 107 BARBIC M, Single domain magnets in bio-medical applications, *Eur. Cells Mater.*, 2002, 3, 132–134.
- 108 HALLIDAY, R, *Phys. Patr II*, 1968, 820.
- 109 HUANG S, DAI L, MAU AWH, *J. Phys. Chem. B*, 1999, 103, 4223.
- 110 HIHARA T, ONODERA H, SUMIYAMA K, SUZUKI K, KASUYA A, NISHINA Y, SAITO Y, YOSHIKAWA T, OKUDA M, Magnetic properties of iron in nanocapsules, *Jpn. J. Appl. Phys.*, 1994, 33, L24–L25.
- 111 SUN X, GUTIERREZ A, YACKMANN MJ, DONG X, JIN S, Investigations on magnetic properties and structure for carbon encapsulated nanoparticles of Fe, Co, Ni, *Mater. Sci. Eng. A*, 2000, 286, 157–160.
- 112 SEBERINO C, BERTRAM HN, *IEEE Trans. Magn.*, 1997, MAG-33, 3055–3057.
- 113 ROSS CA, HWANG M, SHIMA M, CHENG JY, FARHOUD M, SAVAS TA, SMITH HI, SCHWARZACHER W, ROSS FM, REDJDAL M, HUMPHREY FB, Micromagnetic behavior of electro-deposited cylinder arrays, *Phys. Rev. B (Condensed Matter Mater. Phys.)*, 2002, 65, 144 417–144 418.
- 114 GANGOPADHYAY S, HADJIPANAYIS GC, DALE B, SORENSEN CM, KLABUNDE KJ, PAPAETHYMIU V, KOSTIKAS A, Magnetic properties of ultrafine iron particles, *Phys. Rev. B*, 1992, 45, 9778–9787.
- 115 WANG SX, TARATORIN AM, Magnetic information storage technology, in *Magnetic Information Storage Technology*, Academic Press, San Diego, 1999.
- 116 WIRTH S, VON MOLNAR S, Hall cross size scaling and its application to measurements on nanometer-size iron particle arrays, *Appl. Phys. Lett.*, 2000, 76, 3283–3285.
- 117 SKOMSKI R, ZENG H, SELLMYER DJ, Incoherent magnetization reversal in nanowires, *J. Magn. Mater.*, 2002, 249, 175–180.

- 118 STONER EC, WOHLFARTH EP, A mechanism of magnetic hysteresis in heterogeneous alloys, *Phil. Trans. Royal Soc. London; Ser. A Math. Phys. Sci.*, **1948**, 240, 599–642.
- 119 KNELLER E, Theory of the magnetization curve of small crystals, in *Encyclopedia of Physics*, vol. XVIII/2, *Ferromagnetism*, ed. WIJN HPJ, Springer Verlag, New York, **1966**.
- 120 HERGT R, ANDRA W, D'AMBLY CG, HILGER I, KAISER W, RICHTER U, SCHMIDT H-G, Physical limits of hyperthermia using magnetite fine particles, *IEEE Trans. Magn.*, **1998**, 34, 3745–3754.
- 121 SEBERINO C, BERTRAM HN, Numerical study of hysteresis and morphology in elongated tape particles, *J. Appl. Phys.*, **1999**, 85(8), 5543–5545.
- 122 ZHAO B, KOZHUHAROVA R, MÜHL T, MÖNCH I, VINZELBERG H, RITSCHEL M, GRAFF A, HUHLE M, LICHTHE H, SCHNEIDER CM, Magnetic systems with carbon nanotubes, in *Structural and Electronic Properties of Molecular Nanostructures*, ed. KUZMANY H, American Institute of Physics, Springer, Heidelberg, **2002**, pp 583–587.
- 123 SCHNEIDER CM, ZHAO B, KOZHUHAROVA R, GROUDEVA-ZOTOVA S, MUHL T, RITSCHEL M, MONCH I, VINZELBERG H, ELEFANT D, GRAFF A, Towards molecular spintronics: Magnetotransport and magnetism in carbon nanotube-based systems, *Diamond Relat. Mater.*, **2004**, 13, 215–220.
- 124 CHOU SY, WEI MS, KRAUSS PR, FISCHER PB, Single-domain magnetic pillar array of 35 nm diameter and 65 Gbits/in.<sup>2</sup> density for ultrahigh density quantum magnetic storage, *J. Appl. Phys.*, **1994**, 76, 6673–6675.
- 125 DREIKORN J, DREYER L, MICHALOWSKY L, ROSSEL J, SICKER U, *J. Phys. IV (Proc. Soft Magn. Mater. 13)*, **1998**, Pr2-457–460.
- 126 JONES SK, GRAY BN, BURTON MA, CODDE JP, STREET R, Evaluation of ferromagnetic materials for low-frequency hysteresis heating of tumours, *Phys. Med. Biol.*, **1992**, 37, 293–299.
- 127 ROTH S, Polymer mit eingelagerten Magnetiteilchen, IFW-Dresden, personal communication.
- 128 ROSENSWEIG RE, Heating magnetic fluid with alternating magnetic field, *J. Magn. Magn. Mater.*, **2002**, 252, 370–374.
- 129 OLESON JR, A review of magnetic induction methods for hyperthermia treatment of cancer, *IEEE Trans. Biomed. Eng.*, **1984**, BME-31, 91–97.
- 130 GILCHRIST RK, MEDAL R, SHOREY WD, HANSELMAN RC, PARROTT JC, TAYLOR CB, Selective inductive heating of lymph nodes, *Ann. Surg.*, **1957**, 146, 596–606.
- 131 STAUFFER PR, CETAS TC, FLETCHER AM, DEYOUNG DW, DEWHIRST MW, OLESON JR, ROEMER RB, Observations on the use of ferromagnetic implants for inducing hyperthermia, *IEEE Trans. Biomed. Eng.*, **1984**, BME-31, 76–90.
- 132 STAUFFER PR, CETAS TC, JONES RC, Magnetic induction heating of ferromagnetic implants for inducing localized hyperthermia in deep-seated tumors, *IEEE Trans. Biomed. Eng.*, **1984**, BME-31, 235–251.
- 133 ATKINSON WJ, BREZOVICH IA, CHAKRABORTY DP, Usable frequencies in hyperthermia with thermal seeds, *IEEE Trans. Biomed. Eng.*, **1984**, 31, 70–75.
- 134 GORDON RT, HINES JR, GORDON D, Intracellular hyperthermia – A biophysical approach to cancer treatment via intracellular temperature and biophysical alterations, *Med. Hypotheses*, **1979**, 5, 83–102.
- 135 TARTAJ P, MORALES MP, GONZALEZ-CARRENO T, VEINTEMILLAS-VERDAGUER S, SERNA CJ, Advances in magnetic nanoparticles for biotechnology applications, *J. Magn. Magn. Mater.*, **2005**, 290–291, 28–34.
- 136 MUHL T, ELEFANT D, GRAFF A, KOZHUHAROVA R, LEONHARDT A, MONCH I, RITSCHEL M, SIMON P, GROUDEVA-ZOTOVA S, SCHNEIDER CM, Magnetic properties of aligned Fe-filled carbon nanotubes, *J. Appl. Phys.*, **2003**, 93, 7894–7896.
- 137 JORDAN A, SCHOLZ R, WUST P,



- FAHLING H, ROLAND F, Magnetic fluid hyperthermia (MFH): Cancer treatment with AC magnetic field induced excitation of biocompatible superparamagnetic nanoparticles, *J. Magn. Magn. Mater.*, **1999**, 201, 413–419.
- 138 JONES SK, GRAY BN, BURTON MA, CODDE JP, STREET R, *Phys. Med., Biol.*, **1992**, 37, 293–299.
- 139 PANKHURST QA, CONNOLLY J, JONES SK, DOBSON J, Applications of magnetic nanoparticles in biomedicine, *J. Phys. D, Appl. Phys.*, **2003**, R167–R181.
- 140 JORDAN A, WUST P, FÄHLING H, JOHN W, HINZ A, FELIX R, Inductive heating of ferrimagnetic particles and magnetic fluids: Physical evaluation of their potential for hyperthermia, *Int. J. Hyperthermia*, **1993**, 9, 51–68.
- 141 HILGER I, HERGT R, KAISER W, Use of magnetic nanoparticle heating in the treatment of breast cancer, *IEE Proc.-Nanobiotechnol.*, **2005**, 152, 33–39.
- 142 HILGER I, ANDRA W, HERGT R, HIERGEIST R, SCHUBERT H, KAISER W, Electromagnetic heating of breast tumors in interventional radiology: In vitro and in vivo studies in human cadavers and mice, *Radiology*, **2001**, 218, 570–575.
- 143 ANDRA W, D'AMBLY CG, HERGT R, HILGER I, KAISER WA, Temperature distribution as function of time around a small spherical heat source of local magnetic hyperthermia, *J. Magn. Magn. Mater.*, **1999**, 194, 197–203.
- 144 JORDAN A, SCHOLZ R, MAIER-HAUFF K, JOHANNSEN M, WUST P, NADOBNY J, SCHIRRA H, SCHMIDT H, DEGER S, LOENING S, Presentation of a new magnetic field therapy system for the treatment of human solid tumors with magnetic fluid hyperthermia, *J. Magn. Magn. Mater.*, **2001**, 225, 118–126.
- 145 MAEHARA T, KONISHI K, KAMIMORI T, AONO H, NAOHARA T, KIKKAWA H, WATANABE Y, KAWACHI K, Heating of ferrite powder by an AC magnetic field for local hyperthermia, *Jpn. J. Appl. Phys.*, **2002**, 41, 1620–1621.
- 146 BABINCOVA M, LESZCZYNSKA D, SOURIVONG P, CÍCMANEC P, BABINEC P, Superparamagnetic gel as a novel material for electromagnetically induced hyperthermia, *J. Magn. Magn. Mater.*, **2001**, 225, 109–112.
- 147 JOHANNSEN M, GNEVECKOW U, ECKELT L, FEUSSNER A, WALDÖFNER N, SCHOLZ R, DEGER S, WUST P, LOENING SA, JORDAN A, Clinical hyperthermia of prostate cancer using magnetic nanoparticles: Presentation of a new interstitial technique, *Int. J. Hyperthermia*, preview article, **2005**, 1–11.
- 148 HILGER I, ANDRA W, BAHRING R, DAUM A, HERGT R, KAISER WA, Evaluation of temperature increase with different amounts of magnetite in liver tissue samples, *Invest. Radiol.*, **1997**, 32, 705–712.
- 149 HILGER I, KIEBLING A, ROMANUS E, HIERGEIST R, HERGT R, ANDRA W, ROSKOS M, LINSS W, WEBER P, WEITSCHIES W, KAISER W, Magnetic nanoparticles for selective heating of magnetically labelled cells in culture: Preliminary investigation, *Nanotechnology*, **2004**, 15, 1027–1032.
- 150 JORDAN A, WUST P, SCHOLZ R, TESCHE B, FÄHLING H, MITROVICS T, VOGEL T, CERVOS-NAVARRO J, FELIX R, Cellular uptake of magnetic fluid particles and their effects on human adenocarcinoma cells exposed to AC magnetic fields in vitro, *Int. J. Hyperthermia*, **1996**, 12, 705–722.
- 151 JORDAN A, SCHOLZ R, WUST P, SCHIRRA H, THOMAS S, SCHMIDT H, FELIX R, Endocytosis of dextran and silan-coated magnetite nanoparticles and the effect of intracellular hyperthermia on human mammary carcinoma cells in vitro, *J. Magn. Magn. Mater.*, **1999**, 194, 185–196.
- 152 LI GC, MIVECHI NF, WEITZEL G, Heat shock proteins, thermotolerance, and their relevance to clinical hyperthermia, *Int. J. Hyperthermia*, **1995**, 11, 459–488.
- 153 MOROZ P, JONES SK, GRAY BN, Tumor response to arterial embolization hyperthermia and direct injection hyperthermia in a rabbit liver tumor model, *J. Surg. Oncol.*, **2002**, 80, 148–156.

- 154 MOROZ P, JONES SK, GRAY BN, Status of hyperthermia in the treatment of advanced liver cancer, *J. Surg. Oncol.*, **2001**, 77, 259–269.
- 155 MOROZ P, JONES SK, WINTER J, GRAY BN, Targeting liver tumors with hyperthermia: Ferromagnetic embolization in a rabbit liver tumor model, *J. Surg. Oncol.*, **2001**, 78, 22–29.
- 156 HILGER I, HERGT R, KAISER WA, Effects of magnetic thermoablation in muscle tissue using iron oxide particles: An in vitro study, *Investig. Radiol.*, **2000**, 35, 170–179.
- 157 BREZOVICH IA, MEREDITH RF, Practical aspects of ferromagnetic thermoseed hyperthermia, *Radiol. Clin. North Am.*, **1989**, 1, 589–602.
- 158 KUZNETSOV AA, SHLYAKHTIN OA, BRUSENTOV NA, KUZNETSOV NA, “Smart” mediators for self-controlled inductive heating, *Eur. Cells Mater.*, **2002**, 3, 75–77.
- 159 CETAS TC, GROSS EJ, CONTRACTOR Y, *IEEE Trans. Biomed. Eng.*, **1998**, 45, 68.
- 160 HÄFELI UO, Magnetically modulated therapeutic systems, *Int. J. Pharmaceut.*, **2004**, 277, 19–24.
- 161 HIERGEIST R, ANDRA W, BUSKE N, HERGT R, HILGER I, RICHTER U, KAISER W, Application of magnetic ferrofluids for hyperthermia, *J. Magn. Magn. Mater.*, **1999**, 201, 420–422.
- 162 HUBER DL, Synthesis, properties, and applications of iron nanoparticles, *Small*, **2005**, 1, 482–501.
- 163 KIM DK, ZHANG Y, VOIT W, RAO KV, MUHAMMED M, Synthesis and characterization of surfactant-coated superparamagnetic monodispersed iron oxide nanoparticles, *J. Magn. Magn. Mater.*, **2001**, 225, 30–36.
- 164 KIM DK, MIKHAYLOVA M, ZHANG Y, MUHAMMED M, Protective coating of superparamagnetic iron oxide nanoparticles, *Chem. Mater.*, **2003**, 15, 1617–1627.
- 165 JAIN KT, MORALES MA, SAHOO SK, LESLIE-PELECKY DL, Labhasetwar, Iron oxide nanoparticles for sustained delivery of anticancer agents, *Mol. Pharmaceut.*, **2005**, 2, 194–205.
- 166 BÖNNEMANN H, BRANDT RA, BRIJOUX W, HOFSTADT H-W, FRERICHS M, KEPTER V, MAUS-FRIEDRICHS W, MATOUSSEVITCH N, NAGABHUSHANA KS, VOIGTS F, CAPS V, Air stable Fe and Fe-Co magnetic fluids – synthesis and characterization, *Appl. Organomet. Chem.*, **2005**, 19, 790–796.
- 167 BÖNNEMANN H, A review – How nanoparticles emerged from organometallic chemistry, *Appl. Organomet. Chem.*, **2004**, 18, 566–572.
- 168 CANNON WR, DANFORTH SC, FLINT JH, HAGGERTY JS, MARRA RA, *J. Am. Ceram. Soc.*, **1982**, 65, 324.
- 169 KUZNETSOV AA, FILIPPOV VI, KUZNETSOV OA, GERLIVANOV VG, DOBRINSKY EK, MALASHIN SI, New ferro-carbon adsorbents for magnetically guided transport of anti-cancer drugs, *J. Magn. Magn. Mater.*, **1999**, 194, 22–30.
- 170 RACKA K, GICH M, SŁAWSKA-WANIEWSKA A, ROIG A, MOLINS E, Magnetic properties of Fe nanoparticle systems, *J. Magn. Magn. Mater.*, **2005**, 290–291, 127–130.
- 171 MOHADDES-ARDABILI L, ZHENG H, OGALE SB, HANNOYER B, TIAN W, WANG J, LOFLAND SE, SHINDE SR, ZHAO T, JIA Y, SALAMANCA-RIBA L, SCHLOM DG, WUTTIG M, RAMESH R, Self-assembled single-crystal ferromagnetic iron nanowires formed by decomposition, *Nat. Mater.*, **2004**, 3, 533–538.
- 172 HWANG J-h, DRAVID VP, TENG MH, HOST JJ, ELLIOTT BR, JOHNSON DL, MASON TO, Magnetic properties of graphitically encapsulated nickel nanocrystals, *J. Mater. Res.*, **1997**, 12, 1076–1082.
- 173 CHOU C-K, Use of heating rate and specific absorption rate in the hyperthermia clinic, *Int. J. Hyperthermia*, **1990**, 6, 367–370.
- 174 GNEVECKOW U, JORDAN A, SCHOLZ R, BRÜß V, WALDÖFNER N, RICKE J, FEUSSNER A, HILDEBRANDT B, RAU B, WUST P, Description and characterization of the novel hyperthermia- and thermoablation-system MFH 300F for clinical magnetic fluid hyperthermia, *Med. Phys.*, **2004**, 31, 1444–1451.
- 175 BRUSENTOV NA, GOGOSOV VV,

- BRUSENTOVA TN, SERGEEV AV, JURCHENKO NY, KUZNETSOV AA, KUZNETSOV OA, SHUMAKOV LI, Evaluation of ferromagnetic fluids and suspensions for the site-specific radiofrequency-induced hyperthermia of MX11 sarcoma cells in vitro, *J. Magn. Magn. Mater.*, **2001**, 225, 113–117.
- 176 BRUSENTOVA NA, NIKITIN LV, BRUSENTOVA TN, KUZNETSOV AA, BAYBURTSKIY FS, SHUMAKOV LI, JURCHENKO NY, Magnetic fluid hyperthermia of the mouse experimental tumor, *J. Magn. Magn. Mater.*, **2002**, 252, 378–380.
- 177 BRUSENTOVA NA, KOMISSAROVA LK, KSNETZOV AA, et al., Evaluation of ferrifluids containing photosensitizer, *Eur. Cells Mater.*, **2002**, 3, 70–73.
- 178 HERGT R, HIERGEIST R, HILGER I, KAISER W, Magnetic nanoparticles for thermoablation, in *Recent Research Developments in Materials Science*, ed. PANDALAI SG, Research Signpost, Trivandrum, India, **2002**, vol. 3, pp. 723–742.
- 179 RABIN Y, Is intracellular hyperthermia superior to extracellular hyperthermia in the thermal sense? *Int. J. Hyperthermia*, **2002**, 18, 194–202.
- 180 PANTAROTTO D, SHINGH R, MCCARTHY D, ERHARDT M, BRIAND J-P, PRATO M, KOSTARELOS K, BIANCO A, Functionalized carbon nanotubes for plasmid DNA gene delivery, *Angew. Chem.*, **2004**, 116, 5354–5358.
- 181 CHERUKURI P, BACHILLO SM, LITOVSKY SH, WEISMAN RB, Near-infrared fluorescence microscopy of single-walled carbon nanotubes in phagocytic cells, *J. Am. Chem. Soc.*, **2004**, 126, 15 638–15 639.
- 182 LU X, TIAN F, XU X, WANG N, ZHANG Q, A theoretical exploration of the 1,3-dipolar cycloadditions onto the sidewalls of (n,n) armchair single-wall carbon nanotubes, *J. Am. Chem. Soc.*, **2003**, 125, 10 459–10 464.
- 183 BIANCO A, KOSTARELOS K, PARTIDOS CD, PRATO M, Biomedical applications of functionalised carbon nanotubes, *Chem. Commun. (Camb)*, **2005**, 571–577.
- 184 BIANCO A, KOSTARELOS K, PRATO M, Applications of carbon nanotubes in drug delivery, *Curr. Opin. Chem. Biol.*, **2005**.
- 185 KAM NWS, DAI H, Carbon nanotubes as intracellular protein transporters, generality and biological functionality, *J. Am. Chem. Soc.*, **2005**, 127, 6021–6026.
- 186 KAM NWS, JESSOP TC, WENDER PA, DAI H, Nanotube molecular transporters: Internalization of carbon nanotube-protein conjugates into mammalian cells, *J. Am. Chem. Soc.*, **2004**, 126, 6850–6851.
- 187 MEYE A, et al., submitted for publication, **2005**.
- 188 MÖNCH I, MEYE A, LEONHARDT A, ELEFANT D, HAMPEL S, MÜLLER C, WIRTH MP, BÜCHNER B, et al. submitted for publication, **2005**.
- 189 SELBMANN D, KRELLMANN M, LEONHARDT A, EICKEMEYER J, *J. Phys. IV*, **2000**, Pr2-27.
- 190 BIANCO A, HOEBEKE J, GODEFROY S, CHALOIN O, PANTAROTTO D, BRIAND JP, MULLER S, PRATO M, PARTIDOS CD, Cationic carbon nanotubes bind to CpG oligodeoxynucleotides and enhance their immunostimulatory properties, *J. Am. Chem. Soc.*, **2005**, 127, 58–59.
- 191 KAM NW, LIU Z, DAI H, Functionalization of carbon nanotubes via cleavable disulfide bonds for efficient intracellular delivery of siRNA and potent gene silencing, *J. Am. Chem. Soc.*, **2005**, 127, 12 492–12 493.
- 192 PANTAROTTO D, BRIAND JP, PRATO M, BIANCO A, Translocation of bioactive peptides across cell membranes by carbon nanotubes, *Chem. Commun. (Camb)*, **2004**, 16–17.
- 193 GEORGAKILAS V, TAGMATARCHIS N, PANTAROTTO D, BIANCO A, BRIAND JP, PRATO M, Amino acid functionalisation of water soluble carbon nanotubes, *Chem. Commun. (Camb)*, **2002**, 3050–3051.
- 194 ZHENG M, JAGOTA A, STRANO MS, SANTOS AP, BARONE P, CHOU SG, DINER BA, DRESSSELHAUS MS, MCLEAN RS, ONOA GB, SAMSONIDZE GG, SEMKE ED, USREY M, WALLS DJ,

- Structure-based carbon nanotube sorting by sequence-dependent DNA assembly, *Science*, **2003**, 302, 1545–1548.
- 195 ZHENG M, JAGOTA A, SEMKE ED, DINER BA, McLEAN RS, LUSTIG SR, RICHARDSON RE, TASSI NG, DNA-assisted dispersion and separation of carbon nanotubes, *Nat. Mater.*, **2003**, 2, 338–342.
- 196 SINGH R, PANTAROTTO D, MCCARTHY D, CHALOIN O, HOEBEKE J, PARTIDOS CD, BRIAND JP, PRATO M, BIANCO A, KOSTARELOS K, Binding and condensation of plasmid DNA onto functionalized carbon nanotubes: Toward the construction of nanotube-based gene delivery vectors, *J. Am. Chem. Soc.*, **2005**, 127, 4388–4396.
- 197 JOHANNSEN M, THIESEN B, GNEVECKOW U, TAYMOORIAN K, WALDOFNER N, SCHOLZ R, DEGER S, JUNG K, LOENING SA, JORDAN A, Thermotherapy using magnetic nanoparticles combined with external radiation in an orthotopic rat model of prostate cancer, *Prostate*, **2005**.
- 198 JOHANNSEN M, THIESEN B, JORDAN A, TAYMOORIAN K, GNEVECKOW U, WALDOFNER N, SCHOLZ R, KOCH M, LEIN M, JUNG K, LOENING SA, Magnetic fluid hyperthermia (MFH) reduces prostate cancer growth in the orthotopic Dunning R3327 rat model, *Prostate*, **2005**, 64, 283–292.
- 199 LIU B, WEI L, DING Q, YAO J, Synthesis and magnetic study for Fe-doped carbon nanotubes (CNTs), *J. Crystal Growth*, **2005**, 277, 293–297.
- 200 FUJIWARA Y, TAKEGAWA H, SATO H, MAEDA K, SAITO Y, KOBAYASHI T, SHIOMI S, Magnetic properties of carbon nanotubes grown on Fe catalyst layer by microwave plasma enhanced chemical vapor deposition, *J. Appl. Phys.*, **2004**, 95, 11, 7118–7120.
- 201 BAO J, TIE C, XU Z, SUO Z, ZHOU Q, HONG J, A facile method for creating an array of metal-filled carbon nanotubes, *Adv. Mater.*, **2002**, 14, 1483–1486.
- 202 BAO J, ZHOU Q, HONG J, XU Z, Synthesis and magnetic behavior of an array of nickel-filled carbon nanotubes, *Appl. Phys. Lett.*, **2002**, 81, 4592–4594.
- 203 TYAGI PK, SINGH MK, MISRA A, PALNITKAR U, MISRA DS, TITUS E, ALI N, CABRAL G, GRACIO J, ROY M, KULSHRESHTHA SK, Preparation of Ni-filled carbon nanotubes for key potential applications in nanotechnology, *Thin Solid Films*, **2004**, 469–470, 127–130.
- 204 BENKOWSKY G, *Induktionserwärmung*, Verlag Technik, Berlin, **1977**.
- 205 CHAN DCF, KIRPOTIN DB, BRUNN JR. PA, Synthesis and evaluation of colloidal magnetic iron oxides for the site-specific radiofrequency-induced hyperthermia of cancer, *J. Magn. Magn. Mater.*, **1993**, 122, 374–378.
- 206 HERGT R, HIERGEIST R, ZEISBERGER M, GLÖCKL G, WEITSCHIES W, RAMIREZ LP, HILGER I, KAISER WA, Enhancement of AC-losses of magnetic nanoparticles for heating applications, *J. Magn. Magn. Mater.*, **2004**, 280, 358–368.
- 207 GEORGAKILAS V, KORDATOS K, PRATO M, GULDI DM, HOLZINGER M, HIRSCH A, Organic functionalization of carbon nanotubes, *J. Am. Chem. Soc.*, **2002**, 124, 760–761.
- 208 KAM NW, LIU Z, DAI H, Functionalization of carbon nanotubes via cleavable disulfide bonds for efficient intracellular delivery of siRNA and potent gene silencing, *J. Am. Chem. Soc.*, **2005**, 127, 12 492–12 493.
- 209 PANTAROTTO D, PARTIDOS CD, HOEBEKE J, BROWN F, KRAMER E, BRIAND JP, MULLER S, PRATO M, BIANCO A, Immunization with peptide-functionalized carbon nanotubes enhances virus-specific neutralizing antibody responses, *Chem. Biol.*, **2003**, 10, 961–966.
- 210 PANTAROTTO D, PARTIDOS CD, GRAFF R, HOEBEKE J, BRIAND JP, PRATO M, BIANCO A, Synthesis, structural characterization, and immunological properties of carbon nanotubes functionalized with peptides, *J. Am. Chem. Soc.*, **2003**, 125, 6160–6164.
- 211 KAM NW, DAI H, Carbon nanotubes as intracellular protein transporters: Generality and biological functionality,

- J. Am. Chem. Soc.*, **2005**, *127*, 6021–6026.
- 212 SINGH R, PATAROTTO D, MCCARTHY D, CHALOIN O, HOEBEKE J, PARTIDOS CD, BRIAND J-P, PRATO M, BIANCO A, KOSTARELOS K, Binding and condensation of plasmid DNA onto functionalized carbon nanotubes: Toward the construction of nanotube-based gene delivery vectors, *J. Am. Chem. Soc.*, **2005**, *127*, 4388–4396.
- 213 CAI Y, JIANG G, LIU J, ZHOU Q, Multiwalled carbon nanotubes as a solid-phase extraction adsorbent for the determination of bisphenol A, 4-n-nonylphenol, and 4-tert-octylphenol, *Anal. Chem.*, **2003**, *75*, 2517–2521.
- 214 CAI H, CAO X, JIANG Y, HE P, FANG Y, Carbon nanotube-enhanced electrochemical DNA biosensor for DNA hybridization detection, *Anal. Bioanal. Chem.*, **2003**, *375*, 287–293.
- 215 GOODING JJ, WIBOWO R, LIU J, YANG W, LOSIC D, ORBONS S, MEARNES FJ, SHAPTER JG, HIBBERT DB, Protein electrochemistry using aligned carbon nanotube arrays, *J. Am. Chem. Soc.*, **2003**, *125*, 9006–9007.
- 216 WANG SG, WANG R, SELLIN PJ, ZHANG Q, DNA biosensors based on self-assembled carbon nanotubes, *Biochem. Biophys. Res. Commun.*, **2004**, *325*, 1433–1437.
- 217 WANG J, KAWDE AN, JAN MR, Carbon-nanotube-modified electrodes for amplified enzyme-based electrical detection of DNA hybridization, *Biosens. Bioelectron.*, **2004**, *20*, 995–1000.
- 218 WANG Y, LI Q, HU S, A multiwall carbon nanotubes film-modified carbon fiber ultramicroelectrode for the determination of nitric oxide radical in liver mitochondria, *Bioelectrochemistry*, **2005**, *65*, 135–142.
- 219 CHEN RS, HUANG WH, TONG H, WANG ZL, CHENG JK, Carbon fiber nanoelectrodes modified by single-walled carbon nanotubes, *Anal. Chem.*, **2003**, *75*, 6341–6345.
- 220 CHEN RJ, BANGSARUNTIP S, DROUVALAKIS KA, KAM NW, SHIM M, LI Y, KIM W, UTZ PJ, DAI H, Noncovalent functionalization of carbon nanotubes for highly specific electronic biosensors, *Proc. Natl. Acad. Sci. U.S.A.*, **2003**, *100*, 4984–4989.
- 221 SALVADOR-MORALES C, FLAHAUT E, SIM E, SLOAN J, GREEN MLH, SIM RB, Complement activation and protein adsorption by carbon nanotubes, *Mol. Immunol.*, **2006**, *43*, 193–201.
- 222 SCHNITZLER GR, CHEUNG CL, HAFNER JH, SAURIN AJ, KINGSTON RE, LIEBER CM, Direct imaging of human SWI/SNF-remodeled mono- and polynucleosomes by atomic force microscopy employing carbon nanotube tips, *Mol. Cell. Biol.*, **2001**, *21*, 8504–8511.
- 223 HAFNER JH, CHEUNG CL, WOOLLEY AT, LIEBER CM, Structural and functional imaging with carbon nanotube AFM probes, *Prog. Biophys. Mol. Biol.*, **2001**, *77*, 73–110.
- 224 MOGHIMI SM, SZE BENI J, Stealth liposomes and long circulating nanoparticles: Critical issues in pharmacokinetics, opsonization and protein-binding properties, *Prog. Lipid Res.*, **2003**, *42*, 463–478.
- 225 PARK J, PASUPATHY AN, GOLDSMITH JI, CHANG C, YAISH Y, PETTA JR, RINKOSKI M, SETHNA JP, ABRUNA HD, MCEUEN PL, RALPH DC, Coulomb blockade and the Kondo effect in single-atom transistors, *Nature*, **2002**, *417*, 722–725.
- 226 WEISMAN RB, Carbon nanotubes: Four degrees of separation, *Nat. Mater.*, **2003**, *2*, 569–570.
- 227 SERVICE RF, Molecular electronics. Nanodevices make fresh strides toward reality, *Science*, **2003**, *302*, 1310.
- 228 SERVICE RF, Nanotechnology. Sorting technique may boost nanotube research, *Science*, **2003**, *300*, 2018.
- 229 JAVEY A, GUO J, WANG Q, LUNDSTROM M, DAI H, Ballistic carbon nanotube field-effect transistors, *Nature*, **2003**, *424*, 654–657.
- 230 BARTSCH K, LEONHARDT A, An approach to the structural diversity of aligned grown multi-walled carbon nanotubes on catalyst layers, *Carbon*, **2004**, *42*, 1731–1736.

- 231 DUPUIS AC, *Progr. Mater. Sci.*, **2005**, 50, 929–961.
- 232 MÖNCH I, LEONHARDT A, BÜCHNER B, Medical application of filled nanotubes, spin-off: *SYSTEMANIX. Annual Report 2004*, Leibniz-Institute for Solid State and Materials Research Dresden; <http://www.ifw-dresden.de/forsch/jb2004/Techtrans.pdf>, **2004**, 46.
- 233 VOSTROWSKY O, HIRSCH A, Forscher gucken durch die Nano-Röhre – nanotubes aus Kohlenstoff abayfor-Zukunft im Brennpunkt, **2003**; [http://www.abayfor.de/abayfor/\\_media/pdf/ZIB2/zib2\\_vostrowsky.pdf](http://www.abayfor.de/abayfor/_media/pdf/ZIB2/zib2_vostrowsky.pdf), **2003**, 85–88.
- 234 ZHANG X, CAO A, LI Y, XU C, LIANG J, WU D, WEI B, Self-organized arrays of carbon nanotube ropes, *Chem. Phys. Lett.*, **2002**, 351, 183–188.

## 10 Liposomes, Dendrimers and other Polymeric Nanoparticles for Targeted Delivery of Anticancer Agents – A Comparative Study

Yong Zhang and Dev K. Chatterjee

### 10.1 Introduction

Cancer management through chemotherapy, surgery and radiotherapy often fails because of high toxicity and poor target selectivity. Nanotechnology, through the synthesis and modification of nanoparticles, has the potential to overcome these barriers by providing drug molecule stability in circulation, reduced toxicity and better targeting of tumors.

Several excellent reviews deal with the anti-tumor activities of nanoparticles. A look at recent ones in this fast changing field shows that most have tackled the wider issue of nanotechnology as a tool against cancer. In an excellent review, Ferrari has dealt with the whole field of cancer nanotechnology, including *in vitro* diagnostics as well as *in vivo* targeting [1]. In a very recent review Jain (of Jain PharmaBiotech in Switzerland) has focused on the field of “nanobiotechnologies” and its effect on drug delivery in cancer [2]. The same author has also reviewed nanotechnology in the setting of the diagnostic clinical laboratory [3]. Another recent review, by McNeil, deals more widely with the ramifications of nanotechnology for the biologist [4]. A similar review by Fortina et al. details the uses and promises of nanobiotechnology in the whole field of molecular recognition, mainly for enhanced *in vitro* molecular diagnostics [5]. As these and other examples show, most reviews deal either with the wider aspects of nanotechnology or with different subsets.

This chapter focuses specifically on the targeting of drug-loaded nanoparticles to tumor sites. This is perhaps the most important aspect of anticancer therapy with nanoparticles. However, even with a wish to limit ourselves to detailing the means of targeting nanoparticles and discussing and comparing current reports about the three major types of nanoparticles, we find it imperative to include short introductions, wherever applicable, so that even recent entrants to the field can peruse this chapter.

Nanoparticles that are currently under consideration as drug delivery vehicles can be considered to be of three major types: liposomes, dendrimers and other polymeric nanoparticles. When modified with certain chemicals, mainly poly(ethylene

glycol), they enjoy long circulation times and selectively accumulate at tumor sites due to an enhanced permeation and retention (EPR) effect. When a targeting ligand or antibody is attached this selectivity is enhanced. Suitable targets include antigens of the neo-angiogenic process associated with tumor growth, altered antigens specific for tumors (tumor specific antigens) and growth factor receptors such as transferrin and folic acid receptors. Drugs delivered to the site include conventional anti-neoplastic drugs such as doxorubicin and paclitaxel, and also other biological response modifiers such as cytokines and antibodies. Corporate interest in the future of this technology has resulted in a few start ups that have already marketed a few anti-tumor nanoparticles formulations; hope for a better future is appreciably high.

Section 10.2 deals with the effectiveness of chemotherapy and other conventional therapies and discusses their limitations in halting tumor growth. We introduce the concept of targeted drug delivery in Section 10.3 and elaborate on targeting ligands in Section 10.4. Section 10.5 deals with the achievements of each of the three major types of nanoparticles. Section 10.6 wraps up the review with a look at the overall picture that is emerging and ends on an optimistic note.

## 10.2

### Cancer Chemotherapy: so Far, but not so Good

The fundamental differences between cancer cells and normal human cells are still not clear. None of the empirically developed anti-neoplastic drugs in conventional use appear to involve a mechanism or target that is completely unique to the cancer cell. They appear to achieve some degree of selectivity in their action by acting on certain characteristics that are found altered in cancerous tissues as compared to normal ones. These include a rapid rate of cell division, differences in the rate of uptake of or the sensitivity to the drug in different types of cells, and occasional presence in the cancer cells of hormonal responses characteristic of the original cells from which they developed.

All cells undergo divisions in a cyclical manner. This cell cycle has been divided into several phases. Very broadly, cells can undergo DNA synthesis (S phase) and mitotic and cytokinetic activity (M phase) while dividing; or can be in a dormant non-dividing state ( $G_0$  phase). Anti-neoplastic drugs can be broadly classified according to whether they are cycle sensitive or insensitive. Cycle sensitive agents act on dividing cells, during the M or S phase, and have first-order kinetics and exponential dose–response curves. They are highly active on rapidly dividing tumor cells, but fail to kill cells that are dormant or dividing slowly.

The selection of drugs for a particular cancer depends on several factors: the type of cancer, the stage and grade of the tumor, the condition of the patient, and the ability to afford the therapy. The selected regimen may aim for palliation, i.e., reduction in the severity or extent of the disease, or remission, i.e., complete absence of cancerous growth clinically and with laboratory tests. Current cancer therapy suffers from the serious disadvantage of high toxicity to the patient's normal body



tissues. The effectiveness of therapeutic regimens has to be balanced against their side effects. Poor selectivity for cancer cells by the anticancer drugs is the underlying cause.

The major reason for poor selectivity is the relative paucity of marker molecules that will unequivocally distinguish neoplastic from non-neoplastic cells. Most cancer chemotherapeutic drugs interfere with the mechanism of cell division. Some cancers are intrinsically highly drug-sensitive, such as childhood acute lymphoblastic leukemia (ALL), Hodgkin's disease, some non-Hodgkin's lymphomas, and testicular cancer. For these, relatively lower doses of chemotherapy may be effective. However, for most other cancers, promiscuous interaction of significant amounts of potent drug molecules with normal cells cannot fail to have serious consequences. The immune system, hematopoietic system and the internal lining of the gastrointestinal tract are the major sufferers as they have the highest cell turnovers. Side effects of therapy can be acute or delayed. Acute complications include nausea, vomiting, diarrhea, anorexia, allergic reactions and anaphylaxis. Delayed toxicities include myelosuppression, which can cause neutropenia and repeated infections, anemia from multiple causes, and hemorrhagic manifestations from thrombocytopenia. As a consequence of all these, and perhaps other unknown causes, the patient may develop a severe form of cachexia that is almost exclusively found in advanced cancers.

To avoid or reduce toxicities, several approaches have been adopted. Supportive therapy in cancer aims to reduce the specific toxicities of the drugs. Potent antiemetics for gastrointestinal toxicities, diuretics for nephrotoxic agents such as cisplatin, anti-histaminics for allergic reactions, and the more recently introduced recombinant therapies such as erythropoietin and GM-CSF to treat myelosuppression are a few examples. Another is the use of several drugs at lower doses for a single cancer, rather than a single drug in high doses. Multidrug regimens, or protocols, have become the norm in cancer treatment. This is advantageous because the anticancer effects of the drugs will be additive when the drugs have different mechanisms of action, while the side effects will be distributive if their toxic effects are on different cells. Combination of a cycle-specific and non-specific drug may prevent tumor resistance by killing actively dividing as well as dormant cells. Combination chemotherapy also suppresses drug resistance, which is another major drawback of conventional chemotherapy.

Drug resistance, or the lack of responsiveness to the chemotherapeutic agent, can be due to several causes. The drug may not be reaching the tumor site at effective concentrations, either because of poor blood flow, or even after reaching the site may not achieve high enough concentration in the cell due to poor absorption, metabolic degradation, or rapid excretion from the cell (pharmacokinetic resistance). Failure to achieve total cell kills result in cytokinetic resistance: a population of survivors serve as source for repeated proliferation of the tumor. Tumor cells can evolve under these conditions to develop biochemical resistance by altering uptake and target molecules, developing or upgrading drug metabolism and excretion pathways, increasing the intracellular concentration of the drug-affected molecule, or incorporating protective genetic changes.

When multidrug regimens are not effective on their own, they are supplemented with radiotherapy and surgery. Unfortunately, radiotherapy also has the same depressive effect on the immune system and dividing cells, and results in nausea, vomiting, diarrhea and anemia. Surgery in early stages in some cancers can be curative, with only limited associated morbidity and very low fatality. However, most deep-seated cancers in the body are detected after they have metastasized, while some cancers, notably those of intracranial origin, are not easily approachable surgically, and carry high mortality and morbidity risks. Various ingenious combinations of the above, such as adjuvant (and neo-adjuvant) chemotherapy and radiotherapy with surgery to reduce tumor size or treat disseminated tumor cell nests, have been used to maximize the benefit to the patient.

In recent years, in recognition of the limited success of “classical” chemotherapy to treat cancers, several new methods have been investigated. Most important among them are gene therapy for correcting the altered genetic profile in cancer cells; and the biologic response modifiers that aim to enhance the innate anti-tumor immunity of the human body. Nonspecific immune modulators like BCG (for bladder cancer) and cimetidine (for melanoma) have shown limited efficacy. Better results have been obtained with the introduction of lymphokines and cytokines (IL-1, IL-2, TNF and more recently CCL21). These are natural human molecules produced in minute quantities for the purpose of signaling among immune cells. However, nonspecific use of these cytokines, especially IL-2 and TNF, has shown unacceptable levels of toxicity. This is primarily because of the short half-lives of these small molecules. To achieve acceptable levels inside the tumor micro-environment, very high doses need to be introduced: a common theme in cancer therapy regimens. A way to increase the stability of these molecules in circulation, along with the means to target them to selective neoplastic tissue, has become the current need.

### 10.3

#### **Nanoparticles and Drug Delivery in Cancer: a new Road**

##### 10.3.1

##### **Importance of Nanoparticles in Cancer Therapy**

Nanotechnology, especially nanoparticulate drug delivery systems, may provide the solution to the problems facing current cancer therapy. Nanoparticles can be defined as spherical (or spherical-like) particles with at least one dimension less than 100 nm [6]. The history and technology involved in nanoparticle synthesis can be found elsewhere (e.g. [6]). Nanoparticles, along with liposomes and block copolymer micelles, form the group of submicron sized colloidal systems used as targeted drug delivery vehicles (Fig. 10.1). Their small size allows intravenous administration without the risk of embolization, and passage through capillary vessels [7] and mucosae [8], while affording special properties of large surface

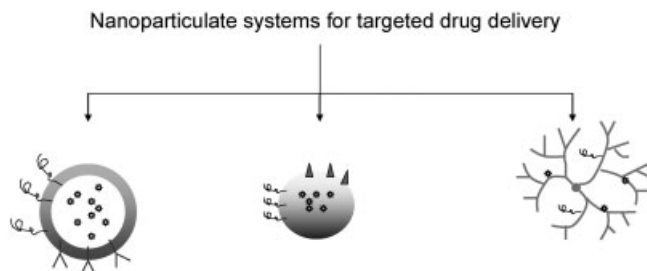


**Fig. 10.1.** Types of nanoparticulate drug delivery systems and their common targeting methods. Left to right: Liposomes with enclosed drug molecules; other polymeric nanoparticles, and dendrimers.

area, significant surface properties, greater solubility (especially for oil-based drugs) and better tissue adhesion [9].

Nanoparticles can have several roles in cancer therapy. They can be useful in targeting the tumor and achieving local therapeutic concentration of the toxic drug while keeping circulating levels of free drug fairly low, thus reducing systemic toxicity. They can stabilize lipophilic drugs in circulation, and help them enter previously inaccessible regions of the body like the central nervous system by crossing the blood–brain barrier, and treat previously untreatable tumors and reach “tumor sanctuaries”. They can increase the circulatory period of drugs by controlled release, thus overcoming the toxicity associated with initial high concentrations in periodic doses. They can also, conceivably, overcome multidrug resistance by a combination of these effects [6]. Apart from their therapeutic benefits, nanoparticles – as fluorescent nanoparticles and quantum dots – can also help in the early detection of tumors.

Therapeutic effects of nanoparticles can be achieved by “physical”, “chemical” or “biological” means. Physical means include the recently developed methods of hyperthermia and magnetic therapy. Chemical means include the delivery of more conventional chemotherapeutic drugs to the tumor sites. Biological response modifiers like immunotherapeutic agents are also gaining favor.

It is debatable whether the term “nanoparticles” applies only to the more recently developed polymeric nanoparticles or if, applying the definition in a broader sense, it should encompass block copolymer micelles and liposomes. Taking the emerging field of targeted drug delivery to cancer as the leit motif of this chapter, and acknowledging the significant roles played by both these types of “nanoparticles” in the development of this important branch of cancer therapeutics, we have included short subsections on both. The reader will thus get a better overview of the current state of knowledge and can peruse the reference section to further his/her interest. However, henceforth, we use the term “nanoparticles” in the narrower sense of polymeric spherical coiled particles, whether modified or unmodified.

## 10.3.2

**An Overview of Targeting Methods**

In this chapter we concentrate on the methods and materials by which nanoparticles are targeted to neoplastic tissue. Targeting can be loosely defined in this context as any means that increases the specificity of localization of nanoparticles in tumor cell masses. Targeting does not intrinsically imply improved sensitivity but, as we shall see, the different methods employed to increase the specificity allow administration of higher doses of the drugs, thus also favorably increasing sensitivity. Also, as mentioned earlier, the ability of nanoparticles to cross the blood–brain barrier and other impediments to conventional therapy increases its volume of distribution. This also results in increased sensitivity.

Targeting can be divided into two major types – passive and active. Passive targeting involves modifications of nanoparticles that increase the circulation time without addition of any component/involvement of any method that is specific to the tumor; increased circulation time helps in accumulation of the particles in the tumor by an EPR effect described below. Active targeting of tumors can be divided into “physical” and “chemical/biological” targeting. Physical targeting involves directing magnetic nanoparticles to tumor sites under the influence of an external magnetic field. Chemical/biological targeting involves the modification of nanoparticles’ surfaces with tumor-specific ligands.

Notably, any of these methods can be used in conjunction with others. For example, common modifications for passive targeting, such as PEGylation, are frequently used with more “active” modifications like antibodies. The methods are almost independent of each other, and can be judiciously combined to increase the effectiveness of the drugs.

This chapter does not deal extensively with the magnetic therapy of cancer and induced hyperthermic killing of tumor cells (see Chapters 5, 8 and 9). However, in keeping with the idea of overviewing the whole field of targeting, we have incorporated a short discussion of physical targeting by magnetically directing particles to tumor tissues.

## 10.4

**Means to the End: Methods for Targeting**

## 10.4.1

**Passive Targeting**

Here we must make a clearer distinction between what can be described as “active” and “passive” targeting. In general terms, a targeted drug can be defined as one modified in a fashion that allows its preferential uptake in the desired cells/tissues, in this case cancer. Evidence has been provided that many nanoparticles, especially long circulating ones, will show a preferential distribution to cancer sites over healthy tissues, even without any specific targeting molecule. This was demon-

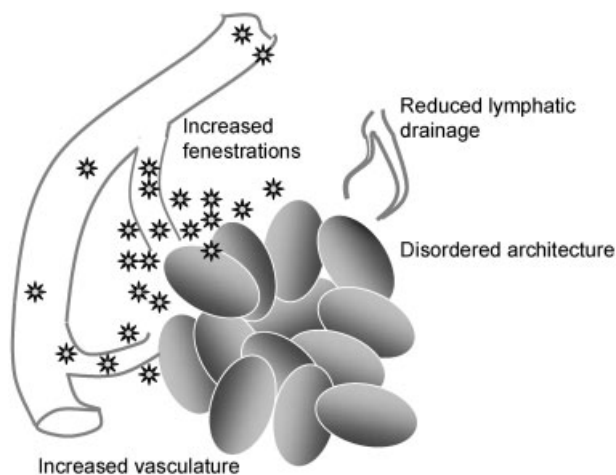


**Fig. 10.2.** The enhanced permeation and retention (EPR) effect accumulates nanoparticles to tumor sites without active targeting.

strated for the first time by Matsumura and Maeda [10]. This is likely due to the increased vasculature of these regions, larger fenestrations in the capillary walls for rapid delivery of nutrients, general disordered architecture that is symbolic of the neoplastic process, and the reduced lymphatic drainage in these regions. All these factors lead to the enhanced permeation and retention effect (EPR) [11, 12] (Fig. 10.2). This fortuitous distribution has been taken advantage of by numerous researchers in designing targeted drug delivery systems. As an example, in a recent study tamoxifen was encapsulated in poly(ethylene oxide)-modified poly( $\epsilon$ -caprolactone) (PEO-PCL) nanoparticles and administered to a murine model of breast cancer [13]. The poly(ethylene oxide) (PEO) coating made it a “stealth nanoparticle”, i.e., able to avoid detection by the body’s MPS system for a considerable time. The PEO surface modified nanoparticles showed significantly increased levels of accumulation within tumor with time than did the native drug or surface unmodified nanoparticles. An earlier effort by one of the authors to incorporate tamoxifen in nanoparticles for preferential uptake by estrogen receptor (ER) positive breast cancer cells had been shown to be successful *in vitro* [14]. However, to translate that success *in vivo*, a long-circulating nanoparticle was necessary. Another current example is the incorporation of cisplatin in liposomal formulations [15] with poly(ethylene glycol) (PEG) coating for gastric tumors: in preclinical and clinical trials, this formulation has been demonstrated to have longer half-life in circulation without the attendant side effects.

This targeted distribution of nanoparticles, together with the controlled release of anticancer drugs, can bring about a type of “passive” but effective targeted delivery. The other type of targeting is by specific ligand–receptor interaction. Possibly,

better specificity and sensitivity can only be achieved by this more “active” means. However, the introduction of a biological entity on the surface of the nanoparticle can create several problems: the size and complexity will increase, with attendant complexities of synthesis and characterization; the biomolecule may react adversely with the immune system or any of the other myriad proteins in the blood and tissues. This may give rise to unpredictable adverse reactions.

However, potential advantages include the ability to deliver larger amounts of drug per target biorecognition event; increase selectivity by including more than one type of targeting molecule, better avoidance of barriers by using different avoidance methods and the ability to administer “localized integrated combination therapy” by including multiple drugs in the same nanoparticle [1].

A method for enhancing this passive delivery to the cancer using nanoparticles is by the use of pH- and heat-sensitive nanoparticles. The fact that the pH in the region of cancerous growth is lower than in the rest of body, while the temperature is raised locally because of enhanced metabolism and ongoing inflammation, has been used to design pH-responsive nanoparticles: a lower pH causes enhanced drug release. Wei et al. have given a recent example of this [16]. The temperature- and pH-sensitive amphiphilic polymer poly(*N*-isopropylacrylamide-*co*-acrylic acid-*co*-cholesteryl acrylate) [P(NIPAAm-*co*-AA-*co*-CHA)] was synthesized and used to encapsulate paclitaxel in core-shell nanoparticles fabricated by a membrane dialysis method. The spherical nanoparticles are below 200 nm and have a pH-dependent lower critical solution temperature (LCST). *In vitro* release of paclitaxel from the nanoparticles was responsive to external pH changes, and was faster in a lower pH environment.

#### 10.4.2

#### Magnetic Targeting of Nanoparticles

Magnetic drug targeting has been defined as “the specific delivery of chemotherapeutic agents to their desired targets, e.g., tumors, by using magnetic nanoparticles (ferrofluids) bound to these agents and an external magnetic field which is focused on the tumor” [17]. This type of tumor targeting is aimed at concentrating the toxic drug at the cancer, hence enhancing its efficacy and reducing systemic side effects from high doses.

Gilchrist et al. described the first magnetic nanoparticles in 1957 [18]. These are generally 10–200 nm in diameter, magnetic or superparamagnetic and usually composed of iron oxide, magnetite, nickel, cobalt or neodymium; of these, magnetite ( $\text{Fe}_3\text{O}_4$ ) and maghemite ( $\gamma\text{-Fe}_2\text{O}_3$ ) are more biocompatible and preferred. Iron oxide is degradable in the body and has been shown to be safe for *in vivo* applications [6]. However, to be effective, magnetic nanoparticles should demonstrate high magnetization for external magnetic field control and should exceed linear blood flow rates of  $10 \text{ cm s}^{-1}$  in arteries and  $0.05 \text{ cm s}^{-1}$  in capillaries. For this purpose, particles composed of, for example, 20% magnetite require a field of 0.8 Tesla. Tissue depth is a limiting factor in active targeting, with deeply localized tumors being hard to access.

Lubbe et al. have utilized a complex of 4-epirubicin bound to ferrofluids in the treatment of squamous carcinoma of the breast or head and neck [19]. They used a field of 0.5–0.8 T at the tumor site while infusing the particles. Results showed accumulation in tumors in 6 of 14 patients with reduced toxicity, a transient rise of serum iron, but no demonstrable damage to kidney or hepatic function. Alexiou et al. have used mitoxantrone complexed to 100 nm ferromagnetic particles against VX2 squamous cell carcinoma among rabbits to demonstrate the superiority of intra-arterial infusion to other routes of delivery, especially the intravenous route where the particles are removed from circulation by the reticulo-endothelial system [20]. They have also demonstrated that circulating mitoxantrone becomes concentrated at the tumor tissue when complexed to ferrofluids; a higher concentration of the complexed drug (compared to the free drug) is achieved at the tumor site using only a half to one-fifth dose [17]. The drug mainly resides in the intraluminal space, the tumor interstitium and peritumoral area (region surrounding the tumor  $\leq 1$  cm). Other researchers have investigated ferrous nanoparticles in glioblastoma (a tumor of the brain), and demonstrated that these particles effectively cross the blood–brain barrier [21].

The clinical applications of magnetic drug targeting have been reviewed in more detail [22].

#### 10.4.3

#### **Ligands for Active Targeting**

Cancer cells arise from normal cells through a complex series of genetic events. Unlike infectious agents like bacteria, they largely share the same proteins as normal cells. However, some proteins are found in much larger numbers on cancer cells than in normal cells [23]. These overexpressed antigens are called tumor-associated antigens (TAA). Some proteins derived from normally silent genes or mutated forms of normal proteins are found exclusively on cancer cells. These are known as tumor-specific antigens (TSA). The obvious targets for targeted cancer therapy are TSAs. However, TSAs are often difficult to characterize for a particular tumor. When found, they are usually not extensive, i.e., they are not found in all patients affected by the tumor, nor are they found in all the cells in a particular tumor in the same patient. The aberrantly expressed tumor specific antigens are produced by aberrant glycosylation in glycolipids, glycoproteins, proteoglycans, and mucin [24]. For example, the glycosylation pattern of MUC1 membrane mucin of breast cancer epithelial cells differs from normal breast epithelial cells, possibly as a result of changes in expression of glycosyltransferases [25]. TAG-72 is a mucin-like tumor-associated glycoprotein [26] that is found in some epithelial tumors. Melanoma cells aberrantly express GM3 ganglioside on their surface [27]. Gastrointestinal cancer cells abnormally express LeX antigens [28].

Tumor-associated antigens are often growth factor receptors on the tumor that are overexpressed to meet the rapidly dividing neoplastic cells' demands. A classic example is folic acid and congeners. These are low molecular weight pterin-based

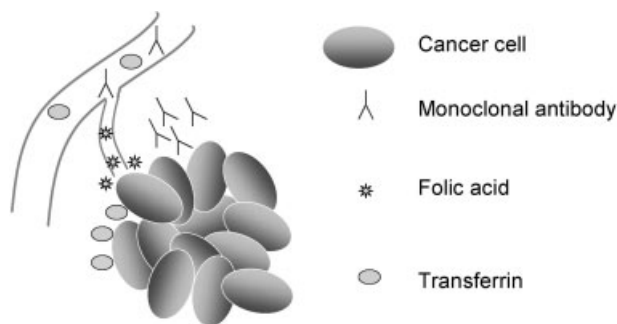


**Fig. 10.3.** Cancer cell antigens are targeted with monoclonal antibodies; ligands such as folic acid and transferrin also show specificity.

vitamins essential for carbon metabolism and *de novo* nucleotide synthesis. The presence of elevated levels of folate receptors has been demonstrated from epithelial tumors of various organs such as the colon, lungs, prostate, ovaries, mammary glands, and brain [29–40]. These present attractive targets for drug delivery. Another promising tumor receptor target is Her2<sub>neu</sub>, also known as c-erbB-2. This is a transmembrane protein with an epidermal growth factor receptor that possesses intrinsic tyrosine kinase activity [41–43]. The normal human Her-2<sub>neu</sub> proto-oncogene is frequently found to be overexpressed in breast and ovarian cancers among others. Its level may correlate with the metastatic potential of the cancer cells [44, 45].

Another such membrane-associated tumor antigen is the transferrin receptor. This is overexpressed in different types of cancers [46]. The levels may also correlate with the malignant potential of these cells [47] (Fig. 10.3).

The presence of various other tumor antigens has been demonstrated: membrane-associated Carcinoembryonic antigen; CD10 or CALLA in leukemias, melanomas and myelomas [48, 49]; CD20 in B cell malignancies [50]; etc. Many others are being recognized routinely. They all represent potential goals for targeted drug delivery.

#### 10.4.3.1 Monoclonal Antibodies against Tumor-specific Antigens

Specific targeting became a possibility with the discovery of monoclonal antibodies in 1975 [51]. As the name suggests, these are antibodies derived from a single clone of cells. They can be mass produced in the laboratory from a single clone and recognize only one antigen. Monoclonal antibodies are usually made by fusing a short-lived, antibody-producing B cell to a fast-growing cell, such as a cancer cell. The resulting hybrid cell, or hybridoma, multiplies rapidly, creating a clone that produces large quantities of the antibody. It was hoped that monoclonal antibodies would be able to target specific antigens on the surface of cancer cells, and initially



raised high hopes for targeted cancer therapy. Animal-origin monoclonal antibodies such as murine antibodies were strongly immunogenic; to avoid this, chimeric antibodies [52] and humanized antibodies [53, 54] were produced. More recently, completely human monoclonal antibodies and single-chain human antibody fragments [55] have been introduced for immunotherapy and targeted drug delivery.

Antigen targets for monoclonal antibody therapy (or for any other targeted anti-cancer therapies) must have the property of specificity, i.e., present only on the cancer cell surface and be absent from the surfaces of all normal cells; they should be extensive, i.e., present on all the cells in a given tumor, preferably on all such tumors in every patient; there should not be any mutation or structural variation of the antigen; and they should be preferably involved with a critical function of the cell, so that adaptive response of the cancer to therapy by losing the antigen can be prevented [56]. However, naturally, such a perfect antigen is rarely, if ever, found. Several good candidates have been discovered, and monoclonal antibodies against these have been marketed. Examples include anti-CD20 antibody for relapsed/refractory CD20 positive B-cell non-Hodgkin's lymphoma and low-grade or follicular-type lymphoma, anti-CD53 antibody for relapsed/refractory AML, and anti-CD52 antibody for B-cell chronic lymphocytic leukemia [56, 57]. Recently, Zhou et al. have utilized BDI-1 monoclonal antibodies to target highly toxic to bladder cancer cells *in vitro* [58]. To improve therapeutic efficacy and decrease toxicity, we prepared arsenic trioxide-loaded aluminates immuno-nanospheres [As<sub>2</sub>O<sub>3</sub>-(HAS-NS)-BDI-1] targeted with monoclonal antibody (McAb) BDI-1 and tested its specific killing effect against bladder cancer cells.

**Identifying Monoclonal Antibodies** One strategy to identify ideal targets for monoclonal antibodies is to select the internalizing antibodies from phage libraries; accordingly, two antibodies to the breast cancer cell line SK-BR-3 which bind to ErbB2 have been identified [59]. Nielsen et al. have demonstrated the use of single-chain Fv (scFv) antibodies for internalization of nanoparticles in target cells [60]. The antibodies were recovered from a non-immune phage library and the scFv specific for ErbB2 (F5) was re-engineered and attached to liposomes. Doxorubicin loaded in these immunoliposomes was selectively active on ErbB2 positive breast cancer cells and showed targeted cancer cell cytotoxicity.

Liu et al. have described a method to map the "epitope space" of a tumor using monoclonal antibody libraries [61]. The expressed epitopes on the cell surface, which constitute the "epitope space", is essential to targeted drug delivery. This is "highly complex, composed of proteins, carbohydrates, and other membrane-associated determinants including post-translational modification products, which are difficult to probe by approaches based on gene expression" [61]. The authors used monoclonal antibody libraries against prostate cancer cells and identified over 90 antibodies, which bind to the cancer cells selectively, with little or no binding to normal human cells. This approach does not attempt to identify the tumor-specific antigens, but rather takes a functional approach to the problem of tumor-target identification.

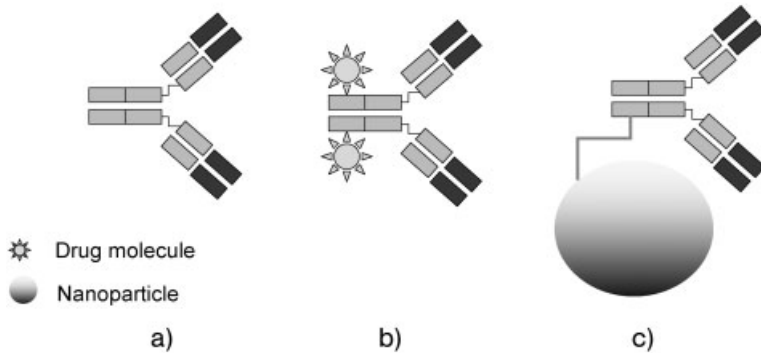


**Fig. 10.4.** Monoclonal antibodies against cancer were originally used either by themselves (A) or attached to drug molecules (B). However, attachment to nanoparticles (C) provides longer circulation times and lower toxicity.

**Monoclonal Antibodies and Nanoparticles** Monoclonal antibodies were initially hailed as therapy for cancers in their own right (Fig. 10.4). To introduce more cancer cell killing ability, they can also be conjugated with anticancer drugs. This complex can also be formulated as a prodrug, which is cleaved to release the anticancer agent at the cancer site. Usually, the link between the molecules would be peptidase cleavable, in order to separate inside the cancer cell. However, such formulations are not very stable *in vivo*, and may undergo early cleavage. The absence or reduction of cleavage at the site will, clearly, lower the potency of the anticancer agent.

The greatest difficulty in using monoclonal antibodies for cancer therapy is their rapid clearance from the bloodstream by the immune mechanisms of the body. Li et al. have estimated that <0.01% of the administered dose of antibodies reaches the target sites [62]. This has two serious drawbacks: firstly, monoclonal antibodies are relatively costly, and a large dose of the therapy becomes prohibitively expensive; secondly, the excess antibody can have serious toxic effects on rest of the patient's body. As we discussed in the introductory section on chemotherapy, this problem, in various proportions, dogs all current therapies of cancer. Hence, monoclonal antibodies by themselves provide no advantage over general anticancer drugs. Attachment of the molecules to nanoparticles circumvents some of these problems.

#### 10.4.3.2 Targeting the Angiogenic Process

Judah Folkman discussed one of the prime candidates for targeted cancer therapy, angiogenic factors, in 1989 [63]. Cancer cells require a significant amount of nutrition to keep growing and reproducing. To obtain this they promote the ingrowth of capillary vessels into the tumor site. This is known as angiogenesis. Tumor cells secrete chemicals that promote angiogenesis. Since active promotion of angiogenesis is unnecessary in most body cells, the associated antigens are of interest

in targeted therapies. The anti-VEGF (vascular endothelial growth factor) drug Avastin® has shown moderate effectiveness in several solid tumors. This has led to a gene-therapeutic approach to anti-angiogenesis using liposomes [64] and cationic nanoparticles [65]. In the latter, an integrin-targeting ligand was used for specific delivery of a mutant Raf gene, and selectivity was demonstrated.

Hallahan et al. have described novel targets that depend on targeting radiation-induced neoantigens in the cancer microvasculature [66]. They demonstrated the presence of an RGD-containing amino acid sequence in phage-displayed peptides obtained from irradiated tumors. This peptide binds to integrins. Immunohistochemical examination confirmed the presence of the fibrinogen receptor integrin in irradiated tumors. Targeting this receptor by fibrinogen-containing nanoparticles showed enhanced anti-tumor effects.

The Intradigm Corporation (MD, USA) has utilized the RGD sequence attached to PEG to target their siRNA-containing nanoparticles to the integrins present in the tumor microvasculature [67]. The siRNA provide potent selective gene inhibition with high specificity. They delivered siRNA-inhibiting vascular endothelial growth factor receptor-2 (VEGF R2) expression and, thereby, tumor angiogenesis to a mouse tumor model using PEI-PEG nanoparticles. The siRNA was found to be active in a highly cell-selective manner. They demonstrated that selectivity could be incorporated in the drug itself, along with the ligand–receptor interaction.

Nucleic acid conjugates have been favored as targeting ligands for their exquisite specificity for the targeted molecule. Farokhzad et al. have utilized nucleic acid ligands (aptamers) to target cells expressing prostate-specific membrane antigen, a tumor marker for prostate cancer acinar epithelial cells [68]. They created PEG-containing PLA nanoparticles that bind to aptamers by surface negative charge. These aptamer conjugated nanoparticles showed 77× greater uptake by the cancer cells than unmodified nanoparticles.

Other efforts [69] have demonstrated nanoparticle targeting to angiogenic epithelium using the  $\alpha_v\beta_3$ -integrin, which is found on endothelial cells. Anti-angiogenic effects were demonstrated in mouse models of melanoma and adenocarcinoma.

#### 10.4.3.3 Folic Acid and Cancer Targeting

Perhaps the most interesting molecule to attract attention for its targeting abilities in recent times is the humble folic acid. Most normal human cells take up this molecule in its reduced form (Fig. 10.5). One of the notable exceptions is the

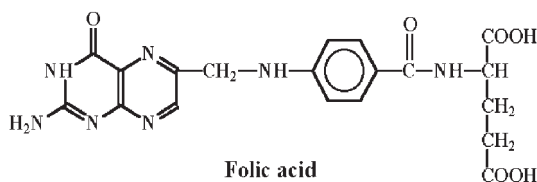


Fig. 10.5. Molecular structure of folic acid.

luminal sides of the gut endothelial layer, which take up the folic acid present in food, convert it into folate, and release it into our bloodstream. Many types of cancer cells, however, take up folic acid in its oxidized form. Since intravenously administered nanoparticles will only come into contact with the abluminal side of the gut epithelium, selectivity for tumor cells is very high. As mentioned above, several endothelial tumors (e.g., derived from the ovaries, mammary glands, colon, lungs, prostate and brain) possess elevated levels of folic acid receptors on their surface [29, 30, 32, 33, 36–40]. Already, a large body of research has accumulated regarding the use of folic acid receptors as cancer targets. Since folic acid, the natural choice for ligand to the folic acid receptor, can be quite easily coupled to the nanoparticle surface, it has been used for targeting these to cancer cells.

Hattori and Maitani have reported *in vitro* studies of folate-linked nanoparticles in human cancer cells [31]. They synthesized DC cholesterol–Tween 80 nanoparticles with incorporated folate-PEG conjugates for steric stability and targeting. The nanoparticles were complexed with plasmid DNA. They showed enhanced uptake in human oral cancer cells by a folate-dependent route. Human prostate cancer cells also showed high uptake of the nanoparticle–DNA complexes. However, based on their results, the authors suggest that the route of uptake may be different for the two cell types.

Oyewumi and Mumper have reported the cellular uptake, distribution and tumor retention of folate-coated and PEG-coated gadolinium nanoparticles in mice models of human nasopharyngeal carcinomas [34]. While this was more for imaging than therapeutic purposes, their results also indicate the efficacy of using folate as a targeting agent. Baker et al. at the Center for Biologic Nanotechnology, University of Michigan Medical School have focused on the use of dendrimers as targeted delivery vehicles (described in detail later). They used folic acid as targeting element to deliver a triplex-forming growth-inhibitory oligonucleotide to breast, ovarian and prostate cell lines [35]. A very recent example of folic acid receptor targeting in squamous cell carcinoma has been demonstrated by Santra et al. [70], who employed a novel technique that uses fluorescent silica nanoparticles (FSNPs) to detect overexpressed folate receptors.

Folic acid targeting to cancer cells has also been demonstrated in our own Cellular and Molecular Bioengineering Laboratory in the National University of Singapore. Although the use of folate as a targeting agent has been extensively reported, little has been done to continuously track the intracellular delivery of nanoparticles grafted with folate using imaging techniques such as confocal microscope. This is possibly due to the short lifetime of most biological fluorescent labels. The problem has been tackled using quantum dots (QDs).

QDs have several advantages over conventional fluorescent dyes and proteins like the Green Fluorescent Protein. They exhibit a strong fluorescence emission, a broad absorption spectra and a narrow, symmetric emission spectrum, and are photochemically stable. The most exciting finding is that QDs also exhibit a wide range of colors, which is exquisitely controlled by their size; a broad absorption spectra means that a series of different-colored dots can be activated using a single laser. These properties of QDs raise the possibility of using them to tag biomole-

cules with an optical coding technology. This can, for example, create QD bar codes, and the use of six colors and ten intensity levels can theoretically encode one million biomolecules. Techniques have been developed to incorporate QDs into polymer beads, to solve problems relating to their surface chemistry. In general, quantum dots exhibit water insolubility, poor biocompatibility, and low chemical stability in physiological media; encapsulation in polymer nanoparticles can reduce these problems. In their work, Zhang et al. have incorporated luminescent CdSe/ZnS QDs into polystyrene (PS) nanoparticles grafted with carboxyl groups using an emulsion polymerization method. Nanoscale QD-incorporated PS nanoparticles (30 nm diameter) were separated by centrifugation at high speed in viscous solution.

Finally, the nanoparticles were modified with folic acid on their surface and their intracellular uptake into NIH-3T3 (an immortalized epithelial cell line) and HT-29 (colon cancer epithelial cell line) cells was investigated using a confocal laser scanning microscope.

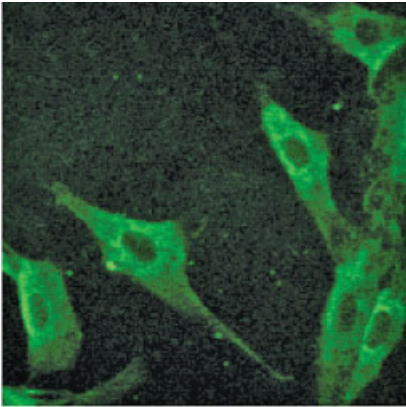
For nanoparticles without a folate cover, fluorescence was observed in the cytoplasm of the cells but not in the nuclei of most cells, indicating that the nanoparticles have difficulty in reaching the nuclei on their own. After surface modification of the nanoparticles with folic acid, fluorescence appeared in the nuclei of some cells (Fig. 10.6). This suggested that intranuclear uptake of the nanoparticles may be affected by the folic acid attached to the surface.

It took three hours of incubation for the PS-encapsulated QDs with folate-modified surfaces to spread throughout the cytoplasm of cells. Folic acid modified nanoparticles first attached to the folate receptors expressed on the cell membrane after 0.5 h incubation. After 1 h, more fluorescence was found on the cells' membranes and some fluorescence spots were already seen in the cytoplasm, indicating early migration of the nanoparticles into cells. After 1.5 h, more fluorescence was observed inside the cytoplasm. Throughout the observation period, fluorescence was seen on the cell membranes. This can be explained by the fact that internalized nanoparticles were rapidly replaced by nanoparticles from the surrounding media. This seems to argue in favor of a receptor-mediated endocytosis process. In contrast, slight cytoplasmic fluorescence was observed with unmodified nano-

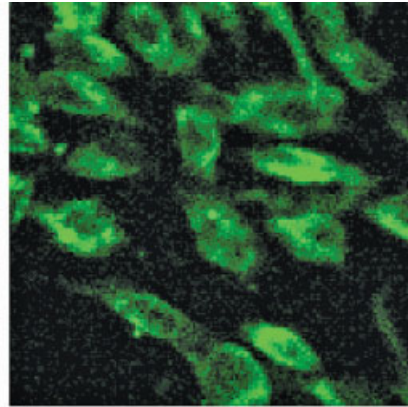
---

**Fig. 10.6.** (top) Confocal images of NIH-3T3 cells after culture with (a) unmodified and (b) folic acid modified nanoparticles and (c, d) their corresponding bright field images.

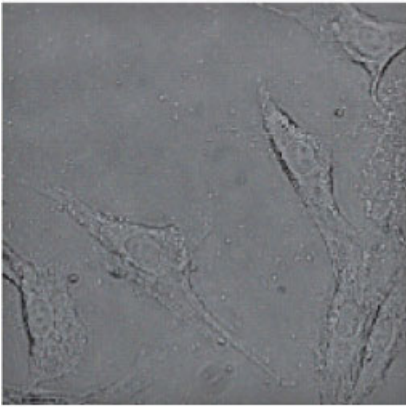
**Fig. 10.7.** (bottom) Transferrin and its receptor. The levels of these receptors are elevated in several tumors. (Source: The protein data bank; [http://www.rcsb.org/pdb/molecules/pdb35\\_2.html](http://www.rcsb.org/pdb/molecules/pdb35_2.html))



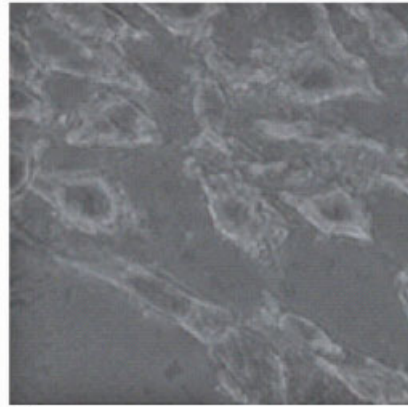
a)



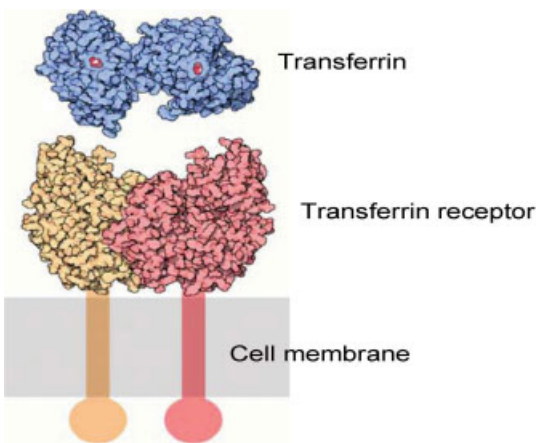
b)



c)



d)



Transferrin

Transferrin receptor

Cell membrane

particles, and did not change throughout the observation period. This uptake was possibly by non-specific endocytosis of the PS beads by the cells.

#### 10.4.3.4 Transferrin as a Targeting Ligand

Approximately 3 mg or 0.1% of body iron in the adult male circulates in the plasma as an exchangeable store. Essentially all circulating plasma iron normally is bound to an 80 kDa glycoprotein called transferrin. Plasma transferrin is synthesized by the liver and secreted into plasma. It has two homologous N-terminal and C-terminal iron-binding domains [71] (Fig. 10.7). This iron-protein chelate serves three functions: it makes iron soluble under physiologic conditions, it prevents iron-mediated free radical toxicity, and it facilitates transport of iron into cells. Transferrin is the most important physiological source of iron for red cells [72]. The liver synthesizes transferrin and secretes it into the plasma. Transferrin is a suitable ligand for tumor targeting because of the upregulation of its receptors in many cancers [46] in which their levels correlate with the malignant potential [47].

Insert Therapeutics (California, USA) have reported transferrin based targeting. They demonstrated tumor targeting in mice by transferrin-modified nanoparticles containing DNAzymes (short catalytic single-stranded DNA molecules) [73]. They synthesized  $\beta$ -cyclodextrin polymer-DNAzyme nanoparticles. Steric stabilization was obtained by adamantane-PEG conjugates complexed to the surface by adamantane-cyclodextrin interaction. Transferrin was included for targeting transferrin receptor expressing tumors. While the uptake of unmodified nanoparticles was demonstrated *in vivo* in nude mice, transfer modification was demonstrated to be necessary for intracellular delivery of the DNAzyme.

Previously, the same group demonstrated [74] the uptake of transferrin-modified cyclodextrin-adamantane inclusion complex nanoparticles to leukemia cells, which was competitively inhibited by excess free transferrin.

#### 10.4.3.5 Other Targeting Ligands

Another targeting molecule used is biotin (vitamin H). Na et al. have incorporated this molecule into a hydrophobically modified polysaccharide, pullulan acetate, loaded with adriamycin [75]. The biotinylated nanoparticles exhibited very strong adsorption to the HepG2 cells, while the unmodified nanoparticles showed no significant interaction. Uptake was confirmed by confocal microscopy. While the degree of interaction increased with increasing vitamin H content, drug uptake by the nanoparticle was inversely related to the vitamin H content.

Various other ligands have been studied as probable candidates for targeted drug delivery in tumors. These include antibodies against tumor-associated antigens [76], lectins [77], and glycoproteins [78]. Recently, Yu et al. from Japan have detailed the use of the surface antigen (sAg) of the hepatitis B virus to accomplish liver-specific delivery of genes and drugs. They describe the association of approximately 110 molecules of this protein to form a polymeric capsule (which they call a "BioNanoCapsule" or BNC) with an average diameter of 130 nm. The nanoparticles that were produced delivered emerald green fluorescent protein (EGFP) to human hepatoma cells [79].

## 10.5 Targeting with Different Types of Nanoparticles

### 10.5.1

#### Liposomes in Cancer Targeting

Currently, the most exciting event in targeted drug delivery systems is undoubtedly the ongoing clinical trial of the world's first tumor-targeted gene delivery vector, Rexin-G™, marketed by Epeius Biotechnologies Corporation. This nanoparticle formulation combines a proprietary vector system with a proprietary anticancer gene controlling cell cycle. The company website claims that "when given by intravenous infusions, Rexin-G™ has been shown to eradicate remote metastatic cancers in mice and to arrest cancer growth with shrinkage and necrosis of solid tumors in humans – determined by CT Scan and MRI – without eliciting systemic side effects." The first clinical trials were started in 2003 in Manila, Philippines; and following FDA approval shortly thereafter, clinical trials were started in New York from April, 2005 for metastatic pancreatic and colon cancer. Initial reports are favorable and results of ongoing studies are eagerly awaited [3, 80, 81].

In this context, a few words regarding immunoliposomes are in order. In our initial classification of colloid based systems, we separated nanoparticles from liposomes and block copolymer micelles. Many authors consider them part and parcel of the same package [1, 82]. Hence, in the interest of topicality and completeness, we consider both in some measure.

Liposomes (and, in some instances, micelles) have long been used for targeted delivery of drugs. Of all the proposed nanoparticulate drug delivery systems, liposome-based agents, particularly liposomal anthracyclines, have had the greatest impact on oncology to date [82]. These lipid based formulations have several advantages as drug carriers: they are amphiphilic, hence allowing the carriage of lipophilic drugs in plasma; they fuse with cell membranes and transfer their load inside cells; and they can be embedded with targeting molecules like antibodies on their outer surface. They have been likened to the Trojan horse in Greek mythology: the cancer cells fuse to the liposomal membrane and takes up the contents of the liposome, which contains the anticancer formulations (the company that is conducting the liposomal targeted-gene delivery trials has been appropriately named after Epeius, the maker of the original Trojan horse).

Several problems have dogged liposomal drug delivery systems from its conception and implementation. These include a short half-life in circulation, instability *in vivo*, and lack of target selectivity. Liposomes are removed rapidly from the circulation by the reticulo-endothelial system (RES) [83]. Stability and circulation times were increased, as in nanoparticles, by the introduction of a steric stabilizer on the surface, usually PEG [84]. Like other nanoparticles, enhanced passive uptake of liposomes has been demonstrated with longer circulation times. PEGylation has increased therapeutic efficacy of the liposomal formulations [85, 86]. These innovations, affording longer and stable circulation times, have resulted in approval of some liposomal formulations for clinical use [87]. The passive increase of lipo-



somes in cancer sites was recognized as a means of delivering toxic, poorly soluble drugs. Liposome-encapsulated doxorubicin was approved for use in Kaposi's sarcoma more than a decade ago. Formulations are available now for breast and ovarian cancers. The most recent instance deals with liposomes encapsulating cisplatin; this has been demonstrated in preclinical and phase 1 clinical trials in humans to have almost negligible nephrotoxicity, ototoxicity and neurotoxicity, which are the major side-effects of free cisplatin in circulation [15].

Improved target selectivity has been demonstrated using ligands and antibodies. Active targeting of liposomes using ligands for tumor-associated receptors, and antibodies against tumor-associated antigens, has been investigated as a means of improving selectivity. Liposome-antibody complexes (immunoliposomes) have received most attention [88]. The problem of rapid removal by the RES is compounded by the attachment of antibodies [89, 90]. However, PEGylation has created a generation of "stealth" immunoliposomes that can effectively hide from the RES for long periods. In this context, immunoliposomes can be classified into two groups based on the relation of the antibody to the PEG group on the liposomal surface: antibody coupled to lipid head group 76 and antibody coupled to the distal end of PEG [91]. The latter composition has been considered to be better for efficient antibody-target coupling because of the absence of interference from PEG chains [92]. At optimal compositions of both types of formulations, antibodies do not interfere with PEG function and long circulation times have been demonstrated; conversely, PEG does not interfere with antibody function, and active targeting is unimpaired. Immunoliposomes complexed with PEG have been successfully demonstrated for *in vivo* targeting of brain [93] and lung [91] tumors.

Immunoliposomes with cancer targeting antibodies have been shown to be cytotoxic to cancer cells *in vitro* [94]. However, this did not translate to *in vivo* success. This was because not all antibodies used to target the cancer cells result in uptake and internalization of the liposome. The use of more specific internalizing antibodies aided in uptake and cytotoxic effects *in vitro*. As an example, the anticancer antibody anti-ErbB2 did not increase cytotoxicity of the liposome [95]; but when the anti-ErbB2 Fab fragment was used, the liposome was internalized and had high efficacy of cancer kill [96, 97]. More recently, scFV (single-chain Fv) antibodies against ErbB2 have been utilized for cancer targeting with doxorubicin-loaded liposomal formulations. The antibodies are selected from a phage display library, and demonstrate higher internalization efficacy [98–100]. Ongoing research by Park et al. at UCSF comprehensive cancer centre [82, 101] aims to develop immunoliposomes with antibodies targeted to HER 2, overexpressed in breast cancer, and EGFR, overexpressed in several cancers such as lung, pancreas and prostate. The targeted liposomes have been loaded with anticancer drugs like doxorubicin and vinorelbine. The loaded immunoliposomes have shown increased effectiveness and reduced toxicity compared with conventional chemotherapy.

The issue of internalization can be circumvented by a two-step method to release the anticancer drugs from the liposome near the tumor. This antibody-directed enzyme pro-drug therapy (ADEPT) involves first administering an enzyme-antibody conjugate that preferentially targets cancer cells, followed by administration of a

non-toxic prodrug that is activated by the bound enzyme and releases the toxic product close to the cancer cells [102]. An improvement of the ADEPT method using immunoliposomes to carry the enzyme shows greater stability in the body and has been tested pre-clinically [103].

#### 10.5.1.1 Beyond Immunoliposomes

Similar to the development of nanoparticles, scientists have looked beyond monoclonal antibodies as a means of targeting liposome to cancer. This was to avoid the intrinsic immunogenic nature of antibodies, their high cost, and the ease of procurement of ligands for overexpressed growth receptors on the tumor surface. Folic acid coupled liposomes have been developed and tested against various cancer cells both *in vitro* and *in vivo* [85, 104, 105]. Transferrin has also been evaluated as a targeting ligand for anticancer drug carrying liposomes [106].

Targeting with transferrin and folic acid has also been used to deliver anticancer genes to tumor cells. Cationic liposome–DNA complexes (lipoplexes) that are formed spontaneously by charge interaction exhibit the best gene-transfer efficiency. However, cationic liposomes were found to be unsuitable for active cancer cell targeting. Hence, a new anionic liposome–polyplex (anionic liposome-entrapped polycation-condensed DNA, LPD-II) was introduced for the gene therapy of cancer. Cationic lipoplexes containing liposomes and DNA were better internalized and transfected when transferrin was conjugated [107] and demonstrated selectivity for myeloblast cells [108], adenocarcinomas and squamous cell carcinomas [109]. Folic acid has also been used for tumor targeting the LPD-II polyplexes [110]; and systemic administration of anticancer gene therapy for selective uptake in squamous cell carcinomas of the head and neck, and breast cancer xenografts have been demonstrated [109].

### 10.5.2

#### Dendrimers

Block copolymers or dendrimers were described as far back as 1985. Initial studies elucidated the physical and chemical properties of these new materials. However, their entry into the field of targeted cancer therapy is relatively recent.

Dendrimers are globular macromolecules that have a “starburst”-like shape, with multiple branches radiating from a central core. The stepwise synthesis of dendrimers makes it possible to fine-tune its highly regular branched structure with defined peripheral groups and adjust physical properties such as the high molecular weight and low polydispersity index. Dendrimers have several advantages over polymeric nanoparticles derived from linear chains. Dendrimers are multivalent: several different drug molecules, targeting agents and other groups can be attached in a predefined fashion. Dendrimers have low polydispersity: all the synthesized molecules have molecular weights within a narrow range; this makes their behavior highly reproducible. Dendrimers have a globular rather than random coil structure, which could lead to better biologic properties [111]. Various types of

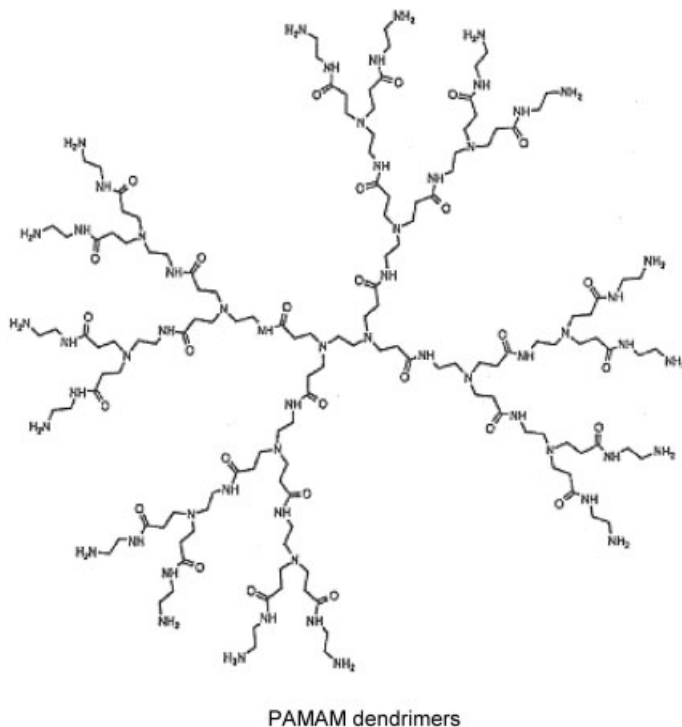


**Fig. 10.8.** PAMAM dendrimers are the most common dendrimer nanoparticles currently used in drug delivery. (Source: <http://www.dendritech.com/pamam.html>)

dendrimers have been synthesized. The most common is the polyamidoamine (PAMAM) dendrimers developed by Tomalia and coworkers [112] (Fig. 10.8), which uses a divergent growth approach. Other types include polypropyleneimine dendrimers [113], polyaryl ether dendrimers [114] and peptide-based dendrimers, such as polylysine-based ones [115].

Passive targeting can be achieved by dendrimers having long circulation times. Unlike polymeric micelles, dendritic unimolecular micelles maintain their structure at all concentrations because of the covalent linkage [111]. This increased stability has the disadvantage that drug release from the central core cannot be controlled. This can be circumvented by attaching the drug molecule covalently to the periphery of the radiating arms of the dendrimer molecule. The amount of drug conjugated can be controlled by the number of generations (which increases the length of the radiating arms) and the release can be ensured by making the drug-dendrimer linkage easily degradable. Attachment of cisplatin to PAMAM dendrimers has been demonstrated by Duncan et al. [116]. Another of type of passive

targeting that utilizes the lowered pH of the intracellular endosomal and lysosomal microenvironment for drug release has been demonstrated [117]. Doxorubicin was conjugated to hybrid dendrimers using hydrazone linkages; these are stable at normal physiologic pHs, but break down after uptake in the mildly acidic endosomes and lysosomes. They demonstrate longer circulation times and toxicity to several tumors [118].

Active targeting of dendrimers using folic acid conjugates has been demonstrated by Frechet and coworkers [119] using dendrimer folate and dendrimer methotrexate conjugates. Quintana et al. have created analogous PAMAM–methotrexate conjugates with degradable amide and ester linkages [35]. Folic acid conjugation enhanced cellular uptake of these compounds, resulting in increased cancer cell cytotoxicity and efficacy of the anticancer drug as compared with the free drug *in vivo*.

Dendrimers have enormous potential in targeted drug delivery systems because of their reproducibility, controlled synthesis, and multivalent structure, which ensures incorporation of different functions like targeting, imaging and multidrug delivery. However, relatively less literature is available on these exciting molecules and they suffer from lower circulation times and drug release rates than those of more established nanoparticles and liposomes, and their biodistribution is still being investigated. With time and experience, these technical obstacles will, hopefully, be solved and they will have an even wider impact on targeted drug delivery.

### 10.5.3

#### **Other Polymeric Nanoparticles**

Historically, nanoparticles were first introduced by Birrenbach and Speiser [120]. They were later developed to become drug delivery systems as a substitute for liposomes. Initial formulations were made by emulsion polymerizations [120]. However, later methods were developed (like phase separation, controlled gelation, etc.) that made use of preformed polymers with already characterized physicochemical properties. This allowed better control over the properties of the nanoparticles.

The most common polymers used as core material for polymeric nanoparticles are poly(alkyl cyanoacrylate), poly(lactide) derivatives and chitosan. However, several other materials have also been investigated, as noted in other volumes of this series. Recently, Gilbert et al. have developed fluorescent virus-like nanoparticles (fVLPs) from fusion protein VP2 and GFP that may serve as a model for the development of vehicles that can be designed for the delivery of large biomolecules to cancer cells [121]. These are taken up with high efficiency and transferred to the nucleus using the microtubular network. In another very recent example, Mo et al. have developed a novel lectin-conjugated isopropyl myristate (IPM)-incorporated PLGA nanoparticle for the local delivery of paclitaxel to the lungs [122].

Nanoparticles can be nanospheres or nanocapsules, the basic difference being that nanospheres have a matrix structure, while the capsules have a core-and-shell structure. While a wide range of sizes are available and have been tried, generally,

the particles should be less than 100 nm in diameter [123]. The greater surface area of the nanoparticles allows attachment of targeting molecules and anticancer agents; alternatively, the drug may form the core of the nanocapsule with a polymeric shell.

Nanoparticles as vehicles of targeted drug delivery enjoy several advantages. Primarily, the attachment of different molecules to the same platform confers bi- and multi-functionality. This is important because conjugating targeting molecules directly to the anticancer drug may cause decreased functionality of either or both. Nanoparticles can be modified to incorporate not only two but more functions. One of could report the presence of the tumor using, for example, quantum dots.

Secondly, attachment to the nanoparticle surface increases the stability of molecules. This is particularly important with peptides, nucleic acids (like anti-HA-*ras* [124]) and anti-Ewing sarcoma [125] and small proteins (like antibodies), which are easily removed from the circulation in the free form. It is also important for carrying poorly soluble drugs (e.g., muramyl tripeptide cholesterol [126]) in significant quantities without the usual side effects. Controlled release can be achieved to ensure a long-term, high level of the drug without encountering the loading dose problem. This has been shown in the use of doxorubicin-loaded nanoparticles. Doxorubicin can cause acute and chronic cardiomyopathy at high levels. By attachment to nanoparticles, high levels of doxorubicin were achieved in the circulation, with reduced cardiac levels and, consequently, less toxic effects and increased effectiveness against the metastatic cancer.

Chemotherapy fails *in vivo* even when the cancer is shown to be highly sensitive to the drug *in vitro* because of cellular “sanctuaries”. For example, the recurrence of acute lymphoblastic leukemia has been attributed to cell nests in the CNS. Intravenous drug formulations fail to cross the blood–brain barrier. Nanoparticles, however, can accomplish this feat, perhaps by trans-cellular movement after endocytosis by the endothelial cells. Some examples of this include the use of polysorbate 80-coated nanospheres to deliver Kytorphin, turbocurarine NMDA antagonist and doxorubicin to the brain. Polysorbate 80 adsorbs apolipoprotein E from the circulation and becomes attached to the low-density lipoprotein receptors on the endothelial surface.

The major drawback of nanoparticles is their propensity to be taken up by the macrophages lodged in the organs of the mononuclear phagocytic system (MPS). After intravenous administration, most of the nanoparticles accumulate in the spleen and the liver, and to a lesser extent in the bone marrow. Steric stabilization has been devised to avoid this. The attachment of PEG to the nanoparticle surface allows them to “hide” from the MPS and stay longer in circulation, eventually finding their way to the targeted regions. Poloxamine has been proposed as an alternative to PEG for producing steric stabilization.

In fact, PEG-coated poly(cyanoacrylate) (pCA) nanoparticles – made by a copolymer inculcating both – have such a long circulating time that they penetrated the brain more than any other modifications, including coating by polysorbate. This uptake was increased in pathological situations with, presumably, higher blood–brain barrier permeability.

Modeling of nanoparticle delivery and effects has raised the question of “diffusional instability”. Vittorio Cristini et al. have shown that the delivery of cytotoxic agents to tumors, particularly anti-angiogenic drugs, might fractionate the lesion into multiple satellite neoplasms [127]. This is likely due to the rearrangement of the sources of oxygen and nutrient supply because of the anti-angiogenic therapy.

The other difficulty is the issue of control. Especially with synthetic methods derived from microencapsulation techniques, there may be considerable difficulty in encapsulating the drug and then controlling its release after encapsulation.

To summarize, a nanoparticle designed for targeted delivery of anticancer agents will have three essential components: (a) the capsule or matrix or core that provides the platform to bind or contain; (b) the drug or anticancer agent, which binds on the surface; and (c) the targeting molecule. This whole arrangement must be made immune from the attacks of the immune system by steric stabilization, usually by the attachment of PEG to the surface.

Mauro Ferrari has labeled these modified nanoparticles as “nanovectors” [1]. The name is appropriate as an indication of their function as carriers of large therapeutic payloads to target sites. He points out that while antibody conjugated therapies can only deliver single molecules of drug per recognition event, nanovectors can deposit a much larger amount. This makes nanoparticles particularly attractive when dealing with toxic drugs.

In the described tripartite arrangement, an optimum combination of matrix, drug and surface recognition element is required. As stated above and described elsewhere, many matrix polymers have been tested for their drug uptake and surface modification abilities (for a review see Ref. [128]). Targeting has ranged from “active” targeting, using antibodies, radiation-induced vascular neo-antigens, folic acid receptors and transferrin, to passive targeting that depends on surface modification with PEG and enhanced fenestrations of tumor vasculature to selectively deliver the drug.

The role of the surface-modified matrix and the targeting molecule is to effectively deliver the drug to the target site. For this, they must provide stability to peptides and others drugs with short half-lives in circulation, avoid uptake by the MPS or RES, circumvent the endothelial and blood–brain barrier, be non-toxic to normal body tissues and, finally, deliver the drug to the tumor cells, avoiding the enhanced osmotic pressure in tumor regions [129] and ensuring uptake and action.

However, a nanoparticle may have yet further uses. As demonstrated by Baker et al., dendrimer-based nanoparticles can be modified to not only avoid obstacles and target tumors but also to “report” on the presence and extent of the tumor by the means of an attached “reporter” molecule, in this case fluorescein [35]. In a similar vein, Loo et al. have demonstrated the dual functional ability of immunotargeted nanoshells for integrated cancer imaging and therapy [130]. They define nanoshells as “a novel class of optically tunable nanoparticles that consist of a dielectric core surrounded by a thin gold shell”. The relative dimensions of the shell thickness and core radius allow nanoshells to either scatter and/or absorb light over a broad spectral range, including the near-infrared (NIR). The NIR is a wavelength region that provides maximal penetration of light through human tissue. Thus,

with attachment of suitable antibodies, these nanoshells offer the opportunity to design vehicles that provide, in a single nanoparticle, both diagnostic and therapeutic capabilities.

Targeting can be enhanced or achieved by other factors, too. One of these is the use of drugs that act preferentially on tumor cells. While most conventional chemotherapeutic drugs now in use have greater or lesser degrees of tumor selectivity (usually by targeting the rapid proliferation of tumor cells), greater selectivity may be achieved by using siRNA that are specific for tumor antigens (see below). Another type of targeting, demonstrated by Potineni, et al. [131], describes a method to utilize pH differences to release drugs at tumor sites. They demonstrated the *in vitro* release of the anticancer drug paclitaxel by biodegradable poly(ethylene oxide)-modified poly( $\beta$ -amino ester) nanoparticles. This can theoretically be reproduced at cancer sites, which have high metabolic rates and altered pH.

## 10.6

### Conclusion

As far back as the late 19<sup>th</sup> century, Paul Ehrlich (1854–1915) – Nobel laureate for Physiology or Medicine in 1908 for his pioneering work in immunology and chemotherapy and for the discovery of the first effective therapy for syphilis – propounded and popularized the concept of a “magic bullet”. This is a drug that targets and destroys diseased cells selectively, to the exclusion of all others, like a bullet that finds its mark every time. His invention, preparation 606, later called Salvarsan, was highly effective against syphilis and harmless despite a large arsenic content. This drug was also found to be successful in curing several other diseases. Indeed, it seemed that a “magic bullet” had indeed been found [132]. We, of course, realize that despite its effectiveness, arsenical-based therapy of syphilis can not accurately qualify for the label of magic bullet. Indeed, for years scientists have searched in vain for such a drug for cancer, but as our understanding of the complexities of the cancer cell and the diverse nature of the neoplastic process grows, more than one researcher has denounced this concept as an unachievable objective. The search for the magic bullet for cancer has become a sort of Holy Grail for cancer researchers worldwide – to be sought for, but not to be found. Each new advance and discovery in this field has been accompanied by hopes that finally the grail has been found, but in all cases these hopes have been shattered by the realities of failure rates. On the bright side, very large strides have been made in cancer treatment, and average life expectancy after detection has increased for most cancers, and several treatments have chalked up impressive cure rates.

The field of nanotechnology was famously introduced by another Nobel laureate, Richard P. Feynmann, in his lecture “There is plenty of room at the bottom” at the annual meeting of the American Physical Society at the California Institute of Technology in 1959. Many nanotechnology researchers consider this talk to be the inspiration for their work. Feynmann, in this lecture, proposed two challenges to future nanotechnologists, but neither, however, was related to the field of biology.

Lipid based formulations, especially liposome encapsulated doxorubicin, first raised visions of a route to the magic bullet. However, it was still just a drug modification that allowed the transfer of toxic but effective drugs in the serum. The introduction of monoclonal antibodies suddenly made active targeting an attractive possibility. However, the high cost of these antibodies, the large amounts needed to counter their rapid removal from circulation, and the single molecule of drug they carried, all presented technical difficulties for their widespread use. An ant can carry 10–20× its body weight of food; imagine how ineffective it would be if it could carry only a mouthful at a time! Nanoparticles – introduced in the 1970s – seemed to be the probable replacement for liposomes. However, they soon came up against the same problem that monoclonal antibodies faced: they were rapidly cleared from circulation by the mononuclear phagocytic system in the liver and spleen. Scientists innovatively tried to turn this drawback into an advantage, by using nanoparticles to target the liver specifically, e.g., to transfect genes to produce essential proteins, but in the end the goal of targeted delivery seemed to be as far away as before.

The discovery of the steric stabilization effect of poly(ethylene glycol) (PEG) solved that major problem. While “PEGylating” nanoparticles increased their circulation time dramatically, it also reaped an unexpected harvest. The local environment of the tumor supports extravasation of nanoparticles through large endothelial fenestrations and disordered neoplastic tissue architecture. Their retention is ensured by a low lymphatic drainage. This enhanced permeation and retention (EPR) effect had a dramatic influence on the distribution of long-circulating nanoparticles: they collected at tumor sites to the exclusion of other body tissues even without any “active” targeting molecules. Long time of circulation and the EPR effect ensured that nanoparticles circumvented the blood–brain barrier, with important implications for the treatment of resistant tumors with cell sanctuaries in the brain.

Innovations continue to increase almost daily. Not satisfied with costly monoclonal antibodies for tumor targeting, researchers have turned to such mundane molecules as folic acid, transferrin and biotin for enhanced selective uptake in tumors. Folic acid in particular has a relatively long history of tumor targeting abilities, and preferential uptake in a large number of solid tumors.

The drug carried to the tumor site is not restricted to the more traditional doxorubicins and paclitaxels. There had been considerable interest in a possible gene therapy of cancer. Indeed, at one time it had been hyped as the elusive “magic bullet”. *In vitro* studies have conclusively demonstrated repetitively the effectiveness of this approach against a wide variety of cancer. The obstacle had always been an appropriate vehicle that can effectively deliver sufficient amounts of the gene to the cancer cells. Direct injection of the naked DNA into muscle cells (the so-called “gene gun”) showed considerable uptake and expression. But for the ultimate delivery vehicle, man decided to trust the vector that Nature’s evolutionary process has skillfully crafted over millions of years for this very purpose: viruses. Initial experiments with harmless adenoviridae *in vitro* promised success; however, clinical trials (to supplement the mutated p53 in ovarian cancer) failed to demonstrate any



advantage over conventional therapy [133]. On September 17, 1999, eighteen-year-old Jesse Gelsinger died during a gene therapy clinical trial for ornithine transcarbamylase (OTC) deficiency, a rare metabolic disorder that is marked by dangerous levels of ammonia in the bloodstream. He died after a vector injected into his liver triggered an immune response that led to multiple organ failure. This incident seemed to ring the death knell to virus-delivered gene therapy.

Gene therapists turned to non-viral means of delivery – the obvious solution appeared to be nanoparticles. They can be modified to carry biological macromolecules, are themselves harmless, and can help protect the gene from the immune system till the cancerous tissue is reached. The complex of genetic material, especially siRNA, and targeted nanoparticle vector brought together a double selectivity process: the targeting ligand ensures selective uptake to cancer cells, and the siRNA ensures that even if some non-cancerous cells have taken up the particle, only the cancer cells are affected.

The excellent results with nanoparticulate gene vector complexes brought back the old nanoparticle workhorse, liposomes, to the forefront. Ease of DNA uptake by the cationic liposomes, and their uptake by fusion to membranes, ensures efficient transfection. With added targeting ligands, the complex promises to be the answer to many cancer therapy problems. Another nano-sized colloidal drug delivery system made its entry into the field more recently: block copolymer micelles or dendrimers.

With nearly all the components finally at hand, the assembly of the actively targeted nanoparticle against cancer was but a matter of time. Several such complexes have already shown promise. In a natural spin off, several start-up companies have already begun early research into human applications. Endocyte, Inc. has taken up folic acid as their solution, while Baker has established the Center for Biologic Nanotechnology at the University of Michigan to espouse the cause of dendrimers. Arguably the most exciting is the performance of Epeius Biotechnologies Corporation's liposomal based active targeting system that delivers genetic material to treat several cancers, including pancreatic head carcinoma, which has one of the worst prognoses among all neoplasms.

It may be that nanoparticles fail to provide us the “magic bullet” against all cancers. However, if current interest, effort and progress in the field of nanoparticulate targeted drug delivery systems are any indication, we may be heading towards an era of more effective chemotherapy with less morbidity and higher cure rates.

## References

- 1 FERRARI, M., Cancer nanotechnology: Opportunities and challenges, *Nat. Rev. Cancer*, **2005**, 5, 161–171.
- 2 JAIN, K. K., Nanotechnology-based drug delivery for cancer, *Technol. Cancer Res. Treat.*, **2005**, 4, 407–416.
- 3 JAIN, K. K., Nanotechnology in clinical laboratory diagnostics, *Clin. Chim. Acta*, **2005**, 358, 37–54.
- 4 MCNEIL, S. E., Nanotechnology for the biologist, *J. Leukoc. Biol.*, **2005**.
- 5 FORTINA, P., KRICKA, L. J., SURREY, S., GRODZINSKI, P., Nanobiotechnology: The promise and reality of new

- approaches to molecular recognition, *Trends Biotechnol.*, **2005**, *23*, 168–173.
- 6 LEUSCHNER, C., KUMAR, C. S. S. R., in *Nanofabrication Towards Biomedical Applications*, eds. KUMAR C. S. S. R., HORMES J., LEUSCHNER C., Wiley-VCH, Verlag, Weinheim, **2005**, pp. 289–326.
  - 7 COURVREUR, P. G. L., LENAERTS, V., BRASSEUR, F., GUIOT, P., BIORNACKI, A., *Biodegradable Polymeric Nanoparticles as Drug Carrier for Antitumor Agents*, ed. GUIOT, P. C. P., CRC Press, Boca Raton, **1986**.
  - 8 FLORENCE, A. T., HUSSAIN, N., Transcytosis of nanoparticle and dendrimer delivery systems: Evolving vistas, *Adv. Drug Deliv. Rev.*, **2001**, *50*(Suppl 1), S69–89.
  - 9 KAWASHIMA, Y., Nanoparticulate systems for improved drug delivery, *Adv. Drug Deliv. Rev.*, **2001**, *47*, 1–2.
  - 10 MATSUMURA, Y., MAEDA, H., A new concept for macromolecular therapeutics in cancer chemotherapy: Mechanism of tumorotropic accumulation of proteins and the antitumor agent smancs, *Cancer Res.*, **1986**, *46*, 6387–6392.
  - 11 SLEDGE, G. W., JR., MILLER, K. D., Exploiting the hallmarks of cancer: The future conquest of breast cancer, *Eur. J. Cancer*, **2003**, *39*, 1668–1675.
  - 12 TEICHER, B. A., Molecular targets and cancer therapeutics: Discovery, development and clinical validation, *Drug Resist. Updat.*, **2000**, *3*, 67–73.
  - 13 SHENOY, D. B., AMIJI, M. M., Poly(ethylene oxide)-modified poly(epsilon-caprolactone) nanoparticles for targeted delivery of tamoxifen in breast cancer, *Int. J. Pharm.*, **2005**, *293*, 261–270.
  - 14 CHAWLA, J. S., AMIJI, M. M., Biodegradable poly(epsilon-caprolactone) nanoparticles for tumor-targeted delivery of tamoxifen, *Int. J. Pharm.*, **2002**, *249*, 127–138.
  - 15 BOULIKAS, T., STATHOPOULOS, G. P., VOLAKAKIS, N., VOUGIOUKA, M., Systemic Lipoplatin infusion results in preferential tumor uptake in human studies, *Anticancer Res.*, **2005**, *25*, 3031–3039.
  - 16 WEI, J. S. et al., Temperature- and pH-sensitive core-shell nanoparticles self-assembled from poly(n-isopropylacrylamide-co-acrylic acid-co-cholesterol acrylate) for intracellular delivery of anticancer drugs, *Front Biosci.*, **2005**, *10*, 3058–3067.
  - 17 ALEXIOU, C. et al., Magnetic drug targeting – biodistribution of the magnetic carrier and the chemotherapeutic agent mitoxantrone after locoregional cancer treatment, *J. Drug Target*, **2003**, *11*, 139–149.
  - 18 GILCHRIST, R. K. et al., Selective inductive heating of lymph nodes, *Ann. Surg.*, **1957**, *146*, 596–606.
  - 19 LUBBE, A. S. et al., Clinical experiences with magnetic drug targeting: A phase I study with 4'-epidoxorubicin in 14 patients with advanced solid tumors, *Cancer Res.*, **1996**, *56*, 4686–4693.
  - 20 ALEXIOU, C. et al., Locoregional cancer treatment with magnetic drug targeting, *Cancer Res.*, **2000**, *60*, 6641–6648.
  - 21 MOORE, A., MARECOS, E., BOGDANOV, A., JR., WEISSLEDER, R., Tumoral distribution of long-circulating dextran-coated iron oxide nanoparticles in a rodent model, *Radiology*, **2000**, *214*, 568–574.
  - 22 LUBBE, A. S., ALEXIOU, C., BERGEMANN, C., Clinical applications of magnetic drug targeting, *J. Surg. Res.*, **2001**, *95*, 200–206.
  - 23 BROWNING, M., *The Cancer Cell and the Immune System*, ed. VILE, R. G., John Wiley & Sons, New York, **1995**.
  - 24 HAKOMORI, S., *Tumor-associated Carbohydrate Markers: Chemical and Physical Basis and Cell Biological Implications*, ed. SELL, S., The Humana Press, Totowa, NJ, **1992**.
  - 25 TAYLOR-PAPADIMITRIOU, J., BURCHELL, J., MILES, D. W., DALZIEL, M., MUC1 and cancer, *Biochim. Biophys. Acta*, **1999**, *1455*, 301–313.
  - 26 COLCHER, D., MILENIC, D. E., FERRONI, P., ROSELLI, M., SCHLOM, J., In vivo and in vitro clinical applications of monoclonal antibodies against TAG-72, *Int. J. Rad. Appl. Instrum. B*, **1991**, *18*, 395–401.
  - 27 HIRABAYASHI, Y. et al., Syngeneic

- monoclonal antibody against melanoma antigen with interspecies cross-reactivity recognizes GM3, a prominent ganglioside of B16 melanoma, *J. Biol. Chem.*, **1985**, *260*, 13 328–13 333.
- 28 HAKOMORI, S., Tumor malignancy defined by aberrant glycosylation and sphingo(glyco)lipid metabolism, *Cancer Res.*, **1996**, *56*, 5309–5318.
- 29 CONEY, L. R. et al., Cloning of a tumor-associated antigen: MOv18 and MOv19 antibodies recognize a folate-binding protein, *Cancer Res.*, **1991**, *51*, 6125–6132.
- 30 GARIN-CHESA, P. et al., Trophoblast and ovarian cancer antigen LK26. Sensitivity and specificity in immunopathology and molecular identification as a folate-binding protein, *Am. J. Pathol.*, **1993**, *142*, 557–567.
- 31 HATTORI, Y., MAITANI, Y., Enhanced in vitro DNA transfection efficiency by novel folate-linked nanoparticles in human prostate cancer and oral cancer, *J. Controlled Release*, **2004**, *97*, 173–183.
- 32 HOLM, J., HANSEN, S. I., HOIER-MADSEN, M., High-affinity folate binding in human liver membranes, *Biosci. Rep.*, **1991**, *11*, 139–145.
- 33 MATTES, M. J. et al., Patterns of antigen distribution in human carcinomas, *Cancer Res.*, **1990**, *50*, 880s–884s.
- 34 OYEWUMI, M. O., YOKEL, R. A., JAY, M., COAKLEY, T., MUMPER, R. J., Comparison of cell uptake, biodistribution and tumor retention of folate-coated and PEG-coated gadolinium nanoparticles in tumor-bearing mice, *J. Controlled Release*, **2004**, *95*, 613–626.
- 35 QUINTANA, A. et al., Design and function of a dendrimer-based therapeutic nanodevice targeted to tumor cells through the folate receptor, *Pharm. Res.*, **2002**, *19*, 1310–1316.
- 36 ROSS, J. F., CHAUDHURI, P. K., RATNAM, M., Differential regulation of folate receptor isoforms in normal and malignant tissues in vivo and in established cell lines. Physiologic and clinical implications, *Cancer*, **1994**, *73*, 2432–2443.
- 37 TOFFOLI, G. et al., Overexpression of folate binding protein in ovarian cancers, *Int. J. Cancer*, **1997**, *74*, 193–198.
- 38 WEITMAN, S. D., FRAZIER, K. M., KAMEN, B. A., The folate receptor in central nervous system malignancies of childhood, *J. Neurooncol.*, **1994**, *21*, 107–112.
- 39 WEITMAN, S. D. et al., Distribution of the folate receptor GP38 in normal and malignant cell lines and tissues, *Cancer Res.*, **1992**, *52*, 3396–3401.
- 40 WEITMAN, S. D. et al., Cellular localization of the folate receptor: Potential role in drug toxicity and folate homeostasis, *Cancer Res.*, **1992**, *52*, 6708–6711.
- 41 COUSSENS, L. et al., Tyrosine kinase receptor with extensive homology to EGF receptor shares chromosomal location with neu oncogene, *Science*, **1985**, *230*, 1132–1139.
- 42 BARGMANN, C. I., HUNG, M. C., WEINBERG, R. A., The neu oncogene encodes an epidermal growth factor receptor-related protein, *Nature*, **1986**, *319*, 226–230.
- 43 YAMAMOTO, T. et al., Similarity of protein encoded by the human c-erbB-2 gene to epidermal growth factor receptor, *Nature*, **1986**, *319*, 230–234.
- 44 SLAMON, D. J. et al., Human breast cancer: Correlation of relapse and survival with amplification of the HER-2/neu oncogene, *Science*, **1987**, *235*, 177–182.
- 45 BORG, A. et al., HER-2/neu amplification predicts poor survival in node-positive breast cancer, *Cancer Res.*, **1990**, *50*, 4332–4337.
- 46 KEER, H. N. et al., Elevated transferrin receptor content in human prostate cancer cell lines assessed in vitro and in vivo, *J. Urol.*, **1990**, *143*, 381–385.
- 47 ELLIOTT, R. L., ELLIOTT, M. C., WANG, F., HEAD, J. F., Breast carcinoma and the role of iron metabolism. A cytochemical, tissue culture, and ultrastructural study, *Ann. New York Acad. Sci.*, **1993**, *698*, 159–166.
- 48 LEBIEN, T. W., MCCORMACK, R. T., The common acute lymphoblastic leukemia antigen (CD10) –

- emancipation from a functional enigma, *Blood*, **1989**, 73, 625–635.
- 49 CARREL, S., ZOGRAFOS, L., SCHREYER, M., RIMOLDI, D., Expression of CALLA/CD10 on human melanoma cells, *Melanoma Res.*, **1993**, 3, 319–323.
  - 50 VERVOORDELDONK, S. F., MERLE, P. A., VAN LEEUWEN, E. F., VON DEM BORNE, A. E., SLAPER-CORTENBACH, I. C., Preclinical studies with radiolabeled monoclonal antibodies for treatment of patients with B-cell malignancies, *Cancer*, **1994**, 73, 1006–1011.
  - 51 KOHLER, G., MILSTEIN, C., Continuous cultures of fused cells secreting antibody of predefined specificity, *J. Immunol.*, **2005**, 174, 2453–2455.
  - 52 BUSKE, C., FEURING-BUSKE, M., UNTERHALT, M., HIDDEMANN, W., Monoclonal antibody therapy for B cell non-Hodgkin's lymphomas: Emerging concepts of a tumour-targeted strategy, *Eur. J. Cancer*, **1999**, 35, 549–557.
  - 53 JONES, P. T., DEAR, P. H., FOOTE, J., NEUBERGER, M. S., WINTER, G., Replacing the complementarity-determining regions in a human antibody with those from a mouse, *Nature*, **1986**, 321, 522–525.
  - 54 RIECHMANN, L., CLARK, M., WALDMANN, H., WINTER, G., Reshaping human antibodies for therapy, *Nature*, **1988**, 332, 323–327.
  - 55 MARKS, J. D. et al., By-passing immunization. Human antibodies from V-gene libraries displayed on phage, *J. Mol. Biol.*, **1991**, 222, 581–597.
  - 56 ABOU-JAWDE, R., CHOUERI, T., ALEMANY, C., MEKHAL, T., An overview of targeted treatments in cancer, *Clin Ther.*, **2003**, 25, 2121–2137.
  - 57 GLENNIE, M. J., VAN DE WINKEL, J. G., Renaissance of cancer therapeutic antibodies, *Drug Discov Today*, **2003**, 8, 503–510.
  - 58 ZHOU, J. et al., Preparation of arsenic trioxide-loaded albuminates immunonanospheres and its specific killing effect on bladder cancer cell in vitro, *Chin. Med. J. (Engl.)*, **2005**, 118, 50–55.
  - 59 BECERRIL, B., POUL, M. A., MARKS, J. D., Toward selection of internalizing antibodies from phage libraries, *Biochem. Biophys. Res. Commun.*, **1999**, 255, 386–393.
  - 60 NIELSEN, U. B. et al., Therapeutic efficacy of anti-ErbB2 immunoliposomes targeted by a phage antibody selected for cellular endocytosis, *Biochim. Biophys. Acta*, **2002**, 1591, 109–118.
  - 61 LIU, B., CONRAD, F., COOPERBERG, M. R., KIRPOTIN, D. B., MARKS, J. D., Mapping tumor epitope space by direct selection of single-chain Fv antibody libraries on prostate cancer cells, *Cancer Res.*, **2004**, 64, 704–710.
  - 62 LI, K. C., PANDIT, S. D., GUCCIONE, S., BEDNARSKI, M. D., Molecular imaging applications in nanomedicine, *Biomed. Microdevices*, **2004**, 6, 113–116.
  - 63 FOLKMAN, J., Successful treatment of an angiogenic disease, *N. Engl. J. Med.*, **1989**, 320, 1211–1212.
  - 64 CHEN, Q. R., ZHANG, L., GASPER, W., MIXSON, A. J., Targeting tumor angiogenesis with gene therapy, *Mol. Genet. Metab.*, **2001**, 74, 120–127.
  - 65 HOOD, J. D. et al., Tumor regression by targeted gene delivery to the neovasculature, *Science*, **2002**, 296, 2404–2407.
  - 66 HALLAHAN, D. et al., Integrin-mediated targeting of drug delivery to irradiated tumor blood vessels, *Cancer Cell*, **2003**, 3, 63–74.
  - 67 SCHIFFELERS, R. M. et al., Transporting silence: Design of carriers for siRNA to angiogenic endothelium, *J. Controlled Release*, **2005**.
  - 68 FAROKHZAD, O. C. et al., Nanoparticle-aptamer bioconjugates: A new approach for targeting prostate cancer cells, *Cancer Res.*, **2004**, 64, 7668–7672.
  - 69 LI, L. et al., A novel antiangiogenesis therapy using an integrin antagonist or anti-Flk-1 antibody coated 90Y-labeled nanoparticles, *Int. J. Radiat. Oncol. Biol. Phys.*, **2004**, 58, 1215–1227.
  - 70 SANTRA, S. et al., Folate conjugated fluorescent silica nanoparticles for labeling neoplastic cells, *J. Nanosci. Nanotechnol.*, **2005**, 5, 899–904.
  - 71 HUEBERS, H. A., FINCH, C. A., The physiology of transferrin and

- transferrin receptors, *Physiol. Rev.*, **1987**, 67, 520–582.
- 72 PONKA, P., Tissue-specific regulation of iron metabolism and heme synthesis: Distinct control mechanisms in erythroid cells, *Blood*, **1997**, 89, 1–25.
- 73 PUN, S. H. et al., Targeted delivery of RNA-cleaving DNA enzyme (DNAzyme) to tumor tissue by transferrin-modified, cyclodextrin-based particles, *Cancer Biol. Ther.*, **2004**, 3, 641–650.
- 74 BELLOCQ, N. C., PUN, S. H., JENSEN, G. S., DAVIS, M. E., Transferrin-containing, cyclodextrin polymer-based particles for tumor-targeted gene delivery, *Bioconj. Chem.*, **2003**, 14, 1122–1132.
- 75 NA, K. et al., Self-assembled nanoparticles of hydrophobically-modified polysaccharide bearing vitamin H as a targeted anti-cancer drug delivery system, *Eur. J. Pharm. Sci.*, **2003**, 18, 165–173.
- 76 MARUYAMA, K. et al., Characterization of in vivo immunoliposome targeting to pulmonary endothelium, *J. Pharm. Sci.*, **1990**, 79, 978–984.
- 77 HUTCHINSON, F. J., FRANCIS, S. E., LYLE, I. G., JONES, M. N., The characterisation of liposomes with covalently attached proteins, *Biochim. Biophys. Acta*, **1989**, 978, 17–24.
- 78 SARKAR, D. P., BLUMENTHAL, R., The role of the target membrane structure in fusion with Sendai virus, *Membr. Biochem.*, **1987**, 7, 231–247.
- 79 YU, D. et al., The specific delivery of proteins to human liver cells by engineered bio-nanocapsules, *FEBS J.*, **2005**, 272, 3651–3660.
- 80 GORDON, E. M., HALL, F. L., Nanotechnology blooms, at last (Review), *Oncol. Rep.*, **2005**, 13, 1003–1007.
- 81 GORDON, E. M. et al., First clinical experience using a “pathotropic” injectable retroviral vector (Rexin-G) as intervention for stage IV pancreatic cancer, *Int. J. Oncol.*, **2004**, 24, 177–185.
- 82 PARK, J. W., BENZ, C. C., MARTIN, F. J., Future directions of liposome- and immunoliposome-based cancer therapeutics, *Semin. Oncol.*, **2004**, 31, 196–205.
- 83 SENIOR, J. H., Fate and behavior of liposomes in vivo: A review of controlling factors, *Crit. Rev. Ther. Drug Carrier Syst.*, **1987**, 3, 123–193.
- 84 KLIBANOV, A. L., MARUYAMA, K., TORCHILIN, V. P., HUANG, L., Amphipathic polyethyleneglycols effectively prolong the circulation time of liposomes, *FEBS Lett.*, **1990**, 268, 235–237.
- 85 GABIZON, A. et al., Targeting folate receptor with folate linked to extremities of poly(ethylene glycol)-grafted liposomes: In vitro studies, *Bioconj. Chem.*, **1999**, 10, 289–298.
- 86 STORM, G., TEN KATE, M. T., WORKING, P. K., BAKKER-WOUDENBERG, I. A., Doxorubicin entrapped in sterically stabilized liposomes: Effects on bacterial blood clearance capacity of the mononuclear phagocyte system, *Clin. Cancer Res.*, **1998**, 4, 111–115.
- 87 MUGGIA, F. M. et al., Phase II study of liposomal doxorubicin in refractory ovarian cancer: Antitumor activity and toxicity modification by liposomal encapsulation, *J. Clin. Oncol.*, **1997**, 15, 987–993.
- 88 LASIC, D. D., PAPAHAJDOPOULOS, D., Liposomes revisited, *Science*, **1995**, 267, 1275–1276.
- 89 ARAGNOL, D., LESERMAN, L. D., Immune clearance of liposomes inhibited by an anti-Fc receptor antibody in vivo, *Proc. Natl. Acad. Sci. U.S.A.*, **1986**, 83, 2699–2703.
- 90 DERKSEN, J. T., MORSELT, H. W., SCHERPHOF, G. L., Uptake and processing of immunoglobulin-coated liposomes by subpopulations of rat liver macrophages, *Biochim. Biophys. Acta*, **1988**, 971, 127–136.
- 91 MARUYAMA, K. et al., Targetability of novel immunoliposomes modified with amphipathic poly(ethylene glycol)s conjugated at their distal terminals to monoclonal antibodies, *Biochim. Biophys. Acta*, **1995**, 1234, 74–80.
- 92 MARUYAMA, K., ISHIDA, O., TAKIZAWA, T., MORIBE, K., Possibility of active

- targeting to tumor tissues with liposomes, *Adv. Drug Deliv. Rev.*, **1999**, *40*, 89–102.
- 93 HUWYLER, J., WU, D., PARDRIDGE, W. M., Brain drug delivery of small molecules using immunoliposomes, *Proc. Natl. Acad. Sci. U.S.A.*, **1996**, *93*, 14 164–14 169.
- 94 BERINSTEIN, N., MATTHAY, K. K., PAPAHAJIOPOULOS, D., LEVY, R., SIKIC, B. I., Antibody-directed targeting of liposomes to human cell lines: Role of binding and internalization on growth inhibition, *Cancer Res.*, **1987**, *47*, 5954–5959.
- 95 GOREN, D. et al., Targeting of stealth liposomes to erbB-2 (Her/2) receptor. In vitro and in vivo studies, *Br. J. Cancer*, **1996**, *74*, 1749–1756.
- 96 PARK, J. W. et al., Development of anti-p185HER2 immunoliposomes for cancer therapy, *Proc. Natl. Acad. Sci. U.S.A.*, **1995**, *92*, 1327–1331.
- 97 PARK, J. W. et al., Anti-HER2 immunoliposomes for targeted therapy of human tumors, *Cancer Lett.*, **1997**, *118*, 153–160.
- 98 POUL, M. A., BECERRIL, B., NIELSEN, U. B., MORISSON, P., MARKS, J. D., Selection of tumor-specific internalizing human antibodies from phage libraries, *J. Mol. Biol.*, **2000**, *301*, 1149–1161.
- 99 WINTER, G., GRIFFITHS, A. D., HAWKINS, R. E., HOOGENBOOM, H. R., Making antibodies by phage display technology, *Annu. Rev. Immunol.*, **1994**, *12*, 433–455.
- 100 SCHIER, R. et al., Isolation of picomolar affinity anti-c-erbB-2 single-chain Fv by molecular evolution of the complementarity determining regions in the center of the antibody binding site, *J. Mol. Biol.*, **1996**, *263*, 551–567.
- 101 PARK, J. W., Liposome-based drug delivery in breast cancer treatment, *Breast Cancer Res.*, **2002**, *4*, 95–99.
- 102 SPRINGER, C. J., NICULESCU-DUVAZ, I., Approaches to gene-directed enzyme prodrug therapy (GDEPT), *Adv. Exp. Med. Biol.*, **2000**, *465*, 403–409.
- 103 VINGERHOEDS, M. H. et al., A new application for liposomes in cancer therapy. Immunoliposomes bearing enzymes (immuno-enzymosomes) for site-specific activation of prodrugs, *FEBS Lett.*, **1993**, *336*, 485–490.
- 104 LEE, R. J., Low, P. S., Delivery of liposomes into cultured KB cells via folate receptor-mediated endocytosis, *J. Biol. Chem.*, **1994**, *269*, 3198–3204.
- 105 LEE, R. J., Low, P. S., Folate-mediated tumor cell targeting of liposome-entrapped doxorubicin in vitro, *Biochim. Biophys. Acta*, **1995**, *1233*, 134–144.
- 106 KIRPOTIN, D. et al., Sterically stabilized anti-HER2 immunoliposomes: Design and targeting to human breast cancer cells in vitro, *Biochemistry*, **1997**, *36*, 66–75.
- 107 MORRISON, S. L., Transfectomas provide novel chimeric antibodies, *Science*, **1985**, *229*, 1202–1207.
- 108 FEERO, W. G. et al., Selection and use of ligands for receptor-mediated gene delivery to myogenic cells, *Gene Ther.*, **1997**, *4*, 664–674.
- 109 XU, L., PIROLLO, K. F., TANG, W. H., RAIT, A., CHANG, E. H., Transferrin-liposome-mediated systemic p53 gene therapy in combination with radiation results in regression of human head and neck cancer xenografts, *Hum Gene Ther.*, **1999**, *10*, 2941–2952.
- 110 LEE, R. J., HUANG, L., Folate-targeted, anionic liposome-entrapped polylysine-condensed DNA for tumor cell-specific gene transfer, *J. Biol. Chem.*, **1996**, *271*, 8481–8487.
- 111 FRÉCHET, J. M. J., TOMALIA, D. A., *Dendrimers Dendritic Polym.*, **2001**.
- 112 ESFAND, R., TOMALIA, D. A., Poly(amidoamine) (PAMAM) dendrimers: From biomimicry to drug delivery and biomedical applications, *Dendrimers Dendritic Polym.*, **2001**, *6*, 427–436.
- 113 MALIK, N. et al., Dendrimers: Relationship between structure and biocompatibility in vitro, and preliminary studies on the biodistribution of 125I-labelled polyamidoamine dendrimers in vivo, *J. Controlled Release*, **2000**, *65*, 133–148.
- 114 BOSMAN, A. W., VESTBERG, R., HEUMANN, A., FRECHET, J. M., HAWKER, C. J., A modular approach

- toward functionalized three-dimensional macromolecules: From synthetic concepts to practical applications, *J. Am. Chem. Soc.*, **2003**, *125*, 715–728.
- 115 DEWEY, R. S. et al., The synthesis of peptides in aqueous medium. VII. The preparation and use of 2,5-thiazolidinediones in peptide synthesis, *J. Org. Chem.*, **1971**, *36*, 49–59.
- 116 MALIK, N., EVAGOROU, E. G., DUNCAN, R., Dendrimer-platinate: A novel approach to cancer chemotherapy, *Anticancer Drugs*, **1999**, *10*, 767–776.
- 117 GREENFIELD, R. S. et al., Evaluation in vitro of adriamycin immun-conjugates synthesized using an acid-sensitive hydrazone linker, *Cancer Res.*, **1990**, *50*, 6600–6607.
- 118 PADILLA DE JESUS, O. L., IHRE, H. R., GAGNE, L., FRECHET, J. M., SZOKA, F. C., JR., Polyester dendritic systems for drug delivery applications: In vitro and in vivo evaluation, *Bioconj. Chem.*, **2002**, *13*, 453–461.
- 119 KONO, K., LIU, M., FRECHET, J. M., Design of dendritic macromolecules containing folate or methotrexate residues, *Bioconj. Chem.*, **1999**, *10*, 1115–1121.
- 120 BIRRENBACH, G., SPEISER, P. P., Polymerized micelles and their use as adjuvants in immunology, *J. Pharm. Sci.*, **1976**, *65*, 1763–1766.
- 121 GILBERT, L. et al., Molecular and structural characterization of fluorescent human parvovirus B19 virus-like particles, *Biochem. Biophys. Res. Commun.*, **2005**, *331*, 527–535.
- 122 MO, Y., LIM, L. Y., Preparation and in vitro anticancer activity of wheat germ agglutinin (WGA)-conjugated PLGA nanoparticles loaded with paclitaxel and isopropyl myristate, *J. Controlled Release*, **2005**.
- 123 BRIGGER, I., DUBERNET, C., COUVREUR, P., Nanoparticles in cancer therapy and diagnosis, *Adv. Drug Deliv. Rev.*, **2002**, *54*, 631–651.
- 124 SCHWAB, G. et al., Antisense oligonucleotides adsorbed to polyalkylcyanoacrylate nanoparticles specifically inhibit mutated Ha-ras-mediated cell proliferation and tumorigenicity in nude mice, *Proc. Natl. Acad. Sci. U.S.A.*, **1994**, *91*, 10460–10464.
- 125 LAMBERT, G. et al., EWS fli-1 antisense nanocapsules inhibits Ewing sarcoma-related tumor in mice, *Biochem. Biophys. Res. Commun.*, **2000**, *279*, 401–406.
- 126 MORIN, C., BARRATT, G., FESSI, H., DEVISSAGUET, J. P., PUISIEUX, F., Improved intracellular delivery of a muramyl dipeptide analog by means of nanocapsules, *Int. J. Immunopharmacol.*, **1994**, *16*, 451–456.
- 127 SINEK, J., FRIEBOES, H., ZHENG, X., CRISTINI, V., Two-dimensional chemotherapy simulations demonstrate fundamental transport and tumor response limitations involving nanoparticles, *Biomed. Microdevices*, **2004**, *6*, 297–309.
- 128 DUNCAN, R., The dawning era of polymer therapeutics, *Nat. Rev. Drug Discov.*, **2003**, *2*, 347–360.
- 129 NETTI, P. A., BAXTER, L. T., BOUCHER, Y., SKALAK, R., JAIN, R. K., Time-dependent behavior of interstitial fluid pressure in solid tumors: Implications for drug delivery, *Cancer Res.*, **1995**, *55*, 5451–5458.
- 130 LOO, C., LOWERY, A., HALAS, N., WEST, J., DREZEK, R., Immunotargeted nanoshells for integrated cancer imaging and therapy, *Nano Lett.*, **2005**, *5*, 709–711.
- 131 POTINENI, A., LYNN, D. M., LANGER, R., AMIJI, M. M., Poly(ethylene oxide)-modified poly(beta-amino ester) nanoparticles as a pH-sensitive biodegradable system for paclitaxel delivery, *J. Controlled Release*, **2003**, *86*, 223–234.
- 132 EHRlich, PAUL, Encyclopaedia Britannica, **2006**, Encyclopaedia Britannica Premium Service, 31 Mar 2006, <http://www.britannica.com/eb/article-9032103>.
- 133 ZEIMET, A. G., MARTH, C., Why did p53 gene therapy fail in ovarian cancer? *Lancet Oncol.*, **2003**, *4*, 415–422.
- 134 ZHANG, Y., HUANG N., Intracellular uptake of CdSe-ZnS/polystyrene nanobeads, *J. Biomed. Mater. Res. B, Appl. Biomater.*, **2006**, *76*(1), 161–168.

## 11

# Colloidal Systems for the Delivery of Anticancer Agents in Breast Cancer and Multiple Myeloma

*Sébastien Maillard, Elias Fattal, Véronique Marsaud, Brigitte Sola, and Jack-Michel Renoir*

### 11.1

#### Introduction

The success of cancer treatments depends on an active drug concentration at the tumor sites. In fact, drug dispatch remains the objective of clinicians and drug delivery has been the subject of a tremendous amount of research during the past four decades [1, 2]. Indeed, most used anticancer drugs have great toxicity, including for normal tissues, and it is crucial to minimize massive damage to the rest of the body after their administration. Moreover, despite poor water solubility, owing to a high hydrophobicity, some chemotherapeutic drugs were initially given orally. However, drug administration, particularly for antitumor drugs, increasingly required intravenous perfusion, leading to a poor amount reaching the tumors and to important side effects because high doses are often administered. This poor specificity creates a toxicological problem that constitutes a serious obstacle to effective antitumor therapy. Thus, a crucial problem remains the addressing of the drug to the site of action, i.e., being more tumor selective.

Undoubtedly, intravenous administration of anticancer drugs could be of great help but it remains limited by the capture of the drug by macrophages of the mononuclear phagocytes system (MPS), leading to drug destruction in the liver, spleen, lung and bone marrow. If the propensity of MPS macrophages for endocytosis/phagocytosis provides an opportunity to deliver efficiently therapeutic agents to these organs, the targeting of non-MPS organs remains a priority. One strategy consists of associating antitumor drugs with colloidal systems engineered to resist the MPS and to increase the selectivity of drugs towards cancer cells while reducing their toxicity towards normal tissues. Various injectable delivery systems, nanoparticles, emulsions and liposomes (conventional drug delivery systems, CDDS), have been developed but only a few are clinically used. To avoid their recognition by opsonins (immunoglobulins, proteins from the complement) and their degradation by the MPS organs, hydrophilic polymers may be grafted [2, 3] at the surface of these colloidal systems [4, 5], rendering them capable of long circula-



tion times in the blood stream, thus constituting “Stealth” drug delivery systems (SDDS) [6].

Another important issue is the capacity of formulations to cross the vascular endothelium (extravasation process). Vascularization of solid tumors is heterogeneous, with regions of necrosis and other areas that are densely vascularized in order to supply the tumor cells with nutrients for tumor growth. The formation of new capillaries from pre-existing vessels (angiogenesis) also contributes to tumor growth. Tumor blood vessels present various abnormalities (increased tortuosity, deficiency in pericytes, aberrant basement membrane formation [1, 7]) that result in an enhanced permeability of tumor vasculature. This enhancement is thought to be regulated by various mediators, such as vascular endothelium growth factor (VEGF), nitric oxide, prostaglandins and metalloproteinases [8, 9]. Macromolecules cross tumor vessels through open gaps (interendothelial junctions and transendothelial channels), vesicular endothelial organelles and fenestrations [10]. The pore size cut-off of various solid tumor models usually lies in the range 380–800 nm [2, 9–13], which is compatible with the extravasation of SDDS.

Thus, to deliver therapeutic agents to tumor cells following i.v. injection one must: (a) avoid the opsonization process and resulting destruction by the MPS; (b) realize a stealth formulation incorporating high amounts of drug; (c) dispatch a high and active drug concentration at the tumor level; (d) overcome drug resistance mechanisms. This chapter focuses on two types of cancer, which differ in the sort of cells they affect and in their morphology, i.e., breast cancers and multiple myeloma, and we describe how new antiestrogen drug delivery devices strongly inhibit tumor growth in xenograft models.

Besides their essential function in female reproduction, estrogens exert various responses in target cells, including promotion of tissue differentiation, morphogenesis, mitogenic activity and development of the mammary gland. They are also beneficial hormones in the regulation of bone mineral density, through effects on the osteoclast/osteoblast balance, in the prevention of atheromatous plaque, and in the nervous system. Importantly, they are also implicated in oncogenesis and maintenance of some tumor growth. In fact, estrogens are regulators of several proto-oncogenes coding for nuclear proteins [14]. Estrogens act on cells via interaction with two types of intracellular receptors, ER $\alpha$  [15, 16] and ER $\beta$  [17–19]. Like all steroid hormone receptors, ERs are trans-acting transcription enhancer factors that are activated by binding of their ligands. They become, therefore, capable of interacting with specific cis-acting enhancer elements that are usually located with the 5'-flanking regions of target genes. This classical mechanism of action was thought for many years to be unique. However, following recent findings reporting the membrane localization of ER, “non-genomic” mechanisms involving mitogen-activated protein kinase (MAPK) activation have emerged [20, 21].

Half of breast cancers are intrinsically estrogen sensitive and, therefore, respond to antiestrogens [22, 23]. To treat these estrogen-dependent cancers, pharmacologists have aimed to develop antiestrogens, i.e., compounds capable of blocking the effects of estradiol without displaying any estrogenic activity on their own. Numer-

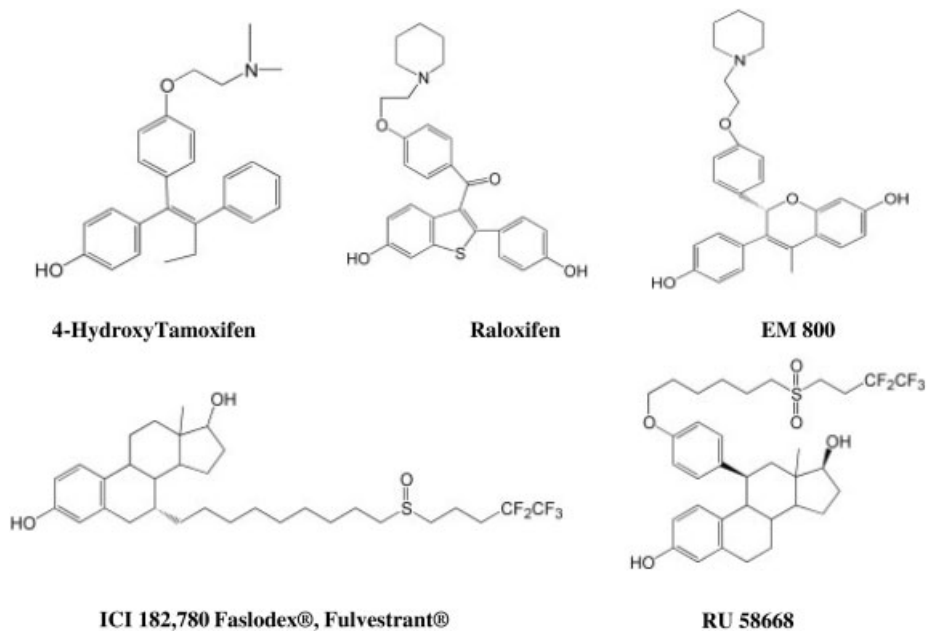


**Fig. 11.1.** Structure of the most commonly studied antiestrogens: The most commonly used SERMs (Tamoxifen and raloxifen) and three pure antiestrogens (ICI 182,780, RU 58 668 and EM 800) are shown. Among them

only ICI 182,780 (Faslodex®), by deep i.m. oily injection in tamoxifen-resistant breast cancers. RU 58 668 development has been stopped and EM 800 is in phase II clinical trials [183, 184].

ous molecules (Fig. 11.1) behave both as agonists or antagonists of estradiol, depending on the tissue, the promoter and the type of the ER [22, 24]. These compounds have been classified as “selective estrogen receptor modulators” (SERMs). Recently, a few compounds able to bind ER and to abrogate all effects of estrogens in a competitive manner have been elaborated [24]. These so-called “pure antiestrogens” were expected to be very useful for estradiol-dependent cancer treatment. In addition to their ability to inhibit all the effects of estradiol, one other important characteristic is their capacity to target ERs to proteasome-mediated degradation in human breast cancer cells [25–27]. On the basis of this property, “pure antiestrogens” have been called selective ER down-regulators (SERDs). However, recent findings in various cancer cell lines prompted reconsideration of this notion, because it has been observed that any kind of antiestrogen, both SERMs and “pure antiestrogens”, behave as inducers of transcription through the activating protein 1 (AP<sub>1</sub>) pathway [28–30].

Multiple myeloma (MM) is a B-cell malignancy characterized by the clonal expansion of tumoral plasma cells in the bone marrow. This accumulation of malignant cells synthesizing immunoglobulins results in hyperproteinemia, renal

dysfunctions, bone lesions and immunodeficiency [31]. This pathology, which accounts for 2% of all cancer deaths per year in occidental countries, remains largely incurable despite novel therapeutic approaches involving the targeting of both MM cells and the bone-marrow environment [32]. Previous studies have established that both ER $\alpha$  and  $\beta$  isotypes are expressed in some MM cells [33–36]. Surprisingly, and differing strongly from breast cancer cells, estradiol as well as SERMs and SERDs induce a decrease of MM cell proliferation, and at a micromolar concentration preclude a classical recruitment of ERs. However, SERMs and SERDs induce breast cancer and MM cell cycle arrest as well as apoptosis. Therefore, they all can be considered as potent anticancer drugs.

Other work relating to the use of anticancer drug delivery systems has shown the importance of this approach in developing new anticancer treatments. However, most work describes the use of drug delivery systems containing highly cytotoxic drugs devoid of specific cellular target, leading to ubiquitous effects and high toxicity [37, 38]. A physicochemical DDS containing an anticancer drug implies knowledge of the physicochemical properties of the drug, its exact mechanism of action in the pathology to be treated, and the physiology of the pathology itself. Here, we point out the importance of delivering a molecule endowed with a very specific intracellular target.

Thus, we focus first (Section 11.2.1) on the importance of estrogens in breast cancer development. The different roles of estrogens will be discussed by presenting the classical ER-ligand and ERE-dependant, ERE-independent, ER-ligand independent, and “non-genomic” pathways. Knowledge of these precise mechanisms has led to the use of various families of antiestrogens (AEs), the properties of which differ (Section 11.2.2). The benefits of AE encapsulation, to improve anti-tumoral activities *in vivo* and to limit side effects, are discussed in Section 11.2.3.

In Section 11.3, we focus on another pathology, multiple myeloma (MM), describing current treatments and new biological therapies as well as the promising use of AEs.

Whatever the concerned pathology, we will develop in Section 11.4 the requirement for a specific drug delivery system. Thus, the use of passive targeting long-circulating drug delivery systems in different types of xenografts are detailed, such as nanoparticles for breast cancer (Section 11.4.1) and liposomes for MM (Section 11.4.2). Finally, we discuss the potential improvement of these systems on acquiring a specific tumoral recognition element (Section 11.4.3).

## 11.2

### Hormone Therapy in Breast Cancers

Two important general ways have been imagined for eliminating the mitogenic activity of estradiol in estrogen-dependent breast cancers: blocking the site of an estrogenic specific target (the estradiol receptor) or blocking the synthesis of estradiol. For the first case, antiestrogenic compounds are used, and for the second case aromatase inhibitors have been developed [39].

## 11.2.1

**Molecular Mechanisms of Estrogen Action in Breast Cancers****11.2.1.1 Classical ER-ligand and ERE-dependent Mechanism**

The general mechanism by which estrogens transduce their mitogenic activity results from their binding to the two nuclear receptors from the steroid/thyroid superfamily of transcription factors, ER $\alpha$  and ER $\beta$  [40, 41]. In addition to binding estrogens with a high affinity, ERs bind to specific DNA sequences called estrogen responsive elements (EREs), possess defined activating functions (AF1 in the N-terminal domain and AF2 in the ligand binding domain), and interact with various protein partners [22, 24, 42–44]. In target cells unexposed to estradiol (E<sub>2</sub>) or growth factors, ER $\alpha$  is part of a large complex in which molecular chaperones such as heat shock proteins (hsp) and co-chaperones are present (for a review see Ref. [44]). The major chaperones that favors the efficient folding of ER $\alpha$  are hsp90 and hsp70 [44–47]. Another important partner of this supramolecular complex is p23 [48, 49], a N-terminal interacting client protein of hsp90 [50], the overexpression of which decreases the transactivation capacity and ligand binding of ER $\alpha$  [51]. In fact, this p23 is a prostaglandin-E<sub>2</sub> synthase and its degradation is an apoptosis indicator [52, 53].

Following E<sub>2</sub> binding, a change in ER $\alpha$  conformation occurs, promoting the dissociation of hsp90 and other proteins from the molecular chaperone complex. Phosphorylation of ER $\alpha$  increases in response to estradiol binding prior to transcriptional enhancement [54]. This rapid process leads to dimerization of ER $\alpha$ , to its tight association with the nucleus [55] and to its interaction with specific nucleotide sequences of the specific EREs in gene promoters. This leads to enhancement of transcription through the recruitment of co-activators, some of which carry a histone acetyl transferase (HAT) activity (Fig. 11.2A), like SRC<sub>1</sub> and CBP/p300 [41, 56, 57]. Histone acetylation leads to chromatin opening and to repositioning of nucleosomes [58]. Other modifications of the ER state and of some co-regulators and the specific DNA sequences (like phosphorylations, methylation, ubiquitination, acetylation) also take place in the sequentially and processivity of transactivation [O'Malley, B. W., NURSA e-journal (2003) 1, ID# 3.11052003.1; ISSN 1550-7629]. This interaction of ER with DNA leads to activation of transcription [40, 42]. Recently, the concept of a “transcriptional clock” that directs and achieves the sequential and combinatorial assembly of 46 co-activators at a specific E<sub>2</sub>-inducible (pS2) promoter in human breast cancer MCF-7 cells was defined [59, 60]. Following the pS2 promoter transactivation, the E<sub>2</sub>-ER complex is polyubiquitinated, leading to its proteasome-mediated destruction [60, 61].

With binding of a SERM, cofactors different from those recruited upon E<sub>2</sub> binding associate with the ER $\alpha$ /DNA complex (Fig. 11.2A). Co-repressors, such as N-COR, SMRT and REA (specific for ER $\alpha$ ), are present in these complexes [56, 57, 62]. The co-repressors are associated with a histone deacetylase activity (HDAC), which re-compacts chromatin followed by nucleosome re-positioning, leading to blockade of transcription of specific genes. It has also been proposed that, in the absence of ligand, ER $\alpha$  could be sequestered in complexes containing

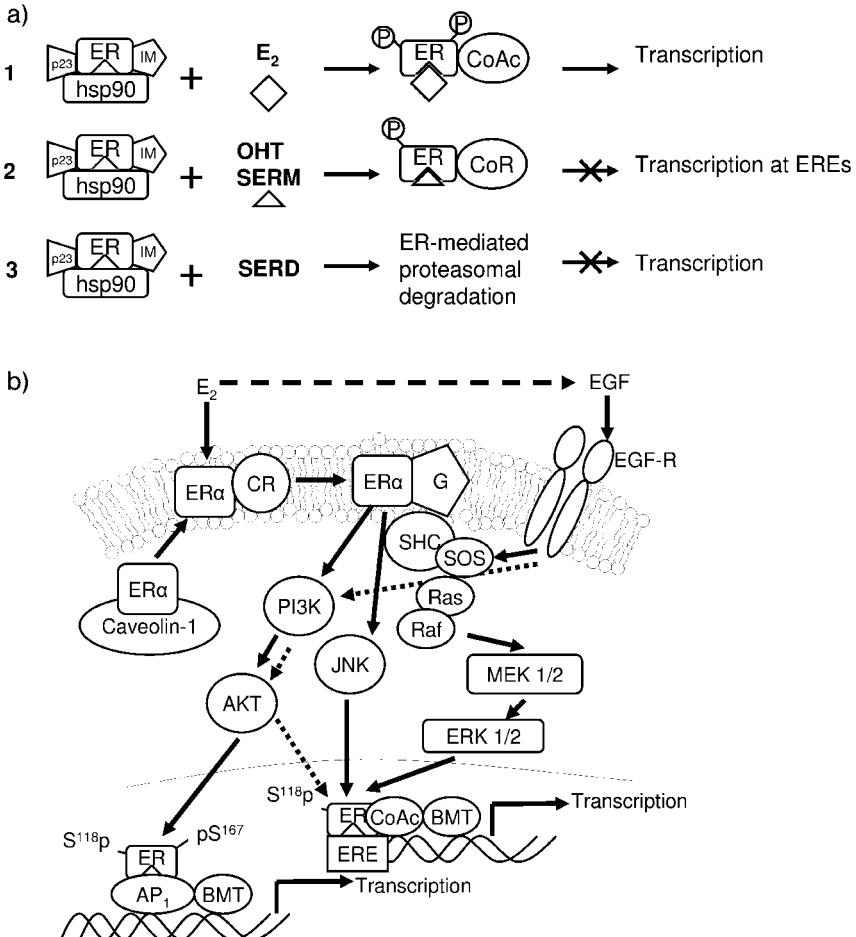


**Fig. 11.2.** Mechanisms of action of estradiol and antiestrogens: (A) In the classical genomic mechanism of ER, the inactivated receptor (1) is sequestered in a supramolecular chaperone complex (organized around hsp90, p23 and immunophilins). E<sub>2</sub> binds to inactivated ER, changes its conformation, promotes both its phosphorylation by different kinases and its release from the molecular chaperones, helps in the sequential recruitment of a set of co-activators, among which are histone acetyl transferases (HAT), which modify the chromatin structure en route to transcription. When a SERM like OH-tamoxifen (OHT) binds to ER (2), the induced conformational change and the phosphorylation state of ER differ from

those induced by E<sub>2</sub> binding. Co-repressors instead of co-activators are recruited, among which are histone deacetylases (HDAC), which re-compact the chromatin and preclude interaction with the basal machinery of transcription (BMT) at an ERE, allowing activation of the polymerase and leading to inhibition of the transcription. With an AP<sub>1</sub>-containing promoter, the SERM-ER $\beta$  complex activates transcription while the E<sub>2</sub>-ER complex inhibits AP<sub>1</sub>-mediated transcription. If a SERD like RU or Faslodex complexes with ER $\alpha$  (3) a delocalization of ER and its fast proteasome-mediated destruction occurs, precluding binding to DNA.

these repressors (or some of them), maintaining the receptor in an inactive state [63].

#### 11.2.1.2 ERE-independent Pathway

In addition to the classical transactivation pathway that results in binding of the  $E_2$ /ER $\alpha$ -complex to EREs, tamoxifen and other SERMs also activate target genes (like collagenase gene) through binding at an activating protein-1 (AP-1) site; this is observed in uterine cells but not in breast tumor cells [28]. It occurs through direct binding of ER- $E_2$  complex to the heterodimer c-fos/c-jun at AP-1 binding sites and is mainly mediated via ER $\beta$ , the major ER form in the endometrium (Fig. 11.2B). Remarkably, the pharmacology of ER ligands bound to ER $\beta$  is reversed at an AP-1 element. Bound to ER $\beta$ , the antiestrogens, including the “pure antiestrogens” Faslodex® and RU 58668 (RU) (Gougelet, A., Marsaud, V., Renoir, J.-M., in preparation), act as transcriptional activators and  $E_2$  behaves as a transcription inhibitor. These features may explain the incidence of uterine cancers following long-term tamoxifen treatment of  $E_2$ -dependent breast cancers, and could be involved in the acquisition of tamoxifen resistance in breast tumors [24]. Similarly, other genes containing GC-rich promoter sequences are activated via an ER-SP1 complex [64, 65].

#### 11.2.1.3 ER-ligand-independent Pathway

There is accumulating evidence that ER-mediated transcription activation occurs also in the absence of ER-ligand binding in response to cell surface growth factor receptors and the intracellular signaling cascades that they activate [66–68]. Indeed, growth factors or cyclic adenosine monophosphate (cAMP) activate intracellular kinase pathways, leading to phosphorylation and activation of ER at ERE-containing promoters in a ligand-independent manner, possibly via p42/44 MAPK activation [69–71]. Similarly, phorbol-12-myristate-13-acetate (PMA) through the stimulation of adenylate cyclase also increases the ER-mediated transcription. Therefore, the genomic activity of ER can be induced by numerous different stimuli, ER agonists themselves but also activators of various kinases of the EGF receptor family as well as activators of PI3-K, PKA and PKC [54]. These variable processes target ER to different sequences present in  $E_2$ - and/or PMA-inducible promoters to affect gene expression. However, the crosstalk between the classical activation  $E_2$ -dependent pathways and other pathways has considerably helped our understanding of the complicated multifaceted mechanism of action of estrogens.

← (B) ER $\alpha$  can also be rapidly phosphorylated on Ser118 by the MAPKinase pathway following activation of the EGF receptor which, through the Ras,Raf, MEK, ERK cascade, leads to an ERE-dependent, ER-ligand-independent transactivation activity, or an ERE-independent, ER-ligand-independent-PI3K/AKT-dependent activation process. The “non-genomic” activation process by which ER $\alpha$  can be

activated proceeds through binding of  $E_2$  to a cytosoluble ER bound to caveolin-1, to translocation of the caveolin-1/ER $\alpha$  complex to the membrane, leading to association with a caveolin-1 receptor (CR), allowing contact with small G proteins, which acts to activate the MAPK cascade and gene expression without any DNA binding of ER $\alpha$ .

#### 11.2.1.4 “Non-genomic” Pathway

Besides this general and well-accepted genomic mechanism (representing direct or indirect binding of ER to DNA), estrogens may induce effects occurring within minutes (“non-genomic effects”), which is incompatible with a process requiring DNA and transcription (Fig. 11.2B). For instance, estrogen-induced vasodilatation is rapid and relies on the activation of nitric oxide synthase by a mechanism involving trimeric G proteins [72] and Akt via the PI3-K pathway [73]. Direct interaction between ER and PI3-K has been demonstrated [74]. Rapid activation by E<sub>2</sub> of protein kinase C in MCF-7 ER-positive (ER+) cells as well as in other human breast cancers lacking ER is membrane mediated and inhibited by tamoxifen [75]. Several groups have reported that E<sub>2</sub> induces a rapid activation of MAPK/ERK in breast cancer cells [76–78] as well as a rapid non-transcriptional activation of PI3-K [79]. However, this E<sub>2</sub>-induced activation of both MAPK and PI3-K in human ER+ breast cancer cells such as MCF-7 and ZR75.1 has been severely criticized by several laboratories, who have questioned the non-genomic mitogenic activity of E<sub>2</sub> [80–83]. In fact, it is now accepted that a small amount of ER $\alpha$  exists as a functional non-traditional G-protein coupled receptor (GPCR) at the plasma membrane [78, 84–86]. Such a membrane localization of ER $\alpha$  is thought to be the consequence of the S522A mutation, which convert the receptor into a dominant-negative form [86]. This GPCR is now known as the endoplasmic reticulum GPR30 [84], which under direct E<sub>2</sub> binding results in intracellular calcium mobilization and synthesis of phosphatidylinositol 3,4,5-triphosphate in the nucleus [87].

#### 11.2.2

#### Differential Activity of Antiestrogens

Evidently, from several reports emanating from various laboratories, an efficient way to inhibit the E<sub>2</sub>-mediated mitogenic effects in breast tumors could be the suppression of the biological activity of ER. This is possible through different pathways that block ER-mediated transcription, as realized with SERMs and SERDs, but also by inhibiting ER protein expression. Introduced as a new approach for targeted therapy with few side effects compared with traditional cytotoxic chemotherapy, hormone therapy is based on the use of non-steroidal antiestrogens, the archetype of which is tamoxifen (Tam), which has been used clinically with success since the 1970s. Initially investigated in the late 1960s these antiestrogens are partial estrogen antagonists or SERMs (Fig. 11.1).

In terms of breast cancer growth, Tam as well as several other SERMs are anti-estrogenic, whereas they exert estrogen-like actions in bone, the cardiovascular system, and in the regulation of circulating low density lipoproteins (LDL) [22, 23]. Unfortunately, the SERMs are agonist in the uterus and can enhance the growth of human endometrial tumors implanted into immune deficient mice [88]. SERMs such as tamoxifen and raloxifen induce an accumulation of ER $\alpha$  in breast cancer cells [25–27, 89, 90]. In contrast to tamoxifen, both ICI 182,780 (Faslodex®) and RU 58668 treatment of human breast cancer cells results in rapid delocalization

and a fast destruction of endogenous ER $\alpha$  through the 26S proteasome pathway [25–27, 61, 86, 89, 90]. Such pure antiestrogen-induced down-regulation of ER $\alpha$  expression takes place in a nuclear compartment from which ER $\alpha$  is difficult to extract [27, 78, 91] and is recovered with the nuclear matrix [55]. The CSN5/Job1, a subunit of the COP9 signalosome, is involved in ligand-dependent degradation of ER $\alpha$  by the proteasome [92]. Interestingly, any alteration of the activity of various kinases known to affect signaling involved in cell cycle progression targets ER $\alpha$  to the 26S proteasome-mediated degradation [27]. Similarly, several co-activators involved in the activation of ER-mediated transcription are also degraded through the proteasome pathway [61]. Contrarily to ER $\alpha$ , ER $\beta$  stably expressed in ER-negative MDA-MB-231 cells is more slowly degraded by the SERDs than the ER $\alpha$  isotype and still conserves a high expression level [93].

In addition to SERDs, hsp90 inhibitors are also able to trigger ER $\alpha$  to proteasomal degradation [94]. Both N-terminal hsp90 ligands such as geldanamycin and radicicol, as well as C-terminal hsp90 ligands such as novobiocin, target not only ER $\alpha$  but also ER $\beta$  [93] to degradation through the proteasome pathway. Thus, destabilization of steroid receptors by hsp90-binding drugs constitutes a ligand-independent approach to hormonal therapy of breast cancer [95, 96]. In general, any compound with high inhibitory ability of the activity of one (or more) of the proteins implicated in the mechanism of action of ERs could be a potential anti-cancer drug (SERDs for ER $\alpha$ , HDAC inhibitors, proteasome inhibitors, hsp90 inhibitors, immunosuppressors, p23 inhibitors).

### 11.2.3

#### The Need to Encapsulate Antiestrogens

We have already mentioned the large spectrum of activity of SERMs. Actually, their use in postmenopausal women treated for estrogen-dependent breast cancer is based on a daily oral administration of Tam (20 mg day<sup>-1</sup>). Sometimes, detrimental side effects occur, leading often to hot flushes and more rarely to endometrium cancers (1–2%). Nevertheless, tamoxifen is still clinically used and, in addition, it is of benefit for osteoporosis and cardiovascular disease due to its agonistic activity in bones and vessels. Pure antiestrogens were first reported nearly 20 years ago [97]. Nevertheless, concern about the increased risk of osteoporosis and coronary heart disease, as well as problems with drug delivery, is similar to that caused by aromatase inhibitors developed as an alternative strategy for antiestrogen therapy [98]. Delivery of these molecules to their site of action at the desired rate is a challenge because their transport through compartmental barriers (endothelium or epithelium) in the body is inefficient and/or because they are rapidly metabolized. For controlled release or for site-specific delivery, new delivery systems will be required (as only oral tablets and an oil solution for i.m. injection of Faslodex® are currently available). Furthermore, alkyl estradiol derivatives are difficult to synthesize, and their oral bioavailability is very low. Therefore, a targeted drug delivery system of both SERMs and SERDs for breast cancer treatment could be of benefit.



### 11.3

#### Multiple Myeloma

Despite new insights into the biology of MM, the major prognostic for such pathology was not significantly improved. Thus, for several years, research into novel approaches, implying new therapeutic targets, has increased. We focus here on the new biological strategies and, particularly, on the promising outcomes of the estrogens and antiestrogens regimen.

##### 11.3.1

#### Current Treatments

Addition of glucocorticoids (which trigger apoptosis) to the oral alkylating agent melphalan [melphalan-prednisone (MP) regimen] constituted the mainstay of therapy for many years, although remissions were rare (<5%) and median survival did not exceed three years. Addition of other alkylating agents such as anthracyclines and vinca alkaloids to MP did not improve patient survival. The further developed therapeutic management of MM for the last two decades has mainly involved regimens based on the use of glucocorticoids (dexamethasone) and cytotoxic chemotherapeutic drugs [99, 100]. The standard therapy for MM, at least for younger patients, is considered to be autologous peripheral blood stem cell (PBSC)-supported high-dose melphalan [101].

##### 11.3.2

#### New Biological Therapies for MM Treatment

The need for efficient therapy has become obvious and several new agents seem very promising [102, 103]. Among them, SU 5416 [104], an inhibitor of VEGF-induced MM proliferation, and thalidomide, an inhibitor of tumor necrosis factor (TNF $\alpha$ ) and VEGF production, which is in phase II trials, could be of great interest [105–107]. As many regulators of cell proliferation or apoptosis are degraded by the ubiquitin-proteasome pathway, proteasome inhibitors such as bortezomib (PS-341) [108–111] (Velcade; Millennium, Cambridge, MA) may be promising. Inhibiting the Ras/Raf/MAPK signaling pathway with farnesyltransferase inhibitors like R115777 [112–114] or promoting growth arrest and apoptosis by HDAC [115] and 2-methoxyestradiol [116, 117], which induce apoptosis in numerous cancers by producing reactive oxygen species as well as hsp90 ATPase inhibitors, are other areas of clinical development. All these drugs/inhibitors represent potential anticancer agents [93, 95, 96] alone and in combination with dexamethasone or other drugs. However, they are highly toxic and great care must be given to their administration so as to avoid healthy tissues. For example, the strong cardio-toxicity of anthracyclines must be suppressed as much as possible. This has been successfully realized with the incorporation of doxorubicin in numerous stealth liposomes. Among them caelix/doxil [118] is actually clinically used for different cancer therapies (breast, ovary, myeloma) alone or in combination with vincristine and

dexamethasone [119]. Liposomal vincristine and liposomal cisplatin have also been clinically evaluated on various cancers [120]. Despite progress in delineating the activity of such regimens, at either conventional or high dose, MM has remained incurable. No substantial improvement of the median survival was obtained, even from new promising attempts.

### 11.3.3

#### **Incidence of Estrogens and Antiestrogens on Multiple Myeloma**

Both isotypes of ER have been identified in several MM cell lines as well as in cells isolated from patients [33–36], and both SERMs like OH-tamoxifen, the active metabolite of tamoxifen, and two pure antiestrogens (Faslodex® and RU 58668) have been shown to block the cell cycle progression of MM cells and to induce apoptosis [34, 36, 121]. Interestingly, 4-OH-tamoxifen-induced apoptosis in several ER-positive MM cells is a mitochondrial process [121]. Such an event, in conjunction with the high doses needed to obtain apoptosis in these MM cells (as compared with lower doses giving the same effect in ER-positive breast cancer cells), raised the question of the ER specificity of antiestrogens in MM. Even if the pathway(s) that conduct MM cells to apoptosis under antiestrogens is (are) not totally elucidated at present, this has prompted us to evaluate the efficacy of liposomal formulations loaded with RU in a xenograft model of MM.

## 11.4

### **Colloidal Systems for Antiestrogen Delivery**

#### 11.4.1

##### **Nanoparticles Charged with AEs in Breast Cancer**

The first strategy employed to obtain a controlled release of the 11 $\beta$ -alkylestradiol derivatives manufactured by Schering was the use of a polyacrylate-based matrix transdermal system [122, 123]. Pretreatment of the skin with a fluid permeation enhancer of propylene glycol–lauric acid should enhance absorption of transdermally administered antiestrogens. Drugs that permeate easily through the skin must be small molecules with moderate lipophilicity. Nanoparticles for intravenous administration of drugs have since been developed. Because the usefulness of conventional nanoparticles is limited by their rapid and massive capture by macrophages of the MPS after i.v. administration, different nanoparticle devices have been considered to target tumors that are not localized in the MPS organs. Several studies have been devoted to the development of so-called “stealth” particles, which are “invisible” to macrophages [6, 124]. These stealth nanoparticles are characterized by a prolonged half-life in the blood compartment, allowing them to extravasate in pathological sites like tumors or inflamed regions with a leaky vasculature [125, 126]. The size of the colloidal carriers and their surface characteristics are the keys for the biological fate of nanoparticles, since these parameters can prevent

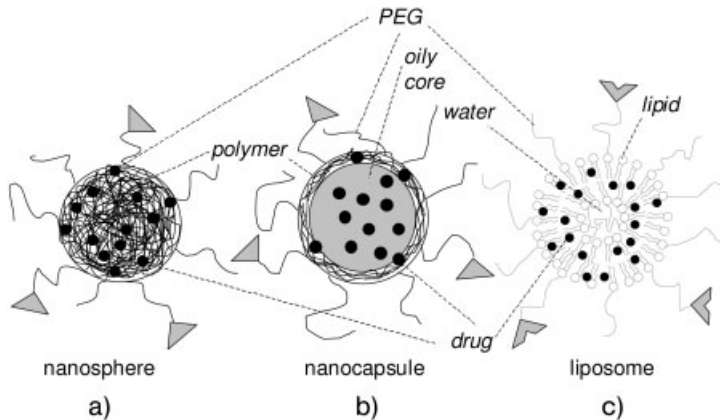


**Fig. 11.3.** Schematic structures of colloidal systems used for antiestrogen incorporation: Nanospheres (A), nanocapsules (B) and liposomes (C) are the drug delivery systems used to encapsulate antiestrogens. Nanospheres are composed of a polymeric matrix in which the ligand (●) can be encapsulated; nanocapsules consist of the same polymer surrounding an oily core, allowing solubilization of hydrophobic

compounds. PEG-PLA or PEG-PLGA or PEG- $\epsilon$ -caprolactone copolymers were also used. Liposomes (C) made of various phospholipid compositions containing a water core were also employed. The antiestrogens were presumed to be located in the lipid bilayer. Tumor recognition molecules are shown as shaded triangles (A and B), and the ligand and antibody as shaded solid Vs (C).

their uptake by the MPS. A high curvature, small size (<100–200 nm) and a hydrophilic surface (as opposed to the hydrophobic surface of conventional nanoparticles) reduce opsonization and subsequent clearance by macrophages [2, 124].

A major breakthrough came with the use of hydrophilic polymers [poly(ethylene glycol) (PEG), poloxamines, poloxamers, polysaccharides] to coat the surface of nanoparticles [6, 127] (Fig. 11.3). Such coatings provide a dynamic “cloud” of hydrophilic and neutral chains at the surface of the particles, repelling plasma proteins and avoiding opsonization. Two ways have been used to introduce hydrophilic polymers at the surface of nanoparticles: either adsorption of surfactants or the use of branched copolymers [6, 127–130]. The second strategy, consisting of the covalent linkage of amphiphilic copolymers, is generally preferred for obtaining a protective hydrophilic cloud on nanoparticles, as it avoids the possibility of rapid coating desorption upon dilution or after contact with blood components. This approach has been employed with poly(lactic acid) (PLA), poly(caprolactone) and poly(cyanoacrylate) polymers, which were chemically coupled to PEG [125, 131–134]. This type of DDS has been used to incorporate antiestrogens in the studies described here.

The “pure antiestrogen” RU 58 668 [135, 136], referred as to RU below, is highly hydrophobic and could be trapped in the lipidic skin layer, avoiding its access

to targets localized in other tissues. Colloidal particles may be used as drug carriers to obtain a site-specific drug delivery. The vascular endothelium in solid tumors is discontinuous [10], and nanoparticles are able to cross this discontinuous endothelium in a process called extravasation. Such a strategy has been already employed in the case of Tam, but the drug release was too fast and its loading too low to obtain significant effects *in vivo*. In fact, poly( $\epsilon$ -caprolactone) and poly(MePEGcyanoacrylate-co-hexadecyl cyanoacrylate) nanoparticles failed to encapsulate Tam correctly, with a maximum loading efficiency of 64% and most of the drug being adsorbed onto the particle surface [137–139]. In contrast, the highly promising pure antiestrogen RU has been successfully incorporated with a high loading efficiency in polyester-PEG nanospheres [140]. These small nanoparticulate systems (~150–200 nm) showed reduced drug release *in vitro*, and reduced protein adsorption in the presence of serum, two features compatible with increased persistence in blood [141]. These parenteral delivery systems inhibited estradiol-promoted tumor growth *in vivo* that correlated with an arrest of cell cycle proliferation in MCF-7 cells [142]. Accumulation of these nanoparticles in tumor sites following i.v. administration has been demonstrated by the use of radioactive polymer [142].

The recent antiestrogen-containing formulations we have synthesized represent, to our knowledge, the first drug delivery systems loaded with an antiestrogen that have been successfully evaluated biologically in animal models. They are made of copolymers that are organized as nanospheres or nanocapsules (Fig. 11.3); in the latter case, the antiestrogen is solubilized in an oily core. Two types of copolymers were employed, affording nanoparticles with a small size that is compatible with good extravasation (Table 11.1). Tamoxifen-loaded PEG-poly(alkyl cyanoacrylate) (PEG-PACA) nanospheres contained only a small amount of drug ( $1.8 \mu\text{g mL}^{-1}$ ) [137], whereas RU-loaded PEG-poly(lactic acid) (PEG-PLA) nanocapsules (NC) and nanospheres (NS) contained at least  $3\times$  more drug ( $5$  and  $33 \mu\text{g mL}^{-1}$ , respectively) [140, 142]. In addition, PEG-PLA nanoparticles are devoid of any intrinsic toxicity, which is not the case for the PACA-based copolymer [143, 144]. RU-charged PEG-PLA nanoparticles in MCF-7 cells show greater toxicity than free RU, and flow cytometry experiments have revealed a strong increase of MCF-7 cells in apoptosis after treatment with RU-loaded NS and NC. Interestingly, following i.v. administration to mice bearing MCF-7 breast cancer xenografts, nanospheres loaded with RU were highly efficient at inhibiting  $\text{E}_2$ -induced tumor growth at a dosage 50 to  $100\times$  lower than that at which free RU is active [142, 145] (Fig. 11.4). Comparatively, RU-loaded nanocapsules possessed a strong potency to reduce the  $\text{E}_2$ -induced tumor growth in this model as well as in xenografts of MCF-7/ras tumors [142]. They also prolonged the anti-uterotrophic activity of RU [142] at a low dose.

Tamoxifen-loaded PEG-PLA nanospheres also possess a high potency for inhibiting  $\text{E}_2$ -induced growth in MCF-7 tumors (Fig. 11.4). Analysis of the cell cycle proteins and proteins involved in apoptosis in tumor extracts from mice injected with nanospheres or nanocapsules containing RU indicated that both cyclin dependent

**Tab. 11.1.** Physicochemical characteristics and biological parameters of antiestrogen-loaded colloidal systems. The size and zeta potential of nanospheres nanocapsules and liposomes loaded with either RU or OH-Tam are indicated, together with the encapsulation rates of the drugs. Interestingly, the change in zeta potential for nanoparticles loaded with OH-Tam indicates that some drug is located at their surface, unlike RU-nanoparticles and liposomes.

	RU	4HT	Mean diameter (nm)	Zeta potential (mV)	Encapsulation efficiency	Encapsulation percentage (%)	Estrogen-induced inhibitory activity half-life (min)
Nanoparticles							
PLA NS	-	-	200 ± 50	-28 ± 3	nd	nd	
PLA NS	+	-	170 ± 30	-3.1 ± 0.7	32.8	≥98	
PLA NS	-	+	172 ± 33	4.1 ± 0.6	19	98	
PEG-PLA NS	-	-	133 ± 48	-26.1 ± 0.9	nd	nd	
PEG-PLA NS	+	-	160 ± 30	-24.7 ± 0.6	32.8	96	1900
PEG-PLA NS	-	+	137 ± 47	1.2 ± 0.7	18.1	97.6	1800
PLA NC	-	-	245 ± 90	-50 ± 1.1	nd	nd	
PLA NC	+	-	233 ± 75	-5.2 ± 4	5.3	≥99	
PEG-PLA NC	-	-	233 ± 67	-44.4 ± 1.3	nd	nd	
PEG-PLA NC	+	-	245 ± 87	-42.2 ± 2.3	5.3	98	2300
Liposomes							
EPC/DSPE-PEG <sup>2000</sup> (94:6)	-	-	110 ± 33	-23.5 ± 5.8	nd	nd	
EPC/DSPE-PEG <sup>2000</sup> (94:6)	+	-	111 ± 31	-24.0 ± 5.8	3.609	≥90	90
EPC/CHOL/DSPE-PEG <sup>2000</sup> (94:30:6)	-	-	106 ± 29.7	-25.6 ± 5.9	nd	nd	
EPC/CHOL/DSPE-PEG <sup>2000</sup> (64:30:6)	+	-	94.7 ± 32.2	-26.5 ± 5.8	3.205	≥90	300

Half-lives were determined following a 24 h-treatment of MELN cells with E<sub>2</sub> (0.1 nM) in the presence or not of 0.5 nM RU; results represent the times at which 50% luciferase expression was inhibited. Empty liposomes had no effects [154]. nd: not defined.

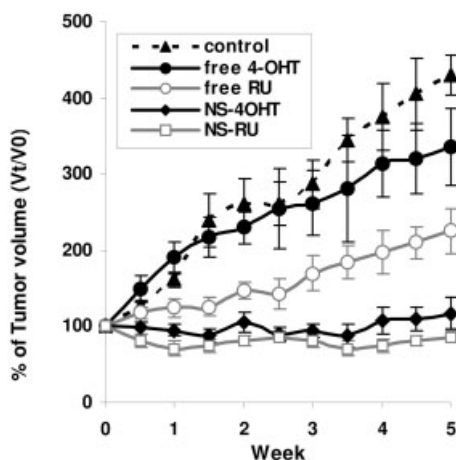


**Fig. 11.4.** Tumor evolution of MCF-7 breast cancer xenografts i.v. injected with RU- and OH-Tam-nanospheres. Bi-weekly i.v. injections of RU-PEG-PLA nanospheres (NS) and of 4-OH-Tam-PEG-PLA nanospheres ( $12 \text{ mg kg}^{-1} \text{ week}^{-1}$  each) were performed in mice ( $n = 10$  per group) bearing MCF-7 tumors (ranging

from  $0.8$  to  $1 \text{ cm}^3$ ). Identical amounts of free antiestrogen in 5% glucose were i.v. injected as controls. All groups received  $0.5 \text{ mg-E}_2 \text{ kg}^{-1} \text{ week}^{-1}$  following skin deposition of an  $\text{E}_2$  solution in ethanol. Tumors were measured each week.

kinase inhibitors  $\text{p}21^{\text{WAF-1/CIP1}}$  and  $\text{p}27^{\text{kip1}}$  (CDKIs) were dramatically augmented (Ameller, T., Marsaud, V., Legrand, P., Renoir, J.-M., manuscript in preparation). This was not seen in tumor extracts from mice having received encapsulated 4-OHT. This finding supports the concept that delivery of RU incorporated in long-circulating formulations is able to arrest tumor growth by a mechanism in which both CDKIs are overexpressed [142]. This agrees with the need for an elevated level of  $\text{p}27^{\text{kip1}}$  for cells to remain quiescent, an effect produced by pure antiestrogens in human breast cancer cells [146] but not by SERMs such as 4-OHT. Additionally, immunological analysis of MCF-7 cells tumors exposed to both nanospheres and nanocapsules containing RU revealed a strong destruction of the  $\text{ER}\alpha$  content, contrary to tumors exposed to nanospheres loaded with OH-Tamoxifen. In the former, TUNEL experiments indicated a strong apoptosis while a weaker one was detected in the latter. These data correlate with the proteasome-mediated degradation of  $\text{ER}\alpha$  under RU, concomitantly with apoptosis induction.

Finally, s.c. administration of trapped RU in mice bearing MCF-7 tumors was as efficient as the i.v. route at the same dose of RU (Fig. 11.5). This finding led to the hypothesis that nanospheres could behave like a reservoir from which the drug could diffuse and release slowly in the interstitium before reaching the tumor. In that case it is intriguing that the efficiency was similar to that obtained by i.v. More research is necessary to elucidate this mechanism, in particular to find out how the administration of an antiestrogen through a stealth DDS affects its pharmacokinetics and biodistribution as well as its bioavailability.

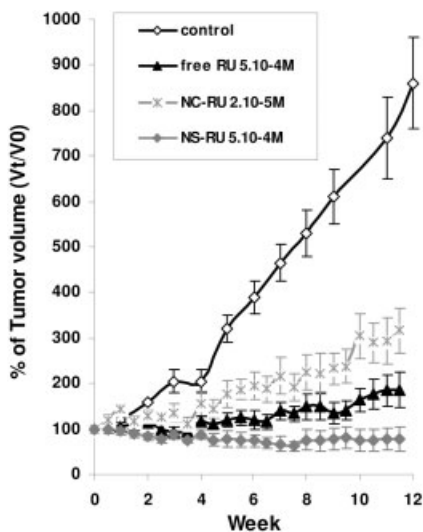


**Fig. 11.5.** Tumor evolution of MCF-7 breast cancer xenografts s.c. injected with RU-nanospheres and RU-nanocapsules. Bi-weekly subcutaneous injection of PEG-PLA-RU loaded nanocapsules and of PEG-PLA-RU-loaded nanospheres [containing, respectively,  $2 \times 10^{-5}$  M ( $0.3 \text{ mg kg}^{-1} \text{ week}^{-1}$ ) and  $5 \times 10^{-4}$  M RU ( $4.3 \text{ mg kg}^{-1} \text{ week}^{-1}$ )] was performed in nude mice bearing MCF-7 tumors ( $n = 8$  mice per group), in addition to  $0.5 \text{ mg kg}^{-1} \text{ week}^{-1}$  by skin deposition. Free RU at the highest concentration was s.c. injected at  $4.3 \text{ mg kg}^{-1} \text{ week}^{-1}$ . Control group received only  $E_2$ .

#### 11.4.2

#### Liposomes Charged with RU 58668 in MM

Several liposomal formulations have been elaborated for the delivery of highly cytotoxic anticancer drugs such as doxorubicin and platinum-based agents [4, 147–151]. These formulations utilized liposomes capable of circulating with very long half-lives (referred to as sterically stabilized liposomes) [152, 153] that avoid the opsonization process when injected in the blood stream. Similarly to nanoparticles, opsonization is reduced by coupling phospholipids to hydrophilic polymers such as PEG. PEG-liposomes can be injected either intravenously or subcutaneously.

From *in vitro* experiments, we have established that high antiestrogen amounts are able to trigger cell cycle arrest in MM cells as well as to induce apoptosis [121, 154]. We then incorporated RU in liposomes known to have a better incorporation capacity than nanoparticles. Table 11.1 summarizes the physicochemical characteristics of the different formulations obtained and their biological properties in terms of drug loading and *in vitro* release. At least  $10\times$  more RU was incorporated into liposomes of EPC/DSPE-PEG<sup>2000</sup> than in nanospheres of PEG-PLA. Coupling of PEG did not modify any of the characteristics of liposomes but addition of cholesterol enhanced vesicle stability of the liposomes and strongly decreased the RU re-

lease measured *in vitro*. RU release from liposomes was comparatively faster than that of RU from nanoparticles (Table 11.1). Flow cytometry experiments carried out on various MM cell lines (LP1, NCI-H929, RPMI8226, OPM-2 and U266) exposed to increasing amounts of RU revealed that in all MM cells RU blocks the cell cycle progression in the G0/G1 phase and/or induced apoptosis (except in OPM-2). This occurred at up to 5  $\mu\text{M}$  RU, a concentration far above (100 $\times$ ) that at which the antiestrogen induced apoptosis in breast cancer ER+ cancer cells. Interestingly, the extent of apoptosis in cells exposed to RU-loaded liposomes is strongly augmented in all MM cells (Fig. 11.6).

Intravenously injected in a RPMI8226 MM xenograft model, RU-charged liposomes inhibited strongly the tumor growth even when injected at 12 mg kg<sup>-1</sup> week<sup>-1</sup> in a single injection (Fig. 11.7). Conversely, free RU at this dose had no effect, as well as empty liposomes. This suggests that the release of RU is slow and that its potency in inhibiting the growth of the MM tumor is enhanced by incorporation in the liposome system. Another interesting observation made in RPMI8226 xenografts was the enhanced anti-angiogenesis activity following RU-charged liposomes (Maillard, S., Gauduchon, J., Gouilleux, F. Marsaud, V., Connault, E., Opolon, P., Fattal, E., Sola, B., Renoir, J.-M., submitted for publication), which is consistent with the inhibition of VEGF by RU in the MM cells (our unpublished work) as well as in human breast cancer cells [155, 156], an effect mediated by ER $\alpha$  contained in the endothelium membranes. In addition, in all of the MM and breast cancer xenograft models we used, no apparent toxicity (liver, lung, bone) was noticed. Interestingly, the size of the xenograft uteri injected with RU-PEG-PLA nanospheres was not decreased, contrary to that of healthy mature mice having received RU at 12 mg kg<sup>-1</sup> week<sup>-1</sup> for at least 5 weeks (RPMI8226 xenografts) and 4.3 mg kg<sup>-1</sup> week<sup>-1</sup> (MCF-7 xenografts) [142, 145, 154]. This strongly suggest that, although being passive, some tumor targeting is produced when stealth DDS are employed.

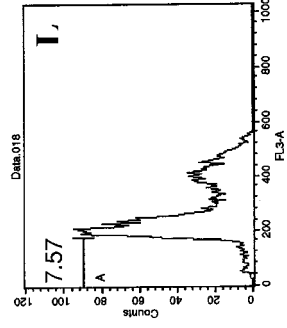
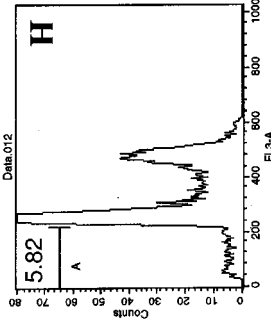
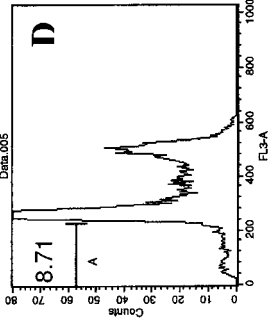
### 11.4.3

#### Tumor-targeted Drug-loaded Colloidal Systems

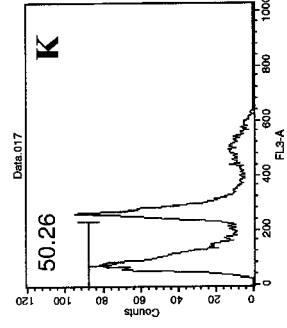
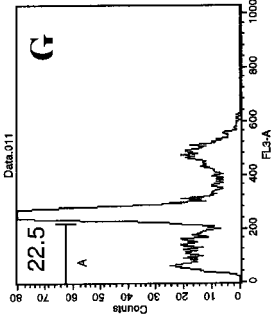
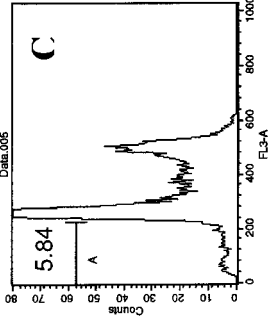
Targeting of drugs to specific tissues of the body has been the major focus of research in recent decades in an attempt to improve selectivity in cancer treatment. The PEG stabilizing effect results from local surface concentration of highly hydrated groups that sterically inhibit both hydrophobic and electrostatic interactions of various blood components at the carrier surface [152, 153, 157]. “Active targeting” of either nanoparticles or liposomes is generally attempted by conjugating ligands, to the carrier surface, that possess high affinity for the tumor cells [158]. Several types of ligands have been used, including antibody fragments [159–161], vitamins [162–164], glycoproteins [165], peptides (RGD-sequences) [166], and oligonucleotides aptamers [158]. The concept is actually over 25 years old, but only small improvements have been obtained. In fact many difficulties are encountered. The major one, besides the complexity of such conjugation chemistry, is the dilemma of preserving the stealth property of the formulation, by leaving enough



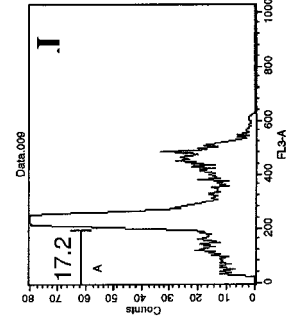
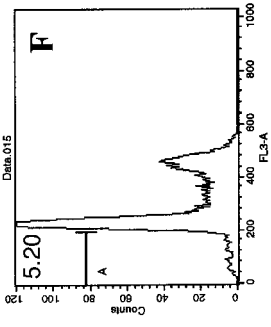
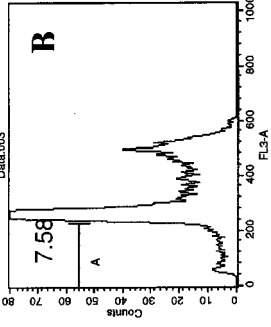
Unloaded liposomes



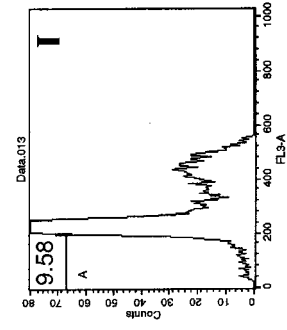
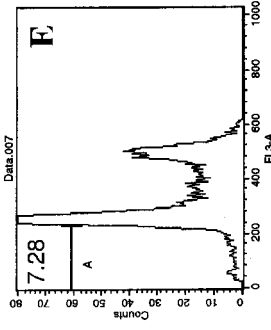
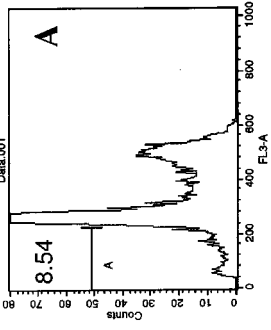
RU-loaded liposomes



Free RU



Control



24h

48h

72h

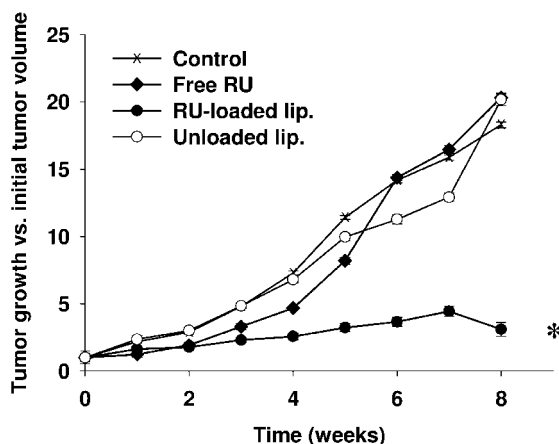


**Fig. 11.7.** Tumor evolution of multiple myeloma xenografts i.v. injected with RU-liposomes. RPMI8226 xenografted nude mice received, or not, a weekly injection of free RU or RU-loaded liposomes (12 mg per kg per

week of RU) or unloaded liposomes at the same lipidic concentration as that containing RU. Tumor volume was measured and tumor evolution plotted as a function of the time of injection. \* $p < 0.01$  with regard to control.

free PEG chains grafted at the surface, while also obtaining enough tumor grafted ligand molecules capable of binding to the tumor cell receptors (Fig. 11.3).

In some cases, “active targeting” may take advantage of the overexpression of a membrane receptor. This is, in particular, the case with breast cancer cells that are insensitive to antiestrogens because they are ER-negative. In that case, a tyrosine kinase membrane receptor of the EGFR family, HER2-Neu or Erb-B2, is overexpressed [24]. Overexpression of Erb-B2 remains a major risk factor in non-metastatic breast cancers treated with high-dose alkylating agents and autologous stem cell transplantation. The activity of Erb-B2 is blocked by a specific antibody, herceptin (trastuzumab), which enhances tumor necrosis factor-related apoptosis-inducing ligand-mediated apoptosis in breast and ovarian cancer cell lines [167]. In MM cells, Erb-B2 is also overexpressed, representing a major risk [168]. Then, coupling trastuzumab on PEG chains of PEGylated nanoparticles and liposomes loaded with an antiestrogen could be of great benefit for breast cancers and MM since both the “piloting” grafted recognition molecule and the encapsulating drug

**Fig. 11.6.** Flow cytometry: NCI-H929 MM cells (50% confluence) were grown and exposed or not to RU ( $1 \mu\text{M}$ ) free or encapsulated, or to empty liposomes (at the same lipid concentration as that used in RU-loaded liposomes) for various periods. Cells ( $10^4$ ) were then analyzed by FACS. Cell cycle profiles and the percentage of cells in the sub-

G1 fraction obtained without treatment (control) are indicated in panels A, E, I for 24, 48 and 72 h, respectively. Panels B, F, J show the same parameters obtained after treatment with free RU. Similarly, panels C, G, K and D, H, L show the profiles obtained for cells treated with RU-loaded liposomes and unloaded liposomes, respectively.

can conduct tumor cells to apoptosis. Several sterically stabilized anti-Erb-B2 immunoliposomes have been synthesized to date [161, 169–173], all of which seem promising.

Another interesting and simple molecule to couple at the end of PEG chains is folic acid [174, 175]. Several malignant cells, including KB3-1 cells, endometrial Ishikawa cells and also some MM cells (but, unfortunately, not breast cancer cells), overexpress a folate receptor [176] that mediates internalization. Folate linked to PEGylated cyanoacrylate nanoparticles show a ten-fold higher apparent affinity for the folate membrane receptor than free folate does. The particles represent a multivalent form of free folic acid and the folate receptor(s) is (are) often disposed in clusters [175]. As a result, conjugated nanoparticles could display a multivalent and hence stronger interaction with the surface of the malignant cells [177]. Moreover, confocal microscopy has demonstrated that folate nanoparticles, compared with non-conjugated nanoparticles, were selectively taken up by the folate receptor-bearing KB3-1 cells, but not by MCF-7 cells. In the former case, the folate nanoparticles were located in the cell cytoplasm, as a consequence of receptor-mediated endocytosis [176]. Very recently, the improved therapeutic response of folate-nanoparticles charged with methotrexate demonstrated a marked decrease in toxicity and increase in antitumor capacity [178].

## 11.5

### Conclusions and Perspectives

The potential use of pure antiestrogens in anticancer therapy leads again to the question of how they must be administered to avoid side effects. Altogether, the data obtained with AE-loaded colloidal systems demonstrate that drug delivery of this type of anticancer drug either i.v. or s.c. administered enhances the apoptotic activity of the drug, decreases the side effects and behaves as long-lasting delivery systems, although probably acting through different process. For example, while it is likely that PEGylated nanoparticles concentrate at tumor sites via a passive targeting, liposomes are believed to deliver the encapsulated RU through an endocytosis process (Fig. 11.8). Several novel drug delivery systems for steroid hormones have been developed, including intra-uterine delivery systems, implants and steroid-loaded vaginal rings [145]. However, what is needed for the delivery of anticancer drugs in general, and for antiestrogens in particular, is a specific targeting of tumor cells with maximum avoidance of normal cells. The challenge is not to reach the pathological cells with a high dose of drug but rather to incorporate at these sites the optimal drug concentration necessary to completely inhibit the activity of the target. If this condition is attained, little of the drug will be disseminated at other sites of the organism, thus minimizing undesirable side effects.

In fact, another way to inhibit ER $\alpha$  activity has emerged recently from Gustafsson's group, who have described ER $\beta$  as a potent dominant negative variant of ER $\alpha$  [179, 180]. This has been confirmed by other groups [181, 182]. Thus, delivery of the cDNA encoding ER $\beta$  or of silencing RNA directed against ER $\alpha$  concomi-

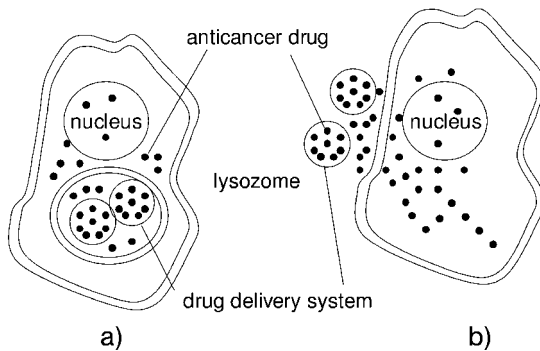


**Fig. 11.8.** Antiestrogen-release mechanisms from colloidal systems. The antiestrogen (●) is located inside the lipid bilayer of liposomes (A), which are internalized in lysosomes in cells capable of endocytosis. The drug is then released in the cell after degradation of the lysosomes. In nanospheres and in nano-

capsules (B) the antiestrogen is trapped in the polymer matrix and/or in the oily core; they also can be submitted to endocytosis as in (A). The encapsulated drug can be released near the tumor cells, allowing its passive diffusion. In both cases, an increased intracellular antiestrogen concentration occurs.

tantly with RU could be a helpful approach since it can reduce, on the one hand, the activity of ER $\alpha$  and, on the other hand, destroys the ER $\alpha$  protein itself, preserving ER $\beta$ .

The results obtained are encouraging and we strongly believe that the drug delivery approach is promising not only for the administration of antiestrogens in estrogen-dependent breast cancers and MM but also for the delivery of much more toxic anticancer agents such as taxol, thalidomide, bortezomib, VEGF inhibitors, farnesyltransferase inhibitors, histone transferase inhibitors and hsp90 inhibitors.

### Acknowledgments

We greatly appreciate the support of the Ligue Nationale contre le Cancer (Cher, Indre and Manche departments Comities), P. Van de Velde for the gift of RU 58 668 and the SCEA of IGR (Villejuif, France) for animal experiments.

### References

- 1 JAIN, R. K., Delivery of molecular and cellular medicine to solid tumors, *Adv. Drug Deliv. Rev.*, **1997**, 26, 71–90.
- 2 MOGHIMI, S. M., SZE BENI, J., Stealth liposomes and long circulating nanoparticles, critical issues in pharmacokinetics, opsonization and protein-binding properties, *Prog. Lipid Res.*, **2003**, 42, 463–478.
- 3 DRUMMOND, D. C., MEYER, O., HONG, K., KIRPOTIN, D. B., PAPAHDJOPOULOS, D., Optimizing

- liposomes for delivery of chemotherapeutic agents to solid tumors, *Pharmacol Rev.*, **1999**, 51, 691–743.
- 4 GABIZON, A., PAPAHDJOPOULOS, D., Liposome formulations with prolonged circulation time in blood and enhanced uptake by tumors, *Proc. Natl. Acad. Sci. U.S.A.*, **1988**, 85, 6949–6953.
  - 5 ALLEN, T. M., HANSEN, C., MARTIN, F., REDEMANN, C., YAU-YOUNG, A., Liposomes containing synthetic lipid derivatives of poly(ethylene glycol) show prolonged circulation half-lives in vivo, *Biochim. Biophys. Acta*, **1991**, 1066, 29–36.
  - 6 STORM, G., BELLLOT, S. O., DAEMEN, T., LASIC, D. D., Surface modification of nanoparticles to oppose uptake by the mononuclear phagocyte system, *Adv. Drug Deliv. Rev.*, **1995**, 17, 31–48.
  - 7 SEYMOUR, L. W., Passive tumor targeting of soluble macromolecules and drug conjugates, *Crit. Rev. Ther. Drug Carrier Syst.*, **1992**, 9, 135–187.
  - 8 BABAN, D. F., SEYMOUR, L. W., Control of tumour vascular permeability, *Adv. Drug Deliv. Rev.*, **1998**, 34, 109–119.
  - 9 MAEDA, H., The enhanced permeability and retention (EPR) effect in tumor vasculature, the key role of tumor-selective macromolecular drug targeting, *Adv. Enzyme Regul.*, **2001**, 41, 189–207.
  - 10 HOBBS, S. K., MONSKY, W. L., YUAN, F., ROBERTS, W. G., GRIFFITH, L., TORCHILIN, V. P., JAIN, R. K., Regulation of transport pathways in tumor vessels, role of tumor type and microenvironment, *Proc. Natl. Acad. Sci. U.S.A.*, **1998**, 95, 4607–4612.
  - 11 YUAN, F., DELLIAN, M., FUKUMURA, D., LEUNIG, M., BERK, D. A., TORCHILIN, V. P., JAIN, R. K., Vascular permeability in a human tumor xenograft, molecular size dependence and cutoff size, *Cancer Res.*, **1995**, 55, 3752–3956.
  - 12 YUAN, F., LEUNIG, M., HUANG, S. K., BERK, D. A., PAPAHDJOPOULOS, D., JAIN, R. K., Microvascular permeability and interstitial penetration of sterically stabilized (stealth) liposomes in a human tumor xenograft, *Cancer Res.*, **1994**, 54, 3352–3356.
  - 13 MONSKI, W. L., FUKUMURA, D., GOHONGI, T., ANCUKIEWCZ, M., WEICH, H. A., TORCHILIN, V. P., YUAN, F., JAIN, R. K., Augmentation of transvascular transport of macromolecules and nanoparticles in tumors using vascular endothelial growth factor, *Cancer Res.*, **1999**, 59, 4129–4135.
  - 14 WEISZ, A., BRESCIANI, F., Estrogen regulation of proto-oncogenes coding for nuclear proteins, *Crit. Rev. Oncog.*, **1993**, 4, 361–388.
  - 15 JENSEN, E. V., On the mechanism of estrogen action, *Perspect. Biol. Med.*, **1962**, 6, 47–59.
  - 16 TOFT, D., GORSKI, J., A receptor molecule for estrogens, isolation from the rat uterus and preliminary characterization, *Proc. Natl. Acad. Sci. U.S.A.*, **1966**, 55, 1574–1581.
  - 17 KUIPER, G. G., ENMARK, E., PELTO-HUIKKO, M., NILSSON, S., GUSTAFSSON, J. A., Cloning of a novel receptor expressed in rat prostate and ovary, *Proc. Natl. Acad. Sci. U.S.A.*, **1996**, 93, 5925–5930.
  - 18 MOSSELMAN, S., POLMAN, J., DIJKEMA, R., ER beta, identification and characterization of a novel human estrogen receptor, *FEBS Lett.*, **1996**, 392, 49–53.
  - 19 KATZENELLENBOGEN, B. S., KORACH, K. S., A new actor in the estrogen receptor drama – enter ER-beta, *Endocrinology*, **1997**, 138, 861–862.
  - 20 KOUSTENI, S., BELLIDO, T., PLOTKIN, L. I., O'BRIEN, C. A., BODENNER, D. L., HAN, L., HAN, K., DIGREGORIO, G. B., KATZENELLENBOGEN, J. A., KATZENELLENBOGEN, B. S., ROBERSON, P. K., WEINSTEIN, R. S., JILKA, R. L., MANOLAGAS, S. C., Nongenotropic, sex-nonspecific signaling through the estrogen or androgen receptors, dissociation from transcriptional activity, *Cell*, **2001**, 104, 719–730.
  - 21 MARINO, M., ACCONCIA, F., BRESCIANI, F., WEISZ, A., TRENTALANCE, A., Distinct nongenomic signal transduction pathways controlled by 17beta-

- estradiol regulate DNA synthesis and cyclin D(1) gene transcription in HepG2 cells, *Mol. Biol. Cell.*, **2002**, *13*, 3720–3729.
- 22** MACGREGOR, J. I., JORDAN, V. C., Basic guide to the mechanisms of antiestrogen action, *Pharmacol Rev.*, **1998**, *50*, 151–196.
- 23** CLARKE, R., LEONESSA, F., WELCH, J. N., SKAAR, T. C., Cellular and molecular pharmacology of antiestrogen action and resistance, *Pharmacol Rev.*, **2001**, *53*, 25–71.
- 24** JORDAN, V. C., Antiestrogens and selective estrogen receptor modulators as multifunctional medicines. 2. Clinical considerations and new agents, *J. Med. Chem.*, **2003**, *46*, 1081–1111.
- 25** WIJAYARATNE, A. L., McDONNELL, D. P., The human estrogen receptor- $\alpha$  is a ubiquitinated protein whose stability is affected differentially by agonists, antagonists, and selective estrogen receptor modulators, *J. Biol. Chem.*, **2001**, *276*, 35 684–35 692.
- 26** EL KHISSIN, A., LECLERCQ, G., Implication of proteasome in estrogen receptor degradation, *FEBS Lett.*, **1999**, *448*, 160–166.
- 27** MARSAUD, V., GOUGELET, A., MAILLARD, S., RENOIR, J. M., Various phosphorylation pathways, depending on agonist and antagonist binding to endogenous estrogen receptor  $\alpha$  (ER $\alpha$ ), differentially affect ER $\alpha$  extractability, proteasome-mediated stability, and transcriptional activity in human breast cancer cells, *Mol. Endocrinol.*, **2003**, *17*, 2013–2027.
- 28** WEBB, P., LOPEZ, G. N., UHT, R. M., KUSHNER, P. J., Tamoxifen activation of the estrogen receptor/AP-1 pathway, potential origin for the cell-specific estrogen-like effects of antiestrogens, *Mol. Endocrinol.*, **1995**, *9*, 443–456.
- 29** PAECH, K., WEBB, P., KUIPER, G. G., NILSSON, S., GUSTAFSSON, J., KUSHNER, P. J., SCANLAN, T. S., Differential ligand activation of estrogen receptors ER $\alpha$  and ER $\beta$  at AP1 sites, *Science*, **1997**, *277*, 1508–1510.
- 30** KUSHNER, P. J., AGARD, D. A., GREENE, G. L., SCANLAN, T. S., SHIAU, A. K., UHT, R. M., WEBB, P., Estrogen receptor pathways to AP-1, *J. Steroid Biochem. Mol. Biol.*, **2000**, *74*, 311–317.
- 31** HALLEK, M., BERGSAGEL, P. L., ANDERSON, K. C., Multiple myeloma, increasing evidence for a multistep transformation process, *Blood*, **1998**, *91*, 3–21.
- 32** HIDEHIMA, T., ANDERSON, K. C., Molecular mechanisms of novel therapeutic approaches for multiple myeloma, *Nat. Rev. Cancer*, **2002**, *2*, 927–937.
- 33** DANIEL, L., VINCENT, C., ROUSSET, F., KLEIN, B., BATAILLE, R., FLACHER, M., DURIE, B. G., REVILLARD, J. P., Estrogen and progesterone receptors in some human myeloma cell lines and murine hybridomas, *J. Steroid Biochem.*, **1988**, *30*, 363–367.
- 34** TREON, S. P., TEOH, G., URASHIMA, M., OGATA, A., CHAUHAN, D., WEBB, I. J., ANDERSON, K. C., Anti-estrogens induce apoptosis of multiple myeloma cells, *Blood*, **1998**, *92*, 1749–1757.
- 35** OTSUKI, T., YAMADA, O., KUREBAYASHI, J., MORIYA, T., SAKAGUCHI, H., KUNISUE, H., YATA, K., UNO, M., YAWATA, Y., UEKI, A., Estrogen receptors in human myeloma cells, *Cancer Res.*, **2001**, *60*, 1434–1441.
- 36** GAUDUCHON, J., GOUILLEUX, F., MAILLARD, S., MARSAUD, V., RENOIR, M. J., SOLA, B., The selective estrogen receptor modulator 4-hydroxy tamoxifen induces G1 arrest and apoptosis of multiple myeloma cell lines, *Ann. New York Acad. Sci.*, **2003**, *1010*, 321–325.
- 37** BRIGGER, I., DUBERNET, C., COUVREUR, P., Nanoparticles in cancer therapy and diagnosis, *Adv. Drug Deliv. Rev.*, **2002**, *54*, 631–651.
- 38** BRANNON-PEPPAS, L., BLANCHETTE, J. O., Nanoparticle and targeted systems for cancer therapy, *Adv. Drug Deliv. Rev.*, **2004**, *56*, 1649–1659.
- 39** SMITH, I. E., DOWSETT, M., Aromatase inhibitors in breast cancer, *N. Engl. J. Med.*, **2003**, *348*, 2431–2442.
- 40** BEATO, M., HERRLICH, P., SCHUTZ, G., Steroid hormone receptors, many

- actors in search of a plot, *Cell*, **1995**, 83, 851–857.
- 41 MCKENNA, N. J., O'MALLEY, B. W., Combinatorial control of gene expression by nuclear receptors and coregulators, *Cell*, **2002**, 108, 465–474.
- 42 TSAI, M. J., O'MALLEY, B. W., Molecular mechanisms of action of steroid/thyroid receptor superfamily members, *Annu. Rev. Biochem.*, **1994**, 63, 451–486.
- 43 NILSSON, S., MAKELA, S., TREUTER, E., TUJAGUE, M., THOMSEN, J., ANDERSSON, G., ENMARK, E., PETTERSSON, K., WARNER, M., GUSTAFSSON, J. A., Mechanisms of estrogen action, *Physiol. Rev.*, **2001**, 81, 1535–1565.
- 44 PRATT, W. B., TOFT, D. O., Steroid receptor interactions with heat shock protein and immunophilin chaperones, *Endocrinol. Rev.*, **1997**, 18, 306–360.
- 45 JOAB, I., RADANYI, C., RENOIR, M., BUCHOU, T., CATELLI, M. G., BINART, N., MESTER, J., BAULIEU, E. E., Common non-hormone binding component in non-transformed chick oviduct receptors of four steroid hormones, *Nature*, **1984**, 308, 850–853.
- 46 CATELLI, M. G., BINART, N., JUNG-TESTAS, I., RENOIR, J. M., BAULIEU, E. E., FERAMISCO, J. R., WELCH, W. J., The common 90-kd protein component of non-transformed '8S' steroid receptors is a heat-shock protein, *EMBO J.*, **1985**, 4, 3131–3135.
- 47 PRATT, W. B., The role of the hsp90-based chaperone system in signal transduction by nuclear receptors and receptors signaling via MAP kinase, *Annu. Rev. Pharmacol. Toxicol.*, **1997**, 37, 297–326.
- 48 JOHNSON, J. L., TOFT, D. O., A novel chaperone complex for steroid receptors involving heat shock proteins, immunophilins, and p23, *J. Biol. Chem.*, **1994**, 269, 24989–24993.
- 49 JOHNSON, J. L., BEITO, T. G., KRCO, C. J., TOFT, D. O., Characterization of a novel 23-kilodalton protein of unactive progesterone receptor complexes, *Mol. Cell Biol.*, **1994**, 14, 1956–1963.
- 50 GRENER, J. P., SULLIVAN, W. P., FADDEN, P., HAYSTEAD, T. A., CLARK, J., MIMNAUGH, E., KRUTZSCH, H., OCHEL, H. J., SCHULTE, T. W., SAUSVILLE, E., NECKERS, L. M., TOFT, D. O., The amino-terminal domain of heat shock protein 90 (hsp90) that binds geldanamycin is an ATP/ADP switch domain that regulates hsp90 conformation, *J. Biol. Chem.*, **1997**, 272, 23843–23850.
- 51 FREEMAN, B. C., FELTS, S. J., TOFT, D. O., YAMAMOTO, K. R., The p23 molecular chaperones act at a late step in intracellular receptor action to differentially affect ligand efficacies, *Genes Dev.*, **2000**, 14, 422–434.
- 52 TANIOKA, T., NAKATANI, Y., SEMMYO, N., MURAKAMI, M., KUDO, I., Molecular identification of cytosolic prostaglandin E2 synthase that is functionally coupled with cyclooxygenase-1 in immediate prostaglandin E2 biosynthesis, *J. Biol. Chem.*, **2000**, 275, 32775–32782.
- 53 MOLLERUP, J., KROGH, T. N., NIELSEN, P. F., BERCHTOLD, M. W., Properties of the co-chaperone protein p23 erroneously attributed to ALG-2 (apoptosis-linked gene 2), *FEBS Lett.*, **2003**, 555, 478–482.
- 54 WEIGEL, N. L., Steroid hormone receptors and their regulation by phosphorylation, *Biochem. J.*, **1996**, 319(Pt 3), 657–667.
- 55 STENOIEN, D. L., PATEL, K., MANCINI, M. G., DUTERTRE, M., SMITH, C. L., O'MALLEY, B. W., MANCINI, M. A., FRAP reveals that mobility of oestrogen receptor-alpha is ligand- and proteasome-dependent, *Nat. Cell Biol.*, **2001**, 3, 15–23.
- 56 KLINGE, C. M., Estrogen receptor interaction with co-activators and corepressors, *Steroids*, **2000**, 65, 227–251.
- 57 ROBYR, D., WOLFFE, A. P., WAHLI, W., Nuclear hormone receptor coregulators in action, diversity for shared tasks, *Mol. Endocrinol.*, **2000**, 14, 329–347.
- 58 SPENCER, T. E., JENSTER, G., BURCIN, M. M., ALLIS, C. D., ZHOU, J.,

- MIZZEN, C. A., MCKENNA, N. J., ONATE, S. A., TSAI, S. Y., TSAI, M. J., O'MALLEY, B. W., Steroid receptor coactivator-1 is a histone acetyltransferase, *Nature*, **1997**, 389, 194–198.
- 59 METIVIER, R., PENOT, G., HUBNER, M. R., REID, G., BRAND, H., KOS, M., GANNON, F., Estrogen receptor-alpha directs ordered, cyclical, and combinatorial recruitment of cofactors on a natural target promoter, *Cell*, **2003**, 115, 751–763.
- 60 REID, G., HUBNER, M. R., METIVIER, R., BRAND, H., DENGEL, S., MANU, D., BEAUDOUIN, J., ELLENBERG, J., GANNON, F., Cyclic, proteasome-mediated turnover of unliganded and liganded ERalpha on responsive promoters is an integral feature of estrogen signaling, *Mol. Cell.*, **2003**, 11, 695–707.
- 61 LONARD, D. M., NAWAZ, Z., SMITH, C. L., O'MALLEY, B. W., The 26S proteasome is required for estrogen receptor-alpha and coactivator turnover and for efficient estrogen receptor-alpha transactivation, *Mol. Cell.*, **2000**, 5, 939–948.
- 62 MONTANO, M. M., EKENA, K., DELAGE-MOURROUX, R., CHANG, W., MARTINI, P., KATZENELLENBOGEN, B. S., An estrogen receptor-selective coregulator that potentiates the effectiveness of antiestrogens and represses the activity of estrogens, *Proc. Natl. Acad. Sci. U.S.A.*, **1999**, 96, 6947–6952.
- 63 CHEN, H., LIN, R. J., SCHILTZ, R. L., CHAKRAVARTI, D., NASH, A., NAGY, L., PRIVALSKY, M. L., NAKATANI, Y., EVANS, R. M., Nuclear receptor coactivator ACTR is a novel histone acetyltransferase and forms a multimeric activation complex with P/CAF and CBP/p300, *Cell*, **1997**, 90, 569–580.
- 64 PORTER, W., SAVILLE, B., HOIVIK, D., SAFE, S., Functional synergy between the transcription factor Sp1 and the estrogen receptor, *Mol. Endocrinol.*, **1997**, 11, 1569–1580.
- 65 SAVILLE, B., WORMKE, M., WANG, F., NGUYEN, T., ENMARK, E., KUIPER, G., GUSTAFSSON, J. A., SAFE, S., Ligand-, cell-, and estrogen receptor subtype (alpha/beta)-dependent activation at GC-rich (Sp1) promoter elements, *J. Biol. Chem.*, **2000**, 275, 5379–5387.
- 66 LEE, H., JIANG, F., WANG, Q., NICOSIA, S. V., YANG, J., SU, B., BAI, W., MEKK1 activation of human estrogen receptor alpha and stimulation of the agonistic activity of 4-hydroxytamoxifen in endometrial and ovarian cancer cells, *Mol. Endocrinol.*, **2000**, 14, 1882–1896.
- 67 HALL, J. M., COUSE, J. F., KORACH, K. S., The multifaceted mechanisms of estradiol and estrogen receptor signaling, *J. Biol. Chem.*, **2001**, 276, 36 869–36 872.
- 68 CAMPBELL, R. A., BHAT-NAKSHATRI, P., PATEL, N. M., CONSTANTINIDOU, D., ALI, S., NAKSHATRI, H., Phosphatidylinositol 3-kinase/AKT-mediated activation of estrogen receptor alpha, a new model for anti-estrogen resistance, *J. Biol. Chem.*, **2001**, 276, 9817–9824.
- 69 ARONICA, S. M., KRAUS, W. L., KATZENELLENBOGEN, B. S., Estrogen action via the cAMP signaling pathway, stimulation of adenylate cyclase and cAMP-regulated gene transcription, *Proc. Natl. Acad. Sci. U.S.A.*, **1994**, 91, 8517–8521.
- 70 BUNONE, G., BRIAND, P. A., MIKSICEK, R. J., PICARD, D., Activation of the unliganded estrogen receptor by EGF involves the MAP kinase pathway and direct phosphorylation, *EMBO J.*, **1996**, 15, 2174–2183.
- 71 JOEL, P. B., TRAIASH, A. M., LANNIGAN, D. A., Estradiol-induced phosphorylation of serine 118 in the estrogen receptor is independent of p42/p44 mitogen-activated protein kinase, *J. Biol. Chem.*, **1998**, 273, 13 317–13 323.
- 72 WYCKOFF, M. H., CHAMBLISS, K. L., MINEO, C., YUHANNA, I. S., MENDELSON, M. E., MUMBY, S. M., SHAUL, P. W., Plasma membrane estrogen receptors are coupled to endothelial nitric-oxide synthase through Galpha(i), *J. Biol. Chem.*, **2001**, 276, 27 071–27 076.
- 73 HISAMOTO, K., OHMICHI, M., KANDA, Y., ADACHI, K., NISHIO, Y., HAYAKAWA, J., MABUCHI, S.,



- TAKAHASHI, K., TASAKA, K., MIYAMOTO, Y., TANIGUCHI, N., MURATA, Y., Induction of endothelial nitric-oxide synthase phosphorylation by the raloxifene analog LY117018 is differentially mediated by Akt and extracellular signal-regulated protein kinase in vascular endothelial cells, *J. Biol. Chem.*, **2001**, 276, 47 642–47 649.
- 74 SIMONCINI, T., HAFEZI-MOGHADAM, A., BRAZIL, D. P., LEY, K., CHIN, W. W., LIAO, J. K., Interaction of oestrogen receptor with the regulatory subunit of phosphatidylinositol-3-OH kinase, *Nature*, **2000**, 407, 538–541.
- 75 BOYAN, B. D., SYLVIA, V. L., FRAMBACH, T., LOHMANN, C. H., DIETL, J., DEAN, D. D., SCHWARTZ, Z., Estrogen-dependent rapid activation of protein kinase C in estrogen receptor-positive MCF-7 breast cancer cells and estrogen receptor-negative HCC38 cells is membrane-mediated and inhibited by tamoxifen, *Endocrinology*, **2003**, 144, 1812–1824.
- 76 MIGLIACCIO, A., PICCOLO, D., CASTORIA, G., DI DOMENICO, M., BILANCIO, A., LOMBARDI, M., GONG, W., BEATO, M., AURICCHIO, F., Activation of the Src/p21ras/Erk pathway by progesterone receptor via cross-talk with estrogen receptor, *EMBO J.*, **1998**, 17, 2008–2018.
- 77 IMPROTA-BREARS, T., WHORTON, A. R., CODAZZI, F., YORK, J. D., MEYER, T., MCDONNELL, D. P., Estrogen-induced activation of mitogen-activated protein kinase requires mobilization of intracellular calcium, *Proc. Natl. Acad. Sci. U.S.A.*, **1999**, 96, 4686–4691.
- 78 RAZANDI, M., PEDRAM, A., GREENE, G. L., LEVIN, E. R., Cell membrane and nuclear estrogen receptors (ERs) originate from a single transcript, studies of ERalpha and ERbeta expressed in Chinese hamster ovary cells, *Mol. Endocrinol.*, **1999**, 13, 307–319.
- 79 CASTORIA, G., MIGLIACCIO, A., BILANCIO, A., DI DOMENICO, M., DE FALCO, A., LOMBARDI, M., FIORENTINO, R., VARRICCHIO, L., BARONE, M. V., AURICCHIO, F., PI3-kinase in concert with Src promotes the S-phase entry of oestradiol-stimulated MCF-7 cells, *EMBO J.*, **2001**, 20, 6050–6059.
- 80 CARISTI, S., GALERA, J. L., MATARESE, F., IMAI, M., CAPORALI, S., CANCEMI, M., ALTUCCI, L., CICATIELLO, L., TETI, D., BRESCIANI, F., WEISZ, A., Estrogens do not modify MAP kinase-dependent nuclear signaling during stimulation of early G(1) progression in human breast cancer cells, *Cancer Res.*, **2001**, 61, 6360–6366.
- 81 LOBHOFER, E. K., MARKS, J. R., Estrogen-induced mitogenesis of MCF-7 cells does not require the induction of mitogen-activated protein kinase activity, *J. Steroid. Biochem. Mol. Biol.*, **2000**, 75, 11–20.
- 82 LOBHOFER, E. K., HUPER, G., IGLEHART, J. D., MARKS, J. R., Inhibition of mitogen-activated protein kinase and phosphatidylinositol 3-kinase activity in MCF-7 cells prevents estrogen-induced mitogenesis, *Cell Growth Differ.*, **2000**, 11, 99–110.
- 83 GABEN, A. M., SAUCIER, C., BEDIN, M., REDEUILH, G., MESTER, J., Mitogenic activity of estrogens in human breast cancer cells does not rely on direct induction of mitogen-activated protein kinase/extracellularly regulated kinase or phosphatidylinositol 3-kinase, *Mol. Endocrinol.*, **2004**, 18, 2700–2713.
- 84 FILARDO, E. J., QUINN, J. A., BLAND, K. I., FRACKELTON, A. R., JR., Estrogen-induced activation of Erk-1 and Erk-2 requires the G protein-coupled receptor homolog, GPR30, and occurs via trans-activation of the epidermal growth factor receptor through release of HB-EGF, *Mol. Endocrinol.*, **2000**, 14, 1649–1660.
- 85 FILARDO, E. J., QUINN, J. A., FRACKELTON, A. R., JR., BLAND, K. I., Estrogen action via the G protein-coupled receptor, GPR30, stimulation of adenylyl cyclase and cAMP-mediated attenuation of the epidermal growth factor receptor-to-MAPK signaling axis, *Mol. Endocrinol.*, **2002**, 16, 70–84.
- 86 RAZANDI, M., ALTON, G., PEDRAM, A.,

- GHONSHANI, S., WEBB, P., LEVIN, E. R., Identification of a structural determinant necessary for the localization and function of estrogen receptor alpha at the plasma membrane, *Mol. Cell Biol.*, **2003**, 23, 1633–1646.
- 87 REVANKAR, C. M., CIMINO, D. F., SKLAR, L. A., ARTERBURN, J. B., PROSSNITZ, E. R., A transmembrane intracellular estrogen receptor mediates rapid cell signaling, *Science*, **2005**, 307, 1625–1630.
- 88 GOTTARDIS, M. M., ROBINSON, S. P., SATYASWAROOP, P. G., JORDAN, V. C., Contrasting actions of tamoxifen on endometrial and breast tumor growth in the athymic mouse, *Cancer Res.*, **1988**, 48, 812–815.
- 89 NAWAZ, Z., LONARD, D. M., DENNIS, A. P., SMITH, C. L., O'MALLEY, B. W., Proteasome-dependent degradation of the human estrogen receptor, *Proc. Natl. Acad. Sci. U.S.A.*, **1999**, 96, 1858–1862.
- 90 ALARID, E. T., BAKOPOULOS, N., SOLODIN, N., Proteasome-mediated proteolysis of estrogen receptor, a novel component in autologous down-regulation, *Mol. Endocrinol.*, **1999**, 13, 1522–1534.
- 91 GIAMARCHI, C., CHAILLEUX, C., CALLIGE, M., ROCHAIX, P., TROUCHE, D., RICHARD-FOY, H., Two antiestrogens affect differently chromatin remodeling of trefoil factor 1 (pS2) gene and the fate of estrogen receptor in MCF7 cells, *Biochim. Biophys. Acta*, **2002**, 1578, 12–20.
- 92 CALLIGE, M., KIEFFER, I., RICHARD-FOY, H., CSN5/Jab1 is involved in ligand-dependent degradation of estrogen receptor {alpha} by the proteasome, *Mol. Cell Biol.*, **2005**, 25, 4349–4358.
- 93 GOUGELET, A., BOUCLIER, C., MARSAUD, V., MAILLARD, S., MUELLER, S. O., KORACH, K. S., RENOIR, J. M., Estrogen receptor alpha and beta subtype expression and transactivation capacity are differentially affected by receptor-, hsp90- and immunophilin-ligands in human breast cancer cells, *J. Steroid Biochem. Mol. Biol.*, **2005**, 94, 71–81.
- 94 SEGNITZ, B., GEHRING, U., The function of steroid hormone receptors is inhibited by the hsp90-specific compound geldanamycin, *J. Biol. Chem.*, **1997**, 272, 18 694–18 701.
- 95 BAGATELL, R., KHAN, O., PAINE-MURRIETA, G., TAYLOR, C. W., AKINAGA, S., WHITESSELL, L., Destabilization of steroid receptors by heat shock protein 90-binding drugs, a ligand-independent approach to hormonal therapy of breast cancer, *Clin. Cancer Res.*, **2001**, 7, 2076–2084.
- 96 NECKERS, L., Hsp90 inhibitors as novel cancer chemotherapeutic agents, *Trends Mol. Med.*, **2002**, 8, S55–61.
- 97 WAKELING, A. E., BOWLER, J., Steroidal pure antioestrogens, *J. Endocrinol.*, **1987**, 112, R7–10.
- 98 BRODIE, A., Aromatase inhibitors in breast cancer, *Trends Endocrinol. Metab.*, **2002**, 13, 61–65.
- 99 ATTAL, M., HAROUSSEAU, J. L., Randomized trial experience of the Intergroupe Francophone du Myelome, *Semin. Hematol.*, **2001**, 38, 226–230.
- 100 DESIKAN, R., BARLOGIE, B., SAWYER, J., AYERS, D., TRICOT, G., BADROS, A., ZANGARI, M., MUNSHI, N. C., ANAISSIE, E., SPOON, D., SIEGEL, D., JAGANNATH, S., VESOLE, D., EPSTEIN, J., SHAUGHNESSY, J., FASSAS, A., LIM, S., ROBERSON, P., CROWLEY, J., Results of high-dose therapy for 1000 patients with multiple myeloma, durable complete remissions and superior survival in the absence of chromosome 13 abnormalities, *Blood*, **2000**, 95, 4008–4010.
- 101 BARLOGIE, B., ZANGARI, M., SPENCER, T., FASSAS, A., ANAISSIE, E., BADROS, A., CROMER, J., TRICOT, G., Thalidomide in the management of multiple myeloma, *Semin. Hematol.*, **2001**, 38, 250–259.
- 102 BRUNO, B., ROTA, M., GIACCONE, L., MASSAIA, M., BERTOLA, A., PALUMBO, A., BOCCADORO, M., New drugs for treatment of multiple myeloma, *Lancet Oncol.*, **2004**, 5, 430–442.
- 103 RICHARDSON, P. G., MITSIADES, C. S., HIDESHIMA, T., ANDERSON, K. C., Novel biological therapies for the

- treatment of multiple myeloma, *Best Pract. Res. Clin. Haematol.*, **2005**, *18*, 619–634.
- 104** ZANGARI, M., ANAISSIE, E., STOPECK, A., MORIMOTO, A., TAN, N., LANCET, J., COOPER, M., HANNAH, A., GARCIA-MANERO, G., FADERL, S., KANTARJIAN, H., CHERRINGTON, J., ALBITAR, M., GILES, F. J., Phase II study of SU5416, a small molecule vascular endothelial growth factor tyrosine kinase receptor inhibitor, in patients with refractory multiple myeloma, *Clin. Cancer Res.*, **2004**, *10*, 88–95.
- 105** HIDESHIMA, T., CHAUHAN, D., SHIMA, Y., RAJE, N., DAVIES, F. E., TAI, Y. T., TREON, S. P., LIN, B., SCHLOSSMAN, R. L., RICHARDSON, P., MULLER, G., STIRLING, D. I., ANDERSON, K. C., Thalidomide and its analogs overcome drug resistance of human multiple myeloma cells to conventional therapy, *Blood*, **2000**, *96*, 2943–2950.
- 106** OSMAN, K., COMENZO, R., RAJKUMAR, S. V., Deep venous thrombosis and thalidomide therapy for multiple myeloma, *N. Engl. J. Med.*, **2001**, *344*, 1951–1952.
- 107** ZERVAS, K., DIMOPOULOS, M. A., HATZICHARISSI, E., ANAGNOSTOPOULOS, A., PAPAIOANNOU, M., MITSOU, C., PANAGIOTIDIS, P., KORANTZIS, J., TZILIANOS, M., MANIATIS, A., Primary treatment of multiple myeloma with thalidomide, vincristine, liposomal doxorubicin and dexamethasone (T-VAD doxil), a phase II multicenter study, *Ann. Oncol.*, **2004**, *15*, 134–138.
- 108** ADAMS, J., PALOMBELLA, V. J., SAUSVILLE, E. A., JOHNSON, J., DESTREE, A., LAZARUS, D. D., MAAS, J., PIEN, C. S., PRAKASH, S., ELLIOTT, P. J., Proteasome inhibitors, a novel class of potent and effective antitumor agents, *Cancer Res.*, **1999**, *59*, 2615–2622.
- 109** HIDESHIMA, T., RICHARDSON, P., CHAUHAN, D., PALOMBELLA, V. J., ELLIOTT, P. J., ADAMS, J., ANDERSON, K. C., The proteasome inhibitor PS-341 inhibits growth, induces apoptosis, and overcomes drug resistance in human multiple myeloma cells, *Cancer Res.*, **2001**, *61*, 3071–3076.
- 110** MITSIADES, C. S., MITSIADES, N., RICHARDSON, P. G., TREON, S. P., ANDERSON, K. C., Novel biologically based therapies for Waldenström's macroglobulinemia, *Semin Oncol.*, **2003**, *30*, 309–312.
- 111** ORLOWSKI, R. Z., Proteasome inhibitors in cancer therapy, *Methods Mol. Biol.*, **2005**, *301*, 339–350.
- 112** LE GOUILL, S., PELLAT-DECEUNYNCK, C., HAROUSSEAU, J. L., RAPP, M. J., ROBILLARD, N., BATAILLE, R., AMIOT, M., Farnesyl transferase inhibitor R115777 induces apoptosis of human myeloma cells, *Leukemia*, **2002**, *16*, 1664–1667.
- 113** OCHIAI, N., UCHIDA, R., FUCHIDA, S., OKANO, A., OKAMOTO, M., ASHIHARA, E., INABA, T., FUJITA, N., MATSUBARA, H., SHIMAZAKI, C., Effect of farnesyl transferase inhibitor R115777 on the growth of fresh and cloned myeloma cells in vitro, *Blood*, **2003**, *102*, 3349–3353.
- 114** DOISNEAU-SIXOU, S. F., CESTAC, P., FAYE, J. C., FAVRE, G., SUTHERLAND, R. L., Additive effects of tamoxifen and the farnesyl transferase inhibitor FTI-277 on inhibition of MCF-7 breast cancer cell-cycle progression, *Int. J. Cancer*, **2003**, *106*, 789–798.
- 115** MITSIADES, C. S., MITSIADES, N. S., McMULLEN, C. J., POULAKI, V., SHRINGARPURE, R., HIDESHIMA, T., AKIYAMA, M., CHAUHAN, D., MUNSHI, N., GU, X., BAILEY, C., JOSEPH, M., LIBERMANN, T. A., RICHON, V. M., MARKS, P. A., ANDERSON, K. C., Transcriptional signature of histone deacetylase inhibition in multiple myeloma, biological and clinical implications, *Proc. Natl. Acad. Sci. U.S.A.*, **2004**, *101*, 540–545.
- 116** BANERJEEI, S. K., ZOUBINE, M. N., SARKAR, D. K., WESTON, A. P., SHAH, J. H., CAMPBELL, D. R., 2-Methoxyestradiol blocks estrogen-induced rat pituitary tumor growth and tumor angiogenesis, possible role of vascular endothelial growth factor, *Anticancer Res.*, **2000**, *20*, 2641–2645.
- 117** CHAUHAN, D., CATLEY, L., HIDESHIMA,

- T., LI, G., LEBLANC, R., GUPTA, D., SATTLER, M., RICHARDSON, P., SCHLOSSMAN, R. L., PODAR, K., WELLER, E., MUNSHI, N., ANDERSON, K. C., 2-Methoxyestradiol overcomes drug resistance in multiple myeloma cells, *Blood*, **2002**, 100, 2187–2194.
- 118 HARRINGTON, K. J., LEWANSKI, C., NORTHCOTE, A. D., WHITTAKER, J., PETERS, A. M., VILE, R. G., STEWART, J. S., Phase II study of pegylated liposomal doxorubicin (Caelyx) as induction chemotherapy for patients with squamous cell cancer of the head and neck, *Eur. J. Cancer*, **2001**, 37, 2015–2022.
- 119 HARRINGTON, K. J., Liposomal cancer chemotherapy, current clinical applications and future prospects, *Expert Opin. Investig. Drugs*, **2001**, 10, 1045–1061.
- 120 HARRINGTON, K. J., LEWANSKI, C. R., NORTHCOTE, A. D., WHITTAKER, J., WELLBANK, H., VILE, R. G., PETERS, A. M., STEWART, J. S., Phase I-II study of pegylated liposomal cisplatin (SPI-077) in patients with inoperable head and neck cancer, *Ann. Oncol.*, **2001**, 12, 493–496.
- 121 GAUDUCHON, J., GOUILLEUX, F., MAILLARD, S., MARSAUD, V., RENOIR, J. M., SOLA, B., The 4-hydroxytamoxifen inhibits proliferation of multiple myeloma cells in vitro and in vivo through down-regulation of c-Myc, up-regulation of p27Kip1 and modulation of Bcl-2 family members, *Clin. Cancer Res.*, **2005**, 11, 2345–2354.
- 122 FUNKE, A. P., SCHILLER, R., MOTZKUS, H. W., GUNTHER, C., MULLER, R. H., LIPP, R., Transdermal delivery of highly lipophilic drugs, in vitro fluxes of antiestrogens, permeation enhancers, and solvents from liquid formulations, *Pharm. Res.*, **2002**, 19, 661–668.
- 123 FUNKE, A. P., GUNTHER, C., MULLER, R. H., LIPP, R., In-vitro release and transdermal fluxes of a highly lipophilic drug and of enhancers from matrix TDS, *J. Controlled Release*, **2002**, 82, 63–70.
- 124 STORM, G., CROMMELIAN, D. J. A., Liposomes, quo vadis, *Pharm. Sci. Technol. Today*, **1998**, 1, 19–31.
- 125 GREF, R., MINAMITAKE, Y., PERACCHIA, M. T., TRUBETSKOY, V., TORCHILIN, V., LANGER, R., Biodegradable long-circulating polymeric nanospheres, *Science*, **1994**, 263, 1600–1603.
- 126 MOGHIMI, S. M., HUNTER, A. C., MURRAY, J. C., Long-circulating and target-specific nanoparticles, theory to practice, *Pharmacol. Rev.*, **2001**, 53, 283–318.
- 127 TORCHILIN, V. P., TRUBETSKOY, V. S., WHITEMAN, K. R., CALICETI, P., FERRUTI, P., VERONESE, F. M., New synthetic amphiphilic polymers for steric protection of liposomes in vivo, *J. Pharm. Sci.*, **1995**, 84, 1049–1053.
- 128 STOLNIK, S., DUNN, S. E., GARNETT, M. C., DAVIES, M. C., COOMBES, A. G., TAYLOR, D. C., IRVING, M. P., PURKISS, S. C., TADROS, T. F., DAVIS, S. S. et al., Surface modification of poly(lactide-co-glycolide) nanospheres by biodegradable poly(lactide)-poly(ethylene glycol) copolymers, *Pharm. Res.*, **1994**, 11, 1800–1808.
- 129 GREF, R., MINAMITAKE, Y., PERACCHIA, M. T., DOMB, A., TRUBETSKOY, V., TORCHILIN, V., LANGER, R., Poly(ethylene glycol)-coated nanospheres, potential carriers for intravenous drug administration, *Pharm. Biotechnol.*, **1997**, 10, 167–198.
- 130 VAUTHIER, C., DUBERNET, C., FATTAL, E., PINTO-ALPHANDARY, H., COUVREUR, P., Poly(alkylcyanoacrylates) as biodegradable materials for biomedical applications, *Adv. Drug Deliv. Rev.*, **2003**, 55, 519–548.
- 131 LANDRY, F. B., BAZILE, D. V., SPENLEHAUER, G., VEILLARD, M., KREUTER, J., Degradation of poly(D,L-lactic acid) nanoparticles coated with albumin in model digestive fluids (USP XXII), *Biomaterials*, **1996**, 17, 715–723.
- 132 BAZILE, D., PRUD'HOMME, C., BASSOULLET, M. T., MARLARD, M., SPENLEHAUER, G., VEILLARD, M., Stealth Me.PEG-PLA nanoparticles avoid uptake by the mononuclear phagocytes system, *J. Pharm. Sci.*, **1995**, 84, 493–498.

- 133 PERACCHIA, M. T., VAUTHIER, C., PUISIEUX, F., COUVREUR, P., Development of sterically stabilized poly(isobutyl 2-cyanoacrylate) nanoparticles by chemical coupling of poly(ethylene glycol), *J. Biomed. Mater. Res.*, **1997**, *34*, 317–326.
- 134 PERACCHIA, M. T., VAUTHIER, C., DESMAELE, D., GULIK, A., DEDIEU, J. C., DEMOY, M., D'ANGELO, J., COUVREUR, P., Pegylated nanoparticles from a novel methoxypolyethylene glycol cyanoacrylate-hexadecyl cyanoacrylate amphiphilic copolymer, *Pharm. Res.*, **1998**, *15*, 550–556.
- 135 VAN DE VELDE, P., NIQUE, F., BOUCHOUX, F., BREMAUD, J., HAMEAU, M. C., LUCAS, D., MORATILLE, C., VIET, S., PHILIBERT, D., TEUTSCH, G., RU 58,668, a new pure antiestrogen inducing a regression of human mammary carcinoma implanted in nude mice, *J. Steroid Biochem. Mol. Biol.*, **1994**, *48*, 187–196.
- 136 VAN DE VELDE, P., NIQUE, F., PLANCHON, P., PREVOST, G., BREMAUD, J., HAMEAU, M. C., MAGNIEN, V., PHILIBERT, D., TEUTSCH, G., RU 58668, further in vitro and in vivo pharmacological data related to its antitumoral activity, *J. Steroid Biochem. Mol. Biol.*, **1996**, *59*, 449–457.
- 137 BRIGGER, I., CHAMINADE, P., MARSAUD, V., APPEL, M., BESNARD, M., GURNY, R., RENOIR, M., COUVREUR, P., Tamoxifen encapsulation within polyethylene glycol-coated nanospheres. A new antiestrogen formulation, *Int. J. Pharm.*, **2001**, *214*, 37–42.
- 138 CHAWLA, J. S., AMIJI, M. M., Biodegradable poly(epsilon-caprolactone) nanoparticles for tumor-targeted delivery of tamoxifen, *Int. J. Pharm.*, **2002**, *249*, 127–138.
- 139 CHAWLA, J. S., AMIJI, M. M., Cellular uptake and concentrations of tamoxifen upon administration in poly(epsilon-caprolactone) nanoparticles, *AAPS PharmSci.*, **2003**, *5*, E3.
- 140 AMELLER, T., MARSAUD, V., LEGRAND, P., GREF, R., BARRATT, G., RENOIR, J. M., Polyester-poly(ethylene glycol) nanoparticles loaded with the pure antiestrogen RU 58668, physico-chemical and opsonization properties, *Pharm. Res.*, **2003**, *20*, 1063–1070.
- 141 AMELLER, T., MARSAUD, V., LEGRAND, P., GREF, R., RENOIR, J. M., Pure antiestrogen RU 58668-loaded nanospheres, morphology, cell activity and toxicity studies, *Eur. J. Pharm. Sci.*, **2004**, *21*, 361–370.
- 142 AMELLER, T., MARSAUD, V., LEGRAND, P., GREF, R., RENOIR, J. M., In vitro and in vivo biologic evaluation of long-circulating biodegradable drug carriers loaded with the pure antiestrogen RU 58668, *Int. J. Cancer*, **2003**, *106*, 446–454.
- 143 CRUZ, T., GASPAS, R., DONATO, A., LOPES, C., Interaction between polyalkylcyanoacrylate nanoparticles and peritoneal macrophages, MTT metabolism, NBT reduction, and NO production, *Pharm. Res.*, **1997**, *14*, 73–79.
- 144 EVANS, C. E., LEES, G. C., TRAIL, I. A., Cytotoxicity of cyanoacrylate adhesives to cultured tendon cells, *J. Hand Surg. [Br]*, **1999**, *24*, 658–661.
- 145 AMELLER, T., LEGRAND, P., MARSAUD, V., RENOIR, J. M., Drug delivery systems for oestrogenic hormones and antagonists, the need for selective targeting in estradiol-dependent cancers, *J. Steroid Biochem. Mol. Biol.*, **2004**, *92*, 1–18.
- 146 CARROLL, J. S., LYNCH, D. K., SWARBRICK, A., RENOIR, J. M., SARCEVIC, B., DALY, R. J., MUSGROVE, E. A., SUTHERLAND, R. L., p27(Kip1) induces quiescence and growth factor insensitivity in tamoxifen-treated breast cancer cells, *Cancer Res.*, **2003**, *63*, 4322–4326.
- 147 UZIELY, B., JEFFERS, S., ISACSON, R., KUTSCH, K., WEI-TSAO, D., YEHOSHUA, Z., LIBSON, E., MUGGIA, F. M., GABIZON, A., Liposomal doxorubicin, antitumor activity and unique toxicities during two complementary phase I studies, *J. Clin. Oncol.*, **1995**, *13*, 1777–1785.
- 148 GABIZON, A., MARTIN, F., Polyethylene glycol-coated (pegylated) liposomal doxorubicin. Rationale for use in solid

- tumours, *Drugs*, **1997**, 54(Suppl 4), 15–21.
- 149 SYMON, Z., PEYSER, A., TZEMACH, D., LYASS, O., SUCHER, E., SHEZEN, E., GABIZON, A., Selective delivery of doxorubicin to patients with breast carcinoma metastases by stealth liposomes, *Cancer*, **1999**, 86, 72–78.
- 150 LOPES DE MENEZES, D. E., PILARSKI, L. M., BELCH, A. R., ALLEN, T. M., Selective targeting of immunoliposomal doxorubicin against human multiple myeloma in vitro and ex vivo, *Biochim. Biophys. Acta*, **2000**, 1466, 205–220.
- 151 BURGER, K. N., STAFFHORST, R. W., DE VIJLDER, H. C., VELINOVA, M. J., BOMANS, P. H., FREDERIK, P. M., DE KRUIJFF, B., Nanocapsules, lipid-coated aggregates of cisplatin with high cytotoxicity, *Nat. Med.*, **2002**, 8, 81–84.
- 152 PAPAHDJOPoulos, D., ALLEN, T. M., GABIZON, A., MAYHEW, E., MATTHAY, K., HUANG, S. K., LEE, K. D., WOODLE, M. C., LASIC, D. D., REDEMANN, C. et al., Sterically stabilized liposomes, improvements in pharmacokinetics and antitumor therapeutic efficacy, *Proc. Natl. Acad. Sci. U.S.A.*, **1991**, 88, 11 460–11 464.
- 153 LASIC, D. D., MARTIN, F. J., GABIZON, A., HUANG, S. K., PAPAHDJOPoulos, D., Sterically stabilized liposomes, a hypothesis on the molecular origin of the extended circulation times, *Biochim. Biophys. Acta*, **1991**, 1070, 187–192.
- 154 MAILLARD, S., AMELLER, T., GAUDUCHON, J., GOUGELET, A., GOUILLEUX, F., LEGRAND, P., MARSAUD, V., FATTAL, E., SOLA, B., RENOIR, J. M., Innovative drug delivery nanosystems improve the anti-tumor activity in vitro and in vivo of anti-estrogens in human breast cancer and multiple myeloma, *J. Steroid Biochem. Mol. Biol.*, **2005**, 94, 111–121.
- 155 BUTEAU-LOZANO, H., ANCELIN, M., LARDEUX, B., MILANINI, J., PERROT-APPLANAT, M., Transcriptional regulation of vascular endothelial growth factor by estradiol and tamoxifen in breast cancer cells, a complex interplay between estrogen receptors alpha and beta, *Cancer Res.*, **2002**, 62, 4977–4984.
- 156 SENGUPTA, K., BANERJEE, S., SAXENA, N., BANERJEE, S. K., Estradiol-induced vascular endothelial growth factor-A expression in breast tumor cells is biphasic and regulated by estrogen receptor-alpha dependent pathway, *Int. J. Oncol.*, **2003**, 22, 609–614.
- 157 WOODLE, M. C., LASIC, D. D., Sterically stabilized liposomes, *Biochim. Biophys. Acta*, **1992**, 1113, 171–199.
- 158 WILLIS, M., FORSSEN, E., Ligand-targeted liposomes, *Adv. Drug Deliv. Rev.*, **1998**, 29, 249–271.
- 159 HEATH, T. D., BRAGMAN, K. S., MATTHAY, K. K., LOPEZ-STRAUBINGER, N. G., PAPAHDJOPoulos, D., Antibody-directed liposomes, the development of a cell-specific cytotoxic agent, *Biochem. Soc. Trans.*, **1984**, 12, 340–342.
- 160 ALLEN, T. M., BRANDEIS, E., HANSEN, C. B., KAO, G. Y., ZALIPSKY, S., A new strategy for attachment of antibodies to sterically stabilized liposomes resulting in efficient targeting to cancer cells, *Biochim. Biophys. Acta*, **1995**, 1237, 99–108.
- 161 HANSEN, C. B., KAO, G. Y., MOASE, E. H., ZALIPSKY, S., ALLEN, T. M., Attachment of antibodies to sterically stabilized liposomes, evaluation, comparison and optimization of coupling procedures, *Biochim. Biophys. Acta*, **1995**, 1239, 133–144.
- 162 LEE, R. J., LOW, P. S., Folate-mediated tumor cell targeting of liposome-entrapped doxorubicin in vitro, *Biochim. Biophys. Acta*, **1995**, 1233, 134–144.
- 163 MASTROBATTISTA, E., KONING, G. A., STORM, G., Immunoliposomes for the targeted delivery of antitumor drugs, *Adv. Drug Deliv. Rev.*, **1999**, 40, 103–127.
- 164 STEPHENSON, S. M., LOW, P. S., LEE, R. J., Folate receptor-mediated targeting of liposomal drugs to cancer cells, *Methods Enzymol.*, **2004**, 387, 33–50.
- 165 KIKUCHI, A., SUGAYA, S., UEDA, H.,

- TANAKA, K., ARAMAKI, Y., HARA, T., ARIMA, H., TSUCHIYA, S., FUWA, T., Efficient gene transfer to EGF receptor overexpressing cancer cells by means of EGF-labeled cationic liposomes, *Biochem. Biophys. Res. Commun.*, **1996**, 227, 666–671.
- 166 GYONGYOSSY-ISSA, M. I., MULLER, W., DEVINE, D. V., The covalent coupling of Arg-Gly-Asp-containing peptides to liposomes, purification and biochemical function of the lipopeptide, *Arch. Biochem. Biophys.*, **1998**, 353, 101–108.
- 167 CUELLO, M., ETTENBERG, S. A., CLARK, A. S., KEANE, M. M., POSNER, R. H., NAU, M. M., DENNIS, P. A., LIPKOWITZ, S., Down-regulation of the erbB-2 receptor by trastuzumab (herceptin) enhances tumor necrosis factor-related apoptosis-inducing ligand-mediated apoptosis in breast and ovarian cancer cell lines that overexpress erbB-2, *Cancer Res.*, **2001**, 61, 4892–4900.
- 168 BRAUD, A. C., MATHOULIN PORTIER, M. P., BARDOU, V. J., BERTUCCI, F., GRAVIS, G., CAMERLO, J., BEGUE, M., HOUVENAEGHEL, G., MARANINCHI, D., JACQUEMIER, J., VIENS, P., Overexpression of erb B2 remains a major risk factor in non-metastatic breast cancers treated with high-dose alkylating agents and autologous stem cell transplantation, *Bone Marrow Transplant.*, **2002**, 29, 753–757.
- 169 PARK, J. W., HONG, K., CARTER, P., ASGARI, H., GUO, L. Y., KELLER, G. A., WIRTH, C., SHALABY, R., KOTTS, C., WOOD, W. I. et al., Development of anti-p185HER2 immunoliposomes for cancer therapy, *Proc. Natl. Acad. Sci. U.S.A.*, **1995**, 92, 1327–1331.
- 170 KIRPOTIN, D., PARK, J. W., HONG, K., ZALIPSKY, S., LI, W. L., CARTER, P., BENZ, C. C., PAPAHDJOPOULOS, D., Sterically stabilized anti-HER2 immunoliposomes, design and targeting to human breast cancer cells in vitro, *Biochemistry*, **1997**, 36, 66–75.
- 171 PARK, J. W., KIRPOTIN, D. B., HONG, K., SHALABY, R., SHAO, Y., NIELSEN, U. B., MARKS, J. D., PAPAHDJOPOULOS, D., BENZ, C. C., Tumor targeting using anti-her2 immunoliposomes, *J. Controlled Release*, **2001**, 74, 95–113.
- 172 PARK, J. W., HONG, K., KIRPOTIN, D. B., COLBERN, G., SHALABY, R., BASELGA, J., SHAO, Y., NIELSEN, U. B., MARKS, J. D., MOORE, D., PAPAHDJOPOULOS, D., BENZ, C. C., Anti-HER2 immunoliposomes, enhanced efficacy attributable to targeted delivery, *Clin. Cancer Res.*, **2002**, 8, 1172–1181.
- 173 NIELSEN, U. B., KIRPOTIN, D. B., PICKERING, E. M., HONG, K., PARK, J. W., REFAAT SHALABY, M., SHAO, Y., BENZ, C. C., MARKS, J. D., Therapeutic efficacy of anti-ErbB2 immunoliposomes targeted by a phage antibody selected for cellular endocytosis, *Biochim. Biophys. Acta*, **2002**, 1591, 109–118.
- 174 GABIZON, A., HOROWITZ, A. T., GOREN, D., TZEMACH, D., MANDELBAUM-SHAVIT, F., QAZEN, M. M., ZALIPSKY, S., Targeting folate receptor with folate linked to extremities of poly(ethylene glycol)-grafted liposomes, in vitro studies, *Bioconj. Chem.*, **1999**, 10, 289–298.
- 175 LU, Y., LOW, P. S., Folate-mediated delivery of macromolecular anticancer therapeutic agents, *Adv. Drug Deliv. Rev.*, **2002**, 54, 675–693.
- 176 STELLA, B., MARSAUD, V., COUVREUR, P., ARPICCO, S., PERACCHIA, M. T., GERAUD, G., IMMORDINO, M. L., CATTEL, L., RENOIR, J. M., Biological characterization of the folic acid-nanoparticles in cellular models, The 28th International Symposium on Controlled Release of Bioactive Materials, San Diego, June 2001, 23–27, Abstract N° 5200.
- 177 STELLA, B., ARPICCO, S., PERACCHIA, M. T., DESMAELE, D., HOEBEKE, J., RENOIR, M., D'ANGELO, J., CATTEL, L., COUVREUR, P., Design of folic acid-conjugated nanoparticles for drug targeting, *J. Pharm. Sci.*, **2000**, 89, 1452–1464.
- 178 KUKOWSKA-LATALLO, J. F., CANDIDO, K. A., CAO, Z., NIGAVEKAR, S. S., MAJOROS, I. J., THOMAS, T. P.,

- BALOGH, L. P., KHAN, M. K., BAKER, J. R., JR., Nanoparticle targeting of anticancer drug improves therapeutic response in animal model of human epithelial cancer, *Cancer Res.*, **2005**, 65, 5317–5324.
- 179 PETERSSON, K., DELAUNAY, F., GUSTAFSSON, J. A., Estrogen receptor beta acts as a dominant regulator of estrogen signaling, *Oncogene*, **2000**, 19, 4970–4978.
- 180 DELAUNAY, F., PETERSSON, K., TUJAGUE, M., GUSTAFSSON, J. A., Functional differences between the amino-terminal domains of estrogen receptors alpha and beta, *Mol. Pharmacol.*, **2000**, 58, 584–590.
- 181 HALL, J. M., McDONNELL, D. P., The estrogen receptor beta-isoform (ERbeta) of the human estrogen receptor modulates ERalpha transcriptional activity and is a key regulator of the cellular response to estrogens and antiestrogens, *Endocrinology*, **1999**, 140, 5566–5578.
- 182 LAZENNEC, G., BRESSON, D., LUCAS, A., CHAUVEAU, C., VIGNON, F., ER beta inhibits proliferation and invasion of breast cancer cells, *Endocrinology*, **2001**, 142, 4120–4130.
- 183 TREMBLAY, A., TREMBLAY, G. B., LABRIE, C., LABRIE, F., GIGUERE, V., EM-800, a novel antiestrogen, acts as a pure antagonist of the transcriptional functions of estrogen receptors alpha and beta, *Endocrinology*, **1998**, 139, 111–118.
- 184 LABRIE, F., LABRIE, C., BELANGER, A., SIMARD, J., GIGUERE, V., TREMBLAY, A., TREMBLAY, G., EM-652 (SCH57068), a pure SERM having complete antiestrogenic activity in the mammary gland and endometrium, *J. Steroid Biochem. Mol. Biol.*, **2001**, 79, 213–225.



## Index

### **a**

accumulation, ff-MWCNTs 322  
 aclacinomycin, cancer treatment 9  
 Acridine 138  
   – Immunoliposomes 137–138  
 Actinomycin D 190  
 active targeting 223–225  
   – circumstantial 221  
   – ligands 346–354  
   – molecular 221  
   – nanoparticles 8–10  
 administration, drug nanoparticles  
   routes 10–12  
 advanced generation nanoparticles 172  
 adverse effects, cancer treatment 74–75  
 AE *see* antiestrogens  
 albumin-microspheres, local  
   chemotherapy 160  
 alkylating agents, anticancer agents  
   release 187–188  
 alpha particles, boron neutron capture therapy  
   (BNCT) 122  
 ammonium-functionalized SWCNTs and  
   MWCNTs 319  
 amphiphilic copolymers 8  
 angiogenic factors, cancer cell targeting  
   349–350  
 anisotropy, magnetic 283–284  
 anthracyclines 12–19  
   – MM treatment 380  
   – nucleic acids synthesis inhibition 211  
 anti-metabolites, cancer treatment 20–21  
 antibodies  
   – coupled to PEG 225, 356  
   – monoclonal 126–127  
   – targeting 225  
 anticancer agents  
   – colloidal systems 371–392  
   – controlled release 168, 186–191

  – kinetics 181  
   – targeted delivery 338–364  
 anticancer antibiotics 190–191  
 anticancer drug delivery 3–5  
   – inorganic nanoparticles 180  
   – nanoparticles 12, 209–211  
 anticancer therapies, critical analysis  
   200–202  
 anticancer treatment strategies, ferromagnetic  
   filled carbon nanotubes 259–324  
 antiestrogen delivery  
   – characteristics 384  
   – colloidal systems 381–390  
 antiestrogens (AE) 19–20, 373–374  
   – differential activity 378–379  
   – encapsulation 379  
   – multiple myeloma 381  
   – nanoparticles charged with 381–386  
   – pure 382–387  
 antimetabolic agent 188  
 arsenic trioxide, cancer treatment 26  
 Au@PNAL, fabrication strategy 178

### **b**

<sup>10</sup>B, neutron capture therapy 88  
 BBB *see* blood brain barrier  
 biocompatible drug-loaded nanoparticles 218  
 biodegradable nanoparticles  
   – polymeric 57  
   – drug-loaded 218  
 biodegradable polymers 5–12  
   – preparation 58–61  
 biodistribution  
   – conventional nanoparticles 5  
   – gadolinium 98–101  
   – photosensitizer-nanoparticle couples 70–71  
 biological drug delivery 208  
 biological therapies, multiple myeloma  
   380–381

- biomedical applications, anticancer agents 170–174
- biotin 354
- bladder cancer, paclitaxel therapy 24
- Bleomycin, anticancer antibiotics 190
- block-copolymers, cancer chemotherapy 203
- blood brain barrier
  - anthracyclines 16
  - boron neutron capture therapy (BNCT) 142
  - cancer therapy 341
  - drug delivery nanoparticulate systems 210
  - magnetic drug nanovectors 219
  - Paclitaxel 25
  - targeting methods 343
- BNCT *see* boron neutron capture therapy
- boranes, liposomal encapsulation 134–136
- boron clusters, monoclonal antibodies 126
- boron compounds, delivery 141
- boron-containing macromolecules, tumor delivery 142–143
- boron delivery
  - dextrans 139–141
  - general requirements 124–125
  - liposomes 130
  - targeted liposomes 137–139
- boron neutron capture therapy (BNCT) 88–93, 122–145
- boronated dendrimers 130
  - attachment 126–127
  - boron neutron capture therapy (BNCT) 126–127
  - receptor ligands 127
- boronophenylalanine, liposomal encapsulation 133–136
- brain metastases, paclitaxel therapy 25
- brain tumors, boron neutron capture therapy (BNCT) 142–143
- breast cancer
  - cisplatin therapy 24
  - colloidal systems 371
  - hormone therapy 374–379
- butyric acid, cancer treatment 26
- C**
- calcium hydroxyapatite, drug delivery vectors design 180
- camptothecins 20–21, 214
- cancer-associated cells, targeting 223
- cancer cells, multidrug resistance 17–19
- cancer chemotherapy 339–341
- cancer markers, targeting 224
- cancer therapy
  - critical analysis 199–232
  - local 156–167
  - neutron capture 87–113
  - new experimental 214–215
  - resistance mechanisms 227–229
- cancer treatment, drug nanoparticles 1–40
- cancer vasculature, targeting 223
- carbohydrates, targeting 225
- carbohydrates-ceramic nanoparticles 204
- carbon nanotubes (CNTs)
  - compared to other nanoparticles 315
  - description 264–277
  - ferromagnetic filled 259–324
  - functionality 315
  - heat generation 290–309
  - magnetism 277–290
  - morphology 315
- carboranes, liposomal encapsulation 134–136
- carmustine, anticancer agents release 188
- carrier characteristics, cancer cells 63
- CDDS *see* conventional drug delivery systems
- CED *see* convection-enhanced delivery
- cell models, polymeric nanoparticles 61–70
- cell separation, magnetic 158
- cellular “sanctuaries”, chemotherapy 360
- ceramic nanoparticles, photodynamic therapy 55–56
- cetyltrimethylammonium bromide (CTAB) 28
- chamber model, administration and characterization of ff-MWCNTs 313–314
- chemical drug delivery 208
- chemical vapor deposition (CVD) 312–313
- chemotherapeutic drug nanoparticles 1–40
- chemotherapy
  - cancer 339–341
  - local 156–158
- chitosan 105–109, 180
  - clinical drug delivery 212
  - neutron capture therapy 68
  - polymeric nanoparticles 180, 359
  - preparation methods 104
- chitosan nanoparticles, gadolinium delivery 104–113
- chitosan-type polymers, gene therapy 215–216
- chlorambucil, anticancer agents release 187–188
- 1-[p-chlorobenzoyl]-2-methyl-5-methoxy-3-indoleacetic acid 183
- circumstantial targeting, active 221
- cisplatin 213–214
  - cancer treatment 21

- clinical considerations, boron neutron capture therapy (BNCT) 144–145
  - clinical use, nanoparticulate drug delivery 211–214
  - clusters, CNTs 319
  - CNTs *see* carbon nanotubes
  - Co, magnetic characteristics 280
  - co-surfactants
    - gadolinium biodistribution 99
    - Gd-nanoLE 98
  - coercivities, ferromagnetic filled multiwalled CNTs 289
  - colloidal Au, drug delivery vectors design 181
  - colloidal systems
    - antiestrogen-loaded 384
    - delivery of anticancer agents 371–392
    - drug carriers 11
    - drug delivery 209
    - drug-loaded 387–390
  - concentration gradient, anticancer agents kinetics 182
  - controlled release, anticancer agents 168, 181
  - convection-enhanced delivery (CED), boron neutron capture therapy 143
  - conventional drug delivery systems (CDDS) 371
  - conventional nanoparticles, cancer treatment 5–12
  - core-shell nanoparticles, intelligent 219
  - coronary plaque removal, anticancer agents 173
  - cremophor EL 21–23
  - critical analysis
    - anticancer therapies 200–202
    - cancer therapy 199–232
    - drug delivery systems 207–220
    - nanoparticles 202–207
    - nanovectors 207–220
    - resistance to therapy 227–229
    - targeting 220–227
    - toxicity issues 229–230
  - CTAB *see* cetyltrimethylammonium bromide
  - CuX zeolite, drug delivery vectors design 180
  - CVD *see* chemical vapor deposition
  - cyclophosphamide, anticancer agents release 187–188
  - cystatins, cancer treatment 26
  - cytarabine, antimetabolic agent 188–189
- d**
- daunorubicin, anticancer antibiotics 191
  - DDS *see* drug delivery system
  - delivery agents
    - boron neutron capture therapy 122–145
    - dendrimer-related 125–130
  - dendrimer-related delivery agents, boron neutron capture therapy 125–130
  - dendrimers 204
    - boron neutron capture therapy 125–126
    - boronated 126–127
    - cancer cell targeting 357–359
    - structure 132
    - targeted delivery of anticancer agents 338, 342, 357–361
  - 2-devinyl-2-(1-hexyloxyethyl) pyropheophorbide (HPPH) 55
  - dextran-coated magnetite-particles 244
  - dextrans, boron delivery 139–141
  - diagnostics, *in vitro* 338
  - diethylenetriaminepentaacetic acid, cancer treatment 26
  - diffusion model, anticancer agents kinetics 182–183
  - direct intracerebral delivery, brain tumors 142–143
  - dissolution model 183–186
  - DNA
    - interaction with CNTs 318–319
    - nanoparticle complexes 351–352
  - domains, magnetic 280–283
  - DOTAP 29
  - doxorubicin 12–19
  - drug biodistribution profile 5–6
  - drug concentration, photocytotoxicity 64
  - drug-conjugated delivery systems 209
  - drug delivery
    - anticancer 209–211
    - intracellular 210, 225–226
    - nanoparticulate 211–214, 341–343
  - drug delivery systems (DDS) 90
    - cancer treatment 4
    - critical analysis 207–220
    - future directions 191
    - polymer materials 174–175
  - drug delivery target 2–4
  - drug delivery vectors, design 175–181
  - drug-loaded nanoparticles
    - biocompatible and biodegradable 218
    - colloidal systems 387–390
    - different types 58
    - toxicity 217
  - drug-nanocarrier linkers 227–228
  - drug nanoparticles
    - chemotherapeutic 1–40
    - routes 10–12
  - drug resistance mechanisms 211
  - drug targeting, magnetic 156–167

- drug transport vectors, brain tumors 142–143
- drugs
  - new experimental 214–215
  - tumor selectivity 362
- e**
- eddy current losses, ff-MWCNTs 293
- EGF *see* epidermal growth factors
- EGFR targeted liposomes, Acridine 138
- embolization hyperthermia, ferromagnetic 248–249
- emulsion/solid lipid nanoparticles, drug delivery 209
- endocytosis
  - Fe-MWCNTs 309–311
  - ff-MWCNT uptake 309–311
- endothelial growth factor, vascular 129–130
- enhanced permeation and retention (EPR) effect 3, 343–344, 363
- epidermal growth factors (EGF) 128–129
- EPR *see* enhanced permeation and retention (EPR) effect
- ER *see* estrogen receptor
- ER-ligands, molecular mechanisms 375–377
- ERE *see* estrogen responsive elements
- estrogen action in breast cancers, molecular mechanisms 375–378
- estrogen receptor (ER) 344
  - colloidal systems 372–396
- estrogen responsive elements (EREs) 375–377
- estrogens
  - breast cancer 372–374
  - multiple myeloma 381
- f**
- f-MWCNTs *see* filled multiwalled CNTs
- FACS *see* FSC-SSC scatter flow cytometric analysis
- Fe, magnetic characteristics 280
- feasibility studies, thermotherapy 249–254
- ferrimagnetic particles, hyperthermia 297
- ferrofluids, anticancer agents
- ferromagnetic embolization hyperthermia 248–249
- ferromagnetic filled carbon nanotubes 259–324
- ferromagnetic filled multiwalled CNTs (ff-MWCNTs) 259
  - accumulation 322
  - evaluation for anticancer applications 313–324
  - *in vitro* and *in vivo* applications 309–324
  - lipid-mediated uptake 309–311
  - magnetic properties 285–290
  - production 312–313
- ferromagnetic particles, hyperthermia 297
- ferromagnetism 278
- ff-MWCNTs *see* ferromagnetic filled multiwalled CNTs
- fff-MWCNTs *see* functionalized and ferromagnetic filled multiwalled CNTs
- Fick's second law, anticancer agents kinetics 182
- filled carbon nanotubes, ferromagnetic 259–324
- filled multiwalled CNTs (f-MWCNTs)
  - filling and closing 275–277
  - growth 271–275
  - structure 269–270
  - synthesis 266–269
- first generation nanoparticles, anticancer agents 171
- flow cytometric analysis *see* FSC-SSC scatter flow cytometric analysis
- flower-state magnetization 281–282
- fluorescence 41
- fluorouracil (FU) 213
  - antimetabolic agent 189
- folate, targeting 224
- folate-overexpressing HeLa cancer cells 316–317
- folate receptor (FR)
  - boron neutron capture therapy 129
  - targeted liposomes 138
- folic acid, cancer cell targeting 350–352
- FR *see* folate receptor
- FR expressing tumor cells, laser radiation 317
- FSC-SSC scatter flow cytometric analysis (FACS) 309–310
- FU *see* fluorouracil
- functional nanoparticles, anticancer agents 172
- functionality, CNTs 315
- functionalization, CNTs 316
- functionalized and ferromagnetic filled multiwalled CNTs (fff-MWCNTs) 259
- functionalized MWCNTs, improved 313–324
- functionalized SWNTs, selective targeting 317
- g**
- G-protein coupled receptor (GPCR) 378
- gadobutrol, GdNCT 94
- gadolinium biodistribution 98–101
  - intravenous administration 101–104

- gadolinium delivery
    - chitosan nanoparticles 104–113
    - lipid emulsion 95–104
  - gadolinium neutron capture therapy (GdNCT) 87
  - GBM *see* glioblastoma multiforme
  - <sup>157</sup>Gd, neutron capture therapy 88
  - Gd accumulation, tumor tissue 102
  - Gd concentration, *in vivo* growth suppression 110
  - Gd-DTPA-SA 96
    - bioadhesion 109–113
    - Gd-DTPA release property 107–108
    - preparation 105–107
    - uptake 109–113
  - Gd-nanoCP 104–113
  - Gd-DTPA release property 107–108
  - preparation 105–107
  - uptake 109–113
  - Gd-nanoLE *see* gadolinium delivery
    - intraperitoneal administration 98–101
    - intravenous administration 101–104
    - preparation 95–98
  - GdNCT *see* gadolinium neutron capture therapy
    - therapeutic potential 93–112
    - typical research 94–95
  - gel drug carriers 219
  - gene therapy 27, 215–216
    - cancer 363–364
  - Gliadel®, anticancer agents release 188
  - glioblastoma multiforme (GBM)
    - boron neutron capture therapy 123
    - thermotherapy 247, 250–251
  - gliomas
    - boron neutron capture therapy 123
    - cyclophosphamide 187
    - paclitaxel therapy 25
    - thermotherapy 244, 250
  - GPCR *see* G-protein coupled receptor
  - Greene's melanoma, gadolinium biodistribution 99
  - growth suppression, melanoma solid tumor 108–109
- h**
- Haematoporphyrin derivative (HpD) 45
  - HCO-60, gadolinium biodistribution 99–100
  - heat generation, carbon nanotubes 290–309
  - HeLa cancer cells, folate-overexpressing 316–317
  - high molecular weight (HMW) delivery agents 122–145
    - boron 125–130
  - HMW *see* high molecular weight (HMW) delivery agents
  - hormone therapy, breast cancer 374–379
  - HpD *see* Haematoporphyrin derivative
  - HPPH *see* 2-devinyl-2-(1-hexyloxyethyl) pyropheophorbide
  - HT *see* hyperthermia therapy
  - hydrophile–lipophile balance value, photosensitizers 44, 66
  - hyperthermia
    - AC-heating 322–323
    - development of materials 296–300
    - embolization 248–249
    - magnetic particle 263
  - hyperthermia therapy (HT), synergetical effects 54
  - hysteresis loop
    - Fe-MWCNTs 302
    - ferromagnetic materials 279, 282, 287–289
    - hyperthermia 299–300
    - well- and ill-conditioned 300
  - hysteresis losses, ff-MWCNTs 293
- i**
- ICP-AES *see* inductively coupled plasma atomic emission spectroscopy
  - ill-conditioned hysteresis loop 300
  - IMC *see* indomethacin (IMC) release
  - immunoliposomes 357
    - boron neutron capture therapy (BNCT) 137–139
  - immunoreaction, gadolinium biodistribution 102
  - in situ* polymerization, biodegradable polymeric nanoparticles 58–59
  - in vitro* efficacy assay, polymeric nanoparticles 62
  - in vitro* molecular diagnostics 338
  - incubation medium, cell viability 63
  - incubation time, *in vivo* growth suppression 110
  - indomethacin (IMC) release, kinetics 183
  - inductively coupled plasma atomic emission spectroscopy (ICP-AES) 99
  - inorganic components, nano-sized 170
  - inorganic nanoparticles, drug delivery vectors 180–180
  - intelligent core–shell nanoparticles 219
  - internalization, ferromagnetic filled multiwalled CNTs (ff-MWCNTs) 309–311
  - intracellular drug delivery 210, 225–226
  - intracellular localization, photosensitizers 68
  - intracerebral delivery, brain tumors 142–143
  - intravenous administration, gadolinium biodistribution 101–104
  - intravenously injected nanoparticles 205–206
  - iron oxide crystals, superparamagnetic 204

- iron oxide nanoparticles, superparamagnetic 169–173
- k**
- Kaplan–Meier survival curves, doxorubicin 15
- l**
- laser radiation, folate receptor expressing tumor cells 317
- ligands, active targeting 346–354
- linkers, drug–nanocarrier 227–228
- lipid addition, *in vitro* 309–311
- lipid emulsion, gadolinium delivery 95–104
- liposomal encapsulation, boron neutron capture therapy 133–136
- liposomes
- antiestrogen incorporation 382
  - boron neutron capture therapy 130
  - cancer cell targeting 355–357
  - cancer chemotherapy 203
  - charged with RU 58668 386–388
  - drug delivery 209
  - non-targeted 133–134
  - receptor-targeted 138
  - structure 132
  - targeted 137–139, 338–364
- liquid source chemical vapor deposition (LSCVD) 312–313
- LMW *see* low molecular weight
- local cancer therapy 156–167
- local chemotherapy 156–158
- locoregional adjuvant therapy 219
- low molecular weight (LMW) boron delivery agents 122–125
- LSCVD *see* liquid source chemical vapor deposition
- m**
- mAb *see* monoclonal antibodies
- macromolecular transport pathways, cancer treatment 2–4
- macromolecules, brain tumors 142–143
- macrophages, targeting 223
- MagForce nanotherapy 249–254
- magic bullet 362–364
- magnetic anisotropy 283–284
- magnetic cell separation, local chemotherapy 158
- magnetic domains 280–283
- magnetic drug delivery, local chemotherapy 158–163
- magnetic drug nanovectors 219–220
- magnetic drug targeting (MDT) 156–167
- magnetic fluid hyperthermia thermotherapy (MFH) 323
- magnetic microspheres, local chemotherapy 159
- magnetic nanoparticle therapy, clinical experiences 249–254
- magnetic nanoparticles 156–167, 244–247
- magnetic particle hyperthermia 263
- magnetic reversal 284–285
- magnetic targeting 345–346
- magnetism, nano-sized materials 277–290
- magnetite-particles, dextran-coated 244
- magnetization distribution, nanoparticles 279–283
- Magnetofection™, local chemotherapy 158
- magnetoliposomes, local chemotherapy 159
- Magnevist®
- comparative studies 112
  - *in vivo* growth suppression 108
- malignant tissue suppression 43
- MDT *see* magnetic drug targeting
- melanoma cells, GdNCT 94
- melanoma solid tumor, *in vivo* growth suppression 108–109
- metallic nanoparticles
- drug delivery vectors design 181
  - photodynamic therapy (PDT) 54–55
- metastatic lymph nodes, local chemotherapy 160
- methotrexate 214
- antimetabolic agent 189–190
- methoxy poly(ethylene glycol)-poly(dl-lactic acid), antitumor characteristics 20
- MFH *see* magnetic fluid hyperthermia thermotherapy
- micelles
- cancer chemotherapy 203
  - polymeric 209
- microspheres, magnetic 159
- miscellaneous agents, cancer treatment 26
- mitoxantrone 27
- MM *see* multiple myeloma
- model chamber, administration and characterization of ff-MWCNTs 313–314
- molecular targeting, active 221
- monoclonal antibodies
- boron neutron capture therapy 126–127
  - boronated dendrimers 126–127
  - cancer cell targeting 346–350
  - conjugation scheme 128
- mononuclear phagocytic system (MPS) 360, 371
- morphology, CNTs 315
- MPS *see* mononuclear phagocytic system

- m*-tetra(hydroxyphenyl)chlorin (mTHPC) 55
  - cell uptake 67
- mTHPC *see m*-tetra(hydroxyphenyl)chlorin
- multi-domain particles, magnetic 280–283
- multidrug resistance 6
  - cancer cells 17–19
- multifunctional nanocontainers 260
- multiple myeloma (MM)
  - colloidal systems 371
  - new biological therapies 380–381
- multiwalled CNTs (MWCNTs) 259
  - ammonium-functionalized 319
  - functionalized 313–324
  - *see also* ferromagnetic filled multiwalled CNTs
- MWCNT model 263
- MWCNTs *see* multiwalled CNTs
  
- n**
- nano-sized materials, magnetism 277–290
- nanocapsules 59
  - advanced generation nanoparticles 172
  - anticancer therapies 202
  - antiestrogen incorporation 382
  - colloidal systems 381–386
  - polymerization 58
- nanocarriers, thermosensitive 177
- nanoencapsulation, polymeric nanoparticles 61
- nanomagnets 278, 283–285
- nanomedicine 231
- nanoparticle targeting, passive or active 206–207
- nanoparticle–DNA complexes 351
- nanoparticles
  - actively targetable 8–10
  - antiestrogen incorporation 381–386
  - biocompatible and biodegradable 218
  - biodegradable polymeric 57
  - cancer treatment 1–40
  - carbohydrates-ceramic 204
  - compared to CNTs 315
  - critical analysis 202–220
  - drug delivery in cancer 341–343
  - emulsion/solid lipid 209
  - generations 171–172
  - intelligent core–shell 219
  - intravenously injected 205–206
  - magnetic 244–247
  - magnetic drug targeting 156–167
  - magnetic targeting 345–346
  - non-biodegradable 54–57
  - oxidation-sensitive 219
  - polymeric 338–364
  - sterically stabilized 6–8
  - superparamagnetic iron oxide 219–220
  - targeting methods 343–364
  - thermoresponsive 219
  - thermotherapy 242–254
- nanoparticulate drug delivery systems
  - clinical use 211–214
  - targeted drugs 210
  - types 342
- nanoshells 361
- nanospheres
  - antiestrogen incorporation 382
  - cancer chemotherapy 204
  - polymeric 209
- nanotechnology 338
- nanotube–protein conjugates 318
- nanotubes, carbon *see* carbon nanotubes
- nanovectors 203–205, 361
  - anticancer agents 173
  - critical analysis 207–220
- nanovehicles, boron neutron capture therapy (BNCT) 122–145
- NCT *see* neutron capture therapy
- neutron capture cross section 88
- neutron capture therapy (NCT) 87–113
  - principle 88–89
- NI, magnetic characteristics 280
- non-biodegradable nanoparticles 54–57
- non-biodegradable polymers 56–57
- non-chitosan-type polymers, gene therapy 216
- nucleic acids, interaction with CNTs 318–319
  
- o**
- oils, Gd-nanoLE 97
- oxidation-sensitive nanoparticles 219
  
- p**
- P-glycoprotein 3
  - multidrug resistance 17–19
- PAA *see* polyacrylamide
- PACA *see* poly(alkyl cyanoacrylates)
- paclitaxel 212–213
  - cancer treatment 21
- PAMAM *see* polyamidoamine dendrimers
  - structure 126
- particle size, polymeric nanoparticles 65
- passive targeting 221–223
- PCa *see* prostate cancer
- PDT *see* photodynamic therapy
- PEG *see* poly(ethylene glycol)
- PEGylation 133, 206, 355–356, 390
- penetration depth, magnetic field 293–294
- PEO *see* poly(ethylene oxide)

- pharmacokinetics, photosensitizer-nanoparticle couples 70–71  
 photodetection 41–55  
 photodiagnosis 41  
 photodynamic therapy (PDT) 215
  - biodegradable polymeric nanoparticles 57
  - cancer therapy 40–89
  - induced damage 72
  - limitations 51–54
  - non-biodegradable nanoparticles 54–57
  - polymeric nanoparticles 61–70
  - polymeric nanoparticles *in vivo* relevance 70–74
 Photofrin® 45, 56  
 photosensitizers (PS) 45
  - adverse effects 52
  - biodistribution 70–71
  - cancer therapy 40–41
  - clinical trials 48–49
  - conventional 45–47
  - coupled to nanoparticles 70–71
  - formulations 53–54
  - intracellular localization 68
  - pharmacokinetics 70–71
  - photodynamic therapy (PDT) 215
  - tumor uptake 43
  - uptake 66–70
 phototoxic effects 41  
 physicochemical drug delivery 208  
 PLA *see* poly(lactic acid)  
 PLGA *see* poly(lactic-co-glycolic acid)  
 PNAL *see* poly[(NIPAAm-*r*-AAm)-co-lactic acid]  
 poly(alkyl cyanoacrylates) (PACA) 58  
 poly(ethylene glycol) (PEG)
  - cancer targeting 355
  - cancer treatment 8–11, 19–21
  - chains 7, 389
  - CNT stabilization 343–364
  - coating 205
  - drug delivery 217–218
  - drug delivery systems 213
  - folate receptor targeting agents 129
  - nanoparticle coating 382
  - non-biodegradable polymers 56
  - passive targeting 344
  - photosensitizers uptake 69
  - RU coupled 386
  - steric stabilization effect 363
  - targetable nanoparticles 8
 poly(ethylene oxide) (PEO), nanoparticle coating 344  
 poly(lactic acid) (PLA)
  - biodegradable polymeric nanoparticles 59
  - nanoparticle coating 382
 poly(lactic-co-glycolic acid) (PLGA), biodegradable polymeric nanoparticles 60  
 poly[(NIPAAm-*r*-AAm)-co-lactic acid] (PNAL) 177  
 poly[ $\beta$ -(1  $\rightarrow$  4)-2-amino-2-deoxy-D-glucopyranose] *see* chitosan  
 polyacrylamide (PAA) 56  
 polyamidoamine (PAMAM) dendrimers 358  
 polymer gels 219  
 polymer materials, anticancer agents 174–175  
 polymer modifications, polymeric nanoparticles 63  
 polymer therapeutics 202  
 polymeric micelles 209  
 polymeric nanoparticles
  - biodegradable 57
  - cancer cell targeting 359–362
  - drug delivery vectors design 175–180
  - *in vitro* relevance 61–70
  - *in vivo* relevance 70–74
  - targeted delivery of anticancer agents 338, 342, 361–362
 polymeric nanospheres, drug delivery 209  
 polymerization, *in situ* 58–59  
 polymers
  - biological characteristics 204
  - dispersion 59–61
  - non-biodegradable 56–57
 porous materials, drug delivery vectors design 180  
 porphyrin derivatives, polymeric nanoparticles *in vivo* 72  
 porphyrins, photosensitizer structure 46  
 preformed polymer, dispersion 59–61  
 prostate cancer, description 260–264  
 prostate carcinoma, recurrent 253–254  
 protein–nanotube conjugates 318  
 PS *see* photosensitizers  
 PSA, serum marker 261–262  
 pure antiestrogen, RU 58 668 382–387
- q**  
 QD *see* quantum dots  
 quantum dots (QDs) 47
  - cancer cell targeting 351–352
- r**  
 radiation-producing element, <sup>10</sup>B 88  
 radiotherapy, neutron capture therapy 87  
 reactive oxygen species (ROS) 42
  - cell uptake 68
 receptor ligands, boronated dendrimers 127



- receptor-mediated tumor cell targeting 137
- recurrent glioblastoma multiforme,
  - thermotherapy 250–251
- recurrent prostate carcinoma 253–254
- release, controlled 168
- residual tumors, thermotherapy 251–253
- resistance to therapy, critical analysis 227–229
- reticuloendothelial system (RES) 129
  - nanocarrier uptake 69
- reversal, magnetic 284–285
- ROS *see* reactive oxygen species
- routes, drug-loaded nanoparticles 10–12
- RU 58668 382–387
  
- s**
- SAR *see* specific absorption rate
- SDDS *see* stealth drug delivery systems
- second generation nanoparticles, anticancer agents 171–172
- secondary tumors, chemotherapy 157
- selective estrogen receptor down-regulators (SERDs) 373–374
- selective estrogen receptor modulators (SERMS) 373–374
- selective tumor-targeting 313, 317
- self-regulating thermoseeds,
  - hyperthermia 297
- semiconductors, photosensitizers 47
- SERD *see* selective ER down-regulators
- SERM *see* selective estrogen receptor modulators
- serum marker, PSA 261–262
- “shell-in-shell” structures 176
- silicon substrate, ferromagnetic filled
  - multiwalled CNTs 287–288
- single-domain particles, magnetic 280–283
- single-walled carbon nanotubes (SWCNTs) 264–265
  - ammonium-functionalized 319
  - functionalized 315–319
  - uptake 316–318
- skin damage, *in vivo* growth suppression 108
- skin photosensitivity scoring system 74
- SLN *see* solid lipid nanoparticles
- sodium borocaptate, liposomal encapsulation 133–136
- solid lipid nanoparticles (SLN) , 20
- solid source CVD (SSCVD) 312
- specific absorption rate (SAR) 300–309
- SPIONs *see* superparamagnetic iron oxide nanoparticles
- SPM *see* superparamagnetic material
- SSCVD *see* solid source CVD
- stabilized nanoparticles, cancer treatment 6–8
- stealth drug delivery systems (SDDS) 372
- Stealth particles, biodegradable polymeric nanoparticles 60–61
- steric stabilization effect, PEG 363
- sterically stabilized nanoparticles 6–8
- superparamagnetic iron oxide crystals 204
- superparamagnetic iron oxide nanoparticles (SPIONs) 169–173, 219–220
- superparamagnetic material (SPM) 298–299
- superparamagnetic nanoparticles 160
  - hyperthermia 297
- superparamagnetism 282
- surface modifications, polymeric nanoparticles 63
- survival rate, cancer cells 63
- SWCNTs *see* single-walled carbon nanotubes
  
- t**
- TAA *see* tumor-associated antigens
- tamoxifen 19, 213
- targeted delivery, anticancer agents 199
- targeted drug delivery nanoparticulate systems 210
- targeted liposomes
  - boron delivery 137–139
  - EGFR 138
- targeted nanoparticles, biodegradable polymeric 60–61
- targeting
  - critical analysis 220–227
  - nanoparticles in cancer therapy 206–207, 343–364
- taxol *see* paclitaxel
- thermoreponsive nanoparticles 219
- thermoseeds, self-regulating 297
- thermosensitive nanocarriers 177
- thermotherapy
  - clinical experiences 249–254
  - feasibility studies 249–254
  - ferromagnetic embolization hyperthermia 248–249
  - MagForce nanotherapy 249–254
  - magnetic nanoparticles 244–247
  - nanoparticles 242–254
  - recurrent glioblastoma multiforme 250–251
  - recurrent prostate carcinoma 253–254
- toxicity
  - doxorubicin 13

- drug-loaded nanoparticles 217
  - MWCNTs 319–323
  - toxicity issues, critical analysis 229–230
  - transferrin
    - cancer cell targeting 352–354
    - cancer treatment 9
  - transferrin receptors, targeting 225
  - transmission electron microscopy (TEM),  
*in vivo* growth suppression 110
  - TSA *see* tumor-specific antigens
  - tumor-associated antigens (TAA) 346
  - tumor selectivity, drugs 362
  - tumor-specific antigens (TSA) 346–350
  - tumor suppression effects, *in vivo*  
efficacy 73–74
  - tumor-targeting, selective 313, 317
  - tumor tissues
    - characterization 44
    - light penetration 53
    - oxygenation 53
  - tumor uptake, selective 43
- u**
- uptake, ferromagnetic filled multiwalled  
CNTs 309–311
- v**
- vascular effects, polymeric nanoparticles  
*in vivo* 71
  - vascular endothelium growth factor  
(VEGF) 129–130
    - angiogenic process 323
    - colloidal systems 371
    - preparation 133
    - targeting cancer vasculature 223
  - VEGF *see* vascular endothelium growth  
factor
  - vitamin H *see* biotin
  - vortex structure, magnetic domains 281
- w**
- well-conditioned hysteresis loop 300

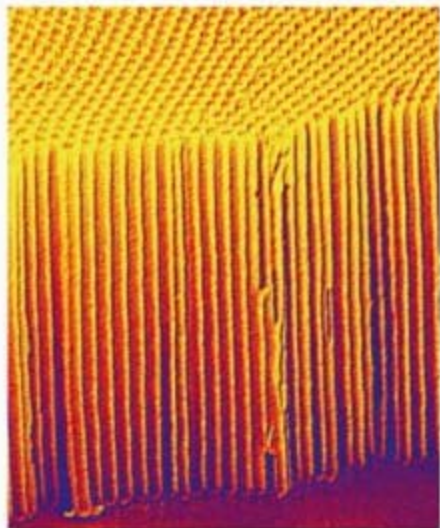


Nanotechnologies for the Life Sciences

Edited by Challa Kumar

 WILEY-VCH

# Nanomaterials for Cancer Diagnosis



**NLS** 

## Contents

<b>Preface</b>	<i>XVII</i>
<b>List of Authors</b>	<i>XXI</i>
<b>1 Dendrimers in Cancer Treatment and Diagnosis</b>	<b>1</b>
<i>Srinivasa-Gopalan Sampathkumar, and Kevin J. Yarema</i>	
1.1	Overview 1
1.2	Introduction 1
1.3	Basic Properties and Applications of Dendrimers 3
1.3.1	Structural Features and Chemical and Biological Properties 3
1.3.1.1	Basic Features of Dendritic Macromolecules are Inspired by Nature 3
1.3.1.2	Comparison of the Properties of Dendrimers and Conventional Synthetic Polymers 5
1.3.1.3	Comparison of the Properties of Dendrimers and Proteins (a Biological Polymer) 6
1.3.2	Dendritic Macromolecules Possess a Wealth of Possible Applications 8
1.4	Methods for Dendrimer Synthesis 10
1.4.1	History and Basic Strategies 10
1.4.1.1	Cascade Reactions are the Foundation of Dendrimer Synthesis 10
1.4.1.2	Dendrimer Synthesis has Expanded Dramatically in the Past Two Decades 12
1.4.2	Strategies, Cores, and Building Blocks for Dendritic Macromolecules 12
1.4.2.1	Dendrimers are Constructed from Simple “Building Blocks” 12
1.4.2.2	The Synthesis of Dendrimers Follows Either a Divergent or Convergent Approach 13
1.4.3	Heterogeneously-functionalized Dendrimers 13
1.4.3.1	Basic Description and Synthetic Considerations 13
1.4.3.2	Glycosylation is an Example of Surface Modification with Multiple Bioactivities 14
1.5	Dendrimers in Drug Delivery 15
1.5.1	Dendrimers are Versatile Nano-devices for the Delivery of Diverse Classes of Drugs 15

VIII | Contents

1.5.2	Dendritic Drug Delivery: Encapsulation of Guest Molecules	16
1.5.2.1	Dendrimers have Internal Cavities that can Host Encapsulated Guest Molecules	16
1.5.2.2	Using Dendrimers for Gene Delivery	16
1.5.2.3	Release of Encapsulated “Pro-drugs”	17
1.5.3	Covalent Conjugation Strategies	17
1.5.3.1	Dendrimers Overcome many Limitations Inherent in Polymeric Conjugation Strategies	17
1.5.3.2	Dendrimer Conjugates can be Used as Vaccines	19
1.5.3.3	Release of Covalently-delivered “Pro-drugs”	19
1.5.4	Fine-tuning Dendrimer Properties to Facilitate Delivery and Ensure Bioactivity	20
1.5.4.1	Delivery Requires Avoiding Non-specific Uptake	20
1.5.4.2	“Local” Considerations: Contact with, and Uptake by, the Target Cell	21
1.5.5	Drug Delivery: Ensuring the Biocompatibility of Dendritic Delivery Vehicles	22
1.5.5.1	Biocompatibility Entails Avoiding “Side Effects” such as Toxicity and Immunogenicity	22
1.5.5.2	Water Solubility and Immunogenicity	22
1.5.5.3	Inherent and Induced Toxicity	23
1.6	Dendrimers in Cancer Diagnosis and Treatment	24
1.6.1	Dendrimers have Attractive Properties for Cancer Treatment	24
1.6.2	Dendrimer-sized Particles Passively Accumulate at the Sites of Tumors	24
1.6.3	Multifunctional Dendrimers can Selectively Target Biomarkers found on Cancer Cells	25
1.6.3.1	Methods for Targeting Specific Biomarkers of Cancer	25
1.6.3.2	Targeting by Folate, a Small Molecule Ligand	26
1.6.3.3	Targeting by Monoclonal Antibodies	26
1.6.4	Dendrimers in Cancer Diagnosis and Imaging	28
1.6.4.1	Labeled Dendrimers are Important Research Tools for Biodistribution Studies	28
1.6.4.2	Towards Clinical Use: MRI Imaging Agents	28
1.6.5	Steps Towards the Clinical Realization of Dendrimer-based Cancer Therapies	29
1.6.5.1	The Stage is now set for Dendrimer-based Cancer Therapy	29
1.6.5.2	Boron Neutron Capture Therapy	29
1.6.6	Innovations Promise to Speed Progress	30
1.6.6.1	“Mix-and-Match” Strategy of Bifunctional Dendritic Clusters	30
1.6.6.2	Towards Therapeutic Exploitation of Glycosylation Abnormalities found in Cancer	31
1.6.6.3	Towards Targeting Metabolically-engineered Carbohydrate Epitopes	31
1.7	Concluding Remarks	33

	Acknowledgments	33
	References	33
<b>2</b>	<b>Nanoparticles for Optical Imaging of Cancer</b>	<b>44</b>
	<i>Swadeshmukul Santra and Debamitra Dutta</i>	
2.1	Introduction	44
2.2	Cancer Imaging Techniques	46
2.2.1	Computed Tomography (CT) Scanning	47
2.2.2	Magnetic Resonance (MR)	47
2.2.3	Positron Emission Tomography (PET)	47
2.2.4	Single-photon Emission CT (SPECT)	48
2.2.5	Ultrasonography (US)	48
2.3	Optical Imaging	48
2.3.1	Basics of Optical Imaging	48
2.3.2	Optical Imaging Techniques	49
2.3.3	Optical Contrast Agents	50
2.4	Nanoparticles for Optical Imaging	51
2.4.1	Why Nanoparticles for Optical Imaging?	51
2.4.2	Development of Nanoparticle-based Contrast Agents	53
2.4.2.1	Quantum Dots	53
2.4.2.2	Gold Nanoparticles	57
2.4.2.3	Dye-doped Silica Nanoparticles	61
2.5	Optical Imaging of Cancer with Nanoparticles	65
2.5.1	Active Targeting	65
2.5.2	Passive Targeting	66
2.5.3	Cancer Imaging with Quantum Dots	66
2.5.4	Cancer Imaging with Gold Nanoparticles	68
2.5.5	Cancer Imaging with Dye-doped Silica Nanoparticles	69
2.6	Other Nanoparticle-based Optical Contrast Agents	70
2.7	Conclusions and Perspectives	70
	Acknowledgments	72
	References	72
<b>3</b>	<b>Nanogold in Cancer Therapy and Diagnosis</b>	<b>86</b>
	<i>Priyabrata Mukherjee, Resham Bhattacharya, Chitta Ranjan Patra, and Debabrata Mukhopadhyay</i>	
3.1	Introduction	86
3.2	Medicinal use of Gold: A Historical Perspective	87
3.3	Application of Gold Nanoparticles in Cancer	88
3.3.1	Angiogenesis and Cancer	88
3.3.1.1	Agents that Inhibit Endothelial Proliferation or Response	90
3.3.1.2	Agents that Block Activation of Angiogenesis	91
3.3.1.3	Agents that Block Extracellular Matrix Breakdown	91
3.3.1.4	Unique Anti-angiogenic Properties of Gold Nanoparticles	91

3.3.1.5	Gold Nanoparticles Inactivate VEGF165	92
3.3.1.6	What is the Mechanism of Action?	93
3.3.1.7	Effect of Gold Nanoparticles on the Activity of VEGF165, VEGF121, bFGF and EGF	94
3.3.1.8	Effect of Gold Nanoparticles on Signaling Events of VEGF165	94
3.3.1.9	Effect of Nanogold on Downstream Signaling events of VEGF165	95
3.3.1.10	Effect of Gold Nanoparticles on Migration of HUVEC Cells	95
3.3.1.11	Effect of Gold Nanoparticles on Angiogenesis <i>in vivo</i>	95
3.3.1.12	Gold Radioisotopes in Cancer Treatment	96
3.3.2	Application of Gold Conjugates in the Treatment of Cancer	96
3.3.2.1	Gold–TNF Conjugate in Cancer Therapeutics	96
3.3.2.2	“2 in 1” System in Cancer Therapeutics	97
3.4	Biocompatibility of Gold Nanoparticles	99
3.4.1	Cellular Adhesion Effects	99
3.4.2	Local Biological Effects	99
3.4.3	Systemic and Remote Effects	99
3.4.4	Effects of the Host on the Implant	100
3.4.5	Addressing the Biocompatibility of Gold Nanoparticles using DNA Microarray Analysis	100
3.4.6	Internalization of Gold Nanoparticles by HUVECs	101
3.4.7	Nanogold Particles do not Alter Global Pattern of Transcription by HUVEC Cells under Serum-free Conditions	101
3.4.8	Nanogold Particles do not Alter the Global Pattern of Transcription by HUVECs in Near-normal Culture Conditions	103
3.5	Synthetic Approaches to Gold Nanoparticles	105
3.5.1	Chemical Methods	105
3.5.2	Physical Methods	105
3.5.3	Biological Methods	106
3.6	Nanotechnology in Detection and Diagnosis with Gold Nanoparticles	106
3.6.1	Cancer Detection	106
3.6.2	Detection in DNA	107
3.6.2.1	Single-mismatch Detection in DNA	107
3.7	Future Direction	109
	Acknowledgments	110
	References	110
<b>4</b>	<b>Nanoparticles for Magnetic Resonance Imaging of Tumors</b>	<b>121</b>
	<i>Tillmann Cyrus, Shelton D. Caruthers, Samuel A. Wickline, and Gregory M. Lanza</i>	
4.1	Introduction	121
4.2	Magnetic Resonance Imaging (MRI)	121
4.3	Targeting Mechanisms	124
4.3.1	Passive versus Active Targeting	124
4.4	Superparamagnetic Nanoparticles	126
4.4.1	Ligand-directed Targeting of Iron Oxides	127



4.4.2	Cell Tracking of Iron Oxides	128
4.5	Paramagnetic Nanoparticles	128
4.5.1	Perfluorocarbon Nanoparticles	129
4.5.2	Liposomes	131
4.5.3	Fullerenes	132
4.5.4	Nanotubes	133
4.5.5	Dendrimers	133
4.6	Quantum Dots	133
4.7	Polymer Nanoparticles	134
4.8	Conclusion	135
	References	138
<b>5</b>	<b>Magnetic Resonance Nanoparticle Probes for Cancer Imaging</b>	<b>147</b>
	<i>Young-wook Jun, Jung-tak Jang, and Jinwoo Cheon</i>	
5.1	Introduction	147
5.2	Magnetic Nanoparticle Contrast Agents	150
5.2.1	Silica- or Dextran-coated Iron Oxide Contrast Agents	150
5.2.2	Magnetoferritin	152
5.2.3	Magnetodendrimers and Magnetoliposomes	152
5.2.4	New Type of Contrast Agent: Non-hydrolytically Synthesized High Quality Iron Oxide Nanoparticles	154
5.3	Iron Oxide Nanoparticles in Molecular MR Imaging	157
5.3.1	Infarct and Inflammation	158
5.3.2	Angiogenesis	159
5.3.3	Apoptosis	160
5.3.4	Gene Expression	161
5.3.5	Cancer Imaging	163
5.4	Summary and Outlook	166
	References	169
<b>6</b>	<b>LHRH Conjugated Magnetic Nanoparticles for Diagnosis and Treatment of Cancers</b>	<b>174</b>
	<i>Carola Leuschner</i>	
6.1	Introduction	174
6.2	Cancer	175
6.2.1	Conventional Approaches to Cancer/Metastases Detection	177
6.2.2	Current Chemotherapeutic Approaches and their Disadvantages in Cancer Treatments	179
6.2.2.1	Multidrug Resistance	179
6.2.2.2	Drug Delivery to Tumors	180
6.3	Nanoparticles as Vehicles for Drug Delivery and Diagnosis	181
6.3.1	Targeting Tumor Cells	183
6.3.1.1	Passive Targeting	183
6.3.1.2	Active Targeting	185
6.3.2	Detection of Tumors and Metastases using Nanoparticles	186

6.3.2.1	Nanoparticles for Magnetic Resonance Imaging	186
6.3.2.2	Targeted Delivery of Nanoparticles to Increase Cellular Uptake for Higher MRI Resolution	188
6.4	LHRH and its Receptors	189
6.4.1	The Ligand Luteinizing Hormone Releasing Hormone – LHRH	189
6.4.2	Analogues of LHRH	192
6.4.3	Receptors for LHRH	193
6.4.4	Function–Signal Transduction Pathways	194
6.4.5	LHRH Receptor-mediated Uptake	197
6.4.6	LHRH Receptor Type II	198
6.5	LHRH-bound Magnetic Nanoparticles	201
6.5.1	Synthesis and Characterization	201
6.5.2	Treatment using Hyperthermia	202
6.5.3	Treatment using Lytic Peptides	203
6.5.3.1	Destruction of Metastases through LHRH-SPION-Hecate	203
6.5.4	Detection of Tumors and Metastases	204
6.5.4.1	Targeted Delivery of SPION Contrast Agents for MRI	204
6.5.4.2	<i>In Vitro</i> Studies on Receptor-targeted LHRH-SPION Uptake	205
6.5.4.3	<i>In Vivo</i> Studies on Receptor-targeted LHRH-SPION Uptake	206
6.6	Future Outlook	210
	Acknowledgments	212
	Abbreviations	212
	References	213
<b>7</b>	<b>Carbon Nanotubes in Cancer Therapy and Diagnosis</b>	<b>232</b>
	<i>Pu Chun Ke and Lyndon L. Larcom</i>	
7.1	Overview	232
7.2	SWNT Modification for Solubility and Biocompatibility	234
7.2.1	Chemical Modifications of SWNTs for Solubility	234
7.2.1.1	Functionalization of SWNTs through Oxidation	235
7.2.1.2	Functionalization of SWNTs through Covalent Modifications	236
7.2.2	Noncovalent Modifications of SWNTs for Solubility	237
7.2.2.1	Solubilization of SWNTs Using Lysophospholipids Enables Cellular Studies	239
7.3	Diffusion of SWNT–Biomolecular Complexes	247
7.4	Gene and Drug Delivery with SWNT Transporters	252
7.4.1	RNA Translocation with SWNT Transporters	253
7.4.2	Gene Transfection with SWNT Transporters	258
7.4.3	Gene Transfection with SWNT Transporters for RNA Interference	261
7.4.4	Drug Delivery with SWNT Transporters	263
7.4.4.1	Vaccine Delivery by SWNTs	263
7.4.4.2	Protein Delivery by SWNTs	266
7.4.4.3	Biosensing by SWNTs	269
7.5	Sensing and Treating Cancer Cells Utilizing SWNTs	269
7.6	Cytotoxicity of SWNTs	272

7.7	Cancers and SWNTs	275
7.8	Summary	277
	Acknowledgments	278
	References	278
<b>8</b>	<b>Nanotubes, Nanowires, Nanocantilevers and Nanorods in Cancer Treatment and Diagnosis</b>	<b>285</b>
	<i>Kiyotaka Shiba</i>	
8.1	Introduction	285
8.2	Nanotubes, Nanowires and Nanorods	285
8.2.1	Carbon Nanotubes	286
8.2.2	Noncarbon Nanotubes	287
8.2.3	Single-wall Carbon Nanohorns	287
8.2.4	Nanorods and Nanowires	288
8.2.5	Self-assembled Nanotubes	289
8.3	Cancer Diagnosis	290
8.3.1	Carbon Nanotube-based Detection System	290
8.3.2	Non-carbon Nanotube-based Detection Systems	291
8.3.3	Microcantilevers	292
8.3.4	Nano-tag made of Nanorods	293
8.4	Cancer Treatment	293
8.4.1	Carriers for Drug Delivery Systems	294
8.4.2	Imaging Agents	294
8.5	Conclusions	295
	References	296
<b>9</b>	<b>Multifunctional Nanotubes and Nanowires for Cancer Diagnosis and Therapy</b>	<b>304</b>
	<i>Sang Bok Lee and Sang Jun Son</i>	
9.1	Introduction	304
9.2	Advanced Technologies in Magnetic Nanoparticles for Biomedical Applications	305
9.2.1	MRI and Therapeutic Application of Magnetic Nanoparticles	305
9.2.2	Biomedical Diagnostic Application of Magnetic Nanoparticles	307
9.3	Carbon Nanotubes	310
9.3.1	Carbon Nanotubes for Targeted Cancer Cell Death	310
9.3.2	Carbon Nanotubes for Detection of Cancer Cell	312
9.3.3	Carbon Nanotubes for Targeted Delivery	313
9.4	Nanotubes and Nanowires Composed of Artificial Peptides	315
9.4.1	Peptide Nanotubes	315
9.4.2	Peptide-Amphiphile Nanofibers	316
9.5	Template-synthesized Nanotubes and Nanorods	318
9.5.1	Differential Functionalization of Nanotube	319
9.5.2	Selective Extraction of Drug Molecules	320
9.5.3	Silica Nanotube Carrier for DNA Transfection	322

9.5.4	DNA Nanotubes	323
9.5.5	Nanobarcodes for Multiplexing Diagnosis	325
9.5.6	Magnetic Nanotubes	328
9.5.6.1	Synthesis and Characterization of Magnetic Nanotubes	328
9.5.6.2	Magnetic Field-assisted Chemical Separation and Biointeraction	329
9.5.6.3	Drug Uptake and Controlled Release	330
9.6	Conclusion	332
	References	333
<b>10</b>	<b>Nanoprobe-based Affinity Mass Spectrometry for Cancer Marker Protein Profiling</b>	<b>338</b>
	<i>Li-Shing Huang, Yuh-Yih Chien, Shu-Hua Chen, Po-Chiao Lin, Kai-Yi Wang, Po-Hung Chou, Chun-Cheng Lin, and Yu-Ju Chen</i>	
10.1	Introduction	338
10.2	Fabrication and Biomedical Applications of Nanoparticles	339
10.2.1	Fabrications and Properties of Nanoparticles	339
10.2.2	Metal Nanoparticles in Cancer Diagnosis	343
10.3	Principles of Mass Spectrometry	348
10.3.1	Matrix-assisted Laser Desorption/Ionization Time-of-flight Mass Spectrometry	348
10.3.2	Affinity Mass Spectrometry	349
10.4	Nanoprobe-based Affinity Mass Spectrometry (NBAMS)	350
10.4.1	Preparation of Nanoprobes and Workflow	351
10.4.2	Proof-of-principle Experiment	353
10.4.3	Kinetic Study of the Nanoscale Immunoreaction	356
10.4.4	Detection Limit and Concentration Effect of Nanoprobe-based Immunoassay	356
10.5	Human Plasma and Whole Blood Analysis by Nanoprobe-based Affinity Mass Spectrometry	359
10.5.1	Selected Protein Profiling from Human Plasma	359
10.5.2	Comparison of Nanoscale and Microscale Immunoassay	359
10.5.3	Suppression of Nonspecific Binding on Magnetic Nanoparticles	361
10.5.4	Enrichment of Target Antigen in Human Plasma	362
10.5.5	Plasma Protein Profiling in Normal Individuals and in Patients	364
10.6	Multiplex Assay	364
10.6.1	Workflow of Multiplexed Assay	366
10.6.2	Screening for Patient and Healthy Individuals	367
10.7	Future Outlook	369
	Acknowledgments	369
	References	369

<b>11</b>	<b>Nanotechnological Approaches to Cancer Diagnosis: Imaging and Quantification of Pericellular Proteolytic Activity</b>	<b>377</b>
	<i>Thomas Ludwig</i>	
11.1	Introduction	377
11.2	Quantification of Local Proteolytic Activity – an Objective	380
11.2.1	Regulation of Protease Activity	382
11.2.1.1	Secretion	382
11.2.1.2	Activation	382
11.2.1.3	Inactivation	383
11.2.1.4	Endogenous Protease Inhibitors	383
11.2.1.5	Glycosylation	384
11.2.1.6	Oligomerization	384
11.2.1.7	Protein Trafficking	385
11.2.2	Mechanisms of Confining Proteolytic Activity	385
11.2.2.1	Membrane-type Matrix Metalloproteinases	386
11.2.2.2	Cell Surface Receptors for Protease Binding	387
11.2.2.3	ECM Binding of Proteases	387
11.2.2.4	Cellular Microdomains	388
11.2.2.5	The Tumor–Host Conspiracy	388
11.2.3	Local Proteolytic Activity Regulates Complex Cellular Functions	389
11.2.3.1	Local Proteolytic Activity in Cancer Cell Migration	389
11.2.3.2	Local Proteolytic Activity and Cell Signaling	389
11.2.3.3	Functional Insights from Matrix-metalloprotease Deficient Mice	390
11.3	Evaluation of Classical Methods for Quantification of Net Proteolytic Activity	391
11.3.1	Functional Detection of Local Proteolytic Activity by <i>In Situ</i> Zymography	392
11.3.2	Tumor Cell Invasion Assays	393
11.3.2.1	Electrical Resistance Breakdown Assay	394
11.3.3	<i>In vivo</i> Detection of Proteolytic Activity	394
11.3.4	Multiphoton Microscopy and Second-harmonic Generation	395
11.3.5	<i>In vitro</i> Detection of Local Proteolytic Activity by Labeled Substrates	396
11.4	Novel Approaches to Local Proteolytic Activity	396
11.5	Conclusions and Perspectives	400
	Acknowledgments	401
	Abbreviations	401
	References	401
	<b>Index</b>	<b>413</b>



## Preface

Two volumes (6 & 7) in the ten-volume series *Nanotechnologies for the Life Sciences* have been dedicated to the application of nanotechnology in cancer. The first of these two has captured nanotechnological approaches for the treatment of cancer and is already published. I do hope you had a chance to read it. This is the second of the pair, bringing out the utility of nanotechnology in developing tools and materials for sensitive and early diagnosis of cancer. These two volumes are timely as it is projected that cancer will be the leading cause of death, overtaking heart diseases, in the near future. One of the major goals of the American Cancer Society is early and sensitive detection of cancer. It is astonishing to note that the five year survival rate for breast cancer patients, if the cancer is diagnosed at localized stage, is 97.5%. Currently only 63.5% of breast cancers are diagnosed at the localized stage and there is no sensitive diagnostic tool for detecting micro-metastases, where the survival rate is less than 30%. Having made only limited progress in early and sensitive diagnosis of cancer using traditional methods, a paradigm shift in our approach is required in order to develop imaging agents and diagnostics for detecting cancer in its earliest and pre-symptomatic stage when it can be treated most easily. Needless to say, nanotechnology is offering this new approach and investigations reported so far demonstrate its immense potential. Since these investigations are being published in a very broad range of journals, this book provides a unique collection of consolidated and up-to-date information on nanotechnological diagnostic tools for the detection of cancer.

It is my pleasure to present, on behalf of the eminent contributors, the 7<sup>th</sup> volume in the series, entitled *Nanomaterials for Cancer Diagnosis*. The uniqueness of nanotechnological approaches in the battle against cancer is a distinct possibility to create technologies for simultaneous diagnosis and treatment of cancer. Therefore, you will find some of the chapters covering both these aspects while focusing primarily on diagnosis. I am grateful to all the contributors who made this book into a comprehensive source of information on the impact of a variety of nanomaterials on a number of diagnostic tools. A book of this magnitude is not possible but for their scholarly contributions. At this point, I also would like to gratefully acknowledge the support of a number of others, especially my employer, family, friends and Wiley VCH publishers for this timely publication.

The book is divided into eleven chapters, encompassing a number of diagnostic approaches for cancer through use of a variety of nanomaterials such as dendrimers, quantum dots, gold nanoparticles, dye-doped silica nanoparticles, superparamagnetic iron oxide nanoparticles (SPIONs), liposomes, fullerenes, carbon nanotubes, nanowires, nanorods, and so on.

The book begins with a chapter reviewing the progress that has been made to date on dendrimers – nano-sized, radially symmetric molecules with well-defined, homogeneous and monodisperse structure consisting of tree-like arms or branches – and dendrimer-based nanomaterials in the diagnosis and treatment of cancer. The authors, Srinivasa-Gopalan Sampathkumar and Kevin J. Yarema from the Johns Hopkins University in Baltimore, USA, have done an excellent job in collating pertinent information on how several different attributes of dendrimers are being utilized to fine-tune their biological activity in order to obtain effective solutions to long standing problems in diagnosis and treatment of cancer. The chapter, *Dendrimers in Cancer Treatment and Diagnosis*, is valuable for all those interested in acquiring knowledge on this exciting and most promising class of nanomaterials in cancer nanotechnology. The second chapter, *Nanoparticles for Optical Imaging of Cancer*, has been contributed from the laboratories of University of Central Florida in Orlando, USA. Authors Swadeshmukul Santra and Debamitra Dutta provide a broad overview on various existing cancer-imaging techniques followed by a detailed description on optical imaging in general and nanoparticle-based optical imaging in particular. This chapter will provide readers with all the necessary information that is required for them to obtain a grasp of this exciting and continuously evolving field of nanoparticle-based optical contrast agents. More specifically, readers will have an opportunity to obtain a broader perspective on applications of quantum dots, dye-doped nanoparticles, gold nanoparticles, phosphors & fluorescent polymer particles as potential contrast agents in optical imaging of cancer. Of all the nanomaterials with optical properties, gold nanoparticles are the most widely investigated materials and therefore, a complete chapter is dedicated to the utility of gold nanoparticles in cancer diagnosis. The third chapter, *Nanogold in Cancer Therapy and Diagnosis*, a contribution from the laboratories of Debabrata Mukhopadhyay from Mayo Clinic Cancer Center in Rochester, USA, brings out the importance of gold nanoparticles in cancer diagnosis and therapy. The authors also have reviewed relevant information on synthetic methods, biocompatibility and the mechanism of action of gold nanoparticles.

Moving from nanomaterials-based optical imaging techniques for diagnosis of cancer, the next three chapters describe investigations into utilization of magnetic nanoparticles for enhancing the sensitivity of detection of tumors using magnetic resonance imaging (MRI). Of the existing non-invasive diagnostic tools such as Computed Tomography (CT), Positron Emission Tomography (PET), Single Photon Emission CT (SPECT), Ultrasound (US) and optical imaging, MRI appears to be the most promising and sensitive technique. It is gaining more importance with the discovery of nanomaterials-based contrast agents. Researchers from the Washington University Medical School in St. Louis, USA, contributed the fourth chapter wherein an overview of the MRI technology and principle targeting mechanisms



are described, followed by a detailed discussion on the application of superparamagnetic and paramagnetic nanoparticles. The chapter, *Nanoparticles for Magnetic Resonance Imaging of Tumors*, brings out clearly the differences between the superparamagnetic nanoparticles, which are mainly SPIONs and paramagnetic nanoparticles belonging to groups such as liposomes, perfluorocarbon nanoparticles, fullerenes, and others. The chapter contributed by Tillmann Cyrus, Shelton D. Caruthers, Samuel A. Wickline, and Gregory M. Lanza also provides up-to-date information on rapidly evolving hybrid technologies using quantum dots for non-invasive imaging with MRI and intraoperative direct visualization. While the fourth chapter provides an overview of nanomaterials being developed for MRI, the fifth chapter primarily focuses on superparamagnetic iron oxide nanoparticles. This chapter, *Magnetic Resonance Nanoparticle Probes for Cancer Imaging*, contributed by Young-Wook Jun, Jung-tak Jang, and Jinwoo Cheon from Yonsei University in Seoul, Korea, reviews recently developed biocompatible magnetic nanoparticles and their utilization in molecular MRI. The final chapter on the application of SPIONs in MRI, the sixth chapter in the book, is from the laboratories of Carola Leuschner, Pennington Biomedical Research Center at Baton Rouge, USA. Being one of my close collaborators and having closely associated with the development of Leutenizing Hormone and Releasing Hormone (LHRH)-conjugated SPIONs, I can confidently say that this chapter is very unique and provides readers with all the information that is available on LHRH-conjugated magnetic nanoparticles. The chapter, *LHRH-conjugated Magnetic Nanoparticles for Diagnosis and Treatment of Cancers*, provides an elaborate account of the role of LHRH and LHRH receptors in malignant tissue. The central theme of the chapter is a description of comparative advantages of LHRH-SPIONs with other targeting agents in targeting specifically primary tumors and metastases, thereby demonstrating the potential for LHRH-SPIONs in dramatically improving the sensitivity of MRI.

Switching gears from nanoparticles, chapter seven written by Pu Chun Ke and Lyndon L. Larcom from Clemson University in Clemson, USA, is a testimony to the ever-increasing number of applications of carbon nanotubes. Not surprisingly, single-walled carbon nanotubes (SWNTs) have already shown promise in cancer diagnosis and therapy and have distinct advantages over multi-walled carbon nanotubes (MWNTs). The chapter, *Carbon Nanotubes in Cancer Therapy and Diagnosis*, captures up-to-date information available in the literature on functionalization for solubility and biocompatibility, cytotoxicity, gene and drug delivery, and sensing of cancer cells utilizing SWNTs. Following this chapter, Kiyotaka Shiba from the Cancer Institute of the Japanese Foundation for Cancer Research in Tokyo, Japan, has brought out a thorough review on the application of “non-spherical” nanomaterials in cancer treatment and diagnosis. The theme of this 8<sup>th</sup> chapter, truly reflected in the title *Nanotubes, Nanowires, Nanocantilevers and Nanorods in Cancer Treatment and Diagnosis*, is the current status of carbonaceous as well as non-carbonaceous nanotubes, nanowires, and nanorods with respect to their potential applications in cancer diagnosis and treatment. In the ninth chapter, *Multifunctional Nanotubes and Nanowires for Cancer Diagnosis and Therapy*, authors Sang Bok Lee and Sang Jun Son from the University of Maryland at College Park, USA, describe in detail

the importance of carbon nanotubes, nanotubes and nanowires composed of artificial peptides, and template-synthesized silica and magnetic nanotubes in general for various biomedical applications and in particular related to cancer. The authors demonstrate that tubular nanomaterials have several advantages over spherical nanoparticles, especially when multifunctionality is needed as nanotubes have distinctive inner and outer surfaces that can be modified and utilized differently, enabling them to be equipped with the right function in the right position.

The last two chapters of this volume are testimony to the breadth of nanotechnological approaches for cancer diagnosis. The penultimate chapter, *Nanoprobe-based Affinity Mass Spectrometry for Cancer Marker Protein Profiling*, provides an overview on a recently developed technique – nanoprobe-based affinity mass spectrometry (NBAMS) – for the screening of normal individual and cancer patients. The chapter is a contribution from the Institute of Chemistry and Genomic Research Center of the Academia Sinica in Taipei, Taiwan, authored by Yu-Ju Chen and co-workers. This chapter provides fundamental principles in mass spectrometry and the detection method in NBAMS, in addition to details of the design, workflow and performance of NBAMS. The final chapter is presented by Thomas Ludwig from Yale University at New Haven, USA. The author points out some of the challenges in cancer diagnosis by focusing on local, nanoscale processes for in vitro and in vivo diagnostics. The chapter, *Nanotechnological Approaches to Cancer Diagnosis: Imaging and Quantification of Pericellular Proteolytic Activity*, is an interesting chapter on how development of improved nanotechnology enabled methods that are likely to provide real-time high-resolution imaging and quantification of local enzymatic activities will play a major role in the design of new drugs and the understanding of basic principles in tumor cell invasion.

This book concludes the two volumes dedicated to cancer nanotechnology. I do realize that there are some topics that have not been covered and also some topics that have been covered are not exhaustive enough. I am hoping that the next edition of this book series will fill these gaps and also will take into consideration suggestions from the readers. I am looking forward to hearing from you.

As I end this preface, I am pleased to note that the first six volumes of the ten volume series have already been published and the next four volumes are in print. I am also pleased to know that the *Nanotechnologies for the Life Sciences* in general is being well received.

September 2006  
Baton Rouge, USA

*Challa S. S. R. Kumar*

## 1

**Dendrimers in Cancer Treatment and Diagnosis**

*Srinivasa-Gopalan Sampathkumar, and Kevin J. Yarema*

## 1.1

**Overview**

Dendrimers are nano-sized, radially symmetric molecules with well-defined, homogeneous and monodisperse structure consisting of tree-like arms or branches. Over the past two decades since the term “dendrimer” was formally defined, research interest in these molecules has gradually evolved from a primary focus on overcoming purely synthetic challenges to include aesthetic and theoretical perspectives, and, more recently, with the ongoing flurry of “nanobiotechnology” advances, to develop practical and commercial applications for these elegant nano-devices. Today, a critical mass of knowledge exists to synthetically control the physicochemical properties of dendrimers and thereby govern their ensuing biological behaviors. These fundamental scientific advances, coupled with practical methods to covalently conjugate a wide range of bioactive molecules to the surface of a dendrimer or encapsulate them as guest molecules within void spaces, provide a highly versatile and potentially extremely powerful technological platform for drug delivery. This chapter recaps synthetic advances in dendrimer construction and summarizes the many features of these fascinating macromolecules that endow them with favorable properties for drug delivery applications. Finally, with this enticing technology having matured to the point where it is ready to confront “real-world” challenges, a synopsis is outlined of the prospects for exploiting dendrimer-based nanodevices for one of the most intractable medical challenges, the diagnosis and treatment of cancer.

## 1.2

**Introduction**

The discovery, design, and development of anticancer therapeutic agents have proven to be remarkably intractable despite intense efforts at the research and clinical levels over many decades. A brief consideration of the challenges facing an

anticancer drug illustrates some of the reasons for frustratingly-slow progress: first the drug must be able to seek out subtle changes that distinguish a transformed cell from the other 200 or so types of healthy cells found in the body and then provide a sufficiently high dose of a toxic agent to kill the cell. The difficulty of this task is amplified by the potential metastasis of cancer cells to widely-spread niches throughout the body, each with unique properties. Furthermore, to successfully cure a patient, each and every cancer cell must be eradicated because even one in a thousand – often harboring latent resistance – can re-grow into a second tumor refractory to therapeutic intervention.

Readers of this chapter, contained within a volume devoted to the development of novel cancer therapeutics, do not require convincing of the difficulty of combating cancer and this issue will not be labored here. Instead, this chapter provides a broad overview of dendrimer-based nanotechnologies for the treatment of cancer with a consideration of their synthesis, the encapsulation and covalent attachment of drugs, and various strategies used for tumor specific targeting, imaging, and therapy. The discussion of specific topics begins with a description of the basic properties of dendrimers in Section 1.3 to highlight how these molecules lie at the interface between conventional synthetic polymers and the archetypical nano-sized biological polymers, proteins. Section 1.4 briefly outlines the synthesis of dendrimers; exhaustive review articles (referenced therein) provide a wealth of synthetic detail beyond the scope of this discussion. This chapter aims to provide the reader with the knowledge that, by control of design parameters, the attributes of dendrimers can be tuned to incorporate the most desired features of synthetic polymers and proteins and, thereby, gain exquisite control of biological activity.

Upon having established that dendrimers are synthetically-tractable, biologically-compatible nano-devices, their unique suitability for drug delivery will be delineated in some detail in Section 1.5. Specific topics covered include the alternative drug-carrying strategies of encapsulation (Section 1.5.2) and covalent conjugation (Section 1.5.3), as well as design features needed to ensure bioactivity of the drug (Section 1.5.4) and the biocompatibility of the dendrimer (Section 1.5.5). Finally, with the multi-disciplinary set of tools required for dendrimer-based drug delivery now reaching maturity, this area of investigation is undergoing transformation from the developmental stage to “real-world” applications. Accordingly, Section 1.6 discusses the prospects for using dendrimer-based nanotechnologies to overcome arguably the most difficult biomedical problem now faced, the diagnosis and treatment of cancer. In particular, the general properties of dendrimers that make them attractive for cancer treatment will be outlined in Section 1.6.1, with a specific benefit – exploitation of the enhanced permeability and retention effect that allows passive accumulation at the sites of tumors – discussed in Section 1.6.2. The ability of dendrimers to serve as a technological platform for multifunctional nano-devices that include targeting, imaging, and/or cytotoxic modalities is discussed in Section 1.6.3 and their prospects for diagnosis and therapeutic applications are given in Sections 1.6.4 and 1.6.5, respectively. Finally, Section 1.6.6 gives a brief synopsis of innovations that promise to speed progress in the near future.

Together – while broader in scope than the typical discussion of dendrimers, drug delivery, or cancer therapy – this chapter provides an integrated look at the many considerations required for successful application of dendrimers for cancer therapy. For a more-in-depth consideration of any particular sub-topic, the interested reader is urged to consult the many original research reports and review articles cited throughout.

## 1.3

### Basic Properties and Applications of Dendrimers

#### 1.3.1

##### Structural Features and Chemical and Biological Properties

###### 1.3.1.1 Basic Features of Dendritic Macromolecules are Inspired by Nature

Dendritic structures, characterized by hyperbranched subunits, are widely found in nature. Indeed, the word dendrimer is based on the Greek words “dendron” meaning “tree” or “branch” and “meros” meaning “part” [1, 2]. Taken literally, similarities with dendrimer macromolecules are illustrated by a tree, where the leaves of a tree are maximally displayed on a highly-branched scaffold to maximize their accessibility to the outside world to optimize functions such as light harvesting. The branches of a tree can modify the environment within them, similarly the core/interior encapsulated within a dendrimer can provide a sheltered microenvironment with tailored chemical properties and reactivities [2]. In addition to actual trees, Nature has scaled dendrimeric structures down to the multi-centimeter level (the intricate neural pathways found in the brain), the millimeter level (ice crystals and snowflakes), and yet further to the micron level (the dendritic outgrowths of neurons). At a molecular, “nano-size” level, dendrimer-like molecules, such as branching polysaccharides, provide an elegant solution to a cell's need to stably store high energy molecules like monosaccharides; the presence of many chain ends allows the rapid release of large numbers of glucose monomers when needed [3].

Unlike Nature, which provides dendritic structures in a range of sizes from real trees to the namesake molecular nano-sized structures, this chapter focuses exclusively on dendritic macromolecules that are of a synthetically tractable scale and appropriate for cancer therapy. Starburst® clusters [4], made of poly(amidoamine) (PAMAM) units, are arguably the most-thoroughly characterized and extensively-utilized dendrimers [5]. A basic characteristic of these molecules is their layered composition – known as “cascades” or “generations” [1] (Fig. 1.1). The overall shapes of dendrimers range from spheres to flattened spheroids (disks) to amoeba-like structures, especially in cases where surface charges exist and give the macromolecule a “starfish”-like shape [6].

The exact morphology of a dendrimer depends both on its chemical composition (the chemical composition of PAMAM dendrimers is shown in Fig. 1.1) as well as on the generation number, as exemplified by PAMAM where the lowest generation

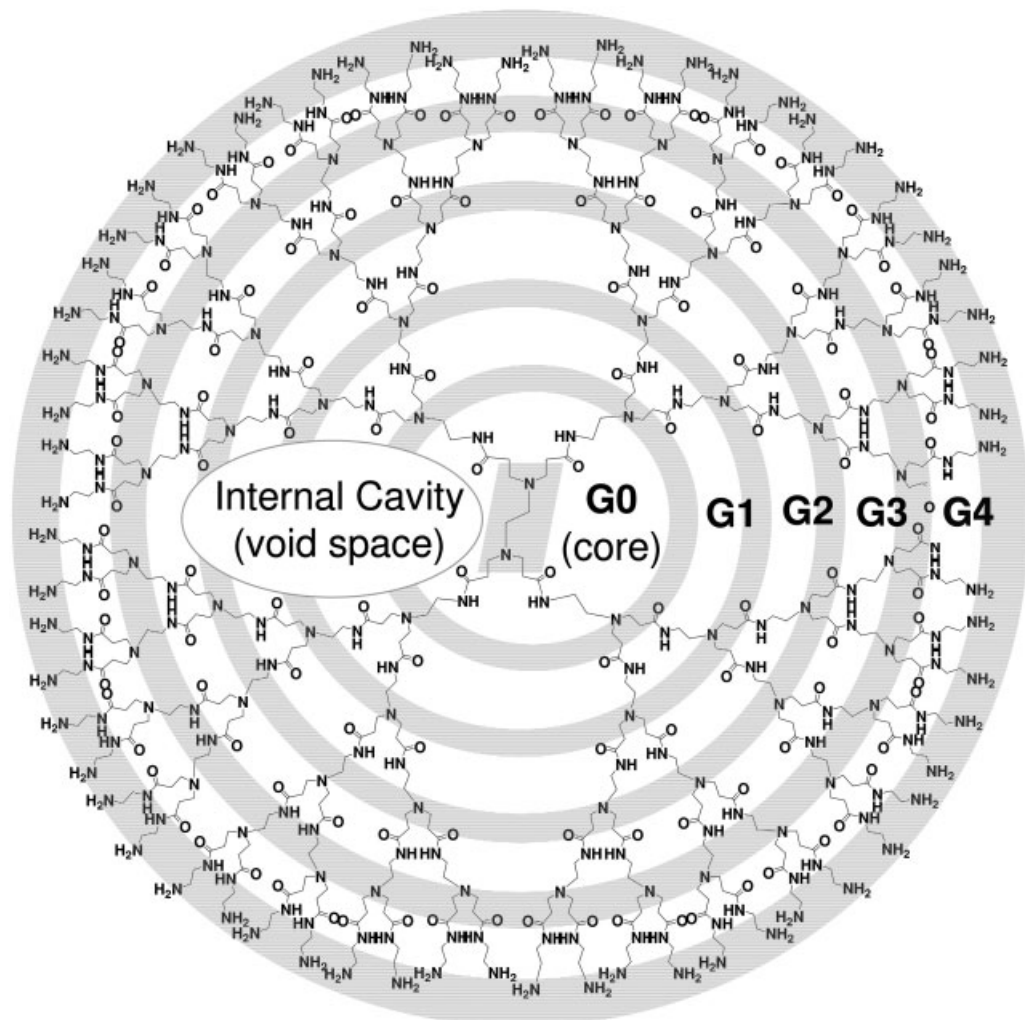


**Fig. 1.1.** Schematic representation of a generation G4 dendrimer with 64 amino groups at the periphery. This dendrimer starts from an ethylene diamine core; the branches or arms were attached by exhaustive Michael addition to methyl acrylate followed by exhaustive aminolysis of the resulting methyl ester using ethylene diamine [36]. This sequence of reactions was applied in an iterative fashion to increase the level of

generations. The periphery of successive generations is marked by grey circles, starting from G0, G1, G2, G3 and G4. Of note, distinctive features of dendrimers, including the densely-packed membrane-like arrangement of surface functional groups, the formation of internal cavities, and the condensation into globular structures (not shown), are typically manifest at the G4 stage (and amplified in successive generations, Table 1.1).

structure (e.g., G0 and G1) have highly asymmetric shapes and possess open structures compared with higher-generation structures that first appear to be disk-like and then progress to increasingly spherical geometries [5] as they assume globular structures with a significant reduction in hydrodynamic volume [7]. In addition to sphere-like dendrimers – based on a “dot-like” core (Fig. 1.1) – increasing interest is developing in cylindrical dendrimers that are based on “rod-like” cores. These interesting spin-off macromolecules have been compared with spaghetti because they can be rigid like the uncooked form of this pasta or highly flexible like the cooked form; these properties can be tuned based on the chemical composition and density of packing of the dendritic branches [6]. Additional features of dendrimers are discussed below, by comparison with the two classes of molecules they are most often likened to, i.e., “conventional” synthetic polymers and, the most extensively studied biological polymer, proteins.

### 1.3.1.2 Comparison of the Properties of Dendrimers and Conventional Synthetic Polymers

Dendrimers have both similarities and differences when compared with traditional polymers. One similarity is the vast diversity in the basic monomeric building blocks used to create both classes of molecules and to provide the final macromolecular products with a wide range of chemical, mechanical, and biological properties. Until recently, polymer chemistry has been focused on the production of linear polymers that often have a degree of branching or crosslinking; this property, however, is dramatically limited by comparison to dendrimers whose entire identity is wrapped up in their hyperbranched character. Interestingly, highly-branched polymers of the same material can be vastly different from conventional polymers of a similar molecular weight and composition; in particular, as dendritic macromolecules progress in size, usually when becoming larger than the third generation (G3), they assume globular structures and occupy considerably smaller hydrodynamic volumes than linear polymers [1].

When dendrimers condense into globular structures, a feat rarely achieved with linear synthetic polymers, their many termini become fixed into an outwards orientation and also form a densely packed, membrane-like surface (Fig. 1.1). This structural arrangement provides numerous attachment points for covalent conjugation of bioactive molecules on the surface as well as enclosed cavities for occlusion of guest molecules within the dendrimer. This tight packing ultimately results in the reaching of a critical branched state – known as the “starburst effect” [4] – where growth of the dendritic macromolecule is dramatically hindered by steric constraints [8] (this state is reached at G10 or G11 for PAMAM, Table 1.1). Dendrimers also have dramatically different rheological properties than conventional polymers; viscosity tends to increase continuously with molecular mass for linear macromolecules whereas the intrinsic viscosity of dendrimers goes through a maximum at approximately the fourth generation and then declines [8, 9]. Finally, dendrimers have a negligible degree of polydispersity because, unlike classical polymerization that is random in nature and produces molecules of various sizes, the size of dendrimers can be carefully controlled during synthesis. Under ideal condi-

**Tab. 1.1.** Generation by generation specifications for PAMAM Starburst® dendrimers. (Adapted from Ref. [5].)

Generation	Physical or structural parameter			
	Molecular weight (Daltons)	Diameter (Å)	Surface groups (-NH <sub>2</sub> )	Radius of gyration (Å)
G0	517	15	4	4.93
G1	1430	22	8	7.46
G2	3256	29	16	9.17
G3	6909	36	32	11.2
G4	14 215	45	64	14.5
G5	28 826	54	128	18.3
G6	58 048	67	256	22.4
G7	116 493	81	512	29.1
G8	233 383	97	1024	36.4
G9	467 162	114	2048	46.0
G10	934 720	135	4096	55.2
G11	1 869 780	167	8192	68.3

tions, preparations of dendrimers are monodisperse, which is to say they have one molecular weight instead of the range, over tens or even hundreds of kDa, often seen for traditional synthetic polymers. Indeed, the homogeneity and uniformity of dendrimers of successive generations becomes strikingly obvious as shown by the tunneling electron microscopy (TEM) images for G5 to G10 PAMAM (Fig. 1.2) [10].

### 1.3.1.3 Comparison of the Properties of Dendrimers and Proteins (a Biological Polymer)

As discussed above, dendrimers have unusual, often dramatically different, characteristics compared with conventional synthetic polymers. In fact dendritic molecules have often been compared with proteins, which are the workhorse biological polymers. Both classes of macromolecules are globular, are composed of precisely controlled monomeric units, have defined architectures, are of comparable size (Table 1.1), and have surfaces with chemically-reactive sites that can be endowed with biologically-compatible ligands found on proteins (such as glycosylation, Section 1.4.3.2). Moreover, the interior of a dendritic molecule, reminiscent of a protein, can harbor unique microenvironments, providing behaviors like redox chemistry, molecular recognition, ligand and substrate binding, and catalysis [11, 12]. The ability to create and exploit isolated nanoenvironments within a dendritic shell is derived from two main properties of a dendrimer. First, dendritic macromolecules adopt a semi-globular or fully globular character containing internal void



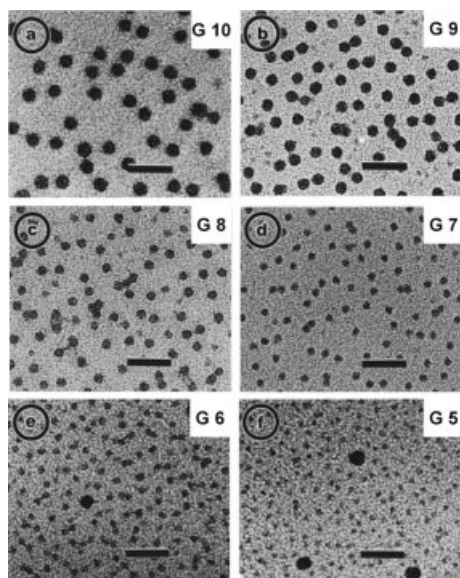


**Fig. 1.2.** Transmission electron microscopy (TEM) of PAMAM dendrimers. Dendrimers were positively stained with aqueous sodium phosphotungstate and imaged by conventional TEM: (a) G10, (b) G9, (c) G8, (d) G7, (e) G6, (f) G5. The scale bars indicate 50 nm, and a

small amount of G10 has been added as a focusing aid for G6 and G5. (Reprinted with permission from Jackson and coauthors [10]. Copyright 1998 by the American Chemical Society.)

spaces once they reach the fourth generation in size (Fig. 1.1) [8], enabling the encapsulation of protein-like functions, including catalysis [13, 14]. Second, these molecules have molecular flexibility and can undergo deformations, leading to rudimentary “lock and key” molecular recognition of the type vitally important to protein functions [15, 16].

Molecular recognition between molecules is a fundamental process in biology and chemistry without which life could not exist. The concept of molecular recognition, based on complementarity between the receptors and substrates, is very similar to the “lock and key” function first described by Emil Fischer over 100 years ago. In biology, the “lock” is the molecular receptor such as a protein or enzyme and the “key” can be regarded as a substrate such as a drug or ligand that is recognized to give a defined receptor–substrate complex [15]. In proteins, molecular recognition is largely driven by non-covalent forces such as hydrogen bonding, electrostatics, van der Waals forces,  $\pi$ - $\pi$  interactions, solvent-dependent interactions including hydration forces, and conformational energy [17]; notably, all of these parameters can be controlled in dendrimers through synthetic design. The inherent ability of dendrimers to achieve molecular recognition of biological features, if it can be successfully developed to a level of sophistication where it can be exploited for the recognition of the surface biomarkers that distinguish cancer

cells from healthy cells (Section 1.6.3), has important – and extremely beneficial – implications for drug delivery (Section 1.5).

Although sharing many superficial features, a close inspection reveals important differences between dendrimers and proteins. For example, remaining on the topic of deformability and flexibility, the linear, folded chain of a protein is more tightly packed but also has a greater *potential* for flexibility (when a comparison is made between the fully folded and unfolded states of a peptide chain) than is possible for the branches of a dendrimer. Only a small proportion of the potential flexibility of a protein, however, is usually available for “induced fit” interactions because the extensive unfolding of a protein is highly thermodynamically unfavorable. By comparison, although the extensive covalent bond networks within a dendrimer prevents complete unfolding under any condition, this arrangement does provide sufficient flexibility to allow dramatic – albeit somewhat thermodynamically unfavorable – deformations fairly readily [18]. Next, to consider dendrimer surfaces in comparison with proteins, synthetic dendritic macromolecules can be given a significant repertoire of tunable characteristics not found on natural proteins; this feature has greatly propelled the development of practical applications for these molecules. In particular, the surface of a protein contains a relative sparse complement of chemically reactive and accessible functional groups because most amino acid side chains are buried with the globular structure of the protein. By contrast, virtually all of the termini of dendritic branches, which can be customized with a wide range of chemical functionalities (Fig. 1.3), are oriented outward and are highly accessible on the surface of the dendrimer (Fig. 1.1). The consequent ability of a dendrimer to be functionalized with far more surface groups than a protein of comparable size [1, 19] has provided impetus to their widespread use as drug delivery vehicles.

### 1.3.2

#### **Dendritic Macromolecules Possess a Wealth of Possible Applications**

Within the past decade, the success of chemists in synthesizing mimics of natural dendrimers with a plethora of interesting physicochemical properties at the nanoscale has spurred efforts to find practical uses for these versatile nanodevices. Now that efforts to synthesize these molecules have reached fruition, there is a pleasing circularity that certain applications mirror natural processes considering that dendritic molecules were initially inspired by nature. In a dramatic example, a primary function of the leaves of real trees is for light harvesting; now, synthetic dendrimers have been created with highly-efficient light-harvesting antennae as well [8, 20]. Similarly, the dendritic network of hairs found on the Gecko foot that allows amazingly strong attachment to many types of surfaces through van der Waals forces [21] has led to efforts to create new forms of adhesives that are unaffected by the roughness, smoothness, wetness, or other macroscopic properties of the surface while providing strong but reversible adhesion. In addition to these two examples, many novel applications such as the exploitation of organometallic dendrimers as quantum dots for imaging, the solubilization of hydrophilic dyes in

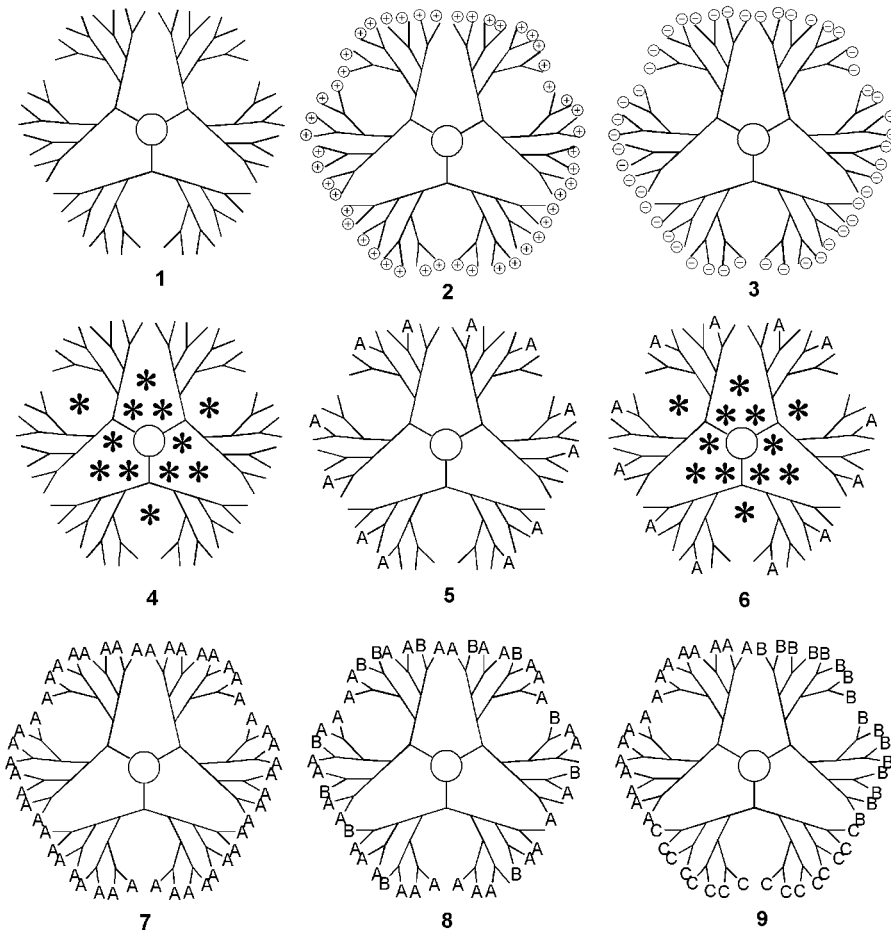


**Fig. 1.3.** Structural options for dendrimer-based drug delivery. Dendrimers can be synthesized with neutral surfaces (1) and positive (2) or negative (3) charges at the periphery; moreover, dendritic macromolecules, generally when larger than G3, can harbor non-covalently encapsulated guest/drug molecules [4 and discussion in Section 1.5.2]. An alternative strategy for drug delivery is through covalent conjugation of ligands ("A" in 5) to the surface of the dendrimer (Section 1.5.3). The versatility of dendrimers for drug delivery is illustrated by considering that "A" could be a targeting

ligand (Section 1.6.6.3) and the active drug could be encapsulated within the same macromolecule (6). Synthetic strategies are now available for providing dendritic clusters with extremely high densities of surface ligands (7) and for providing more than one type of surface ligand, either in a random orientation (8), or in blocks (9). The latter dendrimers are now being exploited in sophisticated cancer cell targeting (Fig. 1.4) and drug release (Section 1.5.3.3) strategies where A, B, and C can be any combination of targeting agents, drugs, contrast agents, or functional groups that improve pharmacological properties.

apolar dendritic “solvents” [22], use as chemical catalysts, and in electronics as insulated molecular wires, light-emitting diodes, or fiber optics [12, 23, 24] have been reported. Besides their use for drug delivery and cancer therapy, the many emerging chemical, synthetic, research, and industrial uses for dendrimers are outside the scope of this article and will not be discussed further; the interested reader can consult chapter articles [1, 2, 11].

## 1.4

### Methods for Dendrimer Synthesis

#### 1.4.1

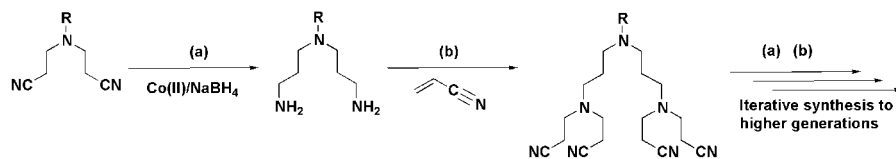
##### History and Basic Strategies

The ability to create homogeneous molecules with defined dendritic architecture and novel physicochemical properties at the sub-nano to nano-size scales occurred in chronological synchrony with the wide-spread application of nanobiotechnology to biology and medicine. Consequently, the parallel development of synthetic chemical methodology and the ever-increasing application of nano-tools in biomedicine triggered an explosive growth in the new field of dendrimer synthesis. This growth is evidenced by a cursory search for “dendrimers and synthesis” in the Web of Science database, which reveals that ~2000 articles have been published on this topic since 1986. Clearly, a full discussion is beyond the scope of this report; excellent accounts and review articles on the synthesis of dendrimers by pioneers of the field have appeared at regular intervals [25–32] and are cited throughout this chapter. Nonetheless, a working knowledge of the chemical properties of dendrimers is critical to successfully devise efficacious therapeutic strategies with these versatile, but temperamental, macromolecules (as described in detail in Sections 1.5 and 1.6). Accordingly, we next provide an outline of the basic strategies and building blocks employed in dendrimer synthesis, with an emphasis on families of dendritic molecules that possess special properties – such as possessing cavities in their interiors suitable for host–guest complexation similar to enzyme–substrate complexes or displaying several functional groups on their surface appropriate for sophisticated drug delivery strategies – relevant to the field of biology and medicine.

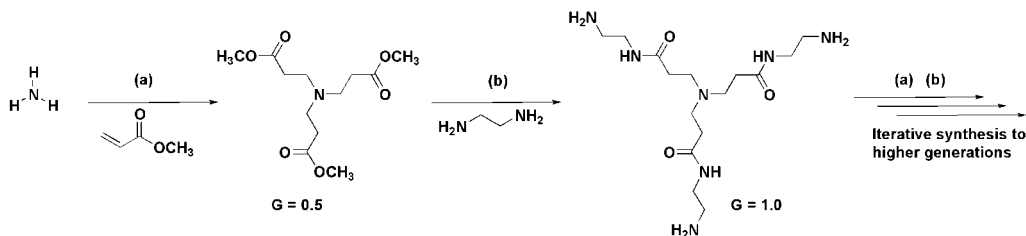
##### 1.4.1.1 Cascade Reactions are the Foundation of Dendrimer Synthesis

Although the term “dendrimer” was coined by Tomalia and coworkers less than two decades ago, the basic cascade or iterative methods that are currently employed for synthesis were known to chemists much earlier. For example, similar schemes form the basis of solid phase peptide synthesis. In turn, biology has long exploited similar iterative strategies in biochemical synthetic pathways; one example is provided by fatty acid biosynthesis [33]. Focusing on dendrimers, these macromolecules are constructed by performing simple chemical reactions in a repetitive or iterative manner by using small building blocks. In 1978 Vögtle and coworkers re-

## A. Cascade synthesis of polyaza compounds by Vögtle and coworkers (1978)



## B. Divergent synthesis of poly(amidoamine) dendrimers (PAMAM) by Tomalia and coworkers (1986)



## C. Convergent synthesis of aryl ether dendrimers by Fréchet and coworkers (1990)

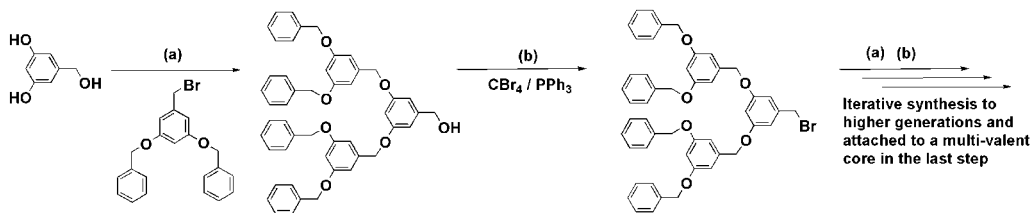


**Fig. 1.4.** Synthetic approaches to dendrimers. (A) Cascade reaction sequences developed for the synthesis of “non-skid-chain like” polyaza macrocyclic compounds [34]. (B) Divergent approach – synthesis of radially symmetric PAMAM dendrimers using ammonia as the trivalent core; the generations are added at each synthetic cycle (two steps), leading

to an exponential increase in the number of surface functional groups [36]. (C) Convergent approach – synthesis of dendrons or wedges or branches that will become the periphery of the dendrimer when coupled to a multivalent core in the last step of the synthesis [40].

ported a similar approach, termed as cascade reactions, for the construction of nonskid-chain-like poly-aza macrocyclic molecules with well-defined architectures. Cascade synthesis is defined as “reactions where a functional group (e.g., amine) is made to react in such a way as to appear twice in the subsequent molecule or product” [34] (Fig. 1.4A). In the first step of the synthesis a primary or secondary amine was reacted with excess acrylonitrile in a Michael reaction to obtain a product with two arms [bis(2-cyanoethyl)amines]. In the second step the nitrile groups were reduced using cobalt(II)/sodium borohydride to generate a new set of primary amine groups on both arms. The newly generated amino groups were then subject to identical reaction sequences iteratively to obtain the desired oligo-amine compounds.

In 1985 Newkome and coworkers reported the synthesis of cascade molecules consisting of hydrocarbon core and shell with alcohol groups on the surface. These synthetic efforts were inspired by the Leuwenberg model of arboreal design; hence they named their synthetic macromolecular tree-like molecules “arborols” (Latin: arbor = tree). Interestingly, characterization of these molecules showed they could be considered to be unimolecular micelles possessing cavities for encapsulation [35], a property that foreshadowed today’s efforts to use dendrimers for the delivery of encapsulated small molecule drug candidates (Section 1.5.2).

#### 1.4.1.2 Dendrimer Synthesis has Expanded Dramatically in the Past Two Decades

In 1986, Tomalia and coworkers coined the now popular name “dendrimers” (Greek: dendron = branch or tree-like) for radially symmetric branched molecules and reported the application of cascade synthesis for the synthesis of starburst dendrimers [36]. These researchers obtained homogeneous dendrimers by using a synthetic sequence of two simple reactions: (a) exhaustive Michael addition of ammonia to methyl acrylate and (b) exhaustive aminolysis of the resulting tri-ester derivative by ethylene diamine. The acrylate addition and aminolysis were repeated in an iterative manner, with excellent yields in each step, to prepare various molecules with increasing molecular weight and generations (Fig. 1.4B). The products with ester groups at the exterior were defined as  $G(m + 0.5)$  generations and those with amine groups at the exterior were defined as  $G(m)$  (Fig. 1.1). This simple methodology is both powerful and versatile as it provided the ability to synthesize dendrimers with various surface properties. For instance, the ester groups could be hydrolyzed to present negatively charged carboxylate functional groups at the periphery or the amine groups could be protonated to present positive charges at the periphery. Electron micrographic studies showed the dendrimer with carboxylate groups of generation,  $G = 4.5$ , to be highly monodispersed with a diameter of  $88 \pm 10 \text{ \AA}$ , compared with the theoretical value of  $\sim 78 \text{ \AA}$ . These dendrimers, when covalently attached to a polymeric backbone, were called “starburst polymers” or, less commonly, “cauliflower polymers” [7, 28].

### 1.4.2

#### Strategies, Cores, and Building Blocks for Dendritic Macromolecules

##### 1.4.2.1 Dendrimers are Constructed from Simple “Building Blocks”

In terms of synthesis, dendrimers can be constructed by using simple chemical reactions and building blocks reminiscent to the modular assembly of “LEGO” toys. Due to the ease, simplicity and repetitive nature of the synthetic methods, dendrimers based on organic, inorganic and organometallic molecular building blocks with greater than hundred different compositions are currently known, and new designs continue to be reported at a fast pace. In general, dendrimers consists of three major regions – (a) an initiator core, (b) a shell with extending arms or branches made of building blocks and (c) the exterior or outer-most surface groups on the termini of the branches.

There are innumerable ways of designing dendrimers [37–39]. For instance, the symmetry of the initiator core (Fig. 1.1) can be varied by using a wide range of molecules, which have included ammonia,  $\alpha,\omega$ -diaminoalkanes, tri-substituted benzene, oligo- or polyalcohols, nucleic acids, amino acids, lipids, carbohydrates, or heteroatoms; many additional permutations are possible, e.g., the number of branching units in the initiator can be increased (tri- or tetra- or higher valency cores have been reported). Once the core moiety has been selected, options for the synthesis of the dendritic branches are equally numerous as various types of building blocks can be used, either singly or in combination with each other in the same dendritic macromolecule. The lengths of the dendritic arms, the nature of the surface, and the display of terminal functional groups can all be customized.

#### 1.4.2.2 The Synthesis of Dendrimers Follows Either a Divergent or Convergent Approach

Dendrimers can be synthesized by two major approaches. In the divergent approach, used in early periods, the synthesis starts from the core of the dendrimer to which the arms are attached by adding building blocks in an exhaustive and step-wise manner. This process provides dendrimers with incrementally increasing generation numbers. However, only one type of reaction can be performed at each step, giving a uniform display of only one functional group on the exterior surface; moreover, defects in successive generations can arise due to incomplete reactions or steric hindrance (Fig. 1.4B).

In the convergent approach, pioneered by Fréchet and coworkers [40], synthesis starts from the exterior, beginning with the molecular structure that ultimately becomes the outer-most arm of the final dendrimer (Fig. 1.4C). In this strategy, the final generation number is pre-determined, necessitating the synthesis of branches of the various requisite sizes beforehand for each generation [31]. Small branches or dendrons are synthesized starting from the building blocks containing surface groups; these assemblies are then condensed with a multivalent core. This approach is versatile in the sense that branches of different molecular composition can be linked to a single core molecule, introducing regional variations on the final dendrimer (Fig. 1.3); this strategy also minimizes the introduction of defects at various stages of synthesis.

### 1.4.3

#### Heterogeneously-functionalized Dendrimers

##### 1.4.3.1 Basic Description and Synthetic Considerations

By simultaneously conjugating appropriate targeting moieties, drugs, and imaging agents to dendritic polymers, “smart” drug-delivery nanodevices can be developed to target, deliver, and monitor the progression of therapy. For example, as will be described in greater detail below, a dendrimer intended for cancer therapy needs to be functionalized with the drug itself, display a moiety for targeting to the tumor cells, as well as include surface groups designed to improve the pharmacological

properties (e.g., to ensure water solubility, avoid non-specific uptake or immunogenicity). Several synthetic strategies – primarily the convergent method discussed above (Section 1.4.2.2) – have been developed that enable multiple species to be added to a dendritic surface in an ordered manner [41] and thereby achieve multiple functionalities within the same dendritic nanodevice (Fig. 1.3). The ability to create multi-functional nanodevices based on dendritic scaffolds, however, remains a challenging endeavor because conjugating several types of different molecules to a dendrimer is likely to change its physicochemical properties and resulting biological activity. Practically, additional synthetic steps required to fine-tune bioactivity and remedy bioincompatibility if it arises may render the whole process cost-inefficient at best and, more troublesomely, lead to loss of product uniformity, thereby negating a key benefit of dendrimers, i.e., their monodisperse, fully defined nature [42].

#### 1.4.3.2 Glycosylation is an Example of Surface Modification with Multiple Bioactivities

An outstanding demonstration of the synthetic power of decorating the surface of dendrimers with “interesting” molecules comes, once again, by way of comparison of these nanodevices with proteins. Proteins, which have had the opportunity to evolve biocompatibility and systemic functions in multicellular organisms over hundreds of millions of years, have found it advantageous to decorate their surfaces with complex carbohydrates when they are displayed on the cell surface or secreted into the extracellular milieu. In the past few years, it has become clear that these sugars play many key roles in molecular recognition over short distances, such as interactions with the extracellular matrix and with neighboring cells, as well providing system-wide communication (e.g., almost all protein hormones are glycosylated). When developing dendritic nanotools requiring bioactivity similar to that found in proteins, including the ability needed by a drug candidate to seek out and evoke responses at a specific but far-removed cell type in the body, it is wise to learn from nature and consider the inclusion of sugars to be an important design parameter.

The ability to provide dendrimers with oligosaccharide coatings has been facilitated by the many functional groups that can be displayed on the surface and function as chemical handles for covalent attachment of a second group. A pioneering example of sugar display on a dendritic scaffold was provided by the unusual nine-carbon sugar sialic acid [43, 44]. This sugar, when displayed on human cells, serves as a critical binding epitope for the influenza virus. The virus, however, does not bind to soluble sialic acid, or sialic acid appended to a conventional polymer. Because these forms of sialic acid do not serve as effective binding elements, they are unable to act as a molecular decoys [45] and prevent the virus from binding to its real target, sialic acid on the human cell. By contrast, when sialic acid was conjugated to the surface of a dendritic polymer, it functioned as an effective and efficient binding decoy [46, 47], opening the door to the development of new diagnostic devices and novel anti-viral therapies [48, 49]. The molecular basis of the preferential recognition of sialic acid by the influenza virus when this sugar was



displayed on a highly structured dendritic scaffold was traced to the “cluster glycoside effect” [50]. Over the past decade it has become firmly established that carbohydrate-based recognition depends on multiple simultaneous interactions to increase specificity and affinity [45, 51]. The demonstration that dendrimers provide an ideal synthetic platform for the appropriate display of carbohydrates to achieve the cluster glycoside response [52–54], along with improved methodology to synthesize glycoconjugated-dendrimers [43, 55], has driven the expansion of this approach from a single monosaccharide to a sugar-amino acid couple (the Tn antigen, which is *N*-acetylgalactosamine linked to serine [56]) to disaccharides (lactose [57] and the T-antigen [58]), and, finally, to tetrasaccharides (the sialyl Lewis X epitope [59]).

## 1.5

### Dendrimers in Drug Delivery

#### 1.5.1

#### Dendrimers are Versatile Nano-devices for the Delivery of Diverse Classes of Drugs

A successful drug must perform the demanding tasks of selectively recognizing and binding to a molecular target, then triggering an appropriate biological response, all the while possessing pharmacological properties that render it “drug-like”. In some cases, nature has supplied compounds – such as aspirin or penicillin – that can be used directly as drugs but the more common situation is that many otherwise promising therapeutic agents are not successful in the clinic because of their poor pharmacological properties. The properties of dendrimers, in particular the synthetic ability to provide them with many different biological properties, along with their capacity to carry conjugated surface molecules or encapsulated guest molecules, make them immediately attractive as potential vehicles for drug delivery.

Drug delivery efforts are complicated by the diversity of molecules that hold potential therapeutic or diagnostic value; briefly reviewing three classes of drug candidates based on size demonstrates the wide applicability of dendrimers to drug delivery. First, regarding “small molecules”, many low molecular weight drug candidates are limited by poor solubility in aqueous environments or, if they are soluble, face rapid elimination from the bloodstream through filtration in the kidney. In the past, efforts have been made to modify the molecule itself, often following the “rule-of-five” guidelines developed by Lipinski to raise awareness of the properties and structural features that render molecules more or less “drug-like” [60]. Dendrimers present an attractive alternative strategy to the redesign of the drug because they allow unfavorable properties of a small molecule, such as insolubility, to be overcome by the larger characteristics of the macromolecule. An approach for improving the pharmacological properties of higher molecular weight drug candidates, analogous to Lipinski’s guidelines for the modification of small molecule drugs, has been applied for protein therapeutics such as recombinant antibodies

and protein toxins used in cancer treatment. In these cases, the amino acid sequences of recombinant proteins have been “humanized” by genetic engineering to avoid immunogenicity [61, 62] and their glycosylation patterns have been modified to increase serum half-life [63, 64]. These efforts, undertaken with actual proteins, illuminate design features that can benefit the development of protein mimics, dendrimers. In particular, the “humanizing” experiments show that small changes, such as the substitution of a single amino acid for another, can avoid significant problems like undesired systemic immune responses. In the same manner, small changes in the surface properties of dendrimers, such as the addition of poly(ethylene glycol) (PEG), can avoid unwanted immunogenicity. Finally, even extremely large therapeutic candidates, notably plasmids or naked viral DNAs used for non-viral gene delivery that are well beyond the size of traditional drugs, are also benefiting from dendrimer-assisted delivery. The next section outlines specific approaches for the delivery of both small and large drug candidates by dendrimers.

### 1.5.2

#### **Dendritic Drug Delivery: Encapsulation of Guest Molecules**

##### **1.5.2.1 Dendrimers have Internal Cavities that can Host Encapsulated Guest Molecules**

The flexible branches of a dendrimer, when constructed appropriately, can provide a tailored sanctuary containing voids that provide a refuge from the outside environment [2] wherein drug molecules can be physically trapped [65] (Figs. 1.1 and 1.3). Encapsulation of hydrophilic, hydrophobic, or even amphiphilic compounds as guest molecules within a dendrimer [66] can be enhanced by providing various degrees of multiple hydrogen bonding sites or ionic interactions [65, 67] or highly hydrophobic interior void spaces [68, 69]. A wide variety of molecules have been successfully encapsulated inside dendrimers. In early experiments, compounds used to demonstrate the “guest molecule” concept included easy-to-visualize dye molecules such as rose bengal [66] and Reichardt’s dye [69] as well as pyridine [65] and peptides [67]. More recently, actual drugs, including 5-fluorouracil [70], 5-amino salicylic acid, pyridine, mefenamic acid and diclofenac [65], paclitaxel [71, 72], docetaxel [73], as well as the anticancer agent 10-hydroxycamptothecin [69], have been successfully encapsulated. Together, these results demonstrate that encapsulation is a general strategy for the delivery of low molecular weight compounds by dendrimers. This method is anticipated to be of particular value when display of the bioactive molecule on the surface of the dendrimer induces unwanted immunogenicity or reduces biocompatibility (Section 1.5.5).

##### **1.5.2.2 Using Dendrimers for Gene Delivery**

The delivery of small molecules complexed as guest molecules in internal void spaces of dendrimers is, at least in retrospect, intuitively obvious. By contrast, the delivery of extremely large macromolecules, such as MDA-sized plasmid DNA for non-viral gene therapy, is counter-intuitive because the encapsulation of a “guest” molecule many times the molecular weight of the dendrimer itself appears impos-

sible. Nonetheless, experimental evidence had demonstrated that gene delivery strategies also benefit from the participation of dendrimers [74]. For example, from its original discovery of efficacy for gene delivery [75], the fractured form of PAMAM, known as Superfect™, is now a commercially-available transfection agent for *in vitro* applications [76]. Typical approaches to optimize dendritic gene delivery for *in vivo* use have involved the surface modification of a PAMAM backbone, either with arginine [77] or hydroxyl groups [78]. Alternatively, the results reported by Kim and coworkers, who demonstrated improved gene delivery with a novel PAMAM-PEG-PAMAM triblock copolymer, show that construction of dendrimers composed of new building blocks is warranted [76]. Although still in their infancy, there are efforts afoot to exploit dendrimers for the delivery of smaller nucleic acids such as antisense oligonucleotides and short interfering RNAs (siRNA); the success of these applications is likely to depend on the continuing development of novel materials for dendrimer synthesis [79].

### 1.5.2.3 Release of Encapsulated “Pro-drugs”

Once a dendrimer carrying an encapsulated drug reaches the intended site of action, the guest molecule generally must be released to gain bioactivity. Indeed, a concern is that the active drug would “leak” out prematurely, thereby reducing the amount available for the intended therapeutic intervention, or more ominously, result in systemic toxicity. Reassuringly, early experiments showed that the close packing of dendritic branches on the surface of the macromolecule (Fig. 1.1) effectively formed a “membrane” that reduced diffusion to immeasurably slow rates [66]. In other cases, the release of encapsulated guest molecules was relatively faster, occurring over a few hours, apparently through hydrolytic degradation of the dendrimer in aqueous conditions [65]. The observation that guest molecules could be liberated at different rates demonstrated that viable opportunities exist to tailor the release for either slow or rapid delivery (Fig. 1.5). At present, additional control of delivery rates is being sought; for instance, the ability of a dendrimer to instantaneously release its entire drug payload upon reaching its cellular target would be valuable. Promising steps in this direction are being taken by the development of pH-sensitive materials [65], the fine tuning of hydrolytic release conditions, and the selective liberation of guest molecules on the basis of their size or shape [80].

## 1.5.3

### Covalent Conjugation Strategies

#### 1.5.3.1 Dendrimers Overcome many Limitations Inherent in Polymeric Conjugation Strategies

The strategy of coupling small molecules to polymeric scaffolds by covalent linkages to improve their pharmacological properties has been under experimental test for over three decades [81–84]. Unfortunately, conventional linear polymers typically used in these efforts are plagued by inherent properties that render them distinctly “un-drug-like”, including high polydispersity and size distributions, a

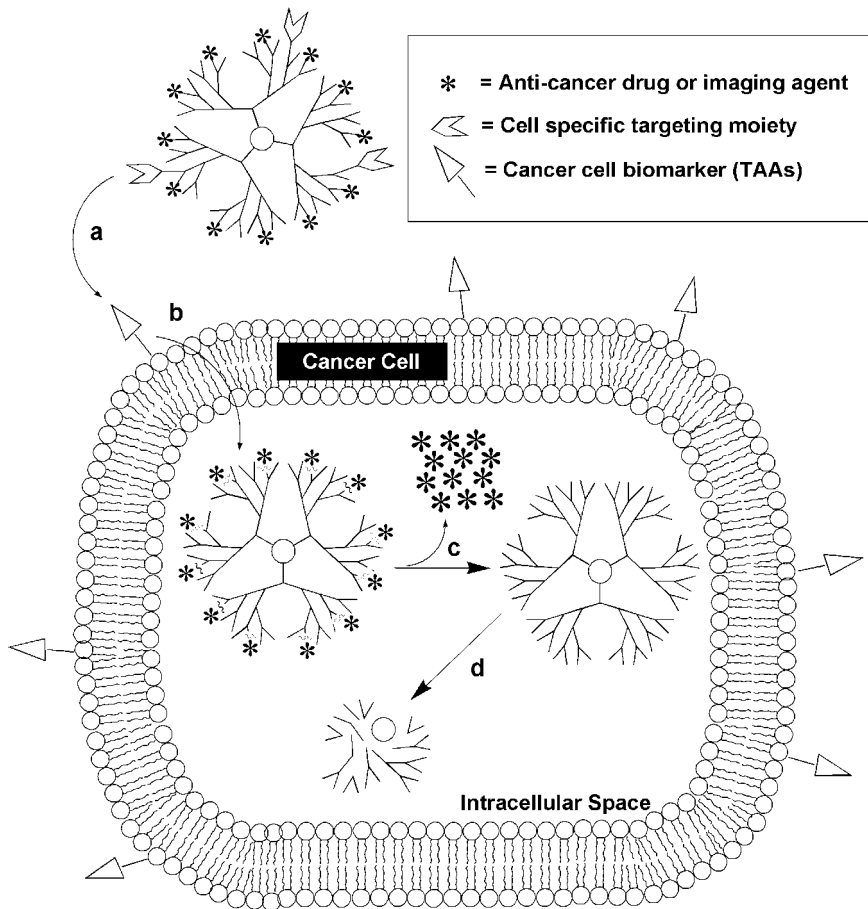


**Fig. 1.5.** Requirements for dendrimer-based, cancer-targeted drug delivery. (a) Dendrimers with multiple surface functional groups (Section 1.4.3) can be directed to cancer cells by tumor-targeting entities that include folate or antibodies specific for tumor-associated antigens (TAAs). (b) The next step is intake into the cell, which in the case of folate

targeting occurs by membrane receptor-mediated endocytosis (Section 1.6.3.2). (c) Once inside the cell, the drug generally must be released from the dendrimer, which, for the self-immolative method (Section 1.5.3.3), results in the simultaneous disintegration of the dendritic scaffold (d).

lack of defined structure, and a low density of drug payload per unit volume or mass. Properties of dendrimers that overcome these problems include monodispersity that results in the ability to select the precise sizes of nanoparticle required to a specific application (Table 1.1), a fully defined structure that allows the presentation of attached conjugates in a defined architecture, a high ratio of drug payload to volume, and enhanced control over drug release rates. Unsurprisingly, based on these many beneficial features, a wide range of biologically active molecules have

already been covalently attached to dendrimers. These conjugates range from small molecule drugs, such as ibuprofen [85], fluorescent and radioactive imaging agents (Section 1.6.4), oligonucleotides, oligosaccharides and peptides, as well as much larger molecules such as monoclonal antibodies (Section 1.6.3). Biologically active molecules attached to dendrimers can have two fundamentally different relationships to the host molecule. In some cases, exemplified by vaccine applications, there is no need to liberate active drug from the dendrimer (indeed, the success of antibody production usually depends on the unique display characteristics achieved by conjugation to the dendrimer). In most cases, however, the conjugated dendritic assembly functions as “pro-drug” where, upon internalization into the target cell, the conjugate must be liberated to activate the drug.

### 1.5.3.2 Dendrimer Conjugates can be Used as Vaccines

Most low molecular weight substances are not immunogenic; consequently, when it is desired to raise antibodies against small molecules, they must be conjugated to a macromolecule. In the past, natural proteins have commonly been used as carriers to generate antibodies to small molecules; now an alternative strategy using dendrimers has been demonstrated. In particular, unmodified PAMAM dendrimers that fail to elicit an antibody response on their own become haptized upon protein conjugation and generate a dendrimer-dependent antigenic response [86, 87]. A specific example of this technique is provided by the dendrimeric presentation of antigenic HIV peptides, which proved superior to other multimeric presentation strategies, such as conjugation to dextran [88]. Notably, the immunogenicity of dendrimer conjugates is not limited to peptides antigens; in one study antibodies were produced against densely penicilloylated dendrimers that were subsequently used for the diagnostic testing of patients with potential allergy to  $\beta$ -lactam antibiotics [89]. Finally, although carbohydrate-conjugated dendrimers (Section 1.4.3.2) are typically non-immunogenic [1], antibodies can be successfully elicited against cancer-specific oligosaccharides displayed on a dendritic scaffold, offering a method for generation of a new class of cancer vaccines (Section 1.6.6.2).

### 1.5.3.3 Release of Covalently-delivered “Pro-drugs”

Similar to encapsulated guest molecules that generally require release from the void spaces of a dendrimer to gain bioactivity (Section 1.5.2.3), a covalently delivered dendritic conjugate must also be cleaved within the target cell to regenerate the active cytotoxic agent (Fig. 1.5). At the same time, to ensure systemic non-toxicity, the covalent linker must be stable in circulation [90]. Several strategies are being pursued to ensure the successful cleavage and activation of the pro-drug in the target cell or tissue while avoiding systemic release. These include activation by low pH found in endosomal vesicles, installation of enzyme-cleavable ester linkages into the linkers that attach the pro-drug to the dendritic macromolecule, or disulfide bonds that are liberated in the reducing environment of the endoplasmic reticulum, photoactivation, or sensitivity to ultrasound [1].

Briefly returning to the benefits of dendritic clusters over conventional polymers for drug delivery, problems with the delivery of covalent conjugates when conven-

tional polymers, such as poly(lactic acid) (PLA) or its copolymer with glycolide (PLGA), are used include a lack of sustained drug release [91]. Generally, these and other linear, randomly oriented polymers have an initial burst where as much as 50% of drug is released followed by a dramatic drop-off. An advantage of dendrimers is that their release rates are more consistent, which has been demonstrated by polylactide-PAMAM dendrimers [91] and dendrimer-platinite [92]. Consistent release from dendrimers is likely an inherent feature of their defined three-dimensional structure as their sites of drug attachment are continuously exposed to solvent, compared with random polymers where conjugated pro-drug moieties can be internalized randomly. The unique architectural features of dendrimers offer additional elegant strategies to gain exquisite control over release of active drug. In particular, the production of dendrimers functionalized with catalytic antibodies [68] has spurred the development of dendrimers capable of “self-immolation” [93–95].

Self-immolative dendrimers provide an attractive potential platform for multi-drug delivery. To briefly explain, these unique assemblies have the ability to release all of their tail units (i.e., the active drug) through a self-immolative chain fragmentation, which is initiated by a single cleavage at the dendrimer’s core [96]. The first generation of dendritic prodrugs was demonstrated by Shamis and coworkers who synthesized doxorubicin and camptothecin as tail units and designed a retro-aldol retro-Michael focal trigger provided by action of the catalytic antibody 38C2 [94]. This method showed a dramatic increase in toxicity to tumor cells upon bioactivation of the pro-drug compared with tests done in the absence of the activating antibody. This technology, when fully developed into a complete chemical adaptor system that combines a tumor-targeting device (Section 1.6.3), a pro-drug, and pro-drug activation trigger, provides a sophisticated platform for future research efforts and the development of drugs for *in vivo* use [93].

#### 1.5.4

### Fine-tuning Dendrimer Properties to Facilitate Delivery and Ensure Bioactivity

#### 1.5.4.1 Delivery Requires Avoiding Non-specific Uptake

From the initial entry into the body, a drug candidate confronts many barriers and diversions on its route to the site of intended bioactivity. Uptake by oral ingestion is ideal for patient comfort and, while still largely speculative for dendrimers [97], there is now evidence that uptake occurs in the rat gut [98]; this route is enticing based on an increasing recognition that nanoparticle uptake across the gut is largely governed by the physicochemical properties and surface chemistries of oral drug delivery vehicles [99]. Typically, to get to the target site in the body, the drug candidate must avoid becoming trapped with the extracellular matrix, which has been shown to hinder cellular uptake and reduce the efficiency of other nano-sized delivery vehicles [100]; instead entry into the bloodstream is generally required for transit to the intended site of action.

Once in the bloodstream, either by successful navigation of an oral route or through direct injection, dendrimers below a certain size are at risk of filtration

and removal by the kidney. This pitfall, however, can be avoided by ensuring that sufficiently large dendrimers are used. Indeed an important design feature and overriding impetus to use dendrimer delivery vehicles is to prevent the filtration of these drug candidates by the kidney. A second, off-target “trap” for dendrimers has been identified in a study that showed sequestration of dendrimers in the liver and spleen, in part due to their surface properties and in part due to their size [101]. As discussed elsewhere, both of these parameters can be controlled with exquisite sensitivity for dendritic macromolecules, allowing longer residence times in the blood (the longer the serum half-life, the greater the opportunity to reach the intended site of action).

#### 1.5.4.2 “Local” Considerations: Contact with, and Uptake by, the Target Cell

Once a dendrimer has successfully entered the bloodstream and has been designed to minimize undue accumulation in non-target organs or tissues, it still faces the challenge of seeking out and interacting with its targeted site of action. The diversity of cell surface targets available for a nanodevice to bind to is vast; here we limit ourselves to specific examples related to cancer (Section 1.6.3). We will jump ahead to the point when a dendrimer has made “first contact” with a cell and reflect on how it interacts with the membrane. In this regard, there are provocative studies with PAMAM polymers that suggest that binding to the cell surface is facilitated by the deformable properties of dendrimers [15, 16, 18] (Section 1.3.1.3). Cell-binding induced deformations, if they prove real, have important implications for drug delivery. For example, the flattened forms of dendrimers lose their internal voids where guest molecules – such as drug payloads – are sequestered [6]. If this step occurs too soon, i.e., outside of the target cell, the drug might be ineffective, whereas if it occurs at the right moment, i.e., in the cytosol for cytosolic-acting drugs, it would provide an additional design parameter to exploit in the drug release process (Section 1.5.2.3). Notably, the deformations proposed to occur upon the interaction of a dendrimer with a cell, where the dendrimer shifts from a canonical “spherical” shape to a flattened disk with a significant loss in volume, have been most-extensively investigated at the dendrimer–mica interface. Clearly, the plasma membrane of a cell shares few biophysical characteristics with an extremely flat and rigid surface of mica, therefore, combined with the thermodynamically unfavorable aspects of the putative shape change, the extrapolation to drug delivery in biological systems should not be overstated. Encouragingly, shape changes also have been observed – but not thoroughly characterized – for dendrimers encountering the air–water interface, which is a better model for biological systems. Regardless of the current lack of concrete information, the intriguing nature of this potential mechanism for cell targeting and drug release merits its discussion here and also warrants further experimental investigation.

Once a dendrimer is in contact with a cell, there is strong experimental evidence that the exact surface properties of the dendrimer influence cellular uptake [102]. Therefore, the ability to modulate the chemical properties of a dendrimer provides additional options for controlling the uptake of a dendritic drug delivery device into a cell and even partitioning pro-drug release into specific organelles. To elaborate

by briefly recapitulating a series of elegant experiment from the Banaszak Holl group, these researchers used a battery of assays, ranging from dye leakage to atomic force microscopy, to demonstrate that G5–G7 PAMAM dendrimers disrupt lipid bilayers and form holes large enough (5–40 nm) to account for dendrimer internalization. Moreover, the hole formation could be tuned by the exact size of the dendrimer, as well as surface chemical properties. To be specific, G7 amine-terminated PAMAM initiated hole formation while its G5 counterpart did not. The smaller G5 dendrimer, however, did expand holes at existing defects; by contrast, acetamide terminated G5 PAMAM neither initiated hole formation nor expanded existing defects [102, 103]. The mechanism of hole formation in membranes by PAMAM was proposed to involve the removal of lipid molecules from the membrane to form aggregates consisting of a dendrimer surrounded by lipid molecules [103]. Once inside a cell, there are early indications that the precise properties of a dendrimer can influence subcellular trafficking. Eventually, if these processes can be better understood and controlled, their exploitation for drug delivery will be very attractive considering that some entities, such as dendrimer-delivered ibuprofen, need to only gain access to the cytosol [85], whereas other class of drugs, such as dendrimer-delivered plasmid DNAs, have the more-demanding task of reaching the nucleus [104].

#### 1.5.5

### **Drug Delivery: Ensuring the Biocompatibility of Dendritic Delivery Vehicles**

#### **1.5.5.1 Biocompatibility Entails Avoiding “Side Effects” such as Toxicity and Immunogenicity**

To briefly reiterate, properties of dendritic polymers important for drug delivery include negligible polydispersity, a high-density payload of pro-drug, and the ability to selectively release the active form of drug precisely at its intended site of action. Although dendrimers are capable of each of these tasks, their advantages are for naught if the final dendritic complex is not “biocompatible.” Biocompatibility, a broad term with numerous meanings, will be considered here from three perspectives, water solubility, lack of immunogenicity, and toxicity.

#### **1.5.5.2 Water Solubility and Immunogenicity**

The first two biocompatibility issues mentioned above, namely water solubility and immunogenicity, are closely related insofar as highly-hydrated macromolecules tend to be less immunogenic. With dendrimers, there are many options available to overcome difficulties that arise in these areas. For example, solubility can be readily adjusted by surface modifications to surface chemistry or by the addition of conjugated ligands (Section 1.5.3, Fig. 1.3). Moreover, dendrimers such as the commonly used G3, G5, and G7 PAMAM clusters are not inherently immunogenic [105]. Derivatized PAMAM such as the G4D-(1B4M-Gd)<sub>62</sub> magnetic resonance imaging (MRI) contrast dendrimer, however, can become immunogenic (which is not surprising considering the deliberate efforts to render small molecules immunogenic through presentation on a dendritic scaffold). This problem –



once again tying together the concepts of solubility and immunity – was overcome in one study by conjugation of poly(ethylene glycol) (PEG) to the surface of the dendrimer. Notably, PEG also had the positive effect of decreasing non-specific clearance from the blood, likely due to the increased hydration and resulting solubility of the particle [106].

### 1.5.5.3 Inherent and Induced Toxicity

A basic issue in drug delivery is the avoidance of non-specific, systemic, or off-target toxicity. At its simplest this issue, when applied to dendrimers, involves the biological effects of the material used to construct the polymer. Ideally, the building blocks themselves, as well as their degradation products upon delivery and release of the drug payload, are non-toxic. One strategy is to directly use natural biological molecules, such as carbohydrates [59, 107], amino acids and peptides [108], nucleic acids [109–113], or lipids [114, 115] as the building blocks. To provide additional synthetic flexibility, while maintaining biocompatibility, an increasing number of biologically compatible and generally-regarded as safe (GRAS) materials are being used in dendrimer construction. Examples include dendritic polyglycerol [116], melamine [117]; phosphate [118], polyglycerols [39], a polyester dendrimer based on poly(ethylene oxide) that has tunable molecular weights and architectures [84], and dendrimers composed of citric acid and poly(ethylene glycol) [65].

The pioneering PAMAM-based dendrimers illustrate a second issue beyond inherent toxicity of the material or breakdown products, namely “induced” toxicity. The PAMAM family (Table 1.1), although not explicitly designed for biocompatibility, was found to be non-toxic when generations 1 through 5 were tested [105]. Evaluation of G7 dendrimers, however, showed potential biological complications, including dose-dependent toxicity [105], thereby illustrating that, while the basic material of PAMAM is inherently non-toxic, deleterious outcomes could be “induced” by factors such as the size or structure of the nanodevice. Smaller generation, non-toxic, dendrimers are sufficient for some applications but larger clusters are needed to fully exploit the enhanced permeation and retention (EPR) effect important in the treatment of cancer with macromolecular therapeutics (Section 1.6.2); consequently, toxicity cannot simply be avoided by restricting use to small, safe-sized particles. Instead, one strategy devised to avoid toxicity was the re-design of the building blocks of PAMAM-based material [76, 119] while another strategy involved the development of completely new polymeric backbones [120].

The selection of “safe” building blocks to avoid deleterious effects in dendrimer construction is unlikely to prevent all problems. To illustrate, even very safe building blocks, such as amino acids, can be highly toxic or immunogenic when assembled into large macromolecules – in this case proteins – in the “wrong” way. Indeed, the toxicity of dendrimers could be the result of several factors beyond the simple properties of the unloaded scaffold. For instance, with cancer drugs intended to kill cells, systemic toxicity could result if the drug is taken up by the wrong cellular target (i.e., a healthy cell or tissue, rather than a cancer cell or tumor) or if the nanodevice was “leaky” (i.e., if the pro-drug was released systemically before reaching the target cell). Fortunately, many strategies exist for prevent-

ing toxicity, including directing a drug to its intended site of action by targeting moieties (Section 1.6.3) and developing sophisticated release strategies (Section 1.5.3.3). Problems that arise from the surface properties of the conjugated dendrimer can be ameliorated by masking the surface with something as simple as PEG or, in more advanced schemes, by coating with sugars or peptides to make glycodendrimers or peptide dendrimers, respectively (discussed in Ref. [121]) to mimic proteins naturally found in circulation (Section 1.4.3.2).

## 1.6

### Dendrimers in Cancer Diagnosis and Treatment

#### 1.6.1

##### Dendrimers have Attractive Properties for Cancer Treatment

Cancer epitomizes the challenges faced during drug delivery: an anticancer drug must be able to seek out subtle changes that distinguish a transformed cell from the other 200 or so types of healthy cells found in the body and then provide a sufficiently high dose of a toxic agent to selectively kill the cell while not harming its healthy neighbors. Therefore, even though dendrimers can be endowed with many favorable properties for drug delivery (Section 1.5), an ultimate challenge – ergo, a “real-world” test – of these versatile nano-devices will be whether they can successfully meet the formidable tasks of diagnosing and treating of malignant disease. As described in Section 1.7, although significant work remains in several areas, prospects now appear bright for dendrimer-based approaches to cancer treatment.

#### 1.6.2

##### Dendrimer-sized Particles Passively Accumulate at the Sites of Tumors

To begin the discussion of properties that make dendrimers attractive vehicles for cancer treatment, we revisit the concept that encapsulation (Section 1.5.2) or covalent linkage (Section 1.5.3) of small molecule drug candidates to a dendrimer enhances the pharmacological properties of the drug. In cancer chemotherapy, these desirable size-based features are reinforced by the enhanced permeability and retention (EPR) effect that improves the delivery of macromolecules to tumors. The EPR effect is based on unique pathophysiological features of a solid tumor, such as extensive angiogenesis resulting in hyper-vascularization, limited lymphatic drainage, and increased permeability to lipids and macromolecules. These features, which help ensure adequate nutrient supply to meet the metabolic requirements of rapidly growing tumors [122, 123], can be turned to the tumor’s disadvantage by the use of nano-sized therapeutic agents.

The EPR effect was discovered when selective accumulation of the SMANCS conjugate (styrene-maleic anhydride-neocarzinostatin) was observed at the site of tumors while similar accumulation was not seen with neocarzinostatin alone

[124, 125]. The EPR response was subsequently demonstrated for similarly-sized liposomes, thereby establishing that this effect was largely a function of particle size and did not solely depend on the chemical or biophysical properties of the macromolecule. Specifically, in one study optimal tumor delivery occurred for liposomes having a size distribution between 70 and 200 nm in diameter [126]. An independent study showed efficacy for liposomes loaded with daunorubicin in the same size range; specifically, those ~142 nm in diameter exhibited an inhibitory effect against Yoshida sarcoma whereas smaller (~57–58 nm) and larger (~272 nm) liposomes had weaker or no effect [127]. Over time, cautionary notes were raised that tempered initial enthusiasm for exploiting the EPR effect for cancer treatment. For example, the porosity of the vasculature in tumors can be highly variable even with a single vessel that can be leaky to one size of particle in one region but not in another [128]. Experimentally addressing this issue was complicated by the size polydispersity of traditional nanoparticles used to exploit the EPR effect, which were typically either lipids or conventional polymers that rendered a significant proportion of intended drug inactive. Fortunately this issue – the ability to match exact and uniform sizes needed to target an individual tumor – is highly tractable with dendrimers because selection of an exactly-sized entity is possible (Table 1.1) compared with the large size distributions that plague liposome and most polymeric materials [42].

The ability to construct monodisperse populations of dendrimers in the size range needed to exploit the EPR effect is an encouraging step towards the passive exploitation of tumor properties. Once the basic issue of size was resolved, however, secondary challenges (and opportunities) arose from observations that the chemical properties of the nano-sized particle can play significant roles in modulating the EPR effect. By way of a specific example, “conventional” polymeric materials showed efficacy at a smaller size range, occurring at ~60 nm for both water-soluble and hydrogel forms of poly(vinyl alcohol) (PVA) [129], whereas almost identically-sized 57 nm egg phosphatidylcholine (EPC)-liposomes were ineffective [127]. As reported above, liposomes about twice this size showed maximal efficacy, so it was not unexpected that the EPC-liposomes were ineffective. Interestingly, however, hydrogenated egg phosphatidylcholine (HEPC)-liposomes in this size range (specifically, 58 nm) were active [127], illustrating that the exact chemical properties of the material is a critical design parameter. In this respect, the many options for dendrimer “building blocks”, as well as the ability to further tune surface properties provide many opportunities to endow dendrimers with favorable “passive” properties for tumor targeting.

### 1.6.3

#### **Multifunctional Dendrimers can Selectively Target Biomarkers found on Cancer Cells**

##### **1.6.3.1 Methods for Targeting Specific Biomarkers of Cancer**

As discussed above, dendrimers can achieve passive EPR-mediated targeting to a tumor simply by control of their size and physicochemical properties. Passive tar-

getting, which localizes the nano-particle in the close vicinity of a cancer cell, can be immediately useful for diagnostic purposes (Section 1.6.4) or for the delivery of radioisotopes capable of killing any cell within a defined radius. In general, however, most delivery strategies require that the anticancer agent directly attached to, or be taken up by, the target cell. The ability to append more than one type of functionality to a dendrimer (Fig. 1.3) allows the inclusion of ligands intended to bind specifically to cancer cells in the design of a multi-functional drug-delivery nanodevice (Fig. 1.5). Although a wide range of targeting ligands have been considered, including natural biopolymers such as oligopeptides, oligosaccharides, and polysaccharides such as hyaluronic acid, or polyunsaturated fatty acids [90, 130], discussion here is limited to folate, which is an exemplary small molecule tumor-targeting agent [42], as well as monoclonal antibodies directed against tumor associated antigens (TAAs).

#### 1.6.3.2 Targeting by Folate, a Small Molecule Ligand

Folate is an attractive small molecule for use as a tumor targeting ligand because the membrane-bound folate receptor (FR) is overexpressed on a wide range of human cancers, including those originating in ovary, lung, breast, endometrium, kidney and brain [131]. As a small molecule, it is presumed to be non-immunogenic, it has good solubility, binds to its receptor with high affinity when conjugated to a wide array of conjugates, including protein toxins, radioactive imaging agents, MRI contrast agents, liposomes, gene transfer vectors, antisense oligonucleotides, ribozymes, antibodies [131, 132] and even activated T-cells [133]. Upon binding to the folate receptor, folate-conjugated drug conjugates are shuttled into the cell via an endocytic mechanism, resulting in major enhancements in cancer cell specificity and selectivity over their non-targeted formulation counterparts [131, 132]. Recently, folate has been enlisted in an innovative dendrimer-based targeting schemes ([42, 134], Section 1.6.6.1).

#### 1.6.3.3 Targeting by Monoclonal Antibodies

Of the many strategies devised to selectively direct drugs to cancer cells, perhaps the most elegant (and demanding!) is the use of monoclonal antibodies that recognize and selectively bind to tumor associated antigens (TAAs) [135–138]. TAA-targeting monoclonal antibodies have been exploited as delivery agents for conjugated “payloads” such as small molecule drugs and prodrugs, radioisotopes, and cytokines [139, 140]. The field of “immunotherapy” envisioned almost a hundred years ago, and given renewed impetus a quarter century ago by the development of monoclonal antibody technologies, has nonetheless progressed erratically over the past two decades as many pitfalls have been encountered [139]. Current prospects remain mixed but hopeful; optimistically, progress marked by commercial interest with companies providing their immunotherapeutic drug candidates with flashy trademarked names, such as “Armed Antibodies™” [141]. Similarly, the rosy opinion that this field is “on the verge of clinical fruition” has been published recently [142]. Perhaps, more realistically, one recent synopsis

holds out “hope” for a major clinical impact for this strategy within the next 10 years [136].

Although a detailed discussion of the many pitfalls encountered in immunotherapy efforts is beyond the scope of this chapter, one key issue – readily addressed by dendrimers – is the requirement that an extremely potent cytotoxic drug be used in targeted antibody therapy. This point is illustrated by the fact that the greatest progress in this field has occurred for immunotoxins, which are antibody–toxin chimeric molecules that kill cancer cells via binding to a surface antigen, internalization and delivery of the toxin moiety to the cell cytosol. In the cytosol, protein toxins, such as those from diphtheria or pseudomonas, catalytically inhibit a critical cell function and cause cell death [143]. The high potency of immunotoxins for killing cancer cells is dramatically illustrated by ricin, where the catalytic activity of this ribosome-inactivating enzyme allows a single immunotoxin conjugate to kill a cell upon successful uptake and trafficking to the site of action [144, 145].

A drawback of immunotoxins is their significant immunogenicity, which limits repeated use [136]; from a broader perspective, their repeated use is made necessary by difficulties in providing a sufficiently high drug load to eradicate all cancer cells despite the high potency of conjugated toxin. An alternative approach of radioimmunotherapy, where high energy radionuclides are conjugated to TAA-targeting antibodies, also shows promise [146] but suffers from indiscriminate toxicity (the surrounding healthy tissues, as well as off-target tissues, become irradiated in addition to the target cancer cells). A third possible approach for immunotherapy, the conjugation of commonly-used small molecule drugs to TAAs, is hindered by the relatively low potency of most low molecular weight therapeutics. To illustrate this point, ~10 000 TAAs occur on a typical cancer cell [101], making this number the upper limit for the number of targeting antibodies that can bind to the cell. The widely used anticancer drug cisplatin, to give one example, requires internalization of at least 50× this level of drug molecules for therapeutic efficacy.

A numerical analysis of the cisplatin example presented above indicates that each tumor-targeting antibody would have to be modified with a large number of small molecules to be effective as an anticancer drug (in this case, roughly 50 cisplatin molecules upon superficial analysis). Modification of an antibody with multiple radioisotopes, toxins, or even small molecules to increase the efficacy of cell killing, however, diminishes or eliminates the inherent specific antigen-binding affinity of an antibody. Therefore, to maximize drug loading while minimizing the deleterious effects on the biological integrity of the host antibody, an attractive approach is to use a linker molecule, such as a dendrimer, that can be highly conjugated (or internally loaded) with drug while modifying only a single site on the surface of the antibody [147]. Methodology to covalently attach antibodies to dendrimers that preserve the activity of the antigen–antibody binding site [148, 149], e.g., by chemical modification of their carbohydrates and subsequent linkage to PAMAM [150], has opened the door for the inclusion of dendrimers in immunotherapy [151, 152], thereby enhancing the future prospects of this chronically “almost-there” strategy.

## 1.6.4

**Dendrimers in Cancer Diagnosis and Imaging****1.6.4.1 Labeled Dendrimers are Important Research Tools for Biodistribution Studies**

The synthetic ability to attach both a tumor-targeting antibody and a potent payload of anticancer drugs to the same dendritic molecule provides a platform for multi-functional nano-scale drug delivery devices (Fig. 1.5). Before this technology can be applied in the clinic, however, its safety and efficacy must be demonstrated; towards this end, fluorescently-modified dendritic conjugates have been used extensively to characterize cell targeting, surface binding, uptake and internalization, and even sub-cellular localization [85, 151, 152]. The radiolabeled counterparts appropriate for animal studies have allowed detailed examination of the biodistribution of dendrimers. Several radio-isotopes have been conjugated to dendrimers, including  $^3\text{H}$  [153],  $^{14}\text{C}$  [105],  $^{88}\text{Y}$  [154],  $^{111}\text{In}$  [154, 155], and  $^{125}\text{I}$  [98, 149, 156–158]. These studies have established that the chemical and physical properties of dendrimers can be tuned to favor distribution to or away from specific organs and, ultimately, to achieve favorable biodistribution to tumors. The methods used in these experiments, however, typically requiring post-administration dissection of the host animal to allow the analysis of organ sequestration and tissue distribution of the radioisotope, are clearly not applicable to clinical practice. Instead, they have served as an important stepping stone along the path towards non- or minimally-invasive diagnostic procedures, which are proceeding mainly by the development of MRI contrast agents.

**1.6.4.2 Towards Clinical Use: MRI Imaging Agents**

Upon successful demonstration of the selective accumulation of dendrimers at the sites of tumors in animal models, a natural extension of this approach was to substitute gadolinium for the previously-tested isotopes or fluorophores. Gadolinium ( $^{153}\text{Gd}$ ) is the best known and most extensively utilized magnetic resonance (MR) contrast agent [159, 160] and has previously been shown to be valuable for the improved diagnosis of cancer [161, 162]. Importantly, the *in vivo* efficacy of gadolinium is greatly enhanced when used as part of a macromolecular system [159]; in the past, attempts to create macromolecular gadolinium platforms have included the conjugation of chelators for this metal to both proteins [163] and conventional polymers [164]. These efforts have met with mixed (but generally limited) success. By contrast, Kobayashi and Brechbiel report that, by conjugating gadolinium to dendrimers, the unique properties of these polymers, such as exquisite size control, allowed selective targeting and imaging of the kidney, vascular, liver, or tumors [159]. Of note, tumor specific targeting and accumulation of gadolinium contrast agents is possible by use of either the folate receptor [165] or TAAs [159]. A drawback of the initial PAMAM-based MR contrast agents was their long residence time in the body; this problem, however, can be met by modifying both the surface properties [106] and basic chemical composition of the dendrimer. Specifically, diaminobutane (DAB) dendrimer-based chelators were more rapidly excreted from the

body, illustrating that the development of clinically-acceptable dendrimer MR platforms is realistic [166].

### 1.6.5

#### Steps Towards the Clinical Realization of Dendrimer-based Cancer Therapies

##### 1.6.5.1 The Stage is now set for Dendrimer-based Cancer Therapy

The use of dendrimers for cancer treatment is still in its infancy with few, if any, applications successfully translated to the clinic. Consequently, their use as diagnostic agents constitutes both an important goal in and of itself, and also a valuable “baby step” towards the ultimate goal of curing cancer. As discussed, the process of actual killing cancer cells entails the complicated process of drug uptake followed by release of the drug into the cytoplasm or nucleus and is clearly a more demanding process than cell surface labeling, or even localization to the vicinity of the tumor, sufficient for diagnostic purposes. Nonetheless, in some cases, the transition from imaging to therapy will be closely linked, as evidenced by efforts now underway to combine antibody-targeted MR imaging nanoparticles with the delivery of antiangiogenic genes intended to inhibit the vascularization to the V2 carcinoma model in rabbits [167]. Another promising strategy – boron neutron capture therapy – has undergone impressive development over the past decade and is presented next as a successful demonstration of the promise of dendrimer-based cancer therapies.

##### 1.6.5.2 Boron Neutron Capture Therapy

Cisplatin-based therapies illustrate the need for multiple conjugations of small molecules – estimated at 50 for this platinum drug – to a targeting antibody (Section 1.6.3.3). While some efforts are underway to use dendrimeric strategies for platinum drug delivery [168], an even more demanding situation, where thousands of ligands are required per targeting antibody, is provided by boron neutron capture therapy (BNCT). Accordingly, BNCT will be discussed here as an illustrative example of how dendrimers can help overcome high hurdles in the development of innovative cancer therapies. As a brief background, BNCT is based on the nuclear reaction that occurs when boron-10, a stable isotope, is irradiated with low energy ( $\leq 0.025$  eV) or thermal neutrons to yield alpha particles and recoiling lithium-7 nuclei. A major requirement for the success of BNCT is the selective delivery of a sufficient number of boron atoms ( $\sim 10^9$ ) to individual cancer cells to sustain a lethal  $^{10}\text{B}(n, \alpha) \rightarrow ^7\text{Li}$  capture reaction [169, 170]. Considering that the maximal number of antigenic sites per tumor cell is in the range of 100 000, and more commonly only  $1/10^{\text{th}}$  that level, an a priori calculation suggests that each targeting antibody must be linked to at least 2000, but preferably closer to 5000, boron atoms [101]. Clearly, a single TAA-targeting antibody cannot be directly conjugated at this level and conventional polymers – e.g., polylysine conjugated with  $\sim 1700$  boron derivatives and linked to a targeting antibody – caused the antibody to lose *in vivo* tumor localizing properties [171]. By contrast, when a

PAMAM dendrimer was used for polyvalent boron conjugation, the linked antibody maintained immuno-recognition (although *in vivo* tumor targeting remained problematic because the conjugated dendrimer had a strong propensity to mis-localize in the spleen and liver) [101]. Over the decade since these pioneering efforts were first reported, continued progress has been made to solve problems such as off-target tissue localization, which was traced to the size of the dendrimer and presence of a large number of amine groups on the surface of PAMAM, by exploiting the versatility of dendrimer chemistry. In short, the re-design of boronated, anti-body-targeted dendrimers has culminated in the successful treatment of gliomas in the rat [158, 169, 172] and laid the foundation for translation of this technology into clinical tests in the foreseeable future.

#### 1.6.6

### Innovations Promise to Speed Progress

#### 1.6.6.1 “Mix-and-Match” Strategy of Bifunctional Dendritic Clusters

Two lessons are immediately apparent from the dedicated efforts to bring dendrimer-based BNCT to fruition. One is that dendritic technologies, while still at an early developmental stage, hold tremendous promise and merit continued investigation. The second is that the coupling of one treatment modality (BNCT) with one targeting strategy (antibodies to a specific type of glioma) required a staggering amount of effort. The growing realization that cancer is hundreds, if not thousands, of unique diseases at the cellular and molecular level, suggests that a commensurate number of therapeutic strategies are needed. The diversity of targeting strategies (which are not limited to folate and TAAs discussed here), coupled with the many “payload” possibilities (beside radioisotopes, boron, and cisplatin discussed here) used to diagnose and kill cancer cells, means that there are literally tens of thousands of individually customized therapies required to fully confront the myriad clinical manifestations of cancer. The sobering reality is that, if each of these customized treatments will require a decade long effort by a large team of researchers and clinicians, the large problem of cancer treatment will not be solved for a long time.

Choi and coworkers [134] have come up with an innovative mix-and-match scheme that promises to offset this gloomy prediction. These researchers have recently reported a cancer-targeting strategy that is reminiscent of the antibody-toxin/immunoconjugate strategy where distinct, but linked, entities are used to first recognize and bind and then subsequently modify a cancer cell. Their strategy, however, has great potential to improve on both the “targeting” and “payload” aspects of cancer therapy by, at first seemingly paradoxically, completely dividing these functions into separate dendritic clusters (Fig. 1.6). The key to this approach was to include a DNA “zipper” on each dendrimer that allows the targeting cluster, composed of folate-derivatized PAMAM in proof-of-concept experiments [173], to be readily combined with the imaging or drug-carrying dendrimer by way of the complementary DNA strand [134]. It can be envisioned that the production of libraries of dendrimers targeted to different cancer-specific biomarkers can be pro-



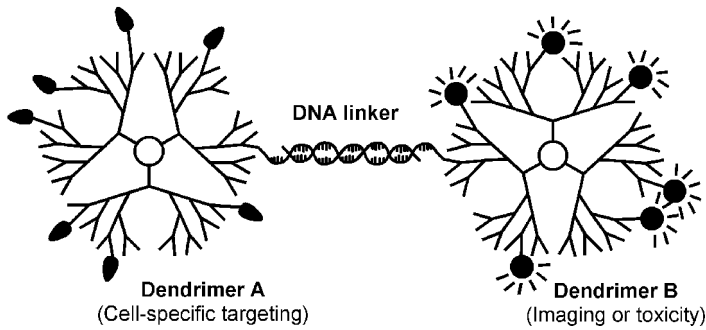


**Fig. 1.6.** DNA–dendrimer conjugates as potential cancer targeting imaging agents or therapeutics. (Adapted from Ref. [189].) Differentially functionalized dendrimers covalently conjugated to complementary deoxy-oligonucleotides can readily form duplex combinatorial nanoclusters that possess

cancer cell-specific ligands hybridized to an imaging agent or drug. Cell-specific targeting ligands (e.g., folic acid in one study) are appended to Dendrimer A, and Dendrimer B is conjugated with an imaging agent or drug [134].

duced by a “mix-and-matched” strategy by combining “off-the-shelf” targeting and drug clusters as needed [42]. Development of easily-customizable nanomedicine platforms that exploit the facile duplex DNA formation for the generation of hybrid nano-clusters, thus circumventing the tedious synthesis of multiply-functionalized dendrimers, offers hope that the next ten years will witness rapid expansion of dendrimer technologies that build on the painstaking advances of the past decade.

#### 1.6.6.2 Towards Therapeutic Exploitation of Glycosylation Abnormalities found in Cancer

Aberrant glycosylation, where the patterns of complex carbohydrate glycoforms found on the surfaces of cancer cells are dramatically different from those on healthy cells, is a hallmark of cancer [174–178]. Efforts to exploit these changes therapeutically, however, have long been stymied by the difficulty of controlling these complex and diverse molecules in an artificial synthetic setting. Today, with new technologies such as dendrimers that provide a platform for physiologically-relevant display of carbohydrates, new vistas are opening up for exploiting these molecules to intervene in malignant disease. Promising – but still early-stage – efforts in this direction include the presentation of oligosaccharides found only in cancer cells [53, 56, 58, 179–181] on a dendritic scaffold (Section 1.4.3.2) for vaccine development (Section 1.5.3.2).

#### 1.6.6.3 Towards Targeting Metabolically-engineered Carbohydrate Epitopes

As discussed above, one area of rapidly-expanding investigation is the abnormal glycosylation associated with the cancer cells; in particular dendrimeric scaffolds provide a unique platform to control the multimeric carbohydrate presentation needed to enact the “cluster glycoside effect” [45, 50, 51], which is crucial for tar-

getting diseased tissues found in malignant diseases [1, 24]. Another approach to exploiting glycosylation for the treatment of cancer is through “chemical biology” strategies, such as the ability to express non-natural sialic acids on the cell surface through the use of *N*-acetylmannosamine (ManNAc) analogs [49, 182, 183] (Fig. 1.7). By appropriate design of the ManNAc analog, sialic acids, which are interesting nine-carbon sugars often overexpressed on cancer cells [175], can be provided with a “chemical handle” – such as a ketone, azide, or thiol [184–186] – for tar-

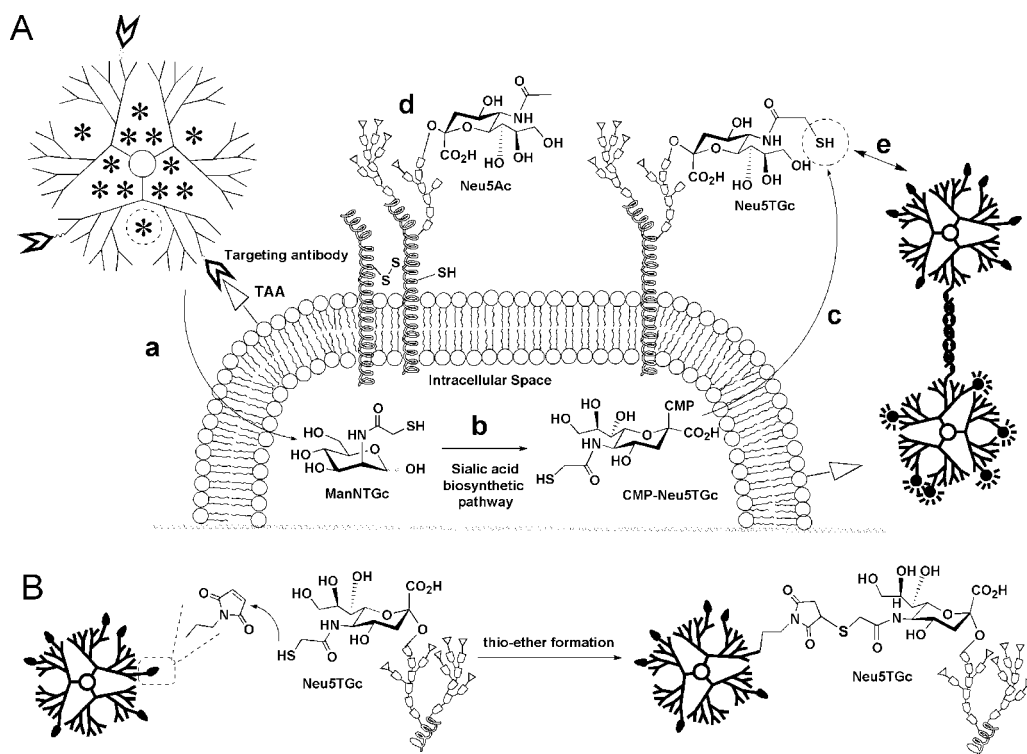


Fig. 1.7. Chemoselective targeting of drug-loaded dendrimers to the cell surface. (A) Overview of sialic acid engineering. (a) A dendrimer can encapsulate and assist the delivery of *N*-acetylmannosamine (ManNAc) analogs, such as the thiol-containing sugar “ManNTGc” (shown as “\*”) into a cell (Section 1.5.2). (b) Once inside the cell, ManNTGc can be metabolically converted into CMP-Neu5TGc, a compound that serves as a sugar-nucleotide needed for the glycosylation process (c) where “Neu5TGc” a non-natural form of sialic acid, is installed into cell surface glycoconjugates. Overall, this process replaces

natural sialic acids, such as “Neu5Ac”, with their thiol-containing counterparts (d), which can then be targeted by dendritic assemblies such as the bifunctional “targeting” and “payload” clusters shown in Fig. 1.6. (B) Details of the “chemoselective ligation reaction” required for targeting the appropriately derivatized dendrimeric assembly to the cell. In this case, a maleimide-conjugated targeting capsule will selectively interact with the sialic acid-display thiols to covalently bind the dendrimer to the cell surface via thio-ether bond formation.

geted delivery of a second agent such as the ricin A-chain used in immunotoxins [187] or small molecule anticancer drugs [188]. Dendrimers offer assistance at several steps in this process of translating early-stage anticancer strategies like “sialic acid engineering” from the laboratory to clinical relevance. An enticing proposition is that the starting material – ManNAc, which like all sugars has notoriously poor pharmacological properties – can be made “drug-like” by encapsulation (or covalent ligation). Subsequently, after display of the target epitope on the cell surface, which is a modified thiol-bearing sialic acid in the case shown in Fig. 1.7, this can benefit from the high local density of dendritic display of maleimide to increase the rate of drug binding to the cell surface, which occurs over an unacceptably long period of several hours for current covalent coupling schemes [188]. This strategy, under evaluation in our laboratory, coupled with a high drug payload on the DNA-hybridized cluster (Fig. 1.6), provides renewed impetus for the already promising application of sugar-based therapeutic approaches to cancer. A particularly attractive aspect of this approach is that  $\sim 10^8$  sialic acids exist on cancer cells, greatly improving prospects to deliver adequate levels of drug to achieve therapeutic efficacy compared with TAA-targeting schemes (Section 1.6.3).

## 1.7

### Concluding Remarks

Dendrimers, chemically-defined entities with tunable biological properties, have advanced over the past two decades to the point where they stand on the cusp of major contributions to the treatment of cancer in a meaningful way. Although, as has been apparent by the many instances cited throughout this chapter where gaps in knowledge still remain and that must be plugged before dendrimers are ready for wide clinical use, their extreme versatility combined with the extensive research efforts now underway are sure to add sophistication to drugs already in use as well as spur the development of entirely new classes of anticancer therapy.

### Acknowledgments

Funding was provided by the Whitaker Biomedical Engineering Institute and Department of Biomedical Engineering at The Johns Hopkins University, the Arnold and Mabel Beckman Foundation, and The National Institutes of Health.

### References

- 1 U. BOAS, P. M. H. HEEGAARD, Dendrimers in drug research. *Chem. Soc. Rev.* **2004**, 33, 43–63.
- 2 G. M. DYKES, Dendrimers: A review of their appeal and applications. *J. Chem. Technol. Biotechnol.* **2001**, 76, 903–918.
- 3 A. SUNDER, J. HEINEMANN, H. FREY, Controlling the growth of polymer trees: Concepts and perspectives for

- hyperbranched polymers. *Chem. Eur. J.* **2000.** 6, 2499–2506.
- 4 “Starburst®” is an official trademark owned by Dow Chemical that covers PAMAM based dendrimers but the term “starburst” is often also used generically to describe the properties of certain dendritic macromolecules.
  - 5 P. K. MAITI, T. ÇAGIN, G. WANG, W. A. GODDARD III, Structure of PAMAM dendrimers: Generations 1 through 11. *Macromolecules* **2004.** 37, 6236–6254.
  - 6 A. D. SCHLÜTER, J. P. RABE, Dendronized polymers: Synthesis, characterization, assembly at interfaces, and manipulation. *Angew. Chem. Int. Ed.* **2000.** 39, 864–883.
  - 7 P. G. DE GENNES, H. HERVET, Statistics of “starburst” polymers. *J. Phys. Lett.* **1983.** 44, L351–L360.
  - 8 B. KLAJNERT, M. BRYZIEWSKA, Dendrimers: Properties and applications. *Acta Biochim. Pol.* **2001.** 48, 199–208.
  - 9 J. M. J. FRÉCHET, Functional polymers and dendrimers: Reactivity, molecular architecture, and interfacial energy. *Science* **1994.** 263, 1710–1715.
  - 10 C. L. JACKSON, H. D. CHANZY, F. P. BOOY, B. J. DRAKE, D. A. TOMALIA, B. J. BAUER, E. J. AMIS, Visualization of dendrimer molecules by transmission electron microscopy (TEM): Staining methods and Cryo-TEM of vitrified solutions. *Macromolecules* **1998.** 31, 6259–6265.
  - 11 D. K. SMITH, F. DIEDERICH, Functional dendrimers: Unique biological mimics. *Chem. Eur. J.* **1998.** 4, 1353–1361.
  - 12 S. HECHT, J. M. J. FRÉCHET, Dendritic encapsulation of function: Applying Nature’s site isolation principle from biomimetics to materials science. *Angew. Chem. Int. Ed.* **2001.** 40, 74–91.
  - 13 A. ESPOSITO, E. DELORT, D. LAGNOUX, F. DJOJO, J.-L. REYMOND, Catalytic peptide dendrimers. *Angew. Chem. Int. Ed.* **2003.** 42, 1381–1383.
  - 14 A. CLOUET, T. DARBRE, J.-L. REYMOND, A combinatorial approach to catalytic peptide dendrimers. *Angew. Chem. Int. Ed.* **2004.** 43, 4612–4615.
  - 15 B. CHEN, S. PILETSKY, A. P. TURNER, High molecular recognition: Design of “Keys”. *Comb. Chem. High Throughput Screen.* **2002.** 5, 409–427.
  - 16 C. S. GOH, D. MILBURN, M. GERSTEIN, Conformational changes associated with protein-protein interactions. *Curr. Opin. Struct. Biol.* **2004.** 14, 104–109.
  - 17 P. O. GLANTZ, T. ARNEBRANT, T. NYLANDER, R. E. BAIER, Bioadhesion – A phenomenon with multiple dimensions. *Acta Odontol. Scand.* **1999.** 57(5), 238–241.
  - 18 A. MECKE, I. LEE, J. R. BAKER JR, M. M. HOLL, B. G. ORR, Deformability of poly(amidoamine) dendrimers. *Eur. Phys. J. E Soft Matter* **2004.** 14, 7–16.
  - 19 D. FARIN, D. AVNIR, Surface fractality of dendrimers. *Angew. Chem. Int. Ed. Engl.* **1991.** 30, 1377–1379.
  - 20 S. L. GILAT, A. ADRONOV, J. M. J. FRÉCHET, Light harvesting and energy transfer in novel convergently constructed dendrimers. *Angew. Chem. Int. Ed.* **1999.** 38, 1422–1427.
  - 21 K. AUTUMN, Y. A. LIANG, S. T. HSIEH, W. ZESCH, W. P. CHAN, T. W. KENNY, R. FEARING, R. J. FULL, Adhesive force of a single gecko foot-hair. *Nature* **2000.** 405, 681–185.
  - 22 G. M. DYKES, L. J. BRIERLEY, D. K. SMITH, T. MCGRAIL, G. J. SEELEY, Supramolecular solubilisation of hydrophilic dyes by using individual dendritic branches. *Chem. Eur. J.* **2001.** 7, 4730–4739.
  - 23 R. ESFAND, D. A. TOMALIA, Poly(amidoamine) (PAMAM) dendrimers: from biomimicry to drug delivery and biomedical applications. *Drug Discovery Today* **2001.** 6, 427–436.
  - 24 M. OZKAN, Quantum dots and other nanoparticles: What can they offer to drug discovery? *Drug Discovery Today* **2004.** 9, 1065–1071.
  - 25 D. A. TOMALIA, A. M. NAYLOR, W. A. GODDARD III, Starburst dendrimers: Molecular-level control of size, shape, surface chemistry, topology, and flexibility from atoms to macroscopic matter. *Angew. Chem. Int. Ed. Engl.* **1990.** 29, 138–175.

- 26 H.-B. MEKELBURGER, W. JAWAREK, F. VÖGTLE, Dendrimers, arborols, and cascade molecules: Breakthrough into generations of new materials. *Angew. Chem. Int. Ed. Engl.* **1992**, *31*, 1571–1576.
- 27 J. ISSBERNER, R. MOORS, F. VÖGTLE, Dendrimers: From generations and functional groups to functions. *Angew. Chem. Int. Ed. Engl.* **1994**, *33*, 2413–2420.
- 28 D. GUDAT, Inorganic cauliflower: Functional main group element dendrimers constructed from phosphorus- and silicon-based building blocks. *Angew. Chem. Int. Ed. Engl.* **1997**, *36*, 1951–1955.
- 29 M. FISCHER, F. VÖGTLE, Dendrimers: From design to application – A progress report. *Angew. Chem. Int. Ed.* **1999**, *38*, 884–905.
- 30 G. R. NEWKOME, C. N. MOOREFIELD, F. VÖGTLE, *Dendrimers and Dendrons: Concepts, Syntheses, Applications*. **2001**, Weinheim, Wiley-VCH.
- 31 S. M. GRAYSON, J. M. J. FRÉCHET, Convergent dendrons and dendrimers: From synthesis to applications. *Chem. Rev.* **2001**, *101*, 3819–3868.
- 32 I. GITSOV, C. LIN, Dendrimers – Nanoparticles with precisely engineered surfaces. *Curr. Org. Chem.* **2005**, *9*, 1025–1051.
- 33 N. FEUERBACHER, F. VÖGTLE, Iterative synthesis in organic chemistry. *Top. Curr. Chem.* **1998**, *197*, 1–18.
- 34 E. BUHLEIER, W. WEHNER, F. VÖGTLE, “Cascade”- and “nonskid-chain-like” synthesis of molecular cavity topologies. *Synthesis* **1978**, 155–158.
- 35 G. R. NEWKOME, Z. YAO, G. R. BAKER, V. K. GUPTA, Micelles. Part 1. Cascade molecules: A new approach to micelles. A [27]-arborol. *J. Org. Chem.* **1985**, *50*, 2003–2004.
- 36 D. A. TOMALIA, H. BAKER, J. DEWALD, M. HALL, G. KALLOS, S. MARTIN, J. ROECK, J. RYDER, P. SMITH, Dendritic macromolecules: Synthesis of starburst dendrimers. *Macromolecules* **1986**, *19*, 2466–2468.
- 37 D. A. TOMALIA, H. D. DURST, Genealogically directed synthesis – Starburst cascade dendrimers and hyperbranched structures. *Top. Curr. Chem.* **1993**, *165*, 193–313.
- 38 T. M. MILLER, T. X. NEENAN, Convergent synthesis of monodisperse dendrimers based upon 1,3,5-trisubstituted benzenes. *Chem. Mater.* **1990**, *2*, 346–349.
- 39 R. HAAG, J.-F. STUMBÉ, A. SUNDER, H. FREY, A. HEBEL, An approach to core-shell-type architectures in hyperbranched polyglycerols by selective chemical differentiation. *Macromolecules* **2000**, *33*, 8158–8166.
- 40 C. J. HAWKER, J. M. J. FRÉCHET, Preparation of polymers with controlled molecular architecture. A new convergent approach to dendritic macromolecules. *J. Am. Chem. Soc.* **1990**, *112*, 7638–7647.
- 41 J. R. MORGAN, M. J. CLONINGER, Heterogeneously functionalized dendrimers. *Curr. Opin. Drug Discov. Devel.* **2002**, *5*, 966–973.
- 42 Y. CHOI, J. R. BAKER JR, Targeting cancer cells with DNA-assembled dendrimers: A mix-and-match strategy for cancer. *Cell Cycle* **2005**, *4*, 669–671.
- 43 M. MELDAL, P. M. ST HILAIRE, Synthetic methods of glycopeptide assembly, and biological analysis of glycopeptide products. *Curr. Opin. Chem. Biol.* **1997**, *1*, 552–563.
- 44 D. ZANINI, R. ROY, Synthesis of new a-thiosialodendrimers and their binding properties to the sialic acid specific lectin from *Limax flavus*. *J. Am. Chem. Soc.* **1997**, *119*, 2088–2095.
- 45 K. J. YAREMA, C. R. BERTOZZI, Chemical approaches to glycobiology and emerging carbohydrate-based therapeutic agents. *Curr. Opin. Chem. Biol.* **1998**, *2*, 49–61.
- 46 J. J. LANDERS, Z. CAO, I. LEE, L. T. PIEHLER, P. P. MYC, A. MYC, T. HAMOUDA, A. T. GALECKI, J. R. J. BAKER JR, Prevention of influenza pneumonitis by sialic acid-conjugated dendritic polymers. *J. Infect. Dis.* **2002**, *186*, 1222–1230.
- 47 J. D. REUTER, A. MYC, M. M. HAYES, Z. GAN, R. ROY, D. QIN, R. YIN, L. T. PIEHLER, R. ESFAND, D. A. TOMALIA, J. R. BAKER JR, Inhibition of viral

- adhesion and infection by sialic-acid-conjugated dendritic polymers. *Bioconjugate Chem.* **1999.** 10, 271–278.
- 48 D. H. CHARYCH, J. O. NAGY, W. SPEVAK, M. D. BEDNARSKI, Direct colorimetric detection of a receptor-ligand interaction by a polymerized bilayer assembly. *Science* **1993.** 261, 585–588.
- 49 O. T. KEPPLER, R. HORSTKORTE, M. PAWLITA, C. SCHMIDT, W. REUTTER, Biochemical engineering of the *N*-acyl side chain of sialic acid: Biological implications. *Glycobiology* **2001.** 11, 11R–18R.
- 50 J. J. LUNDQUIST, E. J. TOONE, The cluster glycoside effect. *Chem. Rev.* **2002.** 102, 555–578.
- 51 L. L. KIESSLING, S. POHL, Strength in numbers: Non-natural polyvalent carbohydrate derivatives. *Chem. Biol.* **1996.** 3, 71–77.
- 52 W. B. TURNBULL, J. F. STODDART, Design and synthesis of glycodendrimers. *J. Biotechnol.* **2002.** 90, 231–255.
- 53 R. ROY, M. G. BAEK, Glycodendrimers: Novel glycotope isosteres unmasking sugar coding. Case study with T-antigen markers from breast cancer MUC1 glycoprotein. *J. Biotechnol.* **2002.** 90, 291–309.
- 54 R. ROY, Synthesis and some applications of chemically defined multivalent glycoconjugates. *Curr. Opin. Struct. Biol.* **1996.** 6, 692–702.
- 55 P. R. ASHTON, S. E. BOYD, C. L. BROWN, N. JAYARAMAN, J. F. STODDART, A convergent synthesis of a carbohydrate-containing dendrimer. *Angew. Chem. Int. Ed. Engl.* **1997.** 36, 732–735.
- 56 T. TOYOKUNI, S.-i. HAKOMORI, A. K. SINGHAL, Synthetic carbohydrate vaccines: Synthesis and immunogenicity of Tn antigen conjugates. *Bioorg. Med. Chem.* **1994.** 2, 1119–1132.
- 57 S. ANDRÉ, P. J. ORTEGA, M. A. PEREZ, R. ROY, H.-J. GABIUS, Lactose-containing starburst dendrimers: Influence of dendrimer generation and binding-site orientation of receptors (plant/animal lectins and immunoglobulins) on binding properties. *Glycobiology* **1999.** 9, 1253–1261.
- 58 R. ROY, M.-G. BAEK, K. RITTENHOUSE-OLSON, Synthesis of *N,N'*-bis(acrylamido)acetic acid-based T-antigen glycodendrimers and their mouse monoclonal IgG antibody binding properties. *J. Am. Chem. Soc.* **2001.** 123, 1809–1816.
- 59 M. M. PALCIC, H. LI, D. ZANINI, R. S. BHELLA, R. ROY, Chemoenzymatic synthesis of dendritic sialyl Lewis(x). *Carbohydr. Res.* **1997.** 305, 433–442.
- 60 M. S. LAJINESS, M. VIETH, J. ERICKSON, Molecular properties that influence oral drug-like behavior. *Curr. Opin. Drug Discov. Devel.* **2004.** 7, 470–474.
- 61 N. R. GONZALES, R. DE PASCALIS, J. SCHLOM, S. V. S. KASHMIRI, Minimizing the immunogenicity of antibodies for clinical application. *Tumour Biol.* **2005.** 26, 31–43.
- 62 B. MATTHEY, A. ENGERT, S. BARTH, Recombinant immunotoxins for the treatment of Hodgkin's disease (Review). *Int. J. Mol. Med.* **2000.** 6, 509–514.
- 63 K. VISWANATHAN, S. LAWRENCE, S. HINDERLICH, K. J. YAREMA, Y. C. LEE, M. BETENBAUGH, Engineering sialic acid synthetic ability into insect cells: Identifying metabolic bottlenecks and devising strategies to overcome them. *Biochemistry* **2003.** 42, 15 215–15 225.
- 64 M. J. BETENBAUGH, N. TOMIYA, S. NARANG, J. T. A. HSU, Y. C. LEE, Biosynthesis of human-type *N*-glycans in heterologous systems. *Curr. Opin. Struct. Biol.* **2004.** 14, 601–606.
- 65 H. NAMAZI, M. ADELI, Dendrimers of citric acid and poly (ethylene glycol) as the new drug-delivery agents. *Biomaterials* **2005.** 26, 1175–1183.
- 66 J. F. G. A. JANSEN, E. M. M. DE BRABANDER-VAN DEN BERG, E. W. MEIJER, Encapsulation of guest molecules into a dendritic box. *Science* **1994.** 266, 1226–1229.
- 67 U. BOAS, S. H. M. SÖNTJENS, K. J. JENSEN, J. B. CHRISTENSEN, E. W. MEIJER, New dendrimer-peptide host-guest complexes: Towards dendrimers

- as peptide carriers. *ChemBioChem* **2002**. 3, 433–439.
- 68 A. CORDOVA, K. D. JANDA, Synthesis and catalytic antibody functionalization of dendrimers. *J. Am. Chem. Soc.* **2001**. 123, 8248–8259.
- 69 M. T. MORGAN, M. A. CARNAHAN, C. E. IMMOOS, A. A. RIBEIRO, S. FINKELSTEIN, S. J. LEE, M. W. GRINSTAFF, Dendritic molecular capsules for hydrophobic compounds. *J. Am. Chem. Soc.* **2003**. 125, 15 485–15 489.
- 70 P. K. TRIPATHI, A. J. KHOPADE, S. NAGAICH, S. SHRIVASTAVA, S. JAIN, N. K. JAIN, Dendrimer grafts for delivery of 5-fluorouracil. *Pharmazie* **2002**. 57, 261–264.
- 71 T. OOYA, J. LEE, K. PARK, Effects of ethylene glycol-based graft, star-shaped, and dendritic polymers on solubilization and controlled release of paclitaxel. *J. Controlled Release* **2003**. 93, 121–127.
- 72 T. OOYA, J. LEE, K. PARK, Hydrotropic dendrimers of generations 4 and 5: Synthesis, characterization, and hydrotropic solubilization of paclitaxel. *Bioconjugate Chem.* **2004**. 15, 1221–1229.
- 73 J. M. BENITO, M. GOMEZ-GARCIA, C. ORTIZ MELLET, I. BAUSSANNE, J. DEFAYE, J. M. GARCIA FERNANDEZ, Optimizing saccharide-directed molecular delivery to biological receptors: Design, synthesis, and biological evaluation of glycodendrimer-cyclodextrin conjugates. *J. Am. Chem. Soc.* **2004**. 126, 10 355–10 363.
- 74 T. HUDDE, S. A. RAYNER, R. M. COMER, M. WEBER, J. D. ISAACS, H. WALDMANN, D. F. LARKIN, A. J. GEORGE, Activated polyamidoamine dendrimers, a non-viral vector for gene transfer to the corneal endothelium. *Gene Ther.* **1999**. 6, 939–943.
- 75 J. HAENSLER, F. C. SZOKA JR, Polyamidoamine cascade polymers mediate efficient transfection of cells in culture. *Bioconjugate Chem.* **1993**. 4, 372–379.
- 76 T.-i. KIM, H. J. SEO, J. S. CHOI, H.-S. JANG, J.-u. BAEK, K. KIM, J.-S. PARK, PAMAM-PEG-PAMAM: Novel triblock copolymer as a biocompatible and efficient gene delivery carrier. *Biomacromolecules* **2004**. 5, 2487–2492.
- 77 J. S. CHOI, K. NAM, J.-y. PARK, J.-B. KIM, J.-K. LEE, J.-s. PARK, Enhanced transfection efficiency of PAMAM dendrimer by surface modification with L-arginine. *J. Controlled Release* **2004**. 99, 445–456.
- 78 J. H. LEE, Y.-b. LIM, J. S. CHOI, Y. LEE, T.-i. KIM, H. J. KIM, J. K. YOON, K. KIM, J.-s. PARK, Polyplexes assembled with internally quaternized PAMAM-OH dendrimer and plasmid DNA have a neutral surface and gene delivery potency. *Bioconjugate Chem.* **2003**. 14, 1214–1221.
- 79 M. HUSSAIN, M. SHCHEPINOV, M. SOHAIL, I. F. BENTER, A. J. HOLLINS, E. M. SOUTHERN, S. AKHTAR, A novel anionic dendrimer for improved cellular delivery of antisense oligonucleotides. *J. Controlled Release* **2004**. 99, 139–155.
- 80 J. F. G. A. JANSEN, E. W. MEIJER, E. M. M. DE BRABANDER-VAN DEN BERG, The dendritic box: Shape-selective liberation of encapsulated guests. *J. Am. Chem. Soc.* **1995**. 117, 4417–4418.
- 81 H. RINGSDORF, Structure and properties of pharmacologically active polymers. *J. Polym. Sci. Polym. Symp.* **1975**. 51, 135–153.
- 82 H. BADER, H. RINGSDORF, B. SCHMIDT, Water-soluble polymers in medicine. *Angew. Makromol. Chem.* **1984**. 123/124, 457–485.
- 83 J. KOPACEK, Soluble biomedical polymers. *Polym. Med.* **1977**. 7, 191–221.
- 84 E. R. GILLIES, E. DY, J. M. J. FRÉCHET, F. C. SZOKA, Biological evaluation of polyester dendrimer: Poly(ethylene oxide) “bow-tie” hybrids with tunable molecular weight and architecture. *Mol. Pharm.* **2005**. 2, 129–138.
- 85 P. KOLHE, J. KHANDARE, O. PILLAI, S. KANNAN, M. LIEH-LAI, R. M. KANNAN, Preparation, cellular transport, and activity of polyamidoamine-based dendritic nanodevices with a high drug payload. *Biomaterials* **2006**. 27, 660–669.

- 86 S. C. LEE, R. PARTHASARATHY, K. BOTWIN, D. KUNNEMAN, E. ROWOLD, G. LANGE, J. KLOVER, A. ABEGG, J. ZOBEL, T. BECK, T. MILLER, W. HOOD, J. MONAHAN, J. P. MCKEARN, R. JANSSON, C. F. VOLIVA, Biochemical and immunological properties of cytokines conjugated to dendritic polymers. *Biomed. Microdevices* **2004**, 6, 191–202.
- 87 F. CHAVES, J. C. CALVO, C. CARVAJAL, Z. RIVERA, L. RAMIREZ, M. PINTO, M. TRUJILLO, F. GUZMAN, M. E. PATARROYO, Synthesis, isolation and characterization of Plasmodium falciparum antigenic tetrabranched peptide dendrimers obtained by thiazolidine linkages. *J. Pept. Res.* **2001**, 58, 307–316.
- 88 L. J. CRUZ, E. IGLESIAS, J. C. AGUILAR, L. J. GONZÁLEZ, O. REYES, F. ALBERICIO, D. ANDREU, A comparative study of different presentation strategies for an HIV peptide immunogen. *Bioconjugate Chem.* **2004**, 15, 112–120.
- 89 F. SÁNCHEZ-SANCHO, E. PÉREZ-INESTROSA, R. SUAÚ, C. MAYORGA, M. J. TORRES, M. BLANCA, Dendrimers as carrier protein mimetics for IgE antibody recognition. Synthesis and characterization of densely penicilloylated dendrimers. *Bioconjugate Chem.* **2002**, 13, 647–653.
- 90 S. JARACZ, J. CHEN, L. V. KUZNETSOVA, I. OJIMA, Recent advances in tumor-targeting anticancer drug conjugates. *Bioorg. Med. Chem.* **2005**, 13, 5043–5054.
- 91 Q. CAI, Y. ZHAO, J. BEI, F. XI, S. WANG, Synthesis and properties of star-shaped polylactide attached to poly(amidoamine) dendrimer. *Biomacromolecules* **2003**, 4, 828–834.
- 92 N. MALIK, E. G. EVAGOROU, R. DUNCAN, Dendrimer-platinate: A novel approach to cancer chemotherapy. *Anticancer Drugs* **1999**, 10, 767–776.
- 93 D. SHABAT, R. J. AMIR, A. GOPIN, N. PESSAH, M. SHAMIS, Chemical adaptor systems. *Chem. Eur. J.* **2004**, 10, 2626–2634.
- 94 M. SHAMIS, H. N. LODE, D. SHABAT, Bioactivation of self-immolative dendritic prodrugs by catalytic antibody 38C2. *J. Am. Chem. Soc.* **2004**, 126, 1726–1731.
- 95 R. J. AMIR, N. PESSAH, M. SHAMIS, D. SHABAT, Self-immolative dendrimers. *Angew. Chem. Int. Ed.* **2003**, 42, 4494–4499.
- 96 F. M. H. DE GROOT, C. ALBRECHT, R. KOEKKOEK, P. H. BEUSKER, H. W. SCHEEREN, “Cascade-release dendrimers” liberate all end groups upon a single triggering event in the dendritic core. *Angew. Chem. Int. Ed.* **2003**, 42, 4940–4944.
- 97 A. T. FLORENCE, T. SAKTHIVEL, I. TOH, Oral uptake and translocation of a polylysine dendrimer with a lipid surface. *J. Controlled Release* **2000**, 65, 253–259.
- 98 R. WIWATTANAPATAPEE, B. CARREÑO-GÓMEZ, N. MALIK, R. DUNCAN, Anionic PAMAM dendrimers rapidly cross adult rat intestine in vitro: A potential oral delivery system? *Pharm. Res.* **2000**, 17, 991–998.
- 99 A. T. FLORENCE, N. HUSSAIN, Transcytosis of nanoparticle and dendrimer delivery systems: Evolving vistas. *Adv. Drug Delivery Rev.* **2001**, 50, S69–S89.
- 100 M. RUPONEN, P. HONKAKOSKI, S. RÖNKKÖ, J. PELKONEN, M. TAMMI, A. URTTI, Extracellular and intracellular barriers in non-viral gene delivery. *J. Controlled Release* **2003**, 93, 213–217.
- 101 R. F. BARTH, D. M. ADAMS, A. H. SOLOWAY, F. ALAM, M. V. DARBY, Boronated starburst dendrimer-mono-clonal antibody immun-conjugates: Evaluation as a potential delivery system for neutron capture therapy. *Bioconjugate Chem.* **1994**, 5, 58–66.
- 102 S. HONG, A. U. BIELINSKA, A. MECKE, B. KEZSLER, J. L. BEALS, X. SHI, L. BALOGH, B. ORR, J. R. BAKER JR, M. M. BANASZAK HOLL, Interaction of poly(amidoamine) dendrimers with supported lipid bilayers and cells: Hole formation and the relation to transport. *Bioconjugate Chem.* **2004**, 15, 774–782.
- 103 A. MECKE, S. UPPULURI, T. M. SASSANELLA, D.-K. LEE, A.



- RAMAMOORTHY, J. R. BAKER JR, B. G. ORR, M. M. BANASZAK HOLL, Direct observation of lipid bilayer disruption by poly(amidoamine) dendrimers. *Chem. Phys. Lipids* **2004**. 132, 3–14.
- 104 G.-D. ZHANG, A. HARADA, N. NISHIYAMA, D.-L. JIANG, H. KOYAM, T. AIDA, K. KATAOK, Polyion complex micelles entrapping cationic dendrimer porphyrin: Effective photosensitizer for photodynamic therapy of cancer. *J. Controlled Release* **2003**. 93, 141–150.
- 105 J. C. ROBERTS, M. K. BHARGAT, R. T. ZERA, Preliminary biological evaluation of polyamidoamine (PAMAM) Starburst™ dendrimers. *J. Biomed. Mater. Res.* **1996**. 30, 53–65.
- 106 H. KOBAYASHI, S. KAWAMOTO, T. SAGA, N. SATO, A. HIRAGA, T. ISHIMORI, J. KONISHI, K. TOGASHI, M. W. BRECHBIEL, Positive effects of polyethylene glycol conjugation to generation-4 polyamidoamine dendrimers as macromolecular MR contrast agents. *Magn. Reson. Med.* **2001**. 46, 781–788.
- 107 N. RÖCKENDORF, T. K. LINDHORST, Glycodendrimers. *Top. Curr. Chem.* **2001**. 217, 201–238.
- 108 L. CRESPO, G. SANCLIMENS, M. PONS, E. GIRALT, M. ROHO, F. ALBERICIO, Peptide and amide bond-containing dendrimers. *Chem. Rev.* **2005**. 105, 1663–1681.
- 109 M. S. SHCHEPINOV, I. A. UDALOVA, A. J. BRIGMAN, E. M. SOUTHERN, Oligonucleotide dendrimers: Synthesis and use as polylabelled DNA probes. *Nucleic Acids Res.* **1997**. 25, 4447–4454.
- 110 T. W. NILSEN, J. GRAYZEL, W. PRENSKY, Dendritic nucleic acid structures. *J. Theoret. Biol.* **1997**. 187, 273–284.
- 111 R. H. E. HUDSON, M. J. DAMHA, Nucleic acid dendrimers: Novel biopolymer structures. *J. Am. Chem. Soc.* **1998**. 115, 2119–2124.
- 112 Y. SUZUKI, T. OTOMO, H. OKAZI, H. SAWAI, Synthesis and properties of a new type DNA dendrimer. *Nucleic Acids Symp. Ser.* **2000**. 44, 125–126.
- 113 Y. LI, Y. D. TSENG, S. Y. KWON, L. D'ESPAUX, J. S. BUNCH, P. L. MCEUEN, D. LUO, Controlled assembly of dendrimer-like DNA. *Nat. Mater.* **2004**. 3, 38–42.
- 114 K. T. AL-JAMAL, T. SAKTHIVEL, A. T. FLORENCE, Dendrisomes: Vesicular structures derived from a cationic lipidic dendron. *J. Pharm. Sci.* **2005**. 94, 102–113.
- 115 S. TAKEOKA, K. MORI, H. OHKAWA, K. SOU, E. TSUCHIDA, Synthesis and assembly of poly(ethylene glycol)-lipids with mono-, di-, and tetraacyl chains and a poly(ethylene glycol) chain of various molecular weights. *J. Am. Chem. Soc.* **2000**. 122, 7927–7935.
- 116 H. FREY, R. HAAG, Dendritic polyglycerol: A new versatile biocompatible-material. *J. Biotechnol.* **2002**. 90, 257–267.
- 117 M. F. NEERMAN, W. ZHANG, A. R. PARRISH, E. E. SIMANEK, In vitro and in vivo evaluation of a melamine dendrimer as a vehicle for drug delivery. *Int. J. Pharm.* **2004**. 281, 129–132.
- 118 A.-M. CAMINADE, J.-P. MAJORAL, Nanomaterials based on phosphorus dendrimers. *Acc. Chem. Res.* **2004**. 37, 341–348.
- 119 X.-Y. WU, S.-W. HUANG, J.-T. ZHANG, R.-X. ZHUO, Preparation and characterization of novel physically cross-linked hydrogels composed of poly(vinyl alcohol) and amine-terminated polyamidoamine dendrimer. *Macromol. Biosci.* **2004**. 4, 71–75.
- 120 H. R. IHRE, O. L. PADILLA DE JESÚS, F. C. SZOKA JR, J. M. J. FRÉCHET, Polyester dendritic systems for drug delivery applications: Design, synthesis, and characterization. *Bioconjugate Chem.* **2002**. 13, 443–452.
- 121 M. J. CLONINGER, Biological applications of dendrimers. *Curr. Opin. Chem. Biol.* **2002**. 6, 742–748.
- 122 L. S. HEUSER, F. N. MILLER, Differential macromolecular leakage from the vasculature of tumors. *Cancer* **1986**. 57, 461–464.
- 123 H. MAEDA, J. WU, T. SAWA, Y. MATSUMURA, K. HORI, Tumor vascular permeability and the EPR effect in

- macromolecular therapeutics: A review. *J. Controlled Release* **2000**. 65, 271–284.
- 124 Y. MATSUMURA, H. MAEDA, A new concept for macromolecular therapeutics in cancer chemotherapy: Mechanism of tumorotropic accumulation of proteins and the antitumor agent smancs. *Cancer Res.* **1986**. 46, 6387–6392.
- 125 L. W. SEYMOUR, Passive tumor targeting of soluble macromolecules and drug conjugates. *Crit. Rev. Ther. Drug Carrier Syst.* **1992**. 9, 135–187.
- 126 D. LIU, A. MORI, L. HUANG, Role of liposome size and RES blockade in controlling biodistribution and tumor uptake of GM1-containing liposomes. *Biochim. Biophys. Acta* **1992**. 1104, 95–101.
- 127 A. NAGAYASU, T. SHIMOOKA, Y. KINOCHI, K. UCHIYAMA, Y. TAKEICHI, H. KIWADA, Effects of fluidity and vesicle size on antitumor activity and myelosuppressive activity of liposomes loaded with daunorubicin. *Biol. Pharm. Bull.* **1994**. 17, 935–939.
- 128 R. K. JAIN, Barriers to drug-delivery in solid tumors. *Sci. Am.* **1994**. 271, 58–65.
- 129 Y. TABATA, Y. MURAKAMI, Y. IKADA, Tumor accumulation of poly(vinyl alcohol) of different sizes after intravenous injection. *J. Controlled Release* **1998**. 50, 123–133.
- 130 S. ZALIPSKY, N. MULLAH, J. A. HARDING, J. GITTELMAN, L. GUO, S. A. DEFREES, Poly(ethylene glycol)-grafted liposomes with oligopeptide or oligosaccharide ligands appended to the termini of the polymer chains. *Bioconjugate Chem.* **1997**. 8, 111–118.
- 131 J. A. REDDY, V. M. ALLAGADDA, C. P. LEAMON, Targeting therapeutic and imaging agents to folate receptor positive tumors. *Curr. Pharm. Biotechnol.* **2005**. 6, 131–150.
- 132 C. P. LEAMON, J. A. REDDY, Folate-targeted chemotherapy. *Adv. Drug Delivery Rev.* **2004**. 56, 1127–1141.
- 133 E. J. ROY, U. GAWLICK, B. A. ORR, D. M. KRANZ, Folate-mediated targeting of T cells to tumors. *Adv. Drug Delivery Rev.* **2004**. 56, 1219–1231.
- 134 Y. CHOI, T. THOMAS, A. KOTLYAR, M. T. ISLAM, J. R. BAKER, Synthesis and functional evaluation of DNA-assembled polyamidoamine (PAMAM) dendrimer clusters with cancer cell-specific targeting. *Chem. Biol.* **2005**. 12, 35–43.
- 135 D. LAHERU, E. M. JAFFEE, Immunotherapy for pancreatic cancer – science driving clinical progress. *Nat. Rev. Cancer* **2005**. 5, 549–467.
- 136 M. HARRIS, Monoclonal antibodies as therapeutic agents for cancer. *Lancet Oncol.* **2004**. 5, 292–302.
- 137 M. Z. LIN, M. A. TEITELL, G. J. SCHILLER, The evolution of antibodies into versatile tumor-targeting agents. *Clin. Cancer Res.* **2005**. 11, 129–138.
- 138 J.-Y. ZHANG, Tumor-associated antigen arrays to enhance antibody detection for cancer diagnosis. *Cancer Detect. Prev.* **2004**. 28, 114–118.
- 139 R. E. KONTERMANN, Recombinant bispecific antibodies for cancer therapy. *Acta Pharmacol. Sin.* **2005**. 26, 1–9.
- 140 P. A. TRAIL, D. H. KING, G. M. DUBOWCHIK, Monoclonal antibody drug immunoconjugates for targeted treatment of cancer. *Cancer Immunol. Immunother.* **2003**. 52, 328–337.
- 141 G. C. McDONALD, N. GLOVER, Effective tumor targeting: Strategies for the delivery of armed antibodies. *Curr. Opin. Drug Discov. Devel.* **2005**. 8, 177–183.
- 142 S. V. GOVINDAN, G. L. GRIFFITHS, H. J. HANSEN, I. D. HORAK, D. M. GOLDENBERG, Cancer therapy with radiolabeled and drug/toxin-conjugated antibodies. *Technol. Cancer Res. Treat.* **2005**. 4, 375–392.
- 143 D. J. FITZGERALD, R. KREITMAN, W. WILSON, D. SQUIRES, I. PASTAN, Recombinant immunotoxins for treating cancer. *Int. J. Med. Microbiol.* **2004**. 293, 577–582.
- 144 K. SANDVIG, S. GRIMMER, T. G. IVERSEN, K. RODAL, M. L. TORGERSEN, P. NICOZIANI, B. VAN DEURS, Ricin transport into cells: Studies of endocytosis and intracellular

- transport. *Int. J. Med. Microbiol.* **2000.** 290, 415–420.
- 145 S. OLSNES, The history of ricin, abrin and related toxins. *Toxicon* **2004.** 44, 361–370.
- 146 A. GRUAZ-GUYON, O. RAGUIN, J. BARBET, Recent advances in pretargeted radioimmunotherapy. *Curr. Med. Chem.* **2005.** 12, 319–338.
- 147 J. C. ROBERTS, Y. E. ADAMS, D. A. TOMALIA, J. A. MERCER-SMITH, D. K. LAVALLEE, Using starburst dendrimers as linker molecules to radiolabel antibodies. *Bioconjugate Chem.* **1990.** 1, 305–308.
- 148 P. SINGH, Terminal groups in Starburst dendrimers: Activation and reactions with proteins. *Bioconjugate Chem.* **1998.** 9, 54–63.
- 149 H. KOBAYASHI, N. SATO, T. SAGA, Y. NAKAMOTO, T. ISHIMORI, S. TOYAMA, K. TOGASHI, J. KONISHI, M. W. BRECHBIEL, Monoclonal antibody-dendrimer conjugates enable radiolabeling of antibody with markedly high specific activity with minimal loss of immunoreactivity. *Eur. J. Nucl. Med. Mol. Imaging* **2000.** 27, 1334–1339.
- 150 N. FISCHER-DURAND, M. SALMAIN, B. RUDOLF, A. VESSIÈRES, J. ZAKRZEWSKI, G. JAOUEN, Synthesis of metal-carbonyl-dendrimer-antibody immunoconjugates: Towards a new format for carbonyl metallo immunoassay. *ChemBioChem* **2004.** 5, 519–525.
- 151 T. P. THOMAS, A. K. PATRI, A. MYC, M. T. MYAING, J. Y. YE, T. B. NORRIS, J. R. BAKER JR, In vitro targeting of synthesized antibody-conjugated dendrimer nanoparticles. *Biomacromolecules* **2004.** 5, 2269–2274.
- 152 A. K. PATRI, A. MYC, J. BEALS, T. P. THOMAS, N. H. BANDER, J. R. BAKER JR, Synthesis and in vitro testing of J591 antibody-dendrimer conjugates for targeted prostate cancer therapy. *Bioconjugate Chem.* **2004.** 15, 1174–1181.
- 153 S. S. NIGAVEKAR, L. Y. SUNG, M. LLANES, A. EL-JAWAHRI, T. S. LAWRENCE, C. W. BECKER, L. BALOGH, M. K. KHAN, <sup>3</sup>H Dendrimer nanoparticle organ/tumor distribution. *Pharm. Res.* **2004.** 21, 476–483.
- 154 H. KOBAYASHI, C. WU, M.-K. KIM, C. H. PAIK, J. A. CARRASQUILLO, M. W. BRECHBIEL, Evaluation of the in vivo biodistribution of indium-111 and yttrium-88 labeled dendrimer-1B4M-DTPA and its conjugation with anti-Tac monoclonal antibody. *Bioconjugate Chem.* **1999.** 10, 103–111.
- 155 M. MAMEDE, T. SAGA, H. KOBAYASHI, T. ISHIMORI, T. HIGASHI, N. SATO, M. W. BRECHBIEL, J. KONISHI, Radiolabeling of avidin with very high specific activity for internal radiation therapy of intraperitoneally disseminated tumors. *Clin. Cancer Res.* **2003.** 9, 3756–3762.
- 156 D. S. WILBUR, P. M. PATHARE, D. K. HAMLIN, K. R. BUHLER, R. L. VESSELLA, Biotin reagents for antibody pretargeting. 3. Synthesis, radioiodination, and evaluation of biotinylated starburst dendrimers. *Bioconjugate Chem.* **1998.** 9, 813–825.
- 157 N. MALIK, R. WIWATTANAPATAPEE, R. KLOPSCH, K. LORENZ, H. FREY, J. W. WEENER, E. W. MEIJER, W. PAULUS, R. DUNCAN, Dendrimers: Relationship between structure and biocompatibility in vitro, and preliminary studies on the biodistribution of <sup>125</sup>I-labelled polyamidoamine dendrimers in vivo. *J. Controlled Release* **2000.** 65, 133–148.
- 158 W. YANG, R. F. BARTH, G. WU, A. K. BANDYOPADHYAYA, B. T. S. THIRUMAMAGAL, W. TJARKS, P. J. BINNS, K. J. RILEY, H. PATEL, J. A. CODERRE, M. J. CIESIELSKI, R. A. FENSTERMAKER, Boronated epidermal growth factor as a delivery agent for neutron capture therapy of EGF receptor positive gliomas. *Appl. Radiat. Isot.* **2004.** 61, 981–985.
- 159 H. KOBAYASHI, M. W. BRECHBIEL, Dendrimer-based macromolecular MRI contrast agents: Characteristics and application. *Mol. Imaging* **2003.** 2, 1–10.
- 160 S.-E. STIRIBA, H. FREY, R. HAAG, Dendritic polymers in biomedical applications: From potential to clinical use in diagnostics and therapy. *Angew. Chem. Int. Ed.* **2002.** 41, 1329–1334.

- 161 T. KAMINAGA, T. TAKESHITA, I. KIMURA, Role of magnetic resonance imaging for evaluation of tumors in the cardiac region. *Eur. Radiol.* **2003**. 13(Suppl 4), L1–L10.
- 162 P. DE GRAAF, F. BARKHOF, A. C. MOLL, S. M. IMHOF, D. L. KNOL, P. VAN DER VALK, J. A. CASTELIJNS, Retinoblastoma: MR imaging parameters in detection of tumor extent. *Radiology* **2005**. 235, 197–207.
- 163 M. D. OGAN, U. SCHMIEDL, M. E. MOSELY, W. GRODD, H. PAAJANEN, R. C. BRASCH, Albumin labeled with Gd-DTPA. An intravascular contrast-enhancing agent for magnetic resonance blood pool imaging: Preparation and characterization. *Invest. Radiol.* **1987**. 22, 665–671.
- 164 L. D. MARGERUM, B. K. CAMPION, M. KOO, N. SHARGILL, J. LAI, A. MARUMOTO, P. C. SONTUM, Gadolinium(III) DO31 macrocycles and polyethylene glycol coupled to dendrimers. Effect of molecular weight on physical and biological properties of macromolecular magnetic resonance imaging agents. *J. Alloys Compd.* **1997**. 249, 185–190.
- 165 S. D. KONDA, S. WANG, M. BRECHBIEL, E. C. WIENER, Biodistribution of a 153 Gd-folate dendrimer, generation = 4, in mice with folate-receptor positive and negative ovarian tumor xenografts. *Invest. Radiol.* **2002**. 37, 199–204.
- 166 H. KOBAYASHI, S. KAWAMOTO, S.-K. JO, H. L. BRYANT JR, M. W. BRECHBIEL, R. A. STAR, Macromolecular MRI contrast agents with small dendrimers: Pharmacokinetic differences between sizes and cores. *Bioconjugate Chem.* **2003**. 14, 388–394.
- 167 S. GUCCIONE, K. C. LI, M. D. BEDNARSKI, Molecular imaging and therapy directed at the neovasculature in pathologies. How imaging can be incorporated into vascular-targeted delivery systems to generate active therapeutic agents. *IEEE Eng. Med. Biol. Mag.* **2004**. 23, 50–60.
- 168 K. ONITSUKA, M. FUJIMOTO, H. KITAJIMA, N. OHSHIRO, F. TAKEI, S. TAKAHASHI, Convergent synthesis of platinum-acetylide dendrimers. *Chem. Eur. J.* **2004**. 10, 6433–6446.
- 169 R. F. BARTH, A. H. SOLOWAY, Boron neutron capture therapy of primary and metastatic brain tumors. *Mol. Chem. Neuropathol.* **1994**. 21, 139–154.
- 170 L. LIU, R. F. BARTH, D. M. ADAMS, A. H. SOLOWAY, R. A. REISFELD, Bispecific antibodies as targeting agents for boron neutron capture therapy of brain tumors. *J. Hematother.* **1995**. 4, 477–483.
- 171 F. ALAM, A. H. SOLOWAY, R. F. BARTH, N. MAFUNE, D. M. ADAMS, W. H. KNOTH, Boron neutron capture therapy: Linkage of a boronated macromolecule to monoclonal antibodies directed against tumor-associated antigens. *J. Med. Chem.* **1989**. 32, 2326–2330.
- 172 R. F. BARTH, G. WU, W. YANG, P. J. BINNS, K. J. RILEY, H. PATEL, J. A. CODERRE, W. TJARKS, A. K. BANDYOPADHYAYA, B. T. S. THIRUMAMAGAL, M. J. CIESIELSKI, R. A. FENSTERMAKER, Neutron capture therapy of epidermal growth factor (+) gliomas using boronated cetuximab (IMC-C225) as a delivery agent. *Appl. Radiat. Isot.* **2004**. 61, 899–903.
- 173 A. QUINTANA, E. RACZKA, L. PIEHLER, I. LEE, A. MYC, I. MAJOROS, A. K. PATRI, T. THOMAS, J. MULÉ, J. R. BAKER JR, Design and function of a dendrimer-based therapeutic nanodevice targeted to tumor cells through the folate receptor. *Pharm. Res.* **2002**. 19, 1306–1310.
- 174 J. W. DENNIS, S. LAFERTE, C. WAGHORNE, M. L. BREITMAN, R. S. KERBEL, R1-6 branching of Asn-linked oligosaccharides is directly associated with metastasis. *Science* **1987**. 236, 236–239.
- 175 S. SELL, Cancer-associated carbohydrates identified by monoclonal antibodies. *Hum. Pathol.* **1990**. 21, 1003–1019.
- 176 A. KOBATA, J. AMANO, Altered glycosylation of proteins produced by malignant cells, and application for the diagnosis and immunotherapy of tumours. *Immunol. Cell Biol.* **2005**. 83, 429–439.

- 177 J. W. DENNIS, M. GRANOVSKY, C. E. WARREN, Protein glycosylation in development and disease. *BioEssays* **1999**, 21, 412–421.
- 178 L. TONG, G. BASKARAN, M. B. JONES, J. K. RHEE, K. J. YAREMA, Glycosylation changes as markers for the diagnosis and treatment of human disease, in *Biochemical and Genetic Engineering Reviews*, S. HARDING (Ed.), **2003**, Intercept Limited, Andover, Hampshire, UK. pp. 199–244.
- 179 J. R. ALLEN, C. R. HARRIS, S. J. DANISHEFSKY, Pursuit of optimal carbohydrate-based anticancer vaccines: Preparation of a multi-antigenic unimolecular glycopeptide containing the Tn, MBr1, and LewisY antigens. *J. Am. Chem. Soc.* **2001**, 123, 1890–1897.
- 180 J. R. ALLEN, J. G. ALLEN, X. F. ZHANG, L. J. WILLIAMS, A. ZATORSKI, G. RAGUPATHI, P. O. LIVINGSTON, S. J. DANISHEFSKY, A second generation synthesis of the MBr1 (Globo-H) breast tumor antigen: New application of the *N*-pentenyl glycoside method for achieving complex carbohydrate protein linkages. *Chemistry* **2000**, 6, 1366–1375.
- 181 V. KUDRYASHOV, P. W. GLUNZ, L. J. WILLIAMS, S. HINTERMANN, S. J. DANISHEFSKY, K. O. LLOYD, Toward optimized carbohydrate-based anticancer vaccines: Epitope clustering, carrier structure, and adjuvant all influence antibody responses to LewisY conjugates in mice. *Proc. Natl. Acad. Sci. U.S.A.* **2001**, 98, 3264–3269.
- 182 H. KAYSER, R. ZEITLER, C. KANNICHT, D. GRUNOW, R. NUCK, W. REUTTER, Biosynthesis of a nonphysiological sialic acid in different rat organs, using *N*-propanoyl-D-hexosamines as precursors. *J. Biol. Chem.* **1992**, 267, 16 934–16 938.
- 183 K. J. YAREMA, L. K. MAHAL, R. E. BRUEHL, E. C. RODRIGUEZ, C. R. BERTOZZI, Metabolic delivery of ketone groups to sialic acid residues. Application to cell surface glycoform engineering. *J. Biol. Chem.* **1998**, 273, 31 168–31 179.
- 184 L. K. MAHAL, K. J. YAREMA, C. R. BERTOZZI, Engineering chemical reactivity on cell surfaces through oligosaccharide biosynthesis. *Science* **1997**, 276, 1125–1128.
- 185 E. SAXON, C. R. BERTOZZI, Cell surface engineering by a modified Staudinger reaction. *Science* **2000**, 287, 2007–2010.
- 186 S.-G. SAMPATHKUMAR, A. V. LI, M. B. JONES, Z. SUN, K. J. YAREMA, Metabolic installation of thiols into sialic acid modulates adhesion and stem cell biology. *Nat. Chem. Biol.* **2006**, 2, 149–152.
- 187 L. K. MAHAL, K. J. YAREMA, G. A. LEMIEUX, C. R. BERTOZZI, Chemical approaches to glycobiology: Engineering cell surface sialic acids for tumor targeting, in *Sialobiology and Other Novel Forms of Glycosylation*, Y. INOUE, Y. C. LEE, F. A. TROY II (Eds.), 1999, Gakushin Publishing Company, Osaka, Japan, pp. 273–280.
- 188 D. A. NAUMAN, C. R. BERTOZZI, Kinetic parameters for small-molecule drug delivery by covalent cell surface targeting. *Biochim. Biophys. Acta* **2001**, 1568, 147–154.
- 189 S.-G. SAMPATHKUMAR, K. J. YAREMA, Targeting cancer cells with dendrimers. *Chem. Biol.* **2005**, 12, 5–6.

## 2

# Nanoparticles for Optical Imaging of Cancer

*Swadeshmukul Santra and Debamitra Dutta*

### 2.1

#### Introduction

The word “cancer” comes from the Latin word for crab. Historically, an ancient physician from Greece noticed the resemblance of the swollen mass of blood vessels around a malignant tumor to the shape of a crab and so named the disease. The malignant tumor is also seen to adhere to surrounding tissues that it can seize upon in a stubborn manner, similar to a crab.

Human cancer consists of more than 200 different diseases [1] in which cells multiply at an exponential growth rate in an uncontrolled fashion. This abnormal growth rate leads to the formation of a lump, called malignant tumor. Gradually the tumor tissue grows and invades the adjacent tissues and organs, obstructing normal physiological functions. In some cases, the cancerous cells can detach from its origin and migrate through circulation to different parts of the body, forming a new tumor site. This is termed as cancer metastasis. Over a period of time, malignant tumors cause malfunctioning of various organs, which turns fatal.

According to the American Cancer Society’s annual report [2], about 570 280 people are expected to die of various cancers in the year 2005 in the United States of America (USA). During the last century, cancer has slowly advanced to become the leading cause of death for patients below the age of 85 in USA, despite rapid advances in global cancer research towards the understanding of cancer biology in the past several decades.

The formation of malignant tumors is associated with six different cellular characteristics [3, 4], each of which is unique for cancer development. These characteristics are self-sufficiency in growth signals, evading apoptosis (a process by which a cell is “commanded” by the environment to die), insensitivity to anti-growth signals (an inherent mechanism for preventing undesirable cell growth), sustained angiogenesis (a process of growth of new blood vessels), tissue invasion and metastasis and limitless replicative potential.

Cancer can develop in any living organ or tissue in the body. The part of the body in which the cancer first develops is referred to as the primary site. The most common cancer developing sites include the skin, lungs, female breasts, prostate, co-

lon and rectum, and corpus uteri. The secondary site refers to the body part where metastasized cancer cells grow and form secondary tumors. Even if a cancer has spread to another part of the body, it is always described with respect to the primary site. For example, advanced breast cancer that has spread to the lymph nodes under the arm and to the lungs is always considered breast cancer.

The diagnosis of cancer means an attempt to accurately identify the anatomical site of origin of the malignancy and the type of cells involved. The presence of cancer may be preliminarily suspected by some other disease-like symptoms. For example, weight loss and abdominal pain can be caused by stomach cancer or an ulcer. However, to confirm the diagnosis of cancer, a biopsy (removal of tissue for microscopic evaluation) is usually done. Biopsies can provide information about histological type, classification, grade, potential aggressiveness and other information that may help determine the best treatment. A biopsy together with advanced imaging technologies, can not only confirm the presence of cancer, but also can pinpoint the primary and secondary cancer sites.

Early cancer diagnosis, in combination with the precise cancer therapies, could eventually save millions of lives. The diagnosis of cancer at the early stage is extremely challenging and has been an active research area of great interest in current times. If the tumor is located near the body's surface, a tissue sample can be easily retrieved for a biopsy (removal of tissue for microscopic evaluation) and the tissue abnormality can be confirmed at the cellular level. However, if the tumor mass is inaccessible for a biopsy, one has to then rely upon the existing imaging techniques for the detection of the tumor location. Existing diagnostic non-invasive imaging techniques such as Computed Tomography (CT), Magnetic Resonance (MR), Positron Emission Tomography (PET), Single Photon emission CT (SPECT), Ultrasound (US) and optical imaging are effective for macroscopic visualization of tumors. However, none of these techniques are sensitive enough for the diagnosis of abnormalities in the microscopic level. Substantial research efforts are being made for the development of better cancer imaging techniques. Of them, optical imaging has shown a great promise with respect to the image resolution [5]. The feasibility of developing optical imaging technique for the sensitive detection of cancer has been recently demonstrated [6, 7] using nanoparticle-based highly sensitive optical contrast agents.

This chapter provides a knowledge base platform to readers interested in learning about nanoparticle technology and its implications in diagnostic cancer imaging. An overview of existing cancer imaging techniques with special emphasis on optical-based imaging techniques has been incorporated. Optical imaging has strong potential in becoming an attractive alternative to existing cancer imaging techniques. Optical imaging is a highly sensitive, non-invasive, non-ionizing, relatively inexpensive and simple technique. With the aid of better contrast agents, this imaging technology could be transferred to a clinical setup for human applications for early cancer diagnosis in the near future. Recent developments which are directly associated with the improvement of optical image contrast, such as the use of sophisticated laser technology, highly sensitive charged-coupled device (CCD) technology and powerful mathematical modeling of light propagation through the

biological systems, have been integrated into the imaging components. However, presently, significantly limited numbers of appropriate *in vivo* optical contrast agents are available. Therefore, there is a great demand of developing highly sensitive, stable and clinically safe *in vivo* optical contrast agents.

Nanoscience and nanotechnology is an interdisciplinary research area that brings various traditional disciplines such as chemistry, physics, materials science, biomedical, molecular biology, and many others together under one umbrella. Several edited books [8–12] on nanoscience and nanotechnology include the development of various nanoparticles such as metals, semiconductors, etc. for biological applications. Several review articles [5, 7, 9, 13–22] have recently reported advance research highlights on optical-based contrast agents [15–17, 21], some of which emphasize nanoparticle-based optical contrast agents [7, 18–20, 22] for bioimaging. However, none of these articles captured thoroughly recent developments on nanoparticle-based optical contrast agents suitable for cancer imaging. In this chapter, we made every effort to provide extensive details of nanoparticle-based contrast agents developments, including separate sections on nanoparticle design, synthesis strategies, nanoparticle dispersion, surface modification, bioconjugations and cancer imaging applications. We hope that this chapter will be useful for students, teachers, research scientists, general audiences who are interested in learning more about early cancer diagnosis and others. We have attempted to explain each section and sub-section of this chapter in a simple manner so that readers could easily grasp the general strategy of various nanoparticle-based optical contrast agent development.

Since the field of cancer imaging is expanding rapidly, we start with an introduction to highlight the contents of this chapter (Section 2.1). Section 2.2 briefly overviews various existing cancer-imaging techniques, allowing readers to understand merits and demerits of these techniques. Section 2.3 describes the basics of optical imaging, optical imaging techniques and optical contrast agents. This chapter provides a clear understanding of the merits and challenges of developing optical-based imaging techniques and contrast agents. Section 2.4 details recent advances in nanoparticle-based optical contrast agents. While Section 2.4.1 provides the reasons for developing such contrast agents, Section 2.4.2 provides some literature review on the development of nanoparticle-based various contrast agents such as quantum dots, dye-doped nanoparticles and gold nanoparticles. Various cancer imaging applications using nanoparticles are reviewed in Section 2.5. Section 2.6 covers some miscellaneous nanoparticles such as up-converting phosphors, fluorescent polymer particles, etc. that are potential contrast agents. Section 2.7 provides concluding remarks and the perspectives of nanoparticle-based optical imaging of cancers.

## 2.2 Cancer Imaging Techniques

Some of the major imaging techniques routinely used in hospital setup for cancer imaging in humans are briefly described below.



### 2.2.1

#### **Computed Tomography (CT) Scanning**

The detection components of a typical CT scanner include the X-ray tube, detectors, image reconstruction computer and visual display monitor. The X-ray tube generates a beam of X-rays that are made to pass through the body of the patient. The detectors are positioned to absorb the X-rays coming out through the body. While processing the information, the reconstruction computer takes into consideration that X-rays passing through denser tissues like bones are attenuated to a higher extent than those passing through softer tissue such as lungs. Thus the X-ray beams of varying strengths that come out from the body create a differential profile. This profile is measured by the detectors and finally imaged by the display monitor. The complete setup rotates around the patient and acquires about 1000 snapshots for every 360° rotation, when a slice is completed. After each rotation, the information from the detectors is collected together and processed by the computer to construct a two-dimensional image (slice) on the display monitor. Image resolution is on the order of 50–100 μm with data acquisition time varying from 5 to 30 min. Recently, there have been continuing efforts to merge the CT modality with other modules like nuclear imaging modalities, which have limited spatial resolution, to generate better images.

### 2.2.2

#### **Magnetic Resonance (MR)**

In this technique, patients are placed in a strong electromagnetic field that causes the hydrogen atoms of water molecules present in the body fluid to align with the field. A short, powerful radio signal is then sent through the body at a desired level (slice) perpendicular to the original field. Hydrogen atoms with similar frequencies resonate with the radio signal and get excited. When the radio signal is switched off, the excited atoms will release their excitation energy in the form of radio waves and return to their normal state. The time taken for the hydrogen atoms to release their energy is characteristic of the physical properties of the tissue. These radio waves are detected and the time taken is measured and analyzed by a computer to construct an image of the tissues. Usually, it is difficult to distinguish tumors from normal tissues in the body using an MR image. Therefore, patients are injected with contrast agents that selectively highlight the tumors. Standard MR images (1.5 Tesla, the magnetic field strength) provide a spatial resolution of 1 mm, which could be increased to about 10 μm with certain modifications.

### 2.2.3

#### **Positron Emission Tomography (PET)**

In this technique, a positron-emitting isotope ( $^{11}\text{C}$  or  $^{18}\text{F}$ ) is attached to a biological molecule that has an affinity to tumor cells and introduced into the patients. The decaying isotopes emit positrons, which collide with a nearby electron and annihilate to release  $\gamma$ -rays. These rays are detected and analyzed by a computer. The po-

sition of the tumor in the body can be located by tracking the density of the positrons in a particular region.

#### 2.2.4

#### **Single-photon Emission CT (SPECT)**

This imaging technique is similar to PET, except that the SPECT isotope itself emits a single  $\gamma$ -ray instead of a positron. This technique is very inexpensive when compared with PET. However the spatial resolution is not as good as PET.

#### 2.2.5

#### **Ultrasonography (US)**

In this form of imaging, ultrasonic sound waves are sent through the body. The waves are partially reflected from the interfaces of different tissues. The intensity of reflected waves depends on the density of the tissues. The time taken for the reflected wave to reach the detector gives a measure of the depth of the tissue location. The advantage of ultrasonography is that the images are generated in real time with very high temporal resolution. However, ultrasonic waves cannot travel through bone and therefore cannot detect tissues behind bony structures such as the brain behind the skull.

### 2.3

#### **Optical Imaging**

##### 2.3.1

#### **Basics of Optical Imaging**

Optical imaging is a sensitive, non-invasive, non-ionizing (clinically safe) and relatively inexpensive technique that has strong potential for diagnostic cancer imaging. Two major components are associated with an optical imaging system: an imaging component and an optical contrast-enhancing component (i.e., contrast agent). Recent advances in optical imaging have utilized sophisticated laser technology, highly sensitive charged-coupled device (CCD) technology and powerful mathematical modeling of light propagation through the biological systems; all these developments have formed a solid basis for the imaging component. Molecular fluorescent probes have been successfully used as optical contrast agents for imaging various cancer tissues in the past [5, 15–17, 23–27]. However, the sensitivity of the contrast agent has become the major obstacle in obtaining a high-resolution image. Again, *in vivo* deep tissue optical imaging has been limited because of the low penetration depth of the light in the ultraviolet (UV) and visible spectral range (the approximate tissue penetration depth is about 1–2 mm). Near-infrared (NIR) light in the spectral range 650–900 nm can, however, penetrate much deeper (up to several centimeters) into the tissue and skull [5, 15]. This is due to the relatively low absorption of tissue components (water and hemoglobin)

in the NIR spectral range. Therefore, the development of an NIR-based optical imaging system has attracted tremendous attention in the cancer imaging community in recent years.

For developing optical-based imaging system, it is important to understand how light interacts with biological tissues. Simply, a tissue can interact with light photons by absorption, scattering and reflection. Since biological tissue represents a complex system in terms of light propagation, it is expected that the optical image would be somewhat distorted. A robust mathematical modeling is thus necessary to improve image quality. Again, all biological tissues somewhat autofluoresce upon interaction with the light in the UV and visible spectrum. The tissue autofluorescence originates from the natural tissue fluorescent molecules such as nicotinamide, flavins, collagen, and elastin [25]. To develop a robust optical imaging system it is thus important to address all sorts of light interaction with tissue as well as tissue autofluorescence.

### 2.3.2

#### Optical Imaging Techniques

Optical-based imaging methods such as confocal imaging, multiphoton imaging, microscopic imaging by intravital microscopy or total internal reflection fluorescence microscopy have been used traditionally to image fluorescence events that originates *in vivo* from surface and subsurface region. Recently, advanced imaging technologies that use photographic systems with continuous or intensity-modulated light and tomographic systems have shown great potential for deep tissue imaging. With the aid of highly sensitive contrast agents such as nanoparticles, it may be possible to transfer optical imaging technology to human application. There are several potential optical imaging techniques, such as reflectance fluorescence imaging and fluorescence-mediated molecular tomography (FMT), that use the diffuse component of light for probing molecular events deep in tissue samples. These techniques are briefly described below.

In a typical reflectance imaging technique, a simple “photographic method” is used where the light source and the detector reside on the same side of the imaging object (e.g., an animal). This technique is currently used for *in vivo* assessment of fluorescent dyes [such as green fluorescent proteins (GFP), bioluminescent molecules, etc.]. In a reflectance imaging system, the light source can be either an appropriate laser for the target fluorescent molecules or a white light with the appropriate low-pass filter. The laser excitation source is preferable because it provides a narrow and well-defined spectral window ( $\pm 3$  nm) when compared with white light ( $\pm 10$  nm). A high-sensitivity CCD camera is usually used as detector. Reflectance imaging has been successfully used to image cathepsin B [28], cathepsin D [29], matrix metalloproteinase 2 (MMP-2) [30], using activatable probes that are dark in the native (quenched) state and fluoresce upon interaction with a specific enzyme. This technique has been used for the elucidation of MMP-2 (a biomarker) expression levels in two different breast cancers, MMP-2 positive human HT1080 fibrosarcoma and MMP-2 negative BT20 mammary adenocarcinoma [31]. A NIR probe was activated upon interaction with both the tumors. The level of MMP-2

expression was directly related to the number of probe molecule activation. As expected, great probe activation was found in human HT1080 fibrosarcoma. Reflectance imaging technique has also been used for targeting cell-surface receptors *in vivo* using peptide-NIR dye conjugate [26, 32] and for studying gene expression [33]. Reflectance imaging is a simple, fast and highly sensitive imaging and screening technique for capturing surface fluorescent events *in vivo* or in excised tissues. This imaging system can be, inexpensively, made portable for the laboratory bench. However, this technique has several limitations. Firstly, the technique will allow imaging of a few millimeters thick tissue. As a result, the appearance of deeper lesions is significantly blurred. Secondly, quantitative information cannot be extracted from the reflectance imaging technique. For example, the surface appearance of a small structure with high dye loading that is located in a deeper tissue could be similar with a larger structure of low dye loading that is closer to the surface.

Fluorescence-mediated molecular tomography is a powerful technique to resolve and quantify deep tissue fluorescence signal. This technique, usually termed as diffuse optical tomography (DOT) utilizes advanced photon sources, a detection system and rigorous mathematical modeling of light propagation in tissue. The DOT technique uses multiple projections and measures light around the boundary of the illuminated body followed by a complex mathematical modeling to construct the three-dimensional tomographic image. This technique has recently been applied clinically for imaging tissue oxy- and deoxy-hemoglobin concentration and blood saturation [34–37]. Based on the same principle, fluorescence molecular tomography (FMT) has been developed where measurements of fluorescent molecular probes at both the emission and excitation wavelengths were considered. The FMT technique has been recently used for imaging cathepsin B activity in deep tissue structure of 9L gliosarcomas [38–40]. An optical imaging system that can image both reflected light and fluorescence light to generate multi-spectral digital imaging of tissue morphology from a large field of view with mm resolution has also been developed [21]. Readers are encouraged to read a few recent review articles [5, 21, 41] that describe the topic on optical imaging techniques.

### 2.3.3

#### **Optical Contrast Agents**

Optical tissue contrast agents are used in biological systems (e.g., cells, tissues, etc.) to enhance the optical contrast by virtue of their contrast enhancing properties (e.g., fluorescence, scattering, etc.). Tissue contrast agents, for example, are capable of reducing the background signal and improving the image resolution. Fluorescent molecular contrast agents, mostly organic fluorescent compounds, possess high extinction coefficient and quantum yield and have the potential to drastically suppress tissue autofluorescence and hence background signal. Effective delivery (loading) of these contrast agents to the target tissue has also been realized to be one of the most important factors for achieving better image contrast, other than its intrinsic fluorescent characteristics (extinction coefficients, quantum yield, etc.). The concentration of contrast agent per unit volume of target tissue would

determine the signal strength. Therefore, a higher loading of contrast agent is always desirable for better image resolution and hence in obtaining a sharp marginal contrast between the normal and the pathological (e.g., a tumor) tissues.

A few important features of contrast agents have to be kept in mind prior to using or developing new contrast agents for diagnostic cancer imaging. Firstly, contrast agents with the excitation and emission band maxima in the NIR range (650 to 900 nm) are highly preferable for deep tissue imaging. Secondly, contrast agents should have a high extinction coefficient for effective absorption and a high quantum yield for obtaining strong fluorescence signal. Thirdly, they should be photostable and should not have any photo-sensitizing effects (i.e., photodynamic effect causing the damage of cellular DNA and hence cell death; also termed as photo-sensitized cell death). Fourthly, contrast agents should be hydrophilic so that an aqueous-based formulation can be easily made. Fifthly, contrast agents should have low toxicity so that they can be administered safely. Lastly, for cancer imaging, contrast agents should be attached to appropriate cancer specific delivery systems (e.g., antibodies, peptides, folates, etc.) for targeting.

Organic fluorescent contrast agents, although studied extensively for various bio-imaging applications [42], starting from cellular to tissues to whole animal fluorescence imaging have, however, several limitations for them to be considered as robust contrast agents. Firstly, organic fluorescent contrast agents (dyes) rapidly undergo photobleaching. As a result, the fluorescence signal fades away when exposed to the excitation light source (particularly when a laser is used for the excitation), limiting sensitive detection of the target. Secondly, fluorescent dyes are usually hydrophobic. To make aqueous-based formulation, chemical modifications (e.g., sodium salt) are often required that sometimes compromises their spectral characteristics. Thirdly, a handful of fluorescent compounds have been shown to possess low toxicity. Lastly, a few dyes have excitation and emission bands in the NIR spectral range (e.g., cyanine dyes). Another class of fluorescent contrast agents is fluorescent proteins. Fluorescent proteins such as green fluorescent protein (GFP) represent one class of imaging marker genes (IMG, artificial genes) with an optical signature where GFP is the transcriptional product of IMG. The GFP-based optical imaging has been successfully used to study various gene expressions *in vivo*. For example, human and rodent tumor cell lines, transected with GFP, could be visualized *in vivo* for monitoring tumor growth and metastasis [43–45]. The major drawback of GFP is limited penetration depth since the tissue can highly absorb the green emission of GFP.

## 2.4 Nanoparticles for Optical Imaging

### 2.4.1 Why Nanoparticles for Optical Imaging?

Nanoparticle (NP)-based contrast agents present a whole new class of robust nanometer size (between 1 and 100 nm) particulate materials that has strong potential

for optical imaging of cancer. The use of NPs for bioimaging applications has several advantages.

Firstly, the sensitivity of the optical imaging could be greatly improved using nanoparticle-based contrast agents. A classic example is the fluorescent quantum dots (Qdots) and their applications in cancer imaging [6, 13, 21, 46–65]. Qdots are usually crystalline cadmium sulfide (CdS) and cadmium selenide (CdSe)-based semiconductor particulate materials. They are small (<5 nm) and bright, having a broad excitation band but a narrow emission band. Dye-doped nanoparticles (NPs) such as dye-doped silica [66–69], dye-doped polymer particles [70–72], present another class of materials for sensitive cancer detection. In dye-doped NPs, each particle carries thousands of dye molecules, thus greatly enhancing the fluorescence signal. Dye-doped NPs are usually smaller (about two to three orders of magnitude) than cells, which make them suitable for cellular application. Gold nanoparticles have been well studied and have also been used for sensitive cancer cell imaging [21, 47, 73–75]. They possess a strong surface plasmon band that originates from efficient light scattering by the nanosize particles.

Secondly, nanoparticle-based contrast agents have better photostability than traditional organic dye-based contrast agents. This has tremendous potential for sensitive and real-time monitoring of cancer progression (e.g., monitoring cancer growth and metastasis). Photostable nanoparticles will allow non-invasive imaging of cancer tissue multiple times for monitoring tumor growth and also the effect of cancer drugs during cancer therapy. For example, Qdots are extremely photostable. The effective surface passivation of Qdots with a wide bandgap material such as zinc sulfide (ZnS) or zinc selenide (ZnSe) makes them photostable. In dye-doped NPs, dye molecules remain encapsulated by the particle-matrix that protects them from photobleaching. This is because the particle-matrix can, somewhat, prevent the penetration of oxygen molecules that cause dye degradation. Usually, Qdot materials are more photostable than dye doped NPs. Gold nanoparticles efficiently scatter light and, therefore, do not fade away via photobleaching process [76–78].

Lastly, multiple imaging modalities can be integrated into nanoparticle-based contrast agents (also called as multifunctional nanoparticles [79–88]), making them suitable for imaging using multiple modalities (such as fluorescence, X-ray, MRI, etc. [86, 89, 90]). This would have great importance for *in vivo* cancer imaging applications. Once labeled with the multimodal contrast agents, tumors could be imaged non-invasively using a CT scan or MRI for the pre-surgical assessment. During the surgical procedure, tumor tissue could be directly visualized in real-time by the optical property (e.g., fluorescence) of the contrast agent. This mode of tumor visualization would provide direct guidance to surgeons for the effective tumor resection, enabling them to demarcate the boundary between the tumor and normal tissues. Nanoparticle surface is usually modified to obtain multiple functional groups/ligands to improve aqueous dispersibility, specific targeting (e.g., cancer targeting), biocompatibility, etc. [6, 20, 66, 67, 84, 86, 89–95].

Nanoparticles-based contrast agents have strong potential for early cancer diagnosis since they are bright and photostable. For *in vivo* cancer diagnosis, NIR-based nanoparticle contrast agents will be required. The following sub-sections describe

in detail the design, synthesis, surface modification, and cancer targeting of various nanoparticle-based contrast agents (e.g., Qdots, dye-doped NPs, gold, etc.).

#### 2.4.2

#### Development of Nanoparticle-based Contrast Agents

A robust nanoparticle design is the key step for the synthesis of highly sensitive optical contrast agents. In a typical nanoparticle-based optical contrast agent design, the optical core is encapsulated by an intermediate coating followed by an outermost layer containing appropriate functional groups for bioconjugation. Figure 2.1 shows a general schematic representation of nanoparticle design. For cancer labeling, these particles are then attached to cancer cell targeting agents (e.g., folates, antibodies, etc.). The resulting nanoparticles can be used as cancer imaging probes (Fig. 2.2).

##### 2.4.2.1 Quantum Dots

Fluorescent Qdots are ultra-small (2–8 nm diameter) semiconductor nanocrystals, having broad absorption band with narrow and symmetric emission band (full-width at half-maximum  $\sim 25\text{--}40$  nm), that typically emit in the visible to NIR spectral range [7, 18, 96]. Qdots absorption is associated with the promotion of electrons from the conduction band to the valence band when the excitation energy exceeds that band gap energy between two electronic bands (semiconductor band gap), resulting in the formation of an electron–hole pair, called an exciton. In con-

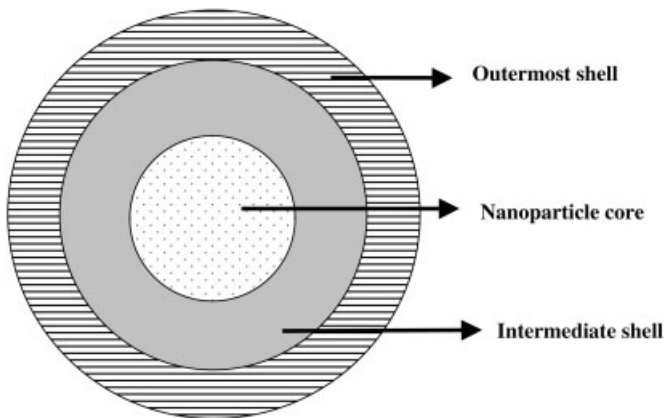


**Fig. 2.1.** Schematic representation of core–shell nanoparticle design. The nanoparticle core (e.g., quantum dot, gold nanoparticle, dye-doped silica nanoparticle, etc.) is the primary source of an optical signal. The intermediate shell (e.g., ZnS surface passivation followed by polymer/silica coating,

pure/hybrid silica coating, etc.) is designed to protect the nanoparticle core. The outermost shell contains appropriate surface functional groups (e.g., carboxyls, amines, thiols, etc.) for biomolecule/ligand (e.g., antibodies, peptides, proteins, sugars, folates, etc.) attachment.

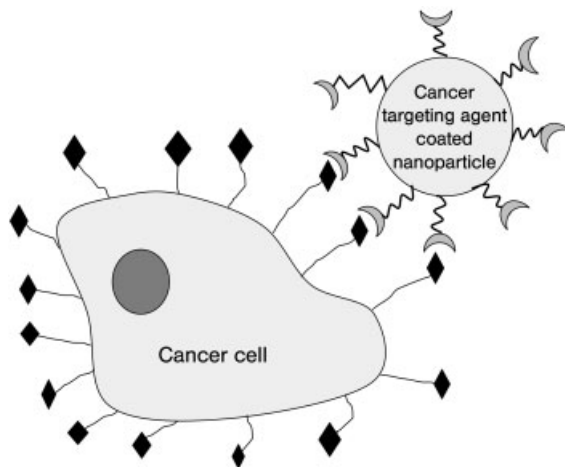


**Fig. 2.2.** Schematic representation showing a typical nanoparticle-based cell-labeling strategy. In this strategy cancer-targeting agents (e.g., folates, antibodies, etc.) are coated onto nanoparticle surface. The resulting coated particles are capable of recognizing cancer cells.

trast to organic fluorescent molecules, the absorption probability of Qdot nanocrystals increases at shorter wavelengths (higher energy), resulting in a broadband absorption spectrum. When the Qdot is smaller than the Bohr exciton radius (which is typically a few nanometers), the quantum confinement effect is observed in such nanocrystals [97]. In this situation, Qdot energy levels are quantized, with values directly related to the Qdot size. Qdot emission is due to a radiative recombination of an exciton, which is characterized by a long lifetime [98] ( $>10$  ns), leading to the emission of a photon in a narrow and symmetric energy band. These spectral characteristics of Qdot materials are different from a typical organic fluorescent molecule with red-tailed broad emission band and short fluorescence lifetimes. In comparison to traditional fluorescent molecules (fluorophores) or fluorescent proteins (e.g., GFP), Qdots have several attractive optical features that are desirable for long-term, multi-target and highly sensitive bioimaging applications. Some of the major optical features of Qdots are described below.

(a) Large molar extinction coefficient: Qdots are highly sensitive fluorescent agents (or fluorescent tags) for labeling cells and tissues. Unlike organic fluorescent compounds, Qdots have very large molar extinction coefficients [99], typically of the order of  $0.5\text{--}5 \times 10^6 \text{ M}^{-1} \text{ cm}^{-1}$  which means that Qdots are capable of absorbing excitation photons very efficiently (the absorption rate is approximately 10–50 $\times$  faster than organic dyes). The higher rate of absorption is directly correlated to the Qdot brightness and it has been found that Qdots are approximately 10–20 $\times$  brighter than organic dyes [100–102], allowing highly sensitive fluorescence imaging.



(b) Excellent photostability: Qdots are several thousand times more photostable than organic dyes. This feature allows real-time monitoring of biological processes over a long period.

(c) Much longer lifetime: Qdots are highly suitable for time-correlated lifetime imaging spectroscopy. This is possible due to the longer excited state lifetime of Qdots (about one order of magnitude longer than that of organic dyes), allowing effective separation of Qdot fluorescence from the background fluorescence. This will improve the image contrast by reducing the signal-to-noise ratio dramatically [103, 104] in the time-delayed data acquisition mode.

(d) Large Stokes shift: Unlike in organic dyes, the excitation and emission spectra of Qdots are well separated (i.e., large Stokes shift value; up to 400 nm, depending on the wavelength of the excitation light). This allows further improvement of sensitivity of the detection by reducing the high autofluorescence background often seen in biological specimens [6].

(e) Multiple targeting capability. The wavelength of Qdot emission is size dependent. This is a unique feature of Qdot materials in comparison to organic fluorescent dyes. The size dependent emission of Qdots allows imaging and tracking of multiple targets simultaneously using a single excitation source. This feature is particularly important in tracking a panel of disease-specific molecular biomarkers simultaneously, allowing classification and differentiation of various complex human diseases [105].

The development of Qdot-based fluorescent probes involves a multi-step process: synthesis, surface capping and bioconjugation. Each step is described below in detail.

**Qdot Synthesis** Qdot nanocrystals are made out of hundreds to thousands of atoms that typically belong to group II and VI elements or group III and V elements in the periodic table. For example, CdSe, CdTe, and ZnSe are group II–VI semiconductor Qdots, whereas InP and InAs Qdots are group III–V semiconductors. The Qdot emission can be continuously tuned from 400 to 2000 nm by changing both the particle size and chemical composition. Herein, we briefly describe two robust synthesis techniques that produce high quality Qdots.

**Hot Solution-phase Mediated Qdot Synthesis** This is most popular technique of synthesizing high quality Qdots. Typically, Qdots are synthesized at elevated temperature in high boiling point non-polar organic solvents. Bawendi's group have reported [106] the synthesis of highly crystalline and monodisperse (size distribution 8–11%) CdSe Qdots using high-temperature growth solvents/ligands (mixture of trioctylphosphine/trioctylphosphine oxide, TOP/TOPO). A combination of TOPO and hexadecylamine can also be used [96]. The purpose of using hydrophobic organic molecules as mixed solvents or as a solvent/ligand mixture is two-fold. The mixture serves as a robust reaction medium and also coordinates with unsaturated metal atoms on the Qdot surface to prevent the formation of bulk semiconductors. Following a similar synthesis strategy, Qu et al. have reported the formation high

quality CdSe nanocrystals having fluorescence quantum yields as high as 85% at room temperature [107].

**Reverse-micelle Mediated Qdot Synthesis** The reverse micelle synthesis of high quality CdS:Mn/ZnS core-shell Qdots has been reported [86, 89, 90, 108–110]. Reverse micelles [also called water-in-oil (W/O) microemulsion system] are an isotropic, thermodynamically stable homogeneous mixture of oil, water and surfactant molecules where the surfactant capped (stabilized) water droplets remain uniformly dispersed in the bulk oil phase. The water droplets serve as a tiny reactor (nano-reactor) for the synthesis of Qdots. This is a simple procedure that does not require extreme reaction conditions such as high temperature or high pressure. This is a robust method that allows room temperature synthesis of monodisperse Qdots at normal atmospheric pressure. Yang et al. have reported the synthesis of manganese-doped cadmium sulfide core and zinc sulfide shell (CdS:Mn/ZnS) Qdots using AOT (dioctylsulfosuccinate sodium salt, a surfactant)/heptane (an oil)/water reverse micelle system [90, 108, 109]. The bright yellow emitting CdS:Mn/ZnS Qdots are small (average Qdot size was 3.2 nm) and highly photostable.

**Qdot Surface Passivation and Aqueous Stabilization** Effective surface passivation of the Qdot nanocrystal core with wide bandgap semiconductor materials (shell) is extremely important [100, 111] for the following reasons. For example, with cadmium selenide/zinc sulfide (CdSe/ZnS) core-shell Qdots, the epitaxially matched ZnS layer effectively passivates the surface defects of the CdSe core [100, 108, 112], protects the core from oxidation, prevents leaching of highly toxic Cd<sup>2+</sup> ions, and also drastically improves the quantum yield by reducing surface defects (that act as exciton traps, leading to non-radiative recombination processes). Surface passivation with silica is effective for the CdSe core [90, 113, 114] nanocrystals.

TOP/TOPO-capped Qdots prepared using hot solution phase mediated synthesis route are hydrophobic. For biological applications, however, it is necessary to obtain aqueous dispersible Qdots. Therefore, phase transfer from the organic (e.g., toluene, hexanes, chloroform) to aqueous solution is usually performed by surface functionalization with hydrophilic ligands. There are three major routes to surface functionalization. Firstly, the “cap exchange” route that involves replacement of TOP/TOPO capping with bifunctional ligands. The bifunctional ligands [102, 115–118] have two functional moieties, Qdot surface anchoring (e.g., thiol) and hydrophilic moieties (e.g., hydroxyl, carboxyl). Secondly, the formation of a hydrophilic silica shell [86, 89, 90, 101, 108, 119] that encapsulates the Qdot. Lastly, the over-coating of TOP/TOPO-capped Qdots with amphiphilic “diblock” and “triblock” copolymers and phospholipids [6, 64, 120–124].

Notably, Qdots capped with mono-mercapto ligands have short shelf-lives, about a week, due the weak (dynamic) thiol-ZnS interaction [125], although polydentate thiolated ligands (containing more than one thiol groups) afford better stability (from a week to a couple of years) [116, 118, 125]. Applying a silica shell over the Qdots has several advantages with respect to long-term stability (shelf-life) and bio-

compatibility. Also, a silica coating remains stable upon pH fluctuation (below pH 8) and a further coating with a multifunctional hybrid silica is possible using appropriate silane reagents [86, 89]. The polymer/phospholipid encapsulation is also robust in terms of long-term stability. Both the silica and the polymer/phospholipid coating increase the particle size (~20–30 nm). However, Yang et al. reported the W/O microemulsion-mediated synthesis of silica-overcoated CdS:Mn/ZnS Qdots [90] where the silica shell thickness was approximately 2–3 nm.

**Qdot Bioconjugation** Qdot bioconjugation represents the attachment of biomolecules (e.g., proteins, antibodies, peptides, DNA, etc.) to the Qdot surface, forming a hybrid structure, interfacing both the inorganic and the biological materials, for targeting to biological systems such as cells, tissues, etc. either specifically or non-specifically. Qdots are comparable or slightly larger than many proteins. For example, a 510 nm green-emitting Qdot size is comparable to GFP and a 650 nm red-emitting Qdot size is comparable to DyRed (a red-emitting fluorescent protein) [126]. Medintz et al. have shown that about 15–20 maltose binding proteins ( $M_r \sim 44$  kDa) can be conjugated to a single 6-nm Qdot [127]. There are three major ways to attach proteins to Qdot surface. Firstly, using carbodiimide [e.g., EDC, 1-ethyl-3-(3-dimethylaminopropyl) carbodiimide] coupling chemistry, carboxylated Qdots are covalently conjugated to the protein molecules through the formation of stable amide bond. Secondly, disulfide bonds can be formed between Qdot surface sulfur atoms (from the ZnS surface) and peptides containing cysteine residues [128, 129]. Histidine-expressing proteins [130] or peptides containing polyhistidine residues [131–133] can also be directly attached to the Zn atom on the Qdot surface. Lastly, engineered proteins containing positively charged domains can be non-covalently adsorbed onto the negatively charged Qdot surface via electrostatic interaction [116, 134, 135]. Although various bioconjugation strategies have been tested, none of them can control the ratios of proteins per Qdots. There is certainly a lack of experimental tools with which to discern the orientation of a protein immobilized on a Qdot surface. For specific targeting, it is highly desirable that the delivery proteins (e.g., antibody) are properly oriented and fully functional. The Qdot bioconjugation step is, therefore, extremely important in obtaining success in bioimaging.

#### 2.4.2.2 Gold Nanoparticles

For over 30 years, nanometer-sized gold particles have been used to stain cells and tissue samples for electron microscopy. The basic principle of interactions between gold particles and biomolecules, like proteins, has been well studied for immunocytochemical staining applications. Although nanosize metals like gold and silver do not fluoresce they can effectively scatter light due to the collective oscillation of the conduction electrons induced by the incident electric field (light). This is known as “surface plasmon resonance” [20]. Thus, colloidal gold particles exhibit a range of intense colors in the visible and NIR spectral regions.

Gold nanoparticles, because of their strong SPR properties, have attracted considerable attention in bioimaging in recent years. The SPR signal originates from

the collective oscillation of conduction electrons upon interaction with absorption photons [136]. The SPR frequency depends on various factors, e.g., particle size [137] shape [138–140], dielectric properties [141, 142], aggregate morphology [143–146], surface functionalization [147, 148] and the refractive index of the surrounding medium [149–152]. Gold nanoparticles have high absorption [146, 151, 153] and scattering cross section [154, 155]. For example, the absorption cross section of a 5 nm diameter gold particle is about 3 nm [156] at a wavelength of 514 nm [136], which is about two orders of magnitude higher than that of organic fluorescent molecules at room temperature. The scattering cross section of gold nanoparticles is much larger than polymeric spherical particles of similar size, especially in the red region of the spectrum, i.e., red to NIR range, having potential in deep tissue imaging. For example, using composite core–shell gold (dielectric silica core and gold shell) particles, it is possible to tune the scattering from 600 to 1200 nm [141]. Due to excellent biocompatibility [157–159], gold nanoparticles have been widely used in immunohistochemistry (gold-based staining) and in ultra-sensitive DNA detection assays [146, 160, 161]. However, a few literature reports are available on gold nanoparticle-based cancers imaging.

**Gold Nanoparticle Synthesis** Various methods have been reported for the synthesis of gold nanoparticles. There are two general approaches (so-called “top-down” and “bottom-up”) that primarily categorize most reported synthesis strategies.

Synthesis of gold nanoparticles by employing laser ablation technique is an example of a “top-down” approach, where the embryonic (nascent) particles are formed from the ionized gold atoms via nucleation and growth processes. The challenge still remains how to stabilize particles in the solution phase. Using a surfactant-based capping agent (sodium dodecylsulfate, an ionic surfactant), Kondow et al. have successfully stabilized ultrafine (~5 nm) particles [162]. The capping agents, in general, control the particle size and size distribution, prevents particle aggregation, and stabilize particle solution (such as in aqueous-based medium).

In the “bottom up” approach, gold nanoparticles and gold nanocomposites (e.g., composite of gold and silica) have been chemically synthesized by reducing gold precursors. Various reduction methods have been reported. The major synthesis routes are as follows.

(a) Reduction of gold precursors (e.g., hydrochloroauric acid,  $\text{HAuCl}_4$ ) using appropriate reducing agents, such as citrate [163–166], sodium borohydride [167], ascorbic acid [168], etc. The citrate reduction of the gold(III) ions has been widely used. While sodium citrate reduces  $[\text{AuCl}_4]^-$  ions in hot aqueous solution, it forms a colloid. The reported average particle size is about 20 nm. Both the citrate ions and the oxidation products (e.g., acetone dicarboxylate) act as capping agents [163–165]. In conjunction with citrate ions, amphiphile surfactants have also been used that allowed particle size tuning upon varying the gold/stabilizer ratio [166]. A two-phase synthesis of gold nanoparticles (the Brust–Schiffrin method) has been reported in which a phase-transfer agent (tetraoctylammonium bromide) is used to transfer  $[\text{AuCl}_4]^-$  ions from an aqueous phase to an organic phase (tol-

uene) containing alkanethiol stabilizer. The Au(III) in organic phase is reduced by the addition of aqueous sodium borohydride. The resulting Au clusters are then capped immediately by alkanethiols. The Brust–Schiffrin method produces monodisperse particles (approx  $1.4 \pm 0.4$  nm) in the diameter range 1.5–5.2 nm [167, 169].

(b) Microemulsions [170–172], copolymer micelles [173], reversed micelles [172], surfactant, membranes, and other amphiphiles have been widely used for the synthesis of stabilized gold nanoparticles. Wilcoxon and coworkers have studied the synthesis of gold nanoparticles formed in aqueous media and in reverse micelles, using chemical and photolytic reduction [174]. The chemical reduction method was achieved using reduction agents such as hydrazine, sodium borohydride, and metallic sodium. The advantages of using reverse micelles for the synthesis of gold nanoparticles are (i) it produces monodisperse particles, (ii) particles remain coated by surfactant molecules that prevent particle aggregation surrounding the molecule and (iii) the size of the nanoparticles can be easily varied by changing reaction parameters such as concentrations of the reagents, water-to-surfactant molar ratio, temperature, time allowed for ripening of particles, etc.

(c) Another popular, long standing, method is the seed mediated route [175]. Indeed, the use of preformed metallic seeds as nucleation centers in nanoparticle synthesis has a long history [175–182]. Various references are available on the seed mediated growth of gold nanoparticles and also of gold nanorods [183–189]. Further nucleation during the “growth” part of the reaction often leads to non-uniform size distribution [190, 191]. The presence of seeds appears to cause additional nucleation (sometimes referred to as secondary nucleation) [184]. The step-by-step particle enlargement is considered more effective than the one-step seeding method to avoid additional nucleation [192]. More recently a modification of seed mediated method was used by Loo et al. [193] to achieve gold coating on the silica nanoparticles. Gold shells were grown using the method of Duff et al. [194]. Briefly, small gold colloid (1–3 nm) was adsorbed onto the aminated (amine functionalized) silica nanoparticle surface. More gold was then reduced onto these colloid nucleation sites using potassium carbonate and HAuCl<sub>4</sub> in the presence of formaldehyde. Gold shell particles have been used for whole blood immunoassay [195], photothermal tumor ablation [196] molecular imaging in live cells [197] and for cancer imaging and therapy [198].

(d) Reduction of gold precursors using a combination of appropriate reducing agents and radiation such as UV [188, 199–201], ultrasound [202–207], heat [208–210].

The UV irradiation method has been used to prepare gold nanoparticles [188, 199, 200, 211, 212], including when in synergy with micelles [211] or seeds [188]. The “gold seed particles” are prepared photochemically by UV irradiation, preferably in the presence of a neutral micelle of a non-ionic surfactant, Triton X-100 [poly(oxyethylene) iso-octyl phenyl ether] [201]. The seed particles subsequently grow by successive addition of metal ions and, again, exposure to UV irradiation under the same experimental conditions.

Several reports are available on the sonochemical synthesis (chemical synthesis using ultrasound radiation) of gold nanoparticles [202–207]. The general mecha-

nism of reduction is briefly described here. When a solution is exposed to ultrasound radiation of sufficient intensity it produces a cavitation field made up of a large distribution of vapor and gas-filled bubbles, which pulsate continuously. When the pressure inside the bubble falls below the vapor pressure of the liquid the bubble fills with vapor and grows. At a certain point when the pressure turns positive the bubble collapses, resulting in extreme temperatures and pressures in the interior. The localized hot point causes ionization of molecular species present within the interior of the collapsing bubble. For water vapor, this dissociation results in the production of H and OH radicals [213]. The radicals produced in the interior of the bubble can then diffuse into the bulk solution and reduce metal ions, yielding nanosized metallic particles such as gold nanoparticles.

Gold has also been fabricated by employing thermolysis [208–210] of organic derivatives of gold. This novel strategy involves the reductive elimination of thiolate ligands with simultaneous attachment of an organic moiety on the growing nuclei [210].

**Surface Functionalization and Bioconjugation** As mentioned in the previous section, gold nanoparticles have been widely used as immunostaining agents for labeling cell, tissue section, blots, etc. In general, protein conjugated gold nanoparticles are mostly used as labeling probes. Although the actual mechanism of macromolecule (e.g., proteins) binding to gold particles is poorly understood, some of the accepted mechanisms are [214]:

- (1) Protein binding via electrostatic (ionic) interaction. Negatively charged gold nanoparticles can bind to positively charged protein domains via electrostatic interactions.
- (2) Protein binding via hydrophobic interaction. Hydrophobic domains present in the protein structure can interact with the metal surface of the particle.
- (3) Protein binding via chemical interaction. Protein molecules containing sulfhydryl ( $-S-H$ ) groups can chemically interact with the gold atoms. This is also called dative binding.

Other biomolecules, such as protein A, antibodies, lectins, avidins (or streptavidins), etc., have also been conjugated to gold nanoparticles to be used as sensitive probes. Some of the binding strategies are described below.

**Protein A–Gold Conjugate** Protein A–gold conjugates are generally prepared by adsorbing protein A onto the gold surface. Following a similar method, many other immunoglobulin binding proteins can also be attached to gold nanoparticles. These probes have been used as “universal” probes for labeling cells, tissue sections and various blots. In a typical tissue labeling experiment, primary antibodies are specifically targeted to the tissue antigens. In the following step, protein A–gold conjugates bind to the antibodies. The advantage of this labeling technique is that the same protein A–gold conjugate can be used for various immunochemical procedures.

**Antibody–Gold Conjugate** Antibody–gold conjugated probes are prepared by coating antibodies directly on to the gold nanoparticle surface. These probes have been successfully used for the detection, localization and quantification of antigens on the target specimens. This is a powerful technique for detection of pathogens, intracellular foreign substances, monitoring cellular metabolic processes, etc.

**Lectin–Gold Conjugate** Lectin-coated gold nanoparticle probes have been used for the detection of sugar-binding receptors that are expressed on the cell membranes. Lectin molecules have specific carbohydrate binding sites. In this assay, a specific carbohydrate molecule is sandwiched between the lectin molecule and the cellular receptor. The objective of this assay is to localize glycoproteins, glycolipids, etc. on cell surfaces.

**Avidin (or Streptavidin)–Gold Conjugate** Avidin–gold conjugated probes have been used to localize, detect and quantify biotin molecules. This assay is similar to protein A–gold complex-based assays except that the primary antibodies are attached to biotin molecules.

#### 2.4.2.3 Dye-doped Silica Nanoparticles

Amorphous silica (silicon dioxide) nanoparticles that are produced via Stober's sol–gel [67, 215, 216] or microemulsion technique [66, 68, 91, 93, 217–225] have recently found applications in the area of bioimaging. Unlike Qdots or gold nanoparticles, silica does not have inherent strong fluorescence that can be exploited for sensitive imaging applications. However, silica nanoparticles can be made fluorescent by incorporating fluorescent dye molecules inside the silica matrix (dye-doping). Another approach could be attaching fluorescent dye molecules (via covalent binding) on the silica surface.

For bioimaging applications, it is preferable that dye molecules remain encapsulated by the silica matrix for the following reasons. Silica-based nanoparticles exhibit several attractive features, e.g., silica is water dispersible and is resistant to microbial attack. The size of silica particles remains unchanged by changing solvent polarity (i.e., resistant to swelling) and, therefore, silica porosity remains unaltered in a wide selection of solvents, including aqueous-based neutral and acidic solutions. A silica matrix is optically transparent, allowing excitation and emission light to pass through efficiently. Moreover, fluorescent dyes can be effectively entrapped inside the silica particles. The spectral characteristics of the dye molecules remain almost intact. Silica encapsulation provides a protective layer around dye molecules, reducing oxygen molecule penetration (which causes photodegradation of dye molecules) both in air and in aqueous medium (in the latter case dissolved oxygen). As a result, photostability of dye molecules increases substantially compared with bare dyes in solution. Amorphous silica appears to be a biocompatible [22] and non-toxic [23] material, and has potential biological applications.

The surface of a silica particle can be easily modified to attach biomolecules such as proteins, peptides, antibodies, oligonucleotides, etc., using conventional silane-based chemistry. For example, carboxylated silica nanoparticles can be covalently

attached to the amine groups of proteins, antibodies etc. through the formation of stable amide bond [216]. Peptides containing a cysteine residue (through a  $-S-H$  group) can be attached to the aminated silica nanoparticles [89] through (SPDP) coupling chemistry.

A general synthesis strategy of fluorescent silica nanoparticles is the incorporation of organic or metalloorganic dye molecules inside the silica matrix [66, 93, 226–231]. For example, a metalloorganic dye, tris(2,2'-bipyridyl)dichlororuthenium(II) (Rubpy), has been entrapped inside silica nanoparticles using a reverse microemulsion-based synthesis approach [66] where the positively charged Rubpy molecules were electrostatically bound to the negatively charged silica matrix. Dye-doped silica-based imaging probes are non-isotopic, sensitive and relatively photostable in the physiological environment. Additionally, the interaction potential of the silica surface can be easily manipulated to facilitate the interaction with cells [232–234]. Due to these novel features, functionalized silica nanoparticles (FSNPs) have found widespread applications in bioanalysis and bioimaging applications.

**Synthesis** There are two reported synthesis routes to dye-doped silica nanoparticles: Stober's sol-gel method and the reverse microemulsion method.

**Stober's Method** In a typical Stober's method, alkoxysilane compounds [e.g., tetraethylorthosilicate (TEOS), tetramethylorthosilicate (TMOS), various TEOS or TMOS derivatives, etc.] undergo base-catalyzed hydrolysis and condensation in an ammonia-ethanol-water mixture, forming a stable alcohol. This method has been widely used for synthesizing both pure and hybrid (when more than one silane compound are used, such as dye-doped silica particles) silica nanoparticles with particle diameters ranging from a few tens to several hundreds of nanometers (sub-micron size). Following Stober's protocol with a slight modification, fairly monodisperse organic dye doped fluorescent silica nanoparticles have been synthesized. Since organic dyes are normally hydrophobic, doping them inside the hydrophilic silica matrix is not straightforward. Typically, a reactive derivative of organic dye (e.g., amine-reactive fluorescein isothiocyanate, FITC) is first reacted with an amine-containing silane compound (e.g., APTS), forming a stable thiourea linkage. Then FITC conjugated APTS and TEOS are allowed to hydrolyze and condense to form FITC conjugated silica particles. Note that particles so formed will have some amount of bare dye molecules on the particle surface that is covalently attached. These bare dyes, due to their hydrophobic nature, will somewhat compromise the overall particle aqueous dispersibility and, also, they will be prone to photobleaching. Therefore, an additional coating with pure silica is usually applied around the dye-conjugated silica nanoparticles. Using Stober's method, bulk amounts (kilograms) of silica particles can be easily produced in a typical laboratory setup.

**Reverse Microemulsion (W/O) Method** This method is used for the synthesis of pure silica, as well as inorganic and organic dye-doped silica nanoparticles. Figure 2.3 shows a schematic representation of dye-doped silica nanoparticle synthesis steps. The W/O microemulsion is a robust technique for producing monodisperse



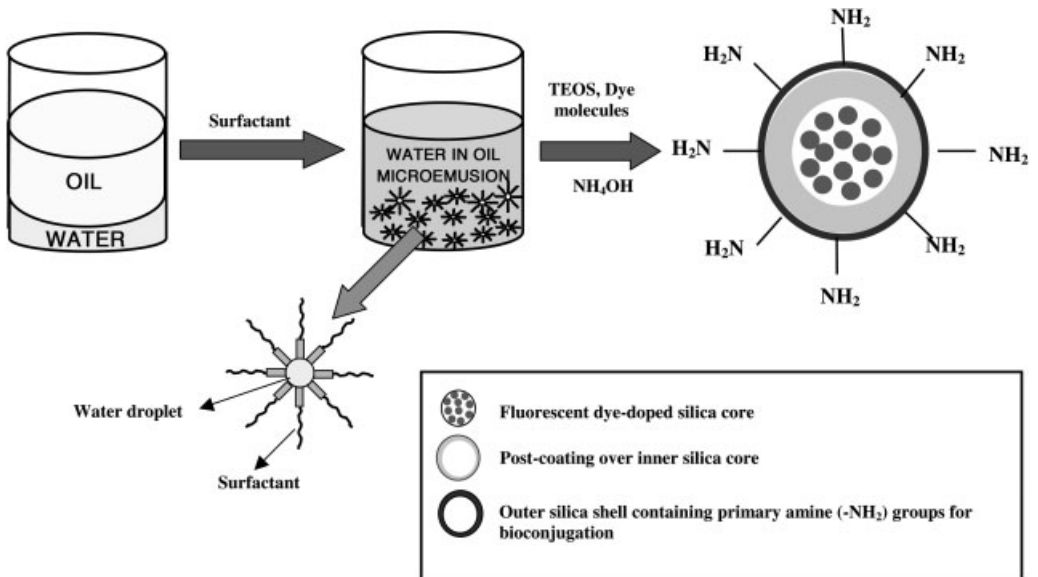


**Fig. 2.3.** Scheme of a water-in-oil (W/O) microemulsion mediated synthesis of dye-doped silica nanoparticles. (A) An immiscible mixture of water and oil (bulk phase). Upon addition of an appropriate surfactant, a W/O microemulsion is formed (B), where each tiny water droplet (nanosize water pool) is stabilized in the bulk oil phase with a surfactant coating (C). In reality each nanosize

water droplet serves as a nanoreactor for the synthesis of nanoparticles (D). The nanoparticle core (shown as filled circles), intermediate shell (inner ring) and outermost shell (outer ring) of the dye-doped silica nanoparticles are constructed in modular fashion by adding appropriate silane-based reagents at various stages of the synthesis process.

particles in the nanometer size range (tens to a few hundred nanometers). Figure 2.4 shows a typical transmission electron microscopic image of dye-doped silica nanoparticles synthesized using the W/O microemulsion technique. The W/O microemulsion is an isotropic, single-phase system that consists of surfactant, oil (as the bulk phase) and water (as nanosize droplets). Each surfactant-coated water droplet that is stabilized in the oil phase serves as an individual nanoreactor for the synthesis of silica nanoparticles. The water droplets undergo rapid and spontaneous collision and coalescence (fusion followed by separation) processes. As a result droplet contents (e.g., water-soluble reagents) are mixed together and chemical reactions (e.g., precipitation, hydrolysis and condensation reactions, etc.) take place. The surfactant present at the interface of oil and water nanodroplet is responsible for the thermodynamic stability of the W/O microemulsion system. Nucleation and growth processes are carried out inside the confined spherical volume of the nanoreactor. Varying the water-to-surfactant molar ratio and the dynamic properties of the microemulsion system helps to control the size of the nanoparticles.

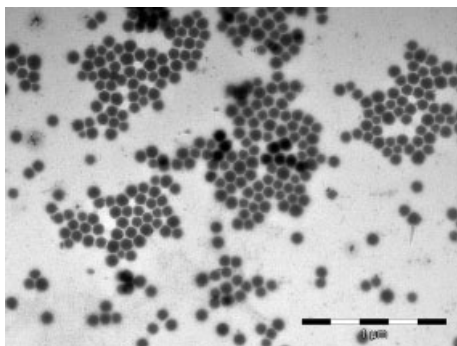


**Fig. 2.4.** Typical transmission electron microscopic image of dye-doped silica nanoparticles about 100 nm in size. Particles were synthesized using the water-in-oil (W/O) microemulsion technique. As expected, nanoparticles were highly monodisperse,

confirming that the W/O microemulsion is a robust technique for the synthesis of dye-doped silica nanoparticles. This technique can be easily adopted to produce other types of nanoparticles such as quantum dots and multimodal nanoparticles.

The fluorescence brightness of dye-doped silica nanoparticles can be improved by incorporating high-quantum-yield organic dyes having large absorption coefficients. In other words, brighter probes will improve the image resolution if encapsulated fluorescent dyes do not experience substantial photobleaching during imaging.

**Surface Functionalization and Bioconjugation** For bioimaging (e.g., cancer imaging), it is highly desirable that dye-doped silica nanoparticles are appropriately surface modified with cancer targeting molecules such as cancer specific antibodies, folates. This surface modification involves a few steps. Firstly, the particle surface should be modified to obtain appropriate functional groups such as, amines, carboxyls, thiols, etc. Secondly, using suitable coupling reagents, nanoparticles are attached to the bio-recognition molecules (such as antibodies, folates, etc.). Lastly, bioconjugated particles are targeted to cancers. Note that all these steps are usually carried out in aqueous-based solutions. A few bioconjugation methods are briefly mentioned below.

- (1) Bioconjugation with carboxylated particles. This is one of the most common bioconjugation techniques to immobilize protein molecules on silica nanoparticles. The surface of the nanoparticle is modified to obtain carboxyl groups ( $-\text{COOH}$ ) by using a carboxylated silane reagent. Biomolecules such as proteins, antibodies, etc. containing free amine functional groups are then covalently attached to the carboxyl functionalized nanoparticle, using carbodiimide-coupling chemistry [235].
- (2) Bioconjugation with aminated particles: Many cancer cells overexpress folate receptors. Cancer targeting with folate-conjugated nanoparticles has been

recently reported [67]. Folates are chemically attached to aminated silica nanoparticles using carbodiimide chemistry.

- (3) Bioconjugation with avidin–biotin binding: Avidin is a protein molecule that contains four specific binding pockets for biotin molecules. A strong binding affinity exists between avidin and biotin molecules, which is comparable to covalent binding. Avidin-coated nanoparticles are typically attached to biotinylated molecules such as antibodies, proteins, etc. [236].
- (4) Bioconjugation through disulfide bonding: Sulfhydryl-modified nanoparticles are conjugated to disulfide-linked oligonucleotides (e.g., DNAs). In this method, oligonucleotides are attached to nanoparticles through di-sulfide bond formation [237].
- (5) Bioconjugation using cyanogen bromide chemistry: Nanoparticles with hydroxyl groups (such as silica) can be activated with cyanogen bromide to form a reactive  $-OCN$  derivative of the nanoparticles. The  $OCN$  derivative then readily reacts with proteins (via amine groups), forming a “zero-length” bioconjugate as there is no spacer between the particle surface and the protein molecule [66].

## 2.5

### Optical Imaging of Cancer with Nanoparticles

Here we discuss the use of nanoparticle-based optical contrast agents in *in vitro* and *in vivo* experiments to image cancerous tissues. These nanoparticle-based contrast agents should provide a new gateway to characterize cancer at the molecular level. As we have already realized, these ultra-sensitive and specific probes provide a viable alternative to rapidly and non-invasively image the uptake, distribution and binding of nanoparticles to tumors. To establish the widespread use, it is important to understand the delivery, interaction and recognition mechanism of these contrast agents with cancer cells.

Various delivery vehicles with varying specificity have been used to target cancer tissues, mainly for drug delivery applications, some of which are folates, antibodies, lectins, growth factors, cytokines, hormones and low-density lipoproteins. Obviously, most of these carriers can be similarly used for molecular imaging applications. These can be broadly classified [6, 238] as active and passive targeting.

#### 2.5.1

##### Active Targeting

This refers to the conjugation of targeting ligands to nanoparticles to provide preferential accumulation into the tumor antigens and blood vessels with high affinity and specificity. This relies on specific interactive forces between lectins–carbohydrate, ligand–receptors and antibody–antigens [214].

Lectins can recognize and bind to glycoproteins that occur on the surface of cells. These proteins can bind to certain carbohydrates in a specific manner. Direct

and reverse lectin targeting have made use of these specific interactions to receptors or antigens expressed by the plasma membrane.

Folate receptor-based interactions are an excellent example of ligand–receptor based active targeting. Folate receptors are overexpressed on the surface of various cancers like those of the brain, ovary, kidney, breast and lungs. Confocal microscopic studies have demonstrated the selective intake and receptor-mediated endocytosis of folate-conjugated nanoparticles by tumor cells.

Antibody-mediated tumor targeting has been performed for detecting the presence of antigenic moieties on the surface of cancer cells. Tumor targeting ligands like monoclonal antibodies are attached to nanoparticles to target the specific receptors. These moieties are minimally present on the surface of normal tissues. Only certain antigens are actually tumor-specific and are referred to as tumor-specific antigens.

### 2.5.2

#### **Passive Targeting**

This mode of targeting particles to tumors includes strategies like using the enhanced permeation and retention (EPR) effect, use of a unique tumor environment and a direct local delivery of imaging agents to tumors.

In the EPR strategy, nanoparticles with a hydrophilic surface and diameter < 100 nm are made to accumulate at the tumors. The nanoparticles are engineered to prevent their uptake by the reticuloendothelial system, resulting in faster circulation and enhanced targeting ability in the physiological environment.

Various researchers have demonstrated the strategy of exploiting the unique tumor environment to trigger the release of therapeutic drugs. The drug is conjugated to tumor specific ligands and remains inactive till it reaches its target site. On reaching the tumor, the linkages are hydrolyzed either by the enzymes present, or by a change in pH and the drug is released by the nanoparticles.

Sometimes the imaging agents can be locally delivered to avoid its systemic circulation. But this is a challenging procedure as it involves the precise delivery using injections or surgical procedures that can be frequently cumbersome.

### 2.5.3

#### **Cancer Imaging with Quantum Dots**

Surface-functionalized quantum dots have been used to image various tumor cells and tissues in *in vitro* and *in vivo* experiments. Some of the different cell lines that have been used are human mammary epithelial tumor (MDA-MB-231) [239], human breast cancer (MDA-MB-435S [240], MDA-MD-435 [129], MCF 7 [240], and SK-BR-3 [64]), human prostate cancer [6], squamous carcinoma [19, 241] B16 melanoma (skin cancer) [56], human neuroblastoma (SK-N-SH) [242], colon tumor (SW480) [240], lung tumor (NCI H1299) [240], and bone tumor (Saos-2) [240] cells.

In 2002, Parak and coworkers used water-soluble [119] siloxane-coated quantum dots of two different sizes (2.8 and 4.1 nm cores), functionalized with thiol and/or amine groups, to label human mammary epithelial tumor cells (MDA-MB-231) [239]. These Qdots emitted at 554 and 626 nm, respectively, and were more photo-stable than ordinary organic dyes. Confocal microscopic images verified the presence of nanocrystals ingested rapidly inside the cells, and not on the surface. The quantum dot crystals were found in the perinuclear region of the cells even after a week. Almost at the same time, Ackerman and coworkers [129] incubated human breast carcinoma MDA-MD-435 cells with peptide coated quantum dots. These cells were then injected into mice to create tumor grafts. The mice were imaged 8–12 weeks after tumor inoculation. Although quantum dot probes were not detected inside the mice, *in vitro* tests showed that peptide-coated Qdots could specifically target tumor cells. Wu et al. have used streptavidin-conjugated commercial Qdots, QD 560 (emission maximum 560 nm) and QD 608 (emission max. 608 nm), to detect Her2 cancer markers on the surface of human breast cancer cells (SK-BR-3) [64]. The nanocrystals effectively labeled the cancer cells with negligible affinity to normal cells.

Recently, Nie and coworkers [6] have developed multifunctional nanoparticle probes (2.5 nm radius core protected by a 1-nm TOPO cap with 2-nm polymer coating and 5 nm PEG/affinity ligand shell) for imaging. The quantum dots were used for *in vivo* imaging to target to tumor sites either through a slow passive targeting process or a more efficient active targeting process. Squamous carcinoma cells have been labeled with quantum dots conjugated to epidermal growth factors (EGF) [19, 241]. These probes with a broad fluorescence peak in the NIR at 770 nm can specifically bind and activate the EGF receptors [241] of cancer cells in C3H mice [19]. Similarly dihydroxyliipoic acid (DHLA)-capped quantum dots can be efficiently delivered into B16 melanoma (skin cancer) cells [56]. The melanoma cells were labeled with the Qdots and injected into live mice to track tumor cell extravasation. The Qdots did not pose a detectable threat [56] to the labeled cells or the host animal and behaved as “inert fluorescent tags.” Quantum dots have also been used to detect integrin  $\alpha_v$  subunits in human neuroblastoma cells (SK-N-SH) [242] and label mouse lymphocytes (EL-4 cells derived from murine T-cell lymphoma) [243].

*In vivo* imaging to map sentinel lymph nodes (SLN) in rats and pigs has also been achieved using Qdots [238, 244, 245]. The presence of lymph node metastases is an early warning signal for breast and lung cancer. NIR nanocrystals with oligomeric phosphine coating (for solubility in aqueous buffers) was used to guide a surgeon during cancer surgery.

A new quantum dot based tool, called “Quantum Dot Phagokinetic Track assay” has been developed [240] to quantify the invasive potential of different tumor cells. When cancer cells move through a bed of Qdots, they engulf the nanocrystals and leave behind a phagokinetic trail depleted in Qdots. Cells with higher metastatic potential engulf more Qdots and leave a clearer trail than those with weak metastatic potential. Seven different cancerous and non-cancerous cell lines were used

to compare the different invasive potentials, including breast epithelial MCF 10A, breast tumor MDA-MB-231, MDA-MB-435S, MCF 7, colon tumor SW480, lung tumor NCI H1299, and bone tumor Saos-2. This assay rapidly discriminates between invasive and non-invasive cancer cell lines with greater sensitivity than the conventional Boyden chamber invasion assay.

#### 2.5.4

#### Cancer Imaging with Gold Nanoparticles

Gold bioconjugates have been used for vital imaging of precancerous and cancerous cells by researchers for *in vitro* and *in vivo* experiments. The unique optical property of the metal in the nanosized range has been used for detecting breast carcinoma cells (SK-BR-3) [246] breast cancer markers like HER2, oral epithelial live cancer cells (HOC 313 clone 8 and HSC 3) [73] and neoplastic cervical biopsies [75].

Gold nanocages <40 nm can be used for specific targeting of breast cancer cells [246]. Gold-bioconjugates with surface plasmon resonance peaks at 800 nm were synthesized and used to label breast cancer cells (SK-BR-3) that overexpresses epidermal growth factor receptor 2 (EGFR2 or HER2). Primary antibodies (monoclonal anti-HER2 antibody from mouse) were immobilized on the SK-BR-3 cells. Secondary antibody (e.g., anti-mouse immunoglobulin G or IgG) conjugated gold nanocages were added to the cancer cells bound with anti-HER2 antibodies and imaged. A gold nanoshell based contrast agent [198] has also been used to image breast cancer cells. The nanoshell consists of a dielectric core surrounded by a thin gold shell. The dimensions were maintained to obtain an optical scattering peak in the NIR region at around 800 nm. In this case, anti-HER2 was attached to a PEG linker, and then attached to the nanoshell surface using a sulfur-containing group. The nanoshells successfully detected the HER2-positive SKBr3 breast adenocarcinoma cells.

SPR scattering imaging or SPR absorption spectroscopy can be used with antibody-conjugated gold nanoparticles for imaging oral epithelial living cancer cells *in vivo* and *in vitro* [73]. Two malignant oral epithelial cell lines (HOC 313 clone 8 and HSC 3) and a non-malignant cell line (HaCaT) were incubated with the gold nanoparticles. The cell cytoplasm contained dispersed and aggregated forms of the colloidal gold nanoparticles, with non-specific uptake for malignant cells. The gold nanoparticles conjugated to monoclonal anti-EGFR antibodies specifically and homogeneously bound to the cancer cell with enormously greater affinity than to non-cancerous cells. A relatively sharper SPR absorption band with a redshifted maximum was obtained for specific binding compared with that obtained for noncancerous cells.

Sokolov and coworkers [75] have reported the use of gold bioconjugates with monoclonal antibodies against EGFR for the real-time vital optical imaging of precancerous cells and tissues. Cervical epithelial cancer cells (SiHa cells) and 3D tissue constructs and normal and cancerous cervical biopsies were used for *in vivo*

imaging. They have shown the topical delivery of gold conjugates for imaging the whole epithelium.

### 2.5.5

#### Cancer Imaging with Dye-doped Silica Nanoparticles

Dye-doped silica nanoparticles have been used for *in vitro* imaging of cancer cells. Researchers have demonstrated their use in labeling human leukemia [66, 92, 93], HepG liver cancer [68], human oral carcinoma [67] and lung carcinoma cells [91, 217]. Figure 2.5 shows a confocal image of human lung cancer cells labeled with folate-conjugated FITC-doped 100-nm silica nanoparticles. Tan and coworkers have used 60-nm dye-doped silica nanoparticles, doped with Rubpy dye to label human leukemia cells [66, 92, 93]. Similarly, He and coworkers [68] have reported a method to recognize HepG liver cancer cells using FITC-APTS-doped silica nanoparticles. More recently, FITC-APTS-doped folate-conjugated silica nanoparticles were used to target overexpressed folate receptors in human oral carcinoma [67] and lung carcinoma cells [91, 217]. The dye-doped silica nanoparticles were covalently attached to folic acid molecules by a carbodiimide coupling reaction. The affinity of folate immobilized conjugates for folate receptors on the cancer cell surface were utilized for imaging [67]. The nanoparticles were detected using fluorescent techniques and imaged using a confocal microscope.

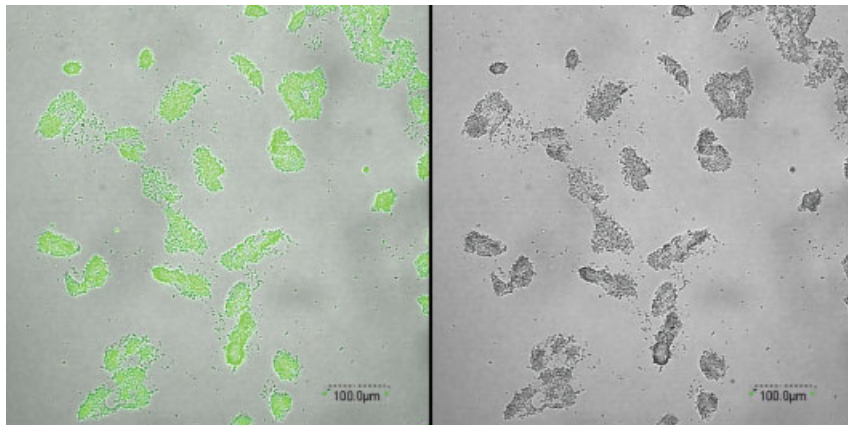


**Fig. 2.5.** Folate conjugated FITC-doped 100-nm silica nanoparticles were targeted to human lung cancer cells. Confocal microscopic images (left: fluorescence, right: transmission) showed that folate-conjugated nanoparticles successfully labeled cancer cells. This nanoparticle-based cancer labeling strategy

could be extended further to image other type of cancer cells that overexpress folate receptors. Note that nanoparticles were taken up by the cancer cells via receptor-mediated endocytosis. The extracellular nanoparticle concentration was  $50 \mu\text{g mL}^{-1}$  and the incubation time was 2 h.

## 2.6

### Other Nanoparticle-based Optical Contrast Agents

Up-converting phosphors, dye-doped polymer particles are also considered as optical nanoparticle probes. However, application of these particles for cancer imaging is yet to be explored.

In up-converting phosphor nanoparticles both the absorber and the emitter ions are present in the crystal lattice. The absorber is excited by the energy of the infrared (IR) light source. The absorber transfers this energy to the emitter ion that emits a detectable photon. The up-conversion of light is caused by multiphoton process. The unique feature of converting IR light into visible radiation of the phosphors has shown great promise as a new type of fluorescence reporter for bioanalysis [247, 248]. Their emission bandwidths are generally very narrow (25–50 nm). There are several advantages of using up-converting phosphor technology (UPT) for bioanalysis. First, emission occurs at discrete wavelengths with a large anti-Stokes shift. Second, the emission is strong and does not fade away. Third, excitation wavelength is in the IR range, which reduces the background signal drastically by completely eliminating autofluorescence from the biological samples. Fourth, it has simultaneous detection capability for multiple target analytes. Fifth, the instrumentation requires low cost microscope modifications for IR excitation and visible emission. Zijlmans et al. have reported application of the phosphor probe for the sensitive detection of antigens in tissue sections or on cell membranes [248]. They conjugated phosphor [green-emitting ytterbium/erbium (Y.Yb.Er) $O_2S$  and a blue-emitting ytterbium/thulium (Y.Yb.Tm) $_2O_2S$ ] particles to NeutrAvidin (Pierce, Rockford, IL) first and then successfully targeted in a model system consisting of prostate-specific antigen in tissue sections and the CD4 membrane antigen on human lymphocytes.

Various fluorescent polymers particles have been reported for bioimaging applications, such as long-lifetime europium chelate complex-doped 107-nm polystyrene particles [249–251], fluorescein isothiocyanate labeled poly(butyl cyanoacrylate) nanoparticles [252], and fluorescent gelatin NPs [253]. Multimodal (fluorescent and paramagnetic) nanoparticles have been prepared where a NIR dye (Cy5.5) and iron oxide nanoparticles were co-doped in dextran particles. These particles were used in constructing quantitative 3D tomographic NIR fluorescence imaging combined with MR imaging to yield highly detailed anatomic and molecular information in living organisms [254].

## 2.7

### Conclusions and Perspectives

Early diagnosis can prevent cancer and possibly cure cancer patients. However, currently available techniques such as CT scan, MRI scan, PET scan, etc. are not sensitive enough to diagnose cancers at the early stage. The challenge is to develop sophisticated *in vivo* imaging techniques that could precisely detect the presence of a



few abnormal cells in the body. Optical-based imaging systems have potential for early cancer diagnosis. To achieve better resolution, a sensitive optical imaging system must be coupled with highly sensitive image-enhancing optical contrast agents. Unlike organic-based dyes, nanoparticle-based contrast agents such as quantum dots, gold nanoparticles, and dye-doped silica nanoparticles have shown great promise for highly sensitive optical imaging of cancers. As described in this chapter, most successful experiments were conducted *in vitro* using various cancer cell lines. So far, few animal experiments have been performed that demonstrate that quantum dots have strong potential for *in vivo* cancer imaging.

The future of nanoparticle-based *in vivo* optical contrast agents and cancer imaging will rely upon many factors.

Firstly, the toxicity of nanoparticles needs to be thoroughly investigated. There are no straightforward answers to the toxicity of quantum dots, gold- and silica-based nanomaterials. Cadmium ions from cadmium sulfide and cadmium selenide-based quantum dots are highly toxic to cells. Although effective surface passivation with zinc sulfide and further coating with polymer, silica, etc. can reduce the release of cadmium ions, the long-term fate of these materials is highly uncertain, especially under *in vivo* conditions. Gold- and silica-based materials are biocompatible substances. However, their long-term *in vivo* behavior in the nanoscale size regime is also uncertain. Again, these particles are not digestible, meaning that if they are not naturally cleared by the body, they will be accumulated somewhere. This might cause additional threats in terms of secondary toxic effect.

Secondly, the size of the particle would play a critical role. It is probably better to work with smaller particles, as they can be easily loaded intra-cellularly. Small particles (<10 nm) may be excreted naturally through the body (via kidney and spleen). Despite these advantages, smaller particles would have some limitations with respect to image resolution. As cancer cells divide rapidly, the concentration of particles in daughter cells will be diluted. As a result, image resolution will be compromised with time.

Thirdly, development of nanoparticles with NIR excitation and emission would be extremely important for deep tissue imaging. Tumors that are present in a deeper tissue area can be imaged using NIR nanoparticles. A few NIR quantum dots have been tested in animal models recently. However, little work has been performed on the development of NIR silica or gold nanoparticles.

Fourthly, nanoparticles with high extinction coefficients, quantum yields and photostability would be highly desirable for sensitive cancer imaging. Quantum dots are likely to be better candidates than gold- and silica-based nanoparticles. Further improvement towards effective surface passivation would be important. The spectral characteristics of gold nanoparticles are highly sensitive to the surface-capping agents and therefore, robust surface capping would be necessary for stable spectral output. As silica is porous, dye-doped silica nanoparticles would experience photobleaching as well as fluorescence quenching to some extent.

Lastly, effective surface modification and bioconjugation for nanoparticle delivery are highly desirable. No matter how robust the nanoparticles are, the ultimate image contrast would also depend on the nanoparticle loading efficiency. The selec-

tion of specific cancer targeting strategies would thus play a crucial role. We envision that this part of the research and development would attract substantial attention in the near future.

Nanoparticle-based optical contrast agents have a bright future in cancer imaging. However, the key is how to make them smart in all the aspects mentioned above for human applications. Although there is no straightforward route to such smart particles, research progress in this area over the last few years has been overwhelming.

## Acknowledgments

We acknowledge the Particle Engineering Research Center (PERC) at the University of Florida for the entire support. Both SS and DD express sincere thanks to Dr. Parvesh Sharma, PERC, for his generous help during the preparation of the manuscript.

## References

- 1 TANNOCK, I. F., HILL, R. P. (Eds.), *The Basic Science of Oncology*, 3rd edn., McGraw-Hill, Health Professions Division, New York, 1998.
- 2 *Cancer Facts & Figures 2005*. American Cancer Society, Atlanta, 2005, p. 1.
- 3 HANAHAN, D., WEINBERG, R. A., The hallmarks of cancer. *Cell* 2000, 100, 57–70.
- 4 SCHULZ, W. A., *Molecular Biology of Human Cancers: An Advanced Student's Textbook*. Springer, New York, NY, 2005, pp. 11–17.
- 5 BREMER, C., NTZIACHRISTOS, V., WEISSLEDER, R., Optical-based molecular imaging: Contrast agents and potential medical applications. *Eur. Radiol.* 2003, 13, 231–243.
- 6 GAO, X. H., CUI, Y. Y., LEVENSON, R. M., CHUNG, L. W. K., NIE, S. M., In vivo cancer targeting and imaging with semiconductor quantum dots. *Nat. Biotechnol.* 2004, 22, 969–976.
- 7 MEDINTZ, I. L., UYEDA, H. T., GOLDMAN, E. R., MATTOUSSI, H., Quantum dot bioconjugates for imaging, labelling and sensing. *Nat. Mater.* 2005, 4, 435–446.
- 8 NALWA, H. R. (Ed.), *Encyclopedia of Nanoscience and Nanotechnology*, American Scientific Publishers, Stevenson Ranch, CA, 2004.
- 9 FELDHEIN, D. L., FOSS, C. A. (Eds.), *Metal Nanoparticles: Synthesis, Characterization & Applications*, 1st edn., Marcel Dekker, New York, NY, 2001.
- 10 SCHMID, G. (Ed.), *Nanoparticles: From Theory to Application*, John Wiley & Sons, Hoboken, NJ, 2004.
- 11 ROTELLO, V., *Nanoparticles: Building Blocks for Nanotechnology*, in *Nanostructure Science and Technology*, LOCKWOOD, D. J. (Ed.), 1st edn., Springer, New York, NY, 2003, 1–300.
- 12 NIEMEYER, C. M., MIRKIN, C. A. (Eds.), *Nanobiotechnology: Concepts, Applications and Perspectives*, John Wiley & Sons, Hoboken, NJ, 2004.
- 13 BEN-ARI, E. T., Nanoscale quantum dots hold promise for cancer applications. *J. Natl. Cancer Institute* 2003, 95, 502–504.
- 14 BRIGGER, I., DUBERNET, C., COUVREUR, P., Nanoparticles in cancer therapy and diagnosis. *Adv. Drug Delivery Rev.* 2002, 54, 631–651.
- 15 LICHA, K., *Contrast Agents for Optical Imaging*, in *Contrast Agents II*, Springer, Berlin, Heidelberg, 2002, 1–29.

- 16 LICHA, K., OLBRICH, C., Optical imaging in drug discovery and diagnostic applications. *Adv. Drug Delivery Rev.* **2005**, *57*, 1087–1108.
- 17 LICHA, K., RIEFKE, B., EBERT, B., GROTZINGER, C., Cyanine dyes as contrast agents in biomedical optical imaging. *Acad. Radiol.* **2002**, *9*, S320–S322.
- 18 MICHALET, X., PINAUD, F. F., BENTOLILA, L. A., TSAY, J. M., DOOSE, S., LI, J. J., SUNDARESAN, G., WU, A. M., GAMBHIR, S. S., WEISS, S., Quantum dots for live cells, in vivo imaging, and diagnostics. *Science* **2005**, *307*, 538–544.
- 19 MORGAN, N. Y., ENGLISH, S., CHEN, W., CHERNOMORDIK, V., RUSSO, A., SMITH, P. D., GANDBAKHCHE, A., Real time in vivo non-invasive optical imaging using near-infrared fluorescent quantum dots. *Acad. Radiol.* **2005**, *12*, 313–323.
- 20 SANTRA, S., XU, J. S., WANG, K. M., TAN, W. H., Luminescent nanoparticle probes for bioimaging. *J. Nanosci. Nanotechnol.* **2004**, *4*, 590–599.
- 21 SOKOLOV, K., AARON, J., HSU, B., NIDA, D., GILLENWATER, A., FOLLEN, M., MACAULAY, C., ADLER-STORTHZ, K., KORGEL, B., DESCOUR, M., PASQUALINI, R., ARAP, W., LAM, W., RICHARDS-KORTUM, R., Optical systems for in vivo molecular imaging of cancer. *Technol. Cancer Res. Treatment* **2003**, *2*, 491–504.
- 22 ROSI, N. L., MIRKIN, C. A., Nanostructures in biodiagnostics. *Chem. Rev.* **2005**, *105*, 1547–1562.
- 23 SMITH, P. W., Fluorescence emission-based detection and diagnosis of malignancy. *J. Cell. Biochem.* **2002**, *54*–59.
- 24 WEISSLEDER, R., Scaling down imaging: Molecular mapping of cancer in mice. *Nat. Rev. Cancer* **2002**, *2*, 11–18.
- 25 BORNHOP, D. J., CONTAG, C. H., LICHA, K., MURPHY, C. J., Advances in contrast agents, reporters, and detection. *J. Biomed. Opt.* **2001**, *6*, 106–110.
- 26 BECKER, A., HESSENIUS, C., LICHA, K., EBERT, B., SUKOWSKI, U., SEMMLER, W., WIEDENMANN, B., GROTZINGER, C., Receptor-targeted optical imaging of tumors with near-infrared fluorescent ligands. *Nat. Biotechnol.* **2001**, *19*, 327–331.
- 27 BECKER, A., RIEFKE, B., EBERT, B., SUKOWSKI, U., RINNEBERG, H., SEMMLER, W., LICHA, K., Macromolecular contrast agents for optical imaging of tumors: Comparison of indotricarbocyanine-labeled human serum albumin and transferrin. *Photochem. Photobiol.* **2000**, *72*, 234–241.
- 28 WEISSLEDER, R., TUNG, C. H., MAHMOOD, U., BOGDANOV, A., In vivo imaging of tumors with protease-activated near-infrared fluorescent probes. *Nat. Biotechnol.* **1999**, *17*, 375–378.
- 29 TUNG, C. H., MAHMOOD, U., BREDOW, S., WEISSLEDER, R., In vivo imaging of proteolytic enzyme activity using a novel molecular reporter. *Cancer Res.* **2000**, *60*, 4953–4958.
- 30 BREMER, C., TUNG, C. H., WEISSLEDER, R., In vivo molecular target assessment of matrix metalloproteinase inhibition. *Nat. Med.* **2001**, *7*, 743–748.
- 31 BREMER, C., BREDOW, S., MAHMOOD, U., WEISSLEDER, R., TUNG, C. H., Optical imaging of matrix metalloproteinase-2 activity in tumors: Feasibility study in a mouse model. *Radiology* **2001**, *221*, 523–529.
- 32 ACHILEFU, S., DORSHOW, R. B., BUGAJ, J. E., RAJAGOPALAN, R., Novel receptor-targeted fluorescent contrast agents for in vivo tumor imaging. *Investigative Radiol.* **2000**, *35*, 479–485.
- 33 SWEENEY, T. J., MAILANDER, V., TUCKER, A. A., OLOMU, A. B., ZHANG, W. S., CAO, Y. A., NEGRIN, R. S., CONTAG, C. H., Visualizing the kinetics of tumor-cell clearance in living animals. *Proc. Natl. Acad. Sci. U.S.A.* **1999**, *96*, 12 044–12 049.
- 34 HILLMAN, E. M. C., HEBDEN, J. C., SCHWEIGER, M., DEGHANI, H., SCHMIDT, F. E. W., DELPY, D. T., ARRIDGE, S. R., Time resolved optical tomography of the human forearm. *Phys. Med. Biol.* **2001**, *46*, 1117–1130.
- 35 POGUE, B. W., POPLACK, S. P., MCBRIDE, T. O., WELLS, W. A.,

- OSTERMAN, K. S., OSTERBERG, U. L., PAULSEN, K. D., Quantitative hemoglobin tomography with diffuse near-infrared spectroscopy: Pilot results in the breast. *Radiology* **2001**, *218*, 261–266.
- 36 BENARON, D. A., HINTZ, S. R., VILLRINGER, A., BOAS, D., KLEINSCHMIDT, A., FRAHM, J., HIRTH, C., OBRIG, H., VAN HOUTEN, J. C., KERMIT, E. L., CHEONG, W. F., STEVENSON, D. K., Noninvasive functional imaging of human brain using light. *J. Cerebral Blood Flow Metab.* **2000**, *20*, 469–477.
- 37 POGUE, B. W., POPLACK, S. P., MCBRIDE, T. O., WELLS, W. A., OSTERMAN, K. S., OSTERBERG, U. L., Hemoglobin imaging of breast tumors with near-infrared tomography. *Radiology* **2000**, *214*, 609–609.
- 38 DEMCHIK, L. L., SAMENI, M., NELSON, K., MIKKELSEN, T., SLOANE, B. F., Cathepsin B and glioma invasion. *Int. J. Developmental Neurosci.* **1999**, *17*, 483–494.
- 39 YAN, S. Q., SAMENI, M., SLOANE, B. F., Cathepsin B and human tumor progression. *Biol. Chem.* **1998**, *379*, 113–123.
- 40 REMPEL, S. A., ROSENBLUM, M. L., MIKKELSEN, T., YAN, P. S., ELLIS, K. D., GOLEMBIESKI, W. A., SAMENI, M., ROZHIN, J., ZIEGLER, G., SLOANE, B. F., Cathepsin-B expression and localization in glioma progression and invasion. *Cancer Res.* **1994**, *54*, 6027–6031.
- 41 NTZIACHRISTOS, V., BREMER, C., WEISSLEDER, R., Fluorescence imaging with near-infrared light: New technological advances that enable in vivo molecular imaging. *Eur. Radiol.* **2003**, *13*, 195–208.
- 42 HAUGLAND, R. P. *Handbook of Fluorescent Probes and Research Products*, Molecular Probes, Eugene, OR, **2003**.
- 43 YANG, M., BARANOV, E., JIANG, P., SUN, F. X., LI, X. M., LI, L. N., HASEGAWA, S., BOUVET, M., AL-TUWAIJRI, M., CHISHIMA, T., SHIMADA, H., MOOSSA, A. R., PENMAN, S., HOFFMAN, R. M., Whole-body optical imaging of green fluorescent protein-expressing tumors and metastases. *Proc. Natl. Acad. Sci. U.S.A.* **2000**, *97*, 1206–1211.
- 44 MOORE, A., SERGEYEV, N., BREDOW, S., WEISSLEDER, R., A model system to quantitate tumor burden in locoregional lymph nodes during cancer spread. *Invasion & Metastasis* **1999**, *18*, 192–197.
- 45 MOORE, A., MARECOS, E., SIMONOVA, M., WEISSLEDER, R., BOGDANOV, A., Novel gliosarcoma cell line expressing green fluorescent protein: A model for quantitative assessment of angiogenesis. *Microvascular Res.* **1998**, *56*, 145–153.
- 46 STROH, M., ZIMMER, J. P., DUDA, D. G., LEVCHENKO, T. S., COHEN, K. S., BROWN, E. B., SCADDEN, D. T., TORCHILIN, V. P., BAWENDI, M. G., FUKUMURA, D., JAIN, R. K., Quantum dots spectrally distinguish multiple species within the tumor milieu in vivo. *Nat. Med.* **2005**, *11*, 678–682.
- 47 SONVICO, F., DUBERNET, C., COLOMBO, P., COUVREUR, P., Metallic colloid nanotechnology, applications in diagnosis and therapeutics. *Curr. Pharmaceut. Design* **2005**, *11*, 2091–2105.
- 48 DRESSLER, C., MINET, O., NOVKOV, V., MULLER, G., BEUTHAN, J., Combination of bioactive quantum dots with an organic fluorescent dye for two-color labeling of cancer cells – Comparison between laser-induced and lamp-induced fluorescence. *Laser Phys.* **2005**, *15*, 536–544.
- 49 PARUNGO, C. P., OHNISHI, S., KIM, S. W., KIM, S., LAURENCE, R. G., SOLTESZ, E. G., CHEN, F. Y., COLSON, Y. L., COHN, L. H., BAWENDI, M. G., FRANGIONI, J. V., Intraoperative identification of esophageal sentinel lymph nodes with near-infrared fluorescence imaging. *J. Thoracic Cardiovascular Surgery* **2005**, *129*, 844–850.
- 50 BALLOU, B., ERNST, L. A., WAGGONER, A. S., Fluorescence imaging of tumors in vivo. *Curr. Med. Chem.* **2005**, *12*, 795–805.
- 51 FERRARI, M., Cancer nanotechnology: Opportunities and challenges. *Nat. Rev. Cancer* **2005**, *5*, 161–171.

- 52 LYONS, S. K., Advances in imaging mouse tumour models in vivo. *J. Pathol.* **2005**, *205*, 194–205.
- 53 JIANG, W., PAPA, E., FISCHER, H., MARDYANI, S., CHAN, W. C. W., Semiconductor quantum dots as contrast agents for whole animal imaging. *Trends Biotechnol.* **2004**, *22*, 607–609.
- 54 SAGE, L., Finding cancer cells with quantum dots. *Anal. Chem.* **2004**, *76*, 453A.
- 55 CHEN, G. Y. J., YAO, S. Q., Lighting up cancer cells with “dots”. *Lancet* **2004**, *364*, 2001–2003.
- 56 VOURA, E. B., JAISWAL, J. K., MATTOUSSI, H., SIMON, S. M., Tracking metastatic tumor cell extravasation with quantum dot nanocrystals and fluorescence emission-scanning microscopy. *Nat. Med.* **2004**, *10*, 993–998.
- 57 WU, X. Y., HARPER, T. F., NG, C. H., Simultaneous detection of HER2 gene amplification and HER2 protein expression in breast cancer cells with semiconductor nanocrystal quantum dots. *FASEB J.* **2004**, *18*, C103–C103.
- 58 Quantum dots target, image cancer cells. *Chem. Eng. News* **2004**, *82*, 40–40.
- 59 MINET, O., DRESSLER, C., BEUTHAN, J., Heat stress induced redistribution of fluorescent quantum dots in breast tumor cells. *J. Fluorescence* **2004**, *14*, 241–247.
- 60 BEUTHAN, J., DRESSLER, C., MINET, O., Laser-induced fluorescence detection of quantum dots redistributed in thermally stressed tumor cells. *Laser Phys.* **2004**, *14*, 213–219.
- 61 UREN, R. F., Cancer surgery joins the dots. *Nat. Biotechnol.* **2004**, *22*, 38–39.
- 62 KIM, S., LIM, Y. T., SOLTESZ, E. G., DE GRAND, A. M., LEE, J., NAKAYAMA, A., PARKER, J. A., MIHALJEVIC, T., LAURENCE, R. G., DOR, D. M., COHN, L. H., BAWENDI, M. G., FRANGIONI, J. V., Near-infrared fluorescent type II quantum dots for sentinel lymph node mapping. *Nat. Biotechnol.* **2004**, *22*, 93–97.
- 63 WU, X. Y., LIU, H. J., LIU, J. Q., HALEY, K. N., TREADWAY, J. A., LARSON, J. P., GE, N. F., PEALE, F., BRUCHEZ, M. P., Immunofluorescent labeling of cancer marker Her2 and other cellular targets with semiconductor quantum dots. *Nat. Biotechnol.* **2003**, *21*, 452–452.
- 64 WU, X. Y., LIU, H. J., LIU, J. Q., HALEY, K. N., TREADWAY, J. A., LARSON, J. P., GE, N. F., PEALE, F., BRUCHEZ, M. P., Immunofluorescent labeling of cancer marker Her2 and other cellular targets with semiconductor quantum dots. *Nat. Biotechnol.* **2003**, *21*, 41–46.
- 65 LAVAN, D. A., LYNN, D. M., LANGER, R., Moving smaller in drug discovery and delivery. *Nat. Rev. Drug Discov.* **2002**, *1*, 77–84.
- 66 SANTRA, S., ZHANG, P., WANG, K. M., TAPEC, R., TAN, W. H., Conjugation of biomolecules with luminophore-doped silica nanoparticles for photostable biomarkers. *Anal. Chem.* **2001**, *73*, 4988–4993.
- 67 SANTRA, S., LIESENFELD, B., DUTTA, D., CHATEL, D., BATICH, C. D., TAN, W. H., MOUDGIL, B. M., MERICLE, R. A., Folate conjugated fluorescent silica nanoparticles for labeling neoplastic cells. *J. Nanosci. Nanotechnol.* **2005**, *5*, 899–904.
- 68 HE, X. X., DUAN, J. H., WANG, K. M., TAN, W. H., LIN, X., HE, C. M., A novel fluorescent label based on organic dye-doped silica nanoparticles for HepG liver cancer cell recognition. *J. Nanosci. Nanotechnol.* **2004**, *4*, 585–589.
- 69 HE, X. X., WANG, K. M., TAN, W. H., LI, J., YANG, X. H., HUANG, S. S., LI, D., XIAO, D., Photostable luminescent nanoparticles as biological label for cell recognition of system lupus erythematosus patients. *J. Nanosci. Nanotechnol.* **2002**, *2*, 317–320.
- 70 STSIAPURA, V., SUKHANOVA, A., ARTEMYEV, M., PLUOT, M., COHEN, J. H. M., BARANOV, A. V., OLEINIKOV, V., NABIEV, I., Functionalized nanocrystal-tagged fluorescent polymer beads: Synthesis, physicochemical characterization, and immunolabeling application. *Anal. Biochem.* **2004**, *334*, 257–265.
- 71 PAN, X. Q., LEE, R. J., RATNAM, M., Penetration into solid tumor tissue

- of fluorescent latex microspheres: A mimic of liposome particles. *Anticancer Res.* **2004**, *24*, 3005–3008.
- 72 UENO, H., HIHARA, J., SHIMIZU, K., OSAKI, A., YAMASHITA, Y., YOSHIDA, K., TOGE, T., Experimental study on fluorescent microspheres as a tracer for sentinel node detection. *Anticancer Res.* **2005**, *25*, 821–825.
- 73 EL-SAYED, I. H., HUANG, X. H., EL-SAYED, M. A., Surface plasmon resonance scattering and absorption of anti-EGFR antibody conjugated gold nanoparticles in cancer diagnostics: Applications in oral cancer. *Nano Lett.* **2005**, *5*, 829–834.
- 74 COPLAND, J. A., EGHTEHARI, M., POPOV, V. L., KOTOV, N., MAMEDOVA, N., MOTAMEDI, M., ORAEVSKY, A. A., Bioconjugated gold nanoparticles as a molecular based contrast agent: Implications for imaging of deep tumors using optoacoustic tomography. *Mol. Imaging Biol.* **2004**, *6*, 341–349.
- 75 SOKOLOV, K., FOLLEN, M., AARON, J., PAVLOVA, I., MALPICA, A., LOTAN, R., RICHARDS-KORTUM, R., Real-time vital optical imaging of precancer using anti-epidermal growth factor receptor antibodies conjugated to gold nanoparticles. *Cancer Res.* **2003**, *63*, 1999–2004.
- 76 SCHULTZ, S., SMITH, D. R., MOCK, J. J., SCHULTZ, D. A., Single-target molecule detection with nonbleaching multicolor optical immunolabels. *Proc. Natl. Acad. Sci. U.S.A.* **2000**, *97*, 996–1001.
- 77 SCHULTZ, S., MOCK, J., SMITH, D. R., SCHULTZ, D. A., Nanoparticle based biological assays. *J. Clinical Ligand Assay* **1999**, *22*, 214–216.
- 78 YGUERABIDE, J., YGUERABIDE, E. E., Resonance light scattering particles as ultrasensitive labels for detection of analytes in a wide range of applications. *J. Cell. Biochem.* **2001**(Suppl.), 71–81.
- 79 GUO, J., YANG, W. L., DENG, Y. H., WANG, C. C., FU, S. K., Organic-dye-coupled magnetic nanoparticles encaged inside thermoresponsive PNIPAM microcapsules. *Small* **2005**, *1*, 737–743.
- 80 VEISEH, O., SUN, C., GUNN, J., KOHLER, N., GABIKIAN, P., LEE, D., BHATTARAI, N., ELLENBOGEN, R., SZE, R., HALLAHAN, A., OLSON, J., ZHANG, M. Q., Optical and MRI multifunctional nanoprobe for targeting gliomas. *Nano Lett.* **2005**, *5*, 1003–1008.
- 81 DEL CAMPO, A., SEN, T., LELLOUCHE, J. P., BRUCE, I. J., Multifunctional magnetite and silica-magnetite nanoparticles: Synthesis, surface activation and applications in life sciences. *J. Magn. Magn. Mater.* **2005**, *293*, 33–40.
- 82 KOPELMAN, R., KOO, Y. E. L., PHILBERT, M., MOFFAT, B. A., REDDY, G. R., MCCONVILLE, P., HALL, D. E., CHENEVERT, T. L., BHOJANI, M. S., BUCK, S. M., REHEMTULLA, A., ROSS, B. D., Multifunctional nanoparticle platforms for in vivo MRI enhancement and photodynamic therapy of a rat brain cancer. *J. Magn. Magn. Mater.* **2005**, *293*, 404–410.
- 83 SPASOVA, M., SALGUEIRINO-MACEIRA, V., SCHLACHTER, A., HILGENDORFF, M., GIERSIG, M., LIZ-MARZAN, L. M., FARLE, M., Magnetic and optical tunable microspheres with a magnetite/gold nanoparticle shell. *J. Mater. Chem.* **2005**, *15*, 2095–2098.
- 84 PELLEGRINO, T., KUDERA, S., LIEDL, T., JAVIER, A. M., MANNA, L., PARAK, W. J., On the development of colloidal nanoparticles towards multifunctional structures and their possible use for biological applications. *Small* **2005**, *1*, 48–63.
- 85 XIE, H. Y., ZUO, C., LIU, Y., ZHANG, Z. L., PANG, D. W., LI, X. L., GONG, J. P., DICKINSON, C., ZHOU, W. Z., Cell-targeting multifunctional nanospheres with both fluorescence and magnetism. *Small* **2005**, *1*, 506–509.
- 86 SANTRA, S., YANG, H. S., HOLLOWAY, P. H., STANLEY, J. T., MERICLE, R. A., Synthesis of water-dispersible fluorescent, radio-opaque, and paramagnetic CdS:Mn/ZnS quantum dots: A multifunctional probe for bioimaging. *J. Am. Chem. Soc.* **2005**, *127*, 1656–1657.

- 87 KIRCHER, M. F., MAHMOOD, U., KING, R. S., WEISSLEDER, R., JOSEPHSON, L., A multimodal nanoparticle for preoperative magnetic resonance imaging and intraoperative optical brain tumor delineation. *Cancer Res.* **2003**, *63*, 8122–8125.
- 88 HUBER, M. M., STAUBLI, A. B., KUSTEDJO, K., GRAY, M. H. B., SHIH, J., FRASER, S. E., JACOBS, R. E., MEADE, T. J., Fluorescently detectable magnetic resonance imaging agents. *Bioconjugate Chem.* **1998**, *9*, 242–249.
- 89 SANTRA, S., YANG, H., STANLEY, J. T., HOLLOWAY, P. H., MOUDGIL, B. M., WALTER, G., MERICLE, R. A., Rapid and effective labeling of brain tissue using TAT-conjugated CdS: Mn/ZnS quantum dots. *Chem. Commun.* **2005**, 3144–3146.
- 90 YANG, H. S., HOLLOWAY, P. H., SANTRA, S., Water-soluble silica-overcoated CdS:Mn/ZnS semiconductor quantum dots. *J. Chem. Phys.* **2004**, *121*, 7421–7426.
- 91 SANTRA, S., YANG, H., DUTTA, D., STANLEY, J. T., HOLLOWAY, P. H., TAN, W. H., MOUDGIL, B. M., MERICLE, R. A., TAT conjugated, FITC doped silica nanoparticles for bioimaging applications. *Chem. Commun.* **2004**, 2810–2811.
- 92 QHOBOSHEANE, M., SANTRA, S., ZHANG, P., TAN, W. H., Biochemically functionalized silica nanoparticles. *Analyst* **2001**, *126*, 1274–1278.
- 93 SANTRA, S., WANG, K. M., TAPEC, R., TAN, W. H., Development of novel dye-doped silica nanoparticles for biomarker application. *J. Biomed. Opt.* **2001**, *6*, 160–166.
- 94 LEVY, L., SAHOO, Y., KIM, K. S., BERGEY, E. J., PRASAD, P. N., Nanochemistry: Synthesis and characterization of multifunctional nanoclinics for biological applications. *Chem. Mater.* **2002**, *14*, 3715–3721.
- 95 WANG, Z., LEVY, R., FERNIG, D. G., BRUST, M., The peptide route to multifunctional gold nanoparticles. *Bioconjugate Chem.* **2005**, *16*, 497–500.
- 96 GAO, X. H., YANG, L. L., PETROS, J. A., MARSHAL, F. F., SIMONS, J. W., NIE, S. M., In vivo molecular and cellular imaging with quantum dots. *Curr. Opin. Biotechnol.* **2005**, *16*, 63–72.
- 97 ALIVISATOS, A. P., Semiconductor clusters, nanocrystals, and quantum dots. *Science* **1996**, *271*, 933–937.
- 98 EFROS, A. L., ROSEN, M., The electronic structure of semiconductor nanocrystals. *Annu. Rev. Mater. Sci.* **2000**, *30*, 475–521.
- 99 LEATHERDALE, C. A., WOO, W. K., MIKULEC, F. V., BAWENDI, M. G., On the absorption cross section of CdSe nanocrystal quantum dots. *J. Phys. Chem. B* **2002**, *106*, 7619–7622.
- 100 DABBOUSI, B. O., RODRIGUEZVIEJO, J., MIKULEC, F. V., HEINE, J. R., MATTOUSSI, H., OBER, R., JENSEN, K. F., BAWENDI, M. G., (CdSe)ZnS core-shell quantum dots: Synthesis and characterization of a size series of highly luminescent nanocrystallites. *J. Phys. Chem. B* **1997**, *101*, 9463–9475.
- 101 BRUCHEZ, M., MORONNE, M., GIN, P., WEISS, S., ALIVISATOS, A. P., Semiconductor nanocrystals as fluorescent biological labels. *Science* **1998**, *281*, 2013–2016.
- 102 CHAN, W. C. W., NIE, S. M., Quantum dot bioconjugates for ultrasensitive nonisotopic detection. *Science* **1998**, *281*, 2016–2018.
- 103 JAKOBS, S., SUBRAMANIAM, V., SCHONLE, A., JOVIN, T. M., HELL, S. W., EGFP and DsRed expressing cultures of Escherichia coli imaged by confocal, two-photon and fluorescence lifetime microscopy. *FEBS Lett.* **2000**, *479*, 131–135.
- 104 PEPPERKOK, R., SQUIRE, A., GELEY, S., BASTIAENS, P. I., Simultaneous detection of multiple green fluorescent proteins in live cells by fluorescence lifetime imaging microscopy. *Curr. Biol.* **1999**, *9*, 269–272.
- 105 GAO, X. H., NIE, S. M., Molecular profiling of single cells and tissue specimens with quantum dots. *Trends Biotechnol.* **2003**, *21*, 371–373.
- 106 MURRAY, C. B., NORRIS, D. J., BAWENDI, M. G., Synthesis and characterization of nearly mono-disperse CdE (E = S, Se, Te) semi-

- conductor nanocrystallites. *J. Am. Chem. Soc.* **1993**, 115, 8706–8715.
- 107 QU, L., PENG, X., Control of photoluminescence properties of CdSe nanocrystals in growth. *J. Am. Chem. Soc.* **2002**, 124, 2049–2055.
- 108 YANG, H., SANTRA, S., HOLLOWAY, P. H., Synthesis and application of Mn-doped II–VI semiconductor nanocrystals. *J. Nanosci. Nanotechnol.* **2005**, 5, 1364–1375.
- 109 YANG, H. S., HOLLOWAY, P. H., CUNNINGHAM, G., SCHANZE, K. S., CdS:Mn nanocrystals passivated by ZnS: Synthesis and luminescent properties. *J. Chem. Phys.* **2004**, 121, 10 233–10 240.
- 110 YANG, H., HOLLOWAY, P. H., Efficient and photostable ZnS-Passivated CdS:Mn luminescent nanocrystals. *Adv. Functional Mater.* **2004**, 14, 152–156.
- 111 HINES, M. A., GUYOT-SIONNEST, P., Synthesis and characterization of strongly luminescing ZnS-capped CdSe nanocrystals. *J. Phys. Chem.* **1996**, 100, 468–471.
- 112 CHEN, F. Q., GERION, D., Fluorescent CdSe/ZnS nanocrystal-peptide conjugates for long-term, nontoxic imaging and nuclear targeting in living cells. *Nano Lett.* **2004**, 4, 1827–1832.
- 113 SELVAN, S. T., LI, C. L., ANDO, M., MURASE, N., Formation of luminescent CdTe-silica nanoparticles through an inverse microemulsion technique. *Chem. Lett.* **2004**, 33, 434–435.
- 114 SELVAN, S. T., TAN, T. T., YING, J. Y., Robust, non-cytotoxic, silica-coated CdSe quantum dots with efficient photoluminescence. *Adv. Mater.* **2005**, 17, 1620–1625.
- 115 GOLDMAN, E. R., BALIGHIAN, E. D., MATTOUSSI, H., KUNO, M. K., MAURO, J. M., TRAN, P. T., ANDERSON, G. P., Avidin: A natural bridge for quantum dot-antibody conjugates. *J. Am. Chem. Soc.* **2002**, 124, 6378–6382.
- 116 MATTOUSSI, H., MAURO, J. M., GOLDMAN, E. R., ANDERSON, G. P., SUNDAR, V. C., MIKULEC, F. V., BAWENDI, M. G., Self-assembly of CdSe-ZnS quantum dot bioconjugates using an engineered recombinant protein. *J. Am. Chem. Soc.* **2000**, 122, 12 142–12 150.
- 117 MITCHELL, G. P., MIRKIN, C. A., LETSINGER, R. L., Programmed assembly of DNA functionalized quantum dots. *J. Am. Chem. Soc.* **1999**, 121, 8122–8123.
- 118 UYEDA, H. T., MEDINTZ, I. L., JAISWAL, J. K., SIMON, S. M., MATTOUSSI, H., Synthesis of compact multidentate ligands to prepare stable hydrophilic quantum dot fluorophores. *J. Am. Chem. Soc.* **2005**, 127, 3870–3878.
- 119 GERION, D., PINAUD, F., WILLIAMS, S. C., PARAK, W. J., ZANCHET, D., WEISS, S., ALIVISATOS, A. P., Synthesis and properties of biocompatible water-soluble silica-coated CdSe/ZnS semiconductor quantum dots. *J. Phys. Chem. B* **2001**, 105, 8861–8871.
- 120 OSAKI, F., KANAMORI, T., SANDO, S., SERA, T., AOYAMA, Y., A quantum dot conjugated sugar ball and its cellular uptake on the size effects of endocytosis in the subviral region. *J. Am. Chem. Soc.* **2004**, 126, 6520–6521.
- 121 PELLEGRINO, T., MANNA, L., KUDERA, S., LIEDI, T., KOKTYSH, D., ROGACH, A. L., KELLER, S., RADLER, J., NATILE, G., PARAK, W. J., Hydrophobic nanocrystals coated with an amphiphilic polymer shell: A general route to water soluble nanocrystals. *Nano Lett.* **2004**, 4, 703–707.
- 122 MATTHEAKIS, L. C., DIAS, J. M., CHOI, Y. J., GONG, J., BRUCHEZ, M. P., LIU, J. Q., WANG, E., Optical coding of mammalian cells using semiconductor quantum dots. *Anal. Biochem.* **2004**, 327, 200–208.
- 123 BALLOU, B., LAGERHOLM, B. C., ERNST, L. A., BRUCHEZ, M. P., WAGGONER, A. S., Noninvasive imaging of quantum dots in mice. *Bioconjugate Chem.* **2004**, 15, 79–86.
- 124 DUBERTRET, B., SKOURIDES, P., NORRIS, D. J., NOIREAUX, V., BRIVANLOU, A. H., LIBCHABER, A., In vivo imaging of quantum dots encapsulated in phospholipid micelles. *Science* **2002**, 298, 1759–1762.



- 125 PARAK, W. J., GERION, D., PELLEGRINO, T., ZANCHET, D., MICHEEL, C., WILLIAMS, S. C., BOUDREAU, R., LE GROS, M. A., LARABELL, C. A., ALIVISATOS, A. P., Biological applications of colloidal nanocrystals. *Nanotechnology* **2003**, *14*, R15–R27.
- 126 JAISWAL, J. K., SIMON, S. M., Potentials and pitfalls of fluorescent quantum dots for biological imaging. *Trends Cell Biol.* **2004**, *14*, 497–504.
- 127 MEDINTZ, I. L., CLAPP, A. R., MATTOUSSI, H., GOLDMAN, E. R., FISHER, B., MAURO, J. M., Self-assembled nanoscale biosensors based on quantum dot FRET donors. *Nat. Mater.* **2003**, *2*, 630–638.
- 128 PINAUD, F., KING, D., MOORE, H. P., WEISS, S., Bioactivation and cell targeting of semiconductor CdSe/ZnS nanocrystals with phytochelatin-related peptides. *J. Am. Chem. Soc.* **2004**, *126*, 6115–6123.
- 129 ACKERMAN, M. E., CHAN, W. C. W., LAKKONEN, P., BHATIA, S. N., RUOSLAHTI, E., Nanocrystal targeting in vivo. *Proc. Natl. Acad. Sci. U.S.A.* **2002**, *99*, 12617–12621.
- 130 HAINFELD, J. F., LIU, W. Q., HALSEY, C. M. R., FREIMUTH, P., POWELL, R. D., Ni-NTA-gold clusters target His-tagged proteins. *J. Struct. Biol.* **1999**, *127*, 185–198.
- 131 SLOCIK, J. M., MOORE, J. T., WRIGHT, D. W., Monoclonal antibody recognition of histidine-rich peptide encapsulated nanoclusters. *Nano Lett.* **2002**, *2*, 169–173.
- 132 MEDINTZ, I. L., KONNERT, J. H., CLAPP, A. R., STANISH, I., TWIGG, M. E., MATTOUSSI, H., MAURO, J. M., DESCHAMPS, J. R., A fluorescence resonance energy transfer-derived structure of a quantum dot-protein bioconjugate nanoassembly. *Proc. Natl. Acad. Sci. U.S.A.* **2004**, *101*, 9612–9617.
- 133 MEDINTZ, I. L., TRAMMELL, S. A., MATTOUSSI, H., MAURO, J. M., Reversible modulation of quantum dot photoluminescence using a protein-bound photochromic fluorescence resonance energy transfer acceptor. *J. Am. Chem. Soc.* **2004**, *126*, 30–31.
- 134 HANAKI, K., MOMO, A., OKU, T., KOMOTO, A., MAENOSONO, S., YAMAGUCHI, Y., YAMAMOTO, K., Semiconductor quantum dot/albumin complex is a long-life and highly photostable endosome marker. *Biochem. Biophys. Res. Commun.* **2003**, *302*, 496–501.
- 135 GOLDMAN, E. R., ANDERSON, G. P., TRAN, P. T., MATTOUSSI, H., CHARLES, P. T., MAURO, J. M., Conjugation of luminescent quantum dots with antibodies using an engineered adaptor protein to provide new reagents for fluoroimmunoassays. *Anal. Chem.* **2002**, *74*, 841–847.
- 136 BOHREN, C. F., HUFFMAN, D. R., Absorption and scattering of light by small particles. Wiley-VCH, Berlin **1983**, 3–476.
- 137 KREIBIG, U., GENZEL, L., Optical-absorption of small metallic particles. *Surf. Sci.* **1985**, *156*, 678–700.
- 138 SARKAR, D., HALAS, N. J., General vector basis function solution of Maxwell's equations. *Phys. Rev. E* **1997**, *56*, 1102–1112.
- 139 MURPHY, C. J., JANA, N. R., Controlling the aspect ratio of inorganic nanorods and nanowires. *Adv. Mater.* **2002**, *14*, 80–82.
- 140 JIN, R. C., CAO, Y. W., MIRKIN, C. A., KELLY, K. L., SCHATZ, G. C., ZHENG, J. G., Photoinduced conversion of silver nanospheres to nanoprisms. *Science* **2001**, *294*, 1901–1903.
- 141 OLDENBURG, S. J., AVERITT, R. D., WESTCOTT, S. L., HALAS, N. J., Nanoengineering of optical resonances. *Chem. Phys. Lett.* **1998**, *288*, 243–247.
- 142 HAYNES, C. L., VAN DUYN, R. P., Nanosphere lithography: A versatile nanofabrication tool for studies of size-dependent nanoparticle optics. *J. Phys. Chem. B* **2001**, *105*, 5599–5611.
- 143 NOVAK, J. P., FELDHEIM, D. L., Assembly of phenylacetylene-bridged silver and gold nanoparticle arrays. *J. Am. Chem. Soc.* **2000**, *122*, 3979–3980.
- 144 NOVAK, J. P., NICKERSON, C., FRANZEN, S., FELDHEIM, D. L., Purification of molecularly bridged metal nanopar-

- article arrays by centrifugation and size exclusion chromatography. *Anal. Chem.* **2001**, *73*, 5758–5761.
- 145 BROUSSEAU, L. C., NOVAK, J. P., MARINAKOS, S. M., FELDHEIM, D. L., Assembly of phenylacetylene-bridged gold nanocluster dimers and trimers. *Adv. Mater.* **1999**, *11*, 447–449.
- 146 ELGHANIAN, R., STORHOFF, J. J., MUCIC, R. C., LETSINGER, R. L., MIRKIN, C. A., Selective colorimetric detection of polynucleotides based on the distance-dependent optical properties of gold nanoparticles. *Science* **1997**, *277*, 1078–1081.
- 147 CARUSO, R. A., ANTONIETTI, M., Sol-gel nanocoating: An approach to the preparation of structured materials. *Chem. Mater.* **2001**, *13*, 3272–3282.
- 148 MARINAKOS, S. M., NOVAK, J. P., BROUSSEAU, L. C., HOUSE, A. B., EDEKI, E. M., FELDHAUS, J. C., FELDHEIM, D. L., Gold particles as templates for the synthesis of hollow polymer capsules. Control of capsule dimensions and guest encapsulation. *J. Am. Chem. Soc.* **1999**, *121*, 8518–8522.
- 149 MALINSKY, M. D., KELLY, K. L., SCHATZ, G. C., VAN DUYN, R. P., Chain length dependence and sensing capabilities of the localized surface plasmon resonance of silver nanoparticles chemically modified with alkanethiol self-assembled monolayers. *J. Am. Chem. Soc.* **2001**, *123*, 1471–1482.
- 150 COCCHINI, F., BASSANI, F., BOURG, M., Model calculation of the optical-properties of metallic particles in a dielectric medium. *Surf. Sci.* **1985**, *156*, 851–858.
- 151 MULVANEY, P., LIZ-MARZAN, L. M., GIERSIG, M., UNG, T., Silica encapsulation of quantum dots and metal clusters. *J. Mater. Chem.* **2000**, *10*, 1259–1270.
- 152 UNDERWOOD, S., MULVANEY, P., Effect of the solution refractive-index on the color of gold colloids. *Langmuir* **1994**, *10*, 3427–3430.
- 153 HAYAT, M. A., *Colloidal Gold: Principles, Methods and Applications*. Elsevier, Burlington, MA, 1989.
- 154 SAUTHIER, M. L., CARROLL, R. L., GORMAN, C. B., FRANZEN, S., Nanoparticle layers assembled through DNA hybridization: Characterization and optimization. *Langmuir* **2002**, *18*, 1825–1830.
- 155 EL-SAYED, M. A., Some interesting properties of metals confined in time and nanometer space of different shapes. *Acc. Chem. Res.* **2001**, *34*, 257–264.
- 156 TAYLOR, J. R., FANG, M. M., NIE, S. M., Probing specific sequences on single DNA molecules with bioconjugated fluorescent nanoparticles. *Anal. Chem.* **2000**, *72*, 1979–1986.
- 157 MANN, S., SHENTON, W., LI, M., CONNOLLY, S., FITZMAURICE, D., Biologically programmed nanoparticle assembly. *Adv. Mater.* **2000**, *12*, 147–150.
- 158 MRKSICH, M., A surface chemistry approach to studying cell adhesion. *Chem. Soc. Rev.* **2000**, *29*, 267–273.
- 159 BRIGHT, R. M., WALTER, D. G., MUSICK, M. D., JACKSON, M. A., ALLISON, K. J., NATAN, M. J., Chemical and electrochemical Ag deposition onto preformed Au colloid monolayers: Approaches to uniformly-sized surface features with Ag-like optical properties. *Langmuir* **1996**, *12*, 810–817.
- 160 TATON, T. A., LU, G., MIRKIN, C. A., Two-color labeling of oligonucleotide arrays via size-selective scattering of nanoparticle probes. *J. Am. Chem. Soc.* **2001**, *123*, 5164–5165.
- 161 TATON, T. A., MIRKIN, C. A., LETSINGER, R. L., Scanometric DNA array detection with nanoparticle probes. *Science* **2000**, *289*, 1757–1760.
- 162 MAFUNE, F., KOHNO, J. Y., TAKEDA, Y., KONDOW, T., Full physical preparation of size-selected gold nanoparticles in solution: Laser ablation and laser-induced size control. *J. Phys. Chem. B* **2002**, *106*, 7575–7577.
- 163 TURKEVITCH, J., STEVENSON, P. C., HILLIER, J., *Faraday Soc.* **1951**, *11*, 55.
- 164 HENGLEIN, A., GIERSIG, M., Formation of colloidal silver nanoparticles: Capping action of

- citrate. *J. Phys. Chem. B* **1999**, *103*, 9533–9539.
- 165** LINK, S., WANG, Z. L., EL-SAYED, M. A., Alloy formation of gold-silver nanoparticles and the dependence of the plasmon absorption on their composition. *J. Phys. Chem. B* **1999**, *103*, 3529–3533.
- 166** YONEZAWA, T., KUNITAKE, T., Practical preparation of anionic mercapto ligand-stabilized gold nanoparticles and their immobilization. *Colloids Surf. A-Physicochem. Eng. Aspects* **1999**, *149*, 193–199.
- 167** BRUST, M., FINK, J., BETHELL, D., SCHIFFRIN, D. J., KIELY, C., Synthesis and reactions of functionalized gold nanoparticles. *J. Chem. Soc., Chem. Commun.* **1995**, 1655–1656.
- 168** KOHLER, J. M., WAGNER, J., ALBERT, J., Formation of isolated and clustered Au nanoparticles in the presence of polyelectrolyte molecules using a flow-through Si chip reactor. *J. Mater. Chem.* **2005**, *15*, 1924–1930.
- 169** BRUST, M., WALKER, M., BETHELL, D., SCHIFFRIN, D. J., WHYMAN, R., Synthesis of thiol-derivatized gold nanoparticles in a 2-phase liquid-liquid system. *J. Chem. Soc., Chem. Commun.* **1994**, 801–802.
- 170** LIN, J., ZHOU, W. L., O'CONNOR, C. J., Formation of ordered arrays of gold nanoparticles from CTAB reverse micelles. *Mater. Lett.* **2001**, *49*, 282–286.
- 171** CHIANG, C. L., Controlled growth of gold nanoparticles in AOT/C12E4/ isooctane mixed reverse micelles. *J. Colloid Interface Sci.* **2001**, *239*, 334–341.
- 172** CHEN, F. X., XU, G. Q., HOR, T. S. A., Preparation and assembly of colloidal gold nanoparticles in CTAB-stabilized reverse microemulsion. *Mater. Lett.* **2003**, *57*, 3282–3286.
- 173** SOHN, B. H., CHOI, J. M., YOO, S. I., YUN, S. H., ZIN, W. C., JUNG, J. C., KANEHARA, M., HIRATA, T., TERANISHI, T., Directed self-assembly of two kinds of nanoparticles utilizing monolayer films of diblock copolymer micelles. *J. Am. Chem. Soc.* **2003**, *125*, 6368–6369.
- 174** WILCOXON, J. P., WILLIAMSON, R. L., BAUGHMAN, R., Optical-properties of gold colloids formed in inverse micelles. *J. Chem. Phys.* **1993**, *98*, 9933–9950.
- 175** ZSIGMONDY, R., THIESSEN, P., *Das Kolloide Gold*. Verlagsges. Leipzig, **1925**.
- 176** HENGLEIN, A., Formation and absorption spectrum of copper nanoparticles from the radiolytic reduction of Cu(CN)<sub>2</sub>(-). *J. Phys. Chem. B* **2000**, *104*, 1206–1211.
- 177** TERANISHI, T., HOSOE, M., TANAKA, T., MIYAKE, M., Size control of monodispersed Pt nanoparticles and their 2D organization by electrophoretic deposition. *J. Phys. Chem. B* **1999**, *103*, 3818–3827.
- 178** TERANISHI, T., MIYAKE, M., Size control of palladium nanoparticles and their crystal structures. *Chem. Mater.* **1998**, *10*, 594–600.
- 179** BROWN, K. R., NATAN, M. J., Hydroxylamine seeding of colloidal Au nanoparticles in solution and on surfaces. *Langmuir* **1998**, *14*, 726–728.
- 180** SHIRTCLIFFE, N., NICKEL, U., SCHNEIDER, S., Reproducible preparation of silver sols with small particle size using borohydride reduction: For use as nuclei for preparation of larger particles. *J. Colloid Interface Sci.* **1999**, *211*, 122–129.
- 181** SCHNEIDER, S., HALBIG, P., GRAU, H., NICKEL, U., Reproducible preparation of silver sols with uniform particle-size for application in surface-enhanced Raman-spectroscopy. *Photochem. Photobiol.* **1994**, *60*, 605–610.
- 182** BROWN, K. R., WALTER, D. G., NATAN, M. J., Seeding of colloidal Au nanoparticle solutions. 2. Improved control of particle size and shape. *Chem. Mater.* **2000**, *12*, 306–313.
- 183** LU, L. H., WANG, H. S., ZHOU, Y. H., XI, S. Q., ZHANG, H. J., JIAWEN, H. B. W., ZHAO, B., Seed-mediated growth of large, monodisperse core-shell gold-silver nanoparticles with Ag-like optical properties. *Chem. Commun.* **2002**, 144–145.
- 184** JANA, N. R., GEARHEART, L., MURPHY, C. J., Evidence for seed-mediated

- nucleation in the chemical reduction of gold salts to gold nanoparticles. *Chem. Mater.* **2001**, *13*, 2313–2322.
- 185** JANA, N. R., GEARHEART, L., MURPHY, C. J., Seed-mediated growth approach for shape-controlled synthesis of spheroidal and rod-like gold nanoparticles using a surfactant template. *Adv. Mater.* **2001**, *13*, 1389–1393.
- 186** MIESZAWSKA, A. J., ZAMBORINI, F. P., Gold nanorods grown directly on surfaces from microscale patterns of gold seeds. *Chem. Mater.* **2005**, *17*, 3415–3420.
- 187** WEI, Z. Q., ZAMBORINI, F. P., Directly monitoring the growth of gold nanoparticle seeds into gold nanorods. *Langmuir* **2004**, *20*, 11 301–11 304.
- 188** SAU, T. K., PAL, A., JANA, N. R., WANG, Z. L., PAL, T., Size controlled synthesis of gold nanoparticles using photochemically prepared seed particles. *J. Nanoparticle Res.* **2001**, *3*, 257–261.
- 189** PRADHAN, N., JANA, N. R., KAUSHIK, M., TARASHANKAR, P., Seed mediated growth: A convenient way for size control in nanoparticle synthesis. *J. Surf. Sci. Technol.* **2000**, *16*, 188–199.
- 190** WIESNER, J., WOKAUN, A., Anisometric gold colloids – Preparation, characterization, and optical-properties. *Chem. Phys. Lett.* **1989**, *157*, 569–575.
- 191** WAITZKY, M. A., FINKE, R. G., Nanocluster size-control and “magic number” investigations, experimental tests of the “living-metal polymer” concept and of mechanism-based size-control predictions leading to the syntheses of iridium(0) nanoclusters centering about four sequential magic numbers. *Chem. Mater.* **1997**, *9*, 3083–3095.
- 192** CARROT, G., VALMALETTE, J. C., PLUMMER, C. J. G., SCHOLZ, S. M., DUTTA, J., HOFMANN, H., HILBORN, J. G., Gold nanoparticle synthesis in graft copolymer micelles. *Colloid Polym. Sci.* **1998**, *276*, 853–859.
- 193** LOO, C., LIN, A., HIRSCH, L., LEE, M. H., BARTON, J., HALAS, N., WEST, J., DREZEK, R., Nanoshell-enabled photonics-based imaging and therapy of cancer. *Technol. Cancer Res. Treatment* **2004**, *3*, 33–40.
- 194** DUFF, D. G., BAIKER, A., EDWARDS, P. P., A new hydrosol of gold clusters. 1. Formation and particle-size variation. *Langmuir* **1993**, *9*, 2301–2309.
- 195** HIRSCH, L. R., HALAS, N. J., WEST, J. L., Whole-blood immunoassay facilitated by gold-nanoshell-conjugate antibodies. *Nanobiotechnol. Protocols* **2005**, *303*, 101–111.
- 196** O’NEAL, D. P., HIRSCH, L. R., HALAS, N. J., PAYNE, J. D., WEST, J. L., Photothermal tumor ablation in mice using near infrared-absorbing nanoparticles. *Cancer Lett.* **2004**, *209*, 171–176.
- 197** LOO, C., HIRSCH, L., LEE, M. H., CHANG, E., WEST, J., HALAS, N., DREZEK, R., Gold nanoshell bioconjugates for molecular imaging in living cells. *Opt. Lett.* **2005**, *30*, 1012–1014.
- 198** LOO, C., LOWERY, A., HALAS, N., WEST, J., DREZEK, R., Immunotargeted nanoshells for integrated cancer imaging and therapy. *Nano Lett.* **2005**, *5*, 709–711.
- 199** MALLICK, K., WANG, Z. L., PAL, T., Seed-mediated successive growth of gold particles accomplished by UV irradiation: a photochemical approach for size-controlled synthesis. *J. Photochem. Photobiol. A Chem.* **2001**, *140*, 75–80.
- 200** ZHOU, Y., WANG, C. Y., ZHU, Y. R., CHEN, Z. Y., A novel ultraviolet irradiation technique for shape-controlled synthesis of gold nanoparticles at room temperature. *Chem. Mater.* **1999**, *11*, 2310–2312.
- 201** PAL, A., Photoinitiated gold sol generation in aqueous Triton X-100 and its analytical application for spectrophotometric determination of gold. *Talanta* **1998**, *46*, 583–587.
- 202** REED, J. A., COOK, A., HALAAS, D. J., PARAZZOLI, P., ROBINSON, A., MATULA, T. J., GRIESER, F., The effects of microgravity on nanoparticle size distributions generated by the ultrasonic reduction of an aqueous

- gold-chloride solution. *Ultrasonics Sonochem.* **2003**, *10*, 285–289.
- 203** POL, V. G., GEDANKEN, A., CALDERON-MORENO, J., Deposition of gold nanoparticles on silica spheres: A sonochemical approach. *Chem. Mater.* **2003**, *15*, 1111–1118.
- 204** OKITSU, K., YUE, A., TANABE, S., MATSUMOTO, H., YOBIKO, Y., YOO, Y., Sonolytic control of rate of gold(III) reduction and size of formed gold nanoparticles: Relation between reduction rates and sizes of formed nanoparticles. *Bull. Chem. Soc. Jpn.* **2002**, *75*, 2289–2296.
- 205** OKITSU, K., YUE, A., TANABE, S., MATSUMOTO, H., YOBIKO, Y., Formation of colloidal gold nanoparticles in an ultrasonic field: Control of rate of gold(III) reduction and size of formed gold particles. *Langmuir* **2001**, *17*, 7717–7720.
- 206** CHEN, W., CAI, W. P., ZHANG, L., WANG, G. Z., ZHANG, L. D., Sonochemical processes and formation of gold nanoparticles within pores of mesoporous silica. *J. Colloid Interface Sci.* **2001**, *238*, 291–295.
- 207** CHEN, W., CAI, W. P., LIANG, C. H., ZHANG, L. D., Synthesis of gold nanoparticles dispersed within pores of mesoporous silica induced by ultrasonic irradiation and its characterization. *Mater. Res. Bull.* **2001**, *36*, 335–342.
- 208** SHIMIZU, T., TERANISHI, T., HASEGAWA, S., MIYAKE, M., Size evolution of alkanethiol-protected gold nanoparticles by heat treatment in the solid state. *J. Phys. Chem. B* **2003**, *107*, 2719–2724.
- 209** TERANISHI, T., HASEGAWA, S., SHIMIZU, T., MIYAKE, M., Heat-induced size evolution of gold nanoparticles in the solid state. *Adv. Mater.* **2001**, *13*, 1699–1701.
- 210** NAKAMOTO, M., YAMAMOTO, M., FUKUSUMI, M., Thermolysis of gold(I) thiolate complexes producing novel gold nanoparticles passivated by alkyl groups. *Chem. Commun.* **2002**, 1622–1623.
- 211** MOSSMER, S., SPATZ, J. P., MOLLER, M., ABERLE, T., SCHMIDT, J., BURCHARD, W., Solution behavior of poly(styrene)-block-poly(2-vinylpyridine) micelles containing gold nanoparticles. *Macromolecules* **2000**, *33*, 4791–4798.
- 212** MELTZER, S., RESCH, R., KOEL, B. E., THOMPSON, M. E., MADHUKAR, A., REQUICHA, A. A. G., WILL, P., Fabrication of nanostructures by hydroxylamine seeding of gold nanoparticle templates. *Langmuir* **2001**, *17*, 1713–1718.
- 213** GRIESER, F., in *Semiconductor Nanoclusters – Physical, Chemical, and Catalytic Aspects*, KAMAT, P. V., MEISEL, D. (Ed.), **1997**, Vol. 103, pp. 57–77.
- 214** HERMANSON, G. T., *Bioconjugation Techniques.* **1996**, 593–604.
- 215** STOBER, W., FINK, A., BOHN, E., Controlled growth of monodisperse silica spheres in micron size range. *J. Colloid Interface Sci.* **1968**, *26*, 62–67.
- 216** QHOBOSHEANE, M., ZHANG, P., TAN, W. H., Assembly of silica nanoparticles for two-dimensional nanomaterials. *J. Nanosci. Nanotechnol.* **2004**, *4*, 635–640.
- 217** SANTRA, S., DUTTA, D., MOUDGIL, B. M., Functional dye-doped silica nanoparticles for bioimaging, diagnostics and therapeutics. *Food Bioproducts Process.* **2005**, *83*, 136–140.
- 218** WANG, L., YANG, C. Y., TAN, W. H., Dual-luminophore-doped silica nanoparticles for multiplexed signaling. *Nano Lett.* **2005**, *5*, 37–43.
- 219** LIAN, W., LITHERLAND, S. A., BADRANE, H., TAN, W. H., WU, D. H., BAKER, H. V., GULIG, P. A., LIM, D. V., JIN, S. G., Ultrasensitive detection of biomolecules with fluorescent dye-doped nanoparticles. *Anal. Biochem.* **2004**, *334*, 135–144.
- 220** TAN, M. Q., WANG, G. L., HAI, X. D., YE, Z. Q., YUAN, J. L., Development of functionalized fluorescent europium nanoparticles for biolabeling and time-resolved fluorometric applications. *J. Mater. Chem.* **2004**, *14*, 2896–2901.
- 221** BAGWE, R. P., YANG, C. Y., HILLIARD, L. R., TAN, W. H., Optimization of dye-doped silica nanoparticles prepared using a reverse micro-

- emulsion method. *Langmuir* **2004**, *20*, 8336–8342.
- 222** TAN, M. Q., YE, Z. Q., WANG, G. L., YUAN, J. L., Preparation and time-resolved fluorometric application of luminescent europium nanoparticles. *Chem. Mater.* **2004**, *16*, 2494–2498.
- 223** YE, Z. Q., TAN, M. Q., WANG, G. L., YUAN, J. L., Novel fluorescent europium chelate-doped silica nanoparticles: Preparation, characterization and time-resolved fluorometric application. *J. Mater. Chem.* **2004**, *14*, 851–856.
- 224** ZHAO, X. J., BAGWE, R. P., TAN, W. H., Development of organic-dye-doped silica nanoparticles in a reverse microemulsion. *Adv. Mater.* **2004**, *16*, 173–176.
- 225** SANTRA, S., TAPEC, R., THEODOROPULOU, N., DOBSON, J., HEBARD, A., TAN, W. H., Synthesis and characterization of silica-coated iron oxide nanoparticles in microemulsion: The effect of nonionic surfactants. *Langmuir* **2001**, *17*, 2900–2906.
- 226** HARMA, H., SOUKKA, T., LOVGREN, T., Europium nanoparticles and time-resolved fluorescence for ultrasensitive detection of prostate-specific antigen. *Clin. Chem.* **2001**, *47*, 561–568.
- 227** GAO, H. F., ZHAO, Y. Q., FU, S. K., LI, B., LI, M. Q., Preparation of a novel polymeric fluorescent nanoparticle. *Colloid Polym. Sci.* **2002**, *280*, 653–660.
- 228** MAKAROVA, O. V., OSTAFIN, A. E., MIYOSHI, H., NORRIS, J. R., MEISEL, D., Adsorption and encapsulation of fluorescent probes in nanoparticles. *J. Phys. Chem. B* **1999**, *103*, 9080–9084.
- 229** SCHLUPEN, J., HAEGEL, F. H., KUHLMANN, J., GEISLER, H., SCHWUGER, M. J., Sorption hysteresis of pyrene on zeolite. *Colloids Surf. A-Physicochem. Eng. Aspects* **1999**, *156*, 335–347.
- 230** CHARREYRE, M. T., YEKTA, A., WINNIK, M. A., DELAIR, T., PICHOT, C., Fluorescence energy-transfer from fluorescein to tetramethylrhodamine covalently bound to the surface of polystyrene latex-particles. *Langmuir* **1995**, *11*, 2423–2428.
- 231** CHARREYRE, M. T., ZHANG, P., WINNIK, M. A., PICHOT, C., GRILLAT, C., Adsorption of Rhodamine-60 onto polystyrene latex-particles with sulfate groups at the surface. *J. Colloid Interface Sci.* **1995**, *170*, 374–382.
- 232** LIU, X. J., TAN, W. H., A fiber-optic evanescent wave DNA biosensor based on novel molecular beacons. *Anal. Chem.* **1999**, *71*, 5054–5059.
- 233** CORDEK, J., WANG, X. W., TAN, W. H., Direct immobilization of glutamate dehydrogenase on optical fiber probes for ultrasensitive glutamate detection. *Anal. Chem.* **1999**, *71*, 1529–1533.
- 234** FANG, X. H., LIU, X. J., SCHUSTER, S., TAN, W. H., Designing a novel molecular beacon for surface-immobilized DNA hybridization studies. *J. Am. Chem. Soc.* **1999**, *121*, 2921–2922.
- 235** WANG, S., LOW, P. S., Folate-mediated targeting of antineoplastic drugs, imaging agents, and nucleic acids to cancer cells. *J. Controlled Release* **1998**, *53*, 39–48.
- 236** ZHAO, X. J., HILLIARD, L. R., MECHERY, S. J., WANG, Y. P., BAGWE, R. P., JIN, S. G., TAN, W. H., A rapid bioassay for single bacterial cell quantitation using bioconjugated nanoparticles. *Proc. Natl. Acad. Sci. U.S.A.* **2004**, *101*, 15 027–15 032.
- 237** TAPEC, R., ZHAO, X. J., TAN, W. H., Development of organic dye-doped silica nanoparticles for bioanalysis and biosensors. *J. Nanosci. Nanotechnol.* **2002**, *2*, 405–409.
- 238** KIM, G. J., NIE, S., Targeted cancer nanotherapy. *Nanotoday* **2005**, *8*, 28–33.
- 239** PARAK, W. J., BOUDREAU, R., LE GROS, M., GERION, D., ZANCHET, D., MICHEEL, C. M., WILLIAMS, S. C., ALIVISATOS, A. P., LARABELL, C., Cell motility and metastatic potential studies based on quantum dot imaging of phagokinetic tracks. *Adv. Mater.* **2002**, *14*, 882–885.
- 240** PELLEGRINO, T., PARAK, W. J., BOUDREAU, R., LE GROS, M. A., GERION, D., ALIVISATOS, A. P., LARABELL, C. A., Quantum dot-based cell motility assay. *Differentiation* **2003**, *71*, 542–548.

- 241 LIDKE, D. S., NAGY, P., HEINTZMANN, R., ARNDT-JOVIN, D. J., POST, J. N., GRECCO, H. E., JARES-ERIJMAN, E. A., JOVIN, T. M., Quantum dot ligands provide new insights into erbB/HER receptor-mediated signal transduction. *Nat. Biotechnol.* **2004**, *22*, 198–203.
- 242 WINTER, J. O., LIU, T. Y., KORGEL, B. A., SCHMIDT, C. E., Recognition molecule directed interfacing between semiconductor quantum dots and nerve cells. *Adv. Mater.* **2001**, *13*, 1673–1677.
- 243 HOSHINO, A., HANAKI, K., SUZUKI, K., YAMAMOTO, K., Applications of T-lymphoma labeled with fluorescent quantum dots to cell tracing markers in mouse body. *Biochem. Biophys. Res. Commun.* **2004**, *314*, 46–53.
- 244 SOLTESZ, E., KIM, S., LAURENCE, R., DEGRAND, A., PARUNGO, C., DOR, D., COHN, L., BAWENDI, M., FRANGIONI, J., MIHALJEVIC, T., Intraoperative sentinel lymph node mapping of the lung using near-infrared fluorescent quantum dots. *Ann. Thoracic Surgery* **2005**, *79*, 269–277.
- 245 PARUNGO, C. P., COLSON, Y. L., KIM, S. W., KIM, S., COHN, L. H., BAWENDI, M. G., FRANGIONI, J. V., Sentinel lymph node mapping of the pleural space. *Chest* **2005**, *127*, 1799–1804.
- 246 CHEN, J., SAEKI, F., WILEY, B. J., CANG, H., COBB, M. J., LI, Z. Y., AU, L., ZHANG, H., KIMMEY, M. B., LI, X. D., XIA, Y., Gold nanocages: Bioconjugation and their potential use as optical imaging contrast agents. *Nano Lett.* **2005**, *5*, 473–477.
- 247 VAN DE RIJKE, F., ZIJLMANS, H., LI, S., VAIL, T., RAAP, A. K., NIEDBALA, R. S., TANKE, H. J., Up-converting phosphor reporters for nucleic acid microarrays. *Nat. Biotechnol.* **2001**, *19*, 273–276.
- 248 ZIJLMANS, H. J. M. A. A., BONNET, J., BURTON, J., KARDOS, K., VAIL, T., NIEDBALA, R. S., TANKE, H. J., Detection of cell and tissue surface antigens using up-converting phosphors: A new reporter technology. *Anal. Biochem.* **1999**, *267*, 30–36.
- 249 SOUKKA, T., HARMA, H., PAUKKUNEN, J., LOVGREN, T., Utilization of kinetically enhanced monovalent binding affinity by immunoassays based on multivalent nanoparticle-antibody bioconjugates. *Anal. Chem.* **2001**, *73*, 2254–2260.
- 250 SOUKKA, T., ANTONEN, K., HARMA, H., PELKKIKANGAS, A. M., HUHTINEN, P., LOVGREN, T., Highly sensitive immunoassay of free prostate-specific antigen in serum using europium(III) nanoparticle label technology. *Clin. Chim. Acta* **2003**, *328*, 45–58.
- 251 SOUKKA, T., PAUKKUNEN, J., HARMA, H., LONNBERG, S., LINDROOS, H., LOVGREN, T., Supersensitive time-resolved immunofluorometric assay of free prostate-specific antigen with nanoparticle label technology. *Clin. Chem.* **2001**, *47*, 1269–1278.
- 252 ALYAUDTIN, R. N., REICHEL, A., LOBENBERG, R., RAMGE, P., KREUTER, J., BEGLEY, D. J., Interaction of poly(butylcyanoacrylate) nanoparticles with the blood-brain barrier in vivo and in vitro. *J. Drug Targeting* **2001**, *9*, 209–221.
- 253 COESTER, C. J., LANGER, K., VON BRIESEN, H., KREUTER, J., Gelatin nanoparticles by two step desolvation – A new preparation method, surface modifications and cell uptake. *J. Microencapsulation* **2000**, *17*, 187–193.
- 254 JOSEPHSON, L., KIRCHER, M. F., MAHMOOD, U., TANG, Y., WEISSELEDER, R., Near-infrared fluorescent nanoparticles as combined MR/optical imaging probes. *Bioconjugate Chem.* **2002**, *13*, 554–560.

### 3

## Nanogold in Cancer Therapy and Diagnosis

*Priyabrata Mukherjee, Resham Bhattacharya, Chitta Ranjan Patra,  
and Debabrata Mukhopadhyay*

### 3.1

#### Introduction

Cancer is the second leading cause of death in the United States. Nearly half of all men and a little over one-third of all women in the United States will develop cancer during their lifetimes. Today, millions of people live with cancer or have had cancer.

The uncontrolled division of cells is termed as cancer. Cancer cells are different from normal cells in that they continue to grow, divide and form new abnormal cells. Cancer cells usually accumulate in an organ to form solid tumors; however, non-tumor forming cancer of the fluid connective tissue, blood, also occurs such as leukemia. Cancer cells can travel to other parts of the body from their primary site of growth and this is called metastasis. Cancer can grow in various sites in the human body such as bladder, breast, colon, kidney (renal cell), lung, skin (melanoma), pancreas, prostate and thyroid [1]. Therapies differ considerably, depending upon the site and stage of tumor formation. Besides conventional treatments such as surgery, chemotherapy and radiation several other alternative approaches have been examined, such as laser therapy, photodynamic therapy, gene therapy, stem cell transplantation and anti-angiogenic therapy [2–5].

Due to the highly heterogeneous nature of the disease, the main challenge to cancer therapists today is to deliver drugs that can be specifically targeted to the different “hallmarks” of cancer growth. Unfortunately, common anticancer as well as new generation of anti-angiogenic or anti-stromal agents have several limitations: they are usually associated with high toxicity; several of them are non-specific and target both normal as well as malignant cells; have poor bioavailability; and last but not least, they have poor half-lives and fast clearance from the body. An ideal therapeutic approach in cancer would be to deliver multi-drugs specifically to the primary tumor, as well as to the site of metastasis and its micro-environment while simultaneously monitoring the prognosis through noninvasive approaches.



Recently, several groups, including ours, have shown that nanoparticles possess enormous potential to improve the efficacy of cancer treatment [6]. Hence, our long-term goal is to develop nanotherapeutics with multifunctional capabilities. This method of drug administration might significantly reduce the dosage of the drugs and this in turn may lead to better specificity, low toxicities, better bioavailability, in a targeted manner with real-time detection by non-invasive imaging. Our recent published and preliminary data support at least part of this hypothesis, as we have shown that when conventional anticancer drugs are loaded with gold-nanoparticles alone or in combination with other drugs such as an anti-angiogenic agent, the efficacy of each drug was intact or even better when tested in respective assays [7–9]. Our goal is to put together all the components to develop “*smart*” drug(s) that will target all the “*hallmarks*” of cancer growth and thereby inhibit tumor progression and metastasis. In this chapter, we emphasize potential targets of the angiogenesis component of the tumor and discuss the current standing with respect to nanotechnology.

### 3.2

#### Medicinal use of Gold: A Historical Perspective

Gold has a long history of use [10, 11]. The therapeutic use of gold can be traced back to the Chinese in 2500 BC. They were the first to prepare and use red colloidal gold as the “drug of longevity.” Red colloidal gold is still in use today in India in the form of Ayurvedic medicine for rejuvenation and revitalization during old age under the name of Swarna Bhasma (“Swarna” meaning gold, “Bhasma” meaning ash) [12]. Mahdihassan has explored the historical use of gold in eastern traditions, especially in India and China [13]. In India cinnabar-gold is known as “Makaradh-waja”. Makaradh-waja means emblem of god of fertility, a drug for vigor of youth [14]. Gold also has a long history of use in the western world as nerving, a substance that could revitalize people suffering from nervous conditions [12]. In the 16<sup>th</sup> century gold was recommended for the treatment of epilepsy [15]. At the beginning of the 19<sup>th</sup> century gold was the drug of choice for the treatment of syphilis [16]. Several books describing the medicinal use of gold came out at the beginning of 19<sup>th</sup> century [17–21].

The discovery by Robert Koch of the bacteriostatic effect of gold cyanide towards the tubercle bacillus marked the beginning of the modern day medicinal use of gold. Following Koch’s discovery, gold therapy for tuberculosis was introduced in the 1920s [22]. The major clinical uses of gold compounds are in the treatment of rheumatic diseases, including psoriasis, juvenile arthritis, palindromic rheumatism and discoid lupus erythematosus [23]. Gold compounds that were mainly used for the treatment of rheumatoid arthritis were gold thiolates (AuSR), where gold is unipositively charged. Sodium aurothiomalate and aurothioglucose are two prime examples of gold thiolates mainly used for rheumatoid arthritis. These drugs are water soluble and administered as deep intramuscular injection. Follow-

ing such injection these drugs get rapidly adsorbed and, at the same time, gold is rapidly cleared from the circulation and distributed to various organs such as kidney, liver, spleen and so on [22]. The adsorption of gold in the kidney causes nephrotoxicity, a major side effect. Other toxic reactions include mouth ulcers, skin reactions, blood disorder and liver toxicity [23–25]. To overcome the poor pharmacokinetics and toxicity, a second-generation gold drug, auranofin, was introduced in 1985 for arthritis [26–29]. The presence of phosphine ligands makes auranofin more lyophilic with better retention in the circulation. The adsorption of gold in the kidney was also reduced, with significant reduction in the nephrotoxicity.

The antitumor activity of cis-platin was discovered in 1969, prompting the discovery of other metal-containing antitumor drugs. Gold has also been included in the search on the basis of three rationales [30–33]: (a) both Pt(II) and Au(III) form analogous square-planar complexes with a  $d^8$  configuration of the central ions, (b) analogy to the immunomodulatory effects of gold(I) antiarthritic agents, and (c) complexation of known antitumor agents with gold(I) and gold(III) to produce compounds with enhanced activity. Auranofin showed activity against HeLa cells *in vitro* and P388 cells *in vivo*. This discovery led to the screening of many phosphine-containing gold drugs, of particular interest are bis(diphos)gold(I) complexes [34, 35]. These complexes showed promising antitumor properties but exhibited cardiovascular toxicity that precluded their use in clinical trials. The mechanism of action of these gold drugs is poorly understood. However, it is thought that, under biological conditions, gold(I) and gold(III) species are reduced to gold(0), which may be the active species. Hardly any report describes the use of gold nanoparticles as anticancer agent. However, recently we have shown, for the first time, the anti-angiogenic property of gold nanoparticles.

### 3.3

#### Application of Gold Nanoparticles in Cancer

The biological application of gold nanoparticles began almost three decades ago in the form of immunogold staining procedure. Since then, gold nanoconjugates have been extensively used to detect cellular components using electron microscopy as an indirect passive component. However, the use of these gold nanoparticles for *in vivo* drug delivery has never been described. This section discusses the application of “naked” gold nanoparticles as well as in the form of their nanoconjugates in the treatment of cancer.

##### 3.3.1

#### Angiogenesis and Cancer

Angiogenesis, the formation of new blood vessels from existing one's, plays an important role in the growth and spread of cancer. New blood vessels “feed” the cancer cells with oxygen and nutrients, allowing these cells to grow, invade nearby

tissue, spread to other parts of the body, and form solid tumors [36]. In the early 1970s Dr. J. Folkman first showed that solid tumors are angiogenic and require vascularization for growth [37, 38]. The central concept that tumor growth is “angiogenesis dependent” is well accepted today, with more than 2500 scientific reports showing angiogenesis linked to tumor growth. Angiogenesis is tightly regulated by a balance between endogenous proangiogenic growth factors like Vascular Endothelial Growth Factor (VEGF), Placental Growth Factor (PLGF), Platelet Derived Growth Factor (PDGF), Tumor Growth Factor-beta (TGF- $\beta$ ) and Angiopoietin-1 (Ang-1) and antiangiogenic factors like thrombospondin-1 (TSP-1), somatostatin, endostatin, angiostatin, interleukins, interferons and tissue inhibitors of matrix metalloproteinases (TIMPs) [39, 40]. In this chapter we briefly discuss angiogenesis in relation to cancer to provide a basis for understanding the fabrication and targets for nanodrug synthesis and use. For a detailed review on angiogenesis and cancer please refer to Refs. [1–44]. The angiogenic response in the microvasculature is associated with changes in cellular adhesive interactions between adjacent endothelial cells (ECs), pericytes, fibroblasts, and immune mediators express many different cytokines and growth factors that react with other cells or extra cellular matrix (ECM) components to affect EC migration, proliferation, tube formation, and vessel stabilization. During tumor growth this balance is disrupted and the scale tips towards the tumor-secreted angiogenic growth factors that interact with their surface receptors expressed on ECs (Fig. 3.1).

Folkman has propounded the idea that inhibiting angiogenesis could inhibit the growth of tumors [41]. Since then considerable effort has been invested in the discovery of agents that block the development of tumor vasculature. Yet only recently have the differences between the vasculature of the normal tissue and the tumor been realized. The tumor vasculature is strikingly tortuous, vessels have poor pericyte cover and numerous shunts, making it often difficult to distinguish between arterioles and venules. Blood flow through the tumor capillaries is sluggish and sometimes stationary, leading to the entire microenvironment, including red blood cells and endothelium, being highly hypoxic [42–44].

Although the idea of targeting and disrupting tumor vasculature as an anti-cancer therapy has been around for sometime, experimental evidence of efficacy was absent until Burrows et al., targeted the toxin ricin to the tumor vasculature in a mouse neuroblastoma model [45]. Since then several different antiangiogenic agents have been developed and used to treat cancer. These include drugs that directly target specific molecules involved in neo-vessel formation, such as antibodies to VEGF, or others that indirectly inhibit endothelial cell function like inhibitors of matrix metalloproteinase (MMP) breakdown [46, 47]. Other strategies include the use of cytotoxic drugs such as thalidomide that appear to have both antiangiogenic as well as tumor cell killing properties; however, the specific mechanism of action of these drugs is not known [48, 49]. Camptothecin analogs, 9-amino-20(*S*)-camptothecin, topotecan, CPT-11, are inhibitors of topoisomerase I and also decrease tumor angiogenesis [50]. Paclitaxel, a microtubule inhibitor, has shown anti-proliferative action in *in vivo* models [51, 52].

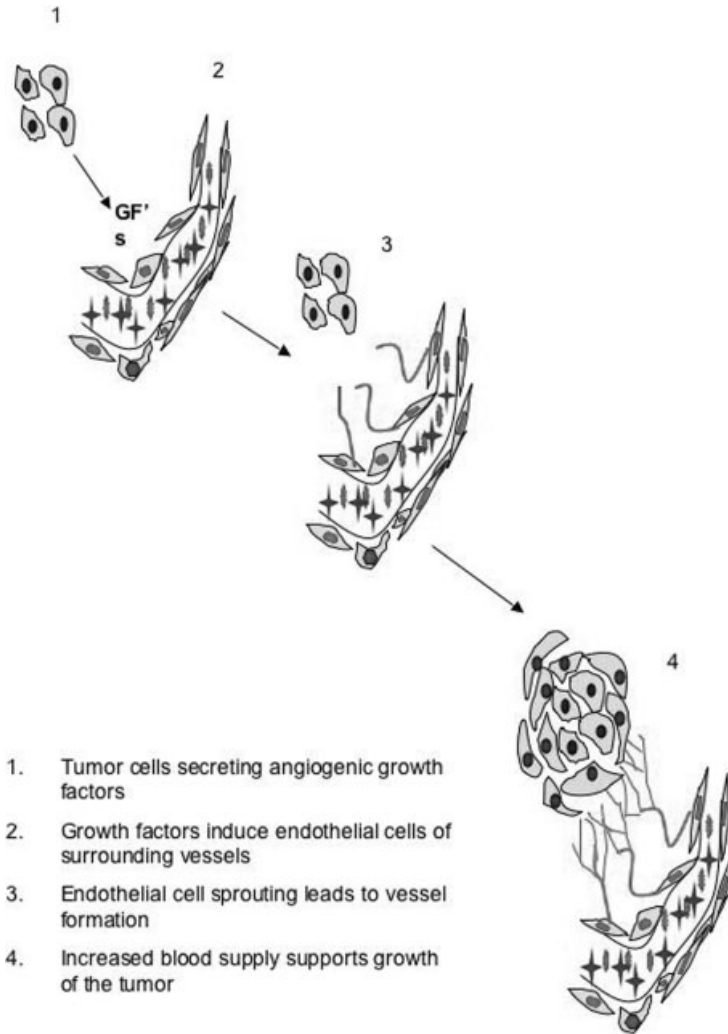


**Fig. 3.1.** Schematic diagram showing the role of angiogenesis in tumor growth and blood vessel formation.

#### 3.3.1.1 Agents that Inhibit Endothelial Proliferation or Response

Such targets include endoglin, integrins, dominant negative receptors and agents that prevent the release or activation of FGF. Direct administration of endogenous angiogenic inhibitors such as angiostatin, endostatin, and gene therapy using DNA that encodes for angiogenesis inhibitors, including angiostatin and platelet factor 4, are being evaluated. Administration of synthetic angiogenic inhibitors that specifically prevent endothelial cell division include derivatives of fumagillin, such as TNP-470 [53, 54]; combrestatin phosphate, which induces apoptosis in proliferat-

ing endothelial cells and causes tubulin destabilization [55]; and vitaxin, which is a humanized monoclonal antibody to alpha5-beta3 integrin present on endothelial cell surface, and EMD 121974 a small molecule blocker of alpha5-beta3 integrins [56–58].

### 3.3.1.2 Agents that Block Activation of Angiogenesis

Interferon alpha has demonstrated a 30% response rate in patients with AIDS-related Kaposi sarcoma and has been shown to be active in the treatment of hemangiomas, chronic myeloid leukemia, myeloma, melanoma, lymphoma and renal cell carcinoma [59–61]. SU5416, a small molecule blocker of VEGF-receptor2 signaling, is in Phase II clinical trial for metastatic colorectal cancer, non-small cell lung cancer and von Hippel-Lindau disease [62]. SU6668, a small molecule blocker of VEGF, FGF and PDGF receptor signaling, is in Phase I trial for selected advanced tumors [63]. Humanized monoclonal antibody to VEGF is now in clinical trials for several cancers, including metastatic renal cancer, advanced prostate cancer, non-small cell lung cancer, colorectal cancer and other solid cancers [46].

### 3.3.1.3 Agents that Block Extracellular Matrix Breakdown

Clinical trials have been ongoing for seven MMP inhibitors. Marimastat, a synthetic inhibitor that blocks TNF- $\alpha$  convertase, has shown clinical activity when combined with chemotherapy in colorectal, ovarian, prostate, gastric and pancreatic cancer [64]. Phase I studies with AG3340 in combination with other chemotherapeutic agents have been well tolerated in patients with advanced prostate and other solid tumors [65, 66]. Bay12-9566 and MM1270, synthetic MMP inhibitors, have undergone Phase I trials as single agents in pancreatic, ovarian and colorectal cancers [67, 68].

Although studies with antiangiogenic molecules have been elegant and results encouraging yet these advances should be viewed with cautious optimism as side effects that occur in some patients include hypertension, thrombosis, proteinuria, and even fatal hemorrhage. Therefore, selectivity, delivering drugs to specific targets on the tumor endothelium, has remained an obstacle in the development of better antiangiogenic therapy. Gold nanoparticles provide an avenue for targeted delivery of bioactive molecules to the tumor microenvironment by means of binding molecules such as antibodies that are specific for tumor-associated markers. Recent reports have demonstrated the potential utility of gold nanoparticles that served as a payload for delivery of DNA, proteins and imaging compounds to the tumor.

### 3.3.1.4 Unique Anti-angiogenic Properties of Gold Nanoparticles

Gold nanoparticles have been extensively used in biological applications due to their biocompatibility [69], dimensions (<50 nm), ease of characterization [70, 71] and their rich history of surface chemistry that can be easily exploited to better suit the needs of biomedical applications [72]. VEGFs are mitogenic for vascular endothelial cells [73] and act as potent angiogenic factors and blood vessel permeabilizing agents [73–76] *in vivo*. Four isoforms of VEGF containing 121, 165, 189 and

206 amino acids are produced from a single gene as a result of alternate splicing [76]. The 121 amino acid form of VEGF induces the proliferation of endothelial cells but, in contrast to VEGF 165, lacks the heparin binding ability [77]. Many anti-angiogenic approaches have been developed to block the interaction of VEGFs with their receptors in order to inhibit angiogenesis and tumor growth that include monoclonal antibodies targeting VEGF [78, 79] and the use of soluble decoy receptors blocking the binding of VEGF to its receptors [80]. We have shown, for the first time, that gold nanoparticles bind and inhibit the activity of Vascular Permeability Factor/Vascular Endothelial Growth Factor 165 (VPF/VEGF-165), an endothelial cell (ECs) mitogen and a prime mediator of angiogenesis that plays a tremendous role in pathological neo-vascularization, including rheumatoid arthritis, chronic inflammation and neoplastic disorders.

Gold nanoparticles used in this study were prepared by the reduction of aqueous chloroaurate ions with sodium and characterized using UV/Visible spectroscopy (UV/Vis), because of the presence of characteristic surface plasmon resonance band (Fig. 3.2), and transmission electron microscopy (TEM). The TEM image clearly showed that gold nanoparticles  $\sim 5$  nm in diameter were formed by this method (Fig. 3.3).

#### 3.3.1.5 Gold Nanoparticles Inactivate VEGF165

Whether gold nanoparticles had any effect on VEGF165 was tested on VEGF165-induced HUVEC proliferation. VEGF165 was pre-incubated with various concentrations of gold nanoparticles (67, 335, 670 nM) overnight at 4 °C and then added them to serum-starved HUVECs followed by [ $^3$ H]-thymidine incorporation. Gold nanoparticles inhibited VEGF165-induced proliferation ( $p < 0.0001$ ). However,

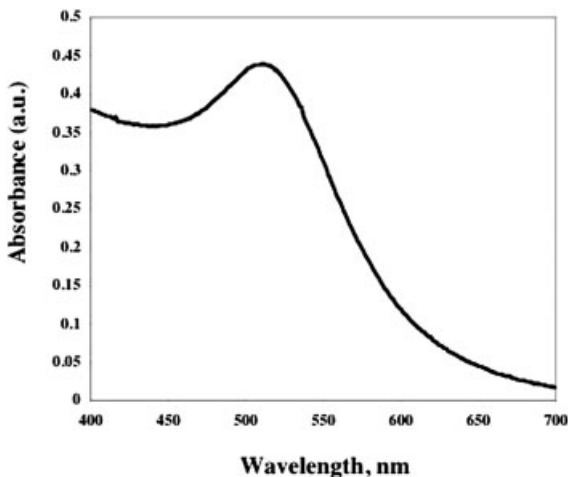
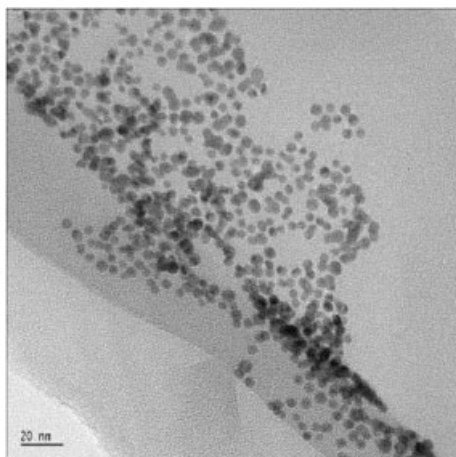


Fig. 3.2. UV/Vis spectrum of gold nanoparticles obtained by sodium borohydride reduction of tetrachloroauric acid.



**Fig. 3.3.** Transmission electron micrograph of gold nanoparticles obtained by borohydride reduction of gold salts.

gold nanoparticles did not inhibit non-heparin binding VEGF121-induced proliferation of HUVEC cells. Importantly, the gold nanoparticles were not toxic to HUVECs, where no inhibition in proliferation was observed in the only nano-gold treated samples compared to the control. Numerous examples of surface modifications of gold nanoparticles with alkanethiols aromatic thiols, and primary amines have been reported [81–85]. Such an ionic/pseudo-covalent reaction may explain the interaction between the gold nanoparticles and VEGF165 that led to the inhibition of its activity. However, the inability of gold nanoparticles to inhibit the activity of VEGF121 suggested that the presence of a heparin-binding domain was necessary to be inactivated by gold nanoparticles.

#### 3.3.1.6 What is the Mechanism of Action?

To prove that gold nanoparticles bind to the heparin-binding domain of VEGF165, gold nanoparticles at different concentrations (335, 670 and 1340 nM) were pre-incubated with VEGF165 overnight at 4 °C. VEGF165 was then precipitated from this complex with a saturating concentration of heparin-sepharose. In the absence of gold, all VEGF165 was bound to heparin-sepharose and was detected only in the precipitated fraction while none was detected in the supernatant fraction.

Heparin sepharose binds to the heparin binding domain of a heparin binding protein and precipitates it from the solution. The results of the pre-incubation experiments with heparin sepharose conclusively proved that VEGF165 in the supernatant fraction was in the gold-bound form and thus could not interact with the heparin-sepharose. From these results, it was concluded that gold nanoparticles inhibited VEGF165 from binding to heparin-sepharose because gold itself binds to VEGF165 through the heparin-binding domain. Signaling events of VEGF165 leading to proliferation were initiated by its association with cell surface receptors, mainly KDR, where the heparin-binding domain plays an important role. Pre-

incubation experiments with heparin sepharose clearly proved that blocking the heparin-binding domain of VEGF165 gold nanoparticles inhibited its association with KDR and, thereby, inhibited its activity.

Direct binding of VEGF165 to gold nanoparticles was confirmed by XPS analysis. The presence of a single Au  $4f_{7/2}$  peak at 83.9 eV clearly demonstrated only one form of Au present in solution and that it is Au(0) [86]. The presence of two sulfur peaks, at 162.7 and 167.1 eV, represented two chemically distinct sulfur species. The peak at 162.7 eV was assigned to gold-bound sulfur and that at higher BE was assigned to oxidized sulfur species such as in sulfones. The nitrogen 1s peak at 399.6 eV was likely due to unionized, non-protonated nitrogen [87]. However, the possibility of gold nanoparticles binding to VEGF165 through nitrogen as well could not be ruled out. Hence it was concluded that the direct binding of VEGF165 to gold nanoparticles occurred through sulfur and/or nitrogen, both present in the heparin-binding domain of VEGF165.

We have described earlier that angiogenesis plays a central role in the growth and progression of tumor [69, 70]. This process is also important for the promotion and maintenance of other diseases like neoplasia and rheumatoid arthritis [71]. As there are several reports that indicate that gold salts can retard the progression of rheumatoid arthritis [72], we reasoned that gold nanoparticles might also inhibit angiogenesis. Because VEGF/VPF [73, 74] and bFGF [75] are two critical cytokines for the induction of angiogenesis, we investigated whether nontoxic novel gold nanoparticles [76] being used at present in several biomedical applications can inhibit the functions of these two important proangiogenic growth factors.

#### **3.3.1.7 Effect of Gold Nanoparticles on the Activity of VEGF165, VEGF121, bFGF and EGF**

The effects of gold nanoparticles on the activity of VEGF165, VEGF121, bFGF and EGF were tested on two different cell lines, namely HUVEC (for VEGF165 and VEGF121) and 3T3 (for EGF and bFGF). The gold nanoparticles inhibited VEGF165-induced proliferation of HUVECs- and bFGF-induced proliferation of 3T3 cells but did not inhibit either VEGF121- or EGF-induced proliferation. Gold nanoparticles are not toxic to either cell line as no inhibition in proliferation was observed in the only nanogold treated samples compared with the control. The inhibition of proliferative activity of two heparin binding growth factors, namely VEGF165 and bFGF, by nanogold and its inability to inactivate non-heparin binding growth factors, namely VEGF121 and EGF, clearly suggested that the heparin-binding domain of VEGF165 and bFGF played the crucial role for their interactions with nanogold and, hence, inactivation.

#### **3.3.1.8 Effect of Gold Nanoparticles on Signaling Events of VEGF165**

With the addition of 335–670 nm nanogold, VEGF165-induced phosphorylation of VEGFR-2 was profoundly inhibited. However, at 67 nm nanogold ~40% inhibition of phosphorylation was evident [from densitometry quantitation using NIH Image software,  $p < 0.0001$ ]. Almost complete inhibition of VEGFR-2 phosphory-



lation was observed at concentrations of 335 and 670 nM nanogold. The results of receptor phosphorylation clearly suggested that nanogold binds directly to VEGF165 and inhibited its interaction with cell surface receptors hence inhibiting phosphorylation.

#### 3.3.1.9 Effect of Nanogold on Downstream Signaling events of VEGF165

To further support the hypothesis that nanogold binds to VEGF165 and inactivates its signaling capability, an intracellular calcium release experiment in HUVECs was performed. A gold concentration of 67 nM gave ~34% inhibition (determined by comparing the length of the upstroke of VEGF165 induced sample to the nanogold-treated samples) and complete inhibition was observed at 335–670 nM ( $p < 0.05$ ). The VEGF receptors on the HUVECs were still functional as evidenced by an increase in calcium release comparable to the control when VEGF was added after 300 s. These observations also clearly demonstrated that gold nanoparticles bind directly to VEGF165 and inhibited its signaling events but did not perturb the receptor functions.

#### 3.3.1.10 Effect of Gold Nanoparticles on Migration of HUVEC Cells

Nanogold inhibited VEGF165-induced migration of HUVECs. Rho A activity was also completely inhibited at 670 nM nanogold, further confirming the hypothesis that nanogold binds directly with the heparin binding growth factor through the heparin binding domain and inhibits its signaling activity.

#### 3.3.1.11 Effect of Gold Nanoparticles on Angiogenesis *in vivo*

The efficacy of nanogold in inhibiting VEGF165-induced permeability and angiogenesis *in vivo* was tested in a nude mouse ear model. Ad-VEGF injected mice treated with nanogold developed lesser edema than mice treated with Ad-VEGF only. As shown, 30 min after injection of Evan's blue dye into the tail vein of these treated mice, a decrease in permeability was also observed. In the MOT model, less fluid accumulation in the peritoneal cavity was observed in nanogold treated samples than in controls.

Taken together, our results showed that gold nanoparticles selectively inhibited VEGF165- and bFGF-induced proliferation of HUVECs and fibroblasts, respectively. In a similar fashion, nanogold also inhibited the activity of placental growth factor (PIGF) (unpublished results). Gold nanoparticles directly bind heparin-binding growth factors, presumably through cysteine residues of the heparin-binding domain, and inhibit growth factor mediated signaling. Gold binds strongly with thiols and amines [85–87]. Such an ionic/pseudo-covalent reaction may explain the interaction between the gold nanoparticles and VEGF that led to a decrease in its proliferative activity. Gold nanoparticles also inhibit VEGF-induced angiogenesis and permeability *in vivo* as well as causing lesser ascites fluid accumulation in a MOT model where VEGF/VPF activity is primarily responsible for fluid accumulation in the peritoneal cavity. Here, we mention, briefly, the toxicity of nanogold. Because metal poisoning is associated with renal and hepatic toxicities, we determined the effect of nanogold administration on liver and renal func-

tion tests. Normal mice were injected with same dose of nanogold as in MOT model intraperitoneally for 7 consecutive days. On day 8, the mice were sacrificed and serum was collected. There were no significant differences between serum levels of creatinine, blood urea nitrogen, bilirubin alkaline phosphatase, ALT (Alanine Aminotransferase) and AST (Aspartate Aminotransferase) between the nanogold treated and untreated control animals. This finding is significant because growth factor-mediated proliferation and angiogenesis have a central role in many pathological conditions, including neoplasia, rheumatoid arthritis and chronic inflammation. The low production cost and relative ease in modifying nanogold make them a feasible choice in future biomedical applications.

#### 3.3.1.12 Gold Radioisotopes in Cancer Treatment

Radioisotopes of gold have also long been used for the treatment of different types of cancer. A cumulative survival of 96.3% was achieved in the treatment of stage Ia ovarian cancer with radiogold [88]. In addition, Ehrlich ascites tumor has been prevented by intraperitoneal injection of colloidal  $^{198}\text{Au}$  [89]. In the treatment of limited epithelial carcinoma of the ovary, 104 patients received intraperitoneal radiocolloid [90]. Fifty six of these patients also received external beam radiation therapy to the pelvis. Five year actuarial no-evidence-of-disease survival rates were 95% for stage Iai, 82% for stage Iaii, 73% for stage Ib, 67% for Ic, 67% for Iia, 67% for Iib without gross residual tumor (GRT) and so on. Radioactive gold has also been used to prevent hepatic metastasis by intravenous administration [91]. Recently, gold nanoparticles have been used to increase radiotherapy in mice [92]. Mice bearing subcutaneous EMT-6 mammary carcinomas received a single intravenous injection of 1.9-nm gold particles (up to 2.7 g-Au per kg body weight). The gold content of the tumor elevated by this treatment to 7 mg-Au per g in tumor. The mice were then subjected to 250 kVp X-ray therapy for several minutes. The one-year survival rate was found to be 86% versus 20% with X-rays alone and 0% with gold alone.

### 3.3.2

#### Application of Gold Conjugates in the Treatment of Cancer

The biological application of gold nanoparticles began in 1971 when Faulk and Taylor invented the immunogold staining procedure [93]. Since then gold nanoconjugates have been extensively used to detect cellular components using electron microscopy. Mostly gold nanoconjugates were seen as passive components, used only to visualize different cellular components. However, the use of these gold nanoparticles for *in vivo* drug delivery has never been described. Recently, gold nanoconjugates have been used as more active components that can interfere with the biological activities [94–98].

#### 3.3.2.1 Gold–TNF Conjugate in Cancer Therapeutics

Recently, colloidal gold, a sol composed of nanoparticles of  $\text{Au}^0$ , has been used as a therapeutic for the treatment of cancer as well as an indicator for immunodiagnos-

tics. However, the use of these gold nanoparticles for *in vivo* drug delivery has not been described. The development of a colloidal gold (cAu) nanoparticle vector that targets the delivery of tumor necrosis factor (TNF) to a solid tumor growing in mice has been reported [99]. The optimal vector, designated PT-cAu-TNF, consists of molecules of thiol-derivatized PEG (PT) and recombinant human TNF that are directly bound onto the surface of the gold nanoparticles. Following intravenous administration, PT-cAu-TNF rapidly accumulates in MC-38 colon carcinoma tumors and shows little to no accumulation in the livers, spleens (i.e., the RES) or other healthy organs of the animals. Tumor accumulation was evidenced by a marked change in color of the tumor as it acquired the bright red/purple of the colloidal gold sol and was coincident with the active and tumor-specific sequestration of TNF. Finally, PT-cAu-TNF was less toxic and more effective in reducing tumor burden than native TNF since maximal antitumor responses were achieved at lower doses of drug.

### 3.3.2.2 “2 in 1” System in Cancer Therapeutics

Recently, our group has reported the fabrication of a “2 in 1” system containing functional anti-angiogenic agent and cytotoxic drug. Angiogenesis, the formation of new blood vessels from a pre-existing vessel, is a necessary step for tumor growth and metastasis [99–102]. This provides the basis for anti-angiogenic therapy – depriving tumor cells the nutrients essential for their growth by blocking their blood supply. Although this treatment may restrict tumor growth, anti-angiogenic therapy alone might not be enough to prevent tumor growth and cause increased cell killing. Therefore, to achieve maximal therapeutic benefit it is necessary to use anti-angiogenic agents in combination with other modalities such as anticancer drugs [103]. One of the problems in the use of anticancer drugs is that they have short half-lives, sometimes with extensive systemic toxicity [104]. When delivered in a gold-conjugated form, these molecules might have increased retention in the body with reduced systemic toxicity. VEGF-antibody attached on gold nanoparticles may facilitate delivery of the drugs to the site of tumor, as many tumors are known to produce VEGF [105, 106]. We hypothesize that use of a cytotoxic agent such as gemcitabine along with VEGF antibody will not only allow tumor cell killing but also give rise to more “normalized” blood vessels, resulting in better drug delivery [107]. This study employed a nano-composite system consisting of a nanogold core, bearing a functional anti-angiogenic molecule, VEGF antibody-2C3 (AbVF), and an anticancer drug, gemcitabine. This provides a unique “2 in 1” system where two components with different functions have been attached onto a single gold core, yet the functional activity of the individual components are retained.

To attach multiple components onto a single gold core, it is essential to determine the saturation concentration of the individual components [108]. The saturation concentration of AbVF was determined after incubating it with gold nanoparticles with increasing concentrations of AbVF for 30 min followed by treatment with 100  $\mu$ L of 10% NaCl solution to test for aggregation [109]. Gemcitabine was similarly attached to nanogold. Without any protection, gold nanoparticles aggre-

gate immediately upon addition of a 10% NaCl solution. The extent of aggregation, however, should decrease with increasing protection of the nanogold surface either by antibody or by gemcitabine. Increased stabilization of nanogold dispersions was observed with increasing concentrations of AbVF. In the absence of antibody but in the presence of NaCl, gold nanoparticles completely aggregated and, as expected, their absorbance dropped to zero [109]. Next, the saturation concentration of gemcitabine on gold nanoparticles was determined, similarly as above. Gold nanoparticles were incubated with different concentrations of gemcitabine for 30 min and their UV/Vis spectra were recorded. Absorbance of nanogold gradually increased with increasing concentrations of gemcitabine until it reached a maximum at  $20 \mu\text{g mL}^{-1}$ . According to the Mie theory, the observed shift in  $Y_{\text{max}}$  with an increase in plasmon resonance coincides with a rising dielectric constant of the medium surrounding the gold nanoparticles [110]. At doses higher than  $20 \mu\text{g mL}^{-1}$ , the absorbance of the nanocomposite gradually decreased, alongside a gradual increase in redshift in  $Y_{\text{max}}$ . This relationship, along with a broadening of the spectra, may be attributed to the aggregation of gold nanoparticles upon the addition of gemcitabine beyond the  $20 \mu\text{g mL}^{-1}$  limit. To attach both gemcitabine and AbVF on nanogold surface, incubation experiments were carried out below the 50% saturation concentration for AbVF and gemcitabine. Gold nanoparticles were first incubated for 30 min at room temperature with  $10 \mu\text{g mL}^{-1}$  of gemcitabine followed by another 30 min incubation with  $2 \mu\text{g mL}^{-1}$  of VEGF antibody. Aggregation tests were performed to confirm the attachment of both the components.

The functional activities of gemcitabine and AbVF were tested by *in vitro* cell culture assays. The activity of gemcitabine was tested on 786-O cells using a BrdU proliferation assay. The observed activity of gemcitabine combined with AbVF on nanogold surfaces was comparable to gemcitabine alone at the same concentration. In the control experiments with gold or AbVF alone or gold-AbVF, no inhibition 786-O proliferation was observed. Therefore, the inhibition in proliferation was due to the presence of gemcitabine within the nanocomposite and the presence of AbVF on the same nanocomposite did not exert any negative influence on the activity of gemcitabine.

The functional activity of AbVF was determined on VEGF165 induced calcium release in HUVEC cells. HUVECs release calcium into the cytoplasm when induced with VEGF165 [6]. AbVF attached to nanogold surfaces with gemcitabine inhibited calcium release more efficiently than the same dose of AbVF alone. At  $10 \text{ ng mL}^{-1}$ , almost no inhibition of VEGF165-induced calcium release was observed in the samples of AbVF alone but a moderate inhibition and delay was observed with AbVF in the nanocomposite form. At  $20 \text{ ng mL}^{-1}$ , moderate inhibition was observed in samples with only AbVF but complete inhibition of calcium release was observed for the nanocomposite. This suggested an optimal threshold concentration requirement for VEGF to be able to induce calcium release. To further confirm that the inhibition in calcium release was due to AbVF, the nanogold surface was blocked with gemcitabine and control mouse IgG. VEGF165-induced calcium release was not inhibited by this nanocomposite. From

the calcium release assay, it was concluded that AbVF retained its functional activity in the AbVF–gold–gemcitabine nanocomposite form and gemcitabine did not had no negative influence on the activity of VEGF antibody.

This study was a unique example of a “2 in 1” system where anti-angiogenic molecule, VEGF antibody and cytotoxic drug (gemcitabine) were attached on the same nanogold surface, with potential implication in cancer therapeutics.

### 3.4

#### **Biocompatibility of Gold Nanoparticles**

The biocompatibility of nanoparticles in general is discussed in detail elsewhere [110–114]. Here, recent efforts addressing the issue related to gold nanoparticles will be discussed briefly. The issue of biocompatibility arises when any foreign body is introduced inside the human body for medical purposes or otherwise [111–114]. In most general terms biocompatibility can be defined as “the ability of a material to perform with an appropriate host response in a specific application” or “the exploitation by materials of the proteins and cells of the body to meet a specific performance goal”. Interactions between the foreign body and the host can be classified in four general categories (a) cellular adhesion effects, (b) local biological effects, (c) systemic and remote effects, and (d) effects of the host on the implant.

#### 3.4.1

##### **Cellular Adhesion Effects**

The interaction of the foreign body, direct or indirect, weak or strong, specific or non-specific, receptor mediated or non-mediated with the host may influence the biocompatibility of the foreign body.

#### 3.4.2

##### **Local Biological Effects**

Local biological effects include cell viability, cell mitotic function such as proliferation, cell cycle phases, etc., plasma membrane integrity, toxicity and modification or normal wound healing.

#### 3.4.3

##### **Systemic and Remote Effects**

Systemic and remote effects include systemic toxicity (such as kidney failure, liver failure, etc.), elevation of unusual components in the blood, allergic, pyrogenic, carcinogenic and teratogenic responses.

## 3.4.4

**Effects of the Host on the Implant**

This mainly includes immune responses, such as inflammation, fibrosis, etc., around the implant, physical and mechanical effects, stability and biological degradation processes.

## 3.4.5

**Addressing the Biocompatibility of Gold Nanoparticles using DNA Microarray Analysis**

Nanotechnology is a rapidly evolving multidisciplinary branch of science involving systems and/or device manufacturing at the nano-scale level [115, 116]. Nanoparticle-aided strategies have been implemented to address a diverse array of issues, including drug delivery, targeting and monitoring of molecules/cells/tissues, and development of novel drug regimens [117–119]. A modified variety of nanoparticles, known as quantum dots, which are highly fluorescent semiconductor particles measuring roughly the size of an average protein, have been developed and shown to be valuable for monitoring metastatic tumor cells in an animal model [120]. These fluorescent quantum dots are reported to be active for over a month inside the body, allowing one to monitor migration and localization of the probe over a long period of time [121, 122].

Conceptually, nanoparticles can have effects, both desired and unintended, on an organism through acting directly and/or indirectly on individual cells. Since all investigations employing nanotechnology were performed related to specific questions, efforts to assess potential global effects remain virtually unanswered. However, some recent reports involving nanotechnology have generated widespread concerns regarding the effect of nanoparticles on the ecosystem and ultimately to human health [123–125]. Several recently published papers showed the toxicological effects of carbon nanotubes [126, 127]. It is, however, not known if all nanoparticles have similar biological effects; it is also not known if the same nanoparticle will have the same effect on different organisms. In fact, the overall consensus among scientists working on various aspects of nanoparticles is that very little is known about the potential impacts of nanoparticles on health and environment. Evidently, a thorough evaluation of the underlying issues needs to be systematically performed to distinguish reality from mere extrapolation of inadequate data. Metallic gold is known to be biocompatible; however, facts regarding the biocompatibility of gold nanoparticles are rare. Recently efforts have been made to address the biocompatibility issue of gold nanoparticles. Significant damage to the cell membrane was observed by cationically modified gold nanoparticles and they were shown to be moderately toxic, whereas anionic particles were quite non-toxic. A series of gold nanoparticles with various surface modifications were tested recently for uptake and acute toxicity in human leukemia cell lines. The authors concluded that although some precursor of nanoparticles might cause toxicity, the nanoparticles themselves are not toxic, further strengthening our findings [128]. The

effects observed in those cases may be due to the presence of the surface modifier and not because of the gold nanoparticles. To find out the effect of bare gold nanoparticles, our laboratory has focused on the genotropic effects of gold nanoparticles on normal human cell lines. We hypothesize that the overall physiology of a cell is equivalent to its global transcriptional profile. Consequently, we speculate that the expression signature of a cell in the presence or in absence of a given nanoparticle can generate valuable information regarding the potential effect of a nanoparticle on the target cell. However, a given nanoparticle can, possibly, interact with cellular components directly and elicit an effect or interact with non-cellular components first, which, in turn, may produce an effect on the target cell (an indirect effect). These so-called “direct” and “indirect” effects, if any, will need to be distinguished to ascertain the full spectrum of effects of nanoparticles on target cells (or on non-target cells). We have previously shown that gold nanoparticles effectively blocked the effect of vascular endothelial growth factor (VEGF)-mediated signaling by HUVECs (Human Umbilical Vein Endothelial Cells) and also inhibited angiogenesis *in vivo* in a mouse ovarian tumor model [10]. We have evaluated the potential direct effect of gold “naked” nanoparticles on HUVECs.

#### 3.4.6

##### **Internalization of Gold Nanoparticles by HUVECs**

To discern the effect of any nanoparticles on any cell lines, it is important to know the location of the nanoparticles, whether most of them are outside or inside the cells, and to find out if the nanoparticles change size upon internalization. To address the localization of gold nanoparticles, transmission electron microscopy was performed after incubating HUVECs with gold nanoparticles for 1 and 24 h under serum-free conditions and in the presence of serum. TEM clearly demonstrated the internalization of gold nanoparticles at both time points under such conditions, and no significant difference on the distribution of the gold nanoparticles was observed (Fig. 3.4). The size of gold nanoparticles did not alter significantly upon internalization. The distribution of gold nanoparticles under serum-free conditions and in the presence of serum was similar. No significant difference in the distribution of gold nanoparticles at 1 and 24 h was observed, confirming that 1 h incubation was enough for gold nanoparticles to be taken up HUVECs.

#### 3.4.7

##### **Nanogold Particles do not Alter Global Pattern of Transcription by HUVEC Cells under Serum-free Conditions**

Since serum contains a host of heparin-binding domain containing proteins, including growth factors, with which nanogold can potentially interact and block their functions [9], which, in turn, can have an (indirect) effect on cells in culture, it was necessary to exclude serum (FBS) in an attempt to evaluate a direct effect of gold nanoparticles on HUVECs. Therefore, cells were first cultured in serum-containing media until they were about 80% confluent, after which the cells were

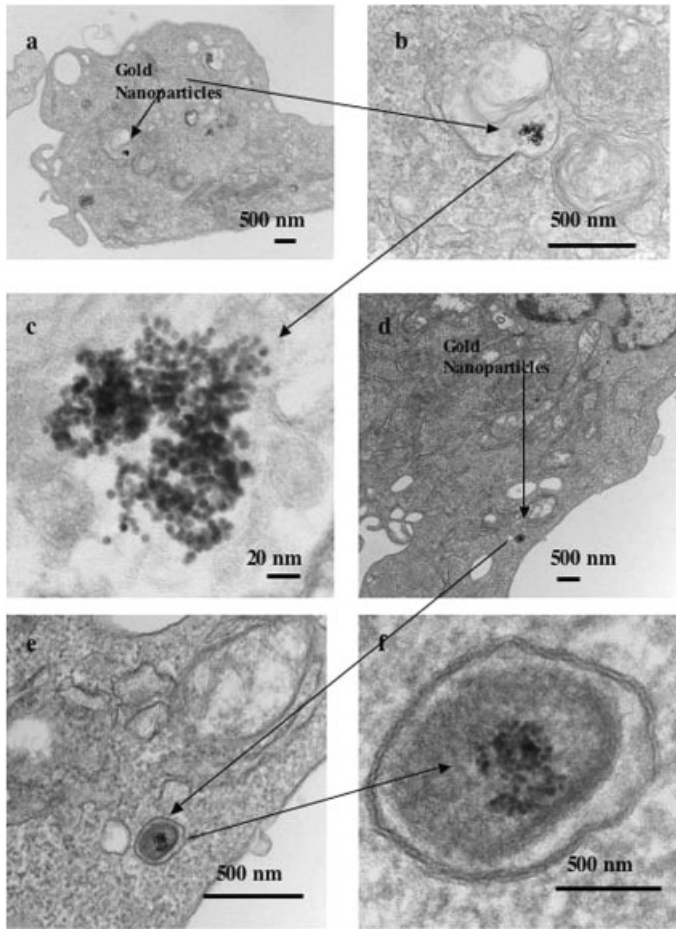


**Fig. 3.4.** Internalization of gold nanoparticles by HUVECs, (a) internalization under serum-free conditions after 4 h incubation; (b) and (c) higher magnification images of (a). (d) Internalization of gold nanoparticles in the presence of serum after 4 h incubation; (e) and (f) higher magnification images of (d).

washed repeatedly with PBS to get rid of serum. The cells were then incubated in serum-free media for 24 h, after which gold nanoparticles were added and the culture continued for 1 and 24 h, respectively. Total RNA extracted from such cells was subjected to microarray analysis. The expression level of genes determined through microarray was subjected to Scatter plot analysis. The results indicated a strikingly similar pattern of gene expression at both 1 and 24 h by cells cultured with or without nanogold particles. The correlation coefficients were 0.98 for 1 h and 0.97 for 24 h, respectively. These observations strongly attest to the similarities



of gene expression, indicating that 5-nm gold nanoparticles have no effect on gene expression by HUVECs. It is possible that a small number of genes truly undergoing differential expression in the presence of gold nanoparticles were missed by the Scatter plot analysis. To eliminate this possibility, the microarray-based expression results were manually checked and seven genes were selected to show expression difference of at least 1.5 fold and having expression values of >300 either for control or for cells treated with gold. RT-PCR was performed for all these genes to validate their mRNA expression status in cells cultured with and without gold nanoparticles. The results showed no significant difference in the mRNA expression levels of any of the seven genes, supporting the observation made through Scatter plot analysis.

#### 3.4.8

#### **Nanogold Particles do not Alter the Global Pattern of Transcription by HUVECs in Near-normal Culture Conditions**

The lack of an effect of gold nanoparticles on HUVECs as observed under serum-free conditions could be due to the possibility that cells exposed to serum-free media preclude any potential effect of the gold nanoparticles on cell transcription. To eliminate this possibility, the first step was omitted completely (culturing cells in serum-free media for 24 h before adding gold particles) and confined incubation of cells with gold for up to 4 h. Briefly, cells were first grown in the presence of serum to near confluency, then repeatedly washed with serum-free media, nanogold particles were then added followed by incubation in serum-free media for 1 and 4 h.

RNA isolated from cells at indicated times (1 and 4 h after exposure to gold particles) was subjected to microarray analysis as above. Scatter plot analysis of the data showed no effect of gold particles on the global transcriptional pattern of HUVECs even when the cells were not exposed to serum-free conditions for a long time. Correlation coefficients obtained from these experiments were 0.995 for 1 h and 0.994 for the 4 h, further supporting this observation. The data was also manually scanned to identify cases of differentially expressed genes not evident in the Scatter plot analysis. Nine genes were identified based on the criteria mentioned earlier. RT-PCR was performed for these genes to validate their mRNA expression level in cells cultured with and without nanogold for 1 and 4 h. The RT-PCR results did not suggest any difference in the mRNA expression levels of these genes in HUVECs not exposed to serum-free conditions prior to adding nanogold in the culture, supporting the results from Scatter plot analysis. Thus, all of the experiments suggested a lack of a direct effect of gold nanoparticles on the transcriptional program of HUVECs.

Conceptually, any agent, physical, chemical or biological, can have an effect on a cell/organism; the magnitude of the effect, however, will depend on a diverse array of known and unknown parameters. Whether such an effect can be measured by

standard means depends on the resolution and sensitivity of a given method. We have previously shown changes in the level of gene expression due to the effect of sound waves on cultured cells [128, 129]. Thus, measurement of gene expression can document subtle intracellular changes caused by the extracellular environment of a cell. DNA-microarray has rapidly become a useful tool for measuring gene expression at the global level – this is, probably, because the resolution of the microarray can be very high (the one used in this study contains probes for virtually all known and predicted human genes) and the sensitivity is within an acceptable range.

However, with such a tool, we did not observe any effect (positive or negative) of gold nanoparticles on the global transcriptional pattern of HUVEC cells. Some genes selected by manual screening of the microarray data appeared to be differentially expressed between HUVEC cells cultured with and without gold nanoparticles. However, repeated RT-PCR failed to document differential expression for any of these genes. Thus, both RT-PCR and microarray-based results strongly suggest a lack of effect of gold nanoparticles on mRNA expression.

Recently, we have demonstrated that nanogold particles can not only bind to VEGF but also can inhibit VEGF-dependent HUVEC proliferation and ascites fluid accumulation in a mouse ovarian tumor model, illustrating a unique mechanism of deactivation of heparin binding growth factors by gold nanoparticles on a complex biological process [7]. Note that VEGF has cysteine residues on its heparin-binding domain, which can easily become conjugated with gold nanoparticles through covalent interaction, causing sequestration and/or inactivation of the growth factor [8]. Since, the experiments reported herein were not VEGF-dependent, no such indirect effect of nanogold should be expected (in agreement with our previous reports where we did not see any toxic effects of gold nanoparticles on HUVEC). The results presented in this study enabled some important inferences. First, although the results could not rule out subtle effects of 5-nm gold nanoparticles or effects beyond the time points investigated under conditions tested, 5-nm naked gold nanoparticles with no surface modifications may indeed have no direct effect on human cells. Second, gold nanoparticles of smaller size were expected to be more “active” than particles of larger size; however, it would be interesting to see if nanoparticles of different sizes with no surface modification have any significant direct effect on biological processes. Finally, since 5 nm nanoparticles appeared to have no effect (toxic or non-toxic) on HUVECs, such particles may be ideal to realize at least some of the promises of nanotechnology, assuming a similar effect of such particles on other types of cells. Notably, the potential genotropic effects of gold nanoparticles have been evaluated in this study; however, such particles may also exert non-genotropic effects (such as membrane protein cycling) on target cells. Such a possibility will need to be addressed to evaluate comprehensively the direct effect of nanoparticles on cell metabolism. We believe our approach provides a general experimental strategy for screening a diverse array of nanoparticles for their potential global effects on any type of target cells/tissues under diverse experimental conditions.

## 3.5

### Synthetic Approaches to Gold Nanoparticles

Even though this chapter focuses on the application of nanogold in cancer therapy and diagnosis, it would be incomplete without a description of the synthesis of gold nanoparticles, since the synthesis procedure may effect the properties of the gold nanoparticles and, hence, their application in the treatment of cancer. Here we describe briefly the general synthesis process for the preparation of gold nanoparticles. There are basically two synthetic methods: chemical and physical.

#### 3.5.1

##### Chemical Methods

In 1857, Faraday first reported the synthesis of gold nanoparticles by reduction of chloroaurate ions by phosphorous in carbon disulfide [130]. Among all the methods that are applied for the reduction of  $\text{HAuCl}_4$  to gold nanoparticles, the citrate reduction and borohydride reduction methods are most commonly used. The citrate reduction method, first introduced by Turkevitch in 1951, yields AuNPs approximately 20 nm in diameter [131]. Recently, it was shown that the size of AuNPs formed by the citrate reduction method can be controlled by the use of a stabilizer along with the reducing agent and by manipulating the ratio of gold salts to reducing agent/stabilizer [132].

In 1994, Brust and Schiffrin introduced a novel method for the synthesis of thiol-capped gold nanoparticles using sodium borohydride as a reducing agent [133]. Nanoparticles so-formed are thermally stable, air stable, with reduced dispersity and a size ranging from 1.5 to 5 nm. Spontaneous reduction of gold salts to gold nanoparticles by an inorganic matrix such as fumed silica has also been reported [134, 135]. These matrices not only reduce the gold salts to gold nanoparticles but also provide them with a solid support. Such conjugates exhibit interesting catalytic properties.

#### 3.5.2

##### Physical Methods

The most common physical methods for the synthesis of gold nanoparticles include UV, irradiation, NIR irradiation, sonochemical method, radiolysis and thermolysis. UV irradiation can improve the quality of the gold nanoparticles formed when it is used in the presence of micelles or seeds [136–139]. Near-IR irradiation produces a large size growth of thiol-stabilized gold nanoparticles [140]. The rate of  $\text{AuCl}_4^-$  reduction in aqueous solution as well as sizes of gold nanoparticles formed can be controlled by using an ultrasonic field of 200 kHz [141, 142]. Radiolysis has also been used to control the sizes of gold nanoparticles or when they are synthesized in the presence of radicals [143, 144]. Gold nanoparticles have also been produced by the thermolysis of gold salts [144, 145].

## 3.5.3

**Biological Methods**

Biological methods for the synthesis of nanoparticles have been reported recently. Some living microorganisms, such as fungus, can reduce metal salts to metal nanoparticles. Both extracellular and intracellular synthesis of metal nanoparticles have been reported using fungus [146, 147]. Cadmium sulfide nanoparticles has also been synthesized [148].

## 3.6

**Nanotechnology in Detection and Diagnosis with Gold Nanoparticles**

Nanotechnology [149] combined with biology is the most advanced technology both from an academic viewpoint and for commercial applications. The integration of nanotechnology with biology and medicine is expected to produce major advances in molecular diagnostics, therapeutics, molecular biology, and bioengineering [150–158]. Optical [159] and magnetic [160] properties of metals, semiconductors, polymers and magnetic nanoparticles, and quantum dots (small devices that contain free electrons and have typical dimensions between nanometers to micrometers – these tiny crystals glow when stimulated by ultraviolet light, e.g., ZnS, ZnSe, CdSe, CdTe, PbSe, etc.) are being used for DNA detection, cancer diagnostics, drug discovery and clinical therapy in biomedical research [121, 154, 161–179].

Among inorganic nanoparticles and quantum dots, colloidal gold nanoparticles have attracted significant research and practical attention in biology. Due to fascinating colors, size-dependent properties and dimensional similarities to biomacromolecule, these colloidal gold nanoparticles are widely used in biomedical research such as DNA detection [150, 177(b), 180], highly sensitive diagnostics [177(a), 181], thermal ablation and radiotherapy enhancement [182], as well as drug and gene delivery [183]. For instance, antibody-modified gold nanoparticles, when used for detection of prostate specific antigen, had an almost one million-fold higher sensitivity than a conventional ELISA-based assay [164]. Near-infrared radiation absorbing gold–silica nanoshells have been prepared and evaluated for thermal ablation of tumors after systemic administration [92, 182].

## 3.6.1

**Cancer Detection**

Sayed et al. have reported that binding gold nanoparticles to a specific antibody for cancer cells could make cancer detection much easier using a simple microscope [177(a)]. Their technique for detection of cancer cells is very simple, clean, faster, economically very cheap and eco-friendly/non-toxic.

They proposed that the very good scattering and light absorption properties of gold nanoparticles could be used to easily distinguish healthy from cancerous

cells with the help of a very simple microscope. Many cancer cells have a protein, known as Epidermal Growth Factor Receptor (EGFR), all over their surface, while healthy cells typically do not express the protein as strongly. By conjugating, or binding, the gold nanoparticles to an antibody for EGFR, suitably named anti-EGFR, they were able to get the nanoparticles to attach themselves to the cancer cells. When they added the conjugated nanoparticle solution to healthy cells and cancerous cells, they observed with a simple microscope that the whole cancer cell shines. In contrast, healthy cells did not bind to the nanoparticles specifically and, consequently, they did not shine.

In this promising technique, they found that the gold nanoparticles have a 600% greater affinity for cancer cells than for noncancerous cells. The gold nanoparticles that worked the best were 35 nm in size. Researchers tested their technique using cell cultures of two different types of oral cancer and one nonmalignant cell line. The shape of the strong absorption spectrum of the gold nanoparticles is also found to distinguish between cancer cells and noncancerous cells.

### 3.6.2

#### **Detection in DNA**

Several studies suggest that nanoparticle-based technology could enable sensitive detection of sequence variation in DNA [180]. Early studies demonstrated array-based DNA discrimination by allele-specific oligonucleotide hybridization using gold nanoparticle reporters containing bound oligonucleotides for hybridization to complementary targets [180(a)]. Detection was achieved by silver enhancement, resulting in deposition of silver on the surface of the nanoparticles, which enabled scanometric detection to define the location of the gold nanoparticles on an array [180(b)]. Attachment of a dye close to the surface of the nanoparticles via linkage to the oligonucleotide also enabled detection after silver enhancement by surface-enhanced Raman spectroscopy (SERS) [180(c)].

##### **3.6.2.1 Single-mismatch Detection in DNA**

Maxwell et al. have demonstrated the design and feasibility of bio-conjugated gold nanoparticles for recognizing and detecting specific DNA sequences in a single step [150]. According to their method, colloidal gold nanocrystals 2.5 nm in size have been used to develop a new class of nanobiosensors that can recognize and detect specific DNA sequences and single-base mutations in a homogeneous format. The 2.5-nm gold nanoparticles function as both a nano-scaffold and a nano-quencher (efficient energy receptor).

They proposed that single-stranded DNA is conformationally flexible. Conversely, two oligonucleotide molecules (oligos) are self-assembled in a constrained conformation (arch-like structure) on each gold particle (2.5 nm in diameter) A T6 spacer (six thymines) is inserted at both the 3' and 5' ends to reduce steric hindrance. In the assembled (closed) state, the fluorophore is quenched by the nanoparticle because of the stable arch-like structure. Upon target binding, the constrained conformation opens, the fluorophore leaves the surface because of the

structural rigidity of the hybridized DNA (double stranded), and fluorescence is restored. In the open state, the fluorophore is separated from the particle surface by about 10 nm.

In this novel method gold nanoparticles represent a new class of universal fluorescence quenchers that are substantially different from DABCYL (4,4'-dimethylaminophenylazobenzoic acid) and should find new applications in molecular engineering and biosensor development and homogeneous bioassays that are not possible by DABCYL.

In another method, Dubertret et al. have shown that gold-quenched nucleic acid probes (gold-oligonucleotide-dye) can be more sensitive than other probes currently available for mismatch detection. With their developed probes a point mutation can be selectively detected in the presence of random sequences even if only 1 out of 50 sequences has one mutation. They have developed a hybrid material composed of a 25-nucleotide long single-stranded DNA (ssDNA) molecule, a 1.4 nm diameter gold nanoparticle, and a fluorophore (an organic dye) that is highly quenched by nanoparticle through a distance-dependent process. This hybrid material can form the hairpin structure that brings the fluorophore and the gold particle in close proximity (within a few angstroms). In this conformation, the gold cluster quenches the fluorescence of the dye. Through sequence-specific hybridization to a single-stranded target DNA, the hairpin structure changes to a rod-like structure (on the right), which maintains the fluorophore and the quencher far apart and thus restores the fluorescence. They reported that 1.4-nm diameter gold nanoparticles are better than a conventional fluorescence quencher, such as DABCYL, because gold nanoparticles quench fluorescence as much as 100× better and have higher quenching efficiency than dyes emitting in the near-infrared region.

As well the above examples of the use of gold nanoparticles in cancer and DNA detection, numerous recent reports relate the biological applications of gold nanoparticles in imaging and in therapy [8, 184–193]. A few are described here very briefly.

Chen et al. have demonstrated a novel nanoshell-based all-optical platform technology for integrating cancer imaging and therapy applications [184]. Immunotargeted nanoshells are engineered to both scatter light in the NIR enabling optical molecular cancer imaging, and to absorb light, allowing selective destruction of targeted carcinoma cells through photothermal therapy. They have shown that dual imaging/therapy immunotargeted nanoshells can be used to detect and destroy breast carcinoma cells that overexpress HER2, a clinically relevant cancer biomarker.

Bioconjugated with antibodies, gold nanocages (<40 nm) have also been used for specific targeting of breast cancer cells [185]. These gold nanocages have a moderate scattering cross-section of  $\sim 8.10 \text{ \AA} \sim 10\text{--}16 \text{ m}^2$  but a very large absorption cross-section of  $\sim 7.26 \text{ \AA} \sim 10\text{--}15 \text{ m}^2$ , suggesting their potential use as a new class of contrast agents for optical imaging.

Surface-enhanced Raman scattering (SERS) studies have been reported on indocyanine green (ICG) on colloidal silver and gold nanoparticles, demonstrating a

novel optical probe for applications in living cells [186]. The ICG gold nanoprobe delivers spatially localized chemical information from its biological environment by employing SERS in the local optical fields of the gold nanoparticles.

Applications of nanostructures including gold nanoparticles in biodiagnostics have been thoroughly reviewed recently [187]. Prostate-specific antigen (PSA) is a valuable biomarker for prostate cancer screening. Huang et al. have developed a PSA immunoassay on a commercially available surface plasmon resonance biosensor [188]. They have developed a sandwich assay with gold nanoparticles for a major enhancement in sensitivity of PSA detection. The assay enables the detection of total PSA levels at clinically relevant concentrations. Gold nanoparticles can be used as an amplifying payload strategy for adenoviral cancer gene therapy [189]. Colloidal gold nanoparticles can be used as a versatile platform for developing tumor targeted cancer therapies [8, 190–192].

On the basis of theoretical and experimental results, a new dynamic mode – the bubbles-overlapping mode (BOM) – has been reported for the selective killing of cancer cells to whose cell membrane nanoparticles conjugated with specific antibodies have been attached [192].

### 3.7

#### Future Direction

Nanotechnology can be used in cancer detection and diagnosis. To improve cancer treatment, detection of cancer at an early stage is a very critical step. Presently, detection and diagnosis of cancer usually depend on molecular changes in cells and tissues that are detected by a doctor's physical examination or imaging expertise. Nanotechnology is uniquely promising as an early detection tool for cancer treatment for several reasons:

To successfully detect cancer at its earliest stages, scientists must be able to detect molecular changes even when they occur only in a small percentage of cells. This means the necessary tools must be extremely sensitive. The potential for nanostructures to enter and analyze single cells suggests they could meet this need.

Many nanotechnology tools will make it possible for clinicians to run tests without physically altering the cells or tissue they take from a patient. This is important because the samples clinicians use to screen for cancer are often in limited supply. Scientists would like to perform tests without altering cells, so they can be used again if further tests are needed.

Other technologies will focus on improved methods of reading the genetic code on single strands of DNA to detect errors that may contribute to cancer. Scientists believe nanopores, tiny holes that allow DNA to pass through one strand at a time, will make DNA sequencing more efficient. As DNA passes through a nanopore, scientists can monitor the shape and electrical properties of each base on the strand. Because these properties are unique for each of the four bases that make up the genetic code, scientists can use the passage of DNA through a nanopore to

decipher the encoded information, including errors in the code known to be associated with cancer.

To detect cancer, scientists can design beads containing quantum dots to bind to sequences of DNA that are associated with cancer. When the quantum dots are stimulated with light, they will emit their unique barcodes, or labels, making the critical, cancer-associated DNA sequences visible. The vast number of possible combinations of quantum dots means that scientists can create many unique labels, which can be used at the same time. This will allow scientists to look simultaneously at numerous regions of DNA. This will be important in the detection of cancer, which results from many different changes within a cell.

These technologies are in various stages of discovery and development. Experts believe that quantum dots, nanopores and other devices for detection and diagnosis may be available for clinical use in 5–15 years. Therapeutic agents are expected to be available within a similar time frame. Devices that integrate detection and therapy could be used clinically in about 15 or 20 years.

### Acknowledgments

This work was partly supported by NIH CA-78383 and HL-70567 and also by a grant from the American Cancer Society to DM. The authors are grateful to D. Lecy for her help in revising the manuscript.

### References

- 1 American Cancer Society: *Cancer Facts and Figures 2005*. Atlanta, GA, American Cancer Society, 2005.
- 2 D. E. J. G. J. DOLMANS, D. FUKUMURA, R. K. JAIN. Photodynamic therapy for cancer. *Nat. Rev. Cancer* 2003, 3(5), 380–387.
- 3 E. J. LEE, J. L. JAMESON. Gene therapy of pituitary diseases. *J. Endocrinol.* 2005, 185(3), 353–362.
- 4 A. PERILLO, G. FERRANDINA, L. PIERELLI, G. BONANNO, G. SCAMBIA, S. MANCUSO. Stem cell-based treatments for gynecological solid tumors. *Eur. Rev. Med. Pharmacol. Sci.* 2005, 9(2), 93–102.
- 5 M. DHANABAL, M. JEFFERS, W. J. LAROCHELLE. Anti-angiogenic therapy as a cancer treatment paradigm. *Curr Med. Chem. Anti-Canc Agents.* 2005, 5(2), 115–130.
- 6 P. MUKHERJEE, R. BHATTACHARYA, D. MUKHOPADHYAY. Gold nanoparticles bearing functional anti-cancer drug and anti-angiogenic agent: a “2 in 1” system with potential application in cancer therapeutics. *J. Biomed. Nanotechnol.* 2005, 1, 1–5.
- 7 R. BHATTACHARYA, P. MUKHERJEE, Z. XIONG, A. ATALA, S. SOKER, D. MUKHOPADHYAY. Gold nanoparticles inhibit VEGF165-induced proliferation of HUVEC cells. *Nano Lett.* 2004, 4(12), 2479–2481.
- 8 G. F. PACIOTTI, L. MYER, D. WEINREICH, D. GOIA, N. PAVEL, R. E. McLAUGHLIN, L. TAMARKIN. Colloidal gold: A novel nanoparticle vector for tumor directed drug delivery. *Drug Deliv.* 2004, 11(3), 169–183.
- 9 P. MUKHERJEE, R. BHATTACHARYA, P. WANG, L. WANG, S. BASU, J. A. NAGY, A. ATALA, D. MUKHOPADHYAY, S. SOKER. Antiangiogenic properties of gold nanoparticles. *Clin. Cancer Res.* 2005, 11(9), 3530–3534.



- 10 G. J. HIGBY. Gold in medicine: A review of its use in the West before 1900. *Gold Bull.* **1982**, *15*, 130–140.
- 11 R. G. BUCKLEY, A. M. ELSOME, S. P. FRICKER, G. R. HENDERSON, B. R. THEOBALD, R. V. PARISH, B. P. HOWE, L. R. KELLAND, Antitumor properties of some 2-[(dimethylamino)methyl]-phenylgold(III) complexes, *J. Med. Chem.* **1996**, *39*, 5208–5214.
- 12 D. G. RICHARDS, D. L. McMILLIN, E. A. MEIN, C. D. NELSON. Gold and its relationship to neurological/glandular conditions. *Int. J. Neurosci.* **2002**, *112*, 31–53.
- 13 S. MAHDIHASSAN. Tan, cinnabar, as drug of longevity prior to alchemy. *Am. J. Chin. Med.* **1984**, *12*, 50–54.
- 14 S. MAHDIHASSAN. Cinnabar-gold as the best alchemical drug of longevity, called Makaradhwaia in India. *Am. J. Chin. Med.* **1985**, *13*, 93–108.
- 15 O. TEMKIN. *The Failing Sickness. A History of Epilepsy from the Greeks to the beginnings of Modern Neurology.* Baltimore, Johns Hopkins Press.
- 16 S. P. FRICKER. Medical uses of gold compounds: past, present and future. *Gold Bull.* **1996**, *29*, 53–59.
- 17 J. C. BURNETT. *Gold as a remedy in disease*, Gould, London 1895.
- 18 H. EICHHORST. *Handbook of Practical Medicine.* Volume 1, *Diseases of the Circulatory and Respiratory Apparatus.* William Wood and Company, New York, 1886.
- 19 S. O. L. POTTER. *A Compend of Material Medica, Therapeutics, and Prescription Writing, with Especial Reference to the Physiological Actions of Drugs.* Sixth Edition **1902**. P. Blakiston's Sons & Co, Philadelphia, 1894.
- 20 H. A. HARE. *A Text Book of Practical Therapeutics.* 14<sup>th</sup> edition, Lea & Febiger, Philadelphia, 1912.
- 21 S. T. GERBER. *Stedman's Practical Medical Dictionary.* Williams & Wilkins, Baltimore, 1942.
- 22 KOCH, R. *Dtsch. Med. Wochenstr.* **1890**, *16*, 756–757.
- 23 D. A. GORDON, in *Textbook of Rheumatology*, W. W. KELLY, E. D. HARRIS, D. RUDDY, C. B. SLEDGE (Eds.), W. B. Saunders, New York, **1989**, Ch. 48, p. 804.
- 24 D. T. FELSON, J. J. ANDERSON, R. F. MEENAN. The comparative efficacy and toxicity of second-line drugs in rheumatoid arthritis. Results of two metaanalyses. *Arthritis Rheum.* **1990**, *33*, 1449–1461.
- 25 C. F. SHAW III. Gold-based therapeutic agents. *Chem. Rev.* **1999**, *99*, 2589–2600.
- 26 D. T. HILL, B. M. SUTTON. *Cryst. Struct. Commun.* **1980**, *9*, 679.
- 27 Y. Y. TONG, A. J. L. POMBIERRO, D. L. HUGHES, R. L. RICHARDS, Synthesis and properties of the gold(I) complexes with bulky thiolates [Au(SR)](6) and [Au(SR)(PPH(3))] (R=C(6)H(2)ME(3)-2,4,6 or C<sub>6</sub>H<sub>2</sub>PR<sub>3</sub>I-2,4,6), (R = C<sub>6</sub>H<sub>2</sub>ME<sub>3</sub>-246 or C<sub>6</sub>H<sub>2</sub>PR<sub>3</sub>I-2,4,6), and the molecular-structure of [AU(SC<sub>6</sub>H<sub>2</sub>PR<sub>3</sub>I-2,4,6)(PPH(3))], *Transition Met. Chem.* **1995**, *20*, 372–375.
- 28 M. NAKAMOTO, W. HILLER, H. SCHMIDBAUR, Preparation and crystal structures of gold(I) complexes of a series of benzothiolates-pair formation by gold-gold interactions of (Benzenethiolate)(triphenylphosphane) gold(I), *Chem. Ber.* **1993**, *126*, 605–610.
- 29 R. BAU, Crystal structure of the antiarthritic drug gold thiomalate (myochrysin): A double-helical geometry in the solid state, *J. Am. Chem. Soc.* **1998**, *120*, 9380–9381.
- 30 C. F. SHAW III, in *Metal Compounds in Cancer Therapy*, S. P. FRICKER (Ed.), Chapman & Hall, London, **1994**, p. 46.
- 31 I. HAIDUC, C. SILVESTRU. Rhodium, iridium, copper and gold antitumor organometallic compounds (review). *In Vivo*, **1989**, *3*, 285–293.
- 32 S. J. BERNERS-PRICE, P. J. SADLER, *Struct. Bonding* **1988**, *70*, 27.
- 33 P. J. SADLER, M. NASR, V. L. NARAYANAN, in *Platinum Coordination Complexes in Cancer Chemotherapy*, M. P. HACKER, E. B. DOUPLE, I. H. KRAKOFF (Eds.), Martinus Nijhoff Publishing, Boston, **1984**, p. 209.
- 34 S. J. BERNERS-PRICE, P. S. JARRET, P. J. SADLER, 31P NMR Studies of

- [Au $\mu$ (pdppe)]<sup>2+</sup> antitumor complexes. Conversion into [A~(dppe)~]<sup>+</sup> induced by thiols and blood plasma, *Inorg. Chem.* **1987**, 26, 3074–3077.
- 35 R. G. BUCKLEY, A. M. ELSOME, S. P. FRICKER, G. R. HANDERSON, B. R. C. THEOBALD, R. V. PARISH, B. P. HOWE, L. R. J. KELLAND. Antitumor properties of some 2-[(dimethylamino)methyl]-phenylgold(III) complexes. *Med. Chem.* **1996**, 39, 5208–5214.
- 36 F. BUSSOLINO, A. MANTOVANI, G. PERSICO. Molecular mechanisms of blood vessel formation. *Trends Biochem. Sci.* **1997**, 22(7), 251–256.
- 37 J. FOLKMAN. Tumor angiogenesis. *Adv. Cancer Res.* **1974**, 19(0), 331–358.
- 38 J. FOLKMAN. Tumor angiogenesis: Role in regulation of tumor growth. *Symp. Soc. Dev. Biol.* **1974**, 30(0), 43–52.
- 39 M. K. GUPTA, R. Y. QIN. Mechanism and its regulation of tumor-induced angiogenesis. *World J. Gastroenterol.* **2003**, 9(6), 1144–1155.
- 40 P. NYBERG, L. XIE, R. KALLURI. Endogenous inhibitors of angiogenesis. *Cancer Res.* **2005**, 65(10), 3967–3979.
- 41 R. LANGER, H. CONN, J. VACANTI, C. HAUDENSCHILD, J. FOLKMAN. Control of tumor growth in animals by infusion of an angiogenesis inhibitor. *Proc. Natl. Acad. Sci. U.S.A.* **1980**, 77(7), 4331–4335.
- 42 M. A. KONERDING, E. FAIT, A. GAUMANN. 3D microvascular architecture of pre-cancerous lesions and invasive carcinomas of the colon. *Br. J. Cancer.* **2001**, 84(10), 1354–1362.
- 43 A. EBERHARD, S. KAHLERT, V. GOEDE, B. HEMMERLEIN, K. H. PLATE, H. G. AUGUSTIN. Heterogeneity of angiogenesis and blood vessel maturation in human tumors: Implications for antiangiogenic tumor therapies. *Cancer Res.* **2000**, 60(5), 1388–1393.
- 44 D. M. McDONALD, P. L. CHOYKE. Imaging of angiogenesis: From microscope to clinic. *Nat. Med.* **2003**, 9(6), 713–725.
- 45 F. J. BURROWS, P. E. THORPE. Eradication of large solid tumors in mice with an immunotoxin directed against tumor vasculature. *Proc. Natl. Acad. Sci. U.S.A.* **1993**, 90(19), 8996–9000.
- 46 L. M. ELLIS. Bevacizumab. *Nat. Rev. Drug Discov.* **2005**, Suppl, S8–9.
- 47 F. MANNELLO, G. TONTI, S. PAPA. Matrix metalloproteinase inhibitors as anticancer therapeutics. *Curr. Cancer Drug Targets.* **2005**, 5(4), 285–298.
- 48 R. NEUBERT, A. C. NOGUEIRA, D. NEUBERT. Thalidomide derivatives and the immune system. I. Changes in the pattern of integrin receptors and other surface markers on T lymphocyte subpopulations of marmoset blood. *Arch. Toxicol.* **1993**, 67(1), 1–17.
- 49 M. F. MCCARTY. Thalidomide may impede cell migration in primates by down-regulating integrin beta-chains: Potential therapeutic utility in solid malignancies, proliferative retinopathy, inflammatory disorders, neointimal hyperplasia, and osteoporosis. *Med. Hypotheses.* **1997**, 49(2), 123–131.
- 50 J. J. O'LEARY, R. L. SHAPIRO, C. J. REN, N. CHUANG, H. W. COHEN, M. POTMESIL. Antiangiogenic effects of camptothecin analogues 9-amino-20(S)-camptothecin, topotecan, and CPT-11 studied in the mouse cornea model. *Clin. Cancer Res.* **1999**, 5(1), 181–187.
- 51 N. KLAUBER, S. PARANGI, E. FLYNN, E. HAMEL, R. J. D'AMATO. Inhibition of angiogenesis and breast cancer in mice by the microtubule inhibitors 2-methoxyestradiol and taxol. *Cancer Res.* **1997**, 57(1), 81–86.
- 52 D. BELOTTI, V. VERGANI, T. DRUDIS, P. BORSOTTI, M. R. PITELLI, G. VIALE, R. GIAVAZZI, G. TARABOLETTI. The microtubule-affecting drug paclitaxel has antiangiogenic activity. *Clin. Cancer Res.* **1996**, 2(11), 1843–1849.
- 53 B. E. TURK, Z. SU, J. O. LIU. Synthetic analogues of TNP-470 and ovalicin reveal a common molecular basis for inhibition of angiogenesis and immunosuppression. *Bioorg. Med. Chem.* **1998**, 6, 1163–1169.
- 54 T. YOSHIDA, Y. KANEKO, A. TSUKAMOTO, K. HAN, M. ICHINOSE, S. KIMURA. Suppression of hepatoma

- growth and angiogenesis by a fumagillin derivative TNP470: Possible involvement of nitric oxide synthase. *Cancer Res.* **1998**, *58*, 3751–3756.
- 55 Y. ZHENG, J. HUA, K. G. PINNEY, C. M. GARNER, R. R. KANE, J. A. PREZIOSO, D. J. CHAPLIN, K. EDVARSDEN. Combretastatin family member OXI4503 induces tumor vascular collapse through the induction of endothelial apoptosis. *Int. J. Cancer.* **2004**, *111*(4), 604–610.
- 56 G. C. TUCKER. Alpha v integrin inhibitors and cancer therapy. *Curr. Opin. Investig. Drugs.* **2003**, *4*(6), 722–731.
- 57 J. A. POSEY, M. B. KHAZAEI, A. DELGROSSO, M. N. SALEH, C. Y. LIN, W. HUSE, A. F. LOBUGLIO. A pilot trial of Vitaxin, a humanized anti-vitronectin receptor (anti alpha v beta 3) antibody in patients with metastatic cancer. *Cancer Biother. Radiopharm.* **2001**, *16*(2), 125–132.
- 58 T. TAGA, A. SUZUKI, I. GONZALEZ-GOMEZ, F. H. GILLES, M. STINS, H. SHIMADA, L. BARSKY, K. I. WEINBERG, W. E. LAUG. Alpha v-Integrin antagonist EMD 121974 induces apoptosis in brain tumor cells growing on vitronectin and tenascin. *Int. J. Cancer* **2002**, *98*(5), 690–697.
- 59 L. M. EVANS, L. M. ITRI, M. CAMPION, R. WYLER-PLAUT, S. E. KROWN, J. E. GROOPMAN, H. GOLDSWEIG, P. A. VOLBERDING, S. B. WEST, R. T. MITSUYASU, et al. Interferon-alpha 2a in the treatment of acquired immunodeficiency syndrome-related Kaposi's sarcoma. *J. Immunother.* **1991**, *10*, 39–50.
- 60 M. A. FISCHL, D. M. FINKELSTEIN, W. HE, W. G. POWDERLY, P. L. TRIOZZI, R. T. STEIGBIGEL. A phase II study of recombinant human interferon-alpha 2a and zidovudine in patients with AIDS-related Kaposi's sarcoma. AIDS Clinical Trials Group. *J. Acquir. Immune Defic. Syndr. Hum. Retrovirol.* **1996**, *11*, 379–384.
- 61 A. K. MORRIS, A. W. VALLEY. Overview of the management of AIDS-related Kaposi's sarcoma. *Ann Pharmacother.* **1996**, *30*, 1150–1163.
- 62 L. ROSEN, M. MULAY, A. MAYERS, et al. Phase I dose-escalating trial of SU5416, a novel angiogenesis inhibitor in patients with advanced malignancies. *J. Clin. Oncol.* **1999**, *18*, 161a.
- 63 K. YOROZUYA, T. KUBOTA, M. WATANABE, H. HASEGAWA, S. OZAWA, M. KITAJIMA, L. M. CHIKAHISA, Y. YAMADA. TSU-68 (SU6668) inhibits local tumor growth and liver metastasis of human colon cancer xenografts via anti-angiogenesis. *Oncol. Rep.* **2005**, *14*(3), 677–682.
- 64 W. P. STEWARD. Marimastat (BB2516): Current status of development. *Cancer Chemother. Pharmacol.* **1999**, *43*(suppl), S56–S60.
- 65 G. WILDING, E. SMALL, M. COLLIER, et al. A phase I pharmacokinetic evaluation of the matrix metalloproteinase (MMP) inhibitor AG3340 in combination with mitoxantrone and prednisone in patients with advanced prostate cancer. *J. Clin. Oncol.* **1999**, *18*, 323a.
- 66 J. D'OLIMPIO, K. HANDE, M. COLLIER, et al. Phase I study of the matrix metalloproteinase inhibitor AG3340 in combination with paclitaxel and carboplatin for the treatment of patients with advanced solid tumors. *J. Clin. Oncol.* **1999**, *18*, 160a.
- 67 R. GOEL, H. HIRTE, P. MAJOR, et al. Clinical pharmacology of the metalloproteinase (MMP) and angiogenesis inhibitor Bayer 12-9566 in cancer patients. *J. Clin. Oncol.* **1999**, *18*, 160a.
- 68 M. EATOCK, J. CASSIDY, J. JOHNSON, et al. A phase I study of the matrix metalloproteinase inhibitor MM1270 (previously termed CGS270231) with 5FU and folinic acid. *J. Clin. Oncol.* **1999**, *18*, 209a.
- 69 W. RISAU. Angiogenesis and endothelial cell function. *Arzneimittelforschung*, **1994**, *44*, 417–417.
- 70 P. CARMELIET, R. K. JAIN. Angiogenesis in cancer and other diseases. *Nature* **2000**, *407*, 249–257.
- 71 Z. SZEKANECZ, G. SZEGEDI, A. E. KOCH. Angiogenesis in rheumatoid arthritis: Pathogenic and clinical

- significance. *J. Invest. Med.* **1998**, *46*, 27–41.
- 72 T. PINCUS, G. FERRACCIOLI, T. SOKKA, A. LARSEN, R. RAU, I. KUSHNER, F. WOLFE. Evidence from clinical trials and long-term observational studies that disease-modifying anti-rheumatic drugs slow radiographic progression in rheumatoid arthritis: Updating a 1983 review. *Rheumatology* **2002**, *41*, 1346–1356.
- 73 D. R. SENGER, C. A. PERRUZZI, J. FEDER, H. F. DVORAK. A highly conserved vascular permeability factor secreted by a variety of human and rodent tumor cell lines. *Cancer Res.* **1986**, *46*, 5629–5632.
- 74 D. W. LEUNG, G. CACHIANES, W. J. KUANG, D. V. GOEDEL, N. FERRARA. Vascular endothelial growth factor is a secreted angiogenic mitogen. *Science* **1989**, *246*, 1306–1309.
- 75 W. RISAU. Mechanisms of angiogenesis. *Nature* **1997**, *386*, 671–674.
- 76 L. R. HIRSCH, R. J. STAFFORD, J. A. BANKSON, S. R. SERSHEN, B. RIVERA, R. E. PRICE, J. D. HAZLE, N. J. HALAS, J. L. WEST. Nanoshell-mediated near-infrared thermal therapy of tumors under magnetic resonance guidance. *Proc. Natl. Acad. Sci. U.S.A.* **2003**, *100*, 13 549–13 554.
- 77 A. KUMAR, S. MANDAL, P. R. SELVAKANNAN, R. PASRICHA, A. B. MANDALE, M. SASTRY, *Langmuir* **2003**, *19*, 6277.
- 78 S. BASU, J. A. NAGY, S. PAL, E. VASILE, I. A. ECKELHOEFER, V. S. BLISS, E. J. MANSEAU, P. S. DASGUPTA, H. F. DVORAK, D. MUKHOPADHYAY. The neurotransmitter dopamine inhibits angiogenesis induced by vascular permeability factor/vascular endothelial growth factor. *Nat. Med.* **2001**, *7*, 569–574.
- 79 D. FAMBROUGH, K. MCCLURE, A. KAZLAUSKAS, E. S. LANDER. Diverse signaling pathways activated by growth factor receptors induce broadly overlapping, rather than independent, sets of genes. *Cell* **1999**, *97*, 727–741.
- 80 H. ZENG, D. ZHAO, D. MUKHOPADHYAY. Flt-1-mediated down-regulation of endothelial cell proliferation through pertussis toxin-sensitive G proteins, beta gamma subunits, small GTPase CDC42, and partly by Rac-1. *J. Biol. Chem.* **2002**, *277*, 4003–4009.
- 81 L. WANG, H. ZENG, P. WANG, S. SOKER, D. MUKHOPADHYAY. Neuropilin-1-mediated vascular permeability factor/vascular endothelial growth factor-dependent endothelial cell migration. *J. Biol. Chem.* **2003**, *49*, 48 848–48 860.
- 82 A. PETTERSSON, J. A. NAGY, L. F. BROWN, C. SUNDBERG, E. MORGAN, S. JUNGLES, R. CARTER, J. E. KRIEGER, E. J. MANSEAU, V. S. HARVEY, I. A. ECKELHOEFER, D. FENG, A. M. DVORAK, R. C. MULLIGAN, H. F. DVORAK. Heterogeneity of the angiogenic response induced in different normal adult tissues by vascular permeability factor/vascular endothelial growth factor. *Lab. Invest.* **2000**, *80*, 99–115.
- 83 J. A. NAGY, K. T. HERZBERG, J. M. DVORAK, H. F. DVORAK. Pathogenesis of malignant ascites formation: Initiating events that lead to fluid accumulation. *Cancer Res.* **1993**, *53*, 2631–2643.
- 84 R. ELGHANIAN, J. J. STORHOFF, R. C. MUCIC, R. L. LETSINGER, C. A. MIRKIN. Selective colorimetric detection of polynucleotides based on the distance-dependent optical properties of gold nanoparticles. *Science* **1997**, *277*, 1078–1081.
- 85 A. ULMAN, *An Introduction to Ultrathin Organic Films: From Langmuir–Blodgett to Self-assembly*, Academic Press, New York, **1991**.
- 86 A. LON, J. R. PORTER, J. I. DAVID, S. L. WESTCOTT, M. GRAUPE, R. S. CZERNUSZEWICZ, N. J. HALAS, R. T. LEE. Alkanethiol molecules containing an aromatic moiety self-assembled onto gold clusters, *Langmuir* **1998**, *14*, 7378.
- 87 S. R. JOHNSON, S. D. EVANS, S. W. MAHON, A. ULMAN. Alkanethiol molecules containing an aromatic moiety self-assembled onto gold clusters, *Langmuir* **1997**, *13*, 51–57.

- 88 H. J. BUCHSBAUM, W. C. KEETTEL. Radioisotopes in treatment of stage Ia ovarian cancer. *Natl. Cancer Inst. Monogr.* **1975**, *42*, 127–128.
- 89 E. E. ROGOFF, R. ROMANO, E. W. HAHN. The prevention of Ehrlich ascites tumor using intraperitoneal colloidal <sup>198</sup>Au. Dose vs. size of inoculum. *Radiology* **1975**, *114*, 225–226.
- 90 R. D. PEZNER, K. R. STEVENS JR, D. TONG, C. V. ALLEN. Limited epithelial carcinoma of the ovary treated with curative intent by the intraperitoneal installation of radiocolloids. *Cancer* **1978**, *42*, 2563–2571.
- 91 A. E. ALFANZO, A. HASSAN, B. GARDNER, S. STEIN, J. PATTI, N. A. SOLOMON, J. MCCARTHY, J. STEIGMAN. Prevention of hepatic metastases by intravenous radioactive gold. *Cancer Res.* **1978**, *38*, 2740–2744.
- 92 J. F. HAINFELD, D. N. SLATKIN, H. M. SMILOWITZ. The use of gold nanoparticles to enhance radiotherapy in mice. *Phys. Med. Biol.* **2004**, *49*, N309–N315.
- 93 W. P. FAULK, G. M. TAYLOR. An immunocolloid method for the electron microscope. *Immunochemistry* **1971**, *8*, 1081–1083.
- 94 A. M. GOBIN, D. P. O'NEAL, D. M. WATKINS, N. J. HALAS, R. A. DREZEK, J. L. WEST. Near infrared laser-tissue welding using nanoshells as an exogenous absorber. *Lasers Surg. Med.* **2005**, *37*, 123–129.
- 95 S. J. OLDENBERG, R. D. AVERITT, S. L. WESTCOTT, N. J. HALAS. Nanoengineering of optical resonances. *Chem. Phys. Lett.* **1998**, *228*, 243–247.
- 96 R. D. AVERITT, S. L. WESTCOTT, N. J. HALAS. Linear optical properties of gold nanoshells. *J. Opt. Soc. Am. B* **1999**, *16*, 1824–1832.
- 97 S. J. OLDENBURG, J. B. JACKSON, S. L. WESTCOTT, N. J. HALAS. Light scattering from dipole and quadrupole nanoshell antennas. *Appl. Phys. Lett.* **1999**, *75*, 1063–1065.
- 98 D. P. O'NEAL, L. R. HIRSCH, N. J. HALAS, J. D. PAYNE, J. L. WEST. Photothermal tumor ablation in mice using near infrared-absorbing nanoparticles. *Cancer Lett.* **2004**, *209*, 171.
- 99 D. R. SENGER, S. J. GALLI, A. M. DVORAK, C. A. PERRUZZI, V. S. HARVEY, H. F. DVORAK. Tumor cells secrete a vascular permeability factor that promotes accumulation of ascites fluid. *Science* **1983**, *219*, 983–985.
- 100 H. C. LICHTENBELD, N. FERARRA, R. K. JAIN, L. L. MUNN. Effect of local anti-VEGF antibody treatment on tumor microvessel permeability. *Microvasc. Res.* **1999**, *57*, 358–362.
- 101 P. J. KECK, D. D. HAUSER, G. KRIVI, K. SANZO, T. WARREN, J. FEDER, D. T. CONOLLY. Vascular permeability factor, an endothelial cell mitogen related to PDGF. *Science* **1989**, *246*, 1309–1312.
- 102 N. FERRARA, K. HOUCK, L. JAKEMAN, D. W. LEUNG. Molecular and biological properties of the vascular endothelial growth factor family of proteins. *Endocr. Rev.* **1992**, *13*, 18–32.
- 103 R. K. JAIN, P. CARMELIET. Vessels of death or life? *Sci. Am.* **2001**, *285*, 38–45.
- 104 M. A. MOSES, H. BREM, R. LANGER. Advancing the field of drug delivery: Taking aim at cancer. *Cancer Cell* **2003**, *4*(5), 337–341.
- 105 A. S. ZAHN, M. DE VILLIERS, M. V. PISHKO. Encapsulation of drug nanoparticles in self-assembled macromolecular nanoshells. *Langmuir* **2005**, *21*, 403–410.
- 106 R. A. BREKKEN, P. J. OVERHOLSER, V. A. STASTNY, J. WALTEBERGER, J. D. MINNA, P. E. THORPE. Selective inhibition of vascular endothelial growth factor (VEGF) receptor 2 (KDR/Flk-1) activity by a monoclonal anti-VEGF antibody blocks tumor growth in mice. *Cancer Res.* **2000**, *60*, 5117–5124.
- 107 H. OKINO, R. MAEYAMA, T. MANABE, T. MATSUDA, M. TANAKA. Trans-tissue, sustained release of gemcitabine from photocured gelatin gel inhibits the growth of heterotopic human pancreatic tumor in nude mice. *Clin. Cancer. Res.* **2003**, *9*, 5786–5793.
- 108 C. MANGENY, F. FERRAGE, I. AUJARD, V. MARCHI-ARTZNER, L. JULLIEN, O. OUARI, E. D. REKAI, A. LASCHEWSKY, I.

- VIKHOLM, J. W. SADOWSKI, Synthesis and properties of water-soluble gold colloids covalently derivatized with neutral polymer monolayers. *J. Am. Chem. Soc.* **2002**, 124, 5811–5821.
- 109 S. R. JOHNSON, S. D. EVANS, S. W. MAHON, A. ULMAN, Alkanethiol molecules containing an aromatic moiety self-assembled onto gold clusters, *Langmuir* **1997**, 13, 51–57.
- 110 R. A. FREITAS JR., *Nanomedicine*, Volume IIA: *Biocompatibility*, Landes Bioscience, Austin, TX, **2003**.
- 111 B. JONATHAN, *Biological Performance of Materials: Fundamentals of Biocompatibility*, 3rd edition, Marcel Dekker, New York, **1999**.
- 112 D. F. WILLIAMS (Ed.), *Fundamental Aspects of Biocompatibility*, Vols I, II, CRC Press, Boca Raton, FL, **1981**.
- 113 J. L. BRAYBROOK (Ed.), *Biocompatibility Assessment of Medical Devices and Materials*, John Wiley and Sons, New York, **1997**.
- 114 H. S. FREDERIC, D. L. CHRISTIANSEN, *Biomaterials Science and Biocompatibility*, Springer Verlag, New York, **1999**.
- 115 A. P. ALIVISATOS, Semiconductor clusters, nanocrystals, and quantum dots. *Science* **1996**, 271, 933–937.
- 116 M. C. DANIEL, D. ASTRUC, Gold nanoparticles: Assembly, supra-molecular chemistry, quantum-size-related properties, and applications toward biology, catalysis, and nanotechnology. *Chem. Rev.* **2004**, 104, 293–346.
- 117 D. F. EMERICH, C. G. THANOS, Nanotechnology and medicine. *Expert Opin. Biol. Ther.* **2003**, 3, 1–9.
- 118 P. L. BRANNON, J. O. BLANCHETTE, Nanoparticle and targeted systems for cancer therapy. *Adv. Drug Delivery Rev.* **2004**, 56, 1649–1659.
- 119 M. FERRARI, Cancer nanotechnology: Opportunities and challenges. *Nat. Rev. Cancer* **2005**, 5, 161–171.
- 120 G. Y. J. CHEN, S. Q. YAO, Lighting up cancer cells with “dots”. *Lancet* **2004**, 364, 2001–2003.
- 121 E. B. VOURA, J. K. JAISWAL, H. MATTOUSSI, S. M. SIMON, Tracking metastatic tumor cell extravasation with quantum dot nanocrystals and fluorescence emission-scanning microscopy. *Nat. Med.* **2004**, 10, 993–998.
- 122 X. GAO, Y. CUI, R. M. LEVENSON, L. W. CHUNG, S. NIE, In vivo cancer targeting and imaging with semiconductor quantum dots. *Nat. Biotechnol.* **2004**, 22, 959–960.
- 123 R. F. SERVICE, Nanotechnology grows up. *Science* **2004**, 304, 1732–1734.
- 124 D. VERGANO, Nano proponents square off against specter of ‘gray gool’. *USA Today*, September 27, **2004**.
- 125 V. L. COLVIN, The potential environmental impact of engineered nanomaterials. *Nat. Biotechnol.* **2003**, 21, 1166–1170.
- 126 E. OBERDORSTER, Manufactured nanomaterials (fullerenes, C60) induce oxidative stress in the brain of juvenile largemouth bass. *Environ. Health Perspect.* **2004**, 112, 1058–1062.
- 127 A. D. MAYNARD, P. A. BARON, M. FOLEY, A. A. SHVEDOVA, E. R. KISIN, V. CASTRANOVA, Exposure to carbon nanotube material: Aerosol release during the handling of unrefined single-walled carbon nanotube material. *J. Toxicol. Environ. Health A* **2004**, 67, 87–107.
- 128 J. PARVIZI, C. C. WU, D. G. LEWALLEN, J. F. GREENLEAF, M. E. BOLANDER, Low-intensity ultrasound stimulates proteoglycan synthesis in rat chondrocytes by increasing aggrecan gene expression. *J. Orthop. Res.* **1999**, 17, 488.
- 129 H. HATANO, H. J. SIEGEL, H. YAMAGIWA, J. T. BRONK, R. T. TURNER, M. E. BOLANDER, G. SARKAR, Identification of estrogen-regulated genes during fracture healing, using DNA microarray. *J. Bone Miner. Metab.* **2004**, 22, 224.
- 130 M. FARADAY, Experimental relations of gold (and other metals) to light. *Philos Trans.* **1857**, 147, 145–181.
- 131 J. TURKEVITCH, P. C. STEVENSON, J. HILLER, Nucleation and growth process in the synthesis of colloidal gold, *Discuss. Faraday. Soc.* **1951**, 11, 55.

- 132 T. YONEZAWA, T. KUNITAKE, Practical preparation of anionic mercapto ligand stabilized gold nanoparticles and their immobilization. *Colloids Surf. A: Physicochem. Eng. Asp.* **1999**, 149, 193.
- 133 M. BRUST, M. WALKER, D. BETHEL, D. J. SCHIFFRIN, R. J. WHYMAN. Synthesis of thiol derivatized gold nanoparticles in a two phase liquid-liquid system. *J. Chem. Soc., Chem. Commun.* **1994**, 801.
- 134 P. MUKHERJEE, C. R. PATRA, A. GHOSH, R. KUMAR, M. SASTRY, Characterization and catalytic activity of gold nanoparticles synthesized by autoreduction of aqueous chloroaurate ions with fumed silica, *Chem. Mater.* **2002**, 14, 1678.
- 135 K. ESUMI, A. SUZUKI, A. YAMAHIRA, K. TORIGOE, Role of poly(amidoamine) dendrimers for preparing nanoparticles of gold, platinum and silver, *Langmuir* **2001**, 16, 2604.
- 136 S. MOSSMER, J. P. SPATZ, M. MOELLER, T. ABERLE, J. SCHMIDT, W. BURCHARD, Solution behaviour of poly(styrene)-block-poly(2-vinylpyridine) micelles containing gold nanoparticles, *Macromolecules* **2000**, 33, 4791.
- 137 T. K. SAU, A. PAL, N. R. JANA, Z. L. WANG, T. PAL, Size controlled synthesis of gold nanoparticles using photochemically prepared seed particles, *J. Nanopart. Res.* **2001**, 13, 257.
- 138 S. MELTZER, R. RESCH, B. E. KOEL, M. E. THOMPSON, A. MADHUKUMAR, A. A. G. REQUICHA, P. WILL, Fabrication of nanostructures by hydroxylamine seeding of gold nanoparticle templates, *Langmuir* **2001**, 17, 1713.
- 139 K. MALLICK, Z. L. WANG, T. PAL, Seed mediated successive growth of gold nanoparticles accomplished by UV-irradiation: A photochemical approach for size controlled synthesis, *J. Photochem. Photobiol.* **2001**, 140, 75.
- 140 Y. ZHOU, C. Y. WANG, Y. R. ZHU, Z. Y. CHEN, A. Novel ultraviolet irradiation technique for shape controlled synthesis of gold nanoparticles at room temperature, *Chem. Mater.* **1999**, 11, 2310.
- 141 Y. NIIDOME, A. HORI, T. SATO, S. YAMADA, Enormous size growth of thiol passivated gold nanoparticles induced by near IR laser light. *Chem. Lett.* **2000**, 310.
- 142 A. HENGLEIN, D. MEISEL, Radiolytic control of the size of colloidal gold nanoparticles, *Langmuir* **1998**, 14, 7392.
- 143 E. GACHARD, H. REMITA, J. KHATOURI, B. KEITA, L. NADJO, J. BELLONI, Radiation induced and chemical formation of gold clusters, *New J. Chem.* **1998**, 1257.
- 144 M. NAKAMOTO, M. YAMAMOTO, M. FUKUSUMI, Thermolysis of gold(I) thiolate complexes producing novel gold nanoparticles passivated by alkyl groups, *Chem. Commun.* **2002**, 1622.
- 145 T. SHIMIZU, T. TERANISHI, S. HASEGAWA, M. MIYAKE, Size evolution of alkanethiol-protected gold nanoparticles by heat treatment in the solid state, *J. Phys. Chem. B* **2003**, 107, 2719.
- 146 P. MUKHERJEE, A. AHMAD, D. MANDAL, S. SENAPATI, S. R. SAINKAR, M. I. KHAN, R. RAMANI, R. PARISCHA, P. V. AJAYAKUMAR, M. ALAM, M. SASTRY R. KUMAR, *Angew. Chem. Int. Ed.* **2001**, 40, 3585.
- 147 P. MUKHERJEE, S. SENAPATI, D. MANDAL, A. AHMAD, M. I. KHAN, R. KUMAR, M. SASTRY, *Chem. Biochem.* **2002**, 3, 461.
- 148 A. AHMAD, P. MUKHERJEE, D. MANDAL, S. SENAPATI, M. I. KHAN, R. KUMAR, M. SASTRY, *J. Am. Chem. Soc.* **2002**, 124, 12 108.
- 149 R. FEYNMAN, There's plenty of room at the bottom, *Science* **1991**, 254, 1300–1301.
- 150 D. J. MAXWELL, J. R. TAYLOR, S. NIE, Self-assembled nanoparticle probes for recognition and detection of biomolecules, *J. Am. Chem. Soc.* **2002**, 124, 9606–9612.
- 151 D. A. LAVAN, D. M. LNN, R. LANGER, Moving smaller in drug discovery and delivery, *Nat. Rev. Drug. Discov.* **2002**, 1, 77–84.

- 152 W. C. W. CHAN, D. J. MAXWELL, X. GAO, R. E. BAILEY, M. Y. HAN, S. NIE, *Curr. Opin. Biotechnol.* Luminescent quantum dots for multiplexed biological detection and imaging, **2002**, 13, 40–46.
- 153 C. M. NIEMEYER, Nanoparticles, proteins, and nucleic acids: Biotechnology meets materials science, *Angew. Chem., Int. Ed.* **2001**, 40, 4128–4158.
- 154 O. V. SALATA, Applications of nanomaterials in biology and medicine. *J. Nanobiotechnol.* **2004**, 2, 3.
- 155 W. FU, D. SHENOY, J. LI, C. CRASTO, G. JONES, C. DIMARZIO, S. SRIDHAR, M. AMIJI, Biomedical applications of gold nanoparticles functionalized using hetero-bifunctional poly(ethylene glycol) spacer, *Mater. Res. Soc. Symp. Proc.* **2005**, 845, AA5.4.1
- 156 C. ZANDONELLA, Cell nanotechnology: The tiny toolkit, *Nature* **2003**, 423, 10–12.
- 157 J. L. WEST, N. J. HALAS, Applications of nanotechnology to biotechnology: Commentary, *Curr. Opin. Biotechnol.* **2000**, 11, 215–217.
- 158 S. K. SAHOO, V. LABHASETWAR. Nanotech approaches to drug delivery and imaging, *Drug Disc. Today* **2003**, 8, 1112–1120.
- 159 W. J. PARAK, D. GERION, T. PELLEGRINO, D. ZANCHET, C. MICHEEL, C. S. WILLIAMS, R. BOUDREAU, M. A. LE GROS, C. A. LARABELL, A. P. ALIVISATOS, Biological applications of colloidal nanocrystals, *Nanotechnology* **2003**, 14, R15–R27.
- 160 Q. A. PANKHURST, J. CONNOLLY, S. K. JONES, J. DOBSON, Applications of magnetic nanoparticles in biomedicine. *J. Phys. D: Appl. Phys.* **2003**, 36, R167–R181.
- 161 (a) M. BRUCHEZ, M. MORONNE, P. GIN, S. WEISS, A. P. ALIVISATOS, Semiconductor nanocrystals as fluorescent biological labels, *Science* **1998**, 281, 2013–2016. (b) W. C. W. CHAN, S. M. NIE, Quantum dot bioconjugates for ultrasensitive nonisotopic detection, *Science* **1998**, 281, 2016–2018. (c) S. WANG, N. MAMEDOVA, N. A. KOTOV, W. CHEN, J. STUDER, Antigen/antibody immunocomplex from CdTe nanoparticle bioconjugates, *Nano Lett.* **2002**, 2, 817–822.
- 162 (a) C. MAH, I. ZOLOTUKHIN, T. J. FRAITE, J. DOBSON, C. BATICH, B. J. BYRNE, Microsphere-mediated delivery of recombinant AAV vectors *in vitro* and *in vivo*, *Mol. Therapy* **2000**, 1, S239. (b) D. PANATAROTTO, C. D. PRITIDOS, J. HOEBEKE, F. BROWN, E. KRAMER, J. P. BRIAND, S. MULLER, M. PRATO, A. BIANCO, Immunization with peptide-functionalized carbon nanotubes enhances virus-specific neutralizing antibody responses, *Chem. Biol.* **2003**, 10, 961–966.
- 163 R. L. EDELSTEIN, C. R. TAMANAHA, P. E. SHEEHAN, M. M. MILLER, D. R. BASELT, L. J. WHITMAN, R. J. COLTON, The BARC biosensor applied to the detection of biological warfare agents, *Biosensors Bioelectron.* **2000**, 14, 805–813.
- 164 J. M. NAM, C. C. THAXTON, C. A. MIRKIN, Nanoparticles-based bio-bar codes for the ultrasensitive detection of proteins, *Science* **2003**, 301, 1884–1886.
- 165 R. MAHTAB, J. P. ROGERS, C. J. MURPHY, Protein-sized quantum dot luminescence can distinguish between “straight”, “bent”, and “kinked” oligonucleotides, *J. Am. Chem. Soc.* **1995**, 117, 9099–9100.
- 166 (a) J. MA, H. WONG, L. B. KONG, K. W. PENG, Biomimetic processing of nanocrystallite bioactive apatite coating on titanium, *Nanotechnology* **2003**, 14, 619–623. (b) A. DE LA ISLA, W. BROSTOW, B. BUJARD, M. ESTEVEZ, J. R. RODRIGUEZ, S. VARGAS, V. M. CASTANO, Nanohybrid scratch resistant coating for teeth and bone viscoelasticity manifested in tribology, *Mater. Resr Innovat.* **2003**, 7, 110–114.
- 167 J. YOSHIDA, T. KOBAYASHI, Intracellular hyperthermia for cancer using magnetite cationic liposomes, *J. Magn. Magn. Mater.* **1999**, 194, 176–184.
- 168 R. S. MOLDAY, D. MACKENZIE, Immunospecific ferromagnetic iron



- dextran reagents for the labeling and magnetic separation of cells, *J. Immunol. Methods* **1982**, *52*, 353–367.
- 169 R. WEISSELER, G. ELIZONDO, J. WITTENBURG, C. A. RABITO, H. H. BENGELE, L. JOSEPHSON, Ultrasmall superparamagnetic iron oxide: Characterization of a new class of contrast agents for MR imaging, *Radiology* **1990**, *175*, 489–493.
- 170 W. J. PARAK, R. BOUDREAU, M. L. GROS, D. GERION, D. ZANCHET, C. M. MICHEEL, S. C. WILLIAMS, A. P. ALIVISATOS, C. A. LARABELL, Cell motility and metastatic potential studies based on quantum dot imaging of phagokinetic tracks, *Adv. Mater.* **2002**, *14*, 882–885.
- 171 R. M. PENNER, Hybrid electro-chemical/chemical synthesis of quantum dots, *Acc. Chem. Res.* **2000**, *33*, 78–86.
- 172 X. ZHAO, L. R. HILLIARD, S. J. MECHERY, Y. WANG, R. P. BAGWE, S. JIN, W. TAN, A rapid bioassay for single bacterial cell quantitation using bioconjugated nanoparticles, *Proc. Natl. Acad. Sci. U.S.A.* **2004**, *101*, 15 027–15 032.
- 173 X. GAO, S. NIE, Molecular profiling of single cells and tissue specimens with quantum dots, *Trends Biotechnol.* **2003**, *21*, 371–373.
- 174 X. WU, H. LIU, J. LIU, K. N. HALEY, J. A. TREADWAY, J. P. LARSON, N. GE, F. PEALE, M. P. BRUCHEZ, Immunofluorescent labeling of cancer marker Her2 and other cellular targets with semiconductor quantum dots, *Nat. Biotechnol.* **2003**, *21*, 41–46.
- 175 B. DUBERTRET, P. SKOURIDES, D. J. NORRIS, V. NOIREAUX, A. H. BRIVANLOU, A. LIBCHABER, In vivo imaging of quantum dots encapsulated in phospholipid micelles, *Science* **2002**, *298*, 1759–1762.
- 176 Y. W. JUN, Y. M. HUH, J. S. CHOI, J. H. LEE, H. T. SONG, S. KIM, S. YOON, K. S. KIM, J. S. SHIN, J. S. SUH, J. CHEON, Nanoscale size effect of magnetic nanocrystals and their utilization for cancer diagnosis via magnetic resonance imaging, *J. Am. Chem. Soc.* **2005**, *127*, 5732–5733.
- 177 (a) I. H. EL-SAYED, X. HUANG, M. A. EL-SAYED, Surface plasmon resonance scattering and absorption of anti-egfr antibody conjugated gold nanoparticles in cancer diagnostics: Applications in oral cancer, *Nano Lett.* **2005**, *5*, 829–834. (b) B. DUBERTRET, M. CALAME, A. J. LIBCHABER, Single-mismatch detection using gold-quenched fluorescent oligonucleotides, *Nat. Biotechnol.* **2001**, *19*, 365–370.
- 178 I. L. MEDINTZ, H. T. UYEDA, E. R. GOLDMAN, H. MATTOUSSI, Quantum dot bioconjugates for imaging, labeling and sensing, *Nat. Mater.* **2005**, *4*, 435–446.
- 179 X. GAO, Y. CUI, R. M. LEVENSON, L. W. K. CHUNG, S. NIE, In vivo cancer targeting and imaging with semiconductor quantum dots, *Nat. Biotechnol.* **2004**, *22*, 969–975.
- 180 (a) C. A. MIRKIN, R. L. LETSINGER, R. C. MUCIC, J. J. STORHOFF, A DNA based method for rationally assembling nanoparticles into macroscopic materials, *Nature* **1996**, *382*, 607–609. (b) T. A. TATON, C. A. MIRKIN, R. L. LETSINGER, Scanometric DNA array detection with nanoparticle probes, *Science* **2000**, *289*, 1757–1760. (c) Y. C. CAO, R. JIN, C. A. MIRKIN, Nanoparticles with Raman spectroscopic fingerprints for DNA and RNA detection, *Science* **2002**, *297*, 1536–1540. (d) J. M. NAM, SAVKA I. STOEVA, C. A. MIRKIN, Bio-bar-code-based DNA detection with PCR-like sensitivity, *J. Am. Chem. Soc.* **2004**, *126*, 5932–5933. (e) P. FORTINA, L. J. KRICKA, S. SURREY, P. GRODZINSKI, Nanobiotechnology: The promise and reality of new approaches to molecular recognition, *Trends Biotechnol.* **2005**, *168*–173.
- 181 (a) K. K. JAIN, Nanotechnology in clinical laboratory diagnostics, *Clin. Chim. Acta* **2005**, *358*, 37–54. (b) C. M. GOODMAN, C. D. MCCUSKER, T. YILMAZ, V. M. ROTELLO, Toxicity of gold nanoparticles functionalized with cationic and anionic side chains,

- Bioconjugate Chem.* **2004**, 15, 897–900.
- 182** L. R. HIRSCH, R. J. STAFFORD, J. A. BANKSON, S. R. SHERSEN, B. RIVERA, R. E. PRICE, J. D. HAZLE, N. J. HALAS, J. L. WEST, Nanoshell-mediated near-infrared thermal therapy of tumors under magnetic resonance guidance, *Proc. Natl. Acad. Sci. U.S.A.* **2003**, 100, 13 549–13 553.
- 183** M. THOMAS, A. KLIBANOV, Conjugation to gold nanoparticles enhances polyethylenimines transfer of plasmid DNA into mammalian cells, *Proc. Natl. Acad. Sci., U.S.A.* **2003**, 100, 9138–9143.
- 184** C. LOO, A. LOWERY, N. HALAS, J. WEST, R. DREZEK, Immunotargeted nanoshells for integrated cancer imaging and therapy, *Nano Lett.* **2005**, 5, 709–711.
- 185** J. CHEN, F. SAEKI, B. J. WILEY, H. CANG, M. J. COBB, Z.-Y. LI, L. AU, H. ZHANG, M. B. KIMMEY, X. D. LI, Y. XIA, Gold nanocages: Bioconjugation and their potential use as optical imaging contrast agents, *Nano Lett.* **2005**, 5, 473–477.
- 186** J. KNEIPP, H. KNEIPP, W. L. RICE, K. KNEIPP, Optical probes for biological applications based on surface-enhanced Raman scattering from indocyanine green on gold nanoparticles, *Anal. Chem.* **2005**, 77, 2381–2385.
- 187** N. L. ROSI, C. A. MIRKIN, Nanostructures in biodiagnostics, *Chem. Rev.* **2005**, 105, 1547–1562.
- 188** L. HUANG, G. REEKMANS, D. SAERENS, J.-M. FRIEDT, F. FREDERIX, L. FRANCIS, S. MUYLDERMANS, A. CAMPITELLI, C.-V. HOOF, Prostate-specific antigen immunosensing based on mixed self-assembled monolayers, camel antibodies and colloidal gold enhanced sandwich assays, *Biosensors Bioelectron.* **2005**, 21, 483–490.
- 189** M. EVERTS, J. L. LEDDON, R. J. KOK, M. A. PREUSS, C. L. MILLICAN, D. E. NIKLES, D.-T. JOHNSON and D.-T. CURIEL, Gold nanoparticles as an amplifying payload strategy for adenoviral cancer gene therapy, *Mol. Therapy* **2005**, 11, 342.
- 190** G. F. PACIOTTI, L. MYER, D. G. I. KINGSTON, T. GANESH, L. TAMARKIN, Colloidal gold nanoparticles: A versatile platform for developing tumor targeted cancer therapies, Nanotech 2005, NSTI Nanotechnology Conference and Trade Show, NSTI, Anaheim, CA, 2005, 1, 7–10.
- 191** G.-F. PACIOTTI, L.-D. MYER, T.-H. KIM, S. WANG, H.-R. ALEXANDER, D. WEINREICH, L. TAMARKIN, Colloidal gold: A novel colloidal nanoparticle vector for tumor-directed drug delivery, *Clin. Cancer Res.* **2001**, 7, 3673S–3674S.
- 192** V. P. ZHAROV, R. R. LETFULLIN, E. N. GALITOVSKAYA, Microbubbles-overlapping mode for laser killing of cancer cells with absorbing nanoparticle clusters, *J. Phys. D: Appl. Phys.* **2005**, 38, 2571–2581.
- 193** E. E. CONNOR, J. MWAMUKA, A. GOLE, C.-J. MURPHY, M. D. WYATT, Gold nanoparticles are taken up by human cells but do not cause acute cytotoxicity, *Small* **2005**, 1, 325–327.

## 4

# Nanoparticles for Magnetic Resonance Imaging of Tumors

*Tillmann Cyrus, Shelton D. Caruthers, Samuel A. Wickline, and Gregory M. Lanza*

### 4.1

#### Introduction

Molecular imaging with nanoparticulate agents represents a novel tool that will allow the detection of tumors and metastases in early stages that evade conventional imaging technologies. Several of these nanoparticulate agents are also undergoing development to deliver drugs locally, thus increasing therapeutic effects at the tumor site while minimizing systemic adverse effects that are often limitations of conventional chemotherapy. The combination of molecular imaging and local delivery of therapeutic agents is unique to nanoparticulate agents and regarding tumor detection and treatment will likely change the current medical paradigm of “see and treat” to a “detect and prevent” strategy. An overview of this technology is given here, focusing on particles that are available for non-invasive magnetic resonance imaging (MRI). Principle targeting mechanisms are described, followed by superparamagnetic nanoparticles, which create negative or dark contrast effects on MRI, and paramagnetic nanoparticles, which produce positive or bright contrast effects. Superparamagnetic nanoparticles all contain magnetic elements, mostly iron oxides, and are sub-classified according to molecular modifications and size. Paramagnetic nanoparticles differ substantially and thus are presented according to their principal groups, such as liposomes, perfluorocarbon nanoparticles, fullerenes, and others. Finally, hybrid technologies using quantum dots are presented, which allow non-invasive imaging with MRI and intraoperative direct visualization. As these technologies are rapidly evolving, particular emphasis is given to the most current developments.

### 4.2

#### Magnetic Resonance Imaging (MRI)

Originally developed as a noninvasive method using a magnetic field and radio waves to generate detailed images of the inside of the human body, MRI is based

on the principles of nuclear magnetic resonance (NMR). Atoms consist of protons, electrons, and often neutrons. All of these particles possess a spin. Depending on its composition, some nuclei have a net spin that, when placed in an external magnetic field ( $\mathbf{B}_0$ ), aligns with the external magnetic field, somewhat like a magnet with a north and south pole would. For a hydrogen nucleus, for example, there are two possible energy states: the lower energy configuration is parallel to the external magnetic field (e.g., N-S-N-S), and the higher energy state is anti-parallel (e.g., N-N-S-S). For a given nuclei, the energy of separation between spin states depends on the magnitude of  $\mathbf{B}_0$ . The parallel state is slightly favored, on the order of a few parts per million, and is described by Boltzmann statistics (as a function of the energy of separation and temperature). Thus, for about every one million nuclei, there is one extra aligned with the  $\mathbf{B}_0$  field resulting in a net magnetization pointing in the direction of the main magnetic field; these spinning nuclei do not perfectly align with  $\mathbf{B}_0$  but rather precess about it at their resonance frequency, also called the Larmor Frequency, which is defined as the product of the gyromagnetic ratio ( $\gamma$ ) of the nucleus and the external magnetic field. Typically, these individual “spins” are thought of collectively as a net magnetic vector, aligned with  $\mathbf{B}_0$ . Individual particles can undergo a transition from the lower to the higher energy state by absorbing a photon, and vice versa by emitting one. In MRI, the required frequency for this photon is in the radiofrequency (RF) range at the resonance or Larmor frequency, which is the product of the gyromagnetic ratio and  $\mathbf{B}_0$ . When exposed to RF energy at this frequency the nuclei change spin states and, when thought of *en masse*, can be represented by a net magnetic vector, which “rotates” away from the longitudinal axis, but returns to alignment once the external RF transmission is ceased. The rate of this return to equilibrium (known as longitudinal or spin–lattice relaxation) is exponential and can be described by the time constant T1. When the net magnetic vector is aligned with  $\mathbf{B}_0$ , an MR signal cannot be measured. But with the net magnetic vector “tipped” out of alignment, the component of the magnetization vector in the transverse plane ( $\mathbf{M}_{xy}$ ) can be measured as an MR signal (using an external RF antenna such as a coil of wire tuned to the correct resonance frequency). Since the individual spins comprising the net vector experience slightly different magnetic milieus, the spins have slightly different precessional frequencies and, thus, the magnitude of  $\mathbf{M}_{xy}$  (transverse magnetization) decays over time (independently of longitudinal relaxation). This signal decay is also exponential, with time constant T2. The detected signal, created by exciting the spins out of longitudinal alignment with  $\mathbf{B}_0$ , is the source for MR image generation is based on the absorption and emission of energy in the radiofrequency range of the electromagnetic spectrum. Hence, the signal in MRI results from the difference between the energy absorbed by the spins that make a transition from the lower energy state to the higher energy state and the energy emitted by the spins that simultaneously make a transition from the higher energy state to the lower one.

Although highly sensitive, NMR can only be performed on isotopes whose natural and biological abundance is high enough to be detected. The hydrogen in water

is an ideal atom in this respect. Its nucleus contains a single proton and has a large magnetic moment. Of the three hydrogen isotopes, the natural abundance of  $^1\text{H}$  is 99.985%. The  $^1\text{H}$  nuclei in water have an MR signal, and the human body consists primarily of water. While bones only contain about 22% water, muscle is 75% and blood up to 83% water, explaining the advantage of MR in imaging soft tissues including tumors. To generate an image, the MRI machine applies an RF pulse ( $\mathbf{B}_1$ ) at the specific resonance frequency of hydrogen. This excitation pulse is localized toward the area of the body that is of interest by simultaneously superimposing a secondary magnetic field, which is a function of position (i.e., gradient magnetic field). This gradient magnetic field causes the resonance frequency of hydrogen nuclei to vary as a function of position within the MRI magnet; thus, a finite “slice” of interest can be excited to give MR signal since the nuclei can absorb energy (to change spin state) only at their resonance frequency. As described earlier, once this RF excitation pulse is turned off, the  $^1\text{H}$  nuclei begin to return to equilibrium with  $\mathbf{B}_0$ . But while some transverse magnetization remains, the signal that will ultimately be reconstructed into the MR image can be detected. This signal is already localized upon excitation, via “slice selection,” in one dimension. The remaining two dimensions are encoded by quickly switching on and off other gradient magnetic fields before (phase encoding) and during (frequency encoding) the readout of the generated signal. By repeating this process multiple times, data is collected until the signal is completely spatially encoded and the final image can be reconstructed.

The signal intensity for each location in the image (volume element, or voxel) is dependent on multiple things, including the number of  $^1\text{H}$  nuclei present (proton density), and the T1 and T2 of the tissue present. T1 relaxation is characterized by the longitudinal return of the net magnetization to its ground state in the direction of the main magnetic field. It also depends on the main magnetic field strength, i.e., higher magnetic fields are generally associated with longer T1. T2 relaxation occurs when spins in the high and low energy state exchange energy but do not lose it to the surrounding area. Thus, transverse magnetization is lost. In pure water, T1 and T2 are approximately the same, but in biological tissues T2 is considerably shorter. These differences are exploited in conjunction with imaging sequence timing parameters to obtain either T1- or T2-weighted images.

Similarly to other imaging technologies, MR imaging benefits from the usage of contrast agents. Conventional MR contrast agents work by altering the local magnetic field and relaxation parameters in the tissue being examined. Superparamagnetic iron oxide particles, for instance, generate image contrast by shortening the MR relaxation times with a predominant effect on apparent T2 relaxivity, which leaves dark contrast effects (i.e., signal voids; Fig. 4.1). Paramagnetic particles such as gadolinium chelates, however, produce bright contrast in T1-weighted MR images (Fig. 4.2). The advent of nanoparticulate contrast agents afforded a dramatic improvement in imaging. These agents, which are described in this chapter, can passively or actively target epitopes within the body, enhance imaging, and, in some cases, even deliver drugs locally.

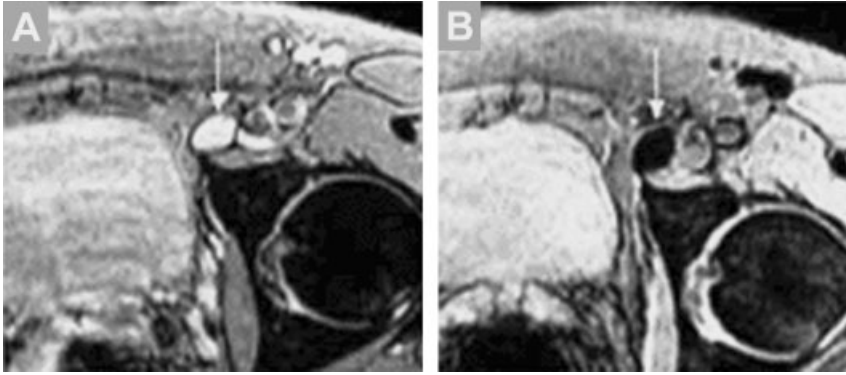


**Fig. 4.1.** T2-weighted MRI. (A) Conventional MRI and (B) MRI obtained 24 h after the administration of lymphotropic superparamagnetic nanoparticles. The accumulation of the iron-containing

superparamagnetic nanoparticles leads to a homogeneous decrease in signal intensity in a lymph node in the left iliac region (arrow). (Reproduced with permission from Ref. [27].)

### 4.3 Targeting Mechanisms

#### 4.3.1

#### Passive versus Active Targeting

Nanoparticulate agents concentrate within a site by passive and/or active targeting mechanisms (Fig. 4.3). Passive targeting refers to the accumulation within or the extravasation through a tumor neovasculature distinguished by a dismorphic, fenestrated architecture [1]. Vascular endothelial and basic fibroblast growth factors produced by tumors accelerate angiogenic sprouting with endothelial pores between 200 and 780 nm in diameter that entrap or permit extravasation of macro-

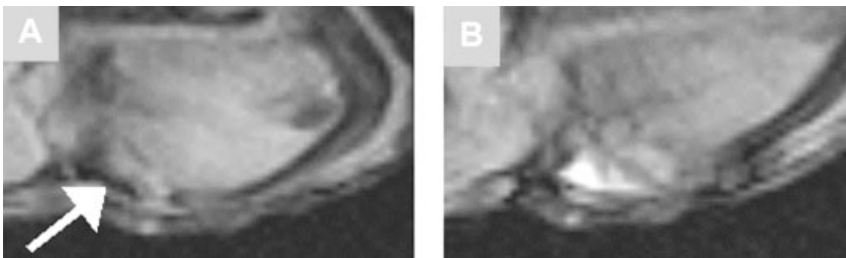


**Fig. 4.2.** T1-weighted MRI. (A) Conventional MRI and (B) MRI obtained 30 min after the administration of perfluorocarbon nanoparticles. C32 tumor in an athymic nude

mouse (arrow in A). Signal enhancement of angiogenic vasculature as detected by  $\alpha_v\beta_3$ -targeted paramagnetic nanoparticles (B).

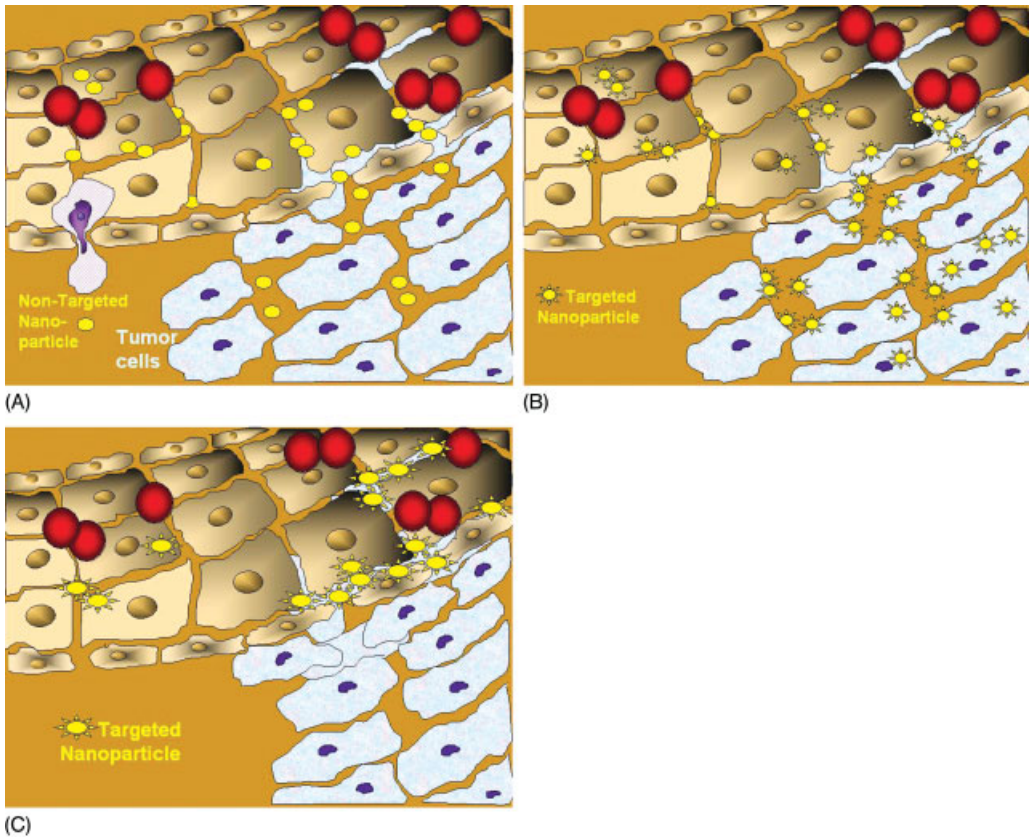


**Fig. 4.3.** Schematic illustration of passive and active targeting with nanoparticles. (A) Passive targeting, via the enhanced permeability and retention (EPR) effect due to pathological endothelialization of angiogenic vessels in tumors, allowing the leakage of very small nanoparticles into the subendothelium and into the space between tumor cells. (B) Active targeting with very small ligand-targeted nanoparticles. These particles bind respective epitopes on tumor cells. (C) Active targeting with ligand targeted nanoparticles with nominal diameters  $> 150$  nm.

molecules and nanoparticles [2, 3], dependent on size. In many tumors, ineffective lymphatic drainage further contributes to the passive, local retention of nanoparticles [4]. This combination enhances the permeability and retention (EPR) effect [4, 5]. In some situations phagocytic cells, naturally responsible for particle clearance, ingest the agent while migrating into the tumors core.

Particles are removed from the circulation in a size-dependent hierarchy by the lung (largest), spleen, liver, and bone marrow (smallest). Opsonization (i.e., biological tagging) with blood proteins such as immunoglobulins, complement proteins, or non-immune serum factors can enhance macrophage recognition, phagocytosis, and further accelerate circulatory clearance. While complement fixation promotes liver sequestration, the presence of antibody Fc receptors favors splenic removal.

Active targeting encompasses ligand-directed, site-specific accumulation of nanoparticulate agents. Antibodies, peptides, polysaccharides, aptamers, and drugs, may be utilized to home nanoparticles specifically to cellular biomarkers. These ligands may be attached covalently (i.e., chemical conjugation) or non-covalently (e.g., avidin–biotin interactions) to the contrast agent. Further surface chemistry modifications, such as incorporation of surface poly(ethylene glycol) or crosslinking of surfactants, are employed to delay rapid systemic destruction or clearance of the agents. Homing-ligands increase contrast signal and therapeutic uptake in target organs beyond the concentrations achieved with passive approaches – benefits usually achieved with active ingredient dosages orders of magnitude less than what would be given in the clinic today.

#### 4.4

#### Superparamagnetic Nanoparticles

Superparamagnetic iron oxide nanoparticles generate contrast by shortening the MR relaxation times with a predominant effect on T2 relaxivity leaving dark or negative contrast effects (Fig. 4.1). These particles are categorized, based upon nominal diameter, into superparamagnetic iron oxides (SPIO, 50 to 500 nm) and ultra-small superparamagnetic iron oxides (USPIO, <50 nm). The variation in size results in different physicochemical and pharmacokinetic properties. SPIO nanoparticles with maghemite or magnetite cores have to be coated with molecules such as dextran, phospholipids, or poly(amino acids) to prevent aggregation. These particles passively localize to normal liver and spleen parenchyma, causing a loss of signal on MR images [6–12]. In contrast, pathological changes in the liver, such as benign tumors, primary hepatic carcinoma, or metastases, have decreased reticuloendothelial system (RES) function, thus avoiding absorption of SPIO particles and retaining their intrinsic signal intensity on MR images. The resulting MR images depict decreased MR signal intensity of the normal liver and spleen tissues and enhanced contrast of focal disease areas. Modifying SPIOs to allow targeting of asialoglycoprotein receptors on hepatocytes can further enhance absorption by native liver cells. These nanoparticles are coated with asialofetuin [13] or galactose [14, 15].

A water-dispersible oleic acid (OA)-pluronic-coated iron oxide magnetic nanoparticle formulation, which can be loaded with high doses of hydrophobic anticancer agents like doxorubicin, has recently been developed [16]. The formulation increased the average particle diameter of the iron oxide particles from 9.3 to 193 nm, but had no effect on the magnetic properties of the core. These nanoparticles demonstrated sustained intracellular drug retention and dose-dependent antiproliferative effect over a period of two weeks *in vitro*.

Ultrasmall particles of iron oxide (USPIOs) with a mean diameter of 10 to 50  $\mu\text{m}$  are cleared slower by the RES than SPIOs, thus increasing their intravascular half-life [17]. Moreover, their small size allows them to migrate through interendothelial junctions and capillary pores or fissures [18, 19] to potentially accumu-



late in the vascular wall. Such USPIOs are phagocytosed by macrophages in atherosclerotic plaque of WHHL rabbits in quantities sufficient to be detected by MRI [20], and have been shown to detect atherosclerotic plaque *in vivo* [21]. Extravasation of USPIOs has been imaged by MRI in the setting of capillary damage associated with infections [22] and inflammation [23], human ischemic stroke [23], angiogenesis associated with atherosclerosis [21], and neovascularity induced by solid tumors [24–26].

#### 4.4.1

#### Ligand-directed Targeting of Iron Oxides

Monocrystalline iron oxide nanoparticles (MION) have been developed to address the limitations of passive tissue accumulation and phagocytosis by macrophages and the RES system. These particles have an average core diameter of 3 nm and can be directly coupled to homing ligands to specifically target epitopes in the tissue of interest. An early clinical trial was based on MION without such ligands at the time [27]. Starting in 1999, patients with prostate cancer were selected to receive MION, delivering 2.6 mg kg<sup>-1</sup> body weight. The investigators were able to demonstrate non-invasive detection by MRI of clinically occult lymph node metastases.

Dextran-coated MION coupled to human holo-transferrin (Tf-MION) have been used to visualize transgene expression in a gliosarcoma mouse model *in vivo* [28]. In these experiments, the cellular uptake of MION was increased approximately 500% relative to control cells following overexpression of engineered transferrin receptor. In other experiments MION have been used to indirectly assess angiogenesis through estimates of blood volume distribution in brain tumors [29]. The targeting efficiency of iron oxide particles was further improved with the development of dextran crosslinked iron oxide (CLIO) particles [30]. These have since been used with various ligands, including e-selectin [31], a peptide sequence from the transactivator protein (Tat) of HIV-1 [32–35], and annexin V [36].

Another example of targeted iron oxide nanoparticles are SPIO coupled to humanized biotinylated monoclonal antibody (Herceptin) that was targeted to the human Her-2/neu (c-erb B-2) tyrosine kinase receptor expressed by human breast cancer cell lines [37]. This formulation yielded contrast proportional to the expression level of Her-2/neu receptors. Other investigators have employed polyacrylamide to encapsulate 10–15 crystals of iron oxide within the particle matrix, for blood pool imaging of gliomas [38]. Future applications of these nanoparticles may include direct targeting of ligands.

The combination of superparamagnetic and non-superparamagnetic nanoparticle technologies such as near-infrared fluorescent (NIRF) probes, which can be targeted to different proteases in tissues [39, 40], has also been employed. Upon phagocytosis by macrophages, detection is facilitated by light scattering with charge-coupled device (CCD) cameras [41] or fluorescence-mediated tomography (FMT) [42, 43]. CLIO-NIRF nanoprobe have been used to coincidentally localize axillary and brachial lymph nodes by MRI and NIRF imaging following intravenous

injection into C57BL/6 mice [44]. The utilization of CLIO-NIRF for non-invasive preoperative and subsequently intraoperative localization of brain tumors has also been established. In experiments with a Fisher 344 gliosarcoma model with stably green fluorescence protein expressing 9L glioma cells, non-invasive brain tumor localization of the superparamagnetic particles with MRI was followed later by intraoperative direct visualization of the fluorescent activity [45]. In conjunction with T2-weighted imaging, magnetite particles can be used to augment targeting through external field placement and create vibratory release of drug at localized sites [46]. One early agent pursuing this development path targets luteinizing hormone releasing hormone (LHRH) overexpressing breast cancer cells and releases a lytic peptide load when the particles fracture in response to magnetic field changes [47].

#### 4.4.2

#### Cell Tracking of Iron Oxides

Magnetic labeling of individual cells prior to reaching their target location allows advantage to be taken of the strong effects of iron oxide on T2 relaxation while increasing spatial resolution due to diminished background disturbance. The concept of cellular tracking became feasible once augmentation of cytoplasmic endocytosis of iron oxide particles was accomplished. An early example of this technology resulted from the exploitation of cell surface proteins, such as the transferrin receptor [48]. In these experiments, dextran-coated MION were incubated with CG-4 rat central nervous system glial precursor cells *in vitro* and then the cells were grafted into the spinal cord of rats. The migration, implantation, and remyelination process was imaged non-invasively by MR and corroborated by histology 10–14 days after transplantation. Subsequently, MION coated with various transfection agents have been used to nonspecifically label human mesenchymal stem cells, mouse lymphocytes, rat oligodendrocyte progenitor cells, and human cervical carcinoma cells [49]. Non-invasive tracking of human mesenchymal and neuronal stem cells has also been reported for iron oxide nanoparticles encapsulated within cationic dendrimers [50]. CD8+ T-cells have been labeled with CLIO derivatized with monoclonal antibodies in a mouse melanoma model [51], and stem cell homing to bone marrow has been tracked after labeling with CLIO coupled with HIV-Tat peptides. Particle uptake has been increased over 100-fold using such specific targeting conjugates [33, 52].

#### 4.5

#### Paramagnetic Nanoparticles

Paramagnetic nanoparticles produce “bright” contrast in T1-weighted MR images (Fig. 4.2). This allows subtle anatomical features to be discerned near the contrast agent. Nanoparticles can carry large paramagnetic payloads on the surface to provide adequate signal for noninvasive MR imaging at clinically relevant field

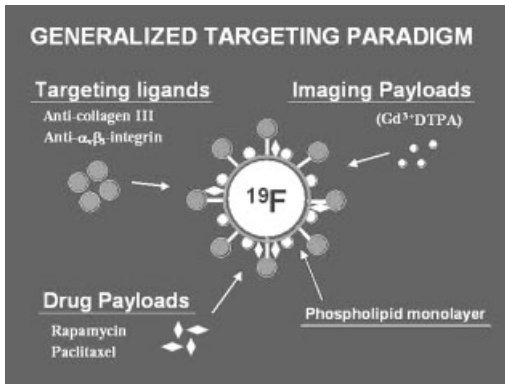


**Fig. 4.4.** Schematic illustration of a perfluorocarbon nanoparticle. Imaging agents such as gadolinium, targeting ligands, and drugs are covalently bound into the phospholipid monolayer. Phospholipids and drugs

within the nanoparticle surfactant exchange with lipids of the target membrane through a convection process after successful targeting. (Nominal particle diameter is 250 nm.)

strengths. Linking these nanoparticles with ligands to specific epitopes facilitates active targeting. Perfluorocarbon emulsions, dendrimers, fullerenes, and liposomes are the most prevalent paramagnetic nanoparticle technologies currently in various stages of development for clinical applications.

#### 4.5.1

##### Perfluorocarbon Nanoparticles

The large lipid surface area of perfluorocarbon (PFC) nanoparticles can be functionalized with magnetic labels for imaging, with homing ligands for specific tissue targeting, and with hydrophobic drugs for local delivery of treatment (Fig. 4.4). Due to the nominal size of the PFC nanoparticles (250 nm diameter), their utility is geared toward vascular-accessible targets, such as thrombosis, atherosclerosis, restenosis, and other angiogenic-dependent diseases, such as most tumors. Access beyond the circulation is sterically precluded, which prevents the unintended targeting of other cell types expressing the same biomarkers. Each nanoparticle can be coupled to several diverse ligands to afford polyvalent binding, which can amplify the signal from either microscopic pathology, where epitope concentrations are low, or where biologic temporal variation requires multiple bio-signature recognition for robustness. Binding to multiple ligands also enhances binding avidity and improves targeting, which also reduces the particle dissociation rate from the biomarker and provides more persistent MR contrast for convenient imaging in a clinical setting.

PFC nanoparticle emulsion technology offers the particular advantage of multimodal imaging. The inherent acoustic contrast of PFC nanoparticles allows detection of these emulsions when targeted and bound *in vivo* or *in vitro* due to the

markedly decreased speed of sound of the PFC core versus the surrounding water-like media [53, 54]. The high  $^{19}\text{F}$  concentrations of the perfluorocarbon provide a unique signal, which can be used for both imaging and spectroscopy. In addition, the integration of fluorine imaging with proton imaging provides an independent validation of the targeted contrast, quantitative assessment of biomarker concentration, and dosimetry of local therapeutic delivery.

For MRI imaging, each bound paramagnetic nanoparticle delivers 50 000 to 90 000+ gadolinium ions [55, 56]. These can be detected with low-resolution scans in routine clinical practice. The relaxivity of paramagnetic nanoparticles allows the calculation of “ionic relaxivity” with respect to absolute Gd concentration, and the determination of “molecular relaxivity” referring to the collective relaxivity of the entire paramagnetic nanoparticle. For applications with a 1.5 T scanner, perfluorocarbon nanoparticles have an ionic relaxivity of  $\sim 30 \text{ mM}^{-1} \text{ s}^{-1}$  and a molecular relaxivity of greater than  $2 \times 10^6 \text{ mM}^{-1} \text{ s}^{-1}$ , which is many fold greater than the ionic and molecular relaxivity of Gd-DTPA alone ( $\sim 5 \text{ mM}^{-1} \text{ s}^{-1}$ ) [57]. Due to this extraordinarily high relaxivity a voxel with as few as 100 pm of nanoparticles can be detected conspicuously with a contrast-to-noise ratio (CNR) of 5 [58]. Consequently, even single layers of cells can be imaged [59].

Various molecular epitopes, including high-density epitopes such as fibrin in thrombi and very sparse biomarkers such as integrins in neovascular beds have been targeted with perfluorocarbon nanoparticles. In angiogenic states,  $\alpha_v\beta_3$ -integrin is expressed on the luminal surface of activated endothelial cells and smooth muscle cells but not on mature quiescent cells. Nanoparticles targeted to  $\alpha_v\beta_3$ -integrin sensitively detect angiogenic endothelium at 1.5 T in New Zealand White rabbits bearing 12d Vx-2 tumors ( $<1.0 \text{ cm}$ ) [60]. In these experiments, the expression of  $\alpha_v\beta_3$ -integrin was obtained with MRI molecular imaging and paralleled by immuno-histochemical staining, which revealed an asymmetric distribution along the border of the tumor capsule where the popliteal fossa mass abutted the muscle border. The MRI signal from tumor vasculature was enhanced by 126% within 2 h of injection of  $\alpha_v\beta_3$ -integrin-targeted nanoparticles. Additional *in vivo* competition-blockade studies diminished targeted signal enhancement by more than 50%, which supports specificity of the  $\alpha_v\beta_3$ -targeted paramagnetic agent. In different experiments,  $\alpha_v\beta_3$ -integrin-targeted nanoparticles were administered systemically into athymic mice implanted with human melanoma xenografts (C-32, ATCC). The MR signal enhancement from the targeted angiogenic vasculature was apparent in 0.5 h and became progressively more prominent through the next 2 h (177%). Here too, *in vivo* competition studies and immuno-histology corroborated the specific localization of  $\alpha_v\beta_3$ -targeted nanoparticles (Fig. 4.5).

Recent studies have demonstrated the unique drug delivery capability of these agents to locally deliver antiangiogenic therapy through a process we term “contact facilitated drug delivery”. Atherosclerotic rabbits were treated with  $\alpha_v\beta_3$ -targeted paramagnetic nanoparticles including 0 or 0.2 mol% fumagillin. MRI signal enhancement averaged over all imaged slices from the renal artery to the diaphragm at 2-h post injection provided quantitative assessments of neovascular proliferation within the aortic wall. MR baseline aortic wall signal enhancement produced

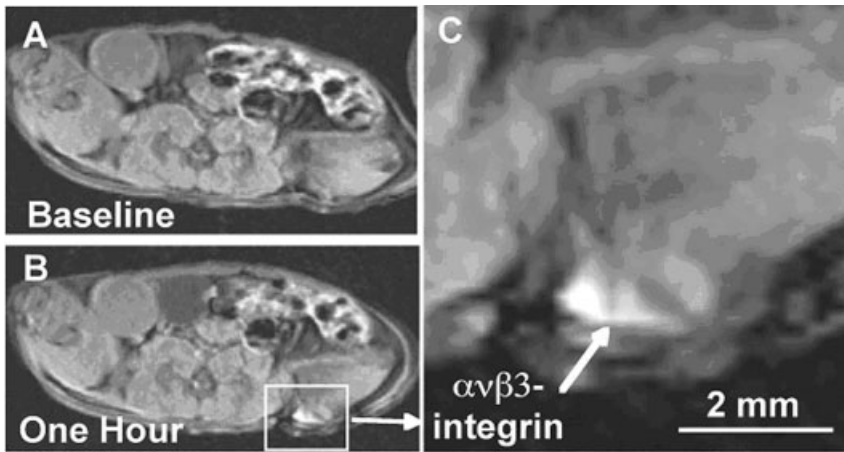


**Fig. 4.5.** (A) Full slice baseline T<sub>1</sub>-weighted MR image (axial view) of an athymic nude mouse. (B) Full slice T<sub>1</sub>-weighted MR image (axial view) of athymic nude mouse 1 h after injection of targeted PFC nanoparticle. (C) Enlarged section of MR image (B). T<sub>1</sub>-weighted signal enhancement of angiogenic vasculature of early tumor at 1 h as detected by  $\alpha_v\beta_3$ -targeted paramagnetic nanoparticles (arrow). [Reproduced with permission from G. M. Lanza et al. *J. Nucl. Cardiol.* 11(6) (2004) 733–743.]

by  $\alpha_v\beta_3$ -targeted paramagnetic nanoparticles was heterogeneously distributed throughout the great vessel and averaged  $16.7 \pm 1.1\%$  and  $16.7 \pm 1.6\%$  in animals receiving fumagillin or control nanoparticles, respectively. Reassessment 7 days later of residual aortic angiogenic activity with  $\alpha_v\beta_3$ -targeted paramagnetic nanoparticles (no drug) revealed that MR signal enhancement in rabbits given  $\alpha_v\beta_3$ -targeted fumagillin nanoparticles was markedly reduced ( $2.9 \pm 1.6\%$ ;  $p < 0.05$ ), whereas the aortic wall enhancement from the control animals was unchanged ( $18.1 \pm 2.1\%$ ). The combination of MR molecular imaging with drug delivery permits local therapeutic concentrations to be estimated, i.e., rational drug dosing, by quantitative MR <sup>19</sup>F spectroscopy [58, 59]. Hence, targeted paramagnetic nanoparticles can serve as a platform to diagnose, treat, and monitor therapy.

#### 4.5.2

##### Liposomes

Liposomes were first described in 1963 following the demonstration that phospholipids in water form closed bilayer vesicles with an aqueous core [61, 62]. The size of these liposomes can reach  $>700$  nm, dependent on the size of the core components and the number of bilayers. Hydrophilic payloads may be stored in the inner aqueous core, hydrophobic ones can be embedded in the phospholipid bilayer and small proteins may be carried on the outer surface. The clinical potential of liposome technology was previously hampered by the short circulation half-lives secondary to rapid phagocytosis by macrophages of the reticuloendothelial

systems. However, the adoption of surface PEGylation and phospholipid crosslinking has helped to reduce the rapid *in vivo* destruction and clearance of liposomes [63–65].

Numerous studies have investigated various liposome formulations in their potential to target and treat cancer in animal models (reviewed in Ref. [66]). Using catheter-based techniques, liposome formulations were shown to deliver genes *in vivo* [67, 68] and, more recently, taking advantage of developments in molecular biology, liposome-mediated drug and gene transfer has been demonstrated for lipid prodrug liposomes [69], and small interfering RNA (siRNA) cationic liposomes [70, 71]. Several studies in humans have led to the approval of liposomal formulations based on doxorubicin, (Doxil™, ALZA Corporation, Tibotec Therapeutics, NJ) for treatment ovarian cancer and AIDS-related Kaposi's sarcoma, and daunorubicin (DaunoXome®, Gilead Sciences Ltd., UK) for the treatment of advanced Kaposi's sarcoma. Many more applications are being investigated in phase II trials [72, 73]. Generally, these liposomal agents accumulate in tumor tissues via passive targeting using the EPR effect. In the treatment of brain tumor models, direct injection and convection-enhanced delivery (CED) to overcome the blood–brain barrier have been employed [74, 75]. Because many cancer cells overexpress certain receptors compared with healthy tissues, avenues of active targeting with liposomes that have been fused with agonists to these receptors have been explored. For instance, liposomes have been fused with low-density lipoprotein (LDL) particles, thereby enhancing uptake into cancer cells, which frequently overexpress these receptors [76], and haloperidol-associated stealth liposomes have been used successfully to deliver genes to breast cancer cells [77].

MRI facilitated *in vivo* monitoring of a liposomal doxorubicin formulation utilizing MnSO<sub>4</sub> as the paramagnetic metal was recently investigated in a murine flank tumor model. This novel thermal-sensitive liposomal formulation took advantage of the relaxivity of Mn, which is similar to Gd. Visualization was possible within minutes following IV liposomal infusion as the temperature-sensitive particles entered the heated tumor, ruptured, and released MnSO<sub>4</sub> locally [78].

Rabbit adenocarcinoma neovasculature has been imaged with a newly developed  $\alpha_v\beta_3$ -targeted paramagnetic UV polymerized liposome. In these experiments, adequate tumor contrast was appreciated 24 h after injection [79], reflecting both the prolonged circulatory persistence of the nanovesicles and the time required to extravasate adequately into the tumor. After incorporation of cationic phospholipids into the polymerized bilayer, delivery of a mutant Raf gene to the neovasculature of M21-L melanoma was accomplished in athymic WEHI mice [80]. ATPmu-Raf, the mutant antisense gene, resulted in apoptosis of the tumor-associated endothelium and ultimately induced tumor regression.

#### 4.5.3

##### Fullerenes

Fullerenes, also referred to as buckyballs due to their characteristic geodesic structure, have unique physical, electrochemical, and photochemical properties [81]. These unique geodesic structures can be formulated to encapsulate gadolinium

atoms for imaging with MRI and have been functionalized for usage as receptor agonists and antagonists, free radical scavengers, and bactericidal agents [82]. Prolonged circulation, up to 48 h, has been demonstrated following intravenous injection for water-soluble gadolinium endohedral metallofullerenes [83, 84]. Recently, fullerene formulations have been developed that can influence proton relaxivities by manipulation of the pH [85]. A remaining challenge is the homing of paramagnetic buckyballs to important biochemical epitopes for molecular imaging at clinically relevant field strengths [86] as well as elucidation of their interaction with blood constituents, biodistribution, metabolism, and safety.

#### 4.5.4

##### **Nanotubes**

Ultrashort single-walled carbon nanotubes (20–100 nm), which are linear superparamagnetic “molecular magnets”, have been loaded with gadolinium ions for possible usage as MRI contrast agents. The relaxivities ( $\sim 170 \text{ mm}^{-1} \text{ s}^{-1}$ ) of these nanotubes are greater than for other gadolinium-based contrast agents currently in clinical use [87]. Studies are ongoing regarding the ideal length for biomedical applications, biocompatibility, and exploitation of the tube exterior to anchor targeting ligands and/or drugs.

#### 4.5.5

##### **Dendrimers**

Dendrimers are hyperbranched, structurally well-defined polymers. They are based upon polyamines, polyamides, or polyaryl-ether subunits, and have varying core structures such as carbohydrate or calixarene [88]. Paramagnetic polyamidoamine (PAMAM) and diaminobutane (DAB) dendrimers have been developed for MRI applications. Several spherically branched molecules [89] have been evaluated in several animal models to detect intratumoral vasculature [90] and lymph vessels [91–93] with high-resolution MRI on clinical 1.5 T MRI scanners. Blood pool imaging has been accomplished with conjugated dendrimers [94, 95]. However, conjugation with antibodies for targeting has tended to unfavorably alter their pharmacokinetics [96]. Recently, improved kinetics have been obtained with small molecule, e.g., folate, based targeting applications [97, 98]. Future formulations need to address the question of toxicity, which can be high, especially for dendrimers with cationic surface groups and amino-terminated dendrimers [99, 100]. The most promise for medical applications has been shown for anionic PAMAM dendrimers and hydroxy- and methoxy-terminated dendrimers [101–103].

## 4.6

### **Quantum Dots**

Semiconductor nanocrystals, also known as quantum dots, absorb light over a very broad spectral range, depending on the particle composition and size (typically 2–8 nm in diameter). This allows for the excitation of a broad spectrum of colors using

a single excitation laser wavelength [104]. When conjugated to targeting proteins such as transferrin or antibodies, these nanocrystals can bind to surface receptors on cells [105], be incorporated by cells [106], and even nuclear localization has been demonstrated [104]. Thus, their use for *in vitro* diagnostic applications has been extended to include *in vivo* small animal imaging applications. Recently, *in vivo* cancer targeting has been demonstrated in a mouse model growing human prostate cancer [107]. In these experiments, antibodies against prostate-specific membrane antigen were conjugated to nanocrystals, allowing for active targeting. Currently, linking quantum dots to therapeutic, e.g., anticancer, agents is being investigated for applicability. Unlike other nanoparticles, which can carry targeting ligands and therapeutic agents, semiconductor nanocrystals, due to their small size, will likely have to be conjugated to other nanoparticles to achieve specific targeting, while allowing for real-time imaging and drug delivery. The first such multimodality probes have recently been developed by integrating quantum dots with superparamagnetic nanoparticles [108, 109].

The main concerns with quantum dot technology, however, are biocompatibility, biodistribution, metabolism and biosafety. Nanocrystals can contain elements such as cadmium and indium and various techniques have been employed to make these particles more water-soluble and safer. One method is to modify the particles by growing a silica layer onto the surface of the quantum dots [110] or coating the dots with amphiphilic polymers [111, 112]. Another avenue of protecting the non-biocompatible elements of the quantum dots involves conjugation with targeting molecules [111, 112]. While polymer-encapsulated nanocrystals may be biocompatible for immediate imaging, the issue of toxicity during breakdown and elimination of these particles from the body requires further study.

## 4.7

### Polymer Nanoparticles

Nanoparticles formulated from poly(hydroxy acids) such as the copolymer of poly(lactic acid) (PLA) and poly(D,L-lactide-co-glycolide) (PLGA) have been investigated for localized drug and gene delivery [113, 114]. These particles are biodegradable, like absorbable suture materials, and result in a similar inflammatory response during degradation [115]. Drugs can be encapsulated into the nanoparticles during the emulsification process and are later released during the decay of the nanoparticle. Depending on size, the entire nanoparticle can be incorporated into cells through phagocytosis. Degradation kinetics, and thus drug release, can be adjusted by changing copolymer composition and molecular weights [116]. In recent experiments, transferrin targeted nanoparticles containing doxorubicin afforded prolonged survival in a murine prostate cancer model [117]. The particle size averaged 220 nm and the treatment was given as a single direct intratumoral injection into the subcutaneously grown prostate cancer in athymic nude mice. Sustained release of drug was observed, as compared with the paclitaxel Cremophor® EL formulation, and complete regression of tumor was observed with the higher nanoparticle associated paclitaxel dosage (24 mg kg<sup>-1</sup>) compared



with (in order of decreasing survival) lower dosage (12 mg kg<sup>-1</sup>), non-transferrin targeted paclitaxel nanoparticles, paclitaxel Cremophor® EL, or Cremophor® EL alone and control nanoparticles. These researchers took advantage of the over-expression of transferrin receptors by many tumors, yet the nanoparticles were still injected directly into the tumor in these experiments and systemic application may prove less effective since many normal tissues express transferrin receptors [118]. Recently shell-crosslinked nanoparticles derivatized with gadolinium were studied for their capability for polyvalent targeting [119]. These particles demonstrated large ionic relaxivities (~39 mM<sup>-1</sup> s<sup>-1</sup>) and a high molecular relaxivity of 20 000 mM<sup>-1</sup> s<sup>-1</sup>. Such particles have been conjugated with folate and shown to result in higher tumor uptake in small tumors overexpressing the folate receptor than controls [120]. Furthermore, folate nanoparticle uptake in the smaller tumors was competitively inhibited by excess folate, supporting ligand-based targeting.

#### 4.8

#### Conclusion

Nanoparticulate agents, such as superparamagnetic agents, perfluorocarbon nanoparticle emulsions, liposomes, fullerenes, dendrimers, are being intensively studied for various clinically relevant applications, particularly for magnetic resonance imaging (Table 4.1). The detection of tumor or metastasis development in the early stages appears feasible with nanoparticles targeted to unique or abundant epitopes on tumor tissues (Table 4.2). Nanoparticle-facilitated signal enhancement

Tab. 4.1. Nanoparticle classification.

Nanoparticles	Ref.	Nanoparticles	Ref.
Superparamagnetic		Paramagnetic	
SPIO	16, 37	PFC	53–60
USPIO	24–26		
MION	27, 28, 49	Liposomes	63, 66, 70–80, 121
CLIO	44, 45, 51		
PAM	38	Fullerenes	83–86
Magnetite	46, 47	Nanotubes	87, 122
Magneto-fluorescent			
NIRF	39–45	Dendrimers	89–95, 97–99, 102, 103
Fluorescent			
Quantum dots	107, 112	Polymer nanoparticles	114, 117, 119, 120

SPIO – Superparamagnetic iron oxides; USPIO – ultrasmall superparamagnetic iron oxides; MION – monocrystalline iron oxide nanoparticles; CLIO – crosslinked iron oxide nanoparticles; PAM – polyacrylamide magnetic nanoparticles; NIRF – near-infrared fluorescent nanoparticles; PFC – liquid perfluorocarbon nanoparticles.

Tab. 4.2. MRI applications of nanoparticles for cancer diagnosis and treatment.

Nanoparticle	Species/model	Cancer	Targeting: active (A); passive (P)	Treatment	Ref.
SPIO	<i>In vitro</i>	Breast and prostate cancer	P	Doxorubicin	16
SPIO	<i>In vitro</i>	Human Her-2/neu receptor expressing breast cancer cells	A	N/A	37
USPIO	Mice	VEGF-expressing Mel57 (human melanoma) tumors in mouse brains	P	N/A	24
USPIO	Rats	Breast cancer	P	N/A	25, 26
MION	Mice	Transferrin receptor expressing 9L gliosarcoma	A	N/A	28
MION	<i>In vitro</i>	Human cervical carcinoma cells	Cellular labeling	N/A	49
MION	Human trial	Prostate cancer	P	N/A	27
CLIO	Rats	9L gliosarcoma	A	N/A	45
CLIO	Mice	Melanoma	Cellular labeling	N/A	51
PAM	Rats	9L gliomas	P	N/A	38
Magnetite	Mice	LHRH expressing human breast cancer cells	A	Lytic peptide	47
PFC	Rabbits	Vx-2 tumors	A	N/A	60
Quantum dots	Mice	Subcutaneously implanted human prostate cancer	A	N/A	107
Quantum dots	<i>In vitro</i>	Human SK-BR-3 breast cancer cells	A	N/A	112

Polymer nanoparticles	Mice	Subcutaneously implanted human prostate cancer	A	Intratumoral injection Paclitaxel	117
Liposomes	<i>In vitro</i>	CV1-P kidney cell line	A	Methotrexate	76
Liposomes	<i>In vitro</i>	MCF-7 human breast cancer cells	A	N/A (reporter gene delivery)	77
Liposomes	Rats	Subcutaneously implanted rat fibrosarcoma	P	Doxorubicin delivered upon tumor heating	78
Liposomes	Rabbits	V2 squamous cell carcinoma	A	N/A	79
Liposomes	Mice	M21-L melanomas	A	Systemic injection. Mutant Raf gene	80
Liposomes	Mice	Melanoma B16 tumors	A	Doxorubicin	121
Dendrimers	Mice rats	Human skin carcinoma Rat prostate carcinoma	P	N/A	90
Dendrimers	<i>In vitro</i>	Folate receptor expressing KB tumor cells	A	Methotrexate	98
Dendrimers	<i>In vitro</i> Mice	Melanoma and breast cancer cell lines Healthy CD-1 mice	P	Doxorubicin	102

will allow the imaging of tumors in size ranges that are undetectable with conventional imaging protocols. Importantly, delivery of drugs by nanocarriers specifically to tumor tissues will allow for localized therapy in dosage ranges that cannot be achieved with conventional systemic chemotherapy due to side effects. Ushering in the era of “personalized medicine” these nanoparticulate technologies will ultimately allow physicians to diagnose disease in asymptomatic individuals and treat pathology early and custom-tailored to the individual patient.

## References

- 1 S. SHARMA, M. C. SHARMA, C. SARKAR, Morphology of angiogenesis in human cancer: A conceptual overview, histoprognostic perspective and significance of neoangiogenesis, *Histopathology* 46 (2005) 481–489.
- 2 M. DELLIAN, B. WITWER, H. SALEHI, F. YUAN, R. JAIN, Quantitation and physiological characterization of angiogenic vessels in mice: Effect of basic fibroblast growth factor, vascular endothelial growth factor/vascular permeability factor, and host microenvironment, *Am. J. Pathol.* 149 (1996) 59–71.
- 3 S. K. HOBBS, W. L. MONSKY, F. YUAN, W. G. ROBERTS, L. GRIFFITH, V. P. TORCHILIN, R. K. JAIN, Regulation of transport pathways in tumor vessels: Role of tumor type and microenvironment, *Proc. Natl. Acad. Sci. U.S.A.* 95 (1998) 4607–4612.
- 4 Y. MATSUMURA, H. MAEDA, A new concept for macromolecular therapeutics in cancer chemotherapy: Mechanism of tumorotropic accumulation of proteins and the antitumor agent smancs, *Cancer Res.* 46 (1986) 6387–6392.
- 5 H. MAEDA, L. W. SEYMOUR, Y. MIYAMOTO, Conjugates of anticancer agents and polymers: Advantages of macromolecular therapeutics in vivo, *Bioconjugate Chem.* 3 (1992) 351–362.
- 6 R. C. SEMELKA, J. K. LEE, S. WORAWATTANAKUL, T. C. NOONE, R. H. PATT, S. M. ASCHER, Sequential use of ferumoxide particles and gadolinium chelate for the evaluation of focal liver lesions on MRI, *J. Magn. Reson. Imaging* 8 (1998) 670–674.
- 7 J. SCOTT, J. WARD, J. A. GUTHRIE, D. WILSON, P. J. ROBINSON, MRI of liver: A comparison of CNR enhancement using high dose and low dose ferumoxide infusion in patients with colorectal liver metastases, *Magn. Reson. Imaging* 18 (2000) 297–303.
- 8 M. NAKAYAMA, Y. YAMASHITA, K. MITSUZAKI, T. YI, A. ARAKAWA, K. KATAHIRA, Y. NAKAYAMA, M. TAKAHASHI, Improved tissue characterization of focal liver lesions with ferumoxide-enhanced T1 and T2-weighted MR imaging, *J. Magn. Reson. Imaging* 11 (2000) 647–654.
- 9 K. IMAM, D. A. BLUEMKE, MR imaging in the evaluation of hepatic metastases, *Magn. Reson. Imaging Clin. N. Am.* 8 (2000) 741–756.
- 10 H. KATO, M. KANEMATSU, H. KONDO, S. GOSHIMA, M. MATSUO, H. HOSHI, N. MORIYAMA, Ferumoxide-enhanced MR imaging of hepatocellular carcinoma: Correlation with histologic tumor grade and tumor vascularity, *J. Magn. Reson. Imaging* 19 (2004) 76–81.
- 11 T. ARAKI, SPIO-MRI in the detection of hepatocellular carcinoma, *J. Gastroenterol.* 35 (2000) 874–876.
- 12 H. NAKAMURA, N. ITO, F. KOTAKE, Y. MIZOKAMI, T. MATSUOKA, Tumor-detecting capacity and clinical usefulness of SPIO-MRI in patients with hepatocellular carcinoma, *J. Gastroenterol.* 35 (2000) 849–855.
- 13 M. STISKAL, H. C. SCHWICKERT, F. DEMSAR, T. P. ROBERTS, D. SZOLAR, R. WEISSLEDER, R. C. BRASCH, Contrast enhancement in experimental radiation-induced liver injury:

- Comparison of hepatocellular and reticuloendothelial particulate contrast agents, *J. Magn. Reson. Imaging* 6 (1996) 286–290.
- 14 R. WEISSLEDER, P. REIMER, A. S. LEE, J. WITTENBERG, T. J. BRADY, MR receptor imaging: Ultrasmall iron oxide particles targeted to asialoglyco-protein receptors, *Am. J. Roentgenol.* 155 (1990) 1161–1167.
  - 15 P. REIMER, R. WEISSLEDER, T. J. BRADY, A. E. YEAGER, B. H. BALDWIN, B. C. TENNANT, J. WITTENBERG, Experimental hepatocellular carcinoma: MR receptor imaging, *Radiology* 180 (1991) 641–645.
  - 16 T. K. JAIN, M. A. MORALES, S. K. SAHOO, D. L. LESLIE-PELECKY, V. LABHASSETWAR, Iron oxide nanoparticles for sustained delivery of anticancer agents, *Mol. Pharmaceutics* 2 (2005) 194–205.
  - 17 R. WEISSLEDER, G. ELIZONDO, J. WITTENBERG, C. A. RABITO, H. H. BENGEL, L. JOSEPHSON, Ultrasmall superparamagnetic iron oxide: Characterization of a new class of contrast agents for MR imaging, *Radiology* 175 (1990) 489–493.
  - 18 E. M. RENKIN, Multiple pathways of capillary permeability, *Circulation Res.* 41 (1977) 735–743.
  - 19 V. W. M. VAN HINSBERGH, Endothelial permeability for macromolecules: Mechanistic aspects of pathophysiological modulation, *Arterioscler. Thromb. Vasc. Biol.* 17 (1997) 1018–1023.
  - 20 S. G. RUEHM, C. COROT, P. VOGT, S. KOLB, J. F. DEBATIN, Magnetic resonance imaging of atherosclerotic plaque with ultrasmall superparamagnetic particles of iron oxide in hyperlipidemic rabbits, *Circulation* 103 (2001) 415–422.
  - 21 M. E. KOOF, V. C. CAPPENDIJK, K. B. J. M. CLEUTJENS, A. G. H. KESSELS, P. J. E. H. M. KITSLAAR, M. BORGENS, P. M. FREDERIK, M. J. A. P. DAEMEN, J. M. A. VAN ENGELSHOVEN, Accumulation of ultrasmall superparamagnetic particles of iron oxide in human atherosclerotic plaques can be detected by in vivo magnetic resonance imaging, *Circulation* 107 (2003) 2453–2458.
  - 22 J. GELLISSSEN, C. AXMANN, A. PRESCHER, K. BOHNDORF, K. P. LODEMANN, Extra- and intracellular accumulation of ultrasmall superparamagnetic iron oxides (USPIO) in experimentally induced abscesses of the peripheral soft tissues and their effects on magnetic resonance imaging, *Magn. Resonan. Imaging* 17 (1999) 557–567.
  - 23 A. SALEH, M. SCHROETER, C. JONKMANN, H.-P. HARTUNG, U. MODDER, S. JANDER, In vivo MRI of brain inflammation in human ischaemic stroke, *Brain* 127 (2004) 1670–1677.
  - 24 W. LEENDERS, B. KUSTERS, J. PIKKEMAAT, P. WESSELING, D. RUITER, A. HEERSCHAP, J. BARENTSZ, R. M. DE WAAL, Vascular endothelial growth factor-A determines detectability of experimental melanoma brain metastasis in GD-DTPA-enhanced MRI, *Int. J. Cancer* 105 (2003) 437–434.
  - 25 K. TURETSCHKEK, T. P. ROBERTS, E. FLOYD, A. PREDA, V. NOVIKOV, D. M. SHAMES, W. O. CARTER, R. C. BRASCH, Tumor microvascular characterization using ultrasmall superparamagnetic iron oxide particles (USPIO) in an experimental breast cancer model, *J. Magn. Reson. Imaging* 13 (2001) 882–888.
  - 26 K. TURETSCHKEK, S. HUBER, E. FLOYD, T. HELBICH, T. P. L. ROBERTS, D. M. SHAMES, K. S. TARLO, M. F. WENDLAND, R. C. BRASCH, MR imaging characterization of microvessels in experimental breast tumors by using a particulate contrast agent with histopathologic correlation, *Radiology* 218 (2001) 562–569.
  - 27 M. G. HARISINGHANI, J. BARENTSZ, P. F. HAHN, W. M. DESERNO, S. TABATABAEI, C. H. VAN DE KAA, J. DE LA ROSETTE, R. WEISSLEDER, Noninvasive detection of clinically occult lymph-node metastases in prostate cancer, *New Engl. J. Med.* 348 (2003) 2491–2499.
  - 28 R. WEISSLEDER, A. MOORE, U. MAHMOOD, R. BHORADE, H.

- BENVENISTE, E. A. CHIOCCA, J. P. BASILION, In vivo magnetic resonance imaging of transgenic expression, *Nat. Med.* 6 (2000) 351–355.
- 29 J. F. DUNN, M. A. ROCHE, R. SPRINGETT, M. ABAJIAN, J. MERLIS, C. P. DAGHLIAN, S. Y. LU, M. MAKKI, Monitoring angiogenesis in brain using steady-state quantification of DeltaR2 with MION infusion, *Magn. Resonan. Med.* 51 (2004) 55–61.
- 30 D. HOGEMANN, L. JOSEPHSON, R. WEISSLEDER, J. P. BASILION, Improvement of MRI probes to allow efficient detection of gene expression, *Bioconjugate Chem.* 11 (2000) 941–946.
- 31 H. W. KANG, L. JOSEPHSON, A. PETROVSKY, R. WEISSLEDER, A. J. BOGDANOV, Magnetic resonance imaging of inducible E-selectin expression in human endothelial cell culture, *Bioconjugate Chem.* 13 (2002) 122–127.
- 32 A. M. KOCH, F. REYNOLDS, M. F. KIRCHER, H. P. MERKLE, R. WEISSLEDER, L. JOSEPHSON, Uptake and metabolism of a dual fluorochrome Tat-nanoparticle in HeLa cells, *Bioconjugate Chem.* 14 (2003) 1115–1121.
- 33 L. JOSEPHSON, C.-H. TUNG, A. MOORE, R. WEISSLEDER, High-efficiency intracellular magnetic labelling with novel superparamagnetic-Tat peptide conjugates, *Bioconjugate Chem.* 10 (1999) 186–191.
- 34 C. H. DODD, H. C. HSU, W. J. CHU, P. YANG, H. G. ZHANG, J. D. J. MOUNTZ, K. ZINN, J. FORDER, L. JOSEPHSON, R. WEISSLEDER, J. M. MOUNTZ, J. D. MOUNTZ, Normal T-cell response and in vivo magnetic resonance imaging of T cells loaded with HIV transactivator-peptide-derived superparamagnetic nanoparticles, *J. Immunol. Methods* 256 (2001) 89–105.
- 35 M. LEWIN, N. CARLESSO, C.-H. TUNG, X.-W. TANG, D. CORY, D. T. SCADDEN, R. WEISSLEDER, Tat peptide-derivatized magnetic nanoparticles allow in vivo tracking and recovery of progenitor cells, *Nat. Biotechnol.* 18 (2000) 410–414.
- 36 E. A. SCHELLENBERGER, A. J. BOGDANOV, D. HOGEMANN, J. TAIT, R. WEISSLEDER, L. JOSEPHSON, Annexin V-Clio: A nanoparticle for detecting apoptosis by MRI, *Mol. Imaging* 1 (2002) 102–107.
- 37 D. ARTEMOV, N. MORI, B. OKOLLIE, Z. M. BHUJWALLA, MR molecular imaging of the Her-2/neu receptor in breast cancer cells using targeted iron oxide nanoparticles, *Magn. Resonan. Med.* 49 (2003) 403–408.
- 38 B. A. MOFFAT, G. R. REDDY, P. MCCONVILLE, D. E. HALL, T. L. CHENEVERT, R. R. KOPELMAN, M. PHILBERT, R. WEISSLEDER, A. REHEMTULLA, B. D. ROSS, A novel polyacrylamide magnetic nanoparticle contrast agent for molecular imaging using MRI, *Mol. Imaging* 2 (2003) 324–332.
- 39 C.-H. TUNG, U. MAHMOOD, S. BREDOW, R. WEISSLEDER, In vivo imaging of proteolytic enzyme activity using a novel molecular reporter, *Cancer Res.* 60 (2000) 4953–4958.
- 40 C. BREMER, C.-H. TUNG, R. WEISSLEDER, In vivo molecular target assessment of matrix metalloproteinase inhibition, *Nat. Med.* 7 (2001) 743–748.
- 41 U. MAHMOOD, C.-H. TUNG, A. BOGDANOV, JR., R. WEISSLEDER, Near-infrared optical imaging of protease activity for tumor detection, *Radiology* 213 (1999) 866–870.
- 42 V. NTZIACHRISTOS, R. WEISSLEDER, Experimental three-dimensional fluorescence reconstruction of diffuse media by use of a normalized Born approximation, *Optics Lett.* 26 (2001) 893–895.
- 43 V. NTZIACHRISTOS, A. G. YODH, M. SCHNALL, B. CHANCE, Concurrent MRI and diffuse optical tomography of breast after indocyanine green enhancement, *Proc. Natl. Acad. Sci. U.S.A.* 97 (2000) 2767–2772.
- 44 L. JOSEPHSON, M. F. KIRCHNER, U. MAHMOOD, Y. TANG, R. WEISSLEDER, Near-infrared fluorescent nanoparticles as combined MR/optical imaging probes, *Bioconjugate Chem.* 13 (2002) 554–560.

- 45 M. F. KIRCHER, U. MAHMOOD, R. S. KING, R. WEISSELEDER, L. JOSEPHSON, A multimodal nanoparticle for preoperative resonance imaging and intraoperative optical brain tumor delineation, *Cancer Res.* 63 (2003) 8122–8125.
- 46 C. S. KUMAR, C. LEUSCHNER, E. E. DOOMES, L. HENRY, M. JUBAN, J. HORMES, Efficacy of lytic peptide-bound magnetite nanoparticles in destroying breast cancer cells, *J. Nanosci. Nanotechnol.* 4 (2005) 245–249.
- 47 C. LEUSCHNER, C. S. S. R. KUMAR, W. HANSEL, J. HORMES, Targeting breast cancer cells and their metastases through luteinizing hormone releasing hormone (LHRH) receptors using magnetic nanoparticles, *J. Biomed. Nanotechnol.* 1 (2005) 229–233.
- 48 J. W. M. BULTE, S.-C. ZHANG, P. VAN GELDEREN, V. HERYNEK, E. K. JORDAN, I. D. DUNCAN, J. A. FRANK, Neurotransplantation of magnetically labeled oligodendrocyte progenitors: Magnetic resonance tracking of cell migration and myelination, *Proc. Natl. Acad. Sci. U.S.A.* 96 (1999) 15 256–15 261.
- 49 J. A. FRANK, B. R. MILLER, A. S. ARBAB, H. A. ZYWICKE, E. K. JORDAN, B. K. LEWIS, L. H. BRYANT, JR, J. W. M. BULTE, Clinically applicable labeling of mammalian and stem cells by combining superparamagnetic iron oxides and transfection agents, *Radiology* 228 (2003) 480–487.
- 50 J. W. M. BULTE, T. DOUGLAS, B. WITWER, S.-C. ZHANG, B. K. LEWIS, P. VAN GELDEREN, H. ZYWICKE, I. D. DUNCAN, J. A. FRANK, Monitoring stem cell therapy in vivo using magnetodendrimers as a new class of cellular MR contrast agents, *Acad. Radiol.* 9 (2002) S332–S335.
- 51 M. F. KIRCHER, J. R. ALLPORT, E. E. GRAVES, V. LOVE, L. JOSEPHSON, A. H. LICHTMAN, R. WEISSELEDER, In vivo high resolution three-dimensional imaging of antigen-specific cytotoxic T-lymphocyte trafficking to tumors, *Cancer Res.* 63 (2003) 6838–6846.
- 52 P. WUNDERBALDINGER, L. JOSEPHSON, R. WEISSELEDER, Tat peptide directs enhanced clearance and hepatic permeability of magnetic nanoparticles, *Bioconjugate Chem.* 13 (2002) 264–268.
- 53 G. M. LANZA, K. D. WALLACE, M. J. SCOTT, W. P. CACHERIS, D. R. ABENDSCHEIN, D. H. CHRISTY, A. M. SHARKEY, J. G. MILLER, P. J. GAFFNEY, A. WICKLINE, A novel site-targeted ultrasonic contrast agent with broad biomedical application, *Circulation* 94 (1996) 3334–3340.
- 54 G. M. LANZA, D. R. ABENDSCHEIN, C. S. HALL, M. J. SCOTT, D. E. SCHERRER, A. HOUSEMAN, J. G. MILLER, S. A. WICKLINE, In vivo molecular imaging of stretch-induced tissue factor in carotid arteries with ligand-targeted nanoparticles, *J. Am. Soc. Echocardiography* 13 (2000) 608–614.
- 55 S. FLACKE, S. FISCHER, M. J. SCOTT, R. J. FUHRHOP, J. S. ALLEN, M. MCLEAN, P. WINTER, G. A. SICARD, P. J. GAFFNEY, S. A. WICKLINE, G. M. LANZA, Novel MRI contrast agent for molecular imaging of fibrin: Implications for detecting vulnerable plaques, *Circulation* 104 (2001) 1280–1285.
- 56 G. M. LANZA, C. H. LORENZ, S. E. FISCHER, M. J. SCOTT, W. P. CACHERIS, R. J. KAUFMANN, P. J. GAFFNEY, S. A. WICKLINE, Enhanced detection of thrombi with a novel fibrin-targeted magnetic resonance imaging agent, *Acad. Radiol.* 5(Suppl. 1) (1998) S173–S176.
- 57 P. M. WINTER, S. D. CARUTHERS, X. YU, S.-K. SONG, J. CHEN, B. MILLER, J. W. M. BULTE, J. D. ROBERTSON, P. J. GAFFNEY, S. A. WICKLINE, G. M. LANZA, Improved molecular imaging contrast agent for detection of human thrombus, *Magn. Resonan. Med.* 50 (2003) 411–416.
- 58 A. M. MORAWSKI, P. WINTER, K. C. CROWDER, S. D. CARUTHERS, R. J. FUHRHOP, M. J. SCOTT, J. D. ROBERTSON, D. R. ABENDSCHEIN, G. M. LANZA, S. A. WICKLINE, Targeted nanoparticles for quantitative imaging of sparse molecular epitopes with MRI, *Magn. Resonan. Med.* 51 (2004) 480–486.

- 59 G. M. LANZA, X. YU, P. M. WINTER, D. R. ABENDSCHEIN, K. K. KARUKSTIS, M. J. SCOTT, L. K. CHINEN, R. W. FUHRHOP, D. E. SCHERRER, S. A. WICKLINE, Targeted antiproliferative drug delivery to vascular smooth muscle cells with a magnetic resonance imaging nanoparticle contrast agent: Implications for rational therapy of restenosis, *Circulation* 106 (2002) 2842–2847.
- 60 P. M. WINTER, S. D. CARUTHERS, A. KASSNER, T. D. HARRIS, L. K. CHINEN, J. S. ALLEN, E. K. LACY, H. ZHANG, J. D. ROBERTSON, S. A. WICKLINE, G. M. LANZA, Molecular imaging of angiogenesis in nascent Vx-2 rabbit tumors using a novel  $a_n b_3$ -targeted nanoparticle and 1.5 Tesla magnetic resonance imaging, *Cancer Res.* 63 (2003) 5838–5843.
- 61 A. D. BANGHAM, Membrane models with phospholipids, *Progr. Biophys. Mol. Biol.* 18 (1968) 29–36.
- 62 M. J. HOPE, M. B. BALLY, L. D. MAYER, A. S. JANOFF, P. R. CULLIS, Generation of multilamellar and unilamellar phospholipid vesicles, *Chem. Phys. Lipids* 40 (1986) 89–107.
- 63 A. GABIZON, D. PAPAHAJOPOULOS, Liposome formulations with prolonged circulation time in blood and enhanced uptake by tumors, *Proc. Natl. Acad. Sci. U.S.A.* 85 (1988) 6949–6953.
- 64 M. C. WOODLE, D. D. LASIC, Sterically stabilized liposomes, *Biochim. Biophys. Acta* 1113 (1992) 171–199.
- 65 A. S. ULRICH, Biophysical aspects of using liposomes as delivery vehicles, *Biosci. Rep.* 22 (2002) 129–150.
- 66 K. J. HARRINGTON, K. N. SYRIGOS, R. G. VILE, Liposomally targeted cytotoxic drugs for the treatment of cancer, *J. Pharm. Pharmacol.* 54 (2002) 1573–1600.
- 67 E. G. NABEL, G. PLAUTZ, G. J. NABEL, Site-specific gene expression in vivo by direct gene transfer into the arterial wall, *Science* 249 (1990) 1285–1288.
- 68 V. J. POMPILI, D. GORDON, H. SAN, Z. YANG, D. W. M. MULLER, G. J. NABEL, E. G. NABEL, Expression and function of a recombinant PDGF B gene in porcine arteries, *Arterioscler. Thromb. Vasc. Biol.* 15 (1995) 2254–2264.
- 69 S. S. JENSEN, T. L. ANDRESEN, J. DAVIDSEN, P. HOYRUP, S. D. SHNYDER, M. C. BIBBY, J. H. GILL, K. JORGENSEN, Secretory phospholipase A2 as a tumor-specific trigger for targeted delivery of a novel class of liposomal prodrug anticancer etherlipids, *Mol. Cancer Ther.* 3 (2004) 1451–1458.
- 70 M. NOGAWA, T. YUASA, S. KIMURA, M. TANAKA, J. KURODA, K. SATO, A. YOKOTA, H. SEGAWA, Y. TODA, S. KAGEYAMA, T. YOSHIKI, Y. OKADA, T. MAEKAWA, Intravesical administration of small interfering RNA targeting PLK-1 successfully prevents the growth of bladder cancer, *J. Clin. Invest.* 115 (2005) 978–985.
- 71 J. YANO, K. HIRABAYASHI, S.-i. NAKAGAWA, T. YAMAGUCHI, M. NOGAWA, I. KASHIMORI, H. NAITO, H. KITAGAWA, K. ISHIYAMA, T. OHGI, T. IRIMURA, Antitumor activity of small interfering RNA/cationic liposome complex in mouse models of cancer, *Clin. Cancer Res.* 10 (2004) 7721–7726.
- 72 S. U. GNAD-VOGT, R.-D. HOFHEINZ, S. SAUSSELE, S. KREIL, A. WILLER, F. WILLEKE, L. PILZ, R. HEHLMANN, A. HOCHHAUS, Pegylated liposomal doxorubicin and mitomycin C in combination with infusional 5-fluorouracil and sodium folinic acid in the treatment of advanced gastric cancer: Results of phase II trial, *Anti-Cancer Drugs* 16 (2005) 435–440.
- 73 D. KATSAROS, M. V. OLETTI, I. A. RIGAUULT DE LA LONGRAIS, A. FERRERO, A. CELANO, S. FRACCHIOLI, M. DONADIO, R. PASSERA, L. CATTEL, C. BUMMA, Clinical and pharmacokinetic phase II study of pegylated liposomal doxorubicin and vinorelbine in heavily pretreated recurrent ovarian carcinoma, *Ann. Oncol.* 16 (2005) 300–306.
- 74 C. MAMOT, J. B. NGUYEN, M. POURDEHNAD, P. HADACZEK, R. SAITO, J. R. BRINGAS, D. C. DRUMMOND, K. HONG, D. B. KIRPOTIN, T. R.



- McKNIGHT, M. S. BERGER, J. W. PARK, K. S. BANKIEWICZ, Extensive distribution of liposomes in rodent brains and brain tumors following convection-enhanced delivery, *J. Neuro-Oncol.* 68 (2004) 1–9.
- 75 R. SAITO, J. R. BRINGAS, T. R. McKNIGHT, M. F. WENDLAND, C. MAMOT, D. C. DRUMMOND, D. B. KIRPOTIN, J. W. PARK, M. S. BERGER, K. S. BANKIEWICZ, Distribution of liposomes into brain and rat brain tumor models by convection-enhanced delivery monitored with magnetic resonance imaging, *Cancer Res.* 64 (2004) 2572–2579.
- 76 K. AMIN, K.-Y. NG, C. BROWN, M. BRUNO, T. HEATH, LDL induced association of anionic liposomes with cells and delivery of contents as shown by the increase in potency of liposome dependent drugs, *Pharmaceutical Res.* 18 (2001) 914–921.
- 77 A. MUKHERJEE, T. K. PRASAD, N. M. RAO, R. BANERJEE, Haloperidol-associated stealth liposomes: A potent carrier for delivering genes to human breast cancer cells, *J. Biol. Chem.* 280 (2005) 15 619–15 627.
- 78 B. L. VIGLIANTI, S. A. ABRAHAM, C. R. MICHELICH, P. S. YARMOLENKO, J. R. MACFALL, M. B. BALLY, M. W. DEWHIRST, In vivo monitoring of tissue pharmacokinetics of liposome/drug using MRI: Illustration of targeted delivery, *Magn. Resonan. Imaging* 51 (2004) 1153–1162.
- 79 D. A. SIPKINS, D. A. CHERESH, M. R. KAZEMI, L. M. NEVIN, M. D. BEDNARSKI, K. C. LI, Detection of tumor angiogenesis in vivo by  $\alpha_n\beta_3$ -targeted magnetic resonance imaging, *Nat. Med.* 4 (1998) 623–626.
- 80 J. D. HOOD, M. BEDNARSKI, R. FRAUSTO, S. GUCCIONE, R. A. REISFELD, R. XIANG, D. A. CHERESH, Tumor regression by targeted gene delivery to the neovasculature, *Science* 296 (2002) 2404–2407.
- 81 S. R. WILSON, Biological applications of fullerene derivatives: A brief overview, in *The Fullerene Handbook*, KADISH, K., RUOFF, R. (Eds.), Wiley, New York, 2000, pp. 437–465.
- 82 S. BOSI, T. DA ROS, G. SPALLUTO, M. PRATO, Fullerene derivatives: An attractive tool for biological applications, *Eur. J. Med. Chem.* 38 (2003) 913–923.
- 83 L. QINGNUAN, X. YAN, Z. XIAODONG, L. RUILI, D. QIEQIE, S. XIAOGUANG, C. SHAOLIANG, L. WENXIN, Preparation of (99m)Tc-C(60)(OH)(x) and its biodistribution studies, *Nucl. Med. Biol.* 29 (2002) 707–710.
- 84 M. MIKAWA, H. KATO, M. OKAMURA, M. NARAZAKI, Y. KANAZAWA, N. MIWA, H. SHINOHARA, Paramagnetic water-soluble metallofullerenes having the highest relaxivity for MRI contrast agents, *Bioconjugate Chem.* 12 (2001) 510–514.
- 85 E. TOTH, R. D. BOLSKAR, A. BOREL, G. GONZALEZ, L. HELM, A. E. MERBACH, B. SITHARAMAN, L. J. WILSON, Water-soluble gadofullerenes: Toward high-relaxivity, pH-responsive MRI contrast agents, *J. Am. Chem. Soc.* 127 (2005) 799–805.
- 86 R. D. BOLSKAR, A. F. BENEDETTO, L. O. HUSEBO, R. E. PRICE, E. F. JACKSON, S. WALLACE, L. J. WILSON, J. M. ALFORD, First soluble M@C60 derivatives provide enhanced access to metallofullerenes and permit in vivo evaluation of Gd@C60 [C(COOH)<sub>2</sub>]<sub>10</sub> as a MRI contrast agent, *J. Am. Chem. Soc.* 125 (2003) 5471–5478.
- 87 B. SITHARAMAN, K. R. KISSELL, K. B. HARTMAN, L. A. TRAN, A. BAIKALOV, I. RUSAKOVA, Y. SUN, H. A. KHANT, S. J. LUDTKE, W. CHIU, S. LAUS, E. TOTH, L. HELM, A. E. MERBACH, L. J. WILSON, Superparamagnetic gadonanotubes are high-performance MRI contrast agents, *Chem. Commun.* (2005) 3915–3917.
- 88 U. BOAS, P. M. H. HEEGAARD, Dendrimers in drug research, *Chem. Soc. Rev.* 33 (2004) 43–63.
- 89 B. MISSELWITZ, H. SCHMITT-WILICH, W. EBERT, T. FRENZEL, H. J. WEINMANN, Pharmacokinetics of Gadomer-17, a new dendritic magnetic contrast agent, *Magma* 12 (2001) 128–134.
- 90 C. FINK, F. KIESSLING, M. BOCK, M. P. LICHY, B. MISSELWITZ, P. PESCHKE,

- N. E. FUSENIG, R. GROBHOIZ, S. DELORME, High-resolution three-dimensional MR angiography of rodent tumors: Morphologic characterization of intratumoral vasculature, *J. Magn. Reson. Imaging* 18 (2003) 59–65.
- 91 G. STAATS, E. SPUNTRUP, A. BUCKER, J. VAZQUEZ-JIMENEZ, O. J. LIAKOPOULOS, D. PFLUGER, S. GROSSKORTENHAUS, B. MISSELWITZ, R. W. GUNTHER, Interstitial T1-weighted MR lymph fistulography with Gadomer-17 in an experimental animal model, ROFO-Fortsch. Gebiet Rontgenstrahlen Bildgebenden Verfah. 175 (2003) 275–281.
- 92 M. G. TORCHIA, B. MISSELWITZ, Combined MR lymphangiography and MR imaging-guided needle localization of sentinel lymph nodes using Gadomer-17, *Am. J. Roentgenol.* 179 (2002) 1561–1565.
- 93 B. MISSELWITZ, H. SCHMITT-WILLICH, M. MICHAELIS, J. J. OELLINGER, Interstitial magnetic resonance lymphography using a polymeric T1 contrast agent: Initial experience with Gadomer-17, *Invest. Radiol.* 37 (2002) 146–151.
- 94 N. SATO, H. KOBAYASHI, A. HIRAGA, T. SAGA, K. TOGASHI, J. KONISHI, M. W. BRECHBIEL, Pharmacokinetics and enhancement patterns of macromolecular MR contrast agents with various sizes of polyamidoamine dendrimer cores, *Magn. Reson. Med.* 46 (2001) 1169–1173.
- 95 H. KOBAYASHI, N. SATO, A. HIRAGA, T. SAGA, Y. NAKAMOTO, H. UEDA, J. KONISHI, K. TOGASHI, M. W. BRECHBIEL, 3D-micro-MR angiography of mice using macromolecular MR contrast agents with polyamidoamine dendrimer core with reference to their pharmacokinetic properties, *Magn. Reson. Med.* 45 (2001) 454–460.
- 96 H. KOBAYASHI, C. WU, M.-K. KIM, C. PAIK, H., J. A. CARRASQUILLO, M. W. BRECHBIEL, Evaluation of the in vivo biodistribution of indium-111 and yttrium-88 labeled dendrimer-1B4M-DTPA and its conjugation with Anti-Tac monoclonal antibody, *Bioconjugate Chem.* 10 (1999) 103–111.
- 97 G. A. WISEMAN, E. KORNMEHL, B. LEIGH, W. D. ERWIN, D. A. PODOLOFF, S. SPIES, R. B. SPARKS, M. G. STABIN, T. WITZIG, C. A. WHITE, Radiation dosimetry results and safety correlations from 90 Y-ibritumomab tiuxetan radioimmunotherapy for relapsed or refractory non-Hodgkin's lymphoma: Combined data from 4 clinical trials, *J. Nucl. Med.* 44 (2003) 465–474.
- 98 A. QUINTANA, E. RACZKA, L. PIEHLER, I. LEE, A. MYC, I. MAJOROS, A. PATRI, T. THOMAS, J. MULE, J. J. BAKER, Design and function of a dendrimer-based therapeutic nanodevice targeted to tumor cells through the folate receptor, *Pharm. Res.* 19 (2002) 1310–1316.
- 99 N. MALIK, R. WIWATTANAPATAPEE, R. KLOPSCH, K. LORENZ, H. FREY, J. W. WEENER, E. W. MEIJER, W. PAULUS, R. DUNCAN, Dendrimers: Relationship between structure and biocompatibility in vitro, and preliminary studies on the biodistribution of 125I-labelled polyamidoamine dendrimers in vivo, *J. Controlled Release* 65 (2000) 133–148.
- 100 N. BOURNE, L. R. STANBERRY, E. R. KERN, G. HOLAN, B. MATTHEWS, D. I. BERNSTEIN, Dendrimers, a new class of candidate topical microbicides with activity against herpes simplex virus infection, *Antimicrob. Agents Chemother.* 44 (2000) 2471–2474.
- 101 H. R. IHRE, O. L. PADILLA DE JESUS, F. C. J. SZOKA, J. M. J. FRECHET, Polyester dendritic systems for drug delivery applications: Design, synthesis, and characterization, *Bioconjugate Chem.* 13 (2002) 443–452.
- 102 O. L. PADILLA DE JESUS, H. R. IHRE, L. GAGNE, J. M. J. FRECHET, F. C. J. SZOKA, Polyester dendritic systems for drug delivery applications: In vitro and in vivo evaluation, *Bioconjugate Chem.* 13 (2002) 453–461.
- 103 G.-P. YAN, B. HU, M.-L. LIU, L.-Y. LI, Synthesis and evaluation of gado-

- linium complexes based on PAMAM as MRI contrast agents, *J. Pharm. Pharmacol.* 57 (2005) 351–357.
- 104 M. BRUCHEZ, JR., M. MORONNE, P. GIN, S. WEISS, A. P. ALIVISATOS, Semiconductor nanocrystals as fluorescent biological labels, *Science* 281 (1998) 2013–2016.
- 105 M. DAHAN, S. LEVI, C. LUCCARDINI, P. ROSTAING, B. RIVEAU, A. TRILLER, Diffusion dynamics of glycine receptors revealed by single-quantum dot tracking, *Science* 302 (2003) 442–445.
- 106 D. S. LIDKE, P. NAGY, R. HEINTZMANN, D. J. ARNDT-JOVIN, J. N. POST, H. E. GRECCO, E. A. JARES-ERIJMAN, T. M. JOVIN, Quantum dot ligands provide new insights into erbB/HER receptor-mediated signal transduction, *Nat. Biotech.* 22 (2004) 198–203.
- 107 X. GAO, Y. CUI, R. M. LEVENSON, L. W. K. CHUNG, S. NIE, In vivo cancer targeting and imaging with semiconductor quantum dots, *Nat. Biotech.* 22 (2004) 969–976.
- 108 D. WANG, J. HE, N. ROSENZWEIG, Z. ROSENZWEIG, Superparamagnetic Fe<sub>2</sub>O<sub>3</sub> Beads-CdSe/ZnS quantum dots core-shell nanocomposite particles for cell separation, *Nano Lett.* 4 (2004) 409–413.
- 109 H. GU, R. ZHENG, X. ZHANG, B. XU, Facile One-pot synthesis of bifunctional heterodimers of nanoparticles: A conjugate of quantum dot and magnetic nanoparticles, *J. Am. Chem. Soc.* 126 (2004) 5664–5665.
- 110 M. A. CORREA-DUARTE, Y. KOBAYASHI, R. A. CARUSO, L. M. LIZ-MARZAN, Photodegradation of SiO<sub>2</sub>-coated CdS nanoparticles with silica gels, *J. Nanosci. Nanotechnol.* 1 (2001) 95–99.
- 111 W. C. W. CHAN, S. NIE, Quantum dot bioconjugates for ultrasensitive nonisotopic detection, *Science* 281 (1998) 2016–2018.
- 112 X. WU, H. LIU, J. LIU, K. N. HALEY, J. A. TREADWAY, J. P. LARSON, N. GE, F. PEALE, M. P. BRUCHEZ, Immunofluorescent labeling of cancer marker Her2 and other cellular targets with semiconductor quantum dots, *Nat. Biotechnol.* 21 (2003) 41–46.
- 113 I. FISHBEIN, M. CHORNY, S. BANAI, A. LEVITZKI, H. D. DANENBERG, J. GAO, X. CHEN, E. MOERMAN, I. GATI, V. GOLDWASSER, G. GOLOMB, Formulation and delivery mode affect disposition and activity of tyrphostin-loaded nanoparticles in the rat carotid model, *Arterioscler. Thromb. Vasc. Biol.* 21 (2001) 1434–1439.
- 114 H. COHEN, R. J. LEVY, J. GAO, I. FISHBEIN, V. KOUSAEV, S. SOSNOWSKI, S. SŁOMKOSWSKI, G. GOLOMB, Sustained delivery and expression of DNA encapsulated in polymeric nanoparticles, *Gene Therapy* 7 (2000) 1896–1905.
- 115 J. M. ANDERSON, M. S. SHIVE, Biodegradation and biocompatibility of PLA and PLGA microspheres, *Adv. Drug Delivery Rev.* 28 (1997) 5–24.
- 116 S. Y. LIN, K. S. CHEN, H. H. TENG, M. J. LI, In vitro degradation and dissolution behaviours of microspheres prepared by three low molecular weight polyesters, *J. Microencapsulation* 17 (2000) 577–586.
- 117 S. K. SAHOO, W. MA, V. LABHASETWAR, Efficacy of transferrin-conjugated paclitaxel-loaded nanoparticles in a murine model of prostate cancer, *Int. J. Cancer* 112 (2004) 335–340.
- 118 K. GATTER, G. BROWN, I. TROWBRIDGE, R. WOOLSTON, D. MASON, Transferrin receptors in human tissues: Their distribution and possible clinical relevance, *J. Clin. Pathol.* 36 (1983) 539–545.
- 119 J. L. TURNER, D. PAN, R. PLUMMER, Z. Y. CHEN, A. K. WHITTAKER, K. L. WOOLEY, Synthesis of gadolinium-labeled shell crosslinked nanoparticles for magnetic resonance imaging applications, *Adv. Functional Mater.* 15 (2005) 1248–1254.
- 120 R. ROSSIN, D. PAN, K. QI, J. L. TURNER, X. SUN, K. L. WOOLEY, M. J. WELCH, <sup>64</sup>Cu-Labeled folate-conjugated shell cross-linked nanoparticles for tumor imaging and

- radiotherapy: Synthesis, radiolabeling, and biologic evaluation, *J. Nucl. Med.* 46 (2005) 1210–1218.
- 121 X.-B. XIONG, Y. HUANG, W.-I. LU, X. ZHANG, H. ZHANG, T. NAGAI, Q. ZHANG, Enhanced intracellular delivery and improved antitumor efficacy of doxorubicin by sterically stabilized liposomes modified with a synthetic RGD mimetic, *J. Controlled Release* 107 (2005) 262–275.
- 122 C. R. MARTIN, P. KOHLI, The emerging field of nanotube biotechnology, *Nat. Rev. Drug Discov.* 2 (2003) 29–37.

## 5

# Magnetic Resonance Nanoparticle Probes for Cancer Imaging

*Young-wook Jun, Jung-tak Jang, and Jinwoo Cheon*

### 5.1

#### Introduction

Inorganic nanoparticles exhibit unique optical, magnetic, and electronic properties arising from nanoscale quantum effect and are emerging as key materials for next-generation device applications [1]. When these nanoparticles are applied to biological systems, they have the potential to improve modern imaging techniques, such as X-ray imaging, computed tomography (CT), near-IR fluorescence imaging, positron emission spectroscopy (PET), and magnetic resonance imaging (MRI) [2–4]. Although such modern imaging techniques provide excellent anatomical information of living objects, they have difficulties in detecting molecular and cellular events. Considering that most biological processes and disease attacks are related to molecular and cellular events, precise observations of detailed biological processes are important [5, 6]. Inorganic nanoparticles, upon conjugation with biomolecular markers, can report such molecular and sub-cellular events. In addition, their nanoscale materials properties can lead to the significant enhancements in detection sensitivity and resolution.

Semiconductor quantum dots are a good example of such nanoparticle probes. Quantum dots exhibit better fluorescence properties, such as high quantum yield, multicolor emissions by single excitation, and high photo-stability, than conventional organic fluorophores [7–9]. Such enhanced properties have allowed the imaging of cell signaling, cell evolution, cell trafficking, and *in vivo* cancer detection [10–13].

In contrast, magnetic nanoparticles with unique superparamagnetism can serve as excellent probes in magnetic resonance imaging (MRI). MRI detects subtle change in the relaxation time of the proton nuclear spins of water molecules, which make up from 70 to 90% of most tissues. Although this is one of the most powerful medical diagnostic tools due to its non-invasive nature, multidimensional tomographic capabilities, and high spatial resolution [14], MRI has a lower sensitivity than other tools [6]. Such weakness can be significantly improved by using magnetic nanoparticle probes [15, 16]. Under an applied magnetic field, magnetized nanoparticles generate an induced magnetic field, which perturbs the mag-

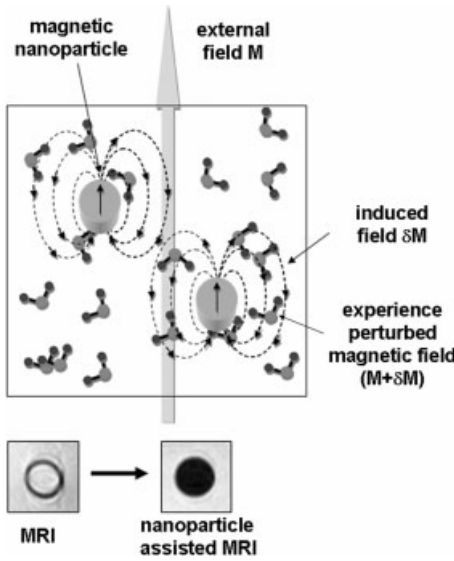


**Fig. 5.1.** MR contrast effects of magnetic nanoparticles. Under an applied magnetic field ( $M$ ), magnetic nanoparticles are magnetized and generate an induced magnetic field ( $\delta M$ ),

which perturbs the magnetic relaxation processes of the proton in water molecules, which is reflected as dark MR contrast.

netic relaxation processes of the protons in water molecules surrounding the magnetic nanoparticles. This leads to a shortening of the spin–spin relaxation time ( $T_2$ ) of the proton, which results in darkening of the MR images (Fig. 5.1).

According to the outer sphere spin–spin relaxation formula of solvent protons by solute magnetic particles, the spin–spin relaxation time of the proton is given by Eq. (1), where  $\gamma_1$  is the gyromagnetic ratio of protons in water,  $m$  is the molarity of magnetic nanoparticles,  $r$  is their radius,  $N_A$  is Avogadro's number,  $\mu$  is the magnetic moment of the nanoparticle,  $\omega_s$  and  $\omega_1$  are the respective Larmor angular precession frequencies of the solute electronic and water proton magnetic moments, the functions  $j_n(\omega, \tau)$  are spectral density functions, and  $\tau (= r^2/D)$  is the time scale of fluctuations in the particle–water proton magnetic dipolar interaction arising from the relative diffusive motion ( $D$ ) of a particle and water molecules [17].

$$\frac{1}{T_2} = \left( \frac{32\pi N_A [M]}{405000rD} \right) \gamma_1^2 \mu^2 \{ 6.5j_2(\omega_s, \tau) + 1.5j_1(\omega_1, \tau) + j_1(0, \tau) \} \quad (1)$$

Therefore,  $T_2$  is shortened by increasing the magnetic moment of the nanoparticles. Recently, Cheon, Suh, and coworkers experimentally demonstrated such magnetic moment effects on  $T_2$  by elucidating the correlated nanoscale effects of iron oxide nanoparticles between size, magnetism, and  $T_2$  relaxivity [18]. Figure

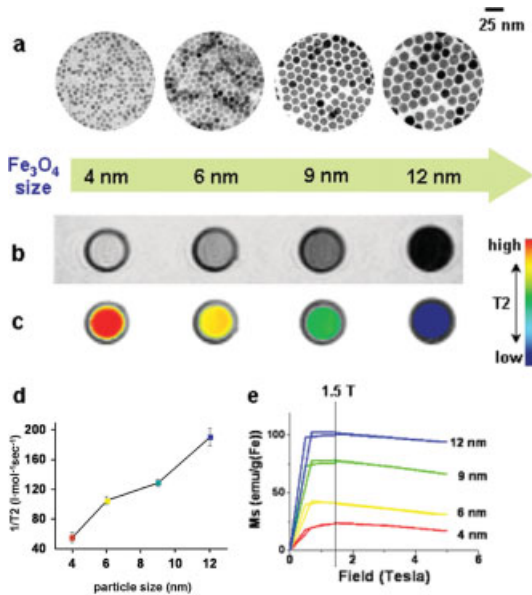


**Fig. 5.2.** Nanoscale size effects of iron oxide nanoparticles on magnetism and induced magnetic resonance (MR) signals. (a) TEM images of Fe<sub>3</sub>O<sub>4</sub> nanocrystals of 4, 6, 9, and 12 nm. (b) Size-dependent T<sub>2</sub>-weighted MR images of iron oxide nanoparticles in aqueous solution at 1.5 Tesla. (c) Size-dependent MR images color-coded by T<sub>2</sub> values. (d) Graph of 1/T<sub>2</sub> relaxivity versus iron oxide nanoparticle size. (e) Magnetization of iron oxide nanoparticles measured by a SQUID magnetometer. (From Ref. [18], with permission.)

5.2(a) shows transmission electron microscopic images of highly monodispersed iron oxide nanoparticles, 4, 6, 9, and 12 nm. These magnetic nanoparticles exhibit size-dependent magnetic moments and as the nanoparticle size is increased from 4 to 6, 9, and to 12 nm, the mass magnetization at 1.5 T changes from 25 to 43, 80, and 102 emu (g-Fe)<sup>-1</sup> (Fig. 5.2e). Such a trend is clearly reflected in the T<sub>2</sub>-weighted MR images. The 1/T<sub>2</sub> relaxivity gradually increases from 56 to 106, 130, and to 190 M<sup>-1</sup> s<sup>-1</sup>, which is imaged by the gradual change of the MR contrast from white to black through gray (Fig. 5.2b–d).

Such effect of magnetic nanoparticles on MR contrast gives them the ability to report various biological events. For example, magnetic nanoparticles >30 nm have been used for phagocytosis imaging [19, 20]. When phagocytes uptake magnetic nanoparticles, they are imaged as dark contrast. But tumor cells without phagocytic ability are imaged as white contrast. By utilizing such an effect, liver metastasis [21, 22], spleen [23], and lymph node detection [24] have been performed.

In contrast, when smaller nanoparticles (e.g., 10 nm) can easily escape from phagocytes, magnetic nanoparticles, upon conjugation with a target specific biomolecule, can detect target tissues through molecular interactions between

nanoparticle–biomolecule conjugates and molecular markers expressed from target tissues [24, 25]. Various types of clinically benign iron oxide based magnetic nanoparticles [e.g., superparamagnetic iron oxide (SPIO)] have been explored, and imaging has been reported of infarct [26–28], angiogenesis [29], apoptosis [30], gene expression [31, 32], and cancer [18, 33–36]. However, MR signal sensitivity and specificity of nanoparticle probes to the target tissue are still unsatisfactory for clinical applications and further efforts are needed to make them better. This chapter briefly reviews recently developed biocompatible magnetic nanoparticles and their utilization in molecular MRI.

## 5.2

### Magnetic Nanoparticle Contrast Agents

For their successful utilization as molecular MR contrast agents, magnetic nanoparticles must fulfill the following requirements: (a) uniform and high superparamagnetic moment, (b) high colloidal stability under physiological conditions (e.g., high salt concentration and pH changes), (c) the ability to escape the reticuloendothelial system (RES), (d) low toxicity and biocompatibility, and (e) possession of functionality to be linked to biologically active species (e.g., nucleic acid, proteins). Since these properties are highly related to their size, stoichiometry, and surface structures, various types of iron oxide nanoparticles have been developed.

#### 5.2.1

##### Silica- or Dextran-coated Iron Oxide Contrast Agents

For conventional MR contrast agents, iron oxide nanoparticles are synthesized through the precipitation of iron oxide in an aqueous solution containing ferrous salt by adding an alkaline solution [37]. Such iron oxide nanoparticles are usually insoluble as-is and a coating material is required for them to be soluble in aqueous media. In early attempts to make them water soluble, silica was used as a coating material [38]. The size of the core magnetic iron oxide can vary between 4 to 10 nm and the total particle size varies from 10 nm to 1  $\mu\text{m}$ , including coating materials. Since these nanoparticles have a broad size distribution, further size sorting procedures, including differential centrifugation and dialysis, are required. A representative silica-coated iron oxide contrast agent is AMI-121 (generic name: Ferumoxsil), which is now commercially available as Lumirem<sup>®</sup> (Guerbet) and Gastromark<sup>®</sup> (Advanced Magnetics) (Table 5.1). The core is  $\sim 10$  nm-sized polycrystalline iron oxide and the hydrodynamic size is  $\sim 300$  nm. This agent is delivered orally and used for abdomen MRI [39].

Although silica-coated iron oxide nanoparticles are reasonably stable in aqueous media, they tend to aggregate in blood and, therefore, are inadequate for blood injection. To enhance the colloidal stability of iron oxide nanoparticles, another type of coating agent, dextran or carbodextran, has been developed [40] (Table 5.1). Since dextran possesses high colloidal stability against harsh physiological condi-



Tab. 5.1. Various silica- or dextran-coated iron oxide contrast agents.

Agent	Iron oxide core size (nm)	Total size (nm)	Coating material	Magnetization at 1.5 T (emu g <sup>-1</sup> )	T2 relaxivity (m <sup>-1</sup> s <sup>-1</sup> )	Blood half-life
AMI-121 <sup>[a]</sup> [36], Lumiren, Gastromark	10	~300	Silica	N/A	72	<5 min
AMI-25 <sup>[a]</sup> [38], Feridex Endorem	5–6	80–150	Dextran	78	98	~6 min
SHU 555A <sup>[a]</sup> [39], Resovist	~4.2	~62	Carbodextran	N/A	151	3 min
AMI-227 <sup>[a]</sup> [41], Combidex, Sinerem	4–6	20–40	Dextran	69.8	53	>24 h
MION [42–44], CLIO	2.8	10–30	Dextran	60–68	69	~10 h

<sup>a</sup>Commercialized.

tions, dextran-coated iron oxide nanoparticles can have good stability. Such nanoparticles are prepared through a co-precipitation method from aqueous solution containing ferrous salt and dextran by adding an alkaline solution [37]. There are three representative dextran-coated iron oxide nanoparticles: AMI-25 [Feridex<sup>®</sup> (Berlex Lab.) and Endorem<sup>®</sup> (Guerbet)], SHU 555A [Resovist<sup>®</sup> (Schering)], and AMI-227 [Combidex<sup>®</sup> (Advanced Magnetics) and Sinerem<sup>®</sup> (Guerbet)]. AMI-25 is composed of a ~5-nm iron oxide core and dextran coating materials. The total size is between 80 and 150 nm with a T2 relaxivity of ~98.3 mm<sup>-1</sup> s<sup>-1</sup> [41]. SHU 555A has an ~4.2-nm iron oxide core coated with carbodextran, with total size of ~62 nm; Resovist has a higher T2 relaxivity of 151.0 mm<sup>-1</sup> s<sup>-1</sup> [42] and has no known side effects after fast intravenous injection [43]. These magnetic contrast agents are generally trapped and accumulated by the reticuloendothelial cells in the liver with a short blood half-life of less than 10 min and, therefore, are used for liver imaging [20]. Compared with these two iron oxide contrast agents, AMI-227 has similar iron oxide core size (~5 nm) but a smaller overall size of 20–40 nm. Although AMI-227 has lower T2 contrast effects (T2 relaxivity of ~53 mm<sup>-1</sup> s<sup>-1</sup>), its smaller size provides a much higher blood half-life of ~24 h, which enables MR angiography and lymph node detection [44].

Smaller dextran-coated iron oxide nanoparticles, including monocrystalline iron oxide (MION) and its derivative, crosslinked iron oxide (CLIO) are composed of a ~2.8-nm core iron oxide and dextran shell with a total size of 10–30 nm [45–47].

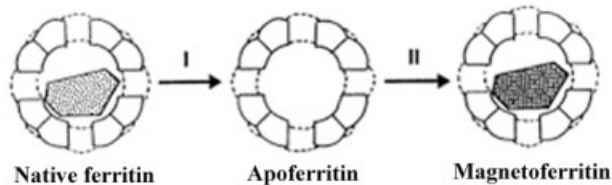


**Fig. 5.3.** Synthesis scheme of magnetoferritin. Removal of ferrihydrite from native ferritin produces apoferritin and subsequent formation of magnetite nanoparticles inside apoferritin affords magnetoferritin. (From Ref. [49], with permission.)

Since these nanoparticles are relatively small and have a long blood half-life, and their surface can be readily linked with biologically active molecules, they are useful for *in vivo* molecular MRI of biological targets [45] (Section 5.3.1).

### 5.2.2

#### Magnetoferritin

Ferritin is a well-known iron storage protein used to sequester and store iron, which is composed of a  $\sim 6$  nm hydrated iron oxide, ferrihydrite ( $5\text{Fe}_2\text{O}_3 \cdot 9\text{H}_2\text{O}$ ), core and polypeptide apoferritin shell [48]. Ferritin has been used as an efficient synthesizer for other magnetic materials [49–51]. For example, magnetically less useful ferrihydrite can be replaced by iron sulfide or magnetite nanoparticles (Fig. 5.3) [49]. Researchers have also utilized magnetoferritin as contrast agents for MRI. Magnetoferritin possesses a reasonably high T2 relaxation of  $157 \text{ mM}^{-1} \text{ s}^{-1}$  [52]. Although magnetoferritin is expected to have high biocompatibility and colloidal stability in the blood when considering that they mimic naturally-occurring ferritin, actual results are contradictory. These magnetoferritin particles are rapidly cleared from the blood circulation (blood half-life of less than 10 min) by the reticuloendothelial system in the liver, spleen, and lymph nodes [52]. Therefore, magnetoferritins are only suitable for liver, spleen, and lymph-node detection rather than molecular imaging.

### 5.2.3

#### Magnetodendrimers and Magnetoliposomes

The unique pore structures and multiple functional end-groups of dendrimers make them useful as host materials in drug and gene delivery. Similarly, dendrimers can efficiently deliver magnetic nanoparticles to cells. Bulte, Frank, and coworkers have demonstrated carboxy-terminated dendrimer ( $G = 4.5$ ) coated iron oxide contrast agents [53, 54]. Typically, magnetodendrimers are synthesized through the pH-controlled reaction of a ferrous salt and a trimethylamine oxide

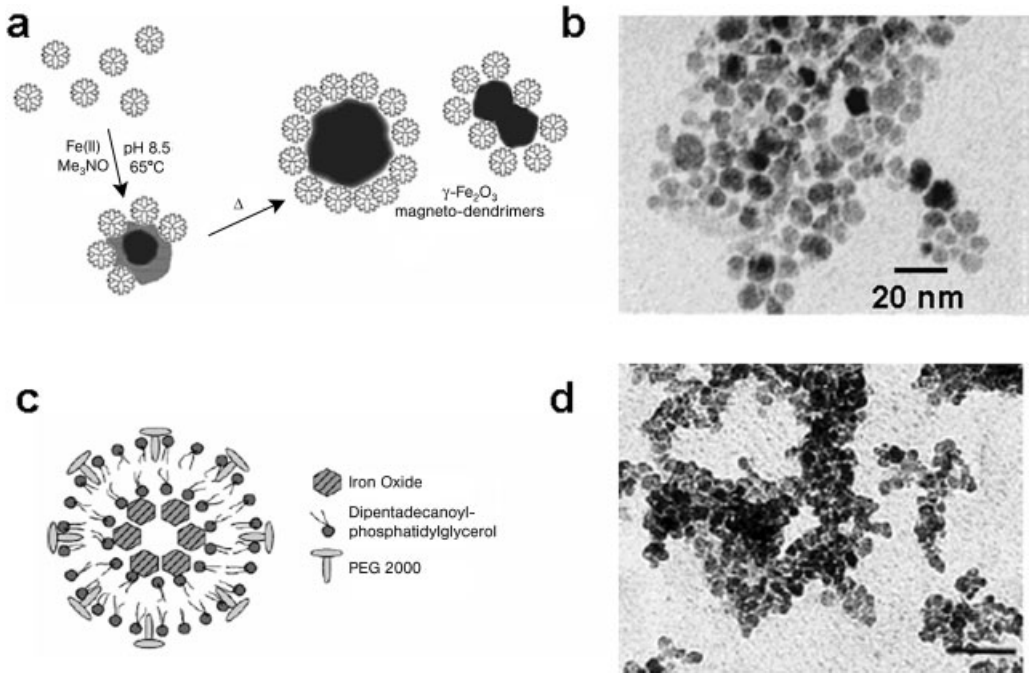


**Fig. 5.4.** Schematics and TEM images of (a, b) magnetodendrimers and (c, d) magnetoliposomes. (From Refs. [54 and 55], with permission.)

oxidant in a methanol/water mixture containing polyamidoamine dendrimers (Fig. 5.4a). The core size of the magnetodendrimers is 7–8 nm and they tend to aggregate to oligomers 20–30 nm in size (Fig. 5.4b). Magnetodendrimers show enhanced magnetic properties [saturation magnetism:  $\sim 94 \text{ emu (g-Fe)}^{-1}$ ] and a high T2 relaxivity of  $200\text{--}406 \text{ M}^{-1} \text{ s}^{-1}$  [53], compared with those of dextran-coated MION. Since dendrimers can be efficiently transfected to cells without any transfection agents, these magnetodendrimers can be used as labelers for cellular MR imaging and trafficking [53].

Similarly, liposomes, which are also widely used for drug and gene delivery, can be good coating materials to solubilize iron oxide nanoparticles. Liposomes have a bilayer assembly of surfactant molecules with a hydrophilic head and a hydrophobic tail. As shown in Fig. 5.4(c), the hydrophilic ends of the inner layer surfactants encapsulate the iron oxide nanoparticles and the hydrophilic head of the outer layer surfactant make them soluble in water. Bulte, Frank, and coworkers have reported that such magnetoliposome can be utilized for bone marrow MR contrast agents [55]. The iron oxide core size of the magnetoliposomes is  $\sim 16 \text{ nm}$ , and the entire size is  $\sim 40 \text{ nm}$  (Fig. 5.4d) with a T2 relaxivity of  $\sim 240 \text{ mM}^{-1} \text{ s}^{-1}$ .

## 5.2.4

**New Type of Contrast Agent: Non-hydrolytically Synthesized High Quality Iron Oxide Nanoparticles**

With the exception of MION and CLIO, previously developed iron oxide MR contrast agents undergo rapid uptake by the reticuloendothelial systems (RES) and, therefore, are effectively for liver, spleen, and lymph node detection. Consequently, researchers have encountered difficulties when they are utilized for molecular MRI [19–23]. Successful molecular imaging requires high-performance magnetic nanoparticle systems that exhibit excellent magnetic properties, the ability to escape from the RES, and possess active functionality that can be linked with biologically active molecules [15]. Since magnetic properties of nanoparticles depend highly on the materials properties such as size, shape, stoichiometry, and crystallinity [18, 56, 57], it is critical to be able to control such properties. However, conventional water-phase protocols, which have been widely adopted for superparamagnetic iron oxide (SPIO) contrast agents, generally lack precise size-controllability and monodispersity, and afford poor crystallinity and non-stoichiometric compositions [37]. In contrast, nonhydrolytic high-temperature growth methods allow one to have size-controllability, high single crystallinity, and good stoichiometry [18, 57–60]. For example, the nanoparticle size can be easily controlled from 4 to ~20 nm with a very narrow size distribution ( $\sigma < 8\%$ ) by controlling the growth conditions [18, 57]. One difficulty that must be overcome before their utilization as MR contrast agents is obtaining water-solubility since nonhydrolytically synthesized iron oxide nanoparticles are soluble only in organic media. Various surface modification methods have been developed, including bifunctional ligand [18, 36, 61], micellar [62, 63], polymer [64–66], and siloxane-linking procedures [67, 68]. For example, nonhydrolytically synthesized nanoparticles can be transferred to aqueous media by overcoating the nanoparticles with poly(ethylene glycol)-(PEG)-ylated phospholipid micelles. Such a micellar coating strategy has been demonstrated with quantum dots [69], and Bao and coworkers have successfully extended this strategy to make water-soluble iron oxide nanoparticles (Fig. 5.5) [63]. The PEGylated nanoparticles can be further linked to cellular transfection Tat peptides and utilized for MR cellular labeling [63].

Bawendi and coworkers have proposed another approach to transfer iron oxide nanoparticles from organic to aqueous media by coating them with polymeric phosphine oxide ligands [70]. These polymeric ligands can tightly bind to the iron oxide nanoparticle surface through multidentate bondings (Fig. 5.6).

The siloxane linkage to a metal oxide surface is efficient and strong. Zhang and coworkers have successfully applied this strategy for the synthesis of water-soluble iron oxide nanoparticles [71]. Refluxing toluene solution containing triethoxysilyl-terminated PEG ligands and nonhydrolytically synthesized iron oxide nanoparticles provides iron oxide nanoparticles with high colloidal stability in aqueous media (Fig. 5.7).

The major advantage of these nonhydrolytic synthesized iron oxide nanoparticles, as mentioned above, is the precise size control with high monodispersity.

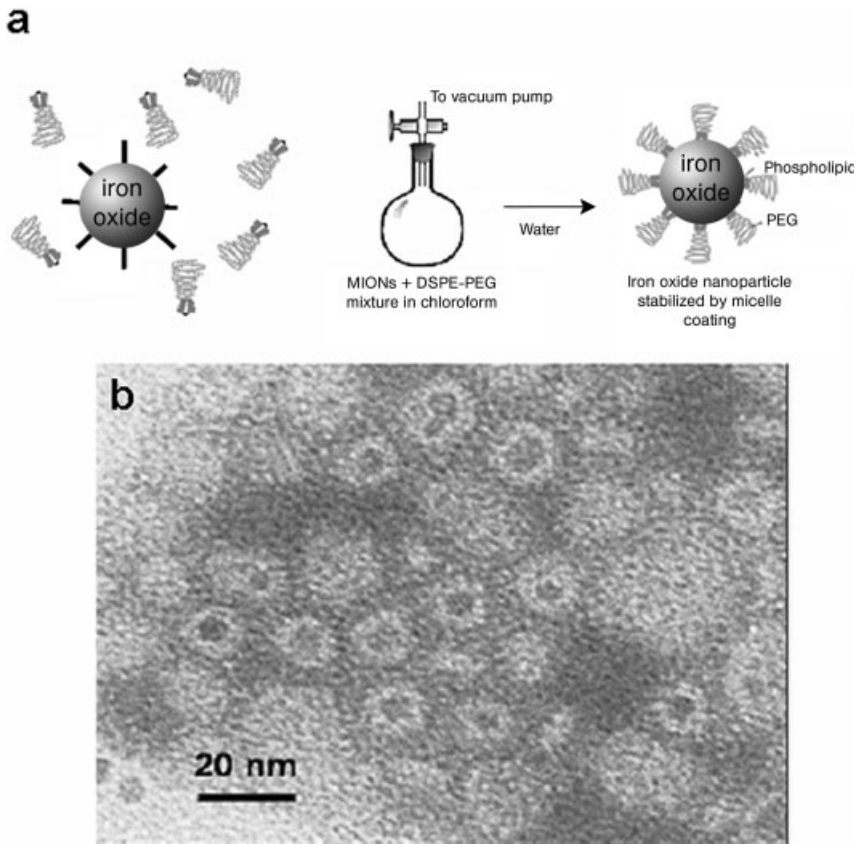


**Fig. 5.5.** (a) Synthetic scheme and (b) TEM image of poly(ethylene glycol) (PEG)-ylated iron oxide nanoparticles. (From Ref. [63], with permission.)

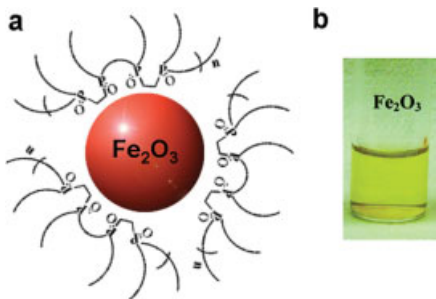


**Fig. 5.6.** Multidentate phosphine oxide ligand approach for the synthesis iron oxide nanoparticles. (a) The phosphine oxide functional groups bind to the surface of iron oxide and exposed PEG groups make them water soluble. (b) Iron oxide nanoparticles dissolved in water. (From Ref. [70], with permission.)

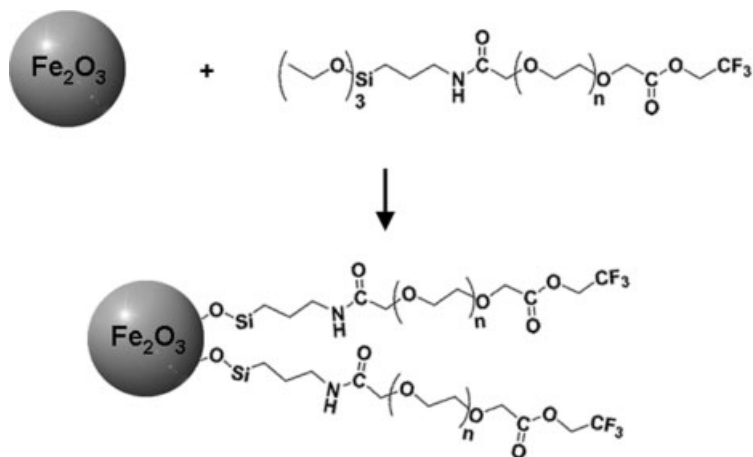


**Fig. 5.7.** Siloxane–poly(ethylene glycol) (PEG) coated iron oxide nanoparticles. Silanization of terminal ethoxysilane groups of the PEG ligand on top of iron oxide nanoparticles induces the formation of PEG-coated iron oxide nanoparticles. (From Ref. [71], with permission.)

Cheon, Suh, and coworkers have demonstrated such advantages for the synthesis of iron oxide MR contrast agents [18, 36, 61]. As shown by transmission electron microscopy (Fig. 5.8), nanoparticles obtained are  $\sim 9$  nm, with a narrow size distribution ( $\sigma < 8\%$ ). HR-TEM and X-ray analyses show that the nanoparticles are single-crystalline stoichiometric  $\text{Fe}_3\text{O}_4$ . Water-soluble iron oxide nanoparticles (WSIO) are then obtained by introducing 2,3-dimercaptosuccinic acid (DMSA) ligand onto the nanoparticle surface. This ligand endows the surface with high

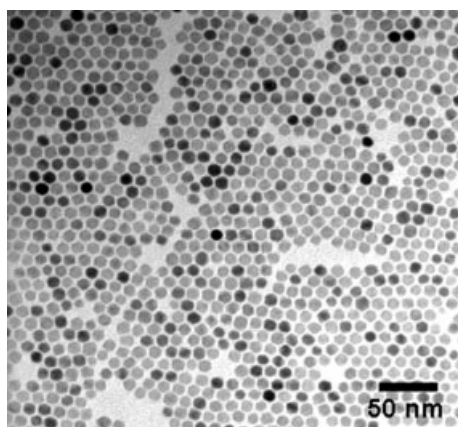


**Fig. 5.8.** TEM image of  $\sim 9$ -nm  $\text{Fe}_3\text{O}_4$  nanoparticles.

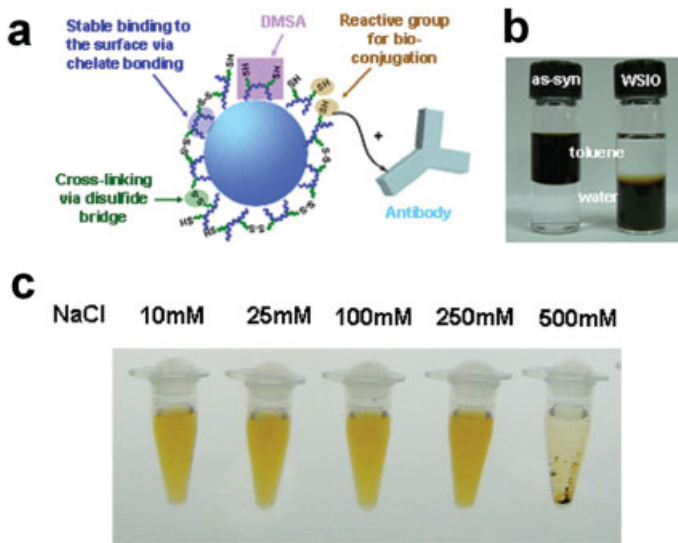


**Fig. 5.9.** (a) Schematic of 2,3-dimercaptosuccinic acid (DMSA)-coated iron oxide nanoparticles. The carboxylic ends of DMSA bind to the surface iron oxide nanoparticles and are further stabilized through interligand disulfide crosslinkages. Remaining free thiol can be used for further

conjugation for biomolecules such as antibody. (b) Solubility test of as-synthesized (as-syn) and DMSA-coated iron oxide nanoparticles (WSIO = water-soluble iron oxide nanoparticles). (c) Stability test of WSIO in various concentrations of NaCl solution. (From Ref. [18], with permission.)

water-phase stability through (a) carboxylate chelate bonding to iron and (b) disulfide crosslinkages between the ligands (Fig. 5.9a) [18]. Furthermore, the remaining free thiol group of the ligand can be used to attach target-specific biomolecules. So-obtained  $\text{Fe}_3\text{O}_4$  nanocrystals with the DMSA ligand are fairly stable in water and phosphate-buffered saline (PBS) up to an NaCl concentration of 250 mM without any aggregation. These nanoparticles have been utilized as MR probes, upon conjugation with cancer targeting antibody, not only for the *in vitro* detection of cancer cells but also for *in vivo* imaging of cancer implanted in a mouse [18, 36] (Section 5.3.5).

### 5.3 Iron Oxide Nanoparticles in Molecular MR Imaging

When iron oxide nanoparticles are conjugated with biologically active materials (e.g., antibody), the resulting iron oxide–biomolecule conjugates possess dual functionalities of both the MR contrast enhancers and molecular recognition capability. These conjugates act as molecular imaging probes that can efficiently report on various molecular/biological events occurring in region-of-interest targets (Fig.

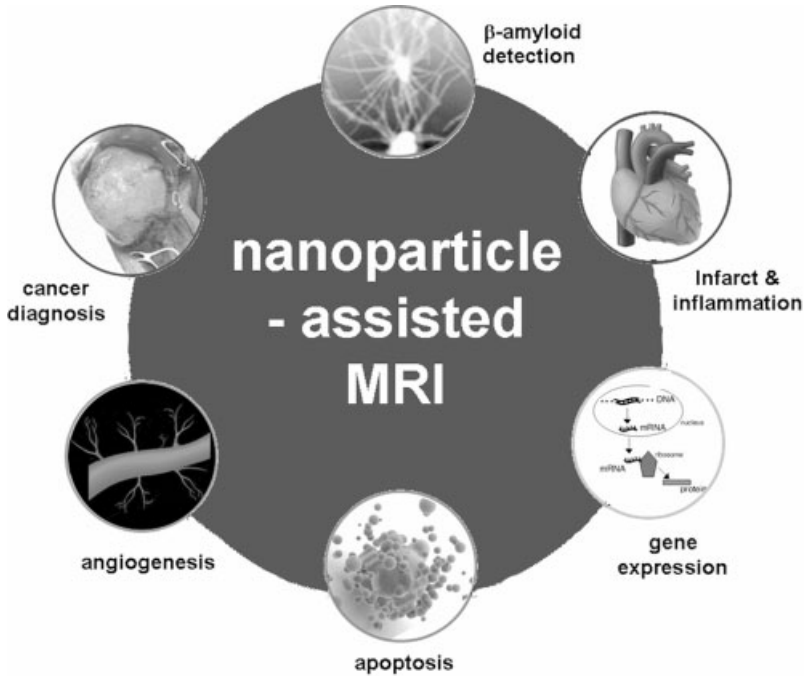


Fig. 5.10. Nanoparticle-assisted molecular MR imaging of biological systems.

5.10). Molecular MRI studies utilizing such iron oxide–biomolecule conjugates include the imaging of inflammation [72, 73], infarct [26–28], angiogenesis [29], apoptosis [30], gene expression [31, 32],  $\beta$ -amyloid plaques [74], and cancer [18, 33–36].

### 5.3.1

#### Infarct and Inflammation

For imaging of infarcts and inflammations, monocrystalline iron oxide (MION) nanoparticles are conjugated with specific antibodies through electrostatic interactions or covalent linkages by the reaction of potassium periodate-activated surface hydroxyl groups with lysine residues of antibodies. For example,  $R_{11}D_{10}$  antimyosin Fab was electrostatically conjugated to hydroxyl groups on MION surfaces for cardiac infarct imaging [27]. Since infarcted cardiac cells have increased porosity compared with normal cells, iron oxide–antimyosin Fab conjugates can efficiently be transported into damaged cells and recognize myosin. Figure 5.11 shows T2-weighted MR images of a mouse with cardiac infarct after injection of MION- $R_{11}D_{10}$  antimyosin Fab conjugates. The infarcted region is clearly observed as dark MR images, while no contrast effect was seen when unconjugated MIONs were administered. Such a targeting effect of MION- $R_{11}D_{10}$  antimyosin Fab conju-



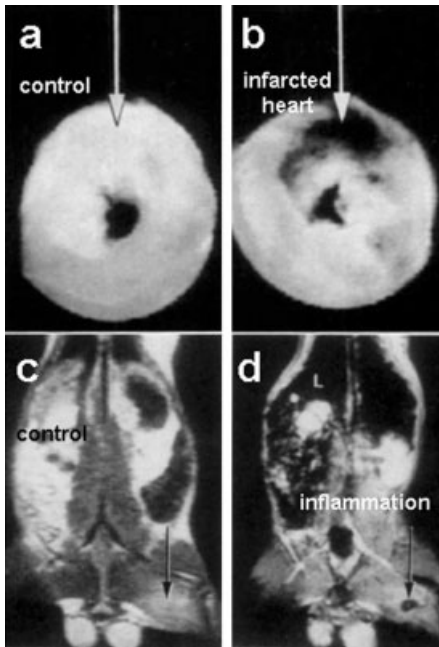


**Fig. 5.11.** MR detection of (a, b) cardiac infarct and (c, d) inflammation of a mouse. After intravenous injection of iron oxide–antimyosin antibody, dark MR contrast in the infarcted area is observed. Similarly,

inflammation is not imaged at the control mouse but an inflammation site is clearly shown as dark contrast. (From Refs. [27 and 72], with permission.)

gates was evaluated through *ex vivo* immunohistological analyses through Prussian blue staining. Weissleder and coworkers further extended this strategy for the detection of inflammation by conjugating MIONs with polyclonal human immunoglobulin G. MION-IgG conjugates consistently detected the area of inflammation in T2-weighted spin-echo MR images (Fig. 5.11c,d), which was also further confirmed by a histological Prussian blue staining study [72].

### 5.3.2

#### Angiogenesis

Angiogenesis is a fundamental growth process of new blood vessels for development, reproduction, and wound repair. This process is also related to the progression of tumor growth. Therefore, the development of anti-angiogenic agents can be a potential pathway to efficient cancer treatment. Imaging of angiogenesis is also related to the cancer diagnosis and the evaluation of anti-cancer agents. Several molecular markers are involved in angiogenesis: vascular endothelial growth factor (VEGF), fibroblast growth factors (FGF), platelet-derived endothelial cell growth

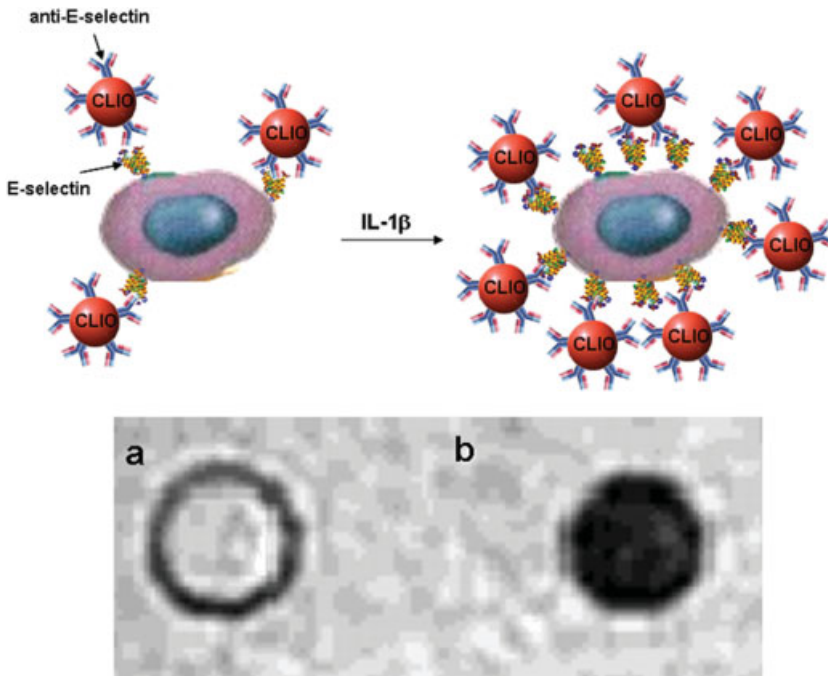


**Fig. 5.12.** *In vitro* MR detection of E-selectin stimulated by interleukin-1 $\beta$ . (a) Without interleukin 1 $\beta$ , a white MR image is obtained from HUVEC treated only with CLIO–anti-E-selectin antibody. (b) In contrast, after

interleukin 1 $\beta$  and CLIO–anti-E-selectin are sequentially dosed to HUVEC, E-selectin expression is clearly imaged as a dark MR image. (From Ref. [29], with permission.)

factor (PD-EDGF), Tie-2 receptor, integrin, and E-selectin [75]. Among the various angiogenesis markers, VEGF, Tie 2 receptor, and integrin have been extensively studied [76–78]. Bogdanov and coworkers have reported that E-selectin expression in human endothelial cells can be imaged by using crosslinked iron oxide (CLIO)–monoclonal anti-human E-selectin antibody conjugate MR contrast agent [29]. When only CLIO–antibody conjugates are treated to endothelial cells with a low E-selectin expression level, an MR contrast effect is hardly detected (Fig. 5.12a). In contrast, treatment of cells with interleukin-1 $\beta$ , which stimulates the expression of E-selectin, followed by nanoparticle–antibody dosing results in a significant MR contrast effect (Fig. 5.12b).

### 5.3.3

#### Apoptosis

Apoptosis is an active process of programmed self-destruction of cells. In the early stages of apoptosis, the redistribution of phosphatidylserine in the cell membrane occurs and the detection of such processes can be an indicators of the programmed

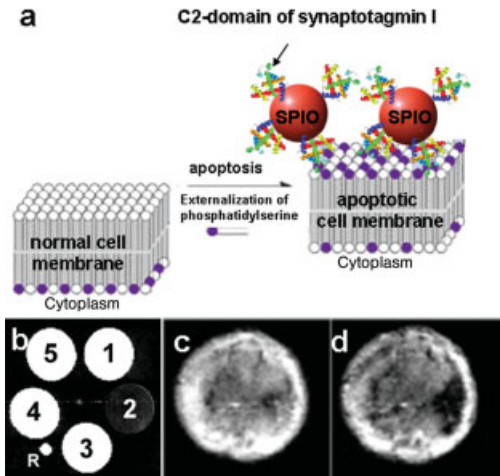


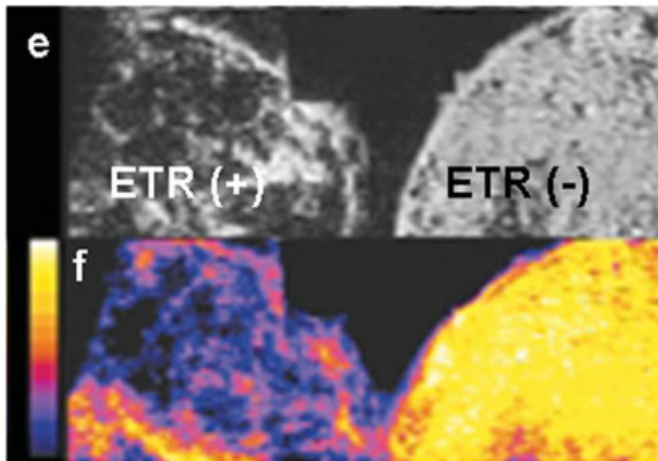
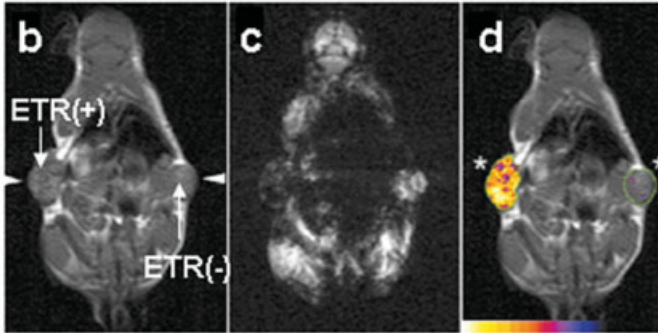
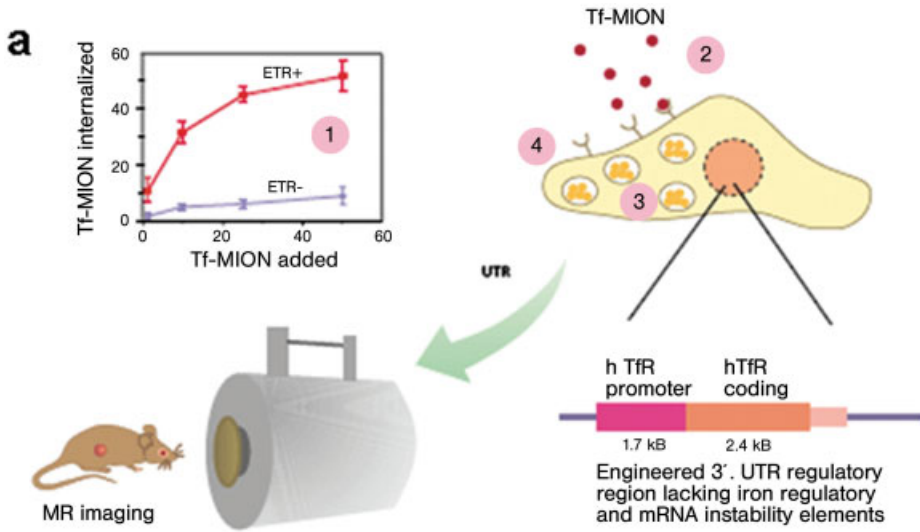
**Fig. 5.13.** (a) MR imaging of apoptosis using the SPIO–C2 domain of synaptotagmin I. (b) T2-weighted MR images of (b, 1) water, (b, 2) SPIO–C2 conjugate, (b, 3) SPIO–BSA control conjugate, (b, 4) SPIO only treated apoptotic cells, and (b, 5) SPIO–C2 conjugate treated normal cells. *In vivo* MR images of tumors implanted in a mouse (c) before and (d) after drug treatment. (From Ref. [30], with permission.)

cell death. Representative binding proteins to phosphatidylserine are annexin V and synaptotagmin I. Although imaging of apoptosis using these antibodies has been already performed through radio-isotope techniques [79], the spatial resolution is only  $\sim 1\text{--}3$  mm and needs improvement. Brindle and coworkers have shown that conjugates of the SPIO and C2 domain of synaptotagmin I (C2-SPIO) can detect apoptotic cells through MRI with  $\sim 0.1$  mm resolution [30]. While there are no MR signals for nonspecific SPIO (BSA-SPIO) [Fig. 5.13b(3)], SPIO-only treated apoptotic cells [Fig. 5.13b(4)], and C2-SPIO treated normal cells [Fig. 5.13b(5)], C2-SPIO treated apoptotic cells [Fig. 5.13b(2)] clearly show dark MR contrast with a significant change in T2 ( $\Delta T_2 = \sim 90\%$ ). Further extension of this strategy to an *in vivo* animal study was also successful. When C2-SPIO was intravenously injected to drug-treated tumor-bearing mice, the nanoparticle conjugates are able to detect apoptotic regions with a significant MR signal change (Fig. 5.13c,d).

#### 5.3.4

##### Gene Expression

Gene expression is an emerging field in biomedical sciences, and the imaging of such expression is of importance. Although several approaches to detect *in vivo* gene expression have been performed through optical [80, 81] and radioisotope imaging techniques [82], there have been limitations such as low-penetration depth of light for optical imaging and poor spatial resolution of radioisotope imaging. Weissleder and coworkers have demonstrated that MR detection of transgene



expression of engineered transferrin receptor (ETR) in tumors is possible by using MION-transferrin (MION-Tf) contrast agents [32]. When MION-Tf is treated to the cells with various ETR expression levels, a gradual decrease in T2 is observed as the ETR expression levels of cells are increased due to proportional binding of MION-Tf conjugates to the expressed ETR. These workers also determined whether ETR expression can be detected in *in vivo* live mice with ETR positive tumors and ETR negative tumors. The results show that the MR contrast effect is only observed for ETR positive tumors (Fig. 5.14b–d). *Ex vivo* MRI of excised tumors shows more dramatic differences between these two tumors (Fig. 5.14e,f).

### 5.3.5

#### Cancer Imaging

Non-invasive detection of cancer in its early stages is of great interest since early detection of cancer can significantly increase the survival rate of patients. With conventional MRI techniques, the present detectable size of cancer is roughly  $\sim 1 \text{ cm}^3$ . If nanoparticle contrast agents can specifically recognize cancer cells through molecular interaction, selective enhancement of the MR signal of cancer cells can provide one with a way to clearly distinguish cancer from normal tissues. Tiefenauer and coworkers have reported that the detection of cancers is possible through such molecular recognition of superparamagnetic iron oxide (SPIO) nanoparticle–antibody conjugates [35]. Conjugation of poly(glutamic acid-lysine-tyrosine)-coated nanoparticles with anti-carcinoembryonic antigen (CEA) antibody is performed through a conventional sulfo-MBS crosslinking method. In the T2-weighted MR images, dark contrast is imaged at the CEA-expressed tumors, although the contrast difference is not highly pronounced (Fig. 5.15). Artemov and coworkers have utilized another approach to detect cancer cells [34]. Since the avidin–biotin interaction is strongly binding, avidin conjugated SPIO can efficiently detect biotinylated cancer specific antibodies that bind to the cancer cells (Fig. 5.16a). Their *in vitro* fluorescence-assisted cell sorting analyses and MRI confirm cancer detection (Fig. 5.16b). Au-565 cells with high expression of HER2/neu cancer markers are imaged as dark MR contrast, while no contrast effect is obtained from MDA-MB-231 cells with low HER2/neu expression.

Recently, Cheon, Suh, and coworkers have achieved highly efficient cancer targeting by using high quality, small-sized water-soluble iron oxide (WSIO) nanoparticle–antibody conjugates [36]. The WSIO nanoparticles have high magnetic momentum [ $\sim 100 \text{ emu (g-Fe)}^{-1}$ ] and small hydrodynamic size ( $\sim 9 \text{ nm}$ ), which are advantageous for both *in vitro* and *in vivo* cancer imaging. When these



**Fig. 5.14.** *In vivo* and *ex vivo* imaging of engineered transferrin receptor (ETR) expression in tumors. (a) Schematic of MRI, (b, c) *in vivo* imaging of ETR(+) and ETR(–) tumor implanted mouse before (b) and after

(c, d) the injection of MION-transferrin. *Ex vivo* imaging of excised ETR(+) and ETR(–) tumors (e) and their color maps based on T2 (f). (From Ref. [32], with permission.)

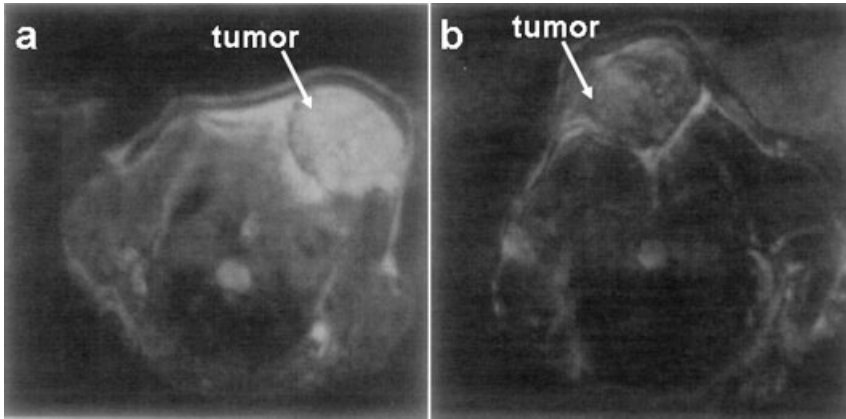


**Fig. 5.15.** MR detection of carcinoembryonic antigen (CEA) overexpressed tumors by using iron oxide–CEA antibody conjugates. MR images before (a) and after (b) injection of SPIO–CEA antibody. (From Ref. [35], with permission.)

nanoparticles are conjugated with Herceptin, they successfully detect cancer cells (SK-BR-3) as dark MR image (Fig. 5.17b) through molecular interaction between nanoparticle surface-bound Herceptin and HER2/neu cancer markers, compared with non-treated (Fig. 5.17a) and WSIO-irrelevant conjugate treated cells (Fig. 5.17c). This MRI result is also confirmed by an optical technique where vivid green fluorescence from the fluorescein (FITC) is clearly observed only for FITC-WSIO-Herceptin probe conjugate treated cells (Fig. 5.17d,e). Furthermore, WSIO nanoparticles enable the detection of various cell lines with different levels of HER2/

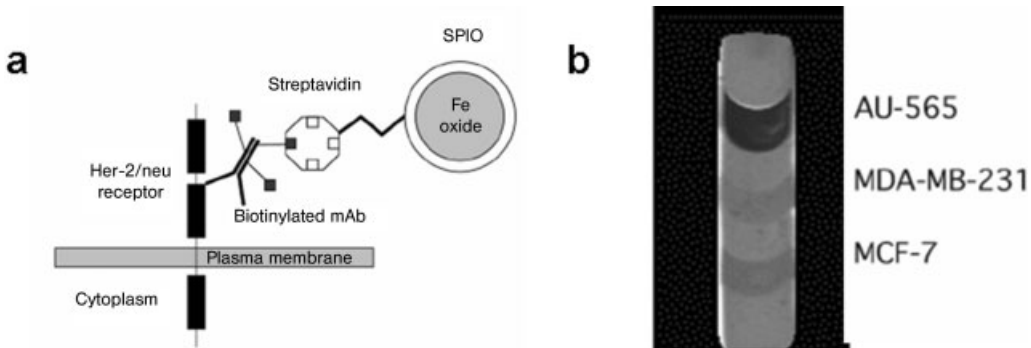


**Fig. 5.16.** *In vitro* MR detection of HER2/neu overexpressed cancer cells by using avidin-coated SPIO and biotinylated Herceptin. (a) Schematic and (b) MR images of SPIO–avidin conjugate treated cells (AU-565, MDA-MB-231, MCF-7). (From Ref. [34], with permission.)

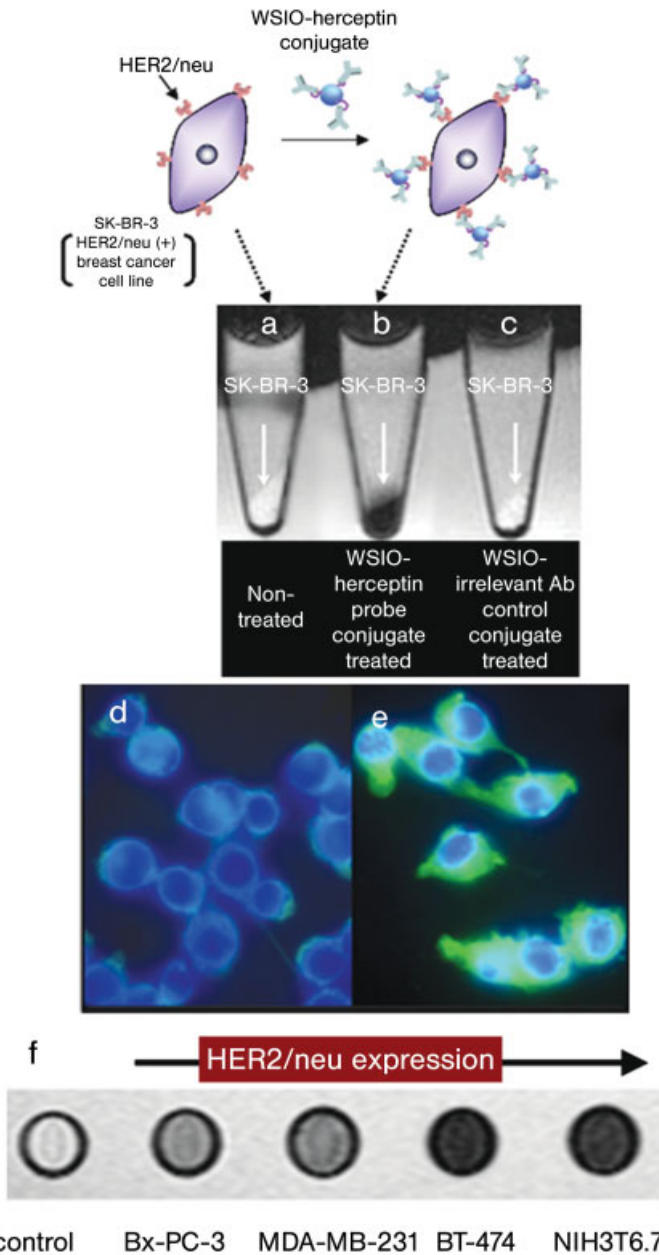


**Fig. 5.17.** *In vitro* cancer detection using water-soluble iron oxide (WSIO)–Herceptin conjugates. MR images of (a) non-treated, (b) WSIO–Herceptin treated, (c) WSIO-irrelevant antibody treated breast cancer cells (SK-BR-3). (d) MR image of WSIO–Herceptin

conjugate treated cell lines with increasing expression levels of HER2/*neu* receptors: Bx-PC-3, MDA-MB-231, BT-474, and NIH3T6.7 cell lines. Control conjugates are treated to Bx-PC-3 cell lines. (From Ref. [36], with permission.)

neu cancer marker expression: Bx-PC-3, MDA-MB-231, BT-474, and NIH3T6.7 cell lines, which are arranged in the order of increasing HER2/*neu* expression level. T2-weighted MR signals of the cell lines treated with WSIO–Herceptin probe conjugates become darker as the expression level of the HER2/*neu* receptors is increased (Fig. 5.17f). Notably, the MR signal intensities of the cell lines treated with WSIO–Herceptin probe conjugates show a marked difference from that of control conjugates, indicating excellent specific binding efficiency of the probe conjugates.

These magnetic probes have been successfully extended to the *in vivo* detection of cancer cells implanted in mouse [36]. When these WSIO–Herceptin conjugates are intravenously injected into a mouse, they successfully reach and recognize HER2/*neu* receptors overexpressed from cancer cells which results in a significant MR contrast effect in the tumor sites, with a ~20% decrease in T2 compared with control experiments (Fig. 5.18a–c). In high-resolution MR images of WSIO–Herceptin conjugate treated mouse measured at 9.4-T MRI, a dark MR image initially appears near the bottom region of the tumor and then gradually grows and spreads to the central and upper region of the tumor as time elapses (Fig. 5.18d). They found that such a time-dependent MR signal change reveals the heterogeneous pattern of the intratumoral vasculatures, where the bottom side of the tumor has well-developed vascular structures.

## 5.4

### Summary and Outlook

Although there has been much progress in the development of magnetic nanoparticle contrast agents for molecular MRI in the past few years, their successful utilization is limited to *in vitro* systems, except for a few *in vivo* cases. The main difficulties lie in their poor MR contrast effects and limited stability under *in vivo* conditions. The MR signal enhancing effect of conventional iron oxide-based nanoparticles is unsatisfactory, compared with other diagnostic tools such as fluorescence and PET, and needs to be improved. Therefore, it is important to develop new types of magnetic nanoparticle contrast agents that can significantly improve contrast effects. Since nanoparticles with higher magnetization values provide stronger MR contrast effects, the development of novel nanoparticles with superior magnetism is the first prerequisite. Concurrently, since the MR contrast effects of nanoparticles are strongly correlated with a material's characteristics in terms of their size, shape, composition, single crystallinity, and magnetism, it is important to have a good nanoparticle model system that can clearly describe the relationship between nanoscale material characteristics and MR contrast effects (Fig. 5.19a).

The next required step is to impart high colloidal stability and biocompatibility to the magnetic nanoparticles. As described in previous sections, various coating materials have been developed for such applications, but it is still necessary to develop general and more reliable protocols for tailoring nanoparticle surfaces with desired coating materials. Since a smaller overall size is advantageous for escaping the re-



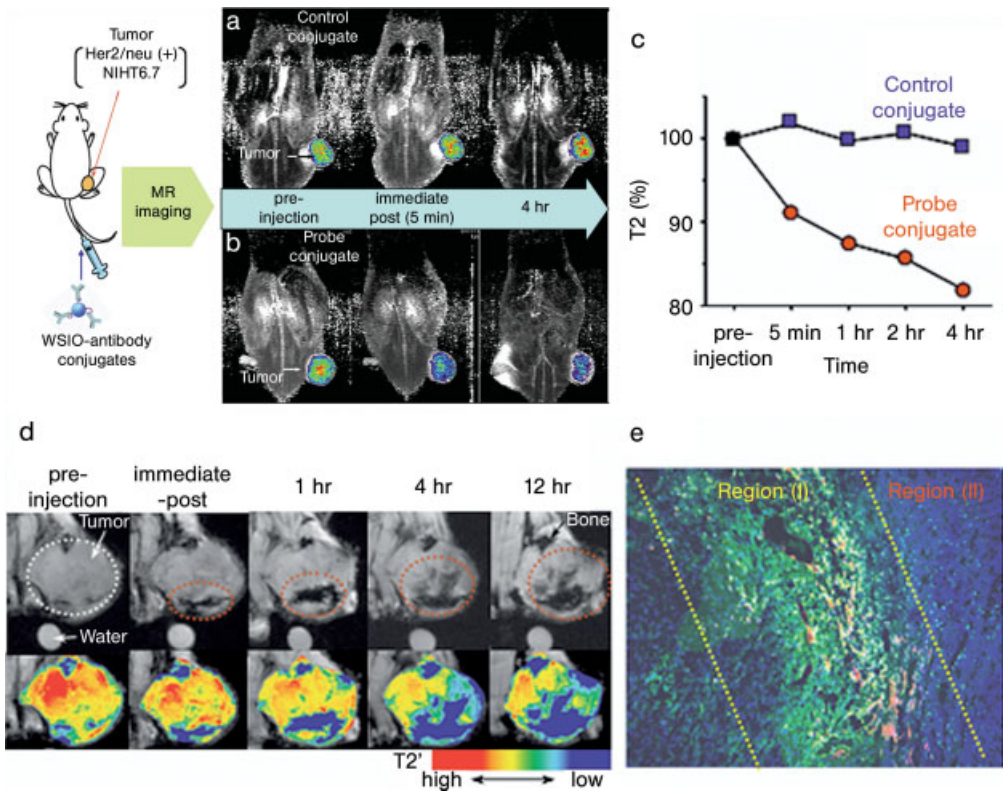


**Fig. 5.18.** *In vivo* MRI of cancer targeting events of WSIO–Herceptin conjugates. Color maps of T2-weighted MR images of cancer cell implanted (NIH3T6.7) mice at different temporal points (pre-injection, immediate post, 4 h) after the intravenous injection of (a) WSIO-irrelevant antibody control conjugates and (b) WSIO–Herceptin probe conjugates. (c) T2 versus time after the injection of WSIO-antibody conjugates in (a) and (b) samples. (d) T2\*-weighted MR images of cancer cell implanted (NIH3T6.7) mouse at 9.4 Tesla and

their color maps at different temporal points after probe conjugate injection. Tumor area is circled with white dotted lines. A dark MR image gradually grows and spreads from the bottom region of the tumor to the central and upper region of the tumor (red circles). (e) Fluorescence immunohistochemical analyses of an excised tumor slice. Endothelial vessels were stained with Rhodamine-anti-CD31 (red fluorescence) and probe conjugates were stained with FITC-anti-human IgG (green fluorescence). (From Ref. [36], with permission.)

ticuloendothelial system, the coating materials should be as small as possible while possessing high colloidal stability without any aggregation under physiological conditions (Fig. 5.19b).

The toxicity of magnetic nanoparticles is also a very important issue that needs to be resolved before clinical utilization. Although iron oxide nanoparticles have been regarded as clinically benign materials, potential cytotoxicity arising from their size, shape, and coating materials should also be examined, along with

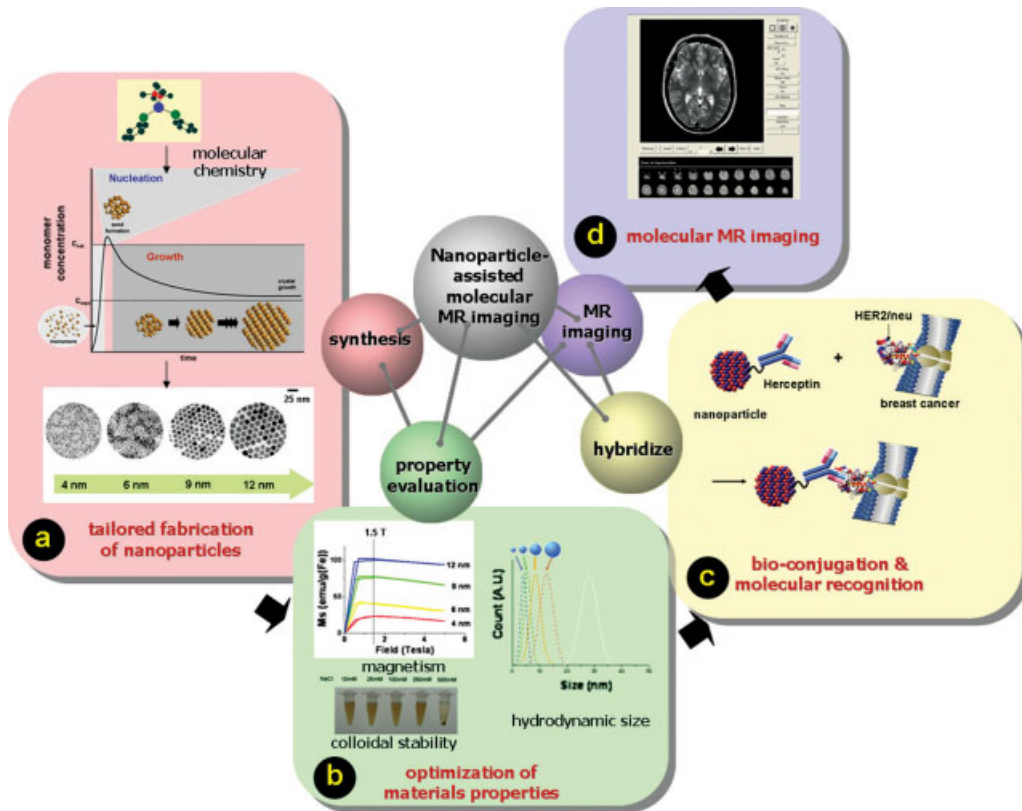


**Fig. 5.19.** Nanoparticle-assisted molecular MRI. (a) Modern molecular chemistry approach enables the tailored synthesis of high quality magnetic nanoparticles with desired sizes and monodispersity. (b) Then, evaluation and optimization of materials properties such as magnetism, hydrodynamic size, and colloidal and biostabilities are important. (c) When these nanoparticles are conjugated

to biomolecules, the resulting nanoparticle–biomolecule conjugates possess the capabilities of both MR contrast effects and molecular recognition of target biosystems. (d) This enables molecular MRI that can report various biological events, such as pinpointing cancer diagnosis, cell migration, cell signaling, and genetic developments, with high sensitivity and specificity.

systematic guidelines for the nano-toxicity evaluation of newly developed novel nanoparticles.

Once novel nanoparticles with highly enhanced magnetism, small size, and high colloidal and biostability are developed, significant improvements in MR detection sensitivity and target specificity are expected (Fig. 5.19c,d). This can bring huge advances in current cancer diagnosis and biomedical imaging fields. For example, highly enhanced MR contrast of a biological target through the molecular recognition of such nanoparticle contrast agents will promise *in vivo* diagnosis of early-stage cancer with sub-millimeter dimension. In addition, many unrevealed

biological processes, such as *in vivo* pathways of cell evolutions, cell differentiations, cell-to-cell interactions, molecular signaling pathways, could be precisely monitored at the molecular level by using next-generation nanoparticle contrast agents.

## References

- ALIVISATOS, A. P. Semiconductors clusters, nanocrystals, and quantum dots, *Science* **1996**, 271, 933–937.
- LA VAN, D. A., LYNN, D. M., LANGER, R. Moving smaller in drug discovery and delivery, *Nat. Rev. Drug. Discov.* **2002**, 1, 77–84.
- LA CONTE, L., NITIN, N., BAO, G. Magnetic nanoparticle probes, *Nanotoday* **2005**, 8, 32–38.
- ALIVISATOS, A. P. *Nat. Biotechnol.* **2004**, 22, 47.
- WEISSLEDER, R., MAHMOOD, U. Molecular imaging, *Radiology* **2001**, 219, 316–333.
- MASSOUD, T. F., GAMBHIR, S. S. Molecular imaging in living subjects: Seeing fundamental biological processes in a new light, *Gene Dev.* **2003**, 17, 545–580.
- WU, X., LIU, H., LIU, J., HALEY, K. N., TREADWAY, J. A., LARSON, J. P., GE, N., PEALE, F., BRUCHEZ, M. P. Immuno-fluorescent labeling of cancer marker Her2 and other cellular targets with semiconductor quantum dots, *Nat. Biotechnol.* **2003**, 21, 41–46.
- BRUCHEZ, JR., M., MORONNE, M. M., GIN, P., WEISS, S., ALIVISATOS, A. P. Semiconductor nanocrystals as fluorescent biological labels, *Science* **1998**, 281, 2013.
- WARREN, C. W. C. and NIE, S. Quantum dot bioconjugates for ultrasensitive nonisotopic detection, *Science* **1998**, 281, 2016.
- MICHALET, X., PINAUD, F. F., BENTOLILA, L. A., TSAY, J. M., DOOSE, S., LI, J. J., SUNDARESAN, G., WU, A. M., GAMBHIR, S. S., WEISS, S. Quantum dots for live cells, in vivo imaging, and diagnostics, *Science* **2005**, 307, 538–544.
- BRUCHEZ, M., MORONNE, M., GIN, P., WEISS, S., ALIVISATOS, A. P. Semiconductor nanocrystals as fluorescent biological labels, *Science* **1998**, 281, 2013–2016.
- CHAN, W. C. W., NIE, S. Quantum dot bioconjugates for ultrasensitive nonisotopic detection, *Science* **1998**, 281, 2016–2018.
- HAN, M., GAO, X., SU, J. Z., NIE, S. Quantum-dot-tagged microbeads for multiplexed optical coding of biomolecules, *Nat. Biotechnol.* **2001**, 19, 631–635.
- MITCHELL, D. G. *MRI Principles*, W.B. Saunders Company, Philadelphia, **1999**.
- BULTE, J. W. M., KRAITCHMAN, D. L. Iron oxide MR contrast agents for molecular and cellular imaging, *NMR Biomed.* **2004**, 17, 484–499.
- WANG, Y.-X. J., HUSSAIN, S. M., KRESTIN, G. P. Superparamagnetic iron oxide contrast agents: Physico-chemical characteristics and applications in MR imaging, *Eur. Radiol.* **2001**, 11, 2319–2331.
- KOENIG, S. H., KELLER, K. E. Theory of  $1/T_1$  and  $1/T_2$  NMRD profiles of solutions of magnetic nanoparticles, *Magn. Reson. Med.* **1995**, 34, 227–233.
- JUN, Y.-w., HUH, Y.-M., CHOI, J.-s., LEE, J.-H., SONG, H.-T., KIM, S., YOON, S., KIM, K.-S., SHIN, J.-S., SUH, J.-S., CHEON, J. Nanoscale size effect of magnetic nanocrystals and their utilization for cancer diagnosis via magnetic resonance imaging, *J. Am. Chem. Soc.* **2005**, 127, 5732–5733.
- HAMM, B., STAKS, T., TAUPITZ, M., MAIBAUER, R., SPEIDEL, A., HUPPERTZ, A., FRENZEL, T., LAWACZEK, R., WOLF,

- K. J., LANGE, L. J. *Magn. Reson. Imag.* **1994**, *4*, 659–668.
- 20 REIMER, P., TOMBACH, B. Hepatic MRI with SPIO: Detection and characterization of focal liver lesions, *Eur. Radiol.* **1998**, *8*, 1198–1204.
- 21 MCLACHLAN, S. J., MORRIS, M. R., LUCAS, M. A., FISCO, R. A., EAKINS, M. N., FOWLER, D. R., SCHEETZ, R. B., OLUKOTUN, A. Y. *J. Magn. Reson. Imag.* **1994**, *4*, 301–307.
- 22 WEISSELEDER, R. Liver MR imaging with iron oxides: Toward consensus and clinical practice, *Radiology* **1994**, *193*, 593–595.
- 23 BENGEL, H. H., PALMACCI, S., ROGERS, J., JUNG, C. W., CRENSHAW, J., JOSEPHSON, L. Biodistribution of an ultrasmall superparamagnetic iron oxide colloid, BMS 180549, by different routes of administration, *Magn. Reson. Imag.* **1994**, *12*, 433–442.
- 24 SUWA, T., OZAWA, S., UEDA, M., ANDO, N., KITAJIMA, M. Magnetic resonance imaging of esophageal squamous cell carcinoma using magnetite particles coated with anti-epidermal growth factor receptor antibody, *Int. J. Cancer* **1998**, *75*, 626–634.
- 25 KRESSE, M., WAGNER, S., PFEFFERER, D., LAWACZECK, R., ELSTE, V., SEMMLER, W. Targeting of ultrasmall superparamagnetic iron oxide (USPIO) particles to tumor cells in vivo by using transferrin receptor pathways, *Magn. Reson. Med.* **1998**, *40*, 236–242.
- 26 KRIEG, F. M., ANDRES, R. Y., WINTERHALTER, K. H. Superparamagnetically labelled neutrophils as potential abscess-specific contrast agent for MRI, *Magn. Reson. Imag.* **1995**, *13*, 393–400.
- 27 WEISSELEDER, R., LEE, A. S., KHAW, B. A., SHEN, T., BRADY, T. J. Antimyosin-labeled monocrySTALLINE iron oxide allows detection of myocardial infarct: MR antibody imaging, *Radiology* **1992**, *182*, 381–385.
- 28 KRAITCHMAN, D. L., HELDMAN, A. W., ATALAR, E., AMADO, L. C., MARTIN, B. J., PITTENGER, M. F., HARE, J. M., BULTE, J. W. M. In vivo magnetic resonance imaging of mesenchymal stem cells in myocardial infarction, *Circulation* **2003**, *107*, 2290–2293.
- 29 KANG, H. W., JOSEPHSON, L., PETROVSKY, A., WEISSELEDER, R., BOGDANOV, A., JR. Magnetic resonance imaging of inducible E-selectin expression in human endothelial cell culture, *Bioconjugate Chem.* **2002**, *13*, 122–127.
- 30 ZHAO, M., BEAUREGARD, D. A., LOIZOU, L., DAVLETOV, B., BRINDLE, K. M. Non-invasive detection of apoptosis using magnetic resonance imaging and a targeted contrast agent, *Nat. Med.* **2001**, *7*, 1241–1244.
- 31 HÖGEMANN, D., JOSEPHSON, L., WEISSELEDER, R., BASILION, J. P. Improvement of MRI probes to allow efficient detection of gene expression, *Bioconjugate Chem.* **2000**, *11*, 941–946.
- 32 WEISSELEDER, R., MOORE, A., MAHMOOD, U., BHORADE, R., BENVENISTE, H., CHIOCCA, E. A., BASILION, J. P. In vivo magnetic resonance imaging of transgene expression, *Nat. Med.* **2000**, *6*, 351–355.
- 33 TIEFENAUER, L. X., KÜHNE, G., ANDRES, R. Y. Antibody-magnetite nanoparticles: In vitro characterization of a potential tumor-specific contrast agent for magnetic resonance imaging, *Bioconjugate Chem.* **1993**, *4*, 347–352.
- 34 ARTEMOV, D., MORI, N., OKOLLIE, B., BHUJWALLA, Z. M. MR molecular imaging of the Her-2/neu receptor in breast cancer cells using targeted iron oxide nanoparticles, *Magn. Reson. Med.* **2003**, *49*, 403–408.
- 35 TIEFENAUER, L. X., TSCHIRKY, A., IWHNE, G., ANDRES, R. Y. In vivo evaluation of magnetite nanoparticles for use as a tumor contrast agent in MRI, *Magn. Reson. Imag.* **1996**, *14*, 391–402.
- 36 HUH, Y.-M., JUN, Y.-W., SONG, H.-T., KIM, S., CHOI, J.-S., LEE, J.-H., YOON, S., KIM, K.-S., SHIN, J.-S., SUH, J.-S., CHEON, J. In vivo magnetic resonance detection of cancer by using multi-functional magnetic nanocrystals, *J. Am. Chem. Soc.* **2005**, *127*, 12 387–12 391.

- 37 SJÖGREN, C. E., JOHANSSON, C., NAEVESTAD, A., SONTUM, P. C., BRILEY-SAEBO, K., FAHLVIK, A. K. Crystal size and properties of superparamagnetic iron oxide (SPIO) particles, *Magn. Reson. Imag.* **1997**, *15*, 55–67.
- 38 HAHN, P. F., STARK, D. D., LEWIS, J. M., SAINI, S., ELIZONDO, G., WEISSELEDER, R., FRETZ, C. J., FERRUCCI, J. T. First clinical trial of a new superparamagnetic iron oxide for use as an oral gastrointestinal contrast agent in MR imaging, *Radiology* **1990**, *175*, 695–700.
- 39 BACH-GANSMO, T. *Acta Radiol.* [Suppl] **1993**, *387*, 1–30.
- 40 WEISSELEDER, R., ELIZONDO, G., JOSEPHSON, L., COMPTON, C. C., FRETZ, C. J., STARK, D. D., FERRUCCI, J. T. Experimental lymph node metastases: Enhanced detection with MR lymphography, *Radiology* **1989**, *171*, 835–839.
- 41 WEISSELEDER, R., STARK, D. D., ENGELSTAD, B. L., BACON, B. R., COMPTON, C. C., WHITE, D. L., JACOBS, P., LEWIS, J. Superparamagnetic iron oxide: Pharmacokinetics and toxicity, *Am. J. Roentgenol.* **1989**, *152*, 167–173.
- 42 REIMER, P., RUMMENY, E. J., DALDRUP, H. E., BALZER, T., TOMBACH, B., BERNIS, T., PETERS, P. E. Clinical results with resovist: A Phase 2 clinical trial, *Radiology* **1995**, *195*, 489–496.
- 43 GRUBNIC, S., PADHANI, A. R., REVELL, P. B., HUSBAND, J. E. Comparative efficacy of and sequence choice for two oral contrast agents used during MR imaging, *Am. J. Roentgenol.* **1999**, *173*, 173–178.
- 44 BARTOLOZZI, C., LENCIONI, R., DONATI, F., CIONI, D. Abdominal MR: Liver and pancreas, *Eur. Radiol.* **1999**, *9*, 1496–1512.
- 45 MOORE, A., MARECOS, E., BOGDANOV, A., WEISSELEDER, R. Tumoral distribution of long-circulating dextran-coated iron oxide nanoparticles in a rodent model, *Radiology* **2000**, *214*, 568–574.
- 46 PALMACCI, S., JOSEPHSON, L. *U.S. Patent* **1993**, 5,262,176.
- 47 SHEN, T., WEISSELEDER, R., PAPISOV, M., BOGDANOV, A., BRADY, T. J. Monocrystalline iron oxide nanocompounds (MION): Physicochemical properties, *Magn. Reson. Med.* **1993**, *29*, 599–604.
- 48 FORD, G. C. Ferritin: Design and formation of an iron-storage molecule, *Philos. Trans. R. London Ser. B.* **1984**, *304*, 551.
- 49 MELDRUM, F. C., HEYWOOD, B. R., MANN, S. Magnetoferritin: In vitro synthesis of a novel magnetic protein, *Science* **1992**, *257*, 522–523.
- 50 BULTE, J. W. M., DOUGLAS, T., MANN, S., FRANKEL, R. B., MOSKOWITZ, B. M., BROOKS, R. A., BAUMGARNER, C. D., VYMAZAL, J., STRUB, M.-P., FRANK, J. A. *J. Magn. Reson. Imag.* **1994**, *4*, 497–505.
- 51 MELDRUM, F. C., WADE, V. J., NIMMO, D. L., HEYWOOD, B. R., MANN, S. Synthesis of inorganic nanophase materials in supramolecular protein cages, *Nature* **1991**, *349*, 684–687.
- 52 BULTE, J. W. M., DOUGLAS, T., MANN, S., VYMAZAL, J., LAUGHLIN, P. G., FRANK, J. A. Initial assessment of magnetoferritin biokinetics and proton relaxation enhancement in rats, *Acad. Radiol.* **1995**, *2*, 871–878.
- 53 BULTE, J. W. M., DOUGLAS, T., WITWER, B., ZHANG, S.-C., STRABLE, E., LEWIS, B. K., ZYVICKE, H., MILLER, B., GELDEREN, P., MOSKOWITZ, B. M., DUNCAN, I. D., FRANK, J. A. Magnetodendrimers allow endosomal magnetic labeling and in vivo tracking of stem cells, *Nat. Biotechnol.* **2001**, *19*, 1141–1147.
- 54 STRABLE, E., BULTE, J. W. M., MOSKOWITZ, B., VIVEKANANDAN, K., ALLEN, M., DOUGLAS, T. Synthesis and characterization of soluble iron oxide-dendrimer composites, *Chem. Mater.* **2001**, *13*, 2201–2209.
- 55 BULTE, M., CUYPER, J. W., DE, M., DESPRES, D. and FRANK, J. A. Short- vs. long-circulating magnetoliposomes as bone marrow-seeking MR contrast agents, *J. Magn. Reson. Imag.* **1999**, *9*, 329–335.
- 56 CHEON, J., KANG, N.-J., LEE, S.-M., LEE, J.-H., YOON, J.-H., OH, S. J.

- Shape evolution of single-crystalline iron oxide nanocrystals, *J. Am. Chem. Soc.* **2004**, *126*, 1950–1951.
- 57 SUN, S., ZENG, H. Size-controlled synthesis of magnetite nanoparticles, *J. Am. Chem. Soc.* **2002**, *124*, 8204–8205.
- 58 REDL, F. X., BLACK, C. T., PAPAETHYMIU, G. C., SANDSTROM, R. L., YIN, M., ZENG, H., MURRAY, C. B., O'BRIEN, S. P. Magnetic, electronic, and structural characterization of nonstoichiometric iron oxides at the nanoscale, *J. Am. Chem. Soc.* **2004**, *126*, 14 583–14 599.
- 59 PARK, J., AN, K., HWANG, Y., PARK, J.-G., NOH, H.-J., KIM, J.-Y., PARK, J.-H., HWANG, N.-M., HYEON, T. Ultra-large-scale syntheses of monodisperse nanocrystals, *Nat. Mater.* **2004**, *3*, 891–895.
- 60 JANA, N. R., CHEN, Y., PENG, X. Size- and shape-controlled magnetic (Cr, Mn, Fe, Co, Ni) oxide nanocrystals via a simple and general approach, *Chem. Mater.* **2004**, *16*, 3931–3935.
- 61 SONG, H.-T., CHOI, J.-s., HUH, Y.-M., KIM, S., JUN, Y.-w., SUH, J.-S., CHEON, J. Surface modulation of magnetic nanocrystals in the development of highly efficient magnetic resonance probes for intracellular labeling, *J. Am. Chem. Soc.* **2005**, *127*, 9992–9993.
- 62 PILENI, M.-P. *Nat. Mater.* **2003**, *2*, 145–150.
- 63 NITIN, N., LA CONTE, L. E. W., ZURKIYA, O., HU, X., BAO, G. Functionalization and peptide-based delivery of magnetic nanoparticles as an intracellular MRI contrast agent, *J. Biol. Inorg. Chem.* **2004**, *9*, 706–712.
- 64 YEE, C., KATBY, G., ULMAN, A., PROZOROV, T., WHITE, H., KING, A., RAFAILOVICH, M., SOKOLOV, J., GEDANKEN, A. Self-assembled monolayers of alkanesulfonic and -phosphonic acids on amorphous iron oxide nanoparticles, *Langmuir* **1999**, *15*, 7111–7115.
- 65 HARRIS, L. A., GOFF, J. D., CARMICHAEL, A. Y., RIFFLE, J. S., HARBURN, J. J., PIERRE, T. G. St., SAUNDERS, M. Magnetite nanoparticle dispersions stabilized with triblock copolymers, *Chem. Mater.* **2003**, *15*, 1367–1377.
- 66 BURKE, N. A. D., STOVER, H. D. H., DAWSON, F. P. Magnetic nanocomposites: Preparation and characterization of polymer-coated iron nanoparticles, *Chem. Mater.* **2002**, *14*, 4752–4761.
- 67 LU, Y., YIN, Y., MAYERS, B. T., XIA, Y. Modifying the surface properties of superparamagnetic iron oxide nanoparticles through a sol-gel approach, *Nano Lett.* **2002**, *2*, 183–186.
- 68 SANTRA, S., TAPEC, R., THEODOROPOULOU, N., DOBSON, J., HEBARD, A., TAN, W. Synthesis and characterization of silica-coated iron oxide nanoparticles in microemulsion: The effect of nonionic surfactants, *Langmuir* **2001**, *17*, 2900–2906.
- 69 DUBERTRET, B., SKOURIDES, P., NORRIS, D. J., NOIREAUX, V., BRIVANLOU, A. H., LIBCHABER, A. In vivo imaging of quantum dots encapsulated in phospholipid micelles, *Science* **2002**, *298*, 1759–1762.
- 70 KIM, S.-W., KIM, S., TRACY, J. B., JASANOFF, A., BAWENDI, M. G. Phosphine oxide polymer for water-soluble nanoparticles, *J. Am. Chem. Soc.* **2005**, *127*, 4556–4557.
- 71 KOHLER, N., FRYKELL, G. E., ZHANG, M. A Bifunctional poly(ethylene glycol) silane immobilized on metallic oxide-based nanoparticles for conjugation with cell targeting agents, *J. Am. Chem. Soc.* **2004**, *126*, 7206–7211.
- 72 WEISSLEDER, R., LEE, A. S., FISCHMAN, A. J., REIMER, P., SHEN, T., WILKINSON, R., CALLAHAN, R., BRADY, T. J. Polyclonal human immunoglobulin G labeled with polymeric iron oxide: Antibody MR imaging, *Radiology* **1991**, *181*, 245–249.
- 73 SCHMITZ, S. A., TAUPITZ, M., WAGNER, S., WOLF, K.-J., BEYERSDORFF, D., HAMM, B. J. *Magn. Reson. Imag.* **2001**, *14*, 355–361.
- 74 WADGHIRI, Y. Z., SIGURDSSON, E. M., SADOWSKI, M., ELLIOTT, J. I., LI, Y., SCHOLTZOVA, H., TANG, C. Y., AGUINALDO, G., PAPPOLA, M., DUFF, K., WISNIEWSKI, T., TURNBULL, D. H.

- Detection of Alzheimer's amyloid in transgenic mice using magnetic resonance microimaging, *Magn. Reson. Med.* **2003**, 50, 293–302.
- 75 RISAU, W. Mechanisms of angiogenesis, *Nature* **1997**, 386, 671–674.
- 76 VEIKKOLA, T., KARKKAINEN, M., CLAESSION-WELSH, L., ALITALO, K. Regulation of angiogenesis via vascular endothelial growth factor receptors, *Cancer Res.* **2000**, 60, 203–212.
- 77 KIM, I., KIM, H. G., SI, J. N., KIM, J. H., KWAK, H. J., KOH, G. Y. Angiopoietin-1 regulates endothelial cell survival through the phosphatidylinositol 3'-kinase/Akt signal transduction pathway, *Circ. Res.* **2000**, 86, 24–29.
- 78 SAEED, M., WENDLAND, M. F., ENGELBRECHT, M., SAKUNA, H., HIGGINS, C. B. Value of blood pool contrast agents in magnetic resonance angiography of the pelvis and lower extremities, *Eur. Radiol.* **1998**, 8, 1047–1053.
- 79 LAHORTE, C. M., VANDERHEYDEN, J. L., STEINMETZ, N., VAN DE WIELE, C., DIERCKX, R. A., SLEGGERS, G. Apoptosis-detecting radioligands: Current state of the art and future perspectives, *Eur. J. Nucl. Med. Mol. Imag.* **2004**, 31, 887–919.
- 80 SHAH, K., WEISSLEDER, R. Molecular optical imaging: Applications leading to the development of present day therapeutics, *NeuroRx.* **2005**, 2, 215–225.
- 81 GROSS, S., PIWNICA-WORMS, D. Spying on cancer: Molecular imaging in vivo with genetically encoded reporters, *Cancer Cell* **2005**, 7, 5–15.
- 82 HABERKORN, U., ALTMANN, A. Functional genomics and radioisotope-based imaging procedures, *Ann. Med.* **2003**, 35, 370–379.

## 6

# LHRH Conjugated Magnetic Nanoparticles for Diagnosis and Treatment of Cancers

*Carola Leuschner*

### 6.1 Introduction

Despite new discoveries of drugs and treatment combinations for cancer the mortality rate has not improved in recent decades. There is an urgent need to improve treatment and imaging in patients diagnosed with distant metastatic cancers. Cancer as a confined disease is treatable today; in contrast, distant metastatic disease outcome has not improved over the past 30 years and most patients succumb to this severe, devastating form of the disease. Furthermore, new drugs and contrast agents need to be developed to monitor the efficacy of response to treatments. Nanotechnology for treatment and diagnostics has been the focus of developmental research in the past 10 years and continues to grow exponentially. This thriving field of research focuses on materials that are on the nanometer scale, opening up new avenues that can lead to the development of highly specific compounds for treatment and imaging. Several reviews focus on the fabrication of nanoparticles for various applications, including encapsulation of drugs, and mainly summarize the latest developments for untargeted nanoparticles that are distinguishable by different coating materials, nanomaterials and various sizes and shapes. Nanoparticles open new opportunities to treat cancers by hyperthermia, to encapsulate drugs like doxorubicin, camptotecin or radiolabeled compounds that can be functionalized for higher specificity to reduce systemic exposure, and to deliver specifically nanoparticles to tumors, metastases peripheral organs and the brain.

The specific targeting of tumor cells and metastases has been more intensely under investigation. Several receptors overexpressed in cancer cells have been targeted. Although with different success with respect to specificity (some of these targets are also expressed in peripheral tissue), targeting of tumor cells can be surface binding only or by receptor-mediated endocytotic uptake of delivered compounds, which was observed to various extents, depending on the type of receptor.

Among targeting moieties on cancer cells, tumors and metastases the receptors for luteinizing hormone releasing hormone (LHRH) have been studied in detail since 1980.



The importance of LHRH receptors as specific targeting moiety for cancer treatments and diagnosis has become evident as peripheral organs express little or no receptors; however, most human cancer cells that belong to cancers of the highest incidence and death rates have tested positive for LHRH receptors. Most importantly, this chapter overviews specific targeting of nanoparticles using LHRH receptors for specific delivery, higher efficiency and faster accumulation of nanoparticles within tumor cells. Current applications in nanotechnology targeting the LHRH receptor for treatment and imaging will be explained and the latest findings and discoveries will be summarized for this highly important receptor.

Several reviews and book chapters have been published over the past decade that summarize LHRH receptors and their function in gonadal and pituitary tissues. This chapter tries to connect the current knowledge of LHRH and LHRH receptors in malignant tissue to specifically target nanoparticles through LHRH receptors to primary tumors and metastases. The current literature regarding LHRH receptors in malignancies will be reviewed and the latest findings in the development of targeted treatment and diagnosis will be discussed, with emphasis on nanoparticle construction and their consequences *in vitro* and *in vivo*.

## 6.2 Cancer

Cancer is the second leading cause of death, with 10.9 million newly diagnosed cases worldwide in 2005, claiming a total of 6.7 million lives [1]. In the USA, one in four deaths are caused by cancer [2].

Despite new drugs and treatment combinations for cancer the mortality rate has not improved in recent decades. Of 1 372 910 new diagnosed cases for all cancers in 2005 in the USA 570 380 Americans died [2]. The highest mortality rate of all occurring deaths in the United States in men and women was lung cancer, claiming the life of 28% of patients [3]. Since 1974 the survival rate has increased by only 13% as more sensitive diagnostic techniques have made very early detection of cancers possible. The yearly cancer death rates in men and women over the past 70 years has not improved despite new treatment regimens [1, 3]. The reason for this poor development becomes apparent in looking at the 5-year survival rates of cancer patients (Table 6.1, [4–29]).

Cancer death is dependent on the disease stage, whether the tumor is confined to the organ of origin and can be resected surgically, treated with radiation therapy or with systemic chemotherapeutics. The table clearly depicts the problem occurring in the distant, metastatic disease of cancer, which significantly reduces the 5-year survival rate of the patients to single digits compared with the organ-confined disease stage (Table 6.1).

This serious situation can be explained for prostate and breast cancers as examples: The second leading cause of cancer death in men is prostatic adenocarcinoma, and in women mammary carcinoma. Both cancers develop mixed popula-

**Tab. 6.1.** Occurrence of cancer by organ, survival rates in local and distant metastatic disease and their LHRH-receptor expression.

Cancer type	New cases	Deaths	5-year survival rate (%)		LHRH-receptors expressed (%)	Ref.
			Metastatic disease	Localized disease		
Lung	186 550	165 130	2.1	49	N.D.	
Prostate	230 110	29 900	34	100 (86% discovered)	86	4–7
Breast	217 440	40 580	23	97	52	8–12
Colon	106 370	56 730	9	90 (only 38% discovered)	Yes	13, 14
Pancreas	31 860	31 270	1.6	16	67	9, 15, 16
Ovary	25 580	16 090	30	94 (only 29% discovered)	80	17–21
Leukemia	33 440	23 300	64			
Non-Hodgkin's lymphoma	54 370	19 410	56	84	Yes	23
Esophagus	14 250	13 300	2.2	29.1	Yes	24
Liver	18 920	14 270	1.9	16.3	Yes	25
Uterine corpus (Endometrium) (Cervix)	40 320 10 370	7 090 3 710	26 17	96 92	80	18, 19, 26
Urinary bladder	60 240	12 710	6	94		
Melanoma	55 100	7 910	13.8	96.7	Yes	22, 27
Kidney	35 710	12 480	9.1	89	Yes	28
Brain	18 400	12 690			Yes	29

1 368 030 newly diagnosed cancer cases in the USA in 2004, 563 700 Americans die. The numbers are stated for the most frequent cancer types for men and women combined [3].

Survival rates are given for patients with localized (malignancy entirely confined to the organ of origin) and distant (malignancy has invaded lymph nodes or organs remote from the primary tumor) disease.

tions of hormone (estrogen/androgen) dependent and independent cells, which are poorly to well differentiated, and have variable proliferation rates. The preferred treatment for men with organ-confined disease is radical prostatectomy, while in women it is mastectomy. Initially, patients are treated with radiation and/or chemotherapy (cyclophosphamide, doxorubicin, 5-fluorouracil) [30, 31], in addition to hormone ablation. Although androgen ablation in prostate cancer patients (LHRH agonists, Leuprolide) [32] leads to a reduction of the primary tumor, and to its partial regression, within 2 years the disease can re-emerge in a poorly differentiated, androgen-independent form, after which there is no therapy available to prolong the patient's life [33]. In breast cancer patients estrogen ablation is achieved by tamoxifen treatment [34] or ovariectomy. Surgical removal of the primary tumor is invasive and has side effects, depending on the area of resection, on the tumor (encapsulated or invasive), and can even lead to increased proliferation of metastases as single metastatic cells and dormant cancer cells start to proliferate [35]. At the time of diagnosis up to 70% of prostate cancer patients [36, 37] and 40% of breast cancer patients have already developed occult metastases [38]. Bone and lymph node metastases occur in 26% of prostate adenocarcinomas [39] and in 23% of breast cancer patients [38]. More than 70% of patients die from skeletal metastases [40]. Often removal of the primary tumor can promote metastatic growth, and dormant cancer cells can become secondary, often more aggressive, tumors [35].

Current treatments are palliative and can only prolong the life of patients, they do not cure patients. Often, high doses of chemotherapeutics administered systemically are necessary to achieve the pharmacological effective concentration. Even to maintain a state of remission in the disease a high dose chemotherapy is required over a long period [41]. Because of the high toxicity and poor specificity of currently used drugs, an increase in chemotherapeutic dosages is not desirable. The administration of high drug concentrations has disadvantages regarding side effects as chemotherapeutics not only destroy malignant tumors but also healthy tissue and organs, which eventually forces an end to such treatment. Often, patients in recurrent disease do not respond to chemotherapy. This is due to an acquired drug-resistance, which decreases the efficacy of chemotherapy. Dormant metastatic disease is not treatable with chemo- or radiation-therapy as these destroy only fast proliferating cells [38, 42, 43].

Currently used chemotherapeutic drugs are systemically active and cannot target single dormant cancer cells, or slow growing tumors [38, 44], because most chemotherapeutic drugs are not selective for cancer cells and destroy only rapidly dividing cells.

### 6.2.1

#### **Conventional Approaches to Cancer/Metastases Detection**

Sensitive non-invasive detection and monitoring tools are needed for early tumor detection and for monitoring disease progression, efficacy of treatment regimens and responses to treatments. Higher resolution and improved imaging techniques are needed to detect single, disseminated cancer cells or even small cancer cell

clusters in peripheral organs, bones and lymph nodes at the earliest stage before development of secondary tumors. Current detection methods are invasive and lack the sensitivity to detect micrometastases.

Clinically, metastases have been quantified by counting macroscopic nodules from biopsy specimen or tumor cell colonies in histological sections. The detection rates with these methods is 1–2% [45–47]. These approaches are invasive and lack the sensitivity necessary to detect micrometastases or single disseminated cells and cell clusters in peripheral organs. The use of immunocytochemistry techniques increased the detection rate of bone metastases in bone marrow aspirates up to 30% [48–50]. RT-PCR techniques (reverse transcriptase polymerase chain reaction) have been developed to detect cytokeratin 18 in bone marrow, with a sensitivity of a single cell in  $2 \times 10^7$  bone marrow cells [51]. Although these techniques are superior to histological examinations they involve invasive procedures and can take up to 7 days for a final diagnosis.

Non-invasive detection methods include X-ray, Mammography, Ultrasound, Magnetic Resonance Imaging (MRI), and nuclear imaging techniques such as Positron Emission Tomography (PET), SPECT (single-photon emission tomography) and Computed Tomography (CT). PET, SPECT and CT techniques require radiochemicals, which can have significant systemic toxicity. Unlike mammography and ultrasound, MRI and CT are independent of tissue depth. They exploit pure tissue–energy interactions and do not require isotopes. Mammography has high false positive rates (70%), whereas MRI is costly and ultrasound has a low spatial resolution and is dependent on tissue depth. The accuracy for detection of tumors from breast cancer by mammography was 36%, by ultrasound 33% and by MRI 77% [52, 53]. Contrast agents like ferrofluids enhanced the detection of tumors by 35% compared with unenhanced MRI (6%) or dynamic CT (14%). Intraoperative ultrasound detected liver metastases as small as 5 mm [54] and reduced false-positive diagnosis [55]. MRI can distinguish metastases from hemangiomas and cysts and is potentially valuable for the detection of occult metastatic disease in the sub-centimeter size [56, 57]. Micrometastases as small as 2 mm were detected; PET imaging for pelvic lymph nodes detected metastases as small as 6 mm [58].

Clinically used contrast agents for MRI are gadolinium chelates and iron oxide based particles (superparamagnetic iron oxide nanoparticles = SPIONs) [55, 59]. SPIONs have important advantages over gadolinium chelates: they have low toxicity (in some instances toxicities were reported at concentrations more than 100-fold above the clinically effective dosage [59]) and their detection limit in MRI is in the subnanomolar range, exceeding Gd imaging by a factor of 100 [60]. The accumulation and binding of the nanoparticles to the target cells was either absent or non-specific and, therefore, insufficient and limited the diagnostic applications to liver, spleen, and bone marrow, all of which are dependent on the reticulo-endothelial system (RES). In the past decade, contrast agents that enhance MR imaging have been used for imaging liver [61, 62], spleen [61, 62], gastrointestinal tracts, cardiovascular diseases, cancer [63, 64] and even lymph node metastases [65–67]. The contrast agent accumulated in healthy tissue and enhanced the resolution of MRI between malignant and healthy tissue [65–67].

### 6.2.2

#### **Current Chemotherapeutic Approaches and their Disadvantages in Cancer Treatments**

Currently used chemotherapeutic drugs are systemically active, have severe side effects and do not target specifically tumors or single dormant cancer cells. Most current chemotherapeutics interfere with the proliferation machinery of fast growing cells – they are not effective on slow growing tumors or dormant cancer cells [38, 43, 44]. Most chemotherapeutic drugs are not selective for cancer cells and do not discriminate between healthy and diseased tissue. However, because they interfere with the proliferation machinery of the cancer cells they show a relatively high efficacy on fast proliferating cells: Cyclophosphamide (Cytosan) destroys genetic material that controls tumor cell growth; methotrexate and 5-fluorouracil (5FU) are antimetabolites that interfere with cancer cell division; antimicrotubule reagents prevent cell division by acting on the microtubules, among them are paclitaxel (Taxol), docetaxel (Taxotere), vincristine (Oncovin), vinblastine (Velban); doxorubicin (Adriamycin) is a tumor antibiotic. To be effective these drugs need to enter, and accumulate in, the tumor cells. High systemic dosages are required to reach therapeutically effective concentrations at the tumor site, which causes severe side effects and peripheral tissue damage. Among the side effects are destruction of bone marrow cells, which impairs the production of erythrocytes, causes cardiotoxicity, nephrotoxicity, hepatotoxicity and hematotoxicity. Because bone marrow cells produce erythrocytes for oxygen transport, patients become anemic as a result of bone marrow destruction. Hematotoxicity includes the destruction of platelets needed for blood clotting and leukocytes to fight infections. Immediate side effects are nausea, alopecia, and fatigue. Longer lasting effects are the increased risk for infections, which persists until the immune system has recovered from the chemotherapy (4–6 weeks).

##### **6.2.2.1 Multidrug Resistance**

High-dose chemotherapy does not necessarily cure the patient. Many patients relapse. Cancer can recur after high-dose chemotherapy, often with a lack of response to further chemotherapy, which in turn leads to terminal disease even after several years of apparent disease-free state. This phenomenon is defined as multidrug-resistance (MDR) and is attributed to multiple mechanisms [68, 69].

Most cancers, like colon, kidney, breast, ovarian, prostatic, lung cancers, over-express the p-glycoprotein gene (also known as the multidrug resistance gene). Its gene product is the protein p-glycoprotein (Pgp), which is located in membranes, Golgi apparatus and nucleus [70, 71]. Pgp is a transmembrane efflux pump that actively excretes cytotoxic drugs of different molecular structure through an ATPase mechanism [72], thus decreasing intracellular drug concentrations. Modulators for Pgp pumps have been reported and include Verapamil, a compound that competes with the drug efflux pump.

During differentiation and progression, cancer cells can acquire the ability to remove the administered drug through such a pump mechanism. Other mechanisms include alteration of enzymatic activities like topoisomerase or glutathione

S-reductase activity, altered apoptosis regulation, altered transport or alteration of intracellular drug distribution due to increased sequestration of cytoplasmic vesicles [73].

The severity of side effects during administration of chemotherapeutic drugs and the occurrence of MDR emerges as non-responsive or refractory disease to chemotherapeutic drugs.

#### 6.2.2.2 Drug Delivery to Tumors

Tumor morphology is differently organized with normal tissue, to meet the physiological requirements for fast growth. Table 6.2 summarizes some of the key characteristics of tumor tissue compared with normal tissue. Consequently, tumor tissue shows certain characteristics that distinguishes it from normal tissue. Malignant tissues have adapted to their increased requirement of nutrients and oxygen by the following characteristics: angiogenesis, tortuous vasculature, leaky basement membranes, lack of lymphatic system (Table 6.2).

Fast growing tumors require high amounts of nutrients, which need to be transported to the fast growing tissues and metabolic waste products need to be eliminated at a higher rates than with normal cells. Newly growing tumors can only meet their nutrient requirements until an average tumor volume of  $2 \text{ mm}^3$ , beyond that the tumoral diffusion limit restricts further growth [74]. Further tumor growth requires the formation of neovasculature, a process called angiogenesis. The highly increased “fuel” requirement leads to specific morphologic characteristics in tumors vasculature, which is tortuous, chaotic and lacks the hierarchic

**Tab. 6.2.** Differences between tumors and normal tissues.

	Normal tissue	Tumor tissue
Cell growth	Low proliferation	High proliferation
Vasculature	No or little angiogenesis	High angiogenesis
	Normal proliferation	Chaotic
	None	High proliferation of endothelial cells
		Occlusions
	Not hypoxic	Hypoxic
	Low permeability	High permeability
Lymphatic system	Functional	Lacking
Interstitial pressure	Normal	High
Pore size (nm)	2–60	100–780

branching pattern found in normal vasculature [75–77]. The fast proliferating tumor cells causes occlusion of the capillary vasculature, which leads to hypoxia and eventually necrosis of tumor tissue [77]. The basement membranes of tumor vasculature is often aberrant, leading to leakiness and increased permeability [76, 78] to counterbalance the high oxygen and nutrient requirements for the fast proliferating tumors [79]. In addition the lack of lymphatic drainage system [80, 81] in conjunction with aberrant cell proliferation and occlusion of capillary vessels increases drastically the interstitial pressure in tumor tissue, which is filled with hyaluronate and proteoglycan-containing fluids. Ideally, removal of the drug from the interstitial into the intracellular compartment of the tumor cell would create the necessary concentration gradient to the plasma to allow further extravasation of the drug.

Increased interstitial pressure in the tumor tissue interferes with extravasation of the drugs, causing an increase in drug concentration in the tumor interstitium. The dense packing of tumor cells further reduces diffusion of compounds in solid tumors [41]. This phenomenon is explained by the enhanced permeability and retention effect (EPR) and is characterized by the accumulation of a compound in the interstitium. At this stage, further delivery of drug to the tumor cells is stagnant when the accumulation of the drug in the interstitium exceeds the drug concentration in the plasma [82, 83].

### 6.3

#### Nanoparticles as Vehicles for Drug Delivery and Diagnosis

The delivery of drugs using nanoparticles can improve current drug administration and treatment. Presently, nanoparticles are under development that can be used for hyperthermic destruction of tumor cells, may incorporate drugs that are slowly released, and at the same time protect the pharmaceutical compound from destruction, alteration in the plasma, and, moreover, opens a possibility to deliver highly lipophilic compounds.

Delivery of drugs through nanoparticles needs to take into account the *in vivo* distribution of systemically injected particles. The biodistribution and circulation time of contrast agents is determined by several factors, including size, charge, and surface chemistry [84, 85] (Fig. 6.1).

Charged particles are rapidly coated with plasma proteins, known as opsonization, aggregate and have an increased phagocytotic index [8, 86]. Opsonized particles and nanoparticles exceeding a diameter of 100 nm are easily recognized by macrophages of the reticuloendothelial system (RES) and preferentially delivered into liver, spleen, lymph nodes, microglia and bones, and reside and accumulate within the macrophages in these organs as fast as 5 min [87–93]. During this process nanoparticles are removed from the circulation and the drug is inaccessible to treat tumor tissues. Nanoparticles can be specifically designed for increased uptake by macrophages that deliver them through the RES system of liver (Kupffer cells),

spleen, lymph nodes (perivascular macrophages), nervous system (microglia) and bones (osteoclasts) [87, 88]. This clearance can occur within 0.5–5 min [90], thus removing the active nanoparticles from the circulation and prevent their access to the tumor tissue.

Coating of nanoparticles with polymers alters their distribution *in vivo*. For example, a hydrophilic coating increases the circulation time by preventing interaction with the RES.

Nanoparticles with a hydrophilic coating, neutral charge and that are <100 nm show characteristics that render them unrecognizable by the macrophage system [94]. These particles then access the tumor tissue through their hyperpermeable vasculature, accumulate in the interstitial compartment and are retained therein due to the lack of a functional lymphatic drainage (EPR effect) [83, 84, 95, 96]. If nanoparticles are biodegraded in the interstitium the drug can be released and enter the tumor cells through diffusion.

Nanoparticles can enter the tumor cells from the interstitial tumoral compartment. Depending on the surface and ligand characteristics the particles can enter by different pathways, among which are pinocytosis or endocytosis [97–99].

Figure 6.1 illustrates the different routes nanoparticles may encounter *in vivo*, depending on their size.

In summary, nanoparticles for the delivery of drugs to tumors offer an attractive possibility for avoiding obstacles that occur during conventional systemic drug ad-

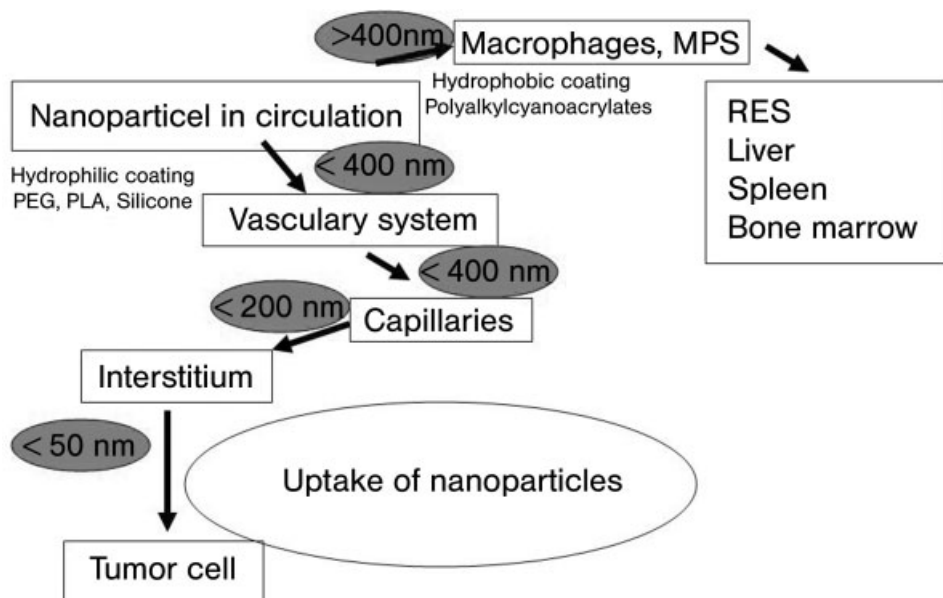


Fig. 6.1. *In vivo* distribution of nanoparticles by size.



ministration. However, new obstacles come into play, when nanoparticles are introduced into the system. The route of administration, particle size and composition, degradable coatings, biologically acceptable coatings, endocytosis properties, and stability in physiological salinity all determine the fate of nanoparticles. Nanoparticles injected into biological systems should not agglomerate to avoid not only macrophage uptake but, most importantly, thrombosis. The accumulation of nanoparticles at the target can be enhanced by either attaching ligands onto the surface of the nanoparticles or, in the case of magnetic nanoparticles, by using an external magnetic field.

### 6.3.1

#### **Targeting Tumor Cells**

Cancer therapy, ideally, should only destroy malignant cells, whether they are singly spread in the periphery or confined in an organ as a tumor. The conjugation of drug molecules with tumor specific ligands could facilitate targeting to the tumor cells and avoid uptake from normal cells: the normal cell would be spared and remain undestroyed whereas the tumor cells could accumulate and concentrate drug molecules, reaching the pharmacologically required concentration. This approach could overcome drug resistance, and side effects to vital organs can be eradicated or minimized through reduced systemic exposure. Malignant cells can be destroyed more effectively: even tumor cells inaccessible to surgery can be destroyed. The specific targeting of drug molecules can lower the plasma concentration and, at the same time, increase the efficacy through concentration of the drugs at the tumor cells.

The overall goal of active targeting is to increase the specificity of a drug to the tumor cells, to increase the concentration of the compound at the target cells and to incorporate and retain the drug or compound within the tumor cells (e.g., in the case of contrast agents). High efficiency internalizing and recycling receptors could improve cellular uptake through receptor-mediated endocytosis. This process is highly specific and efficient in cells expressing sufficient numbers of receptors and having sufficient receptor capacities.

Nanoparticles can be directed to the tumors by passive or active targeting. Passive targeting can be achieved by changing the size/hydrophobicity or other physicochemical characteristics of the newly designed nanoparticles to target the reticulo-endothelial system. Active targeting involves the direction of magnetic particles by using an external magnetic field or by using ligand-conjugated nanoparticles.

#### **6.3.1.1 Passive Targeting**

Passive targeting can be achieved by using nanoparticles of less than 100 nm size and free of charge, which determines the delivery to the tumors and metastases in peripheral organs through enhanced circulation time and at the site of the tumor cells through increased incorporation and concentration. The circulation time is

enhanced by hydrophilic coating of nanoparticles, whereas a hydrophobic coating ensures delivery to the liver and spleen. Examples for the delivery of nanoparticles through the RES include Endorem and AMI25, dextran-coated iron oxide nanoparticles of 62–150 nm diameter, which accumulated in liver and spleen after intravenous injection and have been clinically used for liver diagnostics as they accumulate up to 80% in the liver [100–102, 62]. Bone marrow imaging for tumor detection has been studied with AMI25 iron particles, which were delivered through the RES to the bone marrow [63, 64, 67]. Recently, occult lymph node metastases from prostate, bladder, breast, renal, penile, rectal and testicular cancer patients were diagnosed using dextran-coated nanoparticles (hydrodynamic size 30 nm) [65, 66]. This application exploits the difference between normal and malignant lymph nodes by delivering iron oxide nanoparticles through macrophages. In malignant lymph, nodes macrophages cannot infiltrate the tumor cells. Consequently, malignant lymph nodes do not accumulate macrophage delivered iron oxide nanoparticles.

Other examples of passive targeting include polyacrylcianoacrylate particles loaded with insulin, which have been orally administered into rats and were incorporated via the Peyer's patches in the intestinal lining into the lymphatic system [103], and the delivery of cucurbitan to cervical lymph nodes [104]. Gadolinium lipid nanoemulsions (70–90 nm) are an example of nanoparticles with increased circulation time. The nanoemulsion was synthesized from hydrogenated phosphatidylcholine, and gadolinium-diethylenetriaminepentaacetic acid (Gd-DTPA), which had been coated with polyoxyethylene to create a hydrophilic moiety. Bioavailability was determined for different routes of administration. Intravenous injection was advantageous over i.p. injections with respect to bioavailability, tumor retention and increased accumulation. Tumor accumulation was 49.7  $\mu\text{g-Gd}$  per g-tumor at 24 h compared with 21  $\mu\text{g-Gd}$  per g-tumor at 12 h in the i.p. treated groups. However, intravenous administration resulted in higher Gd accumulation in liver and spleen, lung and kidney compared with i.p. injected groups. Repeated injection with a two-fold enriched formulation led to 100  $\mu\text{g-Gd}$  per g-wt.-tissue [105]. The increased efficacy was due to prolonged circulation of the particles, reduced interaction with the RES, and reduced excretion of the compound Gd and increased retention in the tumor tissue. Polymeric nanoparticles (28 nm) prepared through polymer–metal complex formation between cisplatinum (CDDP) and poly(ethylene glycol)-poly(glutamic acid) block copolymers were tested for their efficacy in delivering cisplatinum to tumors. Lewis lung carcinoma bearing mice were injected i.v. with free CDDP (4 mg  $\text{kg}^{-1}$ ) or CDDP/m. CDDP/m had prolonged blood circulation time, and accumulated in the tumors 20-fold higher compared with free CDDP, whereas the accumulation in normal tissue was reduced [106]. These data clearly show the advantages of drug encapsulation and coating and size selection of nanoparticles with respect of increased bioavailability, increased target accumulation, and reduced accumulation in normal organs.

In the above applications the accumulation and binding of nanoparticles to the target cells was either absent or non-specific and, therefore, insufficient, and limited the diagnostic applications to liver and lymph nodes.

Not only drugs could be delivered to the tumors and cancer cells, but nanoparticles like iron oxide nanoparticles can also be used for imaging procedures.

#### 6.3.1.2 Active Targeting

In the past 5 years more attention has been paid to the identification and development of specific antigens and receptors that are unique to cancer cells. The ideal targeting moiety should be expressed on all tumor cells, including metastatic cells in the periphery, but not on healthy, normal cells. Targeting of nanoparticles or drugs has to meet the following characteristics:

- Specificity – to exclusively target cancer cells.
- Efficiency – faster uptake through receptor-mediated endocytosis, systemic delivered compounds concentrate on tumor cells, no involvement of peripheral tissues, faster delivery to tumor cells.
- Stability – the ligand should not be degraded.
- Functionality – receptor-mediated endocytosis, specific binding to tumor cells through receptors, facilitating increased uptake.
- Neutral surface coating – nanoparticles should not be recognized by macrophages.
- Increased retention through compartmentalization.

The decoration of nanoparticles with tumor targeting molecules, such as hormones, growth factors etc., can increase the efficacy of a treatment regimen by increasing the concentration of the drug at the tumor site, reducing the requirement of systemically administered drug for therapeutic efficacy, and can facilitate sustained intracellular retention of the drug. Antibodies for targeting malignancies have been approved and include Anti-CD 20 (Rituxan®, non-Hodgkins lymphoma), Anti-Her-2 (Herceptin®, metastatic breast cancer), Anti CD 33 (Mylotarg® myelogenous leukemia), and Gefitinib (Iressa®, non-small cell lung cancer) [107]. Other targets under intense investigation include antiangiogenesis compounds to specifically destroy tumor vasculature and eventually starve the tumor tissue. Angiogenesis is a complex process and the number of potential targets includes compounds for limiting endothelial proliferation, expression of angiogenesis inhibitors, and a decrease of angiogenesis stimulatory factors often secreted by tumor cells. The most prominent candidate for targeting vasculature is the vascular endothelial growth factor (VEGF) and an integrin for which antibodies have been developed for the use in conjugation in vascular imaging and tumor vasculature specific drug delivery.

Several specific receptors are overexpressed on tumor cells and have been identified and targeted with drug–ligand complexes or ligand–nanoparticle constructs. Some examples, which include lactoferrin [108, 109], ceruloplasmin [108, 109] and insulin [110], have been studied as targeting moieties; the ligands had strong surface binding on tumor cells, yet were not phagocytosed. High efficiency internalizing receptors could improve cellular uptake through receptor-mediated endo-

cytosis and increase dramatically the specificity of uptake in cancer cells, avoiding uptake in peripheral and healthy tissue.

Ligands that are endocytosed and recycled include transferrin [111–115], folate [116, 117], TGF alpha [118], nerve growth factor [119], Her2/neu [120], somatostatin, bombesin [121], steroid hormones, CD-8 [122], and HIV-1 tat [123, 124].

This chapter reviews in detail the use of Luteinizing Hormone Releasing Hormone (LHRH) as ligand to target the cancer cells. The following outline describes the characteristics and function of LHRH and its receptors regarding tumor treatment and detection.

Drugs delivered in conjugation with LHRH, studied over the past 20 years, include doxorubicin conjugates, studied intensely by Schally and co-investigators [22–24, 121, 125–129], lytic peptides conjugated to LHRH [8, 130], CPT-11 conjugated to LHRH and to pokeweed antiviral protein [159, 160]. Conjugates of lytic peptides or doxorubicin/doxorubicin derivatives with LHRH specifically target and destroy prostate, ovarian and breast cancer cells and their metastases, all of which express LHRH receptors *in vitro* and *in vivo* [22–24, 121, 125–130]. Metastases and disseminated cells derived from breast cancer xenografts of estrogen-independent MDA-MB-435S.luc cells, in the presence and absence of the primary tumor, have been detected, characterized and successfully targeted by CG/LHRH–lytic peptide conjugates [161–164, 318]. Schally et al. have treated several cancers with LHRH–doxorubicin conjugates and have developed a drug, which is currently in Phase III clinical trials (personal communication). These studies clearly demonstrate that tumors can be specifically targeted *in vivo* in experimental xenograft-bearing mice and rats. Moreover, in the above experiments none of the reported side effects of the free compounds were observed, suggesting increased specificity, targeting and efficacy with decreased systemic exposure. In studies using LHRH cytotoxic conjugates of doxorubicin the anterior pituitary did not show any permanent damage – complete recovery of pituitary function was observed [128, 129].

### 6.3.2

#### Detection of Tumors and Metastases using Nanoparticles

##### 6.3.2.1 Nanoparticles for Magnetic Resonance Imaging

The MRI signal in magnetic particles is created through the interaction of total water signal and the magnetic properties of longitudinal (T1) and transversal (T2) relaxivity.

MRI resolution can be increased by: (a) extending the scan time, (b) using high efficiency coils, (c) increasing field strengths, (d) increasing accumulation of contrast agent in cells or tissue, (e) compartmentalization of particles within the target cells, and (f) retention of particles.

To acquire the best image the signal-to-noise ratio must be optimized. An increase in field strength can cause neurological side effects like seizure, and/or cardiovascular effects. Clinically, MRI is conducted at 1.5 T, which is without side effects and well tolerated. MRI requires long imaging times, which can last up to 1 h. To enhance MRI sensitivities, contrast agents must accumulate in the target

cells, without leaking into surrounding tissue, at sufficient concentrations to increase relaxation times and must be retained within the tissue during the imaging procedure. In MRI, the signal can be amplified through an increase in intracellular concentration of the contrast agent [131, 132].

Clinically used contrast agents are paramagnetic gadolinium chelates (DTPA = diethyl tetraminepentaacetic acid) or ferrofluids. The use of superparamagnetic iron-based particles for magnetic resonance imaging has several advantages [133]:

Image enhancement with regard to relaxation time is greater in superparamagnetic particles – the change in T1 relaxation time is seven-fold, T2 relaxation time 16-fold, compared with gadolinium DTPA [134]. Gd is highly water-soluble and it is readily excreted, which allows only a short time for imaging and reduces cellular uptake [135, 136]. Superparamagnetic particles are less likely to aggregate because they lack remnant magnetization [137] and retain their physical characteristics even when chemically inert materials are attached [138]. Magnetite can adsorb or attach chemically to inert material without changing the characteristics of T2 relaxivity [138].

To significantly reduce relaxation time, gadolinium chelates have to be administered at high concentrations [139]. *In vitro*, increased Gd payloads resulted in increased T1 relaxivities and increased the resolution of fibrin clots [137]. In addition, superparamagnetic iron oxide particles have a much more favorable ratio of efficacy dose to LD<sub>50</sub>: 1/2400 compared with 1/50 for Gd-DTPA contrast agents [140]; in some instances toxicities were reported at concentrations 100-fold above the clinically effective dosage [139].

Monocrystalline Fe requires up to 1 mg of Fe per kg of tissue for MRI [141, 142]. In liver, up to 2.5 mg-Fe per kg of tissue showed a linear relationship with T2 relaxation [143]. Best imaging was obtained at 5–50 mg-Fe per kg of tissue sample [144]. A four-fold increase of the dose of superparamagnetic iron particles resulted in a decrease of signal loss by a factor of 10 [145].

Iron oxide nanoparticles are biologically safe and show no toxicity [139]. They are metabolized into elemental iron and oxygen by hydrolytic enzymes and the iron joins the normal body stores and is subsequently incorporated into hemoglobin. Iron homeostasis is controlled by absorption, excretion and storage. Acute toxicity has not been observed, in rats or human clinical trials. The administered iron was excreted over a period of four weeks [146]. Renal function, hepatic parameters, serum electrolytes, lactate dehydrogenase remained unchanged from baseline parameters after treatment with ferrofluids [146]. The elevation of serum iron levels persisted for a maximum of 48 h and caused no symptoms. In rats, 250 mg per kg of iron particles injected intravenously caused no side effects, in mice 350 mg kg<sup>-1</sup> were well tolerated [147].

In the past decade, contrast agents that enhance MRI have been tested for various applications, such as imaging of liver, spleen, gastrointestinal tracts, cardiovascular diseases and cancer detection. Administered systemically, the accumulation of unconjugated nanoparticles has been confined to liver, spleen, and bone marrow, all of which are dependent on the reticulo-endothelial system (RES), and did not directly accumulate in the tumor cells.

In these applications, the biodistribution of nanoparticulate contrast agents was exclusively determined by size, charge and surface chemistry (Fig. 6.1) [84, 85]. Systemically administered nanoparticles that are non-specific were incorporated by the MPS system, or they enter cells through endocytotic pathways involving clathrin-coated pit formation, sequestration and accumulation in vacuolar or lysosomal compartments of the cells [98, 99, 148]. Endocytotic cellular up-take of dextran-coated iron-oxide nanoparticles has been shown for tumor cells *in vitro* to range from 0.01 to 100 ng of iron per  $10^6$  cells within 1 h. In contrast macrophage uptake was about nine times higher [149, 150]. For example, occult lymph node metastases from prostate, bladder, breast, renal, penile, rectal and testicular cancer patients have been diagnosed using dextran-coated nanoparticles (hydrodynamic size 30 nm) [65, 66]. This application exploited the difference between normal and malignant lymph nodes by delivering iron oxide nanoparticles through macrophages. In malignant lymph nodes, macrophages could not infiltrate the tumor cells. Consequently, malignant lymph nodes did not accumulate macrophage-delivered iron oxide nanoparticles, and so they were not labeled.

The accumulation and binding of the nanoparticles to the tumor cells was either absent or non-specific and therefore insufficient and limited the diagnostic applications to liver and lymph nodes with limited sensitivity.

#### 6.3.2.2 Targeted Delivery of Nanoparticles to Increase Cellular Uptake for Higher MRI Resolution

Targeted delivery of nanoparticles can enhance the cellular accumulation of the contrast agent within the cancer cells, can increase the retention and thereby improve the resolution and specificity in imaging modalities.

The MRI signal can be amplified through an increase of the intracellular concentration of the contrast agent [131, 132]. Relaxation times in the acquisition of magnetic resonance imaging, i.e., the contrast of the image, increase with larger particles [151]. Compartmentalized particles and clusters have larger relaxation rates than free dispersed particles [152]. If the target cells are sufficiently loaded with iron oxide particles the MRI resolution can be as high as  $25\ \mu\text{m}$  [153].

This task requires specifically designed particles that concentrate in the target cells. A pre-requisite of the target cells is that they express high efficiency, internalizing, and functional receptors on their surface, to promote accumulation of the particles in the target cells, without leaking into surrounding tissue. Particle accumulation can be increased by targeting specific receptors on the cancer cells to facilitate receptor-mediated endocytosis of the delivered iron particle or to bind and accumulate the particles on the cell surface. Ideally, the injected nanoparticles should not be recognized by macrophages.

Examples for targeted uptake include dextran-coated monocrystalline iron oxide nanoparticles (MIONs) linked to transferrin [115] or to folate [116, 117].

Antibody-coupled paramagnetic liposomes targeting integrin  $\alpha V\beta 3$  of endothelial vascular cells greatly increased the MRI of angiogenic vasculature in rabbit carcinoma [154]. The  $\alpha V\beta 3$ -conjugated nanoparticles increased the signal enhancement

post-injection much faster than untargeted nanoparticle delivery (2 versus 24 h) [155, 156].

Dextran-coated nanoparticles have been conjugated to target Her2/neu receptors [158]. Folate-linked iron oxide nanoparticles accumulated in folate receptor expressing KB cells [116] and reached a maximal level of 75 pg-Fe per cell in BT20 breast cancer cell incubation and were poorly incorporated by macrophages [117]. CD-8 conjugated crosslinked iron oxide nanoparticles have been incorporated into T cells after 1 h of incubation at concentrations up to 100 pg-Fe per cell [122]. LHRH iron oxide nanoparticles coated with a silica shell specifically targeted and accumulated in MC-F7 human breast cancer cells *in vitro* [157]. Basically, the main purpose for targeted delivery of drugs or contrast agents is the improved specificity for a particular cell type, reduced requirement of the compound necessary to gain the desired effect, and the possibility to directly incorporate the desired compound into the target cells, and a sustained retention of the particles within the target cells. The design of nanoparticles carrying specific ligands reduces and avoids the uptake in non-target cells and tissue.

## 6.4

### LHRH and its Receptors

#### 6.4.1

#### The Ligand Luteinizing Hormone Releasing Hormone – LHRH

Luteinizing hormone releasing hormone (LHRH), also referred to as gonadotropin releasing hormone (GnRH), was purified 30 years ago and its isolation was honored with the Nobel Prize of Medicine that the laureates Schally and Guellerin received in 1977 for their discovery of peptide hormones in the brain.

LHRH is excreted from the arcuate nucleus of the hypothalamus into the pituitary gland in a pulsatile manner [165]. In gonadotrophic cells of the adenohypophysis, LHRH stimulates the release of luteinizing hormone and follicle stimulating hormone, which are released into the main body circulation and regulate the production of sex hormones (estradiol and testosterone) and, thereby, the function of normal reproduction in mammals, humans and mice. This relationship is called the pituitary/gonadal axis (Fig. 6.2). The pulsatile release of LHRH is crucial for maintaining its function on the pituitary/gonadal axis and ensuring the optimal function of reproductive organs and maintaining fertility [166–168]. Sustained administration of LHRH or its analogs to patients suppressed steroid hormone production and downregulated and desensitized the LHRH receptor in the pituitary [166, 167]. This observation was exploited for treatments of hormone-dependent cancers; steroid hormone suppression using Leuprolide, which binds to the LHRH receptor, stopped the release of testosterone and inhibited the proliferation of the cancers. Over the last 30 years more than a thousand LHRH agonists and

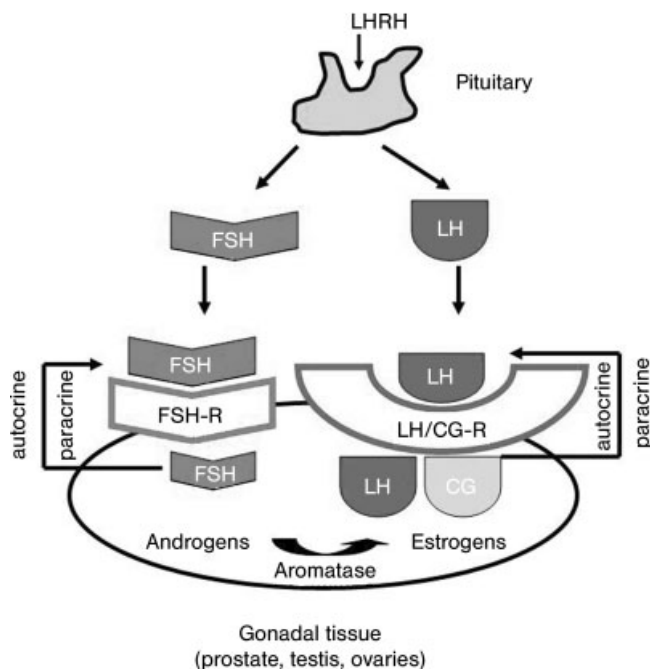


Fig. 6.2. Gonadal/pituitary axis and interaction of LHRH with gonadal function.

antagonists have been developed, and are used in the clinic to treat hormone-dependent cancers [169] (Table 6.3). The common mechanism of action is the ablation of hormones by administration of these pituitary acting antagonists. Suppression of gonadal steroid secretion reduced the growth of these hormone-dependent tumors (Fig. 6.2). Hormone ablation was considered to be the only mechanism of action for LHRH agonists, but recent identification of a second LHRH receptor and the expression of LHRH receptors in malignancies explained why LHRH also had a direct effect on the proliferation and metastatic behavior of cancers [12, 170–173].

In 1971, type I LHRH was isolated from the pituitary of pigs and its structure was revealed [174]. The gonadotropin hormone LHRH is also expressed in gonadal peripheral tissue like Leydig cells in the testes and ovarian cells as well as in numerous malignancies. The decapeptide LHRH is produced in numerous species with astonishing homology during evolution. To date 23 different forms have been identified with highly conserved sequences [170–181].

All these peptides consist of 10 amino acids and share at least 50% sequence identity, with the main differences occurring in amino acids 5–8 (Table 6.3) [170, 182–184]. The different isoforms of LHRH were named after the species of its isolation. Two different forms of LHRH coexist in vertebrates, LHRH I and LHRH II. LHRH I (mLHRH) has been isolated from the hypothalamus in pigs [174]; and



Tab. 6.3. Amino acid sequences of LHRH forms and synthetic analogs [170].

LHRH forms	Naturally occurring LHRH										
	1	2	3	4	5	6	7	8	9	10	
mLHRH (LHRH-I)	pGlu	His	Trp	Ser	Tyr	Gly	Leu	Arg	Pro	Gly	NH <sub>2</sub>
cLHRH (LHRH II)	pGlu	His	Trp	Ser	His	Gly	Trp	Tyr	Pro	Gly	NH <sub>2</sub>
lLHRH (LHRH III)	pGlu	His	Trp	Ser	His	Asp	Trp	Lys	Pro	Gly	NH <sub>2</sub>
rLHRH	pGlu	His	Trp	Ser	Tyr	Gly	Leu	Trp	Pro	Gly	NH <sub>2</sub>
cflLHRH	pGlu	His	Trp	Ser	His	Gly	Leu	Pro	Pro	Gly	NH <sub>2</sub>
LHRH agonists											
Lupron <sup>[a]</sup> (TAP)	pGlu	His	Trp	Ser	Tyr	D Leu	Leu	Arg	Pro	NEt	
Zoladex <sup>[a]</sup> (Zeneca)	pGlu	His	Trp	Ser	Tyr	D Ser (tBu)	Leu	Arg	Pro	Gly	NH <sub>2</sub>
Supprelin <sup>[a]</sup> (Roberts)	pGlu	His	Trp	Ser	Tyr	D His (ImBzl)	Leu	Arg	Pro	Gly	NH <sub>2</sub>
Synarel <sup>[a]</sup> (Searle)	pGlu	His	Trp	Ser	Tyr	D Nal	Leu	Arg	Pro	Gly	NH <sub>2</sub>
Triptorelin <sup>[a]</sup> (Ferring)	pGlu	His	Trp	Ser	Tyr	D Trp	Leu	Arg	Pro	Gly	NH <sub>2</sub>
Buserelin <sup>[a]</sup> (Hoechst)	pGlu	His	Trp	Ser	Tyr	D Ser (tBu)	Leu	Arg	Pro	NEt	
LHRH antagonists											
Centroxel <sup>[a]</sup> (Asta Medica)	D Nal	D Cpa	D Pal	Ser	Tyr	D Cit	Leu	Arg	Pro	D Ala	NH <sub>2</sub>
Ganirelix <sup>[a]</sup> (Organon)	D Nal	D Cpa	D Pal	Ser	Tyr	D hArg (Et) <sub>2</sub>	Leu	D hArg (Et) <sub>2</sub>	Pro	D Ala	NH <sub>2</sub>
Abarelix <sup>[b]</sup> (Praecis)	D Nal	D Cpa	D Pal	Ser	N Me Tyr	D Asn	Leu	Lys (iPr)	Pro	D Ala	NH <sub>2</sub>
Antidel <sup>[c]</sup> (Ares Serono)	D Nal	D Cpa	D Pal	Ser	Lys (Nic)	D Cit	Leu	Lys (iPr)	Pro	D Ala	NH <sub>2</sub>
Teverelix <sup>[d]</sup> (Ardana)	D Nal	D Cpa	D Pal	Ser	Tyr	D hCit	Leu	Lys (iPr)	Pro	D Ala	NH <sub>2</sub>
Fe 200486 <sup>[c]</sup> (Ferring)	D Nal	D Cpa	D Pal	Ser	Aph (Hor)	D Aph (Cba)	Leu	Lys (iPr)	Pro	D Ala	NH <sub>2</sub>
Nal-Glu <sup>[c]</sup> (NIH)	D Nal	D Cpa	D Pal	Ser	Arg	D Glu (AA)	Leu	Arg	Pro	D Ala	NH <sub>2</sub>

[a] = Market, [b] = Phase I, [c] = Phase II, [d] = Phase III

LHRH II (cLHRH) has been isolated from chicken [182] and from the forebrain of the teleost fish, the lamprey eel. LHRH III (lLHRH) has also been identified and characterized [183–185]. LHRH II has been conserved from fish to humans [170, 182–184]. In humans, LHRH II is synthesized in several extrapituitary tissues like kidney, bone marrow, and prostate at significant higher levels [186] and in the female reproductive tract such as placenta, endometrium, breast, ovary and granulosa cells [187–189].

LHRH hormones have manifold functions besides reproductive maintenance, including neuroendocrine (growth hormone release in fish), paracrine (placenta and gonads), autocrine (LHRH neurons, immune cells, breast and prostate cancer cells), neurotransmitter in central and peripheral nervous system (sympathetic ganglion, mid brain), energy and feeding behavior [175–178, 184, 190–194].

Direct effects of LHRH agonists and antagonists have been studied – most importantly, the antiproliferative effects of LHRH I on hormone-dependent and -independent tumor cells, including gonadal cancers like ovarian, endometrial, prostate and breast and non-gonadal cancers like melanoma. In endometrial, ovarian, breast and prostate cancers *in vitro* proliferation was inhibited by agonists and antagonists of LHRH I in a time and dose dependent manner [195–197]. Interestingly, the effects on LHRH agonists/antagonists seem to be different in tumor tissue of the reproductive tract, where LHRH antagonists have agonistic effects on the LHRH receptor type II [195]. Further functions of LHRH in gonadal malignancies and melanoma were antimetastatic, through effects on IGF-I, EGF and c-fos expression and antimetastatic-affecting matrix metalloproteinases, adhesion molecules, and plasminogen activator in prostate cancer cells [198].

#### 6.4.2

##### **Analogs of LHRH**

The highly conserved sequence of the amino (pGlu His Trp Ser) and carboxy (Pro Gly NH<sub>2</sub>) termini suggests that these amino acids are critical for receptor binding and activation. The amino terminus is involved in receptor binding and activation, whereas the carboxy terminus contains regions for receptor binding only. Structural changes in these particular amino acids created agonists and antagonists that had been clinically exploited for the stimulation of hormone production, for contraception and treatment of hormone-dependent cancers and diseases [170]. Substitution of amino acids at the amino terminal produced compounds with analogous antagonistic properties, including Cetrorelix and Ganirelix, which are currently marketed. Agonists on the market include Lupron, Zoladex, Sepprelin, Triptorelin and Buserelin (for sequences see Millar et al. 2004 [170]). Substitution of amino acid 6 by D-Gly enhances activity in the pituitary receptor [170] (Table 6.3). Table 6.3 lists amino acid sequences for various agonists and antagonists. Analogs of LHRH are applied for hormonal ablation, whereas antagonists (like Cetrorelix) seem to have antiproliferative effects on ovarian and endometrial cancers rather than the agonist Triptorelin.

## 6.4.3

**Receptors for LHRH**

LHRH affects the proliferation and metastatic potential of many cancers directly [171–173]. Autocrine/paracrine loops were identified and studied in breast cancer [199, 200], prostate cancer [201], ovarian cancer [202] and melanoma cell lines [172]. LHRH receptors not only are expressed in gonadal malignancies like prostate [4, 5, 203], breast [10], ovarian [204–208], endometrial cancers [26, 209], but have also been detected in several non-gonadal malignancies, such as laryngeal cancers [24] renal [28], pancreatic [15, 16], brain [29], melanoma [22, 27] liver [25], colon [13, 14, 210] and recently in non-Hodgkin's lymphoma [23] (Table 6.1). These findings suggest that there may be a connection between cancer and LHRH receptor expression. LHRH receptors are very widespread among malignancies rather than healthy tissues.

Consequently, LHRH seems to be a very appropriate candidate for specific targeting of malignancies. Most tumors overexpress LHRH receptors in much higher concentrations than normal tissue (where they can be entirely absent) [125, 211]. Non-malignant tissue of lung, liver, skeletal muscle, pancreas, other visceral organs and kidney express little or no LHRH receptors [11, 203, 212, 213].

Although LHRH-receptor transcripts detected in breast and ovarian cancers are identical to those in pituitary [214] the receptors may differ functionally. In binding studies [12], pituitary LHRH-receptors showed high affinity for agonists such as buserelin (nanomolar  $K_d$ ), whereas most LHRH-receptors in extrapituitary sites, including malignancies, have low affinity (micromolar  $K_d$ ) but show higher receptor capacities (Table 6.4).

For example, LHRH receptors were found in 57% of patients with pancreatic cancers and 67% in pancreatic inflammatory disease, compared with normal tissue with only 9% [16]. Pancreatic cancers showed low-affinity binding sites for LHRH in the membrane, and high-affinity binding sites in the nuclei [9]. In melanoma cells the LHRH receptor type I has high affinity/low capacity [172].

LHRH receptors have been cloned from mouse, rat, sheep, cow and human with an amino acid sequence homology of >85% [213–222]. The nucleotide sequence of LHRH receptors from breast, ovarian, endometrial and prostate cancers is identical to that of the pituitary receptor [5, 197, 213–215, 223–228].

The LHRH receptor belongs to the large superfamily of the seven-transmembrane domain receptors that bind G-proteins (G-protein binding receptors, GPBR) (Fig. 6.3) [229–232]. Typically, GPBRs contain a C-terminal cytoplasmic tail, which is lacking in the LHRH receptor type I. This C-terminal tail is phosphorylated by ligand binding and facilitates the binding of  $\beta$ -arrestins, G protein activation, desensitization and internalization of the receptor, and down-regulation via endocytosis and processing [233]. The internalization kinetics of LHRH-receptor type I [234] showed a 20-fold increase in uptake rate constants of the bound radioligand within 1 h compared with kinetics in wild-type TSH receptor, another member of the GBP receptor family (with cytoplasmic tail).

Tab. 6.4. LHRH-receptor binding affinities and capacities.

Cell type	High affinity LHRH-receptor		Low affinity LHRH-receptor	
	$B_{max}$ (fmol/ $10^6$ cells)	$K_d$ (nM)	$B_{max}$ (pmol/ $10^6$ cells)	$K_d$ ( $\mu$ M)
$\alpha$ T3-1 <sup>[a]</sup>	$231.9 \pm 53.7$	$0.867 \pm 0.26$		
PC-3 <sup>[a]</sup>	$8.6 \pm 3.3$	$0.185 \pm 0.08$		
PC-3 <sup>[b]</sup>	$97.2 \pm 10$	$15.3 \pm 1.5$	$118.2 \pm 24$	$0.625 \pm 0.022$
LNCaP <sup>[b]</sup>	$355.3 \pm 19$	$12.8 \pm 2.5$	$203 \pm 31$	$0.438 \pm 0.016$
MCF-7 <sup>[c]</sup>	$307 \pm 21$	$10.8 \pm 3.1$	$138 \pm 26$	$0.358 \pm 0.041$
MDA-MB-435S <sup>[c]</sup>	$64.6 \pm 10$	$14.38 \pm 1.8$	$298 \pm 36$	$0.936 \pm 0.054$
Hec1B	72	1.5	42	3.1
NIH-OVCAR3	49	2.3	73	2.4

<sup>a</sup>Yang [160] passage # not reported.

<sup>b</sup>Leuschner [130] – # 20.

<sup>c</sup>Leuschner unpublished data – # 237.

<sup>d</sup>Gründker [279].

$\alpha$ T3-1 (mouse pituitary, endogenous LHRH receptors, Kaiser [280]);

Hec1B [d] endometrial cancer cell line; NIH-OVCAR3 [d] ovarian cancer cell line.

#### 6.4.4

#### Function–Signal Transduction Pathways

Signal transduction pathways activated by binding of LHRH to a tumor's receptor are quite different to the classical pituitary binding. The physiological significance of this remains under investigation (Fig. 6.4).

In the pituitary, binding of LHRH to its receptor (type I) initiates coupling to  $G_{\alpha q/11}$  binding followed by activation of phospholipase C (PLC), and hydrolysis

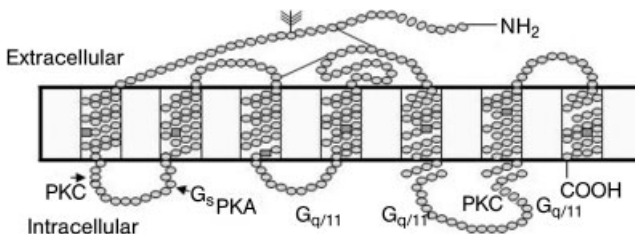
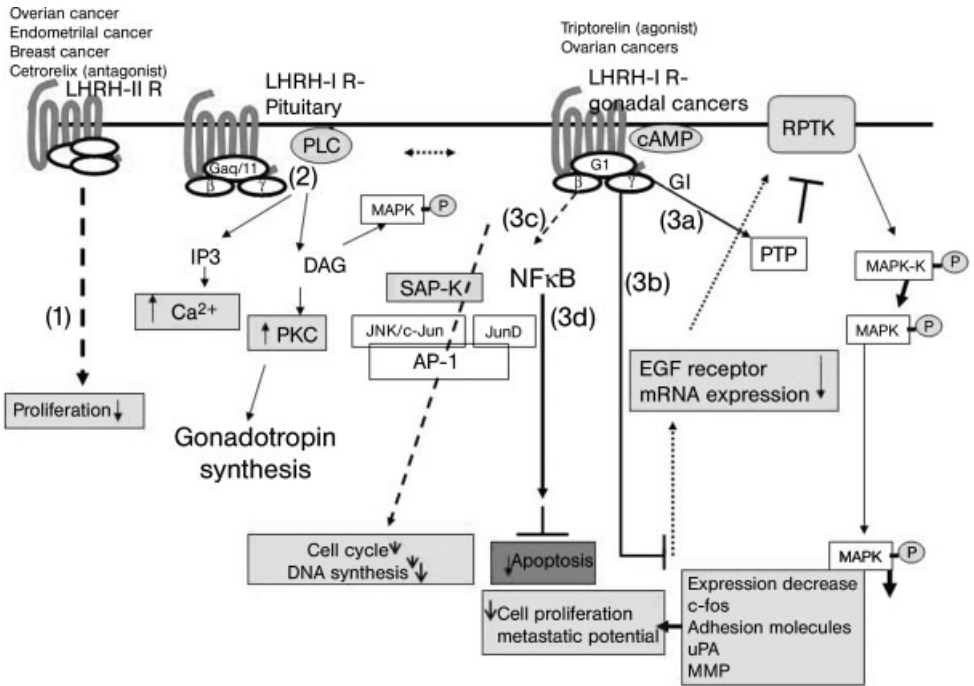


Fig. 6.3. Schematic of the human LHRH-receptor as an example of a seven-transmembrane receptor G protein binding receptor [170].



**Fig. 6.4.** Signal transduction pathways activated by LHRH-receptor binding in pituitary, gonadal and cancerous tissue. (1) Unknown signaling cascade leading to reduction of cell proliferation; (2) signal transduction pathway in pituitary for gonadal function; (3) signaling cascades for LHRH receptor I in malignancies: (3a) signaling resulting in decrease of cell proliferation

through MAP kinase pathway, (3b) signaling interferes with EGF receptor expression, (3c) signaling cascade that result in reduction of cell cycle and reduction of DNA synthesis, (3d) signaling cascade that reduces apoptosis. Abbreviations are defined at the end of this chapter. (Based on Ref. [207] with modification from Refs. [173, 206, 244, 245, 253, 281].)

of phosphoinositide to diacylglycerol (DAG) and inositol 1,4,5-triphosphate (IP3). These secondary messengers mobilize calcium from intracellular stores and activate PKC (protein kinase C) [235, 236]. LHRH also activates PLA2 (phospholipase A2), PLD and MAP-kinases (mitogen-activated protein), providing signals for gene expression for gonadotropin synthesis and secretion [235, 236]. The physiological function for this difference is unresolved.

Binding of LHRH to gonadal and receptors on cancer cells activates different signal transduction cascades. In malignant tissue, LHRH receptors have been suggested to regulate cell proliferation and the metastatic potential in tumors. LHRH receptor expression in tumors is associated with the phosphorylation of the epidermal growth factor receptor: the activated EGF receptor phosphorylates a protein corresponding to the LHRH receptor [237, 238]. Growth factor receptor expression can be reduced in the presence of LHRH most likely by phosphotyrosine phosphatase

tase (PTP), which in turn is connected to the G-protein  $\alpha_i$  in tumors [239, 240] (Fig. 6.4).

In cancer cells, LHRH receptor coupling occurred to multiple G proteins and the activation of multiple effectors has been reported. In prostate cancer cells, LHRH I binding facilitates the coupling of  $G\alpha_i$  protein [241], and human gynecological cancer coupling of  $G\alpha_q$  and  $G\alpha_i$  was demonstrated in ovarian and uterine cancer cells [20, 240].  $G\alpha_i$  coupling is prevalent in cancers, such as in ovarian [239, 240, 242], uterine leiomyosarcomas, uterine endometrial carcinomas and human prostate cancers [241]. Coupling to  $G\alpha_i$  protein is poorly understood and it is suggested that  $G\alpha_i$  activation underlies the antiproliferative effects of LHRH in cancers [240, 243].  $G\alpha_i$  coupling can be activated by both agonist and antagonists of LHRH, suggesting the involvement of an additional form of LHRH receptor distinct from the pituitary receptor type [239, 241]. Antiproliferative action in choriocarcinoma, benign prostate hyperplasia and human embryonic kidney cells, all of which express LHRH receptor type I, was demonstrated with agonists and some antagonists through activation of  $G\alpha_i$  coupling. The signal transduction resulted in activation of caspase and trans-membrane transfer of phosphatidylserine to the outer membrane, JNK and p38 [244].

In hormone-dependent tumors, binding of LHRH to its receptor decreased cyclic AMP levels, which is followed by an activation of phosphotyrosine phosphatase (PTP). This event interferes with the mitogenic signal transduction pathways, which normally activate growth factor cascades such as MAP kinase. The transcription is affected downstream, which include genes such as matrix metalloproteinases, urokinase plasminogen activator (genes for metastatic potency), c-fos (a protooncogene), and cell adhesion molecules. The overall result is reduction of proliferation and interference with the metastatic potential of the cancer cells.

Antagonistic LHRH analogs inhibited  $G\alpha_q/11$ -based signaling, suggesting that their antiproliferative effect on reproductive tumors could be dependent on ligand-selective activation on a  $G\alpha_i$  form of LHRH-receptor I through stress-activated protein kinase pathways (SAP-K) [244].

In hormone-dependent and -independent prostate cancers the antiproliferative effects of LHRH I were attributed through EGF and IGF receptor reduction initiated by different molecular mechanisms, dependent on hormone requirements of these types of cancer. In hormone-dependent prostate cancer cells LHRH I counteracts the stimulatory effects of epidermal growth factor (EGF) by decreasing the EGF receptors and insulin-like growth factors (IGF) [245, 281].

In breast, ovarian and endometrial cancers LHRH can bind to either  $G\alpha_q$  or  $G\alpha_i$ , the latter inhibiting proliferation. Emons et al. have found that endometrial and ovarian cancer cells PTP (phosphotyrosine phosphatase) are activated by LHRH/LHRH-receptor action, which counteracts the phosphorylation of EGF receptors, affects the growth factor signal transduction cascade (MAP-K, c-fos), and interferes with cell proliferation [239, 246–248] (Fig. 6.4). Positive correlation between EGF receptor activation and LHRH receptors were observed in various LHRH receptor expressing cancers [6, 24]. Consequently, EGF receptors can be downregulated to-

gether with LHRH receptors through LHRH-analogs or LHRH-targeting treatments [6, 249–251].

LHRH can influence apoptosis in cancer cells through activation of nuclear factor  $\kappa$ B [252, 253]: LHRH agonists can activate the cJun N-terminal kinase/activator protein 1 (AP-1) pathway, protein kinase C (PKC) or mitogen-activated protein kinase (MAPK/ERK) [20]. In contrast, when the antagonist cetorelix was tested in ovarian and endometrial cancer cells the antiproliferative effects were not mediated through LHRH receptor type I, suggesting binding to, therefore, LHRH receptor type II. The signal transduction pathway of LHRH II is still unknown [20].

#### 6.4.5

#### LHRH Receptor-mediated Uptake

Extensive internalization and downregulation of the receptor via endocytosis and processing has been studied and described in detail for the pituitary receptor [233]. Receptor internalization is highly influenced by the second intracellular loop of the seven-transmembrane receptor [254].

The COOH-terminal tail, which is lacking in the pituitary LHRH-receptor, determines the internalization and the recycling kinetics and causes resistance of the receptor to desensitization. Several examples of this observation have been reported. For example, deletion of the cytoplasmatic tail in TSH receptors decreased the internalization [255]. The chicken LHRH receptor showed rapid internalization that was dependent on the cytoplasmatic tail [256]. As mentioned earlier the pituitary LHRH receptor (type I) lacks the cytoplasmatic tail; however, the receptor still internalized and recycled, and is resistant to desensitization [257, 258]. These turnovers are much slower than with other GPCRs: While angiotensin II internalized 50–60% [259] and GRP receptors up to 80% [260, 261] of their agonists within 1 h, the LHRH receptor type I internalized only 26% [254]. This agrees with results for the LHRH-II receptor in the marmoset and rhesus monkey containing a C-terminal, cytoplasmatic tail that facilitated a more rapid internalization [262, 263].

Receptor-mediated endocytosis can be described with the four-compartment model [264] that includes (1) receptor endocytosis from cell surface to endosome, (2) recycling from endosome to plasma membrane, (3) receptor movement from endosome to lysosome for degradation, and (4) delivery of *de novo* synthesized receptors to the plasma membrane (Fig. 6.5). The classical pathway involves GPCR kinases,  $\beta$ -arrestin, clathrin-coated pits and GTPase dynamin.

As a representative mode for receptor internalization and recycling the process is described here for the type I receptor. Despite the lack of cytoplasmatic tail the LHRH receptor type I displays distinct characteristics described for other GPCRs that internalized via a clathrin-dependent mechanism, appeared to be independent of  $\beta$ -arrestin levels and recycled through an acidified endosomal compartment (Fig. 6.5).

LHRH incubation showed internalization of the ligand–receptor complex and redistributed into vesicular compartments [234]. The internalization was tempera-

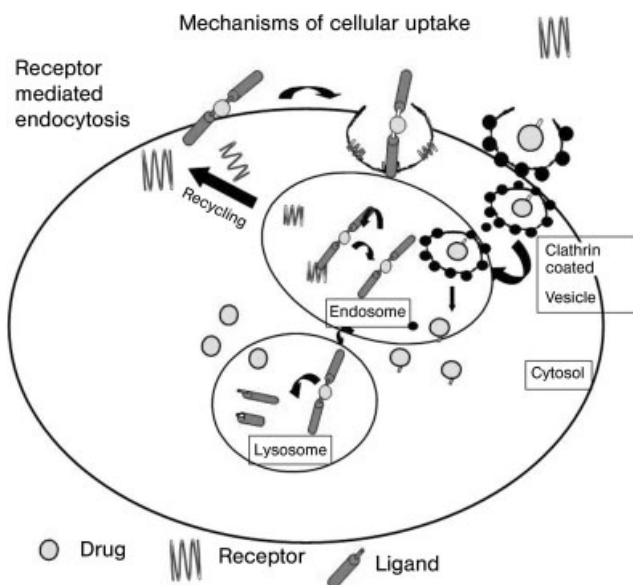


Fig. 6.5. Receptor-mediated endocytosis and recycling of the receptor.

ture and time dependent and was suppressed at 4 °C; internalization was observed after 20 min and reached its maximum after 1–2 h.

The uptake mechanisms through LHRH receptors are cell type dependent and dependent on the type of LHRH receptor. In HeLa cells, internalization of the receptor was independent of dynamin; clathrin mediation was involved in the internalization of the receptor [265]. Receptor recycling to the plasma membrane in HEK 293 cells (human embryonic cells) was observed as early as 15 min and completed after 1 h. The intracellular pool of receptors was decreased by 68% due to reappearance of receptors at the plasma membrane. The reappearance of plasma membrane receptors was clearly due to recycling of the receptor rather than by *de novo* synthesis. Recycling of the receptors caused a loss of 10% of the initially detected surface receptors. When kinetics of LHRH and TSH (retained cytoplasmatic tail) receptors were compared, significantly lower rates were determined in HEK 293 cells for the endocytotic rate (16-fold), recycling (2.5-fold) and degradation rates (30-fold) for the LHRH receptor [234].

#### 6.4.6

#### LHRH Receptor Type II

The existence of two LHRH isoforms in human tissue led to a search for a second LHRH receptor in human tissue. These studies were supported by the following



observations: Effects on LHRH agonists/antagonists were different in tumor tissue of the reproductive tract, where LHRH antagonists have agonistic effects on the LHRH receptor type II. A recent study on human endometrial cancers and ovarian cancer cell lines demonstrated that the proliferation of these human cancer cells was dose and time dependent, but independent of the LHRH receptor I, suggesting the existence of a second LHRH receptor [206]. LHRH type II has been found in ovarian cancer cell lines [266] and had antiproliferative activity. In human malignant tumors *in vitro*, LHRH I agonists and antagonists inhibited the cell proliferation in a dose and time dependent manner. LHRH type II has antiproliferative effects on gynecological cancers to a much higher efficacy than triptorelin [267]. RTPCR and Southern Blot analysis showed the expression of LHRH receptor II mRNA in ovarian and endometrial cancer cell lines [266]. In addition, these cell lines responded to LHRH II with reduction in proliferation, to a much higher degree than with LHRH I or triptorelin [267]. In breast cancer cells the antiproliferative effects of Triptorelin (a LHRH-antagonist) and a LHRH II analog inhibited epidermal growth factor induced signal transduction and restored sensitivity to tamoxifen [313]. Recently, in a clinical study, primary and metastatic stromal sarcoma tested positive for LHRH receptor I and II expression using immunohistochemistry methods [209]. Interestingly, recurrent tumors had the highest levels in LHRH receptor I and II expression, suggesting a link between malignancy and LHRH receptors types [209].

Studies on human prostate cancer cells *in vitro* showed the existence of an 80-kDa protein that specifically bound to LHRH II in addition to the conventional LHRH I receptor. In this study, efficacy and function was studied and the authors found that a novel LHRH II antagonist completely inhibited Ca increase and induced, at high concentrations, cell death through apoptotic processes [268].

In ovarian and endometrial cancers, LHRH II is a more potent inhibitor for cell proliferation [252], receptors of type II have a higher sensitivity to LHRH II ligand [269, 270], and LHRH agonists and antagonists inhibited tumor growth [272]. Type II LHRH receptor has been cloned from monkeys and was highly selective to LHRH II [212, 263, 271]. To date, a functional form of the LHRH receptor type II has not been found in humans, although several observations suggest its existence. Therefore, it is referred to as a putative receptor. Millar found that the type II receptor was more widely distributed: mRNA for LHRH receptor-type II was found in numerous pituitary, brain, mammary glands, uterus, testes, prostate, seminal vesicles, thyroid, heart, pancreas and adrenal tissue, including ovarian and endometrial cancers [193, 212, 242, 268, 273]. In prostate cancer, a novel LHRH II binding protein was detected recently [268], suggesting the existence of a type II receptor in prostate cancer cells. In human pituitary and brain, immunoreactivity to the LHRH receptor type II was demonstrated [212].

Humans may be particularly unusual with respect to the LHRH control of their reproductive axis in that they possess two distinct LHRH precursor genes, on chromosomes 8p11-p21 and 20p13, but only one conventional LHRH receptor subtype

(type I LHRH receptor) encoded within the genome, on chromosome 4. A disrupted human type II LHRH receptor gene homologue is present on chromosome 1q12. In humans, on chromosome 1 and 14 in various tissues a gene for the LHRH receptor II was found, which is not expressed because it contained a premature stop codon [275, 276]. Evidence in support of this concept is available following the characterization of the chromosomal loci encoding the human type II LHRH receptor homologue, a rat type II LHRH receptor gene remnant (on rat chromosome 18) and a mouse type II LHRH ligand precursor gene remnant (on mouse chromosome 2) [277]. The lack of the C-terminal tail causes the type I LHRH receptor to be slowly internalized and to be resistant to desensitization [257, 258]. In contrast, type II LHRH receptors are rapidly internalized and desensitized, contain the c-Terminal tail, and activated a different signal transduction cascade [257, 278]. The LHRH type II specifically induces an intracellular  $Ca^{2+}$  increase that was inhibited by triptorelix in prostate cancers [268]; LHRH receptor type II was found in monkeys, prostate cancer cells show a  $G_{\alpha i}$  linked activation signaling cascade [241]. In ovarian cancer the LHRH-receptor II coupled to the  $G_{\alpha q}/11$  and activated extracellular signal regulated kinase (ERK1/2), but differs in activating p38 and mitogen-activated protein (MAP) kinase [19].

The above-summarized results and the fact that endometrial, ovarian, breast and prostate cancer cells have two types of LHRH binding sites (low- and high-affinity/low- and high-capacity) indicate the existence of a second LHRH receptor type. Only the high-affinity/low-capacity receptor type resembles the LHRH receptor type I form of the pituitary. There are reasons to believe that the low affinity binding site on these cancer cells is the putative LHRH receptor II. mRNA for the LHRH receptor type II is expressed in human endometrial and ovarian cancer cells. LHRH II was more potent in its antiproliferative effect than LHRH I agonists [19]. Leung et al. found similar results in ovarian cancers [273]. In pancreatic cancers the low-affinity receptor was located in the cell membrane, whereas the high-affinity receptor was in the nuclear membrane [9] (Table 6.4).

In summary, LHRH is a most appropriate ligand for targeting cancers, as there are receptors overexpressed in gonadal tissue, multiple cancers and pituitary. In addition, the LHRH receptor signal transduction pathway in tumor cells is different to normal cells in that the classical PLC/PKC pathway from pituitary is not activated by LHRH binding to a LHRH receptor in a tumor cell; multiple G protein subgroups can be activated. The LHRH binding activates signals to mitogenic signal transduction pathways related to growth factor receptors and tyrosine kinase activities as well as the activation of antimetastatic signals [247, 281].

The expression of LHRH II in malignant cells and tumors could be exploited by targeting even more specifically malignancies, increasing uptake through activation of tumor-specific signal transduction cascades and improving the intracellular delivery of nanoparticles conjugated with LHRH to highest efficiency.

The next section reviews the use of nanoparticles linked to LHRH for magnetic resonance imaging, treatment and drug delivery, with emphasis on specific properties of the *in vivo* use of these nanoparticles.

## 6.5 LHRH-bound Magnetic Nanoparticles

### 6.5.1 Synthesis and Characterization

The nanoparticles referred to here are superparamagnetic iron oxide nanoparticles (SPIONs) that were fabricated, by wet chemical synthesis, with amine groups on their surface, which facilitated the binding of LHRH through carbodiimide activation. The binding of LHRH or Hecate to SPIONs was confirmed by FTIR (Fourier-transformation infrared) spectroscopy and HPLC analysis. The SPION surface was saturated by the LHRH peptide, as FTIR spectral analysis of peptide bound magnetite nanoparticles revealed the absence of characteristic bands of  $-\text{NH}_2$  ( $3200$  and  $1625\text{ cm}^{-1}$ ) present in unbound nanoparticles [297, 300]. The LHRH-SPIONs were monodisperse under transmission electron micrographs and had an average diameter of  $10\text{--}20\text{ nm}$ . Both free SPIONs and LHRH-SPIONs retained the cubic spinel structure. Moreover, the particles remained superparamagnetic, regardless of binding to the ligand (Fig. 6.6). Unconjugated SPIONs showed a higher saturation magnetization than LHRH-SPIONs ( $M_s = 72.1$  compared with  $30.6\text{ emu g}^{-1}$ ). The coercivity for LHRH-SPIONs was greater than for SPIONs alone (Fig. 6.6). Zeta potential measurements revealed that SPIONs were positively charged ( $\zeta = 28.5 \pm 1.93\text{ mV}$ ), whereas LHRH-SPIONs were almost neutral ( $\zeta = -2.2 \pm 0.58\text{ mV}$ ). Similar values were reported by Shieh et al. [301] for nanoparticles of similar surface chemistry ( $\zeta = 23.3\text{ mV}$ ). Magnetic data were calculated per g of powder of both SPIONs and LHRH-SPIONs.

In another study LHRH conjugated nanoshells were prepared for treatment with hyperthermia. To increase the iron particle concentration within the tumor tissue,

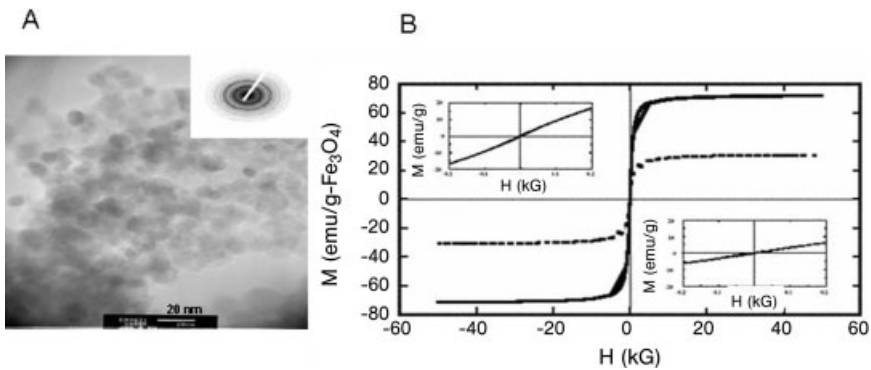


**Fig. 6.6.** (A) TEM micrograph of LHRH-SPION nanoparticles. Inset: electron diffraction pattern. (B) Hysteresis and saturation magnetization at 300 K for LHRH-SPIONs (dashed line) and SPION nanoparticles (solid line).

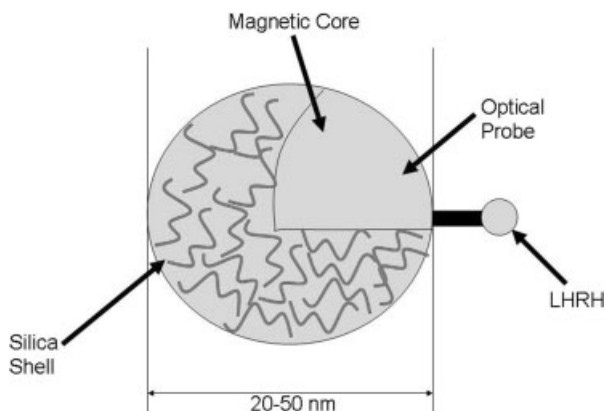


Fig. 6.7. Nanoclinics for hyperthermia treatment [157].

nanoparticles were decorated with LHRH to target the cancer cells and increase the cellular accumulation. Bergey et al. have developed a specific targeting device [157]. The particle consisted of a silica shell (7 nm thick) that housed inside a magnetic core of  $\text{Fe}_2\text{O}_3$  (18 nm diameter), a two-photon optical probe and, on the outside, carried the ligand LHRH (DLys6) as targeting moiety; the optical probe served as a tracking device. The final particle diameter ranged between 20 and 50 nm – small enough to diffuse into tissue without destroying the cells. The ligands were covalently attached to the silica surface through spacer molecules (Fig. 6.7). In this nanoclinic, the ligands consisted of an analog of LHRH that has higher binding affinity to the LHRH receptor due to exchange of amino acid 6 into D-Lys.

### 6.5.2

#### Treatment using Hyperthermia

Tumor cells are more sensitive to temperatures above  $42^\circ\text{C}$  than normal cells [282, 283] and can be destroyed by increasing locally the temperature to  $41\text{--}42^\circ\text{C}$  for 30 min [284–287]. Magnetic particles generate heat when exposed to an alternating magnetic field (AMF) by hysteresis loss [287–289]. These exposures require high power to elicit heat.

The increase of temperature occurs during the thermal loss resulting from re-orientation of the magnetism of the magnetic material with low electrical conductivity [288]. The size of the magnetic particle, which can be controlled by appropriate synthesis methods, determines the heating potential, as nanoparticulate size compared with micro size and degree of dispersion reduces the required AC power [290, 291]. Specific absorption power rates (SAR) have been determined in suspensions of magnetite nanoparticles of various size and coating. SAR of dextran ferrites were  $180\text{--}210\text{ W (g-Fe)}^{-1}$  (120 nm), sonicated dextran ferrites ranged from 12 to  $240\text{ W (g-Fe)}^{-1}$ , uncoated ferro-suspension  $0\text{--}45\text{ W (g-Fe)}^{-1}$  (6–10 nm). Ultrasonification caused dispersion of agglomerated particles and can destroy in

part the dextran coating. Carboxymethyldextran magnetite particles (130 nm) had an SAR of  $90 \text{ W (g-Fe)}^{-1}$ . SAR data allow an estimate of the amount of particles necessary to heat human tissues [292, 293]. Ferrofluids directly injected into tumor tissue destroyed tumor cells after exposure to the magnetic field [289]. This effect was highly specific and cell destruction was only observed in cells containing the magnetic particles [294]. This process is known as magnetocytolysis.

Similar to the diagnostic magnetic resonance imaging approach, an increase in intracellular particle number and concentration increases the efficacy of tumor destruction through hyperthermia.

*In vitro*, LHRH expressing human breast cancer cells, MCF-7, and the receptor negative ovarian cancer cell line were incubated with nanoclinics linked to LHRH or nanoclinics alone. The LHRH-nanoclinic uptake was time dependent, and nanoshells accumulated within 30 min. In contrast, a human ovarian cancer cell line that did not express LHRH receptors did not incorporate LHRH-nanoshells.

LHRH decorated nanoparticles were eight times more potent in destroying MCF-7 cells. The number of lysed cells was linearly dependent on the magnetic field exposure time and the concentration of nanoparticles. The same nanoshells without LHRH resulted in comparable cell lysis in MCF-7 and UCI 107 cells. Up-regulation of LHRH receptors through EGF increased magnetocytolysis two-fold, whereas downregulation of receptors decreased the treatment effect 2.5-fold.

Several crucial observations were made that support the high specificity of these ligand-conjugated nanoclinics: (a) the LHRH-nanoclinics specifically entered the receptor-expressing MCF-7 cells; (b) nanoclinics without the ligand only incorporated particles to a significantly lower amount and were independent of the cell type used; and (c) LHRH-receptor positive MCF-7 cells incorporated higher amounts of LHRH-nanoclinics when LHRH receptors were upregulated through EGF, and lower amounts after downregulation of receptors. These data showed the importance of highly selective nanoclinic uptake.

These studies demonstrated specific targeting of cancer cells and incorporation of magnetic nanoparticles conjugated to LHRH and showed *in vitro* accumulation of magnetic nanoparticles through receptor-mediated endocytosis. These results suggest that specific targeting can increase the efficacy of hyperthermic therapy and keep other organs unaffected.

### 6.5.3

#### Treatment using Lytic Peptides

##### 6.5.3.1 Destruction of Metastases through LHRH-SPION-Hecate

Recent studies on LHRH-SPIONs conjugated with Hecate, a membrane destroying peptide [6, 295, 315–317], resulted in tumor destruction and elimination of lung metastases in nude mice bearing LHRH receptor expressing MDA-MB-435S.luc breast cancer xenografts. Tumor bearing mice were injected once a week for 3 weeks with LHRH-SPION-Hecate conjugates in the presence and absence of LHRH, SPION-Hecate or saline. At necropsy tumor cells were determined in lung homogenates, and iron contents were also determined. In mice treated with

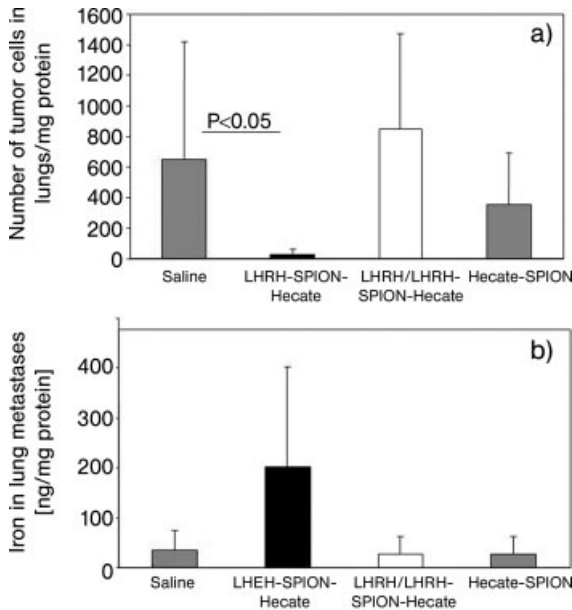


**Fig. 6.8.** LHRH-SPION-Hecate destroys lung metastases in MDA-MB-435S.luc tumor-bearing mice; co-injection with LHRH or Hecate-SPIONs does not destroy lung metastases (A). Iron is detectable in targeted treatment groups after 1 week (B).

LHRH-SPION-Hecate, tumor cell death occurred in primary tumors and lung metastases. Unconjugated SPION Hecate did not reduce the number metastatic cells in lungs (Fig. 6.8) or destroy the primary tumors when compared with saline controls. Iron oxide particles in the treated organs were still detectable 1 week after injections, suggesting that LHRH-SPION-Hecate may be useful in imaging and treating the cancer, most importantly serving as a monitoring tool for treatment response [318].

#### 6.5.4

#### Detection of Tumors and Metastases

##### 6.5.4.1 Targeted Delivery of SPION Contrast Agents for MRI

The development of iron oxide nanoparticles as a contrast agent for MR images requires high accumulation of nanoparticles in the cells of the target tissue. Relaxation times in the acquisition of magnetic resonance imaging, i.e., the contrast of the image, is increased with larger particles [151]. Compartmentalized particles and clusters have larger relaxation rates than free dispersed particles [152]. Highly efficient receptors were required on human breast cancer cells to increase the iron accumulation within the cells. Furthermore, the particles were designed to provide

target specificity, a long circulation time and low opsonization to escape macrophage recognition.

The following outline describes the development of LHRH-targeted nanoparticles to human breast cancer cells. The increase of cellular accumulation of iron oxide nanoparticles in LHRH receptor positive human breast cancer cells and their metastases iron oxide nanoparticles were developed, which carried LHRH as targeting moiety. Human breast cancer cells overexpress LHRH receptors. Recently, the targeted destruction of primary tumors and metastases had been shown in human breast cancer cells, MDA-MB-435S.luc, both *in vitro* and *in vivo* [8, 295–299].

#### 6.5.4.2 *In Vitro* Studies on Receptor-targeted LHRH-SPION Uptake

The accumulation of ligand conjugated and unconjugated SPIONs was compared in MDA-MB-435S.luc, TM4 mouse Sertoli cells to determine whether the iron accumulation was specific for individual receptors on the target cells (Fig. 6.9A). In

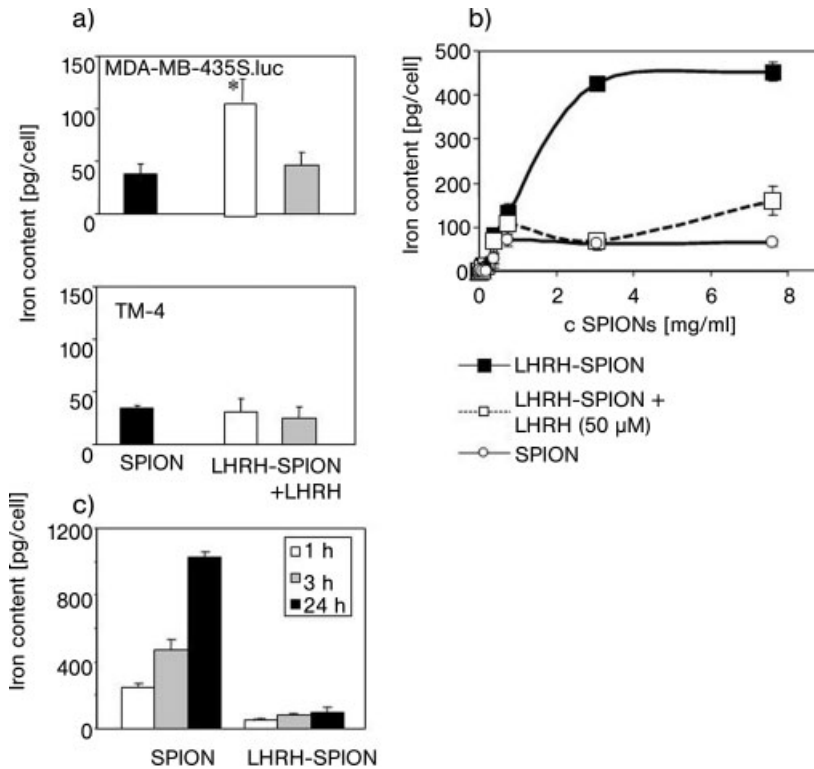


**Fig. 6.9.** (A) Iron uptake from SPIONs, LHRH-SPIONs and LHRH-SPIONs plus LHRH in LHRH receptor expressing breast cancer cells (MDA-MB-435S.luc) and receptor

negative mouse Sertoli cells (TM4). (B) Saturation kinetics in MDA-MB-435S.luc cells. (C) Incorporation of SPIONs or LHRH-SPIONs into THP-1 macrophages [297].

LHRH receptor overexpressing human breast cancer cells LHRH-SPIONs accumulated quickly and reached an intracellular iron concentration of  $452 \text{ pg cell}^{-1}$  whereas free SPIONs reached  $51 \text{ pg cell}^{-1}$  as the highest concentration (Fig. 6.9B). Blocking of the LHRH receptor significantly prevented LHRH-SPION uptake, suggesting that specific receptor-mediated uptake was the mechanism of uptake. Maximal concentrations within the breast cancer cells were reached within 1 h, whereas low temperature ( $4 \text{ }^{\circ}\text{C}$ ) prevented receptor-mediated iron uptake to less than  $1.1 \text{ pg cell}^{-1}$ . The mouse Sertoli cell line showed, at all concentrations, iron uptake between 29 and  $37 \text{ pg cell}^{-1}$  irrespective of LHRH conjugation (Fig. 6.9A).

Most importantly, macrophages incorporated significantly less LHRH-SPIONs ( $85 \text{ pg cell}^{-1}$ ) than free SPIONs ( $246 \text{ pg cell}^{-1}$ ) (Fig. 6.9C), suggesting that LHRH provided a coating as well a targeting moiety. This was expected as LHRH-SPIONs were neutral, while SPIONs were positively charged. Others have shown that neutral nanoparticles are less easily incorporated by macrophages than are charged nanoparticles, predicting an increased circulation time *in vivo* [86, 297–299].

TEM sections from human breast cancer cells *in vitro* showed that LHRH-SPION accumulation in the breast cancer cells resulted in cluster formation in the cytosol and the nucleus. In contrast, no iron particles were observed in cells incubated at  $4 \text{ }^{\circ}\text{C}$  [297–299]. Compared with other ligand conjugated nanoparticles LHRH-SPION uptake was highly efficient and resulted in the highest iron contents in LHRH receptor expressing cancer cells. Dextran-coated nanoparticles  $<10 \text{ nm}$  in diameter resulted in  $0.9\text{--}1.3 \text{ pg-Fe per cell}$  [120], whereas Her2/neu targeting of the same cells increased the uptake by a factor of 2.6 pg-Fe per cell. Folate-linked iron oxide nanoparticles reached a maximal level of  $75 \text{ pg-Fe per cell}$  in BT20 breast cancer cell incubation [117]. CD-8 conjugated crosslinked iron oxide nanoparticles were incorporated into T cells after 1 h of incubation at concentrations up to  $100 \text{ pg-Fe per cell}$  [122]. The targeted up-take of nanoparticles in cancer cells has been demonstrated for ferrofluids: dextran-coated Monocrystalline Iron Oxide Nanoparticles (MIONs) linked to transferrin resulted in a 10-fold increase in accumulation in rat glioma cells compared with free MIONs [111]. In contrast, human fibroblasts did not incorporate transferrin-linked MIONs; the particles were only bound to the membranes, but not internalized [302]. LHRH iron oxide nanoparticles coated with a silica shell specifically targeted and accumulated in MC-F7 human breast cancer cells *in vitro* [157].

Anionic maghemite chelate dimercaptosuccinic acid particles were incorporated in macrophages at up to  $6 \text{ pg-Fe per cell}$ , and in HeLa cancer cells up to  $40 \text{ pg-Fe per cell}$ , and showed saturation kinetics [152]. HIV-1 tat dextran-coated SPIONs were incorporated into CD34 cells up to  $30 \text{ pg cell}^{-1}$  [303, 304].

#### 6.5.4.3 *In Vivo* Studies on Receptor-targeted LHRH-SPION Uptake

When SPIONs and LHRH-SPIONs were injected intravenously into human breast cancer (MDA-MB-435S.luc) xenograft-bearing nude mice, up to 59.1% of iron particles accumulated in tumors of LHRH-SPION injected mice compared with 8% in groups injected with SPIONs (Fig. 6.10A, B). Lung tissue from tumor-bearing



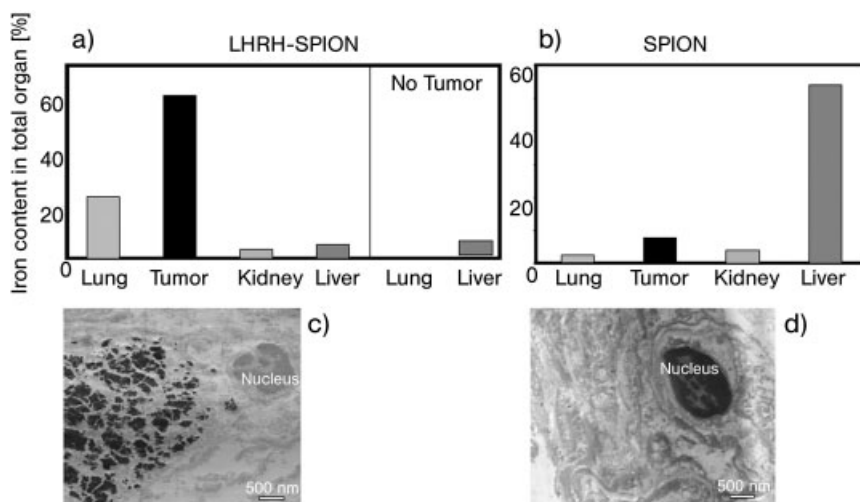


**Fig. 6.10.** Relative iron distribution in human breast cancer xenograft-bearing mice after injection of SPIONs and LHRH-SPIONs. (A) Iron contents in organs and tumors after LHRH-SPION injection, (B) after SPION injection (100% = 5 mg-Fe per mouse). TEM micrographs (C) from lung section with metastases after LHRH-SPION injection and (D) after SPION injection [297].

mice, which contained significant numbers of metastatic breast cancer cells, accumulated up to 20% LHRH-SPIONs and only 2% SPIONs (Fig. 6.10A, B). Neither lungs nor livers of normal mice accumulated LHRH-SPIONs, suggesting that LHRH-SPIONs were not incorporated into macrophages *in vivo* as predicted from low *in vitro* macrophage uptake (Fig. 6.10). LHRH-SPIONs were either incorporated into tumors or metastatic cells or they were excreted as observed in normal mice. The high accumulation of SPIONs in the livers suggested that these particles were incorporated by macrophages and transported therein to the liver, where they accumulated to 55%.

Unconjugated SPIONs accumulated to 8% in tumors ( $p < 0.00006$ ), 55% in the livers, ( $p < 0.00006$ ), 2% in lungs, ( $p < 0.031$ ), and 3.3% in kidneys, ( $p < 0.33$ ) (Fig. 6.10B).

When lung sections from LHRH-SPION- and SPION-injected mice were stained for iron, only lungs from mice injected with LHRH-SPIONs tested positive [298, 299]. The iron contents of lungs correlated directly with the number of metastatic cells (Fig. 6.11) [297]. The average iron content per lung cancer cell was calculated to be  $77.8 \pm 23.5$  pg Fe per metastatic cell in lungs. Lung sections from tumor-bearing mice showed iron clusters in groups after LHRH-SPION treatment. No iron clusters were observed in SPION-injected groups (Fig. 6.10C, D).

The specific targeting of tumors and metastases and the low accumulation in the livers seemed to be a combination of ligand conjugation and physical characteristics of the LHRH-SPIONs. The LHRH-SPIONs had a sufficiently long circulation

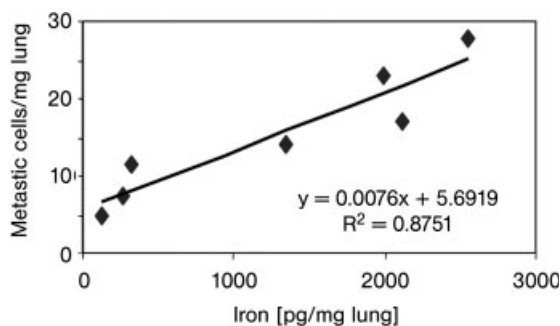


Fig. 6.11. Linear relationship between the metastatic cells in lungs and the iron content in tissue [297].

time, similar to albumin-coated particles with neutral zeta potential [305]. Most important, neutral particles were less prone to accumulate in liver (20%) [86], because they showed the lowest opsonization and were, therefore, not recognized by macrophages of the RES. Coating nanoparticles with short peptides increased the colloidal stage and decreased the non-specific binding to fibronectin, an effect that was similar to PEG coating [274, 306]. It is highly likely that LHRH served as coating itself, considering the low liver accumulation of LHRH-SPIONs in normal (non-tumor) bearing mice.

The biodistribution and circulation time of contrast agents is determined by several factors, such as size, charge, and surface chemistry [84, 85]. Nanoparticles of hydrodynamic size greater than 50 nm, and hydrophilic surface and high charges are eliminated from the circulation within minutes by phagocytotic cells of the reticulo-endothelial system (RES). Therefore, the accumulation of such particles was observed in liver, spleen, bone marrow, and were less likely to accumulate in other organs such as breast tissue, lymph nodes, intestinal tissue or gonads [301, 307, 308]. Coating iron oxide nanoparticles of <50 nm diameter with poly(ethylene glycol) (PEG), sialic acid, neuraminic acid, mucin or glycoporphin increased the circulation time [309]. Dextran-coated nanoparticles of <50 nm were detected to 82% in the livers of rats after intravenous injection [310]. Ligand decoration with LHRH was highly superior in increasing SPION concentration in target cells lowering liver accumulation. Other *in vivo* studies delivered PEG-coated particles decorated with carcinoembryonic antigen, which resulted in 1% tumor, 54% liver and 22% spleen accumulation [309]. Transferrin-decorated MION particles accumulated in rat glioma cells, passing the blood–brain barrier, and were detectable in xenografts [311, 312].

#### Subcellular Distribution of LHRH and SPIONs in Tissues, Metastases and Tumors

The subcellular distribution of LHRH-SPIONs in tumors showed clusters of sub-microsize, which were absent in tumors of mice injected with SPIONs alone [296].

TEM images of the MDA-MB-435S.luc tumors, lungs, liver and kidneys confirmed previous observations. Sections containing LHRH-SPIONs were compared with those of mice injected with unconjugated SPIONs [296–298]. Iron oxide nanoparticles were detected in the cytoplasm of the tumor cells. The regions containing the nanoparticles were identified as iron in energy dispersive X-ray spectroscopy analysis; large nanoparticle clusters were formed in the breast cancer xenografts of nude mice injected with LHRH-SPIONs, whereas single nanoparticles were observed in the tumors of the mice injected with SPIONs. At higher magnification these clusters appeared to be monodisperse [296–298]. Similar observations were made in lung sections of tumor-bearing mice; lungs from mice injected with LHRH-SPIONs with metastases had iron particle clusters in their metastases (Fig. 6.10C). These clusters were absent in lung metastases of mice with SPION injections (Fig. 6.10D) [296–298]. TEM images from livers showed high iron accumulation in SPION injected groups, and no visible iron accumulation in kidneys of either LHRH-SPION or SPION injected groups [296].

In summary, the LHRH-SPION particles accumulated at high concentrations in cells expressing functional LHRH receptors. Neutral particles are less prone to accumulate in the liver due to escape from macrophages of the RES. LHRH-SPIONs were poorly recognized and incorporated into macrophages, which improves iron accumulation in tumors and metastases. Metastases incorporate specifically LHRH-SPIONs. Iron cluster formation suggests a good possibility to increase the relaxation times during MRI. LHRH has a dual function: coating and targeting.

**Enhancement of Magnetic Resonance Images in Tumors and Metastases** Preliminary magnetic resonance images of tumors and lung sections containing metastases have also been obtained from the 7 T animal MRI and were analyzed using acquisition of multiple orders of intermolecular multiple-quantum coherence (iMQC) in a multi-CRAZED sequence. The multi-CRAZED sequence is an imaging pulse sequence that consists of  $90^\circ$ -{delay  $\tau$ }-{gradient pulse, area  $GT$ }- $\Theta$ -{gradient pulse, area  $nGT$ }-{delay  $TE$ }- $180^\circ$ -{delay( $TE-n\tau$ )}acquisitions, that uses the difference in echo timing to acquire multiple echoes and results in up to five echoes that are separated by  $\tau$ , described as DQC ( $+/-2$  quantum coherence), SQC ( $+/-1$  quantum coherence) and ZQC (zero-quantum coherence) (Fig. 6.12 [314]). Tumors and lung sections containing metastatic cells have been analyzed using different acquisition modalities.

The images in Fig. 6.13(A, B) were obtained from tumor pieces of 1–2 cm of tumor samples with LHRH-SPION nanoparticles, while the images at the bottom correspond to 1–2 cm of tumor sample from mice, injected with saline. Due to the heterogeneity of tumor tissue, significant contrast differences are needed to reveal the presence of tumors or the attachment of the magnetic nanoparticles. Hence, classical MRI, such as the T2 images shown in Fig. 6.13(A) [314], did not reveal significant contrast differences between the tumors with or without LHRH-SPIONs, i.e., they did not overcome tissue heterogeneity. Increased contrast was observed in the T2\* image acquisition. Multi-CRAZED images show the contrast for each

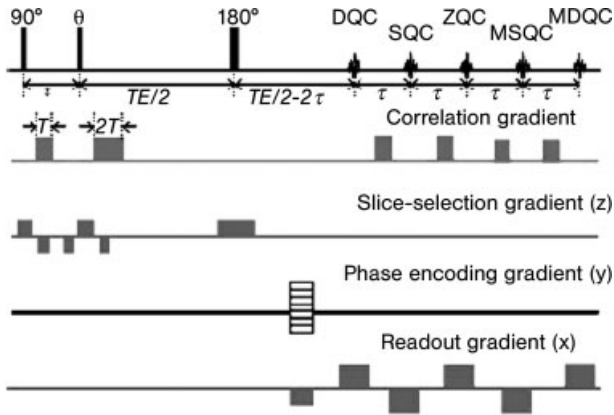


**Fig. 6.12.** The multi-CRAZED sequence uses its echo timing to acquire multiple echoes that result in up to five echoes that are separated by  $\tau$ , described as DQC ( $\pm 2$  quantum coherence), SQC ( $\pm 1$  quantum coherence) and ZQC (zero-quantum coherence) [314]. The +SQC (+1 or single-quantum coherence) and MSQC ( $-1$  or single-quantum coherence)

images have primarily conventional contrast; the DQC ( $+2$ -quantum), ZQC (0-quantum) and MDQC (2-quantum) coherences have contrast from subvoxel variations in magnetization density or resonance frequency. Additional gradient pulses permit image acquisition in the standard way (single-line acquisition shown here) [314].

of the five images and resulted in enhanced contrast in LHRH-SPION-containing tumors for DQC and ZQC images (Fig. 6.13C).

Similar results were obtained with sections from lungs containing metastases from mice injected with LHRH-SPIONs or saline (Fig. 6.14 [319]).

This may be due to the increased concentration of the LHRH particles and formation of clusters, as shown in the TEM image in Fig. 6.10(C). Such particle clusters should give rise to increased contrast due to increased magnetic moments, and their effects on the surrounding water molecules [314].

## 6.6

### Future Outlook

In summary, LHRH is a most appropriate ligand for targeting cancers, as there are receptors overexpressed in gonadal tissue, multiple cancers, their metastases and pituitary. In addition, the LHRH receptor signal transduction pathway in tumor cells is different to normal cells in that that the classical PLC/PKC pathway from the pituitary is not activated by LHRH binding to a LHRH receptor in a tumor cell, and multiple G protein subgroups can be activated. The LHRH binding activates signals to mitogenic signal transduction pathways related to growth factor receptors and tyrosine kinase activities as well as the activation of antimetastatic sig-

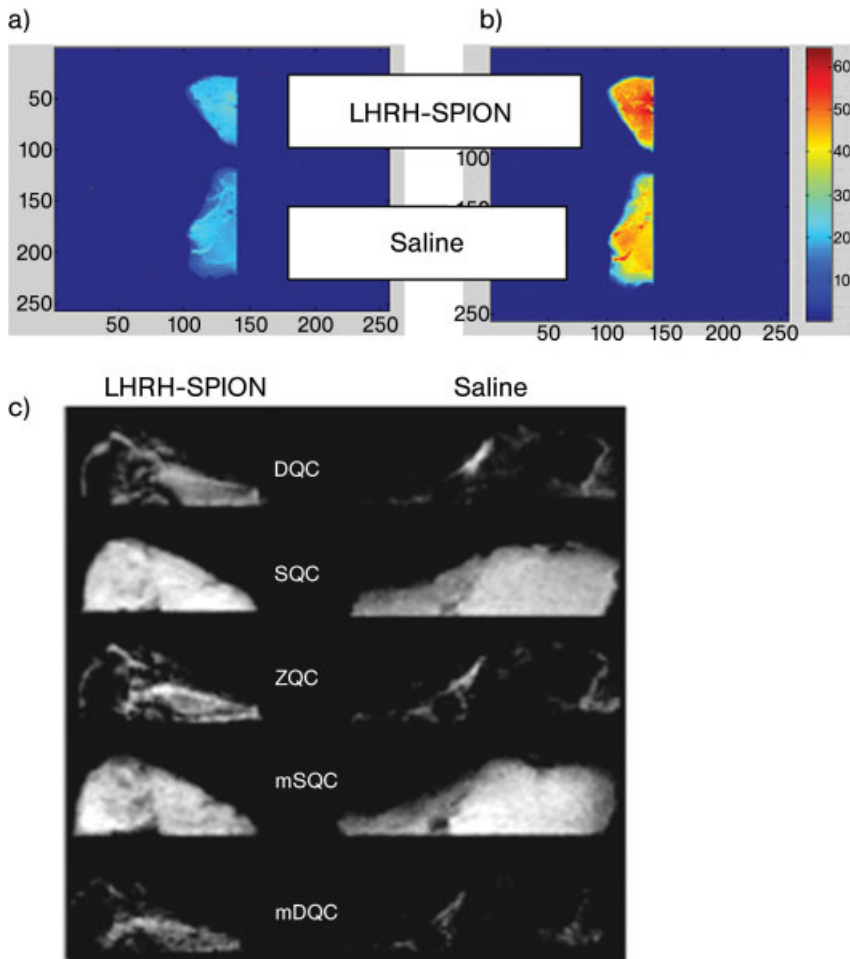


**Fig. 6.13.** (A) Conventional T2 scans obtained from tumor sites in nude mice inoculated with saline (bottom image) and LHRH-SPIONs (top image). Tumor pieces ca. 1–2 cm. (B) Presence of LHRH-SPIONs revealed by T2\* MRI of nude mice xenograft after injection of saline (bottom image) and LHRH-SPIONs (top image) using multi-CRAZED analysis [314]. (C) Multi-CRAZED images of a mouse breast tumor embedded with nanoparticles (left) and without nanoparticles (right): 0-quantum (ZQC image); 1-quantum (SQC image); 2-quantum (DQC image); –1-quantum (MSQC image); –2-quantum (MDQC image) [314].

nals, which can be exploited in designing the LHRH targeting of nanoparticles for cancer treatment [247, 281].

The expression of LHRH II in malignant cells and tumors could be exploited by targeting even more specifically malignancies, increasing uptake through activation of tumor specific signal transduction cascades, and improving specifically tar-

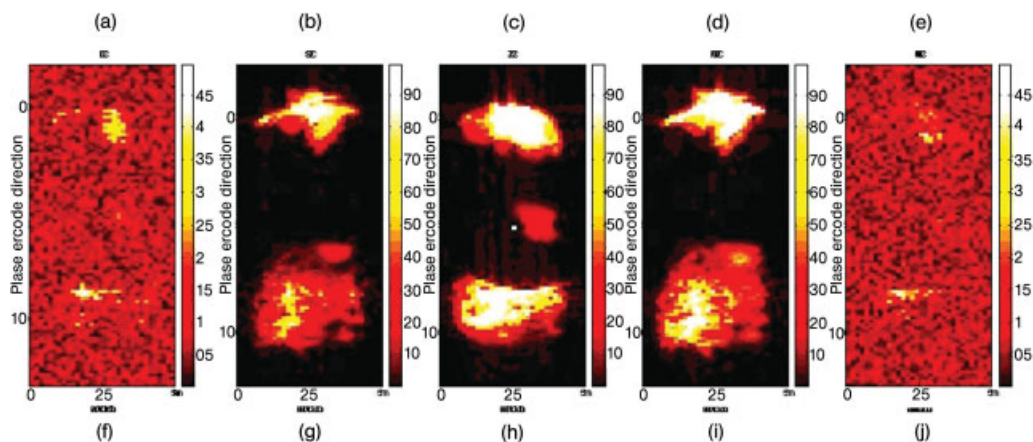


**Fig. 6.14.** Multi-CRAZED images from metastases containing lung tissue from tumor-bearing mice. Images (a)–(e) are lung sections from saline controls, and (f)–(j) are lung sections from mice injected with LHRH-SPIONs. (a) and (f) are 0-quantum

(ZQC image); (b) and (g) are 1-quantum (SQC image); (c) and (h) are 2-quantum (DQC image); (d) and (i) are  $-1$ -quantum (MSQC image); (e) and (j) are  $-2$ -quantum (MDQC image) [319].

geted and intracellular delivery of nanoparticles conjugated with LHRH with highest efficiency. These characteristics could lead to a new era of targeted imaging and treatment and increase the potential of nanoparticle applications in the future.

### Acknowledgments

The author thanks Dr. Challa Kumar and Dr. Franz Josef Hormes, Center for Advanced Microstructures and Devices, for fruitful discussion and enthusiasm in our collaborations. The support of Dr. William Hansel, Pennington Biomedical Research Center is gratefully acknowledged. The expertise in preparing TEM images of Dr. Jikou Zhou, Lawrence Livermore Laboratory, Berkeley, Dr. Wole Soboyejo, Princeton University, and the preparation of MR images by Dr. Warren Warren, Duke University, are gratefully acknowledged. Daniel Lazzaro helped in the preparation of some figures.

### Abbreviations

AP-1	Activator protein 1
CT	Computed tomography
EGF	Epidermal growth factor
EGF-R	Epidermal growth factor receptor
FSH	Follicle stimulating hormone
GnRH	Gonadotropin-releasing hormone

GPCR	G protein-coupled receptor
Jak-Stat	Janus kinase signal transducers and activators of transcription
JNK	cJun N-terminal kinase
LHRH	Luteinizing hormone releasing hormone
MAPK	Mitogen-activated protein kinase
MDR	Multidrug resistance
MRI	Magnetic resonance imaging
MMP	Matrix metallo proteinases
Nrf2	Nuclear factor erythroid 2-related factor 2
NF- $\kappa$ B	Nuclear factor $\kappa$ B
PET	Positron emission tomography
PI-3 K	Phosphatidylinositol 3-kinase
PKC	Protein kinase C
PTP	Phosphotyrosine phosphatase
RPTK	Phosphotyrosine Kinase Receptor
RT-PCR	Reverse transcriptase polymerase chain reaction
SAP-K	Stress activator activated protein kinase
SPECT	Single-photon emission tomography
SPIONs	Superparamagnetic iron oxide nanoparticles
TSH	Thyroid stimulating hormone
TRH	Thyrotropin releasing hormone
uPa	Urokinase plasminogen activator

## References

- 1 Global Cancer Statistics, www.cancer.org. 2002.
- 2 A. JEMAL, T. MURRAY, E. WARD, A. SAMUELS, R.C. TIWARI, A. GHAFOR, E.J. FEUER, M.J. THUN. Cancer statistics, *CA Cancer J. Clin.* **2005**, 54, 10–30.
- 3 Cancer Facts and Figures 2004, American Cancer Society, www.acs.org.
- 4 A. QAYUM, W. GULLICK, R. CLAYTON, K. SIKORA, J. WAXMAN. The effects of gnrh analogues in prostate cancer are mediated through tumor receptors, *Br. J. Cancer.* **1990**, 62, 96–99.
- 5 G. HALMOS, J. ARENCIBIA, A. SCHALLY, R. DAVIS, D. BOSTWICK. High incidence of receptors for luteinizing hormone-releasing hormone (LHRH) and LHRH receptor gene expression in human prostate cancers, *J. Urol.* **2000**, 163(2), 623–629.
- 6 C. LEUSCHNER, F. ENRIGHT, B. GAWRONSKA-KOZAK, W. HANSEL. Human prostate cancer cells and xenografts are targeted and destroyed through LHRH receptors, *Prostate.* **2003**, 56, 239–249.
- 7 B. STRAUB, M. MULLER, H. KRAUSE, M. SCHRADER, C. GOESSL, R. HEICAPPELL, K. MILLER. Increased incidence of luteinizing hormone-releasing hormone receptor gene messenger RNA expression in hormone-refractory human prostate cancers. *Clin. Cancer Res.* **2001**, Aug 7(8), 2340–2343.
- 8 C. LEUSCHNER, C. KUMAR, W. HANSEL, J. HORMES. Targeting breast cancer cells and their metastases through luteinizing hormone releasing hormone (LHRH) using magnetic nanoparticles, *J. Biomed. Nanotechnol.* **2005**, 1, 1–5.
- 9 B. SZENDE, G. SRKALOVIC, J. TIMAR, J. MULCHAHEY, J. NEILL, K. LAPIS, A. CSIKOS, K. SZEPESHAZI, A. SCHALLY.

- Localization of receptors for LHRH in pancreatic and mammary cancer cells, *Proc. Natl. Acad. Sci. U.S.A.* **1991**, *88*, 4153–4160.
- 10 K. BAUMANN, L. KIESEL, M. KAUFMANN, G. BASTERT, B. RUNNEBAUM. Characterization of binding sites for a GnRH-agonist (buserelin) in human breast cancer biopsies and their distribution in relation to tumor parameters, *Breast Cancer Res. Treat.* **1993**(25), *1*, 37–46.
  - 11 M. FEKETE, J.L. WILLIFF, A.V. SCHALLY. Characteristics and distribution of receptors for [D-Trp<sup>6</sup>]-luteinizing hormone releasing hormone, somatostatin, epidermal growth factor and sex steroids in 500 biopsy samples of human breast cancer, *J. Clin. Lab. Anal.* **1989**, *3*, 137–147.
  - 12 K. EIDNE, C. FLANAGAN, R. MILLAR. Gonadotropin releasing hormone binding sites in human breast carcinoma, *Science.* **1985**, *229*, 989–999.
  - 13 A. BEN-YEHUDAH, S. YARKONE, A. NECHUSHTAN, R. BELOSTOTSKY, H. LORBERBOUM-GALSKI. Linker based LhRH-PE chimeric proteins inhibit cancer growth in nude mice, *Med. Oncol.* **1999**, *16*, 38–45.
  - 14 A. BEN-YEHUDAH, D. PRUS, H. LORBERBOUM-GALSKI. IV administration of L-GNRH-PE66 efficiently inhibits growth of colon adenocarcinoma xenografts in nude mice. *Int. J. Cancer* **2001**, *92*, 263–268.
  - 15 M. FEKETE, A. ZALATNAI, A. COMARU SCHALLY, A. SCHALLY. Membrane receptors for peptides in experimental and human pancreatic cancers, *Pancreas.* **1989**, *4*, 521–528.
  - 16 H. FRIESS, M. BUCHLER, L. KIESEL, M. KRUGER, H. BEGER. LHRH receptors in the human pancreas: Basis for antihormonal treatment ductas carcinoma of the pancreas, *Int. J. Panreatol.* **1991**, *10*, 151–159.
  - 17 G. EMONS, O. ORTMANN, M. BECKER, G. IRMER, B. SPRINGER, R. LAUN, F. HOLZEL, K. SCHULZ, A. SCHALLY. High affinity binding and direct antiproliferative effects of LHRH analogs I human ovarian cancer cell lines, *Cancer Res.* **1993**, *53*, 5439–5446.
  - 18 P. VOLKER, C. GRUNDKER, O. SCHMIDT, K.D. SCHULZ, G. EMONS. Expression of receptors for luteinizing hormone-releasing hormone in human ovarian and endometrial cancers: Frequency, autoregulation, and correlation with direct anti-proliferative activity of luteinizing hormone-releasing hormone analogues. *Am. J. Obstet. Gynecol.* **2002**, *186*, 171–179.
  - 19 C. GRUNDKER, A. GUNTHER, R. MILLAR, G. EMONS. Expression of gonadotropin releasing Hormone II receptor in human endometrial and ovarian cancer cells and effects of gnrh II on tumor cell proliferation, *J. Clin. Endocrinol. Metab.* **2002**, *87*, 1427–1430.
  - 20 C. GRUNDKER, G. EMONS. Role of gonadotropin-releasing hormone (GnRH) in ovarian cancer, *Reprod. Biol. Endocrinol.* **2003**, *65*, 1–7.
  - 21 C. VERSCHRAEGEN, S. WESTPHALEN, W. HU, E. LOYER, A. KUDELKA, P. VOLKER, J. KAVANAGH, M. STEGER, K. SCHULZ, G. EMONS. Phase II study of cetrorelix, a luteinizing hormone-releasing hormone antagonist in patients with platinum-resistant ovarian cancer, *Gynecol. Oncol.* **2003**, *90*(3), 552–559.
  - 22 G. KELLER, A. SCHALLY, T. GAISER, A. NAGY, B. BAKER, G. WESTPHAL, G. HALMOS, J. ENGEL. Human malignant melanomas express receptors for luteinizing hormone releasing hormone allowing targeted therapy with cytotoxic luteinizing hormone releasing hormone analogue, *Cancer Res.* **2005**, *65*, 5857–5863.
  - 23 G. KELLER, A. SCHALLY, T. GAISER, A. NAGY, B. BAKER, G. HALMOS, J.B. ENGEL. Receptors for LHRH expressed in human non-Hodgkins lymphomas can be targeted for therapy with the cytotoxic LHRH analogue AN 207, *Eur. J. Cancer.* **2005**, *41*, 2196–2202.
  - 24 L. KREBS, X. WANG, A. NAGY, A. SCHALLY, P. PRASAD, C. LIEBOW. A conjugate of doxorubicin and an analog of IHRH shows increased



- efficacy against oral and laryngeal cancers, *Oral Oncol.* **2002**, *38*, 657–663.
- 25 S. GONG, G. ZHAO, H. ZHAO, W. LU, G. LIU, P. ZHU. Ability of luteinizing hormone releasing hormone-Pseudomonas aeruginosa exotoxin 40 binding to LHRH receptor on human liver cancer cells, *World J. Gastroenterol.* **2004**, *10*(19), 2870–2873.
  - 26 A. IMAI, T. OHNO, K. LIDA, T. FUSEYA, T. FUEUI, T. TAMAYA. Presence of gnrh receptor and its messenger ribonucleic acid in endometrial carcinoma and endometrium, *Gynecol. Oncol.* **1994**, *55*, 144–148.
  - 27 R. MORETTI, M. MONTAGNANI, J. VON GROENINGHEN, P. LIMONTA. Locally expressed LHRH receptors mediate the oncostatic and antimetastatic activity of LHRH agonists on melanoma cells, *J. Clin. Endocrinol. Metab.* **2002**, *87*, 3791–3797.
  - 28 N. SION-VARDI, J. KANETI, T. SEGAL-ABRAMSON, J. GIAT, J. LEVY, Y. SHARONI. Gonadotropin-releasing hormone specific binding sites in normal and malignant renal tissue, *J. Urol.* **1992**, *148*(5), 1568–1570.
  - 29 J. VAN GROENINGHEN, L. KIESEL, D. WINKLER, M. ZWIRNER. Effects of LHRH in nervous system tumours, *Lancet.* **1998**, *352*, 372–373.
  - 30 M. DE LENA, C. BRAMBILLA, A. MORABITO, G. BONADONNA. Adriamycin plus vincristine compared to and combined with cyclophosphamide, methotrexate and 5-fluorouracil for advanced breast cancer, *Cancer.* **1975**, *35*, 1108–1115.
  - 31 J. BULL, D. TORMEY, S. LI, P. CARBONE, G. FALKSON, J. BLUM, E. PERLIN, R. SIMON. A randomized comparative trial of adriamycin versus methotrexate in combination drug therapy, *Cancer.* **1978**, *41*, 1649–1657.
  - 32 R. SANTEN. Endocrine treatment of prostate cancer, *J. Clin. Endocrinol. Metab.* **1992**, *75*, 685–689.
  - 33 J. EMMET, L. GREENE, A. PAPANTONIOU. Endocrine therapy in carcinoma of the prostate gland: 10 year survival studies, *J. Urol.* **1960**, *83*, 471–484.
  - 34 R. O'REGAN, V. JORDAN. Tamoxifen to raloxifene and beyond, *Semin. Oncol.* **2001**, *28*, 260–273.
  - 35 M. O'REILLY, L. HOLMGREN, Y. SHING, C. CHEN, R. ROSENTHAL, M. MOSES, W. LANE, Y. CAO, E. SAGE, J. FOLKMAN. Angiostatin: A novel angiogenesis inhibitor that mediates the suppression of metastases by a Lewis lung carcinoma, *Cell.* **1994**, *79*, 315–328.
  - 36 S. ECCLES, G. BOX, W. COURT, J. SANDLE, C. DEAN. Preclinical models for the evaluation of targeted therapies of metastatic disease, *Cell Biophys.* **1994**, *24–25*, 279–291.
  - 37 H. WALTER. Simultaneous occurrence of malignant tumors and systemic diseases, *Radiol. Clin.* **1951**, *20*, 405–512.
  - 38 K. PANTEL, M. OTTE. Occult micro-metastasis: Enrichment, identification and characterization of single disseminated tumour cells, *Semin. Cancer Biol.* **2001**, *11*, 327–337.
  - 39 C. METTLIN, G. MURPHY, R. HO, H. MENCK. The National Cancer data base report on longitudinal observations on prostate cancer, *Cancer.* **1996**, *77*, 2162–2166.
  - 40 C. GALASKO. The anatomy and pathways of skeletal metastases, in *Bone Metastases*, L. WEISS, A.H. GILBERT (Eds.), Boston, GK Hall, **1981**, pp. 49–63.
  - 41 S. JANG, M. WIJENTJES, D. LU, J. AU. Drug delivery and transport to solid tumors, *Pharm. Res.* **2003**, *20*, 1337–1350.
  - 42 S. HONIG. Hormonal therapy and chemotherapy, in *Diseases of the Breast*, J.R. HARRIS, M.E. LIPPMAN, M. MORROW, S. HELLMAN (Eds.), Lippincott-Raven Publishers, Philadelphia, **1996**, pp. 669–734.
  - 43 K. PANTEL, R. COTE, O. FODSTADT. Detection and clinical importance of micrometastatic disease, *J. Natl. Cancer Inst.* **1999**, *91*, 1113–1124.
  - 44 S. BRAUN, K. PANTEL. Biological characteristics in micrometastatic cancer cells in bone marrow, *Cancer Metastasis Rev.* **1999**, *18*, 75–90.

- 45 S. BRAUN, K. PANTEL, P. MULLER, W. JANNI, F. HEPP, C. KENTENICH, S. GASTROPH, A. WISCHNIK, T. DIMPFL, G. KINDERMANN, G. RIETHMÜLLER, G. SCHLIMOK. Cytokeratin-positive cells in the bone marrow and survival of patients with stage I, II, or III breast cancer, *N. Engl. J. Med.* **2000**, 342, 525–533.
- 46 I. DIEL, B. KREMPIEN, M. KAUFMANN, S. COSTA, R. GOERNER, D. VON FOURNIER, G. BASTERT. Ergebnisse von Beckenkammbiopsien von 475 Patientinnen mit primärem und metastasiertem Mammakarzinom, *Tumor Diagn. Ther.* **1992**, 13, 85–90.
- 47 K. MORIKAWA, S. WALKER, M. NAKAJIMA, S. PATHAK, J. JESSUP, I. FIDLER. Influence of organ environment on the growth selection and metastasis of human colon carcinoma cells in nude mice, *Cancer Res.* **1988**, 48, 6863–6871.
- 48 K. PANTEL, R. COTE, O. FODSTADT. Detection and clinical importance of micrometastatic disease, *J. Natl. Cancer Inst.* **1999**, 91, 1113–1124.
- 49 K. PANTEL, V. MUELLER, M. AUER, N. NUSSE, N. HARBECK, S. BRAUN. Detection and clinical implications of early systemic tumor cell dissemination in breast cancer, *Clin. Cancer Res.* **2003**, 9, 6326–6334.
- 50 D. DEARNALEY, J. SLOANE, M. ORMEROD, K. STEELE, R. COOMBS. Clink Hmc, Powles TJ, Ford HT, Neville AM: Increased detection of mammary carcinoma cells in marrow smears using antisera to epithelial membrane antigen, *Br. J. Cancer.* **1981**, 44, 85–90.
- 51 P. TSCHENTSCHER, C. WAGENER, M. NEUMAIER. Sensitive and specific cytokeratin 18 reverse transcriptase-polymerase chain reaction that excludes amplification of processed pseudogenes from contaminating genomic DNA, *Clin. Chem.* **1997**, 43, 2244–2250.
- 52 M. ROBSEN ME. K. OFFIT. Breast MRI for women with hereditary cancer risk. *JAMA.* **2004**, 292, 1368.
- 53 E. WARNER, D. PLEWES, K. HILL, P. CAUSER, J. ZUBOVITS, R. JONG, M. CUTRARA, G. DEBOER, M. YAFFE, S. MESSNER, W. MESCHINO, C. PIRON, S. NAROD. Surveillance of BRCA1 and BRCA2 mutation carriers with magnetic resonance imaging, ultrasound, mammography, and clinical breast examination, *JAMA.* **2004**, 292(11), 1317–1325.
- 54 K. HAGSPIEL, K. NEIDL, A. EICHENBERGER, W. WEDER, B. MARINCEK. Detection of liver metastases: Comparison of superparamagnetic iron oxide-enhanced and unenhanced MR imaging at 1.5 T with dynamic CT, intraoperative US, and percutaneous, *US. Radiol.* **1995**, 196(2), 471–478.
- 55 O. CLEMENT, N. SIAUWE. Liver imaging with ferrumxodides. *Top. Magn. Res. Imaging.* **1998**, 9, 167–182.
- 56 E. MORRIS, L. SCHWARTZ, D. DERSHAW. MR imaging of the breast in patients with occult primary breast carcinoma, *Radiology.* **1997**, 205, 437–440.
- 57 C. SCHORN, U. FISCHER. MRI of the breast in patients with metastatic disease of unknown primary, *Eur. Radiol.* **1999**, 9, 470–473.
- 58 J. DE JONG, J. PRUIM, P. ELSINGA, W. VAALBURG, H. MENSINK. Visualization of prostate cancer with 11C choline positron emission tomography, *Eur. Urol.* **2002**, 442, 18–23.
- 59 Y. WANG, S. HUSSAIN, G. KRESTING. Superparamagnetic iron oxide contrast agents: Physicochemical characteristics and applications in MR imaging, *Eur. Radiol.* **2001**, 11, 2319–2331.
- 60 R. WEISSELEDER, G. ELIZONDO, J. WITTENBERG, C. RABITO, H. BENGEL, L. JOSEPHSON. Ultrasmall superparamagnetic iron oxide: Characterization of a new class of contrast agents for MR imaging, *Radiology.* **1990**, 175(2), 489–493.
- 61 R. WEISSELEDER, D. STARK, B. ENGELSTAD, B. BACON, C. COMPTON, D. WHITE, P. JACOBAS, J. LEWIS. Superparamagnetic iron oxide: Pharmacokinetics and toxicity, *Am. J. Roentgenol.* **1989**, 152, 167–173.

- 62 B. BONNEMAIN. Superparamagnetic agents in magnetic resonance imaging: Physicochemical characteristics and clinical applications, *J. Drug Target.* **1998**, 6, 167–174.
- 63 H. DALDRUP, T. LINK, S. BLASIUS, A. STROZYK, S. KONEMANN, H. JURGENS, E. RUMMENY. Monitoring radiation induced changes in bone marrow histopathology with ultra small superparamagnetic iron oxide (USPIO) enhanced MRI, *J. Magn. Reson. Imag.* **1999**, 9, 643–652.
- 64 B. VAN DE BERG, F. LECOVERT, J. KANKU, J. JAMART, B. VAN BEERS, B. MALDAGUE, J. MALGHEM. Ferrum-oxides enhanced quantitative magnetic resonance imaging of the normal and abnormal bone marrow. Preliminary assessment, *J. Magn. Reson. Imag.* **1999**, 9, 322–328.
- 65 M. HARISINGHANI, J. BARENTSZ, P. HAHN, W. DESERNO, S. TABATABAEI, C. HULSBERGEN, J. ROSETTE, R. WEISSELER. Noninvasive detection of clinically occult lymph node metastases in prostate cancer, *N. Engl. J. Med.* **2003**, 348, 2491–2499.
- 66 M.G. HARISINGHANI, M.A. SAKSENA, P.F. HAHN, B. KING, J. KIM, M.T. TORABI, R. WEISSELER. Ferumoxtran-10-enhanced MR lymphangiography: Does contrast enhanced imaging alone suffice for accurate lymph node characterization? *Amer. J. Roentgenol.* **2006**, 186, 144–148.
- 67 J. MINTOROVICH, K. SHANSI, EOVIST. Injection and Reovist injection, Two liver specific contrast agents for MRI, *Oncol. Supp.* **2000**(3), 14, 37–40.
- 68 M. KAVELLARIS, D. KUO, C. BURKHART, D. REGL, M. NORRIS, M. HABER, S. HORWITZ. Taxol resistant epithelial ovarian tumors are associated with altered expression of specific beta tubulin isotypes, *J. Clin. Invest.* **1997**, 100, 1282–1293.
- 69 M. LEHNERT, S. EMERSON, W. DALTON, R. DE GUILI, S. SALMON. In vitro evaluation of chemosensitizers for clinical reversal of p-glycoprotein associated: Taxol resistance. *J. Natl. Cancer Inst. Mongr.* **1993**, 15, 63–67.
- 70 N. BALDINI, K. SCOTLANDI, M. SERRA, T. SHIKITA, N. ZINI, A. OGNIBENE, S. SANTI, R. FERRACINI, N.M. MARALDI. Nuclear immunolocalization of P-glycoprotein in multidrug-resistant cell lines showing similar mechanisms of doxorubicin distribution. *Eur. J. Cell Biol.* **1995**, 68, 226–239.
- 71 A. MOLINARI, A. CALCABRINI, S. MESCHINI, A. STRINGARO, D. DEL BUFALO, M. CIANFRIGLIA, G. ARANCIA. Detection of P-glycoprotein in the Golgi apparatus of drug-untreated human melanoma cells. *Int. J. Cancer.* **1998**, 75, 885–893.
- 72 J. HAMADA, T. TSURUO. Characterization of the ATPase activity of the 170 to 180 kilodalton membrane glycoprotein associated with multi-drug resistance: the 170 to 180 kilodalton membrane glycoprotein is an ATPase, *J. Biol. Chem.* **1988**, 263, 1454–1458.
- 73 R. KRISHNA, L. MAYER. Multidrug resistance (MDR) in cancer-mechanisms reversal using modulators of MDR and the role of MDR modulators in influencing the pharmacokinetics of anticancer drugs. *Eur. J. Cancer Sci.* **2000**, 11, 265–283.
- 74 A. JONES, A. HARRIS. New developments in angiogenesis: a major mechanism for tumor growth and target for therapy, *Cancer J. from Sci. Am.* **1998**, 4, 209–217.
- 75 J. MURRAY, J. CARMICHAEL. Targeting solid tumours: Challenges, disappointments and opportunities. *Adv. Drug Delivery Rev.* **1995**, 17, 117–127.
- 76 R. JAIN. Molecular regulation of vessel maturation. *Nat. Med.* **2003**, 9, 685–93.
- 77 T.P. PADERA, B.R. STOLL, J.B. TOOREDMAN, D. CAPEN, E. DI TOMASO, R.K. JAIN. Pathology: Cancer cells compress intratumour vessels. *Nature* **2004**, 427, 695.
- 78 K. WEINDEL, J.R. MORINGLANE, D. MARME, H.A. WEICH. Detection and quantification of vascular endothelial growth factor/vascular permeability factor in brain tumor tissue and cyst fluid: the key to angiogenesis? *Neurosurgery* **1994**, 35, 439–449.

- 79 S.P. OLESEN. Rapid increase in blood brain barrier permeability during severe hypoxia and metabolic inhibition. *Brain Res.* **1986**, 368, 24–29.
- 80 Y. BOUCHER, M. LEUNIG, R.K. JAIN. Tumor angiogenesis and interstitial hypertension. *Cancer Res.* **1996**, 56, 4264–4266.
- 81 G. HELMLINGER, P.A. NETTI, H.C. LICHTENBELD, R.J. MELDER, R.K. JAIN. Solid stress inhibits the growth of multicellular tumor spheroids. *Nat. Biotechnol.* **1997**, 15, 778–783.
- 82 H. MAEDA. The enhanced permeability and retention effect in tumor vasculature, the key role of tumor sensitive macromolecular drug targeting. *Adv. Enzyme Regul.* **2001**, 41, 189–207.
- 83 H. MAEDA. Tumor vascular permeability and the EPR effect in macromolecular therapeutics: A review. *J. Controlled Release.* **2000**, 65, 271–284.
- 84 E. SENETERRE, R. WEISSELEDER, D. JARAMILLO, P. REIMER, A. LEE, T. BRADY, J. WITTENBERG. Bone marrow: Ultrasmall superparamagnetic iron oxide for MR imaging. *Radiology.* **1991**, 179(2), 529–533.
- 85 D. POULIQUEN, I. LUCET, C. CHOULY, R. PERDRISOT, J. LE JEUNE, P. JALLET. Liver-directed superparamagnetic iron oxide: Quantitation of T2 relaxation effects. *Magn. Reson. Imag.* **1993**, 11, 219–228.
- 86 C. CHOULY, D. POULIQUEN, J. LUCET, J. JEUNE, P. JALLET. Development of superparamagnetic nanoparticles for MRI: Effect of particle size, charge and surface nature on biodistribution. *J. Microencapsul.* **1996**, 13, 245–255.
- 87 J. KREUTER. Drug targeting with nanoparticles. *Eur. J. Drug Metab. Pharmacokine.* **1994**, 19, 253–256.
- 88 L. ARAUJO, R. LOBENBERG, J. KREUTER. Influence of the surfactant concentration of the body distribution of nanoparticles. *J. Drug Target.* **1999**, 6, 373–385.
- 89 V. LENAERTS, J. NAGELKERKE, T. VAN BERKEL, P. COUVREUR, L. GRISLAIN, M. ROLAND, P. SPEISER. In vivo uptake of polyisobutyl cyanoacrylate nanoparticles by rat liver Kupffer, endothelial, and parenchymal cells. *J. Pharm. Sci.* **1984**, 73, 980–982.
- 90 P. COUVREUR, B. KANTE, V. LENAERTS, V. SCAILTEUR, M. ROLAND, P. SPEISER. Tissue distribution of antitumor drugs associated with polyalkylcyanoacrylate nanoparticles. *J. Pharm. Sci.* **1980**, 69, 199–202.
- 91 J. PANYAM, V. LABHASETWAR. Biodegradable nanoparticles for drug and gene delivery to cells and tissue. *Adv. Drug Del. Rev.* **2003**, 55, 329–347.
- 92 M. FERRARI. Cancer nanotechnology: opportunities and challenges. *Nat. Rev.* **2005**, 5, 161–171.
- 93 J. VASIR, V. LABHASETWAR. Targeted drug delivery in cancer therapy. *Technol. Cancer Res. Treatment.* **2005**, 4, 363–374.
- 94 A. CHONN, S. SEMPLÉ, P. CULLIS. Separation of large unilamellar liposomes from blood components by a spin column procedure: Towards identifying plasma proteins which mediate liposome clearance in vivo. *Biochim. Biophys. Acta.* **1991**, 1070, 215–222.
- 95 F. YUAN. Transvascular drug delivery in solid tumors. *Semin. Radiat. Oncol.* **1998**, 8, 164–175.
- 96 Y. NOGUCHI, J. WU, R. DUNCAN, J. STROHALLM, K. ULBRICH, T. AKAIKE, H. MAEDA. Early phase tumor accumulation of macromolecules: A great difference in clearance rate between tumor and normal tissues. *Jpn. J. Cancer Res.* **1998**, 89, 307–314.
- 97 R. WEISSELEDER, H. CHENG, A. BOGDANOVA, A. BOGDANOV. Magnetically labeled cells can be detected by MR imaging. *J. Magn. Reson. Imag.* **1997**, 7, 258–263.
- 98 T. YEH, W. ZHANG, S. ILDSTAD, C. HO. Intracellular labeling of T-cells with superparamagnetic contrast agents. *Magn. Reson. Med.* **1993**, 5, 617–625.
- 99 U. SCHOEPF, E. MARECOS, R. MELDER, R. JAIN, R. WEISSELEDER. Intracellular magnetic labeling of lymphocytes for in vivo trafficking studies,

- Biotechniques*. 1998, 24(4), 642–646, 648–651.
- 100 R. WEISSLEDER, D. STARK, B. ENGELSTAD, B. BACON, C. COMPTON, D. WHITE, P. JACOBS, J. LEWIS. Superparamagnetic iron oxide: Pharmacokinetics and toxicity, *Am. J. Roentgenol.* 1989, 152, 167–173.
- 101 P. REIMER, E. RUMMENY, H. DALDRUP, T. BALZER, B. TOMACH, T. BERNS, P. PETERS. Clinical results with Resovist: A phase 2 clinical trial, *Radiology*. 1995, 195, 489–496.
- 102 P. ROBINSON. Imaging liver metastases: Current limitations and future prospects, *Br. J. Radiol.* 2000, 73, 234–241.
- 103 Y. NISHIOKA, H. YOSHINO. Lymphatic targeting with nanoparticulate system, *Adv. Drug Delivery Rev.* 2001, 47, 55–64.
- 104 K. YANG, Y. WEN, L. LI, C. WANG, S. HOU, C. LI. Preparation of cucurbitacinBE polylactic acid nanoparticles for targeting cervical lymph nodes, *Hua Xi Kou Qiang Yi Xue Za Zhi*. 2001, 19, 347–350.
- 105 T. WATANABE, H. ICHIKAWA, M. FUKUMORI. Tumor accumulation of gadolinium in lipid nanoparticles intravenously injected for neutron capture therapy in cancer, *Eur. J. Pharmaceut. Biopharmaceut.* 2002, 54, 119–124.
- 106 N. NISHIYAMA, S. OKAZAKI, H. CABRAL, M. MIYAMOTO, Y. KATO, Y. SUGIYAMA, K. NISHIO, Y. MATSUMURA, K. KATAOKA. Novel cisplatin-incorporated polymeric micelles can eradicate solid tumors in mice, *Cancer Res.* 2003, 63, 8977–8983.
- 107 R. ABOU-JAWDE, T. CHOUERI, C. ALEMANY, T. MEKHAIL. An overview of targeted treatments in cancer, *Clin. Therapeut.* 2005, 25, 2121–2137.
- 108 A. GUPTA, A. CURTIS. Lactoferrin and ceruloplasmin derivatized superparamagnetic iron oxide nanoparticles for targeting cell surface receptors, *Biomaterials*. 2004, 25, 3029–3040.
- 109 A. GUPTA, M. GUPTA. Synthesis and surface engineering of ironoxide nanoparticles for biomedical applications, *Biomaterials*. 2005, 26, 3995–4021.
- 110 A. GUPTA, C. BERRY, M. GUPTA, A. CURTIS. Receptor mediated targeting of magnetic nanoparticles using insulin as a surface ligand to prevent endocytosis, *IEEE Trans. Nanobiosci.* 2003, 2, 256–261.
- 111 Z. QIAN, H. LI, H. SUN, K. HO. Targeted drug delivery via transferring receptor mediated endocytosis pathway, *Pharmacol. Rev.* 2002, 54, 561–587.
- 112 A. MOORE, J. BASILION, E. CHIOCCA, R. WEISSLEDER. Measuring transferring receptor gene expression by NMR imaging, *Biochim. Biophys. Acta*. 1998, 1402, 239–249.
- 113 A. MOORE, L. JOSEPHSON, R. BHOREADE, J. BASILION, R. WEISSLEDER. Human transferring receptor gene as a marker gene for MR imaging, *Radiology*. 2001, 221, 244–250.
- 114 C. BERRY, S. CHARLES, S. WELLS, M. D.ABY, A. CURTIS. The influence of transferring stabilized magnetic nanoparticles on human dermal fibroblasts in culture, *Int. J. Pharm.* 2004, 269, 211.
- 115 D. HOGEMANN, L. JOSEPHSON, R. WEISSLEDER, J. BASILION. Improvement of MRI probes to allow efficient detection of gene expression, *Bioconjugate Chem.* 2000, 11(6), 941–946.
- 116 H. CHOI, S. CHOI, R. ZHOU, H. KUNG, I. CHEN. Iron oxide nanoparticles as magnetic resonance contrast agent for tumor imaging via folate receptor-targeted delivery, *Acad. Radiol.* 2004, 11, 996–1004.
- 117 Y. ZHANG, N. KOHLER, M. ZHANG. Surface modification of superparamagnetic magnetite nanoparticles and their intracellular uptake, *Biomaterials*. 2002, 23, 1553–1561.
- 118 N. TANJI, K. AOKI, M. YOKOYAMA. Growth factors: Roles in andrology, *Arch. Androl.* 2001, 47, 1–7.
- 119 M. BOYLE, M. LAWMAN, A. GEE, M. YOUNG. Nerve growth factor: A chemotactic factor for polymorphonuclear leukocytes in vivo, *J. Immunol.* 1985, 134, 564–568.

- 120 M. FUNOVICS, B. KAPPELLER, C. HOELLER, H. SU, R. KUNSTFELD, S. PUIG, K. MACFELDA. MR imaging of the her2/neu and 9.2.27 tumor antigens using immunospecific contrast agents, *Magn. Reson. Imag.* **2004**, *22*, 843-M.
- 121 A. NAGY, A. SCHALLY. Targeting cytotoxic conjugates of somatostatin, luteinizing hormone releasing hormone and bombesin to cancers expressing their receptors: A smarter chemotherapy, *Curr. Pharmaceut. Design.* **2005**, *11*, 1167–1180.
- 122 M. KIRCHER, U. MAHMOOD, R. KING, R. WEISSLEDER, L. JOSEPHSON. A multimodal nanoparticle for preoperative magnetic resonance imaging and intraoperative optical brain tumor delineation, *Cancer Res.* **2003**, *63*, 8122–8125.
- 123 L. JOSEPHSON, C. TUNG, A. MOORE, R. WEISSLEDER. High efficiency intracellular magnetic labeling with novel superparamagnetic-tat peptide conjugates, *Bioconjugate Chem.* **1999**, *10*, 186–191.
- 124 C. DODD, H. HSU, W. CHU, P. YANG, H. ZHANG, J. MOUNTZ, K. ZINN, J. FORDER, L. JOSEPHSON, R. WEISSLEDER, J. MOUNTZ, J. MOUNTZ. Normal T-cell response and in vivo magnetic resonance imaging of T cells loaded with HIV transactivator-peptide-derived superparamagnetic nanoparticles, *J. Immunol. Methods.* **2001**, *256*, 89–105.
- 125 A. SCHALLY, A. NAGY. Cancer chemotherapy based on targeting of cytotoxic peptide conjugates to their receptors on tumors, *Eur. J. Endocrinol.* **1999**, *141*(1), 1–14.
- 126 A. NAGY, A. SCHALLY. Targeting cytotoxic luteinizing hormone releasing hormone analogs to breast, ovarian, endometrial and prostate cancers, *Biol. Reprod.* **2005**, *73*, 851–859.
- 127 L. CHATZISTAMOU, A. SCHALLY, A. NAGY, K. SZEPESHAZI, G. HALMOS. Effective treatment of metastatic MDA-MB 435 human estrogen independent breast carcinomas with a targeted cytotoxic analogue of luteinizing hormone releasing hormone AN-207, *Clin. Cancer Res.* **2000**, *6*, 4158–4168.
- 128 M. KOVACS, A. SCHALLY, B. CSERNUS, R. BUSTO, Z. REKASI, A. NAGY. Targeted cytotoxic analogue of LHRH only transiently decreases the gene expression of pituitary receptors for LHRH, *J. Neuroendocrinol.* **2002**, *14*, 5–13.
- 129 M. KOVACS, A. SCHALLY, A. NAGY, M. KOPPAN, K. GROOT. Recovery of pituitary function after treatment with a targeted cytotoxic analog of LHRH, *Proc. Natl. Acad. Sci. U.S.A.* **1997**, *94*, 1420–1425.
- 130 C. LEUSCHNER, F. ENRIGHT, B. GAWRONSKA-KOZAK, W. HANSEL. Human prostate cancer cells and xenografts are targeted and destroyed through LHRH receptors, *Prostate.* **2003**, *56*, 239–249.
- 131 P. FOSTER-GAREAU, C. HEYN, A. ALEJSKI, B.K. RUTT. Imaging single mammalian cells with a 1.5 T clinical MRI scanner, *Magn. Reson. Med.*, **2003**, *49*, 968–971.
- 132 K.A. HINDS, J.M. HILL, E.M. SHAPIRO, M.O. LAUKKANEN, A.C. SILVA, C.A. COMBS, T.R. VARNEY, R.S. BALABAN, A.P. KORETSKY, C.E. DUNBAR. Highly efficient endosomal labeling of progenitor and stem cells with large magnetic particles allows magnetic resonance imaging of single cells, *Blood* **2003**, *102*, 867–872.
- 133 A. MERBACH, E. TOTH. *The Chemistry of Contrast Agents in Medical Magnetic Resonance Imaging*, **2001**, Wiley, Chichester.
- 134 C. SIMONSEN, L. OSTERGAARD, P. VESTERGAARD-POULSEN, L. ROHL, A. BJORNERUD, C. GYLDENSTED. CBF and CBV measurements by USPIO bolus tracking: Reproducibility and comparison with Gd based values, *J. Magn. Reson. Imag.* **1999**, *9*, 342–347.
- 135 R. Low. MR imaging in liver using gadolinium chelates, *Magn. Reson. Imag. Clin. N. Am.* **2001**, *9*, 372–374.
- 136 C. JUNG, P. JACOBS. Physical and chemical properties of superparamagnetic iron oxide MR contrast

- agents: ferumoxides, ferumoxtran, ferumoxsil, *Magn. Reson. Imag.* **1995**, 13, 661–674.
- 137 S. FLACKE, S. FISCHER, M. SCOTT, R. FUHRHOP, J. ALLEN, M. MCLEAN, P. WINTER, G. SICARD, P. GAFFNEY, S. WICKLINE, G. LANZA. Novel MRI contrast agent for molecular imaging of fibrin: Implications for detecting vulnerable plaques, *Circulation.* **2001**, 104, 1280–1285.
- 138 T. SUWA, S. OZAWA, M. UEDA, N. ANDO, M. KITAJIMA. Magnetic resonance imaging of esophageal squamous cell carcinoma using magnetite particles coated with anti-epidermal growth factor receptor antibody, *Int. J. Cancer.* **1998**, 75, 626–634.
- 139 Y. WANG, S. HUSSAIN, G. KRESTING. Superparamagnetic iron oxide contrast agents: Physicochemical characteristics and applications in MR imaging, *Eur. Radiol.* **2001**, 11, 2319–2331.
- 140 D. POULIQUEN, R. PERDRISOT, A. ERMAS, S. AKOKA, P. JALLET, J. LE JEUNE. Superparamagnetic iron oxide nanoparticles as a liver MRI contrast agent: Contribution of microencapsulation to improved biodistribution, *Magn. Reson. Imag.* **1989**, 7, 619–627.
- 141 R. WEISSLEDER, A. LEE, B. KHAW, T. SHEN, T. BRADY. Antimyosin labeled monocrystalline iron oxide allows detection of myocardial infarct: MR antibody imaging, *Radiology.* **1992**, 182, 281–285.
- 142 R. WEISSLEDER, A. LEE, A. FISCHMAN, P. REIMER, T. SHEN, R. WILKINSON, R. CALLAHAN, T. BRADY. Polyclonal human immunoglobulin G labeled with polymeric iron oxide: Antibody MR imaging, *Radiology.* **1991**, 181, 245–249.
- 143 P. MOROZ, H. PARDOE, S. JONES, T. ST PIERRE, S. SONG, B. GRAY. Arterial embolization hyperthermia: Hepatic iron particle distribution and its potential determination by magnetic resonance imaging, *Phys. Med. Biol.* **2002**, 47, 1591–1602.
- 144 H. PARDOE, W. CHUA-ANUSORN, T. ST PIERRE, J. DOBSEN. Detection limits for ferromagnetic particle concentrations using magnetic resonance imaging based proton transverse relaxation rate measurements, *Phys. Med. Biol.* **2003**, 48, N89–N95.
- 145 S. SCHMITZ, S. COUPLAND, R. GUST. Superparamagnetic iron oxide enhanced MRI of arteriosclerotic plaques in Watanabe rabbits, *Invest. Radiol.* **2000**, 35, 460–471.
- 146 A. LUEBBE, C. BERGEMAN, H. RIESS, F. SCHRIEVER, P. REICHARDT, K. POSSINGER, M. MATTHIA, B. DOERKEN, F. HERRMANN, R. GUERTLER, P. HOHENBERGER, N. HAAS, R. SOHR, B. SANDER, A. LEMKE, D. OHLENDORF, W. HUHNT, D. HUHNT. Clinical experiences with magnetic drug targeting: A Phase I study with 4-epidoxorubicin in 14 patients with advanced solid tumors, *Cancer Res.* **1996**, 56, 4686–4693.
- 147 B. BACON, D. STARK, C. PARK, S. SAINI, E. GROMAN, P. HAHN, C. COMPTON, J. FERRUCCI. Ferrite particles: A new magnetic resonance imaging contrast agent. Lack of acute or chronic hepatotoxicity after intravenous administration, *J. Lab. Clin. Med.* **1987**, 110, 164–171.
- 148 D. SCHAFFER. Coupling dynamics and membrane dynamics during endocytosis, *Curr. Opin. Cell Biol.* **2002**, 14, 76–81.
- 149 A. MOORE, R. WEISSLEDER, A. BOGDANOV. Uptake of dextran-coated monocrystalline iron oxides in tumor cells and macrophages, *J. Magn. Reson. Imag.* **1997**, 7, 1140–1145.
- 150 A. MOORE, E. MARECOS, A. BOGDANOV, R. WEISSLEDER. Tumoral distribution of long-circulating dextran coated iron oxide nanoparticles in a rodent model, *Radiology.* **2000**, 214, 568–574.
- 151 E. SHAPIRO, S. SKRTIC, K. SHARER, J. HILL, C. DUNBAR, A. KORETSKY. MRI detection of single particles for cellular imaging, *Proc. Natl. Acad. Sci. U.S.A.* **2004**, 101, 10 901–10 906.
- 152 C. BILLOTEY, C. WILHELM, M. DEVAUD, J. BACRI, J. BITTOUN, F. GAZEAU. Cell internalization of anionic maghemite nanoparticles: Quantitative effect on

- magnetic resonance imaging, *Magn. Reson. Med.* **2003**, 49, 646–654.
- 153 J. BULTE, I. DUNCAN, J. FANK. In vivo tracking of magnetically labeled cells following transplantation, *J. Cereb. Blood Flow Metab.* **2002**, 22, 899–907.
- 154 D. SIPKINS. Detection of tumor angiogenesis in vivo by  $\alpha V\beta 3$ -targeted magnetic resonance imaging, *Nat. Med.* **1998**, 4, 623–626.
- 155 P. WINTER. Nanotechnology in cancer drug delivery, in *Nanofabrication for Biomedical Applications*, J. HORMES, C. KUMAR, C. LEUSCHNER (Eds.), Wiley-VCH, Weinheim, **2004**.
- 156 P. WINTER, S. CARUTHERS, A. KASSNER, T. HARRIS, L. CHINEN, J. ALLEN, E. LACY, H. ZHANG, J. ROBERTSON, S. WICKLINE, G. LANZA. Molecular imaging of angiogenesis in nascent Vx-2 rabbit tumors using a novel alpha (nu)beta3-targeted nanoparticle and 1.5 tesla magnetic resonance imaging, *Cancer Res.* **2003**, 263, 5838–5843.
- 157 E. BERGEY, L. LEVY, X. WANG, L. KREBS, M. LAL, K. KIM, S. PAKATCHI, C. LIEBOW, P. PRASAD. DC Magnetic field induced magnetocytolysis of cancer cells targeted by LH-RH magnetic nanoparticles in vitro, *Biomed. Microdevices.* **2002**, 4, 293–299.
- 158 M. FUNOVICS, B. KAPPELLER, C. HOELLER, H. SU, R. KUNSTFELD, S. PUIG, K. MACFELDA. MR imaging of the her2/neu and 9.2.27 tumor antigens using immunospecific contrast agents, *Magn. Reson. Imaging.* **2004**, 22, 843-M.
- 159 S. DHARAP, Y. WANG, J. KHANDARE, B. QIU, S. GUNASEELAN, P. SINKO, S. STEIN, A. FARMANFARMAIAN, T. MINKO. Tumor specific targeting of an anticancer drug delivery system by LHRH peptide, *Proc. Natl. Acad. Sci. U.S.A.* **2005**, 102, 12 962–12 967.
- 160 W. YANG, M. WIECZORCK, M. ALLEN, T. NETT. Cytotoxic activity of gonadotropin releasing hormone Pokeweed antiviral protein conjugates in cell lines expressing GnRH receptors, *Endocrinology.* **2003**, 144, 1456–1463.
- 161 C. LEUSCHNER, F. ENRIGHT, B. GAWRONSKA, J. KEENER, W. HANSEL. Lytic peptide conjugated to luteinizing hormone kills breast cancer cells in vivo and in vitro. AACR-NCI-EORTC International conference, Molecular Targets and Cancer Therapeutics. **2001**, Miami, FL, Abstract 489.
- 162 C. LEUSCHNER, F. ENRIGHT, P. MELROSE, W. HANSEL. Targeted destruction of androgen-sensitive and insensitive prostate cancer cells and xenografts through luteinizing hormone receptors, *Prostate.* **2001**, 46, 116–125.
- 163 B. GAWRONSKA, C. LEUSCHNER, F. ENRIGHT, W. HANSEL. Effects of a lytic peptide conjugated to beta hCG on ovarian cancer studies in vitro and in vivo, *Gynecol. Oncol.* **2002**, 85, 45–52.
- 164 C. LEUSCHNER, F. ENRIGHT, B. GAWRONSKA, W. HANSEL. Membrane disrupting lytic peptide conjugates destroy hormone dependent and independent breast cancer cells in vitro and in vivo, *Breast Cancer Res. Treatment.* **2003**, 78, 17–27.
- 165 G. FINK. Gonadotropin secretion and its control, in *The Physiology of Reproduction*, E. KNOBIL, J. NEILL (Eds.), Raven Press, New York, **1988**, 1349–1377.
- 166 S. KALRA. Mandatory neuropeptide steroid signaling for the preovulatory luteinizing hormone releasing hormone discharge, *Endocrine Rev.* **1993**, 14, 507–538.
- 167 A. SCHALLY. Hypothalamic hormones from neuroendocrinology to cancer therapy, *Anticancer Drugs.* **1994**, 5, 115–130.
- 168 S. STOJILKOVIĆ, K. CATT. Expression and signal transduction pathways of gonadotropin releasing hormone receptors, *Recent Progr. Hormone Res.* **1995**, 30, 161–205.
- 169 A. SCHALLY, A. COMARU SCHALLY, A. NAGY, M. KOVACS, K. SZEPASHIZAI, A. PLONOWSKI, J. VARGA, G. HALMOS. Hypothalamic hormones and cancer, *Frontiers Neuroendocrinol.* **2001**, 22, 248–291.
- 170 R. MILLAR, A. LU, A. PAWSON, C. FLANAGAN, K. MORGAN, S. MAUDSLEY. Gonadotropin releasing hormone



- receptors, *Endocrine Rev.* **2004**, *25*, 235–275.
- 171 P. LIMONTA, R. MORETTI, M. MARELLI, M. MOTTA. The biology of gonadotropin hormone releasing hormone: Role in the control of tumor growth and progression in humans, *Frontiers Neuroendocrinol.* **2003**, *24*, 279–295.
- 172 R. MORETTI, M. MONTAGNANI, J. VON GROENINGHEN, P. LIMONTA. Locally expressed LHRH receptors mediate the oncostatic and antimetastatic activity of LHRH agonists on melanoma cells, *J. Clin. Endocrinol. Metab.* **2002**, *87*, 3791–3797.
- 173 R.M. MORETTI, M.M. MARELLI, J.C. VAN GROENINGHEN, M. MOTTA, P. LIMONTA. Inhibitory activity of luteinizing hormone releasing hormone on tumor growth and progression. *Endocrine Relat. Cancers*, **2003**, *10*, 161–167.
- 174 H. MATSUO, Y. BABA, R. NAIR, A. ARIMURA, A. SCHALLY. Structure of the porcine LH and FSH releasing hormone. I. The proposed amino acid sequence, *Biochem. Biophys. Res. Commun.* **1971**, *43*, 1334–1339.
- 175 J. KING, R. MILLAR. Structural and functional evolution of gonadotropin releasing hormone, *Int. Rev. Cytol.* **1987**, *106*, 149–182.
- 176 J. KING, R. MILLAR. Evolutionary aspects of gonadotropin releasing hormone and its receptor, *Cell Mol. Neurobiol.* **1995**, *15*, 5–23.
- 177 R. MILLAR, B. TROSKIE, Y. SUN, T. OTT, I. WAKEFIELD, D. MYVURTH, A. PAWSON, J. DAVIDSON, A. KATZ, J. HAPGOOD, N. ILLING, W. HEINSTEIN, S. SEALFON, R. PETER, E. TERASAWA, J. KING. Plasticity in the structural and functional evolution of GnRH: A peptide for all seasons. Advances in comparative endocrinology, *Proc. XIII International Congress of Comparative Endocrinology*. Yokohama, Japan, **1997**, pp. 15–27.
- 178 N. SHERWOOD. The GnRH family of peptides, *Trends Neurosci.* **1987**, *10*, 129–132.
- 179 M. JIMINEZ-LINAN, B. RUBIN, J. KING. Examination of guinea pig luteinizing hormone releasing hormone gene reveals a unique decapeptide and existence of two transcripts in the brain, *Endocrinology*. **1997**, *138*, 423–430.
- 180 M. YOO, H. KANG, H. CHOI, J. KIM, B. TROSKIE, R. MILLAR, H. KWON. Molecular cloning, distribution and pharmacological characterization of a novel gonadotropin-releasing hormone ([Trp<sup>8</sup>]GnRH) in frog brain, *Mol. Cell Endocrinol.* **2000**, *164*, 197–204.
- 181 B. ADAMS, J. TELLO, J. ERCHEGEYI, C. WARBY, D. HONG, K. AKINSANYA, G. MACKIE, W. VALE, J. RIVIER, N. SHERWOOD. Six novel gonadotropin releasing hormones are encoded as triplets on each of two genes in a protochordate, *Ciona interstitialis*. *Endocrinology*. **2003**, *144*, 1907–1919.
- 182 E. DUBOIS, M. ZANDBERGEN, J. PEUTE, H. GOOS. Evolutionary development of three gonadotropin releasing hormone systems in vertebrates, *Brain Res. Bull.* **2002**, *57*, 413–418.
- 183 W. YU, S. KARANTH, S. SOWER, A. PARLOW, S. McCANN. The similarity of FSH releasing factor to lamprey gonadotropin releasing hormone III (GnRH III), *Proc. Soc. Exp. Biol. Med.* **2002**, *224*, 87–92.
- 184 K. MIYAMOTO, Y. HASEGAWA, M. NOMURA, M. IGARASHI, K. KANGAWA, H. MATSUE. Identification of the second gonadotropin releasing hormone in chicken hypothalamus evidence that gonadotropin secretion is probably controlled by two distinct gonadotropin releasing hormones in avian species, *Proc. Natl. Acad. Sci. U.S.A.* **1984**, *81*, 3874–3878.
- 185 S. SOWER, Y. CHIANG, S. LOVAS, J. CONLON. Primary structure and biological activity of a third gonadotropin releasing hormone from the lamprey brain, *Endocrinology*. **1993**, *132*, 1125–1131.
- 186 R. WHITE, J. EISEN, T. KASTEN, R. FERNALD. Second gene for gonadotropin releasing hormone in humans, *Proc. Natl. Acad. Sci. U.S.A.* **1998**, *95*, 305–309.
- 187 S. KANG, C. TAI, P. NATHWANI, P. LEUNG. Differential regulation of two forms of GnRH messenger RNA in

- human granulose luteal cells, *Endocrinology*. **2001**, 142, 182–192.
- 188** K. CHOI, N. AUERSPERG, P. LEUNG. Expression and antiproliferative effect of a second form of gonadotropin releasing hormone in normal and neoplastic ovarian surface epithelial cells, *J. Clin. Endocrinol. Metab.* **2001**, 86, 5075–5078.
- 189** S. KHOSRAVI, P. LEUNG. Differential regulation of gonadotropin releasing hormone (GnRH I) and GnRH II messenger ribonucleic acid by gonadal steroids in human granulose luteal cells, *J. Clin. Endocrinol. Metab.* **2003**, 88, 663–372.
- 190** G. EMONS, A. SCHALLY. The use of luteinizing hormone releasing hormone agonists and antagonists in gynaecological cancers, *Hum. Reprod.* **1994**, 9, 1364–1379.
- 191** S. SEALFON, H. WEINSTEIN, R. MILLAR. Molecular mechanisms of ligand interaction with the gonadotropin releasing hormone receptor, *Endocrinol. Rev.* **1997**, 18, 180–205.
- 192** A. HSUEH, J. SCHAEFFER. Gonadotropin releasing hormone as a paracrine hormone and neurotransmitter in extra-pituitary sites, *J. Steroid Biochem.* **1985**, 23, 757–764.
- 193** R. MILLAR. GnRH II and type II GnRH receptors, *Trends Endocrinol. Metab.* **2003**, 14, 35–43.
- 194** J. TEMPLE, R. MILLAR, E. RISSMAN. An evolutionarily conserved form of gonadotropin-releasing hormone coordinates energy and reproductive behavior, *Endocrinology*. **2003**, 144(1), 13–19.
- 195** G. EMONS, O. ORTMANN, K. SCHULZ, A. SCHALLY. Growth inhibitory actions of LHRH on tumor cells. *Trends Endocrinol. Metab.* **1997**, 8, 355–362.
- 196** G. EMONS, S. WEIS, O. ORTMANN, C. GRUNDKER, K. SCHULZ. LHRH might act as a negative autocrine regulator of proliferation of human ovarian cancer, *Eur. J. Endocrinol.* **2000**, 142, 665–670.
- 197** D. DONDI, P. LIMONTA, R. MOTETTI, M. MARELLI, E. GARATTINI, M. MOTTA. Antiproliferative effects of LHRH agonists on human androgen independent prostate cancer cell line DU145: Evidence for an autocrine inhibitory LHRH loop, *Cancer Res.* **1994**, 54, 4091–4095.
- 198** R.M. MORETTI, M. MONTAGNANI MARELLI, J.C. VAN GROHNIGNHEN, M. MOTTA, P. LIMONTA. Inhibitory activity of luteinizing hormone releasing hormone on tumor growth and progression, *Endocrine Relat. Cancer.* **2003**, 10, 161–167.
- 199** W. MILLER, W. SCOTT, R. MORRIS, H. FRASER, R. SHARP. Growth of human breast cancer cells inhibited by a luteinizing hormone releasing hormone agonist, *Nature*. **1985**, 313, 231–233.
- 200** K. EIDNE, C. FLANAGAN, R. MILLAR. Gonadotropin releasing hormone binding sites in human breast carcinoma, *Science*. **1985**, 229, 989–999.
- 201** D. DONDI, P. LIMONTA, R. MORETTI, M. MONTAGNANI MOTTA. Anti-proliferative effects of lutei rele agonists on human androgen independent prostate cancer cell line DU 145: Evidence for an autocrine-inhibitory loop, *Cancer Res.* **1994**, 54, 4091–4095.
- 202** G. EMONS, S. WEISS, O. ORTMANN. LHRH might act as a negative autocrine regulator of proliferation of human ovarian cancer, *Eur. J. Endocrinol.* **2000**, 142, 665–670.
- 203** A. TIEVA, P. STATTIN, P. WIKSTROM, A. BERGH, J. DAMBER. Gonadotropin-releasing hormone receptor expression in the human prostate, *Prostate*. **2001**, 47(4), 276–284.
- 204** G. EMONS, O. ORTMANN, M. BECKER, G. IRMER, B. SPRINGER, R. LAUN, F. HOIZEL, K. SCHULZ, A. SCHALLY. High affinity binding and direct antiproliferative effects of LHRH analogs I human ovarian cancer cell lines, *Cancer Res.* **1993**, 53, 5439–5446.
- 205** A. GUNTHER, C. GRUNDKER, B. BOTTCHE, G. EMONS. Luteinizing hormone-releasing hormone (LHRH) inhibits apoptosis induced by cytotoxic agent and UV-light but not apoptosis mediated through CD95 in human ovarian and endometrial cancer cells,

- Anticancer Res.* **2004**, 24(3a), 1727–1732.
- 206 C. GRUNDKER, L. SCHLOTAWA, V. VIREECK, N. EICKE, A. HORST, B. KAIRIES, G. EMONS. Antiproliferative effects of the GnRH antagonist cetorelix and of GnRH-II on human endometrial and ovarian cancer cells are not mediated through the GnRH type I receptor, *Eur. J. Endocrinol.* **2004**, 151, 141–149.
- 207 C. GRUNDKER, G. EMONS. Role of gonadotropin-releasing hormone (GnRH) in ovarian cancer, *Reprod. Biol. Endocrinol.* **2003**, 7, 1, 65.
- 208 C. VERSCHRAEGEN, S. WESTPHALEN, W. HU, E. LOYER, A. KUDELKA, P. VOLKER, J. KAVANAGH, M. STEGER, K. SCHULZ, G. EMONS. Phase II study of cetorelix, a luteinizing hormone-releasing hormone antagonist in patients with platinum-resistant ovarian cancer, *Gynecol. Oncol.* **2003**, 90(3), 552–559.
- 209 O. REICH, F. NOGALES, S. REGAUER. Gonadotropin-releasing hormone receptor expression in endometrial stromal sarcomas: An immunohistochemical study, *Mod. Pathol.* **2005**, 18(4), 573–576.
- 210 R. EAVERI, A. BEN-YEHUDAH, H. LORBERBOUM-GALSKI. Surface antigens/receptors for targeted cancer treatment: The GnRH receptor/binding site for targeted adenocarcinoma therapy, *Curr. Cancer Drug Targets.* **2004**, 4(8), 673–687.
- 211 J. REUBI. Peptide receptors as molecular targets for cancer diagnosis and therapy, *Endocrine Rev.* **2003**, 24, 389–427.
- 212 R. MILLAR, S. LOWE, D. CONKLIN, A. PAWSON, S. MAUDSLEY, B. TROSKIE, T. OTT, M. MILLAR, G. LINCOLN, R. SELLAR, B. FAURHOLM, G. SCOBIE, R. KUESTNER, E. TERASAWA. A novel mammalian receptor for the evolutionarily conserved type II GnRH, *Proc. Natl. Acad. Sci. U.S.A.* **2001**, 98, 9636–9641.
- 213 L. CHI, W. ZHOU, A. PRIKHOZAN, C. FLANAGAN, K. DAVIDSON. Cloning and characterization of the human gonadotropin releasing hormone receptor, *Mol. Cell. Endocrinol.* **1993**, 91, R1–6.
- 214 S. KAKAR, L. MUSGROVE, D. DEVOR, J. SELLERS, J. NEILL. Cloning sequencing and expression of human GnRH receptor, *Biochem. Biophys. Res. Commun.* **1992**, 189, 289–295.
- 215 M. TSUTSUMI, W. ZHOU, R. MILLER, P. MELLON, J. ROBERTS, C. FLANAGAN, K. DONG, B. GILLO, S. SEALFON. Cloning and functional expression of a mouse gonadotropin releasing hormone receptor, *Mol. Endocrinol.* **1992**, 6, 1163–1169.
- 216 J. REINHART, L. MERTZ, K. CATT. Molecular cloning and expression of CDNA encoding the murine gonadotropin-releasing hormone receptor, *J. Biol. Chem.* **1992**, 267, 21 281–21 284.
- 217 U. KAISER, D. ZHAO, G. CARDONA, W. CHIN. Isolation and characterization of cDNAs encoding the rat pituitary gonadotropin-releasing hormone receptor, *Biochem. Biophys. Res. Commun.* **1992**, 189, 1645–1652.
- 218 K. EIDNE, R. SELLAR, G. COUPER, L. ANDERSON, P. TAYLOR. Molecular cloning and characterization of the rat pituitary gonadotropin releasing hormone (GnRH) receptor, *Mol. Cell. Endocrinol.* **1992**, 90, R5–R9.
- 219 M. PERRIN, L. BILEZEKJIAN, C. HOEGER, C. DONALDSON, J. RIVIER, Y. HAAS, W. VALE. Molecular and functional characterization of GnRH receptors cloned from rat pituitary and a mouse pituitary tumor cell line, *Biochem. Biophys. Res. Commun.* **1993**, 191, 1139–1144.
- 220 J. BROOKS, P. TAYLOR, P. SAUNDERS, K. EIDNE, W. STRUTHERS, A. MCNEILLY. Cloning and sequencing of the sheep pituitary gonadotropin releasing hormone receptor and changes in expression of its mRNA during the estrous cycle, *Mol. Cell. Endocrinol.* **1993**, 94, R23–R27.
- 221 N. ILLING, G. JACOBS, I. BECKER, C. FLANAGAN, J. DAVIDSON, R. MILLAR. Comparative sequence analysis and functional characterization of the cloned sheep gonadotropin releasing hormone receptor reveal differences

- in primary structure and ligand specificity among mammalian receptors. *Biochem. Biophys. Res. Commun.* **1993**, *196*, 745–751.
- 222** S. KAKAR, C. RAHE, J. NEILL. Molecular cloning sequencing and characterizing the bovine receptor for gonadotropin releasing hormone (GnRH), *Domest. Anim. Endocrinol.* **1993**, *10*, 335–342.
- 223** S. KAKAR, W. GRIZZLE, J. NEILL. The nucleotide sequence of human GnRH receptors in breast and ovarian tumors are identical with that found in the pituitary, *Mol. Cell Endocrinol.* **1994**, *106*, 145–149.
- 224** S. SEALFON, R. MILLAR. Functional domains of the gonadotropin releasing hormone receptor, *Cell Mol. Neurobiol.* **1995**, *15*, 25–42.
- 225** S. SEALFON, R. MILLAR. The gonadotropin releasing hormone receptor: Structural determinations and regulatory control, *Human Reprod Update.* **1995**, *1*, 216–230.
- 226** G. HALMOS, A. NAGY, N. LAMHARZI, A. SCHALLY. Cytotoxic analogs of luteinizing hormone releasing hormone bind with high affinity to human breast cancers, *Cancer Lett.* **1999**, *136*, 129–136.
- 227** G. IRMER, C. BURGER, R. MULLER, O. ORTMANN, U. PETER, S. KAKAR, J. NEILL, K. SCHULZ, G. EMONS. Expression of the messenger RNAs for luteinizing hormone-releasing hormone (LHRH) and its receptor in human ovarian epithelial carcinoma, *Cancer Res.* **1995**, *55*(4), 817–822.
- 228** P. LIMONTA, D. DONDI, R. MORETTI, R. MAGGI, M. MOTTA. Antiproliferative effects of luteinizing hormone-releasing hormone agonists on the human prostatic cancer cell line LNCaP, *J. Clin. Endocrinol. Metab.* **1992**, *75*(1), 207–212.
- 229** S. STOJILKOVIC, J. REINHART, K. CATT. GnRH receptors: Structure and signal transduction pathways, *Endocrine Rev.* **1994**, *15*, 462–499.
- 230** E. NEER. Heterotrimeric G proteins: Organizers of transmembrane signals, *Cell.* **1995**, *80*, 249–257.
- 231** C. HELDIN. Dimerization of cell surface receptors in signal transduction, *Cell.* **1995**, *80*, 213–223.
- 232** K. HSIEH, T. MARTIN. Thyrotropin releasing hormone and gonadotropin releasing hormone receptors activate phospholipase C by coupling to the guanosine triphosphate binding proteins Gq and G11, *Mol. Endocrinol.* **1992**, *6*, 1673–1681.
- 233** E. LOUMAYE, K. CATT. Agonist induced regulation of pituitary receptors for gonadotropin releasing hormone. Dissociation of receptor recruitment from hormone release in cultured gonadotrophs. *J. Biol. Chem.* **1983**, *258*, 12 002–12 009.
- 234** M. VRECL, L. ANDERSON, A. HANYALOGU, A. MCGREGOR, A. GROARKE, G. MILLIGAN, P. TAYLOR, K. EIDNE. Agonist induced endocytosis and recycling of the gonadotropin releasing hormone receptor: Effect of b-arrestin on internalization kinetics, *Mol. Endocrinol.* **1998**, *12*, 1818–1829.
- 235** S. KRAUS, Z. NAOR, R. SEGER. Intracellular signaling pathways mediated by the gnRH receptor, *Arch. Med. Res.* **2001**, *32*, 499–509.
- 236** Z. NAOR, D. HARRIS, S. SHACHAM. Mechanism of gnRH receptor signaling: Combinatorial cross talk of ca and protein kinase C. *Frontiers Neuroendocrinol.* **1998**, *19*, 1–19.
- 237** C. LIEBOW, M. LEE, A. KAMER, A. SCHALLY. Regulation of luteinizing hormone releasing hormone by heterologous and autologous receptor stimulated tyrosine phosphorylation. *Proc. Natl. Acad. Sci. U.S.A.* **1991**, *88*, 2244–2248.
- 238** C. GRUNDKER, P. VOLKER, K. SCHULZ, G. EMONS. Luteinizing hormone-releasing hormone agonist triptorelin and antagonist cetrorelix inhibit EGF-induced c-fos expression in human gynecological cancers, *Gynecol. Oncol.* **2000**, *78*(2), 194–202.
- 239** G. GRUNDKER, P. VOLKER, G. EMONS. Antiproliferative signaling of LHRH in human endometrial and ovarian cancer cells through G protein alpha(1) mediated activation of phosphotyrosine phosphatase,

- Endocrinology*. **2001**, 142, 2369–2380.
- 240** A. IMAI, H. TKAGI, S. HORIBE, T. FUSEYA, T. TAMAYA. Coupling of gonadotropin releasing hormone receptor to Gi protein in human reproductive tract tumors. *J. Clin. Endocrinol. Metab.* **1996**, 81, 3249–3253.
- 241** M. MARELLI, R.M. MORETTI, D. DONDI, M. MOTTA, P. LIMONTA. Luteinizing hormone releasing hormone agonists interfere with the mitogenic activity of the insulin-like growth factor system in androgen-independent prostate cancer cells. *Endocrinology*. **1999**, 140, 5250–5256.
- 242** C. GRUNDKER, K. SCHULZ, A.R. GUNTHERT, G. EMONS. Luteinizing hormone-releasing hormone induces nuclear factor kappaB-activation and inhibits apoptosis in ovarian cancer cells. *J. Clin. Endocrinol. Metab.* **2000**, 85, 3815–3820.
- 243** H. EVEREST, J. HISLP, T. HARDING, J. UNEY, A. FLYNN, R. MILLAR, C. McARDLE. Signalling and anti-proliferative effects mediated by GnRH receptors after expression in breast cancer cells using recombinant adenovirus. *Endocrinology*. **2001**, 142, 4663–4672.
- 244** S. MAUDSLEY, L. DAVIDSON, A. PAWSON, R. CHAN, R. LOPEZ DE MATURANA, R. MILLAR. Gonadotropin releasing hormone antagonists promote proapoptotic signaling in peripheral reproductive tumor cells by activating a Gai coupling state of the type I GNRH receptor. *Cancer Res.* **2004**, 64, 7533–7544.
- 245** P. LIMONTA, R.M. MORETTI, M.M. MARELLI, M. MOTTA. The biology of gonadotropin hormone-releasing hormone: Role in the control of tumor growth and progression in humans. *Front Neuroendocrinol.* **2003**, 24, 279–295.
- 246** C. GRUNDKER, A.R. GUNTHERT, S. WESTPHALEN, G. EMONS. Biology of the gonadotropin-releasing hormone system in gynecological cancers. *Eur. J. Endocrinol.* **2002**, 146, 1–14.
- 247** G. EMONS, V. MULLER, O. ORTMANN, G. GROSSMANN, U. TAUTNER, B. VON STUCKRAD, K. SCHULZ, A. SCHALLY. Luteinizing hormone releasing hormone agonist triptorelin antagonizes signal transduction and mitogenic activity of epidermal growth factor in human ovarian and endometrial cancer cell lines. *Int. J. Oncol.* **1996**, 9, 1129–1137.
- 248** M. LEE, C. LIEBOW, A. KRAMER, A. SCHALLY. Effects of epidermal growth factor and analogues of luteinizing hormone releasing hormone and somatostatin on phosphorylation of tyrosine residues of specific substrates in various tumors. *Proc. Natl. Acad. Sci. U.S.A.* **1991**, 88, 1656–1660.
- 249** L. KREBS, X. WANG, H. PUDAVAR, E. BERGEY, A. SCHALLY, A. NAGY, P. PRASAD, C. LIEBOW. Regulation of targeted chemotherapy with cytotoxic luteinizing hormone-releasing hormone analogue by epidermal growth factor. *Cancer Res.* **2000**, 60(15), 4194–4199.
- 250** A. NAGY, A.V. SCHALLY. Cytotoxic analogs of luteinizing hormone releasing hormone (LHRH); a new approach to targeted chemotherapy. *Drug Future* **2002**, 27, 389–370.
- 251** J.M. ARENCIBIA, A.V. SCHALLY, M. KRUPA, A.M. BAJO, A. NAGY, K. SZEPESHAZI, A. PLONOWSKI. Targeting of doxorubicin to ES-2 human ovarian cancers in nude mice by linking to an analog of luteinizing hormone-releasing hormone improves its effectiveness. *Int. J. Oncol.* **2001**, 19, 571–577.
- 252** G. EMONS, C. GRUNDKER, A.R. GUNTHERT, S. WESTPHALEN, J. KAVANAGH, C. VERSCHRAEGEN. GnRH antagonists in the treatment of gynecological and breast cancers. *Endocrine Relat. Cancer*, **2003**, 10, 291–299.
- 253** C. GRUNDKER, A. HUSCHMAND NIA, G. EMONS. Gonadotropin-releasing hormone receptor-targeted gene therapy of gynecologic cancers. *Mol. Cancer Ther.* **2005**, 4, 225–231.
- 254** K. ARORA, A. SAKAI, K. CATT. Effects of second intracellular loop mutations

- on signal transduction and internalization of the gonadotropin releasing hormone receptor, *J. Biol. Chem.* **1995**, *270*, 22 820–22 826.
- 255** D. NUSSENVEIG, M. HEINFLINK, M. GERSHENGORN. Agonist-stimulated internalization of the thyrotropin-releasing hormone receptor is dependent on two domains in the receptor carboxyl terminus, *J. Biol. Chem.* **1993**, *268*, 2389–2392.
- 256** A. PAWSON, A. KATZ, Y. SUN, J. LOPES, N. ILLING, R. MILLAR, J. DAVIDSON. Contrasting internalization kinetics of human and chicken gonadotropin releasing hormone receptors mediated by c-terminal tail, *J. Endocrinol.* **1998**, *156*, R9–R12.
- 257** C. McARDLE, J. FRANKLIN, L. GREEN, J. HISLOP. Signaling cycling and desensitization of gnRH receptors, *J. Endocrinol.* **2002**, *173*, 1–11.
- 258** A. HEDING, M. VREEL, J. BOGERD, A. MCGREGOR, R. SELLAR, P. TAYLOR, K. EIDNE. GnRH receptors with intracellular carboxyl terminal tails undergo acute desensitization of total inositol phosphate production and exhibit accelerated internalization kinetics, *J. Biol. Chem.* **1998**, *273*, 11 472–11 477.
- 259** L. HUNYADY, A. BAUKAL, T. BALLA, K. CATT. Independence of type I angiotensin II receptor endocytosis from G protein coupling and signal transduction, *J. Biol. Chem.* **1994**, *269*, 24 798–24 804.
- 260** R. BENYA, Z. FATHI, J. BATTEY, R. JENSEN. Serines and threonines in the gastrin-releasing peptide receptor carboxyl terminus mediate internalization, *J. Biol. Chem.* **1993**, *268*, 20 285–20 290.
- 261** R.T. JENSEN, Z. FATHI, J. BATTEY, R. JENSEN. Serines and threonines in the gastrin-releasing peptide receptor carboxyl terminus mediate internalization. *J. Biol. Chem.* **1993**, *268*, 20 285–20 290.
- 262** R. MILLAR, S. LOWE, D. CONKLIN, A. PAWSON, S. MAUDSLEY, B. TROSKIE, T. OTT, M. MILLAR, G. LINCOLN, R. SELLAR, B. FAURHOLM, G. SCOBIE, R. KUESTNER, E. TERASAWA, A. KATZ. A novel mammalian receptor for the evolutionarily conserved type II GnRH, *Proc. Natl. Acad. Sci. U.S.A.* **2001**, *98*, 9636–9641.
- 263** J. NEILL, L. DUCK, J. SELLERS, L. MUSGROVE. A gonadotropin-releasing hormone (GnRH) receptor specific for GnRH II in primates, *Biochem. Biophys. Res. Commun.* **2001**, *282*, 1012–1018.
- 264** J. KOENIG, J. EDWARDSON. Endocytosis and recycling of G protein coupled receptors, *Trends Pharmacol. Sci.* **1997**, *18*, 276–287.
- 265** J. HISLOP, H. EVEREST, A. FLYNN, T. HARDING, J. UNEY, B. TROSKIE, R. MILLAR, C. McARDLE. Differential internalization of mammalian and non-mammalian gonadotropin releasing hormone receptors: Uncoupling of dynamin dependent internalization from mitogen activated protein kinase signaling, *J. Biol. Chem.* **2001**, *276*, 39 685–39 694.
- 266** C. GRUNDKER, A. GUNTHERT, R. MILLAR, G. EMONS. Expression of GnRH II receptor in human endometrial and ovarian cancer cells and effects of GnRH II on tumor cell proliferation, *J. Clin. Endocrinol. Metab.* **2002**, *87*, 1427–1430.
- 267** C. GRUNDKER, A.R. GUNTHERT, M. HELLRIGEL, G. EMONS. Gonadotropin-releasing hormone (GnRH) agonist triptorelin inhibits estradiol-induced serum response element (SRE) activation and c-fos expression in human endometrial, ovarian and breast cancer cells. *Eur. J. Endocrinol.* **2004**, *151*, 619–628.
- 268** K. MAITI, Y. OH, J. MOON. Differential effects of gonadotropin releasing hormone I and II on prostate cancer cell signaling and cell death, *J. Clin. Endocrinol. Metab.* **2005**, *90*, 4287–4298.
- 269** N. ILLING, B. TROSKIE, C. NAHORNIA, J. HAPGOOD, R. PETER, R. MILLAR. Two gonadotropin releasing hormone receptor subtypes with distinct ligand selectivity and differential distribution in brain and pituitary in the goldfish (*Carassius auratus*), *Proc. Natl. Acad. Sci. U.S.A.*, **1999**, *96*, 2526–2531.

- 270 L. WANG, J. BOGERD, H. CHOI, J. SEONG, J. SOH, S. CHUN, M. BLOMENROHR, B. TROSKIE, R. MILLAR, W. YU, S. McCANN, H. KWON. Three distinct types of GnRH receptor characterized in the bull frog, *Proc. Natl. Acad. Sci. U.S.A.* **2001**, *98*, 361–366.
- 271 A. WANG, J. LI, K. MAITI, W. KIM, H. KANG, J. SEONG, H. KWON. Preferential ligand selectivity of the monkey type II gonadotropin releasing hormone receptor for GnRH 2 and its analogs, *Mol. Cell Endocrinol.* **2003**, *209*, 33–42.
- 272 G. EMONS, O. ORTMANN, K.D. SCHULZ, A.V. SCHALLY. Growth inhibitory actions of LHRH on tumor cells, *Trends Endocrinol. Metab.* **1997**, *8*, 355–362.
- 273 P. LEUNG, C. CHENG, X. ZHU. Multifactorial role of GnRH I and GnRH II in the human ovary, *Mol. Cell Endocrinol.* **2003**, *202*, 145–153.
- 274 S.-F. CHENG, L.-K. CHAU. Colloidal gold-modified optical fiber for chemical and biochemical sensing. *Anal. Chem.* **2003**, *75*, 16.
- 275 B. FAURHOLM, R. MILLAR, A. KATZ. The genes encoding the type II gonadotropin releasing hormone receptor and the ribonucleoprotein RBM8A in human overlap in two genomic loci, *Genomics.* **2001**, *78*, 15–18.
- 276 J. NEILL. GnRH and GnRH receptor genes in the human genome, *Endocrinology.* **2002**, *143*, 737–743.
- 277 A. PAWSON, K. MORGAN, S. MAUDSLEY, R. MILLAR. Type II gonadotrophin-releasing hormone (GnRH-II) in reproductive biology, *Reproduction.* **2003**, *126*(3), 271–278.
- 278 S. ACHARJEE, K. MAITI. *Cells.* **2002**, *14*, 101–107.
- 279 C. GRUNDKER, P. VOLKER, F. GRIESINGER, A. RAMASWAMY, A. NAGY, A. SCHALLY, G. EMONS. Antitumor effects of the cytotoxic luteinizing hormone-releasing hormone analog AN-152 on human endometrial and ovarian cancers xenografted on nude mice, *Am. J. Obstet. Gynecol.* **2002**, *187*, 528–537.
- 280 U. KAISER, P. CONN, W. CHIN. Studies of gonadotropin releasing hormone (GnRH) action using GnRH receptor expressing pituitary cell lines, *Endocrinol. Rev.* **1997**, *18*, 46–70.
- 281 R. MORETTI, M. MARELLI, D. DONDI. LHRH agonists interfere with the stimulatory actions of egf in human prostate cancer cell lines LNCaP and DU 145, *J. Clin. Endocrinol. Metab.* **1996**, *81*, 3930–3937.
- 282 M. HIRAOKA, S. JO, K. AKUTA, Y. NISHIMURA, M. TAKAHASHI, M. ABE. Radiofrequency capacitive hyperthermia for deep-seated tumors. II. Effects of thermoradiotherapy. *Cancer.* **1987**, *60*, 128–135.
- 283 R. CAVALIERE, E.C. CIOCATTO, B.C. GIOVANELLA, C. HEIDELBERGER, R.O. JOHNSON, M. MARGOTTINI, B. MONDOVI, G. MORICCA, A. ROSSI-FANELLI. Selective heat sensitivity of cancer cells. Biochemical and clinical studies. *Cancer.* **1967**, *20*, 1351–1381.
- 284 P. WUST, B. HILDEBRANDT, G. SREENIVASA, B. RAU, J. GELLERMANN, H. RIESS, R. FELIX, P.M. SCHLAG. Hyperthermia in combined treatment of cancer. *Lancet Oncol.* **2002**, *3*, 487–497.
- 285 A. JORDAN, R. SCHOLZ, P. WUST, H. FAEHLING, R. FELIX. Magnetic fluid hyperthermia (MFH): Cancer treatment with AC magnetic field induced excitation of biocompatible superparamagnetic nanoparticles. *J. Magn. Magn. Mater.* **1999**, *201*, 413–419.
- 286 I. HILGER, R. HERGT, W.A. KAISER. Effects of magnetic thermoablation in muscle tissue using iron oxide particles: An in vitro study. *Invest. Radiol.* **2000**, *35*, 170–179.
- 287 M. SHINKAI, M. MATSUI, T. KOBAYASHI. Heat properties of magnetoliposomes for local hyperthermia. *Jpn. J. Hyperthermic Oncol.* **1994**, *10*, 168–177.
- 288 R. HIERGEIST, W. ANDRAE, N. BUSKE, R. HERGT, I. HILGER, U. RICHTER, W. KAISER. Application of magnetite ferrofluids for hyperthermia. *J. Magn. Magn. Mater.* **1999**, *201*, 420–422.

- 289 W. SCHUTT, C. GRUTTNER, U. HAFELI, M. ZBOROWSKI, J. TELLER, H. PUTZAR, C. SCHUMICHEN. Applications of magnetic targeting in diagnosis and therapy – possibilities and limitations: A mini-review. *Hybridoma*. 1997, 16, 109.
- 290 I. HILGER, K. FRUHAUF, W. ANDRA, R. HIERGEIST, R. HERGT, W.A. KAISER. Heating potential of iron oxides for therapeutic purposes in interventional radiology. *Acad. Radiol.* 2002, 9, 198–202.
- 291 R.E. ROSENZWEIG. Heating magnetic fluid with alternating magnetic field. *J. Magn. Magn. Mater.* 2002, 252, 370–374.
- 292 A.V. BRUSENTOV, V.V. GOGOSOV, T.N. BUNTSOVA, A.V. SERGEEV, N.Y. JURCHENKO, A. KUZNETSOW, O. KUZNETSOW, L.I. SHUMAKOV. Evaluation of ferromagnetic fluids and suspensions for the site-specific radiofrequency-induced hyperthermia of MX11 sarcoma cells in vitro. *J. Magn. Magn. Mater.* 2001, 225, 113–119.
- 293 A. JORDAN, R. SCHOLZ, P. WUST, H. FAHLING, J. KRAUSE, W. WŁODARCZYK, B. SANDER, T. VOGL, R. FELIX. Effects of magnetic fluid hyperthermia (MFH) on C3H mammary carcinoma in vivo. *Int. J. Hyperthermia* 1997, 13, 587–605.
- 294 A. HALBREICH, J. RODGER, J.N. PONS, D. GELDWERTH, M.F. DA SILVA, M. ROUDIER, J.C. BACRI, *Biochimie* 1998, 80, 379.
- 295 W. HANSEL, C. LEUSCHNER, F. ENRIGHT. Targeted destruction of prostate cancers and their metastases by lytic peptide conjugates. *Mol. Cell Endocrinol*, 2005, in the press.
- 296 J. ZHOU, C. LEUSCHNER, C. KUMAR, J. HORMES, W. SOBOYEJO. Subcellular accumulation of magnetic nanoparticles in breast tumors and metastases. *Biomaterials*, 2006, 27, 2001–2008.
- 297 C. LEUSCHNER, C. KUMAR, W. HANSEL, J. ZHOU, W. SOBOYEJO, J. HORMES. Ligand conjugated superparamagnetic iron oxide nanoparticles for early detection of metastases. *Breast Cancer Res. Treatment*, 2006, 99, 2, 163–176.
- 298 C. LEUSCHNER, C. KUMAR, J. HORMES, W. HANSEL. Targeting breast cancer cells and their metastases through luteinizing hormone releasing hormone receptors using magnetic nanoparticles. *J. Biomed. Nanotechnol.*, 2005, 2, 229–233.
- 299 C. LEUSCHNER, C. KUMAR, M. URBINA, J. ZHOU, W. SOBOYEJO, W. HANSEL, F. HORMES. The use of ligand conjugated superparamagnetic iron oxide nanoparticles (SPION) for early detection of metastases. *NSTI Nanotechnol. Technical Proc.*, 2005, 1, 5–6.
- 300 C. KUMAR, C. LEUSCHNER, E. DOOMES, L. HENRY, M. JUBAN, J. HORMES. Efficacy of lytic peptide bound magnetite nanoparticles in destroying breast cancer cells, *J. Nanosci. Nanotechnol.* 2004, 4, 245–249.
- 301 D. SHIEH, F. CHEN, C. SU, C. YEH, M. WU, Y. WU, C. TSAI, D. WU, D. CHEN, C. CHOU. Aqueous dispersions of magnetite nanoparticles with NH<sup>+</sup> surfaces for magnetic manipulations of biomolecules and MRI contrast agents, *Biomaterials*. 2005, 26, 7183–7191.
- 302 C. BERRY, S. CHARLES, S. WELLS, M. DABY, A. CURTIS. The influence of transferring stabilized magnetic nanoparticles on human dermal fibroblasts in culture, *Int. J. Pharm.* 2004, 269, 211.
- 303 L. JOSEPHSON, C. TUNG, A. MOORE, R. WEISSELER. High efficiency intracellular magnetic labeling with novel superparamagnetic-tat peptide conjugates, *Bioconjugate Chem.* 1999, 10, 186–191.
- 304 C. DODD, H. HSU, W. CHU, P. YANG, H. ZHANG, J. MOUNTZ, K. ZINN, J. FORDER, L. JOSEPHSON, R. WEISSELER, J. MOUNTZ, J. MOUNTZ. Normal T-cell response and in vivo magnetic resonance imaging of T cells loaded with HIV transactivator-peptide-derived superparamagnetic nanoparticles, *J. Immunol. Methods*. 2001, 256, 89–105.
- 305 M. ROSER, D. FISCHER, T. KISSEL. Surface-modified biodegradable



- albumin nano- and microspheres. II: Effect of surface charges on in vitro phagocytosis and biodistribution in rats, *Eur. J. Pharm. Biopharm.* **1998**, *46*, 255–263.
- 306 F. PINEAUD, D. KING. Bioactivation and cell targeting of semiconductor CdSe, *J. Am. Chem. Soc.* **2004**, *126*, 6115–6123.
- 307 D. POULIQUEN, J. LE JEUNE, R. PERDRISOT, A. ERMAS, P. JALLET. Iron oxide nanoparticles for use as an MRI contrast agent: Pharmacokinetics and metabolism, *Magn. Reson. Imag.* **1991**, *9*, 275–283.
- 308 S. SAINI, D. STARK, P. HAHN, J. WITTENBERG, T. BRADY, J. FERRUCCI. Ferrite particles: A superparamagnetic MR contrast agent for the reticulo-endothelial system, *Radiology.* **1987**, *162*, 211–216.
- 309 L. TIEFENAUER, A. TSCHIRKY, G. KUHNE, R. ANDRES. In vivo evaluation of magnetite nanoparticles for use as a tumor contrast agent in MRI, *Magn. Reson. Imag.* **1996**, *14*, 391–402.
- 310 R. WEISSLEDER, D. STARK, B. ENGELSTAD, B. BACON, C. COMPTON, D. WHITE, P. JACOBS, J. LEWIS. Superparamagnetic iron oxide: Pharmacokinetics and toxicity, *Am. J. Roentgenol.* **1989**, *152*, 167–173.
- 311 A. MOORE, L. JOSEPHSON, R. BHORADE, J. BASILION, R. WEISSLEDER. Human transferrin receptor gene as a marker gene for MR imaging, *Radiology.* **2001**, *221*, 244–250.
- 312 A. MOORE, E. MARECOS, A. BOGDANOV, R. WEISSLEDER. Tumoral distribution of long-circulating dextran coated iron oxide nanoparticles in a rodent model, *Radiology.* **2000**, *214*, 568–574.
- 313 A.R. GUNTHER, C. GRUNDKER, A. OLOTA, J. LASCHE, N. EICKE, G. EMONS. Analogs of GnRH-I and GnRH-II inhibit epidermal growth factor-induced signal transduction and resensitize resistant human breast cancer cells to 4OH-tamoxifen. *Eur. J. Endocrinol.* **2005**, *153*, 613–625.
- 314 K.L. SHANNON, R.T. BRANCA, G. GALIANA, S. CENZANO, L.S. BOUCHARD, W. SOBOYEYO, W. WARREN. Simultaneous acquisition of multiple orders of intermolecular multiple-quantum coherence images in vivo. *Magn. Reson. Imaging.* **2004**, *22*, 1407–1412.
- 315 M. ZALESKA, G. BODEK, B. JANA, W. HANSEL, A.J. ZIECIK. Targeted destruction of normal and cancer cells through lutropin/choriogonadotropin receptors using hecate- $\beta$ CG conjugate. *Exp. Clin. Endocrinol. Diabetes.* **2003**, *111*, 146–153.
- 316 G. BODEK, N.A. RAHMAN, M. ZALESKA, R. SOLIYMANI, H. LANKINEN, W. HANSEL, I. HUHTANIEMI, A.J. ZIECIK. A novel approach of targeted ablation of mammary carcinoma cells through luteinizing hormone receptors using Hecate-CG $\beta$  conjugate. *Breast Cancer Res. Treat.* **2003**, *79*, 1–10.
- 317 C. LEUSCHNER, W. HANSEL. Membrane disrupting lytic peptides for cancer treatments. *Curr. Pharm. Des.* **2004**, *10*, 2299–2310.
- 318 C. LEUSCHNER, C. KUMAR, W. HANSEL, F.J. HORMES. Targeting breast cancers and metastases with LHRH and a lytic peptide bound to iron oxide nanoparticles. *Clin. Cancer Res.* **2005**, *11*, B 262, 9097s.
- 319 J. MENG, G. GALIANA, T. BRANCA, J. ZHOU, C. LEUSCHNER, C. KUMAR, J. HORMES, T. OTITI, A. BEYE, W. WARREN, W.O. SOBOYEJO. LHRH-functionalized superparamagnetic ironoxide nanoparticles (SPIONs) for contrast enhancement in MRI, **2006**, in preparation.

## 7

# Carbon Nanotubes in Cancer Therapy and Diagnosis

*Pu Chun Ke and Lyndon L. Larcom*

### 7.1

#### Overview

Integrating nanomaterials and biomedicine is a recent endeavor that aims to provide highly localized detection and treatment for cancers and diseases. Understanding the intricate interplay of nanomaterials and biological components and biological systems necessitates combining materials science, nanotechnology, physics, chemistry, biology, and biomedicine. The impact of this grand exploration touches areas of fundamental science and engineering, health care, and environmental control and protection. Recent advances in our understanding of carcinogenesis have led us to consider taking advantage of the special characteristics of both cancer cells and nanomaterials to detect and treat tumors. Integrating cancer therapy and nanomaterials captivates scientific imagination, offers new hope for human well-being, and unavoidably invites controversy and debate as experienced by many scientific and technological developments during their infancy.

Carbon nanotubes (CNTs) are mosaics of carbon atoms synthesized into cylinders of single or multiple layers [1]. The astonishingly simple and plain structures of CNTs transcend the most important classes of nanomaterials owing to their unsurpassed stiffness, easy accommodation of chemical and biological versatility, and rich quantum electronic properties [2–7]. Since their discovery a mere decade ago, CNTs have orchestrated a broad array of applications, including novel composites [8, 9], electrochemical sensors [10, 11], field emission [12, 13], memory, and nanoscale devices [14–16], just to name a few. In the rapidly growing field of biotechnology, CNTs have been utilized as platforms for ultrasensitive recognition of antibodies (Fig. 7.1, left) [17], as nucleic acids sequencers [18], and as bioseparators, biocatalysts [19], and ion channel blockers (Fig. 7.1, right) [20] for facilitating biochemical reactions and biological processes. Within the realm of nanomedicine, an emerging field of utilizing nanomaterials and nanostructures for medicine, CNTs have been transformed into scaffolds for neuronal and ligamentous tissue growth for regenerative interventions of the central nervous system and orthopedic sites [21–23], substrates for detecting antibodies associated with human autoimmune diseases with high specificity [24], and carriers of contrast agent aquated

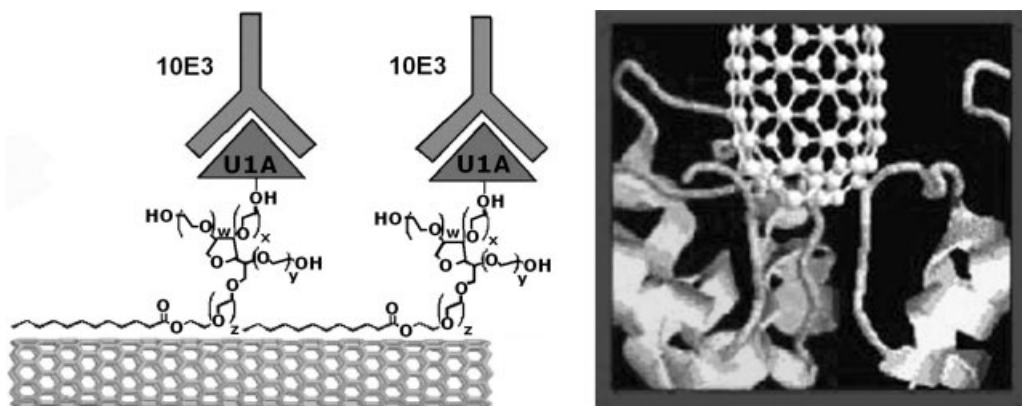


**Fig. 7.1.** (Left) Scheme for specific recognition of 10E3 mAb with an SWNT device coated with a U1A antigen–Tween conjugate [17]. (© National Academy of Sciences.) (Right)

Docking simulation shows a capped SWNT of 0.9 nm in diameter fitting into a selective K-channel [20]. (© The American Society for Biochemistry and Molecular Biology, Inc.)

Gd<sup>3+</sup>-ion clusters for greatly enhanced magnetic resonance imaging [25]. Once covalently or noncovalently attached by nucleic acids (DNA or RNA including short-stranded RNA for gene silencing) [26, 27], vaccines (e.g., B cell epitopes) [28], and proteins [29, 30], CNTs have shown to be effective gene and drug delivery vectors that may someday co-exist with or challenge conventional viral and particulate systems [31]. Selective destruction of cancer cells using functionalized CNTs as transporters and near-infrared (NIR) heat inducing agents, as reported by Dai's group [32], highlights research towards nanomedicine for cancer diagnosis and therapy.

To propel research in nanomedicine, the new “Nanotechnology for Cancer Diagnosis and Therapy” initiative was announced by the National Cancer Institute (NCI) in September 2005 [33]. Nanoscience with its implications for biomedicine has been highlighted as one of the “Priority Areas” of the National Science Foundation (NSF) [34] and in the “Roadmap” of the National Institutes of Health (NIH) [35]. It is not beyond our wildest dream that within the next decade or so we might be able to determine to what extent the atomic world obeys the laws of quantum mechanics, resolve the passionate debate between Drexler and Smalley on “the fat fingers” of nanobots and molecular assemblies [36], and witness how nature selectively embraces the “smart” creatures such as CNTs, buckyballs, dendrimers, quantum dots, and other nanoparticles offered by mankind.

This chapter reviews, for the first time to our knowledge, the state-of-the-art in cancer diagnosis and therapy from the perspective of single-walled carbon nanotubes (SWNTs). Through the introduction of these early developments we wish to present a panorama of how SWNTs can be used for biomedicine. There are many reasons for using SWNTs instead of multiwalled carbon nanotubes (MWNTs) as our model systems. They resemble nucleic acids in physical dimensions and present excellent platforms for biosensing and biocompatibility, as compared with viral

and particulate gene and drug delivery vectors. They possess an enormously high aspect ratio, which allows for efficient permeation of their attached drug loads through tissues and cells. Their large surface areas are able to carry many biomolecules to their respective targets for sensing, sequencing, and therapy. Their stability, flexibility, and non-immunogenicity may prolong the circulation and availability of attached drugs. Their hydrophobicity may facilitate interaction with cell membranes, and the rich electronic properties of SWNTs may open up new routes and methodologies for probing and imaging the states of cancerous tissues and cells.

Because nanotechnology is such a rapidly changing field and because nanomedicine is still in its very infancy, it is beyond our ability to grasp and thus to convey all of the exciting frontiers and aspects of this new science. Instead, we will elucidate only a few of these innovations in this chapter, which is organized into the following sections: Section 7.1 gives an overview; Section 7.2 covers SWNT modification for solubility and biocompatibility; Section 7.3 deals with diffusion of SWNT–biomolecular complexes; Section 7.4 covers gene and drug delivery with SWNT transporters; Section 7.5 deals with sensing and treating cancer cells utilizing SWNTs; Section 7.6 covers the cytotoxicity of SWNTs; Section 7.7 deals cancers and SWNTs; and Section 7.8 provides a summary.

## 7.2

### SWNT Modification for Solubility and Biocompatibility

Pristine SWNTs in aqueous solution form bundles due to the hydrophobic interactions, van der Waals attractions, and  $\pi$ -stacking among individual tubes. Bundle formation presents a major hurdle for the applications of SWNTs in biological systems and medicine. Solutions to this problem include two major routes, covalent and noncovalent modifications of SWNTs. Covalent modification of SWNTs involves esterification or amidation of acid-oxidized nanotubes and side-wall covalent attachment of functional groups [37–41]. These covalent schemes are often characterized by uncertainties in determining reaction efficacy and by undesirable modifications in the physical and chemical properties of SWNTs [28, 42, 43]. In comparison, the noncovalent modifications of SWNTs employ nonspecific attachment of proteins [17, 30], linear bio- and synthetic polymers [DNA, RNA, poly(vinyl pyrrolidone), polystyrene sulfonate], and surfactants [sodium dodecyl sulfate (SDS) etc.] [42–49]. Many surfactants, organic solvents, and residues, however, cause cytotoxicity [50] and/or other side effects that limit the biocompatibility of SWNTs. Developing alternative schemes is thus crucial for facilitating the full range of biological and biomedical applications for SWNTs and their derivatives.

#### 7.2.1

##### Chemical Modifications of SWNTs for Solubility

Chemical modification of SWNTs is an emerging research area in the fields of materials science and nanotechnology, and is pertinent to the biological applications

of SWNTs when it is deemed necessary to attach fluorescent tags, drugs, and proteins. These modifications include the functionalization of oxidized SWNTs and covalent modification of SWNTs. Organic chemistry plays a major role in these approaches.

#### 7.2.1.1 Functionalization of SWNTs through Oxidation

Functionalization of SWNTs utilizing acidic media (e.g., 3:1 mixture of concentrated sulfuric to concentrated nitric acids) may open the ends of the SWNTs and create functionalities suitable for further derivatization at these acid-induced defect sites. Long-chain alkylamines may be coupled with the carboxylic groups present on the surface of oxidized SWNTs. The coupling of organic acids with amines is a well-known reaction, but tends to proceed only at relatively high temperatures. This reaction is often facilitated by converting the acids into a more reactive moiety, usually a mixed anhydride  $R(\text{CO})\text{O}(\text{CO})R'$  or acid chloride  $\text{RCOCl}$ . The acid chloride is generally highly reactive, hydrolyzes upon exposure to air (or the humidity therein), and degrades back to carboxylic acid. Activation of the carboxyl moieties with thionyl chloride and their subsequent reaction with amines are feasible. Alternatively, oxidized SWNTs can be condensed directly with amines. Typically, the solubility of such modified SWNTs is approximately  $0.5 \text{ mg mL}^{-1}$  in organic solvents such as tetrahydrofuran or dichlorobenzene [51]. However, the electronic properties of these functionalized SWNTs are often deviated or even lost. In most cases, the SWNTs are greatly shortened [52].

Functionalization of SWNTs creates charge polarity to the tubes and may lead to their separation from pristine SWNT clusters in polar solvents. This separation is desirable since it breaks the persistent hydrophobic forces and van der Waals interactions among the tubes and renders SWNTs soluble, thus enabling their further incorporation by biological systems. This functionalization process also facilitates the characterization and purification of single SWNTs. The presence of the functional addends at the defect sites of oxidized CNTs can be monitored by either Raman or IR spectroscopy, which easily identify amide- or ester-bond formation. Regarding biosensing, oxidized SWNTs may, for example, react with an alkyl thiol with a subsequent chemical attachment to gold particles [52–54]. These SWNT–gold particle complexes can be used to construct microelectrode arrays. Potential applications of these microelectrode arrays include developing bio-electrochemical sensors and designing novel molecular-recognition electrodes [51].

One scheme that could lead to gene sequencing and recognition is the attachment of peptide nucleic acids (PNA) via N-hydroxysuccinimide (NHS) esters formed on carboxylated SWNTs, as demonstrated by Williams et al. [55] in 2002 (Fig. 7.2). There are several rationales for using PNA to construct such complexes. First, PNA molecules are uncharged DNA analogues that can be hybridized with complementary DNA, and these PNA attached SWNTs may be incorporated into larger electronic devices by recognition-based assembly. PNA treated SWNTs may also serve in biological systems as probes based on sequence-specific attachment. Second, PNA is compatible with the most convenient solvents such as DMF, though less soluble in aqueous solutions. Third, PNA is not susceptible to enzy-

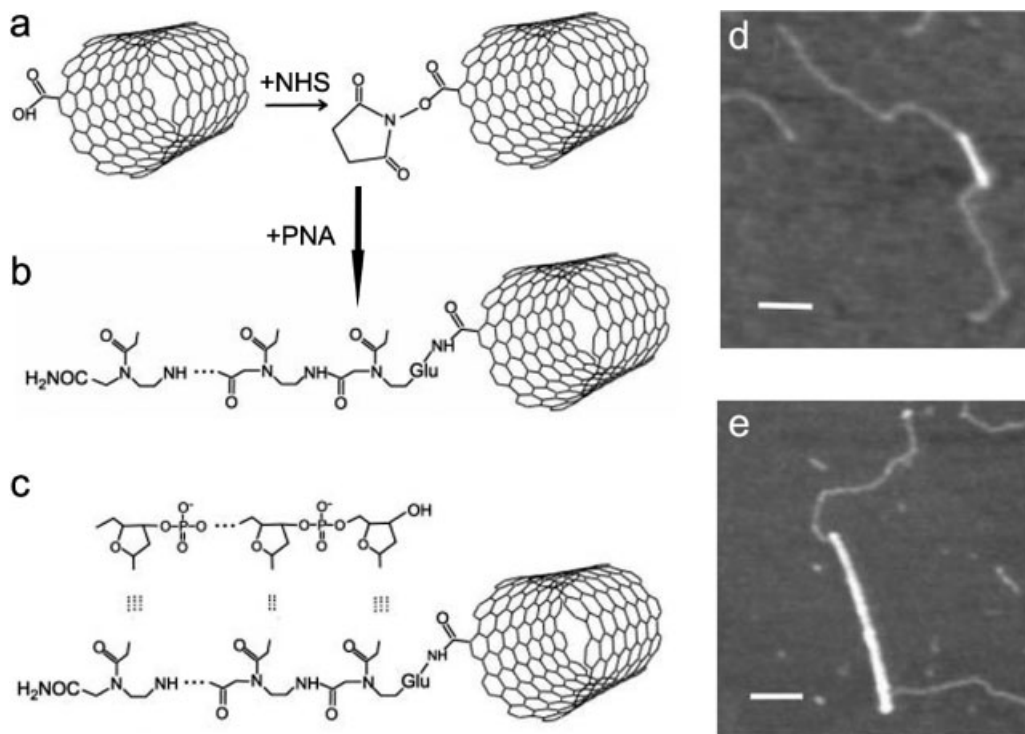


**Fig. 7.2.** Attachment of DNA to carbon nanotubes. (a, b) *N*-Hydroxysuccinimide (NHS) esters formed on carboxylated SWNTs are displaced by PNA, forming an amide linkage. (c) A DNA fragment with a single-stranded, "sticky" end hybridizes by base-

pairing to the PNA-SWNT. (d, e) Atomic-force microscope (tapping mode) images of PNA-SWNTs. SWNTs appear as bright lines; the paler strands represent bound DNA. Scale bars: 100 nm; nanotube diameters: (d) 0.9 and (e) 1.6 nm [55]. (© Nature Publishing Group.)

matic degradation due to its synthetic status. Lastly, PNA-DNA duplexes are thermally more stable than their DNA-DNA counterparts because PNA is neutral and does not induce electrostatic repulsion. The higher thermal stability of PNA-DNA suggests that shorter sticky ends are required for room-temperature hybridization, which reduces nonspecific electrostatic interactions with metallic electrodes, or with silicon oxide, which is desirable for lithography [55].

#### 7.2.1.2 Functionalization of SWNTs through Covalent Modifications

Apart from oxidation, SWNTs also can be treated with dichlorocarbene, which can be induced by chloroform-sodium hydroxide interaction or phenyl(bromodichloromethyl)mercury [56, 57]. SWNTs react with molecular fluorine at 150–600 °C, and these derivatized SWNTs can be retrieved with hydrazine [51]. SWNTs functionalized through this procedure dissolve well in polar solvents, although the fluorine atoms may be substituted by alkyl groups for higher solubility [58]. Fluorination

can also shorten the SWNT to less than 50 nm [51, 59], which has broad implications should the permeation of nuclear membrane pores by SWNTs and their derivatives be desirable.

SWNTs may be functionalized through aryl diazonium chemistry [60], and be derivatized with C–C bonds by the electrochemical reduction of various diazonium salts. In addition, because the oxidative coupling of amines can result in their attachment to SWNT surfaces [51, 61], these nanotube-bound amine moieties have great versatility for use as gene and drug carriers.

Another covalent SWNT functionalization is derived from the chemical processing of fullerenes [62], which is accomplished by the addition of nitrenes, carbenes, or radicals. Functionalized SWNTs may also be constructed via electrophilic addition by adding chloroform to the side walls of SWNTs during a mechanochemical reaction with  $\text{AlCl}_3$ . Hydroxyl groups may replace the chlorine atoms, which then may be esterified to yield corresponding esters [51]. This method not only produces soluble SWNTs but also adds free functional groups for further linking to biomacromolecules.

Based on the methodology of 1,3-dipolar cycloaddition of azomethine ylides, Prato et al. have devised a route for covalently attaching pyrrolidine rings substituted with chemical functions to the side walls of SWNTs [63, 64]. They chose the triethylene glycol group as the N-substituent of the  $\alpha$ -amino acid due to its high solubilizing power. These SWNTs were soluble in chlorinated solvents, acetone, and alcohols but insoluble in diethyl ether or hexane. In particular, the solubility of these functionalized SWNTs in dichloromethane or chloroform was as high as  $50 \text{ mg mL}^{-1}$ , suggesting an average covalent attachment of one pyrrolidine ring to every one hundred carbon atoms of the SWNTs. Moreover, the covalent attachment of pyrrolidine rings to pristine SWNTs quenches their signature NIR band of van Hove transitions [51, 64]. Water-soluble SWNTs can also be obtained by exposing the tubes to N-substituted  $\alpha$ -amino acid with a terminated amino tert-butoxycarbonyl (Boc) protected group and paraformaldehyde. Upon treatment with gaseous hydrochloric acid, the N-Boc groups can be removed by treating the SWNTs with hydrochloric acid, which further releases the corresponding ammonium salts from the water-soluble SWNTs [51, 65].

### 7.2.2

#### **Noncovalent Modifications of SWNTs for Solubility**

Noncovalent solubilization of SWNTs has recently gained recognition partly due to the growing concern over the covalent schemes, including their induced alteration to and/or the loss of the mechanical and electronic properties of SWNTs. Noncovalent schemes are also attractive because of their relative ease of releasing load from the tubes, though this release may sometimes act against the purpose of application, causing uncertainties in quantifying gene and drug transfection. This route of solubilization schemes is unlimited to the field of organic chemistry and often embraces the contributions from researchers in materials sciences, biochemistry, and biophysics. Smalley's group first proposed the idea that SWNTs could be solu-

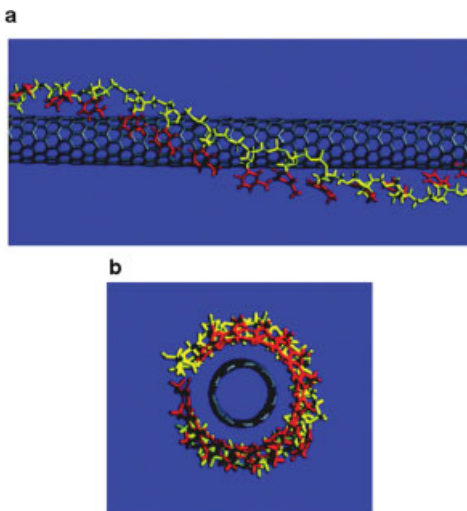


**Fig. 7.3.** Binding model of a (10,0) SWNT wrapped by a poly(T) sequence of ssDNA. (a) The right-handed helical structure shown here is one of several binding structures found, including left-handed helices and linearly adsorbed structures. In all cases, the bases (red) orient to stack with the surface of the

nanotube, and extend away from the sugar-phosphate backbone (yellow). (b) The DNA wraps to provide a tube within which the SWNT can reside, hence converting it into a water-soluble object [49]. (© Nature Publishing Group.)

bilized in aqueous media of amphiphilic molecules such as surfactants [45]. The hydrophobic moieties of the surfactants were hypothesized to interact through wrapping with the hydrophobic surfaces of the SWNTs. This interaction was understood to be facilitated by the van der Waals attractions between the surfactants and the SWNTs in close proximity. Zheng et al. extended this simple scheme to include biomacromolecules such as single-stranded DNA (ssDNA) for the solubilization of SWNTs and sorting of metallic nanotubes from semiconducting ones (Fig. 7.3) [49]. The underlining binding mechanism is the hydrophobic interaction between the nitrogenous bases of the ssDNA and the side walls of the SWNTs, attributed by the  $\pi$ -stacking of the nitrogenous bases and the  $\pi$ -electrons of the carbon atoms on the SWNTs. Poly(A) and poly(C) have lower dispersion efficiencies than poly(T), possibly because these nucleotides tend to strongly self-stack in solution and therefore have smaller free energies for binding to SWNTs. In addition to using nucleic acids, a few groups, most notably Dai's group at Stanford, have dispersed SWNTs in solutions of peptides and proteins such as bovine serum albumin (BSA) and streptavidin [17, 30]. These research efforts have formed the basis for creating biocompatible nanomaterials for biosensing and therapeutics. However, a direct comparison of the solubility from the noncovalent methods with that from the covalent schemes is unavailable, since most noncovalent studies were conducted through visualization rather than quantification.



Recently, our group reported the solubilization of SWNTs using RNA polymers [66]. The structure of this RNA resembles that of ssDNA except that it possesses a hydroxyl group instead of a hydrogen atom at the 2' of their nucleotides. This structural difference, though seemingly minute, opens the door for many exciting applications, including using RNA as catalysts for inorganic particle growth and organic chemical reactions, and as agents for RNA interference (RNAi) for gene silencing. Using single-molecule fluorescence microscopy our group observed that poly(rU) RNA molecules, when exposed to SWNTs immobilized on a quartz substrate, bound to SWNTs instead of randomly distributing on the substrate. The surface property of this substrate changed from hydrophilic to hydrophobic during the chemical deposition of SWNTs. This suggests that  $\pi$ -stacking may dominate the hydrophobic interaction when nucleic acids are noncovalently attached to SWNTs (Figs. 7.4a, b) [46].

The binding induced changes in Raman spectra are shown in Fig. 7.4(c). The samples were prepared using the same protocol as described for fluorescence imaging except that the labeling was omitted to prevent the strong fluorescence signal of labeled poly(rU) from masking the Raman signal of SWNTs. The Raman spectra were excited with a 647.1 nm laser line and the laser power was maintained at approximately 1 mW to avoid heating. A Leica microscope equipped with a 50 $\times$  dry objective (NA = 0.75) was used to focus the laser beam at various spots on the pristine and poly(rU)-bound isolated SWNTs. The Raman scattered light was collected using an ISA Triax 550 spectrometer equipped with a liquid-nitrogen cooled CCD. The bottom spectrum corresponds to pristine SWNTs, while the top spectrum corresponds to poly(rU) bound isolated SWNTs. The frequency positions of the RBM, *D*, and *G* bands were determined from a Lorentzian line shape analysis. The characteristic RBM was observed between 190–290  $\text{cm}^{-1}$ , while the *G* band frequency was centered at 1593  $\text{cm}^{-1}$ . No significant shift in the peak positions was found in the spectrum of poly(rU) bound SWNT as compared with that of the pristine SWNTs, possibly because the charge transfer from the poly(rU) molecules to the SWNT was too minute to discern. The Raman spectrum of SWNT-poly(rU) hybrids exhibits a noticeable decrease in the intensity of the RBM band and a small enhancement in the *D* band intensity compared with the corresponding peaks of the spectrum for isolated SWNTs alone. These changes in Raman spectra are indicative of the effective binding of poly(rU) with SWNTs [46].

#### 7.2.2.1 Solubilization of SWNTs Using Lysophospholipids Enables Cellular Studies [67]

This section details a new approach for solubilizing SWNTs using single-chained phospholipids, or lysophospholipids. This approach is promising because it enables cellular studies using SWNTs and other nanomaterials. The potential applications of lysophospholipid solubilized SWNTs and their biofunctionalized derivatives include *in vivo* imaging, biosensing, and gene and drug delivery for biomedicine.

We first obtained pristine SWNTs using the arc-deposition method. The average diameter of the SWNTs was approximately 1.4 nm measured by Raman spectroscopy.

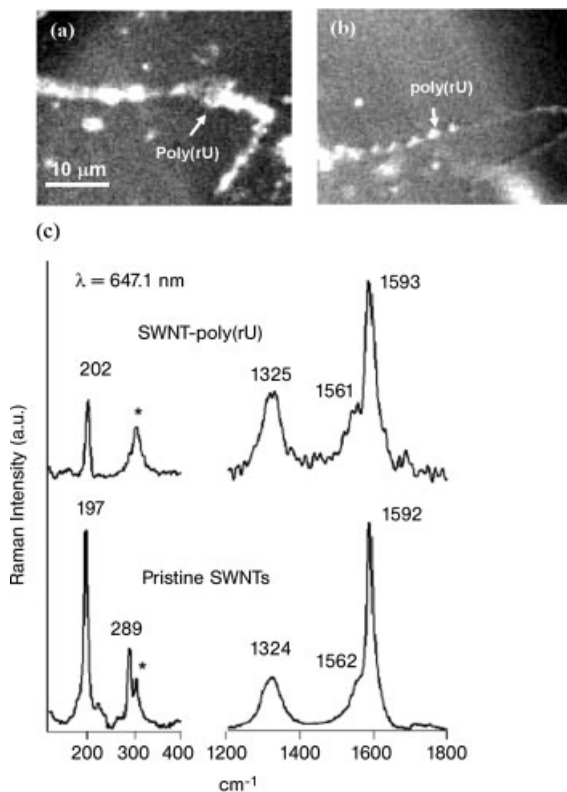


**Fig. 7.4.** (a, b) Fluorescence images of SWNT-poly(rU) hybrids. Individual poly(rU) molecules are visible as small blobs in (b) due to the relatively low concentration. SWNTs in both panels are over 50  $\mu\text{m}$  long. (c) Raman spectra collected at a laser excitation wavelength of 647.1 nm from pristine (bottom) and poly(rU) bound isolated SWNTs (top) on silicon substrates. Plots are normalized with respect to the amplitudes of the G bands. The asterisks at 305  $\text{cm}^{-1}$  correspond to the Raman lines of the silicon substrates [46]. (© American Institute of Physics.)

copy, with an average molecular weight of  $1 \times 10^6$  Dalton (Da), estimated from TEM. To measure the solubility provided by pure phospholipids, SWNTs were dispersed in phosphate-buffered saline (PBS, pH 7.4) containing phospholipids of varying amounts. After sonication for 1 h at room temperature, SWNTs were found to be completely solubilized by LPC 18:0 (Fig. 7.5), and by cell growth mediums (Fig. 7.6a). The weight ratio of solubilized SWNTs to LPC was approximately 1:10, corresponding to a molar ratio of 1:20 000 at saturation (Fig. 7.6b), indicating their high binding capacity. Comparable solubility of SWNTs was also obtained with LPA 16:0 (Fig. 7.5), and LPG 18:0 (Fig. 7.5), based on the same treatments.

Approximately half of the soluble SWNTs were sedimented at 16 060g RCF at tip, based on measured optical densities (Fig. 7.6c), indicating their heterogeneous size

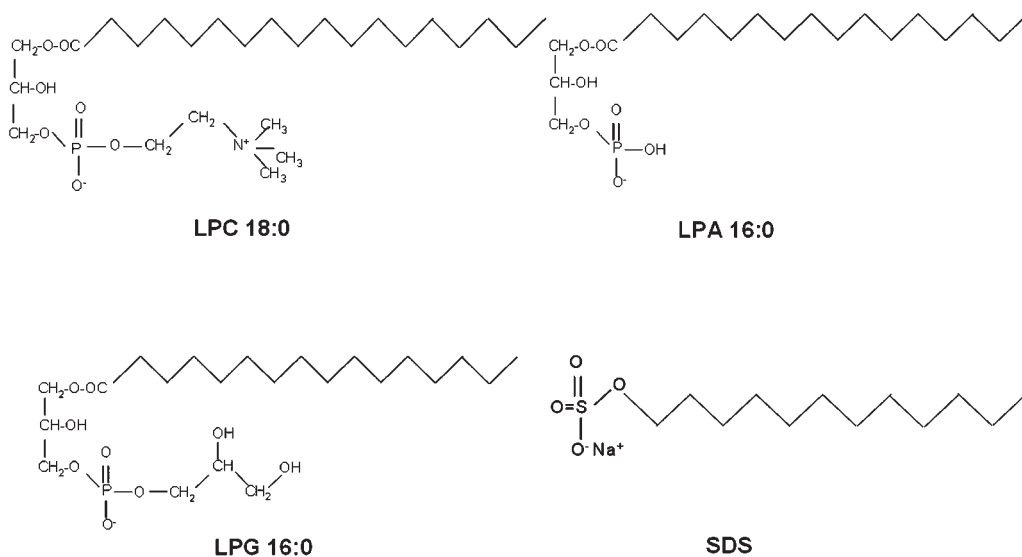


**Fig. 7.5.** Structures of lysophospholipids LPC 18:0, LPA 16:0, and LPG 16:0 and SDS. LPC: lysophosphatidylcholine; LPA: lysophosphatidic acid; LPG: lysophosphatidylglycerol. The numbers 18 and 0 in LPC 18:0 denote the total number of carbon atoms and the total number of double bonds, respectively, contained in the sum of the fatty acyl chains [67]. (© American Chemical Society.)

distribution. From elution volumes measured with chromatography, we estimated that the SWNT-LPC and the SWNT-LPA complexes had an average molecular weight of  $14 \times 10^6$  Da and  $18 \times 10^6$  Da, respectively (Fig. 7.6d). Since each SWNT carries approximately 20 000 LPC molecules and the molecular weight of each LPC is 523.7 Da, the “molecular weight” of each SWNT-LPC complex is estimated at  $11.5 \times 10^6$  Da, which agrees with our measured value of  $14 \times 10^6$  Da. The discrepancy is mainly caused by the heterogeneous size distribution of the SWNTs and the occurrence of small SWNT bundles.

Figure 7.6(e) compares SWNT solubility for LPC, LPG, and the surfactant SDS (Fig. 7.5), a routine solvent for SWNTs [45]. At 6177g RCF at tip, on a per molecule basis, LPC is approximately  $2.5\times$  more effective than SDS in dispersing SWNTs in PBS. At 16060g RCF at tip, LPC is approximately  $10\times$  more effective than SDS in dispersing SWNTs, possibly because the resulting micelles differ in size. This difference might be because LPC has a bulkier head group for interfacing with water and a longer acyl chain for binding with SWNTs. SWNTs with LPG are slightly more soluble than with SDS. Solubilization of SWNTs with lysophospholipids was also more effective than with nucleic acids [47, 49, 68], and was far more effective than with proteins [29, 39]. The aqueous SWNT-lysophospholipid solutions were exceptionally stable for months at room temperature, a promising feature in regards to possible applications in both biology and medicine.

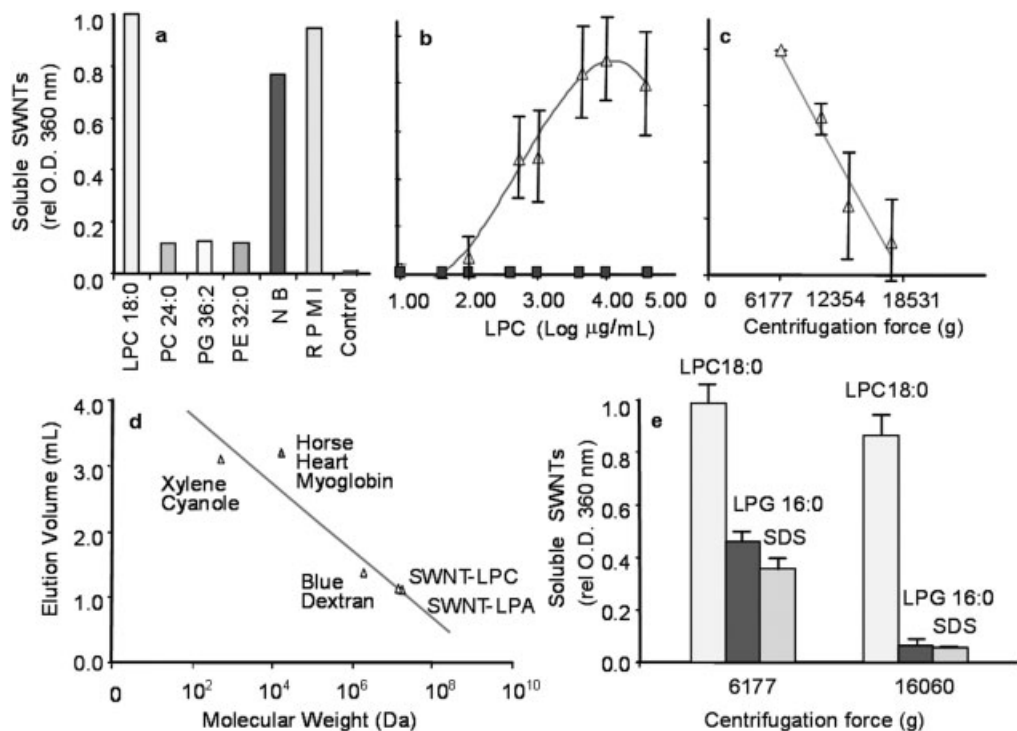


**Fig. 7.6.** Characteristics of SWNTs solubilized with phospholipids. (a) Comparison of SWNT solubility with different aqueous phospholipid solutions and cell growth mediums, RPMI supplemented with 10% fetal bovine serum (FBS) and nutrient broth (NB). SWNTs (1 mg) were treated with phospholipids (10 mg) in PBS (1 mL) or growth medium (1 mL). After bath sonication at room temperature for 1 h and centrifugation for 3 min at 6177g, the absorbance was observed at 360 nm as a measure of the amount of SWNTs solubilized. The label “rel O.D.” on the y-axis denotes relative optical density. (b) LPC solubilized SWNTs. SWNTs (1 mg) were treated with increasing concentrations of LPC 18:0, sonicated, and centrifuged as above, with an absorbance observed at 360 nm. Filled triangles: SWNTs with LPC; filled squares: LPC

alone as a control for micelles. The latter showed negligible absorbance at 360 nm. (c) Sedimentation of LPC-solubilized SWNTs, prepared as above with SWNTs (1 mg) and LPC (10 mg). (d) Size-exclusion chromatography measurements of SWNT-LPC 18:0 (centrifuged at 16 060g for 3 min) and SWNT-LPA 16:0 complexes (centrifuged at 6177g for 3 min). A linear relationship between compound log(molecular weight) and elution volume in mL was established using xylene cyanole FF with blue color (538.6 Da), horse heart myoglobin with reddish color (16951.5 Da), and blue dextran with blue color ( $2 \times 10^6$  Da). (e) Comparison of SWNT solubility in LPC, LPG, and SDS solutions, prepared from SWNTs (1 mg) and detergents (10 mg) as above [67]. (© American Chemical Society.)

To probe the mechanism of SWNT-lysophospholipid binding, zwitterionic LPC and net negatively charged LPG at physiological pH were bound to SWNTs and imaged with TEM (Figs. 7.6a–c). One can see the formation of areas of tightly packed lysophospholipids in the dark/grey areas, our termed “lipid phase”, in

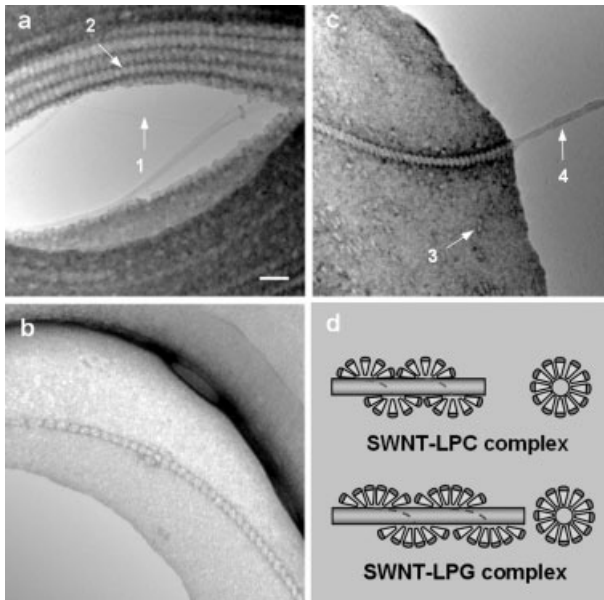


**Fig. 7.7.** TEM images of SWNT-LPC (a and c) and SWNT-LPG (b) complexes. Recorded with an Hitachi 7600 and stained with uranyl acetate. Numbers 1–4 in (a) and (c) correspond to (1) an isolated SWNT in the vacuum phase, (2) an LPC striation on an SWNT/SWNT bundle, (3) possibly an LPC micelle on the substrate in the lipid phase, and (4) an uncoated SWNT bundle in the vacuum phase. Note the less organized and wider striations of SWNT-LPG complexes in (b), as compared with those in (a) and (c) for SWNT-

LPC. Scale bar (a–c): 20 nm. (d) Hypothesized microscopic binding modes of LPC and LPG with SWNTs. The lysophospholipids are shown as truncated triangles, their head groups are at the base of the triangles, and the SWNTs are the inner circles and tubes. The left-hand side illustrates the proposed lipid spiral wrapping along the tube axis while the right-hand side shows their possible binding around the circumference of the tubes [67]. (© American Chemical Society.)

Figs. 7.7(a–c). The light/blank areas in Figs. 7.7(a–c) correspond to lysophospholipid free regions or our termed “vacuum phase”. In the lipid phase SWNTs are wrapped by striations of ~5 nm for LPC and 5–7 nm for LPG. Such organizations were previously reported for the binding of SDS and synthetic lipids on CNTs [69]. However, in the vacuum phase (Figs. 7.7a, c) SWNTs are practically naked, indicating that the binding of lysophospholipids to SWNTs is controlled by the local lysophospholipid environment rather than by specific interactions between lysophospholipids and SWNTs.

Neither LPC nor LPG binds to SWNTs in the vacuum phase, while both coat SWNTs in the lipid phase. LPC on an SWNT or an SWNT bundle displays such a consistent organized pattern along the tube(s) that striations remain approximately the same size (Figs. 7.7a, c). By contrast, the binding of LPG to SWNTs in the lipid phase does not follow the same pattern (Fig. 7.7b). The size and orientation of the

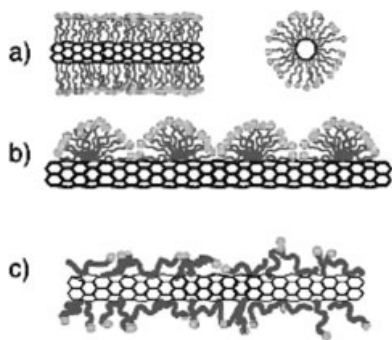


**Fig. 7.8.** Schematic representations of the mechanisms by which surfactants help disperse SWNTs. (a) SWNT encapsulated in a cylindrical surfactant micelle; right-hand side: cross section; left-hand side: side view.

(b) Half-cylinder adsorption of surfactant molecules on a SWNT. (c) Random adsorption of surfactant molecules on an SWNT [42].  
(© American Chemical Society.)

striations change along the axis of SWNTs. These differences could be related to the different lysophospholipid organizations shown in their respective backgrounds. Figures 7.7(a) and (c) show that the lipid phase of LPC is composed of many large objects of  $\sim 5$  nm, which are probably micelles, while the lipid phase of LPG is homogeneous, most probably composed of individual lysophospholipids. Another major difference in the binding of LPC vs. LPG in the lipid phase is the shape of the striations. The crests of striations are approximately 0.2 nm above the surface of SWNT(s) for SWNTs, while the clefts almost touch the surface of SWNT(s) for LPC.

There has been an ongoing debate on the binding mode of amphiphilic surfactants and cylindrical SWNTs [42, 43, 69]. Surfactants are hypothesized in the literature as adopting one of three configurations: (a) micelles; (b) half-cylinders; and (c) random adsorption (Fig. 7.8) [42]. The periodic wrapping in the lipid phase, as observed in our experiment, strongly suggests that the microscopic binding mode is the “half-cylinders” (Fig. 7.7d). Note that the macroscopic arcs formed by lysophospholipids along the SWNT axis are not semi-spherical but are extended arcs, because the ends of lysophospholipid tails within an arc can not occupy the same point and must be offset along the tube axis. Furthermore, LPC on SWNTs (Fig. 7.7a, c) exhibits macroscopic spirals possibly resulting from the wrapping of deformed lipid-composed long half-cylinder(s). In some cases, the step of the spiral is equal to the width of the half-cylinder; thus a single half-cylinder can provide a complete coating of the tube surface. For SWNT bundles, we observed binding with a larger step corresponding to double spiral wrapping. We also noticed that, in some cases, the ring binding mode and the rings were tilted with respect to the tube axis. As long as the tube diameter remains static, the wrapping mode is conserved along the tube. However, the wrapping mode may change when the bundle size varies (Fig. 7.7a). In contrast, the TEM images with LPG (Fig. 7.7b) exhibit alterations of the wrapping mode down the tube axis. In addition, the average width

of the LPG striations is noticeably larger than that of LPC (Fig. 7.7b vs. Fig. 7.7a) owing to a net negative charge of LPG head groups. A macroscopic configuration, like LPG head groups in consecutive half-cylinders, paired and in contact with weakly polarizable SWNT surfaces is energetically unfavorable. To reduce the repulsion between LPG head groups, the SWNT-LPG system must pay an “energy penalty” by distorting and/or broadening the striations (Fig. 7.7d, lower section). Indeed, our experimental data revealed that LPC bound better to SWNTs than LPG (Fig. 7.6e).

To confirm our observation, we tested double-chained phospholipids for their SWNT solubility. The phospholipids used were dimyristoylphosphatidylcholine (PC 24:0), which is zwitterionic at physiological pH; and 1,2-dioleoylphosphatidylglycerol (PG 36:2) and 1,2-dipalmitoylphosphatidylethanolamine (PE 32:0), both of which are negatively charged at physiological pH. None of the above phospholipids provided good solubility for SWNTs.

From a geometrical perspective the three-dimensional (3D) structures of lysophospholipids and detergent molecules can be approximated as cones (Fig. 7.7d). The packing of conical objects normally results in spherically shaped objects, e.g., micelles, due to their curvophilicity. In contrast, double-chained phospholipids are considered to be curvophobic [70], their 3D structures are approximated as cylinders and their packing assumes bilayers. Obviously, wrapping around a cylindrical object, i.e., an SWNT, is geometrically preferential for curvophilic lysophospholipids but not for curvophobic phospholipids.

The geometrical considerations further support the microscopic binding mode shown in Fig. 7.7(d). “Half-cylinder” wrapping is the only microscopic mode that results in semi-spherical curvature along the SWNT axis and SWNT circumference. In addition to the packing consideration, we calculated the average number of LPC necessary for coating an average SWNT, assuming tight packing and the LPC head group size of 0.6 nm. We found that “half-cylinder” binding will result in a lipids-to-tube ratio of 21 000:1 – in excellent agreement with our experimentally estimated ratio of 20 000:1.

Free lysophospholipids and micelles in SWNT-lysophospholipid solution were removed by filtration through 100 kDa *Microcon* (Amicon, Inc) centrifugation tubes and washed four times. The resulting lysophospholipid-free and micelle-free SWNT-LPC complexes were tested by *in vivo* bioassay using colon cancer (CACO-2) and macrophage (THP-1) cell lines. Each cell line was incubated in its own eight-well chamber slide (LabTek) for 48 h at 37 °C in a CO<sub>2</sub> incubator. Before treatment, cell adhesion was checked by differential interference contrast (DIC) microscopy using a Zeiss 135 Axiovert inverted microscope. Treatments ranging from 5 to 40 ppm of lysophospholipid-free and micelle-free SWNT-LPC complexes were added to each adherent cell line and incubated for 3 h at 37 °C in a CO<sub>2</sub> incubator. After incubation, control and treated cells were fixed with 4% paraformaldehyde for 30 min, washed in PBS and subjected to an APO-BrdU TUNEL assay (Invitrogen). This assay detects the onset of apoptosis by fluorescent detection of nuclear DNA fragments or DNA breaks. Cells were labeled with deoxythymidine analogue 5-bromo-2'-deoxyuridine-5'-triphosphate (BrdUTP) followed by the addi-

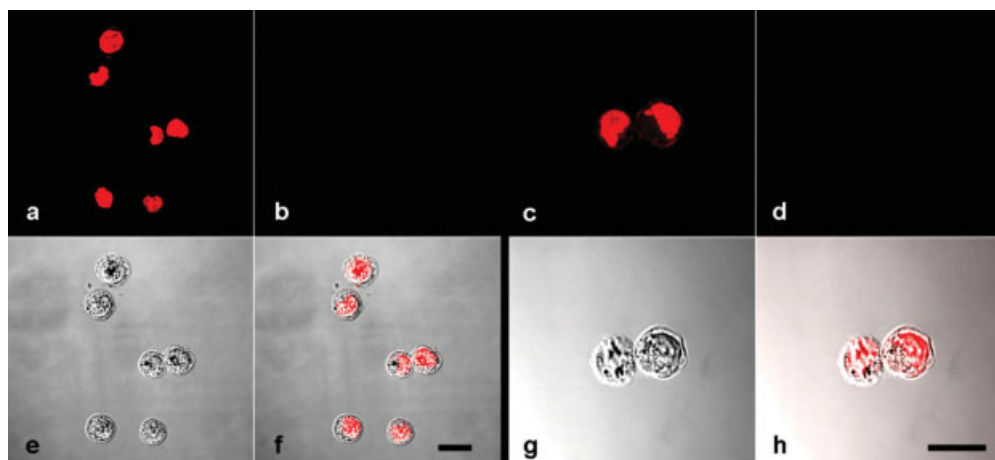


**Fig. 7.9.** Fixed CACO-2 cells incubated with SWNT-LPC for 3 h and examined for apoptosis by APO-BrdU TUNEL assay. Panels (a, b, e, f) show control cells and (c, d, g, h) show cells that have been incubated with 20 ppm of SWNT-LPC. The merged areas shows cells with intact plasma and nuclear membranes in control (f) and in treatments (h). PI staining revealed intact cell nuclei in control (a) and treated cells (c). Neither control (b) nor treated cells (d) appear apoptotic since there was an absence of anti-BrdU antibody labeled staining in the FITC channel. The DIC channel shows intact plasma membranes in both control (e) and treated cells (g). Scale bars: 20  $\mu$ m.

tion of Alexa-Fluor 488 labeled anti-BrdU antibody. Propidium iodide (PI) was used to image the total DNA content of cells. The prepared cells were imaged using a Zeiss 510 LSM confocal fluorescence microscope.

Our bioassays showed no loss of cell viability (Figs. 7.9 and 7.10) when both colon cancer cells (CACO-2) and macrophage (THP-1) cell lines were treated with 20–40 ppm of lysophospholipid-free and micelle-free SWNT-LPC. CACO-2 cell nuclei remained unaffected by treatment of 20 ppm SWNT-LPC (Fig. 7.9c), which was also the case for the macrophage THP-1 cell line treated with 40 ppm SWNT-LPC (Fig. 7.10c). Cell plasma membranes remained intact in both CACO-2 cells (Fig. 7.9e) and THP-1 cells (Fig. 7.10e), and the onset of apoptosis by Apo-BrdU TUNEL assay was not detected in either cell line (Fig. 7.9d and Fig. 7.10d). Motile THP-1 cells treated at 40 ppm SWNT-LPC exhibited elongated cell bodies (Fig. 7.10h), which is thought to be due to SWNT-LPC disruption of plasma membranes or cytoskeleton.

SWNTs, otherwise a collection of hydrophobic synthetic nanoparticles, have been solubilized in aqueous lysophospholipid solutions with extended stability. The biocompatibility of lysophospholipids is unsurpassed since they occur naturally in the cell membrane. The signaling capacity of lysophospholipids and the electronic property of SWNTs may be combined for disease detection. The strong absorbance of isolated SWNTs in NIR [44] can be utilized for noninvasive imaging and sensing. Furthermore, since the head groups of lysophospholipids can be functional-



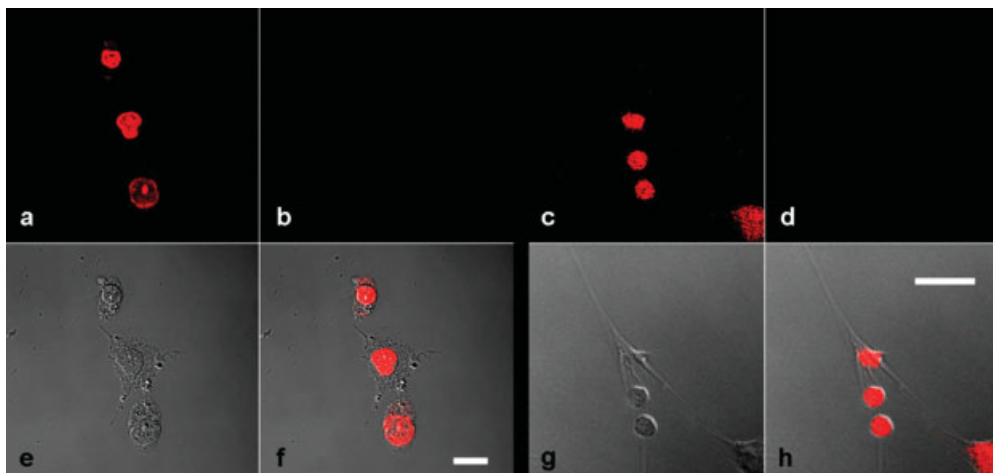


**Fig. 7.10.** Confocal images of fixed macrophages (THP-1) incubated with SWNT-LPC for 3 h and examined for apoptosis by APO-BrdU TUNEL assay. Panels (a, b, e, f) are control cells and (c, d, g, h) are treated cells that have been incubated with 40 ppm of lysophospholipid-free and micelle-free SWNT-LPC. The merged areas show cells with intact plasma and nuclear membranes in control (f)

and in treated cells (h). The treated cells have become elongated. PI staining revealed intact cell nuclei in control (a) and treated cells (c). Neither control (b) nor treated cells (d) appear apoptotic since there was an absence of anti-BrdU antibody labeled staining in the FITC channel. The DIC channel shows intact cell membranes in control (e) and treatments with elongated cell bodies (g). Scale bars: 20  $\mu\text{m}$ .

ized with tags such as quantum dots, antioxidants, and monoclonal antibodies, this solubility method opens the door for utilizing nanomaterials for *in vivo* imaging, cancer diagnosis and therapy, and novel nanomedicines.

### 7.3

#### Diffusion of SWNT–Biomolecular Complexes

The enhanced elucidation of gene function in human health has led to the need for more effective and robust means for delivering therapeutic genes to target cells. While no single gene transfection method developed to date has been found to be optimal for all cells, SWNTs offer a promising alternative since they can be treated or functionalized for biocompatibility [30]. Recent biochemical assays and theoretical studies have indicated that the nonspecific binding of DNA with SWNTs is realized through the  $\pi$ -stacking between the bases of DNA and the  $\pi$ -electrons of carbon atoms as well as the hydrophobic interaction between the bases of DNA and the sidewalls of SWNTs [49, 71]. Helical wrapping of ssDNA on SWNTs is energetically favorable and sequence dependent [49, 71, 72]. While current efforts on interfacing SWNTs with nucleic acids have focused almost exclusively on DNA,

equal attention should be paid to RNA due to its biological significance. For example: (a) messenger RNAs (mRNAs) are the physical gene transcripts that are translated to functional proteins at the ribosomal level; (b) some RNAs act as enzymes to catalyze various cellular biochemical pathways, they serve as mediators for various organic reactions [73–76] and are often utilized as templates for the growth of inorganic-particles [77]; and (c) small interfering RNAs (siRNAs), which disrupt mRNAs prior to translation, will cause the silencing of a specific post-transcriptional gene's expression. The use of siRNA is a powerful research tool that has a pivotal role in deciphering the functions and interactions of thousands of unknown genes [78]. Albumin, in contrast, is one of the most abundant serum proteins present in the mammalian circulatory system, contributing over 80% of the colloid osmotic pressure [79]. Indeed, the nonspecific binding of SWNTs to BSA has been elucidated as a general phenomenon [17]. In this section, we introduce the first study by our group on the diffusion of SWNT-poly(rU) and SWNT-BSA hybrids, two of the most elementary synthetic biomolecular complexes. This study provides a physical guidance to gene delivery using SWNT as transporters.

Diffusion refers to the process by which particles intermingle as a result of their kinetic energy of random motion. It plays a central role in the transportation of small particles across cell membranes, in cytoplasm, and in nuclei. For the applications of gene and drug delivery, the innate hydrophobicity of SWNTs causes the tubes to aggregate or clump, presenting a major challenge for cellular studies. The addition of nucleic acids or proteins mediates the separation of pristine SWNTs through  $\pi$ -stacking and/or by decreasing the degree of hydrophobic interactions, thus markedly enhancing the solubility of the nanotubes. Further, nucleic acids and proteins can be labeled with fluorescent dye molecules and, consequently, SWNTs can be visualized when bound with these biomolecules. Single-molecule fluorescence microscopy (SMFM) has been utilized for the diffusion studies of phospholipids in biomembranes [80, 81]. Superior to confocal microscopy, wide-field SMFM simultaneously collects significant statistics without averaging or losing molecular individuality [80–82]. Unlike scanning electron microscopy (SEM) and crystallography, SMFM is non-invasive and is, therefore, suitable for *in vitro* and *in vivo* studies of biological processes.

In SMFM, the trajectories of fluorescently labeled biomolecules can be followed at nanometer resolution. Based on the displacement of the centre of mass (COM) of a molecule, the mean-square-displacement (MSD) [83] of the molecule can be obtained with Eq. (1), where  $x_i$  and  $y_i$  are the positional coordinates of the COM of the molecule in frame  $i$ , and  $n$  denotes the frame number with time interval  $\Delta t$ .

$$\text{MSD}(\Delta t) = \langle (x_{i+n} - x_i)^2 + (y_{i+n} - y_i)^2 \rangle \quad (1)$$

The diffusion coefficient  $D$  of the molecule undergoing a two-dimensional (2D) random walk is given as  $D = \text{MSD}/4\Delta t$ .

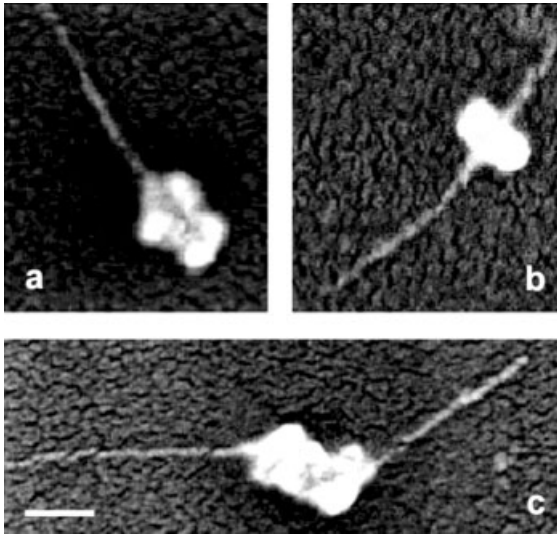
For diffusion studies, pristine SWNTs were first synthesized using the arc-deposition method [84]. The average diameter of the SWNTs was 1.4 nm, as confirmed by Raman spectroscopy and transmission electron microscopy. The sample

of SWNT-poly(rU) hybrids was prepared by modifying the protocol used by Zheng et al. [49], employing the following procedure. A mixture of poly(rU) ( $0.2 \mu\text{g } \mu\text{L}^{-1}$ , lyophilized polyuridylic acid, Midland, 500–2600 nucleotides) and SWNTs ( $0.01 \mu\text{g } \mu\text{L}^{-1}$ ) in TE buffer (10 mM Tris, 1 mM EDTA, pH 7.3) was first placed on ice and probe-sonicated at 10 W for 30 min (VC 130 PB, Sonics). The resultant SWNT-poly(rU) suspension was then centrifuged at 5000 rpm for 10 min to pellet the poly(rU)-wrapped and bare SWNTs. The supernatant of unbound poly(rU) was removed and the pellet resuspended in TE buffer. The sample was then labeled with OliGreen (Molecular Probes, absorption 500 nm, emission 520 nm), which fluoresces strongly only when bound to nucleic acids, and which specifically exhibits a large fluorescence enhancement when bound to the U bases in poly(rU). SWNT-BSA hybrids were prepared by the same procedure as that for the SWNT-poly(rU) hybrids, except labeling since BSA was pre-labeled with TRITC (Sigma, absorption 550 nm, emission 570 nm).

Binding of SWNTs and poly(rU) was analyzed by SEM (S4700, Hitachi), and a drop of the solution containing poly(rU) ( $0.2 \mu\text{g } \mu\text{L}^{-1}$ ) and SWNTs ( $0.01 \mu\text{g } \mu\text{L}^{-1}$ ) in TE buffer was dispersed on a silicon substrate after probe-sonication. The substrate was left to dry overnight then coated with chromium prior to imaging. An SEM analysis revealed that the average length of the SWNTs was approximately 400 nm with a standard deviation of 50 nm for the 50 hybrids examined. As shown in Fig. 7.11, poly(rU) molecules are seen bound at (a) the end or (b) midpoint of an SWNT(s). In Fig. 7.11(c), possibly two SWNT-poly(rU) hybrids are joined together. Figure 7.11 suggests that poly(rU) molecules remain bound to SWNTs even in dry conditions. However, the poly(rU) appear mostly as globules and no helical wrapping of poly(rU) on SWNTs is evident due to the possible lack of hydrogen bonds with water molecules [66].

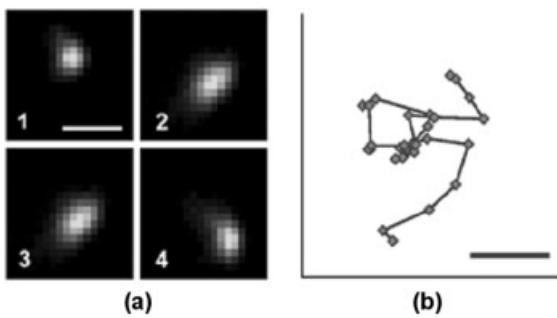
Diffusing poly(rU), SWNT-poly(rU), and SWNT-BSA were imaged on an EPI fluorescence microscope. The excitation source of the microscope was a mercury lamp (PTI). Fluorescence was collected with a water immersion objective (Olympus,  $60\times$ ,  $NA = 1.2$ ) that was then focused onto a CCD camera (Roper, Cascade 512B). The imaging of poly(rU) and SWNT-poly(rU) was excited with blue light while that of SWNT-BSA was excited with green light. Approximately 100 poly(rU), SWNT-poly(rU), and SWNT-BSA hybrids were tracked, respectively, at a rate of six frames per second. The intensity of possible photoluminescence for isolated SWNTs [44, 85, 86] is expected to be much weaker than the fluorescence of the ultrasensitive OliGreen dye (approximately five bases of poly(rU) per dye) with a wavelength shifting to NIR. Our control experiments confirmed this phenomenon in which isolated SWNTs or SWNT hybrids were not visible without fluorescence labeling.

Figure 7.12(a) shows a fluorescence image sequence of an SWNT-poly(rU) hybrid diffusing in TE buffer with a time interval of 1.5 s. Figure 7.12(b) displays the corresponding 2D time trajectory of the SWNT-poly(rU) hybrid. The time interval between the consecutive steps is 0.167 s. The diamonds in the trajectory represent the COMs of the hybrid in individual image frames. The histogram of the bootstrap diffusion coefficients [87] as an ensemble was calculated for 1000 sam-



**Fig. 7.11.** SEM images of a poly(rU) molecule bound at (a) the end and (b) midpoint of an SWNT(s); (c) possibly, two SWNT-poly(rU) hybrids joined together. Scale bar: 100 nm. The SWNTs are seen individually or in very small bundles ( $\leq 10$  nm in diameter). Tertiary structures of the poly(rU) may prevent their

nitrogenous bases from fully binding to the SWNT sidewalls. However, limited by the instrument resolution ( $\sim 2.5$  nm), these fine structures were not clearly resolvable. The background structure is due to the chromium coating used to enhance image contrast [66]. (© American Institute of Physics.)



**Fig. 7.12.** (a) Fluorescence sequence of an SWNT-poly(rU) hybrid diffusing in TE buffer (1-4). Time interval: 1.5 s; (b) corresponding random walk of the SWNT-RNA hybrid in (a). Time interval: 0.167 s. Scale bars: 1  $\mu$ m [66]. (© American Institute of Physics.)

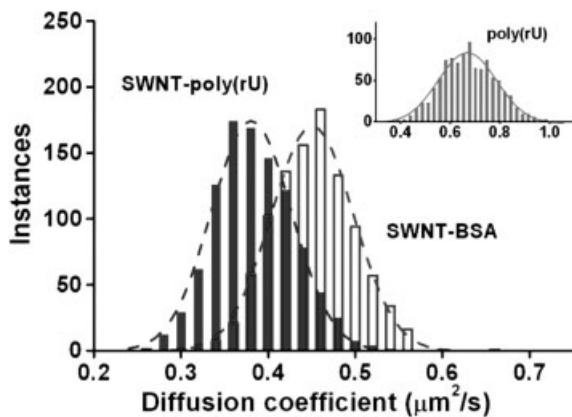


**Fig. 7.13.** Bootstrap histograms of the diffusion coefficients of SWNT-poly(rU) (solid bars) and SWNT-BSA (hollow bars) in TE buffer. Inset: bootstrap histogram of the diffusion coefficient of poly(rU) in TE buffer.

For each case, approximately 100 hybrids were tracked with 1000 instances of bootstrap sampling. Also illustrated are the Gaussian fitting curves for the three cases [66].

(© American Institute of Physics.)

pling instances based on a linear fitting of the MSD versus time interval  $\Delta t$ . The stability/resolution of the imaging system was calibrated to be  $5 \times 10^{-5} \mu\text{m}^2 \text{s}^{-1}$  with fluorescence beads immobilized on glass slides. As shown in Figure 7.13, the diffusion coefficients  $D_{\text{SWNT-poly(rU)}}$  and  $D_{\text{SWNT-BSA}}$  of the SWNT-poly(rU) and the SWNT-BSA hybrids were measured to be  $0.374 \pm 0.045$  and  $0.442 \pm 0.046 \mu\text{m}^2 \text{s}^{-1}$ , respectively. The numbers after “ $\pm$ ” give the standard deviations of the means. By comparison, the mean diffusion coefficient  $D_{\text{poly(rU)}}$  of poly(rU) alone (inset of Fig. 7.13) was found to be  $0.661 \pm 0.110 \mu\text{m}^2 \text{s}^{-1}$ , almost twice that for the SWNT-poly(rU) hybrids due to their different conformations [66].

The diffusion coefficient of a small particle in solution, according to Einstein’s relation, can be described by  $D = k_B T / k_{\text{drag}}$ , where  $k_B$  is the Boltzmann constant,  $T$  is the temperature of the solution, and  $k_{\text{drag}}$  is the drag coefficient. For a rod-like particle,  $k_{\text{drag}} \propto \eta d$ , where  $\eta$  is the viscosity of the solution, and  $d$  is the longest dimension of the particle [88], which is approximately 400 nm for the SWNTs used in our diffusion experiment. The SWNT-poly(rU) hybrids, compared with SWNT-BSA, exhibit a relatively smaller mean diffusion coefficient that may be induced by the overhangs of the poly(rU) extruding from the ends of the SWNTs (refer to Fig. 7.11a). While the radius of gyration  $R_G$  of BSA is merely 3 nm [89], as opposed to an order of tens of nanometers for the  $R_G$  of poly(rU), the diffusion of SWNT-BSA is less affected. Here  $\Delta D$  is defined as the full-width at half-maximum for the distribution of diffusion coefficient. By Gaussian fitting,  $\Delta D_{\text{poly(rU)}}$  is found to be  $0.235 \mu\text{m}^2 \text{s}^{-1}$  (inset of Fig. 7.13), a broad distribution attributed to the length variation (500–2600 nucleotides), the instability, and the conformational changes of the poly(rU) molecules (in transient linear stretches, globules, and other tertiary structures).  $\Delta D_{\text{SWNT-poly(rU)}}$  and  $\Delta D_{\text{SWNT-BSA}}$  for the two hybrids obtained from the Gaussian fittings in Fig. 7.13 are  $0.092$  and  $0.094 \mu\text{m}^2 \text{s}^{-1}$ , respectively. In compar-

ison with poly(rU), the narrower distributions of the diffusion coefficients for the two hybrids possibly result from the rod-like structure of the SWNTs, which is expected to dominate the diffusion of the hybrids. Following Einstein's relation and based on the rule of error analysis, it can be derived that  $S_d = \bar{d}S_D/\bar{D}$ , where  $S_d$  and  $S_D$  are the standard deviations of  $d$  and  $D$ , and  $\bar{d}$  and  $\bar{D}$  are the means of  $d$  and  $D$ , respectively. Using the measured diffusion coefficients of SWNT-poly(rU), it can be calculated that the standard deviation  $S_d$  of the length of SWNT ( $d$ ) is approximately 48 nm. This deviation agrees with the SEM observation, which found a 12.5% deviation for the length distribution of the SWNT-poly(rU) hybrids. In that regard, a single-molecule diffusion study can be used as a measure for the structural information of SWNTs and their hybrids [66].

The measured mean diffusion coefficients suggest that a SWNT hybrid would take approximately 1–2 min to diffuse across a cell 10  $\mu\text{m}$  in diameter, consistent with the known diffusion coefficients of DNA and proteins within the cell's cytoplasm [89]. Faster diffusion can be achieved with SWNT hybrids prepared using extended probe-sonication. In future diffusion studies, the persistence length [90], a parameter that describes bending stiffness and flexibility, will be measured for SWNTs. The effect of the binding of nucleic acids and proteins on the persistence length of SWNTs will be also evaluated. These studies will provide knowledge on the flexibility of SWNTs in comparison with biomacromolecules, such as flexible double-stranded DNA, semiflexible actin filaments, or rigid microtubules. These diffusion studies on SWNTs can be extended to cell membranes and nuclei where hindered diffusion [81, 88] and reptation [88, 91, 92] may be significant. These studies facilitate, from a physical viewpoint, the applications of gene transfection using SWNTs as transporters.

#### 7.4

#### Gene and Drug Delivery with SWNT Transporters

Gene delivery and transfection, or the introduction and expression of foreign DNA, continue to draw strong interest because of their potential for gene therapy and disease prevention potential [93]. One of the greatest challenges for gene delivery is the physicochemical properties of DNA such as its negative charge and hydrodynamic volume. Transporters for DNA must be developed for gene delivery and gene transfection. Solutions to this problem have included viral (retroviral, lentiviral, and adenoviral) vectors and non-viral transfection vectors, including cationic lipids [94], polyethylenimine (PEI), and other cationic polymers [93, 95]. The viral transfection vectors have proven to be the most effective due to their natural ability to introduce foreign genetic information into cells. However, these viral vectors often provoke immune responses from cells, preventing successful gene delivery. Non-viral transfection vectors can avoid immune responses but are often hindered by low efficiency rates for nuclear membrane penetration and gene expression. Even though a few of the cationic polymers such as PEI boost relatively high efficiency rates for non-viral vectors, they exhibit cytotoxicity [96].

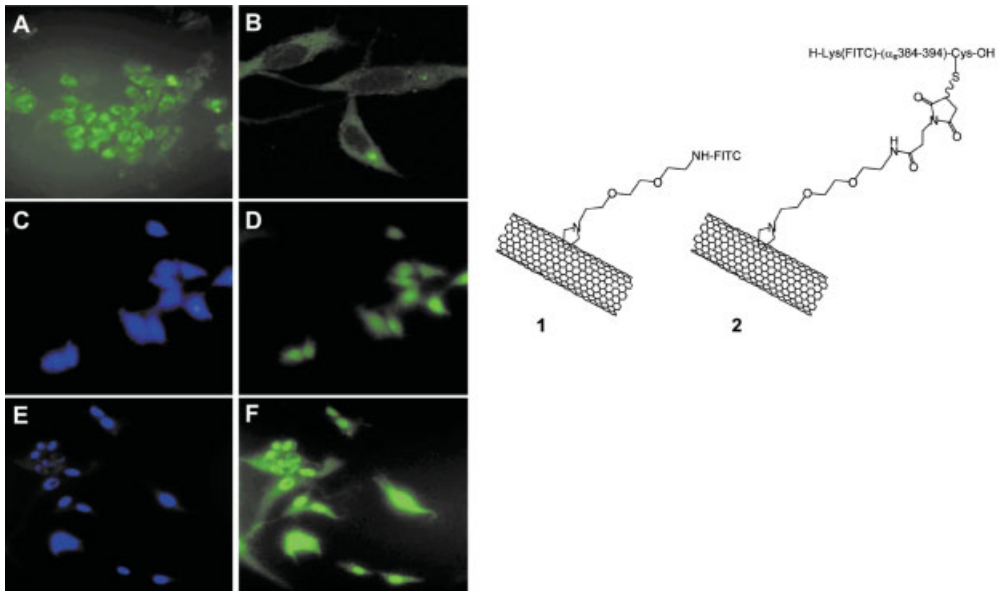


**Fig. 7.14.** EPI-fluorescence (A) and confocal microscopy (B) images of 3T3 cells incubated at 37 °C with 1 and 5  $\mu$ M concentration of CNT 1, respectively. EPI fluorescence microscopy images of 3T6 cells incubated at 37 °C

with 1 (C, D) and 5  $\mu$ M (E, F) concentration of CNT 2. The nucleus is stained with DAPI (C and E) [97]. (© The Royal Society of Chemistry.)

Since none of the current transfection vectors are ideal, alternative vectors must be sought through the exploration of new materials and methods, and SWNTs are one possibility. They possess versatile electronic and mechanical properties and have found numerous applications in both nanotechnology and materials science. Because SWNTs have a large surface area, stability, flexibility, and biocompatibility, they have excellent prospects for effective drug and gene delivery, and therapies [28]. Recently, Pantarotto et al. showed that fluorescently labeled SWNTs that covalently bind with bioactive peptides can penetrate cellular and nuclear membranes (Fig. 7.14) [97]. However, the mechanism for the translocation of SWNTs has yet to be determined and, therefore, can only be speculated upon. Shi Kam et al. have reported the appearance of SWNT–streptavidin conjugates within promyelocytic leukemia and T cells via the endocytosis pathway (Fig. 7.15) [98].

#### 7.4.1

#### RNA Translocation with SWNT Transporters

To explore the possibilities of SWNTs as transporters for gene delivery and transfection, we conducted a novel examination of the translocation of nucleic acid RNA polymer poly(rU) into breast cancer cells (MCF7). The non-specific binding

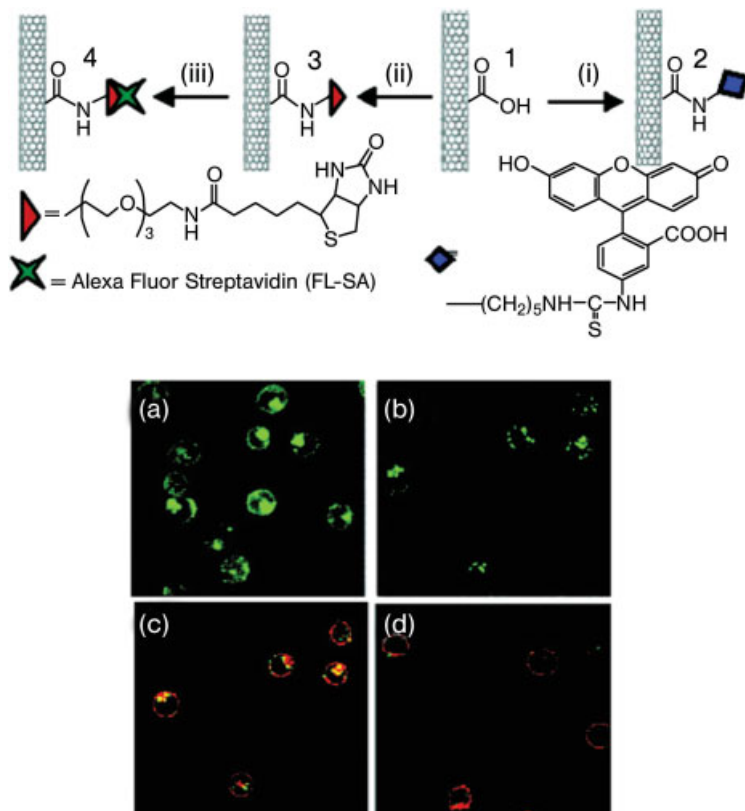


**Fig. 7.15.** (Top) Synthesis and schematic of various SWNT conjugates. (i) EDC, 5-(5-aminopentyl)thioureidyl fluorescein, phosphate buffer; (ii) EDC, biotin-LC-PEO-amine, phosphate buffer; (iii) fluoresceinated streptavidin. (Bottom) Confocal images of cells after incubation in solutions of SWNT conjugates: (a) after incubation in **2**; (b) after

incubation in a mixture of **4** (green due to SA) and the red endocytosis marker FM 4-64 at 37 °C (image shows fluorescence in the green region only); (c) same as (b) with additional red fluorescence shown due to FM 4-64 stained endosomes; and (d) same as (b) after incubation at 4 °C [98]. (© American Chemical Society.)

mechanism for SWNTs and poly(rU) in our study, as opposed to the covalent binding scheme by Pantarotto et al. and Shi Kam et al. in their respective peptide and protein delivery studies [97, 98], may offer more options and flexibility for the release of the load carried by SWNTs upon delivery. The sectioning property of confocal fluorescence microscopy in our study allows for axial discrimination of fluorescently labeled SWNT-poly(rU) hybrids on cell membranes, within either the cytoplasm, or the nucleus. In addition to confocal fluorescence imaging of SWNT-poly(rU) incubated with MCF7 breast cancer cells, we performed radioisotope labeling, cell enumeration, and an MTS [3-(4,5-dimethylthiazol-2-yl)-5-(3-carboxymethoxyphenyl)-2-(4-sulphophenyl)-2H-tetrazolium] assay, which measures



cellular metabolic activity through absorption. These additional studies quantitatively evaluate the direct cellular uptake and the cytotoxicity of SWNTs.

In our studies, SWNT bundles were synthesized using the arc-deposition method, with the dominant SWNT diameter of  $\sim 1.4$  nm [84]. SWNT bundles were probe-sonicated (VC 130 PB, Sonics & Materials) at 8 W for 90 min on ice in 10% FBS/PBS buffer. The SWNTs at a concentration of  $0.4$  mg mL<sup>-1</sup> were filtered through a  $0.45$   $\mu$ m filter before incubating with MCF7. Both the control cells and the cells treated with SWNTs were enumerated at 24, 48, and 72 h. The cell growth medium was RPMI supplemented with 10% FBS and 1% penicillin streptomycin. After the designated time of incubation, cells were released by trypsin-EDTA treatment (5 min) and counted with hemocytometry. Precautions were also taken to prevent contamination in preparing the SWNTs, including filtration to remove the bacteria and sterilization of the instruments in contact with the sample. The MTS assay was performed after treating MCF7 cells with various concentrations of SWNTs (0, 0.0125, 0.025, 0.05, 0.1, 0.125, 0.25, 0.5, and 1 mg mL<sup>-1</sup>). After 24 h of incubation, the growth medium was removed from the 96-well-plate and PBS (200  $\mu$ L) was used to wash the cells twice. RPMI-1640 medium without phenol red (approx. 200  $\mu$ L) and MTS (25  $\mu$ L) were added to each cell well, followed by incubation at 37 °C for 3 h. The absorbance in each well was measured using a spectrophotometric plate reader (Benchmark Microplate Reader, Bio-Rad) at a wavelength of 490 nm.

The translocation of SWNTs into cells was confirmed by radioisotope labeling assay. SWNTs were probe-sonicated in RPMI-1640 growth medium and incubated with radioactive [methyl-<sup>3</sup>H]thymidine overnight. The radioactively labeled SWNTs were collected by centrifugation and re-suspended in PBS before incubating with MCF7 cells. After incubation, the cells were released by trypsin-EDTA and re-collected as pellet by centrifugation. The pellet of MCF7 cells was thoroughly washed with PBS buffer twice to remove excess SWNTs and thymidine bound on the cell surface. The scintillation counts (Beckman Coulter, LS6500) read from the MCF7 cells, as opposed to those from the supernatants and the PBS washing buffer, yielded the translocation efficiencies of the radioactively labeled SWNTs at 1.3%, 6.3%, 10.7%, and 15.4% for incubation times of 0.5, 1, 2, and 4 h, respectively [67]. This result confirms that SWNTs alone can penetrate through cellular membranes with an increased efficiency over time, and concurs with the general understanding that cell membranes intake small hydrophobic particles.

For the imaging experiment, the SWNT-poly(rU) hybrids were prepared as follows. A mixture of poly(rU) ( $0.5$  mg mL<sup>-1</sup>) and SWNTs ( $0.125$  mg mL<sup>-1</sup>) in TE (10 mM Tris-HCl, 1 mM EDTA) buffer was probe-sonicated. From scanning electron microscopy and single-molecule diffusion studies, the prepared SWNT-poly(rU) hybrids were characterized in small bundles or isolated form with an average length of 400 nm [66].

To visualize the SWNT-poly(rU) hybrids, poly(rU) was fluorescently labeled with PI, which has an excitation peak at 535 nm and an emission peak at 617 nm. PI intercalates between the base pairs of nucleic acids, it is membrane impermeable, and is generally excluded by viable cells. To achieve fluorescent labeling, PI

(0.05 mL mL<sup>-1</sup>) in TE buffer was incubated with SWNT-poly(rU) hybrids at a volume ratio of 1:20 for at least 15 min. Excess PI and unbound poly(rU) were removed by cassette dialysis (Slide-A-Lyzer, 10,000 MWCO, Pierce) for a total of 36 h with three changes of buffer solution.

Approximately 10 000 MCF7 cells were deposited in each well of an eight-chambered slide to form a sparsely distributed layer of cells to ensure good exposure of cell membranes to SWNT-poly(rU) hybrids. Cells were directly cultured on the chamber glass slide using RPMI-1640 growth medium at 37 °C under 5% CO<sub>2</sub>. All cells were incubated for 24 h until an approximate 60% confluence was achieved. Twenty μL of PI, PI+poly(rU), or PI-labeled SWNT-poly(rU) hybrids (0.05 mL mL<sup>-1</sup>) was added to the chamber slide, and the cells were incubated for 2, 3, or 4 h. After incubation, the cells were washed twice with growth medium (200 μL) and kept in PBS (400 μL) before imaging with the confocal fluorescence microscope (LSM510, Zeiss, objective NA = 1.3, oil). Fluorescence from PI was collected in the TRITC channel, and the background was recorded from the bright-field channel of the microscope.

The confocal fluorescence images of the two controls, PI and PI+poly(rU), showed little to no fluorescence after incubation and the MCF7 cells appeared elongated and healthy (Fig. 7.16). In contrast, the PI control (Fig. 7.16a) showed one instance of intense fluorescence from a PI stained circular unhealthy cell. The minimal fluorescence intensity surrounding the cellular membrane for the PI+poly(rU) (Fig. 7.16b) was probably due to electrostatic interactions between the charged poly(rU) and cellular membrane.

The confocal fluorescence images of the MCF7 cells that were incubated with the SWNT-poly(rU) hybrids for 2 h showed translocation into the cytoplasm without accumulation of SWNT-poly(rU) hybrids on the outside of the cellular membrane. Figure 7.17 shows MCF7 cells appearing to retain the SWNT-poly(rU) hybrids after an incubation of 3 h. All the images were taken from a stack of slices scanned through the cells with a full scanning depth of approximately 10 μm and

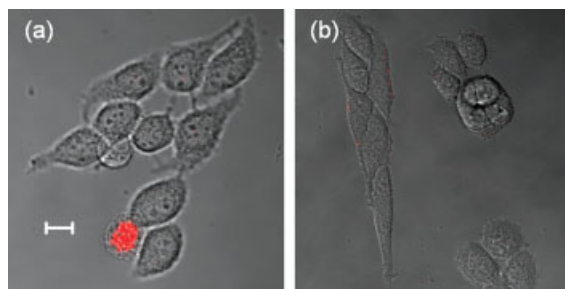


**Fig. 7.16.** Control experiments showing little to no uptake of (a) PI, except in the dying circular cell, and (b) PI+poly(rU). Scale bar = 10 μm [68]. (© American Chemical Society.)

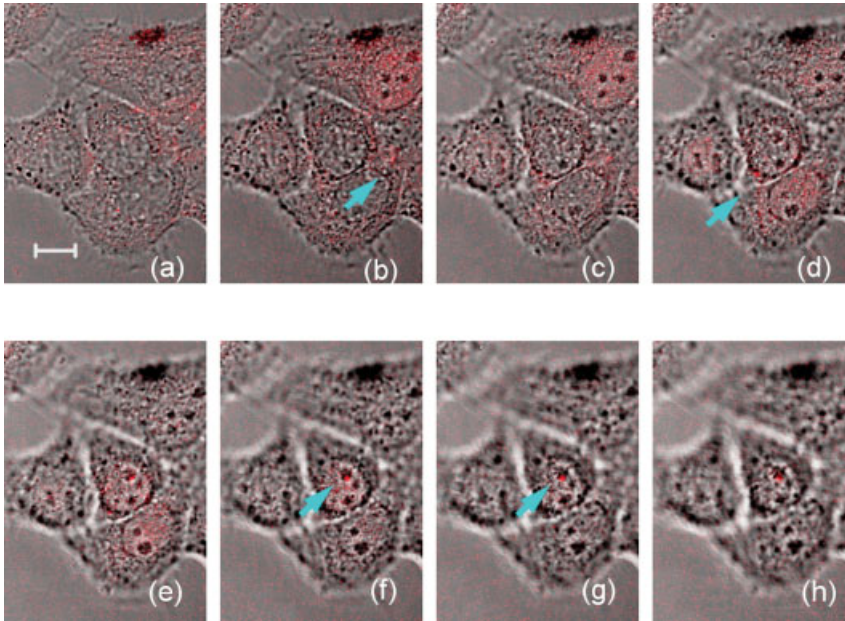


**Fig. 7.17.** Confocal fluorescence images of MCF7 cells incubated with  $0.05 \text{ mL mL}^{-1}$  of PI-labeled SWNT-poly(rU) for 3 h. Images (a)–(h) were acquired at different depths ( $z = 0.5, 1.51, 2.52, 3.53, 4.54, 5.55, 6.56, 7.57$

$\mu\text{m}$ ), across the z-axis normal to the chamber slide surface. The arrows point to the fluorescent spots where large SWNT-poly(rU) hybrids are localized. Scale bar =  $10 \mu\text{m}$  [68]. (© American Chemical Society.)

a scanning step of  $1.01 \mu\text{m}$ . Smaller red spots with low intensities as shown in Figs. 7.17(a–e) are thought to be small soluble SWNT-poly(rU) hybrids and/or PI-labeled poly(rU) dissociated from SWNTs after translocation. Their gradual disappearance (Figs. 7.17f–h) implies the uneven distribution of SWNT-poly(rU) hybrids in cytoplasm and/or possibly the defocusing of the hybrids. Figure 7.17(b) shows the uptake of an SWNT-poly(rU) hybrid in the cytoplasm, as indicated by the arrow. Figure 7.17(d) shows an instance of an SWNT-poly(rU) hybrid appearing in the vicinity of cell membrane; however, whether the exact location of the hybrid is within or on the cell membrane is unclear. In Figs. 7.17(f) and (g), the fluorescent spot was observed to co-localize with the nucleus, which supports the possibility that the SWNT-poly(rU) hybrid could have penetrated through the nuclear membrane. The observed fluorescence in Figs. 7.17(f) and (g) could also be from PI-labeled poly(rU) released from SWNTs due to dissociation kinetics and the change of pH between cytosol and nucleus [68].

The released nucleic acids may be used as templates for transfection at a later stage. Energetically, the fluorescence in the nucleus is unlikely to be from either free PI or PI dissociated from poly(rU) and then re-intercalated with the host

DNA or RNA. However, the binding dynamics of SWNTs and nucleic acids are beyond the scope of this chapter. The strong fluorescence in Figs. 7.17(f) and (g) fades gradually [Figs. 7.17(e) and (h)], which further indicates that the SWNT-poly(rU) hybrid was localized within the cell. From the depth information, we estimate that this large SWNT-poly(rU) hybrid is less than 2  $\mu\text{m}$  long. This length is consistent with that of the SWNTs obtained with probe sonication, confirming that the observed fluorescence was from the SWNT-poly(rU) hybrid. After 4 h of incubation the SWNTs were still present within the MCF7 cytoplasm and nucleus [68].

The uptake of the SWNTs-poly(rU) is hypothesized to be a result of amphipathic properties of both the cellular membrane and the SWNT-poly(rU) hybrids. Due to thermal agitation, lateral diffusion of phospholipids within the biomembrane may contribute to the translocation of SWNT-poly(rU) hybrids by allowing hydrophobic interactions between the hydrocarbon chains and SWNTs within the bilayer. The uptake of the SWNTs by the nuclear membrane is attributed to passive ratchet diffusion [99]. Cell mitosis might also play a significant role in the internalization of the SWNT-poly(rU) hybrids. During cell division, the nuclear envelope breaks down into multiple small vesicles early in mitosis, which may allow the translocation of SWNT-poly(rU) hybrids. In the telophase, the last mitotic stage, the nuclear envelope reforms, possibly incorporating the SWNT-poly(rU) hybrids. Once the SWNT-poly(rU) hybrids are within the MCF7 cells, it is possible that endosomes in the cytoplasm store SWNTs after poly(rU) translocation.

In summary, we have demonstrated the delivery of RNA polymer using SWNTs as transporters [68]. Translocation of SWNTs into MCF7 cells was confirmed by radioisotope labeling assay. Based on the sectioning property of confocal microscopy, fluorescently labeled SWNT-poly(rU) hybrids were found across the cellular and the nuclear membranes of MCF7 cells while the controls were excluded. Both cell growth and MTS studies have shown no cytotoxicity in either MCF7 breast cancer cells or d2C keratinocytes for concentrations up to 1  $\text{mg mL}^{-1}$ . These studies show the potential of using SWNTs as transporters for gene delivery, but further biophysical and biochemical studies must be conducted to better decipher the mechanisms of SWNT translocation across cellular and nuclear membranes. Assays on gene transfection using SWNT transporters need to be performed to move towards the final goal of gene therapy and disease prevention.

#### 7.4.2

##### **Gene Transfection with SWNT Transporters**

Limited literature is available on gene transfection with CNT transporters, with the only proofs of concept being reported by Pantarotto et al. [100] and Liu et al. [101]. The efficiencies of DNA transfection in mammalian cells were not optimal in these preliminary studies, yet they showed at least one order of magnitude enhancement over DNA alone.

Pantarotto [100] revealed that both SWNTs and MWNTs were covalently modified by pyrrolidine rings, each bearing a free amino-terminal oligoethylene glycol moiety attached to the nitrogen atom. The concentration of the functional groups

was 0.55 and 0.90 mmol g<sup>-1</sup> for functionalized-SWNTs and MWNTs, respectively. The presence of these functional groups led to a much increased solubility of the CNTs in aqueous solution. The electrostatic interaction of positively charged ammonium functionalized CNTs with the negatively charged phosphate backbone of plasmid DNA was confirmed by TEM. Plasmid DNA molecules, encoded with marker gene ( $\beta$ -galactosidase;  $\beta$ -gal) were seen adopting spherical, toroidal, or supercoiled structures 15–300 nm in diameter when exposed to the positively charged groups [100]. The varying degree of plasmid condensation could be related to the charge density, the hydrophobic character of the interaction, and the number of plasmid DNA molecules in the condensate [102]. Tighter packing of functionalized SWNTs was noticeable in regions of larger CNT bundles.

The interaction of functionalized CNTs with HeLa cells was also visualized by TEM. HeLa cells were incubated with ammonium functionalized CNTs at a concentration of 2.5 mg mL<sup>-1</sup> for 1 h and the mixture was then embedded in an epoxy resin. Solidified resin was sliced by an ultramicrotome and the slices were examined by TEM. CNTs were spotted inside the cells; higher magnifications provided more convincing evidence of their internalization. Nuclear localization and the translocation of CNTs through plasma cell membranes were also seen. The mechanism hereby was believed to be the binding of the cationic functional groups on the CNTs to the cell membranes, which could be facilitated by spontaneous insertion of the CNTs across the cell membranes. Subsequent translocation and diffusion of the functionalized CNTs within the intracellular space could occur following these nonendocytotic processes [100].

The ability of ammonium-functionalized SWNTs to enter cells and potentially reach their nuclei resulted in the delivery of plasmid DNA to CHO cells. Hypothetically, these functionalized SWNTs entered the cells via a spontaneous mechanism in which the tubes pierced through the cell membranes due to their enormous aspect ratio. This model is consistent with molecular dynamics simulations which predicted that hydrophobic CNTs with hydrophilic functional groups could spontaneously insert into a lipid bilayer. Both the hydrophobicity of SWNTs and the rapid lateral diffusion of lipids in the membrane bilayer could contribute to the uptake of SWNT-plasmid DNA complexes [100].

The rate of gene transfection depended on the charge ratio of the ammonium groups on the SWNT surface to the phosphate groups of the DNA backbone. Gene expression efficiencies 5–10 $\times$  higher than those without the presence of SWNTs were obtained when the charge ratio was maintained within the range of 2:1 to 6:1. Gene expression also increased with incubation time of up to 3 h and decreased thereafter. Although the measured transfection efficiency was far from optimal, functionalized SWNTs seem to offer ample opportunities for chemical and biological modifications than do cationic macromolecules such as peptides, dendrimers, and liposomes. The other significant advantage that functionalized SWNTs have over conventional gene and drug delivery methods is their significantly reduced cytotoxicity [100].

In the study conducted by Liu et al. [101], dendritic polyethylenimine (PEI), a most efficient and popular polymer for gene delivery, was grafted onto MWNTs to

anchor DNA. Carboxylic acid groups were first created on the side walls of the MWNTs by heating the tubes at reflux in 3 M nitric acid. The carboxylic acid groups were then transformed into acyl chloride groups by consecutive treatments of thionyl chloride and ethylenediamine [26, 57]. PEI was then grafted onto MWNTs based on the activated monomer mechanism or the activated chain mechanism. Protonated aziridine monomers or the terminal iminium ion groups of propagation chains were transferred to amines on the surface of the MWNTs to form PEI-g-MWNTs complexes. DNA encoded with pCMV-Luc gene was then immobilized securely onto the complexes through strong electrostatic interactions arising from the amines. The formation of DNA-PEI-g-MWNT complexes was confirmed by the total inhibition of DNA migration in gel electrophoresis [101].

The PEI obtained by cationic polymerization of aziridine had a dendritic structure that contained primary, secondary, and tertiary amines with a molar ratio of about 1:2:1 [103]. The polymer chemistry of the PEI should not have been affected by their grafting onto the surface of MWNTs. Grafted PEI with a high content of primary, secondary, and tertiary amines could function as anchor points for the immobilization of DNA onto the surface of MWNTs. Consequently, the migration of DNA was totally inhibited in gel electrophoresis when the weight ratio of PEI-g-MWNTs to DNA was about 4:1. By comparison, the control experiments using MWNTs and NH<sub>2</sub>-MWNTs showed little inhibition on the migration of DNA, even at a high weight ratio of 100:1. This is because the nonspecific adsorption of PEI on the surface of MWNTs did not facilitate the secure anchoring of DNA, possibly due to weak interactions between the PEI and MWNTs [101].

The PEI-g-MWNTs gene transporters created in the Liu study [101] yielded more encouraging results than the Pantarotto scheme [100], which used functionalized SWNTs. Figure 7.18 details a head-to-head comparison of transfection efficiency in human embryonic kidney 293 cells for DNA-PEI (25 kDa), DNA-PEI-g-MWNTs, and DNA alone. Under the optimal conditions, the transfection efficiency using PEI-g-MWNTs was three times higher than that using PEI, and, remarkably, four orders of magnitude higher than that using naked DNA. Transfection efficiencies using PEI-g-MWNTs in COS7 and HepG2 cells, under optimal conditions, were consistently 2½ times greater than efficiencies using PEI, and were much higher than efficiencies using DNA [101].

The mechanisms proposed and speculated upon in the literature for CNT uptake or their derivatives by cells include phagocytosis, endocytosis, insertion, or passive diffusion. Liu et al. [101] attributed DNA uptake to endocytosis because PEI-g-MWNTs, once labeled with fluorescein isothiocyanate and left incubating in cells for 1 h, significantly reduced their presence in cells with increasing temperature. The high transfection efficiency obtained using PEI-g-MWNTs was perhaps due to the secure anchoring of DNA onto the surface of MWNTs. The proton-sponge effect of the grafted PEI could allow the DNA-PEI-g-MWNTs complexes to escape easily from highly acidic endosomes or other vesicles in cells. The larger complexes of DNA-PEI-g-MWNTs could have improved the proton-sponge effect of PEI and facilitated a more effective sedimentation onto the cells [101].

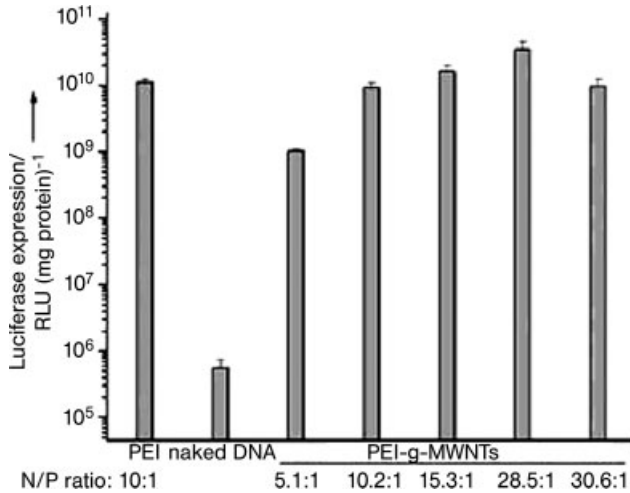


**Fig. 7.18.** Transfection efficiency of PEI-g-MWNTs for DNA delivery relative to that of PEI and naked DNA in 293 cells. The level of pCMV-Luc gene expression is given in RLU per mg of protein for quadruplicate runs [101]. (© Wiley-VCH Verlag GmbH & Co. KGaA, Weinheim.)

### 7.4.3

#### Gene Transfection with SWNT Transporters for RNA Interference

In addition to its fundamental roles in gene transcription and translation, RNA has been used for two decades to reduce (or interfere with) expression of targeted genes in various systems such as plants, fungi and higher organisms. This process, known as RNAi, is a natural defense mechanism that is thought to have evolved to protect organisms from viral diseases. Many viruses have a genetic blueprint made from RNA instead of DNA. The genetic information of many viruses is held in the form of double-stranded RNA and an enzyme known as Dicer first chops the double-stranded RNA of invaded viruses into small segments of genetic code of approximately 22 bases long. These segments, known as siRNAs, are surprisingly stable and, unlike ssDNA or RNA anti-sense oligonucleotides, do not need extensive modification to survive in tissue culture media or even within living cells. These newly formed siRNA then separate into single strands and some bind to intact lengths of single-stranded viral RNA. Finally, proteins target this tagged viral RNA and destroy it. As a result, RNAi shuts off key viral genes, potentially nipping infections in the bud. In theory, RNAi can be used to treat any disease such as cancer, which is an overactive gene or genes, or HIV, a virus with no cure and vaccine.

In one of the most exciting developments thus far, Dai's group reported gene silencing with SWNT delivered siRNA [104]. Phospholipids (PL) were adsorbed

onto SWNTs and the head groups of the PL were covalently linked by single-chained poly(ethylene glycol) (PEG, MW = 2000) with terminal amine or maleimide groups (PL-PEG-NH<sub>2</sub> or PL-PEG-maleimide). The PL-PEG bound to SWNTs via van der Waals and hydrophobic interactions between the fatty alkyl chains of the PL and the side walls of the SWNTs. Although double-chained PL molecules do not solubilize SWNTs, the presence of the PEG greatly increased the hydrophilic moiety of the PL-PEG-SWNT complexes, rendering SWNTs soluble in an aqueous solution. The amine or maleimide terminal on the PL-PEG immobilized on SWNTs was used to conjugate biofunctionalities such as DNA and siRNA. A crosslinker, sulfosuccinimidyl 6-(3'-[2-pyridyldithio]propionamido)hexanoate (sulfo-LC-SSDP), was attached to a thiol-containing biomolecule (X) to form SWNT-PL-PEG-SS-X (1-X). The biomolecule X was either 1-DNA (15-mer DNA with fluorescence label Cy3) or 1-siRNA. No disulfide linkage was employed in the control experiments [104].

In the study by Dai's group, biomolecules DNA or siRNA were transported by functionalized SWNTs into mammalian cells. SWNTs and their derivatives, after the cellular internalization of biomolecules, were believed to be allocated in endosomes and/or lysosomes. The disulfide bonds linking the biomolecules and the PL-PEI complexes were cleaved and the biomolecules were released by enzymes in lysosomal compartments whose pH (~5) is significantly lower than that of the cytosol (pH 7.2). Translocation of SWNT complexes across the cell membranes was believed to result from endocytosis [104]. Active releasing of endocytosed species from endosomes or lysosomes allows molecule cargoes to reach their intended destinations, thus preventing degradation inside the endosomes or lysosomes [105]. No effect on cell viability or proliferation was found by the presence of SWNTs in this study.

Both 1-siRNA and 2-siRNA were prepared where the siRNA was capable of silencing the gene encoding lamin A/C protein present inside the nuclear lamina of cells. HeLa cells were again used to incubate with 1-siRNA (50–500 nM) for up to 24 h. The concentration of SWNTs was 10 nM and cells of 40 000 per well in the presence of 5% FBS were fixed 48–72 h later. The cells were then stained with anti-lamin and fluorescently labeled secondary antibodies. The commercial transfecting agent lipofectamine (1 mg L<sup>-1</sup>) was used for comparison with the SWNT delivery system.

Minimal fluorescence was observed in the experiment (Fig. 7.19b) compared with that of the untreated control (Fig. 7.19a), indicating a significant reduction in the expression of lamin A/C proteins by 1-siRNA. The potency of RNAi was characterized using flow cytometry in the order 1-siRNA, 2-siRNA, and lipofectamine-siRNA, for a given concentration of siRNA (Fig. 7.19c). The higher silencing potency with 1-siRNA than 2-siRNA is possibly due to the release of siRNA from SWNTs by breaking their linking disulfide bonds. This released and subsequently more effective siRNA can then readily escape from endosomes or lysosomes. This two-fold increase in the silencing potency using 1-siRNA compared with lipofectamine was attributed to the high surface area of SWNTs for siRNA cargo loading, the high intracellular transporting ability of SWNTs, and the high degree of



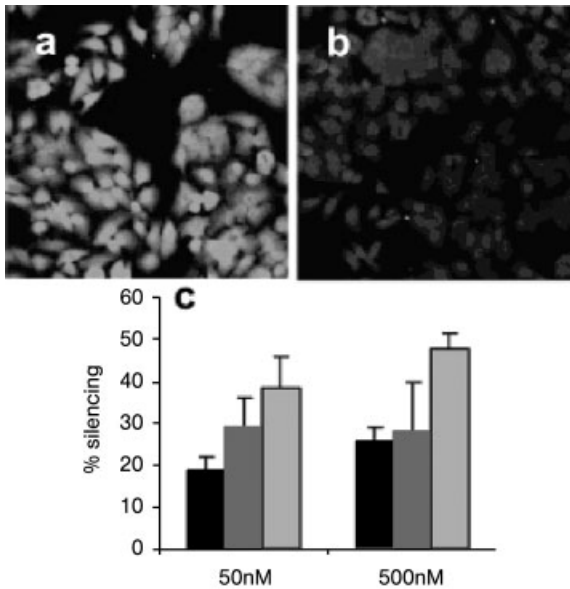


**Fig. 7.19.** Confocal microscopy RNAi assay for (a) untreated control HeLa cells and (b) cells incubated with 1-siRNA, the latter showing a much weaker fluorescence than (a) due to silencing of the expression of lamin protein by RNAi. (c) Silencing efficiency of lipofectamin-siRNA (left-hand bars), 2-siRNA (middle bars) and 1-siRNA (right-hand bars) for 50 and 500 nM siRNA concentrations. Cells were fixed and stained with anti-lamin and a fluorescently labeled secondary antibody prior to analysis. The confocal images were captured at similar experimental settings for (a) and (b) [104]. (© American Chemical Society.)

endosome/lysosome escape owing to the breakage of the disulfide bond. Excellent siRNA delivery and silencing of the luciferase gene were also observed [104]. This study has shown great promise for using SWNT as molecular transporters for gene therapy.

#### 7.4.4

#### Drug Delivery with SWNT Transporters

This section reviews recent developments in drug delivery with SWNT transporters, and highlights the research by Pantarotto et al. on immunization with peptide-functionalized SWNTs for enhancing virus-specific neutralizing antibody responses [28], and the research by Dai's group on intracellular protein transport for inducing apoptosis and on the highly sensitive electronic detection of antibodies associated with human autoimmune diseases [106].

##### 7.4.4.1 Vaccine Delivery by SWNTs

Developing new and effective delivery approaches is of paramount importance for administering protective antigens. SWNTs could serve as excellent transporters for

the effective utilization of antigens that have previously been unable to induce adequate or appropriate responses, thus providing significant means of enhancing and modulating immune responses. In vaccine delivery, conserving the conformation of antigen is crucial. This conservation, in turn, yields the induction of antibody responses with the right specificity. Therefore, the presence of SWNTs should not change the biofunctionality of the antigen when they are linked together. Pantarotto et al. evaluated the capacity of mono- and bis-derivatized SWNTs to present B cell epitope from the VP1 coat protein of FMDV [107]. The knowledge obtained from this study served to enhance the neutralizing potential of the B cell epitope.

The chemical route for obtaining water-soluble SWNTs is based on the methodology described in Section 7.2.1.2. SWNTs were functionalized with a pyrrolidine ring through the 1,3-dipolar cycloaddition of azomethine ylides [108]. The amino-derivatized SWNTs were subsequently used to covalently link a series of peptides by different strategies. In one approach, B cell epitope, a peptide corresponding to the sequence 141-159 derived from VP1 protein of FMDV, was coupled to functionalized SWNTs, employing a selective chemical ligation to obtain the mono-conjugate 2 [28]. In another approach, functionalized SWNTs were covalently attached to two FMDV peptides to yield the bis-conjugate 3. The latter approach involved a derivatization of the free amino groups of SWNT 1 using an excess of Boc-Lys(Boc)-OH activated with DIC (diisopropylcarbodiimide) and HOBt (1-hydroxybenzotriazole) in DMF, and subsequent cleavage of Boc (tert-butyloxycarbonyl) with TFA (trifluoroacetic acid). The free amino groups were neutralized with DIEA (diisopropylethylamine) and coupled with *N*-succinimidyl 3-maleimidopropionate in DMF [108]. Excess reagent was removed by adding an amino-PEGA resin. The *N*-terminal acetylated FMDV 141-159 peptide, with an additional cysteine, was dissolved in water and linked to the two maleimido moieties [109]. Unreacted peptides were removed using a scavenger resin, and reverse-phase HPLC confirmed a peptide covalent bond formation to the SWNTs. The solubilities of the mono-conjugate 2 and the bis-conjugate 3, were 18.0 and 12.5 mg mL<sup>-1</sup>, respectively [28].

The activity of the FMDV 141-159 peptide was confirmed using a monoclonal assay. Anti-FMDV 141-159 peptide mAb was presented to a covalently linked anti-mouse Fc $\gamma$  antibody. SWNTs alone did not react with mAb, while free peptides, mono-conjugates 2, and bis-conjugates 3 all interacted with mAb in increasing masses [28]. However, an analysis of the three sensorgrams showed no difference in the association rate constants and only a small decrease of the dissociation rate constant for the bis-conjugate 3, which might be ascribed to the avidity of the bivalent reagent [28]. Thus both mono- and bis-conjugates preserve the conformation of their attached peptides.

An immunization protocol was tested on the coupling of nonimmunogenic peptides to SWNTs. Anti-peptide antibody responses were measured by ELISA using BSA-conjugated FMDV141-159 peptide as antigen (Fig. 7.20 left). The sensitivity of the ELISA was greater than that for the free peptides. The anti-FMDV 141-159 antibody response slightly increased when OVA was injected with the mono-conjugate 2. Using the bis-conjugate 3 as an immunogen (Fig. 7.20 left) also

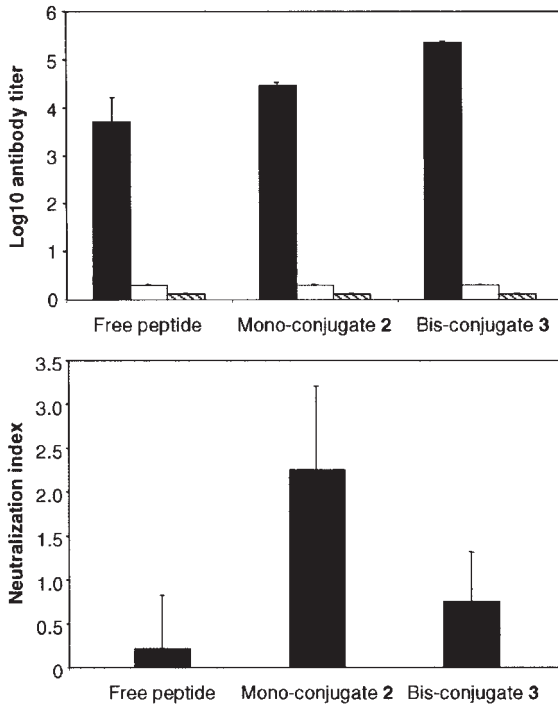


**Fig. 7.20.** (Left-hand side): Anti-peptide antibody responses following immunization with peptides and peptide–SWNTs. Groups of BALB/c mice were co-immunized intraperitoneally with OVA and free FMDV 141-159 peptide, mono-conjugate 2, or bis-conjugate 3 in Freund's adjuvant emulsion. Serum samples collected 2 weeks after the booster immunization (on day 14 post priming) were screened by ELISA for the presence of antibodies using FMDV 141-159 peptide conjugated to BSA (solid bars), or control peptide conjugated to BSA (open bars), or

SWNT 1 functionalized with maleimido group without peptide (hashed bars) as solid-phase antigens. Data represent mean of  $\log_{10}$ (antibody titers) from five mice per group. (Right-hand side): Neutralization indices of serum samples of immunized mice. Serum samples were collected 2 weeks after the boost of mice co-immunized intraperitoneally with OVA and free FMDV 141-159 peptide, mono-conjugate 2, or bis-conjugate 3 in Freund's emulsion. Data represent the mean of antibody titers from five mice per group [28]. (© Elsevier Science Ltd.)

significantly elevated the anti-peptide antibody titers. Antibody responses were specific to the FMDV 141-159 peptides but not to the functional groups linking peptides to the SWNTs, because serum antibodies showed little reactivity to control peptides conjugated to BSA (Fig. 7.20 left). Both the peptide conjugates and OVA were sampled by antigen-presenting cells. Assistance from the OVA-specific T helper cells enabled the B cells to produce antibodies that recognized the FMDV 141-159 peptides. No anti-SWNT antibodies were detected (Fig. 7.20 left) [28]. The bystander help provided by the carrier (OVA) should be directed to the covalently

attached peptides and not to the SWNTs. This study indicated that SWNTs alone do not possess intrinsic immunogenicity.

Mono-conjugate 2 elicited virus-neutralizing antibody responses in mice (Fig. 7.20 right), which were significantly higher than those induced by the bis-conjugate 3 or the control free peptide. An increased number of epitopes at the surface of SWNTs enhanced the immunogenicity of the attached peptides while decreasing the neutralizing titers. It was hypothesized that both copies of the FMDV peptides of the bis-conjugate 3 assumed different conformations than that of their native state, thus failing to invoke antibody responses with the correct specificity [28]. The preferential induction of peptide-specific antibodies with enhanced virus neutralizing capacity using mono-conjugate 2, coupled with the non-responsiveness to the attached SWNTs, demonstrated the presentation of the attached peptides *in vivo*, suggesting their possible use as antigen delivery systems since no anti-carbon antibodies were elicited that could influence immune responses to their attached peptides.

#### 7.4.4.2 Protein Delivery by SWNTs

The Shi Kam and Dai study [106] explored protein delivery with SWNTs. The proteins used, including streptavidin (SA), protein A (SpA), BSA, and cytochrome *c* (cytc), were fluorescently labeled and bound to the side walls of SWNTs via a non-covalent and nonspecific mechanism (Section 7.2.2). Translocation of these proteins in mammalian cell lines, including HeLa, NIH-3T3 fibroblast, HL60, and Jurkats, cells was observed by confocal fluorescence microscopy. Endocytosis, an energy dependent internalization mechanism based on the engulfing of the foreign particles, was believed to be responsible since the uptake showed a distinct temperature dependence. For example, incubating the cells in protein-SWNTs conjugates at 4 °C yielded little uptake [106].

Cellular uptake of large proteins (molecular weight > 80 kDa) was poor, while the binding and intracellular protein transport by SWNTs appeared general for small- and medium-sized proteins [106]. Figure 7.21 compares the fluorescence level detected for cells incubated with proteins alone, and for cells incubated with protein-SWNTs; this suggests that while proteins in solutions were unable to traverse across cell membranes, SWNTs were able to transport protein cargoes inside cells possibly due to their hydrophobicity and high aspect ratio. SWNT-protein conjugates, once internalized within the cells, were found co-localized with red endocytosis endosome marker FM 4-64 [98], suggesting the confinement of the conjugates in endosomal lipid vesicles. Once within cells, the endosomes could fuse with lysosomes, and cause the degradation of the internalized species in the acidic lysosomes. To prevent lysosomal degradation, chloroquine was added to the cell medium during the incubation of cells in protein-SWNT conjugates to trigger an endosomal release of internalized molecules into the cell cytoplasm. Chloroquine is a membrane-permeable base that can localize inside endosomes and cause increases in pH. The resulting osmotic pressure led to swelling and eventual rupture of the endosomal compartments (Fig. 7.22). This phenomenon suggests that it is possible to create biological functionality for these internalized “cargo” molecules.

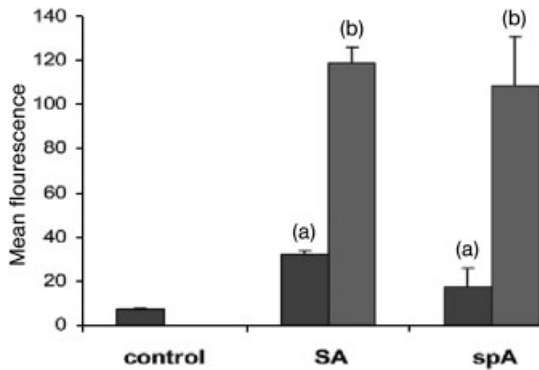


**Fig. 7.21.** Cell cytometry data for untreated HL60 cells (labeled as “control”), and for HL60 cells incubated in solutions of fluorescently labeled SA and SpA (a), and treated with the respective fluorescent protein–SWNT conjugates (b). Cells were incubated in protein–SWNTs solutions for 2 h [106]. (© American Chemical Society.)

HeLa and NIH-3T3 cell lines, known to undergo *cyt-c*-induced apoptosis [110], were used for intracellular transport of *cyt-c* with SWNTs and for apoptosis assay. After cell incubation in the *cyt-c*-SWNT conjugates, apoptosis was analyzed using fluorescently (FITC) labeled Annexin V. Annexin V-FITC is an efficient marker for early stage apoptosis as it binds to the phospholipid flipped from the inner to the outer leaflet of the plasma membrane during apoptosis. For NIH-3T3 cells in the presence of chloroquine and incubated, respectively, with *cyt-c*-SWNT conjugates and with *cyt-c* alone, the degree of Annexin V staining was characterized by both confocal microscopy (Fig. 7.23a, b) and cell flow cytometry (Fig. 7.23c). Significantly higher percentages of apoptosed cells were observed when incubated with *cyt-c*-SWNT conjugates than with *cyt-c* alone [106]. Figure 7.23(c; inset) shows the

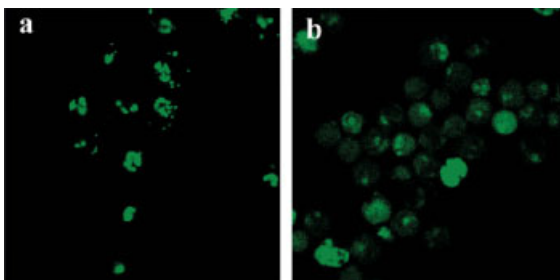


**Fig. 7.22.** Endosomal rupture. Cells were incubated with (a) *cyt-c*-SWNT conjugate and (b) *cyt-c*-SWNT + 100  $\mu\text{M}$  of chloroquine at 37  $^{\circ}\text{C}$  and 5%  $\text{CO}_2$ . Confocal images were taken immediately after incubation and washing.

These images indicate the release of protein–SWNT conjugates from the endosome: overall green color across the cell in (b) vs. green individualized spots inside the cells in (a) [106]. (© American Chemical Society.)

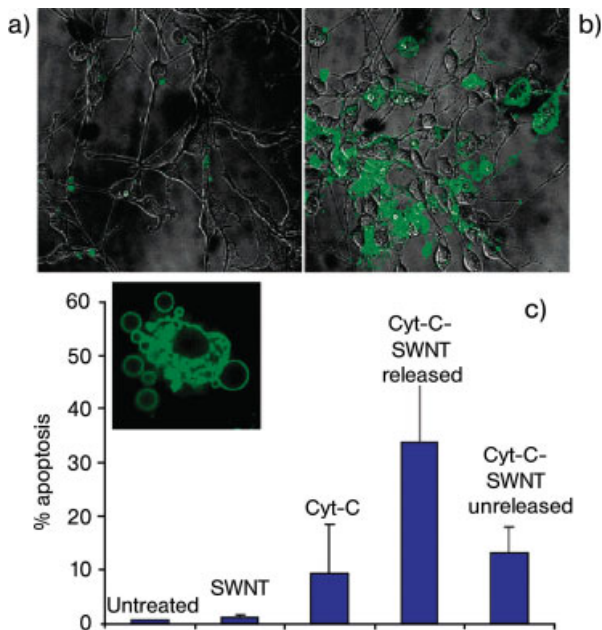


**Fig. 7.23.** Apoptosis induction by cytochrome *c* cargos transported inside cells by SWNTs. (a) Confocal image of NIH-3T3 cells after 3 h incubation in 50  $\mu\text{M}$  cytochrome *c* alone (no SWNT present) and 20 min staining by Annexin V-FITC (green fluorescent). (b) Cell images after incubation in 50  $\mu\text{M}$  cytochrome *c*-SWNTs in the presence of 100  $\mu\text{M}$  chloroquine and after Annexin V-FITC staining. (c) Cytometry data of the percentage of cells undergoing early stage apoptosis (as stained by Annexin V-FITC) after exposure to 100  $\mu\text{M}$  chloroquine only (labeled “untreated”),

SWNT + 100  $\mu\text{M}$  of chloroquine, 10  $\mu\text{M}$  cyt-*c* + 100  $\mu\text{M}$  chloroquine, 10  $\mu\text{M}$  cyt-*c*-SWNT + 100  $\mu\text{M}$  chloroquine, and cyt-*c*-SWNT without chloroquine. Inset: representative confocal image of the blebbing of the cellular membrane (stained by Annexin V-FITC) as the cell undergoes apoptosis. Note that PI co-staining was used, and all data shown here excluded PI-positive cells and were recorded 4–5 h after exposure to chloroquine. The level of PI staining for all cells was a normal ~4–6% out of ~10 000 [106]. (© American Chemical Society.)

blebbing of the cellular membrane stained by Annexin V-FITC, a phenomenon associated with cells undergoing apoptosis.

To investigate the effect of endosomal release on the efficiency of apoptosis induction by cyt-*c* transported by SWNTs, cells were incubated in cyt-*c*-SWNT in both the presence and absence of chloroquine. Higher degrees of apoptosis were consistently observed for cells treated with cyt-*c*-SWNT in the presence of chloroquine (Fig. 7.23c). This higher degree of apoptosis is due to the more efficient endosomal releasing of proteins, suggesting that the cytochrome *c* bound and transported inside cells by SWNT carriers remained biologically active for apoptosis induction [106]. However, it is unclear if the functionality of cytochrome *c* was ob-

tained after detaching from the SWNTs, or if it remained effective even when proteins were still bound to the SWNTs.

#### 7.4.4.3 Biosensing by SWNTs

In a separate study by Dai's group [17], SWNTs were employed as biosensors for potential medical diagnostic and biological applications. In this scheme (Fig. 7.1 left), SWNTs were coated with U1A antigen-Tween conjugates and the immobilized antigens were recognized by 10E3 mAbs. The U1A RNA splicing factor is a prominent autoantigen target in systemic lupus erythematosus and mixed connective tissue disease, and detection of its autoantibodies by ELISA forms a clinical fluorescence assay. With SWNT sensors, binding can be monitored in real-time electronically without labeling, with the resulting sensitivity at a remarkable 1 nm or less.

Similar results were obtained with two other U1A-specific mAbs. In contrast, two different mAbs (3E6 and 6E3) specifically used for TIAR (a structurally related but different RNA binding protein autoantigen) failed to recognize the U1A splicing factor. This result compares favorably with fluorescence-based detection of immobilized antigens, where the limit of detection was found to be 2.3 nm [17]. In addition to offering a higher sensitivity, Dai's scheme also permitted sample preparation and detection to be performed in solution without protein denaturation. This study serves as a proof of concept that SWNT devices can detect clinically and biologically important interactions, with a potential for screening assays of mAb panels for use as reagents or therapeutics. Since the human proteome contains more than 300 000 different protein isoforms, methods for high-throughput screening of mAbs are crucial for their identification. Furthermore, multiplex analysis of autoantibodies may be performed with arrays of SWNT devices to diagnose patients with autoimmune diseases such as HIV, complementing or overtaking other recently developed techniques such as planar array-based methods [17].

## 7.5

### Sensing and Treating Cancer Cells Utilizing SWNTs

A milestone in the possible use of SWNTs to diagnose and treat cancer was recently reported by Dai et al. [32]. They demonstrated how several unique characteristics of SWNTs could be combined to serve the purpose of selectively causing cancer cell destruction. SWNTs functioned as multifunctional biological transporters for cargoes such as Cy3-DNA, various phospholipids, and folate moiety. The destruction of the cancer cells was due to the strong absorbance of translocated SWNTs in the NIR range (700–1100 nm) because of distinct first and second van Hove optical transitions (Fig. 7.24) [44].

*Ex vitro* studies showed an increase to approximately 70 °C after heating SWNTs of various concentrations for 2 min with continuous 808 nm laser light [32]. Heating was caused from optical stimulation of electronic excitations of SWNTs that was transferred to molecular vibration energies and heat. The transfer to molecular

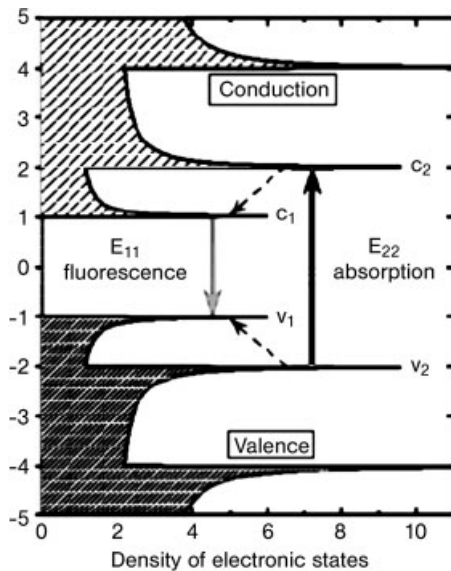


**Fig. 7.24.** Semiconducting SWNTs electronic structure and density diagram of electronic states. Optical emission and excitation transitions are represented by solid arrows; dashed arrows show non-radiative relaxation of

the electron in the conduction band and of the hole in the valence band before emission [86].  
(© American Association for the Advancement of Science.)

vibration energies and heat has another interesting effect if pulsed NIR laser light is discharged. The pulsed optical stimulation of SWNTs seemed to cause the release of their cargoes, as demonstrated with confocal fluorescent images of Cy3-DNA-SWNT complexes (Fig. 7.25).

Perhaps more important than the demonstration of SWNT complex translocation is the preservation of cell viability. As previously shown, SWNT complexes below certain concentrations have no adverse affect on cell viability, and biological systems like cells experience limited or no damage because they are completely transparent to continuous NIR light. These two noninvasive aspects were combined to induce the destruction of cancer cells. Once cancer cells internalized SWNT complexes and were exposed to continuous NIR laser light, they experienced excessive heating and eventual death [32]. After exposure to this treatment, cells appeared round with aggregated SWNT complexes appearing within the growth medium (Fig. 7.26 left).

Another key issue involving cell viability in this experiment is the ability of cancer cells to selectively internalize SWNTs, thus ensuring that they can destroy harmful cells while preserving healthy ones. Specifically, SWNTs were conjugated with various phospholipids (PL), a poly(ethylene glycol) (PEG) moiety, and terminal folic acid (FA) group that provided specificity for this selective internalization (Fig. 7.27). Additionally, the preparation of cancer cells required some ingenuity



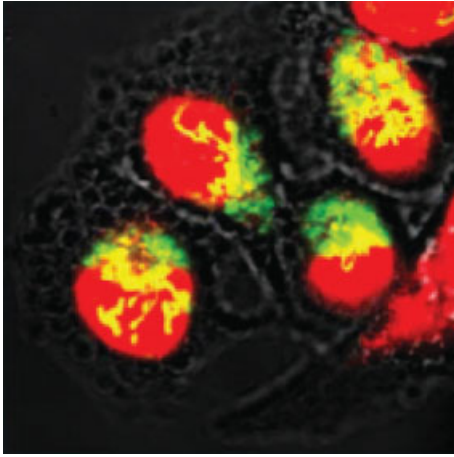


**Fig. 7.25.** NIR laser light excitation of Cy3-DNA-SWNT complexes causing DNA release and nuclear translocation. Confocal image of HeLa cells after 12 h incubation with  $2.5\text{--}5\text{ mg L}^{-1}$  Cy3-DNA-SWNT complexes and

radiation with six NIR pulses at 808 nm and intensity of  $1.4\text{ W cm}^{-2}$  for 10 s. Yellow coloring represents colocalization of green Cy3-DNA and red DRAQ5 in cell nuclei [32]. (© National Academy of Sciences.)

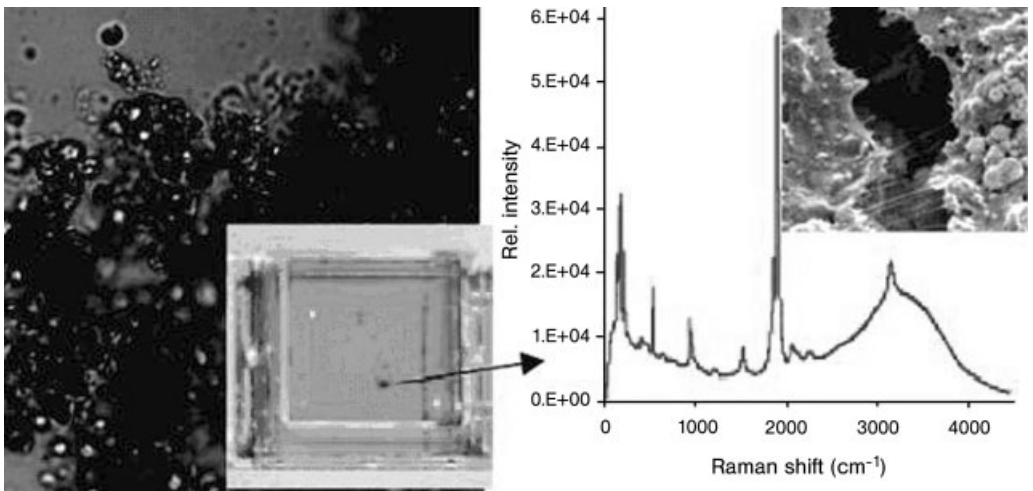


**Fig. 7.26.** Image of dead and aggregated cells after internalization of DNA-SWNT and continuous NIR laser radiation exposure for 2 min at  $1.4\text{ W cm}^{-2}$ . The dead cells show round and aggregated morphology 24 h after laser activated cell death. Black aggregates of

SWNTs are released from dead cells and could visually be seen floating. Raman data and SEM image of black aggregates ( $\times 36\,000$ ) confirm aggregates are SWNTs [32]. (© National Academy of Sciences.)

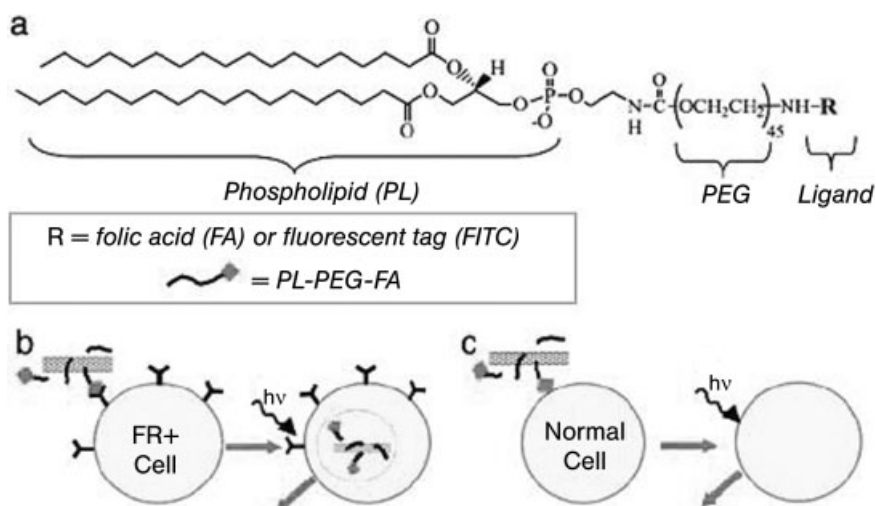


**Fig. 7.27.** Chemical structures of the cancer cell targeting scheme. (a) PL-PEG-FA and PL-PEG-FITC are conjugated with SWNTs and synthesized by conjugating PL-PEG-NH<sub>2</sub> with FA or FITC. (b) Diagram of selective internalization of PL-PEG-FA-SWNTs into folate-starved cells with increased folate receptors (FR). (c) No internalization of PL-PEG-FA-SWNTs into normal cells without folate receptors [32]. (© National Academy of Sciences.)

that included folate moiety starvation to increase the number of folate receptors on the membranes of these cells. SWNTs conjugated with folate moiety were selectively internalized by cancer cells with folate receptor markers, and then bombarded with continuous NIR laser, which heated these internalized SWNTs, which in turn destroyed the cancer cells. Whereas the folate-starved cancer cells were destroyed (Fig. 7.28), healthy cells without SWNTs complexes were transparent to the laser light and remained viable [32].

Though much more research is necessary, this study clearly demonstrated the amazing transporting potential for functionalized SWNTs to deliver both drugs and cancer therapies due to their unique chemical and optical properties.

## 7.6

### Cytotoxicity of SWNTs

Toxicity has been a controversial issue, shadowing the science of nanotechnology. An improved understanding of the cytotoxicity of SWNTs will undoubtedly benefit research on the biological and biomedical aspects of nanomaterials. An early study by Shvedova et al. determined that transition metal catalysts such as iron and nickel at SWNT concentrations of 0.06 mg mL<sup>-1</sup> and higher were toxic to human epidermal keratinocytes [111]. Indeed, inhaling SWNTs, perplexingly, caused the

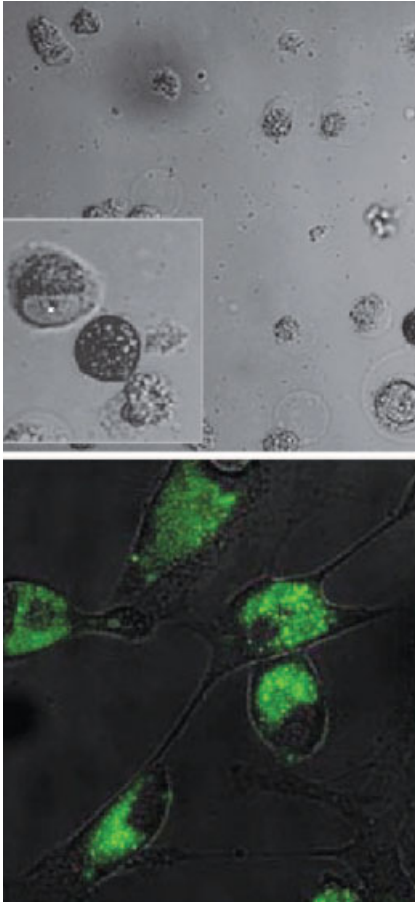


**Fig. 7.28.** Images of SWNT complexes internalized by folate-starved cells. (Top): Confocal image showing the round cell morphology of dead cells. (Bottom): Confocal fluorescence image of SWNTs carrying two cargoes, PL-PEG-FA and PL-PEG-FITC,

internalized within folate-starved cancer cells. The green FITC fluorescence represents the internalization of SWNT with FA and FITC cargoes [32]. (© National Academy of Sciences.)

growth of granulomas in the lungs of rats, and in the total absence of such pulmonary biomarkers as inflammation, cell proliferation, and cytotoxicity [112, 113]. Another study by Colvin's group using the buckyball  $C_{60}$ , a cousin of SWNTs, revealed that nano- $C_{60}$  had a greater toxicity to human skin cells than  $C_{60}(OH)_{24}$  – the fullerene molecules containing most additional chemical groups on their surfaces. However, fullerene molecules with a higher degree of surface modification were far less toxic due to their inability to generate oxygen radicals [114]. Colvin et al. also found that the toxicity of water-soluble SWNTs to human dermal fibroblasts decreased as the functionalization of the tubes increased [115]. Their specific func-

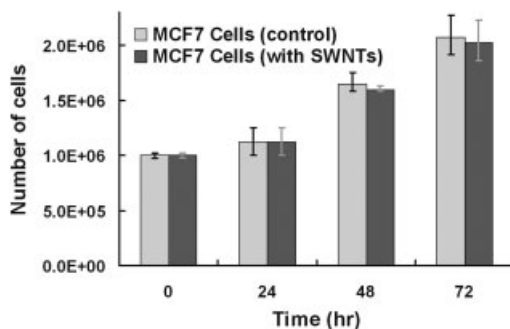
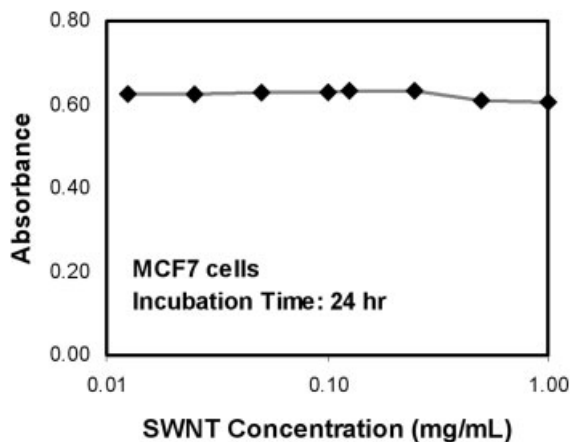


Fig. 7.29. Cell growth curves for MCF7 cells without (control; left-hand bars) and with SWNTs ( $0.04 \text{ mg mL}^{-1}$ ). Incubation time was 72 h [68]. (© American Chemical Society.)

tionalizations included SWNT-phenyl-SO<sub>3</sub>X ratios of 18, 41, and 80 and SWNT-phenyl-(COOH)<sub>2</sub> with a carbon/-phenyl-(COOH)<sub>2</sub> ratio of 23. The cytotoxicity of unfunctionalized SWNTs was 200 parts per billion (ppb), ten times lower than unfunctionalized fullerenes, and modified SWNTs were found to be noncytotoxic. Therefore, while cell death did increase with dose concentration, it did not exceed 50% for concentrations of modified SWNTs up to 2000 ppm [115]. Pantarotto et al. supported this supposition, consistently finding that 90% of fibroblasts remained alive when incubated with SWNTs of  $5 \mu\text{M}$  [97]. Shi Kam et al. have reported that promyelocytic leukemia cells were viable when the SWNT concentrations were below  $1.25 \mu\text{M}$  [98].

Figure 7.29 shows cell growth for MCF7 cells both with and without SWNTs ( $0.4 \text{ mg mL}^{-1}$ ) [68]. A similar result was observed for d2C keratinocytes cells (data not shown). In both cases, no significant difference in growth was observed for SWNTs treated MCF7 or d2C cells over a 3 day period. The cell count for the MCF7 cells with SWNTs showed only a minimal decrease in the number of cells for day 2 and day 3; however, the overall trend mirrored the cell count for the control MCF7 cells. An MTS assay for cellular metabolism (Fig. 7.30) on the absorbance of MCF7 cells was performed on cultures without SWNTs (control) and with SWNTs of various concentrations. Absorbance was similar for the control cells (0.631) and for those of various concentrations of SWNTs (0.607 to 0.631). The highest concentrations of SWNTs (1 and  $0.5 \text{ mg mL}^{-1}$ ) have the largest drop in absorbance (0.024 and 0.021, respectively). However, at concentrations lower than  $0.5 \text{ mg mL}^{-1}$ , the absorbances have variances of less than 0.01. Our results suggest that SWNT of a concentration as high as  $1 \text{ mg mL}^{-1}$  has no effect on metabolism and cell viability, suggesting some general trends in biological responses to nanoparticles. Nonetheless, notably, a comprehensive risk assessment of SWNTs should go beyond cytotoxicity and account for such crucial issues as exposure rates, uptake mechanisms, and cellular transport of SWNTs and their derivatives. These studies formulate the practice of nanomedicine, guide scientific and technological advancement, and have profound impacts on workplace protection and environment control.



**Fig. 7.30.** MTS assay of MCF7 cell absorbance vs. SWNT concentration. The control cell absorbance was measured to be 0.630. Cell absorbance ranges from 0.607 to 0.631 for SWNT concentrations of 0.0125–1 mg mL<sup>-1</sup> [68]. (© American Chemical Society.)

## 7.7

### Cancers and SWNTs

An estimated almost 1.4 million new cases of cancer will be diagnosed in 2005 and over 1500 people will die of the disease per day. Despite intensive research, progress in treatment of the disease has been slow and very few significant advances have been made since President Nixon declared his “War on Cancer” and passage of the National Cancer Act in 1971. Traditional chemotherapy and radiotherapy protocols result in actual cures only infrequently and are often accompanied by serious side effects, some of which are permanent. Since therapy for metastatic cancer requires a method that will destroy cancer cells distant from the primary neoplasm, an effective therapy must involve widespread, but specific tumor cell destruction. There are several causes for the failure of current therapies to cure cancer. While cancer cells are more sensitive than their healthy counterparts to radiation and the drugs used for chemotherapy, the differential between the two is not sufficiently large to allow destruction of all of the cancer cells without damaging the healthy ones. Frequently, even in cases where most of the cancer cells are destroyed, some transformed cells escape detection and survive to establish secondary tumors – sometimes years later. In the process of destroying the tumor, cells of the immune system can be damaged, leading to immunosuppression and eventually tolerance of the tumor. Patients can suffer permanent damage, resulting in neuropathies and arthropathies. A dose that will destroy the tumor, yet not severely damage the host is difficult to determine; and in many cases, it may be impossible to obtain. In addition, cells surviving an initial attack will be stimulated to mutate,

resulting in a more aggressive phenotype. Current evidence indicates that metastatic tumor cells have several mutations. Usually, at least one of these involves a gene coding for DNA repair. This facilitates further mutation and allows the cells to evolve mechanisms for evading destruction. The aim of our current research is to overcome these complications by using nanotubes to target tumor cells with greater specificity so that physical, chemical and genetic therapies can selectively destroy tumor cells, allowing more effective killing without damaging sensitive healthy tissue.

As previously described, the work of Dai et al. [106] represents the first major step toward the direct application of SWNTs for cancer therapy. Here, cells were killed by laser irradiation of engulfed SWNTs, raising the temperature to 70 °C. Internalization of the SWNTs was stimulated by starving the cells for folate and conjugation of the SWNTs with folic acid. While the studies were performed in a somewhat artificial system *in vitro*, modifications of the technique could make this approach a valuable contribution to the anti-tumor armamentarium. The value of hyperthermia as an anti-cancer therapy has long been recognized and current studies indicate that it can lead to significant improvement in response when combined with radiation or chemotherapy. In these studies only temperatures in the range 41–43 °C are required. Van der Heijden et al. [116] found that raising the temperature to only 43 °C was synergistic with four different drugs for the killing of four different human bladder transitional carcinoma cell lines. Raaphorst and Yang [117] found that a temperature of only 41 °C sensitized human cells to killing with cisplatin. The mechanism of enhanced killing involved inhibition of DNA repair, and increased intracellular drug concentrations [118]. In a recent study of sixty eight patients with advanced cervical cancer, Westermann et al. [119] achieved complete remission in 90% of the patients by combining hyperthermia with both radiation and chemotherapy. After 538 days, 74% of the patients remained alive without signs of recurrence. Here the temperature was raised to 41 °C. Hence only moderate heating by laser irradiation of intracellular SWNTs could enhance tumor destruction. The synergistic interaction of hyperthermia and chemotherapy could be utilized if SWNT drug delivery vehicles were also to serve as infrared targets for heating.

Another use of SWNTs for enhancing radiation therapy has been suggested by Yinghuai et al. [120], who have successfully attached C(2)B(10) carborane cages to SWNTs. These could be used to increase concentrations of boron in tumor cells relative to blood and other organs, resulting in sensitization of the tumors for neutron capture therapy.

An obvious method for targeting SWNTs to tumor cells is to attach antibodies specific for the tumor cell surface. Cancer therapy with monoclonal antibodies alone has had minimal success; the best results having been found with trastuzumab (Herceptin) for treatment of her2/nu positive breast cancers [121] and with antibodies against CD20 for non-Hodgkin's lymphoma (Rituxan, Zevalin, Bexxar [122]). While the coupling of monoclonals with radioisotopes or toxins (e.g., ricin) is also being explored, a problem with these approaches is that the antibodies are usually produced in mice, causing them to be recognized as foreign by the

immune system of the patient and destroyed. Conjugating antibodies to SWNTs could extend their lifetimes while targeting the SWNTs to the site of the primary tumor and to metastatic sites. Binding of a toxin to the nanotube or laser heating would then increase the effectiveness of killing. Anti-angiogenesis therapies are also being explored. While these produced promising results during early development, at present they have had limited effectiveness clinically. Recent data indicate the anionic phospholipids, particularly phosphatidylserine, become exposed on the external surface of the vascular endothelial cells in tumors. An antibody produced against these phospholipids localizes in the tumor vasculature and slows the growth of tumors in mice [123]. This effect can be enhanced by pretreatment with docetaxel [124]. Conjugation of this type of antibody to SWNTs would serve to target the SWNTs to the tumor. In this case, blood supply to the tumor would be inhibited by the antibody while additional destruction of the tumor vasculature and the surrounding tissue could be done with laser heating.

The possible uses of SWNTs as delivery vehicles for genes or siRNAs are too numerous to be reviewed here. Transfection of the tumor suppressor gene p53 should be attempted, since this is the most commonly mutated tumor suppressor gene in human cancers. Mutated forms of p53 appear in almost 50% of some tumor types. Both transfection of the p53 gene and transfection of siRNA against the apoptosis inhibitor bcl-2 should drive tumor to self-destruction. Transfection of siRNA the p-glycoprotein coded for by the multidrug resistance gene MDR1 would restore sensitivity of resistant cancer cells to chemotherapeutic drugs. It is possible to attach multiple moieties to SWNTs because of their structure. This will allow almost limitless possibilities for combinations of targeting ligands and inducers of apoptosis or necrosis.

## 7.8 Summary

Iijima could not possibly have imagined, in 1991 [125], the subsequent flurry of enchanting scientific endeavors surrounding CNTs whose impact seems to have increasingly touched every corner of our life. Perhaps no other nanostructure or nanomaterial invented so far has attracted this grand level of attention and fervent study. Much remains to be done to offer high sensitivity and localized treatment for cancers and diseases with functionalized and thus intelligent nanostructures and nanomaterials. The realization of this dream demands joint efforts by researchers in the fields of materials science, physical science, and life science, as nature never intends to favor the description of any specific discipline. It is to our best hope that, after reading this chapter, you may start to envision shuttling biomolecules and drug loads through fluidic cell membranes, reporting complex pathogenic pathways, sensing the pH, ionic strength, and temperature of nano-scale bioenvironment, detecting, treating, and preventing cancers and diseases, all with this synthetic wonder material called CNT.

## Acknowledgments

The authors thank J. M. Moore for assistance. One of the authors, P. C. Ke, dedicates this chapter to his loved ones.

## References

- DRESSELHAUS, M. S., DRESSELHAUS, G., AVOURIS, P. Eds., *Carbon Nanotubes: Synthesis. Structure, Properties, and Applications*, 2001, Springer-Verlag, Berlin.
- DALTON, A. B., COLLINS, S., MUNOZ, E., RAZAL, J. M., EBRO, V. H., FERRARIS, J. P., COLEMAN, J. N., KIM, B. G., BAUGHMAN, R. H. Super-tough carbon-nanotube fibres. *Nature* 2003, 423, 703.
- BARONE, P. W., BAIK, S., HELLER, D. A., STRANO, M. S. Near-infrared optical sensors based on single-walled carbon nanotubes. *Nat. Mater.* 2005, 4, 86–92.
- CHERUKURI, P., BACHILO, S. M., LITOVSKY, S. H., WEISMAN, R. B. Near-infrared fluorescence microscopy of single-walled carbon nanotubes in phagocytic cells. *J. Am. Chem. Soc.* 2004, 126, 15 638–15 639.
- AZAMIAN, B. R., DAVIS, J. J., COLEMAN, K. S., BAGSHAW, C. B., GREEN, M. L. Bioelectrochemical single-walled carbon nanotubes. *J. Am. Chem. Soc.* 2002, 124, 12 664–12 665.
- BELAVOINE, F., SCHULTZ, P., RICHARD, C., MALLOUH, V., EBBESEN, T. W., MIOSKOWSKI, C. Helical crystallization of proteins on carbon nanotubes: A first step towards the development of new biosensors. *Angew. Chem. Int. Ed.* 1999, 38, 1912–1915.
- BAUGHMAN, R., ZAKHIDOV, A., DE HEER, W. Carbon nanotubes – the route toward applications. *Science* 2002, 297, 787–792.
- BIERCUK, M. J., LLAGUNO, M. C., RADOSAVLJEVIC, M., HYUN, J. K., JOHNSON, A. T., FISCHER, J. E. Carbon nanotube composites for thermal management. *Appl. Phys. Lett.* 2002, 80, 2767–2769.
- KEMPA, K., KIMBALL, B., RYBCZYNSKI, J., HUANG, Z. P., WU, P. F., STEEVES, D., SENNETT, M., GIERSIG, M., RAO, D. V. G. L. N., CARNAHAN, D. L., WANG, D. Z., LAO, J. Y., LI, W. Z., REN, Z. F. Photonic crystals based on periodic arrays of aligned carbon nanotubes. *Nano Lett.* 2003, 3, 13–18.
- ZHAO, Y. D., ZHANG, W. D., CHEN, H., LUO, Q. M. Direct electron transfer of glucose oxidase molecules adsorbed onto carbon nanotube powder microelectrode. *Anal. Sci.* 2002, 18, 939–941.
- GOODING, J. J., EROKHIN, P., HIBBERT, D. B. Parameters important in tuning the response of monolayer enzyme electrodes fabricated using self-assembled monolayers of alkanethiols. *Biosens. Bioelectron.* 2000, 15, 229–239.
- DE HEER, W. A., CHATELAIN, A., UGARTE, D. A carbon nanotube field-emission electron source. *Science* 1995, 270, 1179–1180.
- RINZLER, A. G., HAFNER, J. H., NIKOLAEV, P., LOU, L., KIM, S. G., TOMANEK, D., NORDLANDER, P., COLBERT, D. T., SMALLEY, R. E. Unravelling nanotubes: Field emission from an atomic wire. *Science* 1995, 269, 1550–1553.
- BACHTOLD, A., HADLEY, P., NAKANISHI, T., DEKKER, C. Logic circuits with carbon nanotube transistors. *Science* 2001, 294, 1317–1320.
- YAO, Z., CH. POSTMA, H. W., BALENTS, L., DEKKER, C. Crossed nanotube intramolecular junctions. *Nature* 1999, 402, 273–276.
- FUHRER, M. S., NYGARD, J., SHIH, L., FORERO, M., YOON, Y. G., MAZZONI, M. S. C., CHOI, H. J., IHM, J., LOUIE,



- S. G., ZETTL, A., MCEUEN, P. L. Crossed nanotube junctions. *Science* **2000**, *288*, 494–497.
- 17 CHEN, R. J., BANGSARUNTIP, S., DROUVALAKIS, K. A., SHI KAM, N. W., SHIM, M., LI, Y., KIM, W., UTZ, P. J., DAI, H. J. Noncovalent functionalization of carbon nanotubes for highly specific electronic biosensors. *Proc. Natl. Acad. Sci. U.S.A.* **2003**, *100*, 4984–4989.
- 18 WANG, J., LIU, G., JAN, M. R., ZHU, Q. Electrochemical detection of DNA hybridization based on carbon-nanotubes loaded with CdS tags. *Electrochem. Commun.* **2003**, *5*, 1000–1004.
- 19 MITCHELL, D. T., LEE, S. B., TROFIN, L., LI, N., NEVANEN, T. K., SÖDERLUND, H., MARTIN, C. R. Smart nanotubes for bioseparations and biocatalysis. *J. Am. Chem. Soc.* **2002**, *124*, 11 864–11 865.
- 20 PARK, K. H., CHHOWALLA, M., IQBAL, Z., SESTI, F. Single-walled carbon nanotubes are a new class of ion channel blockers. *J. Biol. Chem.* **2003**, *278*, 50 212–50 216.
- 21 HU, H., NI, Y., MONTANA, V., HADDON, R. C., PARPURA, V. Chemically functionalized carbon nanotubes as substrates for neuronal growth. *Nano Lett.* **2004**, *4*, 507–511.
- 22 MATTERSON, M. P., HADDON, R. C., RAO, A. M. Molecular functionalization of carbon nanotubes and use as substrates for neuronal growth. *J. Mol. Neurosci.* **2000**, *14*, 175–182.
- 23 MCKENZIE, J. L., WAID, M. C., SHI, R., WEBSTER, T. J. Decreased functions of astrocytes on carbon nanofiber materials. *Biomaterials* **2004**, *25*, 1309–1317.
- 24 WANG, J., LIU, G., JAN, M. R. Ultrasensitive electrical biosensing of proteins and DNA: Carbon-nanotube derived amplification of the recognition and transduction events. *J. Am. Chem. Soc.* **2004**, *126*, 3010–3011.
- 25 SITHARAMAN, B., KISSELL, K. R., HARTMAN, K. B., TRAN, L. A., BAIKALOV, A., RUSAKOVA, I., SUN, Y., KHANT, H. A., LUDTKE, S. J., CHIU, W., LAUS, S., TÓTH, É., HELM, L., MERBACH, A. E., WILSON, L. J. Superparamagnetic gadonanotubes are high performance MRI contrast agents. *Chem. Commun.* **2005**, 3915–1917.
- 26 DWYER, C., GUTHOLD, M., FALVO, M., WASHBURN, S., SUPERFINE, R., ERIE, D. DNA-functionalized single-walled carbon nanotubes. *Nanotechnology* **2002**, *13*, 601–604.
- 27 CAI, H., CAO, X. N., JIANG, Y., HE, P. G., FANG, Y. Z. Carbon nanotube-enhanced electrochemical DNA biosensor for DNA hybridization detection. *Anal. Bioanal. Chem.* **2003**, *375*, 287–293.
- 28 PANTAROTTO, D., PARTIDOS, C. D., HOEBEKE, J., BROWN, F., KRAMER, E., BRIAND, J.-P., MULLER, S., PRATO, M., BIANCO, A. Immunization with peptide-functionalized carbon nanotubes enhances virus-specific neutralizing antibody responses. *Chem. Biol.* **2003**, *10*, 961–966.
- 29 CHEN, R. J., ZHANG, Y., WANG, D., DAI, H. J. Noncovalent sidewall functionalization of single-walled carbon nanotubes for proteins immobilization. *J. Am. Chem. Soc.* **2001**, *123*, 3838–3839.
- 30 SHIM, M., SHI KAM, N. W., CHEN, R. J., DAI, H. J. Functionalization of carbon nanotubes for biocompatibility and biomolecular recognition. *Nano Lett.* **2002**, *2*, 285–288.
- 31 DUBRUEL, P., CHRISTIAENS, B., ROSSENEU, M., VANDEKERCKHOVE, J., GROOTEN, J., GOOSSENS, V., SCHACHT, E. Buffering properties of cationic polymethacrylates are not the only key to successful gene delivery. *Biomacromolecules* **2004**, *5*, 379–388.
- 32 SHI KAM, N. W., O'CONNELL, M., WISDOM, J. A., DAI, H. J. Carbon nanotubes as multifunctional biological transporters and near-infrared agents for selective cancer cell destruction. *Proc. Natl. Acad. Sci. U.S.A.* **2005**, *102*, 11 600–11 605.
- 33 <http://nano.cancer.gov/>
- 34 [http://www.nsf.gov/news/priority\\_areas/](http://www.nsf.gov/news/priority_areas/)

- 35 <http://nihroadmap.nih.gov/>
- 36 <http://pubs.acs.org/cen/coverstory/8148/8148counterpoint.html>
- 37 SANO, M., KAMINO, A., OKAMURA, J., SHINKAI, S. Self-organization of PEO-graft-single-walled carbon nanotubes in solutions and Langmuir-Blodgett films. *Langmuir* **2001**, *17*, 5125–5128.
- 38 BANERJEE, S., WONG, S. S. Structural characterization, optical properties, and improved solubility of carbon nanotubes functionalized with Wilkinson's catalyst. *J. Am. Chem. Soc.* **2002**, *124*, 8940–8948.
- 39 POMPEO, F., RESASCO, D. E. Water solubilization of single-walled carbon nanotubes by functionalization with glucosamine. *Nano Lett.* **2002**, *2*, 369–373.
- 40 BAHR, J. L., MICKELSON, E. T., BRONIKOWSKI, M. J., SMALLEY, R. E., TOUR, J. M. Dissolution of small diameter single-wall carbon nanotubes in organic solvents? *Chem. Commun.* **2001**, *1*, 193–194.
- 41 SUN, Y., WILSON, S. R., SCHUSTER, D. I. High dissolution and strong light emission of carbon nanotubes in aromatic amine solvents. *J. Am. Chem. Soc.* **2001**, *123*, 5348–5349.
- 42 YURELI, K., MITCHELL, C. A., KRISHNAMOORTI, R. Small-angle neutron scattering from surfactant-assisted aqueous dispersions of carbon nanotubes. *J. Am. Chem. Soc.* **2004**, *126*, 9902–9903.
- 43 MATARREDONA, O., RHOADS, H., LI, Z. R., HARWELL, J. H., BALZANO, L., RESASCO, D. E. Dispersion of single-walled carbon nanotubes in aqueous solutions of the anionic surfactant NaDDBS. *J. Phys. Chem. B* **2003**, *107*, 13 357–13 367.
- 44 O'CONNELL, M. J., BACHILO, S. M., HUFFMAN, C. B., MOORE, V. C., STRANO, M. S., HAROZ, E. H., RIALON, K. L., BOUL, P. J., NOON, W. H., KITTRELL, C., MA, J., HAUGE, R. H., WEISMAN, R. B., SMALLEY, R. E. Band gap fluorescence from individual single-walled carbon nanotubes. *Science* **2002**, *297*, 593–596.
- 45 O'CONNELL, M. J., BOUL, P., ERICSON, L. M., HUFFMAN, C., WANG, Y., HAROZ, E., KUPER, C., TOUR, J., AUSMAN, K. D., SMALLEY, R. E. Reversible water-solubilization of single-walled carbon nanotubes by polymer wrapping. *Chem. Phys. Lett.* **2001**, *342*, 265–271.
- 46 RAO, R., LEE, J., LU, Q., KESKAR, G., FREEDMAN, K. O., FLOYD, W. C., RAO, A. M., KE, P. C. Single-molecule fluorescence microscopy and Raman spectroscopy studies of RNA bound carbon nanotubes. *Appl. Phys. Lett.* **2004**, *85*, 4228–4230.
- 47 STRANO, M. S., ZHENG, M., JAGOTA, A., ONOA, G. B., HELLER, D. A., BARONE, P. W., USREY, M. L. Understanding the nature of the DNA-assisted separation of single-walled carbon nanotubes using fluorescence and Raman spectroscopy. *Nano Lett.* **2004**, *4*, 543–550.
- 48 WANG, H., ZHOU, W., HO, D. L., WINEY, K. I., FISCHER, J. E., GLINKA, C. J., HOBBI, E. K. Dispersing single-walled carbon nanotubes with surfactants: A small angle neutron scattering study. *Nano Lett.* **2004**, *4*, 1789–1793.
- 49 ZHENG, M., JAGOTA, A., SEMKE, E. D., DINER, B. A., MCLEAN, R. S., LUSTIG, S. R., RICHARDSON, R. E., TASSI, N. G. DNA-assisted dispersion and separation of carbon nanotubes. *Nat. Mater.* **2003**, *2*, 338–342.
- 50 JELINEK, A. and KLOCKING, H. P. In vitro toxicity of surfactants in U937 cells: Cell membrane integrity and mitochondrial function. *Exp. Toxicol. Pathol.* **1998**, *50*, 472–476.
- 51 TASIS, D., TAGMATARCHIS, N., GEORGAKILAS, V., PRATO, M. Soluble carbon nanotubes. *Chem. Eur. J.* **2003**, *9*, 4000–4008.
- 52 LIU, J., RINZLER, A. G., DAI, H., HAFNER, J. H., BRADLEY, R. K., BOUL, P. J., LU, A., IVERSON, T., SHELIMOV, K., HUFFMAN, C. B., RODRIGUEZ-MACIAS, F., SHON, Y.-S., LEE, T. R., COLBERT, D. T., SMALLEY, R. E. Fullerene pipes. *Science* **1998**, *280*, 1253–1255.
- 53 LIU, Z., SHEN, Z., ZHU, T., HOU, S., YING, L., SHI, Z., GU, Z. Organizing single-walled carbon nanotubes on

- gold using a wet chemical self-assembling technique. *Langmuir* **2000**, *16*, 3569–3573.
- 54 DIAO, P., LIU, Z., WU, B., NAN, X., ZHANG, J., WEI, Z. Chemically assembled single-wall carbon nanotubes and their electrochemistry. *ChemPhysChem* **2002**, *3*, 898–901.
- 55 WILLIAMS, K. A., VEENHUIZEN, P. T. M., DE LA TORRE, B. G., ERITJA, R., DEKKER, C. Carbon nanotubes with DNA recognition. *Nature* **2002**, *420*, 761.
- 56 CHEN, Y., HADDON, R. C., FANG, S., RAO, A. M., EKLUND, P. C., LEE, W. H., DICKEY, E. C., GRULKE, E. A., PENDERGRASS, J. C., CHAVAN, A., HALEY, B. E., SMALLEY, R. E. Chemical attachment of organic functional groups to single-walled carbon nanotube material. *J. Mater. Res.* **1998**, *13*, 2423–2431.
- 57 CHEN, J., HAMON, M. A., HU, H., CHEN, Y., RAO, A. M., EKLUND, P. C., HADDON, R. C. Solution properties of single-walled carbon nanotubes. *Science* **1998**, *282*, 95–98.
- 58 BOUL, P. J., LIU, J., MICKELSON, E. T., HUFFMAN, C. B., ERICSON, L. M., CHIANG, I. W., SMITH, K. A., COLBERT, D. T., HAUGE, R. H., MARGRAVE, J. L., SMALLEY, R. E. Reversible sidewall functionalization of buckytubes. *Chem. Phys. Lett.* **1999**, *310*, 367–372.
- 59 GU, Z., PENG, H., HAUGE, R. H., SMALLEY, R. E., MARGRAVE, J. L. Cutting single-wall carbon nanotubes through fluorination. *Nano Lett.* **2002**, *2*, 1009–1013.
- 60 BAHR, J. L., TOUR, J. M. Covalent chemistry of single-wall carbon nanotubes. *J. Mater. Chem.* **2002**, *12*, 1952–1958.
- 61 KOOI, S. E., SCHLECHT, U., BURGHARD, M., KERN, K. Electrochemical modification of single carbon nanotubes. *Angew. Chem.* **2002**, *114*, 1409–1411.
- 62 HIRSCH, A. Funktionalisierung von einwandigen Kohlenstoffnanoröhren. *Angew. Chem.* **2002**, *114*, 1933–1999.
- 63 AHN, C. C., YE, Y., RATNAKUMAR, B. V., WITHAM, C., BOWMAN, JR., R. C., MAGGINI, M., SCORRANO, G., PRATO, M. Addition of azomethine ylides to C60: Synthesis, characterization, and functionalization of fullerene pytrollidines. *J. Am. Chem. Soc.* **1993**, *115*, 9798–9799.
- 64 CHOI, M., DOWNES, P., HULMAN, M., ROTH, S., STEPANEK, I., BERNIER, P., GEORGAKILAS, V., KORDATOS, K., PRATO, M., GULDI, D. M., HOLZINGER, M., HIRSCH, A. Organic functionalization of carbon nanotubes. *J. Am. Chem. Soc.* **2002**, *124*, 760–761.
- 65 KORDATOS, K., DA ROS, T., BOSI, S., VAZQUEZ, E., BERGAMIN, M., CUSAN, C., PELLARINI, F., TOMBERLI, V., BAITI, B., PANTAROTTO, D., GEORGAKILAS, V., SPALLUTO, G., PRATO, M. Novel versatile fullerene synthons. *J. Org. Chem.* **2001**, *66*, 4915–4920.
- 66 LU, Q., FREEDMAN, K. O., RAO, R., HUANG, G., LEE, J., LARCOM, L. L., RAO, A. M., KE, P. C. Diffusion of carbon nanotubes with single-molecule fluorescence microscopy. *J. Appl. Phys.* **2004**, *96*, 6772–6775.
- 67 WU, Y., HUDSON, J. S., LU, Q., MOORE, J. M., MOUNT, A. S., RAO, A. M., ALEXOV, E., KE, P. C. Coating single-walled carbon nanotubes with phospholipids. *J. Phys. Chem. B* **2006**, *110*, 2475–2478.
- 68 LU, Q., MOORE, J. M., HUANG, G., MOUNT, A. S., RAO, A. M., LARCOM, L. L., KE, P. C. RNA polymer translocation with single-walled carbon nanotubes. *Nano Lett.* **2004**, *4*, 2473–2477.
- 69 RICHARD, C., BALAVOINE, F., SCHULTZ, P., EBBESEN, T. W., MIOSKOWSKI, C. Supramolecular self-assembly of lipid derivatives on carbon nanotubes. *Science* **2003**, *300*, 775–778.
- 70 LICHTENBERG, D., GONI, F. M., HEERKLOTZ, H. Detergent-resistant membranes should not be identified with membrane rafts. *Trends Biochem. Sci.* **2005**, *30*, 430–436.
- 71 GAO, H., KONG, Y., CUI, D. Detergent-resistant membranes should not be identified with membrane rafts. *Nano Lett.* **2003**, *3*, 471–473.
- 72 ZHENG, M., JAGOTA, A., STRANO, M. S., SANTOS, A. P., BARONE, P., CHOU,

- S. G., DINER, B. A., DRESSELHAUS, M. S., MCLEAN, R. S., ONOA, G. B., SAMSONIDZE, G. G., SEMKE, E. D., USREY, M., WALLS, D. J. Structure-based carbon nanotube sorting by sequence-dependent DNA assembly. *Science* **2003**, 302, 1545–1548.
- 73 ILLANGASEKARE, M., SANCHEZ, G., NICKLES, T., YARUS, M. Aminoacyl-RNA synthesis catalyzed by an RNA. *Science* **1995**, 267, 643–647.
- 74 LOHSE, P. A., SZOSTAK, J. W. Ribozyme-catalysed amino-acid transfer reactions. *Nature* **1996**, 381, 442–444.
- 75 TARASOW, T. M., TARASOW, S. L., EATON, B. E. RNA-catalysed carbon-carbon bond formation. *Nature* **1997**, 389, 54–57.
- 76 ZHANG, B. L., CECH, T. R. Peptide bond formation by in vitro selected ribozymes. *Nature* **1997**, 390, 96–100.
- 77 GUGLIOTTI, L. A., FELDHEIM, D. L., EATON, B. E. RNA-mediated metal-metal bond formation in the synthesis of hexagonal palladium nanoparticles. *Science* **2004**, 304, 850–852.
- 78 MCMANUS, M. T., SHARP, P. A. Gene silencing in mammals by small interfering RNAs. *Nat. Rev./Genet.* **2002**, 3, 737–747.
- 79 CARTER, D. C., HO, J. X. Structure of serum albumin. *Protein Chem.* **1994**, 45, 153–203.
- 80 SCHULTZ, G. J., SCHINDLER, H., SCHMIDT, T. Single-molecule microscopy on model membranes reveals anomalous diffusion. *Biophys. J.* **1997**, 73, 1073–1080.
- 81 KE, P. C., NAUMANN, C. A. Hindered diffusion in polymer-tethered phospholipid monolayers at the air-water interface: A single molecule fluorescence imaging study. *Langmuir* **2001**, 17, 5076–5081.
- 82 ISHIJIMA, A., YANAGIDA, T. Single molecule nanobioscience. *Trends Biochem. Sci.* **2001**, 26, 438–444.
- 83 SAXTON, M. J. Anomalous diffusion due to obstacles – A Monte-Carlo study. *Biophys. J.* **1994**, 66, 394–401.
- 84 JOURNET, C., MASER, W. K., BERNIER, P., LOISEAU, A., DELA CHAPELLE, M. L., LEFRANT, S., DENAIRD, P., LEE, R., FISCHER, J. E. Large-scale production of single-walled carbon nanotubes by the electric-arc technique. *Nature* **1997**, 388, 756–758.
- 85 HARTSCHUH, A., PEDROSA, H. N., NOVOTNY, L., KRAUSS, T. D. Simultaneous fluorescence and Raman scattering from single carbon nanotubes. *Science* **2003**, 301, 1354–1356.
- 86 BACHILO, S. M., STRANO, M. S., KITTRELL, C., HAUGE, R. H., SMALLEY, R. E., WEISMAN, R. B. Structure-assisted optical spectra of single-walled carbon nanotubes. *Science* **2002**, 298, 2361–2366.
- 87 EFRON, B., TIBSHIRANI, R. Statistical data analysis in the computer age. *Science* **1991**, 253, 390–395.
- 88 DOI, M., EDWARDS, S. *The Theory of Polymer Dynamics*, Clarendon, Oxford, **1986**.
- 89 TANFORD, C. *Physical Chemistry of Macromolecules*, John Wiley and Sons, New York, **1961**.
- 90 BUSTAMANTE, C., SMITH, S. B., LIPHARD, J., SMITH, D. E. Single-molecule studies of DNA mechanics. *Curr. Opin. Struct. Biol.* **2000**, 10, 279–284.
- 91 DE GENNES, P. G. *Scaling Concepts in Polymer Physics*, 1979, Cornell UP, Ithaca, New York.
- 92 SMITH, D. E., PERKINS, T. T., CHU, S. Self-diffusion of an entangled DNA molecule by reptation. *Phys. Rev. Lett.* **1995**, 75, 4146–4149.
- 93 DUBRUEL, P., CHRISTIAENS, B., ROSSENEU, M., VANDEKERCKHOVE, J., GROOTEN, J., GOOSSENS, V., SCHACHT, E. Buffering properties of cationic polymethacrylates are not the only key to successful gene delivery. *Biomacromolecules* **2004**, 5, 379–388.
- 94 AISSAOUI, A., OUDRHIRI, N., PETIT, L., HAUCHECORNE, M., KAN, E., SAINLOS, M., JULIA, S., NAVARRO, J., VIGNERON, J. P., LEHN, J. M., LEHN, P. Progress in gene delivery by cationic lipids: Guanidinium-cholesterol-based systems as an example. *Curr. Drug Targets* **2002**, 3, 1–16.
- 95 ALLEN, T. M., CULLIS, P. R. Drug delivery systems: Entering the main stream. *Science* **2004**, 303, 1818–1822.

- 96 VERMA, I., SOMIA, N. Gene therapy-promise, problems, and prospects. *Nature* **1997**, *389*, 239–242.
- 97 PANTAROTTO, D., BRIAND, J., PRATO, M., BIANCO, A. Translocation of bioactive peptides across cell membranes by carbon nanotubes. *Chem. Commun.* **2004**, *1*, 16–17.
- 98 SHI KAM, N. W., JESSOP, T. C., WENDER, P. A., DAI, H. J. Nanotube molecular transporters: Internalization of carbon nanotube-protein conjugates into mammalian cells. *J. Am. Chem. Soc.* **2004**, *126*, 6850–6851.
- 99 SALMAN, H., ZBAIDA, D., RABIN, Y., CHATENAY, D., ELBAUM, M. Kinetics and mechanism of DNA uptake into the cell nucleus. *Proc. Natl. Acad. Sci. U.S.A.* **2001**, *98*, 7247–7252.
- 100 PANTAROTTO, D., SINGH, R., MCCARTHY, D., ERHARDT, M., BRAIND, J.-P., PRATO, M., KOSTARELOS, K., BIANCO, A. Functionalized carbon nanotubes for plasmid DNA gene delivery. *Angew. Chem.* **2004**, *43*, 5242–5246.
- 101 LIU, Y., WU, D. C., ZHANG, W. D., JIANG, X., HE, C. B., CHUNG, T. S., GOH, S. H., LEONG, K. W. Poly-ethylenimine-grafted multiwalled carbon nanotubes for secure noncovalent immobilization and efficient delivery of DNA. *Angew. Chem.* **2005**, *44*, 4782–4785.
- 102 WILSON, R. W., BLOOMFIELD, V. A. Counterion-induced condensation of deoxyribonucleic acid. A light-scattering study. *Biochemistry* **1979**, *18*, 2192–2196.
- 103 HARPE, A. V., PETERSEN, H., LI, Y. X., KISSEL, T. Characterization of commercially available and synthesized polyethylenimines for gene delivery. *J. Controlled Release* **2000**, *69*, 309–322.
- 104 SHI KAM, N. W., LIU, Z., DAI, H. J. Functionalization of carbon nanotubes via cleavable disulfide bonds for efficient Intracellular delivery of siRNA and potent gene silencing. *J. Am. Chem. Soc.* **2005**, *127*, 12 492–12 493.
- 105 GILLIES, E. R., FRÉCHET, J. J. M. pH-responsive copolymer assemblies for controlled release of doxorubicin. *Bioconjugate Chem.* **2005**, *16*, 361–368.
- 106 SHI KAM, N. W., DAI, H. J. Carbon nanotubes as intracellular protein transporters: Generality and biological functionality. *J. Am. Chem. Soc.* **2005**, *127*, 6021–6026.
- 107 PANTAROTTO, D., PARTIDOS, C. D., GRAFF, R., HOEBEKE, J., BRIAND, J.-P., PRATO, M., BIANCO, A. Synthesis, structural characterization, and immunological properties of carbon nanotubes functionalized with peptides. *J. Am. Chem. Soc.* **2003**, *125*, 6160–6164.
- 108 GEORGAKILAS, V., TAGMATARCHIS, N., PANTAROTTO, D., BIANCO, A., BRIAND, J.-P., PRATO, M. Amino acid functionalization of water soluble carbon nanotubes. *Chem. Commun.* **2002**, 3050–3051.
- 109 NIELSEN, O., BUCHARDT, O. Facile synthesis of reagents containing a terminal maleimido ligand linked to an active ester. *Synthesis* **1991**, 819–821.
- 110 CAI, J., YANG, J., JONES, D. P. Mitochondrial control of apoptosis: The role of cytochrome c. *Biochim. Biophys. Acta* **1998**, *1366*, 139–149.
- 111 SHVEDOVA, A. A., CASTRANOVA, V., KISIN, E. R., SCHWEGLER-BERRY, D., MURRAY, A. R., GANDELSMAN, V. Z., MAYNARD, A., BARON, P. Exposure to carbon nanotube material; assessment of nanotube cytotoxicity using human keratinocyte cells. *J. Toxicol. Environ. Health, Part A* **2003**, *66*, 1909–1926.
- 112 WARHEIT, D. B., LAURENCE, B. R., REED, K. L., ROACH, D. H., REYNOLDS, G. A. M., WEBB, T. R. Comparative pulmonary toxicity assessment of single-wall carbon nanotubes in rats. *Toxicity Sci.* **2004**, *77*, 117–125.
- 113 LAM, C. W., JAMES, J. T., MCCLUSKEY, R., HUNTER, R. L. Pulmonary toxicity of single-wall carbon nanotubes in mice 7 and 90 days after intratracheal instillation. *Toxicity Sci.* **2004**, *77*, 126–134.
- 114 SAYES, C. M., FORTNER, J. D., GUO, W., LYON, D., BOYD, A. M., AUSMAN, K. D., TAO, Y. J., SITHARAMAN, B., WILSON, L. J., HUGHES, J. B., WEST,

- J. L., COLVIN, V. L. The differential cytotoxicity of water-soluble fullerenes. *Nano Lett.* **2004**, *4*, 1881–1887.
- 115 <http://nanotechweb.org/articles/news/4/11/3/1>
- 116 VAN DER HEIJDEN, A. G., VERHAEGH, G., JANSEN, C. F., SCHALKEN, J. A., WITJES, J. A. The effect of hyperthermia on mitomycin-C induced cytotoxicity in four human bladder cancer cell lines. *J. Urol.* **2005**, *173*, 1375–1380.
- 117 RAAPHORST, G. P., YANG, D. P. The evaluation of thermal cisplatin sensitization in normal and XP human cells using mild hyperthermia at 40 and 41. *Anticancer Res.* **2005**, *25*, 2649–2653.
- 118 TAKAHASHI, I., EMI, Y., HASUDA, S., KAKEJI, Y., MAEHARA, Y., SUGIMACHI, K. Clinical application of hyperthermia combined with anticancer drugs for the treatment of solid tumors. *Surgery*, **2002**, *131*, S78–S84.
- 119 WESTERMANN, A. M., JONES, E. L., SCHEM, B. C., VAN DER STEEN-BANASIK, KOPER, P., MELLA, O., UITTERHOEVE, A. L., DE WIT, R., VAN DER VELDEN, J., BERGER, C., VAN DER WILT, C. L., DAHL, O., PROSNITZ, L. R., VAN DER ZEE, J. First results of triple-modality treatment combining radiotherapy, chemotherapy, and hyperthermia for the treatment of patients with stage IIB, III, and IVA cervical carcinoma. *Cancer*, **2005**, *104*, 763–770.
- 120 YINGHUI, Z., PENG, A. T., CARPENTER, K., MAGUIRE, J. A., HOSMANE, N. S., TAKAGAKI, M. Substituted carborane-appended water-soluble single-wall carbon nanotubes: New approach to boron neutron capture therapy drug delivery. *J. Am. Chem. Soc.*, **2005**, *127*, 9875–9880.
- 121 WILLEMS, A., GAUGER, K., HENRICH, C., HARBECK, N. Antibody therapy for breast cancer. *Anticancer Res.*, **2005**, *25*, 1483–1489.
- 122 JAZIREHI, A. R., BONAVIDA, B. Cellular and molecular signal transduction pathways modulated by rituximab (rituxan, anti-CD20 mAb) in non-Hodgkin's lymphoma: Implications in chemosensitization and therapeutic intervention. *Oncogene*, **2005**, *24*, 2121–2143.
- 123 RAN, S., HE, J., HUANG, X., SOARES, M., SCOTHORN, D., THORPE, P. E. Antitumor effects of a monoclonal antibody that binds anionic phospholipids on the surface of tumor blood vessels in mice. *Clin. Cancer Res.*, **2005**, *11*, 1551–1562.
- 124 HUANG, X., BENNETT, M., THORPE, P. E. A monoclonal antibody that binds anionic phospholipids on tumor blood vessels enhances the antitumor effect of docetaxel on human breast tumors in mice. *Cancer Res.*, **2005**, *65*, 4408–4416.
- 125 IJIMA, S. Helical microtubules of graphitic carbon. *Nature* **1991**, *354*, 56–58.

## 8

# Nanotubes, Nanowires, Nanocantilevers and Nanorods in Cancer Treatment and Diagnosis

*Kiyotaka Shiba*

### 8.1

#### Introduction

The elimination of cancer-related suffering and death remains an unachieved goal of modern medicine, biology, pharmaceutical science and medical engineering. For this fervent wish to become a reality, what is needed is continued progress, and even ground-breaking innovation, in both the diagnosis of cancer and its treatment. Nanotechnologies have come into the spotlight because of their potential for use as novel diagnostic tools that enable detection of primary cancers at their earliest stages, and in new therapeutic protocols that effectively and selectively exterminate malignant cells. The present chapter introduces the current status of efforts to develop nanomaterials for cancer diagnosis and therapy, mainly by focusing on nonspherical (non-particulate) nanomaterials such as nanotubes, nanowires and nanorods. Because various nanomaterials have been discovered since the first observation of carbon nanotubes, the physicochemical properties of carbonaceous as well as non-carbonaceous nanomaterials are introduced first (Section 8.2). Subsequent sections present potential applications of these molecules in cancer diagnosis (Section 8.3) and treatment (Section 8.4). Progress in the development of spherical nanoparticles for these purposes is reviewed in other chapters of this volume.

### 8.2

#### Nanotubes, Nanowires and Nanorods

Nanotubes, nanowires, nanorods, nanotubules, nanoribbons, nanobelts, nano-onion, nanocapsule, graphite cones, nanopolyhedrons and bamboo tubes, among others, are the names that have been given to various, mostly one-dimensional, nanomaterials. Some of them are composed of graphitic tubes (carbon nanomaterials), but others consist of noncarbonic elements. Some are covalently linked molecules, while others are noncovalently linked assemblages of macromolecules.

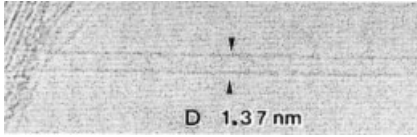


**Fig. 8.1.** Electron micrograph of a single-wall carbon nanotube. (From Ref. [4], with permission.)

This section an overviews the properties of these nonspherical nanomaterials, giving a clue as to their potentially unparalleled utility in some applications.

### 8.2.1

#### Carbon Nanotubes

The discovery of multi-wall carbon nanotubes (MWNTs) by Iijima in 1991 [1] stands as the first of a cascade of brilliant discoveries of various nanomaterials [2, 3]. In 1993, the single-wall carbon nanotube (SWNT), which can be regarded as the simplest form of MWNT, was discovered by Iijima's and other groups [4, 5]. A SWNT is made up of a single layer of graphite molecules rolled up into a hollow cylinder (Fig. 8.1). Though the diameters of these tubes typically range from 1.0 to 1.5 nm [4], nanotubes with diameters of as little as 0.43 nm have been reported [6–8]. MWNTs are tubes composed of two or more concentric cylinders (Fig. 8.2). Those consisting of only two cylinders are often referred to as double-wall carbon nanotubes [9]. Carbon nanotubes are synthesized by (a) laser ablation [10], (b) high-pressure CO conversion (HiPCO) [11], or (c) an

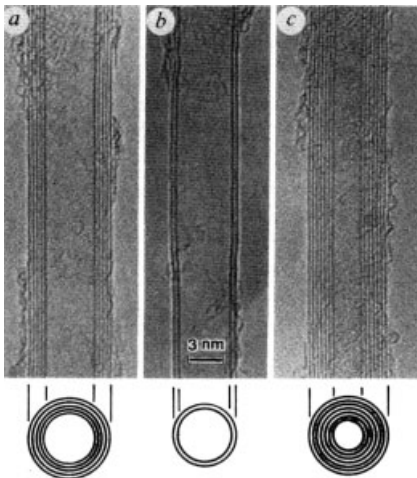


**Fig. 8.2.** Electron micrographs of multi-wall carbon nanotubes. (From Ref. [1], with permission.)



arc-discharge technique [12], and their structures can be dramatically influenced by the conditions under which they are produced, including the metal catalyst used, the temperature, the atmosphere etc. Thus, by applying the appropriate conditions, various SWNT and MWNT derivatives can be obtained, including the nano-onion [13], nanocapsule [14, 15], nanopolyhedron [16], bamboo tube [17], graphite cone [18] and nanohorn [19].

Attractive properties of carbon nanotubes include their high electrical and thermal conductivity, their great tensile strength and their very high elastic modulus [20]. In particular, the electrical properties of nanotubes have received a great deal of attention in nanodevice research. SWNTs can be metallic or semiconducting, depending upon their diameter and chiral angle [21–23], which means that they can act as a molecular wire [24, 25] or as a transistor [26–28]. Indeed, a logic circuit composed of SWNT field-effect transistors (FETs) has been developed [29], and the bottom-up fabrication of such nanoscale block units is expected to break the size limitation that current lithographic technology is encountering.

The electrical conductance [30–33] and capacitance [34], the optical properties [35] and the stiffness [36] of nanotubes have all been shown to be altered by surface adsorption of various molecules. In addition, by integrating the sensing abilities of nanotubes into logic circuits, nanoscale biosensors could be designed that simultaneously quantitate different biomolecules (e.g., mRNAs, proteins and metabolic products) and then give a cue for action (e.g., drug release or signal generation) based on programmed logic. The advent of such devices should revolutionize cancer diagnosis and treatment (Section 8.3.1).

The strength and stiffness of SWNT or MWNTs [37] have also been explored with the aim of developing novel materials, such as carbon nanotube paper [38, 39], film [40, 41], fibers [42], gel [43], nanotube–collagen composite [44], and nanotube–polyurethane composites [45]. One possible use of these materials is as a scaffold for cell growth [46–49], which may indirectly affect cancer treatment as well as regenerative medicine.

### 8.2.2

#### **Noncarbon Nanotubes**

Graphite-like layered structures can also be formed from elements other than carbon, and an array of noncarbon nanotubes have been fabricated from boron nitride (BN) [50, 51], nickel chloride ( $\text{NiCl}_2$ ), niobium disulfide ( $\text{NbS}_2$ ) [52] and molybdenum disulfide ( $\text{MoS}_2$ ) [53], and even a multielement (boron nitride and carbon) coaxial nanotube [54] has been synthesized. Applications that take advantage of the unique properties of these materials are currently being explored.

### 8.2.3

#### **Single-wall Carbon Nanohorns**

Single-wall nanohorns (SWNHs) were discovered in 1999 and are thus relatively new members of the carbon nanomaterial family [19]. They are spherical struc-

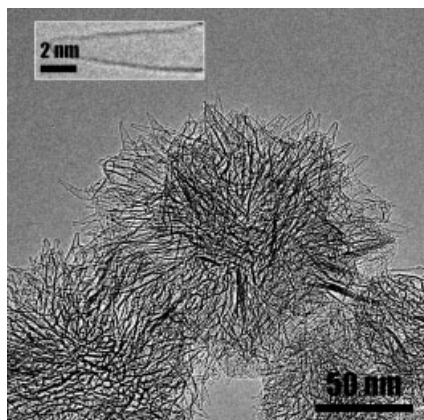


**Fig. 8.3.** Electron micrograph of single-wall carbon nanohorns. (Courtesy of Professor S. Iijima and Dr. M. Yudasaka.)

tures with diameters of 80–100 nm, but their constituent parts are graphene nanotubes – i.e., they are spherical aggregates of carbon nanotubes (Fig. 8.3). The constitutive tubes have closed ends with cone-shaped caps (horns) and have diameters of 2–3 nm, which is larger than the typical SWNT. SWNHs have extensive surface areas and multitudes of horn interstices, which enable large numbers of guest molecules to be adsorbed. In addition, as with carbon nanotubes [55, 56], oxidation or acid treatment can be used to create nano-windows in the walls of SWNHs, through which small molecules (e.g.,  $N_2$ , Ar,  $C_{60}$  etc.) can infiltrate their interior space. Furthermore, the size of the pores can be controlled by appropriately controlling the treatment conditions, enabling the preparation of a series of oxidized SWNHs (oxSWNHs) having distinct molecular sieving effects. Oxidation also introduces functional oxygen groups (e.g., carboxyl and quinone groups) at the pore-edges of oxSWNHs, to which various chemical compounds [e.g., biotin and poly(ethylene glycol)] can be coupled to functionalize the surfaces.

In contrast to the synthesis of other carbon nanomaterials, the synthesis of SWNHs (laser ablation of graphite) does not require a metal catalyst. This enables production of extremely pure preparations with no potential for toxicity from contaminating metals. These unique properties are particularly noteworthy because they suggest the feasibility of using SWNHs as carriers in drug delivery systems (see Section 8.4.1).

#### 8.2.4

#### **Nanorods and Nanowires**

Whereas nanotubes are hollow cylinders composed of rolled-up single molecular layers, nanorods and nanowires are not hollow. One way to form these structures is to use capillary action to fill the interior space of carbon nanotubes, e.g., with

lead [57] or bismuth [55]. Arc discharge in the presence of metals has also been used to fill carbon nanotubes with Y [58], Mn [59], Gd [60], T, Cr, Fe, Cp, Ni, Cu, Zn, Mo, Pd, Sn Ta, W, Dy or Yb [61]. In addition, reacting carbon nanotubes with volatile metal or nonmetal complexes produces carbide (TiC, NbC, Fe<sub>3</sub>C, SiC and BC) nanorods [62]. Similarly, reacting Ga<sub>2</sub>O vapor with NH<sub>3</sub> gas in the presence of carbon nanotubes yields GaN nanorods [63], while analogous reactions have been used to synthesize Si<sub>3</sub>N<sub>4</sub> nanorods [63] and oriented silicon carbide nanowires [64].

Various other approaches to the fabrication of nanorods (nanowires) that do not require nanotubes have also been developed, yielding GaN nanorods [65, 66], silicon nanowires (SiNW) [67, 68] and indium phosphate nanowires [69]. The nanorods obtained were either single crystal [62, 63, 65–67, 70], polycrystalline [62] or amorphous [62], depending upon the method and materials used [62].

### 8.2.5

#### Self-assembled Nanotubes

Self-assembly from smaller molecular blocks is an alternative approach to synthesizing nanotubular structures. Formation of such structures from lipid molecules was first reported some time ago [71, 72], and has recently been garnering attention as a tool for microfabrication [73–75]. Peptides represent another set of molecules that can be assembled into tubular structures [76, 77]. In contrast to lipid tubes, peptide tubes are nanometer scale structures, the diameters of which can be fine tuned through appropriate design [78]. What is more, casting ionic metal into a peptide nanotube fabricated from dipeptide building blocks has been used to form metal nanowires with diameters of only 20 nm [79] (Fig. 8.4). Block copolymers are also versatile for fabricating various types of microstructures, including tubes [80, 81], vesicles [82] and toroidal structures [83], among others.

Lipid, peptide and polymer self-assemblages, along with natural proteinous assemblages, are generally highly biocompatible, so their utility as nano-carriers of drugs, antigens and genes is currently being investigated. They also have been used as templates for inorganic wires fabricated through deposition of various inorganic nanocrystals upon them [84–92].

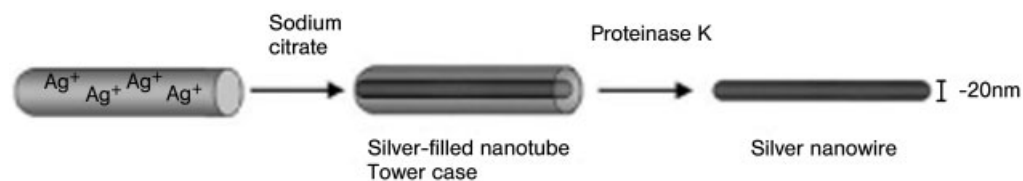


**Fig. 8.4.** Silver nanowires were formed by the reduction of silver ions within the peptide nanotubes, followed by enzymatic degradation of the peptide mold. (From Ref. [79], with permission.)

### 8.3 Cancer Diagnosis

The recent and rapid progress in genomic medicine has required innovative solutions for high-throughput and parallel identification and/or quantification of large numbers of biomolecules, including mRNA, proteins and metabolites [93, 94]. Microarray technology combined with fluorescence detection would be one of the most popular tools for such high-throughput genomic analysis [95–97]; however, that methodology does not yet have sufficient sensitivity or usability. But by using nanomaterials, a new type of ultrasensitive high-density sensor array could be fabricated. Although such next-generation nanosensors are still in an early phase of development, some elemental technologies have already been shown to work.

#### 8.3.1 Carbon Nanotube-based Detection System

As described in Section 8.2.1, the physicochemical properties of carbon nanotubes can be changed by adsorption of molecules onto their surfaces. The nanotube sensor was first demonstrated as a FET-based gas sensor, in which the electrical resistance of a semiconducting SWNT was altered by exposure to electron-withdrawing  $\text{NO}_2$  or  $\text{O}_2$  or to electron-donating  $\text{NH}_3$  molecules [30, 31, 98]. Since then, SWNT-based FETs have been exploited as biosensors through functionalization of the tube surfaces using various biomolecules. For instance, when the surface was modified with biotin, the electronic properties of the resultant biotin–SWNT were altered upon addition of streptavidin (a protein that strongly binds to biotin) [99]. Similarly, when glucose oxidase was immobilized on the surface of SWNTs, the resultant sensor showed increased conductance upon addition of 0.1 M glucose (a substrate of glucose oxidase), probably reflecting a conformational change in the enzyme [100] (Fig. 8.5). Finally, human U1A RNA splicing factor is an antigen in autoimmune diseases such as systemic lupus erythematosus, and detection of autoantibodies against this protein is a diagnostic criterion for the disease. When U1A protein was immobilized on the surface of SWNTs, the binding of a monoclonal anti-U1A antibody at concentrations of less than 1 nM was detected as an electric signal [33], making this construct suitable for development of an ultrasensitive and label-free diagnostic system.

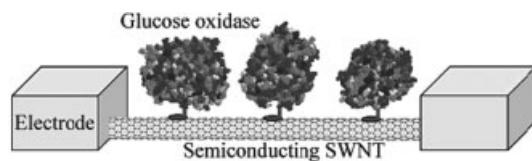


**Fig. 8.5.** Enzyme-coated carbon nanotubes as biosensors. Two electrodes connect a semiconducting SWNT with glucose oxidase immobilized on its surfaces. (From Ref. [100], with permission.)

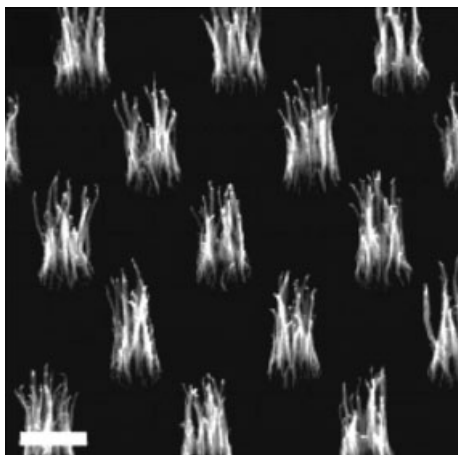


**Fig. 8.6.** Carbon nanotube nanoelectrode array. MWNT arrays were grown on Ni spots defined by UV lithography. (From Ref. [104], with permission.)

RNA, DNA and peptide molecules that bind to specific target substances are termed aptamers [101–103]. They are artificially created using *in vitro* evolution systems in the order-made manner, and a myriad of aptamers have already been generated against a wide variety of biomacromolecules and inorganic substances. Such aptamers can be used to functionalize the surface of nanotubes to prepare sensors for target substances. For instance, when a DNA aptamer against thrombin [102] was immobilized on the surfaces of SWNTs, the aptamer–SWNT FETs worked as a thrombin sensor. In addition, because aptamers are generally much smaller than antibodies, they could be used to fabricate sensors that are both cheaper and more space-efficient than those fabricated from antibodies.

Another type of ultrasensitive DNA/RNA sensor that has been proposed is one in which nanoelectrode arrays composed of MWNTs having one tip modified with oligonucleotides with specifically designed sequences are fabricated on a SiO<sub>2</sub> matrix [104] (Fig. 8.6). The hybridization of sub-attomole amounts of single strand DNAs could then be detected as a electronic signal using the Ru(bpy)<sub>3</sub><sup>2+</sup>-mediated guanine oxidation method [105]. Such arrays of nanotubes should be easy to construct on silicon tips, thereby providing the opportunity to develop multiplexed detection systems [104].

### 8.3.2

#### **Non-carbon Nanotube-based Detection Systems**

Though carbon nanotubes are highly promising materials with which to construct nanosensors, they also have some limitations. For instance, existing methods of synthesis produce mixtures of metallic and semiconducting SWNTs, necessitating their efficient separation before defined nanosensors can be constructed. This

makes noncarbonaceous tubes or wires attractive, as most of them require no separation step. For instance, silicon nanowires (SiNWs, Section 8.2.4) [67, 68] are always semiconducting, and their surfaces are easily modified. When the surfaces of boron-doped SiNWs are modified with 3-aminopropyltriethoxysilane (APTES) and connected to source and drain electrodes, the nanowires function as pH-sensing FETs [106]. Similarly, biotin- and calmodulin-immobilized SiNWs function, respectively, as anti-biotin antibodies and  $\text{Ca}^{2+}$  FET sensors. A SiNW-based ultrasensitive DNA sensor has also been developed by functionalizing the surfaces of SiNWs with a PNA (peptide nucleic acid) that recognizes the gene for the cystic fibrosis transmembrane receptor [107]. Here, the conductance of the nanowire increased upon PNA–DNA hybridization. Thus, highly sensitive, real-time nanosensors can be fabricated using SiNW [106].

In addition to SiNW, metal oxide nanowires are also attractive candidates for the fabrication of nanosensors. For instance,  $\text{In}_2\text{O}_3$  NWs with immobilized anti-PSA (prostate-specific antigen) antibodies on their surfaces showed enhanced conductivity upon exposure to PSA [108]. Interestingly, a similar SWNT-based sensor showed suppressed conductivity upon exposure to PSA, enabling complementary detection of PSA antigen with these two devices [108].

### 8.3.3

#### Microcantilevers

Whereas nanotube- or nanowire-based sensors transduce biomolecular recognition into changes in electrical conductance [30, 31] and capacitance [34] or changes in optical properties [35], microcantilevers transduce that recognition into the nanomechanical bending of a cantilever, which can be measured *in situ* using optical beam detection [109–111]. Microcantilevers are generally made of silicon nitride that is coated on one side with a thin film of gold (Fig. 8.7). They can be constructed using low-cost semiconductor microfabrication processes, thus offering an ideal platform for high-throughput molecular analysis. For instance, a cantilever on which anti-PSA antibody was immobilized could detect free PSA at a concentration of  $0.2 \text{ ng mL}^{-1}$  against a background of human serum albumin and plasminogen at concentrations of  $1 \text{ mg mL}^{-1}$ . Thus, this technique could compete with

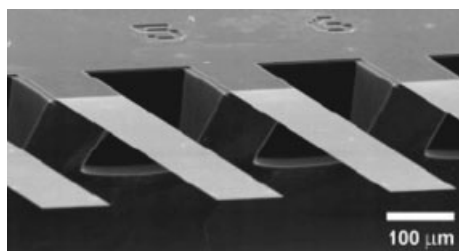


**Fig. 8.7.** Scanning electron micrograph of a section of silicon nanocantilever. (From Ref. [110], with permission.)

ELISA-based diagnoses. Notably, however, although the movement of these cantilevers is on a nanometer scale, a typical microcantilever is 200  $\mu\text{m}$  long, 0.5  $\mu\text{m}$  thick and 20  $\mu\text{m}$  wide, making it difficult to prepare dense arrays of such sensors.

### 8.3.4

#### Nano-tag made of Nanorods

Arraying addressable sensors on a miniaturized tip is one approach to constructing a multiplexed detection system. Other approaches include the simultaneous labeling of several biomolecules with distinctive molecular barcodes, which could be produced with the necessary diversity using nanorods [112, 113]. Sequential electrochemical deposition enables construction of combinatorial striping patterns using gold and silver nanorods, which then could be detected and read using light microscopy (Fig. 8.8). Theoretically, 4160 signatures could be generated from 13-segment, 6.5- $\mu\text{m}$ -long barcodes.

## 8.4

### Cancer Treatment

While nanotube-based diagnosis systems are still at their early stages of development, nanotube-based approaches to cancer treatment are at the experimental

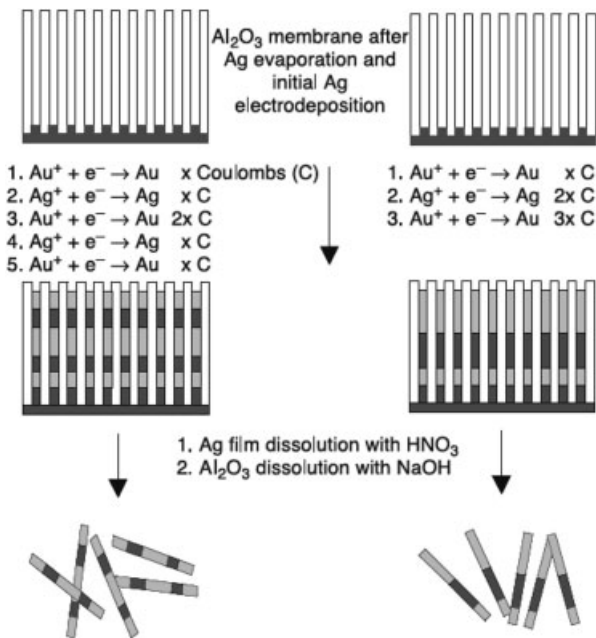


Fig. 8.8. Synthesis of multimetal barcodes. (From Ref. [112], with permission.)

stage. By focusing on drug delivery and imaging systems, several ongoing efforts to make the most of the potential of nanotubes in this area will be introduced.

#### 8.4.1

##### **Carriers for Drug Delivery Systems**

Although synthetic polymers, lipids and peptides are attracting much attention from those involved in the development of drug delivery systems, new classes of materials constructed from carbon nanotubes may also be suitable for drug, protein and gene delivery. Early observations have shown that fluorescently labeled nanotubes are automatically taken up by cells [114]. This internalization of SWNTs, e.g., by HL60 and Jurkat cells, appears to be mediated by endocytosis, leading to accumulation of SWNTs in the cytoplasm [115]. Moreover, when SWNTs are covalently modified with a peptide from the foot-and-mouth disease virus, they elicit a humoral immune response in mice [116]. Likewise, nanotube-based systems also have been shown to mediate gene delivery in similar fashion [117–119]. In addition to genes and DNA, unmethylated CpG motif [120], which is known to confer nonspecific protection against various intracellular pathogens and siRNAs [121] (small RNAs that interfere with the expression of a target gene), has been linked to SWNTs that were then used to deliver the motif into mammalian cells.

SWNHs (Section 8.2.3) are unique among nanomaterials because their constituent parts clearly belong to the nanotube-family, but their overall structure is spherical (Fig. 8.3). The diameters of these spheres, about 80–100 nm, suggests they could show enhanced permeation and retention (EPR) effects [122, 123] and thus could accumulate within solid tumors showing neovascularity. Furthermore, as the synthesis of SWNHs does not require a metal catalyst [124], extremely pure preparations with no contaminating metals can be obtained [125], which would seem to make SWNHs an excellent candidate to be a carrier in a drug delivery system. Indeed, it already has been shown that oxidized SWNHs can adsorb dexamethasone to approximately  $200 \text{ mg mL}^{-1}$  and then slowly release the drug in saline buffer [126]. In addition, peptide aptamers [127] could be used to functionalize the surface of SWNHs and prepare composite materials having multifunctionality [128].

#### 8.4.2

##### **Imaging Agents**

New imaging agents that utilize nanomaterials have also been developed, and one using spherical nanoparticles has already shown good results. For example, dextran-coated ultrasmall superparamagnetic iron oxide (USPIO) nanoparticles have been used to image lymph nodes containing micrometastases in patients with prostate cancer [129]. The development of nanotube-based imaging agents is still at a primitive stage, but the intrinsic near-infrared (NIR) fluorescence of SWNTs [130–132] is an attractive property, as tissue and biological fluids are transparent to NIR light [133], perhaps making it possible to use SWNTs as a new class of bioprobe [134, 135] (Fig. 8.9).



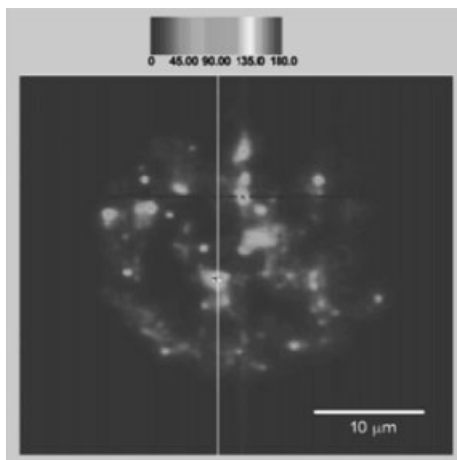


**Fig. 8.9.** Fluorescence image of cell-engulfed SWNT between 1125 and 1600 nm with excitation at 660 nm. (From Ref. [134], with permission.)

Multifunctional molecules that can be used for both diagnosis and treatment should be the ultimate objective of nano-medical material development [136]. For instance, spherical multimodal composites composed of gold-coated nanoparticles containing a dielectric silicon core coated with PEG and a cancer-targeting ligand, Her2, have already been developed. Through illumination with NIR, this composite material has been successfully used to reveal microscopic tumors in breast, and then, by increasing the power of the NIR beam (820 nm), the particle's temperature was increased enough to induce irreversible heat damage to the carcinoma cells [137]. Recently, a similar multifunctional agent was constructed from SWNTs [135]. In that case, SWNTs were functionalized with a folate moiety known to target tumor-associated antigen [138], and were selectively taken up by cells expressing folate receptor. Cells that internalized the SWNT were killed by irradiation with NIR [135].

## 8.5

### Conclusions

Carbon nanotubes and related structures (e.g., nanowires and nanorods) are a recent discovery, and it will take time before materials and protocols that are clinically applicable for the diagnosis and treatment of cancer are developed. Nevertheless, these materials obviously have unique properties, which should soon lead to the development of radically new nanodevices.

Although not introduced in this chapter, a family of nanotubes is currently being investigated with the aim of making new devices that could indirectly influence

cancer diagnosis and cancer therapy. These include probe tips for atomic-force microscopy (AFM) [139–141], ion channel blockers [142], and microcantilevers for medical catheter applications [36], among others.

Finally, careful attention needs to be paid to the potential toxicity of nanomaterials. So far, studies of their toxicity have produced conflicting results [143–148]. Clearly, much additional study of the metabolic pathway taken by nanomaterials in the body [149] and their potential toxicity will need to be carried out before their clinical use becomes practical.

## References

- 1 IIJIMA, S., Helical microtubules of graphitic carbon., *Nature* **1991**, 354, 56–58.
- 2 IIJIMA, S., Carbon nanotubes: Past, present, and future., *Physica B* **2002**, 323, 1–5.
- 3 TENNE, R., RAO, C. N., Inorganic nanotubes., *Phil. Trans. R. Soc. London A* **2004**, 362, 2099–2125.
- 4 IIJIMA, S., ICHIHASHI, T., Single-shell carbon nanotubes of 1-nm diameter., *Nature* **1993**, 363, 603–605.
- 5 BETHUNE, D. S., KIANG, C. H., DeVRIES, M. S., GORMAN, G., SAVOY, R., BEYERS, R., Cobalt-catalysed growth of carbon nanotubes with single-atomic-layer walls., *Nature* **1993**, 363, 605–607.
- 6 QIN, L.-C., ZHAO, X., HIRAHARA, K., MIYAMOTO, Y., ANDO, Y., IIJIMA, S., The smallest carbon nanotube., *Nature* **2000**, 408, 50.
- 7 WANG, N., TANG, Z. K., LI, G. D., CHEN, J. S., Single-walled 4 Å carbon nanotube arrays., *Nature* **2000**, 408, 50–51.
- 8 HAYASHI, T., KIM, Y. A., MATOBA, T., ESAKA, M., NISHIMURA, K., TSUKADA, T., ENDO, M., DRESSSELHAUS, M. S., Smallest freestanding single-walled carbon nanotube., *Nano Lett.* **2003**, 3, 887–889.
- 9 BANDOW, S., TAKIZAWA, M., HIRAHARA, K., YUDASAKA, M., IIJIMA, S., Raman scattering study of double-wall carbon nanotubes derived from the chains in single-wall carbon nanotubes., *Chem. Phys. Lett.* **2001**, 337, 48–54.
- 10 GUO, T., NIKOLAEV, P., THESS, A., COLBERT, D. T., SMALLEY, R. E., Catalytic growth of single-walled nanotubes by laser vaporization., *Chem. Phys. Lett.* **1995**, 243, 49–54.
- 11 COLOMER, J.-F., STEPHAN, C., LEFRANT, S., TENDELOO, G. V., WILLEMS, I., KONYA, Z., FONSECA, A., LAURENT, C., NAGY, J. B., Large-scale synthesis of single-wall carbon nanotubes by catalytic chemical vapor deposition (CCVD) method., *Chem. Phys. Lett.* **2000**, 317, 83–89.
- 12 JOURNET, C., MASER, W. K., BERNIER, P., LOISEAU, A., CHAPELLE, M. L. d. l., LEFRANT, S., DENIARD, P., LEE, R., FISCHER, J. E., Large-scale production of single-walled carbon nanotubes by the electric-arc technique., *Nature* **1997**, 388, 756–758.
- 13 UGARTE, D., Curling and closure of graphitic networks under electron-beam irradiation., *Nature* **1992**, 359, 707–709.
- 14 RUOFF, R. S., LORENTS, D. C., CHAN, B., MALHOTRA, R., Single crystal metals encapsulated in carbon nanoparticles., *Science* **1993**, 259, 346–348.
- 15 TOMITA, M., SAITO, Y., HAYASHI, T., LaC<sub>2</sub> encapsulated in graphite nanoparticle., *Jpn. J. Appl. Phys.* **1993**, 32, L280–L282.
- 16 SAITO, Y., YOSHIKAWA, T., INAGAKI, M., TOMITA, M., HAYASHI, T., Growth and structure of graphitic tubules and polyhedral particles in arc discharge., *Chem. Phys. Lett.* **1993**, 204, 277–282.

- 17 SAITO, Y., YOSHIKAWA, T., Bamboo-shaped carbon tube filled partially with nickel., *J. Cryst. Growth* **1993**, 134, 154–156.
- 18 ZHANG, G., JIANG, X., WANG, E., Tubular graphite cones., *Science* **2003**, 300, 472–474.
- 19 IJIMA, S., YUDASAKA, M., YAMADA, R., BANDOW, S., SUENAGA, K., KOKAI, F., TAKAHASHI, K., Nano-aggregates of single-walled graphitic carbon nanohorns., *Chem. Phys. Lett.* **1999**, 309, 165–170.
- 20 BAUGHMAN, R. H., ZAKHIDOV, A. A., DE HEER, W. A., Carbon nanotubes – The route toward applications., *Science* **2002**, 297, 787–792.
- 21 SAITO, R., DRESSSELHAUS, G., DRESSSELHAUS, M. S., *Physical Properties of Carbon Nanotubes*, Imperial College Press, London, **1998**.
- 22 EBBESEN, T. W., LEZEC, H. J., HIURA, H., BENNETT, J. W., GHAEMI, H. F., THIO, T., Electrical conductivity of individual carbon nanotubes., *Nature* **1996**, 382, 54–56.
- 23 OUYANG, M., HUANG, J. L., CHEUNG, C. L., LIEBER, C. M., Energy gaps in “metallic” single-walled carbon nanotubes., *Science* **2001**, 292, 702–705.
- 24 TANS, S. J., DEVORET, M. H., DAI, H., THESS, A., SMALLEY, R. E., GEERLIGS, L. J., DEKKER, C., Individual single-wall nanotubes as quantum wires., *Nature* **1997**, 386, 474–477.
- 25 BOCKRATH, M., COBDEN, D. H., McEuen, P. L., CHOPRA, N. G., ZETTL, A., THESS, A., SMALLEY, R. E., Single-electron transport in ropes of carbon nanotubes., *Science* **1997**, 275, 1922–1925.
- 26 TANS, S. J., VERSCHUEREN, A. R. M., DEKKER, C., Room-temperature transistor based on a single carbon nanotube., *Nature* **1998**, 393, 49–52.
- 27 POSTMA, H. W., TEEPEN, T., YAO, Z., GRIFONI, M., DEKKER, C., Carbon nanotube single-electron transistors at room temperature., *Science* **2001**, 293, 76–79.
- 28 MARTEL, R., SCHMIDT, T., SHEA, H. R., HERTEL, T., AVOURIS, P., Single- and multi-wall carbon nanotube field-effect transistors., *Appl. Phys. Lett.* **1998**, 73, 2447–2449.
- 29 BACHTOLD, A., HADLEY, P., NAKANISHI, T., DEKKER, C., Logic circuits with carbon nanotube transistors., *Science* **2001**, 294, 1317–1320.
- 30 KONG, J., FRANKLIN, N. R., ZHOU, C., CHAPLINE, M. G., PENG, S., CHO, K., DAI, H., Nanotube molecular wires as chemical sensors., *Science* **2000**, 287, 622–625.
- 31 COLLINS, P. G., BRADLEY, K., ISHIGAMI, M., ZETTL, A., Extreme oxygen sensitivity of electronic properties of carbon nanotubes., *Science* **2000**, 287, 1801–1804.
- 32 SHIM, M., JAVEY, A., KAM, N. W., DAI, H., Polymer functionalization for air-stable n-type carbon nanotube field-effect transistors., *J. Am. Chem. Soc.* **2001**, 123, 11 512–11 513.
- 33 CHEN, R. J., BANGSARUNTIP, S., DROUVALAKIS, K. A., KAM, N. W. S., SHIM, M., LI, Y., KIM, W., UTZ, P. J., DAI, H., Noncovalent functionalization of carbon nanotubes for highly specific electronic biosensors., *Proc. Natl. Acad. Sci. U.S.A.* **2003**, 100, 4984–4989.
- 34 SNOW, E. S., PERKINS, F. K., HOUSER, E. J., BADESCU, S. C., REINECKE, T. L., Chemical detection with a single-walled carbon nanotube capacitor., *Science* **2005**, 307, 1942–1945.
- 35 BARONE, P. W., BAIK, S., HELLER, D. A., STRANO, M. S., Near-infrared optical sensors based on single-walled carbon nanotubes., *Nat. Mater.* **2005**, 4, 86–92.
- 36 BAUGHMAN, R. H., CUI, C., ZAKHIDOV, A. A., IQBAL, Z., BARISCI, J. N., SPINKS, G. M., WALLACE, G. G., MAZZOLDI, A., DE ROSSI, D., RINZLER, A. G., JASCHINSKI, O., ROTH, S., KERTESZ, M., Carbon nanotube actuators., *Science* **1999**, 284, 1340–1344.
- 37 TREACY, M. M. J., EBBESEN, T. W., GIBSON, J. M., Exceptionally high Young’s modulus observed for individual carbon nanotubes., *Nature* **1996**, 381, 678–680.
- 38 ZHANG, M., FANG, S., ZAKHIDOV, A. A., LEE, S. B., ALIEV, A. E.,

- WILLIAMS, C. D., ATKINSON, K. R., BAUGHMAN, R. H., Strong, transparent, multifunctional, carbon nanotube sheets., *Science* **2005**, 309, 1215–1219.
- 39 ENDO, M., MURAMATSU, H., HAYASHI, T., KIM, Y. A., TERRONES, M., DRESSELHAUS, M. S., 'Buckypaper' from coaxial nanotubes., *Nature* **2005**, 433, 476.
- 40 SREEKUMAR, T. V., LIU, T., KUMAR, S., Single-wall carbon nanotube films., *Chem. Mater.*, **2003**, 15, 175–178.
- 41 WU, Z., CHEN, Z., DU, X., LOGAN, J. M., SIPPEL, J., NIKOLOU, M., KAMARAS, K., REYNOLDS, J. R., TANNER, D. B., HEBARD, A. F., RINZLER, A. G., Transparent, conductive carbon nanotube films., *Science* **2004**, 305, 1273–1276.
- 42 VIGOLO, B., PENICAUD, A., COULON, C., SAUDER, C., PAILLER, R., JOURNET, C., BERNIER, P., POULIN, P., Macroscopic fibers and ribbons of oriented carbon nanotubes., *Science* **2000**, 290, 1331–1334.
- 43 FUKUSHIMA, T., KOSAKA, A., ISHIMURA, Y., YAMAMOTO, T., TAKIGAWA, T., ISHII, N., AIDA, T., Molecular ordering of organic molten salts triggered by single-walled carbon nanotubes., *Science* **2003**, 300, 2072–2074.
- 44 MACDONALD, R. A., LAURENZI, B. F., VISWANATHAN, G., AJAYAN, P. M., STEGEMANN, J. P., Collagen-carbon nanotube composite materials as scaffolds in tissue engineering., *J. Biomed. Mater. Res. A* **2005**, 74, 489–496.
- 45 MENG, J., KONG, H., XU, H. Y., SONG, L., WANG, C. Y., XIE, S. S., Improving the blood compatibility of polyurethane using carbon nanotubes as fillers and its implications to cardiovascular surgery., *J. Biomed. Mater. Res. A* **2005**, 74, 208–214.
- 46 MATTSON, M. P., HADDON, R. C., RAO, A. M., Molecular functionalization of carbon nanotubes and use as substrates for neuronal growth., *J. Mol. Neurosci.* **2000**, 14, 175–182.
- 47 SUPRONOWICZ, P. R., AJAYAN, P. M., ULLMANN, K. R., ARULANANDAM, B. P., METZGER, D. W., BIZIOS, R., Novel current-conducting composite substrates for exposing osteoblasts to alternating current stimulation., *J. Biomed. Mater. Res.* **2002**, 59, 499–506.
- 48 CORREA-DUARTE, M. A., WAGNER, N., ROJAS-CHAPANA, J., MORSZCEK, C., THIE, M., GIERSIG, M., Fabrication and biocompatibility of carbon nanotube-based 3D networks as scaffolds for cell seeding and growth., *Nano Lett.* **2004**, 4, 2233–2236.
- 49 HU, H. N. Y., MONTANA, V., HADDON, R. C., PARPURA, V., Chemically functionalized carbon nanotubes as substrates for neuronal growth., *Nano Lett.* **2004**, 4, 507–511.
- 50 CHOPRA, N. G., LUYKEN, R., CHERREY, K., CRESPI, V., COHEN, M., LOUIE, S., ZETTL, A., Boron-nitride nanotubes., *Science* **1995**, 269, 966–967.
- 51 TERRONES, M., HSUA, W. K., TERRONES, H., ZHANG, J. P., RAMOS, S., HAREA, J. P., CASTILLO, R., PRASSIDES, K., CHEETHAM, A. K., KROTO, H. W., WALTON, D. R. M., Metal particle catalysed production of nanoscale BN structures., *Chem. Phys. Lett.* **1996**, 259, 568–573.
- 52 SEIFERT, G., TERRONES, H., TERRONES, M., FRAUENHEIM, T., Novel NbS<sub>2</sub> metallic nanotubes., *Solid State Commun.* **2000**, 115, 635–638.
- 53 REMSKAR, M., MRZEL, A., SKRABA, Z., JESIH, A., CEH, M., DEMSAR, J., STADELMANN, P., LEVY, F., MIHAILOVIC, D., Self-assembly of subnanometer-diameter single-wall MoS<sub>2</sub> nanotubes., *Science* **2001**, 292, 479–481.
- 54 ZHANG, Y., SUENAGA, K., COLLIEX, C., IJIMA, S., Coaxial nanocable: Silicon carbide and silicon oxide sheathed with boron nitride and carbon., *Science* **1998**, 281, 973–975.
- 55 AJAYAN, P. M., EBBESEN, T. W., ICHIHASHI, T., IJIMA, S., TANIGAKI, K., HIURA, H., Opening carbon nanotubes with oxygen and implications for filling., *Nature* **1993**, 362, 522–524.
- 56 TSANG, S. C., CHEN, Y. K., HARRIS, P. J. F., GREEN, M. L. H., A simple

- chemical method of opening and filing carbon nanotubes., *Nature* **1994**, 372, 159–162.
- 57 AJAYAN, P. M., IJIMA, S., Capillarity induced filling in carbon nanotubes., *Nature* **1993**, 361, 333–334.
- 58 SERAPHIN, S., ZHOU, D., JIAO, J., WITHERS, J. C., LOUTFY, R., Yttrium carbide in nanotubes., *Nature* **1993**, 362, 503.
- 59 AJAYAN, P. M., COLLIEX, C., LAMBERT, J. M., BERNIER, P., BARBEDETTE, L., TENCE, M., STEPHAN, O., Growth of manganese filled carbon nanofibers in the vapor phase., *Phys. Rev. Lett.* **1994**, 72, 1722–1725.
- 60 SUBRAMONEY, S. R., RODNEY, S., LORENTS, D. C., CHAN, B., RIPUDAMAN, M., DYER, M. J., PARVIN, K., Magnetic separation of GdC<sub>2</sub> encapsulated in carbon nanoparticles., *Carbon* **1994**, 32, 507–513.
- 61 GUERRET-PIÉCOURT, C., BOUAR, Y. L., LOISEAU, A., PASCARD, H., Relation between metal electronic structure and morphology of metal compounds inside carbon nanotubes., *Nature* **1994**, 372, 761–765.
- 62 DAI, H., WONG, E. W., LU, Y. Z., FAN, S., LIEBER, C. M., Synthesis and characterization of carbide nanorods., *Nature* **1995**, 375, 769–772.
- 63 HAN, W., FAN, S., LI, Q., HU, Y., Synthesis of gallium nitride nanorods through a carbon nanotube-confined reaction., *Science* **1997**, 277, 1287–1289.
- 64 PAN, Z., LAI, H.-L., AU, F. C. K., DUAN, X., ZHOU, W., SHI, W., WANG, N., LEE, C.-S., WONG, N.-B., LEE, S.-T., XIE, S., Oriented silicon carbide nanowires: Synthesis and field emission properties., *Adv. Mater.* **2000**, 12, 1186–1190.
- 65 DUAN, X., LIEBER, C. M., Laser-assisted catalytic growth of single crystal GaN nanowires., *J. Am. Chem. Soc.* **2000**, 122, 188–189.
- 66 GOLDBERGER, J., HE, R., ZHANG, Y., LEE, S., YAN, H., CHOI, H. J., YANG, P., Single-crystal gallium nitride nanotubes., *Nature* **2003**, 422, 599–602.
- 67 CUI, Y., DUAN, X., HU, J., LIEBER, C. M., Doping and electrical transport in silicon nanowires., *J. Phys. Chem. B* **2000**, 104, 5213–5216.
- 68 CUI, Y., LIEBER, C. M., Functional nanoscale electronic devices assembled using silicon nanowire building blocks., *Science* **2001**, 291, 851–853.
- 69 DUAN, X., HUANG, Y., CUI, Y., WANG, J., LIEBER, C. M., Indium phosphide nanowires as building blocks for nanoscale electronic and optoelectronic devices., *Nature* **2001**, 409, 66–69.
- 70 ZHOU, D., SERAPHIN, S., Production of silicon carbide whiskers from carbon nanoclusters., *Chem. Phys. Lett.* **1994**, 222, 233–238.
- 71 YAGER, P., SCHOEN, P. E., Formation of tubules by a polymerizable surfactant., *Mol. Cryst. Liq. Cryst.* **1984**, 106, 371–381.
- 72 NAKASHIMA, N., ASAKUMA, S., KUNITAKE, T., Optical microscopic study of helical superstructures of chiral bilayer membranes., *J. Am. Chem. Soc.* **1985**, 107, 509–510.
- 73 SCHNUR, J. M., Lipid tubules: A paradigm for molecularly engineered structures., *Science* **1993**, 262, 1669–1676.
- 74 KARLSSON, A., KARLSSON, R., KARLSSON, M., CANS, A. S., STROMBERG, A., RYTTSEN, F., ORWAR, O., Networks of nanotubes and containers., *Nature* **2001**, 409, 150–152.
- 75 KARLSSON, M., SOTT, K., DAVIDSON, M., CANS, A. S., LINDERHOLM, P., CHIU, D., ORWAR, O., Formation of geometrically complex lipid nanotube-vesicle networks of higher-order topologies., *Proc. Natl. Acad. Sci. U.S.A.* **2002**, 99, 11573–11578.
- 76 GHADIRI, M. R., TIRRELL, D. A., Chemistry at the crossroads., *Curr. Opin. Chem. Biol.* **2000**, 4, 661–662.
- 77 MATSUI, H., GOLOGAN, B., Crystalline glycyglycinebolaamphiphile tubules and their pH-sensitive structural transformation., *J. Phys. Chem. B* **2000**, 104, 3383–3386.
- 78 KHAZANOVICH, N., GRANJA, J. R., MCRREE, D. E., RONALD, A., MILLIGAN, GHADIRI, M. R., Nanoscale tubular

- ensembles with specified internal diameters. Design of a self-assembled nanotube with a 13 Å pore, *J. Am. Chem. Soc.* **1994**, *116*, 6011–6012.
- 79** RECHES, M., GAZIT, E., Casting metal nanowires within discrete self-assembled peptide nanotubes., *Science* **2003**, *300*, 625–627.
- 80** YU, K., ZHANG, L., EISENBERG, A., Novel morphologies of “crew-cut” aggregates of amphiphilic diblock copolymers in dilute solution., *Langmuir* **1996**, *12*, 5980–5984.
- 81** RAEZ, J. M., I., WINNIK, M. A., Nanotubes from the self-assembly of asymmetric crystalline-coil poly(ferrocenylsilane-siloxane) block copolymers., *J. Am. Chem. Soc.* **2002**, *124*, 10 381–10 395.
- 82** DISCHER, B. M., WON, Y. Y., EGE, D. S., LEE, J. C., BATES, F. S., DISCHER, D. E., HAMMER, D. A., Polymersomes: Tough vesicles made from diblock copolymers., *Science* **1999**, *284*, 1143–1146.
- 83** POCHAN, D. J., CHEN, Z., CUI, H., HALES, K., QI, K., WOOLEY, K. L., Toroidal triblock copolymer assemblies., *Science* **2004**, *306*, 94–97.
- 84** CHA, J. N., STUCKY, G. D., MORSE, D. E., DEMING, T. J., Biomimetic synthesis of ordered silica structures mediated by block copolypeptides., *Nature* **2000**, *403*, 289–292.
- 85** LEE, S. W., MAO, C., FLYNN, C. E., BELCHER, A. M., Ordering of quantum dots using genetically engineered viruses., *Science* **2002**, *296*, 892–895.
- 86** BANERJEE, I. A., YU, L., MATSUI, H., Cu nanocrystal growth on peptide nanotubes by biomimetalization: Size control of Cu nanocrystals by tuning peptide conformation., *Proc. Natl. Acad. Sci. U.S.A.* **2003**, *100*, 14 678–14 682.
- 87** DJALALI, R., CHEN, Y. F., MATSUI, H., Au nanocrystal growth on nanotubes controlled by conformations and charges of sequenced peptide templates., *J. Am. Chem. Soc.* **2003**, *125*, 5873–5879.
- 88** MAO, C., FLYNN, C. E., HAYHURST, A., SWEENEY, R., QI, J., GEORGIU, G., IVERSON, B., BELCHER, A. M., Viral assembly of oriented quantum dot nanowires., *Proc. Natl. Acad. Sci. U.S.A.* **2003**, *100*, 6946–6951.
- 89** SCHEMBRI, M. A., KJAERGAARD, K., KLEMM, P., Bioaccumulation of heavy metals by fimbrial designer adhesins., *FEMS Microbiol. Lett.* **1999**, *170*, 363–371.
- 90** MAO, C., SOLIS, D. J., REISS, B. D., KOTTMANN, S. T., SWEENEY, R. Y., HAYHURST, A., GEORGIU, G., IVERSON, B., BELCHER, A. M., Virus-based toolkit for the directed synthesis of magnetic and semiconducting nanowires., *Science* **2004**, *303*, 213–217.
- 91** REISS, B. D., MAO, C., SOLIS, D. J., RYAN, K. S., THOMSON, T., BELCHER, A. M., Biological routes to metal alloy ferromagnetic nanostructures., *Nano Lett.* **2004**, *4*, 1127–1132.
- 92** WAGNER, D. E., PHILLIPS, C. L., ALI, W. M., NYBAKKEN, G. E., CRAWFORD, E. D., SCHWAB, A. D., SMITH, W. F., FAIRMAN, R., Toward the development of peptide nanofilaments and nanoropes as smart materials., *Proc. Natl. Acad. Sci. U.S.A.* **2005**, *102*, 12 656–12 661.
- 93** SANDER, C., Genomic medicine and the future of health care., *Science* **2000**, *287*, 1977–1978.
- 94** KITANO, H., Cancer as a robust system: Implications for anticancer therapy., *Nat. Rev. Cancer* **2004**, *4*, 227–235.
- 95** SCHENA, M., SHALON, D., DAVIS, R. W., BROWN, P. O., Quantitative monitoring of gene expression patterns with a complementary DNA microarray., *Science* **1995**, *270*, 467–470.
- 96** DERISI, J. L., IYER, V. R., BROWN, P. O., Exploring the metabolic and genetic control of gene expression on a genomic scale., *Science* **1997**, *278*, 680–686.
- 97** LOCKHART, D. J., WINZELER, E. A., Genomics, gene expression and DNA arrays., *Nature* **2000**, *405*, 827–836.
- 98** LI, J., LU, Y., YE, Q., CINKE, M., HAN, J., MEYAPPAN, M., Carbon nanotube sensors for gas and organic vapor

- detection., *Nano Lett.* **2003**, *3*, 929–933.
- 99** STAR, A., GABRIEL, J.-C. P., BRADLEY, K., GRUNER, G., Electronic detection of specific protein binding using nanotube FET devices., *Nano Lett.* **2003**, *3*, 459–463.
- 100** BESTEMAN, K. L., LEE, J.-O., WIERTZ, F. G. M., HEERING, H. A., DEKKER, C., Enzyme-coated carbon nanotubes as single-molecule biosensors., *Nano Lett.* **2003**, *3*, 727–730.
- 101** ELLINGTON, A. D., SZOSTAK, J. W., *In vitro* selection of RNA molecules that bind specific ligands., *Nature* **1990**, *346*, 818–822.
- 102** BOCK, L. C., GRIFFIN, L. C., LATHAM, J. A., VERMAAS, E. H., TOOLE, J. J., Selection of single-stranded DNA molecules that bind and inhibit human thrombin., *Nature* **1992**, *355*, 564–566.
- 103** SCOTT, J. K., SMITH, G. P., Searching for peptide ligands with an epitope library., *Science* **1990**, *249*, 386–390.
- 104** LI, J., NG, H. T., CASSELL, A. F., W., CHEN, H. Y., Q., KOEHNE, J., HAN, J., MEYAPPAN, M., Carbon nanotube nanoelectrode array for ultrasensitive DNA detection., *Nano Lett.* **2003**, *3*, 597–602.
- 105** SISTARE, M. F., HOLMBERG, R. C.; THORP, H. H., Electrochemical studies of polynucleotide binding and oxidation by metal complexes: Effects of scan rate, concentration, and sequence., *J. Phys. Chem. B* **1999**, *103*, 10718–10728.
- 106** CUI, Y., WEI, Q., PARK, H., LIEBER, C. M., Nanowire nanosensors for highly sensitive and selective detection of biological and chemical species., *Science* **2001**, *293*, 1289–1292.
- 107** HAHM, J.-I. LIEBER, C. M., Direct ultrasensitive electrical detection of DNA and DNA sequence variations using nanowire nanosensors., *Nano Lett.* **2004**, *4*, 51–54.
- 108** LI, C., CURRELI, M., LIN, H., LEI, B., ISHIKAWA, F. N., DATAR, R., COTE, R. J., THOMPSON, M. E., ZHOU, C., Complementary detection of prostate-specific antigen using In<sub>2</sub>O<sub>3</sub> nanowires and carbon nanotubes., *J. Am. Chem. Soc.* **2005**, *127*, 12484–12485.
- 109** RAITERI, R., NELLES, G., BUTT, H.-J., KNOLL, W., SKLADAL, P., Sensing of biological substances based on the bending of microfabricated cantilevers., *Sens. Actuators B* **1999**, *61*, 213–217.
- 110** FRITZ, J., BALLER, M. K., LANG, H. P., ROTHUIZEN, H., VETTINGER, P., MEYER, E., GUNTHERODT, H., GERBER, C., GIMZEWSKI, J. K., Translating biomolecular recognition into nanomechanics., *Science* **2000**, *288*, 316–318.
- 111** WU, G., JI, H., HANSEN, K., THUNDAT, T., DATAR, R., COTE, R., HAGAN, M. F., CHAKRABORTY, A. K., MAJUMDAR, A., Origin of nanomechanical cantilever motion generated from biomolecular interactions., *Proc. Natl. Acad. Sci. U.S.A.* **2001**, *98*, 1560–1564.
- 112** NICEWARNER-PENA, S. R., FREEMAN, R. G., REISS, B. D., HE, L., PENNA, D. J., WALTON, I. D., CROMER, R., KEATING, C. D., NATAN, M. J., Submicrometer metallic barcodes., *Science* **2001**, *294*, 137–141.
- 113** FREEMAN, R. G., RAJU, P. A., NORTON, S. M., WALTON, I. D., SMITH, P. C., HE, L., NATAN, M. J., SHA, M. Y., PENN, S. G., Use of nanobarcode particles in bioassays., *Methods Mol. Biol.* **2005**, *303*, 73–83.
- 114** PANTAROTTO, D., BRIAND, J. P., PRATO, M., BIANCO, A., Translocation of bioactive peptides across cell membranes by carbon nanotubes., *Chem. Comm.* **2004**, 16–17.
- 115** PANTAROTTO, D., PARTIDOS, C. D., GRAFF, R., HOEBEKE, J., BRIAND, J. P., PRATO, M., BIANCO, A., Synthesis, structural characterization, and immunological properties of carbon nanotubes functionalized with peptides., *J. Am. Chem. Soc.* **2003**, *125*, 6160–6164.
- 116** KAM, N. W. S., JESSOP, T. C., WENDER, P. A., DAI, H., Nanotube molecular transporters: Internalization of carbon nanotube-protein conjugates into mammalian cells., *J. Am. Chem. Soc.* **2004**, *126*, 6850–6851.
- 117** LU, Q., MOORE, J. M., HUANG, G., MOUNT, A. S., RAO, A. M., LARCOM,

- L. L., KE, P. C., RNA polymer translocation with single-walled carbon nanotubes., *Nano Lett.* **2004**, *4*, 2473–2477.
- 118 PANTAROTTO, D., SINGH, R., MCCARTHY, D., ERHARDT, M., BRIAND, J. P., PRATO, M., KOSTARELOS, K., BIANCO, A., Functionalized carbon nanotubes for plasmid DNA gene delivery., *Angew. Chem. Int. Ed.* **2004**, *43*, 5242–5246.
- 119 SINGH, R., PANTAROTTO, D., MCCARTHY, D., CHALOIN, O., HOEBEKE, J., PARTIDOS, C. D., BRIAND, J. P., PRATO, M., BIANCO, A., KOSTARELOS, K., Binding and condensation of plasmid DNA onto functionalized carbon nanotubes: Toward the construction of nanotube-based gene delivery vectors., *J. Am. Chem. Soc.* **2005**, *127*, 4388–4396.
- 120 BIANCO, A., HOEBEKE, J., GODEFROY, S., CHALOIN, O., PANTAROTTO, D., BRIAND, J. P., MULLER, S., PRATO, M., PARTIDOS, C. D., Cationic carbon nanotubes bind to CpG oligodeoxynucleotides and enhance their immunostimulatory properties., *J. Am. Chem. Soc.* **2005**, *127*, 58–59.
- 121 KAM, N. W. S., LIU, Z., DAI, H., Functionalization of carbon nanotubes via cleavable disulfide bonds for efficient intracellular delivery of siRNA and potent gene silencing., *J. Am. Chem. Soc.* **2005**, *127*, 12 492–12 493.
- 122 MAEDA, H., WU, J., SAWA, T., MATSUMURA, Y., HOR, i. K., Tumour vascular permeability and the EPR effect in macromolecular therapeutics., *J. Controlled Release* **2000**, *65*, 271–284.
- 123 MATSUMURA, Y., MAEDA, H., A new concept for macromolecular therapeutics in cancer chemotherapy: Mechanism of tumortropic accumulation of proteins and the antitumor agent SMANCS., *Cancer Res.* **1986**, *46*, 6387–6392.
- 124 KASUYA, D., YUDASAKA, M., TAKAHASHI, K., KOKAI, F., IJIMA, S., Selective production of single-wall carbon nanohorn aggregates and their formation mechanism., *J. Phys. Chem. B* **2002**, *106*, 4947–4951.
- 125 SHVEDOVA, A. A., CASTRANOVA, V., KISIN, E. R., SCHWEGLER-BERRY, D., MURRAY, A. R., GANDELSMAN, V. Z., MAYNARD, A., BARON, P., Exposure to carbon nanotube material: Assessment of nanotube cytotoxicity using human keratinocyte cells., *J. Toxicol. Environ. Health A* **2003**, *66*, 1909–1926.
- 126 MURAKAMI, T., AJIMA, K., MIYAWAKI, J., YUDASAKA, M., IJIMA, S., SHIBA, K., Drug-loaded carbon nanohorns: Adsorption and release of dexamethasone *in vitro.*, *Mol. Pharm.* **2004**, *1*, 399–405.
- 127 KASE, D., KULP, J. L., 3rd, YUDASAKA, M., EVANS, J. S., IJIMA, S., SHIBA, K., Affinity selection of peptide phage libraries against single-wall carbon nanohorns identifies a peptide aptamer with conformational variability., *Langmuir* **2004**, *20*, 8939–8941.
- 128 SANO, K., AJIMA, K., IWAHORI, K., YUDASAKA, M., IJIMA, S., YAMASHITA, I., SHIBA, K., Endowing a ferritin-like cage protein with high affinity and selectivity for certain inorganic materials., *Small* **2005**, *1*, 826–832.
- 129 HARISINGHANI, M. G., BARENTSZ, J., HAHN, P. F., DESERNO, W. M., TABATABAEI, S., VAN DE KAA, C. H., DE LA ROSETTE, J., WEISSLEDER, R., Noninvasive detection of clinically occult lymph-node metastases in prostate cancer., *N. Engl. J. Med.* **2003**, *348*, 2491–2499.
- 130 O'CONNELL, M. J., BACHILO, S. M., HUFFMAN, C. B., MOORE, V. C., STRANO, M. S., HAROZ, E. H., RIALON, K. L., BOUL, P. J., NOON, W. H., KITTRELL, C., MA, J., HAUGE, R. H., WEISMAN, R. B., SMALLEY, R. E., Band gap fluorescence from individual single-walled carbon nanotubes., *Science* **2002**, *297*, 593–596.
- 131 BACHILO, S. M., STRANO, M. S., KITTRELL, C., HAUGE, R. H., SMALLEY, R. E., WEISMAN, R. B., Structure-assigned optical spectra of single-walled carbon nanotubes., *Science* **2002**, *298*, 2361–2366.
- 132 HARTSCHUH, A., PEDROSA, H. N., NOVOTNY, L., KRAUSS, T. D., Simultaneous fluorescence and



- Raman scattering from single carbon nanotubes., *Science* **2003**, 301, 1354–1356.
- 133 KIM, S., LIM, Y. T., SOLTESZ, E. G., DE GRAND, A. M., LEE, J., NAKAYAMA, A., PARKER, J. A., MIHALJEVIC, T., LAURENCE, R. G., DOR, D. M., COHN, L. H., BAWENDI, M. G., FRANGIONI, J. V., Near-infrared fluorescent type II quantum dots for sentinel lymph node mapping., *Nat. Biotechnol.* **2004**, 22, 93–97.
- 134 CHERUKURI, P., BACHILO, S. M., LITOVSKY, S. H., WEISMAN, R. B., Near-infrared fluorescence microscopy of single-walled carbon nanotubes in phagocytic cells., *J. Am. Chem. Soc.* **2004**, 126, 15 638–15 639.
- 135 KAM, N. W. S., O'CONNELL, M., WISDOM, J. A., DAI, H., Carbon nanotubes as multifunctional biological transporters and near-infrared agents for selective cancer cell destruction., *Proc. Natl. Acad. Sci. U.S.A.* **2005**, 102, 11 600–11 605.
- 136 KIRCHER, M. F., MAHMOOD, U., KING, R. S., WEISSELEDER, R., JOSEPHSON, L., A multimodal nanoparticle for preoperative magnetic resonance imaging and intraoperative optical brain tumor delineation., *Cancer Res.* **2003**, 63, 8122–8125.
- 137 HIRSCH, L. R., STAFFORD, R. J., BANKSON, J. A., SERSHEN, S. R., RIVERA, B., PRICE, R. E., HAZLE, J. D., HALAS, N. J., WEST, J. L., Nanoshell-mediated near-infrared thermal therapy of tumors under magnetic resonance guidance., *Proc. Natl. Acad. Sci. U.S.A.* **2003**, 100, 13 549–13 554.
- 138 LU, Y., SEGA, E., LEAMON, C. P., LOW, P. S., Folate receptor-targeted immunotherapy of cancer: Mechanism and therapeutic potential., *Adv. Drug Delivery Rev.* **2004**, 56, 1161–1176.
- 139 DAI, H., HAFNER, J. H., RINZLER, A. G., COLBERT, D. T., SMALLEY, R. E., Nanotubes as nanoprobe in scanning probe microscopy., *Nature* **1996**, 384, 147–150.
- 140 WONG, S. S., JOSELEVICH, E., WOOLLEY, A. T., CHEUNG, C. L., LIEBER, C. M., Covalently functionalized nanotubes as nanometre-sized probes in chemistry and biology., *Nature* **1998**, 394, 52–55.
- 141 WOOLLEY, A. T., CHEUNG, C. L., HAFNER, J. H., LIEBER, C. M., Structural biology with carbon nanotube AFM probes., *Chem. Biol.* **2000**, 7, R193–204.
- 142 PARKS, G. A., The isoelectric points of solid oxides, solid hydroxides, and aqueous hydroxo complex systems., *Chem. Rev.* **1965**, 65, 177–198.
- 143 WARHEIT, D. B., LAURENCE, B. R., REED, K. L., ROACH, D. H., REYNOLDS, G. A., WEBB, T. R., Comparative pulmonary toxicity assessment of single-wall carbon nanotubes in rats., *Toxicol. Sci.* **2004**, 77, 117–125.
- 144 LAM, C. W., JAMES, J. T., MCCCLUSKEY, R., HUNTER, R. L., Pulmonary toxicity of single-wall carbon nanotubes in mice 7 and 90 days after intratracheal instillation., *Toxicol. Sci.* **2004**, 77, 126–134.
- 145 HUCZKO, A., LANGE, H., CALKO, E., GRUBEK-JAWORSKA, H., DROSCZ, P., Physiological testing of carbon nanotubes: Are they asbestos-like?, *Fullerene Sci. Technol.* **2001**, 9, 251–254.
- 146 CUI, D., TIAN, F., OZKAN, C. S., WANG, M., GAO, H., Effect of single wall carbon nanotubes on human HEK293 cells., *Toxicol. Lett.* **2005**, 155, 73–85.
- 147 MONTEIRO-RIVIERE, N. A., NEMANICH, R. J., INMAN, A. O., WANG, Y. Y., RIVIERE, J. E., Multi-walled carbon nanotube interactions with human epidermal keratinocytes., *Toxicol. Lett.* **2005**, 155, 377–384.
- 148 MANNA, S. K., SARKAR, S., BARR, J., WISE, K., BARRERA, E. V., JEJELOWO, O., RICE-FICHT, A. C., RAMESH, G. T., Single-walled carbon nanotube induces oxidative stress and activates nuclear transcription factor-kB in human keratinocytes., *Nano Lett.* **2005**, 5, 1676–1684.
- 149 WANG, H., WANG, J., DENG, X., SUN, H., SHI, Z., GU, Z., LIU, Y., ZHAO, Y., Biodistribution of carbon single-wall carbon nanotubes in mice., *J. Nanosci. Nanotechnol.* **2004**, 4, 1019–1024.

## 9 Multifunctional Nanotubes and Nanowires for Cancer Diagnosis and Therapy

*Sang Bok Lee and Sang Jun Son*

### 9.1 Introduction

Nanomaterials have been one of the most widely studied and attractive subjects for the last decade in the field of biomedical and biotechnological applications, such as MRI contrasting agent [1], DNA transfection [2], biosensors [3], and drug delivery [4]. These nanoparticles are particularly interesting because many of their properties, such as electronic and optical properties, are quite different from those of bulk material. These new properties have provided new opportunities to develop ideal diagnostic/therapeutic systems and to overcome existing biological barriers such as that only very small amounts of monoclonal antibodies can find their targets *in vivo* system [5]. For example, liposomes, the simplest biologically friendly form of nanoparticles, are being used to increase drug concentration at tumor sites; their doxorubicin-embedded complex was approved by the FDA 10 years ago for the treatment of Kaposi's sarcoma, and now they are used in treating breast cancer [6]. While liposomes deal mainly with sizes, not with unique physical properties, for their application, inorganic nanoparticles, such as gold nanoparticles [7], gold nanoshells [8], and quantum dots [9], use the unique electronic and optical properties of nanoscale materials. They are now in commercial use and development as diagnostic and therapeutic tools. All of these nanoparticles can be filled with anti-cancer drugs and detection agents for the targeted gene therapy and early stage cancer diagnosis [10].

Typically, spherical nanoparticles have been used for most nanobiotechnological applications because they are easy to make. However, spherical nanoparticles still need to be improved in terms of controlling particle sizes, surface functionalization, and environmental compatibility due to their structural limitations when multifunctionality is required, especially on their surfaces. The spherical nanoparticle is not an ideal platform for multifunctional nanomaterials because it has a single surface, so that every surface modification for the multifunctionality takes place at the same surface, which can lead to malfunction or interruption between multifunctional components. Tubular nanoparticles have become highly attractive for multifunctional purposes due to their structural attributes, such as distinctive

inner and outer surfaces, over conventional spherical nanoparticles. Inner voids can be used for capturing, concentrating, and releasing species ranging in size from large proteins to small molecules because tube dimensions can be easily controlled by template synthesis. Distinctive outer surfaces can be differentially functionalized with environmentally friendly and/or probe molecules to a specific target. These differentially functionalized, or multifunctionalized, nanotubes have enormous potential in biomedical application, including therapeutic tools [11], drug delivery [12], bioseparations, and biocatalysis [13, 14], and have provided a model system to study wetting and diffusion problems in nanoscale containers [15]. In addition to these nanotubes, nanowires or nanorods have also been highlighted with respect to multifunctionality for biotechnological application [16, 17]. Although nanotubes and nanowires offer huge opportunities and might prove to be useful in bio-nanotechnology – most likely cancer technology, such as early detection and targeted drug delivery for cancer tumors – there are as yet few example applications of diagnostic and therapeutic tools. From this viewpoint, the present chapter includes (a) the most recent success story of magnetic nanoparticles, (b) carbon nanotubes, (c) nanotubes and nanowires composed of artificial peptides, and (d) template-synthesized nanotubes, such as silica and magnetic nanotubes, for the various biomedical applications.

## 9.2

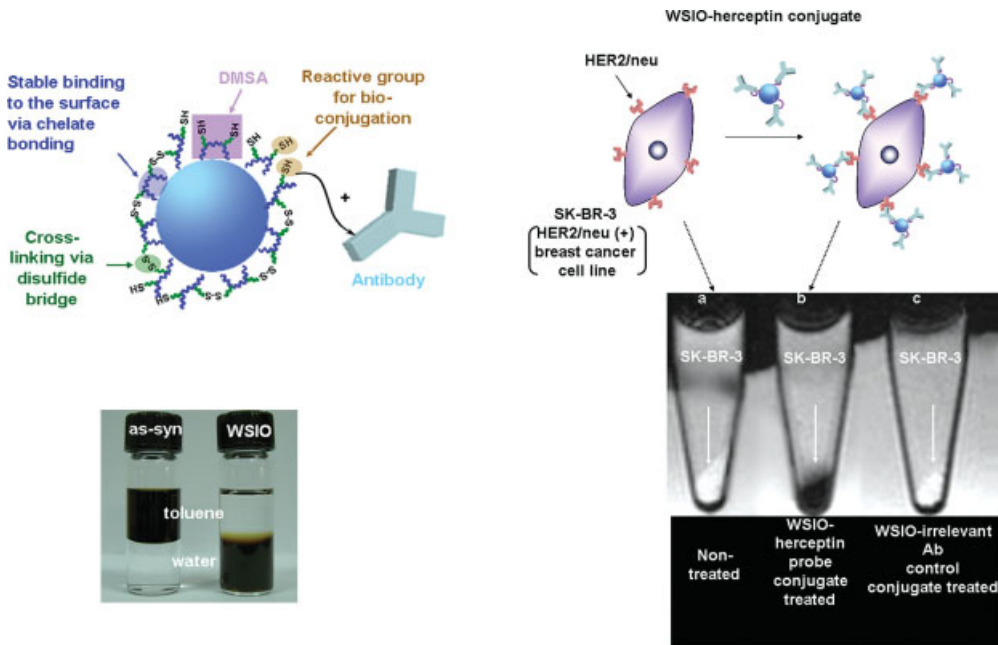
### Advanced Technologies in Magnetic Nanoparticles for Biomedical Applications

Magnetic particles have been extensively studied in the field of biomedical and biotechnological applications, including drug delivery, biosensors, chemical and biochemical separation and concentration of trace amount of specific targets, such as bacteria or leukocytes, enzyme encapsulation, and contrast enhancement in magnetic resonance imaging (MRI) [18–20]. Practically, magnetic nanoparticles are ideal candidate materials for the early detection of cancer and targeted drug delivery due to their natural MRI capability, together with the ability to modify the particle surface with targeting moieties [21]. In addition, new synthetic methods have been recently reported to improve control over particle sizes up to 1-nm scale for mass production [22–24].

#### 9.2.1

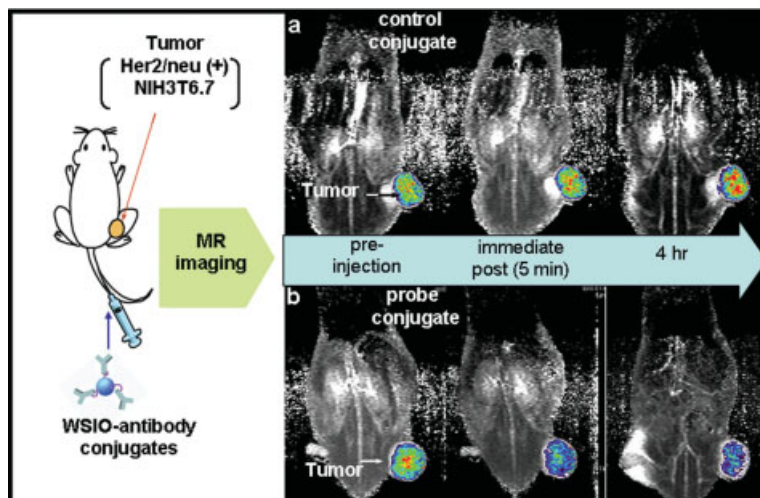
##### MRI and Therapeutic Application of Magnetic Nanoparticles

Recently, a team of Korean scientists have reported that magnetic nanoparticles can be successfully used for cancer diagnosis both *in vitro* and *in vivo* [23, 25, 26]. Magnetic nanoparticles can play a key role in magnetic resonance (MR) diagnosis of early state cancer, which requires sensitive and selective detection techniques because of their strong enhancement in MR signal. In addition, nano-scale size is favorable for more specific and active targeting toward cancer cells due to the leaky and small porous structure of such cells. The team, directed by Jinwoo Cheon, re-



**Fig. 9.1.** Schematic illustration of 2,3-dimercaptosuccinic acid (DMSA)-coated water-soluble  $\text{Fe}_3\text{O}_4$  iron oxide (WSIO) nanocrystals and their solubility test (left-hand side) and *in vitro* cancer diagnosis assisted by WSIO–Herceptin probe conjugate (right-hand side). (From Ref. [26].)

ported that 9 nm water-soluble  $\text{Fe}_3\text{O}_4$  iron oxide (WSIO) nanoparticles are ideal material for cancer diagnosis. Magnetic  $\text{Fe}_3\text{O}_4$  nanoparticles were synthesized through thermal decomposition of  $\text{Fe}(\text{acac})_3$  (acac = acetylacetonate) in a hot organic solvent and their surface was covered with 2,3-dimercaptosuccinic acid (DMSA). The carboxylic group of DMSA ligand is coordinated to the metal surface and disulfide crosslinkage between the ligands stabilizes the ligand shell. This ligand increases the solubility in water, and remaining free thiol groups can be used to attach target-specific antibodies (Fig. 9.1). In this report, the DMSA ligand shell was conjugated with the cancer-targeting antibody Herceptin, which has specific binding properties against a HER2/new receptor overexpressed from breast cancer cells. For *in vitro* study, they examined the binding specificity by treating WSIO–Herceptin probe to a breast cancer cell line, SK-BR-3, and performing an MRI measurement. There was significant darkening of the MR image of the cell line treated with WSIO–Herceptin, while no noticeable difference was observed between the nontreated and WSIO-irrelevant antibody control conjugate-treated cells. The capability of WSIO with multifunctionality for *in vivo* use was further tested with a set of nude mouse implanted at their proximal thigh region with NIH3T6.7 cell lines overexpressed with HER2/neu cancer markers.



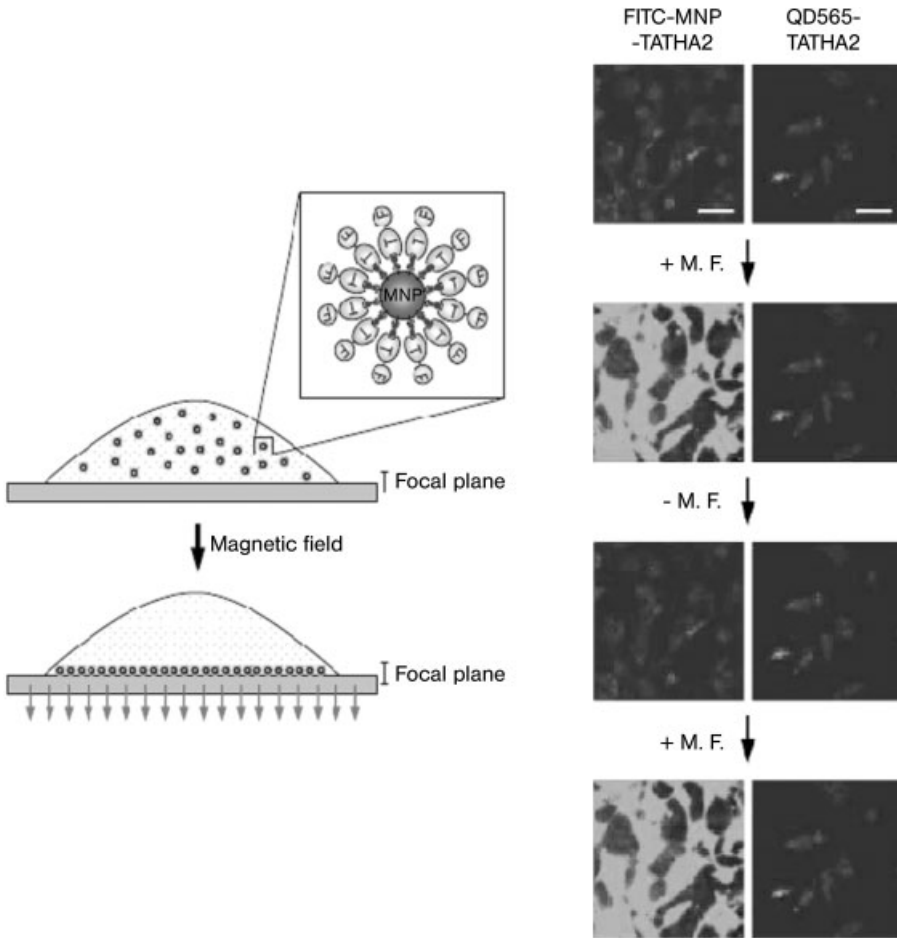
**Fig. 9.2.** *In vivo* MRI of cancer-targeting events of WSIO-irrelevant antibody conjugate (a) and WSIO-Herceptin probe conjugates (b). (From Ref. [25].)

Figure 9.2 shows *in vivo* MRI of cancer-targeting events of WSIO-antibody conjugates. Color maps of T2-weighted MR images of cancer cell implanted (NIH3T6.7) mice at different temporal points (preinjection, immediate post, 4 h) after the intravenous injection of WSIO-irrelevant antibody control conjugates (a) and WSIO-Herceptin probe conjugates (b) reveals that WSIO-Herceptin conjugates induce an immediate color change in the color-mapped MR signal at the tumor site within 5 min. This implies that the WSIO-Herceptin probe conjugates successfully reach and bind to the target cancer cells at the proximal thigh. In the control experiment with WSIO-irrelevant antibody conjugates, however, no change was observed, confirming minimal nonspecific binding to the tumor site.

### 9.2.2

#### Biomedical Diagnostic Application of Magnetic Nanoparticles

Another interesting application of magnetic nanoparticles (MNPs) was reported in *Science* in 2005 by Kim's group [27]. They developed a technology called magnetism-based interaction capture (MAGIC) for the detection of molecular interactions in live cells. Combined with confocal microscopy, which has a very narrow focal plane, the induced movement of superparamagnetic nanoparticles was adapted to detect the molecular interaction of interest or to identify molecular targets. As seen in Fig. 9.3, after internalization of MNPs coated with target-specific probes into live cells, application of a magnetic field can induce concentration of MNPs and associated target proteins at the focal plane, and the translocation of the fluorescent signal can be used to determine whether binding events occur in-



**Fig. 9.3.** Schematic of magnetism-base interaction capture (MAGIC) (left-hand side) and fluorescence microscope images showing translocation of MNPs coated with FITC and TAT-HA2 inside cells by the magnetic field (right-hand side). (From Ref. [27].)

side cells between probe molecule and target proteins. In this study, streptavidin-conjugated MNPs were used as generic reagent for the attachment of biotinylated molecules to the nanoprobe, and efficient intracellular uptake of nanoparticles was mediated by transducible fusogenic TAT-HA2 peptide, which has a high density of cationic residues and thus causes an electrostatic interaction with the negatively charged cell surface. To visualize and track the distribution of MNPs within cells, MNPs coated with fluorescein isothiocyanate (FITC) and TAT-HA2 were prepared; when a magnetic field was applied, specific translocation of MNPs was observed inside cells. Furthermore, this translocation was reversible; the MNPs rapidly dif-

fused away upon removal of the magnetic field and were redirected when it was reapplied. The authors tested whether the MAGIC principle could be used to detect a specific intracellular target for Asp-Glu-Val-Asp (DEVD), an apoptosis inhibitor known to bind caspase-3. After MNPs modified with DEVD and TAT-HA2 were incubated with HeLa cells transfected with caspase-3 fused to red fluorescent protein (mRFP), the red signal translocated in the direction of the magnetic field. As a systematic target identification (ID) experiment for a bioactive small molecule, a normalized EGFP-tagged cDNA library was expressed in HeLa cells by retroviral transduction, and MNPs coated with FK506 were introduced into these cells to identify the receptors for an immunosuppressant, FK506. They identified 19 positive clones that exhibited specific translocation of EGFP in the direction of the magnetic field, and several known FK506-binding proteins and proteins of unknown function were found in these clones. This MAGIC principle can also be used to probe intercellular signaling processes, such as signal-induced phosphorylation and interaction of the NF- $\kappa$ B/I $\kappa$ B.

Enzymes, when immobilized on magnetic nanoparticles (MNPs), can be easily separated from the reaction medium, stored, and reused with consistent results [28]. This system offers a relatively simple technique for separating and reusing enzymes over a longer period than that for both free enzymes alone and enzymes immobilized by physisorption. The most significant advantage of enzyme immobilization on magnetic nanoparticles is their long-term stability, such as reported by Gross's group using *Candida rugosa* lipase (E.C.3.1.1.3) immobilized on  $\gamma$ -Fe<sub>2</sub>O<sub>3</sub> magnetic nanoparticles. Lipases are frequently employed enzymes as they are commonly used for the synthesis of enantio-enriched monomers and macromers and for polymerization reactions [29]. MNPs (20 nm) were prepared by sonication of Fe(CO) in decalin and the subsequent annealing of amorphous Fe<sub>2</sub>O<sub>3</sub> nanoparticles. Acetylated thiophene on MNPs was reacted directly with the enzyme. The enzymatic activity of the immobilized lipase was determined by following the ester cleavage of 4-nitrophenyl butyrate. The activity of *Candida rugosa* lipase immobilized on MNPs turned out to be lower than that for the free enzyme, but constant activity over one month was seen in the case of lipase immobilized on MNPs.

Using bifunctional MNPs, Xu's group reported an instant and sensitive detection method for pathogens at ultralow concentration [30]. Compared with magnetic microbeads used in biological separation, MNPs promise high performance because of their large surface/volume ratios and easy entry into cells. For fast pathogen detection, FePt nanoparticles modified with vancomycin, a broad spectrum antibiotic, were prepared as a system that combines two kinds of interactions: magnetic dipole interactions that aggregate the MNPs under an applied magnetic field and specific multi-ligand-receptor interactions. Figure 9.4 shows a schematic illustration for the capture of bacteria by vancomycin-conjugated magnetic nanoparticles. Vancomycin was used to detect pathogens because it can bind to the terminal peptide, D-Ala-D-Ala, on the cell wall of a Gram-positive bacterium via hydrogen bonds. After mixing the solution of MNPs modified with vancomycin with a solution of bacterium, a point magnet was used to capture the "magnetized" bacteria and aggregates were analyzed using a microscopic method. The optical and SEM results

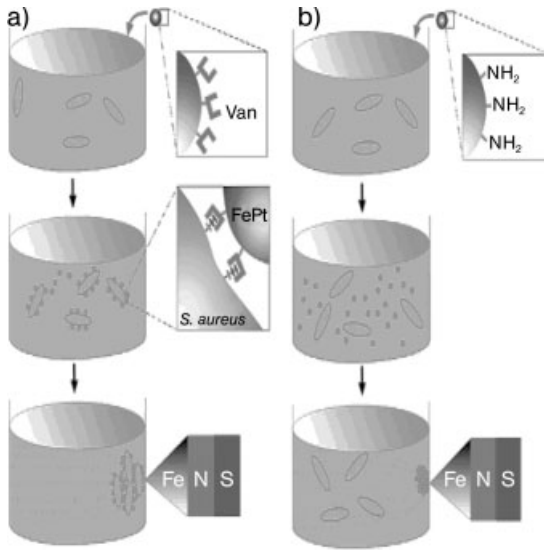


**Fig. 9.4.** Illustration of the capture of bacteria by vancomycin-conjugated magnetic nanoparticles (A), via a plausible multivalent interaction, and the corresponding control experiment (B). (From Ref. [30].)

show that MNPs modified with vancomycin selectively bind to most Gram-positive bacteria and vancomycin-resistant enterococci (VRE).

### 9.3

#### Carbon Nanotubes

Since Iijima discovered the first carbon nanotubes, using the arc discharge method, in 1991 [31], many nanoparticle-based catalytic methods have been developed and have contributed to the improvement in quality and size control of carbon nanotubes [32, 33]. Typically, carbon nanotubes are one to tens of nanometers in diameter and one to hundreds of micrometers long. Although interest in the application of carbon nanotubes has focused mainly on microelectronic devices [34–38], tremendous public concern has pressurized research into their effect on human health. Scientists have begun this bio-related research with the immobilization of biomolecules on carbon nanotube surfaces [39–42].

##### 9.3.1

#### Carbon Nanotubes for Targeted Cancer Cell Death

Hongjie Dai's group have reported that single-wall carbon nanotubes (SWNTs) can be a good multifunctional biological transporter and near-infrared agent for drug



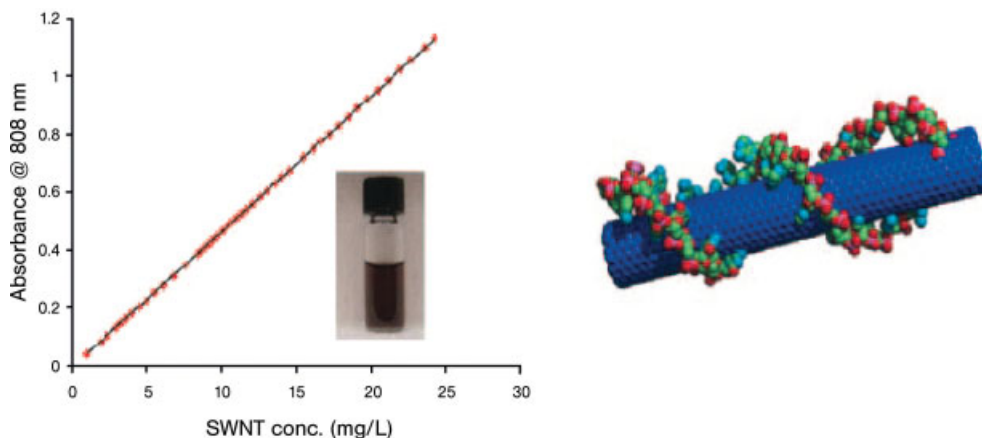


**Fig. 9.5.** NIR absorbance of SWNT at 808 nm vs. SWNT concentrations (left-hand side) and schematic of Cy3-DNA-functionalized SWNT (right-hand side). (From Ref. [43].)

delivery and cancer therapy [43]. SWNTs prepared from high-pressure CO conversion (Hipco) [44] have strong optical absorbance in the near-infrared (NIR) spectral window to which biological systems are highly transparent [45] and this property can be used for optical stimulation of nanotubes inside living cells to release their cargoes such as DNA and drug molecules or destroy cancer cell selectively. Figure 9.5 shows NIR absorbance of SWNT at 808 nm vs. SWNT concentrations; the molar extinction coefficient of the solubilized SWNTs (molecular mass  $\approx 170$  kDa, length  $\approx 150$  nm, diameter  $\approx 1.2$  nm) measured at  $\lambda = 808$  nm in the NIR was  $\epsilon \approx 7.9 \times 10^6 \text{ M}^{-1} \text{ cm}^{-1}$ . The high absorbance of SWNTs in the NIR originates from electronic transitions between the first or second van Hove singularities of the nanotubes. This work exploited the high optical absorbance of SWNTs in the 700–1100 nm NIR window transparent to biological systems at a single wavelength by using an 808-nm laser for *in vitro* radiation [46]. For the DNA transfection experiment, Hipco SWNTs were conjugated with Cy3-DNA by noncovalent adsorption and incubated with HeLa cells at 37 °C.

As seen in Fig. 9.6, the green color in confocal fluorescence image was observed in the cytoplasm region of HeLa, which implies that DNA–SWNT conjugates were internalized inside the cells, but not the nucleus, with nanotubes as the transporter. Upon irradiating the HeLa cells with NIR after DNA–SWNT uptake, colocalization of fluorescence of Cy3-DNA in the cell nucleus was detected, indicating the release of DNA cargoes from SWNT transporters and nuclear translocation after the laser pulses. Conversely, experiments carried out at 4 °C found no uptake of Cy3-DNA–SWNT conjugates inside cells, suggesting an energy-dependent endocytosis mechanism [47] for the uptake observed at 37 °C. For selective cancer cell destruction *in vitro*, SWNTs were noncovalently functionalized with phospholipids that had a poly(ethylene glycol) (PEG) moiety and folic acid (FA) terminal group and then in-

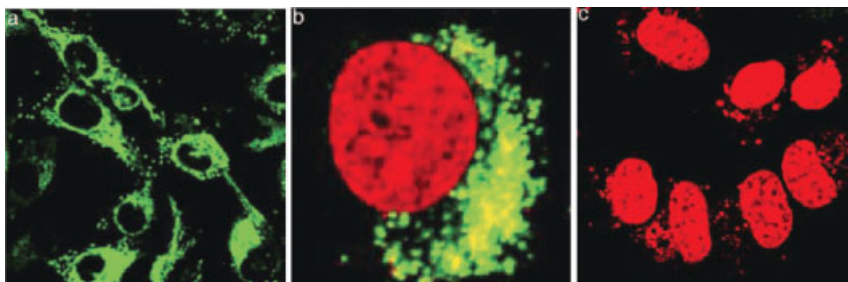


**Fig. 9.6.** Confocal fluorescence images of HeLa cells showing transporting DNA inside living cells by SWNTs: (a) After incubation with Cy3-DNA-SWNT (green); (b) after nucleus staining of HeLa cells by DRAQ5 (red); and (c) after incubation within a Cy3-DNA-SWNT at the low temperature of 4 °C and nucleus staining. (From Ref. [43].)

cubated with folate receptor (FR)-overexpressed HeLa cell and normal cells, respectively. FRs are common tumor markers expressed at high levels on the surfaces of various cancer cells and facilitate cellular internalization of folate-containing species by receptor-mediated endocytosis. After NIR irradiation, extensive cell death for the FR-overexpressed HeLa cells was evidenced by drastic cell morphology changes, whereas the normal cells remained intact. The selective destruction of FR-overexpressed cells was a result of selective binding of FA-functionalized SWNTs and FRs on FR-overexpressed cell surfaces and receptor-mediated endocytosis. This shows that SWNTs are molecular transporters or carriers with very high optical absorbance in the NIR regime where biological systems are transparent. Compared to Au nanoshells employed by Halas, West, and coworkers [48], the SWNTs can be the better NIR absorbing material for cancer cell destruction as lower laser power and shorter radiation times are needed.

### 9.3.2

#### Carbon Nanotubes for Detection of Cancer Cell

Carbon nanotubes have been integrated into a biosensor for the detection of prostate cancer by Chongwu Zhou's group [49]. Figure 9.7 shows, schematically, a device where an active channel made up of nanowires and nanotubes bridges the source/drain electrodes, and the silicon substrate can be used as a gate. They used n-type  $\text{In}_2\text{O}_3$  nanowires (NW) and p-type carbon nanotubes for the complementary detection of prostate specific antigen (PSA), a known oncological marker for the presence of prostate cancer. To detect PSA, they modified the outer surface of NW or SWNT with anti-PSA monoclonal antibody (PSA-AB), a specific ligand for PSA protein. As shown in Fig. 9.7(b), the surface of  $\text{In}_2\text{O}_3$  NW was functionalized with 3-phosphonopropionic acid, which has a COOH group at one end that was used to immobilize PSA-AB by forming amide bonds. The SWNT surface was first functionalized with 1-purenbutanoic acid succinimidyl ester and then treated with the PSA-AB solution (Fig. 9.7c). To investigate the chemical gating effect of PSA on the

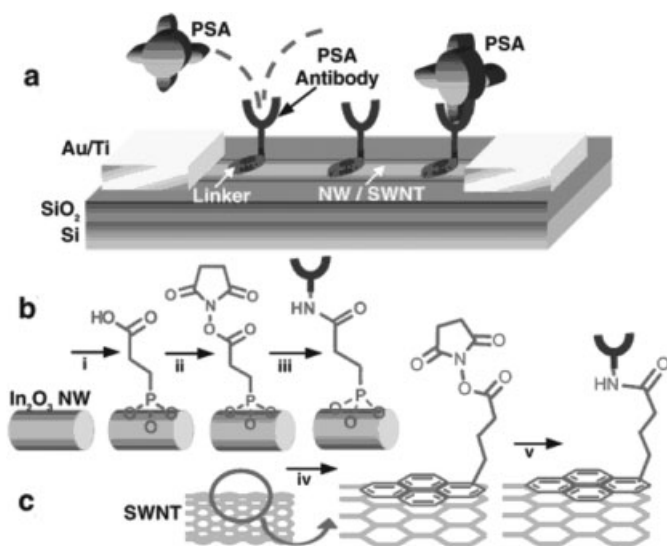


**Fig. 9.7.** (a) Schematic of a nanosensor. (b) Reaction scheme for the modification of In<sub>2</sub>O<sub>3</sub> NW. (c) Reaction scheme for the modification of SWNT. (From Ref. [49].)

devices, they incubated devices consisting of both individual NWs and individual semiconducting SWNTs in a PBS-buffered solution containing PSA for 15 h. The electrical properties of the devices, including both current–voltage ( $I$ - $V_{ds}$ ) and current–gate voltage ( $I$ - $V_g$ ) characteristics, were then measured in air before and after the PSA incubation. In this experiment, the authors consistently observed enhanced conductance for NW devices and reduced conductance for SWNT devices after PSA incubation. This complementary response in conductance arises because In<sub>2</sub>O<sub>3</sub> NWs are n-type and SWNTs are p-type semiconductors. As a result, a chemical gating effect of PSA introduces carriers into In<sub>2</sub>O<sub>3</sub> NWs, while the PSA binding decreases the carrier concentration in nanotubes, thus reducing conductance. Furthermore, the authors performed real-time PSA detection and succeeded in detecting PSA with a sensitivity of 5 ng mL<sup>-1</sup>, a level used for the clinical diagnosis of prostate cancer [50].

### 9.3.3

#### Carbon Nanotubes for Targeted Delivery

As new vectors for the delivery of therapeutic molecules, carbon nanotubes (CNTs) have attracted increasing attention due to the ease of translocation across cell membranes and lower toxicity [51, 52]. The use of functionalized carbon nanotubes (f-CNTs) for drug delivery of small molecules and an alternative strategy for the introduction of two different and orthogonal functionalizations to CNTs have been investigated by the group of Alberto Bianco [53]. The orthogonal methodol-

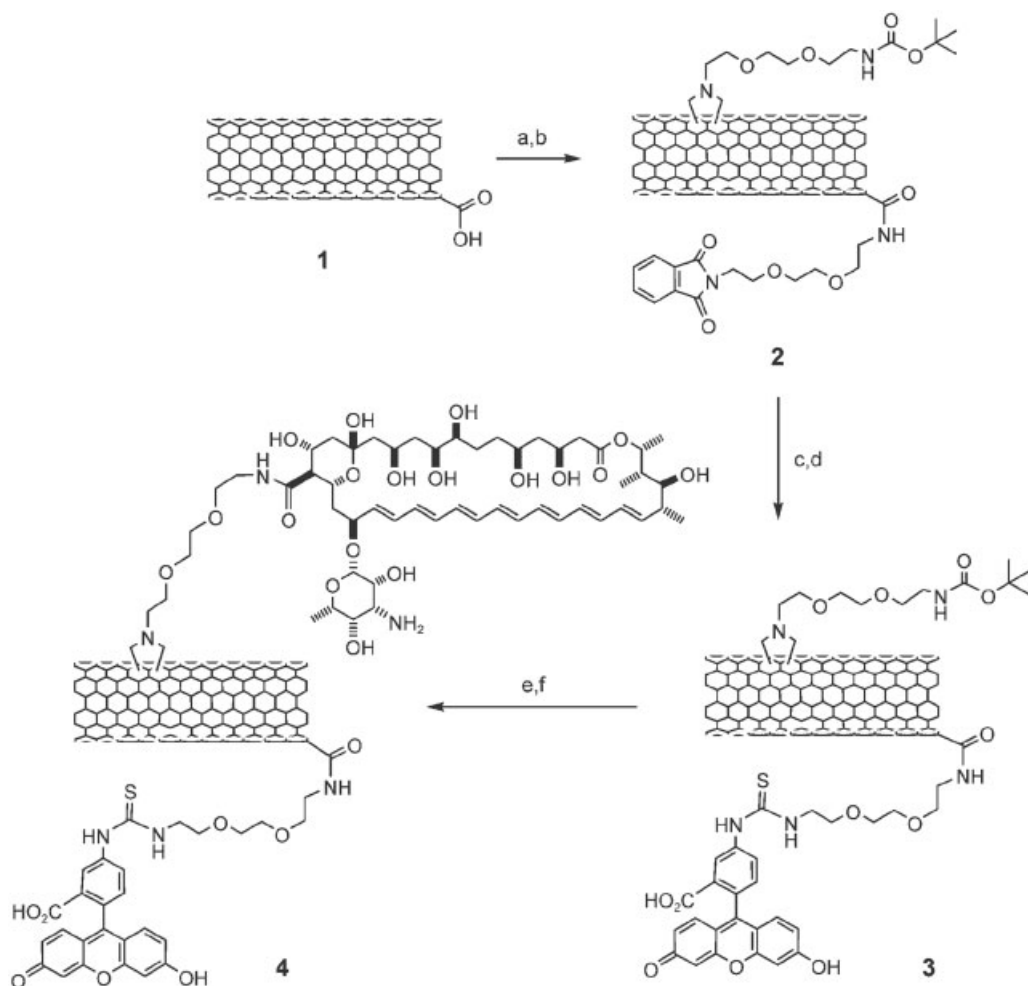


**Fig. 9.8.** Scheme for two different orthogonal CNT modifications. (a) Neat  $(\text{COCl})_2$ ; Pht- $\text{N}(\text{CH}_2\text{CH}_2\text{O})_2\text{CH}_2\text{CH}_2\text{NH}_2$ , dry THF, reflux; (b) Boc- $\text{NH}(\text{CH}_2\text{CH}_2\text{O})_2\text{CH}_2\text{CH}_2\text{NHCH}_2\text{COOH}/$

$(\text{CH}_2\text{O})_n$ , DMF, 125 $^\circ\text{C}$ ; (c) hydrated  $\text{NH}_2\text{NH}_2$ , EtOH, reflux; (d) FTIC, DMF; (e) HCl 4 m in dioxane; (f) Fmoc-AmB, HOBT/EDCHHCl/DIPEA, DMF; 25% piperidine in DMF. (From Ref. [53].)

ogy allows the selection and control of the attachment of active molecules to side-walls and tips of the CNTs. Oxidized MWNTs were activated as the acid chlorides and treated with diaminetriethylene glycol (mono-protected as phthalimide) (Fig. 9.8). The Boc-protected amine group was then introduced to the sidewalls of the MWNTs through 1,3-dipolar cycloaddition. The phthalimide group is particularly useful because it is stable to harsh acidic conditions and orthogonal to the Boc group. Thus FITC and amphotericin B (AmB) can be attached to the tips and side-

walls, respectively, of the CNTs. Fluorescein and AmB were chosen for tracking the uptake of material and as an antibiotic moiety, the active molecule, respectively. AmB is the most effective antibiotic, but is highly toxic to mammalian cells, originating from the formation of aggregates as a result of its lower solubility in water [54]. From the Human Jurkat lymphoma T cell viability test with either FITC-AmB-modified MWNTs (FITC-AmB-MWNTs) or AmB as control, the authors observed the conjugation of AmB to CNTs remarkably reduced the toxic effects. In addition, maximum fluorescence was observed after only 1 h of incubation, indicating rapid cell uptake of FITC-AmB-MWNTs. Most conjugates were found in cytoplasm and around the nuclear membrane. They excluded endocytosis for the mechanism of cell membrane penetration because  $\text{NaN}_3$  did not show remarkable influence on the penetration capacity of MWNT; instead, they proposed a spontaneous mechanism: MWNTs behave like nanoneedles and pass through the cell membrane without causing cell death [55]. They supposed the ability of CNTs to internalize AmB rapidly into the cytoplasm of Jurkat cells reduces the possibility of disruption of the cell membrane structure, thus reducing toxicity. They proved that covalent attachment of AmB to the nanotubes not only prevents the aggregation phenomena that the drug typically displays in solution but also that it has little effect on the antifungal activity.

## 9.4

### Nanotubes and Nanowires Composed of Artificial Peptides

#### 9.4.1

##### Peptide Nanotubes

In 2001, Ghadiri and coworkers reported peptide nanotubes [56–58] that have a new class of antibacterial activities on Gram-positive and/or Gram-negative bacteria [59]. This strategy is based on the self-assembly of ring-shaped cyclic peptide subunits that consist of six or eight alternating D- and L-amino acids. Hydrogen bonding between unit cyclic peptides allows well-defined tubular structures having a uniform internal diameter, which is adjustable by changing the number of amino acid residues in the ring; upon adsorption onto lipid membrane of bacteria, the cyclic peptides can stack to form hollow tubular structures that are open-ended, resulting in an increase in membrane permeability, collapse of transmembrane ion potential, and rapid cell death. Figure 9.9 shows the  $\beta$ -sheet-like, hydrogen-bonded tubular architecture of the self-assembled, eight-residue cyclic D,L- $\alpha$ -peptide, and the modes of membrane permeation accessible to peptide nanotubes. Self-assembly of an eight-residue cyclic D,L- $\alpha$ -peptide subunit is directed by intersubunit backbone-backbone hydrogen bonding to give  $\beta$ -sheet-like, tubular supramolecular structures that are open and hollow. Cyclic D,L- $\alpha$ -peptide nanotubes can display sequence-dependent modes of membrane permeation: intramolecular pore, barrel stave, and carpet-like (cyclic peptides are depicted as ring structures). Peptide nanotubes operating through the carpet-like mode of action could have a greater potential for

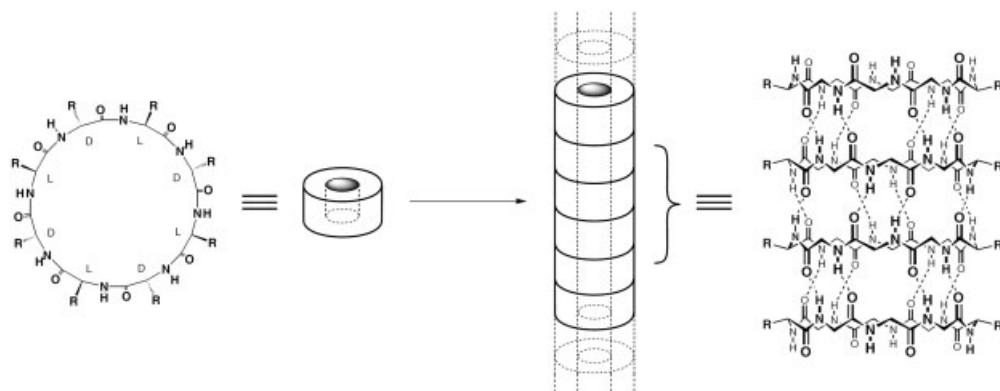


**Fig. 9.9.** Chemical structure of the cyclic D,L- $\alpha$ -peptides and schematic representation of the mode of interaction of the tube caps in forming heterometric transmembrane channels. (From Ref. [56].)

membrane discrimination because of their polyvalent display of surface-exposed hydrophilic side chains for potential interactions with various membrane constituents. For antibacterial activity test, a series of six- and eight-residue amphiphilic cyclic D,L- $\alpha$ -peptides was treated against *Escherichia coli* and methicillin-resistant *S. aureus* (MRSA), and each peptide was designed to bear at least one basic residue to enhance its target specificity towards negatively charged bacterial membranes. *In vitro* activity tests revealed that single amino-acid substitution changed membrane selectivity and activity. In addition, the high efficacy observed against lethal MRSA infections in mice indicates that this new class of abiotic structure, the cyclic peptide, and its quick bactericidal action may contribute to limit temporal acquirement of drug-resistant bacteria.

#### 9.4.2

##### Peptide-Amphiphile Nanofibers

Peptide-amphiphile (PA) nanofibers have been prepared by Stupp's group using self-assembly [60]. A PA is composed of several peptide residues, which can be customized through the peptide sequence for specific purposes, and an alkyl tail with 16 carbon atoms that pack in the center of the micelle, leaving the peptide segments exposed to the aqueous environment. Figure 9.10(A) shows the chemical structure of one example of PAs used in experiments. Here, the PA consists of five key structural features. Region 1 is a long alkyl tail that conveys hydrophobic character to the molecule and, when combined with the peptide region, makes the molecule amphiphilic. Region 2 is composed of four consecutive cysteine residues that when oxidized may form disulfide bonds to polymerize the self-assembled structure. Region 3 is a flexible linker region of three glycine residues to provide the hydrophilic head group flexibility from the more rigid crosslinked region. Re-

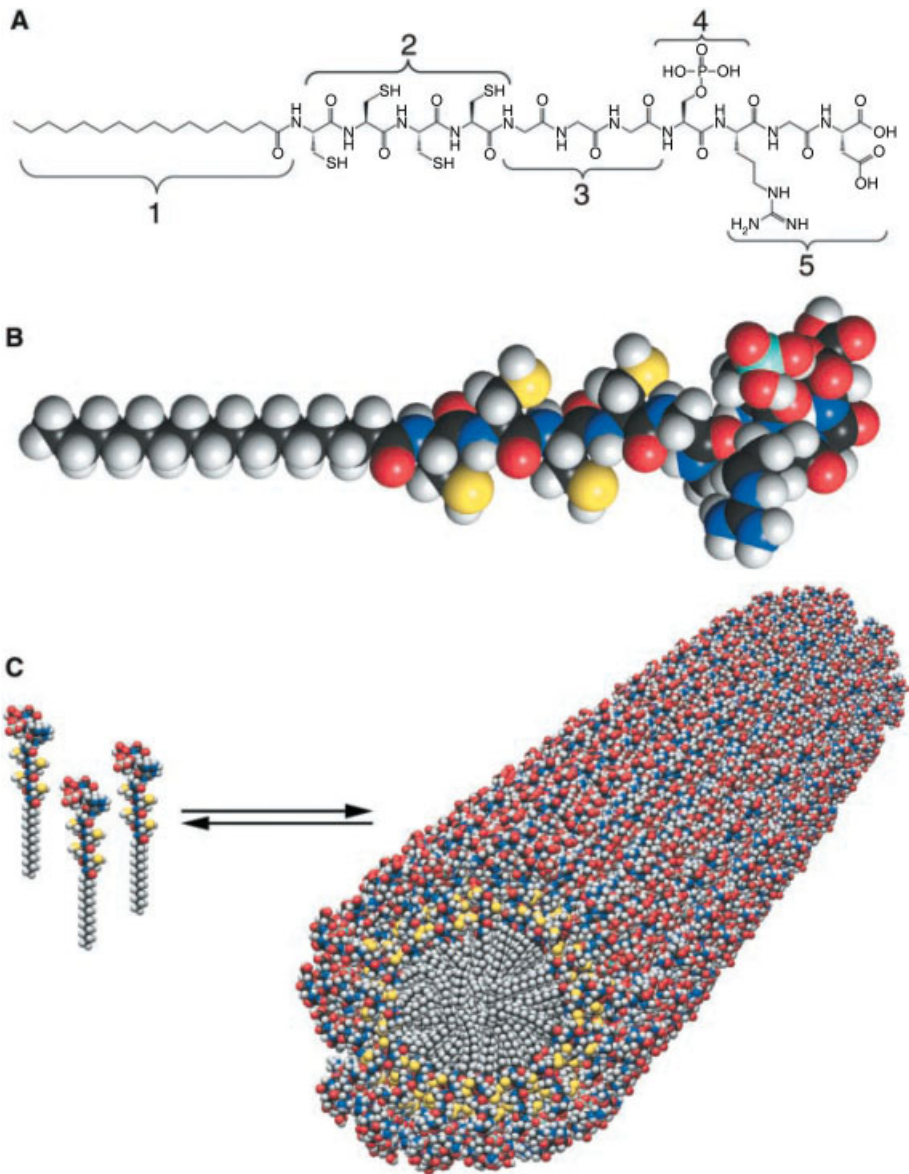


**Fig. 9.10.** (A) Chemical structure of the peptide amphiphiles (PA). (B) Molecular model of PA. (C) Schematic showing the self-assembly of PA. (From Ref. [60].)

gions 4 and 5 are variable regions and can be modified for specific functionalities. These PAs self-assemble at acidic pH into cylindrical fibers ~6–8 nm in diameter and interior cysteine groups are crosslinked through disulfide bonds to yield pH-stable nanofibers. Stupp and colleagues have shown many useful applications for these PA nanofibers, with various functional molecules coupled to the peptide residues of PA for specific applications. For example, 1,4,7,10-tetraazacyclododecane-1,4,7,10-tetraacetic acid (DOTA) was conjugated to PA to yield PA nanofibers for the magnetic resonance imaging (MRI) [61]. When the Gd(III) ion is chelated to the DOTA, Gd(III) is detoxified and the complex acts as a strong MR agent. A peptide nucleic acid/PA conjugate (PNA-PA) has been prepared to develop isolation tools for the poly A-containing mRNAs and biotin has been incorporated into PA for the high densities of binding sites on their surface [62, 63]. Carbon nanotubes were successfully encapsulated into PA nanofiber without degradation of their structural, electronic, and optical properties [64]. The most interesting application is as a cell differentiator. The authors showed that PA nanofiber composed of the pentapeptide epitope isoleucine-lysine-valine-alanine-valine (IKVAV), which was known to promote neurite sprouting and direct neurite growth, can be used to direct the differentiation of neural progenitor cells largely into neurons while suppressing astrocyte differentiation [65]. Once neural progenitor cells are encapsulated within a three-dimensional network of PA nanofiber it is possible to present to cells the neurite-promoting laminin epitope, which is the peptide element of the PA, at nearly van der Waals density. As a result, the nanofibers can achieve amplification of bioactive epitope presentation to cells.

## 9.5

### Template-synthesized Nanotubes and Nanorods

Carbon nanotubes, self-assembled lipid tubes, and peptide nanotubes have been successfully used in some biomedical applications; however, it is difficult to control their tube diameter or length and some nanotubes such as the lipid tubes must be coated with ceramic or metal to make them rugged enough for biomedical use [66]. Since Martin and coworkers have pioneered a technology, called template synthesis, for preparing *monodisperse* nanotubes of nearly any size and composed of nearly any material, tubular structures have become highly attractive for multifunctional nanoparticles [67]. The template method is a general approach for preparing nanomaterials that involves the synthesis or deposition of the desired material within the cylindrical and monodisperse pores of a nanopore membrane or other solid surface [68]. Fig. 9.11 shows an alumina template that has a cylindrical nanopore with monodisperse diameters and lengths. Porous alumina template can be obtained by well-established electrochemical anodization on aluminum plate. These pore dimensions can be typically controlled, ranging from 5 to a few hundred nanometers in diameter and from tens of nanometers to hundreds of micrometers in length. Depending on the membrane and synthetic method used, such as chemical or electrochemical deposition of desired material, solid



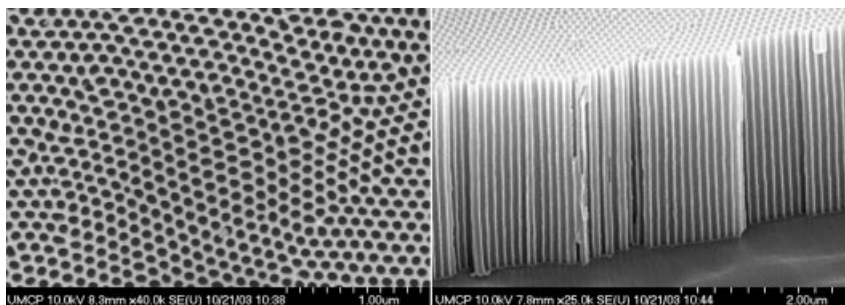


**Fig. 9.11.** Field emission scanning electron micrograph (FESEM) of a home-made alumina template (60-nm in diameter). Top (left-hand side) and cross sectional (right-hand side) images. (Unpublished data prepared by the authors.)

nanowires or hollow nanotubes can be produced. This method has been used to prepare nanowires and nanotubes composed of many types of material, including metals, polymers, semiconductors and carbons. In addition, the template method can be used to prepare composite nanostructures, including concentric tubular composites.

Several unique properties make these nanotubes potential candidate for biotechnological applications. First, their inner voids can be filled with large amounts of interesting materials, such as fluorophores for high optical signal, drug molecules to deliver, magnetic materials for *in vivo* imaging. Second, the distinct outer surfaces can be easily modified with biomolecules. Finally, these nanotubes can be made out of nearly any material. This technology offers tremendous flexibility in making nanotubes with a desired biological property such as biocompatibility or biodegradability [69].

### 9.5.1

#### Differential Functionalization of Nanotube

As another beautiful example of template synthesis, Martin's group recently reported a very important technology, so-called *differential functionalization* between the inner and outer surfaces of nanotubes based on a silica nanotube [13]. They used silica nanotubes for proof-of-concept experiments because they are easy to make, readily suspend in aqueous solution, and because silica surfaces can be easily modified using simple silane chemistry with commercially available reagents. The silica walls of nanotubes are completely transparent for UV/Vis light in the range 200–800 nm, allowing it to pass through to the inner materials. Silica nanotubes were synthesized within the pores of nanopore alumina template membranes using a sol-gel method [70]. The authors have developed the following simple procedure for applying different functional groups to the inner versus outer surfaces of these nanotubes (Fig. 9.12). Before being liberated from the template membrane, the inner surface of a nanotube is modified with the first silane. The

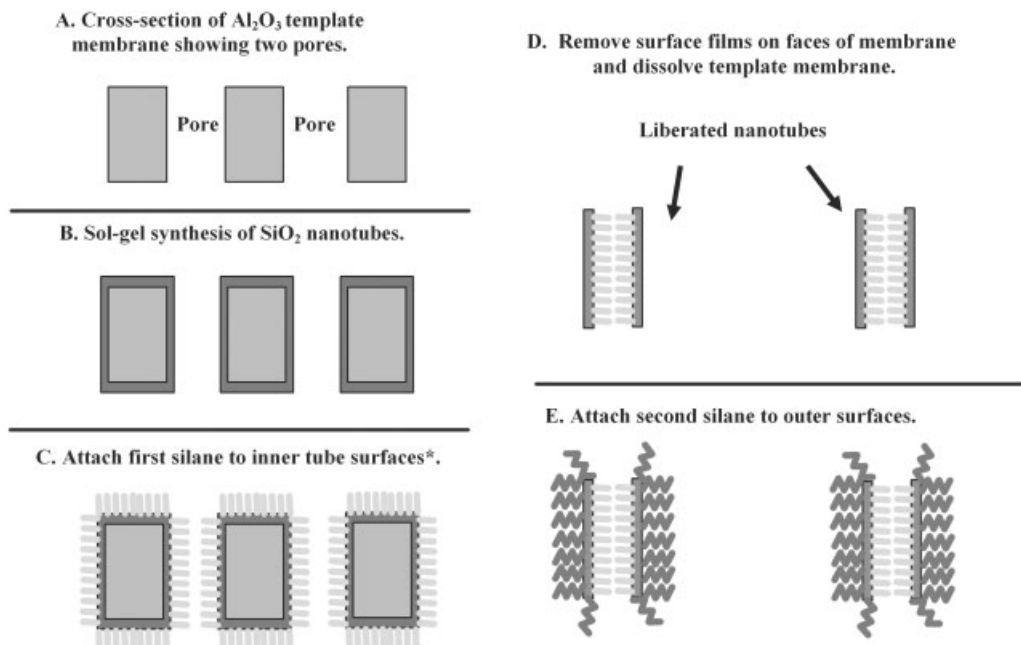


**Fig. 9.12.** Schematic of the differential modification procedure. \* Membrane surfaces also. (From Ref. [13].)

outer surfaces of nanotubes are not modified because they are in contact with the membrane template. The template is then dissolved to liberate the nanotubes, affording free outer surfaces that are then modified with a second silane.

To demonstrate this differential functionalization, two sets of nanotubes were prepared: (a) with the green fluorescent silane *N*-(triethoxysilylpropyl)dansylamide attached to inner surfaces and the hydrophobic octadecylsilane (C18) to the outer surfaces and (b) with the blue fluorescent silane triethoxysilylpropylquinineurethane on the inner surfaces and the bare native (hydrophilic) outer surface. Each of these nanotubes were added to a vial containing water and the immiscible organic solvent cyclohexane. The solvents were then mixed and allowed to separate. The green nanotubes with hydrophobic outer surfaces partition into the (upper) cyclohexane phase (Fig. 9.13A), while blue fluorescence is seen only from the aqueous phase with the hydrophilic nanotubes (Fig. 9.11B). When both sets of nanotubes are added to the solvent mixture in the same vial, tubes with the C18 outer surface chemistry partition into cyclohexane and those with the silica outer surface chemistry partition into water (Fig. 9.11C).

### 9.5.2

#### Selective Extraction of Drug Molecules

Antibody-functionalized nanotubes can be used to extract selectively one enantiomer from a racemic mixture. Fab fragments of antibody produced against the drug 4-[3-(4-fluorophenyl)-2-hydroxy-1-[1,2,4]-triazol-1-yl-propyl]benzotrile (FTB,

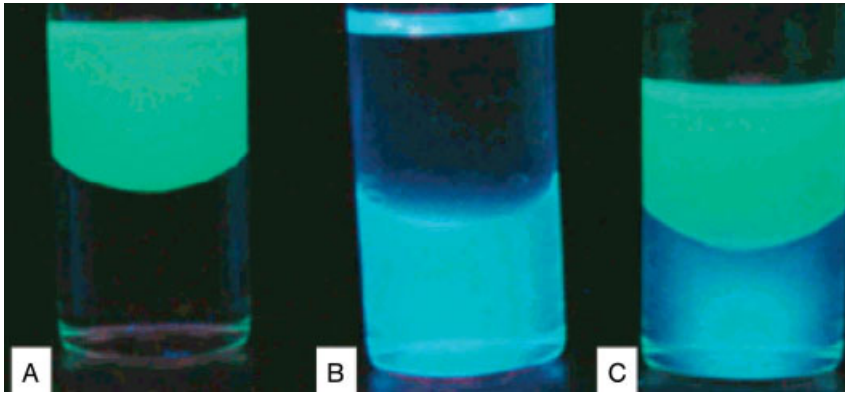


**Fig. 9.13.** Vials containing cyclohexane (upper) and water (lower) under UV light excitation after addition of 10 mg of nanotubes with (A) dansylamide on inner and C18 on outer surfaces and (B) quinineurethane on inner and no silane on outer surfaces; (C) 10 mg of both A and B nanotubes; 200-nm diameter nanotubes were used. (From Ref. [13].)

Fig. 9.14) [71] were immobilized on both inner and outer surfaces of silica nanotubes by attaching an aldehyde silane to both surfaces of free-standing silica nanotubes liberated from membrane template; the aldehyde group of this silane reacts with free amino groups on the Fab fragment of antibody via Schiff base chemistry. After racemic mixtures of the SR and RS enantiomers of FTB were incubated with Fab-functionalized nanotubes, the tubes were then collected by filtration, and the amounts of two enantiomers in the filtrate solution were measured by a chiral HPLC method. Figure 9.14 shows chromatograms both before (chromatogram I)

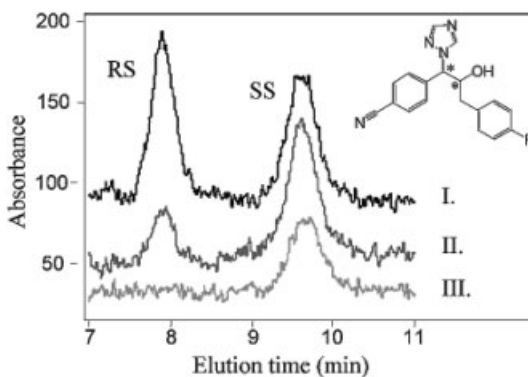


**Fig. 9.14.** Chiral HPLC chromatograms for racemic mixtures of FTB before (I) and after (II, III) extraction with  $18 \text{ mg mL}^{-1}$  of 200-nm Fab-containing nanotubes. (From Ref. [13].)

and after (chromatogram II) exposure of a solution that contained 20  $\mu\text{M}$  of both enantiomers to the Fab-functionalized nanotubes. They found that 75% of the RS enantiomer and none of the SR enantiomer were removed by the nanotubes and that all of the RS enantiomer was removed (chromatogram III) when the concentration of the racemic mixture was dropped to 10  $\mu\text{M}$ . A control experiment with bare silica nanotubes containing no Fab fragment showed negligible extraction of both enantiomers from a 20  $\mu\text{M}$  solution.

Silica nanotubes containing Fab on only the inner surface were prepared by differential functionalization. While nanotubes are still embedded within the pores of template membrane, aminopropyltrimethoxysilane was used to functionalize the inside of the nanotubes with an amine group. After dissolution of the template, the resultant nanotubes were treated with glutaraldehyde, a well-known Schiff base crosslinker, and Fab fragments were immobilized inside the nanotubes through another imine bond between the primary amine of the Fab antibody and the remaining aldehyde group of glutaraldehyde. When a racemic mixture of the drug was incubated with these interior-only Fab-modified nanotubes, 80% of the RS (and none of the SR) enantiomer was extracted, corresponding to almost half the amount extracted by nanotubes with Fab on both their inner and outer surfaces.

### 9.5.3

#### Silica Nanotube Carrier for DNA Transfection

The use of silica nanotubes as a biomolecule carrier, such as a DNA transporter, has been explored by Wu and coworkers [72]. They used the template synthesis method to fabricate silica nanotubes (SNT) that can transport DNA molecules to cells. First, silica nanotubes were prepared inside the pores of 200-nm diameter commercial alumina membrane using a sol-gel process involving tetraethyl orthosilicate. The inner silica layer was then modified with 3-aminopropyltriethoxysilane (APTS) to generate the polycationic surface required to hold CdSe/ZnS core-shell quantum dots (QDs) or DNAs through the electrostatic forces. Figure 9.15 shows, briefly, the preparation of fluorescent silica nanotubes and their use for

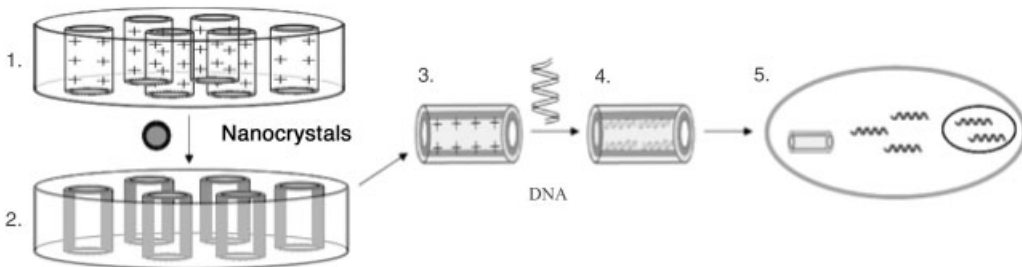


**Fig. 9.15.** Schematic illustration of a fluorescent silica nanotube and its application in gene delivery. (From Ref. [72].)

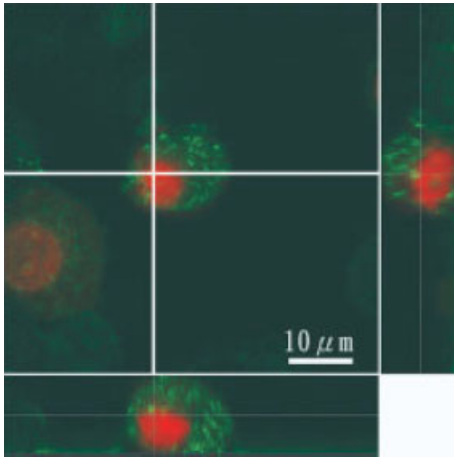


**Fig. 9.16.** Fluorescence microscopy image of COS-7 cells incubated with green QD-silica nanotube after nucleus staining (red) with propidium iodide. (From Ref. [72].)

gene delivery. Before the gene delivery experiment, cultured mammalian cells such as monkey kidney COS-7 cells were treated with green fluorescent silica nanotubes (gfSNTs) to test the cell membrane permeability of silica nanotubes. They found, by confocal microscopy, that the gfSNT entered about 60–70% of the cells by endocytosis and were mostly localized in the cytoplasm (Fig. 9.16). Cytotox-

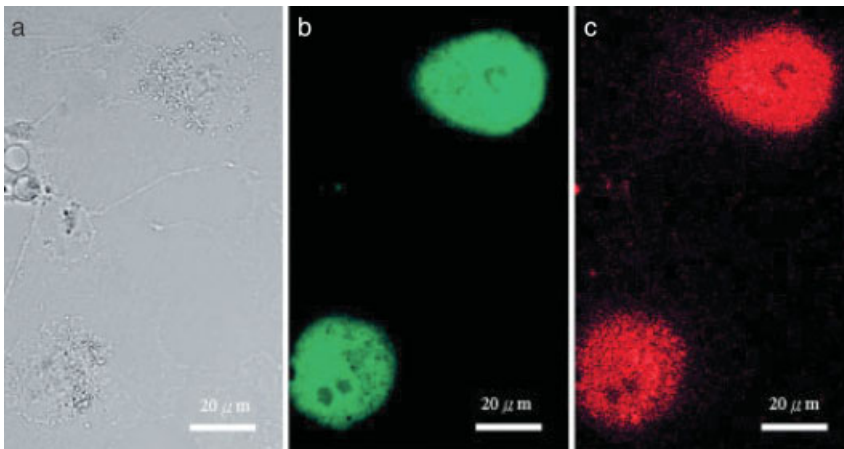


**Fig. 9.17.** (A) Bright-field image of COS-7 cells incubated with DNA/silica nanotube complex. Fluorescence image of the same cells (B) showing GFP expression and (C) incubated with GFP-DAN and red-fluorescent silica nanotube. (From Ref. [72].)

icity tests on nanotubes in the cells, using the 3-(4,5-dimethylthiazol-2-yl)-2,5-diphenyltetrazolium bromide (MTT) assay, revealed that approximately 80% of the cells were still viable after treatment with gfsNT, indicating that silica nanotubes are not especially toxic under the experimental conditions. For a gene delivery experiment, plasmid DNA was inserted into the nanotube to form a DNA/SNT complex, and the complex was added to COS-7 cells. Cells treated with the DNA/SNT complex showed cytoplasmic GFP expression (Figure 9.17), whereas cells treated with free DNA or red fsNT as a control experiment did not. Although the efficiency of SNT-mediated DNA transfection (ca. 10–20%) is less than that of conventional calcium phosphate (ca. 60–70%), the advantage of this strategy is that SNTs can carry other biomolecules such as RNA or proteins.

#### 9.5.4

#### DNA Nanotubes

Unlike the previous DNA-functionalized nanotubes [73, 74], Martin's group have reported DNA nanotubes composed entirely, or predominately, of DNA itself, based on the template synthesis method and DNA hybridization [75]. First, a template membrane was treated with Mallouk's alternating  $\alpha,\omega$ -diorganophosphonate ( $\alpha,\omega$ -DOP) Zr(IV) to form the outer skin of a DNA nanotube, which guides the growth of a DNA layer [76]. As seen in Fig. 9.18, DNA layers were integrated subsequently into the nanotube from the ( $\alpha,\omega$ -DOP) Zr(IV) skin with the alternating hybridization of the two 15-base segments up to five layers. The nanotubes were then liberated by dissolution of the template in a solution of diluted phosphoric acid and 2 M NaCl at 0 °C and collected by centrifugation. A TEM image shows liberated five-layer DNA nanotubes and shorter nanotubes than the alumina template, which is 36  $\mu\text{m}$  thick, indicating that the tubes were broken during membrane dissolution and centrifugation. Because these DNA nanotubes are made of

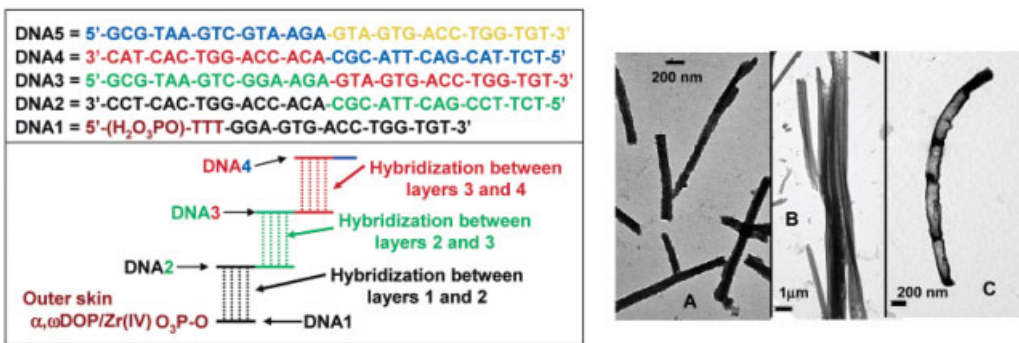
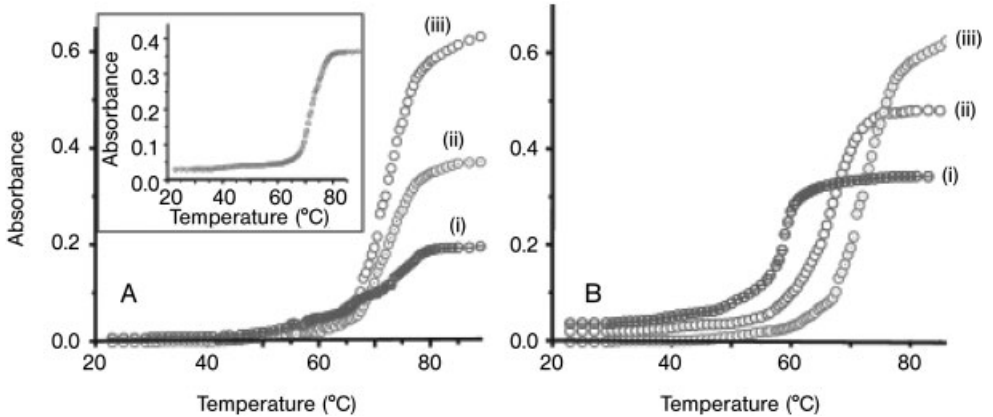


Fig. 9.18. Scheme of DNA hybridization and TEM image of five tubes with (A) one-layer and (B) three-layer  $\alpha,\omega$ -DOP/Zr(IV) skins. (C) Same as for (A) but after heating to 85 °C. (From Ref. [75].)



**Fig. 9.19.** Thermal decomposition curves for (A) nanotubes composed of the DNAs in Fig. 9.18. Number of DNA layers: (i) 2, (ii) 3, (iii) 5. Nanotubes were embedded within the pores of the template. Inset: five-layer tubes liberated from the template. (B) Five-layer nanotubes composed of hybridized 8 (i), 12 (ii) and 15 (iii) base duplexes. (From Ref. [75].)

double-stranded DNA (dsDNA), they can be heated above the melting point at which dsDNA releases the dehybridized ssDNA chains from the tube, which means this strategy can be used to transport DNA. Consequently, DNA release from the DNA-nanotube-containing alumina membranes into buffer solution was investigated, by UV absorbance (260 nm), upon heating from 23 to 85 °C. Figure 9.19 shows that there was, initially, no DNA in solution because the nanotubes were sequestered within the pores of template; however, above the melting temperature, the release of ssDNA was detected. The same DNA release experiment carried out for nanotubes liberated from the template membrane gave analogous data. This result shows that a new family of layer-by-layer template-synthesized DNA nanotubes can be used for DNA transport and that their release can be controlled by melting the DNA duplexes.

#### 9.5.5

#### Nanobarcodes for Multiplexing Diagnosis

In 2001, Keating and Natan's group exploited metallic nanobarcodes that have alternating metal stripes in a nanorod shape for bioanalysis [16]. Multiplexing and miniaturization is big issues in cancer diagnosis, and in any other bioanalysis. To develop innovative devices that can measure ever-increasing numbers of species from smaller and smaller samples volumes, microarray [77] and encoded microbeads [78], or nanoparticles with distinctive fluorescent signatures [79] have been investigated. Microarrays can encode large numbers of analysis based on position, but slow diffusion of analytes to the surface is an intrinsic problem of planar microarray and the range of analyte concentrations that may be detected at the same time is limited. Although an array of beads in solution, such as microbeads or

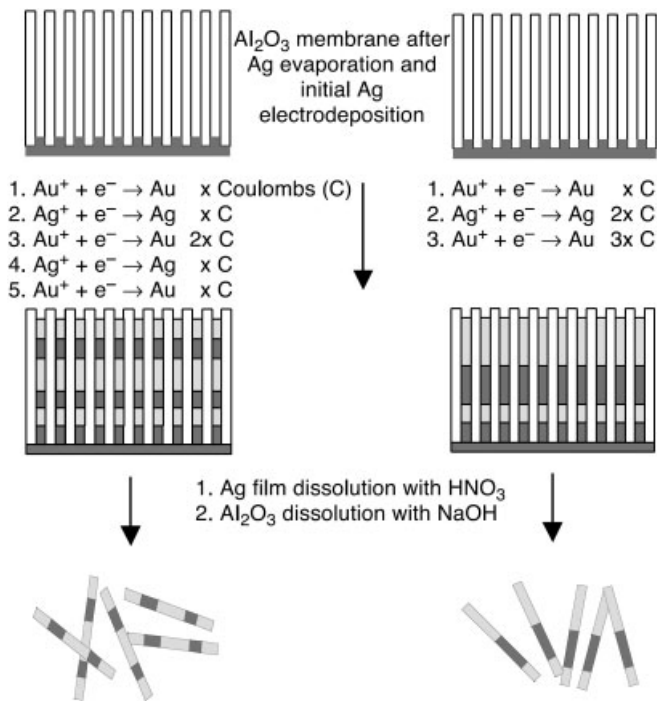


Fig. 9.20. Schematic of the synthesis of nanobarcodes. (From Ref. [16].)

nanoparticles, may circumvent the shortcomings of planar microarrays for assay, the number of previously reported bead-based assays that can be performed simultaneously is limited by the number of spectrally distinguishable fluorophores. However, metallic barcodes enable a wide variety of bioanalytical measurements because many thousands of uniquely identifiable particles can be prepared and then used in fluorescence- and mass spectrometry-based assays. Such nanobarcodes have been manufactured electrochemically in the pores of alumina or polycarbonate using the template synthesis method (Fig. 9.20). Striped, cylindrical metal nanoparticles were optically characterized by the pattern of differential reflectivity of adjacent stripes. For example, a metallic nanobarcode composed of Au, Ag, Ni, Pd, and Pt shows different patterns of optical reflectivity, corresponding to their own identity, with respect to the wavelength of illumination light (Fig. 9.21). Figure 9.22 shows that barcoded rods can be used as supports for bioassays, and the selective detection of DNA hybridization on single optically encoded particles was successfully demonstrated for an important first step towards multiplexed hybridization assays. The authors adapted DNA hybridization and immunoassays for use on barcodes. A 24-mer analyte DNA binds to a 12-mer capture DNA immobilized on the surface of a nanobarcode and is later detected by addition of a 12-mer probe DNA that is complementary to the remaining 12 nucleotides and carries a fluores-



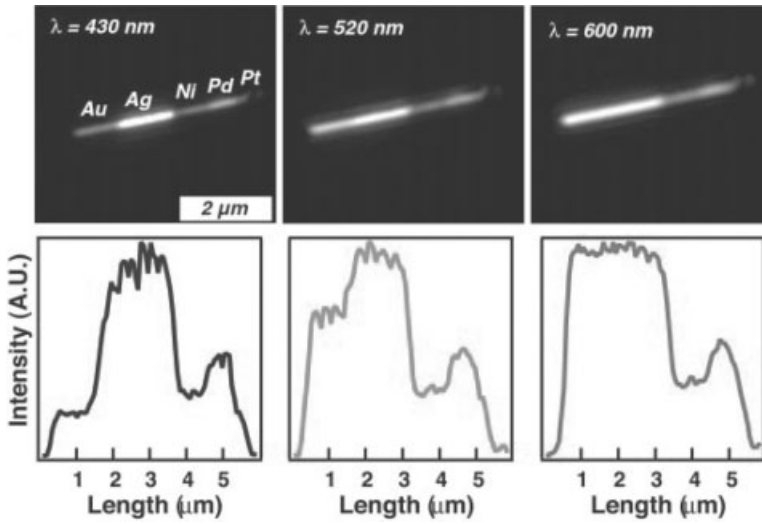


Fig. 9.21. Reflectance optical microscopy images and line profiles for a particle of composition Au-Ni-Pd-Pt with illumination at 430, 520 and 600 nm. (From Ref. [16].)

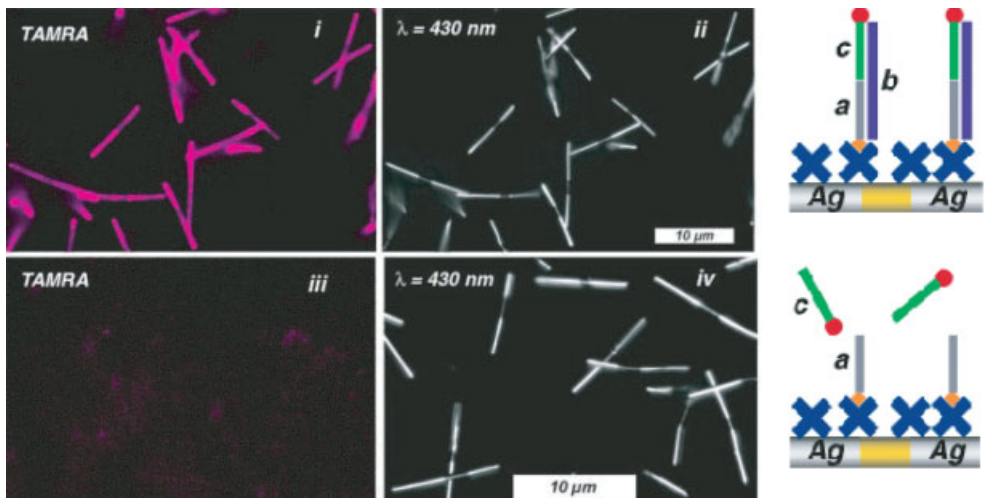


Fig. 9.22. Sandwich DNA hybridization assay. (i) Fluorescence readout; (ii) shows the rod ID. The analyte (b) was omitted in the controls (iii) and (iv). (From Ref. [16].)

cent tag. Each particle can be seen in both the fluorescence (i) and reflectivity (ii) images. In a control experiment, in which the analyte is omitted, a very low fluorescence background is observed (iii) and particles are visible only in the reflectivity image (iv).

### 9.5.6

#### Magnetic Nanotubes

Magnetic nanoparticles have been intensively studied for various biomedical applications, such as early detection of cancer and targeted drug delivery, due to their unique magnetic field-assisted properties like magnetic resonance imaging (MRI) and controlled movement in a magnetic field. Therefore, by combining the attractive magnetic properties with a tubular structure, magnetic nanotubes (MNTs) can be an ideal candidate for multifunctional nanomaterials in biomedical applications, such as targeted drug delivery and MRI. In 2005 Lee's group reported another interesting nanotube based on the template synthesis method [12]. They showed that MNTs can provide another type of useful tool for biomedical and biotechnological applications, including magnetic-field-assisted bioseparation, biointeraction, drug delivery and MRI. Inner voids of MNTs can be used for capturing, concentrating, and releasing species ranging in size from large proteins to small molecules because the tube dimensions can be easily controlled by template synthesis. Distinctive outer surfaces can be differentially functionalized with environmentally friendly and/or probe molecules for a specific target. The group described the synthesis of MNTs and their uses for magnetic-field-assisted chemical and biochemical separations, immunobinding, and drug delivery.

##### 9.5.6.1 Synthesis and Characterization of Magnetic Nanotubes

Silica nanotubes have been synthesized with a layer of magnetite ( $\text{Fe}_3\text{O}_4$ ) nanoparticles on the inner surface of the nanotube using porous alumina film as template (60 and 200 nm pore diameter). To form the layer of magnetite nanoparticles, the silica-nanotube alumina film was dip-coated with a 4:1 mixture solution of  $\text{FeCl}_3$  (1 M) and  $\text{FeCl}_2$  (2 M), dried in an Ar stream, and immersed in  $\text{NH}_4\text{OH}$  [80]. For the differential functionalization of MNTs, the inner nanotube surface was treated with octadecyltriethoxysilane (C18) while MNTs were still embedded in the pores of alumina template. Free-standing MNTs were obtained after polishing both sides of the template film mechanically and dissolving the alumina template in a 0.1 M NaOH solution. After the template was dissolved completely, MNTs were collected by filtration. Transmission electron microscopy (TEM) images of MNTs (Fig. 9.23) show clearly the magnetite layers on the inner surface of the nanotubes; bare silica nanotubes have smooth tubular wall surfaces. Room-temperature magnetization curves of MNTs obtained by superconducting quantum interference device (SQUID) showed that both 60- and 200-nm diameter MNTs exhibit superparamagnetic characteristics and their saturation magnetizations are 2.7 and 2.9  $\text{emu g}^{-1}$ , respectively. Energy dispersive X-ray (EDX) analysis revealed that these magnetic nanotubes consist mainly of Fe and Si.

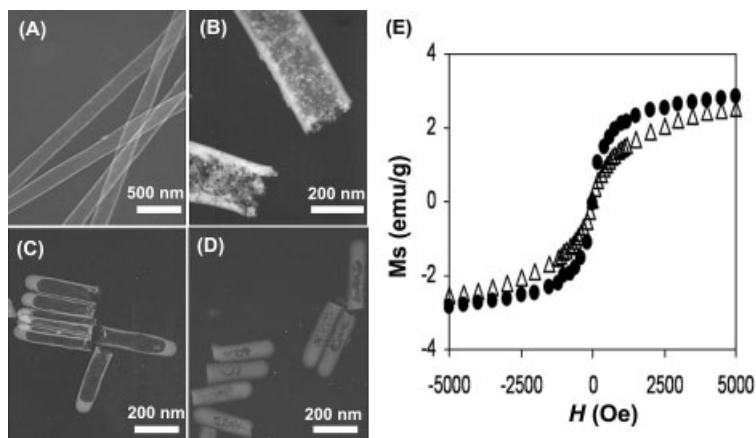


**Fig. 9.23.** Transmission electron micrographs (TEM) of (A, B) 200 and (C, D) 60-nm diameter silica nanotubes without magnetite (A, C) and magnetic nanotubes (MNTs) with magnetite (B, D). (E) Room temperature magnetization curves of MNTs. (From Ref. [12].)

#### 9.5.6.2 Magnetic Field-assisted Chemical Separation and Biointeraction

In an exemplary chemical extraction and separation experiment, MNTs ( $\sim 10^9$ ) functionalized inside with C18 were added to a solution of 1.1'-dioctadecyl-3,3,3',3'-tetramethylindocarbocyanine perchlorate ( $\text{DiIC}_{18}$ , 38  $\mu\text{M}$ ) in water/methanol (9:1 v/v, 1 mL). The mixture was then shaken and allowed to stand for 10 min so that the dye molecules could enter the MNTs by the strong hydrophobic interaction. These nanotubes are completely suspendible in aqueous phases (even in pure water) due to their outer hydrophilic silica surfaces. A strong magnet was then used to separate the nanotubes, and thus the  $\text{DiIC}_{18}$  molecules, from the solution. Figure 9.24 show that magnetic separation turns an initially red solution, containing the red dye ( $\text{DiIC}_{18}$ ), almost transparent and clear. UV/Vis spectroscopy and fluorescence microscopy studies were further performed to show that more than 95% of the  $\text{DiIC}_{18}$  was removed from solution and the hydrophobic dye was extracted inside the MNTs. As a control experiment, when MNTs without an inner C18 layer were incubated with  $\text{DiIC}_{18}$ , no detectable change was observed. The above results tell us that these MNTs can be used for the extraction, separation, release, and analysis of trace amounts of extremely hydrophobic toxic chemicals, such as polychlorinated biphenyls (PCBs) and polycyclic aromatic hydrocarbons (PAHs), in water [81].

MNTs with human IgG inside were prepared and added to a mixed solution (2 mL, pink color) of fluorescein-labeled anti-bovine IgG [green, 0.71  $\mu\text{M}$  in 0.1  $\text{M}$  phosphate-buffered saline (PBS), pH 7.4] and Cy3-labeled anti-human IgG (red, 0.67  $\mu\text{M}$ ) to show a magnetic bioseparation using antigen–antibody interaction. BSA-derivatized MNTs (BSA-MNTs) were prepared as well to show a nonspecific

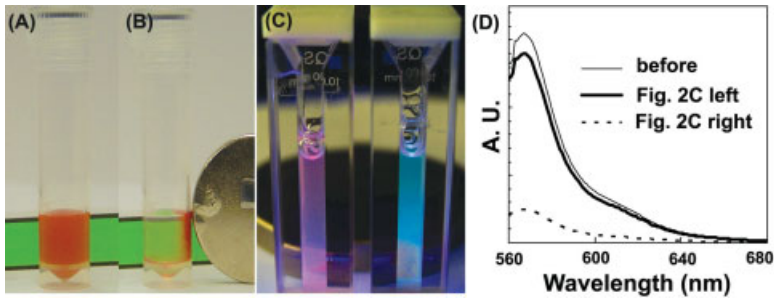


**Fig. 9.24.** A vial containing C-18 modified MNTs before (A) and after (B) magnetic separation for 2 min. (C) A solution containing green FITC-labeled anti-bovine IgG and red Cy3-labeled anti-human IgG after magnetic separation with BSA-MNTs (left) and human IgG-MNTs (right). (D) Fluorescence spectra for measuring the amount of remaining red Cy3-labeled anti-human IgG in solution. (From Ref. [12].)

biointeraction. The outer surfaces of all the MNTs were functionalized with poly(ethylene glycol) (PEG) silane to prevent nonspecific adsorptions on silica surfaces. After magnetic separation, the solution changes from the original pink to greenish blue only when MNTs with human IgG inside are added, while the solution with BSA-MNTs remains pink. This means that red Cy3-labeled anti-human IgG was separated specifically from the solution by human IgG-MNTs. Fluorescence spectra show that 84% of the Cy3-labeled anti-human IgG was separated by human IgG-MNTs but only 9% by BSA-MNTs.

Very interestingly, the magnetic properties of MNTs can be used to facilitate and enhance biointeractions between the outer surfaces of MNTs and a specific target surface. As a potential application, the drug delivery efficiency might be greatly improved by magnetic field-assisted biointeraction when the MNTs carry the drug inside and have probe molecules, such as antibody, on the outer surfaces. In a proof-of-concept experiment, onto a anti-rabbit IgG-modified glass slide, 60-nm diameter MNTs with FITC-modified inner surfaces and rabbit IgG-modified outer surfaces were added and incubated for 10 min both with and without a magnetic field applied to the bottom of the glass slide. After washing the unbound nanotubes, the number of bound nanotubes were counted at five different regions of fluorescence microscopy images (Fig. 9.25) and then averaged. A ca. 4.2-fold binding enhancement was observed for the antigen–antibody interactions in the presence of a magnetic field, showing that the efficiency of antigen–antibody interactions can be controlled spatially by means of an external magnetic field.

#### 9.5.6.3 Drug Uptake and Controlled Release

MNTs functionalized on their inner surface with an aminosilane (aminopropyltriethoxysilane, APTS) have been prepared for drug delivery experiments. The MNTs were treated with APTS while still embedded inside the template, which was then dissolved, and the nanotubes were collected by filtration. 5-Fluorouracil (5-FU), 4-nitrophenol, and ibuprofen were then loaded in an organic solvent, such as etha-

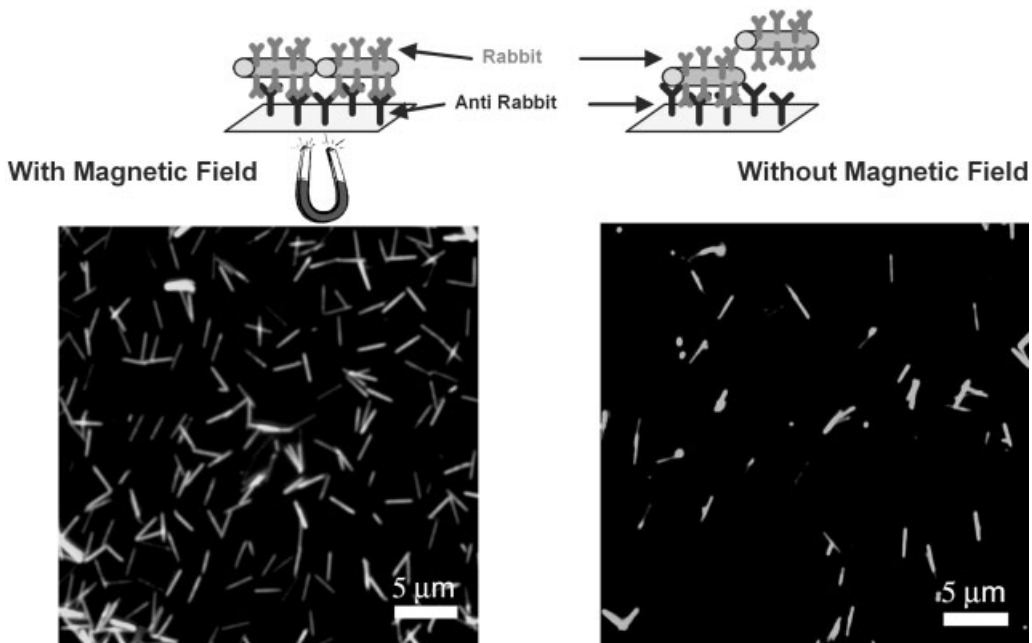


**Fig. 9.25.** Fluorescence microscope images of bound FITC-MNTs-Rabbit IgG (60 nm in diameter, 3  $\mu\text{m}$ ) following incubation with anti-rabbit IgG-modified glass with and without the application of a magnetic field under the glass substrate. (From Ref. [12].)

nol or hexane, as model drug molecules into the pores of MNTs functionalized with APTS to study the effect of charged hydrogen bonding interactions between the drug and the inner pore surfaces on loading and release. To remove the drug molecules bound onto the outer surface of MNTs, and weakly bound drugs, drug-loaded MNTs were washed with PBS (1 mL) and filtered quickly twice, and redispersed in pH 7.4 PBS and incubated at room temperature on a rocking platform. After separation of MNTs from solution using either a strong NdFeB magnet or centrifugation, the amount of released drug was determined by UV/Vis spectroscopy by monitoring changes in absorbance at 264 nm (ibuprofen), 400 nm (4-nitrophenol), and 266 nm (5-FU). The percentage release of loaded drug was estimated by measuring the absorbance of drug-released solution after 5 days. UV/Vis spectrophotometry showed that the number of molecules loaded per nanotube was  $\sim 10^7$  for ibuprofen,  $\sim 10^6$  for 4-nitrophenol, and  $\sim 10^7$  for 5-FU. The value for ibuprofen is about twice the monolayer coverage of the MNT inner surface area. Figure 9.26 shows the drug release rate: <10% of ibuprofen was released in 1 h and 80% was released after 24 h. For 5-FU and 4-nitrophenol, however, more than 90% was released in 1 h. Although several factors have to be considered, such as hydrogen bonding, hydrophobic interaction, and solubility, the ionic interaction between

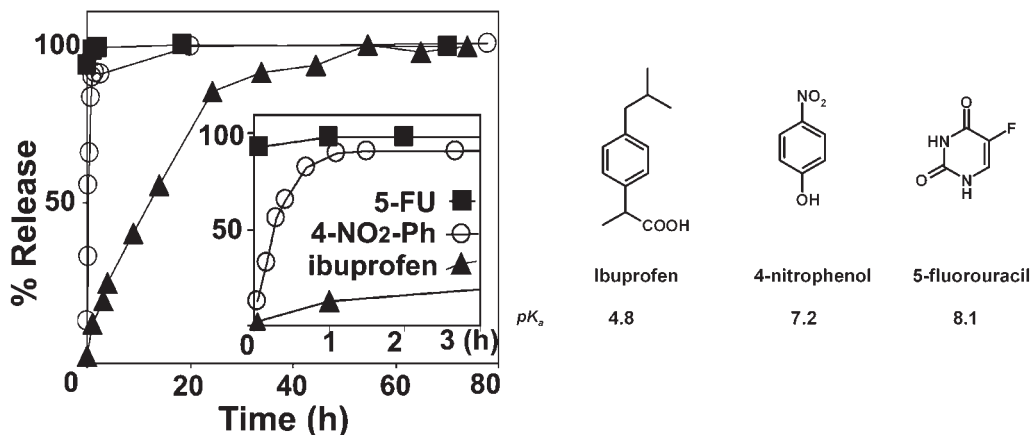


Fig. 9.26. *In vitro* release of ibuprofen, 4-nitrophenol (4-NO<sub>2</sub>-Ph), and 5-fluorouracil (5-FU) from MNTs (60 nm diameter, 250 nm long), and the pK<sub>a</sub> of each drug. (From Ref. [12].)

the inner surface of MNTs and drug molecule is a plausible explanation for this tendency. At pH 7.4, ibuprofen (pK<sub>a</sub> 4.8) is fully ionized so that Coulomb interaction between negatively-charged ibuprofen and protonated aminopropyl groups on the interior of MNTs contributes considerably to retardation of drug release. With 4-nitrophenol (pK<sub>a</sub> 7.2) and 5-FU (pK<sub>a</sub> 8.1), however, the contribution of Coulomb interactions is moderate (4-nitrophenol) or almost negligible (5-FU) because the degree of ionization is less than that of ibuprofen. These results show that the hollow tubular structure of magnetic particles is one of the most promising candidates for various applications, including chemical and biochemical separations and drug delivery, and MNTs with drug-friendly interiors and target-specific exteriors may open up a new field of materials for multifunctional targeted drug delivery.

## 9.6

### Conclusion

We believe that nanotubes or nanowires – with inner chemistry that can be utilized – can be attractive alternatives to spherical nanoparticles – which utilize a single surface – for biomedical and biotechnological applications. Tubular nanoparticles provide more options than spherical ones, especially when multifunctionality is needed because nanotubes have distinctive inner and outer surfaces that can be modified and utilized differentially, enabling them to be equipped with the right function at the right position. The fabrication of nanotubes has been greatly improved by the template synthesis, which affords monodisperse nanotubes with controllable dimensional parameters, such as diameter, length, and wall thickness, together with the differential functionalization technique. However, since the field of

nanotubes and nanowires is still in the early stages of biotechnological applications, much fundamental research is needed to solve challenging problems before commercialization of the technology. For example, although nanotubes can accommodate drugs or biomolecules in their inner space, only their inner surface, and not the whole inner volume, is used in chemical bonds or interactions with chemicals. As Martin mentioned in his review [68], capped nanotubes for which the cap can block the nanotube pore and fall off reversibly according to a chemical or biochemical signal might be one way to overcome such biotechnological problems.

As shown in magnetic particles used for early-stage cancer diagnosis [26] and magnetism-based interaction capture (MAGIC) [27], or peptide nanotubes used for a new class of antibacterial agent [59], combining the properties of a nanomaterial with an existing technology, such as magnetic resonance (MR) imaging, optical or electronic methods, enables us to exploit a novel concept that can not be attained with the conventional technology. Therefore, by combining properties originating from a tubular structure with existing well-understood technology, nanotubes can open up new opportunities to develop a new class of therapeutic and diagnostic tools and to resolve existing biotechnological problems.

## References

- 1 PEREZ, J. M., JOSEPHSON, L., WEISSELEDER, R., Viral-induced self-assembly of magnetic nanoparticles allows the detection of viral particles in biological media., *J. Am. Chem. Soc.*, **2003**, 125, 10192–10193.
- 2 RADLER, J., KOLTOVER, I., SALDITT, T., SAFINYA, C. R., Structure of DNA-cationic liposome complexes: DNA intercalation in multilamellar membranes in distinct interhelical packing regimes., *Science*, **1997**, 275, 810–814.
- 3 PARK, S. J., TATON, T. A., MIRKIN, C. A., Array-based electrical detection with nanoparticles probes., *Science*, **2002**, 295, 1503–1506.
- 4 MURTHY, N., THNG, Y. X., SCHUCK, S., XU, M. C., FRECHET, J. M., A novel strategy for encapsulation and release of proteins: Hydrogels and microgels with acid-labile acetal cross-linkers., *J. Am. Chem. Soc.*, **2002**, 124, 12398–12399.
- 5 LI, K. C. P., PANDIT, S. D., GUCCIONE, S., BEDNARSKI, M. D., Molecular imaging applications in nanomedicine., *Biomed. Microdevices*, **2005**, 6, 113–116.
- 6 PARK, J. W., Liposome-based drug delivery in breast cancer treatment., *Breast Cancer Res.*, **2002**, 4, 95–99.
- 7 CAO, Y. W. C., JIN, R. C., MIRKIN, C. A., Nanoparticles with Raman spectroscopic fingerprints for DNA and RNA detection., *Science*, **2002**, 297, 1536–1540.
- 8 HIRSCH, L. R., HALAS, N. J., WEST, J. L., A whole blood immunoassay using gold nanoshells., *Anal. Chem.*, **2003**, 75, 2377–2381.
- 9 VOURA, E. B., JAISWAL J. K., MATTOUSSI, H., SIMON, S., Tracking metastatic tumor cell extravasation with quantum dot nanocrystals and fluorescence emission-scanning microscopy. *Nat. Med.* **2004**, 10, 993–998.
- 10 FERRARI, M., Cancer nanotechnology: Opportunities and challenges, *Nat. Rev. Cancer*, **2005**, 5, 161–171.
- 11 YINGHUI, Z., PENG, A. T., CARPENTER, K., MAGUIRE, J. A., HOSMANE, N. S., TAKAGAKI, M.,

- Substituted carborane-appended water-soluble single-wall carbon nanotubes: New approach to boron neutron capture therapy drug delivery., *J. Am. Chem. Soc.*, **2005**, *127*, 9875–9880.
- 12 SON, S. J., REICHEL, J., HE, B., SCHUCHMAN, M., LEE, S. B., Magnetic nanotubes for magnetic-field-assisted bioseparation, biointeraction, and drug delivery., *J. Am. Chem. Soc.*, **2005**, *127*, 7316–7317.
  - 13 MITCHELL, D. T., LEE, S. B., TROFIN, L., LI, N., NEVANEN, T. K., SODERLUND, H., MARTIN, C. R., Smart nanotubes for bioseparations and biocatalysis., *J. Am. Chem. Soc.* **2002**, *124*, 11864.
  - 14 BUCAK, S., JONES, D. A., LAIBINIS, P. E., HATTON, T. A., Protein separations using colloidal magnetic nanoparticles., *Biotechnol. Prog.*, **2003**, *19*, 477.
  - 15 OKAMOTO, K., SHOOK, C. J., BIVONA, L., LEE, S. B., ENGLISH, D. S., Direct observation of wetting and diffusion in the hydrophobic interior of silica nanotubes., *Nano Lett.*, **2004**, *4*, 233–239.
  - 16 NICEWARNER-PENA, S. R., FREEMAN, R. G., REISS, B. D., HE, L., PENNA, D. J., WALTON, I. D., CROMER, R., KEATING, C. D., NATAN, M. J., Submicrometer metallic barcodes, *Science*, **2001**, *294*, 137–141.
  - 17 HARTGERINK, J. D., BENIASH, E., STUPP, S. I., Self-assembly and mineralization of peptide-amphiphile nanofibers, *Science*, **2001**, *294*, 1684–1687.
  - 18 KIRCHER, M. F., MAHMOOD, U., KING, R. S., WEISSLEDER, R., JOSEPHSON, L., A multimodal nanoparticle for preoperative magnetic resonance imaging and intraoperative optical brain tumor delineation., *Cancer Res.* **2003**, *63*, 8122–8125.
  - 19 KOBAYASHI, H., CHOYKE, P. L., BRECHBIEL, M. W., WALDMANN, T. A., Lymphatic drainage imaging of breast cancer in mice by micro-magnetic resonance lymphangiography using a nano-size paramagnetic contrast agent., *J. Natl. Cancer Inst.* **2004**, *96*, 703–708.
  - 20 NEUWALT, E. A., VARALLYAY, P., BAGO, A. G., MULDOON, L. L., NESBIT, G., NIXON, R., Imaging of iron oxide nanoparticles with MR and light microscopy in patients with malignant brain tumors., *Neuropathol. Appl. Neurobiol.*, **2004**, *5*, 456–471.
  - 21 LEWIN, M., CARLESSO, N., TUNG, C. H., TANG, X. W., CORY, D., SCADDEN, D. T., WEISSLEDER, R., Tat peptide-derivatized magnetic nanoparticles allow in vivo tracking and recovery of progenitor cells. *Nat. Biotechnol.* **2000**, *18*, 410–414.
  - 22 CHEON, J., KANG, N.-J., LEE, S.-M., LEE, J.-H., YOON, J.-H., OH, S. J., Shape evolution of single-crystalline iron oxide nanocrystals., *J. Am. Chem. Soc.*, **2004**, *126*, 1950–1951.
  - 23 SONG, H.-T., CHOI, J.-S., HUH, Y.-M., KIM, S., JUN, Y.-W., SUH, J.-S., CHEON, J., Surface modulation of magnetic nanocrystals in the development of highly efficient magnetic resonance probes for intracellular labeling., *J. Am. Chem. Soc.*, **2005**, *127*, 9992–9993.
  - 24 PARK, J., LEE, E., HWANG, N.-M., KANG, M., KIM, S. C., HWANG, Y., PARK, J.-G., NOH, H.-J., KIM, J.-Y., PARK, J.-H., HYEON, T., One-nanometer-scale size-controlled synthesis of monodisperse magnetic iron oxide nanoparticles., *Angew. Chem., Int. Ed.*, **2005**, *44*, 2872–2877.
  - 25 HUH, Y.-M., JUN, Y.-w., SONG, H.-T., KIM, S., CHOI, J.-s., LEE, J.-H., YOON, S., KIM, K.-S., SHIN, J.-S., SUH, J.-S., CHEON, J., In vivo magnetic resonance detection of cancer by using multifunctional magnetic nanocrystals., *J. Am. Chem. Soc.* **2005**, *127*, 12 387–12 391.
  - 26 JUN, Y.-w., HUH, Y.-M., CHOI, J.-s., LEE, J.-H., SONG, H.-T., KIM, S.-j., YOON, S., KIM, K.-S., SHIN, J.-S., SUH, J.-S., CHEON, J., Nanoscale size effect of magnetic nanocrystals and their utilization for cancer diagnosis via magnetic resonance imaging., *J. Am. Chem. Soc.* **2005**, *127*, 5732–5733.
  - 27 WON, J., KIM, M., YI, Y.-W., KIM, Y. H., JUNG, N., KIM, T. K., A magnetic nanoprobe technology for



- detecting molecular interactions in live cells., *Science* **2005**, 309, 121–125.
- 28 DYAL, A., LOOS, K., NOTO, M., CHANG, S. W., SPAGNOLI, C., SHAFI, K. V. P. M., ULMAN, A., COWMAN, M., GROSS, R. A., Activity of *Candida rugosa* lipase immobilized on  $\gamma$ -Fe<sub>2</sub>O<sub>3</sub> magnetic nanoparticles., *J. Am. Chem. Soc.* **2003**, 125, 1684–1685.
  - 29 GROSS, R. A., KUMAR, A., KALRA, B., Polymer synthesis by in vitro enzyme catalysis., *Chem. Rev.*, **2001**, 101, 2097–2124.
  - 30 GU, H., HO, P.-L., TSANG, K. W. T., WANG, L., XU, B., Using biofunctional magnetic nanoparticles to capture vancomycin-resistant enterococci and other gram-positive bacteria at ultralow concentration., *J. Am. Chem. Soc.* **2003**, 125, 15 702–15 703.
  - 31 IIJIMA, S., Helical microtubules of graphitic carbon. *Nature* **1991**, 354, 56–58.
  - 32 AJAYAN, P. M., Nanotubes from carbon., *Chem. Rev.*, **1999**, 99, 1787–1800.
  - 33 DAI, H., KONG, J., ZHOU, C., FRANKLIN, N., TOMBLER, T., CASSELL, A., FAN, S., CHAPLINE, M., Controlled chemical routes to nanotube architectures, physics, and devices., *J. Phys. Chem. B*, **1999**, 103, 11 246–11 255.
  - 34 ZHOU, C., KONG, J., YENILMEZ, E., DAI, H., Modulated chemical doping of individual carbon nanotubes. *Science*, **2000**, 290, 1552–1555.
  - 35 FAN, S., CHAPLINE, M. G., FRANKLIN, N. R., TOMBLER, T. W., CASSELL, A. M., DAI, H., Self-oriented regular arrays of carbon nanotubes and their field emission properties., *Science*, **1999**, 283, 512–514.
  - 36 KONG, JING, SOH, HYONGSOK T., CASSELL, ALAN M., QUATE, CALVIN F., DAI, HONGJIE, Synthesis of individual single-walled carbon nanotubes on patterned silicon wafers., *Nature*, **1998**, 395, 878–881.
  - 37 DUERKOP, T., KIM, B. M., FUHRER, M. S., Properties and applications of high-mobility semiconducting nanotubes., *J. Phys.: Condensed Matter*, **2004**, 16, R553–R580.
  - 38 HINES, D. R., MEZHENNY, S., BREBAN, M., WILLIAMS, E. D., BALLAROTTO, V. W., ESEN, G., SOUTHARD, A., FUHRER, M. S., Nanotransfer printing of organic and carbon nanotube thin-film transistors on plastic substrates., *Appl. Phys. Lett.*, **2005**, 86, 163 101–163 101.
  - 39 CHEN, R. J., ZHANG, Y., WANG, D., DAI, H., Noncovalent sidewall functionalization of single-walled carbon nanotubes for protein immobilization., *J. Am. Chem. Soc.*, **2001**, 123, 3838–3839.
  - 40 CHEN, R. J., HONGJIE, D., Noncovalent functionalization of carbon nanotubes for highly specific electronic biosensors., *Proc. Natl Acad. Sci. U.S.A.*, **2003**, 100, 4984–4989.
  - 41 AZAMIAN, B. R., DAVIS, J. J., COLEMAN, K. S., BAGSHAW, C. B., GREEN, M. L. H., Biochemical single-walled carbon nanotubes., *J. Am. Chem. Soc.*, **2002**, 124, 12664–12665.
  - 42 WONG, S. S., JOSELEVICH, E., WOOLLEY, A. T., CHEUNG, C. L., LIEBER, C. M., Covalently functionalized nanotubes as nanometer-size probes in chemistry and biology., *Nature*, **1998**, 394, 52–55.
  - 43 KAM, N. W. S., O'CONNELL, M., WISDOM, J. A., DAI, H., Carbon nanotubes as multifunctional biological transporters and near-infrared agents for selective cancer cell destruction., *Proc. Natl. Acad. Sci. U.S.A.* **2005**, 102, 11 600–11 605.
  - 44 NIKOLAEV, P., BRONIKOWSKI, M. J., BRADLEY, R. K., ROHMUND, F., COLBERT, D. T., SMITH, K. A., SMALLEY, R. E., Gas-phase catalytic growth of single-walled carbon nanotubes from carbon monoxide., *Chem. Phys. Lett.*, **1999**, 313, 91–97.
  - 45 O'CONNELL, M. J., BACHILO, S. M., HUFFMAN, C. B., MOORE, V. C., STRANO, M. S., HAROZ, E. H., RIALON, K. L., BOUL, P. J., NOON, W. H., KITTRELL, C., MA, J., HAUGE, R. H., WEISMAN, R. B., SMALLEY, R. E., Band gap fluorescence from individual single-walled carbon nanotubes., *Science*, **2002**, 297, 593–596.

- 46 KOENIG, K., Two-photon excited lifetime imaging of autofluorescence in cells during UVA and NIR photostress., *J. Microsc.*, **1996**, 183, 197–204.
- 47 MUKHERJEE, S., GHOSH, R. N., MAXFIELD, F. R., Endocytosis, *Physiol. Rev.*, **1997**, 77, 759–803.
- 48 HIRSCH, L. R., STAFFORD, R. J., BANKSON, J. A., SERSHEN, S. R., RIVERA, B., PRICE, R. E., HAZLE, J. D., HALAS, N. J., WEST, J. L., Nanoshell-mediated near-infrared thermal therapy of tumors under magnetic resonance guidance. *Proc. Natl. Acad. Sci. U.S.A.*, **2003**, 100, 13 549–13 554.
- 49 LI, C., CURRELI, M., LIN, H., LEI, B., ISHIKAWA, F. N., DATAR, R., COTE, R. J., THOMPSON, M. E., ZHOU, C., Complementary detection of prostate-specific antigen using In<sub>2</sub>O<sub>3</sub> nanowires and carbon nanotubes., *J. Am. Chem. Soc.*, **2005**, 127, 12 484–12 585.
- 50 LI, X., ZHANG, Y. P., KIM, H. S., BAE, K. H., STANTZ, K. M., LEE, S. J., JUNG, C., JIMENEZ, J. A., GARDNER, T. A., JENG, M. H., KAO, C., Gene Therapy for prostate cancer by controlling adenovirus *E1a* and *E4* gene expression with pses enhancer., *Cancer Res.*, **2005**, 65, 1941–1951.
- 51 BIANCO, A., PRATO, M., Can carbon nanotubes be considered useful tools for biological applications?, *Adv. Mater.* **2003**, 15, 1765–1768.
- 52 BIANCO, A., KOSTARELOS, K., PARTIDOS, C. D., PRATO, M., Biomedical applications of functionalized carbon nanotubes., *Chem. Commun.* **2005**, 571–577.
- 53 WU, W., WIECKOWSKI, S., PASTORIN, G., BENINCASA, M., KLUMPP, C., BRIAND, J.-P., GENNARO, R., PRATO, M., BIANCO, A., Targeted delivery of amphotericin B to cells by using functionalized carbon nanotubes., *Angew. Chem., Int. Ed.* **2005**, 44, 6358–6362.
- 54 ZOTCHEV, S. B., Olyene macrolide antibiotics and their applications in human., *Curr. Med. Chem.*, **2003**, 10, 211–223.
- 55 CAI, D., MATARAZA, J. M., QIN, Z.-H., HUANG, Z., HUANG, J., CHILES, T. C., CARNAHAN, D., KEMPA, K., REN, Z., Highly efficient molecular delivery into mammalian cells using carbon nanotube spearing., *Nat. Methods*, **2005**, 2, 449–454.
- 56 BONG, D. T., CLARK, T. D., GRANJA, J. R., GHADIRI, M. R., Self-assembling organic nanotubes., *Angew. Chem., Int. Ed.* **2001**, 40, 988–1011.
- 57 KIM, H. S., HARTGERINK, J. D., GHADIRI, M. R., Oriented self-assembly of cyclic peptide nanotubes in lipid membranes., *J. Am. Chem. Soc.*, **1998**, 120, 4417–4424.
- 58 HORNE, W. S., STOUT, C. D., GHADIRI, M. R., A heterocyclic peptide nanotube., *J. Am. Chem. Soc.*, **2003**, 125, 9372–9376.
- 59 FERNANDEZ-LOPEZ, S., KIM, H.-S., CHOI, E. C., DELGADO, M., GRANJA, J. R., KHASANOV, A., KRAEHNBUHL, K., LONG, G., WEINBERGER, D. A., WILCOXEN, K. M., GHADIRI, M. R., Antibacterial agents based on the cyclic D,L- $\alpha$ -peptide architecture., *Nature* **2001**, 412, 452–456.
- 60 HARTGERINK, J. D., BENIASH, E., STUPP, S. I., Self-assembly and mineralization of peptide-amphiphile nanofibers., *Science*, **2001**, 294, 1684–1688.
- 61 BULL, S. R., GULER, M. O., BRAS, R. E., MEADE, T. J., STUPP, S. I., Self-assembled peptide amphiphile nanofibers conjugated to MRI contrast agents., *Nano Lett.*, **2005**, 5, 1–4.
- 62 GULER, M. O., POKORSKI, J. K., APPELLA, D. H., STUPP, S. I., Enhanced oligonucleotide binding to self-assembled nanofibers., *Bioconjugate Chem.*, **2005**, 16, 501–503.
- 63 GULER, M. O., SOUKASENE, S., HULVAT, J. F., STUPP, S. I., Presentation and recognition of biotin on nanofibers formed by branched peptide amphiphiles., *Nano Lett.*, **2005**, 5, 249–252.
- 64 ARNOLD, M. S., GULER, M. O., HERSAM, M. C., STUPP, S. I., Encapsulation of carbon nanotubes by self-assembling peptide amphiphiles., *Langmuir*, **2005**, 21, 4705–4709.

- 65 SILVA, G. A., CZEISLER, C., NIECE, K. L., BENIASH, D., HARRINGTON, D. A., KESSLER, J. A., STUPP, S. I., Selective differentiation of neural progenitor cells by high-epitope density nanofibers., *Science*, **2004**, 303, 1352–1355.
- 66 SPECTOR, M. S., SELINGER, J. V., SINGH, A., RODRIGUEZ, J. M., PRICE, R. R., SCHNUR, J. M., Controlling the morphology of chiral lipid tubules., *Langmuir*, **1998**, 14, 3493–3500.
- 67 MARTIN, C. R., Nanomaterials: A membrane-based synthetic approach., *Science* **1994**, 266, 1961–1966.
- 68 MARTIN, C. R., KOHLI, P., The emerging field of nanotube biotechnology., *Nat. Rev. Drug Discov.* **2003**, 2, 29–37.
- 69 MILLER, S. A., YOUNG, V. Y., MARTIN, C. R., Electroosmotic flow in template-prepared carbon nanotube membranes., *J. Am. Chem. Soc.* **2001**, 123, 12 335–12 342.
- 70 STEINLE, E. D., MITCHELL, D. T., WIRTZ, M., LEE, S. B., YOUNG, V. Y., MARTIN, C. R., Ion channel mimetic micropore and nanotube membrane sensors., *Anal. Chem.* **2002**, 74, 2416–2422.
- 71 LEE, S. B., MITCHELL, D. T., TROFIN, L., NEVANEN, T. K., SODERLUND, H., MARTIN, C. R., Antibody-based bio-nanotube membranes for enantiomeric drug separations., *Science* **2002**, 296, 2198–2200.
- 72 CHEN, C.-C., LIU, Y.-C., WU, C.-H., YEH, C.-C., SU, M.-T., WU, Y.-C., Preparation of fluorescent silica nanotubes and their application in gene delivery, *Adv. Mater.*, **2005**, 17, 404–407.
- 73 PANTAROTTO, D., SINGH, R., MCCARTHY, D., ERHARDT, M., BRIAND, J.-P., PRATO, M., KOSTARELOS, K., BIANCO, A., Functionalized carbon nanotubes for plasmid DNA gene delivery., *Angew. Chem., Int. Ed.* **2004**, 43, 5242–5246.
- 74 ZHENG, M., JAGOTA, A., STRANO, M. A., SANTOS, A. P., BARONE, P. S., CHOU, G., DINER, B. A., DRESSSELHAUS, M. S., MCLEAN, R. S., ONOA, G. B., SAMSONIDZE, G. G., SEMKE, E. D., USREY, M., WALLS, D. J., Structure-based carbon nanotube sorting by sequence-dependent DNA assembly., *Science* **2003**, 302, 1545–1548.
- 75 HOU, S., WANG, J., MARTIN, C. R., Template-synthesized DNA nanotubes, *J. Am. Chem. Soc.*, **2005**, 127, 8586–8587.
- 76 LEE, H., KEPLEY, L. J., HONG, H. G., AKHTER, S., MALLOUK, T. E., Adsorption of ordered zirconium phosphonate multilayer films on silicon and gold surfaces., *J. Phys. Chem.* **1988**, 92, 2597–2601.
- 77 CHEUNG, V. G., MORLEY, M., AGUILAR, F., MASSIMI, A., KUCHERLAPATI, R., CHILDS, G., Making and reading microarrays., *Nat. Genet.*, **1999**, 21, 15–19.
- 78 WALT, D. R., Techview: Molecular biology. Bead-based fiber-optic arrays., *Science*, **2000**, 287, 451–452.
- 79 HAN, M., GAO, X., SU, J. Z., NIE, S., Quantum-dot-tagged microbeads for multiplexed optical coding of biomolecules. *Nat. Biotechnol.*, **2001**, 19, 631–635.
- 80 ENZEL, P., ADELMAN, N. B., BECKMAN, K. J., CAMPBELL, D. J., ELLIS, A. B., LISENSKY, G. C., Preparation and properties of an aqueous ferrofluid., *J. Chem. Educ.*, **1999**, 76, 943–946.
- 81 BUEHLER, S. S., BASU, I., HITES, R. A., A comparison of PAH, PCB, and pesticide concentrations in air at two rural sites on lake superior., *Environ. Sci. Technol.* **2001**, 35, 2417–2422.

## 10 Nanoprobe-based Affinity Mass Spectrometry for Cancer Marker Protein Profiling

*Li-Shing Huang, Yuh-Yih Chien, Shu-Hua Chen, Po-Chiao Lin,  
Kai-Yi Wang, Po-Hung Chou, Chun-Cheng Lin, and Yu-Ju Chen*

### 10.1 Introduction

Traditionally, cancer has been considered as a genetic disease; but functionally, it is the altered protein networks and signaling pathways that drive cancer growth, cell survival, tumor invasion, and distant metastasis [1]. Although high-throughput genomic profiling has offered information regarding genomic signature pattern associated with sub-classification of tumor types, these techniques suffer a severe limitation in monitoring the changes in protein levels, which are the actual molecules of action within the cell. In contrast, proteins as the ultimate effectors of gene function directly participate in biological processes to govern cellular growth, differentiation and survival. The change in protein expression patterns in a given disease state should reflect the pathologic processes taking place within the cells. Many studies have shown that the differentially expressed levels of proteins are associated with cancer progression [2, 3]. Protein biomarkers are becoming increasingly important in cancer diagnosis. According to the FDA, biomarkers can be defined as endogenous molecules that are a measurable indicator specifically associated with a particular disease or disease state and are able to differentiate the different physiological states of an individual. More precisely, different types of markers can be used for early detection of disease, for monitoring effects of therapy, for detecting disease recurrence, and for prognosis. Table 10.1 shows a few examples of characteristics of FDA-approved serum tumor markers [4–14]. Although there are only a few types of cancer that can be identified by a single tumor-specific serum marker [15], their expression levels may correlate the progression of cancer with different detection sensitivity and specificity. For example, prostate-specific antigen (PSA) [14, 16] is a specific marker and can be routinely used for screening high-risk population. In contrast, the change in expression pattern of some markers are clinically associated with multi types of cancer (Table 10.1).

In the post-genome era, in particular, proteomics opens up new horizons because it promises to accelerate the discovery of new protein disease marker. The completion of the human genome project has catalyzed advances in proteomics to

investigate cellular function at the protein level. Particularly, increasingly sophisticated techniques have been rapidly developed for discovering disease biomarkers via large-scale differential profiling [17, 18]. The recognition that every disease induces a specific pattern of change in proteomic microenvironments has important clinical implications for the early detection and progression of disease [19, 20]. Tumors also induce dramatic changes in surrounding stroma, cell–cell contact and angiogenesis. During the changes, plasma, urine, and saliva are readily available samples whose protein content reflects the environment encountered by the blood during its journey through tissues and the circulatory system [21]. Ideally, standard biological sources, such as the above-mentioned body fluids, could be used for identifying biomarkers. A rapid, simple, accurate and inexpensive detection of the relevant marker should be available, together with a measurable and standard baseline as a reference point for diagnosis. However, body fluid-derived proteomes are complex, with a wide range in protein abundance that imposes extreme analytical difficulties for medical studies or clinical diagnoses. Thus, with the advent of a growing number of candidate protein biomarkers for disease diagnosis, it is expected that the number and value of molecular diagnostics, prognosis, and treatment monitoring using protein markers will increase. The development of sensitive techniques with great potential to monitor disease onset is urgently needed for the next phase of cancer diagnosis and monitoring.

This chapter overviews a recently developed technique – nanoprobe-based affinity mass spectrometry (NBAMS) – for the characterization of serum protein markers. Section 10.2 summarizes the fabrication of different types of metal nanoparticle and applications in biology and medical science. The principle of mass spectrometry, the detection method in NBAMS, will be described in Section 10.3. Section 10.4 describes the design, workflow, and performance of NBAMS; the advantages of nanoscale probes such as rapid kinetics, specific detection, and high sensitivity are addressed. Section 10.5 reviews the application of NBAMS technology for selected protein pattern analysis in human plasma/blood. Finally, using NBAMS as a multiplexed immunoassay is demonstrated in Section 10.6 for screening of normal individual and cancer patients.

## 10.2

### Fabrication and Biomedical Applications of Nanoparticles

#### 10.2.1

##### Fabrications and Properties of Nanoparticles

Biomolecule-conjugated nanoparticles (NPs) have been demonstrated to have promising applications in bioanalysis. Among NPs, colloidal gold has attracted the attention of scientists for many years [22, 23]. In general, the synthesis of colloidal gold involves the use of different reducing agents with an aqueous solution of tetrachloroauric acid ( $\text{HAuCl}_4$ ). By controlling the formation of nuclei and the

Tab. 10.1. Characteristics of some approved serum tumor markers [4, 5].

Protein name	Biochemical properties	Molecular weight (kDa)	Primary clinical applications	Upper limit of healthy adults	Other related cancer type	Other related conditions
Alpha-fetoprotein (AFP)	Oncofetal protein, glycoprotein	70	Hepatocellular carcinoma (HCC) and germ-cell (nonseminoma) tumor monitoring and diagnosing	10 ng mL <sup>-1</sup>		Pregnancy, hepatitis, and cirrhosis
CA 15-3	Mucin identified by monoclonal antibodies	300–450	Breast [6, 7] cancer monitoring	25 U mL <sup>-1</sup>	Colorectal, liver, lung, ovarian [8, 9], pancreatic cancer	Benign breast, liver disease
CA 19-9	Blood group antigen identified by monoclonal antibodies, glycoprotein complex	200–1000	Colorectal [10] and pancreatic cancer monitoring	37 U mL <sup>-1</sup>	Breast, gastric, hepatobiliary, hepatocellular, and ovarian [8] cancer	Pancreatitis and benign gastrointestinal diseases
CA 72-4	Glycoprotein identified by monoclonal antibodies	48	Gastrointestinal and ovarian cancer monitoring	6 U mL <sup>-1</sup>	Lung and ovarian [8, 9] cancer	Benign gastrointestinal disease

CA 125	Mucin identified by monoclonal antibodies	200	Endometrial and ovarian [8, 9, 11] cancer monitoring	35 U mL <sup>-1</sup>	Breast, cervical, colorectal, gastrointestinal, lung, pancreatic cancer	Follicular phase of menstrual cycle, early pregnancy, cirrhosis, hepatitis, endometriosis, pericarditis
Carcinoembryonic antigen (CEA)	Oncofetal antigen, a family of related cell-surface glycoproteins	150–300	Colorectal [10], lung, and breast [6, 7] cancer monitoring	3 ng mL <sup>-1</sup> (5 ng mL <sup>-1</sup> for smokers)	Gastric, pancreatic, ovarian [8], uterine cancer	Benign breast disease, cirrhosis, pulmonary emphysema, rectal polyp, ulcerative colitis
Human chorionic gonadotrophin (hCG), hCG b-subunit (hCGb)	Hormone, glycoprotein consisting of 2 non-covalently bound subunits (a and b)	36 (hCG)	Trophoblastic and testis cancer monitoring	5 U L <sup>-1</sup> for men and pre-menopausal women; 10 U L <sup>-1</sup> for post-menopausal women	Breast, gastrointestinal, lung and ovarian cancer	Pregnancy, hydatidiform moles, cirrhosis, duodenal ulcer, and inflammatory bowel disease
Prostate specific antigen (PSA)	Enzyme, glycoprotein serine protease, total PSA (tPSA) in blood consisting of 2 major forms: PSA-ACT (a1-antitrypsin complex & free PSA (fPSA))	28	Prostate [12–14] cancer monitoring and diagnosing	tPSA: 2.5–6.5 ng mL <sup>-1</sup> (by age); fPSA/tPSA = 0.25		Benign prostate hyperplasia

amount of gold for shell growth, i.e., the conditions of reduction, NPs of variant size could be prepared. For example, small size particles can be formed by using strong reducing agents such as sodium borohydride and white phosphorus [24–29]. Depending on the reduction conditions, gold nanoparticles (AuNPs) can be synthesized in the size range 0.82–150 nm [30, 31]. Under inert gas conditions, thiol ligands can be assembled on the surface of AuNP by forming the covalent Au–S bond. Besides Au–S formation, the surface of AuNP can also be modified by charge–charge absorption to attach proteins under suitable pH. Antibody-conjugated AuNPs fabricated by charge–charge absorption have been applied in specific cell and tissue labeling that can be visualized under electronic transmission microscopy (TEM) [27]. NPs can also be increased in size by silver enhancement so as to be observed under optical microscopy [32]. In addition, BIA core can be applied to detect the AuNP because the surface plasma resonance (SPR) absorption peaks of gold colloids display in the visible range, 510–550 nm [33]. The aggregation of AuNPs induces a redshift in the SPR peak, which has been applied in many bioassay [34], including DNA–DNA hybridization [35], carbohydrate–protein interactions [36], and carbohydrate–carbohydrate interactions [37]. Recently, gold colloids have been further explored as affinity probes and used with mass spectrometry in biomaterial analysis [38–40].

Besides AuNPs, magnetic nanoparticles (MNPs) have also attracted great attention due to their unique magnetic properties [41–43]. Quantum size effects and the large surface area to volume ratio of MNPs significantly change their magnetic properties and superparamagnetic characteristics [44]. The magnetic properties of iron oxide MNP depend on the particle size [45, 46]. Small particles (<15 nm) show superparamagnetic character, while large particles are ferromagnetic. MNPs of different sizes can be synthesized by changing the reaction parameters, such as the reaction time, temperature, and the concentrations of reagents and stabilizing surfactants. Because of their special properties, MNPs have been utilized in many applications, such as specific cell targeting, virus separation [47], drug delivery [48, 49], magnetic resonance imaging (MRI) [50, 51], and hyperthermia in cancer therapy [52].

MNPs can be fabricated in aqueous or organic solvent conditions. In the aqueous solvent method [53], MNPs are prepared by stirring the mixture of  $\text{FeCl}_2$ ,  $\text{FeCl}_3$  and  $\text{NH}_4\text{OH}$  (pH adjusting solution) in an ice bath under air. Introduction of air bubbles using a pipette into the mixed solution results in the oxidation of  $\text{Fe}^{2+}$  ions to  $\text{Fe}^{3+}$ , to give  $\text{Fe}_3\text{O}_4$  MNPs. Iron oxide NPs synthesized under organic conditions are better dispersed [54]. In this method, an iron oleic acid metal complex is prepared by the thermal decomposition of pentacarbonyl-iron in the presence of oleic acid at 100 °C. Then, iron oxide NPs are generated by ageing the iron complex at 300 °C. The size distribution of monodisperse NPs synthesized under these conditions ranges from 4 to 20 nm. When the ratio between pentacarbonyl-iron and oleic acid is changed from 1:2 to 1:3, the particle size is tuned from 7 to 11 nm.

In addition to iron oxide MNPs, many alloy MNPs have been synthesized recently. For example, FePt NPs are effective NPs that are easily modified with thiol ligands [55]. The FePt was synthesized by dissolving platinum acetylacetonate and



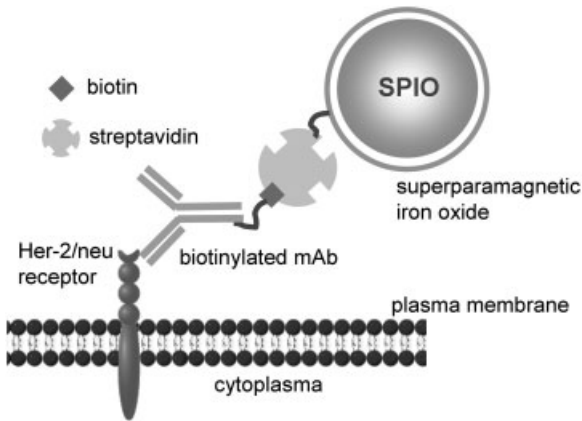


**Fig. 10.1.** The Her-2/neu expressing cell was pre-labeled with biotinylated antibody and then selectively bound to streptavidin-conjugated SPIO NP, which acted as contrast agent in  $T_2$ -weighted MR imaging. (From Ref. [65].)

hexadecane-1,2-diol in dioctyl ether under inert gas and then heating the resulting solution to  $100\text{ }^\circ\text{C}$ . Oleic acid, oleyl amine, and  $\text{Fe}(\text{CO})_5$  were then added to the reaction mixture, followed by heating at  $300\text{ }^\circ\text{C}$  for 30 min. After cooling the reaction mixture, ethanol was added to precipitate the FePt NPs.

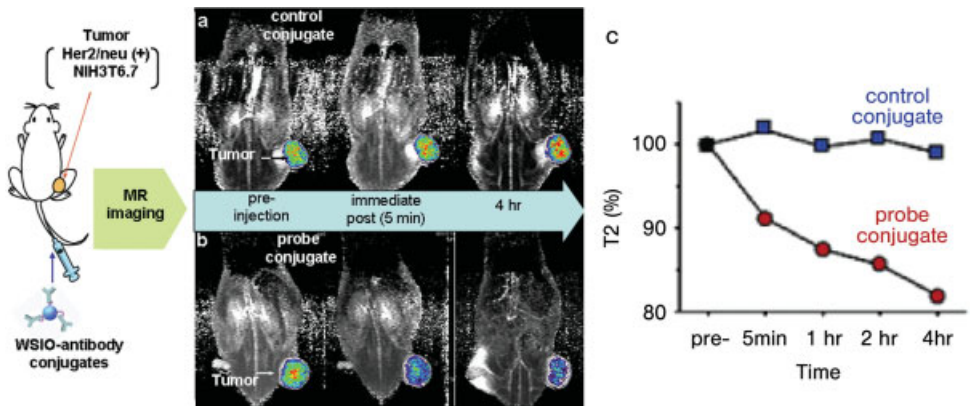


**Fig. 10.2.** *In vivo* MR detection of cancer-targeting event of WSIO-antibody conjugates (a and b). Color maps of  $T_2$ -weighted MR images of cancer cell implanted (NIH3T6.7) mice at different temporal points (preinjection, immediate post, 4 h) after the intravenous injection of WSIO-irrelevant antibody control conjugates (a) and WSIO-Herceptin probe

conjugates (b). Whereas no difference is seen in the color-mapped MRI for the control conjugate (a), an immediate (5 min) color change to blue at the tumor site is evident with the probe conjugate (b). (c)  $T_2$  versus time after the injection of WSIO-antibody conjugates in (a) and (b) samples. (From Ref. [66].)

Semiconductor quantum dots (QDs) are another type of important NPs developed to have many bio-applications, such as medical diagnosis, *in vivo* cell imaging, and molecular recognition [56]. Not only their good size distribution and uniform shape but also the unique quantum properties makes QDs excellent fluorescent tags. The optical properties of QDs are determined by their sizes. As the particle size decreases, the spacing between two energy levels increases and the wavelength of fluorescence becomes shorter. QDs are synthesized by using semiconductor materials, such as cadmium sulfide, cadmium selenide, cadmium telluride [57], or gallium arsenide [58], under organic or aqueous conditions. QDs with a uniform-size distribution are usually synthesized in organic solvent at high temperature. Trioctylphosphine oxide (TOPO) was first heated followed immediately by injecting the metal precursor (dimethyl cadmium and selenium powder in tributylphosphine) using a syringe. CdSe NPs were then nucleated and the resulting solution became colored. The size of NPs can be modulated by changing the amount of metal precursor and reaction time. QDs so-prepared are hydrophobic due to the surface surfactant layer, TOPO.

CdSe NP, one of the most commonly used semiconductor NPs, possesses useful optical properties, including photo-stability, a wide-range excitation, and no red tail in the emission spectrum. Its quantum yield can be increased by coating with a higher band-gap material such as ZnS to form core-shell QDs [59]. Based on these special fluorescent properties, QDs serve as a convenient and effective dye carrier to be monitored either *in vitro* or *in vivo*. Recently, DNA encapsulated QD is used as a nanosensor to capture target DNA and the binding signal is amplified by fluorescent resonant energy transfer (FRET) through an external fluorescent tag [60]. Interestingly, various color-coded QDs have been applied in the real-time detection of biomolecule and virus in a microfluidic device [61]. QDs also act as a strong tracing marker in *in vivo* cell imaging, which facilitates monitoring of the biomolecule distribution [62].

### 10.2.2

#### **Metal Nanoparticles in Cancer Diagnosis**

Sensitive immunoassay methods are being continuously developed and used in clinical diagnostics to measure specific markers with extremely low concentrations in highly complex biofluids or to detect the premalignant and malignant lesions in early stages. Advances in nanotechnology have facilitated the development of novel ultrasensitive assays for cancer diagnosis in more efficient and economic ways. This section reviews a few iron oxide and gold nanoparticles to illustrate the applications of metal nanoparticles in cancer diagnosis. More information is given in recent reviews [43, 63, 64].

Her-2/neu tyrosine kinase receptor is a 185 kDa protein expressed in approximately 25% of breast cancer cell surface and is an important target in staging and treating breast cancer. Artemov's laboratory [65] have used a two-step labeling protocol to label the Her-2/neu receptor on a breast cancer cell line (AU-565). As shown in Fig. 10.1, the receptors on cancer cells were first prelabeled with biotiny-

lated humanized mAb (Herceptin, anti Her-2/neu antibody), and then streptavidin superparamagnetic iron oxide microbeads (SPIO-MBs) used as  $T_2$  weighted MR contrast agent were selectively bound to the prelabeled receptors. Because the large sizes of SPIO-MBs significantly restricted their delivery and diffusion into cell by passive endocytosis or active transporter system, the particles could remain on the cell surface, facilitating MR imaging. Labeling extracellular receptors is an important advantage for the *in vivo* application of this method because of the lower probability of modulating cell physiology.

A similar approach with the use of nanometer-size magnetic nanoparticles (MNPs) has also been demonstrated *in vivo* for diagnosis of cancer. Cheon and workers [66] have coated Herceptin on 9-nm  $Fe_3O_4$  to give 28 nm sized water-soluble magnetic iron oxide (WSIO)–Herceptin probes. These probes were injected into mice with an implanted fibroblast cell line, NIH3T6.7, which possessed over-expressed Her-2/neu cancer markers. Figure 10.2 showed the  $T_2$ -weighted MR images obtained at the different temporal points after the intravenous tail injection. No change in the color-mapped MR signal (Fig. 10.2a) and  $T_2$  values (Fig. 10.2c) at the tumor site was observed in the control experiment. In contrast, an immediate color change to blue, at the tumor site, became evident within 5 min of the injection of probes. Cheon's results successfully demonstrated the application of antibody-conjugated MNPs for *in vivo* MR diagnosis of human cancer cells implanted in live mice. Notably, the  $T_2$ -weighted MR signal intensity was dependent on the size of WSIO. When the MNPs increased in size, the MR signal intensity decreased [67].

Nanoparticles can also be combined with ELISA assay to develop a more sensitive and efficient assay. Cui and coworkers [68] have fabricated  $Fe_3O_4/Au$  nanoparticles (GoldMag NPs) with core–shell structure and demonstrated that antibody immobilization efficiency on GoldMag NPs (nanometer scale) was higher than that on Dynal bead (micrometer scale). The anti-HBV (hepatitis B virus) antibody-conjugated GoldMag (anti-HBV GoldMag) was used to detect HBV antigen in blood by ELISA type assay. As shown in Fig. 10.3, the anti-HBV GoldMag NPs were incubated with HBV positive serum first. After a washing step, the HRP (horseradish peroxidase) labeled antibody and its substrate were added into the antibody–nanoparticle complex. By applying an external magnetic field for separation, the liquid phase was measured by UV/Vis spectroscopy. The absorbance at 280 nm showed a 12-fold difference between positive serum and negative serum for HBV antibody.

Beside MNPs, AuNPs alone can also be used as contrast reagents for vital optical imaging of precancers and cancers based on their abilities to resonantly scatter visible and near-infrared light. Richards-Kortum and coworkers [69] used bioconjugates of gold nanoparticles (12 nm in diameter) with monoclonal antibodies against epidermal growth factor receptor (EGFR), a transmembrane glycoprotein that is highly overexpressed in epithelial cancers, for molecular specific optical imaging. Because the aggregation of AuNP increased in scattering cross-section per particle, this property produced a large optical contrast between isolated AuNPs and assemblies of AuNPs, and made it suitable for vital optical imaging. Light scat-

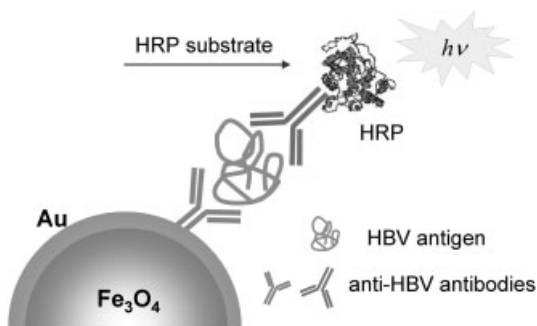


**Fig. 10.3.** Schematic of immunoassay using GoldMag NPs for HBV antigen detection. The GoldMag NPs coupled with anti-HBV antibody can capture the HBV antigen by immuno-

reaction, be isolated from liquid by a magnet, and detected by UV/Vis spectrometry after adding HRP-labeled anti-HBV antibody and HRP substrate. (From Ref. [68].)

tering from the labeled cells was very strong and could be easily observed using low-magnification optics and an inexpensive light source such as a laser pointer. Richards-Kortum's laboratory has applied anti-EGFR AuNPs to the top of engineered tissue constructs and utilized PVP to help AuNP penetrate the tissue layer and reach the cervical cancer cell layer. Transmittance and reflectance images of engineered tissue constructs labeled with anti-EGFR AuNPs (Fig. 10.4) clearly show the distribution of EGFR expression in living neoplastic cervical tissue. The advantage of using AuNP as contrast reagent is that, as many markers are not uniquely expressed in disease cells but are over- or under-expressed, the scattering from closely spaced aggregates associated with overexpression can magnify the signal difference owing to moderate levels of overexpression.

PSA is an important serum marker for the diagnosis and monitoring of prostate cancer. Mirkin and coworkers have developed an ultrasensitive method for detecting PSA using barcode assay [70]. This assay relied on using two particles: a magnetic microparticle for capture target protein and DNA-labeled AuNP for signal amplification. Monoclonal anti-PSA antibody coated magnetic microparticle probes were used to specifically bind target PSA from bio-mediate. The AuNP probes functionalized with hybridized barcode DNA strands and polyclonal antibodies to PSA were used to label microparticle probes through antigen-antibody interaction. Magnetic separation of the complexed probes and PSA was followed by dehybridization of the dsDNA on the AuNP probe to release barcode DNA. Because the AuNP probe carried many DNAs per protein binding event, the binding signal was amplified and PSA could be detected at 30 attomolar concentration. The barcode assay was six orders of magnitude more sensitive than the clinically used ELISA assay for PSA. The same laboratory further discovered that an even more sensitive assay was developed by replacing the AuNPs with polystyrene microparticles, which were loaded with more barcode DNAs to provide a better amplification effect (Fig. 10.5) [71].

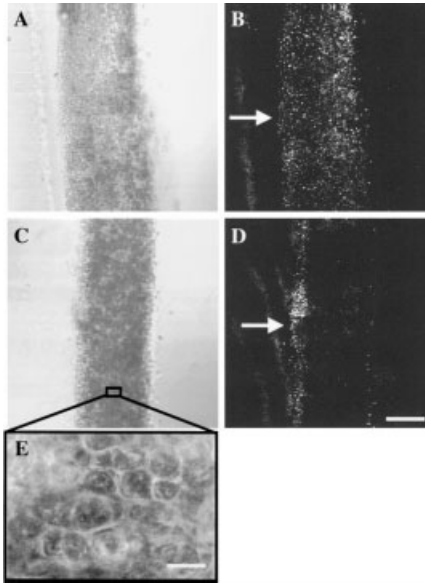


**Fig. 10.4.** Transmittance (A, C, and E) and reflectance (B and D) images of engineered tissue constructs labeled with anti-EGFR/gold conjugated. The tissue constructs consist of densely packed multiple layers of cervical cancer (SiHa) cells. The contrast agents were added on top of the tissue phantoms in 10% PVP solution in PBS (A and B) or in pure PBS (C and D). After incubation for ~30 min at room temperature, the phantoms were transversely sectioned with a Krumdieck tissue

slicer, and the sections were imaged using a Zeiss Leica inverted laser scanning confocal microscope with a  $\times 10$  (A–D) objective. A small spot on a tissue construct was imaged using a  $\times 40$  oil immersion objective to show high density of the epithelial cell in the phantom. Reflectance images were obtained with 647 nm excitation. Arrows show the surfaces exposed to the contrast agents. Scale bars are  $\sim 200 \mu\text{m}$  (A–D) and  $\sim 20 \mu\text{m}$  (E). (From Ref. [69].)

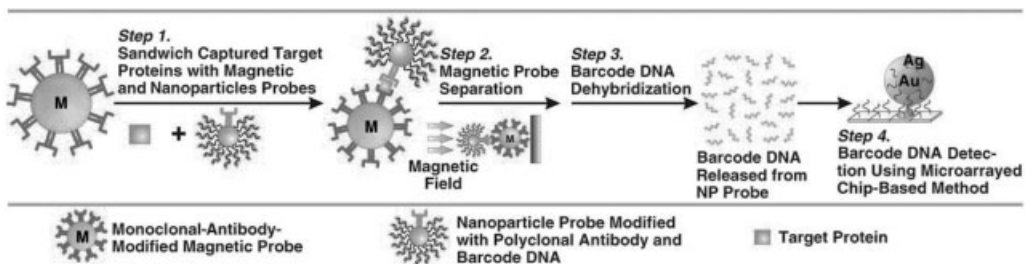


**Fig. 10.5.** Conventional bio-barcode amplification assay. (From Ref. [71].)

## 10.3

## Principles of Mass Spectrometry

Mass spectrometry is a technique that measures the mass-to-charge ratio ( $m/z$ ) of molecules. There are three basic components, ion source, mass analyzer and ion detector, in a typical mass spectrometer. Gaseous ions are formed with sample molecules in the ion source and then introduced into the mass analyzer for separation according to their different  $m/z$ . Finally, the ions that pass through the mass analyzer are detected by the ion detector and the molecular weight of the analyte can be derived. For the analysis of target protein, mass spectrometry has become the choice of tool for protein characterization. Over the last decade, mass spectrometry has not only advanced technologically but has also greatly expanded in applications to unknown protein identification, post-translational modification and protein quantitation in biological and biomedical research.

## 10.3.1

## Matrix-assisted Laser Desorption/Ionization Time-of-flight Mass Spectrometry

Among various types of mass spectrometers, matrix-assisted laser desorption/ionization time-of-flight mass spectrometry (MALDI-TOF MS) has become one of the popular tools for protein detection [72, 73]. As shown in Fig. 10.6, the first step involves mixing and co-crystallizing of the sample and excess molar of “matrix” compounds, which are low molecular weight weak organic acids that strongly absorb UV radiation. Even though the exact mechanism of desorption/ionization is not clear, it is generally considered that the matrix absorbs photoenergy from the laser pulse, resulting in energy transfer and desorption/ionization of matrix and

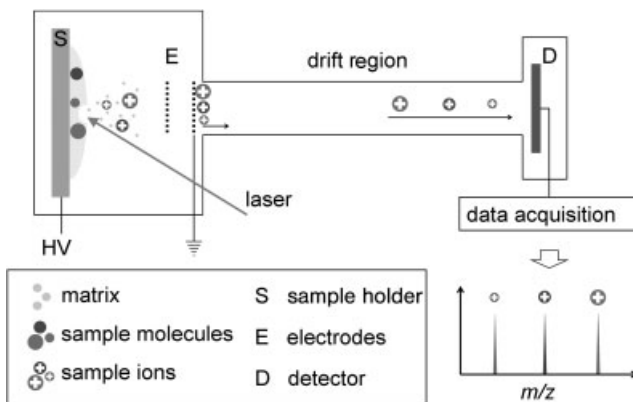


**Fig. 10.6.** Schematic of matrix-assisted laser desorption/ionization time-of-flight mass spectrometer (MALDI-TOF MS). Analyte ions are generated by irradiation of laser in the

MALDI ion source and accelerated into the drift region of TOF mass analyzer. The  $m/z$  of the ions are determined according to their arrival time at the detector.

sample molecules from the condensed phase into gaseous phase. Singly and/or doubly charged sample ions are, therefore, formed during this process. The pulsed nature of MALDI is often coupled with analysis with a time-of-flight (TOF) mass analyzer. Ions generated in the MALDI ion source are accelerated electrically into the drift region, a long, straight and electric field-free tube, and drift to the detector at the opposite end. Because ions with different mass are given the same kinetic energy in the ionization region, the lighter and heavier ions will reach the detector at different times. The  $m/z$  of an ion can be calculated according to the time, distance of flight and the accelerating voltage.

Furthermore, the introduction of peptide mass fingerprints (PMFs) has had a significant impact on unknown protein identification [74]. Based on the properties of the specific enzymatic-hydrolysis of protein and MALDI-TOF MS, protein can be identified simply and rapidly. The protein of interest, which is in many cases purified by gel electrophoresis, is enzymatically or chemically cleaved into a specific set of peptides, and the peptide mixture is analyzed by MALDI-TOF MS. The resulting PMF spectrum is subsequently compared with “virtual” fingerprints obtained by theoretical cleavage of protein sequences stored in databases in a search to identify of possible candidate proteins [75]. Due to its high sensitivity, tolerance to impurities, high speed, and the ability to provide molecule weight information on intact molecule, MALDI-TOF MS has become one of the primary techniques for protein/peptide profiling and protein identification.

### 10.3.2

#### **Affinity Mass Spectrometry**

Recently, surface-enhanced laser desorption/ionization (SELDI) has evolved rapidly as a new frontier for biomarker discovery and clinical diagnoses based on proteomic pattern analysis [76, 77]. The major difference between SELDI and MALDI is the use of a protein chip array that is composed of a chromatographic surface to retain proteins of interest. SELDI shows diverse applications due its flexibility for surface modification. Despite its advantages of high sensitivity and high throughput, however, the pattern recognition platform, unfortunately, suffers from laboratory-to-laboratory variance due to differences in sample preparation, handling, and analysis software. Many complications may result from suppression effects, a wide dynamic range of protein concentration during simultaneous detection of many proteins in sample.

As an alternative to the above approaches, MALDI-TOF MS can be combined with a biologically active probe to rapidly and specifically target, separate, and pre-concentrate proteins of interest. This targeted approach, named affinity mass spectrometry, can accelerate research for class-specific proteins or biomarkers. Several analytical affinity capture techniques have been developed for affinity mass spectrometry. The research group of Hutchens and Yip was one of first to demonstrate MS-based affinity capture by immobilization of “bait” DNA on agarose beads for direct MALDI-TOF MS analysis of targeted proteins from complex biofluids [78]. The concept was further tailored by Nelson and coworkers to develop a mass spec-

trometric immunoassay (MSIA) [79]. They used affinity pipette tips (MSIA tips) to selectively retrieve proteins from biological fluids, demonstrating high-throughput quantitative protein analysis as well as screening of heterogeneous glycan structures in plasma proteins [80–82]. Furthermore, ligands and antibodies can also be immobilized or captured on the surface of gold and organic polymer film as probes [83–85]. Other variations of the biologically active probe for affinity mass spectrometry include the assay of direct desorption/ionization on silicon [86, 87] and self-assembled monolayers [88]. Despite the rapid evolution of efficient chip-based or microbead-based assays for biomedical research, protein chip technologies face some technical challenges such as the special requirement of immobilization chemistry and instruments and denaturing/alternating the native bait proteins caused by the chip/bead surface properties.

In recent years, nanomaterials have begun to serve as biologically active probes in affinity mass spectrometry and show great potential for application in various biology systems. Chen et al. have used gold nanoparticles immobilized on magnetic particles (Au@magnetic particles) and carbon nanotubes (CNTs) to probe proteins and peptides [38, 89]. Magnetic NPs that conjugated with antibodies were also used to probe pathogenic bacteria by Chen's group [90]. Chang et al. used high-affinity diamond NPs to extract and preconcentrate proteins from diluted solution and human serum [91]. In addition, Harrison et al. have introduced the C18 functionalized silica NP and aptamer conjugated MNPs as probes [92].

When affinity molecules are coupled to such NPs, they can function as sensitive biosensors that show superior separation capabilities compared with microbeads [93, 94]. There are more advantages of using NPs as ligand carriers [95]. First, there are simple and facile means of anchoring molecules to the nanoscale surface to form versatile and covalently stable conjugates with the capability of specifically interacting with targeted biomolecules. Second, the large surface area-to-volume ratio and the globular shape of an NP allow multivalent and three-dimensional interactions between ligands and receptors without hindrance. Finally, compared with conventional microarray methods using planar solid supports, functionalized NPs can be used as “water-soluble” probes in biological assays in solution. In principle, these “suspension arrays” should improve assay homogeneity and reduce assay time. In our recent report, sugar-conjugated gold NPs were demonstrated as an affinity probe for efficient separation and enrichment of target protein, and then protein identification and epitope mapping in carbohydrate–lectin recognition [40].

#### 10.4

##### **Nanoprobe-based Affinity Mass Spectrometry (NBAMS)**

During the past few years, we have focused on developing a versatile, sensitive analytical platform based on surface-engineered NPs and mass spectrometry analysis [96, 97]. The principle of nanoprobe-based affinity mass spectrometry (NBAMS) is to use MNPs as an affinity probe to effectively extract and enrich target protein for direct MALDI-TOF MS detection. The probe, derived from antibody-conjugated



MNPs, was designed for protein profiling in human plasma. Three serum proteins with different concentrations, C-reactive protein (CRP), serum amyloid A (SAA), and serum amyloid P component (SAP), have been selected as target proteins to demonstrate the general applicability of the method. Both CRP [98, 99] and SAA [100] are exquisitely sensitive systemic markers of acute phase response and present about  $1 \text{ mg L}^{-1}$  and  $3 \text{ mg L}^{-1}$  in the blood of healthy human, respectively. Overexpression of SAA was also found to be associated with gastric cancer in a recent report [101]. SAP is a biomarker related to Alzheimer's disease and type 2 diabetes [102], with a concentration about  $40 \text{ mg L}^{-1}$  in blood of healthy humans [82, 103].

#### 10.4.1

##### Preparation of Nanoprobes and Workflow

Figure 10.7 illustrates the synthesis of antibody-conjugated iron oxide NPs. The iron oxide ( $\text{Fe}_3\text{O}_4$ ) NPs (MNP 1) were obtained by co-precipitation of  $\text{FeCl}_2$  and

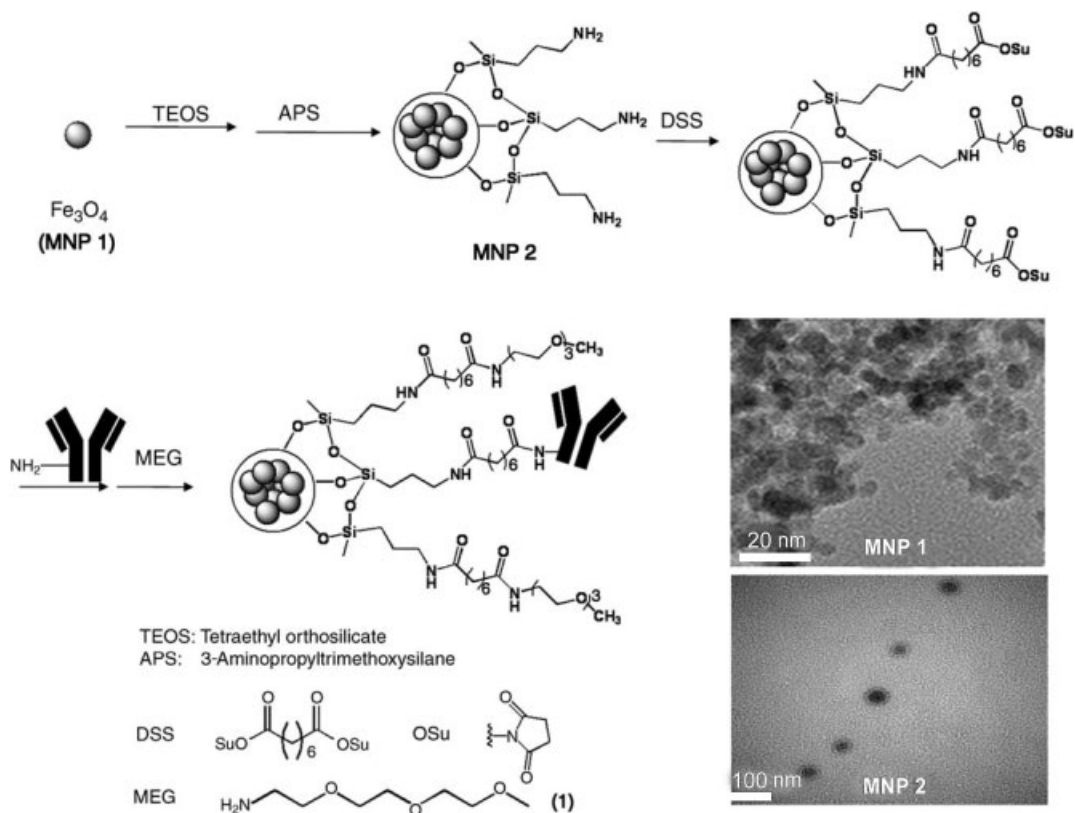


**Fig. 10.7.** Preparation and characterization of MEG-protected antibody-conjugated MNPs. (From Ref. [97].)

$\text{FeCl}_3$  under basic conditions and then dispersed in acidic solution [104]. The particle surface was transformed into an amino functionality by the sol-gel process using tetraethyl orthosilicate (TEOS) followed by addition of 3-aminopropyltrimethoxysilane (APS) to give **MNP 2**, which contains amine terminal groups [105]. Transmission electron microscopy (TEM) revealed that the diameter of **MNP 1** is in the range of 5–15 nm while the average diameter of the iron oxide core of **MNP 2** was 50 nm with a relatively narrow size distribution (Fig. 10.7). Enlargement of the metal core is due to the aggregation of iron oxide during silanization, and the silica shell is visible as a faint circle outside the core. For antibody conjugating, **MNP 2** was treated with a crosslinker, bis(*N*-hydroxysuccinimide ester) (DSS), to crosslink the aminosilane MNPs with antibody [106]. To avoid non-specific binding on the surface of antibody-conjugated MNPs, the resulting MNPs were protected by a blocking reagent, i.e., terminal aminated methoxy-ethylene glycol (MEG). The final products, MEG-protected antibody-conjugated MNPs, were washed and ready to use for NBAMS.

Figure 10.8 shows the workflow of NBAMS. Phosphate-buffered saline (PBS, pH 7.4) diluted plasma sample is incubated with antibody-conjugated MNPs at room temperature. After immunoaffinity capture of antigens, the antigen-captured MNPs are collected by a magnet, and the unbound, non-antigenic components were subsequently removed by a series of washes, abrogating the need for purification and desalting. For subsequent MS analysis, the MNPs were directly mixed with MALDI matrix and directly spotted onto the sample plate for MALDI-TOF MS measurement.

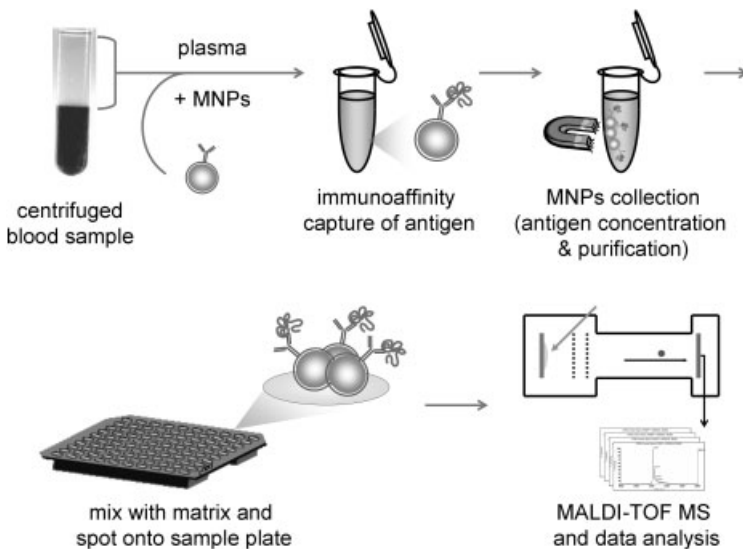


**Fig. 10.8.** Workflow of nanoprobe-based affinity mass spectrometry (NBAMS). The target antigen is specifically extracted from plasma sample by antibody-conjugated MNPs.

After separation by magnet, the isolated, antigen-captured MNPs are directly spotted onto a sample plate and analyzed by MALDI-TOF MS.

## 10.4.2

## Proof-of-principle Experiment

The feasibility of the NBAMS strategy was first evaluated with a protein mixture composed of antigenic proteins (SAP, 20% molar fraction and CRP, 3% molar fraction) and two other “nonantigenic” proteins, myoglobin (Myo, 15%) and enolase (Eno, 62%). The abundance of the targeted antigenic proteins was purposely reduced in mixture to test the extraction efficiency of the targeted protein. As shown in Fig. 10.9(A), the MALDI-TOF mass spectrum of the protein mixture displayed the complexity of the mixture, in which one of the targeted antigens, CRP, was not ob-

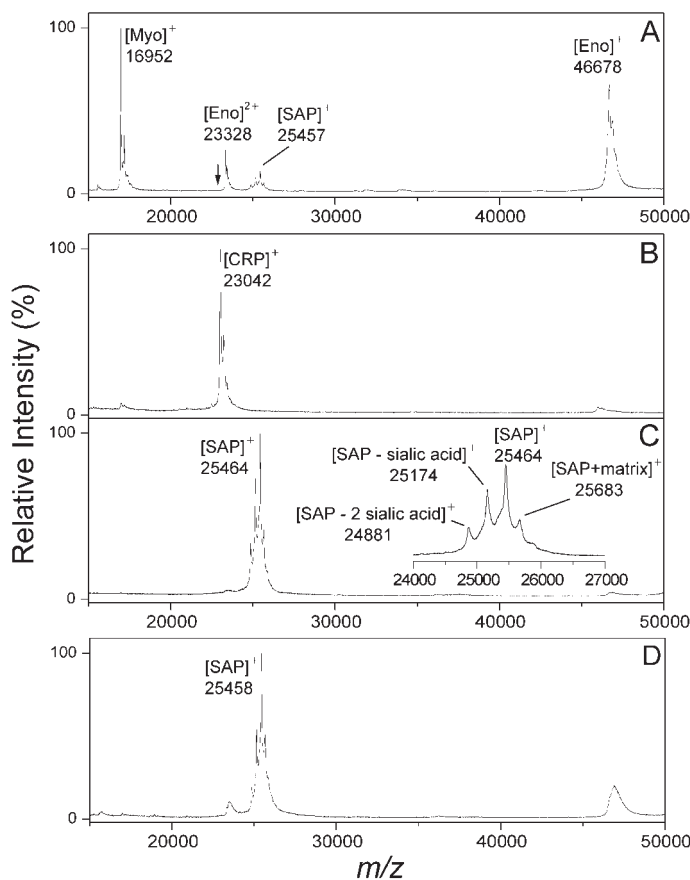


**Fig. 10.9.** MALDI-TOF mass spectra of a protein mixture before (A) and after using (B) anti-CRP-conjugated MNPs, (C) anti-SAP-conjugated MNPs, and (D) anti-SAP-encapsulated AuNPs to extract a specific protein. The protein solution (60  $\mu$ L) was composed of 0.5  $\mu$ M myoglobin (Myo), 0.1  $\mu$ M

C-reactive protein (CRP), 0.67  $\mu$ M serum amyloid P component (SAP), and 2.1  $\mu$ M enolase (Eno). The arrow in (A) indicates the theoretical  $m/z$  of CRP. The inset of (C) shows detailed protein expression profiles of wild-type, monosialo-, and asialo-SAP. (From Ref. [96].)

served due to its low abundance (3% molar fraction) and the ion suppression effect [107]. Suppression effects are commonly observed in MALDI-TOF MS due to the presence of salts, buffer, or other more abundant species in complex biological media [108]. The suppression effect can result in reduced signal intensity or even the disappearance of the signal of targeted analyte. Figure 10.9(B) revealed the specificity of the NBAMS methodology, where CRP was extracted and detected with an excellent signal-to-noise ratio of 822. No background peak between  $m/z$  5000 and 50 000 was observed in control experiments before the addition of the protein mixture, showing no “chemical noise” arising from the antibody-conjugated MNPs. The absence of other abundant proteins excluded nonspecific binding arising from electrostatic attraction or hydrogen bonding. The use of nanoprobe-based immunoassay overcomes the suppression effect because the salt and abundant non-antigenic proteins are removed and targeted proteins are selectively concentrated on the MNPs. The strong peak of target protein in mass spectrum without background demonstrates the advantages of nanoprobe-based affinity extraction in providing simultaneous protein isolation, enrichment, and sample desalting without the necessity of additional purification steps.

Mass spectrometric detection is also ideal for characterizing post-translational modifications that cannot be predicted from genomic information. The MALDI-TOF mass spectrum in Fig. 10.9(C) showed a cluster of peaks corresponding to several SAP variants from the affinity extraction using anti-SAP-conjugated MNPs. The expanded view shows that the mass spectrum is dominated by the mass of  $25464 \pm 4$  Da, which is consistent with the theoretical value of 25462 Da, as calculated from the known sequence [109]. Accompanying the major peak were two peaks at 25174 and 24881 Da, corresponding to mass shifts of 290 and 583 Da, respectively. Within experimental uncertainty, the shifts can be attributed to the loss of one or two sialic acid residues (mass of each residue: 291 Da) [82].

In addition to MNPs, surface-engineering gold nanoparticles (AuNPs) can also be an affinity probe [40]. The test of AuNP for immunoreaction was performed with 13-nm AuNPs. Antibody-encapsulated AuNPs were prepared as follows. The pH of a gold colloid was adjusted to 8.5 with 0.1 M  $K_2CO_3$ , followed by addition of antibody in the solution. The reaction was performed on ice for 60 min and the antibody-encapsulated AuNP was separated by centrifugation. The anti-SAP encapsulated AuNPs were incubated with the same protein pool (Fig. 10.9A). After immunoaffinity extraction, the pellet of AuNP containing targeted antigen was subsequently analyzed by MALDI-TOF MS. Figure 10.9(D) shows the extracted SAP from the mixture; however, signal from the enolase was also observed due to the “unoccupied sites” on AuNP. After further modification with bovine serum albumin on the AuNP surface, the co-extraction of enolase can be diminished (data not shown).

In general, antibody–antigen interactions are strong, with dissociation constants ( $K_d$ ) ranging from  $10^{-7}$  to  $10^{-11}$  M. Most antibody–antigen complexes can be dissociated at extreme pH (i.e.,  $pH < 2$  or  $pH > 12$ ). Direct MALDI-TOF MS analysis is performed where particles are placed directly on the MALDI sample plate with addition of matrix. The pH of matrix (SA) solutions is typically less than 2 and thus may serve to elute the antigen bound to the antibody-conjugated MNPs. The direct

MALDI-TOF MS approach provides rapid and sensitive analysis of affinity-bound analyte, avoiding the potential risk of sample loss. In the linear mode of MALDI-TOF MS, the mass resolution did not deteriorate when the antigen-bound MNPs were deposited on the MALDI probe. Similarly, a mass accuracy of 0.02% could be routinely obtained by external calibration, comparable to the mass accuracy of conventional MALDI-TOF MS detection. Thus, the “direct” analysis of nanoscale particles does not diminish the performance of the MALDI-TOF MS.

To confirm the identity of the captured protein, the MNPs pellet was directly subjected to *in situ* digestion with trypsin and analyzed by MALDI-TOF MS. A database search of the peptide mass fingerprinting map with the MS-Fit program (<http://us.expasy.org/uniprot/P02743>) unambiguously matched to serum amyloid P component precursor (Swiss-Prot P02743, see Fig. 10.10). The unique advantage of on-probe protein identification provides potential applications of functionalized MNPs in discovering unknown class-specific proteins.

Theory (m/z)	Experiment (m/z)	Peptide sequence	Missed cleavages	Theory (m/z)	Experiment (m/z)	Peptide sequence	Missed cleavages
1156.59	1156.11	87-96	0	1441.74	1440.91	85-96	1
1166.58	1166.08	140-149	0	1492.79	1491.88	137-149	1
1168.70	1169.08	97-106	2	1811.89	1810.62	150-165	1
1286.78	1286.14	213-223	0	2381.17	2381.18	65-84	1
1393.69	1392.96	150-162	0	5323.62	5321.13	166-212	0
1406.66	1405.90	65-76	0				

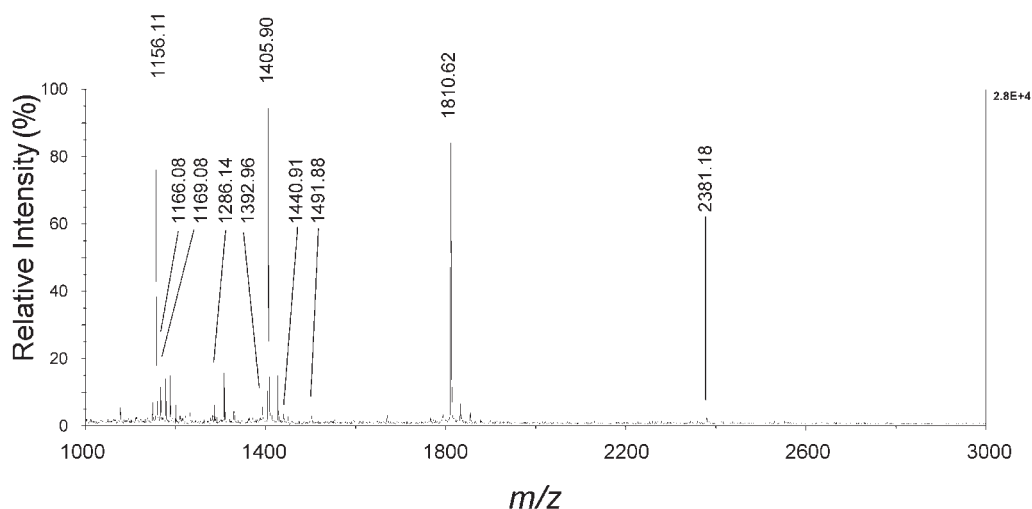


**Fig. 10.10.** Assignment of observed peptides from *in situ* trypsin-digestion of antigen-captured MNPs and their corresponding sequences matched to serum amyloid P component precursor (SAP, P02743 in the SwissProt sequence database). The sequence coverage is 58%. (From Ref. [97].)

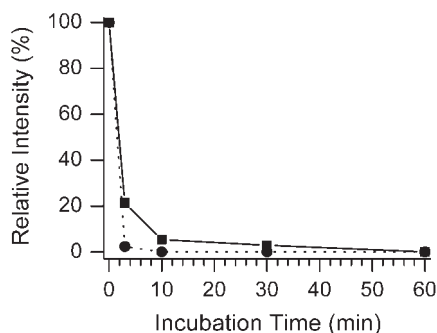


**Fig. 10.11.** Effect of incubation time on antibody–antigen recognition using antibody-conjugated MNPs. To investigate the time course of antibody–antigen recognition on MNPs, 1  $\mu$ L of supernatant was sampled from a 60- $\mu$ L reaction after different incubation times. The MNPs were conjugated with anti-

SAP (filled squares with solid line) and anti-CRP (filled circles with dashed line). After incubation (3–60 min), the quantities of the antigen remaining in the supernatant were detected by MALDI-TOF MS, and the peak intensities were plotted as a function of incubation time. (From Ref. [96].)

#### 10.4.3

#### Kinetic Study of the Nanoscale Immunoreaction

In traditional immunoassays, the incubation of antibody and antigen is often the rate-limiting step (e.g., 30 min to overnight for conventional ELISA) [110, 111]. The high density of surface antibody should, in principle, speed up antibody–antigen interaction. Figure 10.11 shows the required incubation time of NBAMS approach. The peak intensities, corresponding to unbound antigen (SAP) in solution, decreased dramatically as a function of incubation time over 10 min, at which time free SAP was barely detectable (signal-to-noise ratio was  $<3$ ). Significantly, the binding of CRP was almost completed in an even shorter incubation time ( $<3$  min). Unlike conventional immunoassays such as ELISA, for which the overall process usually requires at least 4 h, the nanoscale immunoassay can be shortened to within 15–20 min. In addition to high antibody density on MNPs, the rapid immunoreaction may be attributed to the water-soluble MNPs; the “suspension arrays” improves the assay homogeneity and reduces sample handling time. The NBAMS approach directly detected specific antibody-captured antigens by MALDI-TOF MS without using a secondary antibody or a reporter reaction. Thus, this rapid and sensitive approach may be amenable to clinical applications such as high-throughput or population screening.

#### 10.4.4

#### Detection Limit and Concentration Effect of Nanoprobe-based Immunoassay

The NBAMS assay also reveals high detection sensitivity. Figure 10.12(A–C) shows that the CRP signals decrease progressively with decreasing concentration, ranging

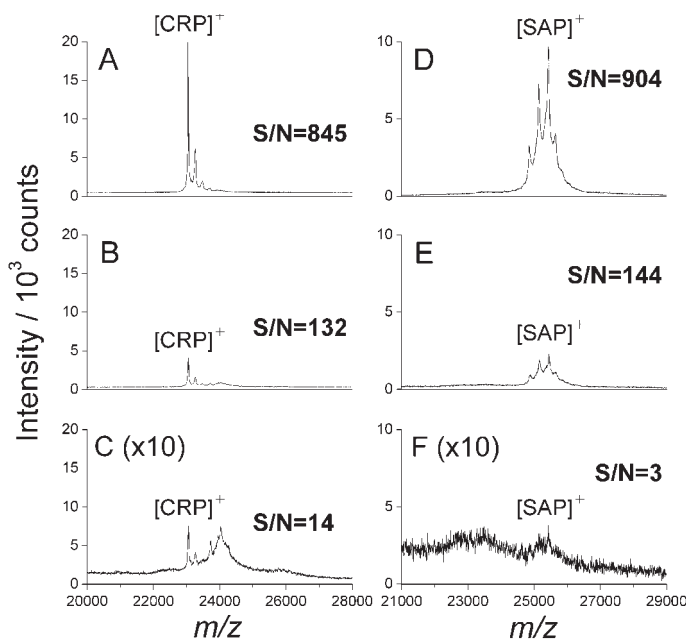


**Fig. 10.12.** Mass spectra of CRP extracted from 60  $\mu\text{L}$  of protein solution of (A) 145, (B) 29, and (C) 6 nM, using anti-CRP-conjugated MNPs; and spectra of SAP extracted from (D) 1.9  $\mu\text{M}$ , (E) 15 nM, (F) 0.6 nM, using anti-SAP-conjugated MNPs. (From Ref. [96].)

from 145 to 6 nM, and the current assay detection limit for CRP is 6 nM (Fig. 10.12C). Similarly, Fig. 10.12(D–F) shows the mass spectra of SAP extracted from a series of dilutions of 60  $\mu\text{L}$  PBS, ranging from 1.9  $\mu\text{M}$  to 0.6 nM. Strong peak intensities were observed in all spectra except that for the 0.6 nM solution (signal-to-noise ratio of 3). The better detection limit of SAP compared with CRP may be attributed to the different amounts of antibody on MNPs (the rate of anti-SAP to anti-CRP was 1.4). Theoretically, the assay sensitivity of the NBAMS approach depends on the MALDI-TOF MS detection limit and the efficiency of affinity extraction. Assuming full recovery of all the SAP present in the 60  $\mu\text{L}$  of diluted solution (0.6 nM in Fig. 10.12F), the absolute detection limit is estimated to be 36 fmol, which is comparable to the detection limit by direct deposition of SAP onto the MALDI probe (data not shown). Notably, SAP and CRP levels in sera from healthy individuals were about 1.6  $\mu\text{M}$  and 40 nM, respectively [112, 113]. Considering current progress in the detection limit, the nanoscale immunoassay is capable, with reasonable enrichment, of detecting plasma proteins at the subnanomolar level (0.6 nM).

Another advantage of the nanoprobe-based immunoassay is the ability to preconcentrate the antigen from diluted medium to a small volume of MNPs. The concentration effect was demonstrated with a series of solutions with different SAP concentration (8–160 nM). Figure 10.13 shows the MALDI-TOF mass spectra of ex-

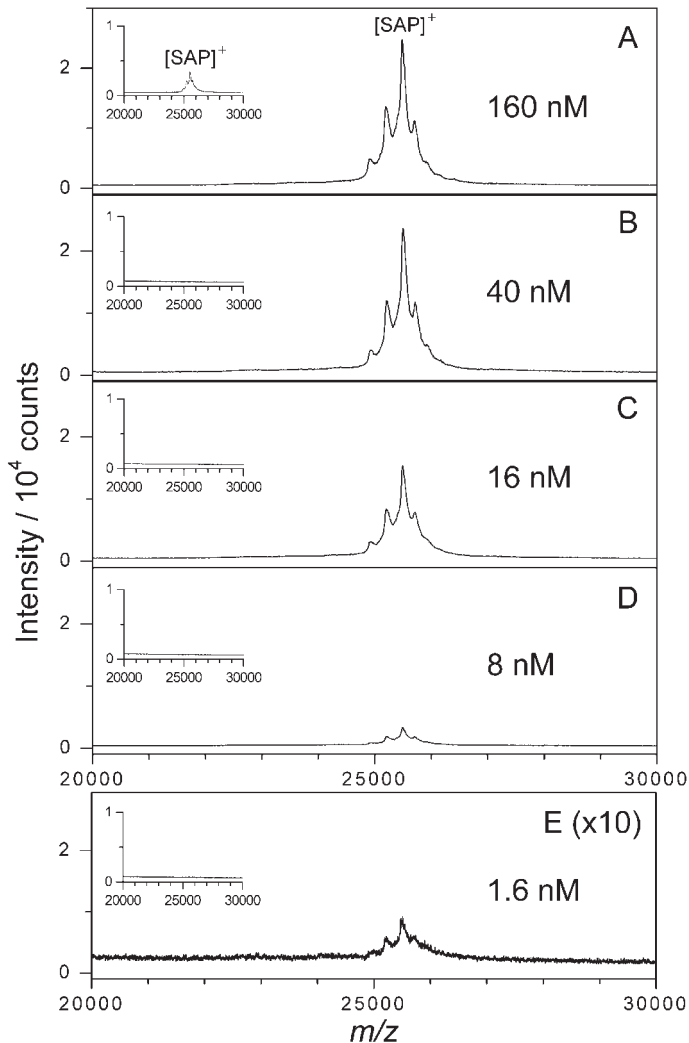


**Fig. 10.13.** Mass spectra of SAP extracted from diluted solution using anti-SAP-conjugated MNPs: (A) 160 nM SAP, 50  $\mu\text{L}$ ; (B) 40 nM, 200  $\mu\text{L}$ ; (C) 16 nM, 500  $\mu\text{L}$ ; (D) 8 nM, 1000  $\mu\text{L}$ ; (E) 1.6 nM, 1000  $\mu\text{L}$ . The inset of each panel shows the mass spectrum of solution prior to extraction. (From Ref. [96].)

tracted SAP after preconcentration using anti-SAP-conjugated MNPs. By contrast, the SAP peak was barely discernible (or not detected) when the diluted samples were analyzed by conventional MALDI-TOF MS, as shown in the inset of each panel. Similarly, Fig. 10.13(E) shows that as low as 1.6 nM SAP in a 1000  $\mu\text{L}$  solution was detectable with a signal-to-noise ratio of 13, and this concentration was



comparable to the detection limit of SAP extracted by MNPs (Fig. 10.12F). All the results demonstrate the MNPs are effective probes that provide simultaneous protein cleaning and concentrating for analyte with very low concentration.

## 10.5

### Human Plasma and Whole Blood Analysis by Nanoprobe-based Affinity Mass Spectrometry

#### 10.5.1

##### Selected Protein Profiling from Human Plasma

Human plasma proteome is the most attractive biological medium containing secreted disease-related markers, holding promise in both disease diagnosis and therapeutic aspects [21]. However, it is a very complex mixture of proteins having a wide and dynamic range of abundance of more than  $10^{12}$ . Indeed, 22 high-abundance proteins constitute 99% of the protein content in plasma, with the remaining 1% that are of great interest as potential biomarkers [114]. In the NBAMS immunoassay, specificity is one of the key components to analyze the low-abundance proteins. The NBAMS platform has been applied to human plasma to investigate whether the approach can directly detect low-level proteins in plasma. Before immunoaffinity extraction, no protein profile could be obtained from the crude plasma in healthy individual due to the interference of salt and other plasma components (Fig. 10.14A). After a 200-fold dilution of the plasma sample to reduce the salt concentration, the protein profile in Fig. 10.14(B) shows the commonly observed abundant plasma proteins, including human serum albumin (HSA), apolipoprotein A-I (Apo A-I), hemoglobin  $\alpha$ -chain (Hb-A), hemoglobin  $\beta$ -chain (Hb-B), and transthyretin (TTR). After immunoaffinity extraction, SAP was detected with concomitant depletion of other proteins of higher concentration (Fig. 10.14C). Similarly, Fig. 10.14(D) shows an apparent peak for CRP, even though the level of this protein is 40-fold lower than that of SAP in healthy individuals. Although the analysis showed minor peaks due to nonspecific binding of other high-abundance plasma proteins, they did not interfere with the unambiguous identification of CRP and SAP by mass spectrometry.

#### 10.5.2

##### Comparison of Nanoscale and Microscale Immunoassay

To compare the advantages of magnetic nano-size particles with those of magnetic microbeads (MMP), commercially aminated magnetic microbeads (DYNAL BIOTECH, 2.8  $\mu\text{m}$ ) were conjugated with anti-SAP antibody to obtain anti-SAP MMP by the same modification process used for MNP. With an equal amount of antibody on the particle surface, the signal intensity and signal-to-noise ratio were dramatically reduced in the mass spectrum of MMP compared with MNP experiments. These results indicate that MNPs afford better affinity extraction of the tar-

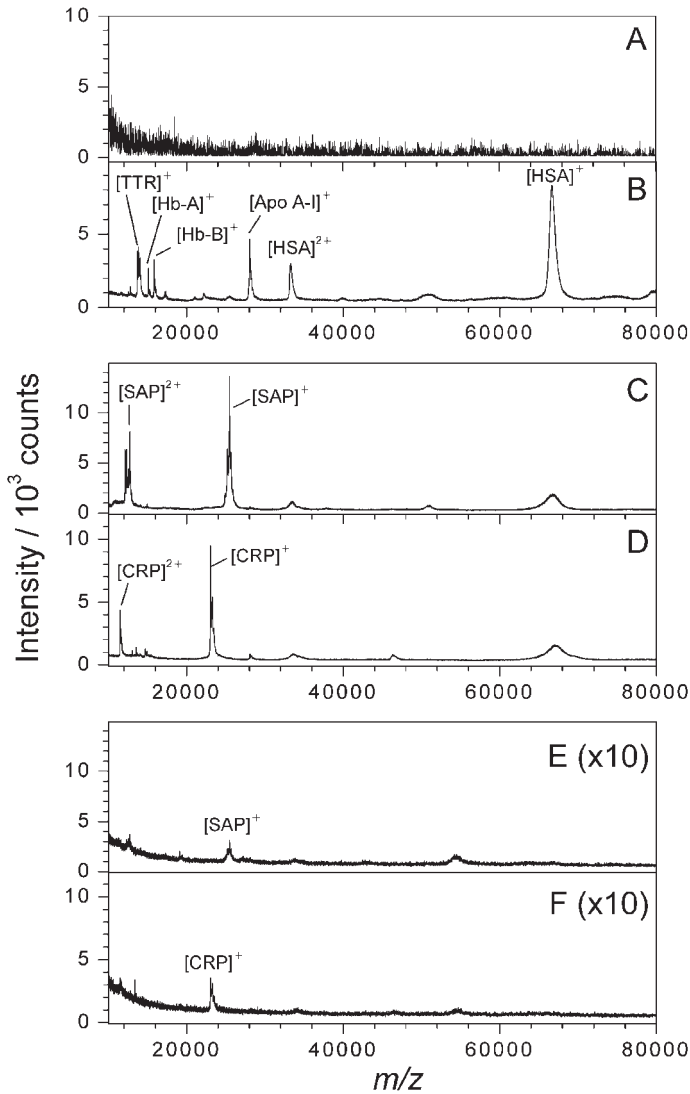


**Fig. 10.14.** Comparison of immunoaffinity extraction performance between antibody-conjugated MNPs and magnetic microbeads. Mass spectra showed human plasma (A) without dilution; (B) with 200-fold dilution. High-abundance proteins were so dominant that the signals from SAP or CRP were buried

in the spectrum. Representative mass spectra of (C) for SAP and (D) for CRP were obtained after extraction using antibody-conjugated MNPs. Spectra for antibody-conjugated microbeads are shown in (E) for SAP and (F) for CRP. (From Ref. [96].)

get protein, thereby improving the detection. The superior efficiency of MNP could be attributed to its large surface area-to-volume ratio, good reaction homogeneity and fast reaction kinetics in suspension array. Additionally, the mass spectrum of affinity extraction with MNPs preserved good spectral resolution and peak profiles without apparent peak broadening and mass shift.

### 10.5.3

#### Suppression of Nonspecific Binding on Magnetic Nanoparticles

Antibody-conjugated MNPs could effectively enhance the target protein signal for MALDI-TOF MS detection. However, nonspecific binding from other non-antigenic protein on the surface of MNPs interferes with the sensitivity and accuracy of MALDI-TOF MS detection. As shown in Fig. 10.15(A), HSA is the major abundant protein present in human plasma and was coextracted by antibody-conjugated MNPs. To avoid nonspecific binding, bovine serum albumin (BSA) was first tested

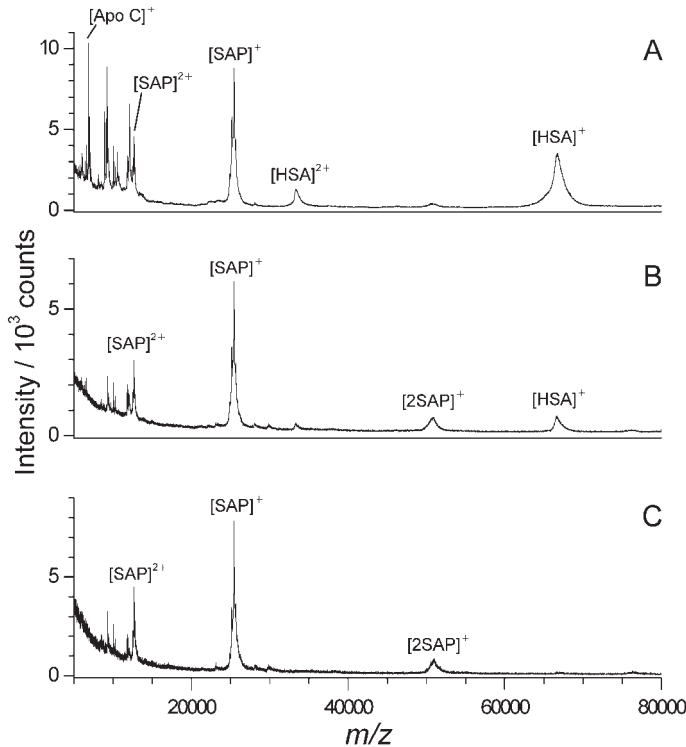


**Fig. 10.15.** Mass spectra of nanoscale immunoaffinity extraction of plasma SAP from a 1- $\mu$ L plasma sample with anti-SAP MNPs (A) without blocking, (B) with BSA blocking and (C) with 40 mM MEG blocking. (From Ref. [97].)

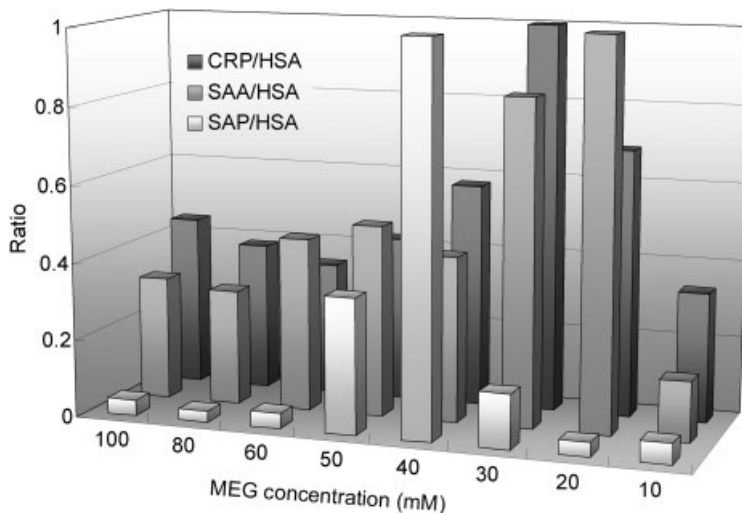


**Fig. 10.16.** Concentration effect of MEG on suppression of non-specific binding; the maximum value of target/HSA ratio is normalized as 1.0. (From Ref. [97].)

as a blocking agent to protect the anti-SAP MNPs. However, BSA did not yield good suppression of the HSA peak. Recently, Huang and Zheng [115] have reported that the short molecule, ethylene glycol, is biocompatible material with good resistance to nonspecific binding with biological molecules. The short terminal aminated methoxy-ethylene glycol (MEG) linker was tested as the surface blocking spacer to suppress the serious nonspecific binding effect. Indeed, MEG-protected antibody-conjugated MNPs can significantly reduce non-specific binding during the affinity separation of protein biomarkers in human plasma.

By modulating the MEG coupling concentration, the inhibition of nonspecific binding was found to be concentration-dependent (10–100 mM). In Fig. 10.16, three different protein markers, including SAP, CRP, SAA, could be obviously enhanced with the least nonspecific interference from the MEG coupling concentration between 20 and 40 mM. Notably, the amount of antibody on the MNP surface was not affected by the incubation time and the concentration of MEG. Based on above results, moderate surface blocking plays a key role in the enhanced detection specificity of the NBAMS approach.

#### 10.5.4

##### Enrichment of Target Antigen in Human Plasma

The major advantage of NBAMS methodology is the simultaneous selection and preconcentration of targeted protein onto the MNPs, even in a complex biological medium. The concentration effect of NBAMS in human plasma was evaluated with equal amounts of plasma (1  $\mu$ L from each subject) diluted 50-, 500-, and

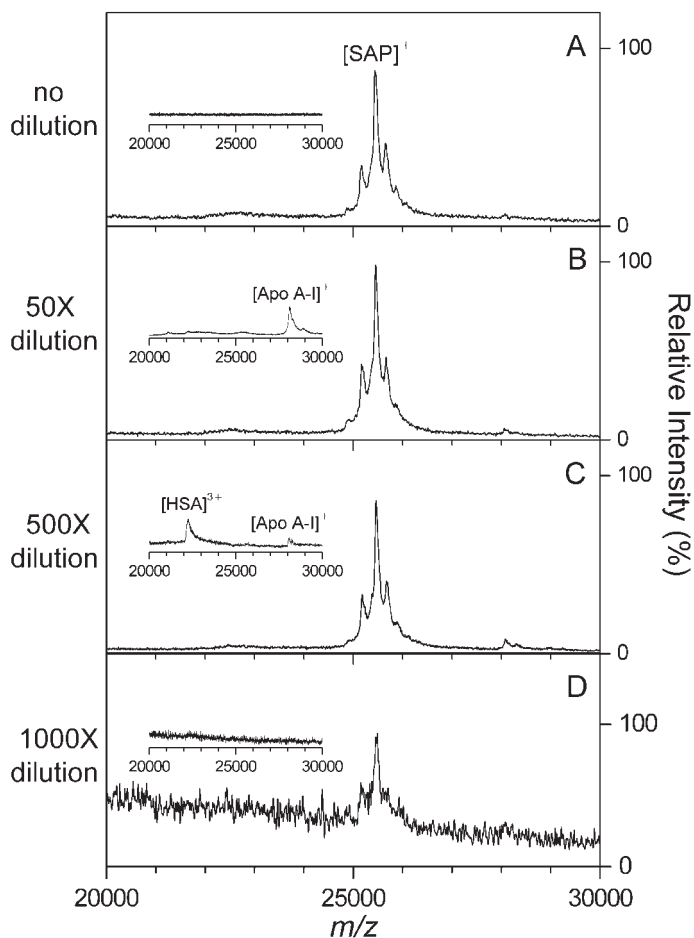


**Fig. 10.17.** Mass spectra of SAP extracted from human plasma (1  $\mu$ L), undiluted (A), and diluted 50-fold (B), 500-fold (C), or 1000-fold (D), using anti-SAP-conjugated MNPs extraction. Inset of each panel shows the mass spectrum of solution before extraction. (From Ref. [96].)

1000-fold in PBS and analyzed using the nanoprobe-based immunoassay. Figure 10.17 shows the MALDI-TOF mass spectra of plasma SAP extracted from each diluted sample. Incubation of the diluted plasma samples with the antibody-conjugated MNPs resulted in antigen selection and concentration, as demonstrated by the similar mass spectra profiles up to 500-fold dilution (Fig. 10.17C). In the 1000-fold diluted sample (1.8 nM SAP), however, the captured antigen showed significantly lower intensity in the mass spectrum (Fig. 10.17D). This decreased recovery may arise from the incomplete collection of the MNPs from the curved wall of the microcentrifuge tube during the washing steps. Despite the decreased

recovery at 1000-fold dilution, the detection sensitivity in human plasma (estimated to be 1.8 nM) was comparable to the performance of NBAMS in a protein standard (SAP, 0.6 nM in Fig. 10.12F), demonstrating that the nanoscale immunoassay is refractory to the presence of highly abundant nonantigenic proteins, salts, and buffers in plasma. All these results display the general applicability of NBAMS methodology, namely, that concentrations with a 1000-fold difference can be detected successfully. By the good concentration effect, 1  $\mu$ L of plasma is sufficient to unambiguously identify an antigen of interest.

In the NBAMS immunoassay, the rate-limiting step of the total procedure for diseased-related protein analysis by NBAMS is the separation of plasma from blood (30–60 min). To speed up the analysis, the NBAMS approach was performed in a blood sample without prior centrifugation. Figure 10.18(A) shows the profile of the major proteins in human blood, containing Hb-A, Hb-B and HSA. After treatment with anti-SAP- and anti-CRP-conjugated MNPs sequentially, the extracted SAP and CRP was shown in Fig. 10.18(B, C, respectively). Although the highly abundant Hb-A, Hb-B and HSA were coextracted, CRP and SAP were unambiguously identified through mass spectrometric detection within 20 min without interference from the highly abundant contaminants. This demonstrates the feasibility of the NBAMS approach in blood sample analysis and holds promise in speeding up clinical applications.

#### 10.5.5

##### **Plasma Protein Profiling in Normal Individuals and in Patients**

The NBAMS approach has been performed with authentic clinical samples plasma (20  $\mu$ L) from six healthy individuals and four patients with gastric cancer [97]. All sample preparation, washing and on-nanoprobe analysis were performed in parallel batches. CRP and SAP were detected successfully in all the healthy individuals, despite the fact that the levels of a few of them were below the detection limit of ELISA ( $<0.159$  mg L<sup>-1</sup>) [101]. The results in Fig. 10.19 illustrate the measured intensities for CRP and SAP, showing significant upregulation and down-regulation in expression levels, respectively. These observed differences in protein levels are consistent with the literature [116, 117] and the ion intensity measured by the nanoprobe-based assay correlated with the concentration measured by ELISA [101], suggesting that the NBAMS approach shows promise for quantitative protein profiling. Analysis with more clinical samples is required for further evaluation on quantitation accuracy.

#### 10.6

##### **Multiplex Assay**

Because of the complex natures of disease, diagnosis using single protein assay often results in insufficient detection specificity. To improve detection specificity and sensitivity to determine disease onset, the utility of multivariant protein

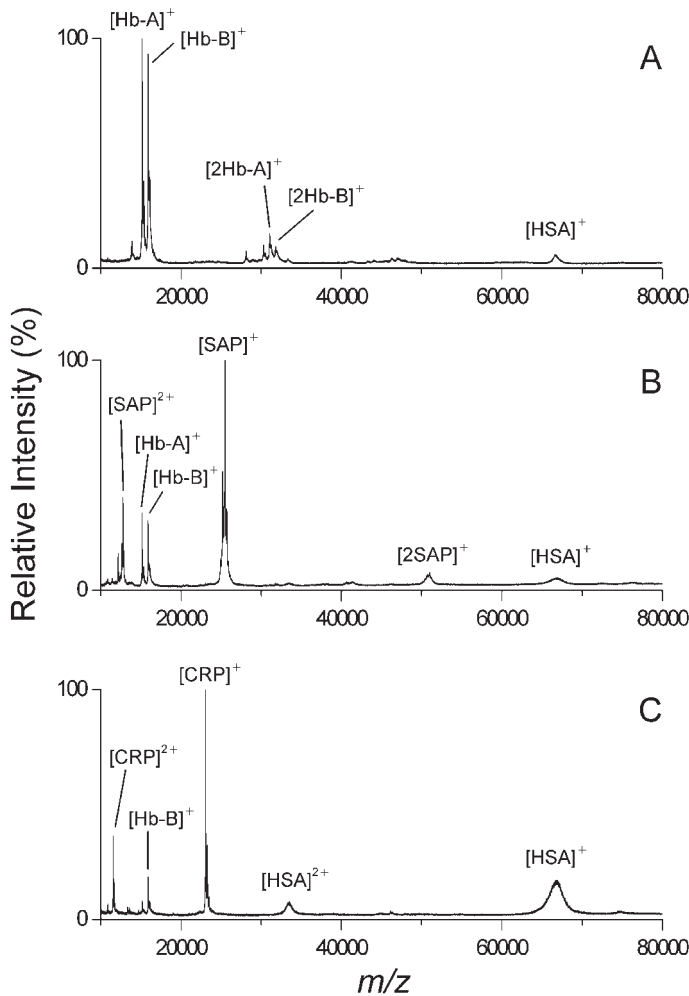


**Fig. 10.18.** Mass spectra of a human blood sample (20  $\mu$ L) from a patient with stroke before (A) and after using (B) anti-SAP-conjugated MNPs or (C) anti-CRP-conjugated MNPs extraction.

markers as disease signature present an evolving direction in diagnosis. Developing multiplexed assays that can simultaneously screen multiple protein biomarkers is a rapidly expanding trend in characterizing disease states [118]. For example, Lokshin et al. [119] have developed new profiling technology, LabMAP, which combines the principle of a sandwich immunoassay with fluorescent-bead-based technology to detect tumor markers and cytokines in serum samples. The sensitivity, around 80–90% specificity, of discriminating early-stage ovarian cancer from

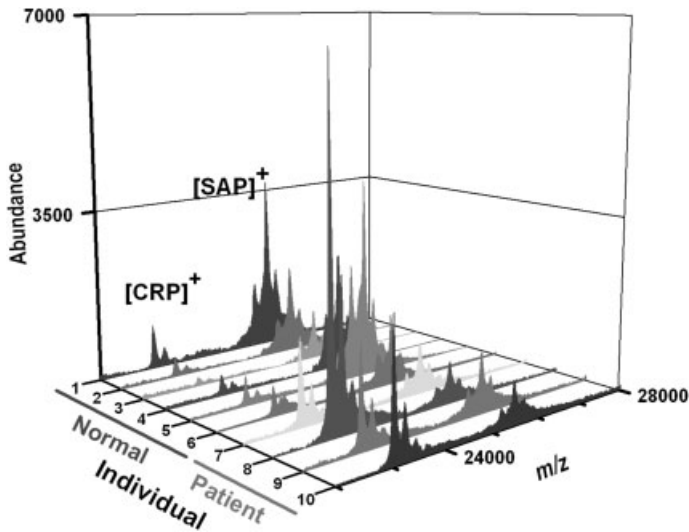


**Fig. 10.19.** Screening of SAP and CRP in human plasma from healthy individuals and patients with gastric cancer using nanoprobe-based affinity mass spectrometry. The mass

spectrum of CRP ( $m/z$  23 kDa) and SAP ( $m/z$  25 kDa) show significant upregulation and down-regulation, respectively. (From Ref. [97].)

healthy controls was increased from 70 to 80% by using CA 125 alone to 90–100% by using the combination of five markers. In addition to the fluorescence-based immunoassay, Wilson has reported antibody-immobilized electrodes as electrochemical immunosensors. Quantitation can be performed simultaneously for two tumor markers, CEA and AFP, in standard protein solution [120]. Lieber's group have developed an antibody-labeled silicon-nanowire sensor array for multiplex electrical detection of PSA, PSA-ACT complex, CEA, and mucin-1. This technology allowed highly selective and sensitive detection of  $0.9 \text{ pg mL}^{-1}$  of PSA in undiluted serum samples [121].

#### 10.6.1

##### Workflow of Multiplexed Assay

In past work, the NBAMS technology has also been successfully demonstrated as a multiplexed immunoassay [97]. Three model proteins, SAA, SAP, and CRP, were still selected as target antigens. Figure 10.20 shows the multiplex immunoassay workflow. Plasma is diluted by PBS, mixed with a mixture of anti-SAA-, anti-CRP-, and anti-SAP-MNPs, and incubated at room temperature. In the same way as described previously, MNPs are isolated, washed, and subjected to MALDI-TOF MS analysis after immunoaffinity capture of antigens. This immunoextraction and subsequent analysis can be completed in 1 h.



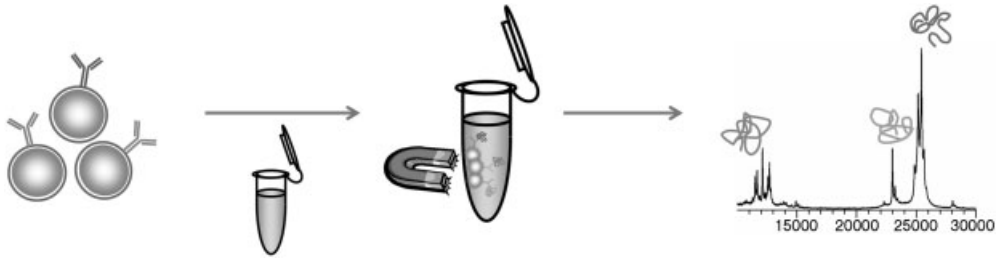


**Fig. 10.20.** Workflow of multiplexed immunoassay. For simultaneous analysis of multiple antigens, various antibody-conjugated MNPs are mixed in the appropriate ratio, and incubated with plasma sample. After separation by magnet, the isolated, antigen-captured MNPs are directly spotted onto a sample plate and analyzed by MALDI-TOF MS.

### 10.6.2

#### Screening for Patient and Healthy Individuals

A total of 18 samples, including nine normal controls and nine gastric cancer patients, have been analyzed by the NBAMS multiplexed immunoassay. Figure 10.21 shows representative results of the multiplex assay for SAA, SAP, and CRP from human plasma. Obvious differences can be observed in the protein profile between the two spectra obtained from healthy control (Fig. 10.21A) and gastric cancer patients (Fig. 10.21B). The measured intensities for both SAA and CRP are considerably higher in the gastric cancer patient sample than in the healthy individual. The relative SAA and CRP intensities are consistent with the concentration measured by ELISA (data not shown), and suggest that our immunoassay shows promise for quantitative protein profiling.

The normal and gastric cancer groups can be differentiated with a scatterplot of relative SAA and CRP intensities (Fig. 10.21C). Obviously, the data distribution falls into two clusters in the diagram. A “virtual diagnosis pattern” of the SAA/SAP and CRP/SAP ratio provides a group separation. The low relative SAA and CRP abundances were observed in plasma from the healthy group, whereas higher ratios were observed for gastric cancer cases. The distribution is consistent with the groups of normal and gastric cancer.

It has been increasingly recognized that multivariate parameters characterize disease states better than a single protein assay. By using a mixture of MNPs conjugated with different antibodies, the NBAMS technology demonstrated the capability of simultaneous multiplex protein profiling in complex mixtures like human plasma. Furthermore, this assay provides the speed, high sensitivity, and detection specificity required by disease diagnosis and monitoring. This preliminary data showed the promise for application of rapid screening targeted protein profile for disease diagnosis and monitoring. However, the potential implementation of NBAMS awaits further considerations. Generally, the diagnosis specificity not only depends on the detection specificity but also on statistical specificity of the protein marker. In terms of accuracy and reproducibility of analysis, more samples

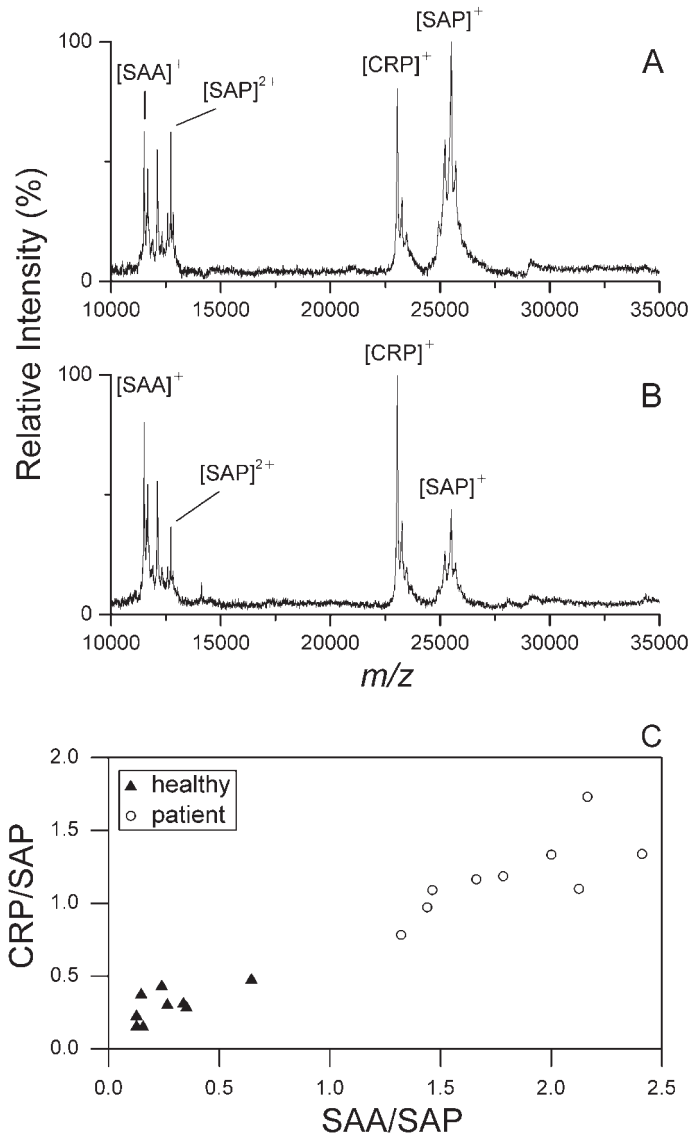


**Fig. 10.21.** Representative protein profiles of human plasma from (A) healthy control (from Ref. [97]) and (B) gastric cancer patient obtained by multiplexed immunoassay. (C) Scatter-plot of relative SAA and CRP intensities shows a differentiation between normal and gastric cancer groups.

are required for further evaluation. Further study for quantitative profiling is currently on-going.

## 10.7

### Future Outlook

Surface-conjugated nanoparticles have been shown to act as specific affinity nanoprobes for the multiplexed detection of target proteins in human plasma. Such nanoprobes are envisaged to become excellent tools for the separation and enrichment of low-abundant protein biomarkers. Analysis by MALDI-TOF MS provides unambiguous identification of target antigen. In combination with the ongoing quantitative analysis of plasma protein profiling, this nanoprobe-based immunoassay holds great potential for the early diagnosis of disease, inflammatory events, and eventually cancers. From proof-of-concept experiments to widespread use, as always, the quantification sensitivity, specificity, and reproducibility have to be further evaluated with a large set of clinical specimens. For large-scale analysis, advances in instrumentation will become imperative for the automation of sample preparation, nanoprobe detection, and data analysis. The specificity, speed, and flexibility of the nanoprobe-based affinity assay can easily be adapted for the detection of other class-specific proteins in biological research, clinical proteomics and diagnostics.

### Acknowledgments

The authors acknowledge financial support from Academia Sinica Research Project on Nanoscience and Technology and the National Science Council, Taiwan. The authors thank Mr. Li-Li Wen at En Chu Kong Hospital for ELISA analysis, Dr. H.-M. Lin for TEM measurement, and the Institute of Biomedical Sciences, Academia Sinica, Taiwan for the use of MALDI-TOF MS.

### References

- 1 ROSENBLATT, K. P., BRYANT-GREENWOOD, P., KILLIAN, J. K., MEHTA, A., GEHO, D., ESPINA, V., PETRICOIN, E. F., 3rd, LIOTTA, L. A. Serum proteomics in cancer diagnosis and management, *Annu. Rev. Med.* **2004**, *55*, 97–112.
- 2 JONES, M. B., KRUTZSCH, H., SHU, H., ZHAO, Y., LIOTTA, L. A., KOHN, E. C., PETRICOIN, E. F., 3rd Proteomic analysis and identification of new biomarkers and therapeutic targets for invasive ovarian cancer, *Proteomics* **2002**, *2*, 76–84.
- 3 ZHOU, G., LI, H., DeCAMP, D., CHEN, S., SHU, H., GONG, Y., FLAIG, M., GILLESPIE, J. W., HU, N., TAYLOR, P. R., EMMERT-BUCK, M. R., LIOTTA, L. A., PETRICOIN, E. F., 3rd, ZHAO, Y. 2D differential in-gel electrophoresis for the identification of esophageal scans cell cancer-specific protein

- markers, *Mol. Cell. Proteomics* **2002**, 1, 117–124.
- 4 BURTIS, C. A., ASHWOOD, E. R., in *Tietz Fundamentals of Clinical Chemistry*, 5th edn., W. B. SAUNDERS, Philadelphia, **2001**, pp. 390–413.
  - 5 [Anon] European Group on Tumour Markers (EGTM), *Anticancer Res.* **1999**, 19, 2785–2820.
  - 6 SOLETORMOS, G., NIELSEN, D., SCHIOLER, V., MOURIDSEN, H., DOMBERNOWSKY, P. Monitoring different stages of breast cancer using tumour markers CA 15-3, CEA and TPA, *Eur. J. Cancer* **2004**, 40, 481–486.
  - 7 MOLINA, R., BARAK, V., VAN DALEN, A., DUFFY, M. J., EINARSSON, R., GION, M., GOIKE, H., LAMERZ, R., NAP, M., SOLETORMOS, G., STIEBER, P. Tumor markers in breast cancer – European Group on Tumor Markers recommendations, *Tumor Biol.* **2005**, 26, 281–293.
  - 8 TERRY, K. L., SLUSS, P. M., SKATES, S. J., MOK, S. C., YE, B., VITONIS, A. F., CRAMER, D. W. Blood and urine markers for ovarian cancer: A comprehensive review, *Dis. Markers* **2004**, 20, 53–70.
  - 9 SKATES, S. J., HORICK, N., YU, Y., XU, F. J., BERCHUCK, A., HAVRILESKY, L. J., DE BRUIJN, H. W., VAN DER ZEE, A. G., WOOLAS, R. P., JACOBS, I. J., ZHANG, Z., BAST, R. C., JR. Preoperative sensitivity and specificity for early-stage ovarian cancer when combining cancer antigen CA-125II, CA 15-3, CA 72-4, and macrophage colony-stimulating factor using mixtures of multivariate normal distributions, *J. Clin. Oncol.* **2004**, 22, 4059–4066.
  - 10 DUFFY, M. J., VAN DALEN, A., HAGLUND, C., HANSSON, L., KLAPDOR, R., LAMERZ, R., NILSSON, O., STURGEON, C., TOPOLCAN, O. Clinical utility of biochemical markers in colorectal cancer: European Group on Tumour Markers (EGTM) guidelines, *Eur. J. Cancer* **2003**, 39, 718–727.
  - 11 DUFFY, M. J., BONFRER, J. M., KULPA, J., RUSTIN, G. J., SOLETORMOS, G., TORRE, G. C., TUXEN, M. K., ZWIRNER, M. CA125 in ovarian cancer: European Group on Tumor Markers guidelines for clinical use, *Int. J. Gynecol. Cancer* **2005**, 15, 679–691.
  - 12 CATALONA, W. J., PARTIN, A. W., SLAWIN, K. M., BRAWER, M. K., FLANIGAN, R. C., PATEL, A., RICHIE, J. P., DEKERNION, J. B., WALSH, P. C., SCARDINO, P. T., LANGE, P. H., SUBONG, E. N., PARSON, R. E., GASIOR, G. H., LOVELAND, K. G., SOUTHWICK, P. C. Use of the percentage of free prostate-specific antigen to enhance differentiation of prostate cancer from benign prostatic disease: A prospective multicenter clinical trial, *J. Am. Med. Assoc.* **1998**, 279, 1542–1547.
  - 13 THAKUR, V., SINGH, P. P., TALWAR, M., MUKHERJEE, U. Utility of free/total prostate specific antigen (f/t PSA) ratio in diagnosis of prostate carcinoma, *Dis. Markers* **2003**, 19, 287–292.
  - 14 HERNANDEZ, J., THOMPSON, I. M. Prostate-specific antigen: A review of the validation of the most commonly used cancer biomarker, *Cancer* **2004**, 101, 894–904.
  - 15 EBERT, M. P., KORC, M., MALFERTHEINER, P., ROCKEN, C. Advances, challenges, and limitations in serum-proteome-based cancer diagnosis, *J. Proteome Res.* **2006**, 5, 19–25.
  - 16 PAVLENKO, M., ROOS, A. K., LUNDQVIST, A., PALMBORG, A., MILLER, A. M., OZENCI, V., BERGMAN, B., EGEVAD, L., HELLSTROM, M., KIESSLING, R., MASUCCI, G., WERSALL, P., NILSSON, S., PISA, P. A phase I trial of DNA vaccination with a plasmid expressing prostate-specific antigen in patients with hormone-refractory prostate cancer, *Br. J. Cancer* **2004**, 91, 688–694.
  - 17 KANTOR, A. B., WANG, W., LIN, H., GOVINDARAJAN, H., ANDERLE, M., PERRONE, A., BECKER, C. Biomarker discovery by comprehensive phenotyping for autoimmune diseases, *Clin. Immunol.* **2004**, 111, 186–195.
  - 18 PETRICOIN, E., WULFKUHLE, J., ESPINA, V., LIOTTA, L. A. Clinical proteomics: Revolutionizing disease

- detection and patient tailoring therapy, *J. Proteome Res.* **2004**, *3*, 209–217.
- 19 LIOTTA, L. A., KOHN, E. C. The microenvironment of the tumour-host interface, *Nature* **2001**, *411*, 375–379.
  - 20 HANASH, S. Disease proteomics, *Nature* **2003**, *422*, 226–232.
  - 21 ANDERSON, N. L., ANDERSON, N. G. The human plasma proteome: History, character, and diagnostic prospects, *Mol. Cell. Proteomics* **2002**, *1*, 845–867.
  - 22 HAYAT, M. A. *Colloidal Gold: Principles, Methods, and Applications*, Academic Press, San Diego, **1989**.
  - 23 DANIEL, M. C., ASTRUC, D. Gold nanoparticles: Assembly, supra-molecular chemistry, quantum-size-related properties, and applications toward biology, catalysis, and nanotechnology, *Chem. Rev.* **2004**, *104*, 293–346.
  - 24 TSCHOPP, J., PODACK, E. R., MULLER-EBERHARD, H. J. Ultrastructure of the membrane attack complex of complement: Detection of the tetrameric C9-polymerizing complex C5b-8, *Proc. Natl. Acad. Sci. U.S.A.* **1982**, *79*, 7474–7478.
  - 25 FAULK, W. P., TAYLOR, G. M. An immunocolloid method for the electron microscope, *Immunochemistry* **1971**, *8*, 1081–1083.
  - 26 SAFER, D., HAINFELD, J., WALL, J. S., REARDON, J. E. Biospecific labeling with undecagold: Visualization of the biotin-binding site on avidin, *Science* **1982**, *218*, 290–291.
  - 27 HORISBERGER, M., ROSSET, J. Colloidal gold, a useful marker for transmission and scanning electron microscopy, *J. Histochem. Cytochem.* **1977**, *25*, 295–305.
  - 28 BIRRELL, G. B., HEDBERG, K. K., GRIFFITH, O. H. Pitfalls of immunogold labeling: Analysis by light microscopy, transmission electron microscopy, and photoelectron microscopy, *J. Histochem. Cytochem.* **1987**, *35*, 843–853.
  - 29 BONNARD, C., PAPERMASTER, D. S., KRAEHNBUHL, J. P. in *Immuno-labelling for Electron Microscopy*, POLAK, J. M., VARDELL, I. M. (Eds.), Elsevier, New York, **1984**, pp. 95–111.
  - 30 TURKEVICH, J., STEVENSON, P. C., HILLIER, J. A study of the nucleation and growth progress in the synthesis of colloidal gold, *Discuss. Faraday Soc.* **1951**, *11*, 55–75.
  - 31 FRENS, G. Controlled nucleation for the regulation of the particle size in monodisperse gold suspensions, *Nat. Phys. Sci.* **1973**, *241*, 20–22.
  - 32 HOLGATE, C. S., JACKSON, P., COWEN, P. N., BIRD, C. C. Immunogold-silver staining: New method of immunostaining with enhanced sensitivity, *J. Histochem. Cytochem.* **1983**, *31*, 938–944.
  - 33 LINK, S., EL-SAYED, M. A. Shape and size dependence of radiative, non-radiative and photothermal properties of gold nanocrystals, *Int. Rev. Phys. Chem.* **2000**, *19*, 409–453.
  - 34 NIEMEYER, C. M. Nanoparticles, proteins, and nucleic acids: Biotechnology meets materials science, *Angew. Chem. Int. Ed.* **2001**, *40*, 4128–4158.
  - 35 MIRKIN, C. A., LETSINGER, R. L., MUCIC, R. C., STORHOFF, J. J. A DNA-based method for rationally assembling nanoparticles into macroscopic materials, *Nature* **1996**, *382*, 607–609.
  - 36 LIN, C. C., YEH, Y. C., YANG, C. Y., CHEN, G. F., CHEN, Y. C., WU, Y. C., CHEN, C. C. Quantitative analysis of multivalent interactions of carbohydrate-encapsulated gold nanoparticles with concanavalin A, *Chem. Commun.* **2003**, 2920–2921.
  - 37 DE LA FUENTE, J. M., BARRIENTOS, A. G., ROJAS, T. C., ROJO, J., CANADA, J., FERNANDEZ, A., PENADES, S. Gold glyconanoparticles as water-soluble polyvalent models to study carbohydrate interactions, *Angew. Chem. Int. Ed.* **2001**, *40*, 2257–2261.
  - 38 TENG, C. H., HO, K. C., LIN, Y. S., CHEN, Y. C. Gold nanoparticles as selective and concentrating probes for samples in MALDI MS analysis, *Anal. Chem.* **2004**, *76*, 4337–4342.
  - 39 NEGISHI, Y., NOBUSADA, K., TSUKUDA, T. Glutathione-protected gold clusters

- revisited: Bridging the gap between gold(I)-thiolate complexes and thiolate-protected gold nanocrystals, *J. Am. Chem. Soc.* **2005**, *127*, 5261–5270.
- 40 CHEN, Y. J., CHEN, S. H., CHIEN, Y. Y., CHANG, Y. W., LIAO, H. K., CHANG, C. Y., JAN, M. D., WANG, K. T., LIN, C. C. Carbohydrate-encapsulated gold nanoparticles for rapid target-protein identification and binding-epitope mapping, *ChemBioChem* **2005**, *6*, 1169–1173.
- 41 HAFELI, U., in *Magnetism in Medicine: A Handbook*, ANDRA, W., NOWAK, H. (Eds.), Wiley-VCH Verlag GmbH, Berlin, **1998**, p. 15.
- 42 WEISSELEDER, R., ELIZONDO, G., WITTENBERG, J., RABITO, C. A., BENGELE, H. H., JOSEPHSON, L. Ultrasmall superparamagnetic iron oxide: Characterization of a new class of contrast agents for MR imaging, *Radiology* **1990**, *175*, 489–493.
- 43 GUPTA, A. K., GUPTA, M. Synthesis and surface engineering of iron oxide nanoparticles for biomedical applications, *Biomaterials* **2005**, *26*, 3995–4021.
- 44 GOYA, G. F., BERQUO, T. S., FONSECA, F. C., MORALES, M. P. Static and dynamic magnetic properties of spherical magnetite nanoparticles, *J. Appl. Phys.* **2003**, *94*, 3520–3528.
- 45 BEAN, C. P., LIVINGSTONE, J. D. Superparamagnetism, *J. Appl. Phys.* **1959**, *30*, 120S–129S.
- 46 LEFEBURE, S., DUBOIS, E., CABUIL, V., NEVEU, S., MASSART, R. Monodisperse magnetic nanoparticles: Preparation and dispersion in water and oils, *J. Mater. Res.* **1998**, *13*, 2975–2981.
- 47 OLSVIK, O., POPOVIC, T., SKJERVE, E., CUDJOE, K. S., HORNES, E., UGELSTAD, J., UHLEN, M. Magnetic separation techniques in diagnostic microbiology, *Clin. Microbiol. Rev.* **1994**, *7*, 43–54.
- 48 ZHANG, Y., KOHLER, N., ZHANG, M. Surface modification of superparamagnetic magnetite nanoparticles and their intracellular uptake, *Biomaterials* **2002**, *23*, 1553–1561.
- 49 WIDDER, K. J., SENYEI, A. E., RANNEY, D. F. In vitro release of biologically active adriamycin by magnetically responsive albumin microspheres, *Cancer Res.* **1980**, *40*, 3512–3517.
- 50 REIMER, P., WEISSELEDER, R. Development and experimental use of receptor-specific MR contrast media, *Radiologe* **1996**, *36*, 153–163.
- 51 PANKHURST, Q. A., CONNOLLY, J., JONES, S. K., DOBSON, J. Applications of magnetic nanoparticles in biomedicine, *J. Phys. D: Appl. Phys.* **2003**, *36*, R167–R181.
- 52 LUDERER, A. A., BORRELLI, N. F., PANZARINO, J. N., MANSFIELD, G. R., HESS, D. M., BROWN, J. L., BARNETT, E. H., HAHN, E. W. Glass-ceramic-mediated, magnetic-field-induced localized hyperthermia: Response of a murine mammary carcinoma, *Radiat. Res.* **1983**, *94*, 190–198.
- 53 SCHWERTMANN, U., CORNELL, R. M. *Iron Oxides in the Laboratory: Preparation and Characterization*, Wiley-VCH, New York, **1991**.
- 54 HYEON, T., LEE, S. S., PARK, J., CHUNG, Y., NA, H. B. Synthesis of highly crystalline and monodisperse maghemite nanocrystallites without a size-selection process, *J. Am. Chem. Soc.* **2001**, *123*, 12798–12801.
- 55 SUN, S., MURRAY, C. B., WELLER, D., FOLKS, L., MOSER, A. Monodisperse FePt nanoparticles and ferromagnetic FePt nanocrystal superlattices, *Science* **2000**, *287*, 1989–1992.
- 56 PARAK, W. J., GERION, D., PELLEGRINO, T., ZANCHET, D., MICHEEL, C., WILLIAMS, S. C., BOUDREAU, R., GROS, M. A. L., LARABELL, C. A., ALIVISATOS, A. P. Biological applications of colloidal nanocrystals, *Nanotechnology* **2003**, *14*, R15–R27.
- 57 MURRAY, C. B., NORRIS, D. J., BAWENDI, M. G. Synthesis and characterization of nearly monodisperse CdE (E = S, Se, Te) semiconductor nanocrystallites, *J. Am. Chem. Soc.* **1993**, *115*, 8706–8715.
- 58 OLSHAVSKY, M. A., GOLDSTEIN, A. N., ALIVISATOS, A. P. Organometallic synthesis of GaAs crystallites exhibiting quantum confinement, *J. Am. Chem. Soc.* **1990**, *112*, 9438–9439.

- 59 SEYDACK, M. Nanoparticle labels in immunosensing using optical detection methods, *Biosens. Bioelectron.* **2005**, *20*, 2454–2469.
- 60 DUBERTRET, B. Quantum dots: DNA detectives, *Nat. Mater.* **2005**, *4*, 797–798.
- 61 AGRAWAL, A., ZHANG, C., BYASSE, T., TRIPP, R. A., NIE, S. Counting single native biomolecules and intact viruses with color-coded nanoparticles, *Anal. Chem.* **2006**, *78*, 1061–1070.
- 62 BRUCHEZ, M., JR., MORONNE, M., GIN, P., WEISS, S., ALIVISATOS, A. P. Semiconductor nanocrystals as fluorescent biological labels, *Science* **1998**, *281*, 2013–2016.
- 63 ITO, A., SHINKAI, M., HONDA, H., KOBAYASHI, T. Medical application of functionalized magnetic nanoparticles, *J. Biosci. Bioeng.* **2005**, *100*, 1–11.
- 64 MORNET, S., VASSEUR, S., GRASSET, F., DUGUET, E. Magnetic nanoparticle design for medical diagnosis and therapy, *J. Mater. Chem.* **2004**, *14*, 2161–2175.
- 65 ARTEMOV, D., MORI, N., OKOLLIE, B., BHUJWALLA, Z. M. MR molecular imaging of the Her-2/neu receptor in breast cancer cells using targeted iron oxide nanoparticles, *Mag. Reson. Med.* **2003**, *49*, 403–408.
- 66 HUH, Y. M., JUN, Y. W., SONG, H. T., KIM, S., CHOI, J. S., LEE, J. H., YOON, S., KIM, K. S., SHIN, J. S., SUH, J. S., CHEON, J. In vivo magnetic resonance detection of cancer by using multi-functional magnetic nanocrystals, *J. Am. Chem. Soc.* **2005**, *127*, 12 387–12 391.
- 67 JUN, Y. W., HUH, Y. M., CHOI, J. S., LEE, J. H., SONG, H. T., KIM, S., YOON, S., KIM, K. S., SHIN, J. S., SUH, J. S., CHEON, J. Nanoscale size effect of magnetic nanocrystals and their utilization for cancer diagnosis via magnetic resonance imaging, *J. Am. Chem. Soc.* **2005**, *127*, 5732–5733.
- 68 CUI, Y., WANG, Y., HUI, W., ZHANG, Z., XIN, X., CHEN, C. The synthesis of GoldMag nano-particles and their application for antibody immobilization, *Biomed. Microdevices* **2005**, *7*, 153–156.
- 69 SOKOLOV, K., FOLLEN, M., AARON, J., PAVLOVA, I., MALPICA, A., LOTAN, R., RICHARDS-KORTUM, R. Real-time vital optical imaging of precancer using anti-epidermal growth factor receptor antibodies conjugated to gold nanoparticles, *Cancer Res.* **2003**, *63*, 1999–2004.
- 70 NAM, J. M., THAXTON, C. S., MIRKIN, C. A. Nanoparticle-based bio-bar codes for the ultrasensitive detection of proteins, *Science* **2003**, *301*, 1884–1886.
- 71 OH, B.-K., NAM, J.-M., LEE, S. W., MIRKIN, C. A. A Fluorophore-based bio-barcode amplification assay for proteins, *Small* **2006**, *2*, 103–108.
- 72 MANN, M., HENDRICKSON, R. C., PANDEY, A. Analysis of proteins and proteomes by mass spectrometry, *Annu. Rev. Biochem.* **2001**, *70*, 437–473.
- 73 AEBERSOLD, R., MANN, M. Mass spectrometry-based proteomics, *Nature* **2003**, *422*, 198–207.
- 74 HENZEL, W. J., WATANABE, C., STULTS, J. T. Protein identification: The origins of peptide mass fingerprinting, *J. Am. Soc. Mass Spectrom.* **2003**, *14*, 931–942.
- 75 GEVAERT, K., VANDEKERCKHOVE, J. Protein identification methods in proteomics, *Electrophoresis* **2000**, *21*, 1145–1154.
- 76 TANG, N., TORNATORE, P., WEINBERGER, S. R. Current developments in SELDI affinity technology, *Mass Spectrom. Rev.* **2004**, *23*, 34–44.
- 77 ISSAQ, H. J., CONRADS, T. P., PRIETO, D. A., TIRUMALAI, R., VEENSTRA, T. D. SELDI-TOF MS for diagnostic proteomics, *Anal. Chem.* **2003**, *75*, 148A–155A.
- 78 HUTCHENS, T. W., YIP, T. T. New desorption strategies for the mass-spectrometric analysis of macromolecules, *Rapid Commun. Mass Spectrom.* **1993**, *7*, 576–580.
- 79 NELSON, R. W., KRONE, J. R., BIEBER, A. L., WILLIAMS, P. Mass spectrometric immunoassay, *Anal. Chem.* **1995**, *67*, 1153–1158.

- 80 TUBBS, K. A., NEDELKOV, D., NELSON, R. W. Detection and quantification of beta-2-microglobulin using mass spectrometric immunoassay, *Anal. Biochem.* **2001**, *289*, 26–35.
- 81 NEDELKOV, D., TUBBS, K. A., NIEDERKOFER, E. E., KIERNAN, U. A., NELSON, R. W. High-throughput comprehensive analysis of human plasma proteins: A step toward population proteomics, *Anal. Chem.* **2004**, *76*, 1733–1737.
- 82 KIERNAN, U. A., NEDELKOV, D., TUBBS, K. A., NIEDERKOFER, E. E., NELSON, R. W. Proteomic characterization of novel serum amyloid P component variants from human plasma and urine, *Proteomics* **2004**, *4*, 1825–1829.
- 83 BROCKMAN, A. H., ORLANDO, R. Probe-immobilized affinity chromatography/mass spectrometry, *Anal. Chem.* **1995**, *67*, 4581–4585.
- 84 BROCKMAN, A. H., ORLANDO, R. New immobilization chemistry for probe affinity mass spectrometry, *Rapid Commun. Mass Spectrom.* **1996**, *10*, 1688–1692.
- 85 CHING, J., VOIVODOV, K. I., HUTCHENS, T. W. Polymers as surface-based tethers with photolytic triggers enabling laser-induced release/desorption of covalently bound molecules, *Bioconjugate Chem.* **1996**, *7*, 525–528.
- 86 WEI, J., BURIK, J. M., SIUZDAK, G. Desorption-ionization mass spectrometry on porous silicon, *Nature* **1999**, *399*, 243–246.
- 87 ZOU, H., ZHANG, Q., GUO, Z., GUO, B., ZHANG, Q., CHEN, X. A mass spectrometry based direct-binding assay for screening binding partners of proteins, *Angew. Chem. Int. Ed.* **2002**, *41*, 646–648.
- 88 SU, J., MRKSICH, M. Using mass spectrometry to characterize self-assembled monolayers presenting peptides, proteins, and carbohydrates, *Angew. Chem. Int. Ed.* **2002**, *41*, 4715–4718.
- 89 CHEN, W. Y., WANG, L. S., CHIU, H. T., CHEN, Y. C., LEE, C. Y. Carbon nanotubes as affinity probes for peptides and proteins in MALDI MS analysis, *J. Am. Soc. Mass Spectrom.* **2004**, *15*, 1629–1635.
- 90 HO, K. C., TSAI, P. J., LIN, Y. S., CHEN, Y. C. Using biofunctionalized nanoparticles to probe pathogenic bacteria, *Anal. Chem.* **2004**, *76*, 7162–7168.
- 91 KONG, X. L., HUANG, L. C., HSU, C. M., CHEN, W. H., HAN, C. C., CHANG, H. C. High-affinity capture of proteins by diamond nanoparticles for mass spectrometric analysis, *Anal. Chem.* **2005**, *77*, 259–265.
- 92 TURNER, K., DRAKE, T. J., SMITH, J. E., TAN, W., HARRISON, W. W. Functionalized nanoparticles for liquid atmospheric pressure matrix-assisted laser desorption/ionization peptide analysis, *Rapid Commun. Mass Spectrom.* **2004**, *18*, 2367–2374.
- 93 GU, H. W., HO, P. L., TSANG, K. W. T., WANG, L., XU, B. Using biofunctional magnetic nanoparticles to capture vancomycin-resistant enterococci and other gram-positive bacteria at ultralow concentration, *J. Am. Chem. Soc.* **2003**, *125*, 15702–15703.
- 94 XU, C. J., XU, K. M., GU, H. W., ZHONG, X. F., GUO, Z. H., ZHENG, R. K., ZHANG, X. X., XU, B. Nitrilotriacetic acid-modified magnetic nanoparticles as a general agent to bind histidine-tagged proteins, *J. Am. Chem. Soc.* **2004**, *126*, 3392–3393.
- 95 HAMLEY, I. W. Nanotechnology with soft materials, *Angew. Chem. Int. Ed.* **2003**, *42*, 1692–1712.
- 96 CHOU, P. H., CHEN, S. H., LIAO, H. K., LIN, P. C., HER, G. R., LAI, A. C., CHEN, J. H., LIN, C. C., CHEN, Y. J. Nanoprobe-based affinity mass spectrometry for selected protein profiling in human plasma, *Anal. Chem.* **2005**, *77*, 5990–5997.
- 97 LIN, P. C., CHOU, P. H., CHEN, S. H., LIAO, H. K., WANG, K. Y., CHEN, Y. J., LIN, C. C. Ethylene glycol-protected magnetic nanoparticles for a multiplexed immunoassay in human plasma, *Small* **2006**, *2*, 485–489.
- 98 BERTON, G., CORDIANO, R., PALMIERI, R., PIANCA, S., PAGLIARA, V., PALATINI, P. C-reactive protein in



- acute myocardial infarction: Association with heart failure, *Am. Heart J.* **2003**, 145, 1094–1101.
- 99 KUHN, E., WU, J., KARL, J., LIAO, H., ZOLG, W., GUILD, B. Quantification of C-reactive protein in the serum of patients with rheumatoid arthritis using multiple reaction monitoring mass spectrometry and <sup>13</sup>C-labeled peptide standards, *Proteomics* **2004**, 4, 1175–1186.
- 100 UHLAR, C. M., WHITEHEAD, A. S. Serum amyloid A, the major vertebrate acute-phase reactant, *Eur. J. Biochem.* **1999**, 265, 501–523.
- 101 JUAN, H. F., CHEN, J. H., HSU, W. T., HUANG, S. C., CHEN, S. T., YI-CHUNG LIN, J., CHANG, Y. W., CHIANG, C. Y., WEN, L. L., CHAN, D. C., LIU, Y. C., CHEN, Y. J. Identification of tumor-associated plasma biomarkers using proteomic techniques: From mouse to human, *Proteomics* **2004**, 4, 2766–2775.
- 102 PEPYS, M. B., HERBERT, J., HUTCHINSON, W. L., TENNENT, G. A., LACHMANN, H. J., GALLIMORE, J. R., LOVAT, L. B., BARTFAI, T., ALANINE, A., HERTEL, C., HOFFMANN, T., JAKOB-ROETNE, R., NORCROSS, R. D., KEMP, J. A., YAMAMURA, K., SUZUKI, M., TAYLOR, G. W., MURRAY, S., THOMPSON, D., PURVIS, A., KOLSTOE, S., WOOD, S. P., HAWKINS, P. N. Targeted pharmacological depletion of serum amyloid P component for treatment of human amyloidosis, *Nature* **2002**, 417, 254–259.
- 103 CHEN, S.-H. Affinity Mass Spectrometry for Targeted Proteomics. Master's Thesis, Department of Chemistry, National Taiwan University, Taipei, Taiwan, **2005**.
- 104 KANG, Y. S., RISBUD, S., RABOLT, J. F., STROEVE, P. Synthesis and characterization of nanometer-size Fe<sub>3</sub>O<sub>4</sub> and gamma-Fe<sub>2</sub>O<sub>3</sub> particles, *Chem. Mater.* **1996**, 8, 2209–2211.
- 105 LIU, X. Q., MA, Z. Y., XING, J. M., LIU, H. Z. Preparation and characterization of amino-silane modified superparamagnetic silica nanospheres, *J. Magn. Mater.* **2004**, 270, 1–6.
- 106 PEREZ, J. M., SIMEONE, F. J., SAEKI, Y., JOSEPHSON, L., WEISSLEDER, R. Viral-induced self-assembly of magnetic nanoparticles allows the detection of viral particles in biological media, *J. Am. Chem. Soc.* **2003**, 125, 10192–10193.
- 107 KRAUSE, E., WENSCHUH, H., JUNGBLUT, P. R. The dominance of arginine-containing peptides in MALDI-derived tryptic mass fingerprints of proteins, *Anal. Chem.* **1999**, 71, 4160–4165.
- 108 KNOCHENMUSS, R., ZENOBI, R. MALDI ionization: The role of in-plume processes, *Chem. Rev.* **2003**, 103, 441–452.
- 109 PEPYS, M. B., RADEMACHER, T. W., AMATAYAKUL-CHANTLER, S., WILLIAMS, P., NOBLE, G. E., HUTCHINSON, W. L., HAWKINS, P. N., NELSON, S. R., GALLIMORE, J. R., HERBERT, J., HUTTON, T., DWEK, R. A. Human serum amyloid P component is an invariant constituent of amyloid deposits and has a uniquely homogeneous glycostructure, *Proc. Natl. Acad. Sci. U.S.A.* **1994**, 91, 5602–5606.
- 110 FU, J. Y., MULLER, D. Simple, rapid enzyme-linked immunosorbent assay (ELISA) for the determination of rat osteocalcin, *Calcif. Tissue Int.* **1999**, 64, 229–233.
- 111 WANG, X., CHEN, F., WAN, P. J., HUANG, G. Development of monoclonal antibody-based enzyme-linked immunosorbent assay for gossypol analysis in cottonseed meals, *J. Agric. Food Chem.* **2004**, 52, 7793–7797.
- 112 PEPYS, M. B., HIRSCHFELD, G. M. C-reactive protein: A critical update, *J. Clin. Invest.* **2003**, 111, 1805–1812.
- 113 PEPYS, M. B., DASH, A. C., MARKHAM, R. E., THOMAS, H. C., WILLIAMS, B. D., PETRIE, A. Comparative clinical study of protein SAP (amyloid P component) and C-reactive protein in serum, *Clin. Exp. Immunol.* **1978**, 32, 119–124.
- 114 TIRUMALAI, R. S., CHAN, K. C., PRIETO, D. A., ISSAQ, H. J., CONRADS,

- T. P., VEENSTRA, T. D. Characterization of the low molecular weight human serum proteome, *Mol. Cell. Proteomics* **2003**, *2*, 1096–1103.
- 115 ZHENG, M., HUANG, X. Nanoparticles comprising a mixed monolayer for specific bindings with biomolecules, *J. Am. Chem. Soc.* **2004**, *126*, 12 047–12 054.
- 116 JANG, J. S., CHO, H. Y., LEE, Y. J., HA, W. S., KIM, H. W. The differential proteome profile of stomach cancer: Identification of the biomarker candidates, *Oncol. Res.* **2004**, *14*, 491–499.
- 117 SOLAKIDI, S., DESSYPRIS, A., STATHOPOULOS, G. P., ANDROULAKIS, G., SEKERIS, C. E. Trypsin inhibitor; Kazal pancreatic; Tumor markers; biological; carcinoembryonic antigen; C-reactive protein;  $\alpha$ 1-antitrypsin; gastrointestinal neoplasms, *Clin. Biochem.* **2004**, *37*, 56–60.
- 118 KINGSMORE, S. F., PATEL, D. D. Multiplexed protein profiling on antibody-based microarrays by rolling circle amplification, *Curr. Opin. Biotechnol.* **2003**, *14*, 74–81.
- 119 GORELIK, E., LANDSITTEL, D. P., MARRANGONI, A. M., MODUGNO, F., VELIKOKHATNAYA, L., WINANS, M. T., BIGBEE, W. L., HERBERMAN, R. B., LOKSHIN, A. E. Multiplexed immunobead-based cytokine profiling for early detection of ovarian cancer, *Cancer Epidemiol. Biomarkers Prev.* **2005**, *14*, 981–987.
- 120 WILSON, M. S. Electrochemical immunosensors for the simultaneous detection of two tumor markers, *Anal. Chem.* **2005**, *77*, 1496–1502.
- 121 ZHENG, G., PATOLSKY, F., CUI, Y., WANG, W. U., LIEBER, C. M. Multiplexed electrical detection of cancer markers with nanowire sensor arrays, *Nat. Biotechnol.* **2005**, *23*, 1294–1301.

## 11

# Nanotechnological Approaches to Cancer Diagnosis: Imaging and Quantification of Pericellular Proteolytic Activity

Thomas Ludwig

### 11.1

#### Introduction

Most cancer related deaths are not caused by the growth of a tumor in its primary location. Metastasis with subsequent local tissue invasion accounts for more than 90% of all lethal outcomes in cancer (reviewed in Refs. [1, 2]). Despite great efforts to improve our understanding of the metastatic cascade (Figs. 11.1 and 11.2) and the accumulation of detailed knowledge about single aspects of this process, comparably little has resulted in patient benefits so far (reviewed in Ref. [3]).

This chapter outlines reasons for this dilemma by analyzing the challenges that result from local, nanoscale processes for *in vitro* and *in vivo* diagnostics. It combines, for the first time, a thorough review of the biological basis of proteolytic activity as the prototype of a highly regulated and spatially restricted process in cancer with a critical analysis of conventional state of the art methods and how the application of nanotechnology creates unique opportunities to further both our understanding and treatment of malignancies.

The mechanisms that confine and concentrate protease activity in the pericellular microenvironment of cancer cells are prerequisites of tumor cell invasion and key factors in the regulation of tumor microecology. This chapter starts with a detailed description of these mechanisms with a special emphasis on the technical problems related to them and how this is connected to the obvious gaps in our knowledge regarding their regulation.

With a reference to the biological background, the next section of the chapter provides the reader with information about the principles and disadvantages of conventional state of the art methods applied in this field. The current imperfections of most methods offer unique opportunities for innovative nanotechnological approaches. As one recent example, atomic-force microscopy is presented as a technique for the nanoscale imaging and quantification of proteolytic activity in the pericellular microenvironment of cancer cells *in vitro*.

In general, techniques that enable real-time, high resolution imaging or precise quantification of local proteolytic activity *in vitro* and *in vivo* remain major chal-

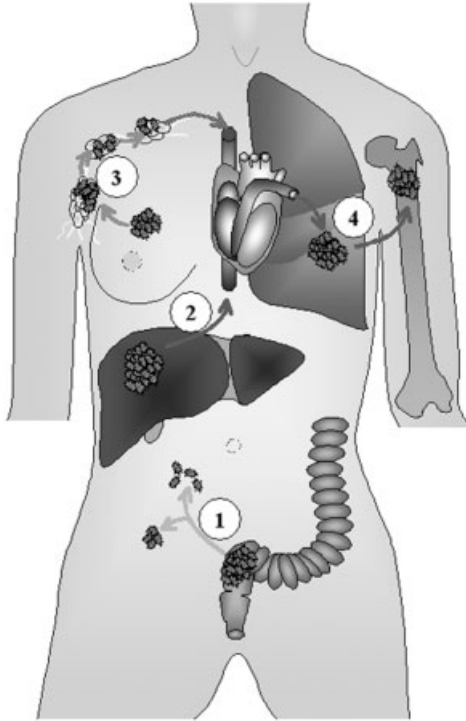


**Fig. 11.1.** Metastasis: The formation of metastasis is a complex and highly dynamic process. It is characterized by the spreading of tumor cells through vessels (2 and 4), lymphatic ducts (3) or cavities (1) to form

new colonies away from their origin. It is undoubtedly a topic of high clinical relevance as it accounts for over 90% of all lethal outcomes in cancer.

lenges. These methods will play an important role in cancer diagnosis, the understanding of basic principles in metastasis, the identification of new therapeutical and targets and, hence drug design in the near future.

The immediate need for these methods has been demonstrated by the results from clinical protease inhibitor trials. Although extensive preclinical data supported the inhibition of protease activity as a promising strategy for cancer therapy, clinical trials with various protease inhibitors, i.e., matrix metalloproteinase-inhibitors (MMPi), did not bring the expected breakthrough in cancer treatment [4, 5] (reviewed in Refs. [6–9]). It might be too early to abandon the concept of protease inhibition in cancer therapy in general, as the design of these clinical trials must be considered. MMPi had to compete, for example, against cytotoxic drugs in late-stage cancer patients. More recent insights into protease function in cancer development and angiogenesis indicate that protease inhibition is unlikely to provide considerable patient benefits in this setting, since proteases are crucial for

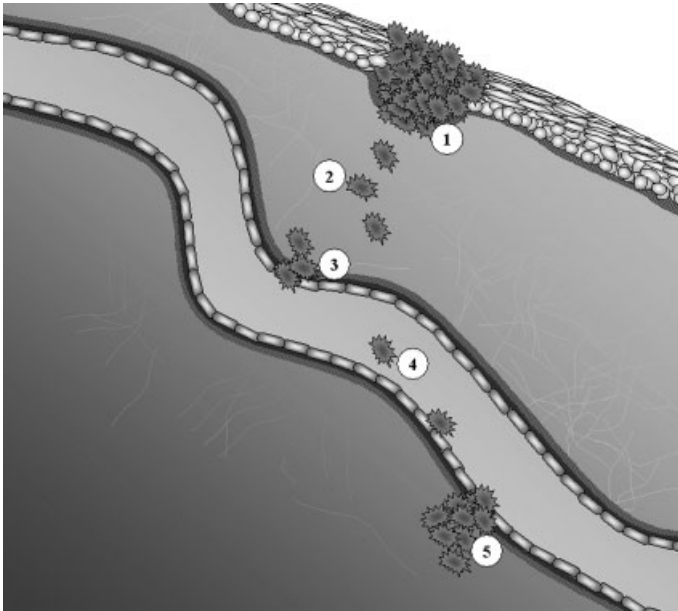


**Fig. 11.2.** Cancer cell invasion. Metastasis depends essentially on the ability of cancer cells to invade intact tissue structures (2), and to overcome physiological barriers such as basement membranes upon intra- (3) and extravasation (4). In skin cancer, as depicted here, the breach of the epidermal basement membrane (1) by cancer cells is a defining step with far reaching consequences in terms

of treatment and prognosis of the patient. The upper layer of the skin is free of lymph and blood vessels. No metastasis can be found until the basement membrane has been crossed by the cancer cells. Patients can therefore be healed by total excision of the tumor and no further treatment such as chemotherapy is necessary at this stage.

establishing new metastasis and may not be necessary to maintain them. Animal studies support this position as MMPI treatment was most effective in early stages of cancer [10]. It seems therefore reasonable to initiate new trials that employ protease inhibition early in cancer treatment or in addition to established treatments like surgery and radiation.

Nonetheless, the principle drawback in the clinical application and evaluation of protease inhibitors is the significant gap in our understanding of the complex regulation mechanisms of local proteolytic activity due to methodological obstacles. In addition, there is a serious lack of reliable techniques and parameters to assess protease inhibitor effectiveness *in vivo*. None of the patient trials proved so far that the administered drug dose was sufficient to target local proteolytic activity *in situ*. Surrogate markers, such as serum gelatinase activity, have proven unreliable for tumor screening purposes and were, therefore, inappropriate for monitoring substance response. These results from clinical trials illustrate the necessity to develop

functional methods to test drug efficacy by the quantification of local proteolytic activity.

## 11.2

### Quantification of Local Proteolytic Activity – an Objective

Cancer metastasis is a complex, highly dynamic multistep process that includes:

- Cell detachment from the primary tumor mass,
- migration within and intrusion into surrounding tissue structures and ECM,
- degradation of physiological barriers such as endothelial basement membranes,
- penetration into the vascular lumen (intravasation),
- distribution by the blood stream and survival in the circulation,
- adhesion to distant endothelia and extravasation.

and, finally, establishment of a colony in a new environment distant from the cancer cells origin (Figs. 11.1 and 11.2) [11] (reviewed in Refs. [12–14]). The expression of proteases and the development of proteolytic activity is a prerequisite for tumor cells to achieve these aims. Regardless of their diverse etiology, the function of proteases in tumor cell spreading constitutes a final common pathway of all invasive malignancies. In agreement, high concentrations and activities of proteases have been found more often in and around cancers than in normal, benign or pre-malignant tissues.

Most proteases are produced as inactive proenzymes that undergo proteolytic cleavage for their activation. Once activated, their activity is modified by several cellular mechanisms and biochemical factors such as protein trafficking and endogenous inhibitors. The excessive post-translational modification of protease activity is responsible for the critical difference between the concentration of proteases and their activity. This limits the application of many conventional methods, which cannot reliably distinguish between the active or inactive protease.

Proteolytic activity in cancer cell invasion is a very local phenomenon. Although a protease can be widely expressed throughout a tumor, it may, for example, only be active at the leading edge in a small subset of cells at the tumor–stroma interface. Specific mechanisms localize and concentrate protease activity in the pericellular microenvironment of cells. This spatial restriction challenges the maximum achievable resolution of common *in situ* imaging techniques and *in vitro* diagnostics. Until now, no method has proven sensitive enough to employ proteolytic activity in cancer for serum diagnostics and screening purposes.

General considerations can be applied to evaluate the quality of diagnostic tools (reviewed in Ref. [15]). For example, numerous methods and assays have been described for the investigation of enzymatic activity *in vitro* as well as *in vivo*. Despite their heterogeneity in terms of strategy and aims, they can be grouped considering aspects of their primarily targeted parameters. These are qualitative or quantitative evaluation of the local, or total, concentration or activity of one or several enzymes

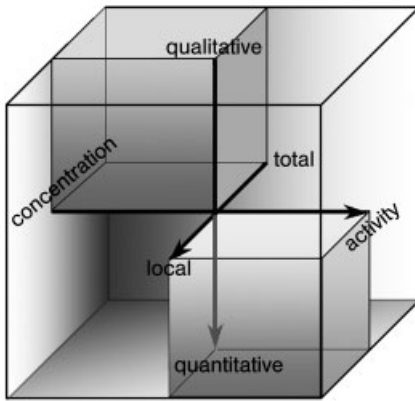


**Fig. 11.3.** Evaluation parameters of assay methods. Several criteria can be applied to assess diagnostic tools such as protease assays. Most proteases are secreted as inactive proenzymes, and enzymatic activity is additionally regulated by endogenous inhibitors. Proteolytic activity is usually restricted to the pericellular microenvironment of cancer and stromal cells, and may only be present in a small fraction of a sample. Assays detecting protease concentrations (top left-hand side box, at the back) give, therefore, only indirect clues to functionally relevant local proteolytic activity (bottom right-hand side box, at the front). Usually, several complementary methods have to be employed

in combination to understand results in the context of proteolytic orchestration. As an example, western blot analysis of cell lysates can determine the overall concentration of a single protease at a time, but is usually not capable of determining the active fraction of this enzyme. The presence of a broad variety of proteases and inhibitors, in the same spot or separate compartments, gives rise to a complex interplay that cannot be assessed by this method. *In situ* zymography is able to localize proteolytic activity, but it must be considered that the activity observed with a specific substrate may not be of particular functional relevance for the investigated microenvironment.

(Fig. 11.3). The usefulness of an assay depends as much on its sensitivity and specificity as it does on its compatibility for a particular question and application. In most cases, a combination of complementary techniques is required to get an oversight of the functional relevance of a result.

As an example, the most valuable functional information is usually derived from the quantitative evaluation of local enzymatic activity (lower, right-hand box in Fig. 11.3); it is also important to get additional information about the spatial distribution and overall concentration, i.e., of a protease in a specimen (upper, left-hand box in Fig. 11.3). The functional context is derived from the knowledge of the quantitative relationship between concentration and activity and the total to local ratio. Hence, the aim must be to develop dynamic high-resolution imaging techniques or methods that enable precise quantification of local activities *in vivo*.

Investigation of the function of proteases and their utilization for diagnostic purposes in cancer faces two major obstacles – post-translational regulation and spatial restriction.

## 11.2.1

**Regulation of Protease Activity**

Protease activity is tightly regulated at the:

- transcriptional,
- translational and
- post-translational level.

The transcription of MMPs (matrix metalloproteinases) can, for example, be up- or down-regulated by various stimuli such as extracellular matrix proteins, phorbol esters and cell stress [16–19] (reviewed in Refs. [20, 21]). It has been demonstrated for MMP-9 that expression can be increased post-transcriptionally through an enhancement of translational efficiency [22].

Most methodological problems are related to the post-translational regulation of proteases, due to the crucial difference between *concentration* and *activity* (Fig. 11.3).

The activity of proteases is post-translationally regulated by diverse, principle mechanisms:

- Secretion
- activation
- inactivation
- endogenous protease inhibitors
- glycosylation
- oligomerization and
- protein trafficking.

11.2.1.1 **Secretion**

Secretion of most proteases seems to be constitutive, which means that they are secreted once they were synthesized. Strong indicators suggest that, at least in inflammatory cells, MMPs can be stored in vesicles and secreted upon stimulation [23]. Although described for cancer cells, aspects of the regulation of this rapid response to environmental stimuli remain vague [24].

11.2.1.2 **Activation**

As most proteases are secreted as latent enzymes, their activation becomes a critical control point. Extracellular activation of proteases can be initiated by other already active proteolytic enzymes. This is usually obtained by the removal of a peptide that helps to maintain latency. For instance, MMPs are activated by a mechanism generally known as the “cysteine switch” [25, 26]. This model suggests that a cysteine coordinates the active-site zinc atom in the latent enzyme. All identified modes of MMP activation lead to a dissociation of this cysteine residue, which is accompanied by exposure of the active site.

Few proteases – among them MMP-11, MMP-13, and MT-MMPs (membrane type-MMPs) – are activated intracellularly, which makes these proteases important



pacemakers of proteolytic cascades by subsequent activation of other proteases [27–30]. The molecular basis of this intracellular activation is the presence of a specific motif between the propeptide and catalytic domain of these proteases that is recognized by proprotein convertases that process secretory precursor proteins in the trans-Golgi network.

### 11.2.1.3 Inactivation

Proteases can be inactivated by proteolysis, protease inhibitors and removal from the extracellular space or plasma membrane. Although similar in principle, the proteolytic processing of proteases leading to their inactivation is far less understood than the proteolytic processing leading to their activation.

In addition to their irreversible inactivation, limited proteolysis of MMPs can also modify their distribution, substrate specificity and ability to be inhibited. Cleavage of a sequence close to the transmembrane domain of MT-MMPs can generate, for example, soluble subspecies of these proteases [31–34]. Although these shed proteases are catalytically active and may now act as soluble proteases, they have lost most of their invasion promoting activity and effects on cell function [35, 36]. Obviously, protease action must occur in the immediate cellular surrounding to contribute significantly to the regulation of the pericellular microenvironment.

MT-1MMP cannot only undergo autocatalytic shedding. Overexpression can lead, furthermore, to an autocatalytic inactivation that results in a truncated membrane-bound remnant that has lost its catalytic domain [31, 37, 38]. Autocatalytic inactivation could serve as a self-limiting mechanism to down-regulate excessive proteolytic activity. The proteolytic processing of many proteases varies, depending on the prevalence of the activity of other proteases.

Summarizing, the presence and interaction of many different representatives of proteases from distinct families, that have

1. different substrate affinities, concentrations and actual states of activity, that are
2. in addition capable of rapidly activating and inactivating themselves and each other and
3. coexist in a tiny space of only several  $\text{nm}^3$  with
4. a no less complex and dynamic mixture of substrates (Fig. 11.7 below)

leads to a complex and fragile balanced composite that determines the functional relevant net proteolytic activity for this micro-compartment.

### 11.2.1.4 Endogenous Protease Inhibitors

Protease activity is modified on the post-translational level by various endogenous inhibitors. For example, the activity of MMPs is tightly regulated by tissue inhibitors of metalloproteases (TIMPs). To date, four structurally related TIMPs have been identified. The upregulation of TIMPs has been shown to attenuate the invasive behavior of several tumors, whereas reduction in TIMP-levels by means of antisense RNA can confer tumorigenicity to non-invasive cells [39].

TIMPs are clearly multifunctional proteins [40, 41]. TIMP-1 was isolated from fibroblasts and initially characterized to inhibit collagenase activity [42]. Soon after its discovery, TIMP-1 turned out to be identical to a known growth factor that was described to have erythroid-potentiating activity in previous studies [43]. Besides their MMP-inhibiting properties and erythroid-stimulating activity, other growth promoting activities of TIMPs have been reported [44].

Paradoxically, the presence of endogenous protease inhibitors can be of significant importance for the activation of some proteases. TIMP-2 was shown to be required for efficient proMMP-2 activation by MT1-MMP both *in vivo* and *in vitro* [37, 45, 46].

Besides being inhibited by TIMPs, MMP activity is regulated by the recently identified membrane-bound MMP-inhibitor RECK (reversion-inducing cysteine-rich protein with Kazal motifs) and other abundant inhibitors such as  $\alpha_2$ -macroglobulin [47].

#### 11.2.1.5 Glycosylation

Glycosylation has recently been discovered as an alternative way of protease activity regulation. Data provide evidence that the glycosylation of proteases may regulate their substrate targeting. In MT-1MMP, O-glycosylation seems to determine whether the protease can degrade ECM and activate MMP-2 or can only cleave ECM components [48]. This might have drastic consequences on local proteolytic activity, as MT-1MMP is considered to be one of the key activators of proteolytic cascades.

Technically, this aspect has far reaching consequences. It limits the use of simple indicator probes of proteolytic activity, as subtle but functionally crucial differences in specificity of a protease can easily be overseen.

Glycosylation is not only relevant for the “fine tuning” of proteases. Moreover, it is important for the suppression of tumor cell invasion that is mediated by the membrane-bound inhibitor RECK [49]. N-Glycosylation of RECK acts through multiple mechanisms such as suppressing MMP-9 secretion and inhibiting MMP-2 activation, which appear to be regulated independently by the glycosylation at different sites [49].

#### 11.2.1.6 Oligomerization

Multimeric complexes of membrane-bound proteases facilitate their autocatalytic processing and the activation of other proteases. The homo-oligomerization of MT1-MMP is stimulated by at least three of its domains and takes part in the regulation of its activity and turnover [50–52]. The formation of homo-oligomers of MT1-MMP turns out to be of particular relevance for the activation of proMMP-2 [50–52]. It has been hypothesized that other regulatory proteins may be involved in this by facilitating protease clustering [53].

These findings reveal that the oligomerization of proteases further determines the “functional activity” that a protease can unfold in a given context and demonstrate that the nanoscale surrounding of a single protease can determine its actual function.

### 11.2.1.7 Protein Trafficking

The internalization of membrane-bound proteases provides cells with an effective way to regulate the proteolytic activity on their surface. Most studies regarding this mechanism have been carried out for MT1-MMP. Endocytosis of this prominent protease can be mediated by at least two distinct pathways – clathrin-coated pits and caveolae [54–57]. Caveolae are not only involved in the internalization of MT1-MMP in cancer cells, but are an issue in the regulation of MT1-MMP in endothelial cells as well [55].

The rapid internalization of MT1-MMP via clathrin-coated pits is dynamin mediated and depends on the cytoplasmic tail of the protease [51, 54, 58–60]. Once internalized, MT1-MMP can be recycled to the surface [54, 61]. The rapid trafficking of MT1-MMP has the potential to regulate MMP-2 activation and thus represents an extra path of proteolytic cascade initiation [24]. Interestingly, internalization and dynamic turnover of proteases are necessary to maintain their proper function [62].

Besides internalization, trafficking deep within the cancer cells can participate in the regulation of events on the cell surface. For instance, internalized MT1-MMP can be transported to CD63-positive lysosomes for its degradation [63]. The tetraspanin CD63, a well investigated resident of late endosomal and lysosomal membranes, promotes thereby the internalization, lysosomal targeting and proteolysis of the protease [63].

Despite proliferating knowledge about the trafficking of proteases, it is still ill-defined as to how it affects local proteolytic activity quantitatively. It is, for example, still not known whether specific sub-fractions of proteases, which means active, inactivated or inhibitor complexed proteases, are internalized and how this might be regulated. Conceivably, the internalization route might differ for these subtypes of a protease and could ultimately determine whether a protease is degraded or recycled.

One reason for this gap in our current understanding has been the already mentioned, namely, inherent problems in the nanoscale quantification of complex local processes – here proteolytic activity.

## 11.2.2

### Mechanisms of Confining Proteolytic Activity

An important concept of tumor cell invasion is that cells do not indiscriminately release proteases (Fig. 11.4). Several specific mechanisms that confine and concentrate protease activity in the pericellular microenvironment and cellular sub-domains of tumor cells have been identified (reviewed in Refs. [15, 20, 51, 64–69]).

These mechanisms are prerequisites of tumor cell invasion and key factors in the regulation of tumor microecology and consist of

- Expression of membrane anchored proteases;
- the binding of soluble proteases by membrane-bound receptors;
- local activation of soluble proteases by membrane-associated activators;

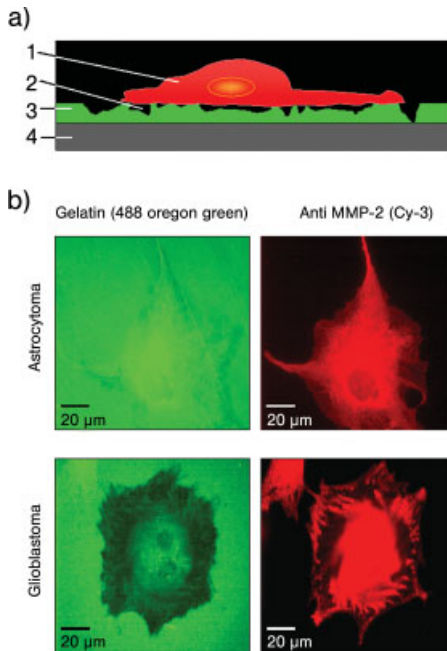


**Fig. 11.4.** Detection of local proteolytic activity by fluorescence-labeled gelatin. In cancer cells, proteolytic activity is a locally restricted phenomenon. It can be detected and visualized by surface-bound indicator substrates. (a) Tumor cells (1) were seeded on coverslips (4) coated with fluorescence-labeled gelatin (3). Proteolytic matrix cleavage (2) causes focal loss of fluorescence. (b) Glioblastoma and astrocytoma cells from primary cultures were fixed 48 h after seeding them on fluorescence-labeled gelatin (green). Dark spots in the gelatin coating reflect areas of proteolytic activity. Cells were labeled by indirect immunofluorescence for MMP-2 using Cy3-conjugated secondary antibodies (red).

- the presence of cell surface receptors for protease activating enzymes;
- the regulated localization of receptors and proteases to distinct subcellular domains (i.e., invadopodia);
- specific binding of latent proteases by ECM components;
- induction of proteases expression at the tumor–stroma interface.

#### 11.2.2.1 Membrane-type Matrix Metalloproteinases

The most obvious mediators of cell surface bound proteolytic activity are undoubtedly the transmembrane- and GPI-anchored membrane type (MT) matrix metalloproteinases (MMPs). The first MT-MMP (MT1-MMP) was discovered by Hiroshi Sato and colleagues in 1994, and was thought to act primarily as a membrane-bound activator of the gelatinase MMP-2 [70]. Besides its crucial role in activation of soluble proteases, MT1-MMP itself is now credited for its important contribu-

tion to ECM macromolecule cleavage and its broad-spectrum proteolytic capacities [71].

To date, six MT-MMPs have been identified that are linked to the plasma membrane by a transmembrane domain or a glycosylphosphatidyl inositol (GPI) anchor. The importance of localized proteolytic activity is demonstrated by the observation that expression of either wild-type MT1- or MT2-MMP confers invasiveness to COS-1 cells, whereas the expression of truncated, soluble forms of these transmembrane domain proteases has no invasion promoting effect [36]. Expression of MT1-MMP in cancer cells amplifies their metastatic potential, and constitutively expressing cell lines are generally more invasive than non-expressing cell lines [51, 72, 73].

Besides the pivotal role of MT1-MMP in tumor cell invasion, expression of this protease appears to be of critical importance for a diversity of physiological functions. It is, for example, crucial for the fibrin-invasive activity of endothelial cells during angiogenesis and wound healing [74, 75]. MT1-MMP deficient mice present the most severe phenotype observed in MMP deficient mice so far. Although these mice are born with no grossly abnormal features, the loss of MT1-MMP interferes with normal postnatal development. MT1-MMP deficient mice develop various bone and joint disorders, like dwarfism, osteopenia and arthritis, which suggest a severe impairment of the remodeling of collagen-rich tissues [69, 76].

#### 11.2.2.2 Cell Surface Receptors for Protease Binding

Non-MT-MMPs are bound to the membrane or localized to invadopodia by specific interactions with integrins or other cell surface receptors. For example, MMP-2 is bound by the  $\alpha_v\beta_3$  integrin [77], and CD44 mediates docking of MMP-9 to the plasma membrane [78]. Impressively, CD147 (extracellular matrix metalloproteinase inducer, EMMPRIN) is capable of both induction of MMP expression in stromal cells and subsequent binding of these proteases [79, 80].

Besides MMPs, accumulating evidence indicates the responsibility of serine proteases for the metastatic phenotype of many tumors. The urokinase-type plasminogen activator (uPA) drives the plasmin cascade system, and its expression is elevated in glioblastomas and correlates with malignant progression of astrocytomas [81]. The uPA receptor (uPAR) can tie uPA to the surface of tumor cells. Results indicate that only cell-bound, not soluble, uPA can effectively generate plasmin for the activation of gelatinases (MMP-2 and MMP-9) [82].

#### 11.2.2.3 ECM Binding of Proteases

Physiologically, binding of MMPs to ECM components can prevent loss of the secreted enzyme via diffusion, provide a reservoir of latent enzyme at the target site for rapid activation and might facilitate cellular regulation of local proteolytic activity. Several specific interactions of latent MMPs and ECM proteins on cells or in the extracellular space have been described. For example, heparan sulfate proteoglycans, common components of the ECM, can bind proMMP-7 [83], and

proMMP-9 can form a complex with  $\alpha 1$  and  $\alpha 2$  chains of collagen IV on cells [84, 85].

#### 11.2.2.4 Cellular Microdomains

During cancer cell invasion, membrane-bound proteases are not randomly distributed on the cell's surface. Cancer cells can accumulate proteases in specialized regions such as the leading edge or invadopodia – a term derived from “invasive pseudopodia”. These subcellular domains have proven to be “hotspots” of ECM degradation during cancer cell invasion.

MT1-MMP is concentrated at the lamellipodium through interaction with CD44, which links the protease, furthermore, directly to F-actin [86]. CD44 also recruits MMP-9 to this subcellular localization [87]. At invadopodia, particularly MMP-2, MMP-9 and MT1-MMP can be found. The clustering of active MMP-2 at invadopodia is directly mediated by the  $\alpha_v\beta_3$  integrin [88]. The cytoplasmic tail of MT1-MMP has been identified to regulate its docking to invadopodia and has been suggested to be a prerequisite for the subsequent focal ECM degradation by this protease [89].

Lipid rafts have been discussed in connection with the organization of membrane proteases in cellular microdomains. Interestingly, the aberrant and persistent inclusion into caveolin-enriched lipid rafts limits the tumorigenic function of MT1-MMP in malignant cells [90]. Although cell membranes are certainly not homogeneous mixtures of lipids and proteins, almost all aspects of lipid rafts – their size, composition and turnover – remain controversial (reviewed in Ref. [91]). Despite this, there is a broad consent about their overall biological relevance (reviewed in Ref. [92]). Most aspects of the dispute around the concept of these cellular microdomains are clearly size and resolution related methodical difficulties. Nanotechniques like AFM (atomic-force microscopy) have proven useful for the investigation of lipid rafts in artificial lipid bilayers *in vitro*, but direct investigation in cells is far more difficult [93].

One important function of microdomains in cancer cell invasion could be the partitioning of proteases into distinct cellular localizations, which then serve as platforms for the regulation of local proteolytic activity via protein oligomerization and trafficking. The restriction of proteolytic activity to small subcellular regions can increase the effectiveness and economy of local ECM degradation, but further complicates the detection of these activities.

#### 11.2.2.5 The Tumor–Host Conspiracy

The local host tissue is a constant and active participant during tumor development and metastasis. The extracellular matrix and stromal cells form a complex microenvironment that can limit or even unwillingly facilitate tumor cell invasion (reviewed in Ref. [94]). A striking example of tumor–stroma cooperation is the contribution of matrix-degrading enzymes by the host itself. For example, MMP-11 (stromelysin-3) was discovered in stromal cells of breast carcinomas [95], before its production by tumor cells was described. Most interesting findings originate from studies in MMP knockout mice (Section 11.2.3.3).

Cancer cells can harbor the ability to induce the production of proteases in stromal cells by factors such as EMMPRIN [79, 80, 96]. In agreement with this, expression levels of matrix degrading enzymes are usually strongly elevated at the invasive front of the tumor–stroma interface [97].

### 11.2.3

#### **Local Proteolytic Activity Regulates Complex Cellular Functions**

Proteolytic cleavage of extracellular matrix (ECM) is a potent regulator of many physiological and pathological events [20, 65, 98–100]. It affects fundamental processes such as cell growth, differentiation, apoptosis, and migration. The mechanisms that localize and concentrate protease activity in the pericellular micro-environment of cells are prerequisites for processes like angiogenesis, bone development and inflammation. The role of local proteolytic activity in tumor cell invasion and all these other processes is not restricted to the function of breaking down the ECM by means of a path clearing process [101].

##### **11.2.3.1 Local Proteolytic Activity in Cancer Cell Migration**

To overcome barriers, cells must be able to move actively to their new location. Several direct and indirect effects of proteolytic activity on tumor cell migration can be observed. The ability of cells to migrate on Laminin-5 is positively correlated with the expression of plasma membrane bound MT1-MMP [102]. The same MMP confers the ability to migrate on myelin substrates to transfected 3T3 fibroblasts [103]. Other results indicate that MT1-MMP plays an important role in glioma cell spreading and migration on white matter [103]. For cancer cell migration in 2D systems, there is virtually no need to cleave the ECM as a barrier. Despite this, a synthetic MMP-inhibitor, tissue inhibitor of metalloproteinases-1 and -2, and the COOH-terminal hemopexin-like domain of MMP-2 inhibit the migration of adenocarcinoma cells on gelatin matrix-coated coverslips [104].

The specific extinction of proteins by small interfering RNAs (siRNAs) has been utilized to target the expression of MMP-9 in a Ewing's sarcoma cell line, constitutively expressing this protein [105]. Silencing of MMP-9 resulted in a migratory-adhesive switch, marked by decreased spreading on extracellular matrix coatings and inhibition of migration towards fibronectin [105]. As migratory behavior was unchanged by gelatinase inhibitors, the authors conclude that the migration-promoting activity of proMMP-9 may be independent of its proteolytic activity [105].

##### **11.2.3.2 Local Proteolytic Activity and Cell Signaling**

It has been suggested that all cancers acquire the same capabilities during their development [1]. These include

- limitless replicative potential,
- sustained angiogenesis,
- tissue invasion and metastasis,

- insensitivity to growth inhibiting signals,
- self-sufficiency in growth signals, and
- the ability to evade apoptosis-inducing signals.

All of these aspects seem to be affected by local proteolytic activity, if not entirely dependent upon it, as local proteolysis during tumor cell invasion is not restricted to cleavage of ECM components [20, 65]. Several other molecules have been identified as important targets of tumor cell associated proteases. Among these are chemokines and their receptors, adhesion molecules, clotting factors and protease inhibitors. For example, the association of MMP-7 with CD44v3 regulates heparin-binding epidermal growth factor (HB-EGF) precursor processing [106]. Subsequent HB-EGF binding to its receptor (ErbB4) might regulate other cellular events, such as cell survival [106]. Fas ligand cleavage by the same protease [107] also has a significant effect on tumor cell survival and is implied in protecting tumor cells from chemotherapeutic drug cytotoxicity [108]. Furthermore, most of the ADAM (a disintegrin and metalloproteinase) family of metalloproteinases are membrane bound and involved in cleavage of diverse surface associated molecules, such as TNF- $\alpha$  [109–111].

#### 11.2.3.3 Functional Insights from Matrix-metalloprotease Deficient Mice

Mice, deficient for single MMPs, helped to shed light on functions of these proteases in physiology and disease. The putative central physiological role of several MMPs *in vivo*, which was deduced from their involvement in pathological processes and their abundance during development, proved to be wrong. Many knockout mice, which are the MMP-2 [112], MMP-3 [113], MMP-7 [114], MMP-9 [115], MMP-11 [116], MMP-12 [117] and MMP-20 [118] deficient mice, display no dramatic phenotype (reviewed in Ref. [69]). It must be considered that MMPs have broadly overlapping substrate specificities. Hence, the lack of dramatic phenotypes in these mice probably demonstrates the redundancy of vital mechanisms, rather than their uniqueness.

Obviously, only a few MMPs are indispensable. Given the importance of MT-MMPs for local proteolytic activity and their potential role as triggers of proteolytic cascades, unsurprisingly, MT1-MMP deficient mice bring along the most severe phenotype observed in MMP deficient mice so far. Although these mice are born with no grossly abnormal features, the loss of MT1-MMP is obviously incompatible with normal postnatal development. These mice develop various bone and joint disorders, like dwarfism, osteopenia and arthritis [69, 76].

Despite the absence of lethal phenotypes, mouse models uncovered specific physiological functions of single MMPs. For example, MMP-20 (enamelysin) null mice develop a profound tooth phenotype [118]. MMP-20 is a tooth-specific protease that is only expressed during the early through middle stages of enamel development [118]. Its substrates are enamel specific matrix proteins that are also expressed during this developmental time period [118].

Although MMP deficient mice might not be considered a major breakthrough for proving the overall importance of all MMPs in development, they made a major



contribution to the understanding of host-derived MMPs for tumor cell invasion and metastasis.

MMP-2 and MMP-9 deficient mice develop normally, but in these mice the number of metastatic colonies formed by intravenously injected B16-BL6 melanoma or Lewis lung carcinoma cells is dramatically decreased [112, 119, 120]. MMP-9 knockout mice show a decreased incidence of invasive tumors, but bone marrow transplantation reconstitutes many properties of carcinogenesis in these mice [121].

Mice heterozygous for the ApcMin allele (Min/+) are susceptible to benign intestinal tumors [114]. In this mouse model, MMP-7 ablation by gene targeting and homologous recombination resulted in a reduction of tumor frequency and diameter [114]. Similarly, anthracene derivative induced tumorigenesis is reduced in MMP-11 (stromelysin-3) null mice, and fibroblasts from these mice fail to support metastasis formation by breast cancer cells (MCF-7) upon co-implantation in a nude mice model [116]. Macrophages secrete a selection of proteases, but macrophages lacking MMP-12 (macrophage metalloelastase) from the corresponding null mice are unable to penetrate reconstituted basement membranes *in vitro* and *in vivo* [117].

### 11.3

#### Evaluation of Classical Methods for Quantification of Net Proteolytic Activity

Classic biochemical methods can be employed to investigate the expression of enzymes and their inhibitors on the transcriptional and translational level. Enzyme expression can be quantified in cell and tissue extracts by real-time reverse transcription-polymerase chain reaction (RT-PCR) and northern blot analysis, whereas *in situ* hybridization is useful to localize mRNA expression in tissue sections. ELISA, Western blot, immunocyto- and histochemistry are useful to evaluate the concentration or distribution of any given protein, but it is not possible to deduce enzymatic activity from its mere concentration in a tissue section or extract (Fig. 11.3) (reviewed in Ref. [15]).

As previously stated, most proteases, such as MMPs, are produced as inactive proenzymes and their activity is additionally regulated by natural inhibitors [21]. Most antibodies for immunohistochemistry cannot distinguish between the activated, inactivated or pro-form of a protease [122]. In general, antibodies recognize structural epitopes, not function.

Thus, RT-PCR, *in situ* hybridization and immunological methods may be suitable to localize or quantify the expression and production of proteases and their inhibitors, but do not indicate the resulting matrix degrading activity.

Various chromogenic, fluorogenic and radioactive assays have been developed to detect and quantify protease activity in tissue extracts [123–125]. Additionally, antibodies can recognize neo-epitopes, e.g., on collagens or aggrecan, that are generated by their proteolytic cleavage. Several ELISA assays exploit the formation of these specific neo-epitopes as an indicator for proteolytic activity (“substrate cleav-

age ELISAs”) [126, 127]. The biological function of cryptic fragments and neo-epitopes has been reviewed elsewhere [128, 129].

Gel enzymography – also referred as substrate zymography – [130] and reverse enzymography [42] offer a way to analyze the activities of MMPs and TIMPs in complex biological samples. Enzymography can detect both the proenzyme and the active MMP. In short, zymography involves gel SDS electrophoresis of samples under nonreducing conditions. Protease substrates such as gelatin or casein are incorporated in the gel and retained during electrophoresis. After SDS is removed from the gel by washing, MMPs refold, regain their activity and digest the substrate incorporated in the gel. By staining the gel, usually with Coomassie Blue, proteolytic activity is evident as an unstained band at the corresponding weight of the protease.

One advantage of gel enzymography is the activation of proenzymes after electrophoresis, which enables convenient quantification of the ratio of pro-MMPs to overall activated MMPs. It is, however, impossible to assess net MMP activity *in situ* with this technique, as MMP-TIMP complexes are separated upon electrophoresis.

As a modification of zymography, reverse zymography was developed to detect protease inhibitors such as TIMPs [42]. After electrophoresis and washing, the gel is either incubated in conditioned media, containing soluble proteases, or proteases were added to the gel before polymerization. The activity of protease inhibitors is visualized by Coomassie Blue staining. The result is a dark band, consisting of partially undegraded substrate protected from proteolysis in the presence of the inhibitor.

Summarizing, the above assays can determine net MMP activity, but there are numerous limitations regarding the quantification of the endogenous and local balance of specific matrix degrading activity and inhibition *in situ*. Most assays cannot distinguish between different enzymes, as most ECM-cleaving proteases have broadly overlapping substrates. Preparation of sample extracts precludes, furthermore, the localization of enzyme activity and real-time quantification. Also, tissue homogenization leads to artificial interactions of inhibitors and proteases that were located within different compartments in tissues and cells. Functionally important, high local proteolytic activity that is only present in a small proportion of a tissue section (i.e., tumor–stroma interface) might be underestimated or not be recognized after dilution in the entire tissue extract upon homogenization (Fig. 11.3, total versus local activity).

### 11.3.1

#### **Functional Detection of Local Proteolytic Activity by *In Situ* Zymography**

*In situ* zymography (ISZ) overcomes some of the limitations of conventional zymography and other biochemical assays. It enables both localization and estimation of net MMP activity in tissue sections, and preserves sample histology.

The method has undergone innumerable modifications and adaptations, but the basic principle remains unchanged. In short, ISZ can be seen as an adaptation of zymography to frozen tissue sections. Sections are placed on a surface coated with a protease substrate (e.g. gelatin on microscope slides). After incubation and washing, uncleaved substrate is detected by protein staining of the coating. Proteolytic activity results in unstained spots. The most commonly used techniques today are either photographic emulsion-based or fluorescence-labeled substrate-based ISZ [122, 125]. Photographic emulsion ISZ utilizes the effect of gelatin to release a thiol group containing propeptide upon cleavage. This thiol group induces a structural change in colloidal silver, which results in a change of color. In fluorescence-labeled substrate-based ISZ, thin coatings of fluorescence-labeled substrates indicate proteolytic activity by local loss of fluorescence after proteolytic cleavage.

ISZ has almost exclusively been used for the localization of MMP activities, especially the gelatinases (MMP-2 and MMP-9), although it can be adjusted to virtually any protease group. Most studies that employ ISZ used complementary techniques to provide accurate insights into the function of a specific protease. Several of these studies confirmed that proteolytic activity was not restricted to the tumor cells, but could also be found in the stroma surrounding the tumor [131, 132], stressing once more the regulatory function of tumor–host interaction for invasion and metastasis.

Although ISZ and related techniques can localize even subtle increases of proteolytic activity and enable one to assess the balance between activated proteases and inhibitors, only three to four levels of proteolytic activity can be classified for quantification purposes [131, 133]. It can be concluded that ISZ is a semi-quantitative method for the detection of local proteolytic activity and acts as a complement to, but does not replace, gel zymography and other biochemical assay methods (Fig. 11.3). However, the major disadvantage of ISZ is the restriction of its application to excised specimen after invasive procedures, which greatly limits its application for any screening purpose or early diagnosis of cancer.

### 11.3.2

#### **Tumor Cell Invasion Assays**

The ability of cancer cells to invade the surrounding stromal microenvironment and breach formerly restrictive basement membrane boundaries is a defining step in tumor progression and a hallmark in the development of the metastatic phenotype (reviewed in Ref. [1]). Invasion is a complex, multifactorial event, that requires directed migration and proteolytic activity to degrade extracellular matrix barriers (reviewed in Refs. [134–136]). Diverse *in vitro* assays have been developed to simulate *in vivo* conditions and understand key regulators of this process. Most experimental setups are variations of a modified Boyden chamber assay, introduced in 1987 by Albini and colleagues [137]. The original assay, published by Boyden 1962 for the analysis of leukocyte chemotaxis, is based on a chamber of two medium-filled compartments, separated by a microfilter membrane [138]. In general, cells

migrate from the upper medium compartment through the pores of the filter membrane to the lower medium compartment, which contains chemotactic agents. At the end of the assay the number of cells that have migrated to the lower side of the membrane is determined by fixation and staining of the membrane.

For tumor cell invasion assays, the filter membrane is coated with an ECM preparation – most commonly matrigel – to resemble the basement membrane. NIH 3T3 conditioned media or FCS is usually used as a chemoattractant to stimulate directed migration [139–141].

In all these assays, invasion is not only dependent on local proteolytic activity, but also on matrix composition [142, 143], the ability of the cells to adhere and detach from this matrix [144–146], and the resulting and intrinsic ability of these cells to migrate [147] (reviewed in Refs. [135, 148, 149]).

#### 11.3.2.1 Electrical Resistance Breakdown Assay

In addition to protease substrate based assay systems, local proteolytic activity can be quantified by an innovative, electrophysiological and indicator cell based assay. The electrical resistance breakdown assay offers a complex but stable cell based model system for the dynamic quantification of tumor cell-associated local proteolytic activity, cancer cell invasiveness and the investigation of basic mechanisms in this process. The system can be used for large and even heterogeneous tumor cell populations from primary tumor cultures and cell lines.

Setups, application and the theoretical background of this assay have been described elsewhere in detail [150–155].

### 11.3.3

#### ***In vivo* Detection of Proteolytic Activity**

The early detection of small primary tumors is still the most promising method to improve cancer survival rates and represents the working basis for extensive screening programs of common tumors. Several high-affinity substances targeted against tumor associated markers or angiogenesis have been used to detect solid tumors in animal models and clinical trials. The targeting of tumors by functional imaging with sufficient sensitivity and specificity is a diagnostic challenge. The limiting factor is the tumor-to-background ratio, which results from the lack of specific processes exclusively found in tumors.

There has been a major drive to design biocompatible probes for *in vivo* detection and imaging of cancer cells. The rationale of this approach is based on the specific binding of easily detectable molecules to proteins that are predominantly expressed by tumor cells.

The development of protease activated near-infrared fluorescent (NIRF) probes has been a huge step towards the functional imaging of tumors. The increased and localized proteolytic activity in invading cancer cells is exploited by these small, synthetic substrates. Optically quenched NIRF probes generate a strong NIRF signal after enzymatic cleavage, and have proved capable of detecting and imaging differential protease expression in nude mice *in vivo*. For example, protease

specific NIRF probes were designed to be either activated by cathepsin-B [156] or cathepsin-D [157]. Tissue studies of breast cancer patients link aggressive tumor behavior and high expression levels of these proteases [158, 159].

In principle, NIRF probes seem to have the potential to evolve to a functional method for protease activity monitoring in clinical applications and MMPI trials. The feasibility of this approach has already been demonstrated by direct imaging of MMP-2 activity in response to an MMPI (prinomastat) in a nude mice model [160].

Despite the achievements of NIRF probes in detecting proteolytic activity, small synthetic substrates do not resemble complex protease–ECM interactions. The cleavage of a synthetic substrate by a single protease or protease group does not imply functional relevance of this activity for the heterogeneous ECM micromilieu that surrounds a tumor cell. At present, it is not possible with this technique to relate the detected proteolytic activity to the net ability of living tumor cells to digest specific, local ECM compositions (Fig. 11.7 below) *in situ*.

#### 11.3.4

#### Multiphoton Microscopy and Second-harmonic Generation

Multiphoton microscopy (MPM) has become a preferred fluorescence imaging technique for *in vivo* studies, due to its ability to image processes deep within living tissues and its extremely low out of focal plane excitation. In standard fluorescence microscopy, a single photon causes excitation of a fluorescent dye. Multiphoton microscopy (MPM) is based on the simultaneous absorption of multiple low energy photons to evoke an electronic transition that is equivalent to the absorption of one single high-energy photon. For example, the simultaneous absorption of two red photons (two-photon excited fluorescence) can cause an excitation that is usually caused by a single photon in the range of UV-light. Multiphoton excitation occurs only at the beam focus.

Without using dyes, intrinsic signals of molecules can be utilized for coherent nonlinear photon microscopic techniques, such as second-harmonic generation (SHG) imaging microscopy. Processes like SHG are based on photon scattering rather than photon absorption. With SHG, the first order hyperpolarizability of a sample enables two incident photons of a given wavelength to scatter coherently and produce a photon of half the wavelength (twice the energy). In fluorescence microscopy a proportion of the excitation energy is lost during relaxation of the excited state. Other than this, SHG involves neither excitation of molecules nor absorption of energy. Hence, it shows no photobleaching and theoretically no phototoxicity. SHG does not need exogenous dyes, but is confined to sources that lack a center of symmetry. Higher-ordered structures in biological specimen such as myosin, collagen, and microtubules fulfill this requirement.

MPM and SHG are noninvasive techniques that can be used to image cancer cell induced ECM remodeling, as they permit three-dimensional (3D) reconstruction and investigation of tissues [161], ECM morphology [162], cell metabolism [163] and tumors [164] *in vivo*.

The full theory of SHG and multiphoton microscopy and their application in biological systems are beyond the scope of this chapter, but have been thoroughly reviewed elsewhere [163, 165–169].

### 11.3.5

#### ***In vitro* Detection of Local Proteolytic Activity by Labeled Substrates**

Although detection of proteolytic activity on the subcellular level is not feasible by *in situ* zymography, the thin fluorescence labeled substrate coatings can be utilized to detect and image local proteolytic activity in the microenvironment of cells under tissue culture conditions (Fig. 11.4). The method was developed to detect focal, proteolytic ECM degradation below cells [170], and facilitated functional investigation of the regulation of proteolytic activity at invadopodia. It was used, for example, to demonstrate that invadopodial docking of MT-MMP1 is dependent on its transmembrane and cytoplasmic domain [89]. Overexpression of MT-MMP1 without invadopodial localization failed in these experiments to initiate ECM degradation [89]. A similar experimental setup proved the ability of integrins to direct proteases to sites of invasion, which gave further insights in the connection between integrins, adhesion and proteolysis [171]. Furthermore, fluorescence labeled protease substrates were used to localize local matrix degradation in the microenvironment of melanoma cells in a combined setup of fluorescence microscopy and atomic-force microscopy [172].

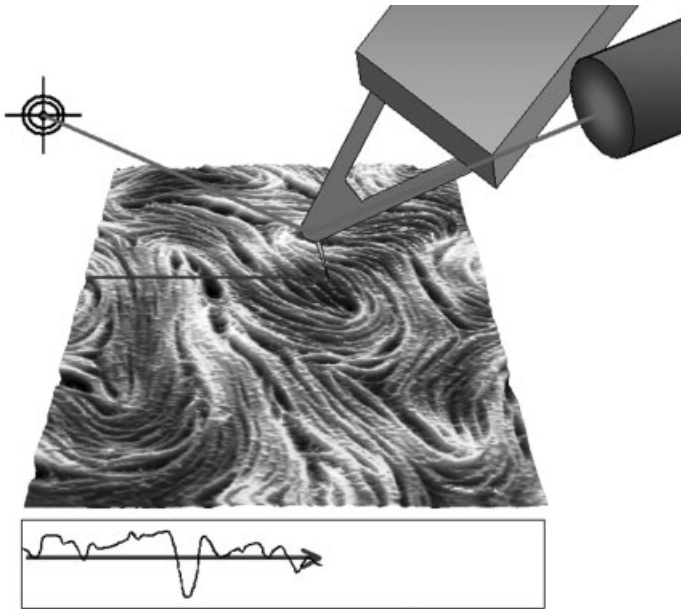
Instead of detecting proteolysis by loss of fluorescence, intramolecularly quenched substrates can be used. Cleavage causes an increase of fluorescence emission in these substrates. Results from functional imaging of proteolytic activity in living cells with quenched substrates supported the previously suggested functional importance of intracellular protease activity for matrix degradation [173]. Studies with DQ-collagen IV confirmed that proteolysis of ECM proteins occurs, for example, intracellularly in glioma [174] and breast cancer cells [175]. In addition to the described applications, “quenched substrates” offer crucial advantages for imaging of proteolytic activity within 3D matrix systems [176].

### 11.4

#### **Novel Approaches to Local Proteolytic Activity**

Atomic-force microscopy offers an interesting and novel approach for high-resolution imaging and nanoscale quantification of local proteolytic activity in the microenvironment of live cancer cells [172]. By moving a fine tip across the sample, the AFM detects height changes and produces a 3D image of surface topography (Fig. 11.5). The atomic-force microscope (AFM) was developed by Binnig and coworkers [177], and evolved from the scanning tunneling microscope (STM) [178].

The possibility of scanning native biological samples (i.e., live cells) under physiological conditions – that means in most cases in liquid at 37 °C – opened up a



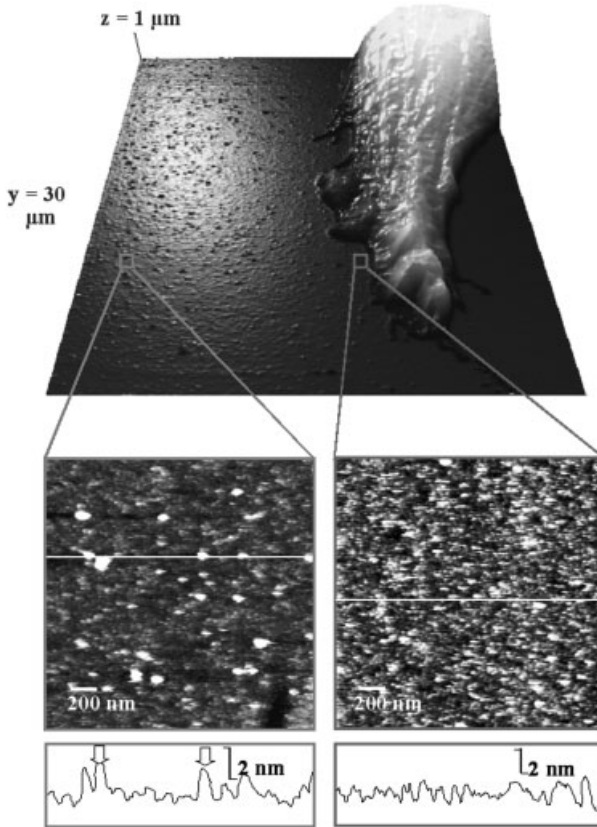
**Fig. 11.5.** Schematic setup for atomic-force microscopy. AFM utilizes the deflection of a thin silicon nitride spring with a fine probe at its end to reconstruct a 3D topographical map of sample surfaces (here native rat tail tendon in fluid). A laser beam is focused at the end of the triangular spring. Deflection of the spring is registered by a photo detector (hair cross on left-hand side). A feedback loop couples the

photo detector to a piezo tube at the other end of the silicon spring (not shown). The corresponding height is calculated from the physical constants of the piezo-crystal and the voltage that must be applied to it to bring the laser beam back into the center of the photo detector. The AFM tip is moved line wise (horizontal arrow) across the sample to collect  $x$ ,  $y$  and  $z$  data.

whole new perspective for biological, medical and biomaterial research. STM was the first instrument to generate real-space images of surfaces with atomic resolution, but was initially unable to image in fluids or scan non-conducting biological samples [179].

Since that time, AFM has become a rapidly emerging technique in biomedical research (e.g. Fig. 11.6). A wide range of biological samples have been successfully studied under native conditions with the AFM, ranging from proteins incorporated in artificial [180] and native lipid bilayers [181], to whole cells, their mechanical properties, subcellular structures and dynamic changes [151, 182–185].

Nanoscale images of, and structural insights into, the ECM have been obtained by AFM. It was used for example to investigate the interaction of basement membrane macromolecules [186], the surface ultrastructure of collagen fibrils and their association in human cornea and sclera [187], the assembly mechanism of fibrous long spacing collagen [188], the substructure of native, hydrated rat tail tendon ECM [189] and imaging of collagen III polymerization in solution [190]. Among



**Fig. 11.6.** Nanoscale imaging of local proteolytic activity by atomic-force microscopy. The image displays the leading edge of a melanoma cell on a gelatin-coated coverslip (principles shown in Figs. 11.4 and 11.5). By stepwise reduction of the scanned matrix area, the AFM tip is directed to the pericellular microenvironment of the tumor

cell (right) and distant control areas (left). Images of pericellular gelatin (right) illustrate the decrease in size and frequency of larger protein structures compared to intact matrix (arrows in left-hand image). These morphometric alterations can automatically be quantified with the AFM software.

various other applications, AFM was used to examine the structure of single collagen XVI molecules on mica [191].

AFM of normal human skin basement membrane preparations [192] displays the structural diversity of different fibrillar networks and the close meshed, underlying laminin-collagen IV net. Imaging of ECM compositions illustrates the high spatial resolution of the AFM in biological samples (Fig. 11.7).

The ability of the AFM to image ECM-components with high resolution has been exploited in an investigation of protease–substrate interactions *in vitro*. For example, Sun et al. have revealed by AFM the existence of several non-specific



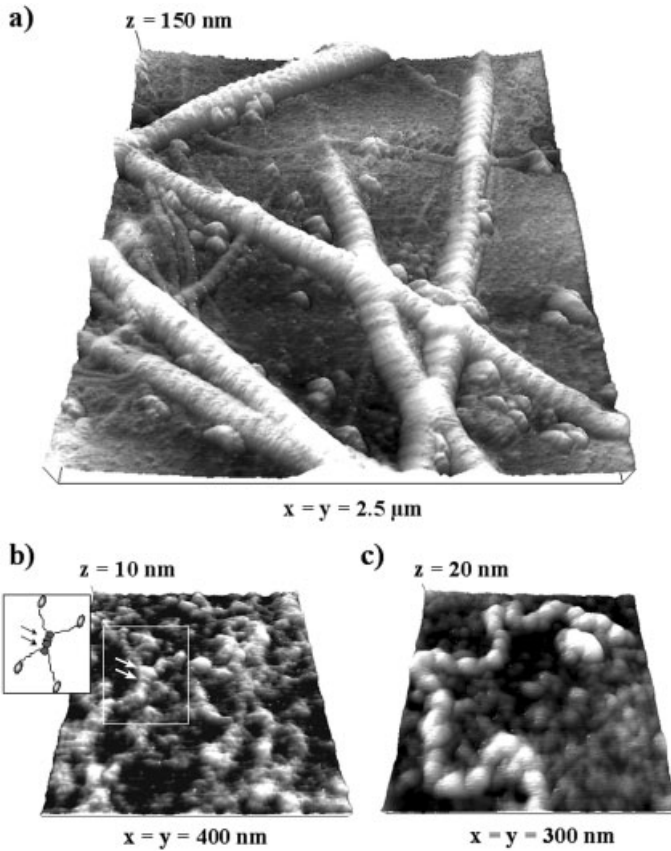


**Fig. 11.7.** 3D reconstruction of AFM images of normal human skin preparations, enriched in basement membranes. The images depict the molecular diversity and complexity of native ECM compositions. (a) Larger scale

magnification; (b) collagen-IV/laminin-V network with typical collagen IV conformations. Arrows: NC-1 domains of collagen IV. (c) Macromolecules such as fibrillin can be identified by their structure.

binding sites for MMP-8 on single type II collagen helices, but only one specific cleavage site for this enzyme [193]. Lin and colleagues demonstrated AFM imaging of real-time proteolysis of single collagen I molecules in fluid [194].

AFM was used alone and in combination with fluorescence microscopy for imaging of local proteolytic activity in the pericellular microenvironment of cancer cells (Figs. 11.2 and 11.4) [172]. Amelanotic melanoma cells were seeded on thin coatings of fluorescence-labeled gelatin or collagen IV (setup comparable to Fig. 11.4). Local loss of fluorescence due to ECM protein cleavage was used for fluorescence microscopic detection of proteolysis and localizing the AFM tip, and served as a positive control. Additional experiments proved that fluorescence microscopy

is not a prerequisite for this approach, as AFM imaging of pericellular matrix is sufficient to detect proteolysis on a subcellular level. As the AFM acquires primarily  $x$ -,  $y$ - and  $z$ -data during scanning, it is very easy to calculate and analyze differences in height and volume of subnanometer structures. AFM depicted significant differences in average height, volume and molecular weight distribution of pericellular matrix proteins between the microenvironment of invasive cancer cells and distant control areas [172]. By treating it as the segment of a sphere, the molecular weight of a protein imaged by AFM can be calculated from the molecular volume of the structure. In these experiments, the AFM registered significant changes in average matrix volume as little as  $0.003 \text{ fl } \mu\text{m}^{-2}$  and decreases in average height of less than 0.5 nm. By focusing on the complex composition of ECM, the possibility of time lapse AFM of primary tumor cell cultures on native human basement membranes is currently being evaluated (Fig. 11.7).

In summary, the AFM can image and quantify nanoscale ECM alterations in the microenvironment of cancer cells. Considering that direct measurement of local proteolytic activity and high-resolution imaging of ECM remodeling have proven difficult, this method is particularly advantageous as it enables nanoscale resolution and functional investigations on the subcellular level.

The advantages of AFM as a rapidly evolving nanotechnique for functional high resolution imaging under physiological conditions are striking, as it can provide functional data in addition to 3D nanoscale images of local phenomena. Current advances in making the AFM a high-resolution tool for simultaneous topography and specific functional recognition imaging of single molecules (“molecular recognition”) like integrins or cellular microdomains such as lipid rafts opens up interesting perspectives [93, 195]. Furthermore, physical parameters such as cell traction, elasticity of membrane compartments and ECM compositions or the binding forces of ligand–receptor complexes can be quantified with nanoscale resolution and integrated in the molecular recognition maps.

## 11.5

### Conclusions and Perspectives

The most devastating process in cancer is metastasis, as it represents the milestone of an irreversible stage of progression that inevitably determines disease prognosis. Regardless of the advancement of therapies for cancer that has already spread, the early diagnosis and removal of the malignancy is still the most promising strategy. The limitations of conventional state of the art methods offer unique opportunities for innovative, nanotechnology based approaches. The development of improved methods that enable real-time high-resolution imaging and quantification of local enzymatic activities will play a major role in the design of new drugs and the understanding of basic principles in tumor cell invasion. These methods themselves harbor the potential to contribute directly to patient benefits due to earlier diagnosis of malignancies and functional monitoring following clinical interventions.

## Acknowledgments

As it is sometimes not possible to cite all relevant articles on a subject, several references have been used as examples to illustrate major principles. I thank Uwe Hansen for the generous supply with various matrix proteins, Sylvia Puttman and Volker Senner for their cooperation and contribution of primary brain tumor cells, and Helga Bertram and Stephan Kusick for their excellent technical assistance in tissue culture and Atomic Force Microscopy. I thank Joerg Hinnerwisch, Mark Lal, Hans Oberleithner, Val Prasad and Michael J. Morton for revising and improving the original manuscript and for interesting discussions. Excerpts of this chapter have been previously published as a review [15]. This work was supported by the Deutsche Forschungsgemeinschaft (LU 854/2-1 and LU 854/3-1) and “Innovative Medizinische Forschung” (LU 110343) of the University of Münster.

## Abbreviations

AFM	Atomic-force microscope
ECM	Extracellular matrix
EMMPRIN	Extracellular matrix metalloproteinase inducer
HSPG	Heparan sulfate proteoglycan
ISZ	<i>In situ</i> zymography
MMP	Matrix metalloproteinase
MT-MMP	Membrane type-matrix metalloproteinase
MMPI	Matrix metalloproteinase inhibitor
MPM	Multi-photon microscopy
NIRF	Near-infrared fluorescence
RECK	Reversion-inducing cysteine-rich protein with Kazal motifs
SHG	Second-harmonic generation
TIMP	Tissue inhibitor of matrix metalloproteinases
uPA	Urokinase-type plasminogen activator

## References

- 1 HANAHAN D, WEINBERG RA. The hallmarks of cancer. *Cell* 100, 57–70, 2000.
- 2 SPORN MB. The war on cancer: A review. *Ann. New York Acad. Sci.* 833, 137–146, 1997.
- 3 SPORN MB. The war on cancer. *Lancet* 347, 1377–1381, 1996.
- 4 WANG X, FU X, BROWN PD, CRIMMIN MJ, HOFFMAN RM. Matrix metalloproteinase inhibitor BB-94 (batimastat) inhibits human colon tumor growth and spread in a patient-like orthotopic model in nude mice. *Cancer Res.* 54, 4726–4728, 1994.
- 5 BROWN PD. Matrix metalloproteinase inhibitors: A novel class of anticancer agents. *Adv. Enzyme Regul.* 35, 293–301, 1995.
- 6 BAKER AH, EDWARDS DR, MURPHY G. Metalloproteinase inhibitors: Biological actions and therapeutic

- opportunities. *J. Cell Sci.* 115, 3719–3727, 2002.
- 7 BRINCKERHOFF CE, MATRISIAN LM. Matrix metalloproteinases: A tail of a frog that became a prince. *Nat. Rev. Mol. Cell Biol.* 3, 207–214, 2002.
  - 8 COUSSENS LM, FINGLETON B, MATRISIAN LM. Matrix metalloproteinase inhibitors and cancer: Trials and tribulations. *Science* 295, 2387–2392, 2002.
  - 9 OVERALL CM, LOPEZ-OTIN C. Strategies for mmp inhibition in cancer: Innovations for the post-trial era. *Nat. Rev. Cancer* 2, 657–672, 2002.
  - 10 BERGERS G, JAVAHERIAN K, LO KM, FOLKMAN J, HANAHAN D. Effects of angiogenesis inhibitors on multistage carcinogenesis in mice. *Science* 284, 808–812, 1999.
  - 11 AL-MEHDI AB, TOZAWA K, FISHER AB, SHIENTAG L, LEE A, MUSCHEL RJ. Intravascular origin of metastasis from the proliferation of endothelium-attached tumor cells: A new model for metastasis [In Process Citation]. *Nat. Med.* 6, 100–102, 2000.
  - 12 BOGENRIEDER T, HERLYN M. Axis of evil: Molecular mechanisms of cancer metastasis. *Oncogene* 22, 6524–6536, 2003.
  - 13 MURPHY PM. Chemokines and the molecular basis of cancer metastasis. *N. Engl. J. Med.* 345, 833–835, 2001.
  - 14 CHAMBERS AF, GROOM AC, MACDONALD IC. Dissemination and growth of cancer cells in metastatic sites. *Nat. Rev. Cancer* 2, 563–572, 2002.
  - 15 LUDWIG T. Local proteolytic activity in tumor cell invasion and metastasis. *Bioessays* 27, 1181–1191, 2005.
  - 16 SHRIVASTAVA A, RADZIEJEWSKI C, CAMPBELL E, KOVAC L, MCGLYNN M, RYAN TE, DAVIS S, GOLDFARB MP, GLASS DJ, LEMKE G, YANCOPOULOS GD. An orphan receptor tyrosine kinase family whose members serve as nonintegrin collagen receptors. *Mol. Cell.* 1, 25–34, 1997.
  - 17 VOGEL W, GISH GD, ALVES F, PAWSON T. The discoidin domain receptor tyrosine kinases are activated by collagen. *Mol. Cell.* 1, 13–23, 1997.
  - 18 KHERADMAND F, WERNER E, TREMBLE P, SYMONS M, WERB Z. Role of Rac1 and oxygen radicals in collagenase-1 expression induced by cell shape change. *Science* 280, 898–902, 1998.
  - 19 FAISAL KHAN KM, LAURIE GW, MCCAFFREY TA, FALCONE DJ. Exposure of cryptic domains in the alpha 1-chain of laminin-1 by elastase stimulates macrophages urokinase and matrix metalloproteinase-9 expression. *J. Biol. Chem.* 277, 13 778–13 786, 2002.
  - 20 STERNLICHT MD, WERB Z. How matrix metalloproteinases regulate cell behavior. *Annu. Rev. Cell Dev. Biol.* 17, 463–516, 2001.
  - 21 CHAKRABORTI S, MANDAL M, DAS S, MANDAL A, CHAKRABORTI T. Regulation of matrix metalloproteinases: An overview. *Mol. Cell Biochem.* 253, 269–285, 2003.
  - 22 FAHLING M, STEEGE A, PERLEWITZ A, NAFZ B, MROWKA R, PERSSON PB, THIELE BJ. Role of nucleolin in posttranscriptional control of MMP-9 expression. *Biochim. Biophys. Acta* 1731, 32–40, 2005.
  - 23 RAZA SL, NEHRING LC, SHAPIRO SD, CORNELIUS LA. Proteinase-activated receptor-1 regulation of macrophage elastase (MMP-12) secretion by serine proteinases. *J. Biol. Chem.* 275, 41 243–41 250, 2000.
  - 24 ZUCKER S, HYMOWITZ M, CONNER CE, DIYANNI EA, CAO J. Rapid trafficking of membrane type 1-matrix metalloproteinase to the cell surface regulates progelatinase a activation. *Lab. Invest.* 82, 1673–1684, 2002.
  - 25 VAN WART HE, BIRKEDAL-HANSEN H. The cysteine switch: A principle of regulation of metalloproteinase activity with potential applicability to the entire matrix metalloproteinase gene family. *Proc. Natl. Acad. Sci. U.S.A.* 87, 5578–5582, 1990.
  - 26 SPRINGMAN EB, ANGLETON EL, BIRKEDAL-HANSEN H, VAN WART HE. Multiple modes of activation of latent human fibroblast collagenase: Evidence for the role of a Cys73 active-site zinc complex in latency and a “cysteine switch” mechanism for

- activation. *Proc. Natl. Acad. Sci. U.S.A.* 87, 364–368, 1990.
- 27 YANA I, WEISS SJ. Regulation of membrane type-1 matrix metalloproteinase activation by proprotein convertases. *Mol. Biol. Cell.* 11, 2387–2401, 2000.
  - 28 PEI D, WEISS SJ. Furin-dependent intracellular activation of the human stromelysin-3 zymogen. *Nature* 375, 244–247, 1995.
  - 29 KANG T, NAGASE H, PEI D. Activation of membrane-type matrix metalloproteinase 3 zymogen by the proprotein convertase furin in the trans-Golgi network. *Cancer Res.* 62, 675–681, 2002.
  - 30 ILLMAN SA, KESKI-OJA J, PARKS WC, LOHI J. The mouse matrix metalloproteinase, epilysin (MMP-28), is alternatively spliced and processed by a furin-like proprotein convertase. *Biochem. J.* 375, 191–197, 2003.
  - 31 OSENKOWSKI P, TOTH M, FRIDMAN R. Processing, shedding, and endocytosis of membrane type 1-matrix metalloproteinase (MT1-MMP). *J. Cell Physiol.* 200, 2–10, 2004.
  - 32 ITOH Y, SEIKI M. MT1-MMP: An enzyme with multidimensional regulation. *Trends Biochem. Sci.* 29, 285–289, 2004.
  - 33 HERNANDEZ-BARRANTES S, BERNARDO M, TOTH M, FRIDMAN R. Regulation of membrane type-matrix metalloproteinases. *Semin. Cancer Biol.* 12, 131–138, 2002.
  - 34 TOTH M, OSENKOWSKI P, HESSEK D, BROWN S, MEROUEH S, SAKR W, MOBASHERY S, FRIDMAN R. Cleavage at the stem region releases an active ectodomain of the membrane type 1 matrix metalloproteinase. *Biochem. J.* 387, 497–506, 2005.
  - 35 CAO J, SATO H, TAKINO T, SEIKI M. The C-terminal region of membrane type matrix metalloproteinase is a functional transmembrane domain required for pro-gelatinase A activation. *J. Biol. Chem.* 270, 801–805, 1995.
  - 36 HOTARY K, ALLEN E, PUNTURIERI A, YANA I, WEISS SJ. Regulation of cell invasion and morphogenesis in a three-dimensional type I collagen matrix by membrane-type matrix metalloproteinases 1, 2, and 3. *J. Cell Biol.* 149, 1309–1323, 2000.
  - 37 LEHTI K, LOHI J, VALTANEN H, KESKI-OJA J. Proteolytic processing of membrane-type-1 matrix metalloproteinase is associated with gelatinase A activation at the cell surface. *Biochem. J.* 334(Pt 2), 345–353, 1998.
  - 38 TOTH M, HERNANDEZ-BARRANTES S, OSENKOWSKI P, BERNARDO MM, GERVASI DC, SHIMURA Y, MEROUEH O, KOTRA LP, GALVEZ BG, ARROYO AG, MOBASHERY S, FRIDMAN R. Complex pattern of membrane type 1 matrix metalloproteinase shedding. Regulation by autocatalytic cells surface inactivation of active enzyme. *J. Biol. Chem.* 277, 26 340–26 350, 2002.
  - 39 KHOKHA R, WATERHOUSE P, YAGEL S, LALA PK, OVERALL CM, NORTON G, DENHARDT DT. Antisense RNA-induced reduction in murine TIMP levels confers oncogenicity on Swiss 3T3 cells. *Science* 243, 947–950, 1989.
  - 40 JIANG Y, GOLDBERG ID, SHI YE. Complex roles of tissue inhibitors of metalloproteinases in cancer. *Oncogene* 21, 2245–2252, 2002.
  - 41 MURPHY G, WILLENBROCK F. Tissue inhibitors of matrix metalloendopeptidases. *Methods Enzymol.* 248, 496–510, 1995.
  - 42 WELGUS HG, STRICKLIN GP, EISEN AZ, BAUER EA, COONEY RV, JEFFREY JJ. A specific inhibitor of vertebrate collagenase produced by human skin fibroblasts. *J. Biol. Chem.* 254, 1938–1943, 1979.
  - 43 DOCHERTY AJ, LYONS A, SMITH BJ, WRIGHT EM, STEPHENS PE, HARRIS TJ, MURPHY G, REYNOLDS JJ. Sequence of human tissue inhibitor of metalloproteinases and its identity to erythroid-potentiating activity. *Nature* 318, 66–69, 1985.
  - 44 HAYAKAWA T, YAMASHITA K, TANZAWA K, UCHIJIMA E, IWATA K. Growth-promoting activity of tissue inhibitor of metalloproteinases-1 (TIMP-1) for a wide range of cells. A possible new growth factor in serum. *FEBS Lett.* 298, 29–32, 1992.

- 45 BUTLER GS, BUTLER MJ, ATKINSON SJ, WILL H, TAMURA T, VAN WESTRUM SS, CRABBE T, CLEMENTS J, D'ORTHO MP, MURPHY G. The TIMP2 membrane type 1 metalloproteinase "receptor" regulates the concentration and efficient activation of progelatinase A. A kinetic study. *J. Biol. Chem.* 273, 871–880, 1998.
- 46 WANG Z, JUTTERMANN R, SOLOWAY PD. TIMP-2 is required for efficient activation of proMMP-2 in vivo. *J. Biol. Chem.* 275, 26411–26415, 2000.
- 47 OH J, TAKAHASHI R, KONDO S, MIZOGUCHI A, ADACHI E, SASAHARA RM, NISHIMURA S, IMAMURA Y, KITAYAMA H, ALEXANDER DB, IDE C, HORAN TP, ARAKAWA T, YOSHIDA H, NISHIKAWA S, ITOH Y, SEIKI M, ITOHARA S, TAKAHASHI C, NODA M. The membrane-anchored MMP inhibitor RECK is a key regulator of extracellular matrix integrity and angiogenesis. *Cell* 107, 789–800, 2001.
- 48 WU YI, MUNSHI HG, SEN R, SNIPAS SJ, SALVESEN GS, FRIDMAN R, STACK MS. Glycosylation broadens the substrate profile of membrane type 1 matrix metalloproteinase. *J. Biol. Chem.* 279, 8278–8289, 2004.
- 49 SIMIZU S, TAKAGI S, TAMURA Y, OSADA H. RECK-mediated suppression of tumor cell invasion is regulated by glycosylation in human tumor cell lines. *Cancer Res.* 65, 7455–7461, 2005.
- 50 ROZANOV DV, DERYUGINA EI, RATNIKOV BI, MONOSOV EZ, MARCHENKO GN, QUIGLEY JP, STRONGIN AY. Mutation analysis of membrane type-1 matrix metalloproteinase (MT1-MMP). The role of the cytoplasmic tail Cys(574), the active site Glu(240), and furin cleavage motifs in oligomerization, processing, and self-proteolysis of MT1-MMP expressed in breast carcinoma cells. *J. Biol. Chem.* 276, 25705–25714, 2001.
- 51 SEIKI M, KOSHIKAWA N, YANA I. Role of pericellular proteolysis by membrane-type 1 matrix metalloproteinase in cancer invasion and angiogenesis. *Cancer Metastasis Rev.* 22, 129–143, 2003.
- 52 ITOH Y, TAKAMURA A, ITO N, MARU Y, SATO H, SUENAGA N, AOKI T, SEIKI M. Homophilic complex formation of MT1-MMP facilitates proMMP-2 activation on the cell surface and promotes tumor cell invasion. *EMBO J.* 20, 4782–4793, 2001.
- 53 ITOH Y, SEIKI M. MT1-MMP: A potent modifier of pericellular microenvironment. *J. Cell Physiol.* 206, 1–8, 2006.
- 54 REMACLE A, MURPHY G, ROGHI C. Membrane type I-matrix metalloproteinase (MT1-MMP) is internalised by two different pathways and is recycled to the cell surface. *J. Cell Sci.* 116, 3905–3916, 2003.
- 55 GALVEZ BG, MATIAS-ROMAN S, YANEZ-MO M, VICENTE-MANZANARES M, SANCHEZ-MADRID F, ARROYO AG. Caveolae are a novel pathway for membrane-type 1 matrix metalloproteinase traffic in human endothelial cells. *Mol. Biol. Cell.* 15, 678–687, 2004.
- 56 ANNABI B, LACHAMBRE M, BOUSQUET-GAGNON N, PAGE M, GINGRAS D, BELIVEAU R. Localization of membrane-type 1 matrix metalloproteinase in caveolae membrane domains. *Biochem. J.* 353, 547–553, 2001.
- 57 WILLIAMS TM, MEDINA F, BADANO I, HAZAN RB, HUTCHINSON J, MULLER WJ, CHOPRA NG, SCHERER PE, PESTELL RG, LISANTI MP. Caveolin-1 gene disruption promotes mammary tumorigenesis and dramatically enhances lung metastasis in vivo. Role of Cav-1 in cell invasiveness and matrix metalloproteinase (MMP-2/9) secretion. *J. Biol. Chem.* 279, 51630–51646, 2004.
- 58 REMACLE AG, ROZANOV DV, BACIU PC, CHEKANOV AV, GOLUBKOV VS, STRONGIN AY. The transmembrane domain is essential for the microtubular trafficking of membrane type-1 matrix metalloproteinase (MT1-MMP). *J. Cell Sci.* 118, 4975–4984, 2005.
- 59 LEHTI K, VALTANEN H, WICKSTROM S, LOHI J, KESKI-OJA J. Regulation of membrane-type-1 matrix metalloproteinase activity by its cytoplasmic

- domain. *J. Biol. Chem.* 275, 15 006–15 013, 2000.
- 60 JIANG A, LEHTI K, WANG X, WEISS SJ, KESKI-OJA J, PEI D. Regulation of membrane-type matrix metalloproteinase 1 activity by dynamin-mediated endocytosis. *Proc. Natl. Acad. Sci. U.S.A.* 98, 13 693–13 698, 2001.
- 61 WANG X, MA D, KESKI-OJA J, PEI D. Co-recycling of MT1-MMP and MT3-MMP through the trans-Golgi network. Identification of DKV582 as a recycling signal. *J. Biol. Chem.* 279, 9331–9336, 2004.
- 62 UEKITA T, ITOH Y, YANA I, OHNO H, SEIKI M. Cytoplasmic tail-dependent internalization of membrane-type 1 matrix metalloproteinase is important for its invasion-promoting activity. *J. Cell Biol.* 155, 1345–1356, 2001.
- 63 TAKINO T, MIYAMORI H, KAWAGUCHI N, UEKITA T, SEIKI M, SATO H. Tetraspanin CD63 promotes targeting and lysosomal proteolysis of membrane-type 1 matrix metalloproteinase. *Biochem. Biophys. Res. Commun.* 304, 160–166, 2003.
- 64 WERB Z. ECM and cell surface proteolysis: Regulating cellular ecology. *Cell* 91, 439–442, 1997.
- 65 EGEBLAD M, WERB Z. New functions for the matrix metalloproteinases in cancer progression. *Nat. Rev. Cancer* 2, 161–174, 2002.
- 66 STAMENKOVIC I. Matrix metalloproteinases in tumor invasion and metastasis. *Semin. Cancer Biol.* 10, 415–433, 2000.
- 67 YANA I, SEIKI M. MT-MMPs play pivotal roles in cancer dissemination. *Clin. Exp. Metastasis* 19, 209–215, 2002.
- 68 ELLERBROEK SM, STACK MS. Membrane associated matrix metalloproteinases in metastasis. *Bioessays* 21, 940–949, 1999.
- 69 HOLMBECK K, BIANCO P, YAMADA S, BIRKEDAL-HANSEN H. MT1-MMP: A tethered collagenase. *J. Cell Physiol.* 200, 11–19, 2004.
- 70 SATO H, TAKINO T, OKADA Y, CAO J, SHINAGAWA A, YAMAMOTO E, SEIKI M. A matrix metalloproteinase expressed on the surface of invasive tumour cells. *Nature* 370, 61–65, 1994.
- 71 OHUCHI E, IMAI K, FUJII Y, SATO H, SEIKI M, OKADA Y. Membrane type 1 matrix metalloproteinase digests interstitial collagens and other extracellular matrix macromolecules. *J. Biol. Chem.* 272, 2446–2451, 1997.
- 72 SEIKI M. Membrane-type matrix metalloproteinases. *APMIS* 107, 137–143, 1999.
- 73 TSUNEZUKA Y, KINOH H, TAKINO T, WATANABE Y, OKADA Y, SHINAGAWA A, SATO H, SEIKI M. Expression of membrane-type matrix metalloproteinase 1 (MT1-MMP) in tumor cells enhances pulmonary metastasis in an experimental metastasis assay. *Cancer Res.* 56, 5678–5683, 1996.
- 74 LAFLEUR MA, HANDSLEY MM, KNAUPER V, MURPHY G, EDWARDS DR. Endothelial tubulogenesis within fibrin gels specifically requires the activity of membrane-type-matrix metalloproteinases (MT-MMPs). *J. Cell Sci.* 115, 3427–3438, 2002.
- 75 COLLEN A, HANEMAAIJER R, LUPU F, QUAX PH, VAN LENT N, GRIMBERGEN J, PETERS E, KOOLWIJK P, VAN HINSBERGH VW. Membrane-type matrix metalloproteinase-mediated angiogenesis in a fibrin-collagen matrix. *Blood* 101, 1810–1817, 2003.
- 76 HOLMBECK K, BIANCO P, CATERINA J, YAMADA S, KROMER M, KUZNETSOV SA, MANKANI M, ROBEY PG, POOLE AR, PIDOUX I, WARD JM, BIRKEDAL-HANSEN H. MT1-MMP-deficient mice develop dwarfism, osteopenia, arthritis, and connective tissue disease due to inadequate collagen turnover. *Cell* 99, 81–92, 1999.
- 77 BROOKS PC, STROMBLAD S, SANDERS LC, VON SCHALSCHA TL, AIMES RT, STETLER-STEVENSON WG, QUIGLEY JP, CHERESH DA. Localization of matrix metalloproteinase MMP-2 to the surface of invasive cells by interaction with integrin alpha v beta 3. *Cell* 85, 683–693, 1996.
- 78 YU Q, STAMENKOVIC I. Cell surface-localized matrix metalloproteinase-9 proteolytically activates TGF-beta and promotes tumor invasion and angiogenesis. *Genes Dev.* 14, 163–176, 2000.

- 79 SUN J, HEMLER ME. Regulation of MMP-1 and MMP-2 production through CD147/extracellular matrix metalloproteinase inducer interactions. *Cancer Res.* 61, 2276–2281, 2001.
- 80 GUO H, LI R, ZUCKER S, TOOLE BP. EMMPRIN (CD147), an inducer of matrix metalloproteinase synthesis, also binds interstitial collagenase to the tumor cell surface. *Cancer Res.* 60, 888–891, 2000.
- 81 YAMAMOTO M, SAWAYA R, MOHANAM S, BINDAL AK, BRUNER JM, OKA K, RAO VH, TOMONAGA M, NICOLSON GL, RAO JS. Expression and localization of urokinase-type plasminogen activator in human astrocytomas in vivo. *Cancer Res.* 54, 3656–3661, 1994.
- 82 FESTUCCIA C, DOLO V, GUERRA F, VIOLINI S, MUZI P, PAVAN A, BOLOGNA M. Plasminogen activator system modulates invasive capacity and proliferation in prostatic tumor cells. *Clin. Exp. Metastasis* 16, 513–528, 1998.
- 83 YU WH, WOESSNER JF, JR. Heparan sulfate proteoglycans as extracellular docking molecules for matrilysin (matrix metalloproteinase 7). *J. Biol. Chem.* 275, 4183–4191, 2000.
- 84 OLSON MW, TOTH M, GERVASI DC, SADO Y, NINOMIYA Y, FRIDMAN R. High affinity binding of latent matrix metalloproteinase-9 to the alpha2(IV) chain of collagen IV. *J. Biol. Chem.* 273, 10672–10681, 1998.
- 85 TOTH M, SADO Y, NINOMIYA Y, FRIDMAN R. Biosynthesis of alpha2(IV) and alpha1(IV) chains of collagen IV and interactions with matrix metalloproteinase-9. *J. Cell Physiol.* 180, 131–139, 1999.
- 86 MORI H, TOMARI T, KOSHIKAWA N, KAJITA M, ITOH Y, SATO H, TOJO H, YANA I, SEIKI M. CD44 directs membrane-type 1 matrix metalloproteinase to lamellipodia by associating with its hemopexin-like domain. *EMBO J.* 21, 3949–3959, 2002.
- 87 BOURGUIGNON LY, GUNJA-SMITH Z, IDA N, ZHU HB, YOUNG LJ, MULLER WJ, CARDIFF RD. CD44v(3,8-10) is involved in cytoskeleton-mediated tumor cell migration and matrix metalloproteinase (MMP-9) association in metastatic breast cancer cells. *J. Cell Physiol.* 176, 206–215, 1998.
- 88 DERUGINA EI, RATNIKOV B, MONOSOV E, POSTNOVA TI, DISCIPIO R, SMITH JW, STRONGIN AY. MT1-MMP initiates activation of pro-MMP-2 and integrin alpha5beta3 promotes maturation of MMP-2 in breast carcinoma cells. *Exp. Cell Res.* 263, 209–223, 2001.
- 89 NAKAHARA H, HOWARD L, THOMPSON EW, SATO H, SEIKI M, YEH Y, CHEN WT. Transmembrane/cytoplasmic domain-mediated membrane type 1-matrix metalloprotease docking to invadopodia is required for cell invasion. *Proc. Natl. Acad. Sci. U.S.A.* 94, 7959–7964, 1997.
- 90 ROZANOV DV, DERUGINA EI, MONOSOV EZ, MARCHENKO ND, STRONGIN AY. Aberrant, persistent inclusion into lipid rafts limits the tumorigenic function of membrane type-1 matrix metalloproteinase in malignant cells. *Exp. Cell Res.* 293, 81–95, 2004.
- 91 LAI EC. Lipid rafts make for slippery platforms. *J. Cell Biol.* 162, 365–370, 2003.
- 92 EDIDIN M. The state of lipid rafts: From model membranes to cells. *Annu. Rev. Biophys. Biomol. Struct.* 32, 257–283, 2003.
- 93 HENDERSON RM, EDWARDSON JM, GEISSE NA, SASLOWSKY DE. Lipid rafts: Feeling is believing. *News Physiol. Sci.* 19, 39–43, 2004.
- 94 MUELLER MM, FUSENIG NE. Friends or foes – bipolar effects of the tumour stroma in cancer. *Nat. Rev. Cancer* 4, 839–849, 2004.
- 95 BASSET P, BELLOQC JP, WOLF C, STOLL I, HUTIN P, LIMACHER JM, PODHAJECER OL, CHENARD MP, RIO MC, CHAMBON P. A novel metalloproteinase gene specifically expressed in stromal cells of breast carcinomas. *Nature* 348, 699–704, 1990.
- 96 TANG Y, KESAVAN P, NAKADA MT, YAN L. Tumor-stroma interaction: Positive



- feedback regulation of extracellular matrix metalloproteinase inducer (EMMPRIN) expression and matrix metalloproteinase-dependent generation of soluble EMMPRIN. *Mol. Cancer Res.* 2, 73–80, 2004.
- 97 HOFMANN UB, EGGERT AA, BLASS K, BROCKER EB, BECKER JC. Expression of matrix metalloproteinases in the microenvironment of spontaneous and experimental melanoma metastases reflects the requirements for tumor formation. *Cancer Res.* 63, 8221–8225, 2003.
- 98 STAMENKOVIC I. Extracellular matrix remodelling: The role of matrix metalloproteinases. *J. Pathol.* 200, 448–464, 2003.
- 99 CHANG C, WERB Z. The many faces of metalloproteases: Cell growth, invasion, angiogenesis and metastasis. *Trends Cell Biol.* 11, S37–S43, 2001.
- 100 GINGRAS D, BOUSQUET-GAGNON N, LANGLOIS S, LACHAMBRE MP, ANNABI B, BELIVEAU R. Activation of the extracellular signal-regulated protein kinase (ERK) cascade by membrane-type-1 matrix metalloproteinase (MT1-MMP). *FEBS Lett.* 507, 231–236, 2001.
- 101 McCRAWLEY LJ, MATRISIAN LM. Matrix metalloproteinases: They're not just for matrix anymore! *Curr. Opin. Cell Biol.* 13, 534–540, 2001.
- 102 KOSHIKAWA N, GIANNELLI G, CIRULLI V, MIYAZAKI K, QUARANTA V. Role of cell surface metalloprotease MT1-MMP in epithelial cell migration over laminin-5. *J. Cell Biol.* 148, 615–624, 2000.
- 103 BELIEN AT, PAGANETTI PA, SCHWAB ME. Membrane-type 1 matrix metalloprotease (MT1-MMP) enables invasive migration of glioma cells in central nervous system white matter. *J. Cell Biol.* 144, 373–384, 1999.
- 104 NABESHIMA K, INOUE T, SHIMAO Y, OKADA Y, ITOH Y, SEIKI M, KOONO M. Front-cell-specific expression of membrane-type 1 matrix metalloproteinase and gelatinase A during cohort migration of colon carcinoma cells induced by hepatocyte growth factor/scatter factor. *Cancer Res.* 60, 3364–3369, 2000.
- 105 SANCEAU J, TRUCHET S, BAUVOIS B. Matrix metalloproteinase-9 silencing by RNA interference triggers the migratory-adhesive switch in Ewing's sarcoma cells. *J. Biol. Chem.* 278, 36 537–36 546, 2003.
- 106 YU WH, WOESSNER JF, JR., MCNEISH JD, STAMENKOVIC I. CD44 anchors the assembly of matrilysin/MMP-7 with heparin-binding epidermal growth factor precursor and ErbB4 and regulates female reproductive organ remodeling. *Genes Dev.* 16, 307–323, 2002.
- 107 POWELL WC, FINGLETON B, WILSON CL, BOOTHBY M, MATRISIAN LM. The metalloproteinase matrilysin proteolytically generates active soluble Fas ligand and potentiates epithelial cell apoptosis. *Curr. Biol.* 9, 1441–1447, 1999.
- 108 MITSIADES N, YU WH, POULAKI V, TSOKOS M, STAMENKOVIC I. Matrix metalloproteinase-7-mediated cleavage of Fas ligand protects tumor cells from chemotherapeutic drug cytotoxicity. *Cancer Res.* 61, 577–581, 2001.
- 109 SCHLONDORFF J, BLOBEL CP. Metalloprotease-disintegrins: Modular proteins capable of promoting cell-cell interactions and triggering signals by protein-ectodomain shedding. *J. Cell Sci.* 112(Pt 21), 3603–3617, 1999.
- 110 MOSS ML, LAMBERT MH. Shedding of membrane proteins by ADAM family proteases. *Essays Biochem.* 38, 141–153, 2002.
- 111 BLACK RA, RAUCH CT, KOZLOSZY CJ, PESCHON JJ, SLACK JL, WOLFSON MF, CASTNER BJ, STOCKING KL, REDDY P, SRINIVASAN S, NELSON N, BOIANI N, SCHOOLEY KA, GERHART M, DAVIS R, FITZNER JN, JOHNSON RS, PAXTON RJ, MARCH CJ, CERRETTI DP. A metalloproteinase disintegrin that releases tumour-necrosis factor-alpha from cells. *Nature* 385, 729–733, 1997.
- 112 ITOH T, IKEDA T, GOMI H, NAKAO S, SUZUKI T, ITOHARA S. Unaltered secretion of beta-amyloid precursor protein in gelatinase A (matrix metalloproteinase 2)-deficient mice. *J. Biol. Chem.* 272, 22 389–22 392, 1997.

- 113 MUDGETT JS, HUTCHINSON NI, CHARTRAIN NA, FORSYTH AJ, McDONNELL J, SINGER II, BAYNE EK, FLANAGAN J, KAWKA D, SHEN CF, STEVENS K, CHEN H, TRUMBAUER M, VISCO DM. Susceptibility of stromelysin 1-deficient mice to collagen-induced arthritis and cartilage destruction. *Arthritis Rheum.* 41, 110–121, **1998**.
- 114 WILSON CL, HEPPNER KJ, LABOSKY PA, HOGAN BL, MATRISIAN LM. Intestinal tumorigenesis is suppressed in mice lacking the metalloproteinase matrilysin. *Proc. Natl. Acad. Sci. U.S.A.* 94, 1402–1407, **1997**.
- 115 VU TH, SHIPLEY JM, BERGERS G, BERGER JE, HELMS JA, HANAHAH D, SHAPIRO SD, SENIOR RM, WERB Z. MMP-9/gelatinase B is a key regulator of growth plate angiogenesis and apoptosis of hypertrophic chondrocytes. *Cell* 93, 411–422, **1998**.
- 116 MASSON R, LEFEBVRE O, NOEL A, FAHIME ME, CHENARD MP, WENDLING C, KEBERS F, LEMEUR M, DIERICH A, FOIDART JM, BASSET P, RIO MC. In vivo evidence that the stromelysin-3 metalloproteinase contributes in a paracrine manner to epithelial cell malignancy. *J. Cell Biol.* 140, 1535–1541, **1998**.
- 117 SHIPLEY JM, WESSELSCHMIDT RL, KOBAYASHI DK, LEY TJ, SHAPIRO SD. Metalloelastase is required for macrophage-mediated proteolysis and matrix invasion in mice. *Proc. Natl. Acad. Sci. U.S.A.* 93, 3942–3946, **1996**.
- 118 CATERINA JJ, SKOBE Z, SHI J, DING Y, SIMMER JP, BIRKEDAL-HANSEN H, BARTLETT JD. Enamelysin (matrix metalloproteinase 20)-deficient mice display an amelogenesis imperfecta phenotype. *J. Biol. Chem.* 277, 49 598–49 604, **2002**.
- 119 ITOH T, TANIOKA M, MATSUDA H, NISHIMOTO H, YOSHIOKA T, SUZUKI R, UEHIRA M. Experimental metastasis is suppressed in MMP-9-deficient mice. *Clin. Exp. Metastasis* 17, 177–181, **1999**.
- 120 ITOH T, TANIOKA M, YOSHIDA H, YOSHIOKA T, NISHIMOTO H, ITOHARA S. Reduced angiogenesis and tumor progression in gelatinase A-deficient mice. *Cancer Res.* 58, 1048–1051, **1998**.
- 121 COUSSENS LM, TINKLE CL, HANAHAH D, WERB Z. MMP-9 supplied by bone marrow-derived cells contributes to skin carcinogenesis. *Cell* 103, 481–490, **2000**.
- 122 YAN SJ, BLOMME EA. In situ zymography: A molecular pathology technique to localize endogenous protease activity in tissue sections. *Vet Pathol.* 40, 227–236, **2003**.
- 123 CATTERALL JB, CAWSTON TE. Assays of matrix metalloproteinases (MMPs) and MMP inhibitors: Bioassays and immunoassays applicable to cell culture medium, serum, and synovial fluid. *Methods Mol. Biol.* 225, 353–364, **2003**.
- 124 LOPEZ-OTIN C, OVERALL CM. Protease degradomics: A new challenge for proteomics. *Nat. Rev. Mol. Cell Biol.* 3, 509–519, **2002**.
- 125 FREDERIKS WM, MOOK OR. Metabolic mapping of proteinase activity with emphasis on in situ zymography of gelatinases: Review and protocols. *J. Histochem. Cytochem.* 52, 711–722, **2004**.
- 126 BILLINGHURST RC, IONESCU M, POOLE AR. Immunoassay for collagenase-mediated cleavage of types I and II collagens. *Methods Mol. Biol.* 151, 457–472, **2001**.
- 127 FOSANG AJ, LAST K, JACKSON DC, BROWN L. Antibodies to MMP-cleaved aggrecan. *Methods Mol. Biol.* 151, 425–449, **2001**.
- 128 MOTT JD, WERB Z. Regulation of matrix biology by matrix metalloproteinases. *Curr. Opin. Cell Biol.* 16, 558–564, **2004**.
- 129 SCHENK S, QUARANTA V. Tales from the crypt[ic] sites of the extracellular matrix. *Trends Cell Biol.* 13, 366–375, **2003**.
- 130 HEUSSEN C, DOWDLE EB. Electrophoretic analysis of plasminogen activators in polyacrylamide gels containing sodium dodecyl sulfate and copolymerized substrates. *Anal. Biochem.* 102, 196–202, **1980**.

- 131 MINAMI R, TSUNODA H, IIJIMA T, YOSHIKAWA H, NEMORI R, NOGUCHI M. Early acquisition of gelatinolytic activity in carcinogenesis of the uterine cervix. *Mod. Pathol.* 16, 1164–1170, 2003.
- 132 DI NEZZA LA, MISAJON A, ZHANG J, JOBLING T, QUINN MA, OSTOR AG, NIE G, LOPATA A, SALAMONSEN LA. Presence of active gelatinases in endometrial carcinoma and correlation of matrix metalloproteinase expression with increasing tumor grade and invasion. *Cancer* 94, 1466–1475, 2002.
- 133 KAWAMURA K, KAMIYA N, SUYAMA T, SHIMBO M, OOSUMI N, SUZUKI H, UEDA T, TOBE T, IGARASHI T, ITO H, ISHIKURA H. In situ gelatinolytic activity correlates with tumor progression and prognosis in patients with bladder cancer. *J. Urol.* 172, 1480–1484, 2004.
- 134 CURRAN S, MURRAY GI. Matrix metalloproteinases in tumour invasion and metastasis. *J. Pathol.* 189, 300–308, 1999.
- 135 FRIEDL P, HEGERFELDT Y, TUSCH M. Collective cell migration in morphogenesis and cancer. *Int. J. Dev. Biol.* 48, 441–449, 2004.
- 136 MURPHY G, GAVRILOVIC J. Proteolysis and cell migration: Creating a path? *Curr. Opin. Cell Biol.* 11, 614–621, 1999.
- 137 ALBINI A, IWAMOTO Y, KLEINMAN HK, MARTIN GR, AARONSON SA, KOZLOWSKI JM, McEWAN RN. A rapid in vitro assay for quantitating the invasive potential of tumor cells. *Cancer Res.* 47, 3239–3245, 1987.
- 138 BOYDEN S. The chemotactic effect of mixtures of antibody and antigen on polymorphonuclear leucocytes. *J. Exp. Med.* 115, 453–466, 1962.
- 139 CHEN HC. Boyden chamber assay. *Methods Mol. Biol.* 294, 15–22, 2004.
- 140 SHAW LM. Tumor cell invasion assays. *Methods Mol. Biol.* 294, 97–106, 2004.
- 141 BENBOW U, ORNDORFF KA, GIVAN AL. Invasion assays and matrix metalloproteinases. Quantification of cellular invasion using propidium iodide labeling and confocal laser scanning microscopy. *Methods Mol. Biol.* 151, 485–494, 2001.
- 142 SHANG M, KOSHIKAWA N, SCHENK S, QUARANTA V. The LG3 module of laminin-5 harbors a binding site for integrin alpha3beta1 that promotes cell adhesion, spreading, and migration. *J. Biol. Chem.* 276, 33 045–33 053, 2001.
- 143 KURATOMI Y, NOMIZU M, TANAKA K, PONCE ML, KOMIYAMA S, KLEINMAN HK, YAMADA Y. Laminin gamma 1 chain peptide, C-16 (KAFDITYVRLKF), promotes migration, MMP-9 secretion, and pulmonary metastasis of B16-F10 mouse melanoma cells. *Br. J. Cancer* 86, 1169–1173, 2002.
- 144 RAY JM, STETLER-STEVENSON WG. Gelatinase A activity directly modulates melanoma cell adhesion and spreading. *EMBO J.* 14, 908–917, 1995.
- 145 YAN L, MOSES MA, HUANG S, INGBER DE. Adhesion-dependent control of matrix metalloproteinase-2 activation in human capillary endothelial cells. *J. Cell Sci.* 2000.
- 146 KUCIK DF, WU C. Cell-adhesion assays. *Methods Mol. Biol.* 294, 43–54, 2004.
- 147 SIEUWERTS AM, KLIJN JG, FOEKENS JA. Assessment of the invasive potential of human gynecological tumor cell lines with the in vitro Boyden chamber assay: Influences of the ability of cells to migrate through the filter membrane. *Clin. Exp. Metastasis* 15, 53–62, 1997.
- 148 HOOD JD, CHERESH DA. Role of integrins in cell invasion and migration. *Nat. Rev. Cancer* 2, 91–100, 2002.
- 149 BUSSEMAKERS MJ, SCHALKEN JA. The role of cell adhesion molecules and proteases in tumor invasion and metastasis. *World J. Urol.* 14, 151–156, 1996.
- 150 LUDWIG T, PUTTMANN S, BERTRAM H, TATENHORST L, PAULUS W, OBERLEITHNER H, SENNER V. Functional measurement of local proteolytic activity in living cells of

- invasive and non-invasive tumors. *J. Cell Physiol.* 202, 690–697, 2005.
- 151 LUDWIG T, OSSIG R, GRAESSEL S, WILHELMI M, OBERLEITHNER H, SCHNEIDER SW. The electrical resistance breakdown assay determines the role of proteinases in tumor cell invasion. *Am. J. Physiol. Renal. Physiol.* 283, F319–F327, 2002.
- 152 SCHNAEKER EM, OSSIG R, LUDWIG T, DREIER R, OBERLEITHNER H, WILHELMI M, SCHNEIDER SW. Microtubule-dependent matrix metalloproteinase-2/matrix metalloproteinase-9 exocytosis: Prerequisite in human melanoma cell invasion. *Cancer Res.* 64, 8924–8931, 2004.
- 153 SCHNEIDER SW, LUDWIG T, TATENHORST L, BRAUNE S, OBERLEITHNER H, SENNER V, PAULUS W. Glioblastoma cells release factors that disrupt blood-brain barrier features. *Acta Neuropathol. (Berl)* 107, 272–276, 2004.
- 154 ZAK J, SCHNEIDER SW, EUE I, LUDWIG T, OBERLEITHNER H. High-resistance MDCK-C7 monolayers used for measuring invasive potency of tumour cells. *Pflugers Arch.* 440, 179–183, 2000.
- 155 LUDWIG T, FAKIH S, KREBS B, OBERLEITHNER H. Platinum complex cytotoxicity tested by the electrical resistance breakdown assay. *Cell Physiol. Biochem.* 14, 425–430, 2004.
- 156 BREMER C, TUNG CH, BOGDANOV A, JR., WEISSLEDER R. Imaging of differential protease expression in breast cancers for detection of aggressive tumor phenotypes. *Radiology* 222, 814–818, 2002.
- 157 TUNG CH, MAHMOOD U, BREDOW S, WEISSLEDER R. In vivo imaging of proteolytic enzyme activity using a novel molecular reporter. *Cancer Res.* 60, 4953–4958, 2000.
- 158 POOLE AR, TILTMAN KJ, RECKLIES AD, STOKER TA. Differences in secretion of the proteinase cathepsin B at the edges of human breast carcinomas and fibroadenomas. *Nature* 273, 545–547, 1978.
- 159 THORPE SM, ROCHEFORT H, GARCIA M, FREISS G, CHRISTENSEN IJ, KHALAF S, PAOLUCCI F, PAU B, RASMUSSEN BB, ROSE C. Association between high concentrations of Mr 52,000 cathepsin D and poor prognosis in primary human breast cancer. *Cancer Res.* 49, 6008–6014, 1989.
- 160 BREMER C, TUNG CH, WEISSLEDER R. In vivo molecular target assessment of matrix metalloproteinase inhibition. *Nat. Med.* 7, 743–748, 2001.
- 161 ZIPFEL WR, WILLIAMS RM, CHRISTIE R, NIKITIN AY, HYMAN BT, WEBB WW. Live tissue intrinsic emission microscopy using multiphoton-excited native fluorescence and second harmonic generation. *Proc. Natl. Acad. Sci. U.S.A.* 100, 7075–7080, 2003.
- 162 BROWN E, MCKEE T, DITOMASO E, PLUEN A, SEED B, BOUCHER Y, JAIN RK. Dynamic imaging of collagen and its modulation in tumors in vivo using second-harmonic generation. *Nat. Med.* 9, 796–800, 2003.
- 163 RICHARDS-KORTUM R, SEVICK-MURACA E. Quantitative optical spectroscopy for tissue diagnosis. *Annu. Rev. Phys. Chem.* 47, 555–606, 1996.
- 164 WANG W, WYCKOFF JB, FROHLICH VC, OLEYNIKOV Y, HUTTELMAIER S, ZAVADIL J, CERMAK L, BOTTINGER EP, SINGER RH, WHITE JG, SEGALL JE, CONDEELIS JS. Single cell behavior in metastatic primary mammary tumors correlated with gene expression patterns revealed by molecular profiling. *Cancer Res.* 62, 6278–6288, 2002.
- 165 FRIEDL P. Dynamic imaging of cellular interactions with extracellular matrix. *Histochem. Cell Biol.* 122, 183–190, 2004.
- 166 MOHLER W, MILLARD AC, CAMPAGNOLA PJ. Second harmonic generation imaging of endogenous structural proteins. *Methods* 29, 97–109, 2003.
- 167 MOREAUX L, SANDRE O, CHARPAK S, BLANCHARD-DESCE M, MERTZ J. Coherent scattering in multi-harmonic light microscopy. *Biophys. J.* 80, 1568–1574, 2001.
- 168 WILLIAMS RM, ZIPFEL WR, WEBB WW. Multiphoton microscopy in biological research. *Curr. Opin. Chem. Biol.* 5, 603–608, 2001.

- 169 CAMPAGNOLA PJ, LOEW LM. Second-harmonic imaging microscopy for visualizing biomolecular arrays in cells, tissues and organisms. *Nat. Biotechnol.* 21, 1356–1360, 2003.
- 170 MONSKY WL, LIN CY, AOYAMA A, KELLY T, AKIYAMA SK, MUELLER SC, CHEN WT. A potential marker protease of invasiveness, seprase, is localized on invadopodia of human malignant melanoma cells. *Cancer Res.* 54, 5702–5710, 1994.
- 171 MUELLER SC, GHERSI G, AKIYAMA SK, SANG QX, HOWARD L, PINEIRO-SANCHEZ M, NAKAHARA H, YEH Y, CHEN WT. A novel protease-docking function of integrin at invadopodia. *J. Biol. Chem.* 274, 24 947–24 952, 1999.
- 172 KUSICK S, BERTRAM H, OBERLEITHNER H, LUDWIG T. Nanoscale imaging and quantification of local proteolytic activity. *J. Cell Physiol.*, 204, 767–774, 2005.
- 173 SZPADERSKA AM, FRANKFATER A. An intracellular form of cathepsin B contributes to invasiveness in cancer. *Cancer Res.* 61, 3493–3500, 2001.
- 174 SAMENI M, DOSESCU J, SLOANE BF. Imaging proteolysis by living human glioma cells. *Biol. Chem.* 382, 785–788, 2001.
- 175 SAMENI M, MOIN K, SLOANE BF. Imaging proteolysis by living human breast cancer cells. *Neoplasia* 2, 496–504, 2000.
- 176 HORINO K, KINDEZELSKII AL, ELNER VM, HUGHES BA, PETTY HR. Tumor cell invasion of model 3-dimensional matrices: Demonstration of migratory pathways, collagen disruption, and intercellular cooperation. *FASEB J.* 15, 932–939, 2001.
- 177 BINNIG G, QUATE CF, GERBER Ch. Atomic force microscope. *Phys. Rev. Lett.* 56, 930–933, 1986.
- 178 BARO AM, MIRANDA R, ALAMAN J, GARCIA N, BINNIG G, ROHRER H, GERBER C, CARRASCOSA JL. Determination of surface topography of biological specimens at high resolution by scanning tunnelling microscopy. *Nature* 315, 253–254, 1985.
- 179 BINNIG G, ROHER H, GERBER Ch, WEIBEL E. Surface studies by scanning tunneling microscopy. *Phys. Rev. Lett.* 49, 57–61, 1982.
- 180 MULLER DJ, ENGEL A, MATTHEY U, MEIER T, DIMROTH P, SUDA K. Observing membrane protein diffusion at subnanometer resolution. *J. Mol. Biol.* 327, 925–930, 2003.
- 181 SCHILLERS H, DANKER T, MADEJA M, OBERLEITHNER H. Plasma membrane protein clusters appear in CFTR-expressing *Xenopus laevis* oocytes after cAMP stimulation. *J. Membr. Biol.* 180, 205–212, 2001.
- 182 OBERLEITHNER H, LUDWIG T, RIETHMULLER C, HILLEBRAND U, ALBERMANN L, SCHAFER C, SHAHIN V, SCHILLERS H. Human endothelium: Target for aldosterone. *Hypertension* 43, 952–956, 2004.
- 183 LUDWIG T, OBERLEITHNER H. Platinum complex toxicity in cultured renal epithelia. *Cell Physiol. Biochem.* 14, 431–440, 2004.
- 184 ENGEL A, MULLER DJ. Observing single biomolecules at work with the atomic force microscope. *Nat. Struct. Biol.* 7, 715–718, 2000.
- 185 SANTOS NC, CASTANHO MA. An overview of the biophysical applications of atomic force microscopy. *Biophys. Chem.* 107, 133–149, 2004.
- 186 CHEN CH, HANSMA HG. Basement membrane macromolecules: Insights from atomic force microscopy. *J. Struct. Biol.* 131, 44–55, 2000.
- 187 MIYAGAWA A, KOBAYASHI M, FUJITA Y, HAMDY O, HIRANO K, NAKAMURA M, MIYAKE Y. Surface ultrastructure of collagen fibrils and their association with proteoglycans in human cornea and sclera by atomic force microscopy and energy-filtering transmission electron microscopy. *Cornea* 20, 651–656, 2001.
- 188 PAIGE MF, RAINEY JK, GOH MC. A study of fibrous long spacing collagen ultrastructure and assembly by atomic force microscopy. *Micron* 32, 341–353, 2001.
- 189 RASPANTI M, CONGIU T, GUIZZARDI S. Tapping-mode atomic force

- microscopy in fluid of hydrated extracellular matrix. *Matrix Biol.* 20, 601–604, 2001.
- 190 TAATJES DJ, QUINN AS, BOVILL EG. Imaging of collagen type III in fluid by atomic force microscopy. *Microsc. Res. Tech.* 44, 347–352, 1999.
- 191 KASSNER A, TIEDEMANN K, NOTBOHM H, LUDWIG T, MORGELIN M, REINHARDT DP, CHU ML, BRUCKNER P, GRASSEL S. Molecular structure and interaction of recombinant human type XVI collagen. *J. Mol. Biol.* 339, 835–853, 2004.
- 192 KASSNER A, HANSEN U, MIOGGE N, REINHARDT DP, AIGNER T, BRUCKNER-TUDERMAN L, BRUCKNER P, GRASSEL S. Discrete integration of collagen XVI into tissue-specific collagen fibrils or beaded microfibrils. *Matrix Biol.* 22, 131–143, 2003.
- 193 SUN HB, SMITH GN, JR., HASTY KA, YOKOTA H. Atomic force microscopy-based detection of binding and cleavage site of matrix metalloproteinase on individual type II collagen helices. *Anal. Biochem.* 283, 153–158, 2000.
- 194 LIN H, CLEGG DO, LAI R. Imaging real-time proteolysis of single collagen I molecules with an atomic force microscope. *Biochemistry* 38, 9956–9963, 1999.
- 195 STROH C, WANG H, BASH R, ASHCROFT B, NELSON J, GRUBER H, LOHR D, LINDSAY SM, HINTERDORFER P. Single-molecule recognition imaging microscopy. *Proc. Natl. Acad. Sci. U.S.A.* 101, 12 503–12 507, 2004.

## Index

- 2-in-1 system, gold nanoparticles 97–98
- a**
- AbVF *see* VEGF antibody-2C3
- active targeting 65, 124, 185
- folate receptors 66
  - lectins 65
- affinity mass spectrometry
- nanoprobe-based 338–369
  - principles 349
- AFM *see* atomic-force microscopy
- agonists, LHRH 192
- AMI-121 (Ferumoxsil) 150–151
- AMI-227 (Combix) 151
- AMI-25 (Feridex) 151
- AMI25 iron particles 184
- aminated particles, bioconjugation 64
- amine-containing silane compound (APTS) 62
- amine-reactive fluorescein isothiocyanate 62
- aminopropyltriethoxysilane (APTS) 330–331
- amorphous silica nanoparticles 61–65
- angiogenesis
- and cancer 88–96
  - blocked extracellular matrix breakdown 91
  - molecular MRI 159
- Annexin V-FITC 267–268
- antibodies 27
- monoclonal 26–27
- antibody–gold conjugate 61
- antibody-2C3 97–98
- antibody-functionalized nanotubes 320
- antibody-mediated tumor targeting 66
- anti-carcinoembryonic antigen (CEA) antibody 163–164
- APO-BrdU TUNEL assay 245–247
- apoptosis
- cyt-c-induced 267–268
  - molecular MRI 160
- APTS *see* aminopropyltriethoxysilane
- artificial peptides, nanotubes 315–317
- assay methods 381
- atomic-force microscopy (AFM), proteolytic activity detection 396–400
- Au NP *see* gold nanoparticles
- avidin–biotin binding, bioconjugation 65
- avidin–gold conjugate 61
- b**
- barcodes
- multimetal 293
  - nano 325–327
- bFGF, activity 94
- bifunctional dendritic clusters 30
- bioactivity, dendrimers 20–21
- bio-barcode amplification assay 347
- biocompatibility
- dendrimers 22
  - gold nanoparticles 99–104
- bioconjugation, gold nanoparticles 60, 64–65
- Qdot 57
- biodistribution studies 28
- biointeraction, magnetic field-assisted 329
- biomarkers, targeting 25–27
- biomolecule-conjugated nanoparticles 339
- biosensors, SWNTs 269, 312–313
- blood analysis, nanoprobe-based affinity mass spectrometry 359–364
- BNCT *see* boron neutron capture therapy
- BOM *see* bubbles-overlapping mode (BOM)
- boron neutron capture therapy (BNCT) 29
- bovine serum albumin (BSA) 238, 248–252, 361–362
- breast cancer cells (MCF7) 253–258
- breast cancer markers 68
- BSA *see* bovine serum albumin
- BSA-MNTs 329–330
- bubbles-overlapping mode (BOM) 109

- buckyball C<sub>60</sub> 273
- building blocks, dendrimers 12–13
- c**
- C<sub>60</sub> 273
- CACO-2 cells 245–246
- cadmium selenide (CdSe) 52
- cadmium sulfide (CdS), crystalline 52
- cancer
  - chemotherapeutic approaches 179
  - conventional approaches to detection 177–178
  - multidrug resistance 179
  - statistics 175–176
- cancer cell death, targeted 310–311
- cancer cell migration, local proteolytic activity 389
- cancer detection, nanotechnology 106–108
- cancer diagnosis
  - carbon nanotubes 290–293
  - nanotechnological approaches 377–400
- cancer imaging 44–72
  - magnetic resonance nanoparticle probes 147–168
  - molecular MRI 163–165
  - techniques 46–48
- cancer marker protein profiling, nanoprobe-based 338–369
- Candida rugosa* lipase 309
- carbohydrate epitopes, metabolically-engineered 31
- carbon nanotubes (CNTs) 232–277, 285–295, 310–314
  - cancer diagnosis 290–293
  - cancer treatment 293–295
  - differential functionalization 319–320
  - drug delivery systems 294
  - enzyme-coated 290
  - functionalized 313–315
  - monodisperse 318
- carboxylated particles, bioconjugation 64
- carcinoembryonic antigen (CEA) 163–164
- cardiac infarct 158–159
- cascade reactions, dendrimer synthesis 10–11
- CCD *see* charged-coupled device
- CDDP 184
- CdSe NP 343
- CEA *see* carcinoembryonic antigen
- cell signaling, local proteolytic activity 389
- cell surface receptors, for protease binding 386
- cell tracking, iron oxides 128
- cell-labeling, nanoparticle-based 55
- cellular functions, local proteolytic activity 389–390
- cellular microdomains, proteolytic activity 388
- cellular uptake, of nanoparticles 188
- charged-coupled device (CCD) technology 48
- chemical separation, magnetic field-assisted 329
- chemoselective ligation reaction 32
- chemoselective targeting, drugloaded dendrimers 32
- chemotherapeutic approaches, cancer 179
- cis-platin 88
- CLIO *see* crosslinked iron oxides
- CLIO–antibody conjugates 160
- coated nanoparticles 181
- colon cancer (CACO-2) 245–246
- Combixid (AMI-227) 151
- computed tomography (CT) scanning 47
- confining proteolytic activity, mechanisms 385–388
- confocal fluorescence images, MCF7 cells 256–257
- conjugation strategies, polymeric 17–18
- contrast agents
  - magnetic nanoparticle 150–156
  - nanoparticle-based 53–64
  - nanoparticles-based 52
  - non-hydrolytically synthesized 154–156
  - optical 50
  - silica- or dextran-coated iron oxide 150–151
  - SPION 204
- controlled drug release, magnetic nanotubes 330–331
- conventional synthetic polymers, comparison to dendrimers 5
- convergent synthesis, of dendrimers 11
- core–shell nanoparticle design 54
- COS-7 cells 323
- covalent conjugation strategies, dendrimers 17–19
- C-reactive protein (CRP) 353–354, 356–358, 363–364
- crosslinked iron oxide (CLIO) particles 127–128
- CRP *see* C-reactive protein
- crystalline cadmium sulfide (CdS) 52
- CT *see* computed tomography
- Cy3-DNA functionalized SWNT 311–312
- Cy3-DNA-SWNT complexes, NIR laser light excitation 271
- cyanogen bromide chemistry, bioconjugation 65



- cyclic peptides 316  
 cysteine switch 382  
 cyt-c-induced apoptosis 267–268  
 cytochrome c 267–268  
 cytotoxicity, SWNTs 272–275
- d**
- DABCYL (4,4'-dimethylaminophenylazobenzoic acid) 108  
 deformability, of dendrimers 8  
 dendrimer-based cancer-targeted drug delivery 18  
 dendrimer-based drug delivery 9  
 dendrimers 1–33  
 – basic properties and applications 3–9  
 – bioactivity 20–21  
 – biocompatibility 22  
 – building blocks 12–13  
 – cascade reactions 10–11  
 – cascade synthesis 11  
 – chemoselective targeting 32  
 – comparison to conventional synthetic polymers 5  
 – comparison to proteins 6–7  
 – convergent synthesis 11  
 – covalent conjugation strategies 17–19  
 – deformability 8  
 – divergent synthesis 11  
 – drug delivery 15–23  
 – encapsulation of guest molecules 16–17  
 – flexibility 8  
 – gene delivery 16  
 – generations 3–5  
 – heterogeneously-functionalized 13–14  
 – immunogenicity 22  
 – internal cavities 16  
 – kidney filtered 21  
 – labeled 28  
 – magneto 152–153  
 – multifunctional 25–27  
 – oligosaccharide coatings 14  
 – paramagnetic 133  
 – paramagnetic polyamidoamine 133  
 – passive accumulation 24  
 – self-immolative 20  
 – surface modification 14  
 – synthesis 10–14  
 – toxicity 22–23  
 – vaccines 19  
 – water solubility 22  
 dendritic clusters, bifunctional 30  
 dendritic PEI 259–260  
 dextran crosslinked iron oxide (CLIO) particles 127–128  
 dextran-coated iron oxide contrast agents 150–151  
 dextran-coated MIONs 188  
 dextran-coated USPIOs 294  
 DHLA *see* dihydroxyloipoic acid  
 diethyl tetraminepentaacetic acid (DTPA) 187  
 differential functionalization, of nanotubes 319–320  
 diffuse optical tomography (DOT) 50  
 dihydroxyloipoic acid (DHLA)-capped quantum dots 67  
 2,3-dimercaptosuccinic acid (DMSA) 156–157  
 2,3-dimercaptosuccinic acid (DMSA)-coated water-soluble Fe<sub>3</sub>O<sub>4</sub> iron oxide (WSIO) nanocrystals 306  
 4,4'-dimethylaminophenylazobenzoic acid (DABCYL) 108  
 disulfide bonding, bioconjugation 65  
 divergent synthesis, of dendrimers 11  
 DMSA *see* 2,3-dimercaptosuccinic acid  
 DNA, single-stranded  
 DNA hybridization 326–327  
 DNA microarray analysis 100  
 DNA nanotubes 324–325  
 DNA-dendrimer conjugates 31  
 DOT *see* diffuse optical tomography  
 DOTA *see* 1,4,7,10-tetraazacyclododecane-1,4,7,10-tetraacetic acid  
 drug delivery  
 – dendrimer-based 9  
 – dendrimer-based cancer-targeted 18  
 – dendrimers 15–23  
 – nanoparticles as vehicles 181–188  
 – SWNT transporters 252–269  
 – targeted 313–314  
 – to tumors 179  
 drug delivery systems, carbon nanotubes 294  
 drug molecules, selective extraction 320–321  
 drug release, controlled 330–331  
 drug uptake, magnetic nanotubes 330–331  
 DTPA *see* diethyl tetraminepentaacetic acid  
 dye-doped nanoparticles 52  
 dye-doped silica nanoparticles  
 – cancer imaging 69  
 – contrast agents 61–64
- e**
- ECM *see* extra cellular matrix  
 ECM binding, of proteases 387  
 ECM-components, atomic-force microscopy (AFM) 397–400  
 EFGR *see* epidermal growth factor receptor

- EGF 94, activity 94  
 electrical resistance breakdown assay 394  
 electronic structure, semiconducting SWNTs 270  
 ELISA *see* enzyme linked immunosorbent assay  
 encapsulation, of guest molecules 16–17  
 endocytosis, receptor-mediated 197–198  
 endogenous protease inhibitors 383  
 endosomal rupture 267  
 endothelial proliferation, inhibition 90  
 engineered transferrin receptor (ETR) 163  
 enhanced permeability and retention (EPR)  
 – effect 24–25, 125  
 – passive targeting 66  
 enzyme linked immunosorbent assay (ELISA) 264–265, 345–346, 356, 364, 391  
 enzyme-coated carbon nanotubes 290  
 epidermal growth factor receptor (EGFR) 107  
 epidermal growth factor receptor (EGFR) 345–346  
 EPR *see* enhanced permeability and retention  
 extra cellular matrix (ECM) components  
 – AFM 396–400  
 – angiogenesis 89
- f**
- Fab (fragment binding antigen) conjugates 158, 320–322  
 FePt NP 342  
 Feridex (AMI-25) 151  
 ferrofluids 187  
 Ferumoxsil (AMI-121) 150–151  
 FET *see* field-effect transistor  
 field-effect transistors (FETs), SWNT 287, 290–291  
 FITC *see* fluorescein isothiocyanate  
 FITC-AmB modified MWNTs 315  
 FITC-doped silica nanoparticles 69  
 flexibility, of dendrimers 8  
 fluorescein isothiocyanate (FITC) 308  
 – amine-reactive 62  
 fluorescence microscopy, single-molecule 248–250, 253  
 fluorescence-mediated molecular tomography (FMT) 49–50  
 fluorescent quantum dots 52  
 4-[3-(4-fluorophenyl)-2-hydroxy-1-[1,2,4]-triazol-1-yl-propyl]benzotrile (FTB) 321  
 5-Fluorouracil (5-FU) 330–331  
 FMDV *see* foot and mouth disease virus  
 FMT *see* fluorescence-mediated molecular tomography
- folate, targeting 26  
 folate receptor (FR)  
 – active targeting 66  
 – HeLa cells 312  
 foot and mouth disease virus (FMDV), peptides 264–265  
 fragment binding antigen *see* Fab  
 FTP *see* 4-[3-(4-fluorophenyl)-2-hydroxy-1-[1,2,4]-triazol-1-yl-propyl]benzotrile  
 fullerenes, paramagnetic 132  
 functionalized carbon nanotubes 313–315  
 – antibody 320  
 – differentially 319–320  
 – *see also* single-wall nanotubes (SWNT)  
 functionalized SWNT, Cy3-DNA 311–312
- g**
- gadolinium chelates 187  
 gadolinium-diethylenetriaminepentaacetic acid (Gd-DTPA) 184, 187  
 Gd-DTPA *see* gadolinium-diethylenetriaminepentaacetic acid  
 gene delivery  
 – dendrimers 16  
 – SWNT transporters 252–269  
 gene expression, molecular MRI 161–162  
 gene transfection, SWNT transporters 258–262  
 generations, of dendrimers 3–5  
 GFP *see* green fluorescent proteins  
 gfSNTs *see* green fluorescent silica nanotubes  
 glycosylation 14  
 – protease activity 384  
 glycosylation abnormalities 31  
 GnRH *see* gonadotropin releasing hormone  
 – *see also* ligand luteinizing hormone releasing hormone  
 gold conjugates 96–98  
 gold nanoparticles (Au NPs) 86–110, 342–346, 354  
 – anti-angiogenic properties 91  
 – biocompatibility 99–104  
 – bioconjugation 64–65  
 – cancer imaging 68  
 – cellular adhesion effects 99  
 – conjugates 60–61  
 – contrast agents 57–60  
 – internalization 101  
 – in-vivo effects on angiogenesis 95  
 – local biological effects 99  
 – near-normal culture conditions 103–104  
 – serum-free conditions 101–102  
 – synthesis 58–59

- synthetic approaches 105–106
- systemic and remote effects 99
- transcription pattern 101–104
- VEGF165 92–95
- gold precursors 58
- gold radioisotopes 96
- gold–TNF conjugates 96
- gonadotropin releasing hormone (GnRH) *see*
- ligand luteinizing hormone releasing hormone
- GPBR *see* G-protein binding receptor
- G-protein binding receptor (GPBR) 193–196
- green fluorescent proteins (GFP) 49, 51
- green fluorescent silica nanotubes (gfSNTs) 323–324
- guest molecules, encapsulation 16–17

**h**

- half-cylinder wrapping 243–245
- HBV *see* hepatitis B virus
- HEK 293 cells 198
- HeLa cells 259, 311–312
- heparin sepharose 93
- hepatitis B virus (HBV) antibody 345–346
- HER2 68
- Her-2/neu receptor 343–344
- Herceptin conjugates, WSIO 164–167
- heterogeneously-functionalized dendrimers 13–14
- HL60 cells 267
- host, effects on the implant 100
- hot solution-phase mediated Qdot synthesis 55
- HSA *see* human serum albumin
- human breast cancer
  - LHRH-SPION uptake 206–207
  - MDA-MB-435 67
- human embryonic cells *see* HEK 293 cells
- human IgG 329–330
- human mammary epithelial tumor (MDA-MB-231) 67
- human plasma, enrichment of target antigen 362–363
- human plasma analysis, nanoprobe-based
  - affinity mass spectrometry 359–364
- human serum albumin (HSA) 361–362
- HUVEC cells 93–94, 160
  - gold nanoparticles 101–104
  - migration 95
  - transcription pattern 101–104
- hydrochloroauric acid 58
- hyperthermia, LHRH-bound magnetic nanoparticles 202

**i**

- ibuprofen 330–331
- IKVAV *see* isoleucine-lysine-valine-alanine-valine
- imaging
  - of pericellular proteolytic activity 377–400
  - optical 44–72
  - with dendrimers 28
- imaging agents, cancer treatment 294
- immunoassay
  - nanoprobe-based 356–358
  - nanoscale 359–360
- immunocytochemistry techniques, metastase detection 178
- immunotherapy 26–27
- implant, effects by host 100
- iMQC *see* intermolecular multiple-quantum coherence
- In<sub>2</sub>O<sub>3</sub> nanowires 312–313
- induced toxicity 23
- infarct, molecular MRI 158
- inflammation, molecular MRI 158
- $\alpha_v\beta_3$ -integrin, MRI 130
- intermolecular multiple-quantum coherence (iMQC) 209–210
- internal cavities, dendrimers 16
- internalization, gold nanoparticles 101
- invasion assays, tumor cell 393–394
- iron oxide contrast agents, silica- or dextran-coated 150–151
- iron oxide MNPs 342, 344
- iron oxide nanoparticles 187
  - cell tracking 128
  - ligand-directed targeting 127
  - molecular MRI 157–165
  - non-hydrolytically synthesized 154–156
  - poly(ethylene glycol) (PEG)-ylated 155
  - siloxane–poly(ethylene glycol) (PEG) coated 156
  - superparamagnetic 203–209
  - ultrasmall superparamagnetic 294
  - water-soluble 156–157
- isoleucine-lysine-valine-alanine-valine (IKVAV) 318
- ISZ *see in situ* zymography

**k**

- kidney, dendrimer filter 21

**l**

- labeled dendrimers 28
- labeled substrates, proteolytic activity detection 396
- lectin–gold conjugate 61

- lectins, active targeting 65
  - LHRH *see* luteinizing hormone releasing hormone
  - LHRH conjugated magnetic nanoparticles 174–211
  - LHRH receptors 175, 189–200
    - cancer types 176
  - LHRH-bound magnetic nanoparticles 201–209
  - LHRH-SPION nanoparticles 201
    - subcellular distribution 208
  - LHRH-SPION uptake, receptor-targeted 205–209
  - LHRH-SPION-hecate, destruction of metastases 203
  - ligand-directed targeting, iron oxides 127
  - ligation reaction, chemoselective 32
  - lipid rafts 388
  - liposomes
    - magneto 152–153
    - paramagnetic 131
  - local proteolytic activity 380–390
  - lock and key function 7
  - LPA *see* lysophosphatidic acid
  - LPC *see* lysophosphatidylcholine
  - LPG *see* lysophosphatidylglycerol
  - luteinizing hormone releasing hormone (LHRH) 174–211
    - agonists 192
    - amino acid sequences 191
    - analogs 192
    - function–signal transduction pathways 194–196
    - ligand 189–200
  - lysophosphatidic acid (LPA) 241
  - lysophosphatidylcholine (LPC) 241–247
  - lysophosphatidylglycerol (LPG) 241–245
  - lysophospholipids, single-wall nanotubes (SWNT) 239–246
  - lytic peptides, LHRH-bound magnetic nanoparticles 203
- m**
- macrophage (THP-1) cells 245–246
  - MAGIC *see* magnetism-base interaction capture
  - magnetic field-assisted chemical separation 329
  - magnetic microbeads (MMP) 359–360
  - magnetic nanoparticles (MNP) 342–344
    - biomedical diagnostic applications 307–309
    - contrast agents 150–156
    - for biomedical applications 305–309
    - LHRH conjugated 174–211
    - LHRH-bound 201–209
    - suppression of nonspecific binding 361
    - vancomycin-conjugated 309–310
    - MEG-protected antibody-conjugated 350–351
  - magnetic nanotubes (MNT) 328–332
  - magnetic resonance (MR) 47, 148
  - magnetic resonance imaging (MRI) 121–138
    - higher resolution 188
    - magnetic nanoparticles 305–306
    - molecular 157–165
    - nanoparticle probes 147–168
    - nanoparticles 186–187
    - SPION contrast agents 204
    - targeting mechanisms 124–125
  - magnetism-base interaction capture (MAGIC) 308–309
  - magnetodendrimers 152–153
  - magnetoferritin 152
  - magnetoliposomes 152–153
  - MALDI-TOF MS *see* matrix-assisted laser desorption/ionization time-of-flight mass spectrometry
  - mass spectrometric immunoassay (MSIA) 349–350
  - mass spectrometry
    - nanoprobe-based 338–369
    - principles 348–349
    - time-of-flight 348
  - matrix breakdown, extracellular 91
  - matrix metalloproteinase 2 (MMP-2) 49
  - matrix metalloproteinase inhibitors (MMPi) 378–379
  - matrix metalloproteinases (MMPs) 382–396
    - membrane-type 386
  - matrix-assisted laser desorption/ionization time-of-flight mass spectrometry (MALDI-TOF MS), principles 348
  - matrix-metalloprotease deficient mice 390
  - MCF7 cells 253–258, 274–275
  - MCF-7 cells 202
  - MDA-MB-231 67
  - MDA-MB-435 67
  - MDA-MB-435S.luc cancers 206–209
  - MEG *see* methoxy-ethylene glycol
  - MEG-protected antibody-conjugated MNPs 362
  - membrane-type matrix metalloproteinases (MT-MMPs) 386–391, 396
  - metabolically-engineered carbohydrate epitopes 31
  - metal nanoparticles 344–347

- metalloproteinases, membrane-type 386  
 metastase detection 177–178  
 – nanoparticles 186–188  
 metastasis, formation 377–379  
 methicillin-resistant *S. aureus* (MRSA) 316  
 methoxy-ethylene glycol (MEG) 350–351  
 microarray analysis, DNA 100  
 microbeads, SPIO 345  
 microcantilevers, cancer diagnosis 292  
 microemulsion (W/O) method, reverse 62  
 microscale immunoassay, comparison to  
 nanoscale immunoassay 359–360  
 MION *see* monocrySTALLINE iron oxide  
 nanoparticles  
 mix-and-match strategy, bifunctional dendritic  
 clusters 30  
 MMP *see* matrix metalloproteinase  
 MMP-2 *see* matrix metalloproteinase 2  
 MMP-9 389  
 MMPI *see* matrix metalloproteinase inhibitor  
 MNT *see* magnetic nanotubes  
 molecular MRI, iron oxides 157–165  
 molecular recognition 7  
 monoclonal antibodies, targeting 26–27  
 monocrySTALLINE iron oxide nanoparticles  
 (MION) 127, 206  
 – dextran-coated 188  
 monodisperse nanotubes 318  
 MR *see* magnetic resonance  
 MRI *see* magnetic resonance imaging  
 MRI imaging agents 28  
 MRSA *see* methicillin-resistant *S. aureus*  
 MT-MMPs *see* membrane-type matrix  
 metalloproteinases  
 multi-CRAZED sequence 209–210  
 multidentate phosphine oxide ligands 155  
 multidrug resistance, cancer 179  
 multifunctional dendrimers 25–27  
 multifunctional nanoparticles 52  
 multifunctional nanotubes 304–332  
 multimetal barcodes 293  
 multiphoton microscopy, proteolytic activity  
 detection 395  
 multiphoton microscopy (MPM) 395  
 multiplex assay 364–369  
 – screening for patient and healthy individuals  
 367–368  
 – workflow 366  
 multiplexing diagnosis, nanobarcodeS 325–  
 327  
 multi-wall nanotubes (MWNT) 286–287  
 – functionalized 314–315  
 – PEI 258–260  
 MWNTs *see* multi-wall nanotubes
- n**  
 nanobarcodeS, for multiplexing diagnosis  
 325–327  
 nanocantilevers 285–295  
 nanocrystals 306  
 nano-devices, dendrimers 15  
 nanogold *see* gold nanoparticles  
 nanoparticle design, core-shell 54  
 nanoparticle-based cell-labeling 55  
 nanoparticle-based contrast agents 53–64  
 nanoparticle-based optical contrast agents 70  
 nanoparticles  
 – as vehicles for drug delivery and diagnosis  
 181–188  
 – biomolecule-conjugated 339  
 – classification 135  
 – coated 181  
 – dye-doped 52  
 – fabrication and biomedical applications  
 339–347  
 – iron oxide 187  
 – LHRH conjugated magnetic 174–211  
 – LHRH-bound magnetic 201–209  
 – LHRH-SPION 201  
 – magnetic 305–309, 361  
 – metallic 344–347  
 – metastase detection 186–188  
 – MRI 305–306  
 – multifunctional 52  
 – non-hydrolytically synthesized iron oxide  
 154–156  
 – optical imaging 44–72  
 – paramagnetic 128–133  
 – perfluorocarbon 129–130  
 – phosphor 70  
 – poly(ethylene glycol) (PEG)-ylated iron oxide  
 155  
 – polymer 134  
 – siloxane-poly(ethylene glycol) (PEG) coated  
 iron oxide 156  
 – superparamagnetic 126–128  
 – tumor detection 186–188  
 – ultrasmall superparamagnetic iron oxide 294  
 – vancomycin-conjugated magnetic 309–310  
 – water-soluble iron oxide 156–157  
 nanoparticleS-based contrast agents 52  
 nanoprobe-based affinity mass spectrometry  
 (NBAMS)  
 – for cancer marker protein profiling 338–  
 369  
 – kinetic study of the nanoscale  
 immunoreaction 356  
 – proof-of-principle experiment 353–355  
 – workflow 351–352

- nanoprobe-based immunoassay 356–358
  - nanorods 285–295
    - template-synthesized 318–332
  - nanoscale immunoassay, comparison to microscale immunoassay 359–360
  - nanoscale immunoreaction, kinetic study 356
  - nanosensors, SWNT 312–313
  - nanotechnology, cancer detection 106–108
  - Nanotechnology for Cancer Diagnosis and Therapy initiative 233
  - nanotube carriers, silica 322
  - nanotubes 285–295
    - carbon 285–295
    - differential functionalization 319
    - DNA 323–324
    - magnetic 328–332
    - multifunctional 304–332
    - noncarbon 287
    - paramagnetic 133
    - self-assembled 289
    - template-synthesized 318–332
  - nanowires 285–295
    - multifunctional 304–332
  - nanowires (NW), In<sub>2</sub>O<sub>3</sub> 312–313
  - NBAMS *see* nanoprobe-based affinity mass spectrometry
  - nearinfrared (NIR) light 48
  - near-infrared fluorescent (NIRF) probes 394–395
  - net proteolytic activity, classical methods for quantification 391–396
  - NHS *see* N-hydroxysuccinimide
  - N-hydroxysuccinimide (NHS) 235
  - NIR *see* nearinfrared
  - NIR laser light excitation, Cy3-DNA-SWNT complexes 271
  - 4-nitrophenol 330–331
  - NMR *see* nuclear magnetic resonance
  - noncarbon nanotubes 287
    - cancer diagnosis 291
  - non-hydrolytically synthesized iron oxide nanoparticles 154–156
  - non-invasive techniques, metastase detection 178
  - nonspecific binding, on magnetic nanoparticles 361
  - NP *see* nanoparticles
  - nuclear magnetic resonance (NMR) 122
    - *see also* magnetic resonance
- O**
- oligomerization, protease activity 384
  - oligosaccharide coatings, of dendrimers 14
  - opsonization 181
  - optical contrast agents 50
    - nanoparticle-based 70
  - optical imaging
    - contrast agents 50
    - of cancer 44–72
- P**
- PA *see* peptide-amphiphile
  - PAMAM *see* poly(amidoamine)
  - paramagnetic nanoparticles 128–133
  - paramagnetic polyamidoamine dendrimers 133
  - passive targeting 66, 124, 183–184
  - PEG *see* poly(ethylene glycol)
  - PEI *see* polyethylenimine
  - peptide coated quantum dots 67
  - peptide nanotubes 315
  - peptide nucleic acids (PNA) 235
  - peptide-amphiphile (PA) nanofibers 316–317
  - peptides, artificial 315–317
  - perfluorocarbon (PFC) nanoparticles 129–130
  - pericellular proteolytic activity,
    - nanotechnological approaches 377–400
  - PET *see* positron emission tomography
  - PFC *see* perfluorocarbon
  - phagokinetic track assay, quantum dot 67
  - phosphine oxide ligands, multidentate 155
  - phospholipids (PL) 261–262
    - single-chained 239
  - phosphor nanoparticles, up-converting 70
  - phosphotyrosine phosphatase (PTP) 196
  - PL *see* phospholipids
  - plasma protein profiling, in normal individuals and in patients 364
  - PL-PEG-SWNT complexes 261–262
  - PNA *see* peptide nucleic acids
  - poly(amidoamine) (PAMAM) 3–7
    - chemical composition 11
    - induced toxicity 23
    - paramagnetic dendrimers 133
    - uptake by target cell 21–22
  - poly(ethylene glycol) (PEG)
  - poly(ethylene glycol) (PEG)-ylated iron oxide nanoparticles 155
  - poly(rU) RNA 239, 248–258
  - polyethylenimine (PEI), dendritic 259–260
  - polymer nanoparticles 134
  - polymers
    - conjugation strategies 17–18
    - conventional synthetic 5
  - positron emission tomography (PET) 47
  - pro-drugs

- covalently-delivered 19
  - encapsulated 17
  - proof-of-principle experiment, affinity mass spectrometry 353–355
  - prostate specific antigen (PSA) 312–313
  - prostate-specific antigen (PSA) 109, 292, 346
  - protease activity, regulation 382–385
  - protease assays 381
  - protease binding
    - cell surface receptors 386
    - ECM 387
  - protease inhibitors, endogenous 383
  - protein A–gold conjugates 60
  - protein delivery, SWNTs 266–268
  - protein profiling
    - human plasma analysis 359
    - nanoprobe-based 338–369
  - protein trafficking 385
  - proteins, comparison to dendrimers 6–7
  - proteolytic activity
    - AFM 396–400
    - classical methods for quantification 391–396
    - confining 385–388
    - *in vitro* detection 396
    - *in vivo* detection 394–396
    - local 380–390
    - pericellular 377–400
  - PSA *see* prostate-specific antigen
  - PT *see* thiol-derivatized PEG
  - PTP *see* phosphotyrosine phosphatase
  - PT-PCR 103–104
- q**
- Qdot synthesis
    - hot solution-phase mediated 55
    - reverse-micelle mediated 56
  - quantum dots (Qdots) 133
    - bioconjugation 57
    - cancer imaging 66–67
    - contrast agents 53–56
    - fluorescent 52
    - peptide coated 67
    - phagokinetic track assay 67
    - semiconductor 344
    - surface passivation 56
    - TOP/TOPO-capped 56
- r**
- radioisotope labeling assay 255–258
  - radioisotopes, gold 96
  - receptor-mediated endocytosis 197–198
  - reflectance fluorescence imaging 49
  - relaxation times, MRI 123, 148
  - RES *see* reticuloendothelial system
  - reticuloendothelial system (RES) 126, 154
  - reverse microemulsion (W/O) method, dye-doped silica nanoparticles 62
  - reverse transcriptase polymerase chain reaction (RT-PCR) 103–104
  - reverse-micelle mediated Qdot synthesis 56
  - RNA
    - HUVEC cells 103
    - poly(rU) 239, 248–252
    - small interfering 248
  - RNA interference, SWNT transporters 261–262
  - RNA polymers, solubilization of SWNTs 239
  - RNA translocation, SWNT transporters 253–257
  - RT-PCR 391
    - metastase detection 178
  - rule-of-five guidelines 15
- s**
- SAP *see* serum amyloid P
  - second-harmonic generation (SHG)
    - imaging microscopy 395–396
    - proteolytic activity detection 395
  - seed mediated route, gold nanoparticle synthesis 59
  - SELDI *see* surface-enhanced laser desorption/ionization
  - self-assembled nanotubes 289
  - self-immolative dendrimers 20
  - semiconducting SWNTs, electronic structure 270
  - semiconductor quantum dots 344
  - sensors *see* biosensors
  - SERS *see* surface-enhanced Raman scattering
  - serum amyloid P (SAP) 351, 353, 356–358, 363–364
  - serum tumor markers 340–341
  - shell-crosslinked nanoparticles 135
  - SHG *see* second-harmonic generation
  - sialic acid engineering 32
  - silica nanoparticles, dye-doped 61–64, 69
    - FITC-doped 69
  - silica nanotube carriers, for DNA transfection 322
  - silica nanotubes, green fluorescent 323–324
  - silica-coated iron oxide contrast agents 150–151
  - silicon dioxide nanoparticles 61–65
  - silicon nanowires (SiNWs) 292
  - siloxane–poly(ethylene glycol) (PEG) coated iron oxide nanoparticles 156

- silver nanowires 289
  - single-chained phospholipids 239
  - single-mismatch detection, of cancer 107
  - single-molecule fluorescence microscopy (SMFM) 248–250, 253
  - single-photon emission CT (SPECT) 48
  - single-stranded DNA (ssDNA) 238–239
  - single-wall nanohorns (SWNHs) 287
  - single-wall nanotubes (SWNT) 232–277
    - biocompatibility 233–246
    - biomolecular complexes 247–251
    - biosensing 269
    - cancer treatment 269–277
    - covalent modifications 236
    - Cy3-DNA functionalized 311–312
    - cytotoxicity 272–275
    - functionalization 235–237, 311–312
    - gene and drug delivery 252–269
    - lysophospholipids 239–246
    - nanosensors 312–313
    - noncovalent modifications 237–246
    - oxidation 235
    - protein delivery 266–268
    - semiconducting SWNTs 270
    - solubility 234–246
    - water-soluble 237–239
  - SiNWs *see* silicon nanowires
  - siRNA *see* small interfering RNA
  - small interfering RNAs (siRNAs) 248, 261–263
  - SMFM *see* single-molecule fluorescence microscopy
  - solubilization of SWNTs 237–247
  - SPECT *see* single-photon emission CT
  - SPIO *see* superparamagnetic iron oxides
  - SPIO microbeads (SPIO-MBs) 345
  - SPIO–C2 conjugates 161
  - SPION *see* superparamagnetic iron oxide nanoparticles
  - SPION contrast agents, targeted delivery 204
  - SPR *see* surface plasmon resonance
  - ssDNA *see* single-stranded DNA
  - Starburst clusters 3
  - Stober's method, dye-doped silica nanoparticles 62
  - streptavidin–gold conjugate 61
  - subcellular distribution, of LHRH-SPIONs 208
  - superparamagnetic iron oxide nanoparticles (SPION) 201
    - LHRH 203–209
  - superparamagnetic iron oxides (SPIO) 126
    - superparamagnetic nanoparticles 126–128
    - surface modification, dendrimers 14
    - surface plasmon resonance (SPR) 58
    - surface-enhanced laser desorption/ionization (SELDI) 349
    - surface-enhanced Raman scattering (SERS) 108
    - surfactants, solubilization of SWNTs 244
    - SWNHs *see* single-wall nanohorns
    - SWNT *see* single-wall nanotubes
    - SWNT field-effect transistors (FETs) 287, 290–291
    - SWNT transporters, gene and drug delivery 252–269
    - SWNT–biomolecular complexes, diffusion 247–251
    - SWNT-BSA complex 248–252
    - SWNT-Cy3-DNA complexes, NIR laser light excitation 271
    - SWNT-LPC complex 241–247
    - SWNT-LPG complex 241–245
    - SWNT-PL-PEG complexes 261–262, 272
    - SWNT-poly(rU) complex 248–258
- t**
- TAAAs *see* tumor associated antigens
  - target antigen, human plasma 362–363
  - target cells 21
  - targeted cancer cell death, carbon nanotubes 310–311
  - targeted delivery, of nanoparticles 188
  - targeted drug delivery, carbon nanotubes 313–314
  - targeting, active 65, 185
    - chemoselective 32
    - ligand-directed 127
    - of metabolically-engineered carbohydrate epitopes 31
    - of specific biomarkers 25–27
    - passive 66, 183–184
    - tumor cells 182–185
  - targeting mechanisms, MRI 124–125
  - TAT-HA2 peptide 308
  - template-synthesized nanotubes and nanorods 318–332
  - TEOS *see* tetraethylorthosilicate
  - 1,4,7,10-tetraazacyclododecane-1,4,7,10-tetraacetic acid (DOTA) 318
  - tetrachloroauric acid (HAuCl<sub>4</sub>) 339
  - tetraethylorthosilicate (TEOS) 62
  - tetramethylorthosilicate (TMOS) 62
  - thiol-derivatized PEG (PT) 97
  - THP-1 cells 245–246



- time-of-flight (TOF) mass spectrometry, matrix-assisted laser desorption/ionization 348
- TIMPs *see* tissue inhibitors of metalloproteases
- tissue inhibitors of metalloproteases (TIMPs) 383–384
- TMOS *see* tetramethylorthosilicate
- TNF *see* tumor necrosis factor
- TOF *see* time-of-flight
- TOP/TOPO-capped Qdots 56
- TOPO *see* trioctylphosphine oxide
- transcription, global pattern 101–104
- trioctylphosphine oxide (TOPO) 344
- tumor associated antigens (TAAs) 26
- tumor cell invasion assays 393–394
- tumor detection, nanoparticles 186–188
- tumor markers 340–341
- tumor morphology 180
- tumor necrosis factor (TNF) 97
- tumor targeting 182–185
- antibody-mediated 66
- tumor–host conspiracy 388
- u**
- U1A antigen-Tween conjugates 269
- ultrasmall superparamagnetic iron oxide (USPIO) nanoparticles 126
- dextran-coated 294
- ultrasonography (US) 48
- up-converting phosphor nanoparticles 70
- urokinase-type plasminogen activator (uPA) 387
- US *see* ultrasonography
- USPIO *see* ultrasmall superparamagnetic iron oxide
- v**
- vaccine delivery, SWNTs 263–265
- vaccines, dendrimer conjugates 19
- vancomycin-conjugated magnetic nanoparticles 309–310
- vascular endothelial growth factor (VEGF) 89, 159–160
- VEGF *see* vascular endothelial growth factor
- VEGF antibody-2C3 (AbVF) 97–98
- VEGF121, activity 94
- VEGF165
- activity 94
- inactivation 92
- signaling events 94–95
- w**
- W/O *see* water-in-oil (W/O)
- water-in-oil (W/O) microemulsion 63
- water-soluble Fe<sub>3</sub>O<sub>4</sub> iron oxide (WSIO) nanocrystals, 2,3-dimercaptosuccinic acid (DMSA)-coated 306
- water-soluble iron oxide nanoparticles (WSIO) 156–157
- water-soluble SWNTs 237–239
- whole blood analysis, nanoprobe-based affinity mass spectrometry 359–364
- WSIO *see* water-soluble iron oxide nanoparticles
- WSIO–antibody conjugates 343
- WSIO–Herceptin conjugates 164–167, 307
- z**
- zinc selenide (ZnSe) 52
- zinc sulfide (ZnS) 52
- in situ* zymography (ISZ) 392–393

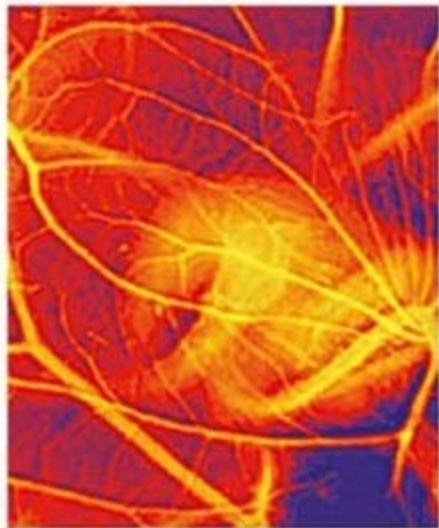


Nanotechnologies for the Life Sciences

Edited by Challa Kumar

WILEY-VCH

# Nanomaterials for Biosensors



**NLS** 

## Contents

**Preface** XV

**List of Authors** XIX

<b>1</b>	<b>Biosensing using Carbon Nanotube Field-effect Transistors</b>	<b>1</b>
	<i>Padmakar D. Kichambare and Alexander Star</i>	
1.1	Overview	1
1.2	Introduction	1
1.3	Carbon Nanotube Field-effect Transistors (NTFETs)	3
1.3.1	Carbon Nanotubes	3
1.3.2	Nanotube Synthesis	4
1.3.3	Fabrication of NTFETs	6
1.4	Sensor Applications of NTFETs	9
1.4.1	Sensitivity of NTFETs to Chemical Environment	9
1.4.2	Bioconjugates of Carbon Nanotubes	12
1.4.3	Protein Detection	14
1.4.4	Detection of Antibody–Antigen Interactions	15
1.4.5	DNA Detection	17
1.4.6	Enzymatic Reactions	19
1.4.7	Glucose Detection	20
1.5	Conclusion and Outlook	21
	References	21
<b>2</b>	<b>Carbon Nanotube-based Sensor</b>	<b>27</b>
	<i>Jian-Shan Ye and Fwu-Shan Sheu</i>	
2.1	Overview	27
2.2	Introduction of Carbon Nanotubes	27
2.3	Growth of Carbon Nanotubes	29
2.4	Methods to Prepare CNTs-based Sensors and Biosensors	29
2.4.1	Individual MWCNTs as Nanoelectrodes	29
2.4.2	Randomly Distributed CNT Electrodes	30
2.4.3	Well-aligned Carbon Nanotube Electrodes	30
2.4.4	Carbon Nanotube Paste Electrodes	31

2.4.5	Screen-printing Carbon Nanotubes	32
2.4.6	Self-assembly of Carbon Nanotubes	33
2.4.7	Carbon Nanotube-packaged Microelectrodes	34
2.5	Application of CNTs-based Electrochemical Sensors and Biosensors	34
2.5.1	Electrochemical and Electrocatalytical Properties of Carbon Nanotubes	34
2.5.2	CNTs-based Electrochemical Biosensors	37
2.6	Functionalization of CNTs	39
2.6.1	Biological Functionalization of CNTs	39
2.6.2	Self-assembly of Surfactant and Lipid Molecules at CNTs	39
2.6.3	Electrochemical Functionalization of CNTs	42
2.6.4	Electrochemical Application of Functionalized CNTs	43
2.6.4.1	Application of Lipid–CNT Nanomaterials in Electrochemical Sensors	43
2.6.4.2	Achieving direct Electron Transfer to Redox Proteins by Functional CNTs	44
2.6.4.3	Biomolecule-functionalized CNTs for Electrochemical Sensors and Biosensors	45
2.7	Conclusions and Future Prospects	48
	Acknowledgments	49
	References	49
<b>3</b>	<b>Nanotubes, Nanowires, and Nanocantilevers in Biosensor Development</b>	<b>56</b>
	<i>Jun Wang, Guodong Liu, and Yuehe Lin</i>	
3.1	Introduction	56
3.2	Carbon Nanotubes in Biosensor Development	57
3.2.1	Preparation and Purification of CNTs	58
3.2.2	Construction of CNT-based Biosensors	60
3.2.2.1	Dispersion and Stabilization by Oxidative Acids	60
3.2.2.2	Dispersion by Surfactant Interaction	61
3.2.2.3	Polymer-assisted Solubilization	61
3.2.2.4	CNT Adsorption on the Transducer Substrate	61
3.2.2.5	Surface Functionalization of CNTs	62
3.2.2.6	Composite Entrapment and CNTs Bulky Electrode Material	63
3.2.2.7	More Sophisticated Surface Tailoring Based on Combination of Co-adsorption, Integration, Prohibition, Spacing, Linkage, Sandwich, Tagging, and other Anchoring Approaches	66
3.2.3	CNT-based Electrochemical Biosensors	69
3.2.3.1	Direct Electrochemistry of Biomolecules on Carbon Nanotubes	69
3.2.3.2	Enzyme/CNTs Biosensors	72
3.2.3.3	DNA and Protein Biosensors	73
3.2.3.4	Immunosensors	74
3.2.4	Flow-injection Analysis	75
3.2.5	Carbon Nanotube Array-based Biosensors	76
3.2.6	Chemiluminescence	80

3.2.7	Field-effect Transistor and Bioelectronics	81
3.3	Nanowires in Biosensor Development	84
3.3.1	Silicon Nanowire-based Biosensors	84
3.3.2	Conducting Polymer Nanowire-based Biosensors	86
3.3.3	Metal Oxide Nanowire-based Biosensors	89
3.4	Nanocantilevers for Biosensors	89
3.5	Summary	90
	Acknowledgments	91
	Glossary	91
	Abbreviations	92
	References	93
<b>4</b>	<b>Fullerene-based Electrochemical Detection Methods for Biosensing</b>	<b>101</b>
	<i>Nikos Chaniotakis</i>	
4.1	Introduction	101
4.2	Aims of the Chapter	101
4.3	Electrochemical Biosensing	103
4.3.1	Making a Biosensor	105
4.4	Evolution of Biosensors	105
4.5	Mediation Process in Biosensors	106
4.5.1	Case A: Non-mediated Biosensor	107
4.5.2	Case B: Mediated Biosensor	108
4.6	Fullerenes	109
4.6.1	Synthesis of Fullerenes	109
4.6.2	Biofunctionalization of Fullerenes	109
4.6.3	Electrochemistry of Fullerenes	113
4.7	Fullerene-mediated Biosensing	114
4.8	Conclusions	118
	References	118
<b>5</b>	<b>Optical Biosensing Based on Metal and Semiconductor Colloidal Nanocrystals</b>	<b>123</b>
	<i>Roberto Comparelli, Maria Lucia Curri, Pantaleo Davide Cozzoli, and Marinella Striccoli</i>	
5.1	Overview	123
5.2	Introduction	123
5.3	Colloidal Nanocrystals	127
5.3.1	Size-dependent Optical Properties	127
5.3.2	Chemical Synthesis	131
5.4	Nanocrystal Functionalization for Biosensing	134
5.4.1	Surface Capping Exchange	135
5.4.2	Coating with a Silica Shell	137
5.4.3	Surface Modification through Hydrophobic Interactions	137
5.5	Optical Techniques	139
5.5.1	Colorimetric Tests	139

5.5.2	Fluorescence	139
5.5.3	Fluorescence Resonance Energy Transfer	141
5.5.4	Fluorescence Lifetime	142
5.5.5	Multiphoton Techniques	145
5.5.6	Metal-enhanced Fluorescence	145
5.5.7	Surface Plasmon Resonance	146
5.5.8	Surface-enhanced Resonance Spectroscopy	149
5.6	Advantages and Disadvantages of Nanocrystals in Optical Detection	152
5.7	Applications	153
5.7.1	Biosensing with Semiconductor Nanocrystals	153
5.7.2	Biosensing with Metallic Nanoparticles	157
5.8	Towards Marketing	162
5.9	Conclusions	164
	References	164
<b>6</b>	<b>Quantum Dot-based Nanobiohybrids for Fluorescent Detection of Molecular and Cellular Biological Targets</b>	<b>175</b>
	<i>Zhivko Zhelev, Rumiana Bakalova, Hideki Ohba, and Yoshinobu Baba</i>	
6.1	Introduction	175
6.2	Quantum Dots – Basic Principles of Design and Synthesis, Optical Properties, and Advantages over Classical Fluorophores	176
6.2.1	Basic Principles of Design and Synthesis of Quantum Dots	176
6.2.2	Optical and Chemical Properties – Advantages Compared with Classical Fluorophores	178
6.3	Quantum Dots for Fluorescent Labeling and Imaging	181
6.3.1	Structure of Quantum Dot Nanobiohybrids for Fluorescent Microscopic Imaging	181
6.3.2	Quantum Dots for Fluorescent Cell Imaging	182
6.3.3	Quantum Dots for Fluorescent Deep-tissue Imaging <i>In Vivo</i>	184
6.3.4	Potential of Quantum Dots for Positron Emission Tomography (PET) and functional Magnetic Resonance Imaging (fMRI)	191
6.4	Quantum Dots for Immunoblot Analysis with Fluorescent Detection	192
6.4.1	Basic Principles of Classical and QD-based Immunoblot Analyses	192
6.4.2	QD-based Immunoblot Analysis of “tracer” Proteins – Privileges over Classical Immunoblot Analysis	194
6.5	Quantum Dots for FRET Analyses, Time-resolved Fluorimetry, and Development of Optical Recognition-based Biosensors	196
6.5.1	Quantum Dots for FRET-based Bioanalyses	196
6.5.2	Quantum Dots for Time-resolved Fluorimetry	197
6.5.3	Quantum Dots for development of New Generation Optical Recognition-based Biosensors	197
6.6	Quantum Dots as New Fluorescent Standards for the Thin Calibration of Fluorescent Instrumentation	201
	References	201

<b>7</b>	<b>Detection of Biological Materials by Gold Nano-biosensor-based Electrochemical Method</b>	<b>208</b>
	<i>Juan Jiang, Manju Basu, Sara Seggerson, Albert Miller, Michael Pugia, and Subhash Basu</i>	
7.1	Introduction	208
7.2	Template Synthesis of Gold Nano-wire Arrays for Biosensor Applications	209
7.2.1	General Template Synthesis	209
7.2.2	Template Formation	212
7.2.3	Fabrication of Gold Nano-wire Arrays (GNW)	214
7.3	Synthesis of a Linker and its Attachment to Gold Posts of GNW followed by Binding to Specific Antibodies	220
7.4	Development of Electrochemical Nano-biosensor for Bacteria Detection	224
7.4.1	General Detections for Biosensors	224
7.4.2	Experimental Conditions	226
7.4.3	Electrochemical Impedance (EIS) Detection of <i>E. coli</i>	227
7.4.3.1	EIS on Flat Gold Surfaces	228
7.4.3.2	EIS on GNW	230
7.4.3.3	EIS on GNW with Al <sub>2</sub> O <sub>3</sub>	230
7.4.4	Summary of EIS Detection of <i>E. coli</i> Bacteria	233
7.5	Conclusions	235
	Acknowledgments	235
	References	236
<b>8</b>	<b>Dendrimer-based Electrochemical Detection Methods</b>	<b>240</b>
	<i>Hak-Sung Kim and Hyun C. Yoon</i>	
8.1	Overview	240
8.2	Introduction	240
8.2.1	Background	240
8.2.2	Dendrimers as a new Constituent of Biocomposite Structures	241
8.3	Applications for Biosensors	242
8.3.1	Bioelectrocatalytic Enzyme Electrodes based on LBL (layer-by-layer) Assembly with Dendrimers	243
8.3.2	Bioelectrocatalytic Immunosensors based on the Dendrimer-associated SAMs	244
8.3.2.1	Affinity Recognition Surface based on the Dendrimer-associated SAMs	244
8.3.2.2	Electrochemical Signaling from Affinity Recognition Reactions	248
8.3.3	Protein Micropatterning on Sensor Surfaces for Multiplexed Analysis	253
8.4	Conclusions	256
	Acknowledgments	256
	References	256



<b>9</b>	<b>Coordinated Biosensors: Integrated Systems for Ultrasensitive Detection of Biomarkers</b>	<b>259</b>
	<i>Joanne I. Yeh</i>	
9.1	Overview	259
9.2	Introduction	260
9.3	Elements of a Nanobiosensor	262
9.3.1	Biomolecular Components	262
9.3.2	Nanoparticles	263
9.3.3	Nanoelectrodes	264
9.4	Coordinated Biosensors	265
9.4.1	Biomolecular Conduits: Signal Transducing Mediators	265
9.4.2	NADH Peroxidase: the Biocatalytic Element	267
9.4.3	Undecagold Nanoparticle: Role in Alignment and Directing Electron Flow	270
9.4.4	Integrated Signals	270
9.5	Conclusion	272
	Acknowledgments	274
	References	274
<b>10</b>	<b>Protein-based Biosensors using Nanomaterials</b>	<b>278</b>
	<i>Genxi Li</i>	
10.1	Introduction	278
10.2	Metal Nanoparticles	279
10.2.1	Gold Nanoparticles	279
10.2.2	Silver Nanoparticles	284
10.2.3	Other Metal Nanomaterials	285
10.3	Metallic Oxide Nanoparticles	285
10.4	Carbon Nanotubes	286
10.5	Nanocomposite Materials	292
10.6	Nanoparticles with Special Functions	293
10.6.1	Semiconductor Nanoparticles	293
10.6.2	Magnetic Nanoparticles	295
10.7	Other Nanomaterials	295
10.8	Conclusion	297
	References	297
<b>11</b>	<b>Biomimetic Nanosensors</b>	<b>311</b>
	<i>Raz Jelinek and Sofiya Kolusheva</i>	
11.1	Introduction	311
11.2	Nanostructures in Biosensor Design	312
11.3	Nanosensors for Probing Biological and Cellular Systems	317
11.4	Biological Components in Nanosensors	323
11.5	Nano-biotechnology and Biomedical Diagnosis	327
11.6	Conclusions and Future Directions	329
	Abbreviations	330
	References	330

<b>12</b>	<b>Reagentless Biosensors Based on Nanoparticles</b>	<b>337</b>
	<i>David E. Benson</i>	
12.1	Introduction	337
12.2	Surface Dielectric Enhancement	339
12.2.1	Gold Nanoparticle Enhanced Surface Plasmon Resonance	340
12.2.2	Carbon Nanotube and Silicon Nanowire Enhanced Conductivity	343
12.2.3	Advantages and Caveats	346
12.3	Catalytic Activation	346
12.3.1	Electrocatalytic Detection	347
12.3.2	Catalytically Enabled Optical and Magnetic Detection	349
12.3.3	Advantages and Caveats	350
12.4	Biomolecule Conformational Modulated Effects	351
12.4.1	Biosensors Based on DNA Conformation Changes	352
12.4.2	Biosensors Based on Protein Conformation Changes	355
12.5	Conclusion	361
	Acknowledgments	362
	References	362
<b>13</b>	<b>Pico/Nanoliter Chamber Array Chips for Single-cell, DNA and Protein Analyses</b>	<b>368</b>
	<i>Shohei Yamamura, Ramachandra Rao Sathuluri, and Eiichi Tamiya</i>	
13.1	Introduction	368
13.2	Multiplexed Polymerase Chain Reaction from A Single Copy DNA using Nanoliter-volume Microchamber Array	369
13.2.1	PCR Microchamber Array Chip System	371
13.2.1.1	Microchamber Array Chip Fabrication	371
13.2.1.2	Sample Loading with a Nanoliter Dispenser	372
13.2.2	Multiplexed Detection of Different Target DNA on a Single Chip	373
13.2.3	On-chip Quantification of Amplified DNA	376
13.3	On-chip Cell-free Protein Synthesis using A Picoliter Chamber Array	378
13.3.1	Cell-free Protein Synthesis Chip Fabrication	379
13.3.2	Cell-free Protein Synthesis using a Microchamber Array	381
13.4	High-throughput Single-cell Analysis System using Pico-liter Microarray	384
13.4.1	Single-cell Microarray Chip Fabrication	386
13.4.2	Pico-liter Microarray for Single-cell Studies	388
13.4.3	Single-cell Microarray System for Analysis of Antigen-specific Single B-cells	389
13.5	Conclusions	392
	Acknowledgments	393
	References	393
	<b>Index</b>	<b>398</b>



## Preface

As we come closer to the completion of the ten-volume series on *Nanotechnologies for the Life Sciences*, I am reminded of a statement by the great scientist Arthur C Clarke who said: “Any sufficiently advanced technology is indistinguishable from magic.” This statement is particularly true in molecular biosensing based on nanomaterials where the detection limits are ‘magically’ becoming smaller and smaller, even reaching zeptomolar concentrations in addition to opening up possibilities for ultra-sensitive multiplexed detection. Thanks to the development of novel concepts such as bio-bar-code assays, nanomaterials-based companies are revolutionizing the commercialization of molecular diagnostics at breathtaking speeds. Therefore, on behalf of a great team of nano researchers who have been involved in the development of nanomaterials for biosensing and particularly those who have contributed to this specific volume, I am pleased to introduce you the 8<sup>th</sup> volume of the series, *Nanomaterials for Biosensors*. We have come a long way in our journey since the publication of the first volume of the series, *Biofunctionalization of Nanomaterials*, into bringing the existing knowledge base of applications of nanotechnologies in biology, biotechnology and medicine on a single platform. The eighth volume has thirteen chapters covering various aspects of biomolecular sensing using a variety of nanomaterials such as carbon nanotubes, nanowires, nanocantilevers, fullerenes, dendrimers in addition to metallic and quantum dot nanoparticles. The most exciting and unique aspect of the book is that it deals with the utilization of nanomaterials not only for enhancing the capabilities in conventional biosensing platforms, but also brings out newer approaches such as biomimetic and reagent-less biosensing.

The first four chapters of the book are dedicated to various modes of biosensing using carbon-based nanomaterials. The first chapter by Padmakar D. Kichambare and Alexander Star from the University of Pittsburgh, USA, provides an overview of recent advances in biodetection using single-walled carbon nanotube field-effect transistors (NTFETs) focusing primarily on fabrication of NTFET devices and how carbon nanotubes can be effectively integrated into conventional electronics for biosensor applications, for example, antibody–antigen interactions, DNA hybridization, glucose detection and enzymatic reactions. The chapter entitled *Biosensing using Carbon Nanotube Field-effect Transistors* provides a promising outlook for novel sensing applications of carbon nanotubes in living systems as

well as new opportunities for CNT-based bioelectronics. In addition to the utility of CNTs as field effect transistors, they can also be used as material of construction as nanoelectrodes, which can be utilized as electrochemical sensing systems. The second chapter, *Carbon Nanotube-based Sensors*, contributed by Jian-Shan Ye and Fwu-Shan Sheu from the National University of Singapore, brings out the importance of various methods utilized for preparing CNT electrodes and different ways to functionalize them for biosensing applications. Particularly interesting in this chapter is the discussion on mechanistic aspects of electrocatalysis by CNTs. The chapter will be very useful for those who are interested in exploiting the electrochemistry of CNTs in molecular diagnostics. Though CNTs are the most well-studied amongst one-dimensional nanomaterials, there are a considerable number of research investigations into exploiting the potential of other 1D nanomaterials like semiconducting nanowires and cantilevers. The third chapter, therefore, is a comprehensive review on silicon nanowires, conducting polymer nanowires, metal oxide nanowires, and nanocantilevers with reference to carbon nanotubes. The chapter, *Nanotubes, Nanowires, and Nanocantilevers in Biosensor Development*, contributed by Jun Wang, Guodong Liu, and Yuehe Lin from Pacific Northwest National Laboratory in Richland, USA, provides up to date information on the development of 1D-nanomaterial-based biosensors. The fourth and final chapter on carbon nanomaterials for biosensing is *Fullerene-based Electrochemical Detection Methods for Biosensing* presented by Nikos Chaniotakis from the University of Crete, Greece. Fullerenes have not received as much attention as CNTs as suitable materials for biosensing, mainly because their physicochemical characteristics are still not very well understood. However, the chapter provides a complete picture on several possibilities for fullerenes to offer new and powerful tools as electrochemical biosensors especially in signal mediation, protein and enzyme functionalization, and light-induced switching.

Nanomaterials also offer opportunities for ultra-sensitive biomolecular sensing through their local field optical effects, which are several orders of magnitude higher than the corresponding bulk effects. Optically active metallic and quantum dot nanomaterials have opened up avenues for newer techniques such as local surface plasmon resonance (LSPR), surface-enhanced Raman scattering (SERS), surface-enhanced fluorescence (SEF), fluorescence resonance energy transfer (FRET), time-resolved fluorimetry, and others. The next two chapters in the book provide an overview of these technologies. The fifth chapter, *Optical Biosensing Based on Metal and Semiconductor Colloidal Nanocrystals* by R. Comparelli, L. Curri, P. D. Cozzoli, and M. Striccoli from the Italian National Research Council's Institute of Physicochemical Processes of CNR in Bari, focuses in general on metal and quantum dot-based optical biosensing, providing a comparative assessment of recent developments categorized into various novel and/or improved optical techniques with traditional methods. The sixth chapter is exclusively dedicated to optical biosensing by quantum dots. Authors Rumiana Bakalova, Zhivko Zhelev, Hideki Ohba, and Yoshinobu Baba from the AIST-Kyushu National Institute of Advanced Science and Technology in Saga and Nagoya University, both in Japan, present an overview on the current status and future trends of QD-based biosensor develop-

ment. The chapter, *Quantum Dot-based Nanobiohybrids for Fluorescent Detection of Molecular and Cellular Biological Targets*, covers not only the basic principles of design and synthesis of highly fluorescent QDs, but also intricacies of *in vitro* and *in vivo* cellular and deep-tissue imaging.

The utility of gold nanoparticles in optical biosensing is very well known and already finding several commercial applications. However, the application of gold nanomaterials' capability as amperometric sensor is only recently being recognized as very promising and powerful tools in bio-fluid or biomaterial investigations and their associated clinical studies. The seventh chapter, *Detection of Biological Materials by Gold Nano-biosensor-based Electrochemical Methods*, provides a review on gold nanowire arrays and their utility as biosensors in bacterial detection. The authors, Juan Jiang, Manju Basu, Sara Seggerson, Albert Miller, Michael Puglia, and Subhash Basu from the university of Notre Dame in Indiana, USA, provides an in-depth analysis of the application of electrochemical impedance spectroscopy (EIS) in gold nanomaterial-based biosensing and demonstrates the technique's potential in clinical laboratories, environmental monitoring and the food industry to achieve rapid and sensitive detection. Continuing on a similar theme related to electrochemical sensing but utilizing dendrimeric nanomaterials, authors Hak-Sung Kim and Hyun C. Yoon from KAIST at Daejeon, Korea, cover various facets of bioelectrocatalytic enzyme sensors in the eighth chapter. *Dendrimer-based Electrochemical Detection Methods* is a must for readers interested in the fabrication of dendrimer-based biocomposite mono-/multilayers and their biosensing applications.

Each of the last five chapters in the book brings out several fascinating facets of nanomaterial-based biosensing very different from what we have seen so far in the first eight chapters. The author of the ninth chapter, *Coordination Biosensors: Integrated Systems for Ultrasensitive Detection of Biomarkers*, Joanne Yeh from the University of Pittsburgh Medical School, USA, presents altogether a different approach to biosensing, utilizing newer concepts to align the signal transduction centers to enhance the kinetics of reactions leading to improved sensitivity of detection. It has been observed that there is a direct electrochemical and catalytic activity of many proteins at electrodes modified with various nanomaterials such as  $\text{TiO}_2$ ,  $\text{ZrO}_2$ ,  $\text{SiO}_2$ ,  $\text{Fe}_3\text{O}_4$ , metal nanoparticles and carbon nanotubes. In the tenth chapter, the author Genxi Li from Nanjing University in China reviews the literature to demonstrate that nanomaterials can not only provide a friendly platform for the assembly of protein molecules but also enhance the electron-transfer process between protein molecules and the electrode. The chapter entitled *Protein-based Biosensors using Nanomaterials* brings out the advantages of combining proteins and nanomaterials to develop sensitive biosensor elements. Proteins and in general various nano-size structures in the field of life sciences provide testimony to the endless possibilities and elegant applications in our day to day world. Therefore, it is not very surprising that a new branch of science, 'Biomimetics', has roots in a variety of scientific disciplines, and the field of biosensors is not an exception. In the eleventh chapter, authors Raz Jelinek and Sofiya Kulusheva from Ben Gurion University of the Negev in Beer-Sheva, Israel, brings out the utility of concepts and methodologies from the biological world into the laboratory. The

chapter, *Biomimetic Nanosensors*, provides a broader perspective on bio-inspired devices and applications related to nanomaterial-based biosensing.

As the title indicates, the twelfth chapter, *Reagentless Biosensors Based on Nanoparticles*, provides the readers with yet another novel concept in biosensing, where sensing tools are being developed based on perturbation of nanoparticle properties, without the need for reagents, in order to produce unique yet sensitive signals for biomeoclecular sensing. The author, David Benson from Wayne State University in Detroit, USA, provides a strong case for adaptation of reagentless concepts that provide sensors that can be adapted to various detection platforms. The book concludes with its thirteenth chapter, wherein the authors, Shohei Yamamura, Sathuluri Ramachandra Rao, and Eiichi Tamiya from Japan Advanced Institute of Science and Technology at Nomi, Japan, bring us closer to biosensing devices incorporating highly integrated microarray systems that can perform assays at pico- and nano-liter volume level. In this chapter, *Pico/Nanoliter Chamber Array Chips for Single-cell, DNA and Protein Analyses*, the authors discuss three very important topics – novel multiplexed PCR, cell-free protein synthesis, and high-throughput single-cell analysis systems using nanolitre microarray platforms.

Nanotechnology embodies the spirit of interdisciplinary approaches and teams. I am, therefore, very grateful to all the authors who have shared my enthusiasm and vision by contributing high-quality manuscripts keeping in tune with the theme of this volume. It is primarily due to their scholarly contributions that this book comes into existence. I am thankful to my employer, the Center for Advanced Microstructures and Devices (CAMD), for providing me with an opportunity to undertake this enormous project. No words can express the understanding of my family, friends, mentors and most importantly the readers who are now an integral part of my existence and continue to shape my life and I am indebted to them. Finally, Wiley-VCH publishers have done a remarkable job and I am grateful for their support.

September 2006  
Baton Rouge

*Challa S. S. R. Kumar*

## 1

## Biosensing using Carbon Nanotube Field-effect Transistors

*Padmakar D. Kichambare and Alexander Star*

## 1.1

### Overview

This chapter covers recent advances in biodetection using single-walled carbon nanotube field-effect transistors (NTFETs). In particular, we describe fabrication of NTFET devices and their application for electronic detection of biomolecules. A typical NTFET fabrication process consists of combination of chemical vapor deposition (CVD) and complementary metal oxide semiconductor (CMOS) processes. The NTFET devices have electronic properties comparable to traditional metal oxide semiconductor field-effect transistors (MOSFETs) and readily respond to changes in the chemical environment, enabling a direct and reliable pathway for detection of biomolecules with extreme sensitivity and selectivity. We address the challenges in effective integration of carbon nanotubes into conventional electronics for biosensor applications. We also discuss in detail recent applications of NTFETs for label-free electronic detection of antibody–antigen interactions, DNA hybridization, and enzymatic reactions.

## 1.2

### Introduction

The interplay between nanomaterials and biological systems forms an emerging research field of broad importance. In particular, novel biosensors based on nanomaterials have received considerable attention [1–4]. Integration of one-dimensional (1D) nanomaterials, such as nanowires, into electric devices offers substantial advantages for the detection of biological species and has significant advantages over the conventional optical biodetection methods [5]. The first advantage is related to size compatibility: Electronic circuits in which the component parts are comparable in size to biological entities ensure appropriate size compatibility between the detector and the detected biological species. The second advantage to developing nanomaterial based electronic detection is that most biological processes involve electrostatic interactions and charge transfer, which are directly



detected by electronic nanocircuits. Nanowire-based electronic devices, therefore, eventually integrate the biology and electronics into a common platform suitable for electronic control and biological sensing as well as bioelectronically driven nanoassembly [6].

One promising approach for the direct electrical detection of biomolecules uses nanowires configured as field-effect transistors (FETs). FETs readily change their conductance upon binding of charged target biomolecules to their receptor linked to the device surfaces. For example, recent studies by Lieber's group have demonstrated the use of silicon nanowire FETs for detecting proteins [7], DNA hybrids [8], and viruses [9]. This biodetection approach may allow in principle selective detection at a single particle levels [10, 11]. Nanowires hold the possibility of very high sensitivity detection owing to the depletion or accumulation of charge carriers, which are caused by binding of a charged biomolecules at the surface. This surface binding can affect the entire cross-sectional conduction pathway of these nanostructures. For some nanowires, such as hollow carbon nanotubes, every atom is on the surface and exposed to the environment; even small changes in the charge environment can drastically change their electrical properties. Thus, among different nanomaterials, carbon nanotubes have a great potential for biosensing.

Among numerous applications of carbon nanotubes [12–14], carbon nanotube based sensing technology is rapidly emerging into an independent research field. As for any new research field, there is no yet consensus in the literature about the exact sensing mechanism. In this chapter, in addition to selected examples of carbon nanotube based sensors, we address the controversial carbon nanotube sensing mechanism.

To date, sensor applications of carbon nanotubes have been summarized and discussed in several excellent review articles [15–17], which primarily focus on carbon nanotube based electrochemical sensors. This chapter covers only recent advances in biodetection using carbon nanotube field-effect transistors (NTFETs). It is divided into two large sections: NTFET fabrication and their sensor applications. Section 1.3 gives a detailed description of NTFET device structure, its fabrication method and introduces device characteristics. This section also addresses technical challenges in effective integration of carbon nanotubes into CMOS electronics. Section 1.4, which focuses on sensor applications of NTFETs, is divided into several subsections. Before discussing NTFET application for biological detection we describe the effect of environmental conditions on NTFET device characteristics. We give selected examples of NTFET sensitivity for small molecules, mobile ions, and water (relative humidity). The effect of these factors should be well understood before NTFET biodetection is reviewed. We also briefly describe the operation of NTFETs in conducting media, which is particularly important for biosensor applications. Then we briefly summarize interactions of carbon nanotubes with biomolecules (e.g., polysaccharides, DNA and proteins) to set a stage for the subsequent subsections that describe in great details recent applications of NTFETs for label-free electronic detection of proteins, antibody–antigen interactions, DNA hybridization, and enzymatic reactions.

### 1.3

## Carbon Nanotube Field-effect Transistors (NTFETs)

### 1.3.1

#### Carbon Nanotubes

Since their discovery by Iijima over a decade ago [18], interest in carbon nanotubes has grown considerably [19]. Recent advances in the synthesis and purification of carbon nanotubes have turned them into commercially available materials. Subsequently, several experiments have been undertaken to study the physical and electrical properties of carbon nanotubes on the individual and macroscopic scale [20–23]. On the macroscopic scale, spectroscopic and optical absorption measurements have been carried out to test the purity of the carbon nanotubes [24, 25]. For electronic transport measurements it is particularly interesting to perform experiments on isolated, individual carbon nanotubes. The properties of carbon nanotubes depend strongly on physical aspects such as their diameter, length, and presence of residual catalyst [12]. The properties measured from a large quantity of nanotubes could be an average of all nanotubes in the sample, so that the unique characteristics of individual carbon nanotubes could be shadowed. Experiments on individual nanotubes are very challenging due to their small size, which prohibits the application of well-established testing techniques. Moreover, their small size also makes their manipulation rather difficult. Specialized techniques are needed to mount or grow an individual carbon nanotube on the electrode with sub-micron precision.

Carbon nanotubes are hollow cylinders made of sheets of carbon atoms and can be divided into single-walled carbon nanotubes (SWNTs) and multi-walled carbon nanotubes (MWNTs). SWNTs possess a cylindrical nanostructure with a high aspect ratio, formed by rolling up a single graphite sheet into a tube (Fig. 1.1). SWNTs are, typically, a few nanometers in diameter and up to several microns long. MWNTs consist of several layers of graphene cylinders that are concentrically nested like rings of a tree trunk, with an interlayer spacing of  $3.4 \text{ \AA}$  [26]. Because of their unique properties, carbon nanotubes have become a material that has generated substantial interest on nanoelectronic devices and nanosensors [27, 28]. These properties are largely dependent upon physical aspects such as diameter, length, presence of catalyst and chirality. For example, SWNT can be metallic or semiconducting, depending upon the intrinsic band gap and helicity [29]. Semiconducting SWNTs can be used to fabricate FET devices, as demonstrated by Dekker and co-workers [30]. In addition, semiconducting SWNTs exhibit significant conductance changes in response to the physisorption of different gases [24, 31, 32]. Therefore, SWNT-based nanosensors can be fabricated based on FET layout, where the solid-state gate is replaced by adsorbed molecules that modulate the nanotube conductance [33]. Since semiconducting SWNTs have a very high mobility and, because all their atoms are located at the surface, they are the perfect nanomaterial for sensors. These sensors offer several advantages for the detection of biological species. First, carbon nanotubes form the conducting channel in a transistor configura-

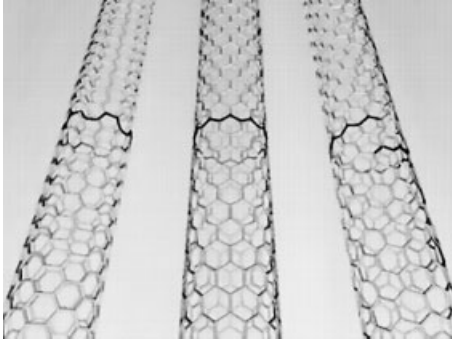


**Fig. 1.1.** A seamlessly rolled-up single graphite sheet forms a single-walled carbon nanotube (SWNT). SWNTs are, typically, a few nanometers in diameter and up to several micrometers long. They can be either metallic

or semiconducting, depending on their helicity and diameter. Semiconducting SWNTs are used for the fabrication of nanotube field-effect transistors (NTFETs). (Adapted with permission from Ref. [4], © Wiley-VCH Verlag).

tion. Second, the nanotubes are typically located on the surface of the supporting substrate and are in direct contact with the environment. This device geometry contrasts with traditional metal oxide semiconductor field-effect transistors (MOSFETs) where the conducting channel is buried in the bulk material in which the depletion layer is formed. Lastly, all of the electrical current flows at the surface of nanotubes. All these remarkable characteristics lead to a FET device configuration that is extremely sensitive to minute variations in the surrounding environment.

### 1.3.2

#### Nanotube Synthesis

Several synthesis methods are used to produce carbon nanotubes [34]. The three most commonly used methods are the arc discharge, laser ablation, and chemical vapor deposition (CVD) techniques. While the arc and laser methods can produce large quantities of carbon nanotubes they lead to resilient contaminants, including pyrolytic and amorphous carbon [35, 36], which are difficult to remove from the sample. Such impurities result in low recovery yield for the carbon nanotube product. However, recent advances in scaling up these methods, as well as development new fabrication methods such as high pressure carbon monoxide (HiPCO), have created commercial supplies of carbon nanotubes with more than 90% purity with competitive prices. In contrast, the less scalable CVD process offers the best chance of obtaining controllable routes for the selective production of carbon nanotubes with defined properties [37]. CVD is catalytically driven, wherein a metal catalyst is used in conjunction with the thermal decomposition of hydrocarbon feedstock gases to produce carbon nanotubes. In most cases, the resultant growth of nanotubes occurs on a fixed substrate within the process. Figure 1.2 illustrates a typical CVD process for the generation of SWNTs. SWNTs are synthesized by the

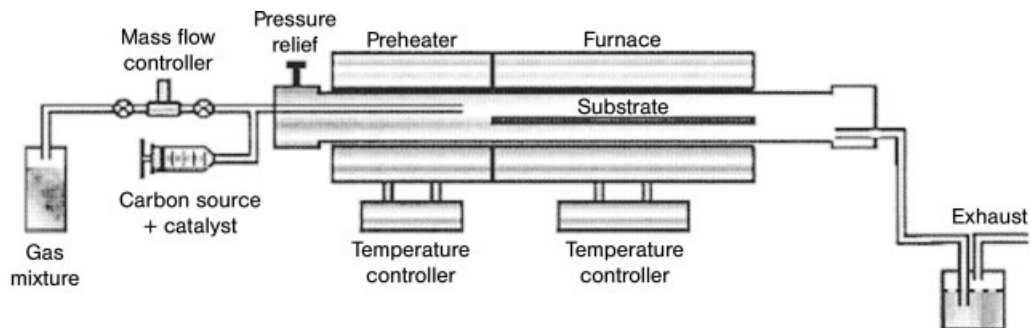


**Fig. 1.2.** Schematic of a chemical vapor deposition (CVD) reactor that uses a two-zone furnace. Carbon nanotubes grow on the substrate placed inside the quartz tube. (Reprinted with permission from Ref. [34], © 2001, CRC Press).

reaction of a hydrocarbon (e.g.,  $\text{CH}_4$ ) vapor over a dispersed Fe catalyst. The synthesis apparatus consists of a quartz tube reactor inside a combined preheater and furnace set-up. The preheat section is operated at  $\sim 200^\circ\text{C}$ . The catalysts are deposited and then hydrocarbon vapors are carried into the reaction zone of the furnace. An  $\text{Ar}/(10\%)\text{-H}_2$  carrier gas is used that controls the partial pressure inside the quartz tube reactor. Reaction temperatures are typically in the range  $900\text{--}1000^\circ\text{C}$ . The SWNTs grow on the substrates (Fig. 1.3) and form thick mats that are readily harvested. This process produces highly pure SWNTs at a yield approaching 50% conversion of all hydrocarbon feedstock into carbon nanotube product. Similarly, a CVD processes sometimes utilize a feed of hydrocarbon-catalyst liquid for the production of nanotubes, and for this purpose a syringe pump is used to allow the continuous injection of this solution into a preheat section. Various gaseous feed-stocks are used to produce nanotubes, ranging from  $\text{CH}_4$  to  $\text{C}_2\text{H}_2$ . A wide range of transition metals and rare earth promoters have been investigated for the synthesis of SWNTs by CVD. In general, a transition metal is the major component in the catalyst particles used regardless of the catalyst support. The most common metals found to be successful in the growth of SWNTs are Fe, Co, and Ni [38, 39]. However, bimetallic catalysts consisting of Fe/Ni, Co/Ni, or Co/Pt [40] are re-



**Fig. 1.3.** Transmission electron microscopy (TEM) image of an SWNT synthesized by chemical vapor deposition (CVD). (Reprinted with permission from Ref. [37], © 2001, The American Chemical Society).

ported to give the best yield of nanotubes, in addition to some rare earth metals that have also been studied [41].

Despite challenges, the understanding the growth mechanism of SWNTs is crucial for, ultimately, tailoring the production of SWNTs with known lengths, diameters, helical structures and placement of SWNTs at the desired location. Presently, efforts are underway to understand the mechanism of catalytic growth of SWNTs on surfaces and the role of impurities and to increase nanotube yield by varying the substrate, catalyst, and growth conditions [42]. Directional growth of SWNTs has been achieved by electric fields [43, 44], gas flow [45], lattice directions [46], and atomic steps [47].

### 1.3.3

#### Fabrication of NTFETs

To date carbon nanotubes have been used to fabricate various devices, including nanotube-based mechanical devices [48] and field emission devices [13]. This section focuses specifically on fabrication of carbon nanotube field-effect transistors (NTFETs). Figure 1.4(a) shows a schematic drawing of NTFET. A semiconducting carbon nanotube is contacted by source and drain electrodes while the gate elec-

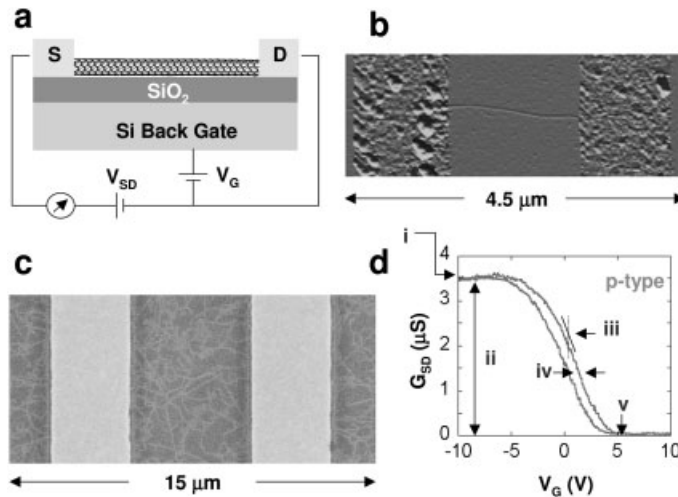


**Fig. 1.4.** (a) Schematic representation of a nanotube field-effect transistor (NTFET) device with a semiconducting SWNT contacted by two Ti/Au electrodes, representing the source (S) and the drain (D) with a Si back gate separated by a SiO<sub>2</sub> insulating layer in a transistor-configured circuit. (b) Atomic force microscopy (AFM) image of a typical NTFET device consisting of a single semiconducting

SWNT. (c) Scanning electron microscopy (SEM) image of a typical NTFET device consisting of a random array of carbon nanotubes. (d) Typical NTFET transfer characteristic – dependence of the source-drain conductance ( $G_{SD}$ ) on the gate voltage ( $V_G$ ) – (i) maximum conductance, (ii) modulation, (iii) transconductance, (iv) hysteresis, and (v) threshold voltage.

trode, which is electrically insulated from the nanotube channel, is used to manipulate the nanotube's conductivity. Depending on the particular method of nanotube fabrication, a NTFET can be structured in different ways [49]. However, most publications on nanotube transistors report the use of a degenerately doped Si-substrate with a comparatively thick (100–500 nm) thermally grown oxide layer [30, 50–53]. Silicon substrates are readily available and can be used with both bulk-produced nanotubes and nanotubes grown directly on the Si-substrate by CVD. If doped highly, the Si substrate stays conductive even at low temperatures, making it usable as a so-called back-gate with the  $\text{SiO}_2$  as a stable, if low-k, gate dielectric. Bulk produced nanotubes (laser ablation [54] or HiPCO [55]) are usually purified and deposited onto Si substrates by suspending them in organic solvents (e.g., chloroform, dichloroethane, etc.) and then spin-coating or drop casting on the substrates. In this approach the nanotubes create a random network over the substrate surface. Alignment of the nanotubes is possible, if an AC dielectric field is applied during deposition [56]. Generally, two different configurations of NTFETs, regarding source and drain contacts, are possible. By patterning the contacts before nanotube deposition [30] one can contact nanotubes in bulk, whereas by depositing the contacts onto the nanotubes one contacts only the ends of nanotubes [57], because depositing contact material on top of the nanotube normally destroys the nanotubes underneath the contacts. The second configuration usually guarantees a lower contact resistance than what is achievable in bulk-contacted devices [58]. Room temperature NTFET manufacturing methods, while compatible with CMOS, are limited by ability to disperse effectively carbon nanotubes in the solution and deposit them without further aggregation on device surfaces [59]. Nanotube bundle formation may decrease the semiconducting character of NTFET due to the occasional presence of nanotube bundles containing metallic nanotubes.

For CVD grown carbon nanotubes metal contacts are deposited onto the nanotubes [60, 61], because typical contact materials cannot withstand CVD temperatures, thus making it impossible to grow carbon nanotubes on CMOS structures. Often, the metal contacts are annealed to lower contact resistance [62]. Several studies have tried to optimize the material used for the contacts, including Cr/Au [49] and Pt [30], but only the Cr/Au contacts have been used widely. In this type of contact the chromium layer is a thin (1–3 nm) adhesion layer that facilitates adhesion of the gold to  $\text{SiO}_2$ . An adhesion layer of Ti [63], especially when annealed, allows deposition of smooth films of many metals onto carbon nanotubes because Ti forms titanium carbide at the interface with the nanotube. For this reason, Ti/Au-contacts are another frequently used combination of contact materials. Many publications investigating Schottky barriers between a nanotube and its contacts [61, 64] have employed such contacts. Palladium (Pd) is another material investigated that wets nanotubes well and has been used recently to produce NTFETs with ohmic contacts, i.e., contacts without Schottky barriers [52, 63].

Depending on the number of carbon nanotubes connecting the source and drain electrodes, there are two different device architectures. In the first device architecture, a single nanotube connects the source and drain (Fig. 1.4b). These devices have been used for biosensing with excellent sensitivity. However, there is substan-

tial variation between the different devices that are fabricated and this variation is reflected in the electronic characteristics of individual nanotubes. In addition, the interface between the nanotube and the metallic contact may vary from device to device. Specialized techniques are needed either to mount or grow an individual carbon nanotube at a predetermined location. Placement is difficult and impractical for mass fabrication of NTFETs. For example, although the process of attaching a carbon nanotube strand via arc-discharge or contact method to sharp metal probe is fast, simple and economical it suffers from low yield. Therefore, it is difficult to determine the quality of carbon nanotube strand attached to metal tip unless examined under SEM. When checked under SEM a large percentage of the metal probes have multiple nanotubes attached or clusters of amorphous carbon accompanying the carbon nanotubes [65]. Hence random networks of SWNTs have been explored as an alternative [66].

Nanotube networks take up more space than individual SWNTs, but they are much easier to fabricate and show great promise towards simple mass fabrication of NTFETs. In this second configuration, the devices contain a random array of nanotubes between source and drain electrodes (Fig. 1.4c). In this configuration, current flows along several conducting channels that determine the overall device resistance. The device characteristics depend on the number of nanotubes and density of the nanotube network. It is reported that the conductance drops are associated with junctions formed by crossed semiconducting and metallic nanotubes. Local conductance is more dependent on the number of connections to the specific area; clusters of nanotubes with many paths to the electrode have significantly higher conductance than those parts of the network connected through fewer paths. Areas with low conductance typically only have two to three connections to the network, thus it is likely that these connections are dominated by the presence of highly resistive metallic/semiconducting junctions. When a sufficient back gate voltage is applied to the sample, current flow through the semiconducting tubes is suppressed. Using this technique, differences between metallic and semiconducting SWNT can be distinguished. This type of device configuration, containing a network of conducting nanotube channels, is less sensitive than devices made of single nanotubes. In both types of device configurations, the parameter used for detection is the transfer characteristic – the dependence of either the source-drain current ( $I_{SD}$ ) or conductance ( $G_{SD}$ ) (for a fixed source-drain voltage  $V_{SD}$ ) on the gate voltage ( $V_G$ ) (Fig. 1.4d).

NTFETs can operate as p-type or n-type transistors. The mode of operation can be changed from the pristine p-type to n-type by either adding electron donor molecules (n-doping) or removing adsorbed oxygen by annealing the contacts under vacuum [67]. Polymer-gated NTFETs can also tune their modes of operation: a change in the chemical group of the polymer changes the NTFET from p-type to n-type [68, 69]. Oxygen doping was attributed to the fact that the oxygen interacts with the nanotube–metal junction and causes the p-type characteristic for NTFETs in air by pinning the metal's Fermi level near the nanotube's valance band maximum [33]. However, there is no apparent consensus in the literature about the exact mechanism of chemical sensitivity of NTFETs.

## 1.4

### Sensor Applications of NTFETs

Before discussing NTFET applications for biological detection we first describe the effect of small molecules, relative humidity, and conductive liquid media on NTFET devices characteristics. Effect of these factors should be well understood before NTFET biodetection is reviewed.

#### 1.4.1

#### Sensitivity of NTFETs to Chemical Environment

Generally, the molecular species in the ambient environment have a significant impact on the electrical properties of NTFETs. The conductance of semiconducting SWNTs can be substantially increased or decreased by exposure to  $\text{NO}_2$  or  $\text{NH}_3$  [24]. Exposure to  $\text{NH}_3$  effectively shifts the valance band of the nanotube away from the Fermi level, resulting in hole depletion and reduced conductance. In contrast, on exposure to  $\text{NO}_2$  molecules the conductance of nanotubes increases by three orders of magnitude [70]. Here, exposure of the initially depleted sample to  $\text{NO}_2$  resulted in the nanotube Fermi level shifting closer to the valence band. This caused enriched hole carriers in the nanotube and enhanced sample conductance. These results show that molecular gating effects can shift the Fermi level of semiconducting SWNTs and modulate the resistance of the sample by several orders of magnitude.

The electronic properties of SWNTs are also extremely sensitive to air or oxygen exposure [33]. Isolated semiconducting nanotubes can be converted into apparent metals through room temperature exposure to oxygen. As the surrounding medium was cycled between vacuum and air, a rapid and reversible change in the SWNT resistance occurred in step with the changing environment. Initially, in a pure atmospheric pressure oxygen environment, the thermoelectric power (TEP)  $S$  was positive with a magnitude of nearly  $+20 \text{ mV K}^{-1}$ . This relatively large positive TEP is consistent with that reported for pristine SWNTs near room temperature [71]. As oxygen was gradually removed from the chamber, the TEP changed continuously from positive to negative, with a final equilibrium value of approximately  $-10 \text{ } \mu\text{V K}^{-1}$ . When oxygen was reintroduced into the chamber, the TEP reversed sign and once again became positive. These dramatic 10–15% variations in  $R$  and change in sign of the TEP demonstrate that SWNTs are exceptionally sensitive to oxygen.

In the carbon nanotubes sensors mentioned above, chemical sensing experiments have been conducted with devices in which both nanotubes and nanotube–metal contacts were directly exposed to the environment. The sensing could be dominated by the interaction of molecules with the metal contacts or the contact interfaces. Adsorbed molecules would modify the metal work functions and, thereby, the Schottky barrier [72, 73]. Heinze et al. [64] have assigned the effect of oxygen to the Schottky barrier. Recently, a new device architecture has been studied in which the interface between the metallic contacts and nanotubes is covered by a



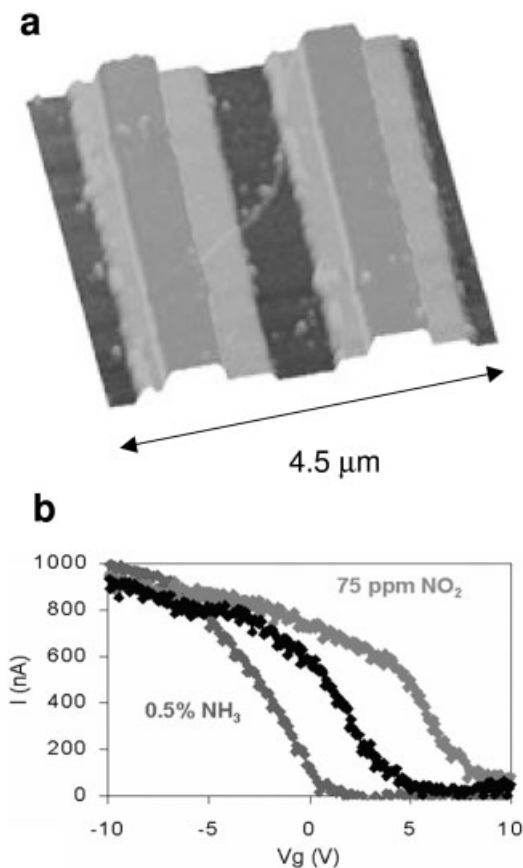


**Fig. 1.5.** (a) AFM image of a contact passivated NTFET device covered with poly(ethylene imine). (b)  $I_{SD}-V_G$  dependence for the device in vacuum (center curve), as well as in  $\text{NH}_3$  and  $\text{NO}_2$  gases. (Adapted with permission from Ref. [74], © 2003 American Institute of Physics).

passivation layer, referred to as contact-passivated [74]. In this configuration, with the junction isolated and only the central length of the nanotube channels exposed, the contacts should be isolated from the effect of chemicals. At the same time, the section of the device that is open to the environment can be doped via charge transfer. NTFETs with such configuration have been investigated by measuring sensitivity to  $\text{NH}_3$ ,  $\text{NO}_2$ , and poly(ethylene imine) (Fig. 1.5).

The NTFET devices were fabricated using SWNTs grown by CVD on 200 nm of silicon dioxide on doped silicon from iron nanoparticles as described in Section 1.3.1. These particles were exposed to flowing hydrocarbon to grow carbon nanotubes, and after growth optical lithography was used to pattern electrical leads (35 nm titanium capped with 5 nm gold) on top of the nanotubes. Contact passiva-

tion was achieved by 70 nm silicon monoxide layer. Source and drain electrodes were separated by nearly a micrometer. The dependence of the source-drain current ( $I_{SD}$ ) as function of the gate voltage ( $V_G$ ) was measured from +10 to -10 V using a semiconductor parameter analyzer in air/water/gas mixtures. The low concentrations of gas mixtures could be introduced to the devices by mixing different proportions of air and gases. The contact-passivated devices demonstrated  $\text{NH}_3$  and  $\text{NO}_2$  sensitivity similar to regular NTFETs. Poly(ethylene imine) also produced negative threshold shifts of tens of volts, despite being in contact with only the center region of devices. Thus, the NTFET sensor character was preserved despite isolating Schottky barriers.

Several groups have reported that NTFET fabricated on  $\text{SiO}_2/\text{Si}$  substrates exhibits hysteresis in current versus gate-voltage characteristics and attributed the hysteresis to charge traps in bulk  $\text{SiO}_2$ , oxygen-related defect trap sites near nanotubes, or the traps at the  $\text{SiO}_2/\text{Si}$  interface. It is mentioned that thermally grown  $\text{SiO}_2$  surface consists of Si-OH silanol groups and is hydrated by a network of water molecules that are hydrogen bonded to the silanols. The CVD nanotube growth condition (900 °C) may dehydrate the surface and condense to form Si-O-Si siloxanes. When such a surface is exposed to and stored in ambient air, the surface siloxanes on the substrate react with water and gradually revert to Si-OH, after which the substrate becomes rehydrated. Heating under dry conditions significantly removes water and reduces hysteresis in the transistors.

Kim et al. have reported that the hysteresis in electrical characteristics of NTFETs is due to charge trapping by water molecules around the nanotubes, including  $\text{SiO}_2$  surface-bound water proximal to the nanotubes [75]. They have demonstrated that coating nanotube devices with PMMA can afford nearly hysteresis-free NTFETs [75]. This passivation is attributed to two factors. First, the ester groups of poly(methyl methacrylate) (PMMA) can hydrogen bond with silanol group on  $\text{SiO}_2$ . Baking at 150 °C combined with the polymer-SiO<sub>2</sub> interaction can significantly remove the silanol-bound water. Second, PMMA is hydrophobic and can keep water in the environment from permeating the PMMA and adsorbing on the nanotube in a significant manner.

Bradley et al. have attributed hysteresis in NTFET devices to cation diffusion [76], based on the following experiments. First, NTFET devices that exhibit very small hysteresis were fabricated. Subsequently, these devices were modified by the addition of an electrolyte coating that created mobile ions on the surface of the device and resulted in the large hysteresis. Experiments were also conducted to explore possible mechanisms for cation-induced hysteresis by varying the humidity that changes the hydration layer around the nanotubes, thus leading to the increase of the ionic mobility. The hysteresis has been found to be sensitive to humidity on sub-second time scales, showing promise as a humidity sensor [77].

Sensitivity of NTFETs to charges as well as NTFET operation in conducting liquid media is important for biosensor design where the sensor should operate in physiological buffers with complex mixtures of biomolecules. Figure 1.6 shows a typical transfer characteristic of NTFET measured in air and water using the silicon and water as the gate electrode, respectively. The change in device characteris-

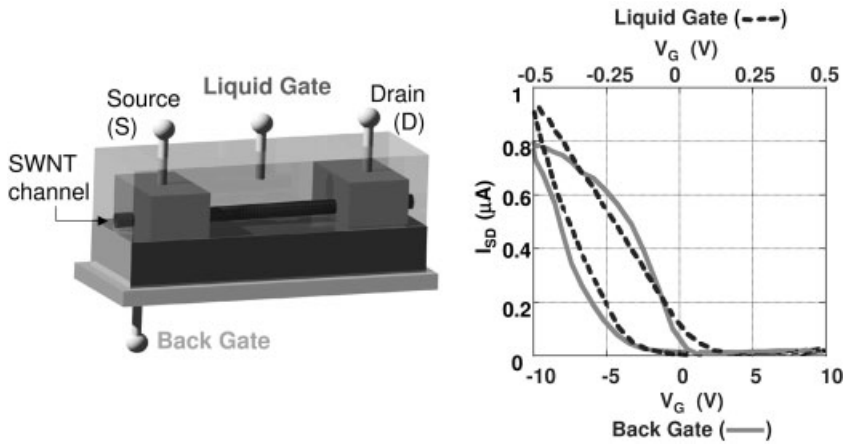


**Fig. 1.6.** (a) Detection in liquid with NTFET devices by using either the back gate or liquid gate configuration. (b) NTFET transfer characteristics in air (solid line), using the back gate, and in water (dashed line), using

the liquid gate. Note the different x-scales for the back and liquid gates. (Adapted with permission from Ref. [93], © 2003, The American Physical Society.)

tics upon exposure to a water/gas mixture is reflected in the transfer characteristics. Saline or electrolytes can also gate NTFETs and give high transconductance [62, 78].

#### 1.4.2

#### Bioconjugates of Carbon Nanotubes

Numerous reports demonstrate the ability to chemically functionalize nanotubes for biological applications [79, 80]. Such chemistry is readily transferable to many applications, ranging from sensors [81, 82] to electronic devices [83]. SWNTs are chemically stable and highly hydrophobic. Therefore, they require surface modification to establish effective SWNT–biomolecule interaction.

So far, two methods of exohedral functionalization of SWNTs have been developed – namely covalent and noncovalent. While covalent modifications [84] are often effective at introducing functionality, they impair the desirable mechanical and electronic properties of SWNTs. Noncovalent modifications [85], however, not only improve the solubility of SWNTs in water, but they also constitute non-destructive processes, which preserve the primary structures of the SWNTs, along with their unique mechanical and electronic properties.

Previously, it has been shown that polysaccharides such as starch [86, 82, 83], gum Arabic [84], and the  $\beta$ -1,3-glucans, curdlan and schizophyllan [85], will solubilize SWNTs in water. It has been proposed that at least some of these polymers achieve their goal by wrapping themselves in helical fashion around SWNTs (Fig.

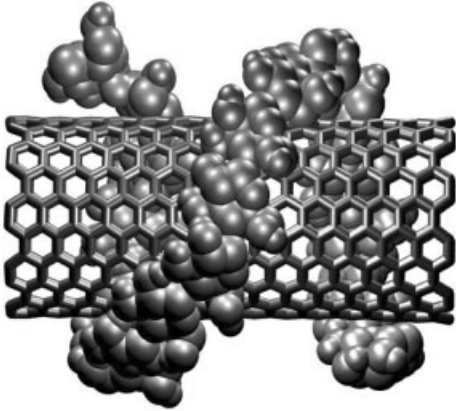


Fig. 1.7. Molecular model of SWNT wrapped in an amylose coil. (Reprinted from Ref. [79], © 2002, The American Chemical Society.)

1.7). Solubilization of the SWNTs with cyclodextrins (CD), which are macrocyclic polysaccharides, has been also investigated [86]. The observed aqueous solubility of SWNTs with  $\gamma$ -CD is unlikely due to encapsulation because the inner cavity dimensions of this CD are far too small to allow it to thread onto even the smallest diameter SWNTs. More recently, however, it has been shown [87] that  $\eta$ -CD, which has 12  $\alpha$ 1,4-linked D-glucopyranose residues and therefore is large enough, does thread onto SWNTs in water, not only solubilizing the NTs but also permitting some partial separations according to their diameters.

Nucleic acids, such as single-stranded DNA, short double-stranded DNA, and some total RNA can also disperse SWNTs in water [88, 89]. Molecular modeling has shown [20] that the non-specific DNA–SWNT interactions in water are from the nucleic acid–base stacking on the nanotube surface, resulting in the hydrophilic sugar–phosphate backbone pointing to the exterior to achieve the solubility in water. The mode of interaction could be helical wrapping or simple surface adsorption. The charge differences among the DNA–SWNT conjugates, which are associated with the negatively charged phosphate groups of DNA and the different electronic properties of SWNTs, have allowed post-production preparation of samples enriched in metallic and semiconducting SWNTs.

Various proteins can also strongly bind to the nanotube exterior surface via non-specific adsorption. Proteins such as streptavidin and HupR crystallize in helical fashion, resulting in ordered arrays of proteins on the nanotube surface [90]. Mechanistically, the non-specific adsorption of proteins onto the nanotube surface may be more complicated than the widely attributed hydrophobic interactions. Quite possibly, the observed substantial protein adsorption is, at least in part, associated with the amino affinity of carbon nanotubes, as was demonstrated recently by monitoring the conductance change in the carbon nanotube [91]. Also, inter-

molecular interactions involving aromatic amino acids, i.e., histidine and tryptophan, in the polypeptide chains of the proteins can contribute to the observed affinity of the peptides to carbon nanotubes [92].

### 1.4.3

#### Protein Detection

Carbon nanotube interactions with proteins have been explored by NTFET devices [91]. In NTFET devices, the ability to measure the electronic properties of the nanotube allowed to query the electronic state of the immobilization substrate. In that work two types of measurements of the device transfer characteristics were performed. In the first measurement, referred to as a substrate-gate transfer characteristic, the current through the drain contact (at fixed source-drain bias) was monitored while a variable gate voltage was applied through a metallic gate buried underneath the SiO<sub>2</sub> substrate. In the second measurement, referred to as liquid-gate transfer characteristics, the device was immersed in a buffer solution and a variable gate voltage was applied through a platinum electrode. The current was passed through the drain contact and a silver reference electrode in the solution. During these measurements, the assembly was shaken gently, using a lab rotator at 3 Hz. The effect of protein adsorption was studied with both measurements. Devices were incubated with streptavidin (40 nm) in 15 mM phosphate buffer at 25 °C. Liquid-gate transfer characteristics were measured continually during the incubations. After 10 h, the devices were rinsed with distilled water and blown dry, and the substrate-gated transfer characteristics of the dried devices were measured.

These results were discussed in terms of a simple model in which adsorbed streptavidin coats the single-walled nanotube (Fig. 1.8). The gradual shift in the threshold voltage is assumed to result from the slow accumulation of a full monolayer of adsorbed protein. This coverage-dependent threshold shift is analogous

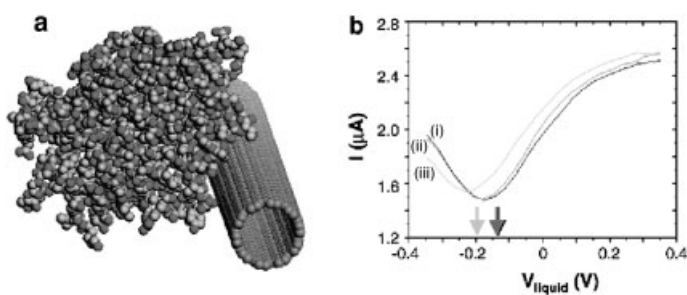


**Fig. 1.8.** (a) Size comparison between a carbon nanotube and a streptavidin molecule. (b) Current versus gate voltage for a nanotube device;  $V_{\text{SD}} = 10$  mV. (ii) In phosphate buffer before streptavidin addition. (i) same conditions, to measure the uncertainty in the

threshold voltage. (iii) After 10 h of incubation with streptavidin. Arrows indicate the threshold voltages for the three curves [the arrow for (i) is behind that for (ii)]. (Adapted with permission from Ref. [91], © 2003, The American Chemical Society.)

to the concentration-dependent shift observed when such devices are exposed to aqueous ammonia [93]. The protein adsorbate equilibrates over several hours so that only the full monolayer can be conclusively determined. Such protein monolayers form under various conditions at interfaces that permit protein crystallization, including sidewalls of MWNTs [90, 94]. The results support the proposal that conductance changes are due to charge injection or field effects caused by proteins adsorbed solely along the lengths of the nanotubes.

Protein adsorption on NTFET leads to appreciable changes in the electrical conductance of the devices that can be exploited for label-free detection of biomolecules with a high potential for miniaturization. For example, Dai and coworkers [95] have used a sensor design consisting of an array of four NTFET sensors on SiO<sub>2</sub>/Si chips. Each NTFET consists of multiple SWNTs connected roughly in parallel across two closely spaced bridging metal electrodes. Three types of devices with different surface functional groups were prepared for the investigation of the biosensing: (1) unmodified as-made devices, (2) devices fabricated with mPEG-SH SAMs formed on, and only on, the metal contact electrodes and, lastly, (3) devices with mPEG-SH SAMs on the metal contacts and a Tween 20 coating on the carbon nanotubes. Electrical conductance of these devices upon the addition of various protein molecules was monitored. While device type 1 showed a significant conductance change with protein adsorption, device type 2 with an mPEG-SH SAM on the metal electrodes did not give any conductance change, except in the case of the protein avidin. It was reported that the metal–nanotube interface or contact region is highly susceptible to modulation by adsorbed species [64]. Modulation of metal work function can alter the Schottky barrier of the metal–nanotube interface, thus leading to a significant change in the nature of contacts and, consequently, a change in the conductance of the devices.

*In situ* detection of a small number of proteins by directly measuring the electron transport properties of a single SWNT has been reported by Nagahara and coworkers [96]. Cytochrome *c* (cytc) adsorption onto individual NTFET has been detected via the changes in the electron transport properties of the transistors. The adsorption of cytc induces a decrease in the conductance of the NTFET devices, corresponding to a few tens of molecules. This experiment was carried out by measuring the conductance versus electrochemical potential of the SWNT with respect to a reference electrode inserted in the solution, and observed a negative shift in the conductance versus potential plot upon protein adsorption. The number of adsorbed proteins has been estimated from this shift.

#### 1.4.4

#### Detection of Antibody–Antigen Interactions

Specific sensitivity can be achieved by employing recognition layers that induce chemical reactions and modify the transfer characteristics. In this two-layer architecture carbon nanotubes function as extremely sensitive transducers while the recognition layer provides chemical selectivity and prevents non-specific binding that is common for complex biological samples.

Following this design, nanotubes have been functionalized to be biocompatible and to be capable of recognizing proteins. This functionalization has involved noncovalent binding between a bifunctional molecule and a nanotube to anchor a bioreceptor molecule with a high degree of control and specificity. Star and co-workers have fabricated [97] NTFET devices sensitive to streptavidin using a biotin-functionalized carbon nanotube bridging two microelectrodes (source and drain, Fig. 1.9a). The SWNT in the NTFET device was coated with a mixture of two polymers, poly(ethyleneimine) and poly(ethylene glycol). The former provided amino groups for the coupling of biotin-*N*-hydroxysuccinimide ester (Fig. 1.9b) and the latter prevented the nonspecific adsorption of proteins on the functionalized carbon nanotube. Figure 1.9(c) shows an AFM image of the device after its exposure to streptavidin labeled with gold nanoparticles (10 nm). Lighter dots represent gold nanoparticles and indicate the presence of streptavidin bound to the

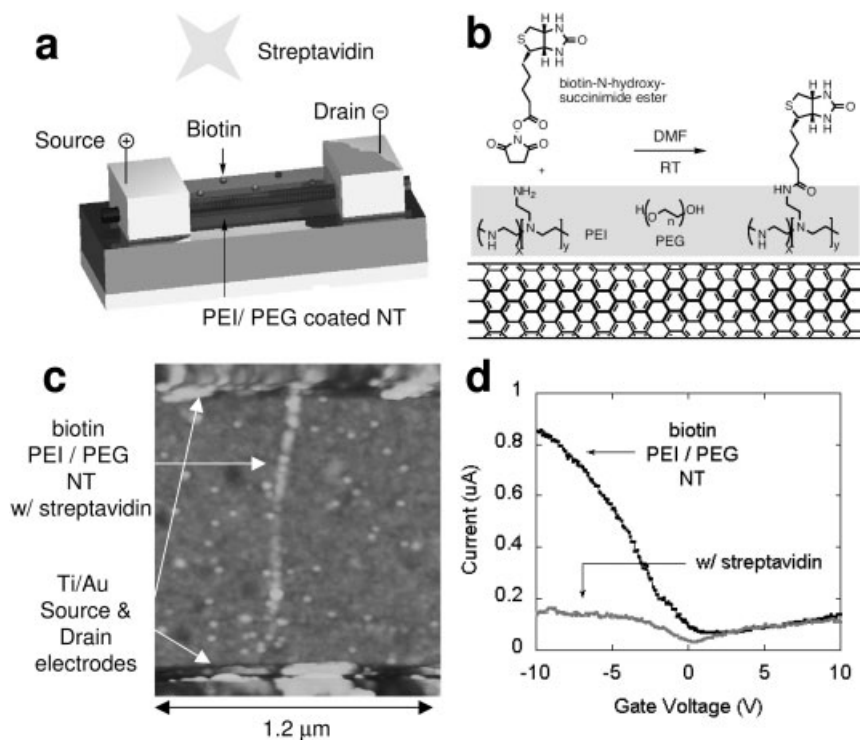


**Fig. 1.9.** (a) Schematic of NTFET coated with a biotinylated polymer layer for specific streptavidin binding. (b) Biotinylation reaction of the polymer layer (PEI/PEG) on the side-wall of the SWNT. (c) AFM image of the polymer-coated and biotinylated NTFET device after exposure to streptavidin labeled with gold

nanoparticles (10 nm in diameter). (d) Source-drain current dependence on gate voltage of the NTFET device based on SWNTs functionalized with biotin in both the absence and presence of streptavidin. (Adapted with permission from Ref. [97], © 2003, The American Chemical Society.)

biotinylated carbon nanotube. The source-drain current dependence on the gate voltage of the NTFET shows a significant change upon the streptavidin binding to the biotin-functionalized carbon nanotube (Fig. 1.9d). The experiments reveal the specific binding of the streptavidin, which occurs only at the biotinylated interface.

The mechanism of the biodetection was explained in terms of the effect of the electron doping of the carbon nanotube channel upon the binding of the charged streptavidin molecules. Dai and coworkers [98] have also analyzed specific antigen–antibody interactions using NTFET devices. In particular, they have studied the affinity binding of 10E3 mAbs antibody (a prototype target of the autoimmune response in patients with systematic lupus erythematosus and mixed connective tissue disease) to human auto antigen U1A.

#### 1.4.5

#### DNA Detection

DNA biosensors based on nucleic acid recognition processes are quickly being developed towards the goal of rapid, simple and inexpensive testing of genetic and infectious diseases. To date, there are several reports on the electrochemical detection of DNA hybridization using multi-walled carbon nanotube (MWNT) electrodes [99]. Whereas electrochemical methods rely on the electrochemical behavior of the labels, measurements of the direct electron transfer between SWNTs and DNA molecules paves the way for label-free DNA detection (Fig. 1.10). To illustrate the practical utility of this new nanoelectronic detection method, an allele-specific assay to detect the presence of SNPs using NTFETs has been recently developed [100]. This DNA assay targeted the H63D polymorphism in the human HFE gene, which is associated with hereditary hemochromatosis, a common and easily treated disease of iron metabolism [101, 102].

DNA sensing mechanism using NTFETs has been recently explored by selective attachment of DNA molecules at different device segments. Tang et al. [103] have found that DNA hybridization on gold electrodes rather than on SWNT sidewalls is mainly responsible for NTFET detection due to Schottky barrier modulation. In another approach, DNA hybridization occurs on the surface at the gate of NTFET [104]. As a result, the conductance in SWNTs was changed through the gate insulators. In the work, the 5' end-amino modified peptide nucleic acid (PNA) oligonucleotides were covalently immobilized onto the Au surfaces of the back gate of NTFETs. PNA is a synthetic analog of DNA, in which both the phosphate and the deoxyribose of the DNA backbone are replaced by a polypeptide. PNA mimics the behavior of DNA and hybridizes with complementary DNA or RNA sequences, thus enabling PNA chips to be used in biosensors. The micro-flow chip was fabricated by using poly(dimethylsiloxane) (PDMS) prepolymer. The NTFET nano-sensor array was placed onto the PDMS chip in such a way that the PNA probe-modified Au side was positioned to face the open chamber for the introduction of solutions and the electrical measurements. A PNA probe with the base sequence 5'-NH<sub>2</sub>-ACC ACC ACT TC-3', which was fully complementary to the tumor necro-



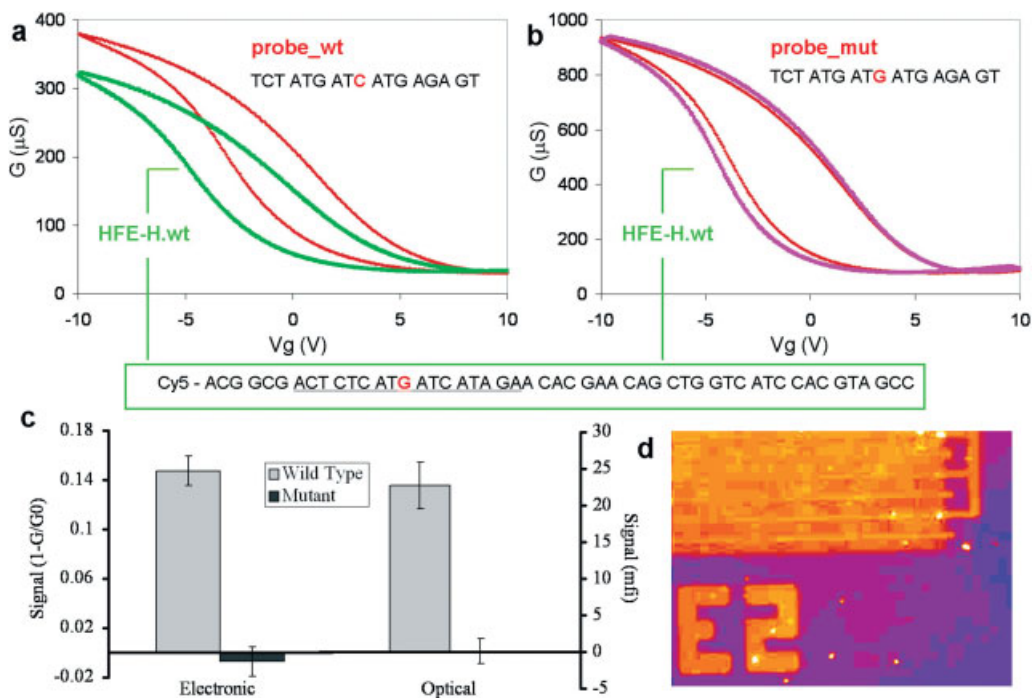


**Fig. 1.10.** Label-free detection of DNA hybridization using NTFET devices. (a)  $G-V_g$  curves after incubation with allele-specific wild-type capture probe and after challenging the device with wild-type synthetic HFE target (50 nm). (b)  $G-V_g$  curves in the experiment with mutant capture probe. (c) Graph with electronic ( $1 - G/G_0$ ) and fluorescent

responses in SNP detection assays. (d) Fluorescence microscopy image of the NTFET network device, with the electrodes 10 nm apart, after incubation with Cy5-labeled DNA molecules. (Adapted with permission from Ref. [100], © 2006, The National Academy of Sciences of the USA.)

sis factor- $\alpha$  (TNF- $\alpha$ ) gene sequence, was used as a model system. The base sequence for full complementary target DNA was 5'-GGT TTC GAA GTG GTG GTC TTG-3' while the non-complementary DNA oligonucleotide sequence was 5'-CCC TAA GCC CCC AA-3'.

The electrical properties of the NTFET devices were measured at room temperature in air. First, the blank PBS solution was introduced into the PDMS-based micro flow chip, revealing that no substantial change in the source-drain current of NTFET was obtained. The current increased dramatically while monitoring in real time for about 3 h. The increase in conductance for the p-type NTFET device was consistent with an increase in negative surface charge density associated with binding of negatively charged oligonucleotides at the surface. DNA hybridization can be detected by measuring the electrical characteristics of NTFETs, and SWNT based FET can be employed for label-free, direct real time electrical detection of biomolecule binding.

## 1.4.6

**Enzymatic Reactions**

SWNTs can be made water soluble by wrapping in amylose (linear component of starch) [86]. These SWNT solutions are stable for weeks, provided nobody spits on them. Indeed, the addition of saliva, which contains  $\alpha$ -amylase, precipitates the nanotubes as the enzyme breaks amylose down into smaller carbohydrate fragments, finally resulting in the formation of glucose. The enzymatic degradation of starch has been recently monitored electronically using NTFETs [105]. Figure 1.11(a) shows the experimental setup used for this study. NTFET devices display transconductance and source-drain current–voltage characteristics typical of the p-type device behavior. The device characteristics, i.e., the source-drain current  $I_{SD}$  as a function of the gate voltage  $V_G$ , were measured to evaluate the effect of starch deposition and the subsequent enzymatic degradation of the starch layer on the carbon nanotubes.

Starch was deposited onto the FET by soaking the silicon wafer in a 5% aqueous starch solution and the device characteristics were found to be shifted by approxi-

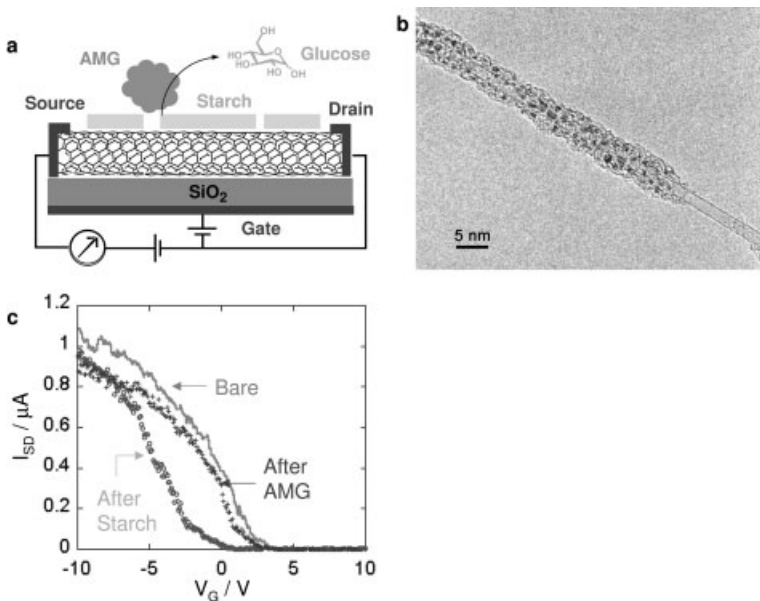


**Fig. 1.11.** (a) NTFET device for electronic monitoring of the enzymatic degradation of starch with amyloglucosidase (AMG) to glucose. (b) High-resolution transmission electron microscopy (HRTEM) image of a SWNT (2.0 nm diameter) after treatment with a drop of a 1% of an aqueous solution of starch. The starch had been stained with  $\text{RuO}_4$

vapor. (c) NTFET device characteristics in the form of  $I_{SD}-V_G$  curves measured from +10 to  $-10$  V gate voltage with a +0.6 V bias voltage before (bare) and after starch deposition, as well as after hydrolysis with AMG. (Adapted with permission from Ref. [104], © 2004, The American Chemical Society.)

mately 2 V toward more negative gate voltages. The direction of the shift equates with electron doping of the nanotube channel by the polysaccharide. Quantitatively similar doping effects have been observed when carbon nanotube FET devices were exposed to  $\text{NH}_3$  gas, amines [106], poly(ethylene imine) (PEI) [107], and proteins [91]. After the enzyme-catalyzed reaction had been performed on the starch-functionalized devices and washed with buffer, the  $I_{\text{SD}}$  vs.  $V_{\text{G}}$  characteristics recovered almost completely to the trace recorded before starch deposition (Fig. 1.11). This indicates that, during the enzyme-catalyzed reaction, nearly all the starch deposited on the surface of the nanotube device is hydrolyzed to glucose which is washed off by the buffer prior to the electronic measurements.

#### 1.4.7

##### Glucose Detection

The diagnosis and management of diabetes mellitus requires a tight monitoring of blood glucose levels. Dekker and coworkers have demonstrated the use of individual semiconducting SWNT as a versatile biosensor [108]. The redox enzyme glucose oxidase ( $\text{GO}_x$ ) that catalyses the oxidation of  $\beta$ -D-glucose ( $\text{C}_6\text{H}_{12}\text{O}_6$ ) to D-glucono-1,5-lactone ( $\text{C}_6\text{H}_{10}\text{O}_6$ ) has been studied. The redox enzymes go through a catalytic reaction cycle where groups in the enzyme temporarily change their charge state and conformational changes occur in the enzyme that can be detected using NTFET devices.

In addition to pH sensitivity,  $\text{GO}_x$ -coated semiconducting SWNTs appeared to be sensitive to glucose, the substrate of  $\text{GO}_x$ . Figure 1.12 exhibits real-time measure-

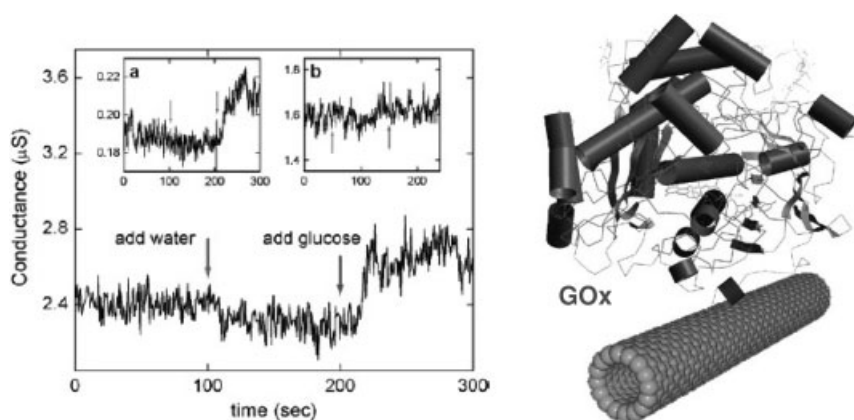


**Fig. 1.12.** Real time electronic response of the NTFET sensor to glucose, the substrate of glucose oxidase ( $\text{GO}_x$ ). The conductance of a semiconducting SWNT with immobilized  $\text{GO}_x$  is measured as a function of time in 5  $\mu\text{L}$  milli-Q water. The conductance of the  $\text{GO}_x$ -coated SWNT increases upon addition of glucose to the liquid. Inset: (a) the same measurement on

a second device where the conductance was a factor of 10 lower; (b) the same measurement on a semiconducting SWNT without  $\text{GO}_x$ ; no conductance increase is observed in this case. (Reprinted with permission from Ref. [107], © 2003, The American Chemical Society.) (B) Schematic of  $\text{GO}_x$  immobilized on SWNT for electronic glucose detection.

ments where the conductance of a GOx-coated semiconducting SWNT in milli-Q water has been recorded in the liquid (left-hand arrow in each graph in Fig. 1.12). No significant change in conductance was observed as a result of water addition. When 0.1 M glucose in milli-Q water was added to the liquid (right-hand arrow in each graph), however, the conductance of the tube increased by about 10%. A similar 10% conductance change was observed for another device (Fig. 1.12a inset), which had a factor 10 lower conductance. Glucose did not change the conductance of the bare SWNT but did increase the device conductance after GOx was immobilized. Inset (b) of Fig. 1.12 shows such measurement on a bare semiconducting SWNT. These measurements clearly indicate that the GOx activity is responsible for the observed increase in conductance upon glucose addition, thus rendering such nanodevices as feasible enzymatic-activity sensors.

## 1.5

### Conclusion and Outlook

Recent advances in the rapidly developing area of biomolecule detection using carbon nanotube systems have been summarized here. SWNTs appear as structurally defined components for various electronic devices. The semiconductive properties of SWNTs are of special interest as these SWNTs have been applied to fabricate FETs for sensing applications. This area requires further development, particularly related to the fabrication of FETs based on individual SWNTs. The use of carbon nanotubes as nanocircuitry elements is particularly interesting. Biomaterials linked to nanotubes may be used as binding elements for the specific linkage of the nanotube to surface in the form of addressable structures.

Important chemical means to functionalize SWNTs with other electronic materials such as conductive polymers or nanoparticles is anticipated to generate materials of new properties and functions. The localized nanoscale contacts of SWNTs with bio-surfaces will be a major advance in understanding and exploring the new applications. The use of nanodevices to monitor various biologically significant reactions is envisioned. In future, it should be possible to connect the living cells directly to these nanoelectronic devices to measure the electronic responses of living systems. The combination of the unique electronic properties of SWNTs and catalytic features of biological system could provide new opportunities for carbon nanotubes based bioelectronics.

### References

- 1 PARK, S., TATON, T. A., MIRKIN, C. A. Array-based electrical detection of DNA with nanoparticle probes., *Science* **2002**, 295, 1503–1506.
- 2 HE, L., MUSICK, M. D., NICEWARNER, S. R., SALINAS, F. G., BENKOVIC, S. J., NATAN, M. J., KEATING, C. D. Colloidal Au-enhanced surface plasmon resonance for ultrasensitive detection of DNA hybridization., *J. Am. Chem. Soc.* **2000**, 122, 9071–9077.

- 3 MCFARLAND, A. D., VAN DUYN, R. P. Single silver nanoparticles as real-time optical sensors with zeptomole sensitivity., *Nano Lett.* **2003**, *3*, 1057–1062.
- 4 GRAHAM, A. P., DUESBERG, G. S., SEIDEL, R. V., LIEBAU, M., UNGER, E., PAMLER, W., KREUPL, F., HOENLEIN, W. Carbon nanotubes for microelectronics?, *Small* **2005**, *1*, 382–390.
- 5 GRÜNER, G. Carbon nanotube transistors for biosensing applications., *Anal. & Bioanal. Chem.*, **2006**, *384*, 322–335.
- 6 WILLNER, I. Biomaterials for sensors, fuel cells, and circuitry., *Science* **2002**, *298*, 2407–2408.
- 7 CUI, Y., WEI, Q., PARK, H., LIEBER, C. M. Nanowire nanosensors for highly sensitive and selective detection of biological and chemical species., *Science* **2001**, *293*, 1289–1292.
- 8 HAHM, J., LIEBER, C. M. Direct ultrasensitive electrical detection of DNA and DNA sequence variations using nanowire nanosensors., *Nano Lett.* **2004**, *4*, 51–54.
- 9 PATOLSKY, F., ZHENG, G., HAYDEN, O., LAKADAMYALI, M., ZHUNG, X., LIEBER, C. M. Electrical detection of single viruses, *Proc. Natl. Acad. Sci. U.S.A.* **2004**, *101*, 14017–14022.
- 10 WEISS, S. Measuring conformational dynamics of biomolecules by single molecule fluorescence spectroscopy., *Nat. Struct. Biol.* **2000**, *7*, 724–729.
- 11 ZHUANG, X. W., RIEF, M. Single-molecule folding., *Curr. Opin. Struct. Biol.* **2003**, *13*, 88–97.
- 12 AJAYAN, P. M. Nanotubes from carbon., *Chem. Rev.* **1999**, *99*, 1787–1799.
- 13 AJAYAN, P. M., ZHOU, O. Z. Applications of carbon nanotubes., *Top. Appl. Phys.* **2001**, *80*, 391–425.
- 14 Special issue on carbon nanotubes, *Acc. Chem. Res.* **2002**, vol. 35.
- 15 WANG, J. Carbon-nanotube based electrochemical biosensors: A review., *Electroanalysis* **2005**, *17*, 7–14.
- 16 LIN, Y., TAYLOR, S., LI, H., SHIRAL FERNANDO, K. A., QU, L., WANG, W., GU, L., ZHOU, B., SUN, Y. P. Advances toward bioapplications of carbon nanotubes., *J. Mater. Chem.* **2004**, *14*, 527–541.
- 17 KATZ, E., WILLNER, I. Biomolecule-functionalized carbon nanotubes: applications in nanobioelectronics., *ChemPhysChem* **2004**, *5*, 1084–1104.
- 18 IIJIMA, S. Helical microtubules of graphitic carbon., *Nature (London)* **1991**, *354*, 56–58.
- 19 DRESSSELHAUS, M. S., DRESSSELHAUS, G., EKLUND, P. C. *Science of Fullerenes and Carbon Nanotubes*, Academic Press, San Diego, **1996**.
- 20 SAITO, R., DRESSSELHAUS, G., DRESSSELHAUS, M. S. *Physical Properties of Carbon Nanotubes*, Imperial College Press, London, **1999**.
- 21 DE JONGE, N., LAMY, Y., SCHOOTS, K., OOSTERKAMP, T. H. High brightness electron beam from a multi-walled carbon nanotube, *Nature (London)* **2002**, *420*, 393–395.
- 22 FRANSEN, M. J., VAN ROOY, Th. L., KRUIT, P. Field emission energy distributions from individual multiwalled carbon nanotubes., *Appl. Surf. Sci.* **1999**, *146*, 312–327.
- 23 WANG, Z. L., PONCHARAL, P., DE HEER, W. A. Measuring physical and mechanical properties of individual carbon nanotubes by in situ TEM., *J. Phys. Chem. Solids* **2000**, *61*, 1025–1030.
- 24 KONG, J., FRANKLIN, N. R., ZHOU, C. W., CHAPLINE, M. G., PENG, S., CHO, K., DAI, H. Nanotube molecular wires as chemical sensors., *Science* **2000**, *287*, 622–625.
- 25 SUGIE, H., TANEMURA, M., FILIP, V., IWATA, K., TAKAHASHI, K., OKUYAMA, F. Carbon nanotubes as electron source in an x-ray tube., *Appl. Phys. Lett.* **2001**, *78*, 2578–2580.
- 26 BAUGHMAN, R. H., ZAKHIDOV, A., DE HEER, W. A. Carbon nanotubes – the route toward applications., *Science* **2002**, *297*, 787–792.
- 27 DEKKER, C. Carbon nanotubes as molecular quantum wires., *Phys. Today* **1999**, *52*, 22–28.
- 28 MCEUEN, P. L., FUHRER, M. S., PARK, H. Single-walled carbon nanotube electronics., *IEEE Trans. Nanotechnol.* **2002**, *1*, 78–85.

- 29 DRESSELHAUS, M. S. Burn and interrogate., *Science* **2001**, 292, 650–651.
- 30 TANS, S. J., VERSCHUEREN, A. R. M., DEKKER, C. Room-temperature transistor based on a single carbon nanotube., *Nature* **1998**, 393, 49–52.
- 31 VALENTINI, L., ARMENTANO, I., KENNY, J. M., CANTALINI, C., LOZZI, L., SANTUCCI, S. Sensor for sub-ppm NO<sub>2</sub> gas detection based on carbon nanotube thin films., *Appl. Phys. Lett.* **2003**, 82, 961–963.
- 32 LI, J., LU, Y. J., YE, Q., CINKE, M., HAN, J., MEYYAPPAN, M. Carbon nanotube sensors for gas and organic vapor detection, *Nano Lett.* **2003**, 3, 929–933.
- 33 COLLINS, P. G., BRADLEY, K., ISHIGAMI, M., ZETTL, A. Extreme oxygen sensitivity of electronic properties of carbon nanotubes., *Science* **2000**, 287, 1801–1804.
- 34 SINNOTT, S. B., ANDREWS, R. Carbon nanotubes: Synthesis, properties, and applications., *Crit. Rev. Solid State Mater. Sci.* **2001**, 26, 145–249.
- 35 KOKAI, F., TAKAHASHI, K., YUDASAKA, M., YAMADA, R., ICHIHASHI, T. and IJIMA, S. Laser ablation of graphite-Co/Ni and growth of single-wall carbon nanotubes in vortexes formed in an Ar atmosphere, *J. Phys. Chem. B* **2000**, 104, 6777–6784.
- 36 TAKIZAWA, M., BANDOW, S., YUDASAKA, M., ANDO, Y., SHIMOYAMA, H., IJIMA, S. Change of tube diameter distribution of single-wall carbon nanotubes induced by changing the bimetallic ratio of Ni and Y catalysts., *Chem. Phys. Lett.* **2000**, 326, 351–357.
- 37 LI, Y., KIM, W., ZHANG, Y., ROLANDI, M., WANG, W., DAI, H. Growth of single-walled carbon nanotubes from discrete catalytic nanoparticles of various sizes., *J. Phys. Chem. B* **2001**, 105, 11 424–11 431.
- 38 IJIMA, S., ICHIHASHI, T. Single-shell carbon nanotubes of 1-nm diameter., *Nature (London)* **1993**, 363, 603–605.
- 39 BETHUNE, D. S., KIANG, C. H., DE VIRE, M. S., GORMAN, G., SAVOY, R., VAZQUEZ, J., BEYERS, R. Cobalt-catalysed growth of carbon nanotubes with single-atomic-layer walls, *Nature (London)* **1993**, 363, 605–607.
- 40 SERAPHIN, S., ZHOU, D. Single-walled carbon nanotubes produced at high yield by mixed catalyst, *Appl. Phys. Lett.* **1994**, 64, 2087–2089.
- 41 WILLEMS, I., KÓNYA, Z., COLOMER, J.-F., VAN TENDELOO, G., NAGARAJU, N., FONSECA, A. and NAGY, J. B. Control of the outer diameter of thin carbon nanotubes synthesized by catalytic decomposition of hydrocarbon, *Chem. Phys. Lett.* **2000**, 317, 71–76.
- 42 HATA, K., FUTABA, D. N., MIZUNO, K., NAMAI, T., YUMURA, M., IJIMA, S. Water-assisted highly efficient synthesis of impurity-free single-walled carbon nanotubes., *Science* **2004**, 306, 1362–1364.
- 43 JOSELEVICH, E., LIEBER, C. M. Vectorial growth of metallic and semiconducting single-wall carbon nanotubes, *Nano Lett.* **2002**, 2, 1137–1141.
- 44 URAL, A., LI, Y., DAI, H. Electric-field-aligned growth of single-walled carbon nanotubes on surfaces., *Appl. Phys. Lett.* **2002**, 81, 3464–3466.
- 45 GAO, J., YU, A., ITKIS, M. E., BEKYAROVA, E., ZHAO, B., NIYOGI, S., HADDON, R. C. Large-scale fabrication of aligned single-walled carbon nanotube array and hierarchical single-walled carbon nanotube assembly., *J. Am. Chem. Soc.* **2004**, 126, 16 698–16 699.
- 46 SU, M., LI, Y., MAYNOR, B., BWLDUM, A., LU, J. P., LIU, J. Lattice-oriented growth of single-walled carbon nanotubes, *J. Phys. Chem. B* **2000**, 104, 6505–6508.
- 47 ISMAOH, A., SERGEV, L., WACHTEL, E., JOSELEVICH, E. Atomic-step-templated formation of single wall carbon nanotube patterns, *Angew. Chem, Int. Ed.* **2004**, 43, 6140–6143.
- 48 QIAN, D., WAGNER, G. J., LIU, W. K., YU, M. F., RUOFF, R. S. Mechanics of carbon nanotubes., *Appl. Mechanics Rev.* **2002**, 55, 495–533.
- 49 DURKÖP, T., Electronic Properties of carbon nanotubes studied in field-effect transistor geometries, PhD thesis 2004.

- 50 MARTEL, R., SCHMIDT, T., SHEA, H. R., HERTEL, T., AVOURIS, Ph. Single- and multi-wall carbon nanotube field-effect transistors., *Appl. Phys. Lett.* **1998**, *73*, 2447–2449.
- 51 FUHRER, M. S., KIM, B. M., CHEN, Y. F., DURKÖP, T., BRINTLINGER, T. High-mobility nanotube transistor memory., *Nano Lett.* **2002**, *2*, 755–759.
- 52 JAVEY, A., GUO, J., WANG, Q., LUNDSTROM, M., DAI, H. Ballistic carbon nanotube field-effect transistors, *Nature* **2003**, *424*, 654–657.
- 53 DURKÖP, T., GETTY, S. A., COBAS, E., FUHRER, M. S. Extraordinary mobility in semiconducting carbon nanotubes., *Nano Lett.* **2004**, *4*, 35–39.
- 54 THESS, A., LEE, R., NIKOLAEV, P., DAI, H., PETIT, P., ROBERT, J., XU, C., LEE, Y. H., KIM, S. G., RINZLER, A. G., COLBERT, D. T., SCUSERIA, G. E., TOMANEK, D., FISHER, J. E., SMALLEY, R. E. Crystalline ropes of metallic carbon nanotubes, *Science* **1996**, *273*, 483–487.
- 55 BRONIKOWSKI, M. J., WILLIS, P. A., COLBERT, D. T., SMITH, K. A., SMALLEY, R. E. Gas-phase production of carbon single-walled nanotubes from carbon monoxide via the HiPco process: A parametric study., *J. Vac. Sci. Technol. A* **2001**, *19*, 1800–1805.
- 56 DIEHL, M. R., YALIRAKI, S. N., BECKMAN, R. A., BARAHONA, M., HEATH, J. R. Self-assembled, deterministic carbon nanotube wiring networks., *Angew. Chem. Int. Ed.* **2002**, *41*, 353–356.
- 57 MARTEL, R., DERYCKE, V., LAVOIE, C., APPENZELLER, J., CHAN, K. K., TERSOFF, J., AVOURIS, Ph. Ambipolar electrical transport in semiconducting single-wall carbon nanotubes., *Phys. Rev. Lett.* **2001**, *87*, 256805-1–256805-4.
- 58 BOCKRATH, M., COBDEN, D. H., LIU, J., RINZLER, A. G., SMALLEY, R. E., BALENTS, L., MCEUEN, P. L. Luttinger-liquid behaviour in carbon nanotubes., *Nature* **1999**, *397*, 598–601.
- 59 HU, L., HECHT, D. S., GRÜNER, G. Percolation in transparent and conducting carbon nanotube networks., *Nano Lett.* **2004**, *4*, 2513–2517.
- 60 RADOSAVLJEVIC, M., FREITAG, M., THADANI, K. V., JOHNSON, A. T. Nonvolatile molecular memory elements based on ambipolar nanotube field effect transistors., *Nano Lett.* **2002**, *2*, 761–764.
- 61 APPENZELLER, J., KNOCH, J., DERYCKE, V., MARTEL, R., WIND, S., AVOURIS, Ph. Field-modulated carrier transport in carbon nanotube transistors., *Phys. Rev. Lett.* **2002**, *89*, 126801-1–126801-4.
- 62 ROSENBLATT, S., YAISH, Y., PARK, J., GORE, J., SAZONOVA, V., MCEUEN, P. L. High performance electrolyte gated carbon nanotube transistors., *Nano Lett.* **2002**, *2*, 869–872.
- 63 ZHANG, Y., DAI, H. Formation of metal nanowires on suspended single-walled carbon nanotubes, *Appl. Phys. Lett.* **2000**, *77*, 3015–3017.
- 64 HEINZE, S., TERSOFF, J., MARTEL, R., DERYCKE, V., APPENZELLER, J., AVOURIS, Ph. Carbon nanotubes as Schottky barrier transistors., *Phys. Rev. Lett.* **2002**, *89*, 106801-1–106801-4.
- 65 DE JONGE, N., VAN DRUTEN, N. J. Field emission from individual multiwalled carbon nanotubes prepared in an electron microscope., *Ultramicroscopy* **2003**, *95*, 85–91.
- 66 STADERMANN, M., PAPADAKIS, S. J., FALVO, M. R., NOVAK, J., SNOW, E., FU, Q., LIU, J., FRIDMAN, Y., BOLAND, J. J., SUPERFINE, R., WASHBURN, S. Nanoscale study of conduction through carbon nanotube networks., *Phys. Rev. B* **2004**, *69*, 201402-1–201402-3.
- 67 DERYCKE, V., MARTEL, R., APPENZELLER, J., AVOURIS, Ph. Controlling doping and carrier injection in carbon nanotube transistors., *Appl. Phys. Lett.* **2002**, *80*, 2773–2775.
- 68 LU, C., FU, Q., HUANG, S., LIU, J. Polymer electrolyte-gated carbon nanotube field-effect transistor., *Nano Lett.* **2004**, *4*, 623–627.
- 69 SIDDONS, G. P., MERCHIN, D., BACK, J. H., JEONG, J. K., SHIM, M. Highly efficient gating and doping of carbon nanotubes with polymer electrolytes., *Nano Lett.* **2004**, *4*, 927–931.
- 70 MARTEL, R., SCHMIDT, T., SHEA, H. R., HERTEL, T., AVOURIS, Ph. Single- and

- multi-wall carbon nanotube field-effect transistors., *Appl. Phys. Lett.* **1998**, *73*, 2447–2449.
- 71 HONE, J., ELLWOOD, I., MUNO, M., MIZEL, A., COHEN, M. L., ZETTL, A., RINZLER, A. G., SMALLEY, R. E. Thermoelectric power of single-walled carbon nanotubes., *Phys. Rev. Lett.* **1998**, *80*, 1042–1045.
- 72 NAKANISHI, T., BACHTOLD, A., DEKKER, C. Transport through the interface between a semiconducting carbon nanotube and a metal electrode., *Phys. Rev. B* **2002**, *66*, 073 307-1–073 307-4.
- 73 FREITAG, M., JOHNSON, A. T., KALININ, S., BONNELL, D. Role of single defects in electronic transport through carbon nanotube field-effect transistors., *Phys. Rev. Lett.* **2002**, *89*, 216 801-1–216 801-4.
- 74 BRADLEY, K., GABRIEL, J.-C. P., STAR, A., GRÜNER, G. Short-channel effects in contact-passivated nanotube chemical sensors., *Appl. Phys. Lett.* **2003**, *83*, 3821–3823.
- 75 KIM, W., JAVERY, A., VERMESH, O., WANG, Q., LI, Y., DAI, H. Hysteresis caused by water molecules in carbon nanotube field-effect transistors., *Nano Lett.* **2003**, *3*, 193–198.
- 76 BRADLEY, K., CUMINGS, J., STAR, A., GABRIEL, J.-C. P., GRÜNER, G. Influence of mobile ions on nanotube based FET devices., *Nano Lett.* **2003**, *3*, 639–641.
- 77 STAR, A., HAN, T.-R., JOSHI, V., STETTER, J. R. Sensing with nafion coated carbon nanotube field-effect transistors., *Electroanalysis* **2004**, *16*, 108–112.
- 78 KRUGER, M., BUITELAAR, M. R., NUSSBAUMER, T., SCHONENBERGER, C., FORRO, L. Electrochemical carbon nanotube field-effect transistor., *Appl. Phys. Lett.* **2001**, *78*, 1291–1293.
- 79 DAGANI, R. DNA matches., *Chem. Eng. News* **2002**, *80*, 8.
- 80 KIM, O.-K., JE, J., BALDWIN, J. W., KOOI, S., PEHRSSON, P. E., BUCKLEY, L. Solubilization of single-wall carbon nanotubes by supramolecular encapsulation of helical amylose., *J. Am. Chem. Soc.* **2003**, *125*, 4426–4427.
- 81 BANDYOPADHYAYA, R., NATIV-ROTH, E., REGEV, O., YERUSHALMI-ROZEN, R. Stabilization of individual carbon nanotubes in aqueous solutions., *Nano Lett.* **2002**, *2*, 25–28.
- 82 NUMATA, M., ASAI, M., KANEKO, K., HASEGAWA, T., FUJITA, N., KITADA, Y., SAKURAI, K., SHINKAI, S. Curdlan and schizophyllan (beta-1,3-glucans) can entrap single-wall carbon nanotubes in their helical superstructure, *Chem. Lett.* **2004**, *33*, 232–233.
- 83 CHEN, J., DYER, M. J., YU, M.-F. Cyclodextrin-mediated soft cutting of single-walled carbon nanotubes., *J. Am. Chem. Soc.* **2001**, *123*, 6201–6202.
- 84 CHEN, J., HAMON, M. A., HIU, H., CHEN, Y., RAO, A. M., EKLUND, P. C., HADDON, R. C. Solution properties of single-walled carbon nanotubes., *Science* **1998**, *282*, 95–98.
- 85 STAR, A., STODDART, J. F., STEUERMAN, D., DIEHL, M., BOUKAI, A., WONG, E. W., YANG, X., CHUNG, S. W., HEATH, J. R. Preparation and properties of polymer-wrapped single-walled carbon nanotubes., *Angew. Chem. Int. Ed.* **2001**, *40*, 1721–1725.
- 86 STAR, A., STEUERMAN, D. W., HEATH, J. R., STODDART, J. F. Starched carbon nanotubes., *Angew. Chem. Int. Ed.* **2002**, *41*, 2508–2512.
- 87 DODZIUK, H., EJCHART, A., ANCZEWSKI, W., UEDA, H., KRINICHNAYA, E., DOLGONOS, G., KUTNER, W. Water solubilization, determination of the number of different types of single-wall carbon nanotubes and their partial separation with respect to diameters by complexation with  $\eta$ -cyclodextrin., *Chem. Commun.* **2003**, 986–987.
- 88 ZHENG, M., JAGOTA, A., SEMKE, E. D., DINER, B. A., MCLEAN, R. S., LUSTIG, S. R., RICHARDSON, R. E., TASSI, N. G. DNA-assisted dispersion and separation of carbon nanotubes., *Nat. Mater.* **2003**, *2*, 338–342.
- 89 ZHENG, M., JAGOTA, A., STRANO, M. S., SANTOS, A. P., BARONE, P., CHOU, S. G., DINER, B. A., DRESSELHAUS, M. S., MCLEAN, R. S., ONOA, G. B., SAMSONIDZE, G. G., SEMKE, E. D., USREY, M., WALLS, D. J. Structure-



- based carbon nanotube sorting by sequence-dependent DNA assembly., *Science* **2003**, 302, 1545–1548.
- 90 BALAVOINE, F., SCHULTZ, P., RICHARD, C., MALLOUH, V., EBBESEN, T. W., MIOSKOWSKI, C. Helical crystallization of proteins on carbon nanotubes: A first step towards the development of new biosensors., *Angew. Chem. Int. Ed.* **1999**, 38, 1912–1915.
- 91 BRADLEY, K., BRIMAN, M., STAR, A., GRÜNER, G. Charge transfer from adsorbed proteins., *Nano Lett.* **2004**, 4, 253–256.
- 92 WANG, S., HUMPHREYS, E. S., CHUNG, S.-Y., DELDUCCO, D. F., LUSTIG, S. R., WANG, H., PARKER, K. N., RIZZO, N. W., SUBRAMONEY, S., CHIANG, Y.-M., JAGOTA, A. Peptides with selective affinity for carbon nanotubes., *Nat. Mater.* **2003**, 2, 196–200.
- 93 BRADLEY, K., GABRIEL, J.-C. P., BRIMAN, M., STAR, A., GRÜNER, G. Charge transfer from ammonia physisorbed on nanotubes., *Phys. Rev. Lett.* **2003**, 91, 218 301-1–218 301-4.
- 94 WILSON-KUBALEK, E. M., BROWN, R. E., CELIA, H., MILLIGAN, R. A. Lipid nanotubes as substrates for helical crystallization of macromolecules., *Proc. Natl. Acad. Sci. U.S.A.* **1998**, 95, 8040–8045.
- 95 CHEN, R. J., CHOI, H. C., BANGSARUNTIP, S., YENILMEZ, E., TANG, X., WANG, Q., CHANG, Y. L., DAI, H. An investigation of the mechanisms of electronic sensing of protein adsorption on carbon nanotube devices., *J. Am. Chem. Soc.* **2004**, 126, 1563–1568.
- 96 BOUSSAAD, S., TAO, N. J., ZHANG, R., HOPSON, T., NAGAHARA, L. A. *In situ* detection of cytochrome c adsorption with single walled carbon nanotube device., *Chem. Comm.* **2003**, 1502–1503.
- 97 STAR, A., GABRIEL, J.-C. P., BRADLEY, K., GRÜNER, G. Electronic detection of specific protein binding using nanotube FET devices., *Nano Lett.* **2003**, 3, 459–463.
- 98 CHEN, R. J., BANGSARUNTIP, S., DROUVALAKIS, K. A., WONG SHI KAM, N., SHIM, M., LI, Y., KIM, W., UTZ, P. J., DAI, H. Noncovalent functionalization of carbon nanotubes for highly specific electronic biosensors., *Proc. Natl. Acad. Sci. U.S.A.* **2003**, 100, 4984–4989.
- 99 LI, H., NG, H. T., CASSELL, A., FAN, W., CHEN, H., YE, Q., KOEHNE, J., HAN, J., MEYAPPAN, M. Carbon nanotube nanoelectrode array for ultrasensitive DNA detection., *Nano Lett.* **2003**, 3, 597–602.
- 100 STAR, A., TU, E., NIEMANN, J., GABRIEL, J.-C. P., JOINER, C. S., VALCKE, C. Label-free detection of DNA hybridization using carbon nanotube field-effect transistors., *Proc. Natl. Acad. Sci. U.S.A.* **2006**, 103, 921–926.
- 101 LIMDI, J. K., CRAMPTON, J. R. Hereditary haemochromatosis., *Q. J. Med.* **2004**, 97, 315–324.
- 102 FRANCHINI, M., VENERI, D. Recent advances in hereditary hemochromatosis., *Ann. Hematol.* **2005**, 84, 347–352.
- 103 TANG, X., BANGSARUNTIP, S., NAKAYAMA, N., YENILMEZ, E., CHANG, Y.-I., WANG, Q. Carbon nanotube DNA sensor and sensing mechanism., *Nano Lett.* **2006**, 6, 1632–1636.
- 104 MAEHASHI, K., MATSUMOTO, K., KERMAN, K., TAKAMURA, Y., TAMIYA, E. Ultrasensitive detection of DNA hybridization using carbon nanotube field-effect transistors., *Jpn. J. Appl. Phys.* **2004**, 43, L 1558–L 1560.
- 105 STAR, A., JOSHI, V., HAN, T. R., ALTOE, V. P., GRÜNER, G., STODDART, J. F. Electronic detection of the enzymatic degradation of starch., *Org. Lett.* **2004**, 6, 2089–2092.
- 106 KONG, J., DAI, H. Full and modulated chemical gating of individual carbon nanotubes by organic amine compounds., *J. Phys. Chem B* **2001**, 105, 2890–2893.
- 107 SHIM, M., JAVEY, A., KAM, N. W. S., DAI, H. Polymer functionalization for air-stable n-type carbon nanotube field-effect transistors., *J. Am. Chem. Soc.* **2001**, 123, 11 512–11 513.
- 108 BESTEMAN, K., LEE, J. O., WIERTZ, F. G. M., HEERING, H. A., DEKKER, C. Enzyme-coated carbon nanotubes as single-molecule biosensors., *Nano Lett.* **2003**, 3, 727–730.

## 2

### Carbon Nanotube-based Sensor

*Jian-Shan Ye and Fwu-Shan Sheu*

#### 2.1

##### Overview

Carbon nanotubes (CNTs) possess high electrical conductivity, high chemical stability, and extremely high mechanical strength and modulus. These special properties of both single-walled carbon nanotubes (SWCNTs) and multiwalled carbon nanotubes (MWCNTs) have attracted much attention in electrochemistry. To develop nanostructured macroscopic electrodes, randomly dispersed nanotubes, well-aligned CNTs, CNT paste, screen-printing CNTs, self-assembly of CNT, and CNT-packaged microelectrodes have been used. Furthermore, single and long MWCNTs, after formation, can be used as a nanoelectrode. The resultant nanotube-based electrodes have been used successfully for electroanalytical purposes such as the development of sensors and biosensors. We outline here the unique electrochemical and electrocatalytical properties of CNTs-based sensors/biosensors and discuss novel applications as well as future challenge of CNTs in electrochemical sensors.

Functionalization of CNTs is one of the most active fields in nanotube research, which provides an effective tool to broaden the electrochemical application spectrum of CNTs. In this chapter, we summarize various approaches to functionalize CNTs for the development of novel electrochemical sensors. Particular emphasis is directed to the use of lipid-functionalized CNTs for sensors and biosensors and for the synthesis of photoswitched-functional devices. Functionalization of nanotubes generates a novel, interesting class of nanomaterials, which combines the properties of the nanotubes and the functional moiety, thus offering new opportunities in the development of electrochemical sensors.

#### 2.2

##### Introduction of Carbon Nanotubes

Carbon nanotubes (CNTs) have captured the imagination of researchers worldwide since they were first observed by Iijima in 1991 [1]. With 100× the tensile strength of steel, a thermal conductivity better than all but the purest diamond, and electrical conductivity similar to copper, but with the ability to carry much higher cur-

rents, CNTs are very interesting and promising nanomaterials. Their small dimensions, unique structures, strength, and remarkable physical properties make them a unique material with a wide range of potential applications.

CNTs, consisting of only  $sp^2$  hybridized carbon atoms, are cylindrical nanostructures with a diameter ranging from 1 nm to several nanometers, and a length of tens of micrometers. They are made of graphene sheets wrapped into a hollow cylinder and capped by fullerene-like structures. There are two typical types of nanotubes, SWCNTs and MWCNTs. The latter consist of several to tens of concentric cylinders of these graphitic shells with a layer spacing of 0.3–0.4 nm. MWCNTs tend to have diameters in the range 2–500 nm, depending on the method of synthesis. An MWCNT can be considered as a mesoscale graphite system, whereas a SWCNT is truly a large single molecule. High-resolution transmission electron microscope (HRTEM) results showed that the first observed CNTs by Iijima in 1991 [1] were fullerene-like tubes consisting of coaxial multiple shells. These tubes were MWCNTs. The interlayer spacing is 0.34 nm, which is slightly greater than that of graphite (0.335 nm) due to a combination of tubule curvature and van der Waals force interactions between successive graphene layers.

After two years, it was discovered that the use of transition metals as catalysts afforded CNTs with a single shell or wall only [2]. These nanotubes were SWCNTs. An ideal SWCNT can be viewed as an “extended” fullerene, and consists of a single graphite layer wrapped into one seamless hollow cylinder. Closure of the cylinder is the result of pentagon inclusion in the hexagonal carbon network of the nanotube walls during the growth process. SWCNTs normally have a narrow diameter distribution (with diameter of the order of 1 nm) but tend to assemble in nanotube bundles during the growth process [3]. This corresponds to the theoretically predicted lower limit for stable SWCNT formation based on considerations of the stress energy built into the cylindrical structure of the SWCNT.

There are three types of SWCNTs: “arm-chair” ( $n, m$ ) tubes where  $n = m$ , “zig-zag” ( $n, 0$ ) tubes and chiral (all other tubes with independent  $n$  and  $m$ ) tubes. Theoretical calculations indicate that the electronic properties for a single-walled nanotube will vary as a function of its diameter and helicity [4–6]. A SWCNT may behave as a semiconductor or metal, and a slight change in the chirality can transform a nanotube from a metal to a semiconductor. In general, about one-third of SWCNTs are metallic, characterized with wrapping vectors of  $n - m = 3l$  ( $l = 0, 1, 2, \dots$ ). All other tubes are semiconductors [7, 8].

Carbon–carbon covalent bonds are one of the strongest in nature, and a structure based on a perfect arrangement of these bonds oriented along the axis of nanotubes would produce an exceedingly strong material. Early theoretical work and recent experiments on individual nanotubes have confirmed that nanotubes are one of the stiffest structures ever made [9–11].

CNTs possess high electrical conductivity, high chemical stability, and extremely high mechanical strength and modulus. These special properties of both SWCNTs and MWCNTs have attracted much attention in electrocatalysis [12–17] and as chemical sensors/biosensors [18–24].

The present chapter only covers particular aspects related to CNTs-based electrochemical sensing systems. Different methods of preparing CNT electrodes and the

possible ways to functionalize CNTs are described, with the major part devoted to the use of lipid-functionalized CNTs for sensors and biosensors and for the fabrication of photoswitched-functional devices. Furthermore, the possible mechanism of electrocatalysis by CNTs is discussed.

### 2.3

#### Growth of Carbon Nanotubes

CNTs are generally produced by three main techniques, arc discharge, laser ablation, and chemical vapor deposition (CVD). The arc discharge method, initially used for producing  $C_{60}$  fullerenes, is the most common and perhaps easiest way to produce CNTs, as it is rather simple to undertake [25]. During arc discharge, a vapor is created by an arc discharge between two carbon electrodes with or without catalyst. Nanotubes self-assemble from the resulting carbon vapor. This technique produces a mixture of components and requires the separation of nanotubes from the soot and catalytic metals present in the crude product. In the laser ablation technique [26], a high-power laser beam impinges on a volume of carbon-containing feedstock gas (methane or carbon monoxide). Presently, laser ablation produces a small amount of clean nanotubes, whereas arc discharge methods generally produce large quantities of impure material. CVD is achieved by putting a carbon source in the gas phase and using an energy source, such as plasma or a resistively heated coil, to transfer energy to a gaseous carbon molecule. CVD nanotube synthesis is essentially a two-step process, consisting of a catalyst preparation step followed by the actual synthesis of the nanotube. The catalyst is generally prepared by sputtering a transition metal onto a substrate and then using either chemical etching or thermal annealing to induce catalyst particle nucleation. Thermal annealing results in cluster formation on the substrate, from which the nanotubes will grow. Excellent alignment, as well as positional control on the nanometer scale, can be achieved by using CVD [27, 28].

Even though much progress on CNT growth has been made in the past decade, it is still challenging to produce CNTs with desired properties for specific applications. In particular, new methods are desired that can be directly integrated into device fabrication. With continued effort in the development of growth techniques, it is expected that CNTs with desired properties, quality, and quantity could be obtained for various applications.

### 2.4

#### Methods to Prepare CNTs-based Sensors and Biosensors

##### 2.4.1

##### Individual MWCNTs as Nanoelectrodes

MWCNTs are tiny electrodes made of carbon, metals or semiconducting materials having typical dimensions of 1–100 nm. MWCNTs can be used as a new material for the construction of nanoelectrodes. Campbell et al. have reported the fabrica-

tion and characterization of electrodes constructed from single MWCNTs [29]. To construct a nanoelectrode, single nanotubes were attached to a mechanically cut Pt tip, using Ag epoxy, and subsequently cleaned by immersion in a fresh piranha solution (3:1 concentrated  $\text{H}_2\text{SO}_4$ :30%  $\text{H}_2\text{O}_2$ ). The sigmoidal voltammetric response of these nanotubular electrodes is characteristic of steady-state radial diffusion. The limiting current of uninsulated electrodes scales linearly with the depth of immersion into electrolyte solutions. However, the walls of nanotubular electrodes can be selectively insulated with a thin layer of polyphenol so that electrochemical activity is limited to the tip region. In this case the limiting current is essentially independent of immersion depth. These nanotubular electrodes are robust, can be fabricated in high yield, and are of uniform diameter. Most importantly, their great strength and high length-to-diameter aspect ratio will be particularly valuable for applications such as scanning electrochemical microscopy (SECM) and electrochemical analysis of biological materials.

#### 2.4.2

##### **Randomly Distributed CNT Electrodes**

To prepare CNT electrodes, randomly distributed CNTs can be casted at the surface of the electrode. Before casting, the concentrated solutions of CNTs in sulfuric acid [20], dimethylformamide [30], concentrated nitric acid, or a Nafion/water mixture [31] are prepared. Coated electrodes were are at high temperature (e.g., 200 °C for 3 h) and then readied for use after careful washing. The randomly deposited CNTs are less mechanically stable and have worse electrical contact to the underneath electrodes than the vertically aligned CNTs directly grown on conductive substrates.

#### 2.4.3

##### **Well-aligned Carbon Nanotube Electrodes**

To construct a CNT electrode, SWCNTs are shaped into an electrode by filtering suspension of nanotubes on a membrane filter [32] to form a nanotube sheet. Another method is casting the SWCNT suspension on the surface of solid electrodes such as Pt, Au, or glassy carbon [33–36]. In contrast, to construct a MWCNT electrode, the MWCNTs are usually mixed with bromoform [12], mineral oil [15], or packed into the cavity at the tip of a microelectrode to form a CNT powder microelectrode [36] as discussed above. MWCNT electrodes prepared by these methods may suffer from mechanical instability during detection, thus limiting their practical application. Fortunately, high-density well-aligned CNTs, which are multi-walled and vertically aligned on a large area of substrates (Fig. 2.1), can be readily synthesized [37, 38]. These CNTs aligned on the substrate are very stable and can be used as photoswitched functional devices [39], electrochemical sensors/biosensors [40–44] and supercapacitors [45]. In particular, this well-aligned MWCNT electrode has been successfully used as a novel candidate for non-enzymatic glucose sensors with the resistance to toxicity by chloride ions [46].

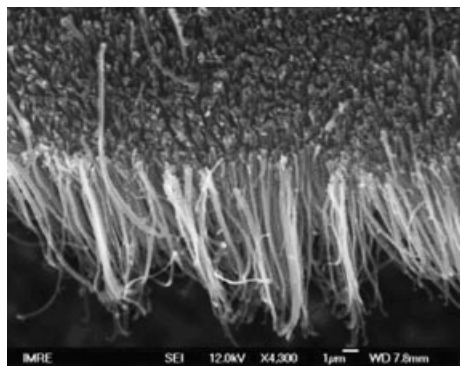


Fig. 2.1. A vertical well-aligned MWCNT electrode. (Adapted from Ref. [44] with permission.)

#### 2.4.4

##### Carbon Nanotube Paste Electrodes

Carbon paste electrodes (CPEs) belong to a special group of heterogeneous carbon electrodes. To prepare CPEs, carbon paste, i.e., a mixture prepared from carbon (graphite) powder and a suitable liquid binder is packed into a suitably designed electrode body. CNT-based CPEs were first reported by Britto et al. [12]. To study the electrochemical response, nanotubes were initially dispersed in bromoform as a binder material and packed into a glass tube. The resultant electrode had randomly distributed tubes with no control over the alignment of the nanotubes. Subsequently, numerous approaches have enabled the random distribution of nanotubes on electrodes, either by dispersing the tubes with a binder, such as dihexadecyl hydrogen phosphate [47], Nafion [21], or forming the nanotube equivalent of a carbon paste [48, 49] that can be screen printed [50], forming a nanotube/Teflon composite [22].

Due to numerous advantageous properties and characteristics, CPEs are widely used in amperometry, coulometry, and potentiometry. CNTs-based CPEs are easily obtainable at minimal costs and are especially suitable for preparing an electrode materials with desired composition and, hence, with pre-determined properties. Electrodes made in this way are usually intended to be used as highly selective sensors and/or biosensors for both inorganic and organic electrochemistry. The rapid development of new nanomaterials and nanotechnologies has provided many new opportunities for electrochemical application. In particular, the immobilization and adsorption of biomolecules on electrode surfaces is of great importance and interest for biosensor and bioelectronic applications. Recent studies have demonstrated that CNTs can enhance the electrochemical reactivity of biomolecules and promote the electron-transfer reactions of proteins. These properties make CNTs an efficient material for use in a wide range of electrochemical biosensors, ranging from amperometric enzyme electrodes to DNA hybridization biosensors. Rubianes and Rivas have recently described the performance of CNT paste electrodes prepared by dispersion of MWCNTs within mineral oil [48]. The resulting paste electrode shows excellent electrocatalytic activity toward ascorbic acid, uric acid, dopamine,

3,4-dihydroxyphenylacetic acid (dopac) and hydrogen peroxide. These properties permit an important decrease in the overvoltage for the oxidation of ascorbic acid (230 mV), uric acid (160 mV) and hydrogen peroxide (300 mV) as well as a dramatic improvement in the reversibility of the redox behavior of dopamine and dopac, in comparison with classic carbon (graphite) paste electrodes (CPE). The substantial decrease in the overvoltage of the hydrogen peroxide reduction (400 mV) associated with a successful incorporation of glucose oxidase (GOD) into the composite material allows the development of a highly selective and sensitive glucose biosensor, without using any metal, redox mediator, or anti-interference membrane. Such excellent performance of CNTPEs toward hydrogen peroxide, represents a very good alternative for developing other enzymatic biosensors. To determinate homocysteine, Lawrence et al. [51] have provided an effective means by using a CNT paste electrodes. A decrease of ca. 120 mV in the overpotential for the oxidation of homocysteine, compared with a traditional carbon paste electrode, is reported along with greatly enhanced signal-to-noise characteristics. The analytical parameters have been assessed with a linear range from 5 to 200  $\mu\text{M}$ , and a detection limit of 4.6  $\mu\text{M}$ . Furthermore, the generic nature of this increased reactivity of the CNT surface towards thiol moieties has been demonstrated with cysteine, glutathione, and n-acetylcysteine, providing a greatly enhanced electrochemical response compared with the carbon paste electrode. Pedano et al. have reported that CNTs paste electrodes are suitable for adsorptive stripping potentiometric measurements of trace levels of nucleic acids [52]. Compared with that obtained at carbon (graphite) paste electrode (CPE), the guanine oxidation signal is greatly enhanced due to the electroactivity inherent to CNTs. Trace ( $\mu\text{g L}^{-1}$ ) levels of the oligonucleotides and polynucleotides can be readily detected following short accumulation periods, with detection limits of 2.0  $\mu\text{g L}^{-1}$  for a 21-base oligonucleotide and 170  $\mu\text{g L}^{-1}$  for calf thymus dsDNA.

SWCNTs have also been used for the development of CPEs. Ricci et al. have used Prussian blue modified-SWCNTs for successive assembling of paste electrodes [53]. The electrochemical feature of such electrodes has been fully evaluated with cyclic voltammetry (CV) and amperometric experiments. The result showed that Prussian blue-modified CNT paste electrodes have a high sensitivity towards hydrogen peroxide with a detection limit of  $7.4 \times 10^{-6}$  M. The Prussian blue-modified CNT paste electrode also possessed strong stability even at basic pHs (i.e., pH 9 and 10), demonstrating no significant loss of signal after three days continuous work. In addition, the loading in the paste mixture of GOD has brought a sensitive tool for the detection of glucose in a range between 0.1 and 50 mM. More recently, Antiochia et al. have studied the electrocatalytic oxidation of NADH at SWCNT CPEs for use in a redox mediator in solution and dissolved in the paste [54].

#### 2.4.5

#### Screen-printing Carbon Nanotubes

Screen-printing technology is particularly attractive for the production of disposable sensors [50]. Recently, Trojanowicz et al. have successfully prepared CNT-

modified screen-printed electrodes for chemical sensors and biosensors [55]. They found that MWCNTs can be used to modify working graphite ink electrodes of the three-electrode screen-printed sensing stripe. Modification has been made by evaporating on the graphite surface a solution of MWCNT in dimethylformamide. The effect of such treatment on reversibility of the electrode process of the system hexacyanoferrate(II)/(III) has been shown, along with an improvement in sensitivity of detection of the pesticide paraoxon with biosensors containing organophosphorus hydrolase immobilized by adsorption on the nanotube-modified graphite ink electrode. The catalytic sensing of methanol has also been demonstrated with the use of a screen-printed sensor modified with MWCNT and Co(II) salt present in the measuring solution. More recently, Guan et al. have prepared a disposable electrochemical biosensor for glucose monitoring [56]. The sensor was based on MWCNTs immobilized with GOD upon a screen printed carbon electrode. The effect of MWCNTs on the response of amperometric GOD electrodes for glucose was examined. Results obtained, of interest for basic and applied biochemistry, represent a first step in construction of a MWCNT-enzyme electrode biosensor with potential application in the biosensor area.

#### 2.4.6

#### **Self-assembly of Carbon Nanotubes**

Self-assembly is the fundamental principle that generates structural organization on all scales from molecules to galaxies. Self-assembly is also a manufacturing method used to construct things at the nanometer scale. The conjugation of CNT with biomolecules and nanoparticles is an emerging field of research that has important potential applications in bionanotechnology. For example, the metallic/semiconductive properties of CNTs have been exploited to produce functional, technologically relevant devices such as sensors [57]. Electrostatic matching can be used to coat CNTs with layers of oppositely charged polyelectrolytes [58]. By using a similar strategy, Mann and his colleagues [59] have described a layer-by-layer procedure based on programmed biomolecular assembly to produce a multi-component, multi-layered CNT-based conjugate. The conjugate consists of a multi-walled CNT core coated with four functionalized layers that successively comprise protein-encapsulated iron oxide nanoparticles [biotinylated ferritin (bFn)], the tetra-valent biotin-binding protein, streptavidin (SA), 24-base three-stranded biotin-terminated oligonucleotide duplexes, and oligonucleotide coupled Au nanoparticles. They demonstrated that the core/multi-shell architecture can be constructed stepwise by specific recognition processes involving biotin–SA binding or DNA duplexation, and that these interactions can be exploited for reversible assembly/disassembly of the Au nanoparticle layer. A recent study showed that CNTs can be self-assembled at the electrode surface for the development of a sensor and biosensor.

Shimoda et al. have reported the formation of macroscopically ordered CNT membranes on a substrate by self-assembly [60]. To form the ordered SWCNTs, SWCNTs produced by the laser ablation method and purified by reflux and filtra-



tion were chemically etched to short bundles by ultrasonic-assisted oxidation. After removing the acid by filtration, the processed SWCNTs were dispersed in deionized water. A thin film appears on the surface of a soaked glass substrate in the SWCNTs/water dispersion with natural vaporization of water. Transmission electron microscopy measurements show that the SWCNT bundles are uniaxially aligned. The self-assembly of SWCNTs at gold electrodes can also be achieved by thiolation [61]. Recently, effective CNT coating was obtained by self-assembling short SWCNTs at an electrode surface [23, 24]. Such vertically aligned SWCNTs act as molecular wires to allow electrical communication between the underlying electrode and a redox enzyme. Direct electron transfer between the prosthetic group of the enzyme and an electron surface obviates the need for redox mediators and is thus extremely attractive for developing reagentless sensing devices. More recently, Wang and Iqbal have reported that thin films of vertically aligned individual SWCNTs can be deposited on silicon using a CVD process [62]. Oriented SWCNT growth was achieved by employing two methods of catalyst precursor self-assembly followed by ethanol CVD. Using the silicon substrate as the working electrode in an electrochemical cell and the enzyme beta-NAD (nicotinamide adenine dinucleotide) synthetase dissolved in a buffered electrolyte solution, the enzyme was attached at the nanotube ends. This was shown using scanning electron microscopy and cyclic voltammetry. Enzyme immobilization on the 1 to 2 nm diameter tube ends of the individual SWCNTs allows for dense packing of the enzyme and utilization of the electrode as an enzymatic sensor in a biofuel cell configuration.

#### 2.4.7

#### **Carbon Nanotube-packaged Microelectrodes**

Packaged microelectrodes are easy to prepare and have been successfully used to prepare electrodes. To fabricate CNT powder microelectrodes, a 76- $\mu\text{m}$  diameter Pt microelectrode was first chemically etched to form a cavity of 10  $\mu\text{m}$  deep, and the etched tip was then grounded on a flat plate (such as glass slide) with CNTs until the micro cavity was filled with CNTs [63, 64]. In this way, the direct electrochemistry of redox enzymes such as GOD [64], horseradish peroxidase [65], as well as the electrocatalytic detection of nitrite [66], cysteine [67], and hydrazine [63] have been reported.

### 2.5

#### **Application of CNTs-based Electrochemical Sensors and Biosensors**

##### 2.5.1

#### **Electrochemical and Electrocatalytical Properties of Carbon Nanotubes**

CNTs combine, uniquely, high electrical conductivity, high chemical stability, and extremely high mechanical strength. These special properties of both SWCNTs

and MWCNTs have attracted the interest of many researchers in the field of electrochemical sensors. Many advances in producing, modifying, characterizing and integrating CNTs into electrochemical sensing systems have been achieved [68]. CNTs, new materials for electrochemical sensing, can be either used as single probes after formation *in situ*, or even individually, when attached onto a proper transducing surface after synthesis. Both SWCNTs and MWCNTs can be used to modify several electrode surfaces in either vertically oriented “nanotube forests” or even a non-oriented way. They can be also used in sensors after mixing them with a polymer matrix to form CNT composites [69].

To find new electrocatalytic surfaces, a suitable electrode substrate, such as glassy carbon or gold, is modified with a film or layer of CNTs. Several methods have achieved the electroanalysis of different analytes by using CNT modified electrodes. Benefits of low detection limits, increased sensitivity, decreased overpotentials and resistance to surface fouling are found by these CNTs-based electrodes [69].

Electrochemistry implies the transfer of charge from one electrode to another. Due to the curvature of the carbon graphene sheet in nanotubes, the electron clouds change from a uniform distribution around the C–C backbone in graphite to an asymmetric distribution inside and outside the cylindrical sheets of the nanotube [70]. Because the electron clouds are distorted, a rich  $\pi$ -electron conjugation forms outside the tube, therefore making CNTs electrochemically active (Fig. 2.2).

There are numerous reports of CNT-modified electrodes for the detection of different analytes with low detection limits, decreased overpotentials, and resistance to surface fouling. However, the exact reason for the unique catalytic properties of CNTs remains unknown. In this regard, Compton and his colleagues [71, 72] addressed the question as to why CNTs are catalytic and provided definitive evidence for their electrocatalytic properties. They explored the reduction of the one-electron aqueous redox probe ferricyanide at a CNT film-modified basal plane pyrolytic graphite (BPPG) electrode and compared it with a bare BPPG electrode. Peak-to-

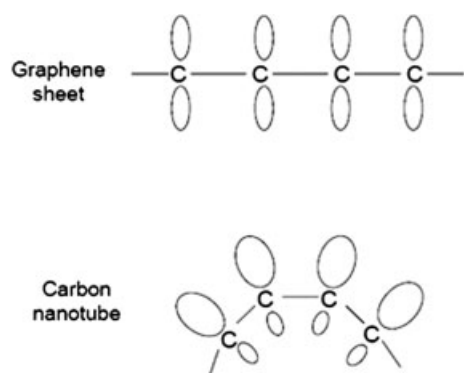
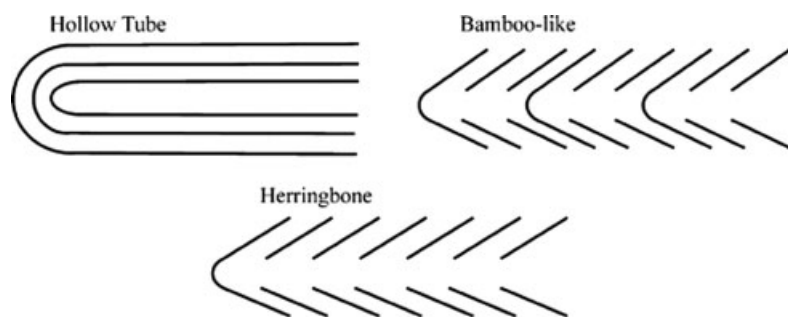


Fig. 2.2. Schematic of the electron distribution along a graphene sheet and around a carbon nanotube (CNT).

peak separations of 58 and 350 mV, respectively, were observed; the peak-to-peak separation is an indication of the heterogeneous charge transfer kinetics, showing that, in this case, CNTs exhibit fast electron transfer [71]. They further compared the electrocatalytic properties of CNTs with an edge plane pyrolytic graphite electrode (EPPG). EPPG electrodes are fabricated by taking a piece of high quality, highly ordered pyrolytic graphite (HOPG) and cutting the desired electrode geometry such that the layers of graphite lie perpendicular to the surface. Conversely, BPPG electrodes are produced by cutting the electrode geometry such that the graphite layers lie parallel to the surface. For voltammetry of ferricyanide at the EPPG electrode, a peak-to-peak separation of 78 mV was observed, suggesting that the electrochemical reaction occurs with a not dissimilar rate constant as at the CNT-modified surface. The slight difference in peak-to-peak separation of the CNTs compared with EPPGs probably reflects the slight impurities at the basal plane in the EPPG electrode. A catalytic response was also seen for the electrochemical oxidation of epinephrine where identical responses were obtained at both the CNT modified electrode and the EPPG; again, slow electrode kinetics was observed at a bare BPPG electrode. Indeed, it has been well documented that the electrode kinetics at EPPG electrodes are at least three times faster than at BPPG electrodes [73], but, seemingly, this was the first comparative approach to provide evidence for electrode kinetic enhancements at CNTs. Edge plane sites/defects are consequently introduced on the electrode surface, resulting in faster electron transfer. This occurs to the point that, after roughening for about a minute, a nearly identical response to that of the EPPG electrode can be observed. This clearly shows that edge plane sites are the dominant sites at which fast electron transfer occurs [74, 75]. The above experiments suggest that edge plane-like sites, which in CNTs occur at the ends and along the tube axis (where graphite sheets terminate at the surface of the tube), are likely to be the reason why nanotubes exhibit fast heterogeneous charge transfer, and explains why they have been widely reported as “electrocatalytic” in the electrochemical literature (Fig. 2.3) [72].

To understand the nature of the electrocatalytic properties and the electrochemical reactivity of CNT, Wang’s group [76] studied the effect of electrochemical pretreatment on CNTs prepared by different processes. They found that anodic pretreatment results in a dramatic improvement in the electrochemical reactivity of ARC-produced CNT, whereas CNTs produced by CVD appear to be resistant to anodic activation. Such a dramatic difference in the pretreatment effect upon ARG and CVD-produced CNTs is illustrated using NADH, ascorbic acid, hydrazine and hydrogen peroxide model redox systems. Differences in the effect of the electrochemical pretreatments are attributed to the anodic preanodization, effectively “breaking” the basal-plane end caps of ARC-CNT, thereby exposing edge plane defects, similar to those already present in the open-end caps of CVD-CNTs. In contrast, Gooding and his colleagues [77] demonstrated the importance of oxygenated species at the ends of CNTs for their favorable electrochemical properties. Definitive evidence is presented for the favorable electrochemical properties of CNT-modified electrodes arising from the ends of SWCNTs due to oxygenated carbon species in general, and carboxylic acid moieties in particular, produced during



**Fig. 2.3.** Schematic representation of the possible variants of CNTs. In both the bamboo and herringbone variations, graphite planes are formed at an angle to the axis of the tube and, therefore, these CNTs have a higher proportion of edge plane sites/defects. (Adapted from Ref. [72] with permission.)

acid purification. Interestingly, large amounts of well-aligned CNTs with open tips have been produced recently by pyrolysis of iron(II) phthalocyanine [78]. The aligned CNTs have an average length of about 10  $\mu\text{m}$  and diameters ranging from 92 to 229 nm. Some of the produced CNTs showed Y-junction structures due to the self-joint growth of two neighboring CNTs. The well-aligned CNTs indicated a bamboo-shaped multiwalled structure and fairly good crystallinity. Availability of the CNTs with open tips will make it possible to further study the electrocatalytic nature of CNTs.

### 2.5.2

#### CNTs-based Electrochemical Biosensors

For use as amperometric enzyme electrodes or DNA hybridization biosensors, CNTs need to be coupled with enzymes or ssDNA probes, respectively. Gooding and his colleagues have successfully self-assembled short SWCNTs to an electrode [24]. The vertically aligned SWCNTs act as molecular wires to allow electrical communication between the underlying electrode and a redox enzyme [23, 24] (Fig. 2.4). Such direct electron transfer between the prosthetic group of the enzyme and an electron surface makes it possible to develop reagentless sensing devices. The direct electron transfer of oxidases and dehydrogenases at CNT-modified electrodes and the dramatic decrease of the overpotential of hydrogen peroxide and NADH indicate great promise for the biosensing of glucose, lactate, cholesterol, amino acids, urate, pyruvate, glutamate, alcohol, hydroxybutyrate, etc. For example, CNT/Nafion/GOD-coated electrodes, coupling the selective reactivity of GOD to glucose with the electrocatalytic detection of hydrogen peroxide and the permselectivity of Nafion, offered a highly selective low-potential (0.05 V vs.  $\text{Ag}|\text{AgCl}$ ) biosensing of glucose [21]. More interestingly, Lin and coworkers [79] reported glucose biosensors based on GOD covalently attached at the free end of vertically-aligned CNTs, which have been grown on a metal-coated silicon substrate. They

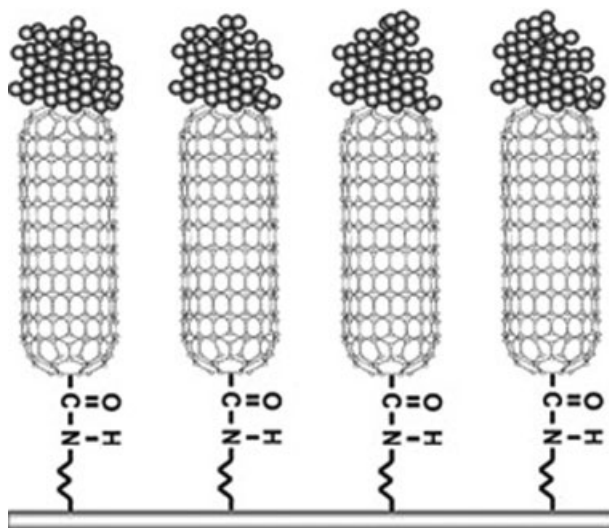


**Fig. 2.4.** Nanoforest of vertically aligned CNT-trees acting as molecular wires. (Adapted from Ref. [24] with permission.)

detected the reduction current of hydrogen peroxide, instead of the oxidation current, at a very low potential ( $-0.2$  V vs. saturated calomel electrode). The low-potential reductive detection of the hydrogen peroxide led to a highly selective amperometric monitoring of the glucose substrate, along with linearity up to  $30$  mM, and a detection limit of  $0.08$  mM. Different from GOD, dehydrogenase-based amperometric devices based on the co-immobilization of dehydrogenases and their  $\text{NAD}^+$  cofactor to electrodes for the biosensing of important substrates such as lactate, alcohol or glucose have also been described [69]. Oxidation of the product (i.e., NADH) serves as the anodic signal and regenerates the  $\text{NAD}^+$  cofactor. Therefore, CNT-modified electrodes, offering an accelerated electron transfer of NADH along with minimization of surface fouling associated with the accumulation of NADH oxidation product [20], provide great promise as dehydrogenase-based enzyme electrodes. For example, Wang and Musameh have reported a low-potential stable detection of ethanol based on the co-immobilization of alcohol dehydrogenase and its  $\text{NAD}^+$  cofactor within a CNT/Teflon matrix [80]. Similar advantages are expected for the biosensing of lactate or glucose in connection with lactate or glucose dehydrogenase, respectively [69]. Deo et al. [81] have reported an amperometric biosensor for organophosphorus (OP) pesticides based on a CNT-modified transducer and an organophosphorus hydrolase (OPH) biocatalyst. To prepare the CNT/OPH biosensor, a bilayer approach with the OPH layer atop of the CNT film was used. The CNT layer leads to a greatly improved anodic detection of the enzymatically generated p-nitrophenol product, including higher sensitivity and stability. The biosensor was used to measure as low as  $0.15$   $\mu\text{M}$  paraoxon and  $0.8$   $\mu\text{M}$  methyl

parathion, with sensitivities of 25 and 6 nA  $\mu\text{M}^{-1}$ , respectively. Li et al. have studied a CNT-modified biosensor for monitoring total cholesterol in blood [82]. The sensor consists of a carbon working electrode and a reference electrode screen-printed on a polycarbonate substrate. Cholesterol esterase, cholesterol oxidase, peroxidase, and potassium ferrocyanide were immobilized on the screen-printed carbon electrodes. MWCNTs were added to prompt electron transfer. Experimental results show that the CNT-modified biosensor offers a reliable calibration profile and stable electrochemical properties.

The remarkable electrocatalytic activity of CNTs, together with the ability to modify CNTs for accumulating important biomolecules, make them extremely attractive for a wide range of electrochemical biosensors, ranging from enzyme-based electrochemical biosensors to DNA hybridization biosensors [69]. CNT-based electrochemical biosensors combine the specificity of enzymes with the electrocatalytic ability of nanotubes, and are expected to be extremely useful for clinical diagnostics and environmental monitoring.

## 2.6

### Functionalization of CNTs

#### 2.6.1

##### Biological Functionalization of CNTs

Biological functionalization of CNTs has come to be of significant interest in recent years due to the possibility of developing sensitive and ultrafast detection systems in biomedical sciences and biotechnological application. CNTs functionalized with biological assays could be the key to novel nano-biosensing techniques. Functionalization of CNT surfaces using proteins and antibodies could enable specific interactions and selective binding to target biomolecules with a very low sample size, often approaching a single protein. Alteration of the surface chemistry of their sidewalls can lead to covalent functionalization and, hence, to their potential application in drug delivery and chemical and biochemical sensing applications [83]. The functionalization of CNTs with proteins like streptavidin and biotin with the help of a polymer coating with poly(ethylene glycol) (PEG), and covalent interactions with its amine-terminated variant, has been demonstrated [84]. Since all the atoms in CNTs are surface atoms, binding proteins or antibodies to surfaces can greatly affect their surface states and, thus, their electrical and optical properties. This effect can be exploited as a basis for detecting biological surface reactions in a single protein or antibody attached to CNT surfaces.

#### 2.6.2

##### Self-assembly of Surfactant and Lipid Molecules at CNTs

Surfactant adsorption at interfaces has been widely studied because of its importance in detergents, lubrication, and colloid stabilization [85]. CNTs are insoluble

in organic solvents and in water, which at present considerably restricts their areas of use. To enhance the solubility of CNTs, detergents are mixed and shaken with nanotubes to form stable suspensions [86]. The chemical adsorption of SDS molecules on the surface of the nanotubes creates a distribution of negative charges that prevents their aggregation and induces stable suspensions in water. The SDS molecules can be oriented perpendicularly to the surface of the nanotube, forming a monolayer. The molecular organization of surfactant at the solid–liquid interface can be (a) the hydrophobic part of SDS is adsorbed on the graphite by van der Waals interactions, likely following the carbon network, and (b) the hydrophilic part of the surfactant is oriented toward the aqueous phase, forming half-cylinders on the surface of the graphite plane [87]. Because CNTs are rolled-up graphene sheets, the SDS molecules may form similar half-cylinders on the surface of the tubes, either oriented parallel or perpendicularly to the tube axis.

The self-assembly of lipids at metallic–aqueous interfaces has been well studied. To determine whether lipid molecules could adsorb and self-organize on CNTs, creating stable assemblies, Richard et al. have designed and synthesized new reagents that form lipidic “rings” made up of supramolecular half-cylinders [88]. TEM results indicated the formation of supramolecular assemblies of these molecules on the surface of the nanotubes. To explore the possibility of functionalizing the surface of CNTs in a noncovalent but permanent way with different reagents, the self-assembly of a series of molecules made of a double lipidic chain was further tested. In contrast to the single-chain lipids, no organization was detected by TEM when an aqueous solution ( $1 \text{ mg mL}^{-1}$ ) of the second series of molecules was directly sonicated with 1 mg of MWCNTs. To investigate whether micelles are necessary to form these supramolecular assemblies, the MWCNTs were sonicated in the presence of mixed micelles. TEM observations showed perfectly organized striations on the CNTs. The size of the striations, determined by TEM, varied from 55 to 75 Å, in perfect agreement with the length of the different lipidic chains. These results are also coherent with a half-cylinder arrangement of the double-chain lipids on the surface of the nanotubes. Hence, the formation of micelles appears to be a key step for the formation of supramolecular assemblies on the CNT surface. This process constitutes a simple, versatile protocol for the non-covalent functionalization of nanotubes.

One of the most exciting applications of CNTs is in the exploration of proteins and cells in aqueous solution. Few of these applications have yet been realized, because of the incompatibility of the CNT surface, which is hydrophobic and prone to nonspecific bioadsorption with biological components such as cells and proteins. In addition, the aqueous environment required for biological materials is not suitable for unfunctionalized CNTs [89]. In nature, cells are faced with a similar challenge of resisting nonspecific biomolecule interactions while engaging in specific molecular recognition. These functions can be simultaneously fulfilled by mucin glycoproteins, defined by their dense clusters of O-linked glycans. Zettl and associates [90] have described a biomimetic surface modification of CNTs using glycosylated polymers designed to mimic natural cell-surface mucins. A  $C_{18}$  lipid at one end of a mucin-mimic polymer is introduced to enable surface modification of

CNTs. Lipids self-assemble on the surface of CNTs through hydrophobic interactions in the presence of water [88] and lipid functionalized glycopolymers form ordered arrays on graphite surfaces [91]. The lipid-functionalized mucin-mimic is self-assembled on CNTs in a similar manner as the organization of native mucins in the cell membrane, with the glycosylated polymers projecting into the aqueous medium. CNTs modified with mucin-mimics were soluble in water, resisted non-specific protein binding, and bound specifically to biomolecules through receptor–ligand interactions. This strategy for biomimetic surface engineering provides a means to bridge CNTs and biological systems.

Several successful strategies using covalent or noncovalent chemistry have been applied to functionalize the sidewall of CNTs. Among these, noncovalent methods are attractive as they may preserve the inherent properties of the nanotubes [88, 92]. Supported bilayer lipid membranes (s-BLMs) have attracted increasing interest due to their potential application as electrochemical biosensors, molecular devices, and for investigating the photoinduced electron transfer in biomembranes [93, 94].

Recently, we [39] successfully self-assembled s-BLM on the surface of MWCNTs using Tien's method [94, 95]. The CV responses of BLMs-coated MWCNTs in PBS were studied. At bare MWCNT electrodes, a large background current  $i$  (in the range of  $10^{-5}$  A) was observed. When the MWCNT electrodes were coated with BLMs, the background current was dramatically reduced to the range of  $10^{-9}$  A, indicating a strong insulation effect of the lipids assembled on the surface of the MWCNTs. Since the membrane capacitance ( $C_m$ ) can be obtained from the background current of the CV ( $C_m = i/v$ ), the thickness of lipid membrane  $T_m$  on MWCNTs can be calculated from  $T_m = 2.2\epsilon_0 A/C_m$  ( $\epsilon_0$ : vacuum dielectric permittivity,  $A$ : surface area).  $T_m$  was thus calculated to be about 4.38 nm, which is approximately double the molecular size of phosphatidylcholine – consistent with a bilayer structure of the lipid membrane [94]. The static water contact angles on the surface of MWCNTs were measured to be  $6\text{--}7^\circ$ , indicating a hydrophilic property of the MWCNT surface. The bilayer lipid membrane can thus be formed with the hydrophilic moiety of one lipid layer absorbed on the surface of MWCNTs, and that of another lipid layer faced to the testing PBS solution. This result agrees with that reported by Kanyó et al. [96] but differs from that found by Richard et al. [88]. Kanyó et al. reported that the surface of MWCNTs, without heating treatment, were hydrophilic [96]. In contrast, Richard et al. reported that a monolayer of synthetic lipid was self-assembled at the surface of CNTs, in which the van der Waals interaction between the hydrophobic part of lipid and the carbon network was suggested [88]. The different hydrophilicity reported may come from the different fabrication methods of the CNTs. When MWCNTs were synthesized from the chemical source of ethylenediamine, chemical elemental analysis indicated that 1.8–2.8% nitrogen existed in the MWCNTs used in the present study [37]. Functional groups containing nitrogen on the MWCNT surface may contribute partly to the hydrophilic property on the MWCNTs synthesized and used here. In addition, it is known that the carbon shell (i.e., each carbon shell of the MWCNT) is closed by various functional groups, most frequently by COOH, –OH, and CO groups. For MWCNTs, the outer shell may often contain discontinuous spots of



imperfection. These local vacancies could also be closed by the functional groups mentioned above [96]. Possibilities exist for these functional groups to confer the hydrophilic surface of the MWCNTs.

### 2.6.3

#### Electrochemical Functionalization of CNTs

The electrochemical functionalization of CNTs has opened up new opportunities to fabricate novel nanostructures by improving both their solubility and processibility. Small-diameter (ca. 0.7 nm) SWCNTs are predicted to display enhanced reactivity relative to larger-diameter nanotubes due to increased curvature strain. Bahr et al. have described the derivatization of these small-diameter nanotubes via electrochemical reduction of various aryl diazonium salts [97]. The estimated degree of functionalization is as high as one out of every 20 carbons in the nanotubes bearing a functionalized moiety. The functionalizing moieties can be removed by heating in an argon atmosphere. Nanotubes derivatized with a 4-*tert*-butylbenzene moiety possessed significantly improved solubility in organic solvents. Functionalization of the nanotubes with a molecular system holds strong promise as useful building blocks for the construction of novel hybrids for nano-sensor applications.

Electrochemical functionalization of CNTs is a selective, clean, and nondestructive chemical method. But it meets difficulties in homogeneous electrografting of SWCNTs in large quantities because the reaction is often localized on a very thin film (ca. 2  $\mu\text{m}$ ). To solve this problem, Zhang et al. have utilized a room-temperature ionic liquid (RTIL)-supported three-dimensional network SWCNT electrode [98]. In their work, large quantities of SWCNTs were considerably untangled in RTILs so as to greatly increase the effective area of the electrode. *N*-Succinimidyl acrylate (NSA), as a model monomer, was dissolved in the supporting RTILs and was electrografted onto SWCNTs (SWCNTs-poly-NSA). As an application example, GOD was covalently anchored on the SWCNT-poly-NSA assembly, and the electrocatalytic oxidation of glucose in this assembly was investigated. RTILs have opened a new path in electrochemical functionalization of CNTs. Recently, we studied the effect of electrochemical oxidation in 0.2 M  $\text{HNO}_3$  for MWCNTs [99]. Scanning electron microscope (SEM) and transmission electron microscope (TEM) images reveal that electrochemical oxidation increases the specific area of MWCNTs by cutting off the nanotube tips. Cyclic voltammetry and constant current charging/discharging was used to characterize the behavior of electrochemical double layer capacitors (EDLCs) of the oxidized MWCNTs in 1.0 M  $\text{H}_2\text{SO}_4$ . The specific capacitance of the oxidized-MWCNTs was remarkably improved. Electrochemical oxidation is, hence, an effective way to improve the performance of MWCNT electrodes in EDLC application. More recently, electrochemical nitration of self-assembled SWCNT sheets with  $-\text{NO}_2$  groups was achieved [100]. A SWCNT sheet, used as the working electrode in 6 M aqueous solution of potassium nitrite, was anodically oxidized to form  $-\text{NO}_2$  groups on the SWCNTs. Attenuated-total-reflection Fourier-transform infrared and micro-Raman spectroscopy showed

the presence of chemisorbed  $-\text{NO}_2$  groups, consistent with transmission electron microscope images of the nanotube bundles after functionalization.

#### 2.6.4

### Electrochemical Application of Functionalized CNTs

#### 2.6.4.1 Application of Lipid–CNT Nanomaterials in Electrochemical Sensors

Sensors represent a most plausible and exciting application area for nanobiotechnology, and nanosensors based on CNTs are expected to emerge in the marketplace in significant volumes over the next ten years. Despite tremendous excitement recently generated by experimental breakthroughs that have led to realistic possibilities of using CNTs in electrochemical sensors, further experimental and theoretical research is necessary. The formation of stable lipid–CNT assemblies offers a simple, efficient method for the development of sensors/biosensors. The supramolecular structure of lipid–CNTs may lead to several applications in the field of nanobiotechnology. For example, it could be used for the development of molecular sensors (biosensors) for detecting the body's molecules. To actualize and optimize the full commercial potential of CNT-based electrochemical sensors, efforts must continue to be devoted to integrate the nanotube-arrays with power, miniaturized and easy-to-use electrochemical instruments for bimolecular sensing, genetic analysis, and drug discovery or screening.

The photoelectric effects of bilayer lipid membranes (BLMs) and electron mediator modified BLMs have been extensively studied, on account of their possible applications in understanding the mechanism of natural photosynthesis, in developing artificial photoelectric devices [101], and in mimicking functionalities of natural photosynthetic systems, which are represented by photoactive groups, electron donors and acceptors [102]. Various attempts have been made to realize an artificial photosynthesis and solar-energy conversion system under laboratory conditions. For example, synthetic dyes have been used to dope BLMs and the corresponding photoresponses have been investigated [103].

Recently, we have described the self-assembly of BLM and  $\text{C}_{60}$ -containing BLM at well-aligned MWCNTs for the development of a novel photoswitchable electrochemical device [39]. The lipid membrane at MWCNTs is estimated to be 4.38 nm thick, which is approximately double the molecular size of phosphatidylcholine, indicating that the BLM at the surface of nanotubes has a bilayer structure. Lipid membrane self-assembled at MWCNTs acts as an insulating layer while the incorporated  $\text{C}_{60}$  can mediate the transport of electrons as well as photocurrent across BLM (Fig. 2.5). The membrane resistance of  $\text{C}_{60}$ -BLM/MWCNTs is 369.3  $\Omega$ , which is much smaller than that of BLM/MWCNTs ( $3.238 \times 10^6 \Omega$ ). Furthermore,  $\text{C}_{60}$ -BLM/MWCNTs possess photoelectric properties due to the electron mediation of  $\text{C}_{60}$  in the lipid membrane. The photoelectric conversion properties of MWCNTs, BLM/MWCNTs, and  $\text{C}_{60}$ -BLM/MWCNTs were thus studied using an amperometric technique. At the lipid interface,  $\text{C}_{60}$  transports about 30–40% of electrons, compared with that of pure MWCNTs, from MWCNTs to the redox species in solu-

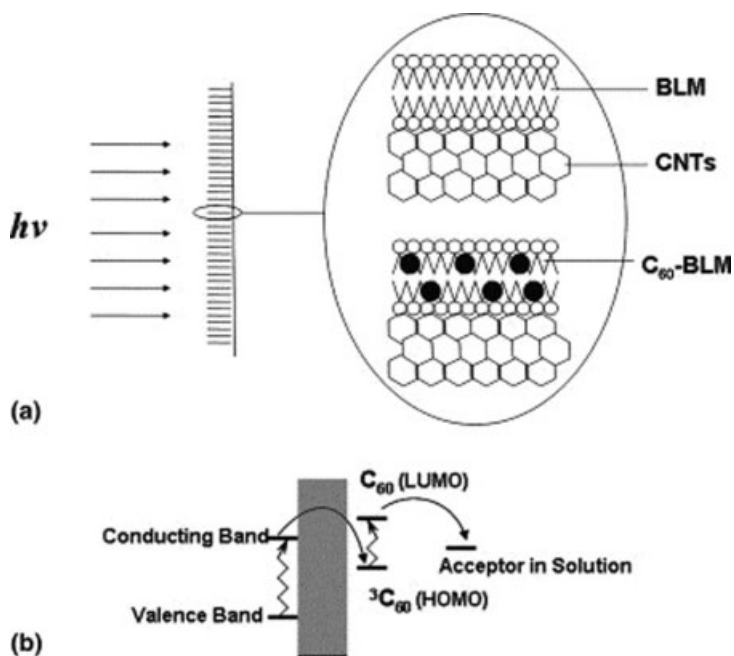


**Fig. 2.5.** (a) Schematic of BLM/MWCNTs and C<sub>60</sub>-BLM/MWCNTs electrode for photocurrent measurement and electrochemical experiments (BLM = bilayer lipid membrane). (b) Possible mechanism of photocurrent generation at the C<sub>60</sub>-BLM/MWCNTs cathode. HOMO, the highest occupied molecular orbital; LUMO, the lowest unoccupied molecular orbital. (Adapted from Ref. [39] with permission.)

tion. The successful self-assembly of BLM and incorporation of C<sub>60</sub> into the BLM at MWCNTs may provide an easy way for construction of new biosensors and bioelectronic materials using BLM/MWCNTs and/or C<sub>60</sub>-BLM/MWCNTs nanocomposites.

#### 2.6.4.2 Achieving direct Electron Transfer to Redox Proteins by Functional CNTs

CNT electrodes have been successfully used to study protein electrochemistry. The novel electrochemical properties and the nanoscale size of CNTs have opened research opportunities in studying hitherto unapproachable phenomena at interfaces and bifaces for redox proteins [23, 24, 104, 105]. The direct electron transfer of proteins such as peroxidases [23, 24, 65], cytochrome *c* [15, 30, 106], myoglobin [107], catalase [108], azurin [15], and GOD [64] have been achieved by the use of CNT electrodes.

Recently, Mao and associates [109] have described the preparation and bioelectrochemical properties of functional nanohybrids through co-assembling of heme-proteins (i.e., horseradish peroxidase, hemoglobin, myoglobin and cytochrome *c*) and surfactants onto CNTs. The prepared protein–surfactant–CNT nanohybrids (Fig. 2.6) possess facilitated interfacial electron transfer of the proteins with en-

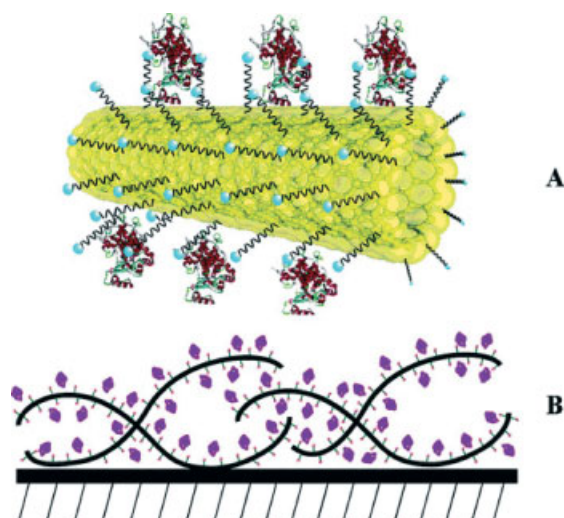


**Fig. 2.6.** Cartoons of (A) bioelectrochemically functional unit through co-assembly of protein and surfactant onto a single MWCNT and (B) nanohybrids consisting of single biofunctional nanotubes deposited onto the glassy carbon electrode. (Adapted from Ref. [109] with permission.)

hanced faradic responses. The enhancements are ascribed to the ability of surfactants to facilitate protein electrochemistry and to the improved portion of electroactive proteins assembled, of which the latter assignment is closely associated with the electrochemical and structural properties of the nanotubes, and the three-dimensional (3D) architecture of the CNT film confined on the glassy carbon electrode. It is proposed that the single and/or small bundles of the nanotubes in the CNT film electrode can be rationally functionalized with surfactants to be functional nanoelectrodes capable of facilitating electron transfer of proteins. The 3D confinement of these functional nanowires onto the GC electrode essentially increases the portion of electroactive proteins assembled in the nanohybrids. These properties of the protein–surfactant–CNT nanohybrids, combined with the bioelectrochemical catalytic activity, could make them useful for development of bioelectronic devices and for the investigation of protein electrochemistry at functional interfaces.

#### 2.6.4.3 Biomolecule-functionalized CNTs for Electrochemical Sensors and Biosensors

Biomolecule-functionalized carbon nanomaterials have been of interest in electrochemical areas in both fundamental research and application. The immobilization of molecules, biomolecules or even nanoparticles on SWCNTs has been exploited, motivated by the prospects of using nanotubes as new types of sensor/biosensor materials [110–113]. In contrast, there are few studies on the modification of

MWCNTs [36, 114–117]. The conducting nature of the MWCNTs, together with their outstanding electronic and mechanical properties, make them attractive for potential applications. Hemin (iron protoporphyrin IX) is the active center of the heme-protein family, such as *b*-type cytochromes, peroxidase, myoglobin and hemoglobin. It contains a porphyrin ring, which can be immobilized at the surface of CNTs through noncovalent functionalization by  $\pi$ - $\pi$  interaction [92]. We have successfully constructed a hemin-modified MWCNT electrode [43] and characterized its electrochemical behavior by CV. The electron-transfer coefficient ( $\alpha$ ) was found to be 0.38, with a heterogeneous electron transfer rate ( $k$ ) of  $2.9 \text{ s}^{-1}$  for the adsorbed hemin. The hemin-modified MWCNT electrodes show ideal reversibility in  $5 \text{ mM K}_3[\text{Fe}(\text{CN})_6]$  in the range  $0.02$ – $1.00 \text{ V s}^{-1}$ , indicating fast electron-transfer kinetics. CV of the hemin-modified MWCNT electrode in pH 7.4 phosphate buffer solution (PBS) clearly shows the dioxygen reduction peaks to be close to  $0 \text{ V}$  (vs.  $\text{Ag}|\text{AgCl}$ ). These results are useful in the development of a novel oxygen sensor for working at a relatively low potential. To improve the sensitivity of CNT-based electrochemical sensors toward hydrogen peroxide, we functionalized MWCNTs with iron-phthalocyanines (FePc) [40]. Highly sensitive and selective glucose sensors can be constructed on FePc-MWCNTs electrodes based on the immobilization of GOD on a poly-*o*-aminophenol (POAP)-electropolymerized electrode surface. SEM images indicate that GOD enzymes trapped in POAP film tend to deposit primarily on the curved tips and evenly disperse along the sidewalls. The GOD@POAP/FePc-MWCNTs biosensor we proposed exhibits excellent performance for glucose with a rapid response (less than 8 s), a wide linear range (up to  $4.0 \times 10^{-3} \text{ M}$ ), low detection limits ( $2.0 \times 10^{-7} \text{ M}$  with signal-to-noise of 3), a highly reproducible response (RSD of 2.6%), and long-term stability (120 days). Such characteristics may be attributed to the catalytic activity of FePc-functionalized CNT, permselectivity of POAP film, as well as the large surface area of CNT materials. Aligned CNT electrode arrays have been used to achieve direct electron transfer to enzymes with redox centers close to the surface of the protein [23, 24]. Most of the electrochemistry was dominated by proteins immobilized on the electroactive ends of the nanotubes. Both horseradish peroxidase and myoglobin functionalized CNTs [23] could be used analytically to detect hydrogen peroxide.

CNTs have generated considerable recent interest in bioelectronics and electrochemistry owing to their unique mechanical, electrical, and chemical properties [69, 118]. The electrocatalytic properties of these materials have been exploited as a means of promoting electron-transfer reactions of a wide range of important biomolecules [107, 119]. For example, the greatly enhanced electrochemical reactivity of hydrogen peroxide and NADH at CNT-modified electrodes makes these nanomaterials extremely attractive for numerous oxidase- and dehydrogenase-based amperometric biosensors [20, 21]. The use of CNT molecular wires offers great promise for achieving efficient electron transfer from electrode surfaces to the redox sites of enzymes [105]. Recently, Georgakilas and colleagues have described the magnetic modification of CNTs [120]. It is expected that the magnetic and catalytic properties of CNTs can be exploited for the magnetoswitchable control of electron transfer reactions with functionalized magnetic particles. Pyrene can be non-

covalently attached on the CNT surface. A carboxylic derivative of pyrene is used as an interlinker for the binding of capped magnetic nanoparticles on the CNTs. The increased organophilic character of the capped nanoparticles induces high solubility in organic media for the modified CNTs.

The unique structure and the outstanding electronic properties of CNTs coupled with the specific recognition properties of DNA would indeed make CNT–DNA bioconjugates widely useful in biosensors [121]. To prepare the bioconjugates, CNTs are treated with concentrated oxidizing acids so as to cover their ends and surfaces with oxygen-containing groups such as carboxyl groups and ether groups. The pretreated CNTs are then dispersed in water or organic solvents with the aid of ultrasonic oscillation. Biomolecules can be linked to CNT-modified electrodes with the aid of 1-ethyl-3-(3-dimethylaminopropyl)carbodiimide (EDC) and/or *N*-hydroxysuccinimide (NHS) through the formation of an amide bond between the carboxylic groups on CNTs and the amino groups in biomolecules. Guo et al. have studied the electrochemical characteristics of the immobilization of DNA on the surface of MWCNTs [122, 123]. Both single strand and double strand calf thymus DNA molecules were attached to MWCNT-modified gold electrodes with the aid of EDC and NHS. The results of CV, electrochemical impedance spectroscopy (EIS), and piezoelectric quartz crystal impedance (PQCI) indicate that calf thymus DNA can be immobilized on MWCNTs via a cationic polyelectrolyte. No matter how DNA molecules were immobilized on MWCNTs, they still remained bioactive and could interact with small molecules such as chlorpromazine hydrochloride and ethidium bromide (EB). Recently, SWCNTs functionalized with amino groups have been prepared via chemical modification of carboxyl groups introduced on the CNT surface [124]. Two different approaches (amide and amine-moieties) were used to produce the amino-functionalized nanotubes. The amino-termination allows further chemistry of the functionalized SWCNTs and makes possible covalent bonding to polymers and biological systems such as DNA and carbohydrates. Wang et al. have attached CdS nanoparticles capped with octadecanethiol (ODT) to SWCNTs, which were dispersed in toluene after pretreatment with acetone, through hydrophobic interactions [125]. Then, streptavidin was anchored to CdS-SWCNTs, followed by combination with biotinylated probe DNA. The resultant SWCNTs-DNA bioconjugates were attached to a microplate through “sandwich” hybridization. Target DNA can be detected via determination of cadmium in CdS nanoparticles dissolved by nitric acid at a mercury film GCE by stripping voltammetry. The detection limit is around  $40 \text{ pg mL}^{-1}$ . With selective functionalization of oligonucleotide probes at the open ends of MWCNTs, Meyyappan’s group [121] reported that a nanoelectrode array based on vertically aligned MWCNTs embedded in  $\text{SiO}_2$  can be used for ultrasensitive DNA detection. Characteristic electrochemical behaviors are observed for measuring bulk and surface-immobilized redox species. Sensitivity is dramatically improved by lowering the nanotube density. More recently, they reported a similar approach for the fabrication of nanoelectrode arrays using vertically aligned MWCNTs embedded within a  $\text{SiO}_2$  matrix [126]. CV and pulse voltammetry were employed to characterize the electrochemical properties of the MWCNT array. The unique graphitic structure of the

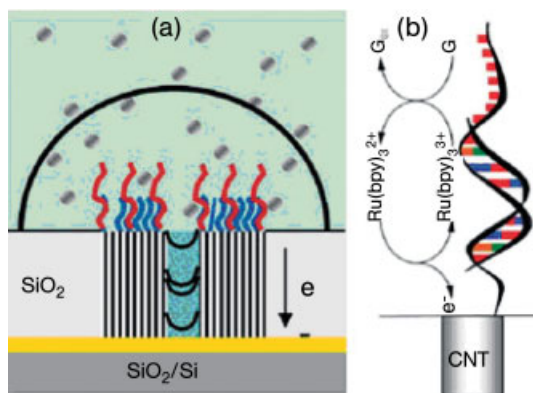


**Fig. 2.7.** (a) and (b) Schematic of the mechanism for DNA/RNA sensing on an inlaid MWCNT nanoelectrode combined with  $\text{Ru}(\text{bpy})_3^{2+}$  mediator amplified guanine oxidation. Short blue lines in (a) represent oligonucleotide probe molecules functionalized

at the open end of MWCNTs, and the longer red lines represent target molecules hybridized with the probe molecules. The hemisphere represents the diffusion layer of  $\text{Ru}(\text{bpy})_3^{2+}$  mediators. (Adapted from Ref. [126] with permission.)

novel MWCNT nanoelectrodes were compared with model systems such as highly oriented pyrolytic graphite and glassy carbon electrodes. Low-density MWCNT nanoelectrode arrays display independent nanoelectrode behavior, showing diffusion-limited steady-state currents in cyclic voltammetry over a wide range of scan rates. Electroactive species can be detected at concentrations as low as a few nm. In addition, ultrasensitive DNA/RNA sensors have been demonstrated using the low-density MWCNT arrays with selectively functionalized oligonucleotide probes (Fig. 2.7). This platform can be widely used in analytical applications as well as fundamental electrochemical studies. In summary, biomolecule-functionalized CNT electrodes can in the future be used as a new type of miniature DNA affinity biosensors [127].

## 2.7

### Conclusions and Future Prospects

We have addressed recent advances in electrochemistry and electrochemical application of CNTs, particularly of the functionalized CNTs with specific properties. The attractive properties of functionalized CNTs have paved the way for the construction of a wide range of electrochemical sensors/biosensors exhibiting attractive analytical behavior. In particular, functionalization of the CNT surface can result in highly soluble materials, which can be further modified with active molecules, making them compatible with biological systems. Therefore, many applications can be envisaged by using functionalized CNTs. With the creation of bifaces and interfaces at lipid-CNTs nanocomposites, progress in CNT technology may

well lead to better insights into biological and physical chemistry processes. This will make it possible to find compounds more compatible with CNT technology and to facilitate more effective use in electrochemical applications. Highly selective and sensitive molecular sensors based on CNTs are set to become commonplace in the near future.

## Acknowledgments

Part of the work conducted in our laboratory and reviewed in this chapter was supported by the Academic Research Grant of the National University of Singapore R-398-000-024-112, and by the Defense Science & Technology Agency of Singapore R-154-000-243-422, to F.-S. S. We are also grateful to many colleagues who have collaborated with our group over the years, contributing heavily to the development of the CNT electrochemical sensors.

## References

- 1 S. IIJIMA, Helical microtubules of graphitic carbon, *Nature* 354 (1991) 56–58.
- 2 S. IIJIMA, T. ICHIHASHI, Single-shell carbon nanotubes of 1-nm diameter, *Nature* 363 (1993) 603–605.
- 3 A. THESS, R. LEE, P. NIKDAEV, H. DAI, P. PETIT, J. ROBERT, C. XU, Y. H. LEE, S. G. KIM, A. G. RINZLER, D. T. COLBERT, G. E. SCUSERIA, D. TOMANEK, J. E. FISCHER, R. E. SMALLEY, Crystalline ropes of metallic carbon nanotubes, *Science* 273 (1996) 483–487.
- 4 R. SAITO, M. FUJITA, G. DRESSELHAUS, M. S. DRESSELHAUS, Electronic structure of grapheme tubules based on C<sub>60</sub>, *Phys. Rev. B* 46 (1992) 1804–1811.
- 5 R. SAITO, M. FUJITA, G. DRESSELHAUS, M. S. DRESSELHAUS, Electronic structure of chiral graphite tubes, *Appl. Phys. Lett.* 60 (1992) 2204–2206.
- 6 J. H. WEAVER, D. M. POIRIER, Solid state properties of fullerenes and fullerene-based materials, *Solid State Phys. – Adv. Res. Applicat.* 48 (1994) 1–108.
- 7 J. W. MINTMIRE, B. I. DUNLAP, C. T. WHITE, Are fullerene tubules metallic, *Phys. Rev. Lett.* 68 (1992) 631–634.
- 8 N. HAMADA, S. SAWADE, A. OSHIYAMA, New one-dimensional conductors: Graphitic microtubules, *Phys. Rev. Lett.* 68 (1992) 1579–1581.
- 9 B. I. YAKOBSON, C. J. BRABEC, J. BERNHOLC, Nanomechanics of carbon tubes: Instabilities beyond linear response, *Phys. Rev. Lett.* 76 (1996) 2511–2514.
- 10 M. M. J. TREACY, T. W. EBBESEN, J. M. GIBSON, Exceptionally high Young's modulus observed for individual carbon nanotubes, *Nature* 381 (1996) 678–680.
- 11 E. W. WONG, P. E. SHEEHAN, C. M. LIEBER, Nanobeam mechanics: Elasticity, strength, and toughness of nanorods and nanotubes, *Science* 277 (1997) 1971–1975.
- 12 P. J. BRITTO, K. S. V. SANTHANAM, P. M. AJAYAN, Carbon nanotube electrode for oxidation of dopamine, *Bioelectrochem. Bioenerg.* 41 (1996) 121–125.
- 13 E. PENNISI, Simple recipe yields fullerene tubules, *Sci. News* 142 (1992) 36.
- 14 Z. H. WANG, J. LIU, Q. L. LIANG, Y. M. WANG, G. LUO, Carbon nanotube-modified electrodes for the simultaneous determination of



- dopamine and ascorbic acid, *Analyst* 127 (2002) 653–658.
- 15 J. J. DAVIS, R. J. COLES, H. A. O. HILL, Protein electrochemistry at carbon nanotube electrodes, *J. Electroanal. Chem.* 440 (1997) 279–282.
  - 16 H. X. LUO, Z. J. SHI, N. Q. LI, Z. N. GU, Q. K. ZHUANG, Investigation of the electrochemical and electrocatalytic behavior of single-wall carbon nanotube film on a glassy carbon electrode, *Anal. Chem.* 73 (2001) 915–920.
  - 17 P. J. BRITTO, K. S. V. SANTHANAM, A. RUBIO, J. A. ALONSO, P. M. AJAYAN, Improved charge transfer at carbon nanotube electrodes, *Adv. Mater.* 11 (1999) 154–157.
  - 18 J. KONG, N. R. FRANKLIN, C. ZHOU, M. G. CHAPLINE, S. PENG, K. CHO, H. DAI, Nanotube molecular wires as chemical sensors, *Science* 287 (2000) 622–625.
  - 19 P. G. COLLINS, K. BRADLEY, M. ISHIGAMI, A. ZETTL, Extreme oxygen sensitivity of electronic properties of carbon nanotubes, *Science* 287 (2000) 1801–1804.
  - 20 M. MUSAMEH, J. WANG, A. MERKOCI, Y. LIN, Low-potential stable NADH detection at carbon-nanotube-modified glassy carbon electrodes, *Electrochem. Commun.* 4 (2002) 743–746.
  - 21 J. WANG, M. MUSAMEH, Y. H. LIN, Solubilization of carbon nanotubes by Nafion toward the preparation of amperometric biosensors, *J. Am. Chem. Soc.* 125 (2003) 2408–2409.
  - 22 J. WANG, M. MUSAMEH, Carbon nanotube/teflon composite electrochemical sensors and biosensors, *Anal. Chem.* 75 (2003) 2075–2079.
  - 23 X. YU, D. CHATTOPADHYAY, I. GALESKA, F. PAPADIMITRAKOPOULOS, J. F. RUSLING, Peroxidase activity of enzymes bound to the ends of single-wall carbon nanotube forest electrodes, *Electrochem. Commun.* 5 (2003) 408–411.
  - 24 J. J. GOODING, R. WIBOWO, J. Q. LIU, W. R. YANG, D. LOSIC, S. ORBONS, F. J. MEARNES, J. G. SHAPTER, D. B. HIBBERT, Protein electrochemistry using aligned carbon nanotube arrays, *J. Am. Chem. Soc.* 125 (2003) 9006–9007.
  - 25 S. J. LEE, H. K. BAIK, J. E. YOO, J. H. HAN, Large-scale synthesis of carbon nanotubes by plasma rotating arc discharge technique, *Diamond Relat. Mater.* 11 (2002) 914–917.
  - 26 T. GUO, P. NIKOLAEV, A. THESS, D. T. COLBERT, R. E. SMALLEY, Catalytic growth of single-walled nanotubes by laser vaporization, *Chem. Phys. Lett.* 243 (1995) 49–54.
  - 27 Z. F. REN, Z. P. HUANG, J. W. XU, J. H. WANG, P. BUSH, M. P. SIEGEL, P. N. PROVENCIO, Synthesis of large arrays of well-aligned carbon nanotubes on glass, *Science* 282 (1998) 1105–1107.
  - 28 Z. F. REN, Z. P. HUANG, D. Z. WANG, J. G. WEN, J. W. XU, J. H. WANG, L. E. CALVET, J. CHEN, J. F. KLEMIC, M. A. REED, Growth of a single freestanding multi-wall carbon nanotube on each nano-nickel dot, *Appl. Phys. Lett.* 75 (1999), 1086–1088.
  - 29 J. K. CAMPBELL, L. SUN, R. M. CROOKS, Electrochemistry using single carbon nanotubes, *J. Am. Chem. Soc.* 121 (1999) 3779–3780.
  - 30 J. X. WANG, M. X. LI, Z. J. SHI, N. Q. LI, Z. N. GU, Direct electrochemistry of cytochrome *c* at a glassy carbon electrode modified with single-wall carbon nanotubes, *Anal. Chem.* 74 (2002) 1993–1997.
  - 31 N. S. LAWRENCE, R. P. DEO, J. WANG, Comparison of the electrochemical reactivity of electrodes modified with carbon nanotubes from different sources, *Electroanalysis* 17 (2005) 65–72.
  - 32 J. N. BARISCI, G. G. WALLACE, R. H. BAUGHMAN, Electrochemical studies of single-wall carbon nanotubes in aqueous solutions, *J. Electroanal. Chem.* 488 (2000) 92–98.
  - 33 C. Y. LIU, A. J. BARD, F. WUDL, I. WEITZ, J. R. HEATH, Electrochemical characterization of films of single-walled carbon nanotubes and their possible application in supercapacitors, *Electrochem. Solid State Lett.* 2 (1999) 577–578.

- 34 C. NIU, E. K. SICHEL, R. HOCH, D. MOY, H. TENNET, High power electrochemical capacitors based on carbon nanotube electrodes, *Appl. Phys. Lett.* 70 (1997) 1480–1482.
- 35 H. LUO, Z. SHI, N. LI, Z. GU, Q. ZHUANG, Investigation on the electrochemical and electrocatalytic behavior of chemically modified electrode of single wall carbon nanotube functionalized with carboxylic acid group, *Chem. J. Chin. Univ.* 21 (2000) 1372–1374.
- 36 P. F. LIU, J. H. HU, Carbon nanotube powder microelectrodes for nitrite detection, *Sens. Actuators B* 84 (2002) 194–199.
- 37 W. D. ZHANG, Y. WEN, S. M. LIN, W. C. TJIU, G. Q. XU, L. M. GAN, Synthesis of vertically aligned carbon nanotubes on metal deposited quartz plates, *Carbon* 40 (2002) 1981–1989.
- 38 W. D. ZHANG, Y. WEN, W. C. TJIU, G. Q. XU, L. M. GAN, Growth of vertically aligned carbon-nanotube array on large area of quartz plates by chemical vapor deposition, *Appl. Phys. A* 74 (2002) 419–422.
- 39 J. S. YE, H. F. CUI, W. D. ZHANG, A. L. OTTOVA, H. T. TIEN, F. S. SHEU, Self-assembly of bilayer lipid membrane at multiwalled carbon nanotubes towards the development of photo-switched functional device, *Electrochem. Commun.* 7 (2005) 81–86.
- 40 J. S. YE, Y. WEN, W. D. ZHANG, H. F. CUI, G. Q. XU, F. S. SHEU, Electrochemical biosensing platforms using phthalocyanine-functionalized carbon nanotube electrode, *Electroanalysis* 17 (2005) 89–96.
- 41 H. F. CUI, J. S. YE, W. D. ZHANG, J. WANG, F. S. SHEU, Electrocatalytic reduction of oxygen by platinum nanoparticle/carbon nanotube composite electrode, *J. Electroanal. Chem.* 577 (2005) 295–302.
- 42 W. C. POH, K. P. LOH, W. D. ZHANG, S. TRIPARTHY, J. S. YE, F. S. SHEU, Biosensing properties of diamond and carbon nanotubes, *Langmuir* 20 (2004) 5484–5492.
- 43 J. S. YE, Y. WEN, W. D. ZHANG, L. M. GAN, G. Q. XU, F. S. SHEU, Application of multi-walled carbon nanotubes functionalized with hemin for oxygen detection in neutral solution, *J. Electroanal. Chem.* 562 (2004) 241–246.
- 44 J. S. YE, Y. WEN, W. D. ZHANG, L. M. GAN, G. Q. XU, F. S. SHEU, Selective voltammetric detection of uric acid in the presence of ascorbic acid at well-aligned carbon nanotube electrode, *Electroanalysis* 15 (2003) 1693–1698.
- 45 J. S. YE, H. F. CUI, X. LIU, T. M. LIM, W. D. ZHANG, F. S. SHEU, Preparation and characterization of well-aligned carbon nanotubes-ruthenium oxide nanocomposites for supercapacitors, *Small* 1 (2005) 560–565.
- 46 J. S. YE, Y. WEN, W. D. ZHANG, L. M. GAN, G. Q. XU, F. S. SHEU, Non-enzymatic glucose detection using multi-walled carbon nanotube electrode, *Electrochem. Commun.* 6 (2004) 66–70.
- 47 K. B. WU, S. S. HU, J. J. FEI, W. BAI, Mercury-free simultaneous determination of cadmium and lead at a glassy carbon electrode modified with multi-wall carbon nanotubes, *Anal. Chim. Acta* 489 (2003) 215–221.
- 48 M. D. RUBIANES, G. A. RIVAS, Carbon nanotubes paste electrode, *Electrochem. Commun.* 5 (2003) 689–694.
- 49 F. VALENTINI, A. AMINE, S. ORLANDUCCI, M. L. TERRANOVA, G. PALLESCHI, Carbon nanotube purification: Preparation and characterization of carbon nanotube paste electrodes, *Anal. Chem.* 75 (2003) 5413–5421.
- 50 J. WANG, M. MUSAMEH, Screen-printed carbon nanotube electrodes, *Analyst* 129 (2004) 1–2.
- 51 N. S. LAWRENCE, R. P. DEO, J. WANG, Detection of homocysteine at carbon nanotube paste electrodes, *Talanta* 63 (2004) 443–449.
- 52 M. L. PEDANO, G. A. RIVAS, Adsorption and electrooxidation of nucleic acids at carbon nanotubes paste electrodes, *Electrochem. Commun.* 6 (2004) 10–16.
- 53 F. RICCI, A. AMINE, D. MOSCONE, G. PALLESCHI, Prussian blue modified

- carbon nanotube paste electrodes: A comparative study and a biochemical application, *Anal. Lett.* 36 (2003) 1921–1938.
- 54 R. ANTIOCHIA, I. LAVAGNINI, F. MAGNO, Electrocatalytic oxidation of NADH at single-wall carbon-nanotube-paste electrodes: Kinetic considerations for use of a redox mediator in solution and dissolved in the paste, *Anal. Bioanal. Chem.* 381 (2005) 1355–1361.
- 55 M. TROJANOWICZ, A. MULCHANDANI, M. MASCINI, Carbon nanotubes-modified screen-printed electrodes for chemical sensors and biosensors, *Anal. Lett.*, 37 (2004) 3185–3204.
- 56 W. J. GUAN, Y. LI, Y. Q. CHEN, X. B. ZHANG, G. Q. HU, Glucose biosensor based on multi-wall carbon nanotubes and screen printed carbon electrodes, *Biosens. Bioelectron.* 21 (2005) 508–512.
- 57 E. KATZ, I. WILLNER, Biomolecule-functionalized carbon nanotubes: Applications in nanobioelectronics, *ChemPhysChem* 5 (2004) 1085–1104.
- 58 A. B. ARTYUKHIN, O. BAKAJIN, P. STROEVE, A. NOY, Layer-by-layer electrostatic self-assembly of polyelectrolyte nanoshells on individual carbon nanotube templates, *Langmuir* 20 (2004) 1442–1448.
- 59 M. LI, E. DUJARDIN, S. MANN, Programmed assembly of multi-layered protein/nanoparticle-carbon nanotube conjugates, *Chem. Commun.* 39 (2005) 4952–4954.
- 60 H. SHIMODA, L. FLEMING, K. HORTON, O. ZHOU, Formation of macroscopically ordered carbon nanotube membranes by self-assembly, *Phys. B Condens. Matter* 323 (2002) 135–136.
- 61 N. O. V. PLANK, R. CHEUNG, R. J. ANDREWS, Thiolation of single-wall carbon nanotubes and their self-assembly, *Appl. Phys. Lett.* 85 (2004) 3229–3231.
- 62 Y. B. WANG, Z. IQBAL, Vertically oriented single-wall carbon nanotube/enzyme on silicon as biosensor electrode, *JOM* 57 (2005) 27–29.
- 63 Y. D. ZHAO, W. D. ZHANG, H. CHEN, Q. M. LUO, Anodic oxidation of hydrazine at carbon nanotube powder microelectrode and its detection, *Talanta* 58 (2002) 529–534.
- 64 Y. D. ZHAO, W. D. ZHANG, H. CHEN, Q. M. LUO, Direct electron transfer of glucose oxidase molecules adsorbed onto carbon nanotube powder microelectrode, *Anal. Sci.* 18 (2002) 939–941.
- 65 Y. D. ZHAO, W. D. ZHANG, H. CHEN, Q. M. LUO, S. F. Y. LI, Direct electrochemistry of horseradish peroxidase at carbon nanotube powder microelectrode, *Sens. Actuators, B* 87 (2002) 168–172.
- 66 Y. D. ZHAO, W. D. ZHANG, Q. M. LUO, S. F. Y. LI, The oxidation and reduction behavior of nitrite at carbon nanotube powder microelectrodes, *Microchem. J.* 75 (2003) 189–198.
- 67 Y. D. ZHAO, W. D. ZHANG, H. CHEN, Q. M. LUO, Electrochemical oxidation of cysteine at carbon nanotube powder microelectrode and its detection, *Sens. Actuators, B* 92 (2003) 279–285.
- 68 A. MERKOCI, M. PUMERA, X. LLOPIS, B. PEREZ, M. DEL VALLE, S. ALEGRET, New materials for electrochemical sensing VI: Carbon nanotubes, *Trends Anal. Chem.* 24 (2005) 826–838.
- 69 J. WANG, Carbon-nanotube based electrochemical biosensors: A review, *Electroanalysis* 17 (2005) 7–14.
- 70 J. LI, in *Carbon Nanotube Applications: Chemical and Physical Sensors, in Carbon Nanotubes Science and Application*, Ed. M. MEYYAPPAN, CRC Press, New York, 2005, 213–233.
- 71 C. E. BANKS, R. R. MOORE, T. J. DAVIES, R. G. COMPTON, Investigation of modified basal plane pyrolytic graphite electrodes: Definitive evidence for the electrocatalytic properties of the ends of carbon nanotubes, *Chem. Commun.* 16 (2004) 1804–1805.
- 72 C. E. BANKS, R. G. COMPTON, New electrodes for old: From carbon nanotubes to edge plane pyrolytic graphite, *Analyst* 131 (2006) 15–21.
- 73 C. E. BANKS, T. J. DAVIES, G. G. WILDGOOSE, R. G. COMPTON, Electrocatalysis at graphite and carbon nanotube modified electrodes: Edge-

- plane sites and tube ends are the reactive sites, *Chem. Commun.* 7 (2005) 829–841.
- 74 C. E. BANKS, R. G. COMPTON, Exploring the electrocatalytic sites of carbon nanotubes for NADH detection: An edge plane pyrolytic graphite electrode study, *Analyst* 130 (2005) 1232–1239.
- 75 T. J. DAVIES, R. R. MOORE, C. E. BANKS, R. G. COMPTON, The cyclic voltammetric response of electrochemically heterogeneous surfaces, *J. Electroanal. Chem.* 574 (2004) 123–152.
- 76 M. MUSAMEH, N. S. LAWRENCE, J. WANG, Electrochemical activation of carbon nanotubes, *Electrochem. Commun.* 7 (2005) 14–18.
- 77 A. CHOU, A. T. BOCKING, N. K. SINGH, J. J. GOODING, Demonstration of the importance of oxygenated species at the ends of carbon nanotubes for their favourable electrochemical properties, *Chem. Commun.* 7 (2005) 842–844.
- 78 T. J. LEE, S. I. JUNG, C. Y. PARK, Y. H. CHOA, C. J. LEE, Synthesis of well-aligned carbon nanotubes with open tips, *Carbon* 43 (2005) 1341–1346.
- 79 Y. H. LIN, F. LU, Y. TU, Z. F. REN, Glucose biosensors based on carbon nanotube nanoelectrode ensembles, *Nano Lett.* 4 (2004) 191–195.
- 80 J. WANG, M. MUSAMEH, A reagentless amperometric alcohol biosensor based on carbon-nanotube/Teflon composite electrodes, *Anal. Lett.* 36 (2003) 2041–2048.
- 81 R. P. DEO, J. WANG, I. BLOCK, A. MULCHANDANI, K. A. JOSHI, M. TROJANOWICZ, F. SCHOLZ, W. CHEN, Y. H. LIN, Determination of organophosphate pesticides at a carbon nanotube/organophosphorus hydrolase electrochemical biosensor, *Anal. Chim. Acta* 530 (2005) 185–189.
- 82 G. LI, J. M. LIAO, G. Q. HU, N. Z. MA, P. J. WU, Study of carbon nanotube modified biosensor for monitoring total cholesterol in blood, *Biosen. Bioelectron.* 20 (2005) 2140–2144.
- 83 J. J. DAVIS, K. S. COLEMAN, B. R. AZAMIAN, C. B. BAGSHAW, M. L. H. GREEN, Chemical and biochemical sensing with modified single walled carbon nanotubes, *Chem. Eur. J.* 9 (2003) 3732–3739.
- 84 M. SHIM, N. W. S. KAM, R. J. CHEN, Y. M. LI, H. J. DAI, Functionalization of carbon nanotubes for biocompatibility and biomolecular recognition, *Nano Lett.* 2 (2002) 285–288.
- 85 A. C. ZETTEMLOYER, *J. Colloid Interface Sci.*, 28 (1968) 343.
- 86 J. M. BONARD, T. STORA, J. P. SALVETAT, F. MAIER, T. STOCKLI, C. DUSCHL, L. FORRO, W. A. DEHEER, A. CHATELAIN, Purification and size-selection of carbon nanotubes, *Adv. Mater.* 9 (1997) 827–831.
- 87 S. MANNE, J. P. CLEVELAND, H. E. GAUB, G. D. STUCKY, P. K. HANSMAN, Direct visualization of surfactant hemimicelles by force microscopy of the electrical double layer, *Langmuir* 10 (1994) 4409–4413.
- 88 C. RICHARD, F. BALAVOIBE, P. SCHULTZ, T. W. EBBESEN, C. MIOSKOWSKI, Supramolecular self-assembly of lipid derivatives on carbon nanotubes, *Science* 300 (2003) 775–778.
- 89 Y. LIN, S. TAYLOR, H. P. LI, K. A. S. FERNANDO, L. W. QU, W. WANG, L. R. GU, B. ZHOU, Y. P. SUN, Advances toward bioapplications of carbon nanotubes, *J. Mater. Chem.*, 14 (2004) 527–541.
- 90 X. CHEN, G. S. LEE, A. ZETTL, C. R. BERTOZZI, Biomimetic engineering of carbon nanotubes by using cell surface mucin mimics, *Angew. Chem. Int. Ed.* 43 (2004) 6111–6116.
- 91 N. B. HOLLAND, Y. X. QIU, M. RUEGSEGGER, R. E. MARCHANT, Biomimetic engineering of non-adhesive glycocalyx-like surfaces using oligosaccharide surfactant polymers, *Nature* 392 (1998) 799–801.
- 92 X. B. WANG, Y. Q. LIU, W. F. QIU, D. ZHU, Immobilization of tetra-tert-butylphthalocyanines on carbon nanotubes: A first step towards the development of new nanomaterials, *J. Mater. Chem.* 12 (2002) 1636–1639.
- 93 C. M. DRAIN, Self-organization of self-assembled photonic materials into

- functional devices: Photo-switched conductors, *Proc. Natl. Acad. Sci. U.S.A.* 99 (2002) 5178–5182.
- 94 H. T. TIEN, L. G. WANG, X. WANG, A. L. OTTOVA, Electronic processes in supported bilayer lipid membranes (s-BLMs) containing a geodesic form of carbon (fullerene C<sub>60</sub>), *Bioelectrochem. Bioenerg.* 42 (1997) 161–167.
- 95 H. T. TIEN, Z. SALAMON, A. L. OTTOVA, Lipid bilayer-based sensors and biomolecular electronics, *Crit. Rev. Biomed. Eng.* 18 (1991) 323–340.
- 96 T. KANYÓ, Z. KÓNYA, A. KUKOVECZ, F. BERGER, I. DÉKÁNY, I. KIRICSI, Quantitative characterization of hydrophilic-hydrophobic properties of MWNTs surfaces, *Langmuir* 20 (2004) 1656–1661.
- 97 J. L. BAHR, J. YANG, D. V. KOSYNKIN, M. J. BRONIKOWSKI, R. E. SMALLEY, J. M. TOUR, Functionalization of carbon nanotubes by electrochemical reduction of aryl diazonium salts: A bucky paper electrode, *J. Am. Chem. Soc.* 123 (2001) 6536–6542.
- 98 Y. J. ZHANG, Y. F. SHEN, J. H. LI, L. NIU, S. J. DONG, A. IVASKA, Electrochemical functionalization of single-walled carbon nanotubes in large quantities at a room-temperature ionic liquid supported three-dimensional network electrode, *Langmuir* 21 (2005) 4797–4800.
- 99 J. S. YE, X. LIU, H. F. CUI, W. D. ZHANG, F. S. SHEU, T. M. LIM, Electrochemical oxidation of multi-walled carbon nanotubes and its application to electrochemical double layer capacitors, *Electrochem. Commun.* 7 (2005) 249–255.
- 100 Y. B. WANG, S. V. MALHOTRA, F. J. OWENS, Z. IQBAL, Electrochemical nitration of single-wall carbon nanotubes, *Chem. Phys. Lett.* 407 (2005) 68–72.
- 101 W. S. XIA, C. H. HUANG, L. B. GAN, H. LI, X. S. ZHAO, Photoelectric response of a bilayer lipid membrane doped with an azo pyridinium compound containing a rare-earth-metal complex, *J. Chem. Soc., Faraday Trans.* 92 (1996) 769–772.
- 102 K. UOSAKI, T. KONDO, X. Q. ZHANG, M. YANAGIDA, Very efficient visible light-induced uphill electron transfer at a self-assembled monolayer with a porphyrin-ferrocene-thiol linked molecule, *J. Am. Chem. Soc.* 119 (1997) 8367–8368.
- 103 H. FUJIWARA, Y. YONEZAWA, Photoelectric response of a black lipid-membrane containing an amphiphilic azobenzene derivative, *Nature* 351 (1991) 724–726.
- 104 J. Q. LIU, A. CHOU, W. RAHMAT, M. N. PADDON-ROW, J. J. GOODING, Achieving direct electrical connection to glucose oxidase using aligned single walled carbon nanotube arrays, *Electroanalysis* 17 (2005) 38–46.
- 105 F. PATOLSKY, Y. WEIZMANN, I. WILLNER, Long-range electrical contacting of redox enzymes by SWCNT connectors, *Angew. Chem.* 43 (2004) 2113–2117.
- 106 G. WANG, J. J. XU, H. Y. CHEN, Interfacing cytochrome *c* to electrodes with a DNA – carbon nanotube composite film, *Electrochem. Commun.* 4 (2002) 506–509.
- 107 G. C. ZHAO, L. ZHANG, X. W. WEI, Z. S. YANG, Myoglobin on multi-walled carbon nanotubes modified electrode: Direct electrochemistry and electrocatalysis, *Electrochem. Commun.* 5 (2003) 825–829.
- 108 L. WANG, J. X. WANG, F. M. ZHOU, Direct electrochemistry of catalase at a gold electrode modified with single-wall carbon nanotubes, *Electroanalysis* 16 (2004) 627–632.
- 109 Y. M. YAN, W. ZHENG, M. N. ZHANG, L. WANG, L. SU, L. Q. MAO, Bioelectrochemically functional nanohybrids through co-assembly of proteins and surfactants onto carbon nanotubes: Facilitated electron transfer of assembled proteins with enhanced faradic response, *Langmuir* 21 (2005) 6560–6566.
- 110 R. J. CHEN, Y. G. ZHANG, D. W. WANG, H. J. DAI, Noncovalent sidewall functionalization of single-walled carbon nanotubes for protein immobilization, *J. Am. Chem. Soc.* 123 (2001) 3838–3839.

- 111 S. E. KOOI, U. SCHLECHT, U. BURGHARD, K. KERN, Electrochemical modification of single carbon nanotubes, *Angew. Chem. Int. Ed.* 41 (2002) 1353–1355.
- 112 H. C. CHOI, M. SHIM, S. BANGSARUNTIP, H. J. DAI, Spontaneous reduction of metal ions on the sidewalls of carbon nanotubes, *J. Am. Chem. Soc.* 124 (2002) 9058–9059.
- 113 J. CHEN, H. LIU, W. A. WEIMER, M. D. HALLS, D. H. WALDECK, G. C. WALKER, Noncovalent engineering of carbon nanotube surfaces by rigid, functional conjugated polymers, *J. Am. Chem. Soc.* 124 (2002) 9034–9035.
- 114 S. HERMANS, J. SLOAN, D. S. SHEPHARD, B. F. G. JOHNSON, M. L. H. GREEN, Bimetallic nanoparticles aligned at the tips of carbon nanotubes, *Chem. Commun.* 3 (2002) 276–277.
- 115 C. DOWNS, J. NUGENT, P. M. AJAYAN, D. J. DUQUETTE, K. S. V. SANTHANAM, Efficient polymerization of aniline at carbon nanotube electrodes, *Adv. Mater.* 11 (1999) 1028–1031.
- 116 J. H. CHEN, Z. P. HUANG, D. Z. WANG, S. X. YANG, W. Z. LI, J. G. WEN, Z. F. REN, Electrochemical synthesis of polypyrrole films over each of well-aligned carbon nanotubes, *Synth. Met.* 125 (2002) 289–294.
- 117 L. DUNSCH, P. JANDA, K. MUKHOPADHYAY, H. SHINOHARA, Electrochemical metal deposition on carbon nanotubes, *New Diam. Front. Carbon Technol.* 11 (2001) 427–435.
- 118 C. N. R. RAO, B. C. SATISHKUMAR, A. GOVINDARAJ, M. NATH, Nanotubes, *ChemPhysChem* 2 (2001) 78–105.
- 119 F. H. WU, G. C. ZHAO, X. W. WEI, Electrocatalytic oxidation of nitric oxide at multi-walled carbon nanotubes modified electrode, *Electrochem. Commun.* 4 (2002) 690–694.
- 120 V. GEORGAKILAS, V. TZITZIOS, D. GOURNIS, D. PETRIDIS, Attachment of magnetic nanoparticles on carbon nanotubes and their soluble derivatives, *Chem. Mater.* 17 (2005) 1613–1617.
- 121 J. LI, H. T. NG, A. CASSELL, W. FAN, H. CHEN, Q. YE, J. KOEHNE, J. HAN, M. MEYYAPPAN, Carbon nanotube nanoelectrode array for ultrasensitive DNA detection, *Nano Lett.* 3 (2003) 597–602.
- 122 M. L. GUO, J. H. CHEN, L. H. NIE, S. Z. YAO, Electrostatic assembly of calf thymus DNA on multi-walled carbon nanotube modified gold electrode and its interaction with chlorpromazine hydrochloride, *Electrochim. Acta* 49 (2004) 2637–2643.
- 123 M. L. GUO, J. H. CHEN, D. Y. LIU, L. H. NIE, S. Z. YAO, Electrochemical characteristics of the immobilization of calf thymus DNA molecules on multi-walled carbon nanotubes, *Bioelectrochemistry* 62 (2004) 29–35.
- 124 T. RAMANATHAN, F. T. FISHER, R. S. RUOFF, L. C. BRINSON, Amino-functionalized carbon nanotubes for binding to polymers and biological systems, *Chem. Mater.*, 17 (2005) 1290–1295.
- 125 J. WANG, G. LIU, M. R. JAN, Q. ZHU, Electrochemical detection of DNA hybridization based on carbon-nanotubes loaded with CdS tags, *Electrochem. Commun.* 5 (2003) 1000–1004.
- 126 J. KOEHNE, J. LI, A. M. CASSELL, H. CHEN, Q. YE, H. T. NG, J. HAN, M. MEYYAPPAN, The fabrication and electrochemical characterization of carbon nanotube nanoelectrode arrays, *J. Mater. Chem.* 14 (2004) 676–684.
- 127 J. LI, J. E. KOEHNE, A. M. CASSELL, H. CHEN, H. T. NG, Q. YE, W. FAN, J. HAN, M. MEYYAPPAN, Inlaid multi-walled carbon nanotube nanoelectrode arrays for electroanalysis, *Electroanalysis* 17 (2005) 15–27.

### 3

## Nanotubes, Nanowires, and Nanocantilevers in Biosensor Development

*Jun Wang, Guodong Liu, and Yuehe Lin*

### 3.1

#### Introduction

Recent developments in designing and synthesizing conducting one-dimensional (1D) nanostructured materials, including carbon nanotubes (CNTs) and nanowires, etc., have attracted much attention across scientific and engineering disciplines because of their great potential for replacing conventional bulk materials in micro- and nanoelectronic devices [1, 2] and in chemical [3, 4] and biological sensors [4–9]. Various methodologies and technologies have been developed to fabricate 1D conducting nanomaterials [10, 11]. For example, chemical methods, including catalytic vapor deposition (CVD) have been widely used to synthesize CNTs [12, 13] and silicon nanowires [14, 15] on catalytically patterned substrates at desired sites with controlled orientations. Microfabrication [10, 11], soft lithography techniques [10, 11], and electric fields [16], etc. have been employed to fabricate highly oriented 1D nanomaterials. Various electrochemical techniques have been developed to fabricate 1D conducting polymer nanowires [17, 18]. New techniques are being explored to synthesize new 1D nanomaterials.

One-dimensional nanostructured materials as building blocks for biosensors are promising because of their unique electronic, optical, chemical, and mechanical properties, which are intrinsically associated with their low dimensionality and the quantum confinement effect. Therefore, 1D nanomaterials have broad applications in developing various types of biosensors, e.g., electrical [19, 20], optical [21], and mechanical [22] (nanocantilever biosensors). For example, CNTs exhibit excellent electronic properties. They can be used as molecular wires for facilitating electron transfer on the surface [23]. One-dimensional nanomaterials have a high aspect ratio, which makes them exhibit extreme sensitivity and superior response. Owing to their high sensitivity, 1D nanomaterials can be used to construct label-free biosensors. This will be very attractive and avoid exhausting and complicated labeling. With the ever-decreasing sizes of these 1D nanostructures, the “bottom-up” chemical approach is playing an increasingly important role because of its capability to make much smaller features compared to the “top-down” approach. So, combined with bottom-up techniques, 1D nanomaterials are ideal building blocks for

constructing miniature biochips. The detection mechanism with these tiny nanosensors is based on chemical interactions between the surface atoms of 1D nanostructured materials and adsorbed molecules. This interaction will provide a direct electronic readout within a few seconds of electron-donating or -withdrawing molecules adsorbing onto the nanomaterials. A miniature biochip based on 1D nanomaterials will be implanted in the body and will detect multiple biological molecules *in vivo*! In general, these 1D nanomaterials are expected to play an important role in the development of various emerging technologies that will improve the way we live.

Biosensors based on 1D nanomaterials have shown great advantages. However, real applications in biological diagnosis are a long way off. A major challenge remains to fully exploit the 1D nanostructure with one lateral dimension between 1 and 100 nm. For example, 1D nanostructured material-based biosensors need to bind biological recognition molecules onto the device. It is a great challenge to individually address high-density biomolecule nanoarrays. There is also a need for deconvolution of noise from the signals. To analyze proteomic signatures, a major challenge will be to identify signatures from low-concentration molecular species in the presence of an extremely high concentration of non-specific proteins.

As a branch of nanotechnology, 1D nanomaterial-based biosensor development has made great progress. Each year, thousands of articles on nano-related biosensors are published, and many reviews have appeared in different journals [24, 25]. The present chapter introduces reviews on biosensor development based on 1D nanomaterials, CNTs, semiconducting nanowires, and some cantilevers. The chapter is comprehensive – previous reviews on nanomaterials-based biosensor development have focused on one of 1D nanomaterials, e.g., either carbon nanotubes or nanowires. The emphasis here, however, is on CNTs and electrochemical/electronic biosensor developments. Section 3.2 gives a detailed description of carbon nanotubes-based biosensor development, from fabrication of carbon nanotubes, the strategies for construction of carbon nanotube based biosensors to their bioapplications. In the section on the applications of CNTs based biosensors, various detection principles, e.g., electrochemical, electronic, and optical method, and their applications are reviewed in detail. Section 3.3 introduces the method for synthesis of semiconducting nanowires, e.g., silicon nanowires, conducting polymer nanowires and metal oxide nanowires and their applications in DNA and proteins sensing. Section 3.4 simply describes the development for nanocantilever-based biosensors and their application in DNA and protein diagnosis. Each section starts with a brief introduction and then goes into details. Finally, Section 3.5 summarizes the development of 1D nanomaterials based biosensors.

### 3.2

#### Carbon Nanotubes in Biosensor Development

CNTs, rolled graphene sheets, were discovered in 1991 by Iijima [26] following the historical finding of the new fascinating member of the carbon family –



“Buckyball” fullerene (carbon nanocage) and other nanocarbon particles [27]. CNTs have basic  $sp^2$  carbon units that comprise a seamless structure with hexagonal honeycomb lattices, being several nanometers in diameter and up to hundreds of microns long. CNTs can be divided into two major groups, i.e., single-wall CNTs (SWCNTs) and multiwall CNTs (MWCNTs). SWCNTs represent a single graphite sheet rolled flawlessly, demonstrating a tube diameter of 1 to 2 nm, whereas MWCNTs show concentric and closed graphite tubules with diameters ranging from 2 to 50 nm and an interlayer distance approximately 0.34 nm [28]. Typical SWCNTs have an open-ended nanostraw or a capped nanohorn tubular structure. Because of the highly oriented architectures, these novel nanostructures exhibit physicochemical properties different from those of bulk graphite and diamond and thus provide their unique electronic, chemical, thermal, and mechanical properties [29, 30]. Since the early 1990s, CNT science has been one of the fastest growing areas of research in chemistry, physics, materials, and life technologies. The important properties and possible potential applications of CNTs have been reviewed recently [31–35].

The first type of CNT-based sensor was prepared by using MWCNTs mixed with bromoform as a binder packed into a glass capillary. This modified electrode exhibited remarkable improvement with regard to the electrochemical oxidation of dopamine [36]. Since then, work has concentrated on their electrocatalytic performance towards the redox behaviors of biomolecules [37, 38], especially towards the fabrication of effective, prototype deoxyribonucleic acid (DNA) and glucose biosensors [39, 40]. Recent summaries of the preparation conditions, interferences, interfacing, comparison, or analytical promise of the CNT-based sensors can be found in more specific reviews [41–43].

### 3.2.1

#### Preparation and Purification of CNTs

CNTs synthesis has mainly involved three major methods: the carbon arc-discharge method, or electric arc discharge (EAD) [26, 44], the laser vaporization of a graphite electrode or laser ablation (LA) [45], and a chemical method, CVD [11, 12]. EAD uses a direct current arc between carbon electrodes within a noble gas, like argon or helium [26]. In CVD, the CNTs are formed by the decomposition of the gaseous hydrocarbon at 700–900 °C and atmospheric pressure [46]. Materials produced by the EAD and LA protocols are in the forms of porous membranes and powders that require further processing. CNTs can be grown directly on substrates by the CVD process. Among these three techniques, the CVD is the most promising synthesis route for economically producing large quantities of CNTs. This is because the catalyst-involved CVD can use a lower temperature to form CNTs than the other two techniques. In addition, the catalyst can be deposited on a substrate, which allows for ordered synthesis and the formation of novel structures. CNT-based research for sensor applications only gained momentum after these highly oriented, large-scale productions emerged.

MWCNTs were first made by Yacaman et al. [47] followed by others [12, 13, 45]. Their experimental set-up usually consists of a high-temperature oven in which the catalysts are placed onto a highly resistant ceramic or metal plate. The nature and yield of the deposit obtained in the reaction are controlled by varying different parameters, such as the nature of the metals and the supports, the hydrocarbon sources, the gas flows, the reaction temperature, and the reaction time. By selecting the proper conditions, both the physical (e.g., length, shape, diameter) and chemical (e.g., number of defects, graphitization) properties of MWCNTs can be designed in advance. The choice of catalysts is vital in growing a good quality of CNTs and has been a subject for several research groups. Supported Co, Ni, and Fe catalysts were found to be the most active in the CVD growth thus far, although the metals and supports demand different temperature ranges [48, 49].

The first SWCNTs were reported by Iijima and Ichihashi when employing the EAD set-up with a low product yield [50]. This synthesis was significantly improved in 1996 when Dai et al. demonstrated that LA can be an effective way to grow highly uniform tubes that have a greater tendency to form aligned bundles than those prepared using EAD [45]. These ordered CNTs were fabricated by laser vaporization of a carbon target in a furnace at 1100 to 1200 °C, which was a much lower temperature than that was previously thought necessary for nanotube formation. A Co-Ni catalyst assists the growth of the nanotubes, presumably because it prevents the ends from being “capped” during synthesis. In a later work, the same group showed that high quality SWCNTs could be produced by CVD decomposition of methane on supported transition metal oxide catalysts [51]. The experimental set-up was similar to apparatus generally producing multiwalled nanotubes; however, some factors, including the catalyst composition, the support, and the hydrocarbon, were different. Fe<sub>2</sub>O<sub>3</sub> was found to be significantly more efficient in SWCNT production than CoO or NiO. Methane was used instead of the generally applied acetylene or ethylene because of its kinetic stability at high temperatures. Since there is no pyrolytic decomposition, the carbon atoms needed for the growth of nanotubes are produced by a catalytic reaction from the methane on the metal surfaces. The reaction time was dramatically reduced from the usually applied hour(s) to 10 min, and thus it prevents the outer surface of the nanotubes from being coated with amorphous carbon. In the following year, Colomer et al. proved, after viewing the nanotube bundles by transmission electron microscopy, that the best yield of SWCNTs is obtained by using a Fe-Co binary mixture supported by alumina [52]. Other groups have explored the possibility of extending their successful approach for MWCNTs into SWCNTs growth, mainly focusing on CVD [12, 13, 46–49].

High-purity CNTs can be, theoretically, achieved by optimizing the synthetic routes, and this should be viewed as part of the overall performance of the proposed preparation protocol. Nevertheless, the as-synthesized CNT materials unavoidably contain significant amounts of impurities, including amorphous carbon, graphite particles, and metal catalysts. The purification schemes that have been developed usually take advantage of differences in the aspect ratio [53] and oxidation

rate [54] between the nanotubes and the impurities. Zhou et al. proposed a method that can reach final product purity over 95% [55]. The protocol combines hydrogen peroxide reflux with filtration that can effectively remove most of the impurities. Recently, Chiang et al. modified a gas-phase purification technique previously reported by Smalley and others [53] that uses a combination of high-temperature oxidations and repeated extractions with hydrochloric acid. This improved procedure significantly reduces the amount of impurities (catalyst and non-nanotube forms of carbon) within the nanotubes, increasing their stability remarkably. The onset of decomposition of the purified nanotubes (determined by thermal gravimetric analysis in air) is more than 300 °C higher than that of the crude nanotubes. Transmission electron microscopy analysis of the purified nanotubes reveals near complete removal of iron catalyst particles. The iron content of the nanotubes was reduced from 22.7 wt.% in the crude nanotubes to less than 0.02 wt.% in the final product. Nanotubes purified by this method can be readily dispersed in common organic solvents, in particular *N,N*-dimethylformamide, using prolonged ultrasonic treatment. These dispersions can then be used to incorporate single-wall CNTs into polymer films.

### 3.2.2

#### **Construction of CNT-based Biosensors**

Interest in exploring CNTs in biosensor fabrication has grown exponentially since the inception of CNTs in 1991 [26] and the first CNT-based sensor report [36]. Following the preparation and purification of a large quantity of CNTs as discussed above, the immobilization of these sensing layers onto the transducer support is introduced below. Basically, these CNT immobilizations have been based on dispersion, solubilization, adsorption, functionalization, composite entrapment, and other surface anchoring protocols.

##### **3.2.2.1 Dispersion and Stabilization by Oxidative Acids**

The well-ordered, all-carbon hollow CNTs possess unique walls and ends and thus resemble the sensing properties of basal planes of pyrolytic graphite (through their walls) and of edge planes of pyrolytic graphite (through their open ends). This sensing mechanism, in addition to their high surface-to-volume ratio, high chemical and thermal stability, high tensile strength, and elastic nanostructures, has made them excellent candidates for sensor fabrication. However, the spontaneous coagulation and the lack of solubility of CNTs in aqueous media is a major challenge for their application. To prevent coagulation of the as-synthesized CNTs, oxidative acid treatments are usually explored, including refluxing and sonication in a concentrated mixture containing sulfuric acid and nitric acid, as reported by Smalley's group [56]. This procedure, while occasionally generating surface defects and tube shortening, can produce abundant carboxylated sites on the CNT walls and caps. A dark stable aqueous suspension of CNTs can be achieved after removing excess acids. More recently, Mallouk's group have reported that a stable SWCNT aqueous dispersion at concentrations above 0.3% can be obtained as a re-

sult of the hydrogel formation. This follows the treatments by a mixture containing  $\text{H}_2\text{SO}_4 + (\text{NH}_4)_2\text{S}_2\text{O}_8 + \text{P}_2\text{O}_5$  and a subsequent mixture with  $\text{H}_2\text{SO}_4 + \text{KMnO}_4$  [57]. Similar approaches have also been reported for a stable aqueous MWCNT hydrogel formation [58].

### 3.2.2.2 Dispersion by Surfactant Interaction

To preserve the intact CNT nanostructures after dispersion, a noncovalent stabilization/immobilization might be attractive. Simple physical stabilization, such as centrifugation, filtration, distillation, and sonication, in coupling with simple immobilization, including evaporation, casting, or spin coating, can be directly applied for respective sensor fabrications [35, 36]. Nevertheless, the hydrophobicity of the CNT walls, which accounts for vast majority of the tubes, is a major barrier when it comes to dispersing and manipulating the sensor surface and anchoring in a controlled manner.

Considering the relatively hydrophilic caps of CNTs, the noncovalent surfactant- and polymer-assisted aqueous dispersion may offer an alternative to overcome the drawbacks of the simple physical stabilization [59, 60]. The systematic study of the SWCNT dispersion in various surfactants has been reported and tabulated by Sun et al. [41], with the CNT solubilities ranging 10–50 mg mL<sup>-1</sup>.

### 3.2.2.3 Polymer-assisted Solubilization

Because of the pseudo-amphiphilic feature of CNTs, due to their hydrophilic carboxylated ends and hydrophobic sidewalls, various ionic and nonionic polymers, such as poly(*p*-phenylenevinylene) [59], poly{(*m*-phenylenevinylene)-*co*-[2,5-dioctyloxy-(*p*-phenylene)-vinylene]}, [60] or poly(ethylene oxide)-poly(propylene oxide)-poly(ethylene oxide) triblock polymers, have been reported to “wrap” CNT in polymeric chains to facilitate dispersing and to stabilize the nanotubes, without impairing their physical properties [59, 60]. Wang et al. developed a method that directly applied Nafion polymer-assisted CNT dispersion in sensor fabrication [61]. Similar to other polymers used to wrap and solubilize CNTs, Nafion bears a polar side chain and can produce a CNT suspension in phosphate buffer or alcohol solution. Increasing the Nafion content from 0.1 to 5 weight percent (wt.%) results in dramatic enhancement of the solubility of both single-wall and multiwall CNTs (Fig. 3.1). A homogeneous solution of the Nafion/CNT complex is observed in Nafion solution, but no such solubilization is observed in ethanol or phosphate-buffer solutions containing no Nafion. The CNT/Nafion association does not impair the electrocatalytic properties of CNTs with respect to the redox reaction of hydrogen peroxide. The Nafion-induced solubilization of CNT thus permits various applications, including the modification of electrode surfaces for preparing amperometric biosensors, and field-effect transistors [62].

### 3.2.2.4 CNT Adsorption on the Transducer Substrate

Although the dispersion and distribution of CNTs in aqueous media have proved to be challenging, some non-polar organic solvents such as *N,N*-dimethylformamide (DMF) cause less coagulation of the tubes and thus permit a greater extent of dis-

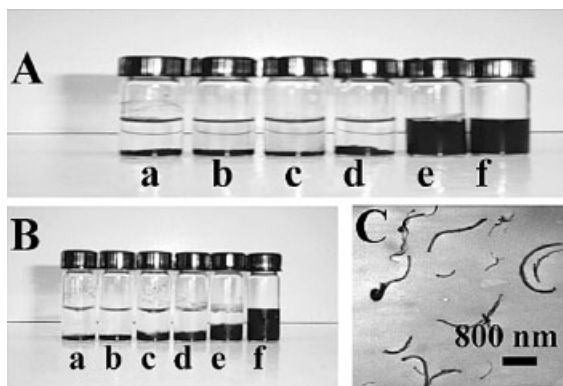


**Fig. 3.1.** Photographs of vials containing  $0.5 \text{ mg mL}^{-1}$  SWCNT (A) and MWCNT (B) in different solutions: phosphate buffer ( $0.05 \text{ M}$ ,  $\text{pH } 7.4$ ) (a), 98% ethanol (b), 10% ethanol in phosphate buffer (c), 0.1% Nafion in phosphate buffer (d), 0.5% Nafion in

phosphate buffer (e), and 5% Nafion in ethanol (f). (C) TEM image of a 0.5% Nafion solution containing MWCNT ( $0.3 \text{ mg mL}^{-1}$ ). (Reprinted with permission from Ref. [61]. © 2003 American Chemical Society.)

persion. This organic solubility offers the possibility for directly coating or spin casting of the CNT organic solution onto the sensor substrate and subsequent solvent evaporation. Re-immersion of these resultant CNT-based sensors into aqueous media showed no loss of operational performance and thus provides proof of strong adsorption on the surface. The first CNT-based sensor by Britto and co-authors was based on nanotubes solubilized in bromoform as a binder material following packing into a glass tube to complete the sensor construction [36]. Presently, many sensors still use this approach because of the ease of fabrication. The most often used substrates are glassy carbon, gold, platinum, carbon fiber, and glass. Lately, a protocol derived to co-incorporate some recognition reagent has been reported [63, 64]. Although these protocols are almost the simplest and most convenient ways to fabricate CNT-based sensors, the non-specific CNT adsorption needs to be addressed to gain greater control over their random distribution if a highly reproducible and stable sensor is demanded.

#### 3.2.2.5 Surface Functionalization of CNTs

Biosensors need specific surface recognition towards targets, and have thus promoted the modification of CNTs. These modifications usually start with the CNTs' sidewalls, ends, and defects, which are rich in nanotube-bound carboxylic groups. The latter are the nondestructive outcome of oxidative acid pretreatment on CNTs. The external-added functional molecules can be as small as simple amino acids or as large as protein macromolecules. Linkages between the nanotubes and the functional components, with or without coupling agents, are based on carboxylate chemistry via amidation and esterification, as well as ionic interaction schemes.

Accordingly, these functionalizations can be covalent or noncovalent bonding in nature.

Liu et al. have used dicyclohexylcarbodiimide (DCC), a coupling reagent which converts the carboxylate ends of the SWCNTs into carbodiimide leaving groups, to react with amines on cysteamine ( $\text{NH}_2\text{CH}_2\text{CH}_2\text{SH}$ ) [65]. The single-walled nanotubes with free thiol terminal groups then covalently attached onto substrate gold surface through a self-assembly process. Although atomic force microscopy (AFM) and transmission electron microscopy (TEM) have revealed different surface morphology of the resultant modified surfaces [66], this functionalization protocol offers control over the spatial distribution, lengths, and other surface patterns of the nanotubes aligned on the substrate by adjusting the assembled amount and time. Gooding and coauthors employed a similar carbodiimide-activated conjugating method in immobilization of microperoxidase (MP-11) onto the perpendicularly aligned nanotubes that were pre-anchored on the cysteamine-modified gold electrode [66]. Other direct bonding or electrostatic complexing approaches include using such as bridging metal ions to connect a polyelectrolyte-modified surface and the carboxylic acid terminated tubes [67] and complexing with an oppositely charged polyelectrolyte [66]. While these approaches provide various patterned nanotubes, a major concern lies in that the aligned tubes have little support and, therefore, the electrodes may lack robustness [67].

To elucidate the covalent, electrostatic, and nonspecific contributions to protein–SWCNT interaction, Davis et al. carried out the experiments of amidation both in the presence and absence of the coupling reagent DCC [69, 70]. They discovered that glucose oxidase is adsorbed along the length of CNTs randomly distributed on a glassy carbon electrode. Though coupling can be controlled, to a degree, through variation of tube oxidative pre-activation chemistry, careful control experiments and observations made by AFM suggest that immobilization is strong, physical, and does not require covalent bonding. Figures 3.2 and 3.3(a) exhibit their proposed protein–nanotube conjugates, which were readily characterized at the molecular level by AFM. Ferrocene monocarboxylic acid behaves as a mediator to promote charge transfer communication between electrode surface and the enzyme molecules. Under such conditions, the glucose signal was  $10\times$  greater than if only glucose oxidase was adsorbed onto the glassy carbon electrode without CNTs (Fig. 3.3b). This approach demonstrated the possible device application; protein attachment appears to occur with retention of the native biological structure. The role of nanotubes in this proposed glucose sensor was to provide (1) the high-aspect ratio electrode to which high capacity glucose oxidase loading was achieved, and thus greater signals were generated from more active enzyme interfacing and (2) provide possible direct electrical communication between a redox-active biomolecule and the delocalized  $\pi$  system of its CNT support [71].

#### 3.2.2.6 Composite Entrapment and CNTs Bulky Electrode Material

The first nanotube composites were prepared by Ajayan and coauthors by mechanically mixing MWCNTs and epoxy resin [72]. Because CNTs themselves could be

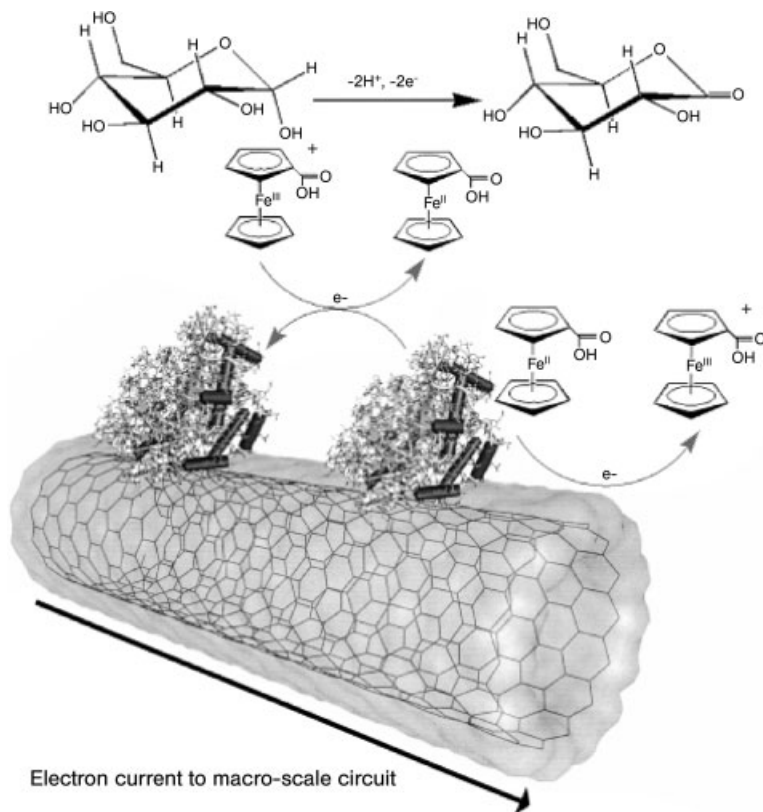


**Fig. 3.2.** Schematic representation of the “SWCNT Glucose Biosensor.” Solution-phase D-glucopyranose is turned over by oxidase enzymes immobilized on the nanotubes. This redox process at the enzyme flavin moieties is “communicated” to the nanotube  $\pi$  system through the diffusive mediator ferrocene

monocarboxylic acid. The redox action of the ferrocenes at the nanotube surface ultimately generates a quantifiable catalytic current that is characteristic of substrate detection and turnover. (Reprinted with permission from Ref. [70]. © 2003 Wiley-VCH.)

viewed as an extreme form of conducting polymer, the combination of nanotubes with conventional  $\pi$ -conjugated conducting polymers offers new electronic properties and high surface area capacity. This well suits the integration of substrate and transducer when making biosensors.

Wallace et al. combined MWCNTs and glucose oxidase to be embedded into polypyrrole (Ppy) with 0.1 M NaClO<sub>4</sub> as supporting electrolyte [73]. Such an enzyme electrode retains its stability at 70% after 3 days storage in the dry state at 4 °C. The use of these 3D electrodes offers advantages in that large accessible enzyme loadings can be obtained within an ultrathin layer. The iron-loaded nanotube tips (generated from CNT preparation) also contribute partial catalytic capacity toward H<sub>2</sub>O<sub>2</sub> oxidation. A biosensor based on Ppy/DNA composite covered CNT under-

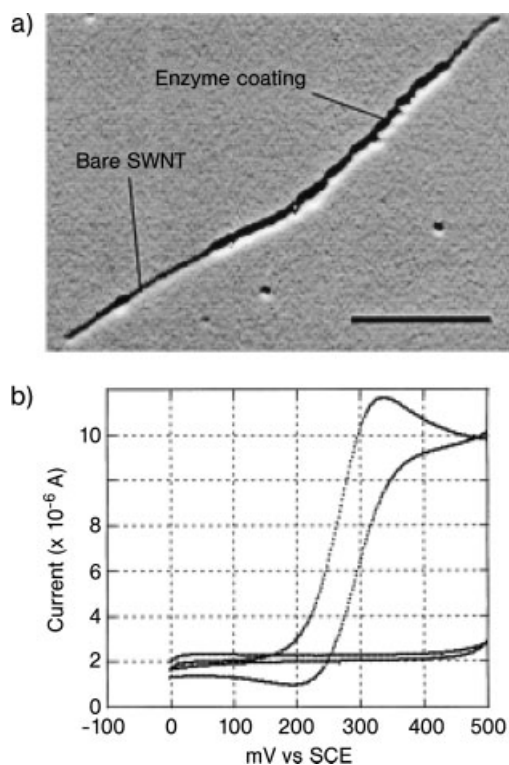


**Fig. 3.3.** (a) TMAFM amplitude micrograph of a GOX-modified SWCNT in which a high degree of enzyme loading is apparent. The scale bar is 200 nm. (b) Voltammetric response of such nanotubes in the absence

(lower curves) and presence (upper curves) of the substrate,  $\beta$ -D-glucose. (TMAFM = tapping-mode atomic force microscopy). (Reprinted with permission from Ref. [70]. © 2003 Wiley-VCH.)

layers was recently provided for DNA sensing [74]. By applying an impedance technique to this two-layer-based sensor, the complementary DNA target can be detected down to  $5 \times 10^{-11}$  M.

Sol-gel chemistry involves the hydrolysis and condensation of suitable alkoxy-silane precursors and has been widely employed for the preparation of inorganic materials (monolithic, hybrid, composites, and chromatographic stationary phase) suitable for various applications. Recently, Bachas and coworkers have applied a CNT sol-gel composite as an enzyme-friendly platform to develop biosensors [75]. Using L-amino acid oxidase as a model enzyme, the biosensors were made in aqueous sol-gel processes involving methyltrimethoxysilane, ethyltrimethoxysilane and propyltrimethoxysilane as precursors. Aliquot amounts of MWCNTs and enzyme were added into the sol when the hydrolysis took place. The resultant sensor proved to be stable and retained more than 50% of its response after 1 month of testing. In such an immobilization protocol, the porous  $-\text{Si}-\text{O}-$  sol-gel network



encapsulates biomolecules while the use of CNTs, as the conductive part of the composite, facilitated fast electron transfer rates.

Because of the unique  $sp^2$  hybrid surface structures, CNTs themselves could be viewed as an extreme form of conducting polymer. The CNT bulky material may be applied directly towards sensor construction without binders or other auxiliary components. Wang and co-authors have developed a simple approach for preparing effective CNT-based biosensors from CNT/Teflon composite material by hand-mixing a certain amount of CNTs in the dry-state with granular Teflon to obtain a desired composition of CNT/Teflon [76]. Carbon composites, based on the dispersion of graphite powder within an insulator, offer convenient bulk modification for the preparation of reagentless and renewable biosensors. Wang et al.'s approach relies on CNTs as the sole conductive component rather than as the modifier cast on other electrode surfaces. The bulk of CNT/Teflon composites hence serve as a reservoir for the enzymes. By comparing the sensors' performance against their respective composite compositions, the CNT content of 40–60 wt.% has been suggested. CNT/Teflon composites combine advantages of CNTs and bulk composite electrodes that permit a wide range of applications without the need for a graphite surface. Certain amounts of enzymes (e.g., glucose oxidase and alcohol dehydrogenase) and cofactor (e.g.,  $NAD^+$ ) can be mixed with the CNT/Teflon composite and used as electrode materials, depending upon specific needs. These biosensor interfacing displayed a marked electrocatalytic action toward hydrogen peroxide and  $\beta$ -nicotinamide adenine dinucleotide (NADH) and, hence, this is promising for the development of biosensors for glucose (in connection with oxidase enzymes) and ethanol (in connection with dehydrogenase enzyme), respectively [76]. Similar approaches have been developed for CNT-based sensor fabrication using nanotube–mineral oil paste, reagent-embedded CNT paste, or powders to determine DNA, glucose, cysteine, and other biomolecules.

Composites consisting of CNTs and other nanotubes or nanoparticles were reported recently for enhancing the catalytic capacity of the sensing devices. Luong's group [77] and Yao's group [78] used platinum nanoparticles combining with CNTs to construct a biosensing platform for glucose oxidase. Wang et al. employed semiconductor CdS nanoparticle-tagged CNTs for DNA hybridization detection [79].

#### 3.2.2.7 More Sophisticated Surface Tailoring Based on Combination of Co-adsorption, Integration, Prohibition, Spacing, Linkage, Sandwich, Tagging, and other Anchoring Approaches

Biosensors involve biomolecules and biorecognition reactions. Their optimal operational performance depends on the maximization of the desired signals while minimizing the side reaction. DNAs, enzymes, antigens, and other biomolecules usually bear charges, depending on the medium pH. CNT biomodifications based on non-specific interaction with DNAs or proteins can be achieved through the sidewall electrostatic interaction, hydrogen bonding, and other mechanisms, as well as the insertion of smaller biomolecules into the tubular channel. The nature of these noncovalent bondings are complicated and were proposed by Dai et al. as

mainly the results of hydrophobic interaction and the  $\pi$ -stacking of the conjugated pyrenyl group of 1-pyrenebutanoic, succinimidyl ester, or coating with some surfactants, such as Triton [80, 81]. More specific binding to functionalize the CNTs can take advantage of covalent bonding, DNA hybridization, coupling agents, and antigen–antibody interactions. Biosensing by these approaches was reported for the CNTs attachment of decorated glucose oxidase [82], thiolated DNA [83], amine-terminated DNA [84], and peptide nucleic acid (PNA) – a DNA mimic [85].

The non-specific adsorption of proteins on nanotubes is not always desirable, especially when tested in real biofluid samples that contain many co-existing proteins. More sophisticated sensors, therefore, need to address issues like target-recognition enhancement, blockage of undesired interference (the co-existing proteins' non-specific adsorption on the nanotube surfaces), long-term storage, etc. Accordingly, CNT surface engineering might be a combination of different tailoring techniques. Dai et al. have presented a typical example [81] (Fig. 3.4). In their approach U1A, a protein involved in the splicing of message ribonucleic acid (mRNA), was covalently linked to Tween-20, a surfactant. The complex was then noncovalently cast onto the single-walled CNT surface. The latter was as-grown on a quartz wafer that was *in situ* monitored by its conductance and frequency response during the sensing measurement.

This CNT modification with the adsorption of biotinylated Tween-20 allowed streptavidin recognition by the specific biotin–streptavidin interaction, but provided resistance toward other protein adsorptions. Under such design, the sensor could detect the binding of 10E3, a specific antibody for recognition of U1A, at concentrations as low as 1 nM (Fig. 3.4), while showing no response toward other existing proteins such as streptavidin, avidin, bovine serum albumin (BSA),  $\alpha$ -glucosidase, staphylococcal protein A (SpA), and immunoglobulin G (IgG) (Fig. 3.4C). The blocking mechanism toward coexisting proteins was proposed as the formation of a nearly uniform layer of surfactant Tween-20 through the favorable hydrophobic interaction on the nanotube surface, with the poly(ethylene glycol) (PEG) segments extending into the aqueous media to provide the observed protein resistance. Noticeably, this protein-resistant assembly may be covalently conjugated to specific antigens to allow sensitive detection of antibodies, or *vice versa* [81]. This proposed real-time immunosensor can thus compare favorably with a standard fluorescence-based assay with immobilized antigens on planar arrays.

Wang et al. have recently developed a CNT-based amplified bioelectronic protocol that uses DNA for linking particles to CNTs [63]. As can be seen in Fig. 3.5(a), the preparation is based on the sandwich hybridization (a) or antigen–antibody (b) binding along with magnetic separation of the analyte-linked magnetic-bead/CNT assembly (A), followed by enzymatic amplification (B), and chronopotentiometric stripping detection of the product at the CNT-modified electrode (C). TEM observations (Fig. 3.5D) indicate that the hybridization event leads to crosslinking of the alkaline phosphatase (ALP)-loaded CNTs and the magnetic beads (with the DNA duplex acting as “glue”). In this new bioaffinity assay, CNTs play a dual amplification role in both the recognition and transduction events, namely as carriers for

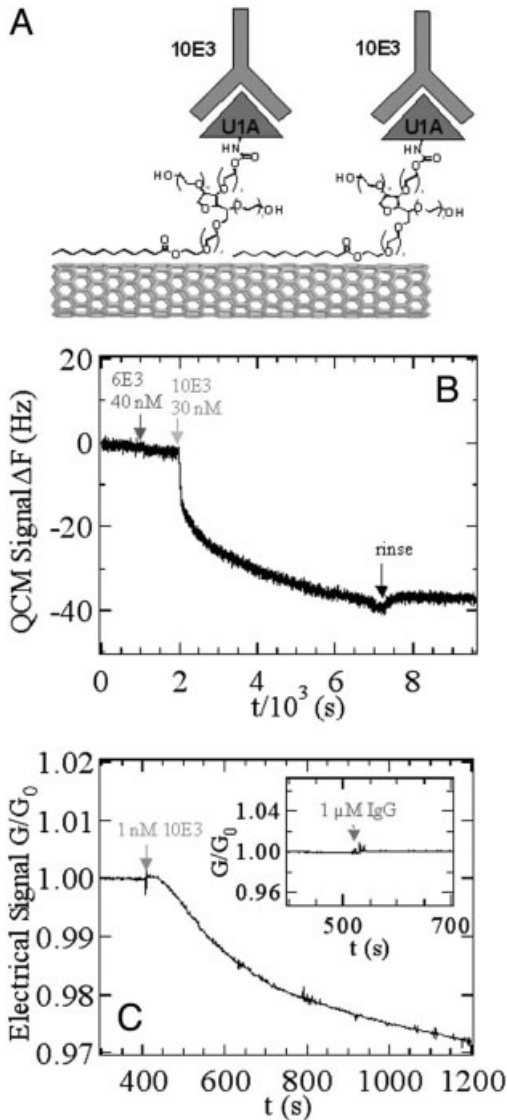


**Fig. 3.4.** Specific detection of mAbs binding to a recombinant human autoantigen. (A) Scheme for specific recognition of 10E3 mAb with a nanotube device coated with a U1A antigen-Tween conjugate. (B) QCM frequency shift vs. time curve showing selective detection of 10E3 while also showing rejection of the antibody 6E3, which recognizes the highly

structurally related autoantigen TIAR. (C) Conductance vs. time curve of a device, revealing a specific response to  $\leq 1$  nM 10E3 while rejecting polyclonal IgG at a much greater concentration of 1  $\mu$ M (inset). (Reprinted with permission from Ref. [81]. © 2003 of National Academy of Sciences, U.S.A.)

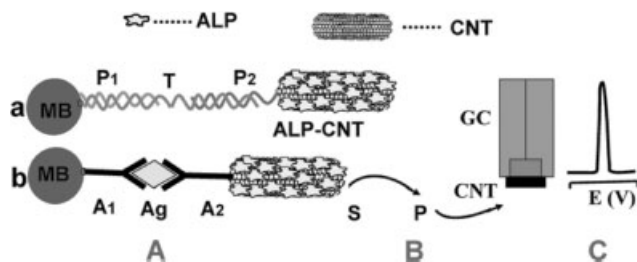


**Fig. 3.5.** Schematic representation of the analytical protocol: (A) Capture of the ALP-loaded CNT tags to the streptavidin-modified magnetic beads by a sandwich DNA hybridization (a) or Ab-Ag-Ab interaction (b). (B) Enzymatic reaction. (C) Electrochemical detection of the product of the enzymatic reaction at the CNT-modified glassy carbon electrode. (D) TEM image of the magnetic beads-DNA-CNT assembly produced following a 20-min hybridization with the  $10 \text{ pg mL}^{-1}$  target sample. Micrographs were taken with a Hitachi H7000 instrument operated at 75 kV

after washing the DNA-linked CNT/particle assembly with autoclaved water, placing a  $5\text{-}\mu\text{L}$  drop of the aggregate sample onto a carbon-coated copper grid (3 mm diameter, 200-mesh), and allowing it to dry. MB, Magnetic beads; P<sub>1</sub>, DNA probe 1; T, DNA target; P<sub>2</sub>, DNA probe 2; Ab<sub>1</sub>, first antibody; Ag, antigen; Ab<sub>2</sub>, secondary antibody; S and P, substrate and product, respectively, of the enzymatic reaction; GC, glassy carbon electrode; CNT, carbon nanotube layer. (Reprinted with permission from Ref. [63]. © 2003 American Chemical Society.)

numerous enzyme tags and for accumulating the product of the enzymatic reactions. With such an assembly, the extraordinarily low detection limits were reported for DNA and IgG of  $1$  and  $500 \text{ fg mL}^{-1}$ , respectively.

### 3.2.3

#### CNT-based Electrochemical Biosensors

Soluble CNTs have been electrochemically and quantum-chemically characterized for their bulk properties [86]. Results showed that the electronic states are not strongly affected when the nanotubes are functionalized. The electronic properties of CNTs range from metallic to semiconductive, depending on the nanotube's own diameter and chirality. These subtle electronic properties offer various electrochemical features for CNT-based sensors after functionalization of the nanotubes.

##### 3.2.3.1 Direct Electrochemistry of Biomolecules on Carbon Nanotubes

Recently, direct electrochemical communications between redox-active macromolecules and conventional electrode substrates mediated by CNTs have received attention because of their potential to lead a mechanistic study of the structure–function relationship of these biomolecules and their guidance toward biosensor design. Wang et al. reported the direct electrochemistry of cytochrome *c* at electrochemically activated SWCNT-modified electrodes [23]. Gooding et al. and Rusling et al. have used aligned nanotubes to promote the direct electrochemistry of redox-active proteins [66, 67]. These studies demonstrate that direct electro-

chemistry of redox-active biomacromolecules can be improved through the use of CNTs.

In addition to the aforementioned charge transfer promotion, there have been reports on the electrocatalytic behavior of CNTs toward some small biomolecules such as cysteine and hemocysteine [87], ascorbic acid [88], uric acid [89], dopamine [90]. The mechanisms of this surface mediation are not currently well understood, and the terminology of electrocatalysis should be exercised cautiously for different electrode material and media. The promoted electrochemical reactions for hydrogen peroxide, NADH, and quinones enable possible sensing schemes for more than 800 enzymes that involve these substrates, products, coenzymes, and cofactors.

Several hundred enzymatic reactions of  $\text{NAD}^+/\text{NADH}$ -dependent dehydrogenases have NADH as a cofactor. The electrochemical oxidation of NADH has thus been the subject of numerous studies related to the development of amperometric biosensors. Problems inherent to such anodic detection are the large overpotential encountered for NADH oxidation at ordinary electrodes and surface fouling associated with the accumulation of reaction products. CNTs have thus been examined in recent work [91] as the new electrode material to alleviate these problems.

Lin et al. have employed CNTs that had been pretreated with dispersion in concentrated sulfuric acid to cast a glassy carbon electrode [91]. Figure 3.6 shows a typical hydrodynamic voltammogram of  $1 \times 10^{-4}$  M NADH in a physiological medium (0.05 M phosphate solution, pH 7.4). This voltammogram demonstrates an electrocatalytic behavior of the CNT coating towards NADH with varying potentials, as evidenced by the MWCNT-coated electrode (B) responding to NADH over

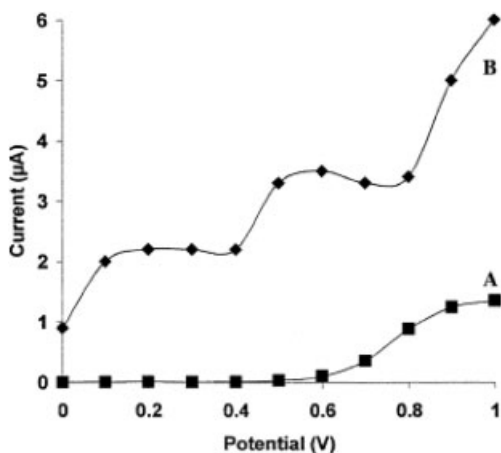


**Fig. 3.6.** Hydrodynamic voltammograms for  $1 \times 10^{-4}$  M NADH at unmodified (A) and MWCNT-modified (B) GC electrodes. Operating conditions: stirring rate, 500 rpm; electrolyte, phosphate buffer (0.05 M, pH 7.4). (Reprinted with permission from Ref. [91]. © 2002 Elsevier.)

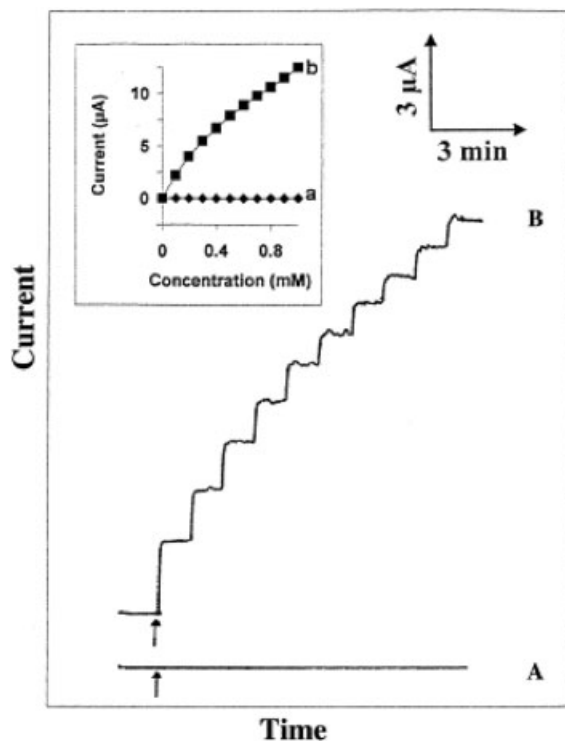


Fig. 3.7. Current–time recordings obtained after increasing the NADH concentration (by  $1 \times 10^{-4}$  M at each step) at unmodified (A) and MWCNT-modified (B) GC electrodes.

Inset: the corresponding calibration curve. Operating conditions: potential, +0.3 V. (Reprinted with permission from Ref. [91]. © 2002 Elsevier.)

the entire 0.0–1.0 V range, whereas the bare electrode (A) responds only at potentials higher than +0.6 V. The modified electrode yields an approximately three-fold larger NADH peak than does the unmodified electrode. Figure 3.7 shows that successive additions of  $1 \times 10^{-4}$  M NADH result in increasing response detected at the CNT-modified electrode (B) but no response at the unmodified electrode (A) when the detection potential was kept low (i.e., 0.3 V). Evidently, the electrocatalytic action of CNT enables the fast response (i.e., 10 s to reach the steady state) to the change of NADH concentrations at the low-detection potential. The amperometric response of  $5 \times 10^{-3}$  M NADH appears to be very stable; the decay of the signal is less than 10% and 25% after a 60-min period at the MWCNT-modified and SWCNT-modified electrodes, compared with 75% and 53% at the graphite-coated and acid-treated electrodes, respectively. This shows the capability of CNTs to resist the fouling effects and prevent the diminishing of signals in successive cyclic voltammetric detections. The oxygen-rich groups on the CNT surface, introduced during the acid dispersion, are perhaps responsible for such electrocatalytic behavior

for the oxidation of NADH. The resistance to fouling of CNT-based electrodes has yet to be understood.

The CNT-coating offers remarkably decreased overvoltage for the NADH oxidation as well as reducing the surface fouling effects of the electrodes. These characteristics indicate the great promise of CNTs for developing highly sensitive, low potential, and stable amperometric biosensors based on dehydrogenase enzymes.

### 3.2.3.2 Enzyme/CNTs Biosensors

Most reported CNT-based biosensors for glucose thus far involve the enzymatic reaction by glucose oxidase (GOx) [61, 69, 70, 76, 78]. Wang and Musameh have employed CNT/Teflon-based electrodes, which are immobilized with GO<sub>x</sub> enzyme [76]. Figure 3.8 compares the amperometric response to successive additions of 2 mM

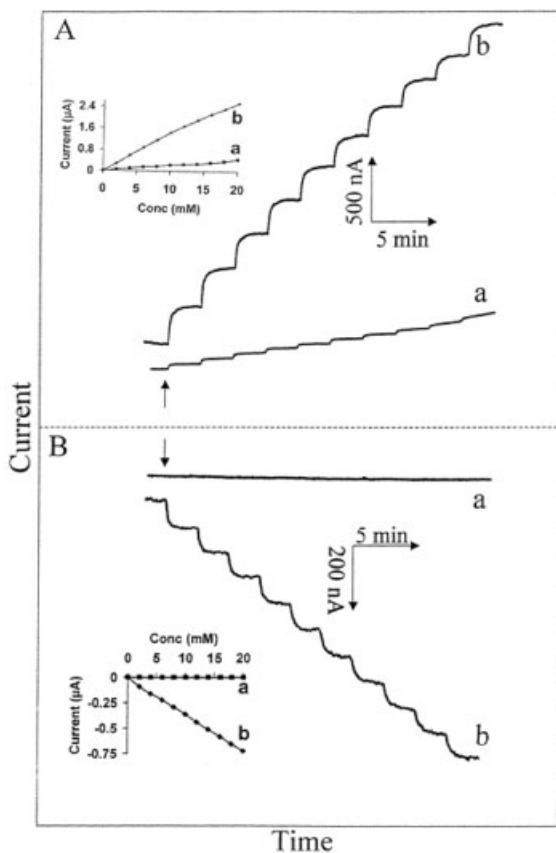


**Fig. 3.8.** Current–time recordings for successive 2-mM additions of glucose at graphite/Teflon/GO<sub>x</sub> (a) and the MWCNT/Teflon/GO<sub>x</sub> (b) electrodes measured at +0.6

(A) and +0.1 V (B). Electrode composition, 30:69:1 wt.% carbon/Teflon/GO<sub>x</sub>. (Reprinted with permission from Ref. [76]. © 2003 American Chemical Society.)

glucose at the graphite/Teflon/ $\text{GO}_x$  (a) and the MWCNT/Teflon/ $\text{GO}_x$  (b) electrodes using operating potentials of +0.6 V (A) and +0.1 V (B). The CNT-based bioelectrode offers substantially larger signals, especially at low potential, reflecting the electrocatalytic activity of CNTs. Such low-potential operation of the CNT-based biosensor results in a highly linear response (over the entire 2–20 mM range) and a slower response time ( $\sim 1$  min vs. 25 s at +0.6 V). The glucose biocomposite based on single-wall CNTs results in a more sensitive but slower response than that based on multiwall CNTs. The low-potential detection also leads to high selectivity (i.e., effective discrimination against coexisting electroactive species). Despite the absence of external (permselective) coating, the glucose response at +0.1 V was not affected by adding the common acetaminophen and uric acid interferences at 0.2 mM [76]. A similar addition of ascorbic acid resulted in a large interference, reflecting the accelerated oxidation of this compound at the CNT surface [88].

Recently, Sheu et al. have reported the non-enzymatic detection of glucose [92]. This approach uses MWCNTs but needs a strong basic media that may not be compatible with the bioenvironment.

### 3.2.3.3 DNA and Protein Biosensors

Interest in the detection of DNA has grown aggressively because of its importance in the diagnosis and treatment of genetic disease, drug discovery, and anti-bioterrorism efforts. The completion of the Human Genome Project offers an abundance of gene mapping and screening. A hybridization recognition scheme, based on the Watson–Crick base pair principle, is the central point when constructing a DNA sensor. The unique electric, thermal, chemical, mechanical, and 3D spatial properties of CNTs make them a natural choice as transducers for hybridization-based DNA sensors. Different attachment protocols for DNA probes (single strand DNA molecules) onto CNTs were introduced, either by unmodified or surface-confined nanotubes [40, 63, 93].

Wang and coworkers have developed an ultrasensitive DNA biosensor based on a “dual amplification route” by using CNTs both as recognition sites and transducers, namely as carriers for numerous enzyme tags and for accumulating the product of the enzymatic reaction [63]. Figure 3.9 displays typical chronopotentiograms for extremely low target DNA concentrations (0.01 to 100  $\text{pg mL}^{-1}$ ; a–e). Well-defined  $\alpha$ -naphthol signals are observed for these low DNA concentrations in connection with 20-min hybridization. The resulting plot of response vs.  $\log[\text{Target}]$  (shown as inset) is linear and suitable for quantitative work. The favorable response of the 5  $\text{fg mL}^{-1}$  DNA target (B) indicates a remarkably low detection limit of around 1  $\text{fg mL}^{-1}$  (54 aM), i.e., 820 copies or 1.3 zmol in the 25- $\mu\text{L}$  sample. Such a low detection limit compares favorably with the lowest values of 5 zmol (3000 copies) and 25 amol reported for electrical DNA detection. The smaller signal observed in a control experiment for a huge ( $\sim 10^6$ ) excess of a non-complementary oligonucleotide (Fig. 3.9C vs. B) reflects the high selectivity associated with the effective magnetic separation. The amplified electrical signal is coupled to a good reproducibility. Two series of six repetitive measurements of



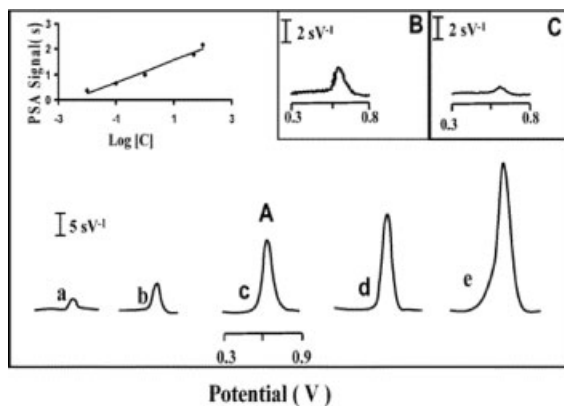


**Fig. 3.9.** Chronopotentiometric signals for increasing levels of the DNA target: (a) 0.01, (b) 0.1, (c) 1, (d) 50, (e) 100  $\text{pg mL}^{-1}$ . Also shown (inset) is the resulting calibration plot (A), and the response for 5  $\text{fg mL}^{-1}$  target

DNA (B) and 10  $\text{ng mL}^{-1}$  non-complementary (NC) oligonucleotide (C). Sample volume, 25 (B) and 50  $\mu\text{L}$  (C). (Reprinted with permission from Ref. [63]. © 2003 American Chemical Society.)

1  $\text{pg mL}^{-1}$  DNA target or 0.8  $\text{ng mL}^{-1}$  IgG yielded reproducible signals with relative standard deviations of 5.6% and 8.9%, respectively [63].

Noticeably, Wang's "dual amplification" mode for the DNA sensor as above has also been applied to an immunosensor for IgG because of the similarity between DNA hybridization and antigen-antibody interaction. An extremely low detection for IgG was reported, as 500  $\text{fg mL}^{-1}$  [63]. In contrast, DNA, RNA, proteins, and enzymes all bear multiple charges, and their adsorption onto the nanotubes is expected to change their electronic properties. These changes, upon adsorption, can be readily transduced into measurable sensing signals [38, 94]. DNA has already been used as a template to localize CNTs to make new building blocks or alignments in electronics and bioelectronics, such as field-effect transistors (FETs) [95]. These functionalized FETs, coupled with advanced sensor array techniques, can therefore serve as a new direction in CNT-based bioassays [77, 80].

#### 3.2.3.4 Immunosensors

Electrochemical immunosensors based on CNTs have been designed [20]. Vertically aligned arrays of single CNTs called SWCNT forests have been developed for amperometric enzyme-linked immunoassays of proteins by Rusling and coworkers [20]. A prototype amperometric immunosensor was evaluated based on the adsorption of antibodies onto perpendicularly oriented assemblies of SWCNT forests. The forests were self-assembled from oxidatively shortened SWCNTs onto Nafion/iron oxide coated pyrolytic graphite electrodes. Anti-biotin antibodies strongly adsorbed to the SWCNT forests. They found that the detection limit for horseradish peroxidase (HRP) labeled biotin was 2.5  $\text{pmol mL}^{-1}$  (2.5  $\text{nM}$ ) in the presence of a soluble mediator. Unlabeled biotin was detected in a competitive approach with a detection

limit of  $16 \text{ nmol mL}^{-1}$  and a relative standard deviation of 12%. The immunosensor showed low non-specific adsorption of biotin-HRP (approx. 0.1%) when blocked with bovine serum albumin. The biosensor platform is also being developed to accommodate flow-through sensor design with direct electron transfer detection of the enzyme label on a CNT matrix. Traditional electrochemical immunosensors were based on mediated electron transfer. However, efficient direct electron transfer will offer some advantages, such as a simple possibility for a reagentless immunoassay. CNTs exhibit excellent electrical properties, and they are a suitable candidate for developing such a reagentless immunoassay.

#### 3.2.4

##### Flow-injection Analysis

Flow detectors have been widely used in process chemistry and online monitoring. It is the core part for real time, *in situ* analysis and for the integration of separation and detection – “lab-on-a-chip.” Microfabricated fluidic devices, particularly used as sensors for capillary electrophoresis (CE) and liquid chromatography (LC), have gained steadily growing attention in recent years [64]. Wang et al. have presented a CNT-based detector for a conventional as well as a miniaturized CE system [64]. CE combines the advantages of high performance, design flexibility, reagent economy, high throughput, miniaturization, and automation. It demands a detector with high sensitivity, inherent miniaturization (of both the detector and control instrumentation), and compatibility with advanced micromachining technologies, and low cost and power requirements [64]. Conventional detectors are based on gold, platinum, and various forms of carbon. A CNT-based electrode offers an alternative for low potential detection, it imparts enhanced sensitivity, and it leads to long-term stability. In this approach, Wang et al. used a Nafion/CNT-coated screen-printed electrode for end-column amperometric detection. After anodic pretreatment (3 min at +1.5 V in 1 M sulfuric acid), this sensor showed substantial electrocatalytic behavior and resistance to surface fouling toward hydrazine, phenol, tyrosine, purine, and amino acids, when compared with the bare surface. The CNT microchip detector also displayed well-defined concentration dependence.

Typical flow detection for glucose, based on the CNT/Nafion/ $\text{GO}_x$  modified gas chromatography (GC) electrode, can be seen in Fig. 3.10 (from the work by Wang's group) [61]. Figure 3.10 compares the amperometric responses for relevant physiological levels of glucose, ascorbic acid, acetaminophen, and uric acid at the CNT/Nafion/ $\text{GO}_x$  modified GC electrode (B) and Nafion/ $\text{GO}_x$  modified GC electrode (A). In Figure 3.10, the accelerated electron-transfer reaction of hydrogen peroxide at the CNT/Nafion/ $\text{GO}_x$  modified GC electrode allows for glucose measurements at very low potentials (i.e.,  $-0.05 \text{ V}$ ) where interfering reactions are minimized. As a result, a well-defined glucose signal (d) is observed, while the signals of acetaminophen (a), uric acid (b), and ascorbic acid (c) are negligible. No such discrimination is obtained at the Nafion/ $\text{GO}_x$  biosensor (without the CNT) (A) held at  $+0.80 \text{ V}$ , where large oxidation peaks are observed for all interferences, indicating that the permselective (charge exclusion) properties of Nafion are not adequate to

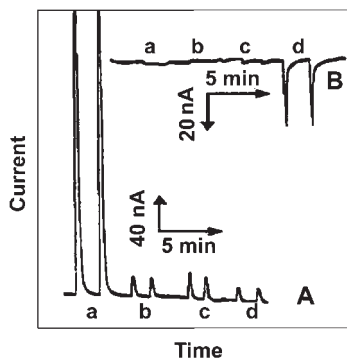


**Fig. 3.10.** Flow-injection signals for  $2 \times 10^{-4}$  M acetaminophen (a),  $2 \times 10^{-4}$  M ascorbic acid (b),  $2 \times 10^{-4}$  M uric acid (c), and  $1 \times 10^{-2}$  M glucose (d) at a Nafion/ $\text{GO}_x$ -modified GC electrode (A) at +0.8 V, and at a

MWCNT/Nafion/ $\text{GO}_x$ -modified GC electrode (B) at  $-0.05$  V, and flow rate of  $1.25 \text{ mL min}^{-1}$ . (Reprinted with permission from Ref. [61]. © 2003 American Chemical Society.)

fully eliminate anionic interferences. In short, the coupling of the permselective properties of Nafion with the electrocatalytic action of CNT allows for glucose detection with effective discrimination against both neutral and anionic redox constituents. Similarly, the CNT/Nafion-coated electrodes have also been demonstrated to dramatically improve the signal of dopamine in the presence of the common ascorbic acid interference [61].

Jin et al. used CNT-based sensors for LC detection [97, 98]. To overcome the aggregation of nanotubes in aqueous and common organic solution, nitric acid was used to treat CNTs to introduce carboxyl groups in the open ends of the MWCNTs. Such functionalized CNTs were cast onto the glassy carbon as the flow detector. Various biofluids containing neurotransmitters were tested using this protocol. The results from real samples such as plasma agreed with those from other methods.

In terms of the mechanism of the CNT-based flow sensor, Ghosh et al. recently found that the flow of a liquid on single-walled CNT bundles induces a voltage in the sample along the direction of the flow [98]. The magnitude of the voltage depended sensitively on the ionic conductivity and on the polar nature of the liquid. The nonlinear response of flow velocity and the voltage was attributed to a direct forcing of the free charge carriers in the nanotubes by the fluctuating Coulombic field of the liquid flowing past the nanotubes. Their work highlighted the potential of a CNT-based device as sensitive flow sensors and for energy conversion [98].

### 3.2.5

#### Carbon Nanotube Array-based Biosensors

Control over the orientation, distribution, and effective sensing sites of the nanotubes have been the subject of CNT-based biosensor research [56, 66]. Several ap-

proaches have been reported to achieve these controlled-density aligned CNTs and CNT arrays. The versatile approach is that of self-assembling aligned nanotube arrays by using oxidative acid treated single walled nanotubes [99]. These shortened tubes then react with DCC to introduce a carbodiimide leaving a group that allows reaction with thiols. Finally, these thiolated nanotubes are self-assembled on the gold surface to form aligned CNT arrays. Alternatively, aligned CNT arrays can be grown off a surface by using pyrolyzing CVD of relevant catalysts and carbon materials, followed by transferring the tubes onto a substrate support [73]. The third approach is to grow directly aligned CNTs onto an electrode surface by using CVDs or plasma, offering a controllable size and a given location for the catalyst spots that allows the growth of a given numbers of nanotubes [93].

Although vertically aligned CNTs have good material properties (e.g., good electrical conductivity, the capability to promote electron transfer reactions) and are of the right size (20 to 200 nm) for nanoelectrode arrays (NEAs), they lack the right spacing, having little support, and, therefore, the electrodes may lack robustness. To make each nanotube work as an individual nanoelectrode, the spacing needs to be sufficiently larger than the diameter of the nanotubes to prevent diffusion layer overlap from the neighboring electrodes [100]. Ren and co-authors recently developed a nonlithography method that allows the fabrication of low site density aligned CNT arrays with an interspacing of more than several micrometers [101]. Figure 3.11 demonstrates the manufacturing process of such aligned CNT arrays: Ni nanoparticles were randomly deposited on a 1-cm<sup>2</sup> Cr-coated silicon substrate

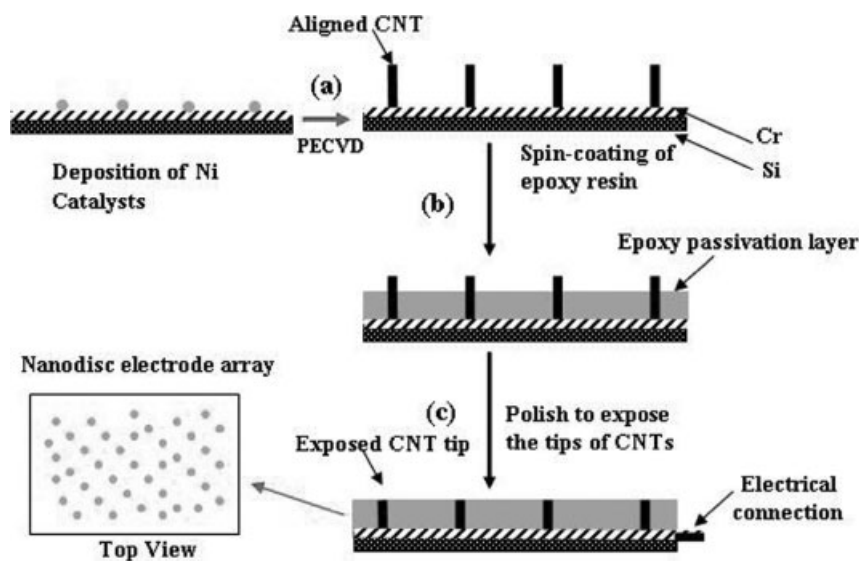


**Fig. 3.11.** Fabrication scheme of a low-site-density aligned CNT nanoelectrode array. (Reprinted with permission from Ref. [101]. © 2003 American Chemical Society.)

(Fig. 3.11a) by applying a pulse current to the substrate in a  $\text{NiSO}_4$  electrolyte solution. The size and the site density of the Ni nanoparticles were controlled by the amplitude and the duration of the pulse current. On these Ni particles, the CNTs were grown (Fig. 3.11b) in the plasma-enhanced chemical vapor deposition (PECVD) system at  $650^\circ\text{C}$  for 8 min with 160 sccm  $\text{NH}_3$  and 40 sccm  $\text{C}_2\text{H}_2$  gases with a total pressure of 15 Torr and a plasma intensity of 170 W. The aligned CNT arrays had a site density of  $1 \times 10^6$ – $3 \times 10^6 \text{ cm}^{-2}$ , a length of 10 to 12  $\mu\text{m}$ , and a diameter of 50–80 nm. A thin layer of Epon epoxy resin 828 (Miller-Stephenson Chemical Co., Inc., Sylmar, CA) was coated on the surface by magnetron sputtering to insulate the Cr layer. This was followed by applying m-phenylenediamine (MPDA) as a hardener. After these steps, the CNTs were half-embedded in the polymer resin, and the protruding part of the CNTs beyond the polymer resin was mechanically removed by polishing with a lens, followed by ultrasonication in water. Then the electronic connection was made on the CNT-Si substrate to make the CNT nanoelectrode arrays (Fig. 3.11c). Finally, the electrode arrays were pretreated by electrochemical etching in 1.0 M NaOH at 1.5 V for 90 s before electrochemical characterizations [101]. Results showed that, within these low site density CNTs, the NEAs consist of millions of nanoelectrodes, with each electrode being less than 100 nm in diameter. There is no degradation of these sensors for several weeks because of the excellent stability of the epoxy layer. Since the total current of the loosely packed electrode arrays is proportional to the total number of individual electrodes, having the number of the electrodes up to millions is highly desirable. The size reduction of each individual electrode and the increased total number of the electrodes result in improved signal-to-noise ratio (S/N) and detection limits.

Ng et al. have developed a soft lithography-mediated selective CVD template approach in preparing the multiwalled CNT membrane [102]. This membrane can be integrated with a flexible elastomeric polydimethylsiloxane framework to fabricate microsensing devices. The presented sensor design can be developed into a generic platform for electrochemical detection and gas sensing, as well as other general purpose sensory systems.

The unmodified and surface-confined aligned CNTs and CNT arrays by different preparation protocols discussed above have all been applied to the study of protein interaction [101, 103], DNA hybridization [104], and enzyme catalysis [66, 102]. Lin et al. have reported typical results for glucose biosensing using a CNT array (Fig. 3.12) [103]. The  $\text{GO}_x$  molecules were attached to the broken tips of the CNTs via carbodiimide chemistry by forming amide linkages between their amine residues and carboxylic acid groups on the CNT tips. Fig. 3.12(a) and (b) compare amperometric responses for 5 mM glucose (G), 0.5 mM ascorbic acid (AA), 0.5 mM acetaminophen (AC), and 0.5 mM uric acid (UA) at the  $\text{GO}_x$ -modified NEA and the potentials of +0.4 V (a) and -0.2 V (b). Well-defined cathodic and anodic glucose responses are obtained at this aligned CNT/ $\text{GO}_x$ -based biosensor at both potentials. However, the glucose detection at a lower operating potential (-0.2 V) is significantly less influenced by the interferences, indicating high selectivity towards the glucose substrate. Such a highly selective response to glucose is obtained

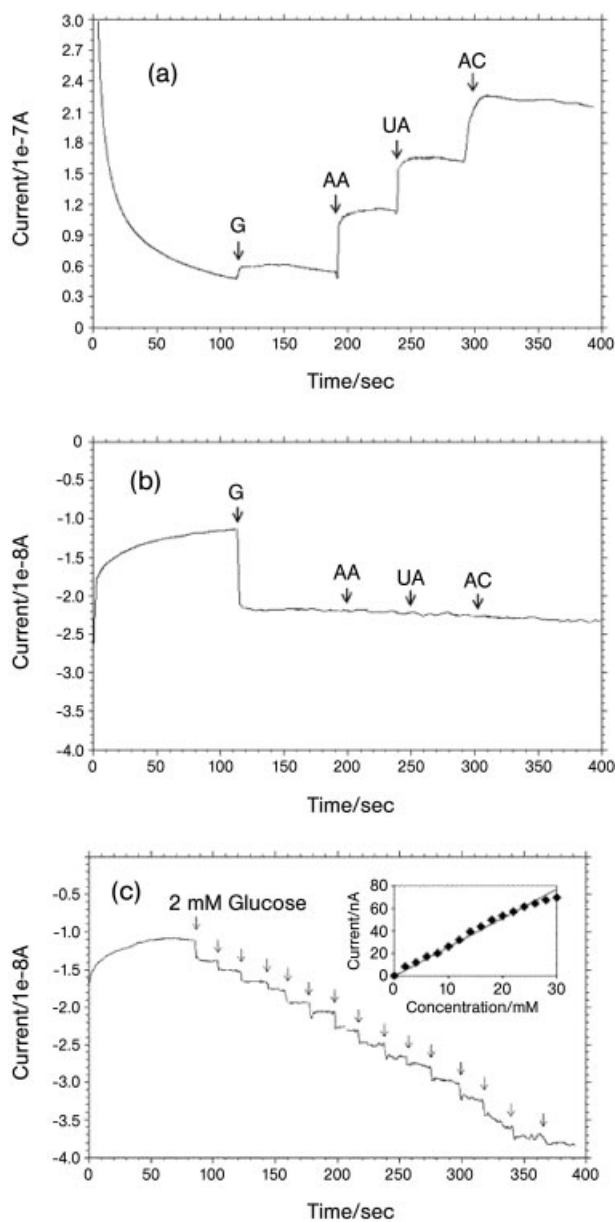


**Fig. 3.12.** (a, b) Amperometric responses for 5 mM glucose (G), 0.5 mM ascorbic acid (AA), 0.5 mM acetaminophen (AC), and 0.5 mM uric acid (UA) at a  $\text{GO}_x$ -modified, CNT-nanoelectrode array and potentials of +0.4 (a) and -0.2 V (b). Electrolyte: 0.1 M phosphate buffer/0.1 M NaCl (pH 7.4). (c) Amperometric

response at the  $\text{GO}_x$ -modified, CNT-nanoelectrode array for each successive addition of 2 mM glucose. Inset: the corresponding calibration curve. Potential: -0.2 V, other conditions are as in (a, b). (Reprinted with permission from Ref. [103]. © 2003 American Chemical Society.)

at this aligned CNT/GO<sub>x</sub>-based biosensor without the use of mediators and permselective membranes. The amperometric response at this sensor for each successive addition of  $2 \times 10^{-3}$  M glucose is presented in Fig. 3.12(c) with the corresponding calibration curve in the inset. The linear response to glucose is up to 30 mM, and steady state is reached within 20 to 30 s [103]. Because of this low potential detection, CNTs eliminate perspective interferences through the preferential detection of hydrogen peroxide at the CNT-based electrodes. Such development of interference-free transducers will significantly simplify the design and fabrication of biosensors. Biosensors based on low-site-density aligned CNTs are also suitable for the highly selective detection of glucose in various biological fluids (e.g., saliva, sweat, urine, and serum) [103].

Rusling et al. reported the first example of enzymes covalently attached onto the ends of vertically oriented SWCNT forest arrays [67]. These arrays were made from their unique methodology of assembling dense orthogonally oriented arrays of shortened SWCNTs. Quasi-reversible Fe<sup>III</sup>/Fe<sup>II</sup> voltammetry was obtained for the iron heme enzymes myoglobin and horseradish peroxidase coupled to the carboxylated ends of the nanotube forests by amide linkages. Their observation suggested that the “trees” in the nanotube forest behaved, electrically, similarly to a metal, conducting electrons from the external circuit to the enzymes. Accordingly, the electrochemically manifested peroxidase activity of myoglobin and horseradish peroxidase attached to the CNT array was demonstrated, showing analytical promise for hydrogen peroxide with a detection limit down to ~100 nM in buffer solutions. The covalently attached enzymes kept their activity for weeks in these prototype SWCNT-forest array biosensors [67]. Gooding and co-authors also observed the direct charge transfer between redox-active enzymes and the aligned CNTs’ surface [66]. Their mechanistic study revealed that the rate of electron transfer remains the same regardless of the lengths of the tubes. These findings enable electroactive molecules to be located several hundred nanometers from a macroscopic substrate electrode with no loss in performance. This might guide future modification of the CNT array for sensor applications.

While most of the array studies have focused on their electrochemical mode, because of the unique electronic properties of individual nanotubes and nanotube arrays, optical sensing based on CNT arrays has also been carried and has been reviewed by Xu [21].

### 3.2.6

#### Chemiluminescence

Miscellaneous CNT sensing applications have been reported recently by using different transducer techniques with various nanotube platforms. As a traditional technique, fluorescence spectroscopy has been widely employed in sensor and bioassay application because of its high sensitivity. However, there have been few reports regarding its study on CNTs, partly because of the limited aqueous solubility or dispersion of CNTs [105, 106]. By using amine-terminated oligonucleotide-functionalized CNTs, Hazani and co-authors were able to enhance nanotube solu-

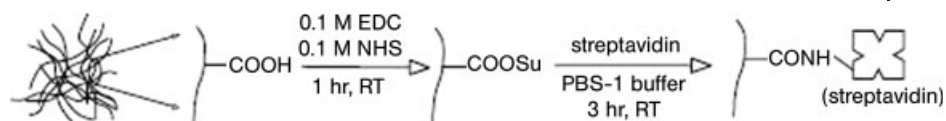


Fig. 3.13. Reaction scheme of immobilization of streptavidin on nanotubes by covalent coupling. (Reprinted with permission from Ref. [105]. Copyright 2003 Wiley-VCH.)

bility to facilitate the confocal fluorescence imaging of the DNA hybridization from a fluorescence dye-tagged complementary sequence [107]. Baker et al. used thiol-terminated oligonucleotide-modified CNTs for the similar assay [108].

A more direct application of CNT based biosensors has been reported by Wohlstadter et al. in their electrogenerated chemiluminescence (ECL) study of immunoassays for  $\alpha$ -fetoprotein (AFP) [105]. Nanotubes possess several characteristics that make them attractive for ECL-based assays: First, they are conductive or semiconductive and hence can act as electrodes to generate ECL in aqueous solutions; second, nanotubes can be surface-functionalized as we discussed before; finally, their high surface area-to-volume ratio and  $sp^2$  network make them feasible for immobilizing biomolecules as well as their associated electrochemistry. Wohlstadter et al. first mixed nanotubes with poly(vinyl acetate) (EVA) to form a nanotube–EVA composite. This composite was then etched with strong acid to produce a densely packed nanotube sheet with available surface carboxylic acid groups. As can be seen in Fig. 3.13, streptavidin was then immobilized on the nanotube sheet by carbodiimide-activated coupling, followed by the attachment of a biotinylated mAb for AFP via the specific biotin–streptavidin interaction. Figure 3.14 shows the whole assay based on this sensor. The capture of AFP resulted in the binding of a  $Ru(bpy)_3^{3+}$  labeled antibody on to the EVA-MWCNTs composite electrode. As the  $Ru(bpy)_3^{3+}$  is chemiluminescent, binding is transduced by the release of light upon applying the electrode at potentials more positive than +1 V. This immunosensor with electrochemiluminescence detection was sensitive at AFP concentrations as low as 0.1 nM, with a linear range up to 30 nM [105].

By using chemiluminescent  $Ru(bpy)_3^{3+}$  as a marker, Dong et al. found that the CNT/Nafion composite possesses ECL sensitivity two orders of magnitude more than that at the silica/Nafion composite and three orders of magnitude more than that at pure Nafion films, again proving that the solubility enhancement for CNTs plays a key role in developing a CNT-based fluorescence sensor [106].

### 3.2.7

#### Field-effect Transistor and Bioelectronics

Advances in electronic detection based on 1D nanomaterials provide the ability for label-free and real time, yet sensitive and selective, sensing biomolecules. The development of CNTs with unique electronic properties has been spotlighted for future solid-state nanoelectronics. Therefore, CNT-based molecular electronics have



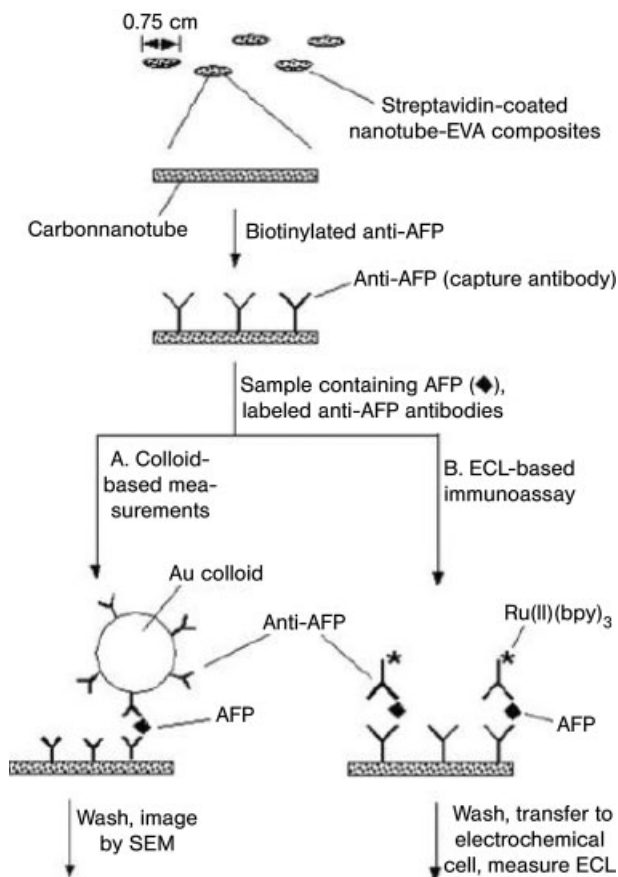
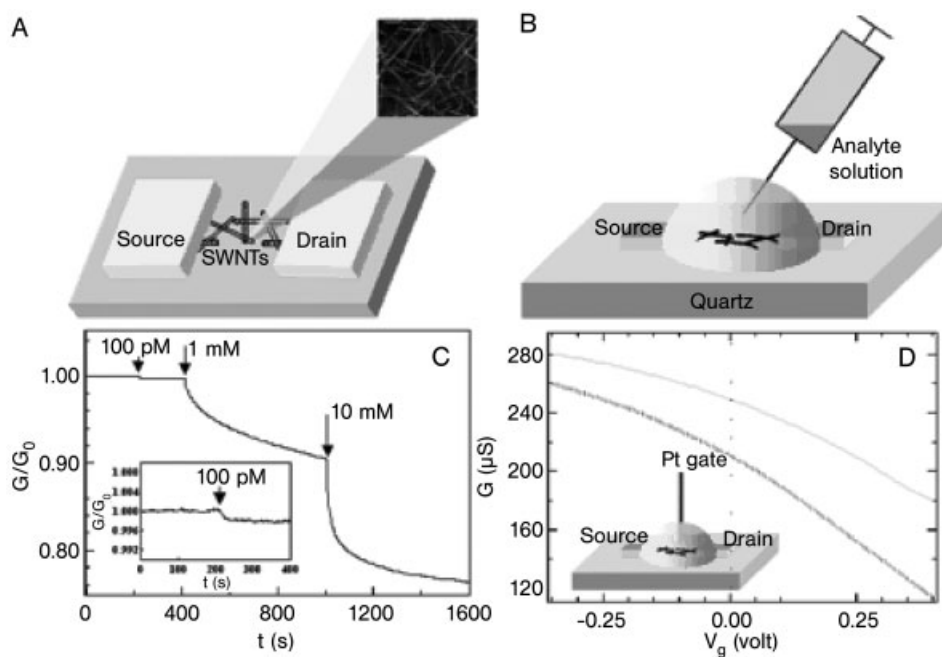


Fig. 3.14. Schematic of procedures for AFP assays based on the CNT-ECL sensor (not to scale). (Reprinted with permission from Ref. [105]. Copyright 2003 Wiley-VCH.)

received wide attention because of the semiconductor features of the nanotubes [109]. Among them, the study of CNT field-effect transistors (CNTFETs) is the core study to compare with the silicon-based transistors. The first CNTFETs were demonstrated by Tans et al. and Martel et al., respectively, in observing the CNTs' exploitable switching behavior [110, 133]. Since then, efforts have been made to improve the electrical characteristics of the CNTFETs. Presently, those explorable features of CNTFETs are the ballistic (scattering-free) and spin-conserving transport of electrons along the nanotubes, their ability to display metallic conducting as well as semiconducting behavior, and their access to the energy gap, which depends on the tube diameter and the rolling orientation of the tubes. CNTs also have extraordinarily high thermal conductivity. These unique properties make them behave similarly to conventional metal-oxide semiconductor field effect transistors

(MOSFETs) as well as differently, with a change from Schottky-barrier modulation at the contacts to bulk switching. These responding multiplicities, coupled with different CNT assembling approaches, offer various possible CNTFETs applications in biological diagnosis, e.g., proteins [5, 81] and cancer cell [111]. Chen and co-workers have demonstrated an exploration of SWCNT as a platform for investigating surface–protein and protein–protein binding and developing a highly specific electronic biosensor. They put SWCNT on a junction (drain and source) as shown in Fig. 3.15 [81]. The SWCNT was modified with polyethylene, which can reduce the non-specific interaction of proteins. A specific receptor was conjugated onto polyethylene-modified SWCNT. Therefore, the device can be highly specific in detecting proteins such as 10E3 m Ab (Fig. 3.4). The detection limit of this method was found to be about  $340 \text{ ng mL}^{-1}$  or 1.0 nM.



**Fig. 3.15.** Carbon nanotubes as electronic devices for sensing in aqueous solutions. (A) Schematic view of the electronic sensing device consisting of interconnected nanotubes bridging two metal electrode pads. An AFM image of a portion of the nanotube network ( $0.5 \mu\text{m}$  on a side) is shown. (B) Schematic setup for sensing in solution. (C) Conductance ( $G$ ) evolution of a device for electronic monitoring of SA adsorption on nanotubes. The conductance is normalized by the initial conductance  $G_0$ . Inset: Sensitivity to a 100-pM

protein solution. (D) Electrical conductance ( $G$ ) vs. gate voltage ( $V_g$ ) for a device in a 10-mM phosphate buffer solution. The gate voltage is applied through a Pt electrode immersed in the solution (inset). The upper (solid) and lower (broken) curves are the  $G$ – $V_g$  characteristics for the device before and after SA binding, respectively. The shift in the two curves suggests a change in the charge environment of the nanotubes. (Reprinted with permission from Ref. [81]. © 2003 NAS).

### 3.3

#### Nanowires in Biosensor Development

Recently, nanowires have been explored as building blocks to fabricate nanoscale electronic devices through self-assembly – a typical bottom-up approach for biosensing [4, 6, 9]. The underlying mechanism for a nanowire biosensor is a field effect that is transduced using a field-effect transistor [4]. This “bottom-up” approach to bionanoelectronics has several attractive features. First, the nanowires are extremely sensitive for detection of biointeractions on their surface because of their high aspect ratio. Second, the electronically switchable properties of semiconducting nanowires provide a sensing modality, a direct and label-free electrical readout, which is exceptionally attractive. Third, the size of the nanowires can be readily tuned to sub-100 nm and smaller, which can lead to a high density of a device on a chip. Therefore, it is feasible for the miniaturized devices to detect multiple samples real time *in vivo*. Fourth, the candidate materials for the nanowires are unlimited, which gives the researcher great flexibility in selecting the right materials for the functionality of the desired device. Presently, the most studied nanowires as a building block for biosensing are semiconducting nanowires, e.g., silicon nanowires [4, 6, 9], conducting polymer nanowires [17, 18], and oxide nanowires [112]. Some metal nanowires have also been developed for sensing. We will focus on semiconducting nanowires for biosensor development here.

#### 3.3.1

##### Silicon Nanowire-based Biosensors

Silicon nanowires are generally fabricated by CVD [14, 15] and template etching [113, 114]. For the purpose of biosensing, the modification of silicon nanowires is through a silanization reaction on the silicon surface, which introduces the active groups, e.g., amino, carboxyl, or biotin, on the surface of the nanowires. Then the receptor, which can specifically recognize the interested analyte, will be immobilized on the surface through those active groups, the interaction between biomolecules and their counterparts on the silicon surface will introduce the conductance change caused by the field effect, and the conductance change can be electronically transduced. Thus far, silicon nanowire-based biosensors have been developed for detection DNA [4, 8, 115, 116], proteins [4, 9], and viruses [6].

Lieber’s group is pioneering the development of silicon nanowire-based biosensors [4, 8]. Biological macromolecules, such as proteins and nucleic acids, are typically charged in aqueous solutions and, as such, can be detected readily by nanowire sensors when appropriate receptors are linked to the nanowire active surface. Figure 3.16 shows the real time detection of proteins and DNA based on silicon nanowires. They modified silicon nanowires with biotin, which has a strong affinity to protein streptavidin on the oxide surface of nanowires [4]. When a solution of streptavidin is delivered to a nanowire sensor device modified with a biotin receptor, they found that the conductance of nanowires increases rapidly to a constant value, and this conductance value is maintained after the addition of pure buffer

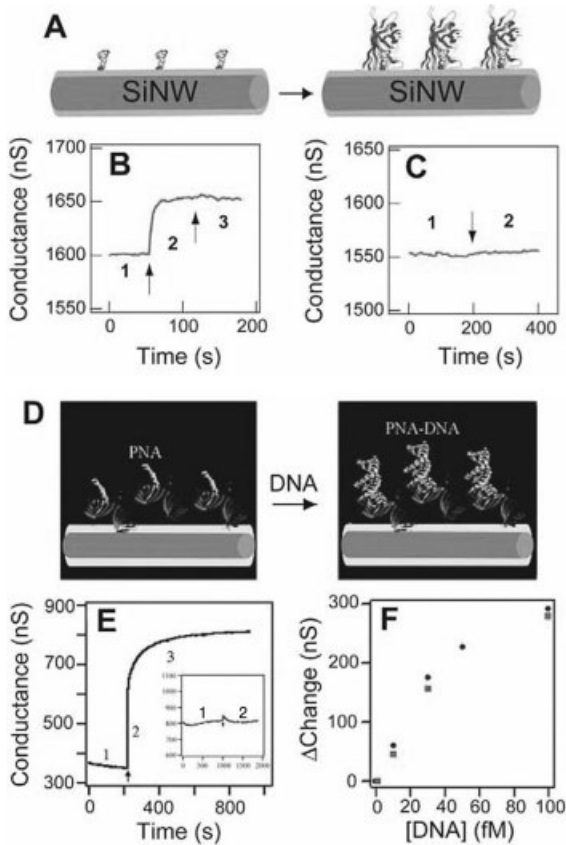


**Fig. 3.16.** Real-time detection of proteins and DNA. (A) Schematic of a biotin-modified Si nanowire and subsequent binding of streptavidin to the modified surface. (B) Conductance versus time for a biotin-modified Si nanowire, where Region 1 corresponds to the buffer solution, Region 2 corresponds to the addition of 250 nm streptavidin, and Region 3 corresponds to pure buffer solution. (C) Conductance versus time for an unmodified Si nanowire; Regions 1 and 2 are the same as in (B). (D) Schematic of a Si

nanowire sensor surface modified with a PNA receptor before and after duplex formation with target DNA. (E) Si nanowire DNA sensing; the arrow corresponds to the addition of a 60-fM complementary DNA sample, and the inset shows the device conductance following addition of 100-fM mutant DNA. (F) Conductance versus DNA concentration; data points indicated by ■ and ● are obtained from two independent devices. (Reprinted with permission from Ref. [4], [8]. (A)–(C) 2001 © AAAS and (D)–(F) 2004 © ACS.)

(Fig. 3.16B). However, adding a streptavidin solution to unmodified silicon nanowires does not produce a change in conductance (Fig. 3.16C). The conductance change is caused by the specific interaction between biotin and streptavidin, and these results are further proved by an experiment in which blocking the streptavidin binding sites leads to an absence of response from biotin-modified silicon nanowires. They also studied the detection limit and found that the electrical detec-

tion could be carried out to 10 pM, which is below the detection level required for a number of disease marker proteins. More recently, a silicon nanowire field effect device has been investigated as a biosensor to detect the sequence of DNA [8]. First, a PNA was immobilized on the surface of the p-type Si nanowires (Fig. 3.16D). When a complementary DNA target was introduced to the device, the hybridization of DNA (Fig. 3.16D) caused the conductance of the nanowires to increase (Fig. 3.16E). PNA was used as a receptor for DNA detection because the uncharged PNA molecules have a greater affinity and stability than the corresponding DNA recognition sequence. They have used this device to detect the wild type versus the DF508 mutation site in the cystic fibrosis transmembrane receptor gene and showed that the conductance increases when adding a 60-fM wild-type DNA sample solution (Fig. 3.16E). The increase in conductance of the Si nanowire device is consistent with the increase in the negative charge density associated with the binding of negatively charged DNA at the surface, and moreover, careful control experiments show that the binding response is specific to the wild-type sequence. Further study shows that the direct electrical detection for DNA is possible down to at least the 10-fM level, and the method is reproducible (Fig. 3.16F).

The same group have also studied the use of the Si nanowire for detecting a single virus and demonstrated that the Si nanowires could be assembled to form arrays for multiplexed detection of samples [6]. Addressable arrays are fabricated by a process that uses a fluid-based assembly, such as microfluidic or Langmuir–Blodgett methods, to align and set the average spacing of nanowires over large areas for photolithography to define interconnections (Fig. 3.17A). They also fabricated a state-of-the art array containing more than 100 addressable elements (Fig. 3.17B). All the of the active nanowire sensor devices are confined to a central rectangular area on the device chip that overlaps with the microfluidic sample delivery channels, as illustrated in the figure. They further demonstrated the use of this nanowire array for detecting two types of virus at the same time. An antibody receptor that is specific either for influenza or for adenovirus was modified on p-type Si nanowires. Simultaneous conductance measurements were obtained when adenovirus, influenza, and a mixture of both viruses were delivered to the device. Other groups have also studied the use of silicon nanowires for DNA and protein analysis [115, 116].

### 3.3.2

#### **Conducting Polymer Nanowire-based Biosensors**

In recent years, conducting polymer-based nanostructured materials have been used extensively in resistive sensors [17]. Because of their promising properties, which include high surface areas, chemical specificities, tunable conductivities, material flexibilities, and easy processing, various methods have been developed to fabricate conducting polymer nanowires. For example, (a) polyaniline nanowires have been obtained through a facile synthesis [117] or by electrospinning methods [118]; (b) template-directed electrochemical processes have been employed to fabricate nanowire junctions that feature robust polymer electrode contacts [119]; and (c) mechanical stretching [120] and magnetic field-assisted assembly [121] pro-

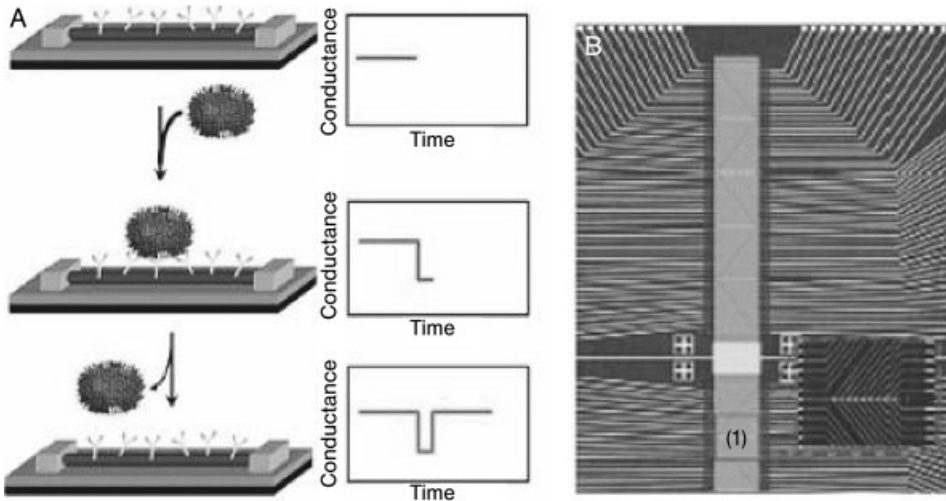


**Fig. 3.17.** (A) Schematic of a single virus binding and unbinding to the surface of a Si nanowire device modified with antibody receptors and the corresponding time-dependent change in conductance. (B) Optical image of the upper portion of a sensor device array, where the inset shows one row of

individually addressable nanowire elements. The rectangle labeled (1) highlights the position of the microfluidic channel used to deliver samples and overlap the active elements. (Reprinted with permission from Ref. [6]. © 2004 NAS).

cesses have produced miniaturized polymer-electrode junctions. A templateless electrochemical assembly of conducting polymer nanowires has also been developed recently [17, 18]. The development of biosensors based on conducting polymer nanowires is still in its infancy. Some examples are introduced as follows.

Tao's group have demonstrated a glucose biosensor using conducting polymer/enzyme junctions and found that a unique feature can arise when shrinking a sensor to a nanometer [122]. Figure 3.18(A) shows the structure of the polymer/enzyme nanojunction sensor. The thickness of the polyaniline in the junction is 20–60 nm. The polyaniline/enzyme nanojunction was prepared by co-polymerization of monomer aniline and GOx in an aqueous solution. The signal transduction mechanism of the sensor is based on the changes in nanojunction conductance as a result of glucose oxidation induced change in the polymer redox state. Because of the small size of the nanojunction, they found that the response to glucose is fast and less than 1.0 s. However, the response time for glucose with a 10  $\mu\text{m}$  gap is up to 10 min. The detection of limit for this method is at the  $\mu\text{M}$  level.

Myung's group has developed a facile technique for synthesizing conducting polymer nanowires by electrodeposition within channels between two electrodes on the surface of silicon wafers. They demonstrated that this technique can fabricate multiple individually addressable conducting polymer nanowires between two junctions. They also demonstrated the capability to create a scalable and high-density array by site-specific positioning of conducting polymer nanowires of the same and different composition on the same chip. Furthermore, the same group

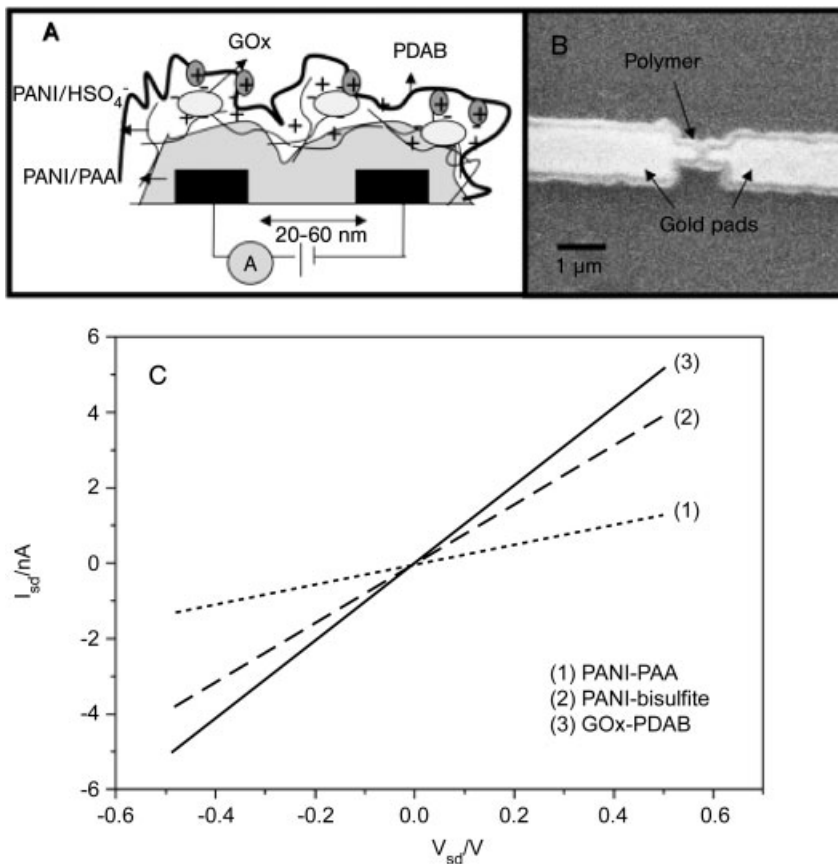


**Fig. 3.18.** (A) Structure of the polymer nanojunction sensor. (B) SEM image of PANI-PAA/PANI-bisulfite/GOx-PDAB films deposited on gold pads with gaps of 20–60 nm. (C)  $I$ – $V$  curves obtained in air after each nanogap modification step: (1) polymerization of PANI-PAA carried out in 0.4 M aniline + 150 mg mL<sup>-1</sup> PAA (MW: 2000) solution with 0.5 M Na<sub>2</sub>SO<sub>4</sub> and 0.5 M H<sub>2</sub>SO<sub>4</sub> by a potential sweep between –0.2 and 0.9 V vs. SCE during the first cycle and between –0.2 and 0.78 V vs. SCE during the following cycles at 0.05 V s<sup>-1</sup>;

(2) polymerization of PANI bisulfite in a 0.4 M aniline + 0.5 M NaHSO<sub>4</sub> solution acidified to pH 0 with H<sub>2</sub>SO<sub>4</sub> by a single potential sweep from –0.2 to 0.9 V vs. SCE; (3) immobilization of GOx-PDAB by exposing the polymer nanojunction to 0.5 M Na<sub>2</sub>SO<sub>4</sub> + 25 mM 1,2-diaminobenzene + 167 μM glucose oxidase in a pH 5 citric acid/Na<sub>2</sub>HPO<sub>4</sub> (McIlvaine) buffer solution for 15 min, followed by electro-deposition of PDAB at +0.4 V vs. SCE for 4 min. (Reprinted with permission from Ref. [122]. © 2004 ACS).

reported bio-affinity sensing using biological functionalized conducting polymer nanowire. The device incorporated with polypyrrole nanowires made by the facile technique can be used for studying protein–protein interaction [123].

Wang et al. demonstrated template-free fabrication of polyaniline nanowire on electrode junctions by electrodeposition, and this method can be extended to syn-

thesize other conducting polymer nanowires, e.g., polypyrrole and poly(Edot). They systematically studied the electron transport properties of these conducting polymer nanowires with an electrolyte gate [124].

### 3.3.3

#### Metal Oxide Nanowire-based Biosensors

Metal oxide nanowires (MONWs) have been used to develop biosensors [112, 125]. They can work as a valid alternative to CNTs or Si NWs. Curreli and co-workers have reported a selective functionalization of  $\text{In}_2\text{O}_3$  nanowires for biosensor applications. They first generated a self-assembled monolayer (SAM) of 4-(1,4-dihydroxybenzene) butyl phosphonic acid (HQ-PA) on the  $\text{In}_2\text{O}_3$  NW surface. Oxidized HQ-PA can react with a range of functional groups, which can be easily incorporated in biomolecules. They have successfully attached DNA on the  $\text{In}_2\text{O}_3$ , and this study opens an avenue for using such metal oxide nanowires for biosensing [112].

## 3.4

### Nanocantilevers for Biosensors

Recently, microfabricated cantilevers have successfully been used for biosensors [126–132]. The adsorption of biomolecules on the surface will induce surface stress, which can be measured with micro/nanocantilevers. Adsorption of two proteins, immunoglobulin (IgG) and albumin (BSA), on a gold surface has been studied in a buffer solution in terms of surface stress measurements. Fritz and coworkers have reported the specific transduction, via surface stress changes, of DNA hybridization and receptor–ligand binding into a direct nanomechanic response of microfabricated cantilevers [126]. Cantilevers were fabricated in arrays and functionalized with a selection of biomolecules. The differential deflections of the cantilever were responses of individual cantilevers. Figure 3.19 illustrates the DNA hybridization on nanocantilevers in solution. First, a different sequence of DNA probe was modified on the surface of cantilevers (Fig. 3.19A), and then target DNA was injected. Only the cantilever that provides the matching sequence was found to have surface stress. It has been demonstrated that a single mismatch between 12-mer oligonucleotide is detectable. This method shows important advantages in that it does not require labeling, optical excitation, or external probes. In addition, the transduction process is repeatable and enables cyclic operation. At the same time, Hansen et al. have reported a cantilever-based optical deflection assay for discrimination of DNA single-nucleotide mismatches [127].

Furthermore, Wu and coworkers have extended this research to a real biological system, disease-related proteins. They reported that microcantilevers of different geometries have been used to detect two forms of prostate-specific antigens (PSAs) over a wide range of concentration range  $0.2 \text{ ng mL}^{-1}$  to  $60 \text{ } \mu\text{g mL}^{-1}$  in a background of human serum albumin and human plasminogen at  $1.0 \text{ mg mL}^{-1}$



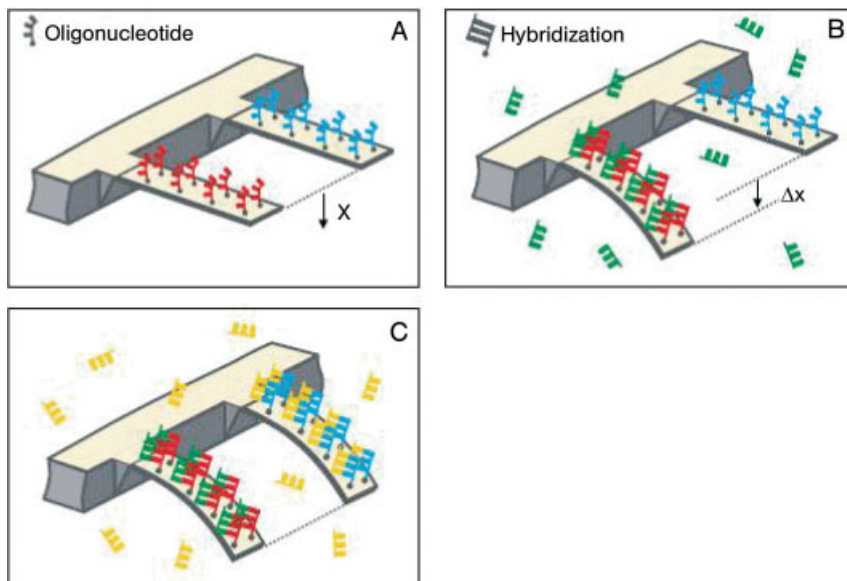


**Fig. 3.19.** Scheme illustrating the hybridization experiment. Each cantilever is functionalized on one side with a different oligonucleotide base sequence (red or blue). (A) The differential signal is set to zero. (B) After injection of the first complementary oligonucleotide (green), hybridization occurs

on the cantilever that provides the matching sequence (red), increasing the differential signal  $\Delta x$ . (C) Injection of the second complementary oligonucleotide (yellow) causes the cantilever functionalized with the second oligonucleotide (blue) to bend.

[129]. This study makes this technique a clinically relevant diagnostic technique for prostate cancer.

### 3.5

#### Summary

One-dimensional nanomaterials, such as CNTs, semiconducting nanowires, and Si-based nanocantilevers have shown promise as new detection platforms that are equal or superior to many other sensing materials. This is mainly attributed to their unique electronic, mechanic, thermal, and chemical properties. The preparation, purification, and dispersion of single-walled and multiwalled nanotubes have, especially, been reviewed. Various sensor fabrication protocols based on those 1D nanomaterials have been discussed in detail. A typical application for DNA and proteins, including enzymes and antibodies, has been described, and the respective responding mechanisms have been addressed in this comprehensive review. Various 1D nanomaterial-based biosensors have found broad application from their

respective designs, including unmodified and surface-confined nanomaterials. Accordingly, biosensing based on amperometric amplification, field-effect transistors, signal-enhanced immunoassay, and non-enzymatic monitoring, and surface stress has been described for various biosensor designs. This research field is experiencing explosive growth, and new reports appear on a daily basis. We anticipate that the high order array design, combined with multiple biorecognition, will be the hotspot for the next stage of the 1D nanomaterial-based sensor studies.

### Acknowledgments

The work performed at Pacific Northwest National Laboratory (PNNL) was supported by the Laboratory Directed Research and Development program, DOE-EMSP, SERDP (Project ID 1297), and NIH/1R01 ES010976-01A2. The authors' research described in this chapter was performed in part at the Environmental Molecular Sciences Laboratory, a national scientific user facility sponsored by the DOE Office of Biological and Environmental Research and located at PNNL. PNNL is operated for DOE by Battelle under Contract DE-AC05-76RL01830.

### Glossary

**Amperometry** An electrochemical technique that measures electrical current at a fixed potential upon adding analyte or titrant into the measuring cell.

**Biosensor** Any probe designed to measure biological molecules' concentration or structures, monitor biological processes, or translate biochemical signals into quantifiable physical signals.

**Carbon nanotube (CNT)** A 1D fullerene with a cylindrical shape that consists of a seamless structure with hexagonal honeycomb lattices, being several nanometers in diameter and up to hundreds of microns long. CNTs can be divided into two major groups, i.e., single-wall carbon nanotubes (SWCNTs) and multiwall carbon nanotubes (MWCNTs). SWCNTs represent a single graphite sheet rolled flawlessly, demonstrating a tube diameter of 1 to 2 nm, whereas MWCNTs show concentric and closed graphite tubules with diameters ranging from 2 to 50 nm and an inter-layer distance of approximately 0.34 nm.

**Catalysis** The acceleration of a chemical reaction by a catalyst.

**Chemiluminescence** A luminescence phenomenon produced by the direct transformation of chemical energy into light energy.

**DNA** Deoxyribonucleic acid. A naturally occurring polymer consisting of a phosphate backbone, sugar rings, and various bases. Usually it is found as single- or double-stranded deoxynucleotides.

**Field effect transistor (FET)** A semiconductor transistor with a region of donor material with two terminals designated as the "source" and the "drain," respectively, and an adjoining region of acceptor material in between, called the "gate."

The voltage between the gate and the substrate controls the current flow between the source and the drain by depleting the donor region of its charge carriers to a greater or lesser extent.

**Enzyme electrode** A type of biosensor that uses an enzyme-anchored electrode setup.

**Hybridization** The process of forming double stranded DNA molecules by combining two complementary single-stranded oligonucleotides.

**Nafion** A brand from a DuPont produced polymer that was synthesized by modifying a Teflon polymer. Like Teflon, Nafion is extremely chemically inert. However, unlike Teflon, Nafion is very ion-conductive because it contains sulfonic acid groups. These unique properties make Nafion useful in ion-exchange membranes, humidity sensors, fuel cells, etc.

**Lithography** A technique that creates chemical patterns on a metal or ceramic surface. It is currently used in making integrated electronic circuits, computer chips, etc.

**Organophosphorus compounds** Organic molecules that contain the element phosphorus. Organophosphorus (OP) compounds are very toxic and are thus widely used as pesticides and chemical-warfare agents (CWAs).

**Polymer** A macromolecule consisting of repeated chemical units.

**Screen printing** A traditional printing method that is used to print everything from T-shirts to coffee mugs and decals. It uses a squeegee to force ink through a stencil created on a mesh fabric onto some type of substrate such as a silk, metal, or stone. It is a mass production method. It has been used for fabricating sensors, such as single-use glucose strips.

**Sol-gel technique** A sol is a homogeneous dispersion of the solid particles (~100 to 1000 nm) in a liquid where only the Brownian motions suspend the particles. A gel is a state where both liquid and solid are dispersed in each other, which presents a solid network containing liquid components. The sol-gel technique is a low-temperature method using chemical precursors that can produce ceramics and glasses with better purity and homogeneity than high-temperature conventional processes. This technique currently has wide application in preparing electronic, optical, and electro-optic devices.

### Abbreviations

1D	One-dimensional
AFM	Atomic-force microscopy
AFP	$\alpha$ -Fetoprotein
ALP	Alkaline phosphatase
BSA	Bovine serum albumin
CE	Capillary electrophoresis
CNT	Carbon nanotube
CNTFET	Carbon nanotube field-effect transistor
CVD	Catalytic vapor deposition

CWA	Chemical-warfare agent
DCC	Dicyclohexylcarbodiimide
DMF	<i>N,N</i> -Dimethylformamide
DNA	Deoxyribonucleic acid
DOE	U.S. Department of Energy
EAD	Electric arc discharge
ECL	Electrogenerated chemiluminescence
EVA	Poly(vinyl acetate)
FET	Field-effect transistor
GC	Gas chromatography
GOx	Glucose oxidase
HQ-PA	4-(1,4-Dihydroxybenzene) butyl phosphonic acid
HRP	Horseradish peroxidase
IgG	Immunoglobulin G
LA	Laser ablation
LC	Liquid chromatography
MONW	Metal oxide nanowire
MOSFET	Metal-oxide-semiconductor field effect transistor
MPDA	<i>m</i> -Phenylenediamine
mRNA	Message ribonucleic acid
MWCNT	Multiwall carbon nanotube
NADH	$\beta$ -Nicotinamide adenine dinucleotide
NEA	Nanoelectrode array
PECVD	Plasma-enhanced chemical vapor deposition
PEG	Poly(ethylene glycol)
PNA	Peptide nucleic acid
PNNL	Pacific Northwest National Laboratory
Ppy	Polypyrrole
PSA	Prostate-specific antigen
RNA	Ribonucleic acid
SAM	Self-assembled monolayer
SpA	Staphylococcal protein A
SWCNT	Single-wall carbon nanotube
TEM	Transmission electron microscopy

## References

- 1 BACHTOLD, A., HADLEY, P., NAKANISHI, T., DEKKER, C. Logic circuits with carbon nanotube transistors, *Science* **2001**, 294, 1317–1320.
- 2 RUECKES, T., KIM, K., JOSELEVICH, E., TSENG, G. Y., CHEUNG, C. L., LIEBER, C. M. Carbon nanotube-based nonvolatile random access memory for molecular computing, *Science* **2000**, 289, 94–97.
- 3 KONG, J., FRANKLIN, N. R., ZHOU, C. W., CHAPLINE, M. G., PENG, S., CHO, K. J., DAI, H. J. Nanotube molecular wires as chemical sensors, *Science* **2000**, 287, 622–625.

- 4 CUI, Y., WEI, Q. Q., PARK, H. K., LIEBER, C. M. Nanowire nanosensors for highly sensitive and selective detection of biological and chemical species, *Science* **2001**, 293, 1289–1292.
- 5 STAR, A., GABRIEL, J. C. P., BRADLEY, K., GRUNER, G. Electronic detection of specific protein binding using nanotube FET devices, *Nano Lett.* **2003**, 3, 459–463.
- 6 PATOLSKY, F., ZHENG, G. F., HAYDEN, O., LAKADAMYALI, M., ZHUANG, X. W., LIEBER, C. M. Electrical detection of single viruses, *Proc. Natl Acad. Sci. U.S.A.* **2004**, 101, 14 017–14 022.
- 7 SO, H. M., WON, K., KIM, Y. H., KIM, B. K., RYU, B. H., NA, P. S., KIM, H., LEE, J. O. Single-walled carbon nanotube biosensors using aptamers as molecular recognition elements, *J. Am Chem. Soc.* **2005**, 127, 11 906–11 907.
- 8 HAHM, J., LIEBER, C. M. Direct ultrasensitive electrical detection of DNA and DNA sequence variations using nanowire nanosensors, *Nano Lett.* **2004**, 4, 51–54.
- 9 WANG, W. U., CHEN, C., LIN, K. H., FANG, Y., LIEBER, C. M. Label-free detection of small-molecule-protein interactions by using nanowire nanosensors, *Proc. Natl Acad. Sci. U.S.A.* **2005**, 102, 3208–3212.
- 10 XIA, Y. N., YANG, P. D., SUN, Y. G., WU, Y. Y., MAYERS, B., GATES, B., YIN, Y. D., KIM, F., YAN, Y. Q. One-dimensional nanostructures: Synthesis, characterization, and applications, *Adv. Mater.* **2003**, 5, 353–389.
- 11 LAW, M., GOLDBERGER, J., YANG, P. D. Semiconductor nanowires and nanotubes, *Ann. Rev. Mater. Res.* **2004**, 34, 83–122.
- 12 NIKOLAEV, P., BRONIKOVSKI, M. J., BRADLEY, K., ROHMUND, F., COLBERT, D. T., SMITH, K. A., SMALLEY, R. E. Gas-phase catalytic growth of single-walled carbon nanotubes from carbon monoxide, *Chem. Phys. Lett.* **1999**, 313, 91–97.
- 13 AMELINCKX, S., ZHANG, B., BERNAERTS, J., ZHANG, X. F., IVANOV, V., NAGY, J. B. A formation mechanism for catalytically grown helix-shaped graphite nanotubes, *Science*, **1996**, 265, 635–639.
- 14 NIU, J. J., SHA, H., WANG, Y. W., MA, X. Y., YANG, D. R. Crystallization and disappearance of defects of the annealed silicon nanowires, *Microelectron. Eng.* **2003**, 66, 65–69.
- 15 WU, Y., FAN, R., YANG, P. D. Block-by-block growth of single-crystalline Si/SiGe superlattice nanowires, *Nano Lett.* **2002**, 2, 83–86.
- 16 CHENG, S. W., CHEUNG, H. F. Role of electric field on formation of silicon nanowires, *J. Appl. Phys.* **2003**, 94, 1190–1194.
- 17 WANG, J., CHAN, S., CARLSON, R. R., LUO, Y., GE, G. L., RIES, R. S., HEATH, J. R., TSENG, H. R. Electrochemically fabricated polyaniline nanoframework electrode junctions that function as resistive sensors, *Nano Lett.* **2004**, 4, 1693–1697.
- 18 LIANG, L., LIU, J., WINDISCH, C. F., EXARHOS, G. J., LIN, Y. H. Direct assembly of large arrays of oriented conducting polymer nanowires, *Angew. Chem. Int. Ed.* **2002**, 41, 3665–3668.
- 19 WANG, J., LIU, G., JAN, M. Ultrasensitive electrical biosensing of proteins and DNA: Carbon-nanotube derived amplification of the recognition and transduction events, *J. Am. Chem. Soc.* **2004**, 126, 3010.
- 20 O'CONNOR, M., KIM, S. N., KILLARD, A. J., FORSTER, R. J., SMYTH, M. R. PAPADIMITRAKOPOULOS, F., RUSLING, J. F. Mediated amperometric immunosensing using single walled carbon nanotube forests, *Analyst* **2004**, 129, 1176–1180.
- 21 XU, J. M. Highly ordered carbon nanotube arrays and IR detection, *Infra. Phys. Tech.* **2001**, 42, 485–491.
- 22 FRITZ, J., BALLER, M. K., LANG, H. P., STRUNZ, T., MEYER, E., GUNTHERODT, H. J., DELAMARCHE, E., GERBER, C., GIMZEWSKI, J. K. Stress at the solid-liquid interface of self-assembled monolayers on gold investigated with a nanomechanical sensor, *Langmuir* **2000**, 16, 9694–9696.
- 23 WANG, J. X., LI, M. X., SHI, Z. J., LI, N. Q., GU, Z. N. Direct electro-

- chemistry of cytochrome c at a glassy carbon electrode modified with single-wall carbon nanotubes, *Anal. Chem.* **2002**, *74*, 1993–1997.
- 24 WANG, J. Nanomaterial-based electrochemical biosensors, *Analyst* **2005**, *130*, 421–426.
- 25 KOHLI, P., WIRTZ, M., MARTIN, C. R. Nanotube membrane based biosensors, *Electroanalysis* **2004**, *16*, 9–18.
- 26 IIJIMA, S. N. Helical microtubules of graphitic carbon, *Nature*, **1991**, *354*, 56–58.
- 27 KROTO, H. W., HEATH, J. R., O'BRIEN, S. C., CURL, R. F., SMALLEY, R. E. C-60 – buckminsterfullerene, *Nature*, **1985**, *318*, 162–163.
- 28 AJAYAN, P. M. Carbon nanotube from carbon, *Chem. Rev.* **1999**, *99*, 1787–1799.
- 29 HARRIS, P. J. F. *Carbon Nanotubes and Related Structures*, Cambridge University Press, Cambridge, UK, **1999**.
- 30 THOSTENSON, E. T., REN, Z. F., CHOU, T. W. C. Advances in the science and technology of carbon nanotubes and their composites: A review, *Compos. Sci. Technol.* **2001**, *61*, 1899–1912.
- 31 POPOV, V. N. Carbon nanotubes: Properties and application, *Mater. Sci. Eng. R: Rep.*, **2004**, *43*, 61–102.
- 32 KOHLI, P., MARTIN, C. R. The emerging field of nanotube biotechnology, *Nat. Rev. Drug Discov.* **2003**, *2*, 29–37.
- 33 SINNOTT, S. B. Chemical functionalization of carbon nanotubes, *J. Nanosci. Nanotechnol.* **2002**, *2*, 113–123.
- 34 BAUGHMAN, R. H., ZAKHIDOV, A. A., DE HEER, W. A. Carbon nanotubes – the route toward applications, *Science*, **2002**, *297*, 787–792.
- 35 OUYANG, M., HUANG, J., LIEBER, C. M. Fundamental electronic properties and applications of single-walled carbon nanotubes, *Acc. Chem. Res.* **2002**, *35*, 1018–1025.
- 36 BRITTO, P. J., SUNTHANAM, K. S. V., AJAYAN, P. M. Carbon nanotube electrode for oxidation of dopamine, *Bioelectrochem. Bioenerg.* **1996**, *41*, 121–125.
- 37 BESTEMAN, K., LEE, J., WIERTZ, F. G. M., HEERING, H. A., DEKKER, C. Enzyme-coated carbon nanotubes as single-molecule biosensors, *Nano Lett.* **2003**, *3*, 727–730.
- 38 SALIMI, A., BANKS, C. E., COMPTON, R. G. Abrasive immobilization of carbon nanotubes on a basal plane pyrolytic graphite electrode: Application to the detection of epinephrine, *Analyst*, **2004**, *129*, 225–228.
- 39 WANG, J., MUSAMEH, M. Carbon nanotube screen-printed electrochemical sensors, *Analyst*, **2004**, *129*, 1–2.
- 40 PEDANO, M. L., RIVAS, G. A. Adsorption and electrooxidation of nucleic acids at carbon nanotubes paste electrodes, *Electrochem. Commun.* **2004**, *6*, 10–16.
- 41 LIN, Y., TAYLOR, S., LI, H. P., FERNANDO, K. A. S., QU, L. W., WANG, W., GU, L. R., ZHOU, B., SUN, Y. P. Advances toward bioapplications of carbon nanotubes, *J. Mater. Chem.* **2004**, *14*, 527–541.
- 42 MARTIN, C. R., KOHLI, P. The emerging field of nanotube biotechnology, *Nat. Rev. Drug Discov.*, **2003**, *2*, 29–37.
- 43 LI, N., WANG, J., LI, M. *Rev. Anal. Chem.* **2003**, *22*, 19.
- 44 ODOM, T. W., HUANG, J. L., LIEBER, C. M. Single-walled carbon nanotubes – From fundamental studies to new device concepts, *Ann. N. Y. Acad. Sci.* **2002**, *960*, 203–215.
- 45 THESS, A., LEE, R., NIKOLAEV, P., DAI, H., PETTIT, H., ROBERT, J., XU, D., LEE, Y. H., KIM, S. G., RINZLER, A. G., COLBERT, D. T., SCUSERIA, G., TOMANEK, D., FISHER, J. E., SMALLEY, R. E. Crystalline ropes of metallic carbon nanotubes, *Science*, **1996**, *273*, 483–487.
- 46 XIE, S., LI, W., AN, Z., CHANG, B., SUN, L. *Mater. Sci. Eng. A*, **2000**, *286*, 11.
- 47 YACAMAN, M. J., YOSHIDA, M. M., RENDON, L., SANTIESTEBAN, J. G. Catalytic growth of carbon microtubules with fullerene structure, *Appl. Phys. Lett.*, **1993**, *62*, 202.
- 48 IVANOV, V., NAGY, J. B., LAMBIN, P., LUCAS, A., ZHANG, X. B., ZHANG,

- X. F., BERNAERTS, D., VAN TENDELOO, G., AMELINCKX, S., VAN LANDUYT, J. The study of carbon nanotubes produced by catalytic method, *Chem. Phys. Lett.* **1994**, 223, 329–335.
- 49 YUDASAKA, M., KITUCHI, R., MATSUI, T., OHKI, Y., YOSHIMURA, S. Specific conditions for Ni catalyzed carbon nanotube growth by chemical vapor deposition, *Appl. Phys. Lett.* **1995**, 67, 2477–2479.
- 50 IJIMA, S., ICHIHASHI, T. Single-shell carbon nanotubes of 1-nm diameter, *Nature*, **1993**, 363, 603–605.
- 51 KONG, J., SOH, H., CASSELL, A. M., QUATE, C. F., DAI, H. J. Synthesis of individual single-walled carbon nanotubes on patterned silicon wafers, *Nature* **1998**, 395, 878–881.
- 52 COLOMER, J. F., BISTER, G., WILLEMS, I., KONYA, Z., FONSECA, A., VAN TENDELOO, G., NAGY, J. B. Synthesis of single-wall carbon nanotubes by catalytic decomposition of hydrocarbons, *Chem. Commun.* **1998**, 1343–1344.
- 53 SHELIMOV, K. B., ESENALIEV, R. O., RINZLER, A. G., HUFFMAN, C. B., SMALLEY, R. E. Purification of single-wall carbon nanotubes by ultrasonically assisted filtration, *Chem. Phys. Lett.* **1998**, 282, 429–434.
- 54 TOHJI, K., GOTO, T., TAKAHASHI, H., SHINODA, Y., SHIMIZU, N., JEYDEVAN, B., SAITO, I., MIASUOKA, Y., KASUYA, A., OHSUNA, T., HIRAGA, K., NASHINA, Y. Purifying single-walled nanotubes, *Nature* **1996**, 383, 679.
- 55 ZHOU, O., GAO, B., BOWER, D., FLEMING, L., SHIMODA, H. Structure and electrochemical properties of carbon nanotube intercalation compounds, *Mol. Cryst. Liq. Cryst.* **2000**, 340, 541.
- 56 LIU, J., RINZLER, A. G., DAI, H., HAFNER, J. H., BRADLEY, R. K., BOUL, P. J., LU, A., IVERSON, T., SHELIMOV, K., HUFFMAN, C. B., RODRIGUEZ-MACIAS, F., SHON, Y. S., LEE, T. R., COLBERT, D. T., SMALLEY, R. E. Fullerene pipes, *Science* **1998**, 280, 1253–1256.
- 57 KOVTYUKHOVA, N. I., MALLOUK, T. E., PAN, L., DICKEY, E. C. Individual single-walled nanotubes and hydrogels made by oxidative exfoliation of carbon nanotube ropes, *J. Am. Chem. Soc.* **2003**, 125, 9761–9769.
- 58 SHAFFER, M. S. P., WINDLE, A. H. Analogies between polymer solutions and carbon nanotube dispersions, *Macromolecules* **1999**, 32, 6864–4866.
- 59 STAR, A., STODDART, J. F., STEUERMAN, D., DIEHL, M., BOUKAI, A., WONG, E. W., YANG, X., CHUNG, S., CHOI, H., HEATH, J. R. Preparation and properties of polymer-wrapped single-walled carbon nanotubes, *Angew. Chem. Int. Ed.* **2001**, 40, 1721–1275.
- 60 RIGGS, J. E., GUO, Z. X., CARROLL, D. L., SUN, Y. P. Strong luminescence of solubilized carbon nanotubes, *J. Am. Chem. Soc.* **2000**, 122, 5879–5880.
- 61 WANG, J., MUSAMEH, M., LIN, Y. Solubilization of carbon nanotubes by Nafion toward the preparation of amperometric biosensors, *J. Am. Chem. Soc.* **2003**, 125, 2408–2409.
- 62 STAR, A., HAN, T., JOSHI, V., STETTER, J. R. Sensing with Nafion coated carbon nanotube field-effect transistors, *Electroanalysis* **2004**, 16, 108–112.
- 63 WANG, J., LIU, G., JAN, M. R. Ultrasensitive electrical biosensing of proteins and DNA: Carbon-nanotube derived amplification of the recognition and transduction events, *J. Am. Chem. Soc.* **2004**, 126, 3010–3011.
- 64 WANG, J., CHEN, G., CHATRATHI, M. P., MUSAMEH, M. Capillary electrophoresis microchip with a carbon nanotube-modified electrochemical detector, *Anal. Chem.* **2004**, 76, 298–302.
- 65 LIU, Z., SHEN, Z., ZHU, T., HOU, S., YING, L., SHI, Z., GU, Z. Organizing single-walled carbon nanotubes on gold using a wet chemical self-assembling technique, *Langmuir* **2003**, 16, 3569–3573.
- 66 GOODING, J. J., WIBOWO, R., LIU, J., YANG, W., LOSIC, D., ORBONS, S., MEARNES, F. J., SHAPTER, J. G., HIBBERT, D. B. Protein electrochemistry using aligned carbon nanotube

- arrays, *J. Am. Chem. Soc.* **2003**, *125*, 9006–9007.
- 67 YU, X., CHATTOPADHYAY, D., GALESKA, I., PAPADIMITRAKOPOULOS, F., RUSLING, J. F. Peroxidase activity of enzymes bound to the ends of single-wall carbon nanotube forest electrodes, *Electrochem. Commun.* **2003**, *5*, 408–411.
- 68 KIM, B., SIGMUND, W. M. Self-alignment of shortened multiwall carbon nanotubes on polyelectrolyte layers, *Langmuir* **2003**, *19*, 4848–4851.
- 69 AZAMIAN, B. R., DAVIS, J. J., COLEMAN, K. S., BAGSHAW, C. B. B., GREEN, M. L. J. Bioelectrochemical single-walled carbon nanotubes, *J. Am. Chem. Soc.* **2002**, *124*, 12 664–12 665.
- 70 DAVIS, J. J., COLEMAN, K. S., AZAMIAN, B. R., BAGSHAW, C. B., GREEN, M. L. H. Mical and biochemical sensing with modified single walled carbon nanotubes, *Chem. Eur. J.* **2003**, *9*, 3732–3739.
- 71 AZAMIAN, B. R., COLEMAN, K. S., DAVIS, J. J., HANSON, N., GREEN, M. L. J. Directly observed covalent coupling of quantum dots to single-wall carbon nanotubes, *Chem. Commun.* **2002**, 366.
- 72 AJAYAN, P. M., STEPHAN, O., COLLIEX, C., TRAUTH, D. Aligned carbon nanotube arrays formed by cutting a polymer resin-nanotube composite, *Science* **1994**, *265*, 1212–1214.
- 73 GAO, M., DAI, L., WALLACE, G. G. Biosensors based on aligned carbon nanotubes coated with inherently conducting polymers, *Electroanalysis* **2003**, *15*, 1089–1094.
- 74 XU, Y., JIANG, Y., CAI, H., HE, P., FANG, Y. Electrochemical impedance detection of DNA hybridization based on the formation of M-DNA on polypyrrole/carbon nanotube modified electrode, *Anal. Chim. Acta* **2004**, *516*, 19–27.
- 75 GAVALAS, V. G., LAW, S. A., CHRISTOPHER, B. J., ANDREWS, R., BACHAS, CARBON, L. G. Nanotube aqueous sol-gel composites: Enzyme-friendly platforms for the development of stable biosensors, *Anal. Biochem.* **2004**, *329*, 247–252.
- 76 WANG, J., MUSAMEH, M. Carbon nanotube/Teflon composite electrochemical sensors and biosensors, *Anal. Chem.* **2003**, *75*, 2075–2079.
- 77 HRAPOVIC, S., LIU, Y., MALE, K. B., LUONG, J. H. Electrochemical biosensing platforms using platinum nanoparticles and carbon nanotubes, *Anal. Chem.* **2004**, *76*, 1083–1088.
- 78 TANG, H., CHEN, J., YAO, S., NIE, L., DENG, G., KUANG, Y. Carbon nanotube aqueous sol-gel composites: Enzyme-friendly platforms for the development of stable biosensors, *Anal. Biochem.* **2004**, *331*, 97–252.
- 79 WANG, J., LIU, G., JAN, M. R., ZHU, Q. Electrochemical detection of DNA hybridization based on carbon-nanotubes loaded with CdS tags, *Electrochem. Commun.* **2003**, *5*, 1000–1004.
- 80 CHEN, R. J., ZHANG, Y., WANG, D., DAI, H. Noncovalent sidewall functionalization of single-walled carbon nanotubes for protein immobilization, *J. Am. Chem. Soc.* **2001**, *123*, 3838–3839.
- 81 CHEN, R. J., BANGSARUNTIP, S., DROUVALAKIS, K. A., KAM, N., SHIM, M., LI, Y., KIM, W., UTZ, P. J., DAI, H. Noncovalent functionalization of carbon nanotubes for highly specific electronic biosensors, *Proc. Natl. Acad. Sci. U.S.A.* **2003**, *100*, 4984–4989.
- 82 BESTEMAN, K., LEE, J.-O., WIERTZ, F. G. M., HEERING, H. A., DEKKER, C. Enzyme-coated carbon nanotubes as single-molecule biosensors, *Nano Lett.* **2003**, *3*, 727–730.
- 83 BAKER, S. E., CAI, W., LASSETER, T. L., WEIDKAMP, K. P., HAMERS, R. J. Covalently bonded adducts of deoxyribonucleic acid (DNA) oligonucleotides with single-wall carbon nanotubes: Synthesis and hybridization, *Nano Lett.*, **2002**, *2*, 1413–1417.
- 84 HAZANI, M., NAAMAN, R., HENNRICH, F., KAPPES, M. M. Confocal fluorescence imaging of DNA-functionalized carbon nanotubes, *Nano Lett.*, **2003**, *3*, 153–155.
- 85 WILLIAMS, K. A., VEENHUIZEN, P. T. M., DE LA TORRE, B. G., ERITJA,



- R., DEKKER, C. Nanotechnology: Carbon nanotubes with DNA recognition, *Nature* **2002**, 420, 761.
- 86 MELLE-FRANCO, M., MARCACCIO, M., PAOLUCCI, D., PAOLUCCI, F., GEORGAKILAS, V. D., GULDI, M., PRATO, M., ZERBETTO, F. Cyclic voltammetry and bulk electronic properties of soluble carbon nanotubes, *J. Am. Chem. Soc.* **2004**, 126, 1646–1647.
- 87 ZHAO, Y., ZHANG, W., CHEN, H., LUO, Q. Electrocatalytic oxidation of cysteine at carbon nanotube powder microelectrode and its detection, *Sens. Actuators, B: Chem.* **2003**, 92, 279–285.
- 88 WANG, Z., LIU, J., LIANG, Q., WANG, Y., LUO, G. Carbon nanotube-modified electrodes for the simultaneous determination of dopamine and ascorbic acid, *Analyst* **2002**, 127, 653.
- 89 WANG, Z., WANG, Y., LUO, G. A selective voltammetric method for uric acid detection at  $\beta$ -cyclodextrin modified electrode incorporating carbon nanotubes, *Analyst*, **2002**, 127, 1353.
- 90 WU, K., FEI, J., HU, S. Simultaneous determination of dopamine and serotonin on a glassy carbon electrode coated with a film of carbon nanotubes, *Anal. Biochem.* **2003**, 318, 100–106.
- 91 MUSAMEH, M., WANG, J., MERKOCI, A., LIN, Y. Low-potential stable NADH detection at carbon-nanotube-modified glassy carbon electrodes, *Electrochem. Commun.* **2002**, 4, 743–746.
- 92 YE, J., WEN, Y., ZHANG, W., GAN, L. M., XU, G., SHEU, F. Nonenzymatic glucose detection using multi-walled carbon nanotube electrodes, *Electrochem. Commun.* **2004**, 6, 66–70.
- 93 LI, J., NG, H. T., CASSELL, A., FAN, W., CHEN, H., YE, Q., KOEHNE, J., HAN, J., MEYAPPAN, M. Carbon nanotube nanoelectrode array for ultrasensitive DNA detection *Nano Lett.* **2003**, 3, 597–602.
- 94 BOUSSAAD, S., TAO, N. J., ZHANG, R., HOPSON, T., NAGAHARA, L. A. *In situ* detection of cytochrome c adsorption with single walled carbon nanotube device, *Chem. Commun.* **2003**, 1502.
- 95 XIN, H., WOOLLEY, A. T. DNA-templated nanotube localization, *J. Am. Chem. Soc.* **2003**, 125, 8710–8711.
- 96 REYES, D. R., IOSSIFIDIS, D., AUROUX, P. A., MANZ, A. Micro total analysis systems. 1. Introduction, theory, and technology, *Anal. Chem.* **2002**, 74, 2623–2636.
- 97 YAMAMOTO, K., SHI, G., ZHOU, T., XU, F., XU, J., KATO, T., JIN, J. Y., JIN, L. Study of carbon nanotubes–HRP modified electrode and its application for novel on-line biosensors, *Analyst*, **2003**, 128, 249.
- 98 GHOSH, S., SOOD, A. K., KUMAR, N. Carbon nanotube flow sensors, *Science*, **2003**, 299, 1042–1044.
- 99 LIN, Y., LU, F., WANG, J. Disposable carbon nanotube modified screen-printed biosensor for amperometric detection of organophosphorus pesticides and nerve agents, *Electroanalysis* **2004**, 16, 145–149.
- 100 MORF, W. E., DE ROOIJ, N. F. Performance of amperometric sensors based on multiple microelectrode arrays, *Sens. Actuators, B-Chem.*, **1997**, 44, 538–541.
- 101 TU, Y., LIN, Y., REN, Z. F. Nanoelectrode arrays based on low site density aligned carbon nanotubes, *Nano Lett.* **2003**, 3, 107–109.
- 102 NG, H. T., FANG, A., LI, J., LI, S. F. Flexible Carbon nanotubes membrane sensory system – A generic platform, *J. Nanosci. Nanotechnol.* **2001**, 1, 375–379.
- 103 LIN, Y., LU, F., TU, Y., REN, Z. Glucose biosensors based on carbon nanotube nanoelectrode ensembles, *Nano Lett.* **2004**, 4, 191–195.
- 104 HE, P., DAI, L. Aligned carbon nanotube–DNA electrochemical sensors, *Chem. Commun.* **2004**, 3, 348.
- 105 WOHLSTADTER, J. N., WILBUR, J. L., SIGAL, G. B., BIEBUYCK, H. A., BILLADEAU, M. A., DONG, L., FISCHER, A. B., GUDIBANDE, S. R., JAMEISON, S. H., KENTEN, J. H., LEGINUS, J., LELAND, J. K., MASSEY, R. J., WOHLSTADTER, S. J. Carbon nanotube-based biosensor, *Adv. Mater.* **2003**, 15, 1184–1187.

- 106 GUO, Z., DONG, S. Electrogenerated chemiluminescence from Ru(Bpy)<sub>3</sub><sup>2+</sup> ion-exchanged in carbon nanotube/perfluorosulfonated ionomer composite films, *Anal. Chem.* **2004**, *76*, 2683–2688.
- 107 HAZANI, M., NAAMAN, R., HENNRICH, F., KAPPES, M. M. Confocal fluorescence imaging of DNA-functionalized carbon nanotubes, *Nano Lett.* **2003**, *3*, 153–155.
- 108 BAKER, S. E., CAI, W., LASSETER, T. L., WEIDKAMP, K. P., HAMERS, R. J. Covalently bonded adducts of deoxyribonucleic acid (DNA) oligonucleotides with single-wall carbon nanotubes: Synthesis and hybridization, *Nano Lett.* **2002**, *2*, 1413–1417.
- 109 DAI, H. Carbon nanotubes: Synthesis, integration, and properties, *Acc. Chem. Res.* **2002**, *35*, 1035–1044.
- 110 TANS, S. J., VERSCHUEREN, A. R. M., DEKKER, C. *Nature*, **1998**, *393*, 49.
- 111 KAM, N. W. S., O'CONNELL, M., WISDOM, J. A., DAI, H. J. Carbon nanotubes as multifunctional biological transporters and near-infrared agents for selective cancer cell destruction, *Proc. Natl. Acad. Soc. U.S.A.* **2005**, *102*, 11 600–11 605.
- 112 CURRELI, M., LI, C., SUN, Y. H., LEI, B., GUNDERSEN, M. A., THOMPSON, M. E., ZHOU, C. W. Selective functionalization of In<sub>2</sub>O<sub>3</sub> nanowire mat devices for biosensing applications, *J. Am. Chem. Soc.* **2005**, *127*, 6922–6923.
- 113 MELOSH, N., BOUKAI, A., DIANA, F., GERARDOT, B., BADOLATO, A., PETROFF, P., HEATH, J. R. Ultrahigh density nanowire lattices and circuits, *Science*, **2003**, *300*, 112.
- 114 JUHASZ, R., ELFSTROM, N., LINNROS, J. Controlled fabrication of silicon nanowires by electron beam lithography and electrochemical size reduction, *Nano Lett.* **2005**, *5*, 275–280.
- 115 LI, Z., CHEN, Y., LI, X., KAMINS, T. I., NAUKA, K., WILLIAMS, R. S. Sequence-specific label-free DNA sensors based on silicon nanowires, *Nano Lett.* **2004**, *4*, 245–247.
- 116 LI, Z., RAJENDRAN, B., KAMINS, T. I., LI, X., CHEN, Y., WILLIAMS, R. S. Silicon nanowires for sequence-specific DNA sensing: Device fabrication and simulation, *Appl. Phys. A-Mater. Sci. Proc.* **2005**, *80*, 1257–1263.
- 117 HUANG, J. X., VIRJI, S., WEILLER, B. H., KANER, R. B. Polyaniline nanofibers: Facile synthesis and chemical sensors, *J. Am. Chem. Soc.* **2003**, *125*, 314–315.
- 118 KAMEOKA, J., VERBRIDGE, S. S., LIU, H. Q., CZAPLEWSKI, D. A., CRAIGHEAD, H. G. Fabrication of suspended silica glass nanofibers from polymeric materials using a scanned electrospinning source, *Nano Lett.* **2004**, *4*, 2105–2108.
- 119 RAMANATHAN, K., BANGAR, M. A., YUN, M. H., CHEN, W. F., MULCHANDANI, A., MYUNG, N. V. Individually addressable conducting polymer nanowires array, *Nano Lett.* **2004**, *4*, 1237–1239.
- 120 HE, H. X., LI, C. Z., TAO, N. J. Conductance of polymer nanowires fabricated by a combined electrodeposition and mechanical break junction method, *Appl. Phys. Lett.* **2001**, *78*, 811–813.
- 121 ZHANG, H., BOUSSAAD, S., LY, N., TAO, N. J. Magnetic field-assisted assembly of metal/polymer/metal junction sensor, *Appl. Phys. Lett.*, **2004**, *84*, 133–135.
- 122 FORZANI, E. S., ZHANG, H. Q., NAGAHARA, L. A., AMLANI, I., TSUI, R., TAO, N. J. A conducting polymer nanojunction sensor for glucose detection, *Nano Lett.* **2004**, *4*, 1785–1788.
- 123 RAMANATHAN, K., BANGAR, M. A., YUN, M., CHEN, W., MYUNG, N. V. MULCHANDANI, A. Bioaffinity sensing using biologically functionalized conducting-polymer nanowire, *J. Am. Chem. Soc.* **2005**, *127*, 496–497.
- 124 ALAM, M. M., WANG, J., GUO, Y. Y., LEE, S. P., TSENG, H. R. Electrolyte-gated transistors based on conducting polymer nanowire junction arrays, *J. Phys. Chem. B* **2005**, *109*, 12 777–12 784.

- 125 ZHANG, D. H., LIU, Z. Q., LI, C., TANG, T., LIU, X. L., HAN, S., LEI, B., ZHOU, C. W. Detection of NO<sub>2</sub> down to ppb levels using individual and multiple In<sub>2</sub>O<sub>3</sub> nanowire devices, *Nano Lett.* **2004**, 4, 1919–1924.
- 126 FRITZ, J., BALLER, M. K., LANG, H. P., ROTHUIZEN, H., VETTIGER, P., MEYER, E., GUNTHERODT, H. J., GERBER, C., GIMZEWSKI, J. K. Translating biomolecular recognition into nanomechanics, *Science* **2000**, 288, 316–318.
- 127 HANSEN, K. M., JI, H. F., WU, G. H., DATAR, R., COTE, R., MAJUMDAR, A., THUNDAT, T. Cantilever-based optical deflection assay for discrimination of DNA single-nucleotide mismatches, *Anal. Chem.* **2001**, 73, 1567–1571.
- 128 STEVENSON, K. A., MEHTA, A., SACHENKO, P., HANSEN, K. M., THUNDAT, T. Nanomechanical effect of enzymatic manipulation of DNA on microcantilever surfaces, *Langmuir* **2002**, 18, 8732–8736.
- 129 WU, G. H., DATAR, R. H., HANSEN, K. M., THUNDAT, T., COTE, R. J., MAJUMDAR, A. Bioassay of prostate-specific antigen (PSA) using microcantilevers, *Nat. Biotechnol.* **2001**, 19, 856–860.
- 130 TIAN, F., HANSEN, K. M., FERRELL, T. L., THUNDAT, T. Dynamic microcantilever sensors for discerning biomolecular interactions, *Anal. Chem.* **2005**, 77, 1601–1606.
- 131 SU, M., LI, S. U., DRAVID, V. P. Microcantilever resonance-based DNA detection with nanoparticle probes, *Appl. Phys. Lett.* **2003**, 82, 3562–3564.
- 132 CHEN, H., HAN, J., LI, J., MEYYAPPAN, M. Microelectronic DNA assay for the detection of BRCA1 gene mutations, *Biomed. Microdev.* **2004**, 6, 55–60.
- 133 MARTEL, R., SCHMIDT, T., SHEA, H. R., HERTEL, T., AVOURIS, PH. Single- and multiwall carbon nanotube field-effect transistors, *Appl. Phys. Lett.* **1998**, 73, 2447–2449.

## 4

# Fullerene-based Electrochemical Detection Methods for Biosensing

*Nikos Chaniotakis*

### 4.1

#### Introduction

The football-like structure of fullerenes was discovered by Harold Kroto, James Heath, Sean O'Brien, Robert Curl, and Richard Smalley in 1985 [1]. These large nanostructures are made up of only carbon atoms, and are called Fullerenes after the American architect Richard Buckminster Fuller [2]. Buckminster Fuller designed large dome-shaped structures, such as the famous geodesic dome in Montreal Canada, built in 1967 for the Expo '67. Geodesic domes have no internal supports; they are light, and rigid, made up of specific geometrical prefabricated panels that can be assembled and taken apart quickly. Similarly, fullerenes have only carbon atoms, in a football like shell, made of five- and six-membered rings that are fused together.

The diameter of  $C_{60}$  Fullerene is so small, approximately  $10 \text{ \AA}$  ( $10^{-10} \text{ m}$ ) [3], that even the state of the art high resolution electron microscope cannot give us a clear image of it. The molecular model and the simulated HRTEM images of  $C_{60}$  fullerene [4] shown in Fig. 4.1 can help us visualize what this material actually looks like, while Fig. 4.2 can help us visualize how small it actually is. The size ratios between the earth ( $d = 1.275 \times 10^{-7} \text{ m}$ ) and the football ( $d = 0.22 \text{ m}$ ) is approximately the same as that between the football and the  $C_{60}$  fullerene.

### 4.2

#### Aims of the Chapter

This chapter addresses the use of the nanostructured fullerenes in the area of electrochemical biosensing, and its implementation to the development of electrochemical biosensors. Therefore, the basic concepts of both the idea of biosensing and the electrochemical properties of fullerenes must be well understood. This knowledge will allow for the understanding of the usefulness of the fullerenes in biosensing, as well as the possibilities provided for future applications. Fullerenes

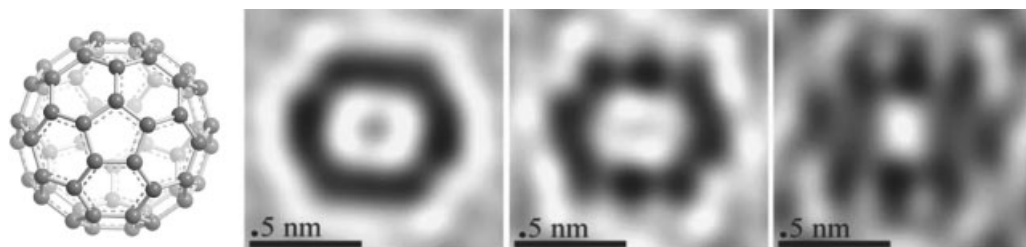


**Fig. 4.1.** Left: Molecular model drawing of  $C_{60}$ . Right: simulated HRTEM images focused at different planes of  $C_{60}$ . (Adopted from Ref. [4].)

are structures, or molecules, that have been at the forefront of research and public interest for more than 20 years now. Despite this, their applications are quite limited, mainly because their physicochemical characteristics are still not very well understood. The use of the fullerenes and their derivatives can provide multi-dimensional advances in the area of chemical sensors and biosensors in particular. Their electrochemical characteristics, combined with their unique physicochemical properties, provide the grounds for such claims, even though the current range of applications in this specific scientific area is rather limited.

This chapter provides a complete overview of fullerene-based electrochemical detection methods with specific emphasis on biosensing. Initially, it provides the background on the development of fullerenes as well as their electrochemical characteristics. This information is followed by a detailed description of the evolution and design characteristics of sensing systems based on biomolecules, the so-called biosensing. This combination provides the reader with well-rounded information on the exact role of the fullerenes in biosensing. Finally, it gives direction on the future role of these and similar nanostructures for possible applications in chemistry and biochemistry, both *in vitro*, and *in vivo*.



**Fig. 4.2.** The relative size of  $C_{60}$  to a football is approximately the same as that of a football to the earth.

### 4.3

#### Electrochemical Biosensing

The monitoring of the chemical and biochemical substances involved in the biological world is one of the important biological functions that make life possible. This is because the detection of substrates, signals and other external stimuli allow for direct interaction of a living system with the environment, and thus make life viable. Such information can also be very useful in many everyday human activities. Health issues, environmental problems, food quality and safety are some of the human activity areas that need direct and selective quantitative biochemical information. For this reason researchers for more than 50 years, and since the introduction of the oxygen electrode [5], have been using biosensing principles for the development of analytical instruments. These efforts have led to the development of a series of analytical devices called “biosensors” [6].

According to IUPAC [7], a biosensor is “A device that uses specific biochemical reactions mediated by isolated enzymes, immunosystems, tissues, organelles or whole cells to detect chemical compounds usually by electrical, thermal or optical signals.” Based on this definition, electrochemical biosensing is the recognition process that is based on the use of a specific biochemical reaction or mediated by isolated enzymes, immunosystems, tissues, organelles or whole cells, and the signal of the processes involved is relayed (transduced) to the analysts using current, potential, or impedance. The transduction is based on the interaction of the activity of electrochemically active species that are in a close contact and adjacent to the working electrode, the transducer. These species are then reduced or oxidized, depending on the experimental conditions, and the resulting signal is monitored. The signal that is obtained is related to the analyte of interest, and thus the analytical information sought is obtained. While the transduction mechanism has to do with the electrode and electronics employed, the difficult task of analyte recognition is undertaken by the biosensing element. The biosensing element is usually a membrane, or a layer of material into which the enzymes, immunosystems, tissues, organelles or whole cells are immobilized.

Electrochemical biosensing methods are characterized by the fact that they can provide continuous, on-line information on the activity of an analyte. Analytes that are usually detected using biosensors are substances that can either take part in an enzyme-catalyzed reaction (catalytic biosensors), or inhibit an enzyme-catalyzed reaction (inhibition biosensors). Electrochemical biosensors can thus provide on-line and continuous quantitative biochemical information on the activity of the analyte, either within a biological system or in the environment surrounding these biological systems. This information is based on the electrochemical signals that result from a biological recognition event, and it is manifested through the electrode, the so-called transducer. The transducer can be any surface or matrix that can interact with the biological recognizing element, relaying the electrochemical recognizing process to the display and the analyst. Figure 4.3 shows a schematic diagram of all the components of a biosensor.

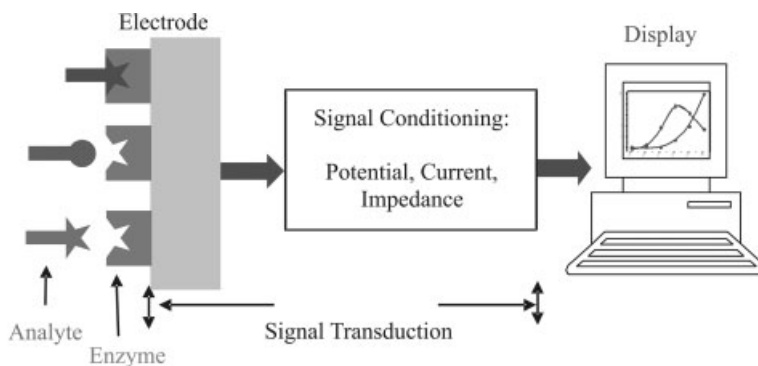


**Fig. 4.3.** Schematic diagram showing the main components of a biosensor. The analyte interacts with the biological recognition element (biocatalyst) and it is converted into product(s). This reaction is monitored by the

signal transduction system, converting it into an electrical signal. The output from the transducer is amplified, processed, and displayed to the analyst.

The role of chemistry and biochemistry is to optimize the biological recognition element, as well as the transducer surface that is in contact with this biosensing element. The biosensing process is usually based on the what is called the lock and key concept [8] or, in a more modern term, the host–guest interaction. The host is the biological molecule or the system that is responsible for the recognition, while the guest is the analyte or the species that we are interested in recognizing and quantitatively measuring its concentration or activity in the sample.

In the electrochemical biosensors the signal transduction takes place using the electrochemical properties of the species involved in the recognition process. Current, potential and resistance are the main parameters that can be utilized for decoding the effect a stimulus has (the analyte) on a recognition element. Clearly, there are various processes involved within a biosensor, which will transform a biochemical information into analytically useful data. For this reason the proper interaction and communication between the biological part, the biochemical processes, the transducers and other materials used is very important. To this, one must add the understanding and control of the electrochemical processes involved throughout the system. Only under these conditions can a biosensor device be designed that will provide analytically useful information on the presence of a specific analyte. At the same time, the proper interaction of these disciplines and materials involved will in the long run determine the stability of the device, the selectivity over other interfering substances, the detection limit that can be achieved, as well as the size of the device and its possible applications. As shown in Fig. 4.3, the sensor element is responsible for recognition of the analyte, while the transducer translates this information into the appropriate signal for recording. These two processes should be spatially very close, especially when electrochemical detection is utilized, without any inverse effects. Electrochemical processes are those involving

the three basic ohms law parameters, that is current ( $I$ ), potential ( $V$ ), and resistance ( $R$ ). Based on these parameters, electrochemical biosensors are categorized as amperometric, potentiometric, or impedometric. The simplicity and the sensitivity of the measurement of these parameters is the basis for the wide range of application of these methods. Electrochemical biosensing has an additional advantage, namely its ability to monitor localized events taking place at the interface between the biosensing element and the system under investigation. For all these reasons, electrochemical biosensors have found a very wide range of applications, while scientists all over the world are still working on improving their characteristics, as well as on finding new applications.

#### 4.3.1

##### **Making a Biosensor**

As an example, an outline of how a biosensor can be made in simple steps is provided here. Even though some technical terms are omitted for simplicity, the system described can be used for the measurement of an analyte such as glucose with very good analytical characteristics.

Making a biosensor has become by now a relatively simple procedure. The main components as described in Fig. 4.3 are:

- 1 The enzyme for the biorecognition.
- 2 The membrane(s) to hold the enzyme and to complete the biosensor element.
- 3 The transducer electrode, which includes the working and the counter electrode and, if possible, a reference electrode.
- 4 The electronic signal processing and display unit.

All these materials and tools are available, at a relatively low cost. A very good detailed description of the procedure can be found in the book *Biosensors. A Practical Approach* [9].

#### 4.4

##### **Evolution of Biosensors**

Electrochemical biosensors have been in continuous development and improvement since their first appearance in 1969 [6]. The development of electrochemical biosensors are concomitant with the three “biosensor generations” that have appeared in the literature. The major factor that determines the successful development of biosensors is the communication between the biosensing element or biomolecule and the transducer. The first-generation electronic coupling between redox enzymes and electrodes achieved this communication with the native enzyme co-factor [10] (Fig. 4.4A). The second-generation replaces this native redox couple with an electrochemically active compound, the mediator [11]. The mediator can be either free in solution or immobilized with the biomolecule (Fig. 4.4B).



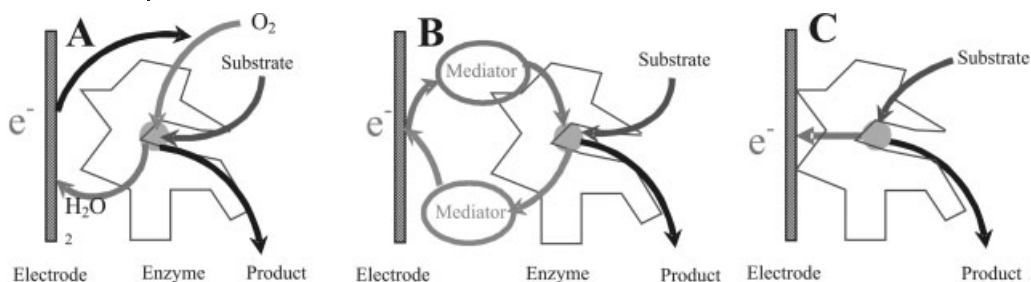


Fig. 4.4. Schematic diagram of (A) first-, (B) second-, and (C) third-generation biosensors.

Third-generation biosensors aim at direct electron transfer between the native enzyme co-factor and the electrode surface [12, 13] (Fig. 4.4C).

A mediator is a substance that acts as the “middle man” in transferring the generated signal from the active site to the transducer. For electrochemical biosensors, a mediator is a redox species (a species that can be easily reduced or oxidized) that is spatially close to both the active center and the transducer, without harmful effects to the biosensing element.

Evidently, from these schematic diagrams of the biosensors, the interaction between the analyte, the catalytic site of the biological element and transducer plays a decisive role in the performance and quality characteristics of the biosensing system. Several processes are involved. Initially, there is a diffusion process of the substrates to the active center and then another diffusion of the products from the active center to the transducer. Alternatively, the product of the reaction can provide the signal to the transducer using either a mediator, or the biomolecule itself. This is one of the main roles that fullerenes are asked to play in biosensing.

#### 4.5

##### Mediation Process in Biosensors

Electrochemical detection in biosensing provides a convenient, efficient means of amplification. For such a process to occur within the closed system of a biosensor, the signal must flow to the transducer regardless of the activity of substances other than either the analyte or the product of the catalytic reaction. This task is usually undertaken by the natural coenzymes and co-factors found in the enzymes. The electrochemical reactions of the redox enzymes are known to have slow electron-transfer kinetics to and from a transducer or electrode. There are three main parameters that determine the kinetics of this electron-transfer mechanism. The first has to do with the physicochemical properties of the active site, such as charge, hydrophobicity and surface active groups. The second is related to the distance of the active site from the outer surface of the protein, while the distance of the protein from the electrode surface is the third determining parameter. For these reasons,

and in order that these biocatalytic reactions can proceed at analytically useful rates, the potential used on the transducer is much larger than that required to actually oxidize or reduce the natural biomolecule mediator. Lowering the redox potential of the substrates involved in these processes will not only increase the reaction rates but, at the same time, it will improve the sensitivity and most importantly the selectivity of the biosensor [14]. Lowering the operating potential will aid in increasing the enzyme stabilization, prolonging its activity, and decreasing the rate of denaturation. To achieve this, artificial mediators or electron relays are employed that can efficiently interact with both the enzyme catalytic site and the electrode surface. Such successful mediators should have lower redox potential than that of the natural enzyme mediator so that they can act as electron acceptors during the enzymatic reaction. Also, they should be compatible with both the transducer surface as well as the biomolecule. Finally, they should be stable, while providing sites for chemical functionalization. Molecules or nanostructures that are good candidates for such electron mediation should also have fast and reversible redox states, they should be stable both in the oxidized and in the reduced form, their redox potentials should be close to those of the enzyme's active site, and they should not react with any of the reactants or products of the enzymatic reaction. The reduced form of the mediator can then transfer the electron to the electrode surface, and after they are oxidized back to its initial state are ready to proceed to the next cycle.

#### 4.5.1

##### Case A: Non-mediated Biosensor

Under normal conditions the electron transfer in enzyme-catalyzed redox reactions takes place with the mediation of natural cofactors such as  $O_2$  and NADH. Figure 4.5 shows this process for the glucose biosensor.

The electron-transfer process is carried out by the natural coenzymes found in the biosystem, and the electrons are transferred to the transducer for the signal

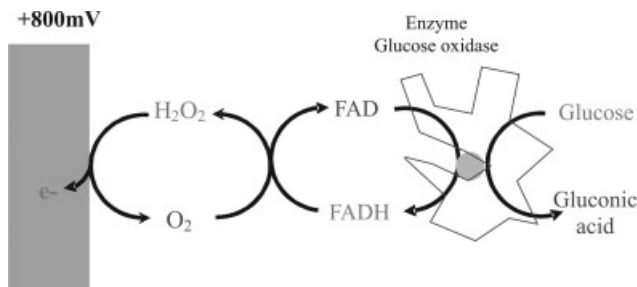


Fig. 4.5. Flowchart of the processes involved in a non-mediated electrochemical biosensor. The operating potential in the case of glucose is +800 mV.

generation. In this case, the mediation is carried out using FAD–FADH and  $\text{H}_2\text{O}_2$ – $\text{O}_2$  electrochemical couples. Since the system is sensitive to the activity of both peroxide and oxygen, oxygen electrodes have been extensively used as transducers in electrochemical biosensors. Evidently, close contact between the enzymes with the transducer surface is mandatory. Such heterogeneous electron-transfer reactions are energetically demanding since the catalytic site of the enzyme is deeply buried within the protein structure and protected by the hydrophobic core of the protein. This is evident by the rather large potential polarization potential of the transducer (+800 mV) required to operate the glucose biosensor (Fig. 4.5). Such large potentials have very detrimental effects on the lifetime and selectivity of the biosensor. This is why, under these potentials, the stability of the enzymes to denaturation and deactivation is drastically decreased, while at the same time all substances that can be oxidized at that potential will seriously interfere during the measurement. Based on these facts a decrease in the operating potential is a very important experimental requirement, and it can be achieved with the use of mediators.

#### 4.5.2

##### Case B: Mediated Biosensor

As mentioned above, the use of mediators in the development of biosensors can provide specific solutions to operational problems of biosensors. Mediators can aid in improving the stability, the reproducibility, the selectivity and thus the range of applications of biosensors. Figure 4.6 shows the flowchart of a mediated biosensor. Numerous compounds have been proposed as mediators in biosensors. Most of them are different ferrocene derivatives or osmium complexes [15, 16]. Figure 4.7 shows two voltammograms of a glucose biosensor without (a) and with (b) the use of mediator. Note that at the operation potential of 400 mV, the signal obtained, and thus the sensitivity of the biosensor, is more than  $5\times$  higher.

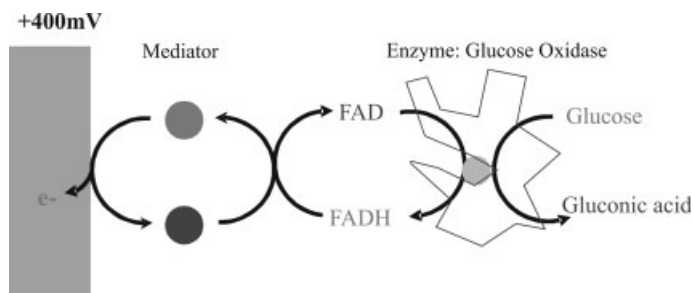


**Fig. 4.6.** Flowchart of the processes involved in a mediated electrochemical biosensor. Note that the operating potential has dropped to +400 mV.

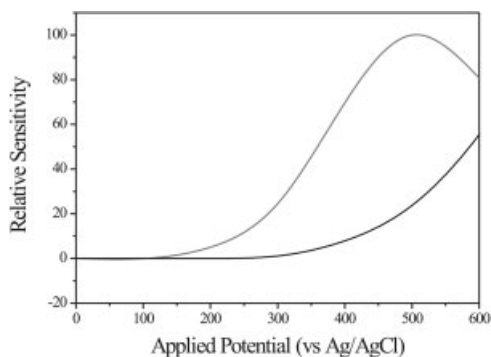


Fig. 4.7. Response of a non-mediated (a) and a mediated (b) glucose biosensor.

## 4.6

### Fullerenes

#### 4.6.1

##### Synthesis of Fullerenes

Fullerenes were discovered by Kroto and Smalley in 1985 in vaporized graphite under inert gas. Since then, several methods for the synthesis of fullerene have been reported. Many of them are based on laser ablation of carbon. Alternatively, graphite can be heated using either high power current source or, instead, an AC or DC arc discharge, to generate a “soot” of various carbon structures. Simple chromatographic separation of the soot provides high purity fullerenes [17, 18]. Based on this technology fullerenes can now be synthesized in large quantities (Fig. 4.8) [19, 20].

After the successful synthesis of  $C_{60}$  by thermal methods, fullerenes have also been synthesized using wet chemistry lab technology. A step-by-step synthesis based on polyne is now also possible [21–23] based on the precursor shown in Fig. 4.9. The synthesis of fullerenes in a step by step procedure provides the capability to control the surface functionalization of the  $C_{60}$ . Such functionalization can add new physicochemical characteristics to these molecules, rendering them, for example, more water soluble, adding sites for covalent bonding with biomolecules, or making them more susceptible to redox reactions.

#### 4.6.2

##### Biofunctionalization of Fullerenes

Fullerenes are very robust, very lipophilic and relatively unreactive nanostructures. There are a lot of instances where the physicochemical characteristics of these structures need to be altered to make them more hydrophilic, to link them to other

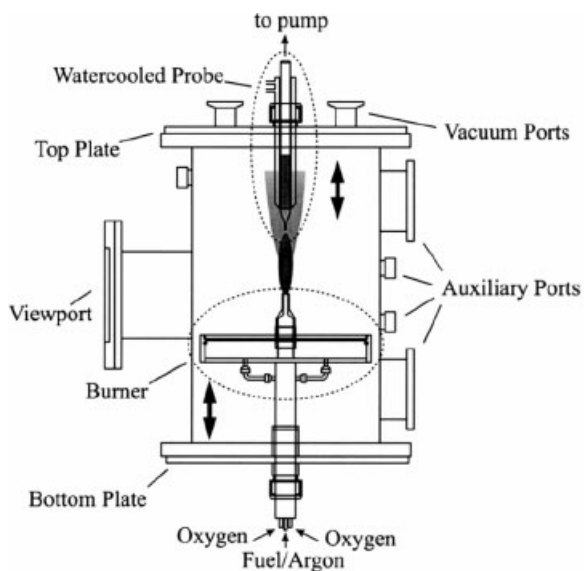


Fig. 4.8. Schematic of apparatus used to synthesize large quantities of fullerenes.

biomolecules, or immobilize them to a protein or other substrates, so that they are more suitable for a specific application. Initially, the functionalization of the fullerenes with organic and organometallic ligands has enabled them to be extensively studied in many fields. Different organic and organometallic ligands have been added by adsorption or covalent immobilization to the shell of the fullerenes, in-

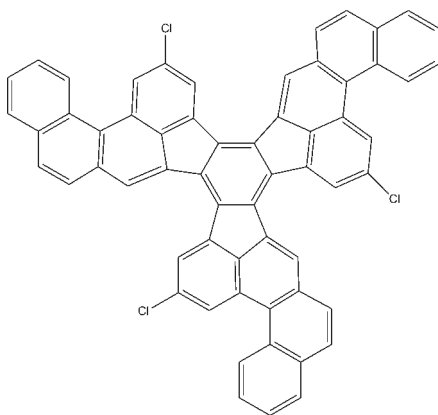


Fig. 4.9. Precursor for the chemical synthesis of  $C_{60}$ . Upon heating, chlorine is liberated, and the molecule folds up to generate  $C_{60}$ .

creasing their hydrophilicity, or altering their optical and electrochemical properties [24–31]. In addition, the ability of the fullerenes to accept and donate electrons to the species surrounding them can also be drastically influenced and elegantly controlled using these functionalization methods [32, 33]. These functionalized nanostructures have already found applications in medicine, electronics and optoelectronics [34] and, recently, biosensing applications.

One of the advantages of grafting the biomolecule onto the surface of the fullerene is the fact that these two units will be spatially very close. Such a close arrangement will allow for direct and efficient interaction of the nanostructure with the biomaterial, and thus increase the efficiency of the processes involved [35].

Various substituted  $C_{60}$  derivatives have been derived to probe DNA reactions [36] or their radical scavenging properties. Unique structures, such as that illustrated in Fig. 4.10, have proved to be very interesting both for their interaction with radicals as well as with cell walls and DNA. Similarly, very interesting water-soluble fullerene derivatives such as the one shown in Fig. 4.11 [37] have appeared in the literature. However, their application in biosensing has not been extensively evaluated. It is, for example, envisioned that such positively charged species will both protect and stabilize proteins and enzymes [38], while at the same time pro-

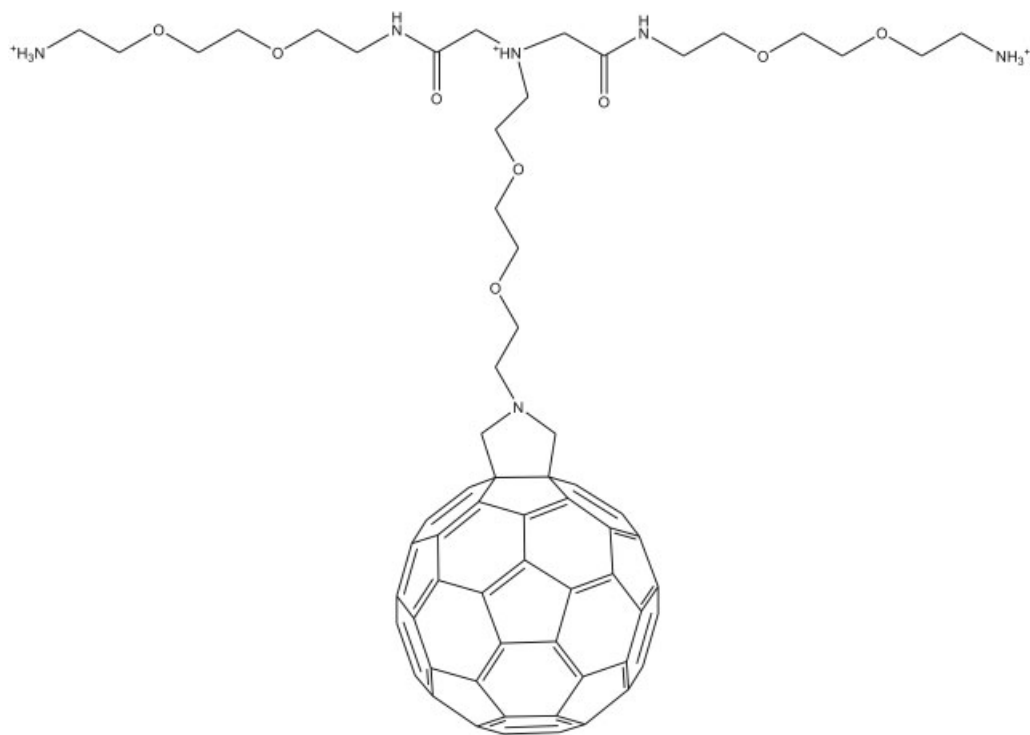


Fig. 4.10. A water-soluble mono-substituted positively charged  $C_{60}$  derivative.

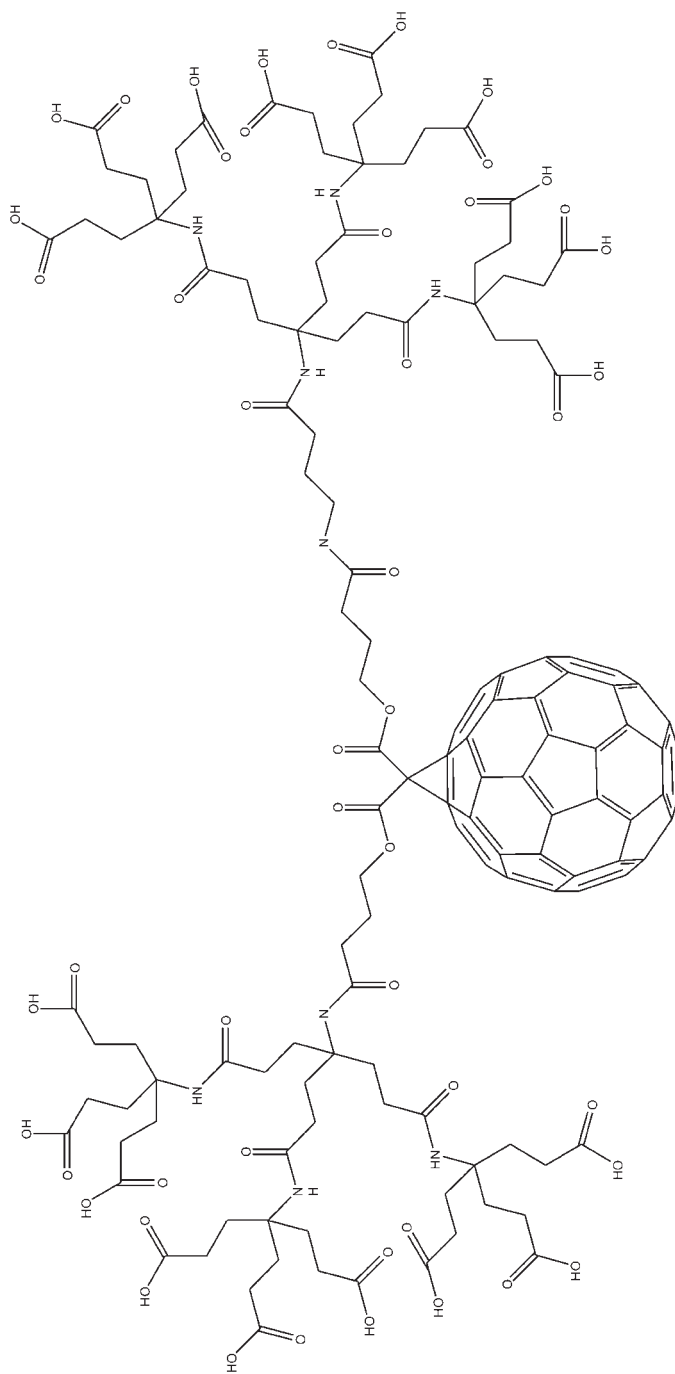
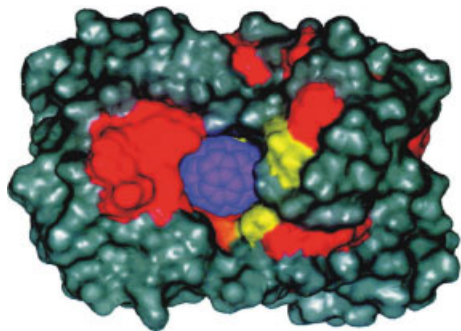


Fig. 4.11. A highly water-soluble dendro[60]fullerene.



**Fig. 4.12.** Model of Van der Waals surface representation of  $C_{60}$  bound to the anti-fullerene antibody.

vide an efficient way for signal transduction and mediation. Finally, the discovery of  $C_{60}$  antibodies [39] (Fig. 4.12) has already paved the way for the application of such systems in piezoelectric crystal immunosensors [40].

#### 4.6.3

#### Electrochemistry of Fullerenes

From the early stages of the discovery of fullerenes their electrochemical characteristics were considered to be very interesting and unique [41]. For this reason the electrochemistry of fullerenes in both solutions and films has been under intensive scientific investigation for many years [42]. Fullerene  $C_{60}$  behaves as an n-type semiconductor with a bandgap in the range of 1.6 eV, and its electron affinity is of the order of 2.7 eV [43]. Fullerenes in general have an expanded network of  $sp^2$  hybridized bonds that allows them to undergo up to six, one-electron reversible reduction reactions between  $-0.61$  and  $1.00$  V vs. SHE. Molecular orbital calculations predict very low lying triply degenerate LUMOs [44, 45]. The electron affinity of  $C_{60}$  can be explained qualitatively by considering its numerous perylene units, which upon receiving two electrons could go from an unstable  $4n$ -system to a stable aromatic  $4n + 2$  system. Moreover, the formation of  $sp^3$ -like anionic centers may lower the energy of the somewhat strained fullerene surface of bent  $sp^2$  carbons [46, 47, 48, 49].

Evidently, these early results show that the fullerene anions are stable due to the large separation between the distinct redox states and are, therefore, attractive oxidizing agents. Since then, there has been a considerable effort to clarify their electrochemical behavior in different solutions and matrices [50]. The bottom line of all these studies is that fullerenes indeed have unique electrochemical characteristics, as shown by the variety of redox couples. As carbonaceous materials, fullerenes are expected to have very unique electrochemical behavior within biological systems.



## 4.7

**Fullerene-mediated Biosensing**

As shown above,  $C_{60}$  fullerenes are nanomaterials with very unique redox characteristics. They are ideal substances for absorbing energy, taking up electrons (reduction), and releasing them (oxidation) with ease to a transducer. They are not harmful to biological materials and proteins, while they are small enough to come at least close to the active site of catalytic enzymes. At the same time they can be chemically modified, so that they can be functionalized to meet the needs of various applications.

For these reasons fullerenes were recognized very early on as materials that can play a decisive role in biocatalysis. Indeed, fullerenes have found applications in the area of biocatalysis and sensors from their early days of existence [51–54]. The idea of introducing a  $C_{60}$  chemically modified electrode to electrochemical research was first presented by Compton and coworkers in 1992 [55]. The sensor was prepared by immobilizing  $C_{60}$  films by drop coating onto surfaces of the noble metal electrodes, which were then coated with the Nafion protecting films. In this way, the amount of  $C_{60}$  required for performing electrochemical experiments was reduced and the signal enhanced compared with using  $C_{60}$  dissolved in solution. Subsequently, the electrochemical behavior of the  $C_{60}$  chemically modified electrodes (CMEs), has been widely investigated, providing the possibility of their electroanalytical applications [56]. Soon after,  $C_{60}$  fullerene film modified electrodes were investigated for the electrochemical reactions of cytochrome *c* using  $C_{60}$  fullerene deposited on glassy carbon (Fig. 4.13) [57, 58]. It was established then that the response of cytochrome *c* was quite independent of the underlying substrate (gold or glassy carbon), indicating that the fullerene film indeed acted as a promoter. Moreover, the molecular sieve type character and the possible effect of negative charges or polar groups on the surface of the films were suggested to be the reasons for the enhanced stability of the electrochemical response observed com-

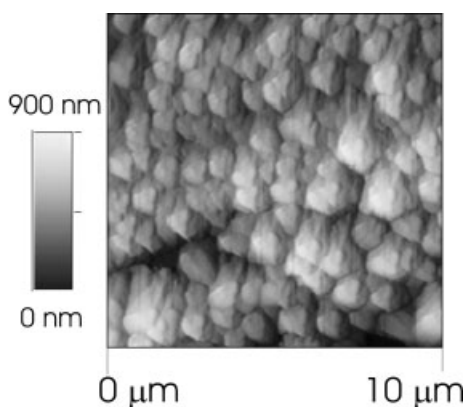


**Fig. 4.13.** AFM picture of a  $C_{60}$  fullerene on glassy carbon. (Adopted from Ref. [57].)

pared with bare electrodes. The rate of electron transfer to cytochrome *c* was drastically improved with the use of fullerenes as electron shuttles between the cytochrome and the carbon electrode.

These very promising initial results in biocatalysis suggested that, indeed, fullerenes can be ideal substances for electron mediation also in biosensors, since they are small, robust, biocompatible and have a wide range of oxidation/reduction potentials. In addition fullerenes are very lipophilic, while at the same time they can be chemically modified by functionalized matrix, and also with the hydrophilic proteins and the active site of the enzymes. All these characteristics make them ideal for use as mediators in electrochemical biosensing. In 1998 [59] carboxylic derivatives of  $C_{60}$  were covalently attached to a cystamine-monolayer-functionalized Au-electrode for the monitoring of biocatalysis transformations. It was then shown that the  $C_{60}$  monolayer can provide electrical communication between the electrode and a soluble glucose oxidase, GOx, with sufficiently high electron-transfer rates. The use of  $C_{60}$  as an electron mediator for electrocatalyzed biotransformations presented in this work set the stage for the direct application of  $C_{60}$  in biosensors. This was followed by reports in which fullerenes were used as mediating agents capable of charge transfer between redox enzymes and electrodes. Fullerene molecules can be used without functionalization, or after immobilization in gold electrodes with good success [60, 61].

Fullerenes has also been suggested as mediators in supported bilayer lipid membrane (s-BLM) biosensors [62–65]. s-BLMs are self-assembled systems that can be used for the design of electrochemical sensors and biosensors. S-BLMs are very thin membranes formed onto a transducer (platinum, gold, etc.) that can come in contact with the system to be analyzed. The introduction of biomolecules into these BLMs makes them suitable for the monitoring of chemical and biological species in systems such as that shown in Fig. 4.14.

Based on this idea, fullerenes have been used for the development of highly sensitive s-BLM-based chemical sensors for  $I^-$  [66]. The increase in sensitivity is because fullerenes change the electrical parameters of s-BLMs and facilitate the electron transfer of  $I^-$  at the metal surface, according to reaction scheme (1):

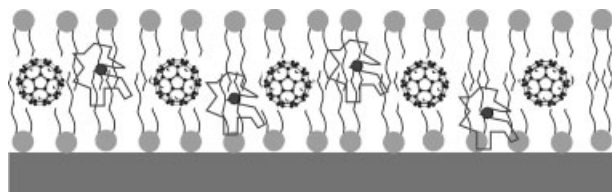
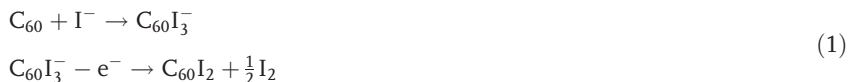
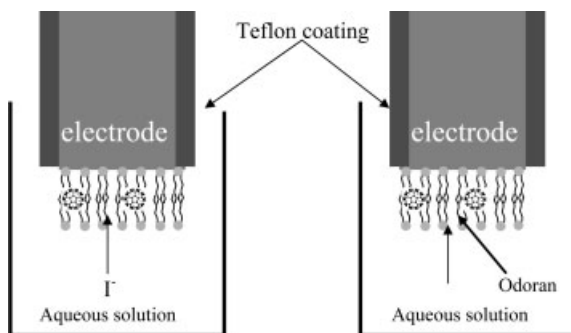


Fig. 4.14. s-BLM incorporating fullerene and enzyme for the construction of a BLM biosensor.



**Fig. 4.15.** Scheme of electrochemical sensor based on C<sub>60</sub>-modified s-BLM for the detection of volatile organic compounds (odorants). (Adopted from Ref. [67].)

The same idea has been applied for the electrochemical detection of volatile organic compounds using a sensor setup such as the one shown in Fig. 4.15 [67].

In these molecular devices fullerenes can also act as light-sensitive dipoles, capable of photoinduced charge separation, which undergo redox reactions across the substrate–hydrophobic lipid bilayer–aqueous solution junctions. Based on this, light addressable devices can be developed. Indeed, recent results [68] have also indicated that the photoinduced activation or switching of electron transfer of the enzyme glucose oxidase to the transducer is possible (Fig. 4.16).

Using fullerenes as an optical nanostructure switch, the biosensor is active only under light illumination, at potentials very close to zero versus Ag/AgCl reference electrode.

The functionalized fullerenes grafted onto polyelectrolytes were shown to be significant tools in biosensor design. Polyelectrolytes are very efficient enzyme stabilization systems.

The controlled interaction with enzymes allows for the protection and stabilization of the protein from denaturation, unfolding and, thus, deactivation [69–73].

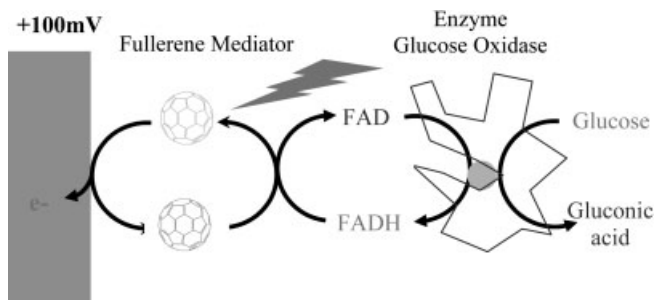


**Fig. 4.16.** Flowchart of the processes involved in a light-induced fullerene-mediated electrochemical biosensor. Note that the operating potential has dropped to +100 mV.

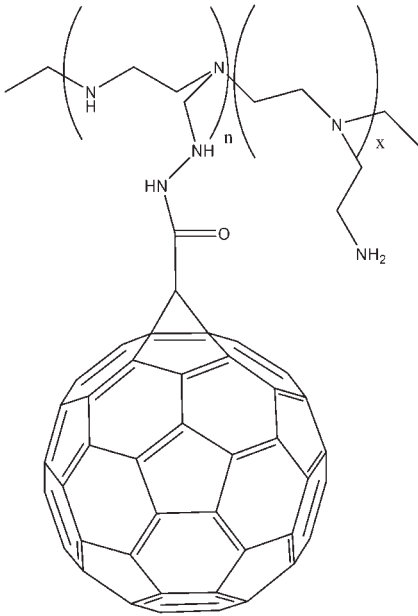


**Fig. 4.17.** Structure of fullerene-functionalized polyethylenimine (PEI-C<sub>60</sub>). Such structures provide both stabilization and signal mediation.

Systems such as polyethylenimine functionalized with fullerenes (Fig. 4.17) via covalent bonding allow for the simultaneous stabilization of the protein, and mediation of the signal [74].

Controlled modification of the fullerene surface with biomolecules is the state of the art method to improve the catalytic redox properties of proteins (Fig. 4.18). Covalent bonding of fullerene onto proteins has significant advantages over direct

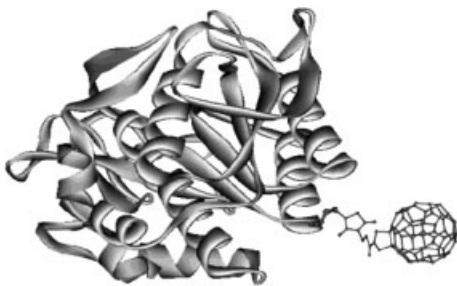


**Fig. 4.18.** Schematic illustration of protein conjugated to *N*-(3-maleimidopropionyl)-3,4-fullerolridine used for the development of subtilisin-based biosensor. (Adopted from Ref. [75].)

immobilization on nonporous silica or similar matrices [75]. The small size of the C<sub>60</sub> molecule makes the active site of the enzyme accessible to the substrate, and thus there is no diffusional limitation for the substrate to reach the active site imposed by the C<sub>60</sub> surface. The enzyme retains its activity and behaves in a similar manner as its free solution form.

#### 4.8

#### Conclusions

Even though the basic physicochemical characteristics of Fullerenes have only recently been realized, they have already contributed significantly in the area of biosensing and nanobiotechnology. In addition, the use of fullerenes and their derivatives have already provided multidimensional advances in the area of electrochemical sensors and biosensors in particular. The electrochemical characteristics of fullerenes, combined with their unique physicochemical properties lend its use in the design of novel biosensor systems, even though the current range of applications in this specific scientific area is still rather limited. Given their signal mediation, protein and enzyme functionalization and light induced switching; fullerenes can potentially provide new and powerful tools in the fabrication of electrochemical biosensors in the future.

#### References

- 1 H. KROTO, C-60 – Buckminsterfullerene. *Nature* **1985**, 318(6042), 162–163.
- 2 <http://www.archinform.net/arch/1098.htm?ID=RQadsJnbeCOBZs1C>.
- 3 S. E. CAMPBELL, G. LUENGO, V. I. SRDANOV, F. WUDL, J. N. ISRAELACHVILI. Very low viscosity at the solid–liquid interface induced by adsorbed C60 monolayers. *Nature* **1996**, 382, 520–522.
- 4 A. GOEL, J. B. HOWARD, J. B. VANDER SANDE. Size analysis of single fullerene molecules by electron microscopy. *Carbon* **2004**, 42, 1907–1915.
- 5 L. C. CLARK JR. Monitor and control of blood and tissue O<sub>2</sub> tensions. *Trans. Am. Soc. Artif. Intern. Organs* **1956**, 2, 41–48.
- 6 S. J. UPDIKE, G. P. HICKS. The enzyme electrode. *Nature* **1967**, 214, 986–988.
- 7 *IUPAC Compendium of Chemical Terminology*, 2nd Edn, **1997**. <http://www.iupac.org/goldbook/B00663.pdf>.
- 8 E. FISCHER. Einfluss der configuration auf die wirkung der enzyme. *Ber. Dtsch. Chem. Ges.* **1894**, 27, 2984–2993.
- 9 A. E. G. CASS. *Biosensors. A Practical Approach*, The Practical Approach Series, Oxford University Press, **1990**.
- 10 A. KARYAKIN, O. GITELMACHER, E. KARYAKINA. Prussian Blue-based first-generation biosensor. A sensitive amperometric electrode for glucose. *Anal. Chem.* **1995**, 67(14), 2419.
- 11 F. SCHELLER, F. SCHUBERT, B. NEUMANN, D. PFEIFFER, R. HINTSCHE, I. DRANSFELD, U. WOLLENBERGER, R. RENNEBERG, A. WARSINKE, G. JOHANSSON, M. SKOOG, X. YANG, V. BOGDANOVSKAYA, A. BÜCKMANN, S. YU. ZAITSEV. Second generation biosensors. *Biosensors Bioelectron.*, **1991**, 6(3), 245–253.
- 12 L. GORTON, A. LINDGREN, T. LARSSON, F. D. MUNTEANU, T. RUZGAS, I. GAZARYAN. Direct electron transfer between heme-containing enzymes and electrodes as basis for third

- generation biosensors. *Anal. Chim. Acta*, **1999**, 400(1–3), 91–108 L.
- 13 T. LOTZBEYER, W. SCHUMANN, H. L. SCHMIDT. Minizymes. A new strategy for the development of reagentless amperometric biosensors based on direct electron-transfer processes. *Biosensors Bioelectron.*, **1997**, 12(9–10), 1–6.
  - 14 W. KUTNER, J. WANG, M. L. X. HER, R. P. BUCK. Analytical aspects of chemically modified electrodes: Classification, critical evaluation and recommendations. *Pure Appl. Chem.*, **1998**, 70, 1301–1318.
  - 15 A. TURNER. Amperometric biosensors based on mediator-modified electrodes. *Methods Enzymol.*, **1988**, 137, 90–103.
  - 16 A. CASS, G. DAVIS, G. FRANCIS, A. HILL, W. ASTON, J. HIGGINS, E. PLOTKIN, L. SCOTT, A. TURNER. Ferrocene mediated enzyme electrode for amperometric determination of glucose. *Anal. Chem.*, **1984**, 56(4), 667–671.
  - 17 E. ROHLFING. High-resolution time-of-flight mass-spectrometry of carbon and carbonaceous clusters. *J. Chem. Phys.* **1990**, 93, 7851.
  - 18 W. CREASY, J. ZIMMERMAN, R. RUOFF. Van de waals binding of fullerenes to a graphite plane. *J. Phys. Chem.* **1993**, 97, 973.
  - 19 W. KRÄTSCHMER, L. D. LAMB, K. FOSTIROPOULOS, D. R. HUFFMAN. Solid C60: A new form of carbon. *Nature*, **1990**, 347, 354–358.
  - 20 P. HEBGEN, A. GOEL, J.-B. HOWARD, L. C. RAINEY, J. B. VANDER SANDE. Synthesis of fullerenes and fullerene nanostructures in a low-pressure benzene/oxygen flame. *Proc. Combustion Institute*, **2000**, 28, 1397–1404.
  - 21 S. W. McELVANY, M. M. ROSS, N. S. GOROF, F. DIEDERICH. Cyclocarbon coalescence: Mechanisms for tailor-made fullerene formation. *Science*, **1993**, 259, 1594–1596.
  - 22 L. SCOTT, M. BOORUM, B. J. McMAHON, S. HAGEN, J. MACK, J. BLANK, H. WEGNER, A. DE MEIJERE. A rational chemical synthesis of C60. *Science*, **2002**, 295, 1500–1503.
  - 23 A. YASUDA. Chemical synthesis scheme for a C60 fullerene. *Carbon*, **2005**, 43(4), 889–892.
  - 24 D. M. GULDI. Fullerene-porphyrin architectures; photosynthetic antenna and reaction center models. *Chem. Soc. Rev.* **2002**, 31, 22–36.
  - 25 B. GOTSCHY. Magnetism in C60 charge transfer complexes. *Fullerene Sci. Technol.*, **1996**, 4, 677–698.
  - 26 D. V. KONAREV, A. YU. KOVALEVSKY, A. L. LITVINOV, N. V. DRICHKO, B. P. TARASOV, P. COPPENS, R. N. LYUBOVSKAYA. Molecular complexes of fullerenes C60 and C70 with saturated amines. *J. Solid State Chem.*, **2002**, 168, 474–485.
  - 27 D. V. KONAREV, R. N. LYUBOVSKAYA, N. V. DRICHKO, E. I. YUDANOVA, YU. M. SHUL'GA, A. L. LITVINOV, V. N. SEMKIN, B. P. TARASOV. Donor-acceptor complexes of fullerene C60 with organic and organometallic donors? *J. Mater. Chem.*, **2000**, 803–818.
  - 28 M. M. OLMSTEAD, D. A. COSTA, K. MAITRA, B. C. NOLL, S. L. PHILLIPS, P. M. VAN CALCAR, A. L. BALCH, J. Interaction of curved and flat molecular surfaces. The structures of crystalline compounds composed of fullerene (C60, C60O, C70, and C120O) and metal octaethylporphyrin units. *J. Am. Chem. Soc.* **1999**, 121, 7090–7097.
  - 29 D. V. KONAREV, I. S. NERETIN, YU. L. SLOVOKHOTOV, E. I. YUDANOVA, N. V. DRICHKO, YU. M. SHUL'GA, B. P. TARASOV, L. L. GUMANOV, A. S. BATSANOV, J. A. K. HOWARD, R. N. LYUBOVSKAYA. New molecular complexes of fullerenes C60 and C70 with tetraphenylporphyrins [M(tpp)], in which M = H2, Mn, Co, Cu, Zn, and FeCl. *Chem. Eur. J.*, **2001**, 7, 2605–2516.
  - 30 D. V. KONAREV, A. YU. KOVALEVSKY, P. COPPENS, R. N. LYUBOVSKAYA. Synthesis and crystal structure of a C60 complex with a bis(ethylenedithio)-tetrathiafulvalene radical cation salt: (BEDT-TTF-13)C60. *Chem. Commun.*, **2000**, 2357–2358.
  - 31 G. L. MARCORIN, T. D. ROS, S. CASTELLANO, G. STEFANCICH,

- I. BONIN, S. MIERTUS, M. PRATO. Design and synthesis of novel [60]fullerene derivatives as potential HIV aspartic protease inhibitors. *Org. Lett.*, **2000**, *2*, 3955–3958.
- 32 D. D. KONAREV, S. S. KHASANOV, A. OTSUKA, G. SAITO, R. N. LYUBOVSKAYA. Crystal structure and magnetic properties of an ionic multi-component complex of fullerene (OMTTF center dot I-3)center dot C-60 – Comparison with OMTTF-I-3 salts. *Synth. Metals*, **2005**, *151*(3), 231–238.
- 33 G. SAITO, T. TERAMOTO, A. OTSUKA, Y. SUGITA, T. BAN, M. KUSUNOKI, K. SAKAGUCHI. Preparation and ionicity of C60 charge transfer complexes. *Synth. Methods*, **1994**, *64*, 359–368.
- 34 A. HIRSCH. *Fullerenes and Related Structures*, Springer, Berlin, **1998**.
- 35 S. BOSI, T. DA ROS, G. SPALLUTO, M. PRATO. Fullerene derivatives: An attractive tool for biological applications, *Eur. J. Med. Chem.*, **2003**, *38*(11–12), 913–923.
- 36 C. CUSAN, T. DA ROS, G. SPALLUTO, S. FOLEY, J.-M. JANOT, P. SETA, C. LARROQUE, M. C. TOMASINI, T. ANTONELLI, L. FERRARO, M. PRATO. Synthesis and molecular modeling studies of fullerene-trimethoxyindole-oligonucleotide conjugates as possible probes for studying photochemical reactions in DNA triple helices. *Eur. J. Org. Chem.*, **2002**, *17*, 2928–2934.
- 37 M. BRETTREICH, A. HIRSCH. A highly water-soluble dendro[60]fullerene. *Tetrahedron Lett.*, **1998**, *39*, 2731–2734.
- 38 N. A. CHANIOTAKIS. Enzyme stabilization strategies based on electrolytes and polyelectrolytes for biosensor applications. *Anal. Bional Chem.*, **2004**, *378*(1), 89–95.
- 39 B. C. BRADEN, F. A. GOLDBAUM, B.-X. CHEN, A. N. KIRSCHNER, S. R. WILSON, B. F. ERLANGER. X-ray crystal structure of an anti-Buckminsterfullerene antibody Fab fragment: Biomolecular recognition of C60. *Proc. Natl. Acad. Sci. U.S.A.*, **2000**, *97*, 12193–12197.
- 40 N. Y. PAN, J. S. SHIH. Piezoelectric crystal immunosensors based on immobilized fullerene C60-antibodies. *Sens. Actuators B-Chem.*, **2004**, *98*(2–3), 180–187.
- 41 R. E. HAUFLE, J. CONCEICAO, L. P. F. CHIBANTE, Y. CHAI, N. E. BYRNE, S. FLANAGAN, M. M. HALEY, S. C. O'BRIEN, C. PAN, et al. Efficient production of C60 (buckminsterfullerene), C60H36, and the solvated buckide ion. *J. Phys. Chem.*, **1990**, *94*(24), 8634–8636.
- 42 C. JEHOULET, A. J. BARD, F. WUDL. Electrochemical reduction and oxidation of C60 films. *J. Am. Chem. Soc.*, **1991**, *113*(14), 5456–5457.
- 43 Y. YANG, F. ARIAS, L. ECHEGOYEN, L. P. F. CHIBANTE, S. FLANAGAN, A. ROBERTSON, L. J. WILSON. Reversible fullerene electrochemistry correlation with the HOMO-LUMO energy difference for C60, C70, C76, C78, and C84. *J. Am. Chem. Soc.*, **1995**, *117*, 7801.
- 44 R. C. HADDON. L. E. BRUS, K. RAGHAVACHARI. Electronic structure and bonding in icosahedral C60. *Chem. Phys. Lett.*, **1986**, *125*, 459.
- 45 R. C. HADDON. Electronic structure, conductivity and superconductivity of alkali metal doped C60. *Acc. Chem. Res.*, **1992**, *25*, 127–133.
- 46 F. WUDL. The chemical properties of buckminsterfullerene (C60) and the birth and infancy of fullerenes. *Acc. Chem. Res.*, **1992**, *25*, 157.
- 47 A. HIRSCH. *Chemistry of the Fullerenes*, Georg Thieme, Stuttgart, **1994**.
- 48 B. MILLER, J. M. ROSAMILIA, G. DABBAGH, R. TYCKO, R. C. HADDON, A. J. MULLER, W. WILSON, D. W. MURPHY, A. F. HEBARD. Photoelectrochemical behavior of C60 films. *J. Am. Chem. Soc.*, **1991**, *113*(16), 6291–6293.
- 49 C. JEHOULET, Y. S. OBENG, Y. T. K. KIM, F. ZHOU, A. J. BARD. Electrochemistry and Langmuir trough studies of fullerene C60 and C70 films. *J. Am. Chem. Soc.*, **1992**, *114*(11), 4237–4247.
- 50 L. ECHEGOYEN, F. DIEDERICH, L. E. ECHEGOYEN. *Fullerenes: Chemistry, Physics, and Technology*, eds K. M. KADISH, R. S. RUOFF, Wiley, New York, **2000**, pp. 1–52.

- 51 *Principles of Chemical and Biological Sensors*, ed. D. DIAMOND, Wiley, New York, 1998.
- 52 A. JENSEN, S. WILSON, D. SCHUSTER. Biological applications of fullerenes. *Bioorg. Med. Chem.*, 1996, 4(6), 767–779.
- 53 D. GUST, T. MOORE, A. MOORE. Fullerenes linked to photosynthetic pigments. *Res. Chem. Intermediates*. 1997, 23(7), 621–651.
- 54 H. IMAHORI, K. HAGIWARA, M. AOKI, T. AKIYAMA, S. TANIGUCHI, T. OKADA, M. SHIRAKAWA, Y. SAKATA. Linkage and solvent dependence of photoinduced electron transfer in zincporphyrin-C60 dyads. *J. Am. Chem. Soc.*, 1996, 118(47), 11 771–11 782.
- 55 R. G. COMPTON, R. A. SPACKMAN, R. G. WELLINGTON, M. L. H. GREEN, J. TURNER. A fullerene(C60)-modified electrode: Electrochemical formation of tetra-butylammonium salts of C60 anions. *Electroanal. Chem.*, 1992, 327, 337–341.
- 56 Á. SZÜCS, M. TÖLGYESI, E. SZÜCS, M. CSISZÁR, A. LOIX, L. LAMBERTS, J. B. NAGY, M. NOVÁK. Electrochemistry of C60 films in aqueous solutions, in *Fullerenes Volume 5, Chapter 42: Recent Advances in the Chemistry and Physics of Fullerenes and Related Materials*, ed. K. M. KADISH, R. S. RUOFF, Electrochemical Society, New Jersey, 1997, 68–81.
- 57 M. CSISZÁR, A. SZÜCS, M. TÖLGYESI, A. MECHLER, J. B. NAGY, M. NOVAK. Electrochemical reactions of cytochrome c on electrodes modified fullerene films. *J. Electroanal. Chem.*, 2001, 497, 69–74.
- 58 M.-X. LI, N.-Q. LI, Z.-N. GU, X.-H. ZHOU, Y.-L. SUN, Y.-Q. WU. Electrocatalysis by a C60- $\gamma$ -cyclodextrin (1:2) and nafion chemically modified electrode of hemoglobin. *Anal. Chim. Acta*, 1997, 356, 225.
- 59 F. PATOLSKY, G. TAO, E. KATZ, I. WILLNER. C60-mediated bioelectro catalyzed oxidation of glucose with glucose oxidase. *J. Electroanal. Chem.*, 1998, 454, 9.
- 60 V. GAVALAS, N. A. CHANIOTAKIS. Fullerene-mediated amperometric biosensors. *Anal. Chim. Acta*, 2000, 409(1–2), 23, 131–135.
- 61 S. SOTIROPOULOU, V. GAVALAS, V. VAMVAKAKI, N. A. CHANIOTAKIS. Novel carbon materials in biosensor systems. *Biosensors Bioelectron.*, 2003, 18(2–3), 211–215.
- 62 H. T. TIEN, L. G. WANG, W. XING, A. L. OTTOVA. Electronic processes in supported bilayer lipid membranes (s-BLMs) containing a geodesic form of carbon (fullerene C60). *Bioelectrochem. Bioenerget.*, 1997, 42, 161–167.
- 63 H. T. TIEN, A. L. OTTOVA. Supported planar lipid bilayers (s-BLMs) as electrochemical biosensors. *Electrochim. Acta*, 1998, 43(23), 3587–3610.
- 64 K. ASAKA, H. T. TIEN, A. OTTOVA. Voltammetric study of charge transfer across supported bilayer lipid membranes (s-BLMs). *J. Biochem. Biophys. Methods*, 1999, 40, 27–37.
- 65 J. S. YE, A. OTTOVA, H. T. TIEN, F. S. SHEU. Nitric oxide enhances the capacitance of self-assembled, supported bilayer lipid membranes. *Electrochem. Commun.*, 2001, 3(10), 580–584.
- 66 H. T. TIEN, R. H. BARISH, L.-Q. GU, A. L. OTTOVA. Supported bilayer lipid membranes as ion and molecular probes. *Anal. Sci.*, 1998, 1(14), 3–18.
- 67 I. SZYMANSKA, H. RADECKA, J. RADECKI, D. KIKUT-LIGAJ. Fullerene modified supported lipid membrane as sensitive element of sensor for odorants. *Biosensors Bioelectron.*, 2001, 16, 911–915.
- 68 S. SOTIROPOULOU, N. A. CHANIOTAKIS. Photoinduced electron transfer (mediation) nano switch between fullerene C60 and glucose oxidase, submitted for publication.
- 69 S. SOTIROPOULOU, V. VAMVAKAKI, N. A. CHANIOTAKIS. Stabilization of enzymes in nanoporous materials for biosensor applications. *Biosensors Bioelectron.*, 2005, 20(8), 1674–1679.
- 70 S. SOTIROPOULOU, V. GAVALAS, V. VAMVAKAKI, N. A. CHANIOTAKIS. Novel carbon materials in biosensor systems. *Biosensors Bioelectron.*, 2003, 18(2–3), 211–215.



- 71 V. G. GAVALAS, N. A. CHANIOTAKIS. Polyelectrolyte stabilized oxidase based biosensors: Effect of diethylaminoethyl-dextran on the stabilization of glucose and lactate oxidases into porous conductive carbon. *Anal. Chim. Acta*, **2000**, 404(1), 10, 67–73.
- 72 V. G. GAVALAS, N. A. CHANIOTAKIS, T. D. GIBSON. Improved operational stability of biosensors based on enzyme-polyelectrolyte complex adsorbed into a porous carbon electrode. *Biosensors Bioelectron.*, **1998**, 13(11), 1205–1211.
- 73 N. A. CHANIOTAKIS. Enzyme stabilization strategies based on electrolytes and polyelectrolytes for biosensor applications. *Anal. Bioanal. Chem.* **2004**, 378(1), 89–95.
- 74 V. GAVALAS. Stabilization of Amperometric Biosensors with DEAED in Porous Carbon Electrodes. Ph.D. Thesis, **2000**.
- 75 P. NEDNOOR, M. CAPACCIO, V. G. GAVALAS, M. S. MEIER, J. E. ANTHONY, L. G. BACHAS. Hybrid nanoparticles based on organized protein immobilization on fullerenes. *Bioconjugate Chem.* **2004**, 15(1), 12–15.

## 5

# Optical Biosensing Based on Metal and Semiconductor Colloidal Nanocrystals

*Roberto Comparelli, Maria Lucia Curri, Pantaleo Davide Cozzoli, and Marinella Striccoli*

### 5.1

#### Overview

Nanomaterial-based optical sensors are among the most advanced class of sensing devices produced in the recent past for the continuous, real-time monitoring of diverse analytes. Following the tremendous impact of the unusual properties of nanoscale matter on present technology, scientific publications dealing with sensing applications have concomitantly proliferated. Research on these topics embraces wide and interdisciplinary fields under intense evolution, making it difficult to provide a comprehensive scenario of the current status of their development. This chapter is specifically intended to offer a critical view on the specific potential of colloidal nanocrystals as a distinguishable class of nanosized materials for biosensing. Especially, it will emphasize how the size-dependent optical properties of nanocrystals can be flexibly tailored by the synthetic tools accessible by modern material chemistry, specifically addressing optical techniques and methods for well-defined sensing purposes.

The review of this subject will therefore be organized as follows: (a) the introduction will focus on the chemical-physical properties that justify the choice of nanocrystals as advantageous in various diagnostic approaches; (b) several optical techniques that can be used as transduction methods for biosensing will then be described in detail; (c) selected examples of specific applications and biochemical studies will be presented; and (d) in the conclusions, a few key issues regarding the commercial development of the presented techniques will be discussed.

### 5.2

#### Introduction

Current interest in both fundamental and practical scientific research is oriented towards the design and engineering of new generations of devices based on nanosized inorganic objects coupled with assembled molecules [1–3]. The tremendous

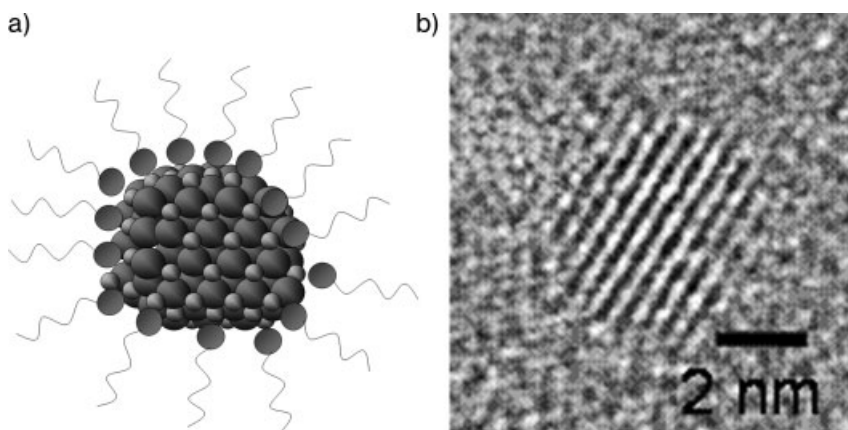


**Fig. 5.1.** (a) Schematic representation of single colloidal nanocrystal coated with organic molecules. (b) High-resolution transmission electron microscope picture of CdS nanocrystal.

efforts in this direction have been motivated by the recognition of size-, shape-, and composition-dependence of the optoelectronic, magnetic, and catalytic properties of matter at the nanoscale [4].

Recent advances in both physical and chemical synthetic approaches have made various nanostructured materials available for novel technological applications (Fig. 5.1).

The unique and intriguing optoelectronic properties of such nanostructured objects can find applications in the fabrication of new and original nanosensors in the wide field of biochemistry. In particular, this chapter emphasizes the impact of semiconductor and noble metal colloidal nanocrystals on the development of optically driven detection methodologies for biosensing purposes.

A “biosensor” can be broadly defined as a sensing device able to measure any property with biological significance or connected with bioactivity by means of biomolecules and/or biologically related structures. More appropriately, a biosensor is a small device that, as the result of a chemical interaction or process occurring between the analyte and the sensing element, transforms quantitative or qualitative chemical or biochemical information into an analytically useful signal. Biosensors are usually considered a subset of chemical sensors because of the peculiar transduction methods associated with them, sometimes referred to as the sensor “platforms”. The fundamental understanding of the physics and chemistry of nanosized metal and semiconductors has stimulated intense efforts to the development of innovative strategies for biosensing devices. Although various sensing mechanisms, based on the changes of magnetic, electrochemical, piezoelectric, and resistivity properties of matter, have been exploited so far, optical transduction has largely been the most preferred tool in many biosensing applications because of its superior advantages and versatility. Especially, optical platforms are technologically appealing, as they offer high detection limits, little sensitivity to electro-

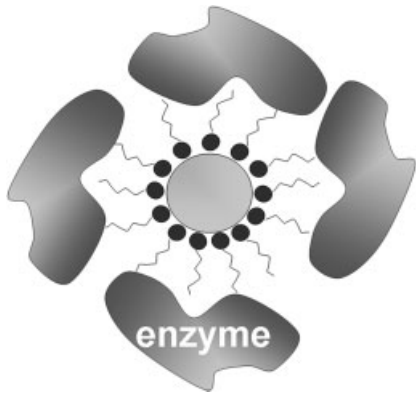


Fig. 5.2. Colloidal nanocrystals are commensurate with biomacromolecules.

magnetic noise, the possibility of remote control and information transfer through optical fibers, long lifetime, and amenability to multiplexing. Such interest is further motivated by the expectation that nanomaterial-based optical biosensors will not only replace conventional sensors, but also enable the fabrication of unprecedented sensing devices. Finally, the recent advantages in photonic technologies and the low cost availability of commercial optical fibers and lasers will certainly encourage access to new frontiers of biosensing.

Inorganic objects on the nanometer scale promise easy integration with many bio-related domains. The fact that nanoparticles share the same size regime (<50 nm) as that of many biomolecules opens access to the fabrication of novel composite nanostructures with the biological and the inorganic components suitably coupled (Fig. 5.2).

Including nanomaterials in a sensing device can be beneficial in that unprecedented transduction modes, relying on their special properties, can be, in principle, developed for any event of biological relevance.

The emerging disciplines of nanoengineering, nanoelectronics, and nanobioelectronics, require suitably sized and functionalized nanosized particles as the “building blocks” with which to construct their architectures and active elements. Especially, colloidal nanocrystals represent attractive precursors for creating various electronic and sensor components due to the ease of their fabrication and to their intrinsic robustness, allowing for further processing. Such objects are composed of a crystalline inorganic core and a protective shell of surface anchored molecules provided by a solution-phase synthesis. Nanocrystals are grown directly in a liquid solution by chemical methods that facilitate their medium-scale production in a reaction flask.

Colloidal nanoparticles differ significantly from other classes of nanostructured materials in that their surface chemistry can be conveniently manipulated to enhance compatibility with biological environments, to achieve nanocrystal immobilization onto substrates, conjugation with selected biomolecules, and/or incorporation into different matrixes (Fig. 5.3).

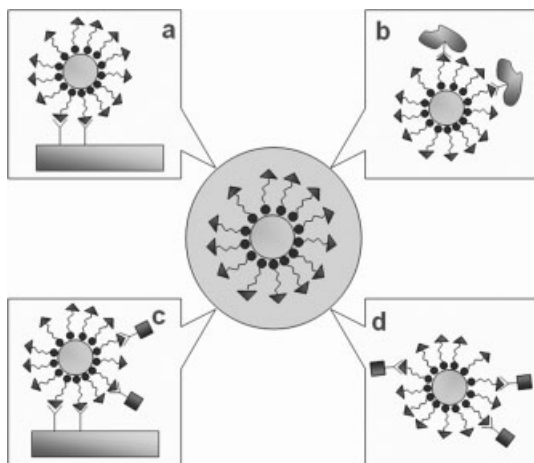


**Fig. 5.3.** Colloidal nanocrystals can be surface functionalized for (a) guided assembly, (b) biomolecular recognition, (c) sensing devices, and (d) solution-based receptors.

Nanoparticles have been used in biosensors for the last two decades. The fabrication and characterization methods for nanomaterials have been progressively refined to the point that deliberate modulation of their size, shape, and composition can be now obtained, thereby permitting a fine control of their properties. Colloidal techniques have long been known, but only recently has a great body of work been devoted to the synthesis of nanocrystals specifically intended for the construction of devices and complex composite nanostructures.

Today, the key goal in nanocrystal-based technology is to reproducibly synthesize nanoparticles having several properties, such as specific size, tailored shapes, crystal phase and crystallographic orientation, well-defined surface chemistry, solubility in any desired solvent, and multifunctional performances. These latter can be achieved by combining different materials in a single hybrid nanostructure, due to novel structural and electronic properties arising from interactions of the single components. A new concept of “purpose-built” nanomaterials has thus emerged, whose basic idea is to model and design materials with the proper morphology, size, shape and surface status to probe, tune and optimize the material’s physical-chemical properties. The ability in tailoring all these characteristics is an essential condition to extend NCs to large-scale technological and industrial applications.

Now, the structure of nanosized noble metals and semiconductors can be systematically engineered to produce materials with specific emissive, absorptive, and light-scattering properties, which make these materials ideal for multiplexed analyte detection. The control of composition and shape can allow for the variation of additional parameters useful in the detection of target analytes.

Furthermore, techniques for surface modification and patterning have advanced to such a great extent that the binding affinity of materials for various biomolecules

can be modulated by suitable chemical tools as much as desired, leading to novel generations of nanoscale arrays of biomacromolecules and small molecules together on surfaces [2a]. The overall ensemble of these capabilities has allowed the design of functional materials that can be implemented into new optical assays in biosensors based on improved modes of signal transduction.

## 5.3

### Colloidal Nanocrystals

#### 5.3.1

##### Size-dependent Optical Properties

Most nanocrystal physical properties evolve as a function of the size and/or shape, approximately following some “scaling laws” [5]. Two major reasons account for this special dependence in nanocrystals: the confinement of charge carrier motion in a small material volume, and the significant fraction of atoms residing at the surface, as compared with that in the corresponding bulk counterpart.

Now, in any material, there will be a size below which a substantial change of fundamental electrical and optical properties occurs with size: these variations will be seen when the energy spacing  $\delta$  of successive quantum levels ( $\delta = 4E_F/3n$ , where  $E_F$  is the Fermi level of the bulk material and  $n$  is the total number of valence electrons in the nanocrystal) exceeds the thermal energy ( $\sim 25$  meV at room temperature). For a given temperature, this occurs at a very large size in semiconductors, as compared with metals, insulators, van der Waals, or molecular crystals.

In semiconductors, the quantum-sized effects result in a widening of the band gap and in the development of well-defined energy levels at the band edges [7]. These facts can be clearly observed in the optical absorption spectra of “quantum dots”: the threshold energy for absorption is shifted to shorter wavelengths with decreasing the particle size and discrete spectral features develop in the spectrum, which correspond to the allowed optical transitions (Fig. 5.4). The positions of the lowest energy absorption peak (which is usually the most defined) as well as that of the luminescence peak are strictly correlated to the average particles size, while their widths reflect, in part, the remaining size distribution. In anisotropic nanocrystals, such as nanorods and tetrapods, the shift behavior of the exciton peak is characteristically dependent on the shortest confined dimension [8] (Fig. 5.5). Furthermore, the size-dependence of semiconductor nanocrystal band-gap provides a tool for tuning the redox potentials of photogenerated holes and electrons, allowing redox process that would be forbidden for extended solids.

In noble metals, the decrease in size below the electron mean free path gives rise to intense absorption in the visible–near-UV region [9]. The optical absorption spectra exhibit absorption peaks that do not derive from quantum confinement effects but result from the collective oscillations of the itinerant free electron gas on the particle surface, that are induced by the incident electromagnetic wave. Such resonances, referred to as surface plasmons (SPs), are seen when the wavelength

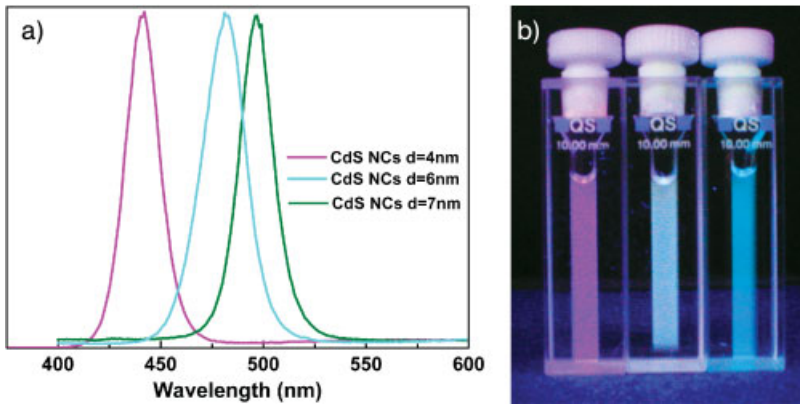


**Fig. 5.4.** (a) Emission spectra of CdS nanocrystals with different sizes. (b) Distinguishable emission colors of CdS nanocrystals in chloroform solution, excited with a near-UV lamp. (From Ref. [6].)

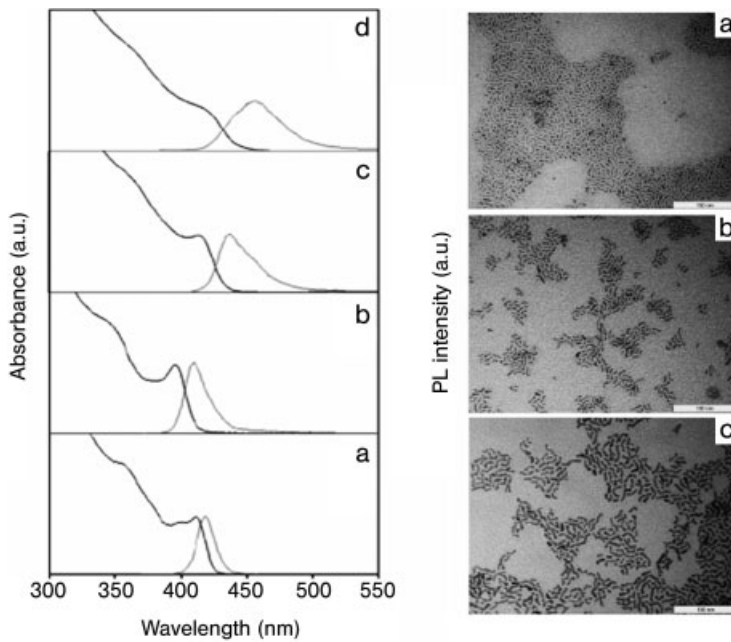


**Fig. 5.5.** Left-hand side: UV/Vis absorption and PL emission spectra of spherical (a) and rod-like ZnSe nanocrystals (b–d) with aspect ratios of 3, 6, and 8, respectively. Right-hand side: TEM overview of ZnSe nanorods with aspect ratios of 4, 10 and 5. (From Ref. [8].)

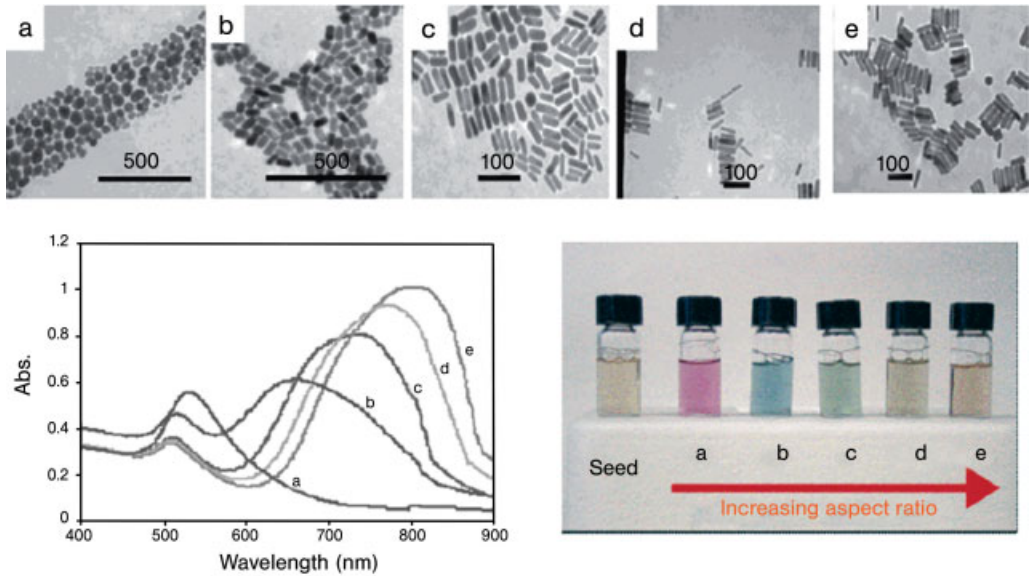


**Fig. 5.6.** TEM images (top), absorption spectra (left), and photographs (right) of aqueous solutions of gold nanorods of various aspect ratios. Seed sample: aspect ratio 1; sample a, aspect ratio 1.35 (0.32); sample b, aspect ratio 1.95 (0.34); sample c, aspect ratio

3.06 (0.28); sample d, aspect ratio 3.50 (0.29); sample e, aspect ratio 4.42 (0.23). Scale bars: 500 nm for a and b, 100 nm for (c–e). The value in parenthesis represents the error in the determination of the aspect ratio. (From Ref. [10].)

of incident light far exceeds the particle diameter. In the “intrinsic size” regime ( $<5$  nm), noble metal nanoparticles do not show any plasmon absorption, while the absorption of particles larger than 50–60 nm (in the “extrinsic size” region) is broad and covers most of the visible region.

The spectrum of anisotropic particles can exhibit several bands (Fig. 5.6) corresponding to multipole SP resonances and becomes further modified by charge accumulation, molecular adsorption, solvent nature, and aggregation status of the particles (Fig. 5.7) [10, 11].

Interestingly, in the nanosized regime noble metals exhibit a considerable shift of their redox potential toward negative values, which makes them work as efficient electron-transfer mediators [12, 13] (Fig. 5.8).

In nanocrystals the number of atoms residing at the surface is a large fraction of the total and the density of bulk defects is rather low [14]. To minimize surface energy, substantial reconstructions in the atomic positions can occur, so that nanocrystal surfaces can be largely disordered, yielding spherical or ellipsoidal shapes, or can expose regular facets, as are present in extended crystals. Surface rearrangement can be more easily visible in extremely small clusters (in the 3–50 atoms range), where, as there is no clearly identifiable interior, unique bonding geometries, distinct from those of the bulk solid, are assumed.



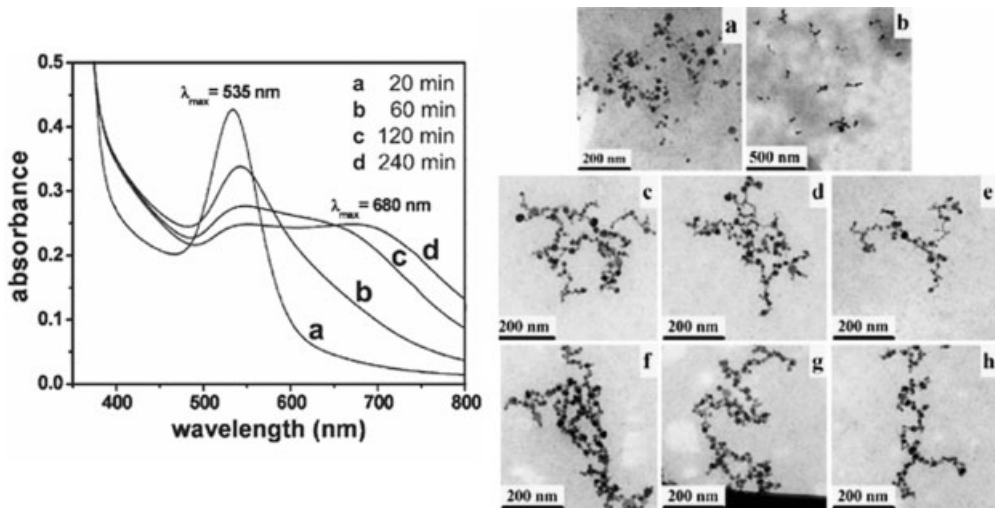


**Fig. 5.7.** The surface plasmon resonance of Au nanoparticles can be modified by their aggregation status. The left-hand side of the figure shows the temporal evolution of the absorption spectrum of gold upon UV-photocatalytic reduction of  $10^{-3}$  M  $\text{HAuCl}_4$  in

the presence of  $5 \times 10^{-2}$  M  $\text{TiO}_2$  nanorods in  $\text{CHCl}_3$ -EtOH. The corresponding TEM images (right-hand side) show the progress of Au nanoparticle assembly after irradiation for (a) 20, (b) 60, (c)–(e) 120, and (d)–(h) 240 min. (From Ref. [11].)

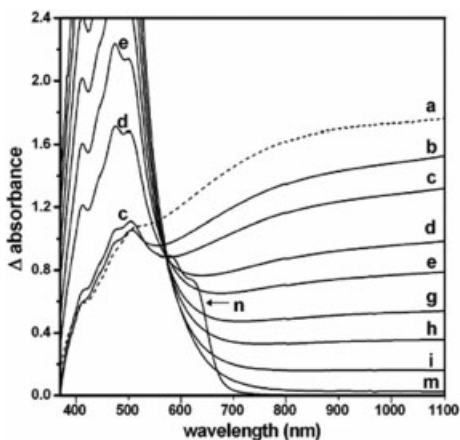


**Fig. 5.8.** An example of electron transfer mediated by nanosized metal nanoparticles, showing the absorption changes occurring to UV pre-irradiated  $\text{TiO}_2$ -stabilized Au NPs (a) upon successive additions (5  $\mu\text{m}$  each) of Uniblue A (UBA), an organic dye, under  $\text{O}_2$ -free conditions (b–m). When all stored electrons are consumed, the absorption

features of unreduced UBA can be observed (spectrum n). Conditions:  $[\text{TiO}_2] = 0.1$  M, nanorods:  $3 \times 25$  nm;  $[\text{Au}] = 5 \times 10^{-7}$  M, metal size:  $15 \pm 3$  nm; pre-irradiation time: 30 min. Spectra were taken using the respective photocatalyst solution as the reference. (From Ref. [12], some spectra have been removed for clarity.)

In nanocrystals having applications in opto-electronic devices, surface states invariably result in energy levels within the forbidden energy gap. They act as traps for electrons or holes, ultimately leading to the degradation of the electrical and optical properties of the material. In contrast, lower coordination surface atoms in metal and semiconductor oxides are usually beneficial toward catalysis and sensing of various chemical reactions [15]. The coordination numbers of surface atoms may vary over wide ranges because different crystallographic faces, edges, steps, point defects, and dislocations may be exposed, resulting in a substantial energetic heterogeneity. Unsaturated valences may be, therefore, completed by adsorbed target molecules, the latter affecting the overall electronic distribution of the nano-sized object. More importantly, the qualitative change in the electronic structure of nanocrystals coupled with chemisorption of suitable substrates can bestow unusual optoelectronic behavior for both the inorganic and organic component.

### 5.3.2

#### Chemical Synthesis

In colloidal approaches, a fine modulation over the NC size and shape is possible by adjusting the balance between the nucleation and the growth stage. To achieve this, in general the key ingredient is the presence of one or more organic molecules in the reactor, broadly termed as “surfactants”. Surfactants are amphiphilic compounds, i.e., molecules composed by one hydrophilic part (a polar or a charged functional group) and one hydrophobic part (in the simplest case, one or several hydrocarbon chains). They can act in two main different ways, described below.

(a) *Organic Templates*: Depending on physical-chemical parameters, such as surfactant concentration, temperature, solvent polarity, additives, ionic strength, amphiphilic compounds tend to assemble into soluble aggregates [16]. These assemblies can have spherical shapes or evolve into rod-like or cylindrical aggregates, flexible bilayers, and planar bilayers. Therefore, the liquid phase can contain hydrophilic or hydrophobic compartments of nanometer size prior to the synthesis, which serve as NC templates. The addition of monomers to the growing cluster is naturally terminated once a NC fills the compartment volume, which predetermines a specified distribution of the NC population close to that of nanocompartments [17] (Fig. 5.9).

In bulk colloidal dispersions, the role of compartments is generally played by direct or reverse micelles, microemulsion droplets, or by the pores (cavities) in any bicontinuous cubic phase of a lipid. A self-assembled amphiphile layer on the interface is also capable of compartmentalizing the accepted reagents, to introduce nanocrystalline structures (so-called membrane mimetic chemistry), and to orient the nanocrystal domains in the nanoreactors [18].

(b) *Terminating agents*: The growth of NCs can be properly controlled in many cases by use of special molecules that behave as “terminating” agents. Such molecules direct the growth of nanostructures by dynamically coordinating their surface under the reaction conditions. Some examples of suitable surfactants include molecules carrying functional groups with electron-donor atoms, such as alkyl thiols,

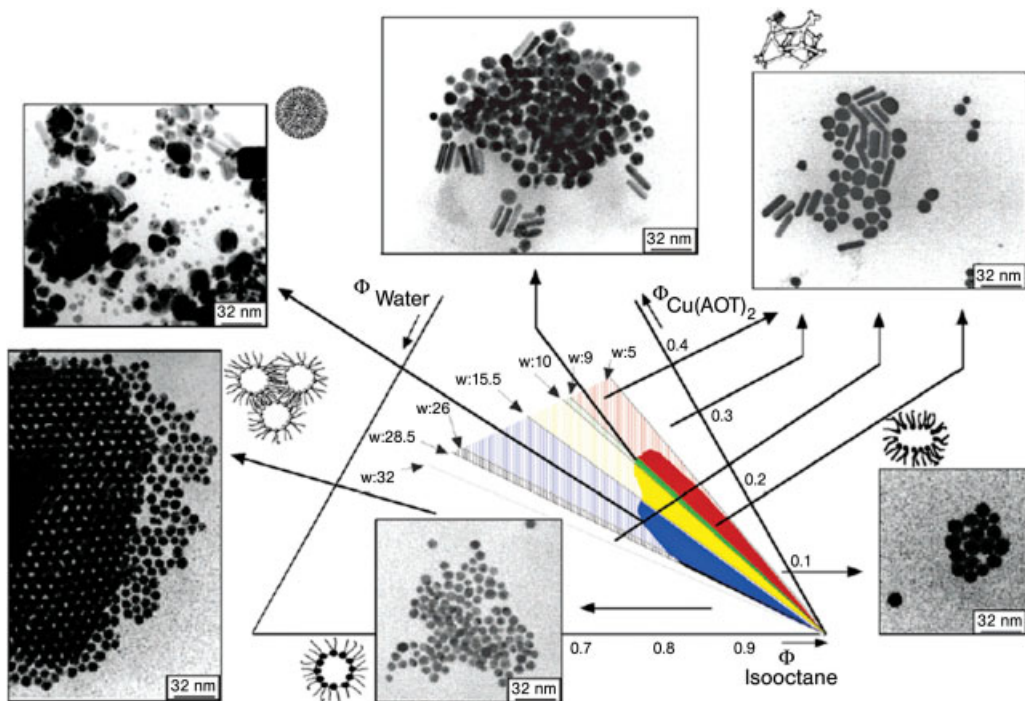


**Fig. 5.9.** Example of nanoparticle shape control achieved by combining the strategy of surfactant-based templating and the capping of salts or molecules. Various shapes of copper nanocrystals are obtained in the various parts of the phase diagram of  $\text{Cu}(\text{AOT})_2$ -water-isoctane in the oil-rich region. (From Ref. [17].)

phosphines, phosphine oxides, phosphates, phosphonates, amides or amines, carboxylic acids, and nitrogen-containing aromatics [17–19].

The choice of surfactants varies from case to case: a molecule that binds too strongly to the surface of the quantum dot is not useful, as it would not allow the nanocrystal to grow. A weakly coordinating molecule, however, would yield large particles, or aggregates. The surfactant molecules must be chemically stable at the reaction temperature to be suitable candidates for controlling growth. At lower temperatures, or more generally, when the growth is stopped, the surfactants are more strongly bound to the surface of the NCs and provide their solubility in a wide range of solvents. More importantly, surface defects (unsaturated valences) that act as traps for electron and holes, in turn degrading their optoelectronic properties, can be effectively passivated through coordination bonds with the surface ligands.

By controlling the mixture of surfactant molecules that are present during the generation and the time growth of the nanocrystals, excellent control of their size and shape is possible for many materials (Fig. 5.10) [20]. Under appropriate conditions, the choice of suitable surfactants can indeed modulate the reactivity of the

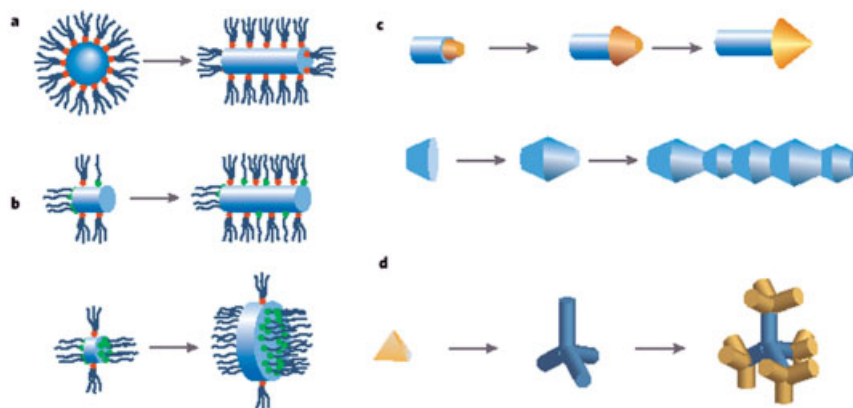


**Fig. 5.10.** Shape control of colloidal nanocrystals. (a) Kinetic shape control at high growth rate. High-energy facets grow more quickly than low energy facets in a kinetic regime, using one type of metal coordinating group. (b) Kinetic shape control through selective adhesion. The introduction of an organic molecule that selectively adheres to a particular crystal facet can be used to slow the growth of that side relative to others, i.e., metal coordinating groups with different affinities to nanocrystal facets are used, leading to the formation of rod- or disk-shaped nanocrystals. (c) More intricate shapes result from sequential elimination of a high-energy

facet. The persistent growth of an intermediate-energy facet eventually eliminates the initial high-energy facet, forming complex structures such as an arrow- or zigzag-shaped nanocrystals. (d) Controlled branching of nanocrystals. The existence of two or more crystal structures in different domains of the same crystal, coupled with the manipulation of surface energy at the nanoscale, can be exploited to produce branched inorganic nanostructures such as tetrapods. Inorganic dendrimers can be further prepared by creating subsequent branch points at defined locations on the existing nanostructures. (From Ref. [20].)

molecular precursors and direct shape changes by adhering selectively to the various facets of the growing crystallites. Delicate control of parameters, such as strain, surface reactivity, interfacial energy, and crystal solubility at the nanoscale [8–21], opens access to various complex NC morphologies and even hybrid architectures, ranging from simple core/shell systems to individual nanostructures with linear and/or branched topology [21], with site-specific deposits of a different material [22], and hetero-groups made of magnetic, metal or fluorescent spherical NCs [21d, 23].

The surfactant coating on the NC surface provides great synthetic flexibility in that it can be exchanged with another coating of organic molecules having different functional groups or polarity.

After the synthesis, colloidal nanocrystals can be further processed (e.g., functionalized with selected biomolecules or coupled with other nanosized objects) and/or transferred to any desired substrate or object.

Many applications of the quantum-mechanical aspects of quantum dots can be found in optics. As the more general case of atoms and molecules, quantum dots

can be excited either optically or electrically. Regardless of the nature of excitation, quantum dots may emit photons when they relax from the excited state to the ground state. Based on these properties, quantum dots may be used as lasing media, as single-photon sources, as optically addressable charge storage devices, or as fluorescent labels.

Colloidal quantum dots have also been used for the development of light-emitting diodes [24] and in the fabrication of photovoltaic devices [25]. In these devices, the nanocrystals are incorporated into a thin film of conducting polymer.

Chemically synthesized quantum dots fluoresce in the visible range with a wavelength tunable by the size of the colloids. The possibility of controlling the onset of absorption and the color of fluorescence by tailoring the size of the nanocrystals makes them interesting objects for the labeling of biological structures [26] as a new class of fluorescent markers. The tunability combined with extremely reduced photobleaching makes colloidal quantum dots an interesting alternative to conventional fluorescent molecules.

#### 5.4 Nanocrystal Functionalization for Biosensing

In general, practical applications can take advantage of some unique properties of NCs, such as that of being conjugable, connectable or anyway joinable with biomaterials, thus enabling biolabeling [29], biosensing [30] and use for biomedical purposes [28c–31].

Sensing processes operated by biomaterials bound to surfaces are commonly practiced in analytical biochemistry. Actually, many recent sensing applications are the result of a natural evolution of the bioconjugation chemistry, which is based on the idea of merging biological and non-biological molecular species and/or systems, to realize novel markers for cellular biology, labeling, and biosensing.

In this perspective, the use of NC-biomaterial conjugates has been demonstrated to provide a general route for the development of optical biosensors, which exploit the newly designed nanomaterial based hybrids.

The synthesis of noble metal NCs (which possess a naturally higher bioaffinity) in the presence of biomolecules has been proposed to provide nanoparticles directly connected to biologically relevant molecules [32]. However, semiconductor nanocrystals, which are typically prepared by non-aqueous routes in organic media, require several post-synthetic treatments to enhance their compatibility with biological environments. Such processing is delicate in that it should preserve the NC optical properties over the desired spectral range.

Therefore, in the last decade several studies have provided the means to obtain water-soluble and biocompatible NCs, while keeping intact their original optical characteristics.

The plethora of nanocrystal functionalization methods reported can be mainly divided into three classes: (a) surface capping exchange (typically with bi-functional agents), (b) coating with siloxane and (c) modification of the pristine capping layer

of NCs via hydrophobic interactions. Figure 5.11 gives a schematic representation describing different surface functionalization methods.

#### 5.4.1

##### Surface Capping Exchange

This approach has been proposed for the functionalization of cadmium and zinc chalcogenide NCs (e.g., CdSe, CdS, ZnS, ZnSe) and of their related core-shell derivatives (CdSe@ZnS, CdSe@ZnSe, CdS@ZnS). The basic idea is the substitution of the pristine organic capping layer with bifunctional ligands. Mercapto-acids (mercapto-acetic, mercapto-succinic, mercapto-propionic, mercapto-benzoic, and so on) have been the most commonly used molecules to this purpose [34]. They interact with the NC surface by means of the thiol group while water solubility is ensured by the outermost exposed carboxylic moiety. A major limitation is that mercaptoacid-capped NCs are highly soluble in water only when the carboxylic group is deprotonated, so that the stability of the particles at acid pHs is poor. More importantly, in comparison with the original NC emission, a reduction in photoluminescence (PL) quantum yield is usually observed, the extent of which depends on the nature of the linker exchanged and on the medium. Also, progressive detachment of thiol ligands from the NC surface due to the established dynamic adsorption-desorption equilibrium can usually result in NC aggregation and precipitation over periods longer than one week [29a–35]. Despite these drawbacks, this simple procedure allows for the preparation of fresh batches in gram scale on an “as-needed” basis. Moreover, if further bioconjugation of such thiol-modified NCs is accomplished, their stability in water can be enhanced [29a].

Bifunctional agents, such as dithiothreitol (DTT) [34] and dihydrolipoic acid (DHLA) [30–36] carrying two thiol moieties per molecule, provide stronger interactions with the NC surface, thus prolonging their stability in water (up to 2 months in the case of DTT and up to 1–2 years with DHLA) [37]. This evidence suggests that polydentate thiolated ligands could be even more effective [35b]. DHLA-capped NCs are stable at pH > 7, while at slightly acid pHs aggregation can occur.

Mercapto-capped NCs can be bioconjugated either by replacing the capping layer with thiol-modified biomolecules (e.g., DNA [30a] or proteins [38, 39]) or by carboxylic group activation. The hydroxyl groups in DTT can be exploited to achieve bioconjugation by just making them react with nucleophilic agents, such as amines. This approach, suitable to different types of NCs [28c], does not require specific coupling agents and allows one to employ commercially available nucleotides. If NCs are stabilized by negatively charged ligands (for instance DHLA or citrate), bioconjugation can be obtained by electrostatic interactions [36a–40].

The surface capping exchange can also be performed directly with biomolecules. For instance, small biomolecules, like serotonin, can replace tri-*n*-octylphosphine oxide (TOPO) on CdSe@ZnS NC [41]. Analogously, these NCs have been functionalized with synthetic phytochelatin-related peptides, providing them with a coating of biotinylated peptides, which efficiently bind to streptavidin [42]. Lysine and biotin have been used to modify Au NPs and to bind them to various proteins [43],

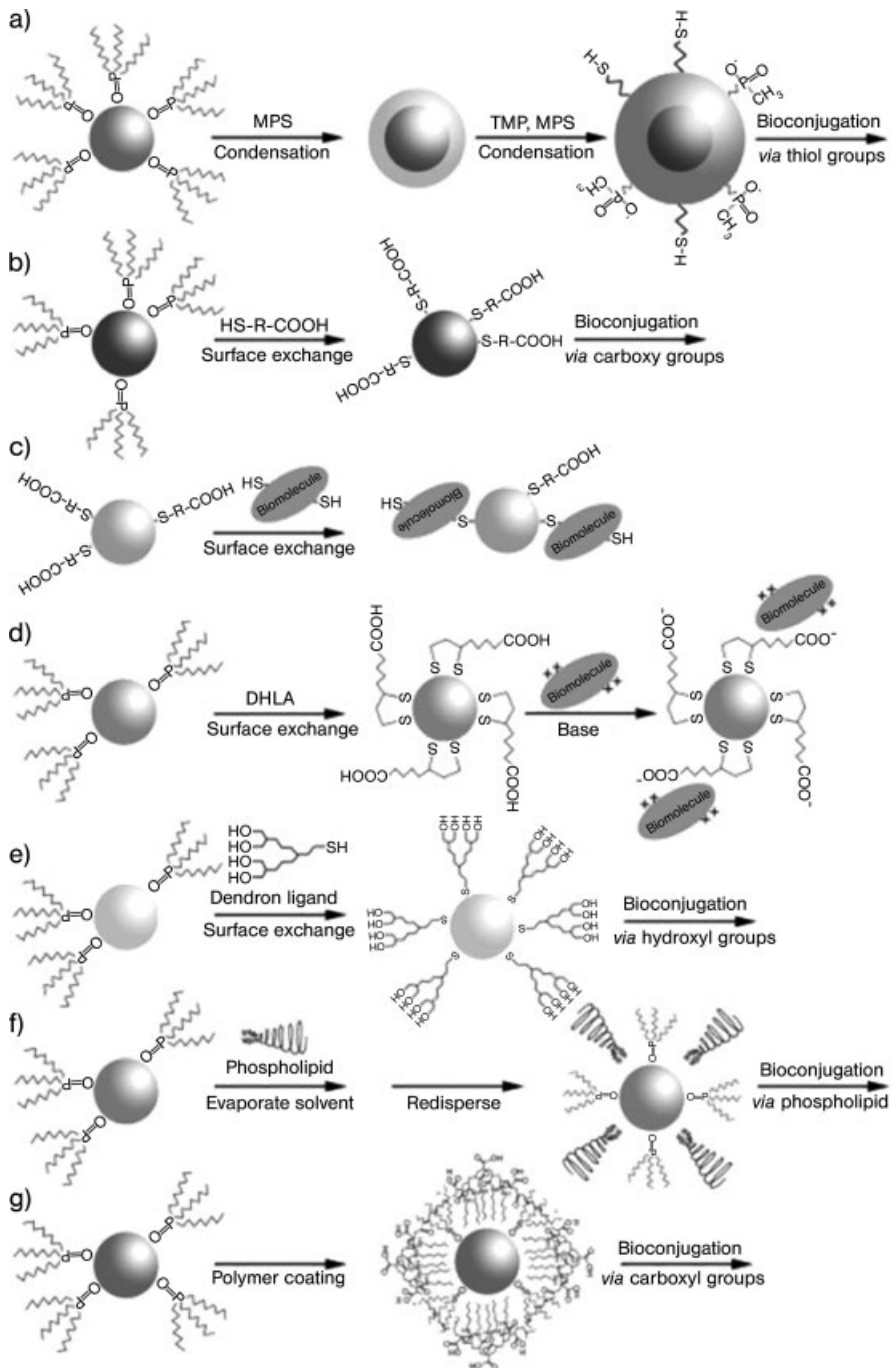


**Fig. 5.11.** Example strategies for nanocrystal surface modification: (a) coating with silica shell; capping exchange with (b) bifunctional linkers, (c) thiolated molecules, (d) bivalent

linkers, (e) and organic dendrons. (f) and (g) Nanocrystal modification via hydrophobic interaction. (From Ref. [33].)

immunoglobulin (IgG), and BSA. This approach is particularly successful for metal particles capped by loosely bound molecules, such as citrate, as demonstrated in the case of Au [44] and Ag [45]. Conversely, in the case of CdS NCs [46] weaker interactions have been observed as well as a luminescence quenching.

Finally, organic dendrons can also replace the native ligand capping on core-shell NCs, leaving the exposed hydroxyl moieties available for bioconjugation in aqueous environment, as reported for TOPO-capped CdSe NCs and Au NPs [47].

#### 5.4.2

##### Coating with a Silica Shell

*Surface silanization* is the procedure through which a hydrophilic silica shell is grown on NCs after displacing the original hydrophobic capping layer, ultimately providing NCs with solubility in water [26a]. In the general approach, the first step accomplishes ligand exchange with mercaptosilanes, usually mercaptopropyltrimethoxysilane (MPS). The mercapto groups ( $-SH$ ) are bound to the NC surface, whereas methoxy groups ( $-OCH_3$ ) are exposed to the solvent. Subsequently, siloxane bonds ( $-Si-O-Si-$ ) can be formed by reacting the methoxysilane moieties with each other under basic conditions. The final result is a highly cross-linked silica shell possessing improved resistance against dissolution [48, 49]. To provide hydrophilicity, in a further step, molecules bearing mercaptosilane groups at one end and hydrophilic groups at the other one are attached to the shell via the formation of siloxane bonds, leading to a multilayered shell. By properly selecting the hydrophilic functional groups in the latter step, it is possible to tailor the NC surface functionality [26a–48a]. Interestingly, negatively charged particles are obtained by providing the surface with phosphonate groups (for instance, by using trihydroxysilylpropylmethylphosphonate, TMP), which prevent the NCs from agglomerating and/or precipitating by means of electrostatic repulsions. Alternatively, by replacing TMP with poly(ethylene glycol) (PEG)–silane, stable neutral NCs can be prepared that repel each other by steric hindrance [50]. Finally, trimethoxysilylpropyl trimethylammonium chloride can be suitably manipulated to confer a small positive charge to the particles [32]. Bioconjugation can occur via conversion of residual MPS thiol groups into amine or carboxyl groups and via reaction with suitable bifunctional linkers, as established in the pertinent literature [28c–31a].

Silanized NCs also do not undergo to aggregation phenomena in electrolytic solutions, while retaining their original optical properties. Unfortunately, the silica shell often suffers for being inhomogeneous [29–32]. More importantly, the chemical complexity and the delicateness of the steps involved in the silanization process render the preparation of silanized NCs extremely difficult to scale up beyond the milligram quantities per batch.

#### 5.4.3

##### Surface Modification through Hydrophobic Interactions

A class of modification techniques allows one to obtain water-soluble NCs without removing the pristine capping layer. Such procedures ensure retention of the orig-



inal optical properties of NCs, as the inorganic core always remains shielded from the external environment. The general strategy relies on exploiting hydrophobic interactions between the pristine NC capping layer and suitable amphiphilic molecules. These latter can intercalate and/or interdigitate with the native capping layer alkyl chains, exposing their hydrophilic head out to the solution. A successful example is represented by phospholipid micelles encapsulating CdSe@ZnS NCs [28c–31a]. The polar head of phospholipids can be used for bioconjugation by reaction with bifunctional agents, like EDC, 1-ethyl-3-(3-(dimethylamino)propyl)-carbodiimide hydrochloride. As drawbacks, aggregation can be induced to some extent by EDC [36a], and the technique is laborious and provides only milligrams quantities per batch. Despite this, the NC optical properties are fully retained after phase transfer [31b–51].

Commercially available amphiphilic polymers bearing hydrophobic alkyl side chains and hydrophilic groups, such as PEG or multiple carboxylate groups, have also been used [52]. Several polymers have been employed: octylamine-modified polyacrylic acid [52a], block copolymers [52b], and polyanhydrides [52c]. Bioconjugation is accomplished by linking biocompatible ligands to polymer-coated NCs by reaction with the hydrophilic heads. PEG-derivatized polymers can also improve biocompatibility and reduce non-specific binding. Carboxylate-functionalized polymers strongly interact with primary amines via condensation, which can be applied to most common proteins in their native form without further modification or activation. In this regard, a high reactivity of polyanhydrides toward primary amines has been observed [52c]. Notably, NCs functionalized with high molecular weight triblock polymers [as those composed of a hydrophobic poly(butyl acrylate) segment, a hydrophobic poly(methacrylate) segment, of a hydrophilic poly(methacrylic acid) segment, and of and a hydrophobic hydrocarbon chain] are so well protected that their optical properties do not change under a broad range of pH (1–14) and salt conditions (0.01 to 1 M), or even upon harsh treatments with concentrated acid [52b]. Nonetheless, both phospholipid micelles and polymer coating can not prevent the NC size from increasing to a great extent, which can limit the intracellular mobility and may preclude fluorescence resonance energy transfer studies [35b].

More recently, host–guest chemistry has been exploited to induce the phase transfer of organic capped metal and semiconductor NCs into water by means of cyclodextrins [53]. Due to their peculiar characteristics [54], cyclodextrin-modified NCs can be very appealing for biological studies. This method deals with the formation of a host–guest complex between the hydrophobic cyclodextrin cavity and the alkyl chains of the surfactants anchored on an NC surface. Among the various classes of cyclodextrins tested,  $\alpha$ -cyclodextrins appear the most suitable for this purpose, since no aggregation or precipitation phenomena have been observed. In an alternative approach, metal NCs have also been synthesized [55] in the presence of modified cyclodextrins behaving as the capping ligands for the particles, while leaving their cavity available to perform host–guest chemistry. In this case, only a broadening of the NC size distribution has been observed during the synthesis.

## 5.5 Optical Techniques

Recent advances have been reported in the development of sensors based on optical detection methods, with remarkable improvements in terms of sensitivity and selectivity. This progress has been triggered by the access to new technical instrumentation and techniques, as well as by the availability of unprecedented materials. The discovery and the fundamental understanding of the peculiar optical properties of nanocrystals have led to a re-evaluation of the potential of well-assessed optical methods (colorimetric assays and fluorescence-based recognition) and, at the same time, have extended the technological opportunities.

Depending on the nature of the optical transduction signals, nanocrystal-based biosensors may be roughly divided into luminescence-based sensors and absorption-based sensors, relying on the changes of the emission and absorbance intensity, respectively [56]. Another possible classification can be made with reference to the chemical composition (metal or semiconductor) of the material used in the sensing process. Such diverse categorization can sometimes merge with each other, resulting in a lack of clarity in the definition. In this section we adopt a more schematic approach by classifying the methods according to the specific optical process that is exploited for the detection process.

### 5.5.1

#### Colorimetric Tests

The simplest method for detecting analytes is by measuring the absorption changes that occur because of some analyte–NC interactions modifying the optical properties of the nanocrystals [57]. Especially, metal nanoparticles are convenient for this purpose, as their surface plasmons are characterized by high extinction coefficients, many orders of magnitude larger than those of organic dyes [58]. The absorption spectrum, primarily reflecting the particle size, shape, composition [59], as well as the dielectric constant of the surrounding medium, can be sensitively affected by any process that alters the surface charge density, like direct adsorption of molecules, or variation in the mean interparticle distance induced by molecular recognition events (e.g., DNA hybridization, antigen–antibody interactions). The resulting shift in the plasmon maximum, and changes in band width and intensity, can be explained qualitatively in terms of particle electromagnetic interactions through simple quasi-static limit scattering models [60].

### 5.5.2

#### Fluorescence

Fluorescence is the optical phenomenon for which a molecule or a material (fluorophore), after gaining excitation by some means, can return to its minimum energy state by emitting light. Excitation and emission processes in a typical mole-

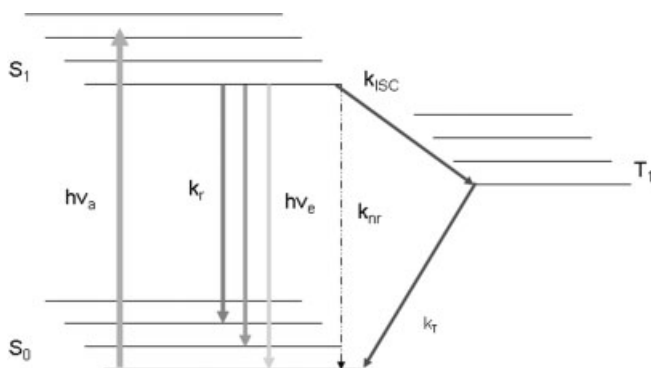


**Fig. 5.12.** Jablonski diagram describing the fluorescence process in a molecule. Upon absorption of a photon of energy ( $h\nu_a = E_{S_1} - E_{S_0}$ ), a molecule in the ground singlet state ( $S_0$ ) is promoted to a vibronic sublevel of the lowest excited singlet state ( $S_1$ ). Nonradiative, fast relaxation brings the molecule down to the lowest  $S_1$  sublevel. Emission of a photon of energy  $h\nu_e < h\nu_a$  with radiative rate  $k_r$  can take place, bringing back

the molecule to one of the vibronic sublevels of the ground state. Alternatively, the molecule can undergo collisional quenching, returning to its ground state without photon emission (nonradiative rate  $k_{nr}$ ). A third type of process is intersystem crossing to the first excited triplet state  $T_1$  (rate  $k_{ISC}$ ). Relaxation to the ground state takes place either by photon emission (phosphorescence) or nonradiative relaxation (rate  $k_{nr}$ ).

cule are represented by a Jablonski diagram, depicting the initial, final, and intermediate electronic and vibrational states of the molecule (Fig. 5.12).

In general, the molecule can be excited, by a one- or multiphoton process, from its electronic ground state  $S_0$  to the first excited state  $S_1$ . Its return to the ground state can be accompanied by the emission of a fluorescence photon. The  $S_1 \pm S_0$  transition competes with another photophysical process, called intersystem crossing, that is responsible for converting the  $S_1$  state into the first excited triplet state  $T_1$ . An irreversible photobleaching can follow the latter event, ultimately preventing a fraction of molecules from contributing to the overall fluorescence signal.

In general, fast intramolecular vibrational relaxations are responsible for the lower energy of the emitted photons with respect to that associated with the incident light. The difference in energy between absorption and emission is named the Stokes shift – it accounts for the wavelength separation of the emitted fluorescence from the excitation light. This phenomenon renders fluorescence a powerful analytical tool. The delay (lifetime) between the absorption step and the detected fluorescence depends on the nature of the fluorophore and on its local environment.

The efficiency of photon absorption is proportional to the local electric field and to the dipole moment of the fluorophore. For an immobilized fluorophore, the spatial orientation of the absorbing molecule dipole can be determined by recording the emitted fluorescence as a function of the direction of the linear polarization of the excitation light. For a mobile molecule, more information is needed, because the emission dipole may change orientation significantly in a short time. Fluctua-

tions that are faster than the fluorescence lifetime lead to a depolarized emission, while fluctuations covering timescales longer than the lifetime but shorter than the instrumental integration time lead to anticorrelation of the two orthogonal emission polarizations. Fluorescence polarization measurements have been used in analytical and clinical chemistry and as a biophysical research tool for studying the mobility of membrane lipids, domain motions in proteins, and interactions at the molecular level. Also, fluorescence polarization-based immunoassays are also extensively utilized for clinical diagnostics.

Measurement of fluorescence intensity is a widely applied technique in biological applications, as it is related to the number of photons emitted by a fluorescing sample upon excitation. Based on fluorescence wavelength and intensity level determination, various molecular or cellular targets can be easily tagged. The fluorescence intensity may be influenced by several factors, such as the excitation intensity thermal fluctuations, self-absorption, self-fluorescence, and fading due to photobleaching of the probe. However, organic fluorophores usually have emission bands with long tails extending to the red part of the visible spectrum. This issue could limit multiplexing and would require the use of interference filters in the optical readout, reducing the dynamic range of intensity levels. In contrast, the emission spectrum of semiconductor nanocrystals is narrow and Gaussian; their absorption spectrum is continuous and extended in the UV, so that a single wavelength can excite nanocrystals of different sizes, yielding several emission colors at once. Therefore, multicolor NC probes can be used to track multiple molecular targets simultaneously.

### 5.5.3

#### Fluorescence Resonance Energy Transfer

Among the most promising optical biodetection techniques, Fluorescence Resonance Energy Transfer (FRET) has been used to carry out analyte recognition and binding, while simultaneously producing useful output signals through an integrated signal transduction system [61]. FRET has been used in carefully designed sensing systems for proteins, peptides, nucleic acids and small molecules.

FRET is one of the few tools available for measuring nanometer scale distances and/or changes in distances, both *in vitro* and *in vivo*. This technique indeed relies on the distance-dependent transfer of energy from a donor fluorophore to an acceptor fluorophore. Recent advances have led to both qualitative and quantitative improvements, including increased spatial resolution, distance range, and sensitivity [62]. This progress has been facilitated by the use of new fluorescent dyes and by novel optical methods and instrumentation.

In FRET, a donor fluorophore is excited by incident light, and if an acceptor is in its close proximity, the excited state energy from the donor can be transferred to the acceptor. This event leads to a reduction in the fluorescence intensity and in the excited state lifetime of the donor, and to a concomitant increase in the emission intensity of the acceptor. The efficiency of the process depends on the inverse sixth-distance between the donor and the acceptor [Eq. (1)], where  $R_0$  is the dis-

tance at which half of the energy is transferred, and depends on the spectral characteristics of the dyes and their relative orientation.

$$\text{efficiency} = 1/\{1 + (R/R_0)^6\} \quad (1)$$

This would allow one to measure: (a) interactions between molecules, e.g., between proteins, between a protein and a ligand or (b) distances between two sites in a macromolecule.

A crucial aspect of FRET biosensor development involves optimizing the relative positions of energy levels of the donor and acceptor dyes to make them operate in concert with the desired recognition elements. Although organic dyes are available to accomplish this, many of them have functional limitations, such as pH dependence, susceptibility to photobleaching, and narrow excitation bands coupled with broad emission peaks, which can compromise sensor performance. The photo-physical properties of nanocrystals, such as size-tunable photoluminescence spectra, broad absorption, narrow emission lines, and high quantum yields, make them good candidates as energy donors able to overcome some of the problems associated with conventional molecular-based FRET systems. Indeed, it has been recently demonstrated [63] that the use of single-NC-incorporated nanosensors for DNA detection can reduce significantly, or even eliminate, the complication of background fluorescence encountered by conventional molecular FRET probes (Fig. 5.13). Further, the target signal is amplified through enhanced energy-transfer efficiency by increasing the number of acceptors linked to a donor. These features allow NC-incorporated nanosensors to generate a very distinct target signal that is easily distinguishable from the background in the presence of low target abundance and a large excess of the probe.

#### 5.5.4

##### Fluorescence Lifetime

The Fluorescence Lifetime (FLT) is a measure of the time a fluorophore spends in the excited state before returning to the ground state by emitting a photon. If a fluorophore population is excited, the lifetime  $\tau$  is the time it takes for the excited molecules to decay to  $1/e$  or 36.8% of the original population. The decay of the intensity as a function of time is given by Eq. (2).

$$I_t = \alpha e^{-t/\tau} \quad (2)$$

where  $I_t$  is the intensity at time  $t$ ,  $\alpha$  is a normalization term (pre-exponential factor) and  $\tau$  is the lifetime of the excited state. Knowledge of the excited state lifetime of a fluorophore is crucial for quantitative interpretations of fluorescence measurements, such as quenching, polarization, and FRET. Excited state lifetimes are measured in the time domain by illuminating the sample with a short pulse of light and recording the temporal behavior of the emission intensity. In pioneering work, these short light pulses having widths on the order of several nanoseconds were

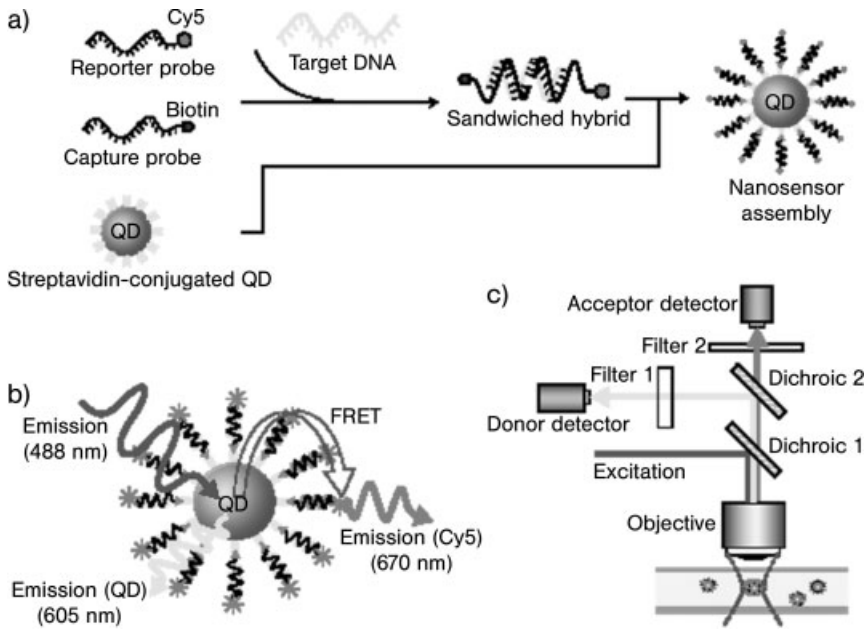


**Fig. 5.13.** Operative principle of single-NC-based DNA nanosensors. (a) Conceptual scheme showing the formation of a nanosensor assembly in the presence of

targets. (b) Fluorescence emission from Cy5 caused by FRET between Cy5 acceptors and a NC donor in a nanosensor assembly. (c) Experimental setup. (From Ref. [63].)

generated using flash lamps. Modern laser sources can now routinely provide pulses with widths on the order of picoseconds or shorter. If the decay is a single exponential and the lifetime is long compared with the exciting light, then the lifetime can be determined directly from the slope of the curve. If the lifetime and the excitation pulse width are comparable, deconvolution methods taking in account the effect of the exciting pulse shape must be used to extract the lifetime.

Fluorescence lifetime is a parameter that is mostly unaffected by inner filter effects, static quenching and variations in the fluorophore concentration. For this reason, FLT can be considered as one of the most robust fluorescence parameters. Therefore, FLT measurements are advantageous in clinical and high-throughput screening applications, where it is necessary to discriminate against the high background fluorescence from biological samples. Also, the decay studies offer a route to multiplexing. The ability to distinguish two fluorophores with similar spectra but different lifetimes is another way to allow an increased number of parameters to be measured (Fig. 5.14).

Several approaches have been used for the development of FLT-based biosensors. For example, in simple binding assays, the binding of two components (one being fluorescently labeled) is accompanied by a change in the fluorescence lifetime. In quench-release type assays, a quenched species, exhibiting low but detectable fluo-

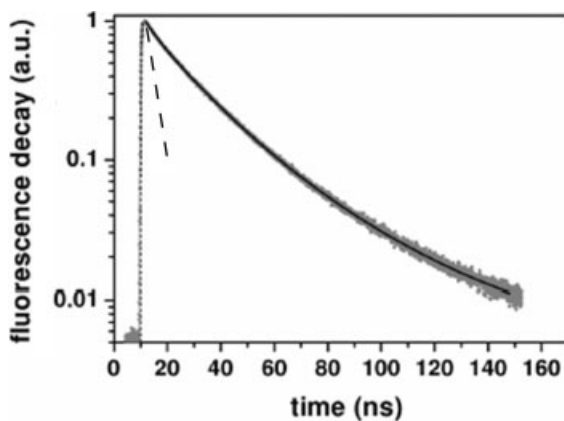


**Fig. 5.14.** Normalized ensemble fluorescence decay of CdSe@ZnS nanocrystals (1.8-nm radius, 575-nm peak emission). The solid curve is a triple exponential fit to the data with components at 3.4, 16.1, and 35.6 ns. The measured fluorescence decay of Rhodamine molecules in water is also displayed (dashed curve) and is well described by a single exponential decay with time constant 4.3 ns. (From Ref. [65].)

rescence, is initially present in large excess. If a fluorescence compound is released (e.g., by binding to a complementary DNA strand or by an enzymatic reaction) the FLT of the system increases. Finally, the study of lifetime is a powerful tool to measure the energy transfer efficiency in FRET assays by using a non-fluorescent acceptor, which helps to circumvent the problem of spectral cross talk between the donor and the acceptor.

FLT measurements offer additional opportunities in fluorescence microscopy, where the local probe concentration can not be controlled. Lifetime microscopy allows image contrast to be created from the fluorescence lifetime of a probe at each point of the image. Typical examples are the mapping of cell parameters, such as pH, ion concentrations or oxygen saturation. To enhance contrast in cellular imaging and analysis by FLT imaging, labeling agents with long lifetime fluorescence are required. Usually, organic dyes undergo radiative emission from allowed singlet–singlet electronic transitions, with typical decay rates of few nanoseconds. Unfortunately, such rapid emission merges with the time scale of short-lived self-fluorescence background from many naturally occurring species in biological specimens. In fact, self-fluorescence of several proteins often precludes observation of small details, unless the target is heavily loaded with dyes (which, in turn, results in phototoxicity problems). Lanthanide chelates with lifetimes in the sub-microsecond to millisecond range have also been successfully used [62]. However, because their FLT is too long, these probes have a limited photon turnover rate and, therefore, low sensitivity. In contrast, nanocrystals are more advantageous, in that they emit light slowly enough to avoid serious interference by self-fluorescence background, but also fast enough to maintain a high photon turnover rate. Indeed, ensemble measurements show a multi-exponential decay after pulsed excitation, which yields decay times between 10 and 40 ns. Benefiting from the long lifetime

of NCs and using fast pulsed laser excitation, it is possible to reject all photons emitted within the first few ns after the pulse, while revealing only those arriving after the decay of fluorescence from all dyes or self-fluorescent proteins (time-gated imaging). Also, the allowed repetition rate of a few megahertz is compatible with rapid cell imaging.

### 5.5.5

#### **Multiphoton Techniques**

Another class of widely used optical methods for biological detection makes use of multiphoton-based approaches [65]. Such nonlinear optical techniques are based on the fact that two or more photons of low energy can be simultaneously absorbed by a fluorophore, producing the emission of a photon with a shorter wavelength. Since multiphoton absorption is a nonlinear effect, it strictly requires a high source intensity and a tightly focused incident beam. To illuminate the sample with the necessary intensity, while preserving it from thermal damage, a femtosecond pulsed laser source is commonly used. The laser beam is then focused through an objective onto a sample treated with a fluorescent dye. Although single photons do not possess enough energy to induce an absorption transition, the photon density is sufficiently high in the centre of the tightly focused laser beam to cause direct absorption of two photons, so that an up-converted emission can result in. The fluorescence signal can be thus only detected in the focus of the laser beam. The focus can be also rasterized through the sample to create a 2D mapping. A typical advantage of this technique is that it suffers little from photobleaching effects. Indeed, irradiation in the far-red and near-infrared (NIR) spectral regions is characterized by low scattering and absorption by the biological environment [66]. More recently, NIR radiation has been used to excite visible CdSe@ZnS core-shell NCs in mouse capillaries using multiphoton fluorescence imaging [67].

### 5.5.6

#### **Metal-enhanced Fluorescence**

The use of metallic materials to favorably alter the intrinsic photo-physical characteristics of fluorophores in a controllable manner is a fairly new concept that has received much attention only in the past few years.

Although fluorescence is a highly sensitive technique, allowing for the detection of single molecules, it exhibits intrinsic detection limits. These latter are typically related to the fact that the detection of a fluorophore is usually limited by its quantum yield, self-fluorescence of the sample, and/or by its photostability. In typical fluorescence measurements, the experimental set-up is such that the sampled area is large relative to the size of the fluorophores and relative to the absorption and emission wavelengths. In this arrangement, the fluorophores irradiate freely in space. Interestingly, for fluorophores close to metallic surfaces or nanoparticles the free-space condition is altered, resulting in dramatic spectral changes. The so-called Metal Enhanced Fluorescence (MEF) [68] arises from the interaction of the



dipole moment of the fluorophore and the surface plasmon field of the metal, resulting in an increase in the radiative decay rate and in stronger fluorescence emission. Indeed, the quantum yield ( $Q_0$ ) and lifetime of the fluorophore ( $\tau_0$ ) in the free-space condition are given by Eqs. (3) and (4), respectively.

$$Q_0 = \Gamma / (\Gamma + k_{nr}) \quad (3)$$

$$\tau_0 = 1 / (\Gamma + k_{nr}) \quad (4)$$

where  $\Gamma$  and  $k_{nr}$  are the radiative and non-radiative decay rate, respectively. Due to the close proximity to a metal surface, the radiative decay rate increases by a term  $\Gamma_m$ . In this case, the quantum yield ( $Q_m$ ) and lifetime of the fluorophore ( $\tau_m$ ) near the metal surface are given by Eqs. (5) and (6) [69]:

$$Q_m = (\Gamma + \Gamma_m) / (\Gamma + \Gamma_m + k_{nr}) \quad (5)$$

$$\tau_m = 1 / (\Gamma + \Gamma_m + k_{nr}) \quad (6)$$

These equations allow the prediction of unusual behavior of a fluorophore near to a metallic surface. Notably, from Eqs. (3)–(6), as  $\Gamma_m$  increases, the quantum yield increases, while the lifetime decreases. These effects have also been justified theoretically [70], being analogous to the increase in Raman signals observed in surface-enhanced Raman scattering. However, a remarkable difference is that fluorescence enhancement is activated by interactions through space and does not require direct contact between the fluorophores and the metal surface.

Remarkably, metal surfaces can affect the radiative decay rates of fluorophores and can also be beneficial to resonance energy transfer. In practice, this means that weakly emitting materials (dyes, proteins, or DNA) with low quantum yields can be transformed into more efficient fluorophores with shorter fluorescence lifetimes. The reduction in fluorescence lifetime associated to MEF implies that molecules spend less time in the excited state, thus reducing photobleaching effects. The dramatic increase in the fluorescence emission occurs for fluorophores located at well-defined distances (50–200 Å) above metal surfaces with nanoscale roughness. This enables the use of photosensitive fluorophores that can hardly be employed in conventional fluorescence studies because of their high susceptibility to photobleaching. Another interesting effect is observed when fluorescence originates from nanomaterials with periodic patterns. In this case, the fluorescence emission can be spatially directed over a small viewing angle [71], which leads to emission sufficiently intense to be revealed by detectors without extensive optics. Such high directional emission combined with the increase in quantum yield offers the potential for efficient MEF-based sensors and microarrays [72].

### 5.5.7

#### Surface Plasmon Resonance

In the past decade, sensing by Surface Plasmon Resonance (SPR) has been demonstrated to be a powerful tool to probe of protein–ligand, protein–protein, and

protein–DNA interactions. More interestingly, this technique provides a means not only to quantify the equilibrium and kinetic constants related to such events, but also for setting up very sensitive, label-free biochemical assays.

This optical technique is based on the detection of change in reflectivity of a laser beam, incident to a metallic thin layer, due to the interaction with surface plasmons propagating on metallic surface. A surface plasmon is a collective surface excitation of conduction electrons in a metal that can be excited by means of photon irradiation [73]. This concept originates in the plasma approach of Maxwell's theory, in which the free electrons of a metal are treated as an electron liquid of high density (plasma) and density fluctuations occurring on the surface of such a liquid are called plasmons, surface plasmons (SP), or surface polaritons. According to Maxwell's theory, surface plasmons can propagate along a metallic surface and are characterized by a spectrum of eigenfrequencies related to the wave-vector by a dispersion relation. Since the dispersion relation of SPs never intersects the dispersion relation of light in air, which can be represented by a straight line, the resonances cannot be excited directly by a freely propagating beam of light incident upon a metal surface. However, if the exciting beam travels through an optically denser medium (e.g., glass) of high dielectric constant, it is possible to decrease the slope of the straight line corresponding to the photon dispersion. If this is the case, plasmons can be excited by p-polarized light undergoing total internal reflection on the glass surface. More precisely, the plasmons are excited by the evanescent wave associated with the internal reflection, which can penetrate deeply even to the metal/air interface (Fig. 5.15). The fields associated with the surface plasmon (SP) extend into the media adjacent to the interface and decay exponentially away from it. Consequently, the SP is sensitive to changes in the environment near the interface and therefore is a sensing probe.

Whenever the momentum of the incoming photon matches with that of the plasmon, surface plasmon resonance is excited. This phenomenon can be inferred

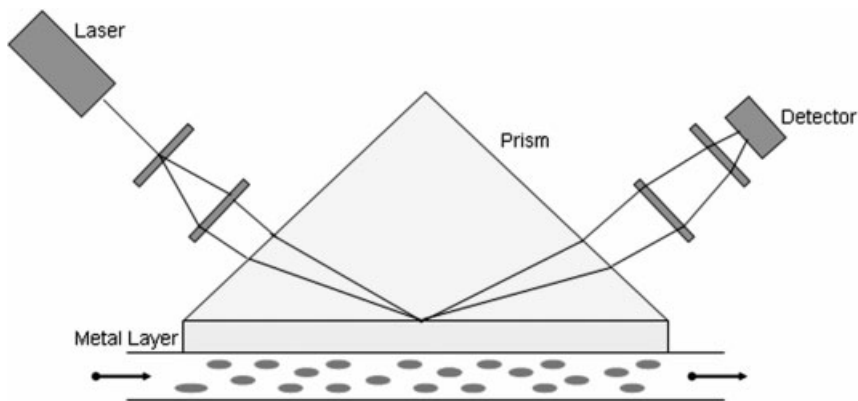


Fig. 5.15. Kretschmann configuration for surface plasmon resonance.

from the drop in intensity of reflected light when a suitable angle for resonance is approached at which an energy transfer between evanescent wave and surface plasmon occurs [74]. The value of the resonant angle is a sensitive function of the dielectric constants of the two contacting media.

The resonance conditions are influenced by the material adsorbed onto the thin metal film. Owing to this property, the surface plasmon resonance can be used to monitor surface reactions, as any organic or inorganic layer deposited on the metal surface causes changes in dielectric function of the medium, determining the new conditions for resonance (i.e., at a different resonance angle). The shape of the whole resonance curve, i.e., its depth and width depends on optical absorption within the metal and on radiation losses resulting from surface roughness. Therefore, optical systems based on SPR can provide a safe, remote, non-destructive means of sensing. SPR has already been used for gas sensing, biosensing, immunosensing and electrochemical studies. A satisfactory linear relationship is found between the resonance energy and the concentration of biochemically relevant molecules, such as proteins, sugars, and DNA [75]. The SPR signal, which is expressed in resonance units, therefore represents a measure of mass concentration at the sensor chip surface. This means that the analyte and ligand association and dissociation can be revealed, while rate constants as well as equilibrium constants can be then calculated.

A fraction of the light energy incident at a sharply defined angle can interact with the delocalized electrons in the metal film (plasmon), thus reducing the reflected light intensity. The precise value of incidence angle at which this occurs is determined by several factors, among which the most relevant is the refractive index of the backside layer of the metal film into which the evanescent wave propagates. This layer is the non-illuminated side of the metal film on which target molecules are immobilized and addressed by ligands in a mobile phase running along a flow cell. When a binding event occurs, the local refractive index is modified, leading to a change in SPR angle, which can be monitored in real-time by detecting changes in the intensity of the reflected light (Fig. 5.16).

The change rates for the SPR signal can be analyzed to extract apparent rate constants for the association and dissociation steps of the monitored reaction. The ratio of these values gives the apparent equilibrium constant (affinity). The magnitude of the change in the SPR signal is directly proportional to the immobilized mass, and can thus be roughly interpreted in terms of the reaction stoichiometry. Signals are easily obtained from sub-microgram quantities of material.

Since the SPR signal depends only on binding to the immobilized template, it is also possible to study binding events from molecules in extracts, i.e., in the presence of poorly purified components. The light source for SPR is a near-infrared light emitting diode that has a fixed range of incident angles. The SPR response is monitored by an array of light sensitive diodes covering the whole wedge of the reflected light. The angle at which minimum reflection occurs is detected and converted into resonance units.

Many biomolecular binding events cause changes in the refractive index at the surface layer, which are detected as changes in the SPR signal. In general, the re-

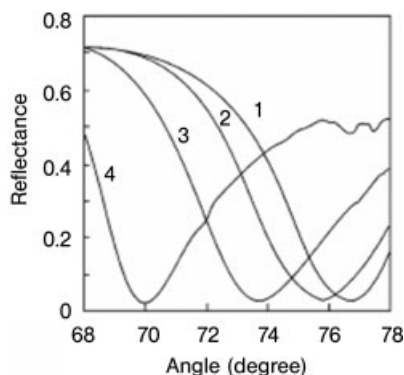


**Fig. 5.16.** Typical SPR curves of surfaces modified with Au-MIP/MIP gel (1), with Au-MIP/MIP of lower nanoparticle density (2), with MIP/MIP (3), and with 11-mercaptoundecanoic acid (4) in water at 30 °C. (From Ref. [76].)

fractive index change for a given change of mass concentration at the surface layer is practically of comparable magnitude for all proteins and peptides, and is similar for glycoproteins, lipids and nucleic acids.

#### 5.5.8

#### Surface-enhanced Resonance Spectroscopy

Raman spectroscopy provides highly resolved vibrational spectra at room temperature without suffering from rapid photobleaching of the investigated molecule. However, Raman scattering is an intrinsically inefficient process with scattering cross sections ( $\sim 10^{-30}$  cm<sup>2</sup> per molecule) approximately 14 orders of magnitude smaller than the absorption cross sections ( $\sim 10^{-16}$  cm<sup>2</sup> per molecule) of fluorescent dye molecules. Therefore, to achieve sensitivity at the single molecule level, the normal Raman scattering efficiency must be enhanced  $10^{14}$ -fold or more. Surface-enhanced Raman Spectroscopy (SERS) is a Raman Spectroscopic technique that provides a greatly enhanced Raman signal from Raman-active molecules that are adsorbed onto suitably prepared metal surfaces. An increase in the intensity of Raman signal of the order of  $10^4$ – $10^6$  has been routinely observed, and can be as high as  $10^8$ – $10^{14}$  for some systems [77]. SERS was first discovered for analytes adsorbed onto Au, Ag, Cu or alkali (Li, Na, K) metal surfaces, with useful excitation wavelength near or in the visible region. Interestingly, a giant signal enhancement has been found using silver and gold faceted nanocrystals, allowing both detection and identification of single, non-fluorescent molecules. Therefore SERS is not only highly sensitive, but it is also selective as a result of enhancement mechanisms operating only at surfaces.

The importance of SERS is that the surface selectivity and sensitivity is extended to various molecular systems that are inaccessible by conventional Raman scatter-

ing, such as to *in situ* and ambient analyses of electrochemical, catalytic, biological, and organic systems. SERS measurements can be carried out under ambient conditions in a broad spectral range. Both electromagnetic-field and chemical-based models have been used to explain the SERS phenomenon. Electromagnetic effects dominate over the chemical effects, which in fact contribute to enhancement by one–two orders of magnitude [78]. Chemical enhancement (CE) involves changes in the electronic states of the analyte following its surface chemisorption [79], while electromagnetic enhancement (EME) is related to the metal surface roughness. The latter can be developed in several ways, such as, for example, by means of (a) oxidation–reduction cycles on electrode surfaces; (b) vapor deposition of metal particles onto substrates; (c) lithographically produced metal spheroid assemblies; (d) metal deposition over a mask of polystyrene nanospheres; (e) metal colloids [80]. All of these methods basically aim to provide rough metal surface for which roughness is actually due to metal nanoparticles or aggregates.

The intensity of the Raman scattered radiation is proportional to the square of the magnitude of the electromagnetic field incident to the analyte [Eq. (7)]:

$$I_R = E^2 \quad (7)$$

where  $I_R$  is the intensity of the Raman field, and  $E$  is the total electromagnetic field associated with the analyte. Moreover,  $E$  is given by Eq. (8):

$$E = E_a + E_p \quad (8)$$

where  $E_a$  is the electromagnetic field on the analyte in the absence of any roughness features and  $E_p$  is the electromagnetic field emitted from the particulate metal roughness feature [81]. Of course, the electromagnetic field of the excitation radiation is incident to the analyte. In normal Raman scattering ( $E_p = 0$ ),  $E_a$  is relatively small since the source of the electromagnetic radiation (the laser) is relatively far away. However, in SERS the roughness features provide an additional field,  $E_p$ , in close proximity to the adsorbate, that is associated with the metal particles. Because of this proximity, any electromagnetic field from the particle will strongly contribute to  $E$ . Thus, the magnitude of the particle field is of crucial importance in determining the overall intensity of the Raman signal. Since the plasmon excitation is also confined in a small material volume (related to the characteristic features of the surface roughness), the field  $E_p$  associated with it is also very intense. The large electromagnetic energy density on the particle effects the scattering  $I_R$ , as described by Eqs. (7) and (8). It follows that analyte molecules adsorbed between two SERS-active particles will yield a higher signal than those molecules being close to only one particle.

Since the surface roughness features are so relevant to SERS, much attention has been devoted to their study. Normal roughening procedures produce heterogeneous surfaces where the particles have various sizes, shapes, and orientations [82]. The frequency of incident light that is most effective in producing an intense field on the particle severely depends on the degree of surface roughness as well as on the nature of metal used. The specific region on the particle where analyte ad-

sorption occurs affects the magnitude of the SERS enhancement, as the EME is strongest where the particle has the highest curvature.

The CE mechanism is less understood than the EME enhancement, but brings about some interesting considerations. The molecule adsorbed onto the surface has necessarily to interact with the surface. CE exists because of this interaction, which has been described in several ways. The proximity of metal adsorbate may allow pathways of electronic coupling from which novel charge-transfer intermediates are formed that have a higher Raman scattering cross-section than that of a non-adsorbed analyte. This fact resembles a resonance Raman effect. Another explanation is that the molecular orbitals of the adsorbate overlap with the conduction band of the metal, thus modifying the analyte chemical properties [83]. Interestingly, the CE effect results in an alteration in the scattering cross-section, whereas the EME effect generally leads to change in the scattering intensity without affecting the scattering cross-section.

The distance dependence of SERS is used in the overlayer technique. An ultrathin solid or liquid film is adsorbed onto the SERS-active substrate, with the analyte within the film taking advantage of the EME of the substrate. It follows that the Raman spectrum of the analyte is greatly enhanced. This makes SERS applicable to various targets, such as organic films, semiconductors, insulators, etc. Spacer layers can be adsorbed onto the substrate, and can alter the chemistry of either the substrate or that of the overlayer, extending the utility of SERS even further. An advantage to the overlayer technique is that it suffers less from the inhibitory effect of metal surface defects, such as pinholes in silver [84].

As most of signal enhancement is due to electromagnetic fields whose intensities decrease with increasing distance from the point source, it follows that an analyte would benefit from SERS substrates even if it were located at some distance away from the active surface. Theoretical calculations have been performed, and the SERS enhancement,  $G$ , has been found to scale with distance according to Eq. (9):

$$G = [r/(r + d)] \quad (9)$$

where  $r$  is the radius of the spherical metal roughness feature, and  $d$  is the distance of the analyte from that feature. Experimentally,  $G$  decreases by a factor of ten at a distance of 2–3 nm, or equivalent to one–two monolayers.

Traditionally, SERS-based sensing has employed roughened metal surfaces or colloidal particles immobilized on a substrate to create relatively large active areas for sensing [85]. More recently, efforts have been focused on the potential of using individual nanoparticles or small clusters of nanoparticles as the sensing elements [86]. This approach has paved the way to a wide range of applications that so far have been difficult to address with conventional chemical sensors. A remarkable example is the possibility of using these probes inside single living cells. The small size of the nanoparticles (50–100 nm in diameter) combined with the highly localized probe volume makes these particles work as localized sensors suitable for monitoring biological processes in living cells.

## 5.6

### Advantages and Disadvantages of Nanocrystals in Optical Detection

Colloidal nanocrystals have several peculiar advantages over organic dyes that are conventionally used in optical bio-detection [29d–87]. Indeed, their wide absorption spectrum, coupled with their extinction cross-section, makes it possible to excite different luminescent nanoparticles with different sizes by one single excitation wavelength. Organic fluorophores, however, exhibit discrete and well-spaced absorption bands with cross-sections nearly an order of magnitude smaller. In addition, most semiconductor nanocrystals have narrow (few tenths of nanometers) symmetric emission peaks that can be finely tuned from blue to red up to the near-infrared region [88]. The high color purity achievable by precise size control represents the main advantage offered by colloidal nanocrystals, especially in multiplexing applications. In contrast, organic dyes are often characterized by asymmetric spectra with distinct phonon progression towards the longer wavelength, which leads to undesirable spectral overlap among different channels in a detecting system for the measurements. Moreover, the typical fluorescence quantum yields of NCs, defined as the ratio of the number of photon emitted in radiative channel to the number of photon absorbed, can be as high as that of organic dyes, approaching values close to 30%. As a further advantage, semiconductor NCs are much less susceptible to photobleaching than organic dyes, which are rapidly and irreversibly photodegraded [52a].

The sensitivity of luminescence of NCs to their surface status (defects and/or dangling bonds) and to the local environment has typically represented the major limitation to technological applications. Now, core–shell heterostructures, where the nanocrystal is coated with a thin inorganic shell of a wider band gap semiconductor, provide increased fluorescence quantum efficiencies (>50%) and greatly improved photochemical stability (Fig. 5.17).

The sensitive detection in thick specimen requires wavelengths such that excitation light can penetrate up to the desired depth, and the emitted light must be able to travel back to a photodetector. Several semiconductor materials have been used to generate bright nanocrystals that emit between 650 and 2000 nm [89]. NCs with emission maxima between 750 and 860 nm have been employed to image the coronary vasculature in a rat model, while NCs emitting in the 840–860 nm region have been used to sentinel lymph-node mapping in cancer [90, 31c]. This use of near-IR emitting NCs can be thus profitably extended for “*in vivo*” biosensing applications, as NCs have been demonstrated to retain their emission in tissues *in vivo* for months.

Colloidal semiconductor nanocrystals represent, therefore, a valid alternative to organic fluorophores and their superior fluorescence properties account for the large success illustrated by several applications as biosensors.

Historical inconveniences of colloidal nanocrystals, such as the loss of emission in aqueous environment or the poor biocompatibility and bioconjugability, have been effectively overcome in recent years by suitable functionalization methods that have been reported in the Section 5.3. A serious difficulty with the large-scale

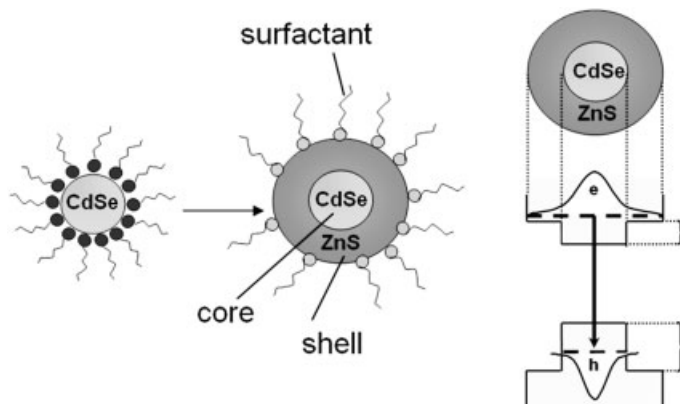


**Fig. 5.17.** Schematic diagram of core–shell nanocrystals of CdSe@ZnS. The growth of a thin layer of ZnS on CdSe nanocrystal cores causes an increased optical confinement.

use of colloidal nanocrystals, especially those subjected to bioconjugation treatments, lies in the still expensive fabrication costs. However, it is expected that commercial expansion of chemical manufacturers will lead to a more competitive environment and, possibly, to lower production costs.

## 5.7 Applications

The impact of nanotechnology on biosensing has been tremendous owing to the availability of the more robust, versatile and efficient materials for sensing. The following subsections review several successful examples of the use of colloidal nanoparticles in optical biosensing.

### 5.7.1

#### Biosensing with Semiconductor Nanocrystals

The broad spectrum of “colors”, which can be obtained by exciting semiconductor NCs of different size with a single excitation laser wavelength, poses the basis for the simultaneous detection of several markers in biosensing and assay applications. NCs can be used as fluorescent labels for immunosensing and DNA sensing, providing tunable wavelength, narrow emission peaks, and 100-fold higher stability than molecular fluorescent dyes [91].

The novel applications of NCs have highlighted their wide potential in present technology. Several examples can be found on the use of luminescent CdSe@ZnS core–shell nanocrystal bioconjugates in quantum dot-based sensors. Biomolecules can be labeled with luminescent NCs. They have been also demonstrated to be in-



volved in efficient fluorescence resonance energy transfer between neighboring NCs of different sizes, while their emission is readily quenched by bound fluorescent dyes. Sensor assemblies have been reported that employ NCs linked to dye-labeled biological receptors to exploit donor–acceptor energy transfer between the NCs and the receptors for detection purposes based on molecular recognition events. The effect of variation in concentration of the energy acceptors bound to a nanocrystal surface on the luminescence quenching of either in soluble and solid phase conditions has been investigated. The obtained results suggest the occurrence of fluorescence quenching between NCs and surface anchored dye–biological receptor [36b].

An application of quantum dots is the multiplexed optical encoding and the high-throughput analysis of genes and proteins. This is a very important issue, because most complex human diseases (such as cancer) involve many genes and proteins. Tracking a panel of molecular markers at the same time will allow scientists to understand, classify and to differentiate such complex human diseases.

The advantageous core–shell nanocrystals have also been exploited in combination with polymers [29c] (Fig. 5.18).

First, polystyrene microspheres doped with single-size CdSe@ZnS nanocrystals in known amounts are prepared and analyzed. Fluorescence intensity analysis of the beads clearly discriminates ten different intensity levels and indicates a high degree of bead uniformity and bead identification accuracy. Next, the beads with three colors of quantum dots are prepared. Significantly, fluorescent resonant energy transfer from the small nanocrystals to the large nanocrystals is not observed. The triple-coded bead is then used to demonstrate a DNA hybridization assay. Overall, these results indicate that a new spectral coding technology with potentially wide application to various biological assays that can be developed using fluorescent nanocrystals, embedded in microspheres. In this regard, NC probes are particularly attractive, because of the simultaneous excitation and continuous tuning by variation of particle size and chemical composition. The use of six colors and ten intensity levels can, theoretically, encode one million protein or nucleic acid sequences. Specific capturing molecules, such as peptides, proteins, and oligonucleotides can be covalently linked to the beads, which encode a specific spectroscopic signature. To determine whether an unknown analyte is captured or not, conventional assay methodologies (similar to direct or sandwich immunoassay) can be applied.

Bioconjugated NCs have also been used successfully in time-gated fluorescence detection of tissue sections. This optical technique is based on lifetime fluorescence microscopy employed for the selective and sensitive characterization of fluorescence species and in biophysical studies of proteins. Silanized nanocrystals were added to a 3T3 mouse fibroblasts cells grown on fibronectin treated coverslips, without signs of toxic response to the presence of NCs in the medium being observed [64].

The use of luminescent colloidal semiconductor nanocrystals as fluorophores have expanded to the range in FRET-based sensing applications [92]. If fully exploited, the unique NC properties should allow development of FRET-based nano-

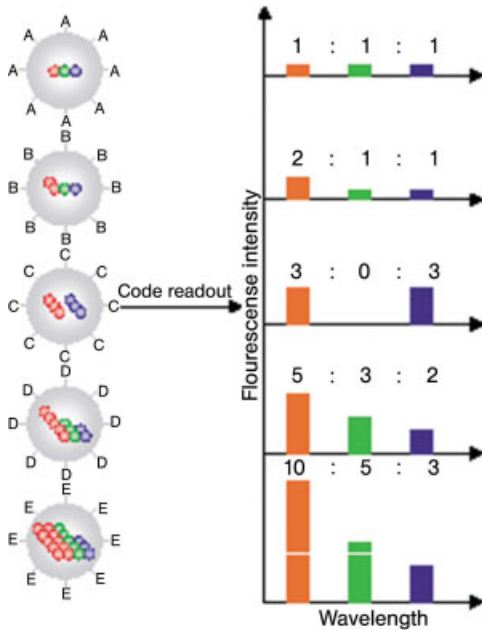


**Fig. 5.18.** Schematic illustration of optical coding based on wavelength and intensity multiplexing. Large spheres represent polymer microbeads, in which small colored spheres (multicolor quantum dots) are embedded according to predetermined intensity ratios. Molecular probes (A–E) are attached to the bead surface for biological binding and recognition, such as DNA–DNA hybridization and antibody–antigen/ligand–receptor interactions. The numbers of colored spheres

(red, green, and blue) do not represent individual NCs, but are used to illustrate the fluorescence intensity levels. Optical readout is accomplished by measuring the fluorescence spectra of single beads. Both absolute intensities and relative intensity ratios at different wavelengths are used for coding purposes; for example, (1:1:1) (2:2:2), and (2:1:1) are distinguishable codes. (From Ref. [29c].)

scale assemblies capable of continuously monitoring target (bio)chemical species in diverse environments [93].

It has been confirmed that semiconductor nanocrystals can be FRET donors, quenchable with efficiencies up to 99%, when using organic fluorophores, non-emissive dyes, gold nanoparticles, or other nanocrystals as acceptors (Fig. 5.19) [94].

NCs conjugated to maltose binding proteins have been used as *in situ* biosensors for carbohydrate detection. A fluorescence quenching is observed by adding a maltose derivative covalently bound to a FRET acceptor dye, while PL emission is recovered upon addition of native maltose, as the sugar–dye compound is displaced. In this work, the recovery of nanocrystal fluorescence upon maltose addition can be directly related to maltose concentration, because of both the physical orientation and stoichiometry of the maltose receptors on the nanocrystals are considered as

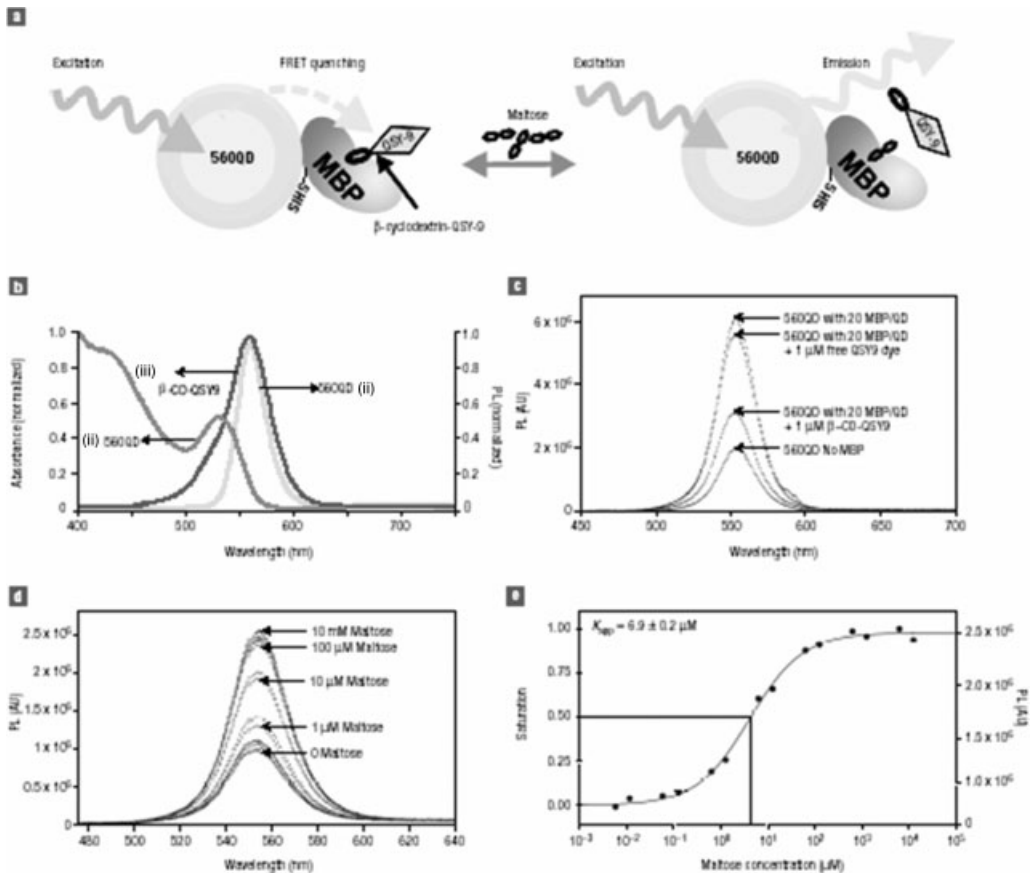


**Fig. 5.19.** Function and properties of a maltose nanosensor. (a) Nanocrystal-MBP nanosensor operation principle. Each NC is surrounded by MBP. The formation of complex NC-MBP with CD-QSY9 (maximum absorption  $\sim 565$  nm) results in quenching of NC emission. Added maltose displaces CD-QSY9 from the sensor assembly, resulting in an increase in direct NC emission. (b) Spectral properties of the nanosensor. Absorption (i) and emission spectra (ii) of MBP-conjugated NC are displayed along with the absorption spectra (iii) of CD-QSY9. (c) Demonstration

of NC-MBP FRET quenching. PL spectra (AU = arbitrary units) were collected from NCs and NCs mixed with an average of 20 MBP/NC, obtaining an increase in PL ( $\sim 300\%$ ). The same NC-MBP conjugates were then mixed with either free QSY9 dye or CD-QSY9. (d) NC-10MBP maltose sensing. Titration of a NC-10MBP/NC conjugate (quantum yield  $\sim 39\%$ ) preassembled with CD-QSY9 with increasing concentrations of maltose. (e) Transformation of titration data. The right-hand axis shows PL at 560 nm, and fractional saturation is shown on the left-hand axis. (From Ref. [94].)

parameters. Although the FRET quenching efficiency was low, this work demonstrates the potential of NC-based *in situ* biosensing.

Other important applications of fluorescent nanocrystals as FRET-based biosensors have been very recently developed for ultrahigh sensitive detection of DNA [63]. The DNA nanosensor can consist of two target-specific oligonucleotide

probes, which include a reporter probe labeled with a fluorophore and a capture probe labeled with biotin, in addition to a NC conjugated with several streptavidins. The nanocrystal works as both a FRET energy donor and a target concentrator, producing an extremely low level of background fluorescence that is difficult to achieve with conventional organic fluorophores. When a target DNA is present in solution, it is sandwiched by the two probes. Several sandwiched hybrids are then captured by a single NC through biotin–streptavidin binding, resulting in a local concentration of targets in a nanoscale domain. The resulting assembly brings the fluorophore acceptors and the nanocrystal donor into close proximity, leading to fluorescence emission by the acceptors by means of FRET upon illumination of the donor, indicating the presence of targets.

### 5.7.2

#### **Biosensing with Metallic Nanoparticles**

The use of gold colloids in biodetection dates back to the early 1970s when the immunogold staining procedure was invented. Since that time, the labeling of targeting molecules, such as antibodies, with gold NCs has deeply modified the approach to detection of biologically relevant components.

The optical transduction of receptor–ligand interactions at the surface of noble metal NCs via changes in their extinction spectrum is attractive for the development of biosensors, because a colorimetric transduction scheme is considerably simpler to implement than conventional, planar SPR.

It has been shown [95] that, for oligonucleotide-functionalized 30-nm Au NCs, the amount of optical absorbance recorded for an array surface of bound particles is directly related to the number of bound particles and to the concentration of hybridizable targets in solution. This study also demonstrates that, using microstructured substrates, DNA-modified areas with dimensions in the micrometer range specifically recognize complementary NC-bound DNA strands, with the signal background from unfunctionalized areas of the chip remaining rather low.

The environmental sensitivity of the color of nanosized gold has been exploited in a first prototype of biosensor in [96]. This study demonstrated the possibility of colorimetrically monitoring the binding of antibody to the surface of Au NCs functionalized with protein antigens.

Highly selective, colorimetric detection methods based on polynucleotide-modified gold particle probes have been also proposed (Fig. 5.20) [97]. Specifically, in the presence of 13-nm Au NCs, the color of the solution changes from red to blue, as a consequence of analyte-induced formation of Au NC aggregates in which the individual surface plasmon resonances are coupled. This simple phenomenon points to the use of metal NCs as DNA detection agents for nucleic acid targets. Actually, it has been found that spotting the solution onto a white support amplifies the colorimetric change and provides a permanent record for each test. Such system can detect about 10 fmol of oligonucleotides.

This type of colorimetric biosensor based on Au NCs has been extensively used in the analysis of biomolecules.

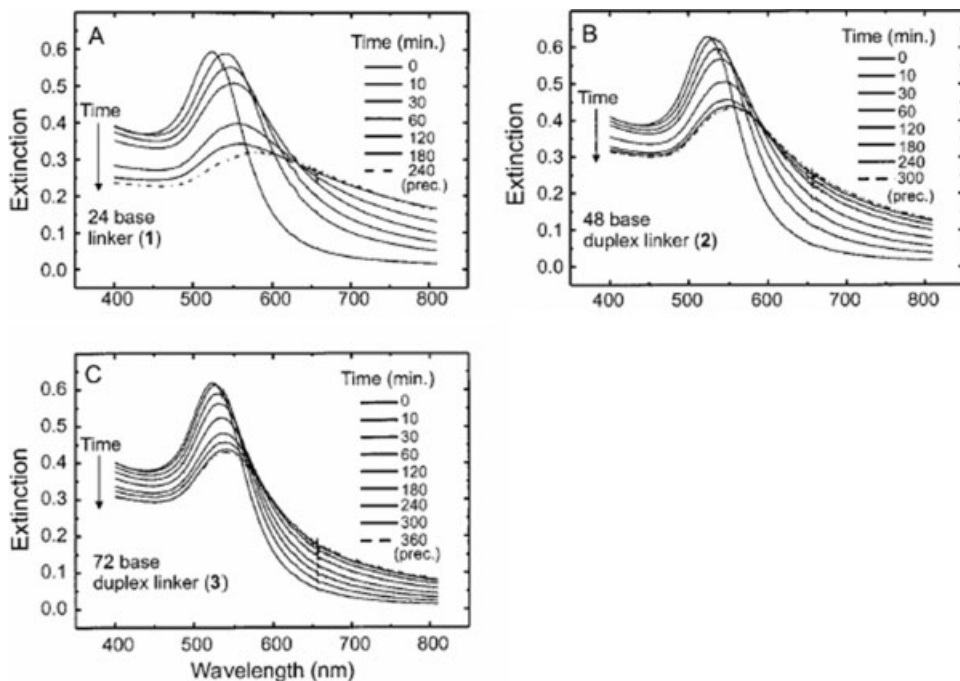


**Fig. 5.20.** Temporal changes in the UV/Vis spectra of nanoparticle aggregates grown from DNA linkers 1–3 (defined in parts A–C, respectively). The y-axes are labeled “extinction” since the larger aggregate structures will contain scattering as well as absorbance components. (From Ref. [97d].)

Gold NCs have been modified with an aptamer, which is specific to a defined growth factor, to allow monitoring of the change in color and extinction coefficient due to NC aggregation [44c]. The color of the aptamer-modified Au NCs significantly changes at low concentrations ( $<400$  nM), while only minor changes are detected at higher concentrations ( $>400$  nM). In addition, the ionic strength of the medium and the NC surface status surface are also important parameters in determining the ultimate sensitivity and specificity of the aptamer–nanoparticle-based probes. Efforts are now focused on the development of aptamer modified Au nanorods, to achieve further sensitivity enhancement. Special precautions must, however, be taken to prevent aspecific adsorption of biomolecules.

The performances of a label-free optical biosensor [98] have been tested in the real-time quantification of biomolecular interactions on a surface in a commercially available UV–visible spectrophotometer and in colorimetric end-point assays with an optical scanner. Such a sensor shows a concentration-dependent binding and a detection limit of 16 nM for streptavidin.

In this perspective, coupling the optical properties of noble metal colloids with improved bioconjugation protocols has the potential to provide excellent detection

capabilities. SPR has been widely used to monitor a broad range of analyte–surface binding reactions, including the adsorption of small molecules, ligand–receptor binding, protein adsorption on self-assembled monolayers, antibody–antigen binding, DNA and RNA hybridization, and protein–DNA interactions [99]. The SPR sensing mechanism relies on the measurement of small changes in refractive index that occur in response to analyte binding at or near the surface of a noble metal (Au, Ag, Cu) thin film. Chemosensors and biosensors based on SPR spectroscopy possess many desirable characteristics: (a) a refractive index sensitivity of the order of  $10^{-1}$  pg mm $^{-2}$ ; (b) a large sensing length scale ( $\sim 200$  nm) dictated by the exponential decay of the evanescent electromagnetic field; (c) multiple instrumental modes of detection (viz., angle shift, wavelength shift, and imaging); (d) real-time detection on the  $10^{-1}$ – $10^{-3}$  s time scale for measurement of binding kinetics; and (e) lateral spatial resolution of the order of  $10$   $\mu$ m allows for multiplexing and miniaturization, especially using the SPR imaging mode of detection [100]. Although SPR spectroscopy is an intrinsically nonselective sensor platform, a high degree of analyte selectivity can be conferred by means of attaching high specificity ligands to the surface and then passivating the sensor surface with non-specific binding molecules. Other practical advantages of SPR can be recognized, such as that of being label-free [101] useful for probing unpurified complex mixtures, such as clinical samples, easy to integrate with the available commercial instrumentation and with advanced microfluidic sample handling [100]. The development of large-scale biosensor arrays composed of highly miniaturized signal transducer elements that enable the real-time, parallel monitoring of multiple species is an important driving force in biosensor research.

Au NCs linked to bioreceptors provide labeled conjugates that can be used to follow the biorecognition event at a biosensor surface. Resonance enhancement of the absorption properties of nanosized metals binding to a surface by biorecognition interactions has also been used as an effective approach for biosensor devices [102]. Au nanoparticles have been extensively applied in bioaffinity binding events based on enhanced SPR. SPR biosensing has been improved dramatically in DNA immunosensing in the presence of Au NCs [103]. A sensor interface has been modified with antibody units, with the surface being functionalized with the complementary antigen component, and, finally, making this affinity assembly react with a secondary antibody labeled with Au NCs. The association of an antigen with its antibody-functionalized surface can be detected by SPR. However, the change in the SPR spectrum is larger if the secondary antibody is bound to the surface. The secondary antibody is, notably, not able to associate with the modified surface, unless the antigen is already bound there, thus providing an amplification route for the primary recognition event. Amplification is dramatically increased when the secondary antibody is labeled with gold. The binding of the Au NCs to the immunosensing interface leads to a large shift in plasmon angle, to a broadening of the plasmon resonance, and to an increase in the minimum reflectance, thereby allowing for picomolar detection of the antigen. Similarly, an enhancement in sensitivity by about 3 orders of magnitude has been obtained in DNA analysis when Au NC-functionalized DNA molecules have been used as probes [76].

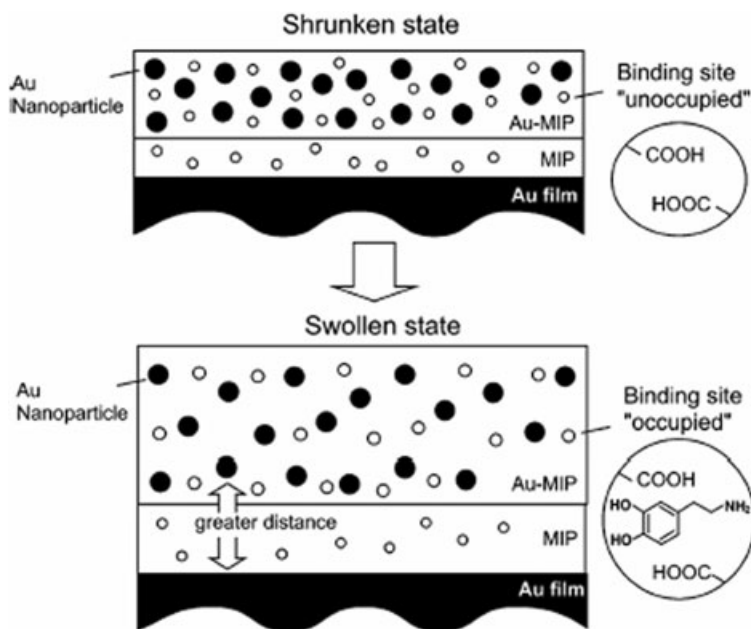


**Fig. 5.21.** Schematic representation of Au-MIP/MIP-coated SPR sensor chip for detection of an analyte, dopamine. (From Ref. [76].)

An SPR sensing device sensitive to a low molecular weight analyte has been fabricated starting from molecularly imprinted polymer gel with embedded Au NCs onto a gold substrate of a chip sensor. The sensing mechanism is based on swelling of the imprinted polymer gel that is triggered by an analyte binding event within the polymer gel (Fig. 5.21). The swelling increases the distance between the Au NCs and substrate, shifting the SPR resonance angle to higher values.

The modified sensor chip shows changes in the SPR angle in response to dopamine concentration, which agrees with the supposed sensing mechanism. The presence of Au NCs has been proven to be essential for enhancing the signal intensity. The analyte-binding process and the consequent swelling appears to be reversible, thus allowing re-use of the sensor chip.

There has been a recent explosion in the use of metallic nanostructures to favorably modify the spectral properties of fluorophores and to alleviate some of the photophysical constraints associated with these fluorophores. The use of fluorophore-metal interactions can lead to ultrabright over-labeled proteins, generating a new class of probes based on MEF proteins covalently labeled with fluorophores to be used as reagents, e.g., in immunoassays or for the immunostaining of biological specimens with specific antibodies. For these applications, the commonly used fluorescein is unfortunately self-quenching, thus resulting in a homo-

transfer process [68]. Self-quenching can be largely avoided by the close proximity to Ag islands [68]. Such a decrease in self-quenching has been ascribed to an increase in the rate of radiative decay. These results suggest the possibility of exploiting ultrabright labeled proteins based on high labeling ratios, and the release of self-quenching through metal enhanced fluorescence.

An approach has also been reported that should provide a readily measurable change in fluorescence intensity in DNA hybridization assays [104] due to the presence of Ag particles. This approach should ensure an intensity enhancement relative to the background with an increase in the number of detected photons per fluorophore molecule by a factor of ten or more. In the presence of thiolated oligonucleotide single-stranded DNA as the capturing sequence bound to Ag particles, an increase in the emission intensity has been observed upon addition of a single strand fluorescein-labeled DNA. This effect can be attributed to the localization of the fluorescein labeled DNA near to the particles by hybridization with the capturing DNA.

A metal-enhanced multiphoton excitation has also been studied. For multiphoton excitation of fluorescence, most of excitation occurs at the focal point of the excitation beam, where the local intensity is the highest. For a two-photon absorption process, the rate of excitation is proportional to the square of the incident intensity. This suggests that two-photon excitation can be greatly enhanced [69–105]. Such an enhancement in the excitation rate is expected to provide selective excitation of fluorophores near to metal islands of colloids, even if the solution contains a considerable concentration of other fluorophores that could undergo two-photon excitation at the same wavelength, but which are more distant from the metal surface. Recently, the enhanced and localized multiphoton excitation of fluorophores adjacent to metallic silver islands has been observed to be accompanied by a reduction in lifetime, as compared with that detected using one-photon excitation. At present, following the widespread use of multiphoton excitation in microscopy and medical imaging, the use of metallic nanostructures appears promising to both enhance and localize fluorescence.

Recent works have demonstrated the effectiveness of MEF in solution-based biosensing applications. Silica-coated Ag colloids can represent enhanced-fluorescence sensing platform as a three- to fivefold enhancement has been observed [106]. It has also been found that oligonucleotide-modified Ag particles and fluorophore-labeled complementary oligonucleotides can yield an increased emission from the fluorophore-labeled complementary oligonucleotide after hybridization, which could allow access to DNA detection based on the aggregation of metallic NCs binding to the fluorophore label [3b].

The unusual optical properties of noble metal NCs have been also used to design a label-free biosensor in a chip format. The NC size affects the sensitivity of the biosensor significantly. The sensor has been fabricated by making Au NCs chemisorbed nanoparticles on amine-functionalized glass. In the investigated size range (12–48 nm), sensors fabricated from 39-nm-diameter Au NCs exhibited the highest sensitivity to the change in the bulk refractive index as well as the largest “analyti-



cal volume”, defined as the region around the nanocrystal within which a change in refractive index induces a change in the optical properties of the immobilized NCs. The detection limit for streptavidin–biotin binding of a sensor fabricated from 39-nm diameter nanoparticles is 20× better than that of a sensor fabricated from 13-nm-diameter gold nanoparticles by another method [101].

Surface-enhanced Raman scattering (SERS) of substrates bound to nanoparticles allows molecular vibrational spectra to be amplified by a factor of  $10^5$  [107]. Although this technique has not been widely applied for detecting biorecognition events on surfaces, a cytochrome *c*–Au NC conjugate associated with silver surface has been revealed by a SERS spectrum [108].

The use of a versatile format based on gold nanoparticles-based microarray demonstrated high selectivity and sensitivity for protein binding and kinase functionality, indicating that the method is based on the fact that specific antibody–protein binding or peptide phosphorylation events can be marked by attaching gold nanoparticles and then depositing silver to enhance the signal. The detection principle is based on the resonance light scattering. The attachment of gold nanoparticles is achieved by standard avidin–biotin chemistry. The obtained results show that a low detection limit for protein binding has been achieved together with a large dynamic range. Similarly, for kinase functionality a high sensitivity has been reached [109]. Recently the SERS response of individual nanoscale pH sensors based on functionalized silver nanoparticles has been tested *in vitro* [110].

The 4-MBA-capped nanoparticles (4-MBA, 4-mercaptobenzoic acid, is a non-resonant molecule) have shown a pH-dependent response in a pH range relevant to biological systems, showing promise for application in intracellular chemical measurements (Fig. 5.22). The nanoparticle sensors can be incorporated into living cells while retaining their functionality and robust signal.

## 5.8

### Towards Marketing

Generally, the term “technological applications” strictly refers to scientific products that can be potentially put on the road towards markets. The combination of biology, material science, and modern optical techniques has certainly great potential in offering a new generation of devices able to solve biosensing problems in a sensitive, selective, fast and high-performance way. Nevertheless, present applications of nanocrystals in the biosensing field are still far from being recognized as commercializable.

Presently, in detection devices relying on chip-based biosensing, the capturing molecules on the chip surfaces are patterned on the microscale. A large parallel screening of diverse analytes can be thus achieved in a small area, which greatly facilitates simultaneous sensing. Further miniaturization in the form of nanoarrays would allow for orders of magnitude larger multiplexed detection, eventually improving detection limits due to the smaller analyte capture area. Several estab-

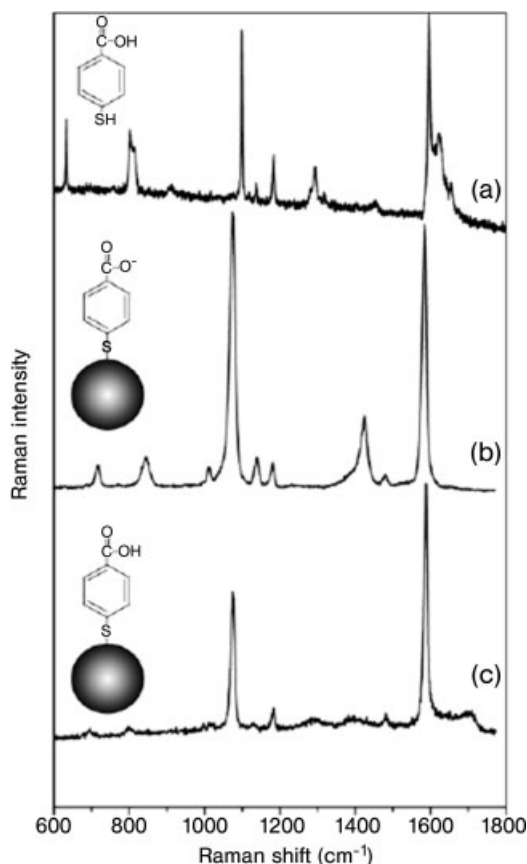


**Fig. 5.22.** Raman spectrum of solid 4-mercaptobenzoic acid (4-MBA) (a) and the SERS spectra of 4-MBA attached to silver nanoparticles at pH 12.3 (b) and at pH 5.0 (c). Insets to the left of each spectra illustrate the dominant state of the molecule under the conditions described. (From Ref. [110].)

lished techniques, as well as emerging technologies, such as dip-pen nanolithography, nanografting, and focused ion beam lithography are possible candidate tools to fabricate nanoscale patterns of biomolecules or hybrid systems.

Lithographic techniques can also be used to fabricate nanoscopic patterns or containers on surfaces that should significantly reduce the sample volume required and, possibly, lower detection limits even more. The development of such nanopatterning techniques can be expected to represent the next step that has to be made towards achieving further miniaturization [3b]. The commercial exploration of nanomaterials for biosensing deals also with the development, the production and the commercialization of nanocrystals suitably engineered. In this regard,

a large progress has been realized, as authenticated by the first related patents [111].

Industrial interest in this direction is indicated by the number of companies that have worked in synergy with academic institutions, where the seed ideas have been generated. Quantum size effects in semiconductor NCs for tagging biomolecules or the use of bio-conjugated noble metal nanoparticles to label and sense biomolecules or bio-related analytes are among the most explored application fields.

Other key issues for the progress of nanomaterial based biosensing are related to material toxicity and safety issues. The properties of colloidal NCs should be better exploited in *in vivo* biosensing devices. In this perspective, the issue of toxicity of the used nanosized material became crucial. The toxicity suspects of many semiconductor nanocrystals have recently alerted the scientific community, becoming also a societal topic of considerable importance and discussion. Indeed, *in vivo* toxicity is likely to be a key factor in determining whether nanoparticles would be approved by regulatory agencies as biosensing probes for clinical use on human beings. For example, a recent study [31c] indicates that CdSe NCs are highly toxic to cultured cells under UV illumination for extended periods of time. This is not surprising because the UV irradiation can break covalent chemical bonds and induce NC photodissolution, ultimately releasing toxic cadmium ions into the culture medium. In the dark, however, NCs protected by a polymer coating have been found to be essentially non-toxic to cells and animals, as no effects on cell division or ATP production have been ascertained. For polymer-encapsulated NCs, chemical or enzymatic degradation of the inorganic cores is unlikely.

Finally, possible toxicity problems associated with long-term exposure of technical human staff devoted to routine production, manipulation, and “*in vitro*” use of NCs for fundamental research purposes must be carefully considered [112].

## 5.9

### Conclusions

The potential of nanomaterial-based optical biosensing has been assessed by recent research developments and implemented into various novel and/or improved optical techniques, competing strongly with traditional methods. The merits of nanocrystals can be recognized in the breakthrough, compared with conventional assays, in terms of both selectivity and sensitivity. Optimization of the physical, chemical and fabrication parameters is necessary to ensure extension of these devices from experimental prototypes to large-scale industrial production.

Future design and engineering of biosensing devices able to detect analytes in complex matrices and environments will, essentially, need close interdisciplinary exchange and stimulating collaborations among material scientists, engineers, analytical, (bio)chemical and biomedical researchers. This can, hopefully, be expected to guarantee the realization of efficient sensors at relatively low cost for easy commercialization.

## References

- 1 (a) BARTL, M. H., BOETTCHER, S. W., FRINDELL, K. L., STUCKY, G. D., Molecular assembly of function in titania-based composite material systems, *Acc. Chem. Res.* **2005**, *38*, 263–271. (b) CAMINADE, A.-M., MAJORAL, J.-P., Nanomaterials based on phosphorus dendrimers, *Acc. Chem. Res.* **2004**, *37*, 341–348.
- 2 (a) SHIPWAY, A. N., KATZ, E., WILLNER, I., Nanoparticle arrays on surfaces for electronic, optical and sensor applications, *Chem. Phys. Chem.* **2000**, *1*, 18–52. (b) HUYNH, W. U., DITTMER, J., ALIVISATOS, A. P., Hybrid nanorod-polymer solar cells, *Science* **2002**, *295*, 2425–2427. (c) NARAYANAN, R., EL-SAYED, M. A., Catalysis with transition metal nanoparticles in colloidal solution: Nanoparticle shape dependence and stability, *J. Phys. Chem. B* **2005**, *109*, 12 663–12 676.
- 3 (a) ALIVISATOS, A. P., Colloidal quantum dots. From scaling laws to biological applications, *Pure Appl. Chem.* **2000**, *72*, 3–9. (b) ROSI, N. L., MIRKIN, C. A., Nanostructures in biodiagnostics, *Chem. Rev.* **2005**, *105*, 1547–1562. (c) HU, J., LI, L.-S., YANG, W., MANNA, L., WANG, L.-W., ALIVISATOS, A. P., Linearly polarized emission from colloidal semiconductor quantum rods, *Science* **2001**, *292*, 2060–2063. (d) BAKALOVA, R., OHBA, H., ZHELEV, Z., ISHIKAWA, M., BABA, Y., Quantum dots as photosensitizers?, *Nat. Biotechnol.* **2004**, *22*, 1360–1361.
- 4 (a) RAO, C. N. R., KULKARNI, G. U., THOMAS, P. J., EDWARDS, P. P., Size-dependent chemistry: Properties of nanocrystals, *Chem. Eur. J.* **2002**, *8*, 28–35. (b) KAMAT, P. V., Photophysical, photochemical and photocatalytic aspects of metal nanoparticles, *J. Phys. Chem. B* **2002**, *106*, 7729–7744. (c) EL-SAYED, M. A., *Acc. Chem. Res.* **2004**, *37*, 326–333. (d) EL-SAYED, M. A., *Acc. Chem. Res.* **2001**, *34*, 257–264.
- 5 (a) ALIVISATOS, A. P., Perspectives on the physical chemistry of semiconductor nanocrystals, *J. Phys. Chem.* **1996**, *100*, 13 226–13 239. (b) BUFFAT, P., BOREL, J. P., Size effect on the melting temperature of gold particles, *Phys. Rev. A* **1976**, *13*, 2287–2298. (c) PETERS, K. F., COHEN, J. B., CHUNG, Y. W., Melting of Pb nanocrystals, *Phys. Rev. B – Condensed Matter* **1998**, *57*, 13 430–13 438. (d) BESSON, J. M., ITIE, J. P., POLIAN, A., WEILL, G., MANSOT, J. L., Gonzalez, High-pressure phase transition and phase diagram of gallium arsenide, *Phys. Rev. B – Condensed Matter* **1991**, *44*, 4214–4234. (e) CHEN, C. C., HERHOLD, A. B., JOHNSON, C. S., ALIVISATOS, A. P., Dependence of structural metastability in semiconductor nanocrystals, *Science* **1997**, *276*, 398–401. (f) HERHOLD, A. B., CHEN, C. C., JOHNSON, C. S., TOLBERT, S. H., ALIVISATOS, A. P., KLEIN, D. L., BOWEN KATARI, J. E., ROTH, R. A., ALIVISATOS, P., MCEUEN P. L., A new approach to electrical studies of single nanocrystals, *Appl. Phys. Lett.* **1996**, *68*, 2574.
- 6 COMPARELLI, R., TAMBORRA, M., STRICCOLI, M., CURRI, M. L., AGOSTIANO A., unpublished results.
- 7 GAPONENKO, S. V., *Optical Properties of Semiconductor Nanocrystals*, Cambridge University Press, Cambridge, UK, **1998**.
- 8 COZZOLI, P. D., MANNA, L., CURRI, M. L., KUDERA, S., GIANNINI, C., STRICCOLI, M., AGOSTIANO, A., Shape and phase control of colloidal ZnSe nanocrystals, *Chem. Mater.* **2005**, *17*, 1296–1306.
- 9 (a) HODAK, J. H., HENGLEIN, A., HARTLAND, G. V., Photophysics and spectroscopy of metal particles, *Pure Appl. Chem.* **2000**, *72*, 189–197. (b) MULVANEY, P., Surface plasmon spectroscopy of nanosized metal particles, *Langmuir* **1996**, *12*, 788–800. (c) LINK, S., EL-SAYED, M. A., Spectral

- properties and relaxation dynamics of surface plasmon electronic oscillations in gold and silver nanodots and nanorods, *J. Phys. Chem. B* **1999**, *103*, 8410–8426. (d) LINK, S., EL-SAYED, M. A., Size and temperature dependence of the plasmon absorption of colloidal gold nanoparticles, *J. Phys. Chem. B* **1999**, *103*, 4212–4217.
- 10 MURPHY, C. J., SAU, C. J., GOLE, T. K., ORENDORFF, A. M., GAO, C. J., GOU, HUNYADI, J., LI, T., Anisotropic metal nanoparticles: Synthesis, assembly, and optical applications, *J. Phys. Chem. B* **2005**, *109*, 13 857–13 870.
- 11 COZZOLI, P. D., FANIZZA, E., CURRI, M. L., LAUB, D., AGOSTIANO, A., Low-dimensional chainlike assemblies of TiO<sub>2</sub> nanorod-stabilized Au nanoparticles, *Chem. Comm.* **2005**, 942–944.
- 12 COZZOLI, P. D., CURRI, M. L., AGOSTIANO, A., Efficient charge storage in photoexcited TiO<sub>2</sub> nanorod-noble metal nanoparticle composite systems, *Chem. Comm.* **2005**, 3186–3188.
- 13 (a) HENGLEIN, A., Small-particle research: Physicochemical properties of extremely small colloidal metal and semiconductor particles, *Chem. Rev.* **1989**, *89*, 1861–1873. (b) HENGLEIN, A., Physicochemical properties of small metal particles in solution: “Microelectrode” reactions, chemisorption, composite metal particles, and the atom-to-metal transition, *J. Phys. Chem.* **1993**, *97*, 5457–5471.
- 14 (a) ROTHLISBERGER, U., ANDREONI, W., PARRINELLO, M., Structure of nanoscale silicon clusters, *Phys. Rev. Lett.* **1994**, *72*, 665–668. (b) MURRAY, C. B., NORRIS, D. B., BAWENDI, M. G., Synthesis and characterization of nearly monodisperse CdE (E = sulfur, selenium, tellurium) semiconductor nanocrystallites, *J. Am. Chem. Soc.* **1993**, *115*, 8706–8715.
- 15 (a) IDRIS, H., PIERCE, K., BARTEAU, M. A., Carbonyl coupling on the titanium dioxide TiO<sub>2</sub>(001) surface, *J. Am. Chem. Soc.* **1991**, *113*, 715–716. (b) IDRIS, H., PIERCE, K., BARTEAU, M. A., Synthesis of stilbene from benzaldehyde by reductive coupling on TiO<sub>2</sub> (001) surfaces, *J. Am. Chem. Soc.* **1994**, *116*, 3063–3074. (c) LEWIS, L. N., Chemical catalysis by colloids and clusters, *Chem. Rev.* **1993**, *93*, 2693–2730. (d) SCHMID, G., Large clusters and colloids. Metals in the embryonic state, *Chem. Rev.* **1992**, *92*, 1709–1727. (e) GATES, B. C., Rotational currents as a measure of excited-state dipole moments, *Chem. Rev.* **1995**, *95*, 511–525. (f) MORENO-MANAS, M., PLEIXATS, R., Formation of carbon-carbon bonds under catalysis by transition-metal nanoparticles, *Acc. Chem. Res.* **2003**, *36*, 638–643. (g) ROUCOUX, A., SCHLUZ, J., PATIN, H., Reduced transition metal colloids: A novel family of reusable catalysts? *Chem. Rev.* **2002**, *102*, 3757–3778.
- 16 SHIOJIRI, S., HIRAI, T., KOMASAWA, I., *J. Chem. Eng. Jpn.* **1997**, *30*, 86. (b) LADE, M., MAYS, H., SCHMIDT, J., WILLUMEIT, R., SCHOMAKER, R., On the nanoparticle synthesis in microemulsions: Detailed characterization of an applied reaction mixture, *Colloids Surf. A* **2000**, *163*, 3–15.
- 17 LISIECKI, I., Size, shape and structural controls of metallic nanocrystals, *J. Phys. Chem. B* **2005**, *109*, 12 231–12 244.
- 18 (a) WONG, E. M., BONEVISH, J. E., SEARSON, P. C., Ultrafast studies of photoexcited electron dynamics in  $\gamma$ - and  $\alpha$ -Fe<sub>2</sub>O<sub>3</sub> semiconductor nanoparticles, *J. Phys. Chem. B* **1998**, *102*, 7770–7775. (b) CURRI, M. L., AGOSTIANO, A., MANNA, L., DELLA MONICA, M., CATALANO, M., CHIAVARONE, L., SPAGNOLO, V., LUGARA, M., Synthesis and characterization of CdS nanoclusters in a quaternary microemulsion: The role of the cosurfactant, *J. Phys. Chem. B* **2000**, *104*, 8391–8397. (c) ADAIR, J. H., LI, T., KIDO, T., HAVEY, K., MOON, J., MECHOLSKY, J., MORRONE, A., TALHAM, D. R., LUDWIG, M. H., WANG, L., Recent developments in the preparation and properties of nanometer-size spherical and platelet-shaped particles and composite particles, *Mater. Sci. Eng. R* **1998**, *23*, 139–242. (d) MACDOUGALL, J. E.,

- ECKERT, H., STUCKY, G. D., HERRON, N., WANG, Y., MOLLER, K., BEIN, T., COX, D., Synthesis and characterization of group III-V semiconductor clusters: Gallium phosphide GaP in zeolite Y, *J. Am. Chem. Soc.* **1989**, 111, 8006–8007.
- 19 (a) MANNA, L., SCHER, E. C., ALIVISATOS, A. P., Shape control of colloidal semiconductor nanocrystals, *J. Clusters Sci.* **2002**, 13, 521–532. (b) LEE, S.-M., CHO, S.-N., CHEON, J., Anisotropic shape control of colloidal inorganic nanocrystals, *Adv. Mater.* **2003**, 15, 441–444. (c) PENG, X., Green chemical approaches toward high-quality semiconductor nanocrystals, *Chem. Eur. J.* **2002**, 8, 334–339. (d) BURDA, C., CHEN, X., NARAYANAN, R., EL-SAYED, M. A., Chemistry and properties of nanocrystals of different shapes, *Chem. Rev.* **2005**, 105, 1025–1102.
- 20 YIN, Y., ALIVISATOS, A. P., Colloidal nanocrystal synthesis and the organic–inorganic interface, *Nature*, **2005**, 437, 664–670.
- 21 (a) MILLIRON, D. J., HUGHES, S. M., CUI, Y., MANNA, L., LI, J., WANG, L.-W., ALIVISATOS, A. P., Colloidal nanocrystal heterostructures with linear and branched topology, *Nature* **2004**, 430, 190–195. (b) SHIEH, F., SAUNDERS, A. E., KORGEL, B. A., General shape control of colloidal CdS, CdSe, CdTe quantum rods and quantum rod heterostructures, *J. Phys. Chem. B* **2005**, 109, 8538–8542. (c) COZZOLI, P. D., KORNOWSKI, A., WELLER, H., Low-temperature synthesis of soluble and processable organic-capped anatase TiO<sub>2</sub> nanorods, *J. Am. Chem. Soc.* **2003**, 125, 14 539–14 548.
- 22 (a) MOKARI, T., ROTHENBERG, E., POPOV, I., COSTI, R., BANIN, U., Selective growth of metal tips onto semiconductor quantum rods and tetrapods, *Science* **2004**, 304, 1787–1790. (b) KUDERA, S., CARBONE, L., CASULA, M. F., CINGOLANI, R., FALQUI, A., SNOECK, E., PARAK, W. J., MANNA, L., Selective growth of PbSe on one or both tips of colloidal semiconductor nanorods, *Nano Lett.* **2005**, 5, 445–449. (c) PACHOLSKI, C., KORNOWSKI, A., WELLER, H., *Angew. Chem.* **2004**, 116, 4878–4881; *Angew. Chem. Int. Ed. Engl.* **2004**, 43, 4774–4777.
- 23 (a) GU, H., YANG, Z., GAO, J., CHANG, C. K., XU, B., Heterodimers of nanoparticles: Formation at a liquid–liquid interface and particle-specific surface modification by functional molecules, *J. Am. Chem. Soc.* **2005**, 127, 34–35. (b) GU, H., ZHENG, R., ZHANG, X., XU, B., Facile one-pot synthesis of bifunctional heterodimers of nanoparticles: A conjugate of quantum dot and magnetic nanoparticles, *J. Am. Chem. Soc.* **2004**, 126, 5664–5665. (c) TERANISHI, T., INOUE, Y., NAKAYA, M., OUMI, Y., SANO, T., Nanoacorns: Anisotropically phase-segregated CoPd sulfide nanoparticles, *J. Am. Chem. Soc.* **2004**, 126, 9914–9915. (d) YU, H., CHEN, M., RICE, P. M., WANG, S. X., WHITE, R. L., SUN, S., Dumbbell-like bifunctional Au-Fe<sub>3</sub>O<sub>4</sub> nanoparticles, *Nano Lett.* **2005**, 5, 379–382. (e) GAO, X., YU, L., MACCUSPIE, R. I., MATSUI, H., Controlled growth of Se nanoparticles on Ag nanoparticles in different ratios, *Adv. Mater.* **2005**, 17, 426–429.
- 24 (a) COLVIN, V. L., SHLAMP, M. C., ALIVISATOS, A. P., Light-emitting diodes made from cadmium selenide nanocrystals and a semiconducting polymer, *Nature* **1994**, 370, 354–357. (b) DABBOUSI, B. O., BAWENDI, M. G., ONOTSUKA, O., RUBNER, M. F., Electroluminescence from CdSe quantum-dot/polymer composites, *Appl. Phys. Lett.* **1995**, 66, 1316–1318.
- 25 HUYNH, W. U., PENG, X., ALIVISATOS, A. P., CdSe nanocrystal rods/poly(3-hexylthiophene) composite photovoltaic devices, *Adv. Mater.* **1999**, 11, 923–927.
- 26 (a) BRUCHEZ, M. J., MORONNE, M., GIN, P., WEISS, S., ALIVISATOS, A. P., Semiconductor nanocrystals as fluorescent biological labels, *Science* **1998**, 281, 2013–2016. (b) CHAN, W. C. W., NIE, S., Quantum dot bioconjugates for ultrasensitive

- nonisotopic detection, *Science* **1998**, 281, 2016–2018.
- 27 (a) MIRKIN, C. A., LETSINGER, R. L., MUCIC, R. C., STORHOFF, J. J., A DNA-based method for rationally assembling nanoparticles into macroscopic materials, *Nature* **1996**, 382, 607–609. (b) LOWETH, C. J., CALDWELL, W. B., PENG, X. G., ALIVISATOS, A. P., DNA-based assembly of gold nanocrystals, *Angew. Chem. Int. Ed.* **1999**, 38, 1808–1812.
- 28 (a) ZANCHET, D., MICHEEL, C. M., PARAK, W. J., GERION, D., WILLIAMS, S. C., ALIVISATOS, A. P., Electrophoretic and structural studies of DNA-directed Au nanoparticle groupings, *J. Phys. Chem. B* **2002**, 106, 11 758–11 763. (b) SHENHAR, R., ROTELLO, V. M., Nanoparticles: Scaffolds and building blocks, *Acc. Chem. Res.* **2003**, 36, 549–561. (c) DUBERTRET, B., SKOURIDES, P., NORRIS, D. J., NOITREAU, V., BRIVANLOU, A. H., LIBCHABER, A., In vivo imaging of quantum dots encapsulated in phospholipid micelles, *Science* **2002**, 298, 1759–1762.
- 29 (a) MITCHELL, G. P., MIRKIN, C. A., LETSINGER, L. R., Programmed assembly of DNA functionalized quantum dots, *J. Am. Chem. Soc.* **1999**, 121, 8122–8123. (b) ROSENTHAL S. J., Bar-coding biomolecules with fluorescent nanocrystals, *Nat. Biotechnol.* **2001**, 19, 621–622. (c) HAN, M., GAO, X., SU, Z. J., NIE, S., Quantum-dot-tagged microbeads for multiplexed optical coding of biomolecules, *Nat. Biotechnol.* **2001**, 19, 631–635. (d) MICHALET, X., PINAUD, F. F., BENTOLILA, L. A., TSAY, J. M., DOOSE, S., LI, J. J., SUNDARESAN, S. G., WU, A. M., GAMBHIR, S. S., WEISS, S., Quantum dots for live cells, In Vivo Imag. Diagnostics, *Science* **2005**, 307, 538–544.
- 30 (a) GOLDMAN, E. R., BALIGHIAN, E. D., MATTOUSSI, H., KUNO, K. M., MAURO, J. M., TRAN, P. T., ANDERSON, G. P., Avidin: A natural bridge for quantum dot-antibody conjugates, *J. Am. Chem. Soc.* **2002**, 124, 6378–6382. (b) GOLDMAN, E. R., ANDERSON, G. P., TRAN, P. T., MATTOUSSI, H., CHARLES, P. T., MAURO, J. M., Conjugation of luminescent quantum dots with antibodies using an engineered adaptor protein to provide new reagents for fluoroimmunoassays, *Anal. Chem.* **2002**, 74, 841–847. (c) WANG, Z., LEE, J., COSSINS, A. R., BRUST, M., Microarray-based detection of protein binding and functionality by gold nanoparticle probes, *Anal. Chem.* **2005**, 77, 5770–5774.
- 31 (a) JAISWAL, J. K., MATTOUSSI, H., MAURO, J. M., SIMON, S. M., Long-term multiple color imaging of live cells using quantum dot bioconjugates, *Nat. Biotechnol.* **2003**, 21, 47–51. (b) FAN, H., LEVE, E. H., SCULLIN, C., GABALDON, J., TALLANT, D., BUNGE, S., BOYLE, T., WILSON, M. C., BRINKER, C. J., Surfactant-assisted synthesis of water-soluble and biocompatible semiconductor quantum dot micelles, *Nano Lett.* **2005**, 5, 645–648. (c) GAO, X., YANG, L., PETROS, J. A., MARSHALL, F. F., SIMONS, J. W., NIE, S., In vivo molecular and cellular imaging with quantum dots, *Curr. Opin. Biotechnol.* **2005**, 16, 63–72.
- 32 MEZIANI, M. J., PATHAK, P., HARRUFF, B. A., HUREZEANU, R., SUN, Y. P., Direct conjugation of semiconductor nanoparticles with proteins, *Langmuir* **2005**, 21, 2008–2011.
- 33 BAILEY, R. E., NIE, S., in *The Chemistry of Nanomaterials: Synthesis, Properties and Applications*, Ed. C. N. R. RAO, A. MULLER, A. K. CHEETNAM, Wiley-VCH Verlag, Weinheim, **2004**, pp. 405–417.
- 34 PATHAK, S., CHOI, S. K., ARNHEIM, N., THOMPSON, M. E., Hydroxylated quantum dots as luminescent probes for in situ hybridization, *J. Am. Chem. Soc.* **2001**, 123, 4103–4104.
- 35 (a) SUTHERLAND, A. J., Quantum dots as luminescent probes in biological systems, *Curr. Opin. Solid State Mater. Sci.* **2002**, 6, 365–370. (b) MEDINTZ, I. G., UYEDA, H. T., GOLDMAN, E. R., MATTOUSSI, H., Quantum dot bioconjugates for imaging, labelling and sensing, *Nat. Biotechnol.* **2005**, 4, 435–446.

- 36 (a) MATTOUSSI, H., MAURO, J. M., GOLDMAN, E. R., ANDERSON, G. P., SUNDAR, V. C., MIKULEC, F. V., BAWENDI, M. G., Self-assembly of CdSe-ZnS quantum dot bioconjugates using an engineered recombinant protein, *J. Am. Chem. Soc.* **2000**, *122*, 12 142–12 150. (b) TRAN, P. T., GOLDMAN, E. R., ANDERSON, G. P., MAURO, J. M., MATTOUSSI, H., Use of luminescent CdSe-ZnS nanocrystal bioconjugate in quantum dot based nanosensor, *Phys. Stat. Sol.* **2002**, *229*, 427–432.
- 37 PARAK, W. J., GERION, D., PELLEGRINO, T., ZANCHET, D., MICHEEL, C., WILLIAMS, S. C., BOUDREAU, R., LE GROS, M. A., LARABELL, C. A., ALIVISATOS, A. P., Biological applications of colloidal nanocrystals, *Nanotechnology* **2003**, *14*, R15–R27.
- 38 UYEDA, H. T., MEDINTZ, I. L., JAISWAL, J. K. SIMON, S. M., MATTOUSSI, H., Synthesis of compact multidentate ligands to prepare stable hydrophilic quantum dot fluorophores, *J. Am. Chem. Soc.* **2005**, *127*, 3870–3878.
- 39 WILLARD, D. M., CARILLO, L. L., JUNG, J., VAN ORDEN, A., CdSe-ZnS quantum dots as resonance energy transfer donors in a model protein-protein binding assay, *Nano Lett.* **2001**, *1*, 469–474.
- 40 SHENTON, W., DAVIS, S. A., MANN, S., Direct self-assembly of nanoparticles into macroscopic materials using antibody-antigen recognition, *Adv. Mater.* **1999**, *11*, 449–452.
- 41 ROSENTHAL, S. J., TOMLINSON, I., ADKINS, E. M., SCHROETER, E. M., ADAMS, S., SWAFFORD, L., MCBRIDE, J., WANG, J. DEFELICE, L. J., BLAKELY, R. D., Targeting cell surface receptors with ligand-conjugated nanocrystals, *J. Am. Chem. Soc.* **2002**, *124*, 4586–4594.
- 42 PINAUD, F., KING, D., MOORE, H.-P., WEISS, S., Bioactivation and cell targeting of semiconductor CdSe/ZnS nanocrystals with phytochelatin-related peptides, *J. Am. Chem. Soc.* **2004**, *126*, 6115–6123.
- 43 GESTWICKI, J. E., STRONG, L. E., KIESSLING, L. L., Visualization of single multivalent receptor-ligand complexes by transmission electron microscopy, *Angew. Chem. Int. Ed.* **2000**, *39*, 4567–4570.
- 44 (a) PARK, S. J., LAZARIDES, A. A., MIRKIN, C. A., BRAZIS, P. W., KANNEWURF, C. R., LETSINGER, R. L., The electrical properties of gold nanoparticle assemblies linked by DNA, *Angew. Chem.* **2000**, *112*, 4003–4006. (b) BARDEA, A., DAGAN, A., BEN-DOV, I., AMIT, B., WILLNER, I., Amplified microgravimetric quartz-crystal-microbalance analyses of oligonucleotide complexes: A route to a Tay-Sachs biosensor device, *Chem. Commun.* **1998**, 839–840. (c) PATOLSKY, F., RANJIT, K. T., LICHTENSTEIN, A., WILLNER, I., Dendritic amplification of DNA analysis by oligonucleotide-functionalized Au-nanoparticles, *Chem. Commun.*, **2000**, 1025–1026. (d) HUANG, C. C., HUANG, Y. F., CAO, Z., TAN, W., CHANG, H. T., Aptamer-modified gold nanoparticles for colorimetric determination of platelet-derived growth factors and their receptors, *Anal. Chem.* **2005**, *77*, 5735–5741. (e) BREWER, S. H., GLOMM, W. R., JOHNSON, M. C., KNAG, M. K., FRANZEN, S., Probing BSA binding to citrate-coated gold nanoparticles and surfaces, *Langmuir* **2005**, *21*, 9303–9307.
- 45 (a) ELECHIGUERRA, J. L., BURT, J. L., MORONES, J. R., CAMACHO-BRAGADO, A., GAO, X., LARA, H. H., YACAMAN, M. J., Interaction of silver nanoparticles with HIV-1, *J. Nanobiotechnol.* **2005**, *3*, 6. (b) MACDONALD, I. D. G., SMITH, W. E., Orientation of cytochrome *c* adsorbed on a citrate-reduced silver colloid surface, *Langmuir* **1996**, *12*, 706–713.
- 46 (a) MAHTAB, R., ROGERS, J. P., MURPHY, C. J., Protein-sized quantum dot luminescence can distinguish between “straight”, “bent”, and “kinked” oligonucleotides, *J. Am. Chem. Soc.* **1995**, *117*, 9099–9100. (b) MAHTAB, R., ROGERS, J. P., SINGLETON, C. P., MURPHY, C. J., Preferential adsorption of a “kinked”



- DNA to a neutral curved surface: Comparisons to and implications for nonspecific DNA-protein interactions, *J. Am. Chem. Soc.* **1996**, *118*, 7028–7032. (c) MAHTAB, R., HARDEN, H. H., MURPHY, C. J., Temperature- and salt-dependent binding of long DNA to protein-sized quantum dots: Thermodynamics of “inorganic protein”-DNA interactions, *J. Am. Chem. Soc.* **2000**, *122*, 14–17.
- 47 WANG, Y. A., LI, J. J., CHEN, H., PENG, X., Stabilization of inorganic nanocrystals by organic dendrons, *J. Am. Chem. Soc.* **2002**, *124*, 2293–2298.
- 48 (a) GERION, D., PINAUD, F., WILLIAMS, S. C., PARAK, W. J., ZANCHET, D., WEISS, S., ALIVISATOS, A. P., Synthesis and properties of biocompatible water-soluble silica-coated CdSe/ZnS semiconductor quantum dots, *J. Phys. Chem. B* **2001**, *105*, 8861–8871. (b) CORREA-DUARTE, M. A., GIERSIG, M., LIZ-MARZAN, L. M., Stabilization of CdS semiconductor nanoparticles against photodegradation by a silica coating procedure, *Chem. Phys. Lett.* **1998**, *286*, 497–501. (c) YANG, Y., GAO, M., Preparation of fluorescent SiO<sub>2</sub> particles with single CdTe nanocrystal cores by the reverse microemulsion method, *Adv. Mater.* **2005**, *17*, 2354–2357.
- 49 PARAK, W. J., PELLEGRINO, T., PLANK, C., Labelling of cells with quantum dots, *Nanotechnology* **2005**, *16*, R9–R25.
- 50 (a) PARAK, W. J., GERION, D., ZANCHET, D., WOERZ, A. S., PELLEGRINO, T., MICHEEL, C., WILLIAMS, S. C., SEITZ, M., BRUEHL, R. E., BRYANT, Z., BUSTAMANTE, C., BERTOZZI, C. R., ALIVISATOS, A. P., Conjugation of DNA to silanized colloidal semiconductor nanocrystalline quantum dots, *Chem. Mater.* **2002**, *14*, 2113–2119. (b) KIRCHNER, C., LIEDL, T., KUDERA, S., PELLEGRINO, T., MUNOZ JAVIER, A., GAUB, H. E., STOLZLE, S., FERTIG, N., PARAK, W. J., Cytotoxicity of colloidal CdSe and CdSe/ZnS nanoparticles, *Nano Lett.* **2005**, *5*, 331–338.
- 51 DEPALO, N., MALLARDI, A., FANIZZA, E., COMPARELLI, R., STRICCOLI, M., CURRI, M. L., AGOSTIANO, A., unpublished results.
- 52 (a) WU, X., LIU, H., LIU, J., HALEY, K. N., TREADWAY, J. A., LARSON, J. P., GE, N., PEALE, F., BRUCHEZ, M. P., Immunofluorescent labelling of cancer marker Her2 and other cellular targets with semiconductor quantum dots, *Nat. Biotechnol.* **2003**, *21*, 41–46. (b) GAO, X., CUI, Y., LEVENSON, R. M., CHUNG, L. W. K., NIE, S., In vivo cancer targeting and imaging with semiconductor quantum dots, *Nat. Biotechnol.* **2004**, *22*, 969–976. (c) PELLEGRINO, T., MANNA, L., KUDERA, S., LIEDL, T., KOKTYSH, D., ROGACH, A. L., KELLER, S., RADLER, J., NATILE, G., PARAK, W. J., Hydrophobic nanocrystals coated with an amphiphilic polymer shell: A general route to water soluble nanocrystals, *Nano Lett.* **2004**, *4*, 703–707.
- 53 (a) WANG, Y., WONG, J. F., TENG, X., LIN, X. Z., YANG, H., “Pulling” nanoparticles into water: Phase transfer of oleic acid stabilized monodisperse nanoparticles into aqueous solutions of  $\alpha$ -cyclodextrin, *Nano Lett.* **2003**, *3*, 1555–1559. (b) DEPALO, N., COMPARELLI, R., CURRI, M. L., STRICCOLI, M., AGOSTIANO, A., Cyclodextrin mediated phase transfer in water of organic capped CdS nanocrystals, *Synth. Met.* **2005**, *148*, 43–46. (c) DEPALO, N., COMPARELLI, R., STRICCOLI, M., CURRI, M. L., CATUCCI, L., AGOSTIANO, A., Water phase transfer of oleic capped semiconductor nanocrystals mediated by  $\alpha$ -cyclodextrins, *Proc. SPIE*, **2005**, vol. 5838, 245–251, Nanotechnology II, ed. PAOLO LUGLI. (d) HOU, Y., KONDOH, H., SHIMOJO, M., SAKO, E. O., OZAKI, N., KOGURE, T., OHTA, T., Inorganic nanocrystal self-assembly via the inclusion interaction of  $\alpha$ -cyclodextrins: Toward 3d spherical magnetite, *J. Phys. Chem. B* **2005**, *109*, 4845–4852.
- 54 DEL VALLE, E. M. M., Cyclodextrins and their uses: A review, *Process*

- Biochem.* **2004**, *39*, 1033–1046 and references therein.
- 55 (a) BONACCHI, D., CANESCHI, A., GATTESCHI, D., SANGREGORIO, C., SESSOLI, R., FALQUI, A., Synthesis and characterisation of metal oxides nanoparticles entrapped in cyclodextrin, *J. Phys. Chem. Solids* **2004**, *65*, 719–722. (b) MAHALINGAM, V., ONCLIN, S., PETER, M., RAVOO, B. J., HUSKENS, J., REINHOUDT, D. N., Directed self-assembly of functionalized silica nanoparticles on molecular printboards through multivalent supramolecular interactions, *Langmuir* **2004**, *20*, 11756–11762. (c) CRESPO-BIEL, O., DORDI, B., REINHOUDT, D. N., HUSKENS, J., Supramolecular layer-by-layer assembly: Alternating adsorptions of guest- and host-functionalized molecules and particles using multivalent supramolecular interactions, *J. Am. Chem. Soc.* **2005**, *127*, 7594–7600. (d) FENG, J., MIEDANER, A., AHRENKIEL, P., HIMMEL, M. E., CURTIS, C., GINLEY, D., Self-assembly of photoactive TiO<sub>2</sub>-cyclodextrin wires, *J. Am. Chem. Soc.* **2005**, *127*, 14968–14969. (e) FENG, J., DING, S. Y., TUCKER, M. P., HIMMEL, M. E., KIM, Y. H., ZHANG, S. B., KEYES, B. M., RUMBLES, G., Cyclodextrin driven hydrophobic/hydrophilic transformation of semiconductor nanoparticles, *Appl. Phys. Lett.* **2005**, *86*, 33108–33111.
- 56 SHI, J., ZHU, Y., ZHANG, X., BAYENS, W. P. G., GARCIA-COMPAN, A. M., Recent developments in nanomaterial optical sensors, *Trends Anal. Chem.* **2004**, *23*, 351–360.
- 57 FRITZSCHE, W., TATON, T. A., Metal nanoparticles as labels for heterogeneous, chip-based DNA detection, *Nanotechnology* **2003**, *14*, R63–R73.
- 58 (a) YGUERABIDE, J., YGUERABIDE, E. E., Light-scattering submicroscopic particles as highly fluorescent analogs and their use as tracer labels in clinical and biological applications. I. Theory, *Anal. Biochem.* **1998**, *262*, 137–156. (b) KREIBIG, U., VOLLMER, M., *Optical Properties of Metal Clusters*, Springer, Berlin, **1995**.
- 59 (a) MIE, G. Beitrage zur optik trueber medien, speziell-kolloidaler metalosungen, *Ann. Phys.* **1908**, *25*, 377–445. (b) KELLY, K. L., CORONADO, E., ZHAO, L. L., SCHATZ, G. C., The optical properties of metal nanoparticles: the influence of size, shape, and dielectric environment, *J. Phys. Chem. B* **2003**, *107*, 668–677.
- 60 KANARAS, A. G., WANG, Z., BATES, A. D., COSSTICK, R., BRUST, M., Towards multistep nanostructure synthesis: Programmed enzymatic self-assembly of DNA/gold systems, *Angew. Chem.* **2003**, *115*, 201–204.
- 61 JARES-ERYMAN, E. A., JOHN, T. M., FRET imaging, *Nat. Biotechnol.* **2003**, *21*, 1387–1395.
- 62 SELVIN, P. R., The renaissance of fluorescence resonance energy transfer, *Nat. Struct. Biol.* **2000**, *7*, 730–734.
- 63 ZHANG, Y., YEH, H. C., KUROKI, M. T., WANG, T. H., Single-quantum-dot-based DNA nanosensor, *Nat. Mater.* **2005**, *4*, 826–831.
- 64 BEWERSDORF, J., PICK, R., HELL, S. W., Multifocal multiphoton microscopy, *Opt. Lett.* **1998**, *23*, 655–657.
- 65 DAHAN, M., LAURENCE, T., PINAUD, F., CHEMLA, D. S., ALIVISATOS, A. P., SAUER, M., WEISS, S., Time-gated biological imaging by use of colloidal quantum dots, *Opt. Lett.* **2001**, *26*, 825–827.
- 66 WEISSLEDER, R., A clearer vision for in vivo imaging, *Nat. Biotechnol.*, **2001**, *19*, 316–317.
- 67 LARSON, D. R., ZIPFEL, W. R., WILLIAMS, R. M., CLARK, S. W., BRUCHEZ, M. P., WISE, F. W., WEBB, W. W., Water soluble quantum dots for multiphoton fluorescence imaging in vivo, *Science* **2003**, *300*, 1434–1436.
- 68 ASLAN, K., GRZYCZYNSKI, I., MALICKA, J., MATVEEVA, E., LAKOWICZ, J. R., GEDDES, C. D., Metal-enhanced fluorescence: An emerging tool in biotechnology, *Curr. Opin. Biotechnol.* **2005**, *16*, 55–62.
- 69 GEDDES, C. D., LAKOWICZ, J. R., Metal enhanced fluorescence, *J. Fluoresc.* **2002**, *12*, 121–129.

- 70 WEITZ, D. A., GAROFF, S., GERSTEN, J. I., NITZAN, A., The enhancement of Raman scattering, resonance Raman scattering and fluorescence from molecules adsorbed on a rough silver surface, *J. Chem. Phys.* **1983**, *78*, 5324–5338.
- 71 KITSON, S. C., BARNES, W. L., SAMBLES, J. R., Photoluminescence from dye molecules on silver gratings, *Opt. Commun.*, **1996**, *122*, 147–154.
- 72 (a) LAKOWICZ, J. R., Radiative decay engineering: Biophysical and biomedical applications, *Anal. Biochem.*, **2001**, *298*, 1–24. (b) LAKOWICZ, J. R., SHEN, Y., D'AURIA, S., MALICKA, J., FANG, J., GRZYCZYNSKI, Z., GRZYCZYNSKI, I., Radiative decay engineering 2. Effects of silver island films on fluorescence intensity, lifetimes, and resonance energy transfer, *Anal. Biochem.* **2002**, *301*, 261–277.
- 73 RAETHER, H., *Surface Plasmons*, Springer-Verlag, Berlin, **1988**.
- 74 (a) HOMOLA, J., YEE, S. S., GAUGLITZ, G., Surface plasmon resonance sensors: Review, *Sens. Actuators B-Chem.*, **1999**, *54*, 3–15. (b) CULLEN, D. C., LOWE, R., A direct surface plasmon-polariton immunosensor: Preliminary investigation of the non-specific adsorption of serum components to the sensor interface, *Sens. Actuators B-Chem.* **1990**, *1*, 576–579.
- 75 JUNG, L. S., JUNG, L. S., CAMPBELL, C. T., CHINOWSKY, T. M., MAR, M. N., YEE, S. S., Quantitative interpretation of the response of surface plasmon resonance sensors to adsorbed films, *Langmuir* **1998**, *14*, 5636–5648.
- 76 MATSUI, J., AKAMATSU, K., HARA, N., MIYOSHI, D., NAWAFUNE, H., TAMAKI, K., SUGIMOTO, N., SPR sensor chip for detection of small molecules using molecularly imprinted polymer with embedded gold nanoparticles, *Anal. Chem.* **2005**, *77*, 4282–4285.
- 77 (a) KNEIPP, K., KNEIPP, H., ITZKAN, I., DASAR, R. R., FELD, M. S., Ultra-sensitive chemical analysis by Raman spectroscopy, *Chem. Rev.* **1999**, *99*, 2957–2975. (b) LECOMTE, S., WACKERBART, H., SOULIMANE, T., BUSE, G., HILDEBRANDT, P., Time-resolved surface-enhanced resonance Raman spectroscopy for studying electron-transfer dynamics of heme proteins, *J. Am. Chem. Soc.* **1998**, *120*, 7381–7382.
- 78 KAMBHAMPATI, P., CHILD, C. M., FOSTER, M. C., CAMPION, A., On the chemical mechanism of surface enhanced Raman scattering: Experiment and theory, *J. Chem. Phys.*, **1998**, *108*, 5013–5026.
- 79 WEAVER, M. J., ZOU, S., CHAN, H. Y. H., The new interfacial ubiquity of surface-enhanced Raman spectroscopy, *Anal. Chem.* **2000**, *72*, 38A–47A.
- 80 JENSEN, T. R., MALINSKY, M. D., HAYNES, C. L., VAN DUYN, R. P., Nanosphere lithography: Tunable localized surface plasmon resonance spectra of silver nanoparticles, *J. Phys. Chem. B* **2000**, *104*, 10 549–10 556.
- 81 MOSKOVITS, M., Surface-enhanced spectroscopy, *Rev. Mod. Phys.* **1985**, *57*, 783–826.
- 82 EMORY, S. R., HASKINS, W. E., NIE, S., Direct observation of size-dependent optical enhancement in single metal nanoparticles, *J. Am. Chem. Soc.* **1998**, *120*, 8009–8010.
- 83 CAMPION, A., KAMBHAMPATI, P., Surface-enhanced Raman scattering, *Chem. Soc. Rev.* **1998**, *27*, 241–250.
- 84 ZOU, S., WILLIAMS, C. T., CHEN, E. K.-Y., WEAVER, M. J., Surface-enhanced Raman scattering as a ubiquitous vibrational probe of transition-metal interfaces: Benzene and related chemisorbates on palladium and rhodium in aqueous solution, *J. Phys. Chem. B* **1998**, *102*, 9039–9049.
- 85 TIAN, Z. Q., REN, B., WU, D. Y. Surface-enhanced Raman scattering: From noble to transition metals and from rough surfaces to ordered nanostructures, *J. Phys. Chem. B* **2002**, *106*, 9463–9483.
- 86 (a) MCFARLAND, A. D., VAN DUYN, R. P., Single silver nanoparticles as real-time optical sensors with zeptomole sensitivity, *Nano Lett.* **2003**,

- 3, 1057–1062. (b) PRIIKULIS, J., SVEDBERG, F., KÄLL, M., ENGER, J., RAMSER, K., GOKSÖR, M., HANSTORP, D., Optical spectroscopy of single trapped metal nanoparticles in solution, *Nano Lett.* **2004**, *4*, 115–118.
- 87 ALIVISATOS, A. P., The use of nanocrystals in biological detection, *Nat. Biotechnol.* **2004**, *22*, 47–52.
- 88 WEST, J. W., HALAS, N. J., Engineered nanomaterials for biophotonics applications: Improving sensing, imaging, and therapeutics, *Annu. Rev. Biomed. Eng.* **2003**, *5*, 285–292.
- 89 HINES, M. A., SCHOLLES, G. D., Colloidal PbS nanocrystals with size-tunable near-infrared emission: Observation of post-synthesis self-narrowing of the particle size distribution, *Adv. Mater.* **2003**, *15*, 1844–1849.
- 90 KIM, S., LIM, Y. T., SOLTESZ, E. G., DE GRAND, A. M., LEE, J., NAKAYAMA, A., PARKER, J. A., MIHALJEVIC, T., LAURENCE, R. G., DOR, D. M., COHN, L. H., BAWENDI, M. G., FRANGIONI, J. V., Near-infrared fluorescent type II quantum dots for sentinel lymph node mapping, *Nat. Biotechnol.* **2004**, *22*, 93–97.
- 91 NIEMEYER, C. M., Nanoparticles, proteins, and nucleic acids: Biotechnology meets materials science, *Angew. Chem. Int. Ed.* **2001**, *40*, 4128–4158.
- 92 CHEN, Q., MA, Q., WAN, Y., SU, X., LIN, Z., JIN, Q., *Luminescence* **2005**, *20*, 251–255.
- 93 CLAPP, A. R., MEDINTZ, I. L., MAURO, J. M., FISHER, B. R., BAWENDI, M. G., MATTOUSSI, H., Fluorescence resonance energy transfer between quantum dot donors and dye labeled protein acceptors, *J. Am. Chem. Soc.* **2004**, *126*, 301–310.
- 94 MEDINTZ, I. L., CLAPP, A. R., MATTOUSSI, H., GOLDMANN, E. R., FISHER, B., MAURO, J. M., Self-assembled nanoscale biosensors based on quantum dot FRET donors, *Nat. Mater.* **2003**, *2*, 630–638.
- 95 REICHERT, J., CSAKI, A., KOHLER, J. M., FRITZSCHE, W., Chip-based optical detection of DNA hybridization by means of nanobead labeling, *Anal. Chem.* **2000**, *72*, 6025–6029.
- 96 ENGLEBIENNE, P., Use of colloidal gold surface plasmon resonance peak shift to infer affinity constants from the interactions between protein antigens and antibodies specific for single or multiple epitopes, *Analyst* **1998**, *123*, 1599–1603.
- 97 (a) ELGHANIAN, R., STORHOFF, J. J., MUCIC, R. C., LETSINGER, R. L., MIRKIN, C. A., Selective colorimetric detection of polynucleotides based on the distance-dependent optical properties of gold nanoparticles, *Science* **1997**, *277*, 1078–1081. (b) STORHOFF, J. J., ELGHANIAN, R., MUCIC, R. C., MIRKIN, C. A., LETSINGER, R. L., One-pot colorimetric differentiation of polynucleotides with single base imperfections using gold nanoparticle probes, *J. Am. Chem. Soc.* **1998**, *120*, 1959–1964. (c) REYNOLDS, R. A., MIRKIN, C. A., LETSINGER, R. L., Homogeneous, nanoparticle-based quantitative colorimetric detection of oligonucleotides, *J. Am. Chem. Soc.* **2000**, *122*, 3795–3796. (d) STORHOFF, J. J., LAZARIDES, A. A., MUCIC, R. C., MIRKIN, C. A., LETSINGER, R. L., SCHATZ, G. C., What controls the optical properties of DNA-linked gold nanoparticle assemblies? *J. Am. Chem. Soc.* **2000**, *122*, 4640–4650.
- 98 NATH, N., CHILKOTI, A., A colorimetric colloidal gold sensor to interrogate biomolecular interactions in real-time on a surface, *Anal. Chem.* **2002**, *74*, 504–509.
- 99 HUTTER, E., FENDLER, J. H., ROY, D., Surface plasmon resonance studies of gold and silver nanoparticles linked to gold and silver substrates by 2-aminoethanethiol and 1,6-hexanedithiol, *J. Phys. Chem. B* **2001**, *105*, 11 159–11 168.
- 100 HAES, A. J., VAN DUYN, R. P., A nanoscale optical biosensor: Sensitivity and selectivity of an approach based on the localized surface plasmon resonance spectroscopy of triangular silver nanoparticles, *J. Am. Chem. Soc.* **2002**, *124*, 10 596–10 604.

- 101 NATH, N., CHILKOTI, A., Label-free biosensing by surface plasmon resonance of nanoparticles on glass: Optimization of nanoparticle size, *Anal. Chem.* **2004**, 76, 5370–5378.
- 102 MU, Y., ZHANG, H., ZHAO, X., SONG, D., WANG, Z., SUN, J., LI, M., Q. JIN, Q., An optical biosensor for monitoring antigen recognition based on surface plasmon resonance using avidin-biotin system, *Sensors* **2001**, 1, 91–101.
- 103 SARKAR, D., SOMASUNDARAN, P., Overcoming contamination in surface plasmon resonance spectroscopy, *Langmuir* **2002**, 18, 8271–8277.
- 104 MALICKA, J., GRZYCZYNSKI, I., LAKOWICZ, J. R., DNA hybridization assays using metal-enhanced fluorescence, *Biochem. Biophys. Res. Commun.* **2003**, 306, 213–218.
- 105 MALIWAL, B. P., MALICKA, J., GRZYCZYNSKI, I., GRZYCZYNSKI, Z., LAKOWICZ, J. R., Fluorescence properties of labeled proteins near silver colloid surfaces, *Biopolymers* **2003**, 70, 585–594.
- 106 NIE, S., EMORY, R., Probing single molecules and single nanoparticles by surface-enhanced Raman scattering, *Science* **1997**, 275, 1102–1106.
- 107 STUART, D. A., HAES, A. J., YONZON, C. R., HICKS, E. M., VAN DUYN, R. P., Biological applications of localised surface plasmonic phenomena, *IEE Proc.-Nanobiotechnol.* **2005**, 152, 13–32.
- 108 KEATING, C. D., KOVALESKI, K. K., NATAN, M. J., Heightened electromagnetic fields between metal nanoparticles: Surface enhanced Raman scattering from metal-cytochrome *c*-metal sandwiches, *J. Phys. Chem. B* **1998**, 102, 9414–9425.
- 109 WHANG, Z., LEE, J., COSSINS, A. R., BRUST, M., Microarray-based detection of protein binding and functionality by gold nanoparticles probes, *Anal. Chem.* **2005**, 77, 5770–5774.
- 110 TALLEY, C. E., JUSINSKI, L., HOLLARS, C. W., LANE, S. M., HUSER, T., Intracellular pH sensors based on surface-enhanced Raman scattering, *Anal. Chem.* **2004**, 76, 7064–7068.
- 111 MATTOUSSI, H., KUNO, M. K., GOLDMAN, E. R., ANDERSON, G. P., MAURO, J. M., in *Optical Biosensors: Present and Future*, eds. LIGLER, F. S., ROWE, C. A., Elsevier, Amsterdam, **2002**, pp. 537–569.
- 112 AITKEN, R. J., CREELY, K. S., TRAN, C. L., *Nanoparticles: An Occupational Hygiene Review*, Institute of Occupational Medicine for the Health and Safety Executive Research Report 274, **2004**.

## 6

# Quantum Dot-based Nanobiohybrids for Fluorescent Detection of Molecular and Cellular Biological Targets

Rumiana Bakalova, Zhivko Zhelev, Hideki Ohba,  
and Yoshinobu Baba

### 6.1 Introduction

Over the last several years, semiconductor quantum dots (QDs) have won recognition as a new generation of fluorophores in bioimaging and biosensing, because of their unique spectral properties compared with traditional organic dyes: high quantum yield (>50% versus 15–50% for classical organic dyes); high molar extinction coefficients ( $\sim 10\text{--}100\times$  that of traditional organic dyes); broad absorption spectra with narrow, symmetric fluorescence spectra (full-width at half-maximum  $\sim 25\text{--}40$  nm) spanning the ultraviolet to near-infrared; large effective excitation/emission Stokes shifts; high resistance to photobleaching and exceptional resistance to photo- and chemical degradation. All these characteristics make QDs brighter fluorescent probes ( $10\text{--}20\times$  brighter than classical organic dyes) under photon-limited *in vivo* and *in situ* conditions, where the light intensities are severely attenuated by scattering and absorption. These novel optical properties can be used to optimize the signal-to-noise (signal-to-background) ratio and to improve the sensitivity of the fluorescence detection devices, as well as to increase the quality of fluorescent cellular and molecular labeling, and deep-tissue *in situ* and *in vivo* fluorescent imaging. Moreover, the size-tunable fluorescent emission (as a function of core size for binary semiconductor materials) and the broad excitation spectra (which allow excitation of mixed QD populations at a single wavelength) give possibilities for application of QDs in multiplexed fluorescent analyses.

The present chapter overviews the current status and future trends of QD-based nanobiohybrids for ultrasensitive fluorescent detection of molecular and cellular biological targets. Section 6.2 outlines the basic principles of design and synthesis of highly fluorescent QDs, appropriate for life science research, with their advantages and drawbacks over classical fluorophores. Section 6.3 summarizes currently data on applications of QD-based nanobioprobes in cellular and deep-tissue imaging *in situ* and *in vivo*, using the following fluorescent detection methods: fluorescent confocal microscopy, two-photon microscopy, fluorescence correlation spectroscopy, single-molecule microscopy. It describes the potential of multifunctional

QDs for positron emission tomography and functional magnetic resonance imaging. Sections 6.4 and 6.5 focus on the application of QDs in several basic fluorescent biotechnologies *in vitro* (e.g., FRET analyses, time-resolved photoluminescence spectroscopy, immunoblotting). These sections describe, for the first time, the great capacity of QDs for improvement and quantification of immunoblot analysis of protein expression, using a fluorescent detection, as well as for development of new generation optical recognition-based biosensors. A new type of QDs possessing a long fluorescence life-time (approximately 90 ns) is also reported. Finally, Section 6.6 briefly describes future trends for QD-based composite materials as novel fluorescent standards for thin calibration of fluorescent instrumentation.

## 6.2

### Quantum Dots – Basic Principles of Design and Synthesis, Optical Properties, and Advantages over Classical Fluorophores

#### 6.2.1

##### Basic Principles of Design and Synthesis of Quantum Dots

QDs are made from inorganic colloidal semiconductors. They are single crystals a few nanometers in diameter whose size and shape can be precisely controlled by the duration, temperature, and ligand molecules used in the synthesis [1]. This process yields QDs that have unique composition- and size-dependent absorption and emission (Fig. 6.1).

Absorption of a photon with energy above the semiconductor band gap energy results in the creation of an exciton. The absorption has an increased probability at higher energies (i.e., shorter wavelengths) and results in a broadband absorption spectrum, in marked contrast to standard fluorophores. For nanocrystals smaller than the so-called Bohr exciton radius (a few nanometers), energy levels are quantized, with values directly related to the QD size – an effect called quantum confinement that gives the name “quantum dots”. The relative recombination of an exciton (characterized by a long life-time, >10 ns) [2] leads to the emission of a photon in a narrow, symmetric energy band.

Surface defects in the QD crystal structure act as temporary “traps” for the electron or hole, preventing their radiative recombination. The alternation of trapping and untrapping events results in intermittent fluorescence (blinking) visible at the single-molecule level [3–5]. This reduces the overall quantum yield (the ratio of emitted to absorbed photons). The way to overcome these problems and to protect surface atoms from oxidation and other chemical reactions is to grow a shell of a few atomic layers of a material with a large band gap on top of the nanocrystal core. The shell can be designed carefully to obtain quantum yields close to 90%. This step also enhances QD’s photostability by several orders of magnitude in comparison with conventional dyes.

For application of QDs in life science experiments, it is necessary to dissolve the core-shell nanocrystals in aqueous solutions at physiological conditions (pH  $\sim$  7–7.4 and physiologically normal ion strength), avoiding aggregation completely.

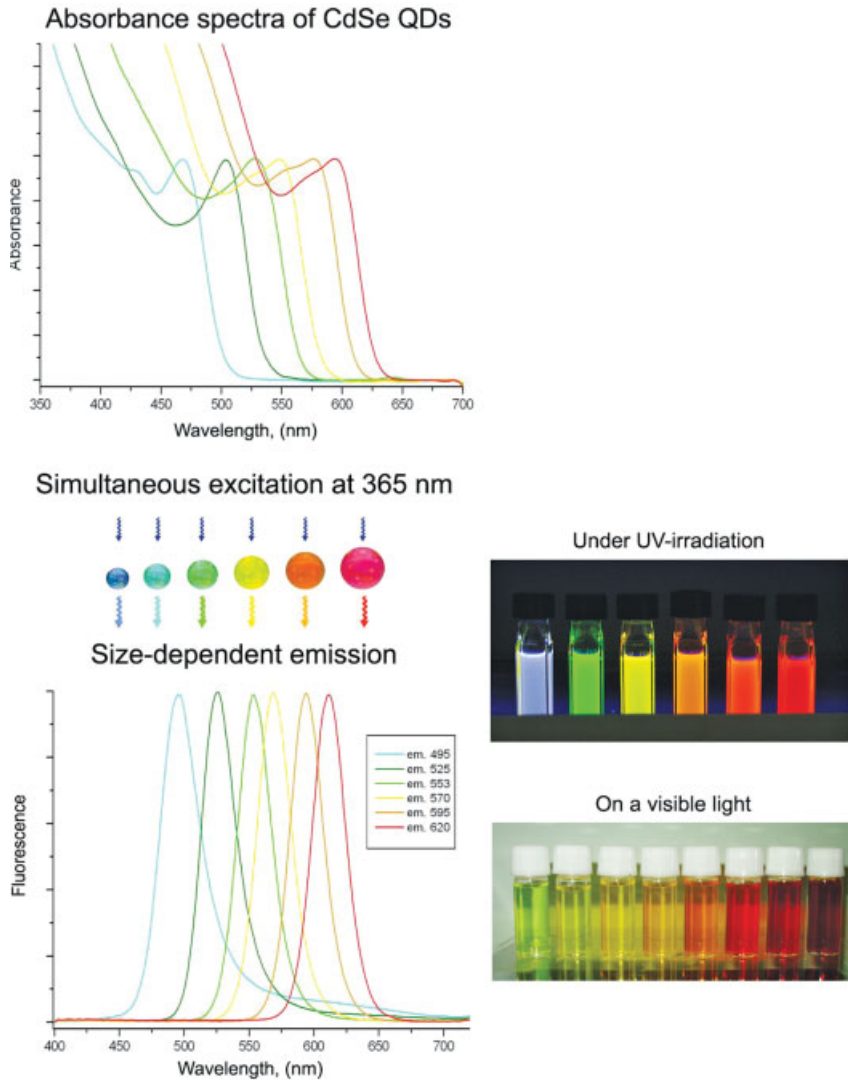


**Fig. 6.1.** Size-dependent absorption and emission of CdSe quantum dots (from  $\sim 2$  to  $\sim 6$  nm in diameter, starting from the blue color).

Presently, the best available QDs for biological applications are made of CdSe cores overcoated with a layer of ZnS. The size of CdSe/ZnS QDs varies from 3 to 10 nm. Their quantum yield is very high in organic solvents ( $\sim 85\%$ ); however, the direct phase-transfer to aqueous solutions using appropriate surface-modifying agents results in a significant decrease or complete loss of their fluorescent proper-



ties (as a result of direct contact between the metal surface and the polar environment). Thus, additional organic coating of CdSe/ZnS QDs is necessary to preserve (at least partially) their high quantum yield in aqueous solutions. The organic (usually polymer) coating is required not only to preserve the quantum yield but, mostly, for isolation of the metal surface, which is sensitive to oxidation. For example, QDs that are covered only with water-soluble surface ligand can be easily oxidized by the oxygen dissolved in aqueous solution. As a result, QDs aggregate, form about 100–500 nm clusters, and lose completely their unique properties. The polymer coat forms a box around single QDs and thus avoids the aggregation and preserves the unique properties of the semiconductor core–shell nanocrystal.

Several excellent reviews summarize the advantages and drawbacks of the synthetic strategies for water-soluble QDs [6–11]. QDs have been synthesized using both two-element systems (binary dots) and three-element systems (ternary alloy dots). The most successful strategy for additional coating of CdSe/ZnS QDs before their subsequent water-solubilization is an organic coating using “diblock” or “triblock” copolymers [8, 12], amine box dendrimers [13], dihydrolipoic acid derivatives [14, 15], modified acrylic acid polymer [16–18]. However, current organic coats have one important shortcoming – the obtained QD particles have a non-defined heterogeneous size after the organic coating. Moreover, the total size of the organic-coated CdSe/ZnS QDs usually varies in the range 15–50 nm – a size that is commensurable with or larger than that of biomolecules (proteins, oligonucleotides, etc.) that the particles have to be conjugated with. Despite their relatively large size, recent life science experiments have shown that bioconjugated QD probes behave like fluorescent proteins and do not suffer from serious binding kinetic or steric hindrance problems and can be used in fluorescent imaging of molecular and cellular targets [8, 9, 12, 19–32]. In this “mesoscopic” size range, QDs also have a greater surface area and a lot of functionalities to develop multifunctional nanoparticles that can be used for linking to multiple diagnostic and therapeutic agents. However, the comparatively large sizes of water-soluble QDs make them inappropriate for several approaches, e.g., FRET-based biosensing technologies (the Forster-radius for effective FRET is calculated as 5–10 nm). Since the organic coating is necessary to avoid aggregation of the metal nanoparticles and to preserve their high quantum yield in aqueous solutions, future expectations have been directed to the development of methods for overcoating of QDs with a maximal size of organic coat of ~8 nm.

### 6.2.2

#### **Optical and Chemical Properties – Advantages Compared with Classical Fluorophores**

Semiconductor QDs have attracted much interest for bioimaging and biosensing, because of their unique spectral properties over traditional organic fluorophores. Briefly, the following characteristics distinguish QDs from the commonly used fluorophores: high quantum yield (more 50% versus 15–50% for standard organic dyes); high molar extinction coefficients (in the order of  $0.5\text{--}5 \times 10^6 \text{ M}^{-1} \text{ cm}^{-1}$ , which is  $\sim 10\text{--}100\times$  larger than those of traditional organic dyes –  $5\text{--}10 \times 10^4$

$M^{-1} \text{ cm}^{-1}$ ) [7, 33]; broad absorption spectra with narrow, symmetric photoluminescence spectra (full-width at half-maximum  $\sim 25\text{--}40 \text{ nm}$ ) spanning the UV to near-infrared; low life-time-limited emission rates for single QDs ( $\sim 5\text{--}10\times$  lower than those of single organic dyes), because of their longer excited state life-times ( $20\text{--}50 \text{ ns}$ ); large effective Stokes shifts; high resistance to photobleaching (several thousand times more stable than organic dyes) and exceptional resistance to photo- and chemical degradation [34–36], which makes them well-suited for continuous tracking studies over a long period of time. All these characteristics make QDs brighter fluorescent probes ( $10\text{--}20\times$  brighter than organic dyes) [37, 38] under photon-limited *in vivo* and *in situ* conditions, where light intensities are severely attenuated by scattering and absorption. These novel optical properties can be used to optimize the signal-to-background (signal-to-noise) ratio. For example, the comparatively long fluorescence life-time of QDs enables the use of time-gated detection to separate their signal from that of shorter lived species, such as background autofluorescence encountered in viable cells and animals. Moreover, the longer excited state life-times of QDs provide a means to separate the QD fluorescence from background fluorescence using a time-domain imaging technique [39, 40]. Figure 6.2 shows a comparison of the excited state decay curves of QDs and organic dyes.

Assuming that the initial fluorescence intensities of QDs and dyes after a pulse excitation are the same and that the fluorescence life-time of QDs is one order of magnitude longer, one can estimate that the QD and dye intensity ratio ( $I_{\text{QD}}/I_{\text{dye}}$ ) will increase rapidly from 1 at time  $t = 0$  to  $\sim 100$  in only  $10 \text{ ns}$  ( $t = 10 \text{ ns}$ ). Thus,

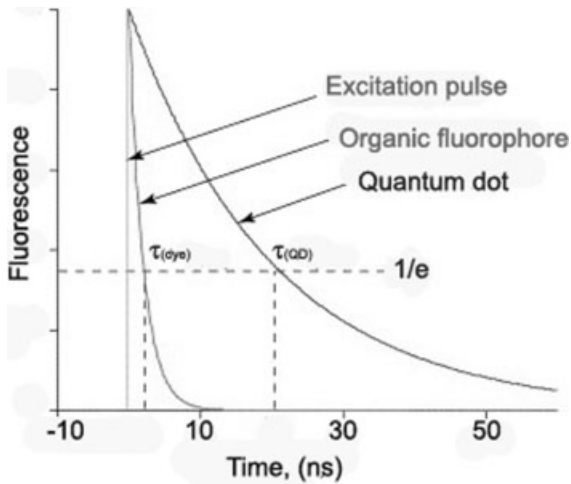


**Fig. 6.2.** Comparison of the excited state decay curves (monoexponential model) of QDs and classical organic dyes. The longer excited state life-time of QDs allows the use of time-domain imaging to discriminate against the background fluorescence (short life-times);

$\tau_{(\text{dye})}$  and  $\tau_{(\text{QD})}$  are the delay times for the fluorescence signals to decrease to  $1/e$  of their original values, where  $e$  is the natural log constant ( $= 2.718$ ). (Kindly provided from X. Gao [8]).

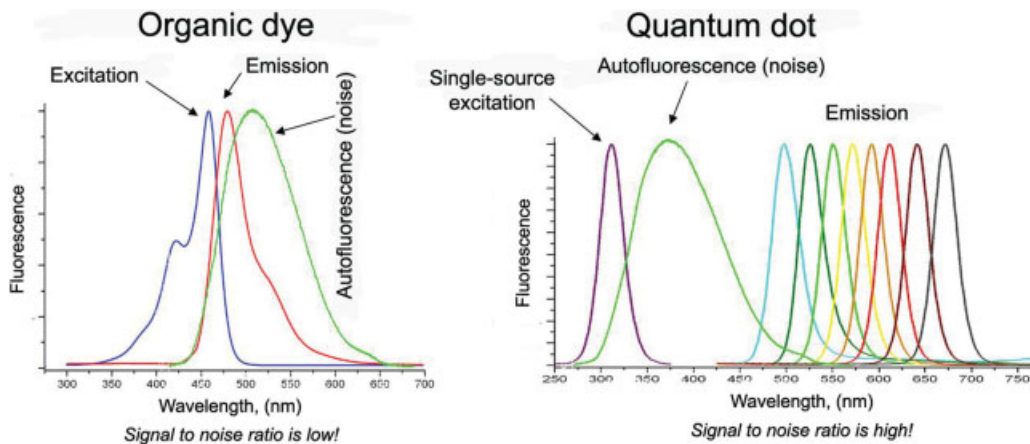


**Fig. 6.3.** Comparison of excitation/emission Stokes shifts between QDs and classical organic dyes – an important issue for optimization of the signal-to-noise (signal-to-background) ratio.

the image contrast (measured by signal-to-noise or signal-to-background ratio) can be markedly improved by time-delayed data acquisition.

The large Stokes shifts of QDs (measured by the distance between the excitation and emission peaks) can be used to further improve detection sensitivity (Fig. 6.3). As shown in Fig. 6.3, the Stokes shifts of QDs can be as large as 300–400 nm, depending on the wavelength of the excitation light. Organic dye signals with a small Stokes shift are often mimicked by strong tissue and cell autofluorescence. In contrast, QD signals with a large Stokes shift are clearly recognizable above the background. This “color contrast” is only available to QD probes, as the signals and background can be separated by wavelength-resolved or spectral imaging [12].

The most attractive features for life science research are the size- and composition-tunable emission of QDs from visible to infrared wavelengths, which give a possibility for their use to image and track multiple molecular targets simultaneously, e.g., combinatorial optical encoding, in which multiple colors and intensities are combined to encode thousands of genes, proteins or small-molecule compounds (a), and simultaneous sensing and imaging of several molecular and more complex targets (b) [17, 41–48].

Single QDs can be observed and tracked over an extended period of time (up to a few hours) with fluorescent confocal microscopy [49], total internal reflection microscopy [50, 51], or basic wide-field epifluorescence microscopy [19, 52]. Single-molecule microscopy is possibly one of the most exciting new capabilities offered to biologists. A related technique, fluorescence correlation spectroscopy, has allowed determination of the brightness per particle and also provides measurement of the average QD size [53]. QDs are also excellent probes for two-photon confocal microscopy [51, 54, 55] because they are characterized by a large absorption cross section. They can be used simultaneously with standard dyes. In particular, QDs

have a largely untapped potential as novel tracers in PET and MRI imaging [9], as customizable donors of a fluorescence resonance energy transfer (FRET) pair [23, 24, 28, 56–61], and as photosensitizers [31, 32, 62]. In the next several subsections we discuss the application of QD-based probes in most usable imaging and sensing methodologies in life science experiments.

### 6.3 Quantum Dots for Fluorescent Labeling and Imaging

The unique optical properties of QDs make them very attractive as novel fluorophores in various life science investigations, in which traditional fluorescent organic dyes fall short of providing long-term stability and simultaneous detection of multiple fluorescent signals. The ability to make QDs water soluble and target them to specific biomolecules has led to promising applications in cellular labeling, deep-tissue imaging, *in vitro* fluorescent assays, and FRET-based techniques.

#### 6.3.1

##### Structure of Quantum Dot Nanobiohybrids for Fluorescent Microscopic Imaging

Since water-soluble QDs have many functional groups ( $\text{NH}_2^-$ ,  $\text{COOH}^-$ ,  $\text{SH}^-$ , etc.) on their surface, they are easily conjugated with different biomolecules (proteins, DNAs, RNAs, small ligands, etc.), as well as with appropriate chemical substances (e.g., drugs). The resulting conjugates combine the properties of both materials, i.e., the spectroscopic characteristics of the nanocrystal and the biomolecular function of the surface-attached entities.

There are two types of conjugates, depending on the QD size. Using QDs with size commensurable with or slightly larger than that of many biomolecules, it is possible to obtain QD-based nanobiohybrids that consist of a single QD with several biomolecules attached on its surface. Thus, the large number (10 to 100) of potential surface attachment groups can be used to “graft” different functionalities to individual QDs, resulting in multifunctional probes. For instance, in addition to a recognition moiety, QDs can be equipped with a membrane-crossing or cell-internalization capability, and/or and enzymatic function.

In contrast, using small QDs (approximately 2–3 nm in diameter) it is possible to obtain nanobiohybrids that consist of several QD particles attached to a single biomolecule (usually protein) [26]. In this case, QDs have an important privilege for fluorescence detection methods in comparison with classical organic dyes – the attachment of several small size QDs on the surface of one protein molecule does not result in fluorescence self-quenching, in contrast to classical dyes (e.g., cyanines, fluorescein, etc.) where the conjugation of several dye molecules with one protein molecule results in a strong fluorescence self-quenching. This assumption is based on our comparative study of the fluorescence intensity of multifunctional PMAM dendrimers conjugated with different numbers of QD particles (~2 nm in diameter) or cyanine 3/cyanine 5 molecules (unpublished data).

Several strategies can be used to manipulate the molecular orientation of the ligands attached on the QD surface as well as their molar ratios with respect to QDs. However, QD probes with precisely controlled ligand orientations and molar ratios are still not available.

Two problems associated with fluorescence microscopy – cell and tissue autofluorescence in the visible spectrum (which can mask the signals from labeled molecules) and the requirement of long observation times – have created a need for new QD probes that emit in the near-infrared (NIR) region (wavelength > 700 nm) and are more photostable than current organic fluorophores [29].

### 6.3.2

#### Quantum Dots for Fluorescent Cell Imaging

QDs have made the most progress and attracted the greatest interest in cellular labeling and imaging. Within the last two-three years, numerous reports have described the ability of one or more “color/size” of biofunctionalized QDs to label cells [20–22, 26, 30, 32, 37, 50, 63–68]. Many of these reports show that QD labeling permits extended visualization of cells under continuous laser illumination as well as multicolor imaging, highlighting the advantages offered by these fluorophores (Fig. 6.4) [20, 22, 26, 65–68].

A clear differentiation can be made between labeling of live and fixed cells (dead with crosslinked components to maintain cellular architecture). Fixed cells can be treated “harshly” to facilitate entry of the QDs by chemically creating pores. To label live cells, the process must be handled softly to maintain cellular viability. Live-cell experiments introduce a few extra levels of complexity, depending on the application: whole-cell QD labeling, labeling of membrane-bound proteins, and cytoplasmic, subcellular or nuclear target labeling. The major impediment is the entry of the relatively large QDs into the cell across the cellular membrane lipid bilayers. For small size water-soluble QDs, the positive charge on the surface can facilitate this process, but for negatively charged QDs this is usually extremely difficult. Such QDs can be delivered into the cells only through some specific (receptor-mediated) transport based on the functional molecules conjugated on the QD surface. The results indicate that large amounts of QDs can be delivered into live mammalian cells via three different mechanisms: non-specific pinocytosis, microinjection, and peptide-induced transport [16, 17, 22, 69–71]. For example, transferrin has been used to facilitate endocytosis of QDs by mammalian cells and to label pathogenic bacteria and yeast cells [38], whereas lectin-conjugated QDs were used to detect specifically Gram-negative bacteria [61, 72]. Different types of QD functionalization have also been explored as a way to target QDs to cell surface proteins. Some examples include streptavidin, secondary or primary antibodies, receptor ligands such as epidermal growth factor or serotonin, recognition peptides, and affinity pairs such as biotin–avidin after engineering of the target protein [19–22, 25, 70, 73, 74]. To reduce the size of QD probes, researchers have used ligands of cell surface receptors bound to QDs via a biotin–streptavidin link or by direct crosslinking [21, 25, 70]. Some cell surface proteins can be recognized by small

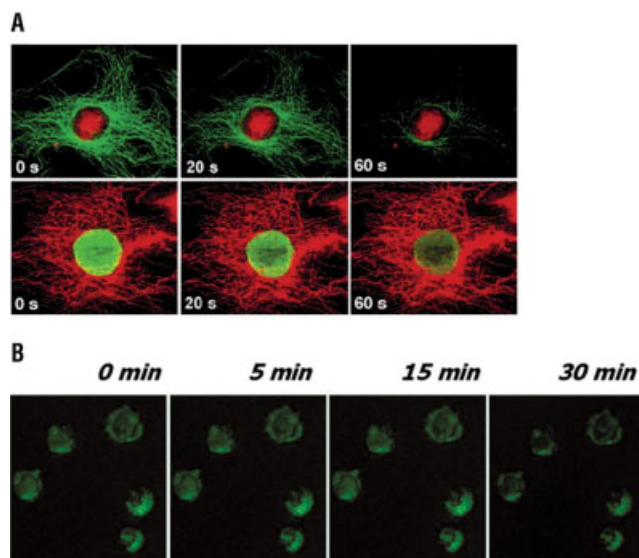


**Fig. 6.4.** Stability of QD fluorescence during continuous laser scanning on a confocal fluorescent microscope. (A) Top row: Nuclear antigens labeled with QD630-streptavidin (red), and microtubules labeled with Alexa-488 conjugated with anti-mouse IgG (green) simultaneously in 3T3 cells. Bottom row: Microtubules labeled with QD630-streptavidin (red), and nuclear antigens stained with Alexa-488 conjugated with anti-human IgG (green). Specimens were continuously illuminated for 1 min with light from a 100 W mercury lamp under a  $100\times 1.30$  oil-immersion objective. An

excitation filter ( $\lambda_{\text{ex}} = 485$  nm) was used to excite both Alexa-488 and QD630. Emission filters at  $\lambda_{\text{em}} = 535$  nm and  $\lambda_{\text{em}} = 635$  nm were used to collect Alexa-488 and QD630 signals, respectively. Images were captured with a CCD camera at 10 s intervals for each color automatically. (According to Wu et al. [20]). (B) Fluorescent microscopic imaging of interaction of QD-lectin conjugates with leukemia cells (green): dynamic of the signal during 30 min scanning. (According to Zhelev et al. [26]).

peptides (screened by phage-display technology) [74], so it is attractive to use peptides for QD functionalization. The same concepts could also be used to label sub-cellular or nuclear targets. However, QDs need to enter the cell cytoplasm and to reach their target without being trapped in the endocytosis. A surprising finding is that two billion QDs could be delivered into the nucleus of a single cell, without compromising its viability, proliferation or migration [8, 16, 71, 75]. The ability to image single-cell migration and differentiation in real time is expected to be important to several research areas such as embryogenesis, cancer metastasis, stem-cell therapeutics and lymphocyte immunology.

The main advantage of QDs in cellular imaging resides in their resistance to photobleaching over long periods of time (minutes to hours), allowing the acquisition of images that are crisp and well contrasted. The increased photostability of QDs is especially useful for acquisition of many consecutive focal-plane images and their reconstruction into a high-resolution three-dimensional (3D) projection,

e.g., for 3D optical sectioning, where a major issue is bleaching of fluorophores during acquisition of successive z-sections. This compromises the correct reconstruction of 3D structures [76]. The very small number of QDs is necessary to produce a fluorescent signal. In addition, QDs are available in a virtually unlimited number of well-separated colors, all excitable by a single wavelength. This property could be used in fluorescent confocal microscopy to perform nanometer-resolution colocalization of multiple-color individual QDs.

### 6.3.3

#### Quantum Dots for Fluorescent Deep-tissue Imaging *In Vivo*

The long-term stability and brightness of QDs make them ideal candidates for *in vivo* fluorescent targeting and imaging. At present, such imaging uses two groups of organic fluorophores: the fluorescent proteins expressed by the cells themselves and fluorescent dyes that are exogenously loaded into the cells. Organic fluorophores have numerous limitations, restricting their usefulness for *in vivo* fluorescent microscopy. A first limitation is the difficulty in simultaneous imaging of multiple independent organic fluorophores, based on two characteristics of these fluorophores. First, they require distinct excitation wavelengths and have a very small Stokes shift between excitation and emission wavelengths (Fig. 6.3). Thus, multiple excitation lines are needed for imaging multiple organic fluorophores and each additional excitation line limits the spectra available for emission collection. Second, they emit over a broad region of the visible spectra. Thus the emission of different fluorophores overlaps with each other and with much of the tissue autofluorescence. A second limitation is the susceptibility of organic fluorophores to photodamage and metabolic degradation, which restricts their use in long-term *in vivo* imaging [53]. Moreover, some organic fluorophores (e.g., fluorescein) have a limited response to multiphoton excitation, which is a particular liability when trying to image into tissues.

QDs completely overcome these limitations. They can be excited by a wide spectrum of single and multiphoton excitation light, which is well separated from their emission spectra. The large Stokes shifts allow the possibility to overcome, or at least to minimize, tissue autofluorescence that appears near the excitation region (Fig. 6.5). Thus, only one excitation wavelength is needed to simultaneously excite several different QD probes. QDs also have narrow emission spectra, which are tunable to any desired wavelength from blue to infrared. Thus from their emission spectra several different QD probes can be easily distinguished. QDs are also virtually resistant to photobleaching and are as bright as the best-known organic fluorophores. Further, they have a good multiphoton absorption between 700 and 1000 nm. These features make QDs desirable for long-term multicolor *in vivo* imaging.

Theoretical modeling studies have indicated that two spectral windows are available for *in vivo* QD imaging – one at 700–900 nm and other at 1200–1600 nm [77–

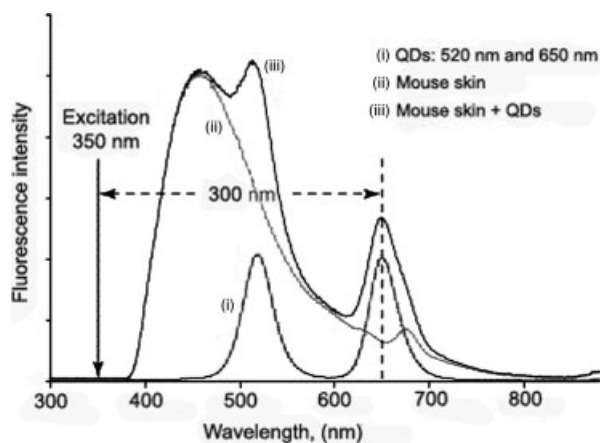
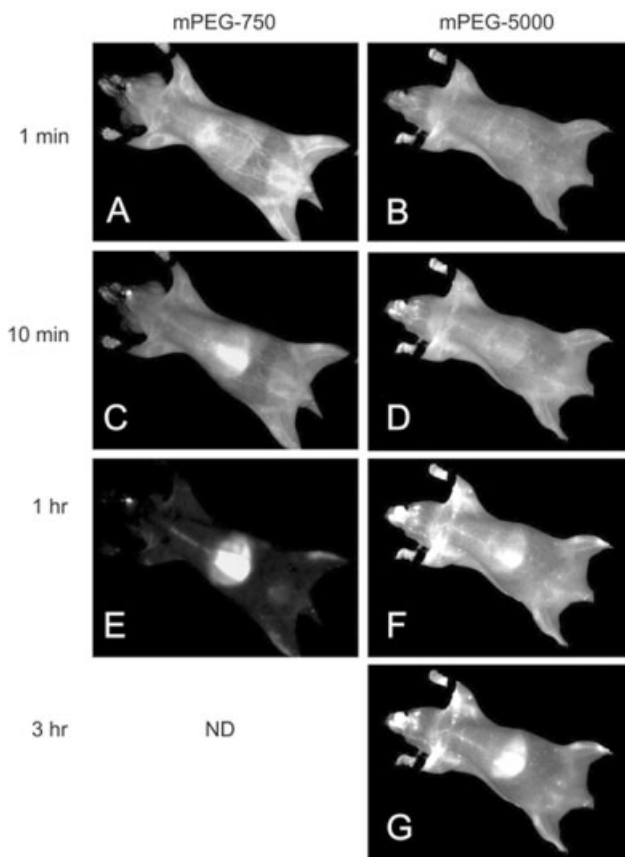


Fig. 6.5. Comparison of mouse skin autofluorescence and QD emission spectra, obtained under excitation at 350 nm. The results demonstrate that QD signals can be shifted to a spectral region where autofluorescence is reduced. (This figure was kindly provided from X. Gao [8].)

79]. There are great expectations for QDs emitting in the near-IR region that are ideal for *in vivo* imaging. In this region of the electromagnetic spectrum there is low tissue scattering and absorption, yielding the greatest tissue penetration depth and optical signal. In this case, QDs offer an excellent alternative to organic fluorophores for *in vivo* animal imaging. However, biocompatible near-IR-emitting organic fluorophores suffer from low QY (quantum yield), broad emission spectra, and an inability to multiplex. Near-IR QDs can, potentially, be designed to have high QYs and molar absorption coefficients, leading to a highly luminescent and useful *in vivo* contrast agent. In fact, high QY near-IR organic soluble QDs have already been designed [29, 80–82] – a major hurdle is the preservation of the optical properties of organic-soluble near-IR QDs after surface modification with biocompatible coatings and water solubilization. The highest reported QY for biocompatible near-IR-emitting QDs made from CdSe/CdTe alloy is 17%.

Another important issue for application of QDs *in vivo* is their overcoating with high molecular weight poly(ethylene glycol) (PEG) molecules that gives a possibility to reduce their accumulation in the liver and bone marrow, and to ensure effective targeting and imaging of the desired tissue *in vivo* (e.g., blood vessels, solid tumors, tumor metastases, lymph nodes, etc.) [12, 16, 18]. In contrast to small organic dyes, which are eliminated from the circulation within minutes after injection, PEG-coated QDs remained in the blood circulation for an extended period of time (half-life more than 3 h) (Fig. 6.6A) [18, 29]. This long-circulating feature can be explained by the unique structural properties of QD nanoparticles. PEG-coated QDs fall within an intermediate size range: they are small enough and sufficiently





**Fig. 6.6.** (A) Noninvasive imaging of 645 nm-emitting mPEG-750 QDs (A, C, E) and 655 nm-emitting mPEG-5000 QDs (B, D, F, G). Nude mice are imaged at different post-injection times. Significant liver uptake is detected using mPEG-750 QDs even at 10 min, while using mPEG-5000 QDs such uptake is visible after 1 h. The same QDs are very stable and can be also detected after 3 h. (Reprinted from Ref. [18] with the permission of ACS Publications).

hydrophilic to slow down opsonization and reticuloendothelial uptake, but are large enough to avoid renal filtration. In this context, near-IR QDs also have great potential to be used in diagnostic blood vessel (e.g., stenosis, aneurism, stroke, etc.).

To guarantee high binding affinities of QD probes to the respective cellular or molecular target *in vivo*, the nanocrystals are usually conjugated with antibodies or small peptides [12, 63]. Antibodies offer higher binding affinity of QDs than peptides, but they add size to the nanoparticles (~5–30 nm). Furthermore, antibodies could limit the co-coating of other molecules (e.g., polymers) onto the surface of QDs. By contrast, peptides are smaller than antibodies – large libraries of targeting peptides for specific diseases can be identified using screening tech-

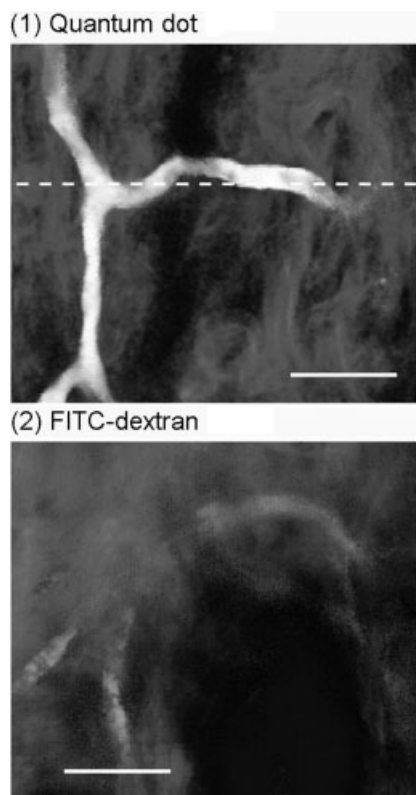


**Fig. 6.6.** (B1) In vivo imaging of vasculature labeled by a tail vein injection of water-soluble QDs (fluorescence wavelength, 550 nm). Fluorescent capillaries, containing  $\sim 1 \mu\text{M}$  QDs, were clearly visible through the skin at the base of the dermis ( $\sim 100 \mu\text{m}$  deep). Blue pseudocolor is collagen imaged via its second

harmonic signal at 450 nm. (B2) Comparison image at the same depth as in (B1), acquired by injecting FITC-dextran at its solubility limit. Scale bars in (B1) and (B2):  $20 \mu\text{m}$ . Excitation is at 880 nm for (B1) and 780 nm for (B2). (Reprinted from ref. [84] with the permission of Science Publishing Group.)

niques, such as phage-display – and provide greater flexibility in QD surface engineering.

Currently, there are several excellent examples for application of QDs in *in vivo* cellular targeting and imaging, including fluorescent deep-tissue imaging. Two-photon laser exciton confocal microscopy has been used to visualize blood vessels in mice after intravenous injection of QDs, showing that higher contrast and imaging depth can be obtained at a lower excitation power than with organic dyes [53]. Larson and coworkers found that the two-photon absorption cross-sections of QDs are two to three orders of magnitude larger than those of traditional organic fluorophores (Fig. 6.6.(B)) [81].

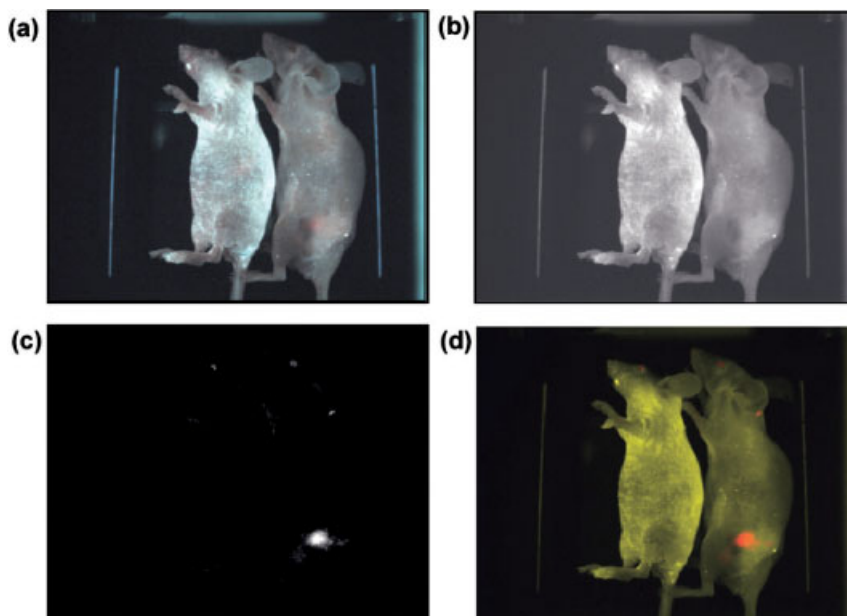


**Fig. 6.7.** *In vivo* fluorescence imaging of QD-PSMA antibody conjugates in mouse bearing C4-2 human prostate tumor. Orange-red fluorescence signals indicate a prostate tumor growing in a live mouse (right-hand mouse). Control studies using a healthy mouse (without tumor) and the same amount of QD

injected showed no localized fluorescence signals (left-hand mouse). (a) Original image; (b) unmixed autofluorescence image; (c) unmixed QD image; (d) super-imposed image. (This figure was kindly provided from X. Gao [12].)

QD-peptide conjugates have been also used to target tissue-specific vascular markers (lung blood vessels and cancer cells) by intravenous injection in mice [18]. Histological sections of different organs after 5 or 20 min of circulation showed that QD-peptide conjugates reach their targets and are internalized by endocytosis in target cells but not in surrounding tissues, probably because of their large size relative to dye molecules (which stain surrounding tissues). *In vivo* imaging of targeted QD delivery has recently been achieved in mice by Gao et al., who intravenously injected PEG-coated QDs functionalized with antibodies to prostate-specific membrane antigen (PSMA) (Fig. 6.7) [12]. However, since their QDs emit in the visible spectrum, the authors use a spectral demixing algorithm to separate tissue autofluorescence from QD signal in grafted tumors.

This problem has been eliminated by Kim et al. [29], who have injected near-IR-emitting QDs intradermally into mice and pigs and demonstrated the visualization of sentinel lymph nodes in these animals via optical imaging (Fig. 6.8).

To improve tissue penetration, Kim et al. have prepared a novel core-shell nanostructure called type II QDs with fairly broad emission at 850 nm and a moderate QY of  $\sim 13\%$  [29]. In contrast to conventional QDs (type I), the shell materials in

type II QDs have valence and coordination band energies both lower than those of the core materials. As a result, the electrons and holes are physically separated and the nanoparticles emit light at reduced energies (longer wavelengths). Injection of only picomolar amounts of the QDs enables visualization of sentinel lymph nodes 1 cm below the skin using excitation rates of only  $5 \text{ mW cm}^{-2}$ . QDs rapidly migrate to nearby lymph nodes and can be imaged virtually background-free, allowing image-guided resection of a lymph node in a pig. The sentinel nodes have been confirmed by a second intradermal injection of blue dye (the current “gold standard”), which also flowed to the same nodes. The advantage of QD over blue dye is the ability to “see” through several centimeters of tissue so that there would be real-time visual guidance of the surgery, with resolution being limited only by the visual acuity of the surgeon. Visual inspection would also allow the surgeon to confirm that all sentinel nodes had been removed from the node field. There is also exciting potential for histopathologists to focus exactly on the part of the sentinel node containing the QDs by using a fluorescent microscope.

Sentinel lymph node biopsy is elegantly simple in concept but quite often very difficult to perform accurately in individual patients. The sentinel nodes can be very deep, up to 10 cm from the skin, and sometimes the nodes are inside the body cavities; situations such as these are considered as problematic for optical imaging using near-IR fluorescence. Therefore, anything that potentially improves the technique is welcome. The work of Kim et al. [29] points to the possibility that QD probes could be used for real-time intra-operative optical imaging, providing an *in situ* visual guide so that a surgeon could locate and remove small lesions (e.g., metastatic tumors) quickly and accurately. At present, however, appropriate high-quality QDs with near-IR-emitting properties are not yet available. Most materials (e.g., PdS, PdSe, CdHgTe and CdSeTe) are either not bright enough or not stable enough for biomedical imaging applications. There is an urgent need to develop bright and stable near-IR-emitting QDs that are broadly tunable in the far-red and IR spectral regions.

**Fig. 6.8.** Near-IR QD sentinel lymph node mapping in mouse and pig. (a) Images of mouse injected intradermally with 10 pmol of near-IR QDs in the left paw. Left-hand side – pre-injected near-IR autofluorescence image; middle – 5 min post-injection white light color video image; right – 5 min post-injection near-IR fluorescence image. An arrow indicates the putative axillary sentinel lymph node. Fluorescence images have identical exposure times and normalization. (b) Images of the mouse obtained 5 min after re-injection with 1% isosulfan blue (standard) and exposure of the actual sentinel lymph node. Left-hand side

– color video; right – near-IR fluorescence images. Isosulfan blue and near-IR QDs are localized in the same lymph node (arrows). (c) Images of the surgical field in a pig injected intradermally with 400 pmol of near-IR QDs in the right groin. Four time points are shown from top to bottom: before injection (autofluorescence), 30 s after injection, 4 min after injection, and during image-guided resection. For each time-point: Left – color video; middle – near-IR fluorescence; and right – color-near-IR merge images. (This figure was kindly provided from J. Frangioni [29].)

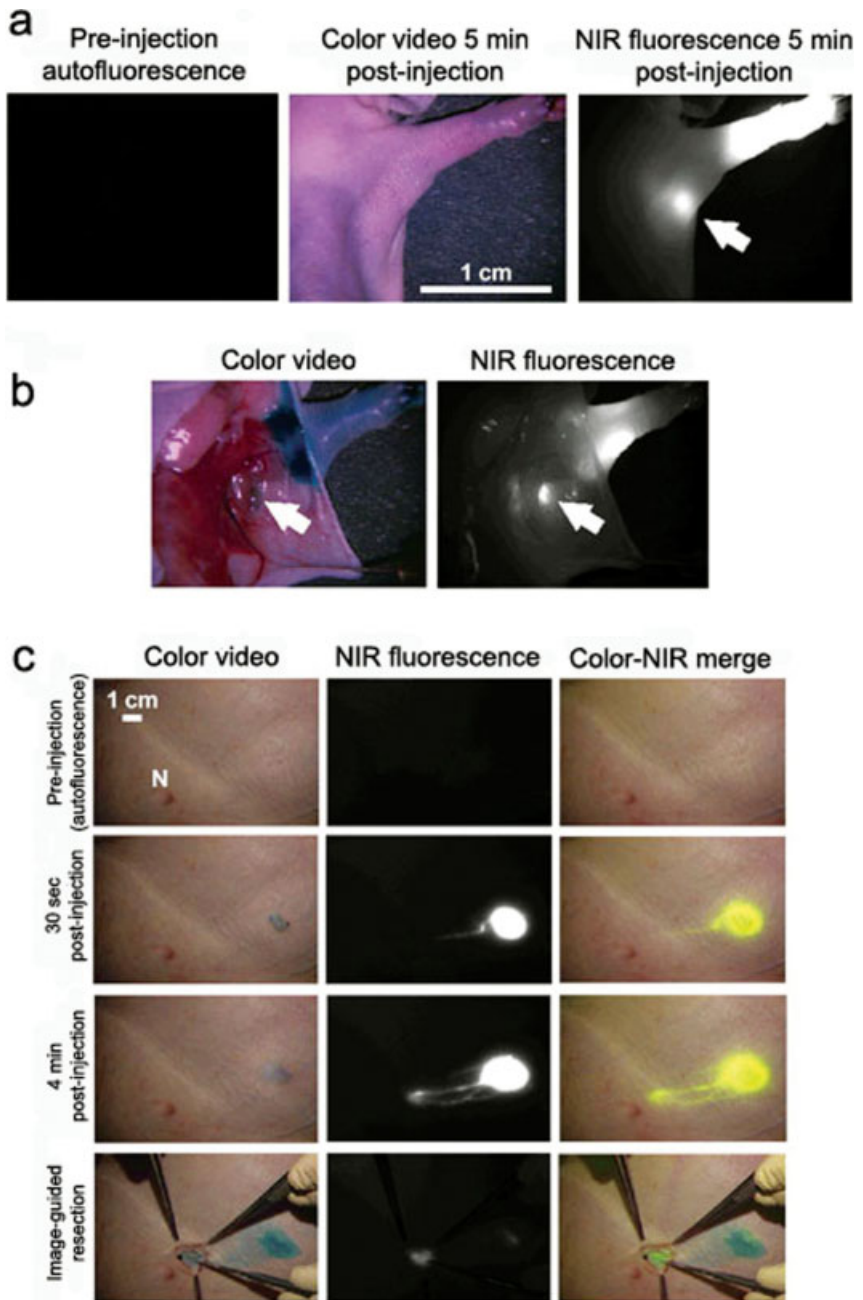


Fig. 6.8

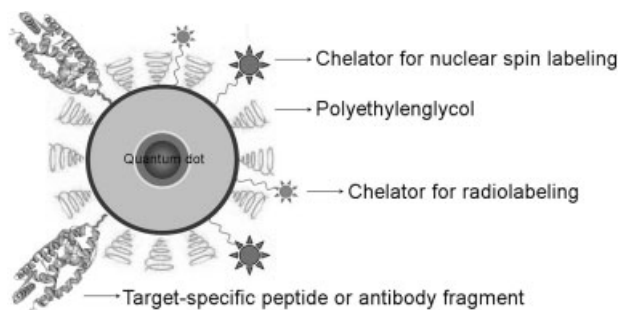


Fig. 6.9. Multifunctional QD-based probes for simultaneous application in different imaging techniques (e.g., fluorescent imaging, MRI, PET).

#### 6.3.4

#### Potential of Quantum Dots for Positron Emission Tomography (PET) and functional Magnetic Resonance Imaging (fMRI)

The ability to design a wide variety of QDs and targeting molecules provides a new set of tools for engineering novel contrast probes for non-invasive imaging techniques such as PET, MRI, and CT. As a research tool, these probes could have many uses, from monitoring tissue implants to studying the real-time dynamics of tumor metastasis.

Despite their relatively large hydrodynamic radii (10–15 nm), bioconjugated QD probes do not suffer from serious binding kinetic or steric-hindrance problems. In this “mesoscopic” size range, QDs also have more surface areas and functionalities that can be used for linking to multiple diagnostic (e.g., radioisotopic or magnetic) and therapeutic (e.g., anticancer) agents. Multimodality imaging probes could be created by integrating QDs with paramagnetic or superparamagnetic agents, as well as with chelators for radioactive isotopes (Figs. 6.9 and 6.10).

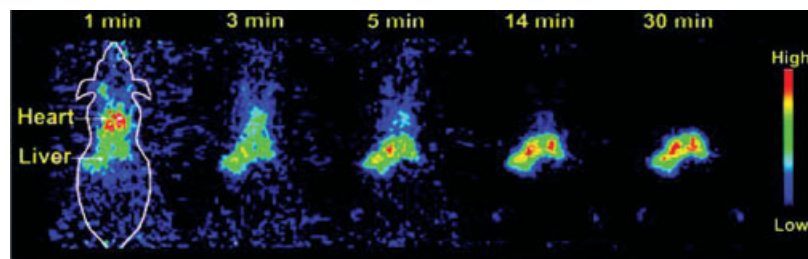


Fig. 6.10. MicroPET imaging of QD uptake in live animals. QDs having DOTA (a chelator for radiolabeling) and PEG on their surface were radiolabeled with  $^{64}\text{Cu}$  (positron-emitted isotope with a half-life of 12.7 h). These QDs were then injected via the tail vein into nude mice ( $\sim 80 \mu\text{Ci}$  per animal) and imaged in a

small animal PET-scanner. Rapid and marked accumulation of QDs in the liver was detected. This could be avoided by functionalizing QDs with higher molecular weight PEG chains. (Reprinted from Ref. [9] with the permission of Science Publishing Group.)

Researchers have recently attached QDs to Fe<sub>2</sub>O<sub>3</sub> and FePt nanoparticles and even to paramagnetic gadolinium chelators [83, 84]. By correlating the deep imaging capabilities of MRI with ultrasensitive optical imaging, a clinician could visually identify tiny tumors or other small lesions during an operation and remove the diseased cells and tissue completely. Medical imaging modalities such as MRI and PET can identify diseases non-invasively, but they do not provide a visual guide during surgery. The development of magnetic or radioactive QD probes has the potential to solve this problem.

## 6.4

### Quantum Dots for Immunoblot Analysis with Fluorescent Detection

#### 6.4.1

##### Basic Principles of Classical and QD-based Immunoblot Analyses

Although immunoblotting technology is about 20 years old it is still a major analytical approach for detection of protein expression in cells and tissues, used in molecular and cellular biology and molecular medicine. Currently, it is one of the basic methodologies (together with northern blot analysis and Light Cycler technology) for microarray data validation and verification in functional genomics and proteomics projects.

Figure 6.11(A) shows the basic principle of classical immunoblot analysis (Western blot).

The protein fractions are separated from cell lysate using gel-electrophoresis and are subsequently transferred to a PVDF membrane. The protein of interest is detected using two-step immunoblotting procedure: incubation of PVDF membrane with primary monoclonal antibody that interacts specifically with the target protein and does not interact with other protein fractions (a); washing of membrane and incubation with secondary antibody, conjugated with enzyme (usually horse radish peroxidase, HRP) (b). The blotted antigen is detected by the chemiluminescence of the HRP-catalyzed reaction of appropriate substrate, exposed to X-ray or Polaroid films.

Notably, despite its widespread and long-standing use, immunoblotting has not been much improved from its initial state 20 years ago. The standard immunoblot analysis suffers from several shortcomings: a semi-quantitative nature; a long duration (usually more 24 h); a poor reproducibility of the obtained data; a risk to reach saturation of the enzyme reaction and to mimic the concentration-dependent difference of the blotted antigens; a low sensitivity for detection of “tracer” proteins – including the impossibility of using directly cell lysates for protein separation and immunoblotting, as well as a necessity to use preliminary procedures for immunoprecipitation and concentration of these proteins (each step holds a risk for accumulation of analytical errors). Every researcher in the genomics/proteomics field has been faced with the difficulties in obtaining reproducible and high quality immunoblot images.

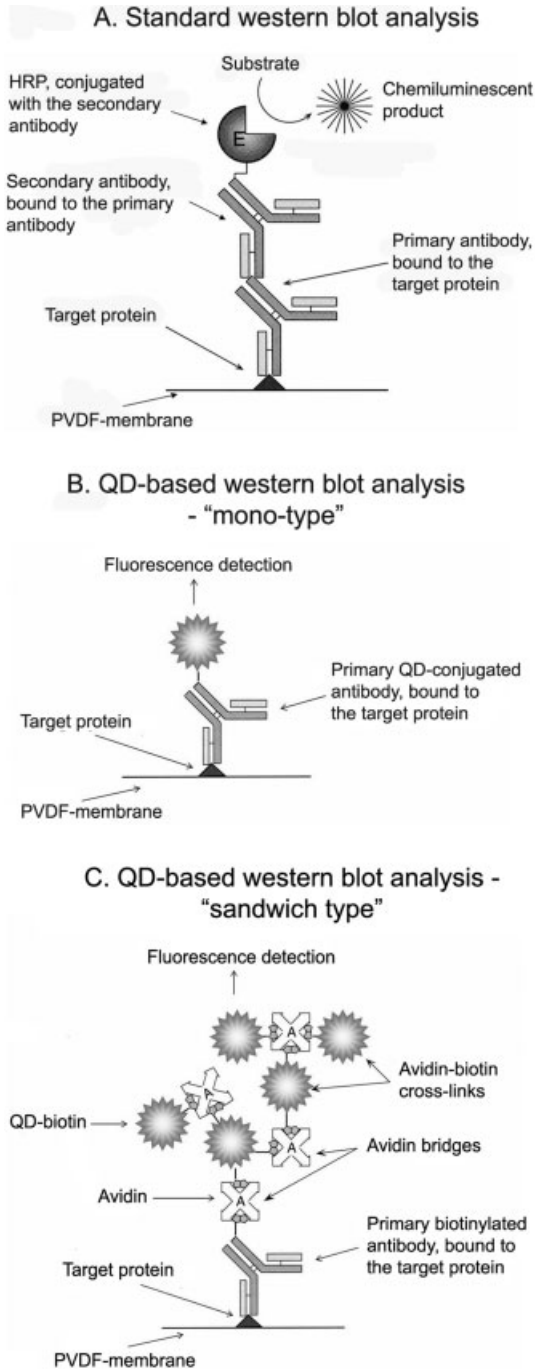


Fig. 6.11. Principle schemes of classical and QD-based immunoblot analyses.



In the middle of August 2004 the Quantum Dot Corporation (USA) offered on the market two western blotting kits, and in the January 2005 issue of *Nature Methods* [85] they undoubtedly demonstrated the potential of QD-based immunoblotting technology in multiplex fluorescent detection of proteins or protein states from a single immunoblot. Their protocol is similar to the classical one; however, the secondary antibody is conjugated with QD instead of enzyme, and the fluorescence of blot images instead of chemiluminescence is detected. The described procedure takes the same time as standard western blot analysis with chemiluminescent detection. However, the narrow emission of QD-labeled protein blots enables simplified image acquisition and quantification that gave a possibility to overcome the semiquantitative nature of western blot analysis. It is possible to store QD-labeled blots in a buffer at 4–8 °C with minimal loss of the fluorescent signal for imaging at a later date.

We have tried to improve QD-based western blotting technology, to simplify and to make it quantitative and applicable for detection of “tracer” proteins directly in cell lysates [27, 86].

Below, we present two immunoblotting protocols, named as “mono type” and “sandwich type” and show the privilege of QD-based western blot analysis in the detection of “tracer” proteins through classical technology with colorimetric detection. Figure 6.11(B, C) presents the principle schemes of both procedures.

#### 6.4.2

##### **QD-based Immunoblot Analysis of “tracer” Proteins – Privileges over Classical Immunoblot Analysis**

QDs with emission maximum at 535 nm were used in this study. Telomere associated proteins, telomeric repeat binding factor (TRF1, a 56 kDa protein) and TRF1-interacting nuclear protein 2 (Tin2, ~40 kDa protein), were selected as proteins of interest. TRF1 and Tin2 are known to be poorly expressed in Philadelphia-positive (Ph+) cells derived from patients with chronic myelogenous leukemia (e.g., K-562 cells) and several modifications of the standard immunoblotting protocol have to be performed to identify these two proteins in K-562 cells. Details are described in Refs. [27, 86]. The blotted QD-labeled antigens (proteins) were detected directly by a fluorescence gel imaging system supplied with an appropriate emission filter. The experimental results in Fig. 6.12 represent typical blots of TRF1 and Tin2, analyzed in cell lysates by classical (C) and QD-based western blotting protocols (A, B).

Using “mono-type” QD-based western blotting technology, it was possible to detect both proteins without preliminary immunoprecipitation and concentration procedures (Fig. 6.12A). However, the fluorescence of QD-labeled TRF1 and Tin2 blots was weak. It was practically impossible to detect these “tracer” proteins directly in cell lysate, without their preliminary immunoprecipitation and concentration (Fig. 6.12C). In contrast, TRF1 and Tin2, detected in K-562 cell lysates by “sandwich type” QD-based western blotting technology, possessed a bright fluorescence as a result of biotin–avidin crosslinks (Fig. 6.12B). The images in Fig.

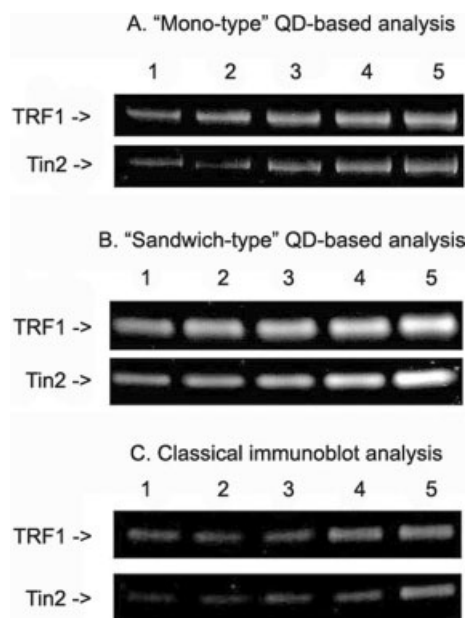


**Fig. 6.12.** Representative blots of “tracer” proteins TRF1 and Tin2, analyzed in K-562 cell lysate using classical (C) and QD-based (A, B) immunoblot analysis. Numbers 1–5 correspond, respectively, to protein concentrations of cell lysates (in  $\mu\text{g}$ ), applied

to each gel patch, of 1–10, 2–20, 3–30, 4–40, and 5–50. In (A) and (B) blot images were obtained by fluorescent detection, and the images in (C) were obtained by chemiluminescent detection.

6.12(A, B) were generated using an identical exposure time (15 min) and excitation/emission settings. Since avidin can interact non-specifically with other non-biotinylated proteins on the PVDF membrane, we recommend the use of neutravidin or streptavidin in “sandwich type” QD-based western blot analysis. Notably, the fluorescent signal was stable during continuous scanning in gel imager. No changes in the blot fluorescence intensity were registered between 5 and 30 min scanning – time enough for membrane imaging and data acquisition.

The higher sensitivity of QD-based methodology in comparison with classical analysis can be explained, at least partially, by the inherent sensitivity of fluorescence compared with chemiluminescence. The QD-labeled membranes can be kept in buffer at 4 °C for a week without loss of image quality. It was also possible to improve markedly the brightness of blots with serial incubations of PVDF-membrane in QD-labeled neutravidin and QD-labeled biotin. However, concentration-dependent saturation of QD-signal was detected at high protein concentrations of cell lysate (applied to each gel patch) and this procedure can be recommended for work with samples containing less than 20  $\mu\text{g}$  protein per gel patch.

The proposed QD-based immunoblotting technologies with fluorescent detection allow the possibility of quantification of the blot fluorescence, and they also

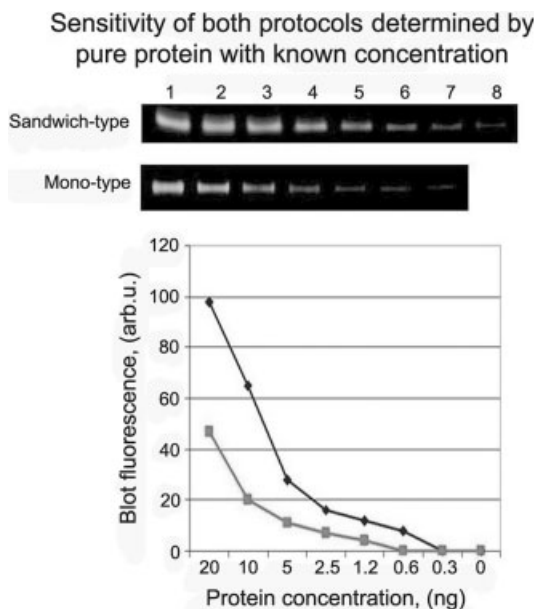


**Fig. 6.13.** Sensitivity of “sandwich type” and “mono-type” QD-based immunoblot analyses, as determined by pure soybean agglutinin (two-serial dilution starting from 20 ng per gel patch – number 1). Upper curve – “sandwich type”; lower curve – “mono type”.

shortened the time of analysis of “tracer” proteins in comparison with the standard methodology. The sensitivity of our protocols was up to 1 and 5 ng of pure protein per gel patch for “sandwich” and “mono” type, respectively (Fig. 6.13). The detection of QD-labeled immunoblotted proteins is simple, in contrast to the detection procedures of the standard western blot analysis. Standard technology requires a transfer of the chemiluminescent signal on Hyperfilms, which is a time- and cost-consuming process. Both technologies in our study were developed for detection of TRF1 and Tin2 in K-562 cells, but they can also be applied for detection of other proteins in different cellular and tissue samples.

## 6.5

### Quantum Dots for FRET Analyses, Time-resolved Fluorimetry, and Development of Optical Recognition-based Biosensors

#### 6.5.1

##### Quantum Dots for FRET-based Bioanalyses

In the past several years, FRET has been involved in many biochemical analyses and applied to the development of simple fluorescence detection techniques, in-

cluding a PCR with real-time FRET measurements; DNA hybridization analyses and formation and dissociation of hairpin structures; an elucidation of the dynamics of telomerization or DNA replication; and an investigation of interactions between proteins, nucleic acids and small molecules [23, 87–90].

The essential requirement for FRET is that the emission spectrum of the donor has to overlap with the absorption spectrum of the acceptor, and distance between donor and acceptor has to be within 1–10 nm. Reports on QDs as FRET-donors in a biological context appeared from 2001 [56, 57]; however, the full potential has not been demonstrated yet. Several elegant studies in this field have been designed and provided recently by the U.S. Naval Research Laboratory [23, 24, 58, 59]. By self-assembling acceptor dye-labeled proteins onto QD donor surfaces, two unique advantages over organic fluorophores for FRET became apparent: QD donor emission could be size-tuned to improve spectral overlap with an acceptor dye (using a size selection, it is possible to obtain QDs with emission maximum corresponding exactly to the excitation maximum of the FRET-acceptor) (a), and several acceptor dyes interacting with a single QD-donor substantially improved FRET efficiency (b). Obviously, the unique optical properties of QDs make them the most appropriate FRET-donors. However, currently there is a serious limitation in the widespread use of QDs in FRET-based bioanalyses related to the size of highly luminescent water-soluble QDs, which is usually beyond the Forster radius. Efforts are being directed to the development of small (up to 10 nm in diameter) highly luminescent water-soluble QDs with optimal FRET capacity.

### 6.5.2

#### **Quantum Dots for Time-resolved Fluorimetry**

Some of the presently described QDs possess a comparatively long fluorescence half-life and can be appropriate for time-resolved fluorimetric analyses. Figure 6.14 demonstrates the fluorescence half-life of water-soluble broad-fluorescent CdSe QDs [86]. The fluorescence half-life varied from 27 to 92 ns, depending of the emission wavelength. Lakowicz and colleagues have described sharp-fluorescent CdSe/ZnS QDs with a mean fluorescence half-life of ~17 ns and a heterogeneous intensity decay curve [91]. For comparison, the reported fluorescence half-life of commercial CdSe/ZnS QDs, dispersed in organic solvents, is approximately 10–12 ns [92–94].

### 6.5.3

#### **Quantum Dots for development of New Generation Optical Recognition-based Biosensors**

The FRET capacity and comparatively long fluorescence half-life of QDs are very promising in the evolution of optical recognition-based biosensors that can monitor rapidly the concentrations of target species in their physiological environment, in a continuous, simple and reliable manner. Presently, the most popular recognition-based optical sensors consist of surface immobilized functional

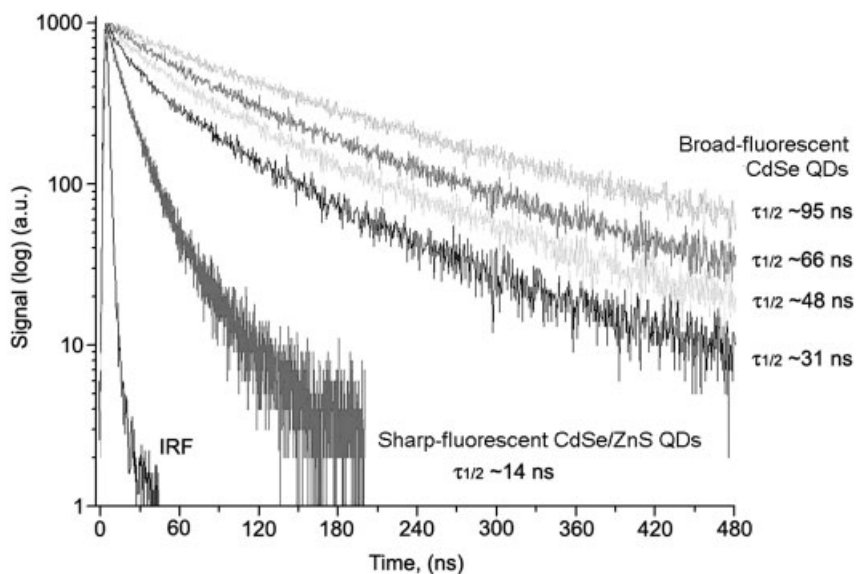


**Fig. 6.14.** Time-resolved fluorescence life-time spectra of water-soluble broad-fluorescent CdSe QDs synthesized at room temperature. For comparison, sharp fluorescent QDs synthesized at high temperature were recorded at an emission wavelength corresponding to

their fluorescent maximum. All data were recorded at an excitation wavelength of 365 nm, frequency 40 kHz, using a Hamamatsu FLS920S spectrometer. IRF = instrumental response function of the nanosecond flash-lamp.

materials – usually a thin polymer film with incorporated hydrophobic organic dye [95, 96]. These sensors possess, predominantly, a pressure or temperature sensing ability, and an ability to detect the concentration of ions and small molecular weight molecules (e.g., oxygen, carbon dioxide, etc.). They do not possess an ability to detect the concentration of middle (100–1000 Da) or high (10–100 kDa) molecular weight molecules and more complex components, since the diffusion of such substances into the film and their accessibility to the dye are strongly restricted. All presently known recognition-based optical sensors work in two dimensions and in a non-aqueous environment. They have no possibility for analysis of complex chemical and biochemical substances, as well as enzyme activities.

The leading tendencies in the development of new generation optical recognition-based biosensors are: to increase the intensity of the specific optical signal; to decrease the intensity of the non-specific noise; to ensure the possibility for detection of water-soluble target compounds in their aqueous environment; and to increase the number of simultaneously analyzed targets in one sensor device.

What can QDs offer to biosensor evolution?

QDs have attracted much attention as one of the most promising nanotransducers that have several advantages over other known nanomaterials. Figures 6.15 and 6.16 represent two common examples for the design of QD-based sensors for detection of chemical or biochemical targets and for detection of enzyme activity.

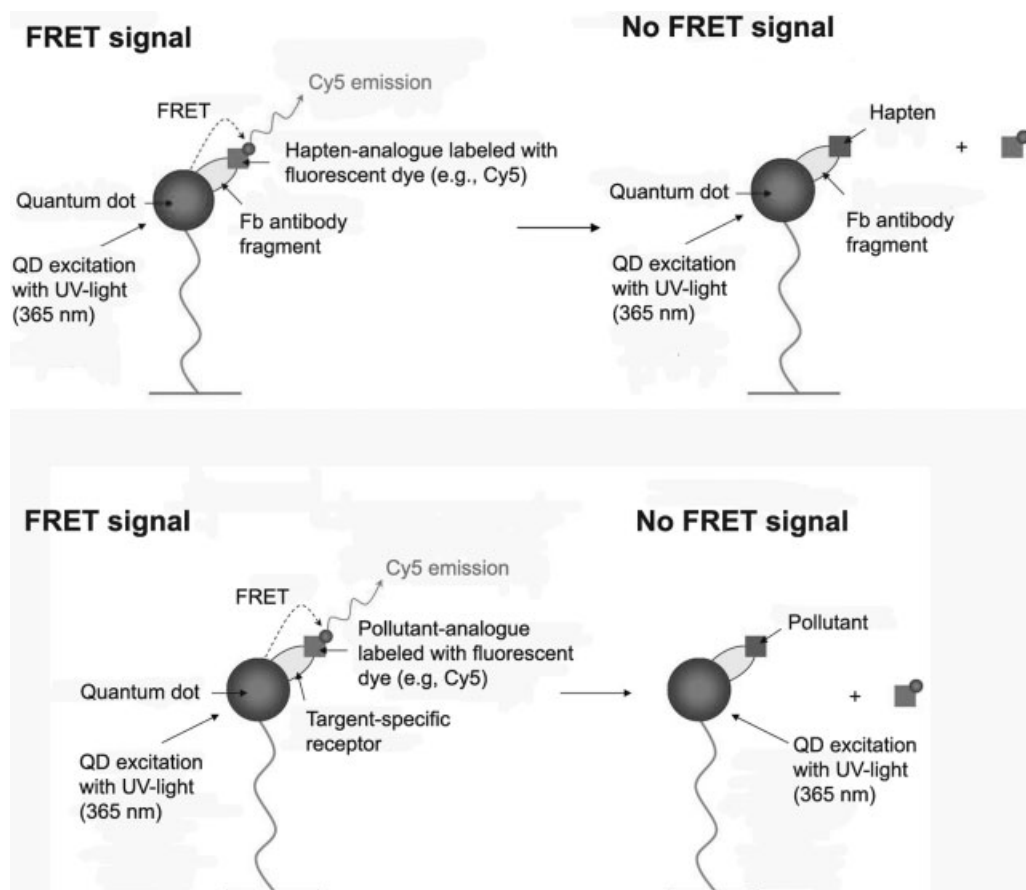


Fig. 6.15. Schemes of QD-based optical sensors for detection of more complex chemical and biochemical targets.

In the first sensor, a QD nanotransducer is conjugated with a receptor-specific for some chemical (or biochemical) target substance that has to be analyzed. The receptor is bound to target analogue, labeled with classical dye (e.g., cyanine). The analytical capacity of the sensor is based on the FRET efficiency between QD and dye. The target analogue has to be with a lower binding affinity to the receptor than the real target. Thus, it can be competitively replaced from the target, which will reflect the FRET signal in a concentration-dependent manner. In the second sensor (biosensor), a quantum dot nanotransducer is conjugated with some enzymatic substrate, e.g., double-stranded RNA (dsRNA) labeled with fluorescent quencher (e.g., black hall quencher, BHQ). The analytical capacity of this biosensor is based on the lack of fluorescence in the presence of quencher near the QD surface and the appearance of fluorescent signal if there is RNase activity leading to a

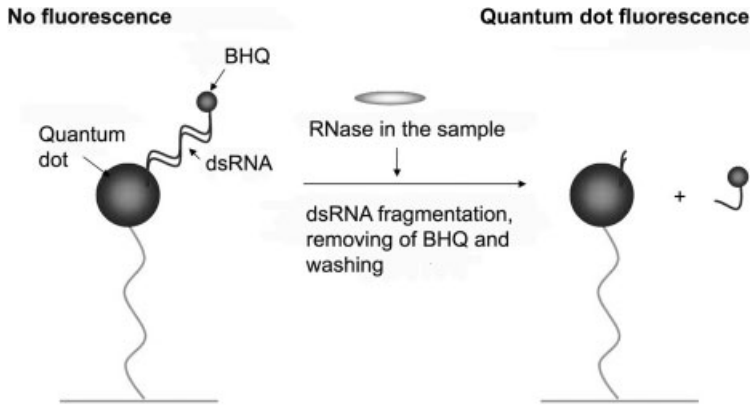


Fig. 6.16. Scheme of QD-based optical sensor for detection of enzyme activity.

fragmentation of dsRNA and removal of the quencher from the QD area. Fluorescence detection in both cases can be realized using fiber optic devices.

QD nanotransducers meet almost all requirements of the leading tendencies in the design and fabrication of new generation recognition-based optical biosensors.

Currently, only QDs manifest a large excitation/emission Stokes shift, which gives an opportunity to overcome the autofluorescence of other components in the sensor device and to minimize the noise, using filter combinations that effectively isolate the desired fluorescent signal. Moreover, the autofluorescence usually appears rapidly, while the FRET-signal appears slower and, using a time-resolved fluorimetry, it is possible additionally to increase the signal-to-noise ratio. The size-dependent multicolor coding properties of QDs render these nanoparticles as an indisputable favorite in multiplex fluorescent analyses. Thus, size-distinguished QD nanotransducers immobilized on 2D or 3D matrices will give an opportunity to develop optical sensor devices for the simultaneous detection of several targets. Presumably, it will be not necessity to separate the size-distinguished QD nanotransducers in the area of matrix platform because the unique fluorescent properties of QDs give a possibility to detect more than six fluorescent signals at the same time. Because different colors QD nanotransducers can be conjugated with different reporters, they can be functionally separated on the matrix.

Finally, the significant progress in the synthesis of highly fluorescent water-soluble QDs makes possible the fabrication of nanobiosensors for detection of biological targets and enzyme activities in their physiological environment, as well as environmental pollutants and food ingredients in aqueous solutions.

Obviously, the bridge between QD technology and fiber optic technology can open up new trends in biosensor evolution, resulting in development of ultrasensitive 3D optical sensors for multiplex detection of low, middle and high molecular weight substances, and enzyme activities, in their natural environment.

## 6.6

**Quantum Dots as New Fluorescent Standards for the Thin Calibration of Fluorescent Instrumentation**

Fluorescence-based measurements are becoming the standard for high-throughput screening technologies, sensing technologies, imaging technologies, forensic determination, genomic research, clinical diagnostics, etc. One of the critical challenges in the measurement of fluorescence is to obtain wavelength calibration. A small discrepancy in wavelength can lead to a large discrepancy in the measured fluorescence intensity. Moreover, absolute fluorescent measurements are also difficult since few fluorescent standards are available. A fluorescence standard is necessary, especially where quantification is required. At present, it is nearly impossible to quantify the fluorescence from an assay. Traditional fluorescing materials, such as organic dyes, lose their fluorescence intensity due to photodegradation and have significant disadvantages as standards. Semiconductor QDs are very promising in this application since they are typically very stable – a characteristic required for a standard. Being composed of simple inorganic compounds they are chemically relatively inert and very resistant to photochemical damage. The size-tunable fluorescent emission of QDs and the large Stokes-shift between excitation and emission give a possibility for application of QD composite materials for the thin calibration of fluorescent instrumentation.

Future efforts are being directed to the development of QD composites (consisting of QDs incorporated in transparent materials such as polymers, silica, etc.) and to applying them in fluorescent measurements – to characterize these materials and to evaluate their possible use as novel fluorescence standards for calibration of biotech instrumentation. This is the priority of all leading institutes in the field of measurements and standardization.

Fluorescent standards based on QD composites will possess the following improved characteristics in comparison with conventional fluorescent standards (based on organic dyes incorporated into transparent composite materials): a higher quantum yield (70–80% vs. 15–50% for classical standards); a higher chemical and photochemical stability; a long fluorescence life-time; a possibility for fabrication of fluorescent standards that have Stokes' shifts of several nanometers for thin calibration of the fluorescent instrumentation, which is impossible with traditional fluorescent standards.

**References**

- 1 ALIVISATOS, A. P., Semiconductor clusters, nanocrystals, and quantum dots, *Science* **1996**, 271, 933–937.
- 2 DAHAN, M., LAURENCE, F., PINAUD, D. S., ALIVISATOS, A. P., SAUER, M., WEISS, S., Time-gated biological imaging by use of colloidal quantum dots, *Opt. Lett.* **2001**, 26, 825–827.
- 3 NIRMAL, M., DABBOUSI, B. O., BAWENDI, M. G., MACKLIN, J. J., TRAUTMAN, J. K., HARRIS, T. D., BRUS, L. I., Fluorescence intermittency in



- single cadmium selenide nanocrystals, *Nature* **1996**, 383, 802–804.
- 4 TANG, J., MARCUS, R. A., Mechanisms of fluorescence blinking in semiconductor nanocrystal quantum dots, *J. Chem. Phys.* **2005**, 123(5), 054704.
  - 5 SHIMIZU, K. T., WOO, W. K., FISHER, B. R., EISLER, H. J., BAWENDI, M. G., Surface-enhanced emission from single semiconductor nanocrystals, *Phys. Rev. Lett.* **2002**, 89(11), 117401.
  - 6 MEDINTZ, I. L., UYEDA, H. T., GOLDMAN, E. R., MATTOUSSI, H., Quantum dot bioconjugates for imaging, labeling and sensing, *Nature Mater.* **2005**, 4(6), 435–446.
  - 7 ALIVISATOS, A. P., GU, W., LARABELL, C., Quantum dots as cellular probes, *Annu. Rev. Biomed. Eng.* **2005**, 7, 55–76.
  - 8 GAO, X., YANG, L., PETROS, J. A., MARSHALL, F. F., SIMONS, J. W., NIE, S., *In vivo* molecular and cellular imaging with quantum dots, *Curr. Opin. Biotechnol.* **2005**, 16(1), 63–72.
  - 9 MICHALET, X., PINAUD, F. F., BENTOLILA, L. A., TSAY, J. M., DOOSE, S., LI, J. J., SUNDARESAN, G., WU, A. M., GAMBHIR, S. S., WEISS, S., Quantum dots for live cells, *in vivo* imaging, and diagnostics, *Science* **2005**, 307(5709), 538–544.
  - 10 JAISWAL, J. K., SIMON, S. M., Potentials and pitfalls of fluorescent quantum dots for biological imaging, *Trends Cell Biol.* **2004**, 14(9), 497–504.
  - 11 PENN, S. G., HE, L., NATAN, M. J., Nanoparticles for bioanalyses, *Curr. Opin. Chem. Biol.* **2003**, 7(5), 609–615.
  - 12 GAO, X. H., CUI, Y. Y., LEVENSON, R. M., CHUNG, L. W. K., NIE, S. M., *In vivo* cancer targeting and imaging with semiconductor quantum dots, *Nat. Biotechnol.* **2004**, 22, 969–976.
  - 13 GAO, W., LI, J. J., WANG, Y. A., PENG, X., Layered structural heme protein magadiite nanocomposites with high enzyme-like peroxidase activity, *Chem. Mater.* **2003**, 15, 3125–3133.
  - 14 MATTOUSSI, H., MAURO, J. M., GOLDMAN, E. R., ANDERSON, G. P., SUNDAR, V. C., MICULEC, F. V., BAWENDI, M. G., Self-assembly of CdSe-ZnS quantum dot bioconjugates using an engineered recombinant protein, *J. Am. Chem. Soc.* **2000**, 122, 12142–12150.
  - 15 UYEDA, H. T., MEDINTZ, I. L., JAISWAL, J. K., SIMON, S. M., MATTOUSSI, H., Synthesis of compact multidentate ligands to prepare stable hydrophilic quantum dot fluorophores, *J. Am. Chem. Soc.* **2005**, 127, 3870–3878.
  - 16 DUBERTRET, B., SKOURIDES, P., NORRIS, D. J., NOIREAUX, V., BRIVANLOU, A. H., LICHBABER, A., *In vivo* imaging of quantum dots encapsulated in phospholipids micelles, *Science* **2002**, 298, 1759–1762.
  - 17 MATTHEAKIS, L. C., DIAS, J. M., CHOI, Y. J., GONG, J., BRUCHEZ, M. P., LIU, J., WANG, E., Optical coding of mammalian cells using semiconductor quantum dots, *Anal. Biochem.* **2004**, 327, 200–208.
  - 18 BALLOU, B., LAGERHOLM, B. C., ERNST, L. A., BRUCHEZ, M. P., WAGGONER, A. S., Noninvasive imaging of quantum dots in mice, *Bioconj. Chem.* **2004**, 15, 79–86.
  - 19 DAHAN, M., LEVI, S., LUCCARDINI, C., ROSTAING, P., RIVEAU, B., TRILLER, A., Diffusion dynamics of glycine receptors revealed by single-quantum dot tracking, *Science* **2003**, 302, 442–445.
  - 20 WU, X. Y., LIU, H. J., LIU, J. Q., HALEY, K. N., TREADWAY, J. A., LARSON, J. P., GE, N. F., PEALE, F., BRUCHEZ, M. P., Immunofluorescent labeling of cancer marker Her2 and other cellular targets with semiconductor quantum dots, *Nat. Biotechnol.* **2003**, 21, 41–46.
  - 21 LIDKE, D. S., NAGY, P., HEINTZMANN, R., ARNDT-JOVIN, D. J., POST, J. N., GRECCO, H. E., JARES-ERJIMAN, E. A., JOVIN, T. M., Quantum dot ligands provide new insights into erbB/HER receptor-mediated signal transduction, *Nat. Biotechnol.* **2004**, 22, 198–203.
  - 22 JAISWAL, J. K., MATTOUSSI, H., MAURO, J. M., SIMON, S. M., Long-term multiple color imaging of live cells using quantum dot bioconjugates, *Nat. Biotechnol.* **2003**, 21, 47–51.

- 23 MEDINTZ, I. L., CLAAP, A. R., MATTOUSSI, H., GOLDMAN, E. R., FISHER, B., MAURO, J. M., Self-assembled nanoscale biosensors based on quantum dot FRET donors, *Nature Mater.* **2003**, *2*, 630–638.
- 24 MEDINTZ, I. L., KONNERT, J. H., CLAAP, A. R., STANISH, I., TWIGG, M. E., MATTOUSSI, H., MAURO, J. M., DESCHAMPS, J. R., A fluorescence resonance energy transfer-derived structure of a quantum dot-protein bioconjugate nanoassembly, *Proc. Natl. Acad. Sci. U.S.A.* **2004**, *101*, 9612–9617.
- 25 ROSENTHAL, S. J., TOMLINSON, I., ADKINS, E. M., SCHROETER, S., ADAMS, S., SWAFFORD, L., MCBRIDE, J., WANG, Y., DEFELICE, L. J., BLAKELY, R. D., Targeting cell surface receptors with ligand-conjugated nanocrystals, *J. Am. Chem. Soc.* **2002**, *124*, 4586–4594.
- 26 ZHELEV, Z., OHBA, H., BAKALOVA, R., JOSE, R., FUKUOKA, S., NAGASE, T., ISHIKAWA, M., BABA, Y., Fabrication of quantum dot-lectin conjugates as novel fluorescent probes for microscopic and flow cytometric identification of leukemia cells from normal lymphocytes, *Chem. Commun.* **2005**, 1980–1982.
- 27 BAKALOVA, R., ZHELEV, Z., OHBA, H., BABA, Y., Quantum dot-based western blot technology for ultrasensitive detection of tracer proteins, *J. Am. Chem. Soc.* **2005**, *127*(26), 9328–9329.
- 28 BAKALOVA, R., ZHELEV, Z., OHBA, H., BABA, Y., Quantum dot-conjugated hybridization probes for preliminary screening of siRNA sequences, *J. Am. Chem. Soc.* **2005**, *127*(32), 11 328–11 335.
- 29 KIM, S., LIM, Y. T., SOLTESZ, E. G., DEGRAND, A. M., LEE, J., NAKAYAMA, A., PARKER, J. A., MIHALJEVIC, T., LAURENCE, R. G., DOR, D. M., COHN, L. H., BAWENDI, M. G., FRANGIONI, J. V., Near-infrared fluorescent type II quantum dots for sentinel lymph node mapping, *Nat. Biotechnol.* **2004**, *22*(1), 93–96.
- 30 OZKAN, M., Quantum dots and other nanoparticles: What can they offer to drug discovery? *Drug Discovery Today* **2004**, *9*(24), 1065–1071.
- 31 BAKALOVA, R., OHBA, H., ZHELEV, Z., ISHIKAWA, M., BABA, Y., Quantum dots as photosensitizers?, *Nat. Biotechnol.* **2004**, *22*(11), 1360–1361.
- 32 BAKALOVA, R., OHBA, H., ZHELEV, Z., NAGASE, T., JOSE, R., ISHIKAWA, M., BABA, Y., Quantum dot anti-CD conjugates: Are they potential photosensitizers or potentiators of classical photosensitizing agents in photodynamic therapy of cancer? *Nano Lett.* **2004**, *4*(9), 1567–1573.
- 33 LEATHERDALE, C. A., WOO, W. K., MIKULEC, F. V., BAWENDI, M. G., On the absorption cross section of CdSe nanocrystal quantum dots, *J. Phys. Chem. B* **2002**, *106*, 7619–7622.
- 34 MURPHY, C. J., Optical sensing with quantum dots, *Anal. Chem.* **2002**, *74*, 520A–526A.
- 35 ALIVISATOS, A. P., The use of nanocrystals in biological detection, *Nat. Biotechnol.* **2004**, *22*, 47–52.
- 36 MATTOUSSI, H., KUNO, M. K., GOLDMAN, E. R., ANDERSON, G. P., MAURO, J. M., in *Optical Biosensors: Present and Future*, E. S. LIGLER, C. A. ROWE (Eds.), Elsevier, Amsterdam, **2002**, pp. 537–569.
- 37 BRUCHEZ, J. M., MORONNE, M., GIN, P., WEISS, S., ALIVISATOS, A. P., Semiconductor nanocrystals as fluorescence biological labels, *Science* **1998**, *281*, 2013–2015.
- 38 CHAN, W. C. W., NIE, S. M., Quantum dot bioconjugates for ultrasensitive nonisotopic detection, *Science* **1998**, *281*, 2016–2018.
- 39 JAKOBS, S., SUBRAMANIAM, V., SCHONLE, A., JOVIN, T. M., HELL, S. W., EFGP and DsRed expressing cultures of Escherichia coli imaged by confocal, two-photon and fluorescence lifetime microscopy, *FEBS Lett.* **2000**, *479*, 131–135.
- 40 PEPPERKOK, R., SQUIRE, A., GELEY, S., BASTIAENS, P. I. H., Simultaneous detection of multiple green fluorescent proteins in live cells by fluorescence lifetime imaging microscopy, *Curr. Biol.* **1999**, *9*, 269–272.

- 41 GAO, X., CHAN, W. C., NIE, S., Quantum dot nanocrystals for ultrasensitive biological labeling and multicolor optical encoding, *J. Biomed. Opt.* **2002**, 7(4), 532–537.
- 42 CUNIN, F., SCHMEDAKE, T. A., LINK, J. R., LI, Y. Y., KOH, J., BHATIA, S. N., SAILOR, M. J., Biomolecular screening with encoded porous-silicon photonic crystals, *Nat. Mater.* **2002**, 1(1), 39–41.
- 43 CHAN, P., YUEN, T., RUF, F., GONZALEZ-MAESO, J., SEALFON, S. C., Method for multiplex cellular detection of mRNAs using quantum dot fluorescent in situ hybridization, *Nucleic Acids Res.* **2005**, 33(18), e161.
- 44 LIANG, R. Q., LI, W., LI, Y., TAN, C. Y., LI, J. X., JIN, Y. X., RUAN, K. C., An oligonucleotide microarray for microRNA expression analysis based on labeling RNA with quantum dot and nanogold probe, *Nucleic Acids Res.* **2005**, 33(2), e17.
- 45 ROBELEK, R., NIU, L., SCHMID, E. L., KNOLL, W., Multiplexed hybridization detection of quantum dot-conjugated DNA sequences using surface plasmon enhanced fluorescence microscopy and spectrometry, *Anal. Chem.* **2004**, 76(20), 6160–6165.
- 46 WANG, J., LIU, G., MERKOZI, A., Electrochemical coding technology for simultaneous detection of multiple DNA targets, *J. Am. Chem. Soc.* **2003**, 125(11), 3214–3215.
- 47 HO, Y. P., KUNG, M. C., YANG, S., WANG, T. H., Multiplexed hybridization detection with multicolor colocalization of quantum dot nanoprobe, *Nano Lett.* **2005**, 5(9), 1693–1697.
- 48 GAO, X., NIE, S., Quantum dot-encoded mesoporous beads with high brightness and uniformity: Rapid readout using flow cytometry, *Anal. Chem.* **2004**, 76(8), 2406–2410.
- 49 LACOSTE, T. D., MICHALET, X., PINAUD, F., CHEMLA, D. S., ALIVISATOS, A. P., WEISS, S., Ultrahigh-resolution multicolor colocalization of single fluorescent probes, *Proc. Natl. Acad. Sci. U.S.A.* **2000**, 97, 9461–9466.
- 50 MICHALET, X., PINAUD, F., LACOSTE, T. D., DAHAN, M., BRUCHEZ, M. P., ALIVISATOS, A. P., WEISS, S., Properties of fluorescent semiconductor nanocrystals and their application to biological labeling, *Single Mol.* **2001**, 2, 261–276.
- 51 POWE, A. M., FLETCHER, K. A., ST. LUCE, N. N., LOWRY, M., NEAL, S., MCCARROLL, M. E., OLDHAM, P. B., MCGOWN, L. B., WARNER, I. M., Molecular fluorescence, phosphorescence, and chemiluminescence spectrometry, *Anal. Chem.* **2004**, 76(16), 4614–4634.
- 52 HOHNG, S., HA, T., Near-complete suppression of quantum dot blinking in ambient conditions, *J. Am. Chem. Soc.* **2004**, 126, 1324–1325.
- 53 LARSON, D., ZIPFEL, W. R., WILLIAMS, R. M., CLARK, S. W., BRUCHEZ, M. P., WISE, F. W., WEBB, W. W., Water-soluble quantum dots for multiphoton fluorescence imaging in vivo, *Science* **2003**, 300, 1434–1436.
- 54 LEE, S., THOMAS, K. R. J., THAYUMANAVAN, S., BARDEEN, C. J., Dependence of the two-photon absorption cross section on the conjugation of the phenylacetylene linker in dipolar donor-bridge-acceptor chromophores, *J. Phys. Chem. A* **2005**, 109(43), 9767–9774.
- 55 BHARALI, D. J., LUCEY, D. W., JAYAKUMAR, H., PUDAVAR, H. E., PRASAD, P. N., Folate-receptor-mediated delivery of InP quantum dots for bioimaging using confocal and two-photon microscopy, *J. Am. Chem. Soc.* **2005**, 127(32), 11364–11371.
- 56 WILLARD, D. M., CARILLO, I. I., JUNG, J., VAN ORDEN, A., CdSe-ZnS quantum dots as resonance energy transfer donors in a model protein-protein binding assay, *Nano Lett.* **2001**, 1, 469–474.
- 57 MAMEDOVA, N. N., KOTOV, N. A., ROGACH, A. L., STUDER, J., Albumin-CdTe nanoparticle bioconjugates: Preparation, structure, and interunit energy transfer with antenna effect, *Nano Lett.* **2001**, 1, 281–286.
- 58 CLAAP, A. R., MEDINTZ, I. L., MAURO, J. M., FISHER, B. R., BAWENDI, M. G., MATTOUSSI, H., Fluorescence

- resonance energy transfer between quantum dot donors and dye-labeled protein acceptors, *J. Am. Chem. Soc.* **2004**, *126*, 301–310.
- 59 CLAAP, A. R., MEDINTZ, I. L., FISHER, B. R., ANDERSON, G. P., MATTOUSSI, H., Can luminescent quantum dots be efficient energy acceptors with organic dye donors? *J. Am. Chem. Soc.* **2005**, *127*(4), 1242–1250.
- 60 EBENSTEIN, Y., MOKARI, T., BANIN, U., Quantum dot-functionalized scanning probes for fluorescence-energy-transfer-based microscopy, *J. Phys. Chem. B* **2004**, *108*(1), 93–99.
- 61 KLOEPFER, J. A., COHEN, N., NADEAU, J. L., FRET between CdSe quantum dots in lipid vesicles and water- and lipid-soluble dyes, *J. Phys. Chem. B* **2004**, *108*(44), 17042–17049.
- 62 SAMIA, A. C. S., CHEN, X., BURDA, C. Semiconductor quantum dots for photodynamic therapy, *J. Am. Chem. Soc.* **2003**, *125*(51), 15736–15737.
- 63 AKERMAN, M. E., CHAN, W. C. W., LAAKKONEN, P., BHATIA, S. N., ROUSLAHTI, E., Nanocrystal targeting *in vivo*, *Proc. Natl. Acad. Sci. U.S.A.* **2002**, *99*, 12617–12621.
- 64 XIAO, Y., BARKER, P. E., Semiconductor nanocrystal probes for human metaphase chromosomes, *Nucleic Acids Res.* **2004**, *32*, e28.
- 65 HANAKI, K., MOMO, A., OKU, T., KOMOTO, A., MAENOSONO, S., YAMAGUCHI, Y., YAMAMOTO, K., Semiconductor quantum dot/albumin complex is a long-life and highly photostable endosome marker, *Biochem. Biophys. Res. Commun.* **2003**, *302*, 496–501.
- 66 SUKHANOVA, A., DEVI, J., VENTEO, L., KAPLAN, H., ARTEMYEV, M., OLEINIKOV, V., KLINOV, D., PLUOT, M., COHEN, J. H., NABIEV, I., Biocompatible fluorescent nanocrystals for immunolabeling of membrane proteins and cells, *Anal. Biochem.* **2004**, *324*, 60–67.
- 67 KAUL, Z., YAGUCHI, T., KAUL, S. C., HIRANO, T., WADHWA, R., TAIRA, K., Mortalin imaging in normal and cancer cells with quantum dot immuno-conjugates, *Cell Res.* **2003**, *13*, 503–507.
- 68 HOSHINO, A., HANAKI, K.-I., SUZUKI, K., YAMAMOTO, K., Applications of T lymphoma labeled with fluorescent quantum dots to cell tracing markers in mouse body, *Biochem. Biophys. Res. Commun.* **2004**, *314*, 46–53.
- 69 CHEN, F., GERION, D., Fluorescent CdSe/ZnS nanocrystal-peptide conjugates for long-term, nontoxic imaging and nuclear targeting in living cells, *Nano Lett.* **2004**, *4*, 1827–1832.
- 70 DERFUS, A. M., CHAN, W. C. W., BHATIA, S. N., Intracellular delivery of quantum dots for live cell labeling and organelle tracking, *Adv. Mater.* **2004**, *16*, 961–966.
- 71 VOURA, E. B., JAISWAL, J. K., MATTOUSSI, H., SIMON, S. M., Tracking early metastatic progression with quantum dots and emission scanning microscopy, *Nat. Med.* **2004**, *10*, 993–998.
- 72 DWARAKANATH, S., BRUNO, J. G., SHASTRY, A., PHILLIPS, T., JOHN, A. A., KUMAR, A., STEPHENSON, L. D., Quantum dot-antibody and aptamer conjugates shift fluorescence upon binding bacteria, *Biochem. Biophys. Res. Commun.* **2005**, *325*(3), 739–743.
- 73 PINAUD, F., KING, D., MOORE, H.-P., WEISS, S., Bioactivation and cell targeting of semiconductor CdSe/ZnS nanocrystals with phytochelatin-related peptides, *J. Am. Chem. Soc.* **2004**, *126*, 6115–6123.
- 74 WINTER, J. O., LIU, T. Y., KORGEL, B. A., SCHMIDT, C. E., Recognition molecule directed interfacing between semiconductor quantum dots and nerve cells, *Adv. Mater.* **2001**, *13*, 1673–1677.
- 75 LEWIN, M., CARLESSO, N., TUNG, C. H., TANG, X. W., CORY, D., SCADDEN, D. T., WEISSLEDER, R., Tat peptide-derivatized magnetic nanoparticles allow *in vivo* tracking and recovery of progenitor cells, *Nat. Biotechnol.* **2000**, *18*, 410–414.
- 76 TOKUMASU, F., DVORAK, J., Development and application of quantum dots

- for immunocytochemistry of human erythrocytes, *J. Microsc.* **2003**, 211, 256–261.
- 77 SMITH, A. M., RUAN, G., RHYNER, M. N., NIE, S., Engineering luminescent quantum dots for in vivo molecular and cellular imaging, *Ann. Biomed. Eng.* **2006**, 34, 3–14.
- 78 PINAUD, F., MICHALET, X., BENTOLILA, L. A., TSAY, J. M., DOOSE, S., LI, J. J., IYER, G., WEISS, S., Advances in fluorescence imaging with quantum dot bio-brobes, *Biomaterials* **2006**, 27, 1679–1687.
- 79 LIM, Y. T., KIM, S., NAKAYAMA, A., STOTT, N. E., BAWENDI, M. G., FRANGIONI, J. V., Selection of quantum dot wavelengths for biomedical assays and imaging, *Mol. Imaging* **2003**, 2, 50–64.
- 80 KIM, S., BAWENDI, M. G., Oligomeric ligands for luminescent and stable nanocrystal quantum dots, *J. Am. Chem. Soc.* **2003**, 125(48), 14 652–14 653.
- 81 LARSON, D. R., ZIPFEL, W. R., WILLIAMS, R. M., CLARK, S. W., BRUCHEZ, M. P., WISE, F. W., WEBB, W. W., Water-soluble quantum dots for multiphoton fluorescence imaging in vivo, *Science* **2003**, 300, 1434–1436.
- 82 ROSENTHAL, S. J., TOMLINSON, I., ADKINS, E. M., SCHROETER, S., ADAMS, S., SWAFFORD, L., MCBRIDE, J., WANG, Y., DEFELICE, L. J., BLAKELY, R. D., Targeting cell surface receptors with ligand-conjugated nanocrystals, *J. Am. Chem. Soc.* **2002**, 124, 4586–4594.
- 83 WANG, D. S., HE, J. B., ROSENZWEIG, N., ROSENZWEIG, Z., Superparamagnetic Fe<sub>2</sub>O<sub>3</sub> beads-CdSe/ZnS quantum dots core-shell nanocomposite particles for cell separation, *Nano Lett.* **2004**, 4, 409–413.
- 84 BAKALOVA, R., ZHELEV, Z., AOKI, I., OHBA, H., IMAI, Y., KANNO, I., Silica-shelled single quantum dot micelles as imaging probes with dual and multimodality, *Anal. Chem.* **2006**, 78(16), 5925–5932.
- 85 ORNBERG, R. L., HARPER, T. F., LIU, H., Western blot analysis with quantum dot fluorescence technology: A sensitive and quantitative method for multiplexed proteomics, *Nat. Methods* **2005**, 2, 79–81.
- 86 ZHELEV, Z., BAKALOVA, R., OHBA, H., JOSE, R., IMAI, Y., BABA, Y., Uncoated, broad-fluorescent, and size-homogenous CdSe quantum dots for bioanalyses, *Anal. Chem.* **2006**, 78(1), 321–330.
- 87 GUDMUNDSSON, B., BJARNADOTTIR, H., KRISTJANSDOTTIR, S., JONSSON, J. J., Quantitative assays for maedi-visna virus genetic sequences and mRNA's based on RT-PCR with real-time FRET measurements, *Virology* **2003**, 307, 135–142.
- 88 YURKE, B., TURBERFIELD, A. J., MILLS, A. P., SIMMEL, F. C., NEUMANN, J. L., A DNA-fuelled molecular machine made of DNA, *Nature* **2000**, 406, 605–608.
- 89 DUBERTRET, B., CALAME, M., LIBCHABER, A. J., Single-mismatch detection using gold-quenched fluorescent oligonucleotides, *Nat. Biotechnol.* **2001**, 19, 365–370.
- 90 PATOLSKY, F., GILL, R., WEIZMANN, Y., MOKARI, T., BANIN, U., WILLNER, I., Lighting-up the dynamics of telomerization and DNA replication by CdSe-ZnS quantum dots, *J. Am. Chem. Soc.* **2003**, 125, 13 918–13 919.
- 91 GRYCZYNSKI, I., MALICKA, J., JIANG, W., FISHER, H., CHAN, W. C. W., GRYCZYNSKI, Z., GRUDZINSKI, W., LAKOWICZ, J. R., Surface-plasmon-coupled emission of quantum dots, *J. Phys. Chem. B* **2005**, 109, 1088–1093.
- 92 WARNER, J. H., THOMSEN, E., WATT, A. R., HECKENBERG, N. R., RUBINSZTEIN-DUNLOP, H., Time-resolved photoluminescence spectroscopy of ligand-capped PbS nanocrystals, *Nanotechnology* **2005**, 16, 175–179.
- 93 LODAHL, P., VAN DRIEL, A. F., NIKOLAEV, I. S., IRMAN, A., OVERGAAG, K., VANMAEKELBERGH, D., VOS, W. L., Controlling the dynamics of spontaneous emission from quantum dots by photonic crystals, *Nature* **2004**, 430, 654–657.

- 94 WOGGON, U., HERZ, E., SCHOPS, O., ARTEMYEV, M. V., ARENS, Ch., ROUSSEAU, N., SCHIKORA, D., LISCHKA, K., LITVINOV, D., GERTHSEN, D., Hybrid epitaxial-colloidal semiconductor nanostructures, *Nano Lett.* **2005**, 5, 483–490.
- 95 ORELLANA, G., MORENO-BONDI, M. C. (Eds.), *Frontiers in Chemical Sensors*, Springer Verlag, Berlin, **2005**, Vol. 3.
- 96 NARAYANASWAMY, R., WOLFBEIS, O. S. (Eds.), *Optical Sensors*, Springer Verlag, Berlin, **2004**, Vol. 1.

## 7

## Detection of Biological Materials by Gold Nano-biosensor-based Electrochemical Method

Juan Jiang, Manju Basu, Sara Seggerson, Albert Miller, Michael Pugia, and Subhash Basu

## 7.1

### Introduction

*Escherichia coli* (*E. coli*) is a fecal coliform bacteria commonly found in the intestine of healthy humans and animals, but disease-causing pathogenic forms such as *E. coli* O157:H7 are responsible for food-borne and water-borne illness because they can rapidly produce a powerful toxin, resulting in hemorrhagic colitis or hemolytic uremic syndrome, which may lead to death, especially in children. Not only *E. coli* but also other pathogenic bacteria produce toxins (such as *Cholera*, *Salmonella*, *Pseudomonas*, etc.) and they divide in human bodies quite rapidly (doubling times are 10 to 15 min). Time, sensitivity, and accuracy of analysis are the most important limitations affecting the usefulness of microbiological methods of detection for pathogenic bacteria. Most of these microbiological detection techniques involve the binding of a non-fluorescent or fluorescent dye to the bacteria and the culturing and screening in the presence of several antibiotics for 2 to 3 days. Thus, while a specific strain is being identified, a patient may die helplessly with kidney infection from *E. coli* or *Salmonella* (from food). A quicker detection method for pathogenic strains of such bacteria is urgently needed to maintain human health around the world.

Gold-based amperometric sensors are now recognized as very promising and powerful tools in bio-fluid or biomaterial investigations and their associated clinical studies. It is expected that such sensors will not only cut down the time of detection but also guide doctors to prescribe specific drug or antibiotic therapy to save a human being without contributing unduly to the growing problem of drug resistance. In addition, subtle changes in adsorbates at electrolyte/electrode interfaces affect the AC capacitance measured in two electrode cell systems by Electrochemical Impedance Spectroscopy (EIS) and could be used to sensitively detect and distinguish any strain of bacteria present on gold surface based biosensors, provided binding specificity can be provided by a surface bound specific antibody. An understanding of the electrical polarization mechanisms in bacteria leading to the AC capacitive response and the database that catalogues this determined capac-

itance behavior of selective antibody-bound bacteria are not available. Until such knowledge is developed, EIS biosensor development will continue to proceed on a case-by-case basis, limiting progress in the next few years.

Section 7.2 of this chapter gives a detailed method for the preparation of various kinds of gold nanowires arrays (GNW), while Section 7.3 describes the method for synthesis and attachment of a linker, dithiobissuccinimidylundecanoate (DSU), to these GNW, which significantly increases the binding capacity of a specific antibody. Section 7.4 details the method of bacteria detection utilizing GNW and Electrochemical Impedance Spectroscopy (EIS). Preliminary results demonstrate the potential applications of this kind of biosensor in clinical laboratories, environmental monitoring, and the food industry to achieve rapid and sensitive detections.

## 7.2

### Template Synthesis of Gold Nano-wire Arrays for Biosensor Applications

#### 7.2.1

##### General Template Synthesis

Template synthesis is one of the ways to form nanostructured materials. The nanostructured materials are formed by confining the nucleation and growth of the material inside the ordered templates. The advantage of this method is that it can be very generally applied. Various nanostructured materials, such as conductive polymer [1–5], metals [6–11], and semiconductors [12–14], can be prepared using the same type of template. Moreover, nanostructured materials with different shapes, such as nano sized wires, rods, tubules and particles, can be prepared by controlling the growth morphology of the materials inside a template cavity [15–18]. With a two-step replication, the template nanostructure can be duplicated in most materials [19]. Template synthesis has been able to produce materials with the dimensions of only several nanometers [20, 21], which are very difficult to make by lithographic methods. Template synthesis is also suitable for mass production.

Most template syntheses reported in the literature have been accomplished by the use of a nanoporous film. To date, there are mainly two types of films: “track-etch” polymeric films and porous alumina films [22, 23]. Track-etch films are made by bombarding a polymeric material to create damaged tracks and then chemically etching these tracks into pores. These porous films are commercially available as microporous or nanoporous polymeric filtration membranes, with pore diameters ranging from 10 nm to several microns [22, 23]. The drawbacks of “track-etch” membrane are randomly distributed pores and a wide distribution of pore diameters. Porous alumina films are produced electrochemically. Masuda et al. [24–26] have reported that, under certain conditions, the pores are self-ordered. All the pores have the same diameter and are uniformly distributed across the surface. The pores are vertically aligned, perpendicular to the film surface, and hexagonally arranged. In addition, the pore diameter is adjustable by controlling the conditions



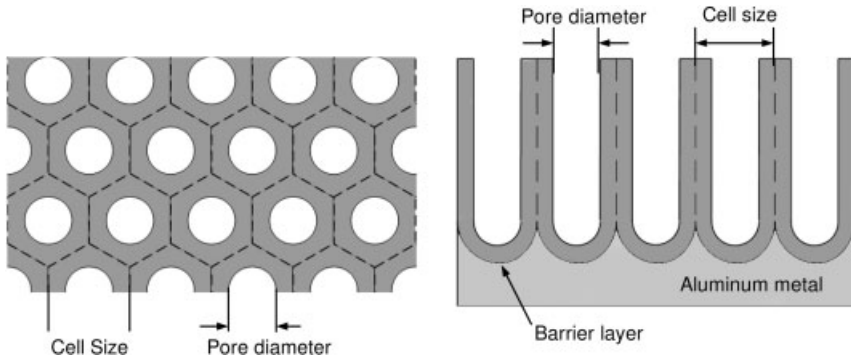


**Fig. 7.1.** Schematic illustration of the porous oxide film that grows on aluminum when it is anodized in acidic electrolytes.

of the electrochemical preparation process. A very high aspect ratio (pore length divided by the pore diameter) can be easily achieved, which is difficult to obtain by conventional lithographic techniques. Because of the regularity of the pore structure and ease of formation, the porous alumina films with pore diameters from 5 nm to more than 200 nm have been used as the template to prepare various nano-materials for applications in optoelectronic, electronic, and magnetic devices, in addition to catalysis.

The ideal structure of an anodized porous aluminum oxide film is a two-dimensional (2D) close-packed array of columnar hexagonal cells, each containing a central pore normal to the underlying metal surface and separated from it by a convex barrier-type film (Fig. 7.1). This porous  $\text{Al}_2\text{O}_3$  film is made by electrochemical anodic oxidation of aluminum in a chilled acid bath. Traditionally,  $\text{Al}_2\text{O}_3$  film is prepared to protect the metal against corrosion and to improve its abrasion and adsorption properties. The more recent and rapidly growing applications of porous anodic alumina in nano material synthesis are due to the self-assembled and well-controllable pore structure, high throughput, and low cost compared with conventional lithographic (electron beam, focused ion beam, X-ray, STM/AFM, etc.) techniques.

Anodic processes consist of the oxidation of metals and the formation of a hard oxide film, the partial dissolution of metals in the electrolyte, and the evolution of gaseous oxygen at the anode. The applied electric field sustains a continued growth of the film by causing metal ions and oxygen ions to be pulled through the growing film in opposite directions.

More than 40 years ago, Hoar and Mott [27] first proposed their field-assisted dissolution model to explain the pore initiation and growth phenomena. This electric field-assisted dissolution theory has been widely accepted since then to explain the steady-state growth of the pores [1, 28, 29]. This theory showed that pore growth is balanced by field-assisted dissolution at the bottom of the advancing pore, whose rate is determined by the local field and by the radius of curvature of

the pore base. Therefore, the applied voltage is the most important factor that affects the formation and growth of the pores. Both pore diameter and pore spacing depend on the cell voltage. Other factors, such as pH and acid aggressiveness, also affect the oxide formation. The ratio of pore diameter to pore separation is found to be independent of voltage but varies with the pH of the electrolyte and at pH higher than 1.77 a nonporous oxide film forms [26]. Relatively non-aggressive electrolytes promote thicker barrier layers, larger cells and larger pores than aggressive electrolytes under constant current density conditions. The acid aggressiveness decreases in the order of sulfuric acid > oxalic acid > phosphoric acid. In sulfuric acid, pore sizes of 15–20 nm are usually formed; while in oxalic acid and phosphoric acid 40–60 nm pores and 120–180 nm pores respectively, are more commonly found.

The reason for the self-organization of the pores is still not very clear. The driving force could be the lateral component of the electrical field at the pore bottom curvature and also, could be the mechanical stress or thermal effects [26, 28, 30]. It is generally agreed that long anodization time and low anodization temperature improve the ordering of the pores. For different acids, the best ordering occurs in different potential regions. The experimental results of Masuda et al. showed that a well-ordered hexagonally arranged pore structure was accomplished with anodization in 0.5 M  $\text{H}_2\text{SO}_4$  at 25 V, or in 0.3 M oxalic acid at 40 V, or in 0.3 M  $\text{H}_3\text{PO}_4$  at 195 V [24, 25, 31]. However, very long-period anodizations, from 16 to 160 h, were used to achieve the best ordering.

The initial surface structure of the metal plays an important role in the pore initiation mechanism [28, 32]. Yue has shown that pores would preferentially nucleate at the bottom of depressions in electropolished aluminum surfaces or at defective sites, such as grain boundaries or cracks [33]. Therefore, improved ordering of the pore structure can be, possibly, obtained in a shorter time by introducing designed “preferred sites” to facilitate the nucleation of pores in a desired way. For example, an almost defect-free porous structure has been achieved by using a SiC stamp with a hexagonally ordered array of convexes to pre-texture the aluminum surface [24]. Two-step anodization can also achieve a better ordering and form well-ordered pores with a very short aspect ratio [19]. A long-term anodization in the first step generates a well-organized porous structure at the pore bottom. After complete removal of the anodic oxide film prepared in the first step by dissolution in the mixture of chromic acid and phosphoric acid, a highly ordered array of dimples remains on the surface of aluminum metal that becomes the pore initiation sites in the second anodization step. However, the overall preparation time is still long.

Previous work has determined that the electrochemically polished aluminum surface can exhibit a very regular pattern of aligned stripes or hexagonal arranged dots, depending on the time of the electropolishing and the voltage applied [33–39]. The patterns are attributed to preferential adsorption of organic molecules on the convex portion of the electrode due to its locally enhanced electric field [39]. The wavelength of the pattern increases monotonically with the applied voltage and also depends on the effective electrolyte polarizability. When the electrochemi-

cally polished patterned surface with the right wavelength has been used for anodization, a well-organized nano-porous oxide structure was formed in a very short time. Therefore, highly ordered nano-porous aluminum oxide template can be fabricated rapidly.

### 7.2.2

#### Template Formation

The porous alumina template was fabricated using 99.999% 0.1 mm thick aluminum foil (Alfa Aesar, Ward Hill, MA). The foil was annealed in nitrogen at 500 °C for 3 h before electropolishing at 40–42 V DC for 60 s in a LECO electropolishing tank EP-50 (LECO Corporation, St. Joseph, MI) with an electrolyte consisting of 70.0 vol.% of ethanol ( $\text{CH}_3\text{CH}_2\text{OH}$ ), 13.8 vol.% distilled water, 10.0 vol.% butyl cellosolve ( $\text{CH}_3(\text{CH}_2)_3\text{OCH}_2\text{CH}_2\text{OH}$ ), and 6.2 vol.% perchloric acid ( $\text{HClO}_4$ ). The electropolishing temperature was 10 °C, controlled by a Julabo® FP30 refrigerated circulating bath (Julabo USA Inc., Allentown, PA). Anodization was performed in 0.3 M oxalic acid (pH 1.6) at a constant voltage of 40 V and 3 °C for 10 min. The reaction was executed in a jacketed glass reactor with vigorous agitation. The anodization process was controlled by a digital acquisition system running a custom LabVIEW® program that logged the anodization current and controlled the applied voltage at a preset level. After anodization, the foil was immersed in 5% (by weight) phosphoric acid (pH 1) with moderate stirring for 45 min to round the pores.

Field emission scanning electron microscopy (SEM, Hitachi, Model S4500) was used to observe the anodized alumina membranes and the nano-structured gold arrays. Atomic force microscope images were taken by a tapping mode atomic force microscope (AFM, Model Dimension 3100, Veeco Instruments, Woodbury, NY). X-Ray diffraction patterns were obtained using Cu  $K\alpha$  radiation (wavelength = 1.5405 Å) on a Scintag X-ray diffractometer (Scintag Inc., Cupertino, CA).

Figure 7.2 shows a typical anodization curve of aluminum in 0.3 M oxalic acid at 40 V, 3 °C. The curve can be divided into three regions. In region I, the current density surges to a very high value in a very short time, representing the barrier oxide layer formation. Once the barrier oxide layer forms, the current starts to drop because of the lower mass transport through the oxide layer. After the current reaches a minimum, it increases again in region II, where pore nucleation occurs. Region III is the pore growth and self-adjustment region in which the dissolution of the aluminum metal and the oxide formation have the same rate.

The ordering near the pore bottom (pore advancing front) was observed to be better than that near the pore opening because of a longer self-adjustment time. Figure 7.3(a) and (b) are SEM images viewed from the top and bottom of a porous alumina film anodized in 0.3 M oxalic acid at 3 °C, 40 V for 16 h. At the pore bottom, the cells have an almost perfect hexagonal shape and uniform size. The average distance from the center of the cell to the center of the neighboring cell is 100 nm, which is also shown in the magnified cross-section image (Fig. 7.3(d)). Al-

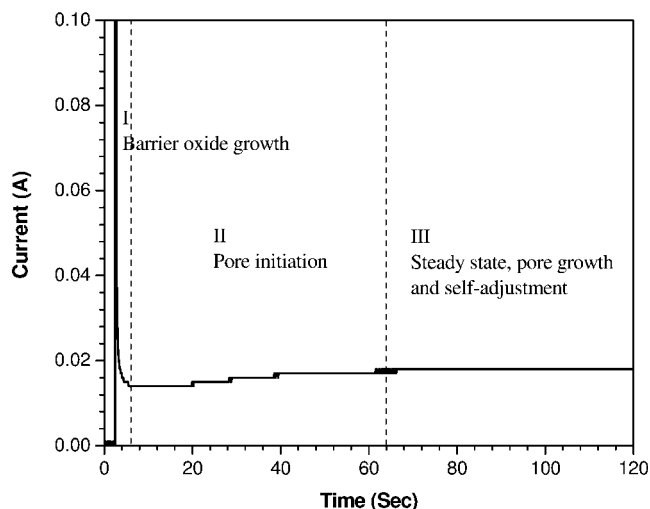
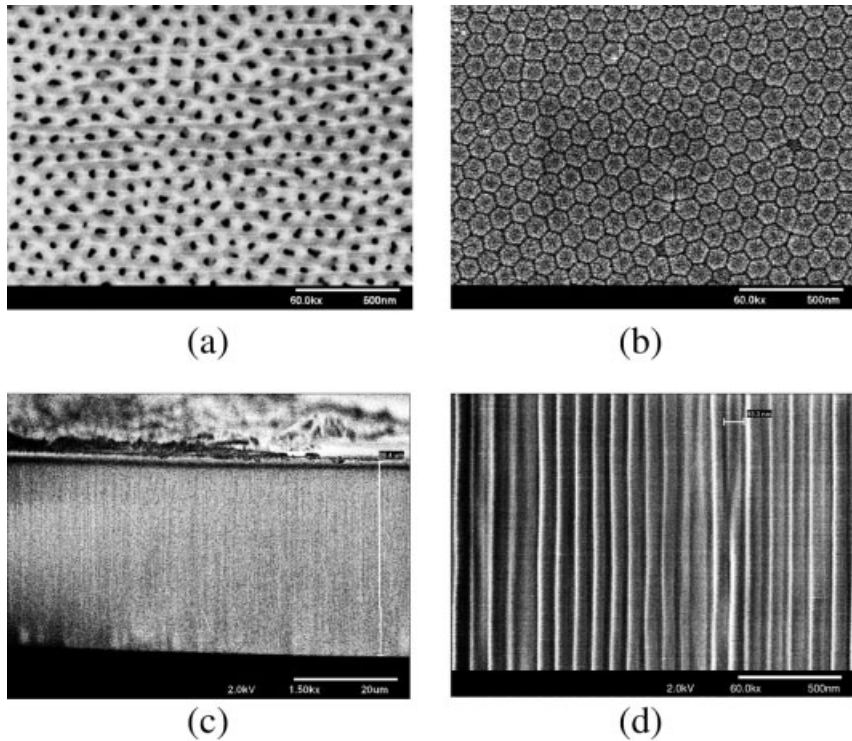


Fig. 7.2. Dependence of anodization current on time for aluminum anodized in 0.3 M oxalic acid at 40 V and 3 °C.

though there are still a couple of defect sites, the ordering at the pore advancing front is much better than that at the pore opening.

Figure 7.4 demonstrates the impact of the initial surface structure of the aluminum metal on the pore ordering of the template. One of the electropolishing patterns containing regular stripes of wavelength of 102 nm was observed when the aluminum foil was electropolished at 41 V, 10 °C for 60 s (Fig. 7.4a). Actually, at this voltage the electropolishing pattern is at the transition from regular stripes to regular hexagons [39]. The onset of the breakdown of the stripes to dots was observed. When this pre-patterned sample was anodized, the prior electropolishing pattern impacted the initial pore nucleation and hence the final pore ordering. Figure 7.4(b) shows one sample anodized in 0.3 M oxalic acid at 40 V, 3 °C for 5 min. The pores are aligned along parallel lines, and the average distance from line to line is about 100 nm, indicating that the pores are preferentially initiated along the valleys of the stripe pattern obtained from electropolishing. For comparison, Fig. 7.4(c) is the porous structure obtained when the aluminum was not electropolished.

The templates discussed here were produced without electropolishing since array order was not important. The aluminum foil was anodized for 10 min in 0.3 M oxalic acid at 3 °C. The pores were then widened and rounded in 5 wt.%  $\text{H}_3\text{PO}_4$  for 45 min. Figure 7.4(c) shows a typical SEM image of an anodized oxide film. The average pore diameter is 65 nm with a standard deviation of 4.3 nm and the separation is 95 nm with a standard deviation of 6.2 nm. The porosity is 43% and the pore density is  $1.4 \times 10^{10} \text{ cm}^{-2}$ . To determine the anodization rate, the thicknesses of the oxide layers were measured by SEM after the aluminum metal was removed in saturated  $\text{HgCl}_2$  solution. The anodized aluminum oxide film was



**Fig. 7.3.** SEM images of an alumina oxide film, anodized in 0.3 M oxalic acid at 40 V, 3 °C for 16 h. (a) View from the top of the oxide film; (b) from the bottom side of the oxide film; (c) a cross-section image that shows that the oxide layer is 37 μm thick; and (d) a higher magnification image of the cross-section, showing the parallel columnar pores.

about 2.5 μm thick for 60-min anodization, 5.3 μm thick for 120-min anodization and 37 μm for 16-h anodization. The calculated average growth rate is about 42 nm min<sup>-1</sup>. Therefore, the estimated pore depth for 10-min anodization is around 420 nm.

### 7.2.3

#### Fabrication of Gold Nano-wire Arrays (GNW)

Gold nanowire arrays were formed by a two-step deposition procedure, which consisted of electrochemical deposition and electroless plating. Electrodeposition was carried out in a CEC/TH electrochemical cell (Radiometer Analytical, Loveland, CO) with a platinum disc counter electrode. The electrolyte was H<sub>2</sub>AuCl<sub>4</sub>·3H<sub>2</sub>O (1 g L<sup>-1</sup>; ACS reagent grade, ICN Biomedicals Inc., Aurora, OH) + H<sub>2</sub>SO<sub>4</sub> (7 g L<sup>-1</sup>). An AC voltage of frequency 60 Hz and RMS amplitude of 15 V was applied at room temperature for 1 min. The electrochemical deposition was used to drive gold ions down to the bottom of the pores and form gold metal nuclei. Electroless

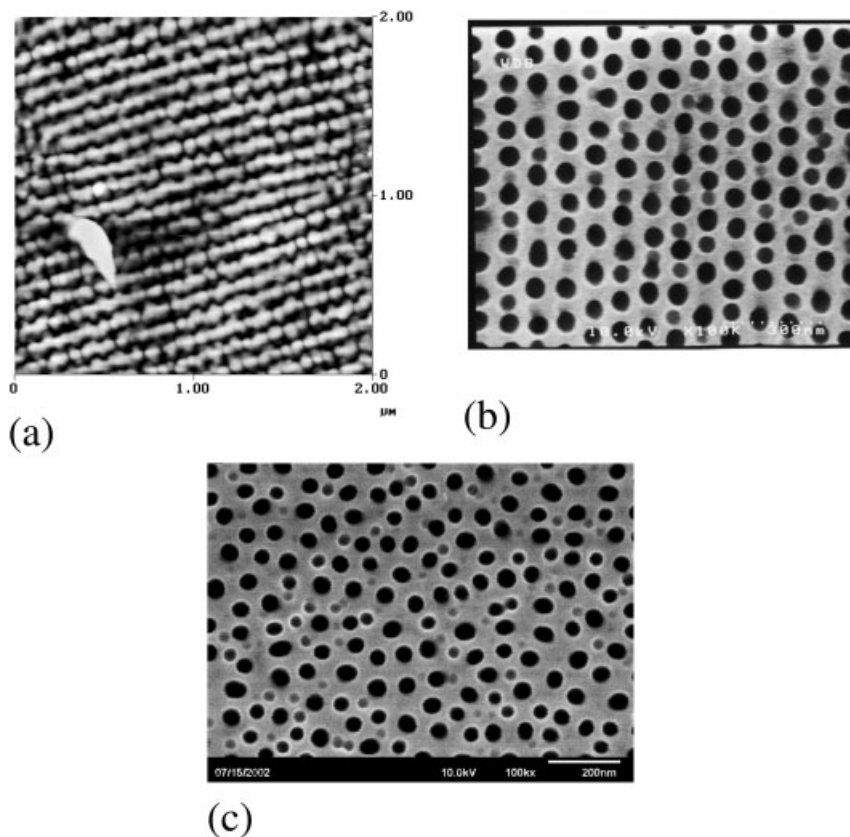


**Fig. 7.4.** (a) AFM image of an aluminum surface electropolished for 60 s at 41 V, 10 °C. A regular striped structure developed. (b, c) Porous alumina oxide formed at 40 V, 3 °C in 0.3 M oxalic acid for 5 min: (b) after electropolishing and (c) without electropolishing.

deposition was used to grow gold nanowires. Electroless deposition used a commercial Neorum TWB gold plating solution (Uyemura International Corporation, Ontario, CA). For the best plating speed and quality, the deposition temperature was controlled in the range of 68–72 °C. No stirring of the solution was supplied.

Two types of gold nanowire arrays were prepared by this template synthesis method. The experimental procedure is described schematically in Fig. 7.5. The first type of structure was formed by filling the pores, so that gold was deposited just to the top of the porous alumina template surface (Fig. 7.5(a)). The gold nanowires were still embedded in the oxide template and separated from the Al metal by a 3-nm thick oxide barrier, with the tips of the wires sticking out to interact with biomolecules for later biosensor applications. The second type of surface was made by a 2.5–3 h electroless plating of gold. After the pores of the template were com-

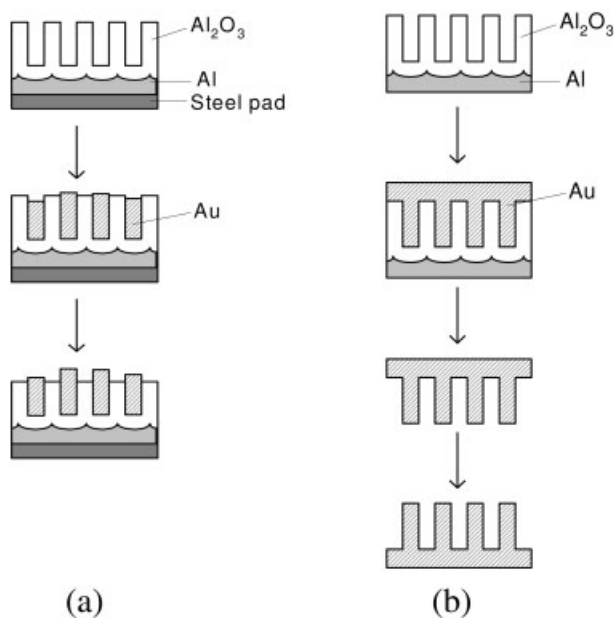


**Fig. 7.5.** Schematic view of the procedure for preparing gold nanowire (GNW) arrays, (a) embedded in the aluminum oxide template (GNW-Al<sub>2</sub>O<sub>3</sub>) and (b) free-standing (GNW).

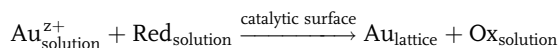
pletely filled with gold, gold was plated onto the top surface of the oxide template. Before use, both the oxide template and the underlying unanodized aluminum metal were removed by immersing the sample in 1.5 M NaOH at 40 °C. After the dissolution, the overplated thin (~5 μm) gold film was left with gold nanowires protruding from the surface like the bristles of a brush (Fig. 7.5b).

For the application of biosensors, the substrate materials should be compatible with and have a good affinity for biological molecules and should also be stable in air or aqueous solution for reliable measurements. Gold is a good candidate for this purpose. Gold has good affinity to biomolecules – functional groups such as thiol (–SH) or amine (–NH<sub>2</sub>) can chemically adsorb onto the gold surface. The bonds are strong enough to survive measurements in flowing liquids and even in a vacuum.

There are two common ways to electroplate metals inside the pores. The first is to electrodeposit metal from a metal ion solution by AC current. Alternating current was needed to deposit metal inside the pores because of the rectifying nature of the Al metal/oxide junction [9, 40, 41]. Another approach is to remove the aluminum metal and etch through the barrier layer of the oxide to get a through-hole oxide membrane. Then a thin layer of metal is evaporated onto one side of the oxide as the cathode, so electrodeposition by DC current can be carried out. Electroless plating has a distinct advantage over electroplating in its capability to coat a surface that is not electronically conductive, such as aluminum oxide. Martin et al.

also discovered that electroless plating allowed for more uniform gold deposition than electrochemical plating [18]. Therefore, a commercial electroless gold plating bath was chosen to grow the gold wires inside the aluminum oxide template. This plating solution is a non-cyanide solution and works at a neutral pH. Most of the conventional electroless gold plating baths are strongly alkaline [42]. However, alumina is only stable in the pH range between 4 and 9. When the pH is above 9,  $\text{Al}_2\text{O}_3$  can be dissolved and form aluminate ion ( $\text{AlO}_2^-$ ). Thereby the porous structure can be damaged.

The basic components of an electroless plating solution are a gold salt ( $\text{Au}^{z+}$ ) and a reducing agent ( $\text{Red}_{\text{solution}}$ ). This reducing agent will reduce gold ion to gold metal ( $\text{Au}_{\text{lattice}}$ ) and form an oxidized species in the solution ( $\text{Ox}_{\text{solution}}$ ) when a catalytic surface is present. The overall reaction is:



Without a catalyst, this reaction is extremely slow and, therefore, prevents gold formation in the solution. A non-catalytic surface to be plated must be activated by generating catalytic metal nuclei on the surface to obtain a practical plating rate. The catalyst metal may be any of Pd, Pt, Au, Ag, or Cu. In this work, gold seeds were put down as the catalytic sites. The deposition of gold seeds was realized by AC electrodeposition. The locally enhanced electric field will drive the metal ions down to the pore bottom and form nuclei there [43]. Gold wires were then grown on these catalytic sites by electroless plating. The length of the wires can be simply controlled by the plating time.

Figure 7.6 is the top view SEM image of an alumina membrane with gold inside the pores. The time used for electrodeposition was 1 min and for electroless deposition it was 5 min. Since the electrodeposition solution was acidic (pH 2), containing  $\text{H}_2\text{SO}_4$ , prolonged immersion in this solution with an AC voltage applied may damage the template; consequently, the electrochemical deposition was performed

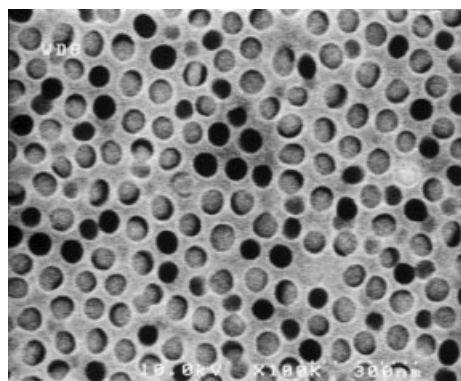


Fig. 7.6. SEM image of an aluminum oxide template with gold deposited inside the pores.



for no longer than 1 min. Notably, not all the pores are filled with gold. This is probably due to the low frequency (60 Hz) of the AC voltage applied. The filling percentage increases as the frequency increased from 100 to 750 Hz for electro-deposition of Ni and Bi inside the pores of alumina films [44]. This is because more nuclei are formed at higher frequencies, promoting the deposition better. This is similar to pulse plating, which has more “throwing” power to facilitate the filling of the pores. However, a lower frequency may be preferred if a uniform growth of the wires is required [45].

Because only the gold nuclei at the pore bottoms produced by electrodeposition were catalytic sites for the electroless plating, gold was only plated inside the pores and not on the top of the oxide layer. After the pores were completely filled with gold, gold began to plate on top of the oxide film. It was found experimentally that the time needed for electroless plating to fill the pore (the average length is  $\sim 420$  nm) was about 5 min, when the temperature of the electroless plating bath was controlled between 68 and 72 °C. Owing to the special optical properties of nano-sized metal-oxide composite, the color of the gold-alumina composite changes depending on the aspect ratio of the gold wire inside the oxide [46–51]. This phenomenon was also observed in this research in that the gold-alumina changed from purple to dark blue, then green and yellow during the filling of the pores (65 nm in diameter, 420 nm long) of the oxide layer with gold.

Figure 7.7(a) and (b) shows top-view SEM images of the free-standing gold nanowires at lower and higher magnifications respectively, after the dissolution of both the alumina and the residual aluminum metal. The electroless plating was carried out for 2.5 to 3 h, resulting in an overplated gold film of about 5  $\mu\text{m}$  thick. The wires stood on this overplated gold film. According to the SEM images, the average diameter of the wire is 62 nm with a standard deviation of 6.4 nm, and the distance from the center of the wire to the center of the neighboring wire is 93 nm, with a standard deviation of 7.5 nm. This is consistent with the pore size and the inter-pore distance of the template. Notably, in Fig. 7.7(a), some gold nanowires are

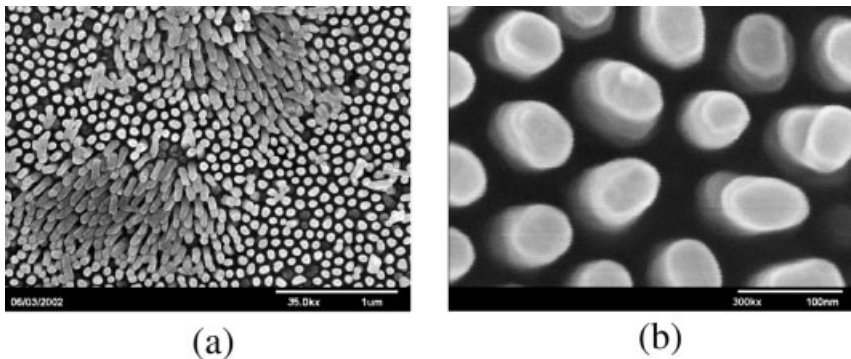
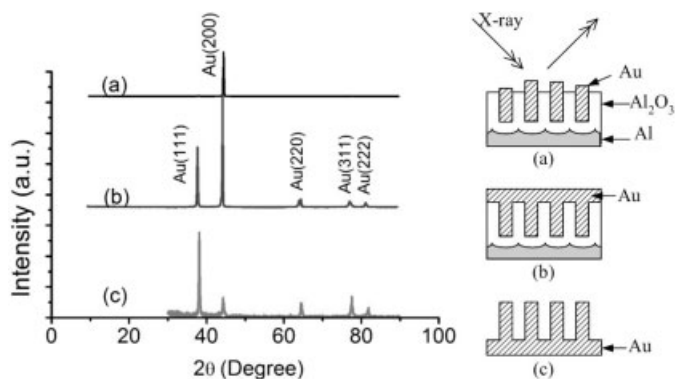


Fig. 7.7. SEM images of the top view of gold nanowires. Magnifications: (a) 60k $\times$ . (b) 300k $\times$ .



**Fig. 7.8.** X-ray diffraction patterns of (a) gold nanowires embedded in a porous alumina template; (b) an electrolessly plated gold film ( $\sim 5 \mu\text{m}$  thick), and (c) free-standing gold nanowire arrays on top of the electrolessly plated gold film. The average length of the wire is about 420 nm.

lying down in two regions. They were deformed intentionally with tweezers in an attempt to measure the length of the wires.

Figure 7.8(a) shows an X-ray diffraction pattern of the gold nanowire arrays inside the alumina template. There is only one peak, at about  $2\theta = 44^\circ$ , which represents the Au(200) crystal plane. No  $\text{Al}_2\text{O}_3$  peaks appeared at this scale, indicating the oxide was probably amorphous. The X-ray diffraction pattern of the electrolessly plated gold film is shown as pattern (b) in Fig. 7.8. The peaks corresponding to Au(111), Au(200), Au(220), Au(311), and Au(222) crystal planes appeared, meaning that this electroless-plated gold film is polycrystalline with a face-centered cubic crystal structure. When the sample with free-standing gold nanowire arrays on top of the electrolessly plated gold film was scanned, again all the gold peaks appeared (pattern (c) in Fig. 7.8). This X-ray diffraction pattern is not only the diffraction pattern of the gold wires but may also have a contribution from the underlying electrolessly overplated gold film.

In this work, nanogold wire arrays were formed based on a template synthesis method. The template was a nano-porous aluminum oxide membrane produced by electrochemical anodization in 0.3 M oxalic acid. Gold nanowires were grown by filling the pores of the template by electrochemical plating and electroless plating. The gold nanowires could either be embedded in the oxide matrix or be free-standing on a thin gold film. The average diameter of the wire was 62 nm, which is consistent with the size of the pores. The wire could be as long as the depth of the pore or shorter, depending on the deposition time.

Gold has selective affinity to some functional groups, such as amine ( $-\text{NH}_2$ ) and thiol ( $-\text{SH}$ ). These functional groups exist extensively in bio-entities, such as enzymes and antibodies, which are common bio-sensing elements for the detection of a particular bio-reaction or bio-interaction. Both kinds of nano-structured gold

surfaces fabricated in this work, including the free-standing gold nanowires and the gold nanowire arrays embedded inside the porous alumina template, could be the substrates for sensor applications. Electrochemical and optical transducers can be applied. The free-standing gold nanowire arrays have a large surface area, which improves the binding capacity of bio-sensing molecules or electrochemically active species; and enhances the reaction current and double-layer charging capacitance that can be detected with electrochemical methods, such as chronoamperometry or impedance spectroscopy. Complete sealing of the cylindrical surface of the gold nanowires inside the aluminum oxide template, with only the end disk-shaped electrode exposed to the electrolyte, enables detection by electrochemical methods, such as cyclic voltammetry, because of the reduced charging current and the enhanced signal-to-noise ratio [18, 52]. The special optical properties of this nano-structured metal-oxide composite may also find use in optical sensors [49, 51].

### 7.3

#### Synthesis of a Linker and its Attachment to Gold Posts of GNW followed by Binding to Specific Antibodies

Figure 7.9 gives the synthesis of DSU [53]. In the first reaction, 11-bromoundecanoic acid (1) was added to  $\text{Na}_2\text{S}_2\text{O}_3$  in 50% aqueous 1,4-dioxane and

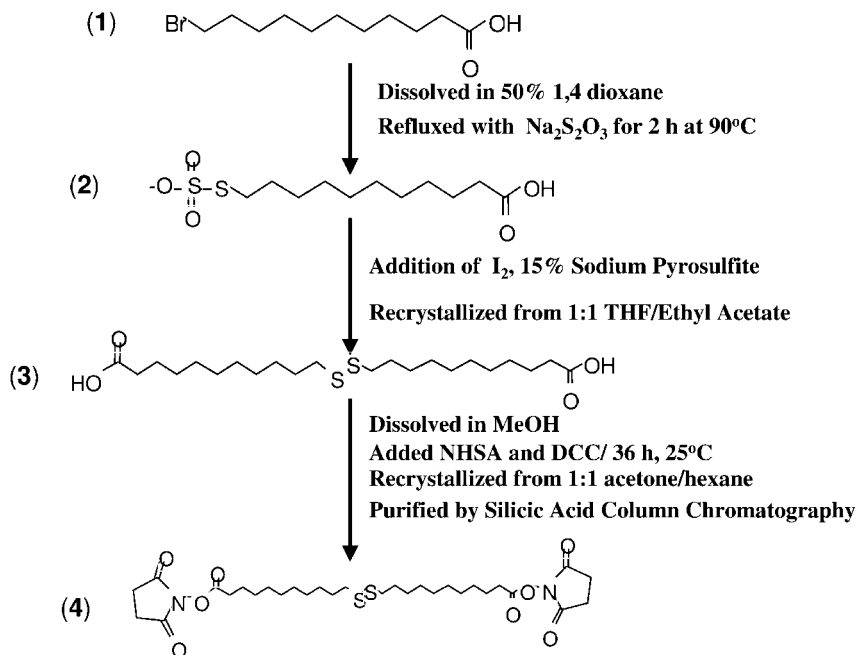


Fig. 7.9. Synthesis of the dithio-bissuccinimidylundecanoate (DSU) linker.

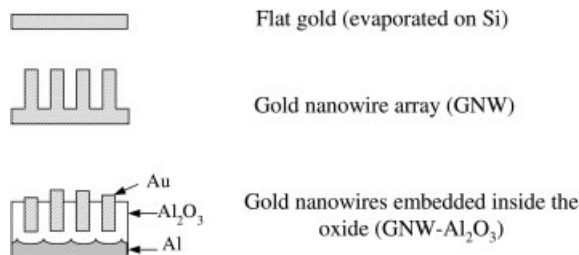
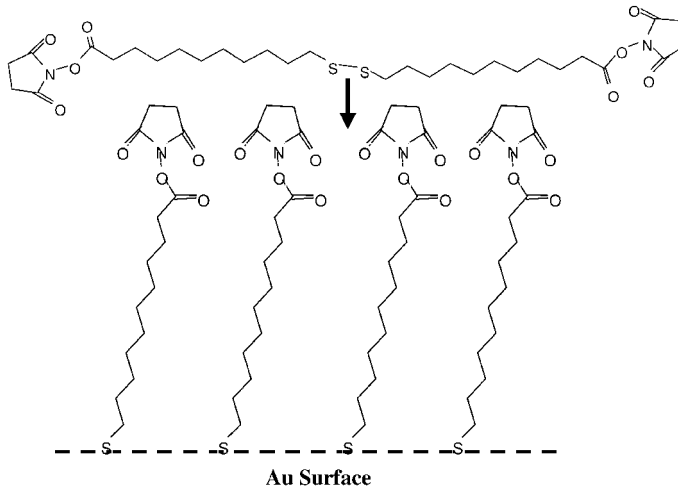


Fig. 7.10. Structures of the surfaces investigated.

refluxed for 2 h at 90 °C to yield the Bunte Salt (2). Oxidation to the disulfide was carried out by adding  $I_2$ . Surplus  $I_2$  was retitrated with 15% aqueous sodium pyrosulfite. The 1,4-dioxane solvent was removed by rotary evaporation and the suspension was filtered to yield dithio-bis(undecanoic acid) (3). Purification was achieved by recrystallization from ethyl acetate/THF(1:1). *N*-Hydroxysuccinimide (NHSA) was added to a solution of (3) in MeOH, followed by the addition of dicyclohexylcarbodiimide (DCC) at 0 °C. The reaction mixture was cooled to 25 °C and stirred for 36 h. MeOH was removed by rotary evaporation, and the product was resuspended in THF and filtered off. The crude final product (4) was purified by recrystallization from 1:1 acetone/hexane, and by silicic acid column chromatography to yield DSU (4). All intermediates were characterized by IR spectroscopy.

Initial studies were carried out using various amounts of (Goat PAb)<sub>*E. coli*</sub> to determine the degrees of direct binding to the gold plate. Competition studies were carried out among three kinds of testing surfaces (as shown in Fig. 7.10): (I) flat gold disc (FGD), (II) free-standing gold nanowire array (GNW), and (III) gold nanowire array surrounded by  $Al_2O_3$  (GNW- $Al_2O_3$ ), to determine which had the higher affinity for antibody binding. The flat gold surface (structure I) was prepared by electron beam evaporation of gold on a Si(100) n-type wafer under a vacuum of about  $1 \times 10^{-6}$  Torr. The deposition speed was around  $10 \text{ \AA s}^{-1}$ . The gold layer was 200 nm thick.

The DSU linker was applied to the surface to covalently immobilize the antibodies. Covalent immobilization of (Goat Pab)<sub>*E. coli*</sub> was accomplished by immersing the gold discs in 1500  $\mu\text{L}$  of a 1 mM DSU in MeOH solution for 30 min at room temperature [54]. After rinsing with MeOH (7 mL), the *N*-hydroxysuccinimide (NHS) terminated monolayers were dried under a stream of nitrogen gas and immediately used for immobilization of *E. coli* antibodies. Figure 7.11 depicts the self-assembly of DSU to form self-assembled monolayers (SAM) on the gold surface. Covalent immobilization takes place when a lysine residue of the antibody comes into contact with the DSU SAM to nucleophilically attack the carbonyl carbon, thereby displacing the *N*-hydroxysuccinimide to form an amide linkage (Fig. 7.12). Covalent immobilization of antibodies via SAM (Fig. 7.12) is desirable because of the tendency to increase the binding capacity of the gold surface for the antibody. This is predicted because the linker has a long carbon chain, protruding directly up from the plate, that can freely rotate in space. This creates a more steri-



**Fig. 7.11.** Formation of self-assembled monolayers with the dithio-bissuccinimidylundecanoate (DSU) linker.

cally favorable condition for the antibodies to bind to monolayers because there is less chance of antibody crowding, whereas when antibodies are directly bound to the gold nanowire surfaces without the SAM there may be crowding on the gold surface that decreases the binding capacity.

Studies of the influence of the linker on antibody binding were also carried out among the same set of three surface types.

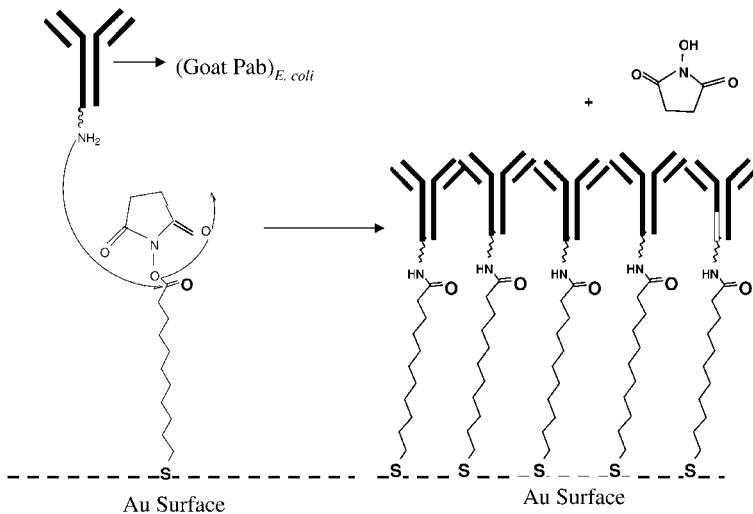


**Fig. 7.12.** Covalent immobilization of antibodies via a DSU self-assembled monolayer.

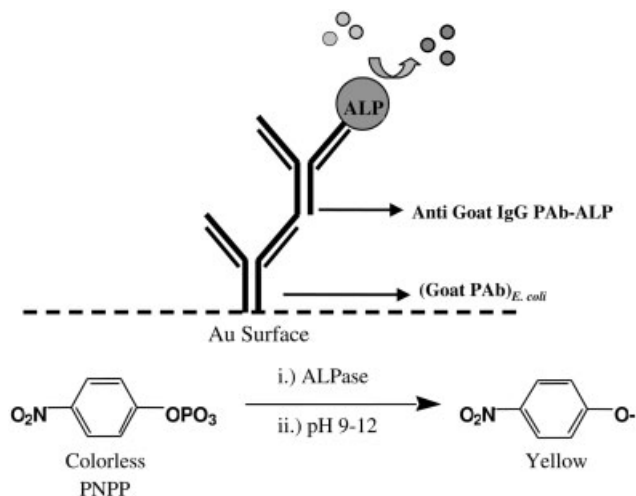


Fig. 7.13. Schematic representation of antibody binding detection by the ELISA sandwich assay.

The binding of anti-*E. coli* antibody was determined optically by enzyme-linked immunosorbent assay (ELISA). Alkaline-phosphatase-conjugated second antibody (rabbit anti-goat IgG) was added to the gold discs after washing off unbound first antibody. The anti-*E. coli* antibody binding to the gold substrates was then quantitated optically by measuring the hydrolysis of *p*-NO<sub>2</sub>-phenylphosphates (Fig. 7.13). Tables 7.1–7.3 give the ELISA results.

From the data it was determined that, without linker, the gold surface with Al<sub>2</sub>O<sub>3</sub> (GNW-Al<sub>2</sub>O<sub>3</sub>) bound the antibodies more efficiently than the gold nanowires (GNW), although gold nanowires have a huge surface area (e.g., GNW-1 vs. GNW-Al<sub>2</sub>O<sub>3</sub>-1). It was inferred that the antibodies are not able to fit completely inside the crevices or between the wires, thereby decreasing the binding capacity. For the surface with Al<sub>2</sub>O<sub>3</sub>, it was hypothesized that the antibodies may be binding to the Al<sub>2</sub>O<sub>3</sub> as well as the Au.

Tab. 7.1. Relative affinity of (Goat PAb)*E. coli* to flat gold discs (FGD) with and without DSU linker.

	1 mM DSU (μL)	1 <sup>st</sup> antibody (μg)	2 <sup>nd</sup> antibody (μg)	O.D. <sub>405 nm</sub>
FGD-1	–	5	6	0.144
FGD-2	–	10	12	0.337
FGD-3	1500	5	6	0.224
FGD-4	1500	10	12	0.510
FGD-5	–	–	6	blank

**Tab. 7.2.** Relative affinity of (Goat PAb)*E. coli* to a gold nanowire array (GNW) with and without DSU linker.

	1 mM DSU ( $\mu\text{L}$ )	1 <sup>st</sup> antibody ( $\mu\text{g}$ )	2 <sup>nd</sup> antibody ( $\mu\text{g}$ )	O.D. <sub>405 nm</sub>
GNW-1	–	5	6	0.127
GNW-2	–	10	12	0.204
GNW-3	1500	5	6	0.648
GNW-4	1500	10	12	0.652
GNW-5	–	–	6	blank

**Tab. 7.3.** Relative affinity of (Goat PAb)*E. coli* to gold nanowire array embedded in Al<sub>2</sub>O<sub>3</sub> (GNW-Al<sub>2</sub>O<sub>3</sub>) with and without DSU linker.

	DSU 1 mM ( $\mu\text{L}$ )	1 <sup>st</sup> antibody ( $\mu\text{g}$ )	2 <sup>nd</sup> antibody ( $\mu\text{g}$ )	O.D. <sub>405 nm</sub>
GNW-Al <sub>2</sub> O <sub>3</sub> -1	–	5	6	0.192
GNW-Al <sub>2</sub> O <sub>3</sub> -2	–	10	12	0.354
GNW-Al <sub>2</sub> O <sub>3</sub> -3	1500	5	6	0.257
GNW-Al <sub>2</sub> O <sub>3</sub> -4	1500	10	12	0.590
GNW-Al <sub>2</sub> O <sub>3</sub> -5	–	–	6	blank

It was determined that the linker greatly enhances antibody binding for the free-standing gold nanowire surfaces (GNW) (e.g., GNW-3 vs. GNW-1). The presence of the linker also enhances antibody binding for the GNW-Al<sub>2</sub>O<sub>3</sub> surfaces (e.g., GNW-Al<sub>2</sub>O<sub>3</sub>-3 vs. GNW-Al<sub>2</sub>O<sub>3</sub>-1). However, the increase in antibody binding is not as great as it was for the gold nanowire surfaces (GNW-3 vs. GNW-Al<sub>2</sub>O<sub>3</sub>-3). For flat gold surfaces, DSU linker also enhances the antibody binding, but the effect is not as great as GNW and GNW-Al<sub>2</sub>O<sub>3</sub> surfaces. This may be because the flat surface does not have the crevice characteristic and, therefore, exhibits a lower binding capacity for antibodies than other kinds of surfaces.

## 7.4

### Development of Electrochemical Nano-biosensor for Bacteria Detection

#### 7.4.1

##### General Detections for Biosensors

Biosensors have attracted considerable attention and have found extensive applications. However, although there is an extensive literature on various combinations

of biological recognition elements and transducers in biosensor configurations, the conventional biosensors generally lack the combination of high-speed detection, high specific sensitivity and the ability to be integrated into a miniaturized sensor [55]. Therefore, in recent years, intensive research has been undertaken to develop the technology of portable, selective and sensitive biosensors capable of immediate results [56, 57]. The development of biosensors in this work was based on electrochemical impedance measurements on nanostructured substrates, with the aim of increasing the sensitivity, and decreasing the response time and the size of the device.

Among various transducers, electrochemical transduction strategies have distinct advantages in that they offer a much higher sensitivity and a simple, fast detection procedure. Owing to the capability of the measurement of nano- or pico-ampere current by conventional instruments, the pretreatment steps, such as separation and pre-enrichment, are no longer necessary. In addition, the equipment required for electrochemical analyses are simple and inexpensive as compared with most other analytical techniques. Furthermore, electrochemical techniques are more suitable for miniaturization, circuit integration and continuous electrical controls. With the development of microelectronics, the integrated circuit industry, nanotechnology and microfluidics, electrochemical transducers could be one of the most promising candidates for future sensor development.

Electrochemical impedance spectroscopy (EIS) was chosen as the main detection method because it is a very sensitive method that facilitates the direct measurement of the antigen–antibody interaction. This method does not require the presence of tags, such as redox probes, fluorophores, dyes or radioactive species, for the detection. This greatly simplifies the detection procedures. Moreover, EIS measurements require only a very small voltage (which is usually less than 20 mV) to be applied to the system. This small voltage applied is beneficial not only because it allows a complicated nonlinear problem to be simplified into a pseudo-linear problem during the analysis, but also because it is less destructive to the biological properties of the biomolecules, such as the activities of enzymes and antibodies, minimizing the impact on the sensitivity, stability and reliability of biosensors employing EIS.

Figure 7.14 depicts a model of the nano-biosensor. The nano-structured substrate, with biological recognition components immobilized, was the working electrode. The nano-structured substrates were gold nanowire arrays, which were fabricated as described in Section 7.2. To detect a specific type of bacteria, the biological recognition component was a bacteria-specific antibody. To enhance the binding strength and capacity, the specific antibody was covalently bound onto the gold surface through an organic “linker” molecule (Section 7.3). *Escherichia coli* (*E. coli*) was the target analyte for this sensor prototype. The reaction scheme at the electrode surface includes: (a) assembling the linker onto the gold substrates; (b) covalent binding of the anti *E. coli* antibody onto the linker; and (c) tethering of the target *E. coli* antigen. The voltage and current signals were recorded when the analyte interacted with the biological recognition component. This study was carried out using both the nano-structured gold substrates and the conventional



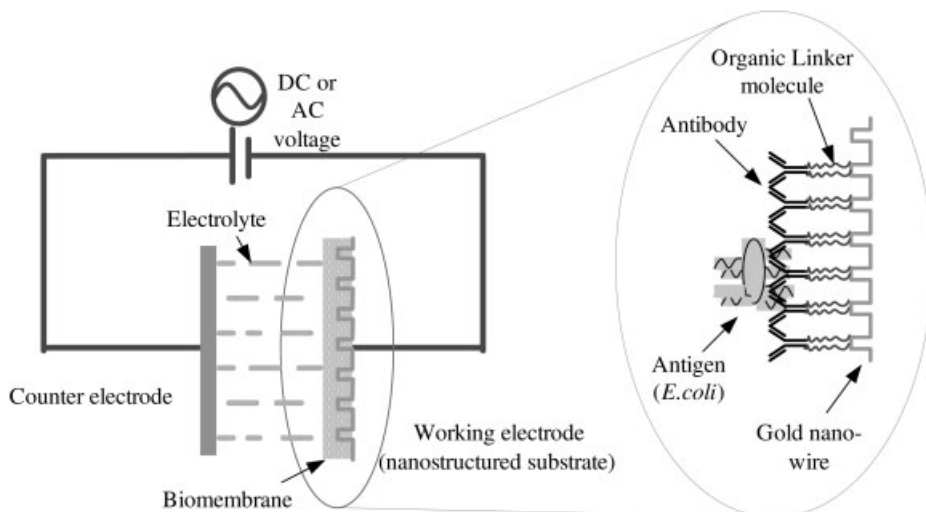


Fig. 7.14. Biosensor model for the detection of *E. coli* bacteria.

e-beam evaporated planar gold substrate. The effect of the nano-scale structure of the substrate on the detection sensitivity was investigated. Optimization of the dimension of the nano-structured gold substrates is expected in the future.

#### 7.4.2

##### Experimental Conditions

*E. coli* antigen was cultured in the Department of Chemical and Biomolecular Engineering at the University of Notre Dame from the strain – ATCC #11775 (American Type Culture Collection, Manassas, VA). The bacteria were suspended in a 0.01 M phosphate saline buffer. The number of bacteria was counted during culturing after serial dilution using an optical microscope.

The antibody used was polyclonal goat anti *E. coli* antibody (catalog # 1091) from ViroStat (Portland, Maine). The concentration of the antibody was  $0.4 \mu\text{g } \mu\text{L}^{-1}$ . Dithio-bissuccinimidylundecanoate (DSU) was synthesized as described in Section 7.3. It was used to covalently link the antibody onto the gold substrate. Thus, it is also called the “linker”. The final concentration of DSU was 1 mM, dissolved in methanol.

All electrochemical measurements were performed using a Gamry FAS1 potentiostat (Gamry Instruments, Warminster, PA). Electrochemical impedance spectroscopy (EIS) was performed in the frequency range  $10^{-2}$ – $10^5$  Hz at an amplitude of 10 mV (RMS) around the open circuit potential. A three-electrode electrochemical cell was used. The reference electrode was a saturated calomel electrode (SCE) and the counter electrode was a platinum disk. The exposed geometric surface area of the working electrode was  $0.2 \text{ cm}^2$ , defined by a silicone rubber washer.

All measurements were performed in 0.01 M phosphate buffer saline (PBS buffer) solution (Sigma, St. Louis, MO), which has a pH of 7.4 at 25 °C. All dilutions were made using Millipore [Millipore, Bedford, MA (18 M $\Omega$ )] water.

Three kinds of surfaces with the same geometric area have been studied for comparison. They are (I) vacuum evaporated gold on Si wafer (FGD); (II) free-standing gold nanowire array (GNW), and (III) gold nanowire array distributed inside the pores of the anodized alumina template (GNW with Al<sub>2</sub>O<sub>3</sub>). Figure 7.10 depicts the structures of the substrates.

The general biomolecule immobilization steps were as follows. First 1 mM DSU (20  $\mu$ L) was added to the substrate. The sample was rested at room temperature for 30 min, followed by washing in methanol. After the sample was dried under an air stream, antibody (10  $\mu$ L, 0.4  $\mu$ g  $\mu$ L<sup>-1</sup>) was added and the sample was rested at room temperature for 2 h to let the antibody interact with the DSU linker. The sample was kept wet by sealing in a glass bottle. If needed, another 10  $\mu$ L of PBS buffer was added to the sample after 1 h. The sample was then rinsed with PBS buffer to remove the loosely bound antibodies. *E. coli* bacteria were added in units from 10 to 25  $\mu$ L, depending on the final surface concentration of bacteria desired and the *E. coli* concentration of the stock solution used. After adding the bacteria, the sample was rested for another 1.5 to 2 h at room temperature to let the antigens attach to the antibodies. Finally, the sample was rinsed with PBS buffer before the electrochemical measurements.

### 7.4.3

#### Electrochemical Impedance (EIS) Detection of *E. coli*

The detection of the *E. coli* antigen was investigated by sequentially adding a certain number of *E. coli* cell onto the antibody/linker coated substrates.

The EIS data can be analyzed by an equivalent circuit model [58, 59]. However, for this *E. coli* sensor device, the equivalent circuit model analysis could be very complicated because:

- There are three layers of molecules that have been immobilized on the surface: linker, antibody and antigen. Each layer may not be completely loaded. Also, in every layer, either the organic linker or the bioentities may be immobilized at different orientations, which also results a nonuniform biomembrane.
- The substrates studied have nanostructured surfaces. These nanostructures can cause an inhomogeneous current distribution along the surface and disturb the double-layer structure.
- There is an electrostatic force between the biomolecules, which changes the polarizability of the system and influences the impedance measurements.

Therefore, this biosensor study used a simplified circuit model that contained only an overall resistance and an overall capacitance connected serially.

It was assumed that the binding of the biomolecules causes the capacitance to change and the measured imaginary part of the impedance comes mainly from

the capacitive behavior of the biomembrane. Therefore, the number of *E. coli* on the surface can be approximately determined from the system capacitance value. This overall capacitance can be calculated by the Eq. (1):

$$C = 1/[2\pi f|Z_{\text{imag}}|] \quad (1)$$

where  $|Z_{\text{imag}}|$  is the magnitude of the imaginary part of the impedance, in ohms,  $f$  is frequency in Hz, and  $C$  is capacitance in farads. Equation (1) can also be rewritten as

$$|Z_{\text{imag}}| = \frac{1}{C}\omega^{-1} \quad (2)$$

where  $\omega^{-1} = 1/2\pi f$ , in  $\text{rad}^{-1} \text{ s}$ . Therefore the capacitance  $C$  can be obtained as the inverse slope of a plot of the imaginary impedance  $Z_{\text{imag}}$  against the reciprocal frequency for the low frequency data.

#### 7.4.3.1 EIS on Flat Gold Surfaces

Figures 6.15 and 6.16 are representative EIS results on an enzyme-coated flat gold electrode with different numbers of *E. coli* bacteria attached. Figure 6.15 is the Nyquist plot. Figure 7.16 is the same result plotted as the imaginary part vs. the frequency.

The capacitances can be calculated by the reciprocal slops of  $|Z_{\text{imag}}|$  vs.  $\omega^{-1}$  (Fig. 7.17a). If the capacitance of the electrode with linker and antibody,  $4.3 \mu\text{F}$ , is

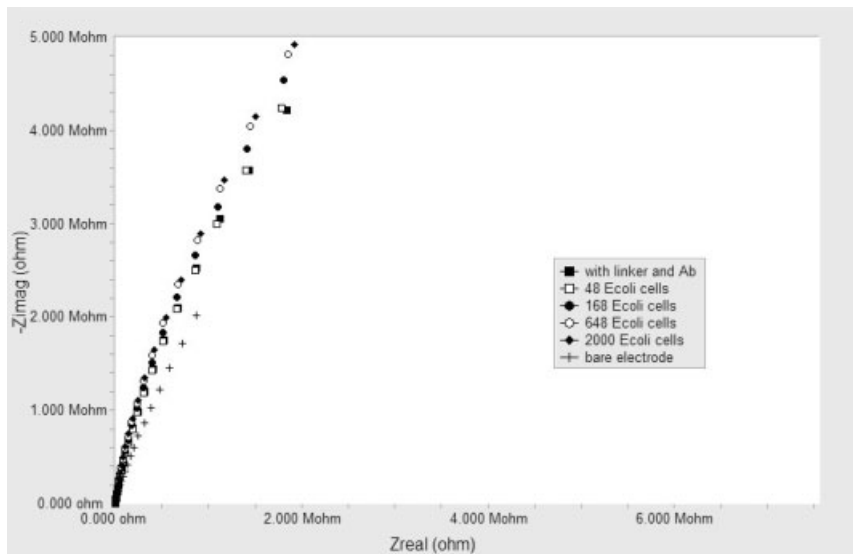


**Fig. 7.15.** Electrochemical impedance spectroscopy (EIS) on a flat gold surface with different amounts of *E. coli* bacteria attached (Nyquist plot).

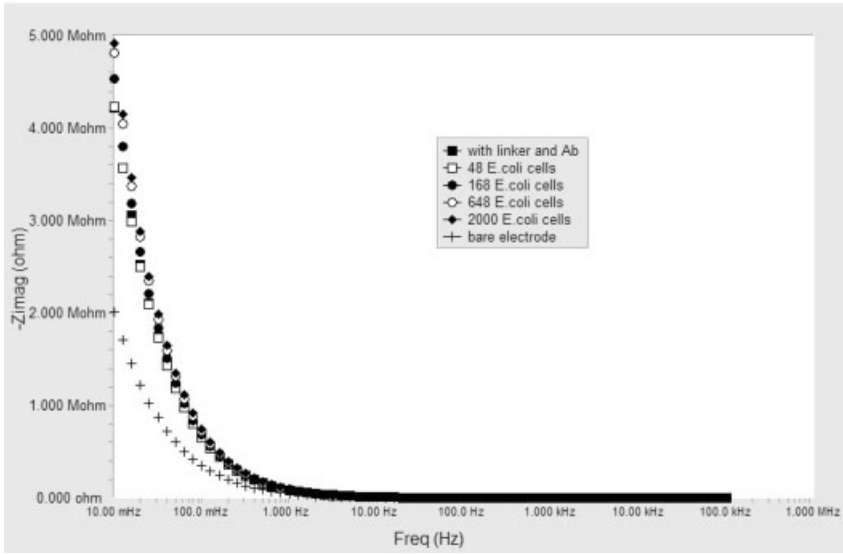


Fig. 7.16. EIS on a flat gold surface with different amounts of *E. coli* bacteria attached ( $-Z_{imag}$  vs. frequency).

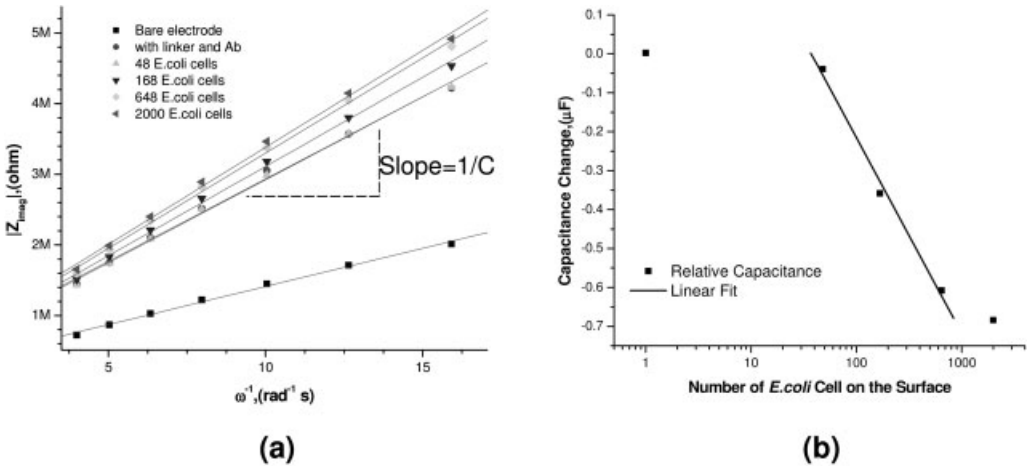


Fig. 7.17. (a)  $|Z_{imag}|$  vs.  $\omega^{-1}$ , and (b) relative capacitance change vs. the number of *E. coli* (log scale) on a flat gold electrode.

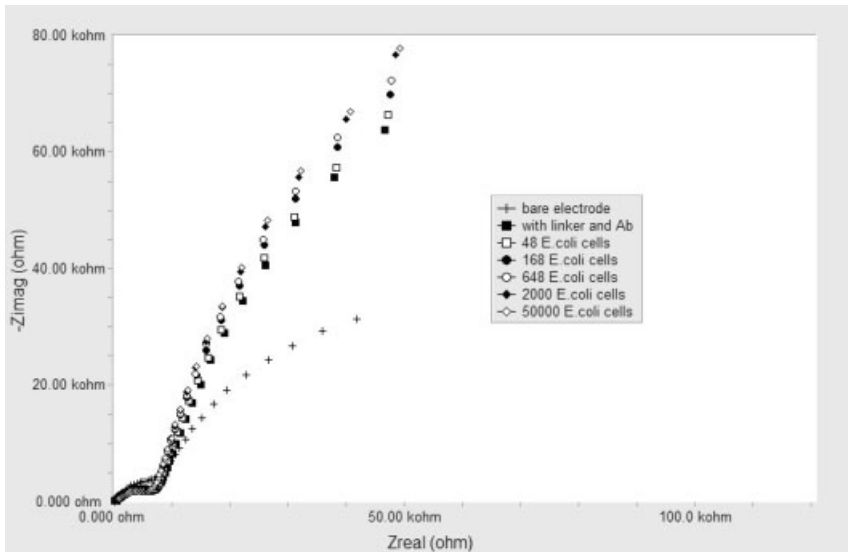


Fig. 7.18. EIS on GNW with different amounts of *E. coli* bacteria attached (Nyquist plot).

considered as a reference capacitance, Fig. 7.17(b) shows the relative capacitance change with the number of *E. coli* bacteria tethered. There is a linear relationship between the change of capacitance and the logarithmic number of *E. coli* cell on the surface when the number of *E. coli* cell is from 50 to 1000. The sensitivity of the capacitance change is about  $-0.5 \mu\text{F}$  per  $\log(\text{number of } E. coli \text{ cells})$ .

#### 7.4.3.2 EIS on GNW

On a free standing gold nanowire array, typical EIS results are shown in Figs. 7.18 and 7.19. The same calculation procedure was applied as that for a flat gold. The imaginary impedance is also linear with the reciprocal radial frequency in the low frequency range (Fig. 7.20(a)). The relative capacitance change because of the binding of the *E. coli* cells is shown in Fig. 7.20(b). A similar linear relationship between the change of the capacitance and the log scale number of *E. coli* was obtained in the concentration range from 50 cells to 2000 cells. The slope was determined to be  $-29.82 \mu\text{F}$  per  $\log(\text{number of } E. coli \text{ cells})$ . The sensor saturates at a higher concentration than a flat gold electrode.

#### 7.4.3.3 EIS on GNW with $\text{Al}_2\text{O}_3$

Figures 7.21 and 7.22 shows a typical set of the impedance results of *E. coli* attached GNW- $\text{Al}_2\text{O}_3$ . The Nyquist plots of this sensor surface have very different shapes from the previous ones. This is because of the different structure of the sensor, in other words, the gold nanowires are embedded in an insulating alumina matrix. The capacitance of this insulating oxide layer also contributes to the system overall capacitance. However, the capacitance of the oxide layer could be assumed

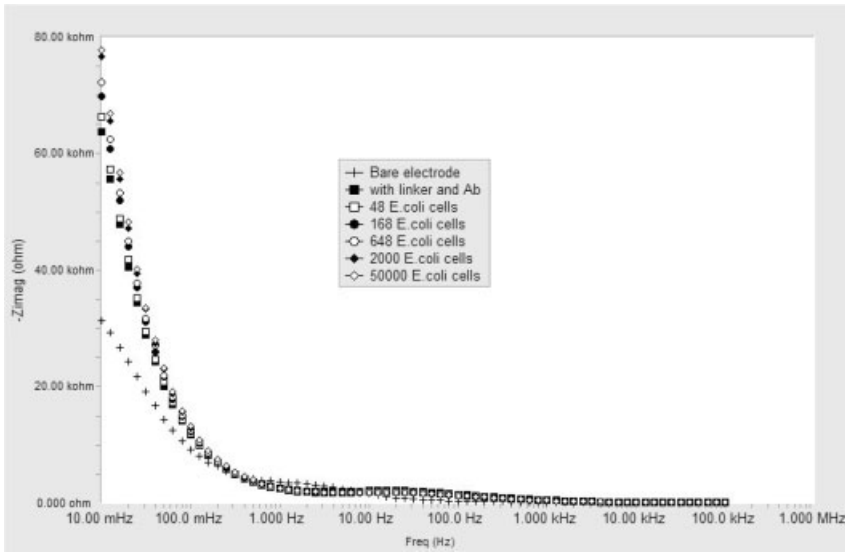


Fig. 7.19. EIS on GNW with different amounts of *E. coli* bacteria attached ( $-Z_{imag}$  vs. frequency).

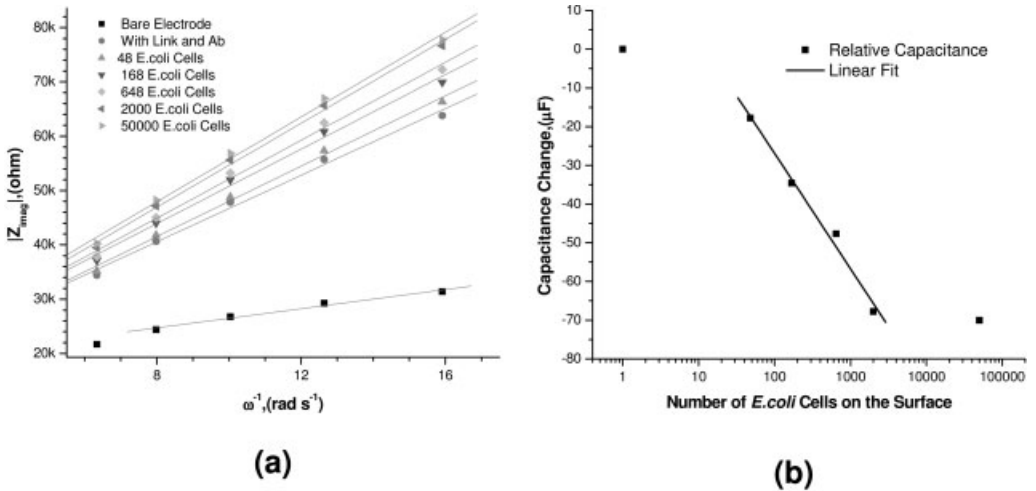


Fig. 7.20. (a)  $|Z_{imag}|$  vs.  $\omega^{-1}$  and (b) relative capacitance change vs. the number of *E. coli* (log scale) on a GNW electrode.

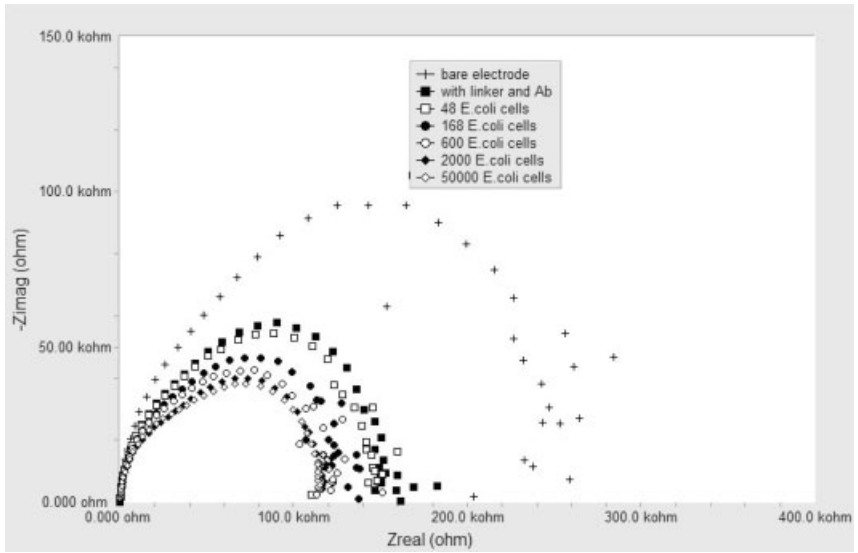


Fig. 7.21. EIS results for a GNW-Al<sub>2</sub>O<sub>3</sub> sample with different amounts of *E. coli* cells attached (Nyquist plot).

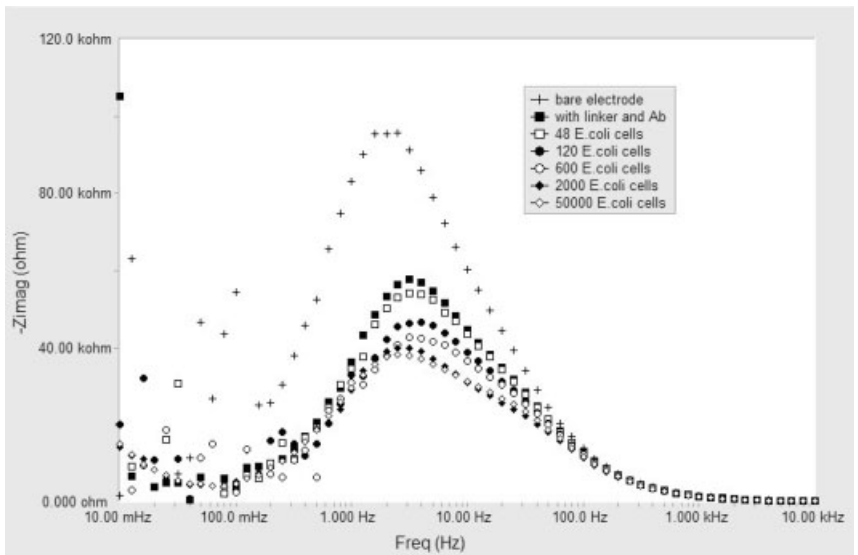
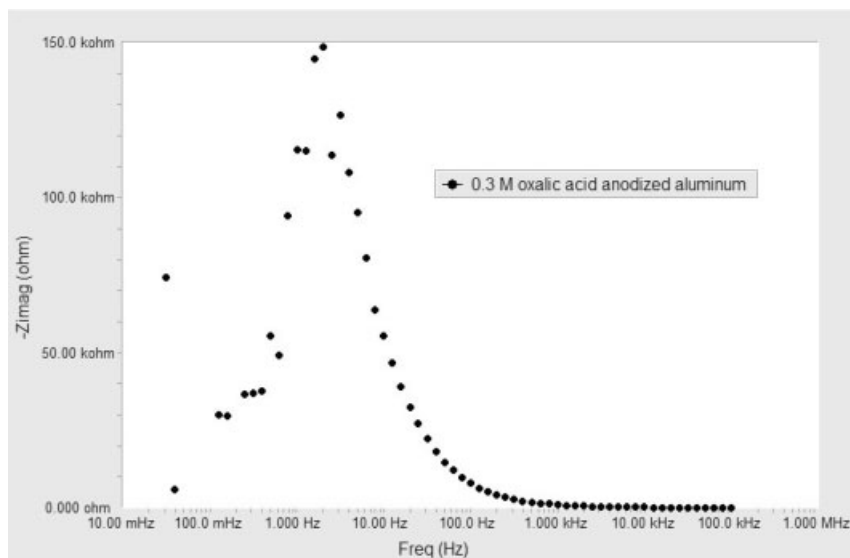


Fig. 7.22. Imaginary part of impedance vs. frequency of a GNW-Al<sub>2</sub>O<sub>3</sub> sample with different amounts of *E. coli* cells attached.



**Fig. 7.23.** Imaginary part of impedance vs. frequency of an anodized  $\text{Al}_2\text{O}_3/\text{Al}$  electrode in 0.01 M PBS buffer.

to be constant before and after the antigens interact with the antibodies, which means that the observed capacitance change is only due to the binding of *E. coli* cells. If the imaginary part of impedance is plotted vs. the frequency, a peak shape curve was obtained (Fig. 7.22). The imaginary impedance vs. frequency curve was a peak shape in many tests for this type of substrate. The peak frequencies for different samples were in the range 1 Hz–100 Hz. This peak is most likely due to the presence of  $\text{Al}_2\text{O}_3$  on the substrate. The impedance results of an anodized  $\text{Al}_2\text{O}_3/\text{Al}$  electrode tested in 0.01 M PBS buffer shown in Fig. 7.23 confirmed this speculation.

The capacitance can be calculated for this type of substrate from the data in the region of the right-half of the peak in the figure. Figure 7.24(a) shows the fitting results. If the capacitance of the electrode with linker and antibody is set as the reference capacitance, the relative capacitance change vs. the number of *E. coli* cells can be plotted as shown in Fig. 7.24(b). An increase of the capacitance with the concentration of *E. coli* has been found. The sensitivity of the linear region is about 0.36  $\mu\text{F}$  per  $\log(\text{number of } E. coli \text{ cells})$ . The reason why the capacitance increases instead of decreases after *E. coli* is bound is still not clear.

#### 7.4.4

##### Summary of EIS Detection of *E. coli* Bacteria

Immunosensors for the detection of *E. coli* bacteria have been developed based on the gold nanowire arrays formed by the template synthesis technique. A specific



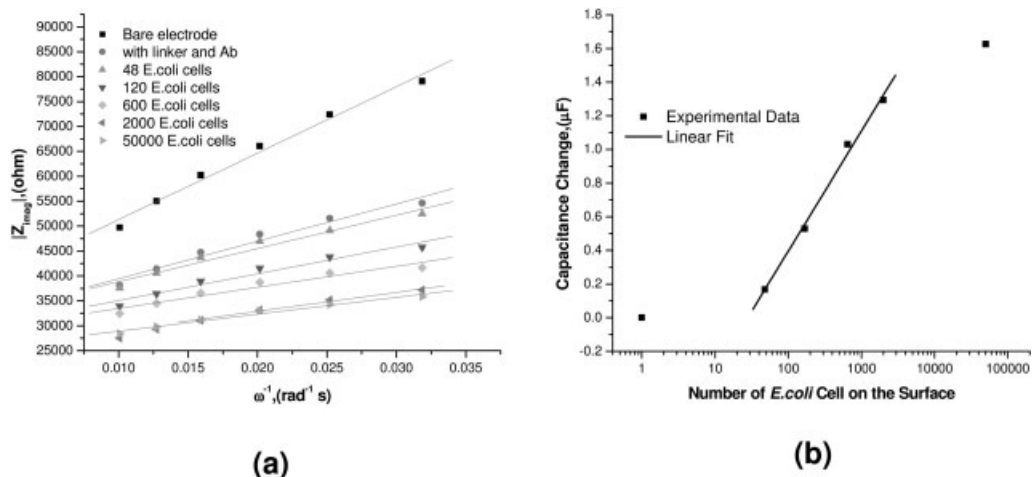


**Fig. 7.24.** (a)  $|Z_{imag}|$  vs.  $\omega^{-1}$ , and (b) relative capacitance change vs. the number of *E. coli* (log scale) on a GNW- $Al_2O_3$  sample.

type of antibody was immobilized on the active gold surface by covalent binding. EIS measurements were carried out to detect the complex formation between the antibodies and antigens. A thiol-containing linker molecule was synthesized to increase the binding capacity and strength of the specific antibody. The binding of *E. coli* results in a change in the overall capacitance. This capacitance change can be monitored by impedance measurements. Different substrate structures result in different working frequency ranges (compare Figs. 17(a), 20(a), and 24(a)). The preliminary results showed that this nano-gold biosensor is able to detect every 50 *E. coli* cells with a sensor area of 0.2 cm<sup>2</sup>. For both planar and nanostructured gold substrates, the change of capacitance ( $\Delta C$ ) was linear with the logarithmic number of *E. coli* cell on the surface. However, the linear range was smaller on a flat gold surface. The detection sensitivities were determined to be the slopes of the linear portion of the curves for all substrates (Table 7.4). It can be seen that the gold

**Tab. 7.4.** Comparison of three substrates studied for *E. coli* sensor application.

Substrate	Detection sensitivity	Sensitive region
Flat gold	$-0.5 \mu F/\log(\text{number of } E. coli \text{ cell})$	50–1000 cells
Gold nanowire array (GNW)	$-29.8 \mu F/\log(\text{number of } E. coli \text{ cell})$	50–2000 cells
Gold nanowire array in the oxide (GNW- $Al_2O_3$ )	$0.36 \mu F/\log(\text{number of } E. coli \text{ cell})$	50–2000 cells

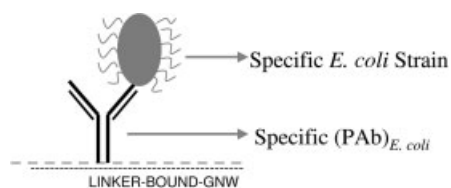


Fig. 7.25. Detection of pathogenic *E. coli* by antibody-linker-GNW biosensors.

nanowire array electrode is the most sensitive substrate according to the obtained capacitance change arising from the binding of the same amount of *E. coli* cells.

The study of the *E. coli* sensor has shown that an impedometric transduction strategy is suitable for detection of *E. coli* at low concentrations. The nanostructured materials can further improve the detection sensitivity. However, the specificity of this sensor device, as well as the long-term stability has not yet been established. The antibody used is not specific to a single strain of *E. coli* bacteria, various strains of *E. coli* can interact with this antibody.

## 7.5

### Conclusions

This chapter has described a quick method for bacteria detection using a gold nanowire based biosensor and electrochemical measurements. Detection methods have been developed with the use of gold nanowire (GNW) substrates attached to a C<sub>11</sub> linker arm in turn attached to the specific *E. coli* antibodies (Fig. 7.25). Preliminary results indicate that the GNW biosensor can detect as few as 50 *E. coli* cells with a sensor area of 0.2 cm<sup>2</sup>. However, this report gives the initial results for this novel procedure to be used in wider applications. The specificity of detection of any cell depends on the availability of a specific antibody directed to the cell surface macromolecules or antigens (Fig. 7.25). This method would be applicable to detect any cancer cells based on the antigens present on cell surfaces, such as human colon and breast cancer cells containing Le<sup>x</sup> and Sialo-Le<sup>x</sup> [60]. Antibodies against these antigens are available commercially. Further studies on the detection of cancer cells by this method are in progress.

### Acknowledgments

This chapter was written on research supported by an NSF-REU grant (Chemistry Department) and a grant-in-aid from the Bayer Corporation to Subhash Bash. Juan Jiang was the recipient of a Bayer Predoctoral Fellowship. Our thanks go to Dr. Patrick J. Boyle, Mr. Rui Ma, Mr. Joshua Henshaw, Ms. Rocio del A. Cordona, Mr. Kunal Saxena and Ms. Clare Lefave for their tireless technical help. Our special

thanks to Mrs. Dorisanne Nielsen for her help in the preparation of the final manuscript.

### References

- 1 CAI, Z. H., MARTIN, C. R., Electronically conductive polymer fibers with mesoscopic diameters show enhanced electronic conductivities. *J. Am. Chem. Soc.* **1989**, 111(11), 4138–4139.
- 2 MARTIN, C. R., PARTHASARATHY, R., MENON, V., Template synthesis of electronically conductive polymers – A new route for achieving higher electronic conductivities. *Synthetic Met.* **1993**, 55(2–3), 1165–1170.
- 3 PARTHASARATHY, R. V., MARTIN, C. R., Synthesis of polymeric microcapsule arrays and their use for enzyme immobilization. *Nature* **1994**, 369(6478), 298–301.
- 4 PENNER, R. M., MARTIN, C. R., Controlling the morphology of electronically conductive polymers. *J. Electrochem. Soc.* **1986**, 133, 2206.
- 5 VANDYKE, L. S., MARTIN, C. R., Electrochemical investigations of electronically conductive polymers. 4. Controlling the supermolecular structure allows charge transport rates to be enhanced. *Langmuir* **1990**, 6(6), 1118–1123.
- 6 JIANG, J., Electrochemical studies of nanostructured materials: The synthesis and size effect dependence of adsorption of organic molecules and applications to biosensors. Ph.D. dissertation, University of Notre Dame, Notre Dame, **2004**.
- 7 GAO, T., MENG, G. W., ZHANG, J., WANG, Y. W., LIANG, C. H., FAN, J. C., ZHANG, L. D., Template synthesis of single-crystal Cu nanowire arrays by electrodeposition. *Appl. Phys. A* **2001**, 73(2), 251–254.
- 8 LI, L., AC anodization of aluminum, electrodeposition of nickel and optical property examination. *Sol. Energy Mater. Sol. Cells* **2000**, 64, 279–289.
- 9 METZGER, R. M., KONOVALOV, V. V., SUN, M., XU, T., ZANGARI, G., XU, B., BENAKLI, M., DOYLE, W. D., Magnetic nanowires in hexagonally ordered pores of alumina. *IEEE Trans. Magn.* **2000**, 36(1), 30–35.
- 10 PENG, Y., QIN, D.-H., ZHOU, R.-J., LI, H.-L., Bismuth quantum-wires arrays fabricated by electrodeposition in nanoporous anodic aluminum oxide and its structural properties. *Mater. Sci. Eng.* **2000**, B77, 246–249.
- 11 SHINGUBARA, S., OKINO, O., SAYAMA, Y., SAKAUE, H., TAKAHAGI, T., Two-dimensional nanowire array formation on Si substrate using self-organized nanoholes of anodically oxidized aluminum. *Solid State Electron.* **1999**, 43, 1143–1146.
- 12 CROUSE, M. M., MILLER, A. E., JIANG, J., CROUSE, D. T., BASU, S. C., Enabling nanostructured materials via multilayer thin film precursor and applications to biosensors. *US Patent 6,869,671 B1*, March 22, **2005**.
- 13 WANG, Z., LI, H. L., Highly ordered zinc oxide nanotubules synthesized within the anodic aluminum oxide template. *Appl. Phys. A* **2002**, 74(2), 201–203.
- 14 XU, D. S., XU, Y. J., CHEN, D. P., GUO, G. L., GUI, L. L., TANG, Y. Q., Preparation and characterization of CdS nanowire arrays by dc electrodeposition in porous anodic aluminum oxide templates. *Chem. Phys. Lett.* **2000**, 325, 340–344.
- 15 BRUMLIK, C. J., MARTIN, C. R., Template synthesis of metal microtubules. *J. Am. Chem. Soc.* **1991**, 113(8), 3174–3175.
- 16 HULTEEN, J. C., CHEN, H. X., CHAMBLISS, C. K., MARTIN, C. R., Template synthesis of carbon nanotubule and nanofiber arrays. *Nanostructured Mater.* **1997**, 9(1–8), 133–136.
- 17 MARTIN, C. R., VANDYKE, L. S., CAI, Z. H., LIANG, W. B., Template synthesis of organic microtubules.

- J. Am. Chem. Soc.* **1990**, 112(24), 8976–8977.
- 18 WIRTZ, M., MARTIN, C. R., Template-fabricated gold nanowires and nanotubes. *Adv. Mater.* **2003**, 15(5), 455–458.
  - 19 MASUDA, H., WATANABE, M., YASUI, K., TRYK, D., RAO, T., FUJISHIMA, A., Fabrication of a nanostructured diamond honeycomb film. *Adv. Mater.* **2000**, 12(6), 444–447.
  - 20 WU, C. G., BEIN, T., Conducting polyaniline filaments in a mesoporous channel host. *Science* **1994**, 264(5166), 1757–1759.
  - 21 WU, C. G., BEIN, T., Conducting carbon wires in ordered, nanometer-sized channels. *Science* **1994**, 266(5187), 1013–1015.
  - 22 MARTIN, C. R., Nanomaterials – A membrane-based synthetic approach. *Science* **1994**, 266(5193), 1961–1966.
  - 23 MARTIN, C. R., Membrane-based synthesis of nanomaterials. *Chem. Mater.* **1996**, 8(8), 1739–1746.
  - 24 MASUDA, H., HASEGAWA, F., ONO, S., Self-ordering of cell arrangement of anodic porous alumina formed in sulfuric acid solution. *J. Electrochem. Soc.* **1997**, 144(5), L127–L130.
  - 25 MASUDA, H., YADA, K., OSAKA, A., Self-ordering of cell configuration of anodic porous alumina with large-size pores in phosphoric acid solution. *Jpn. J. Appl. Phys.* **1998**, 37(Pt.2)(11A), L1340–L1342.
  - 26 THAMIDA, S. K., CHANG, H. C., Nanoscale pore formation dynamics during aluminum anodization. *Chaos* **2002**, 12(1), 240–251.
  - 27 HOAR, T. P., MOTT, N. F., A mechanism for the formation of porous anodic oxide films on aluminum. *Phys. Chem. Solids* **1959**, 9, 97.
  - 28 O'SULLIVAN, J. P., WOOD, G. C., The morphology and mechanism of formation of porous anodic films on aluminum. *Proc. R. Soc. London A* **1970**, 317(1531), 511–543.
  - 29 THOMPSON, G. E., XU, Y., SKELDON, P., SHIMIZU, K., HAN, S. H., WOOD, G. C., Anodic-oxidation of aluminum. *Philos. Mag. B* **1987**, 55(6), 651–667.
  - 30 BA, L., LI, W. S., Influence of anodizing conditions on the ordered pore formation in anodic alumina. *J. Phys. D: Appl. Phys.* **2000**, 33, 2527–2531.
  - 31 MASUDA, H. A. F., Kenjiq, Ordered metal nanohole arrays made by a two-step replication of honeycomb structures of anodic alumina. *Science* **1995**, 268, 1466–1468.
  - 32 DESPIE, A., PARKHUTIK, V. P., Electrochemistry of aluminum in aqueous solutions and physics of its anodic oxide, in *Modern Aspects of Electrochemistry*, BOCKRIS, J. O. M., CONWAY, B. (Eds.), Plenum Press, New York, **1989**, Vol. 20.
  - 33 YUE, D., Electrochemically Synthesized Nanostructures on Aluminum. Ph.D. dissertation, University of Notre Dame, Notre Dame, **1995**.
  - 34 BANDYOPADHYAY, S., MILLER, A. E., CHANG, H. C., BANERJEE, G., YUZHAKOV, V., YUE, D. F., RICKER, R. E., JONES, S., EASTMAN, J. A., BAUGHER, E., CHANDRASEKHAR, M., Electrochemically assembled quasi-periodic quantum dot arrays. *Nanotechnology* **1996**, 7(4), 360–371.
  - 35 CROUSE, D., LO, Y. H., MILLER, A. E., CROUSE, M., Self-ordered pore structure of anodized aluminum on silicon and pattern transfer. *Appl. Phys. Lett.* **2000**, 76(1), 49–51.
  - 36 RICKER, R. E., MILLER, A. E., YUE, D. F., BANERJEE, G., BANDYOPADHYAY, S., Nanofabrication of a quantum dot array: Atomic force microscopy of electropolished aluminum. *J. Electron. Mater.* **1996**, 25(10), 1585–1592.
  - 37 YUE, D. F., BANERJEE, G., MILLER, A. E., BANDYOPADHYAY, S., Giant magnetoresistance in an electrochemically synthesized regimented array of nickel quantum dots. *Superlattices Microstruct.* **1996**, 19(3), 191–195.
  - 38 YUZHAKOV, V. V., CHANG, H. C., MILLER, A. E., Pattern formation during electropolishing. *Phys. Rev. B* **1997**, 56(19), 12 608–12 624.
  - 39 YUZHAKOV, V. V., TAKHISTOV, P. V., MILLER, A. E., CHANG, H. C., Pattern selection during electropolishing due

- to double-layer effects. *Chaos* **1999**, 9(1), 62–77.
- 40 PRESTON, C. K., MOSKOVITES, M., Optical characterization of anodic aluminum oxide films containing electrochemically deposited metal particles. 1. Gold in phosphoric acid anodic aluminum oxide films. *J. Phys. Chem.* **1993**, 97, 8459–8503.
- 41 WANG, Y. H., MO, J. M., CAI, W. L., SHI, G., Mechanism of metal deposited in porous alumina by alternating current. *Acta Phys. Chim. Sin.* **2001**, 17(2), 116–118.
- 42 MORIMOTO, K., TSUJIMOTO, M., YAJI, T., MURAKAMI, T., Electroless gold plating bath. *US* 5,364,460, Nov. 15, 1994.
- 43 MILLER, A. E., BANDYOPADHYAY, S., Electrochemical synthesis of quasi-periodic quantum dot and nanostructure arrays. *US* 5,747,180, **1998**.
- 44 YIN, A. J., LI, J., JIAN, W., BENNETT, A. J., XU, J. M., Fabrication of highly ordered metallic nanowire arrays by electrodeposition. *Appl. Phys. Lett.* **2001**, 79(7), 1039–1041.
- 45 WANG, Z., SU, Y. K., LI, H. L., AFM study of gold nanowire array electrodeposited within anodic aluminum oxide template. *Appl. Phys. A* **2002**, 74, 563–565.
- 46 FOSS, C. A., HORNYAK, G. L., STOCKERT, J. A., MARTIN, C. R., Optical-properties of composite membranes containing arrays of nanoscopic gold cylinders. *J. Phys. Chem.* **1992**, 96(19), 7497–7499.
- 47 FOSS, C. A., HORNYAK, G. L., STOCKERT, J. A., MARTIN, C. R., Template-synthesized nanoscopic gold particles – Optical-spectra and the effects of particle-size and shape. *J. Phys. Chem.* **1994**, 98(11), 2963–2971.
- 48 HORNYAK, G. L., PATRISSI, C. J., MARTIN, C. R., Fabrication, characterization, and optical properties of gold nanoparticle/porous alumina composites: The nonscattering Maxwell-Garnett limit. *J. Phys. Chem. B* **1997**, 101(9), 1548–1555.
- 49 HORNYAK, G. L., PATRISSI, C. J., MARTIN, C. R., VALMALETTE, J. C., DUTTA, J., HOFMANN, H., Dynamical Maxwell-Garnett optical modeling of nanogold porous alumina composites: Mie and kappa influence on absorption maxima. *Nanostruct. Mater.* **1997**, 9(1–8), 575–578.
- 50 HORNYAK, G. L., PHANI, K. L. N., KUNKEL, D. L., MENON, V. P., MARTIN, C. R., Fabrication, characterization and optical theory of aluminum nanometal nanoporous membrane thin film composites. *Nanostruct. Mater.* **1995**, 6(5–8), 839–842.
- 51 HULTEEN, J. C., PATRISSI, C. J., MINER, D. L., CROSTHWAIT, E. R., OBERHAUSER, E. B., MARTIN, C. R., Changes in the shape and optical properties of gold nanoparticles contained within alumina membranes due to low-temperature annealing. *J. Phys. Chem. B* **1997**, 101(39), 7727–7731.
- 52 MARTIN, C. R., MITCHELL, D. T., Template-synthesized nanomaterials in electrochemistry, in *Electro-analytical Chemistry*, **1999**, Vol. 21, pp. 1–74.
- 53 WAGNER, P., HEGNER, M., KERMAN, P., ZUAGG, F., SEMENZA, G., Covalent immobilization of biomolecules on Au via n-OH succinamide ester functionalized self-assembled monolayers for scanning probe microscopy. *Biophys. J.* **1996**, 70, 2052–2066.
- 54 BASU, M., SEGGERSON, S., HENSHAW, J., JIANG, J., CORDONA, R., LEFAVE, C., BOYLE, P. J., MILLER, A., PUGIA, M., BASU, S., Nano-biosensor development for the bacterial detection during human kidney infection. *Glycoconjugate J.* **2004**, 21, 487–496.
- 55 GHINDILIS, A. L., ATANASOV, P., WILKINS, M., WILKINS, E., Immunosensors: Electrochemical sensing and other engineering approaches. *Biosens. Bioelectron.* **1998**, 13(1), 113–131.
- 56 GRIFFITHS, D., HALL, G., Biosensors – What real progress is being made? *Trends Biotechnol.* **1993**, 11, 122–130.
- 57 OWEN, V. M., Market requirements for advanced biosensors in healthcare. *Biosens. Bioelectron.* **1994**, 9, XXIX–XXXV.

- 58 BARD, A. J., FAULKNER, L. R., *Electrochemical Methods: Fundamentals and Applications*, 2nd edn., John Wiley & Sons, Inc., New York, 2001, 833.
- 59 MACDONALD, J. R., *Impedance Spectroscopy*, John Wiley & Sons, New York, 1987.
- 60 BASU, M., HAWES, J. W., LI, Z., GHOSH, S., KHAN, F. A., ZHANG, B. J., BASU, S., Biosynthesis in vitro of SA-Le<sup>x</sup> and SA-diLe<sup>x</sup> by 1-3 fucosyltransferases from colon carcinoma cells and embryonic brain tissues. *Glycobiology*, 1991, 1, 527–535.

## 8

# Dendrimer-based Electrochemical Detection Methods

*Hak-Sung Kim and Hyun C. Yoon*

### 8.1 Overview

The use of molecularly-organized nanoscale interfaces is of great interest in efforts to enhance the analytical capabilities of biosensors. In this regard, dendrimer-based biocomposite structures, including molecularly organized monolayers and multilayers, have been developed for catalytic and affinity biosensing. As a highly organized and plurifunctional macromolecule, dendrimers find wide applications in analytical sciences. The anticipated merits of using dendrimers as the layer-forming materials are based on their structural characteristics such as homogeneity, compatible size with biomolecules, internal porosity, and the high density of functional groups. These unique characteristics make them good candidates for the building units of films on biosensor surfaces, presenting both the advantages of using polymers (plurifunctionality) and molecularly controllable nanomaterials. This chapter focuses on the fabrication of dendrimer-based biocomposite mono-/multilayers and their biosensing applications. Implementations of biointerfaces for the bioelectrocatalytic enzyme sensors with the multilayer configuration and affinity sensors based on either bioelectrocatalytic signal amplification or immunoprecipitation-voltammetric detection principles with dendrimer monolayers are covered.

### 8.2 Introduction

#### 8.2.1 Background

Molecularly organized nanostructures are of great interest in analytical sciences, molecular device technology, and biotechnology [1]. Especially, an enormous amount of research has been devoted to the development of molecularly organized

interfaces containing biomolecules as diagnostic tools (biosensors), biomimetic membranes and, recently, bioelectronic devices [2–4].

With the availability of highly controllable structuring and patterning techniques, especially the self-assembled monolayers (SAMs) methodology [5, 6], the pace of development in the related fields has greatly increased. The pioneering studies of Whitesides group regarding the mixed SAM technology and micropatterning such as microcontact printing have opened a new avenue for the technique [7–9]. By keeping in step with such developments, there have been numerous approaches for the well-organized and active biocomposite assemblies.

However, the quest continues for molecularly organized, structurally rigid, biochemically active and stable biocomposite superstructures. In this regard, the implementation of useful surface bio-functionalization methodologies as well as the introduction of novel materials having unique properties is one of the major subjects of research and development. As a promising molecule for biocomposite nanostructures, highly branched dendrimers draw much attention.

### 8.2.2

#### **Dendrimers as a new Constituent of Biocomposite Structures**

The past decade has seen expanding interest in the newly introduced synthetic dendritic polymers (dendrimers) [10, 11], which are highly branched, fractal-like macromolecules of defined molecular structure, size, and topology. The molecules are synthesized by an iterative sequence of reaction steps, or cascade synthesis, with sophisticated control in reaction conditions [12]. With the development in synthetic methodology, structurally perfect dendrimers with high purity and narrow polydispersity have been produced. The unique characteristics of dendrimers, such as structural homogeneity, molecular integrity, controlled composition, and the multiple homogeneous chain-ends available for consecutive conjugation reaction, have enabled their use as the material of choice in applications such as drug delivery, energy harvesting, ion sensing, catalysis, and information storage [13]. For these objectives, several approaches adopting dendrimers as the building block for the nanostructures have been conducted. These include deposition of dendritic multilayers via Pt-complexation, electrostatic interaction, and reaction with grafted copolymer [14–17]. Characteristics mentioned above, along with the recently recognized biocompatibility [13], merit the use of dendrimers for the fabrication of organized functional biocomposite nanostructures, comparable with those prepared with entangled linear and branched polymers. By us and other groups, the utility of the dendrimer has extended to bio-related fields [18–20].

Our recent reports demonstrate that dendrimers are advantageous as the building block for the construction of the multilayered biocomposite nanostructures and reagentless enzyme or affinity biosensors [18, 21–25]. As a building unit for organic thin films, dendrimers, as highly branched dendritic macromolecules, possess a unique surface of multiple chain-ends, and the number of surface groups can be precisely controlled as a function of synthetic generations (Fig. 8.1). For example,



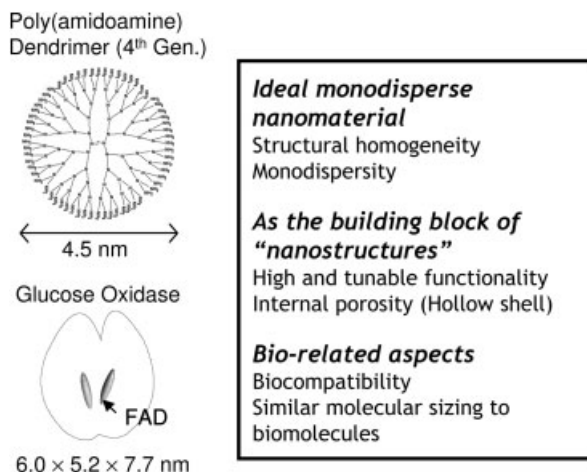


**Fig. 8.1.** Characteristics of fourth-generation (G4) poly(amidoamine) dendrimers. Molecular models for dendrimer and glucose oxidase are shown for size comparison.

fourth generation (G4) poly(amidoamine) dendrimers have 64 surface amine groups. The high concentration of functional end groups of dendrimers enables synthetic modifications of molecularly ordered nanostructures. Dendrimers provide multiple conjugation sites, and the remaining groups, after film formation, are accessible for further modification with functionalization groups for specific purposes. Dendrimers of high generation numbers offer some advantages over linear or partly branched polymers, e.g., structural homogeneity, controllable composition, comparable size to the participating biomolecules, and multiple homogeneous chain-ends groups, valuable for the conjugating reactions [21].

In this respect, we have employed the G4 poly(amidoamine) dendrimer as the underlying-layer for functionalizing or micropatterning ligands on the solid surface. Besides G4 poly(amidoamine) dendrimers, poly-L-lysine and poly(allylamine) and amine-terminated cystamine SAM, all presenting surface amine functionalities, have frequently been used, and we have compared their physicochemical and biochemical properties as thin films for arraying ligands on a solid surface [26].

### 8.3 Applications for Biosensors

In the past decade, self-assembled monolayers, silane-modified layers, Langmuir-Blodgett (LB) layers, and polymer grafting layers compatible with biomolecules have been commonly used for the presentation of ligands or proteins on a solid surface to modulate their interactions with reacting couple molecules. These or-

ganic thin films have an expanded application in biosensors (enzyme electrodes, immunoelectrodes, DNA analyses), artificial biomimetic membranes, and, recently, bioelectronic devices. In this regard, dendrimer-based biocomposite structures, organized mono- and multilayers, have been developed for catalytic and affinity biosensing.

### 8.3.1

#### Bioelectrocatalytic Enzyme Electrodes based on LBL (layer-by-layer) Assembly with Dendrimers

For a catalytic biosensing interface, a new approach to construct a multilayered enzyme film on the electrode surface has been developed [18, 21]. Figure 8.2 shows the schematic procedure to construct a film by alternate layer-by-layer (LBL) depositions of G4 poly(amidoamine) dendrimers and periodate-oxidized glucose oxidase (GOx). Cyclic voltammograms registered from gold electrodes modified with GOx/

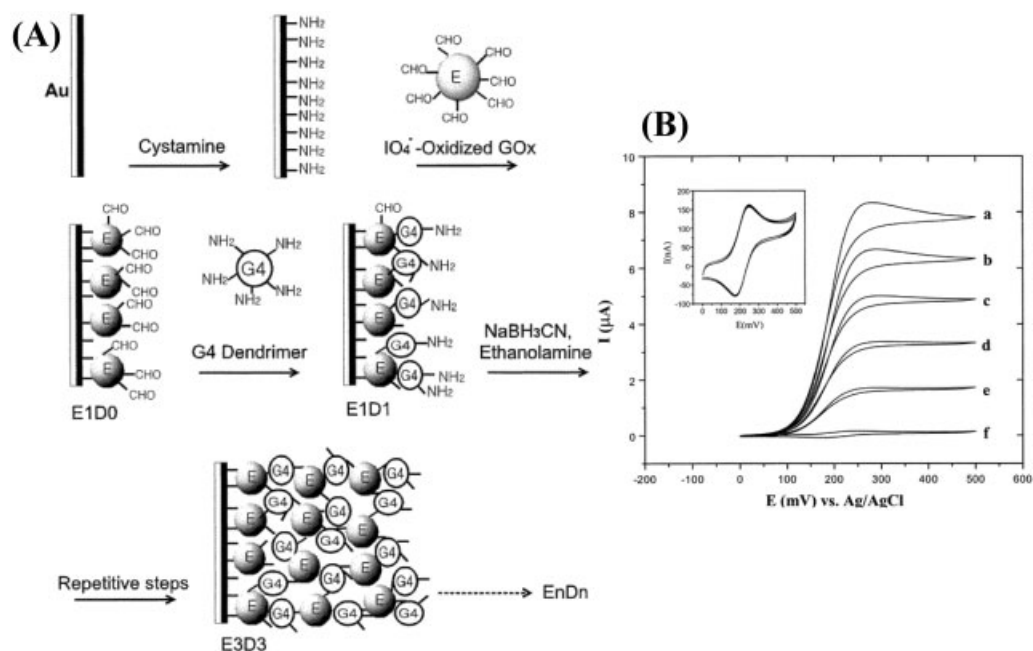


**Fig. 8.2.** (A) Schematic representation of a multilayered GOx/dendrimer network construction on a Au electrode surface. (B) Cyclic voltammograms of the GOx/dendrimer multilayered electrodes in the presence of 0.1 mM ferrocene-methanol as a diffusional electron-transferring mediator: (a) E5D5, (b) E4D4, (c) E3D3, (d) E2D2, and

(e) E1D1 in the presence of 20 mM glucose; (f) E1D1 in the absence of glucose, unmediated. Inset: cyclic voltammograms for each layer numbers in the absence of glucose in solution. All curves were registered in 0.1 M phosphate buffer (pH 8.0) under Ar. Potential scan rate:  $5 \text{ mV s}^{-1}$ . (Modified after Ref. [18]).

dendrimer multilayers revealed that the bioelectrocatalytic response is directly proportional to the number of deposited bilayers, i.e., to the amount of active GOx immobilized on the gold electrode surface. From analysis of electrochemical signals, the amount of active enzyme per GOx/dendrimer bilayer during the multilayer forming steps was calculated, demonstrating that the multilayer is constructed in a spatially-ordered manner. Also, by ellipsometry measurement, a linear increase of the film thickness was observed, supporting formation of the desired multilayer. The five-bilayer associated electrode (E5D5) showed a sensitivity of  $14.7 \mu\text{A} (\text{mM glucose})^{-1} \text{cm}^{-2}$  and remained stable over 20 days under daily calibrations. The proposed method is simple and applicable to the construction of thickness- and sensitivity-controllable biosensing [18].

As an extension of this research, poly(amidoamine) dendrimers having surface ferrocenyl functional groups were prepared and used for the fabrication of a reagentless bioelectrocatalyzed enzyme electrode [21]. Poly(amidoamine) dendrimers having various degrees of tethering with the ferrocenyls were prepared by controlling the molar ratio of ferrocenecarboxaldehyde to amine groups of dendrimers during synthesis (Fig. 8.3A). By LBL depositions of ferrocenyl-tethered dendrimers with periodate-oxidized GOx on gold surface, an electrochemically and enzymatically active multilayer was constructed. The resulting GOx/Fc-D multilayer-associated electrodes were electrochemically characterized, and the density of ferrocenyl groups, active enzyme content, and sensitivity were analyzed. Dendrimers with 32% modification level was found to be an optimum from the analyses in terms of GOx-dendrimer network formation, electrochemical connectivity of ferrocenyls, and electrode sensitivity (Fig. 8.3B, C). With the synthesized Fc(32%)-tethered dendrimers, mono- and multilayered electrodes were constructed, and their electrochemical and catalytic properties were characterized. The bioelectrocatalytic signals from the GOx/Fc-D electrodes were directly proportional to the bilayer numbers. From this result, it seems that the electrode sensitivity is directly controllable, and the multilayer-forming strategy with ferrocenyl-labeled dendrimers is useful for the development of reagentless biosensors.

### 8.3.2

#### **Bioelectrocatalytic Immunosensors based on the Dendrimer-associated SAMs**

##### **8.3.2.1 Affinity Recognition Surface based on the Dendrimer-associated SAMs**

All biological phenomena, such as generation and development, are regulated by functional interactions of protein–protein, receptor–ligand, antigen–antibody, enzyme–substrate, and protein–XNA. Therefore, the understanding of functions of biomolecules that specifically interact with particular proteins or ligands is the main theme in life science. As a tool for the functional study of proteins, affinity recognition chip technology is important. Therefore, we have focused on surface functionalization technology that will arrange and immobilize active proteins on affinity chip surfaces. Immobilization of active proteins on solid supports with an extended lifetime is the major concern of a protein chip.

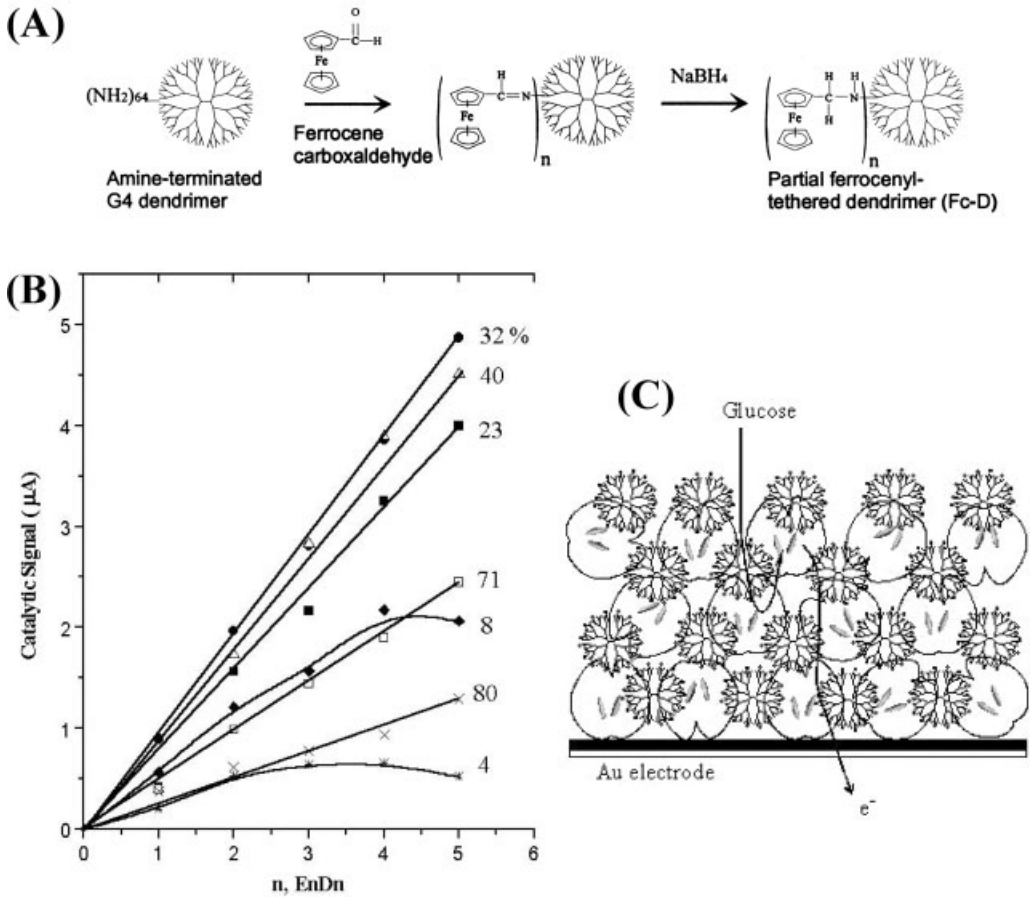


**Fig. 8.3.** (A) Schematic representation of a semi-synthetic preparation of partial ferrocenyl-tethered G4 poly(amidoamine) dendrimer (Fc-D). (B) Bioelectrocatalytic signal amplification for GOx/Fc-D electrodes containing dendrimers with various ferrocenyl functionalization levels as a function of deposited bilayer numbers. Signal values were

sampled at +370 mV vs. Ag/AgCl reference electrode from cyclic voltammetric data in the presence of 20 mM glucose. (C) Schematic representation of the idealized multilayered GOx/Fc-D network on an Au electrode surface and the anticipated biochemical and charge-transfer reactions. (Modified after Ref. [21]).

In this respect, we emphasize three considerations to obtain sufficient sensitivity and accuracy from the affinity sensor. Aside from the signal generation efficacy, which will be covered later, the surface chemistry should be specially optimized to drive efficient immobilization of proteins or ligands. (a) Proteins must be immobilized on a chip surface in a stable and satisfactorily concentrated manner. (b) The orientation of protein should be controlled for favorable bio-specific interactions at

the chip surface. (c) Nonspecific binding of molecules at the chip surface should be adequately circumvented. Additionally, and importantly, a highly sensitive detection system should be developed, by which the derived signal can be analyzed, because, in typical cases, the concentration of immobilized biomolecules on the chip is as low as  $10^{-15}\sim 10^{-14}$  mol/chip surface.

For a biospecific affinity-sensing interface, an affinity biosensor system based on avidin–biotin interaction has been developed [22]. The avidin–biotin interaction, a unique model of strong protein–ligand interaction, exhibits stronger affinity than any other antigen–antibody interactions. As the building block of an affinity sensing monolayer, a G4 poly(amidoamine) dendrimer having partial ferrocenyl-labeled surface groups was synthesized and used. The surface amine groups from dendrimers were also functionalized with biotin amidocaproate, and the biotinylated and electroactive monolayer was used for the affinity-sensing surface interacting with avidin. As shown in Fig. 8.4(A), an electrochemical signal from the affinity biosensor was generated by free enzyme GOx in electrolyte, depending on the degree of coverage of the sensing surface with avidin and subsequent surface shielding. The sensor signal decreased with increasing avidin concentration, and approached a minimum when the sensing surface was fully covered (Fig. 8.4B). The

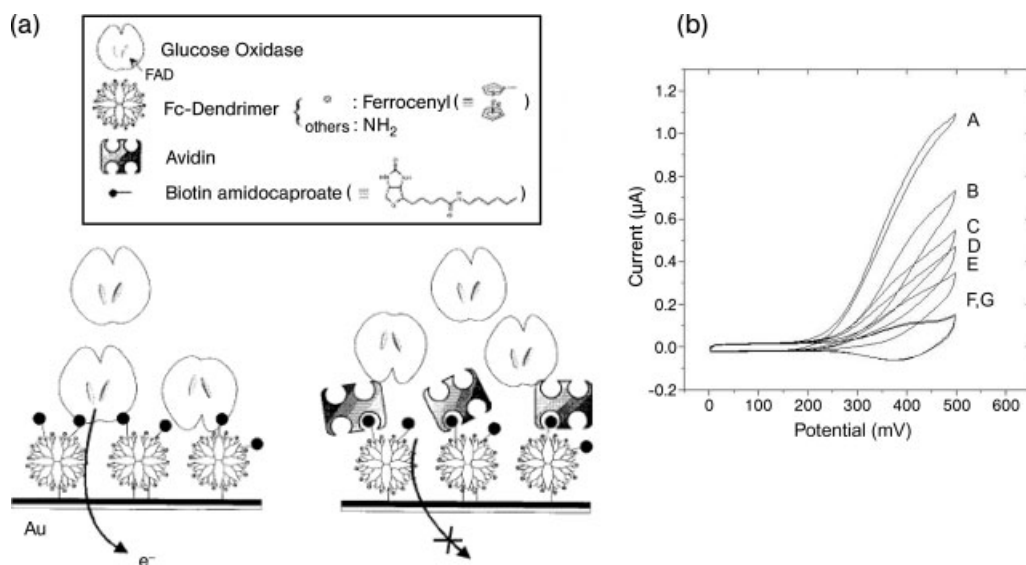


**Fig. 8.4.** (a) Construction and proposed operational principle for an affinity biosensor based on the avidin–biotin interaction on a gold electrode surface. Molecular models of the chemicals used for electrode construction are shown. (b) Cyclic voltammograms of the affinity biosensors as a function of reacted avidin concentration: (A) 0, (B) 1 ng mL<sup>-1</sup>,

(C) 10 ng mL<sup>-1</sup>, (D) 100 ng mL<sup>-1</sup>, (E) 1 mg mL<sup>-1</sup>, and (F) 10 mg mL<sup>-1</sup>. Cyclic voltammograms were obtained in the presence of 30 mg mL<sup>-1</sup> of GOx as a signal generator and 10 mM glucose as a substrate; (G) background voltammogram in the absence of enzyme and substrate. Potential scan rate: 5 mV s<sup>-1</sup>. (Modified after Ref. [22]).

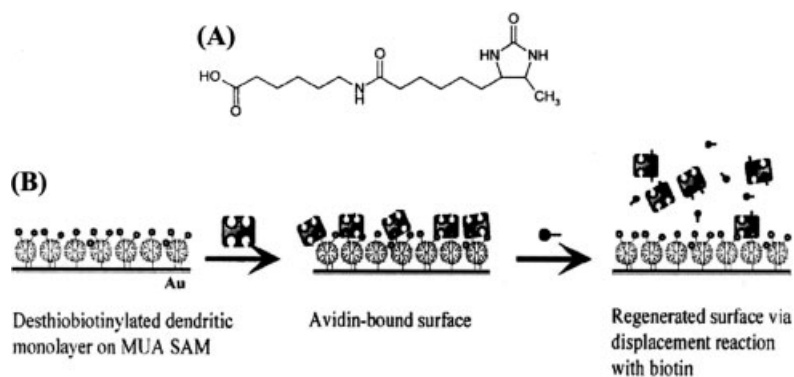


**Fig. 8.5.** (A) Molecular structures of d-desthiobiotin amidocaproate. (B) Schematic representation of the procedure employed for the biospecific association/dissociation of biomolecules at the affinity-sensing electrode surfaces. (Modified after Ref. [23]).

detection limit of avidin was about 4.5 pM, and the sensor signal was linear, ranging from 1.5 pM to 10 nM, under optimal conditions. Based on the kinetic analysis using the biotinylated glucose oxidase, an active enzyme coverage of  $2.5 \times 10^{-12}$  mol cm<sup>-2</sup> on the avidin pretreated surface was calculated, demonstrating the formation of a spatially ordered and compact protein layer on the modified sensing interface.

As an extension of this research, a new approach regarding the development of a repeatedly renewable affinity-sensing surface was presented based on the reversible association/dissociation reactions between avidin and biotin analogues [23] (Fig. 8.5). The surfaces were constructed with dendrimer monolayers, whose surface chain-end groups have been functionalized with a biotin analog, desthiobiotin, which has a reduced affinity toward avidin (Fig. 8.5A). The functionalized monolayers provided an affinity recognition interface for avidin and further biospecific interactions with biotinylated molecules. The desthiobiotin–avidin associates underwent a dissociation (displacement) reaction with free biotin treatment, and this renewed the affinity surface and provided the possibility of repeated utilization of the affinity-sensing surface. Biotinylated glucose oxidase, as a model compound for signal generation, was used for the association reaction onto the avidin preincubated surface, and voltammetric measurements were performed to track the reaction steps by registering the activity of associated enzyme. Efficient association/dissociation reaction cycle traces were found, especially for the desthiobiotin amidocaproate modified electrodes, suggesting steric limitation regarding the ligand length for the biospecific interaction. With the optimized affinity-surface construction steps and reaction conditions, continuous association/dissociation reaction cycles were achieved, which is useful as a regenerable affinity surface.

Reversible affinity interactions at the functionalized electrode have also been extended to antibodies [24]. The surfaces were constructed with dendrimer mono-

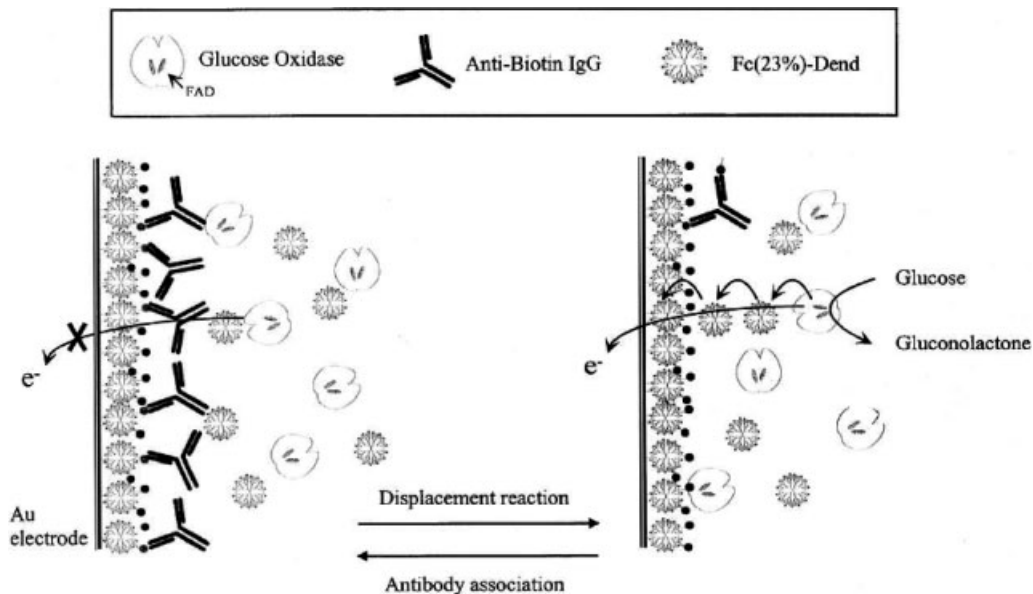


**Fig. 8.6.** Schematic representation of the idealized reactions in electrolyte and at the affinity-sensing electrodes for antibody-associated and regenerated surfaces: enzymatic catalysis, electron mediation with

Fc-D in electrolyte, and charge transfer to Au electrodes. Dimensions of the components are not drawn to scale for simplicity. (From Ref. [24]).

layers, whose surface chain-end groups have been double-functionalized with biotins and ferrocenyls for the biospecific recognition and electron transfer. The functionalized monolayers provide a platform for biospecific recognition with monoclonal anti-biotin antibodies. The bound antibodies were dissociated with free biotin treatment, and the process renewed the affinity surfaces for repeated utilization. Figure 8.6 displays the electrochemical tracking of the association/dissociation reaction cycles, based on the shielding of the electrode surface with bound antibody molecules and subsequent hindrance in electron transfer, with free-diffusing signal generator and mediator. Factors influencing the biospecific interactions and measurements were considered. With the results, continuous association/dissociation reactions have been accomplished, holding great promise for reversible affinity biosensing.

### 8.3.2.2 Electrochemical Signaling from Affinity Recognition Reactions

Affinity sensing has been evolved from the viewpoints of detection of immune-related molecules with minute concentration range and signaling with acceptable quantification capability. Several detection principles for affinity/immuno sensing have been developed. A detection technique such as surface plasmon resonance (SPR) spectroscopy and a quartz crystal microbalance (QCM) can recognize the concentration of bound biomolecules by changes in mass and/or surface density

(molecules/sensor area). However, notably, they are not suitable for application as portable biosensors. For SPR immunosensing, major progress has been made with bench-top scale instruments, enabling high-throughput and multiplexed analysis. In the concept of handheld biosensor/immunosensor, electrochemical methods have received the spotlight due to facile device-miniaturization and sensitive signal-quantification. Especially, recent efforts have focused on integrated devices, the so-called lab-on-a-chips [27, 28], combining the detection part with sample delivery parts based on microfluidics; thus a detection method that necessitates minimum instrumental part is highly desired. In that sense, we have focused on signaling methodologies that fulfill the needs of electrochemical detection and have developed two potential methods, including the immunoprecipitation-mediated signaling and the enzymatic back-filling immunoassay.

A signaling strategy for immunosensors that transduces biospecific affinity recognition reactions into electrochemical signals has been developed. This method combines the relatively well-known immunohistochemical reactions with electrochemistry [25]. As can be seen in Fig. 8.7, the cyclic voltammetric method, tracking the precipitation of insoluble products onto the sensing surface and the subsequent surface shielding and decrement in the electrode area, was employed for signal registration. Precipitation of insolubilities was induced by the catalytic reaction of peroxidase, which were labeled to the biospecifically associated protein or antibody molecules. We have investigated the functionalization of biotin ligand groups to the sensing monolayer and their biospecific interactions with anti-biotin antibody molecules as a model affinity recognition. The immunosensing interface was developed onto dendrimer-activated SAMs, as the base template for the functionalization of the antigen as well as generation. Additionally, the sensing system was applied for biotin/(strept)avidin couples, extending the usage of the developed strategy. With the affinity-sensing interface, a stepwise surface regeneration process has been developed, based on the combination of deposited product thin-film dissolution and bound-protein displacement reactions from the modified sensor surfaces [29]. The results exemplify the usefulness of immunoprecipitation-mediated signaling in terms of sensitivity and repeated use.

By using the developed immunosensing principle, a silicon-based immunosensor chip has been microfabricated and applied for the analysis of real samples such as blood serum [30]. Figure 8.8 shows an array-type gold electrode, which was fabricated on a silicon wafer, containing two electrode geometries of rectangular ( $100 \times 500 \mu\text{m}$ ) and circular (radius:  $50 \mu\text{m}$ ) types. These two types of electrodes showed distinct electrochemical characteristics of bulk and micro-electrodes, respectively, exhibiting different sensing parameters such as operation voltage, sensitivity, and dynamic detection range. Ferritin was employed as a model analyte for immunosensing because it has serological importance as a general marker protein for tumors and cancer recurrence. With the ferritin-functionalized immunosensor chips, biospecific interactions were performed with antiferritin antiserum and secondary antibody samples, followed by electrochemical signaling by an immunoprecipitation reaction with the label peroxidase enzyme. Under the optimized affinity-surface construction steps and signaling conditions, both types of microfabri-



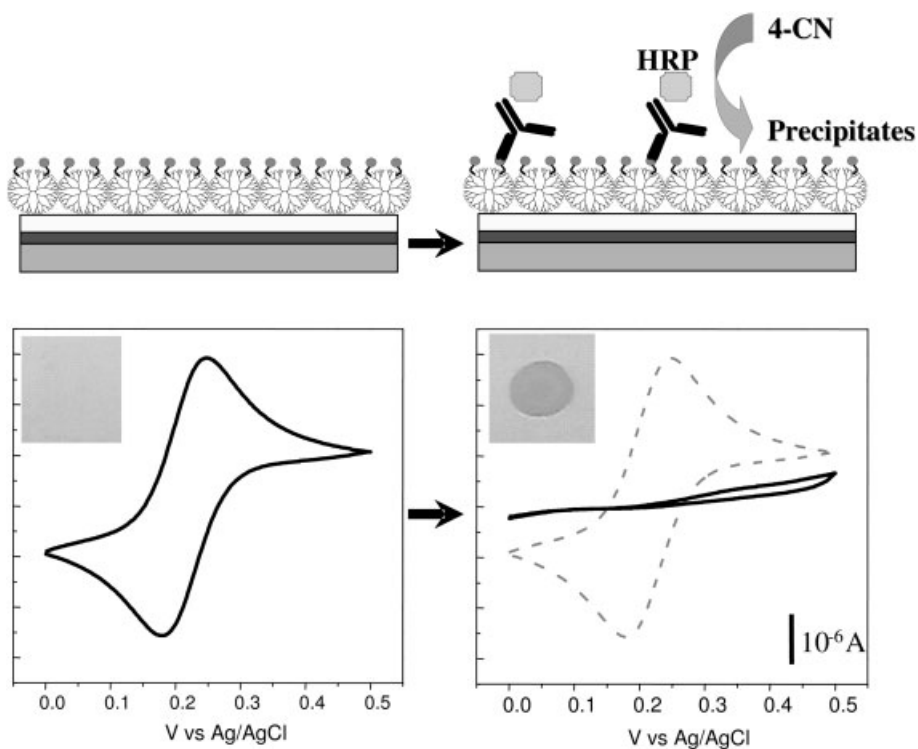


**Fig. 8.7.** (Top) Schematic representation of the affinity biosensor construction and proposed operational principle, and CCD camera images of a representative surface upon signaling reaction (inset). Component dimensions are not drawn to scale for simplicity. (Bottom) Cyclic voltammetric traces for sensor signaling at the dendrimer-assisted

SAM surfaces. A freshly prepared and biotin-functionalized surface before (left) and after target protein association and precipitation reaction steps (right). Curves were registered in a 0.1 M phosphate buffer (pH 7) containing ferrocene-methanol (0.1 mM) as a signal tracer. Potential scan rate:  $50 \text{ mV s}^{-1}$ . (Modified after Ref. [25]).

cated electrodes, including rectangular ( $100 \times 500 \mu\text{m}$ ) and circular (radius:  $50 \mu\text{m}$ ) types, exhibited well-defined calibration results as a function of ferritin concentration in antiserum samples. Furthermore, circular-type micropatterned immunoelectrodes displayed the voltammetric characteristics of microelectrodes, which is advantageous in sensor operation under a fixed potential with low signal drift compared with the bulk-type electrodes. The results support the idea that the employed signaling method with the proposed immunosensor configuration is fit for sensor miniaturization and integration to biomicrosystems and lab-on-a-chips.

The analyte for affinity sensors, especially antibody, is usually bound to the surface-immobilized capture molecule and could cause a significant signal loss during subsequent handling procedures and signaling due to its limited affinity/

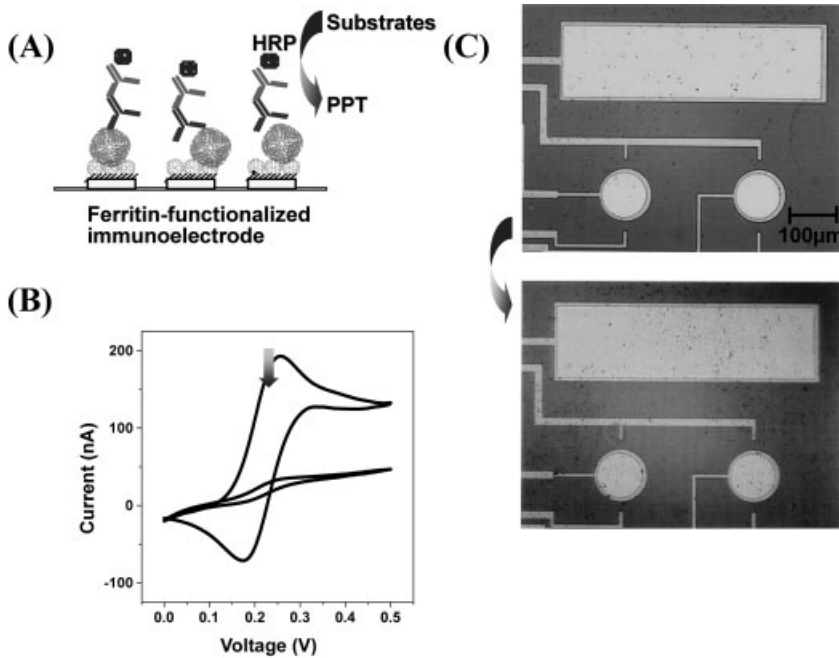


**Fig. 8.8.** (A) Schematic representation of the procedure for bioaffinity interface construction and the biocatalyzed precipitation reaction for signal generation from a ferritin immunosensor. Component dimensions are not drawn to scale for simplicity. (B) Representative voltammetric sensor signal.

(C) Photographs of the signaling result along with the microfabricated immunosensors. Magnified views of an array micropatterned biochip were taken both before and after the signal generation reaction by the biocatalyzed immunoprecipitation. (Modified after Ref. [30]).

stability. Thus, we also focused on the signal stability of affinity sensors. The signal stability from immunosensors is usually not sufficient because the known binding constant between antigens and antibodies are several orders of magnitude lower than the well known and frequently used model of biotin–streptavidin ( $K_a = 1 \times 10^{15} \text{ M}^{-1}$ ) [23, 24]. This suggests that the antibody-bound surface undergoes a gradual change, raising the possibility of antibody detachment and signal variation. Also, supplementary label molecules such as enzymes are applied to generate electrochemical signals from immunosensors. In a typical immunoassay, the detection process requires pre-treatment of ligands or expensive commercial reagent to activate reporter molecules such as secondary antibodies because the signaling mechanism is based on the proper enzymatic labeling. Therefore, a detection strategy for electrochemical immunosensors in which the signal is not dependent on the stability of bound antibody molecules to the sensing interface would be valuable. In this regard, we have developed a signal generation method from bioelectrocatalytic immunosensors that does not require routine and cumber-

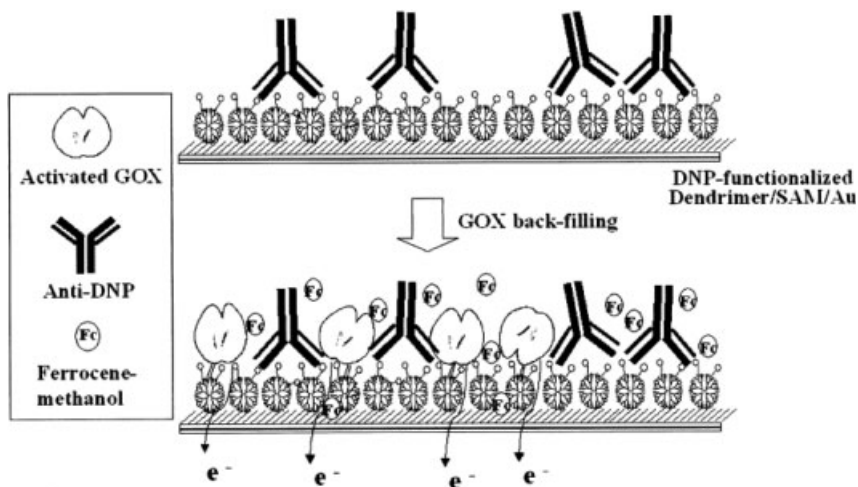


**Fig. 8.9.** Schematic representation of electrochemical immunosensing with the “back-filling” immobilization of enzyme (GOx) and bioelectrocatalysis (component dimensions not drawn to scale for simplicity). (From Ref. [31]).

some processes, including surface activation and antibody labeling or the use of labeled reporter molecules such as secondary antibodies [31]. The signaling method is based on the “back-filling” covalent immobilization of enzymes onto the immunosensor surface, circumventing the use of enzyme-tagged antibody and alleviating the signal instability from low-affinity binding (Fig. 8.9). In the back-filling assay, the electrochemical signal could be maintained despite the analyte dissociation by its low affinity with immobilized ligand because the signal generating enzyme is separated from the analyte.

As a model biorecognition reaction, a dinitrophenyl (DNP) antigen-functionalized immunosensor surface has been fabricated and the anti-DNP antibody was used as a target analyte [31]. For the construction of immunosensing surface, a poly(amidoamine) G4-dendrimer was employed not only as a building block for the electrode surface modification for antigen-functionalization but also as a matrix for binding of signaling enzyme (GOx). The non-labeled native antibody was biospecifically bound to the immobilized ligand, and the enzyme (periodate-activated GOx) reacted and back-filled the remaining surface amine groups on the dendrimer layer by an imine formation reaction. The DNP functionalization reaction was optimized to facilitate the antibody recognition and signaling; 65% displacement of surface amine to DNP was found to be an optimum (Fig. 8.10A). From quartz crystal microbalance measurements, the immunosensing reaction timing and the surface inertness to nonspecific biomolecular binding were investigated. By changing the DNP functionalization level in the calibration experiments, immunosensors exhibited distinct dynamic detection ranges and limits of detection, supporting the capability of parameter modulation (Fig. 8.10B).

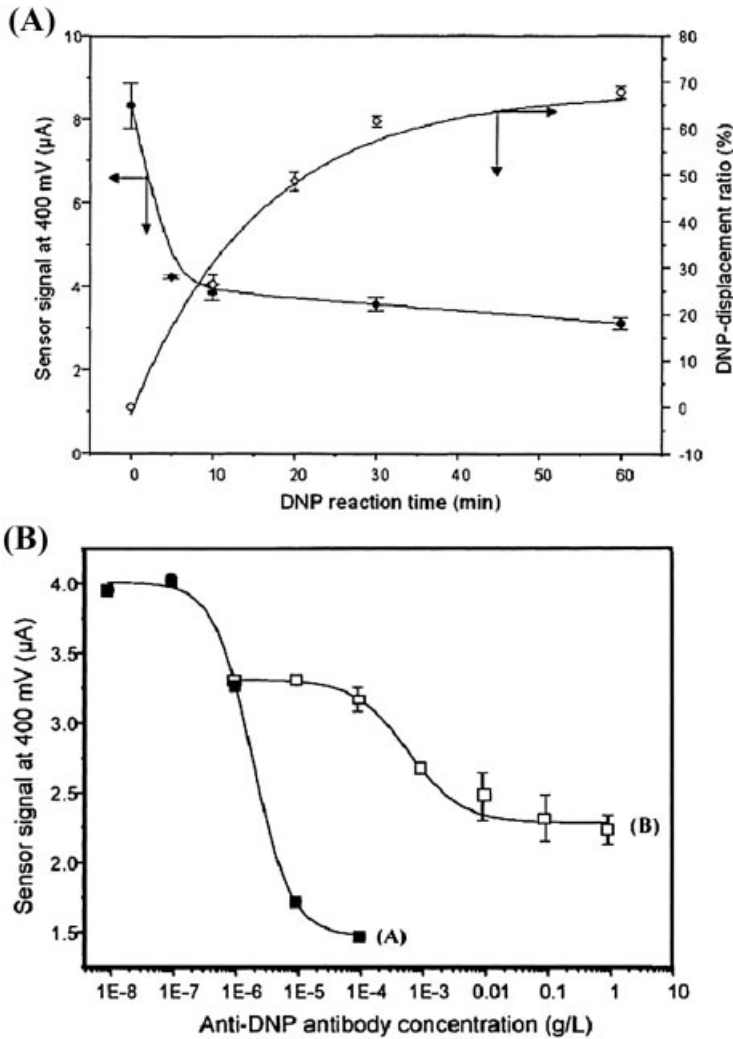


**Fig. 8.10.** (A) Comparison between the DNP displacement ratio (○) and bioelectrocatalyzed signals from the back-filled GOx (●) as a function of reaction time for DNP-functionalization. Error bars represent 95% confidence limits for three tests.

(B) Calibration curves for the DNP/anti-DNP IgG affinity biosensors as a function of target protein concentration. Two types of immunosensors were tested, having different DNP-functionalization ratios of 13% (■) and 65% (□). (Modified after Ref. [31]).

### 8.3.3

#### Protein Micropatterning on Sensor Surfaces for Multiplexed Analysis

Micropatterning of biomolecules on solid surfaces has several applications, including the modulation of cell–substrate interactions in biomaterials and tissue engineering, the fabrication of array-type biosensors for multianalyte detection, and

genomic/proteomic arrays. We have patterned molecularly organized films of dendrimers having a submicrometer edge resolution on solid chip surfaces such as evaporated gold and glass using microcontact printing technique [32]. Microcontact printing is a non-photolithographic technique that is broadly applicable for the generation of micrometer scale patterns on solid surfaces, e.g., gold, silver, copper, and silicon oxide [33]. In this process, an elastomeric stamp, typically made from poly(dimethylsiloxane) (PDMS), is prepared by casting a prepolymer against a master whose surface has been patterned with a complementary relief structure using conventional photolithography. Microcontact printing has been used to pattern alkanethiolates on metallic substrates, alkylamines on reactive SAM of alkanethiolates, alkyltrichlorosilanes on metal oxides, and proteins with submicrometer spatial resolution by area-selective printing [34, 35].

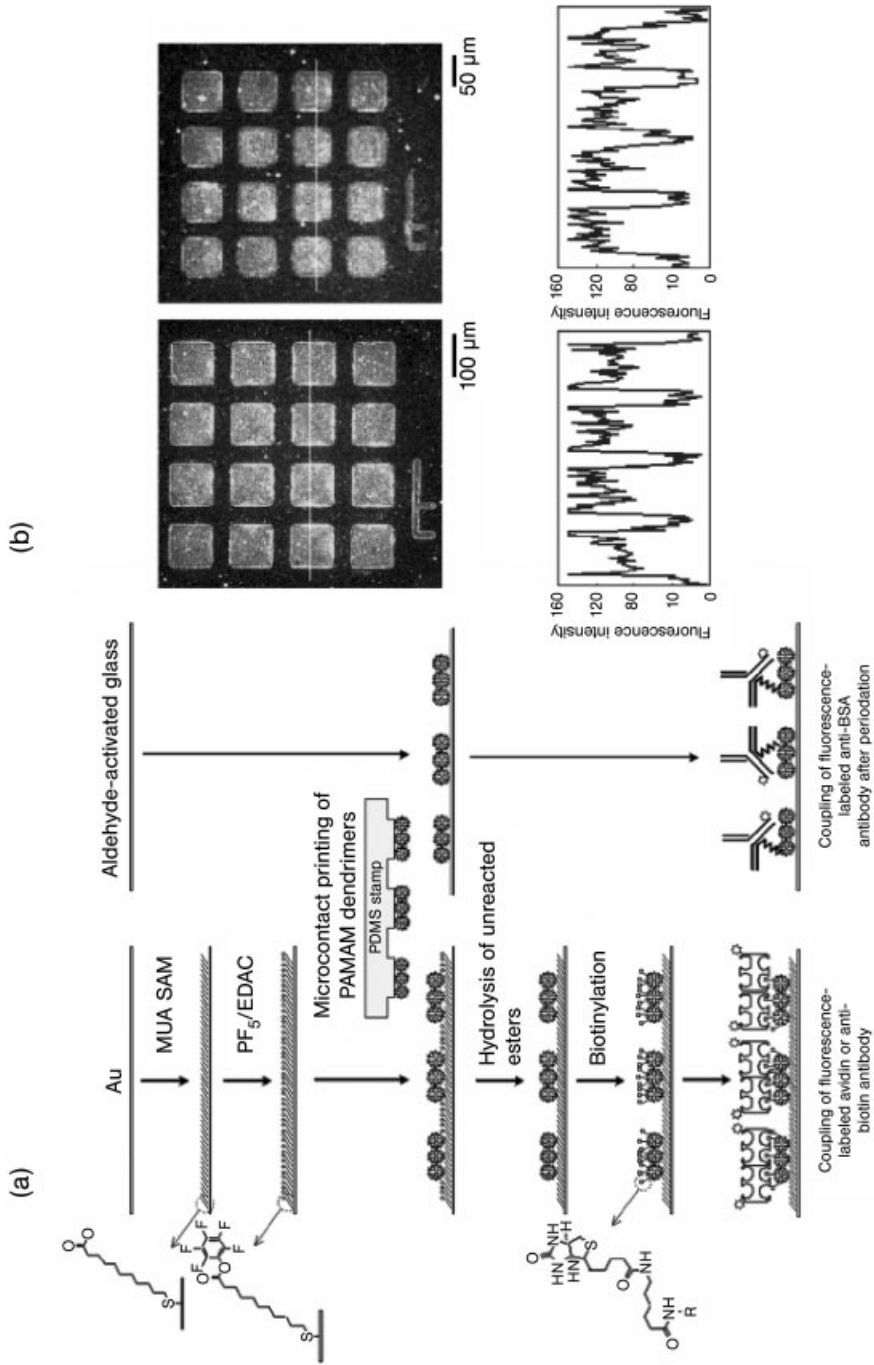
In our report [32], a patterned thin film of dendrimers was used as the underlying platform for ligand modification for the fabrication of protein microarray. Patterning of biological molecules was attempted on both gold and glass surfaces using fourth generation poly(amidoamine) dendrimer as an interfacing layer between solid surfaces and biomolecules to be patterned (Fig. 8.11). An alcoholic solution of dendrimer was employed as the inking material for the PDMS stamp. As for the patterning of avidin and anti-biotin antibody on gold, dendrimers representing amine groups were printed onto the preactivated 11-mercaptoundecanoic acid SAMs by microcontact printing, followed by biotinylation, and reacted with fluorescein-labeled avidin or anti-biotin antibody. Fluorescence analysis revealed that the patterns of avidin and anti-biotin antibody were successfully constructed within the resolution of less than a micrometer. The dendrimers were also printed onto an aldehyde-activated slide glass and reacted directly with anti-bovine serum albumin (BSA) antibodies that had been oxidized with sodium periodate. Also, distinct patterns of the anti-BSA antibodies were made with a comparable edge resolution to that of avidin patterns on gold (Fig. 8.11B). These results clearly show that dendrimers can be adopted as an interfacing layer for the patterning of biological molecules on solid surfaces with micrometer resolution, presenting a highly functionalizable microarray (plurifunctionality) made of a molecularly ordered nanomaterial.

The micropatterning technology of arranging dozens or hundreds of different biomolecules on a chip surface is required to analyze biospecific recognition events in a concurrent and massive manner. For example, 256 corrals of proteins dimensioned by  $50 \times 50 \mu\text{m}$  is made up on a  $1 \times 1 \text{ cm}$  chip surface, and a large pool of biomolecules can be distributed at the chip surface by micro-spotting. By using the developed micropatterning technique with amine-terminated dendrimer, array-

**Fig. 8.11.** (A) Schematic representation of the microcontact printing and patterning of biomolecules on gold and glass. Component dimensions are not drawn to scale for simplicity. MUA = 11-mercaptoundecanoic acid, PF5 = pentafluorophenol, EDAC = 1-ethyl-3-(3-dimethylaminopropyl)carbodiimide hydrochloride, PAMAM = poly(amidoamine),

PDMS = poly(dimethylsiloxane).

(B) Fluorescence images of patterns constructed on the dendrimer-printed gold surface by using FITC-labeled avidin. Fluorescence profiles across the white lines on images are also registered. (Modified after Ref. [32]).



patterned chips could be made having different surface wettability or surface charge between the patterned area and background space, enabling efficient spotting and/or functionalization of target molecules. Multiplexed electrochemical affinity sensing with the micropatterned chips is being pursued, by adopting the aforementioned electrochemical signal generation strategies [25, 31].

## 8.4

### Conclusions

There has been an increasing demand for efficient analytical tools for bioassays in the fields of clinical analysis and biochemical studies. Based on this requirement, a new scientific field in bioassay has been emerging, linking bioanalytical techniques with microelectronics technology. Especially, immuno- or affinity-sensing biochip technology, registering biospecific interactions such as antigen–antibody, ligand–receptor and protein–protein recognition reactions, is under great demand in terms of assay automation and throughput/output. Additionally, recent completion of the human genome project (HGP) and flourishing genomics/proteomics have opened new research fields of high throughput and user-friendly analysis, making the development of biosensing techniques more important.

Current research trends in protein biochips are, mainly, in two directions: the first is the design of biorecognition interfaces/surfaces presenting desired characteristics such as useful surface functionality, adequate immobilization density, biocompatibility, resistance to nonspecific binding, etc. Second is the development of novel transduction techniques, particularly stressing parallel sensing with array-type sensors. In this chapter, we have summarized our recent researches regarding the development of electrochemical biosensors and platform technologies for the effective immobilization of proteins or ligands on solid surfaces. We have developed technologies that use dendrimers as the building unit for biospecific recognition layers based on SAMs technology and accumulated signaling result by using the dendrimer-associated mono-/multilayers. Currently, we are attempting to integrate proteins on chip surfaces in a form of microarrays to prototype the protein chip microsystem.

### Acknowledgments

H.C.Y acknowledges support from the Regional Technology Innovation Program of MOCIE (RTI04-03-05) and the ERC(BSEF)/KOSEF.

### References

- 1 NIEMEYER, C. M., MIRKIN, C. A., *Nanobiotechnology: Concepts, Applications and Perspectives*, Wiley-VCH, Weinheim, 2004.
- 2 SACKMANN, E., TANAKA, M., Supported membranes on soft polymer cushions: Fabrication, characterization and applications, *TIBTECH* 2000, 18, 58–64.

- 3 CORNELL, B. A., BRAACH-MAKSVYTIS, V. L. B., KING, L. G., OSMAN, P. D. J., RAGUSE, B., WIECZOREK, L., PACE, R. J., A biosensor that uses ion-channel switches, *Nature* **1997**, 387, 580–583.
- 4 LIU, Q., WANG, L., FRUTOS, A. G., CONDON, A. E., CORN, R. M., SMITH, L. M., DNA computing on surfaces, *Nature* **2000**, 403, 175–179.
- 5 ULMAN, A., *An Introduction to Ultrathin Organic Films: From Langmuir-Blodgett to Self-assembly*, Academic Press, Boston, **1991**.
- 6 ULMAN, A., Formation and structure of self-assembled monolayers, *Chem. Rev.* **1996**, 96, 1533–1554.
- 7 KUMAR, A., ABBOTT, N. L., KIM, E., BIEBUYCK, H. A., WHITESIDES, G. M., Patterned self-assembled monolayers and meso-scale phenomena, *Acc. Chem. Res.* **1995**, 28, 219–226.
- 8 BAIN, C. D., WHITESIDES, G. M., Depth sensitivity of wetting: Monolayers of mercapto ethers on gold, *J. Am. Chem. Soc.* **1988**, 110, 5897–5898.
- 9 LAHIRI, J., ISAACS, L., GRZYBOWSKI, B., CARBECK, J. D., WHITESIDES, G. M., Biospecific binding of carbonic anhydrase to mixed SAMs presenting benzenesulfonamide ligands: A model system for studying lateral steric effects, *Langmuir* **1999**, 15, 7186–7198.
- 10 TOMALIA, D. A., NAYLOR, A. M., GODDARD, W. A. III, Starburst dendrimers: Molecular-level control of size, shape, surface chemistry, topology, and flexibility from atoms to macroscopic matter, *Angew. Chem., Int. Ed. Engl.* **1990**, 29, 138–175.
- 11 FISCHER, M., VÖGTLE, F., Dendrimers: From design to application – A progress report, *Angew. Chem. Int. Ed. Engl.* **1999**, 38, 884–905.
- 12 CHOW, H.-F., MONG, T. K.-K., NONGRUM, M. F., WAN, C.-W., The synthesis and properties of novel functional dendritic molecules, *Tetrahedron* **1998**, 54, 8543–8660.
- 13 FREEMANTLE, M., Blossoming of dendrimers, *C&EN* **1999**, 77(44), 27–35.
- 14 WATANABE, S., REGEN, S. L., Dendrimers as building blocks for multilayer construction, *J. Am. Chem. Soc.* **1994**, 116, 8855–8856.
- 15 TSUKRUK, V. V., RINDERSPACHER, F., BLIZNYUK, V. N., Self-assembled multilayer films from dendrimers, *Langmuir* **1997**, 13, 2171–2176.
- 16 LIU, Y., BRUENING, M. L., BERGBREITER, D. E., CROOKS, R. M., Multilayer dendrimer-polyanhydride composite films on glass, silicon, and gold wafers, *Angew. Chem., Int. Ed. Engl.* **1997**, 36, 2114–2116.
- 17 ABRUNA, H. D., Redox and photoactive dendrimers in solution and on surfaces, *Anal. Chem.* **2004**, 76, 310A–319A.
- 18 YOON, H. C., KIM, H.-S., Multilayered assembly of dendrimers with enzymes on gold: Thickness-controlled biosensing interface, *Anal. Chem.* **2000**, 72, 922–926.
- 19 ANZAI, J., KOBAYASHI, Y., NAKAMURA, N., NISHIMURA, M., HOSHI, T., Layer-by-layer construction of multilayer thin films composed of avidin and biotin-labeled poly(amine)s, *Langmuir* **1999**, 15, 221–226.
- 20 FRANCHINA, J. G., LACKOWSKI, W. M., DERMODY, D. L., CROOKS, R. M., BERGBREITER, D. E., SIRKAR, K., RUSSELL, R. J., PISHKO, M. V., Electrostatic immobilization of glucose oxidase in a weak acid, polyelectrolyte hyperbranched ultrathin film on gold: Fabrication, characterization, and enzymatic activity, *Anal. Chem.* **1999**, 71, 3133–3139.
- 21 YOON, H. C., HONG, M. Y., KIM, H. S., Functionalization of a poly(amidoamine) dendrimer with ferrocenyls and its application to the construction of a reagentless enzyme electrode, *Anal. Chem.* **2000**, 72, 4420–4427.
- 22 YOON, H. C., HONG, M. Y., KIM, H. S., Affinity biosensor for avidin using a double functionalized dendrimer monolayer on a gold electrode, *Anal. Biochem.* **2000**, 282, 121–128.
- 23 YOON, H. C., HONG, M. Y., KIM, H. S., Reversible association/dissociation reaction of avidin on the dendrimer



- monolayer functionalized with a biotin analogue for a regenerable affinity-sensing surface, *Langmuir* **2001**, *17*, 1234–1239.
- 24 YOON, H. C., LEE, D., KIM, H. S., Reversible affinity interactions of antibody molecules at functionalized dendrimer monolayer: Affinity-sensing surface with reusability, *Anal. Chim. Acta* **2002**, *456*, 209–218.
- 25 YOON, H. C., YANG, H., KIM, Y. T., Biocatalytic precipitation induced by an affinity reaction on dendrimer-activated surfaces for the electrochemical signaling from immunosensors, *The Analyst* **2002**, *127*, 1082–1087.
- 26 HONG, M. Y., YOON, H. C., KIM, H. S., Protein-ligand interactions at poly(amidoamine) dendrimer monolayers on gold, *Langmuir* **2003**, *19*, 416–421.
- 27 BANGE, A., HALSALL, H. B., HEINEMAN, W. R., Microfluidic immunosensor systems, *Biosens. Bioelectron.* **2005**, *20*, 2488–2503.
- 28 KO, J. S., YOON, H. C., YANG, H., PYO, H. B., CHUNG, K. H., KIM, S. J., KIM, Y. T., A polymer-based microfluidic device for immunosensing biochips, *Lab Chip* **2003**, *3*, 106–113.
- 29 YOON, H. C., KO, J. S., YANG, H., KIM, Y. T., Stepwise surface regeneration of electrochemical immunosensors working on biocatalyzed precipitation, *The Analyst* **2002**, *127*, 1576–1579.
- 30 YOON, H. C., YANG, H., BYUN, S. Y., Ferritin immunosensing on micro-fabricated electrodes based on the integration of immunoprecipitation and electrochemical signaling reactions, *Anal. Sci.* **2004**, *20*, 1249–1253.
- 31 WON, B. Y., CHOI, H. G., KIM, K. H., BYUN, S. Y., KIM, H. S., YOON, H. C., Bioelectrocatalytic signaling from immunosensors with back-filling immobilization of glucose oxidase on biorecognition surfaces, *Biotechnol. Bioeng.* **2005**, *89*, 815–821.
- 32 HONG, M. Y., LEE, D., YOON, H. C., KIM, H. S., Patterning biological molecules onto poly(amidoamine) dendrimer on gold and glass, *Bull. Korean Chem. Soc.* **2003**, *24*, 1197–1202.
- 33 GATES, B. D., XU, Q., STEWART, M., RYAN, D., WILSON, C. G., WHITESIDES, G. M., New approaches to nanofabrication: Molding, printing, and other techniques, *Chem. Rev.* **2005**, *105*, 1171–1196.
- 34 KANE, R. S., TAKAYAMA, S., OSTUNI, E., INGBER, D. E., WHITESIDES, G. M., Patterning proteins and cells using soft lithography, *Biomaterials* **1999**, *20*, 2363–2376.
- 35 KUNG, L. A., KAM, L., HOVIS, J. S., BOXER, S. G., Patterning hybrid surfaces of proteins and supported lipid bilayers, *Langmuir* **2000**, *16*, 6773–6776.

## 9

# Coordinated Biosensors: Integrated Systems for Ultrasensitive Detection of Biomarkers

*Joanne I. Yeh*

### 9.1

#### Overview

The ability to monitor biorecognition events and interactions on platforms offers pathways to the application of biological macromolecules as detectors. Coupled to the ability to precisely produce conductive elements on the nanoscale, biosensing offers unprecedented avenues for screening and detection at increasing sensitivities. Although biosensors have been an area of active investigation for several years, full realization of their potential has yet to be reached because the rates of reactions and sensitivities are significantly lower than in endogenous, biological systems. This is likely due to the random nature of how the various signal transducing units are placed relative to the electrode. Consequently, integrating the precise 3D information obtained from X-ray crystal structure analysis with nanotechnology platforms can result in a highly enhanced system. This gain is from optimization of the geometrical parameters that make up the various components of the biosensor. A nanobiosensor involves a biological molecule, linker or mediator, and nanoelectrodes; the various components can be equated with the electronic elements of a sensor as every component has to transduce the signal generated at the source (biomolecule) to the detector (electrode). Consequently, as in enzyme systems, rate improvements can occur from proximity and geometric effects, with potential enhancements of  $10^2$  to  $10^3$  at each junction. The additive consequence can be a gain of several orders of magnitude in rates, concomitantly improving sensitivities. In this chapter, the concept of coordinated biosensors is introduced, as an approach to align the signal transduction centers to enhance the kinetics of reactions. Additionally, nanoparticles are described that can further augment the systems by positioning the bioelement relative to the electrode surface. The various components of a bionanosensor and their role in enhancing the overall response of the system are described, from a structural perspective.

## 9.2

### Introduction

Several recent reviews illustrate, compare and contrast biosensor designs [1–5]. The main focus of this chapter is to provide a brief introduction of the biotechnologies behind these systems and to highlight the improvements that can be gained using an integrated approach, utilizing precise three-dimensional (3D) structural information.

The structure determination of deoxyribonucleic acid (DNA) double helix advanced the scientific world in numerous ways. This discovery led to the understanding of how DNA replication is achieved, resulting in the birth of a new field, molecular biology. The foundation for these discoveries was the X-ray diffraction data from DNA fibers [6]. This scientifically defining result highlights the value structures can have on understanding biological reactions, functions, and states. The ability to explicitly observe the exact positions of atoms of a molecule provides vast insights into important questions, such as how a biomolecule functions, potential interactions to trigger cellular activity, and regulatory mechanisms to control activity. The link between structural biology – the study of the precise conformation and location of the atoms that comprise the molecule and how the molecule folds in three dimensions – and its link to bionanotechnology can be understood from how structural results are used in biotechnological applications. Among the more traditional uses are in structure-based drug design, mutational analysis, and bioengineering. However, a revolutionary approach is to integrate structural results with nanotechnology, as described in this chapter.

Proteins and nucleic acids have diverse roles in the body and studies of their 3D structures teaches us how these function in our bodies and help us understand diseases caused by abnormal forms of these biomolecules. Just as structural biology has provided a definitive fundamental understanding of functional states of biological macromolecules, nanotechnology has provided the platform and a means to bridge the gap between fundamental scientific understanding to enhanced applications [7–11]. A direct connection between the two disciplines can be seen in size: in X-ray crystallography, the resolutions at which molecules are determined are at the atomic dimensions of  $10^{-10}$  m or angstroms (Å). When looking at protein–protein or oligomeric interactions, complexes, and organelles, the working functional “machinery” of a cell, these are on the order of hundreds of angstroms or in the nanometer range. Consequently, there exist complementarities of dimensionalities when linking structural results with nanotechnology applications.

As structural biology has had an immense impact on how scientists visualize biomolecules and their interactions, nanotechnology has changed our concept of working dimensions and applications at the single molecule level. Single eukaryotic cells are at least  $250\times$  larger than the nanodevices that are being developed. As a new field, nanotechnology already has had an immense impact on theoretical as well as empirical areas. In bioanalysis, nanoparticles can overcome many of the significant chemical and spectral limitations of more traditional reagents, leading to the ability to detect and monitor on the single molecule level. Fundamentally,

as single molecule measurements become possible, profound changes to our understanding of biochemical reactions are occurring. With the removal of ensemble averaging, distributions and fluctuations of molecular properties can be characterized, transient intermediates identified, and catalytic mechanisms elucidated. Recently, it has become apparent that models based on data obtained from a population of molecules do not most accurately reflect the true biochemical nature of reactions [12–15]. This is particularly important when applying biomolecules to various applications because the most efficient means of catalyzing a reaction, for example, would not be one based on an averaged reaction but the most active and efficient one. Consequently, the ability to discriminate differences between single molecules allows us to identify the most effective states of a biomolecule, to obtain enhanced reactions and sensitivities.

The ability to precisely see the positions of atoms from crystallographic structural analysis allows for optimally aligning the various components of a nanobiosensor. Orientation and proximity can have immense effects on activity and this can be readily seen in native biological systems. The ultimate catalysts in nature are enzymes, which have the ability to enhance reactions by  $10^5$  to  $10^{17}$ -fold. Enzymes hold reactive molecules in precise configurations one by one, orchestrating the formation and breakage of bonds to form products. Although enzyme biosensors have been under study for several years, their use have been limited by the inability to actively harness signals generated by a binding event, such as the electrons produced from a biochemical reaction. The rate constants in electrode-contacted enzymes are far lower than between enzymes and their natural electron acceptors. This decrease has been largely attributed to nonoptimal positioning of the bioelectrocatalyst with the electrode. This is because the active site of a redox enzyme is buried and electrons produced from a reaction cannot efficiently get out to the surface to be used or are not directed to the electrode so they are lost to solution. Consequently, the decreased rates of reactions and amount of enzyme required to obtain detectable signals make these enzyme-based sensors impractical and limited in their sensitivities. The application of structural insights to precisely align the biological components with nanoplatfoms can more fully realize the vision of exploiting the innate specificities and enhancements of biological reactions in detection applications. This ability to direct the placement of various active centers (e.g., electron transducing sites or other active units), allows the production of systems with enhanced sensitivities and kinetic properties. This capability is firmly rooted in incorporating results from X-ray crystallography or NMR spectroscopy, techniques allowing for the atomic resolution determination of the 3D conformation of molecules. Consequently, detection of molecular events approximating single molecule sensitivity through integrating advances gained in structural biology and nanotechnology is feasible.

### 9.3

#### Elements of a Nanobiosensor

##### 9.3.1

##### Biomolecular Components

Biosensors are chemical sensors capable of biorecognition through biochemical processes. Generally, bionanosensors contain a biological component that can be a protein (e.g. antibodies, enzymes) or nucleic acids or even whole cells [16, 17]. This bioelement is responsible for the binding and recognition of the target analyte, whether a small molecule or a large protein partner. The binding event is the basis for signal generation and a physical element, such as an electrode, captures the signal as the output. As the electrode, this component translates information from the biological element into a chemical or physical output with a defined sensitivity. The information that is detected can be chemical, energetic such as detection of light, or essentially any information that organisms innately process as all of these signals depend on biological molecules for their generation and/or signal detection and transduction. The array of potential sensory detection is vast, as combinatorial integration can potentially result in detection of multiple signals. The bioelement can consist of antibody/antigen; enzymes, particularly redox enzymes; nucleic acids including DNA, RNA; cellular components such as organelles; and synthetic or semi-synthetic materials. Some will be described briefly.

In antigen/antibody biosensing, interactions of immunogenic partners are the events being detected [19, 20]. The innate sensitivity of antibody–antigen complexes are exploited to detect the presence of antigens although conditions are usually manipulated to minimize nonspecific interactions. The structures of several antibodies have been determined to high resolution.

For enzyme-based biosensors, the detection process relies on the catalytic activity of the system. Enzymes are of great interest as they are natural catalysts, typically proteins but can also be catalytic ribonucleic acids (catalytic RNA). Enzymes can accelerate reactions  $10^5$ - to  $10^{17}$ -fold. Such magnitudes of kinetic amplification are possible through various mechanisms, including proximity and geometrical effects. The structures of enzymes show that they are mostly globular, with their active sites buried at the center or at oligomeric (multimeric) interfaces [21]. This serves to protect the active site from reacting with non-productive molecules, including solvent water molecules. This is achieved by protecting their labile active sites from bulk environment, forming a region with limited accessible and a local microenvironment. The catalytic site can thus have substantially perturbed  $pK_a$  and electronegativity values from the bulk solvent; this unique microenvironment is attained through the folded structure of the protein. Accordingly, the catalytic activity of enzymes depends on the integrity of their native protein conformations. Signals and products formed at the active site must somehow be released via a conformational change or through other means. This highlights the essential difficulties in using proteins as the source; immobilizing the protein onto an electrode surface to more directly establish electrical communication between the biocatalyst

and electrode can alter the conformation of the protein. Not only can the biocatalyst not be optimally aligned to the electrode surface upon immobilization but the signals generated in a buried active site may not be efficiently routed to allow facile communication between the biocatalysts and electrodes. Consequently, these can limit applications of enzyme biosensors as the electrode-contacted electron transfer rate constants are far lower than those between the enzymes and their natural electron acceptors [22–24]. This highlights an area of optimization in bioelectrode development, where chemical immobilization method for the enzyme can be modified to maximize the enzyme's active conformation. In addition to immobilizing, the method would provide a means of directing the signals generated at the buried active site of the enzyme to the electrode surface, increasing the signals obtained. The 3D structures of numerous enzymes have been determined and these can be used to enhance both of these important parameters.

Some of the most familiar systems involve the use of DNA-based sensors. Nucleic acid based biosensors (also called genosensors) are numerous and have been shown to detect nucleic acids at very low concentrations [25–27] (attomole levels). These types of sensors combine nucleic acid layers with electrochemical transducers for sensitivity. Several different approaches have been used to amplify signals, many based on electrochemical effects. Advantages of using nucleic acids for biosensing are their endogenous charge characteristics, allowing for electrochemical detection methods that allow for amplification. There are numerous structures of nucleic acids and most adopt canonical conformations that can be predicted based on sequence information.

### 9.3.2

#### **Nanoparticles**

Semiconductor nanoparticles coordinated to native biological macromolecules sensitive to external stimuli are attractive systems for various applications [28, 29]. As labeling reagents, undecagold particles have been used for several years in electron microscopy applications as phasing reagents. Their application in nanobiotech applications is an extension of their material properties, providing facile surface chemistries that can be exploited to further enhance optical, charge, and magnetic properties of the particles. Several types of nanoparticles have been used as biosensor components. Their function in a biosensor varies, from directing the binding of the biomolecular component to functioning as the sensor component itself. They have been used as probes, recognizing and differentiating an analyte of interest for diagnostic and screening purposes [30]. Detection of an interaction event via nanoparticle probes can be through color, mass, or other changes in physical properties [31–34].

Nanoparticles such as quantum dots, metallic nanobeads, and non-metallic particles such as those based on silica and natural materials such as chitosan and carbon nanotubes have been produced [35, 36]. In addition to their role in mediating biomolecular binding and linkage for electrochemical detection, these nanoparticles have been used in various bioanalytical formats. These include quantitation

tags in optical detection of quantum dots, substrates for multiplexed bioassays, mediators of signaling events such as those using gold-based aggregation assays, and potentially as surface catalysts for biological reactions. The sizes of nanoparticles used for most of these applications are from 2 to 50 nm [2, 30].

Another type of nanomaterial is nanopores, molecular sieves that could be transport and possibly serve as inorganic channels. These nanopores have been demonstrated to allow permeation of charged molecules when an external electric field is applied. A protein capable of forming pore structures,  $\alpha$ -hemolysin, has been inserted in lipid bilayers coating nanopores to form selective molecular sieves [37]. Other organic and synthetic nanopores have been fabricated in an attempt to form channels and detection systems capable of high throughput and specificity [38, 39]. These nanopores are typically over 5 nm in diameter and larger.

### 9.3.3

#### Nanoelectrodes

In nanoscale structures, electrons no longer behave like physical objects that flow in a continuous stream but take on wave mechanical and quantum properties and have the ability to tunnel through structures that would ordinarily be insulators. As single molecule measurements become more feasible with the advent of methods sensitive enough to study single molecule kinetics, thermodynamic, and electronics, significant deviations from ensemble measurements have been found. With the removal of ensemble averaging, distributions and fluctuations of molecular properties can be characterized, transient intermediates identified, and catalytic mechanisms elucidated. Towards facilitating single molecule measurements, nanoelectrode platforms have been investigated as nanosensors for enhancing signals.

A viable nanobiosensor must include an electrode surface that allows proteins to be immobilized yet retain their native structure. Proteins approaching a hydrophobic planar surface will denature upon contact. This phenomenon, called surface denaturation, occurs because the platform serves as a catalyst to the cooperative unfolding process whereby hydrophobic residues of a protein will interact with a surface to expose additional hydrophobic groups. Consequently, immobilization of a protein onto an electrode whose dimensions are significantly larger than the hydrodynamic radius of the macromolecule requires a spacer that will prevent or minimize surface denaturation effects. As described in the next section, peptides and DNA have been used for this purpose; furthermore, these have an additional role as a conductive bridge between the protein and electrode. However, nanoelectrode platforms with dimensions of 20–40 nm diameter and 80–100 nm center-to-center distance on an array platform mostly circumvents surface denaturation effects as their sizes and geometrical aspects results in 3D electrodes, bypassing complications that arise from planar surfaces as well as maximizing surface areas for binding proteins.

Nanoelectrodes formed from carbon nanotube and other materials can display altered properties simply by the nature of their dimensionality [40–43]. Reducing to smaller sizes can result in increased reactive surface areas as well as other ef-

fects, such as focusing of electric field due to their geometric configuration [36, 44, 45]. These are desirable effects, enhancing the system through their physical aspects. Carbon nanotube and metallic arrays have been used as electrodes, to promote electron transfer in redox reactions [36, 40, 46].

## 9.4 Coordinated Biosensors

Advantages in sensitivity and enhanced rates of reactions can be gained from integrating atomic resolution structural information with nanoelectrode arrays, to build detection devices of ultrahigh sensitivity and enhanced kinetics of reactions. In this section, a system utilizing a peroxidase consisting of the components described above will be described, to demonstrate how structural results can be applied to enhance nanobiosensors design. The enzyme NADH peroxidase has been used as the specific detector of hydrogen peroxide, converting a biological binding event into an electronic signal [47, 48]. Although this system used an oxidative metabolism enzyme, other redox proteins can be the bioelement, since detection is based on generation of electrons as the detectable signal. In addition to the traditional use of redox enzymes, other non-redox proteins can be used if the binding of a ligand triggers a conformational change that can be detected by an induced electronic event or via optical, thermal or other detectable physical changes. These interactions provide the basis for catalysis (in enzymes), recognition of antigen (with antibodies), in initiating cellular processes and signal transduction (in receptor systems). Alternatively, a virion or particles can theoretically be the bioelement of a sensor as structural information is available for many of these macromolecules. Our strategy integrates desirable properties of the individual components: the protein machinery for sensitivity and specificity of binding, peptide chemistry for aligning the various electron transducing units, and the nanoelectrodes for gain sensitivity in electronic detection.

### 9.4.1

#### **Biomolecular Conduits: Signal Transducing Mediators**

The use of redox enzymes as the source of electronic signals that can be propagated efficiently in response to a specific ligand or other physiological signal has many potential applications, such as amperometric biosensors [17, 18, 49]. A major limitation in using biomolecules in electrodes is that their incorporation is complicated by a lack of efficient pathways for the transport of electrons from their embedded redox sites to an electrode, as described above. Although electrical communication between redox proteins and electrode surfaces has been improved through various approaches [17, 19, 50–52], these methods involve contact of the enzyme at somewhat random conformations with respect to the electron relaying units, ultimately resulting in decreased rates of electron transfer. To produce electroactive biocatalysts in amperometric biosensors with sufficiently high rates of



electron transfer, the relaying units must be linked in a controlled and mechanistically relevant manner [53–57]. The following section describes harnessing of electrons through a modularly formed, redox active assembly consisting of a redox enzyme, a metallized double-helical peptide, and a gold nanoparticle immobilized onto a carbon nanotubes electrode and a gold wire derivatized with a benzenedithiol compound. Each of these components and their role in biosensing has been described before. One unique component of this bioassembly is the use of metallized peptide as the conduit of electronic signals.

Peptides and DNA linkers can be made conductive through binding of metals and functionalized to incorporate specific reactive groups. The overall redox potential is driven by the coordination of the particular metals to the peptide. The reductive potentials reflect the ease or difficulty in transitioning between oxidized and reduced states for a particular metal ion. Imidazolium chemistry is well defined and allows for the binding of divalent metals. Depending on the metal, the potentials needed to drive the oxidative/reductive states of the metals can be shifted through precise ligation [58, 59]. Consequently, application of specific coordination chemistry through various ligation groups of a peptide or DNA allows for the more directed binding and stabilization of a subsequent redox state. This is an important consideration as the peptide or DNA linkers form a junction and functions in transducing the signals from the bioelement to the electrode. Functionalization of peptides and DNA allows for targeting, in principle, of virtually any protein, as long as unique groups (e.g., reactive amines, thiols, hydroxides) are present and assessable. In addition to their roles in linking and signal transduction, they have a physical function of spacing the protein away from the surface of the electrode, helping to minimizing surface denaturation effects.

Using the unique cysteine-sulfenic acid chemistry of the Npx redox center, described below, we designed a metallizable, multi-histidine peptide (MHP), with differentially functionalized termini that linked to a specific component of the signaling assembly (Fig. 9.1) and of sufficient length to penetrate the active site.

A 33-amino acid sequence from the leucine zipper region of the GCN4 transcription factor was used to design metal binding sites along a face of the helix by introducing histidines at  $i$ ,  $i + 4$  positions [60]. These histidines bind divalent metals while still permitting the formation of a stable dimer with metals bound along each face of the double-stranded peptide, as confirmed through circular dichroism analysis. A reduced thiolate moiety at the carboxyl terminus (CT) reacts with the active site sulfenate of Npx to form a cysteine bond. Formation of the enzyme–peptide complex was confirmed by mass spectrometry (Fig. 9.2).

The peptide has a helical axis 47 Å long, sufficient to penetrate into the active site that is buried centrally in the enzyme. Before formation of the peptide–AuNP complex in the next step, cobalt metallization of the peptide was achieved by incubation of the MHP with  $\text{CoCl}_2$ , forming a substituted metallized peptide (CoMHP) (confirmed by mass spectrometry). The stoichiometry of Co to peptide duplex was determined by isothermal titration calorimetry, which resulted in a stoichiometry of 2 to 4.7, depending on conditions and design, Co per peptide strand. Further confirmation of binding to various divalent metals came through X-ray fluores-

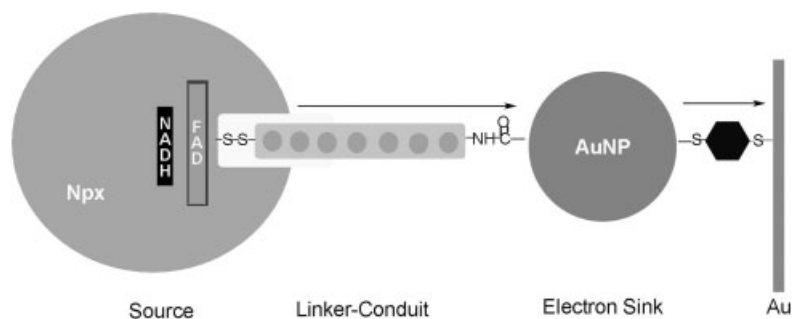


**Fig. 9.1.** Schematic of assembly of AuNP-Co-MHP-Npx electrode through stepwise linkage of each component with adsorption of the AuNP linked complex reconstituted onto a dithiol monolayer associated with an Au electrode. An electroactive monolayer assembly consisting of NADH peroxidase enzyme (“source”), CoMHP, (“linker-conduit”), and AuNP (“electron sink”) was constructed by stepwise linkage of components and covalently connected to a monolayer on a macroscopic Au electrode.

cence spectroscopy (EXAF) measurements performed at beamline X8C at Brookhaven National Laboratory. EXAF results established that the peptide binds  $\text{Ni}^{2+}$ ,  $\text{Zn}^{2+}$ , and  $\text{Co}^{2+}$ . For the assembly, Co was used as the  $\text{Co}^{3+}/\text{Co}^{2+}$  redox couple has reported values of 0.22–0.295 V vs. SCE for imidazolium complexes [58] and 0.37 to 0.4 V for conjugated ring complexes [59]. The mechanism by which electrons are transmitted through this assembly system likely requires the formation of the  $\text{Co}^{3+}$  state, which is transiently reduced back to  $\text{Co}^{2+}$  during the transduction of electrons upon NADH binding. The structure of the MHP peptide in the presence and absence of cobalt have been determined to high resolutions of 1.6 and 1.7 Å. These results show that the peptides not only maintain their structural integrity after mutation to histidines but that their elongated structure is even more pronounced (Fig. 9.3), confirming the design principles originating from the structural results of the intact GCN4 protein.

#### 9.4.2

##### NADH Peroxidase: the Biocatalytic Element

For the peroxidase sensor [61], the assembly incorporated a bacterial NADH peroxidase (Npx), a 49 kDa flavoenzyme, that catalyzes the two-electron reduction of  $\text{H}_2\text{O}_2$  into  $\text{H}_2\text{O}$ . This reduction is initiated upon binding of the cofactor NADH, which donates two electrons through the primary redox center, FAD. Under oxidizing conditions, the electrons are passed onto a molecule of peroxide, bound to the secondary redox center, a thiolate residue. This residue progresses from the reduced thiolate ( $-\text{S}^-$ ) to the oxidized sulfenate ( $-\text{SO}^-$ ) states during the catalytic cycle [48]. The 3D crystal structures of wild-type, oxidized and reduced forms of Npx [61] have been solved to atomic resolution so that the precise conformation of the active site residues and steric limitations within the active site are well-defined.

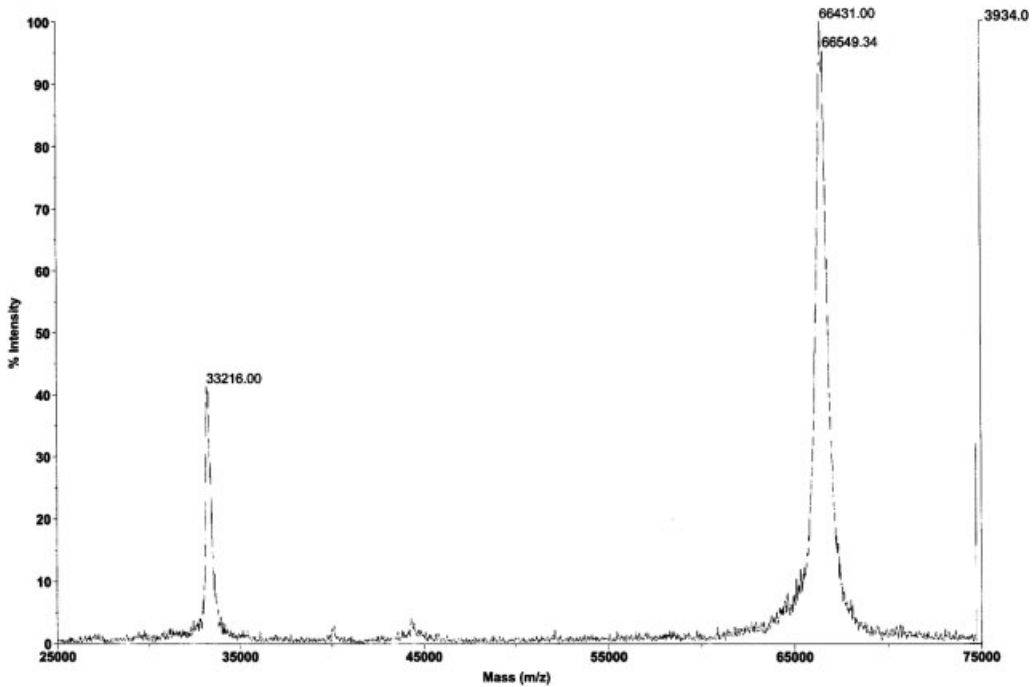


**Fig. 9.2.** Matrix-assisted laser desorption time-of-flight mass spectrometry (MALDI-TOFMS) analysis of the complex formed upon reaction of the peptide with the NADH peroxidase (Npx). A gold nanoparticle was also part of the complex and the resulting complex molecular weight is between 66431 and 66549

daltons (Da). The molecular weights of each component are Npx (49 500 Da), MHP (3934 Da), and gold nanoparticle (13 115 Da). MS analysis can be valuable in confirming the formation of various complexes as the bioassembly consists of multiple components.

The current resulting from NADH binding to Npx and the concomitant electron transfer through the assembly was measured using an electrochemical cell consisting of the biocatalytic molecular wire assembly (“working electrode”) and an Au-wire reference electrode. Solution conditions for current measurements were the same as that used for enzyme activity measurements as these are optimized for NADH binding [47]. Before initiating the reactions, we applied a slight potential of 10 mV to the working electrode, to offset the difference in potential between the reference and working electrodes originating from immobilization of the assembly. It was expected that a charging potential may be necessary to overcome the tunneling barrier that may arise from the dithiol monolayer that bridges the AuNP to the Au bulk electrode, as reported previously [49]. However, other than the 10 mV offset potential applied, additional charging potential did not appear to be necessary in this system.

Once the system was equilibrated in the reaction buffer, an aliquot of  $\text{H}_2\text{O}_2$  solution was added. This generated a signal in the positive Y-direction, indicating that

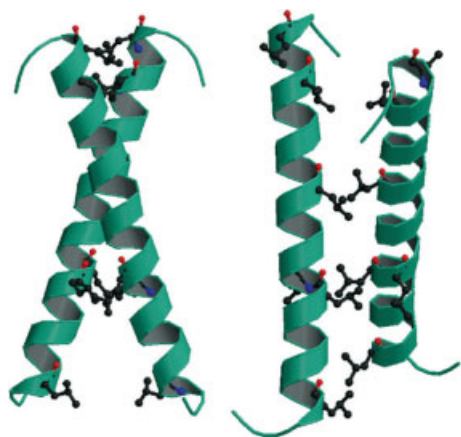


**Fig. 9.3.** Structure of the metallizable peptide (MHP), shown in ribbon depiction, in the absence of metals, refined to 1.6 Å resolution. These structural results confirm the conformational rigidity of the peptide, which is essential for efficient electron transduction. The leucines, which hold the peptide together, are shown in gray ball-and-stick, at the interface of the two strands. Two views are shown, differing by 90° along the helical axis.

electrons were flowing through the circuit toward the working electrode from the reference electrode. The role of hydrogen peroxide is two-fold – to oxidize unreacted free thiols prior to initiating the enzyme-mediated reaction and, more importantly, to generate the  $\text{Co}^{3+}$  oxidation state of the metal. As expected, the reaction of  $\text{H}_2\text{O}_2$  has a time constant longer than that generated by NADH, whose binding initiates the electron transfer reaction mediated through the binding of the cofactor by the enzyme. Hence,  $\text{H}_2\text{O}_2$  current generation represents reactions that are not mediated through the enzyme itself but rather through oxidation effects at the surface and on the metal centers. Oxidation of metals bound in the peptide primes the assembly for electron transduction. This is an important factor and aids in driving the overall reaction from the enzyme active site to the electrode. After the  $\text{H}_2\text{O}_2$  signal returned to the starting baseline value, an aliquot of NADH was added to reach a final concentration of 0.3  $\mu\text{M}$ . The current generated in response to NADH binding reached maximum values within 100 ms, indicating fast kinetics of electron transfer. Anodic current peak density values obtained for electrodes with three different surface areas were 50 nA for an electrode coated with  $10^8$  molecules of assembly and 85  $\mu\text{A}$  for  $10^{11}$  molecules of immobilized assembly. Two concurrent processes appeared to occur with the addition of NADH – a fast electron transfer signal that is transduced through the assembly to the electrode and a slower event that is the reduction of the disulfide bond linkage between the enzyme and the metallized peptide [61]. This reduction resulted in eventual liberation of the enzyme from the assembly and limited the current producing cycles of the assembly, providing additional verification of the route of electron transfer in this system.

## 9.4.3

**Undecagold Nanoparticle: Role in Alignment and Directing Electron Flow**

For the peroxidase sensor described, an undecagold nanoparticle was used to further help align Npx on the electrode surface. A sulfo-N-hydroxysuccinimido activated carboxyl group on the AuNP allows the formation of a covalent link to the MHP through a nucleophilic attack by the amino terminus primary amine group of MHP. The AuNP-CoMHP component is reacted with the Npx enzyme to form a disulfide bond between the carboxy terminal cysteine of the peptide and the redox active cysteine of Npx. For the final reconstitution of the Npx-CoMHP-AuNP assembly onto the Au electrode, a self-assembled monolayer was formed by adsorption of 1,4-benzenedithiol (BDT) onto Au wires. This provided the reaction surface for final immobilization by reaction of the AuNP with thiols of the BDT monolayer. The tri-modular assembly was formed on an Au electrode wire with a geometrical area of  $0.25 \text{ cm}^2$  and a roughness factor of  $\sim 1.2$ , functionalized with the 1,4-benzenedithiol monolayer. Surface coverage of the electrode was determined by cyclic voltammetry scans of the 1,4-benzenedithiol derivatized electrode, which indicated a number density of thiol groups of  $3.2 \times 10^{-10} \text{ mol cm}^{-2}$ . Our first route for assembly formation prior to immobilization on the Au-electrode was non-optimal, which resulted in  $10^8$  molecules of assembly per  $0.25 \text{ cm}^2$  electrode surface. This was found to be due largely to incubation times of 1–2 h for the initial CoMHP-AuNP formation. We have found that increasing the incubation times to overnight at  $4 \text{ }^\circ\text{C}$  resulted in enhanced linkage between the peptide and AuNP, producing an electrode surface coverage of  $10^{11}$  molecules  $\text{cm}^{-2}$ .

Using the gold nanoparticle, we labeled as described above then reacted the assembly through the MHP N-terminus to carbon nanotube arrays. The reaction between the peptide's N-terminus to the carboxyl groups at the tips of carbon nanotube arrays was catalyzed by EDC/NHS chemistry. Scanning electron microscopy of the resulting array shows that the bioassembly is localized to the tips of the electrodes and that this reaction can be quantitated (Fig. 9.4).

## 9.4.4

**Integrated Signals**

Based on reaction rate enhancements reported due to proximity and orientation effects in native enzyme and receptor systems, a coordinated assembly whose components are optimally tethered on an electrode would be expected to enhance rates of reactions by up to  $\sim 100$ -fold [62, 63]. Furthermore, the tethering of a signaling assembly containing the redox enzyme onto an electrode could enhance electronic signal transduction rates by minimizing loss of signal to the solution. Particularly relevant to the formation of a bioelectrocatalytic system is the spatial orientation of the signaling unit and all its components, which must be reconstituted in a conformation that is conducive for charge transfer. Exhibition of enhanced electron transfer rates through the enzyme assembly, compared with the native rate of

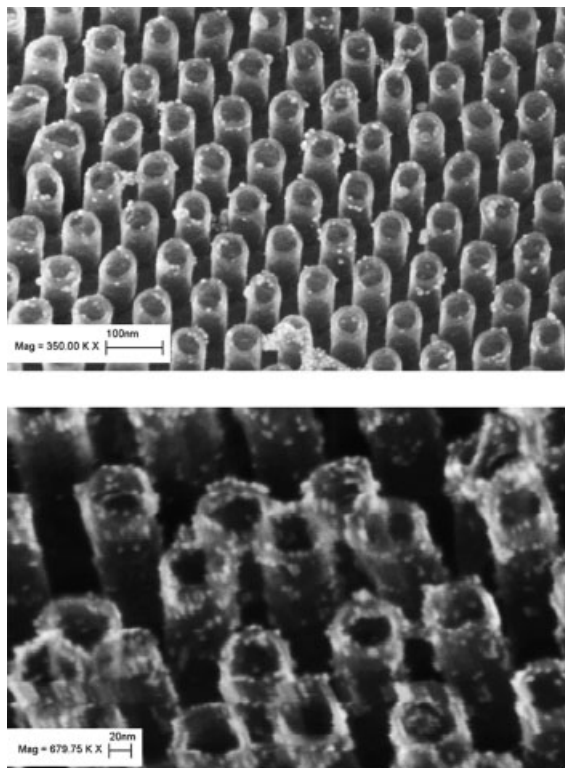


**Fig. 9.4.** Scanning electron microscopy (SEM) of an NADH peroxidase assembly conjugated at the tips of highly ordered carbon nanotubes (CNTs). In the array, the CNTs are 50 nm in diameter, have walls of 3-nm thick, and exhibit an exposed length of 60 nm, a total length of 10  $\mu\text{m}$ , and a center-to-center spacing of 100 nm between adjacent tubes. The reaction conditions can be modified to link quantitatively the bioassembly onto the electrode platform.

unimolecular enzyme reduction by NADH, the electron donor, would suggest that the signaling units are aligned properly for electron transfer.

The currents measured correlate to an electron transfer rate constant on the order of  $3000 \text{ s}^{-1}$  within each assembly. This electron transfer rate is two orders of magnitude higher than the endogenous electron transfer rate from NADH to the native enzyme,  $27 \text{ s}^{-1}$ . This rate indicates that the metallized peptide is in an optimal conformation for electron transfer, and, in conjunction with the nanoparticle, forms effective conduits for the electrical signals.

An advantage to this system is that, in addition to the atomic resolution structures of Npx, the kinetics of this enzyme have been well characterized so that the rate constants of several steps in the reaction cycle are known. This information helps correlate the electron transfer rate constant derived from the assembly cur-

rents measured in this system with the native reaction rates and allows an assessment of the efficiency of the designed assembly in electronic signal transduction. Using the anodic currents and the number of assembly molecules on the electrode surface, we calculate a first-order electron transfer rate constant of  $k_{\text{et}} = 3000 \text{ s}^{-1}$ . This value is more than  $100\times$  larger than that of the reduction of the oxidized enzyme by NADH ( $27 \text{ s}^{-1}$ ), the most comparable unimolecular kinetic step characterized in the native enzyme. We believe that the rate-determining step for electron transfer in this system is the initial binding of NADH, and that subsequent steps in electron transduction are fast compared with this event.

Metallized peptides appear to be an efficient mediator of electrons. The precise mechanism by which electrons are propagated through the peptide remains to be studied although, based on the  $5.2 \text{ \AA}$  distance between cobalt ions modeled into the peptide, a hopping mechanism seems more likely than through-bond transduction. The use of metallized peptides as conduits for electronic signals can be extended to various systems, offering a convenient approach for the design of modular functional linkers. Linking of biomolecules to electronic circuitry can be essential to the design of efficient signal transduction assemblies in bioresponsive systems. The use of metal nanoparticles that act as electrical nanoplugs helps to align the enzyme on the conductive support. In our work, the AuNP appears to channel the current to the electrode to help maximize the efficiency of electron transfer.

This peroxidase biosensor initiates and conducts redox signals in the presence of  $\text{H}_2\text{O}_2$  and NADH. The current generated by the binding of NADH, the electron donor, was transduced through the molecular assembly with high efficiency. A key component of the system is the metallized peptide and the formation of  $\text{M}^{3+}/\text{M}^{2+}$  states that allow for the transduction of the electronic signal. The gain in electron transfer rates and concomitant sensitivity is likely a result of positioning of the electron transducing units (Fig. 9.5), which provides an improvement at each junction, which can additively influence the overall rates of the biocatalytic element.

## 9.5

### Conclusion

Important technological advances in the past few years have provided the tools needed to develop new technologies to monitor biorecognition and interaction events on solid devices and in solution [7, 64]. In conjunction with the ability to fabricate solid substrates with nanoscale features and precisions, biosensing offers unprecedented opportunities for screening and detection. In this chapter, the approach of integrating 3D structural information to align the various signal transducing elements in a nanobiosensor has been described. This can result in coordinated biosensing, where the elements of a biosensor are optimized geometrically to enhance kinetics of reactions.

To illustrate the concepts presented here, the NADH peroxidase biosensor was described as this was one of the first systems that demonstrated the gain that

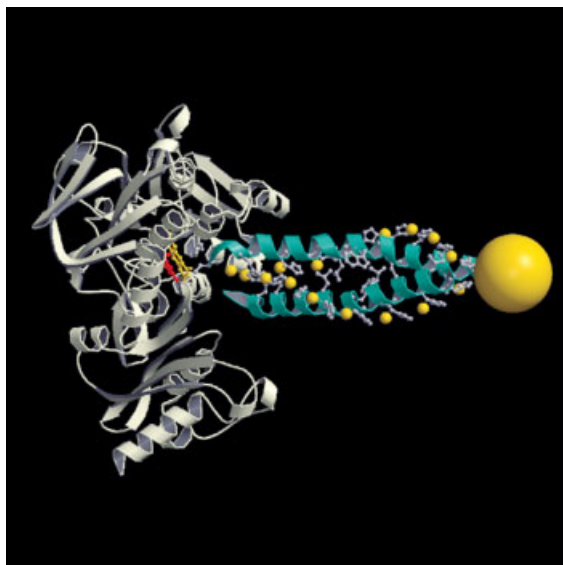


**Fig. 9.5.** Model of the assembly based on the atomic coordinates of the NADH peroxidase and MHP. The peptide coordinates cobalt atoms (small yellow spheres) through the histidine residues at every  $i, i + 4$  positions. AuNP was modeled in as a gold sphere, to

scale with the biological molecules, with a diameter of 14 Å. The cofactors are shown in ball-and-stick, with nicotinamide adenine dinucleotide in red and flavin adenine dinucleotide in yellow.

can be obtained in by applying atomic resolution structural results to align transducing centers. These results highlight the feasibility of using these biosensors in various applications, including nanomedicine, where detecting markers of disease states requires high sensitivity to make them viable in clinical applications. This approach, applying detailed structural information at sub-nanometer resolutions, produces sensors at the nanometer dimensions that fully integrate the various biological and electronic elements to produce ultrasensitive detectors.

The efficiency, specificity, and modularity of biomolecules such as proteins and nucleic acids make them attractive material for designing highly sensitive and intelligent circuitry. Utilization of natural macromolecules as sensors exploits the inherent recognition and diversity of these molecules. Effective integration of biomolecules with nanoelectronic circuitry holds great promise for the design of compact and highly sensitive systems. Direct electronic coupling with high efficiencies between electrodes and enzymes can be achieved through several approaches and highlights the feasibility of fully utilizing biomolecules in nanobiosensors. The new field of nanomedicine, as with other studies on the nanoscale, can lead to substantially new breakthroughs in technologies, leading to new paradigms in medical detection and treatments. Many biomedical applications can benefit substantially from the use of coordinated biosensors.



## Acknowledgments

We thank DARPA (F49620-03-1-0365) and NIH (GM066466) for funding.

## References

- MOSHAROV, E.V., SULZER, D., Analysis of exocytotic events recorded by amperometry. *Nat. Methods* **2005**, *2*, 651–658.
- MEDINTZ, I., UYEDA, H.T., GOLDMAN, E.R., MATTOUSSI, H., Quantum dot bioconjugates for imaging, labeling, and sensing. *Nat. Mater.* **2005**, *4*, 435–446.
- DRUMMOND, T.G., HILL, M.G., BARTON, J.K., Electrochemical DNA sensors. *Nat. Biotechnol.* **2003**, *21*, 1192–1199.
- RAMSEY, M., DNA chips: State-of-the-art. *Nat. Biotechnol.* **1998**, *16*, 40–44.
- ROSENTHAL, S.J., Bar-coding biomolecules with fluorescent nanocrystals. *Nature* **2001**, *7*, 621–622.
- WATSON, J., CRICK, F., A structure for deoxyribose nucleic acid. *Nature* **1953**, *171*, 737–738.
- KUBIK, T., BOGUNIA-KUBIK, K., SUGISAKA, M., Nanotechnology on duty in medical applications. *Curr. Pharm. Biotechnol.* **2005**, *6*, 17–33.
- STORHOFF, J.J., ELGHANIAN, R., MUCIC, R.C., MIRKIN, C.A., LETSINGER, R.L., One-pot colorimetric differentiation of polynucleotides with single base imperfections using gold nanoparticle probes. *J. Am. Chem. Soc.* **2000**, *120*, 1959–1964.
- TATON, T.A., MIRKIN, C.A., LETSINGER, R.L., Scanometric DNA array detection with nanoparticle probes. *Science* **2000**, *289*, 1757–1760.
- KATZ, E., WILLNER, I., Integrated nanoparticle-biomolecule hybrid systems: Synthesis, properties, and applications. *Angew. Chem. Int. Ed.* **2004**, *43*, 6042–6108.
- ARMSTRONG, F.A., Recent developments in dynamic electrochemical studies of adsorbed enzymes and their active sites. *Curr. Opin. Chem. Biol.* **2005**, *9*, 110–117.
- VAN OIJEN, A.M., BLAINNEY, P.C., CRAMPTON, D.J., RICHARDSON, C.C., ELLENBERGER, T., XIE, X.S., Single-molecule kinetics of I exonuclease reveal base dependence and dynamic disorder. *Science* **2003**, *301*, 1235–1238.
- BUSTAMANTE, C., BRYANT, Z., SMITH, S.B., Ten years of tension: Single-molecule DNA mechanics. *Nature* **2003**, *421*, 423–427.
- YASUDA, R., NOJI, H., YOSHIDA, M., KINOSHITA JR., K., ITOH, H., Resolution of distinct rotational substeps by submillisecond kinetic analysis of F1-ATPase. *Nature* **2001**, *410*, 898–904.
- FINER, J.T., SIMMONS, R.M., SPUDICH, J.A., Single myosin molecule mechanics: Piconewton forces and nanometre steps. *Nature* **1994**, *368*, 113–119.
- ARMSTRONG, F.A., WILSON, G.S., *Electrochim. Acta* **2000**, *45*, 263.
- WILLNER, I., KATZ, E., Integration of layered redox proteins and conductive supports for bioelectronic applications. *Angew. Chem. Int. Ed.* **2000**, *39*, 1180–1218.
- HELLER, A., Amperometric biosensors. *Curr. Opin. Biotechnol.* **1996**, *7*, 50–54.
- SLEYTR, U.B., PUM, D., SARA, M., Advances in S-layer nanotechnology and biomimetics. *Adv. Biophys.* **1997**, *34*, 71–79.
- SLEYTR, U.B., BAYLEY, H., SARA, M., BREITWIESER, A., KUPCU, S., MADER, C., WEIGERT, S., UNGER, F.M., MESSNER, P., JAHN-SCHMID, B., SCHUSTER, B., PUM, D., DOUGLAS, K., CLARK, N.A., MOORE, J.T., WINNINGHAM, T.A., LEVY, S., FRITHSEN, I., PANKOVIC, J., BEALE, P.,

- GILLIS, H.P., CHOUTOV, D.A., MARTIN, K.P., Applications of S-layers. *FEMS Microbiol. Rev.* **1997**, *20*, 151–157.
- 21 BRANDEN, C., TOOZE, J., An example of enzyme catalysis: Serine proteases, in *Introduction to Protein Structure*, 2<sup>nd</sup> edn., Garland Publishing, New York, 1999, pp. 205–220.
- 22 GERARD, M., CHAUBEY, A., MALHOTRA, D.B., Application of conducting polymers to biosensors. *Biosens. Bioelectron.* **2002**, *17*, 345–359.
- 23 OHARA, T.J., RAJAGOPALAN, R., HELLER, A., “Wired” enzyme electrodes for amperometric determination of glucose or lactate in the presence of interfering substances. *Anal. Chem.* **1994**, *66*, 2451–2457.
- 24 BADIA, A., CARLINI, R., FERNANDEZ, A., BATTAGLINI, F., MIKKELSEN, S.R., ENGLISH, A.M., Intramolecular electron-transfer rates in ferrocene-derivatized glucose oxidase. *J. Am. Chem. Soc.* **1993**, *115*, 7053.
- 25 WANG, J., POLSKY, R., XU, D.K., Silver-enhanced colloidal gold electrochemical stripping detection of DNA hybridization. *Langmuir* **2001**, *17*, 5739–5741.
- 26 PARK, S.J., TATON, T.A., MIRKIN, C.A., Array-based electrical detection of DNA with nanoparticle probes. *Science*, **2002**, *295*, 1503–1506.
- 27 WANG, J., POLSKY, R., MERKOCI, A., TURNER, K.L., “Electroactive beads” for ultrasensitive DNA detection. *Langmuir* **2003**, *19*, 989–991.
- 28 ANDERSON, J.L., BOWDEN, E.F., PICKUP, P.G., Dynamic electrochemistry: Methodology and application. *Anal. Chem.* **1996**, *68*, 379R–444R.
- 29 HAMAD-SCHIFFERLI, K., SCHWARTZ, J.L., SANTOS, A.T., ZHANG, S., JACOBSON, J.M., Remote electronic control of hybridization through inductive coupling to an attached metal nanocrystal antenna. *Nature* **2002**, *415*, 152–155.
- 30 PENN, S.G., HE, L., NATAN, M.J., Nanoparticles for bioanalysis. *Curr. Opin. Chem. Biol.* **2003**, *7*, 609–615.
- 31 SANTRA, S., ZHANG, P., WANG, K., TAPEC, R., TAN, W., Conjugation of biomolecules with luminophore-doped silica nanoparticles for photostable biomarkers. *Anal. Chem.* **2001**, *73*, 4988–4993.
- 32 HAN, M., GAO, X., SU, J.Z., NIE, S., Quantum-dot-tagged microbeads for multiplexed optical coding of biomolecules. *Nat. Biotechnol.* **2001**, *19*, 631–635.
- 33 VAN DE RIJKE, F., ZIJLMANS, H., LI, S., VAIL, T., RAAP, A.K., NIEBALA, R.S., TANKE, H.J., Up-converting phosphor reporters for nucleic acid microarrays. *Nat. Biotechnol.* **2001**, *19*, 273–276.
- 34 ZHENG, J., DICSON, R.M., Individual water-soluble dendrimer-encapsulated silver nanodot fluorescence. *J. Am. Chem. Soc.* **2002**, *124*, 13 982–13 983.
- 35 YI, H., WU, L.-Q., BENTLY, W.E., GHODSSI, R., RUBLOFF, G.W., CULVER, J.N., PAYNE, G.F., Biofabrication with chitosan. *Biomacromolecules* **2005**, *6*, 2881–2894.
- 36 GRUNER, G., Carbon nanotube transistors for biosensing applications. *Anal. Bioanal. Chem.* **2006**, *384*, 232–335.
- 37 ASTIER, Y., BRAHA, O., BAYLEY, H., Toward single molecule DNA sequencing: Direct identification of ribonucleoside and deoxyribonucleoside 5'-monophosphates by using an engineered protein nanopore equipped with a molecular adapter. *J. Am. Chem. Soc.* **2006**, *128*, 1705–1710.
- 38 LI, N., YU, S., HARRELL, C.C., MARTIN, C.R., Conical nanopore membranes. Preparation and transport properties. *Anal. Chem.* **2004**, *76*, 2025–2030.
- 39 HARRELL, C.C., LEE, S.B., MARTIN, C.R., Synthetic single-nanopore and nanotube membranes. *Anal. Chem.* **2003**, *75*, 6861–6867.
- 40 WITHEY, G.D., LAZARECK, A.D., TZOLOV, M.B., YIN, A., AICH, P., YEH, J.I., XU, J.M., Ultra-high redox enzyme signal transduction using highly ordered carbon nanotube array electrodes. *Biosens. Bioelectron.* **2006**, *21*, 1560–1565.
- 41 SHIM, M., SHI KAM, N.W., CHEN, R.J., LI, Y., DAI, H., Functionalization of carbon nanotubes for biocompati-

- bility and biomolecular recognition. *Nano Lett.* **2002**, *2*, 285.
- 42 HYANG, W., TAYLOR, S., FU, K., LIN, Y., ZHANG, D., HANKS, T.W., RAO, A.M., SUN, Y.-P., Attaching proteins to carbon nanotubes via diimide-activated amidation. *Nano Lett.* **2002**, *2*, 311.
- 43 CHEN, R.J., ZHANG, Y., WANG, D., DAI, H., Noncovalent sidewall functionalization of single-walled carbon nanotubes for protein immobilization. *J. Am. Chem. Soc.* **2001**, *123*, 3838.
- 44 BRADLEY, K., BRIMAN, M., STAR, A., GRUNER, G., Charge transfer from adsorbed proteins. *Nano Lett.* **2004**, *4*, 253.
- 45 STAR, A., BRADLEY, K., GABRIEL, J.-C.P., GRUNER, G., Nanoelectronic sensors: Chemical detection using carbon nanotubes. *Pol. Mater. Sci. Eng.* **2003**, *89*, 204.
- 46 KOHLI, P., HARRELL, C.C., CAO, Z., GASPARAC, R., TAN, W., MARTIN, C.R., DNA-functionalized nanotube membranes with single-base mismatch selectivity. *Science* **2004**, *305*, 984–986.
- 47 PARSONAGE, D., MILLER, H., ROSS, P.R., CLAIBORNE, A., Purification and analysis of streptococcal NADH peroxidase expressed in *E. coli*. *J. Biol. Chem.* **1995**, *268*, 3161–3167.
- 48 POOLE, L.B., CLAIBORNE, A., Interactions of pyridine nucleotides with redox forms of the flavin-containing NADH peroxidase from *Streptococcus faecalis*. *J. Biol. Chem.* **1986**, *261*, 14 525–14 533.
- 49 WANG, J., Amperometric biosensors for clinical and therapeutic drug monitoring: A review. *J. Pharm. Biomed. Anal.* **1999**, *19*, 47–53.
- 50 SCHUHMANN, W., OHARA, T.J., SCHMIDT, H.-L., HELLER, A., Electron transfer between glucose oxidase and electrodes via redox mediators bound with flexible chains to the enzyme surface. *J. Am. Chem. Soc.* **1991**, *113*, 1394.
- 51 WILLNER, I., HELEG-SHABTAI, V., BLONDER, R., KATZ, E., TAO, G., BÜCKMANN, A.F., HELLER, A., Electrical wiring of glucose oxidase by reconstitution of FAD-modified monolayers assembled onto Au-electrodes. *J. Am. Chem. Soc.* **1996**, *118*, 10 321.
- 52 RAJAGOPALAN, R., AOKI, A., HELLER, A., Effect of quaternization of the glucose oxidase “wiring” redox polymer on the maximum current densities of glucose electrodes. *J. Phys. Chem.* **1996**, *100*, 3719.
- 53 MEDVEDEV, D.M., DAIZADEH, I., STUCHEBRUKHOV, A.A., Electron transfer tunneling pathways in bovine heart cytochrome C oxidase. *J. Am. Chem. Soc.* **2000**, *122*, 6571–6582.
- 54 XIAO, Y., PATOLSKY, F., KATZ, E., HAINFELD, J.F., WILLNER, I., “Plugging into enzymes”: Nanowiring of redox enzymes by a gold nanoparticle. *Science* **2003**, *299*, 1877–1881.
- 55 YEH, J.I., ZIMMT, M.B., ZIMMERMAN, A.L., Nanowiring of a redox enzyme by metallized peptides. *Biosens. Bioelectron.* **2005**, *21*, 973–978.
- 56 SCOTT, D.L., BOWDEN, E.F., Enzyme-substrate kinetics of adsorbed cytochrome c peroxidase on pyrolytic graphite electrodes. *Anal. Chem.* **1994**, *66*, 1217–1223.
- 57 NAHIR, T.M., CLARK, R.A., BOWDEN, E.F., Linear-sweep voltammetry of irreversible electron transfer in surface-confined species using the Marcus theory. *Anal. Chem.* **1994**, *66*, 2595–2598.
- 58 BOTTCHEER, A., TAKEUCHI, T., HARDCASTLE, K.I., MEADE, T.J., GRAY, H.B., CWIKEL, D., KAPON, M., DORI, Z., Spectroscopy and electrochemistry of cobalt(III) Schiff base complexes. *Inorg. Chem.* **1997**, *36*, 2498–2504.
- 59 AROUNAGUIRI, S., ESAWARAMOORTHY, D., ASHKKUMAR, A., DATTAGUPTA, A., MAIYA, B.G., Cobalt (III), nickel (II), and ruthenium (II) complexes of 1,10-phenanthroline family of ligands: DNA binding and photocleavage studies. *Proc. Indian Acad. Sci. (Chem. Sci.)* **2000**, *112*, 1–17.
- 60 KRANTZ, B.A., SOSNICK, T.R., Engineered metal binding sites map the heterogeneous folding landscape of a coiled coil. *Nat. Struct. Biol.* **2001**, *12*, 1042–1047.

- 61 YE H, J.I., CLAIBORNE, A., HOL, W.G.J., Structure of the native cysteine-sulfenic acid redox center of enterococcal NADH peroxidase refined at 2.8 Å resolution. *Biochemistry* **1996**, 31, 9951–9957.
- 62 FOUBERT, T.R., BURRITT, J.B., TAYLOR, R.M., JESAITIS, A.J., Structural changes are induced in human neutrophil cytochrome b by NADPH oxidase activators, LDS, SDS, and arachidonate: Intermolecular resonance energy transfer between trisulfopyrenyl-wheat germ agglutinin and cytochrome b(558). *Biochim. Biophys. Acta* **2002**, 1567, 221–231.
- 63 GRAEF, I.A., HOLSINGER, L.J., DIVER, S., SCHREIBER, S.L., CRABTREE, G.R., Proximity and orientation underlie signaling by the non-receptor tyrosine kinase ZAP70. *EMBO J.* **1997**, 16, 5618–5628.
- 64 WANG, J., Amperometric biosensors for clinical and therapeutic drug monitoring: A review. *J. Pharm. Biomed. Anal.* **1999**, 19, 47–53.

## 10

# Protein-based Biosensors using Nanomaterials

*Genxi Li*

### 10.1

#### Introduction

Protein-based biosensors are fabricated based on the electron transfer between proteins (enzymes) and electrodes [1, 2]. However, electron-transfer rates between redox proteins and electrode surfaces are usually prohibitively slow [3]. On the one hand, the electroactive prosthetic groups of most redox proteins are deeply buried in the electrically insulated peptide backbones. On the other hand, unfavorable orientations and adsorptive denaturations of proteins often occur at electrode surfaces. To achieve efficient electrical communication, one approach that has been proposed, and widely employed in previous years, is based on electrochemical mediators, both natural enzyme substrates or products, and artificial redox mediators (first-generation and second-generation biosensors) [1]. First-generation biosensors have many defects, such as possible interference because of the too high applied potential, systematic complexity caused by fluctuation of the concentration of dissolved oxygen, a relatively low detection limited since the tenuity of dissolved oxygen will significantly decrease the electrical currents, etc. [4–6]. Consequently, the idea of artificial mediators has been proposed, leading to the development of second-generation biosensors. Nevertheless, redox mediators used in conjunction with redox proteins are in no way selective but rather general redox catalysts, facilitating not only the electron transfer between electrode and protein but also various interfering reactions [7]. Therefore, third-generation biosensors, which are based on the direct electron transfer of proteins, i.e., the electrical communication between the proteins and signal transducers is accomplished directly without additional mediators, have received more and more attention [2]. Third-generation biosensors are superior in selectivity both because they should be operated in a potential window close to the redox potential of the protein itself, and therefore, are less prone to interfering reactions [4] and also because of the lack of yet another reagent in the reaction sequence.

Recent breakthroughs in nanotechnology have made various nanostructured materials more affordable for a broader range of applications, and nanotechnology is playing an increasingly important role in the development of biosensors [8–11].

Owing to the unique properties of nanomaterials, direct electrochemistry and catalytic activity of many proteins have been observed at electrodes modified with various nanomaterials such as  $\text{TiO}_2$ ,  $\text{ZrO}_2$ ,  $\text{SiO}_2$ ,  $\text{Fe}_3\text{O}_4$ , metal nanoparticles, carbon nanotubes, etc. [12–17]. The sensitivity and performance of biosensors are being improved by using nanomaterials for their construction. Various nanostructures have been examined as hosts for protein immobilization via approaches including protein adsorption, covalent attachment, protein encapsulation, and sophisticated combinations of methods. Studies have shown that nanomaterials can not only provide a friendly platform for the assembly of protein molecules but also enhance the electron-transfer process between protein molecules and the electrode.

We have summarized the sensors fabricated with proteins (enzymes) in a recently published encyclopedia of sensors [1]. Later, we noticed that increasing numbers of protein-based biosensors were being fabricated by using nanomaterials. It has been necessary to focus on the application of nanomaterials in the development of protein-based biosensors. This chapter reviews protein-based biosensors according to the various sorts of nanomaterials used in their fabrication.

## 10.2

### Metal Nanoparticles

Metal nanoparticles have many unique properties: large surface-to-volume ratio, high surface reaction activity, high catalytic efficiency, and strong adsorption ability. Metal nanoparticles have been used to facilitate the electron transfer in nanoelectronic devices owing to the following important functions: the roughening of the conductive sensing interface, the catalytic properties of the nanoparticles, and the conductivity properties of nanoparticles at nanoscale dimensions that allow the electrical contact of redox-centers in proteins with electrode surfaces [8, 18]. Gold nanoparticles and silver nanoparticles are the most intensively studied and applied metal nanoparticles in fabricating biosensors, which will be specially summarized later. Other metal nanoparticles, such as palladium [19] and platinum nanoparticles [20], etc. have also been used.

#### 10.2.1

##### Gold Nanoparticles

Colloidal gold is a metallic colloid whose particles are formed by small octahedral units, called primary particles. The size of gold particles essentially depends on the way the colloid is formed [21]. To improve the stability of these particles, a kind of gold nanoparticle protected by lipid has also been invented [22]. Gold colloid has been widely used as a cytochemical label for the study of macromolecules, with transmission and scanning electron microscopy, light microscopy and freeze-etch electron microscopy, and to improve the signals of both surface-enhanced Raman spectroscopy and surface plasmon resonance [21].

In the last few years, electrochemical biosensors created by coupling biological elements with electrochemical transducers based on or modified with gold nanoparticles have played an increasingly important role in biosensor research. Gold colloid has many advantages for biosensor applications. First, gold nanoparticles can, very usefully, provide a stable surface for the immobilization of biomolecules, such that the molecules retain their biological activities. As is well known, the performance of enzyme biosensors depends not only on the nature of the enzyme molecules but also on the influences imposed on these molecules by immobilization. Modification of an electrode surface with gold nanoparticles provides a micro-environment similar to that of the redox proteins in native systems and offers the protein molecules more freedom in orientation, which can weaken the insulating property of the protein shell for the direct electron transfer and facilitate the electron transfer through the conducting tunnels of colloidal gold [21]. Second, gold nanoparticles can form conducting electrodes and are the site of electron transfer when anchored to the substrate surface, allowing direct electron transfer between redox proteins and electrode surfaces with no mediators required [23]. They can act as an electron-conducting pathway between prosthetic groups and electrode surface. They can provide useful interfaces at which redox processes of biological molecules, such as proteins or NADH, involved in biochemical reactions of analytical significance can be electrocatalyzed [23]. Xiao et al. have that reported the reconstitution of one apo-flavoenzyme, apo-glucose oxidase, on a 1.4-nm gold nanocrystal functionalized with the cofactor flavin adenine dinucleotide and integrated into a conductive film could yield a bioelectrocatalytic system with exceptional electrical contact with the electrode support [24]. Their work shows that electron transfer through the Au nanoparticles is much faster than electron transfer to  $O_2$ . Besides, various characteristics of gold colloid, such as their high surface-to-volume ratio, high surface energy, and ability to decrease the distance between proteins and metal particles, may also facilitate electron transfer between the redox sites of the proteins and electrode surface. The last advantage, but not the least, is that the size and surface morphology (important parameters when applied in biosensing) of gold colloid can be controlled easily experimentally. Colloidal gold surface morphology is vital in establishing the electrical contact between the proteins and the electrodes [25].

Taking horseradish peroxidase (HRP) as an example, although direct, non-mediated electron transfer is well known for some redox proteins and particularly for HRP [26, 27], it is usually very inefficient and is not generally used for practical biosensory devices. Zhao et al. found, in 1992, that a mixed layer of HRP and colloidal gold nanoparticles of 30 nm could be electrocatalytically active for hydrogen peroxide ( $H_2O_2$ ) reduction without the need of electro-transfer mediators [28]. In addition, immobilized HRP was reduced directly on gold colloid through an amplification effect of the enzyme–substrate interaction. It was demonstrated that the utilization of gold nanoparticles in enzyme immobilization could increase the enzyme loading without compromising charge-transfer efficiency [21]. That was to say the small size of gold nanoparticles could allow the conductive material to come into close proximity of the active center of the enzyme, which might facilitate

the electron-transfer process. The nanoparticles could also provide bioelectrocatalytic activity that can be utilized in biosensor devices. This work led to an extensive investigation of the direct electron transfer based on gold nanoparticles and immobilization of proteins, especially enzymes [15, 29–33]. Some related biosensors for  $\text{H}_2\text{O}_2$  [28, 34–38], glucose [34, 39], xanthine and hypoxanthine [34, 40–42], dopamine [43], and cholesterol [44, 45] were also reported. These biosensors exhibited high sensitivity, good reproducibility, and long-term stability.

The catalytic activity of HRP is attributed to its iron heme group, which acts as the electroactive center. Since hemoglobin (Hb) contains four heme groups, it can be utilized as the HRP substitute in the detection of  $\text{H}_2\text{O}_2$ , by virtue of its low cost and stable properties in solution [46]. In the last few years, electrochemical sensors for  $\text{H}_2\text{O}_2$  based on the peroxidase-like activity of Hb incorporated in many different kinds of materials, including colloidal gold, have been fabricated [22, 47–49]. Researchers have also made a novel Hb-based  $\text{H}_2\text{O}_2$  sensor constructed on a gold nanoparticles-modified ITO electrode [50]. Gold nanoparticles, acting as bridges of electron transfer, can greatly promote the direct electron transfer between Hb and the electrode surface without the aid of any electron mediator [51]. Thus, the Hb-immobilized gold nanoparticles-modified electrode can be developed as a third-generation biosensor for the determination of  $\text{H}_2\text{O}_2$ .

Besides HRP and Hb, other heme proteins, such as cytochrome *c* (Cyt *c*), myoglobin (Mb), have also been investigated via being immobilized with gold nanoparticles [52]. Direct electron transfer between immobilized Mb and a colloidal gold modified carbon paste electrode, in addition to a glass carbon electrode, has also been studied [53]. Cyt *c* immobilized on colloidal gold modified carbon paste electrodes can also maintain its activity and electrocatalyze the reduction of  $\text{H}_2\text{O}_2$  [54]. Meanwhile, a chitosan-stabilized gold nanoparticles-modified electrode can also be developed for biosensors [55, 56].

Fabricating a sensitive, stable glucose biosensor has long been of great interest. A novel method to fabricate a glucose biosensor has been proposed by immobilizing glucose oxidase (GOD) on gold nanoparticles, which have self-assembled on Au electrode modified with a thiol-containing three-dimensional (3D) network of silica gel [57] or with a cystamine monolayer [58]. GOD can exhibit excellent bioelectrocatalytic response to the oxidation of glucose. Researchers have also found that aqueous colloidal gold nanoparticles can enhance the activity of aqueous enzymes [59]. Mena. et al. have compared several enzyme biosensor designs, prepared by immobilization of GOD onto different tailored gold nanoparticle-modified electrode surfaces [60].

The immobilization methods for connecting gold nanoparticles with electrodes and with proteins should both be discussed in detail. Generally, there are three ways to prepare gold nanoparticles-modified electrode: (a) by binding with functional groups of self-assembled monolayer (SAMs); (b) by direct deposition of gold colloid onto the electrode surface; (c) by co-modification of mixed gold colloid with other components in the composite electrode matrix [61].

Protein or enzyme can readily be immobilized on colloid gold by dipping a protein solution onto the colloid gold modified electrode surface. The electrostatic in-



teraction between the negatively charged citrate surface of colloidal gold and positively charged groups of the protein leads to the adsorption of protein onto the electrode surface. The prepared electrodes can be characterized by several means such as cyclic voltammetry (CV), transmission electron microscope (TEM), atomic force microscopy (AFM), UV/visible spectroscopy (UV/Vis), surface-enhanced Raman spectroscopy (SERS) and electrochemical impedance spectroscopy (EIS), etc.

SAMs can provide a simple way to tailor surfaces with well-defined compositions, structures and thickness that can then be employed as specific functionalized surfaces for the immobilization of gold nanoparticles and enzymes [62]. Gold nanoparticle-modified electrode surfaces can be prepared by covalently binding gold nanoparticles with surface functional groups ( $-\text{CN}$ ,  $-\text{NH}_2$ , or  $-\text{SH}$ ) of SAMs modified solid surfaces [63–66]. Short-chain molecules, such as cysteamine (Cyst) and 3-mercaptopropionic acid (MPA), can be self-assembled on the gold disk electrode for further binding of gold nanoparticles. Biosensors based on immobilization of enzyme onto Cyst or MPA SAMs that had been previously bound onto gold nanoparticles have also been evaluated and compared [61].

An early work through fabrication of a monolayer of colloidal gold on an indium-doped tin oxide (ITO) support was performed in 1995 [67]. Either (2-aminopropyl)-trimethoxysilane or (3-mercaptopropyl)trimethoxysilane was first attached to the ITO support to yield an amine/thiol-functionalized thin film. The deposited gold thin film was quite stable and provided an active interface for the immobilization or redox-active self-assembled monolayers. The thiol functional group-derived carbon ceramic electrode (CCE) has been used to construct  $\text{H}_2\text{O}_2$  biosensors [68]. Biosensors can also be constructed by immobilizing the proteins by adsorbing them onto the nanoparticles, by crosslinking them with bifunctional agents such as glutaraldehyde, or by mixing them with the other components of composite electrodes. When HRP is immobilized on a colloidal gold monolayer formed at the gold electrode by a long “cysteamine/glutaraldehyde/cysteamine” molecular bridge, it shows an excellent electrocatalytic response to the reduction of  $\text{H}_2\text{O}_2$  [33]. This sensor shows a fast amperometric response, wide linear calibration range and low detection limit for  $\text{H}_2\text{O}_2$  determination. In addition, HRP immobilized on colloidal gold has a high affinity to  $\text{H}_2\text{O}_2$  with no loss of enzymatic activity.

Multilayers of conductive particles can give rise to porous, high-surface-area electrodes, where the local microenvironment can be controlled by the crosslinking elements. Superstructures of a controllable number of colloidal Au particle layers have been formed on a support surface by the alternate interaction of the assembly with a crosslinker and the negatively charged Au particles [69]. A two-dimensional (2D) double layer structure [70] and 3D superstructure consisting of gold nanoparticles for biosensors [71] have also been proposed. The utilization of gold nanoparticles as a building block in the construction of nanoscale functional devices has become a very promising aspect for electrochemical biosensing. The technology of derivatizing Au electrode surface by silica sol-gel and gold nanoparticles takes advantage of both self-assembly, nanoparticles, and the increased surface area of 3D electrodes. Ikeda and coworkers have demonstrated that gold nanoparticles can

self-assemble both inside the network and on the surface of the silica gel [72]. These gold nanoparticles immobilized by a silica gel 3D network can act as tiny conducting centers and facilitate electron transfer between proteins and electrodes. Based on these investigations, a HRP-based  $\text{H}_2\text{O}_2$  sensor and a GOD-based glucose sensor have been developed by embedding gold nanoparticles in thiol-containing silica sol-gel network [73]. An amperometric  $\text{H}_2\text{O}_2$  biosensor has also been reported, based on immobilizing HRP to a nano-Au monolayer supported by a carbon sol-gel derived carbon ceramic electrode [68]. This sol-gel 3D network made it possible to control the effectiveness of the electrocatalytic process, the sensitivity and response rate of the nanoparticle biosensor by controlling the thickness of thiolated polymer or sol-gel, and the number of Au particle layers associated with the electrodes.

Another feasible method to fabricate protein-based biosensor involves covalent attachment of protein molecules to a gold nanoparticle monolayer modified Au electrode, such as GOD/gold nanoparticle systems [58]. Briefly, gold nanoparticles are first self-assembled on a gold electrode by dithiol via Au-S bonds. A cystamine monolayer is then chemisorbed onto those gold nanoparticles and exposed to an array of amino groups, which would further react with aldehyde groups of periodate oxidized GOD via the well-known Schiff base reaction. By this means, GOD could be covalently attached to the gold electrode, resulting in a stable biosensing interface.

Recently, a gold nanoparticle- $\text{CaCO}_3$  hybrid material ( $\text{AuNP-CaCO}_3$ ) has been prepared and applied for sensor preparation [74].  $\text{AuNP-CaCO}_3$  can retain the porous structure and inherits the advantages from its parent materials, such as satisfying biocompatibility and good solubility and dispersibility in water; therefore, it can offer a promising template for enzyme immobilization and biosensor fabrication. HRP has been conjugated with  $\text{AuNP-CaCO}_3$  to fabricate HRP- $\text{AuNP-CaCO}_3$  bioconjugates, which were then embedded into a silica sol-gel matrix to construct a novel biosensor.

There are also many reports on fabricating biosensors by mixing colloidal gold and carbon paste to incorporate colloidal gold into the electrode. A reagentless glucose biosensor based on the direct electron transfer of GOD [75], and a renewable tyrosinase biosensor [76], have been constructed by immobilizing the corresponding enzymes onto electrodes prepared by mixing a colloidal gold solution with the carbon paste components. A renewable reagentless  $\text{H}_2\text{O}_2$  sensor has also been reported based on the direct electron transfer of HRP where HRP is mixed into colloidal gold-modified carbon paste electrodes [15]. Here, the nanoparticles are used to retain the enzymatic activity and facilitate direct electron transfer between HRP and carbon-sensing sites. In addition, nitrite sensors based on a Hb-colloidal gold nanoparticle modified screen-printed electrode and carbon paste electrode have also been developed [77, 78].

In addition to the proteins employed for the fabrication of the above-mentioned biosensors, some other proteins (enzymes) have been used. Xanthine oxidase is reported to be adsorbed onto colloidal gold that was previously evaporated on the surface of glassy carbon, which responds to xanthine or hypoxanthine in the absence

of added mediator by electrochemical oxidation of the enzymatic oxidation product, uric acid [40]. A multi-enzyme biosensor for cholesterol [44] has been constructed to detect cholesterol in serum and whole blood, by making use of HRP and cholesterol oxidase. This sensor gives an electrochemical response that correlates well with the total cholesterol concentration. The biosensor operates at a sufficiently low potential to avoid interference from many sources, and the carrageenan hydrogel enables analysis of whole blood without electrode fouling. A more recent paper reports immobilization of tyrosinase by crosslinking it onto glassy carbon electrodes modified with electrodeposited gold nanoparticles [79]. The immobilized tyrosinase retained a high bioactivity on this electrode material, displaying stable, sensitive responses to various phenolic compounds.

The immobilization of proteins on colloidal gold has also been used for the development of immunological detection methods. An electrochemical method to monitor biotin–streptavidin interaction and determine the concentration of streptavidin has been established by the use of colloidal gold as an electrochemical label [80]. Velev and Kaler have created arrays of biosensors by *in situ* assembly of gold and silver colloidal particles onto micropatterned electrodes and immobilizing antibodies (IgG) on the colloidal particles [81]. Niemeyer and Ceyhan [82] have prepared biofunctionalized nanoparticles by DNA-directed immobilization of proteins at colloidal gold. Biometallic hybrid components can be used in an immunoassay for the detection of proteins. Thanh and Rosenzweig have developed a unique, sensitive and highly specific immunoassay system for antibodies using gold nanoparticles [83]. This assay is based on the aggregation of gold nanoparticles that are coated with protein antigens in the presence of their corresponding antibodies. Au nanoparticles have also been used as electrochemical labels in genetic diagnosis application [84]. *Escherichia coli* single-stranded DNA binding protein (SSB) has been attached onto a SAM of single-stranded oligonucleotide modified Au nanoparticle, and the resulting Au-tagged SSB was used as the hybridization label for the electrochemical detection of DNA hybridization. Changes in the Au oxidation signal were monitored upon binding of Au tagged SSB to probe and hybridization on the electrode surface. These works demonstrate the emergence of a new field of application for colloidal gold in protein immobilization and biosensing.

### 10.2.2

#### **Silver Nanoparticles**

Colloidal silver is another nanomaterial often used for biosensor fabrication. Its synthesis has been well demonstrated [85]. Much attention has also been given to the quantum characteristics of small granule diameter and large specific surface area as well as the ability to quickly transfer photoinduced electrons at the surfaces of colloidal particles [86]. It is also found that surface-assembled silver nanoparticles can act as an electrical bridge that “wire” the fast interfacial electron transfer between Cyt c and pyrolytic graphite electrodes, opening up new opportunities for the *in vitro* electron-transfer process of heme proteins by using silver nanoparticles and for fabricating bioelectronic devices. Furthermore, silver nanoparticles

greatly enhance the electron-transfer reactivity of heme-proteins, such as HRP, Mb, Hb and their catalytic ability toward  $\text{H}_2\text{O}_2$  and nitric oxide [87–89]. Glucose biosensors based on immobilization of GOD in silver nanoparticles have also been fabricated [90, 91]. The studies show that the colloidal silver nanoparticles function as electron-conducting pathways between the prosthetic groups and the electrode surface, therefore the electron-transfer rate between the enzyme and the electrode is increased significantly. In addition, by the vapor deposition method, Hb and colloidal silver nanoparticles can be entrapped in a titania sol-gel matrix on the surface of a glassy carbon electrode – thus a  $\text{NO}_2$  biosensor is prepared [92].

### 10.2.3

#### Other Metal Nanomaterials

One promising metal for nanoparticles is platinum. Platinum nanoparticles with a diameter of 2–3 nm have been used with single-wall carbon nanotubes (SWCNTs) for fabricating electrochemical sensors with Nafion to form a network that connected Pt nanoparticles to the electrode surface [20]. The use of platinized carbon microelectrodes has also been reported for a glucose biosensor [93]. Nanocrystalline diamond exhibits several special properties that make it particularly suitable for biofunctionalization and biosensing [94]. As an improvement, platinum-modified boron-doped diamond microfiber electrodes were fabricated, which exhibited much higher sensitivity [95]. Electrodeposition of highly dispersed palladium nanoparticles on a glassy carbon electrode has also been reported for the construction of a glucose biosensor [96]. Another glucose biosensor has also been reported by co-depositing palladium nanoparticles and GOD onto a Nafion-solubilized carbon nanotube (CNT) film [19]. GOD can retain its biocatalytic activity and offer efficient oxidation and reduction of the enzymatically liberated  $\text{H}_2\text{O}_2$ , allowing for fast and sensitive glucose quantification.

Some glucose biosensors based on non-conducting polymer films have been reported; however, such biosensors always suffer from a low response current and a relatively high detection limit. To solve these problems, Cu nanoparticles are selected to increase the response current because it can electrochemically oxidize glucose [97]. A GOD and Cu nanoparticles-based sensor has a two times lower detection limit, a three times larger maximum current and  $2.5\times$  higher sensitivity than biosensors fabricated with no Cu nanoparticles.

## 10.3

### Metallic Oxide Nanoparticles

Some researchers have used  $\text{MnO}_2$  nanoparticles as eliminators of ascorbic acid interference to amperometric glucose and lactate biosensors [98, 99]. Others have constructed an enzyme field-effect transistor using a GOD membrane doped with  $\text{MnO}_2$  powder [100]. In this configuration,  $\text{MnO}_2$  acts as a catalyst to the decomposition of  $\text{H}_2\text{O}_2$ . Therefore, the produced  $\text{O}_2$  from the decomposition of  $\text{H}_2\text{O}_2$  can

be replenished in the glucose oxidation reaction and the dynamic range of glucose determination is extended. Researchers have also fabricated some glucose biosensors based on the co-immobilization of GOD and  $\text{MnO}_2$  nanoparticles [98, 101].

Nano titanium dioxide ( $\text{TiO}_2$ ) is now an attractive biocompatible material widely used in toothpaste and cosmetics. Due to its unique physiochemical properties and its inclination to selectively combine with some groups of biomolecules, nanosized  $\text{TiO}_2$  has been proposed as a promising interface for the immobilization of biomolecules. Attempts have been made to assemble heme proteins, including Cyt c, Mb and Hb, onto a nanocrystalline  $\text{TiO}_2$  film; the  $\text{TiO}_2$  film can not only offer a friendly platform to assemble the protein molecules, but also enhances the electron-transfer process between the protein molecules and the electrode [12]. The electrochemical characteristics of HRP entrapped in a  $\text{TiO}_2$  nanoparticles film cast on pyrolytic graphite electrode has been examined [102]. The good biocompatibility of  $\text{TiO}_2$  nanoparticles can make HRP retain its native state and show good electrocatalytic activity, which may have potential application in constructing a third-generation electrochemical biosensor.

Zirconium dioxide ( $\text{ZrO}_2$ ) nanoparticles have also been used in protein-based biosensors. As an example,  $\text{ZrO}_2$  nanoparticles 35 nm in diameter have been cast on a pyrolytic graphite electrode by dispersing them in dimethyl sulfoxide to immobilize Hb for fabrication of a  $\text{H}_2\text{O}_2$  sensor [13]. This sensor shows a high thermal stability up to 74 °C. Another example is the treatment of the surface of a platinum electrode with nanoporous  $\text{ZrO}_2$ /chitosan composite matrix to fabricate a glucose biosensor [103]. Other studies reveal that nanoporous  $\text{ZrO}_2$  has general affinity for the binding of proteins because the amine and carboxyl groups on the surface of enzyme can act as ligands to  $\text{ZrO}_2$ . Thus, the usage of glutaraldehyde in crosslinking, which always denatures an enzyme, can be avoided, and a HRP-based biosensor for  $\text{H}_2\text{O}_2$  is correspondingly constructed [104]. Moreover,  $\text{H}_2\text{O}_2$  sensors are constructed based on the self-assembly of  $\text{ZrO}_2$  nanoparticles with heme proteins (Hb and Mb) on a functional glassy carbon electrode [105].

Zinc oxide (ZnO) is another attractive semiconductor material. It has been demonstrated that ZnO with a high isoelectric point ( $\sim 9.5$ ) is suitable for the adsorption of low-isoelectric point proteins [106]. For example, low-isoelectric point tyrosinase is reported to be adsorbed on the surface of such ZnO nanoparticles, facilitated by the electrostatic interactions, and is immobilized on a glassy carbon electrode via film formation to develop a mediator-free phenol biosensor [107]. Therefore, ZnO nanoparticles deserve further investigation as an important promising candidate as support material in the fabrication of biosensors.

#### 10.4

##### Carbon Nanotubes

Carbon nanotubes (CNTs), discovered in 1991, are a new type of carbon material obtained by folding grapheme layers into carbon cylinders. They present a closed topology and tubular structure with diameters of several nanometers and lengths

to several microns. Basically, there are two types of carbon nanotubes, multiwall carbon nanotubes (MWCNTs) and single-wall carbon nanotubes (SWCNTs). They can behave as conductors or semiconductors depending on their structures, mainly on their diameter and helicity.

Carbon nanotubes have received enormous attention for the preparation of electrochemical sensors due to their unique properties, as reviewed in some publications [108–114]. Similar to the conventional electrochemical biosensors, proteins and CNTs based biosensors can also be, generally, divided into three categories: (a) first-generation biosensors via the detection of  $\text{H}_2\text{O}_2$  or  $\text{O}_2$  involved in the enzymatic reaction, (b) second-generation biosensors through the utilization of electron-transfer mediators, and (c) third-generation biosensors based on the direct electron transfer of enzymes or proteins. Especially, CNT materials have been proved to possess electrocatalytic activity toward the oxidation of  $\text{H}_2\text{O}_2$  and the reduction of  $\text{O}_2$  and can facilitate the direct electron transfer of proteins or enzymes. These features make CNTs particularly attractive for the development of first- and third-generation electrochemical biosensors [111]. Many second-generation protein-based biosensors have also been fabricated by using CNTs. For example, organic electrocatalysts, such as polynuclear aromatic dyes, have been employed, which can be stably immobilized onto CNTs and can be further used to accelerate the oxidation of  $\text{H}_2\text{O}_2$  or shuttle electron transfer between the CNTs and enzymes or proteins. Ye et al. have functionalized the MWCNTs with iron-phthalocyanines to redox-catalyze  $\text{H}_2\text{O}_2$  oxidation and have constructed a highly sensitive and selective glucose biosensor [115]. Chen et al. have co-immobilized methylene blue with HRP onto CNTs to shuttle the electron transfer between HRP and the CNTs. The modified electrode exhibited a good bioelectrocatalytic activity toward  $\text{H}_2\text{O}_2$  reduction [116].

The nano-dimensions, graphitic surface chemistry and electronic properties of carbon nanotubes make them an ideal material for use in chemical and biochemical sensing [108–114, 117, 118]. In addition, the fabricated sensors using CNTs usually show high sensitivity and stability of electrocatalysis. Although the mechanism is still not fully understood, some researchers suggest that these advantages may be attributed to the special structure of nanotubes, such as their open ends [119, 120]. The electroactive ends of the nanotubes are readily accessible to species in solution. The opened nanotube ends allow the enzyme to enter the hollow CNTs. In addition, the rigidity of the tubes allows them to be plugged into biomolecules, so enabling electrical connection to the redox centers of the biomolecules. Furthermore, the large surface area per unit volume of CNTs allows a large amount of enzyme to be immobilized within nanotubes.

However, the potential application of CNTs is still limited by (a) the CNTs tend to aggregate in most solvents; (b) electronic communication between proteins and CNTs is rather slow at pristine CNTs; and (c) strong interactions between proteins and CNTs may distort the proteins. Therefore, the biosensing applications of CNTs require rational functionalization of the CNTs to improve their solubility and biocompatibility.

The combination of CNTs with redox active protein (enzymes) appears to offer a convenient platform for a fundamental understanding of biological redox reactions

and for the development of third-generation biosensors. Direct electron transfer and bioelectrocatalysis of many proteins, such as GOD, cyt c, Mb, Hb, HRP, etc., have been investigated with CNTs-modified electrodes and their performance has been found to be much superior to those of other carbon electrodes in terms of reaction rate, reversibility, and detection limit [121–132].

GOD is the major protein employed for sensor fabrication by using CNTs. GOD has been immobilized by coating onto the surface of SWCNTs without a gross loss of enzyme activity [133]. Treatment of this bio-SWCNT sensor with both a diffusive mediator and equilibrated glucose substrate enhanced the catalytic signal by more than one order of magnitude compared with that observed at an activated macro-carbon electrode. This enhanced performance was partly due to the high enzyme loading and partly because of better electrical communication ability of the nanotubes. Other research on MWCNTs has revealed that a MWCNTs-modified glassy carbon electrode can be employed as an amperometric oxygen sensitive electrode to fabricate a glucose biosensor [134]. CNT-based glucose biosensor was also fabricated via polypyrrole [135, 136]. Recently, a CNTs-doped polypyrrole (PPy) glucose biosensor was reported [137]. Unlike other work on glucose biosensors based on CNT/PPy electrodes, where CNT was physically entrapped within the growing film, the PPy/GOD films were formed by using “oxidized” CNT as the sole charge-balancing anionic dopant. This is the first example of anionic CNT acting as dopant in the preparation of conducting-polymer enzyme electrodes. While the concept has been presented within the context of glucose sensing, it could readily be extended to other biocatalytic electrodes based on judicious selection of the enzyme.

Heme proteins have also been extensively employed to fabricate biosensors by using CNTs. The direct electrochemical response of Mb on MWCNT-modified glassy carbon electrode has been reported [16]. Mb exhibited elegant catalytic activity for electrochemical reduction of oxygen, based on which an unmediated biosensor for  $O_2$  was developed. An unmediated  $H_2O_2$  biosensor, based on the peroxidase-like activity of Mb on MWCNTs, has also been constructed [138]. Recently, the same research group reported that Mb can be strongly adsorbed onto the surface of MWCNTs with an approximate monolayer to develop an unmediated NO biosensor, with a low detection limit [139]. HRP is able to adsorb on a carbon nanotube microelectrode to transfer electrons directly with the electrode and retain its catalytic activity toward  $H_2O_2$  [124]. A  $H_2O_2$  biosensor based on Cyt c and MWCNTs has also been fabricated [140]. The enhanced electron-transfer rate was also observed in systems in which microperoxidase (MP-11) was attached to the end of aligned SWCNTs array and MWCNTs [141, 142].

Many other proteins (enzymes) have been employed to prepare various kinds of biosensors by using CNTs. For example, the direct electrochemistry of xanthine oxidase has been achieved on a SWCNTs-modified gold electrode, which may provide an attractive route for the development of biosensors [143]. Table 10.1 gives information on sensors that use other proteins (enzymes).

Understanding the interaction between CNTs and proteins should be helpful in developing protein-based biosensors using CNTs. Usually, proteins (enzymes) are immobilized onto CNTs in three ways, taking GOD as example.

**Tab. 10.1.** Protein-based biosensors using carbon nanotubes.

Protein(enzyme)	CNT	CNT immobilization matrix/electrode	Analyte	Ref.
Acetylcholinesterase (AChE)	MWCNT	Thick film strip electrode	Organophosphorus (OP) insecticides	219
L-Amino acid oxidase	CNT	Alkoxy silane sol-gel	L-Amino acid	220
Urease	CNT	Sol-gel	Urea	221
Acetylcholinesterase	CNT	Sol-gel	Acetylthiocholine	221
L-lactate oxidase	MWCNT	Sol-gel/GCE	L-Lactate	222
Putrescine oxidase	MWCNT	PDDA/GCE	Putrescine	223
Aflatoxin-detoxifizyme (ADTZ)	MWCNT	Au electrode	Sterigmatocystin	224
Choline oxidase (ChOx)	MWCNT	Sol-gel/platinum electrode	Choline	225
Cholesterol oxidase	MWCNT	Sol-gel chitosan hybrid film	Cholesterol	226
Dehydrogenase	CNT	CNT paste electrode	Glucose, NADH	227
		GCE	Glucose, NADH	228
		GCE	NADH	229
Catalase	MWCNT	GCE	H <sub>2</sub> O <sub>2</sub>	230
	SWCNT	Au electrode		231
Microperoxidase (MP-11)	MWCNT	MWCNT-Au NPs nanohybrid film	H <sub>2</sub> O <sub>2</sub>	232
Laccase	CNT	CNT-chitosan composite film	2,2-Azino-bis-(3-ethylbenzthiazoline-6-sulfonic acid) diammonium salt (ABTS), catechol, O <sub>2</sub>	233
lactate oxidase (LOX)	SWCNT	Functionalized CNT-COOH electrode	Lactate	234
Cholesterol esterase, cholesterol oxidase, and peroxidase	MWCNT	Screen-printed carbon electrode	Cholesterol	235



(a) Physical adsorption [144]. GOD immobilized in this way usually maintains its substrate-specific enzyme activity in the presence of glucose. The tubular fibrils become positioned within tunneling distance of the cofactors without too much denaturation of the enzyme.

(b) GOD is covalently attached to the ends of the aligned tubes, which allows close approach to FAD [145]. In addition, some researchers have reported the synthesis of a fully integrated CNT protein composite system with high function density and with direct chemical bonding GOD to functionalized MWCNT under a high degree of control and specificity [146]. Recently, a highly ordered array of CNTs has been reported to serve as a universally direct nanoelectrode interface for redox proteins [147]. The site-selective, covalent docking of GOD on the CNTs tips has a marked effect on enhancing electron transfer properties.

(c) FAD is directly attached to the ends of the tubes [148]. A good example is given by Willner and his coworkers, who covalently immobilized the FAD redox center of GOD on one end of SWCNT, and the other end of the SWCNT was attached to a gold surface or another FAD to accelerate electrical communication between the electrode and redox proteins [149].

CNTs have been extensively employed in preparing different kinds of electrodes for biosensors on a larger scale. Wang et al. have reported a remarkable decrease in overvoltage for the oxidation of NADH using composites obtained by dispersing CNTs in a Teflon binder [150]. Compton et al. have proposed the use of MWCNTs abrasively attached to the basal plane pyrolytic graphite [151]. Unique electrochemistry of soluble molecules and adsorbed proteins on flat mat-like layers of SWCNTs or MWCNTs has been demonstrated. Rusling et al. have reported that Mb was covalently attached onto the ends of vertically oriented SWCNTs forest arrays used as electrodes [121]. The results suggest that the “trees” in the nanotube forest behaved electrically similar to a metal, conducting electrons from the external circuit to the redox sites of the proteins. Huang et al. [152] and Zhao et al. [153] have reported multilayers of MWCNTs and GOD through a layer-by-layer technique. Liu has reported the preparation of enzyme-polyion thin films consisting of GOD alternately assembled with poly(diallyldimethylammonium) chloride polymer on CNTs at a glassy carbon electrode [154].

CNTs have also been used to develop electrochemiluminescence (ECL) biosensors. For instance, Wohlstader et al. have reported ECL biosensors for the assay of  $\alpha$ -fetoprotein [113]. Studies revealed that CNTs were very useful for ECL-based assays. CNTs have also been used to fabricate sensors with screen-printed carbon electrode [155, 156].

CNTs array-based biosensors have also been reported. Aligned MWCNTs grown on a platinum substrate have been described for the development of an amperometric biosensor [114]. The two array systems in this work were either acid treated or air treated. The results showed that chemical etching was more effective in opening the carbon nanotubes and allowing the enzyme to enter the inner channel.

A so-called carbon nanotube paste electrode (CNTPE) has been reported in the fabrication of a glucose biosensor modified with some metallic particles [157]. The bioelectrodes were obtained by dispersing the metal particles, enzyme and

MWCNTs within a mineral oil binder. The resulting CNTPE combines the ability of CNTs to promote electron-transfer reactions with the attractive advantages of composite materials.

Microelectrodes and ultramicroelectrodes are important analytical tools because they exhibit fast response times, significantly improved Faradic-to-capacitive current ratios, and substantially reduced ohmic drops [158, 159]. Therefore, it is reasonable to develop so-called micro-biosensors. The electrocatalytic reduction of dissolved oxygen in acidic medium using microelectrodes constructed from MWCNTs has been reported [160]. Meanwhile, Martin and coworkers [161] have reported that the detection limits obtained at nanoscopic electrodes ensembles are much lower, three orders of magnitude, than the corresponding detection limits for a conventional macroscopic disk electrode. An important consideration in the future advancement of practical sensors is how to develop new immobilization strategies that are appropriate for the construction of miniature sensors, which requires precise control of film deposition on a small electrode. Electrochemical immobilization provides an elegant alternative for the deposition of enzymes on very small area electrodes of defined geometry.

Nanoelectrode ensembles based on low-site density, aligned CNTs have also been fabricated, and the electrochemical characteristics have been investigated [162]. Subsequently, the same research group developed a glucose biosensor based on CNT nanoelectrode ensembles [163]. The operation eliminates the need for permselective membrane barriers or artificial electron mediators, thus greatly simplifying the sensor design and fabrication. The same group have also fabricated CNT nanoelectrode ensembles by another method [164]. Platinum nanoparticles have been used to modify the CNT nanoelectrode ensembles and a new amperometric biosensor, based on adsorption of GOD at the platinum nanoparticle-modified CNT electrode [165]. This work combines the advantages of CNTs with Pt nanoparticles. The excellent electrocatalytic activity and special 3D structure of the enzyme electrode result in good characteristics such as a large determination range (0.1–13.5 mM), a short response time (within 5 s) and stability (73.5% remains after 22 days). Another reported glucose biosensor is also notable, due to its high sensitivity and selectivity coupled to a wide linear range, prolonged lifetime and oxygen independence [166].

CNTs are often used together with other materials (including nanomaterials) for biosensor fabrication. Early in 2002, a novel glassy carbon electrode modified by a gel containing MWCNTs and the ionic liquid 1-butyl-3-methylimidazolium hexafluorophosphate (BMIPF<sub>6</sub>) was reported [167]. Wang et al. have reported on a simple avenue for preparing effective CNT-based electrochemical sensors and biosensors using CNT/Teflon composite materials [150]. Unlike early CNT-modified electrodes, the composite devices rely on the use of CNT as the sole conductive component rather than utilizing it as the modifier in connection with another electrode surface. Another novel glucose biosensor based on CNT epoxy resin biocomposite has also been reported [168]. Experimental results show that the CNT epoxy composite biosensor offers excellent sensitivity, a reliable calibration profile, and stable electrochemical properties together with a significantly lower detection

potential (+0.55 V) than the sensor with no CNT. Recently, a nanobiocomposite material based on a MWCNT-Nafion thin film for bioanalytical application has been proposed [169]. By the combination of MWCNTs, Nafion, and GOD, a novel electroanalytical nanobiocomposite thin film can be produced by simple solvent casting. Compton et al. have proposed another glucose biosensor, fabricated by immobilizing GOD encapsulated in a sol-gel matrix on basal plane pyrolytic graphite modified with MWCNTs [151]. The present carbon nanotube sol-gel biocomposite glucose sensor showed excellent properties for the sensitive determination of glucose. More recently, Yang has used sol-gel solution with highly dispersed Pt nanoparticles as a binder for MWCNTs to fabricate glucose biosensors [170]. In another study by Yang, a CNT-cobalt hexacyanoferrate nanoparticle-chitosan biopolymer system was used in the fabrication of biosensors [171]. With the introduction of CNT, this system could show significant improvement of redox activity of cobalt nanoparticles due to the excellent electron-transfer ability of CNTs. Meanwhile, CNTs have also been doped in organically modified sol-gels (ormosils) to enhance the conductive properties of the sol-gel matrixes, since the conductivity of ormosils is not good, although the porosity and biocompatibility are very favorable. Accordingly,  $\text{H}_2\text{O}_2$  and glucose sensors have been developed by entrapping enzymes in a new ormosil composite doped with ferrocene monocarboxylic acid-bovine serum albumin conjugate and MWCNTs [172, 173].

The insolubility of CNTs in most solvents is one of the limitations in the design of CNTs-based biosensing devices. A stable suspension of CNTs can be obtained by dispersing CNTs in a solution of surfactant, such as cetyltrimethylammonium bromide (CTAB, a cationic surfactant) [174]. CNTs have promotion effects on the direct electron-transfer of GOD immobilized onto the surface of CNTs. Solubilization of CNTs by Nafion, a widely used perfluorosulfonated polymer, has also been reported for both single- and multiwall CNTs [175]. Redox activity has also been dramatically enhanced at CNT/Nafion-coated electrodes. This gives a new way to fabricate amperometric biosensors. A recent interesting observation is that covalently linked composites of MWCNT and GOD composites are highly water soluble [146].

SWCNTs have been reported to combine platinum nanoparticles with a diameter of 2–3 nm for use in fabricating electrochemical sensors with remarkably improved sensitivity toward  $\text{H}_2\text{O}_2$  and glucose [176]. This work demonstrates that it is possible to obtain very small Pt nanoparticles deposited onto Nafion-solubilized SWCNT. Platinum nanoparticles are in electrical contact, through the SWCNT, with the glassy carbon or carbon fiber backing, enabling the composite structure to be used as an electrode. This composite structure may offer an excellent platform for various biosensing applications. Finally, CNTs have been combined with Fe nanoparticles to develop a glucose biosensor [177].

## 10.5 Nanocomposite Materials

Collagen/poly(acrylic acid) bilayers were once reported to be added to nanoparticle CdTe/polycation layer-by-layer films to produce porous collagen bilayers. Such

stratified multilayer systems showed successful cell attachment and survival while native nanoparticle CdTe/polycation films were strongly cytotoxic [178]. Hu et al. have made a detailed electrochemical investigation of Hb incorporated in collagen films [179]. The Hb-collagen film electrodes were also used to catalyze the reduction of nitrite, oxygen and  $H_2O_2$ , indicating potential applications of the films for the fabrication of a new type of biosensor. A novel amperometric glucose biosensor combined with an enzymatic assay of glucose level in rat brain has also been developed based on ferrocene-doped silica (FcDS) nanoparticles conjugated with a biopolymer chitosan (CHIT) membrane [180]. The formation through a water-in-oil (W/O) microemulsion method of such dye-doped silica particles clearly demonstrated their remarkable bioconjugation and photostability.

Gold nanoparticles have been widely used in the electrochemical study of proteins; however, the reversibility of Hb is not so good, because both gold nanoparticles and Hb are positive-charged, and the electrostatic repulsion may result in unfavorable orientation of Hb. It has been reported that  $\alpha$ -zirconium phosphate is an anionic material with good biocompatibility, but direct electron transfer of the anchored protein is not easily realized perhaps for the weak conductivity and lower enzyme-loading ability of ZrP [181]. To solve the problem, Chen et al. have introduced the gold nanoparticles into ZrP, based on which an excellent  $H_2O_2$  biosensor was constructed [182]. Liu et al. have also developed a  $H_2O_2$  biosensor based on the immobilization of HRP to a nano-Au monolayer, which is supported by a PAMAM dendrimer/cystamine modified gold electrode [183]. Meanwhile, Yu et al. have reported a new electrode interface by using L-cysteine-gold particle nanocomposite immobilized in the network of a Nafion membrane on a glassy carbon electrode [184].

## 10.6 Nanoparticles with Special Functions

### 10.6.1 Semiconductor Nanoparticles

Some nanomaterials used for sensors fabrication have several special functions. For instance, semiconductor nanoparticles that have recently been used for sensing applications are a highly luminescent, photostable class of fluorophore [185–187]. Colloidal semiconductor nanocrystals, often referred to as “quantum dots” or “QDs”, are single crystals a few nanometers in diameter whose size and shape can be precisely controlled by the duration, temperature, and ligand molecules used in their synthesis [185]. The synthesis process yields QDs that have composition- and size-dependent absorption and emission. Absorption of a photon with energy above the semiconductor band gap energy results in the creation of an electron-hole pair or exciton. Absorption has an increased probability at higher energies and results in a broadband absorption spectrum, in marked contrast to standard fluorophores. Luminescent QDs have unique spectroscopic properties that

include a broad adsorption spectra: size-tunable, narrow, and symmetric photoluminescence emissions ranging from UV to the near-IR range; and exceptional resistance to chemical and photodegradation along with high photobleaching thresholds [188]. Nanocrystals composed of ZnSe, CdS, CdSe, and CdTe also have emission spectra that span the visible spectrum. Researchers have demonstrated that QDs can function as fluorescence resonance-energy transfer (FRET) donors in prototype hybrid QD–protein sensors [189]. Nanosized semiconductor crystals can be effectively coupled to biomolecular units such as enzyme, to generate novel photoelectrochemical systems [190].

CdSe nanocrystals have broad absorption spectra that progressively shift to longer wavelengths with increasing particle size. These nanocrystals are tunable fluorophores with absorption characteristics that allow simultaneous excitation of different particle sizes at a single wavelength, while they exhibit a luminescent emission that spans a wide range of wavelengths in the visible spectrum [188]. Researchers have fabricated a facile, reagentless method for generating protein-based semiconducting nanoparticle sensors for small molecules using CdSe nanoparticles [187]. They used maltose binding protein (MBP) for the sensor receptor. When MBP binds with maltose, the conformation of MBP is changed, and then the movement prohibits the electron transfer to CdSe, resulting in fluorescence emission. Researchers have also described a novel and direct method for conjugating protein molecules to luminescent CdSe–ZnS core–shell nanocrystals used as bioactive fluorescent probes in sensing, immunoassay, imaging, and other diagnostics applications [188].

CdS is also a promising nanomaterial that has also been used in biosensor fabrication. The direct electrochemistry of GOD adsorbed on CdS nanoparticles-modified pyrolytic graphite electrode has been investigated [191]. The results showed that the fabricated biosensor was sensitive and stable in detecting glucose, indicating that CdS nanoparticles are a good candidate material for the immobilization of enzyme in glucose biosensor construction. Hb has also been immobilized with CdS nanoparticles on pyrolytic graphite electrode to characterize the electrochemical reactivity and peroxidase activity of the protein, and the result demonstrates that good redox waves of Hb can be achieved after this protein is entrapped in CdS nanoparticles [192]. Combined with formaldehyde dehydrogenase enzyme, nanocrystalline CdS has also been immobilized by self-assembling on a gold electrode to prepare a biological–inorganic hybrid to perform catalytic oxidation of formaldehyde [190, 193]. Researchers have also prepared an acetylcholine esterase (AChE)/CdS nanoparticle hybrid system for the photoelectrochemical detection of AChE inhibitors [194]. The photoelectrochemical charging effect of a Au–CdS nanoparticle array has also been employed to develop a sensor for acetylcholine esterase inhibitors [195].

As mentioned above, TiO<sub>2</sub> has been a popular nanomaterial for use in sensor devices. Recently, Li et al. have successfully constructed a Hb-based H<sub>2</sub>O<sub>2</sub> biosensor tuned by the photovoltaic effect of the nanoparticles [196]. The catalytic ability of the protein and the sensitivity of sensor could be greatly enhanced after UV light irradiation on the co-immobilized nanomaterial.

## 10.6.2

**Magnetic Nanoparticles**

Magnetic nanoparticles have been widely applied in various fields of biology and medicine, such as magnetic targeting, magnetic resonance imaging, diagnostics, immunoassays, RNA and DNA purification, gene cloning, and cell separation and purification etc. [197]. Thus, researchers have fabricated magneto-bioelectronics that rely on magnetic nanoparticles. Multilayer films have been prepared on the surface of a glassy carbon electrode by the deposition of chitosan/ $\text{Fe}_3\text{O}_4$  nanoparticles and phytic acid via the layer-by-layer assembly technique [198]. The multilayer films exhibited good biocompatibility, and adsorbed Hb on the film could realize direct electron transfer reactions and maintain high catalytic activity. In contrast, the orientation of magnetic particles can be controlled with a magnet, which can in turn control the electron transfer of protein-based biosensors. Accordingly, a magneto-switchable bioelectrocatalysis glucose biosensor has been prepared with magnetic  $\text{Fe}_3\text{O}_4$  nanoparticles as control factor [199]. Switchable systems that can be used as both  $\text{H}_2\text{O}_2$  biosensor and glucose biosensor have also been prepared with magnetic nanoparticles by the same research group [197]. Other magnetic nanoparticles have also been used in fabricating protein-based biosensors with good characteristics. For example, a phenol biosensor has been developed based on the immobilization of tyrosinase on the surface of modified magnetic  $\text{MgFe}_2\text{O}_4$  nanoparticles attached to the surface of a carbon paste electrode [200].

## 10.7

**Other Nanomaterials**

In addition to the above-mentioned nanomaterials, which have been largely used for sensor fabrication, there are also many other nano-materials, which either have been used for biosensing devices or may have the potential of biosensor application. One such nanostructure material is nanocrystalline silicon, often referred to as porous silicon, which, in fact, has been extensively used in sensors. Since the discovery of its strong visible luminescence at room temperature, porous silicon has attracted considerable interest in its possible use in the construction of biosensors. Its ability to emit light is due to its tiny pores that range from less than 2 nm to micrometer dimensions. In addition, porous silicon possesses a high surface to volume ratio (as much as  $500 \text{ m}^2 \text{ cm}^{-3}$ ) and it can be fabricated easily using some of the established processes of silicon technology. Porous silicon has been used as an optical interferometric transducer for detecting small organic molecules (biotin and digoxigenin), 16-nucleotide DNA oligomers, and proteins (streptavidin and antibodies) at pico- and femtomolar analyte concentrations [201, 202]. Many potentiometric biosensors based on porous silicon have been reported [203–205]. In addition, the enzymes penicillinase and lipase have separately been immobilized on the surface of porous silicon to develop biosensors for penicillin and triglycerides [206].

SiO<sub>2</sub> nanoparticles are another often used nanomaterial. The electrochemical and electrocatalytic properties of heme proteins, including Mb, Hb, and HRP in layer-by-layer films assembled with SiO<sub>2</sub> nanoparticles and the proteins have been investigated. The proteins in the films can display good electrocatalytic activities toward various substrates such as oxygen, H<sub>2</sub>O<sub>2</sub>, trichloroacetic acid, and nitrite, which has showed a potential applicability in fabricating a new kind of biosensor without using mediators [14]. SiO<sub>2</sub> nanoparticles have also been used to immobilize GOD by the sol-gel method. Experimental results show that hydrophobic SiO<sub>2</sub> nanoparticles can immobilize enzyme well, providing a good and simple approach for preparing a high quality glucose biosensor [207, 208]. Moreover, SiO<sub>2</sub> nanoparticles have been introduced into the construction of enzyme field-effect transistors (ENFETs) to create a glucose-sensitive ENFET, and the SiO<sub>2</sub> nanoparticles can provide a biocompatible environment and improve the enzyme activity, and prevent the immobilized enzymes from leakage as well [209]. In addition, boron-doped silicon nanowires (SiNWs) have been reported by Cui et al. to create highly sensitive, real-time electrically based sensors for biological and chemical species [210]. Antigen-functionalized SiNWs showed reversible antibody binding and concentration-dependent detection in real time.

Recently, a disposable glucose biosensor was reported based on co-dispersion of a diffusion polymeric mediator, poly(vinylferroceneco-acrylamide) (PVFcAA), and GOD in an alumina nanoparticulate membrane on a screen-printed carbon electrode [211]. The nanoparticulate membrane served not only biosensing, but also analyte-regulating functions. Since the membrane is highly hydrophilic, the amount of dissolved oxygen, one of the main interferants, is greatly reduced, and, thus, little interference is observed.

Arrays of nanoscopic gold tubes have been prepared by electroless deposition of the metal within the pores of polycarbonate particle track-etched membranes [212]. GOD can be immobilized onto the self-assembled monolayers of gold tubes, via crosslinking with glutaraldehyde or covalent attachment by carbodiimide coupling. Based on a similar method of template synthesis, Miao et al. have immobilized GOD in the polypyrrole nanotubes and produced a biosensor [213]. Compared with conventional techniques, this immobilization strategy greatly enhances the amount of the enzyme immobilized, the retention of the immobilized activity and the sensitivity of the biosensor.

Polyaniline nanoparticles, synthesized with dodecylbenzylsulfonic acid, can be successfully electrodeposited on the surface of glassy carbon electrodes to form nanostructured films suitable as heterogeneous mediators [214], and nanoparticles have been applied to a glassy carbon electrode surface with HRP for H<sub>2</sub>O<sub>2</sub> sensing. A sensitive and selective amperometric glucose biosensor based on platinum microparticles dispersed in nano-fibrous polyaniline has also been developed [215]. PANI has a large specific surface area, good conductivity, high reaction ability, and many microgaps between the fibers, which is very useful for sensor fabrication. This nanofibrous morphology is also beneficial to the dispersion of metal catalyst and the immobilization of enzyme.

Recently, there has been a tendency to extend the study of nanoparticles from metal and inorganic compounds to organic compounds because of the diversity offered by organic molecules [216]. It is expected that organic nanoparticles can be used in constructing sensors, bioprobes, devices, etc. [217, 218].

## 10.8

### Conclusion

Nanobiotechnology has played an increasingly important role in the development of protein-based biosensors. Owing to the unique properties of nanomaterials, such as large surface-to-volume ratio, high surface reaction activity, high catalytic efficiency, and strong adsorption ability, numerous protein-based biosensors have been well constructed with higher selectivity, better stability and a lower detection limit for the detection of even more species. In addition, the special electronic, optical and magnetic characteristics of nanomaterials are providing a platform for fabricating more novel biosensors, which might also open up new topics in the field of protein-based biosensors. Greater achievements and advances will be made by combining nanotechnology with protein science and biosensing.

### References

- 1 LI, G., *Protein-based Voltammetric Sensors*, Encyclopedia of Sensors, Eds. GRIMES, C. A. et al., American Scientific Publishers Stevenson Ranch, CA, 2006, Vol. 8, pp. 301–314.
- 2 ZHANG, W. J., LI, G. X., Third-generation biosensors based on the direct electron transfer of proteins., *Anal. Sci.* 2004, 20, 603–609.
- 3 MACUS, R. A., SUTIN, N., Electron transfers in chemistry and biology., *Biochim. Biophys. Acta*, 1985, 811, 265–322.
- 4 GORTON, L., Carbon paste electrodes modified with enzymes, tissues, and cells., *Electroanalysis* 1995, 7, 23–45.
- 5 HELLER, A., Electrical connection of enzyme redox centers to electrodes., *J. Phys. Chem.* 1992, 96, 3579–3587.
- 6 BARTLETT, P. N., TEBBUTT, P., WHITAKER, R. P., Kinetic aspects of the use of modified electrodes and mediators in bioelectrochemistry., *Progr. React. Kinet.* 1991, 16, 155.
- 7 GORTON, L., A. LINDGREN, T. L., MUNTEANU, F. D., RUZGAS, T., GAZARYAN, I., Direct electron transfer between heme-containing enzymes and electrodes as basis for third generation biosensors., *Anal. Chim. Acta* 1999, 400, 91–108.
- 8 HERNANDEZ-SANTOS, D., GONZALEZ-GARCIA, M. B., GARCIA, A. C., Metal-nanoparticles based electroanalysis., *Electroanalysis* 2002, 14, 1225–1235.
- 9 KIMA, J., GRATEA, J. W., WANG, P., Nanostructures for enzyme stabilization., *Chem. Eng. Sci.* 2006, 61, 1017–1026.
- 10 CHEN, J. R., MIAO, Y. Q., HE, N. Y., WU, X. H., LI, S. J., Nanotechnology and biosensors., *Biotechnol. Adv.* 2004, 22, 505–518.
- 11 VASEASHTA, A., DIMOVA-MALINOVSKA, D., Nanostructured and nanoscale devices, sensors and detectors., *Sci. Technol. Adv. Mater.* 2005, 6, 312–318.
- 12 LI, Q. W., LUO, G., FENG, J., Direct electron transfer for heme proteins assembled on nanocrystalline TiO<sub>2</sub> film., *Electroanalysis* 2001, 13, 359–363.



- 13 LIU, S., DAI, Z., CHEN, H., JU, H., Immobilization of hemoglobin on zirconium dioxide nanoparticles for preparation of a novel hydrogen peroxide biosensor., *Biosens. Bioelectron.* **2004**, 19, 963–969.
- 14 HE, P., HU, N., Electrocatalytic properties of heme proteins in layer-by-layer films assembled with SiO<sub>2</sub> nanoparticles., *Electroanalysis* **2004**, 16, 1122–1131.
- 15 LIU, S. Q., JU, H. X., Renewable reagentless hydrogen peroxide sensor based on direct electron transfer of horseradish peroxidase immobilized on colloidal gold-modified electrode., *Anal. Biochem.* **2002**, 307, 110–116.
- 16 ZHANG, L., ZHAO, G. C., WEI, X. W., YANG, Z. S., Electroreduction of oxygen by myoglobin on multi-walled carbon nanotube-modified glassy carbon electrode., *Chem. Lett.* **2004**, 33, 86–87.
- 17 CAO, D. F., HE, P. L., HU, N. F., Electrochemical biosensors utilising electron transfer in heme proteins immobilised on Fe<sub>3</sub>O<sub>4</sub> nanoparticles., *Analyst* **2003**, 128, 1268–1274.
- 18 KATZ, E., WILLNER, I., WANG, J., Electroanalytical and bioelectroanalytical systems based on metal and semiconductor nanoparticles., *Electroanalysis* **2004**, 16, 19–44.
- 19 LIM, S. H., WEI, J., LIN, J., LI, Q., KUAYOU, J., A glucose biosensor based on electrodeposition of palladium nanoparticles and glucose oxidase onto nafion-solubilized carbon nanotube electrode., *Biosens. Bioelectron.* **2005**, 20, 2341–2346.
- 20 HRAPOVIC, S., LIU, Y., MALE, K. B., LUONG, J. H. T., Electrochemical biosensing platforms using platinum nanoparticles and carbon nanotubes., *Anal. Chem.*, **2004**, 76, 1083–1088.
- 21 LIU, S., LEECH, D., JU, H., Application of colloidal gold in protein immobilization, electron transfer, and biosensing., *Anal. Lett.* **2003**, 36, 1–19.
- 22 HAN, X., CHENG, W., ZHANG, Z., DONG, S., WANG, E., Direct electron transfer between hemoglobin and a glassy carbon electrode facilitated by lipid-protected gold nanoparticles., *Biochim. Biophys. Acta Bioenerg.* **2002**, 1556, 273–277.
- 23 YANEZ-SEDEÑO, P., PINGARRÓN, J. M., Gold nanoparticle-based electrochemical biosensors., *Anal. Bioanal. Chem.* **2005**, 382, 884–886.
- 24 XIAO, Y., PATOLSKY, F., KATZ, E., HAINFELD, J. F., WILLNER, I., Plugging into enzymes: Nanowiring of redox enzymes by a gold nanoparticle. *Science* **2003**, 299, 1877–1881.
- 25 BROWN, K. R., FOX, A. P., NATAN, M. J., Morphology-dependent electrochemistry of cytochrome c at Au colloid-modified SnO<sub>2</sub> electrodes., *J. Am. Chem. Soc.* **1996**, 118, 1154–1157.
- 26 VARFOLOMEEV, S. D., KUROCHKIN, I. N., YAROLOV, A. I., Direct electron transfer effect biosensor. *Biosens. Bioelectron.*, **1996**, 11, 863–871.
- 27 GHINDILIS, A. L., ATANASOV, P., WILKINS, E., Enzyme-catalyzed direct electron transfer: Fundamentals and analytical applications., *Electroanalysis* **1997**, 9, 661–674.
- 28 ZHAO, J., HENKENS, R. W., STONEHUERNER, J., O'DALY, J. P., CRUMBLISS, A. L., Direct electron transfer at horseradish peroxidase-colloidal gold modified electrodes., *J. Electroanal. Chem.* **1992**, 327, 109–119.
- 29 LUO, X. L., XU, J. J., ZHANG, Q., YANG, G. J., CHEN, H. Y., Electrochemically deposited chitosan hydrogel for horseradish peroxidase immobilization through gold nanoparticles self-assembly., *Biosens. Bioelectron.* **2005**, 21, 190–196.
- 30 XU, S., HAN, X., A novel method to construct a third-generation biosensor: Self-assembling gold nanoparticles on thiol-functionalized poly(styrene-co-acrylic acid) nanospheres., *Biosens. Bioelectron.* **2004**, 19, 1117–1120.
- 31 WANG, L., WANG, E., A novel hydrogen peroxide sensor based on horseradish peroxidase immobilized on colloidal Au modified ITO electrode., *Electrochem. Commun.* **2004**, 6, 225–229.
- 32 JIA, J. B., WANG, B. Q., WU, A. G., CHENG, G. J., LI, Z., DONG, S. J., A

- method to construct a third-generation horseradish peroxidase biosensor: Self-assembling gold nanoparticles to three-dimensional sol-gel network., *Anal. Chem.* **2002**, *74*, 2217–2223.
- 33 XIAO, Y., JU, H. X., CHEN, H. Y., Hydrogen peroxide sensor based on horseradish peroxidase-labeled Au colloids immobilized on gold electrode surface by cysteamine monolayer., *Anal. Chim. Acta* **1999**, *391*, 73–82.
- 34 CRUMBLISS, A. L., PERINE, S. C., STONEHUERNER, J., TUBERGEN, K. R., ZHAO, J. G., HENKENS, R. W., O'DALY, J. P., Colloidal gold as a biocompatible immobilization matrix suitable for the fabrication of enzyme electrodes by electrodeposition., *Biotechnol. Bioeng.* **1992**, *40*, 483–490.
- 35 XU, X., LIU, S., JU, H., A novel hydrogen peroxide sensor via the direct electrochemistry of horseradish peroxidase immobilized on colloidal gold modified screen-printed electrode., *Sensors* **2003**, *3*, 350–360.
- 36 LEI, C. X., HU, S. Q., SHEN, G. L., YU, R. Q., Immobilization of horseradish peroxidase to a nano-Au monolayer modified chitosan-entrapped carbon paste electrode for the detection of hydrogen peroxide., *Talanta* **2003**, *59*, 981–988.
- 37 YEH, J. I., ZIMMT, M. B., ZIMMERMAN, A. L., Nanowiring of a redox enzyme by metallized peptides., *Biosens. Bioelectron.* **2005**, *21*, 973–978.
- 38 XIAO, Y., JU, H. X., CHEN, H. Y., Direct electrochemistry of horseradish peroxidase immobilized on a colloid/cysteamine-modified gold electrode., *Anal. Biochem.* **2000**, *278*(1), 22–28.
- 39 LEI, C. X., WANG, H., SHEN, G. L., YU, R. Q., Immobilization of enzymes on the nano-Au film modified glassy carbon electrode for the determination of hydrogen peroxide and glucose., *Electroanalysis* **2004**, *16*, 736–740.
- 40 ZHAO, J., O'DALY, J. P., HENKENS, R. W., STONEHUERNER, J., CRUMBLISS, A. L., A xanthine oxidase/colloidal gold enzyme electrode for amperometric biosensor applications., *Biosens. Bioelectron.* **1996**, *11*, 493–502.
- 41 AGUI, L., MANSO, J., YANEZ-SEDENO, P., PINGARRON, J. M., Amperometric biosensor for hypoxanthine based on immobilized xanthine oxidase on nanocrystal gold-carbon paste electrodes., *Sens. Actuators B* **2006**, *113*, 272–280.
- 42 LIU, Y. J., NIE, L. H., TAO, W. Y., YAO, S. Z., Amperometric study of Au-colloid function on xanthine biosensor based on xanthine oxidase immobilized in polypyrrole layer., *Electroanalysis* **2004**, *16*, 1271–1278.
- 43 MISCORIA, S. A., BARRERA, G. D., RIVAS, G. A., Enzymatic biosensor based on carbon paste electrodes modified with gold nanoparticles and polyphenol oxidase., *Electroanalysis* **2005**, *17*, 1578–1582.
- 44 CRUMBLISS, A. L., STONEHUERNER, J. G., HENKENS, R. W., ZHAO, J., O'DALY, J. P., A carrageenan hydrogel stabilized colloidal gold multienzyme biosensor electrode utilizing immobilized horseradish peroxidase and cholesterol oxidase/cholesterol esterase to detect cholesterol in serum and whole blood., *Biosens. Bioelectron.* **1993**, *8*, 331–337.
- 45 SHUMYANTSEVA, V. V., CARRARA, S., BAVASTRELLO, V., RILEY, D. J., BULKO, T. V., SKRYABIN, K. G., ARCHAKOV, A. I., NICOLINI, C., Direct electron transfer between cytochrome P450scc and gold nanoparticles on screen-printed rhodium-graphite electrodes., *Biosens. Bioelectron.* **2005**, *21*, 217–222.
- 46 YU, J., JU, H., Amperometric biosensor for hydrogen peroxide based on hemoglobin entrapped in titania sol-gel film., *Anal. Chim. Acta* **2003**, *486*, 209–216.
- 47 WANG, H. Y., GUAN, R., FAN, C. H., ZHU, D. X., LI, G. X., A hydrogen peroxide biosensor based on the bioelectrocatalysis of hemoglobin incorporated in a kieselguhr film., *Sens. Actuators B* **2002**, *84*, 214–218.
- 48 DAI, Z., LIU, S., JU, H., CHEN, H., Direct electron transfer and enzymatic activity of hemoglobin in a hexagonal mesoporous silica matrix., *Biosens. Bioelectron.* **2004**, *19*, 861–867.

- 49 GU, H. Y., YU, A. M., CHEN, H. Y., Direct electron transfer and characterization of hemoglobin immobilized on a Au colloid-cysteamine-modified gold electrode., *J. Electroanal. Chem.* **2001**, 516, 119–126.
- 50 ZHANG, J. D., OYAMA, M., A hydrogen peroxide sensor based on the peroxidase activity of hemoglobin immobilized on gold nanoparticles-modified ITO electrode., *Electrochim. Acta* **2004**, 50, 85–90.
- 51 ZHANG, L., JIANG, X., WANG, E., DONG, S., Attachment of gold nanoparticles to glassy carbon electrode and its application for the direct electrochemistry and electrocatalytic behavior of hemoglobin., *Biosens. Bioelectron.* **2005**, 21, 337–345.
- 52 YANG, W. W., LI, Y. C., BAI, Y., SUN, C. Q., Hydrogen peroxide biosensor based on myoglobin/colloidal gold nanoparticles immobilized on glassy carbon electrode by a Nafion film., *Sens. Actuators B* **2006**, 115, 42–48.
- 53 LIU, S. Q., JU, H. X., Electrocatalysis via direct electrochemistry of myoglobin immobilized on colloidal gold nanoparticles., *Electroanalysis* **2003**, 15, 1488–1493.
- 54 JU, H. X., LIU, S. Q., GE, B., LISDAT, F., SCHELLER, F. W., Electrochemistry of cytochrome c immobilized on colloidal gold modified carbon paste electrodes and its electrocatalytic activity., *Electroanalysis* **2002**, 14, 141–147.
- 55 FENG, J. J., ZHAO, G., XU, J. J., CHEN, H. Y., Direct electrochemistry and electrocatalysis of heme proteins immobilized on gold nanoparticles stabilized by chitosan., *Anal. Biochem.* **2005**, 342, 280–286.
- 56 LUO, X. L., XU, J. J., DU, Y., CHEN, H. Y., A glucose biosensor based on chitosan-glucose oxidase-gold nanoparticles biocomposite formed by one-step electrodeposition., *Anal. Biochem.* **2004**, 334, 284–289.
- 57 ZHANG, S. X., WANG, N., NIU, Y. M., SUN, C. Q., Immobilization of glucose oxidase on gold nanoparticles modified Au electrode for the construction of biosensor., *Sens. Actuators B* **2005**, 109, 367–374.
- 58 ZHANG, S. X., WANG, N., YU, H. J., NIU, Y., SUN, C. Q., Covalent attachment of glucose oxidase to an Au electrode modified with gold nanoparticles for use as glucose biosensor. *Bioelectrochemistry* **2005**, 67, 15–22.
- 59 PAN, M., GUO, X. S., CAI, Q., LI, G., CHEN, Y. Q., A novel glucose sensor system with Au nanoparticles based on microdialysis and coenzymes for continuous glucose monitoring., *Sens. Actuators A* **2003**, 108, 258–262.
- 60 MENA, M. L., YANEZ-SEDENO, P., PINGARRON, J. M., A comparison of different strategies for the construction of amperometric enzyme biosensors using gold nanoparticle-modified electrodes., *Anal. Biochem.* **2005**, 336, 20–27.
- 61 YANEZ-SEDENO, P., PINGARRON, J. M., Gold nanoparticle-based electrochemical biosensors., *Anal. Bioanal. Chem.* **2005**, 382, 884–886.
- 62 GOODING, J. J., HIBBERT, D. B., The application of alkanethiol self-assembled monolayers to enzyme electrodes., *Trends Anal. Chem.* **1999**, 18, 525–533.
- 63 GRABAR, K. C., FREEMAN, R. G., HOMMER, M. B., NATAN, M. J., Preparation and characterization of Au colloid monolayers., *Anal. Chem.* **1995**, 67, 735–743.
- 64 GRABAR, K. C., SMITH, P. C., MUSICK, M. D., DAVIS, J. A., WALTER, D. G., JACHSON, M. A., GUTHRIE, A. P., NATAN, M. J., Kinetic control of interparticle spacing in Au colloid-based surfaces: Rational nanometer-scale architecture., *J. Am. Chem. Soc.* **1996**, 118, 1148–1153.
- 65 BLONDER, R., SHEENEY, L., WILLNER, I., Three-dimensional redox-active layered composites of Au–Au, Ag–Ag and Au–Ag colloids., *Chem. Commun.* **1998**, 13, 1393–1394.
- 66 FISHESON, N., SHKROB, I., LEV, O., GUN, J., MODESTOV, A. D., Studies on charge transport in self-assembled

- gold-dithiol films: Conductivity, photoconductivity, and photoelectrochemical measurements., *Langmuir* **2001**, *17*, 403–412.
- 67 DORON, A., KATZ, E., WILLNER, I., Organization of Au colloids as monolayer films onto ITO glass surfaces: Application of the metal colloid films as base interfaces to construct redox-active monolayers., *Langmuir* **1995**, *11*, 1313–1317.
- 68 LEI, C. X., HU, S. Q., GAO, N., SHEN, G. L., YU, R. Q., An amperometric hydrogen peroxide biosensor based on immobilizing horseradish peroxidase to a nano-Au monolayer supported by sol-gel derived carbon ceramic electrode., *Bioelectrochemistry* **2004**, *65*, 33–39.
- 69 SHIPWAY, A. N., LAHAV, M., WILLNER, I., Nanostructured gold colloid electrodes., *Adv. Meterol.* **2000**, *12*, 993–998.
- 70 ZHONG, X., YUAN, R., CHAI, Y., LIU, Y., DAI, J., TANG, D., Glucose biosensor based on self-assembled gold nanoparticles and double-layer 2d-network (3-mercaptopropyl)-trimethoxysilane polymer onto gold substrate., *Sens. Actuators B* **2005**, *104*, 191–198.
- 71 PATOLSKY, F., GABRIEL, T., WILLNER, I., Controlled electrocatalysis by microperoxidase-11 and Au-nanoparticle superstructures on conductive supports., *J. Electroanal. Chem.* **1999**, *479*, 69–73.
- 72 BHARATHI, S., NOGAMI, M., IKEDA, S., Novel electrochemical interfaces with a tunable kinetic barrier by self-assembling organically modified silica gel and gold nanoparticles., *Langmuir* **2001**, *17*, 1–4.
- 73 DI, J. W., SHEN, C. P., PENG, S. H., TU, Y. F., LI, S. J., A one-step method to construct a third-generation biosensor based on horseradish peroxidase and gold nanoparticles embedded in silica sol-gel network on gold modified electrode., *Anal. Chim. Acta* **2005**, *553*, 196–200.
- 74 CAI, W. Y., XU, Q., ZHAO, X. N., ZHU, J. J., CHEN, H. Y., Porous gold-nanoparticle-CaCO<sub>3</sub> hybrid material: Preparation, characterization, and application for horseradish peroxidase assembly and direct electrochemistry., *Chem. Mater.* **2006**, *18*, 279–284.
- 75 LIU, S. Q., JU, H. X., Reagentless glucose biosensor based on direct electron transfer of glucose oxidase immobilized on colloidal gold modified carbon paste electrode., *Biosens. Bioelectron.* **2003**, *19*, 177–183.
- 76 LIU, S. Q., YU, J. H., JU, H. X., Renewable phenol biosensor based on a tyrosinase-colloidal gold modified carbon paste electrode., *J. Electroanal. Chem.* **2003**, *540*, 61–67.
- 77 XU, X. X., LIU, S. Q., LI, B., JU, H. X., Disposable nitrite sensor based on hemoglobin-colloidal gold nanoparticle modified screen-printed electrode., *Anal. Lett.* **2003**, *36*, 2427–2442.
- 78 LIU, S. Q., JU, H. X., Nitrite reduction and detection at a carbon paste electrode containing hemoglobin and colloidal gold., *Analyst* **2003**, *128*, 1420–1424.
- 79 CARRALERO, V., MENA, M. L., GONZALEZ-CORTES, A., YANEZ-SEDENO, P., PINGARRON, J. M., Development of a tyrosinase biosensor based on gold nanoparticles-modified glassy carbon electrodes: Application to the measurement of a bioelectrochemical polyphenols index in wines., *Anal. Chim. Acta* **2005**, *528*, 1–8.
- 80 GONZALEZ-GARCIA, M. B., FERNANDEZ-SANCHEZ, C., COSTA-GARCIA, A., Colloidal gold as an electrochemical label of streptavidin-biotin interaction., *Biosens. Bioelectron.* **2000**, *15*, 315–321.
- 81 VELEV, O. D., KALER, E. W., In situ assembly of colloidal particles into miniaturized biosensors., *Langmuir* **1999**, *25*, 3694–3698.
- 82 NIEMEYER, C. M., CEYHAN, B., DNA-directed functionalization of colloidal gold with proteins., *Angew. Chem. Int. Ed.* **2001**, *40*, 3685–3688.
- 83 THANH, N. T. K., ROSENZWEIG, Z., Development of an aggregation-based immunoassay for anti-protein A using gold nanoparticles., *Anal. Chem.* **2002**, *74*, 1624–1628.

- 84 KERMAN, K., MORITA, Y., TAKAMURA, Y., OZSOZ, M., TAMIYA, E., Modification of Escherichia coli single-stranded DNA binding protein with gold nanoparticles for electrochemical detection of DNA hybridization., *Anal. Chim. Acta* **2004**, 510, 169–174.
- 85 KVITEK, L., PRUCEK, R., The preparation and application of silver nanoparticles., *J. Mater. Sci.*, **2005**, in the press, available online, <http://dx.doi.org/10.2007/s10853-005-0789-2>.
- 86 LIU, T., ZHONG, J., GAN, X., FAN, C., LI, G., MATSUDA, N., Wiring electrons of cytochrome c with silver nanoparticles in layered films., *ChemPhysChem* **2003**, 4, 1364–1366.
- 87 REN, C. B., SONG, Y. H., LI, Z., ZHU, G. Y., Hydrogen peroxide sensor based on horseradish peroxidase immobilized on a silver nanoparticles/cysteamine/gold electrode., *Anal. Bioanal. Chem.* **2005**, 381, 1179–1185.
- 88 GAN, X., LIU, T., ZHONG, J., LIU, X. J., LI, G. X., Effect of silver nanoparticles on the electron transfer reactivity and the catalytic activity of myoglobin., *ChemPhysChem* **2004**, 5, 1686–1691.
- 89 GAN, X., LIU, T., ZHU, X. L., LI, G. X., An electrochemical biosensor for nitric oxide based on silver nanoparticles and hemoglobin., *Anal. Sci.* **2004**, 20, 1271–1275.
- 90 REN, X. L., MENG, X. W., CHEN, D., TANG, F., JIAO, J., Using silver nanoparticle to enhance current response of biosensor., *Biosens. Bioelectron.* **2005**, 21, 433–437.
- 91 REN, X. L., MENG, X. W., TANG, F. Q., Preparation of Ag–Au nanoparticle and its application to glucose biosensor., *Sens. Actuators B* **2005**, 110, 358–363.
- 92 ZHAO, S., ZHANG, K., SUN, Y. Y., SUN, C. Q., Hemoglobin/colloidal silver nanoparticles immobilized in titania sol–gel film on glassy carbon electrode: Direct electrochemistry and electrocatalysis., *Bioelectrochemistry* **2006**, 1, 10–15.
- 93 REYNOLDS, E. R., YACYNICH, A. M., Platinized carbon ultramicroelectrodes as glucose biosensors., *Electroanalysis* **1993**, 5, 405–411.
- 94 HARTL, A., SCHMICH, E., GARRIDO, J., HERNANDO, J., CATHARINO, S. C. R., WALTER, S., FEULNER, P., KROMKA, A., STEINMULLER, D., STUTZMANN, M., Protein-modified nanocrystalline diamond thin films for biosensor applications., *Nat. Mater.* **2004**, 3, 736–742.
- 95 OLIVIA, H., SARADA, B. V., HONDA, K., FUJISHIM, A., Continuous glucose monitoring using enzyme-immobilized platinized diamond microfiber electrodes., *Electrochim. Acta* **2004**, 49, 2069–2076.
- 96 ZHANG, F. F., WAN, Q., LI, C. X., ZHU, Z. Q., XIAN, Y. Z., JIN, L. T., YAMAMOTO, K., A novel glucose biosensor based on palladium nanoparticles and its application in detection of glucose level in urine., *Chin. J. Chem.* **2003**, 21, 1619–1623.
- 97 PAN, D., CHEN, J., YAO, S., NIE, L., XIA, J., TAO, W., Amperometric glucose biosensor based on immobilization of glucose oxidase in electropolymerized o-aminophenol film at copper-modified gold electrode., *Sens. Actuators B* **2005**, 104, 68–74.
- 98 XU, J. J., LUO, X. L., DU, Y., CHEN, H. Y., Application of MnO<sub>2</sub> nanoparticles as an eliminator of ascorbic acid interference to amperometric glucose biosensors., *Electrochem. Commun.* **2004**, 6, 1169–1173.
- 99 WANG, K., XU, J. J., CHEN, H. Y., Biocomposite of cobalt phthalocyanine and lactate oxidase for lactate biosensing with MnO<sub>2</sub> nanoparticles as an eliminator of ascorbic acid interference., *Sens. Actuators B* **2006**, 114, 1052–1058.
- 100 YIN, L. T., CHOU, J. C., CHUNG, W. Y., SUN, T. P., HSIUNG, K. P., HSIUNG, S. K., Glucose ENFET doped with MnO<sub>2</sub> powder., *Sens. Actuators B* **2001**, 76, 187–192.
- 101 LUO, X. L., XU, J. J., ZHAO, W., CHEN, H. Y., A novel glucose ENFET based on the special reactivity of MnO<sub>2</sub> nanoparticles., *Biosens. Bioelectron.*, **2004**, 19, 1295–1300.
- 102 ZHANG, Y., HE, P., HU, N., Horseradish peroxidase immobilized

- in TiO<sub>2</sub> nanoparticle films on pyrolytic graphite electrodes: Direct electrochemistry and bioelectrocatalysis, *Electrochim. Acta* **2004**, 49, 1981–1988.
- 103 YANG, Y., YANG, H., YANG, M., LIU, Y., SHEN, G., YU, R., Amperometric glucose biosensor based on a surface treated nanoporous ZrO<sub>2</sub>/chitosan composite film as immobilization matrix., *Anal. Chim. Acta* **2004**, 525, 213–220.
- 104 LIU, B., CAO, Y., CHEN, D., KONG, J., DENG, J., Amperometric biosensor based on a nanoporous ZrO<sub>2</sub> matrix. *Anal. Chim. Acta* **2003**, 478, 59–66.
- 105 ZHAO, G., FENG, J. J., XU, J. J., CHEN, H. Y., Direct electrochemistry and electrocatalysis of heme proteins immobilized on self-assembled ZrO<sub>2</sub> film., *Electrochem. Commun.* **2005**, 7, 724–729.
- 106 TOPOGLDIS, E., CASS, A. E. G., O'REGAN, B., DURRANT, J. R., Immobilisation and bioelectrochemistry of proteins on nanoporous TiO<sub>2</sub> and ZnO films., *J. Electroanal. Chem.* **2001**, 517, 20–27.
- 107 LI, Y. F., LIU, Z. M., LIU, Y. L., YANG, Y. H., SHEN, G. L., YU, R. Q., A mediator-free phenol biosensor based on immobilizing tyrosinase to ZnO nanoparticles., *Anal. Biochem.* **2006**, 349, 33–40.
- 108 KATZ, E., WILLNER, I., Biomolecule-functionalized carbon nanotubes: Applications in nanobioelectronics., *ChemPhysChem* **2004**, 5, 1084–1104.
- 109 MERKOCI, A., PUMERA, M., LLOPIS, X., PEREZ, B., VALLE, M. D., ALEGRET, S., New materials for electrochemical sensing VI: Carbon nanotubes., *Trends Anal. Chem.* **2005**, 24, 826–838.
- 110 RUBIANES, M. D., RIVAS, G. A., Enzymatic biosensors based on carbon nanotubes paste electrodes., *Electroanalysis* **2005**, 17, 73–78.
- 111 GONG, K. P., YAN, Y. M., ZHANG, M. N., SU, L., XIONG, S. X., MAO, L. Q., Enzymatic biosensors based on carbon nanotubes paste electrodes., *Anal. Sci.* **2005**, 21, 1383–1393.
- 112 LIN, Y. H., YANTASEE, W., WANG, J., Carbon nanotubes (CNTs) for the development of electrochemical biosensors., *Front. Biosci.* **2005**, 10, 492–505.
- 113 WOHLSTADTER, J. N., WILBUR, J. L., SIGAL, G. B., BIEBUYCK, H. A., BILLADEAU, M. A., DONG, L., FISCHER, A. B., GUDIBANDE, S. R., JAMEISON, S. H., KENTEN, J. H., LEGINUS, J., LELAND, J. K., MASSEY, R. J., WOHLSTADTER, S. J., Carbon nanotube-based biosensor., *Adv. Mater.* **2003**, 15, 1184–1187.
- 114 SOTIROPOULOU, S., CHANIOTAKIS, N. A., Carbon nanotube array-based biosensor., *Anal. Bioanal. Chem.* **2003**, 375, 103–105.
- 115 YE, J. S., WEN, Y., ZHANG, W. D., CUI, H. F., XU, G. Q., SHEU, F. S., Electrochemical biosensing platforms using phthalocyanine-functionalized carbon nanotube electrode., *J. Electroanal. Chem.* **2005**, 17, 89–96.
- 116 XU, J. Z., ZHU, J. J., WU, Q., HU, Z., CHEN, H. Y., An amperometric biosensor based on the coimmobilization of horseradish peroxidase and methylene blue on a carbon nanotubes modified electrode., *Electroanalysis* **2003**, 15, 219–224.
- 117 DRESSSELHAUS, M. S., DRESSSELHAUS, G., AVOURIS, P., Carbon nanotubes synthesis, structure, properties, and applications., *Fullerenes, Nanotubes, Carbon Nanostruct.* **2002**, 10(2), 181–182.
- 118 DAVIS, J. J., COLEMAN, K. S., AZAMIAN, B. R., BAGSHAW, C. B., GREEN, M. L. H., Chemical and biochemical sensing with modified single walled carbon nanotubes., *Chem. Eur. J.* **2003**, 9, 3732–3739.
- 119 BANKS, C. E., DAVIES, T. J., WILDGOOSE, G. G., COMPTON, R. G., Electrocatalysis at graphite and carbon nanotube modified electrodes: Edge-plane sites and tube ends are the reactive sites., *Chem. Comm.* **2005**, 7, 829–841.
- 120 WANG, S. G., ZHANG, Q., WANG, R., YOON, S. F., A novel multi-walled carbon nanotube-based biosensor for glucose detection., *Biochem. Biophys. Res. Commun.* **2003**, 311, 572–576.
- 121 YU, X., CHATTOPADHYAY, D., GALESKA, I., PAPADIMITRAKOPOULOS, F.,

- RUSLING, J. F., Peroxidase activity of enzymes bound to the ends of single-wall carbon nanotube forest electrodes., *Electrochem. Commun.* **2003**, 5, 408–411.
- 122 WANG, J., LI, M., SHI, Z., LI, N., GU, Z., Direct electrochemistry of cytochrome c at a glassy carbon electrode modified with single-wall carbon nanotubes., *Anal. Chem.* **2002**, 74, 1993–1997.
- 123 CAI, C., CHEN, J., Direct electron transfer and bioelectrocatalysis of hemoglobin at a carbon nanotube electrode., *Anal. Biochem.* **2004**, 325, 285–292.
- 124 ZHAO, Y., ZHANG, W., CHEN, H., LUO, Q., LI, S., Direct electrochemistry of horseradish peroxidase at carbon nanotube powder microelectrode., *Sens. Actuators B* **2002**, 87, 168–172.
- 125 SOTIROPOULOU, S., GAVALAS, V., VAMVAKAKI, V., CHANIOTAKIS, N. A., Novel carbon materials in biosensor systems., *Biosens. Bioelectron.* **2003**, 18, 211–215.
- 126 ZHAO, G. C., YIN, Z. Z., WEI, X. W., A reagentless biosensor of nitric oxide based on direct electron transfer process of cytochrome c on multi-walled carbon nanotube., *Front. Biosci.* **2005**, 10, 2005–2010.
- 127 ZHAO, G. C., ZHANG, L., WEI, X. W., YANG, Z. S., Myoglobin on multi-walled carbon nanotubes modified electrode: Direct electrochemistry and electrocatalysis., *Electrochem. Commun.* **2003**, 5, 825–829.
- 128 ZHAO, L., LIU, H., HU, N., Electroactive films of heme protein-coated multiwalled carbon nanotubes., *J. Colloid Interface Sci.* **2006**, 296, 204–211.
- 129 QI, H., ZHANG, C., LI, X., Amperometric third-generation hydrogen peroxide biosensor incorporating multiwall carbon nanotubes and hemoglobin., *Sens. Actuators B* **2006**, 114, 364–370.
- 130 LIU, Y., WANG, M., ZHAO, F., XU, Z., DONG, S., The direct electron transfer of glucose oxidase and glucose biosensor based on carbon nanotubes/chitosan matrix., *Biosens. Bioelectron.* **2005**, 21, 984–988.
- 131 YAMAMOTO, K., SHI, G., ZHOU, T. S., XU, F., XU, J. M., KATO, T., JIN, J. Y., JIN, L., Study of carbon nanotubes-HRP modified electrode and its application for novel on-line biosensors., *Analyst* **2003**, 128, 249–254.
- 132 ZHAO, Y. D., BI, Y. H., ZHANG, W. D., LUO, Q. M., The interface behavior of hemoglobin at carbon nanotube and the detection for H<sub>2</sub>O<sub>2</sub>., *Talanta* **2005**, 65, 489–494.
- 133 AZAMIAN, B. R., DAVIS, J. J., COLEMAN, K. S., BAGSHAW, C., GREEN, M. L. H., Bioelectrochemical single-walled carbon nanotubes., *J. Am. Chem. Soc.* **2002**, 64, 124–126.
- 134 DAI, Y. Q., SHIU, K. K., Glucose biosensor based on multi-walled carbon nanotube modified glassy carbon electrode., *Electroanalysis* **2004**, 16, 1697–1703.
- 135 GAO, M., DAI, L., WALLACE, G., Glucose sensors based on glucose-oxidase-containing polypyrrole/aligned carbon nanotube coaxial nanowire electrodes., *Synth. Met.* **2003**, 137, 1393–1394.
- 136 LOH, K. P., ZHAO, S. L., ZHANG, W. D., Diamond and carbon nanotube glucose sensors based on electro-polymerization., *Diamond Relat. Mater.* **2004**, 13, 1075–1079.
- 137 WANG, J., MUSAMEH, M., Carbon-nanotubes doped polypyrrole glucose biosensor., *Anal. Chim. Acta* **2005**, 539, 209–213.
- 138 ZHAO, G. C., ZHANG, L., WEI, X. W., An unmediated H<sub>2</sub>O<sub>2</sub> biosensor based on the enzyme-like activity of myoglobin on multi-walled carbon nanotubes., *Anal. Biochem.* **2004**, 329, 160–161.
- 139 ZHANG, L., ZHAO, G. C., WEI, X. W., YANG, Z. S., A nitric oxide biosensor based on myoglobin adsorbed on multi-walled carbon nanotubes., *Electroanalysis* **2005**, 17, 630–634.
- 140 ZHAO, G. C., YIN, Z. Z., ZHANG, L., WEI, X. W., Direct electrochemistry of cytochrome c on a multi-walled carbon nanotubes modified electrode

- and its electrocatalytic activity for the reduction of  $\text{H}_2\text{O}_2$ ., *Electrochem. Commun.* **2005**, 7, 256–260.
- 141 GOODING, J. J., WIBOWO, R., LIU, J., YANG, W., LOSIC, D., ORBONS, S., MEARNES, F. J., SHAPTER, J. G., HIBBERT, D. B., Protein electrochemistry using aligned carbon nanotube arrays., *J. Am. Chem. Soc.* **2003**, 125, 9006–9007.
- 142 WANG, M. K., SHEN, Y., LIU, Y., WANG, T., ZHAO, F., LIU, B. F., DONG, S. J., Direct electrochemistry of microperoxidase-11 using carbon nanotube modified electrodes., *J. Electroanal. Chem.* **2005**, 578, 121–127.
- 143 WANG, L., YUAN, Z., Direct electrochemistry of xanthine oxidase at a gold electrode modified with single-wall carbon nanotubes., *Anal. Sci.* **2004**, 20, 635–638.
- 144 GUISEPPI-ELI, A., LEI, C., BAUGHMAN, R. H., Direct electron transfer of glucose oxidase on carbon nanotubes., *Nanotechnology* **2002**, 13, 559–564.
- 145 XUE, H., SUN, W., HE, B., SHEN, Z., Single-wall carbon nanotubes as immobilization material for glucose biosensor., *Synth. Met.* **2003**, 135, 831–832.
- 146 LI, J., WANG, Y. B., QIU, J. D., SUN, D. C., XIA, X. H., Biocomposites of covalently linked glucose oxidase on carbon nanotubes for glucose biosensor., *Anal. Bioanal. Chem.* **2005**, 383, 918–922.
- 147 WITHEY, G. D., LAZARECK, A. D., TZOLOV, M. B., YINA, A., AICH, P., YEH, J. I., XUA, J. M., Ultra-high redox enzyme signal transduction using highly ordered carbon nanotube array electrodes., *Biosens. Bioelectron.* **2006**, 21, 1560–1565.
- 148 LIU, J., CHOU, A., RAHMAT, W., PADDON-ROW, M. N., GOODING, J. J., Achieving direct electrical connection to glucose oxidase using aligned single walled carbon nanotube arrays., *Electroanalysis* **2005**, 17, 38–46.
- 149 PATOLSKY, F., WEIZMANN, Y., WILLNER, I., Long-range electrical contacting of redox enzymes by SWCNT connectors., *Angew. Chem. Int. Ed.* **2004**, 43, 2113–2117.
- 150 WANG, J., MUSAMEH, M., Carbon nanotube/teflon composite electrochemical sensors and biosensors., *Anal. Chem.* **2003**, 75, 2075–2079.
- 151 SALIMIA, A., COMPTON, R. G., HALLAJ, R., Glucose biosensor prepared by glucose oxidase encapsulated sol-gel and carbon-nanotube-modified basal plane pyrolytic graphite electrode., *Anal. Biochem.* **2004**, 333, 49–56.
- 152 HUANG, J., YANG, Y., SHI, H., SONG, Z., ZHAO, Z., ANZAI, J. I., OSA, T., CHEN, Q., Multi-walled carbon nanotubes-based glucose biosensor prepared by a layer-by-layer technique., *Mater. Sci. Eng. C* **2006**, 26, 113–117.
- 153 ZHAO, H., JU, H. X., Multilayer membranes for glucose biosensing via layer-by-layer assembly of multiwalled carbon nanotubes and glucose oxidase., *Anal. Biochem.* **2006**, 350, 138–144.
- 154 LIU, G., LIN, Y., Amperometric glucose biosensor based on self-assembling glucose oxidase on carbon nanotubes., *Electrochem. Commun.* **2006**, 8, 251–256.
- 155 WANG, J., MUSAMEH, M., Carbon nanotube screen-printed electrochemical sensors., *Analyst* **2004**, 129, 1–2.
- 156 GUAN, W. J., LI, Y., CHEN, Y. Q., ZHANG, X. B., HU, G. Q., Glucose biosensor based on multi-wall carbon nanotubes and screen printed carbon electrodes., *Biosens. Bioelectron.* **2005**, 21, 508–512.
- 157 LUQUE, G. L., FERREYRA, N. F., RIVAS, G. A., Glucose biosensor based on the use of a carbon nanotube paste electrode modified with metallic particles., *Microchim. Acta* **2006**, 152, 277–283.
- 158 MALINSKI, K., TAHA, Z., Nitric oxide release from a single cell measured in situ by a porphyrinic-based microsensor., *Nature* **1992**, 352, 676–678.
- 159 TROYER, K. P., WIGHTMAN, R. M., Dopamine transport into a single cell in a picoliter., *Vial. Anal. Chem.* **2002**, 74, 5370–5375.



- 160 BRITTO, P. J., SANTHANAM, K. S. V., RUBIO, A., ALONSO, J. A., AJAYAN, P. M., Improved charge transfer at carbon nanotube electrodes., *Adv. Mater.* **1999**, 11, 154–157.
- 161 MENON, V. P., MARTIN, C. R., Fabrication and evaluation of nanoelectrode ensembles., *Anal. Chem.* **1995**, 67, 1920–1928.
- 162 TU, Y., LIN, Y. H., REN, Z. F., Nanoelectrode arrays based on low site density aligned carbon nanotubes., *Nano Lett.* **2003**, 3, 107–109.
- 163 LIN, Y., LU, F., TU, Y., REN, Z., Glucose biosensors based on carbon nanotube nanoelectrode ensembles., *Nano Lett.* **2004**, 4, 191–195.
- 164 TU, Y., HUANG, Z. P., WANG, D. Z., WEN, J. G., REN, Z. F., Growth of aligned carbon nanotubes with controlled site density., *Appl. Phys. Lett.* **2002**, 80, 4018–4020.
- 165 TANG, H., CHEN, J., YAO, S., NIE, L., DENG, G., KUANG, Y., Amperometric glucose biosensor based on adsorption of glucose oxidase at platinum nanoparticle-modified carbon nanotube electrode., *Anal. Biochem.* **2004**, 331, 89–97.
- 166 WANG, J., MUSAMEH, M., Enzyme-dispersed carbon-nanotube electrodes: A needle microsensor for monitoring glucose., *Analyst* **2003**, 128, 1382–1385.
- 167 ZHAO, Q., ZHAN, D. P., MA, H. Y., ZHANG, M. Q., ZHAO, Y. F., JING, P., ZHU, Z. W., WAN, X. H., SHAO, Y. H., ZHUANG, Q. K., Direct proteins electrochemistry based on ionic liquid mediated carbon nanotube modified glassy carbon electrode., *Front. Biosci.* **2002**, 7, 752–764.
- 168 PEREZ, B., PUMERA, M., DEL VALLE, M., MERKOCI, A., ALEGRET, S., Glucose biosensor based on carbon nanotube epoxy composites., *J. Nanosci. Nanotechnol.* **2005**, 5, 1694–1698.
- 169 TSAL, Y. C., LI, S. C., CHEN, J. M., Cast thin film biosensor design based on a nafion backbone, a multiwalled carbon nanotube conduit, and a glucose oxidase function., *Langmuir* **2005**, 21, 3653–3658.
- 170 YANG, M., YANG, Y., LIU, Y., SHEN, G., YU, R., Platinum nanoparticles-doped sol-gel carbon nanotubes composite electrochemical sensors and biosensors., *Biosens. Bioelectron.* **2006**, 21, 1125–1131.
- 171 YANG, M., JIANG, J., YANG, Y., CHEN, X., SHEN, G., YU, R., Carbon nanotube cobalt hexacyanoferrate nanoparticle-biopolymer system for the fabrication of biosensors., *Biosens. Bioelectron.* **2006**, 21, 1791–1797.
- 172 KANDIMALLA, V. B., TRIPATHI, V. S., JU, H. X., A conductive ormosil encapsulated with ferrocene conjugate and multiwall carbon nanotubes for biosensing application., *Biomaterials* **2006**, 27, 1167–1174.
- 173 TRIPATHI, V. S., KANDIMALLA, V. B., JU, H. X., Amperometric biosensor for hydrogen peroxide based on ferrocene-bovine serum albumin and multiwall carbon nanotube modified ormosil composite., *Biosens. Bioelectron.* **2006**, 21, 1529–1535.
- 174 CAI, C., CHEN, J., Direct electron transfer of glucose oxidase promoted by carbon nanotubes., *Anal. Biochem.* **2004**, 332, 75–83.
- 175 WANG, J., MUSAMEH, M., LIN, Y., Solubilization of carbon nanotubes by nafion toward the preparation of amperometric biosensors., *J. Am. Chem. Soc.* **2003**, 125, 2408–2409.
- 176 HRAPOVIC, S., LIU, Y. L., MALE, K. B., LUONG, J. H. T., Electrochemical biosensing platforms using platinum nanoparticles and carbon nanotubes., *Anal. Chem.* **2004**, 76, 1083–1088.
- 177 WU, J., ZOU, Y., GAO, N., JIANG, J., SHEN, G., YU, R., Electrochemical performances of C/Fe nanocomposite and its use for mediator-free glucose biosensor preparation., *Talanta* **2005**, 68, 12–18.
- 178 SINANI, V. A., KOKTYSH, D. S., YUN, B. G., MATTS, R. L., PAPPAS, T. C., MOTAMEDI, M., THOMAS, S. N., KOTOV, N. A., Collagen coating promotes biocompatibility of semiconductor nanoparticles in stratified LBL films., *Nano Lett.* **2003**, 3, 1177–1182.

- 179 LI, M., HE, P. L., ZHANG, Y., HU, N. F., An electrochemical investigation of hemoglobin and catalase incorporated in collagen films., *Biochim. Biophys. Acta* **2005**, 1749, 43–51.
- 180 ZHANG, F. F., WAN, Q., WANG, X. L., SUN, Z. D., ZHU, Z. Q., XIAN, Y. Z., JIN, L. T., YAMAMOTO, K., Amperometric sensor based on ferrocene-doped silica nanoparticles as an electron transfer mediator for the determination of glucose in rat brain coupled to in vivo microdialysis., *J. Electroanal. Chem.* **2004**, 571, 133–138.
- 181 BELLEZZA, F., CIPICIANI, A., COSTANTINO, U., NICOLIS, S., Catalytic activity of myoglobin immobilized on zirconium phosphonates., *Langmuir* **2004**, 20, 5019–5025.
- 182 FENG, J. J., XU, J. J., CHEN, H. Y., Synergistic effect of zirconium phosphate and Au nanoparticles on direct electron transfer of hemoglobin on glassy carbon electrode., *J. Electroanal. Chem.* **2005**, 585, 44–50.
- 183 LIU, Z. M., YANG, Y., WANG, H., LIU, Y. L., SHEN, G. L., YU, R. Q., A hydrogen peroxide biosensor based on nano-Au/PAMAM dendrimer/cystamine modified gold electrode., *Sens. Actuators B* **2005**, 106, 394–400.
- 184 LI, X. L., WU, J., GAO, N., SHEN, G. L., YU, R. Q., Electrochemical performance of L-cysteine–goldparticle nanocomposite electrode interface as applied to preparation of mediator-free enzymatic biosensors., *Sens. Actuators B* **2006**, 177, 35–42.
- 185 MICHALET, X., PINAUD, F. F., BENTOLILLA, L. A., TSAY, J. M., DOOSE, S., LI, J. J., SUNDARESAN, G., WU, A. M., GAMBHIR, S. S., WEISS, S., Quantum dots for livecells, in vivo imaging, and diagnostics., *Science* **2005**, 307, 538–544.
- 186 WANG, Y., TANG, Z., KOTOV, N. A., Bioapplication of nanosemiconductors., *Mater. Today* **2005**, 8, 20–31.
- 187 MARINELLA, G., SANDROS, D. G., BENSON, D. E., A modular nanoparticle-based system for reagentless small molecule biosensing., *J. Am. Chem. Soc.* **2005**, 127, 12 198–12 199.
- 188 MATTOUSSI, H., MAURO, J. M., GOLDMAN, E. R., ANDERSON, G. P., SUNDAR, V. C., MIKULEC, F. V., BAWENDI, M. G., Self-assembly of CdSe-ZnS quantum dot bioconjugates using an engineered recombinant protein., *J. Am. Chem. Soc.* **2000**, 122, 12 142–12 150.
- 189 GOLDMAN, E. R., MEDINTZ, I. L., WHITLEY, J. L., HAYHURST, A., UYEDA, H. T., DESCHAMPS, J. R., LASSMAN, M. E., MATTOUSSI, H., A hybrid quantum dot-antibody fragment fluorescence resonance energy transfer-based TnT sensor., *J. Am. Chem. Soc.* **2005**, 127, 6744–6751.
- 190 CURRI, M. L., AGOSTIAN, A., LEO, G., MALLARDI, A., COSMA, P., MONICA, M. D., Development of a novel enzyme/semiconductor nanoparticles system for biosensor application., *Mater. Sci. Eng. C* **2002**, 22, 449–452.
- 191 HUANG, Y. X., ZHANG, W. J., XIAO, H., LI, G. X., An electrochemical investigation of glucose oxidase at a CdS nanoparticles modified electrode., *Biosens. Bioelectron.* **2005**, 21, 817–821.
- 192 ZHOU, H., GAN, X., LIU, T., YANG, Q. L., LI, G. X., Effect of nano cadmium sulfide on the electron transfer reactivity and peroxidase activity of hemoglobin., *J. Biochem. Biophys. Methods* **2005**, 64, 38–45.
- 193 VASTARELLA, W., NICASTRI, R., Enzyme/semiconductor nanoclusters combined systems for novel amperometric biosensors., *Talanta* **2005**, 66, 627–633.
- 194 PARDO-YISSAR, V., KATZ, E., WASSERMAN, J., WILLNER, I., Acetylcholine esterase-labeled CdS nanoparticles on electrodes: Photoelectrochemical sensing of the enzyme inhibitors., *J. Am. Chem. Soc.* **2003**, 125, 622–623.
- 195 ZAYATS, M., KHARITONOV, A. B., POGORELOVA, S. P., LIUBASHEVSKI, O., KATZ, E., WILLNER, I., Probing photoelectrochemical processes in Au-CdS nanoparticle arrays by surface

- plasmon resonance: Application for the detection of acetylcholine esterase inhibitors., *J. Am. Chem. Soc.* **2003**, 125, 16 006–16 014.
- 196 ZHOU, H., GAN, X., WANG, J., ZHU, X., LI, G., Hemoglobin-based hydrogen peroxide biosensor tuned by the photovoltaic effect of nano titanium dioxide., *Anal. Chem.* **2005**, 77, 6102–6104.
- 197 KATZ, E., WILLNER, I., Switching of directions of bioelectrocatalytic currents and photocurrents at electrode surfaces by using hydrophobic magnetic nanoparticles., *Angew. Chem. Int. Ed.* **2005**, 44, 4791–4794.
- 198 ZHAO, G., XU, J. J., CHEN, H. Y., Fabrication, characterization of Fe<sub>3</sub>O<sub>4</sub> multilayer film and its application in promoting direct electron transfer of hemoglobin., *Electrochem. Commun.* **2006**, 8, 148–154.
- 199 HIRSCH, R., KATZ, E., WILLNER, I., Magneto-switchable bioelectrocatalysis., *J. Am. Chem. Soc.* **2000**, 122, 12 053–12 054.
- 200 LIU, Z., LIU, Y., YANG, H., YANG, Y., SHEN, G., YU, R., A phenol biosensor based on immobilizing tyrosinase to modified core-shell magnetic nanoparticles supported at a carbon paste electrode., *Anal. Chim. Acta* **2005**, 533, 3–9.
- 201 LIN, V. S., MOTESHAREI, K., DANCIL, K. P., SAILOR, M. J., GHADIRI, M. R., A porous silicon-based optical interferometric biosensor., *Science* **1997**, 278, 840–843.
- 202 DI FRANCA, G., QUERCIA, L., LA FERRARA, S., MANZO, S., CHIAVARINI, S., CERULLO, F., DE FILIPPO, F., LA FERRARA, V., MADDALENA, P., VITIELLO, R., *Proceedings of the 2nd Workshop on Chemical Sensors and Biosensors*, AMZZEI, F. ET AL. (eds.), Enea Casaccia, Rome, **1999**, pp. 18–19.
- 203 THUST, M., SCHOENING, M. J., FROHNHOFF, S., ARENS-FISCHER, R., KORDOS, P., LUETH, H., Porous silicon as a substrate material for potentiometric biosensors., *Meas. Sci. Technol.* **1996**, 7, 26–29.
- 204 REDDY, R. R., CHADHA, A., BHATTACHARYA, E., Porous silicon based potentiometric triglyceride biosensor., *Biosens. Bioelectron.* **2001**, 16, 313–317.
- 205 REDDY, R. R. K., BASU, I., BHATTACHARYA, E., CHADHA, A., Estimation of triglycerides by a porous silicon based potentiometric biosensor., *Curr. Appl. Phys.* **2003**, 3, 155–161.
- 206 SCHONING, M. J., KUROWSKI, A., THUST, M., KORDOS, P., SCHULTZE, J. W., LUTH, H., Capacitive microsensors for biochemical sensing based on porous silicon technology., *Sens. Actuators B* **2000**, 64, 59–64.
- 207 LIN, Z., FANGQIONG, T., JINSUO, Y., LONG, J., Preparation of glucose oxidase electrode containing hydrophobic silica nanoparticles by the sol-gel method., *Sci. Chin.* **1995**, 38, 1434–1438.
- 208 YANG, H., ZHU, Y., A high performance glucose biosensor enhanced via nanosized SiO<sub>2</sub>., *Anal. Chim. Acta* **2005**, 554, 92–97.
- 209 LUO, X. L., XU, J. J., ZHAO, W., CHEN, H. Y., A glucose biosensor based on ENFET doped with SiO<sub>2</sub> nanoparticles., *Sens. Actuators B* **2004**, 97, 249–255.
- 210 CUI, Y., WEI, Q., PARK, H., LIEBER, C. M., Nanowire nanosensors for highly sensitive and selective detection of biological and chemical species., *Science* **2001**, 293, 1289–1292.
- 211 GAO, Z. Q., XIE, F., SHARIFF, M., ARSHAD, M., YING, J. Y., A disposable glucose biosensor based on diffusional mediator dispersed in nanoparticulate membrane on screen-printed carbon electrode., *Sens. Actuators B.* **2005**, 111–112, 339–346.
- 212 MARC, D., SOPHIE, D. C., Immobilisation of glucose oxidase within metallic nanotubes arrays for application to enzyme biosensors., *Biosens. Bioelectron.* **2003**, 18, 943–951.
- 213 MIAO, Y. Q., QI, M., ZHAN, S. Z., HE, N. Y., WANG, J., YUAN, C. W., Construction of a glucose biosensor immobilized with glucose oxidase in the film of polypyrrole nanotubules., *Anal. Lett.* **1999**, 32, 1287–1299.
- 214 MORRIN, A., NGAMNA, O., KILLARD, A. J., MOULTON, S. E., SMYTH, M. R.,

- WALLACE, G. G., An amperometric enzyme biosensor fabricated from polyaniline nanoparticles., *Electroanalysis* **2005**, *17*, 423–429.
- 215 ZHOU, H., CHEN, H., LUO, S., CHEN, J., WEI, W., KUANG, Y., Glucose biosensor based on platinum microparticles dispersed in nano-fibrous polyaniline., *Biosens. Bioelectron.* **2005**, *20*, 1305–1311.
- 216 GONG, X., MILIC, T., XU, C., BATTEAS, J. D., DRAIN, C. M., Preparation and characterization of porphyrin nanoparticles., *J. Am. Chem. Soc.* **2002**, *124*, 14290–14291.
- 217 CHEN, H. Z., PAN, C., WANG, M., Characterization and photoconductivity study of tiopc nanoscale particles prepared by liquid phase direct reprecipitation., *NanoStruct. Mater.* **1999**, *11*(4), 523–530.
- 218 WANG, Y., DENG, K., GUI, L., TANG, Y., ZHOU, J., CAI, L., QIU, J., REN, D., WANG, Y., Preparation and characterization of nanoscopic organic semiconductor of oxovanadium phthalocyanine., *J. Colloid Interface Sci.* **1999**, *213*, 270–272.
- 219 JOSHI, K. A., TANG, J., HADDON, R., WANG, J., CHEN, W., MULCHANDANI, A., A disposable biosensor for organophosphorus nerve agents based on carbon nanotubes modified thick film strip electrode., *Electroanalysis* **2005**, *17*, 54–58.
- 220 GAVALAS, V. G., LAW, S. A., BALL, J. C., ANDREWS, R., BACHAS, L. G., Carbon nanotube aqueous sol-gel composites: Enzyme-friendly platforms for the development of stable biosensors., *Anal. Biochem. Biophys. Res. Commun.* **2004**, *329*, 247–252.
- 221 XU, Z., CHEN, X., QU, X., JIA, J., DONG, S., Single-wall carbon nanotube-based voltammetric sensor and biosensor., *Biosens. Bioelectron.* **2004**, *20*, 579–584.
- 222 HUANG, J., SONG, Z., LI, J., YANG, Y., SHI, H. B., WU, B. Y., ANZAI, J. I., OSA, T., CHEN, Q., A highly-sensitive L-lactate biosensor based on sol-gel film combined with multi-walled carbon nanotubes (MWCNTs) modified electrode., *Mater. Sci. Eng. C* **2006**, in the press, available online, <http://dx.doi.org/10.1016/j.msec.2006.01.001>.
- 223 ROCHETTE, J. F., SACHER, E., MEUNIER, M., LUONG, J. H. T., A mediatorless biosensor for putrescine using multiwalled carbon nanotubes. *Anal. Biochem.* **2005**, *336*, 305–311.
- 224 YAO, D. S., CAO, H., WEN, S., LIU, D. L., BAI, Y., ZHENG, W. J., A novel biosensor for sterigmatocystin constructed by multi-walled carbon nanotubes (MWNT) modified with aflatoxin–detoxifzyme (ADTZ)., *Bioelectrochemistry* **2005**, *68*, 131–138.
- 225 SONG, Z., HUANG, J. D., WU, B. Y., SHI, H. B., ANZAI, J. I., CHEN, Q., Amperometric aqueous sol-gel biosensor for low-potential stable choline detection at multi-wall carbon nanotube modified platinum electrode., *Sens. Actuators B* **2006**, *115*, 626–633.
- 226 TAN, X. C., LI, M. J., CAI, P. X., LUO, L. J., ZOU, X. Y., An amperometric cholesterol biosensor based on multiwalled carbon nanotubes and organically modified sol-gel/chitosan hybrid composite film., *Anal. Biochem.* **2005**, *337*, 111–120.
- 227 ANTIOCHIA, R., LAVAGNINI, I., PASTORE, P., MAGNO, F., A comparison between the use of a redox mediator in solution and of surface modified electrodes in the electrocatalytic oxidation of nicotinamide adenine dinucleotide., *Bioelectrochemistry* **2004**, *64*, 157–163.
- 228 ZHANG, M., SMITH, A., GORSKI, W., Carbon nanotube-chitosan system for electrochemical sensing based on dehydrogenase enzymes., *Anal. Chem.* **2004**, *76*, 5045–5050.
- 229 ZHANG, M., GORSKI, W., Electrochemical sensing platform based on the carbon nanotubes/redox mediators-biopolymer system., *J. Am. Chem. Soc.* **2005**, *127*, 2058–2059.
- 230 SALIMI, A., NOORBAKSHSH, A., GHADERMARZ, M., Direct electrochemistry and electrocatalytic activity of catalase incorporated onto multiwall carbon nanotubes-modified glassy carbon electrode., *Anal. Biochem.* **2005**, *344*, 16–24.

- 231 WANG, L., WANG, J. X., ZHOU, F. M., Direct electrochemistry of catalase at a gold electrode modified with single-wall carbon nanotubes. *Electroanalysis* **2004**, 16, 627–632.
- 232 LIU, Y., WANG, M., ZHAO, F., GUO, Z., CHEN, H., DONG, S., Direct electron transfer and electrocatalysis of microperoxidase immobilized on nanohybrid film., *J. Electroanal. Chem.* **2005**, 581, 1–10.
- 233 LIU, Y., QU, X. H., GUO, H. W., CHEN, H. J., LIU, B. F., DONG, S., Facile preparation of amperometric laccase biosensor with multifunction based on the matrix of carbon nanotubes–chitosan composite., *Biosens. Bioelectron.* **2006**, 21, 2195–2201.
- 234 WEBER, J., KUMARC, A., KUMAR, A., BHANSALI, S., Novel lactate and pH biosensor for skin and sweat analysis based on single walled carbon nanotubes., *Sens. Actuators B* **2006**, 117, 308–313.
- 235 LI, G., LIAO, J. M., HU, G. Q., MA, N. Z., WU, P. J., Study of carbon nanotube modified biosensor for monitoring total cholesterol in blood., *Biosens. Bioelectron.* **2005**, 20, 2140–2144.

## 11

### Biomimetic Nanosensors

Raz Jelinek and Sofiya Kolusheva

#### 11.1

##### Introduction

Within the burgeoning field of nanotechnology, *bionanotechnology* is an important area. Bionanotechnology is generally defined as the ability to produce biological devices and materials through molecular manipulation and specific control of the physical, chemical and biological properties of the materials employed. The goals of this increasingly visible discipline focus on the creation of functional systems that could be employed in electronic circuitry and devices, advanced materials, biomedical devices, sensors, and others. Many excellent reviews have been published in recent years on subjects at the interface between biology and nanotechnology, reflecting the increasing interest in its potential for addressing diverse scientific and technological challenges [1].

In the field of *sensor* research and development, bionanotechnology is poised to make significant contributions, and has the potential to radically alter the way sensors are designed, constructed, and implemented. As a rule of thumb, the requirements for miniaturization are ever present and are often critical in sensor design. Accordingly, utilizing bio-inspired concepts and technical approaches and introducing biologically-based detection technologies have already had considerable impact in biosensor development. In particular, the ability to harness molecular recognition in the *literal* sense – employing fewer and fewer recognition units in sensor devices – could revolutionize the way biosensors operate. Several reviews on varied aspects and exciting developments in this field have been published recently [2–6].

The present chapter discusses the nascent but rapidly expanding field of nanobiosensors, putting particular emphasis on the way concepts and methodologies borrowed from the biological world – termed “biomimetics” – contribute and shape the chemical/physical characteristics of sensor devices. Put the other way around – we have also summarized here reports depicting nanosensors designed to analyze biological and cellular systems without interference in their functions or structures. Such goals are sometimes satisfied by nanosensor assemblies that mimic certain components within the biological or cellular system investigated.

*Biomimetic* nanosensors are referred to in a rather broad sense, including various systems and applications that can be depicted as “nanotechnology”, and focusing on the interface between biology and chemistry, physics, or engineering. Similarly, “biomimetic sensors” depicted here represent important concepts, design criteria, or molecular targets that are “biological”, but include innovative components from other disciplines. The explosive growth of publications that touch in different ways on the subject of this chapter (and due to space limitations) necessitated summarizing only selected studies.

Thematically, this chapter is organized according to the roles played by biology and biomimetic assemblies in sensing devices, and mirroring this – the development of nanotechnology-based (or nanotechnology-inspired) sensing of biological and cellular systems. Specifically, Section 11.2 focuses on the description of biosensing applications relying on nanostructures, such as nanoparticles and nanotubes, for studying and detection of biological systems. Emphasis in this section is on the *nanostructures* and how their unique physicochemical properties contribute to bio-sensor designs. The spotlight in Section 11.3 is rather on biological (and cellular) systems, and the solutions nanotechnology offers to detect and elucidate molecular events in those assemblies. Section 11.4 summarizes the contribution of biological molecules as building blocks and structural components in biomimetic nano-scale sensors. Finally, Section 11.5 discusses the increasing prominence of nano-biotechnology in biomedical diagnosis. Certain overlap exists among the topics, primarily due to the interchanging roles of the sensors and biological molecules in many bio-inspired devices and applications.

## 11.2

### Nanostructures in Biosensor Design

For such a young scientific endeavor, nanotechnology has already demonstrated a noticeable role in biosensor research and development. The contributions of nanotechnology can be roughly divided between the more “conceptual” impact – pointing and demonstrating new approaches and models for biosensor design – and the practical utilization of novel or superior physicochemical properties of nanostructures in certain applications. This subsection will discuss examples for both aspects of biomimetic nanotechnology in sensors.

One of the most important recent “meeting points” between nanotechnology and the biological world has been the demonstration that nanoparticles (NPs) can be successfully incorporated and used for detection and imaging biological assemblies and cell systems. Semiconductor nanocrystals or “quantum dots”, in particular, have become an important tool in this field. The concept underlying the use of quantum dots, particularly for biological and cellular imaging, is simple and elegant (Fig. 11.1). Essentially, NPs with different sizes and compositions exhibit distinct optical properties (mainly fluorescence or luminescence) [7, 8]. NPs can be conjugated to varied biological targets, including proteins, enzymes, DNA and others, thus facilitating detection, imaging and functional analysis of biolog-

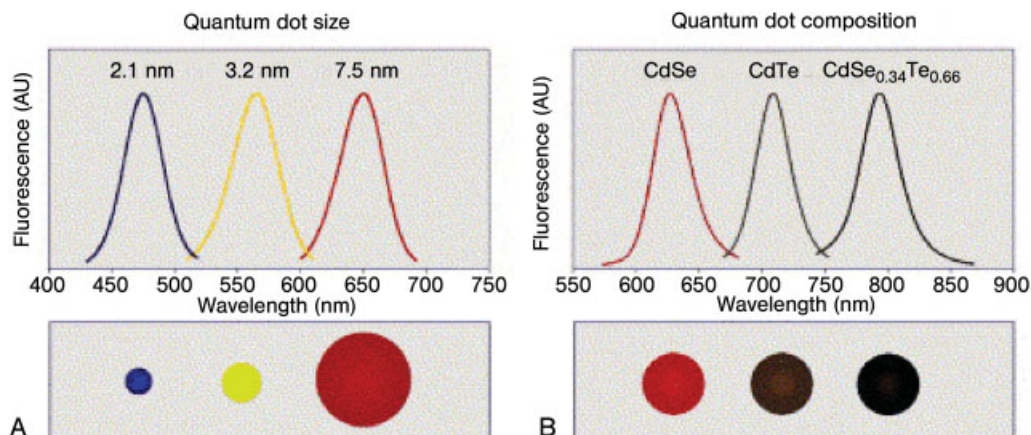


Fig. 11.1. Variation of fluorescence emitted from semiconductor nanoparticles (quantum dots), in relation to particle size and composition. (Reprinted from Ref. [7]. Copyright (2004), with permission from Elsevier.)

ical processes via the differently-labeled NPs [8–11]. Coupling of the NPs to biological molecules provides these nanosensing particulates with means of exploiting the diversity of the biological universe for varied applications. In particular, bioconjugation allows probing and pinpointing specific cellular pathways and physical environments within the cell. Semiconductor NPs were used for imaging of single cells [11], cell components [12], tissues [13], plant cells [14], and living animals [15].

An important advantage of the use of NPs for biological imaging is their often superior spectral and optical properties compared with conventional dyes [16]. In that regard, the ability to tune their optical properties through varying the particle size and molecular composition, the coupling of the recognition element to NPs with different emission wavelengths, and the relative biological inertness of the NP core all make conjugated NPs an attractive labeling tool. Semiconductor NPs are currently widely used in scientific and applied biotechnology research, e.g., for intra- and extra-cellular imaging of cancer markers, and for orthogonal detection of different molecular targets within a cell [16].

Diverse techniques have been developed for making NPs generally biocompatible, and to overcome problems of nonspecific adsorption, aggregation, and intracellular targeting in cell imaging. A simple and innovative approach has been the inclusion of semiconductor NPs within phospholipids micelles, making such assemblies easy to manipulate and introduce into cellular systems [17]. The creation of lipid/NP particles has certain advantages over covalent coupling of NPs to biological molecules. First, the assembly process is simple and does not require formation of chemical bonds between the lipids and the NPs. Furthermore, the small lipid-surrounded particulates can transport into cellular systems and microorganisms without adversely affecting their viability [17].



A critical test for the use of NPs for cellular imaging and analysis is whether these particles can be depicted as “inert” markers of cells (or specific organelles within the cell). Many studies have shown that NP incorporation does not adversely affect cell processes or cell viability [8, 11]. In that sense, NPs can be referred to as “biomimetic” in that they can become part of a biological system (the cell) without affecting its viability and biological functionalities, and augment it through providing the imaging capabilities.

Semiconductor NPs are not the only nano-scale probes used in biological imaging; however, their remarkable biological and optical versatility make them promising components for imaging and bioanalysis applications. Other types of NPs have been reported in biosensing applications. NPs composed of silica or metal atoms, for example, also allow easy surface modification aimed to incorporate labile biological functionalities [18, 19]. Zhao et al. have developed an elegant sensing technique based on bioconjugated silica NPs containing fluorescent dyes [20] (Fig. 11.2). The silica NPs were coupled to recognition elements such as antibodies recognizing specific antigens on bacterial surfaces, and additionally encapsulated high concentration of fluorescence dyes within the NP matrix. Consequently, binding of even a *single* bacterial cell yielded a detectable fluorescence signal from the intensely fluorescent NP. This approach could easily be extended to rapid pathogen detection and high-throughput screening using simple chip devices.

Gold NPs, in particular, exhibit varied uses in biological detection, in some instances comprising the basic building blocks for the biosensors, in other cases as vehicles of transmission of the induced signals. An example of the former design is the use of gold NPs in monolayers for the construction of amperometric immunosensors [21]. Here, the NPs constituted both the sensing interface as well as the substrate for biological immobilization. Another study has described the use of

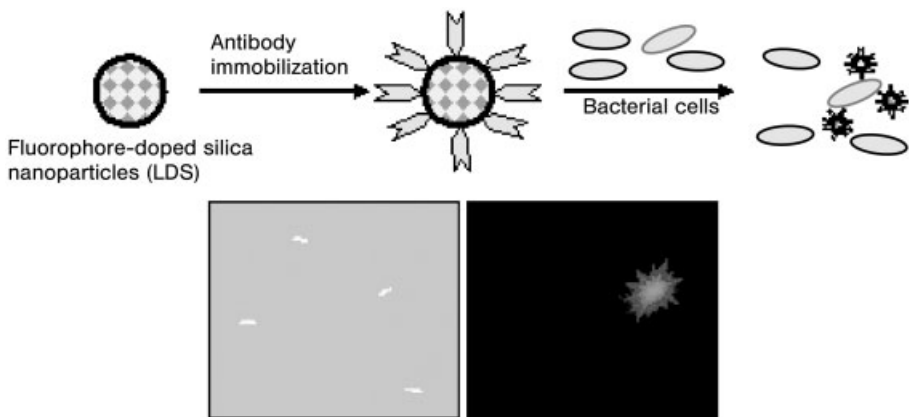


**Fig. 11.2.** Schematic depiction of bacterial detection using fluorophore-containing silica NPs [20]. Binding of bacterial cells to antibody-labeled NPs causes the release of the fluorescence dyes.

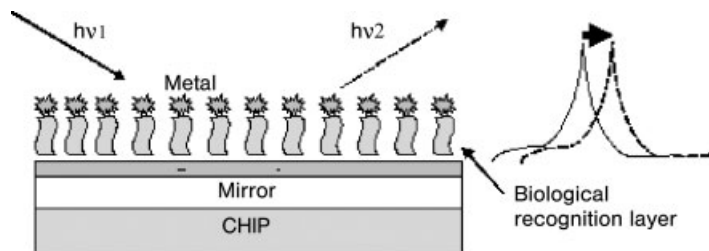


**Fig. 11.3.** A biosensor design based on a metal cluster resonance bio-chip;  $h\nu_1$  and  $h\nu_2$  are the incoming and reflected light, respectively, and the shift in color is caused by

absorption due to mirror–NP layer resonance. Light absorption from the metal layer is modified by the thickness of the biological recognition layer [24].

gold NPs for assembling a surface sensor for DNA hybridization [22]. Silica NPs encapsulating luminescent markers have been prepared and used for biosensing through conjugation with biological molecules and bio-surfaces [23]. The latter work exploited advanced synthesis methods to assemble NP in distinct sizes, thus achieving controlled luminescence. This, in turn, has endowed the system with “molecular encoding” capabilities through multiplexed signaling.

Films composed of NPs forming parts of *biosensor chip* assemblies have been reported [24]. Metal nanoclusters were positioned on top of a biological recognition layer (receptor/ligands) at a nanometer-scale distance from a reflecting layer (Fig. 11.3). The surface-enhanced light absorption by the NP layer was shown to be highly sensitive to the thickness of the biological recognition assembly, thus providing means for sensing biomolecular binding [24]. The simplicity of this application stems from the enhancement of visible signals – essentially color changes detected by the naked eye – through deposition of the NPs on surfaces functionalized with macromolecules. Such bio-chip devices could find varied uses in proteomics applications, and their extension to single molecule detection is possible through surface micro-patterning and nanolithography.

Confining NPs on solid surfaces could facilitate the application of sensitive surface spectroscopic methods in a highly localized manner. Metallic NPs, particularly gold or silver, placed on solid substrates yielded a dramatic increase in the intensity of surface-enhanced Raman scattering (SERS) signals, enabling trace-level detection of varied biological compounds, including, for example, viral DNA [25]. Silver NPs coupled to biological ligands yielded improved localized surface plasmon resonance (LSPR) signals following ligand/receptor binding, making such systems potentially useful in immunoassays [26].

Biologically functionalized magnetic nanoparticles have been also contributed to bio-sensing applications. The sensing schemes in such designs do not involve *optical detection* but rather rely on the modification of the *magnetic properties* of the particles, induced through biological interactions. One such system for sensing biomolecular interactions has utilized biocompatible magnetic NPs onto which biological molecules could be chemically attached [27]. The researchers demon-

strated that differences in the aggregation state of the magnetic NPs, affected through specific biomolecular interactions involving the functionalized NPs, could dramatically alter the magnetic relaxation properties of the particles – making the system a “magnetic relaxation switch” for identification of biological analytes. A notably practical advantage of the technique is that such “relaxation sensing” could be implemented by using conventional magnetic resonance instruments.

One of nanotechnology greatest molecular players – the carbon nanotube – could also form a basis for a wide range of biosensor applications. The remarkable chemical properties of carbon nanotubes [particularly single-wall (SW) nanotubes] have already been exploited in biosensor applications. Particularly important factors when considering carbon nanotubes as nanobiosensors are their nano-scale dimensions, versatile chemical functionalization possibilities, and the ready adsorption of proteins and other biomolecules onto their surface. All these factors make carbon nanotubes ideal candidates for sensing platforms, capable of detecting analytes at extremely low molecular concentrations. Indeed, the field of carbon nanotube sensors has developed rapidly in recent years due in large part to the spectacular progress in nanotube surface chemistries [28]. Biological molecules have been attached to nanotube surfaces through covalent and noncovalent bonding, with and without pre-activation, and through the use of diverse synthetic procedures [28]. Carbon nanotubes derivatized with oligonucleotides and embedded in silica have been used, for example, for ultrasensitive DNA detection [29]. That study and other reports point to an important advantage of carbon nanotubes: their simultaneous role both as *immobilization matrixes* for the detected analytes, as well as mediators of the induced signals (generally amperometric or electrical) within the bio-sensor assemblies [30, 31].

Other recent developments straddling the chemistry/nanotechnology interface point to technologies that could play a role in biomimetic nanosensors. Molecular imprinting, for example, could become a useful tool for biosensor architectures. Molecular imprinting creates recognition sites in polymers by using template molecules; the templates are prepared by initiation of the polymerization processes while specific molecules of a particular analyte (or resembling the analyte) are incorporated within the solidifying polymeric material [32, 33]. Following the removal of the embedded analyte molecules, the polymer essentially becomes a porous framework that selectively adsorbs only the analyte molecules within the pre-shaped binding sites [34]. This kind of “template biosensing” could be compatible with nanosensor design through accurately controlling the pore dimensions, or through manipulation of the recognition surface, for example by using microgel spheres that determine the overall size of the porous framework [35]. Recent studies have employed molecularly imprinted polymers as bio-sensing templates, achieving extremely sensitive (subpicomolar) detection of biological ligands [36]. A potentially useful implementation of molecular imprinting focuses on separation applications, particularly capillary chromatography and electrophoresis [37]. Such techniques, however, often face considerable hurdles when applied to minute sample quantities. Indeed, technical challenges still exist for transforming molecular imprinting into a viable sensing technology.

### 11.3

#### Nanosensors for Probing Biological and Cellular Systems

Nanosensors applied in the context of biological systems can be roughly divided into two broad applications. One route focuses on sensor technologies designed to investigate biological *molecules* and physiological/biological *processes* (rather than the complete “living systems”), while another active research track employs nanosensing for investigating actual *living* cells or tissues. This section summarizes the contribution of nanotechnology to both applications, beginning with sensors aiming to elucidate various aspects in the primary constituents of biology: proteins, nucleic acids, carbohydrates, and others.

The protein world has probably attracted the most intense activity in nanosensor development, undoubtedly due to the broad knowledge-base and the significance of proteins in numerous biochemical and therapeutic processes. The main difference between the established and highly versatile protein bio-assays available and newly introduced nanosensor methodologies is the focus on a very limited number of molecules (preferably, sometimes, single protein molecules) in nanosensor design, rather than looking at greater populations. Similar to fluorescent markers, luminescent dyes, or radioactive tracers, a primary challenge in protein nanosensor research and development is not to affect or interfere with the structural and functional properties of the inspected molecule. Indeed, the unprecedented technical advances in biomolecular manipulation in recent years have greatly contributed to progress in this field. An experiment exemplifying these concepts was the analysis of the molecular interactions in metal transfer by the protein metallothionein. The protein was labeled at two specific locations with a fluorescent-energy donor and an acceptor, respectively [38]. Such labeling was achieved through introducing a mutation in the protein that did not affect the protein properties. Monitoring the fluorescence resonance energy transfer (FRET) between the donor and acceptor bound to the protein allowed probing fine details pertaining to varied molecular processes of the protein.

An innovative method for detection of single antigen–antibody binding events at a bio-chip surfaces has been described recently [39] (Fig. 11.4). The sensing device relied on the fabrication of an artificial pore between two electrode surfaces; the electrical current measured through the pore (or more accurately its resistivity) was sensitive to the passage of streptavidin-derivatized colloids. When antigens, for example, were specifically bound to antibodies crosslinked to the colloid surface, the size change of the colloid was reflected in the recorded current. This microfluidic bio-sensor can be constructed through conventional lithography techniques – and points to the substantial potential of “nanolithography” to produce truly “single molecule” nanosensors.

Oligonucleotide detection has also been at the forefront of nanotechnology-based sensing techniques. This is mostly due to the explosive growth of genomics as a tool for biological research and pharmaceutical R&D. The introduction of the “gene-chip” and the quest for ever higher molecular densities and sophistication of chip surfaces have been major driving forces for new scientific and technical

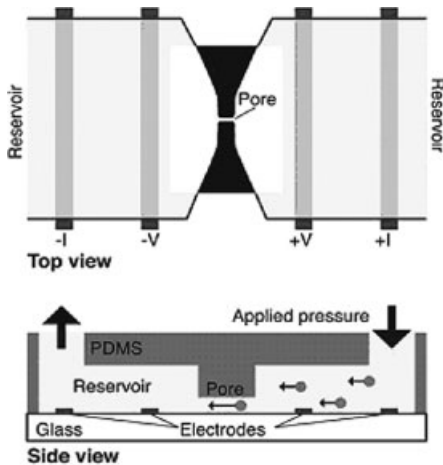


**Fig. 11.4.** Schematic depiction of apparatus designed to detect antigen–antibody interactions through measuring the electrode voltage across a small pore. The measured current was sensitive to the size of antibody-

functionalized colloids passing through the pores; antigen binding to the colloids modified the measured current [39]. (From Ref. [39]. Copyright (2003), National Academy of Science USA.)

breakthroughs involving nanobiosensors. Pioneering work by Letsinger and Mirkin has demonstrated that gold NPs can be used as sensitive probes for single-strand oligonucleotides [40]. The novel detection scheme was based on the colorimetric transitions of the gold NP suspension following the formation of a polymeric network, owing to hybridization between the target solubilized oligonucleotides and complementing oligonucleotide strands attached to the gold NPs. Furthermore, the red–blue transformations of the NPs were highly dependent upon hybridization mismatches – providing a unique tool for detection of DNA damage. Extending the gold NP technology, the same researchers demonstrated a simple scanner-based detection of target DNA segments using derivatized gold NPs [10]. This work also showed that the sensor signal can be further enhanced through addition of *silver* NPs to the surface-immobilized gold NPs. Of particular importance, single nucleotide mismatch could be resolved by achieving heat-induced dissociation of the hybridized gold NP network. These seminal studies have demonstrated the power of nanotechnology to introduce a new tool-kit for DNA sensing in particular, and biological sensing in general.

Other, diverse techniques have been developed to identify DNA strands with high fidelity and sensitivity. A critical requirement in many methods has been amplification of signals arising from recognition events between very dilute DNA analytes and their complementary oligonucleotides. “Nanopores” fabricated in polymer surfaces succeeded in detecting single DNA molecules, and achieved size discrimination based on strand length [41]. Another approach for high sensitivity DNA sensing involves the construction of optical fiber bundles, in which each fiber

within such “nano-arrays” can transmit precise optical signals induced by various physical changes, e.g., complementary strand binding of functionalized nano-beads [42, 43]. Detection of DNA binding through force deflection measurements on a nanomechanical cantilever array has been reported [44].

Carbohydrates appear increasingly important in different biological processes and therapeutic applications. Similar to nucleic acids and proteins, some studies have focused on the integration between carbohydrates and nanometer-size systems and devices, while other efforts were directed to integrate advanced nanotechnology-oriented concepts and instrumentation for specific detection of carbohydrates. In a similar way to the approach described above for protein engineering with fluorescent probes, ribose uptake and metabolism was monitored by flanking a bacterial ribose-binding protein with two variants of the green fluorescent protein (GFP), a popular macromolecular marker [45]. The FRET rate in such a system was inversely correlated to ribose concentration, allowing evaluation of free ribose concentrations within cells.

An intriguing study has described an amperometric biosensor facilitating high-sensitivity detection of carbohydrates through embedding nickel nanoparticles within a graphite-film electrode [46]. Essentially, the dispersion of the Ni nanoparticles within the carbon film yielded an order-of-magnitude lower detection threshold compared with conventional electrode arrangements. Similar to other NP-assisted biosensors described above, the nanoparticles in the device did not participate in the actual detection of the carbohydrate molecules, but rather provided the means for improving technical performance of the electrode. Another report demonstrated that nanometer-size amphiphilic C<sub>60</sub>-dendrimers could be employed in a biosensor construct for achieving improved association between the sensor surface and the carbohydrate analytes [47]. Binding was achieved through creating ordered Langmuir monolayers of the C<sub>60</sub> conjugates. The films could be further transferred to solid quartz surfaces, pointing to their potential applicability in biosensor design.

Atomic force microscopy (AFM), a major driving force in nanotechnology research, has also contributed to development of nanobiosensor for carbohydrates and other biomolecules. Among the most abundant uses of AFM in nanobiosensor research has been imaging of single biomolecules [48–50]. A potential high impact application of AFM has been the introduction of “dip-pen nanolithography” – placing molecules at desired locations on surfaces, and chemically manipulating molecular entities at specific locations using chemically-coated AFM tips [49]. A recent demonstration of dip-pen nanolithography for biosensing application has been the construction of bioactive protein nano-arrays on a conductive surface for detection of protein–protein interactions and proteomics applications [51]. Other biological applications of AFM have been reported. The technique was used as a tool for determination of carbohydrate heterogeneity on bacterial surfaces [52], or the observation of a non-homogeneous distribution of specific oligosaccharide units on the surface of yeast cells through derivatization of the AFM tip with lectins [53]. A novel saccharide “force fingerprinting” technique, based on the single-molecule imaging capabilities of AFM, has been reported [54].

The numerous AFM studies of biomolecules both illustrate the potential of this technique as well as the significant challenges for using single-molecule imaging and force measurements for routine biosensor applications. On the one hand, the atomic-level resolution of AFM could provide “imaging fingerprinting” for varied biological surfaces and surface-bound molecules. It might be possible, for example, to assemble an AFM image database for bacterial surfaces that might be used for rapid pathogen identification. Further contributions could be envisaged from integration of computer-aided image analysis into AFM-biosensor applications. On the other hand, formidable technical difficulties could arise from using AFM for sufficiently fast and reliable detection in biosensors. In particular, the wealth of atomic details and sensitivity of the method might lead to impracticality as a sensing method.

Nanotechnology approaches could yield information on processes occurring within lipid bilayers comprising the cell membrane. Jang et al. have inserted silicon NPs capped with a hydrophobic organic layer into the interior of lipid bilayer vesicles [55]. Photoluminescence from the highly optically-sensitive silicon NPs could be quenched by external quenchers – opening up possibilities to use the technique for detection of membrane properties such as the communication between membrane-embedded species and the external environment of a cell.

The use of biomimetic vesicles themselves as bio-sensing platforms has gained acceptance. Vesicles (also referred to as liposomes), having a simple lipid bilayer structure, can be particularly attractive for bio-sensing applications because they can be created in a range of sizes, and could enclose different dyes and optically-active compounds. Liposomes can also be made reactive/non-reactive to biological molecules, other vesicles, or cells, depending upon their lipid components and the membrane compositions of their biological target [56]. Thus, such aggregates can serve as specific detectors for pre-selected molecules, cell locations, or tissues. Somewhat related to liposomes, newly-developed “nanogels” (Fig. 11.5) consisting of nano-scale polymeric hydrogels coated with phospholipids [57] could be attractive for bio-sensing applications since they both mimic the bilayer membrane as

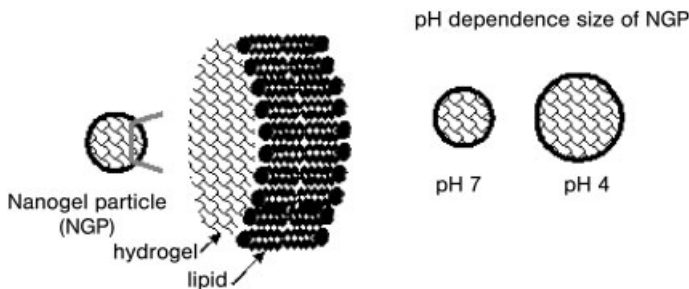


**Fig. 11.5.** “Nanogel” particles employed for bio-sensing applications [57]. The particle size is dependent upon the pH, making it a sensitive probe of different cellular compartments.

well as providing a rigid scaffolding for addition of optical transduction components. Nanogel particles (NGP) were shown to exhibit size sensitivity to the solution pH, making these particles potential sensor for tissue or intracellular pH changes.

Several studies have exploited the properties of *whole microorganisms* for constructing nano-scale sensor assemblies with unique features. Genetic engineering of filamentous bacteriophage allowed expression of a recognition element for ZnS nanoparticles on the phage surface (through peptide selection by affinity screening), and the NPs could then be ordered via a liquid crystal alignment of the phage [58]. This clever design resulted in NP “patterning” that could be further employed in varied nanosensor constructs.

The primary aim of biosensor design for *cellular* sensing technology is the desire to expose biochemical phenomena at the *single cell* level, and, preferably, maintain cell viability throughout the measurement. Indeed, miniaturization constitutes the core of different cellular sensing technologies, and nanotechnology could open new avenues for such applications. An interesting device addressing that goal was a nano-calorimetric sensor for measuring minute temperature changes in isolated cell suspensions, generated by biological or pharmaceutical stimuli [59]. The cellular sensor consisted of a gold and nickel thermoelectric transducer, and could produce signals upon extremely small temperature and heat changes. That report both exemplifies sensor fabrication achievements, as well as the technical and technological challenges nanobiosensor research is still facing.

Because *aqueous* environments are essential for cell viability, development of nanobiosensors for cell activity and cellular processes have greatly benefited from technical advances in micro- and nano-fluidics. Indeed, the increasing sophistication of fluidic biochips and cells has already contributed to demonstrating intriguing biosensor designs up to a single cell level. Detection of metabolic processes in few dozens bacterial cells was achieved using a microfluidic biochip prototype that could hold as little as 5 nL of a bacterial suspension [60]. Such an impedance-based biosensor of cellular metabolism could, in principle, accomplish detection of a single bacterial cell through lithographic design that would decrease the electrode size and distance between the sensor electrodes.

Being a “silent observer” to processes within a cell is a central goal in nanobiosensor research and development. An innovative method for literally “illuminating” the cell interior with biologically-inert nano-capsules has been developed by R. Kopelman [61–63]. The cell-inserted nanoprobe, denoted PEBBLEs (photonic explorers for bioanalysis with biologically localized embedding), have been fabricated from different polymeric matrixes encapsulating both a reference dye and a sensing dye [63, 64]. Owing to their small size (20–100 nm) and biological inertness, PEBBLE nanosensors can be delivered into the cell interior without compromising cell viability. Inside the cell, PEBBLEs essentially mimic cellular compartments, as they interact with and “sense” the intracellular environment. The sensitivity of the encapsulated dyes to ions and molecules have made PEBBLEs a useful platform for measuring intracellular concentrations of protons (pH),  $K^+$ ,  $Mg^{2+}$ ,  $Ca^{2+}$ ,  $Cl^-$ , oxygen, and glucose [65, 66].



Antibody-based nanoprobes have been a recent intriguing nanosensor approach for probing the interior of living cells. These devices utilize extremely thin optical fibers – less than 50 nm in diameter – derivatized with antibodies and inserted into single cells [67]. Similar to PEBBLEs, the unique advantages of these nanoprobes stem from their exceedingly small diameters, making them almost inert and non-perturbing to the inspected cells.

While different methods have been developed for probing cell interior, relatively fewer nanotechnology applications have been designed to explore processes at the cell-surface or at the external membrane of living cells. A recent study has depicted the construction of new membrane-fused fluorescent/colorimetric nano-patches for probing membrane events in living cells [68]. The nano-scale probes in that work were based on a conjugated polymer – polydiacetylene – that changes its visible color and its fluorescence emission following structural perturbations in its vicinity [68, 69]. Polydiacetylene nano-patches were attached to the cell surface through coupling to phospholipid moieties. Such membrane-incorporated lipid/polymer patches do not adversely affect cell viability, and respond to local structural perturbations within the membranes both through induction of fluorescence as well as by undergoing blue–red color changes [67] (Fig. 11.6). These chemo-engineered nanopatch-labeled cells could be used for microscopic imaging and fluorescence or visible spectroscopic analyses of physiological processes affecting the cell membrane, its structure or morphology.

One of the challenges in coupling sensor devices to biological or cellular systems is the efficient transduction of the signals (optical, electronic) from the biological assembly into the recording/analysis units. Varied methods have been developed

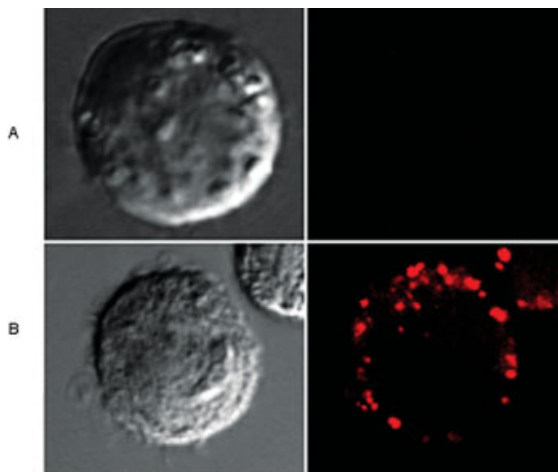


**Fig. 11.6.** Phase contrast microscopic images (left) and fluorescence confocal images (right) of nanopatch-labeled cells [67]. (A) Control “blue” cells; (B) cells treated with a

membrane-active substance (polymyxin-B). Fluorescence spots corresponding to the “red” nanopatches indicate membrane disruption by polymyxin-B.

to interface the biological constructs investigated with opto-electronic detectors, and this is an active field of research. The fabrication of tiny micro-electrodes has been reported, and these were successfully used for monitoring adhesion and movement of different cells [70]. The use of organic dyes as reporters for the biological/inorganic interface has also been described [71]. Surface patterning of biological chips has further allowed fabrication of multi-analyte biosensors, as well as monitoring pathological conditions *in vitro* [70].

The considerable advancement in construction of optical nano-fibers has been central to developing nanosensors for investigating and imaging cell interiors [3]. Coupling of biological recognition elements to optical fibers (generally optical fiber tips) has been another active field of research aiming to efficiently transmit biological signals to opto-electronic detection systems. Varied types of biological molecules were attached to optical fiber surfaces, including enzymes, antibodies, nucleotides, and even whole cells, making this approach highly versatile as a tool for detection of diverse analytes [42]. The increasingly sophisticated technologies for manufacturing thin, resilient optical fibers with highly uniform consistencies should significantly contribute to this nanosensing track.

Several laboratories reported the incorporation of nano-electronic devices *inside* biological systems, thus creating new biosensor designs. Ritter et al. have described the inclusion of nano-electronic sensors in a cellular neural/nonlinear network for investigating fundamental physiological aspects, including image recognition, target tracking, and others [72]. Miniaturization of the devices through nanotechnology makes possible their use as tiny probes within cells and tissues.

Technological progress in cellular nanosensor fabrication also promises to yield important insight into cell metabolite levels, also known as “metabolomics”. The capability for detecting changes in metabolite patterns at a *single cell* level (rather than in *ensembles* of cells as mostly done now) is extremely important for elucidation of specific factors and substances affecting cell functions [73]. In particular, the recent introduction of protein-based nanosensors, expressed via conventional biotechnology methods, could play prominent roles in intracellular metabolite sensing. One successful design was based on the attachment of two fluorescent proteins through a fusion protein, in which one of the proteins had calcium-binding properties [74, 75]. This nanosensor made possible analysis of  $\text{Ca}^{2+}$  levels in isolated cells as well as in living microorganisms. Another reported protein-based nanosensor employed a fluorescent marker (green fluorescent protein) fused to a bacterial periplasmic binding protein, facilitating real-time sensing of a range of cellular metabolites [75].

## 11.4

### Biological Components in Nanosensors

The extraordinary diversity of the biological universe has inspired numerous devices and structures in the materials science realm. This is particularly the case in biosensor design, in which varied biological concepts, or even actual biological

molecules, can be utilized for construction of novel sensing assemblies. In that sense, miniaturization, which constitutes the core of nano-biotechnology and nanobiosensor development, increasingly relies on the incorporation of biomolecules from different sources into the sensing devices. In most instances, biological molecules and entire microorganisms have been used as templates for construction of organized nanostructures.

“Classical” biosensor designs have generally exploited enzymatic reactions as the biological transduction component. Accordingly, enzyme immobilization and maintenance of enzyme activity have been primary tasks in biosensor development. Nanotechnology offers significant advantages and new approaches for enzyme-based biosensors. In a complementary sense, enzymatic redox systems by themselves are ideal candidates for nanobiosensor applications: electron transfer is generally highly localized and can be detected in many instances both electronically and optically. Furthermore, enzymes can be readily chemically and biologically manipulated through self-assembly and protein engineering approaches and can be assembled in modular building blocks [76].

Recent reports have described the incorporation of gold nanoparticles as “mediators” of the electrochemical signals produced by immobilized enzymes in biosensors [77]. The NPs in such studies have the potential not only to improve the electrode performance but also to participate in immobilization of the enzyme and retaining of biological activities. Another study has used the aggregation properties of gold NPs for *indirect detection* of enzyme inhibitors, some of which are known nerve gases [78]. The sensing system relied on prevention of thiocholine-mediated transformation of  $\text{AuCl}_4^-$  into growing nanoparticles through inhibiting the action of the enzyme acetylcholine-esterase needed to produce thiocholine.

Peptides and proteins have also constituted important nano-structural components in sensor systems. Diverse nano-assemblies, some with potential bio-sensor applications, have relied on controlling and manipulating the *self-assembly* properties of short peptide sequences [79]. The extensive and advanced technical capabilities of peptide and protein engineering have facilitated a remarkable plethora of peptide- and protein-based nanostructures, which could furthermore respond to external stimuli by emission of detectable signals – essentially performing a biosensor task [80].

The use of biomimetic receptors in biosensor design has led to development of fascinating hybrid systems. Artificial receptors that mimic ion channel proteins have been used for detection of diverse ionic species [81]. Interestingly, that work has shown that molecules *much larger* than the ions were actually recognized and discriminated by the receptors. A chromatic detection platform for catecholamines (such as adrenaline, noradrenaline, and dopamine) based upon nanoscale vesicles displaying synthetic catecholamine receptors at their surface has been reported recently [82]. The synthetic hosts in the vesicle assembly were incorporated within a matrix that contained both biomimetic membrane bilayers, as well as domains of a chromatic polymer reporter. This new assembly featured remarkable sensitivity and selectivity among similar ligands compared with existing receptor-based catecholamine biosensors.

DNA has been a natural component in diverse assays and sensors because molecular recognition is an intrinsic property of the molecule. The introduction of aptamer technology has been a particularly significant driving force for oligonucleotide-based molecular sensing [83]. Particularly important in this context is the possibility for carrying out various chemical modifications of aptamers, thereby attaching specific probes to the molecules [84]. The DNA ligands could then emit the desired signal (optical, fluorescent, etc.) upon binding their protein target. An example is the construction of “molecular beacon aptamers” for fluorescent detection of even minute amounts of a platelet-derived growth factor through their high affinity binding to the protein [85]. The notable strength of aptamer technology for nano-biosensing applications stems from the versatility of ligands that can be constructed and their high specific affinity, which allows precise localization onto target molecules or even cells and tissues.

An elegant nanosensor design for DNA detection using only biological components has been reported recently [86]. That construct contained an aptamer unit bound tightly to thrombin (through the aptamer peptide recognition element), thereby disrupting the catalytic action of the enzyme towards a fluorescently-labeled peptide. However, in the presence of an oligonucleotide strand complementary to a nucleic acid tethered to the aptamer, the aptamer was released from the binding pocket, facilitating peptide cleavage by thrombin and generation of a fluorescence signal (Fig. 11.7). The important aspect of this nano-scale system is

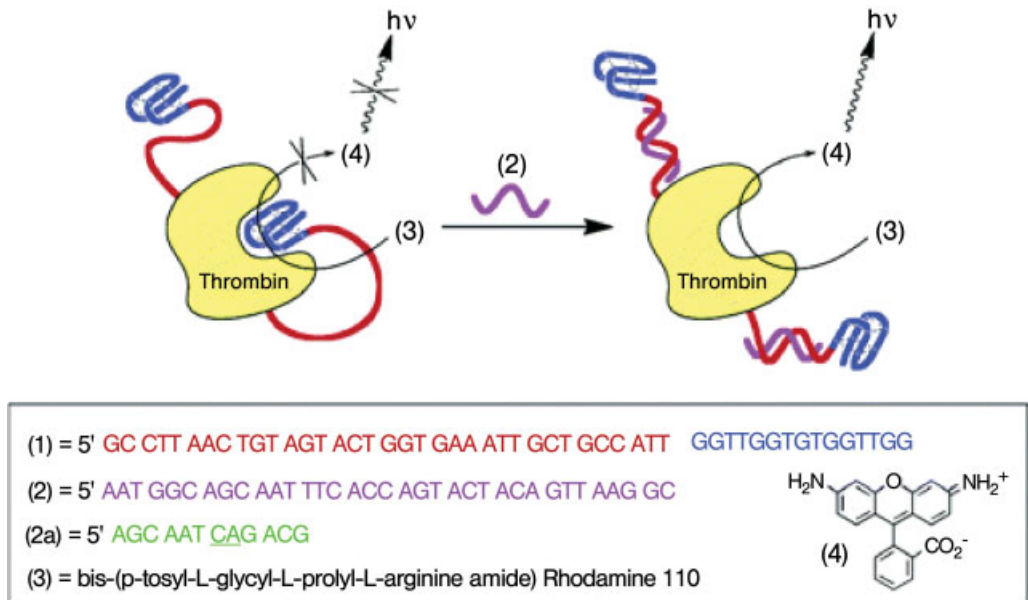


Fig. 11.7. Oligonucleotide detection by an all-biological sensor. Double strand recognition frees the thrombin binding pocket, facilitating enzymatic activity and fluorescence signal. (From Ref. [86]. Copyright (2005), The American Chemical Society.)

the use of only biological building blocks to produce a highly sensitive and specific signal. Such an assembly could be easily coupled to opto-electronic components, making a complete biological DNA nanosensor unit. The same research group has reported the application of magnetic NPs functionalized with sequence-specific DNA as substrates for endonuclease activity both as detector for complementary DNA strands, but also as novel biological “logic” circuitry [87].

DNA and oligonucleotide derivatives have been used for varied other sensing applications. DNA enzymes (referred to also as “DNAzymes”), for example, were the basis for a highly sensitive lead biosensor [88]. This clever application relied on the high specificity of DNA enzymes to metal ions such as  $\text{Pb}^{2+}$ , in which metal binding consequently resulted in a catalytic reaction – generally cleavage of the substrate strand of the DNA. In the reported application, the DNA enzyme formed a cluster of gold NPs; the presence of lead ions resulted in DNA cleavage and prevention of NP aggregation – leading to different visible colors.

DNA was one of the early examples of biological scaffolding for nano-fabrication. The molecular recognition and self-assembly properties inherent in DNA have been powerful tools for assembling complex structures that could have sensing properties. A research group at the Israel Institute of Technology has demonstrated that DNA could form the basis for varied organized nanostructures [89]. These studies demonstrated that creation of highly defined carbon nanotube constructs using DNA as a self-assembled framework had potential for bio-sensing applications [90]. The researchers exploited the “coding” inherent in DNA by directing a DNA-binding protein (a bacterial RecA protein) towards the DNA strand. This groundbreaking experiment demonstrated that DNA can constitute a molecular “toolbox” for assembling organized nonbiological nanostructures.

Nano-scale patterns constructed through “bio-inspired” approaches, such as DNA hybridization, could, indeed, become an important tool in sensor technologies. Such molecular patterning could be crucial for improving sensitivity and selectivity of the sensors, for integrating the biosensor within non-biological assemblies such as silicon chips, and for coupling of the nano-scale sensors to electro-optic devices and circuits. Different techniques have been developed for producing biomolecular patterning, e.g., microelectronic fabrication combined with DNA hybridization and chemical immobilization on chip surfaces [91, 92]. DNA and antibodies have been used for extremely sensitive detection of molecular interactions through attachment to tiny cantilevers [93]. Such sensing devices, conceptually and practically, resemble force microscopes in that the cantilever moves (or changes its shape) in response to molecular attractions between the immobilized biomolecules and their targets. Such constructs could, in principle, facilitate detection at a single molecule level; this property would depend upon the cantilever size and the immobilization methods. The “functionalized cantilever” technology could form the basis of extremely sensitive sensing devices capable of detecting minute analyte concentrations.

Several reports have depicted the coupling between nano-scale assemblies and biological molecules in sensor applications. An interesting, albeit complex, nano-

sensor platform has been described in which the luminescent protein firefly luciferase was used to assemble colloids deposited on an optical sensor surface [94]. The luciferase was utilized in this system for monitoring binding events occurring at the sensor surface, but also as a participant in the sensing mechanisms through its catalytic activity. The integration of whole cells or cell elements into inorganic biosensor devices is another promising avenue for new sensing applications. Recent progress in engineering of molecular circuits has opened the way for construction of microelectronic devices containing whole cells [95]. Indeed, the coupling of nanofabrication and bio-microelectronics could revolutionize microbiological and environmental monitoring [96].

Developments in surface manipulation through microprinting, lithography, and microfluidics continue to contribute significantly to nanobiosensor research. A recent report demonstrated, for example, the construction of a “lab-on-a-chip” using a modular architecture [97]. One of the most remarkable aspects of that work was the creation of an integrated chip for detection of biological markers through the use of highly spatially-defined microfluidic channels and reaction chambers. This device is a fine representative of the large variety of microfluidic labs-on-chips demonstrated or already commercialized for detection of minute amounts of analytes in liquid samples.

## 11.5

### Nano-biotechnology and Biomedical Diagnosis

The emphasis in nanotechnology research on manipulation of ever smaller structures has opened revolutionary new avenues for biomedical applications and strategies, an approach referred to as “nano-medicine” [98]. An often touted futuristic application of nanotechnology in the field of medical diagnosis has been the introduction of tiny “nano-robots” traveling within blood vessels and tissues, scanning for malfunction and disease. Even though such applications are still far off, initial steps towards “molecular diagnostics” have been reported. A fascinating example of a nanosensor for *in vivo* analysis has been the implanting of nanoprobes for monitoring neural tissues and therapeutic treatments of neural diseases [99, 100]. Carbon nanotubes and nanofibers, in particular, are promising candidates for diverse biomedical uses because of their unique chemical and biological reactivity profiles. Several breakthrough studies have demonstrated effects of composites containing carbon nanotubes on functionalities and behavior of nerve cells and bone-forming cells [100].

Cancer diagnosis using nano-scale devices has gained considerable interest. Two main directions are pursued in this field: (a) *in vivo* imaging – using biomimetic nano-constructs for delivering imaging agents to malignant tissues and suspected areas within the body, and (b) *ex vivo* analysis – early detection of precancerous and malignancies in fluids extracted from the body using nanostructures as platforms,

generally in high-throughput screening arrays [101]. NPs are particularly attractive candidates for *in vivo* imaging. In principle, they can undergo “orthogonal” couplings – both to molecular markers, such as fluorophores or radio-isotopes, as well as conjugated with molecular entities necessary for targeting the particles to their cellular or tissue destinations [102]. Furthermore, in addition to *imaging*, NPs can be simultaneously used as vehicles for *delivery* of therapeutic substances to desired targets – making them a highly versatile platform for cancer diagnostics and treatment.

Nanoparticles have been employed for other cancer detection applications. A recent study has described the attachment of biocompatible superparamagnetic iron oxide NPs to nucleotide repeats produced by telomerase – an enzyme for which elevated levels are associated with many malignancies [103]. Intriguingly, such magnetic nanoparticles switched their magnetic state upon binding – facilitating detection of the biologically originated signals using conventional magnetic readers [103]. Such “magnetic illumination” from the bound nanoparticles could be also captured easily by modified magnetic resonance imaging apparatus and forms the basis for high-throughput sample screening.

A different type of NPs – the “nanoshells” – has been implemented in cancer diagnostics and imaging. Nanoshells, spherical metallic shells encapsulating a dielectric core, have been successfully used for tissue imaging because of the remarkable tunability of their optical properties [104]. Specifically, the optical resonance of the particles can be tuned to the near-IR (NIR) range – in which tissues are transparent. Accordingly, bioconjugation of the nanoshells with molecular markers and contrast agents allows illumination of inner body parts and disease diagnostics.

Detection of disease biomarkers, combined with micro-array technologies and biochips, has been an increasingly active field in nanobiosensor research, with significant scientific and commercial potential at stake. Several innovative nanotechnology-based techniques have been reported in recent years for detection of biomarkers for Alzheimer’s disease. Haes et al. have employed LSPR in a nanoscale optical sensor for immunological detection of amyloid-derived ligands [105]. In this application, which is amenable for high-throughput screening, the nanosensor surface successfully mimicked a physiological environment, facilitating antibody–antigen recognition. Nanoparticles have been employed in a recent breakthrough application for detection of a soluble biomarker for Alzheimer’s disease in cerebral spinal fluid [106]. The detection scheme was based on the onset of aggregation by oligonucleotide-modified gold NPs following binding of an Alzheimer’s disease pathogenic peptide to its specific antibody, where the antibody was also attached to the gold NPs (Fig. 11.8). This elegant approach not only achieved very high sensitivity due to signal amplification from the gold NPs, but is also notable for being carried out in an actual physiological solution. Such biomimetic diagnostic systems point to future development of molecular diagnostic kits in which pathogenic markers could be identified at very early stages of disease progression.

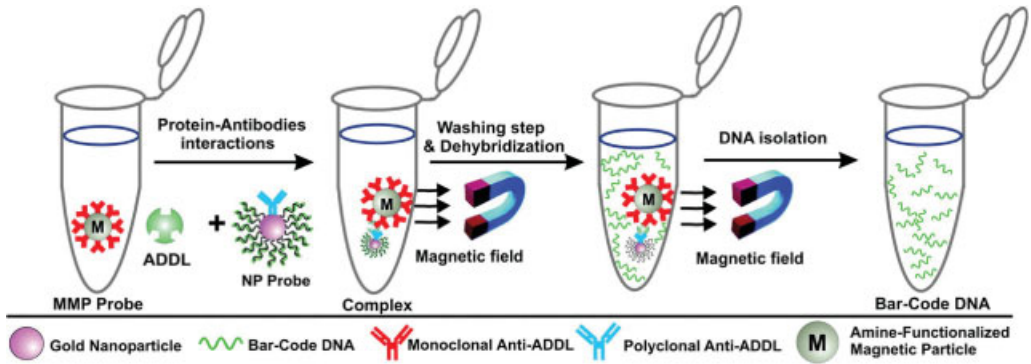


Fig. 11.8. Bio-barcode amplification assay [106]. The assay uses gold nanoparticles functionalized with monoclonal antibodies that recognize and bind a molecular marker for Alzheimer's disease (ADDLs). Following

separation and dehybridization, the oligonucleotides can be identified. (From Ref. [106]. Copyright (2005), the National Academy of Science USA.)

## 11.6

### Conclusions and Future Directions

Biosensors (or “biological detection devices” in the broad sense of the word) are becoming ubiquitous and increasingly complex. The proliferation of biological and biomedical applications and technologies, such as high-throughput screening, biomedical monitoring and diagnosis, and molecular arrays for functional genomics and proteomics analyses, all point to the pressing need for developing new biosensor platforms, technologies, and concepts. The biological and physiological spheres would most likely be increasingly exploited for ideas and building blocks in biosensor design, a process that is already taking place.

Nature provides abundant examples for innovative nanobiosensors. Snakes' “thermal vision” organs [i.e., sensitive to infra-red (IR) electromagnetic radiation] were found to contain an intricate array of nano-pits containing specific IR receptors [107]. The highly-defined spacings between these nano-pits are assumed to play a critical role in selective light absorption at particular wavelengths within the IR spectrum – endowing the snake with environmental sensing and navigation. Elaborate multilayered spheres of IR receptors have been similarly identified in *Melanophila acuminata* beetles [108]. Such dazzling arrays could inspire new sensors and IR observation devices.

In several fields, the advantages offered by nanobiosensors are obvious. The use of nanostructures as platforms for screening of large pool of compounds, i.e., genomics, proteomics, metabolomics, etc., would have a significant impact since this would increase array densities and assay efficiency. In biomedicine and medical diagnosis, nanosensors could have a profound effect on the way diagnosis is carried out, both inside and outside the human body. “Molecular imaging” and “molecular



diagnostics” point to a future in which “smart agents” consisting of tiny molecular entities will circulate in the blood stream, aiming to identify and report on various diseases and pathological conditions. *In vitro* diagnostics will rely on nanostructures to form devices, making possible high-throughput screening and rapid analysis of millions of genetic and other biological markers for identification of disease or health risks in individuals. Such applications could realize the much touted “personalized medicine” revolution.

Close collaboration among biologists, chemists, physicists, and engineers have become a defining feature in nanobiosensor research and development, and promise to open new horizons in the field. Such efforts have led to extraordinary advances in molecular manipulation, using physical, chemical, and biological tools. The general interest in nanotechnology commercialization and increasing activity in this field by industrial entities will undoubtedly shorten the routes from bench-top to commercial applications, a process that is already happening, as witnessed by the proliferation of start-up companies dealing mainly with nanobiosensor development.

### Abbreviations

AFM	Atomic-force microscopy
FRET	Fluorescence resonance energy transfer
GFP	Green fluorescent protein
LSPR	Localized surface plasmon resonance
NP	Nanoparticle
PEBBLE	Photonic explorer for bioanalysis with biologically localized embedding
SERS	Surface-enhanced Raman scattering

### References

- 1 SARIKAYA, M., TAMERLER, C., JEN, A. K.-Y., SCHULTEN, K., BANEYX, F. (2003) Molecular biomimetics: Nanotechnology through biology., *Nat. Mater.* 2, 577–585.
- 2 KATZ, E., WILLNER, I. (2004) Nanobiotechnology: Integrated nanoparticle-biomolecule hybrid systems: Synthesis, properties, and applications., *Angew. Chem. Int. Ed.* 43, 6042–6108.
- 3 CULLUM, B. M., VO-DINH, T. (2000) The development of optical nanosensors for biological measurements., *Trends Biotechnol.* 18, 388–393.
- 4 FORTINA, P., KRICKA, L. J., SURREY, S., GRODZINSKI, P. (2005) Nano-biotechnology: The promise and reality of new approaches to molecular recognition., *Trends Biotechnol.* 23, 168–173.
- 5 ROSI, N. L., MIRKIN, C. A. (2005) Nanostructures in biodiagnostics., *Chem. Rev.* 105, 1547–1562.
- 6 WEST, J., HALAS, N. (2003) Engineered nanomaterials for biophotonics applications: Improving sensing, imaging, and therapeutics., *Annu. Rev. Biomed. Eng.* 5, 285–292.
- 7 BAILEY, R. E., SMITH, A. M., NIE, S. (2004) Quantum dots in biology and medicine, *Physica E.* 25, 1–12.
- 8 CHAN, W. C., NIE, S. (1998) Quantum dot bioconjugates for ultrasensitive

- nonisotopic detection., *Science*. 281, 2016–2018.
- 9 CAO, Y.-W. C., JIN, R., MIRKIN, C. A. (2002) Nanoparticles with Raman spectroscopic fingerprints for DNA and RNA detection., *Science*. 297, 1536–1540.
  - 10 TATON, T. A., MIRKIN, C. A., LETSINGER, R. L. (2000) Scanometric DNA array detection with nanoparticle probes., *Science*. 289, 1751–1760.
  - 11 BRUCHEZ, M. P., MORONNE, M., GIN, P., WEISS, S., ALIVISATOS, A. P. (1998) Semiconductor nanocrystals as fluorescent biological labels., *Science*. 281, 2013–2016.
  - 12 GAO, X., YANG, L., PETROS, J. A., MARSHALL, F. F., SIMONS, J. W., NIE, S. (2005) In vivo molecular and cellular imaging with quantum dots., *Curr. Opin. Biotechnol.* 16, 63–72.
  - 13 GAO, X., NIE, S. (2003) Molecular profiling of single cells and tissue specimens with quantum dots., *Trends Biotechnol.* 21, 371–373.
  - 14 RAVINDRAN, S., KIM, S., MARTIN, R., LORD, E., OZKAN, C. S. (2005) Quantum dots as bio-labels for the localization of a small plant adhesion protein., *Nanotechnology* 16, 1–4.
  - 15 LARSON, D. R., ZIFFEL, W. R., WILLIAMS, R. M., CLARK, S. W., BRUCHEZ, M. P., WISE, F. W., WEBB, W. W. (2003) Water-soluble quantum dots for multiphoton fluorescence imaging in vivo., *Science* 300, 1434–1437.
  - 16 WU, X., LIU, H., LIU, J., HALEY, K. N., TREADWAY, J. A., LARSON, J. P., GE, N., PEALE, F., BRUCHEZ, M. P. (2003) Immunofluorescent labeling of cancer marker Her2 and other cellular targets with semiconductor quantum dots., *Nat. Biotechnol.* 21, 41–46.
  - 17 DUBERTRET, B., SKOURIDES, P., NORRIS, D. J., NOIREAUX, V., BRIVANLOU, A. H., LIBCHABER, A. (2002) In vivo imaging of quantum dots encapsulated in phospholipid micelles., *Science* 298, 1759–1762.
  - 18 TAN, W. B., ZHANG, Y. (2005) Surface modification of gold and quantum dot nanoparticles with chitosan for bioapplications., *J. Biomed. Mater. Res., Part A* 75, 56–62.
  - 19 KIM, D. K., TOPRAK, M., MIKHAILOVA, M., ZHANG, Y., BJELKE, B., KEHR, J., MUHAMMED, M. (2002) Surface modification of superparamagnetic nanoparticles for in-vivo bio-medical applications., *Mater. Res. Soc. Symp. Proc.* 704, 369–374.
  - 20 ZHAO, X., HILLIARD, L. R., MECHERY, S. J., WANG, Y., BAGWE, R. P., JIN, S., TAN, W. (2004) A rapid bioassay for single bacterial cell quantitation using bioconjugated nanoparticles., *Proc. Natl. Acad. Sci. U.S.A.* 101, 15027–15032.
  - 21 LEI, C.-X., YANG, Y., WANG, H., SHEN, G.-L., YU, R.-Q. (2004) Amperometric immunosensor for probing complement III (C3) based on immobilizing C3 antibody to a nano-Au monolayer supported by sol-gel-derived carbon ceramic electrode., *Anal. Chim. Acta.* 513, 379–384.
  - 22 OLOFSSON, L., RINDZEVICIUS, T., PFEIFFER, I., KAELL, M., HOEOEK, F. (2003) Surface-based gold-nanoparticle sensor for specific and quantitative DNA hybridization detection., *Langmuir*. 19, 10414–10419.
  - 23 WANG, L., YANG, C., TAN, W. (2005) Dual-luminophore-doped silica nanoparticles for multiplexed signaling., *Nano Lett.* 5, 37–43.
  - 24 MAYER, C., PALKOVITS, R., BAUER, G., SCHALKHAMMER, T. (2001) Surface enhanced resonance of metal nano clusters: A novel tool for proteomics., *J. Nanoparticle Res.* 3, 361–371.
  - 25 ISOLA, N. R., STOKES, D. L., VO-DINH, T. (1998) Surface-enhanced Raman gene probe for HIV detection., *Anal. Chem.* 70, 1352–1356.
  - 26 RIBOH, J. C., HAES, A. J., MCFARLAND, A. D., YONZON, C. R., VAN DUYN, R. P. (2003) A nanoscale optical biosensor: Real-time immunoassay in physiological buffer enabled by improved nanoparticle adhesion., *J. Phys. Chem. B* 107, 1772–1780.
  - 27 PEREZ, J. M., JOSEPHSON, L., O'LOUGHLIN, T., HOGEMANN, D., WEISSELEDER, R. (2002) Magnetic relaxation switches capable of sensing

- molecular interactions., *Nat. Biotechnol.* 20, 816–820.
- 28 DAVIS, J. J., COLEMAN, K. S., AZAMIAN, B. R., BAGSHAW, C. B., GREEN, M. L. H. (2003) Chemical and biochemical sensing with modified single walled carbon nanotubes., *Chem.-A Eur. J.* 9, 3732–3739.
  - 29 LI, J., NG, H. T., CASSELL, A., FAN, W., CHEN, H., YE, Q., KOEHNE, J., HAN, J., MEYAPPAN, M. (2003) Carbon nanotube nanoelectrode array for ultrasensitive DNA detection., *Nano Lett.* 3, 597–602.
  - 30 SOTIROPOULOU, S., CHANIOTAKIS, N. A. (2003) Carbon nanotube array-based biosensor., *Anal. Bioanal. Chem.* 375, 103–105.
  - 31 VALENTINI, F., ORLANDUCCI, S., TERRANOVA, M. L., AMINE, A., PALLESCHI, G. (2004) Carbon nanotubes as electrode materials for the assembling of new electrochemical biosensors., *Sens. Actuators, B* 100, 117–125.
  - 32 ROYDHOUSE, R. H. (1968) Implant testing of polymerizing materials., *J. Biomed. Mater. Res.* 2, 265–277.
  - 33 LAUN, H. M. (1992) Rheometry towards complex flows: Squeeze flow technique., *Makromol. Chem., Macromol. Symp.* 56, 55–66.
  - 34 LEE, B., KIM, Y., LEE, H., YI, J. (2001) Synthesis of functionalized porous silicas via templating method as heavy metal ion adsorbents: The introduction of surface hydrophilicity onto the surface of adsorbents., *Microporous Mesoporous Mater.* 50, 77–90.
  - 35 YE, L., CORMACK, P. A. G., MOSBACH, K. (2001) Molecular imprinting on microgel spheres., *Anal. Chem. Data* 435, 187–196.
  - 36 DEVANATHAN, S., SALAMON, Z., NAGAR, A., NARANG, S., SCHLEICH, D., DARMAN, P., HRUBY, V., TOLLIN, G. (2005) Subpicomolar sensing of delta-opioid receptor ligands by molecular-imprinted polymers using plasmon-waveguide resonance spectroscopy., *Anal. Chem.* 77, 2569–2574.
  - 37 KIST, T. B. L., MANDAJI, M. (2004) Separation of biomolecules using electrophoresis and nanostructures., *Electrophoresis* 25, 3492–3497.
  - 38 MARET, W. (2003) Cellular zinc and redox states converge in the metallothionein/thionein pair., *J. Nutrition.* 133, 1460S–1462S.
  - 39 SALEH, O. A., SOHN, L. L. (2003) Direct detection of antibody-antigen binding using an on-chip artificial pore., *Proc. Natl. Acad. Sci. U.S.A.* 100, 820–824.
  - 40 ELGHANIAN, R., STORHOFF, J. J., MUCIC, R. C., LETSINGER, R. L., MIRKIN, C. A. (1997) Selective colorimetric detection of polynucleotides based on the distance-dependent optical properties of gold nanoparticles., *Science.* 277, 1078–1080.
  - 41 MARA, A., SIWY, Z., TRAUTMANN, C., WAN, J., KAMME, F. (2004) An asymmetric polymer nanopore for single molecule detection., *Nano Lett.* 4, 497–501.
  - 42 MONK, D. J., WALT, D. R. (2004) Optical fiber-based biosensors., *Anal. Bioanal. Chem.* 379, 931–945.
  - 43 TAM, J. M., SONG, L., WALT, D. R. (2005) Fabrication and optical characterization of imaging fiber-based nanoarrays., *Talanta* 67, 498–502.
  - 44 MCKENDRY, R., ZHANG, J., ARNTZ, Y., STRUNZ, T., HEGNER, M., LANG, H. P., BALLER, M. K., CERTA, U., MEYER, E., GUNTHERODT, H.-J., GERBER, C. (2002) Multiple label-free biodetection and quantitative DNA-binding assays on a nanomechanical cantilever array., *Proc. Natl. Acad. Sci. U.S.A.* 99, 9783–9788.
  - 45 LAGER, I., FEHR, M., FROMMER, W. B., LALONDE, S. (2003) Development of a fluorescent nanosensor for ribose., *FEBS Lett.* 553, 85–89.
  - 46 YOU, T., NIWA, O., CHEN, Z., HAYASHI, K., TOMITA, M., HIRONO, S. (2003) *Anal. Chem.* 75, 5191–5196.
  - 47 CARDULLO, F., DIEDERICH, F., ECHEGOYEN, L., HABICHER, T., JAYARAMAN, N., LEBLANC, R. M., STODDART, J. F., WANG, S. (1998) *Langmuir* 14, 1955–1959.
  - 48 CARDULLO, F., DIEDERICH, F., ECHEGOYEN, L., HABICHER, T., JAYARAMAN, N., LEBLANC, R. M., STODDART, J. F., WANG, S. (1998) Stable Langmuir and Langmuir-

- Blodgett films of fullerene-glycodendron conjugates., *Langmuir* 14, 1955–1959.
- 49 PINER, R. D., ZHU, J., XU, F., HONG, S., MIRKIN, C. A. (1999) “Dip-pen” nanolithography., *Science* 283, 661–663.
- 50 YOU, T., NIWA, O., CHEN, Z., HAYASHI, K., TOMITA, M., HIRONO, S. (2003) An amperometric detector formed of highly dispersed Ni nanoparticles embedded in a graphite-like carbon film electrode for sugar determination., *Anal. Chem.* 75, 5191–5196.
- 51 NAM, J.-M., HAN, S. W., LEE, K.-B., LIU, X., RATNER, M. A., MIRKIN, C. A. (2004) Bioactive protein nanoarrays on nickel oxide surfaces formed by dip-pen nanolithography., *Angew. Chem. Int. Ed.* 43, 1246–1249.
- 52 CAMESANO, T. A., ABU-LAIL, N. I. (2002) Heterogeneity in bacterial surface polysaccharides, probed on a single-molecule basis., *Biomacromolecules* 3, 661–667.
- 53 GAD, M., ITOH, A., IKAI, A. (1997) Mapping cell wall polysaccharides of living microbial cells using atomic force microscopy., *Cell Biol. Int.* 21, 697–706.
- 54 WONG, N. K. C., KANU, N., THANDRAYAN, N., RADEMAKER, G. J., BALDWIN, C. I., RENOUF, D. V., HOUNSELL, E. F. (2002) Microassay analyses of protein glycosylation., *Protein Protocols Handbook*, 841–850.
- 55 JANG, H., PELL, L. E., KORGEL, B. A., ENGLISH, D. S. (2003) Photoluminescence quenching of silicon nanoparticles in phospholipid vesicle bilayers., *J. Photochem. Photobiol., A* 158, 111–117.
- 56 JELINEK, R., KOLUSHEVA, S. (2005) Membrane interactions of host-defense peptides studied in model systems., *Curr. Protein Peptide Sci.* 6, 103–114.
- 57 KAZAKOV, S., KAHOLEK, M., TERAOKA, I., LEVON, K. (2002) UV-induced gelation on nanometer scale using liposome reactor., *Macromolecules* 35, 1911–1920.
- 58 LEE, S.-W., MAO, C., FLYNN, C. E., BELCHER, A. M. (2002) Ordering of quantum dots using genetically engineered viruses., *Science* 296, 892–895.
- 59 JOHANNESSEN, E. A., WEAVER, J. M. R., BOUROVA, L., SVOODA, P., COBBOLD, P. H., COOPER, J. M. (2002) Micromachined nanocalorimetric sensor for ultra-low-volume cell-based assays., *Anal. Chem.* 74, 2190–2197.
- 60 GOMEZ, R., BASHIR, R., BHUNIA, A. K. (2002) Microscale electronic detection of bacterial metabolism., *Sens. Actuators, B* 86, 198–208.
- 61 CLARK, H. A., HOYER, M., PHILBERT, M. A., KOPELMAN, R. (1999) Optical nanosensors for chemical analysis inside single living cells. 1. Fabrication, characterization, and methods for intracellular delivery of PEBBLE sensors., *Anal. Chem.* 71, 4831–4836.
- 62 CLARK, H. A., KOPELMAN, R., TJALKENS, R., PHILBERT, M. A. (1999) Optical nanosensors for chemical analysis inside single living cells. 2. Sensors for pH and calcium and the intracellular application of PEBBLE sensors., *Anal. Chem.* 71, 4837–4843.
- 63 BUCK, S. M., KOO, Y.-E. L., PARK, E., XU, H., PHILBERT, M. A., BRASUEL, M. A., KOPELMAN, R. (2004) Optochemical nanosensor PEBBLES: Photonic explorers for bioanalysis with biologically localized embedding., *Curr. Opin. Chem. Biol.* 8, 540–546.
- 64 BUCK, S. M., XU, H., BRASUEL, M., PHILBERT, M. A., KOPELMAN, R. (2004) Nanoscale probes encapsulated by biologically localized embedding (PEBBLES) for ion sensing and imaging in live cells., *Talanta* 63, 45–59.
- 65 BRASUEL, M., KOPELMAN, R., PHILBERT, M., AYLOTT, J. W., CLARK, H., KASMAN, I., KING, M., MONSON, E., SUMNER, J., HOYER, M., MILLER, T. J., TJALKENS, R. (2002) PEBBLE nanosensors for real time intracellular chemical imaging., *Opt. Biosens.*, 497–536.
- 66 MONSON, E., BRASUEL, M., PHILBERT, M. A., KOPELMAN, R. (2003) PEBBLE

- nanosensors for in vitro bioanalysis., *Biomed. Photonics Handbook*, 59/1–59/14.
- 67 VO-DINH, T., ALARIE, J.-P., CULLUM, B. M., GRIFFIN, G. D. (2000) Antibody-based nanoprobe for measurement of a fluorescent analyte in a single cell., *Nat. Biotechnol.* 18, 764–767.
- 68 ORYNBAYEVA, Z., KOLUSHEVA, S., LIVNEH, E., LICHTENSHEIN, A., NATHAN, I., JELINEK, R. (2005) Visualization of membrane processes in living cells by surface-attached chromatic polymer patches., *Angew. Chem., Int. Edn.* 44, 1092–1096.
- 69 KOLUSHEVA, S., WACHTEL, E., JELINEK, R. (2003) Biomimetic lipid/polymer colorimetric membranes: Molecular and cooperative properties., *J. Lipid Res.* 44, 65–71.
- 70 CONNOLLY, P., MOORES, G. R., MONAGHAN, W., SHEN, J., BRITLAND, S., CLARK, P. (1992) Microelectronic and nanoelectronic interfacing techniques for biological systems., *Sens. Actuators, B* 6, 113–121.
- 71 GOEPEL, W., SCHIERBAUM, K. D. (1991) Specific molecular interactions and detection principles [in chemical and biochemical sensing]. *Sensors* 2, 119–157.
- 72 RITTER, C., HEIKE, F., HERBERT, K., JOSEF, K. F., SUSANNE, L., CHRISTIAN, N., HELMUT, O., GABRIELE, P., BERNHARD, S., MARIELOUISE, S., WOLFGANG, S., GREGOR, S. (2001) Multiparameter miniaturized sensor arrays for multiple use., *Sens. Actuators, B* 76, 220–225.
- 73 FEHR, M., EHRHARDT, D. W., LALONDE, S., FROMMER, W. B. (2004) Minimally invasive dynamic imaging of ions and metabolites in living cells., *Curr. Opin. Plant Biol.* 7, 345–351.
- 74 SCHWALLER, B., DURUSSEL, I., JERMANN, D., HERRMANN, B., COX, J. A. (1997) Comparison of the Ca<sup>2+</sup>-binding properties of human recombinant calretinin-22k and calretinin., *J. Biol. Chem.* 272, 29663–29671.
- 75 FEHR, M., OKUMOTO, S., DEUSCHLE, K., LAGER, I., LOOGER, L. L., PERSSON, J., KOZHUKH, L., LALONDE, S., FROMMER, W. B. (2005) Development and use of fluorescent nanosensors for metabolite imaging in living cells., *Biochem. Soc. Trans.* 33, 287–290.
- 76 GILARDI, G., FANTUZZI, A. (2001) Manipulating redox systems: Application to nanotechnology., *Trends Biotechnol.* 19, 468–476.
- 77 LEI, C.-X., WANG, H., SHEN, G.-L., YU, R.-Q. (2004) Immobilization of enzymes on the nano-Au film modified glassy carbon electrode for the determination of hydrogen peroxide and glucose., *Electroanalysis* 16, 736–740.
- 78 PAVLOV, V., XIAO, Y., WILLNER, I. (2005) Inhibition of the acetylcholine esterase-stimulated growth of Au nanoparticles: Nanotechnology-based sensing of nerve gases., *Nano Lett.* 5, 649–653.
- 79 ZHANG, S., MARINI, D. M., HWANG, W., SANTOSO, S. (2002) Design of nanostructured biological materials through self-assembly of peptides and proteins., *Curr. Opin. Chem. Biol.* 6, 865–871.
- 80 PETKA, W. A., HARDEN, J. L., MCGRATH, K. P., WIRTZ, D., TIRRELL, D. A. (1998) Reversible hydrogels from self-assembling artificial proteins., *Science* 281, 389–392.
- 81 UMEZAWA, Y., ROKI, H. (2004) Ion channel sensors based on artificial receptors., *Anal. Chem.* 76, 320A–326A.
- 82 KOLUSHEVA, S., MOLT, O., HERM, M., SCHRADER, T., JELINEK, R. (2005) Selective detection of catecholamines by synthetic receptors embedded in chromatic polydiacetylene vesicles., *J. Am. Chem. Soc.* 127, 10000–10001.
- 83 SAMPSON, T. (2003) Aptamers and SELEX: The technology., *World Pat. Information* 25, 123–129.
- 84 KANDIMALLA, V. B., JU, H. (2004) New horizons with a multi dimensional tool for applications in analytical chemistry – Aptamer., *Anal. Lett.* 37, 2215–2233.
- 85 VICENS, M. C., SEN, A., VANDERLAAN, A., DRAKE, T. J., TAN, W. (2005) Investigation of molecular beacon

- aptamer-based bioassay for platelet-derived growth factor detection., *Chembiochem* 6, 900–907.
- 86 PAVLOV, V., SHLYAHOVSKY, B., WILLNER, I. (2005) Fluorescence detection of DNA by the catalytic activation of an aptamer/thrombin complex., *J. Am. Chem. Soc.* 127, 6522–6523.
- 87 WEIZMANN, Y., ELNATHAN, R., LIOUBASHEVSKI, O., WILLNER, I. (2005) Endonuclease-based logic gates and sensors using magnetic force-amplified readout of DNA scission on cantilevers., *J. Am. Chem. Soc.* 127, 12 666–12 672.
- 88 LIU, J., LU, Y. (2005) Stimuli-responsive disassembly of nanoparticle aggregates for light-up colorimetric sensing., *J. Am. Chem. Soc.* 127, 12 677–12 683.
- 89 BRAUN, E., EICHEN, Y., SIVAN, U., BEN-YOSEPH, G. (1998) DNA-templated assembly and electrode attachment of a conducting silver wire., *Nature* 391, 775–778.
- 90 KEREN, K., BERMAN, R. S., BUCHSTAB, E., SIVAN, U., BRAUN, E. (2003) DNA-templated carbon nanotube field-effect transistor., *Science* 302, 1380–1382.
- 91 BASHIR, R. (2001) DNA nanobiostuctures., *Mater. Today* 4, 30–39.
- 92 IQBAL, S. M., BALASUNDARAM, G., GHOSH, S., BERGSTROM, D. E., BASHIR, R. (2005) Direct current electrical characterization of ds-DNA in nanogap junctions., *Appl. Phys. Lett.* 86, 153 901/1–153 901/3.
- 93 MORROW, K. J. J. (2002) Nanotechnology: Applications to biotechnology., *Genomic/Proteomic Technol.* 2, 26–29.
- 94 PASTORINO, L., DISAWAL, S., NICOLINI, C., LVOV, Y. M., EROKHIN, V. V. (2003) Complex catalytic colloids on the basis of firefly luciferase as optical nanosensor platform., *Biotechnol. Bioeng.* 84, 286–291.
- 95 SIMPSON, M. L., SAYLER, G. S., APPLIGATE, B. M., RIPP, S., NIVENS, D. E., PAULUS, M. J., JELLISON, G. E. J. (1998) Bioluminescent-bioreporter integrated circuits form novel whole-cell biosensors., *Trends Biotechnol.* 16, 332–338.
- 96 SAYLER, G. S., SIMPSON, M. L., COX, C. D. (2004) Emerging foundations: Nano-engineering and bio-microelectronics for environmental biotechnology., *Curr. Opin. Microbiol.* 7, 267–273.
- 97 SHAIKH, K. A., RYU, K. S., GOLUCH, E. D., NAM, J.-M., LIU, J., THAXTON, C. S., CHIESL, T. N., BARRON, A. E., LU, Y., MIRKIN, C. A., LIU, C. (2005) A modular microfluidic architecture for integrated biochemical analysis., *Proc. Natl. Acad. Sci. U.S.A.* 102, 9745–9750.
- 98 EMERICH, D. F. (2005) Nanomedicine – prospective therapeutic and diagnostic applications., *Expert Opin. Biol. Therap.* 5, 1–5.
- 99 MCKENZIE, J. L., SHI, R., KALKHORAN, N. M., SAMBITO, M. A., WEBSTER, T. J. (2004) In vitro analysis of carbon nanofiber and mesoscale porous silicon materials with nanoscale roughness for neural applications., *Mater. Res. Soc. Symp. Proc.* 311–316.
- 100 WEBSTER, T. J., WAID, M. C., MCKENZIE, J. L., PRICE, R. L., EJIORFOR, J. U. (2004) Nano-biotechnology: Carbon nanofibers as improved neural and orthopedic implants., *Nanotechnology* 15, 48–54.
- 101 FERRARI, M. (2005) Cancer nanotechnology: Opportunities and challenges., *Nat. Rev. Cancer* 5, 161–171.
- 102 SULLIVAN, D. C., FERRARI, M. (2004) Nanotechnology and tumor imaging: Seizing an opportunity., *Mol. Imag.* 3, 364–369.
- 103 GRIMM, J., PEREZ, J. M., JOSEPHSON, L., WEISSLEDER, R. (2004) Novel nanosensors for rapid analysis of telomerase activity., *Cancer Res.* 64, 639–643.
- 104 LOO, C., LIN, A., HIRSCH, L., LEE, M.-H., BARTON, J., HALAS, N., WEST, J., DREZEK, R. (2004) Nanoshell-enabled photonics-based imaging and therapy of cancer., *Technol. Cancer Res. Treatment* 3, 33–40.
- 105 HAES, A. J., CHANG, L., KLEIN, W. L., VAN DUYN, R. P. (2005) Detection of a biomarker for Alzheimer's disease

- from synthetic and clinical samples using a nanoscale optical biosensor., *J. Am. Chem. Soc.* 127, 2264–2271.
- 106 GEORGANOPOULOU, D. G., CHANG, L., NAM, J.-M., THAXTON, C. S., MUFSON, E. J., KLEIN, W. L., MIRKIN, C. A. (2005) Nanoparticle-based detection in cerebral spinal fluid of a soluble pathogenic biomarker for Alzheimer's disease., *Proc. Natl. Acad. Sci. U.S.A.* 102, 2273–2276.
- 107 FUCHIGAMI, N., HAZEL, J., GORBUNOV, V. V., STONE, M., GRACE, M., TSUKRUK, V. V. (2001) Biological thermal detection in infrared imaging snakes. 1. Ultramicrostructure of pit receptor organs., *Biomacromolecules* 2, 757–764.
- 108 HAZEL, J., FUCHIGAMI, N., GORBUNOV, V. V., SCHMITZ, H., STONE, M., TSUKRUK, V. V. (2001) Ultramicrostructure and microthermomechanics of biological IR detectors: Materials properties from a biomimetic perspective., *Biomacromolecules* 2, 304–312.

## 12

# Reagentless Biosensors Based on Nanoparticles

*David E. Benson*

### 12.1

#### Introduction

The reagentless criterion for biosensors is one of the more stringent criteria for biosensor development. However, biosensors based on nanoparticles have progressed to the point that the reagentless criterion can be applied. The advantages of reagentless biosensors are a decreased need for recalibration, increased reproducibility, and minimized leaching of molecules used for analyte detection. From a development standpoint, concepts used for developing reagentless biosensors can be applied to various optical, electrochemical and magnetic detection methods. For a biosensor to be considered reagentless, the entire sensing modality needs to be unimolecular and connected through either covalent or kinetically-stable coordinate bonds. Multimolecular sensor (“non-reagentless”) systems are well known and provide an avenue for rapid concept development. However, artifacts arise from multimolecular systems as one component is diluted more than another. A classic example of this is the constant recalibration required of glucose oxidase-based electrochemical biosensors due to mediator dilution. The advantage of a reagentless biosensor is that differential dilution artifacts have been removed. The solution to the reagentless criterion for biomolecule-modified nanoparticles is addressed through biomolecule adhesion, specifically or non-specifically, to the nanoparticle surface. Certain aspects of attachment chemistry will be discussed in this chapter with regard to the effect on biosensor performance; however, the bulk of this literature is left to other chapters in this book series and many excellent review articles [1–5]. Here we discuss the growing literature of reagentless biosensors that are based on nanoparticles.

Notably, many nanoparticle-based biosensors function well but do not meet the reagentless criteria. One methodology is to encapsulate various chemosensors and biosensors within a nanometer scale liposome or polymer (PEEBLEs) [6–9]. While this methodology is quite successful, it is beyond the scope of this chapter. This chapter covers methods to perturb nanoparticle properties to produce unimolecular biosensors, since this methodology will allow the unique properties of nanoparticulate materials to be harnessed for analytical applications. Additionally,



biotin–streptavidin, DNA hybridization probes and antibody sandwich assays are superb systems for concept demonstration, but do not meet the reagentless criterion for this chapter. Coverage of these assays is left for other chapters in this volume. Finally, several cellular biosensors meet the reagentless criterion [5]. Discussion of these biosensors is deferred to other chapters in that the sensing modality still requires the multimerization of these probes to produce changes in optical absorbance, scattering, and fluorescence. Despite these biosensors being a single molecular species, the multimerization of these species is required for biosensing, which does not meet the reagentless criterion.

Nanoparticle-based reagentless biosensor development tests the current scaling law description of nanoparticulate systems. Creation of a nanoparticle-based reagentless biosensor must center on the nanoparticle as the readout element. The biomolecule–nanoparticle interface must be altered to translate the (bio)molecular–biomolecular binding event into a change in nanoparticle properties. The scaling rules of both nanoparticles and (bio)molecular phenomena must be interlaced for reagentless biosensing with nanoparticles. Thus, the reagentless criterion provides a method to compare nanosystem scaling rules to the scaling rules that are well known for material and molecular systems.

There are three general methods for interlacing nanoparticle and (bio)molecular scaling laws to provide nanoparticle-based reagentless biosensors (Fig. 12.1): surface dielectric enhancement, catalytic activation, and biomolecular conformational modulated effects. Optical, electrochemical, or magnetic detection methods have been reported for at least one of these classes. Additionally, surface immobilized and solution-based biosensors have differential representation in each class. Dielectric enhancement, detected by surface plasmon resonance or electrical conductivity, is induced by the analyte adsorbing to a nanoparticle surface. The nanoparticles in this class are typically surface immobilized or embedded; however, local surface plasmon resonance scaling rules suggest a solution-based approach could work as well. Catalytic activation of a biomolecule–nanoparticle scaffold by a small molecule analyte provides excellent signal responses using optical, electrochemical, and magnetic detection methods. The optical and magnetic detected biosensors from this class are solution-based, while the electrochemical is inherently surface-immobilized. The use of analyte-induced biomolecule conformation changes provides a flexible method for reagentless biosensor design. While, optical solution-state biosensors in this class are typical, nanoparticles are an excellent coupling element for developing electrochemical surface-immobilized biosensors of this class. In each of these reagentless biosensor classes, the analyte–biomolecule interaction must change either the nanoparticle electronic structure or influence the environment surrounding the nanoparticle.

Here we discuss reagentless nanoparticle-based biosensors in the context of three general methods for interlacing nanoparticle and (bio)molecular scaling laws. Classification by these methods will be used to discuss relationships between detection methods, types of analyte–biomolecule interaction, and the nanoparticle scaling rules. A caveats and advantages subsection points out this relationship and finishes the discussion of each general method. Each method relies on one of

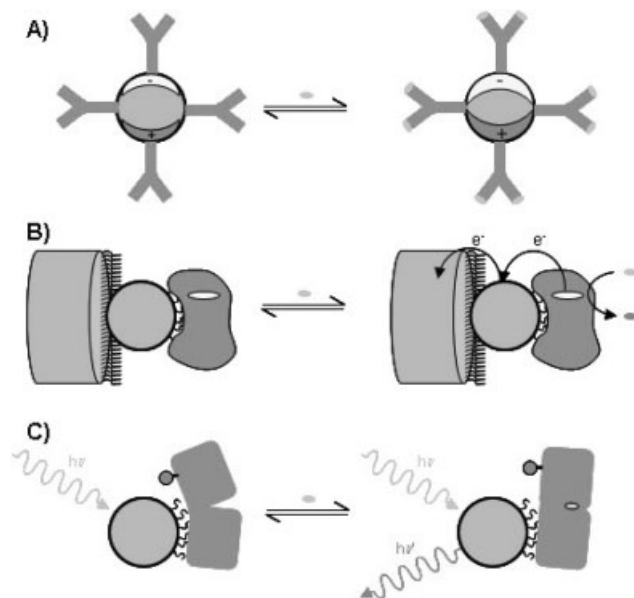


**Fig. 12.1.** Three classes of reagentless nanoparticle-based biosensors. (A) Analyte-induced changes in surface dielectric. The surface plasmon (+/−) is enhanced upon analyte binding to a biomolecule. (B) Catalytic enhancement of nanoparticle-mediated signals. Nanoparticle-facilitated electron ( $e^-$ ) transfer from an enzyme to a working electrode is

shown. (C) Biomolecular conformation changes that alter nanoparticle properties. Analyte-induced changes in protein conformation alters the distance between a nanoparticle and a reporter group, where the reporter group–nanoparticle distance changes the properties of the nanoparticle.

these related aspects more than another, which will be discussed in the conclusion section.

## 12.2

### Surface Dielectric Enhancement

Gold nanoparticles, silicon nanowires, and single-wall carbon nanotubes enhance the sensitivity in detecting analytes at material–liquid interfaces by changes in surface dielectric (Fig. 12.2). Most biosensors in this category are reagentless, in that biomolecule surface immobilization is necessary for providing selectivity. Surface dielectric changes can be detected either by changes in surface plasmon resonance (SPR) of gold coated materials or by changes in electrical conductivity of nanoscale circuits. In each of these approaches, an analyte is concentrated by a biomolecule and the build up of this analyte changes the solvent dielectric at the material–liquid interface. Sensitivity enhancements observed for both techniques come from increasing the number/strength of analyte–material interactions. Thus, intro-

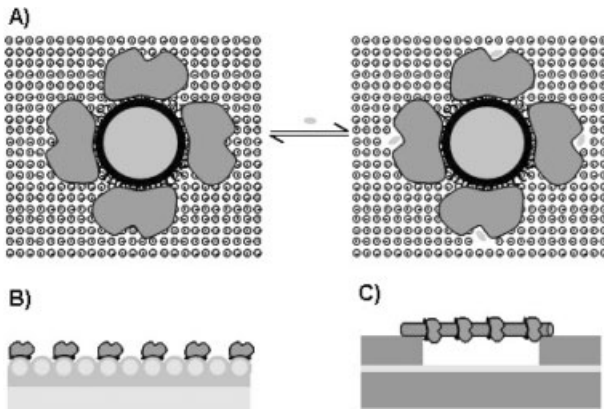


**Fig. 12.2.** Analyte-induced changes in surface solvent dielectric. (A) Upon analyte binding aqueous ions and water molecules are displaced, which alters the solvent dielectric at the nanoparticle surface. Two possible configurations are shown for detection of these effects: (B) Au bilayer films with proteins or nucleic acids attached to the solvent exposed

surface and (C) Si nanowire FET devices, where the bottom is the drain and the *n*- and *p*-gate are on either side of the Si nanowire (top). Proteins or nucleic acids are attached to the Si nanowire or the exposed surface of the Au film to increase solvent and ion displacement upon analyte introduction.

duction of nanoparticles, nanotubes, or nanowires enhance preexisting material properties.

### 12.2.1

#### Gold Nanoparticle Enhanced Surface Plasmon Resonance

Various Au/Ag nanoparticle modified surfaces enhance the SPR effect, but only two primary configurations have been used for reagentless biosensing. Additional localized SPR (LSPR) detection methods have been shown in multimolecular biosensor formats; however, discussion of these methods is left for another chapter in this series [10]. For planar Au/Ag surfaces the surface plasmon propagates along the metal surface, where changes in the refractive index or surface dielectric at the metal–liquid interface will alter plasmon propagation. For Au/Ag nanoparticle templated or fabricated surfaces, the surface plasmon scattering is redirected from within the material through the nanoparticles and into solution. These corrugated Au/Ag surfaces provide enhanced detection of changes in the solvent dielectric above these nanometer scale Au/Ag surface features [11, 12]. Two experimental configurations have been used to measure the LSPR response. The classic measurement determined the minimum absorbance by a Au/Ag coated slide as a function of the angle of incident light. A change in the angle of incidence for minimum absorbance indicates a change in solvent dielectric at the Au/Ag surface. Alternatively, the amount of light reflected at the surface plasmon resonance wavelength of Au/Ag nanoparticles has been determined using a backscattering fiber optic

setup. In this approach, changes in the solvent dielectric around the nanoparticle surface will change the amount of light back-scattered to the fiber optic cable. Backscattered reflection spectra are recorded and the intensity at the surface plasmon resonance peak is monitored. Both detection systems rely on the Au/Ag nanoparticle modified surface changing the SPR response as the analyte binds to surface-immobilized biomolecules.

One reagentless LSPR-based biosensor uses an Au nanoparticle coated quartz slide for optical detection. This work is ultimately based on earlier observations that Au nanoparticles adsorbing to Au surfaces shift the minimum angle of reflection from  $54.2^\circ$  to  $55.8^\circ$  [13]. While the binding of these nucleic acid probes is non-reagentless, reversibility measurements did provide reagentless detection of the *HinF* I restriction enzyme. Discussion of the restriction enzyme reagentless biosensing is left until Section 12.3. However, changes in the intensity of the Au/Ag nanoparticle surface plasmon absorbance can also be used as a detection strategy. Frederix and coworkers [14] have demonstrated LSPR-based human serum albumin (HSA) biosensing using a quartz substrate mounted in a cuvette using a standard UV/Vis spectrophotometer. The quartz substrate had Au nanoparticles adsorbed to the surface through 3-mercaptopropyl triethoxysilane and enlarged the Au nanoparticles under electroless reduction of  $\text{HAuCl}_4$ . Anti-HSA was covalently attached to the Au modified surface [14, 15] causing an increase in surface plasmon resonance ( $\sim 634$  nm, Au;  $\sim 445$  nm, Ag) and, after subtraction of the protein contribution, the interband absorbance (250–400 nm, Au and Ag). Addition of  $2.5 \text{ mg mL}^{-1}$  HSA ( $\sim 40 \text{ }\mu\text{M}$ ) to anti-HSA modified Au nanoparticle surfaces caused a 0.002 and a 0.004 absorbance unit increase after 30 min and overnight incubation in the absence of stirring. These small, but detectable, absorbance signals demonstrated reagentless biosensing could be obtained using common instrumentation. As noted by the authors, addition of stirring to this system will increase mass transport and facilitate a more rapid response. The small absorbance response could be enhanced by using the biotin-immobilized surface shown by Nath and Chilkoti [12] with a tightly packed array of monodisperse Au nanoparticles. This work used a flow cell variant of the Frederix work to increase mass transport, but maintained detection by a UV/Vis spectrophotometer. In this study, a biotin-immobilized array of 39-nm diameter Au nanoparticles on a glass slide showed a 0.050 absorbance increase upon the binding of  $1 \text{ }\mu\text{g mL}^{-1}$  ( $\sim 20 \text{ nM}$ ) streptavidin [12]. Thus, reagentless biosensing by an array of glass-immobilized nanoparticles provides a highly accessible platform for Au nanoparticle-based reagentless biosensor development.

Au bilayer films with 100 nm spherical features allowed for wavelength-resolved backscattered reflectance detection of single-stranded DNA and fibrinogen (Fig. 12.2B) [16, 17]. In these reports, thiobutyric acid coated Au films on glass slides were EDC coupled with 100 nm diameter aminopropyltriethoxysilane coated silica nanoparticles and the second Au layer was vapor deposited over these 100 nm silica particles. Near monolayer coverage of these 100 nm features yielded an optimal LSPR response [17]. The 100 nm features of these surfaces create an array of Au nanoparticle shells that have been shown previously to provide large LSPR enhancements [18]. These Au bilayers are similar, but with larger features, to the

nanoprism arrays on Au surfaces reported by Van Duyne and coworkers [11]. Anti-fibrinogen was immobilized on these structures through biotin–streptavidin chemistry, which increased the reflected absorbance at 560 nm by 0.2 absorbance units. Addition of  $100 \mu\text{g mL}^{-1}$  ( $\sim 2 \mu\text{M}$  of monomers) fibrinogen yielded an additional 0.2 absorbance unit increase, while bovine serum albumin addition (non-specific control) yielded a 0.002 absorbance unit increase. When the neutral backbone peptide nucleic acid (PNA) or DNA is substituted for the antibody, single-stranded nucleic acids were detected in a reagentless format [16]. Biotinylated DNA or PNA probes (10-mers) from the tumor necrosis factor- $\alpha$  gene were attached to the Au corrugated surface, causing a 0.10 to 0.15 increase in absorbance at 550 nm. Addition of a complementary DNA target ( $1 \mu\text{M}$ ) with a single nucleotide mismatch yielded a less than a 0.003 absorbance unit increase, while addition of a completely complementary DNA target ( $1 \mu\text{M}$ ) yielded a 0.15 to 0.2 absorbance unit increase. The limit of detection of both the PNA and DNA immobilized biosensors were 0.1 pM of the target DNA with a 0.03–0.04 absorbance unit increase. PCR-amplified DNA targets were also detected down to  $5 \mu\text{L}$  of the 1:40 dilutions from the initial amplified mixture. Application of this reagentless biosensing strategy to the smaller Au/Ag nanoisland structures fabricated and examined by Van Duyne and coworkers [11, 19] should produce similar absorbance changes, along with over 100 nm redshifts in the surface plasmon absorbance. Therefore, these nanotemplated Au/Ag surfaces provide a surface-immobilized platform for reagentless biosensing with inexpensive instrumentation.

A hybrid photoelectrical SPR-detected device has been constructed for reagentless biosensing of acetylthiocholine [20]. Using an open circuit configured Au electrode, monolayers of Au and CdSe nanoparticles were successively chemisorbed to the Au surface (Au/Au np/CdS np surfaces, Fig. 12.3). A similar surface had been shown previously to display a photoinduced change in the minimum angle of incidence for SPR reflected light under closed circuit constant potential electro-

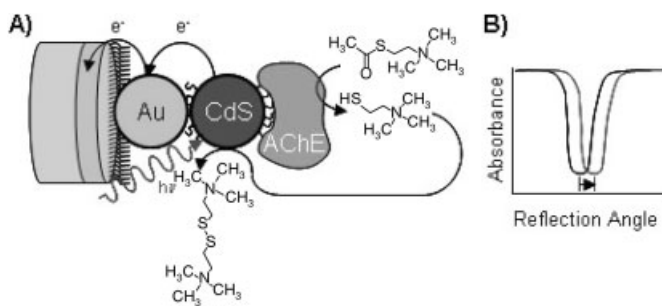


**Fig. 12.3.** Example of a hybrid biosensing device. Enzymatic hydrolysis of acetylthiocholine into thiocholine and thiocholine oxidation provides a pseudo-reagentless method for photoelectrochemical

injections of electrons into thin Au films (A). Electron injection to the Au surface changes the incident angle of surface plasmon resonance (B).

chemical conditions [21]. With these Au/Au np/CdS np surfaces, applying mM concentrations of triethanolamine in the presence of 1.5 mW blue LED source caused up to a  $0.4^\circ$  shift in the angle of incidence minimum. This open circuit photostimulated SPR effect comes from a  $\sim -150$  mV bias across the Au/Au nanoparticle junction and a  $-25$  mV photoinduced potential from the CdSe nanoparticle. The triethanolamine dependence of this process stems from oxidation of triethanolamine by the valence band holes of CdS, which are formed by photoexcitation. Back of the envelope calculations suggests four additional electrons are collected per Au nanoparticle during this photostimulated process. Pseudo-reagentless biosensing was then demonstrated, where acetylcholine esterase was attached to the CdS nanoparticle that in the presence of acetylthiocholine produced thiocholine. The acetylcholine esterase-produced thiocholine then mediated the photostimulated  $0.4^\circ$  shift in the minimal SPR absorbance angle of incidence at 25 mM acetylthiocholine and a 2 mM LOD. The acetylcholine LOD in this system is limited by the  $K_M$  of acetylcholine esterase, as observed by the  $\mu\text{M}$  LOD for an acetylcholine esterase inhibitor. This strategy has also been applied to an electrocatalytic biosensor (Section 12.3.1). This strategy not only demonstrates an exciting hybrid technique for nanoparticle-based reagentless biosensing, but also demonstrates the detection of a low molecular weight analyte and that electrode-immobilized metallic nanoparticles function as electron reservoirs.

### 12.2.2

#### Carbon Nanotube and Silicon Nanowire Enhanced Conductivity

Altering the conductivity of nanometer-scale electrode junctions is an alternative technique to optical surface plasmon resonance techniques for biosensor development (Fig. 12.2C). Single-wall carbon nanotubes (SWCNTs) [22] and Si nanowires (SiNWs) [23] have been used for biosensing [24, 25]. The conductivities of these devices are intimately linked to the electrostatics surrounding the SWCNTs and SiNWs. While there are different scaling effects for SWCNTs [26] and SiNWs [23], these nanotubes increase the sensitivity of conductivity measurements by increasing the interaction between the electrode carriers and the surrounding solution. Electrical conductivity detected biosensing with nanotubes is similar to SPR detected biosensing, in that the non-specific adsorption needs to be carefully excluded. While the sensing methodology is generally similar between SWCNTs and SiNWs, there are differences in device fabrication and biomolecule attachment chemistry.

Carbon nanotubes are attractive as biosensing transducers from a biocompatibility and synthetic standpoint. Covalent modification of SWCNTs for biomolecule attachment is an active area of research [24, 25]. Despite reported methods, biomolecular attachment to SWCNTs for reagentless biosensing has relied on surfactant physisorption with Tween [22]. Covalent coupling between Tween-20 and the biomolecule of interest then provides the specificity for conductivity measurements. Surfactant coating is an important issue in that the sensitivity of the conductivity response is minimized. An additional issue comes from the observation that con-

ductivity detection occurs primarily at the SWCNT–metal electrode junction, or Schottky barrier modulation [26]. Adsorption of biomolecules with an isoelectric point similar to the solution pH to the SWCNT–metal junction will give the largest change in conductivity [26]. If SWCNTs are left untreated, non-specific protein adsorption abounds due to the large hydrophobic surface area of the SWCNTs, as observed by conductivity changes. Tween-20 and other surfactants also adsorb readily and irreversibly to SWCNT surfaces [22], forming the basis for biomolecule selective attachment strategies discussed here.

Selective protein detection has been displayed by SWCNT-based biosensors in a reagentless format. Initial studies from Dai and coworkers were performed with immunoglobulin G (IgG) and the 10E3 antibody that selectively binds the U1A RNA splicing factor [22]. Each of these selective sensors were generated through carbodiimide coupling between SWCNT adsorbed Tween-20 and either staphylococcal protein A (IgG biosensor) or U1A RNA splicing factor (10E3 biosensor). The staphylococcal protein A immobilized sensor showed a 1.02-fold decrease in conductance with the addition of 100 nM IgG after 5–10 min. The IgG LOD could be 20–50 nM for this system. The U1A-immobilized sensor gave a 1.03-fold decrease in conductivity with the addition of 1 nM 10E3 antibody after 10 min, placing the LOD for 10E3 around 200 pM. As a proof of principle after a mechanistic report, human chondriotic gonadotropin (hCG) was immobilized on a SWCNT device to detect a monoclonal antibody that specifically binds hCG, termed  $\alpha$ -hCG. Addition of 10 nM  $\alpha$ -hCG to the hCG immobilized sensor yielded a 1.03-fold decrease in conductivity after 15 min. The  $\alpha$ -hCG LOD is approximately 5 nM from this report. With known solution state affinities for at least the SpA-IgG complex ( $K_D \sim 1$  pM) the sensitivity of these biosensors seems to be limited by the SWCNT conductivity. Recently, SpA and hCG immobilized SWCNT biosensors were reported with 1 pM detection of IgG or  $\alpha$ -hCG, respectively, within one minute [27]. This increased sensitivity was provided by a shadow mask lithography technique, which increased the area of SWCNT-Si/SiO<sub>2</sub> contact and increased the Schottky barrier where detection occurs. An increased conductivity response has been reported for an aptamer-immobilized SWCNT sensor [28]. The thrombin-specific DNA aptamer used in this report is one of the classic protein-specific aptamers [4]. The thrombin aptamer was carbodiimide coupled to Tween-coated SWCNTs, which yielded a sensor with 1.08-fold decrease in conductivity with the addition of 1  $\mu$ M thrombin. The thrombin LOD for this biosensor was 10 nM and the response saturated at 300 nM. Since the thrombin–aptamer dissociation constant is 100 pM in solution the sensitivity of this biosensor can be improved. Finally, glucose/glucose oxidase production of H<sub>2</sub>O<sub>2</sub> has provided a pseudo-reagentless biosensing strategy for glucose [29]. This report immobilized glucose oxidase to SWCNTs through a pyrene-modification so that, in the presence of glucose, O<sub>2</sub> would be converted into H<sub>2</sub>O<sub>2</sub> and increase the conductivity around the Schottky junction. This biosensor showed a 1.12-fold increase in conductivity after the addition of 10  $\mu$ M with a 30 s response time that lasted for at least 10 min. With the advent of SWCNT covalent modification chemistries [30] and the increased Schottky barrier

area fabrication technique [27], the sensitivity and response of SWCNT conductivity sensors can be improved from these exciting reports.

Lieber and coworkers have demonstrated SiNWs as a conductivity detected biosensing platform. SiNW-based sensors rely on the solvent dielectric surrounding the nanowire surface and not the nanowire termini at the device interface. This chemical potential of SiNWs allows for an increased interaction between the solution dielectric and carriers in the nanowire. Thus, SiNWs are potentially more sensitive than SWCNT-based conductivity devices. Additionally, the passivated SiO<sub>2</sub> layer on the SiNW surface allows for facile biomolecule immobilization chemistry. 3-(Trimethoxysilyl)propyl aldehyde treatment is typically used to provide biotin or protein modified surfaces. The increased synthetic control of doping in SiNWs also allows analyte response validation by observing the opposite conductivity response in the oppositely doped SiNW. SiNW-based conductivity devices that detect a metal ion, DNA, and proteins have been reported.

SiNW-based biosensors displayed higher sensitivities but similar conductance changes compared with SWCNT-based biosensors. The initial report of SiNW-based biosensors described a calmodulin-terminated SiNW sensor [23]. This sensor showed a reversible 1.03-fold decrease in conductance within 15 s of 25  $\mu\text{M}$  Ca<sup>2+</sup> ions. Two systems were reported for SiNW-based biosensing of DNA. Li and coworkers used a top-down lithographic method to fabricate larger diameter SiNWs [31]. Chemical immobilization of the probe DNA oligonucleotide to SiNWs yielded a biosensor with a 1.13-fold increase (*p*-type SiNW) and a 1.8-fold decrease (*n*-type SiNW) in conductivity within 30 s of adding 25  $\mu\text{M}$  complementary DNA. Lieber and coworkers used synthetic SiNWs with biotin-modified surfaces. Avidin attachment to these biotinylated SiNWs then facilitated biotinylated PNA immobilization [32]. Despite the larger distance of the probe PNA from the *p*-type SiNW surface, within 5 min a 1.25-fold increase in conductivity was observed with the addition of 100 fM complementary DNA to this biosensor. This biosensor was specific for the complementary DNA over a DNA containing a single base deletion, responsible for cystic fibrosis. A 10 fM detection limit of this PNA-modified SiNW device places this as one of the most sensitive detection methods for DNA. Direct protein adhesion was used for cancer marker biosensing, where monoclonal antibodies for prostate specific antigen (PSA) and carcinoembryonic antigen (CEA) were immobilized through aldehyde crosslinking to an array of *n*-type and *p*-type SiNWs [33]. This sensor showed a 1.10-fold increase (*p*-type) and a 1.12-fold decrease (*n*-type) in conductivity with the addition of 20  $\mu\text{M}$  PSA. The LOD for PSA in buffer was 25 fM (1.01-fold change in conductivity) while a 0.8  $\mu\text{M}$  LOD was found for PSA detection in donkey serum. Immobilization of a protein tyrosine kinase, Abl, to *p*-type SiNWs through aldehyde crosslinking chemistries yielded reagentless ATP biosensors with a 1 nM LOD [34]. The addition of 20 nM ATP caused, surprisingly, a 2.0-fold increase in conductivity. Addition of known Abl inhibitors decreased the ATP-dependent increase of the *p*-type SiNW conductivity to about 25% of the initial increase (1.25-fold increase). Given the large change in conductivity relative to the molecular weight of ATP, a protein conformation change could be responsible



for this large relative increase in conductivity but the lack of site-specific attachment chemistry makes investigation of this point difficult. Taken together, SiNWs provide a versatile platform for biomolecule attachment, microfluidic interfacing, and high analyte sensitivity for reagentless biosensing.

### 12.2.3

#### **Advantages and Caveats**

The ability to directly couple biomolecules to nanoparticles for analytical readout is a clear advantage of the surface dielectric technique. The use of nanoparticles provides an exquisite sensitivity to solvent dielectric changes localized at the nanoparticle surface. Proper attachment of biomolecules to nanoparticle surfaces adds the molecular selectivity necessary for analyte detection. Most of these devices are surface immobilized, which minimize the amount of solution handling for biosensor activation. The surface immobilized nature of these devices allows for multiplexed device fabrication and application to microfluidic separations. Integration of these sensors with microfluidic separation is required due to the necessity of sample clean-up. Changes in surface dielectric effectively increase the local analyte concentration around the nanoparticle surface. Therefore, analyte detection in complex environments will be difficult based on the small signal changes and large changes in bulk solvent dielectric. By comparison of *n*- and *p*-type Si nanowires Lieber and coworkers have addressed this issue [33, 34]; however, performing this analysis in salt water, for example, would be difficult. Therefore, additional methods for reagentless biosensing have been explored to minimize the amount of sample clean-up necessary before analysis.

## 12.3

### **Catalytic Activation**

An alternative method for developing reagentless biosensors is to couple nanoparticle–biopolymer composites with catalytic activity. The nanoparticle scaling rules used by biosensors in this class depends on whether the detection method is electrochemical or optical/magnetic. The distance dependent dissipation of this sensitivity should decay rapidly. Electrochemical biosensors that use nanoparticles take advantage of the improved electron flux at the enzyme–electrode interface that the nanoparticle provides. Scaling laws similar to the previously discussed LSPR-scaling laws are used in optical or magnetic detected biosensors in this class. The catalytic strategy can be readily employed to translate concepts from hybridization-based biosensors into reagentless biosensors for hydrolytic enzymes or reagents. While the surface dielectric methodology provides a method that integrates surface immobilization chemistry with analyte–biomolecule binding, the catalytic methodology translates multimolecular biosensing strategy into a reagentless biosensing strategy.

## 12.3.1

**Electrocatalytic Detection**

Nanoparticle-modified electrode surfaces allow multimolecular electrocatalytic biosensors to be translated into reagentless biosensors. Electrode immobilized glucose oxidase (GOx) is the classic electrocatalytic biosensor example. GOx-based biosensors provide a catalytic amplification of Faradaic current to overwhelm capacitive currents that typically dominate enzyme-immobilized electrochemical responses. Such catalytic enhancement occurs by the detection of  $\text{H}_2\text{O}_2$  resulting from  $\text{O}_2$  reduction during glucose oxidation by GOx. Catalytic amplification stores electron equivalents in small molecular products that are more rapidly transported to the electrode surface. Carbon nanotubes [35–38], Au nanoparticles [39–42], CdS nanoparticles [43], and  $\text{Fe}_3\text{O}_4$  nanoparticles [44] that are immobilized on glassy carbon electrodes also store electron, or hole, equivalents to produce electrocatalytically amplified Faradaic currents for biosensing (Fig. 12.1B). The photovoltaic LSPR biosensing scaffold discussed in the previous section calculated under photostimulated, open circuit conditions that four electrons were injected per Au nanoparticle [20]. Both increased electronic communication and enzyme stability of colloidal Au adsorbed electrodes were demonstrated ten years ago [45–47]. Integration of the reagentless electrocatalytic biosensors discussed here shows a  $\sim$ five-fold integrated current increase, by cyclic voltammetry, in non-mediated background electrocatalytic currents of enzyme-immobilized glass carbon electrodes. Most of these methods employ non-oriented physisorption or crosslinking chemistries for enzyme film formation on the electrode interface. The five-fold Faradaic current increase relative to the uncoated glassy carbon electrode was observed for carbon nanotube [35, 36, 38], Au nanoparticle [39, 42, 48], and  $\text{Fe}_3\text{O}_4$  nanoparticle [44] adsorbed glassy carbon electrodes. The potential for increased enzyme stability and electrode interaction with active enzyme makes the correlation of this five-fold increase in integrated Faradaic current difficult to justify as an increased heterogeneous electron transfer rate. Since surface immobilized electrochemical behavior is not typically observed for bare glassy carbon electrodes, derivation of differences in the heterogeneous electron transfer rate is difficult. While no comparison of Faradaic current increases were provided by adsorbing CdS nanoparticles to glassy carbon electrodes, Willner and coworkers have shown photocatalytic electron transfer in enzymes adsorbed to CdS nanoparticle [21] and CdS nanoparticle–Au nanoparticle [20] modified Au electrodes. These nanoparticle-modified Au electrodes clearly point out that electron injection to Au nanoparticles occurs [20]. Also, photocatalytic electron injection is provided by CdS nanoparticle modified Au electrodes [21]. Finally, enzymatic immobilized versions of nanoparticle-modified electrodes can reversibly activate these photostimulated effects [20, 21]. Therefore, integration of nanoparticles into enzyme immobilized electrodes provides mediator-free electrocatalytic amplification.

For reagentless electrocatalytic biosensors the detectable analytes are predominantly low molecular weight. Glucose oxidase based electrocatalytic biosensors

displayed different LODs for glucose. Single-wall carbon nanotube adsorbed electrodes with GOx have shown an increase in catalytic current with a LOD of 2 mM glucose and a response time of 30 s [35]. CdS nanoparticle modified glassy carbon electrodes were able to detect glucose by a decrease in the reductive current in cyclic voltammetry with a glucose LOD of 2 mM [43]. The decrease in reductive current upon glucose addition demonstrated slow electron injection from CdS for FAD reduction in the absence of photostimulation. The GOx adsorbed Au nanoparticle modified electrodes showed a LOD of 50  $\mu\text{M}$  but a decrease in background current with a  $-600$  mV potential (vs. SCE) upon glucose addition [41]. The Au nanoparticle based biosensor was able to detect accurately blood glucose levels (8.4 mM). Carbon nanotube modified electrodes with alcohol dehydrogenase immobilized showed an ethanol LOD of 1 mM [37], consistent with the  $K_M$  for the enzyme. Immobilization of hemeproteins provides bioelectrochemical sensors for various low molecular weight redox-active analytes. Hydrogen peroxide is a common analyte for these sensors, where the LOD for the multiwall carbon nanotube biosensors [36, 38] was  $\sim 1$  mM. The  $\text{Fe}_3\text{O}_4$  nanoparticle modified electrodes provided a 80  $\mu\text{M}$  LOD for hemoglobin- or myoglobin-immobilized electrodes and a 2  $\mu\text{M}$  LOD for catalase-immobilized electrodes.  $\text{Fe}_3\text{O}_4$  nanoparticle modified electrodes demonstrated that the sensitivity was determined by the enzyme, not the electrode. Nitrite biosensing with these  $\text{Fe}_3\text{O}_4$  nanoparticle modified electrodes [44] and with Au nanoparticle modified electrodes [42] both showed a 200  $\mu\text{M}$  LOD for sodium nitrite in the electrocatalytic mode. However, the Au nanoparticle modified electrode with hemoglobin immobilized showed a 1  $\mu\text{M}$  LOD for nitrite [42] and 50 nM LOD for NO [40] using reversible non-catalytic peak currents from cyclic voltammetry. The final example is the immobilization of the Cu-containing tyrosinase on Au nanoparticle modified electrodes, which demonstrated LODs for phenolic compounds from 150 nM (catechol) to 70  $\mu\text{M}$  (gallic acid) [39]. Tyrosinase-modified electrodes were able to detect the concentration of caffeic acid (LOD 6  $\mu\text{M}$ ) from three red and three white wines, confirmed by a colorimetric test. Overall, LODs that reflect the Michaelis constants of the immobilized enzymes are observed for electrocatalytic biosensors that use nanoparticles as an electron reservoir.

A photoelectrochemical methodology demonstrates the potential for integrating semiconducting nanoparticles into the bioelectrocatalytic systems above. Willner and coworkers have demonstrated that illumination of CdS-modified Au electrodes with acetylcholine esterase attached to the CdS nanoparticle turns on electrocatalytic current [21]. Enzymatic production of thiocholine governs this process, in that thiocholine reduces CdS valance band holes, which are formed upon photoexciting the CdS nanoparticle. Monitoring the current as a function of wavelength (6–30 mM acetylthiocholine) produced an action spectra consistent with the band edge absorbance of the CdS nanoparticles. In the presence of 380 nm wavelength light, a LOD of 5 mM acetylthiocholine was detected, and the response saturated above 30 mM. In comparison, CdS nanoparticles adsorbed on glassy carbon electrodes were able to detect the slow reduction of glucose oxidase FAD in the absence of light and glucose [43]. Taken together these experiments demonstrate that electron flow between CdS and enzymes/substrates is reversible. Application

of photostimulated electron transfer to the electrochemical-based biosensors discussed here provides a method to introduce additional detection selectivity. Semiconducting nanoparticles allow the development of such hybrid techniques, like the photostimulated LSPR effect in Section 12.2 [20], to be developed.

### 12.3.2

#### Catalytically Enabled Optical and Magnetic Detection

Enzymatic cleavage of biomolecule-tethered nanoparticles provides an alternative method for detecting enzymatic activity (Fig. 12.4). In this particular type of sensing, the biomolecule attached to the nanoparticle becomes the substrate to detect the enzyme or reagent catalyzing biomolecule hydrolysis. As biomolecule hydrolysis occurs the physical link between the nanoparticles or nanoparticle–organic fluorophore is broken. Once the nanoparticles or nanoparticle–organic fluorophore assembly dissociate, the properties of the non-modified nanoparticles and fluorophores are restored [1, 10, 49, 50]. Such a strategy has yielded pseudo-reagentless biosensors based on Au nanoparticle quenched CdSe@CdS nanoparticle emission [51], Fe<sub>3</sub>O<sub>4</sub> nanoparticle associated enhancement of spin–spin relaxation time ( $T_2$ ) of adjacent water protons [52], or magnetic field modulated cantilever deflection [53, 54]. This method might be extended to optically detected surface plasmon resonance from an Au nanoparticle assembly. While optical assays based on hydrolysis of DNA-modified Au nanoparticle assemblies exist [55, 56], the assembly and thermal denaturation steps seem to ensure specificity. It is assumed that the forces applied by magnetic field detection methods [52, 53] overcome the need for assembly and thermal denaturation. Since enzymatic cleavage uses an initial associated complex, the more effective scaling laws for nanoparticulate materials can be more readily employed for biosensor development.

To date, there is one example of a reagentless, optically-detected biosensor for collagenase [51]. In this system, a peptide that is specifically degraded by collagenase (GGLGPAGGCG) is covalently coupled between CdSe@CdS nanoparticles on the amino-terminus and Au nanoparticles on the carboxy-terminus. The covalently coupled CdSe@CdS-peptide-Au complex has the CdSe@CdS emission intensity partially quenched by energy transfer to the Au nanoparticles. Incubation with  $\sim 2 \mu\text{M}$  collagenase for 18, 39, and 47 h showed a 1.10, 1.20, and 1.35-fold increase, respectively, in CdSe@CdS emission intensity. While the response times for these

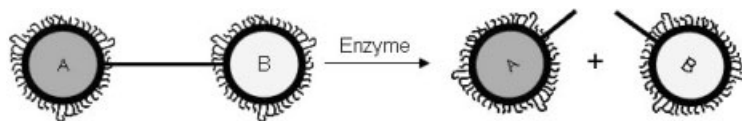


**Fig. 12.4.** Enzymatic cleavage of biomolecule tethered nanoparticle–nanoparticle or reporter group–nanoparticle pairs. Upon cleavage, the pair of chromophores no longer interact and restore the original signal of these chromophores.

collagenase biosensors are slow, the response time could be enhanced through increasing the accessibility of the peptide substrate.

DNA–magnetic nanoparticle assemblies that have been termed magnetic relaxation switches (MRS) provide magnetic resonance imaging (MRI) detected reagentless biosensing [52]. This method hybridizes two pools of covalently modified DNA–Fe<sub>3</sub>O<sub>4</sub> nanoparticle aggregates with complementary nucleotide sequences. Once assembled, the 50–100 nm DNA–nanoparticle aggregates decrease the water spin–spin relaxation time ( $T_2$ ) by two-fold. Duplex DNA formed in these hybridized assemblies contains a recognition site for the BamH I restriction endonuclease. Digestion with BamH I, but not EcoR I digestion, caused a disassembly of the aggregates and a restoration of the original  $T_2$ . Imaging microtiter plate samples within a MRI spectrometer, the Dpn I restriction endonuclease was specifically detected with methylated DNA–Fe<sub>3</sub>O<sub>4</sub> nanoparticle assemblies, while unmethylated DNA–Fe<sub>3</sub>O<sub>4</sub> nanoparticle assemblies showed no change in  $T_2$ . A similar strategy was reported where rennin and matrix metalloprotease-2 proteolytic activities were determined using peptide substrates that were biotinylated at both termini [57]. Unfortunately, the peptide substrate had to be hydrolyzed before nanoparticle assembly occurred, rendering this as a multimolecular assay. Despite the drawbacks of this second assay, catalytic hydrolysis has demonstrated reagentless biosensing can be performed using MRI.

Using larger magnetic particles, Willner and coworkers have demonstrated reagentless biosensors that detect restriction endonucleases with the application of a magnetic field [53, 54]. Atomic force microscope cantilevers were coated with Au and thiol-terminated DNA that was complementary to DNA modified magnetic particles. The duplex DNA formed on the cantilever surface contained recognition sites for restriction endonucleases. The cantilever deflection could be reversibly controlled by application of a magnet to each system. The force experienced by these cantilever systems was around 1–3 nN. In one system, ten units of either Apa I or Mse I restriction endonucleases were detected with a 5 minute response time [53]. In a different set of systems, two restriction enzyme sites were included on one DNA duplex providing an OR logic gate detection for either Apa I or EcoR I [54]. Alternatively, a mixed monolayer of duplex DNA was formed between the cantilever surface and the magnetic particle that contained recognition sites for EcoR I and Asc I on different duplex DNA strands. The mixed monolayer provides an AND logic gate detection of EcoR I and Asc I. The extension of logic gated detection strategies to microarray sensors is a particularly interesting application for biosensor development.

### 12.3.3

#### **Advantages and Caveats**

Catalytic activation schemes for biosensing with nanoparticles enhance the analyte-dependent signal. Enhancement occurs by one of two methods, either using nanoparticles to interface enzymatic electrochemical reactions or to adapt analyte–biomolecule recognition to the scaling laws of nanoparticle mediated effects. These

methods harness the unique properties of nanoparticles to detect analytes in complex mixtures. Analyte specificity, in each case, is provided by the enzymatic amplification of a Faradaic current or enzyme (analyte) mediated cleavage. However, many additional factors contribute to enzyme inhibition and the degree of inhibition varies from enzyme to enzyme. The largest caveat with enzymatic activation schemes is that surface immobilization is necessary for analyte reversible detection. Thus, use of enzymatic activation schemes for reagentless biosensing for fluorescence contrast imaging agents will only provide single-use biosensors. An obvious alternative is to couple analyte-dependent biomolecular conformation changes to provide reversible analyte detection by fluorescence contrast imaging biosensors.

## 12.4

### Biomolecule Conformational Modulated Effects

The final method for reagentless biosensing using nanoparticles is translating ligand-mediated biomolecule conformational motions into changes in nanoparticle properties (Fig. 12.5). While the previous methods have focused on directly coupling the ligand–biomolecule binding event to changes in the analytical signal, this method focuses on the detecting changes in the interaction between a reporter molecule and a nanoparticle. The reporter groups that have been described are organic compounds [58–62], a coordination complex [63, 64], or a nanoparticle [65]. With the reagentless criterion, these reporter groups have to be covalently attached to the biomolecule. Covalent bond formation is carried out through standard nucleophilic modification chemistries [66], where biomolecule-derived primary amines or thiols are modified with the reporter group. Reporter group co-

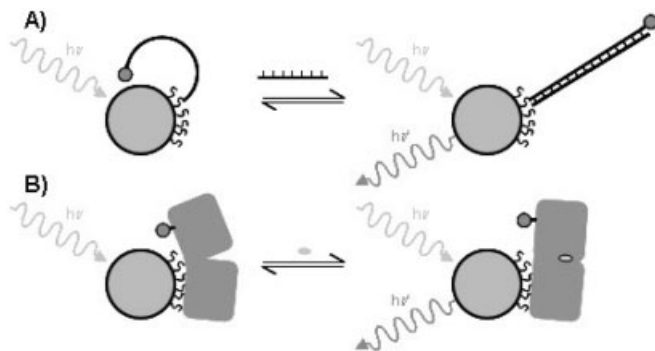


**Fig. 12.5.** Biomolecular conformation changes mediate reagentless nanoparticle-based biosensing. (A) Nucleic acid-based conformation changes will move a reporter group (the smaller ball) by 10 to 50 Å away from the nanoparticle upon complementary nucleic acid binding. (B) Protein-based conformation changes will move a reporter group by 1 to 6 Å away from the nanoparticle upon analyte binding.

valent attachment is necessary for ligand-mediated conformation changes to alter the reporter group–nanoparticle interaction. Since biomolecular conformation changes are the focal point of this method, the nanoparticle has to be site-specifically attached to the biomolecule as well. Thus, strategies for orthogonal site-specific attachment of reporter groups and nanoparticles are necessary for this method [55, 67–69]. These methods either use DNA synthesis and modification chemistry or recombinant DNA technology for protein production followed by modification chemistry. Once generated, the type of reporter compound–nanoparticle interaction that effectively reports analyte concentrations depends on the magnitude of biomolecule motion. DNA duplex formation provides the largest conformation change (10–50 Å, Fig. 12.5A), while analyte-induced protein conformation changes are much more subtle (1–10 Å, Fig. 12.5B). Therefore, this section will be organized based on the type of biomolecule (DNA or protein) used in analyte detection.

#### 12.4.1

##### **Biosensors Based on DNA Conformation Changes**

With the larger analyte-induced conformation change of DNA, more nanoparticle-based detection methods have been reported (Fig. 12.5A). Energy transfer methods are a popular method for detecting changes in biomolecule conformation [70] and provide reagentless biosensors with DNA probes. Organic reporter molecules [58, 60–62] seem to be most effective in reagentless biosensor development. Au–Au nanoparticle interactions have also been used to provide colorimetric pseudo-reagentless biosensors [65]. Three types of analytes have been detected by these DNA–nanoparticle-based biosensors: oligonucleotides, proteins, and small molecules. The oligonucleotide biosensors [58, 60, 62] used base pair recognition for sequence specific recognition. With the development of selection strategies for small molecule and protein dependent conformation changes in nucleic acids (aptamers) [71, 72], small molecule [65] and protein [61] biosensors have been developed for reagentless DNA-nanoparticle based biosensors. Aptamers provide a complementary method for reagentless small molecule and protein biosensing relative to proteins [4]. The drawback of aptamer–nanoparticle based biosensors that are currently reported is that they are pseudo-reagentless where they begin as unimolecular species but after analyte addition part of the initial system is displaced. Irrespective of this critique, these aptamer-based biosensors have introduced an important concept in reagentless nanoparticle-based biosensor development.

Aptamer–nanoparticle based biosensors provide an avenue to rapidly expand the pool of analytes that are detected by reagentless nanoparticle-based biosensors. Using exponential selection strategies (SELEX) [71, 72], various RNA and DNA sequences have been identified that bind small molecules and proteins while inducing a change in nucleic acid tertiary structure [4]. The ligand-bound conformation is typically a stem-loop structure where the base of one of the nucleic acid termini forms a duplexed stem. Stem formation then mediates a reporter molecule that is

attached to the stem forming nucleic acid terminus, moving either away from or towards the nanoparticle surface. As pointed out above, the change in the reporter group–nanoparticle distance can be between 10 to 50 Å in aptamers. Adenosine and cocaine aptamers were attached to Au nanoparticles through a thiolate-modified 3'-end of a 12-mer complementary DNA strand [65]. In the absence of adenosine or cocaine the oligonucleotide existed in an extended conformation allowing a second Au nanoparticle with a 5' thiolate-modified DNA strand complementary to the aptamer DNA. The duplex DNA formed from this second Au nanoparticle DNA was composed of seven bases from the adenosine aptamer sequence and five additional bases used to separate the aptamer sequence from the hybridization sequence of the first Au nanoparticle. When these two pools of DNA-modified Au nanoparticles are combined, the classic redshifted absorbance (~580 nm) of aggregated Au nanoparticles was observed. Due to multiple DNA molecules attached to one Au nanoparticle, a simple two Au nanoparticle complex did not occur but a larger aggregate of Au nanoparticles formed. However, the addition of 0.5 to 5 mM adenosine changed the solution from blue to red within one minute. The equilibrium absorbance ratio between 522 nm (dissociated) and 700 nm (aggregated) increased up to a saturated value of 15 with the addition of adenosine or cocaine to the cognate aptamer assemblies. While the adenosine/cocaine-mediated dissociation kinetics look monoexponential, the absorbance ratios after one minute of reaction showed two binding affinities and saturated absorbance ratios. The low adenosine/cocaine effect could be explained by dissociation of Au nanoparticles on the surface of the Au nanoparticle aggregates. Despite these effects a colorimetric assay for adenosine and cocaine with LODs of 0.5 and 0.1 mM was developed by this strategy.

Thrombin-specific aptamer modified CdSe@ZnS nanoparticles were generated and demonstrated thrombin and DNA biosensing detected by fluorescence [61]. This strategy harnessed the high quantum yield and photostability of semiconducting nanoparticles for low micromolar analyte sensitivity. The system used commercially available streptavidin-coated CdSe@ZnS nanoparticles that emitted at 525 nm. A 5'-biotin modified DNA containing the thrombin aptamer sequence was hybridized with a complementary 12-mer DNA with a proprietary organic quencher ( $\epsilon_{525} \sim 66\,000 \text{ M}^{-1} \text{ cm}^{-1}$ ) attached to the 3'-terminus. Up to 40 quencher-containing DNA equivalents needed to be added per CdSe@ZnS nanoparticle to quench the fluorescence by 95%. Addition of 0.8  $\mu\text{M}$  complementary DNA or 1  $\mu\text{M}$  thrombin to this solution increased the emission intensity by 15- and 19-fold after 50 min. Based on the greater than 15-fold signal response the LODs should be significantly below the micromolar analyte concentrations reported. This report optimized this response by adopting a superquenched approach used for FRET based detection of maltose using maltose binding protein attached to CdSe@ZnS nanoparticles [73, 74]. Clearly, the slow response time of the thrombin aptamer system, relative to the Au nanoparticle aggregate disassembly, is due to the numerous organic quenchers that need to be removed per CdSe nanoparticle for a measurable response. Again, this work presents a pseudo-



reagentless biosensor based on DNA modified CdSe nanoparticles. Nevertheless, the demonstration of a strategy for using aptamers to control the emission properties of semiconducting nanoparticles is highly significant.

The first demonstration of reagentless biosensing with nanoparticles through analyte-mediated biomolecule changes was reported by Nie and coworkers in 2002 [58]. This method was based on the observation of organic fluorophore adsorption to Au colloid surfaces as detected by fluorescence quenching and surface-enhanced Raman scattering [75, 76]. This design used a single DNA probe strand with a 3'-thiol group and a 5'-fluorescein or 5'-tetramethylrhodamine fluorophore. Upon addition of the probe DNA to the Au nanoparticle, the emission intensity from the organic fluorophore was completely quenched. After adding a four-fold excess (10 nM Au nanoparticle, 30 min incubation time, room temperature, 2–10 mM MgCl<sub>2</sub>) of a complementary DNA strand, the emission intensity of tetramethylrhodamine or fluorescein was completely restored. Addition of single-base mismatch complementary DNA strand under the same conditions caused a 50% restoration of the fluorophore emission intensity. This study went on to carefully examine the complementary DNA strand binding kinetics and DNA–Au nanoparticle thermal stabilities. Up to 5 min (40% overall response), the binding kinetics were consistent with a single exponential binding event. After 5 min multiple phases were observed that slowed the response time. Notably, the response time of this biosensor [58] is similar, if not more rapid, than the thrombin biosensor based on aptamer attached CdSe nanoparticles [61]. Thermal stability studies of the probe DNA–Au nanoparticle conjugate showed minimal increase in emission intensity at higher temperatures as opposed to the analogous molecular beacon in solution. These results suggest substantial non-specific Au nanoparticle–DNA interactions, which were clearly defined by this report. Despite these caveats this report showed, for the first time, that biomolecule conformation could be used to couple ligand binding to nanoparticle-based signal enhancements.

This fluorophore modified DNA–Au nanoparticle methodology has been extended to a fluorescence microscopy detected microfluidic device [62]. Fluorescein and Cy3 were used as the fluorophores in this study and attached to the 5' end of the DNA probe. The 3'-end of the DNA probe contained a thiol functional group that provided Au nanoparticle attachment. Au nanoparticle modified microchannels (50–90 μm) were generated by channel microfabrication followed by introducing 3-aminopropyltriethoxysilane, rinsing, and overnight incubation in Au nanoparticle solutions. The fluorophore-modified DNA probe was introduced to these microfluidic channels for 16 h and repeatedly rinsed. Minimal fluorescence was observed above background fluorescence in these rinsed channels. Fluorescence micrographs before and after complementary DNA addition (60 min incubation time) showed a significant increase in emission intensity for channels with 8 ppm of the complementary DNA. This detector was able to discriminate between DNA from denguevirus and enterovirus. This report demonstrates how a solution-based strategy with the DNA–Au nanoparticle based reagentless biosensor can be translated to a surface immobilized strategy.

Surface plasmon enhanced Raman spectroscopy has also been demonstrated for reagentless biosensing of DNA strands [60]. Plasmonic detection was provided by the use of a single strand of probe DNA with Rhodamine 6G attached to the 5'-end and a thiol on the 3' end. The DNA recognition sequence was flanked with 6-mer complementary sequences on each end to induce stem-loop formation in the absence of analyte DNA. These DNA probes were adsorbed to 50 nm diameter Ag nanoparticles and investigated in by Raman spectroscopy with the 632.8 nm line from a HeNe laser excitation source. In the absence of any additional DNA the SERS enhanced spectrum for Rhodamine was observed. Addition of a four-fold excess of complementary analyte DNA caused an eight-fold decrease in the intensity of the prominent  $1512\text{ cm}^{-1}$  vibration. All of the SERS vibrational bands decrease upon the addition; however, the higher energy and intensity bands provided the best spectroscopic handle for analysis. A sensor for the gene product of the HIV *gag* gene was then constructed. PCR amplified DNA (109 bases) was then added to this plasmonic detection biosensor. Addition of HIV *gag* amplified DNA cause a three- to six-fold decrease in SERS band intensities, while the addition of amplified DNA from human placenta (negative control) only caused a 1.5 to 2.5-fold decrease in SERS band intensities. This method removes the worry of reporter group photobleaching, since, even if photooxidation occurs, most of the SERS vibrational bands will be observed.

#### 12.4.2

##### **Biosensors Based on Protein Conformation Changes**

Energy transfer methods are less prolific in reagentless fluorescence detected protein-based biosensors. The rationale for diminished reagentless energy transfer protein-based biosensors is that the ligand-induced atomic movements in proteins are smaller than in DNA. For an energy transfer methodology to function for a reagentless protein-based biosensor the distance for half-maximal energy transfer ( $R_0$ ) must be similar to the ligand-dependent change in interatomic distance. Frommer and coworkers have shown reagentless energy transfer protein-based biosensors for maltose, ribose, and glutamate [77–79]. These systems use green fluorescent proteins (GFPs) that are engineered to absorb and emit at different visible wavelengths, genetically encoded on the amino- and carboxy-terminus of the sensor protein (Fig. 12.6A). The  $R_0$ s for these GFP chromophore pairs are around 20–25 Å. Fluorophore pairs with  $R_0$ s longer than 30 Å are difficult to use as reagentless protein-based biosensing. In this case, reagentless protein-based biosensing has been achieved by intercalating organic fluorophores into cracks in the protein structure that reversibly opens and closes as ligand-induced conformation changes occur [80]. The intercalation strategy has yielded various reagentless biosensors [3, 81]. Despite the success of these reagentless organic fluorophore modified protein-based biosensors, the susceptibility of organic molecules to photodegradation remains a significant difficulty in fluorescence contrast imaging. Semiconducting nanoparticles, of course, have minimal photodecomposition and have been an at-

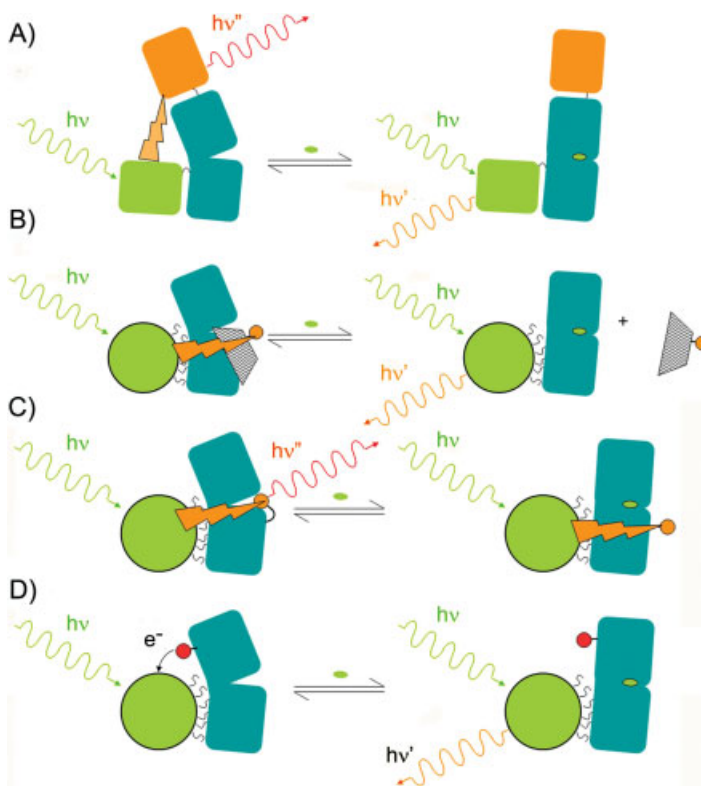


**Fig. 12.6.** Strategies for reagentless biosensing based on changes in protein conformation. (A) GFP-CFP protein chimeric strategy, where energy transfer efficiency from enhanced cyan fluorescent protein (green) to enhanced yellow fluorescent protein (orange) is altered as a function of analyte-induced change in protein conformation. (B) Displacement assay of a fluorescence quencher bound (shaded with orange ball) bound to a protein, where analyte binding displaces this quencher and restores emission intensity of the CdSe nanoparticle (green ball). (C) Method where the emission intensity of an

organic fluorophore (orange ball) is altered as a function of analyte binding, where a CdSe nanoparticle (green ball) is used for photon collection via energy transfer. (D) An electron transfer quenching method where a reductant or oxidant (red ball) is placed close to the CdSe nanoparticle (green ball) surface in one conformation to provide electron transfer quenching (text and Fig. 12.7). Because the protein conformation changes upon analyte binding, the distance between the reductant/oxidant and the nanoparticle will be altered and the nanoparticle emission intensity will change.

tractive target to apply similar methodologies, energy transfer or intercalation, for reagentless protein-based biosensing.

To a first approximation, energy transfer can be used for reagentless protein-attached nanoparticle biosensing. Two energy transfer based biosensing methods using maltose binding protein (MBP) have been published [59, 74]. One system used the maltose selective displacement of  $\beta$ -cyclodextran from MBP as a pseudo-

reagentless strategy (Fig. 12.6B) [74]. For this system, fluorophores were attached to a cyclodextran and energy transfer from the CdSe@ZnS nanoparticle to the cyclodextran-modified fluorophore reported the amount of maltose in solution. A 100 nM LOD for maltose was observed with a 0.1 to 10  $\mu\text{M}$  dynamic range. The dynamic range is typical for this type of strategy; however, the LOD is higher than typical due to the use of a competitive displacement strategy. This report did, though, demonstrate the effectiveness of energy transfer to proteins attached to semiconducting nanoparticles. Clearly, with this system, multiple organic fluorophores need to be adsorbed to the nanoparticle surface to substantially alter the nanoparticle emission intensity. A reagentless method based on nanoparticle–organic fluorophore energy transfer has been reported recently [59]. This report showed that CdSe@ZnS nanoparticles could function as high photon cross-section antenna. Because energy transfer directly couples the nanoparticle emission intensity to the organic fluorophore emission and absorbance properties, the interaction between the organic fluorophore (Cy3) and MBP actually mediated the changes in overall emission intensity (Fig. 12.6C). The linkage between Cy3-modified 41C MBP and emission intensity is similar to that demonstrated by previous studies [82–84]. In the end, maltose binding mediated a “turn off” signal and is still inherently linked to the relatively fast photodecomposition of organic fluorophores. Therefore, an alternative to energy transfer needs to be used for reagentless protein–nanoparticle based biosensing to take full advantage of the photonic properties of semiconducting nanoparticles.

Electron transfer quenching provides a route to reagentless protein–nanoparticle based biosensing that maintains the high photostability of the semiconducting nanoparticle. Electron transfer quenching involves an electron transfer to or from the excited state of a fluorophore followed by a back electron transfer to form the ground state to non-radiatively relax the fluorophore excited state [70]. Two proof-of-principle articles have been published for electron transfer quenching with a  $\text{Ru}^{\text{II}}$  complex modified MBP that was attached to either CdSe [63] or CdSe@ZnS nanoparticles [64]. In this system, the  $\text{Ru}^{\text{II}}$  complex reduces the valence band hole of the CdSe core, while the resulting  $\text{Ru}^{\text{III}}$  complex oxidizes the electron that remains in the conduction band of the *n*-type CdSe nanoparticle core (Fig. 12.7). When the cyclic nature of this reaction scheme is maintained, minimal photodegradation of this material occurs. This electron transfer quenching method has an exponential dependence [85] with respect to the distance between the  $\text{Ru}^{\text{II}}$  complex and the surface of the CdSe nanoparticle core. Energy transfer distance dependence varies as a function of  $R_0^6/(R_0 + r)^6$ , where  $R_0$  is the distance at which half maximal energy transfer occurs [70]. However, the  $r = 0$  point for energy transfer is at the center of the CdSe nanoparticle core [73, 74, 86] while the core–shell interface is the  $r = 0$  point for electron transfer. Based on the  $R_0$ s for energy transfer from core–shell CdSe nanoparticle donors to organic fluorophore acceptors (40–70 Å) [73, 86–88], energy transfer should have a shallow distance dependence relative to electron transfer quenching.

Benson and coworkers have shown electron transfer quenching provides a solution to reagentless small molecule biosensor design using protein–semiconducting

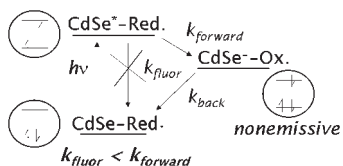


**Fig. 12.7.** Electron transfer quenching methodology. A nanoparticle ground state (CdSe) and a reductant (Red.) are placed close together. Upon photoexcitation ( $h\nu$ ) the CdSe excited state is formed with an electron in the conduction band (upper molecular orbital) and a hole in the valence band (lower molecular orbital). For a close association of the reductant with the CdSe surface, electron (charge) transport can occur from the

reductant to the valence band hole. The charge-separated state that forms ( $\text{CdSe}^-$  and oxidized reductant, Ox.) is non-emissive. The electron in the conduction band of the CdSe core will then reduce the oxidized reductant to reform the ground state. As long as the first electron transfer rate ( $k_{\text{forward}}$ ) is faster than the fluorescence emission rate ( $k_{\text{fluor.}}$ ) the nanoparticle emission intensity will be diminished and the lifetime will be decreased.

nanoparticle assemblies (Fig. 12.6D) [63, 64, 67]. This work relies on the generation of a 1:1 complex between a  $\text{Ru}^{\text{II}}$  complex modified protein and a semiconducting nanoparticle. Such a complex has been obtained through the use of kinetically stable mercaptohexadecanoate capping groups [67], as opposed to the dihydrolipoic acid capping groups used by Medintz, Mattoussi, and coworkers to facilitate multiple proteins attached per semiconducting nanoparticle [74]. Four MBPs with different surface Cys attachment sites were surveyed. When the  $\text{Ru}^{\text{II}}$ -modified MBP was bound to either CdSe or CdSe@ZnS nanoparticles that emitted at 560–570 nm, the emission intensities decreased from 1.5 to 2.3-fold [63] and 1.2 to 1.8-fold [64]. Upon maltose addition to the  $\text{Ru}^{\text{II}}$  modified MBP attached to CdSe or CdSe@ZnS nanoparticles, the emission intensity increased by 1.39 to 1.45-fold [63] or 1.13 to 1.42-fold [64]. Recently, our laboratory has confirmed that maltose-dependent changes in CdSe emission intensities correlate with changes in CdSe emission lifetimes [89] and Faradaic electrochemical currents observed for these proteins adsorbed to Au working electrodes [90]. Maltose titrations yielded dissociation constants ranging from 0.20 to 0.75  $\mu\text{M}$  (LOD 1 to 5 nm) and 0.25 to 1.00  $\mu\text{M}$  (LOD 5 to 10 nm) for the CdSe and CdSe@ZnS nanoparticle systems. The similarity of these dissociation constants to the maltose dissociation constant for MBP in solution ( $K_{\text{D}} \sim 0.70 \mu\text{M}$ ) suggests the function of MBP has not been altered by nanoparticle attachment. This is in direct contrast to the 200 to 800  $\mu\text{M}$  dissociation constants reported for the Cy3-modified 41C MBP attached CdSe@ZnS nanoparticle biosensors [59] and the 0.8 to 8.0  $\mu\text{M}$  dissociation constant determined for the fluorophore modified cyclodextran-MBP-CdSe@ZnS nanoparticle system [74]. The only nanoparticle-based perturbation seen for the  $\text{Ru}^{\text{II}}$  complex labeled systems is in the variation of the sample-to-sample dissociation constant reproducibility [63]. For MBPs that placed the  $\text{Ru}^{\text{II}}$  complex closer to the nanoparticle surface, predicted by quenching efficiency, a higher variation in the dissociation constants was observed. This suggested the  $\text{Ru}^{\text{II}}$  complex might be kinetically trapped in the hydrophobic layer surrounding the nanoparticle, which is formed by the fifteen

methylenes of the capping ligand. However, electron transfer is still observed for MBPs with the  $\text{Ru}^{\text{II}}$  complex placed away from the nanoparticle surface [63, 64]. Using K46C and K25C MBP, where the  $\text{Ru}^{\text{II}}$  complex was away from the nanoparticle surface, these MBP-CdSe@ZnS nanoparticle biosensors were shown to be selective for maltose in a ten-sugar test panel and reversibly detect maltose in an increasing glucose background [64]. Taken together, the use of electron transfer quenching provides reagentless biosensing that modulates nanoparticle emission intensity using protein–semiconducting nanoparticle assemblies.

The distance dependent changes in electron transfer and energy transfer quenching efficiencies, based on reported data, are compared relatively in Fig. 12.8. As stated above, the delocalized hole–electron pair (exciton) density in core–

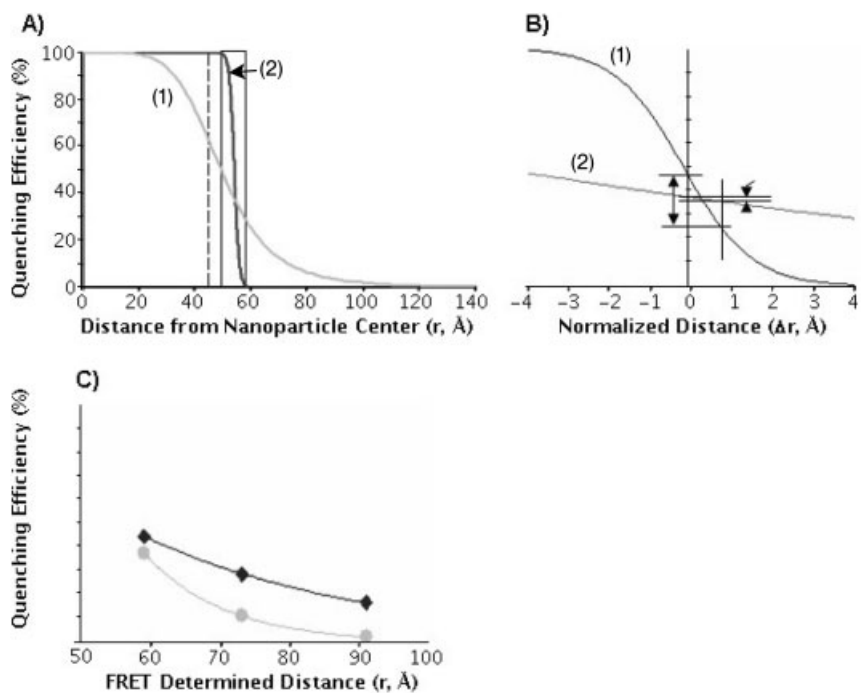


**Fig. 12.8.** Comparison of energy and electron transfer quenching efficiencies in maltose binding protein based biosensors. (A) Overall comparison of energy transfer distance dependence of quenching efficiency (line 1) and electron transfer quenching efficiency (line 2). The dotted line approximates the nanoparticle radius reported by Medintz and coworkers [86]. The range of the energy transfer based distance was calculated from assuming activation-less electron transfer. The area within the box (50–58 Å) is shown in panel B. (B) The region for nanoparticle

distance determined for N282C (line 1,  $r = 0$ ) and D80C (line 2,  $r = 0$ ). Using the change in quenching efficiency for the electron transfer method [64], the expected FRET dependent change was calculated to be one tenth of the measured electron transfer change. (C) Quenching efficiency (electron transfer method [64], diamonds; energy transfer method [86], circles) for three structurally related attachment positions on MBP [64, 86] as a function of the FRET determined distances from the nanoparticle core [86].

shell nanoparticles creates different starting points for distance determinations by energy and electron transfer. Since the average emitted photon density comes from the center of the nanoparticle core the nanoparticle centroid is considered  $r = 0$   $R_o$ . Since exciton delocalization occurs significantly faster than nanoparticle emission, the closest approach for electron transfer is the nanoparticle core–shell interface and functions as the  $r = 0$  for electron transfer. Energy transfer-determined distances have been reported for CdSe@ZnS nanoparticle–Cy3 fluorophore pairs using the derived  $R_o$  of  $53 \pm 3 \text{ \AA}$  [86]. Using this radius the Cy3 quenching efficiencies of 530-nm emitting CdSe@ZnS nanoparticles (2% to 37%) yielded RET-determined distances of 59 to 95  $\text{\AA}$  for six different surface Cys attachment points for Cy3 [86]. The orientation of MBP, in the absence of maltose, on the nanoparticle surface was derived to have both domains interacting with the nanoparticle surface and the maltose binding site pointing away from the nanoparticle surface. For the Ru<sup>II</sup> complex modified MBP system, quenching efficiencies of 16% to 44% were obtained for CdSe@ZnS nanoparticle emission [64]. A rough comparison between these two published systems is presented in Fig. 12.8, where the RET determined distances of structurally related surface Cys attachment sites are compared.

Clearly, all three structurally related surface Cys attachment sites show the Ru<sup>II</sup> complex with a higher quenching efficiency than Cy3. Furthermore, maltose addition decreases the Ru<sup>II</sup> complex quenching efficiencies (–9% to –22%) [64], while no maltose dependent change in Cy3 mediated nanoparticle quenching efficiency has been reported. The differences in maltose-dependent quenching are no surprise based on the distance dependences of electron transfer and energy transfer discussed above. Figure 12.8(B) illustrates for the 282C/80C attachment site the comparison of these scaling rules, where energy transfer has a shallower distance dependence. Additionally, maltose dependent changes in quenching efficiencies for the electron transfer method are consistent with changes in the CdSe core fluorescence lifetimes [89]. However, the surprise in the Ru<sup>II</sup> complex mediated CdSe@ZnS nanoparticle quenching is the shallow distance dependence with respect to RET-derived surface Cys distance to the nanoparticle centroid (Fig. 12.8C). From a technological standpoint the shallow distance dependence of Ru<sup>II</sup> complex mediated quenching efficiencies abrogates [63] the need for Cys scanning mutagenesis methods as with organic fluorophore-MBP based biosensors [3, 81]. From a mechanistic standpoint, the Ru<sup>II</sup> complex based quenching distance dependence might be more similar to protein–protein electron transfer as opposed to intraprotein electron transfer. Beratan and coworkers [91, 92] have recently found constructive interference from structural waters in electron transfer pathways provide very shallow distance dependences in electron transfer. Interestingly, the electron transfer distances calculated ruthenated MBP-CdSe@ZnS systems (8.0 to 9.5  $\text{\AA}$ ) are similar to the distances for the cyt.  $b_5$ –cyt.  $c$  study [92]. In the end, the Ru<sup>II</sup> complex [63, 64] provides reagentless biosensing that modulates the emission intensity of semiconducting nanoparticles in a ligand dependent fashion.

Clearly, from these examples, the scaling laws of the nanoparticle and the reporter group need to be carefully considered for reagentless biosensor construction. The biomolecular conformation change strategy clearly demonstrates this

point. Nucleic acid–nanoparticle based biosensors can provide reagentless biosensors more readily using conformation change, in that the conformation change is typically greater than 10 Å. By moving a reporter group greater than 10 Å a substantial change in energy transfer and surface-enhanced Raman can be expected. Protein–nanoparticle based biosensors require more careful consideration of scaling rules since reporter groups typically are moved by 1–6 Å. Electron transfer quenching takes advantage of a less efficient methodology than energy transfer to provide a higher sensitivity to conformational motion. This is not to say that electron transfer quenching is the only solution to protein–nanoparticle based reagentless biosensing, but that it provides a scaling law that appropriately couples analyte-induced protein conformation motions into changes in the nanoparticle electronic structure.

## 12.5

### Conclusion

The three general concepts outlined here provide reagentless biosensors from biomolecules attached to nanoparticles. As demonstrated by the literature cited in this chapter, these reagentless concepts provide sensors that can be adapted to various detection platforms. More importantly, the instrumentation used for biosensing is relatively inexpensive and modular. Extension of these systems to multiplexed or array assays has been reported and should be able to be extended for various other systems. The idea that the biomolecule provides the analyte sensitivity and selectivity is at the heart of the modular detection strategies. As outlined in this volume and this series, nanoparticles provide unique properties that can be detected by various analytical techniques. The translation between analyte–biomolecule binding and changes in nanoparticle properties requires the selection of a reporting methodology (e.g., FRET, SERRS,  $T_2$  relaxation, electron transfer quenching) with an appropriate scaling law. The high surface area of nanoparticles provides a high sensitivity method to measure changes in local solvent dielectric. Biomolecule attachment to nanoparticle surfaces allows substrates for these biomolecules to alter the local solvent dielectric and properties such as localized surface plasmon absorption and electrical conductivity. Metallic and semiconducting nanoparticles can also be used as electron/hole buffers to increase electrochemical communication between enzymes and working electrodes. This strategy has allowed multimolecular bioelectrochemical sensors to be transformed into reagentless bioelectrochemical sensors. Energy transfer methods are the most popular method for coupling biomolecule and nanoparticle properties by energy transfer from organic fluorophores to metallic nanoparticles, semiconducting nanoparticles to organic fluorophores, or semiconducting nanoparticles to metallic nanoparticles. While energy transfer scaling laws facilitate enzymatic cleavage biosensors and nucleic acid–nanoparticle based biosensors, protein–nanoparticle biosensors require a coupling method with a more sensitive distance dependence. While reagentless protein–nanoparticle based biosensors that use energy transfer have been reported [59], this method



monitors differences in the emission intensity of the organic fluorophore. Electron transfer quenching provides a method to effectively couple changes in protein conformation into changes in nanoparticle emission intensity [63, 64]. Magnetic force and  $T_2$  magnetic relaxation methods, along with nanoparticle surface energy transfer [93, 94], have a much shallower distance dependence that could be used for reagentless biosensor development with enzymatic cleavage (pseudo-reagentless) or nucleic acid conformation changes. Another advantage of using nanoparticles is the advent of hybrid detection schemes, such as endonuclease detection by magnetic force measurements [53, 54], electrochemical surface plasmon resonance [20] and photoelectrochemical detection [21]. Such hybrid detection strategies provide signal selectivity on top of the analyte selectivity provided by the biomolecule. Such selectivity provides additional confidence necessary for device approval and commercialization. Finally, the development of nanoparticle based biosensors that are reagentless and reversible is an exciting frontier that requires a material, biomolecular, and molecular viewpoint that is producing sophisticated biosensors with inexpensive instrumentation.

### Acknowledgments

The financial support of the National Science Foundation (DBI-0508134) is acknowledged. Marinella G. Sandros, Vivekanand Shete, and Kathleen Fleming are acknowledged for their help in bibliographic searches and reference acquisition.

### References

- 1 KATZ, E., WILLNER, I., Nanobiotechnology: Integrated nanoparticle-biomolecule hybrid systems: Synthesis, properties, and applications, *Angew. Chem. Int. Ed.* **2004**, 43, 6042–6108.
- 2 DWYER, M. A., HELLINGA, H. W., Periplasmic binding proteins: A versatile superfamily for protein engineering, *Curr. Opin. Struct. Biol.* **2004**, 14, 495–504.
- 3 FELTUS, A., DAUNERT, S., Genetic engineering of signaling molecules. In *Optical Biosensors: Present and Future*, eds. LIGLER, F. S., LOWE TAITT, C. A., Elsevier, Amsterdam, **2002**, pp. 307–329.
- 4 RAJENDRAN, M., ELLINGTON, A. D., Nucleic acids for reagentless biosensors. In *Optical Biosensors: Present and Future*, eds. LIGLER, F. S., LOWE TAITT, C. A., Elsevier, Amsterdam, **2002**, pp. 369–396.
- 5 MEDINTZ, I. L., UYEDA, H. T., GOLDMAN, E. R., MATTOUSSI, H., Quantum dot bioconjugates for imaging, labelling and sensing, *Nat. Mater.* **2005**, 4, 435–446.
- 6 BRASUEL, M., KOPELMAN, R., AYLOTT, J. W., CLARK, H., XU, H., HOYER, M., MILLER, T. J., TJALKENS, R., PHILBERT, M. A., Production, characteristics and applications of fluorescent PEBBLE nanosensors: Potassium, oxygen, calcium and pH imaging inside live cells, *Sens. Mater.* **2002**, 14, 309–338.
- 7 XU, H., AYLOTT, J. W., KOPELMAN, R., Fluorescent nano-PEBBLE sensors designed for intracellular glucose imaging, *Analyst* **2002**, 127, 1471–1477.
- 8 CLARK, H. A., HOYER, M., PHILBERT, M. A., KOPELMAN, R., Optical nanosensors for chemical analysis inside single living cells. 1.

- Fabrication, characterization, and methods for intracellular delivery of PEBBLE sensors, *Anal. Chem.* **1999**, *71*, 4831–4836.
- 9 ROSENZWEIG, Z., KOPELMAN, R., Analytical properties and sensor size effects of a micrometer-sized optical fiber glucose biosensor, *Anal. Chem.* **1996**, *68*, 1408–1413.
- 10 COMPARELLI, R., CURRI, M. L., COZZOLI, P. D., STRICCOLI, M., Chapter 5 of this volume.
- 11 HAES, A. J., VAN DUYN, R. P., A unified view of propagating and localized surface plasmon resonance biosensors, *Anal. Bioanal. Chem.* **2004**, *379*, 920–930.
- 12 NATH, N., CHILKOTI, A., Label-free biosensing by surface plasmon resonance of nanoparticles on glass: Optimization of nanoparticle size, *Anal. Chem.* **2004**, *76*, 5370–5378.
- 13 HE, L., MUSICK, M. D., NICEWARNER, S. R., SALINAS, F. G., BENKOVIC, S. J., NATAN, M. J., KEATING, C. D., Colloidal Au-enhanced surface plasmon resonance for ultrasensitive detection of DNA hybridization, *J. Am. Chem. Soc.* **2000**, *122*, 9071–9077.
- 14 FREDERIX, F., FRIEDT, J.-M., CHOI, K.-H., LAUREYN, W., CAMPITELLI, A., MONDELAERS, D., MAES, G., BORGHIS, G., Biosensing based on light absorption of nanoscaled gold and silver particles, *Anal. Chem.* **2003**, *75*, 6894–6900.
- 15 FREDERIX, F., BONROY, K., LAUREYN, W., REEKMANS, G., CAMPITELLI, A., DEHAEN, W., MAES, G., Enhanced performance of an affinity biosensor interface based on mixed self-assembled monolayers of thiols on gold, *Langmuir* **2003**, *19*, 4351–4357.
- 16 ENDO, T., KERMAN, K., NAGATANI, N., TAKAMURA, Y., TAMIYA, E., Label-free detection of peptide nucleic acid-DNA hybridization using localized surface plasmon resonance based optical biosensor, *Anal. Chem.* **2005**, *77*, 6976–6984.
- 17 ENDO, T., YAMAMURA, S., NAGATANI, N., MORITA, Y., TAKAMURA, Y., TAMIYA, E., Localized surface plasmon resonance based optical biosensor using surface modified nanoparticle layer for label free monitoring of antigen-antibody reaction, *Sci. Technol. Adv. Mater.* **2005**, *6*, 491–500.
- 18 PRODAN, E., NORDLANDER, P., HALAS, N. J., Electronic structure and optical properties of gold nanoshells, *Nano Lett.* **2003**, *3*, 1411–1415.
- 19 HAES, A. J., ZOU, S., SCHATZ, G. C., VAN DUYN, R. P., A nanoscale optical biosensor: The long range distance dependence of the localized surface plasmon resonance of noble metal nanoparticles, *J. Phys. Chem. B* **2004**, *108*, 109–116.
- 20 ZAYATS, M., KHARITONOV, A. B., POGORELOVA, S. P., LIIOUBASHEVSKI, O., KATZ, E., WILLNER, I., Probing photoelectrochemical processes in Au-CdS nanoparticle arrays by surface plasmon resonance: Application for the detection of acetylcholine esterase inhibitors, *J. Am. Chem. Soc.* **2003**, *125*, 16 006–16 014.
- 21 PARDO-YISSAR, V., KATZ, E., WASSERMAN, J., WILLNER, I., Acetylcholine esterase-labeled CdS nanoparticles on electrodes: Photoelectrochemical sensing of the enzyme inhibitors, *J. Am. Chem. Soc.* **2003**, *125*, 622–623.
- 22 CHEN, R. J., BANGSARUNTIP, S., DROUVALAKIS, K. A., KAM, N. W. S., SHIM, M., LI, Y., KIM, W., UTZ, P. J., DAI, H., Noncovalent functionalization of carbon nanotubes for highly specific electronic biosensors, *Proc. Natl. Acad. Sci.* **2003**, *100*, 4984–4989.
- 23 CUI, Y., WEI, Q., PARK, H., LIEBER, C. M., Nanowire nanosensors for highly sensitive and selective detection of biological and chemical species, *Science* **2001**, *293*, 1289–1292.
- 24 KICHAMBARE, P. D., STAR, A., Chapter 1 of this volume.
- 25 WANG, J., LUI, G., LIN, Y., Chapter 3 of this volume.
- 26 CHEN, R. J., CHOI, H. C., BANGSARUNTIP, S., YENILMEZ, E., TANG, X., WANG, Q., CHANG, Y.-L., DAI, H., An investigation of the mechanisms of electronic sensing of protein adsorption on carbon nanotube devices, *J. Am. Chem. Soc.* **2004**, *126*, 1563–1568.

- 27 BYON, H. R., CHOI, H. C., Network single-walled carbon nanotube-field effect transistors (SWNT-FETs) with increased Schottky contact area for highly sensitive biosensor applications, *J. Am. Chem. Soc.* **2006**, *128*, 2188–2189.
- 28 SO, H.-M., WON, K., KIM, Y. H., KIM, B.-K., RYU, B. H., NA, P. S., KIM, H., LEE, J.-O., Single-walled carbon nanotube biosensors using aptamers as molecular recognition elements, *J. Am. Chem. Soc.* **2005**, *127*, 11 906–11 907.
- 29 BESTEMAN, K., LEE, J.-O., WIERTZ, F. G. M., HEERING, H. A., DEKKER, C., Enzyme-coated carbon nanotubes as single-molecule biosensors, *Nano Lett.* **2003**, *3*, 727–730.
- 30 BANERJEE, S., HEMRAJ-BENNY, T., WONG, S. S., Covalent surface chemistry of single-walled carbon nanotubes, *Adv. Mater.* **2005**, *17*, 17–29.
- 31 LI, Z., CHEN, Y., LI, X., KAMINS, T. I., NAUKA, K., WILLIAMS, R. S., Sequence-specific label-free DNA sensors based on silicon nanowires, *Nano Lett.* **2004**, *4*, 245–247.
- 32 HAHM, J.-i., LIEBER, C. M., Direct ultrasensitive electrical detection of DNA and DNA sequence variations using nanowire nanosensors, *Nano Lett.* **2004**, *4*, 51–54.
- 33 ZHENG, G., PATOLSKY, F., CUI, Y., WANG, W. U., LIEBER, C. M., Multiplexed electrical detection of cancer markers with nanowire sensor arrays, *Nat. Biotechnol.* **2005**, *23*, 1294–1301.
- 34 WANG, W. U., CHEN, C., LIN, K.-h., FANG, Y., LIEBER, C. M., Label-free detection of small-molecule-protein interactions by using nanowire nanosensors, *Proc. Natl. Acad. Sci.* **2005**, *102*, 3208–3212.
- 35 GUISEPPi-ELIE, A., LEI, C., BAUGHMAN, R. H., Direct electron transfer of glucose oxidase on carbon nanotubes, *Nanotechnology* **2002**, *13*, 559–564.
- 36 SALIMI, A., NOORBAKSH, A., GHADERMARZ, M., Direct electrochemistry and electrocatalytic activity of catalase incorporated onto multiwall carbon nanotubes-modified glassy carbon electrode, *Anal. Biochem.* **2005**, *344*, 16–24.
- 37 WANG, J., MUSAMEH, M., A reagentless amperometric alcohol biosensor based on carbon-nanotube/teflon composite electrodes, *Anal. Lett.* **2003**, *36*, 2041–2048.
- 38 ZHAO, G.-C., YIN, Z.-Z., ZHANG, L., WEI, X.-W., Direct electrochemistry of cytochrome c on a multi-walled carbon nanotubes modified electrode and its electrocatalytic activity for the reduction of H<sub>2</sub>O<sub>2</sub>, *Electrochem. Commun.* **2005**, *7*, 256–260.
- 39 CARRALERO SANZ, V., MENA, M. L., GONZALEZ-CORTES, A., YANEZ-SEDENO, P., PINGARRON, J. M., Development of a tyrosinase biosensor based on gold nanoparticles-modified glassy carbon electrodes, *Anal. Chim. Acta* **2005**, *528*, 1–8.
- 40 GU, H.-Y., YU, A.-M., YUAN, S.-S., CHEN, H.-Y., Amperometric nitric oxide biosensor based on the immobilization of hemoglobin on a nanometer-sized gold colloid modified Au electrode, *Anal. Lett.* **2002**, *35*, 647–661.
- 41 LIU, S., JU, H., Reagentless glucose biosensor based on direct electron transfer of glucose oxidase immobilized on colloidal gold modified carbon paste electrode, *Biosens. Bioelectron.* **2003**, *19*, 177–183.
- 42 LIU, S., JU, H., Nitrite reduction and detection at a carbon paste electrode containing hemoglobin and colloidal gold, *Analyst* **2003**, *128*, 1420–1424.
- 43 HUANG, Y., ZHANG, W., XIAO, H., LI, G., An electrochemical investigation of glucose oxidase at a CdS nanoparticles modified electrode, *Biosens. Bioelectron.* **2005**, *21*, 817–821.
- 44 CAO, D., HE, P., HU, N., Electrochemical biosensors utilizing electron transfer in heme proteins immobilised on Fe<sub>3</sub>O<sub>4</sub> nanoparticles, *Analyst* **2003**, *128*, 1268–1274.
- 45 CRUMBLISS, A. L., STONEHUERNER, J., HENKENS, R. W., O'DALY, J. P., ZHAO, J., The use of inorganic materials to control or maintain immobilized

- enzyme activity, *New J. Chem.* **1994**, *18*, 327–339.
- 46 ZHAO, J., HENKENS, R. W., CRUMBLISS, A. L., Mediator-free amperometric determination of toxic substances based on their inhibition of immobilized horseradish peroxidase, *Biotechnol. Prog.* **1996**, *12*, 703–708.
- 47 ZHAO, J., O'DALY, J. P., HENKENS, R. W., STONEHUERNER, J., CRUMBLISS, A. L., A xanthine oxidase/colloidal gold enzyme electrode for amperometric biosensor applications, *Biosens. Bioelectron.* **1996**, *11*, 493–502.
- 48 LIU, J., LU, Y., A colorimetric lead biosensor using DNazyme-directed assembly of gold nanoparticles, *J. Am. Chem. Soc.* **2003**, *125*, 6642–6643.
- 49 GU, H., XU, K., XU, C., XU, B., Biofunctional magnetic nanoparticles for protein separation and pathogen detection, *Chem. Commun.* **2006**, 941–949.
- 50 ZHELEV, Z., BAKALOVA, OHBA, H., BABA, Y., Chapter 6 of this volume.
- 51 CHANG, E., MILLER, J. S., SUN, J., YU, W. W., COLVIN, V. L., DREZEK, R., WEST, J. L., Protease-activated quantum dot probes, *Biochem. Biophys. Res. Commun.* **2005**, *334*, 1317–1321.
- 52 PEREZ, J. M., O'LOUGHIN, T., SIMEONE, F. J., WEISSLEDER, R., JOSEPHSON, L., DNA-based magnetic nanoparticle assembly acts as a magnetic relaxation nanoswitch allowing screening of DNA-cleaving agents, *J. Am. Chem. Soc.* **2002**, *124*, 2856–2857.
- 53 WEIZMANN, Y., ELNATHAN, R., LIOUBASHEVSKI, O., WILLNER, I., Magnetomechanical detection of the specific activities of endonucleases by cantilevers, *Nano Lett.* **2005**, *5*, 741–744.
- 54 WEIZMANN, Y., ELNATHAN, R., LIOUBASHEVSKI, O., WILLNER, I., Endonuclease-based logic gates and sensors using magnetic force-amplified readout of DNA scission on cantilevers, *J. Am. Chem. Soc.* **2005**, *127*, 12666–12672.
- 55 LIU, J., LU, Y., A colorimetric lead biosensor using DNazyme-directed assembly of gold nanoparticles, *J. Am. Chem. Soc.* **2003**, *125*, 6642–6643.
- 56 WANG, Z., KANARAS, A. G., BATES, A. D., COSSTICK, R., BRUST, M., Enzymatic DNA processing on gold nanoparticles, *J. Mater. Chem.* **2004**, *14*, 578–580.
- 57 ZHAO, M., JOSEPHSON, L., TANG, Y., WEISSLEDER, R., Magnetic sensors for protease assays, *Angew. Chem. Int. Ed.* **2003**, *42*, 1375–1378.
- 58 MAXWELL, D. J., TAYLOR, J. R., NIE, S., Self-assembled nanoparticle probes for recognition and detection of biomolecules, *J. Am. Chem. Soc.* **2002**, *124*, 9606–9612.
- 59 MEDINTZ, I. L., CLAPP, A. R., MELINGER, J. S., DESCHAMPS, J. R., MATTOUSSI, H., A reagentless biosensing assembly based on quantum dot-donor Forster resonance energy transfer, *Adv. Mater.* **2005**, *17*, 2450–2455.
- 60 WABUYELE, M. B., VO-DINH, T., Detection of human immunodeficiency virus type 1 DNA sequence using plasmonics nanoprobe, *Anal. Chem.* **2005**, *77*, 7810–7815.
- 61 LEVY, M., CATER, S. F., ELLINGTON, A. D., Quantum-dot aptamer beacons for the detection of proteins, *ChemBioChem* **2005**, *6*, 2163–2166.
- 62 LI, Y.-T., LIU, H.-S., LIN, H.-P., CHEN, S.-H., Gold nanoparticles for microfluidics-based biosensing of PCR products by hybridization-induced fluorescence quenching, *Electrophoresis* **2005**, *26*, 4743–4750.
- 63 SANDROS, M. G., GAO, D., BENSON, D. E., A modular nanoparticle-based system for reagentless small molecule biosensing, *J. Am. Chem. Soc.* **2005**, *127*, 12198–12199.
- 64 SANDROS, M. G., SHETE, V., BENSON, D. E., Selective, reversible, reagentless maltose biosensing with core-shell semiconducting nanoparticles, *Analyst* **2006**, *131*, 229–235.
- 65 LIU, J., LU, Y., Fast colorimetric sensing of adenosine and cocaine based on a general sensor design involving aptamers and nanoparticles, *Angew. Chem. Int. Ed.* **2005**, *45*, 90–94.

- 66 HERMANSON, G. T., *Bioconjugate Techniques*, Academic Press, San Diego, 1996.
- 67 SANDROS, M. G., GAO, D., GOKDEMIR, C., BENSON, D. E., General, high-affinity approach for the synthesis of fluorophore appended protein nanoparticle assemblies. *Chem. Commun.* **2005**, 2832–2834.
- 68 GOLDMAN, E. R., BALIGHIAN, E. D., MATTOUSSI, H., KUNO, M. K., MAURO, J. M., TRAN, P. T., ANDERSON, G. P., Avidin: A natural bridge for quantum dot-antibody conjugates, *J. Am. Chem. Soc.* **2002**, 124, 6378–6382.
- 69 GOLDMAN, E. R., MEDINTZ, I. L., HAYHURST, A., ANDERSON, G. P., MAURO, J. M., IVERSON, B. L., GEORGIOU, G., MATTOUSSI, H., Self-assembled luminescent CdSe-ZnS quantum dot bioconjugates prepared using engineered poly-histidine terminated proteins, *Anal. Chim. Acta* **2005**, 534, 63–67.
- 70 LAKOWICZ, J. R., *Principles of Fluorescence Spectroscopy*. 2nd edn., Klewer Academic, New York, 1999.
- 71 ELLINGTON, A. D., SZOSTAK, J. W., In vitro selection of RNA molecules that bind specific ligands, *Nature* **1990**, 346, 818–822.
- 72 TUERK, C., GOLD, L., Systematic evolution of ligands by exponential enrichment: RNA ligands to bacteriophage T4 DNA polymerase, *Science* **1990**, 249, 505–510.
- 73 CLAPP, A. R., MEDINTZ, I. L., MAURO, J. M., FISHER, B. R., BAWENDI, M. G., MATTOUSSI, H., Fluorescence resonance energy transfer between quantum dot donors and dye-labeled protein acceptors, *J. Am. Chem. Soc.* **2004**, 126, 301–310.
- 74 MEDINTZ, I. L., CLAPP, A. R., MATTOUSSI, H., GOLDMAN, E. R., FISHER, B., MAURO, J. M., Self-assembled nanoscale biosensors based on quantum dot FRET donors, *Nat. Mater.* **2003**, 2, 630–638.
- 75 KRUG, J. T., II, WANG, G. D., EMORY, S. R., NIE, S., Efficient Raman enhancement and intermittent light emission observed in single gold nanocrystals, *J. Am. Chem. Soc.* **1999**, 121, 9208–9214.
- 76 NIE, S., EMORY, S. R., Probing single molecules and single nanoparticles by surface-enhanced Raman scattering, *Science* **1997**, 275, 1102–1106.
- 77 DEUSCHLE, K., OKUMOTO, S., FEHR, M., LOOGER, L. L., KOZHUKH, L., FROMMER, W. B., Construction and optimization of a family of genetically encoded metabolite sensors by semirational protein engineering, *Protein Sci.* **2005**, 14, 2304–2314.
- 78 FEHR, M., FROMMER, W. B., LALONDE, S., Visualization of maltose uptake in living yeast cells by fluorescent nanosensors, *Proc. Natl. Acad. Sci. U.S.A.* **2002**, 99, 9846–9851.
- 79 LAGER, I., FEHR, M., FROMMER, W. B., LALONDE, S., Development of a fluorescent nanosensor for ribose, *FEBS Lett.* **2003**, 553, 85–89.
- 80 DATTELBAUM, J., LOOGER, L., BENSON, D., SALI, K., THOMPSON, R., HELLINGA, H., Analysis of allosteric signal transduction mechanisms in an engineered fluorescent maltose biosensor, *Protein Sci.* **2005**, 14, 284–291.
- 81 DE LORIMIER, R. M., SMITH, J. J., DWYER, M. A., LOOGER, L. L., SALI, K. M., PAAVOILA, C. D., RIZK, S. S., SADIGOV, S., CONRAD, D. W., LOEW, L., HELLINGA, H. W., Construction of a fluorescent biosensor family, *Protein Sci.* **2002**, 11, 2655–2675.
- 82 GILARDI, G., ZHOU, L. Q., HIBBERT, L., CASS, A. E., Engineering the maltose binding protein for reagentless fluorescence sensing, *Anal. Chem.* **1994**, 66, 3840–3847.
- 83 ZHOU, L. Q., CASS, A. E. G., Periplasmic binding protein based biosensors. 1. Preliminary study of maltose binding protein as sensing element for maltose biosensor. *Biosens. Bioelectron.* **1991**, 6, 445–450.
- 84 BRUNE, M., HUNTER, J. L., CORRIE, J. E., WEBB, M. R., Direct, real-time measurement of rapid inorganic phosphate release using a novel fluorescent probe and its application to actomyosin subfragment 1 ATPase, *Biochemistry* **1994**, 33, 8262–8271.
- 85 MARCUS, R. A., SUTIN, N., Electron transfers in chemistry and biology,

- Biochim. Biophys. Acta* **1985**, 811, 265–322.
- 86 MEDINTZ, I. L., KONNERT, J. H., CLAPP, A. R., STANISH, I., TWIGG, M. E., MATTOUSSI, H., MAURO, J. M., DESCHAMPS, J. R., A fluorescence resonance energy transfer-derived structure of a quantum dot-protein bioconjugate nanoassembly, *Proc. Natl. Acad. Sci. U.S.A.* **2004**, 101, 9612–9617.
- 87 WILLARD, D. M., CARILLO, L. L., JUNG, J., VAN ORDEN, A., CdSe-ZnS quantum dots as resonance energy transfer donors in a model protein-protein binding assay, *Nano Lett.* **2001**, 1, 469–474.
- 88 WANG, S., MAMEDOVA, N., KOTOV, N. A., CHEN, W., STUDER, J., Antigen/antibody immunocomplex from CdTe nanoparticle bioconjugates. *Nano Lett.* **2002**, 2, 817–822.
- 89 SHETE, V., SANDROS, M. G., BENSON, D. E., unpublished results.
- 90 HERNANDEZ, F. J., BENSON, D. E., unpublished results.
- 91 KAWATSU, T., BERATAN, D. N., KAKITANI, T., Conformationally averaged score functions for electronic propagation in proteins, *J. Phys. Chem. B* **2006**, 110, 5747–5757.
- 92 LIN, J., BALABIN, I. A., BERATAN, D. N., The nature of aqueous tunneling pathways between electron-transfer proteins, *Science* **2005**, 310, 1311–1313.
- 93 LEE, J., GOVOROV, A. O., KOTOV, N. A., Nanoparticle assemblies with molecular springs: A nanoscale thermometer, *Angew. Chem. Int. Ed.* **2005**, 44, 7439–7442.
- 94 YUN, C. S., JAVIER, A., JENNINGS, T., FISHER, M., HIRA, S., PETERSON, S., HOPKINS, B., REICH, N. O., STROUSE, G. F., Nanometal surface energy transfer in optical rulers, breaking the FRET barrier, *J. Am. Chem. Soc.* **2005**, 127, 3115–3119.

## 13

# Pico/Nanoliter Chamber Array Chips for Single-cell, DNA and Protein Analyses

*Shohei Yamamura, Ramachandra Rao Sathuluri, and Eiichi Tamiya*

### 13.1

#### Introduction

In recent years, miniaturized systems called Lab-on-a-chip or Micro-Total Analysis System ( $\mu$ -TAS) have been examined as new systems for biochemical analyses. These systems are expected to perform DNA, protein and cell analysis for drug screening and development of novel therapies. Especially, microarray and microfluidic types of chip devices have been developed using micro- and nanotechnological techniques. These lab-on-a-chip systems can be used for high-throughput identification of large numbers of potential drug targets, e.g., DNA, protein, chemicals [1, 2]. Recent advances in the human genome project have prompted the use of the miniaturized chip devices for high-throughput analysis of the vast amount of information potentially available. To obtain as much information as possible in a short time with a minimal use of reagents, researchers require highly integrated and sophisticated devices, such as microarrays. Thus, microarrays suitable for different biomaterial assay and detection technologies have been under intense investigation [1, 2]. Microarrays have been mostly applied to the assessment of the presence of a specific base sequence, or which genes are expressed and at what level [3, 4]. They have also been employed in identification of peptides and proteins as pharmaceutical drugs [5, 6]. Although the number of human genes was reported to be approximately 30 000 from the human genomic project, the functions and expression mechanism for most of the genes remain unknown, because the fate of the genes functionality is determined after protein expression, but proteins expression is controlled by cellular function. Therefore, it is necessary to develop the microarray chip devices that can perform high-throughput screening and analysis of proteins and cells at single-cell and single-molecule level.

To achieve single-cell or single-molecule analysis, highly integrated microarray systems that can perform assays at pico- and nano-liter volume level are greatly desirable to realize post-genomic research, such as proteomics and cellomics. Single-cell analysis contributes to elucidate the functional mechanism of genes, proteins and chemical responses, which lead to clinical diagnosis and drug discovery [7]. In

recent work, some researchers reported cellular microarrays using biomaterial spotting techniques for investigating gene expression or differentiation of some kinds of cells [8, 9]. These systems can screen and detect a group of cells but not single-cell based assay from bulk cell suspension, because they have a great possibility of cross-contamination with neighboring cells due to the absence of a physical boundary. Therefore, it is necessary to construct a microarray system that can perform high-throughput analysis of single-molecule or single-cell and quantitative detection.

However, there are no reports available, to the best of our knowledge, that describe high-throughput analysis of DNA, protein and cell at single-molecule and single-cell level together at one place. Therefore, we address the analysis of DNA, protein and cell using pico- or nano-liter chamber array system in this chapter. This chapter is divided into three topics: novel multiplexed PCR, cell-free protein synthesis, and high-throughput single-cell analysis system [10–13]. The chapter ends with a look at future prospects.

## 13.2

### **Multiplexed Polymerase Chain Reaction from A Single Copy DNA using Nanoliter-volume Microchamber Array**

Polymerase chain reaction (PCR)-based techniques have become the most important part of DNA diagnostic laboratories since its first introduction in 1985 [14]. The discovery of this technology has earned its inventor, K. B. Mullis, a Nobel prize for his achievement [15], which has opened up new horizons for a limitless number of DNA-based research possibilities. Since then, qualitative PCR has been a well-established and straightforward technology, but the quantification of specific target DNA sequences in a complex sample has been a difficult task. Several variations, caused by the manipulation of nucleic acids that may occur during sample preparation, storage, or the course of the reaction hampered accurate quantification. The exponential nature of the PCR amplification can significantly magnify even minor variations in reaction conditions. Normalizing the amount of PCR products of the specific template with respect to an internal reference template has been partly successful against these variations. Since the challenge of accurate DNA quantification stimulated many researchers, a great variety of protocols already exist for the utility of quantitative PCR [16–18]. However, these methods are nearly exclusively restricted to be applied for research purposes only because of two factors they have in common: they are difficult tasks and are costly to run.

To supply the demand for faster, more accurate, and more cost-effective PCR devices with a high-throughput capacity, three important properties have directed the development of the next generation of PCR systems: automation, standardization, and miniaturization. Recently, Yang et al. have reported a high-sensitivity PCR assay in polycarbonate plastic, disposable PCR microreactors [19]. At a template concentration as low as 10 *Escherichia coli* cells (equivalent to 50 fg of genomic DNA),



221-bp product was successfully amplified within 30 min. Lee et al. [20] have described a microfabricated PCR device for simultaneous DNA amplification and electrochemical detection on gold or indium tin oxide (ITO) electrodes patterned on a glass substrate. A miniaturized flow-through PCR with different template types in a silicon chip thermocycler has also been reported to have a minimum power consumption [21]. With the flow-through PCR device of Fukuba et al. [22], 580 and 1450 bp of DNA fragments were successfully amplified from *E. coli* genomic DNA and directly from untreated cells. For temperature control of their chip, six heaters made of ITO were placed on a glass substrate to act as three uniform temperature zones. Lee et al. [23] have recently reported a bulk-micromachined PCR chip. They validated that the proposed chip amplified the DNA related to the tumor suppressor gene BRCA 1 (127 bp at 11th exon) after 30 thermal cycles in a 200-nL-volume chamber. Although most of the recent assays are accurate and sensitive, they involve the definition of very stringent limits. The PCR products are usually separated by gel electrophoresis, and the band intensities are quantified by video imaging and densitometry. Additionally, Lagally et al. [24, 25] have shown that microfluidic systems are capable of multiplexed PCR reactions and robust on-chip detection.

Microchamber arrays etched on silicon or glass have also been one of the most reported miniaturized devices for multiple simultaneous DNA amplification [26–28]. The minimum reported size for a microchamber for PCR was demonstrated by Leamon et al. in connection with PCR [29]. They reported a novel platform, namely PicoTiterPlate™, which enabled simultaneous amplification of 300 000 discrete PCR reactions in volumes as small as 39.5 pL. Following the PCR on the PicoTiterPlate™, the solution from each well was recovered, and then quantified by TaqMan assay. As for the easy integration with different applications, solid-phase amplification was also performed on PicoTiterPlate™ by immobilizing the PCR product to a DNA capture bead in each well. Thus, 370 000 beads bound with PCR product were obtained for parallel processing in numerous solid-phase applications. The volume of a microchamber for a successful PCR amplification was reduced to 86 pL by Nagai et al. [26]. However, as the sample volume was decreased, evaporation of sample solution and the introduction method of quite a small amount of solution into the reaction microchamber appeared as the major drawbacks.

In our research, for achieving simultaneous detection of several numbers of target DNA, the feasibility of our microchamber array was further improved by using TaqMan PCR [11, 12]. To the best of our knowledge, three different DNA sequences were amplified from three different DNA templates and detected in the same microchamber array simultaneously for the first time. In addition, the quantification of initial DNA concentration present in a microchamber was achieved from 0 to 12 copies per chamber, not only by monitoring the real-time fluorescence intensity but also by observing the end point fluorescence signal. Therefore, this system proves to be a promising device for the low-cost, high-throughput DNA amplification and detection for point-of-care clinical diagnosis, which can also be handled by non-specialist users.

## 13.2.1

**PCR Microchamber Array Chip System****13.2.1.1 Microchamber Array Chip Fabrication**

The microchamber array chip for DNA amplification was fabricated using micro-machining techniques, including photolithography, and anisotropic wet etching on the optically polished side of a silicon (100) wafer. The chip substrate was designed to be  $2.54 \times 7.62$  cm for compatibility with the dispensing system employed. Figure 13.1 shows the fabrication procedure, giving detailed schematic steps of the silicon chamber array chip.

Before proceeding to microfabrication, the silicon wafer was washed thoroughly with acetone and then immersed in a 60% (v/v) hydrogen fluoride solution and, finally, allowed to dry at room temperature. Subsequently, the silicon wafer surface was oxidized to silicon oxide ( $\text{SiO}_2$ ) by wet thermal oxidation at  $1000^\circ\text{C}$  for 8 h. A photo mask with 1248 chambers having a  $24 \times 52$  pattern was then printed on the surface, after being coated with a positive photoresist (OFPR-800) layer, by a photolithographic process. Soaking the chip substrate in a NMD-3 solution for 5 min removes the light exposed OFPR portions and, followed by treatment with  $\text{HF}/\text{NH}_4\text{F}$  (v/v) 10:60 volumes solution, removed the exposed oxide layer and then remaining portions of photoresist by treating with acetone. The chip substrate was then anisotropically etched with 25% (w/v) tetramethylammonium hydroxide (TMAH) in an aqueous solution to a depth of  $250\ \mu\text{m}$  for 8 h at  $80^\circ\text{C}$ . A layer of  $\text{SiO}_2$  was grown on the surfaces, including the etched chamber walls and then OFPR-800 was spin coated and further photolithography was performed to leave the  $\text{SiO}_2$  layer inside the microchamber walls. The oxidized layer and photoresist were removed by using  $\text{HF}/\text{NH}_4\text{F}$  (v/v) 10:60 volumes of solution and acetone, respectively. The microchamber feature was observed by a color laser 3D profile microscope VK-8500

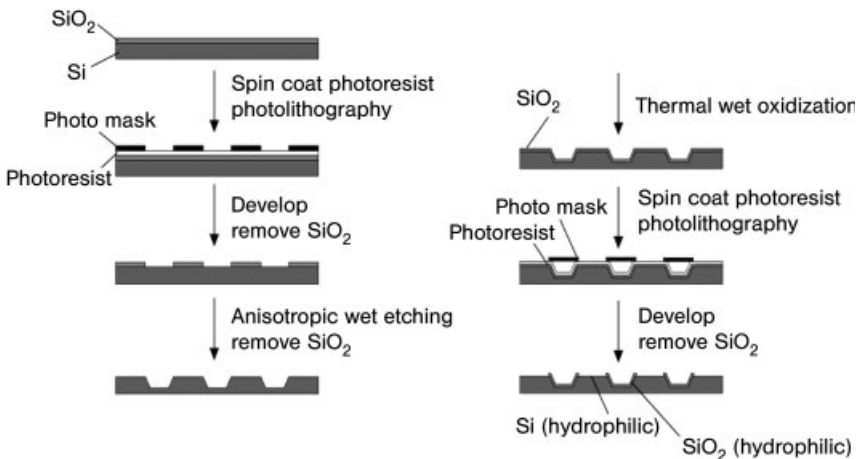
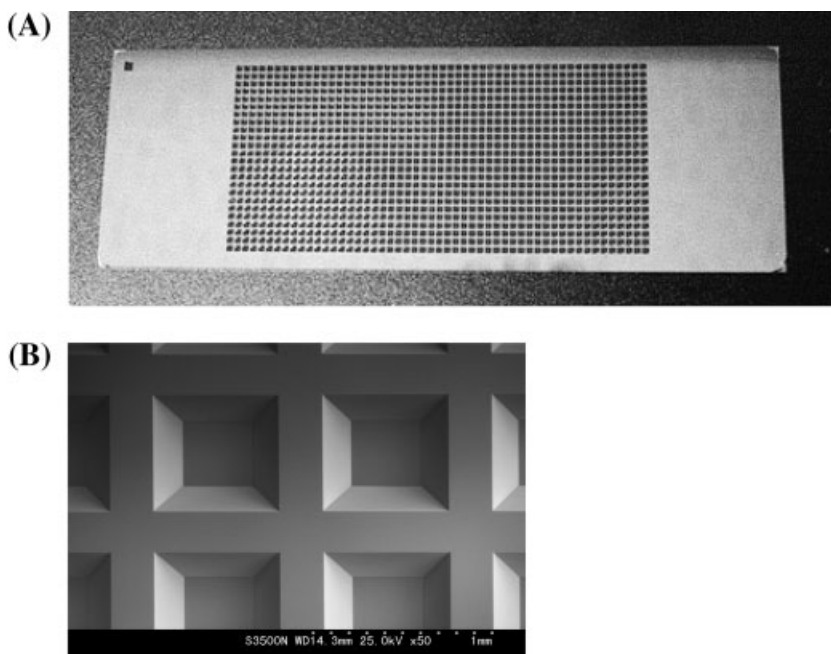


Fig. 13.1. Schematic illustration of microchamber array fabrication procedures.



**Fig. 13.2.** (A) Photographic image of the microchamber array chip. The 1248 microchambers are integrated on the  $1 \times 3$  inch. of a silicon chip. (B) Scanning electron micrograph (SEM) of a silicon microchamber array.

(KEYENCE, Japan) and scanning electron microscope (HITACHI, Japan). Each chamber was parallelepiped with dimensions of  $650 \times 650 \times 200 \mu\text{m}$ , a pitch of each microchamber of  $\sim 900 \mu\text{m}$ , and accommodates 50 nL (Fig. 13.2). The total number of chambers on each chip is of 1248. To achieve precise introduction of sample mixture into the microchamber, only the inner wall surfaces of the microchamber were prepared as hydrophilic by leaving an oxidized layer on them by photolithographic techniques, as described recently by Felbel et al. [30].

#### 13.2.1.2 Sample Loading with a Nanoliter Dispenser

The microchamber array chip was soaked in 1% (w/v) bovine serum albumin (BSA) solution overnight, then rinsed with deionized water, and dried to prevent nonspecific adsorption by coating the chamber wall. The chip was placed onto the dispensing stage of a nanoliter dispenser from Cartesian Technologies. The precise dispensing of nanoliter volumes of solutions exactly at previously determined locations had become very simple by using their technology. The volume of dispensed solution in a single microchamber was 40 nL. Mineral oil as a cover lid was coated onto the template DNA-modified chip, and 40 nL of PCR mixture, which included target-specific primers and probe, was dispensed into all of the microchambers

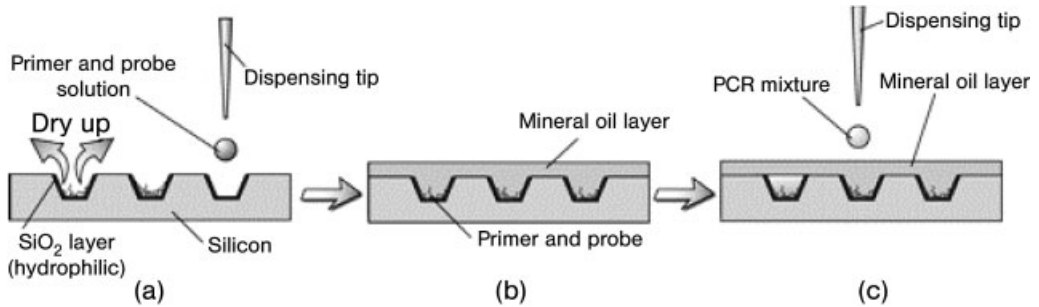


**Fig. 13.3.** Illustration of preparation steps for on-chip DNA amplification: (a) Different types of primers are dispensed into the microchamber and then dried. (b) Mineral oil is coated on the chip after the primer solution

has dried. (c) A PCR mixture (40 nL) with no primers is dispensed in each chamber through the oil layer. The solution sinks to the bottom and then spreads to the microchamber walls.

through the oil layer. After preparing this setup, the chip was placed onto a conventional thermal cycling system to achieve PCR reaction. Thermal cycling was initiated at 94 °C and held for 10 min, followed by 40 cycles of 94 °C for 10 s and 60 °C for 60 s. After the end of PCR amplification, the amplified DNA was observed using a charge-coupled device (CCD) camera (Hamamatsu Photonics, Japan) mounted on a fluorescence microscope (Leica, Heidelberg, Germany). The inner walls of the microchamber were rendered hydrophilic with the formation of an oxidized layer on their surfaces. After coating the microchamber array with mineral oil, the remaining hydrophobic surface of the microchamber prevented the spread of the aqueous solution to the outside of the microchamber. After dispensing of the aqueous sample solution, it first formed a droplet, which in time was replaced with the oil in the microchamber, and settled inside the microchamber with the convection of the oil (Fig. 13.3). The thickness of the oil layer had a significant effect on the protection of nanoliter-scale solutions from evaporation. The oil layer was adjusted by controlling the volume of the oil drop. As the thickness of the oil layer increased, the dispensing of the sample solution became more erroneous (data not shown). The optimum thickness of the oil layer for introduction of the sample mixture was chosen to be ~200  $\mu\text{m}$ .

### 13.2.2

#### Multiplexed Detection of Different Target DNA on a Single Chip

Target DNA sequence was amplified specifically in a nanoliter-volume microchamber, and the microchambers, in which fluorescence signal was released, were counted in consequence to TaqMan PCR. Cross-contamination between chambers was tested by using alternate dispensings of wells containing template and those without template. A high concentration of the template DNA was introduced as alternate dispensings into the microchambers. Fluorescence signals were obtained only from the chambers, into which template DNA was introduced. No fluores-

cence was gained from the remaining chambers, into which no template DNA was dispensed. Thus, it was concluded that the selective distribution of the template DNA into the microchambers was achieved in our system.

There were several inhibition factors, such as nonspecific adhesion of biomaterials, variety in the distribution efficiency of the sample dispensing, and errors caused by PCR itself. Surface treatment of the microchamber was also an important factor affecting the efficiency of the PCR reaction. Shoffner et al. have reported several kinds of surface treatment methods that are useful for avoiding the adsorption of biomaterials on the silicon surface [31]. Erill et al. have reported a systematic analysis of material-related inhibition and adsorption phenomena in glass-silicon PCR chips [32]. Their results suggested that the previously reported inhibition of PCR by silicon-related materials was caused mainly by the adsorption of Taq polymerase at the walls of the chip due to increased surface-to-volume ratios; thus, direct chemical action of silicon-related materials on the PCR mixture was negligible. In contrast to Taq polymerase, DNA was not adsorbed in significant amounts. The net effect of polymerase adsorption could be prevented by the addition of a titrated amount of a competing protein, BSA, and the ensuing reactions could be kinetically optimized to yield efficient PCR amplifications. In our system, we combined these advantageous points of previous reports. The surface of the microchamber walls was first modified by an oxidized layer [30, 31] and then coated with BSA [32]. Only a very low fluorescence signal could be observed, when no BSA coating was employed. Thus, it was found necessary to coat the oxidized walls of the microchambers with BSA, in good agreement with the findings of Erill et al. [32]. To quantify DNA concentration, a certain number of microchambers were used as one region for only one concentration.

Figure 13.4 shows the fluorescence image of the chip after DNA amplification of three different target DNA sequences from three different DNA templates. Visual comparison of the positive fluorescence intensity signals with the negative ones greatly simplified the procedure of distinguishing which chamber contained the target DNA. If the target DNA sequence was present in the dispensed sample, a high fluorescence signal was easily obtained as a result of TaqMan PCR. Additionally, the background fluorescence intensity of the  $\beta$ -actin PCR system was much lower than that of the other two probes by using both our chip and the SmartCycler real-time PCR system (Fig. 13.4B). SmartCycler real-time PCR system results were in good agreement with the results of our chip. The difference in the background fluorescence intensity was caused by the bp distance between FAM and TAMRA dyes of the TaqMan probes. In the TaqMan probe for  $\beta$ -actin gene, FAM was only 6 bp away from TAMRA, but FAM and TAMRA were 26 and 31 bp apart in the probes for SRY and RhD genes, respectively. Such a short distance of 6 bp between the dyes caused the rapid quenching of the signal, and thus, the  $\beta$ -actin system could release much lower fluorescence signals after amplification in comparison with the other systems. Although the PCR systems in this experiment had such different background fluorescence intensities, accurate detection of TaqMan amplification for all systems was achieved by using our chip. Since Rh(-) human female genomic DNA did not contain SRY and RhD genes, almost none

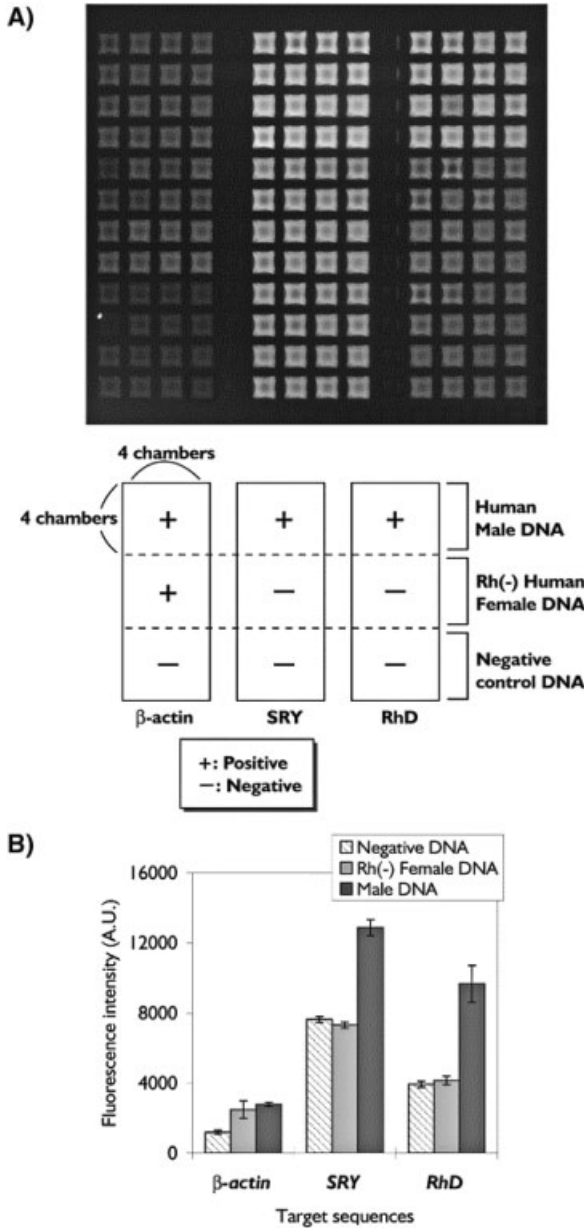


**Fig. 13.4.** Multiple PCR analysis of  $\beta$ -actin, SRY, and RhD genes using three different kinds of template DNA.

(A) Photograph of the microchamber array after multiple TaqMan PCR. (B) Average fluorescence intensity values obtained from 16 microchambers.

of the microchambers showed a fluorescence signal. Both human male and female genomic DNA contained the  $\beta$ -actin gene; thus, a fluorescence signal could be observed successfully in all microchambers of the related area on the chip. The fluorescence intensity of the microchambers was also scanned and evaluated using a DNA microarray scanner and its analysis system. The fluorescence intensity values were obtained from 16 chambers. A remarkable difference between the fluorescence intensities of the positive and negative controls was observed clearly for all three DNA templates. This result indicated that our system can detect different kinds of target DNA sequences from different DNA sources simultaneously. Since TaqMan PCR required the same thermal cycling protocol for the amplification of many kinds of target sequences, it was found to be the most suitable detection technique for microchamber array PCR systems in this report. For example, the detection of genetic diseases such as Down's syndrome [33], 22q11.2 deletion syndrome [34], and  $\beta$ -thalassaemia [35] using TaqMan PCR has already been reported. These clinically important diseases can also be detected simultaneously using our microchamber array-based PCR chip.

### 13.2.3

#### **On-chip Quantification of Amplified DNA**

The initial RhD gene concentration was also quantified by using the microchamber array (Fig. 13.5A). Amplification of the RhD gene was performed by dispensing different concentrations of target DNA into the microchambers. As target DNA was increased from 0 to 12 copies per chamber, the number of the microchambers with positive fluorescence signal also increased. PCR amplification in almost the whole block of the chip was achieved by using eight copies of the target DNA. When 0.4 copies of the target DNA were used, an average of 2 out of 60 chambers ( $n = 3$ ) showed a signal above the threshold level. The average fluorescence intensity value of 1000 AU was determined as the threshold. The high fluorescence released in these two chambers could also be visually detected. Since 0.4 copies of the target DNA were enough to give a readable signal, this concentration was determined as our limit-of-detection. The chambers with positive fluorescence signals, which mean successful PCR amplification, showed easily distinguishable fluorescence intensity (Fig. 13.5A).

Figure 13.5(B) plots the number of chambers with positive fluorescence signal versus input template DNA copy number for the amplification of RhD (B) sequence. As target DNA increased from 0 to 12 copies/chamber, the number of microchambers with a positive fluorescence signal also increased. It was possible to fit the data from 0 to 8 copies/chamber into a straight line with the regression coefficients of 0.9879 for RhD sequence. The system reached a saturation plateau after DNA concentration of 8 copies/chamber, indicating that a trace amount of target DNA was satisfactory for the detection process. PCR amplification in almost the whole block of the chip was achieved by using eight copies of the target DNA. Such a behavior indicated the high detection capacity of our system, so that even a trace amount of DNA copies would be satisfactory for a precise quantification.

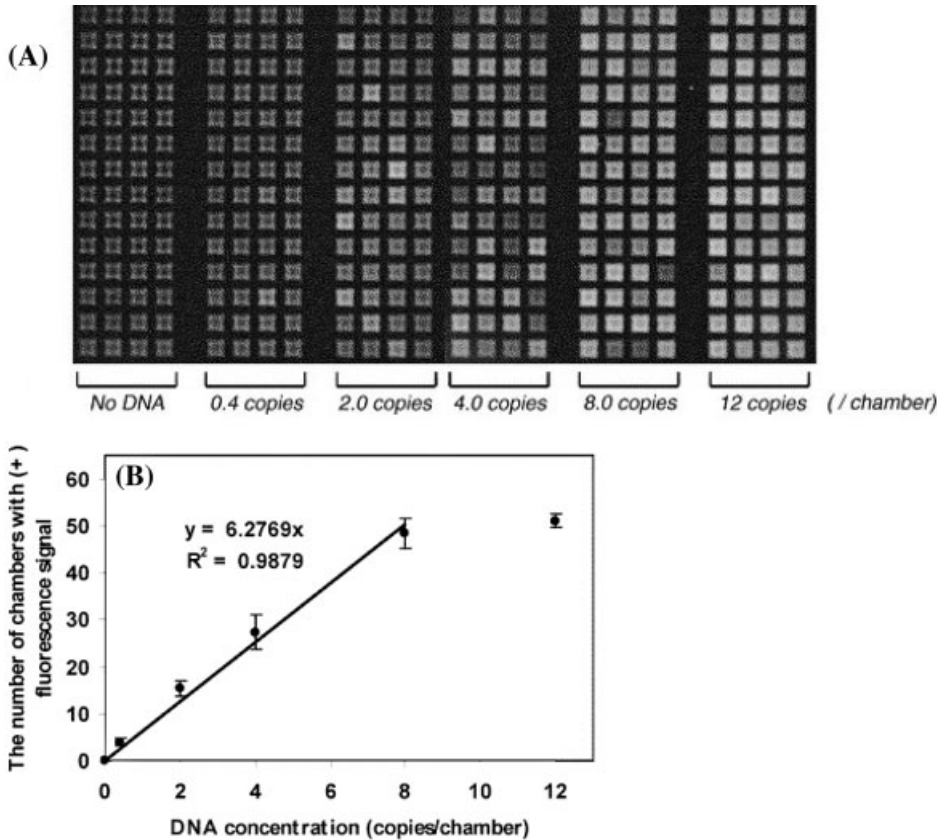


Fig. 13.5. (A) Photograph of fluorescence image for on-chip quantitative analysis of RhD gene. (B) Plot for the average number of chambers within a specific fluorescence signal range versus the number of target DNA copies related to RhD gene after TaqMan PCR.

Copy numbers above eight that would be amplified without any problems but, however, could not be quantified. Even 0.4 copies of the target DNA was enough to give a readable signal, which was determined as our limit of detection. The average fluorescence intensity value of 1000 AU was determined as the threshold. When 0.4 copies were dispensed, only two microchambers reached within the 1000–1200 AU level. One would have expected to get 4 out of 10 microchambers to be positive and 6 to be negative, if we had an average of 0.4 copies/microchamber, and every copy was intact. The polymerase concentration, annealing temperature,  $MgCl_2$  concentration, and the specific primers and TaqMan probes should have been kept under the optimum conditions in 40-nL volumes in the microchamber – a tedious task. Instrumental limitations also added to the inefficiency of PCR, when such a small volume containing such a trace amount of an-



alyte was dispensed on a microchamber array. Thus, the combined negative effects of biochemical (resulting from the TaqMan PCR itself) and instrumental limitations caused the appearance of only two microchambers out of 60 with positive signals after TaqMan PCR on our system. Our method requires only counting the microchambers that show a positive fluorescence signal as a consequence of PCR amplification. No special equipment for the detection of real-time fluorescence intensity is required for determination of DNA copy numbers. Only a simple fluorescence microscope, or a transilluminator used for gel electrophoresis, need be employed for accurate observation of the fluorescence released microchambers with positive signals.

The microchamber array chip presented could be used to amplify multiple DNA targets in combination with a nanoliter dispenser. Theoretically, the chip could be used to amplify and detect ~1200 target DNA simultaneously. The size and total number of the microchambers are determined by the dispensing system. The minimum solution volume that could be dispensed with reliability was optimized as 40 nL for our experiments. If the dispensing instrument could be improved to provide the dispensation of a lesser volume of solution, the microchamber size could become smaller, and the chip would become more integrated with a higher number of microchambers. Such further integration of our microarray PCR chips with a miniaturized thermal cycler unit is in progress in our laboratory. The microarray PCR chip reported here has significant potential to be implemented for a wide range of applications. Overall, this system is a promising candidate for mass microfabrication due to its low-cost and high-throughput detection ability.

### 13.3

#### **On-chip Cell-free Protein Synthesis using A Picoliter Chamber Array**

The progress in analyzing the human genome has shifted the focus of research from genes to proteins [36–40]. Although the number of human genes is reported to be 28 000–38 000 [41], the functions of most of them are remain unknown. A rapid and easy method for synthesizing gene products has yet to be developed. Thus, an *in vitro* protein synthesis system has been designed and constructed on the microarray to make a protein library chip. The chip has proteins arranged in an array, and can detect target molecules. Gene cloning and expression is widely used in the preparation of proteins. However, some kinds of proteins often cannot be expressed well in host cells. Our cell-free protein synthesis system could be suitable for expressing such proteins. This protein synthesis system has other advantages as well, such as labeling proteins with isotopes for detection by NMR spectroscopy [42], easy purification of the synthesized protein, and short protein synthesis time.

A highly integrated protein chip is a powerful tool for accelerating post-genomic research. Our aim is to develop protein chips directly from a DNA library using the *in vitro* protein synthesis system. Recently, a cell-free protein synthesis system

from *Escherichia coli*, rabbit reticulocytes, and wheat germ has been commercialized [43]. In this research, a rapid translation system from *E. coli* was used for protein expression. Previously, we reported the development of a large-scale integrated pico-liter microchamber arrays for PCR [27], the introduction of a novel nano-liter dispensing system suitable for DNA amplification on microchamber array chip [28], the development of a simultaneous multianalyte immunoassay method for detecting human immunoglobulins based on a protein chip and imaging detection [44], and the development of a new approach for manufacturing encoded microstructures used as versatile building blocks for miniaturized multiplex bioassays [45]. Others have reported the construction of protein chips [46, 47] or cell-free protein synthesis in small chambers [48]. Kukar et al. have detected eight samples simultaneously on one chip [46], and Kojima et al. have constructed an electrochemical immunochip including an assembly of 36 electrodes [47].

There have been reports of high-throughput screening of a mutated anti-human serum albumin single-chain antibody (anti-HSA-scFv) using an *in vitro* protein synthesis system [49, 50]. In these reports, two amino acids were mutated randomly, and over 600 mutations were screened on 96-well plates. Our newly developed chip could also be a powerful tool in similar applications.

High-throughput screening is required for the rapid elucidation of protein functions. Microscale reactions have the advantages of short reaction time and the use of a small amount of samples and reagents. Especially in a high-throughput screening system, numerous samples must be analyzed simultaneously and, if possible, economically. Thus, we have made a highly integrated protein microchamber array chip by using micro-fabrication techniques and polydimethylsiloxane (PDMS) [6]. PDMS micro-molding techniques have been used to fabricate microfluidic systems [51, 52]. Unlike traditional micro-fabrication materials, such as silicon and glass, PDMS can be bonded and manufactured easily and efficiently [53]. In addition, PDMS has some properties that are advantageous for biochemical applications such as high transparency in the 230–700 nm wavelength range, and high permeability to gases.

### 13.3.1

#### Cell-free Protein Synthesis Chip Fabrication

Photolithography has been used to fabricate thin microarray sheets using PDMS [53]. A master pattern was formed on a silicon wafer using SU-8 photoresist. The PDMS prepolymer (Sylgard-184: Dow Corning, USA) mixture was poured onto the master and covered with a transparency film (overhead projector sheet). A multi-layer stack of aluminum plates, the master pattern, PDMS, a transparency film, a glass wafer, and rubber sheets were clamped tightly and the PDMS prepolymer was baked and crosslinked at 80 °C for 2 h. The resulting thin PDMS sheet, which has over 200 000 microchambers (micro-holes), was put on a slide glass in acetone and treated with oxygen plasma to bind the sheet to the glass. A reactive ion etching (RIE) system was used for the oxygen plasma treatment. The PDMS sheet has

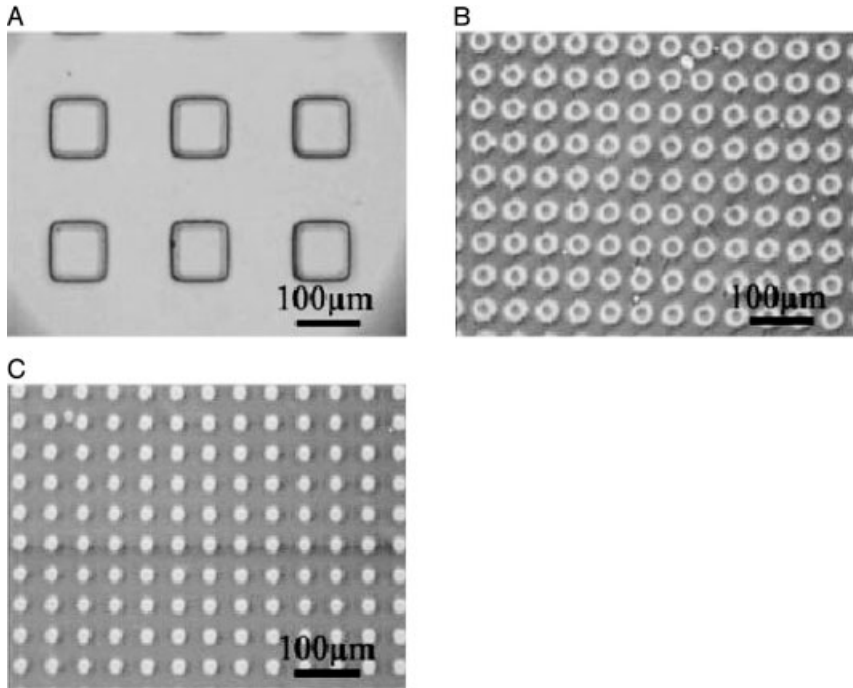


**Fig. 13.6.** Optical images of PDMS/glass complex chambers. (A) Rectangular chambers about  $100 \times 100 \times 15 \mu\text{m}$ ; the volume is about 150 pL. (B) Cylindrical chambers 20  $\mu\text{m}$  in diameter and 15  $\mu\text{m}$  deep; the volume is about 5 pL. (C) Cylindrical chambers 10  $\mu\text{m}$  in diameter and 15  $\mu\text{m}$  deep; the volume is about 1 pL.

micro-holes, and a hydrophobic surface. Thus, only the bottoms of the microchambers were hydrophilic and the solution easily remained in the chambers. Three different types of chips were designed and fabricated (Fig. 13.6).

The PDMS microchamber was used for *in vitro* protein synthesis. The ribosome source was based on a lysate from *E. coli* (RTS-500 kit: Roche, USA). The wild-type GFP gene contained in the kit was used as a reporter gene, and expressed on the chips. Cell-free protein synthesis reagents were prepared according to the supplier's directions. The reaction solution was composed of a mixture of *E. coli* lysate solution (0.25 mL), of the reconstituted reaction mixture (0.75 mL), of the enzyme mixture (50  $\mu\text{L}$ ), and the GFP vector at a final concentration of 10  $\mu\text{g mL}^{-1}$ . First, we dripped the *in vitro* protein synthesis solution on the chip, and removed the surplus. Next, the microchamber chip was covered with a gap cover glass, and sealed to prevent evaporation. A 20  $\mu\text{m}$  gap between the chip surface and the cover glass prevented capillary action among the chambers. The chip was then held at 30  $^{\circ}\text{C}$ , and GFP expression was detected by an optical fluorescence microscope with an FITC filter (excitation: 450–490 nm, emission: 515–565 nm).

## 13.3.2

**Cell-free Protein Synthesis using a Microchamber Array**

RIE treatment (oxygen plasma treatment) was used to bind PDMS to a slide glass. Three different types of PDMS chips were designed and fabricated (Fig. 13.6). Since the PDMS and glass construction gives the chamber structure a hydrophobic surface and a hydrophilic bottom substrate, an aqueous solution poured onto the chip enters through the holes of the array, and remains only in these microchambers. This phenomenon prevents the cross-contamination between the microchambers. This chip is also suitable for optical observations because of its transparency over a wide wavelength range. Protein synthesis was carried out on the microchamber chips with the GFP gene used as a reporter gene. Expression of GFP was detected by fluorescence using an optical microscope. Figure 13.7 shows the results of cell-free protein synthesis on the chip. Fluorescence intensity was detected within 1 h of incubation, and remained constant. In a batch system, protein synthesis is said to be inhibited by a lack of substrate or accumulated waste within 2 h [54]. In our system, cell-free protein synthesis stopped within 2 h. This result agrees with the report of Spirin et al. [54]. However, the formation of the GFP fluorescent group is known to take 1–2 h [54]; thus, it may be considered that protein synthesis stopped before the GFP fluorescence became constant. However, a similar shift in GFP fluorescence was shown in chambers with 10 (Fig. 13.8) or 20  $\mu\text{m}$  i.d.

The lowest concentration of DNA template necessary for the detection of the GFP signal was determined to be only 10 molecules of DNA per chamber. A microchamber array chip with cylindrical chambers 10  $\mu\text{m}$  wide and 15  $\mu\text{m}$  deep was used in this experiment. The volume of this chamber is about 1 pL. Thus, the concentration of a solution containing 10 molecules of DNA is about  $4 \times 10^{-5}$

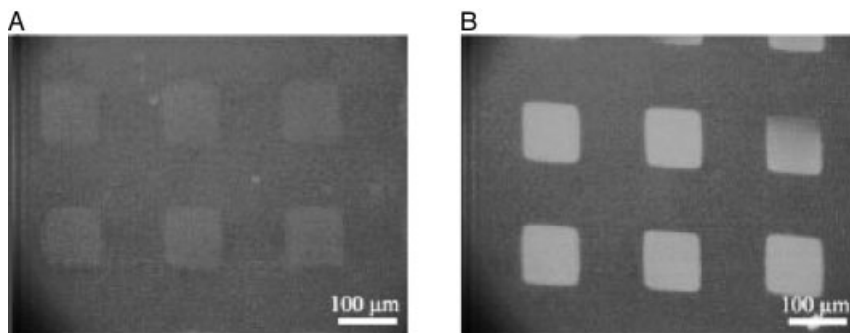


**Fig. 13.7.** Fluorescent images of microchips showing the expressed GFP protein. Chambers on the chip were filled with the cell-free protein synthesis reagents. Fluorescent image of the

chambers after incubation for (A) 0 h and (B) 1 h; GFP expression was detected under an optical microscope with a FITC filter.

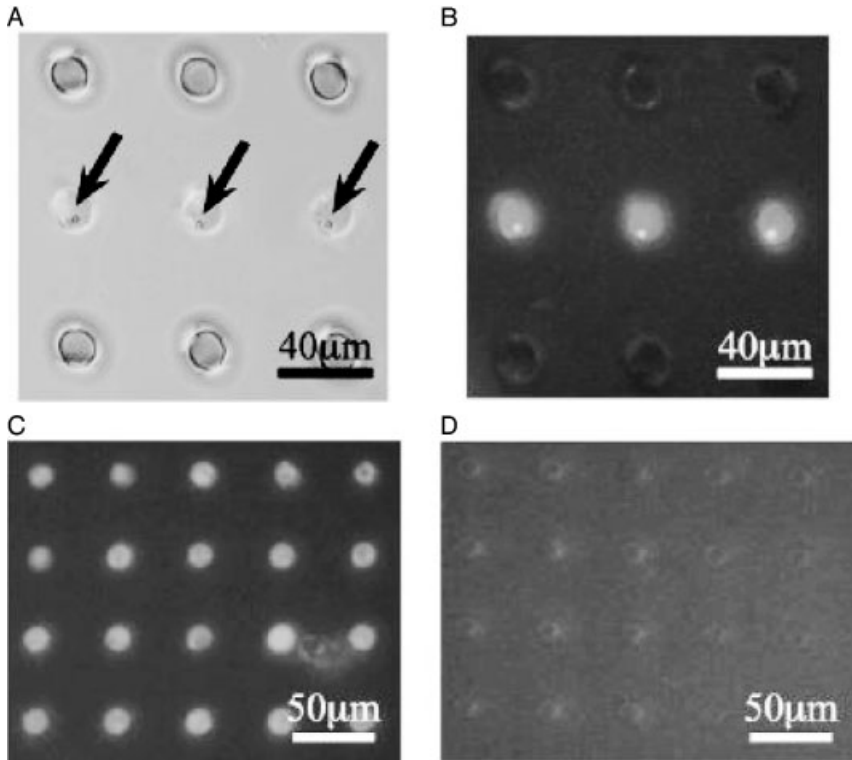


**Fig. 13.8.** Optical images of GFPuv expression from DNA-immobilized beads. (A) Optical image under white light; arrows indicate the presence of beads. (B) Fluorescence image of the chamber,  $\lambda_{ex.} = 400\text{--}440\text{ nm}$ ,  $\lambda_{em.} = 475\text{ nm}$ . (C) Fluorescence image of a positive control containing cell-free protein synthesis reagents with 10 fg per pL pGGFPH vector. (D) Fluorescence image of a negative control containing only cell-free protein synthesis reagents (no template DNA). Cylindrical chambers shown in the figure are 10  $\mu\text{m}$  in diameter.

$\text{mg mL}^{-1}$ . This concentration is about 1/100 to 1/500 compared with the DNA concentration utilized in conventional cell-free protein synthesis protocols. The use of a small volume chamber increases the possibility of contact between DNA and reagents, making it possible to express a protein using a trace amount of DNA.

The distribution of over 10 000 samples using a DNA spotter would take a very long time; therefore, self-layout of samples containing the DNA library was used in this study. DNA-immobilized beads were used as DNA carriers. The amount of DNA immobilized on one bead was about 200 molecules on Dynabeads M-270 Carboxylic Acid, and 10 000 molecules on Dynabeads M-280 Streptavidin (Dyna, USA). A microchamber array chip with a 10  $\mu\text{m}$  i.d. chamber was used for bead arrangement. About 60% of the chambers contained one bead; however, some chambers had multiple beads because the diameter of a bead, which is 2.8  $\mu\text{m}$ , is much smaller than that of the chamber. The design and fabrication of a new chip with

smaller chambers to allow the entry of only one bead into each chamber are currently underway in our laboratory.

With the aid of lipid, it was possible to disperse the beads into the chambers. Rhodamine-modified lipid was used instead of phosphatidylcholine, and the chip covered with lipid solution was observed both in air and in water. Interestingly, the lipid moved into the chamber when the chip was soaked in water. A chip with beads containing the GFP gene was used for *in vitro* protein synthesis. As shown in Fig. 13.8, fluorescence was observed after 1 h of incubation only in chambers that contained DNA beads. As a positive control, pGGFPH vector solution was added to the *in vitro* protein synthesis reagents at  $10 \text{ fg pL}^{-1}$ ; no template DNA was added to the *in vitro* protein synthesis reagents as a negative control. The results of these control experiments are shown in Fig. 13.8. A comparison between DNA immobilized beads and DNA in solution suggests that the amount of protein per DNA molecule in solution is greater than that on DNA-immobilized beads. Nevertheless, easy and fast manipulation of DNA immobilized beads prompted us to use this method. In the experiments shown in Fig. 13.8, DNA immobilized beads with biotin–streptavidin conjugate were used. Similar results were observed when primer-immobilized beads were used. The concentration of GFP solution was about  $10 \text{ } \mu\text{g mL}^{-1}$ , estimated from the intensity of the fluorescence. The amount of GFP protein per chamber was about 10 fg. The GFP solution did not diffuse from the chambers, indicating that the solution in each chamber is physically separated from that in other chambers.

Tabuchi et al. have made a microchamber chip with a chamber volume per chip of  $10 \text{ } \mu\text{L}$  [48]. In our case, the chamber number is much larger and the chamber volume is much smaller, which is advantageous for high-throughput applications. However, the analysis of over  $10^4$  chambers takes a long time. Therefore, a scanner-type analyzer for our system is being developed to enable automatic screening in the near future.

A new method for making a highly integrated protein chip from a DNA library using *in vitro* protein synthesis on a microchamber array has been demonstrated. The chambers are of three types, based on their volume capacity: 1, 5, and 150 pL, and the total number of chambers per chip is 10 000 (150 pL), and 250 000 (both 1 and 5 pL). The array has a hydrophobic surface of PDMS and a hydrophilic glass bottom. These structural properties provide the advantage of preventing cross-contamination among the chambers. *In vitro* protein synthesis using these chambers was achieved. The fluorescence of GFP expressed on the micro chamber was rapidly detected. GFP expression was also achieved using immobilized DNA molecules on polymer beads, which allows easy handling of the DNA molecules. Brenner et al. have described a method for cloning nucleic acid molecules onto the surfaces of  $5 \text{ } \mu\text{m}$  microbeads rather than in biological hosts [55]. A unique tag sequence was attached to each cDNA molecule, and the tagged library was amplified. A unique tag was also attached to each bead, and the tagged library was conjugated with the tagged beads.

This method allows the immobilization of one kind of DNA on a bead. Because such clones are segregated on microbeads, they can be manipulated simul-

taneously and then assayed separately. If this method can be applied to the chip described in this report, it will be possible to analyze easily a whole DNA library on a chip in a short time. In future, this system will be used for the exhaustive expression of proteins included in target cells, the functional analysis of proteins expressed from unknown genes, and the screening of artificially mutated proteins.

In this study, we have reported a highly integrated protein microarray chip using *in vitro* protein synthesis from DNA conjugated microbeads. The protein microarray system made it possible to perform high-throughput screening and analysis for multiplexed gene expression on single beads in each pico-liter chamber. In the future, this system will be applied for the expression analysis of proteins in multiplexed single-cells and the functional analysis of proteins expressed from unknown genes or cells.

### 13.4

#### High-throughput Single-cell Analysis System using Pico-liter Microarray

Cell-based assays are one of the newest tools being used to broaden and strengthen drug discovery for the identification of new therapeutic agents. They are fast becoming the assay format of choice, especially in target validation, lead identification and optimization. Cell-based assay screening is by nature more complex and automation is more difficult than biochemical screening. These assays hold the promise of increasing productivity in the discovery process and the ability to screen out compound failure earlier in the development process. The last few years have seen an increasing number of cell-based assays being used, driving the market to an anticipated \$500 million mark by 2005 [56, 57]. Cell-based assays play a very important role in the post-genomic era focusing on high-throughput functional genomics and drug discovery. High-throughput screening assays play a pivotal role in the search of novel drugs and potential therapeutics. Over the last decade, various scientific advances include the growing number of potential therapeutic targets emerging from the field of functional genomics and the rapid development of large compound libraries derived from parallel and combinatorial chemical synthetic techniques, driven by the need for improved drug discovery screening technology [58, 59]. High-throughput cell-based assays reduce the total cost in screening the specific therapeutic target for a specific disease remarkably reducing the time. High-throughput drug screening methods employed so far involve use of 96- and 384-well microtiter plates and require at least a minimum of 100- $\mu$ L-assay mixture, suggesting further miniaturized assay formats to reduce the total cost of drug screening. Combining miniaturized technology with developments in automation, sensitive signal-detection, plate formats, automated compound-delivery and data management results in highly efficient, and cost-effective, integrated miniaturized ultrahigh-throughput screening (uHTS) systems. The need to screen numerous compounds rapidly, in increasingly automated dispensing systems, and with very small reaction volumes prompted us to carry out

this study. It was of interest to develop a high-throughput cell-based assay using miniaturized microarray chip formats.

For example, each B-cell clone expresses antigen-receptors, antibodies, with a unique antigen-specificity: an antigen-specific monoclonal antibody derived from a single B-cell clone finds applications in antibody medicine and clinical diagnosis. Though each B-cell has  $10^7$  to  $10^8$  varieties of monoclonal antibody on these surfaces only small percentage of B-cells respond and produce a specific monoclonal antibody. Only one or two cells in a total of 10 000 B-cells become active and produce antigen-specific antibodies after stimulation with a hepatitis B virus (HBV) surface antigen (HbsAg) [60]. It would be impossible to make a HbsAg specific antibody taking this ratio of positive B-cells into account using recently available technologies. A flow cytometer allows us to monitor individual cells that flow through sheath fluid, but the signals of the cells become background noise, which consists of 0.1 to sometimes 1% of total cells, thus it is quite difficult to monitor a signal of a minor population of cells whose signals are buried in the noise by a flow cytometer. Further, we cannot compare the states of each cell before and after stimulation by using flow cytometer. In contrast, a fluorescence microscope allows us to observe the states of cells both before and after stimulation. However, it is difficult to observe signals of large number of cells under a microscope. Accordingly, it is difficult to monitor  $\text{Ca}^{2+}$  mobilization of a minor population of cells.

Therefore, it is necessary to construct a microarray platform that can confine a large number of single-cells and detect antigen-specific single B-cells before and after stimulation with an antigen from a bulk cell suspension. For high-throughput single-cell separation and analysis, Thorsen et al. have reported high-density microfluidic chips that contain plumbing networks with thousands of micromechanical valves and hundreds of individually addressable chambers and showed the separation of single *E. coli* cells in each chamber [61]. To achieve single-cell separation, they diluted cells to create a median distribution of 0.2 cells per compartment, so that reliable capturing of cells in each chamber is difficult. In another recent report, Anderson et al. have tested biomaterial microarrays for their effects on human embryonic stem cell growth and differentiation using populations of human embryonic stem cells [8]. However, single-cell based assay seemed to be impossible using this microarray format. Also we have reported recently a microchamber array and microfluidic chip for measuring high-throughput analysis of cellular fluorescence [62–64]. Here, we discuss an improved microchamber array to monitor  $\text{Ca}^{2+}$  mobilization of over 25 000 cells simultaneously at a single-cell level [13]. We have also developed a novel high-throughput screening and analysis system for antigen-specific single B-cells using microarray, which was carried out by detecting antigen-specific single B-cells against an antigen of interest and their retrieval by a micromanipulator for antibody DNA analysis [13]. The single-cell microarray system developed in this study does not need to use myeloma, as in the case of conventional hybridoma technique, and can screen the antigen-specific single B-cells directly from cell suspension and analyze antigen-specific antibody DNA at a single-cell level. This system is simple and easy in its operation, and quick enough for making monoclonal antibodies when compared with conven-



tional techniques. Moreover it can perform high-throughput single-cell analysis using chip devices.

#### 13.4.1

##### Single-cell Microarray Chip Fabrication

The microarray chip is made from polystyrene with over 200 000 microchambers ( $10\ \mu\text{m}$  width,  $12\ \mu\text{m}$  depth, and  $30\ \mu\text{m}$  pitch) by using the Lithographie Galvanoformung (LIGA) process and was performed by the Starlight Co. Ltd., Japan (Fig. 13.9A–D). Using X-ray lithography from synchrotron radiation, a poly(methyl methacrylate) (PMMA) as a resist was exposed and patterned with Au metal mask. After development of the PMMA substrate, the resulting PMMA mold was used for nickel mold construction by electroforming. Finally, a polystyrene microarray chip was fabricated from the nickel mold by injection molding (Fig. 13.9A). Each microarray chip is consisted of 225 ( $15 \times 15$ ) clusters, and each cluster consisted of 900 ( $30 \times 30$ ) microchambers. Each microchamber is cylindrical and can accommodate only a single-cell.

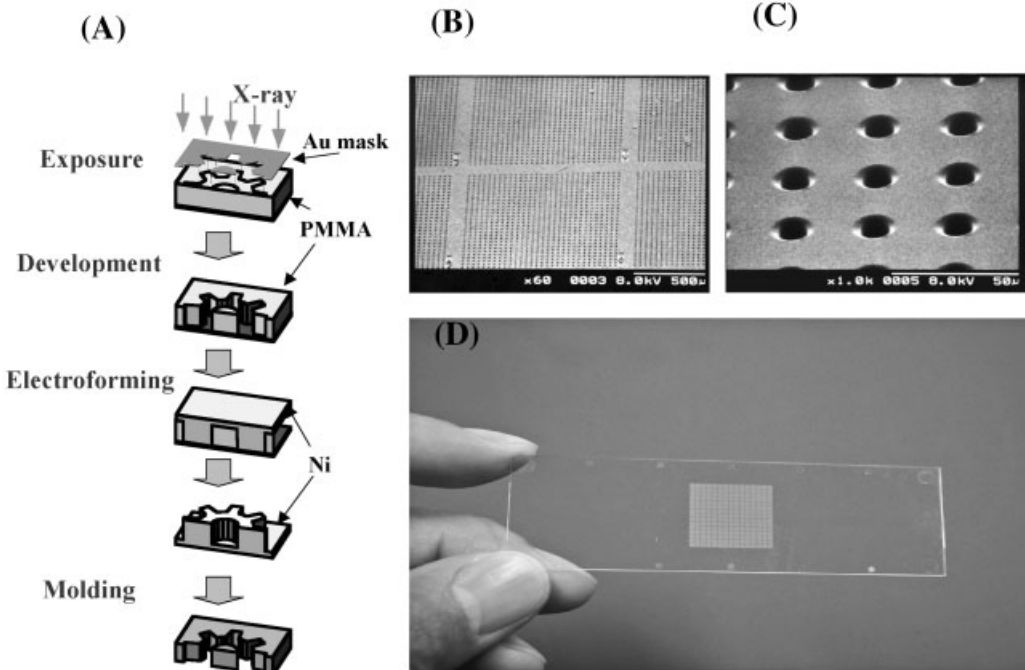


**Fig. 13.9.** Construction of single-cell microarray chip. (A) LIGA process for the fabrication of single-cell microarray chip. (B and C) SEM images and (D) a real picture

of the microarray chip device. The microarray chip is made from polystyrene with over 200 000 microchambers ( $10\ \mu\text{m}$  wide,  $12\ \mu\text{m}$  deep,  $30\ \mu\text{m}$  pitch).

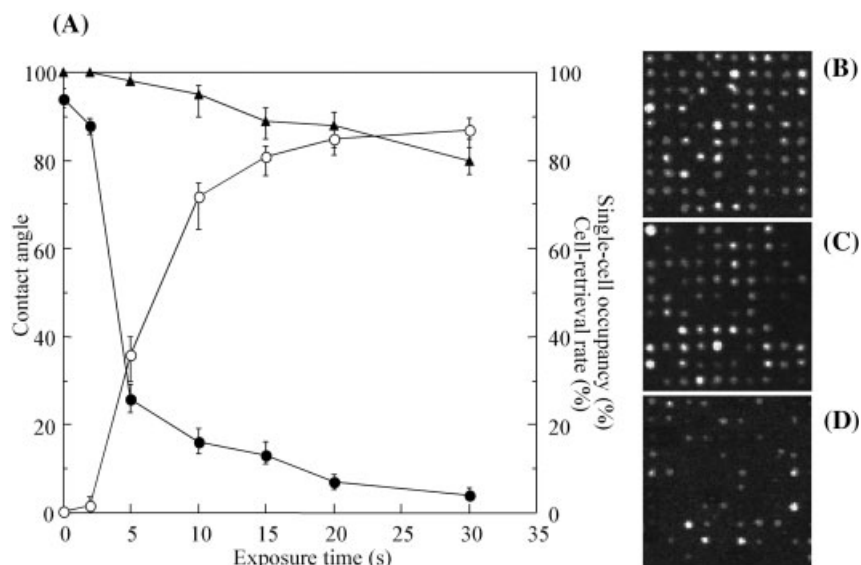


**Fig. 13.10.** Microarray chip surface treatment studies for single-cell confinement and retrieval. (A) Optimization of RIE exposure time of chip surface for single-cell confinement and retrieval from microchambers. Contact angle (●); single-cell occupancy (○); and cell-retrieval rate (▲ closed triangle). Scanned microarray image of single-cells in 100 microchambers after (B) 20, (C) 10 and (D) 5 s RIE exposure. Each treatment showed single-cell occupancy of 83, 73 and 38%, respectively.

The microarray surface was rendered hydrophilic by reactive ion etching (RIE) treatment to make it convenient for cell studies. RIE exposure time controlled the cell adhesion on the chip surface. An increase in RIE exposure time increases the hydrophilicity of the microarray chip surface, which is inversely proportional to the decrease in the contact angle of chip surface (Fig. 13.10A). This condition is suitable for increased levels of single-cell occupancy in the microchambers because RIE treatment keeps the confined single-cell in the microchamber during the washing process, which is shown in Fig. 13.10(B–D). The polystyrene microarray chip maintained hydrophilicity character without alteration for at least one week. However, with increasing hydrophilicity, it becomes difficult to retrieve positive single-cells from microchambers, e.g., over 30-s RIE restricted the retrieval rate to <80% (Fig. 13.10A). This suggests optimization in the exposure time that suits single B-cell occupancy as well as for cell retrieval – determined to be 20 s exposure, which resulted in over 80% of single-cell occupancy and cell-retrieval rate (Fig. 13.10B). To achieve over 80% single-cell occupancy, the cell density should always be  $1 \times 10^6$  cells  $\text{mL}^{-1}$  or more, otherwise a decrease in the percentage of single-cell occupancy was observed. We succeeded in single-cell separation and retrieval on the plastic microarray chip by controlling the chip surface treatment. In contrast, we could not retrieve B-lymphocytes that adhered strongly to the glass

and silicon chip substrates, because these materials have highly hydrophilic surfaces. Further, the transparent nature of a plastic microarray chip, along with its flat bottom-surfaced cylindrical microchambers, made by the LIGA process, is convenient for visualization of single B-cells as well as retrieval of cells from microchambers by a micromanipulator under a light microscope. Thus, the single-cell microarray chip developed in this study was suitable for separation and retrieval of single cells to analyze the antigen-specific single B-cells.

#### 13.4.2

##### **Pico-liter Microarray for Single-cell Studies**

A single-cell microarray chip that was constructed by using LIGA process has over 200 000 flat-bottomed cylindrical microchambers (10  $\mu\text{m}$  diameter, 12  $\mu\text{m}$  depth) in 1.4  $\text{cm}^2$  area on a plastic wafer ( $2 \times 8 \text{ cm}^2$ ) (Fig. 13.9A–D). Characterization of such a microarray chip for single-cell studies was performed using mouse splenic B-lymphocytes. The microchamber design was made such that each chamber allowed entry of single B-cell (approximately 8  $\mu\text{m}$  diameter) and hence there is no possibility of two cells in a single microchamber. To achieve single B-cell confinement in each microchamber as well as cell-retrieval from microchambers, hydrophilicity of the microarray chip surface was controlled by adopting different timings of RIE exposure (Fig. 13.10). As the result of chip surface treatment using RIE, lymphocytes derived from mouse spleen or human blood were spread on the microarray, and over 80% of the microchambers achieved single-cell status. In addition, this novel microarray system demonstrated easy retrieval of positive single B-cells from microchambers by a micromanipulator under microscope.

In this study, we report the data from approximately 30 000 microchambers for detecting antigen-specific single B-cells, because the assay we have adopted, i.e., measurement of increase in the intracellular calcium after antigenic stimulus using Fluo-4, lasts for few minutes. During this short period a microarray scanner could scan the analyzable area of 30 000–40 000 microchambers. This number of microchambers is sufficient to screen and identify below as little as 0.1% of antigen-specific single-cells in a total B-cell population, which is the limitation of flow cytometer, as described above. The ultimate potential of this single-cell microarray can be realized by improving the assay system and the scanning speed of microarray scanner for detecting the total number of microchambers on the microarray chip.

Recently, however, researchers have reported single-cell based cultivation on microchips with the help of optical tweezers [65] and specially designed micropipette [66]. By using these systems, it would be impossible to perform high-throughput single-cell screening and analysis. Other chip systems, microfluidic devices, have been reported to perform single-cell separation and analysis from bulk cell suspension in microchannels under the influence of integrated valves and pumps [67–70], which make these systems complex in handling compared with microarray formats. Despite their complexity these devices could not guarantee capturing a

target cell, moreover they were not compatible for high-throughput analysis. The single-cell microarray developed in the present study could easily separate single-cells from a bulk cell suspension without using specialized tools.

### 13.4.3

#### Single-cell Microarray System for Analysis of Antigen-specific Single B-cells

To evaluate the utility of a novel single-cell microarray system for detecting intracellular calcium, the  $(Ca^{2+})_i$  level of individual cells, we have employed anti-mouse IgM antibody as a stimulant for mouse splenic B-cells, which delivers the signals through B-cell antigen-receptors and induces a transient increase in the  $(Ca^{2+})_i$  levels. Mouse lymphocytes loaded with  $Ca^{2+}$ -indicator, Fluo-4, were applied on the chip and their fluorescence was detected with a microarray scanner before and after stimulation with anti-mouse IgM antibody (Fig. 13.11). Fluo-4 is a standard fluorescent calcium indicator [71], which enters into the cells and generates fluorescence after binding to  $(Ca^{2+})_i$ . It is known that the concentration of  $(Ca^{2+})_i$  increases after B-cells respond to antigenic stimulation [72]. In this experiment, major single B-cells on the microarray showed increases in the  $(Ca^{2+})_i$  after stimulation (Fig. 13.11A). The fluorescence intensity reached to its maximum level after 1 min stimulation, and maintained a high magnitude for 2 min and then decreased gradually (data not shown). Thus, we used a 2 min stable duration for analysis. Scatter plot analysis of individual cell's fluorescence-intensity (Fig. 13.11B) enabled us to discriminate B-cells that were activated with anti-mouse IgM antibody. The data from over 30 000 microchambers in the microarray chip revealed 68% (18 130 cells) of total splenic lymphocytes (26 650 cells) showed more than twice the fluorescence after stimulation with anti-mouse IgM (Fig. 13.11B). While cells with over a  $5\times$  increase in fluorescence (3883 cells) existed in 14% of the total splenic lymphocytes [Fig. 13.11B(I)]. Whereas most lymphocytes incubated with control antibody (anti-human IgM) showed a less than  $5\times$  increase in fluorescence intensities [Fig. 13.11B(II)].

Each B-cell expresses membrane-bound antibodies with unique antigen-specificity as antigen receptors. When B-cells were stimulated with an antigen instead of anti-IgM antibody, only a minor population of total B-cells is stimulated and their  $(Ca^{2+})_i$  increases. Previous studies reported diverse frequencies in the number of antigen-specific B-cells, ranging from 1 in  $10^2$  for rabies virus [73] to 7 in  $10^5$  for myelin basic protein [74]. However, it is quite difficult to screen and identify a minor cell population of antigen-specific single B-cells ( $<0.1\%$ ) with a flow cytometer because fluorescent signals of minor populations of cells are buried in the noise of non-specific cells. Whereas the single-cell microarray platform developed in this study could successfully screen and detect a low frequency of antigen-specific single B-cells using a single chip in one run. In addition, it also analyzes the same single-cells before and after stimulations with antigen, which a flow cytometer could not.

If antibody cDNA is recovered from an antigen-specific single B-cell that is detected with single-cell microarray, antigen-specific monoclonal antibodies can be

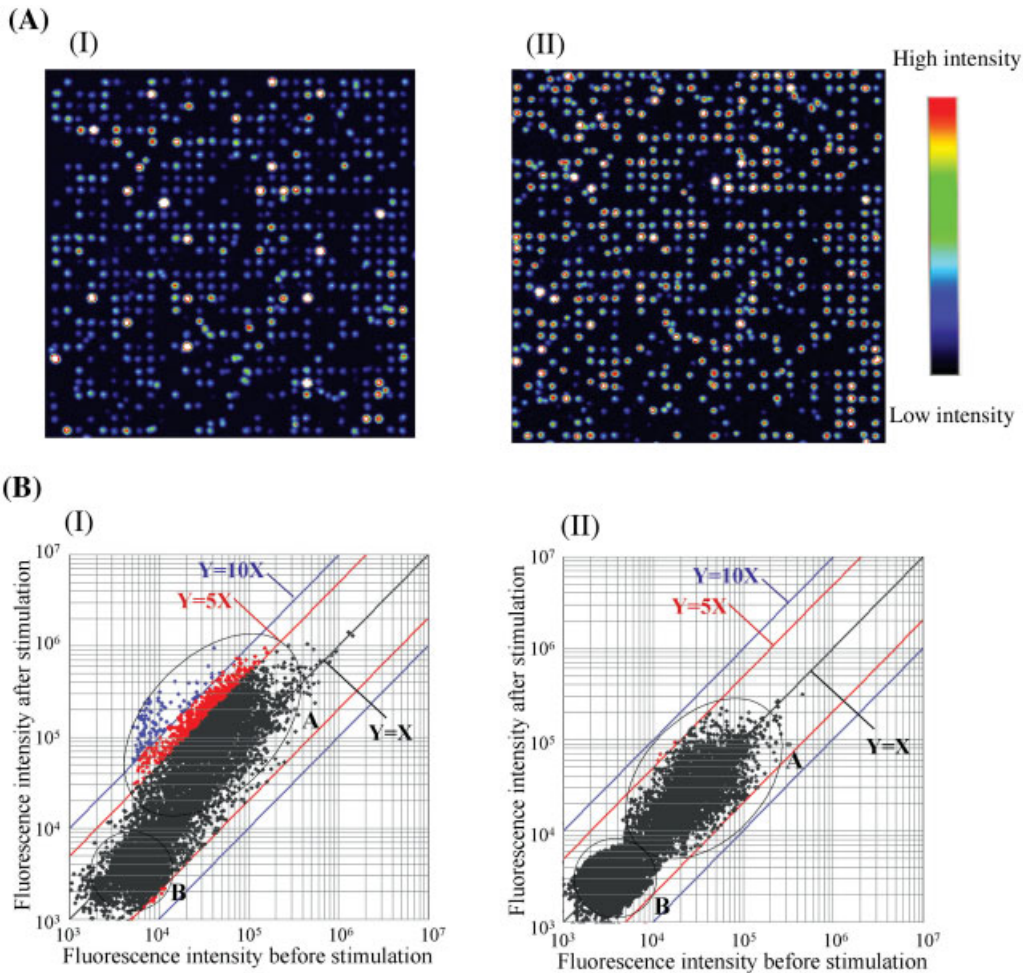


**Fig. 13.11.** Detection of activated single B-cells using Fluo-4 upon stimulation with anti-mouse IgM antibody. (A) Scanned images of single-cells microarray in a single cluster area of 900 ( $30 \times 30$ ) microchambers on a microarray (I) before and (II) after stimulation. Color scale represents the intensity of fluorescence emission. (B) Scattered plot analysis of single B-cell response in 32 400

microchambers area after stimulation with (I) anti-mouse IgM antibody and (II) negative control antibody. Circle A, microchambers with lymphocytes; circle B, empty microchambers; X, fluorescence intensity before stimulation; Y, fluorescence intensity after stimulation; blue line ( $Y = 10X$ ),  $10\times$  higher fluorescence intensity; red line ( $Y = 5X$ ),  $5\times$  higher fluorescence intensity.

developed. To this end, we have successfully performed retrieval of a single B-cell from the microarray by a micromanipulator system under a microscope (Fig. 13.12) and subsequent single-cell RT-PCR amplification to determine its antibody cDNA. Monoclonal antibodies are usually produced using hybridoma techniques

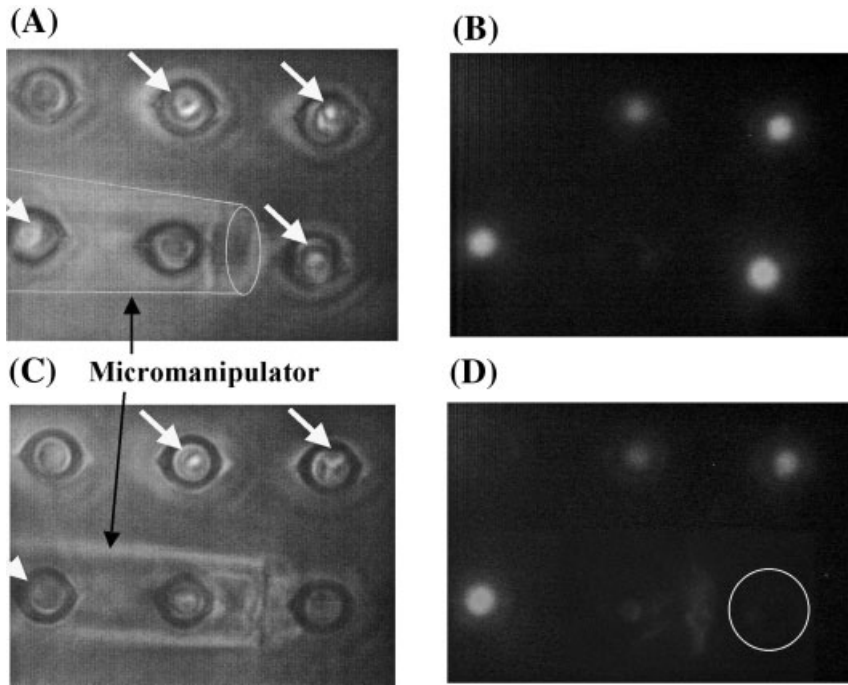


**Fig. 13.12.** Retrieval and antibody cDNA analysis of single B-cells derived from human blood. (A and B) Light and fluorescence microscopic images of the single B-cells on a microarray chip before cell-retrieval using a micromanipulator system. B-cells were treated with CellTracker Orange ( $\lambda_{\text{ex.}} = 541 \text{ nm}$ ,  $\lambda_{\text{em.}} = 565 \text{ nm}$ ) for observation of fluorescence from living cells. The arrows indicate a single-

cell in each microchamber, observed under the  $40\times$  lens of an inverted microscope. (C and D) Light and fluorescence microscopic images after target single-cell retrieval using a micromanipulator. The circle in (D) indicates the disappearance of fluorescence of target a single-cell that was retrieved from the microchambers.

developed by Milstein and Koeller [75]. Using conventional hybridoma methods, one hybridoma is routinely produced from  $10^5$  splenocytes [57] and, therefore, not all B-lymphocytes are screened for antigen-specificity. However, the single-cell microarray system we have developed could screen directly all the B-cell population to detect antigen-specific single B-cells and analyze the antigen-specific antibody DNA at a single-cell level. Our chip system is simple and easy in its operation, and can perform high-throughput single-cells analysis. Moreover, it provides a superior screening system for antigen-specific monoclonal antibodies that provide the source for antibody medicines.

The single-cell microarray system we have developed made it possible to perform high-throughput screening and analysis of intracellular  $\text{Ca}^{2+}$ -response at a single-cell level and analyze multiplexed single-cell status before and after antigenic stimulation on a single platform, which flow cytometry could not. Further, this system

facilitated easy retrieval of antigen-specific single B-cell from the microarray, demonstrating its novelty and superiority over conventional methods in making monoclonal antibody. This explorative study throws more light on a novel high-throughput single-cell analysis system that has tremendous potential to analyze antibody DNA of an antigen-specific single B-cell for developing highly specific monoclonal antibody as antibody medicines. It might also be applicable for detection of antigen-specific T cells, which could lead to immune therapy or gene therapy in the future.

### 13.5

#### Conclusions

Pico- and nano-liter chamber array chips have been developed that show great potential to detect and analyze DNA, protein and cell at single-molecule or single-cell level.

The microchamber (40 nL) array PCR chip presented in this chapter was used to amplify and detect quantitatively multiple DNA targets in combination with a nanoliter dispenser. This demonstrated that a microarray PCR chip can be used to amplify and detect ~1200 target DNAs simultaneously; in addition, target gene analysis at single copy level was achieved. Thus, the microarray PCR chip system has a significant potential to be implemented for a wide range of purposes such as detection of pathogenic microorganisms and clinical diagnosis.

The highly integrated protein microarray chip presented here successfully performed *in vitro* protein synthesis using a pico-liter chamber array. Furthermore, it made it possible to perform screening and analysis for multiplexed gene expression on single beads in each chamber. In future, this system will be applied for high-throughput screening and functional analysis of proteins expressed from unknown genes or cells.

The single-cell microarray system, which can accommodate single-cells in pico-liter chambers, made it possible to perform high-throughput screening and analysis of antigen-specific single B-cells and analyze multiplexed single-cell status before and after antigenic stimulation on a single platform. Further, this system facilitated easy retrieval of positive antigen-specific single B-cell from the microarray, demonstrating its novelty over conventional methods in making monoclonal antibody. The single-cell analysis system has tremendous potential to analyze antibody DNA of an antigen-specific single B-cell for developing highly specific monoclonal antibody as antibody medicines. It might also be applicable for cell therapy as personal diagnosis and development of personalized medicine in future.

Thus, the pico- and nano-liter chamber array systems discussed here could become a potential tool for high-throughput analysis of DNA, protein and cell at single-molecule or single-cell level, which could lead to clinical diagnosis and drug discovery.

## Acknowledgments

Research into *in vitro* protein synthesis on a pico-liter chamber array was supported by the grants of New Energy and Industrial Technology Development Organization (NEDO) and the Japan Society for the Promotion of Science (JSPS). The single-cell microarray chip research was carried out under the Toyama Medical Bio-cluster project, which was sponsored by the Ministry of Education, Culture, Sports, and Science, Japan.

## References

- OOSTERBROEK, E., VAN DEN BERG, A., Lab-on-a-chip: Miniaturized systems for biochemical analysis and synthesis, Elsevier, Amsterdam, 2003.
- FIGEYS, D., PINTO, D., Lab-on-a-chip: A revolution in biological and medical science, *Anal. Chem.*, 2000, 72, 330–335.
- HELLER, M.J., DNA microarray technology: Devices, systems, and applications. *Annu. Rev. Biomed. Eng.*, 2002, 4, 129–153.
- EISEN, M.B., BROWN, P.O., DNA arrays for analysis of gene expression, *Methods Enzymol.*, 1999, 303, 179–205.
- PANICKER, R.C., HUANG, X., YAO, S.Q., Recent advances in peptide-based microarray technologies, *Comb. Chem. High. Throughput. Screen.*, 2004, 7, 547–556.
- FIGEYS, D., Adapting arrays and lab-on-a-chip technology for proteomics, *Proteomics*, 2002, 2, 373–382.
- COTTINGHAM, K., The single-cell scene, *Anal. Chem.*, 2004, 76, 235A–238A.
- ANDERSON, D.G., LEVENBERG, S., LANGER, R., Nanoliter-scale synthesis of arrayed biomaterials and application to human embryonic stem cells, *Nat. Biotechnol.*, 2004, 22, 863–866.
- ZIAUDDIN, J., SABATINI, D.M., Microarrays of cells expressing defined cDNAs, *Nature*, 2001, 411, 107–110.
- KINPARA, T., MIZUNO, R., MURAKAMI, Y., KOBAYASHI, M., YAMAMURA, S., HASAN, Q., MORITA, Y., NAKANO, H., YAMANE, T., TAMIYA, E., A picoliter chamber array for cell-free protein synthesis, *J. Biochem. (Tokyo)*, 2004, 136, 149–154.
- MATSUBARA, Y., KERMAN, K., KOBAYASHI, M., YAMAMURA, S., MORITA, Y., TAKAMURA, Y., TAMIYA, E., On-chip nanoliter-volume multiplex TaqMan polymerase chain reaction from a single copy based on counting fluorescence released microchambers, *Anal. Chem.*, 2004, 76, 6434–6439.
- MATSUBARA, Y., KERMAN, K., KOBAYASHI, M., YAMAMURA, S., MORITA, Y., TAMIYA, E., Microchamber array based DNA quantification and specific sequence detection from a single copy via PCR in nanoliter volumes, *Biosens. Bioelectron.*, 2005, 20, 1482–1490.
- YAMAMURA, S., KISHI, H., TOKIMITSU, Y., KONDO, S., HONDA, R., RAMACHANDRA, R.S., OMORI, M., TAMIYA, E., MURAGUCHI, A., Single-cell microarray for analysing cellular response, *Anal. Chem.*, 2005, 77, 8050–8056.
- SAIKI, R.K., SCHARF, S., FALOONA, F., MULLIS, K.B., HORN, G.T., ERLICH, H.A., ARNHEIM, N., Enzymatic amplification of beta-globin genomic sequences and restriction site analysis for diagnosis of sickle cell anemia, *Science*, 1985, 230, 1350–1354.
- MULLIS, K.B., FALOONA, F.A., Specific synthesis of DNA *in vitro* via a polymerase-catalyzed chain reaction, *Methods Enzymol.*, 1987, 155, 335–350.



- 16 IRINO, T., KITO, T., KOAMI, K., KASHIMA, T., MUKAI, K., TAKEUCHI, E., HONGO, T., NAKAHATA, T., SCHUSTER, S.M., OSAKA, M., Establishment of real-time polymerase chain reaction method for quantitative analysis of asparagine synthetase expression, *J. Mol. Diagn.*, **2004**, *6*, 217–224.
- 17 HIRT, C., SCHULER, F., DOLKEN, L., SCHMIDT, C.A., DOLKEN, G., Low prevalence of circulating t(11,14)(q13,q32) positive cells in the peripheral blood of healthy individuals as detected by real-time quantitative PCR, *Blood*, **2004**, *104*, 904–905.
- 18 NURMI, J., WIKMAN, T., KARP, M., LOVGREN, T., High-performance real-time quantitative RT-PCR using lanthanide probes and a dual-temperature hybridization assay, *Anal. Chem.*, **2002**, *74*, 3525–3532.
- 19 YANG, J., LIU, Y., RAUCH, C.B., STEVENS, R.L., LIU, R.H., LENIGK, R., GRODZINSKI, P., High sensitivity PCR assay in plastic micro reactors, *Lab Chip*, **2002**, *2*, 179–187.
- 20 LEE, T.M.H., CARLES, M.C., HSING, I.M., Microfabricated PCR-electrochemical device for simultaneous DNA amplification and detection, *Lab Chip*, **2003**, *3*, 100–105.
- 21 SCHNEEGASS, I., BRAUTIGAM, R., KOHLER, M., Miniaturized flow-through PCR with different template types in a silicon chip thermocycler, *Lab Chip*, **2001**, *1*, 42–49.
- 22 FUKUBA, T., YAMAMOTO, T., NAGANUMA, T., FUJII, T., Micro-fabricated flow-through device for DNA amplification – towards in situ gene analysis, *Chem. Eng. J.*, **2004**, *101*, 151–156.
- 23 LEE, D.S., PARK, S.H., YANG, H., CHUNG, K.H., YOON, T.H., KIM, S.J., KIM, K., KIM, Y.T., Bulk-micromachined submicroliter-volume PCR chip with very rapid thermal response and low power consumption, *Lab Chip*, **2004**, *4*, 401–407.
- 24 LAGALLY, E.T., EMRICH, C.A., MATHIES, R., Fully integrated PCR-capillary electrophoresis microsystem for DNA analysis, *Lab Chip*, **2001**, *1*, 102–107.
- 25 LAGALLY, E.T., MEDINTZ, I., MATHIES, R.A., Single-molecule DNA amplification and analysis in an integrated microfluidic device, *Anal. Chem.*, **2001**, *73*, 565–570.
- 26 NAGAI, H., MURAKAMI, Y., YOKOYAMA, K., TAMIYA, E., High-throughput PCR in silicon based microchamber array, *Biosens. Bioelectron.*, **2001**, *16*, 1015–1019.
- 27 NAGAI, H., MURAKAMI, Y., MORITA, Y., YOKOYAMA, K., TAMIYA, E., Development of a microchamber array for picoliter PCR, *Anal. Chem.*, **2001**, *73*, 1043–1047.
- 28 MATSUBARA, Y., KOBAYASHI, M., MORITA, Y., TAMIYA, E., Application of a microchamber array for DNA amplification using a novel dispensing method, *Arch. Histol. Cytol.*, **2002**, *65*, 481–488.
- 29 LEAMON, J.H., LEE, W.L., TARTARO, K.R., LANZA, J.R., SARKIS, G.J., DEWINTER, A.D., BERKA, J., LOHMAN, K.L., A massively parallel PicoTiter-Plate™ based platform for discrete picoliter-scale polymerase chain reactions, *Electrophoresis*, **2003**, *24*, 3769–3777.
- 30 FELBEL, J., BIEBER, I., PIPPER, J., KOHLER, J.M., Investigations on the compatibility of chemically oxidized silicon (SiO<sub>x</sub>)-surfaces for applications towards chip-based polymerase chain reaction, *Chem. Eng. J.*, **2004**, *101*, 333–338.
- 31 SHOFFNER, M.A., CHENG, J., HVICHIA, G.E., KRICKA, L.J., WILDING, P., Chip PCR. I. Surface passivation of microfabricated silicon-glass chips for PCR, *Nucleic Acids Res.*, **1996**, *24*, 375–379.
- 32 ERILL, I., CAMPOY, S., ERILL, N., BARBE, J., AGUILO, J., Biochemical analysis and optimization of inhibition and adsorption phenomena in glass-silicon PCR-chips, *Sens. Actuators B*, **2003**, *96*, 685–692.
- 33 ZIMMERMANN, B., HOLZGREVE, W., WENZEL, F., HAHN, S., Novel real-time quantitative PCR test for Trisomy 21, *Clin. Chem.*, **2002**, *48*, 362–363.
- 34 KARIYAZONO, H., OHNO, T., IHARA, K., IGARASHI, H., JOH-O, K., ISHIKAWA, S.,

- HARA, T., Rapid detection of the 22q11.2 deletion with quantitative real-time PCR, *Mol. Cell. Probes*, **2001**, 15, 71–73.
- 35 CHIU, R.W., LAU, T.K., LEUNG, T.N., CHOW, K.C., CHUI, D.H., LO, Y.M., Prenatal exclusion of  $\beta$  thalassaemia major by examination of maternal plasma, *Lancet*, **2002**, 360, 998–1000.
- 36 RUDERT, F., Genomics and proteomics tools for the clinic, *Curr. Opin. Mol. Ther.*, **2000**, 2, 633–642.
- 37 SRINIVAS, P.R., SRIVASTAVA, S., HANASH, S., WRIGHT, G.L., JR., Proteomics in early detection of cancer, *Clin. Chem.*, **2001**, 47, 1901–1911.
- 38 FIGEYS, D., PINTO, D., Proteomics on a chip: Promising developments, *Electrophoresis*, **2001**, 22, 208–216.
- 39 REID, G., GAN, B.S., SHE, Y.M., ENS, W., WEINBERGER, S., HOWARD, J.C., Rapid identification of probiotic lactobacillus biosurfactant proteins by ProteinChip tandem mass spectrometry tryptic peptide sequencing, *Appl. Environ. Microbiol.*, **2002**, 68, 977–980.
- 40 TABUCHI, M., BABA, Y., A novel injection method for high-speed proteome analysis by capillary electrophoresis, *Electrophoresis*, **2002**, 23, 1138–1145.
- 41 VENTER, J.C. et al., The sequence of the human genome, *Science*, **2001**, 291, 1304–1351.
- 42 PAVLOV, M.Y., FREISTROFFER, D.V., EHRENBERG, M., Synthesis of region-labelled proteins for NMR studies by *in vitro* translation of column-coupled mRNAs, *Biochimie*, **1997**, 79, 415–422.
- 43 <http://www.roche-applied-science.com/sis/proteinexpression/>
- 44 ZHI, Z.L., MURAKAMI, Y., MORITA, Y., HASAN, Q., TAMIYA, E., Multianalyte immunoassay with self-assembled addressable microparticle array on a chip, *Anal. Biochem.*, **2003**, 318, 236–243.
- 45 ZHI, Z.L., MORITA, Y., HASAN, Q., TAMIYA, E., Micromachining microcarrier-based biomolecular encoding for miniaturized and multiplexed immunoassay, *Anal. Chem.*, **2003**, 75, 4125–4131.
- 46 KUKAR, T., ECKENRODE, S., GU, Y., LIAN, W., MEGGINSON, M., SHE, J.X., WU, D., Protein microarrays to detect protein–protein interactions using red and green fluorescent proteins, *Anal. Biochem.*, **2002**, 306, 50–54.
- 47 KOJIMA, K., HIRATSUKA, A., SUZUKI, H., YANO, K., IKEBUKURO, K., KARUBE, I., Electrochemical protein chip with arrayed immunosensors with antibodies immobilized in a plasma-polymerized film, *Anal. Chem.*, **2003**, 75, 1116–1122.
- 48 TABUCHI, M., HINO, M., SHINOHARA, Y., BABA, Y., Cellfree protein synthesis on a microchip, *Proteomics*, **2002**, 2, 430–435.
- 49 RUNGPRAGAYPHAN, S., KAWARASAKI, Y., IMAEDA, T., KOHDA, K., NAKANO, H., YAMANE, T., High-throughput, cloning-independent protein library construction by combining single-molecule DNA amplification with *in vitro* expression, *J. Mol. Biol.*, **2002**, 318, 395–405.
- 50 NAKANO, H., OKUMURA, R., GOTO, C., YAMANE, T., *In vitro* combinatorial mutagenesis of the 65th and 222nd positions of the green fluorescent protein of *Aequorea Victoria*, *Biotechnol. Bioprocess Eng.*, **2002**, 7, 311–315.
- 51 McDONALD, J.C., WHITESIDES, G.M., Poly(dimethylsiloxane) as a material for fabricating microfluidic devices, *Acc. Chem. Res.*, **2002**, 35, 491–499.
- 52 NG, J.M., GITLIN, I., STROOCK, A.D., WHITESIDES, G.M., Components for integrated poly(dimethylsiloxane) microfluidic systems, *Electrophoresis*, **2002**, 23, 3461–3473.
- 53 JO, B.H., VAN LERBERGHE, L.M., MOTSEGOOD, K.M., BEEBE, D.J., Three-dimensional micro-channel fabrication in polydimethylsiloxane (PDMS) elastomer, *J. MEMS*, **2000**, 9, 76–81.
- 54 SPIRIN, A.S., BARANOV, V.I., RYABOVA, L.A., OVODOV, S.Y., ALAKHOV, Y.B., A continuous cell-free translation system capable of producing polypeptides in high yield, *Science*, **1988**, 242, 1162–1164.

- 55 BRENNER, S., WILLIAMS, S.R., VERMAAS, E.H., STORCK, T., MOON, K., MCCOLLUM, C., MAO, J.I., LUO, S., KIRCHNER, J.J., ELETR, S., DUBRIDGE, R.B., BURCHAM, T., ALBRECHT, G., *In vitro* cloning of complex mixtures of DNA on microbeads: Physical separation of differentially expressed cDNAs, *Proc. Natl. Acad. Sci. U.S.A.*, **2000**, 97, 1665–1670.
- 56 GIESE, K., KAUFMANN, J., PRONK, G.J., KLIPPEL, A., Unravelling novel intracellular pathways in cell-based assays, *Drug Discovery Today* **2002**, 7, 179–186.
- 57 LATRAITE, S., BIGOT-LASSERRE, D., BARS, R., CARMICHAEL, N., Optimization of cell-based assays for medium throughput screening of oxidative stress, *Toxicol. In Vitro* **2003**, 17, 207–220.
- 58 WOLCKE, J., ULLMANN, D., Miniaturised HTS technologies- $\mu$ HTS, *Drug Discovery Today*, **2001**, 6, 637–646.
- 59 HERTZBERG, R.P., POPE, A.J., High-throughput screening: New technology for the 21<sup>st</sup> century, *Curr. Opin. Biotechnol.*, **2000**, 4, 445–451.
- 60 SHOKRGOZAR, M.A., SHOKRI, F., Enumeration of hepatitis B surface antigen-specific B lymphocytes in responder and non-responder normal individuals vaccinated with recombinant hepatitis B surface antigen, *Immunology*, **2001**, 101, 75–79.
- 61 THORSEN, T., MAERKL, S.J., QUAKE, S.R., Microfluidic large-scale integration, *Science*, **2002**, 298, 580–584.
- 62 AKAGI, Y., RAMACHANDRA RAO, S., MORITA, Y., TAMIYA, E., Optimization of fluorescent cell-based assays for high-throughput analysis using microchamber array chip formats, *Sci. Technol. Adv. Mater.*, **2004**, 5, 343–349.
- 63 YAMAMURA, S., RAMACHANDRA RAO, S., OMORI, M., TOKIMITSU, Y., KONDO, S., KISHI, H., MURAGUCHI, A., TAKAMURA, Y., TAMIYA, E., High-throughput screening and analysis for antigen specific single-cell using microarray, *Proceedings of Micro Total Analysis System ( $\mu$ TAS) 2004*, The Royal Society of Chemistry, Cambridge, **2004**, Vol. 1, pp. 78–80.
- 64 RAMACHANDRA RAO, S., YAMAMURA, S., TAKAMURA, Y., TAMIYA, E., Multiplexed microfluidic devices for single-cell manipulation and analysis, *Proceedings of Micro Total Analysis System ( $\mu$ TAS) 2004*, The Royal Society of Chemistry, Cambridge, **2004**, Vol. 1, pp. 61–63.
- 65 UMEHARA, S., WAKAMOTO, Y., INOUE, I., YASUDA, K., On-chip single-cell microcultivation assay for monitoring environmental effects on isolated cells, *Biochem. Biophys. Res. Commun.*, **2003**, 305, 534–540.
- 66 SUZUKI, I., SUGIO, Y., MORIGUCHI, H., JIMBO, Y., YASUDA, K., Modification of a neuronal network direction using stepwise photo-thermal etching of an agarose architecture, *J. Nanobiotechnol.*, **2004**, 2, 7–14.
- 67 WHEELER, A.R., THRONSET, W.R., WHELAN, R.J., LEACH, A.M., ZARE, R.N., LIAOR, Y.H., FARRELL, K., MANGER, I.D., DARIDON, A., Microfluidic device for single-cell analysis, *Anal. Chem.*, **2003**, 75, 3581–3586.
- 68 HUANG, W.H., CHENG, W., ZHANG, Z., PANG, D.W., CHENG, J.K., CUI, D.F., Transport, location, and quantal release monitoring of single cells on a microfluidic device, *Anal. Chem.*, **2004**, 76, 483–488.
- 69 PENG, X.Y., LI, P.C.H., A three-dimensional flow control concept for single-cell experiments on a microchip. 1. Cell selection, cell retention, cell culture, cell balancing, and cell scanning, *Anal. Chem.*, **2004**, 76, 5273–5281.
- 70 LI, X., LI, P.C., Microfluidic selection and retention of a single cardiac myocyte, on-chip dye loading, cell contraction by chemical stimulation, and quantitative fluorescent analysis of intracellular calcium, *Anal. Chem.*, **2005**, 77, 4315–4322.
- 71 HAUGLAND, R.P., In *Handbook of Fluorescent Probes and Research Products*, 9th edn., Molecular Probes, Inc., USA, **2002**.
- 72 NISHIDA, M., SUGIMOTO, K., HARA, Y., MORI, E., MORII, T., KUROSAKI, T.,

- MORI, Y., Amplification of receptor signaling by  $\text{Ca}^{2+}$  entry-mediated translocation and activation of PLCgamma2 in B lymphocytes, *EMBO J.*, **2003**, 22, 4677–4688.
- 73 UEKI, Y., GOLDFARB, I.S., HARINDRANATH, N., GORE, M., KOPROWSKI, H., NOTKINS, A.L., CASALI, P., Clonal analysis of a human antibody response. Quantitation of precursors of antibody-producing cells and generation and characterization of monoclonal IgM, IgG, and IgA to rabies virus, *J. Exp. Med.*, **1990**, 171, 19–34.
- 74 JINGWU, Z., HENDERIKX, P., YING, C., MEDAER, R., RAUS, J.C.M., A method to establish antibody secreting B cell lines and simultaneously perform frequency analysis, *J. Immunol. Methods*, **1989**, 123, 153–154.
- 75 KOHLER, G., MILSTEIN, C., Continuous cultures of fused cells secreting antibody of predefined specificity, *Nature*, **1975**, 256, 495–497.

## Index

10E3 antibody 344

### **a**

absorption-based sensors 139  
 $\beta$ -actin gene 374–375  
 adsorption, on the transducer substrate 61  
 affinity recognition surface, based on the  
 dendrimer-associated SAMs 244–252  
 AFM *see* atomic force microscopy  
 AFP *see*  $\alpha$ -fetoprotein (AFP)  
 Al<sub>2</sub>O<sub>3</sub>, EIS 230–232  
 Alexa-488 183  
 alkaline phosphatase (ALP)-loaded CNTs  
 67, 69  
 all-biological sensors 325  
 ALP *see* alkaline phosphatase  
 alumina films, porous 209–214  
 Alzheimer's disease (ADDLs), nanosensors  
 329  
 AMG *see* amyloglucosidase  
 amino-functionalized nanotubes 47  
 amperometry 91  
 amplified DNA, on-chip quantification  
 376–377  
 amyloglucosidase (AMG) 19  
 anchoring approaches, CNT-based biosensors  
 66–69  
 anodization  
 – porous alumina films 210–211  
 – two-step 211  
 antibodies  
 – 10E3 344  
 – GNWs 220–223  
 antibody–antigen interactions 15–16  
 antibody-based nanoprobe 322  
 antibody linker, GNWs 208, 220–224  
 antigen–antibody binding, biomimetic  
 nanosensors 317–318  
 antigen/antibody biosensors 262

antigen-specific single B-cells, single-cell  
 microarray system 389–392  
 aptamer–nanoparticle based biosensors 352  
 atomic force microscopy (AFM), biomimetic  
 nanosensors 319–320  
 ATP biosensors, reagentless 345  
 Au/Au np/CdS np surfaces 342–343  
 AuNP-CoMHP 270  
 avidin–biotin interaction 246

### **b**

B-cells 385–387  
 – antigen-specific single 389–392  
 back-filling immobilization 252  
 bacteria, pathogenic 208  
 bacteria detection, electrochemical nano-  
 biosensor 224–235  
 bifunctional agents 135  
 bilayer lipid membranes (BLMs) 41, 43–44  
 bioaffinity interface construction 251  
 bioanalyses  
 – FRET-based 196  
 – immunoblot 192–195  
 – time-resolved fluorimetry 197  
 bioconjugates, carbon nanotubes 12–14  
 bioelectrocatalytic enzyme electrodes, based on  
 LBL (layer-by-layer) assembly with  
 dendrimers 243  
 bioelectrocatalytic immunosensors, based on  
 the dendrimer-associated SAMs 244–252  
 bioelectronics 81–83  
 biological functionalization, CNTs 39  
 biological materials, gold nano-biosensor-  
 based electrochemical detection 208–235  
 biological systems, nanosensor probing 317–  
 322  
 biological transducers 225  
 biology, structural 260  
 biomarkers, ultrasensitive detection 259–273

- biomedical diagnosis, nano-biotechnology 327–329
  - biomimetic nanosensors 311–330
  - biomimetic vesicles 320
  - biomolecular conduits, signal transducing mediators 265–266
  - biomolecular recognition, colloidal nanocrystals 126
  - biomolecule conformational modulated effects
    - nanoparticle scaling laws 338–339
    - reagentless biosensors 351–361
  - biomolecule-functionalized CNTs, for electrochemical sensors and biosensors 45–48
  - biomolecules on CNTs, direct electrochemistry 69–72
  - bionanotechnology 311
  - biosensing
    - electrochemical 103–105
    - fullerene-based electrochemical detection methods 101–118
    - fullerene-mediated 114–118
    - with semiconductor nanocrystals 153–156
  - biosensor chip 315
  - biosensor development 56–90
    - CNTs 57–84
    - nanocantilevers 89–90
    - nanowires 84–89
  - biosensor generations 105–106
  - biosensors
    - according to IUPAC 103
    - antigen/antibody 262
    - applications of dendrimers 242–255
    - based on DNA conformation changes 352–354
    - based on protein conformation changes 355–361
    - biomolecule-functionalized CNTs 45–48
    - classical 324
    - CNT array-based 76–80
    - CNT-based 60–69
    - CNT-based electrochemical 34–38, 69–74
    - conducting polymer nanowire-based 86–88
    - coordinated 259–273
    - definition 125
    - DNA and protein 73
    - DNA-based 263
    - enzyme-based 261–263, 324
    - enzyme–CNT 72
    - evolution 105
    - glucose 87
    - mediation process 106–109
    - metal oxide nanowire-based 89
    - nano- *see* nanobiosensors, 208–235
    - non-reagentless 337
    - optical recognition-based 197–200
    - protein-based 278–297
    - reagentless 337–361
    - s-BLM 115–116
    - silicon nanowire-based 84–85
    - subtilisin-based 117
    - SWCNT glucose 64
  - biotinylated polymer layer, NTFETs 16
  - BLMs *see* bilayer lipid membranes
  - Bohr exciton radius 176
  - branching, colloidal nanocrystals 132
  - Buckyballs 58
- c**
- C<sub>60</sub> chemically modified electrodes (CMEs) 114
  - C<sub>60</sub> fullerene 101–102
    - synthesis 109
    - van der Waals surface representation 113
  - calibration of fluorescent instrumentation, standards 201
  - cancer detection, biomimetic nanosensors 328
  - carbohydrate detection, biomimetic nanosensors 319
  - carbon nanocage 58
  - carbon nanotube field-effect transistors (NTFETs) 1–21
    - coated with a biotinylated polymer layer 16
    - contact-passivated 10
    - fabrication 6–9
    - mode of operation 8
    - passivation layer 10
    - sensitivity to chemical environment 9–12
    - sensor applications 9–20
    - transistor function 8
    - *see also* CNT field-effect transistors
  - carbon nanotube-packaged microelectrodes 34
  - carbon nanotube paste electrode (CNTPE) 290
  - carbon nanotube paste electrode (CPE) 31
  - carbon nanotubes (CNTs) 286–291
    - bioconjugates 12–14
    - biomimetic nanosensors 316
    - biomolecule-functionalized 45–48
    - biosensor development 57–84
    - comparison with a streptavidin molecule 14
    - electrochemical and electrocatalytic properties 34–37
    - enhanced conductivity 343–346
    - functionalization 39–48

- carbon nanotubes (CNTs) (cont.)
  - growth 29
  - introduction 3–4, 27–29
  - preparation and purification 58–59
  - screen-printing 32
  - self-assembly 33
  - sensors 27–49
  - solubility 60–61
  - surface functionalization 62
  - synthesis 4–5
- catalytic activation
  - nanoparticle scaling laws 338–339
  - reagentless biosensors 346–350
- catalytically enabled detection 349–350
- catecholamine biosensors 324
- CdS nanocrystals 124
  - emission spectra 127
- CdS nanoparticles 294, 348
- CdSe nanocrystals 294
- CdSe nanoparticles 356–358
- CdSe/ZnS quantum dots 177–178
- CdSe@ZnS nanocrystals 153–154
- CdSe@ZnS nanoparticles 353, 358–360
- CE *see* chemical enhancement
- cell imaging, fluorescent 182–183
- cell membrane, biomimetic nanosensors 320
- cellular biological targets, fluorescent detection 176–201
- cellular systems, nanosensor probing 317–322
- chemical enhancement (CE) 150–151
- chemical environment, NTFET sensitivity 9–12
- chemical vapor deposition (CVD) 4–5, 29, 77–78
- chemically modified electrodes (CMEs), C<sub>60</sub> 114
- chemiluminescence 80–81
- classical biosensors 324
- classical fluorophores 178–181
- CMEs *see* chemically modified electrodes
- CNT adsorption, on the transducer substrate 61
- CNT array-based biosensors 76–80
- CNT-based biosensors
  - construction 60–69
  - dispersion and stabilization 60
  - dispersion by surfactant interaction 61
  - polymer-assisted solubilization 61
- CNT-based electrochemical biosensors 69–74
- CNT-based electrochemical sensors, applications 34–38
- CNT-based sensors, preparation 29–34
- CNT bulky electrode material, composite entrapment 63–65
- CNT–DNA bioconjugates 47
- CNT electrodes
  - MWCNTs 29
  - paste 31
  - randomly distributed 30
  - well-aligned 30
- CNT field-effect transistors (CNTFETs) 82–83
  - *see also* carbon nanotube field-effect transistors
- CNT-trees 38, 80
- CNT/Teflon composite material 66, 72–73
- CNTFETs *see* CNT field-effect transistors
- CNTPE *see* carbon nanotube paste electrode
- co-adsorption, anchoring approaches 66–69
- coating of nanocrystals, with a silica shell 137
- colloidal nanocrystals
  - branching 132
  - chemical synthesis 131–133
  - metal and semiconductor 123–164
  - optical biosensing based on 123–164
  - shape control 132
  - single 124
  - size-dependent optical properties 127–130
- colloidal quantum dots 133–134
- colorimetric tests, nanocrystals 139
- CoMHP 266–267
- composite entrapment and CNTs bulky electrode material 63–65
- conducting polymer, nanowire-based biosensors 86–88
- conducting polymer/enzyme junction 87
- conformational modulated effects, biomolecular 338–339
- contact-passivated NTFETs 10
- coordinated biosensors
  - integrated signals 270–271
  - NADH peroxidase 267–269
  - signal transducing mediators 265–266
  - ultrasensitive detection of biomarkers 259–273
  - undecagold nanoparticles 270
- core–shell heterostructures 152–153
- covalent functionalization, of SWNTs 12
- CPEs *see* carbon nanotube paste electrodes
- CVD *see* chemical vapor deposition
- cyclic voltammetry 249–250
- cyclodextrins (CD) 138
  - solubilization of SWNTs 13
- cysteine-sulfenic acid chemistry 266
- cytochrome c 281

**d**

DCC *see* dicyclohexylcarbodiimide  
 deep-tissue imaging *in vivo*, Qdots 184–190  
 dendrimer-associated SAMs  
 – affinity recognition surface 244–252  
 – bioelectrocatalytic immunosensors 244–252  
 dendrimer-based electrochemical detection  
 methods 240–256  
 dendrimers  
 – as a new constituent of biocomposite  
 structures 241  
 – biosensors 242–255  
 – G4 poly(amidoamine) 242  
 DHLA *see* dihydroliipoic acid  
 dicyclohexylcarbodiimide (DCC) 63  
 different target DNA, multiplexed detection  
 373–376  
 dihydroliipoic acid (DHLA) 135  
 dinitrophenyl (DNP) 252  
 direct electrochemistry, biomolecules on CNTs  
 69–72  
 disease biomarkers, nanosensors 328  
 dithiobissuccinimidylundecanoate (DSU)  
 220–224  
 dithiothreitol (DTT) 135  
 DNA  
 – amplified 376–377  
 – different target 373–376  
 DNA analyses, pico/nanoliter chamber array  
 chips 368–393  
 DNA–Au nanoparticles, fluorophore modified  
 354  
 DNA-based sensors 263  
 DNA biosensors 73  
 DNA conformation changes, biosensors based  
 on 352–354  
 DNA detection 17  
 – biomimetic nanosensors 325–326  
 DNA duplex formation 350–351  
 DNA enzymes 326  
 DNA hybridization 17, 326  
 DNA linkers 266  
 DNA–magnetic nanoparticle assemblies  
 350  
 DNA–nanoparticle-based biosensors 352–355  
 DNA/RNA sensors 48  
 DNA sensing  
 – biomimetic nanosensors 318  
 – with nanowires 85–86  
 DNA–SWNT conjugates 13  
 DNAszymes *see* DNA enzymes  
 DNP *see* dinitrophenyl

DSU *see* dithiobissuccinimidylundecanoate  
 DTT *see* dithiothreitol  
 dual amplification route 73–74  
 duplex DNA, OR logic gate 350–351

**e**

*E. coli* *see* *Escherichia coli*  
 EAD *see* electric arc discharge  
 ECL *see* electrogenerated chemiluminescence  
 edge plane pyrolytic graphite electrode (EPPG)  
 36  
 EDLCs *see* electrochemical double layer  
 capacitors  
 EIS *see* electrochemical impedance  
 spectroscopy  
 electric arc discharge (EAD) 58  
 electric field-assisted dissolution theory 210–211  
 electrocatalytic detection, reagentless  
 biosensors 347  
 electrochemical biosensors 103–105  
 – CNT-based 69–74  
 electrochemical deposition, GNWs 214–220  
 electrochemical detection methods  
 – dendrimer-based 240–256  
 – fullerene-based 101–118  
 electrochemical double layer capacitors  
 (EDLCs) 42  
 electrochemical functionalization, CNTs  
 42  
 electrochemical impedance spectroscopy (EIS)  
 208, 225  
 – flat gold surfaces 228–229  
 – of *E. coli* 227–235  
 – on GNWs 230–232  
 electrochemical nano-biosensor, bacteria  
 detection 224–235  
 electrochemical sensors  
 – biomolecule-functionalized CNTs 45–48  
 – CNT-based 34–38  
 electrochemical signaling, from affinity  
 recognition reactions 248–252  
 electrochemistry, biomolecules on CNTs 69–72  
 electrochemical detection of biological  
 materials, nano-biosensor-based 208–235  
 electrode material, CNT bulky 63–65  
 electrodes, bioelectrocatalytic enzyme 243  
 electrogenerated chemiluminescence (ECL)  
 81  
 electroless plating, GNWs 214–220  
 electromagnetic enhancement (EME) 150–151



- electron flow, role of undecagold nanoparticles 270
- electron-transfer mechanism, kinetics 106–107
- electron transfer quenching 357–359
- electron transfer to redox proteins, functionalized CNTs 44
- ELISA *see* enzyme-linked immunosorbent assay
- embedded gold nanowire arrays 215–216
- EME *see* electromagnetic enhancement
- enhanced conductivity, carbon nanotube 343–346
- enhanced surface plasmon resonance, gold nanoparticle 340–342
- enzymatic reactions 19–20
- enzyme-based biosensors 261–263, 324  
– *see also* protein-based biosensors
- enzyme–CNT biosensors 72
- enzyme electrodes, bioelectrocatalytic 243
- enzyme-linked immunosorbent assay (ELISA) 223
- enzyme/conducting polymer junction 87
- EPPG *see* edge plane pyrolytic graphite electrode
- Escherichia coli* 208
- electrochemical impedance detection 227–235
- EVA *see* poly(vinyl acetate)
- f**
- Faradaic current increase, electrocatalytic detection 347
- ferrocenylthethered G4 poly(amidoamine) dendrimer (Fc-D) 245
- $\alpha$ -fetoprotein (AFP) 81–82
- field-effect transistors (FETs) 2  
– bioelectronics 81–83  
– carbon nanotube 1–21
- films, nanoporous 209
- flat gold surfaces, EIS 228–229
- flavin-adenin-dinucleotide (FAD) 348  
– CNTs 290
- flow-injection analysis 75–76
- FLT *see* fluorescence lifetime
- Fluo-4 389–390
- fluorescence  
– metal-enhanced 145  
– nanocrystals 139–146  
– quantum dots 313
- fluorescence lifetime (FLT), nanocrystals 142–145
- fluorescence resonance energy transfer (FRET) 141–142  
– quantum dots 197–200
- fluorescent cell imaging, Qdots 182–183
- fluorescent deep-tissue imaging *in vivo*, Qdots 184–190
- fluorescent detection  
– immunoblot analysis 192–195  
– molecular and cellular biological targets 176–201
- fluorescent labeling, Qdots 181–192
- fluorescent microscopic imaging, Qdots 181
- fluorescent standards, thin calibration of fluorescent instrumentation 201
- fluorophore modified DNA–Au nanoparticles 354
- fluorophores  
– compared with Qdots 178–180  
– *see also* organic dyes
- fMRI *see* functional magnetic resonance imaging
- fourth generation (G4) poly(amidoamine) dendrimers 242
- free-standing gold nanowire arrays 215–216
- FRET *see* fluorescence resonance energy transfer
- FRET acceptors 155–157
- FRET-based bioanalyses, Qdots 196–200
- FRET donors 155–157
- fullerene-based electrochemical detection methods, for biosensing 101–118
- fullerene-functionalized polyethylenimine 117
- fullerene-mediated biosensing 114–118
- fullerenes 58, 109–113  
– biofunctionalization 109–113  
– electrochemistry 113  
– synthesis 109
- functional magnetic resonance imaging (fMRI), Qdots 191
- functionalization  
– nanocrystal 134–139  
– of SWNTs 12
- functionalized CNTs 39–48  
– biomolecule- 45–48  
– electrochemical application 43–44  
– electron transfer to redox proteins 44
- g**
- G4 poly(amidoamine) dendrimers 242
- gas chromatography (GC) 75–76
- GCN4 transcription factor 266–267
- GFP *see* green fluorescent proteins
- GFP-CFP protein chimeric strategy 356
- GFP gene 380–383

glucose biosensor 87  
 – SWCNT 64  
 glucose detection 20  
 glucose oxidase (GOD) 32–33, 38, 281, 283, 285–286  
 – CNTs 288, 290, 292  
 – silicon nanoparticles 296  
 glucose oxidase (GOx) 20–21, 243–246, 252–253  
 – electrode immobilized 347–348  
 – modified CNTs 78–80  
 GNWs *see* gold nano-wire arrays  
 (Goat PAb)*E. coli* 221–224  
 GOD *see* glucose oxidase  
 gold nano-biosensor-based electrochemical method, detection of biological materials 208–235  
 gold nano-wire arrays (GNWs)  
 – EIS 230–232  
 – embedded 215–216  
 – free-standing 215–216  
 – specific antibodies 220–223  
 – template synthesis 209–219  
 gold nanocrystals 157–162  
 gold nanoparticle enhanced surface plasmon resonance 340–342  
 gold nanoparticles 279–283, 353–354  
 – biomimetic nanosensors 314, 318  
 – TiO<sub>2</sub>-stabilized 130  
 gold nanorods, emission spectra 128  
 gold posts, GNWs 220–223  
 GOx *see* glucose oxidase  
 GOx/Fc-D electrodes 244–245  
 graphene sheets  
 – electron distribution 35  
 – rolled 57  
 green fluorescent proteins (GFPs) 355–356  
 guided assembly, colloidal nanocrystals 126

**h**

H<sub>2</sub>O<sub>2</sub> biosensors 282–283  
 $\alpha$ -hCG 344  
 heme proteins 44, 46, 281  
 – CNTs 286, 288  
 high-throughput single-cell analysis system, using pico-liter microarray 384–392  
 horseradish peroxidase (HRP) 280, 282–284  
 human serum albumin (HSA), LSPR-based biosensing 341  
 hybrid photoelectrical SPR-detected device 342  
 hybridization 92  
 hydrophobic interactions, nanocrystals 137–139

**i**

IgG *see* immunoglobulin G  
 imaging, Qdots 181–192  
 imaging probes, multimodality 191  
 immunoblot analysis, Qdots 192–195  
 immunoglobulin G (IgG) 344  
 immunosensors 74  
 – bioelectrocatalytic 244–252  
 indium-doped tin oxide (ITO) 281–282  
 integrated signals, coordination biosensors 270–271  
 integration, anchoring approaches 66–69  
 ITO *see* indium-doped tin oxide

**k**

kinetic shape control, colloidal nanocrystals 132  
 kinetics, of electron-transfer mechanism 106–107

**l**

lab-on-a-chip 250, 368  
 labeling  
 – fluorescent 181–192  
 – live-cell 182  
 layer-by-layer (LBL) assembly, with dendrimers 243  
 ligand-mediated biomolecule conformational motions 351  
 linkage, anchoring approaches 66–69  
 linker, antibody 208, 220–224  
 linker synthesis, GNWs 220–223  
 lipid bilayers, biomimetic nanosensors 320  
 lipid-CNT assemblies 43  
 lipid molecules, self-assembly at CNTs 39–42  
 lithography 92  
 live-cell experiments, labeling 182  
 localized SPR (LSPR) 315, 340–341  
 logic gate, duplex DNA 350  
 luciferase, biomimetic nanosensors 327  
 luminescence-based sensors 139

**m**

magnetic detection, catalytically enabled 349–350  
 magnetic nanoparticles 295  
 magnetic relaxation switches (MRS) 350  
 magnetic resonance imaging (MRI) 350  
 – functional 191  
*N*-(3-maleimidopropionyl)-3,4-fullerolindine 117  
 maltose binding protein (MBP) 156, 294, 356–360  
 – semiconductor nanoparticles 294

- maltose nanosensor 156
  - material toxicity 164
  - MBP *see* maltose binding protein
  - mediated biosensor 108–109
    - fullerene- 114–118
  - MEF *see* metal-enhanced fluorescence
  - membrane-fused fluorescent/colorimetric nano-patches 322
  - membranes, bilayer lipid 41
  - mercaptosilanes 137
  - metabolomics 323
  - metal cluster resonance bio-chip 315
  - metal colloidal nanocrystals, optical biosensing based on 123–164
  - metal-enhanced fluorescence (MEF), nanocrystals 145
  - metal oxide nanowire(MONW)-based biosensors 89
  - metal oxide semiconductor field-effect transistors (MOSFETs) 1, 4
  - metallic nanoparticles 279–285
    - biosensing 157–161
    - SAMs 281–282
  - metallic oxide nanoparticles 285–286
  - MHP *see* multi-histidine peptide
  - micro-biosensors 291
  - micro-total analysis system (m-TAS) 368
  - microbiological detection techniques 208
  - microchamber arrays
    - nanoliter-volume 369–377
    - PCR 370
  - microelectrodes, carbon nanotube-packaged 34
  - microflow chip fabrication, PDMS 17
  - microfluidic biochip 321
  - microorganisms, for nanaoscale sensor construction 321
  - micropatterning, protein 253–256
  - microPET imaging 191
  - microscopic imaging, fluorescent 181
  - MnO<sub>2</sub> nanoparticles 286
  - mode of operation, NTFETs 8
  - molecular biological targets, fluorescent detection 176–201
  - molecular wires 38
  - mono-type QD-based western blotting technology 194–196
  - MONW *see* metal oxide nanowire
  - MOSFETs *see* metal oxide semiconductor field-effect transistors
  - mPEG Qdots 186
  - mPEG-SH SAMs 15
  - MRI *see* magnetic resonance imaging
  - MRS *see* magnetic relaxation switches
  - multi-histidine peptide (MHP) 266–269, 273
  - multi-walled carbon nanotubes (MWNTs) 3, 28, 58
    - as nanoelectrodes 29
  - multicolor quantum dots 155
  - multimodality imaging probes 191
  - multiphoton techniques, nanocrystals 145
  - multiple PCR analysis 375
  - multiplexed analysis, protein micropatterning 253–256
  - multiplexed detection, of different target DNA 373–376
  - multiplexed PCR, nanoliter-volume microchamber array 369–377
  - MWCNT-Nafion thin film 292
  - MWNT *see* multi-walled carbon nanotube
  - myoglobin (Mb) 281
    - CNTs 288
- n**
- N-Succinimidyl acrylate (NSA) 42
  - NADH *see* nicotinamide adenine dinucleotide
  - NADH peroxidase 265
    - biocatalytic element 267–269
  - Nafion, MWCNT thin film 292
  - nano-biosensors
    - bacteria detection 224–235
    - electrochemical detection of biological materials 208–235
    - experimental conditions 226
  - nano-biotechnology, biomedical diagnosis 327–329
  - nano-fibers, optical 323
  - nano-patches, membrane-fused fluorescent/colorimetric 322
  - nanobiohybrids
    - quantum dot-based 176–201
  - nanobiosensors, elements of 262–265
  - nanocantilevers, biosensor development 89–90
  - nanocomposite materials 292
  - nanocrystals
    - advantages and disadvantages 152
    - applications 153–161
    - biosensing 153–161
    - coating 137
    - colloidal *see* colloidal nanocrystals
    - colorimetric tests 139
    - fluorescence 139–146
    - fluorescence lifetime 142–145
    - functionalization 134–139
    - marketing 162–163
    - multiphoton techniques 145

- surface-enhanced resonance spectroscopy 149–151
  - surface modification 136
  - surface plasmon resonance 146–149
  - nanoelectrode arrays (NEAs) 77
  - nanoelectrodes, MWCNTs 29
  - nanogel particles (NGPs) 320–321
  - nanoliter dispenser, sample loading 372
  - nanoliter-volume microchamber array, multiplexed PCR 369–377
  - nanomaterials, purpose-built 126
  - nanoparticle scaling laws, interlacing 338–339
  - nanoparticles
    - fluorophore modified DNA–Au 354
    - magnetic 295
    - metal 279–285
    - metallic oxide 285–286
    - reagentless biosensors 337–361
    - semiconductor 293–294
    - with special functions 293–295
  - nanoporous films 209
  - nanoprobes, antibody-based 322
  - nanosensors
    - biological components 323–326
    - biomimetic 311–330
    - for probing biological and cellular systems 317–322
    - PEBBLE 321
  - nanoshells 328
  - nanostructured materials, one-dimensional 56–57
  - nanostructures, in biosensor design 312–317
  - nanotube networks 8
  - nanotubes
    - amino-functionalized 47
    - biosensor development 57–84
  - nanowire arrays, template synthesis 209–219
  - nanowire-based biosensors
    - conducting polymer 86–88
    - metal oxide nanowire-based 89
  - nanowires, biosensor development 84–89
  - near-IR QDs 185–186
  - NEAs *see* nanoelectrode arrays
  - NGP *see* nanogel particles
  - nicotinamide adenine dinucleotide (NADH) 66, 70–72
  - non-mediated biosensor 107
  - non-reagentless biosensors 337
  - noncovalent functionalization, of SWNTs 12
  - Npx-CoMHP-AuNP assembly 270
  - Npx redox center 266
  - NSA *see* N-Succinimidyl acrylate (NSA)
  - NTFET fabrication, SiO<sub>2</sub>/Si substrates 11
  - NTFETs *see* carbon nanotube field-effect transistors
- o**
- oligonucleotide detection
    - all-biological sensor 325
    - biomimetic nanosensors 317
  - on-chip cell-free protein synthesis, picoliter chamber array 378–383
  - on-chip DNA amplification 373
  - on-chip quantification, of amplified DNA 376–377
  - one-dimensional nanostructured materials 56–57
  - optical biosensing, based on metal and semiconductor colloidal nanocrystals 123–164
  - optical detection, catalytically enabled 349–350
  - optical nano-fibers 323
  - optical recognition-based biosensors, new generation 197–200
  - OR logic gate, duplex DNA 350
  - organic dyes 152, 178–181
    - *see also* fluorophores
  - organic templates, surfactants 131
  - organophosphorus compounds 92
  - oxidative acids, dispersion and stabilization of CNT-based biosensors 60
- p**
- passivation layer, NTFETs 10
  - paste electrodes, carbon nanotube 31
  - pathogenic bacteria 208
  - PCR *see* polymerase chain reaction
  - PCR microchamber array chip system 371–377
  - PDMS *see* poly(dimethylsiloxane)
  - PEBBLE (photonic explorers for bioanalysis with biologically localized embedding) nanosensors 321
  - PEG *see* poly(ethylene glycol)
  - peptide–AuNP complex 266
  - peptide nucleic acid (PNA) 17, 342
  - PET *see* positron emission tomography
  - photoelectrical SPR-detected device, hybrid 342
  - photoluminescence (PL)
    - quantum yield 135
    - spectra 156
  - photonic explorers for bioanalysis with biologically localized embedding *see* PEBBLE

- picoliter chamber array, on-chip cell-free protein synthesis 378–383  
 picoliter microarray, single-cell analysis system 384–392  
 pico/nanoliter chamber array chips, for single-cell, DNA and protein analyses 368–393  
 PL *see* photoluminescence  
 platinum nanoparticles 285  
 PMMA *see* poly(methyl methacrylate)  
 PNA *see* peptide nucleic acid  
 POAP *see* poly-o-aminophenol  
 poly-o-aminophenol (POAP)-electropolymerized electrode 46  
 poly(amidoamine) dendrimers, fourth generation 242  
 poly(dimethylsiloxane) (PDMS) 254, 379–380  
   – microflow chip fabrication 17  
 poly(ethylene glycol) (PEG) 39, 138, 185–186, 188, 191  
 poly(methyl methacrylate) (PMMA) 386  
 poly(vinyl acetate) (EVA) 81  
 polymer-assisted solubilization, CNT-based biosensors 61  
 polymer nanojunction sensor 88  
 polymerase chain reaction (PCR), multiplexed 369–377  
 polypyrrole (Ppy) 64  
 porous alumina films 209–214  
 porous silicon 295–296  
 positron emission tomography (PET), Qdots 191  
 Ppy *see* polypyrrole  
 prohibition, anchoring approaches 66–69  
 prostate specific antigen (PSA) 345  
 protein analyses, pico/nanoliter chamber array chips 368–393  
 protein-based biosensors 73  
   – CNTs 289  
   – using nanomaterials 278–297  
   – *see also* enzyme-based biosensors  
 protein conformation changes, biosensors based on 355–361  
 protein detection 14  
   – with nanowires 85–86  
 protein micropatterning, on sensor surfaces for multiplexed analysis 253–256  
 protein nanosensors 317  
 protein synthesis, on-chip cell-free 378–383  
 proteins  
   – Qdot-based immunoblot analysis 194–195  
   – redox 44  
 purification, of CNTs 58–59  
 purpose-built nanomaterials 126
- q**  
 QCM *see* quartz crystal microbalance  
 QD *see* quantum dot  
 QD-based western blotting technology 192–194  
   – mono-type 194–196  
   – sandwich-type 194–196  
*in vivo* QD imaging 185  
 QD-peptide conjugates 188  
 QD630-streptavidin 183  
 Qdot *see* quantum dot  
 Qdot-based immunoblot analysis, of “tracer” proteins 194–195  
 quantum dots  
   – basic principles 176–180  
   – colloidal 133–134  
   – conjugates 181  
   – design and synthesis 176–178  
   – fluorescence 313  
   – fluorescent detection of molecular and cellular biological targets 176–201  
   – fluorescent labeling and imaging 181–192  
   – multicolor 155  
   – nanobiohybrids 176–201  
   – optical and chemical properties 178–180  
   – Stokes shift 180  
   – water-soluble 178  
 quantum yield (QY), quantum dots 185  
 quartz crystal microbalance (QCM) 248  
 QY *see* quantum yield
- r**  
 randomly distributed CNT electrodes 30  
 reactive ion etching (RIE) 387  
 reagentless ATP biosensors 345  
 reagentless biosensors  
   – based on nanoparticles 337–361  
   – biomolecule conformational modulated effects 351–361  
   – catalytic activation 339–346  
   – gold nanoparticle enhanced surface plasmon resonance 340–342  
   – surface dielectric enhancement 340–342  
 redox enzymes, as electrodes 265–266  
 redox proteins, functionalized CNTs 44  
 restriction endonucleases detection 350  
 RhD gene 374–377  
 RIE *see* reactive ion etching  
 rolled graphene sheets 57
- S**  
 s-BLMs *see* supported bilayer lipid membranes

- sample loading, with a nanoliter dispenser 372
- SAMs *see* self-assembled monolayers
- sandwich, anchoring approaches 66–69
- sandwich-type QD-based western blotting technology 194–196
- scaling laws, nanoparticle 338–339
- screen printing 92
- screen-printing carbon nanotubes 32
- SDS molecules 40
- self-assembled monolayers (SAMs),  
dendrimer-associated 241, 244–253
- DSU 221
  - metal nanoparticles 281–282
- self-assembly
- CNTs 33
  - of surfactant and lipid molecules at CNTs 39–42
- semiconductor nanocrystals
- biosensing 153–156
  - colloidal 123–164
- semiconductor nanoparticles 293–294, 314
- fluorescence 313
- sensing devices, colloidal nanocrystals 126
- sensor platforms, definition 125
- sensor surfaces, for multiplexed analysis 253–256
- sensors
- CNT-based 27–49
  - CNT-based electrochemical 34–38
  - DNA/RNA 48
- SERS *see* surface-enhanced Raman scattering
- *see also* surface-enhanced resonance spectroscopy
- shape control, colloidal nanocrystals 132
- shell
- of nanocrystals 137
  - of Qdots 176
- signal transducing mediators, biomolecular conduits 265–266
- silanized nanocrystals 137
- silica NPs, biomimetic nanosensors 314
- silica shell, coating of nanocrystals 137
- silicon, porous 295–296
- silicon nanowire, enhanced conductivity 343–346
- silicon nanowire-based biosensors 84–85, 345
- silver nanoparticles 161, 284
- single B-cells, antigen-specific 389–392
- single-cell analyses
- high-throughput 384–392
  - pico/nanoliter chamber array chips 368–393
- single chip, multiplexed detection of different target DNA 373–376
- single copy DNA, multiplexed PCR 369–377
- single-walled carbon nanotubes (SWNTs) 3, 28, 58
- functionalization 12
  - glucose biosensor 64
  - solubilization 13
  - surface dielectric enhancement 343–345
- SiO<sub>2</sub>/Si substrates, NTFET fabrication 11
- snakes, thermal vision organs 329
- sol-gel chemistry 65
- sol-gel technology 92
- CNT-based biosensors 292
- solubility of CNTs 60–61
- solubilization, polymer-assisted 61
- solution-based receptors, colloidal nanocrystals 126
- spacing, anchoring approaches 66–69
- specific antibodies, linker binding 220–223
- SPR *see* surface plasmon resonance
- SRY gene 374–375
- standards, fluorescent 201
- starch degradation, enzymatic 19
- steady-state growth of pores 210
- Stokes shift, of Qdots 180
- streptavidin molecule, comparison with a carbon nanotube 14
- structural biology 260
- substrates, transducer 61
- subtilisin-based biosensor 117
- supported bilayer lipid membranes (s-BLMs) 41
- biosensors 115–116
- surface capping exchange 135–137
- surface denaturation 264
- surface dielectric enhancement 339–346
- nanoparticle scaling laws 338–339
- surface-enhanced Raman scattering (SERS) 162
- surface-enhanced resonance spectroscopy (SERS), nanocrystals 149–151
- surface functionalization, of CNTs 62
- surface modification, through hydrophobic interactions 137–139
- surface plasmon resonance (SPR) 159–160, 248–249
- gold nanoparticles 130, 340–342
  - nanocrystals 146–149
- surface silanization 137
- surface tailoring, CNT-based biosensors 66–69
- surfactant interaction, CNT-based biosensors 61

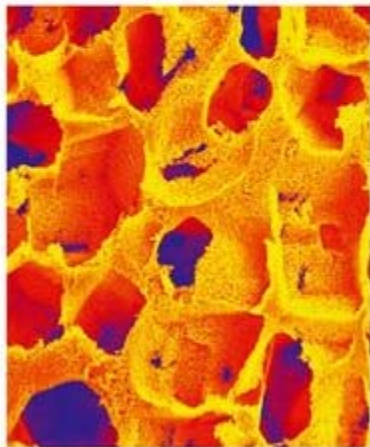
- surfactant molecules, self-assembly at CNTs 39–42
  - surfactants 131
  - SWCNT *see* single-walled carbon nanotube
  - SWNT *see* single-walled carbon nanotube
- t**
- tagging, anchoring approaches 66–69
  - TaqMan PCR 374–378
  - $\mu$ -TAS *see* micro-total analysis system
  - Teflon/CNT composite material *see* CNT/Teflon composite material
  - template synthesis, gold nano-wire arrays 209–219
  - terminating agents 131
  - thermal vision organs, snakes 329
  - time-resolved fluorimetry, Qdots 197
  - TiO<sub>2</sub> nanoparticles 286
  - TiO<sub>2</sub>-stabilized gold nanoparticles 130
  - toxicity, semiconductor colloidal nanocrystals 164
  - tracer proteins, Qdot-based immunoblot analysis 194–195
  - track-etch polymeric films 209
  - transducer substrate, CNT adsorption 61
  - transducers, biological 225
  - transistor function, NTFETs 8
  - Tween-20 67
  - two-step anodization, porous alumina films 211
- u**
- U1A RNA splicing factor 67, 344
  - ultrasensitive detection of biomarkers, coordinated biosensors 259–273
  - undecagold nanoparticles, electron flow 270
- v**
- van der Waals surface representation, C<sub>60</sub> fullerene 113
  - vesicles, biomimetic 320
  - voltammetric detection 247, 249–250
- w**
- water-soluble Qdots 178
  - western blot 192–194
- z**
- ZnO nanoparticles 286
  - ZnSe nanocrystals, emission spectra 127
  - ZrO<sub>2</sub> nanoparticles 286

Nanotechnologies for the Life Sciences

Edited by Challa Kumar

WILEY-VCH

# Tissue, Cell and Organ Engineering



NLS 



## Contents

<b>Preface</b>	XV
<b>List of Authors</b>	XIX
<b>1 Nanotechnology and Tissue Engineering: The Scaffold Based Approach</b>	<b>1</b>
<i>Lakshmi S. Nair, Subhabrata Bhattacharyya, and Cato T. Laurencin</i>	
1.1	Overview 1
1.2	Introduction 1
1.3	The Importance of Scaffolds in Tissue Engineering 4
1.4	Structure and Functions of Natural Extracellular Matrix 12
1.5	Applications of Nanotechnology in Developing Scaffolds for Tissue Engineering 21
1.5.1	Polymeric Nanofiber Scaffolds 23
1.5.1.1	Top-down Approaches in Developing Scaffolds for Nano-based Tissue Engineering 24
1.5.1.2	Bottom-up Approaches in Developing Scaffolds for Nano-based Tissue Engineering 33
1.6	Cell Behavior Towards Nano-based Matrices 39
1.7	Applications of Nano-based Matrices as Scaffolds for Tissue Engineering 43
1.7.1	Stem Cell Adhesion and Differentiation 43
1.7.2	Neural Tissue Engineering 47
1.7.3	Cardiac and Blood Vessel Tissue Engineering 49
1.7.4	Bone, Ligament and Cartilage Tissue Engineering 54
1.8	Conclusions 55
	References 56
<b>2 Polymeric Nanofibers in Tissue Engineering</b>	<b>66</b>
<i>Seow Hoon Saw, Karen Wang, Thomas Yong, and Seeram Ramakrishna</i>	
2.1	Overview 66
2.2	Introduction 67
2.2.1	History of Tissue Engineering and Nanofibers 67
2.3	Classification of Nanofibers 69
2.3.1	Synthetic Polymers 69
2.3.2	Biopolymers 69

VIII | Contents

2.3.3	Copolymers	70
2.3.4	Composite Polymers	70
2.4	Nanofiber Fabrication	70
2.4.1	Drawing	71
2.4.2	Template Synthesis	71
2.4.3	Phase Separation	72
2.4.4	Self-assembly	73
2.4.5	Electrospinning	73
2.5	Degradation and Absorption Kinetics of Nanofiber Scaffolds Compared with Conventional Scaffolds	74
2.6	Advantages and Disadvantages of Nanofiber Scaffolds Compared with Other Conventional Scaffolds	76
2.7	Biocompatibility of Nano-structured Tissue Engineered Implants	82
2.8	Applications of Polymeric Nanofibers in Tissue Engineering	87
2.8.1	Ophthalmology	89
2.8.2	Liver	93
2.8.3	Nerve	93
2.8.4	Skin	99
2.8.5	Bone and Cartilage	102
2.8.6	Heart and Vascular Grafts	105
2.8.7	Stem Cells	109
2.9	Innovations in Nanofiber Scaffolds	111
2.10	Conclusion	115
	References	116

**3 Electrospinning Technology for Nanofibrous Scaffolds in Tissue Engineering** 135

*Wan-Ju Li, Rabie M. Shanti, and Rocky S. Tuan*

3.1	Introduction	135
3.2	Nanofibrous Scaffolds	138
3.2.1	Fabrication Methods for Nanofibrous Scaffolds	138
3.2.1.1	Phase Separation	138
3.2.1.2	Self-assembly	138
3.2.1.3	Electrospinning	139
3.2.2	The Electrospinning Process	140
3.2.2.1	History	140
3.2.2.2	Setup	141
3.2.2.3	Mechanism and Working Parameters	142
3.2.3	Properties of Electrospun Nanofibrous Scaffolds	144
3.2.3.1	Architecture	144
3.2.3.2	Porosity	145
3.2.3.3	Mechanical Properties	146
3.3	Current Development of Electrospun Nanofibrous Scaffolds in Tissue Engineering	146
3.3.1	Evidence Supporting the Use of Nanofibrous Scaffolds in Tissue Engineering	146

3.3.1.1	Nanofibrous Scaffolds Enhance Adsorption of Cell Adhesion Molecules	146
3.3.1.2	Nanofibrous Scaffolds Induce Favorable Cell–ECM Interaction	147
3.3.1.3	Nanofibrous Scaffolds Maintain Cell Phenotype	148
3.3.1.4	Nanofibrous Scaffolds Support Differentiation of Stem Cells	149
3.3.1.5	Nanofibrous Scaffolds Promote <i>in vivo</i> -like 3D Matrix Adhesion and Activate Cell Signaling Pathway	150
3.3.2	Biomaterials Electrospun into Nanofibrous Scaffolds	151
3.3.2.1	Natural Polymeric Nanofibrous Scaffolds	151
3.3.2.2	Synthetic Polymeric Nanofibrous Scaffolds	162
3.3.2.3	Composite Polymeric Nanofibrous Scaffolds	166
3.3.2.4	Nanofibrous Scaffolds Coated with Bioactive Molecules	168
3.3.3	Engineered Tissues using Electrospun Nanofibrous Scaffolds	169
3.3.3.1	Skin	169
3.3.3.2	Blood Vessel	170
3.3.3.3	Cartilage	171
3.3.3.4	Bone	172
3.3.3.5	Muscle	173
3.3.3.6	Ligament	175
3.3.3.7	Nerve	175
3.4	Current Challenges and Future Directions	176
3.5	Conclusion	177
	References	177
<b>4</b>	<b>Nanofibrous Scaffolds and their Biological Effects</b>	<b>188</b>
	<i>Laura A. Smith, Jonathan A. Beck, and Peter X. Ma</i>	
4.1	Overview	188
4.2	Introduction	188
4.3	Methods of Formation	190
4.3.1	Electrospinning	190
4.3.2	Self-assembly	193
4.3.3	Phase Separation	194
4.4	Nanofibrous Composite Scaffolds	198
4.4.1	Inorganic Composites	199
4.4.2	Surface Modification	200
4.4.3	Factor Delivery Scaffolds	201
4.5	Biological Effects of Nanofibers	202
4.5.1	Attachment	202
4.5.2	Proliferation	203
4.5.3	Differentiation	203
4.5.4	Migration	204
4.6	Tissue Formation	205
4.6.1	Connective Tissue	205
4.6.1.1	Ligaments	205
4.6.1.2	Cartilage	205
4.6.1.3	Bone	206

4.6.2	Neural Tissue	207
4.6.3	Cardiovascular Tissue	208
4.6.3.1	Cardiac Muscle	208
4.6.3.2	Blood Vessel	208
4.6.4	Liver Tissue	208
4.7	Conclusion	209
	References	210
<b>5</b>	<b>Nanophase Biomaterials for Tissue Engineering</b>	<b>216</b>
	<i>Ramalingam Murugan and Seeram Ramakrishna</i>	
5.1	Introduction: Problems with Current Therapies	216
5.2	Tissue Engineering: A Potential Solution	219
5.3	Stem Cells: The Essentials	220
5.4	Nanobiomaterials: A New Generation Scaffolding Material	223
5.4.1	Characteristics of Scaffold	225
5.4.2	Types of Scaffolding Materials	227
5.4.2.1	Ceramic Nanobiomaterials	227
5.4.2.2	Polymeric Nanobiomaterials	234
5.5	Nanofibrous Scaffold Processing: Current Scenarios	237
5.5.1	Self-assembly	237
5.5.2	Phase Separation	239
5.5.3	Electrospinning – A New Approach	240
5.5.3.1	Experimental System	240
5.5.3.2	Spinning Mechanism	241
5.5.3.3	Electrospun Nanofibrous Scaffolds	243
5.6	Cell–Matrix (Scaffold) Interactions	244
5.6.1	Cell–Ceramic Scaffold Interactions	244
5.6.2	Cell–Polymer Scaffold Interactions	247
5.7	Concluding Remarks	248
	Acknowledgments	249
	Abbreviations	249
	Glossary	250
	References	252
<b>6</b>	<b>Orthopedic Tissue Engineering Using Nanomaterials</b>	<b>257</b>
	<i>Michiko Sato and Thomas J. Webster</i>	
6.1	Preface	257
6.2	Introduction: Problems with Current Implants	258
6.3	A Potential Solution: Nanotechnology	259
6.3.1	Current Research Efforts to Improve Implant Performance Targeted at the Nanoscale	260
6.3.1.1	Ceramic Nanomaterials	262
6.3.1.2	Metal Nanomaterials	270
6.3.1.3	Polymeric Nanomaterials	270
6.3.1.4	Composite Nanomaterials	274

6.3.2	<i>In Vivo</i> Compared with <i>In Vitro</i> Studies	276
6.4	Considerations and Future Directions	278
	Acknowledgments	279
	References	279
<b>7</b>	<b>Hydroxyapatite Nanocrystals as Bone Tissue Substitute</b>	<b>283</b>
	<i>Norberto Roveri and Barbara Palazzo</i>	
7.1	Overview	283
7.2	Introduction	284
7.3	Biogenic Hydroxyapatite: Bone and Teeth	284
7.4	Biomimetic Hydroxyapatite: Porous and Substituted Apatites	288
7.5	Biologically Inspired Hydroxyapatite: HA–Collagen Composites and Coatings	292
7.6	Functionalized Hydroxyapatite: HA Nanocrystals – Bioactive Molecules	296
7.7	Conclusion and Future Challenges	301
	Acknowledgments	301
	References	302
<b>8</b>	<b>Magnetic Nanoparticles for Tissue Engineering</b>	<b>308</b>
	<i>Akira Ito and Hiroyuki Honda</i>	
8.1	Introduction	308
8.2	Mesenchymal Stem Cell Isolation and Expansion	310
8.2.1	MSC Expansion using MCLs	310
8.2.2	MSC Isolation and Expansion using AMLs	313
8.3	Mag-seeding	316
8.4	Construction of 3D Tissue-like Structure	318
8.4.1	Cell Sheet Engineering using RGD-MCLs	318
8.4.2	Construction of a Keratinocyte Sheet using MCLs	321
8.4.3	Delivery of Mag-tissue Engineered RPE Sheet	323
8.4.4	Construction of a Liver-like Structure using MCLs	326
8.4.5	Construction of Tubular Structures using MCLs	328
8.5	Conclusion	330
	References	331
<b>9</b>	<b>Applications and Implications of Single-walled Carbon Nanotubes in Tissue Engineering</b>	<b>338</b>
	<i>Peter S. McFetridge and Matthias U. Nollert</i>	
9.1	Introduction	338
9.2	Electromagnetic Fields for Tissue Regeneration	339
9.3	Tissue Engineering	340
9.4	SWNT Preparation: Purification and Functionalization	342
9.5	Specific Applications of Carbon Nanotubes in Tissue Engineering	352
9.6	Conclusions	355
	References	355

<b>10</b>	<b>Nanoparticles for Cell Engineering – A Radical Concept</b>	<b>361</b>
	<i>Beverly A. Rzigalinski, Igor Danelisen, Elizabeth T. Strawn, Courtney A. Cohen, and Chengya Liang</i>	
10.1	Introduction and Overview	361
10.2	Free Radicals and Oxidative Stress	362
10.2.1	Sources of Intracellular Free Radicals	362
10.2.2	Oxidative Stress	364
10.2.3	Oxidative Stress and Disease	365
10.3	A Nanotechnological Approach to Oxidative Stress	366
10.3.1	Rare Earth Oxide Nanoparticles – Cerium	367
10.3.1.1	Biological Effects of Cerium	369
10.3.1.2	Biological Effects of Cerium Oxide Nanoparticles	370
10.3.1.3	Other Oxide Nanoparticles	373
10.3.1.4	Fullerene Derivatives and Carbon Nanotubes	373
10.4	Nano-pharmacology	374
10.4.1	Absorption	375
10.4.1.1	Agglomeration	376
10.4.1.2	Dose	376
10.4.2	Distribution, Metabolism, and Excretion	377
10.5	Nanoparticle Antioxidants and Treatment of Disease	377
10.6	Toxicology	379
10.7	Summary	380
	References	380
<b>11</b>	<b>Nanoparticles and Nanowires for Cellular Engineering</b>	<b>388</b>
	<i>Jessica O. Winter</i>	
11.1	Introduction	388
11.2	Biological Opportunities at the Nanoscale	389
11.2.1	Nanostructures and Cells	389
11.2.2	Nanoparticle and Nanowire Synthesis for Biological Systems	390
11.2.2.1	Nanoparticle Synthesis	390
11.2.2.2	Nanowire Synthesis	393
11.2.3	Surface Passivation Strategies	394
11.2.4	Bioconjugation	395
11.2.4.1	Conjugation Strategies to Promote Non-specific Cellular Affinity	396
11.2.4.2	Biomolecular Recognition	397
11.2.4.3	Conjugation Strategies for Antibody-mediated Recognition	397
11.2.4.4	Conjugation Strategies for Protein- and Peptide-mediated Recognition	398
11.2.5	Toxicity (see also Volume 5 of this Series)	399
11.3	Nanostructures to Modify Cell Adhesion and Migration	400
11.3.1	Cell Adhesion at the Nanoscale	401
11.3.2	Cell Adhesion and Nanoscale Physical Topography	402
11.3.3	Cell Adhesion and Nanoscale Chemical Patterns	405

11.3.4	Cytoskeletal Manipulation	406
11.3.5	Future Applications of Nanostructures for Cell Adhesion and Migration	407
11.3.5.1	Future Physical Nanostructures for Cell Adhesion	408
11.3.5.2	Future Chemical Patterns for Cell Adhesion	409
11.3.5.3	Active Investigation of the Cytoskeleton	411
11.4	Nanostructure Cellular Entry	411
11.4.1	Biology of Molecular Delivery	412
11.4.2	Nanostructure Endocytotic Delivery	412
11.4.3	Other Methods of Cellular Entry	415
11.4.4	Nanoparticle Intracellular Sensing	416
11.4.4.1	Semiconductor Quantum Dots	416
11.4.4.2	Magnetic Nanoparticles	418
11.4.5	Future Directions	419
11.4.5.1	Nanostructure Intracellular Delivery	419
11.4.5.2	Intracellular Sensing	420
11.5	Intracellular Transport of Nanostructures	421
11.5.1	Biology of Intracellular Transport	422
11.5.2	Actin-based Nanostructure Transport	423
11.5.3	Microtubule-based Nanostructure Transport	424
11.5.4	Future Directions	424
11.6	Biomolecule Delivery Using Nanostructures	425
11.6.1	Biology of Controlled Delivery	425
11.6.1.1	Drug Delivery	425
11.6.1.2	Gene Therapy	426
11.6.2	Drug Delivery	426
11.6.2.1	Cell Targeting <i>In Vivo</i>	426
11.6.2.2	Drug Delivery for Cancer Treatment	427
11.6.3	Gene Therapy	432
11.6.3.1	Silica Nanocarriers	432
11.6.3.2	Gold Nanocarriers	433
11.6.3.3	Magnetic Nanocarriers	433
11.6.4	Future Directions	434
11.6.4.1	Drug Delivery	434
11.6.4.2	Gene Therapy	436
11.7	Protein Manipulation	437
11.7.1	Biology of Protein Manipulation	438
11.7.2	Manipulation of Free Proteins: Enzymes	438
11.7.3	Manipulation of Bound Proteins: Receptors and Ion Channels	439
11.7.4	Future Directions	440
11.8	Summary and Conclusions	441
11.8.1	Summary	441
11.8.2	Conclusions	443
	References	444

<b>12</b>	<b>Nanoengineering of Biomaterial Surfaces</b>	<b>461</b>
	<i>Ashwath Jayagopal and Venkatram Prasad Shastri</i>	
12.1	Introduction	461
12.2	Conventional Photolithography	462
12.3	Electron-beam Lithography	466
12.4	Soft Lithography	468
12.5	Polymer-demixed Nanotopographies	472
12.6	Star-shaped and other Novel Polymer Structures	474
12.7	Vapor Deposition	476
12.8	Self-assembly	479
12.9	Particle Blasting	482
12.10	Ion Beam and Plasma-guided Surface Engineering	483
12.11	Sol–Gel Technology	486
12.12	Nanolithography	487
12.13	Laser-guided Strategies	489
12.14	Rapid Prototyping Techniques	492
12.15	Conclusions	496
	Acknowledgments	496
	References	497
	<b>Index</b>	<b>506</b>



## Preface

Tissue Cell and Organ Engineering is the title of the ninth volume of the series on Nanotechnologies for the Life Sciences. As the title indicates the book can be considered as an encyclopedia on nanotechnological approaches to tissue, cell and organ engineering. The publication of the book is timely for a number of reasons. First, with the increase in life expectancy there is an unfulfilled demand for replacing non functional tissues and organs. Second, life time for implants and vascular grafts made from conventional synthetic materials (with constituent dimensions greater than 1 micron) is limited ranging from 5 to 15 years. Third, utilization of living tissue/organ for replacement is not a practical solution as evidenced by the fact that millions of surgeries are performed annually to treat tissue and organ failure and the number of people waiting for such transplantations are more than 80,000 at any time. Fourth, there is the ever-increasing cost of health care related to tissue loss or end-stage organ failure exceeding 400 billion US dollars. Furthermore, laboratory experiments to date suggest that nanomaterials have great potential for tissue, cell and organ engineering. Until the publication of this book, there is no single source of information about how nanotechnologies are impacting various facets of tissue engineering. With close to five hundred pages, the book has turned out to be a comprehensive source of information covering different types of nanomaterials being investigated for tissue, cell and organ engineering in addition to innovative strategies for assembling functional and structural artificial tissues.

I am extremely pleased with the final product, which is a tribute to harmonious integration of tissue engineering and nanomaterials science. Such an integration is only possible due to the scholarly presentations from some thirty researchers around the world, spanning twelve chapters. My special thanks to all of them for making this project a reality. I am always grateful to my employer, family, friends and Wiley-VCH publishers, who are part and parcel of this long journey into the union of nanomaterials and life sciences. I am thankful to you, the reader, who has taken time to join this journey. I do hope you will enjoy reading the book and will find it useful in your future endeavors. Let me first give you a bird's eye view of the various facets of tissue engineering being touched by nanomaterials prior to your plunging into the more specific topics.

In comparison with nanomaterials such as nanoparticles and nanotubes, nanofibers are more suitable for use as scaffolds in tissue engineering as they are

morphologically similar to natural scaffolds and possess suitable properties such as high porosity, various pore-size distributions, and high surface-to-volume ratio. The majority of the investigations being carried out by tissue engineering researchers centers on utilization of nanofibers for development of artificial tissues. Therefore, the first four chapters in the book have been dedicated to provide an understanding of various aspects of nanofibers with respect to tissue engineering. The book begins with a chapter on *Nanotechnology and Tissue Engineering: The Scaffold Based Approach* providing an overview of the importance of nanotechnologies in developing scaffolds that closely mimic the structure and functions of the extra cellular matrix (ECM). Lakshmi S. Nair, Subhabrata Bhattacharyya and Cato T. Laurencin from the University of Virginia, USA, have demonstrated the importance of the scaffold approach for utilizing nanostructured materials in engineering ECM replacements. Of the various types of nanofibers currently under investigation for tissue engineering, polymeric nanofibers have been attracting a great deal of attention especially for applications in the area of ophthalmology, hepatic biology, nerve, skin, bone and cartilage regeneration, heart and vascular grafts, and stem cell research. Researchers Seow Hoon Saw, Karen Wang, Thomas Yong and Seeram Ramakrishna from the National University of Singapore have contributed the second chapter by bringing out an exhaustive review on *Polymeric Nanofibers for Tissue Engineering* covering different types of nanofibers, fabrication methodologies, degradation kinetics, biocompatibility and their applications in regeneration of several types of tissues. Focusing more specifically on electrospinning technology, researchers Wan-Ju Li, Rabie M. Shanti and Rocky S. Tuan from the National Institute of Arthritis, and Musculoskeletal and Skin Diseases in Bethesda, USA, demonstrate that this technology is a useful, economical, and easily set-up method for the fabrication of three-dimensional, highly porous and nanofibrous scaffolds which have been shown to support cellular activities and tissue formation. Their contribution in the third chapter, *Electrospinning Technology in Tissue Engineering*, is a thorough review on not only electrospinning technology per se but also on various chemical, physical and biological properties of nanofibers prepared using this technology. In the fourth chapter, electrospinning technology is compared with two other well known approaches, namely self-assembly and phase separation for fabrication of nano-fibrous scaffolds. Researchers from the University of Michigan in Ann Arbor, USA, systematically analyze the differences and unique characteristics of the three approaches for the development of scaffolds and their applications in tissue engineering. This chapter, *Nano-fibrous Scaffolds and their Biological Effects*, reviewed by Laura A. Smith, Jonathan A. Beck and Peter X. Ma provides some useful insights into achieving the dream of engineering three-dimensional tissue formations.

The fifth chapter in the book, *Nanophase Biomaterials for Tissue Engineering*, contributed by R. Murugan and S. Ramakrishna from the National University of Singapore is a source of information on nanoscale biomaterials in particular, ceramic and polymer-based materials that are being investigated for tissue engineering applications. In addition to the fabrication techniques for nanobiomaterials, the chapter also provides information related to their influence on cells and cell growth. In

the next chapter, the sixth, reader's attention is brought to nanotechnologies that are bringing solutions to long-standing problems with current orthopedic implants. The chapter, *Orthopedic Tissue Engineering using Nanomaterials*, written by Michiko Sato and Thomas J. Webster from Purdue University and Brown University respectively in West Lafayette, USA, discusses the effect of ceramic, metallic, polymeric, and composite nanomaterials on cellular functions particularly related to the bone. Norberto Roveri and Barbara Palazzo from the University of Bologna in Italy provide an up to date review on hydroxyapatite nanoparticles, which are being thoroughly investigated as materials for bone substitution. In the seventh chapter, entitled *Hydroxyapatite Nanocrystals as Bone Tissue Substitute*, they describe morphological, structural, chemical-physical, and surface characteristics of hydroxyapatite nanocrystals, followed by research investigations leading to understanding their high bioactivity and ability to induce bone regeneration and remodeling.

Moving away from nanofibers, ceramic nanomaterials and hydroxyapatite nanocrystals, the eighth chapter, *Magnetic Nanoparticles for Tissue Engineering*, authored by Akira Ito and Hiroyuki Honda from Kyushu University and Nagoya University respectively in Japan contains research investigations about application of the magnetic force-based tissue engineering technique (Mag-TE) to cell-seeding (termed "Mag-seeding") and its effectiveness in enhancing cell-seeding efficiency, leading to three-dimensional porous scaffolds for tissue engineering. In addition to magnetic nanomaterials, carbon nanotubes (CNTs) have been attracting the attention of life scientists. Due to their extraordinary physical, chemical, mechanical and electrical properties, in particular single-walled carbon nanotubes (SWNTs) are being touted as materials that have immense potential to interface directly with biological systems leading to innovative applications. In the ninth chapter, Peter S. McFetridge and Matthias U. Nollert from the University of Oklahoma in Norman, USA, delve deeply into the applications of SWNTs in the field of tissue engineering. The chapter, *Applications and Implications of Single-Walled Carbon Nanotubes in Tissue Engineering*, provides the history behind the electrical stimulation of cells and the reasoning behind the use of SWNTs as a conductive material to support or promote organ regeneration with specific examples of applications of SWNT in tissue engineering from the literature.

Cellular engineering is conceptually more fundamental to tissue engineering and nanotechnologies are helping in modulating cellular functions as well. In the tenth chapter, a more specific case of the effect of nanomaterials on cellular engineering related to free radical mediated oxidative stress is examined. The chapter, *Nanoparticles for Cell Engineering—A Radical Concept*, is a contribution from the laboratories of Beverly A. Rzigalinski at Virginia College of Osteopathic Medicine and Virginia Polytechnic & State University in Blacksburg, USA. The authors describe in detail potential application of three nanoparticle redox reagents viz rare earth oxide nanoparticles (particularly cerium), fullerenes and their derivatives and carbon nanotubes in preservation of cellular redox status and treatment of disease. Adding to the specific case of cellular engineering described in the tenth chapter, Jessica Winter from Ohio State University in Columbus, USA, presents in the eleventh chapter an exhaustive review on engineering of cells using nanotechnolo-

gies. The chapter aptly entitled *Nanoparticles and Nanowires for Cellular Engineering* is a one-stop source of information on applications of nanostructures to cellular engineering in general and for manipulating specific cellular components. The chapter deals with a gamut of issues on nanomaterial-based cellular engineering related to a wide spectrum of biomedical applications ranging from tissue engineering, intracellular tracking, biosensing and drug delivery. The final chapter of the book is an excellent review on *Nanoengineering of Biomaterial Surfaces* contributed by Ashwath Jayagopal and V. Prasad Shastri from Vanderbilt University in Nashville, USA. In this chapter, a variety of surface engineering techniques are presented for achieving micro- and nanoscale surface features, in addition to their applicability in the construction of hard and soft materials and three-dimensional geometries relevant to cellular and tissue engineering. This chapter brings to close the first comprehensive treatise on nanotechnological approaches for tissue, cell and organ engineering and I am very confident that the book will be a knowledge base for further advances that are bound to take place in the near future.

June 2006  
Baton Rouge, USA

*Challa S. S. R. Kumar*

## 1

## Nanotechnology and Tissue Engineering: The Scaffold Based Approach

*Lakshmi S. Nair, Subhabrata Bhattacharyya,  
and Cato T. Laurencin*

## 1.1

### Overview

Biodegradable porous three-dimensional (3D) structures have been extensively used as scaffolds for tissue engineering to temporarily mimic the structure and functions of the natural extracellular matrix (ECM). The ECM functions to provide 3D structure with mechanical and biochemical cues to support and control cell organization and functions. Even though macro- and micro-fabrication techniques enabled the development of highly porous 3D scaffolds that could support the adhesion and proliferation of cells, their ability to closely mimic the complex nanostructured topography and biochemical functions of the ECM is far from optimal. However, recent developments in nanofabrication techniques have afforded various nanostructured bioactive scaffolds. These include top-down approaches such as electrospinning and phase separation to develop nanofibrous scaffolds from polymer solutions or bottom-up approaches such as self-assembly to develop nanofibrous scaffolds from specifically designed bioactive peptide motifs. Although significant improvements are needed for these nanofabrication processes to produce scaffolds that could precisely mimic the structure and functions of the ECM, the developments so far have significantly enhanced our ability to recreate the natural cellular environment for regenerating tissues.

## 1.2

### Introduction

Tissue engineering has now emerged from the stage of infancy demonstrating proof of principle and developing various functional tissues using different approaches to the stage of an established scientific discipline capable of developing viable products for clinical applications. Tissue engineered skin can be considered as one of the first commercialized products developed using the principles of tissue engineering. In addition to clinical applications, tissue engineering has also

raised significant interest as a novel tool for investigating cell and developmental biology and developing novel drugs using tissues grown in 3D environments [1].

The ultimate goal of tissue engineering is to address the current organ shortage problem, i.e., development of an alternative therapeutic strategy to autografting and allografting, two common approaches currently used to repair or reconstruct damaged tissues or organs. Autografts and allografts have several shortcomings that significantly limit their applications. These include limited availability and donor site morbidity associated with autografts and risk of infection and immunogenicity associated with allografts [2]. Conversely, regeneration or repair of tissue using tissue engineering approaches attempts to recreate functional tissue using bioresorbable synthetic materials and other required components that can be routinely assembled and reliably integrated into the body without any of the above-mentioned adverse side effects. Tissue engineering thus holds promise to revolutionize current health care approaches to improve the quality of human life in a practical and affordable way.

The term “tissue engineering” was coined in 1987 during a National Science Foundation (NSF) Meeting inspired by a concept presented by Dr. Y.C. Fung of the University of California at San Diego [3]. At a subsequent workshop held by NSF in 1988, tissue engineering was defined as “the application of principles and methods of engineering and life sciences to obtain a fundamental understanding of structure–function relationships in novel and pathological mammalian tissues and the development of biological substitutes to restore, maintain and improve tissue functions” [4]. However, widespread interest of the scientific community in tissue engineering was triggered by two phenomenal reviews: one by Nerem [5] on cellular engineering and another by Langer and Vacanti on tissue engineering [6]. These reviews discuss in depth, for the first time, the possibilities of tissue engineering and presented some of the preliminary studies demonstrating proof of the concept. Figure 1.1 shows the process of tissue engineering [7]. The field of tissue engineering has now developed into a highly interdisciplinary science and has attempted to recreate or regenerate almost every type of human tissue and organ [8]. This was possible within a short time due to the highly multidisciplinary nature of the tissue engineering approach, which makes use of the combined efforts of basic and material scientists, cell biologists, engineers and clinicians. Several different definitions for tissue engineering followed the NSF consensus definition due to the interdisciplinary approach and our laboratory defines tissue engineering as “the application of biological, chemical and engineering principles towards the repair, restoration or regeneration of living tissues using biomaterials, cells and factors, alone or in combination”, describing the different possible approaches for tissue engineering [9]. Thus, three or more approaches are currently used to regenerate tissues using the principles of tissue engineering. One approach is the guided tissue engineering that uses a biomaterial membrane to guide the regeneration of new tissue; another approach called cell transplantation uses the application of isolated cells, manipulated cells (gene therapy) or cell substitutes to promote tissue regeneration. A third approach uses biomaterial in combination with bioactive molecules called growth factors to induce and guide tissue regenera-

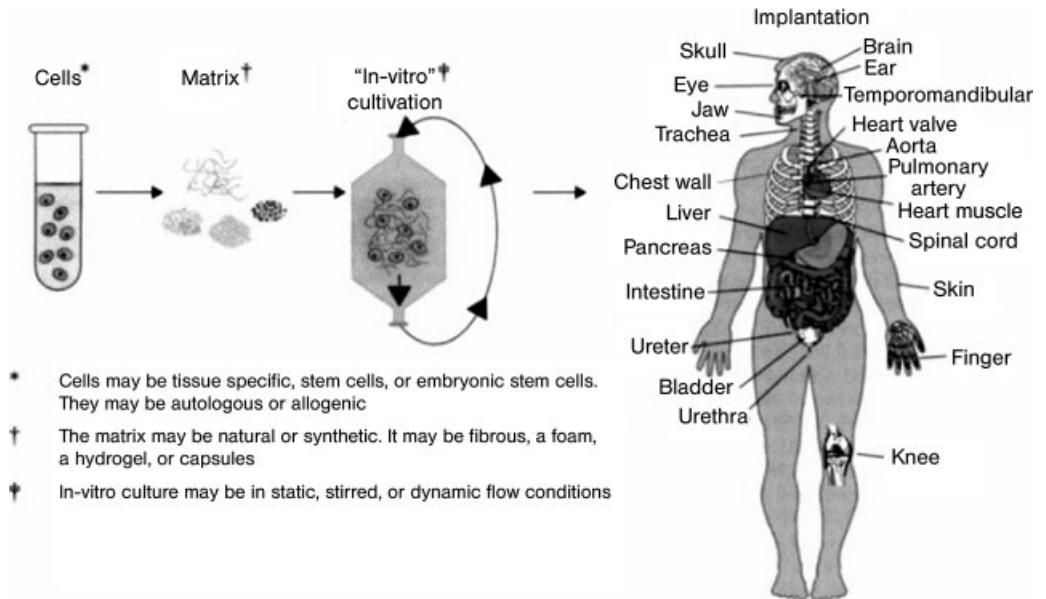


Fig. 1.1. Scheme showing the process of tissue engineering. (Adapted from Ref. [7] with permission from Elsevier.)

tion and a fourth, the most extensively investigated approach, uses biomaterials in combination with cells (with and without biological factors). Within the cell–biomaterial combination approach two different methods are used, a closed system and an open system. In a closed system cells are protected from the immune response of the body by encapsulating in a semi-permeable membrane that can allow nutrient and waste transport to keep them functional. In an open system, the cell–biomaterial construct is developed *in vitro* and is directly implanted in the body. In the open system, biomaterials are used to develop supporting matrices or scaffolds for cell implantation. Bioresorbable polymers (both synthetic and natural polymers) are commonly used for fabricating scaffolds. Several fabrication techniques are used to develop porous 3D scaffolds from these biomaterials. The function of the scaffold is to guide the regeneration of new tissue and to provide appropriate structural support, i.e., to mimic the structure and functions of natural extracellular matrix (ECM). The exogenous cells delivered through the scaffolds along with endogenous cells are used to regenerate or remodel the damaged tissue. During this process the bioresorbable scaffold will degrade and disappear resulting in the formation of remodeled native tissue [8]. Research to date has identified different cell sources, including stem cells that, when combined with degradable, matrices can form 3D living structures. The technique has led to the development of many tissues in the laboratory scale such as bone, ligament, tendon, heart valves, blood vessels, myocardium, esophagus, and trachea. However, several engineering and biological challenges still remain for successful clinical translation of the labo-

ratory research to make tissue engineering a reliable route for organ/tissue regeneration. These include mimicking the complex structure and biology of the ECM using synthetic materials, controlling cell interactions using artificial scaffolds, vascularization of cell–scaffold constructs, development of efficient bioreactors for *in vitro* culture, storage and translation [10]. The present chapter reviews progress made in tissue engineering to overcome some of the engineering and biological challenges in developing ideal 3D synthetic scaffolds by harnessing nanotechnology and material science.

This chapter also overviews the importance of mimicking the structure and functions of the ECM when developing ideal scaffolds for tissue engineering and the recent developments and advantages of nanotechnology assisted techniques to fabricate scaffolds that closely mimic the ECM.

After the present section, which gives a brief introduction to tissue engineering, Section 1.3 lays out the importance of scaffolds in tissue engineering and the need for mimicking the structure and functions of the ECM. Section 1.4 reviews the important aspects of the structure and functions of the ECM that need to be mimicked to develop ideal scaffolds for tissue engineering. Section 1.5 includes in-depth examination of the applications of nanotechnology in developing ECM mimic nanostructured scaffolds for tissue engineering. Section 1.6 reviews some recent studies, demonstrating the advantages of nanostructured scaffolds for tissue engineering, and Section 1.7 overviews some of the current applications of nanostructured scaffolds for engineering different tissues.

### 1.3

#### The Importance of Scaffolds in Tissue Engineering

The importance of the extra-cellular matrix (ECM) in cellular assembly and tissue regeneration was demonstrated by the pioneering works of Mina Bissell along with others [11]. The cells in mammalian tissues are connected to the ECM which provide three-dimensionality, organize cell–cell communications and provide various biochemical and biophysical cues for cellular adhesion, migration, proliferation, differentiation and matrix deposition. Their studies have shown the significant differences in behavior of cells when grown in two-dimensional (2D) and 3D environments [11].

Even though 2D cell culture techniques have been extensively used by cell biologists to derive valuable information regarding cellular processes and cell behavior, in the light of recent studies it is evident that *in vivo* tissue response can be simulated only through 3D cell culture techniques [12]. Considering the complex biomechanical and biochemical interplay between cells and the ECM, it is apparent that tissue engineers will be unable to address the biological subtleties if the cells are grown on 2D biomaterials before implantation in the body.

The strategy of using bioresorbable porous synthetic scaffolds as artificial ECM was introduced by Langer and Vacanti in 1988 [13]. This seminal paper significantly influenced investigators throughout the world in the practical area of scaf-



fold based tissue engineering and has led to hundreds of research articles and patents to date.

A bioresorbable  $\alpha$ -hydroxyester was used as the candidate polymer in the first study by Langer's group for developing the scaffolds. The  $\alpha$ -hydroxyesters being aliphatic polyesters have the ability to undergo hydrolytic degradation *in vivo* and therefore could resorb and disappear once regeneration is complete. Studies that followed have shown that the properties of the biomaterial play a crucial role in the success of the tissue engineered construct. Since the dynamics of different tissues vary significantly, appropriate materials need to be carefully chosen to satisfy the properties required. This knowledge has led to the design and development of several bioresorbable polymeric biomaterials to fabricate scaffolds for engineering different types of tissues [14]. These include synthetic polymers such as  $\alpha$ -hydroxyesters, polyanhydrides, polyphosphazenes, polyphosphoesters and natural polymers such as collagen, gelatin, chitosan and hyaluronic acid [15, 16]. Among these, synthetic polymers are mostly preferred for developing tissue engineering scaffolds due to immunogenic problems and batch by batch variations associated with many of the natural polymers.

Apart from the properties of the materials, the 3D architecture of the scaffold is very important when attempting to mimic the structure and functions of the natural ECM. Several unique fabrication processes have been developed to form 3D porous structures from bioresorbable materials as scaffolds for tissue engineering [9, 17]. These 3D structures have been primarily designed to direct tissue growth by allowing cell attachment, proliferation and differentiation. Most of these fabrication processes have been designed based on a set of criteria that have been identified as crucial to promote cellular infiltration and tissue organization. Some of the basic requirements of scaffolds for tissue engineering, summarized by Agarwal and Ray [18], are that they should be:

- Biocompatible.
- Bioresorbable and hence capable of being remodeled.
- Degrade in tune with the tissue repair or regeneration process.
- Highly porous to allow cell infiltration.
- Highly porous and permeable to allow proper nutrient and gas diffusion.
- Have the appropriate pore sizes for the cell type used.
- Possess the appropriate mechanical properties to provide the correct micro-stress environment for cells.
- Have a surface conducive for cell attachment.
- Encourage the deposition of ECM by promoting cellular functions.
- Able to carry and present biomolecular signals for favorable cellular interactions.

Various studies have been performed so far, using macro- and micro-fabrication techniques, to form 3D scaffolds that could address the requirements listed above to develop ideal synthetic scaffolds with some success. The results of these studies have been extensively reviewed [17, 19–23]. Particulate leaching can be considered as one of the first techniques widely used to develop micro-porous matrices from

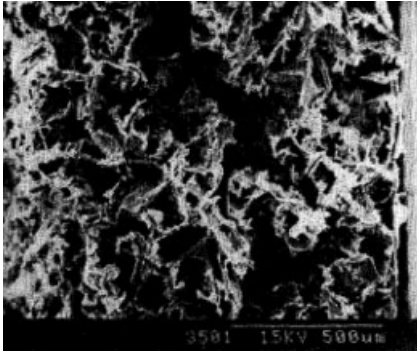


**Fig. 1.2.** Porous bioresorbable poly(L-lactic acid) foams developed by particulate leaching. (Adapted from Ref. [24] with permission from Elsevier.)

biodegradable polymers for tissue engineering applications (Fig. 1.2) [24–26]. The technique has several advantages such as ease of processing, ability to develop foams from wide range of polymers, and the ability to control the pore size by varying the size of the porogen. However, the porogen leaching process has some serious limitations to fabricate scaffolds for tissue engineering, such as the inability to completely remove the porogen from the porous matrix and to control the pore shape and maintain interconnectivity between pores. Consequently, several modifications to the particulate leaching method as well as new fabrication techniques were developed. Some of the newer processes include sintered microsphere process and rapid prototyping.

Sintered microsphere matrix fabrication technique of Laurencin was developed as a robust technique to fabricate 3D porous structures with reproducible porosities and interconnected pore structure [27, 28]. Sintered microsphere matrices are developed by heat sintering bioresorbable polymeric microspheres (Fig. 1.3)

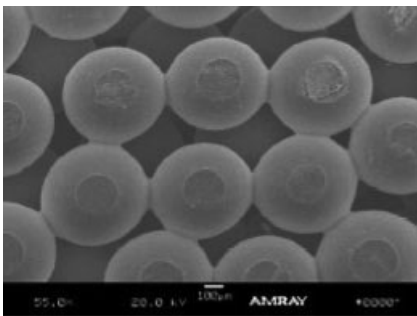


**Fig. 1.3.** SEM showing the 3D porous structure of a PLAGA scaffold formed by the sintered microsphere fabrication process. (Adapted from Ref. [29] with permission from Elsevier.)

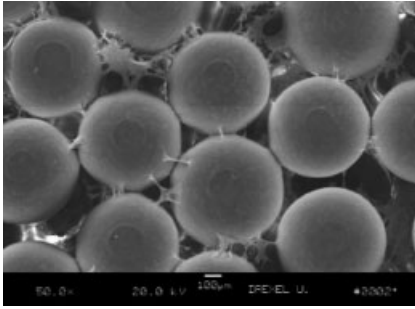


**Fig. 1.4.** SEM showing human osteoblast attachment and infiltration in porous PLAGA sintered microsphere matrix. (Adapted from Ref. [29] with permission from Elsevier.)

[27, 28]. Poly(lactide-*co*-glycolide)s (PLAGA) having different ratios of lactic acid (LA) and glycolic acid (GA) were used as the polymers to develop sintered matrices. Polymeric microspheres are prepared by the commonly used solvent evaporation technique [27, 28]. The sintered microsphere matrices demonstrated controllable pore size and interconnectivity depending on the size of the microspheres used to fabricate the matrices. Thus, the pore size of the scaffolds could be varied from 100 to 300  $\mu\text{m}$ , depending on the size of the microspheres used. The 3D porous sintered microsphere scaffolds were investigated as potential candidates for bone tissue engineering and showed appropriate mechanical properties for orthopedic applications. The osteoconductivity of the porous 3D matrices were evaluated using human osteoblast cells and showed good osteoblast attachment and infiltration (Fig. 1.4) [28, 29]. An *in vivo* evaluation demonstrated the efficacy of the bioresorbable sintered microsphere matrix in healing a critical segmental bone defect in a rabbit model [30]. Figure 1.5 shows the X-ray of a bone defect site implanted with a sintered microsphere matrix after eight weeks of implantation. The study showed the formation of new bone throughout the entire structure of the implant indicating significant bone regeneration at the defect site. The fabrication process led to the development of porous scaffolds having high interconnectivity and good mechanical integrity, with the percentage pore volume of the matrices equal to  $\sim 40\%$ .

Recently, different types of computer-assisted design and manufacturing processes (CAD/CAM) were investigated as potential methods to develop scaffolds

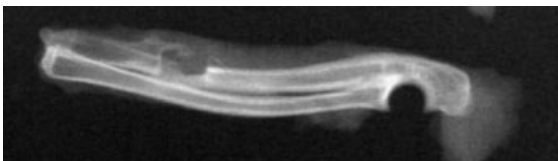


**Fig. 1.5.** Radiograph of a defect site implanted with sintered microsphere matrix, bone marrow cells and BMP-7 after 8 weeks of implantation, showing significant bone regeneration.

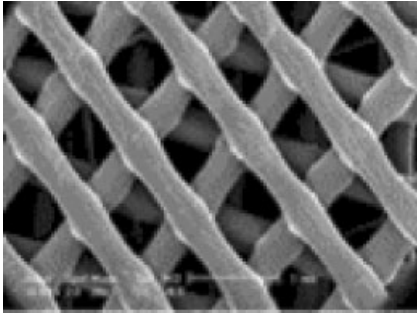


**Fig. 1.6.** SEM showing the porous structure of a polymer scaffold developed by FDM. (Adapted from Ref. [23] with permission from Elsevier.)

having controllable pore size, shape and porosity. One of the first developed computer assisted techniques for scaffold fabrication was solid free form fabrication or 3D printing. In this process a complex 3D structure is first designed using CAD software. An inkjet printing of a binder on appropriate polymer powder layers is then used to fabricate the porous structure based on the computer model. Even though complex structures can be designed and fabricated using this automated process, the preciseness of the technology has various limitations imparted by the size of the polymer particle, size of the binder drop and the type of the nozzle tip [31]. Another rapid prototyping technique extensively investigated for developing porous scaffolds for tissue engineering is fused deposition model (FDM) developed by Hutmacher [22, 23]. The FDM can be used to develop 3D structures from a CAD or an image source such as computer tomography (CT) or magnetic resonance imaging (MRI) of the object. The computer design is then imported into software that mathematically slices the model into different horizontal layers. The FDM extrusion head and the platform are then synchronized to deposit fused polymeric melt based on the computer model, one layer at a time. Figure 1.6 shows a porous 3D structure developed from a bioresorbable polymer poly(caprolactone) (PCL). The FDM process has several advantages, such as the ability to precisely control the pore size, pore morphology and pore interconnectivity. The process enables also the development of multiple-layer designs and different localized pore morphologies needed for multiple tissue types or interfaces. Another advantage of FDM is the good mechanical properties and structural integrity of the scaffolds due to the use of mechanically stable designs and proper fusion between individual material layers. However, the fabrication process has some limitations that make it less than an optimal method for developing porous matrices for tissue engineering applications. These include the limitations associated with the processing technique such as the requirement of temperature, the need for materials that are appropriate for fused deposition, the necessity of supporting structures to construct complex structures, and variable pore openings observed along different axis [32].

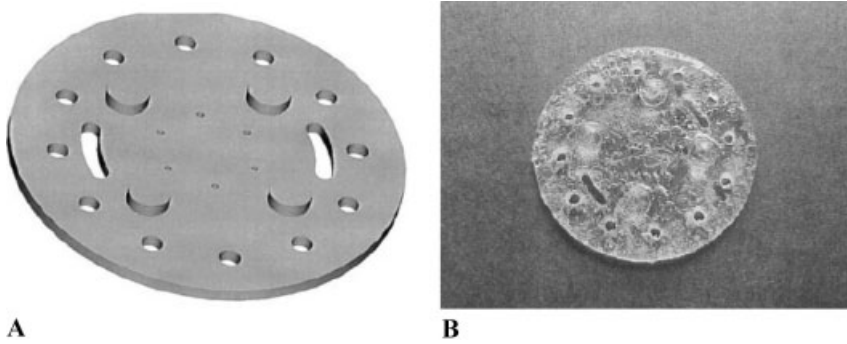


**Fig. 1.7.** (A) Pro/Engineer rendered CAD image of prototype PPF construct. The series of slots and projections test the interslice PPF registration ( $50 \times 4$  mm). (B) Three-dimensional structure developed from CAD model data from PPF. (Adapted from Ref. [33].)

Several stereolithographic techniques were investigated to develop porous 3D matrices from polymers to overcome the problems associated with temperature-assisted fabrication methods. Stereolithographic techniques have been extensively used to develop 3D structures from photopolymerizable polymer solutions such as poly(propylene fumarate) (PPF) in presence of photoinitiators (Fig. 1.7A and B) [33]. Preliminary studies showed the feasibility of developing structures having controlled pore sizes ( $50\text{--}300\ \mu\text{m}$ ) and different layer thicknesses using a highly controlled laser light source.

Most of the techniques described above are used to develop 3D structures from synthetic hydrophobic polymers. However, a wide range of techniques using hydrophilic polymers have also been investigated to develop novel structures as cell delivery vehicles. Hydrophilic polymers are good candidates to develop tissue engineering scaffolds due to their high water content and ability to mimic the properties of various tissues. One such technique is the use of photolithography to pattern hydrogel films with hydrophilic porous structures [34].

The fabrication techniques discussed so far have been developed to fabricate acellular scaffolds that are populated with appropriate cells after fabrication for tissue engineering applications. However, this process has the limitation of obtaining uniform cell distribution throughout the scaffold even with the use of bioreactors during *in vitro* culture. Therefore some studies have also focused to develop materials and fabrication processes to form cellular scaffolds. These studies have led to the development of different types of stimuli sensitive hydrophilic polymers that can be used to encapsulate cells under mild conditions to form cellular scaffolds [35, 36]. Cells can be uniformly distributed in the aqueous stimuli sensitive polymer solutions before the gelling process (Fig. 1.8) [37]. Attempts are currently underway to combine this process with the lithographic techniques to form cell incorporated 3D structures under very mild conditions.

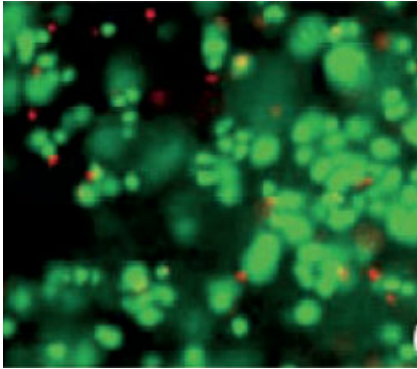


**Fig. 1.8.** Photomicrograph showing chondrocytes encapsulated within a hydrogel after 21 days in culture stained using Live dead stain (green shows live cells and red shows dead cells). (Adapted from Ref. [37] with permission from Elsevier.)

Another strategy recently developed to form structures with uniform distribution of cells throughout the scaffold is cell printing [38]. This approach combines rapid prototyping procedures with microencapsulation to print viable free form structures using bio-ink with custom-modified ink-jet printers. One advantage is the feasibility of placing quickly and precisely various cells layer by layer to develop multi-cell systems. However, the process is still in its infancy and further research is necessary with regards to developing appropriate bio-ink, optimizing the rheologic and surface properties of the inks, and designing printers optimized for these properties [39]. Another strategy is organ printing, which makes use of nature's ability to assemble many tissue forms such as blood vessels. The technology is based on the hypothesis that when cell aggregates are placed in close approximation they can assemble to form a disc or tube of tissue (Fig. 1.9) [40–42]. This process is also still in its infancy, has various scaling up limitations and further studies are needed to demonstrate the potential of the approach.

The previous discussion demonstrates the importance of the ECM in tissue repair and regeneration and serves as a brief overview of the attempts made to mimic the structure of the ECM using polymeric biomaterials and various macro/micro fabrication techniques to develop interconnected porous structures having porosities in the micron range. These studies have led to the design and synthesis of novel bioresorbable materials with unique chemistries, fabrication of 3D structures having different properties and demonstrated the feasibility of growing cells in appropriate 3D forms *in vitro* and *in vivo* with the help of these scaffolds. Figure 1.10(A and B) shows the feasibility of developing an artificial ear on the back of a mouse using a bioresorbable PCL scaffold having the macroscopic shape of an ear seeded with chondrocytes [43].

Even though these materials and fabricated 3D structures showed the feasibility of 3D organization of cells into tissue, they are far from being ideal for develop-

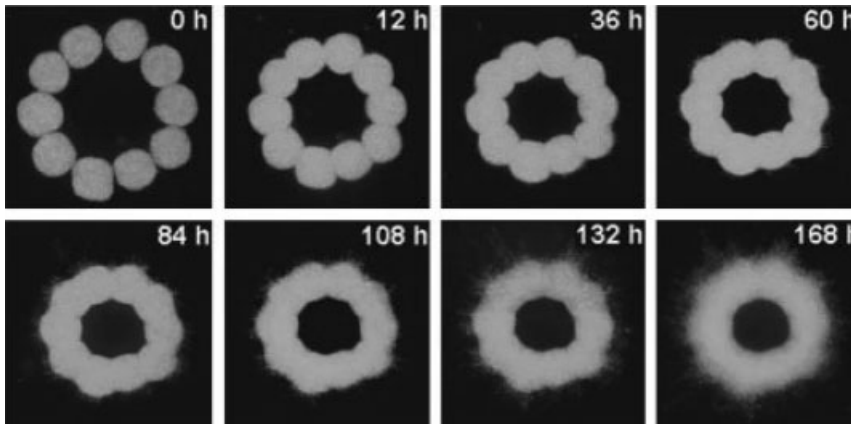


**Fig. 1.9.** Time evolution of the fusion of aggregates of Chinese Hamster Ovary (CHO) cells encapsulated in collagen gel. The nuclei of the cells are fluorescently labeled. Cell

before fusion (top left) and the final disc-like configuration after fusion (bottom right). (Adapted from Ref. [37] with permission from the National Academy of Sciences, USA.)

ing fully functional tissues and organs *in vivo* in a reproducible way under clinical setting.

So far, most of the biomaterial design has focused on developing materials that are capable of degrading at a rate that matches tissue regeneration, have the ability to degrade into non-toxic degradation products and can support the adhesion and proliferation of cells without placing much emphasis on the bioactivity of the materials. Conversely, most fabrication techniques are focused on developing scaffolds with macroscale properties, such as the ability to provide sufficient transport prop-

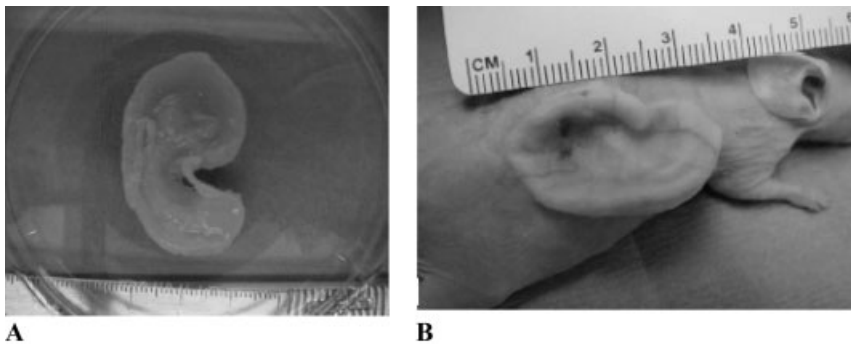


**Fig. 1.10.** (A) Photomicrograph of tissue engineered ear construct developed from chondrocyte-PCL composite after 8 weeks *in vitro* culture. (B) The regenerated ear on the back of athymic mice. (Adapted from Ref. [43] with permission from Elsevier.)

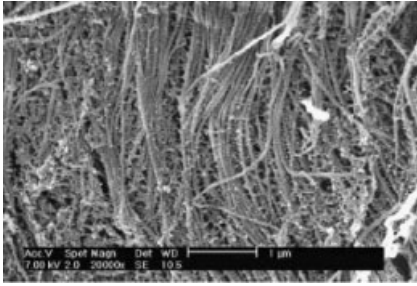


**Fig. 1.11.** High magnification picture of collagen fibrils in human aortic valve. Individual fibrils are separated by a narrow space crossed by interfibrillar bridges formed by small proteoglycans interconnecting adjoining fibrils. (Adapted from Ref. [44] with permission from Elsevier.)

erties (interconnected microporous structure), and adequate mechanical properties (to match the properties of the tissue to be replaced or repaired).

However, the organization of the cells, and hence the properties of the tissue, are highly dependent on the structure of the ECM, which has a hierarchical structure with nano-sized features. Figure 1.11 shows the ultrastructure of collagen fibrils in human aortic valves, illustrating the nanoscale topographic features of the native tissue [44]. Thus, successful fabrication of a fully functional tissue is a far more complex and involved process that requires the creation of an appropriate environment at both a micro- and nano-scale level to allow for cell viability and function along with macroscopic properties [45]. In fact, just as important as these structural features are the biological principles that govern cell–cell and cell–matrix interactions. These interactions form the basis of cellular performance and appropriate tissue organization and are controlled by various biochemical cues present in the natural ECM. The recreation of this process requires the incorporation of various bioactive molecules in synthetic porous scaffolds with molecular precision to mimic the functions of the ECM. Recently, a paradigm shift has been observed from developing macro/micro-structured scaffolds to nanostructured bioactive scaffolds in an attempt to improve tissue design and reconstruction in reparative medicine [46, 47].

#### 1.4

##### Structure and Functions of Natural Extracellular Matrix

Since the ultimate goal of tissue engineering is to develop tissue substitutes that could temporarily mimic the structure and functions of damaged tissue to be replaced, it is crucial that the engineered substitutes mimic the natural tissue structurally and functionally for successful regeneration. Extensive research performed in different areas such as tissue and organ development during embryogenesis, the



normal tissue healing process, tissue structure and functions and development of various characterization techniques at the micro- and nano-scale levels have significantly enhanced our ability to mimic native tissue. The human body is a very complex structure that is organized in a hierarchical way with body composed of systems, systems composed of organs, organs composed of tissues and tissues composed of cells, vasculature and extracellular matrix. In tissues, the ECM provides the structured environment with mechanical and biochemical cues that enable the cells to interact with each other and with the ECM to allow for control of growth, proliferation, differentiation and gene expression.

The ECM is composed of a physical and chemical crosslinked network of fibrous proteins and hydrated proteoglycans with glycosaminoglycan side chains (collectively called the physical signals) in which other small molecules (such as growth factors, chemokines and cytokines) and ions are bound. Figure 1.12 shows the ultrastructural features of an ECM with a condensed basement membrane and the stromal tissue [48]. The ECM proteins are mainly composed of more than 20 different types of collagens as well as elastin, fibrillin, fibronectin, and laminin [49]. In the natural environment these macromolecular ECM components are secreted by the cells and then modified and assembled to form the matrix during the tissue development and repair process. Among the ECM proteins, type I collagen is mainly involved in the formation of the fibrillar and microfibrillar structure of the ECM. Type I collagen molecules ( $\sim 300$  nm long and  $\sim 1.5$  nm in diameter) are packed to form collagen fibrils. Each collagen fibril displays a characteristic

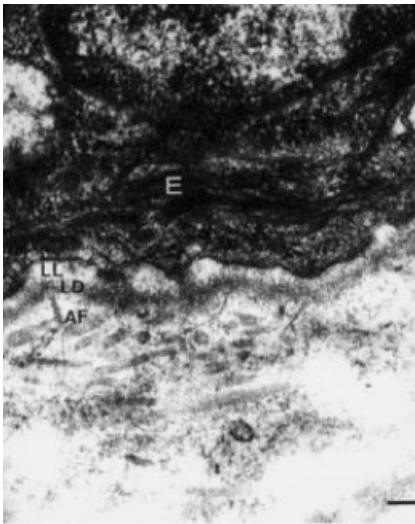


**Fig. 1.12.** Ultrastructure of ECM matrix. Adjacent to an epithelial cell (E) is the basement membrane with its amina lucida (LL) and lamina densa (LD). The interstitial

matrix contains collagen fibrils and is close to the basement membrane anchoring fibrils (AF), composed of type VII collagen fibrils. (Adapted from Ref. [48].)

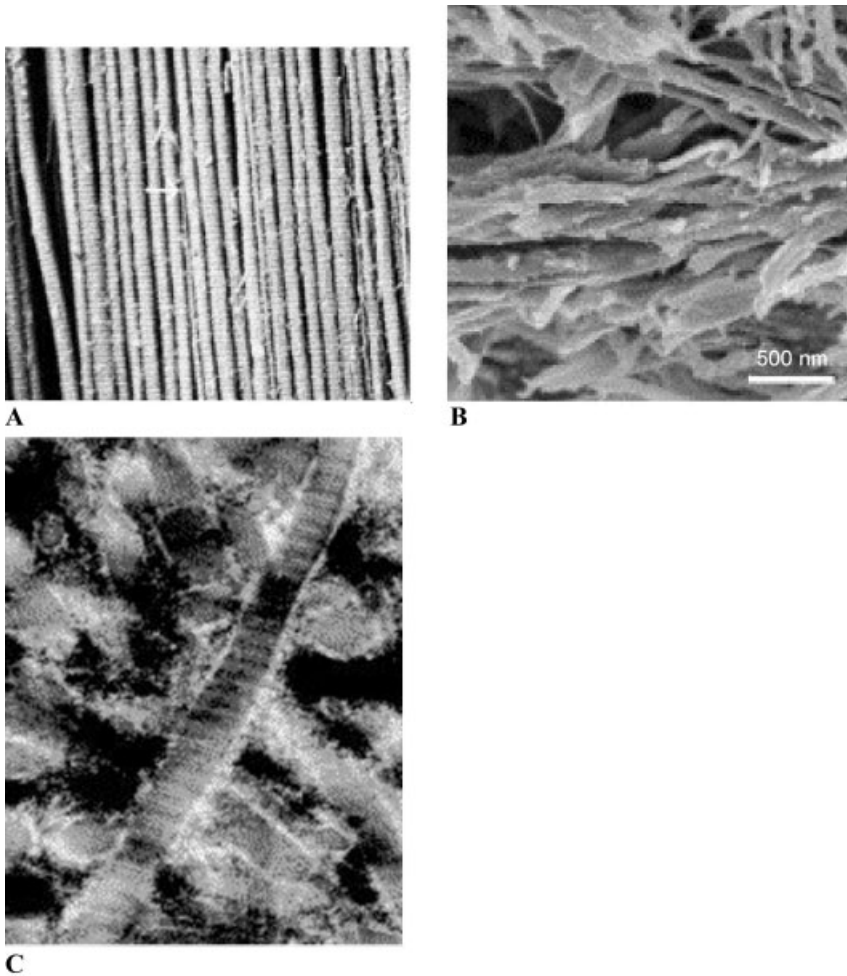


**Fig. 1.13.** Structure and orientation of collagen fibrils of various tissues. (A) Mature rat ligament-collagen fibrils are primarily aligned along the long axis of the ligament. (Adapted from Ref. [51] with permission from

Elsevier.) (B) Mineralized fibrils in trabecular bone without the non-fibrillar matrix. (Adapted from Ref. [52] with permission from Elsevier.) (C) Articular cartilage. (Adapted from Ref. [53] with permission from Elsevier.)

~67 nm D-repeat with uniform or multi-model diameter distribution varying from ~25 to 500 nm and several micrometers in length, depending on the nature of the tissue. All of these molecules are arranged in a unique tissue specific 3D architecture [50]. Figure 1.13 shows the different arrangement patterns of collagen fibrils as observed in three different types of tissues (A: ligament; B: bone; and C: articular cartilage) [51–53]. Fibrils show varied orientation in different tissue types that give the appropriate physical and mechanical properties to the tissue. Collagen fi-

brils are further bundled together to form collagen fibers. The hierarchical structure of the ECM has length scales, varying from a few nanometer (nm) to millimeter (mm) that control the cellular functions and corresponding tissue properties. The fact that cells are highly sensitive to the environmental structural features has been demonstrated using *in vitro* cell culture studies on nanopatterned surfaces fabricated by electron beam lithographic techniques. These studies revealed that the cells are sensitive to nanoscale dimensions and could react to objects as small as 5 nm [54]. This can be attributed to the structural details ECM presents to the cells *in vivo*. Thus, the 3D hierarchical structure of the ECM significantly affects cellular behavior and hence tissue functions through topographical cues.

However, the function of the ECM is not just to provide an inert support for cellular adhesion. Almost all of the molecules present in ECM have both structural and functional roles. The ECM serves mainly to organize cells in space to give them form, provide them with environmental signals, to direct site-specific cellular regulation, and separate one tissue space from another. Thus the orientation and position of cells with respect to each other is dictated by the ECM and the orientation varies with different tissues. This is achieved by providing chemical cues such as insoluble signals or factors of the ECM which could interact with the soluble signals of cells along with the structural features to promote adherence, migration, division and differentiation of cells. In a natural tissue the ultimate decision of cellular processes such as adhesion, proliferation, differentiation, migration and matrix production takes place as a result of this continuous cross-talk between cells and ECM effectors [55]. Figure 1.14 shows a schematic representation of various interactions taking place between cells and ECM during tissue organization and function [50].

At least three mechanisms have been identified through which the ECM can regulate cell behavior. The first mechanism is through the composition of the ECM such as various proteins and glycosaminoglycans, which is highly tissue and cell specific. The second mechanism is through synergistic interactions between growth factors and matrix molecules. The growth factors are found to bind with the ECM through the glycosaminoglycan side chains or protein cores and this increases the stability of growth factors and creates the appropriate cellular environment or niche to regulate cell proliferation and differentiation. The third mechanism is through the cell surface receptors or integrins that mediate cell adhesion to extracellular matrix components [56]. The integrin–ECM ligand interactions play a major role in anchoring cells to the ECM. An integrin is  $\sim 280$  Å long and consists of one  $\alpha$  (150–180 kDa) and one  $\beta$  ( $\sim 90$  kDa) subunit, both of which are type I membrane proteins [57]. About 18 $\alpha$  and 8 $\beta$  subunits that can form 24 different heterodimers have been identified so far and the ligand specificity of the integrin is determined by the specific  $\alpha\beta$  subunit combination [58]. Integrin-mediated cell adhesion to the ECM occurs through a cascade of processes. First cell attachment occurs where cell attach to the surface with ligand binding through integrins to withstand gentle shear forces followed by cell spreading. Next organization of actin into microfilament bundles or stress fibers occurs. In the last stage the formation of focal adhesion occurs, which links the ECM to molecules of the actin

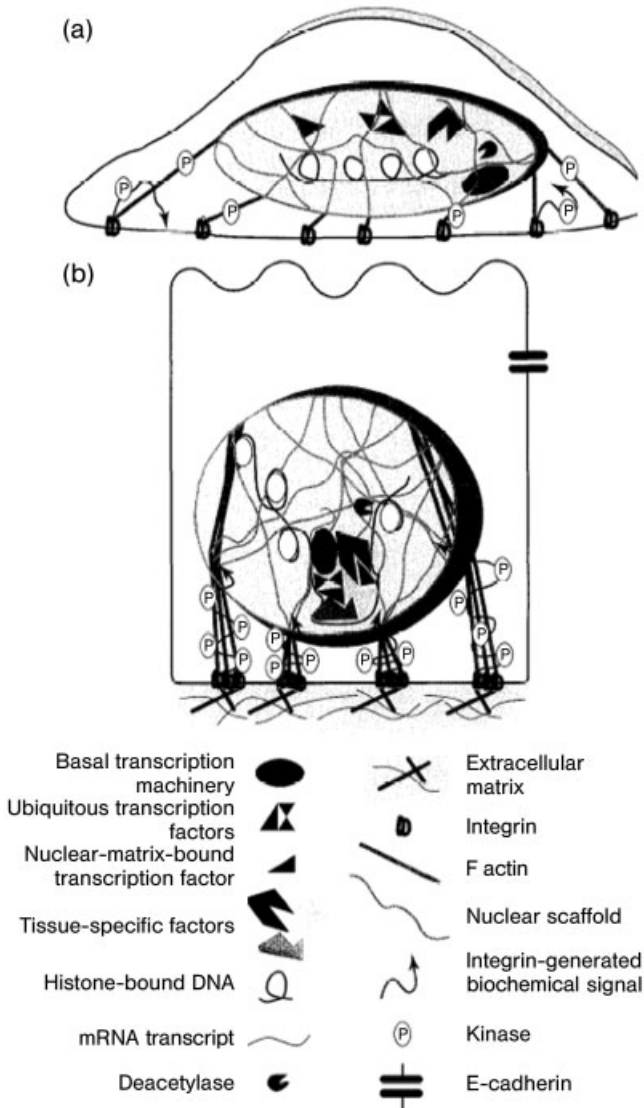


**Fig. 1.14.** Scheme showing the various interactions between cells and the ECM during tissue organization and repair. (a) Flattened cells in the absence of ECM. Due to incompatible cytoskeletal organization no signals originating from integrin receptors can be properly propagated. (b) In the presence of ECM, binding of ECM components to integrin receptors induces integrin clustering and generates biochemical signals. Cytoskeleton filaments intimately associated with the cytoplasmic domains of the integrins are

modified and reorganized to facilitate interaction of the incoming signals with downstream mediators. This reorganized cytoskeleton can evoke further architectural changes via its association with the nuclear matrix. The subsequent nuclear reorganization brings together incoming signaling molecules, transcriptional activators, histone deacetylases, and the basal transcriptional machinery to promote the assembly of a functional transcriptional complex on the gene. (Adapted from Ref. [50] with permission from Elsevier.)

cytoskeleton. The focal adhesion is mainly composed of clustered integrins and other transmembrane molecules. In this process, the integrins have two-fold activities, anchoring the cells to the ECM and signal transduction through the cell membrane [59]. This allows for continuous cross-talk between ECM and cells which is highly crucial for proper tissue functioning [60].

Several studies have been performed to characterize and analyze the largest and most stable types of contacts between the ECM and cells. These include focal adhesions, focal contacts or adhesion plaques, fibrillar adhesions and hemidesmosomes (Table 1.1) [61]. Several morphological criteria have been used to characterize the

**Tab. 1.1.** Characterization of cell–matrix contact structures.  
(Reprinted from Ref. [61] with permission from Birkhäuser Verlag, Basel.)

Contact type	Dimensions	IRM Image separation from substratum	Characteristic associations
Close contact	(Associated with lamellipodium)	Grey in IRM 30–50 nm from substratum	Submembranous densities parallel to F-actin meshwork at plasma membrane
Filopodium	20–200 $\mu\text{m}$ long 0.2–0.5 $\mu\text{m}$ diameter	grey in IRM	core bundle of F-actin, integrins, syndecans
Focal contact/focal adhesion/	0.25 $\mu\text{m}$ wide 1.5 $\mu\text{m}$ long	Black in IRM 10–15 nm from substratum	At termini of microfilaments, contain integrins, syndecan-4, low tensin content
Hemidesmosome	Plaque ca. 0.15 $\mu\text{m}$ by 0.04 $\mu\text{m}$	–	Connect to intermediate filaments, contain $\alpha 6\beta 4$ integrin, plectin, BP230
Matrix assembly sites/fibronexus/fibrillar adhesions	ca. 3–5 $\mu\text{m}$ long	White in IRM 100 nm from substratum	ECM cables align parallel with microfilaments, contain $\alpha 5\beta 1$ and tensin
Podosomes	0.2–0.4 $\mu\text{m}$ diameter	Dark in IRM	Core bundle of actin perpendicular to substratum, in macrophages contain $\beta 2$ integrins, fimbrin
Spike or microspike	2–10 $\mu\text{m}$ long 0.2–0.5 $\mu\text{m}$ diameter	Grey in IRM	Core bundle of F-actin, contain fascin

contact type and size of the contact including evaluation of phase-dark structures detected by phase contrast or interference reflexion microscopy (IRM), electron-dense and organized structures detected by transmission electron microscopy and cell surface topography detected by scanning electron microscopy (SEM) [61]. Table 1.1 shows that even though the size of a cell is  $\sim 10\ \mu\text{m}$ , the activities leading to cell adhesion and the following processes take place mainly at the nanometer level.

Detailed studies on integrin-mediated cell adhesion to the ECM clearly point to the importance of ECM ligands on cell behavior. In addition to the structure and size of the ECM–cell contact points, several studies have been performed to elucidate the biological molecules involved in the interactions. The results of these studies have significantly influenced tissue engineers and have become a great tool in their attempts to recreate a natural cellular environment using synthetic scaffolds. Many of the identified biological molecules have been utilized to decorate synthetic scaffolds to form ligand-functionalized matrices to increase their bioactivity. Various surface modifications or one-dimensional nanotechnological modifications are used to develop ligand functionalized scaffolds [62].

Several cell recognition motifs such as fibronectin, vitronectin, collagen and laminin present in the natural ECM have been used to modify the surface of biomaterial scaffolds to increase their bioactivity [63–65]. Even though preliminary studies show significant promise in developing biomimetic scaffolds, the modification of matrices using bioactive proteins has several limitations. Proteins are bioactive molecules and can elicit an immunological response as they are mostly isolated from different sources and also possess the risk of associated infections. Another serious limitation associated with protein surface modification is that the surface topography and chemistry of the synthetic matrix could influence the orientation and conformation of the attached or adsorbed protein, thereby affecting its functionality. Owing to the low stability of the proteins, the immobilization process as well as subsequent storage could also affect its patency.

The breakthrough research that revolutionized the biomimetic surface modification approach towards biomaterials development is the finding that low molecular peptides from ECM proteins such as the tetrapeptide “arginine-glycine-aspartate-serine” (GRGDS) sequence could significantly modulate cellular behavior [66, 67]. Following this, several RGD-containing sequences were found in other ECM proteins and several other short linear adhesive sequence motifs have also been identified as active molecules to promote cell adhesion, proliferation and migration. Several studies have been performed to elucidate the mechanisms by which these sequences could interact with cells. The tetrapeptide and tripeptide sequences such as arginine-glycine-aspartate can bind to members of the integrin family of the transmembrane receptors, thereby activating a series of signaling events within the bound cells favorably affecting their functions [67–72]. The RGD sequence has been quickly identified as a potential candidate to develop biomimetic scaffolds and extensive research has followed. Because the RGD sequence is present in multiple ECM proteins such as fibronectin, laminin, collagen and vitronectin, a broad range of cell types could respond to this peptide sequence. Furthermore, small peptide sequences are highly stable compared to the corresponding proteins [73], they

are cost effective [74], can be packed densely on surfaces due to their small size, and can selectively address one type of cell adhesion receptors for controlled cell adhesion during multicellular tissue development [68].

Various techniques have been attempted to immobilize these biological motifs on synthetic biomaterial surfaces to increase their bioactivity [75]. Stable immobilization of these ligands to the surface is crucial for proper functioning, as the peptide sequence should be able to withstand the cells contractile forces during initial attachment and prevent internalization by cells [76, 77]. The most extensively investigated approach to covalently immobilize the RGD sequence on surfaces is by using active functional groups such as hydroxyl, carboxyl or amino groups on the RGD and polymer surfaces, involving carbodiimide chemistry [75]. For polymers devoid of these functional groups, several approaches were attempted, such as coating the surface with a polymer having such active groups such as polylysine [75, 78] and coating with RGD modified pluronics via hydrophobic interactions [75, 79]. Another approach to incorporate active groups is by copolymerizing with a monomer having active groups such as acrylic acid [75, 80] or lysine in the case of poly(lactic acid-co-lysine) [75, 81]. Another extensively investigated approach is chemical or physical surface modification of biomaterials such as alkaline hydrolysis [75, 82], oxidation [75, 83], reduction [75, 84], etching [75, 85] or plasma deposition [75, 86].

Even though immobilization via carbodiimide chemistry is a versatile approach to covalently immobilize RGDs on various surfaces, it is not a highly selective process as RGD has two reactive groups (amino and carboxyl) and therefore can lead to various un-wanted side reactions. A recent study has demonstrated the feasibility of incorporating RGDs on the surface of polymers without the various functionalization routes described above. The approach is called chemoselective ligation. Under mild conditions, selected pairs of functional groups are used to form stable bonds with RGD without interfering with other functional groups [87]. Thus thiol-functionalized surfaces can be modified using bromoacetyl containing RGD cyclopeptides [88] or a thiol-containing RGD can be linked to maleinimide-functionalized surfaces under mild conditions [89]. Benzophenone or aromatic azide functionalized RGD has been developed as a versatile technique to immobilize RGDs on the surface [90–92] by streptavidin–biotin capture [93].

In addition to direct linking, attachment of RGD to surfaces using spacers significantly increases the activity of immobilized RGDs. This increased activity has been attributed to the ability of RGD peptide binding site to reach the hollow globular head of an integrin. Several studies have confirmed a spacer length of 35–40 Å is optimal for maximum activity [75, 94]. However, recent studies on the crystal structure of the ligand bound extracellular domain of the  $\alpha V\beta 3$  integrin show the RGD binding site on the surface region of the head of the  $\alpha V\beta 3$  integrin, suggesting that it is only a few angstroms deep [71]. This indicates that spacers may not be needed for the ligand–integrin interaction. The experimental improvement in activity of RGDs with spacers found in some studies has been attributed to the spacer presumably contributing to the surface roughness of the substrates [75].

All of these approaches have shown the feasibility of covalent attachment of

RGDs on the surface of polymeric biomaterials and several studies were also performed to demonstrate the bioactivity of RGD immobilized surfaces. Numerous polymers, various immobilization techniques, different RGD peptides and different cell types were used to investigate the biological activity of biomimetic surfaces. The cell behavior towards RGD modified surfaces has been found to depend on various parameters such as the structure and conformation of RGD as well as the density and arrangement of RGD on the surface. Some of the RGD peptides investigated include RGD, RGDS, GRGD, YRGDS, YRGDG, YGRGD, GRGDSP, GRGDSG, GRGDSY, GRGDSPK, CGRGDSY, GCGYGRGDSPG, and RGDSPASSKP peptides [75]. One study systematically investigated the cell attachment activity of different types of RGDs including RGD, RGDS (from fibronectin), RGDV (from vitronectin) and RGDT (from collagen) immobilized on polymeric surfaces. The study demonstrated that tetrapeptides show distinct increases in cell attachment compared to tripeptides indicating that peptides with higher integrin affinity bear higher cell attachment [80]. No significant differences in cell attachment between the tetrapeptides were observed [80]. Another study showed that cyclic RGD peptides on surfaces can show higher activity than linear molecules, which has been attributed to their higher stability and increased  $\alpha\beta3$  binding of cyclic peptide compared with linear molecules [95].

Another unique application of RGD modified biomaterials is the development of materials that can promote selective adhesion of various cell types. Since it has been found that each cell type has its own typical pattern of different integrins, RGD peptides could be used to promote selective cell adhesion on a surface by modifying the surface with an appropriate RGD [69]. Some *in vitro* studies have demonstrated the feasibility of integrin specificity of RGD leading to selective cell adhesion on RGD modified surfaces [69]. The study showed that fibroblasts rather than endothelial cells preferably adhered to a RGDSPASSKP (which is selective to  $\alpha5\beta1$ ) modified surface [96]. Similarly, enhanced fibroblast attachment was observed to an  $\alpha5\beta1$  integrin selective GRGDSP peptide functionalized surface where as  $\alpha5\beta3$  selective cyclic G\*PenGRGDSPC\*A supported higher smooth muscle cell and endothelial cell densities [97]. However, no data is currently available to show if such modification holds for more complex *in vivo* environments since cells could express more than one type of integrin and also because the integrin expression pattern of a cell is a highly dynamic phenomenon.

The surface density of RGD on the material also has a profound effect on the number of cells attached as well as cell spreading, cell survival, focal contact formation and to some extent proliferation. Studies have shown a sigmoidal increase in cell attachment with RGD concentration on the surface, indicating a critical minimum density for cell response [94]. Thus Neff et al. demonstrated that maximum proliferation of fibroblast occurred on surfaces with intermediate surface concentration ( $\sim 1.33 \text{ pmol cm}^{-2}$ ) [79]. Another study by Massia and Hubbell using RGD functionalized glycophasse glass surface has shown that a minimal amount, as low as  $1 \text{ fmol RGD peptide cm}^{-2}$ , is sufficient for cell spreading on the surface and as low as  $10 \text{ fmol cm}^{-2}$  sufficient for formation of focal contacts and stress fibers [98].



However, a higher RGD peptide concentration requirement has been reported for polymers and has been attributed to the entropic penalty that results from attachment of a peptide to flexible polymer chain compared to a rigid glass surface as well as the inefficient transmission of forces through polymer surfaces [75, 99]. Studies have shown that in addition to surface concentration, the mode of presentation of ligands also could affect integrin behavior [100]. One study by Maheshwari et al. evaluated surfaces with controlled overall peptide density and controlled nanoscale spatial ligand distribution with an overall RGD distribution of 0.15–20.50 nmol cm<sup>-2</sup> [101]. The results demonstrated that a significantly higher fraction of fibroblasts showed higher shear stress resistance and exhibited well-formed stress fibers and focal contacts when the ligand was presented in a clustered versus a random individual format. The use of a higher affinity peptide GRGDSPK afforded a lower RGD density of 0.06–0.88 nmol, showing that activity of the RGD is also very important [102].

Nanoscale RGD clustering on the surface of biomaterials seems to be a promising approach to elicit favorable cell responses with minimal amounts of RGD peptides. Studies are ongoing to determine the technique that could be used to create nanoscale clustering on the surface as well as to determine which arrangement elicits a particular cell response.

Thus the foremost challenge in developing a tissue engineered construct is the development of a resorbable synthetic microenvironment that could closely mimic the complex hierarchical micro-nano architecture of the ECM along with the molecular level spatial organization of biological cues found in native tissue *in vivo*.

## 1.5

### Applications of Nanotechnology in Developing Scaffolds for Tissue Engineering

Nanotechnology has been defined as “research and technology development at the atomic, molecular and macromolecular levels in the length scales of approximately 1–100 nm range, to provide a fundamental understanding of phenomena and materials at the nanoscale and to create and use structures, devices and systems that have novel properties and functions because of their small and/or intermediate size” [103]. Nanotechnology has emerged as an exciting field that deals with both the design and fabrication of structures with molecular precision. Nanotechnology enables the control and manipulation of individual constituent molecules/atoms to have them arranged to form the bulk macroscopic substrate. The uniqueness of the nanotechnological approach is that it considers spatial and temporal scales at the same time, thereby forming an excellent technique to develop hierarchical structures. The biological milieu that tissue engineers attempt to mimic using synthetic materials and techniques is a highly complex system with spatial and temporal levels of organization that span several orders of magnitude, with different levels nested within higher order levels (nm to cm scale). To study and mimic this complex system, highly sophisticated technology is required. For instance, the

visualization and characterization of these biological structures, processes, and their manipulation require sophisticated imaging and quantitative techniques with spatial and temporal control at or below the molecular level.

Recent developments in nanotechnology have revolutionized the visualization and characterization of biological processes in various ways. The capability of imaging living cells after implantation is very crucial in studying cell behavior and processes *in vivo*. The recent developments in nanotechnology assisted fluorescent probes such as quantum dots (QD) have significantly improved our capability of *in vivo* imaging. QDs are nanocrystals or nanoparticles with size ranging from 1 to 10 nm with unique photophysical and photochemical properties not available with conventional organic fluorophores [104].

Similarly, the scanning probe microscopic techniques (SPM) provide a great tool to investigate atomic and molecular level biological phenomena even though its potential in biology is yet to be realized. One of the most extensively investigated SPM techniques for tissue engineering application is atomic force microscopy (AFM). AFM has provided various strategies to investigate the interactions of living cells with the ECM [105]. AFM has also enabled the visualization of nano-scale biomolecules and significantly contributed to the in-depth understanding of their structure and role in biological process [106].

The developments in current nanoscale fabrication techniques have also significantly increased our understanding of nanoscale features on cellular behavior and tissue organization. Several nanoprinting/etching/electron beam lithographic techniques have been developed to form substrates with large areas of controlled nanoscale features. *In vitro* studies using these substrates confirmed the importance of nanoscale topography of scaffolds for developing tissue *in vitro* [107–110]. One study examined the interaction of fibroblasts with nanoscale islands having heights varying from 10 to 95 nm on polymer films. The fibroblasts underwent rapid organization of cytoskeleton and improved adhesion during initial reaction to the islands with concomitant cell spreading. The lamellae of the cells on the islands also showed many filopodia showing better interaction with the islands. Another study by Dalby et al., using nano- and micro-patterned surfaces has demonstrated the importance of nanoscale features in modulating human mesenchymal bone marrow stromal cell (HBMSC) adhesion [111]. HBMSCs were found to be well-spread and attained normal morphologies on polymer thin films similar to the morphology cells attained on flat topographies. However, the cells on nanofeatured surfaces were found to respond to the nanofeatures. This included cells conforming to the shape of the nanosized pits (Fig. 1.15A – 310 nm deep and 30  $\mu$ m wide), filopodia production, contact guidance and production of endogenous extracellular matrix. On nanometer depth grooves, the cells were found to be highly aligned along the groove direction showing pronounced contact guidance (Fig. 1.15B – 500 nm deep and 5  $\mu$ m wide). The study demonstrated that the nanoscale features of the substrates could elicit significant control over cell adhesion, cytoskeletal organization, cell-growth, and production of the osteoblastic markers osteocalcin and osteopontin [111].

To recreate structures having features at the nanoscale level, novel nanotech-

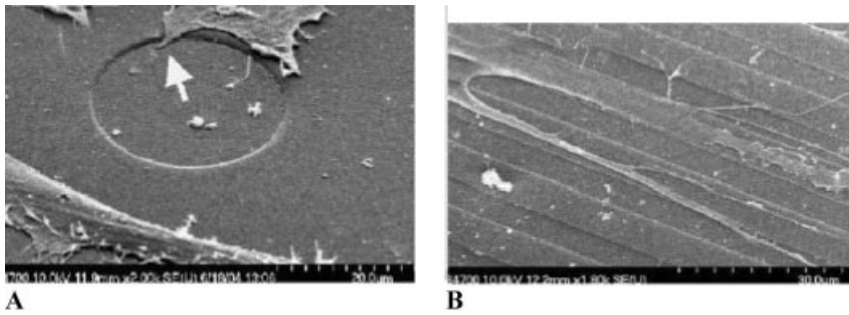


**Fig. 1.15.** Scanning electron micrographs of HBMSCs cultured on polymer surface with pits and grooves having nanometer depth. (A) Cells conforming to a groove edge of a nanopit (arrow). (B) Contact guidance of cells and their filopodia on the narrow grooves. (Adapted from Ref. [111] with permission from Elsevier.)

niques that enable the conversion of existing macromolecules into nanostructured forms or development of novel structures from atomic or molecular constituents with spatial organization of biofunctionality are needed. It is presumed that these developed nanostructures, due to their ability to interact with cells and tissues at a molecular (subcellular) level with a high degree of functional specificity, would allow a greater extent of integration than previously attainable. Thus, research in this direction is ongoing to develop structures that could temporarily mimic the structure and functions of the ECM as ideal scaffolds for tissue engineering using various nanofabrication processes.

Nanofabrication techniques have shown the feasibility to develop nanostructured scaffolds that better mimic the structure of the ECM compared to the structures developed by macro/micro fabrication techniques. Two different approaches are currently under investigation to develop synthetic nanostructured scaffolds that could resemble the structure of nanoscale collagen fibrils of the ECM as scaffolds for tissue engineering. The first approach can be considered as a “top-down approach” which uses synthetic polymeric materials to develop nanostructures using various nanofabrication processes. The second approach can be considered as a “bottom-up approach” and is based on short peptides or block polymers that can assemble into nanofibers by a self-assembly process.

### 1.5.1

#### **Polymeric Nanofiber Scaffolds**

As discussed earlier, collagen fibrils are the major building blocks of the natural ECM and they have diameters in the range 50–500 nm and orientation in different directions depending on the tissues. A logical method to develop scaffolds for tissue engineering is to mimic the structure of collagen fibrils, i.e., by using synthetic polymeric nanofiber matrices. Developments in nanofabrication techniques have

enabled the fabrication of synthetic nanofiber matrices from a wide range of polymers. Polymeric nanofibers have been defined as fibers having diameters less than  $1\ \mu\text{m}$  and are developed from synthetic and natural polymers [112]. Fibers with diameters ranging from 1–1000 nm and a very high surface area can be developed by the nanofabrication processes. Thus a nanofiber with a diameter of 100 nm has a specific surface area of  $1000\ \text{m}^2\ \text{g}^{-1}$  [113]. Porous matrices developed using polymeric nanofibers have excellent structural and mechanical properties, high axial strength combined with extreme flexibility, high surface to volume ratio, high porosity ( $>70\%$ ), and variable pore sizes – all of these properties are highly beneficial for cell adhesion, migration and proliferation.

#### 1.5.1.1 Top-down Approaches in Developing Scaffolds for Nano-based Tissue Engineering

The top-down approach is considered as a classical approach used to size down macrostructures to smaller sizes using various fabrication techniques. Several top-down techniques have been developed to form polymeric nanofibers from preformed macromolecules such as electrospinning, phase separation and templating [112, 114, 115].

**Polymeric Nanofibers by Electrospinning** Electrospinning has developed into a promising, versatile and economical technique to produce nanostructured scaffolds for tissue engineering [112, 116]. Figure 1.16 shows the schematic of the electrospinning process. Briefly in an electrospinning process an electric field is applied to a pendant droplet of polymer solution at the tip of a needle or capillary attached to a syringe or pipette. The polymer solution feed to the needle/capillary is controlled using a syringe pump or allowed to flow under gravity. The electrode can be either inserted in the polymer solution or connected to the tip of the needle. When an electric potential is applied to the droplet, the droplet will be subjected to couple of mutually opposing forces. One set of forces (surface tension and viscoelastic forces) tend to retain the hemispherical shape of the droplet and another set

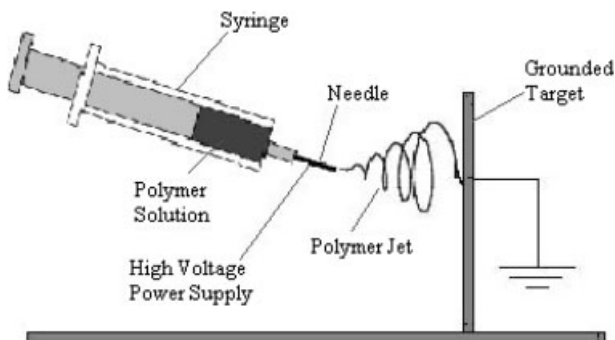


Fig. 1.16. Scheme of the electrospinning process.

of forces (due to the applied electric field) tend to deform the droplet to form a conical shaped “Taylor cone”. Beyond a threshold voltage, the electric forces in the droplet predominate and at that point a narrow charged polymer jet will be ejected from the tip of the Taylor cone. However, the viscosity of the polymer solution plays a crucial role in maintaining the ejected jet. If the viscosity of the polymer solution is low, the ejected jet break into droplets by a process called “electrospraying”. For solutions with higher viscosities, the ejected jet travels in a nearly straight line towards the grounded collector for some time due to the stabilization imparted by the longitudinal stress of the external electrical field on the charge carried by the jet. However, at some point along the course, the jet reaches a point of instability due to the repulsive forces arising from the opposite charges in the jet. The unstable jet then passes through a series of bending instabilities and it tends to bend back and forth following a bending, winding, spiraling and looping path in three dimensions. This bending instability of the jet has been demonstrated using high speed videography. During this process the polymer jet is continuously stretched resulting in significant reduction of the fiber diameter. This, along with the rapid evaporation of the solvent from the ultrathin jets results in the formation of ultrathin fibers that are deposited on a grounded collector surface [117–122].

Extensive studies have been performed to investigate the fundamental aspects of the process of electrospinning to determine the parameters that modulate the morphology and diameter of the electrospun fibers and for determining appropriate conditions for developing fibers from a wide range of polymers [112, 123–126]. These studies have clearly demonstrated the flexibility of the electrospinning process. Electrospun nanofiber scaffolds can be developed from a wide range of polymers with varying physical, chemical, and mechanical properties, thereby creating scaffolds with varying strength, surface chemistry, degradation patterns (in the case of matrix developed from bioresorbable polymers) and physical properties. The electrospinning process also enables co-spinning two or three different polymers, which further extends the ability to control the properties of the resulting scaffolds/matrices. Another advantage of electrospinning process is the feasibility of developing composite nanofiber scaffolds/matrices by incorporating small insoluble particles such as drugs or bioactive particles within polymeric nanofibers. Since the shape of the nanofiber scaffold/matrix depends on the properties of the collector, complex and seamless 3D structures can be developed using the appropriate collectors.

**Parameters that Affect the Electrospinning Process** Extensive studies have been undertaken to determine the parameters/variables that affect the electrospinning process. These include system parameters, solution properties and processing variables. The system parameters include the nature (chemistry and structure) of the polymer, molecular weight of the polymer and molecular weight distribution of the polymer. Solution properties include viscosity, elasticity, conductivity and surface tension of the polymer solution. The processing variables in the electrospinning process are electric potential, flow rate of the polymer solution, concentration of the polymer solution, the distance between the tip and the target,

ambient parameters such as solution temperature, humidity, air velocity in the electrospinning chamber, and motion of the target screen [112, 124, 126].

Most studies correlated the electrospinning parameters/variables to fiber diameter and/morphology. The effect of molecular weight of polymer on the process of electrospinning was evaluated using poly(ethylene oxide)s (PEO) of different molecular weights electrospun under identical conditions and by following the morphology of the fibers [127]. Figure 1.17(A–C) shows the effect of polymer molecular weight on the morphology of resultant nanofibers. In this study viscosity, surface tension and conductivity of all the solutions were kept constant to correlate the morphology of fibers to the molecular weight. Electrospinning of the low molecular weight polymer (20 000) resulted in the formation of mostly beads rather than fibers (Fig. 1.17A). Increasing the molecular weight to 500 000 resulted in the formation of fibers, however, with spindle shaped defect structures or beads (Fig. 1.17B). A further increase in molecular weight to  $4 \times 10^6$  resulted in the formation of bead-free fibers (Fig. 1.17C). The formation of bead-free structures with high molecular weight PEO has been attributed to the increasing entanglement of the polymer chains with high molecular weight polymer.

The effect of electric potential and polymer concentration on the morphology and diameter of electrospun polymer fibers were demonstrated by Katti et al. using a bioresorbable polymer poly(lactide-*co*-glycolide) (PLGA) [128]. PLGA dissolved in a dimethyl formamide–tetrahydrofuran (1:3) mixture was used for electrospinning. The study demonstrated that the concentration of the polymer solution has a significant effect on the diameter and morphology of the electrospun fibers. Figure 1.18(A–C) shows the morphologies of PLGA fibers formed from polymer solutions having different concentrations. A lower polymer concentration ( $0.15 \text{ g mL}^{-1}$ ) resulted in the formation of beaded nanofibers (Fig. 1.18A). Increasing the polymer concentration ( $0.2 \text{ g mL}^{-1}$ ) significantly reduced the probability of bead formation (Fig. 1.18B). The concentration also showed significant effects on the diameter of the resulting fibers. At low concentration ( $0.15 \text{ g mL}^{-1}$ ), fibers having diameters  $\sim 270 \text{ nm}$  with beads were formed and increasing the concentration to  $0.2 \text{ g mL}^{-1}$  increased the diameter of the fibers to  $\sim 340 \text{ nm}$  with minimal amount of beads. A further increase in concentration to  $0.25 \text{ g mL}^{-1}$  resulted in the formation of fibers having diameters  $\sim 1000 \text{ nm}$  with apparently no bead formation (Fig. 1.18C). Increase in fiber diameter with increasing solution concentration followed a power law relationship. The same behavior has been observed for different polymer systems by other investigators [123, 129]. Demir et al., using polyurethane solution, have shown that fiber diameter can be correlated to polymer concentration as proportional to the cube of the polymer concentration [130].

Similarly the electrospinning voltage has a profound effect on the morphology and diameter of the fibers. An increase in electric voltage decreases the diameter of electrospun fibers up to a certain voltage and above that tends to increase the fiber diameter [126, 128]. Spinning voltage has been found to strongly correlate with the formation of beads. Deitzel et al. have shown that an increase in electrical potential increases the feasibility of formation of beads along the fibers [131].

In addition to varying the polymer concentration and the electric potential the

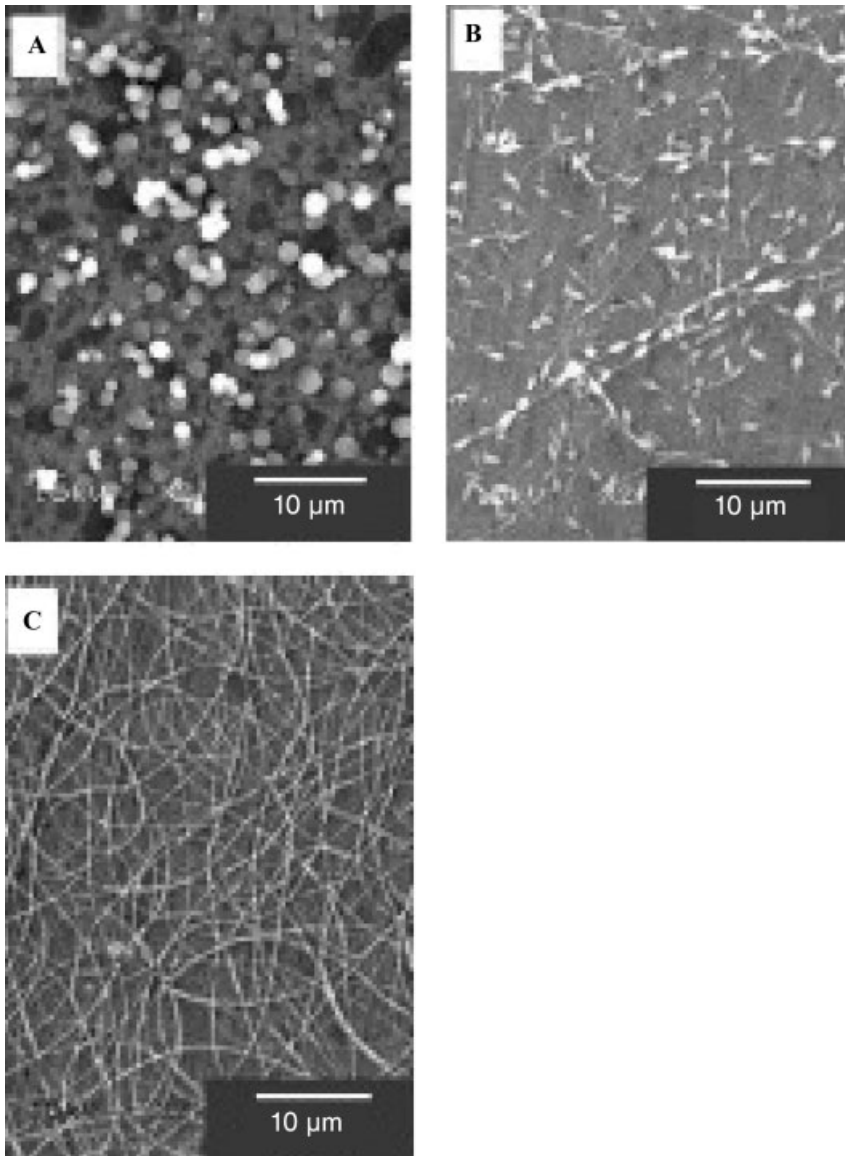


**Fig. 1.17.** Morphology of fibers formed by the electrospinning process using poly(ethylene oxide)s of different molecular weights: (A) 20 000, (B) 500 000, and (C)  $4 \times 10^6$ . (Adapted from Ref. [127] with permission from Elsevier.)

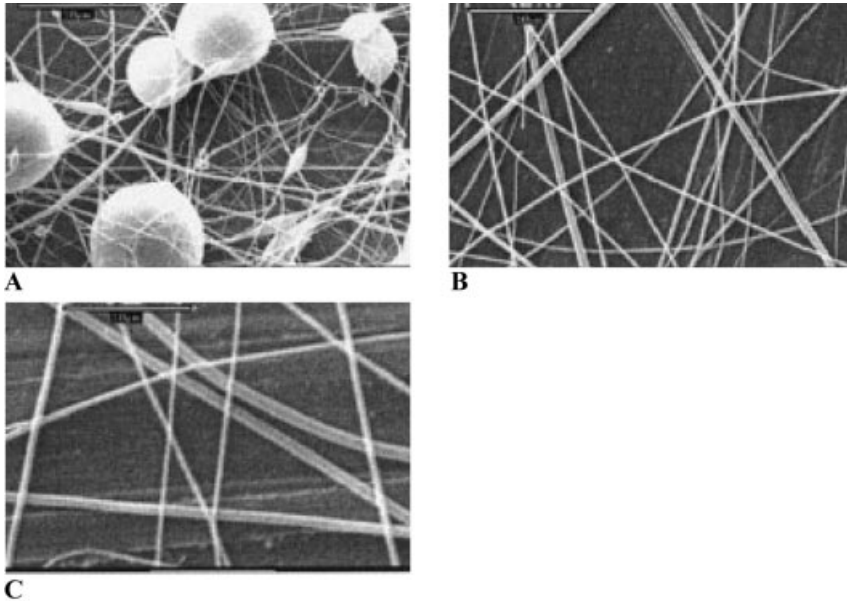


**Fig. 1.18.** Morphology of fibers formed by the electrospinning of PLGA solutions having varying polymer concentrations ( $\text{g mL}^{-1}$ ): (A) 0.15, (B) 0.2, and (C) 0.25. (Adapted from Ref. [128].)

diameter and morphology of electrospun polymer nanofibers can be modulated by the addition of various additives to the spinning solution. One study by Zong et al. has shown that addition of ionic salts to the polymer solution can significantly reduce the bead formation and could result in thinner fibers. This has been attributed to the higher charge density of the jet due to the presence of ionic salts. The higher the charge carried by the jet, the greater will be the pull or elongation force the jet will experience under the electrical field, resulting in fewer beads and thinner fiber [132].

The electrospinning process can also result in the formation of fibers having various cross-sectional features in addition to circular fibers, as demonstrated in the case of various polymers. Fibers having varying shapes have been created such as flat ribbon, bent ribbon, ribbons with other shapes, branched fibers and fibers that were split longitudinally from larger fibers from different polymers and polymer–solvent systems [133]. Figure 1.19 shows the SEM of fibers having varying cross-sectional shapes. The occurrence of skin on the polymer jet accounts for a number of these observations. The phenomenon has been attributed to various causes, including contribution of fluid mechanical effects, electrical charge carried by the jet, and evaporation of solvent from the jet. In addition to varied cross-sectional features, fibers have been found to form with surfaces having varying nanotopographies such as nanopores or ridges. The formation of these structures



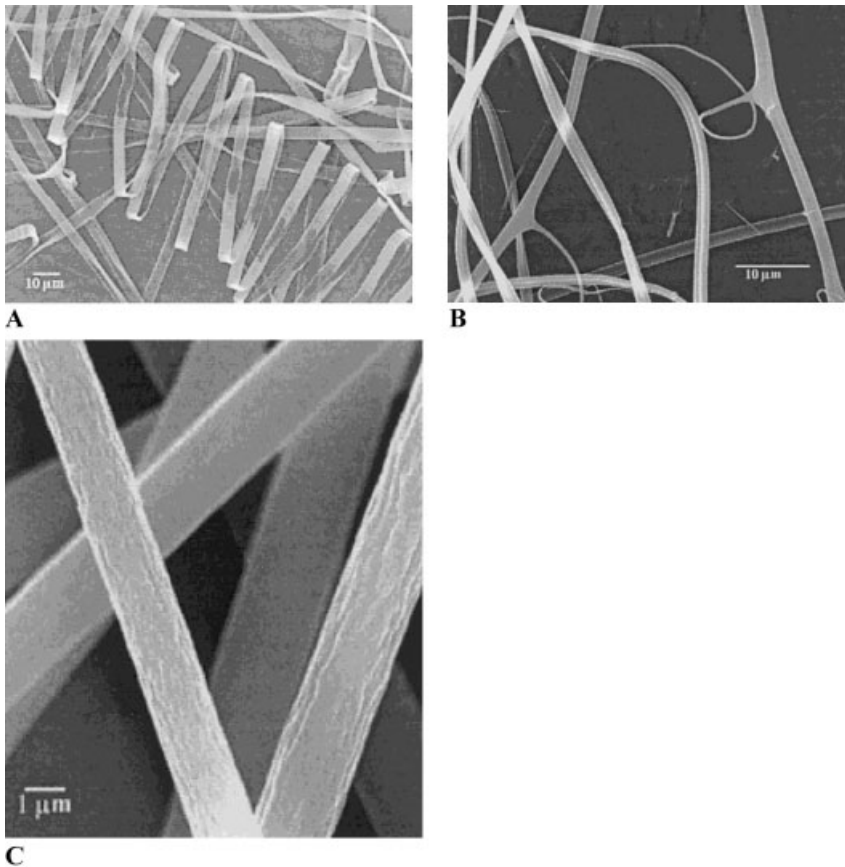


**Fig. 1.19.** SEM showing the fibers having varying cross-sectional shapes. (A) Flat ribbon formed from 10% solution of poly(ether imide). (B) Branched fibers from 16% HEMA. (C) Round fibers with skin collapsed to form longitudinal wrinkles. (Adapted from Ref. [133].)

have been attributed to various parameters such as the nature of the solvent, glass transition temperature of the polymer, solvent–polymer interactions, and environmental parameters such as humidity and temperature [134–136].

Nanofibers deposited by electrospinning using a static target result in the formation of a non-woven matrix composed of randomly oriented fibers. However, properties of fiber matrices can evidently be improved, if the fibers could be aligned in appropriate directions. This is particularly important for developing scaffolds for tissue regeneration as this would enable the development of scaffolds with specific orientation and architecture. Aligning the fibers formed by the process of electrospinning, however, is very difficult to achieve because during electrospinning process the jet trajectory follows a complex 3D whipping and bending path towards

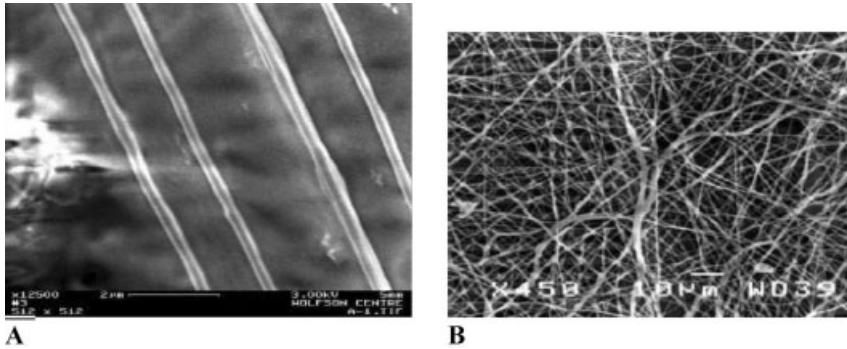


**Fig. 1.20.** SEM showing PEO nanofibers: (A) Aligned fibers and (B) randomly deposited fibers. (Reprinted from Ref. [139] with permission from Institute of Physics Publishing.)

the target rather than a straight line. Several attempts have been performed to develop aligned electrospun polymeric nanofibers. Earlier attempts were performed using a high speed rotating cylinder collector [137]. However, fiber alignment could be achieved only to a certain extent using this process, presumably due to the low control that can be achieved over a polymer jet that undergoes chaotic motion. In another attempt, an auxiliary electrical field was applied to align the fibers which substantially improved the fiber alignment [138]. Another successful approach to align electrospun nanofibers was developed by Theron et al. using a thin wheel with sharp edge device. The thin edge of the wheel helped to concentrate the electrical field so that almost all of the spun nanofibers were attracted and wound to the bobbin edge of the rotating wheel [139]. Figure 1.20(A and B) shows the SEMs of aligned PEO nanofibers developed using the thin wheel with sharp edge collector and randomly deposited fiber matrix using conventional static collector. Another approach investigated is the use of a frame collector and has been found to significantly improve the alignment of nanofibers [140]. In this process, however, the extent of alignment depends significantly on the frame material. Figure 1.21 shows the SEM of aligned PLLA-CL copolymer fibers formed by the frame method.

In addition to the above techniques, several processing techniques were also attempted to increase the versatility of the electrospinning process. These include electrospinning the mixture of polymer with sol-gel solution [141], electrospinning blend polymer solutions [142], electrospinning polymer solution containing nanomaterials to form composite matrices [126], core-shell nanofiber spinning [143] and side by side/multijet electrospinning of different polymers (to increase the rate of fiber deposition and develop matrices having unique properties such as biohybrid matrices) [144–146].

The electrospinning process is a very mild fabrication process. This makes it very attractive for developing structures for biomedical applications. Studies have shown the ability of electrospun fibers to preserve the biological activity of highly sensitive biomolecules encapsulated within the fibers during the electrospinning

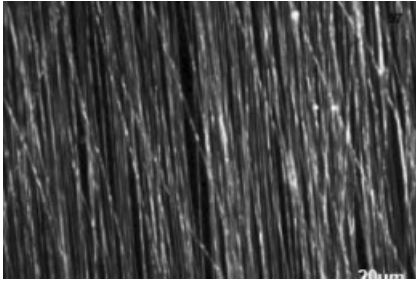


**Fig. 1.21.** Aligned PLLA-CL nanofibers formed by the frame method. (Adapted from Ref. [140] with permission from Elsevier.)

process. Hamdan et al. have encapsulated RNase and trypsin in poly(2-ethyl-2-oxazoline) nanofibers by electrospinning [147]. The enzymes were found to preserve their biological activity after being encapsulated within the nanofibers. Another study by Jiang et al. demonstrated the feasibility of incorporating model proteins such as bovine serum albumin and lysozyme within PCL nanofibers with preservation of their biological activity [148]. A novel electrospinning fabrication process called coaxial spinning was recently developed to encapsulate water-soluble macromolecules within hydrophobic nanofibers [143]. The fibers developed are called core-shell nanofibers where the aqueous phase containing the protein solution forms the core of the fiber surrounded by the hydrophobic polymer layer. The thickness of the core and the shell can be adjusted by the feed rate of the inner dope. Circular dichroism and SDS-PAGE studies on the released lysozyme and BSA encapsulated in the core-shell fibers revealed that both the proteins maintained their structure and bioactivity after encapsulation. The core-shell structures could have several advantages, such as improved protection of the encapsulated molecules and feasibility of achieving their controlled delivery when used as a macromolecular delivery vehicle for biomedical applications, including tissue engineering.

The mechanical properties of non-woven nanofiber matrices developed from bioresorbable polymers have been investigated. Thus, nanofiber matrices developed from PLAGA with LA:GA ratio of 85:15 showed a tensile strength similar to that of natural skin [149]. Ding et al. have demonstrated that the mechanical properties of non-woven nanofiber matrices could be further modulated by developing blend nanofibrous matrices using multi-jet electrospinning [144]. Another study by He et al. has demonstrated the low stiffness of non-woven polymeric nanofiber matrices compared to large diameter dacron grafts using poly(L-lactic acid-co-caprolactone) copolymer (PLLA-CL) nanofiber matrices. The low stiffness of the matrix makes it a suitable candidate for vascular graft applications [150]. The nanofiber matrix developed from PLLA-CL showed an ultimate strain of  $175 \pm 49\%$ . This high distension property has been attributed to the ability of the randomly oriented fibers to rearrange themselves in the direction of the stress. Another study compared the mechanical properties of nanofiber matrices with microfiber matrices developed

from poly(L-lactide-co-caprolactone) [PLCL] by the electrospinning process [151]. Three matrices composed of fibers with diameters of  $\sim 0.3$ ,  $\sim 1.2$ , and  $\sim 7$   $\mu\text{m}$  were investigated. The differences in fiber diameter could lead to differences in specific density of the resultant matrices. The matrix composed of the smallest diameter fibers ( $\sim 0.3$   $\mu\text{m}$ ) gave the densest matrix. Also, the Young's modulus of the densest matrix ( $\sim 0.3$   $\mu\text{m}$ ) was the highest followed by the matrix composed of fibers having diameter 1.2  $\mu\text{m}$ . The matrix composed of fibers with diameter  $\sim 7$   $\mu\text{m}$  showed the lowest Young's modulus. This indicates that nanofiber matrices could show better mechanical performance than microfibrinous matrices of the same material presumably due to the increase in fiber density. In terms of the mechanical properties of aligned nanofiber matrices developed by electrospinning, the nanofiber matrices showed different properties along different directions [152]. The ultimate strength of the aligned polyurethane fiber matrices ( $3520 \pm 30$  kPa) was significantly higher than randomly deposited fiber matrices ( $1130 \pm 21$  kPa) [153].

In summary, these studies demonstrate the feasibility of developing polymeric nanofibers with diameters ranging from 1 to 1000  $\mu\text{m}$  from a wide range of polymers using the process of electrospinning. The diameter and morphology of the nanofibers can be controlled to a great extent by varying the process parameters/variables that govern the electrospinning process. The properties of the matrices fabricated using polymeric nanofibers can be modulated by varying the properties of the polymer, co-spinning or multiple spinning polymer mixtures, incorporating nanoparticles or fillers, varying the rate of deposition as well as varying the properties of the target. The feasibility of aligning the fibers significantly increases the ability to modulate the properties of nanofiber matrices for biomedical applications. Another notable advantage of the electrospinning process is the cost effectiveness compared to other nanofabrication techniques.

**Polymeric Nanofibers by Phase Separation** Phase separation is another type of top-down approach used to develop polymeric nanofiber matrices from different polymer solutions. This technique has been found to be effective in developing nanofibrous matrices having high porosities (up to 98.5%) from biodegradable polymers and has been investigated for tissue engineering applications [154].

Liquid-liquid phase separation can be achieved by lowering the temperature of a polymer solution having an upper critical solution temperature. The phase separation at low temperature could lead to the formation of a continuous polymer-rich and polymer-lean solvent phases. The removal of solvent from the phase separated system at low temperature affords a scaffold with an open porous structure [154, 155]. Thus the development of nanofibrous porous matrices using phase separation of polymer solution takes place in five steps. Polymer dissolution in a solvent system, phase separation and gelation, solvent extraction from the gel with water, freezing and freeze drying under vacuum [114]. Similar to the electrospinning process, various processing variables can be controlled to modulate the properties of the nanofibrous matrices formed by phase separation process. These include type of solvent and polymer, polymer concentration, solvent exchange, thermal treatment and order of procedures [114].

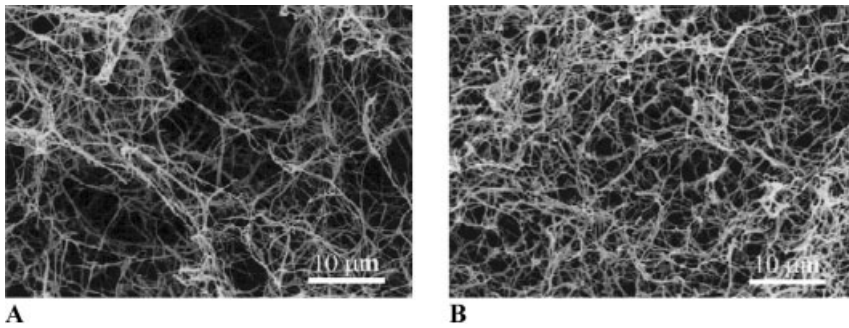


**Fig. 1.22.** SEM micrographs of PLLA fibrous matrices prepared from PLLA/THF solution with different PLLA concentrations at a gelation temperature of 8 °C: (A) 1% and (B) 5% (w/v). (Adapted from Ref. [154].)

Ma and Zhang have developed 3D continuous nanofibrous structures that could mimic the structure of the ECM using biodegradable poly(L-lactic acid) [PLLA]. Fibers of the nanofiber matrix exhibited diameters in the range 50–500 nm. Figure 1.22(A and B) shows the SEM of PLLA fibrous matrices prepared from 1% (w/v) and 5% (w/v) PLLA/THF solution. The figures demonstrate the feasibility of varying the porosity of matrices by varying the concentration of the polymer solution. The higher the concentration of the solution, the lower was the porosity of the matrices formed.

Another advantage of fabricating nanofibrous matrices using the phase separation technique is that it allows for incorporation of macropores along with nanopores in the matrices by adding various porogens such as sugars, inorganic salts or paraffin spheres to the mold with the polymer solution during phase separation [156]. Figure 1.23(A and B) shows macro-nano porous matrices of PLLA fabricated by the combined porogen leaching phase separation method. Thus the phase separation process is a mild processing technique that provides the flexibility to control the properties of the nanofiber matrices such as fiber diameter, interconnectivity, porosity and size of the pores.

### 1.5.1.2 Bottom-up Approaches in Developing Scaffolds for Nano-based Tissue Engineering

Bottom-up approaches are based on self-assembly, a ubiquitous natural phenomenon that harnesses the physical and chemical forces operating at the nanoscale to assemble small building blocks into larger structures. Thus, the basic principle of the bottom-up approach is molecular self-assembly, which is the spontaneous organization of molecules under near thermodynamic equilibrium conditions into structurally well-defined and stable arrangements through non-covalent interactions [157]. These interactions include weak non-covalent bonds, such as hydrogen bonds, ionic bonds, hydrophobic interactions, van der Waals interactions and water-mediated hydrogen bonds [158]. The development of a self-assembling sys-

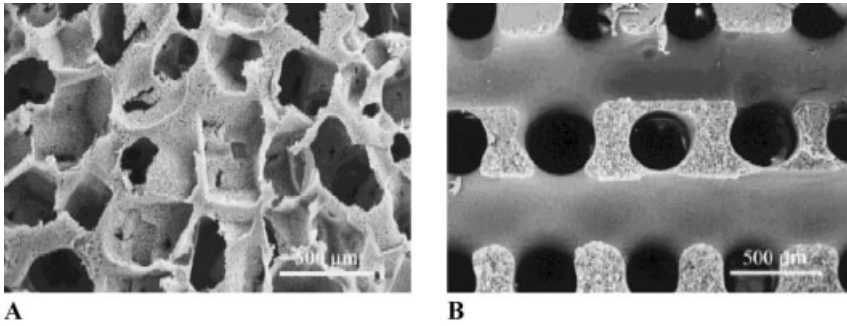


**Fig. 1.23.** (A) SEM micrograph of PLLA nano-fibrous matrix with particulate macropores prepared from PLLA/THF solution and sugar particles; particle size 250–500 nm. (B) SEM micrograph of PLLA nano-fibrous matrix with an orthogonal tubular macropore network prepared from PLLA/THF solution and an orthogonal sugar fiber assembly. (Adapted from Ref. [156].)

tem requires the design and development of small building blocks that can spontaneously self-assemble and be stabilized to form functional nano/microstructures. Recently, there has been significant interest in using self-assembly to develop nanostructured scaffolds for tissue engineering.

The most extensively investigated self-assembled nanostructured scaffolds for tissue engineering application are developed from peptide molecules. In 1993, Zhang et al. demonstrated the feasibility of an aqueous solution of a 16-residue ionic self-complementary peptide to spontaneously associate to form a macroscopic membrane [159]. The ionic complementary oligopeptides used in the study have regular repeating units of positively charged residues (lysine or arginine) and negatively charged residues (aspartate or glutamate) separated by hydrophobic residues (alanine or leucine). The membrane was highly stable to varying pHs and temperatures [159]. SEM of the self-assembled membrane revealed that the structure is composed of nanofibers with diameters ranging from 10 to 15 nm. The study raised interest in self-assembling peptide motifs and led to the development of different self-assembling peptide structures capable of assembling into unique nanostructures. Thus different types of self-assembling peptides have been identified to form different self-assembled structures such as nanofibers, nanotubes, nanowires and nanocoatings. Among these the Type I peptides also called molecular Legos developed by Zhang et al. have been identified as a potential peptide motif for developing self-assembled scaffolds for tissue engineering. These peptide motifs are called molecular Legos because at the nanometer scale they resemble the Lego bricks that have pegs and legs in a precisely determined organization. These peptides form  $\beta$ -sheet structures in aqueous solution resulting in distinct hydrophilic and hydrophobic surfaces [158–160]. The hydrophobic surface shields the peptide motif from water, thereby enabling them to self-assemble as in the case of protein folding *in vivo*. Then complementary ionic bonds will be formed with regular repeats on the hydrophilic surface. The complementary ionic sides have been

classified into different moduli based on the chemistry of the hydrophilic surface, i.e., having alternating positive and negative charged amino acid residues with different intervals. Depending on the moduli, these molecules could undergo ordered self-assembly to form nanofibers. These nanofibers, due to their high aspect ratio, in turn associate to form nanofiber scaffolds that closely mimic the porosity and gross structure of the ECM, making them potential candidates as tissue engineering scaffolds [161]. Figure 1.24(A) illustrates the formation of nanofibrous structures using molecular Lego. “PuraMatrix” a commercially developed ECM mimic self-assembling molecular Lego system has been found to be suitable for performing 3D tissue culture *in vitro*. The nanofiber scaffolds formed from these peptide motifs are formed of interwoven nanofibers with diameter of  $\sim 10$  nm and pores of  $\sim 5$ – $500$  nm with very high water content ( $>99.5\%$ ) (Fig. 1.24B).

Naturally occurring amino acids were used in developing peptide motifs in these studies. However, studies by Stupp et al. demonstrated the feasibility of using building blocks other than natural amino acids to create amphiphilic peptides. The peptide amphiphiles were developed from appropriate amino acids using solid phase peptide chemistry and the NH terminus of the peptide sequence was then alkylated to form the amphiphilic molecule. The amphiphilic peptides (PA) molecules are composed of a peptide segment containing 6–12 amino acids coupled via an amide bond to a fatty acid chain that varies in length from 10 to 22 carbon atoms. Even at very low concentrations of 0.25% (w/v) these molecules can self-assemble to form a gel structure composed of a network of cylindrical nanofibers with diameter ranging from 5 to 8 nm, depending on the length of the self-assembling molecules. The matrices were highly hydrated ( $>99.5\%$ ) and the mechanical integrity of such a highly hydrated matrix has been attributed to the high aspect ratio of the nanofibers composing the matrix. These molecules are custom developed so that they can self-assemble to form nanostructured scaffolds that could structurally and biologically mimic the structure of the ECM of specific tissue type. Thus, a composite nanostructured matrix has been developed as potential scaffolds for bone tissue engineering. The scaffold was designed to mimic the ECM of natural bone by self-assembling peptide motifs with appropriate amino acids and mineralizing the matrix *in vitro* [162]. In this study the peptide amphiphile was designed as follows. To make robust nanofibers four consecutive cysteine amino acids were incorporated in the sequence. The cysteine residues were incorporated as they could form disulfide linkages between adjacent molecules upon oxidation to stabilize the supramolecular structure. The formation of the disulfide linkage, however, is a reversible process. A phosphoserine residue was incorporated into the peptide sequence, so that after self-assembly the resulting fibers will have highly phosphorylated surface. These groups are specifically incorporated in the PA to increase the mineralizing capacity (nucleation and deposition of hydroxyapatite an essential inorganic component of natural bone) of the nanostructured scaffold. Anionic groups are known to promote nucleation and deposition of hydroxyapatite on synthetic materials and phosphorylated groups are particularly important in the formation of calcium phosphate minerals. Thus, the phosphorylated surface of self-assembled nanofibers could promote the nucleation and deposition

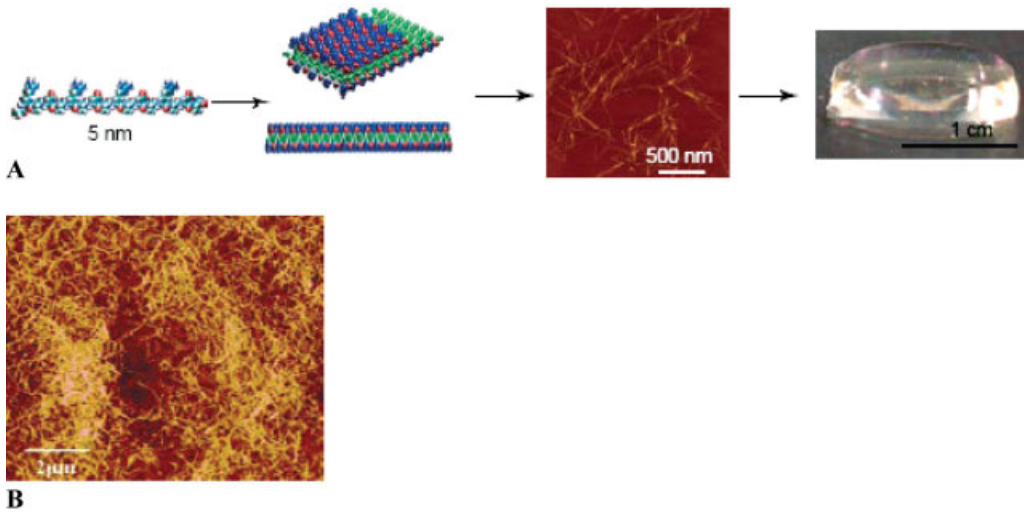


**Fig. 1.24.** Fabrication of various peptide materials. (A) Peptide Lego, also called ionic self-complementary peptide, has 16 amino acids,  $\sim 5$  nm in size, with an alternating polar and nonpolar pattern. The peptide motifs could form stable  $\beta$ -strand and  $\beta$ -sheet structures. The peptide motifs undergo self-assembly to form nanofibers with the nonpolar residues inside (green) and positive (blue) and negative (red) charged residues forming complementary ionic interactions, like a checkerboard. These nanofibers form interwoven matrices that produce a scaffold hydrogel with very high water content ( $\sim 99.5\%$ ). (Adapted from Ref. [161] with permission from Elsevier.) (B) AFM image of the nanofiber scaffold (PuraMatrix). (Adapted from Ref. [161] with permission from Elsevier.)

of hydroxyapatite (HA). To improve the cell adhesivity of the self-assembled nanofiber matrix, an RGD sequence was also incorporated in the peptide. Figure 1.25 shows the structure of the PA molecule designed to self-assemble to form nanofiber scaffold for bone tissue engineering.

The nanofiber scaffold was developed from the PA as follows. The cysteine residues of the PA were first reduced to thiol groups at higher pH. The resulting PA was found to be highly soluble in water. The pH of the aqueous solution was then reduced to 4.0, at that point the material rapidly became insoluble due to the formation of network structure. Cryo-transmission electron microscopy (Cryo-TEM) showed that the gel is composed of a network of fibers that are  $7.6 \pm 1$  nm in diameter and up to several micrometers long. Figure 1.26(A and B) shows the ultrastructure of the gels formed by self-assembly with and without covalent stabilization. The ability of the nanofiber matrix formed from the PA to nucleate hydroxyapatite (HA) along the fiber axis was also demonstrated by incubating the nanofiber matrix in appropriate salt solution (Fig. 1.26C). Another interesting property of the self-assembled gel is its reversibility. The self-assembled matrix could disassemble at higher pHs. Even though the study demonstrated for the first time the feasibility of designing and developing bioactive self-assembled system to mimic the properties of the ECM, it has certain disadvantages. The significant



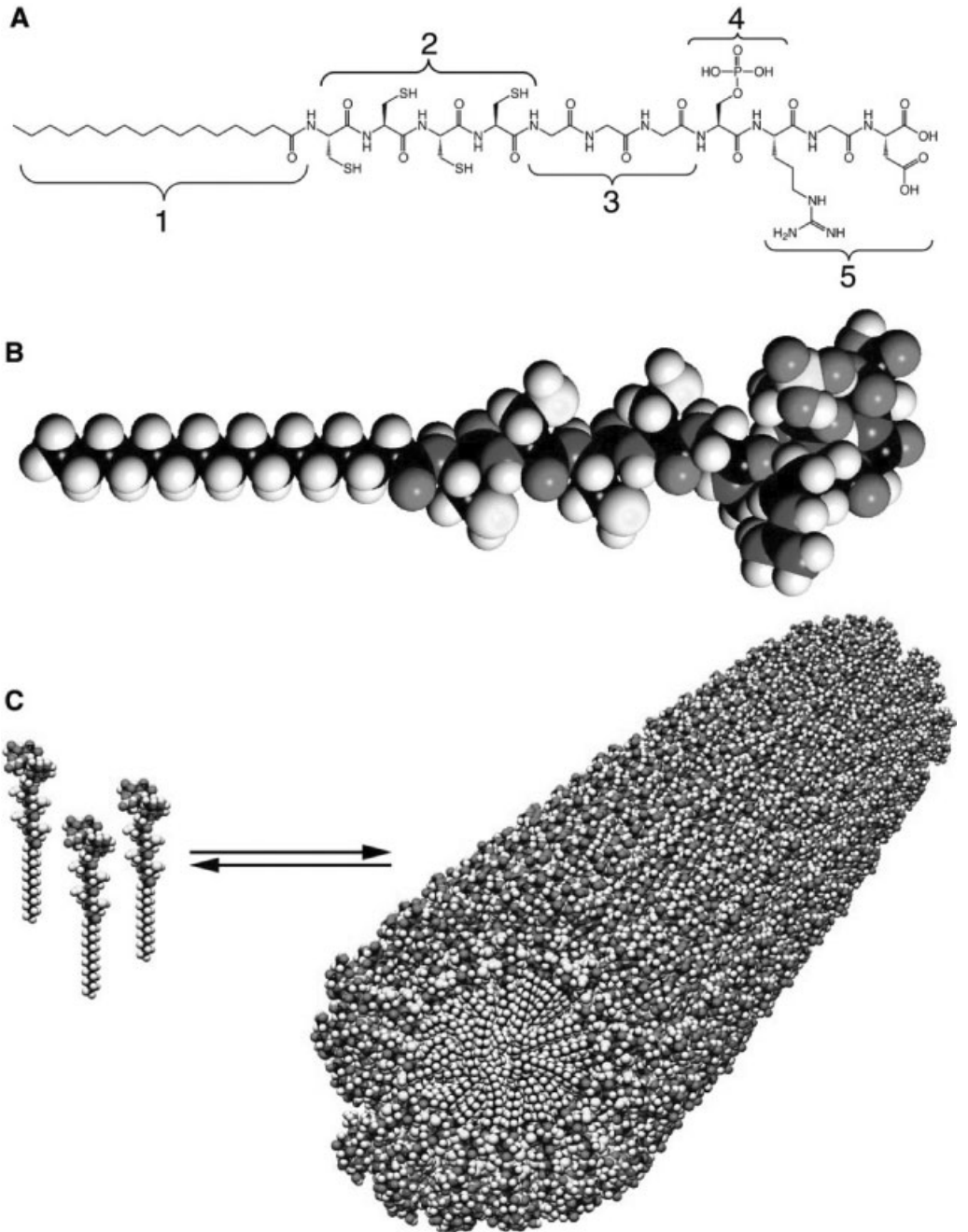


**Fig. 1.25.** (A) Chemical structure of the peptide amphiphile. Region 1 is a long alkyl tail to make the peptide motif amphiphilic. Region 2 is composed of four consecutive cysteine residues for disulfide linkages. Region 3, a flexible linker region of three glycine residues, provides

hydrophilic head group flexibility from the rigid crosslinked region. Region 4 is a single phosphorylated serine residue. Region 5 is a cell adhesion RGD ligand. (B) Molecular model of PA. (C) Scheme showing the self-assembly. (Reprinted with permission from Ref. [162].)

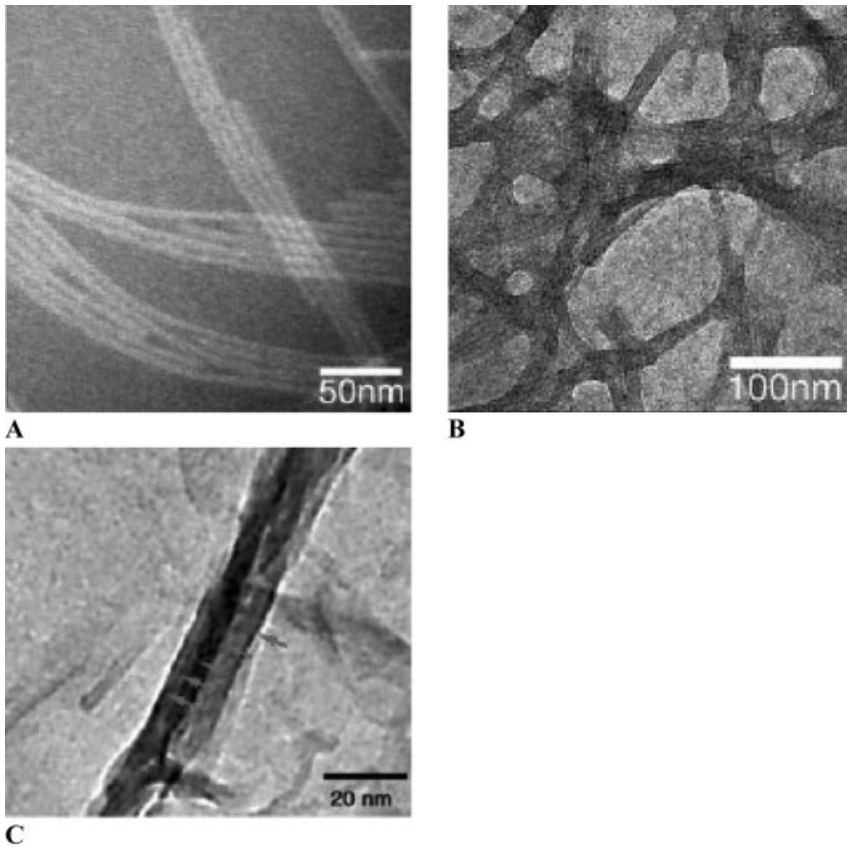


**Fig. 1.26.** TEM of self-assembled nanofibers (A) before and (B) after covalent stabilization. (C) TEM showing PA nanofibers completely covered by mature hydroxyapatite crystals. (Reprinted with permission from Ref. [162].)

disadvantage of this system is the low stability of the self-assembled structure at physiological pH unless internally crosslinked by covalent bonds. Another study was therefore performed to demonstrate the feasibility of developing self-assembled structures that are stable at physiological pH using PAs with opposite charges based on the electrostatic attraction of the opposite charge [163]. Mixed systems having oppositely charged PAs were used to develop self-assembled systems capable of assembling at physiological pH due to electrostatic attraction. This ability of these materials to undergo mild self-assembly and gelation at physiological conditions and the ability to decorate them with bioactive motifs makes them potential candidates for various biomedical applications.

In addition to peptide motifs, synthetic proteins were also investigated to develop self-assembled matrices. Thus Petka et al. used a recombinant DNA method to cre-

ate artificial proteins that can undergo reversible gelation in response to pH or temperature. The developed proteins consist of terminal leucine zipper domains flanking a central flexible water-soluble polyelectrolyte segment [164]. In near neutral solution, a 3D network can be formed by coiled-coil aggregates of the terminal domains and the polyelectrolyte segment prevent precipitation of the chain and retain the solvent. An elevation of pH or temperature leads to dissolution of the gel, resulting in the formation of viscous polymer solution. Similarly Nowak et al. developed a diblock copolypeptide amphiphile containing charged and hydrophobic segments, which were found to form hydrogels with high temperature stability [165]. The ability of this system to form gel under mild conditions makes them potential candidates for biomedical applications.

Both top-down and bottom-up approaches have significantly contributed to the development of nanostructured matrices as scaffolds for tissue engineering. The top-down approaches currently used to develop nanofiber matrices such as electrospinning or phase separation are highly economical and easily scalable processes. Furthermore, nanofiber scaffolds with finely controlled physical and mechanical properties and complex structures can be developed due to the versatility of the fabrication processes. The bottom-up approach even though is a more involved process that requires highly specific building blocks for spontaneous self-assembly has several advantages from a biomaterials point of view. The matrix formation via a mild self-assembling process makes it a very attractive process for *in vivo* applications. Another advantage is the ease of incorporating specific bioactive motifs as the building blocks that when combined with the nanostructured topography of the resulting matrix could better mimic the structure and functions of the extracellular matrix. The major disadvantage of the self-assembly process, however, is its relative inability to generate complex patterns for biological devices due to its homogeneous character.

## 1.6 Cell Behavior Towards Nano-based Matrices

Several studies have confirmed the fact that cells prefer to live in a complex nanostructured environment composed of pores, ridges and fibers of the polymeric nanofiber matrices that mimics the structure of the ECM compared to 2D matrices or microfiber matrices. Kwon et al. have evaluated the adhesion and proliferation potential of human umbilical vein endothelial cells (HUVEC) on three different types of PLL-CL fiber matrices composed of fibers having diameters  $\sim 0.3$ ,  $\sim 1.2$ , and  $7 \mu\text{m}$  [151]. Figure 1.27 shows the SEMs of HUVECs cultured for 1 and 7 days on electrospun matrices having fibers of different diameters (0.3, 1.2, and  $7 \mu\text{m}$ ). The matrix composed of the smallest diameter fibers ( $0.3 \mu\text{m}$ ) and the medium diameter fibers ( $1.2 \mu\text{m}$ ) showed higher cell adhesion and proliferation than matrix composed of fibers having diameter  $7 \mu\text{m}$ . The morphology of the cells on 0.3 and  $1.2 \mu\text{m}$  fiber matrices were comparable but differed significantly from that on the matrix composed of  $7 \mu\text{m}$  diameter nanofibers. Thus the matrices com-

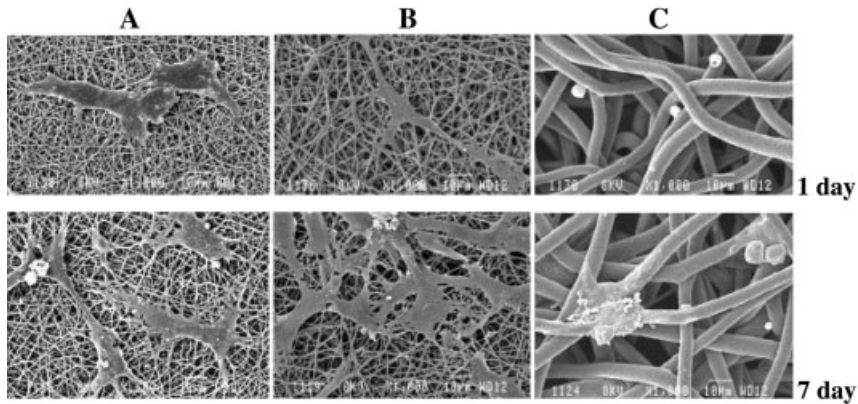


**Fig. 1.27.** SEM showing the morphologies of HUVECs cultured for 1 and 7 days on PLCL (50/50) electro-spun fibers having different diameters ( $\mu\text{m}$ ): (A) 0.3, (B) 1.2, and (C) 7. (Adapted from Ref. [151] with permission from Elsevier.)

posed of 0.3 and 1.2  $\mu\text{m}$  diameter fibers promoted the adhesion, spreading and proliferation of cells and the cells were found to be anchored on many fibers on the surface of the matrices. The quantitative determination of cell adhesion on these two matrices did not show any statistically significant differences in cell proliferation. However, the cells on the 7  $\mu\text{m}$  fiber matrix were found to be rounded and showed significant decrease in cell proliferation compared to the other two matrices. This low cell adhesion and proliferation on microfiber matrix has been attributed to the large interfiber distance or a very low surface density of fibers that could not permit cell adhesion between the neighboring fibers.

Schindler et al. have investigated the ability of nanofibrillar matrix to promote *in vivo*-like organization and morphogenesis of cells in culture [166]. The synthetic nanofibrillar matrices were prepared by electrospinning a polymer solution of polyamide onto glass cover slips. The matrices were found to be composed of fibers of diameters  $\sim 180$  nm and a pore diameter of  $\sim 700$  nm. The surface smoothness of the matrix was found to be within 5 nm over a length of 1.5  $\mu\text{m}$ , which is similar to the 3D organization of fibers in the basement membranes. NIH 3T3 fibroblasts, normal rat kidney (NRK) cells and breast epithelial cells were used for the *in vitro* evaluation. The organizational and structural changes of the intracellular components (actin and focal adhesion components) of the cells were measured as a function of adhesion when cultured on nanofibrous matrices and compared with the responses to cells on glass substrate. Fibroblasts plated on the glass substrate were well spread with an elaborate checkerboard pattern of stress fibers (Fig. 1.28A). Cells on the nanofiber matrix, however, showed significant changes in the morphology and shape. Compared to cells on the glass substrates, the cells on the nanofiber matrices were more elongated and bipolar with thinner actin fibers arranged parallel to the long axis of the cell. Notable increases in the formation of actin-rich lamellipodia, membrane ruffles and cortical actin were also observed

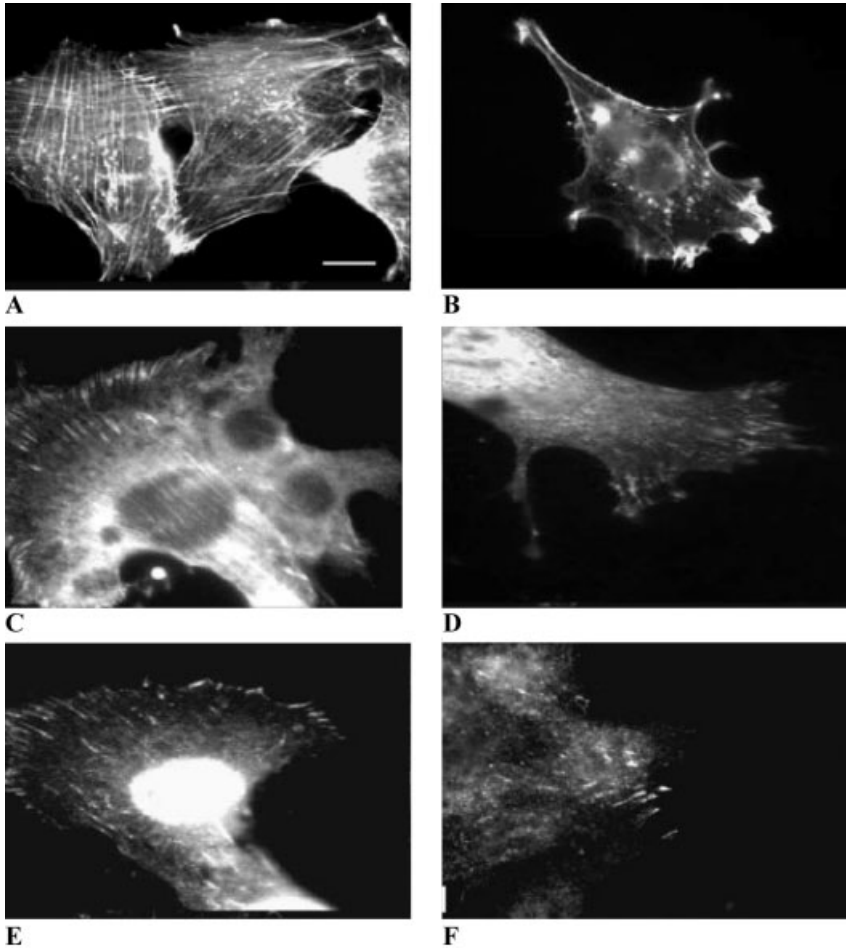


**Fig. 1.28.** Comparison of the F-actin network, focal adhesion components, fibronectin organization and integrin antibodies for NIH 3T3 fibroblasts cultured on glass substrates and nanofiber matrices. (A, C, E, G, I) are cells

on glass substrates and (B, D, F, H and J) are cells on nanofiber matrices (see text for details). (Adapted from Ref. [166] with permission from Elsevier.)

(Fig. 1.28B). Staining of vinculin (a prominent component of focal complexes and focal adhesions that links cytoskeleton, plasma membrane and the ECM) of fibroblasts cultured on glass substrate showed a parallel streaked structure (Fig. 1.28C). However, the streaked staining for vinculin within cells on nanostructured matrix was limited to the edge of the lamellipodia with a more diffuse staining throughout the cell cytoplasm (Fig. 1.28D). Similar to actin distribution, such pattern of vinculin labeling correlates with cellular differentiation and morphogenesis *in vivo*. The cells were also stained for focal adhesion kinase (FAK) which functions as a central mechano-sensing transducer in cells. Cells cultured on glass demon-

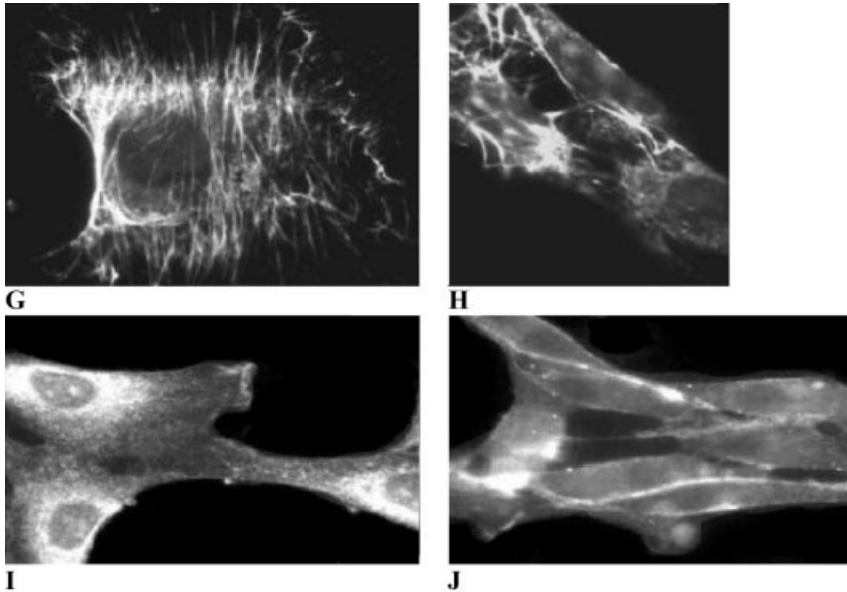
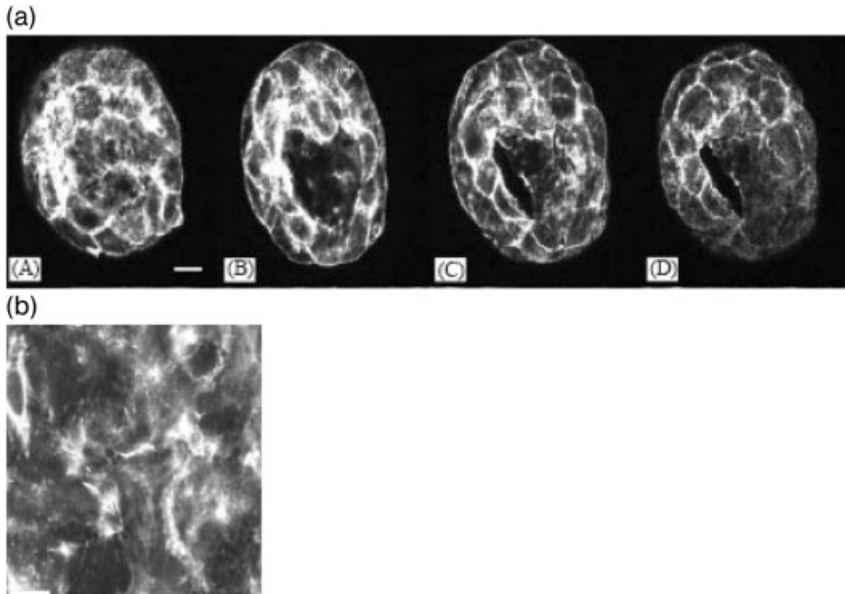


Fig. 1.28 (continued)

strated a streaky pattern of FAK labeling similar to the pattern obtained for vinculin (Fig. 1.28E). However, for cells on nanofiber matrix, the localization of FAK was found to be more punctuated and less well defined (Fig. 1.28F). Previous studies using breast epithelial cells have correlated this loss of FAK localization at focal adhesions to morphogenesis and differentiation [167]. The distribution of fibronectin on the cell surface cultured on glass substrate for 24 h revealed a classic linear pattern of fibrils (Fig. 1.28G). The cells on the nanofiber matrix, however, showed a thicker network of more randomly deposited apically localized fibrils indicating that they are permissive for the assembly of a matrix that can promote the formation of 3D-matrix adhesions (Fig. 1.28H). Staining for  $\beta 1$  integrin for NPK cells was punctuated when cultured on glass substrate for 24 h (Fig. 1.28I). However, the cells on nanofibrous matrix showed an organized long slender aggregate staining pattern, indicating the localization of  $\beta 1$  integrin in focal adhesions (Fig. 1.28J).

The ability of nanofiber matrices to promote morphogenesis was demonstrated by culturing T47D epithelial cells on glass and nanofiber coated glass matrices [166]. The T47D cells were used in the present study as they have been demonstrated to form duct like tubular structures and spheroids under conditions that promote morphogenesis. After 5 days in culture, a mixed population of multicellular structures comprised of tubules and spheroids were found on nanofiber matrix. At day 10, multicellular spheroids were dominant compared to tubules. Figure 1.29(A) shows a confocal series through a multicellular spheroid showing a lumen formed on nanofiber matrix. The figure shows the ability of T47D cells to grow into a complex multilayer structure on a nanofiber matrix. The cells cultured on



**Fig. 1.29.** (a) A series of confocal sections of a multicellular spheroid composed of T47D breast epithelial cells grown on nanofibers and stained with phalloidin-Alexa Fluor (A–D). (b) Cells after 10 days of culture on glass substrate. (Adapted from Ref. [166] with permission from Elsevier.)

glass surface, in contrast, formed a monolayer with groups of F-actin fibers (Fig. 1.29B). These studies demonstrated the advantages of using nanofiber matrices compared to microfiber matrices or 2D surfaces in developing 3D tissues, demonstrating their potential as ideal scaffolds for tissue engineering application.

## 1.7

### Applications of Nano-based Matrices as Scaffolds for Tissue Engineering

Due to the unique properties and favorable cell behavior towards nanofiber matrices, different nanofiber matrices developed by top-down and by bottom-up approaches have been investigated as potential scaffolds for developing various tissues. The following section overviews nanofiber-based matrices as scaffolds for tissue regeneration.

#### 1.7.1

##### Stem Cell Adhesion and Differentiation

As stem cells have been identified as one of the most appropriate cells for tissue engineering, the interaction of nanofiber matrices with stem cells raise significant

interest. The unique ability of nanofiber matrices to support the growth and differentiation of stem cells into appropriate lineages have been demonstrated using self-assembled protein nanofiber matrices. Silva et al. have demonstrated the feasibility of encapsulating neural progenitor cells (NPCs) in self-assembled bioactive peptide amphiphiles and the ability of the cells to differentiate to appropriate lineage [168]. NPCs were selected as they are extensively used to replace lost central nervous system cells after degenerative or traumatic insults. Owing to the design flexibility of peptide amphiphiles as described earlier, unique PA was developed for form self-assembled scaffolds that could provide favorable environment for NPCs. The peptide motif designed to develop the scaffold was composed of a pentapeptide epitope isoleucine-lysine-valine-alanine-valine (IKVAV). The epitope has been selected because it is present in laminin, a cell adhesive protein present in the ECM and known to promote neurite sprouting and direct neurite growth. In addition to the neurite sprouting epitope, a GLu residue was also incorporated in the peptide that could give the peptide a net negative charge at pH 7.4. The rest of the molecule is composed of four Ala and three Gly followed by an alkyl tail of 16 carbon atoms.

The peptide was soluble in aqueous media and upon addition of cell suspension the cations present in the cell culture media screened the electrostatic repulsion, allowing the molecules to self-assemble due to hydrogen bond formation. Upon self-assembly the bioactive motifs were found to be placed on the surface. Figure 1.30 shows the SEM of nanofiber matrix formed by the self-assembly of peptide amphiphiles. A control amphiphile was also developed with a non-physiological sequence of glutamic acid-glutamine-serine (EQS) to compare the cell response to the bioactive self-assembling PA. Even though the control matrices allowed the encapsulation of the progenitor cells by self-assembly, the encapsulated cells did not sprout neuritis or differentiate morphologically or histologically.

The NPCs encapsulated within the peptide amphiphile self-assembled matrix was found to be viable throughout the period of study of 22 days. No differences in cell viability between the encapsulated cells and cells cultured on polylysine 2D

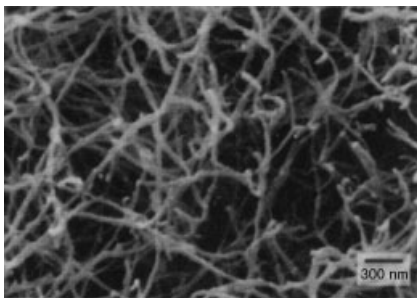


**Fig. 1.30.** SEM showing the morphology of scaffold developed from an IKVAV nanofiber network by adding cell culture media to the peptide amphiphile. The sample is dehydrated

and critical point dried caged in a metal grid to prevent network collapse during sample preparation for SEM. (Reprinted with permission from Ref. [168].)



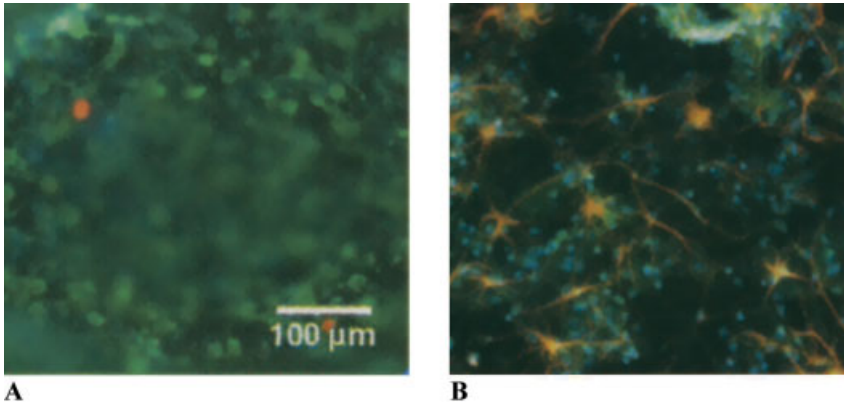
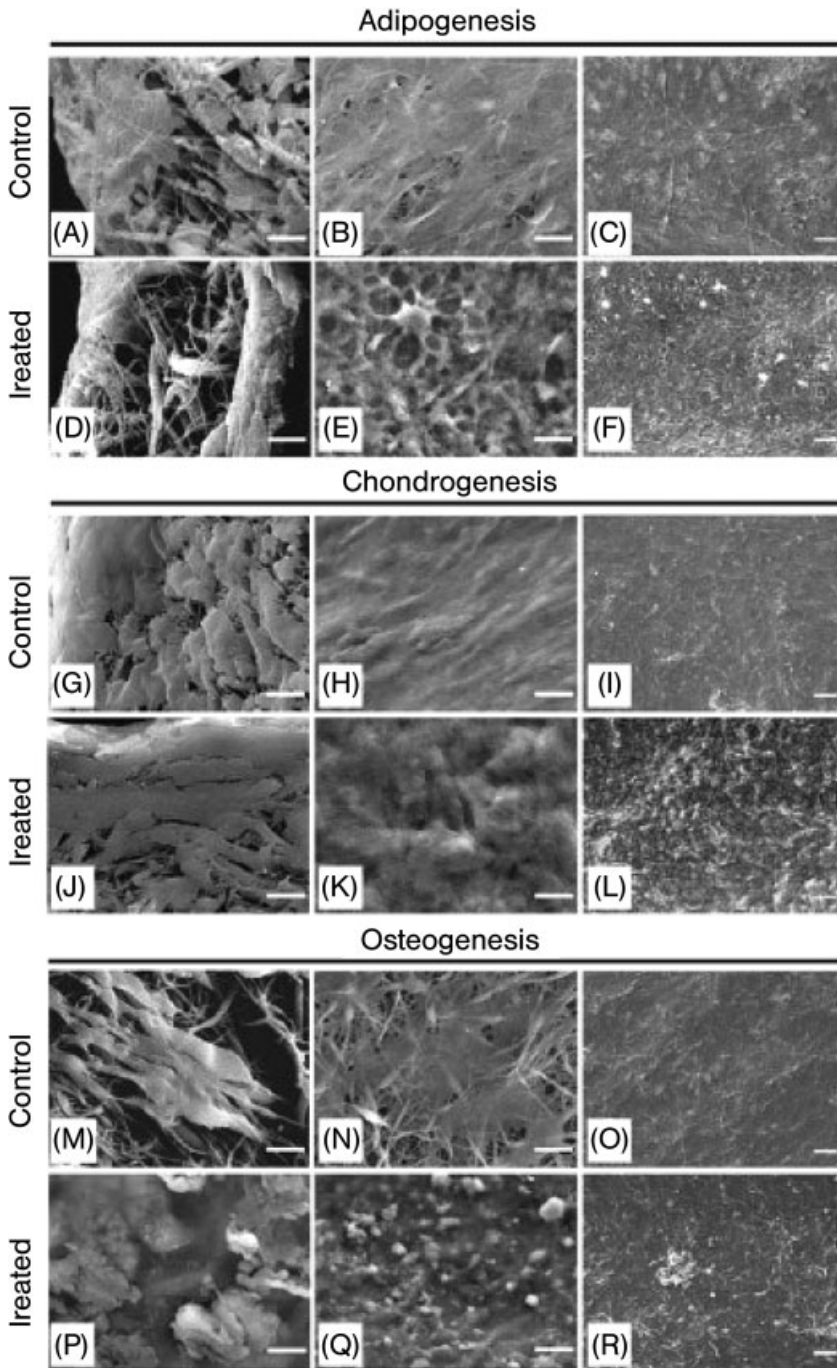


**Fig. 1.31.** Immunohistochemistry showing  $\beta$ -tubulin III of neurons and astrocytes of cells encapsulated in self-assembled bioactive gels (A) (after 1 day in culture) and laminine-coated

cover slips (B) (after 7 days in culture).  $\beta$ -Tubulin III is stained green, differentiated astrocytes (glial cells) are labeled orange. (Reprinted with permission from Ref. [168].)

films were found demonstrating that sufficient diffusion of nutrients, bioactive factors and oxygen is taking place through the highly hydrated nanofiber matrix. Immunocytochemistry demonstrated the differentiation of NPCs encapsulated in the bioactive self-assembled PA matrix to neurons. Furthermore, the results were found to be statistically significant when compared to cells grown on laminin or lysine coated surface. Differentiated neurons were labeled for  $\beta$ -tubulin III and glial fibrillary acidic protein to detect neurons and astrocytes. After only 1 day in culture, 35% of the cells encapsulated within the bioactive nanofiber scaffold stain positive for  $\beta$ -tubulin (Fig. 1.31A). At the same time only less than 5% of the cells in the bioactive scaffold showed astrocyte differentiation even after 7 days in culture (Fig. 1.31A). This is a positive observation since inhibition of astrocyte proliferation is important in the prevention of the glial scar a known barrier to axon elongation following CNS trauma. Cells cultured on 2D laminine coated substrate did not show such differentiation and at the same time showed significant astrocyte proliferation (Fig. 1.31B). Encapsulation in the nanofiber scaffold led to the formation of large neurites after only 1 day ( $57 \pm 26 \mu\text{m}$ ) where as cells grown on laminin or lysine did not form neurites at that time. TEM evaluation of cells encapsulated within the gels after 7 day showed a healthy and normal ultrastructural morphology. The high migrating ability of the cells encapsulated within the gels was also demonstrated by tracking the distance between the center of each neurosphere and cell bodies as a function of time. The study demonstrated the potential of bioactive self-assembling nanofiber scaffolds as stem cell delivery vehicles.

The differentiation ability of progenitor cells into different lineages on polymeric nanofiber matrices developed by electrospinning was demonstrated recently by Li et al., using multipotent human mesenchymal stem cells (MSC). The study demonstrated the feasibility of nanofiber matrices to support the adhesion and differen-



tiation of these cells into different lineages [169]. PCL nanofiber matrices were used for the study. The matrix was found to be composed of randomly oriented nanofibers having diameters  $\sim 700$  nm. The MSCs seeded on the nanofiber matrices were found to attach and remained viable. For multi-lineage differentiation of the cells the MSC seeded nanofiber matrices were placed under specific differentiation promoting culture conditions (Fig. 1.32). Thus, under adipogenic conditions (media with dexamethazone, 3-isobutyl-1-methylxanthine and insulin), the cell-polymer constructs developed into an adipose like tissue with the cells expressing appropriate gene expression. The incubation of the cell seeded nanofiber matrices in chondrogenic media resulted in the formation of a cartilaginous tissue composed of cells showing characteristic chondrocyte phenotypes. The authors observed that the chondrogenic differentiation of MSC on nanofiber matrices takes place even at low cell population compared to 2D cultures or cells encapsulated in hydrogels presumably due to the unique interactions of the cells with the nanostructured topography of the matrix. Incubation of the cell seeded nanofiber matrix in osteogenic media ( $\beta$ -glycerophosphate, ascorbic acid and dexamethasone) resulted in the formation of a dense bone-like tissue with the cells showing characteristic osteoblast phenotypes. The study thus demonstrated that electrospun nanofiber scaffolds can support chondrogenic, osteogenic and adipogenic differentiation and, therefore, are candidate scaffolds for the fabrication of multi-component tissue constructs.

### 1.7.2

#### Neural Tissue Engineering

Nerve tissue engineering can be considered as one of the most promising approaches to restore central nervous system function. Several studies have evaluated the efficacy of nanofibrous matrices as scaffolds for neural tissue engineering. In one study Yang et al. determined the efficacy of PLLA nanofiber matrices developed by phase separation process as scaffold for neural tissue regeneration [170]. The fiber diameters were  $\sim 196$  nm with a matrix porosity of  $\sim 85\%$ . Neural stem cells (NSC) were used in the study. Upon NSC seeding and culturing for a day, the cells were found to randomly spread over the surface of the polymer scaffold without much differentiation. By day 2 the cells had progressively grown throughout the scaffold, with a neurite length twice that of the cell body, and migration of cells

---

**Fig. 1.32.** SEM showing nanofiber-MSC constructs maintained with and without differentiation media (A–F adipogenic; G–L chondrogenic; and M–R osteogenic). (A, D, G, J, M, P) Cross sections; (B, C, E, F, H, I, K, L, N, O, Q, R) top views. In adipogenic cultures (D–F), globular, round cells were evident, while fibroblast-like cells were found in the control cultures (A–C). In chondrogenic cultures (J–L), round chondrocyte-like cells were embedded in a thick layer of ECM that was not found in the control group (G–I). In osteogenic cultures (P–R), mineralized nodules were formed in the constructs. In contrast, control cultures (M–O) contained primarily fibroblast-like cells, and mineralization was not seen [169] with permission from Elsevier.

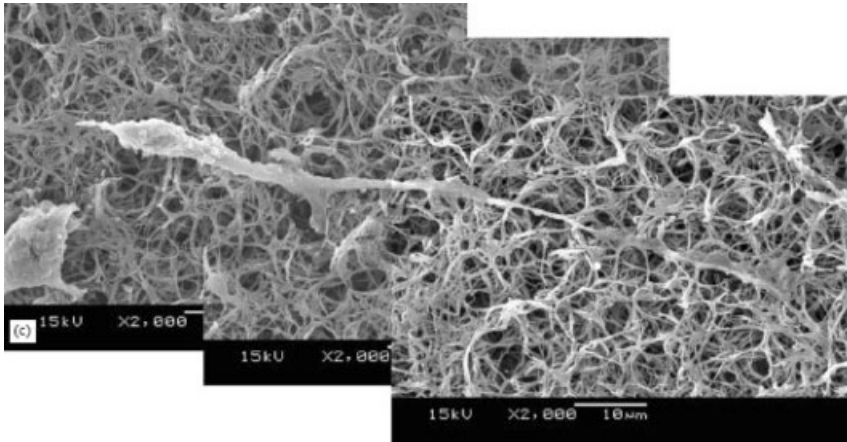


**Fig. 1.33.** SEM showing the magnified view of a differentiated cell with long neurite cultured on a nanofiber matrix developed by phase separation. (Adapted from Ref. [170] with permission from Elsevier.)

into the porous matrix also occurred (Fig. 1.33). The study showed the feasibility of nanofibrous scaffold to act as a positive guidance cue to guide neurite outgrowth.

Efficacy of aligned polymeric nanofiber matrices as a scaffold for the growth and differentiation of neural NSCs was further evaluated by Yang et al. using PLLA nano/microscaffold [171]. The cell adhesion and differentiation pattern on the aligned nanofiber matrices were compared to aligned microfiber matrices formed by electrospinning as well as random micro and nanofiber matrices. The aligned nanofiber matrices were composed of fibers having diameter  $\sim 300$  nm and microfiber matrices were composed of fibers having diameter  $\sim 1.5$   $\mu\text{m}$ . The average fiber diameters of the random nano and microfiber matrices were  $\sim 250$  nm and  $1.25$   $\mu\text{m}$  respectively. NSC attached and formed an elongated spindle-like shape on all the surfaces. The direction of NSC elongation and neurite outgrowth was found to be aligned with the direction of aligned fibers and showed classical contact guidance. The cells on random fiber matrices in contrast showed significantly different phenotype. In terms of differentiation, more cells were found to be differentiated on aligned nanofiber matrix (80%) than on aligned microfiber matrix (40%) demonstrating that nanofiber alignment has profound effect on cell differentiation. Since successful nerve regeneration rely on the extensive growth of axonal process, the neurite length of cells on the matrices was evaluated. The neurite length of NSCs on aligned nanofiber matrix was significantly higher than aligned micromatrix or random matrices. Figure 1.34 shows the SEM micrograph of NSC on aligned nanofiber matrix. The cells body shows an apparent bipolar elongated morphology with the outgrowing neuritis. Both cell elongation and neurite outgrowth followed the same direction of PLLA nanofibers. The figure also shows significant interaction between NSCs and the aligned fibers. Some filament-like



**Fig. 1.34.** SEM showing the interaction of NSC on an aligned PLLA nanofiber matrix. Bar = 5  $\mu\text{m}$ . (Adapted from Ref. [171] with permission from Elsevier.)

structures, presumably focal adhesions, extend out from the NSC cell body and neurite and attach to the nanofiber. This study thus demonstrated that aligned nanofiber matrix could improve NSC differentiation and support neurite out-growth compared to other matrices evaluated.

### 1.7.3

#### **Cardiac and Blood Vessel Tissue Engineering**

One of the major reasons for the failure of synthetic small diameter vascular grafts is adverse blood biomaterials interactions resulting in an acute occlusion followed by a chronic intimal hyperplasia. The ability to engineer vascular grafts using biodegradable scaffolds could lead to the development of synthetic grafts with long-term patency. One of the most extensively investigated approaches to prevent graft occlusion is to improve the antithrombogenicity of graft materials by seeding them with endothelial cells. But the development of a stable endothelial covering on the surface of synthetic materials is difficult due to the high sensitivity of the endothelial cells.

Mo et al. have evaluated the efficacy of polymeric nanofiber matrices as scaffolds for growing endothelial and smooth muscle cells [172]. P(LLA-CL) nanofiber

matrices developed by the process of electrospinning were used as the 3D scaffold in the study. Endothelial cells and smooth muscle cells were cultured on the nanofiber matrices for 7 days. Both SMC and EC adhered and spread on nanofiber matrices with the cell number, showing a significant increase from day 1 to day 7. This indicates the ability of the cell to attach and proliferate on the nanofiber matrix. Immunohistochemical evaluation of adhered ECs on the nanofiber matrix showed appropriate EC phenotype expression, indicating favorable interaction of the cells with the matrix.

Even though self-assembly of bioactive peptide motifs can be considered as the direct method to develop bioactive nanofiber matrices, He et al. have recently demonstrated the feasibility of improving the bioactivity of electrospun nanofibers by surface modification. They modified the surface of a P(LLA-CL) nanofiber matrix to improve the efficacy of the matrix towards endothelial cell attachment and proliferation [150]. The surface of p(LLA-CL) nanofiber matrix was functionalized by plasma modification and the nanofiber matrix surface was then coated with collagen. Human coronary artery endothelial cells (HCAECs) were used to evaluate the efficacy of the coated nanofiber scaffold compared to uncoated scaffold. The cells on uncoated scaffold were rounded in shape without significant spreading (Fig. 1.35A). More cells were found to be attached on the collagen-coated p(LLA-CL) nanofibers than uncoated nanofiber matrix since collagen is the main structural and functional protein present in ECM (Fig. 1.35B). Immunohistochemical evaluation of the cultured cells showed the preservation of endothelial phenotype by the cells on the coated nanofiber matrix.

Similarly a collagen coated PCL nanofiber matrix was evaluated for improve SMC adhesion and interaction [173]. Coating the nanofibers with collagen improved the cell adhesion on the fibers, with cells preserving their characteristic phenotype.

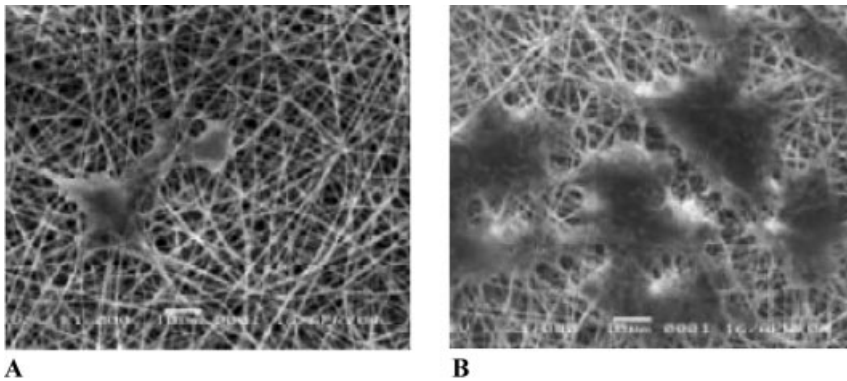


**Fig. 1.35.** SEM images of HCAECs cultured on (A) uncoated P(LLA-CL) nanofiber matrix and (B) collagen-coated p(LLA-CL) nanofiber matrix after 3 days in culture. (Adapted from Ref. [150] with permission from Elsevier.)

Another related study was performed by the same research group to evaluate the effect of cell behavior towards scaffolds that combine nanostructure and bioactivity. Poly(ethylene terephthalate) a non-degradable polymer extensively investigated for developing vascular graft was fabricated into a nanofibrous structure using the process of electrospinning [174]. The nanofibers were then surface modified to attach a bioactive protein gelatin. The surface-modified fiber scaffolds were then seeded with HCAECs and cultured for 7 days. The surface-modified nanofiber matrix showed improved cell adhesion and maintenance of phenotypic activity. These results showed that combining the nanostructure of the scaffold with the bioactive molecule could positively promote cell–matrix and cell–cell interactions, inducing them to express the phenotypic shape.

The effect of fiber orientation on SMC attachment and proliferation of nanofiber matrices was evaluated using aligned nanofiber scaffolds of P(LLA-CL) [140]. Aligned fibers were developed by the process of electrospinning using the wheel with a sharp edge collector. SMCs were found to adhere on aligned nanofiber scaffold as early as within 1 h of seeding and the cells tend to elongate along the direction of the nanofibers. After 3 days in culture, SMCs proliferated approximately along the longitudinal direction of the nanofiber length, which formed an oriented pattern similar to those in native artery. The cell number significantly increased at day 7 and the surface of the nanofibrous scaffold was covered with a continuous SMC monolayer with a regular direction from left to right along the nanofiber alignment. The cell adhesion and proliferation on aligned nanofiber matrix was significantly higher than on 2D film of the same polymer. Figure 1.36 shows the SEM of aligned SMC on aligned nanofiber matrix. Further, the distribution and organization of cytoskeleton proteins inside SMCs were parallel to the direction of the nanofibers (Fig. 1.37). The study demonstrated for the first time the feasibility of using an aligned nanostructured scaffold to mimic natural vessel architecture and the ability of cells to orient along the fiber axis to mimic the natural orientation.

One elegant method to incorporate biofunctionality into nanofiber scaffolds is the use of self-assembling peptides decorated with appropriate protein motifs. Gen-

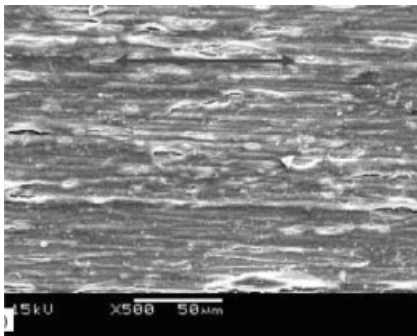


**Fig. 1.36.** SEM showing the alignment of SMCs along the aligned nanofiber matrix. (Adapted from Ref. [140] with permission from Elsevier.)

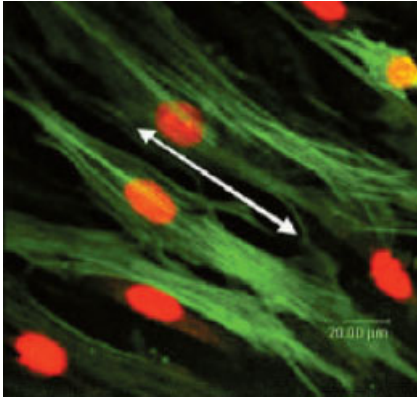


**Fig. 1.37.** LSCM micrograph of immunostained  $\alpha$ -actin filaments in SMC after 1 day of culture on aligned nanofiber matrix. (Adapted from Ref. [140] with permission from Elsevier.)

ove et al. recently developed biomimetic self-assembled peptide scaffolds and evaluated the function of human aortic endothelial cells seeded on the scaffolds [175]. The self-assembling protein motifs were developed based on the functionality of basement membrane, which is composed mainly of laminin and collagen. Two peptide sequences present in laminin (YIGSR and RYVVLPR) are known to promote cell adhesion, cell migration and endothelial cell tubular formation, and a peptide sequence in collagen Type IV (TAGSCLRKFSTM) shown to promote the adhesion and spreading of bovine aortic endothelial cells, were selected to develop novel functionalized peptide motifs for self-assembly. The functionalized peptides were developed by solid-phase synthesis and found to self-assemble to form hydrogel under physiological conditions (Fig. 1.38). Four different scaffolds were investigated in the study, unmodified self-assembled peptide scaffolds, composed of RAD 16-1 (AcN-RADARADARADARADA-CONH<sub>2</sub>), YIG (10%) modified scaffold, RYV (10%) modified scaffold and TAH (10%) modified scaffold. Cell numbers increased about two-fold in modified peptide scaffolds compared to unmodified scaffolds, indicating that cell could sense and respond to the functionalized material. In addition, the matrix could modulate endothelial cell growth only when the sequence was physically attached to the nanofiber matrix, showing the importance of spatial distribution of the bioactive molecules on the nanostructured scaffolds. The peptide scaffolds in general also enhanced the endothelial cell phenotype, such as NO synthesis and deposition of basement membrane components (laminin I and collagen IV), suggesting the potential of these scaffolds in recreating the endothelial microenvironment.

Another application for which biodegradable nanofiber matrices have been evaluated is for developing scaffolds for engineering myocardium. Shin et al. have evaluated the potential of PCL nanofiber matrix as a cardiac graft by assessing the interaction of rat cardiomyocytes with the nanofiber scaffold [176]. The average di-



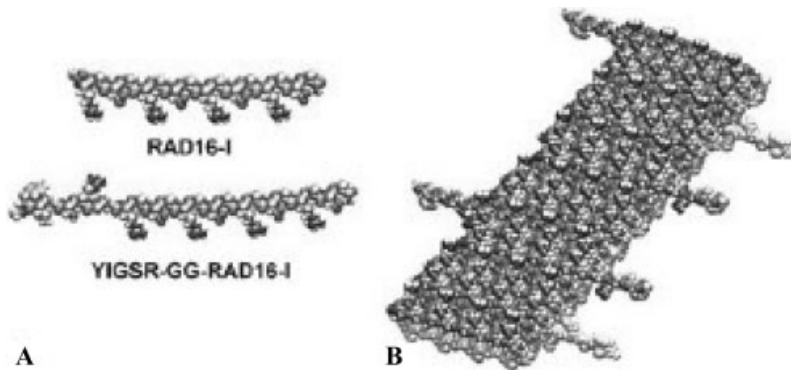


**Fig. 1.38.** (A) Model representing the peptide RAD16-1 (unfunctionalized peptide) and peptide YIG (functionalized). (B) Model representing the double  $\beta$ -sheet tape of a self-assembled peptide nanofiber of a mixture composed of RAD16-1 and YIG (9:1). (Adapted from Ref. [175] with permission from Elsevier.)

ameter of the fibers used to develop the scaffold was  $\sim 250$  nm. The cardiomyocytes attached well on the scaffold and after three days in culture the cardiomyocytes started to contract (Fig. 1.39). The contractions were ubiquitous and synchronized. The mechanical property (softness) of the scaffold was found to be highly appropriate to allow the spontaneous contraction of the cardiomyocytes. The cardiomyocytes were also found to form a tight arrangement and intercellular contacts throughout the entire mesh and stained positive for cardiotypical proteins. However, the system has some limitations for *in vivo* application. The limited thickness of the scaffold might not be able to provide sufficient function when used alone to cover an infarcted area. Therefore, a modified multilayered nanostructured nanofibrous graft was developed [177]. PCL nanofiber matrices composed of fibers having diameters of  $\sim 100$  nm were developed and cardiomyocytes were cultured on nanofiber matrices for 5–7 days. After that layering of the individual grafts (five

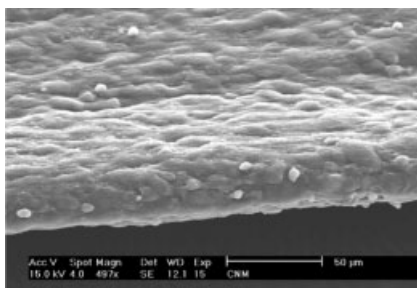


**Fig. 1.39.** SEM of the cross-section of a cardiac nanofibrous mesh, showing complete coverage of the mesh with cardiomyocytes. (Adapted from Ref. [176] with permission from Elsevier.)

layers) were performed by gently placing layers on top of each other. The layered constructs were incubated for 2 h at 37 °C without media for interlayer attachment and then cultured for 14 days in culture media. Multilayered scaffolds initially showed weak and unsynchronized contractions but became stronger and synchronized with time. H&E staining of the constructs demonstrated the interconnections between the layers. The immunohistochemistry study showed the presence of connexin43 in multilayered graft, indicating that the cells are rebuilding gap junctions, and synchronized contractions in multilayered grafts. *In vivo* studies using these grafts are under way.

#### 1.7.4

#### Bone, Ligament and Cartilage Tissue Engineering

Nanofiber matrices were also investigated for developing scaffolds for bone, ligament and cartilage tissue engineering. Li et al. used PLGA nanofiber matrices to culture MSCs and demonstrated that nanofibrous matrices could support the adhesion and proliferation of these cells [149]. Yoshimoto et al. used PCL nanofiber matrices to culture MSCs under dynamic conditions in osteogenic media to evaluate the feasibility of developing bone *in vitro* [178]. The average fiber diameter of the scaffold was ~400 nm. The MSCs were seeded on the nanofiber matrix and cultured for 4 weeks under dynamic conditions. MSCs were found to attach and proliferate throughout the nanofiber matrix. Furthermore, the cells migrated inside the scaffold and produced an extracellular matrix of collagen throughout the scaffold (Fig. 1.40). After 4 weeks in culture the cell polymer construct was noticeably harder and the extracellular matrix was calcified throughout the matrix, as evidenced from histology.

Polyurethane nanofiber scaffold was used to evaluate the effect of nanofiber alignment on the cellular response of human ligament fibroblasts (HLF) and to evaluate the influence of HLF alignment and strain direction on mechanotransduction [153]. A rotating collecting target was used to develop aligned nanofibers. After 3 days in culture, the HLFs on the aligned nanofibers were spindle shaped



**Fig. 1.40.** SEM showing a cell nanofiber construct after 4 weeks in culture. Globular accretions, abundant calcification and collagen bundles can be seen. (Adapted from Ref. [178] with permission from Elsevier.)

and oriented (similar to *in vivo* ligament fibroblast morphology) along the nanofiber direction and the aligned nanofiber formed tissue-like oriented bundles that were confluent over the entire surface within 7 days. The HLFs on randomly oriented nanofiber scaffold were not oriented, but when the scaffold was subjected to uniaxial strain the cells reorganized their spindle shape and became organized. There were significant differences in the ECM production by oriented and un-oriented cells on the matrices, indicating that cell morphology plays a significant role in ECM production. Furthermore, the aligned HLFs on the nanofiber structure were more sensitive to strain in a longitudinal direction. The study demonstrated that aligned nanofiber scaffold forms a promising structure for developing tissue engineered ligament due to its biomimetic structure and the ability to provide a mechanical environment ligament cells encounter *in vivo*.

Li et al. using PCL nanofiber scaffold demonstrated the efficacy of nanofiber scaffold to support the differentiation of MSCs to chondrocytes as a viable method to engineer cartilage *in vitro* [179]. The three-dimensional MSC seeded constructs display a cartilage-like morphology containing chondrocyte like cells surrounded by abundant cartilaginous matrix (Fig. 1.41). The level of MSC chondrogenesis using nanofiber scaffold was found to be higher than in high density pellet cultures commonly used for MSCs. This study demonstrated that biodegradable nanofiber scaffold due to its microstructure resemblance to a native ECM effectively supported MSC chondrogenesis.

A self-assembling peptide hydrogel scaffold has also been investigated as scaffolds for cartilage repair and regeneration [180]. A KLD12 peptide was developed, the aqueous solution of which was found to form a hydrogel when exposed to salt solution or cell culture media. The encapsulated chondrocytes showed a round morphology with cell viability of 89% immediately after encapsulation. Cell division of encapsulated chondrocytes in peptide hydrogel was found to be much higher than agarose control cultures. Histological evaluation of the encapsulated cell-hydrogel construct showed the formation of cartilage-like ECM rich in proteoglycans and type II collagen. Time dependent accumulation of this ECM was paralleled by increase in stiffness of the material showing the deposition of mechanically functional neo-tissue. This study demonstrated the potential of self-assembling peptide hydrogel as a scaffold for the synthesis and accumulation of a true cartilage-like ECM within a 3D cell culture for cartilage tissue repair.

## 1.8

### Conclusions

Nanotechnology assisted fabrication processes are changing the way bioresorbable scaffolds are being developed for tissue engineering. Novel nanofabrication processes have enabled the development of nanostructured scaffolds that could closely resemble the structure of the ECM, and studies using bioactive nanostructured scaffolds have demonstrated the importance of nanostructure in cell-matrix and cell-cell interaction. Even though top-down and bottom-up approaches developed

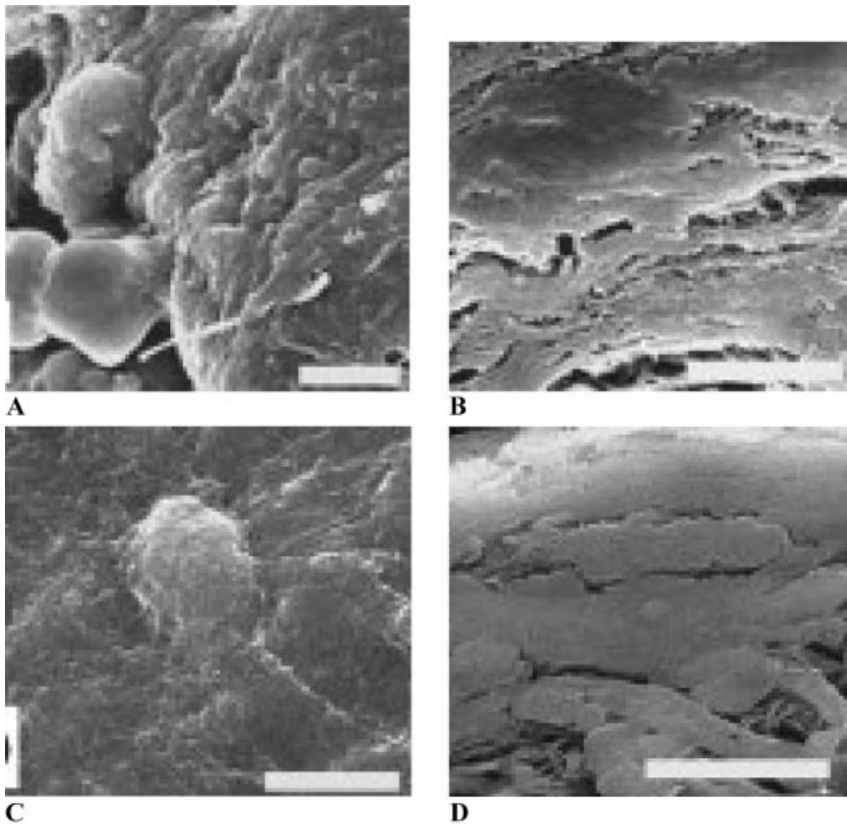


**Fig. 1.41.** Morphology of differentiated chondrocytes in cell pellet (CP) culture and using PCL nanofiber matrix. (A) Top view of CP with round chondrocyte-like cells on the surface. (B) Cross-sectional view of CP, showing thick ECM. (C) Top view of nanofiber

matrix, showing the presence of round, ECM-embedded chondrocyte-like cells. (D) Cross-sectional view of nanofiber matrix, showing a thick, dense ECM-rich layer. (Adapted from Ref. 179] with permission from Elsevier.)

to fabricate nanostructured scaffolds have several advantages of their own, several limitations still hinder the translation of many of these technologies for clinical applications. Future studies will rely on a combination of both approaches as necessary as well as combining these with lithographic techniques to develop hierarchical nanostructures with spatially presented biological cues for developing optimal scaffolds for tissue engineering.

## References

- 1 LEVENBERG S, LANGER R. *Curr. Top. Develop. Biol.* 61, 113–134, 2004.
- 2 BAUER TW, MUSCHLER GF. Bone graft materials An overview of the basic

- science. *Clin. Orthop.* 371, 10–27, 2000.
- 3 HEINEKEN FG, SKALAK R. Tissue engineering: A brief overview. *J. Biomech. Eng.* 113, 111, 1991.
  - 4 SKALAK R, FOX CF (eds.). *Tissue Engineering*. Proceedings for a Workshop held at Granlibakken, Lake Tahoe, California, February 26–29, Alan Liss, New York, 1988.
  - 5 NEREM RM. Cellular engineering. *Ann. Biomed. Eng.* 19, 529–545, 1991.
  - 6 LANGER R, VACANTI JP. Tissue engineering. *Science* 260, 920–926, 1993.
  - 7 VACANTI JP, LANGER R. Tissue engineering: the design and fabrication of living replacement devices for surgical reconstruction and transplantation. *Lancet* 354 (Suppl 1), 32–34, 1999.
  - 8 FUCHS JR, NASSERI BA, VACANTI JP. Tissue engineering: A 21<sup>st</sup> century solution to surgical reconstruction. *Ann. Thorac. Surg.* 72, 577–591, 2001.
  - 9 LAURENCIN CT, AMBORSIO AMA, BORDEN MD, COOPER JA. Tissue engineering: orthopedic application. *Ann. Rev. Biomed. Eng.* 1, 19–46, 1999.
  - 10 SIPE JD. Tissue engineering and reparative medicine. *Ann. New York Acad. Sci.* 961, 1–9, 2002.
  - 11 WEAVER VM, PETERSEN OW, WANG F, LARABELL CA, BRIAND P, DAMSKY C, BISSELL MJ. Reversion of the malignant phenotype of human breast cells in three-dimensional culture and in vivo by integrin blocking antibodies. *J. Cell Biol.* 137, 231–245, 1997.
  - 12 CUKIERMAN E, PANKOV R, STEVENS DR, YAMADA KM. Taking cell-matrix adhesions to third dimensions. *Science* 294, 1708–1712, 2001.
  - 13 VACANTI JP, MORSE MA, SALTZMAN WM, DOMB AJ, PEREZATYDE A, LANGER R. Selective cell transplantation using bioabsorbable artificial polymers as matrices. *J. Pediatr. Surg.* 23, 3–9, 1988.
  - 14 LANGER R, TIRRELL DA. Designing materials for biology and medicine. *Nature* 428, 487–492, 2004.
  - 15 ROSSO F, MARIO G, GIORDANO A, BARBARISI M, PARMEGGIANI D, BARBARUSU A. Smart materials as scaffolds for tissue engineering. *J. Cell Physiol.* 203, 465–470, 2005.
  - 16 MALLAPRAGADA S, NARASIMHAN B (Eds.). *Handbook of Biodegradable Polymeric Materials and their Applications*. American Scientific Publishers, North Lewis Way, 2006.
  - 17 HOLLISTER SJ. Porous scaffold design for tissue engineering. *Nat. Mater.* 4, 518–524, 2005.
  - 18 AGARWAL CM, RAY RB. Biodegradable polymeric scaffolds for musculoskeletal regeneration. *J. Biomed. Mater. Res.* 55, 141–150, 1988.
  - 19 LU L, MIKOS AG. The importance of new processing techniques in tissue engineering. *MRS Bull.* 11, 28, 1996.
  - 20 THOMSON RC, YASZEMSKI MJ, MIKOS AG. Polymer scaffold processing. In: LANZA RP, LANGER R, CHICK WL (Eds.), *Principles of Tissue Engineering*. R.G. Landes Co., Austin, TX, p. 263, 1997.
  - 21 WIDMER MS, MIKOS AG. Fabrication of biodegradable polymer scaffolds for tissue engineering. In: PATRICK JR CW, MIKOS AG, MCINTIRE LV (Eds.), *Frontiers in Tissue Engineering*. Elsevier Science, New York, p. 107, 1998.
  - 22 HUTMACHER DW, ZEIN I, TEOH SH, NG KW, SCHANTZ JT, LEAHY JC. Design and fabrication of a 3D scaffold for tissue engineering bone. In: AGARWAL CM, PARR JE, LIN ST (Eds.), *Synthetic Bioabsorbable Polymers for Implants*, STP 1396. American Society for Testing and Materials, West Conshohocken, PA, p. 152, 2000.
  - 23 HUTMACHER DW, SITTINGER M, RISBUD MV. Scaffold-based tissue engineering: rationale for computer aided design and solid free form fabrication systems. *Trends Biotechnol.* 22, 354–362, 2004.
  - 24 MIKOS AG, THORSEN AJ, CZERWONKA LA, BAO Y, LANGER R, WINSLOW DN, VACANTI JP. Preparation and characterization of poly(L-lactic acid) foams. *Polymer* 35, 1068–1077, 1994.
  - 25 MA, PX, LANGER R. Fabrication of biodegradable polymer foams for cell transplantation and tissue

- engineering. In: MORGAN J, YARMUSH M (Eds.), *Tissue Engineering Methods and Protocols*, Humana Press, NJ, p. 47, **1999**.
- 26 LU L, PETER SJ, LYMAN MD, LAI H, LEITE SM, TAMADA JA, VACANTI JP, LANGER R, MIKOS AJ. *In vitro* degradation of porous poly(L-lactic acid) foams. *Biomaterials* 21, 1595–1605, **2000**.
  - 27 BORDEN MD, KHAN Y, ATTAWIA M, LAURENCIN CT. Tissue engineered microsphere-based matrices for bone repair: Design, evaluation, and optimization. *Biomaterials* 23, 551–9, **2002**.
  - 28 BORDEN M, ATTAWIA M, LAURENCIN CT. The sintered microsphere matrix for bone tissue engineering: In vitro osteoconductivity studies. *J. Biomed. Mater. Res.* 61, 421–429, **2002**.
  - 29 BORDEN MD, EL-AMIN SF, ATTAWIA M, LAURENCIN CT. Structural and human cellular assessment of a novel microsphere based tissue engineered scaffold for bone repair. *Biomaterials*, 24, 597–609, **2003**.
  - 30 BORDEN MD, ATTAWIA M, KHAN Y, EL-AMIN SF, LAURENCIN CT. Tissue-engineered bone formation *in vivo* using a novel sintered polymeric microsphere matrix. *J. Bone Joint Surg. (B)*. 86-B, 1200–1208, **2004**.
  - 31 YANG SF, LEONG KF, DU ZH, CHUA CK. The design of scaffolds for use in tissue engineering: part 1 – Traditional factors. *Tissue Eng.* 7, 679–689, **2001**.
  - 32 LEONG KF, CHEAH CM, CHUA CK. Solid freeform fabrication of three-dimensional scaffolds for engineering replacement tissues and organs, *Biomaterials* 24, 2363–2378, **2003**.
  - 33 COOKE MN, FISHER JP, DEAN D, RIMNAC C, MIKOS AG. Use of stereolithography to manufacture critical-sized 3D biodegradable scaffolds for bone ingrowth, *J. Biomed. Mater. Res.* 64B, 65–69, **2003**.
  - 34 YU T, CHIPELLINI F, SCHMALJOHANN D, SOLARO R, OBER CK. Microfabrication of hydrogels as polymer scaffolds for tissue engineering applications. *Polym. Prepr.* 41, 1699–1700, **2000**.
  - 35 GARIEPY E, LEROUX J. In situ forming hydrogels – Review of temperature sensitive systems. *Eur. J. Pharm. Biopharm.* 58, 409–426, **2004**.
  - 36 GIL ES, HUDSON SM. Stimuli-responsive polymers and their bioconjugates. *Progr. Polym. Sci.* 29, 1173–1222, **2004**.
  - 37 KIM TM, SHARMA B, WILLIAMS CG, RUFFNER MA, MALIK A, MCFARLAND EG, ELISSEFF JH. Experimental model for cartilage tissue engineering to regenerate the zonal organization of articular cartilage. *Osteoarthritis Cartilage* 11, 653–664, **2003**.
  - 38 VARGHESE D, DESHPANDE M, XU T, KESARI P, OHRI S, BOLAND T. Advances in tissue engineering: cell printing. *J. Thor. Card. Surg.* 129, 470–472, **2005**.
  - 39 BOLAND T, MIRONOV V, GUTOWSKA A, ROTH EA, MARKWALD RR. Cell and organ printing 2: Fusion of cell aggregates in three-dimensional gels. *Anat. Rec.* 272A, 497–502, **2003**.
  - 40 NEAGU A, FORGAC G. Fusion of cell aggregates: a mathematical model. In: VOSSOUGH J (Ed.), *Biomedical Engineering. Recent Development*, Medical and Engineering Publishers, Inc., Washington DC, USA, pp. 241–242, **2002**.
  - 41 MIRONOV V, BOLAND T, TRUSK T, FORGACS G, MARKWALD RR. Organ printing: Computer-aided jet-based 3D tissue engineering. *Trends Biotechnol.* 21, 157–161, **2003**.
  - 42 JAKAB K, NEAGU A, MIRONOV V, MARKWALD RR, FORGACS G. Engineering biological structures of prescribed shape using self-assembling multicellular systems, *Proc. Natl. Acad. Sci. U.S.A.* 10, 2864–2869, **2004**.
  - 43 SHIEH S, TERADA S, VACANTI JP. Tissue engineering auricular regeneration: *In vitro* and *in vivo* studies. *Biomaterials.* 25, 1545–1557, **2004**.
  - 44 RASPANTI M, PROTASONI M, MANELLI A, GUIZZARDI S, MANTOVANI V, SALA A. The extracellular matrix of the human aortic wall: Ultrastructural observations by FEG-SEM and by tapping-mode AFM. *Micron.* 37, 81–86, **2006**.
  - 45 GRIFFITH LG. Emerging design

- principles in biomaterials and scaffolds in tissue engineering. *Ann. New York Acad. Sci.* 961, 83–95, 2002.
- 46 SALTZMANN WM, OLBRICHT WL. Building drug delivery into tissue engineering. *Nat. Rev. Drug Discov.* 1, 177–186, 2002.
  - 47 TIRRELL M, KOKKOLI E, BIESALSKI M. The role of surface science in bioengineered materials. *Surf. Sci.* 500, 61–83, 2002.
  - 48 BOSMAN FT, STAMENKOVIC I. Functional structure and composition of the extracellular matrix. *J. Pathol.* 200, 432–428, 2003.
  - 49 OLSEN BR. Matrix molecules and their ligands. In: LANZA RP, LANGER R, CHICK WL (Eds.), *Principles of Tissue Engineering*, 1<sup>st</sup> edition, Academic Press, New York, pp. 47–65, 1997.
  - 50 BOUDREAU N, MYERS C, BISSELL MJ. From laminin to lamin: regulation of tissue-specific gene expression by the ECM. *Trends Cell Biol.* 5, 1–4, 1995.
  - 51 PROVENZANE PP, VANDERBY R. Collagen fibril morphology and organization: Implications for force transmission in ligament and tendon. *Matrix Biol.* 25, 71–84, 2006.
  - 52 FANTNER GE, RABINOVYCH O, SCHITTER G, THURNER P, KINDT JH, FINCH MM, WEAVER JC, GOLDE LS, MORSE DE, LIPMAN EA, RANGELOW IW, HANSMA PK. Hierarchical interconnections in the nanocomposite material bone: Fibrillar cross-links resist fracture on several length scales. *Composites Sci. Technol.* 66, 1205–1211, 2006.
  - 53 GELSE K, POSCHL E, AIGNER T. Collagen Structure, function and biosynthesis. *Adv. Drug Deliv. Rev.* 55, 1531–1546, 2003.
  - 54 CURTIS A, WILKINSON C. Nanotechniques and approaches in biotechnology. *Trends Biotechnol.* 19, 97–101, 2001.
  - 55 LUTOLF MP, HUBBELL JA. Synthetic biomaterials as instructive extracellular microenvironments for morphogenesis in tissue engineering. *Nat. Biotechnol.* 23, 47–55, 2005.
  - 56 ADAMS JC, WATT FM. Regulation of development and differentiation by the extracellular matrix. *Development* 117, 1183–1198, 1993.
  - 57 XIONG J, STEHLE T, DIEFENBACH B, ZHANG R, DUNKER R, SCOTT DL, JOACHIMIAK A, GOODMAN SL, ARNAOUTI MA. Crystal structure of the extracellular segment of integrin  $\alpha V\beta 3$ . *Science* 294, 339–345, 2001.
  - 58 GARCIA AJ. Get a grip. Integrins in cell–biomaterial interactions. *Biomaterials* 26, 7525–7529, 2005.
  - 59 BERSHADSKY AD, BALLESTREM C, CARRAMUSA L, ZILBERMAN Y, GILQUIN B, KHOCHBIN S, ALEXandrova AY, VERKHOVSKY AB, SHEMAH T, KOZLOV MM. Assembly and mechanosensory function of focal adhesions: experiments and models. *Eur. J. Cell Biol.* 85, 165–173, 2006.
  - 60 ROSS RS. Molecular and mechanical synergy: Cross-talk between integrins and growth factor receptors. *Cardiovasc. Res.* 63, 381–390, 2004.
  - 61 ADAMS JC. Cell matrix contact structure. *Cell Mol. Life Sci.* 58, 371–392, 2001.
  - 62 HE L, DEXTER AF, MIDDLEBERG APJ. Biomolecular engineering at interfaces. *Chem. Eng. Sci.* 61, 989–1003, 2006.
  - 63 LI JM, MENCONI MJ, WHEELER HB, ROHRER MJ, KLASSEN VA, ANSELL JE, APPEL MC. Precoating expanded polytetrafluoroethylene grafts alters production of endothelial cell-derived thrombomodulators. *J. Vasc. Surg.* 15, 1010–1017, 1992.
  - 64 KAEHLER J, ZILLA P, FASOL R, DEUTSCH M, KADLETZ M. Precoating substrate and surface configuration determine adherence and spreading of seeded endothelial cells on polytetrafluoroethylene grafts. *J. Vasc. Surg.* 9, 535–41, 1989.
  - 65 SEEGER JM, KLINGMAN N. Improved endothelial cell seeding with cultured cells and fibronectin-coated grafts. *J. Surg. Res.* 38, 641–7, 1985.
  - 66 PIERSCHBACHER MD, RUOSLAHTI E. Cell attachment activity of fibronectin can be duplicated by small synthetic fragments of the molecule. *Nature* 309, 30–33, 1984.
  - 67 RUOSLAHTI E, PIERSCHBACHER MD. New perspectives in cell adhesion:

- RGD and integrins. *Science* 238, 491–497, 1987.
- 68 RUOSLAHTI E. RGD and other recognition sequences for integrins. *Annu. Rev. Cell Dev. Biol.* 12, 697–715, 1996.
- 69 RUOSLAHTI E. The RGD story. A personal account. *Matrix Biol.* 22, 459–465, 2003.
- 70 HYNES RO. Integrins – Versatility, modulation, and signaling in cell-adhesion. *Cell* 69, 11–25, 1992.
- 71 XIONG JP, STEHLE T, ZHANG R, JOACHIMIAK A, FRECH M, GOODMAN SL, ARNAOUT MA. Crystal structure of the extracellular segment of integrin  $\alpha$ v $\beta$ 3 in complex with an Arg–Gly Asp ligand. *Science* 296, 151–155, 2002.
- 72 XIONG J, STEHLE T, GOODMAN SL, ARNAOUTI MA. A novel adaptation of the integrin  $\alpha$ PSI domain revealed from its crystal structure. *J. Biol. Chem.* 279, 40 252–40 254, 2004.
- 73 ITO Y, KAJIHARA M, IMANISHI Y. Materials for enhancing cell adhesion by immobilization of cell-adhesive peptide. *J. Biomed. Mater. Res.* 25, 1325–37, 1991.
- 74 NEFF JA, CALDWELL KD, TRESKO PA. A novel method for surface modification to promote cell attachment to hydrophobic substrates. *J. Biomed. Mater. Res.* 40, 511–519, 1998.
- 75 HERSEL U, DAHMEN C, KESSLER H. RGD modified polymers: Biomaterials for simulated cell adhesion and beyond. *Biomaterials* 24, 4385–4415, 2003.
- 76 PELHAM JR RJ, WANG YL. Cell locomotion and focal adhesions are regulated by the mechanical properties of the substrate. *Biol. Bull.* 194, 348–50, 1998.
- 77 CASTEL S, PAGAN R, MITJANS F, PIULATS J, GOODMAN S, JONCZYK A, HUBER F, VILARO S, REINA M. RGD peptides and monoclonal antibodies, antagonists of  $\alpha$ v $\beta$ 3-integrin, enter the cells by independent endocytic pathways. *Lab. Invest.* 81, 1615–1626, 2001.
- 78 YANG XB, ROACH HI, CLARKE NM, HOWDLE SM, QUIRK R, SHAKESHEFF KM, OREFFO RO. Human osteoprogenitor growth and differentiation on synthetic biodegradable structures after surface modification. *Bone* 29, 523–531, 2001.
- 79 NEFF JA, TRESKO PA, CALDWELL KD. Surface modification for controlled studies of cell–ligand interactions. *Biomaterials* 20, 2377–2393, 1999.
- 80 HIRANO Y, OKUNO M, HAYASHI T, GOTO K, NAKAJIMA A. Cell attachment activities of surface immobilized oligopeptides RGD, RGDS, RGDV, RGDY, and YIGSR toward five cell lines. *J. Biomater. Sci. Polym. Ed.* 4, 235–243, 1993.
- 81 COOK AD, HRKACH JS, GAO NN, JOHNSON IM, PAJVANI UB, CANNIZZARO SM, LANGER R. Characterization and development of RGD-peptide-modified poly(lactic acid-co-lysine) as an interactive, resorbable biomaterial. *J. Biomed. Mater. Res.* 35, 513–523, 1997.
- 82 BREUERS W, KLEE D, HOCKER H, MITTERMAYER C. Immobilization of a fibronectin fragment at the surface of a polyetherurethane film. *J. Mater. Sci. Mater. Med.* 2, 106–109, 1991.
- 83 TONG YW, SHOICHET MS. Peptide surface modification of poly(tetrafluoro-ethylene-co-hexafluoropropylene) enhances its interaction with central nervous system neurons. *J. Biomed. Mater. Res.* 42, 85–95, 1998.
- 84 PORTE-DURRIEU MC, LABRUGERE C, VILLARS F, LEFEBVRE F, DUTOYA S, GUETTE A, BORDENAVE L, BAQUEY C. Development of RGD peptides grafted onto silica surfaces: XPS characterization and human endothelial cell interactions. *J. Biomed. Mater. Res.* 46, 368–375, 1999.
- 85 MARCHAND-BRYNAERT J. Surface modifications and reactivity assays of polymer films and membranes by selective wet chemistry. *Recent Res. Polym. Sci.* 2, 335–361, 1998.
- 86 CARLISLE ES, MARIAPPAN MR, NELSON KD, THOMES BE, TIMMONS RB, CONSTANTINESCU A, EBERHART RC, BANKEY PE. Enhancing hepatocyte adhesion by pulsed plasma deposition and polyethylene glycol coupling. *Tissue Eng.* 6, 45–52, 2000.



- 87 TAM JP, YU Q, MIAO Z. Orthogonal ligation strategies for peptide and protein. *Biopolymers* 51, 311–332, 1999.
- 88 IVANOV B, GRZESIK W, ROBEY FA. Synthesis and use of a new bromoacetyl-derivatized heterotrifunctional amino acid for conjugation of cyclic RGD-containing peptides derived from human bone sialoprotein. *Bioconj. Chem.* 6, 269–277, 1995.
- 89 HOUSEMAN BT, GAWALT ES, MRKSICH M. Maleimide functionalized self-assembled monolayers for the preparation of peptide and carbohydrate biochips. *Langmuir* 19, 1522–1531, 2003.
- 90 HERBERT CB, McLERNON TL, HYPOLITE CL, ADAMS DN, PIKUS L, HUANG CC, FIELDS GB, LETOURNEAU PC, DISTEFANO MD, HU WS. Micropatterning gradients and controlling surface densities of photoactivatable biomolecules on self-assembled monolayers of oligo(ethylene glycol) alkanethiolates. *Chem. Biol.* 4, 731–737, 1997.
- 91 LIN YS, WANG SS, CHUNG TW, WANG YH, CHIOU SH, HSU JJ, CHOU NK, HSIEH KH, CHU SH. Growth of endothelial cells on different concentrations of Gly Arg-Gly Asp photochemically grafted in polyethylene glycol modified polyurethane. *Artif. Organs* 25, 617–621, 2001.
- 92 SUGAWARA T, MATSUDA T. Photochemical surface derivatization of a peptide containing Arg–Gly Asp (RGD). *J. Biomed. Mater. Res.* 29, 1047–1052, 1995.
- 93 REYES CD, GARCIA AJ. Engineering integrin-specific surfaces with a triple helical collagen mimetic peptide. *J. Biomed. Mater. Res. Part A* 65, 511–523, 2003.
- 94 KANTLEHNER M, SCHAFFNER P, FINSINGER D, MEYER J, JONCZYK A, DIEFENBACH B, NIES B, HOLZEMANN G, GOODMAN SL, KESSLER H. Surface coating with cyclic RGD peptides stimulates osteoblast adhesion and proliferation as well as bone formation. *Chem-BioChem* 1, 107–114, 2000.
- 95 DELFORGE D, GILLON B, ART M, DEWELLE J, RAES M, REMACLE J. Design of a synthetic adhesion protein by grafting RGD tailed cyclic peptides on bovine serum albumin. *Letts. Pept Sci.* 5, 87–91, 1998.
- 96 KAO WJ, HUBBELL JA, ANDERSON JM. Protein-mediated macrophage adhesion and activation on biomaterials: A model for modulating cell behavior. *J. Mater. Sci. Mater. Med.* 10, 601–605, 1999.
- 97 MASSIA SP, STARK J. Immobilized RGD peptides on surface grafted dextran promotes biospecific cell attachment. *J. Biomed. Mater. Res.* 56, 390–9, 2001.
- 98 MASSIA SP, HUBBELL JA. An RGD spacing of 440 nm is sufficient for integrin avb3-mediated fibroblast spreading and 140 nm for focal contact fiber formation. *J. Cell. Biol.* 114, 1089–1100, 1991.
- 99 ELBERT DL, HUBBELL JA. Conjugate addition reactions combined with free-radical cross-linking for the design of materials for tissue engineering. *Biomacromolecules* 2, 430–441, 2001.
- 100 IRVINE DJ, HUE KA, MAYES AM, GRIFFITH LG. Simulations of cell-surface integrin binding to nanoscale-clustered adhesion ligands. *Biophys. J.* 82, 120–132, 2002.
- 101 MAHESHWARI G, BROWN G, LAUFFENBURGER DA, WELLS A, GRIFFITH LG. Cell adhesion and motility depend on nanoscale RGD clustering. *J. Cell Sci.* 113, 1677–1686, 2000.
- 102 IRVINE DJ, RUZETTE A-VG, MAYES AM, GRIFFITH LG. Nanoscale clustering of RGD peptides at surfaces using comb polymers – 2. Surface segregation of comb polymers in polylactide. *Biomacromolecules* 2, 545–56, 2001.
- 103 Interagency Working Groups on Nanoscience, and Technology, National Nanotechnology Initiative: Leading to the Next Industrial Revolution. Washington D.C., Committee on Technology, National Science and Technology Council, 2000.
- 104 ALIVISATOS AP. Semiconductor

- clusters, nanocrystals, and quantum dots. *Science* 271, 933–937, 1996.
- 105 SIMON A, DURRIEU M. Strategies and results of atomic force microscopy in the study of cellular adhesion. *Micron* 37, 1–13, 2006.
- 106 WOODCOCK SE, JOHNSON WC, CHEN Z. Collagen adsorption and structure on polymer surfaces observed by atomic force microscopy. *J. Colloid Interface Sci.* 292, 99–107, 2005.
- 107 CURTIS AS, CASEY B, GALLAGHER JO, PASQUI D, WOOD MA, WILKINSON CD. Substratum nanotopography and the adhesion of biological cells. Are symmetry or regularity of nanotopography important? *Biophys. Chem.* 94, 275–283, 2001.
- 108 DALBY MJ, YARWOOD SJ, RIEHLE MO, JOSHSTONE HJH, AFFROSSMAN S, CURTIS ASG. Increasing fibroblast response to materials using nanotopography: morphological and genetic measurements of cells response to 13 mm-high polymer demixed islands. *Exp. Cell Res.* 276, 1–9, 2002.
- 109 DALBY MJ, CHILDS S, RIEHLE MO, JOHNSTONE HJH, AFFROSSMAN S, CURTIS ASG. Fibroblast reaction to island topography; changes in cytoskeleton and morphology with time. *Biomaterials* 24, 927–935, 2003.
- 110 DALBY MJ, GIANNARAS D, RIEHLE MO, GADEGAARD N, AFFROSSMAN S, CURTIS ASG. Rapid fibroblast adhesion to 27 nm high polymer demixed nanotopography. *Biomaterials* 25, 77–83, 2004.
- 111 DALBY MJ, MCCLOY D, ROBERTSON M, WILKINSON CDW, OREFFO ROC. Osteoprogenitor response to defined topographies with nanoscale depths. *Biomaterials* 27, 1306–1315, 2006.
- 112 NAIR LS, BHATTACHARYYA S, LAURENCIN CT. Development of novel tissue engineering scaffolds via electrospinning. *Expert Opin. Biol. Ther.* 4, 1–10, 2004.
- 113 CHRONAKIS IS. Novel nanocomposites and nonoceramics based on polymer nanofibers using electrospinning process – A review. *J. Mater. Process Tec.* 167, 283–293, 2005.
- 114 SMITH LA, MA PX. Nanofibrous scaffolds for tissue engineering. *Collids Surf. B: Biointerfaces* 39, 125–131, 2004.
- 115 MARTIN CR. Membrane based synthesis of nanomaterials. *Chem. Mater.* 8, 1739–1746, 1996.
- 116 JAYARAMAN K, KOTAKI M, ZHANG Y, MO X, RAMAKRISHNA S. Recent advances in polymer nanofibers. *J. Nanosci. Nanotechnol.* 4, 52–65, 2004.
- 117 TAYLOR GI. *Proc. Royal Soc. London* A313, 453, 1969.
- 118 RENEKER JD. Electrospinning process and applications of electrospun fibers. *J. Electrostatics* 35, 151, 1995.
- 119 RENEKER DH, YARIN AL, FONG H, KOOMBHONGSE S, *J. Appl. Phys.* 87, 4531, 2000.
- 120 RENEKER DH, YARIN A, EVANS EA, KATAPHINAN W, RANGKUPAN R, LIU W. *Electrospinning and Nanofibers*, Book of Abstracts. In: New Frontiers in Fiber Science, Spring Meeting 2001. Available from: [http://www.tx.ncsu.edu/jtatm/volume1specialissue/presentations/pres\\_part1.doc](http://www.tx.ncsu.edu/jtatm/volume1specialissue/presentations/pres_part1.doc).
- 121 YARIN AL, RENEKER DH. Taylor cone and jetting from liquid droplets in electrospinning of nanofibers. *J. Appl. Phys.* 90, 4836–4846, 2001.
- 122 SHIN MY, HOHMAN MM, BRENNER M, RUTELDEGE GC. Experimental characterization of electrospinning: The electrically forced jet and instabilities. *Polymer* 42, 9955–9967, 2001.
- 123 NAIR LS, BHATTACHARYYA S, BENDER JD, GREISH YE, BROWN PW, ALLCOCK HR, LAURENCIN CT. Fabrication and optimization of methylphenoxy substituted polyphosphazene nanofibers for biomedical applications. *Biomacromolecules*, 5, 2212–2220, 2004.
- 124 FRENOT A, CHRONAKIS IS. Polymer nanofibers assembled by electrospinning. *Curr. Opin. Colloid Inter. Sci.* 8, 64–75, 2003.
- 125 RENEKER DH, CHUN I. Nanometric diameter fibers of polymer produced by electrospinning. *Nanotechnology*, 7, 216–223, 1996.
- 126 HUANG Z, ZANG YZ, KOTAKI M,

- RAMAKRISHANA S. A review on polymer nanofibers by electrospinning and their applications in nanocomposites. *Composites Sci. Technol.* 63, 2223–2253, 2003.
- 127 MOROTA K, MATSUMOTO H, MIZUKOSHI T, KONOSU Y, MINAGAWA M, TANIOKA A, YA, AGATA Y, INOUE K. Poly(ethylene oxide) thin films produced by electrospray deposition: Morphology control and additive effects of alcohols on nanostructure. *J. Colloid Interface Sci.* 279, 484–492, 2004.
- 128 KATTI DS, ROBINSON KW, KO FK, LAURENICN CT. Bioresorbable nanofiber-based systems for wound healing and drug delivery: Optimization of fabrication parameters. *J. Biomed. Mater. Res. Part B, Appl. Biomater.* 70, 286–296, 2004.
- 129 DEITZEL JM, KLEINMEYER D, HIRVANEN JK, TAN NCB. Controlled deposition of electrospun poly(ethylene oxide) fibers. *Polymer* 42, 8163–8170, 2001.
- 130 DEMIR MM, YILGOR I, YILGOR E, ERMAN B. Electrospinning of polyurethane fibers. *Polymer* 43, 3303–3309, 2002.
- 131 DEITZEL JM, KLEINMEYER J, HARRIS D, TAN NCB. The effect of processing variables on the morphology of electrospun nanofibers and textiles. *Polymer* 42, 261–272, 2001.
- 132 ZONG X, KIM K, FANG D, RAN S, HSIAO BS, CHU B. Structure and process relationship of electrospun bioabsorbable nanofiber membranes. *Polymer* 43, 4403–4412, 2002.
- 133 KOOMBHONGSE S, LIU W, RENEKER DH. Flat ribbons and other shapes by electrospinning. *J. Polym. Sci., Polym. Phys. Ed.* 39, 2598–2606, 2001.
- 134 BOGNITZKI M, CZADO W, FRESE T, SCHAPER A, HELLWEG M, STEINHART M, GREINER A, WENDORFF JH. *Adv. Mater.* 13, 70, 2001.
- 135 MEGELSKI S, STEPHENS JS, CHASE DB, RABOLT JF. Micro- and nanostructured surface morphology on electrospun polymer fibers. *Macromolecules* 35, 8456–8466, 2002.
- 136 CASPER CL, STEPHENS JS, TASSI NG, CHASE DB, RABOLT JF. Controlling surface morphology of electrospun polystyrene fibers: Effect of humidity and molecular weight in the electrospinning process. *Macromolecules* 37, 573–578, 2004.
- 137 MATTHEWS JA, WNEK GE, SIMPSON DG, BOWLIN GL. Electrospinning of collagen nanofibers. *Biomacromolecules* 3, 232–238, 2002.
- 138 BORNAT A. Production of electrostatically spun products. *US Patent* 4689186, 1987.
- 139 THERON A, ZUSSMAN E, YARIN AL. Electrostatic field-assisted alignment of electrospun nanofibers. *Nanotechnology* 12, 384–390, 2001.
- 140 XU CY, INAI R, KOTAKI M, RAMAKRISHNA S. Aligned biodegradable nanofibrous structure: A potential scaffold for blood vessel engineering. *Biomaterials* 25, 877–886, 2004.
- 141 DING B, KIM HY, KIM CK, KHL MS, PARK SJ. *Nanotechnology* 14, 532–537, 2003.
- 142 KENAWY ER, BOWLIN GL, MANSFIELD K, LAMAN J, SIMPSON DG, SANDER EH, WNEK GE. *J. Controlled Release* 81, 57–64, 2002.
- 143 SUN ZC, ZUSSMAN E, YARIN AL, WENDORFF JH, GREINER A. *Adv. Mater.* 15, 1929, 2003.
- 144 DING B, KIMURA E, SATO T, FUJITA S, SHIRATORI S. Fabrication of blend biodegradable nanofibrous nonwoven mats via multijet electrospinning. *Polymer* 45, 1895–1902, 2004.
- 145 GUPTA P, WILKES GL. Some investigations on the fiber formation by utilizing a side-by-side bicomponent electrospinning approach. *Polymer* 44, 6353–6359, 2003.
- 146 STANKUS JJ, GUAN J, WAGNER WR. Fabrication of biodegradable elastomeric scaffolds with sub-micron morphologies. *J. Biomed. Mater. Res.* 70, 603–614, 2004.
- 147 HAMDAN AL, DANIEL SJ, LAURA HM, RENEKER D. Preservation of enzymes in electrospun nanofibers. Technical Papers – American Chemical Society, Rubber Division, Spring Technical Meeting, 163rd, San Francisco, 28–30 April 2003.

- 148 JIANG H, HU Y, LI Y, ZHAO P, ZHU K, CHEN W. A facile technique to prepare biodegradable coaxial electrospun nanofibers for controlled release of bioactive agents. *J. Controlled Release* 108, 237–243, 2005.
- 149 LI WJ, LAURENCIN CT, CATERSON EJ, TUAN RS, KO FK. Electrospun nanofibrous structure: A novel scaffold for tissue engineering. *J. Biomed. Mater. Res.* 60, 613–621, 2002.
- 150 HE W, MA ZW, YONG T, TEO WE, RAMAKRISHNA S. Fabrication of collagen-coated biodegradable polymer nanofiber mesh and its potential for endothelial cells growth. *Biomaterials* 26, 7606–7615, 2005.
- 151 KWON K, KODOAKI S, MATSUDA T. Electrospun nano- to microfiber fabrics made of biodegradable copolyesters: Structural characteristics, mechanical properties and cell adhesion potential. *Biomaterials* 26, 3929–3939, 2005.
- 152 LEE SH, KU BC, WANG X, SAMUELSON LA, KUMAR J. Design, synthesis and electrospinning of a novel fluorescent polymer for optical sensor applications. *Mater. Res. Soc. Symp. Proc.* 708, 403–408, 2002.
- 153 LEE CH, SHIN HJ, CHO IH, KANG YM, KIM IA, PARK KD, SHIN JW. Nanofiber alignment and direction of mechanical strain affect the ECM production of human ACL fibroblast. *Biomaterials* 26, 1261–1270, 2005.
- 154 MA PX, ZHANG R. Synthetic nanoscale fibrous. *J. Biomed. Mater. Res.* 46, 60–72, 1999.
- 155 WEI G, MA PX. Structure and properties of nano-hydroxyapatite/polymer composite scaffolds for bone tissue engineering *Biomaterials* 25, 4749–4757, 2004.
- 156 ZHANG R, MA PX. Synthetic nanofibrillar extracellular matrices with predesigned macroporous architectures. *J. Biomed. Mater. Res.* 52, 430–438, 2000.
- 157 WHITESIDES GA, MATHIAS JP, SETO CT. *Science* 254, 1312, 1991.
- 158 ZHANG S. Building from bottom-up. *Mater. Today* 6, 20–27, 2003.
- 159 ZHANG S, HOLMES T, LOCKSHIN L, RICH A. Spontaneous assembly of a self-complementary oligopeptide to form a stable macroscopic membrane. *Proc. Natl. Acad. Sci. U.S.A.* 90, 3334–3338, 1993.
- 160 ZHANG S. Molecular self-assembly. In: BUSCHON KH et al. (Eds.), *The Encyclopedia of Materials Science and Technology*, Elsevier Science, Oxford, pp. 5822–5829, 2001.
- 161 ZHAO Z, ZHANG S. Fabrication of molecular materials using peptide construction motifs. *Trends Biotechnol.* 22, 470–476, 2004.
- 162 HARTGERINK JD, BENIASH E, STUPP SI. Self assembly and mineralization of peptide amphiphile nanofibers. *Science* 294, 1684–1688, 2001.
- 163 NIECE KL, HARTGERINK JD, DONNORS JJM, STUPP SI. Self assembly combining two bioactive peptide-amphiphile molecules into nanofibers by electrostatic attraction. *J. Am. Chem. Soc.* 125, 7146–7147, 2003.
- 164 PETKA WA, HARDEN JL, MCGRATH KP, WIRTZ D, TIRRELL DA. Reversible hydrogels from self-assembling artificial proteins. *Science* 281, 389–392, 1998.
- 165 NOWAK AP, BREEDVELD V, PAKSTIS L, OZBAS B, PINE DJ, POCHAN D, DEMING TJ. Rapidly recovering hydrogel scaffolds from self assembling diblock copolypeptide amphiphiles. *Nature* 417, 424–428, 2002.
- 166 SCHINDLER M, AHMED I, KAMAL J, NUR-E-KAMAL A, GRAFE TH, CHUNG HY, MEINERS S. A synthetic nanofibrillar matrix to promote *in vivo*-like organization and morphogenesis for cell in culture. *Biomaterials* 26, 5624–5631, 2005.
- 167 WOZNIAK MA, DESAI R, SOLSKI PA, DER CJ, KEELY PJ, ROCK generated contractility regulates breast epithelial cell differentiation in response to the physical properties of a three-dimensional collagen matrix. *J. Cell. Biol.* 163, 583–595, 2003.
- 168 SILVA GA, CZEISLER C, NIECE KL, BENIASH E, HARRINGTON DA, KESSLER JA, STUPP SI. Selective differentiation of neural progenitor cells by high-

- epitope density nanofibers. *Science* 303, 1352–1355, 2004.
- 169 LI W, TULI R, HUANG X, LAQUERRIERE P, TUAN RS. Multilineage differentiation of human mesenchymal stem cells in a three-dimensional nanofibrous scaffold. *Biomaterials* 26, 5158–5166, 2005.
- 170 YANG F, MURUGAN R, RAMAKRISHNA S, WANG X, MA YX, WANG S. Fabrication of nano-structured porous PLLA scaffold intended for nerve tissue engineering. *Biomaterials* 25, 1891–1900, 2004.
- 171 YANG F, MURUGAN R, WANG S, RAMAKRISHNA S. Electrospinning of nano/micro scale poly(L-lactic acid) aligned fibers and their potential in neural tissue engineering. *Biomaterials* 26, 2603–2610, 2005.
- 172 MO ZM, XU CY, KOTAKI M, RAMAKRISHNA S. Electrospin (P(LLA-CL) nanofiber: A biomimetic extracellular matrix for smooth muscle cell and endothelial cell proliferation. *Biomaterials* 25, 1883–1890, 2004.
- 173 VENUGOPAL J, MA LL, YONG T, RAMAKRISHNA S. In vitro study of smooth muscle cells on polycaprolactone and collagen nanofibrous matrices. *Cell Biol. Int.* 29, 861–867, 2005.
- 174 MA Z, KOTAKI M, YONG T, HE W, RAMAKRISHNAN S. Surface engineering of electrospun polyethylene terephthalate (PET) nanofibers towards development of a new material for blood vessel engineering. *Biomaterials* 26, 2527–2536, 2005.
- 175 GENOVE E, SHEN C, ZHANG S, SEMINO CE. The effect of functionalized self-assembling peptide scaffolds on human aortic endothelial cell function. *Biomaterials* 26, 3341–3351, 2005.
- 176 SHIN M, ISHII O, SUEDA T, VACANTI JP. Contractile cardiac grafts using a novel nanofibrous mesh. *Biomaterials* 25, 3717–3723, 2004.
- 177 ISHII O, SHIN M, SUEDA T, VACANTI JP. In vitro tissue engineering of a cardiac graft using a degradable scaffold with an extracellular matrix-like topography. *J. Thor. Cardiovasc. Surg.* 130, 1358–1363, 2005.
- 178 YOSHIMOTO H, SHIN YM, TERAI H, VACANTI JP. A biodegradable nanofiber scaffold by electrospinning and its potential for bone tissue engineering. *Biomaterials*, 24, 2077–2082, 2003.
- 179 LI W, TULI R, HUANG X, OKAFOR C, DERFOUL A, DANIELSON KG, HALL DJ, TUAN RS. A three-dimensional nanofibrous scaffold for cartilage tissue engineering using human mesenchymal stem cells. *Biomaterials* 26, 599–609, 2005.
- 180 KISIDAY J, JIN M, KURZ B, HUNG H, SEMINO C, ZHANG S, GRODZINSKY AJ. Self assembling peptide hydrogel fosters chondrocyte extracellular matrix production and cell division: implications for cartilage tissue repair. *Proc. Natl. Acad. Sci. U.S.A.* 99, 9996–10001, 2002.

## 2

# Polymeric Nanofibers in Tissue Engineering

*Seow Hoon Saw, Karen Wang, Thomas Yong,  
and Seeram Ramakrishna*

### 2.1

#### Overview

Advances in tissue engineering in recent decades has sparked interest in fabricating polymeric fibers, in particular nanofibers, as scaffolds for biomedical applications. The unique properties of nanofibers, such as high surface area, remarkable surface properties and superior mechanical properties, have great potential for a wide variety of applications in medicine, biotechnology and engineering. Among the many features of nanofibers, biocompatibility is the most crucial aspect of tissue engineering. The materials that are mainly used are biopolymer and biodegradable synthetic polymers. Researchers have shown that polymeric nanofibers can be fabricated using various processing techniques such as self-assembly, phase separation and electrospinning.

This chapter reviews the applications of nanofibers in different aspects of tissue engineering. Studies have been carried out to optimize the properties of nanofiber scaffolds for applications in ophthalmology, hepatic biology, nerve, skin, bone and cartilage regeneration, heart and vascular grafts, and stem cell research. Numerous studies have shown that nanofibers that closely mimic the extracellular matrix in natural tissues have potential as scaffolds for tissue regeneration. They provide interconnected pores that facilitate transport of nutrients and growth factors to the cells as well as providing a stable structural support, which are essential for effective tissue engineering.

In nerve regeneration, nanofibers have been shown to effectively control the neurite outgrowth rate and orientation that are critical for the repair of the damaged nervous system. Similarly, the ability to control the morphology, proliferation, adhesion and alignment of smooth muscles cells and endothelial cells cultured on nanofibrous scaffolds provides a possible avenue for successful tissue engineering of blood vessels. Suitable bioactive nanofibers for proliferation of osteoblasts in guided bone regeneration, and dermal fibroblasts for burns and chronic wound treatment have also been reported. Studies on nanofibers for stem cell proliferation

and differentiation are still in their infancy but the potential for biomedical applications is tremendous.

Although most of these studies are at the laboratory level, researchers foresee that polymeric nanofibers have good prospects in the near future. Advances in material science, manufacturing technology and design aspects of polymer nanofibers are necessary to realize their full potential in medicine, biology and engineering.

## 2.2

### Introduction

Nanotechnology is a rapidly expanding field and the products resulting from research have increasingly entered into our daily lives. This chapter reviews potential applications of nanofibers, fiber fabrication techniques, and illustrates some of the current studies carried out to optimize the properties of nanofiber scaffolds for applications in ophthalmology, hepatic biology, nerve, skin, bone and cartilage regeneration, heart and vascular grafts, and stem cell research. The advantages and disadvantages of the nanofiber scaffolds are discussed and compared with conventional scaffolds in terms of their physical properties, performances and functionalities for tissue engineering applications. This chapter will contribute to the understanding of nano-scale polymeric fibers, which will facilitate the development of nanofibers with defined properties for specific applications to accelerate advanced research in tissue engineering.

#### 2.2.1

##### History of Tissue Engineering and Nanofibers

Tissue engineering is a discipline that involves the application of the principles and methods of engineering and life sciences towards a fundamental understanding of structure–function relationships in normal and pathological tissues and the development of biological substitutes to restore, maintain or improve functions [1]. It is a relatively novel and emerging field that involves knowledge of bioengineering, the life sciences, and the clinical sciences with the aim of solving the serious medical problems of tissue loss and organ failure [2]. A new functional living tissue is created with the help of the growth and interaction of cells with a matrix or scaffolding to guide tissue development.

Previously, this area of science was called reconstructive surgery and, later, renamed as tissue engineering when attention was focused on fabricating living replacement parts for the body in the laboratory. Tissue engineering has developed at a logarithmic rate, and with researchers realizing the realistic potentials of this new discipline, many concepts and techniques that can be applied to saving lives

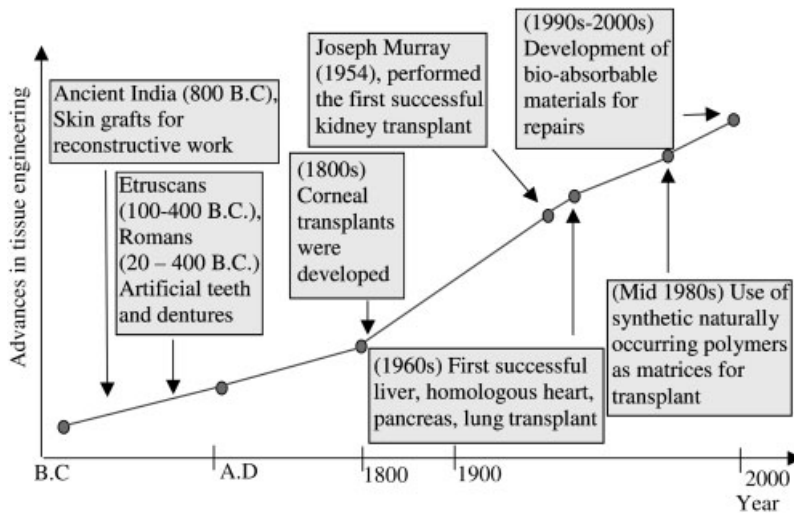


Fig. 2.1. Advances in tissue engineering.

are becoming a reality. Figure 2.1 shows a comprehensive summary of the advances made in tissue engineering.

Scaffolds for tissue engineering are an important aspect as they provide the optimized environment for cell survival, proliferation and differentiation, and also for the formation of tissues for desired tissue engineering applications. Constructing scaffolds for tissue engineering purposes is a challenging task as there are many factors that need to be taken into consideration, e.g., the implants must not be able to induce an immune response that can cause inflammation or rejection, a proper substrate is needed for cell survival and differentiation, and an appropriate environmental condition for tissue maintenance is required [3]. Research in the last decade has aimed to design and develop optimized scaffolds for tissue regeneration.

The field of nanotechnology was introduced by Drexler (1986) [4], and subsequently this has become a highly researched topic and promising area for applications in various industries, in particular biomedical applications. Fibers of nanoscale diameter, called nanofibers, were developed and found to be good candidates in the areas of molecular filters, tissue regeneration, drug delivery system, protective clothing, nanosensors and many more. Researchers have realized that polymeric nanofibers have unique properties such as high surface area, remarkable surface properties and superior mechanical properties, making them good candidates as tissue regeneration scaffolds. Thus, the potential of scaffolds in tissue engineering is enormous and studies have been carried out to gain a better understanding of the interactions between cells and the polymeric nanofibers in order to optimize scaffold designs for tissue engineering applications.



## 2.3

### Classification of Nanofibers

Nanofibers are classified based on the materials of which they are fabricated: biodegradable synthetic polymers, biopolymers, copolymers and composite polymers, which will impart unique properties to the nanofibers for specific applications.

#### 2.3.1

##### Synthetic Polymers

A wide variety of synthetic polymers have been commonly used for fabricating nanofibers. In the area of tissue engineering, using synthetic polymers to fabricate nanofibers provides many advantages. Many studies have been performed to evaluate the potential of using these polymers in different tissue engineering applications. Some synthetic polymers such as aliphatic polyesters, poly(L-lactic acid) (PLLA), poly(glycolic acid) (PGA) and polycaprolactone (PCL) have biodegradable properties that are important for the development of biodegradable implants, scaffolds for tissue engineering, and controlled drug delivery. On the other hand, non-biodegradable synthetic polymers are frequently used for permanent or temporary prostheses in the area of biomedical applications, and are not commonly used as biological grafts. As they are not biodegradable, they satisfy the requirement of being sufficiently strong, flexible and hard to withstand the fatigue due to constant motion and friction. Some examples of commonly used non-biodegradable synthetic polymers are poly(vinyl chloride) (PVC), poly(tetrafluoroethylene) (PTFE) and poly(dimethyl siloxane) (PDMS).

Generally, synthetic polymer nanofibers have a major advantage of being mechanically stronger as well as greater flexibility, therefore making them highly durable scaffolds for replacement of desired tissues. In addition, synthetic polymers have another advantage, i.e., they can be produced relatively easily in large quantity with reproducible properties. This allows a consistency in the quality of scaffolds or devices fabricated for tissue engineering applications where obtaining reproducible results is important for determining future applications of the polymer. The degradation rate of the synthetic polymer would also be easier to determine and refine, making them more specific for desired applications. However, the main disadvantage is that synthetic polymers lack biocompatibility, which is a critical issue in tissue engineering.

#### 2.3.2

##### Biopolymers

In recent years, researches have started using natural biopolymers to fabricate nanofibers. Some of these successfully electrospun biopolymers are silk [5, 6], fibrinogen [7], collagen [8], gelatin [9], chitosan [10] and chitin [11]. Natural biopolymers used in tissue engineering are often components in the extracellular ma-

trix (ECM) produced by cells, giving them a better biocompatibility and providing a better environment for tissue regeneration. This in turn improves the cell attachment and growth on these nanofibers. However, variation in the quality of natural biopolymers is inevitable as they are extracted from different sources, and batch variations are unavoidable even when the biopolymers are extracted from the same source, thus affecting the reproducibility of studies. In addition, it is generally more difficult to obtain submicron or nano-sized fibers from natural biopolymers than from synthetic polymer nanofibers because of the relatively low molecular weight of the polymer and the limited solvent availability to dissolve biopolymers.

### 2.3.3

#### **Copolymers**

To overcome certain limitations of synthetic and natural biopolymer, researchers have developed copolymers and blends to fabricate nanofibers. With their unique and favorable properties combined, this enhances their usefulness as scaffolds in tissue engineering, examples are collagen-blended poly(L-lactide-co- $\epsilon$ -caprolactone) (PLLA-CL) [12], collagen/PCL [13], and gelatin/PCL [9]. Besides copolymers and blended nanofibers, surface modification is another means of improving the biocompatibility of nanofibers for specific tissue engineering applications, some examples are gelatin-grafted poly(ethylene terephthalate) (PET) nanofiber mats [14], collagen type I or gelatin grafted PLLA films [15], collagen-coated PLLA-CL nanofibers [16], concentrated hydrochloric acid treated PGA nanofibers [17], and galactosylated poly( $\epsilon$ -caprolactone-co-ethyl ethylene phosphate) (PCLEEP) nanofiber scaffolds [18].

### 2.3.4

#### **Composite Polymers**

In general, most synthetic and natural biopolymers lack certain properties such as material strength and biocompatibility. Researchers have included additives to the nanofibers to confer beneficial properties, making them specific for tissue engineering applications. Studies have revealed that composite nanofibers have better material strength and performance than synthetic and natural biopolymers nanofibers, and this is mostly due to the high surface area to volume ratio, thus providing a greater interaction between the additives and the nanofibers. In tissue engineering, examples of some composite polymers used to fabricate nanofibers are poly(L-lactide-co-glycolide) (PLGA)/chitin [19], polycarbonate urethane (PCU)/carbon [20], and gelatin/PCL [9].

## 2.4

### **Nanofiber Fabrication**

Polymeric nanofibers can be fabricated by several techniques, including drawing, template synthesis, phase separation, self-assembly and electrospinning.

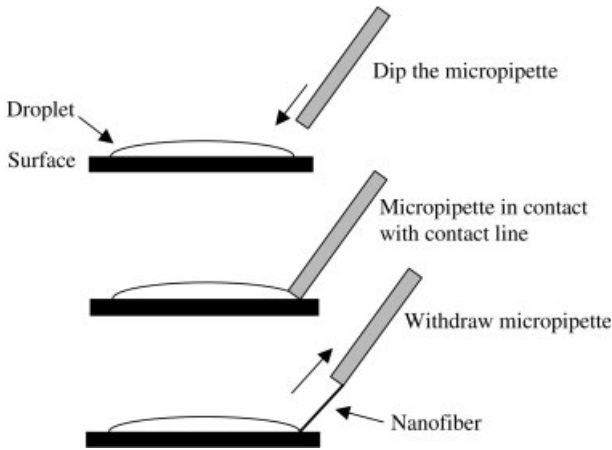


Fig. 2.2. Schematic diagram of the drawing technique.

#### 2.4.1

##### Drawing

Drawing is a process whereby nanofibers are produced when a micropipette with a tip few micrometers in diameter is dipped into a droplet near the contact line using a micromanipulator and then withdrawn from the liquid at about  $1 \times 10^{-4} \text{ m s}^{-1}$  (Fig. 2.2). When the end of the micropipette touches the surface, the drawn nanofiber is then deposited. To draw fibers, a viscoelastic material is required so that it can endure the strong deformation and at the same time it has to be cohesive enough to support the stress that build up in the pulling process. This method can be considered as dry spinning at a molecular level [21]. Nanofibers have been fabricated by the drawing method with citrate molecules [22]. The droplet of solution is deposited on a surface to allow evaporation to take place. After a few minutes of evaporation, due to the capillary flow, the edge of the droplet is more concentrated and the drawing process can begin.

#### 2.4.2

##### Template Synthesis

Template synthesis involves utilizing a template to achieve nanofibers. Aligned polyacrylonitrile nanofibers have been fabricated by this method, using aluminum oxide membrane as the template [23]. In this particular process, when the pressure of the water is increased, it forces the polymer solution through the cylindrical nanopores of the membrane (Fig. 2.3). Once the extruded polymer comes into contact with the solidification solution, it solidifies and forms nanofibers. The diameter of the nanofibers depends on the diameter of the pores of the membrane. This method has been used to obtain nanotubules and nanofibrils of polymers, metals, semiconductors and carbons.

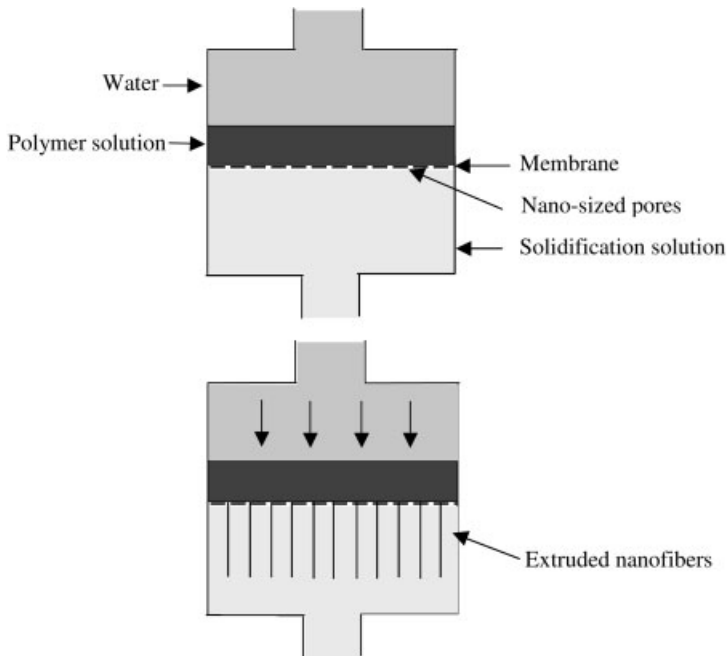


Fig. 2.3. Schematic diagram of template synthesis.

### 2.4.3

#### Phase Separation

Phase separation of a homogenous polymer–solvent solution can be induced in several ways, e.g., thermal induced phase separation (TIPS). When the polymer solution undergoes a decrease in temperature, two phases would form, a polymer-rich phase and a polymer-lean phase. Gradually, gelation would occur causing the polymer-rich phase to form a network structure when the solvent is removed via extraction, sublimation or evaporation. The spaces that were occupied by the solvent in the polymer-lean phase become pores [24] (Fig. 2.4). Generally, matrices made by solid–liquid phase separation have a greater pore size than by liquid–

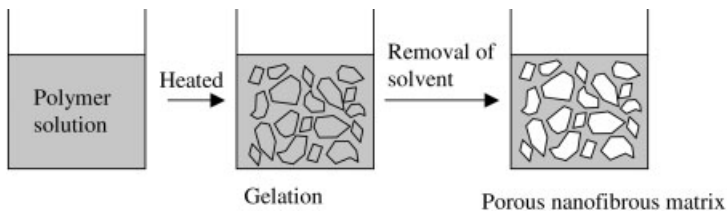


Fig. 2.4. Diagram showing nanofibrous matrix obtained by phase separation.

liquid phase separation. Common materials used for this process are PLLA and PLLA-CL. Fiber dimensions achievable by this process range from 50 to 500 nm [25]. The mechanical properties of nanofibrous mats so-fabricated can be customized by altering the polymer concentration. Various porous structures can be achieved with this method by varying the thermodynamic and kinetic parameters [26]. Although the phase separation method is an easy process, it can only be applied to a few polymers.

#### 2.4.4

##### **Self-assembly**

Self-assembly is a complex process that involves individual, pre-existing components to organizing themselves into desired patterns and functions. Several factors significantly affect this process, including the peptide sequence if the self-assembly is based on protein–ligand interactions, concentration, pH, presence of salt, and time (or kinetics) [27]. By varying these parameters, nano-scale or macro-scale structures with great stability and functionality can be constructed. Polymeric nanofibers have been constructed by self-assembly through multiple processes of polymer chain annealing, crosslinking, dissolution and cleaving [25]. In the annealing process, polymer chains are annealed end to end, and are crosslinked chemically, thermally or by UV irradiation. The crosslinked polymers are immersed in chemicals to dissolve the continuous non-crosslinked polymer phase to disentangle the nanofibers. Further modifications involve cleaving and loading the nanofibers with chemicals to yield desired nanofiber morphology and chemical structures. By this method, nanofibers ranging from a few to 100 nm in diameter have been fabricated.

#### 2.4.5

##### **Electrospinning**

Electrospinning is a technique used to fabricate polymeric nanofibers by means of an electrostatic force [21]. This cost effective and simple method was invented back in 1934 by Formhals [28]. The principle involves applying a high voltage to the surface of the polymer solution, and when the surface tension is overcome, an electrically charged jet is ejected. The electrical forces cause the discharged jet to stretch, forming a long and thin jet. At the same time, the solvent evaporates before the nanofiber is collected on a grounded collector. Figure 2.5 illustrates schematically the electrospinning process. To date, a great variety of polymer nanofibers have been successfully prepared by electrospinning when compared with other methods mentioned above that can fabricate nanofibers from only a limited number of polymers. With further advancement in this technology, electrospinning has the greatest potential for the mass production and industrial processing of nanofibers.

Electrospinning is influenced by many factors: the most significant is the properties of the polymer solution, e.g., viscosity, conductivity, and surface tension. Controlled variables such as distance between the needle tip and the collector, voltage

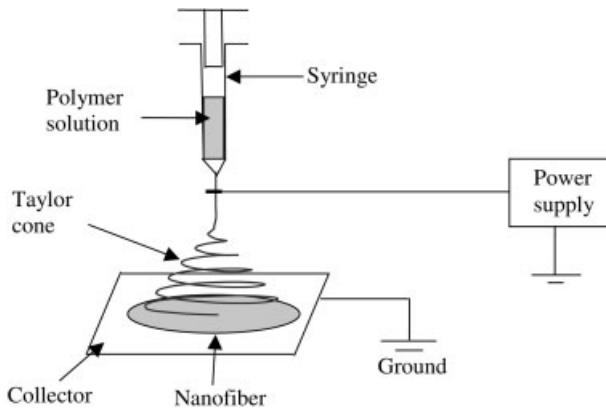


Fig. 2.5. Schematic diagram of the electrospinning technique.

applied, type of collector and feed rate have to be considered, too. Ambient parameters such as humidity, pressure and the type of atmosphere in the electrospinning environment also play a role [29]. With this knowledge, different morphology, structures and arrangements of nanofibers can be achieved by varying the parameters.

As most electrospun nanofibers are in the non-woven form, researchers have spent tremendous time and effort in controlling the alignment of the nanofibers. Several set-ups have been designed, such as the cylinder collector with high rotating speed [8, 30], auxiliary electrode/electrical field [31], parallel conducting collector [32], knife edge disk [33], frame collector [34] and many more. Currently, the thinnest electrospun nanofibers achievable are 3 nm in diameter [25]. Huang et al. (2003) have provided a more comprehensive review of electrospun nanofibers [35].

Comparing all of the above techniques, only drawing, template synthesis, phase separation and electrospinning are simple to perform. However, these processes have a common limitation, i.e., most of the polymeric nanofiber production process is currently only possible at the laboratory level, with the exception for electrospinning, which may be the only technique that has the potential for mass production.

## 2.5

### Degradation and Absorption Kinetics of Nanofiber Scaffolds Compared with Conventional Scaffolds

One of the factors required of a tissue regeneration scaffold is that it needs to be biodegradable. As the tissue grows into the porous structure of the scaffold, it is

difficult to remove the scaffold after the tissue has regenerated. Therefore, the scaffold is only required to maintain its volume, structure and mechanical stability just long enough for adequate tissue formation. The rate of the biodegradation needs to be adjusted so that it is able to match the rate of tissue formation. When degradation occurs, the breakdown products released should not induce any inflammation or cause toxicity to the body [36]. The biodegradation rate of the scaffold is influenced by many factors. One common method used to determine the rate is by placing the scaffold in phosphate-buffered saline (PBS) at 37 °C in an incubator (*in vitro*) or implanted into animals (*in vivo*), and biodegradability can be measured by the amount of mass loss, strength loss and the changes in morphology.

Conventional scaffolds such as hydrogels, sheets, meshes, and foams have been widely used in tissue engineering. Many studies were carried out to evaluate their degradation, e.g., Lee et al. (2004) [37] have shown that poly(aldehyde guluronate) (PAG) hydrogel crosslinked with poly(acrylamide-*co*-hydrazide) (PAH) had a weight loss of about 8% at the end of 60 days in Dulbecco's Modified Eagle Medium (DMEM). Generally, nanofibers have a very high surface area to volume ratio, and this will affect the degradation kinetics when compared to more conventional fibers. Studies showed that PGA nanofibers exhibited a rapid degradation rate and was left with a residual weight of approximately 40% at 20 days in PBS. Even after only 1 day of degradation, some PGA nanofibers have already started to undergo hydrolytic degradation and, after 4 days a significant amount of fibers was degraded. At the end of 12 days of degradation, the nanofiber matrix had become chunks of shorter fiber fragments [38]. In contrast, PGA microfiber non-woven matrix, which has been commercialized as a tissue engineering scaffold, only started to degrade at day 3, as shown by surface defects or microcracks. After several days, the surface defect degraded further to form a rupture in the microfiber [39]. The difference in the degradation rate between the microfiber and the nanofiber is probably due to the fiber diameter, which relates to the surface area. This property of rapid degradation is especially beneficial for temporary tissue regeneration scaffolds. However, studies have shown that the breakdown product from PGA was able to cause dedifferentiation as well as reduce proliferation rate of vascular smooth muscle cells. Therefore, PGA would not be the optimal scaffold for vascular tissue engineering [40]. As PGA nanofibers have a faster degradation rate, more breakdown product would be produced in a shorter period and this would cause more dedifferentiation and reduction of the proliferation rate when compared to conventional scaffolds.

Other degradation kinetic studies include that of Zong et al. (2005) [41], which showed that non-woven PLLA scaffold of an average fiber diameter of 1  $\mu\text{m}$  had 90% remaining weight after about 20 days of degradation. The thickness of the scaffold also plays an important role in the degradation rate. With a reduction in the thickness of PLGA films, the degradation rate significantly decreased as there is faster diffusion of the degraded products, thus minimizing autocatalyzed hydrolysis [42].

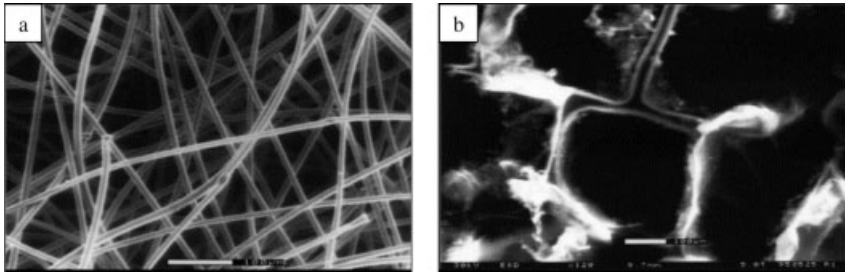


**Fig. 2.6.** (a) Scanning electron micrograph of a PGA non-woven scaffold with a fiber diameter of approximately 15  $\mu\text{m}$  [54]. (b) Scanning electron micrograph of a PLLA foam fabricated using the salt-leaching technique [54].

## 2.6

### Advantages and Disadvantages of Nanofiber Scaffolds Compared with Other Conventional Scaffolds

Textile technologies have been utilized to produce the earlier tissue engineering scaffolds consisting of fibrous biodegradable polymer fabrics with an average diameter of 15  $\mu\text{m}$ . It has been used alone or in combination with other non-woven biodegradable polymers, such as PGA (Fig. 2.6a), PGA/PDLLA and PGA/PLLA for the engineering of cartilage [43, 44–46], tendon [47], ureter [48], intestine [49], blood vessels [50, 51], heart valves [46, 52] and other tissues [46]. However, the limitations of these scaffolds are a lack of structural stability to withstand bio-mechanical loading, low mechanical strength, fast degradation rate, difficulty in controlling pore shape and limited fiber diameter variations [53, 54].

Other conventional scaffolds developed using particulate leaching techniques [55, 56] and phase separation techniques have diameters of the order of a few to tens of microns. The fibers are not uniformly distributed and are not suitable for tissue engineering applications [55]. In the particulate leaching method, a polymer solution is cast into the salt-filled mold with the desired size. After the solvent is allowed to evaporate, the salt crystals are leached away using water to form the pores in the scaffold (Fig. 2.6b). It is relatively easy to prepare, the pore size can be controlled by the size of the salt crystals, and the porosity by the salt/polymer ratio. However, this method of scaffold preparation is not able to control the pore shape and interpore opening of the scaffolds. To improve these aspects, the three-dimensional (3D) printing (free-form fabrication) technique was adopted to fabricate scaffolds. In this process, a binder is ink-jet printed onto sequentially laid polymer powder layers [57] where computer-assisted design and manufacture (CAD/CAM) is used to design complex-shaped objects. This method was initially explored at Massachusetts Institute of Technology, USA [58–60]. The precision of this process is severely limited due to the smallest possible powder particle size achievable and pixel size of the binder drops (usually a few hundred  $\mu\text{m}$ ), and po-



sitioning of the printer nozzle [61]. Membrane lamination is another technique that can be used to fabricate scaffolds by laminating membranes and introducing the peptides and proteins layer by layer during the fabrication process. This method will produce porous 3D structures [62]. The limitations of this process are less interconnected pore networks in the scaffold and the lack in mechanical properties. Solvent cast polymer–salt composites have also been extruded into a tubular geometry [63]. The disadvantages of producing the scaffold using this method are extensive use of highly toxic solvents, long duration for solvent evaporation (days to weeks), labor intensive fabrication process, limitation to thin structures, residual particles in the polymer matrix, irregularly shaped pores, and insufficient interconnectivity.

All the above-mentioned methods do not allow tissue engineers to design and fabricate scaffolds with a completely interconnected pore network, and a highly regular and reproducible scaffold morphology. However, many researchers have successfully developed high-performance polymer fibers with a high degree of fiber orientation using conventional fiber spinning techniques such as wet spinning, dry spinning, melt spinning, and gel spinning. Wet spinning is the oldest of these processes and it involves submerging the polymer solvent into a chemical bath, followed by precipitation and solidification of the polymer fiber. Dry spinning is achieved by evaporating the polymer solution in a stream of air or inert gas to solidify the fibers. In melt spinning, the molten polymer is forced through a spinneret and the fibers are directly solidified by cooling. Gel spinning is achieved by binding the polymer chains at various points in the liquid crystal state and further cooled in liquid bath after passing through air to produce the fibers [64–67]. With these methods, many different high-performance and functional polymer fibers have been produced and commercialized for many applications in the various industries.

Several complex molecular processes are involved in conventional fiber fabrication processes such as the spinning and drawing techniques. The ultimate state of molecular order in the polymer fibers depends on process variables such as stress, strain, temperature, time, length and length-distribution of the molecules [65]. Polymer fibers developed by these techniques have diameters in the range of microns (10–100  $\mu\text{m}$ ) and are classified as microfibers. The advantages of polymer microfiber are its flexibility which is easily controlled during structure formation, and the superior mechanical properties [68]. These fibers have been used in making ropes, satellite tethers, and high-performance sails. Polymer composite microfibers have found applications in aircrafts, boats, automobiles, sporting goods and biomedical implants. Several significant fiber properties such as ultraviolet resistance, electrical conductivity and biodegradability have been brought to good use.

The specific features of microfiber are fully exploited in industry, which exceeded previous performance level, and this led to the research, development and production of nano-diameter fibers or nanofibers with remarkable properties. When a fiber diameter is reduced to the nanometer scale, the surface area to volume ratio is significantly increased and this property has been exploited by many researchers for applications in various industries such as medicine, biotechnology and engi-

neering [36]. There are more than 70 research groups worldwide investigating electrospun polymer nanofibers [69] and this is due to the unique properties of nanofibers when compared with the conventional macromaterials and polymer microfibers. Being as thin as less than 10 nm in diameter [35], nanofibers exhibit a larger surface area per unit mass of the order of  $10^3 \text{ m}^2 \text{ g}^{-1}$  [70], permitting easier addition of surface functionalities as well as providing better mechanical properties. As a result, mats of these nanofibers are being tested for use in filter media, scaffolds for tissue engineering, protective clothing, reinforcement in composite materials and sensors [71]. The increased surface area, micro-scale interstitial space with high interconnectivity, good morphological stability, controlled fiber diameter, and sheet thickness make polymeric nanofibers an ideal scaffold for tissue engineering applications as it allows a significant amount of cell–surface interaction [69]. Polymeric nanofibers as well as other nano-structured materials such as nanotubes, nanowires, nanocrystals, nanorods and nanospheres are actively studied to uncover the many potentially advanced technological applications [72]. Several fabrication techniques are currently being investigated to develop nanofiber matrices from polymers: template synthesis, phase separation, drawing, self-assembly, and electrospinning (Section 2.4). Among these, electrospinning [33] is an efficient method to develop polymeric fibers with diameters in the nanometer range, and has attracted a great deal of attention recently. In addition to the small fiber diameter and pore size, and lightweight scaffolds that can be fabricated, electrospinning is an inexpensive and easy way to produce nanofibers from many types of polymers.

One of most crucial features of nanofibers is the huge availability of surface area per unit mass (Fig. 2.7). It provides a remarkable capacity for the attachment or release of functional groups, absorbed molecules, ions, catalytic moieties and

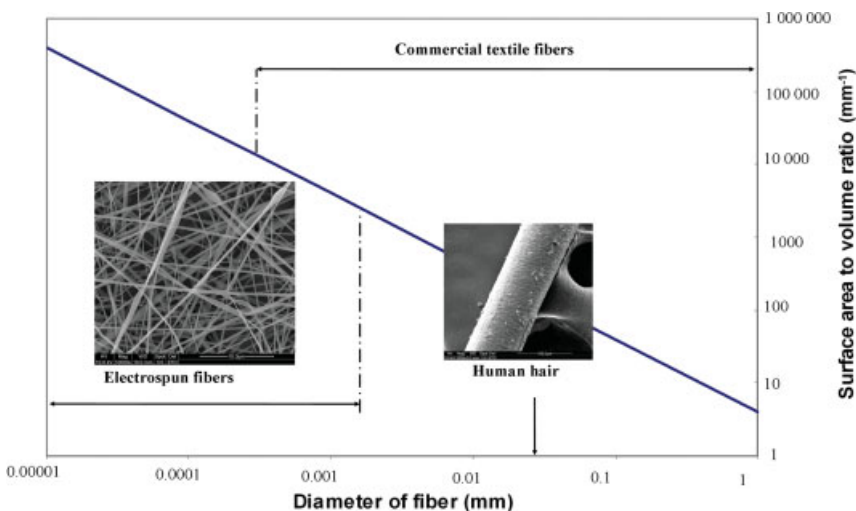
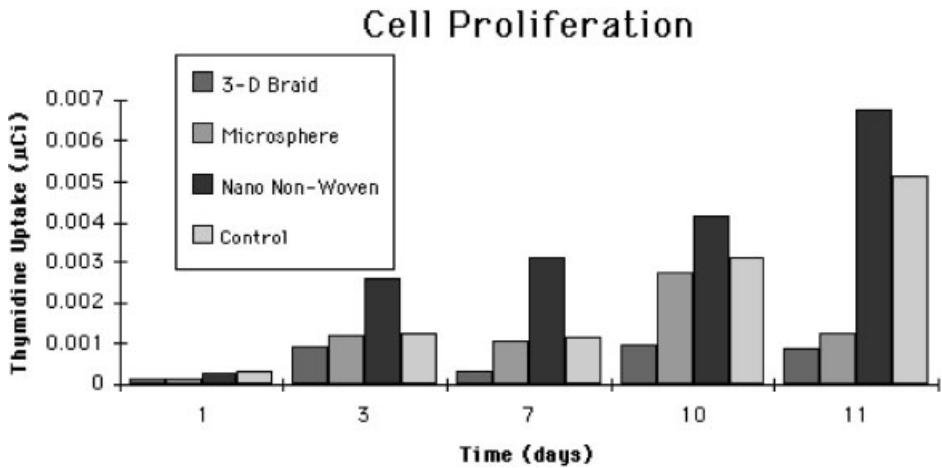


Fig. 2.7. Effect of the fiber diameter on surface area [73].



**Fig. 2.8.** Proliferation of fibroblast cells on four types of scaffolds: (red) 3D braided structure consisting of 20 bundles of 20  $\mu\text{m}$  filaments; (green) 150–300  $\mu\text{m}$  PLGA sintered spheres; (blue) non-woven, consisting of PLGA nanofibrils; (yellow) unidirectional bundles of

20  $\mu\text{m}$  filaments. Proliferation was determined by the thymidine uptake of the cell as a function of time. Clearly, the PLGA nanofiber scaffold is the most favorable for cell growth [73].

nanometer-scale particles of many kinds [73]. The high surface cohesion of nanofibers is capable of trapping tiny particles that are less than 0.5  $\mu\text{m}$  in size. The porosity and pore size of nanofiber membranes are important for application in tissue engineering. Nano-scale fibrous scaffolds can provide an optimal template for cells to attach, migrate, and grow. Mammalian cells can attach and organize well around fibers with diameters smaller than the diameter of the cells [74] and this is mainly due to the nano-scale interaction between the cells and the many biologically functional molecules and extracellular matrix components [54]. In a study of osteoblast bioactivity cultured on matrices consisting of 3D braided filaments, microspheres, non-woven nanofibrils, and microfilaments (Fig. 2.8), nanofibrils had the best support for cell growth and proliferation as determined by thymidine uptake [75]. This study also showed that a small fiber diameter facilitates greater available surfaces for the cell adhesion and migration. Non-woven mats formed from nanofibers have additional advantages of controllable pore size, high porosity, and permeability [76]. These remarkable properties motivate extensive interests in using these materials for applications in industries, especially in the biomedical fields. Composites nanofibers have been identified as potential candidates for high technology applications [35] due to its unique physical and mechanical properties. Hence, nano-featured synthetic scaffold design is one of the exciting new areas in tissue engineering.

Some recent studies showed that electrospun nanofibers can be collected in the form of highly oriented arrays that are able to elicit favorable biological responses due to their ability to mimic the biological microarchitecture and act to support and guide cell growth [33, 35, 67, 77]. Converting biopolymers into fibers and net-

works that mimic native structures will ultimately enhance the utility of these materials, as large diameter fibers do not mimic the morphological characteristics of the native fibrils [65]. The various properties of electrospun nanofibers such as mechanical strength, fiber diameter, porosity, and biocompatibility are dependent on the properties of the polymer type. Electrospun nanofibers fabricated from polyesters, polyurethanes, silicones, and poly(ethylene-co-vinyl acetate) (PEVA) have been identified as potential candidates for medical applications and have been fabricated as drug delivery devices, wound dressings and prosthetic devices such as vascular grafts [78–80] (Section 2.8). In the area of wound healing, electrospun nanofibrous membrane showed good and immediate adherence to wet wound surface where it attained uniform adherence to the wound surface without any fluid accumulation. The rate of epithelialization was increased and the dermis was well organized in the nanofibrous membrane, providing a good support for wound healing. The porosity of the nanofibrous membrane promotes evaporative water loss, excellent oxygen permeability and fluid drainage from the wound [81, 82]. Nanomaterial scaffolds have also been observed to enhance the functions of osteoblasts, such as adhesion, synthesis of alkaline phosphatase, and deposition of calcium-containing mineral compared with conventional scaffolds [83], and promote greater than  $1.7\times$  the osteoblastic cell attachment of conventional scaffolds. Nanofibrous scaffolds have also shown to adsorb four times more serum proteins than conventional scaffolds. More interestingly, the nanofibrous architecture selectively enhanced protein adsorption including fibronectin and vitronectin, even though both scaffolds were made from the same PLLA material. These results demonstrate that the biomimetic nanofibrous architecture serves as superior scaffolding for tissue engineering [84]. However, as-spun nanofibrous matrix can quickly lose its structural integrity or biological functionality in an aqueous environment such as in the human body [85]. Bhattarai et al. (2005) [85] have investigated the cellular compatibility of electrospun chitosan nanofibers incorporated with 40 wt.% poly(ethylene oxide) (PEO) but the nanofibrous matrix swelled readily in water and completely lost its fibrous structure in a few days. This would limit its application where a prolonged material functionality *in vivo* is required. Thus, processing conditions and mechanisms that would yield the desirable nanofibrous structure and material properties need to be investigated in order to construct nanofibrous matrix that exhibit good structural integrity to promote cell attachment and potentially serve as scaffold materials for tissue engineering.

Nanomaterials are unique as they are stronger than bulk materials. As fiber diameter decreases, the strength of the fiber (in this particular case glass fiber) increases exponentially [86] and this is probably due to the reduction in structural flaws of the glass fibers (Fig. 2.9a). Dresslhaus et al. (2000) [87] have described that, in the case of nanotubes, as the radius of matter gets smaller the strain energy per atom increases exponentially (Fig. 2.9b), contributing to over 30 GPa of increased strength. These unique characteristics in addition to their light weight, high permeability and the ability to absorb toxic materials enable these materials to be developed into high-performance filters, catalysis systems as well as for novel military fabrics [35]. Nano-sized fibers that can conduct electrical current and respond to electronic stimuli over metal contacts have also been developed. Norris

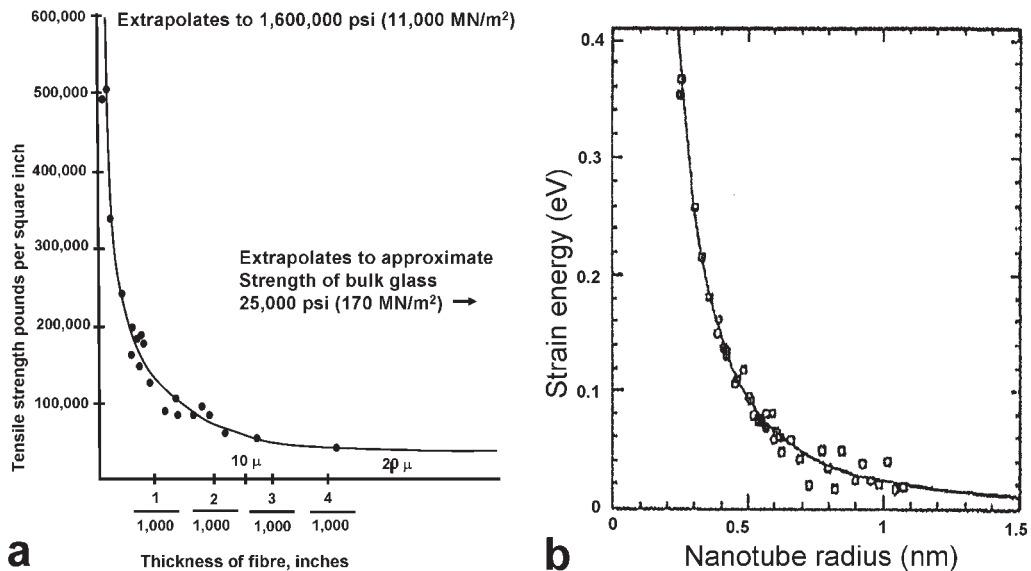


**Fig. 2.9.** Effect of fiber size on strength. (a) Glass fiber diameter versus the tensile strength [86]. (b) Strain energy as a function of nanotube radius [87].

and colleagues (2000) [88] found that polyaniline/PEO sub-micron fibrils have a response time an order of magnitude faster than bulk polyaniline/PEO in a doping–doping experiment. El-Aufy et al. (2003) [89] also demonstrated a significant increase in conductivity using sub-micron polyethylene dioxythiophene (PEDT) conductive fiber mat or when the fiber diameter decreases (Fig. 2.10). This effect is probably attributed to the intrinsic fiber conductivity effect or the geometric surface and packing density effect. However, nanofibers of smaller diameter have also been reported to exhibit lower and less stable conductivities. Zhou et al. (2003) [90] fabricated electrospun polyaniline/PEO nanofibers with diameters below 15 nm and found that the nanofibers were in fact electrically insulating. Many factors play important roles in polyaniline-based conductometric sensors, and one has to balance these factors to fully realize the potential of nano-structured conducting polymers. In some instances, “old-fashioned” materials may provide more desirable sensing characteristics [91]. Although the nanofiber films demonstrated faster responses, they exhibited lower sensitivity than conventional thin films. Researchers have shown that high surface area nanofibril structures do not effectively enhance sensor sensitivity due to the relatively open structure inherent in the many polymeric materials, and the adverse contribution from the interfibrillar contact resistance associated with nanofiber films [92, 93].

Current research focuses on the exploitation of these unique properties of nanofibers to improve their performance and functionalities for various applications. Improvement in the electrospinning technique has also been a focus of many research groups to refine and improve the properties and features of nanofibers. This

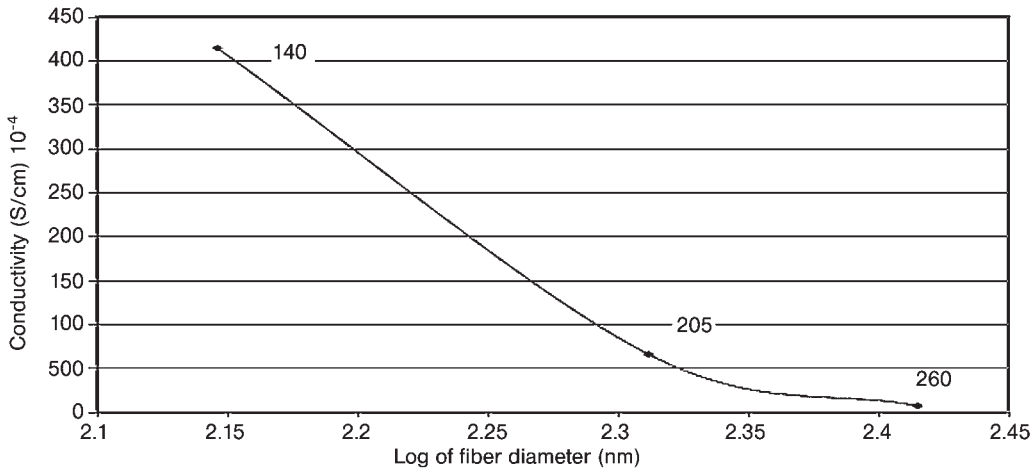


**Fig. 2.10.** Log of fiber diameter (nm) versus conductivity ( $S\text{ cm}^{-1}$ ). As fiber diameter decreases from 260 to 140 nm, the electrical conductivity of PEDT nanofibers showed almost two orders of magnitude increase [89].

is because electrospinning is a simple process to fabricate polymer nanofibrous materials for high-performance applications. Nano-scale fibers have the potential to revolutionize many industries. During the past decade, rapid technological advances in the areas of surface microscopy, silicon fabrication, biochemistry, molecular biology, physical chemistry, and computational engineering have enhanced and enabled research and implementation of nanotechnology in academia and industry. Figure 2.11 summarizes the advantages of nanofibrous scaffolds.

## 2.7

### Biocompatibility of Nano-structured Tissue Engineered Implants

The objective of tissue engineering is to develop reproducible and biocompatible 3D scaffolds that act as bio-matrix composites to support cell in-growth in tissue repair and replacement procedures [65]. Researchers have focused on making such scaffolds with synthetic biopolymers and/or biodegradable polymer nanofibers [94–96]. Polymeric nanofibers have been widely studied as potential tissue engineering materials for biomedical applications. As a matrix, nanofibers mimic the structure and certain functions of the natural extracellular matrix to restore, maintain or improve the function of human tissues. Being biocompatible, nanofibers have been used for the replacement of structurally or physiologically deficient tissues and organs in human [35].

Biocompatibility is described as the ability of an implant (biomaterial, biotextile, prosthesis, artificial organ, biomedical device) to be accepted by the cellular and biological response from the host environment and does not have the potential to

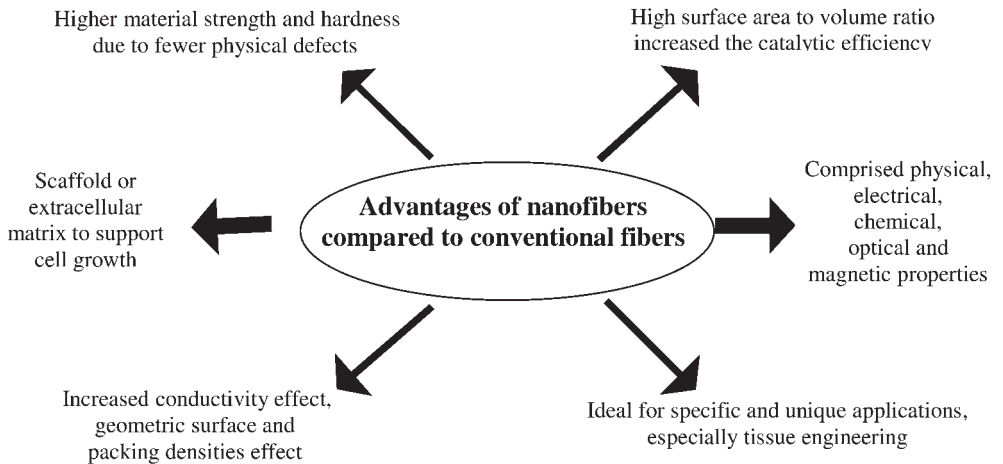


**Fig. 2.11.** The many advantages of nanofibers.

elicit an immunological or clinically detectable primary or secondary foreign body reaction [53, 97, 98]. It should be compatible with tissues in terms of mechanical, chemical, surface and pharmacological properties. *In vivo* biocompatibility testing of the biomaterials requires introduction of the implant into the biological environment to evaluate adverse reactions [99], such as alterations in homeostatic mechanisms, magnitude and duration of these altered homeostatic mechanisms if any, to determine the host biocompatibility response to the implant. If the implants are not rejected by the body, the following phases of recovery will be initiated: resolution (response of the biological environment to the injury and the presence of the implant), restitution (the return of the tissue environment to its normal structure and with the implant) and reorganization (the result of the wound healing response initiated by the injury and the presence of the implant). In addition, the rate of polymer biodegradation will also affect the biocompatibility of the implant in the biological system. Jayaraman and colleagues (2004) [71] have demonstrated that mats made of nanofibers from biodegradable polymers may be helpful in adjusting the degradation rate of specified biomaterials in the *in vivo* environment. Although no reports have been established on the influence of nanofiber diameter on the degradation behavior of polymers in the *in vivo* environment, there is evidence that the diameter of fibers do affect the degradation features and related mechanical properties of the materials [100]. In an *in vivo* study carried out in our laboratory on electrospun PLGA nanofibers tubes [101] that act as nerve guidance conduits, we observed that there was no inflammatory response after a month's implantation of the nanofiber nerve guidance conduit to the right sciatic nerve of the rat. Nerve growth factors or Schwann cells [102, 103] could be introduced into the nanofiber conduits to increase the biocompatibility of the nanofibers and hence improve the quality of the nerve regeneration and lead to clinical applications.

Polymeric nanofibers have been fabricated from various natural and synthetic biodegradable nanofibers [71] and most of the research on nanofibers for tissue engineering applications has centered on *in vitro* cell culturing to evaluate cell adhesion, proliferation, gene expression and extracellular matrix secretion [104]. Natural polymers are generally preferred over synthetic polymers in tissue engineering due to their tissue compatibility and biodegradation products which are readily resorbed into the body. In addition, nanofibers made from natural materials usually have better cell interactions than synthetic polymer nanofibers. Thus, the surface properties of the scaffold have been modified by adding surface coatings of collagen, gelatin, heparin, albumin or pyrolytic carbon to enhance the biocompatibility of the scaffold [69].

The most commonly used naturally derived polymers as tissue engineering scaffolds are collagen and chitosan [105]. Scientists are able to fabricate these nanofibers with diameters in the range of 100 nm to a few microns [8]. Collagen is a natural substrate for cell attachment, growth and differentiation. It provides considerable strength in its natural polymeric state. Collagen is also important in the design of tissue engineered devices [106] and it meets the requirements in wound healing since it has higher gas permeation and is able to protect the wound from infection and dehydration [81]. Venugopal et al. (2005) [107] fabricated nanofiber matrices from biodegradable PCL incorporated with collagen and showed that human dermal fibroblasts were able to grow, proliferate and migrate inside the matrices. These scaffolds support the attachment and proliferation of the cells and can be used as dermal substitutes for skin regeneration. In another study, Matthews et al. (2001) observed that smooth muscle cells cultured on electrospun collagen (calfskin) nanofiber matrix were able to grow into the nanofiber network [8]. Other studies showing infiltration of cells into the nanofiber networks include chondrocyte cultured on electrospun collagen type II scaffolds [108], human bone marrow stromal cell (BMSC) cultured on electrospun silk fibroin based-nanofibers [6], and human keratinocytes and fibroblasts proliferation on silk fibroin-based nanofibers [5].

Chitosan, a biologically renewable, biodegradable, non-antigenic and biocompatible natural polymer [105], is widely studied in wound dressing, wound healing [109], drug delivery systems [110], bone tissue engineering [111–113] and in various tissue engineering applications [114–117]. Electrospun chitosan nanofibers incorporated with synthetic polymers such as chitosan/poly(vinyl alcohol) and ultrathin hybrid nanofibers containing chitosan and PEO have been prepared by Ohkawa et al. (2004) [118], Duan et al. (2004) [119] and Bhattarai et al. (2005) [85]. Chitosan nanofibers with controllable size and alignment to form non-woven mats or 3D porous structures will provide an unlimited source for the development of natural scaffolds for tissue engineering [85]. Elastin, another structural protein of the extracellular matrix, has been successfully electrospun into elastin-mimetic peptide polymer nanofibers. The elastic property of elastin nanofibers has been capitalized on for the engineering of arterial blood vessels [96, 120].

In bone tissue engineering, nano-structured composites consisting of nano-hydroxyapatite and collagen (nHAC) have been developed by co-precipitation of hy-



droxyapatite (HA) and collagen [121], and mineralizing type I collagen sheet with hydroxyapatite [122, 123]. Preliminary *in vitro* and *in vivo* studies indicate that nHAC is bioactive and biodegradable [124]. However, its mechanical properties were too weak for practical application. To improve the mechanical strength, a nano-HA/collagen/PLA (nHAC/PLA) scaffold has been developed [124] which has high biocompatibility and strength, and serve as a promising scaffold in traditional bone-defect repair and in bone tissue engineering. Osteoblast cultured on the nHAC/PLA nano-composites performed well in adhesion, proliferation and maturation that accompanied the morphological change from spindle shaped to predominantly polygonal morphology. To further enhance nHAC mechanical properties, Zhang et al. (2003) [125] integrated nHAC composite with a small fraction of Ca-crosslinked to alginate to produce a porous structure that mimicked the composition of natural bone as well as to increase the osteoconductive activity of the scaffold. Polysaccharide alginate possesses good biocompatibility and provides satisfying mechanical support. Fibroblasts and osteoblasts co-cultured with nHAC/Ca-alginate composite exhibited good cell morphology, adhesion and proliferation, inferring the composite as a good scaffold material for bone tissue engineering. Although the efforts in fabricating natural polymer-based fibrous structures are encouraging, much remains to be explored and improved, especially in *in vivo* applications.

The uses of biocompatible synthetic polymer nanofibers have been widely investigated to evaluate their feasibility as scaffolds for applications in tissue engineering. Materials that have been used are polyesters, polycaprolactone, poly(amino acids), polycarbonates, poly(ethylene glycol) and many more. Polyesters such as PLA, PGA and copolymers of lactide/glycolide are among the most commonly used biomaterials for drug delivery [126] and tissue engineering. They break down to naturally occurring metabolites and degradation requires only water. Fine fibers produced from PLA and PGA by electrospinning for tissue engineering applications have been intensively investigated [30, 127]. ECM-like scaffolds fabricated from PLLA nanofibers by phase separation promote cell growth, proliferation and migration into the interstices of the nanofiber network [128, 129]. A nano-3D PLGA scaffold constructed by solvent casting and salt leaching processes had been shown to be biocompatible and support human bladder smooth muscle cells adhesion, growth and proliferation [130]. Cells cultured on nano-dimensional scaffolds showed a corresponding increase in cellular protein production when compared to cells cultured on conventional, micro-dimensional scaffolds. In addition, evidence in pressure experiments showed that, in general, scaffolds and resident cells experiencing a sustained pressure stimulus of 10 cm-H<sub>2</sub>O functioned similarly to those experiencing atmospheric (control) pressures. These results suggest that the novel porous, nano-dimensional PLGA scaffold is promising for *in vivo* replacements of the urinary bladder wall. Webster et al. (2005) [83] observed that the functions of osteoblasts such as adhesion, synthesis of alkaline phosphatase, and deposition of calcium-containing mineral showed an increase on nanofibrous PLGA scaffolds compared with conventional ceramics. Since both the nanofibrous PLGA and conventional ceramics share the same chemistry, material phase, porosity, and pore

size, the study implies that the surface features created by adding nanophase compared with conventional titania was a key parameter that enhanced functions of osteoblasts. Such nanophase ceramics (or nanomaterials in general) require further attention as orthopedic tissue engineering materials [83].

PCL is compatible with soft and hard tissue and is used as resorbable suture material, in drug delivery systems, and as bone graft substitutes. It has been incorporated into other synthetic polymers to create an ideal scaffold for the cell growth. Fetal bovine chondrocytes seeded on a nanofibrous PCL scaffold and cultured in serum-free medium maintained their chondrocytic phenotype by expressing cartilage-specific extracellular matrix genes that were evaluated by reverse transcription-polymerase chain reaction (RT-PCR). PCL nanofibers not only promoted the phenotypic differentiation but also promoted chondrocyte proliferation when cultures were maintained in serum-containing medium [131]. Adult bone marrow-derived mesenchymal stem cells cultured in a PCL nanofiber scaffold were induced to form chondrocytes in the presence of transforming growth factor- $\beta$ 1 (TGF- $\beta$ 1), as evidenced by chondrocyte-specific gene expression and synthesis of cartilage-associated extracellular matrix proteins. The chondrogenic ability of stem cells cultured in a PCL nanofiber scaffold was comparable to that observed for stem cells maintained as cell aggregates or pellets [132]. Yoshimoto et al. (2003) [133] seeded mesenchymal stem cells (MSCs) derived from the bone marrow of neonatal rats on electrospun PCL nanofibers as well and cultured the cells in osteogenic culture medium under dynamic culture conditions. At 4 weeks, the material was covered by multiple cell layers and mineralization occurs together with the existing type I collagen on the PCL nanofiber. Besides supporting the chondrocytes and stem cells, PCL nanofibers have also been observed to support the attachment of cardiomyocytes. Shin et al. (2004) [134] developed a cardiac nanofibrous mesh by culturing cardiomyocytes on electrospun nanofibrous PCL scaffold. The nanofibrous mesh acted as an extracellular matrix for cell growth and was supported by a wire ring that played a role as a passive load for the contracting cardiomyocytes. The cells on the scaffold were observed to start beating after 3 days of culture. In addition, cells cultured *in vitro* for 14 days were found to attach well on the PCL mesh and expressed cardiac-specific proteins such as  $\alpha$ -myosin heavy chain, connexin43 and cardiac troponin I. Block copolymers of PLLA and PCL (PLLA-CL) electrospun into non-woven and aligned nanofiber scaffolds have been reported to support the adhesion and proliferation of human coronary artery endothelial and smooth muscle cells, with a future application in blood vessel tissue regeneration [135–137]. In addition, PLGA and PCL nanofibers have been successfully utilized by Li et al. [131, 132, 138] to culture fibroblasts, cartilage, and bone marrow-derived mesenchymal stem cells. These reports showed that biocompatible synthetic polymeric nanofiber scaffolds were capable of enhancing cell attachment and proliferation.

Poly(*p*-dioxane) (PPDO) is a hydrophobic polyester that possesses good biocompatibility, flexibility and tensile strength. It degrades to non-toxic compounds and can be used in the body safely [139]. It has been applied to different applications in the medical field [140–142], such as surgical sutures [143] and drug delivery sys-

tem [141]. Poly(ethylene glycol) (PEG) is another widely used biocompatible polymer. PEG is a simple linear polyether that exhibits outstanding physiochemical and biological properties, and possesses good hydrophilicity and solubility in water and organic solvents. It lacks toxicity, and does not induce immunological effect, allowing it to be used for many biomedical and biotechnological applications [144, 145]. When PEG is coupled to PPDO, the conjugated product possesses the beneficial properties of both individual polymers. PLLA conjugated to PEG is another block copolymer that possesses properties desirable for tissue engineering applications [146–148]. The synthesis of a novel biocompatible block copolymer consisting of PPDO, PLLA and PEG (PPDO/PLLA-b-PEG) by Bhattarai et al. (2004) [82] takes advantage of the combined properties of these polymers to further enhance biocompatibility. NIH 3T3 fibroblast cells seeded on the PPDO/PLLA-b-PEG nanofibrous structure were shown to maintain their phenotypic shape and guided growth according to the nanofiber orientation. PEO is another biocompatible polymer that has been used in food, cosmetics, personal care products and pharmaceutical. Electrospun poly(ethylene-co-vinyl alcohol) nanofiber mat can also support the growth of smooth muscle cells and fibroblast [80].

## 2.8

### Applications of Polymeric Nanofibers in Tissue Engineering

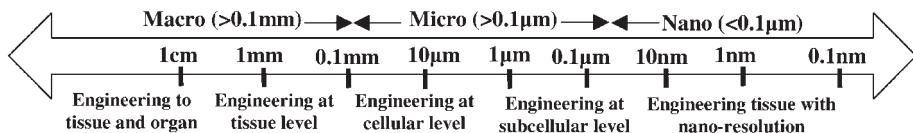
With the advancement in tissue engineering in the past decades, researchers realized that nanofibers have potential as scaffolds in tissue regeneration. These nanofibers can be fabricated from either natural or synthetic polymers for various applications in tissue engineering (Table 2.1). The rationale for using nanofibers is based on the principle that cells organize and attach well around fibers with a diameter smaller than that of the cells [74]. In addition, non-woven polymeric nanofibers mimic the nano-scale fibers that are present in the natural extracellular matrix. They provide interconnected pores that facilitate transport of nutrients and growth factors to the cells as well as providing a stable structural support, which are essential for effective tissue engineering. A unique characteristic of the nanofibers is its huge surface area-to-mass ratio, in the range of  $10\text{--}10^3\text{ m}^2\text{ g}^{-1}$  for a fiber diameter of around 500 nm [98], and this makes them suitable to host various functionalities and be applied to a broad range of applications in life sciences and sensor applications. Therefore, studies have been performed to optimize the properties of the nanofiber scaffolds in the areas of ophthalmology, hepatic biology, nerve, skin, bone and cartilage regeneration, heart and vascular grafts, and stem cell research as well as drug delivery application [149]. Tissues can be engineered at different levels of complexity (Fig. 2.12) [150]. Using this knowledge of nanotechnology, tissue engineered products with highly predictable biological and physical properties can be obtained.

In nerve regeneration, nanofibers have been shown to effectively control the neurite outgrowth rate and orientation that are critical for the repair of the damaged nervous system. Similarly, the ability to control the morphology, proliferation, ad-

**Tab. 2.1.** Different types of biomaterials in the various biomedical applications.

Applications	Biomaterials
Ophthalmic (Intraocular lenses, contact lenses)	PMMA, PHEMA, PEU, PEO, PGMA, PVA, PLGA, collagen
Liver	PLA, PGA, PGLA, polyorthoesters, polyanhydride, PLGA, PCLEEP
Nerve (Hydrocephalus shunts)	PEU, PLGA, PDLA, PLLA-CL, PDMS, PTFE, collagen, glycosaminoglycan, PGA
Skin (Facial and hip prostheses, artificial skin)	PEU, PCL, PTFE, PE, Collagen, PGA, PGLA (Vicryl), nylon, collagen-glycosaminoglycan
Orthopedic and cartilage (Bone cement for fracture fixation, sutures, bone repair)	PMMA, polyamides, PP, hydroxyapatite, PGA, PLLA, PGLA+hydroxyapatite fibers, PCL
Heart (Heart valves, artificial heart, ventricular assist devices, pacemaker leads)	PDMS, PEU, PTFE, PE, PSu, PGA
Vascular graft (Blood substitutes)	PTFE, PVP, Polyester (Dacron), polyurethane, expanded PTFE, PGA, PLA, PGLA, PVC, collagen
Stem cells	PCL, PLA
Drug delivery systems	PDMS, PEVA, PLA, PGA, PLGA

PCL: polycaprolactone; PCLEEP: poly(*ε*-caprolactone-*co*-ethyl ethylene phosphate); PDLA: poly(D,L-lactic acid); PDMS: polydimethylsiloxane, silicone elastomers; PE: polyethylene; PEO: poly(ethylene oxide); PEU: polyurethanes; PGA: poly(glycolic acid); PGLA, PLAGA, PLGA: copolymers of poly(glycolic acid) and poly(lactic acid); PGMA: poly(glyceryl monomethacrylate); PHEMA: poly(2-hydroxyethyl methacrylate); PLA: poly(L-lactic acid); PLLA-CL: copolymer of PLA and PCL; PMMA: poly(methyl methacrylate); PP: polypropylene; PS: polystyrene; PSu: polysulfone; PTFE: poly(tetrafluoroethylene); PVA: poly(vinyl alcohol); PVC: poly(vinyl chloride); PVP: poly(vinyl pyrrolidone); PEVA: poly(ethylene-*co*-vinyl acetate).

**Fig. 2.12.** Tissue engineering at different levels.

hesion and alignment of smooth muscles cells and endothelial cells cultured on nanofibrous scaffolds provides a possible avenue for successful tissue engineering of blood vessels. Suitable bioactive nanofibers for proliferation of osteoblasts in guided bone regeneration, and dermal fibroblasts for burns and chronic wound treatment have also been reported. Studies on nanofibers for stem cell proliferation and differentiation are still in their infancy but the potential for biomedical applications is tremendous.

### 2.8.1

#### **Ophthalmology**

Every part of the human eye plays an important role in providing clear vision. The cornea is the primary component of the ocular optical system that refracts light onto the retina for vision and act as a tough protective barrier for the delicate internal eye tissues [151]. It is an avascular and transparent tissue that consists of three main layers: outer stratified epithelium, stroma of cell network within a hydrated collagen–proteoglycan matrix, and inner endothelial layer. Nerve activity is crucial for the maintenance of overall corneal health. Innervation loss can cause “dry eye” [152], a pathological condition that will decrease the sensitivity of the cornea and/or caused the erosion of the cornea epithelial. When the sensitivity is lost, the cornea can be affected by a wide variety of disorders [153–156] and becomes vulnerable to irreparable injury, ulceration, eventual loss of vision or blindness [157, 158].

Cornea disease is a major cause of vision loss [159] and it affects more than 10 million individuals worldwide [160]. Transplantation of human donor corneal graft is the widely accepted treatment in the hope of visual recovery [151]. However, transplant donors are limited and worldwide demand exceeds supply. This situation will worsen with an aging population and increased used of corrective laser surgery [161]. Patients with conditions such as autoimmune disorders, alkali burns, graft rejection or recurrent graft failures will have a lower success rate in corneal transplantation [162]. Furthermore, there is a risk in the transmission of infectious agent [163]. Therefore, an alternative for these patients is the replacement of the damaged cornea with an artificial substitute. The structural and immunological simplicity of the human cornea, and the importance of nerve innervations for optimal function, make it an ideal tissue for tissue engineering studies. The ideal artificial cornea (keratoprosthesis) should consist of materials and structures that support adhesion and proliferation of cornea epithelial cells in order to form an intact continuous epithelial layer [163]. It should be permeable to provide appropriate exchange of nutrient and fluid, light transparent and non-toxicity to cells.

In the early 1950s until the 1990s, a few synthetic polymers were used extensively for the manufacture of keratoprostheses. Poly(methyl methacrylate) (PMMA) [164–168] was used as intraocular lenses into human patients. Poly(2-hydroxyethyl methacrylate) (PHEMA) hydrogels have a long history of proven biocompatibility in the cornea [169–182]. Polyurethanes [183–185], poly(glyceryl monomethacry-

late) (PGMA) [186–188], PEO, and poly(vinyl alcohol) (PVA) hydrogels [189] were proposed and/or used episodically as keratoprosthesis materials. Corneal epithelial cells have been preseeded onto PVA and transplanted into rabbit corneas, where they remained adherent and proliferated for 1 to 2 weeks [190–193].

Research in synthetic cornea replacement is essential since most artificial cornea is still plagued with poor adhesion to the host tissues and does not promote reinnervation [194]. Scientists from Argus Biomedical, Australia, have claimed to successfully develop an artificial cornea, named Alphacor. It is made of a biocompatible, flexible, hydrogel material similar to a soft contact lens. It contains a central clear zone, consisting of a transparent gel PHEMA that provides refractive power and a peripheral skirt or rim made of an opaque, porous, high-water PHEMA that encourages the eye to heal over the device. Alphacor has been under clinical study since 1998 and was FDA-approved in August 2002. The replacement cornea is designed to minimize the risk of complications, and to replace the scarred or diseased cornea of the eye that has a history of multiple graft failures [195]. Using collagen-copolymer implants, Li et al. (2003) [160] reported successful growth of stratified epithelium and stromal fibroblast, and nerve innervations into the implant. In two other studies, collagen-copolymer scaffolds designed to mimic the natural ECM matrix and crosslinked to TERP5 copolymer synthesized from *N*-isopropylacrylamide were shown to allow cell growth on the surface [196] and as well as cell ingrowths [197]. Cell adhesion factors may be incorporated into the biosynthetic matrices to promote cell growth and nerve innervations.

The retina is the other part of the eye that has received extensive research in tissue engineering. It has a complex, multilayered architecture that consists of polarized photoreceptor cells that are closely related to the retinal pigment epithelium (RPE), nerve innervations, and rich supply of blood capillaries [198]. The integrity of the RPE layer is critical to the survival and functions of photoreceptors and hence patterns the vision. Retinal degeneration such as retinitis pigmentosa (RP) and age-related macular degeneration (AMD) affect over a million people in USA alone, where they suffer from irreversible visual disability. Photoreceptor cells will lose their functions when the degeneration happens at the outer retina and this will affect the cells that connect and support the photoreceptors of the inner nuclear layer. Conventional treatment of the disease such as retinal progenitor cell (RPC) grafts is not sufficient to create the complex cytoarchitecture on a large scale, especially when multiple retinal layers have been lost or disrupted [199, 200]. Studies have shown that delivery of RPCs using typical bolus injection of RPCs leads to a large degree of cell death [201]. In addition, the widespread intraretinal migration frequently observed with these cells may not be desirable in all settings. A tissue engineering approach using a biodegradable polymer scaffold with the appropriate architecture may improve the survival and promote the organized differentiation of grafted RPCs in retinal degeneration and injury.

Recently, RPCs have been isolated from the mature eye [202, 203] to develop retina [204, 205] and these cells may be able to replace photoreceptors [206]. Lavik et al. (2005) [198] (Fig. 2.13) seeded RPCs onto porous degradable PLGA scaffolds fabricated by anisotropic phase inversion [207] and by liquid–liquid phase separa-

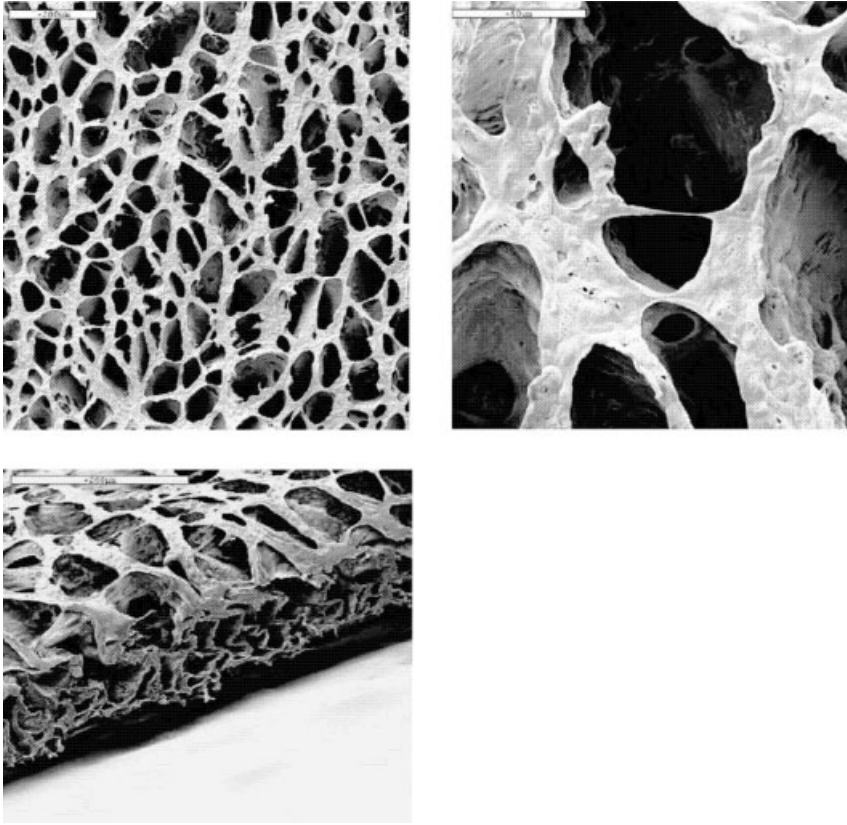
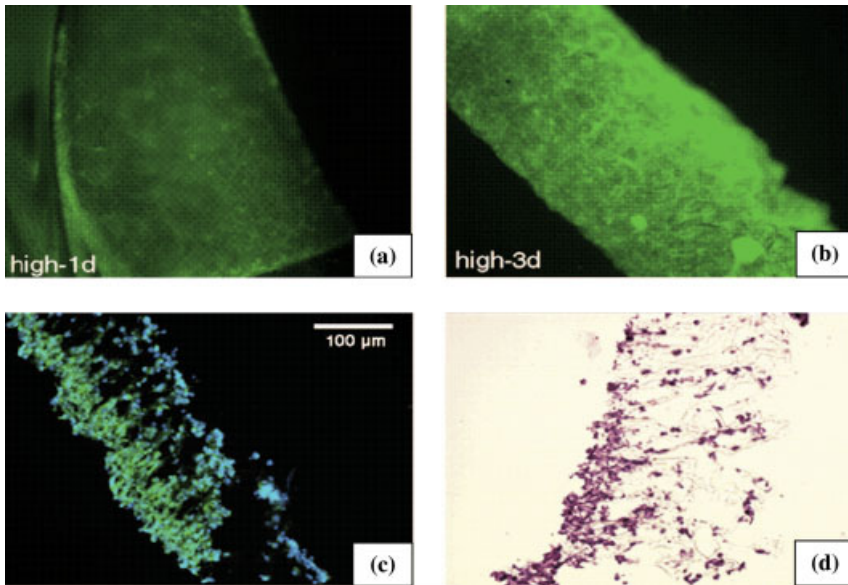


Fig. 2.13. PLGA scaffold prepared using the solid-liquid phase separation technique [198].

tion [208]. The results of this work indicate that degradable polymer scaffolds improve the survival of RPCs in retinal degeneration model, promote differentiation of RPCs, and provide physical guidance to the RPCs resulting in a more normal anatomical organization (Fig. 2.14).

There are very few comprehensive and systematic reports on the functional relationship between nanofibers and applications in ophthalmology. One of the most recent studies is by Zhong et al. (2005) [209] who seeded rabbit conjunctiva fibroblasts (RCF) on electrospun random collagen-glycosaminoglycan (GAG) blended nanofibrous scaffolds with a fiber diameter range 100–600 nm. The results showed that the nano-sized scaffold increased the proliferation of rabbit conjunctiva fibroblast on the scaffolds (Fig. 2.15). Since collagen and GAG are components of the natural ECM, their incorporation into scaffolds has been used extensively for *in vitro* cell-ECM interactions studies and as platform for tissue biosynthesis [210–217]. Traditional collagen gels can self-assemble into a nano-scale fiber-like superstructure [218], but their application is limited due to the poor physical strength. However, aligned nanofibers possess higher mechanical strength than random



**Fig. 2.14.** Seeding of RPCs that are stained green on the solid–liquid phase separated scaffolds for (a) 1 and (b) 3 days. (c) Cross section of the scaffold at 3 days post seeding. The green fluorescence RPCs were

counterstained blue with 4',6-diamidino-2-phenylindole (DAPI). (d) Cross section of the same sample stained with hematoxylin and eosin (H&E) [198].

nanofibers [16], and this fiber alignment feature can be used to increase the physical strength of collagen nanofibers. In a study conducted in our laboratory in collaboration with the Singapore Eye Research Institute [219], it was shown that aligned nanofiber scaffold seeded with RCF exhibited lower cell adhesion but higher cell proliferation than the random scaffold. This is likely due to the aligned

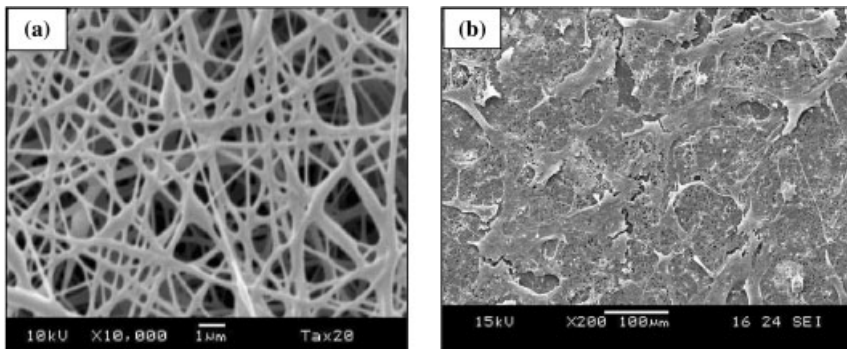


**Fig. 2.15.** Scanning electron microscope (SEM) micrographs of (a) electrospun collagen-GAG scaffolds, and (b) RCFs on collagen-GAG scaffolds after 7 days culture [209].



orientation of the fibers, which may control cell orientation and at the same time strengthen the interaction between cells and fibers. This may indirectly increase the overall physical strength of the biological scaffolds. From these results, application of nano-scale collagen or collagen-GAG scaffolds in ophthalmology is significant as the nano-scale dimension of these electrospun nanofibers mimic that of native ECM found in our body and at the same time promote tissue biosynthesis, guide cell growth, and maximize the rate of tissue regeneration [136, 210–221].

### 2.8.2

#### **Liver**

The cells in the liver are highly organized into structural units called liver lobules. These cells or hepatocytes are radially disposed in the lobules, piling up to form one cell thick layers, alike to the bricks of the wall. These cell plates are directed from the periphery of the lobule to its center. In human, these lobules are in close contact with one another, forming sponge-like structures. A unique feature of the liver is its ability to regenerate following injury or resection and tissue engineering methodologies have been applied to assist in liver regeneration. Nano-structured biomaterials have been used to enhance the development of liver replacement devices [222]. In a study by Chua et al. (2005) [18], growth of primary rat hepatocytes on PCLEEP nanofiber scaffolds conjugated with galactose ligands to achieve a bio-functional construct was evaluated. PCLEEP was shown in earlier reports to have good tissue compatibility and low cytotoxicity to the cells [223–225]. Galactose-conjugated substrates have been reported to mediate hepatocyte adhesion, minimize involvement of integrin-mediated signaling pathways, and reduce the loss of hepatocyte phenotype [226]. In this study, hepatocytes cultured on the galactosylated PCLEEP nanofibrous scaffold exhibited comparable functional profiles in terms of cell attachment, ammonia metabolism, albumin secretion, and cytochrome P450 enzymatic activity, when compared with hepatocytes cultured on functional 2D matrix. In addition, hepatocytes cultured on galactosylated nanofiber scaffold formed smaller aggregates of 20–100  $\mu\text{m}$  that engulfed the functional nanofibers and created an integrated spheroid-nanofiber construct, resulting in reduced cell detachment from the nanofibrous scaffold, and form stable immobilized hepatocyte spheroids throughout the period of culture (Figs. 2.16 and 2.17). Such functional nanofiber scaffolds can be incorporated into a bioartificial liver assist device design, and with their textured and porous nature may promote hepatocyte scaffold interaction, improve the stability of the attached cells, maintain their differentiation functions, and, finally, remain stable against the perfusion and shear forces in the bioreactor.

### 2.8.3

#### **Nerve**

Neural tissue engineering (NTE) is a promising and challenging field that involves various disciplines, such as grafting processes, polymer bioprocess and surface

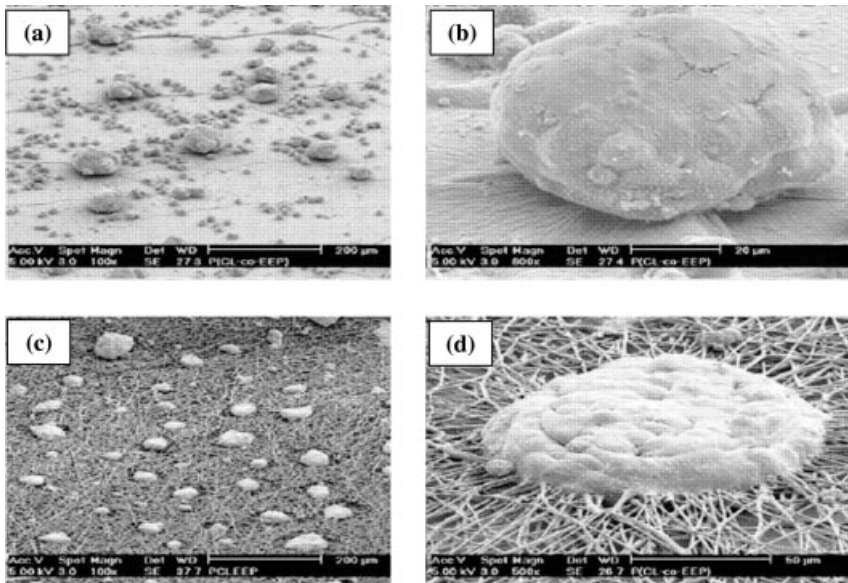


**Fig. 2.16.** SEM images of hepatocytes after 8 days of culture. Hepatocytes cultured on galactosylated film (Gal-film) formed rounded spheroids that did not integrate with the

scaffold (a, b). In contrast, hepatocytes cultured on galactosylated-nanomesh (Gal-nanomesh) showed aggregates that engulfed the functional nanofibers (c, d) [18].

chemistry modifications, as well as involving cell–cell and cell–matrix interactions that occur during development, remodeling and restoration of neural cells [227]. Nerve tissue repair is an important treatment concept in human health care as it directly impacts on the quality of life. However, restoring the nerve function after traumas or diseases has been a great challenge for neurobiologists and neurologists, as the central nervous system (CNS), such as brain and axons, do not regenerate on its own in their native environment. In the peripheral nervous system (PNS), healing of severed peripheral nerves may be impaired by the growth of fibroblastic connective tissues that will disrupt and prevent the proximal neuron from growing towards and reattaching to the distal stump [69]. Attempts to replace lost or dysfunctional neurons using tissue transplantation or peripheral nerve grafting method have been intensely sought for over a century [228]. The purpose is to restore the function in damaged or diseased regions. However, these methods always encountered problems such as donor shortage and immunological problems associated with infectious diseases [229]. To overcome some of these problems, alternative approaches are being investigated that use biomaterials to influence the function and differentiation of cultured or transplanted cells to enhance nerve regeneration [230–233].

The ultimate goal of neural tissue engineering is to achieve suitable biointeractions for a desired cell response that is required to compensate for the loss of tissue function [234] through *in vivo* induction of a neural circuit or *in vitro* fabrication

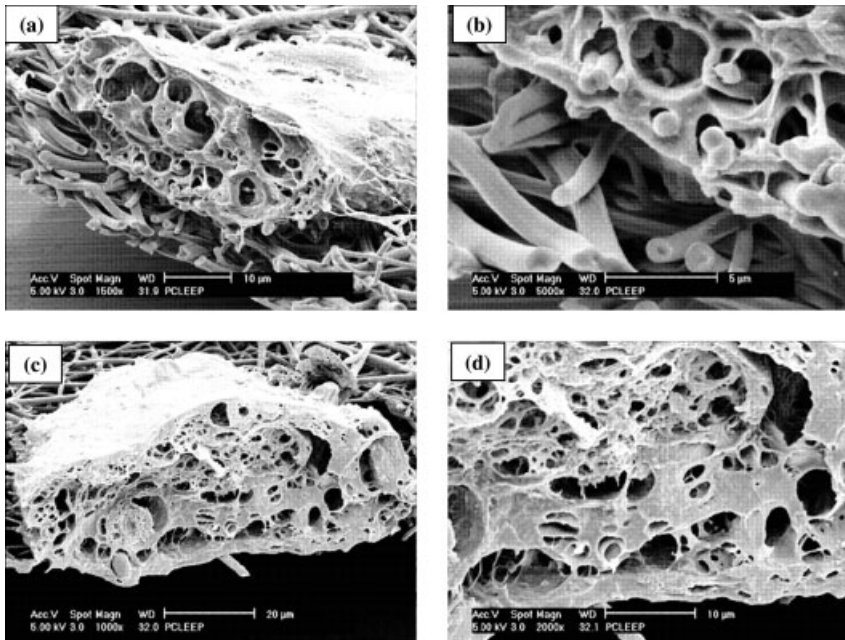


**Fig. 2.17.** SEM images of freeze-fractured hepatocytes on Gal-nanomesh after 8 days of culture. PCLEEP nanofibers can be found within the hepatocyte aggregates (a, b).

However, no fibers were observed in some hepatocyte aggregates, which may be attributed to degradation of the biodegradable PCLEEP nanofibers (c, d) [18].

of a tissue structure. Engineered polymer scaffolds that can serve as extracellular matrix are crucial to support the fundamental cell processes. Recent advances in the NTE provide optimism by creating a permissive environment for nerve regeneration [163, 235–237]. The ECM of the nervous system is crucial in guiding neural outgrowth and may be relevant to the process of regeneration. It consists of the collagen types I, II, III, IV and V, the noncollagenous glycoproteins and the GAGs [238, 239]. A great variety of natural ECM components exist in fibrous form and structure, some examples include collagen, fibronectin and laminin. All of them are characterized by well-organized hierarchical fibrous structures, ranging from nanometer to millimeter scale [240]. Hence, a nano-structured porous scaffold with interconnective pores and large surface area is needed as an alternative to natural ECM for better cell ingrowths in a three-dimensional fashion.

Polymers can be used as scaffold to promote cell adhesion, maintenance of differentiated cell function without interfering proliferation, template to organize and direct the growth of cells and help in the function of extracellular matrix [241]. Several methods have been reported to fabricate polymeric nanofibers or submicron fibers: phase separation [242], electrospinning [243] and self-assembly [244]. Yang et al. (2004) [245] have shown the potential of the PLLA nanofibrous porous scaffold, prepared by phase separation in nerve tissue engineering. The scaffold mim-

icked the structure of the natural ECM and was shown to support neural stem cells differentiation and outgrowth of the neurites. In another study, Spilker et al. (2001) [246] demonstrated that cells obtained from nerve explants were able to construct and restructure the walls of porous collagen-GAG matrices *in vitro*, suggesting that contractile cells may be capable of restructuring the extracellular component of the nerve wound environment *in vivo*. Electrospinning is able to fabricate fibrous scaffolds with desired properties [136, 247] to create biocompatible thin structures with useful coating design and surface properties that can be deposited on implantable devices to facilitate the integration of these devices into the body. This is exemplified in electrospun silk-like polymer with fibronectin functionality for making biocompatible films, which were used on prosthetic devices aimed to be implanted in the central nervous system [94].

Advanced techniques to produce a complex, degradable guidance channels that precisely mimic a natural repairing process in the human body have been investigated [248–251]. Various biomaterials or polymers have also been investigated for their suitability in nerve tissue engineering applications [101]. These synthetic conduits have been fabricated from materials such as polyurethane, polyorthoester, glycolide trimethylene carbonate, PLGA, PGA, poly(D,L-lactic acid) (PDLLA) and PLLA-CL [63] (Table 2.1). Early nerve regeneration studies used biotextile incorporated with appropriate growth factors to join the two neural stumps. The proximal neuron regenerates and can bridge gaps as wide as 8 mm, so as to re-establish distal neural activity [69]. In another study, the bioresorbable implant (trimethylene carbonate-co- $\epsilon$ -caprolactone) seeded with Schwann cells showed a significant increase in growth, ensheathment and peripheral nerve myelination [252]. In a recent study by Bini and colleagues (2004) [101], nerve guidance channel was fabricated by electrospinning PLGA biodegradable polymer nanofibers onto a Teflon mandrel. The biological performance of the conduits was examined in the rat right sciatic nerve model with a 10 mm gap length. There was no inflammatory response after the implantation of the nanofibrous nerve guidance conduit. Five out of eleven rats showed nerve innervation into the conduits after a month of implantation (Fig. 2.18). None of the implanted conduits showed tube breakage. This showed that the nanofibrous nerve guidance conduits have the necessary flexibility to adapt well inside a living system, a porous structure that make it permeable for gaseous and nutrient exchange in the conduit lumen to promote the nerve regeneration, are biocompatible, and showed no inflammatory response, which is clinically desirable in minimizing adhesions of an implanted conduit to surrounding tissues.

Nerve regeneration in the CNS is much more difficult than in the PNS and this is probably due to the glial cells in the CNS, which act as a barrier to the regenerating axons and create an unfavorable environment for axon regeneration after trauma or injury [237, 239]. Another reason would be the dissimilarities in the ECM components between PNS and CNS to assist and promote nervous regeneration [239]. In the PNS, the linear orientation of ECM components at the peripheral stump of a damaged nerve provide terrain well suited for axonal regrowth, whereas such framework is not available in the ECM of the CNS to assist axonal growth



**Fig. 2.18.** The regenerated nerve cable after a month of implantation [101].

[238, 253]. The nanofibrous scaffolds are well suited for CNS tissue engineering due to two unique properties. Firstly, the morphology and architecture are similar to the natural ECM, which is the foundation of creating reproducible and biocompatible 3D scaffolds for cell attachment, differentiation and proliferation. Secondly, the nanofibrous scaffolds are highly porous structures with a wide variety of pore diameters, allowing fluid transportation while inhibiting glial scars. Moreover, with the electrospinning technique, aligned nanofibrous scaffolds can be fabricated to

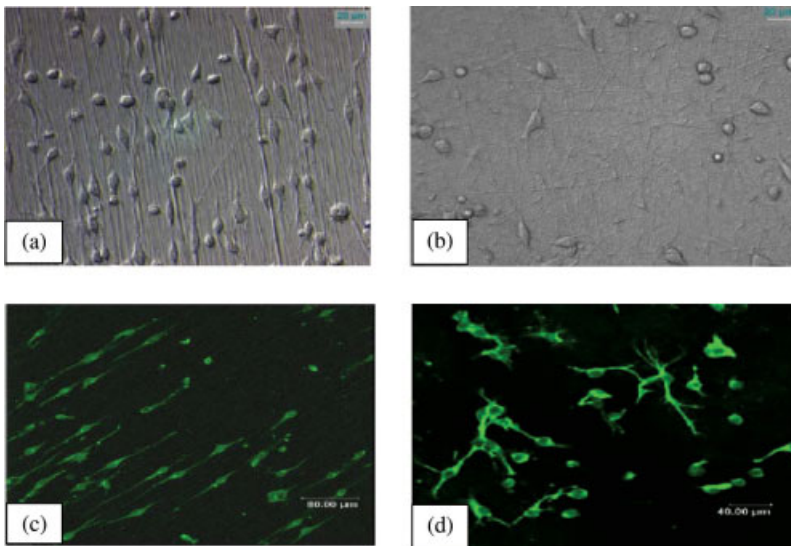


**Fig. 2.19.** C17.2 cells cultured on aligned (a, c) and random (b, d) PLLA nanofiber scaffolds for 1 day (a, b) and 2 days (c, d). Parts (a) and (b) are phase contrast light microscope images of cells attached on aligned nanofibers and random nanofibers, respectively. Parts (c) and (d) are laser scanning confocal micrographs of cells immunostained for neurofilament 200 kDa when cultured on aligned and random nanofibers, respectively [254].

guide neuronal regeneration in both the central and peripheral nervous systems [254].

Yang and colleagues (2005) [254] designed an electrospun aligned PLLA nanofibrous scaffold to evaluate the efficacy in promoting neuron differentiation and guiding neurite outgrowth of C17.2 cells *in vitro*. The aligned nanofiber scaffold is anticipated to provide better contact guidance effects on the neurite outgrowth. C17.2 is a primordial, multipotent self-renewing cell that can be used as neuron precursors, and is involved in the normal development of cerebellum, embryonic neocortex and other structures upon implantation [251, 255, 256]. The cells are capable of differentiating without interaction with adhesion molecules such as laminin, fibronectin, collagen, poly-L-lysine or Matrigel™, which are generally required as permissive substrates in neurite outgrowth. This offers the convenience of investigating the physical effects of PLLA fibrous scaffolds because the coating of adhesive molecules will affect the surface topography of the scaffold. The *in vitro* results of this study showed that the fiber alignment had a strong effect on the cell phenotype: neural cells on aligned fibers grew parallel to the fiber orientation, and the aligned nanofibers improved neurite outgrowth when compared with random or microfibrinous scaffolds (Figs. 2.19 and 2.20). The results suggest that the aligned nanofibrous scaffold may be a suitable nerve guidance channel for both CNS and PNS regeneration.

Researchers have not only explored the use of biomaterials for neural tissue engineering. A silicon-based electronic device for neural network applications has been developed by Fan et al. (2002) [257]. They investigated the adhesion of neural cells from substantia of prenatal rat on silicon wafer with different nanotopographic features of between 20 and 70 nm in dimension produced by etching. The cell adhesion and viability were significantly improved on the nano-featured surface. The results strongly suggested that nanotopography could improve the

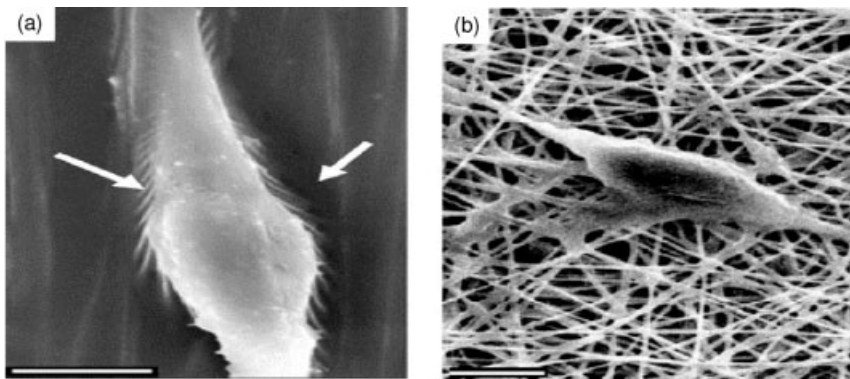


**Fig. 2.20.** SEM micrographs of neural stem cells seeded on (a) aligned and (b) random nanofiber for 2 days, showing the cell–matrix adhesion between the neural stem cells and PLLA fibers. Bar = 5  $\mu\text{m}$  [254].

response of neural cells and be used in designing neurochips as proposed by researchers such as Weis and Fromherz at the Max-Planck Institute for Biochemistry, Germany, and Pine and colleagues at the California Institute of Technology, Pasadena, California [222].

#### 2.8.4

##### **Skin**

Extensive burns or skin damaged by ambustion and injury require comprehensive therapy to repair the conditions, to prevent dehydration and infection. Dressing of wound is aimed to protect, remove exudates, inhibit exogenous microorganism invasion, and improve appearance [81]. Many studies have been done in the past 30 years to develop and enhance the skin regeneration by tissue engineering. In 1962, Winter [258] showed that covering the wound with a polyethylene film significantly improves the epithelialization of the wound in a shorter time. Protection was further accomplished by covering the wound with a dressing such as artificial skin constructed from either natural or synthetic polymers [259]. Wound areas that are kept just damp may heal faster, but accumulation of exudates under the dressing can cause infection [260]. Currently, autograft is a standard treatment in wound dressing. It is done by removing a section of the skin from another part of the body and grafting onto the wound. However, the removal of the dermis and epidermis is a serious operation and the availability of healthy skin can be limited if the burnt areas are widespread [261]. Recent developments in the regeneration of skin by tissue engineering have overcome these difficulties, especially in the use of polymer nanofibers for wound healing.

The objective of tissue engineered wound dressing is to produce an ideal structure, which gives higher porosity and good barrier. The materials must be selected carefully to produce high quality barrier properties and oxygen permeability. Electrospun nanofibrous membranes have potentials as wound dressing. This is because the membrane attained uniform adherence on wet wound surface without any fluid accumulation [82]. It can meet the essential requirements of wound healing such as high gas permeation and protection of wound from infection and dehydration. Khil and colleagues (2003) [81] have shown that the rate of epithelialization was increased and the dermis was well organized in wound covered with electrospun nanofibrous polyurethane membrane, which provided a good support for wound healing. The wound dressing showed controlled evaporative water loss, excellent oxygen permeability and promoted fluid drainage ability due to the porous nature of the nanofibers and the inherent properties of polyurethane. Polyurethane is frequently used in wound dressing because of its good barrier properties and oxygen permeability. Woodley and colleagues (1993) [262] reported that semi-permeable dressings, many of which are constructed from polyurethane, enhanced wound healing. The permeability of the wound dressing is crucial to prevent accumulation of fluid between the wound and the dressing. The fluid absorbed in the wound dressing will keep the wound moist and this will inhibit wound desiccation. Researchers have also tried to determine the effect of occlusive dressings on the

healing of wound prepared by polyurethane [263–266]. The disadvantage of the semiocclusive dressings is that fluid will accumulate under the dressings after a few days [267] and aspiration of the wound is required to prevent leakage and infection.

Another polymer that is frequently used for wound dressing is PCL, a biodegradable polymer characterized by a resorption time in excess of one year [268] but is known to be susceptible to enzymatic degradation [269]. Various degradative enzymes such as collagenases, matrix metalloproteinases, gelatinase A and stromelysin-1, which are secreted by macrophages, epidermal cells and fibroblasts for cell migration and repair during wound healing have been established to degrade PCL [270]. PCL and collagen nanofiber membranes have been used as wound dressings [107]. This structured membrane improves the mechanical integrity of the matrix, and provides a high level of surface area for cells to attach due to its 3D features and high surface area to volume ratio when compared to polymer film (Fig. 2.21). This PCL/collagen membrane will possess both the mechanical properties and cell binding affinity derived from the unique properties of PCL and collagen, respectively. In this study, fibroblasts were shown to migrate inside the collagen nanofibrous matrices mimicking the structure of the dermal substitute. Collagen synthesized by fibroblasts is a good surface active agent and will en-

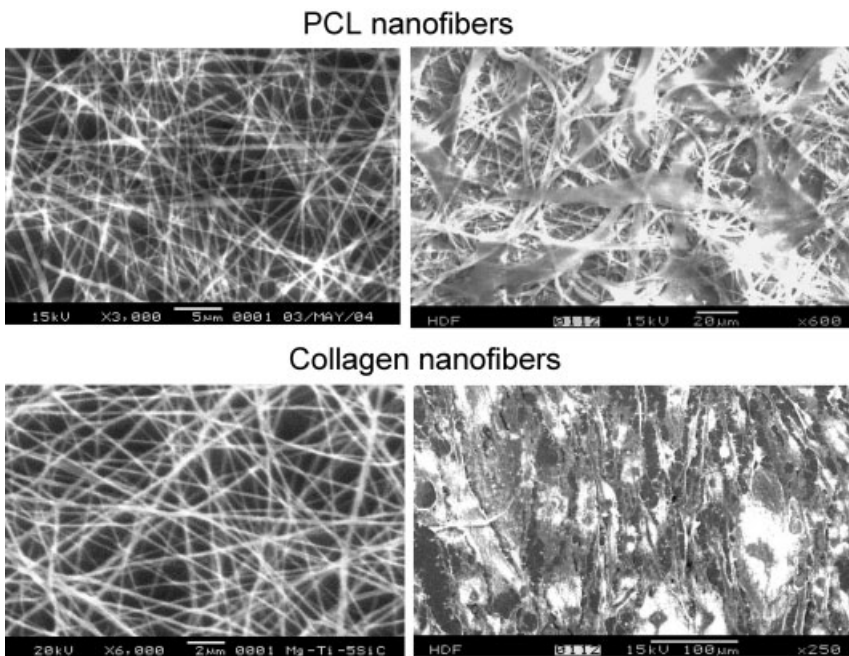


Fig. 2.21. Fibroblast cell attachment and growth on PCL and collagen nanofibers [107].



hance the attachment of keratinocytes to the surface of artificial dermis in serum free medium. It is assumed that the fibroblasts on the artificial dermis can release biologically active substances, such as cytokines, which induce invasion of the wound site by fibroblasts and other immunological cells during the early synthesis of the new skin tissue. The dynamic architecture of the fibers such as pore size and fiber alignment allows the cells to grow into the nanofiber matrices to form a dermal substitute for many types of wound healing. This nanofiber-based fibroblast-cultured dermal substitute maintains the moist environment on the wound surface and thereby promotes wound healing.

The incorporation of collagen in polymer scaffolds has been demonstrated in many studies to promote cell growth and proliferation. Using human osteoblasts, Coombes et al. (2002) [271] demonstrated that PCL composite films consisting of non-crosslinked collagen mats support higher cell growth than unmodified PCL films. In another study, Dai et al. (2004) [272] found that composite films of collagen and PCL are favorable substrates for growth of fibroblasts and keratinocytes and may find utility for skin repair. To improve on this further, Huang and colleagues (2001) [273] developed a convenient, non-toxic, and non-denaturing process to fabricate collagen-containing nanofibers with diameters ranging from 100 to 150 nm, and non-woven fabrics, which they proposed based on the materials excellent properties to have potential applications in wound healing, tissue engineering and as haemostatic agents. Fine fibers of biodegradable polymers have also been developed to be directly sprayed or spun onto the injured location of the skin, forming a nanofibrous mat dressing, which encourages wound healing by the formation of normal skin and elimination of scar tissue that would occur in a conventional treatment [274–277]. Two patents have been filed [278, 279] where researchers produced a skin mask by directly electrospinning fibers that contain pH-adjusting compound onto the skin surface to protect and eventually heal the wound.

The main advantages of non-woven nanofibrous membrane mats for wound dressing are their pore size, usually from 500 nm to 1  $\mu\text{m}$ , which is small enough to protect the wound from bacterial penetration, and the high total nanofiber surface area of 5 to 100  $\text{m}^2 \text{g}^{-1}$ , which is extremely efficient for fluid absorption and dermal delivery. A commonly used wound dressing in hospitals is Tegaderm™ developed by 3M (USA), which is a thin polyurethane membrane that is permeable to both water vapor and oxygen but impermeable to microorganisms. In one study, electrospun nanofibrous membrane showed excellent and immediate adherence to wet wound surface compared with the dermis of wound covered with Tegaderm™ (3M, USA), which was also reported to be inflamed [81]. The rate of epithelialization was increased, the dermis was well organized, and fluid accumulation was not observed in electrospun nanofibrous membrane group [81, 82]. These result indicate that the electrospun nanofibrous membrane provided a good means for wound healing. In addition, histological examination confirmed that epithelialization rate was increased, and the exudates in the dermis were well controlled by covering the wound with the electrospun membrane. Thus, nanofibrous membrane prepared by electrospinning could be properly employed as wound dressings.

## 2.8.5

**Bone and Cartilage**

Only in recent years have researchers gained a better understanding of stem cell biology and their potential for bone and cartilage repairs and regeneration, and this has accelerated the development of biomaterial scaffolds for tissue engineering research in this discipline. The surface properties of biomaterial regulate the cell phenotype through their capacity to support and spatially display the crucial adhesion contacts [280, 281]. Nano-scale features have also been used to design the scaffolds for culture of osteoblasts and mesenchymal stem cells [221]. Recent advances in stem cell biology have shown that MSCs can differentiate into cells of mesenchymal tissues such as bone, cartilage, muscle, tendon, ligament and fat, and are expected to play important roles in the repair of skeletal defects [282, 283]. Osteoblasts derived from MSCs of neonatal rats cultured on poly(D,L-lactide-co-glycolide) foam were observed to deposit minerals and form 3D bone-like structures in the foam [284]. In another report, a non-woven PCL nanofibrous scaffold was fabricated and its potential evaluated in bone tissue engineering with rat mesenchymal stem cells [133, 285]. It was observed that the polymer constructs were covered with multiple cell layers, mineralized, and impregnated with type I collagen. Besides synthetic polymer, researchers have used natural polymers such as silk to produce nanofibrous scaffolds [6]. Human bone marrow stromal cells were cultured on electrospun silk fibroin fibers with an average diameter of 700 nm. These silk matrices supported bone marrow stromal cell attachment and proliferation with higher cell density than for native silk fibroin matrices.

The 3D structure of these nanofibrous scaffolds are characterized by a wide range of pore diameter, high porosity, high surface area to volume ratio, and morphological architectures similar to the natural structural fibrillar proteins in the native ECM. These physical characteristics promote favorable biological responses of cells by enhancing cell attachment and proliferation as demonstrated by Li and colleagues (2002) [138] when they developed an electrospun PLGA nanofibrous scaffold that has potential as a possible alternative replacement for bone, cartilage and skin tissue engineering. Fibroblast and bone marrow-derived mesenchymal stem cells seeded on this structure tend to maintain phenotypic shape and guided growth according to the nanofiber orientation. Li et al. (2003) [131] further evaluated a novel, 3D non-fibrous PCL scaffold composed of electrospun nanofiber for its ability to maintain chondrocytes in a mature functional state. Nanofibrous cultures maintained in the supplemented serum-free medium produced more sulfated proteoglycan-rich cartilaginous matrix, and supported cellular proliferation than monolayer cultures. In another study, Li et al. (2005) [132] evaluated the effects of growth factors incorporated in the scaffolds on cell growth. When the adult human bone marrow-derived MSCs were cultured on a PCL nanofibrous scaffold in the presence of transforming growth factor- $\beta$  (TGF- $\beta$ ), the MSCs differentiated to chondrocytic phenotypes, expressing chondrocyte-specific genes such as collagen type II, IX, and XI, aggrecan, and produced cartilage-associated extracellular matrix proteins. The level of chondrogenesis in the nanofibrous scaffold was com-

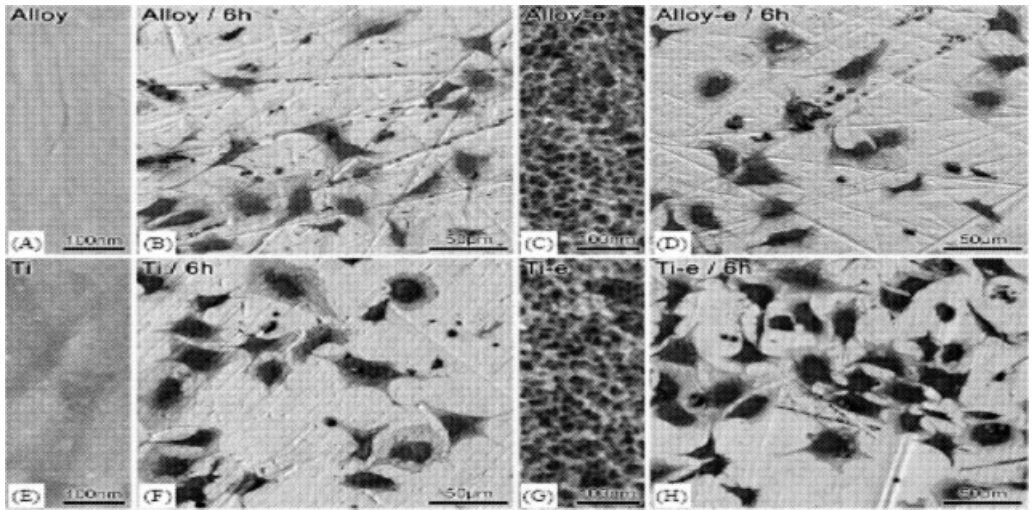


**Fig. 2.22.** SEM images of osteogenic cells grown on diverse titanium surfaces. Control samples, (A) Ti alloy and (E) cpTi, exhibit a smooth surface, while etched ones, (C) Ti alloy and (G) cpTi, are characterized by a unique nanotopography. At 6 h, no significant

differences were detected in cell shape between control (B and F) and nanotextured (D and H) surfaces. The predominant cell shape was polygonal, with cells showing either thin cytoplasmic extensions or large veil-like ones. cp: commercially pure, Ti: titanium [286].

parable to cell aggregates or pellet cultures, which are the established procedures in inducing chondrogenesis. In addition, the mechanical properties of the cell-nanofibrous construct were superior to those developed from pellet cultures. These studies suggested that nanofibrous structure may be a suitable candidate scaffold biomaterial for bone and cartilage tissue engineering applications.

Nanotexturing has also been reported to provide the necessary attachment surfaces on the scaffolds for cell to grow. This was demonstrated by Oliveira et al. (2004) [286] who reported that nanotexturing of titanium-based surfaces upregulates the early expression of bone sialoprotein and osteopontin in osteogenic cell cultures (Fig. 2.22). Badami et al. (2005) [287] determined how chemical and topographical features affect adhesion, morphology, orientation, proliferation, and osteoblastic differentiation of MC3T3-E1 model osteoprogenitor cells, and found that osteoprogenitor cells were able to adhere and proliferate on a random fused fiber topographies and mean fiber diameters ranging from 0.14  $\mu\text{m}$  to 2.1  $\mu\text{m}$ . In the presence of osteogenic factors such as  $\beta$ -glycerophosphate, and L-ascorbate-2-phosphate, cell density on fibers was equal or greater than on smooth surfaces. Cells attached to electrospun substrates exhibited a higher cell aspect ratio than cells on smooth surfaces. This study demonstrated that surface topography introduced by electrospun fibers with an average fiber diameter of 0.14–2.1  $\mu\text{m}$  affects cell morphology and cell proliferation. Carbon nanotubes and nanofibers have several potential properties that make these materials beneficial in the development of

novel devices for bone reconstruction [20]. The dimensions of carbon nanofibers or nanotubes mimic that of collagen fibrils (0.1–8  $\mu\text{m}$  in diameter) in the bone. In one study, Elias et al. (2002) [288] investigated the functions of human osteoblasts cultured on carbon nanofibers with diameters of  $<100$  nm. Osteoblasts were observed to increase in proliferation, synthesis of alkaline phosphatase and deposited more extracellular calcium on carbon nanofiber with diameters  $<100$  nm. The enhanced mineral deposition in this study demonstrated the potential of carbon nanofibers as a material for orthopedic implants. The enhanced function of the osteoblasts is suggested to be due to similarity of the dimension of carbon fibers to that of hydroxyapatite crystals found in physiologic bone. Smaller diameter carbon nanofibers (60–100 nm) have been suggested as suitable for use in orthopedic/dental implant material designs and this may be due to the increase in osteoblast and decrease in osteoblast competitive cells such as fibroblasts, chondrocytes, and smooth muscle cells adhering to the carbon nanofibers [20]. These studies demonstrated that nano-scale carbon fibers could promote osteoblast adhesion, and the application of nanotopography could create an environment favorable for bone cells.

Studies have determined that nanofibrous structure could enhance protein adsorption, including fibronectin and vitronectin, and hence enhance the osteoblast attachment [84, 289]. Woo et al. (2003) [84] hypothesized that nanofibrous PLLA scaffolds, which they developed to mimic the bone extracellular matrix microenvironment, have potential to adsorb serum proteins to enhance cell growth. The 3D porous PLLA scaffolds they developed had interconnected spheroid pores of between 50 and 500 nm with nanofibrous architecture walls. This nanofibrous scaffold adsorbed  $4\times$  more serum protein than the non-fibrous scaffold. In another study, Wei and Ma (2004) constructed a nHAP/polymer composite with high porosity from a dioxane–water mixture solvent system using thermally induced phase separation techniques for bone tissue engineering and observed that the protein adsorption was three-fold higher in the fibrous scaffold compared with non-fibrous scaffold [289]. The adsorbed serum proteins may have a role in enhancing cell attachment and proliferation on nano-structured surfaces compared with micro-structured surfaces [290–295]. Incorporation of chemical additives to the nanofibers has also been reported to enhance cell growth. Recently, Fujihara and colleagues (2005) [296] fabricated a new type of guided bone regeneration membrane from electrospun PCL/ $\text{CaCO}_3$  composite nanofibers (Fig. 2.23). SEM images showed the presence of  $\text{CaCO}_3$  nanoparticles on the surface of the PCL nanofibers. *In vitro* studies showed that osteoblast attachment was encouraged on the composite nanofibrous membrane, and good cell proliferation was observed.

In its native environment, self-healing of articular cartilage is rarely possible [297]. Hence, various clinical procedures have been evaluated in articular cartilage repairs, in particular tissue engineering approaches [298, 299]. Successful cartilage tissue engineering depends on the ability of chondrocytes to accumulate into a 3D architecture. Chondrocytes for articular cartilage therapy are isolated from the cartilage of the patients. However, low numbers of chondrocytes can be harvested from each isolation procedure and expansion of the cells is inevitable [131]. This

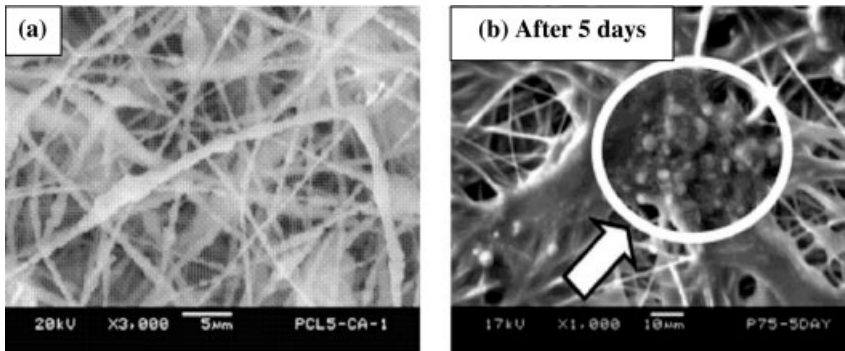


**Fig. 2.23.** (a) PCL/CaCO<sub>3</sub> composite nanofibers, and (b) osteoblast on guided bone regeneration membranes [296].

procedure will also result in the cellular dedifferentiation of the cells [300]. To overcome the dedifferentiation issue, the cells can be redifferentiated upon seeding low passage cells in 3D matrix environments such as alginate, agarose [301, 302] or other scaffolds [303]. Hydrogel formatted biopolymers have limited applications for cartilage tissue engineering and this is due to the lack of long-term mechanical stability and controlled degradation time [303], while synthetic polymers with defined chemical composition provide tailored properties to fit the requirements of engineered tissue scaffolds. The unique architecture of the electrospun 3D synthetic polymer scaffold may provide an ideal environment for both the induction of redifferentiation and the maintenance of differentiated chondrocytes [131]. In cartilage, this synthetic ECM-like structure is crucial to provide mechanical support for the tissue and interacts with the chondrocytes [304, 305].

The above studies implicate the advantages of electrospun nanofibers as scaffolds for bone and cartilage tissue engineering as evidenced by growth of osteoblasts, chondrocytes and mesenchymal stem cells on these fibers. Nanofibrous meshes could provide a better mechanical structure and spatially control cell-scaffold interaction compared with conventional systems. This is based on the observation of osteogenesis and chondrogenesis of the bone marrow-derived stem cells on the nanofibers media.

#### 2.8.6

##### Heart and Vascular Grafts

Blood vessels play important roles in distributing blood to the body for gaseous and nutrient exchange. One of the major causes of mortality in the world is cardiovascular or vascular disease that results when the heart, arteries or veins are dysfunctional. Due to the high statistics of this disease, much effort in tissue engineering has been geared towards developing a viable vascular substitute as an alternative treatment.

Tissue-engineered blood vessels have a long history, beginning with PMMA tubes as vascular grafts back in the late 1940s [306]. In the early 1950s, textile grafts were first introduced with the development of the first fabric graft by Voothees (1952) [307]. This subsequently led to the use of PET (Dacron) as a vascular graft substitute by Julian and DeBakey in 1958 [308] who believed that a woven material would be less thrombogenic than a smooth material. However, numerous studies have shown that absorbable vascular grafts would allow the regeneration of new functional arteries [309, 310]. In 1979, Bowald reported a fully bioresorbable graft made of a rolled sheet of Vicryl as vascular substitutes [311, 312]. Bioresorbable woven PGA grafts were also evaluated as vascular substitutes in rabbit models by Greisler (1982) [313] and Greisler et al. (1985) [314]. All these grafts performed only modestly in terms of patency, immunological tolerance, and thrombogenic response.

Currently, a more practical approach for tissue engineering implantation is to use polymer based vascular conduits. However, vascular grafts constructed from synthetic polymers have only been used successfully for large diameter, but not for small diameter, vessels (<6 mm). To date, there are no acceptable synthetic grafts for small diameter blood vessels and autologous grafts have to be harvested from the patients for transplantation. However, this process is time consuming and complications may arise, increasing the time of recovery for patients. In addition, there is a limit on the number of autologous grafts that can be harvested from the patient for transplantation and, at times, the autologous grafts may be diseased and are not suitable for transplantation.

Understanding the basic structure of the blood vessel is important in order to construct a blood vessel scaffold. It consists of three main layers: *tunica intima* (innermost lining), *tunica media* (middle lining) and *tunica adventitia* (outermost lining). The *tunica intima* includes an endothelial lining and an underlying layer of connective tissue of elastic fibers. The *tunica media* contains concentric sheets of smooth muscle tissue in a structure of loose connective tissue, and the *tunica adventitia* contains collagen and elastic fibers [315]. Constructing a blood vessel scaffold is a complex task, and the chances that thrombosis or hyperplasia may arise are high, resulting in vascular graft failure. Rejections can also be another problem when the cellular and humoral immune system detects the graft as a foreign body.

Endothelization is a promising approach to prevent thrombogenesis and intimal hyperplasia. These endothelial cells secrete bioactive substances such as heparin sulfate and nitric oxide, which prevent the smooth muscle cells from overproliferating, as well as cover the scaffold to minimize attachment of platelets to the scaffold to initiate thrombogenesis. Obtaining an endothelized surface on a biodegradable polymer scaffold has become an attractive model for replacing the small diameter blood vessel. Studying the interaction of endothelial cells and polymeric nanofiber scaffold helps researchers optimize the cell growth conditions on the vascular grafts. Surface roughness is one of the parameters that even subtle differences in can affect endothelization. Studies comparing the adhesion of the human vascular artery endothelial cells on a smooth solvent-cast PLLA surface

and a rough electrospun PLLA surface showed an inverse relationship between surface roughness and endothelial cells adhesion and proliferation rates [316].

Endothelialization is limited when endothelial cells are exposed to blood circulation resulting in cell detachment from the surface. Introduction of biomolecular cell recognition sites on the surface of the vascular graft such as extracellular matrix proteins will enhance cell attachment through receptor–ligand binding with the endothelial cells. In He et al. (2005) [16], human coronary artery endothelial cells (HCAECs) were cultured on collagen-coated PLLA-CL nanofiber mesh (NFM) and its growth compared with cells cultured on PLLA-CL NFM and the tissue culture polystyrene surface (TCPS). The endothelial cells cultured on the collagen-coated NFM had the same typical spreading morphology as the TCPS, in contrast to the rounded morphology of cells cultured on the PLLA-CL NFM (Fig. 2.24). This study clearly demonstrated that the cytocompatibility of PLLA-CL nanofibers was increased when coated with collagen. This is important in achieving an anti-thrombogenic layer for a successful vascular graft. Endothelial cells were cultured on collagen-blended PLLA-CL nanofibers with various PLLA-CL:collagen weight ratios of 4:1, 2:1, 1:1 and 1:2. The cell viability increased with increased collagen content in the blended nanofibers (Fig. 2.25). In addition, there was an enhancement of cell adhesion and spreading on the blended nanofibers when they were grown in culture medium without serum and growth factors [12]. In another

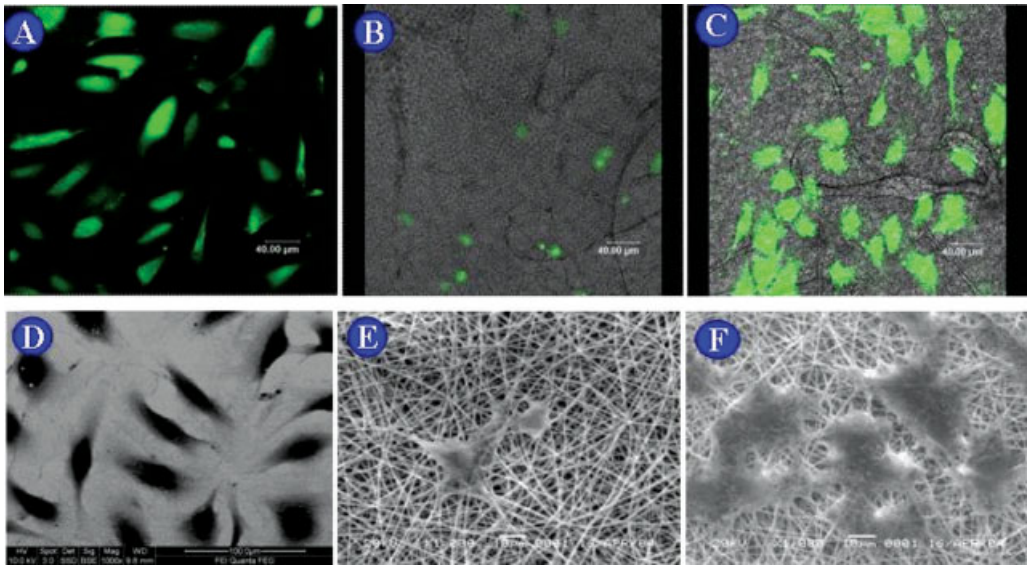


**Fig. 2.24.** (a)–(c) Laser scanning confocal images of endothelial cells, stained with CMFDA (5-chloromethylfluorescein diacetate), that are cultured on TCPS, PLLA-CL nanofiber mats and collagen-coated PLLA-CL nanofiber

mats, respectively. (d)–(f) Scanning electron micrographs of endothelial cells cultured on TCPS, PLLA-CL nanofiber mats and collagen-coated PLLA-CL nanofiber mats, respectively [16].

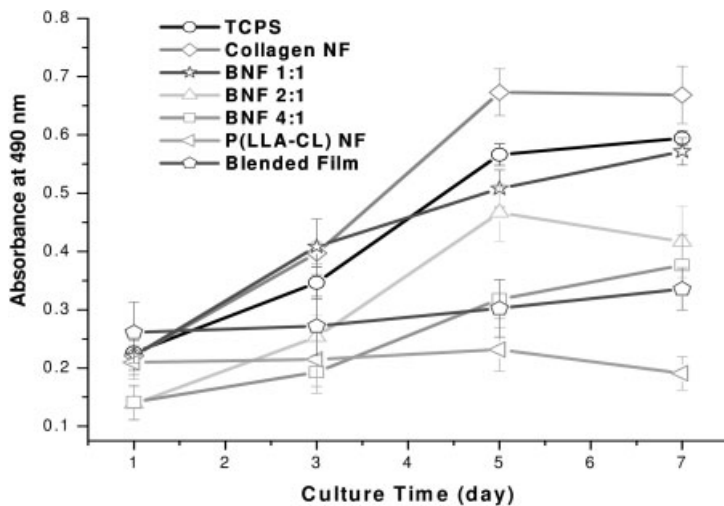


**Fig. 2.25.** Viability of HCAECs grown on TCPS, collagen nanofibers, collagen-blended PLLA-CL nanofibers (BNF) with different weight ratios of PLLA-CL to collagen (BNF 1:1, BNF 2:1, BNF 4:1), PLLA-CL nanofibers, and collagen-blended PLLA-CL film [12].

study, gelatin grafted PET nanofiber mats were shown to improve endothelial cell proliferation and preserved the cell phenotype. On the gelatin grafted PET nanofiber mats, the cells were observed to exhibit polygonal spread out morphology, in contrast to rounded morphology of cells cultured on the PET nanofiber mats [14]. Alternatively, modifying the physical properties of scaffold surface, such as enhancing hydrophilic property, changing the pore size, and altering the surface roughness, have been reported to increase endothelization on the scaffolds [316].

Another important population of cells in the blood vessels is the smooth muscle cells. Studies have shown that human coronary artery smooth muscle cells (HCASMCs) were able to attach and grow in the direction of the axis of the nanofibers, expressing a spindle-like contractile phenotype when cultured on electrospun aligned PLLA-CL nanofibers (Fig. 2.26), which closely mimics the behavior of cells in native vessels. The adhesion and proliferation of the HCASMCs on the aligned nanofibers was significantly increased compared to that on the solvent-cast polymer film. PLLA-CL aligned nanofiber is seen as a potential scaffold for blood vessel engineering applications.

In the native blood vessel, the most abundant proteins are collagen and elastin. Collagen provides the resistance against rupture and elastin confers elasticity. There are studies showing that pretreatment of nanofibers would enhance cell growth. Buttafoco et al. (2005) [317] have reported that collagen-elastin nanofibrous mesh crosslinked with *N*-(3-dimethylaminopropyl)-*N'*-ethylcarbodiimide hydrochloride and *N*-hydroxysuccinimide enabled smooth muscle cells to grow



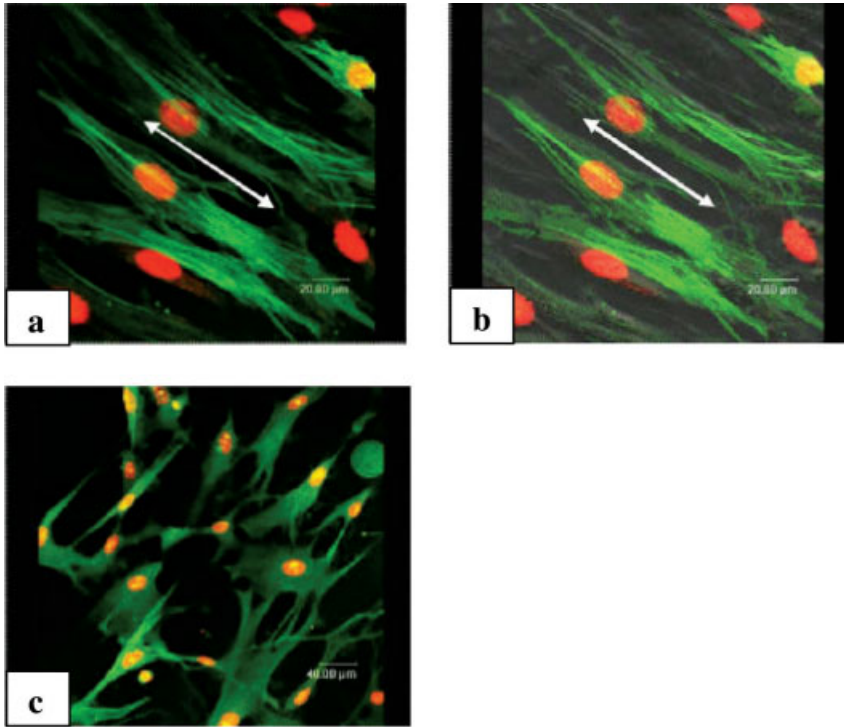


**Fig. 2.26.** Confocal images of HCASMCs immunostained for  $\alpha$ -actin filaments cultured (a) on aligned nanofibrous scaffold, (b) on aligned nanofibrous scaffold, overlay image on the aligned fiber, and (c) on TCPS.

well as a confluent layer. Studies by Boland et al. (2004) [17] showed that pretreatment of small diameter electrospun PGA fibers with concentrated hydrochloric acid significantly increased rat cardiac fibroblast proliferation. To date, constructing a viable blood vessel substitute is a challenging task as many criteria need to be fulfilled. One of the criteria may be the use of nanofiber scaffolds for blood vessel tissue engineering.

### 2.8.7

#### Stem Cells

Stem cells are undifferentiated cells that have the capacity for both self-renewal, proliferate and differentiate to one or more types of specialized cells [318]. These unique characteristics of stem cells are crucial in the applications of *in vivo* therapies such as treating leukemia and repairing injured myocardium by the injection of stem cells that will differentiate and proliferate into the desired cell type. However, this approach relies on the pre-existence of extracellular matrix proteins [319]. The two major types of stem cells are embryonic stem cells, derived from the inner

cell mass of early aborted fetuses and capable of differentiating into almost any cell type, and adult stem cells of hematopoietic or mesenchymal origin, which are less versatile for tissue engineering applications. However, the use of adult stem cells in therapy incurs less ethical and medical issues since the cells are harvested from the patient, incorporated into a tissue engineered construct and then returned to the individual without the need for immunosuppression [318].

The majority of mammalian cells are anchorage dependent and are mostly derived from mesenchymal stem cells [320]. MSCs are multi-potential cells that can differentiate into bone, cartilage, fat, muscle, marrow stroma, and other cell types when induced by the appropriate biological cues *in vitro* [282, 321]. Their potential for expansion, lineage-specific differentiation, and derivation from autologous sources suggest that human mesenchymal stem cells (hMSCs) can be a possible candidate cells for tissue engineering and regenerative therapies [132]. Research has shown that when MSCs are cultured in the presence of suitable media containing differentiation-promoting agents and growth factors the cells differentiated into osteoblasts [322], adipocytes, and chondrocytes [323]. Human MSCs have been isolated from many adult human tissues [324–331], especially from the bone marrow, which is also a major source and reservoir for hematopoietic stem cells [332]. The capture, expansion, and differentiation of these stem cells are required before incorporation into a tissue engineered construct for successful tissue regeneration.

An ideal biomaterial scaffold for stem cell tissue engineering application should be able to support multi-lineage cell types since most tissues and organs are multiphasic in nature [333]. There are a few successful examples of engineered multiphasic tissues such as the osteochondral construct which consists of bone and cartilage tissues [334–338]. The approach involves the integration of the chondral construct and the osteo-construct after they are separately fabricated from stem cells [336] or differentiated cells [337]. Another approach would be using the cell pellet culture system, which has been widely used to investigate the MSC chondrogenesis [323, 324, 339–341]. In two of those studies, human MSCs exhibited chondrogenic properties when cultured in a cell pellet system [323, 324]. However, constructs derived from the cell pellet culture system are small and uniformly weak in mechanical properties, making them unsuitable for repair of larger cartilage defects.

Alternatively, nanofibrous scaffold is a potential candidate scaffold for a cell-based tissue engineering approach as well as a potential carrier for MSC transplantation. In a study, Li et al. (2005) [132] compared the chondrogenic activities of bone marrow-derived MSCs seeded on PCL nanofibrous scaffolds to cell pellet culture system in the presence of TGF- $\beta$ 1 as chondrogenic growth factor. The results showed that the level of MSC chondrogenesis on nanofibrous scaffolds is enhanced compared to the cell pellet culture system (Fig. 2.27). From this observation, it was proposed that the 3D PCL-based nanofibrous scaffold is able to serve as a bioactive carrier for MSC transplantation for cartilage repair. In a later study, Li et al. (2005) [333] tested a 3D PCL nanofibrous scaffold for its ability to support and maintain multi-lineage differentiation of bone marrow-derived human MSCs.

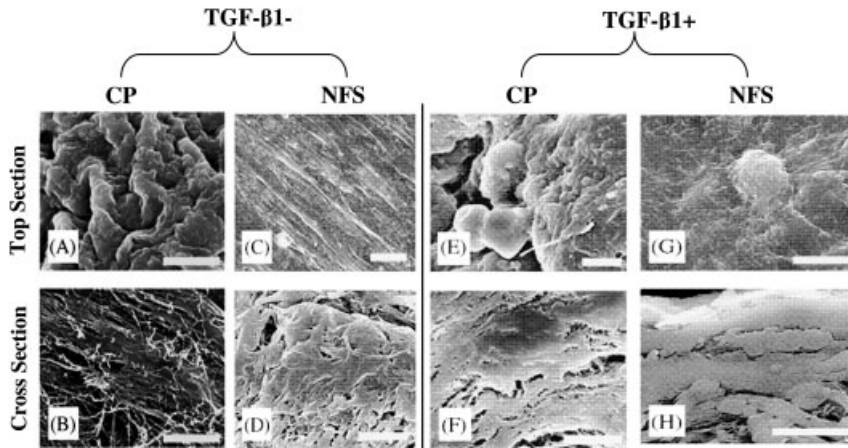


**Fig. 2.27.** Morphology of day 21 cell pellet and nanofibrous scaffold MSC cultures examined by SEM. (A)–(D) cultures maintained without TGF- $\beta$ 1; (E)–(H) cultures treated with TGF- $\beta$ 1. (A) Top view of cell pellet, revealing a roughened surface; (B) cross-sectional view of cell pellet, showing the presence of native collagen-like fibers; (C) top view of nanofibrous scaffold, showing fibroblast-like cells covering the surface; (D) cross-sectional view of nanofibrous scaffold, showing cells covered with ECM, and integrated with PCL nanofibers; (E) top view of cell pellet, with round chondrocyte-like cells on the surface; (F) cross-sectional view of cell pellet, showing thick ECM; (G) top view of nanofibrous scaffold, showing the presence of round, ECM-embedded chondrocyte-like cells; and (H) cross-sectional view of nanofibrous scaffold, showing a thick, dense ECM-rich layer. Bar = 10  $\mu$ m [132].

In this *in vitro* study, the cells seeded onto the scaffold were induced to differentiate along adipogenic, chondrogenic or osteogenic lineages by culturing in specific differentiation media. It was reported that multi-lineage differentiation of MSCs is fully supported within the nanofibrous scaffolds. These two studies suggested that the PCL-based nanofibrous scaffold is a promising candidate scaffold for cell-based, multi-phasic tissue engineering. This is further supported by Boudriot and colleagues (2005) [320] who studied the differentiation of human MSCs when cultured onto 3D electrospun PLLA nanofibers for 21 days. The mesenchymal stem cells clearly preferred a guided growth along the nanofibers and revealed no signs of cell death (Fig. 2.28). In addition, osteogenic differentiation of the mesenchymal stem cells was also observed. The results showed that the use of electrospun nanofibers as scaffolds for stem cells is promising in tissue engineering.

## 2.9 Innovations in Nanofiber Scaffolds

Even though nanofibrous scaffolds are widely used for tissue engineering applications, they are increasingly being used as vectors for controlled delivery systems such as for drugs, and this is due to their high surface area and nano-scale dimen-

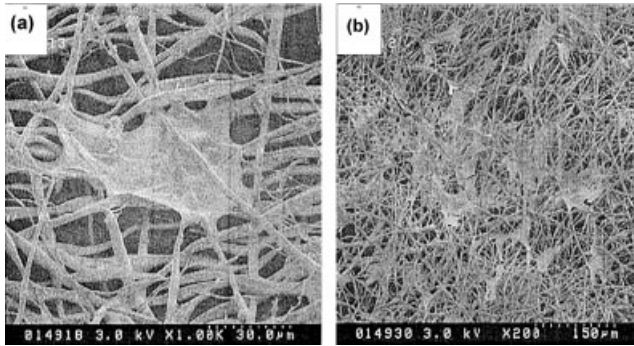


Fig. 2.28. (a) hMSC morphology on nanofiber scaffold; (b) seeded hMSC [320].

sions. Annually, millions of people [342] have been administered with various drugs and proteins such as human growth factors and hormones encapsulated or incorporated with polymers to assist delivery in the treatment of diseases or to improve health [343]. In drug delivery systems, the ideal drug dosage is the minimum amount delivered to the diseased site and effectively absorbed. Uptake of drugs by the body is influenced by the solubility of the compound in aqueous environment, modifications to the compound to assist solubility, and the ease of releasing the drug into the system is facilitated by the degradation of the coating or encapsulating materials of the drugs [35]. Hence, polymeric materials in the form of nano or micro particles, hydrogels and micelle [344] have been developed as vectors for drug delivery. The principle of drug delivery with polymer nanofibers is based on the dissolution rate of a particulate drug which increases with a corresponding increase in the carrier surface area. The nano-dimensions of these polymeric delivery materials will allow the drugs to be more effectively delivered to the target sites and this will improve the therapeutic effects of the drugs and at the same time reduce undesirable side effects associated with the drugs. As such, the usage of polymer nanofiber membranes has become the main focus of research for drug delivery applications [21].

Nanofiber mats prepared from PLA, PEVA and their blend have been incorporated with the drug tetracycline hydrochloride [345, 346]. The PLA nanofibers showed an instantaneous release of the drug while the drug release profiles of PEVA and PLA/PEVA blend gradually increased over 120 h. Zong et al. (2002) [347] have prepared bioabsorbable nanofiber membranes from PDLA incorporated with the antibiotic Mefoxin and a burst drug release profile was observed within the first 3 h, and a 90% release rate was achieved after 50 h. Even though the release profile of the drug is important, it is essential that the drug remains active upon release. Kim et al. (2004) [344] have evaluated the bioactivity of released Mefoxin incorporated in PLGA nanofibrous membrane to inhibit *Staphylococcus aureus* growth. Incorporation of Mefoxin in the polymer did not diminish the antibiotic activity and the released Mefoxin effectively inhibited bacterial growth.

Drugs incorporated into the nanofibers have a tendency to release in a burst profile when administered directly into the biological system, as shown by the earlier studies [344–347]. This release profile may not be suitable for some drugs that have to be released gradually, such as hypertension drugs. In an effort to better control drug release, Verreck et al. (2003) [348] placed the electrospun hydroxypropylmethyl cellulose (HPMC) nanofibrous membranes that contained the drug itraconazole into a hard gelatin capsule that is traditionally used to encapsulate drugs. Nanofibers in the capsule gradually released the drug over 20 h compared with the nanofiber membranes without the capsule, which released 100% of the drug within 4 h. This unique approach using pharmaceutical hard gelatin capsule for drug release from nanofiber is able to control the drug release rate by changing the amount of drug incorporated, minimizing the distribution of fiber diameter, and drug distribution in a nanofiber. The diffusion of drugs through the inter-fiber pores in an aqueous environment is another important issue in order to understand the drug release manner from nanofibers. Verrick et al. (2003) [349] used poorly water-soluble drugs, itraconazole and ketanserin, as model compounds while segmented polyurethane was selected as the non-biodegradable polymer. At low drug loading, itraconazole was released from the nanofibers in a linear function. Initial burst release of the drug was not observed. As for ketanserin, a bi-phasic release pattern was observed where two sequential linear release phases were noted. These release phases may be temporally correlated with drug diffusion through the polymer and through formed aqueous pores, where the latter require some time to materialize in the aqueous environment.

Modification to the polymeric nanofibers is an alternative to control drug release. Zeng et al. (2003) [350] have fabricated PLLA nanofibers with cationic, anionic and nonionic surfactants as additives, to evaluate the release profiles of typical drugs such as rifampin (a drug for tuberculosis) and paclitaxel (an anticancer drug). They found that the surfactants can reduce the diameter of electrospun fibers as well as control the size distribution of the nanofiber diameter. The constant rate of drug release is in-line with the degradation rate of the nanofibers. Therefore, the distribution of fiber diameter may play an important role in controlling the drug release rate. Such nanofibers may find clinical applications. Table 2.2 summarizes studies conducted using nanofibers for the drug delivery system. Electrostatic spinning is an efficient and simple technique to prepare the drug-laden nanofiber for potential use in oral, topical, and even *in vivo* delivery of drugs despite its recent application in the pharmaceutical industry. Several recent publications suggest that it may be of high value in the formulation of poorly water-soluble drugs by combining nanotechnology and solid solution/dispersion methodologies [351].

Current therapies to regenerate or replace various tissues (e.g., bone, blood vessels, skin, liver, eye, and nerve) in the body depend on the delivery of growth factors [352]. Growth factors are crucial to achieve successful tissue regeneration as substitutes for biological functions of damaged and injured organs. These growth factors help to create a more favorable environment to enhance tissue regeneration. In addition to the growth factors, this environment can be achieved by providing various biomaterials as cell scaffolds to promote cell proliferation and differen-

**Tab. 2.2.** Electrospun polymer nanofibers incorporated with different drugs.

Polymer nanofiber	Drug	Function of drug	Ref.
<ul style="list-style-type: none"> <li>• PLLA</li> <li>• PEVA</li> <li>• PLA/PEVA</li> </ul>	Tetracycline hydrochloride	Lyme disease, pneumonia, acne, venereal (sexually transmitted) disease, bladder infections, and ulcers	346
<ul style="list-style-type: none"> <li>• PDLLA</li> <li>• PLGA</li> <li>• PLGA/PEG-b-PLA [poly(ethylene glycol)-<i>b</i>-poly(lactide)]</li> </ul>	Mefoxin	A wide ranging drug against Gram-positive and Gram-negative bacteria	344, 347
<ul style="list-style-type: none"> <li>• Polyurethane</li> <li>• HPMC (Hydroxypropylmethyl cellulose)</li> </ul>	Ketanserin Itraconazole	Treatment for wound healing Treatment of fungal infections, such as aspergillosis, blastomycosis, histoplasmosis, and fungal infection localized to the toenails and fingernails (onychomycosis)	348
<ul style="list-style-type: none"> <li>• PLLA</li> </ul>	Rifampin Paclitaxel	Treats tuberculosis (TB) Treats head and neck cancer, non-small cell lung cancer, small cell lung cancer, and bladder cancer	350

tiation. Growth factors such as fibroblast growth factor (FGF), vascular endothelial growth factor (VEGF), TGF- $\beta$ , platelet derived growth factor (PDGF), and angiopoietins are often required to promote tissue regeneration. This is because they can induce angiogenesis, promoting a sufficient supply of oxygen and nutrients to effectively maintain the biological functions of cells transplanted for organ substitution. Biodegradable polymers have been developed to provide localized and sustained growth factor release [343, 353–358], as well as to introduce plasmid DNA that encodes the growth factors [359, 360], to desirable targets in human body. However, the success rate of current efforts is limited due to the poor *in vivo* stability of the growth factors, the mode of delivery, and the necessity for numerous signals to complete the regeneration process. Ma (2004) [54] has designed a conceptual model using a bioactive scaffold integrating nanofibrous architecture with 3D biomimetic surface modification to control growth factor release (Fig. 2.29). The design uses the architectural features of collagen to provide a high surface area for cell attachment and new matrix deposition, as well as an open structure that will allow an interactive environment for cell–cell, cell–nutrient, cell–matrix, and

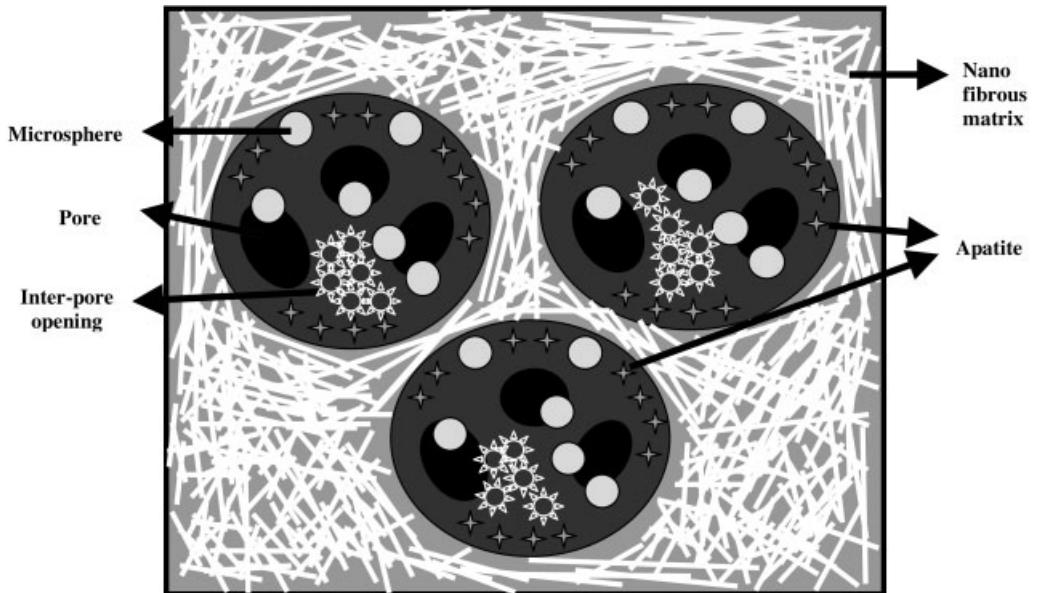


**Fig. 2.29.** Schematic of a “biomimetic nano-scaffold”. The scaffold combines the novel nanofibrous architecture of an interconnected pore network with microspheres for controlled release of putative regenerative factors. (Adapted from Figure 10 of Ma [54].)

cell–signal molecule interactions. The challenge of finding an appropriate delivery mechanism for these signaling proteins, and to determine the time and dosage of delivery, could possibly be achieved by capitalizing on the unique characteristics of nano-scale polymeric fibers.

## 2.10 Conclusion

Nanotechnology is a diverse and interdisciplinary area of research. This research discipline promotes the innovation of new nano-scale materials and devices with improved properties and functionalities. Nanotechnology has the capacity to revolutionize in many areas of applications such as surface microscopy, silicon fabrication, biochemistry, molecular biology, physical chemistry and computational engineering. However, safety concerns of nanomaterials in everyday life and its social, political and regulatory implications have been discussed extensively despite commercialization of some products made of nano-based materials. Nanofiber technology is an important research area in nanotechnology and the understanding of nanofiber processing methodologies is essential for the overall advancement of

nanotechnology. Current research in nanomaterials may not only lead to the development of superior functions but also provide a means to deliver these special functions to higher order structures. Nanofibrous scaffolds designed to elicit specific cellular responses through the incorporation of signaling ligands (e.g., growth factors and adhesion peptides) or DNA fragments are particularly promising for advanced tissue repairs and regeneration, while nanoparticles and nanospheres are able to control the release of therapeutic agents, antibiotics, genes and vaccines to the target cells.

The electrospinning technique provides an inexpensive and convenient method to produce nanofibers from various types of polymers with controlled variations in polymer characteristics such as fiber diameter, pore size, high surface area, and lightweight scaffolds. This technology has made it possible to manufacture products such as permeable nanofiber mats and nanofiber tubes for biomedical applications, which have proven difficult to fabricate before and most probably would not have been in existence using fabrication technologies presently available. The availability of new materials will play a critical role in developing advanced applications in disease diagnosis and treatment. Further research and development is required to improve the biocompatibility and potential applications of nanofiber scaffolds. The incorporation of nanofibers into useful devices requires in-depth understanding of the parameters influencing nanofiber processing and the resulting fiber characteristics, cell–nanofiber interactions in the biological system, and the integrative process to existing technologies or applications. These are some of the many challenges that need to be taken into account when using nanofibers for tissue engineering and biomedical applications.

## References

- 1 SKALAK, R., FOX, C. Preface. In: *Tissue Engineering*, Alan R Liss, Inc, New York, 1988.
- 2 GOOCH, K.J., BLUNK, T.B., VUNJAK-NOVAKOVIC, G., LANGER, R., FREED, L.E., TENNANT, C.J. *Frontiers in Tissue Engineering*, Pergamon Press, New York, USA, 1998.
- 3 LANZA, R.P., LANGER, R., VACANTI, J. *Principles of Tissue Engineering* (2<sup>nd</sup> Edn.), Academic Press, San Diego, USA, 2000.
- 4 DREXLER, K.E. *Engines of Creation: The Coming Era of Nanotechnology*, Anchor Press/Doubleday, New York, 1986.
- 5 MIN, B.M., LEE, G., KIM, S.H., NAM, Y.S., LEE, T.S., PARK, W.H. Electrospinning of silk fibroin nanofibers and its effect on the adhesion and spreading of normal human keratinocytes and fibroblasts *in vitro*. *Biomaterials*. 2004, 25, 1289–1297.
- 6 JIN, H.J., CHEN, J.S., KARAGEORGIU, V., ALTMAN, G.H., KAPLAN, D.L. Human bone marrow stromal cell responses on electrospun silk fibroin mats. *Biomaterials*. 2004, 25, 1039–1047.
- 7 WNEK, G.E., CARR, M.E., SIMPSON, D.G., BOWLIN, G.L. Electrospinning of nanofiber fibrinogen structures. *Nano Lett*. 2003, 3, 213–226.
- 8 MATTHEWS, J.A., WNEK, G.E., SIMPSON, D.G., BOWLIN, G.L., Electrospinning of collagen nanofibers. *Biomacromolecules*. 2001, 3, 232–238.
- 9 ZHANG, Y.Z., OUYANG, H.W., LIM, C.T., RAMAKRISHNA, S. Electro-



- spinning of gelatin fibers and gelatin/PCL composite fibrous scaffolds. *J. Biomed. Mater. Res. Part B: Appl. Biomater.* **2004**, 72B, 156–165.
- 10 GENG, X., KWON, O.H., JANG, J. Electrospinning of chitosan dissolved in concentrated acetic acid solution. *Biomaterials.* **2005**, 26, 5427–5432.
  - 11 MIN, B.M., LEE, S.W., LIM, J.N., YOU, Y., LEE, T.S., KANG, P.H., PARK, W.H. Chitin and chitosan nanofibers: electrospinning of chitin and deacetylation of chitin nanofibers. *Polymer.* **2004**, 45, 7137–7142.
  - 12 HE, W., YONG, T., TEO, W.E., MA, Z. Fabrication and endothelialization of collagen-blended biodegradable polymer nanofibers: Potential vascular graft for the blood vessel tissue engineering. *Tissue Eng.* **2005**, 11, 1575–1589.
  - 13 ZHANG, Y.Z., VENUGOPAL, J., HUANG, Z.M., LIM, C.T., RAMAKRISHNA, S., Characterization of the surface biocompatibility of the electrospun PCL-collagen nanofibers using fibroblasts. *Biomacromolecules.* **2005**, 6, 2583–2589.
  - 14 MA, Z., KOTAKI, M., YONG, T., HE, W., RAMAKRISHNA, S. Surface engineering of electrospun polyethylene terephthalate (PET) nanofibers towards development of a new material for blood vessel engineering. *Biomaterials.* **2005**, 26, 2527–2536.
  - 15 MA, Z.W., GAO, C.Y., JI, J., SHEN, J.C. Protein immobilization on the surface of poly-L-lactic acid films for improvement of cellular interactions. *Eur. Polym. J.* **2002**, 38, 2279–2284.
  - 16 HE, W., MA, Z.W., YONG, T., TEO, W.E., RAMAKRISHNA, S. Fabrication of collagen-coated biodegradable copolymer nanofiber and their potential for endothelial cell growth. *Biomaterials.* **2005**, 26, 7606–7615.
  - 17 BOLAND, E.D., TELEMCO, T.A., SIMPSON, D.G., WNEK, G.E., BOWLIN, G.L. Utilizing acid pretreatment and electrospinning to improve biocompatibility of poly(glycolic acid) for tissue engineering. *J. Biomed Mater Res Part B: Appl. Biomater.* **2004**, 71B, 144–152.
  - 18 CHUA, K.N., LIM, W.S., ZHANG, P., LU, H., WEN, J., RAMAKRISHNA, S., LEONG, K.W., MAO, H.Q. Stable immobilization of rat hepatocyte spheroids on galactosylated nanofiber scaffold. *Biomaterials.* **2005**, 26, 2537–2547.
  - 19 MIN, B.M., YOU, Y., KIM, J.M., LEE, S.J., PARK, W.H. Formation of nanostructured poly(lactic-co-glycolic acid)/chitin matrix and its cellular response to normal human keratinocytes and fibroblasts. *Carbohydr. Polym.* **2004**, 57, 285–292.
  - 20 PRICE, R.L., WAID, M.C., HABERSTROH, K.M., WEBSTER, T.J. Selective bone cell adhesion on formulations containing carbon nanofibers. *Biomaterials.* **2003**, 24, 1877–1887.
  - 21 RAMAKRISHNA, S., FUJIHARA, K., TEO, W.E., LIM, T.C., MA, Z. *An Introduction to Electrospinning and Nanofibers*, World Scientific Publishing Co. Pte. Ltd., Singapore, **2005**.
  - 22 ONDARCUHU, T., JOACHIM, C. Drawing a single nanofiber over hundreds of microns. *Europhys. Lett.* **1998**, 42, 215–220.
  - 23 FENG, L., LI, S., LI, H., ZHAI, J., SONG, Y., JIANG, L., ZHU, D. Superhydrophobic surface of aligned polyacrylonitrile nanofibers. *Angew. Chem. Int. Ed.* **2002**, 41, 1221–1223.
  - 24 ATALA, A., LANZA, R.P. *Methods of Tissue Engineering*, Academic Press, San Diego, USA, **2002**.
  - 25 RAMAKRISHNA, S., JAYARAMAN, K., HUANG, Z.M., ZHANG, Y.Z., MO, X.M. *Advances in Nanoscience & Nanotechnology*, National Institute of Science Communication & Information Resources, New Delhi, **2004**, pp. 113–140.
  - 26 NAM, Y.S., PARK, T.G. Porous biodegradable polymeric scaffolds prepared by thermally induced phase separation. *J. Biomed. Mater. Res.* **1999**, 47, 8–17.
  - 27 CHEN, P. Self-assembly of ionic-complementary peptides: A physicochemical viewpoint. *Colloids Surf. A: Physicochem. Eng. Aspects.* **2005**, 261, 3–24.
  - 28 FORMHALS, A. Process and apparatus

- for preparing artificial threads. *US Patent No 1,975,504*, 1934.
- 29 DOSHI, J., RENEKER, D.H. Electrospinning process and applications of electrospun fibers. *J. Electrostatics*. **1995**, 35, 151–160.
  - 30 BOLAND, E.D., WNEK, G.E., SIMPSON, D.G., PALOWSKI, K.J., BOWLIN, G.L. Tailoring tissue engineering scaffolds using electrostatic processing techniques: A study of poly(glycolic acid) electrospinning. *J. Macromol. Sci. Pure Appl. Chem.* **2001**, A38, 1231–1243.
  - 31 BORNAT, A. Production of electrostatically spun products. *US Patent No. 4,689,186*, 1987.
  - 32 LI, D., WANG, Y., XIA, Y. Electrospinning of polymeric and ceramic nanofibers as uniaxially aligned arrays. *Nano Lett.* **2003**, 3, 1167–1171.
  - 33 THEORON, A., ZUSSMAN, E., YARIN, A.L. Electrostatic field-assisted alignment of electrospun nanofibers. *Nanotechnology*. **2001**, 12, 384–390.
  - 34 DERSCH, R., LIU, T., SCHAPER, A.K., GREINER, A., WENDORFF, J.H. Electrospun nanofibers: Internal structure and intrinsic orientation. *J. Polym. Sci. Pt. B-Polym. Phys.* **2003**, 41, 545–553.
  - 35 HUANG, Z.M., ZHANG, Y.Z., KOTAKI, M., RAMAKRISHNA, S. A review on polymer nanofibers by electrospinning and their applications in nanocomposites. *Composites Sci. Technol.* **2003**, 63, 2223–2253.
  - 36 RAMAKRISHNA, S. *Textile Scaffolds in Tissue Engineering, Smart Fibers, Fabrics, and Clothing: Fundamentals and Applications*, Woodhead Publishing Limited, Cambridge, UK, **2001**.
  - 37 LEE, K.Y., BOUHADIR, K.H., MOONEY, D.J. Controlled degradation of hydrogels using multi-functional cross-linking molecules. *Biomaterials*. **2004**, 25, 2461–2466.
  - 38 YOU, Y., MIN, B.M., LEE, S.J., LEE, T.S., PARK, W.H. *In vitro* degradation behavior of electrospun polyglycolide, polylactide, and poly(lactide-co-glycolide). *J. Appl. Polym. Sci.* **2005**, 95, 193–200.
  - 39 SHUM, A.W.T., MAK, A.F.T. Morphological and biomechanical characterization of poly(glycolic acid) scaffolds after *in vitro* degradation. *Polym. Degradation Stabil.* **2003**, 81, 141–149.
  - 40 HIGGINS, S.P., SOLAN, A.K., NIKLASON, L.E. Effects of polyglycolic acid on porcine smooth muscle cell growth and proliferation. *J. Biomed. Mater. Res.* **2003**, 67A, 295–302.
  - 41 ZONG, X., BIEN, H., CHUNG, C.Y., YIN, L., FANG, D., HSIAO, B.S., CHU, B., ENTCHEVA, E. Electrospun fine-textured scaffolds for heart tissue constructs. *Biomaterials*. **2005**, 26, 5330–5338.
  - 42 LU, L., GARCIA, C.A., MIKOS, A.G. *In vitro* degradation of thin poly(dl-lactico-glycolic acid) films. *J. Biomed. Mater. Res.* **1999**, 46, 236–244.
  - 43 VACANTI, C.A., LANGER, R., SCHLOO, B., VACANTI, J.P. Synthetic polymers seeded with chondrocytes provide a template for new cartilage formation. *Plast. Reconstr. Surg.* **1991**, 88, 753–759.
  - 44 MA, P.X., SCHLOO, B., MOONEY, D., LANGER, R. Development of biomechanical properties and morphogenesis of *in vitro* tissue engineered cartilage. *J. Biomed. Mater. Res.* **1995**, 29, 1587–1595.
  - 45 FREED, L.E., LANGER, R., MARVIN, I., PELLIS, N.R., VUNJAK-NOVAKOVIC, G. Tissue engineering of cartilage in space. *Proc. Natl. Acad. Sci. U.S.A.* **1997**, 94, 13 885–13 890.
  - 46 FREED, L.E., VUNJAK-NOVAKOVIC, G., BIRON, R.J., EAGLES, D.B., LESNOY, D.C., BARLOW, S.K., LANGER, R. Biodegradable polymer scaffolds for tissue engineering. *Biotechnology*. **1994**, 12, 689–693.
  - 47 CAO, Y., VACANTI, J.P., MA, X., PAIGE, K.T., UPTON, J., CHOWANSKI, Z., SCHLOO, B., LANGER, R., VACANTI, C.A. Generation of neo-tendon using synthetic polymers seeded with tenocytes. *Transplant Proc.* **1994**, 26, 3390–3392.
  - 48 ATALA, A., VACANTI, J.P., PETERS, C.A., MANDELL, J., RETIK, A.B., FREEMAN, M.R. Formation of urothelial

- structures in vivo from dissociated cells attached to biodegradable polymer scaffolds in vitro. *J. Urol.* **1992**, *148*, 658–662.
- 49 ORGAN, G.M., MOONEY, D.J., HANSEN, L.K., SCHLOO, B., VACANTI, J.P. Enterocyte transplantation using cell-polymer devices to create intestinal epithelial-lined tubes. *Transplant Proc.* **1993**, *25*, 998.
- 50 SHINOKA, T., SHUM-TIM, D., MA, X.P., TANEL, R.E., ISOGAI, N., LANGER, R., VACANTI, J.P., MAYER, J.E. Creation of viable pulmonary artery autografts through tissue engineering. *J. Thorac. Cardiac Surg.* **1998**, *115*, 536–546.
- 51 NIKLASON, L.E., GAO, J., ABBOTT, W.M., HIRSCHI, K.K., HOUSER, S., MARINI, R., LANGER, R. Functional arteries grown in vitro. *Science.* **1999**, *284*, 489–493.
- 52 SHINOKA, T., MA, P.X., SHUM-TIM, D., BREUER, C.K., CUSICK, R.A., ZUND, G., LANGER, R., VACANTI, J.P., MAYER, J.E. JR. Tissue-engineered heart valves. Autologous valve leaflet replacement study in a lamb model. *Circulation.* **1996**, *94*, 164–168.
- 53 HUTMACHER, D.W. Scaffold design and fabrication technologies for engineering tissues – state of the art and future perspectives. *J. Biomater. Sci. Polym. Edn.* **2001**, *12*, 107–124.
- 54 MA, P.X., Scaffolds for tissue engineering. *Materials Today.* **2004**, *7*, 30–40.
- 55 MA, P.X., LANGER, R. *Tissue Engineering Methods and Protocols.* Humana Press, Totowa, NJ, USA, **1999**.
- 56 LU, L., PETER, S.J., LYMAN, M.D., LAI, H.L., LEITE, S.M., TAMADA, J.A., VACANTI, J.P., LANGER, R., MIKOS, A.G. *In vitro* and *in vivo* degradation of porous poly(DL-lactic-co-glycolic acid) foams. *Biomaterials.* **2000**, *21*, 1595–1605.
- 57 ZELTINGER, J., SHERWOOD, J.K., GRAHAM, D.A., MUELLER, R., GRIFFITH, L.G. Effect of pore size and void fraction on cellular adhesion, proliferation, and matrix deposition. *Tissue Eng.* **2001**, *7*, 557–572.
- 58 YANG, S., LEONG, K.F., DU, Z. and CHUA, C.K. The design of scaffolds for use in tissue engineering. Part II. Rapid prototyping techniques. *Tissue Eng.* **2002**, *8*, 1–11.
- 59 GIORDANO, R.A., WU, B.M., BORLAND, S.W., CIMA, L.G., SACHS, E.M., CIMA, M.J. Mechanical properties of dense polylactic acid structures fabricated by three dimensional printing. *J. Biomater. Sci. Polym.* **1996**, *8*, 63–75.
- 60 PARK, A., WU, B., GRIFFITH, L.G. Integration of surface modification and 3D fabrication techniques to prepare patterned poly(L-lactide) substrates allowing regionally selective cell adhesion. *J. Biomater. Sci., Polym.* **1998**, *9*, 89–110.
- 61 MA, P.X. *Encyclopedia of Polymer Science and Technology.* Vol. 3, John Wiley & Sons, New York, USA, **2004**.
- 62 MIKOS, A.G., SARAOKOS, G., LEITE, S.M., VACANTI, J.P., LANGER, R. Laminated three-dimensional biodegradable foams for use in tissue engineering. *Biomaterials.* **1993**, *14*, 323–330.
- 63 WIDMER, M.S., GUPTA, P.K., LU, L., MESZLENYI, R.K., EVANS, G.R.D., BRANDT, K., SAVEL, T., GURLEK, A., PATRICK, JR. C.W., MIKOS, A.G. Manufacture of porous biodegradable polymer conduits by an extrusion process for guided tissue regeneration. *Biomaterials.* **1998**, *19*, 1945–1955.
- 64 MCINTYRE, J.E., DENTON, M.J. *Encyclopedia of Polymer Science and Engineering.* Vol. 6, Wiley, New York, **1986**.
- 65 KOTAKI, M., HUANG, Z.M., RAMAKRISHNA, S. *Handbook of Nanostructured Biomaterials and Their Application in Nanobiotechnology.* Vol. 2, American Scientific Publishers, Los Angeles, USA, **2005**.
- 66 <http://www.fibersource.com/f-tutor/techpag.htm>.
- 67 FRENOT, A., CHRONAKIS, I.S. Polymer nanofibers assembled by electrospinning. *Curr. Opin. Colloid Interface Sci.* **2003**, *8*, 64–75.
- 68 GUPTA, V.B. *Manufactured Fiber Technology.* Chapman & Hall, London, **1997**.
- 69 SUMANASINGHE, R.D., KING, M.W. New trends in biotextiles – The

- challenge of tissue engineering. *J. Textile Apparel*. **2003**, 3, 1–13.
- 70 GIBSON, P.W., SCHREUDER-GIBSON, H.L., RIVIN, D. Transport properties of porous membranes based on electrospun nanofibers. *Colloids Surf. A: Physicochem. Eng. Aspects*. **2001**, 187, 469–481.
- 71 JAYARAMAN, K., KOTAKI, M., ZHANG, Y.Z., MO, X.M., RAMAKRISHNA, S. Recent advances in polymer nanofibers [Review]. *J. Nanosci. Nanotechnol.* **2004**, 4, 52–65.
- 72 NALWA, H.S. *Handbook of Nanostructured Materials and Nanotechnology*. Academic Press, San Diego, **2000**.
- 73 Ko, F.K. Nanofiber technology: Bridging the gap between nano and macro world. In: *NATO ASI on Nanoengineered Nanofibrous Materials*. Vol. 169, Kluwer Academic Publishers, Anatalia, Turkey, **2003**.
- 74 LAURENCIN, C.T., AMBROSIO, A.M.A., BORDEN, M.D., COOPER, J.A. Tissue engineering: orthopedic applications. *Annu. Rev. Biomed. Eng.* **1999**, 1, 19–46.
- 75 Ko, F.K., LAURENCIN, C.T., BORDEN, M.D., RENEKER, D. The Dynamics of Cell-Fiber Architecture Interaction. Proceedings, Annual Meeting, Biomaterials Research Society, San Diego, USA, April, **1998**.
- 76 NAIR, L.S., BHATTACHARYYA, S., BENDER, J.D., GREISH, Y.E., BROWN, P.W., ALLCOCK, H.R., LAURENCIN, C.T. Fabrication and optimization of methylphenoxy substituted polyphosphazene nanofibers for biomedical applications. *Biomacromolecules*. **2004**, 5, 2212–2220.
- 77 ZUSSMAN, E., THERON, A., YARIN, A.L. Formation of nanofiber crossbars in electrospinning. *Appl. Phys. Lett.* **2003**, 82, 973–975.
- 78 MARTIN, G.E., COCKSHOT, I.D., FILDES, F.J.T. Fibrillar product. *US Patent No 4878908*, **1989**.
- 79 STENOIN, M.D., DRASLER, W.J., SCOTT, R.J., JENSON, M.L. *US Patent No 5866217*, **1999**.
- 80 KENAWY, E.R., LAYMAN, J.M., WATKINS, J.R., BOWLIN, G.L., MATTHEWS, J.A., SIMPSON, D.G., WNEK, G.E. Electrospinning of poly(ethylene-co-vinyl alcohol) fibers. *Biomaterials*. **2003**, 24, 907–913.
- 81 KHIL, M.S., CHA, D.I., KIM, H.Y., KIM, I.S., BHATTARAI, N. Electrospun nanofibrous polyurethane membrane as wound dressing. *J. Biomed. Mater. Res. B Appl. Biomater.* **2003**, 67, 675–679.
- 82 BHATTARAI, S.R., BHATTARAI, N., YI, H.K., HWANG, P.H., CHA, D.I., KIM, H.Y. Novel biodegradable electrospun membrane: scaffold for tissue engineering. *Biomaterials*. **2004**, 25, 2595–2602.
- 83 WEBSTER, T.J., SMITH, T.A. Increased osteoblast function on PLGA composites containing nanophase titania. *J. Biomed. Mater. Res. Part A*. **2005**, 74A, 677–686.
- 84 WOO, K.M., CHEN, V.J., MA, P.X. Nano-fibrous scaffolding architecture selectively enhances protein adsorption contributing to cell attachment. *J. Biomed. Mater. Res. A*. **2003**, 67, 531–537.
- 85 BHATTARAI, N., EDMONDSON, D., VEISEH, O., MATSEN, F.A., ZHANG, M. Electrospun chitosan-based nanofibers and their cellular compatibility. *Biomaterials*. **2005**, 26, 6176–6184.
- 86 GORDON, J.E. *The New Science of Strong Materials or Why you don't Fall through the Floor*. Princeton University Press, Harmondsworth, UK, **1984**.
- 87 DRESSLHAUS, M.S., DRESSLHAUS, G., AVOURIS, P. *Carbon Nanotubes: Synthesis, Structure, Properties, and Applications*. Springer-Verlag, Berlin, **2001**.
- 88 NORRIS, I.D., SHAKER, M., Ko, F.K., MACDIARMID, A.G. Electrostatic fabrication of ultrafine conducting fibers: polyaniline/polyethylene oxide blends. *Synth. Metals*. **2000**, 114, 109–114.
- 89 EL-AUFY, A., NABET, B., Ko, F.K. Carbon nanotube reinforced nanocomposites for wearable electronics. *ACS Polym. Preprints*, **2003**, 44.
- 90 ZHOU, Y., FREITAG, M., HONE, J., STAI, C., JOHNSON, A.T., PINTO, N.J., MACDIARMID, A.G. Fabrication and

- electrical characterization of polyaniline-based nanofibers with diameter below 30 nm. *Appl. Phys. Lett.* **2003**, *83*, 3800–3802.
- 91 LI, G.F., MARTINEZ, C., SEMANCIKA, S., SMITH, J.A., JOSOWICZ, M., JANATA, J. The effect of morphology on the response of polyaniline-based conductometric gas sensors: Nanofibers vs. thin films. *Electrochem. Solid-State Lett.* **2004**, *7*, H44–H47.
- 92 LONG, Y., CHEN, Z., WANG, N., MA, Y., ZHANG, Z., ZHANG, L., WAN, M. Electrical conductivity of a single conducting polyaniline nanotube. *Appl. Phys. Lett.* **2003**, *83*, 1863–1865.
- 93 LONG, Y., ZHANG, L., MA, X., CHEN, Z., WANG, N., ZHANG, Z., WAN, M. Electrical conductivity of an individual polyaniline nanotube synthesized by a self-assembly method. *Macromol. Rapid Commun.* **2003**, *24*, 938–946.
- 94 BUCHKO, C.J., CHEN, L.C., SHEN, Y., MARTIN, D.C. Processing and microstructural characterization of porous biocompatible protein polymer thin films. *Polymer.* **1999**, *40*, 7397–7407.
- 95 FERTALA, A., HAN, W.B., KO, F.K. Mapping critical sites in collagen II for rational design of gene-engineered proteins for cell-supporting materials. *J. Biomed. Mater. Res.* **2001**, *57*, 48–58.
- 96 HUANG, L., McMILLAN, R.A., APKARIAN, R.P., POURDEYHIMI, B., CONTICELLO, V.P., CHAIKOF, E.L. Generation of synthetic elastin-mimetic small diameter fibers and fiber networks. *Macromolecules.* **2000**, *33*, 2989–2997.
- 97 KING, M.W. Overview of opportunities in medical textiles, Part 1. *Can Textile J.* **2001**, *18*, 34–36.
- 98 RAMAKRISHNA, S., MAYER, J., WINTERMANTEL, E., LEONG, K.W. Biomedical applications of polymer-composite materials: A review. *Composites Sci. Technol.* **2001**, *36*, 1189–1224.
- 99 ANDERSON, J.M. Biocompatibility of tissue engineered implants. In: *Frontiers in Tissue Engineering*, PATRICK, C.W.J., MIKOS, A.G. (Eds.), Chapter II.8, Pergamon, Oxford, New York, **1998**.
- 100 MIGLIARESI, C., FAMBRI, L. Processing and degradation of poly(L-lactic acid) fibres. *Macromol. Symp.* **1997**, *123*, 155–161.
- 101 BINI, T.B., GAO, S., TAN, T.C., WANG, S., LIM, A., LIM, B.H., RAMAKRISHNA, S. Electrospun poly(L-lactide-co-glycolide) biodegradable polymer nanofiber tubes for peripheral nerve regeneration. *Nanotechnology.* **2004**, *15*, 1459–1464.
- 102 HADLOCK, T., SUNDBACK, C., HUNTER, D., CHENEY, M., VACANTI, J.P. A polymer foam conduit seeded with Schwann cells promotes guided peripheral nerve regeneration. *Tissue Eng.* **2000**, *6*, 119–127.
- 103 SONDELL, M., LUNDBORG, G., KANJE, M. Vascular endothelial factor stimulates Schwann cell invasion and neovascularization of acellular nerve grafts. *Brain Res.* **1999**, *846*, 219–228.
- 104 MA, Z.W., KOTAKI, M., INAI, R., RAMAKRISHNA, S. Potential of nanofiber matrix as tissue engineering scaffolds. *Tissue Eng.* **2005**, *11*, 101–109.
- 105 KUMAR, M.R. A review of chitin and chitosan applications. *React. Funct. Polym.* **2000**, *46*, 1–27.
- 106 RUSZCZAK, Z. Effect of collagen matrices on dermal wound healing. *Adv. Drug Deliv. Rev.* **2003**, *55*, 1595–1611.
- 107 VENUGOPAL, J., RAMAKRISHNA, S. Biocompatible nanofiber matrices for the engineering of a dermal substitute for skin regeneration. *Tissue Eng.* **2005**, *11*, 847–854.
- 108 MATTHEWS, J.A., BOLAND, E.D., WNEK, G.E., SIMPSON, D.G., BOWLIN, G.L. Electrospinning of collagen type II: A feasibility study. *J. Bioact. Compat. Polym.* **2003**, *18*, 125–134.
- 109 AIEDEH, K., GIANASI, E., ORIENTI, I., ZECCHI, V. Chitosan microcapsules as controlled release systems for insulin. *J. Microencapsul.* **1997**, *14*, 567–576.
- 110 BERGER, J., REIST, M., MAYER, J.M., FELT, O., GURNY, R. Structure and interactions in chitosan hydrogels formed by complexation or

- aggregation for biomedical applications. *Eur. J. Pharm. Biopharm.* **2004**, 57, 35–52.
- 111 PARK, Y.J., LEE, Y.M., PARK, S.N., SHEEN, S.Y., CHUNG, C.P., LEE, S.J. Platelet derived growth factor releasing chitosan sponge for periodontal bone regeneration. *Biomaterials.* **2000**, 21, 153–159.
- 112 KLOKKEVOLD, P.R., VANDEMARK, L., KENNEY, E.B., BERNARD, G.W. Osteogenesis enhanced by chitosan (poly-N-acetyl glucosaminoglycan) *in vitro*. *J. Periodontol.* **1996**, 67, 1170–1175.
- 113 GUTOWSKA, A., JEONG, B., JASIONOWSKI, M. Injectable gels for tissue engineering. *Anat. Rec.* **2001**, 263, 342–349.
- 114 YAGI, K., MICHIBAYASHI, N., KURIKAWA, N., NAKASHIMA, Y., MIZOGUCHI, T., HARADA, A., HIGASHIYAMA, S., MURANAKA, H., KAWASE, M. Effectiveness of fructose-modified chitosan as a scaffold for hepatocyte attachment. *Biol. Pharm. Bull.* **1997**, 20, 1290–1294.
- 115 ZHANG, Y., ZHANG, M.Q. Synthesis and characterization of macroporous chitosan/calcium phosphate composite scaffolds for tissue engineering. *J. Biomed. Mater. Res.* **2001**, 55, 304–312.
- 116 ZHANG, Y., ZHANG, M.Q. Calcium phosphate/chitosan composite scaffolds for controlled *in vitro* antibiotic drug release. *J. Biomed. Mater. Res.* **2002**, 62, 378–386.
- 117 ZHANG, Y., ZHANG, M.Q. Three-dimensional macroporous calcium phosphate bioceramics with nested chitosan sponges for loadbearing bone implants. *J. Biomed. Mater. Res.* **2002**, 61, 1–8.
- 118 OHKAWA, K., CHA, D.I., KIM, H., NISHIDA, A., YAMAMOTO, H. Electrospinning of chitosan. *Macromol. Rapid Commun.* **2004**, 25, 1600–1605.
- 119 DUAN, B., DONG, C.H., YUAN, X.Y., YAO, K.D. Electrospinning of chitosan solutions in acetic acid with poly(ethylene oxide). *J. Biomater. Sci.-Polym. E.* **2004**, 15, 797–811.
- 120 NAGAPUDI, K., BRINKMAN, W.T., LEISEN, J.E., HUANG, L., McMILLAN, R.A., APKARIAN, R.P., CONTICELLO, V.P., CHAIKOF, E.L. Photomediated solid state cross-linking of an elastin-mimetic recombinant protein polymer. *Macromolecules.* **2002**, 35, 1730–1737.
- 121 WANG, R.Z., CUI, F.Z., LU, H.B., WEN, H.D., LI, H.D. Synthesis of nanophase hydroxyapatite/collagen composite. *J. Mater. Sci. Lett.* **1995**, 14, 490–492.
- 122 DU, C., CUI, F.Z., ZHU, X.D., DE GROOT, K. Three-dimensional nano-HAp/collagen matrix loading with osteogenic cells in organ culture. *J. Biomed. Mater. Res.* **1999**, 44, 407–415.
- 123 DU, C., CUI, F.Z., ZHANG, W., FENG, Q.L., ZHU, X.D., DE GROOT, K. Formation of calcium phosphate/collagen composites through mineralization of collagen matrix. *J. Biomed. Mater. Res.* **2000**, 50, 518–527.
- 124 LIAO, S.S., CUI, F.Z., ZHANG, W., FENG, Q.L. Hierarchically biomimetic bone scaffold materials: Nano-HA/collagen/PLA composite. *J. Biomed. Mater. Res. B.* **2002**, 69B, 158–165.
- 125 ZHANG, S.M., CUI, F.Z., LIAO, S.S., ZHU, Y., HAN, L. Synthesis and biocompatibility of porous nano-hydroxyapatite/collagen/alginate composite. *J. Mater. Sci. Mater. Med.* **2003**, 14, 1–5.
- 126 PITT, C.G. Poly-ε-caprolactone and its copolymers. In: *Biodegradable Polymers as Drug Delivery Systems*. CHASIN, M., LANGER, R. (Eds.), New York, Marcel Dekker, **1990**, pp. 71–120.
- 127 STITZEL, J.D., PAWLOWSKI, K.J., WNEK, G.E., SIMPSON, D.G., BOWLIN, G.L. Arterial smooth muscle cell proliferation on a novel biomimicking, biodegradable vascular graft scaffold. *J. Biomater. Appl.* **2001**, 15, 1–12.
- 128 MA, P.X., ZHANG, R. Porous poly(L-Lactic acid)/apatite composites created by biomimetic process. *J. Biomed. Mater. Res.* **1999**, 45, 285–293.
- 129 CHEN, V.J., MA, P.X. Nano-fibrous poly(L-lactic acid) scaffolds with interconnected spherical macropores. *Biomaterials.* **2004**, 25, 2065–2073.

- 130 PATTISON, M.A., WURSTER, S., WEBSTER, T.J., HABERSTROH, K.M. Three-dimensional, nano-structured PLGA scaffolds for bladder tissue replacement applications. *Biomaterials*. **2005**, 26, 2491–500.
- 131 LI, W.J., DANIELSON, K.G., ALEXANDER, P.G., TUAN, R.S. Biological response of chondrocytes cultured in three-dimensional nanofibrous poly(caprolactone) scaffolds. *J. Biomed. Mater. Res.* **2003**, 67A, 1105–1114.
- 132 LI, W.J., TULIA, R., OKAFOR, C., DERFOUL, A., DANIELSON, K.G., HALL, D.J., TUAN, R.S. A three-dimensional nanofibrous scaffold for cartilage tissue engineering using human mesenchymal stem cells. *Biomaterials*. **2005**, 26, 599–609.
- 133 YOSHIMOTO, H., SHIN, Y.M., TERAI, H., VACANTI, J.P. A biodegradable nanofiber scaffold by electrospinning and its potential for bone tissue engineering. *Biomaterials*. **2003**, 24, 2077–2082.
- 134 SHIN, M., ISHII, O., SUED, T., VACANTI, J.P. Contractile cardiac grafts using a novel nanofibrous mesh. *Biomaterials*. **2004**, 25, 3717–3723.
- 135 XU, C.Y., INAI, R., KOTAKI, M., RAMAKRISHNA, S. Electrospun nanofiber fabrication as synthetic extracellular matrix and its potential for vascular tissue engineering. *Tissue Eng.* **2004**, 10, 1160–1168.
- 136 XU, C.Y., INAI, R., KOTAKI, M., RAMAKRISHNA, S. Aligned biodegradable nanofibrous structure: A potential scaffold for blood vessel engineering. *Biomaterials*. **2004**, 25, 877–886.
- 137 MO, X.M., XU, C.Y., KOTAKI, M., RAMAKRISHNA, S. Electrospun P(LLA-CL) nanofiber: A biomimetic extracellular matrix for smooth muscle cell and endothelial cell proliferation. *Biomaterials*. **2004**, 25, 1883–1890.
- 138 LI, W.J., LAURENCIN, C.T., CATERSON, E.J., TUAN, R.S., FRANK, K.K. Electrospun nanofibrous structure: A novel scaffold for tissue engineering. *J. Biomed. Mater. Res.* **2002**, 60, 613–621.
- 139 DODDI, N., VERSFELT, C.C., WASSERMAN, D. *U.S. Patent 4,052,988*, 20, 1977.
- 140 LIPINSKY, E.S., SINCLAIR, R.G., BROWING, J.D. Degradable polydioxanone-based materials, *US Patent No. 5,767,222*, 1998.
- 141 WANG, H., DONG, J.H., QIU, K.U., GU, Z.W. PDON-b-PEG-b-PDON block copolymers and drug delivery system thereof. *J. Appl. Polym. Sci.* **1998**, 68, 2121–2128.
- 142 SALTZMAN, W.M. Introduction to polymers, in *Tissue Engineering, Engineering Principles for the Design of Replacement Organs and Tissues*, 2004, Oxford University Press, New York, USA, p. 453.
- 143 VAINIONPAA, S., ROKKANEN, P., TORMALA, P. Surgical applications of biodegradable polymers in human tissues. *Prog. Polym. Sci.* **1989**, 14, 679–716.
- 144 HEROLD, D.A., KEIL, K., BRUNS, D.E. Oxidation of polyethylene glycols by alcohol dehydrogenase. *Biochem. Pharmacol.* **1989**, 38, 73–76.
- 145 HARRIS, J.M. Synthesis of polyethylene glycol derivatives. *J. Macromol. Sci. Rev. Macromol.* **1985**, C25, 325–373.
- 146 RASHKOV, I., MANOLOVA, N., LI, S.M., ESPARTERO, J.L., VERT, M. Synthesis, characterization, and hydrolytic degradation of PLLA/PEO/PLA triblock copolymers with short poly(L-lactic acid) chains. *Macromolecules*. **1996**, 29, 50–56.
- 147 DU, Y.J., LEMSTRA, P.J., NIJENHUIS, A.J., VAN AERT, H.A.M., BASTIAANSEN, C. ABA type copolymers of lactide with poly(ethylene glycol) kinetic, mechanistic, and model studies. *Macromolecules*. **1995**, 28, 2124–2132.
- 148 MOLINA, K.J., LI, S., MARTINEZ, M.B., VERT, M. Protein release from physically crosslinked hydrogels of the PLA/PEO/PLA triblock copolymer-type. *Biomaterials*. **2001**, 22, 363–369.
- 149 FUKUI, K., SUMPTER, B.G., BARNES, M.D., NOID, D.W. Molecular dynamics studies of the structure and properties of polymer nano-particles. *Comput. Theor. Polym. Sci.* **1999**, 9, 245–254.

- 150 WEN, X., SHI, D., ZHANG, N. Applications of nanotechnology in tissue engineering. In: *Handbook of Nanostructured Biomaterials and their Applications in Nanobiotechnology*, Vol. 1, H.S. NALWA (Eds.), American Scientific Publishers, Los Angeles, USA, 2005, pp. 1–23.
- 151 CHIRILA, T.V., HICKS, C.R., DALTON, P.D., VIJAYASEKARAN, S., LOU, X., HONG, Y., CLAYTON, A.B., ZIEGELAAR, B.W., FITTON, J.H., PLATTEN, S., CRAWFORD, G.F., CONSTABLE, I.J. Artificial cornea. *Progr. Polym. Sci.* 1998, 23, 447–473.
- 152 STERN, M.E., BEUERMAN, R.W., FOX, R.I., GAO, J., MIRCHEFF, A.K. and PFLUGFELDER, S.C. A unified theory of the role of the ocular surface in dry eye. *Adv. Exp. Med. Biol.*, 1998, 438, 643–651.
- 153 HOGAN, M.J., ZIMMERMAN, L.E. *Ophthalmic Pathology. An Atlas and Textbook*. Saunders, Philadelphia, 1962, pp. 277–343.
- 154 GREER, C.H. *Ocular Pathology*, 3rd edn. Blackwell Scientific, Oxford, 1979, pp. 79–115.
- 155 BARRAQUER, J.I., BINDER, P.S., BUXTON, J.N., FINE, M., JONES, D.B., LAIBSON, P.R., NESBUM, A.B., PATON, D., TROUTMAN, R.C. *Symposium on Medical and Surgical Diseases of the Cornea*. Mosby Company, St Louis, New Orleans, 1979.
- 156 LEIBOWITZ, H.M. *Corneal Disorders, Clinical Diagnosis and Management*. Saunders, Philadelphia, 1984.
- 157 LAMBIASE, A., RAMA, P., BONINI, S., CAPRIOGLIO, G., ALOE, L. Topical treatment with nerve growth factor for corneal neurotrophic ulcers. *N. Engl. J. Med.* 1998, 338, 1174–1180.
- 158 GILBARD, J.P., ROSSI, S.R. Tear film and ocular surface changes in a rabbit model of neurotrophic keratitis. *Ophthalmology*. 1990, 97, 308–312.
- 159 WHITCHER, J.P., SRINIVASAN, M., UPADHYAY, M.P. Corneal blindness: A global perspective. *Bull. World Health Organ.* 2001, 79, 214–221.
- 160 LI, F., CARLSSON, D., LOHMANN, C., SUURONEN, E., VASCOTTO, S., KOBUCH, K., SHEARDOWN, H., MUNGER, R., NAKAMURA, M., GRIFFITH, M. Cellular and nerve regeneration within a biosynthetic extracellular matrix for corneal transplantation. *Proc. Natl. Acad. Sci. U.S.A.* 2003, 100, 15 346–15 351.
- 161 Eye Bank Association of America, *Eye Banking Statistical Report*, Washington DC, USA, 1999.
- 162 CHIRILA, T.V. An overview of the development of artificial corneas with porous skirts and the use of PHEMA for such an application. *Biomaterials*. 2001, 22, 3311–3317.
- 163 LANGER, R., VACANTI, J.P. Tissue engineering. *Science*. 1993, 260, 920–926.
- 164 RIDLEY, H. Intra-ocular lenses. *Trans. Ophthalm. Soc. UK*. 1951, 71, 617–621.
- 165 RIDLEY, H. Intraocular acrylic lenses after cataract extraction. *Lancet*. 1952, 1, 118–121.
- 166 RIDLEY, H. Intra-ocular acrylic lenses; a recent development in the surgery of cataract. *Br. J. Ophthalm.* 1952, 36, 113–122.
- 167 CHIRILA, T.V., CONSTABLE, I.J., RUSSO, A.V., LINTON, R.G. Ridley intraocular lens revisited: chemical analysis of residuals in the original lens material. *J. Cataract Refr. Stag.* 1989, 15, 283–288.
- 168 APPLE, D.J., SIMS, J. Harold Ridley and the invention of the intraocular lens. *Surv. Ophthalm.* 1996, 40, 279–292.
- 169 MESTER, U., ROTH, K., DARDENNE, U. Trial with 2-hydroxy-ethyl-methacrylate lenses as keratophakia material. *Ber. Dtsch. Ophthalm. Ges.* 1974, 72, 326–329.
- 170 MESTER, U., STEIN, H.J., MEIER, J. Permeability of hydrogel plastics (PHEMA) to different substances of corneal metabolism (author's transl). *Gruefes. Arch. Klin. Exp. Ophthalm.* 1978, 205, 207–212.
- 171 MCCAREY, B.E., ANDREWS, D.M. Refractive keratoplasty with intrastromal hydrogel lenticular implants. *Invest. Ophthalm. Vis. Sci.* 1981, 21, 107–115.
- 172 MCCAREY, B.E., ANDREWS, D.M., HATCHELL, D.L., PEDERSON, H. Hydrogel implants for refractive



- keratoplasty: Corneal morphology. *Curr. Eye Res.* **1982**, 2, 29–38.
- 173 BINDER, P.S., DEG, J.K., ZAVALA, E.Y., GROSSMAN, K.R. Hydrogel keratophakia in non-human primates. *Curr. Eye Res.* **1982**, 1, 535–542.
- 174 BINDER, P.S. Hydrogel implants for the correction of myopia. *Curr. Eye Res.* **1983**, 2, 435–441.
- 175 WERBLIN, T.P., BLAYDES, J.E., FRYCZKOWSKI, A., PEIFFER, R. Refractive corneal surgery: The use of implantable alloplastic lens material. *Aust. J. Ophthalmol.* **1983**, 11, 325–331.
- 176 SENDELE, D.D., ABELSON, M.B., KENYON, K.R., HANNINEN, L.A. Intracorneal lens implantation. *Arch. Ophthalmol.* **1983**, 101, 940–944.
- 177 SAMPLES, J.R., BINDER, P.S., ZAVALA, E.Y., BAUMGARTNER, S.D., DEG, J.K. Morphology of hydrogel implants used for refractive keratoplasty. *Invest. Ophthalmol. Vis. Sci.* **1984**, 25, 843–850.
- 178 ZAVALA, E.Y., NAYAK, S., DEG, J.K., BINDER, P.S. Keratocyte attachment to hydrogel materials. *Curr. Eye Res.* **1984**, 3, 1253–1262.
- 179 BINDER, P.S., BAUMGARTNER, S.D., DEG, J.K. Hydrogel refractive keratoplasty. Lens removal and exchanges. *CLAO J.* **1984**, 10, 105–111.
- 180 PEIFFER, R.L., WERBLIN, T.P., FRYCZKOWSKI, A.W. Pathology of corneal hydrogel alloplastic implants. *Ophthalmology.* **1985**, 92, 1294–1304.
- 181 WATSKY, M.A., MCCAREY, B.E., BEEKHUIS, W.H. Predicting refractive alterations with hydrogel keratophakia. *Invest. Ophthalmol. Vis. Sci.* **1985**, 26, 240–243.
- 182 MCCAREY, B.E., VAN RIJ, G., BEEKHUIS, W.H. and WARING, G.O. Hydrogel keratophakia: A freehand pocket dissection in the monkey model. *Br. J. Ophthalmol.* **1986**, 70, 187–191.
- 183 SZYCHER, M. Keratoprosthetic polyurethane, U.S. Patent No. 4,285,073, **1981**.
- 184 SZYCHER, M. Process for forming an optically clear polyurethane lens or cornea. U.S. Patent No. 4,386,039, **1983**.
- 185 SZYCHER, M. Keratoprosthetic polyurethane. U.S. Patent No. 4,424,335, **1984**.
- 186 REFOJO, M.F. Glyceryl methacrylate hydrogels. *J. Appl. Polym. Sci.* **1965**, 9, 3161–3170.
- 187 REFOJO, M.F. Permeation of water through some hydrogels. *J. Appl. Polym. Sci.* **1965**, 9, 3417–3426.
- 188 DOHLMAN, C.H., REFOJO, M.F., ROSE, J. Synthetic polymers in corneal surgery. I. Glycerylmetacrylate. *Arch. Ophthalmol.* **1967**, 77, 252–257.
- 189 HYON, S.H., CHA, W.I., IKADA, Y. Preparation of transparent poly(vinyl alcohol) hydrogel. *Polym. Bull.* **1989**, 22, 119–122.
- 190 KOBAYASHI, H., IKADA, Y., MORITERA, T., OGURA, Y., HONDA, Y. Collagen-immobilized hydrogel as a material for lamellar keratoplasty. *J. Appl. Biomater.* **1991**, 2, 261–267.
- 191 TRINKAUS-RANDALL, V., CAPECCHI, J., NEWTON, A., VADASZ, A., LEIBOWITZ, H., FRANZBLAU, C. Development of a biopolymeric keratoprosthetic material. Evaluation in vitro and in vivo. *Invest. Ophthalmol. Vis. Sci.* **1988**, 29, 393–400.
- 192 THOMPSON, K.P., HANNA, K., WARING, G.O. 3rd, GIPSON, I., LIU, Y., GAILITIS, R.P., JOHNSON-WINT, B., GREEN, K. Current status of synthetic epikeratoplasty. *Refractive Corneal Surg.* **1991**, 7, 240–248.
- 193 SIPEHIA, R., GARLINKLE, A., JACKSON, W.B., CHANG, T.M.S. Towards an artificial cornea: surface modifications of optically clear, oxygen permeable soft contact lens materials by ammonia plasma modification technique for the enhanced attachment and growth of corneal epithelial cells. *Biomater. Artif. Cells Artif. Organs.* **1990**, 18, 643–655.
- 194 LEGEAIS, J.M., RENARD, G., PAREL, J.M., SERDAREVIC, O., MUI, M.M., POULIQUEN, Y. Expanded fluorocarbon for keratoprosthetic cellular ingrowth and transparency. *Exp. Eye Res.* **1994**, 58, 41–52.
- 195 WANG, M., SWARTZ, T., CHU, Y.R., BULIANO, M., ABDELMALAK, H., GULANI, A., KARPECKI, P., PEPOSE,

- J.S., YU, K. Peer-reviewed literature: Alphacor. *Cataract Refractive Surg. Today*. **2004**, 23–28.
- 196** YAMATO, M., UTSUMI, M., KUSHIDA, A.I., KONNO, C., KIKUCHI, A., OKANO, T. Thermo-responsive culture dishes allow the intact harvest of multi-layered keratinocyte sheets without disperse by reducing temperature. *Tissue Eng.* **2001**, 7, 473–480.
- 197** STILE, R.A., BURGHARDT, W.R., HEALY, K.E. Synthesis and characterization of injectable poly(N-isopropylacrylamide)-based hydrogels that support tissue formation *in vitro*. *Macromolecules*. **1999**, 32, 7370–7379.
- 198** LAVIK, E.B., KLASSEN, E., WARFVINGE, H., LANGER, R., YOUNG, M.J. Fabrication of degradable polymer scaffolds to direct the integration and differentiation of retinal progenitors *Biomaterials*. **2005**, 26, 3187–3196.
- 199** MARC, R., JONES, B., WATT, C., STRETTOI, E. Neural remodeling in retinal degeneration. *Prog. Eye Res.* **2003**, 22, 607–655.
- 200** KLASSEN, H., SAKAGUCHI, D.S., YOUNG, M. Stem cells and retinal repair. *Prog. Eye Res.* **2004**, 23, 149–181.
- 201** RYAN, S.J. The patho-physiology of proliferative vitreoretinopathy in its management. *Am. J. Ophthalmol.* **1985**, 100, 188–193.
- 202** REH, T.A., LEVINE, E.M. Multi-potential stem cells and progenitors in the vertebrate retina. *J. Neurobiol.* **1998**, 36, 206–220.
- 203** TROPEPE, V., COLES, B.L.K., CHIASSON, B.J., HORSFORD, D.J., ELIA, A.J., MCINNIS, R.R., VAN DER KOY, D. Retinal stem cells in the adult mammalian eye. *Science*. **2000**, 287, 2032–2036.
- 204** SHATOS, M., MIZUMOTO, K., MIZUMOTO, H., KURIMOTO, Y., KLASSEN, H., YOUNG, M. Multipotent stem cells from the brain and retina of green mice. *Regen. Med.* **2001**, 2, 13–15.
- 205** BHATTACHARYA, S., JACKSON, J.D., DAS, A.V., THORESON, W.B., KUSZYNSKI, C., JAMES, J., JOSHI, S., AHMAD, I. Direct identification and enrichment of retinal stem cells/progenitors by Hoechst dye efflux assay. *Invest. Ophthalmol. Visual Sci.* **2003**, 44, 2764–2773.
- 206** AKAGI, T., HARUTA, M., AKITA, J., NISHIDA, A., HONDA, Y., TAKAHASHI, M. Different characteristics of rat retinal progenitor cells from different culture periods. *Neurosci. Lett.* **2003**, 341, 213–216.
- 207** DI LUCCIO, M., NOBREGA, R., BORGES, C.P. Microporous anisotropic phase inversion membranes from bisphenol A polycarbonate: Effect of additives to the polymer solution. *J. Appl. Polym. Sci.* **2002**, 86, 3085–3096.
- 208** SCHURGENS, C., MAQUET, V., GRANDFILS, Ch., JEROME, R., TEYSSIE, Ph. Polylactide macroporous biodegradable implants for cell transplantation. II. Preparation of polylactide foams by liquid–liquid phase separation. *J. Biomed. Mater. Res.* **1996**, 30, 449–4461.
- 209** ZHONG, S., TEO, W.E., ZHU, X., BEUERMAN, R., RAMAKRISHNA, S., YUNG, L.Y.L. Formation of collagen-GAG blended nanofibrous scaffolds and their biological properties. *Biomacromolecules*. **2005**, 6, 2998–3004.
- 210** TAN, W., KRISHNARAJ, R., DESAI, T.A. Evaluation of nanostructured composite collagen-chitosan matrices for tissue engineering. *Tissue Eng.* **2001**, 7, 203–210.
- 211** BELLAMKONDA, R., RANIERI, J.P., BOUCHE, N., AEBISCHER, P. Hydrogel-based 3-dimensional matrix for neural cells. *J. Biomed. Mater. Res.* **1995**, 29, 663–671.
- 212** SAITO, N., OKADA, T., HORIUCHI, H., MURAKAMI, N., TAKAHASHI, J., NAWATA, M., OTA, H., NOZAKI, K., TAKAOKA, K. A biodegradable polymer as a cytokine delivery system for inducing bone formation. *Nat. Biotechnol.* **2001**, 19, 332–335.
- 213** EVANS, G.R.D., BRANDT, K., WIDMER, M.S., LU, L., MESZLENYI, R.K., GUPTA, P.K., MIKOS, A.G., HODGES, J., WILLIAMS, J., GURLEK, A., NABAWI, A., LOHMAN, R., PATRICK, C.W.J. *In vivo* evaluation of poly(L-lactic acid) porous conduits for peripheral nerve

- regeneration. *Biomaterials*. **1999**, *20*, 1109–1115.
- 214** LI, F., CARLSSON, D., LOHMANN, C., SUURONEN, E., VASCOTTO, S., KOBUCH, K., SHEARDOWN, H., MUNGER, R., NAKAMURA, M., GRIFFITH, M. Cellular and nerve regeneration within a biosynthetic extracellular matrix for corneal transplantation. *Proc. Natl. Acad. Sci. U.S.A.* **2003**, *100*, 15 346–15 351.
- 215** PEK, Y.S., SPECTOR, M., YANNAS, M., GIBSON, I.V., TI, L.J. Degradation of a collagen-chondroitin-6-sulfate matrix by collagenase and by chondroitinase. *Biomaterials*. **2004**, *25*, 473–482.
- 216** LEE, C.R., GRODZINSKY, A.J., SPECTOR, M. The effects of cross-linking of collagen-glycosaminoglycan scaffolds on compressive stiffness, chondrocyte-mediated contraction, proliferation and biosynthesis. *Biomaterials*. **2001**, *22*, 3145–3154.
- 217** DOILLON, C.J., WATSKY, M.A., HAKIM, M., WANG, J., MUNGER, R., LAYCOCK, N., OSBORNE, R., GRIFFITH, M. A collagen-based scaffold for a tissue engineered human cornea: Physical and physiological properties. *Int. J. Artif. Organs*. **2003**, *26*, 764–773.
- 218** YUNOKI, S., NAGAI, N., SUZUKI, T., MUNEKATA, M. Novel biomaterial from reinforced salmon collagen gel prepared by fibril formation and cross-linking. *J. Biosci. Bioeng.* **2004**, *98*, 40–47.
- 219** ZHONG, S., TEO, W.E., ZHU, X., BEUERMAN, R., RAMAKRISHNA, S., YUNG, L.Y. A study on characterization of aligned nanofibrous collagen scaffold by electrospinning and its effects on *in vitro* culture, unpublished work.
- 220** ZHU, H.G., JI, J., TAN, Q., BARBOSA, M.A., SHEN, J. Surface engineering of poly(DL-lactide) via electrostatic self-assembly of extracellular matrix-like molecules. *Biomacromolecules*. **2003**, *4*, 378–386.
- 221** ZHANG, R.Y. and MA, P.X. Synthetic nano-fibrillar extracellular matrices with pre-designed macroporous architectures. *J. Biomed. Mater. Res.* **2000**, *52*, 430–438.
- 222** YIM, E.K.F., LEONG, K.W. Significance of synthetic nanostructures in dictating cellular response. *Nanomed.: Nanotechnol., Biol. Med.* **1**, **2005**, 10–21.
- 223** MAO, H.Q., KADIYALA, I., LEONG, K.W., ZHAO, Z., DANG, W. Biodegradable polymers: poly(phosphoester)s. In: *Encyclopedia of Controlled Drug Delivery*, MATHIOWITZ, E. (Ed.), Wiley Inc., New York, **1999**.
- 224** WEN, J., LEONG, K.W. Synthesis and characterization of poly( $\epsilon$ -caprolactone-co-ethyl ethylene phosphate) for tissue engineering. The 29th International Symposium on Controlled Release of Bioactive Materials, Controlled Release Society, Seoul, Korea, **2002**.
- 225** WEN, J., KIM, G.J., LEONG, K.W. Poly(D,L-lactide-co-ethyl ethylene phosphate)s as new drug carriers. *J. Controlled Rel.* **2003**, *92*, 39–48.
- 226** HODGKINSON, C.P., WRIGHT, M.C., PAINE, A.J. Fibronectin-mediated hepatocyte shape change reprograms cytochrome P450 2C11 gene expression via an integrin-signaled induction of ribonuclease activity. *Mol. Pharmacol.* **2000**, *58*, 976–981.
- 227** WOERLY, S., PLANT, G.W., HARVEY, A.R. Neural tissue engineering: From polymer to biohybrid organs. *Biomaterials*. **1996**, *17*, 301–310.
- 228** WOERLY, S., MARCHAND, R. 100 ans de neurotransplantation chez les mammifères. *1 Neurochirurgie* **1990**, *36*, 71–95.
- 229** HUDSON, T., EVANS, G., SCHMIDT, C. Engineering strategies for peripheral nerve repair. *Orthop. Clin. North. Am.* **2000**, *31*, 485–498.
- 230** RANIERI, J.P., BELLAMKONDA, R., JACOB, J., VARGO, T.G., GARDELLA, J.A., AEBISCHER, P. Selective neuronal cell attachment to a covalently patterned monoamine on fluorinated ethylene propylene films. *J. Biomed. Mater. Res.* **1993**, *27*, 917–925.
- 231** RANIERI, J.P., BELLAMKONDA, R., BEKOS, E.J., GARDELLA, J.A. JR., MATHIEU, H.J., RUIZ, L., AEBISCHER, P. Spatial control of neuronal cell attachment and differentiation on covalently patterned laminin

- oligopeptide substrates. *J. Biomed. Mater. Res.* **1994**, 12, 725–735.
- 232** MATSUDA, T., SUGAWARA, T., INOUE, K. An artificial neural circuit based on surface micropattern processing. *ASAIO J.* **1992**, 36, 243–247.
- 233** WOERLY, S., MAGHAMI, G., DUNCAN, R., SUBR, V., ULBRICH, K. Synthetic polymer derivatives as substrata for neuronal adhesion and growth. *Brain Res. Bull.* **1993**, 30, 423–432.
- 234** WOERLY, S., LAROCHE, G., MARCHAND, R., PATO, J., SUBR, V., ULBRICH, K. Intracerebral implantation of hydrogel-coupled adhesion peptides: Tissue reaction. *J. Neural Transplant Plast.* **1995**, 5, 245–255.
- 235** FINE, E.G., VALENTINI, R.E., AEBISCHER, P. Nerve regeneration. In: *Principles of Tissue Engineering*, LANZA, R.P., LANGER, R., VACANTI, J.P. (Eds.), Academic Press, San Diego, **2000**, pp. 785–798.
- 236** TRESKO, P.A. Tissue engineering strategies for nervous system repair. In: *Progress in Brain Research*, SEIL, F.J. (Ed.), Elsevier Science, New York, **2000**, pp. 349–363.
- 237** SCHMIDT, C.E., LEACH, J.B. Neural tissue engineering: Strategies for repair and regeneration. *Biomed. Eng.* **2003**, 5, 293–347.
- 238** RUTKA, J.T., APODACA, G., STERN, R., ROSENBLUM, M. The extracellular matrix of the central and peripheral nervous systems: structure and function. *J. Neurosurg.* **1988**, 69, 155–170.
- 239** CARBONETTO, S. The extracellular matrix of the nervous systems. *Trends Neurosci.* **1984**, 7, 382–387.
- 240** DESAI, T.A. Micro- and nanoscale structures for tissue engineering constructs. *Med. Eng. Phys.* **2000**, 2, 595–606.
- 241** THOMSON, R.C., SHUNG, A.K., YASZEMSKI, M.J., MIKOS, A.G. In: *Principles of Tissue Engineering*, LANZA, R.P., LANGER, R., VACANTI, J.P. (Eds.), Academic Press, San Diego, **2000**, p. 251.
- 242** MA, P.X., ZHANG, R. Synthetic nanoscale fibrous extracellular matrix. *J. Biomed. Mater. Res.* **1999**, 46, 60–72.
- 243** BOGNITZKI, M., CZADO, W., FREESE, T., SCHAPER, A., HELLWIG, M., STEINHART, M., GRENIER, A., WENDORFF, J.H. Nanostructured fibers via electrospinning. *Adv. Mater.* **2001**, 13, 70–76.
- 244** HARTGERINK, D.J., BENIASH, E., STUPP, S.I. Self-assembly and mineralization of peptide-amphiphile nanofibers. *Science*. **2001**, 294, 1684–1687.
- 245** YANG, F., MURUGAN, R., RAMAKRISHNA, S., WANG, X., MA, Y.X. Fabrication of nano-structured porous PLLA scaffold intended for nerve tissue engineering. *Biomaterials*. **2004**, 25, 1891–1900.
- 246** SPILKER, M.H., ASANO, K., YANNAS, I.V., SPECTOR, M. Contraction of collagen-glycosaminoglycan matrices by peripheral nerve cells *in vitro*. *Biomaterials*. **2001**, 22, 1085–1093.
- 247** XU, C.Y., YANG, F., WANG, S., RAMAKRISHNA, S. *In vitro* study of human vascular endothelial cell function on materials with various surface roughness. *J. Biomed. Mater. Res.* **2004**, 71A, 154–161.
- 248** HADLOCK, T., ELISSEFF, J., LANGER, R., VACANTI, J.P., CHENEY, M. A tissue-engineered conduit for peripheral nerve repair. *Arch. Otolaryngol. Head Neck Surg.* **1998**, 124, 1081–1086.
- 249** CEBALLOS, D., NAVARRO, X., DUBEY, N., WENDELSCHAFFER-CRABB, G., KENNEDY, W.R., TRANQUILLO, R.T. Magnetically aligned collagen gel filling a collagen nerve guide improves peripheral nerve regeneration. *Exp. Neurol.* **1999**, 158, 290–300.
- 250** DUBEY, N., LETOURNEAU, P.C., TRANQUILLO, R.T. Neuronal contact guidance in magnetically aligned fibrin gels: Effect of variation in gel mechano-structural properties. *Biomaterials*. **2001**, 22, 1065–1075.
- 251** TENG, Y.D., LAVIK, E.B., QU, X., PARK, K.I., OUREDNIK, J., ZURAKOWSKI, D., LANGER, R., SNYDER, E.Y. Functional recovery following traumatic spinal cord injury mediated by a unique polymer scaffold seeded with neural stem cells. *Proc. Natl. Acad. Sci. U.S.A.* **2002**, 99, 3024–3029.

- 252 KESENCI, K., MOTTA, A., FAMBRI, L., MIGLIARESI, C. Poly( $\epsilon$ -caprolactone-co-D,L-lactide)/silk fibroin particles composite materials: Preparation and characterization. *J. Biomater. Sci. Polym. Ed.* **2001**, 12, 337–351.
- 253 BUNGE, M.B., BUNGE, R.P. Linkage between Schwann cell extracellular matrix production and ensheathment function. *Ann. New York Acad. Sci.* **1986**, 486, 241–247.
- 254 YANG, F., MURUGAN, R., WANG, S., RAMAKRISHNA, S. Electrospinning of nano/micro scale poly(L-lactic acid) aligned fibers and their potential in neural tissue engineering. *Biomaterials.* **2005**, 26, 2603–2610.
- 255 SNYDER, E.Y., DEITCHER, D.L., WALSH, C., ARNOLD-ALDEA, S., HARTWIEG, E.A., CEPKO, C.L. Multipotent neural cell lines can engraft and participate in development of mouse cerebellum. *Cell.* **1992**, 68, 33–51.
- 256 SNYDER, E.Y., YOON, C., FLAX, J.D., MACKLIS, J.D. Multipotent neural precursors can be differentiated toward replacement of neurons undergoing targeted apoptotic degeneration in adult mouse neocortex. *Proc. Natl. Acad. Sci. U.S.A.* **1997**, 94, 11 663–11 668.
- 257 FAN, Y.W., CUI, F.Z., CHEN, L.N., ZHAI, Y., XU, Q.Y., LEE, I.S. Adhesion of neural cells on silicon wafer with nanotopographic surface. *Appl. Surf. Sci.* **2002**, 187, 313–318.
- 258 WINTER, G.D. Formation of scab and the rate of epithelialization in superficial wounds of the domestic pig. *Nature.* **1962**, 193, 293–294.
- 259 YANNAS, I.V., BURKE, J.F. Design of an artificial skin. I. Basic design principles. *J. Biomed. Mater. Res.* **1980**, 14, 65–81.
- 260 MATSUDA, K., SUZUKI, S., ISSHIKI, N., IKADA, Y. Re-freeze dried bilayer artificial skin. *Biomaterials.* **1993**, 14, 1030–1035.
- 261 FREYMAN, T.M., YANNAS, I.V., GIBSON, L.J. Cellular materials as porous scaffolds for tissue engineering. *Progr. Mater. Sci.* **2001**, 46, 273–282.
- 262 WOODLEY, D.T., CHEN, J.D., KIM, J.P., SARRET, Y., IWASAKI, T., KIM, Y., O'KEEFE, E.J. Reepithelialization: Human keratinocyte locomotion. *Dermatol. Clin.* **1993**, 11, 641–646.
- 263 FALANGA, V. Growth factors and wound healing. *Dermatol. Clinics.* **1993**, 11, 667–675.
- 264 JONES, B.C., BRIGGS, C.D., NORTON, D.A. This new type of I.V. dressing can save you time. *Nursing.* **1982**, 12, 70–73.
- 265 LEIPZIGER, L.S., GLUSHKO, V., DIBERNADO, B., SHAFARIE, F., NOBLE, J., NICHOLS, J., ALVAREZ, O.M. Dermal wound repair: Role of collagen matrix implants and synthetic polymer dressing. *J. Am. Acad. Dermatol.* **1985**, 12, 409–419.
- 266 HELFMAN, T.L.O., OVINGTON, L., FALANGA, V. Occlusive dressings and wound healing. *Clin. Dermatol.* **1994**, 12, 121–127.
- 267 STASO, M.A., RASCHBAUM, M., SLATER, H., GOLDFARB, I.W. Experience with omiderm – A new burn dressing. *J. Burn Care Rehab.* **1991**, 12, 209–210.
- 268 PITT, C.G., CHASALOW, F.I., HIBIONADA, Y.M., KLIMAS, D.M., SCHINDLER, A. Aliphatic polyesters. I. The degradation of Poly( $\epsilon$ -caprolactone) in vivo. *J. Appl. Polym. Sci.* **1981**, 26, 3779–3787.
- 269 YANNAS, I.V. Studies on the biological activity of the dermal regeneration template. *Wound Repair. Regen.* **1998**, 6, 518–524.
- 270 CLARK, R.A.F., SINGER, A.J. *Principles of Tissue Engineering.* LANZA, R.P., LANGER, R., VACANTI, J. (Eds.), Academic Press, San Diego, **2000**, p. 857.
- 271 COOMBS, A.G.A., VERDERIO, E., SHAW, B., LI, X., GRIFFIN, M., DOWNES, S. Biocomposites of non-crosslinked natural and synthetic polymers. *Biomaterials.* **2002**, 23, 2113–2118.
- 272 DAI, N.T., WILLIAMSON, M.R., KHAMMO, N., ADAMS, E.F., COOMBS, A.G.A. Composite cell support membranes based on collagen and polycaprolactone for tissue engineering of skin. *Biomaterials.* **2004**, 25, 4263–4271.
- 273 HUANG, L., NAGAPUNDI, K., CHAIKOF,

- E.L. Engineered collagen-PEO nanofibers and fabrics. *J. Biomater. Sci. Polym. Ed.* **2001**, 12, 979–993.
- 274 COFFEE, R.A. PCT/GB97/01968. **1998**.
- 275 MARTINDALE, D. Scar no more. *Sci. Am.* **2000**, 34–36.
- 276 SMITH, D., RENEKER, D.H. PCT/US00/27737. **2001**.
- 277 JIN, H.J., FRIDRIKH, S.V., RUTLEDGE, G.C., KAPLAN, D.L. Electrospinning *Bombyx mori* silk with poly(ethylene oxide). *Biomacromolecules.* **2002**, 3, 1233–1239.
- 278 KATAPHINAN, W., DABNEY, S., RENEKER, D.H., SMITH, D., AKRON, U.O. Electrospun skin masks and uses thereof. *Patent WO0126610*. University of Akron, **2001**.
- 279 SMITH, D.J., RENEKER, D.H., MCMANUS, A.T., SCHREUDER-GIBSON, H.L., MELLO, C., SENNETT, M.S. Electrospun fibers and an apparatus thereof. *US Patent 6753454*. University of Akron, **2004**.
- 280 ANSELME, K. Osteoblast adhesion on biomaterials. *Biomaterials.* **2000**, 21, 667–681.
- 281 BOYAN, B.D., HUMMERT, T.W., DEAN, D.D., SCHWARTZ, Z. Role of material surfaces in regulating bone and cartilage cell response. *Biomaterials.* **1996**, 17, 137–146.
- 282 CAPLAN, A.L. Mesenchymal stem cells. *J. Orthoped. Res.* **1991**, 9, 641–650.
- 283 PITTENGER, M.F., MACKAY, A.M., BECK, S.C., JAISWAL, R.K., DOUGLAS, R., MARSHAK, D.R. Multilineage potential of adult human mesenchymal stem cells. *Science.* **1999**, 284, 143–147.
- 284 TERAJ, T., HANNOUCHE, D., OCHOA, E., YAMANO, Y., VACANTI, J.P. *In vitro* engineering of bone using a rotational oxygen-permeable bioreactor system. *Mater. Sci. Eng. C.* **2002**, 20, 3–8.
- 285 SHIN, M., YOSHIMOTO, H., VACANTI, J.P. *In vivo* bone tissue engineering using mesenchymal stem cells on a novel electrospun nanofibrous scaffold. *Tissue Eng.* **2004**, 10, 33–41.
- 286 DE OLIVEIRA, P.T., NANJI, A. Nanaotexturing of titanium-based surfaces upregulates expression of bone sialoprotein and osteopontin by cultured osteogenic cells. *Biomaterials.* **2004**, 25, 403–413.
- 287 BADAMI, A.S., KREKE, M.R., THOMPSON, M.S., RIFFLE, J.S., GOLDSTEIN, A.S. Effect of fiber diameter on spreading, proliferation, and differentiation of osteoblastic cells on electrospun poly(lactic acid) substrates. *Biomaterials.* **2006**, 27, 596–606.
- 288 ELIAS, K.L., PRICE, R.L., WEBSTER, T.J. Enhanced functions of osteoblasts on nanometer diameter carbon fibers. *Biomaterials.* **2002**, 23, 3279–3287.
- 289 WEI, G., MA, P.X. Structure and properties of nano-hydroxyapatite/polymer composite scaffolds for bone tissue engineering. *Biomaterials.* **2004**, 25, 4749–4757.
- 290 WEBSTER, T.J., SIEGEL, R.W., BIZIOS, R. Osteoblast adhesion on nanophase ceramics. *Biomaterials.* **1999**, 20, 1221–1227.
- 291 WEBSTER, T.J., ERGUN, C., DOREMUS, R.H., SIEGEL, R.W., BIZIOS, R. Specific proteins mediate enhanced osteoblast adhesion on nanophase ceramics. *J. Biomed. Mater. Res.* **2000**, 51, 475–483.
- 292 WEBSTER, T.J., EJIORFOR, J.U. Increased osteoblast adhesion on nanophase metals: Ti, Ti6Al4 V, and CoCrMo. *Biomaterials.* **2004**, 25, 4731–4739.
- 293 THAPA, A., MILLER, D.C., WEBSTER, T.J., HABERSTROH, K.M. Nanostructured polymers enhance bladder smooth muscle cell function. *Biomaterials.* **2003**, 24, 2915–2926.
- 294 THAPA, A., WEBSTER, T.J., HABERSTROH, K.M. Polymers with nano-dimensional surface features enhance bladder smooth muscle cell adhesion. *J. Biomed. Mater. Res.* **2003**, 67A, 1374–1383.
- 295 MILLER, D.C., THAPA, A., HABERSTROH, K.M., WEBSTER, T.J. Endothelial and vascular smooth muscle cell function on poly(lactic-co-glycolic acid) with nano-structured surface features. *Biomaterials.* **2004**, 25, 53–61.
- 296 FUJIHARA, K., KOTAKI, M., RAMAKRISHNA, S. Guided bone regeneration membrane made of polycaprolactone/calcium carbonate

- composite nano-fibers. *Biomaterials*. 2005, 26, 4139–4147.
- 297 USHIDA, T., FURUKAWA, K., TOITA, K., TATEISHI, T. Three dimensional seeding of chondrocytes encapsulated in collagen gel into PLLA scaffolds. *Cell Transplantation*. 2002, 11, 489–494.
- 298 DUNKELMAN, N.S., ZIMBER, M.P., LEBARON, R.G., PAVELEC, R., KWAN, M., PURCHIO, A.F. Cartilage production by rabbit articular chondrocytes on polyglycolic acid scaffolds in a closed bioreactor system. *Biotechnol. Bioeng.* 1995, 46, 299–305.
- 299 FREED, L.E., HOLLANDER, A.P., MARTIN, I., BARRY, J.R., LANGER, R., VUNJAK-NOVAKOVIC, G. Chondrogenesis in a cell polymer-bioreactor system. *Exp. Cell Res.* 1998, 240, 58–65.
- 300 ABBOTT, J., HOLTZER, H. The loss of phenotypic traits by differentiated cells. III. The reversible behavior of chondrocytes in primary cultures. *J. Cell Biol.* 1966, 28, 473–487.
- 301 VAN OSCH, G.J., VAN DER VEEN, S.W., VERWOERD-VERHOEF, H.L. *In vitro* redifferentiation of culture-expanded rabbit and human auricular chondrocytes for cartilage reconstruction. *Plast. Reconstr. Surg.* 2001, 107, 433–440.
- 302 BENYA, P.D., SHAFFER, J.D. Dedifferentiated chondrocytes reexpress the differentiated collagen phenotype when cultured in agarose gels. *Cell*. 1982, 30, 215–224.
- 303 MARTIN, I., VUNJAK-NOVAKOVIC, G., YANG, J., LANGER, R., FREED, L.E. Mammalian chondrocytes expanded in the presence of fibroblast growth factor to maintain the ability to differentiate and regenerate three-dimensional cartilaginous tissue. *Exp. Cell Res.* 1999, 253, 681–688.
- 304 LEE, K.Y., ALSBERG, E., MOONEY, D.J. Degradable and injectable poly(aldehyde guluronate) hydrogels for bone tissue engineering. *J. Biomed. Mater. Res.* 2001, 56, 228–233.
- 305 BUCKWALTER, J.A., MANKIN, H.J. Articular cartilage: Tissue design and chondrocyte–matrix interactions. *J. Bone Joint Surg. Am.* 1997, 79A, 600–611.
- 306 HUFNAGEL, C.A. Permanent intubation of the thoracic aorta. *Arch. Surgery*. 1947, 54, 382.
- 307 VOORHEES, A.B., JR., JARETZKI, A., BLAKEMORE, A.H. The use of tubes constructed from vinyon “N” cloth in bridging arterial defects. *Ann. Surg.* 1952, 135, 332–336.
- 308 XUE, L., GREISLER, H.P. Biomaterials in the development and future of vascular grafts. *J. Vasc. Surg.* 2003, 37, 472–480.
- 309 WESOLOWSKI, S.A., FRIES, C.C., DOMINGO, R.T., LIEBIG, W.J., SAWYER, P.N. The compound prosthetic vascular graft: A pathologic survey. *Surgery*. 1963, 53, 19–44.
- 310 RUDERMAN, R.J., HEGYELI, A.F., HATTLER, B.G., LEONARD, F. A partially biodegradable vascular prosthesis. *Trans. Am. Soc. Artif. Intern. Organs.* 1972, 18, 30–37.
- 311 BOWALD, S., BUSCH, C., ERIKSSON, I. Arterial regeneration following polyglactin 910 suture mesh grafting. *Surgery*. 1979, 86, 722–729.
- 312 BOWALD, S., BUSCH, C., ERIKSSON, I. Absorbable material in vascular prostheses: A new device. *Acta Chir. Scand.* 1980, 146, 391–395.
- 313 GREISLER, H.P. Arterial regeneration over absorbable prostheses. *Arch. Surg.* 1982, 117, 1425–1431.
- 314 GREISLER, H.P., KIM, D.U., PRICE, J.B., VOORHEES, A.B. JR. Arterial regenerative activity after prosthetic implantation. *Arch. Surg.* 1985, 120, 315–323.
- 315 MARTINI, H.F., OBER, W.C., GARRISON, C.W., WELCH, K., HUTCHINGS, R.T. *Fundamentals of Anatomy and Physiology* (4<sup>th</sup> Edn.), Prentice Hall, New Jersey, 1998.
- 316 CHUNG, T.W., LIU, D.Z., WANG, S.Y., WANG, S.S. Enhancement of the growth of human endothelial cells by surface roughness at nanometer scale. *Biomaterials*. 2003, 24, 4655–4661.
- 317 BUTTAFOCO, L., KOLKMAN, N.G., ENGBERS-BUIJTENHUIJS, P., POOT, A.A., DIJKSTRA, P.J., VERMES, I., FEIJEN, J. Electrospinning of collagen

- and elastin for tissue engineering applications. *Biomaterials* **2006**, *27*, 724–734.
- 318** BISHOP, A.E., BUTTERY, L.D.K., POLACK, J.M. Embryonic stem cells. *J. Pathol.* **2002**, *197*, 424–429.
- 319** TABATA, Y. The importance of drug delivery systems in tissue engineering. *Pharm. Sci. Technol. Today.* **2000**, *3*, 80–89.
- 320** BOUDRIOT, U., GOETZ, B., DERSCH, R., GREINER, A., WENDORFF, J.H. Role of electrospun nanofibers in stem cell technologies and tissue engineering. *Macromol. Symp.* **2005**, *225*, 9–16.
- 321** CAPLAN, A.I., BRUDER, S.P. Mesenchymal stem cells: Building blocks for molecular medicine in the 21st century. *Trends Mol. Med.* **2001**, *7*, 259–264.
- 322** HAYNESWORTH, S.E., GOSHIMA, J., GOLDBERG, V.M., CAPLAN, A.I. Characterization of cells with osteogenic potential from human marrow. *Bone.* **1992**, *13*, 81–88.
- 323** JOHNSTONE, B., HERING, T.M., CAPLAN, A.I., GOLDBERG, V.M., YOO, J.U. In vitro chondrogenesis of bone marrow-derived mesenchymal progenitor cells. *Exp Cell Res.* **1998**, *238*, 265–272.
- 324** YOO, J.U., BARTHEL, T.S., NISHIMURA, K., SOLCHAGA, L., CAPLAN, A.I., GOLDBERG, V.M., JOHNSTONE, B. The chondrogenic potential of human bone-marrow-derived mesenchymal progenitor cells. *J. Bone Jt. Surg. Am.* **1998**, *80*, 1745–1757.
- 325** ZUK, P.A., ZHU, M., MIZUNO, H., HUANG, J., FUTRELL, J.W., KATZ, A.J., BENHAIM, P., LORENZ, H.P., HEDRICK, M.H. Multilineage cells from human adipose tissue: Implications for cell-based therapies. *Tissue Eng.* **2001**, *7*, 211–228.
- 326** GIMBLE, J., GUTLAK, F. Adipose-derived adult stem cells: Isolation, characterization, and differentiation potential. *Cytotherapy.* **2003**, *5*, 362–369.
- 327** NOTH, U., OSYCZKA, A.M., TULI, R., HICKOK, N.J., DANIELSON, K.G., TUAN, R.S. Multilineage mesenchymal differentiation potential of human trabecular bone-derived cells. *J. Orthop Res.* **2002**, *20*, 1060–1069.
- 328** JANKOWSKI, R.J., DEASY, B.M., HUARD, J. Muscle-derived stem cells. *Gene Ther.* **2002**, *9*, 642–647.
- 329** DE BARI, C., DELL'ACCIO, F., VANDENABEELE, F., VERMEESCH, J.R., RAYMACKERS, J.M., LUYTEN, F.P. Skeletal muscle repair by adult human mesenchymal stem cells from synovial membrane. *J. Cell Biol.* **2003**, *160*, 909–918.
- 330** CATERSON, E.J., NESTI, L.J., LI, W.J., DANIELSON, K.G., ALBERT, T.J., VACCARO, A.R., TUAN, R.S. Three-dimensional cartilage formation by bone marrow-derived cells seeded in polylactide/alginate amalgam. *J. Biomed. Mater. Res.* **2001**, *57*, 394–403.
- 331** TULI, R., TULI, S., NANDI, S., WANG, M.L., ALEXANDER, P.G., HALEEM-SMITH, H., HOZACK, W.J., MANNER, P.A., DANIELSON, K.G., TUAN, R.S. Characterization of multipotential mesenchymal progenitor cells derived from human trabecular bone. *Stem Cells.* **2003**, *21*, 681–693.
- 332** DEVINE, S.M. Mesenchymal stem cells: Will they have a role in the clinic? *J. Cell Biochem.* **2002**, *38*, 73–79.
- 333** LI, W.J., TULI, R., HUANG, X., LAQUERRIERE, P., TUAN, R.S. Multineage differentiation of human mesenchymal stem cells in a three-dimensional nanofibrous scaffold. *Biomaterials.* **2005**, *26*, 5158–5166.
- 334** ANGELE, P., KUJAT, R., NERLICH, M., YOO, J., GOLDBERG, V., JOHNSTONE, B. Engineering of osteochondral tissue with bone marrow mesenchymal progenitor cells in a derivatized hyaluronan-gelatin composite sponge. *Tissue Eng.* **1999**, *5*, 545–554.
- 335** YAYLAOGLU, M.B., YILDIZ, C., KORKUSUZ, F., HASIRCI, V. A novel osteochondral implant. *Biomaterials.* **1999**, *20*, 1513–1520.
- 336** GAO, J., DENNIS, J.E., SOLCHAGA, L.A., AWADALLAH, A.S., GOLDBERG, V.M., CAPLAN, A.I. Tissue-engineered fabrication of an osteochondral composite graft using rat bone



- marrow-derived mesenchymal stem cells. *Tissue Eng.* **2001**, *7*, 363–371.
- 337 SCHAEFER, D., MARTIN, I., SHASTRI, P., PADERA, R.F., LANGER, R., FREED, L.E., VUNJAK-NOVAKOVIC, G. *In vitro* generation of osteochondral composites. *Biomaterials.* **2000**, *21*, 2599–2606.
- 338 TULI, R., NANDI, S., LI, W.J., TULI, S., HUANG, X., MANNER, P.A., LAQUERRIERE, P., NOTH, U., HALL, D.J., TUAN, R.S. Human mesenchymal progenitor cell-based tissue engineering of a single-unit osteochondral constructs. *Tissue Eng.* **2004**, *10*, 1169–1179.
- 339 MURAGLIA, A., CORSI, A., RIMINUCCI, M., MASTROGIACOMO, M., CANCEDDA, R., BIANCO, P., QUARTO, R. Formation of a chondroosseous rudiment in micromass cultures of human bone-marrow stromal cells. *J. Cell Sci.* **2003**, *116*, 2949–2955.
- 340 OSYCZKA, A.M., NOTH, U., O'CONNOR, J., CATERSON, E.J., YOON, K., DANIELSON, K.G., TUAN, R.S. Multilineage differentiation of adult human bone marrow progenitor cells transduced with human papilloma virus type 16 E6/E7 genes. *Calcif. Tissue Int.* **2002**, *71*, 447–458.
- 341 MURPHY, J.M., DIXON, K., BECK, S., FABIAN, D., FELDMAN, A., BARRY, F. Reduced chondrogenic and adipogenic activity of mesenchymal stem cells from patients with advanced osteoarthritis. *Arthritis Rheum.* **2002**, *46*, 704–713.
- 342 LANGER, R. Where a pill won't reach. *Sci. Am.* **2003**, *288*, 50–57.
- 343 LANGER, R. Drug delivery and targeting. *Nature.* **1998**, *392*, 5–10.
- 344 KIM, K., LUUC, Y.K., CHANG, C., FANG, D., HSIAO, B.S., CHUA, B., HADJIARGYROU, M. Incorporation and controlled release of a hydrophilic antibiotic using poly(lactide-co-glycolide)-based electrospun nanofibrous scaffolds. *J. Controlled Release.* **2004**, *98*, 47–56.
- 345 KENAWY, E.R., BOWLIN, G.L., MANSFIELD, K., LAYMAN, J., SIMPSON, D.G., SANDERS, E.H., WNEK, G.E. Release of tetracycline hydrochloride from electrospun poly(ethylene-co-vinylacetate), poly(lactic-acid), and a blend. *J. Controlled Release.* **2002**, *81*, 57–64.
- 346 KENAWY, E.R., ABDEL-FATTAH, Y.R. Antimicrobial properties of modified and electrospun poly(vinyl phenol). *Macromol. Biosci.* **2002**, *2*, 261–266.
- 347 ZONG, X., KIM, K., FANG, D., RAN, S., HSIAO, B.S., CHU, B. Structure and process relationship of electrospun bioabsorbable nanofiber membranes. *Polymer.* **2002**, *43*, 4403–4412.
- 348 VERRECK, G., CHUN, I., PEETERS, J., ROSENBLATT, J., BREWSTER, M.E. Preparation and characterization of nanofibers containing amorphous drug dispersions generated by electrostatic spinning. *Pharm Res.* **2003**, *20*, 810–817.
- 349 VERRECK, G., CHUN, I., ROSENBLATT, J., PEETERS, J., DIJCK, A.V., MENSCH, J., NOPPE, M., BREWSTER, M.E. Incorporation of drugs in an amorphous state into electrospun nanofibers composed of a water-insoluble, nonbiodegradable polymer. *J. Controlled Release.* **2003**, *92*, 349–360.
- 350 ZENG, J., XU, X., CHEN, X., LIANG, Q., BIAN, X., YANG, L., JING, X. Biodegradable electrospun fibers for drug delivery. *J. Controlled Release.* **2003**, *92*, 227–231.
- 351 BREWSTER, M.E., VERRECK, G., CHUN, I., ROSENBLATT, J., MENSCH, J., VAN DIJCK, A., NOPPE, M., ARIEN, A., BRUINING, M., PEETERS, J. The use of polymer-based electrospun nanofibers containing amorphous drug dispersions for the delivery of poorly water-soluble pharmaceuticals. *Pharmazie.* **2004**, *59*, 387–391.
- 352 RICHARDSON, T.P., MARTIN, C.P., ALESSANDRA, B.E., MOONEY, D.J. Polymeric system for dual growth factor delivery. *Nat. Biotechnol.* **2001**, *19*, 1029–1034.
- 353 MURRAY, J., BROWN, L., LANGE, R. Controlled release of microquantities of macromolecules. *Cancer Drug Deliv.* **1984**, *1*, 119–123.
- 354 EDELMAN, E.R., MATHIOWITZ, E., LANGER, R., KLAGSBRUN, M.

- Controlled and modulated release of basic fibroblast growth factor. *Biomaterials*. **1991**, 12, 619–626.
- 355** GOMBOTZ, W.R., PETTIT, D.K. Biodegradable polymers for protein and peptide drug delivery. *Bioconjug. Chem.* **1995**, 6, 332–351.
- 356** KUO, P.Y.P., SALTZMAN, W.M. Novel systems for controlled delivery of macromolecules. *Crit. Rev. Eukaryot. Gene Expr.* **1996**, 6, 59–73.
- 357** MAHONEY, M., SALTZMAN, W. Millimeter-scale positioning of a nerve-growth-factor source and biological activity in the brain. *Proc. Natl. Acad. Sci. U.S.A.* **1999**, 96, 4536–4539.
- 358** LEE, K.Y., PETERS, M.C., ANDERSON, K.W., MOONEY, D.J. Controlled growth factor release from synthetic extracellular matrices. *Nature*. **2000**, 408, 998–1000.
- 359** SHEA, L.D., SMILEY, E., BONADIO, J., MOONEY, D.J. DNA delivery from polymer matrices for tissue engineering. *Nat. Biotechnol.* **1999**, 17, 551–554.
- 360** LU, D., SALTZMAN, W. Synthetic DNA delivery systems. *Nat. Biotechnol.* **2000**, 18, 33–37.

### 3

## Electrospinning Technology for Nanofibrous Scaffolds in Tissue Engineering

*Wan-Ju Li, Rabie M. Shanti, and Rocky S. Tuan*

### 3.1

#### Introduction

Annually, millions of Americans suffer tissue loss or end-stage organ failure at a health care cost exceeding \$400 billion, representing nearly one-half of all medical related costs in the United States [1]. Approximately 80 000 of these patients will await solid organ transplantation, and based on the figures from the United Network for Organ Sharing (UNOS) only 27 037 solid organs were transplanted in the United States in 2004. Also, according to the American Association of Tissue Banks (AATB), 1.3 million bone grafts and 94 000 soft tissue (e.g., tendon, meniscus) grafts were performed in the United States in 2003. The current standard-of-care for the replacement of lost or damaged organs and tissues includes transplantation of whole organs from one individual to another (allografts), transplantation of a patient's own tissues from one region of the body to another (autografts), or by the utilization of synthetic materials (alloplasts). Although these therapeutic modalities have had much success in clinical practice, each is associated with significant complications. For instance, allografts are restricted due to limited supply of donor organs and tissues, potential sequelae of chronic immunosuppression, and risk of host immunorejection. Alloplasts or synthetic materials, also have the potential of eliciting an adverse body response, and often fail over time due to wear and fatigue. Therefore, tissue engineering has emerged as a promising alternative for the reconstitution of lost or damaged organs and tissues, circumventing the secondary complications associated with autografts, allografts, and alloplasts.

Three general strategies were devised in the early 1990s for the engineering of new tissue: (1) delivery of cells or cell substitutes, (2) local or systemic delivery of tissue inducing substances, (3) and delivery of scaffolds containing both cells and inductive agents [1]. These approaches typically require some sort of carrier in the form of a biomaterial scaffold to guide the delivery of cells, inductive agents, or a combination of the two to the area of interest. In the same capacity, this biomaterial scaffold can also facilitate the growth and regeneration of new tissue. Figure 3.1 illustrates the general concept of tissue engineering based strategy for therapeutic applications. Briefly, target cells (differentiated/undifferentiated) expanded

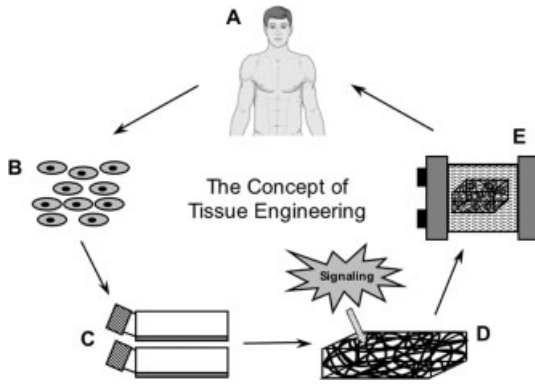


**Fig. 3.1.** The general concept of tissue engineering. (A) Human tissue or cell donors and recipients. (B) Harvested and isolated cells. (C) Cells expanded in tissue cultures. (D) Cells cultured in tissue engineered scaffolds and induced by biochemical and mechanical signals. (E) Cellular constructs maintained in bioreactors.

*in vitro* cultures, usually in cell culture flasks, are cultured in three-dimensional (3D), highly porous biomaterial scaffolds (natural/synthetic) under biologically favored conditions. After a period of culture time, the cellular scaffold receiving chemical and physical growth-needed stimuli turns into a natural tissue-like cellular implant. Furthermore, these biologically functional scaffolds play a critical role in the tissue engineering process, for they provide a 3D structure for cellular functions such as attachment, migration, proliferation, and differentiation and/or serve as vehicles for the delivery of cells to the implant site. The success of this process is determined by the biological and functional similarity of the engineered tissue with native tissue. In summary, whether the biomaterial scaffold serves as a 3D matrix for *in vitro* culture or functions as a template to recruit surrounding host cells to conduct the repair process, a principal objective of scaffold design for tissue engineering is to create a structure that can simulate the native extracellular matrix (ECM) until cells seeded within the scaffold and/or derived from the host tissue can synthesize a new, natural matrix.

To achieve this goal, a scaffold material must be carefully selected and the scaffold architecture should be properly designed to ensure biocompatibility with the seeded cells. Ideal characteristics for a scaffold include (a) biocompatibility (no cell toxicity before and after degradation of the scaffold material); (b) promotion of cellular activities such as cell adhesion; (c) biodegradability with a controlled rate of degradation that corresponds with tissue growth within the scaffold; (d) a 3D highly porous structure with an interconnected network of microscopic spaces to allow tissue growth and permeation of nutrient medium; (e) favorable mechanical properties; and (f) a highly reproducible and adaptable fabrication process for different shapes or sizes. These characteristics are determined by the material selection and the method of scaffold fabrication [2].

Both chemical [3] and physical properties [4] of a scaffold affect cell behavior, ultimately determining the fate of a tissue-engineered scaffold. Progress has been made in the improvement of the chemical biocompatibility of scaffolds through the use of natural polymers [5] or synthetic polymers that incorporate bioactive peptides, such as those containing the arginine-glycine-aspartate (RGD) sequence [6]. Conversely, there has been relatively limited work on the effect of physical properties, such as the 3D architecture of a scaffold, on cell behavior. Cells respond differently to geometrically distinct biomaterial substrates [7]. Specifically, previous studies have demonstrated that cells behave differently when cultured on either two-dimensional (2D) or 3D substrates [8, 9]. For instance, chondrocytes dedifferentiate when cultured on a 2D surface [10], but maintain a stable phenotype when cultured in a 3D agarose hydrogel [11]. Fibroblasts cultured in a 3D environment developed a 3D profile of matrix adhesion, leading to a distinct cytoskeletal organization and induction of specific cell signaling pathways, compared with those cultured on 2D substrates, implying the *in vivo* relevance of 3D matrix adhesion. Similarly, the advantage of using 3D structures for cell culture has also been shown to have an effect on the maintenance and differentiation of embryonic stem cells [12]. For instance, biomimetic 3D cultures significantly increase hematopoietic differentiation efficacy of embryonic stem cells over their 2D counterparts. The biological relevance of 3D cultures is most likely a consequence of cell–matrix interactions that proceed in a complicated, bidirectional (outside-in and inside-out) manner [13], and are likely to be critical for effective tissue engineering or regeneration. While much is known about the biology of cell–matrix interactions in 2D cultures, relatively little is known about this process in 3D matrices. To date, two models of 3D environments have been proposed to elucidate the details of this interaction: substrates with a 3D topography, and 3D scaffolds. The former is useful for studying the effects of geometrical variables on cellular activities, but not directly applicable to tissue engineering. Since 3D scaffolds can be fabricated into desired shapes and form interconnected pores to allow tissue ingrowth, they are readily applicable for tissue engineering.

Recent studies have also shown that cells on substrates with varying topography, fabricated using precisely controllable techniques, behave quite differently, suggesting that cells are able to recognize and distinguish geometric properties of substrates, such as shape and/or roughness. For example, Tuan's and Curtis's groups have reported that surface roughness had an effect on osteoblast, endothelial cell, and fibroblast morphology, cytoskeletal properties, and proliferation [14–16]. Other studies have reported that adhesion, proliferation, synthesis of alkaline phosphatase, and deposition of a calcium-containing mineral were all enhanced when osteoblasts were cultured in a nanophase ceramic, compared with micro-grain size ceramics [17, 18]. Increased functions of osteoblasts have also been correlated with a decrease in the diameter of carbon nanofibers [19]. These observations suggest that a scaffold composed of nanometer-scale components is biologically preferred, which is consistent with previous studies reporting that cells favor nanotopographic biomaterial surfaces [18]. As a result, nanometer structural components should be preferred for the fabrication of functional tissue-engineered scaffolds.

This chapter differs from previously published review articles [20–24] that focus on the electrospinning process and the characterization of electrospun nanofibrous scaffolds by covering in much greater detail the breadth of electrospinning technology and its applications in tissue engineering. Notably, by taking advantage of our research expertise in cell and tissue engineering, we particularly focus on the biological mechanisms and activities enhanced by nanofibers while also reviewing the most up-to-date findings for the development of electrospun nanofibrous scaffolds and the engineering of nanofiber-based tissues. In this chapter, we first emphasize the importance of tissue engineering for clinical applications, introduce electrospun nanofibrous scaffolds by discussing the mechanisms and parameters influencing the properties of electrospun nanofibrous scaffolds, and, finally, review the current development of electrospun nanofibrous scaffolds in tissue engineering applications.

## 3.2

### **Nanofibrous Scaffolds**

Among nanostructures, nanofibers are more suitable for use as the basic component of a scaffold compared with nanoparticles, due to their continuous structure. The advantage of a scaffold composed of ultrafine, continuous fibers are high porosity, variable pore-size distribution, high surface-to-volume ratio, and, most importantly, morphological similarity to natural ECM [25]. The combination of these features makes nanofibrous structures a favorable scaffold for tissue engineering, as shown by several studies described below.

#### 3.2.1

##### **Fabrication Methods for Nanofibrous Scaffolds**

Several techniques based on different physical principles have been used to fabricate nanofibrous scaffolds with unique properties.

###### 3.2.1.1 **Phase Separation**

Phase separation is often utilized as an alternative technique for scaffold fabrication. In most cases, the polymer is dissolved in a solvent at a low temperature, and then the resulting polymer and solvent phases are quenched to create a two-phase solid. The solidified solvent is then removed by sublimation, leaving a porous polymeric scaffold behind. In brief, the polymer is dissolved, gelled, and extracted using various solvents. The advantage of using phase separation to fabricate nanofibrous scaffolds is that the shape and size of the pores can be controlled by the addition of porogens [26]. Conversely, a limitation of the foam-like structures produced by phase separation is their compliance and lack of pore interconnectivity.

###### 3.2.1.2 **Self-assembly**

By definition, self-assembly is the spontaneous organization of molecules into well-defined and macroscopic aggregates [5, 27]. The principle of molecular self-

assembly is ubiquitous in biological systems, e.g., the aggregation of lipid molecules into micelles in an aqueous environment. In contrast to processes such as electrospinning (see below), which are based on a top-down approach (i.e., materials are broken down into their respective components), self-assembly is based on a bottom-up approach (i.e., materials are assembled molecule by molecule).

On a molecular level, self-assembly is mediated by weak, non-covalent bonds, i.e., ionic bonds, hydrophobic interactions, van der Waals interactions, and water-mediated hydrogen bonds [5]. Aside from the balance of these forces, an additional crucial factor of the self-assembly process is complementary shape among the components [27]. To date, much of the work on self-assembly in tissue engineering has focused on the fabrication of 3D nanofibrous structures from amphiphilic peptides. In brief, when placed within an aqueous solution, the hydrophobic and hydrophilic domains within these peptides interact via the aforementioned forces to form distinct strong and fast-recovering hydrogels, with hydrophobic interactions being the principle force that drives the molecules together [28].

Self-assembled 3D nanofibrous scaffolds also closely mimic the porosity and gross structural scale of the natural ECM. Matrices composed of interwoven nanofibers with a diameter of 5–8 nm, and pores of 50–200 nm diameter [28, 29] have been observed by scanning electron microscopy and atomic force microscopy. The biocompatibility of these scaffolds is demonstrated by their ability to support cell proliferation and differentiation [29, 30]. In extended *in vitro* cultures of bovine chondrocytes within a peptide hydrogel, the chondrocytes encapsulated within the 3D scaffold retained their morphology and developed a cartilaginous extracellular matrix rich in proteoglycans and collagen type II, biochemical markers of a stable chondrocyte phenotype [30].

An advantage of using self-assembly to fabricate nanofibers is that the amino acid residues present may be chemically modified for the addition of bioactive moieties. Furthermore, self-assembly is carried out in aqueous salt solution or physiological media, thus avoiding the use of organic solvents and reducing cytotoxicity.

### 3.2.1.3 Electrospinning

Electrospinning technology has become popular for the fabrication of tissue engineering scaffolds in recent years (Fig. 3.2). This is a result of the growing interest in nanotechnology and the unique properties and relative ease of fabricating scaffolds using this process. Scaffolds fabricated by electrospinning have a totally different appearance and structure to those made by self-assembly and phase separation. Furthermore, electrospinning technology is exceptionally useful for the fabrication of tissue engineered scaffolds, for not only is the electrospinning equipment economical, but the preparation and fabrication phases are relatively quick compared with phase separation and self-assembly. In addition, the electrospinning system is easy to set up and can be modified to fabricate nanofibrous scaffolds that meet specific requirements for structural or mechanical needs. The advantages of electrospinning technology make it suitable for both small quantity production for laboratory research use and mass production for industrial use. In terms of the properties of scaffolds produced by the different methods, electrospun

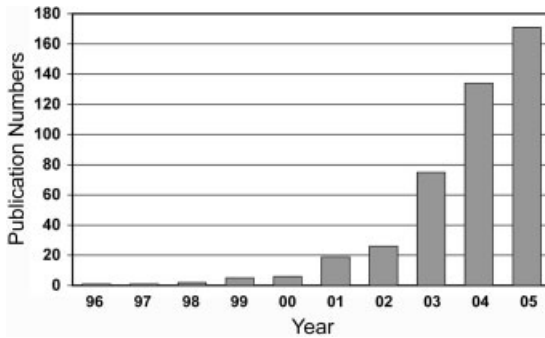


**Fig. 3.2.** Growth of research using electrospinning technology. The increasing number of scientific publications containing the keyword “electrospinning” indicates the upward trend of electrospinning applications.

nanofibrous scaffolds contain interconnected pores, and possess mechanical and structural stability, that provide superiority over scaffolds fabricated by phase separation and self-assembly. The following sections detail the fabrication technique, properties, and clinical applications of electrospun nanofibrous scaffolds.

### 3.2.2

#### The Electrospinning Process

##### 3.2.2.1 History

Electrospinning was developed based on observations of the “electrospray” phenomenon first described by Lord Rayleigh in 1882 [31]. He discovered that a highly charged droplet was unstable and would break down into smaller droplets when passed through a voltage gradient, a property known as the “Rayleigh instability”. Rayleigh proposed that disruption of the droplet surface tension was the result of forces generated through Coulombic repulsion. After this initial study, Zeleny further investigated the electrospaying of aqueous solutions [32, 33], and Dole et al. experimented with electrospays of dilute polymer solutions [34]. In addition, Vonnegut and Neubauer electrospayed water and other liquids [35], and Drozin found that electrospayed droplets resembled a highly dispersed aerosol [36]. These seminal studies laid the foundation for what was to become the electrospinning phenomenon.

Electrospinning is a direct extension of the electrospaying phenomenon, as both processes are based on the same physical and electrical mechanisms. The main difference between the two is that electrospaying produces small droplets, whereas electrospinning produces continuous fibers. In 1934, Formhals electrospun fine fibers from a cellulose acetate solution and was granted a series of U.S. patents on this technology [37]. In 1966, Simons found that more viscous solutions favored the formation of longer fibers [38]. Baumgarten designed an apparatus with an infusion pump to electrospin acrylic fibers, and discovered that the diameter of fibers



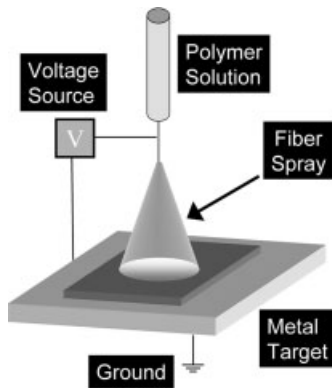


Fig. 3.3. Schema of the electrospinning apparatus (see text for details).

could be controlled by the polymer feed rate from the infusion pump [39]. Finally, Larrondo and Manley electrospun polypropylene and produced polyethylene nanofibers in 1981 [40–42]. The recent, surging interest in nanotechnology has engendered renewed attention to this convenient, economical technology that enables engineers to produce nanofibers for various applications.

#### 3.2.2.2 Setup

The electrospinning apparatus is quite simple, with only three major components: a high voltage power supply, a polymer solution reservoir (e.g., a syringe, with a small diameter needle) with or without a flow control pump, and a metal collecting screen (Fig. 3.3). A high voltage power supply with adjustable control should be able to provide up to 50-kV DC output and, depending on the number of electrospinning jets, multiple outputs that function independently are needed. A reservoir is used to store the polymeric solution and is connected to a power supply to form a charged polymer jet. Either a syringe with a metal needle or a capillary with a metal tip in the polymer solution may be used to charge the polymer solution. Polymer flow can be driven by gravity if the syringe is not horizontally placed. However, to eliminate the experimental variables, a syringe pump is usually used to control the precise flow rate. The fiber collecting screen should be conductive and can be either a stationary plate or a rotary platform or substrate. The plate can produce non-woven fibers, while a rotary platform can produce both non-woven and aligned fibers.

Currently, there are two standard electrospinning setups, vertical and horizontal. With increasing interest in this technology, several research groups have developed more sophisticated systems that can fabricate more complex nanofibrous structures in a more controlled and efficient manner [43, 44]. For example, motor-controlled multiple jets and fiber-collecting targets provide a means for fabricating a single nanofibrous scaffold composed of multiple layers, with each layer derived from a different polymer type. Additionally, this technology can be used to fabricate polymer composite scaffolds where the fibers of each layer represent the amal-

gamation of different polymer types. The multiple jet setup is not only useful for making multi-layer nanofibrous scaffolds, but is also efficient for the production of a large quantity of scaffolding material. Notably, the electrospinning apparatus is usually set up in a chemical fume hood to remove organic vapor. In addition, a closed, non-conductive environment with temperature and humidity control is required to avoid interference from environmental factors, such as air turbulence.

### 3.2.2.3 Mechanism and Working Parameters

To initiate the electrospinning process, a selected polymer material is dissolved in the appropriate solvent and this solution is loaded into a syringe. A high-voltage electric field is created between the needle and the collecting screen by the use of a power supply and electrodes. When the polymer solution is extruded slowly by a syringe pump and/or gravity, a semispherical polymer solution droplet is formed at the tip of the needle. With increasing voltage, the polymer droplet elongates to form a conical shape known as the Taylor cone [45], causing the surface charge on the polymer droplet to increase with time. Once the surface charge overcomes the surface tension of the polymer droplet, a polymer jet is initiated [46]. The solvent in the polymer jet evaporates during travel to the collecting screen, increasing the surface charge on the jet. This increase in surface charge induces instability in the polymer jet as it passes through the electric field [45]. To compensate for this instability, the polymer jet divides geometrically, first into two jets, and then into many more as the process repeats itself. The formation of nanofibers results from the action of the spinning force provided by the electrostatic force on the continuously splitting polymer droplets. Nanofibers are deposited layer-by-layer on the metal target plate, forming a non-woven nanofibrous mat.

Although the electrospinning/electrospinning technology has been utilized for more than a hundred years, the mechanisms by which nanofibers are formed, much less controlled, have yet to be completely elucidated. Although several studies have been carried out to investigate the mechanism of fiber formation to reproducibly control scaffold design, little theoretical clarity has been achieved. During the electrospinning process, a uniform fibrous structure is created only under optimized operating conditions. Both extrinsic and intrinsic parameters are known to affect the structural morphology of the nanofibers [47]. Specifically, extrinsic parameters, such as environmental humidity and temperature, in addition to intrinsic parameters, including applied voltage, working distance, and conductivity and viscosity of the polymer solution, need to be optimized to produce uniform nanofibers. Generally speaking, the intrinsic parameters are more critical in determining the nanofiber structure. Two major structures are usually found in the nanofibrous mat fabricated by the electrospinning process – a uniform, continuous fibrous structure or a bead-containing fibrous structure. Variation in the relative abundance of these two structures is determined by the relative contributions of the four intrinsic parameters during the electrospinning process.

**Polymer Solution Viscosity** Polymer solution viscosity, a parameter directly proportional to the concentration of the polymer solution, is the most critical factor in

controlling the structural morphology of the nanofibrous structure. For fiber formation, polymer viscosity should be in a specific range, depending on the type of polymer and solvent used. Fong et al. used polyethylene oxide (PEO) to study nanofiber formation in different PEO viscosities, and found that a range of viscosity between 1 and 20 poise is suitable for electrospinning uniform nanofibers [48]. Below this range, a bead-containing nanofibrous structure was created. With increasing viscosity, spherical beads became elongated into spindle-shaped ones, and the number of beads in the structure was reduced. Similarly, Liu et al. also reported that a different specific range of viscosity was appropriate for the formation of uniform nanofibers composed of cellulose [49]. In addition, recent studies conducted by Deitzel et al. [50] and Demir et al. [51] have shown that a more viscous polymer solution resulted in larger fibers. Taken together, these studies indicate that there exist polymer-specific, optimal viscosity values for electrospinning.

**Applied Charge Density** Charge density, as the amount of charge per unit surface area of the polymer droplet, is determined by the applied voltage, the working distance, and the conductivity of the polymer solution. Applied voltage is used to provide the driving force to spin fibers by imparting charge to the polymer droplet. The working distance is defined as the distance between the tip of syringe and the collecting plate and, together with the applied voltage, can influence the structural morphology of nanofibers. Demir et al. suggested that when higher voltages are applied more polymer is ejected to form a larger diameter fiber [51]. Similarly, high voltage conditions also created a rougher fiber structure. Zong et al. proposed an approach to increase charge density on the surface of the droplet by adding salt particles to reduce bead formation [52]. However, their conclusion was that a high charge density produced thinner fibers, a finding not corroborated by Demir et al. [51].

**Polymer Solution Conductivity** The conductivity of a polymer solution is mainly determined by the polymer type, solvent used, and the availability of ionizable salts. A more conductive polymer solution carries more electric charge during the electrospinning process, with the as-spun fibers generating a stronger repulsive force, which facilitates the formation of bead-free, uniform fibers. Therefore, the general rule for the production of uniform electrospun nanofibers is to electrospin a highly conductive polymeric solution. Since most synthetic biodegradable polymers such as the commonly used poly( $\alpha$ -hydroxy esters) do not carry a charge, it is preferred to increase the solvent conductivity. As a result, a dipolar aprotic solvent, *N,N*-dimethylformamide (DMF), which has a high dielectric constant and dipole moment, is added to enhance the solution conductivity [53]. An additional approach entails the use of salts to increase chargeable functional groups in polymeric solutions. The addition of benzyl triethylammonium chloride (BTEAC) [54] or sodium chloride [55], for instance, enhances polymer solution conductivity, in turn reducing fiber size, while producing bead-free fibrous structures. Natural polymers, though, such as collagens, which contain functional groups, usually carry charges when dissolved in solution; however, the polyelectrolyte characteristic

and hydrogen bonding potential of natural polymers limit the choice of solvents. The use of highly polar fluorinated or acid-based solvents can prevent complicated polymer–polymer and polymer–solvent interactions to smooth the electrospinning process.

### 3.2.3

#### **Properties of Electrospun Nanofibrous Scaffolds**

##### 3.2.3.1 **Architecture**

An electrospun nanofibrous scaffold has a macro-architecture that is defined by the gross structure of the entire scaffold. The macro-architecture can be machined into a desired dimension and shape, depending on the type of tissue being engineered. However, the micro-architecture is defined by the porous, fibrous structure composed of nanofibers, with the more commonly seen micro-architecture being either a non-woven or an aligned fibrous structure.

**Non-woven Nanofibrous Scaffolds** Upon ejection from the nozzle of a needle, a polymer jet travels spirally at a high speed in the space between the tip of a needle and the fiber-collecting plate. The jet path is a complicated 3D curve and thus nanofibers are deposited on the target platform in a random manner, resulting in a non-woven structure [56]. Nevertheless, under optimal electrospinning conditions, a homogeneous nanofibrous mat will be formed, with fiber direction in the structure being equally oriented in every direction and polygonal, interconnected pores of various sizes formed between nanofibers. Although deposited fibers lay on and barely contact each other, the interlocking between fibers helps to maintain the micro-architecture of the nanofibrous scaffold. Shape and size of pores are altered only when the structure is subjected to loading.

**Aligned Nanofibrous Scaffolds** While such randomly oriented scaffolds are useful, a significant number of natural tissues exhibit a preferred fiber alignment. This fiber alignment endows tissues with unique functional material properties that depend on the testing direction and location. For example, in tendon and ligaments, tensile properties are 200–500× higher along the fiber direction (the direction over which the force is transmitted) than those perpendicular to the fiber direction [3]. In articular cartilage, tensile properties are greatest in the superficial zone of the tissue and highest along the prevailing collagen (split line) direction [4, 5]. As the goal of tissue engineering is to recapitulate the functional properties of the native tissue, new techniques have been developed for engineering tissue anisotropy.

The strategies in controlling nanofiber alignment generally focus on the as-spun fiber-assembly methods, using either an electrostatic field and/or specially designed collectors such as a rotary target [57] and patterned electrodes [58]. Theron et al. have utilized a rotary disc as a fiber collector to electrically and mechanically align nanofibers [57]. The sharp edge of the disc provides a physically sharp point that serves as an electrode to attract positive-charged nanofibers. The sharp point accumulates charge and generates a strong electrostatic field. The rotary sharp edge acts like a continuously moving, charged band that forces nanofibers to align

on a limited strip that winds around the circumference of the disc. In addition, the rotary movement of the disc provides a tangential force, further aligning and stretching nanofibers at the same time. Fiber alignment in this initial study is relatively satisfactory, but the amount of collected aligned nanofiber is limited due to the narrow sharp edge. To increase aligned nanofiber production for tissue engineering applications, it is suggested that a disc is replaced by a drum or a shaft with a large surface area [59]. Doing so will efficiently produce a larger and thicker nanofibrous mat, but without any precise control of fiber alignment. One of the solutions is to increase the rotational speed. Several studies have shown that the nanofiber alignment in a mat is highly dependent on the rotational speed of the drum or shaft [59]. Nanofiber alignment increases with the rotational speed of the collecting surface, and plateaus after reaching an optimal value.

Another practical approach to align nanofibers utilizes a fiber collector consisting of two rectangular conductive electrodes placed on a highly insulating substrate and separated by an air gap [58]. Nanofibers, due to a preferential electrostatic field, are deposited on the electrodes uniaxially across the air gap. The air humidity, in which the electrospinning is carried out, is the major factor affecting the fiber alignment using this approach. Nanofiber alignment increases with the carried charge of as-spun nanofibers and is also enhanced by the reduction of air humidity, since the higher humidity discharges the nanofibers. In addition, fiber orientation is partially determined by the amount of charge left on the deposited nanofibers. The retained charge on deposited nanofibers improves the orientation through electrostatic repulsions between the fibers. Altering the pattern of the electrode array can change the orientation of uniaxial nanofibers and may be useful to fabricate a scaffold with a complicated aligned nanofibrous pattern.

### 3.2.3.2 Porosity

The internal porous structure of void spaces, or porosity, is a physical component of a biomaterial scaffold that is also dependent on the architectural scale. These pores serve as pathways for mass transport (convection and diffusion), while also providing void space for cells to form new tissues [60]. One technique for measuring the pore diameter distribution, total pore volume, and total pore area of a structure is mercury porosimetry. Utilizing this technology, a 91.63% porosity was reported for electrospun nanofibrous scaffolds, indicating a highly porous structure [25]. This study also reported a total pore volume of  $9.69 \text{ mL g}^{-1}$ , a total pore area of  $23.54 \text{ m}^2 \text{ g}^{-1}$ , and a pore diameter ranging broadly from 2 to  $465 \text{ }\mu\text{m}$  [25]. While some of these pores are too small to influence the migration of cells and facilitate invasion of blood vessels within the scaffold, nutrients and metabolic wastes are still able to pass through these nano-sized pores, thus enhancing engineering of the tissues. In addition, the high porosity of these scaffolds should present a wider path for mass transport, improving cell survival within the scaffold [60].

Although precise control of the pore size in nanofibrous scaffolds is challenging, efforts have been made to fabricate large-pore nanofibrous scaffolds in a more controllable manner. Lee et al. have combined electrospinning technology and salt leaching/gas foaming methods for the fabrication of an electrospun fibrous scaffold with dual-sized pores [61]. In addition to intrinsic pores formed between

nanofibers, micro-sized pores created by salt particles are distributed in the scaffolds using this modified approach. As porous scaffolds fabricated by the conventional salt-leaching method, pore sizes in electrospun nanofibrous scaffolds are determined by the dimension of the salt particles. The dual-pore, electrospun nanofibrous scaffolds represent an enhanced porous structure for more efficient cell migration and nutrition/waste exchange.

### 3.2.3.3 Mechanical Properties

As previously discussed, tissue engineering aims to utilize natural and synthetic biomaterials to simulate the 3D environment of the natural ECM. Tissue-engineered scaffolds thus also need to match the mechanical properties of the natural environment. The mechanical properties (strength, toughness, modulus, and ductility) of a scaffold are determined by both its structure (macrostructure, microstructure, and nanostructure) and its material properties [60]. Matching the mechanical properties of a scaffold to that of the natural ECM is critically important so that once grafted the progression of tissue healing is not limited by mechanical failure of the scaffold [60]. Furthermore, the mechanical properties of the scaffold can affect cell morphology, proliferation, and differentiation [62].

The process of electrospinning provides ultrafine nanoscale structures that not only geometrically and topologically simulate the natural ECM, but may also mimic the mechanical properties of the natural tissue microenvironment. To accurately investigate the mechanical behavior of nanofibrous scaffolds, it is essential to measure the mechanical properties of individual fibers that make up the scaffold [63]. Such tensile testers must possess the capability of measuring the small load and elongation required for the deformation of these ultrafine fibers, including individual fibers [63, 64]. In a previous study of the mechanical properties of individual electrospun poly( $\epsilon$ -caprolactone) (PCL) nanofibers, it was shown that mechanical properties varied with fiber diameter, i.e., both tensile strength and yield stress decreased with increased fiber diameter, while an increase in fiber diameter resulted in an increase in strain at break [63]. While in this study it was shown that the strain of break increases with an increase in fiber diameter, yield strain was found to decrease with an increase in fiber diameter, and there was also no apparent correlation between Young's modulus ( $E$ ) and fiber diameter [63]. In summary, the high ductility, and low strength and stiffness of the PCL nanofibers observed in this study depend on the physical properties of the polymer (i.e., low  $T_g$ ) and fiber diameter.

## 3.3

### Current Development of Electrospun Nanofibrous Scaffolds in Tissue Engineering

#### 3.3.1

##### Evidence Supporting the Use of Nanofibrous Scaffolds in Tissue Engineering

#### 3.3.1.1 Nanofibrous Scaffolds Enhance Adsorption of Cell Adhesion Molecules

Cell adhesion is one of the most important aspects of cell interaction with a biomaterial. It is the first cellular event to take place after cells are seeded onto a biomaterial.

terial surface; cell migration, proliferation, and/or differentiation take place only after cells are securely adhered [65]. In native tissues, cells bind via integrins to specific binding sites in the tissue ECM, consisting of specific peptide sequences recognized by the integrins [66]. However, synthetic polymers do not have natural cell binding sites, and cell adhesion to a polymeric scaffold is therefore necessarily mediated by plasma/serum proteins adsorbed onto the polymer surface. Protein adsorption to the polymer surface is affected by the hydrophilicity [67] and the surface energy of the polymer [68]. Cells attach to many ECM proteins, including fibronectin, vitronectin, collagens, and other matrix proteins [69]. Nikolovski et al. showed that vitronectin, compared with fibronectin, was the predominant matrix protein adsorbed from serum-containing medium onto poly(glycolic acid) (PGA) and poly(lactic acid) (PLA) [70]. Woo et al. recently reported that nanofibrous scaffolds for tissue engineering show enhanced adsorption of cell adhesion ECM molecules, which may therefore enhance cell adhesion [71]. The high surface-area-to-volume ratio of electrospun nanofibrous scaffolds should result in higher adsorption of vitronectin and fibronectin molecules than other scaffolds. In fact, approximately four times as much serum proteins adsorbed to nanofibrous scaffolds compared with scaffolds with solid pore walls. Moreover, fibronectin and vitronectin preferentially adsorbed to the nanofibrous scaffold at a level that was 2–4× higher than those adsorbed to the solid-walled scaffold [71]. Although the mechanisms by which a nanofibrous scaffold acts as a selective substrate are not yet known, it is clear that the enhanced adsorption of cell adhesion matrix molecules enhances cell adhesion.

#### 3.3.1.2 Nanofibrous Scaffolds Induce Favorable Cell–ECM Interaction

In a native environment, cells are in contact with the ECM and neighboring cells, and cell–matrix interaction act as key regulators of cellular activities [72]. Cells synthesize, assemble, organize, and maintain ECM macromolecules, while the ECM functions to provide structural protection to the resident cells and acts as a messenger regulating cellular activities such as proliferation or differentiation [73]. In postnatal life, the ECM continuously undergoes dynamic turnover to respond to environmental changes caused by biochemical stimulation or mechanical loading. In particular, mechanical signals are transmitted from the environment via the ECM network to cells, which respond to these signals by remodeling the ECM to adapt to the environmental change [74]. Extrapolating from these native interactions, a scaffold that serves as a functional, temporary ECM must involve optimal cell–matrix interactions, as well as cell–cell interactions.

Several reports have demonstrated that nanofibers as scaffolds are more favorable than microfibers, suggesting cell activities can be regulated by the size of the fiber [75, 76]. One such study evaluated the influence of the structural properties of biomaterial scaffolds on the biological activities of chondrocytes cultured in microfiber- and nanofiber-based scaffolds [75]. The results show that chondrocytes seeded into microfibrous scaffolds display dedifferentiated, fibroblast-like morphology, whereas chondrocytes seeded onto nanofibrous scaffolds maintain a chondrocyte-like morphology (Fig. 3.4). Large, organized stress fibers, commonly found in cells in monolayer culture also appear in cells seeded onto microfibrous

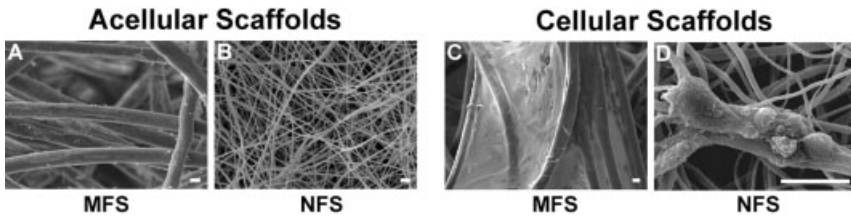


**Fig. 3.4.** Ultrastructural morphology of acellular and cellular PLLA microfibrous and nanofibrous scaffolds examined by SEM. (A) A PLLA microfibrous scaffold showing random orientation of microfibers with a diameter ranging from 15 to 20  $\mu\text{m}$ . (B) A PLLA nanofibrous produced by the electrospinning process, showing random orientation of ultrafine fibers with diameters ranging from

500 to 900 nm, defining a matrix with interconnecting pores. (C) Spread cellular sheets composed of fibroblast-like cells spanned between microfibers in the microfibrous culture after 28 days. (D) Cellular aggregates composed of globular, chondrocyte-like cells grew on nanofibers in the nanofibrous culture after 28 days. Bar = 10  $\mu\text{m}$ .

scaffolds. However, cells seeded in nanofibrous scaffolds do not display a similar cytoskeletal structure. Cell activities such as proliferation and the production of a cartilaginous ECM are enhanced in nanofibrous cultures compared with microfibrous cultures. Overall, these results demonstrate the biological effects of different-sized fibrous biomaterial scaffolds, and suggest that a nanofibrous scaffold is a more effective scaffold for cartilage tissue engineering.

Another study also reported a similar conclusion of nanofibers outperforming microfibers [76], in terms of the biological response of neural stem cells cultured on nanofibrous and microfibrous scaffolds. Unlike the comparison of fibers with a two-order difference in Li's study [75], 300 nm nanofibers were compared with 1.5  $\mu\text{m}$  microfibers. The results of this study show that a greater percentage of neural stem cells cultured on nanofibrous scaffolds exhibit a neuron-like morphology when compared with microfibrous scaffolds. In addition, the average neurite length of neural stem cells on a nanofibrous scaffold is significantly longer than that of cells on a microfibrous scaffold, suggesting that nanofibers enhance the neurite outgrowth.

One possible explanation for the enhanced performance of nanofibrous scaffolds is that nano-scale fibers, smaller than a cell by two-orders resembling native ECM, create the 3D environment that has spatial advantage in promoting cell–matrix interaction, whereas a scaffold composed of micro-scale fibers with the same order size as a cell does not have such an advantage.

### 3.3.1.3 Nanofibrous Scaffolds Maintain Cell Phenotype

Chondrocytes isolated from cartilage and cultured *in vitro* readily undergo dedifferentiation when plated as monolayers, but will redifferentiate and re-express their phenotype maintained in a 3D environment such as collagen gels. Nanofibrous scaffolds have been shown to support the potential of dedifferentiated chondrocytes to redifferentiate *in vitro* [77]. In this study, fetal bovine chondrocytes were



seeded onto nanofibrous scaffolds, or as monolayers on standard tissue culture polystyrene (TCPS) as a control substrate. Gene expression analysis shows that chondrocytes seeded on the nanofibrous scaffold and maintained in a serum-free, ITS+ supplemented medium continuously maintain their chondrocytic phenotype by expressing cartilage specific ECM genes, including collagen types II and IX, aggrecan, and cartilage oligomeric matrix protein (COMP). Specifically, expression of the collagen type IIB splice variant transcript, which is indicative of the mature chondrocyte phenotype, is up-regulated. Chondrocytes exhibit either a spindle or round shape on the nanofibrous scaffold, in contrast to the flat, well-spread morphology seen in monolayer TCPS cultures. Organized cytoskeletal actin stress fibers are only observed in the cytoplasm of cells cultured on TCPS. Histologically, nanofibrous cultures maintained in supplemented serum-free medium produce more sulfated proteoglycan-rich, cartilaginous matrix than monolayer cultures. In addition to promoting phenotypic differentiation, the nanofibrous scaffold also supports cellular proliferation when the cultures are maintained in serum-containing medium. These results indicate that the biological activities of chondrocytes are crucially dependent on the architecture of the extracellular scaffolds as well as the composition of the culture medium, and that the nanofibrous scaffold acts as a biologically preferred scaffold/substrate for proliferation and maintenance of the chondrocytic phenotype.

#### 3.3.1.4 Nanofibrous Scaffolds Support Differentiation of Stem Cells

Stem cells, including embryonic and adult stem cells, are promising cell sources for tissue engineering because of their extensive expansion and differentiation capability. Therefore, the biomaterial scaffold used to culture stem cells should be able to support basic stem cell processes, such as proliferation, self-renewal, and differentiation.

Embryonic stem cells (ESCs), different from mesenchymal stem cells (MSCs) isolated from adult tissues, are derived from the inner cell mass of a blastocyst [78]. ESCs have been considered as having the potential of unlimited differentiation, whereas MSCs are more restricted in their differentiation potential. The technique of controlling the fate of ESCs *in vitro* is complicated and far from mature. One of the requirements for the growth of ESCs is the presence of basement membrane matrix or feeder layers of embryonic fibroblasts. Basement membrane matrix or feeder cell layers provide chemical and physical cues to the ESCs, and maintain their ability to self-renew and differentiate [79]. A nanofibrous structure resembling a basement membrane matrix has been used to culture ESCs to maintain their aforementioned “stemness” properties [80]. The results show that ESC-nanofibrous cultures have significantly larger colonies of undifferentiated cells and enhanced proliferation compared with controls cultured on glass coverslips and same-polymer-films, suggesting that the physical cues from the unique geometry of nanofibrous surfaces regulate cellular activities.

Compared with the uncertain future of ESCs in the clinic, owing to ethical and legal issues, adult stem cells provide a promising cell source for stem cell based-tissue engineering. MSCs are undifferentiated, multipotential cells that are capable

of giving rise to cells characteristic of several tissues, including the connective tissue lineage [81]. Advantages of using MSCs include the fact that MSCs can be isolated from many different adult tissues, such as bone marrow [81], fat [82], umbilical cord blood [83], muscle [84], and synovial membrane [85]. In addition, nanofibrous scaffolds support multi-differentiation of MSCs [86]. In this study, MSCs from bone marrow maintained in nanofibrous scaffolds differentiated along adipogenic, chondrogenic, or osteogenic lineages when induced with specific differentiation media. Gene expression analysis and immunohistochemical detection of lineage-specific marker molecules confirmed the formation of nanofibrous constructs containing cells differentiated into the specified cell types. These results demonstrate the full support of multi-lineage differentiation of MSCs within nanofibrous scaffolds and the feasibility of tissue-engineering multiphasic constructs using a single cell source, which is of particular relevance to the development of multiphasic tissue constructs.

#### 3.3.1.5 Nanofibrous Scaffolds Promote *in vivo*-like 3D Matrix Adhesion and Activate Cell Signaling Pathway

The observations presented above strongly suggest that nanofibrous scaffolds serve as synthetic ECM networks to provide both chemical and physical stimuli to cells via direct interaction with the cells surface. Unique geometric features of the extracellular matrix, especially ultrafine structure, are generally believed to play a direct and/or indirect role in the regulation of cellular activities. However, studies about cell–nanofiber interactions are new, and the specific mechanisms of how the unique properties of nanofibers enhance cellular activities are largely unknown. From the recently published studies, integrin receptors, cytoskeleton, and signal pathways involving focal adhesion kinase (FAK), Rho, Rac, and Cdc42 GTPases are likely to play a significant role in regulating cells cultured on nanofibrous cultures [87, 88]. Schindler et al. have demonstrated that nanofibrous cultures promote *in vivo*-like cell morphology of both fibroblasts and kidney cells [87]. They also showed that both cells cultured on nanofiber surface have less defined, punctate patterns of vinculin and FAK, molecules mediating cell adhesion, at the edge of lamellipodia. In response to the accumulation of cell adhesion molecules at the edge of cells, a notable increase is observed in the formation of actin cytoskeleton-rich lamellipodia, membrane ruffles, and cortical actin. Such cellular response is also found in 3D cultures on basement membrane matrix, but not on 2D cultures. Instead, in a flat culture on glass, more vinculin and FAK are accumulated in a streaky pattern, promoting the formation of well-defined actin filaments. The decrease of FAK at the adhesion site, characteristic for cells in tissue, is called “3D-matrix adhesion”. Different from focal adhesion and fibrillar adhesion commonly formed *in vitro* on flat surfaces, 3D-matrix adhesion takes place in a 3D culture, suggesting that such *in vitro* cultures may bring the cells closer to *in vivo* conditions [13]. Thus, nanofibrous cultures should promote the formation of 3D-matrix adhesion and simulate the *in vivo* microenvironment.

In addition to the formation of 3D-matrix adhesion, nanofibrous cultures also demonstrate different expression profiles of components of cell signaling pathways

that mediate cell morphology and cytoskeletal organization. These components include members of the family of Rho GTPases, Rho, Rac, and Cdc42, each controlling distinct downstream signal pathways [88]. Cells cultured on a nanofibrous surface extensively activate Rac, which consequently enhances cell proliferation rate and increases the deposition of fibrillar fibronectin. The activated Rac is also found to accumulate at the lamellopodial edge, intracellular vesicles, and dorsal membrane ruffles, often formed in migrating cells and cells cultured in other 3D environment. The activation of Rho and Cdc42 is not as significant as that of Rac. Both GTPases were mildly elevated in the nanofibrous culture than on glass at the early phase of cell attachment. However, the extent of Cdc42 mediating cell polarity decreases along the culture. The nanofibrous scaffolds can dramatically induce the preferential activation of Rac GTPase, suggesting that nanofibrous scaffolds can provide physical as well as spatial cues to activate intracellular signaling pathways that are essential to mimic *in vivo*-like tissue growth.

### 3.3.2

#### **Biomaterials Electrospun into Nanofibrous Scaffolds**

Many polymeric biomaterials have been used for tissue engineering applications, including non-biodegradable and biodegradable polymers, with the latter consisting of both natural and synthetic polymers. Non-biodegradable polymers can be utilized to engineer tissues requiring substantial mechanical stability, such as ligament or muscle. However, their long-lasting nature interferes with tissue turnover and remodeling. Therefore, more attention has been devoted to biodegradable polymers in tissue engineering. Polymer biodegradation, by the combined effect of enzymatic and hydrolytic activities, generates space within the scaffold that facilitates cellular processes, such as proliferation and the deposition of newly synthesized ECM. To date, more than one hundred different biodegradable polymers have been successfully electrospun and over thirty of them have been used for various tissue-engineered applications. Table 3.1 summarizes the polymers used in electrospinning, their potential applications, and the evaluation criteria employed in each study.

#### 3.3.2.1 **Natural Polymeric Nanofibrous Scaffolds**

Because of their more biologically favorable polymeric chemistry towards cell and tissue growth, natural polymers have recently been fabricated into various 3D, tissue engineering scaffolds. Two groups of biocompatible natural polymers electrospun into nanofibers have been used for tissue engineering applications: protein-based and carbohydrate-based polymers. Protein-based polymers include collagen, gelatin, elastin, silk fibroin, and fibrinogen, and carbohydrate-based polymers include chitin, chitosan, and hyaluronan. Recently, natural polymers have been electrospun into nano-/micro-fibers that are structurally similar to ECM protein fibers.

**Collagen** Collagen, the most abundant protein family in the body, has been extensively used for *in vitro* and *in vivo* tissue engineering. Among the at least 19 differ-

**Tab. 3.1.** Polymers used in electrospinning, their potential applications, and the evaluation criteria employed.

Study	Biomaterial	Applications	Characterization	Ref.
1	PGA	Nonwoven TE scaffold	SEM, TEM, <i>in vitro</i> rat cardiac fibroblast culture, <i>in vivo</i> rat model	168
2	PGA	Nonwoven, aligned TE scaffold	SEM, mechanical evaluation	129
3	PLGA	Nonwoven TE scaffold	SEM, porosimetry, mechanical evaluation, <i>in vitro</i> human mesenchymal stem cell and mouse fibroblast cultures	25
4	PLGA, PLLA, PDLLA	Biomedical applications	SEM, degradation analysis, DSC, WAXD, SAXS	132
5	PLGA	Biomedical applications	SEM, WAXD, SAXS, degradation analysis	147
6	PLGA	Wound healing, drug delivery	SEM	134
7	PLGA	Biomaterials	SEM	135
8	PLGA	Nonwoven TE scaffold, peripheral nerve	SEM, <i>in vivo</i> rat model	169
9	PLGA/PEG-PLA	Prevention of postsurgical abdominal adhesions	SEM, <i>in vivo</i> rat model	154
10	PCL	Nonwoven TE scaffold	SEM, WAXD, mechanical evaluation	53
11	PCL	Nonwoven TE scaffold bone	SEM, <i>in vitro</i> rat mesenchymal stem cell culture	137
12	PCL	Nonwoven TE scaffold bone	SEM, <i>in vivo</i> rat model	138
13	PCL	Nonwoven TE scaffold cardiac tissue	SEM, <i>in vitro</i> rat cardiomyocyte culture	139
14	PCL	Nonwoven TE scaffold cartilage	SEM, <i>in vitro</i> human mesenchymal stem cell culture	140
15	PCL	Nonwoven TE scaffold cartilage	SEM, <i>in vitro</i> bovine chondrocyte culture	77

Tab. 3.1 (continued)

Study	Biomaterial	Applications	Characterization	Ref.
16	PCL	Nonwoven TE scaffold	SEM, WAXD, mechanical evaluation, <i>in vitro</i> MCF-7 mammary carcinoma cell culture	141
17	PCL	Nonwoven TE scaffold	SEM, <i>in vitro</i> human coronary smooth muscle cell culture	142
18	PCL	Nonwoven, aligned TE scaffold	SEM, surface contact angle test, <i>in vitro</i> human endothelial cell culture	99
19	PCL	Nonwoven TE scaffold	SEM, TEM, <i>in vitro</i> human dermal fibroblast culture	143
20	PCL	Nonwoven TE scaffold skin	SEM, <i>in vitro</i> human dermal fibroblast culture	144
21	PCL, PLA	Nonwoven TE scaffold blood vessel	SEM, mechanical evaluation, <i>in vitro</i> mouse fibroblast and human venous saphenous myofibroblast cultures	145
22	PCL, PCL/ CaCO <sub>3</sub>	Nonwoven TE scaffold bone	SEM, surface contact angle test, mechanical evaluation, <i>in vitro</i> human osteoblast culture	146
23	PCL, PCL/ gelatin, gelatin	Nonwoven TE scaffold	SEM, surface contact angle test, mechanical evaluation, <i>in vitro</i> bone marrow stromal cell culture	170
24	PLLA	3D cell substrate	SEM, <i>in vitro</i> human chondrocyte culture	171
25	PLLA	Nonwoven TE scaffold	SEM, <i>in vitro</i> mouse cerebellum stem cell culture	172
26	PLLA	Surface coating	SEM, AFM, <i>in vitro</i> endothelial cell culture	173
27	PLLA	Nonwoven, aligned TE scaffold nerve	SEM, <i>in vitro</i> mouse cerebellum stem cell culture	76

Tab. 3.1 (continued)

Study	Biomaterial	Applications	Characterization	Ref.
28	PLGA/PEG-PDLLA, PLLA/PLGA, PLLA	Nonwoven, aligned TE scaffold heart	SEM, surface contact angle test, degradation analysis, <i>in vitro</i> rat cardiomyocyte culture	174
29	PDLLA-PEG-PDLLA, PDLLA, PLGA	Biomedical applications	SEM, degradation analysis, surface contact angle test, <i>in vitro</i> mouse calvaria osteoblast culture	175
30	PLLA, PDLLA, PEG-PLLA, PEG-PDLLA	Nonwoven TE scaffold	SEM, surface contact angle test, <i>in vitro</i> mouse calvaria-derived osteoprogenitor culture	176
31	PLLA/MMT	Nonwoven TE scaffold	SEM	177
32	P(LLA-CL)	Aligned TE scaffold blood vessel	SEM, <i>in vitro</i> human coronary artery smooth muscle cell culture	160
33	P(LLA-CL)	Nonwoven TE scaffold	SEM, DSC, XRD, <i>in vitro</i> human coronary artery endothelial and smooth muscle cell cultures	178
34	P(LLA-CL)	Nonwoven TE scaffold	SEM, mechanical evaluation, <i>in vitro</i> human coronary muscle and endothelial cell cultures	179
35	P(LLA-CL)	Nonwoven TE scaffold blood vessel	SEM, flow press analysis, mechanical evaluation	180
36	P(LLA-CL)	Nonwoven TE scaffold blood vessel	SEM, <sup>1</sup> H NMR, porosimetry, mechanical evaluation, <i>in vitro</i> human umbilical vein endothelial cell culture	181
37	P(LLA-CL)	Nonwoven TE scaffold blood vessel	SEM, porosimetry, mechanical evaluation, <i>in vitro</i> human coronary artery endothelial cell culture	157
38	P(CL-EEP)	Nonwoven TE scaffold liver	SEM, <i>in vitro</i> rat hepatocyte culture	182
39	PNmPh	Biomedical applications	SEM, NMR, viscosity analysis, DSC, <i>in vitro</i> mouse calvarial cell culture	183

Tab. 3.1 (continued)

Study	Biomaterial	Applications	Characterization	Ref.
40	PHBV	Nonwoven TE scaffold	SEM, <i>in vitro</i> chondrocyte culture	184
41	PHBV	Nonwoven TE scaffold	SEM, viscosity analysis, degradation analysis	54
42	PHBV	Nonwoven TE scaffold	SEM, surface contact angle test, <i>in vitro</i> monkey kidney cell culture	185
43	PEU	Nonwoven TE scaffold skeletal muscle	SEM, degradation analysis, mechanical evaluation, <i>in vitro</i> murine myoblast, rat myoblast, and human satellite cell cultures	161
44	PEUU	Nonwoven TE scaffold cardiovascular tissues	SEM, mechanical evaluation, <i>in vitro</i> rat vascular smooth muscle cell culture	44
45	PEUU/Col I	Nonwoven TE scaffold soft tissue	SEM, circular dichroism spectroscopy, mechanical evaluation, <i>in vitro</i> vascular smooth muscle cell culture	186
46	PPDO-PLLA-b-PEG	Nonwoven TE scaffold	SEM, porosimetry, mechanical evaluation, degradation analysis, <i>in vitro</i> fibroblast cell culture	187
47	PU	Nonwoven, aligned TE scaffold ligament	SEM, mechanical evaluation, <i>in vitro</i> human ligament fibroblast culture	164
48	PU	Nonwoven tissue template wound healing	SEM, <i>in vivo</i> guinea pig model	188
49	PU	Nonwoven TE scaffold blood vessel	SEM, flow pressure analysis, mechanical evaluation	189
50	PU	Biomaterial	SEM, porosimetry, mechanical evaluation	190
51	PET	Nonwoven TE scaffold blood vessel	SEM, XPS, surface contact angle test, <i>in vitro</i> human coronary artery endothelial cell culture	191

Tab. 3.1 (continued)

Study	Biomaterial	Applications	Characterization	Ref.
52	PEVA	Nonwoven TE scaffold	SEM, <i>in vitro</i> human aortic smooth muscle cell and dermal fibroblast cultures	148
53	PS	Nonwoven TE scaffold skin	SEM, <i>in vitro</i> human fibroblast, keratinocyte, and endothelial single or co-cultures	192
54	PDS	Nonwoven, aligned TE scaffold biomedical applications	SEM, viscosity analysis, mechanical evaluation	193
55	PEG-LMWH/ PLGA, PEG- LMWH/PEO	Biomaterial	SEM, EDX, multiphoton microscopy	194
56	PVA/CA	Biomaterials	SEM, FTIR, WAXD, mechanical evaluation	156
57	Fibrinogen	Nonwoven TE scaffold wound healing	SEM, TEM, mechanical evaluation	115
58	Col I/PEO	Nonwoven TE scaffold wound healing	SEM, TEM, <sup>1</sup> H NMR spectroscopy, mechanical evaluation	152
59	Col I, Col III	Nonwoven TE scaffold	SEM, TEM, mechanical evaluation, <i>in vitro</i> aortic smooth muscle cell culture	91
60	Col I	Nonwoven TE scaffold wound healing	SEM, degradation, porosimetry, mechanical evaluation, <i>in vitro</i> human oral and epidermal keratinocyte cultures, <i>in vivo</i> rat model	92
61	Col I/elastin/ PLGA	Nonwoven TE scaffold blood vessel	SEM, mechanical evaluation, <i>in vitro</i> bovine endothelial and smooth muscle cell cultures	102
62	Col I/elastin/ PEO, Col I/PEO, elastin/PEO	Nonwoven TE scaffold	SEM, surface tension analysis, viscosity analysis, DSC, amino group detection	103
63	Col I, gelatin, PGA, PGA/PLA, PLA	Nonwoven TE scaffold	SEM, <i>in vivo</i> rat model	93



Tab. 3.1 (continued)

Study	Biomaterial	Applications	Characterization	Ref.
64	Col I, Col III, elastin	Nonwoven TE scaffold blood vessel	SEM, <i>in vitro</i> human umbilical vein endothelial cell, aortic smooth muscle cell, and dermal fibroblast cultures	94
65	Col I, gelatin, PU, PEO	Nonwoven TE scaffold	SEM, laser scanning confocal microscopy, mechanical evaluation	43
66	Col I, gelatin, elastin, tropoelastin	Nonwoven TE scaffold	SEM, AFM, mechanical evaluation, <i>in vitro</i> human embryonic palatal mesenchymal cell culture	95
67	Col II	Nonwoven TE scaffold	SEM	96
68	Col II	Nonwoven TE scaffold cartilage	SEM, mechanical evaluation, <i>in vitro</i> adult human articular chondrocyte culture	97
69	Elastin-mimetic	Nonwoven TE scaffold	SEM	104
70	Silk fibroin, silk/PEO	Nonwoven TE scaffold	SEM, FTIR, XPS	105
71	Silk, silk/PEO	Nonwoven TE scaffold	SEM, XPS, DSC, mechanical evaluation, <i>in vitro</i> human bone marrow stromal cell culture	106
72	Silk	Biomedical applications	SEM, <sup>13</sup> C CP/MAS NMR, mechanical evaluation	107
73	Silk	Biomedical applications	SEM, TEM, WAXD	108
74	Silk fibroin	Nonwoven TE scaffold wound healing	SEM, porosimetry, <i>in vitro</i> human keratinocyte and fibroblast cultures	109
75	Silk fibroin	Nonwoven, woven TE scaffold wound healing	SEM, ATR-IR, <sup>13</sup> C CP/MAS NMR, WAXD, NMR, <i>in vitro</i> human keratinocyte culture	110
76	Silk/chitosan	Nonwoven TE scaffold wound dressings	SEM, viscosity analysis, conductivity	111
77	Chitin, chitosan	Wound dressings	SEM, <sup>1</sup> H NMR, FTIR, WAXD, DSC, TGA	120

Tab. 3.1 (continued)

Study	Biomaterial	Applications	Characterization	Ref.
78	Chitosan	Nonwoven, aligned TE scaffold cartilage	SEM, mechanical evaluation, degradation, <i>in vitro</i> canine chondrocyte culture	121
79	Chitosan	Nonwoven biomaterial	SEM	122
80	Chitosan/PEO	Nonwoven TE scaffold, drug delivery, wound healing	SEM, XPS, FTIR, DSC	153
81	Chitosan/PEO	Nonwoven, aligned TE scaffold	SEM, viscosity analysis, <i>in vitro</i> human chondrocyte and osteoblast cultures	195
82	Chitin/PLGA	Nonwoven TE scaffold	SEM, <i>in vitro</i> human oral keratinocyte and epidermal keratinocyte cultures	158
83	Gelatin	Nonwoven TE scaffold wound healing	SEM, mechanical evaluation	101
84	Oxidized cellulose	Adhesion barriers	SEM, FTIR, WAXD, TGA	196
85	HA	Medical implant	SEM	127

PGA = poly(glycolide), PLGA = poly(lactide-co-glycolide), PLLA = poly(L-lactide), PDLLA = poly(D,L-lactide), PEG = poly(ethylene glycol), PCL = poly( $\epsilon$ -caprolactone), MMT = montmorillonite, P(LLA-CL) = poly(L-lactide-co- $\epsilon$ -caprolactone), P(CL-EEP) = poly( $\epsilon$ -caprolactone-co-ethyl ethylene phosphate), PNmPh = poly[bis(*p*-methylphenoxy)phosphazene], PHBV = poly(3-hydroxybutyrate-co-3-hydroxyvalerate), PEU = polyetherurethane, PEUU = poly(ester urethane)urea, PPDO = poly(*p*-dioxanone), PU = polyurethane, PET = polyethylene terephthalate, PEVA = poly(ethylene-co-vinyl alcohol), PS = polystyrene, PDS = polydioxanone, LMWH = low molecular weight heparin, PVA = poly(vinyl alcohol), CA = cellulose acetate, PEO = poly(ethylene oxide), Col I = collagen type I, Col II = collagen type II, Col III = collagen type III, HA = hyaluronic acid, TE = tissue engineering, SEM = scanning electron microscopy, TEM = transmission electron microscopy, DSC = differential scanning calorimetry, WAXD = wide-angle X-ray diffraction, SAXS = small angle X-ray scattering, AFM = atomic force microscopy, XRD = X-ray diffractometry, NMR = nuclear magnetic resonance, XPS = X-ray photoelectron spectroscopy, EDX = energy dispersive X-ray, ATR-IR = attenuated total reflectance infrared spectroscopy, FTIR = Fourier-transform infrared spectroscopy, TGA = thermogravimetric analysis.

ent collagen types, collagen type I is the major collagen in connective tissues and collagen type II is exclusively abundant in hyaline cartilage. Both collagen types I and II have been fabricated into different scaffolds, mostly in a gel-format, to repair tissue defects *in vivo* [89, 90]. Collagen electrospinning provides an *in vitro* method to create a preformed, nanofibrous collagen scaffold that closely mimics the native collagen network [43, 91–97]. For instance, Matthews et al. have demonstrated that, under optimal working parameters, electrospinning can be adapted to fabricate collagen types I and III nanofibers [91]. Electrospun fibers of skin-derived collagen type I and placenta-derived collagen type III were shown to be more uniform than fibers of placenta-derived collagen type I, suggesting that the diameter of electrospun collagen fibers varies with tissue origin and collagen type. Interestingly, electrospun collagen type I nanofibers exhibit the periodic banding pattern typical of native collagen, further demonstrating the potential of electrospinning in the fabrication of natural collagen fibers. Collagen type II has also been successfully electrospun. Being a major fibrous component of the ECM in hyaline cartilage, collagen type II networks are extremely important in cartilage regeneration. Electrospinning collagen type II is a promising approach to reconstruct collagen networks *in vitro*. However, one of the drawbacks on using electrospun collagen scaffolds is their rapid degradation in culture. A study by Shields et al., comparing the properties of crosslinked and non-crosslinked scaffolds using glutaraldehyde as the crosslinking agent, found crosslinking to increase the diameter of collagen fibers as well as the thickness of the scaffold [97]. This study also demonstrated that electrospun collagen type II fibers are relatively larger but mechanically weaker than native collagen fibers. Although not fully recapitulating the properties of the native collagen type II network formed in cartilage, electrospun collagen type II scaffolds still hold promise in cartilage tissue engineering due to their ability to closely mimic the natural ECM.

**Gelatin** Gelatin is the denatured form of collagen type I, a natural protein-based polymer that is extensively used in the biomedical and food industries. Unlike the triple-helical collagen from which it is derived, the denatured protein chain of gelatin is readily soluble in water at room temperature. Tissue engineered scaffolds made of gelatin usually require treatment with a crosslinking agent to maintain their structural integrity in a physiological environment, due to their ready dissociation in physiological solution. It is also common for gelatin to be grafted or blended with other polymers in the preparation of tissue engineering scaffolds [98, 99]. Like most protein polymers, gelatin contains amine and carboxylic groups, which are easily ionized in water to carry charge. This polyelectrolyte property of gelatin, coupled with its strong hydrogen bonding makes electrospinning of a gelatin aqueous solution quite challenging [43, 93, 95, 100]. In a study by Huang et al., highly polar fluorinated solvents were used to prepare a gelatin solution with an optimal concentration for electrospinning [101]. This study also showed that the mechanical performance of a gelatin mat is determined by fiber morphology, which is dependent on polymer concentration. For instance, an increase in the average diameter of gelatin fibers from 100 nm to 1.9  $\mu\text{m}$  was achieved by increasing polymer con-

centration, with smaller uniform fibers being mechanically stronger than larger uniform fibers.

**Elastin** Elastin is a highly water-insoluble protein that functions as a “perfect coil” to provide elasticity to tissues that need to be stretched and recoiled. However, it is rare for elastin to be used alone as a material to fabricate tissue engineering scaffolds [94, 95]. Elastin-containing tissues generally also contain collagen fibers [102, 103]. For instance, tissues such as skin, lung, and blood vessels are composed of collagen fibers for tensile properties and elastin fibers for elastic properties. Nagapudi et al. used a genetic engineering approach to synthesize recombinant elastin-mimetic proteins, and which were electrospun into nanofibers with different properties [104]. Elastin-mimetic proteins dissolved in a highly polar fluorinated solvent were electrospun into smaller fibers, compared with those dissolved in aqueous solution, suggesting that different fibrous morphologies of natural polymers could result from the use of different solvents, such as highly polar fluorinated solvent and water.

**Silk Fibroin** Besides collagen, silk fibroin is another protein-based, natural polymer most commonly used for electrospinning. With a long history of textile use, beginning with the ancient Chinese, silk has recently been applied for the fabrication of tissue engineering scaffolds [105–111]. One of the most significant properties of silk is its excellent mechanical properties. Natural silk is produced by spiders or silkworms, with different composition and properties among species. A study by Ohgo et al. comparing three electrospun silk fibroin nanofibers suggested that silk fibroins from two different silkworms and genetically engineered silk-like protein each required individual optimal polymer concentration for electrospinning [107]. In addition, the engineered silk-like protein nanofibers were reported to be smaller than the natural silk fibroin nanofibers, and the mechanical strength of silk fibroin nanofibrous mats was also dependent on silk fibroin type.

**Fibrinogen** Purified from blood plasma, fibrinogen is a globular protein that plays a critical role in wound healing. In the presence of thrombin, fibrinogen gives rise to fibrin which forms fibrous clots that have found use as a clinical fixative, due to its natural role in wound healing. Fibrin has recently attracted scientific attention for use as a scaffold to deliver cells [112, 113] or growth factors [114] for tissue engineering. Due to the high surface area to volume ratio available for clot formation, electrospun nanofibrous fibrinogen mats are highly suitable for wound dressing and hemostatic products. Wnek et al. have fabricated and characterized electrospun fibrinogen scaffolds [115], and found the fibrinogen mats to be composed of uniform, randomly orientated fibrinogen nanofibers. Notably, the electrospun fibrinogen fiber typically exhibited a granular appearance with 22.5 nm banding, characteristic of native fibrinogen. Consistent with the finding of studies using other polymers, the fiber diameter was shown to increase from 80 to 700 nm with increasing in polymer concentration. The electrospun fibrinogen mats were also shown to have substantial structural integrity and good handling, with an elastic

modulus comparable to that of PGA. The most important characteristic of electrospun fibrinogen mats was their high surface area-to-weight ratio of  $41\,000\text{ cm}^2\text{ g}^{-1}$ , making electrospun fibrinogen mats ideal for wound dressing products. However, the risk of immune cross-reactivity may limit the use of fibrinogen for scaffold applications.

**Chitin and Chitosan** Chitin and chitosan are biocompatible and biodegradable natural polymers, used in biomedical applications and cosmetics. Chitosan (poly-D-glucosamine) is derived from chitin (poly-N-acetyl-D-glucosamine), a polysaccharide formed in shellfish exoskeleton, which has received more attention in biomaterial development than chitin due to its solubility. Therefore, chitosan has been critically considered as a candidate biomaterial for tissue engineering scaffolds [116–118]. Chitosan carries a high cationic charge density and can interact with various anionic polymers, such as chondroitin sulfate, to form a hydrogel scaffold [119]. Different from a hydrated scaffold, an electrospun scaffold is a preformed, nanofiber-based scaffold with a definite structure [120–122]. Min et al. used radiation to depolymerize chitin to increase its solubility for electrospinning [120]. In this study, the electrospun chitin nanofibers started to form at a viscosity at which the required polymer chain entanglement occurs. Fiber diameters vary from 40 to 600 nm, but most fibers are less than 100 nm. The authors also demonstrated that chitosan nanofibrous scaffolds electrospun using deacetylated chitin showed no significant changes in terms of scaffold size and fiber diameter after this transformation. Significantly different from Min's approach, Geng et al. directly electrospun a chitosan solution [122], prepared by dissolving chitosan in concentrated acetic acid, into chitosan nanofibers with an average diameter of 130 nm. The authors suggested that the use of concentrated acetic acid to decrease surface tension of chitosan solution and increase the charge density of the jet, facilitated the formation of uniform chitosan nanofibers. Other factors affecting fiber morphology include chitosan molecular weight, solution concentration, and charge density of electric field. For each parameter, there is a narrow window of optimal working conditions for defect-free nanofiber formation to occur. Generally, a viscous chitosan polymer solution prepared from a higher molecular weight chitosan is preferred, with electrospinning done in a moderate charge density electric field.

**Hyaluronan** The most commonly used carbohydrate-based natural polymer in tissue engineering is hyaluronan (hyaluronic acid), a polysaccharide composed of repeating glucuronic acid and N-acetylglucosamine. Like chitosan, unmodified hyaluronan is hydrophilic and is commonly produced in a gel-format scaffold. A hyaluronan-based scaffold is inherently unstable and thus has limited application in tissue engineering. Thus, approaches have been developed to increase the resistance of hyaluronan to degradation, including esterification [123] and crosslinking [124]. Modified hyaluronan can be fabricated into scaffolds with pre-formed structures, and several *in vitro* and *in vivo* studies have reported cell proliferation and synthesis of ECM using these modified hyaluronan scaffolds [125, 126]. It is difficult to form uniform size fibers from hyaluronan using electrospinning because of

the high viscosity and surface tension of the hyaluronan solution. Um et al. reported on several approaches to prepare a hyaluronan solution that has sufficient molecular entanglement in a rapidly evaporated solvent, while still maintaining low viscosity and surface tension [127]. One of the approaches blended two hyaluronan polymers of low and high molecular weight, resulting in increased molecular entanglement but not viscosity. Another approach consisted of adding ethanol in the polymer solution, which facilitated solvent evaporation as well as reduction in surface tension. However, although the approaches seemed rational, these results, while satisfactory, were limited. Therefore, further approaches entailed adding an air-blow system close to the spinneret, providing both electrical and air-blowing shear forces as well as heat, to facilitate hyaluronan nanofiber formation, and the new setup is named an “electro-blowing” system. In the electro-blowing apparatus, the hyaluronan solution was heated to reduce viscosity and surface tension, and was electrospun by both electrical (voltage) and mechanical (air blow) force. Lastly, air-blowing significantly improved solvent evaporation and fiber stretch, and the electro-blowing system produced hyaluronan nanofibers with a fiber diameter ranging from 49 to 74 nm.

### 3.3.2.2 Synthetic Polymeric Nanofibrous Scaffolds

**Poly( $\alpha$ -hydroxy esters)** The most commonly used biopolymers for nanofiber production are of the biodegradable poly( $\alpha$ -hydroxy ester) based polymer family. PLA, PGA, their co-polymers, poly(lactic-co-glycolic acid) (PLGA), and poly( $\epsilon$ -caprolactone) (PCL) are biodegradable polymers approved by the U.S. Food and Drug Administration, with a long history in medical applications. *In vivo*, complete degradation of poly( $\alpha$ -hydroxy esters) results in the production of natural metabolites, such as lactic acid, which are subsequently converted into CO<sub>2</sub> and water, and eventually removed by the respiratory and urinary systems, respectively [128]. Thus, poly( $\alpha$ -hydroxy esters) are metabolized into non-toxic end-products that are not accumulated in the body.

PGA is a polymer of glycolic acid and has been extensively used in various biomaterial applications. Due to its high crystallinity, it is insoluble in general organic solvents, with highly fluorinated solvents being the only exception. Consistent with the trend found in other polymers, the PGA fiber diameter, ranging from 110 nm to 1.19  $\mu$ m, increases with polymer concentrations from 0.05 to 14.3 wt.%. PGA polymer in a higher concentration solution encounters stronger molecular entanglement, resulting in thicker fibers during the electrospinning [129, 130].

PLA, with the addition of a methyl group, is more hydrophobic and more soluble in organic solvents, and degrades more slowly than PGA [131]. The three stereoisomers of PLA [D, L, and D,L] differ in the position of a methyl group in the lactic acid monomer, and exhibit distinct properties. For example, PLLA has a higher melting temperature than PDLLA because of its higher order crystal structure. However, PDLLA, composed of l and d stereoisomers, degrades faster than PLLA. The properties of various PLA polymers are determined by the stereochemistry of the PLA isomers. PLLA is a semicrystalline polymer, whereas PDLLA is an

amorphous polymer. During the preparation process, both PLLA and PDLLA are soluble in most organic solvents, such as chloroform. Commonly, DMF is added to increase the polymer conductivity, enhancing the fiber formation. Electrospun PDLLA and PLLA fibers share similar morphology, fiber density ( $0.27\text{--}0.31\text{ g cm}^{-3}$ ), and porosity (75–78%) [132]. However, the average diameter of semicrystalline PLLA fibers is larger than that of amorphous PDLLA fibers when both polymers are used at the same concentration, suggesting that a stronger polymer molecular entanglement exists in PLLA fibers.

PLGA is a widely used biodegradable polymer because of its flexibility of copolymerizing different ratios of PLA and PGA. Depending on the ratio of copolymerization, PLGA has different subtypes with each exhibiting different properties. PLGA has been extensively used in medical products and was one of the first biodegradable polymers electrospun for tissue engineering applications [133]. The PLGA copolymer has an amorphous structure, because the constituent PGA and PLA molecules are unable to pack tightly to one another. Katti et al. and Berkland et al. have both used PLGA for electrospinning to investigate the parameters affecting fiber morphology [134, 135]. Their results showed that, in addition to polymer concentration and charge density, orifice diameter also has an effect on the morphology and diameter of electrospun fibers. Smaller nanofibers tend to be produced from smaller orifices. The area density of electrospun fiber mats increases linearly with electrospinning time. Among the working parameters, polymer concentration is the major parameter affecting fiber morphology. Li et al. have shown that nanofibrous PLGA scaffolds have an interconnected-porous structure with more than 90% porosity and sound mechanical properties, ideal properties for tissue engineered scaffolds [25].

Another member of the poly( $\alpha$ -hydroxy ester) family is poly( $\epsilon$ -caprolactone) (PCL), also a semicrystalline biodegradable polymer. Compared to other polyester family members such as PLA, PGA, and PLGA, PCL has been used less frequently as a material for fabricating biomaterial scaffolds, mainly because of concern over its slower degradation kinetics [136]. However, the improved resistance to hydrolytic attack and lower cost than other biodegradable polymers also make PCL an attractive polymer for the fabrication of electrospun nanofibers [53, 77, 99, 100, 137–146]. The rationale for using a biodegradable polymer with a longer half-life is to provide a structurally stable environment that is able to initiate and promote cell growth for a sufficient period of time. Lee et al. characterized the morphology, crystallinity, and mechanical properties of electrospun PCL meshes produced by electrospinning PCL solutions prepared in different solvents; they found that surface tension, viscosity, and electric conductivity of PCL solutions depended on the addition of DMF [53]. DMF can efficiently enhance the electrospinning process by decreasing fiber diameter by decreasing the surface tension and viscosity of the polymeric solution, and also by increasing polymer conductivity and the dielectric constant. It is also known that the electrospinning process reorganizes PCL polymer chains and, compared with unprocessed PCL, electrospun nanofibers have a reduced crystallinity.

Although poly( $\alpha$ -hydroxy ester) members are classified in the same polymer fam-

ily, electrospun scaffolds derived from these polymers exhibit distinct degradation and mechanical properties [25, 129, 132, 147]. Studies comparing the degradation of electrospun nanofibers of various poly( $\alpha$ -hydroxy esters) have shown that PLLA and PCL fibers were able to resist hydrolytic attack for the duration of the study. However, all of the remaining polymers underwent severe degradation, including both structural collapse and gross shrinkage. A similar study conducted by Zong et al. demonstrated that PLGA 75:25 and PDLLA degrades at a much faster rate than PLGA 10:90 and PLLA [132]. One of the reasons for this more rapid degradation could be the high surface area of nanofibrous scaffolds, thereby allowing more water contact at the polymer surface, accounting for the vulnerability of small fibers, like nanofibers, to hydrolytic attack. Zong et al. also proposed that the electrospinning process lowers the glass transition temperature of PLGA copolymers to a value very close to their incubation temperature (37 °C); the relaxation of extended amorphous chains near the glass transition temperature thus causes shrinkage under incubation condition. Given the rapid degradation of some nanofiber formulations, many research groups have focused their efforts on electrospinning PLLA or PCL alone, or copolymerized with other biodegradable polymers, to fabricate polymer scaffolds with more desirable, long term stability.

**Poly(3-hydroxybutyrate-co-3-hydroxyvalerate) (PHBV)** PHBV is a member of the polyester family, and represents a new class of biodegradable polymers, recently attracting attention for tissue engineering applications. The co-polymerization with hydroxyvalerate renders PHBV with enhanced mechanical and degradation properties, thus extending the application to scaffold fabrication. Choi et al. investigated the feasibility of PHBV electrospinning and attempt to reduce fiber diameter by increasing the conductivity of the polymeric solution [54]. PHBV fibers electrospun from various concentrations of polymeric solutions range from 1 to 4  $\mu\text{m}$ . However, efforts to manipulate electrospinning parameters such as voltage and concentration were not effective in bringing the fiber diameter below 1  $\mu\text{m}$ . To increase the conductivity of the polymeric solution, favorable for smaller fiber formation, benzyl triethylammonium chloride (BTEAC) was added to the PHBV solution. The addition of BTEAC resulted in a reduction of the size of the electrospun fibers and the needed polymer concentration for producing uniform fibers, suggesting the conductivity of the PHBV solution plays a major role affecting the fiber diameter and morphology of PHBV fibers. In addition, the degradation of the electrospun fibrous mat is relatively slow in the first 12 days, but the disintegration of the structure accelerates after that, and results in a dramatic weight loss.

**Poly(ethylene-co-vinyl alcohol) (PEVA)** PEVA is a semi-crystalline, biocompatible but not biodegradable polymer. Recently, it has been electrospun and evaluated for its potential in tissue engineering scaffolds. PEVA is a hydrophilic polymer that is insoluble in aqueous solution due to the presence of both vinyl alcohol and ethylene groups. Most hydrophobic polymers have the property of slow degradation, whereas most hydrophilic polymers exhibit a rapid degradation rate. The de-



sired property makes PEVA a potential material ideal for tissue engineering scaffolds. PEVA needs to be dissolved in dimethyl sulfoxide or lower alcohols. Kenawy et al. have prepared the PEVA solution by dissolving PEVA in a 70% alcohol solution (rubbing alcohol) at 65 °C for electrospinning [148]. Interestingly, the polymer tends to precipitate when sitting in room temperature for several hours. Therefore, electrospun PEVA needs to be processed before precipitation occurs, and is carried out in a setup designed to maintain the solution temperature. This study also demonstrated a consistent finding of fiber diameter increasing with increase in solution viscosity. The diameter of fibers electrospun from higher concentrations of polymer solutions is higher than the  $\mu\text{m}$  level. In these structures, fibers are fused at their contact points, instead of being individually stacked, suggesting that strong molecular entanglement exists in the highly concentrated PEVA polymer solution. Another remarkable observation is that PEVA electrospinning is extremely efficient. The usage of PEVA, disinfected by dissolving in rubbing alcohol, combined with the efficiency of the PEVA electrospinning, could be ideal for wound dressing application.

**Poly(ethylene terephthalate) (PET)** PET, referred to also by the trade name “Dacron”, has largely been used in biomaterial applications, especially in blood vessel prostheses, since PET is inert and does not interact with blood cells. Ma et al. investigated how electrospinning time affects the thickness and porosity of electrospun PET scaffolds [98]. The electrospun PET nanofibers fabricated using optimal parameters ranged from 200 to 600 nm. The thickness, mass per area, and porosity of the PET fiber mats all increase with increasing electrospinning time. However, there is no linear relation between these factors. A likely explanation is that not all the as-spun nanofibers were collected onto the sampling area, because, in their setup, there was uneven fiber deposition onto the fiber-collecting surface.

**Polyurethane (PU)** PU is a non-biodegradable biomaterial with good blood and tissue compatibility, which is primarily used in vascular implants or wound dressing. PU is ideal for applications for tissue engineering products that require stable mechanical properties or structural integrity. Unlike most studies in which the polymer concentration was manipulated to control fiber morphology, Khil et al. have optimized fiber morphology by controlling solvent composition [149]. They electrospun a PU solution, prepared from pure DMF or tetrahydrofuran (THF) or mixed solvents with different DMF/THF ratios, and found that the mixed solvent produced more uniform, small fibers. Electrospun fibers prepared from pure DMF were smaller and irregular, whereas those from pure THF were relatively larger and uniform. Solvents could loosen the polymer coil, thereby affecting the viscosity of a polymer solution. In this study, the different solvent compositions loosened the polymer coil to various extents, resulting in different viscosities. The mixed solvent reduced the surface tension and viscosity of PU solution, and the addition of DMF increased the conductivity of the solution, which together contributed to the formation of uniform fibers.

**Poly(ethylene oxide) (PEO)** PEO is a commonly used biomaterial for tissue engineering because of its capability to gel *in situ*. A PEO gel can be directly injected into an irregularly shaped defect site and photopolymerized to help tissue repair [150, 151]. However, the inherent, soft mechanical properties of the PEO hydrogel and the depth limit of the injection site that permits sufficient energy present a major challenge for using PEO hydrogel. Preformed PEO scaffolds with a defined porous structure is another scaffold option. PEO is one of the earliest polymers processed for electrospinning because it is easy to prepare and can be dissolved in both organic and aqueous solvents. Much of the current knowledge on the electrospinning process is in fact based on results using PEO. Because of the ease of forming uniform nanofibers, PEO, is often blended with another polymer in the electrospinning of tissue engineering scaffolds [106, 152, 153].

### 3.3.2.3 Composite Polymeric Nanofibrous Scaffolds

Current scaffold development aims to incorporate many polymer types for the fabrication of biomaterial scaffolds that are able to respond to the biological activities of cells while meeting specific host tissue site requirements. Regardless of whether a double, triple, even quadruple polymer blend/mix is used, a tissue engineering scaffold made of a polymer blend should still retain the properties of each polymer type. Therefore, it is expected that electrospinning of a polymer blend/mix will create novel composite scaffolds with enhanced performance for tissue engineering. Another practical reason for electrospinning a blend of polymers is that often the polymer of interest cannot be electrospun into uniform fibers without the addition of the “electrospinning-driving” polymer. Regardless of the goal, the challenge of electrospinning a polymer blend is to optimize the standard electrospinning parameters, which are further complicated by the interplay of the properties of multiple polymers. Hence, a sound understanding of polymer and solvent chemistry is important in identifying favorable electrospinning parameters. Three general composite nanofibrous scaffolds, natural–natural, synthetic–synthetic, and natural–synthetic, have been developed and characterized for their properties and potential applications.

**Natural–Natural Composites** Electrospinning of multiple natural polymer blends can yield a mixture of natural nanofibers that closely mimic the native ECM. A large percentage of native tissues contains both collagen and elastin fibers that are frequently subjected to tensile and elastic loading, respectively. Electrospun fibrous scaffolds composed of collagen types I and III, and elastin have been fabricated to replicate the native ECM of blood vessels [94]. The fiber diameter found within the native ECM of blood vessels ranges from 270 to 710 nm, which is slightly larger than the 100 to 680 nm diameter range of nanofibers electrospun from blends of collagen types I and III. Aside from protein–protein mixtures, the protein-based silk and carbohydrate-based chitosan blend has been electrospun into nanofibers as well. In the silk fibroin/chitosan blend for electrospinning, the addition of chitosan increases the viscosity and conductivity of the blend solution, thus enhancing the formation of smaller, uniform nanofibers [111]. One possible explanation for

this phenomenon is that chitosan carries ionizable, amino groups, and increases the conductivity of the silk fibroin, which is ideal for electrospinning. Nevertheless, the formation of uniform nanofibers discontinues after excessive chitosan is added. Silk fibroin and chitosan in the blend solution may form hydrogen bonds, suggesting that optimizing the electrospinning of a blend natural polymer is more complicated than for pure natural polymers. It is reasonable to expect that the nanofiber mat is composed of individual, blended nanofibers rather than a mixture of different mono-polymer nanofibers.

**Synthetic–Synthetic Composites** The synthetic–synthetic blend is commonly used to fabricate scaffolds with the combined properties of composite polymers. Polymers, such as PLA and PCL, are biodegradable, biocompatible, and hydrophobic whereas poly(ethylene glycol) (PEG) is hydrophilic, non-immunogenic, and non-biodegradable. In mixing PLA and PEG, the resultant PLA/PEG blend is more hydrophilic than PLA and also more biodegradable than PEG. In addition, the co-existing properties of hydrophilicity and biodegradability can be programmed by manipulating the ratio and the type of composed polymers. For instance, PLGA nanofibrous scaffolds shrink during degradation; thus, by blending of PLGA and PEG-PLA one can effectively resist scaffold shrinkage [154]. In addition to improvements in biodegradation, the polymer blend has been shown to exhibit flexible mechanical properties that can be altered by the ratio of composed polymers. For example, the elastic PEVA nanofibrous mat becomes stiffer after PLA is added for blend electrospinning [155].

**Natural–Synthetic Composites** The mixing of natural and synthetic polymers can be a major challenge for electrospinning since solvents workable for both polymers are limited. Therefore, the choice of solvent becomes a primary consideration after determining the blend components. Many natural polymers are difficult to electrospin into nanofibers, especially when dissolved in water, since their polyelectrolyte characteristic interferes with fiber formation. One alternative is to add synthetic polymers such as PEO to facilitate nanofiber formation. The natural polymer/PEO blend in aqueous solution can be electrospun, and the use of organic solvents may be avoided. Duan et al. have systematically characterized the properties of chitosan/PEO blend solutions and their electrospun fibers [153]. They concluded that the chitosan/PEO blend retains conductivity, surface tension, and viscosity, and favors the formation of smaller, uniform nanofibers, compared with pure chitosan or PEO solutions.

Another completely different blending approach is to physically, rather than chemically, mix two polymer nanofibers together using multiple jet electrospinning. In this approach, natural and synthetic polymers are placed in two separate containers and electrospun simultaneously to form a natural/synthetic nanofibrous composite. For example, poly(vinyl alcohol) (PVA) and cellulose acetate (CA) are electrospun onto the same target area [156]. With this method, PVA and CA nanofibers disperse into each other as a direct result of physical blending. When the PVA/CA ratio of the blend is reduced, mechanical properties, such as tensile

strength and fiber elongation, are decreased, but the average fiber diameter increases. Further investigations are needed to assess whether the mechanical property changes are due to polymer composition, fiber size, or a combination of the two.

#### 3.3.2.4 **Nanofibrous Scaffolds Coated with Bioactive Molecules**

A natural ECM scaffold contains bioactive peptides, such as RGD sequences, but is often mechanically too weak or rapidly degraded for tissue engineering applications. Conversely, a synthetic polymeric scaffold has tailorable properties to meet the physical requirements, but lacks the native biocompatibility. There is, therefore, a need to develop methodologies to incorporate and optimize bioactive motifs, such as the RGD peptide, for the synthesis of biocompatible polymeric scaffolds that possess the advantages of both natural and synthetic polymers. Unlike natural–synthetic composite nanofibrous scaffolds fabricated from electrospinning a blend polymer, nanofibrous scaffolds coated with bioactive molecules are produced by coating natural polymers to the surface of synthetic nanofibrous scaffolds. This after-work addition can avoid alteration of the properties of the natural polymer during the electrospinning. The most commonly used approaches for the incorporation of bioactive agents on a polymeric surface include simple coating and covalent linking. The simple coating process is easy and fast but the coated agents detach shortly, depending on the coating surface properties, whereas the covalent linking process is more laborious but the coating should be more stable.

Collagen coated electrospun scaffolds have been developed by simply placing nanofibrous scaffolds in a collagen solution. The simple coating works for most synthetic polymers, but the efficiency and effectiveness of the coating are dependent on polymer surface properties such as charge, chemistry and geometry. Collagen type I has been coated on PCL [142] and P(LLA-CL) [157] electrospun nanofibrous scaffolds, which are used for culturing different cells for various tissue engineering applications. Although there is no direct measurement to evaluate the efficiency of the collagen coating on the scaffolds, cell response, i.e., the promotion of specific biological activities, indirectly demonstrates the presence of collagen coating on electrospun fibrous scaffolds.

Electrospun nanofibrous scaffolds made of either hydrophobic or hydrophilic synthetic polymers are usually inert and lack functional groups for direct covalent linkage of bioactive peptides or domains. To create functional groups for the covalent bonding, surface processing techniques, such as acid/base treatment, chemical activation, and oxidization, are used. For instance, studies have reported on the modification of PET nanofiber surfaces by gelatin grafting [98]. The process starts with the creation of hydroxyl groups on PET nanofibers using formaldehyde, grafts with methacrylic acid, and covalent linkage of gelatin using carbodiimide. The results show that more gelatin is grafted to PET nanofibers than to the film counterpart, and the grafting occurs throughout the entire scaffold surface. In addition, gelatin grafting significantly increases the hydrophilicity of the PET surface, suggesting that covalently grafting bioactive proteins or peptides to a nanofibrous scaffold is an effective approach for the modification of the hydrophobic properties of the scaffold.

### 3.3.3

## Engineered Tissues using Electrospun Nanofibrous Scaffolds

### 3.3.3.1 Skin

Skin is the largest tissue covering the body and provides physical and chemical protection of the body from harmful sources such as heat and microbial organisms. The top layer is the epidermis containing melanocytes and the dermis lies directly underneath the epidermis.

In the body, cells and tissue matrices interact via complex chemical and physical processes. Due to the sophisticated architecture of the skin with its various layers, it is difficult for current synthetic 3D matrices to simulate such processes. Therefore, electrospinning has been used to spin natural and synthetic polymers to fabricate biomaterial scaffolds that more closely mimic the tissue matrix of skin. In a study by Venugopal et al., PCL, collagen type I, and collagen type I-coated PCL nanofibers were electrospun to fabricate a substitute for skin regeneration [144]. In this study, fibroblasts from normal human skin attached and spread on all three nanofiber matrices; however, the interaction between cells and nanofiber matrices varied with the scaffold material. For instance, collagen nanofiber matrices showed a significantly higher level of fibroblast proliferation than control monolayer culture. Conversely, PCL fibers showed a significantly lower level of cellular proliferation than control monolayer culture. The results of this study also showed normal morphology and confluence of cells on control monolayer culture and collagen nanofibers. However, while PCL nanofibers were able to support cell growth, they showed no confluence compared with collagen coated PCL nanofibers. As a result, this study proved that PCL fibers are able to partially support the growth of skin fibroblasts, while the presence of collagen on the scaffolds greatly enhances the interactions between cells and nanofibers. The advantage of using a collagen coated PCL composite nanofibrous scaffold is to incorporate the biological and mechanical properties of each polymer, with collagen type I providing a favorable milieu for skin fibroblasts and biodegradable PCL improving the mechanical integrity of the matrix. Therefore, electrospun 3D nanometer sized fibers provide a potential scaffold for skin regeneration. Min et al. electrospun silk fibroin into nanofibers and then coated the fibers with collagen type I, fibronectin, and laminin to evaluate cell response to different ECM coatings on silk fibroin nanofibers [109]. In addition, they also used different cell types, human oral and epithelial keratinocytes and gingival fibroblasts, to measure cell attachment and spreading on the nanofibers. In terms of the effect of various ECM coatings, collagen type I coated nanofibers were shown to more actively promote attachment of keratinocytes, compared with laminin or fibronectin coated nanofibers, and, interestingly, even to a polystyrene surface. Cells adhered to and spread on the surface of silk fibroin nanofibers, and then started to migrate along the fibers, forming a 3D cellular network well integrating with nanofibers. The similar cellular response in a nanofiber scaffold is also demonstrated in the previous study using fibroblasts in PLGA nanofibers [25]. Beside the attempt of using silk fibroin nanofibers as scaffolds for skin regeneration, chitin/PLGA nanofibrous scaffolds cultured with keratinocytes

and fibroblasts have also shown great promise in skin tissue engineering since chitin has proved to have good wound healing properties [158]. The chitin/PLGA nanofibrous scaffolds, taking advantages of the desired properties of chitin and PLGA for tissue engineered scaffolds, exhibit improved hydrophilicity and sound mechanical properties. Cells attach better in the chitin/PLGA than the PLGA-only nanofibrous scaffolds. In the preliminary cell study, the same cell types used in the silk fibroin scaffolds show a similar trend of cell attachment and spreading in various ECM coated chitin/PLGA nanofibrous scaffolds. Collagen type I coated chitin/PLGA nanofibrous scaffolds enhances cell attachment and spreading in the scaffolds, which is critical for cellular activities in skin regeneration using the tissue engineering approach.

#### 3.3.3.2 Blood Vessel

Blood vessels are a part of the circulation system, and function as a channel to transport oxygen and nutrient to the body tissues or remove metabolic waste for replenishment. There are three types of blood vessels found in the body: arteries, veins, and capillaries. Each of them has a different structure and various functions. Vascular related disorders are one of the leading fatal diseases around the world, and one of the current treatments is the use of vascular grafts in bypass surgeries. In terms of material types, grafts are either biological (autograft, allograft, and xenograft) or synthetic. Although there is fair success with these conventional grafts, challenges such as the availability of small vascular grafts still remain. Vascular tissue engineering is promising for creating cellular vascular grafts with desired dimensions.

The tissue engineered artery fabricated using electrospun scaffolds has been extensively investigated recently. Boland et al. have fabricated a vascular scaffold by assembling two electrospun nanofibrous tubes composed of different collagen/elastin ratios with cultured dermal fibroblasts, aortic smooth muscle cells, and umbilical vein endothelial cells in the outer, middle, and inner layers of the scaffold, respectively, to simulate the anatomical three layers of an artery [94]. After culturing in a bioreactor, the engineered artery exhibits a tri-cellular layer architecture in cross section. One of the critical requirements for tissue engineered arteries is to have satisfactory mechanical properties to bear compliance strength and burst pressure. Therefore, Stitzel et al. blended PLGA with collagen and elastin to produce an electrospun tri-polymeric fibrous scaffold, thus increasing the strength of the original collagen/elastin scaffold and rendering it mechanically comparable to a native artery [102]. Both endothelial and smooth muscle cells cultured in the scaffolds exhibit favorable cell attachment and growth. Further *in vivo* testing found no signs of toxicity. In addition to studies that focus on the design of a tissue engineered vascular graft, several studies have reported the effects of surface roughness and fiber orientation on the cellular activities of vascular cells [159, 160]. Xu et al. have demonstrated that endothelial cells cultured on electrospun fibrous scaffolds exhibit less-spread cell morphology, compared with those on smooth surfaces [159]. An increase in cell attachment and proliferation was also observed on the smooth surface culture. Another study has shown that smooth

muscle cells exhibit a spindle-like contractile phenotype, while cytoskeletal proteins, such as  $\alpha$ -actin and myosin filaments, are oriented along the direction of aligned nanofibers [160]. Fiber alignment using electrospinning supports the construction of a tissue engineered vascular graft that contains a middle, smooth muscle layer that mimics the circumferentially oriented nature.

### 3.3.3.3 Cartilage

Adult cartilage is formed mainly at the articular joint and is a specialized tissue that consists of chondrocytes, ECM macromolecules, and water. Chondrocytes synthesize and maintain the ECM in cartilage while the ECM functions to provide structural protection to residing cells and to act as a regulatory messenger for cell activities. Cartilage tissue engineering aims to replace damaged cartilage and restore biological function. A main research focus in our laboratory is the development of cartilage tissue engineering using the electrospinning technique.

We have recently compared the biological response of chondrocytes seeded onto 3D PCL nanofibrous scaffolds to that of cells seeded as monolayers on standard tissue culture polystyrene (TCPS) [77]. Gene expression analysis (Fig. 3.5) showed that chondrocytes seeded on the nanofibrous scaffold maintained their chondrocytic phenotype by expressing cartilage-specific ECM genes, including collagen types II and IX, aggrecan, and COMP. Specifically, expression of the collagen type IIB spliced variant transcript, indicative of the mature chondrocyte phenotype, was significantly up-regulated. Chondrocytes exhibited a round shape on the nanofibrous scaffolds, in contrast to a flat, well-spread morphology seen in monolayer

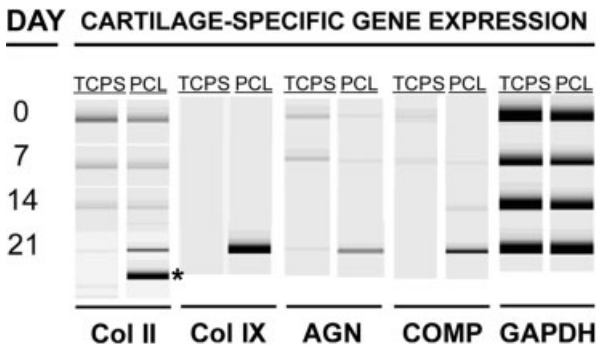


**Fig. 3.5.** Reverse transcription-polymerase chain reaction (RT-PCR) analysis of expression of cartilage associated genes in fetal bovine chondrocytes seeded onto tissue culture polystyrene (TCPS) or PCL nanofibrous scaffolds. On culture days 0, 7, 14, and 21 total RNA was extracted and RT-PCR performed with gene-specific primer pairs, including collagen type II (Col II), collagen IX (Col IX), aggrecan (AGN), cartilage oligomeric matrix protein

(COMP), and glyceraldehyde-3-phosphate dehydrogenase (GAPDH) as a house keeping gene. Cells cultured on nanofibrous scaffolds showed strong induction of mRNA expression of collagen types II and IX, aggrecan, and COMP after 21 days. More importantly, the alternatively spliced mRNA variant of collagen type II, the IIB(\*), was expressed only in the nanofibrous scaffold cultures.

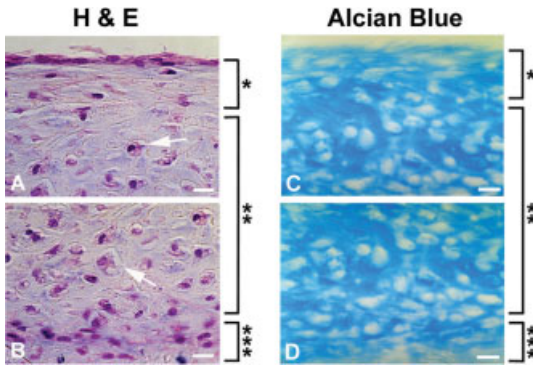


**Fig. 3.6.** Histological analysis of MSC cultures seeded into a PCL nanofibrous scaffold and maintained in a chondrogenic medium supplemented with TGF- $\beta$ 1 for 21 days. Sections from the upper and lower portions of the 3D constructs were stained with hematoxylin and eosin (H&E) (A, B) and Alcian blue (C, D). H&E staining showed flat fibroblast-like cells on the top zone (\*), round chondrocyte-like cells embedded in lacunae (arrows) in the middle zone (\*\*), and small, flat cells at the bottom zone (\*\*\*). Alcian blue staining showed the presence of sulfated proteoglycan-rich ECM in the construct. Bar = 10  $\mu$ m.

cultures on TCPS. Histologically, nanofibrous cultures produced more sulfated proteoglycan-rich, cartilaginous matrix than monolayer cultures. These results indicate that the biological activities of chondrocytes are crucially dependent on the dimensionality of the extracellular scaffolds, and that nanofibrous PCL may be a biologically preferred scaffold/substrate for proliferation and phenotype maintenance of chondrocytes.

In another study [140], we specifically compare the chondrogenic activities of MSC–nanofiber cultures to those of high-density cell pellet cultures, a commonly used culture system for studying chondrogenesis of MSCs *in vitro*. MSCs cultured in nanofibrous scaffolds in the presence of TGF- $\beta$ 1 differentiate into a chondrocytic phenotype, as evidenced by chondrocyte-specific gene expression and the synthesis of cartilage-associated ECM proteins. The level of chondrogenesis observed in MSCs seeded within nanofibrous scaffolds is comparable to that observed for MSCs maintained as cell aggregates or pellets. The 3D MSC-seeded constructs display a cartilage-like morphology, containing chondrocyte-like cells surrounded by abundant cartilaginous matrix (Fig. 3.6). Due to the physical nature and improved mechanical properties of nanofibrous scaffolds, particularly in comparison to cell pellets, these findings suggest that the nanofibrous scaffold is a practical carrier for MSC transplantation, and represents a candidate scaffold for cell-based tissue engineering approaches to cartilage repair.

#### 3.3.3.4 Bone

Bone is a hard, solid connective tissue that provides structure and protection to the body. To support external loading and absorb shocks, bone has a unique structure



and chemical composition. The bone structure is composed of two layers of different density of bones. The outer layer is compact bone and the inner layer being spongy bone. Bone is always undergoing dynamic remodeling carried out by two different cell types, the osteoblast for building bone and the osteoclast for digesting bone. In addition, the bone marrow contains numerous MSCs that are capable of differentiating into various connective tissue cells to replenish them.

Cells used in bone tissue engineering include osteoblasts, osteoprogenitor cells, and MSCs. Each of these cell types, depending on their nature, requires a different culture environment. MSCs are a highly promising cell source for tissue engineering applications because of their multi-differentiation capabilities and their expandability [81]. Applications of MSCs for bone tissue engineering requires that the cells are seeded within electrospun nanofibrous scaffolds that will permit and/or promote osteogenic differentiation. Yoshimoto et al. and Shin et al. have reported on the osteogenic differentiation of MSCs in PCL nanofibrous scaffolds cultured *in vitro* and *in vivo* [137, 138]. In their study, MSCs from rat bone marrow seeded in PCL nanofibrous scaffolds are cultured in a rotatory oxygen-permeable bioreactor with the osteogenic medium. This environment promotes MSCs to differentiate into osteoblast-like cells producing collagen type I and minerals in the scaffold. In addition, the bioreactor improves oxygen and nutrients diffusion, enhancing cell growth in the nanofibrous scaffold. Initial osteogenic differentiation of MSCs is carried out in the *in vitro* model. Further assessment of bone formation included implanting the MSC loaded nanofibrous scaffold pre-induced and -cultured in a bioreactor in a rat model. The new osteo-matrix is deposited throughout the entire harvested cellular constructs, resulting in a white, smooth appearance and stiffer properties. The preliminary results of new bone formation using MSC–nanofiber constructs are encouraging. To actively induce bone formation, osteoconductive calcium carbonate has been coelectrospun with PCL nanofiber to fabricate a nanofibrous composite scaffold. The addition of calcium carbonate increases the mineralization in the cellular constructs, an early sign of bone formation. The composite scaffold combining the osteogenic promotion of nanofibers and the osteoconductivity of calcium carbonate is also suggested for guided bone regeneration therapy to repair jaw and alveolar bone defects.

#### 3.3.3.5 Muscle

Muscles make up most of the body and account for almost half of body weight. Skeletal muscle covering the skeleton functions to move the body, cardiac muscle making up the heart contracts in a rhythmic movement, and smooth muscle forming internal organs perform the unconscious actions. The three types of muscles are composed of different kinds of cells and ECM protein compositions.

Skeletal muscle tissue is composed of bundles of highly oriented and dense muscle fibers, each representing a multinucleated cell derived from myoblasts. Therefore, the engineering of skeletal muscle tissue necessitates the use of a bio-material scaffold that will allow cells to align parallel to one another. Electrospinning, as previously illustrated, provides a technique that not only can generate nanoscale non-woven fibers, but this technique also offers the versatility of align-

ing fibers to yield an ideal scaffold architecture for skeletal muscle tissue engineering. In a study by Riboldi et al., DegraPol®, a degradable block polyesterurethane, was electrospun to fabricate a biomaterial scaffold to engineer skeletal muscle tissue using mouse C2C12 muscle progenitor cells [161]. Preliminary experiments in this study found C2C12 line cells to be compatible with the electrospun scaffold by adhering, proliferating, and differentiation into myotubes on the electrospun scaffolds [161]. More specifically, the authors showed that after 3 days of culture of C2C12 cells in differentiation medium there was formed elongated, multinucleated, myosin heavy chain expressing myotubes that preferentially aligned with the direction of the scaffold fibers. C2C12 cells were also viable on the electrospun scaffold up to 7 days of culture. By aligning myofibers to one another, scaffolds may be engineered with the ability to generate sufficient force for contraction of differentiated C2C12 cells. While the tendency of utilizing microfibrinous polymeric scaffolds has yielded promising results in driving myofibers development and orientation along the scaffold, the high tensile modulus and low-yield elongation of these microfibrinous polymeric scaffolds is inadequate to withstand the mechanical stimulation needed for dynamic culturing methods needed for skeletal muscle tissue engineering [161–163].

A critical factor for successful regeneration of myocardium in a tissue engineered scaffold is that the scaffold structure should be flexible for cardiomyocyte contraction, sustain a reasonable tension for cell morphology maintenance, and have a good integrity for handling. To fulfill this purpose, Shin et al. have cultured primary cardiomyocytes from rat ventricles on PCL nanofiber suspended wire rings [139]. Interestingly, unlike a rigid scaffold, the flexibility of the nanofibrous network applies limited restriction on cell contraction. The cardiomyocytes on the nanofibers start the ubiquitous and synchronized contraction after 3 days of culture. In addition, cells within the scaffold exhibit spindle, multi-angular muscle-cell-like morphology, and also express cardiac-specific markers such as tropomyosin and connexin43. The wire ring applies a tensile force on the suspended nanofibers, which may be transferred to stretch cells, which is critical for the maturation of the cardiomyocyte. In another study, rat cardiac fibroblasts are cultured in acid-treated PGA scaffolds to evaluate the proliferation of cells cultured in PGA scaffolds with different fiber sizes and surface chemistry [130]. Cells proliferate significantly more rapidly in acid treated, smaller nanofibers, suggesting that the acid treated surface exposes more carboxylic and hydroxylic groups that favorably attract cell attachment molecules, such as fibronectins and vitronectins, to enhance cell attachment; thus more cells can grow on a bigger surface area in a scaffold with smaller fibers.

Functional tissue engineered smooth muscle is essential for the development of complex tissue engineered organs. Flexible, anisotropic properties of smooth muscle provide internal organs the capability of constant movement and the expansion for additional content storage. Electrospinning has been applied to microintegrate smooth muscle cells into nanofibrous scaffolds to fabricate a cell–nanofiber composite [44]. The mechanical properties of the composite are in an adequate range to meet the requirements for soft tissue application. After culturing in a perfusion

bioreactor, the cellular composite exhibits a high density of smooth muscle cells in a uniform distribution. The smooth muscle is successfully engineered by the microintegration process based on the electrospinning, which can be adopted to tissue engineer other tissues as well.

#### 3.3.3.6 Ligament

The ability of electrospun nanofibrous scaffolds to mimic the architectural scale of the native ECM provides them with great potential for the engineering of ligaments. The ligament is a tough fibrous band of slightly elastic connective tissue that provides stability to skeletal joints. The specialized cells that make up ligaments are called fibroblasts. The matrix of ligaments is made up of collagen fibrils with a diameter of  $\sim 60$  nm; therefore, nanofibrous scaffolds should provide ligament fibroblasts with a structure that closely mimics the native matrix [164]. A study investigating the effects of fiber alignment on the ECM generation of human ligament fibroblasts (HLF) on PU electrospun nanofibers showed that cells cultured on aligned nanofibers were spindle-shaped and oriented in the nanofiber direction, while cells on non-aligned nanofibers had no directionality [164]. After 7 days of culture, HLF cells on aligned nanofibers showed a significant change in their ECM with increase collagen synthesis compared with non-aligned fibers, although cell proliferation was not affected by fiber directionality [164]. A significant increase in cell attachment and proliferation on nanofiber scaffolds was also observed, as compared with cast PU membranes. Therefore, this study demonstrates that the biomimetic nature of aligned electrospun nanofibers provides an architectural environment similar to that which ligament fibroblasts normally encounter *in vivo*.

#### 3.3.3.7 Nerve

Unlike other parts of the body, the central nervous system (CNS) cannot generate new neurons or regenerate damaged nerves itself. Cell-based tissue engineering strategies using multipotential cells have been investigated as a therapy for specific neurologic disorders (i.e., paralysis of extremities). Due to the complexity of the architectural organization of the CNS, polymeric scaffolds should provide a suitable 3D carrier for cell delivery. Electrospinning presents a sophisticated technique to fabricate an ECM-like matrix. Recent studies have investigated the potential of electrospun 3D scaffolds, both aligned and non-aligned, in neural tissue engineering using a multipotent neural stem cell (NSC) line, C17-2, derived from a neonatal mouse cerebellum [76, 165]. Yang et al. have investigated the morphology and cell adhesion response of NSC to PLLA non-aligned nanofibrous scaffolds [165]. Phase-contrast microscopy revealed that C17-2 cells seeded on the scaffolds adhered to the scaffolds and started to differentiate on the fibrous scaffold 10 h after seeding, and by 24 h around 70% of cells exhibited a spindle-like shape with extended processes. An additional study by Yang et al. compared the response of C17-2 cells to aligned versus non-aligned electrospun PLLA nanofibers [76], and reported that after 2 days of culture significant changes in the phenotype of cells based on directionality had occurred.

Successful nerve regeneration is dependent upon extensive growth of axonal processes. The study by Yang et al. found no significant effect of fiber alignment when comparing aligned (1.5  $\mu\text{m}$ ) and non-aligned (1.25  $\mu\text{m}$ ) microfibrinous scaffolds. However, the directionality did have an effect when comparing aligned (300 nm) and non-aligned (250 nm) nanofibrous scaffolds. The results indicate that the presence or absence of a directionality effect is dependent on architectural scale. The average neurite length of C17-2 cells on aligned nanofibrous scaffolds was calculated as 100  $\mu\text{m}$  and 75–80  $\mu\text{m}$  on aligned and non-aligned microfibrinous scaffolds, respectively. These results show a significant relationship of a decrease in fiber diameter increasing neurite outgrowth.

### 3.4 Current Challenges and Future Directions

To date, many different polymers have been successfully electrospun and characterized for numerous intended applications. However, limited progress has been made on fabricating tissues using nanofibrous scaffolds. Unlike nanofiber applications in composites and electronics, tissue engineering applications of nanofibrous polymeric scaffolds still require further extensive biological analyses in addition to physical characterization to determine if they are suitable for the promotion of tissue growth. Recent studies have focused on the introduction of different new polymers for electrospinning, as well as testing and characterizing the physical properties of electrospun nanofibrous polymeric scaffolds, with less emphasis on biological evaluation. To move to the next developmental phase of nanofibrous scaffold-based tissue engineering, cellular and molecular analyses are necessary to understand the interaction between nanofibers and cells. A better understanding of cell–nanofiber interactions, based on the structural and functional similarity between nanofibers and native ECM, is critical to successful tissue engineering.

Functional nanofibrous scaffolds providing structural and mechanical support for tissue growth as well as actively inducing favorable biological activities should be the future aim of research on electrospun nanofibrous scaffolds. Peptide domains, such as RGD on ECM molecules, bind to cell surface receptors, activating cellular signaling pathways to elicit cellular response. Therefore, to promote cellular activities, efforts should be devoted to developing methodologies to incorporate and optimize bioactive motifs or peptides into the electrospun nanofibrous scaffold, ultimately creating biologically active scaffolds. In addition to matrix-bound signal proteins on ECM, soluble bioactive molecules such as growth factors are important for the regulation of cellular events, including proliferation and differentiation [166]. Biodegradable polymers have long been used as drug delivery systems to deliver therapeutic agents because they can be designed to undergo programmed degradation in a controlled fashion [167]. Incorporation of growth factors, such as transforming growth factor-beta (TGF- $\beta$ ) or insulin-like growth factor (IGF), into a nanofibrous scaffold may be used as an additional strategy for the control of tissue growth. Ideally, it is desirable to fabricate nanofibrous scaffolds

that are capable of releasing, in a controlled manner, one or more growth factors to act on specific cellular functions at different times. A nanofibrous scaffold housing multiple growth factors may be produced using a selected combination of biodegradable polymers, each releasing one or more specifically adsorbed growth factors as a function of its own degradation profile. These characteristics, once optimized and taken together with the “tissue-engineering”-friendly nature of the nanofibrous scaffold, should make this a highly promising candidate scaffold system for tissue regeneration applications.

### 3.5

#### Conclusion

Electrospinning technology is a useful, economical, and easily set-up means of fabricating of 3D, highly porous, nanofibrous scaffolds that have been shown to support cellular activities and tissue formation. Conversely, tissue engineering is a revolutionary, cell-based therapy with a higher promise for clinical applications. Together, tissue engineering and regeneration with the application of electrospun polymeric nanofibers is an exciting example of the power of the rapidly emerging field of nanotechnology.

#### References

- 1 LANGER R, VACANTI JP. Tissue engineering. *Science* **1993**, 260, 920–926.
- 2 HUTMACHER DW. Scaffold design and fabrication technologies for engineering tissues – state of the art and future perspectives. *J. Biomater. Sci. Polym. Ed.* **2001**, 12, 107–124.
- 3 LEE JH, JUNG HW, KANG IK, LEE HB. Cell behaviour on polymer surfaces with different functional groups. *Biomaterials* **1994**, 15, 705–711.
- 4 BHARDWAJ T, PILLIAR RM, GRYNPAS MD, KANDEL RA. Effect of material geometry on cartilagenous tissue formation in vitro. *J. Biomed. Mater. Res.* **2001**, 57, 190–199.
- 5 ZHANG S. Fabrication of novel biomaterials through molecular self-assembly. *Nat. Biotechnol.* **2003**, 21, 1171–1178.
- 6 HERSEL U, DAHMEN C, KESSLER H. RGD modified polymers: biomaterials for stimulated cell adhesion and beyond. *Biomaterials* **2003**, 24, 4385–4415.
- 7 FLEMMING RG, MURPHY CJ, ABRAMS GA, GOODMAN SL, NEALEY PF. Effects of synthetic micro- and nano-structured surfaces on cell behavior. *Biomaterials* **1999**, 20, 573–588.
- 8 ELSDALE T, BARD J. Collagen substrata for studies on cell behavior. *J. Cell Biol.* **1972**, 54, 626–637.
- 9 CUKIERMAN E, PANKOV R, STEVENS DR, YAMADA KM. Taking cell-matrix adhesions to the third dimension. *Science* **2001**, 294, 1708–1712.
- 10 ABBOTT J, HOLTZER H. The loss of phenotypic traits by differentiated cells. 3. The reversible behavior of chondrocytes in primary cultures. *J. Cell Biol.* **1966**, 28, 473–487.
- 11 BENYA PD, SHAFFER JD. Dedifferentiated chondrocytes reexpress the differentiated collagen phenotype when cultured in agarose gels. *Cell* **1982**, 30, 215–224.
- 12 LEVENBERG S, HUANG NF, LAVIK E,

- ROGERS AB, ITSKOVITZ-ELDOR J, LANGER R. Differentiation of human embryonic stem cells on three-dimensional polymer scaffolds. *Proc. Natl. Acad. Sci. U.S.A.* **2003**, *100*, 12 741–12 746.
- 13 CUKIERMAN E, PANKOV R, YAMADA KM. Cell interactions with three-dimensional matrices. *Curr. Opin. Cell Biol.* **2002**, *14*, 633–639.
- 14 SINHA RK, MORRIS F, SHAH SA, TUAN RS. Surface composition of orthopaedic implant metals regulates cell attachment, spreading, and cytoskeletal organization of primary human osteoblasts in vitro. *Clin. Orthop.* **1994**, 258–272.
- 15 DALBY MJ, RIEHLE MO, JOHNSTONE H, AFFROSSMAN S, CURTIS AS. In vitro reaction of endothelial cells to polymer demixed nanotopography. *Biomaterials* **2002**, *23*, 2945–2954.
- 16 DALBY MJ, RIEHLE MO, JOHNSTONE HJ, AFFROSSMAN S, CURTIS AS. Polymer-demixed nanotopography: control of fibroblast spreading and proliferation. *Tissue Eng.* **2002**, *8*, 1099–1108.
- 17 WEBSTER TJ, SIEGEL RW, BIZIOS R. Osteoblast adhesion on nanophase ceramics. *Biomaterials* **1999**, *20*, 1221–1227.
- 18 WEBSTER TJ, ERGUN C, DOREMUS RH, SIEGEL RW, BIZIOS R. Enhanced functions of osteoblasts on nanophase ceramics. *Biomaterials* **2000**, *21*, 1803–1810.
- 19 ELIAS KL, PRICE RL, WEBSTER TJ. Enhanced functions of osteoblasts on nanometer diameter carbon fibers. *Biomaterials* **2002**, *23*, 3279–3287.
- 20 HUANG ZM, ZHANG YZ, KOTAKI M, RAMAKRISHNA S. A review on polymer nanofibers by electrospinning and their applications in nanocomposites. *Composites Sci. Technol.* **2003**, *63*, 2223–2253.
- 21 NAIR LS, BHATTACHARYYA S, LAURENCIN CT. Development of novel tissue engineering scaffolds via electrospinning. *Expert Opin. Biol. Ther.* **2004**, *4*, 659–668.
- 22 LI WJ, MAUCK RL, TUAN RS. Electrospun nanofibrous scaffolds: Production, characterization, and applications for tissue engineering and drug delivery. *J. Biomed. Nanotechnol.* **2005**, *1*, 259–275.
- 23 MA Z, KOTAKI M, INAI R, RAMAKRISHNA S. Potential of nanofiber matrix as tissue-engineering scaffolds. *Tissue Eng.* **2005**, *11*, 101–109.
- 24 VENUGOPAL J, RAMAKRISHNA S. Applications of polymer nanofibers in biomedicine and biotechnology. *Appl. Biochem. Biotechnol.* **2005**, *125*, 147–158.
- 25 LI WJ, LAURENCIN CT, CATERSON EJ, TUAN RS, KO FK. Electrospun nanofibrous structure: A novel scaffold for tissue engineering. *J. Biomed. Mater. Res.* **2002**, *60*, 613–621.
- 26 SMITH LA, MA PX. Nano-fibrous scaffolds for tissue engineering. *Colloids Surf. B Biointerfaces* **2004**, *39*, 125–131.
- 27 WHITESIDES GM, BONCHEVA M. Beyond molecules: self-assembly of mesoscopic and macroscopic components. *Proc. Natl. Acad. Sci. U.S.A.* **2002**, *99*, 4769–4774.
- 28 ZHANG S, MARINI DM, HWANG W, SANTOSO S. Design of nanostructured biological materials through self-assembly of peptides and proteins. *Curr. Opin. Chem. Biol.* **2002**, *6*, 865–871.
- 29 SILVA GA, CZEISLER C, NIECE KL, BENIASH E, HARRINGTON DA, KESSLER JA, STUPP SI. Selective differentiation of neural progenitor cells by high-epitope density nanofibers. *Science* **2004**, *303*, 1352–1355.
- 30 KISIDAY J, JIN M, KURZ B, HUNG H, SEMINO C, ZHANG S, GRODZINSKY AJ. Self-assembling peptide hydrogel fosters chondrocyte extracellular matrix production and cell division: Implications for cartilage tissue repair. *Proc. Natl. Acad. Sci. U.S.A.* **2002**, *99*, 9996–10 001.
- 31 RAYLEIGH JWG. *Lond. Edinburgh Dublin Phil. Mag.* **1882**, *14*, 184.
- 32 ZELENY J. The electrical discharge from liquid points, and a hydrostatic method of measuring the electric intensity at their surface. *Phys. Rev.* **1914**, *3*, 69–91.

- 33 ZELENY J. Instability of electrified liquid surface. *Phys. Rev.* **1917**, 10, 1–6.
- 34 DOLE M, MACK LL, HINES RL. Molecular beams of macroions. *J. Chem. Phys.* **1968**, 49, 2240–2249.
- 35 VONNEGUT B, NEUBAUER RL. *J. Colloid Sci.* **1952**, 7, 616.
- 36 DROZIN VG. The electrical dispersion of liquids as aerosols. *J. Colloid Sci.* **1955**, 7, 616.
- 37 Patent 1,975,504. **1934**.
- 38 Patent 3,280,229. **1966**.
- 39 BAUMGARTEN PK. Electrostatic spinning of acrylic microfibers. *J. Colloid Interface Sci.* **1971**, 36, 71–79.
- 40 LARRONDO L, MANLEY RSJ. Electrostatic fiber spinning from polymer melts. 1. Experimental observations on fiber formation and properties. *J. Polym. Sci. Part B – Polym. Phys.* **1981**, 19, 909–920.
- 41 LARRONDO L, MANLEY RSJ. Electrostatic fiber spinning from polymer melts. 2. Examination of the flow field in an electrically driven jet. *J. Polym. Sci. Part B – Polym. Phys.* **1981**, 19, 921–932.
- 42 LARRONDO L, MANLEY RSJ. Electrostatic fiber spinning from polymer melts. 3. Electrostatic deformation of a pendant drop of polymer melt. *J. Polym. Sci. Part B – Polym. Phys.* **1981**, 19, 933–940.
- 43 KIDOAKI S, KWON IK, MATSUDA T. Mesoscopic spatial designs of nano- and microfiber meshes for tissue-engineering matrix and scaffold based on newly devised multilayering and mixing electrospinning techniques. *Biomaterials* **2005**, 26, 37–46.
- 44 STANKUS JJ, GUAN J, FUJIMOTO K, WAGNER WR. Microintegrating smooth muscle cells into a biodegradable, elastomeric fiber matrix. *Biomaterials* **2006**, 27, 735–744.
- 45 TAYLOR GI. Electrically driven jets. *Proc. R. Soc. (London)* **1969**, 453–475.
- 46 TAYLOR GI. Disintegration of water drops in an electric field. *Proc. R. Soc. (London)* **1964**, 383–397.
- 47 DOSHI J, RENEKER DH. Electrospinning process and applications of electrospun fibers. *J. Electrostatics* **1995**, 35, 151–160.
- 48 FONG H, CHUN I, RENEKER DH. Beaded nanofibers formed during electrospinning. *Polymer* **1999**, 40, 4585–4592.
- 49 LIU HQ, HSIEH YL. Ultrafine fibrous cellulose membranes from electrospinning of cellulose acetate. *J. Polym. Sci. Part B – Polym. Phys.* **2002**, 40, 2119–2129.
- 50 DEITZEL JM, KLEINMEYER J, HARRIS D, TAN NCB. The effect of processing variables on the morphology of electrospun nanofibers and textiles. *Polymer* **2001**, 42, 261–272.
- 51 DEMIR MM, YILGOR I, YILGOR E, ERMAN B. Electrospinning of polyurethane fibers. *Polymer* **2002**, 43, 3303–3309.
- 52 ZONG XH, KIM K, FANG DF, RAN SF, HSIAO BS, CHU B. Structure and process relationship of electrospun bioabsorbable nanofiber membranes. *Polymer* **2002**, 43, 4403–4412.
- 53 LEE KH, KIM HY, KHIL MS, RA YM, LEE DR. Characterization of nanostructured poly( $\epsilon$ -caprolactone) nonwoven mats via electrospinning. *Polymer* **2003**, 44, 1287–1294.
- 54 CHOI JS, LEE SW, JEONG L, BAE SH, MIN BC, YOUK JH, PARK WH. Effect of organosoluble salts on the nanofibrous structure of electrospun poly(3-hydroxybutyrate-co-3-hydroxyvalerate). *Int. J. Biol. Macromol.* **2004**, 34, 249–256.
- 55 ZONG X, KIM K, FANG D, RAN S, HSIAO BS, CHU B. Structure and process relationship of electrospun bioabsorbable nanofiber membranes. *Polymer* **2002**, 43, 4403–4412.
- 56 SHIN YM, HOHMAN MM, BRENNER MP, RUTLEDGE GC. Experimental characterization of electrospinning: The electrically forced jet and instabilities. *Polymer* **2001**, 42, 9955–9967.
- 57 THERON A, ZUSSMAN E, YARIN AL. Electrostatic field-assisted alignment of electrospun nanofibres. *Nanotechnology* **2001**, 12, 384–390.

- 58 LI D, OUYANG G, MCCANN JT, XIA Y. Collecting electrospun nanofibers with patterned electrodes. *Nano Lett.* **2005**, *5*, 913–916.
- 59 LI WJ, MAUCK R, COOPER JA, TUAN RS. Engineering anisotropy in electrospun biodegradable nanofibrous scaffolds for musculoskeletal tissue engineering. In: 5th Combined Meeting of the Orthopaedic Research Societies of Canada, USA, Japan, and Europe, Banff, Alberta, Canada, 2004.
- 60 MUSCHLER GF, NAKAMOTO C, GRIFFITH LG. Engineering principles of clinical cell-based tissue engineering. *J. Bone Joint Surg. Am.* **2004**, *86-A*, 1541–1558.
- 61 LEE YH, LEE JH, AN IG, KIM C, LEE DS, LEE YK, NAM JD. Electrospun dual-porosity structure and biodegradation morphology of montmorillonite reinforced PLLA nanocomposite scaffolds. *Biomaterials* **2005**, *26*, 3165–3172.
- 62 HUBBELL JA. Biomaterials in tissue engineering. *Biotechnology (N Y)* **1995**, *13*, 565–576.
- 63 TAN EP, NG SY, LIM CT. Tensile testing of a single ultrafine polymeric fiber. *Biomaterials* **2005**, *26*, 1453–1456.
- 64 SANDERS JE, NICHOLSON BS, MITCHELL SB, LEDGER RE. Polymer microfiber mechanical properties: A system for assessment and investigation of the link with fibrous capsule formation. *J. Biomed. Mater. Res. A* **2003**, *67*, 1412–1416.
- 65 GRINNELL F. Cellular adhesiveness and extracellular substrata. *Int. Rev. Cytol.* **1978**, *53*, 65–144.
- 66 GIANCOTTI FG, RUOSLAHTI E. Integrin signaling. *Science* **1999**, *285*, 1028–1032.
- 67 SMETANA K, JR. Cell biology of hydrogels. *Biomaterials* **1993**, *14*, 1046–1050.
- 68 BOYAN BD, HUMMERT TW, DEAN DD, SCHWARTZ Z. Role of material surfaces in regulating bone and cartilage cell response. *Biomaterials* **1996**, *17*, 137–146.
- 69 LOESER RF. Chondrocyte integrin expression and function. *Biorheology* **2000**, *37*, 109–116.
- 70 NIKOLOVSKI J, MOONEY DJ. Smooth muscle cell adhesion to tissue engineering scaffolds. *Biomaterials* **2000**, *21*, 2025–2032.
- 71 WOO KM, CHEN VJ, MA PX. Nanofibrous scaffolding architecture selectively enhances protein adsorption contributing to cell attachment. *J. Biomed. Mater. Res.* **2003**, *67A*, 531–537.
- 72 BUCKWALTER JA, MANKIN HJ. Articular cartilage: Tissue design and chondrocyte-matrix interactions. *Instr. Course Lect.* **1998**, *47*, 477–486.
- 73 SCULLY SP, LEE JW, GHERT PMA, QI W. The role of the extracellular matrix in articular chondrocyte regulation. *Clin. Orthop.* **2001**, *S72*–89.
- 74 GRAY ML, PIZZANELLI AM, GRODZINSKY AJ, LEE RC. Mechanical and physicochemical determinants of the chondrocyte biosynthetic response. *J. Orthop. Res.* **1988**, *6*, 777–792.
- 75 LI WJ, JIANG YJ, TUAN RS. Chondrocyte phenotype in engineered fibrous matrix is regulated by fiber size. *Tissue Eng.* in the press.
- 76 YANG F, MURUGAN R, WANG S, RAMAKRISHNA S. Electrospinning of nano/micro scale poly(L-lactic acid) aligned fibers and their potential in neural tissue engineering. *Biomaterials* **2005**, *26*, 2603–2610.
- 77 LI WJ, DANIELSON KG, ALEXANDER PG, TUAN RS. Biological response of chondrocytes cultured in three-dimensional nanofibrous poly(epsilon-caprolactone) scaffolds. *J. Biomed. Mater. Res. A* **2003**, *67*, 1105–1114.
- 78 BURDON T, SMITH A, SAVATIER P. Signalling, cell cycle and pluripotency in embryonic stem cells. *Trends Cell Biol.* **2002**, *12*, 432–438.
- 79 LI S, EDGAR D, FASSLER R, WADSWORTH W, YURCHENCO PD. The role of laminin in embryonic cell polarization and tissue organization. *Dev. Cell* **2003**, *4*, 613–624.
- 80 NUR-E-KAMAL A, AHMED I, KAMAL J, SCHINDLER M, MEINERS S. Three-dimensional nanofibrillar surfaces promote self-renewal in mouse



- embryonic stem cells. *Stem Cells* **2005**, 24, 426–433.
- 81 PITTENGER MF, MACKAY AM, BECK SC, JAISWAL RK, DOUGLAS R, MOSCA JD, MOORMAN MA, SIMONETTI DW, CRAIG S, MARSHAK DR. Multi-lineage potential of adult human mesenchymal stem cells. *Science* **1999**, 284, 143–147.
- 82 ZUK PA, ZHU M, MIZUNO H, HUANG J, FUTRELL JW, KATZ AJ, BENHAIM P, LORENZ HP, HEDRICK MH. Multilineage cells from human adipose tissue: Implications for cell-based therapies. *Tissue Eng.* **2001**, 7, 211–228.
- 83 GOODWIN HS, BICKNESE AR, CHIEN SN, BOGUCKI BD, QUINN CO, WALL DA. Multilineage differentiation activity by cells isolated from umbilical cord blood: Expression of bone, fat, and neural markers. *Biol. Blood Marrow Transplant* **2001**, 7, 581–588.
- 84 YOUNG HE, STEELE TA, BRAY RA, HUDSON J, FLOYD JA, HAWKINS K, THOMAS K, AUSTIN T, EDWARDS C, CUZZOURT J, DUENZL M, LUCAS PA, BLACK AC, JR. Human reserve pluripotent mesenchymal stem cells are present in the connective tissues of skeletal muscle and dermis derived from fetal, adult, and geriatric donors. *Anat. Rec.* **2001**, 264, 51–62.
- 85 DE BARI C, DELL'ACCIO F, TYLZANOWSKI P, LUYTEN FP. Multipotent mesenchymal stem cells from adult human synovial membrane. *Arthritis Rheum.* **2001**, 44, 1928–1942.
- 86 LI WJ, TULI R, HUANG X, LAQUERRIERE P, TUAN RS. Multilineage differentiation of human mesenchymal stem cells in a three-dimensional nanofibrous scaffold. *Biomaterials* **2005**, 26, 5158–5166.
- 87 SCHINDLER M, AHMED I, KAMAL J, NUR EKA, GRAFE TH, YOUNG CHUNG H, MEINERS S. A synthetic nanofibrillar matrix promotes in vivo-like organization and morphogenesis for cells in culture. *Biomaterials* **2005**, 26, 5624–5631.
- 88 NUR EKA, AHMED I, KAMAL J, SCHINDLER M, MEINERS S. Three dimensional nanofibrillar surfaces induce activation of Rac. *Biochem. Biophys. Res. Commun.* **2005**, 331, 428–434.
- 89 FRENKEL SR, TOOLAN B, MENCHE D, PITMAN MI, PACHENCE JM. Chondrocyte transplantation using a collagen bilayer matrix for cartilage repair. *J. Bone Joint Surg. Br.* **1997**, 79, 831–836.
- 90 LEE CR, GRODZINSKY AJ, HSU HP, SPECTOR M. Effects of a cultured autologous chondrocyte-seeded type II collagen scaffold on the healing of a chondral defect in a canine model. *J. Orthop. Res.* **2003**, 21, 272–281.
- 91 MATTHEWS JA, WNEK GE, SIMPSON DG, BOWLIN GL. Electrospinning of collagen nanofibers. *Biomacromolecules* **2002**, 3, 232–238.
- 92 RHO KS, JEONG L, LEE G, SEO BM, PARK YJ, HONG SD, ROH S, CHO JJ, PARK WH, MIN BM. Electrospinning of collagen nanofibers: Effects on the behavior of normal human keratinocytes and early-stage wound healing. *Biomaterials* **2006**, 27, 1452–1461.
- 93 TELEMECO TA, AYRES C, BOWLIN GL, WNEK GE, BOLAND ED, COHEN N, BAUMGARTEN CM, MATHEWS J, SIMPSON DG. Regulation of cellular infiltration into tissue engineering scaffolds composed of micromer diameter fibrils produced by electrospinning. *Acta Biomater.* **2005**, 1, 377–385.
- 94 BOLAND ED, MATTHEWS JA, PAWLOWSKI KJ, SIMPSON DG, WNEK GE, BOWLIN GL. Electrospinning collagen and elastin: Preliminary vascular tissue engineering. *Front Biosci.* **2004**, 9, 1422–1432.
- 95 LI M, MONDRINOS MJ, GANDHI MR, KO FK, WEISS AS, LELKES PI. Electrospun protein fibers as matrices for tissue engineering. *Biomaterials* **2005**, 26, 5999–6008.
- 96 MATTHEWS JA, BOLAND ED, WNEK GE, SIMPSON DG, BOWLIN GL. Electrospinning of collagen type II: A feasibility study. *J. Bioactive Compatible Polymers* **2003**, 18, 125–134.
- 97 SHIELDS KJ, BECKMAN MJ, BOWLIN

- GL, WAYNE JS. Mechanical properties and cellular proliferation of electrospun collagen type II. *Tissue Eng.* **2004**, 10, 1510–1517.
- 98 MA Z, KOTAKI M, YONG T, HE W, RAMAKRISHNA S. Surface engineering of electrospun polyethylene terephthalate (PET) nanofibers towards development of a new material for blood vessel engineering. *Biomaterials* **2005**, 26, 2527–2536.
- 99 MA Z, HE W, YONG T, RAMAKRISHNA S. Grafting of gelatin on electrospun poly(caprolactone) nanofibers to improve endothelial cell spreading and proliferation and to control cell Orientation. *Tissue Eng.* **2005**, 11, 1149–1158.
- 100 ZHANG Y, OUYANG H, LIM CT, RAMAKRISHNA S, HUANG ZM. Electrospinning of gelatin fibers and gelatin/PCL composite fibrous scaffolds. *J. Biomed. Mater. Res. B Appl. Biomater.* **2005**, 72, 156–165.
- 101 HUANG ZM, ZHANG YZ, RAMAKRISHNA S, LIM CT. Electrospinning and mechanical characterization of gelatin nanofibers. *Polymer* **2004**, 45, 5361–5368.
- 102 STITZEL J, LIU J, LEE SJ, KOMURA M, BERRY J, SOKER S, LIM G, VAN DYKE M, CZERW R, YOO JJ, ATALA A. Controlled fabrication of a biological vascular substitute. *Biomaterials* **2006**, 27, 1088–1094.
- 103 BUTTAFOCO L, KOLKMAN NG, ENGBERS-BUIJTENHUIJS P, POOT AA, DIJKSTRA PJ, VERMES I, FEIJEN J. Electrospinning of collagen and elastin for tissue engineering applications. *Biomaterials* **2006**, 27, 724–734.
- 104 NAGAPUDI K, BRINKMAN WT, THOMAS BS, PARK JO, SRINIVASARAO M, WRIGHT E, CONTICELLO VP, CHAIKOF EL. Viscoelastic and mechanical behavior of recombinant protein elastomers. *Biomaterials* **2005**, 26, 4695–4706.
- 105 JIN HJ, FRIDRIKH SV, RUTLEDGE GC, KAPLAN DL. Electrospinning Bombyx mori silk with poly(ethylene oxide). *Biomacromolecules* **2002**, 3, 1233–1239.
- 106 JIN HJ, CHEN J, KARAGEORGIU V, ALTMAN GH, KAPLAN DL. Human bone marrow stromal cell responses on electrospun silk fibroin mats. *Biomaterials* **2004**, 25, 1039–1047.
- 107 OHGO K, ZHAO C, KOBAYASHI M, ASAKURA T. Preparation of non-woven nanofibers of Bombyx mori silk, Samia cynthia ricini silk and recombinant hybrid silk with electrospinning method. *Polymer* **2003**, 44, 841–846.
- 108 ZARKOUB S, EBY RK, RENEKER DH, HUDSON SD, ERTLEY D, ADAMS WW. Structure and morphology of electrospun silk nanofibers. *Polymer* **2004**, 45, 3973–3977.
- 109 MIN BM, LEE G, KIM SH, NAM YS, LEE TS, PARK WH. Electrospinning of silk fibroin nanofibers and its effect on the adhesion and spreading of normal human keratinocytes and fibroblasts in vitro. *Biomaterials* **2004**, 25, 1289–1297.
- 110 MIN BM, JEONG L, NAM YS, KIM JM, KIM JY, PARK WH. Formation of silk fibroin matrices with different texture and its cellular response to normal human keratinocytes. *Int. J. Biol. Macromol.* **2004**, 34, 281–288.
- 111 PARK WH, JEONG L, YOO DI, HUDSON S. Effect of chitosan on morphology and conformation of electrospun silk fibroin nanofibers. *Polymer* **2004**, 45, 7151–7157.
- 112 SILVERMAN RP, PASSARETTI D, HUANG W, RANDOLPH MA, YAREMCHUK MJ. Injectable tissue-engineered cartilage using a fibrin glue polymer. *Plast. Reconstr. Surg.* **1999**, 103, 1809–1818.
- 113 WORSTER AA, BROWER-TOLAND BD, FORTIER LA, BENT SJ, WILLIAMS J, NIXON AJ. Chondrocytic differentiation of mesenchymal stem cells sequentially exposed to transforming growth factor-beta1 in monolayer and insulin-like growth factor-I in a three-dimensional matrix. *J. Orthop. Res.* **2001**, 19, 738–749.
- 114 FORTIER LA, MOHAMMED HO, LUST G, NIXON AJ. Insulin-like growth factor-I enhances cell-based repair of articular cartilage. *J. Bone Joint Surg. Br.* **2002**, 84, 276–288.
- 115 WNEK GE, CARR ME, SIMPSON DG, BOWLIN GL. Electrospinning of

- nanofiber fibrinogen structures. *Nano Lett.* **2003**, 3, 213–216.
- 116 SECHRIEST VF, MIAO YJ, NIYIBIZI C, WESTERHAUSEN-LARSON A, MATTHEW HW, EVANS CH, FU FH, SUH JK. GAG-augmented polysaccharide hydrogel: A novel biocompatible and biodegradable material to support chondrogenesis. *J. Biomed. Mater. Res.* **2000**, 49, 534–541.
- 117 LAHIJI A, SOHRABI A, HUNGERFORD DS, FRONDOZA CG. Chitosan supports the expression of extracellular matrix proteins in human osteoblasts and chondrocytes. *J. Biomed. Mater. Res.* **2000**, 51, 586–595.
- 118 LU JX, PRUDHOMMEAU F, MEUNIER A, SEDEL L, GUILLEMIN G. Effects of chitosan on rat knee cartilages. *Biomaterials* **1999**, 20, 1937–1944.
- 119 DENUZIERE A, FERRIER D, DAMOUR O, DOMARD A. Chitosan-chondroitin sulfate and chitosan-hyaluronate polyelectrolyte complexes: Biological properties. *Biomaterials* **1998**, 19, 1275–1285.
- 120 MIN BM, LEE SW, LIM JN, YOU Y, LEE TS, KANG PH, PARK WH. Chitin and chitosan nanofibers: Electrospinning of chitin and deacetylation of chitin nanofibers. *Polymer* **2004**, 45, 7137–7142.
- 121 SUBRAMANIAN A, LIN HY, VU D, LARSEN G. Synthesis and evaluation of scaffolds prepared from chitosan fibers for potential use in cartilage tissue engineering. *Biomed. Sci. Instrum.* **2004**, 40, 117–122.
- 122 GENG X, KWON OH, JANG J. Electrospinning of chitosan dissolved in concentrated acetic acid solution. *Biomaterials* **2005**, 26, 5427–5432.
- 123 CAMPOCCIA D, DOHERTY P, RADICE M, BRUN P, ABATANGELO G, WILLIAMS DF. Semisynthetic resorbable materials from hyaluronan esterification. *Biomaterials* **1998**, 19, 2101–2127.
- 124 VERCRUYSE KP, MARECAK DM, MARECEK JF, PRESTWICH GD. Synthesis and in vitro degradation of new polyvalent hydrazide cross-linked hydrogels of hyaluronic acid. *Bioconj. Chem.* **1997**, 8, 686–694.
- 125 AIGNER J, TEGELER J, HUTZLER P, CAMPOCCIA D, PAVESIO A, HAMMER C, KASTENBAUER E, NAUMANN A. Cartilage tissue engineering with novel nonwoven structured biomaterial based on hyaluronic acid benzyl ester. *J. Biomed. Mater. Res.* **1998**, 42, 172–181.
- 126 GRIGOLO B, ROSETI L, FIORINI M, FINI M, GIAVARESI G, ALDINI NN, GIARDINO R, FACCHINI A. Transplantation of chondrocytes seeded on a hyaluronan derivative (hyaff-11) into cartilage defects in rabbits. *Biomaterials* **2001**, 22, 2417–2424.
- 127 UM IC, FANG D, HSIAO BS, OKAMOTO A, CHU B. Electrospinning and electro-blowing of hyaluronic acid. *Biomacromolecules* **2004**, 5, 1428–1436.
- 128 HOLLINGER JO. Preliminary report on the osteogenic potential of a biodegradable copolymer of polyactide (PLA) and polyglycolide (PGA). *J. Biomed. Mater. Res.* **1983**, 17, 71–82.
- 129 BOLAND ED, WNEK GE, SIMPSON DG, PAWLOWSKI KJ, BOWLIN GL. Tailoring tissue engineering scaffolds using electrostatic processing techniques: A study of poly(glycolic acid) electrospinning. *J. Macromol. Sci. – Pure Appl. Chem.* **2001**, A38, 1231–1243.
- 130 BOLAND ED, TELEMCO TA, SIMPSON DG, WNEK GE, BOWLIN GL. Utilizing acid pretreatment and electrospinning to improve biocompatibility of poly(glycolic acid) for tissue engineering. *J. Biomed. Mater. Res. B Appl. Biomater.* **2004**, 71, 144–152.
- 131 MIDDLETON JC, TIPTON AJ. Synthetic biodegradable polymers as orthopedic devices. *Biomaterials* **2000**, 21, 2335–2346.
- 132 ZONG X, RAN S, KIM KS, FANG D, HSIAO BS, CHU B. Structure and morphology changes during in vitro degradation of electrospun poly-(glycolide-co-lactide) nanofiber membrane. *Biomacromolecules* **2003**, 4, 416–423.
- 133 KO FK, LI WJ, LAURENCIN CT. Electrospun nanofibrous structure for tissue engineering. In: Sixth World Biomaterials Congress, Kamuela, Hawaii, USA, 2000.

- 134 KATTI DS, ROBINSON KW, KO FK, LAURENCIN CT. Bioresorbable nanofiber-based systems for wound healing and drug delivery: Optimization of fabrication parameters. *J. Biomed. Mater. Res. B* **2004**, *70*, 286–296.
- 135 BERKLAND C, PACK DW, KIM KK. Controlling surface nano-structure using flow-limited field-injection electrostatic spraying (FFESS) of poly(D,L-lactide-co-glycolide). *Biomaterials* **2004**, *25*, 5649–5658.
- 136 PITT CG. Poly-epsilon-caprolactone and its copolymers. In: *Biodegradable Polymers as Drug Delivery Systems*. CHASIN M, LANGER R (Eds.), Marcel Dekker, New York, **1990**, pp. 71–120.
- 137 YOSHIMOTO H, SHIN YM, TERAJI H, VACANTI JP. A biodegradable nanofiber scaffold by electrospinning and its potential for bone tissue engineering. *Biomaterials* **2003**, *24*, 2077–2082.
- 138 SHIN M, YOSHIMOTO H, VACANTI JP. In vivo bone tissue engineering using mesenchymal stem cells on a novel electrospun nanofibrous scaffold. *Tissue Eng.* **2004**, *10*, 33–41.
- 139 SHIN M, ISHII O, SUEDA T, VACANTI JP. Contractile cardiac grafts using a novel nanofibrous mesh. *Biomaterials* **2004**, *25*, 3717–3723.
- 140 LI WJ, TULI R, OKAFOR C, DERFOUL A, DANIELSON KG, HALL DJ, TUAN RS. A three-dimensional nanofibrous scaffold for cartilage tissue engineering using human mesenchymal stem cells. *Biomaterials* **2005**, *26*, 599–609.
- 141 KHIL MS, BHATTARAI SR, KIM HY, KIM SZ, LEE KH. Novel fabricated matrix via electrospinning for tissue engineering. *J. Biomed. Mater. Res. B Appl. Biomater.* **2004**, *72*, 117–124.
- 142 VENUGOPAL J, MA LL, YONG T, RAMAKRISHNA S. In vitro study of smooth muscle cells on polycaprolactone and collagen nanofibrous matrices. *Cell Biol. Int.* **2005**, *29*, 861–867.
- 143 ZHANG YZ, VENUGOPAL J, HUANG ZM, LIM CT, RAMAKRISHNA S. Characterization of the surface biocompatibility of the electrospun PCL-collagen nanofibers using fibroblasts. *Biomacromolecules* **2005**, *6*, 2583–2589.
- 144 VENUGOPAL J, RAMAKRISHNA S. Biocompatible nanofiber matrices for the engineering of a dermal substitute for skin regeneration. *Tissue Eng.* **2005**, *11*, 847–854.
- 145 VAZ CM, TUIJL SV, BOUTEN CVC, BAAIJENS FPT. Design of scaffolds for blood vessel tissue engineering using a multi-layering electrospinning technique. *Acta Biomater.* **2005**, *1*, 575–582.
- 146 FUJIHARA K, KOTAKI M, RAMAKRISHNA S. Guided bone regeneration membrane made of polycaprolactone/calcium carbonate composite nanofibers. *Biomaterials* **2005**, *26*, 4139–4147.
- 147 ZONG X, RAN S, FANG D, HSIAO BS, CHU B. Control of structure, morphology and property in electrospun poly(glycolide-co-lactide) non-woven membranes via post-draw treatments. *Polymer* **2003**, *44*, 4959–4967.
- 148 KENAWY EL R, LAYMAN JM, WATKINS JR, BOWLIN GL, MATTHEWS JA, SIMPSON DG, WNEK GE. Electrospinning of poly(ethylene-co-vinyl alcohol) fibers. *Biomaterials* **2003**, *24*, 907–913.
- 149 KHIL MS, CHA DI, KIM HY, KIM IS, BHATTARAI N. Electrospun nanofibrous polyurethane membrane as wound dressing. *J. Biomed. Mater. Res. B Appl. Biomater.* **2003**, *67*, 675–679.
- 150 ELISSEFF J, ANSETH K, SIMS D, MCINTOSH W, RANDOLPH M, LANGER R. Transdermal photopolymerization for minimally invasive implantation. *Proc. Natl. Acad. Sci. U.S.A.* **1999**, *96*, 3104–3107.
- 151 ELISSEFF J, ANSETH K, SIMS D, MCINTOSH W, RANDOLPH M, YAREMCHUK M, LANGER R. Transdermal photopolymerization of poly(ethylene oxide)-based injectable hydrogels for tissue-engineered cartilage. *Plast. Reconstr. Surg.* **1999**, *104*, 1014–1022.
- 152 HUANG L, NAGAPUDI K, APKARIAN RP, CHAIKOF EL. Engineered collagen-

- PEO nanofibers and fabrics. *J. Biomater. Sci. Polym. Ed.* **2001**, *12*, 979–993.
- 153 DUAN B, DONG C, YUAN X, YAO K. Electrospinning of chitosan solutions in acetic acid with poly(ethylene oxide). *J. Biomater. Sci. Polym. Ed.* **2004**, *15*, 797–811.
- 154 ZONG X, LI S, CHEN E, GARLICK B, KIM KS, FANG D, CHIU J, ZIMMERMAN T, BRATHWAITE C, HSIAO BS, CHU B. Prevention of postsurgery-induced abdominal adhesions by electrospun bioabsorbable nanofibrous poly(lactide-co-glycolide)-based membranes. *Ann. Surg.* **2004**, *240*, 910–915.
- 155 KENAWY EL R, BOWLIN GL, MANSFIELD K, LAYMAN J, SIMPSON DG, SANDERS EH, WNEK GE. Release of tetracycline hydrochloride from electrospun poly(ethylene-co-vinylacetate), poly(lactic acid), and a blend. *J. Controlled Release* **2002**, *81*, 57–64.
- 156 DING B, KIMURA E, SATO T, FUJITA S, SHIRATORI S. Fabrication of blend biodegradable nanofibrous nonwoven mats via multi-jet electrospinning. *Polymer* **2004**, *45*, 1895–1902.
- 157 HE W, MA Z, YONG T, TEO WE, RAMAKRISHNA S. Fabrication of collagen-coated biodegradable polymer nanofiber mesh and its potential for endothelial cells growth. *Biomaterials* **2005**, *26*, 7606–7615.
- 158 MIN BM, YOU Y, KIM JM, LEE SJ, PARK WH. Formation of nanostructured poly(lactic-co-glycolic acid)/chitin matrix and its cellular response to normal human keratinocytes and fibroblasts. *Carbohydr. Polymers* **2004**, *57*, 285–292.
- 159 XU C, YANG F, WANG S, RAMAKRISHNA S. In vitro study of human vascular endothelial cell function on materials with various surface roughness. *J. Biomed. Mater. Res. A* **2004**, *71*, 154–161.
- 160 XU CY, INAI R, KOTAKI M, RAMAKRISHNA S. Aligned biodegradable nanofibrous structure: A potential scaffold for blood vessel engineering. *Biomaterials* **2004**, *25*, 877–886.
- 161 RIBOLDI SA, SAMPALESI M, NEUENSCHWANDER P, COSSU G, MANTERO S. Electrospun degradable polyesterurethane membranes: Potential scaffolds for skeletal muscle tissue engineering. *Biomaterials* **2005**, *26*, 4606–4615.
- 162 NEUMANN T, HAUSCHKA SD, SANDERS JE. Tissue engineering of skeletal muscle using polymer fiber arrays. *Tissue Eng.* **2003**, *9*, 995–1003.
- 163 CRONIN EM, THURMOND FA, BASSELDUBY R, WILLIAMS RS, WRIGHT WE, NELSON KD, GARNER HR. Protein-coated poly(L-lactic acid) fibers provide a substrate for differentiation of human skeletal muscle cells. *J. Biomed. Mater. Res. A* **2004**, *69*, 373–381.
- 164 LEE CH, SHIN HJ, CHO IH, KANG YM, KIM IA, PARK KD, SHIN JW. Nanofiber alignment and direction of mechanical strain affect the ECM production of human ACL fibroblast. *Biomaterials* **2005**, *26*, 1261–1270.
- 165 YANG F, XU CY, KOTAKI M, WANG S, RAMAKRISHNA S. Characterization of neural stem cells on electrospun poly(L-lactic acid) nanofibrous scaffold. *J. Biomater. Sci. Polym. Ed.* **2004**, *15*, 1483–1497.
- 166 TATSUYAMA K, MAEZAWA Y, BABA H, IMAMURA Y, FUKUDA M. Expression of various growth factors for cell proliferation and cytodifferentiation during fracture repair of bone. *Eur. J. Histochem.* **2000**, *44*, 269–278.
- 167 KOST J, LANGER R. Responsive polymeric delivery systems. *Adv. Drug Deliv. Rev.* **2001**, *46*, 125–148.
- 168 BOLAND ED, TELEMCO TA, SIMPSON DG, WNEK GE, BOWLIN GL. Utilizing acid pretreatment and electrospinning to improve biocompatibility of poly(glycolic acid) for tissue engineering. *J. Biomed. Mater. Res. B* **2004**, *71*, 144–152.
- 169 BINI TB, GAO S, XU X, WANG S, RAMAKRISHNA S, LEONG KW. Peripheral nerve regeneration by microbraided poly(L-lactide-co-glycolide) biodegradable polymer fibers. *J. Biomed. Mater. Res. A* **2004**, *68*, 286–295.
- 170 ZHANG Y, OUYANG H, LIM CT, RAMAKRISHNA S, HUANG ZM.

- Electrospinning of gelatin fibers and gelatin/PCL composite fibrous scaffolds. *J. Biomed. Mater. Res. B* **2005**, *72*, 156–165.
- 171 FERTALA A, HAN WB, KO FK. Mapping critical sites in collagen II for rational design of gene-engineered proteins for cell-supporting materials. *J. Biomed. Mater. Res.* **2001**, *57*, 48–58.
- 172 YANG F, MURUGAN R, WANG S, RAMAKRISHNA S. Electrospinning of nano/micro scale poly(L-lactic acid) aligned fibers and their potential in neural tissue engineering. *Biomaterials* **2005**, *26*, 2603–2610.
- 173 XU C, YANG F, WANG S, RAMAKRISHNA S. In vitro study of human vascular endothelial cell function on materials with various surface roughness. *J. Biomed. Mater. Res. A* **2004**, *71*, 154–161.
- 174 ZONG X, BIEN H, CHUNG CY, YIN L, FANG D, HSIAO BS, CHU B, ENTCHEVA E. Electrospun fine-textured scaffolds for heart tissue constructs. *Biomaterials* **2005**, *26*, 5330–5338.
- 175 KIM K, YU M, ZONG X, CHIU J, FANG D, SEO YS, HSIAO BS, CHU B, HADJIARGYROU M. Control of degradation rate and hydrophilicity in electrospun non-woven poly(D,L-lactide) nanofiber scaffolds for biomedical applications. *Biomaterials* **2003**, *24*, 4977–4985.
- 176 BADAMI AS, KREKE MR, THOMPSON MS, RIFFLE JS, GOLDSTEIN AS. Effect of fiber diameter on spreading, proliferation, and differentiation of osteoblastic cells on electrospun poly(lactic acid) substrates. *Biomaterials* **2006**, *27*, 596–606.
- 177 LEE YH, LEE JH, AN IG, KIM C, LEE DS, LEE YK, NAM JD. Electrospun dual-porosity structure and biodegradation morphology of Montmorillonite reinforced PLLA nanocomposite scaffolds. *Biomaterials* **2005**, *26*, 3165–3172.
- 178 MO XM, XU CY, KOTAKI M, RAMAKRISHNA S. Electrospun P(LLA-CL) nanofiber: A biomimetic extracellular matrix for smooth muscle cell and endothelial cell proliferation. *Biomaterials* **2004**, *25*, 1883–1890.
- 179 XU C, INAI R, KOTAKI M, RAMAKRISHNA S. Electrospun nanofiber fabrication as synthetic extracellular matrix and its potential for vascular tissue engineering. *Tissue Eng.* **2004**, *10*, 1160–1168.
- 180 INOGUCHI H, KWON IK, INOUE E, TAKAMIZAWA K, MAEHARA Y, MATSUDA T. Mechanical responses of a compliant electrospun poly(l-lactide-co-epsilon-caprolactone) small-diameter vascular graft. *Biomaterials* **2006**, *27*, 1470–1478.
- 181 KWON IK, KIDOAKI S, MATSUDA T. Electrospun nano- to microfiber fabrics made of biodegradable copolyesters: Structural characteristics, mechanical properties and cell adhesion potential. *Biomaterials* **2005**, *26*, 3929–3939.
- 182 CHUA KN, LIM WS, ZHANG P, LU H, WEN J, RAMAKRISHNA S, LEONG KW, MAO HQ. Stable immobilization of rat hepatocyte spheroids on galactosylated nanofiber scaffold. *Biomaterials* **2005**, *26*, 2537–2547.
- 183 NAIR LS, BHATTACHARYYA S, BENDER JD, GREISH YE, BROWN PW, ALLCOCK HR, LAURENCE CT. Fabrication and optimization of methylphenoxy substituted polyphosphazene nanofibers for biomedical applications. *Biomacromolecules* **2004**, *5*, 2212–2220.
- 184 LEE IS, KWON OH, MENG W, KANG IK. Nanofabrication of microbial polyester by electrospinning promotes cell attachment. *Macromol. Res.* **2004**, *12*, 374–378.
- 185 ITO Y, HASUDA H, KAMITAKAHARA M, OHTSUKI C, TANIHARA M, KANG IK, KWON OH. A composite of hydroxyapatite with electrospun biodegradable nanofibers as a tissue engineering material. *J. Biosci. Bioeng.* **2005**, *100*, 43–49.
- 186 STANKUS JJ, GUAN J, WAGNER WR. Fabrication of biodegradable elastomeric scaffolds with sub-micron morphologies. *J. Biomed. Mater. Res. A* **2004**, *70*, 603–614.
- 187 BHATTARAI SR, BHATTARAI N, YI HK, HWANG PH, CHA DI, KIM HY. Novel biodegradable electrospun membrane:

- Scaffold for tissue engineering. *Biomaterials* **2004**, 25, 2595–2602.
- 188 KHIL MS, CHA DI, KIM HY, KIM IS, BHATTARAI N. Electrospun nanofibrous polyurethane membrane as wound dressing. *J. Biomed. Mater. Res. B* **2003**, 67, 675–679.
- 189 MATSUDA T, IHARA M, INOGUCHI H, KWON IK, TAKAMIZAWA K, KIDOAKI S. Mechano-active scaffold design of small-diameter artificial graft made of electrospun segmented polyurethane fabrics. *J. Biomed. Mater. Res. A* **2005**, 73, 125–131.
- 190 KIDOAKI S, KWON IK, MATSUDA T. Structural features and mechanical properties of in situ-bonded meshes of segmented polyurethane electrospun from mixed solvents. *J. Biomed. Mater. Res. B Appl. Biomater.* **2006**, 76, 219–229.
- 191 MA Z, KOTAKI M, YONG T, HE W, RAMAKRISHNA S. Surface engineering of electrospun polyethylene terephthalate (PET) nanofibers towards development of a new material for blood vessel engineering. *Biomaterials* **2005**, 26, 2527–2536.
- 192 SUN T, MAI S, NORTON D, HAYCOCK JW, RYAN AJ, MACNEIL S. Self organization of skin cells in three-dimensional electrospun polystyrene scaffolds. *Tissue Eng.* **2005**, 11, 1023–1033.
- 193 BOLAND ED, COLEMAN BD, BARNES CP, SIMPSON DG, WNEK GE, BOWLIN GL. Electrospinning polydioxanone for biomedical applications. *Acta Biomater.* **2005**, 1, 115–123.
- 194 CASPER CL, YAMAGUCHI N, KIICK KL, RABOLT JF. Functionalizing electrospun fibers with biologically relevant macromolecules. *Biomacromolecules* **2005**, 6, 1998–2007.
- 195 BHATTARAI N, EDMONDSON D, VEISEH O, MATSEN FA, ZHANG M. Electrospun chitosan-based nanofibers and their cellular compatibility. *Biomaterials* **2005**, 26, 6176–6184.
- 196 SON WK, YOUK JH, PARK WH. Preparation of ultrafine oxidized cellulose mats via electrospinning. *Biomacromolecules* **2004**, 5, 197–201.

## 4 Nanofibrous Scaffolds and their Biological Effects

*Laura A. Smith, Jonathan A. Beck, and Peter X. Ma*

### 4.1 Overview

Natural extracellular matrix (ECM) contains nanofibrous structures. To develop optimal scaffolds (synthetic temporary ECMs) for tissue engineering/regeneration, researchers mimic the natural ECM to recreate fibrous structures at this size scale. These nanofibrous scaffolds may eventually provide a better environment for tissue formation. Three different approaches toward the formation of nanofibrous scaffolds have emerged: self-assembly, electrospinning and phase separation. Each of these approaches is different and has a unique set of characteristics, which lends to its development as a scaffolding system. For instance, self-assembly can generate small diameter nanofibers in the lowest end of the range of natural extracellular matrix collagen, while electrospinning has generated large diameter nanofibers, often on the upper end of the range of natural ECM collagen. Phase separation, however, has generated nanofibers in the same range as natural collagen and allows for the design of macropore structures. Utilizing these three techniques, composite scaffolds have also been formed that contain minerals and biological factors to enable the scaffolds to more effectively mimic the natural ECM's bioactivities. These nanofibrous scaffolds have been shown to promote cellular attachment, proliferation and differentiation when compared to more traditional scaffolds that do not have nanofibrous structures. Nanofibrous scaffolds have been used to engineer various tissues such as cartilage, bone, vascular, cardiac, and neural tissues. This chapter briefly reviews the three fabrication techniques for nanofibrous scaffolds and their applications in tissue engineering.

### 4.2 Introduction

Tissue engineering is an interdisciplinary field that applies the principles of engineering and the life sciences to the development of biological substitutes that restore, maintain, or improve tissue function [1]. Essentially, there are three possible



approaches to tissue engineering [1, 2]: use of isolated cells or cell substitutes to replace the cells that supply a needed function; delivery of tissue-inducing substances such as growth factors to a targeted location; and growing cells in a three-dimensional (3D) scaffold. The first two approaches may be suitable for small, well-contained defects. However, only the third, using a scaffold to direct cell growth, is suitable to engineer larger tissue blocks with predesigned shapes. As such, more tissue engineers are utilizing scaffolds in their studies of neo-tissue formation.

With this approach, biomaterials play a pivotal role [3, 4]. To properly direct cell growth and tissue formation, scaffolds should have certain vital characteristics. The scaffold should provide a suitable surface for the attachment, proliferation, and differentiation of cells and provide an appropriate 3D template to guide the tissue growth to its final shape [5, 6]. To enhance cell adhesion and subsequent tissue formation, a high surface-to-volume ratio is desirable [7, 8]. An open porous network with a suitable pore size should be contained in the scaffold to allow for uniform cell seeding and for mass transport of signaling molecules, nutrients, and removal of metabolic waste. The scaffold should also degrade at the rate of tissue formation, yet have enough mechanical strength to provide temporary support while the tissue is forming. Biocompatibility is important. Neither the scaffold nor its degradation products should be toxic to cells. Finally, because of its importance in cellular behavior with respect to morphology, cytoskeletal structure and functionality, the scaffold should allow cellular interactions similar to those in the natural extracellular matrix (ECM) [9–11]. To meet all these criteria, tissue engineering scaffolds are often designed to mimic the natural ECM until the host cells repopulate and synthesize a new matrix [12, 13].

The most abundant protein in the ECM is collagen. Over 25 distinct collagen chains have been identified, the most abundant of which is type I [14]. Type I collagen molecules are composed of three collagen polypeptide chains wound around each other to form a ropelike superhelix. Collagen molecules assemble further into higher-order polymers called collagen fibrils, which in turn are assembled into collagen fibers. The diameter of collagen fibers typically ranges from 50 to 500 nm.

Type I collagen, as a result of being the primary component of the ECM, has been used in many medical materials, particularly in soft tissue repair [15]. Type I collagen is relatively bioinert because of its helical structure and because the primary sequence of type I collagen is well-conserved across species lines [16]. Despite these advantages, the use of collagen in tissue engineering scaffolds remains questionable for the following reasons: concern of pathogen transmission, difficulties in handling, and limited control of mechanical properties, biodegradability, and batch-to-batch consistency [17]. To combat this, several synthetic tissue engineering scaffolds with nano-scale structures are being developed to mimic the ECM. The success of these scaffolds hinges on their ability to replicate the dimensional scale of living tissue in both the micro- and nanometer scale, which will aid in the maintenance of cell phenotype and provide a structurally, mechanically and biologically compatible cell–material interface [18].

As you progress through this chapter, the methods of forming nanofibrous scaf-

olds are first addressed along with modification methods to further tailor the scaffolds for biological applications. This is followed by the biological effects of nanofibrous architecture on cultured cells and the neo-tissue formation. The chapter follows the linear development of tissue engineering from scaffold to tissue formation, and provides the most up-to-date comprehensive review of the field.

### 4.3

#### Methods of Formation

Three principle methods have been employed in the fabrication of nanofibrous scaffolds for use in tissue engineering. They are self-assembly, electrospinning, and phase separation. Although very different from each other, these approaches are at the cutting edge of technology. Each method is detailed in this section.

#### 4.3.1

##### Electrospinning

Since it was first patented in the 1930s, electrospinning has been used in polymer-processing [19]. It is a relatively simple process in which an electric field is used to draw a polymer solution (melt) from an orifice to a collector. Application of a high voltage (typically 5–30 kV) to the tip of a needle causing the polymer to form a Taylor cone is required for electrospinning. When the electrical field strength exceeds the surface tension (surpassing a critical voltage), a fiber jet is ejected from the Taylor cone to the collector (Fig. 4.1). The solvent evaporates from the polymer solution as the jet travels through the air. This process leaves behind a randomly oriented fiber matrix on the electrically grounded target [20–23].

Electrospinning typically is used to produce thin two-dimensional (2D) non-woven sheets; however, thicker 3D meshes are possible [24]. To maintain nano-

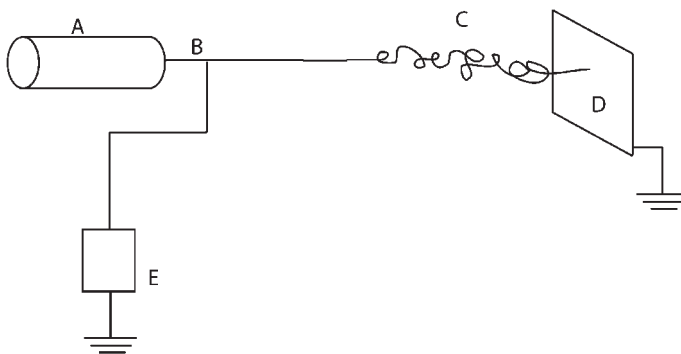


**Fig. 4.1.** Schematic diagram of a typical electrospinning apparatus: (A) Polymer solution loaded into a syringe; (B) syringe needle; (C) polymer nanofiber jet; (D) grounded target, which can be either stationary or rotating; (E) power supply.

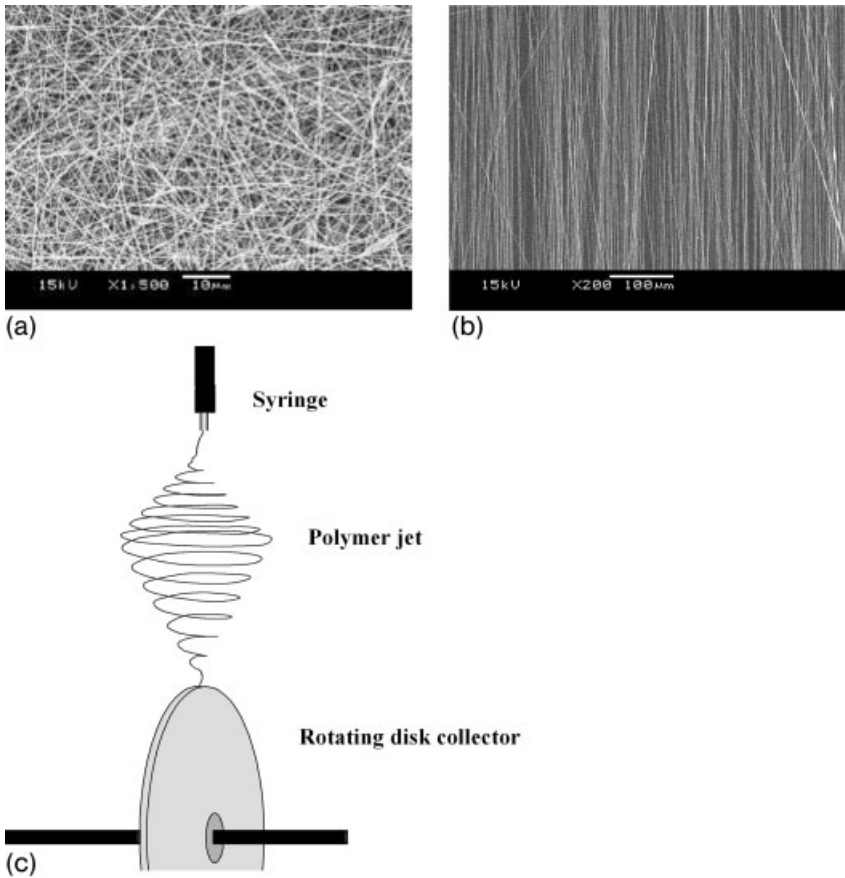


**Fig. 4.2.** (a) Randomly oriented nanofibers are created when a static collector is used. (b) Aligned nanofibers can be manufactured using a rotating collector. (Reprinted with permission from Ref. [25] © 2005, Elsevier.) (c) Diagram of a rotating collector. (Reprinted with permission from Ref. [27] © 2004, Elsevier.)

scale diameters throughout these meshes, a low extrusion rate must be used, leading to long fabrication times. It has been proposed that 3D meshes could more quickly be produced using multiple orifices simultaneously [24]. In this type of arrangement, the rate of mesh formation will be proportional to the number of orifices. Figure 4.2(a) shows SEM micrograms of a typical electrospun nanofibrous mesh [25]. However, electrospinning has yet to produce designed pore structures. Despite such shortcomings, electrospinning has been widely explored due to its capacity of generating nanofibers and the fabrication simplicity.

Electrospinning has been used to form scaffolds from many different biomaterials, including poly(lactic-*co*-glycolic acid) (PLGA), poly(caprolactone) (PCL), poly(ethylene oxide) (PEO) and poly(vinyl alcohol) (PVA) in water or organic solvent [26]. Nanofibrous mats of collagen, silk protein, elastin-mimetic peptide, fibri-

nogen, casein and lipase enzyme, and even DNA have been formed using electrospinning [20–23]. The use of electrospinning with regard to naturally occurring biomaterials has been limited in comparison to synthetic polymers because of the difficulty in finding appropriate solvents.

Typically, electrospun fibers produced are randomly oriented on the collection plate. However, random fiber orientation is not always ideal. Many tissues are anisotropic and have a clearly defined directionality. Examples of anisotropic tissues include muscle, bone, blood vessels, and nerves. Several methods have been developed to create mats with oriented fibers for use in these types of tissue engineering projects. The first method involves the use of a rotating drum as the grounded target rather than a static plate. As the drum spins, the fibers naturally align themselves (Fig. 4.2) [27]. A modification on the rotating drum concept that offers more versatility utilizes modified polymer solution system pushed through a microfluidic chamber in close proximity to a rotating collection grid. This system achieves variable fiber alignment from linear to S shaped curves dependent on the rate of collection grid rotation [28].

Besides dynamic collection grids, post-drawing can also be used to create oriented nanofibers [29]. In this method, the fibers are prepared using a static collection grid. Following electrospinning, the mat is drawn by stretching and then annealed under constant strain. Mats created in this manner not only contain uniaxial oriented fibers but also crystal orientation. Uniaxial oriented fibers can also be created with a special collector composed of two pieces of electrically conductive substrates separated by a gap [30]. The electrostatic fields created by the separated conductors cause the fibers to bridge the gap perpendicularly. This method is limited by the electrostatic interactions between the conducting collectors, meaning that only narrow meshes are possible.

The dimensions of electrospun fibers vary, depending on the material used. However, in general, the diameters of electrospun fibers are at least one order of magnitude smaller than those produced by conventional extrusion techniques [24]. Yet, this is still generally at the upper end of the diameters present in the native ECM. Ko and coworkers created nanofibrous PLGA matrices with fibers having diameters between 500 and 800 nm [26], while Vacanti and coworkers fabricated PCL matrices with an average fiber diameter of 400 nm ( $\pm 200$  nm) [31]. Chaikof and coworkers have also created electrospun nanofibers, with diameters in the 100–150 nm range, by combining collagen and PEO [32]. Pure collagen solutions have also been fabricated using electrospinning techniques [33–35]. Bowlin and coworkers have demonstrated electrospun collagen, with an average diameter of 250 nm, that exhibits the 67-nm banding typical of native collagen fibrils [34].

Although electrospinning is a relatively simple and quick method that can be applied to many different types of biomaterials, there is inherent difficulty in creating scaffolds with well-organized pore architectures with complex geometries. The diameter of most electrospun fibers is near the upper limit for the natural size of collagen fibers (50–500 nm) with some even reaching into the micro-scale. These are the two primary shortcomings of electrospinning.

## 4.3.2

**Self-assembly**

Although molecular self-assembly is a rather new laboratory technique for the formation of nano-scale scaffolds, it is prevalent in the natural world. Molecular self-assembly is a “bottom up”, rather than a “top down” approach. Self-assembly is described as the reversible process by which preexisting parts are organized into an ordered system. By definition, molecular self-assembly is the spontaneous association of molecules under equilibrium conditions into stable, structurally well-defined aggregates joined by non-covalent bonds [36]. Although non-covalent bonds such as hydrogen bonds, ionic bonds, van der Waals interactions, and hydrophobic interactions are rather weak in isolation, taken in concert they govern the self-assembly of biological macromolecules [37].

As mentioned, self-assembled molecules are ubiquitous in nature. One example of molecules that readily self-assemble into higher order structures is phospholipids. Phospholipids are the principal component of the plasma membrane in cells. In aqueous solutions, phospholipids readily self-assemble to form several structures, including vesicles, micelles, and tubules. One advantage of molecular self-assembly is that fiber diameters can be produced that are much smaller than those produced using electrospinning.

Schnur et al. [38] pioneered the work of molecular self-assembly using lipid tubules. Several molecule types have been utilized in molecular self-assembly. Zhang, Rich, Holmes, et al. [39] have created self-assembled structures using ionic self-complementary oligopeptides. These oligopeptides contain alternating regions of hydrophobic and hydrophilic amino acids, and, in water, they freely organize themselves into stable  $\beta$ -sheet structures. Exposure to monovalent alkaline cations or physiological conditions, the oligopeptides can assemble into hydrogels with interwoven 10–20 nm diameter nanofibers and 50–200 nm diameter pores [39–41].

Peptide-amphiphiles (PA) have also been fabricated and will self-assemble to form nano-structured fibers [42, 43]. Stupp and coworkers [42] demonstrated that a molecule composed of a carbon alkyl tail and several peptide regions will self-assemble to form nanofibers with a diameter of  $7.6 \pm 1$  nm. The nanofibrous scaffolds formed by this method are evident in Fig. 4.3. More recently, Stupp and coworkers [44] have reported preliminary results that indicate that PA self-assembled molecules can be used to encourage angiogenesis.

The PA is synthesized using solid-phase chemistry that ends with the alkylation of the N-terminus of the peptide and contains the following features: a long alkyl tail that conveys hydrophobic characteristics to the molecule; four consecutive cysteine residues that form disulfide bonds to polymerize the structure; a linker region containing three glycine residues to provide the hydrophilic head group the flexibility from the rigid crosslinked regions; a phosphorylated serine residue that interacts strongly with calcium ions and helps to direct mineralization; and Arg-Gly-Asp (RGD), a cell adhesion ligand. The cysteine, phosphorylated serine and RGD sequence are specific characteristics of the peptide portion of the PA [42].

Similar to PAs, diblock copolypeptides containing charged and hydrophobic seg-

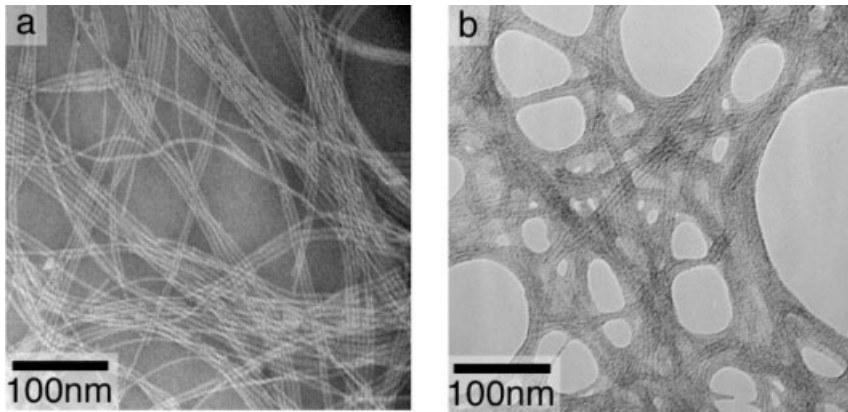


**Fig. 4.3.** TEM images of PA molecule (a) self-assembled by drying directly onto a TEM grid without adjusted pH, and (b) another PA molecule self-assembled by mixing with  $\text{CaCl}_2$ . Image (a) is negatively stained with phosphotungstic acid whereas (b) is positively stained with uranyl acetate. In both cases the same fibrous morphology is observed, as is seen by pH-induced self-assembly. (Ref. [43] © 2002 by National Academy of Science, USA.)

ment have also been utilized to form rigid hydrogels in water for tissue engineering applications [45–47]. These hydrogels contain 1–30  $\mu\text{m}$  water-containing pores surrounded by a nanofibrous gel matrix [46]. The diblock copolypeptides hydrogels are thermally stable under physiological conditions [45] and reorganize quickly after mechanical deformation due to the low molecular mass of the diblock copolypeptides [47]. However, the pore size is on the lower side and may not be ideal for tissue regeneration.

Molecular self-assembly has also been proven using molecules other than peptides or PAs. For example, Liu et al. reported the self-assembly of polyphenylene dendrimers into  $\mu\text{m}$ -long nanofibers [48, 49]. Perutz [50–52] demonstrated the formation of nanotubes from polyglutamines.

As mentioned, tissue engineering scaffolds should ideally have large pore spaces to allow for cell accommodation and mass transport. One of the restrictions of self-assembled scaffolds is the limited ability to form macro size pores. Degradation of self-assembled scaffolds is also an issue that will need to be addressed. In addition, the mechanical properties of these scaffolds will need to be increased before self-assembly can be used in tissue engineering applications that require load bearing. Nevertheless, self-assembled materials are often hydrogels, which are convenient for injection.

#### 4.3.3

#### Phase Separation

Phase separation processes have been used for some years to create porous polymer membranes for filtration and other applications [53]. However, the use of ther-

mally induced phase separation (TIPS) in the preparation of tissue engineering scaffolds is fairly new [54]. In this process, a temperature change results in the separation of the polymer solution into two phases; one having a low polymer concentration (polymer-lean phase) and one having a high polymer concentration (polymer-rich phase). Conversely, the polymer-lean phase is sometimes referred to as the solvent-rich phase and the polymer-rich phase, in this naming methodology, is referred to as the solvent-lean phase. Once the phase separation has occurred, the solvent is removed by extraction, evaporation, or sublimation. As the polymer-rich phase solidifies, this process leaves behind a network of pores referred to as the polymer foam. The properties of the foam can be tailored to meet specific needs. Thermally induced phase separation does not automatically lead to materials with nanometer scale architecture. For example, our laboratory has used TIPS to develop polymer and polymer/bioceramic composite scaffolds that do not have the nanofibrous structure for tissue engineering [55, 56].

Ma and colleagues have recently developed a novel phase separation process to fabricate nanofibrous materials from polymers [13]. A distinct advantage of the phase separation process is that it can be combined with other manufacturing techniques (such as particulate leaching or three-dimensional printing) to design complex 3D structures with well-controlled pore morphologies [6, 12, 57, 58]. The rest of this section will discuss how such phase separation is used for nanofibrous scaffold fabrication for tissue engineering applications.

An appropriate liquid–liquid phase separation seems critical for nanofibrous structure formation, but does not occur in all solvent systems. The selection of solvent system and phase separation temperature are vital to nanofiber formation. When the system and conditions are right, liquid–liquid phase separation can result in a 3D continuous fibrous network with nano-scaled architecture similar to natural type I collagen [59, 60]. The fibers formed in this manner have diameters ranging from 50 to 500 nm and the scaffolds can have a porosity in excess of 98% [13]. Figure 4.4 is an image of a nanofibrous PLLA scaffold, and as can be seen, this scaffold closely resembles collagen in the ECM.

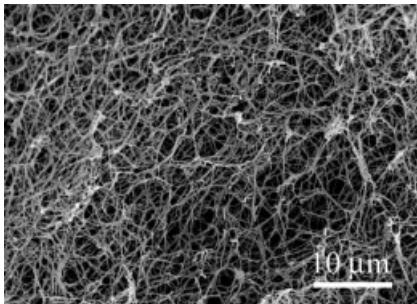


**Fig. 4.4.** SEM micrograph of a nanofibrous PLLA matrix prepared from 5.0% (wt/v) PLLA/THF solution at a gelation temperature of  $-18^{\circ}\text{C}$ . (Ref. [13] © 1999, John Wiley & Sons.)

The TIPS process for nanofibrous structure formation typically occurs in five steps [13]: polymer dissolution, phase separation and gelation, solvent exchange from the gel with water, freezing, and finally freeze-drying (sublimation) under vacuum. Although each step is necessary, gelation is the step that determines the type of structure that will be formed. At high temperatures, the solution is homogeneous. When the polymer solution is cooled, phase separation into a polymer-rich and polymer-lean phase can occur. Liquid–liquid phase separation usually occurs via one of two routes: nucleation and growth or spinodal decomposition [61].

When a polymer that crystallizes, such as PLLA, is used the phase separation process becomes much more complicated. In addition to phase separation, polymer crystallization can also occur. In these cases, kinetics become important because the solution will experience driving forces for both liquid–liquid phase separation and polymer crystallization. When the liquid–liquid phase separation is faster than the polymer crystallization that leads to the nucleation of crystalline domains in the polymer-rich phase, the morphology of the porous network is largely dependent on the initial liquid–liquid phase separation. The selection of phase-separation temperature should accordingly promote the desired liquid–liquid phase separation [62].

As mentioned earlier, proper selection of solvents is critical in liquid–liquid phase separation. The solvent must have a freezing point (crystallization temperature) lower than the liquid–liquid phase separation temperature of the polymer solution. Otherwise, the solvent may crystallize before the liquid–liquid phase separation occurs. In addition to phase separation temperature and solvent selection, the final morphology of the polymer matrix is dependent on the concentration of polymer solution and the molecular weight of the polymer [59]. For example, a very low concentration of polymer will typically result in a powder-like structure, whereas a higher concentration will result in a foam.

Tissue engineers desire scaffolds not only with fibrous networks that mimic the ECM, but also with designed 3D architecture of interconnected pores. In scaffolds, macroscopic pores ( $>100\ \mu\text{m}$ ) are vital for proper cell seeding, distribution, migration, and neovascularization.

Here we present a few examples to illustrate how to combine liquid–liquid phase separation with other technologies to create scaffolds with the proper 3D shape, pore architecture, and nano-scale fibers. To form a nanofibrous matrix with a macroscopic pore network, TIPS can be combined with particulate leaching techniques [12]. For example, a polymer solution can be dripped over salt or sugar crystals. The system is then cooled, inducing liquid–liquid phase separation. Next the scaffold is immersed in water to simultaneously extract the solvent and leach out the salt/sugar crystals. The scaffold is then frozen and, finally, freeze dried. The resulting scaffolds (Fig. 4.5) have a nano-scale fibrous architecture with macroscopic pores. Although sugar/salt leaching creates well-formed pores, it is difficult to control the amount of interconnectivity. Interconnectivity of pores is important for cell migration, cell signaling, and for mass transport (transport of nutrients to the cells and removal of metabolites from the cells).

To better control the interconnectivity of the macroscopic pores in a scaffold, our



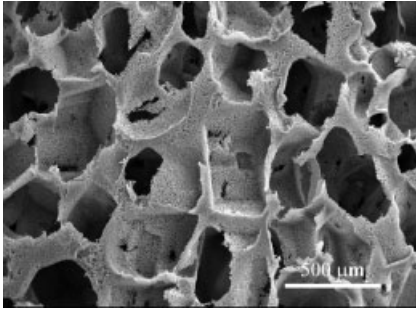
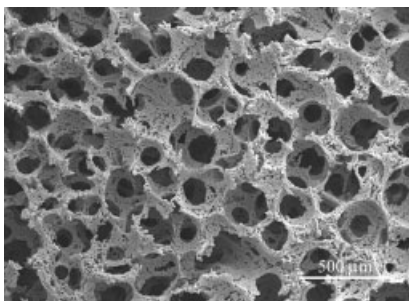


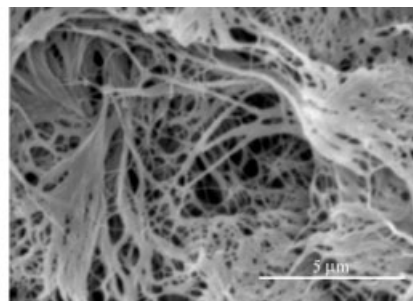
**Fig. 4.5.** SEM micrograph of a PLLA nanofibrous matrix with particulate macropores prepared from PLLA/THF solution and sugar particles. Particle size 250–500  $\mu\text{m}$ , original magnification  $\times 50$ . (Ref. [12] © 2000, John Wiley & Sons.)

laboratory has developed a dispersion technique to create paraffin microspheres to be used as porogens. The interconnectivity of the pores can be controlled through thermal bonding of the paraffin microspheres. Paraffin dissolves in THF, and for this reason, THF cannot be used as the polymer solvent, and alternate solvents must be implemented [6]. Following phase separation, hexane is used to leach out the paraffin. The matrix is then frozen and lyophilized. This process results in a scaffold with well-controlled interconnected spherical macropores and nanofibrous pore walls (Fig. 4.6) [6].

Phase separation can also be combined with rapid prototyping techniques or solid free-form (SFF) fabrication. In SFF fabrication a computer-aided design program is used to design a 3D scaffold. To create a nanofibrous scaffold, a negative mold is first generated using SFF fabrication techniques. The polymer solution is then dripped over this mold. Following phase separation, the mold is leached out



(a)



(b)

**Fig. 4.6.** SEM micrographs of a PLLA nanofibrous matrix with interconnected spherical macropores prepared from a 7.5% (wt/v) PLLA/dioxane/pyridine (dioxane/pyridine = 1:1) solution and paraffin spheres

heat treated for 40 min. Sphere size range  $d = 250\text{--}420\ \mu\text{m}$ . Original magnification (A)  $\times 50$  and (B)  $\times 8000$ . (Reprinted with permission from Ref. © [6] 2004, Elsevier.)

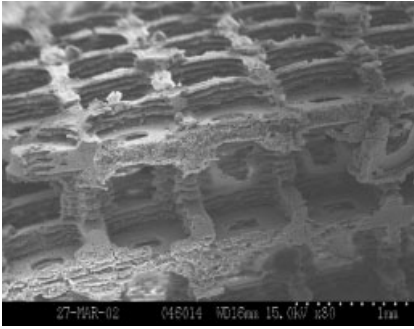


**Fig. 4.7.** SEM micrograph of the internal pore structure of a scaffold fabricated using the reverse SFF fabrication technique. (Ref. [58] © 2003, John Wiley & Sons.)

and the matrix is processed as described previously. SFF fabrication makes possible the construction of scaffolds with complex 3D structures. Figure 4.7 shows an example of a scaffold formed by combining this reverse SFF fabrication and phase separation [58].

In addition to being combinable with other processing techniques to design macropores, phase separation is also a desirable method for forming tissue engineering scaffolds because it can produce nanofibers in the size range similar to that of natural collagen. Furthermore, phase separation does not require expensive equipment or complicated synthesis schemes and can be easily adapted to a small laboratory setting or large-scale industrial production.

Each technique, molecular self-assembly, electrospinning, and phase separation, provides unique strengths in the area of nano-scale tissue engineering scaffolds. As each area develops further, it is likely that niches will be created where a particular method better suits the needs of certain tissue engineers. As scientists better understand and mimic the ECM, scaffolds will undoubtedly be created that provide the characteristics necessary to move tissue engineering off the laboratory bench and into widespread clinical applications.

#### 4.4

#### **Nanofibrous Composite Scaffolds**

Utilizing the above three techniques, composite scaffolds have been formed that contain minerals and biological materials to enable the scaffolds to better mimic the natural ECM's surface chemistry. Although nanofibrous scaffolds provide an improved base architecture, the surface characteristics affect cellular response to a material by influencing the rate and quality of new tissue formation. Specifically, the surface chemistry and topography determine whether protein molecules can adsorb, and the conformation of adsorbed proteins on the surface. This in turn

affects cellular attachment, alignment, proliferation and differentiation. Most materials used to fabricate nanofibrous scaffolds lack the biological recognitions of the ECM on their surface. These scaffolds can be altered through the inclusion of molecules and biological recognition sites to more closely mimic natural ECM of the tissues they are trying to emulate.

#### 4.4.1

#### Inorganic Composites

Most mineralized tissues, like bone, contain both organic and inorganic molecules. In natural mineralized tissues, hydroxyapatite (HAP), a plate or spindle-shaped crystal, is found between collagen fibrils in the ECM [63]. HAP is the main component of the inorganic bone matrix, and the major site of mineral storage in bone and the body. Bone contains 99% of the calcium and 88% of the phosphate in the body. The HAP crystals within the matrix measure up to 200 nm in length and offer a large surface area available for mineral exchange, about 10 m<sup>2</sup> per 1 g of bone [64].

By incorporating HAP into scaffolding, one attempts to increase mineralized tissue formation through mimicking natural mineral content and ECM base architecture. HAP-containing polymer scaffolds possess good mechanical and osteoconductive properties [5]. Nano- and micro-size HAP particles have been incorporated with nanofibrous PLLA scaffolds created by phase separation to yield highly porous scaffolds with improved mechanical strength and increased protein adsorption [65]. Particularly interesting is that the nano-sized HAP provides improved characteristics relative to micro-sized HAP in scaffolds [65].

HAP can also be deposited onto the surface of nanofibrous scaffolds using simulated body fluid. This allows the HAP to have nano-features within the larger deposited masses. This technique has been utilized to deposit HAP on phase separated PLLA scaffolds (Fig. 4.8) [57] and electrospun poly(3-hydroxybutyrate-co-3-hydroxyvalerate) nanofibers [66]. Similarly, electrospun PCL and PLGA nanofibers

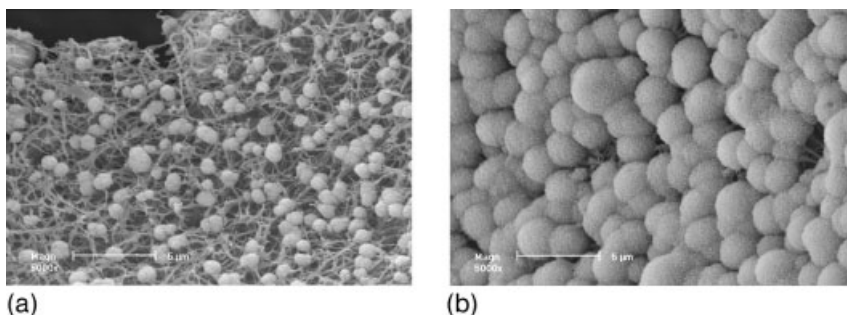


**Fig. 4.8.** SEM micrographs of nanofibrous PLLA/nHAP (90:10) composite scaffolds incubated in 1.5X SBF for varying (a) 4 days and (b) 30 days. (Ref. [57] © 2006, John Wiley & Sons.)

have been combined with calcium carbonate [67], yielding similar advantages for mineralized tissue formation.

#### 4.4.2

#### Surface Modification

When mineralized tissue is not the goal, yet the base polymer used to create the scaffold does not possess the most desirable surface characteristics, the scaffold surface can be modified to obtain more desirable characteristics to promote cell-scaffold interaction. These modifications can be as simple as plasma treatment or allowing ECM proteins to adsorb to the scaffold [68]. For instance, PCL nanofibers have been air-plasma treated to introduce  $-COOH$  groups and then gelatin was allowed to adsorb to the surface [69]. There is a concern over the penetration depth and uniformity of the plasma treatment. More advanced and controlled modifications are desired.

Using electrospinning, a molecule such as gelatin can be blended with polymer and then drawn through the electrospinning process to form nanofibrous scaffolds, as was done by Zhang et al. using PCL and gelatin mixtures [70]. Furthering this concept of multiple species electrospinning, coaxial electrospinning techniques have been developed, which allow for nanofibers to be produced with different core and shell materials. This means that the core and shell material do not necessarily need to be compatible. For instance, Zhang et al. have produced nanofibers with a PCL core and a collagen shell for tissue engineering purposes [71].

Another strategy in surface modification is to use a completely synthetic system. In this approach a biologically active peptide is grafted onto the surface. For instance, a galactose ligand has been covalently conjugated to poly(acrylic acid) spacers, which were UV-grafted onto poly( $\epsilon$ -caprolactone-co-ethyl ethylene phosphate) nanofibers [72]. As such, peptide scaffolds have been made containing the biologically active motifs of laminin I and collagen IV, two important proteins in the basement membrane [73].

Alternatively, peptide amphiphiles containing either biologically active sequences or structures potentially could be assembled on the surface of nanofibrous scaffolds. Fields, Tirrell and coworkers have illustrated the validity of such a coating using PA molecules that consist of a  $\alpha 1$  (IV) 1263-1277 collagen sequence Gly-Val-Lys-Gly-Asp-Lys-Gly-Asn-Pro-Gly-Trp-Pro-Gly-Ala-Pro ([IV-H1]) connected to a long-chain mono- or di-alkyl ester lipid [74–78], which assembles into stable triple helices under physiological conditions [78], and have been shown to favorably support cell adhesion when coated on surfaces [76]. This work illustrates that surface chemistry can be mimicked with this type of PAs. However, it has yet to be developed for scaffold modifications.

In our laboratory, a few easier implementing and effective techniques have been developed for 3D surface modification of complex shaped scaffolds. For example, physical entrapment of gelatin along with chemical crosslinking has been used to modify nanofibrous PLLA scaffolds [79]. This is an advancement beyond adsorp-

tion because it immobilizes the gelatin on the surface of the nanofibrous scaffold, ensuring that the gelatin does not wash away in a tissue culture environment. After 4 weeks of culture, osteoblasts on nanofibrous scaffolds modified with this method showed increased proliferation and collagen fiber bundle formation over the unmodified control scaffolds [79]. This indicates that this surface modification does not have the depth penetration problems that more simplistic modification like plasma-treated surfaces encounter in 3D applications.

An electrostatic layer-by-layer self-assembly technique has also been used to improve the surface characteristics of nanofibrous PLLA scaffolds with gelatin [80]. Similar to physical entrapment with chemical crosslinking, self-assembly has led to increased osteoblast proliferation over unmodified control scaffolds [80]. Histological sections of nanofibrous scaffolds with the self-assembly modification showed a more even distribution of cells throughout the scaffolds after 2 weeks of culture than unmodified control scaffolds [80].

#### 4.4.3

#### Factor Delivery Scaffolds

As the drive to mimic the ECM continues, more nanofibrous scaffolds will likely contain biological modifications to more appropriately tailor their characteristics to the desired application. Similarly, investigators are moving beyond simply mimicking the ECM to incorporating the release of factors to promote healing and tissue formation from the scaffolds. To date, the antibiotic Cefoxitin has been released from nanofibrous PLGA scaffolds by several groups [81, 82]. PDLA nanofibers have been used to release Mefoxin, a similar antibiotic to Cefoxitin, by others [83]. Beyond antibiotics, the lipophilic anti-tumor drugs, doxorubicin and paclitaxel, have been released from PLLA nanofibers studied [84]. Ibuprofen, an anti-inflammatory drug, has had its release from PLGA/PEG-g-chitosan nanofibers [85]. Polyurethane nanofibers have been used to study the release of Ketanserin, a selective 5<sub>2</sub>-setotonin antagonist, and Itraconazole, an anti-fungal drug [86].

The release of plasmid DNA from PLGA and PLA-PEG nanofibrous scaffolds has also been studied [2, 87]. Besides DNA, a few biological growth and differentiation factors have been delivered from nanofibers. Human  $\beta$ -nerve growth factor has been released from electrospun PCL/ethyl ethylene phosphate nanofibers [88]. Systems for the delivery of biologically active proteins are often far more difficult to engineer than those for drug or nucleotide release because of the sensitivity of proteins to conformational changes that render them biologically inactive, thus limiting the available methods and necessitating their protection from harsh conditions. Wei et al. have developed a system for release of platelet derived growth factor (PDGF) and/or other biologically active factors from micro-spheres evenly distributed within nanofibrous PLLA scaffolds [89]. Incorporation of the micro-spheres into the nanofibrous scaffolds decreased the initial burst release of the PDGF and extended the release of biologically active PDGF in a controlled fashion [89].

## 4.5

### Biological Effects of Nanofibers

The ultimate goal of tissue engineering is to develop biological substitutes that restore, maintain or improve tissue function within the body. Developing nanofibrous scaffolds that better mimic the ECM is one step further down the road to achieving functional neo-tissue formation.

Regardless of the method used to form the nanofibrous scaffolds or further process the scaffolds, these scaffolds seem to possess certain advantages over more conventional scaffolds. They seem advantageous when it comes to cellular adhesion, proliferation, migration and differentiation. Increased cellular adhesion and proliferation, along with more rapid differentiation into mature cell types, have been observed with several cell types [17, 27, 90–93]. However, engineering tissues using nanofibrous scaffolds is still at the early stages. Notably, there is limited data and a systematic study of the biological effects of nanofibers on cell function and tissue development has yet to be completed.

#### 4.5.1

##### Attachment

Suitable attachment is the first step to successful neo-tissue formation, since most cell types require anchorage to proliferate, migrate and differentiate [94]. Woo et al. [17] found that the cell adhesion proteins fibronectin, vitronectin, and laminin adsorbed to the nanofibrous scaffolds much more than solid-walled control scaffolds. They also found that this effect is not simply due to increased surface area since different proteins adsorbed at different levels, which suggests the selective interaction of the proteins with the nanofibrous matrix [17].

Cells seem to react to this increased adhesion protein presence on the nanofibers by up-regulating integrins, a family of transmembrane proteins involved in adhesion of cells to the ECM and each other. Specifically, normal rat kidney cells upregulate expression of  $\beta 1$  integrin [91], while chondrocytes upregulate expression of integrin  $\alpha 2$  on nanofibrous surfaces [92]. Beside up-regulation of  $\beta 1$  integrin, normal rat kidney cells organize their  $\beta 1$  integrin in long, slender aggregates on the nanofibers while on glass expression was concentrated in the cell body [91], as seen in Fig. 4.9, on nanofibrous surfaces. Similarly, NIH 3T3 fibroblasts have been shown to express vinculin, a prominent component of focal adhesions that connect the cytoskeleton and plasma membrane with the ECM, strongly in the edge of lamellipodia with more diffuse staining throughout the cell cytoplasm on nanofibrous surfaces [91]. The expression and distribution of these important adhesion molecules are thought to correlate with cellular morphogenesis *in vivo* [91] and the change in cellular interactions between nanofibrous scaffolds and traditional scaffolds, which contain flat walls.

Three days after seeding calvarial cells on both nanofibrous and traditional scaffolds, Woo et al. found that the cells on nanofibrous scaffolds had many long processes that intermingled with the nanofibrous scaffold and connected to neigh-

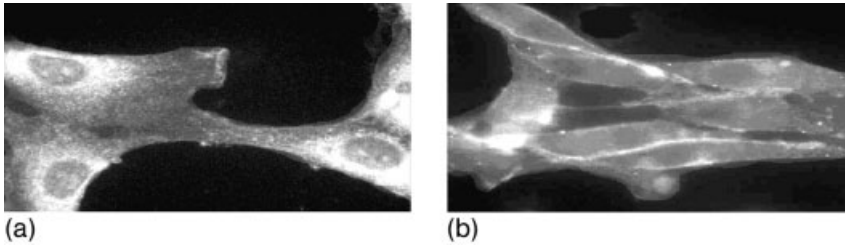


**Fig. 4.9.** Comparison of  $\beta 1$  integrin organization in normal rat kidney cells. Indirect immunofluorescence on (a) glass and (b) nanofibers. (Reprinted with permission from Ref. [91] © 2005, Elsevier.)

boring cells, while cells on traditional scaffolds had only a few processes [95]. Furthermore, cells on the nanofibrous scaffolds were actively synthesizing and secreting molecules [95].

The increased adsorption of adhesion proteins from serum-containing media and the cellular response at least partially explains the increased attachment of numerous cell types on various nanofibrous scaffolds. For instance, neural progenitor cells attach faster to nanofibers than to the control surfaces [90]. Pre-osteoblasts [17], calvarial cells [95], smooth muscle cells [27], fibroblasts [91], normal rat kidney cells [91] and multipotent neural stem cells [90] have also shown preferential adhesion on nanofibers over controls.

#### 4.5.2

##### **Proliferation**

After cells attach to a scaffold, they must reproduce by duplicating their contents and dividing in two to develop into new tissue [94]. Several cell types have shown increased proliferative capability on nanofibers over various time periods [27, 91, 92, 96]. Specifically, normal rat kidney cells have shown increased proliferation on nanofibers relative to control at 24 h [91] and high density chondrocyte cultures increased proliferation over 3 weeks on nanofibrous scaffolds relative to control [92]. The authors have also observed this trend with pre-osteoblasts over the course of 12 days. In the context of neo-tissue formation, quicker proliferation will limit the invasion of scar tissue *in vivo* and lead to faster differentiation and functional tissue formation.

#### 4.5.3

##### **Differentiation**

Differentiation is the process by which cells undergo a change to an overly specialized cell type from a more immature cell type. This process is different for each

cell type. However, nanofibrous materials appear to quicken differentiation of multiple cell types. Fibroblasts have shown more differentiated characteristics on an electrospun nanofibrous substrate [91]. These fibroblasts, along with normal rat kidney cells, express 40–50% less actin on nanofibers than on control substrates at 24 h, which also suggests an increase in differentiated characteristics [91].

Nanofibrous scaffolds have also shown the ability to direct more immature cells to a desired lineage. This has been studied with neural progenitor cells [93], multipotent neural cells [90] and neonatal murine cavariar cells [95]. In these cases, nanofibrous scaffolds have aided in the differentiation of neurons relative to other neuronal support cells. Compared to control scaffolds, nanofibrous scaffolds allow the neonatal murine cavariar cells to differentiate to osteoblasts faster and enhance the expression of phenotypic markers [95]. Specifically, bone sialoprotein was found to be expressed approximately 8–10× higher on nanofibrous scaffolds than on solid-walled scaffolds.

Nanofibrous scaffolds have also shown ability to aid in the redifferentiation of cells that have regressed to a more immature state during cell culture [92]. This particular feature will aid in tissue formation of chondrocytes and hepatocytes, both of which revert to immature cell types during culture.

#### 4.5.4

#### Migration

To form neo-tissue, cells must be able to infiltrate the scaffold and move throughout it. This movement of cells across the scaffold and pore surfaces is a highly complex process that is dependent on the actin-rich cortex beneath the plasma membrane, which pushes the plasma membrane outward to form a leading edge. Next the actin cytoskeleton must attach to the substrate and provide the traction necessary to move the bulk of the cytoplasm [94]. Many ECM proteins, such as fibronectin, are thought to aid in and direct migrating cells toward their final destination [94]. As discussed in the attachment section, the preferential adsorption of attachment proteins including fibronectin, and the concentration of transmembrane attachment proteins and focal adhesion in localized areas could potentially explain the increased migrant capability of cells on nanofibrous scaffolds. This is particularly evident in a study by Semino et al., in which hippocampal slices were cultured on nanofibrous hydrogel scaffolds [97]. The nanofibrous scaffolds allowed for deeper penetration (~500 μm relative to the ~150 μm of the control surface) [97]. Over time the cells migrating into the space were of different lineages. Glia cells were the first to infiltrate the nanofibrous scaffold followed by neural progenitor cells, which then proliferated and differentiated to form a framework for neuron tissue formation within the nanofibrous scaffold [97]. A similar phenomena has been seen by simply placing neural progenitor cells on nanofibrous scaffold [93]. This indicates that cells on nanofibers, independent of tissue type, are capable of increased navigation.



## 4.6

### Tissue Formation

In the human body, tissues and organs are organized into 3D structures. Each tissue or organ has its own specific characteristic architecture depending on its biological function. This architecture provides appropriate channels for mass transport (movement of signaling molecules, nutrients, and metabolic waste) and spatial cellular organization (cell–cell and cell–matrix interactions), both of which are thought to be important for appropriate tissue function [12]. As such, scaffolds for each particular tissue engineering application need to be designed with sensitivity to the cellular requirements of the tissue it is generating.

#### 4.6.1

##### Connective Tissue

Connective tissue mainly functions to bind and support other tissues. As such, connective tissue contains a sparse cell population scattered throughout an ECM composed of fibrous webs embedded in a uniform foundation, all of which is generally secreted by the cell population [98]. However, there is great diversity in the cellular requirements for various connective tissues. In the context of this discussion we will examine three types, ligaments, cartilage and bone.

##### 4.6.1.1 Ligaments

Ligaments are fibrous connective tissue that connects bones together at joints. To do this, ligaments contain numerous collagenous fibers organized into parallel bundles that maximize non-elastic strength [98]. It is this organization that a scaffold must mimic to successfully generate a new ligament. This has been attempted with scaffolds containing oriented nanofibers seeded with human ligament fibroblasts [96]. Shortly after seeding, the human ligament fibroblasts oriented themselves in the direction of the nanofibers and assumed the appropriate spindle-shaped morphology [96]. After 7 days in culture, oriented bundles were present in a tissue-like formation [96] (Fig. 4.10).

##### 4.6.1.2 Cartilage

Rather than acting as a connector like ligaments, cartilage acts as a cushion between vertebrae and the ends of some bones and reinforces tissue such as the windpipe. As such, the ECM of cartilage is much different from that of ligaments and contains an abundance of collagenous fibers embedded in a rubbery matrix of chondroitin sulfate [98].

Overall, cartilage tissue engineering has been relatively successful even with micro-sized fibers [99, 100]. Nanofibrous materials have been reported to promote chondrocyte proliferation [101, 102], differentiation [92] and the secretion of the suitable ECM [101–103]. Interestingly, in a study by Li et al., chondrocytes on nanofibrous scaffolds were the only ones found to express collagen type IIB, a col-

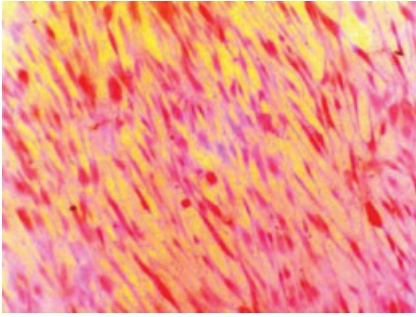


**Fig. 4.10.** Histological sections of ligament regenerated on nanofibrous scaffolds: human ligament fibroblasts on aligned nanofibers after 7 days of culture. (Reprinted with permission from Ref. [96] © 2005, Elsevier.)

lagen type found only in mature chondrocytes [92]. While in another study, Li et al. found collagen X down-regulated on nanofibrous scaffolds, and yet the chondrocytes had morphology similar to native cartilage and still produced the correct sulfated matrix [103]. This seems to suggest that, in this study, the scaffold potentially interacted with the cells in a way similar to that of collagen X, triggering the decrease in its expression.

#### 4.6.1.3 Bone

Bone is a mineralized connective tissue that supports the body and a major skeletal component that is constantly changing and remodeling itself based on the current needs of the organism. This remodeling is done to help bone fulfill one or more of its primary functions within the organism. These functions include supporting and protecting soft tissues, providing the rigidity necessary for locomotion, regulating calcium and phosphate, and providing a site for hematopoiesis [104]. Although bone can remodel and repair itself, it cannot repair large defects caused by trauma or degenerative disease on its own, which is why tissue engineers are interested in *de novo* bone generation.

After 1 week or more of *in vitro* culture on a nanofibrous scaffold, collagen type 1 has been observed throughout the scaffold [31, 95, 105]. After three or more weeks of *in vitro* culture, up-regulation of bone markers such as alkaline phosphatase, bone sialoprotein and osteocalcin on nanofibrous scaffolds relative to control have been observed [103, 106]. The notable exception to this is collagen type I, a major component of the bone ECM [103]. As with cartilage, it is possible that the nanofibrous scaffolds interact with the cells in a similar manner to native collagen, limiting the cells' need to express it. This has been supported by Woo et al., who administered 3,5-dehydroproline to inhibit collagen fibril formation and found alpha-2 integrin and osteogenic markers expressed on the nanofibrous scaffold but not the control scaffolds [95, 106].

In a 10-day study of osteoblastic phenotype development in neonatal murine

cavariar cells,  $\alpha 1$  collagen and Runx2 expression were shown to be initially up-regulated on the nanofibrous scaffolds compared to solid-walled scaffolds. However, as the experiment continued the expression levels for both markers approached the expression levels on the nanofibrous scaffolds, while both bone sialoprotein and osteocalcin once observed were substantially higher on the nanofibrous scaffolds compared with solid-walled scaffolds [95]. The authors have also observed the up-regulation of bone sialoprotein and osteocalcin and the down-regulation of collagen type I over the course of 6 weeks with pre-osteoblasts on nanofibrous scaffolds compared with solid-walled scaffolds.

Small globular mineral deposits have been observed within nanofibrous scaffolds in as early as 2 weeks using primary calvarial cells [95]. In this study, large mineral deposits existed along the nanofibers, indicating mineral development along the nanofibers. This is supported by the authors' own observations of mineralization emanating from within areas of the synthetic nanofibrous scaffold. This architecture allows for cellular penetration within the synthetic matrix [107].

In terms of successful bone generation, Vacanti and coworkers found that after 4 weeks *in vitro* and 4 weeks *in vivo* vascularization, mineralization and embedded osteocyte-like cells can be seen in electrospun nanofibrous scaffolds [105].

#### 4.6.2

#### Neural Tissue

Neural tissue is composed of neurons and support cells. Neurons transmit signals to direct other tissues' function via nerve impulses throughout the body while the support cells provide structure for the tissue and protect, insulate and generally support the neurons. This tissue has a limited capacity to regenerate, but is vital to normal body function.

Nerve impulses are passed from one neuron to the next at synapses where a projection from the first neuron approaches the body of a second neuron [98]. To achieve this sort of order within a scaffold, neurons grow neurite projections with growth cones to interact with other cells. Several nanofibrous scaffolds have showed increased neurite outgrowth relative to control [25, 90, 93, 108]. At times, this increased outgrowth has been as much as 100  $\mu\text{m}$  [25]. It has been generally observed that the nanofibrous scaffold acts as a guide for neurite outgrowth [25, 108]. When the nanofibers are aligned this growth tends to be in the direction parallel to the nanofibers and the cells tend to have a more elongated shape similar to *in vivo* [25].

Since neuronal progenitor cells are difficult to isolate, much of neuronal tissue engineering relies on the migration of progenitor cells from tissue. This has been documented with nanofibrous scaffolds [93, 97]. Once these progenitor cells migrate, they must differentiate to provide the necessary neurons and support cells for proper function of the neuronal tissue. Nanofibrous scaffolds promote increased differentiation compared to control scaffolds [90, 93, 97]. Although complete *de novo* neural tissue has yet to be formed on nanofibrous scaffolds, great potential and interest exist to pursue *de novo* tissue formation of this tissue type.

## 4.6.3

**Cardiovascular Tissue**

The cardiovascular system is responsible for the transport of nutrients and wastes to and from cells. The heart acts as the pump driving the system and the vascular tissue acts as tubes directing the path of collection and exchange of nutrients and waste. As such, disruption in the function of this system is life threatening and must be repaired quickly. This section concentrates on cardiac muscle and blood vessels.

4.6.3.1 **Cardiac Muscle**

The regenerative capability of cardiac muscle is particularly limited, making it the most challenging tissue to regenerate in the cardiovascular system [109]. To combat this, nanofibrous self-assembling RAD12-II peptide scaffolds have been developed by Lee and coworkers that can be injected into the heart to promote cardiac muscle regeneration. When injected into the left ventricle wall of adult mice, endothelial cells invaded, organized and matured into the appropriate structure to support smooth muscle cell migration, which allowed for the formation of arterioles [110]. Red blood cells located within the arterioles indicate that they were functionally connected to the vascular system. This led to the migration of cardiac progenitor cells that differentiated into myocytes [110]. Inclusion of myocytes in the scaffold greatly increases myocyte density within the scaffold over a much shorter period of time. When implanted with embryonic stem cells this same self-assembling RAD12-II peptide scaffold promoted the controlled differentiation of the cells to cardiomyocytes [110]. During *in vitro* cultures, the self-assembling RAD12-II peptide scaffold promoted endothelial and myocardial cell survival and synchronized contraction of the generated muscle [111].

4.6.3.2 **Blood Vessel**

Blood vessels are composed of smooth muscle and endothelial cells. Similar to previously discussed tissue types, alignment of nanofibers aids in blood vessel function. The aligned nanofibrous scaffolds have been shown to prompt the alignment of smooth muscle cells parallel to the fiber direction, which increases vessel strength [27]. This alignment has also been shown to increase initial adhesion and proliferation on the scaffold, which leads to quicker functional blood vessel formation [27].

The second cellular component of blood vessels, endothelial cells, also benefit from culture on nanofibrous scaffolds. Human aortic endothelial cells cultured on nanofibrous scaffolds form confluent layers similar to those formed on collagen type I gel or Matrigel [73]. The scaffolds also promote nitric oxide release which is a marker of endothelial cell phenotype [73].

## 4.6.4

**Liver Tissue**

Liver is a multipurpose organ that aids in the digestion of fats, the uptake and release of glucose, synthesis of plasma proteins and the detoxification of many

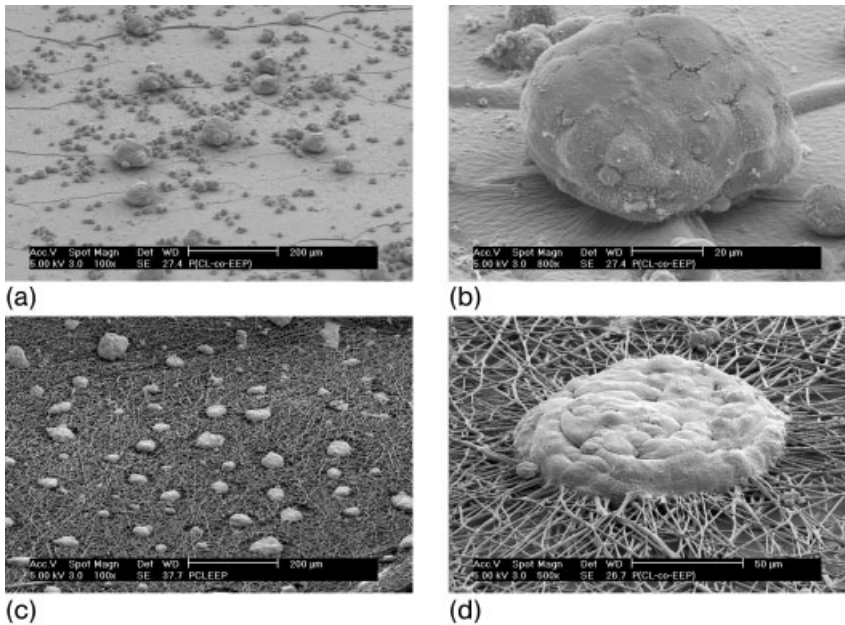


**Fig. 4.11.** SEM images of hepatocytes after 8 days of culture: (a, b) Hepatocytes cultured on a Gal-film formed spheroids that did not integrate with the substrate; (c, d) in contrast,

hepatocytes cultured on Gal-nanomesh afforded aggregates that engulfed the functional nanofibers. (Reprinted with permission from [72] © 2005, Elsevier.)

poisons and metabolic waste [98]. Regeneration of liver tissue in a functional form has proven incredibly difficult. However, nanofibrous scaffolds have brought renewed efforts. Nanofibrous scaffolds appear to increase hepatocyte function in comparison to control scaffolds [72, 112]. Hepatocytes on nanofibrous scaffolds also exhibit a more uniform spheroid-like distribution than on control scaffolds [72]. Figure 4.11 illustrates these differences in interaction between hepatocytes and nanofibrous and non-fibrous materials.

#### 4.7

#### Conclusion

To date the most successful neo-tissue generation has involved connective tissues [100, 101, 113]. As evident by the developments in cardiac muscle formation, headway is being made with more metabolically demanding and complex tissues. However, the holy grail of tissue engineering still remains the development of complete patient-specific organs available on demand [2, 114]. To achieve this, scaffolds must not only provide structural support but also biological cues [115]. Increased knowledge about cellular interactions with the native ECM and nano-structured scaffolds will facilitate more functional scaffold development.

Hopefully, this chapter has provided some insight into the crucial role tissue engineering scaffolding plays in this drive for 3D neo-tissue formation [4, 17, 116] through its focus on nanofibrous scaffolding fabrication and the biological advantages of nanofibrous scaffolding structures in mimicking the ECM.

## References

- 1 LANGER, R., J. VACANTI, Tissue engineering. *Science*, **1993**, 260, 920–926.
- 2 MA, P., Scaffolds for tissue fabrication. *Mater. Today*, **2004**, 7, 30–40.
- 3 MA, P., R. ZHANG, *J. Biomed. Mater. Res.*, **1999**, 46, 60–72.
- 4 HUBBELL, J., *Biotechnology*, **1995**, 13(6), 565–575.
- 5 LIU, X., P. MA, Polymeric scaffolds for bone tissue engineering. *Ann. Biomed. Eng.*, **2004**, 32, 477–486.
- 6 CHEN, V.J., P.X. MA, Nano-fibrous poly(L-lactic acid) scaffolds with interconnected spherical macropores. *Biomaterials*, **2004**, 25(11), 2065–2073.
- 7 ELSDALE, T., J. BARD, *J. Cell Biol.*, **1972**, 54, 626–637.
- 8 MA, P., R. LANGER, Fabrication of biodegradable polymer foams for cell transplantation and tissue engineering, in *Tissue Engineering Methods and Protocols*, M. YARMUSH, J. MORGAN (Eds.), **1999**, Humana Press Inc., Totowa, NJ, pp. 47–56.
- 9 ABBOTT, A., Cell culture: Biology's new dimension. *Nature*, **2003**, 424, 870–872.
- 10 CUKIERMAN, E., R. PANKOV, D. STEVENS, K. YAMADA, Taking Cell-matrix adhesions to the third dimensions. *Science*, **2001**, 294, 1708–1712.
- 11 SCHMEICHEL, K.L., M.J. BISSELL, Modeling tissue-specific signaling and organ function in three dimensions. *J. Cell Sci.*, **2003**, 116(Pt 12), 2377–2388.
- 12 ZHANG, R., P.X. MA, Synthetic nano-fibrillar extracellular matrices with predesigned macroporous architectures. *J. Biomed. Mater. Res.*, **2000**, 52(2), 430–438.
- 13 MA, P.X., R. ZHANG, Synthetic nano-scale fibrous extracellular matrix. *J. Biomed. Mater. Res.*, **1999**, 46(1), 60–72.
- 14 ALBERTS, B., *Molecular Biology of the Cell*, 4th edn. **2002**, Garland Science, New York, xxxiv, 1463.
- 15 PACHENCE, J.M., Collagen-based devices for soft tissue repair. *J. Biomed. Mater. Res.*, **1996**, 33(1), 35–40.
- 16 ANSELME, K., C. BACQUES, G. CHARRIERE, D.J. HARTMANN, D. HERBAGE, R. GARRONE, Tissue reaction to subcutaneous implantation of a collagen sponge. A histological, ultrastructural, and immunological study. *J. Biomed. Mater. Res.*, **1990**, 24(6), 689–703.
- 17 WOO, K.M., V.J. CHEN, P.X. MA, Nano-fibrous scaffolding architecture selectively enhances protein adsorption contributing to cell attachment. *J. Biomed. Mater. Res. A*, **2003**, 67(2), 531–537.
- 18 DESAI, T., Micro- and nanoscale structures for tissue engineering constructs. *Med. Eng. Phys.*, **2000**, 22, 595–606.
- 19 FORMHALS, A., *Process and Apparatus for Preparing Artificial Threads*, U.S.P. Office, Editor. **1934**, Schreiber-Gastell, Richard and Formhals, Anton: United States. pp. 1–7.
- 20 DEITZEL, J.M., J.D. KLEINMEYER, J.K. HIRVONEN, N.C. BECK TAN, Controlled deposition of electrospun poly(ethylene oxide) fibers. *Polymer*, **2001**, 42(19), 8163–8170.
- 21 JAEGER, R., M.M. BERGSHOFF, C. MARTÍN I BATLLE, H. SCHÖNHERR, G.J. VANCISO. Electrospinning of ultrathin polymer fibres. In: *Macromolecular Symposia*. **1998**, 127, 141–150.
- 22 RENEKER, D.H., I. CHUN, Nanometre

- diameter fibres of polymer, produced by electrospinning. *Nanotechnology*, **1996**, 7(3), 216–223.
- 23 KENAWY EL, R., J.M. LAYMAN, J.R. WATKINS, G.L. BOWLIN, J.A. MATTHEWS, D.G. SIMPSON, G.E. WNEK, Electrospinning of poly(ethylene-co-vinyl alcohol) fibers. *Biomaterials*, **2003**, 24(6), 907–913.
  - 24 MA, Z., M. KOTAKI, R. INAI, S. RAMAKRISHNA, Potential of nanofiber matrix as tissue-engineering scaffolds. *Tissue Eng.*, **2005**, 11(1–2), 101–109.
  - 25 YANG, F., R. MURUGAN, S. WANG, S. RAMAKRISHNA, Electrospinning of nano/micro scale poly(L-lactic acid) aligned fibers and their potential in neural tissue engineering. *Biomaterials*, **2005**, 26, 2603–2610.
  - 26 LI, W.J., C.T. LAURENCIN, E.J. CATERSON, R.S. TUAN, F.K. KO, Electrospun nanofibrous structure: A novel scaffold for tissue engineering. *J. Biomed. Mater. Res.*, **2002**, 60(4), 613–621.
  - 27 XU, C., R. INAI, M. KOTAKI, S. RAMAKRISHNA, Aligned biodegradable nanofibrous structure: A potential scaffold for blood vessel engineering. *Biomaterials*, **2004**, 25, 877–886.
  - 28 KAMEOKA, J., H.G. CRAIGHEAD, Fabrication of oriented polymeric nanofibers on planar surfaces by electrospinning. *Appl. Phys. Lett.*, **2003**, 83(2), 371–373.
  - 29 ZONG, X., S. RAN, D. FANG, B.S. HSIAO, B. CHU, Control of structure, morphology and property in electrospun poly(glycolide-co-lactide) non-woven membranes via post-draw treatments. *Polymer*, **2003**, 44(17), 4959–4967.
  - 30 LI, D., Y.L. WANG, Y.N. XIA, Electrospinning of polymeric and ceramic nanofibers as uniaxially aligned arrays. *Nano Lett.*, **2003**, 3(8), 1167–1171.
  - 31 YOSHIMOTO, H., Y.M. SHIN, H. TERAI, J.P. VACANTI, A biodegradable nanofiber scaffold by electrospinning and its potential for bone tissue engineering. *Biomaterials*, **2003**, 24(12), 2077–2082.
  - 32 HUANG, L., K. NAGAPUDI, R.P. APKARIAN, E.L. CHAIKOF, Engineered collagen-PEO nanofibers and fabrics. *J. Biomater. Sci. Polym. Ed.*, **2001**, 12(9), 979–993.
  - 33 LI, M., M. MONDRINOS, M. GANDHI, F. KO, A. WEISS, P. LELKES, Electrospun protein fibers as matrices for tissue engineering. *Biomaterials*, **2005**, 26, 5999–6008.
  - 34 MATTHEWS, J.A., G.E. WNEK, D.G. SIMPSON, G.L. BOWLIN, Electrospinning of collagen nanofibers. *Biomacromolecules*, **2002**, 3(2), 232–238.
  - 35 BOLAND, E., J. MATTHEWS, K. PAWLOWSKI, D. SIMPSON, G. WNEK, G. BOWLIN, Electrospinning collagen and elastin: Preliminary vascular tissue engineering. *Front Biosci.*, **2004**, 9, 1422–1432.
  - 36 ROEMER, D., H.H. BUESCHER, R.C. HILL, J. PLESS, W. BAUER, F. CARDINAUX, A. CLOSSE, D. HAUSER, R. HUGUENIN, A synthetic enkephalin analogue with prolonged parenteral and oral analgesic activity. *Nature*, **1977**, 268(5620), 547–549.
  - 37 ZHANG, S., Fabrication of novel biomaterials through molecular self-assembly. *Nat. Biotechnol.*, **2003**, 21(10), 1171–1178.
  - 38 SCHNUR, J.M., R. PRICE, P. SCHOEN, P. YAGER, J.M. CALVERT, J. GEORGER, A. SINGH, Lipid-based tubule microstructures. *Thin Solid Films*, **1987**, 152(1–2), 181–206.
  - 39 HOLMES, T.C., S. DE LACALLE, X. SU, G. LIU, A. RICH, S. ZHANG, Extensive neurite outgrowth and active synapse formation on self-assembling peptide scaffolds. *Proc. Natl. Acad. Sci. U.S.A.*, **2000**, 97(12), 6728–6733.
  - 40 ZANG, S., T. HOLMES, C. LOCKSHIN, A. RICH, Spontaneous assembly of a self-complementary oligopeptide to form a stable macroscopic membrane. *Proc. Natl. Acad. Sci. U.S.A.*, **1993**, 90, 3334–3338.
  - 41 ZANG, S., T. HOLMES, C. DIPERSIO, R. HYNES, X. SU, A. RICH, Self-complementing oligopeptide matrices support mammalian-cell attachment. *Biomaterials*, **1995**, 16, 1385–1395.
  - 42 HARTGERINK, J.D., E. BENIASH, S.I. STUPP, Self-assembly and mineraliza-

- tion of peptide-amphiphile nanofibers. *Science*, **2001**, 294(5547), 1684–1688.
- 43 HARTGERINK, J., E. BENIASH, S. STUPP, Peptide-amphiphile nanofibers: A versatile scaffold for the preparation of self-assembling materials. *Proc. Natl. Acad. Sci. U.S.A.*, **2002**, 99, 5133–5138.
  - 44 SERVICE, R.F., Nanofibers seed blood vessels. *Science*, **2005**, 308(5718), 44b–45.
  - 45 PAKSTIS, L., B. OZBAS, K. HALES, A. NOWAK, T. BEMING, D. POCHAN, Effect of chemistry and morphology on the biofunctionality of self-assembling diblock copolypeptide hydrogels. *Biomacromolecules*, **2004**, 5, 312–318.
  - 46 POCHAN, D., L. LPAKSTIS, B. OZBAS, SANS and Cryo-TEM study of Self-assembled diblock copolypeptide hydrogels with rich nano-through microscale morphology. *Macromolecules*, **2002**, 35, 5358–5360.
  - 47 NOWAK, A., V. BREEDVELD, L. PAKSTIS, B. OZBAS, D. PINE, D. POCHAN, T. DEMING, Rapidly recovering hydrogel scaffolds from self-assembling diblock copolypeptide amphiphiles. *Nature*, **2002**, 417, 424–428.
  - 48 LIU, D.J., S. DE FEYTER, M. COTLET, U.M. WIESLER, T. WEIL, A. HERRMANN, K. MULLEN, F.C. DE SCHRYVER, Fluorescent self-assembled polyphenylene dendrimer nanofibers. *Macromolecules*, **2003**, 36(22), 8489–8498.
  - 49 LIU, D.J., H. ZHANG, P.C.M. GRIM, S. DE FEYTER, U.M. WIESLER, A.J. BERRESHEIM, K. MULLEN, F.C. DE SCHRYVER, Self-assembly of polyphenylene dendrimers into micrometer long nanofibers: An atomic force microscopy study. *Langmuir*, **2002**, 18(6), 2385–2391.
  - 50 PERUTZ, M.F., A.H. WINDLE, Cause of neural death in neurodegenerative diseases attributable to expansion of glutamine repeats. *Nature*, **2001**, 412(6843), 143–144.
  - 51 PERUTZ, M.F., Glutamine repeats and neurodegenerative diseases. *Brain Res. Bull.*, **1999**, 50(5–6), 467.
  - 52 PERUTZ, M.F., B.J. POPE, D. OWEN, E.E. WANKER, E. SCHERZINGER, Aggregation of proteins with expanded glutamine and alanine repeats of the glutamine-rich and asparagine-rich domains of Sup35 and of the amyloid beta-peptide of amyloid plaques. *Proc. Natl. Acad. Sci. U.S.A.*, **2002**, 99(8), 5596–5600.
  - 53 VAN DE WITTE, P., P.J. DIJKSTRA, J.W.A. VAN DEN BERG, J. FEIJEN, Phase separation processes in polymer solutions in relation to membrane formation. *J. Membr. Sci.*, **1996**, 117(1–2), 1–31.
  - 54 ATALA, A., R.P. LANZA, *Methods of Tissue Engineering*. **2001**, Academic Press, San Diego, xli, 1285 pp.
  - 55 ZHANG, R., P.X. MA, Poly(alpha-hydroxyl acids)/hydroxyapatite porous composites for bone tissue engineering. I. Preparation and morphology. *J. Biomed. Mater. Res.*, **1999**, 44(4), 446–455.
  - 56 MA, P.X., R. ZHANG, G. XIAO, R. FRANCESCHI, Engineering new bone tissue in vitro on highly porous poly(alpha-hydroxyl acids)/hydroxyapatite composite scaffolds. *J. Biomed. Mater. Res.*, **2001**, 54(2), 284–293.
  - 57 WEI, G., P.X. MA, Macro-porous and nano-fibrous polymer scaffolds and polymer/bone-like apatite composite scaffolds generated by sugar spheres. *J. Biomed. Mater. Res.*, **2006**, in the press.
  - 58 MA, P.X., Tissue engineering, in *Encyclopedia of Polymer Science and Technology*, J.I. KROSCWITZ (Ed.), **2003**, John Wiley & Sons, Inc., Hoboken, NJ. p. www.mrw.interscience.wiley.com/epst.
  - 59 ZHANG, R., P.X. MA, Processing of polymer scaffolds: Phase separation, in *Methods of Tissue Engineering*, A. ATALA, R. LANZA (Eds.), **2001**, Academic Press, San Diego, pp. 715–724.
  - 60 CHEN, V.J., P.X. MA, Phase separation for polymer scaffolds, in *Scaffolding in Tissue Engineering*, P.X. MA, J. ELISSEFF (Eds.), CRC Press, Boca Raton, FL, **2005**, pp. 121–133.



- 61 LARSON, R.G., *The Structure and Rheology of Complex Fluids*. Oxford University Press, New York, 1999, xxi, 663 pp.
- 62 CHEN, V., G. WEI, P. MA, Nanostructured scaffolds for tissue engineering and regeneration, in *Handbook of Nanostructured Biomaterials and their Applications in Nanobiotechnology*, H. NALWA (Ed.), American Scientific Publishers, Los Angeles, 2005, pp. 415–435.
- 63 ROSSERT, J., B. DE CROMBUGGHE, Type I collagen: Structure, synthesis, and regulation, in *Principles of Bone Biology*, J. BILEZIKIAN (Ed.), Academic Press, San Diego, 2002, pp. 189–210.
- 64 SALO, J., Bone resorbing osteoclasts reveal two basal plasma membrane domains and transcytosis of degraded matrix material, in *Department of Anatomy and Cell Biology*, 2002, University of Oulu, Oulu, Finland, p. 59.
- 65 WEI, G., P. MA, Structure and properties of nano-hydroxyapatite/polymer composite scaffolds for bone tissue engineering. *Biomaterials*, 2004, 25, 4749–4759.
- 66 ITO, Y., H. HASUDA, M. KAMITAKAHARA, C. OHTSUKI, M. TANIHARA, I. KANG, O. KOWON, A composite of hydroxyapatite with electrospun biodegradable nanofibers as a tissue engineering material. *J. Biosci. Bioeng.*, 2005, 100, 43–49.
- 67 FUJIIHARA, K., M. KOTAKI, S. RAMAKRISHNA, Guided bone regeneration membrane made of polycaprolactone/calcium carbonate composite nano-fibers. *Biomaterials*, 2005, 26, 4139–4147.
- 68 MIN, B., G. LEE, S. KIM, Y. NAM, T. LEE, W. PARK, Electrospinning of silk fibroin nanofibers and its effect on the adhesion and spreading of normal human keratinocytes and fibroblasts in vitro. *Biomaterials*, 2004, 25, 1289–1297.
- 69 MA, Z., W. HE, T. YONG, S. RAMAKRISHNA, Grafting of gelatin on electrospun poly(caprolactone) nanofibers to improve endothelial cell spreading and proliferation and to control cell orientation. *Tissue Eng.*, 2005, 11(7/8), 1149–1158.
- 70 ZHANG, Y., H. OUYANG, C. LIM, S. RAMAKRISHNA, Z. HUANG, Electrospinning of gelatin fibers and gelatin/PCL composite fibrous scaffolds. *J. Biomed. Mater. Res., B* 2005, 72, 156–165.
- 71 ZHANG, Y., J. VENUGOPAL, Z. HUANG, C. LIM, S. RAMAKRISHNA, Characterization of the surface biocompatibility of the electrospun PCL-collagen nanofibers using fibroblasts. *Biomacromolecules*, 2005, 6, 2583–2589.
- 72 CHUA, K., W. LIM, P. ZHANG, H. LU, J. WEN, S. RAMAKRISHNA, K. LEONG, H. MAO, Stable immobilization of rat hepatocyte spheroids on galactosylated nanofibers. *Biomaterials*, 2005, 26, 2537–2547.
- 73 GENOVE, E., C. SHEN, S. ZHANG, C. SEMINO, The effect of functionalized self-assembling peptide scaffolds on human aortic endothelial cell function. *Biomaterials*, 2005, 26, 3341–3351.
- 74 MIKOS, A.G., A.J. THORSEN, L.A. CZERWONKA, Y. BAO, R. LANGER, D.N. WINSLOW, J.P. VACANTI, Preparation and characterization of poly(-lactic acid) foams. *Polymer*, 1994, 35(5), 1068–1077.
- 75 BERNDT, P., G. FIELDS, M. TIRRELL, *J. Am. Chem. Soc.*, 1995, 117, 9515–9522.
- 76 MALKAR, N., J. LAUER-FIELDS, D. JUSKA, G. FIELDS, *Biomacromolecules*, 2003, 4(3), 518–528.
- 77 HAVERSTICK, K., T. PAKALNS, Y. YU, J. MCCARTHY, G. FIELDS, M. TIRRELL, *Polym. Mater. Sci. Eng.*, 1997, 77, 584–585.
- 78 YU, Y., V. ROONTGA, V. DARAGAN, K. MAYO, M. TIRRELL, G. FIELDS, *Biochemistry*, 1999, 38, 1659–1668.
- 79 LIU, X., Y. WON, P. MA, Surface modification of interconnected porous scaffolds. *J. Biomed. Mater. Res., A* 2005, 74, 84–91.
- 80 LIU, X., L. SMITH, G. WEI, Y. WON, P. MA, Surface engineering of nanofibrous poly(L-lactic acid) scaffolds via self-assembly technique for bone

- tissue engineering. *J. Biomed. Nanotechnol.*, **2005**, 1(1), 54–60.
- 81 KIM, K., Y. LUU, C. CHANG, D. FANG, B. HSIAO, B. CHU, M. HADJIARYROU, Incorporation and controlled release of a hydrophilic antibiotic using poly(lactide-co-glycolide)-based electrospun nanofibrous scaffolds. *J. Controlled Release*, **2004**, 98, 47–56.
- 82 KATTI, D., K. ROBINSON, F. KO, C. LAURENCIN, Bioresorbable nanofiber-based systems for wound healing and drug delivery: Optimization of fabrication parameters. *J. Biomed. Mater. Res. Part B: Appl Biomater.*, **2004**, 70, 286–296.
- 83 ZONG, X., K. KIM, D. FANG, S. RAN, B. HSIAO, B. CHU, Structure and process relationship of electrospun bioabsorbable nanofiber membranes. *Polymer*, **2002**, 43, 4403–4412.
- 84 ZENG, J., L. YANG, Q. LIANG, X. ZHANG, H. GUAN, X. XU, X. CHEN, X. JING, Influence of the drug compatibility with polymer solution on the release kinetics of electrospun fiber formulation. *J. Controlled Release*, **2005**, 20, 43–51.
- 85 JIANG, H., D. FANG, B. HSIAO, B. CHU, W. CHEN, Preparation and characterization of ibuprofen-loaded poly(lactid-co-glycolide)/poly(ethylene glycol)-g-chitosan electrospun membranes. *J. Biomater. Sci. Polym. Edn.*, **2004**, 15, 279–296.
- 86 VERRECK, G., I. CHUN, J. ROSENBLATT, J. PEETERS, A. DIJCK, J. MENSCH, M. NOPPE, M. BREWSTER, Incorporation of drugs in an amorphous state into electrospun nanofibers composed of a water-insoluble, nonbiodegradable polymer. *J. Controlled Release*, **2003**, 92, 349–360.
- 87 LUU, Y., K. KIM, B. HSIAO, B. CHU, M. HADJIARYROU, Development of a nanostructured DNA delivery scaffold via electrospinning of PLGA and PLA-PEG block copolymers. *J. Controlled Release*, **2003**, 89, 341–353.
- 88 CHEW, S., J. WEN, E. YIM, K. LEONG, Sustained release of proteins from electrospun biodegradable fibers. *Biomacromolecules*, **2005**, 6, 2017–2024.
- 89 WEI, G., Q. JIN, W. GIANNIBILE, P. MA, Nano-fibrous scaffolds for controlled delivery of recombinant human PDGF-BB. *J. Controlled Release*, **2006**, 112(1), 103–110.
- 90 YANG, F., C. XU, M. KOTAKI, S. WANG, S. RAMAKRISHNA, Characterization of neural stem cells on electrospun poly(L-lactic acid) nanofibrous scaffolds. *J. Biomater. Sci. Polym. Edn.*, **2004**, 15(12), 1483–1497.
- 91 SCHINDLER, M., I. AHMED, J. KAMAL, A. NUR-E-KAMAL, T. GRAFE, H. CHUNG, S. MEINERS, A synthetic nanofibrillar matrix promotes in vivo-like organization and morphogenesis for cells in culture. *Biomaterials*, **2005**, 26, 5624–5631.
- 92 LI, W., K. DANIELSON, P. ALEXANDER, R. TUAN, Biological response of chondrocytes cultured in three-dimensional nanofibrous poly(E-caprolactone) scaffolds. *J. Biomed. Mater. Res. A*, **2003**, 67, 1105–1114.
- 93 SILVA, G., C. CZEISLER, K. NIECE, E. BENIASH, D. HARRINGTON, J. KESSLER, S. STUPP, Selective differentiation of neural progenitor cells by high-epitope density nanofibers. *Science*, **2004**, 303, 1352–1355.
- 94 ALBERTS, B., A. JOHNSON, J. LEWIS, M. RAFF, K. ROBERTS, P. WALTER, *Molecular Biology of the Cell*. 4th edn., Garland Science, New York, **2002**.
- 95 WOO, K., J. JUN, V. CHEN, J. SEO, J. BAEK, H. RYOO, G. KIM, M. SOMERMAN, P. MA, Nano-fibrous scaffolding promotes osteoblast differentiation and biomineralization. *Biomaterials*, **2006**, in press.
- 96 LEE, C., H. SHIN, I. CHO, Y. KANG, I. KIM, K. PARK, J. SHIN, Nanofiber alignment and direction of mechanical strain affect the ECM productions of human ACL fibroblast. *Biomaterials*, **2005**, 26, 1261–1270.
- 97 SEMINO, C., J. KASAHARA, Y. HAYASHI, S. ZHANG, Entrapment of migrating hippocampal neural cells in three-dimensional peptide nanofiber scaffolds. *Tissue Eng.*, **2004**, 10(3/4), 643–655.
- 98 CAMPBELL, N., J. REECE, L. MITCHELL, *Biology*. 5 edn., Benjamin Cummings, Menlo Park, **1999**.

- 99 MA, P.X., B. SCHLOO, D. MOONEY, R. LANGER, Development of biomechanical properties and morphogenesis of in vitro tissue engineered cartilage. *J. Biomed. Mater. Res.*, **1995**, 29(12), 1587–1595.
- 100 MA, P., R. LANGER, Morphology and mechanical function of long-term in vitro engineered cartilage. *J. Biomed. Mater. Res.*, **1999**, 44, 217–221.
- 101 LI, W., R. TULI, C. OKAFOR, A. DERFOUL, K. DANIELSON, D. HALL, R. TUAN, A three-dimensional nanofibrous scaffold for cartilage tissue engineering using human mesenchymal stem cells. *Biomaterials*, **2005**, 26, 599–609.
- 102 KISIDAY, J., M. JIN, B. KURZ, H. HUNG, C. SEMINO, S. ZHANG, A. GRODZINSKY, Self-assembling peptide hydrogel fosters chondrocyte extracellular matrix production and cell division: Implications for cartilage tissue repair. *Proc. Natl. Acad. Sci. U.S.A.*, **2002**, 99, 9996–10001.
- 103 LI, W., R. TULI, X. HUANG, P. LAQUERRIERE, R. TUAN, Multilineage differentiation of human mesenchymal stem cells in a three-dimensional nanofibrous scaffold. *Biomaterials*, **2005**, 26, 5158–5166.
- 104 MARKS, S., P. ODGREN, Structure and development of the skeleton, in *Principles of Bone Biology*, G. RODAN (Ed.), Academic Press, San Diego. **2002**, pp. 3–16.
- 105 SHIN, M., H. YOSHIMOTO, J. VACANTI, In vivo bone tissue engineering using mesenchymal stem cells on a novel electrospun nanofibrous scaffold. *Tissue Eng.*, **2004**, 10(1/2), 33–41.
- 106 WOO, K., J. JUN, V. CHEN, J. BAEK, S. SEO, G. KIM, S. KO, P. MA, Mineralization in the mouse calvarial cell-seeded nano-fibrous scaffolds. *J. Biomed. Mater. Res.*, **2004**, 19, S212.
- 107 CHEN, V.J., L.A. SMITH, P.X. MA, Bone regeneration on computer designed nano-fibrous scaffolds. *Biomaterials*, **2006**, 27(21), 3973–3979.
- 108 YANG, F., R. MURUGAN, S. RAMAKRISHNA, X. WANG, Y. MA, S. WANG, Fabrication of nano-structured porous PLLA scaffold intended for nerve tissue engineering. *Biomaterials*, **2004**, 25, 1891–1900.
- 109 LEOR, J., Y. AMSALEM, S. COHEN, CELLS, scaffolds and molecules for myocardial tissue engineering. *Pharmacol. Therapeut.*, **2005**, 105, 151–161.
- 110 DAVIS, M., B. MOTION, D. NARMONEVA, T. TAKAHASHI, D. HAKUNO, R. KAMM, S. ZHANG, R. LEE, Injectable self-assembling peptide nanofibers create intramyocardial microenvironments for endothelial cells. *Circulation*, **2005**, 111, 442–450.
- 111 NARMONEVA, D., R. VUKMIROVIC, M. DAVIS, R. KAMM, R. LEE, Endothelial cells promote cardiac myocyte survival and spatial reorganization. *Circulation*, **2004**, 110, 962–968.
- 112 SEMINO, C., J. MEROK, G. CRANE, G. PANAGIOTAKOS, S. ZHANG, Functional differentiation of hepatocyte-like spheroid structures from putative liver progenitor cells in three-dimensional peptide scaffolds. *Differentiation*, **2003**, 71, 262–270.
- 113 LI, W., R. TUAN, Polymeric scaffolds for cartilage tissue engineering. *Macromol. Symp.*, **2005**, 227, 65–75.
- 114 MOONEY, D., A. MIKOS, Growing new organs. *Sci. Am.*, **1999**, 280, 60–67.
- 115 LANGER, R., D. TIRRELL, Designing materials for biology and medicine. *Nature*, **2004**, 428, 487–492.
- 116 MA, P., J. CHOI, Biodegradable polymer scaffolds with well-defined interconnected spherical pore network. *Tissue Eng.*, **2001**, 7, 23–33.

## 5 Nanophase Biomaterials for Tissue Engineering

*Ramalingam Murugan and Seeram Ramakrishna*

### 5.1 Introduction: Problems with Current Therapies

Tissue or organ failure, resulting from traumatic or non-traumatic destruction, gives rise to a major health problem that directly affects quality and length of patient's life. These circumstances often call for surgical treatments to repair, replace, maintain or augment the functions of affected tissue or organ using some additional functional components to facilitate quality life to the patient. They have been traditionally treated with the help of tissue or organ procured from the donor site. Depending on the location of reimplantation of the procured tissue or organ (also called graft), they are termed as autograft, allograft, or xenograft (Fig. 5.1) [1]. If the graft is implanted in the same patient, it is termed as autograft and if it is placed in another individual of the same species it is termed as allograft. If the graft is placed in another species, then it is termed as xenograft. Among them, autograft is considered as a gold standard and has long been used with good clinical results, but the supply of autograft is limited. Conversely, allograft and xenograft are not much preferred due to the possibility of pathogen transfer and graft rejection. Furthermore, procurement of living tissue/organ is complex, expensive, and requires an additional surgery. Notably, over 8 million surgical procedures are performed annually to treat tissue and organ failures in the United States of America itself, as per medical statistics [2–4]. Over 80 000 patients are still awaiting tissue and organ transplantations. In this regard, a potential solution is needed to overcome the limitations of traditional tissue transplantation methods and, at the same time, to increase the accessibility and long-time survivability of the tissue implants.

These limitations have instigated the search for alternative approaches and have resulted in the emergence of the concept of tissue engineering, whereby tissue or organ failure is addressed by using synthetic materials cultured with appropriate cells harvested from patient or donor and then implanted in the patient's body where tissue regeneration is required. The synthetic materials used for this purpose are generally called biomaterials. Biomaterial by definition is a substance or a combination of substances, other than drugs, derived either from natural or syn-

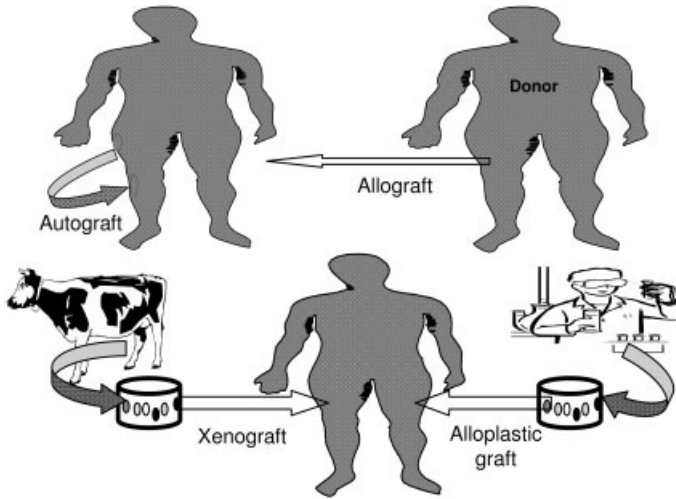
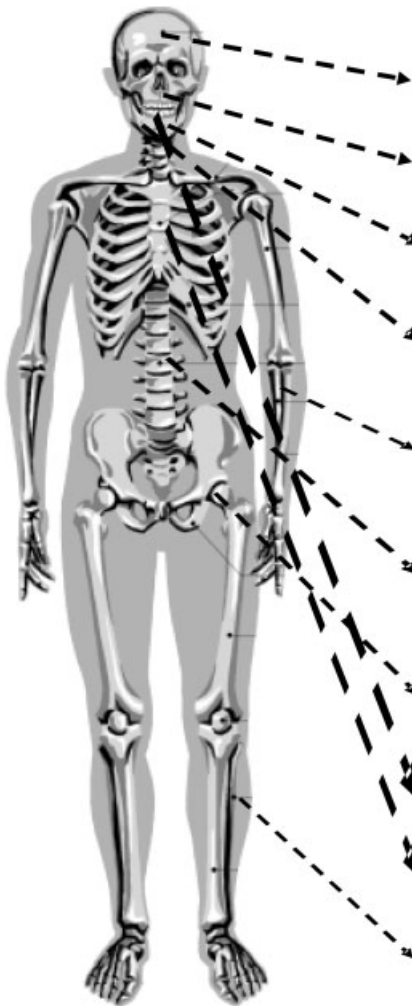


Fig. 5.1. A schematic of tissue transplantation. (Adopted and modified from Ref. [1].)

thetic origin that can be used for any period of time as a whole or as a part of the system that treats, augments, or replaces any tissue, organ, or functions of body [5]. Biomaterials have the advantage of eliminating the surgical process in procuring tissue or organ encountered in the traditional graft procedures, and eliminating the chance of graft rejection or transmission of infectious diseases. In addition, the availability, reproducibility, and cost-effectiveness make the biomaterials more suitable for tissue engineering applications. Figure 5.2 gives some of the clinical uses of biomaterials. Although biomaterials have been used in human health care systems for more than 50 years, the medical community still faces many problematic cases due to the biomaterials' failure before fulfilling their intended functions. There are many reasons for such failure, but one of the prime factors is related to lack of sufficient tissue regeneration around the biomaterials immediately after implantation, which occurs mainly due to the poor surface interaction of biomaterials with the host tissue. In this concern, it is essential to design biomaterials with superior surface properties (e.g., surface area and surface roughness) to facilitate favorable host tissue interactions for their long-term survivability, and to enhance tissue regeneration. High surface area is one of the key properties of biomaterials, which influences cell adhesion and cell density. Surface roughness is another key determinant factor for the occurrence of sufficient host tissue interactions. It has been hypothesized that cell–matrix interactions are governed by surface properties and their imperative interactions found to occur within 1 nm of the implant surface [6]. Apart from surface chemistry, it is also worth mentioning that the cells live in a complex mixture of pores, ridges, and fibers of extra cellular matrix (ECM) in a nano-featured environment. This is because cells attach, organize, and grow well around the fibers with diameters smaller than those of the cells [7]. These information eventually lead to the concept of nanophase biomaterials



Clinical uses	Biomaterials
Cranial bone defects	Bioactive glass, alumina, HA, HA-collagen
Maxillofacial reconstruction	HA, bioactive glass, alumina, zirconia, HA -PE, Bioglass -PE, PTFE -carbon
Alveolar ridge augmentation	HA, TCP, bioglass, Alumina, HA-PLA, HA -collagen, HA -PLGA
Periodontal defects	HA, TCP, bioactive glass, HA -PLA, HA -PLGA, HA -collagen
Bone void fillers	HA, TCP, bicoral, calcium sulfate, PMMA, HA -collagen, bioactive glass -ceramic composite
Spinal surgery	HA, bioactive glass, HA -collagen, PET -silicon, bioglass -PU
Orthopedic prostheses	Alumina, zirconia, stainless steel, Ti, Ti -6Al-4V, Co -Cr -Mo -Ni, A -W glass ceramics, HA -PE, HA-collagen, bioactive glass -coated biomaterials, HA -coated biomaterials, Carbon fibers -PE
Dental implants	Ti, Ti-6Al-4V, stainless steel, PE, alumina, HA
Cardiovascular systems	PU, silicon rubber, carbon, PTFE, PE
Skin substitutes	Collagen, collagen -glycosaminoglycan, collagen -silicon

Fig. 5.2. Clinical uses of biomaterials.

(herein called nanobiomaterials) for tissue repair and regeneration. The nanobiomaterials are therefore perceived to be more beneficial in tissue engineering than their microscale counterparts.

This chapter introduces the role of the nanobiomaterials in the success of tissue engineering. Numerous articles describe the potential of biomaterials in tissue engineering applications, but only a very few studies emphasize the impact of nanobiomaterials in constructing tissues or organs. This chapter focuses mainly on nanobiomaterials, in particular ceramic and polymeric nanobiomaterials, and examines prospects for their applications in tissue engineering. The following sections discuss the basic aspects of tissue engineering and the key factors for their

success, fabrication methodologies and properties of widely used nanobiomaterials, and current scenarios of nanofibrous scaffold processing techniques. The chapter culminates with a discussion on how these materials influence cell growth functions with illustrated experimental examples.

## 5.2

### Tissue Engineering: A Potential Solution

Tissue engineering is emerging as a significant solution for the traditional tissue and organ transplantations. Tissue engineering is a multidisciplinary theme that applies the principles and methods of engineering and life sciences towards the development of viable substitutes capable of repairing or regenerating the functions of damaged tissue that fails to heal spontaneously. Tissue repair is a process, which involves the usual inflammatory cell cascade, followed by matrix deposition and then a remodeling process, which attempts to regenerate the damaged tissue into healthy tissue. In contrast, tissue regeneration involves gradual replacement of damaged tissue with identical healthy tissue. The major advantage of the tissue engineering approach is that tissues can be perfectly reconstructed in such a way that they match exactly the patient's requirements and can be transplanted into the patient's body with a minimal surgical intervention, which eventually conquers several limitations encountered in the conventional tissue transplantations.

The prime concept of tissue engineering is to harvest a small biopsy of specific cells from the donor site, seed them on a scaffold to culture a specific tissue, and transplant the cultured tissue into the defective site of the patient's body that needs tissue regeneration. The ability to satisfy these criteria is largely dependent on three key factors: (a) the cells that create tissue, (b) the scaffold that gives structural support to cells, and (c) cell–matrix (scaffold) interactions that direct the tissue growth (Fig. 5.3). Among them, cells are the prime determinant factor for the success of tissue engineering because they are the basic units of all life. There are different types of cells that could be used for tissue reconstruction, which are commonly categorized as mature cells (non-stem) and stem cells. Although the use of mature cells dates far back, they are generally differentiated cells, which give rise to low rate of proliferation. As an alternative, stem cells have gained much recognition recently, owing to their ability to overcome many of the limitations of mature cells. The potential of stem cells are briefly discussed in Section 5.3, with experimental examples. The scaffold is another important determinant factor for the success of tissue engineering, which basically provides a structural support for the cells to grow in the three-dimensional (3D) space into a specific tissue. The success of the scaffold typically depends on the quality of starting material and the fabrication methodology (much discussed in Sections 5.4 and 5.5, respectively). Cell–matrix (scaffold) interactions is another key determinant factor for the success of tissue engineering because it greatly influences tissue growth. As aforementioned, cell–matrix interactions are governed by surface properties and their imperative interactions found to occur within 1 nm of the implant surface. Furthermore, the

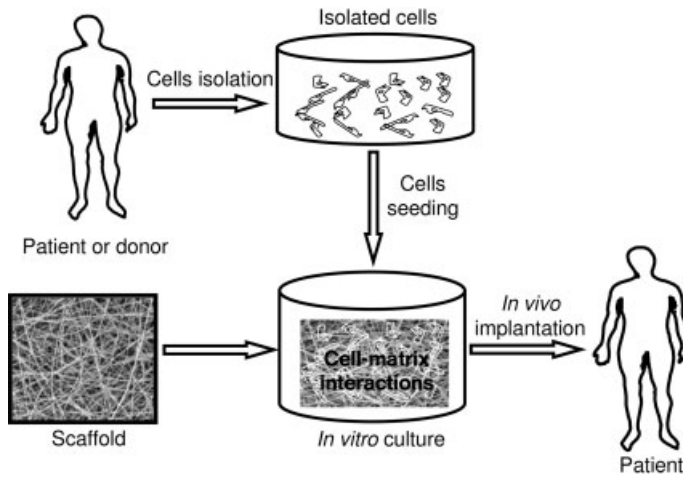


Fig. 5.3. Key factors contributing to the success of tissue engineering.

growth of new tissue depends on the way the seeded cells interact with the scaffold. In this regard, cell seeding density must be optimized to enhance the cell–matrix interactions. However, several growth factors and biological molecules are also involved in the cell–matrix interactions (Section 5.6).

### 5.3

#### Stem Cells: The Essentials

A key factor in tissue engineering approach for repair or regeneration of defective tissue is the use of appropriate cell source. Currently, there are various cells available corresponding to specific tissues. Although the use of mature cells has a successful history and remains an important source for tissue engineering, rapid advances are being made in identifying new cell types that has the capacity to transform into specific cell type that may be required to produce appropriate tissue. Stem cells have recently been recognized as a promising alternative to mature cells owing to their enormous potential in generating a spectrum of tissues with adequate functions. With the advances of cell biology, several well-characterized tissue-specific stem cells are currently available for tissue engineering.

Stem cells, by definition, are immature or undifferentiated cells that are able to renew by themselves and differentiate into more specialized type of cells/tissues in response to appropriate signals and cell plasticity. A diverse range tissues can now be engineered using stem cells, from epithelial surfaces to skeletal tissues. This ability allows them to act as a good repair system for the defective tissue or organ of our body. Stem cells are generally classified into three types: totipotent (e.g., zygote), pluripotent (e.g., embryonic stem cells), and multipotent (e.g., mesenchymal stem cells). The totipotent stem cells are capable of producing any type of cells/tis-



sues. The pluripotent stem cells are capable of producing most of the cells/tissues, whilst multipotent stem cells produce a limited number of cells/tissues with specific functions. Stem cells are also categorized into embryonic or adult cells according to their source of origination. Embryonic stem cells, as their name suggests, are derived from the early stage of an embryo. Although embryonic stem cells research is thought to have much greater potential than adult stem cells, several ethical and legal controversies still exist concerning their use for humans. Besides, some of the important clinical and safety issues also hinder their use to a certain extent. Conversely, adult stem cells have considerable biological and clinical interests. Basically these are undifferentiated cells found in differentiated adult tissues. They are also called somatic stem cells. The potential advantage of using adult stem cells is that the patient's own cells could be easily isolated, expanded in culture with appropriate functions, and then transplanted into the patient's body where tissue regeneration is required. By this approach, there is no chance of immune rejection and certain ethical and legal issues can also be conquered. These cells are typically harvested from bone marrow. The bone marrow chiefly constitutes two distinct stem cells: (a) hematopoietic stem cells (HSCs), which are responsible for the formation of blood cells, and (b) mesenchymal stem cells (MSCs), which are responsible for the formation of bone cells.

Mesenchymal stem cell transplantation is considered as a promising method to improve various tissue functions of mesenchymal origin. MSCs are one of the well-characterized populations of stem cells residing in various adult mesenchymal tissues; thereby they are well adopted for tissue engineering with considerable interest and, subsequently, for clinical practice. These cells were first recognized by Friedenstein and group in the 1960s, wherein they noticed that an adherent, fibroblast-like cell population could have the ability to regenerate the essentials of normal bone [8]. Notably, the early investigations using these cells are mainly focused on bone tissue engineering. Nowadays, these cells are being applied to various tissue engineering, including cartilage, myocardium, liver, nerve, spinal cord, and dermal tissues. The advantages of using MSCs are that they can be easily harvested from the donor site and cultured into a spectrum of tissue-specific phenotypes of mesenchymal origin, such as bone, cartilage, muscle, marrow stroma, and tendon (Fig. 5.4) [9–11]. These features attracted the attention of the biomedical community towards stem cell-based therapy, in particular MSCs. The list of tissues with the potential to be engineered has recently grown progressively due to the advances in stem cell biology and sophisticated characterization techniques, which indicates the prospects for future MSCs-based tissue engineering.

Notably, once cells are isolated from their natural environment, they tend to lose their phenotype and differentiated functions. It is really a great challenge to refurbish the cell phenotypic expression and differentiated functions without hindering proliferation under laboratory conditions. A few studies have reported the direct delivery of cell suspension without using scaffolds [12, 13], but these processes encountered difficulties in having poor control over the localization of transplanted cells; thereby, notably, the cell expression may not be achieved without a suitable scaffold. Numerous investigations have reported the effective delivery of MSCs us-

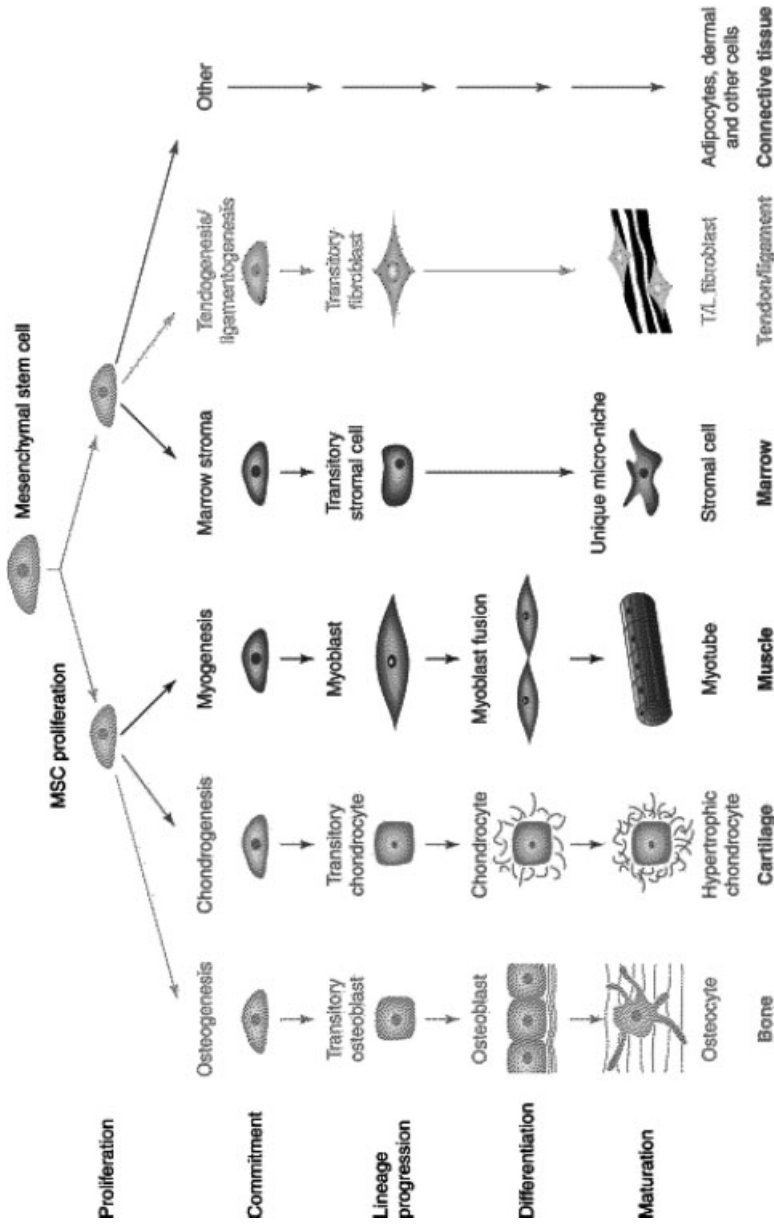


Fig. 5.4. Schematic of mesengenic process, showing stepwise cellular transitions from the putative mesenchymal stem cell to highly differentiated phenotypes. (Adopted with permission from Ref. [11].)

ing scaffolds made of polymers, ceramics, and their composites [14–16]. Recently, Li et al. [17] have reported the ability of MSCs to differentiate into chondrocytic phenotype, a cartilage-specific tissue. First, they fabricated the nanoporous biodegradable polymer scaffolds using poly( $\epsilon$ -caprolactone) (PCL) by the electrospinning method followed by *in vitro* assessment of chondrogenesis, in the presence of transforming growth factor- $\beta$  (TGF- $\beta$ ). The results indicated that the MSCs are capable of giving rise to chondrocytes and also stimulate the synthesis of cartilage-associated ECM proteins throughout the scaffold. Therefore, they suggested that the electrospun PCL scaffold is a practical carrier system for MSCs transplantation in tissue engineering-based cartilage repair. Another interesting study, reported by Yoshimoto et al. [18], demonstrated the ability of MSCs to differentiate into osteoblastic phenotype. To facilitate this, the authors manufactured the nano-featured PCL scaffolds by electrospinning, and their ability of MSCs differentiation was studied under *in vitro* cell culture conditions. They found that the scaffolds provided a suitable environment to stimulate the MSCs to differentiate into osteoblastic phenotype, a bone-specific tissue. Furthermore, the scaffolds supported the synthesis of ECM of type I collagen throughout the matrix, which is a good sign of mineralized tissue formation; thereby, the authors suggested that the PCL scaffold may be a potential candidate for bone tissue engineering. This experimental information suggests that most of the cells are anchorage-dependent and will not survive if delivered without a suitable scaffold. Processing a perfect scaffold with all the qualities similar to natural ECM is, therefore, of great importance for tissue engineering.

#### 5.4

#### Nanobiomaterials: A New Generation Scaffolding Material

Recent progress in nanoscience and nanotechnology has drastically increased the success rate of nanobiomaterials as a scaffolding material in tissue engineering. Scaffold, by definition, is a temporary supporting structure for growing cells and tissues. It is also called synthetic ECM, which plays a significant role in supporting the cells to accommodate. These cells then undergo proliferation, migration, and differentiation in 3D and eventually lead to the formation of a specific tissue with appropriate functions. Numerous studies have reported the prospects of nanobiomaterials as tissue scaffolds. Nanobiomaterials generally refers to biomaterials with the basic structural unit less than 100 nm (nanostructured), crystalline solids with a grain size less than 100 nm (nanocrystals), ultrafine powders with an average particle size less than 100 nm (nanopowders), and extremely small fibers with a diameter less than 100 nm (nanofibers). A nanometer is a billionth of a meter ( $10^{-9}$  m). For ease of understanding, Fig. 5.5 illustrates the scale of some of natural and manmade things, highlighting nanoscale items [19]. Notably, all hard and soft tissues of our body contain plenty of cells living in ECM at the nanoscale hierarchical structure elegantly designed by the Mother Nature. For example, bone tissue can be considered as an assembly of various levels of hierarchical structural

# The scale of things - nanometers and more

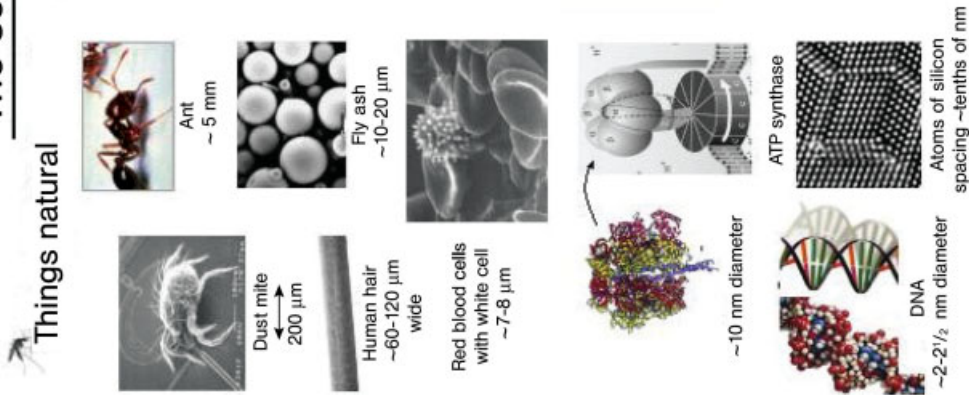
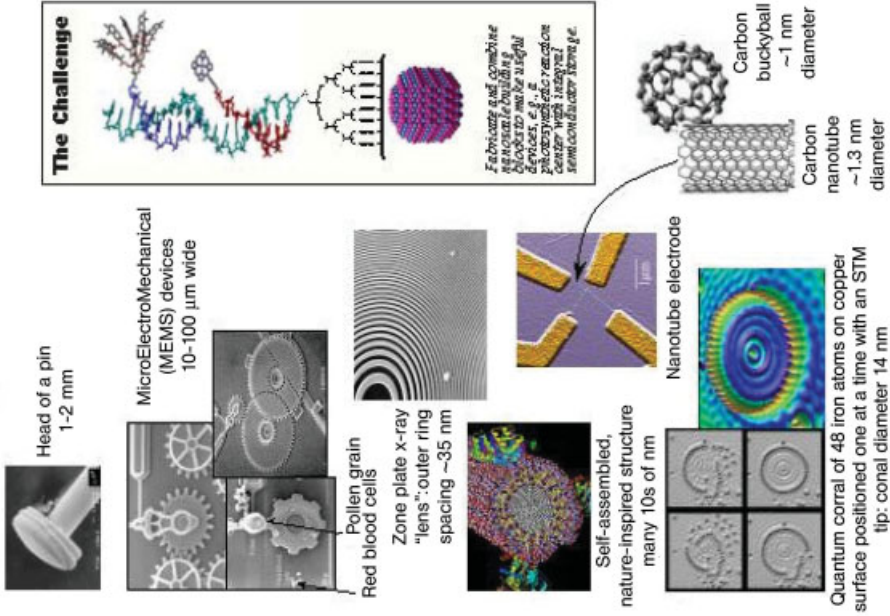
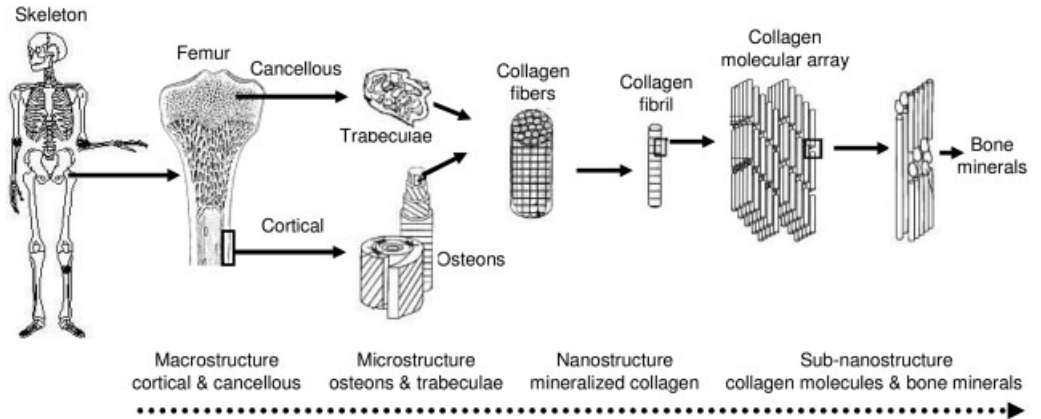


Fig. 5.5. The scale of various natural and manmade things. (Adopted by courtesy from Ref. [19].)

## Things manmade





**Fig. 5.6.** Hierarchical structure of bone, from macro- to nano-assembly. (Adapted with permission from Ref. [20].)

units designed on many length scales ranging from macro to nano, using essential organic and inorganic components, to facilitate multiple functions required for tissue formation (Fig. 5.6) [20]. The nano- or micro-featured environment of the ECM is critical for the proper functions of cells and tissues. The cells can, reportedly, attach and organize better around the nanobiomaterials than around their micro-scale counterparts because of their typical surface properties [21]. The fact is that nanobiomaterials have more atoms and crystal grains at the surfaces, and possess higher surface area to volume ratio, than conventional microscale biomaterials, making the surface of nanobiomaterials more reactive to cultured cells (during *in vitro*) and to host tissue (during *in vivo*), and thus greatly enhancing the cell-matrix interactions, leading to faster tissue regeneration. In this regard, the rate of tissue regeneration will be greater for nanobiomaterials than for conventional biomaterials. Nanobiomaterials are, therefore, perceived to be beneficial for tissue engineering applications as a new generation scaffolding material. To facilitate these measures, the scaffold should possess a few essential characteristics, which are discussed below.

#### 5.4.1

##### Characteristics of Scaffold

The structural and behavioral characteristics of the tissue scaffold are critical to ensure normal cell activities and performance of the cultured tissues. An ideal scaffold for tissue engineering should possess all the qualities of a natural ECM and should function in the same way as that of ECM under physiological conditions. However, there is no clear guideline as to which characteristic defines the so-called ideal scaffold. Notably, the characteristics of a scaffold vary according to the tissue types where the scaffold is to be applied. For example, scaffold for engineering

Tab. 5.1. Characteristics of tissue scaffold.

Characteristics	General remarks
Biocompatible	Biologically compatible to host tissue, i.e., should not provoke any rejection, inflammation, and immune responses
Biodegradable	The rate of degradation must perfectly match the rate of tissue regeneration and the degraded product(s) should not harm the living tissues
Vascular supportive	Should provide channels for blood supply for fast and healthy tissue regeneration
Non-toxic	Should not evoke toxicity to tissues
Non-immunogenic	Should not evoke immunogenic response to tissues
Non-corrosive	Should not corrode at physiological pH and at body temperature
Porosity with interconnected pores	To maximize the space for cellular adhesion, growth, ECM secretion, revascularization, adequate nutrition and oxygen supply without compromising mechanical strength
3D structure	To assist cellular ingrowth and transport of nutrition and oxygen
High surface area to volume ratio	To accommodate high density cells
Surface modifiable	To functionalize chemical or biomolecular groups to improve tissue adhesion
Adequate mechanical strength	To withstand hemodynamic and other biological forces <i>in vivo</i>
Sterilizable	To avoid toxic contamination

bone tissues requires an osteoconductive feature but it is not required for engineering nerve or dermal tissues. Table 5.1 gives some of the basic characteristics of a perfect scaffold for generalized tissue engineering applications. Any scaffold, irrespective of applications, should be biocompatible, meaning that it should not provoke any rejection, inflammation, and immune responses. The scaffold should provide a 3D template with interconnected porous architecture for the maximum loading of cells, tissue in-growth, and transportation of nutrients and oxygen. It should be able to facilitate several biochemical and biological process, in synthesizing specific proteins, required for a healthy tissue growth in the bodily environment. Notably, most tissue engineering applications require scaffolds that are bio-

degradable, but the rate of degradation must match the rate of tissue regeneration. The scaffold should be mechanically strong to withstand hemodynamic and other biological forces *in vivo*, otherwise it may hinder tissue formation. Besides, the scaffold should have high surface area to facilitate better cell adhesion and interaction with each other, and should also have a surface roughness similar to that of natural tissues for the occurrence of enhanced host tissue interactions. The scaffold should also be vascular supportive because cells will not survive without an adequate blood supply. Finally, the scaffold should be stable during storage, and must be sterilizable, to avoid toxic contaminations, without compromising any structural and other related properties. The pragmatic success of tissue scaffold is not only dependent on the above measures but also on appropriate communication between the cells, tissues, and the host system as a whole.

#### 5.4.2

#### **Types of Scaffolding Materials**

The materials used to manufacture scaffold play a key role in supporting the growth of cells, which are cultured on the scaffold. In this regard, selection of materials is of great importance for the success of tissue engineering. Based on the facts discussed in Section 5.4, nanobiomaterials are perceived to be more beneficial than their microscale counterparts owing to their superior surface characteristics. Nanobiomaterials currently investigated as scaffolding materials for tissue engineering applications can be classified into four types: metals, ceramics, polymers, and composites thereof (Table 5.2). Each type of material has its own distinct properties that can be advantageous for specific tissue engineering. The choice of materials depends on the type of tissue to be reconstructed. For example, metals and ceramics are widely used for manufacturing scaffolds for hard tissue applications, whilst polymers are used for soft tissue applications, and composites are considerably used for both the applications due to their mechanical properties (Table 5.3) [22–24]. This information helps clinicians to choose a right material for a specific application. In the following sections we focus on the widely used nanobiomaterials, in particular ceramic and polymeric nanobiomaterials, for tissue engineering applications.

##### 5.4.2.1 **Ceramic Nanobiomaterials**

Ceramics represent a class of nanobiomaterials that is widely used as a scaffolding material in hard tissue repair and regeneration (e.g., bone). The ceramics used in tissue engineering can be classified into three major groups corresponding to their ability to interact with host tissue: (a) bioinert (e.g., alumina and zirconia), (b) bioactive (e.g., HA and bioglass), and (c) bioresorbable [e.g., tricalcium phosphate (TCP)]. It is desirable, for bone tissue engineering, that the scaffolding material mimic the natural bone in chemical composition and phase structure, to facilitate better osteointegration and other related functions. In this regard, HA [hydroxyapatite,  $\text{Ca}_{10}(\text{PO}_4)_6(\text{OH})_2$ ] may be considered a good choice of scaffolding material. We, therefore, focus on the properties and the various processing methodologies of

Tab. 5.2. A broad classification of nanobiomaterials.

Nanobiomaterials	Advantages <sup>a</sup>	Disadvantages	Applications	Examples
Metals & alloys	Strong, tough, ductile	Dense, may corrode, difficult to make	Load-bearing bone implants, dental restoration, etc.	Nanostructured titanium and Ti-6Al-4V alloys
Ceramics	Bioinert Bioactive Bioresorbable High resistance to wear, corrosion resistance	Brittle, low toughness, not resilient	Low weight-bearing bone implants, dental restoration, tissue scaffolds, bone drug delivery, etc.	Nano alumina Nano HA Nano TCP
Polymers	Flexible, low density, resilient, surface modifiable, chemical functional groups	Low stiffness, may degrade	Tissue scaffolds, drug delivery, breast implant, sutures, skin augmentation, blood vessels, heart valves, etc.	Collagen and PLLA nanofibers
Composites	Strong, design flexibility, enhanced mechanical reliability than monolithics	Properties might be varied with respect to fabrication methodology	Tissue scaffolds, drug delivery, dental restoration, spinal surgery, etc.	Nano HA-collagen, nano HA-PLLA

<sup>a</sup> Common characteristics of nanobiomaterials, such as biocompatibility, high surface area, etc. are not highlighted.

HA in detail. HA possesses most of the qualities required for bone tissue engineering, in particular biocompatibility, bioactivity, and osteoconductivity. Table 5.4 gives a compilation of some of the physical, mechanical, chemical, and biological properties of HA that make it an appropriate scaffolding material [1, 23–29]. As per the literature survey, several methods for processing HA, either from natural sources (e.g., coral exo-skeleton and animal bone) or from synthetic sources (e.g., inorganic chemical synthesis), have been reported [30–36], but these studies concentrated on microscale HA.

Recently, nanoscale HA has received much attention owing to its superior surface functional properties over its microscale counterpart, particularly surface area and surface roughness, which are the most imperative properties of nanobiomaterials.



**Tab. 5.3.** Mechanical properties of biological tissues and biomaterials. (Compiled from Refs. [22–24].)

Materials	Young's modulus (GPa)	Tensile strength (MPa)
Soft tissues		
Articular cartilage	10.5	27.5
Fibrocartilage	159.1	10.4
Ligament	303.0	29.5
Tendon	401.5	46.5
Skin	0.1–0.2	7.6
Hard tissues		
Cortical bone	7–30	50–150
Cancellous bone	1–14	7.4
Dentine	11–17	21–53
Enamel	84–131	10
Metals		
Ti	110	300–740
Stainless steel	190	500–950
Ti-6Al-4V alloy	120	860–1140
Co-Cr alloy	210	665–1200
Ceramics		
Alumina	380	310
Zirconia, partially stabilized	200	420
HA	30–100	50–190
Polymers		
Biodegradable		
Poly(L-lactic acid)	2.7	50
Poly(D,L-lactic acid)	1.9	29
Poly(ε-caprolactone)	0.4	16
Non-biodegradable		
Polyethylene	0.88	35
Polyurethane	0.02	35
Poly(methyl methacrylate)	2.55	59
Poly(ethylene terephthalate)	2.85	61
Composites		
HA/PE (40/60)	4.29	20.67
Bioglass/PE (40/60)	2.54	10.15
Glass-ceramic/PE (40/60)	2.84	14.87

**Tab. 5.4.** Physical, mechanical, chemical, and biological properties of HA. (Compiled from Refs. [1, 23–29].)

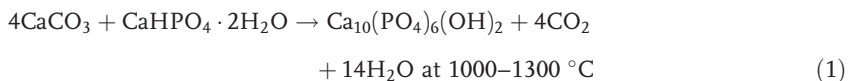
Properties	Experimental data
Chemical composition	$\text{Ca}_{10}(\text{PO}_4)_6(\text{OH})_2$
Ca/P (molar)	1.67
Color	White
Crystal system	Hexagonal
Space group	$P6_3/m$
Cell dimensions (Å)	$a = b = 9.42, c = 6.88$
Young's modulus (GPa)	80–110
Elastic modulus (GPa)	114
Compressive strength (MPa)	400–900
Bending strength (MPa)	115–200
Density ( $\text{g cm}^{-3}$ )	3.16
Relative density (%)	95–99.5
Fracture toughness ( $\text{MPa m}^{-1/2}$ )	0.7–1.2
Hardness (HV)	600
Decomposition temp. ( $^{\circ}\text{C}$ )	>1614
Melting point ( $^{\circ}\text{C}$ )	1000
Dielectric constant	7.40–10.47
Thermal conductivity ( $\text{W cm}^{-1} \text{K}^{-1}$ )	0.013
Biocompatibility	High
Bioactivity	High
Biodegradation	Low
Cellular compatibility	High
Osteoinduction	Nil
Osteoconduction	High

rials because of enhanced cell–matrix interactions. For the past few years, significant research effort has been devoted to the production of nanosize HA [37–39], to obtain high surface reactive materials with enhanced physicochemical and biological properties compared with their microscale counterparts and, at the same time, quite similar to natural bone mineral. It has also been proved that the nano HA, compared with conventional HA, promotes osteoblast adhesion, differentiation and proliferation, which leads to enhanced formation of new bone tissue within a short period [21, 40]. With reference to this information, nano HA may be considered as a unique class of ceramic scaffolding material for bone tissue engineering. The nano HA can be synthesized by many different methods, including solid state [41], wet chemical [42, 43], hydrothermal [44, 45], mechanochemical [46], pH shock wave [47], and microwave processing [48]. Table 5.5 depicts some of the general remarks on these methods, and the detailed processing conditions of nano HA are described in the following sections.

Tab. 5.5. Methods involved in the synthesis of nano HA.

Methods	Grain sizes (nm)	General remarks	Ref.
Solid state	500	Inhomogeneous, large grain sizes, irregular shapes, reaction temp.: 900–1300 °C	41
Wet chemical	20–200	Nano size grains, low crystallinity, homogeneous, reaction conditions: room temp. to 100 °C at elevated pH	42, 43
Hydrothermal	10–25	Homogeneous, ultrafine particles, reaction condition: high temp. and high pressure atmosphere	44, 45
Mechanochemical	<20	Easy production, semi-crystallinity, ultrafine crystals, room temp. process	46
pH shock wave	300	High-energy dispersing, nonporous, monocrystalline particles	47
Microwave	100–300	Uniformity, nanosize particles, time and energy saving	48

**Solid-state Reaction** Solid-state reaction has generally been used for the processing of HA at high temperature. HA powders synthesized by this method usually have irregular shapes with larger grain size, and they quite often exhibit heterogeneity in the phase composition, owing to chemical reactions resulting from small diffusion coefficients of ions within the solid. A general formation of HA using the solid-state method is based on Reaction 1:



The key ingredients of this reaction are basically in the solid phase, in which  $\text{CaCO}_3$  acts as a calcium precursor and  $\text{CaHPO}_4 \cdot 2\text{H}_2\text{O}$  acts as a phosphorous precursor in the formation of HA. The solid-state reaction typically takes place at a very high temperature ( $\sim 1000$  °C). A method for the preparation of HA fibers was introduced using a solid-phase reaction [41]. With this method, the HA fibers were produced by heating a compact consisting of calcium metaphosphate fibers with calcium hydroxide particles at 1000 °C in air, and treated subsequently with dilute aqueous HCl solution to remove unwanted secondary phase substitution such as CaO. The obtained fibers were characterized by various analytical

methods, and the results confirmed the formation of HA with nanostructural features. Therefore, the solid-state reaction can be considered as one of the methods for the production of nano HA.

**Wet Chemical Method** This method is one of the promising methods, widely used in synthesizing nano HA at low temperature, in contrast to the solid-state reaction. HA powders synthesized by using this method have a homogeneous phase composition, but are poorly crystallized owing to the low temperature process. One common wet chemical method of synthesizing HA is based on Reaction (2), which uses calcium hydroxide and orthophosphoric acid as calcium and phosphorous precursors, respectively.



Recently, rod-like nano HA was synthesized by this method [42]. In brief, a  $\text{H}_3\text{PO}_4$  solution (0.3 M) was added drop-wise to a 0.5 M  $\text{Ca}(\text{OH})_2$  solution under continuous stirring at room temperature, while the pH was kept above 10.5 by the addition of ammonia solution. Stirring was maintained for a further 16 h after complete addition of the reactants. The precipitate thus obtained was further aged for a week and was examined for phase purity and chemical composition using various analytical methods. The results indicated the possibility of producing phase pure, nanosize, and rod-like HA by a wet chemical method. Our group, Murugan et al. [38, 43], have also synthesized HA nanoparticles by using this method, and have extensively studied their physicochemical and physiological properties at body pH. The results clearly showed the enhanced resorbable characteristics of nano HA compared with their microscale counterpart, owing to their larger surface area to volume ratio, which ultimately makes the nano HA highly surface reactive. Based on these experimental data, the wet chemical method is one of the most promising methods for the production of nano HA.

**Hydrothermal Process** This hydrothermal process involves the reaction of an aqueous solution of calcium and phosphorous precursors at ambient temperature and pressure for the production of nano HA. It enables the synthesis of crystallized HA with homogenous phase composition. The HA so-prepared is easily sinterable, owing to the effects of high temperature and high pressure aqueous solutions. Zhang and Consalves [44] have synthesized nano HA by precipitating the precursors under hydrothermal conditions, and they studied its thermal stability in detail. By using this approach, they obtained rod-like, nano-sized HA with an average crystal size of 10 to 24 nm, according to the composition of the precursors. They prepared various HA powders with a Ca/P ratio ranging from 1.66 to 1.73. In another interesting study [45], the efficacy of nano HA as filler in fabricating tissue scaffold has been reported. The authors produced nano HA by a hydrothermal method. In brief, 2 g of ammonium phosphate dissolved in 37.5 mL of de-ionized water was added to 5.9 g of calcium nitrate dissolved in 22.5 mL of de-ionized water under stirring, and the pH of solution was adjusted to 12 by adding ammo-

nia. The solution was then autoclaved under hydrothermal conditions (170 °C and 19.5 MPa) and subsequently aged for 5 h. The precipitates thus obtained were cooled to room temperature, repeatedly washed with distilled water to remove traces of ammonia and ammonium nitrate, dried at 80 °C overnight, and then ground to a fine powder. Characterization of the powders indicated the formation and purity of HA. The HA particles were ellipsoidal-shaped with needle-like morphologies. The particles were, on average, approximately 25 nm wide and 150 nm long with aspect ratios ranging from 6 to 8, indicating nanostructure features. The authors further investigated the efficacy of nano HA as filler in polymer matrix in fabricating porous 3D tissue scaffolds. The results showed that the scaffold consisting of nano HA and polymer should be suitable for non-load sharing tissue engineering applications as compared with scaffold made of polymer alone, owing to their enhanced compression modulus.

**Mechanochemical Route** Production of nano HA by the mechanochemical route has gained interest in recent years, owing to its simplicity. The processing conditions involved in this method slightly differ from the conventional wet chemical method. Notably, the purity of material synthesized by conventional wet chemical method depends on the reaction pH, whereas reaction through the mechanochemical route need not be under precise pH control. Nakamura et al. [46] have reported the synthesis of nano HA by using this method. The HA was prepared directly by milling a mixture of  $\text{Ca}(\text{OH})_2$ ,  $\text{H}_3\text{PO}_4$  and a dispersant, an ammonium salt of polyacrylic acid. The reaction was carried out at room temperature. The prepared HA powders have relatively crystallized particles in the nanometer regime. The average crystallite size was 20 nm. The authors suggested some of the merits of this method, which include (a) assisting deprotonation from brushite to form HA and (b) keeping high dispersibility and low viscosity of reaction sol. This method is of particular interest in synthesizing nano HA with ultrafine crystallite sizes.

**pH Shock Wave Method** Another interesting method for the production of nano HA is pH shock wave. Koumoulidis et al. [47] have reported the synthesis of HA in the form of lath-like monocrystalline particles using the precursors of  $\text{Ca}(\text{H}_2\text{PO}_4)_2 \cdot \text{H}_2\text{O}$  and  $\text{CaCl}_2$ . They employed high-energy dispersing equipment to synthesize nano HA. The prepared HA was characterized by various analytical methods to determine the phase composition, structure, and texture. The results showed that the material has a different Ca/P molar ratio (1.43 to 1.66) with respect to processing conditions. The crystal grains of HA were 140–1300 nm long, 20–100 nm wide, and 10–40 nm thick. With reference to experimental results, this method seems to be quite interesting because it creates appropriate hydrodynamic conditions for lath-like particle growth in the [001] direction, which could not be obtained by using conventional mechanical stirring equipment.

**Microwave Processing** Microwave-assisted synthesis of ceramic nanobiomaterials is a relatively new method, which has recently been of interest in synthesizing nano HA. Sarig and Kahana [48] reported the processing conditions for the rapid

formation of nanocrystalline HA. Briefly, the recipe for the synthesis of nano HA is: the HA powder was precipitated from  $\text{CaCl}_2$  10 mM aqueous solution (A) and  $\text{NaH}_2\text{PO}_4$  6 mM aqueous solution (B). The solution A was used without admixture, whereas the solution B was made with a concentration of 25 ppm with respect to L-aspartic acid and 150 ppm with respect to  $\text{NaHCO}_3$ . Both solutions were kept at pH 7.4 by admixture of Trizma. This pH was selected to make the HA appropriate for medical applications. Equal volumes of solutions A and B (250 mL each) were introduced simultaneously into a 1000 mL beaker, which was put into a 2450 MHz microwave oven at maximum power for 5 min. The microwave-irradiated mixture was then quenched in ice for 30 min. The resultant precipitate was filtered off, washed with water, and dried overnight at 55 °C. The powder thus obtained was characterized and found to be bouncy and free-flowing. It was composed of spherulites of about 2–4  $\mu\text{m}$  in diameter, and the spherulite was composed of ultrafine platelets of about 300 nm. Notably, the powder exhibited a quite peculiar behavior on storage, in contrast with commercial apatites. Commercial powders usually tend to aggregate and form large solid lumps, whereas the powder produced by this method remained free-flowing after 3 years of storage in non-hermetically closed containers. Yang et al. [49] further reported the sintering effect of HA by using microwaves. They synthesized HA by precipitating the calcium and phosphorous precursors at 95 °C with a pH of 9 to 11.5. The HA green samples were sintered by microwave heating and the results were compared with other HA green samples sintered by a conventional heating method. The results clearly indicated that the HA prepared by microwave processing was denser and had a finer grain size than those prepared by the conventional heating method, which is the merit of microwave processing. Overall, microwave-assisted synthesis offers the advantages of uniform heating throughout the volume with very efficient transformation energy within a short period; thereby, it may be considered as a suitable method for the production of HA nanocrystals.

#### 5.4.2.2 Polymeric Nanobiomaterials

Polymers, the largest class of biomaterials, are made up of repeated small and simple chemical units called monomers. The term “polymer” was derived from two Greek words, *polys* meaning “many” and *meros* meaning “units”. Polymers in the form of nanofibers are considered as a unique class of scaffolding material and are in demand for various tissue engineering applications compared with other types of nanobiomaterials, owing to their functional properties, design flexibility, and surface modifiability. The polymer nanofibers used for this purpose are commonly called polymeric nanobiomaterials. A nanofiber generally refers to a fiber having a diameter size in the range of 1 to 100 nm. Although the polymer nanofibers have many desirable characteristics, they tend to possess low mechanical strength (e.g., low stiffness) compared with nanophase metals and ceramics; thereby, they are often used in soft tissue reconstructions, but are also used in hard tissue reconstructions in conjunction with nanophase ceramics. The following sections focus on the major classification of polymers and emphasize widely used biodegradable

polymers in the process of nanofibrous scaffolds for tissue engineering applications.

Polymers used in tissue engineering can be grouped into (a) naturally-derived and (b) synthetic polymers. Naturally-derived polymers are biodegradable. Collagen, gelatin, and chitosan are a few notable examples. Synthetic polymers can be either biodegradable or non-biodegradable. Poly(lactic acid) (PLA), poly(glycolic acid) (PGA), and poly(lactic-co-glycolic acid) (PLGA) are notable examples of biodegradable polymers, and poly(ethylene) (PE), poly(ethylene terephthalate) (PET), and poly(tetrafluoroethylene) (PTFE) are notable examples of non-biodegradable polymers. In most circumstances, biodegradable polymers, either from natural or from synthetic origin, are considered as good choice for tissue engineering rather than non-biodegradable polymers. However, degraded products from the biodegradable polymers must be non-toxic and should not elicit any foreign body reaction. Based on their astonishing qualities, we further focus our attention on some of the widely used biodegradable polymers, both naturally-derived and synthetic, in tissue engineering applications.

**Naturally-derived Biodegradable Polymers** Collagen is the most widely used naturally-derived polymer in designing scaffolds for tissue engineering. It is a primary structural protein of the natural ECM and hence natural collagen has various functional characteristics favorable for cells and tissue growth. Although many types of collagen exist in a living organism, the most abundant forms in native tissue are types I and III. Type I collagen is composed of two  $\alpha_1$  (I) chains and one  $\alpha_2$  (I) chain in the triple helix pattern with a fiber diameter of about 50 nm. Type III collagen is composed of three  $\alpha_1$  (III) chains with fibers ranging from 30 to 130 nm in diameter. Structurally, collagen is composed of three polypeptides ( $\alpha$ -chains) that are each coiled into a left-handed helical pattern, and then these three chains are wrapped around each other into a right-handed helical pattern, resulting in well-organized rope-like fibers of great structural strength. The triple-helical domain has a characteristic primary structure, where glycine in every third amino acid generates repeating (Gly X-Y)  $n$  units, where X is alanine or proline, and Y is hydroxyproline. In general, collagen extracted from natural tissues is capable of eliciting an immunogenic response upon implantation; thereby direct use of this type of collagen is limited. Nowadays, a purified form of collagen known as reconstituted collagen, which has relatively lesser immunogenic response, is produced by various biochemical methods and is commercially available for tissue engineering applications.

Gelatin is a denatured form of collagen, obtained by acidic and alkaline process, widely used in tissue engineering as a scaffolding material. There are two types of gelatin, namely A and B, which are identified by the method of processing from the native collagen. Gelatin A can be obtained by the extraction of collagen by acidic treatment, and gelatin B can be obtained by the extraction of collagen by alkaline treatment. Gelatin B has a higher content of carboxylic groups than gelatin A owing to their biochemical processing. Although gelatin is a denatured form of

collagen, it has its own functional properties. Gelatin is a highly biocompatible, bioresorbable, non-toxic, and non-immunogenic natural polymer. It does not elicit any noticeable antigenic response and has a low coagulation activity towards platelets. Based on these characteristics, gelatin has some individual importance as a scaffolding material for various tissue engineering.

Chitosan is also a naturally-derived polymer (polysaccharide), which is obtained by alkaline deacetylation of chitin. The chitin is extracted from the exoskeleton of shellfish. Basically, this process consists of two steps: (a) deproteination of the shells with a dilute sodium hydroxide solution and (b) decalcification with a dilute hydrochloric acid solution. The chitin thus obtained is subjected to N-deacetylation by treatment with a 40–45% of sodium hydroxide solution followed by purification procedures, resulting in chitosan. Chemically, it is a copolymer of  $\beta(1-4)$  linked 2-acetamido-2-deoxy-D-glucopyranose and 2-amino-2-deoxy-D-glucopyranose. It is a weak base and thus it is insoluble in water and in a few organic solvents, but it is soluble in dilute aqueous acidic solution with  $\text{pH} < 6.5$ . It is a biocompatible, biodegradable, and non-toxic polymer. It shows good antimicrobial and antifungal activities. Due to its natural abundance and specific physicochemical and biological properties, it is used in tissue engineering applications. Further, its plasticity and adhesiveness make chitosan a suitable binder for various biomedical applications.

**Synthetic Biodegradable Polymers** Synthetic biodegradable polymers play an increasingly pivotal role in tissue engineering. These polymers offer many advantages over naturally-derived polymers in that they can be easily tailored to provide a wide range of functional properties; in particular, freedom from concerns of immunogenicity. Further, they are easily processable, surface modifiable, and sterilizable. Notably, not all the polymers are widely used in tissue engineering, but there are a few polymers (e.g., PLA, PGA, and PLGA) that have been approved for clinical applications by the US Food and Drug Authority, which can be considered for tissue engineering applications.

PLA is one of the most frequently used synthetic polymers in designing tissue scaffolds, owing to its functional characteristics that favor cell and tissue growth. It has two enantiomeric forms: (a) the left-handed (L-lactide), and (b) the right-handed (D,L-lactide). These two enantiomers have different degradation rates. Hydrolysis is the principal mode of degradation and it is greatly affected by the hydrophilicity and crystallinity of the polymer. The degradation products of PLA are non-toxic. The L-lactide is widely used for tissue engineering applications owing to its superior biocompatibility and prolonged biodegradation compared with D,L-lactide. Furthermore, it possesses high strength and modulus. The D,L-lactide possesses, in contrast, low strength and modulus, and undergoes rapid biodegradation.

PGA is the simplest form of linear aliphatic polyester, being used in various tissue engineering applications. It is also a biocompatible and a biodegradable polymer. It can be synthesized by ring-opening polymerization of glycolic acid, but does not form any enantiomers like PLA. It is highly crystalline and is a hydro-



philic polymer. The percent crystallinity ranges from 45 to 55. Owing to its hydrophilic nature, it is completely absorbed within 4 to 6 months upon implantation. It exhibits a high tensile strength, modulus, and is also stiff, making it suitable for biomedical applications.

PLGA is a copolymer that consists of PLLA and PGA macromolecular units. By changing the composition of copolymeric units, the rate of degradation and mechanical strength of PLGA can be manipulated. This kind of copolymer has less crystallinity and degrades faster than homopolymers. For example, a copolymer of 50% PGA and 50% PLLA degrades much faster than each homopolymer. The composition of copolymer also significantly affects its percent crystallinity. For example, a copolymer of 90% PGA and 10% PLLA has high crystallinity, whereas a PGA-to-PLLA ratio from 25/75 to 75/25 is relatively amorphous. Owing to its biocompatibility and tunable biodegradability, PLGA is widely used in various tissue engineering applications.

## 5.5 Nanofibrous Scaffold Processing: Current Scenarios

Processing nanofibrous scaffolds with structural features similar to natural ECM is essential for tissue engineering. Numerous studies have been conducted in processing tissue scaffolds quite similar to natural ECM in the authors' laboratory [50–52]. These scaffolds possess high surface area, high aspect ratio, high porosity, small pore size, and low density. These features are essential for the improvement of cell adhesion, which is a significant issue in the initial stage of tissue engineering because cell migration, proliferation and differentiation functions typically depend on the cell adhesion. Although tissue scaffolds can be manufactured by multiple methods, very few methods have the ability to produce scaffolds with nanofibrous structure, which include self-assembly [53, 54], phase separation [55, 56], and electrospinning [57, 58]. Table 5.6 depicts the comparative merits and demerits of these methods. Some of the key aspects of these methods, along with illustrated examples, are briefly described in the following sections.

### 5.5.1 Self-assembly

The past few years has seen great interest in self-assembling processes for manufacturing scaffolds suitable for tissue engineering. Self-assembly is simply a process in which individual, pre-existing components organize themselves into an ordered structure required for specific functions without human intervention. The key challenge in self-assembly is to design molecular building blocks that can undergo spontaneous organization into a well-defined pattern that mimics complex biological systems. Self-assembly takes place by non-covalent bonding, which typically includes hydrogen bonding, ionic bonding, hydrophilic and van der Waals

Tab. 5.6. Comparison of various nanofibrous scaffold processing methods.

Scaffold processing methods	General descriptions	Level of processability	Level of productivity	Merits	Demerits
Self-assembly	A process in which atoms, molecules, and supramolecular aggregates organize and arrange themselves into an ordered structure through weak and non-covalent bonds; typically involves a bottom-up approach	Difficult	Lab scale	Mimic the biological process in certain circumstances	Complex process, limited to a few polymers, unable to produce long and continuous fibers with control over fiber orientation
Phase separation	A process that involves various steps, typically raw material dissolution, gelation, solvent extraction, freezing and drying, leading to the formation of nanofibrous foam-like structure	Easy	Lab scale	Simple process, tailorable mechanical properties	Limited to a few polymers, longer processing time, unable to produce long and continuous fibers with control over fiber orientation
Electro-spinning	A process that essentially employs electrostatic forces for the production of polymer nanofibrous scaffolds; typically involves a top-down approach	Relatively easy	Lab and industrial scales	Simple and cost effective process, capable of producing long and continuous fibers with control over fiber orientation; versatile to many polymers	Use of high voltage apparatus

interactions. Although each of these forces is rather weak, their collective interactions could produce a very stable structure that could match the structural features of biological systems.

Recently, peptide-amphiphile (PA) nanofibers were developed by a self-assembling process for cell transplantation [53] and to direct biomineralization of HA [54]. Beniash et al. [53] have demonstrated the feasibility of PA molecules to self-assemble into 3D nanofibrous scaffold under physiological conditions, and their efficacy in cell entrapment was studied. The results indicated that cells entrapped in the nanofibrous network can survive and proliferate well, which suggests that the self-assembled PA system could be used for cell transplantation or other related tissue engineering applications. Hartgerink et al. [54] have further revealed the potential of self-assembled PA nanofibrous scaffold to direct self-biomineralization. They reported a PA molecule that self-assembles into a nanostructural gel and mimics some of the key features of the natural ECM of bone tissue. They processed the PA nanofibers with negatively charged surfaces because it is believed that this promotes biomineralization by establishing local ion supersaturation. The experimental results confirmed that the PA fibers are capable of nucleating HA on their surfaces. It was also noticed that the c-axes of HA crystals are co-aligned with the long axes of PA fiber that nucleates the structural orientation between collagen and HA observed in the natural bone tissues. Therefore, this self-assembled system could be promising for mineralized tissue repair.

### 5.5.2

#### Phase Separation

Phase separation is an interesting method used for manufacturing tissue scaffolds, which involves various processing steps, typically raw material dissolution, gelation, solvent extraction, freezing, and drying. Of course, these steps to convert the polymer into a nanofibrous structure would take a prolonged time. The unique advantage of this method lies in the possibility of designing 3D nanostructures without using any special equipment. Furthermore, the porosity and mechanical properties of scaffold can be controlled to some extent, but it is very difficult and perhaps not feasible to maintain the fiber orientation. Tissue scaffolds using poly(L-lactic acid) (PLLA) were recently fabricated by the authors' group using this phase separation method [55]. They processed scaffolds with highly porous and fibrous structures close to natural ECM. The fiber diameters ranged from 50 to 300 nm with an average of 150 to 250 nm, according with the polymer concentration used in the experimental process. The scaffolds were further evaluated with neural stem cells under *in vitro* cell culture conditions. The results indicated that the cells differentiated well on the nanofibrous scaffolds and the scaffolds served as a positive cue in supporting neurite outgrowth. This study, therefore, suggests that PLLA nanofibrous scaffolds would be promising for neural tissue engineering. Another study, reported by Chen and Ma [56], manufactured nanofibrous PLLA scaffolds with interconnected spherical macropores by a phase separation method, with the aim of mimicking the fibrous architecture of type I collagen protein. By using this

method, they were able to control the structure of the scaffolds, in particular the macroscopic shape, the spherical pore size, interfiber distance, and the fiber diameter at the nanometer size; thereby, the phase separation method has gained considerable interest in processing scaffolds for tissue engineering.

### 5.5.3

#### **Electrospinning – A New Approach**

Although the above methods have been employed to produce nanofibrous scaffolds, they often encountered some difficulties, especially in controlling the fiber orientation of the scaffolds. For the success of tissue engineering, it is desirable to control not only the fiber diameter but also the fiber orientation of scaffolds. For various tissue engineering applications, it is necessary to produce scaffolds with control over fiber orientation because alignment of the fibers predominantly influences the cell growth. Therefore, importance is given to a method that facilitates a well-defined fiber orientation and control over fiber thickness. Recently, considerable efforts have been made world-wide to process nanofibrous scaffolds with fiber orientation by so-called electrospinning.

Electrospinning is a straightforward, cost-effective, and versatile technique that essentially employs electrostatic forces to produce polymer fibers, ranging in diameter from a few microns down to tens of nanometers. This technique was first introduced by Zeleny in 1914 [59]. Later, Formhals contributed much to the development of electrospinning and, prolifically, obtained several patents in the 1930s and 1940s [60–64]. In those days it was called electrostatic spray or electrostatic spinning, and subsequently renamed as electrospinning in the 1990s. However, this technique was not adopted for tissue engineering as a tool for manufacturing tissue scaffolds at the time of invention, but it was used in other industrial applications. Recently, it has been revitalized and has been successfully applied in processing nanofibrous scaffolds suitable for tissue engineering. The precise merit of this technique is that it could produce scaffolds with most of the structural features required for tissue engineering. It also offers many advantages over conventional scaffold methodologies, e.g., it can produce ultrafine fibers with spatial orientation, high aspect ratio, high surface area, and having control over pore geometry. These are some of the favorable characteristics to be considered for better cell growth because they directly influence the cell adhesion, cell expression, and transportation of oxygen and nutrients. In this light, electrospun scaffold can serve as a good tissue scaffold and could provide spatial environment for the growth of new tissue with appropriate functions.

##### **5.5.3.1 Experimental System**

Figure 5.7 illustrates schematically the basic configuration of electrospinning [24], which consists of three major components: (a) a spinneret, (b) a fiber collector, and (c) a high-voltage power system. As illustrated in the figure, the spinneret is directly connected to a syringe, which acts as a reservoir for the polymer solution to be electrospun. This polymer solution can be fed through the spinneret with the

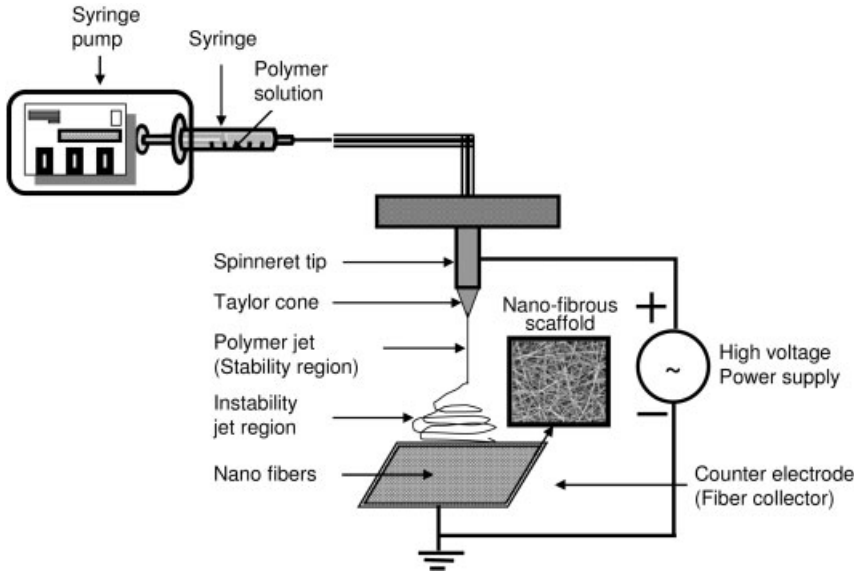


Fig. 5.7. Schematic of the electrospinning system. (Adopted and modified from Ref. [24].)

help of a syringe pump at a steady and controllable feed rate. The feeding rate can be controlled, corresponding to the concentration of polymer solution. Notably, the material to be spun by this technique must be viscous, but the viscosity may vary, depending on the type of materials used. The fiber collecting device is positioned immediately below the spinneret, with an appropriate gap. A high-voltage/low-current power system is required for the conversion of polymer solution into a charged polymer jet. The electric power (usually up to 30 kV) is applied across the spinneret and the grounded metallic counter electrode (fiber collector) to facilitate ejection of the charged jet from the spinneret tip towards the surface of the fiber collector.

### 5.5.3.2 Spinning Mechanism

Although the experimental design and functional components of electrospinning seems to be extremely simple, mechanism involved in the spinning of polymer nanofibers is rather complicated. Upon applying an optimized electric potential to the spinneret, a pendent droplet of the polymer solution at the tip of the spinneret gets electrified, thereby inducing charge accumulation on the surface of the droplet that subsequently allows the droplet to deform into a cone, known as Taylor's cone [65]. This deformation is commonly caused by two electrostatic forces: (a) electrostatic repulsion between the surface charges of the droplet and (b) Columbic force exerted by the strong external electric field applied [66]. Once the applied electric field surpasses a critical value (threshold), the electrostatic force tends to exceed the viscoelastic force and the surface tension of the polymer droplet; thereby, a

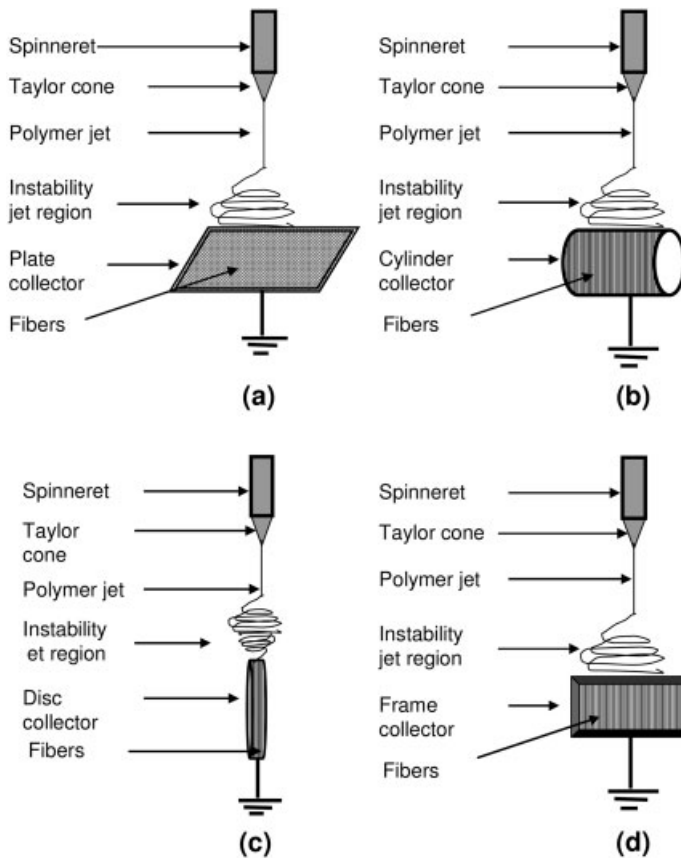
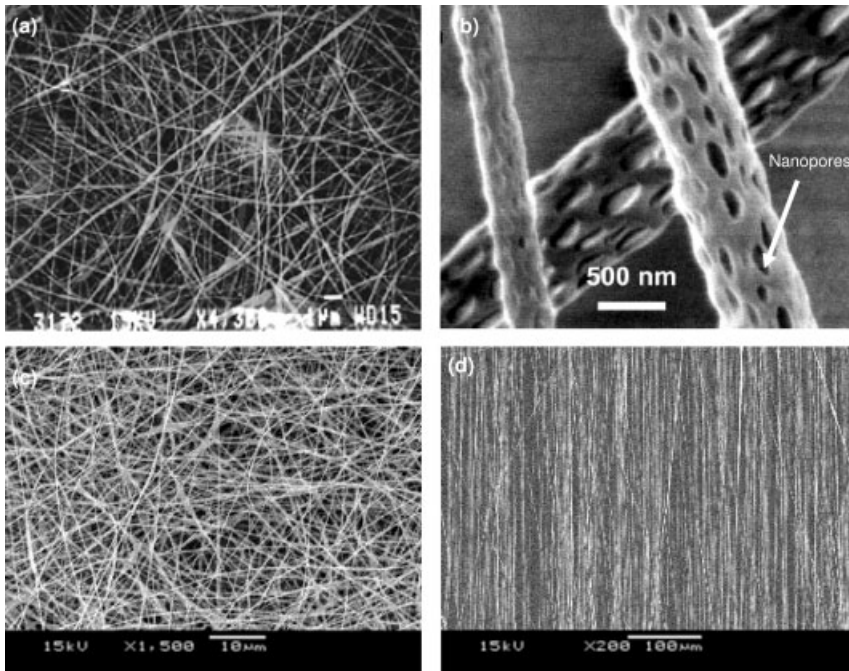


Fig. 5.8. Types of fiber collector.

fine charged polymer jet is forced to eject from the tip of the Taylor cone. This polymer jet then moves toward the counter electrode, accompanied by rapid evaporation of the solvent molecules and, while in transit, the different polymer strands in the jet are separated out due to the mutual repulsion, a phenomenon called “splaying” [67], which gives rise to a series of ultrafine dry fibers. These fibers can be collected on a grounded metallic target (fiber collector) and are typically in the range of a few micrometers to nanometers.

Notably, different types of fiber collectors are available, corresponding to spatial orientation (Fig. 5.8). For example, rotating-type collectors can be used to obtain aligned nanofibers, whilst static-type collectors can be used to obtain random nanofibers. The alignment of the fibers is rather complicated and numerous parameters influence the fiber orientation, including the rotational speed and shape of counter electrode, the concentration of polymer solution, the dielectric constant of the solvent, the strength and shape of the electric field, and the environmental conditions such as relative humidity and temperature.



**Fig. 5.9.** SEM micrographs of electrospun nanofibrous scaffolds made of (a) collagen, (b) poly(L-lactide), showing scattered nanopores, (c) poly(L-lactide), showing randomly-oriented fibers, and (d) poly(L-lactide), showing well-aligned fibers. (Adopted with permission from Refs.[57, 68, 58, and 58], respectively.)

### 5.5.3.3 Electrospun Nanofibrous Scaffolds

This section explicates how electrospinning can be adopted to produce nanofibrous scaffolds using a few biodegradable polymers suitable for tissue engineering. Matthews et al. [57] have processed collagen nanofibrous scaffolds; Fig. 5.9(a) shows a representative scanning electron microscopy (SEM) image of such a scaffold. The results indicate that the scaffold is composed of randomly-oriented nanofibers with an average diameter of  $100 \pm 40$  nm. The morphology of collagen structure is quite analogous to the natural ECM; therefore, they suggested that it may be used as a good scaffolding material in tissue engineering. Bognitzki et al. [68] have revealed the possibility of spinning PLLA nanofibrous scaffolds with nanopores. Figure 5.9(b) is a representative SEM micrograph of such a scaffold, showing that each fiber has a beautiful porous structure with well-defined nanopores. The average pore was 100 nm wide and 250 nm long. The size and density of the pores can be controlled by manipulating the spinning parameters. Elongation of the pores along the fiber axis, which is obvious from the SEM micrograph of Fig. 5.9(b), is the result of a uniaxial extension of the polymer jet in the high electric potential.

Recently, our group, Yang et al. [58], also reported the feasibility of spinning PLLA nanofibrous scaffolds suitable for tissue engineering. A representative SEM

micrograph of the scaffold is shown in Fig. 5.9(c), which provides a complete detail on size, shape, and pores of the scaffold architecture. The average fiber diameter was 700 nm and the fibers are randomly orientated. They revealed that spatial orientation of the nanofibers mainly depends on the concentration of polymer solution and rotational speed of the fiber collector. Yang et al. [58] further reported the feasibility of spinning PLLA nanofibrous scaffolds with well-defined fiber orientation perfectly suitable for tissue engineering. Briefly, the spinning conditions to obtain such scaffolds are: first, PLLA was dissolved in dichloromethane and *N,N*-dimethylformamide (70:30) at a concentration of 2%. The polymer solution was extruded at a constant flow rate ( $1.0 \text{ mL h}^{-1}$ ) by keeping the distance between the spinneret tip and the fiber collector at 10 cm. A high voltage power supply (12 kV) was applied to the tip of the spinneret using a regulated DC power system. Once the applied voltage reaches the threshold, continuous long and ultrafine fibers eject from the spinneret tip and deposit on the surface of the fiber collector. Note that a sharp-edge rotating disc was used as a fiber collector in this study. A representative SEM micrograph of such a nanofibrous scaffold is shown in Fig. 5.9(d). The results show that a high order of alignment on the fiber orientation was obtained, with fiber diameters ranging from 100 to 400 nm (average is 300 nm). The nanofibrous scaffolds with fiber orientation could be potentially ideal for tissue engineering since the fiber orientation of the scaffolds very much influences cell orientation and phenotypic expression [69]. Therefore, manufacturing nanofibrous scaffolds with fiber orientation is of great importance for the success of tissue engineering, which is now practically possible by the so-called electrospinning method.

## 5.6

### Cell–Matrix (Scaffold) Interactions

#### 5.6.1

##### Cell–Ceramic Scaffold Interactions

As mentioned above, ceramic nanobiomaterials, particularly nano HA, have considerable interest in tissue engineering, owing to their excellent cell compatibility and bio-activity. Several studies have reported *in vitro* and *in vivo* assessments of the biological responses to nano HA. Table 5.7 lists a few notable examples of tissue scaffolds made from HA-based nanobiomaterials [70–76]. Recently, Huang et al. [70] have reported the *in vitro* assessment of the biological response to nano HA. They prepared the nano HA by a precipitation reaction, and the nano HA suspension was subsequently electrospayed onto glass substrates using a novel processing route to maintain nanocrystals of HA. The *in vitro* cell-compatibility of nano HA was studied with human osteoblast-like cells. The obtained results are shown in Fig. 5.10. Figure 5.10(a) shows that the prepared HA particles are in the nanometer size range (50–80 nm long), and there are no secondary phase observed as evidenced by X-ray diffraction analysis (Fig. 5.10b), which confirms the phase



Tab. 5.7. Examples of tissue scaffolds made of HA-based nanobiomaterials.

Tissue scaffolds	Cells/growth factors studied	Ref.
Nano HA	Osteoblast-like cells	70
Nano HA	Mesenchymal stem cells	71
Nano HA	Osteoblast cells	72
NanoHA/collagen	Mesenchymal cells	73
NanoHA/collagen	Osteoblast cells/rhBMP-2	74
NanoHA/collagen/PLA	rhBMP-2	75
NanoHA/collagen/PLA	Osteoblast cells	76

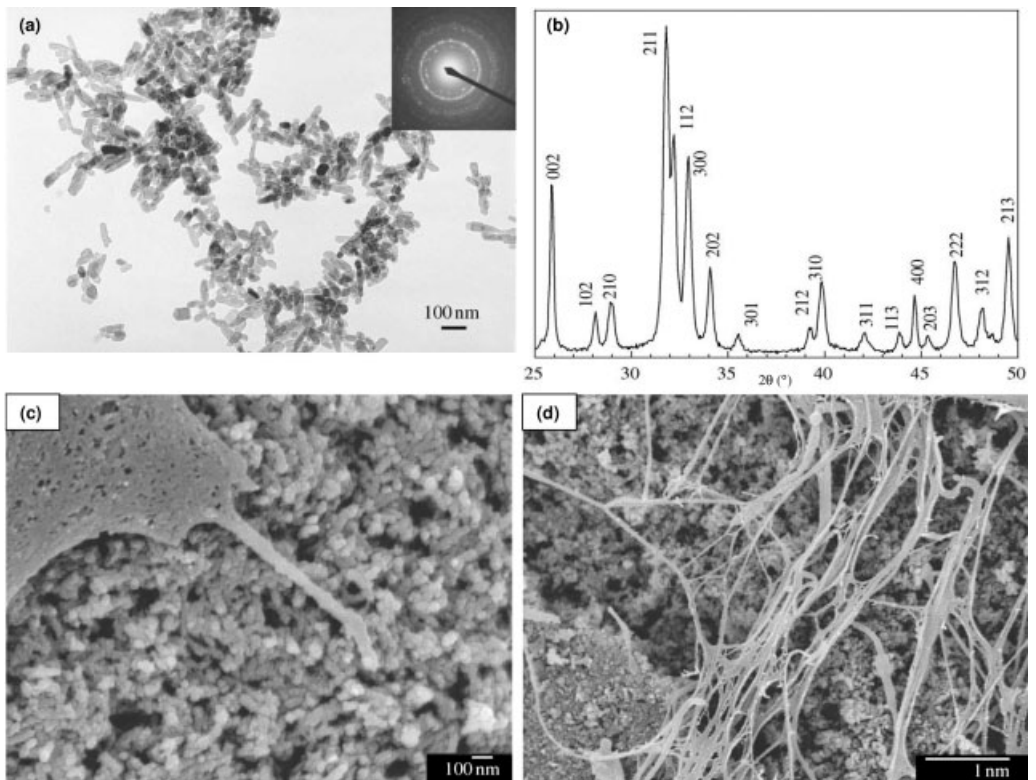


**Fig. 5.10.** Characteristic results of nano HA produced by wet chemical method: (a) transmission electron micrograph and selected area of diffraction pattern (inset) of nano HA, (b) X-ray diffraction pattern of nano HA, and

scanning electron micrographs showing (c) the attachment of human osteoblast-like cells onto nano HA and (d) ECM produced by the cells on nano HA-sprayed glass substrate. (Adopted with permission from Ref. [70].)

purity of nano HA. The results of *in vitro* cell culture studies confirmed the ability of nano HA in supporting cell adhesion and growth. The cells were able to attach to the nano HA surfaces and maintain their osteoblastic morphology with visible filopodia attached to nano HA particles (Fig. 5.10c). There were large areas of confluent cells after seven days of culture and fiber-like ECM was produced (Fig. 5.10d), which provides evidence for the better cell–matrix interactions.

The *in vitro* response of sol–gel derived nano HA with human MSCs was investigated to confirm their biocompatibility and bioactivity [71]. The *in vitro* results showed that the human MSCs adhered to nano HA and exhibited better proliferation signals on their surface. Evidence of proliferation of MSCs was observed with a tendency to spread onto the surface as if forming groups, thus supporting not only biocompatibility but also enhanced bioactivity of the material. This behavior is considered important, since it simulates, on an artificial surface, several steps of the cell-cycle occurring in a tissue environment, with no need for an interfacial protein scaffold. The authors concluded that these surfaces interact with the MSCs in a manner that might be useful for tissue engineers to design scaffolds as an alternative to biological ECM. Porous biomaterials are of great interest in tissue engineering as cells and tissues invade pores for their extensive growth, and they also help the transportation of nutrient and oxygen supply to the cells. Besides, the pores provide a mechanical interlock, thereby leading to a firmer fixation of the biomaterials upon implantation. As bone tissue grows well into the pores, it is expected to increase the strength of the implanted biomaterial. *In vitro* studies on the enhanced functions of osteoblasts (bone-forming cells) on ceramic nanobiomaterials have been reported [72]. The authors extensively studied select functions of osteoblasts on nano HA (with grain size of 67 nm) and conventional HA (with grain size of 179 nm) using *in vitro* cellular models. Osteoblasts were seeded onto the HA substrates and cultured under standard cell culture conditions. The results of cell culture studies provided evidence of increased osteoblast proliferation onto nano HA when compared with conventional HA and with to reference substrate (borosilicate glass). Although the osteoblast proliferation trend was similar on nanophase and conventional HA after 1 day of culture, it was significantly greater on nano HA after 3 and 5 days of culture, indicating that the nanophase provides highly adhesive substrate to facilitate better cell adhesion and long-term cell growth. The results further provided evidence of enhanced long-term functions, in particular synthesis of alkaline phosphatase and concentration of calcium in the ECM, of osteoblasts cultured on nano HA than on conventional HA.

Notably, though the nano HA serves as an excellent bone tissue scaffold, it behaves as a typical brittle material; thereby it is used only in certain bone tissue repair applications. To improve reliability, it is necessary to introduce some biocompatible reinforcement agents or matrix materials. However, introduction of foreign materials may decrease the reliability of HA; thereby, choosing the reinforcement agents or matrix materials is of great importance. A composite of nano HA with collagen is perceived to be beneficial in improving the reliability of nano HA, and, at the same time, both are the key components of natural bone tissue (Fig. 5.6). Osteogenic cell-engineered HA/collagen nanocomposite scaffold structures were

developed using culture techniques as well as conventional methods, and their *in vitro* cellular functions were studied [73]. It was noticed that the scaffolds supported well the cellular growth and related functions, leading to new bone formation. Later, a 3D bone-resembling nanocomposite matrix using nanoHA/collagen/osteoblasts was developed in conjunction with PLA [76]. This system supported cellular adhesion, proliferation, and migration. Interestingly, the cells penetrated deep into the matrix to about 200–400  $\mu\text{m}$  within a short period (12 days), probably owing to its composition and structural similarity to natural bone tissue, thereby providing a promising scaffold for bone tissue engineering. In this light, ceramic nanobiomaterials clearly represent a unique and promising class of scaffolding material for tissue engineering applications, but they are limited to hard tissue repair and regeneration.

### 5.6.2

#### Cell–Polymer Scaffold Interactions

This section briefly describes how the polymer nanofibrous scaffolds influence cell growth and related functions. Matthews et al. [57] have processed collagen nanofibrous scaffolds and the *in vitro* cellular compatibility was studied using smooth muscle cells. The results suggest that the scaffold has excellent biocompatibility, cellular compatibility, and capability of promoting cells in-growth and related functions (Fig. 5.11a). This study thus demonstrated the feasibility of using collagen as a good tissue scaffold. Yang et al. [58] processed the PLLA nanofibrous scaffolds, with randomly-oriented fibers, and the *in vitro* cellular compatibility was studied using neural stem cells. The results suggest that the scaffold has excellent biocompatibility, cellular compatibility, and is highly supportive to cell differentiation and related functions. The results further indicated that most of the cells have a bipolar shape with extended neurites and the neurites outgrowth was randomly spread over the scaffold (Fig. 5.11b), a good sign for cell–matrix interactions under *in vitro* cell culture conditions.

Yang et al. [58] also reported the feasibility of processing PLLA nanofibrous scaffolds with well-aligned fibers and the *in vitro* cellular compatibility was studied using neural stem cells. They observed the influence of fiber orientation on the cell growth. Figure 5.11(c) shows a representative phase contrast light microscopy image of cell cultured scaffold. The results indicated that cells were well attached to the scaffold and showed an extensive neurite-like outgrowth, which is a good sign for their differentiation. Interestingly, the results revealed that the cells elongated and their neurites outgrew along the direction of the fiber orientation, which shows the significance of spatial orientation of the fibers on cellular growth behavior. To observe expression of the cytoskeleton proteins of neural stem cells as well as the relationship between the cytoskeleton proteins and fiber orientation of the scaffolds, laser scanning confocal microscopy (LSCM) was performed; Fig. 5.11(d) shows a representative micrograph. The results show that the cells exhibited a classical contact guidance by growing parallel to the fibers. In addition, most of the differentiated cells show a bipolar shape with two extended neurites, which

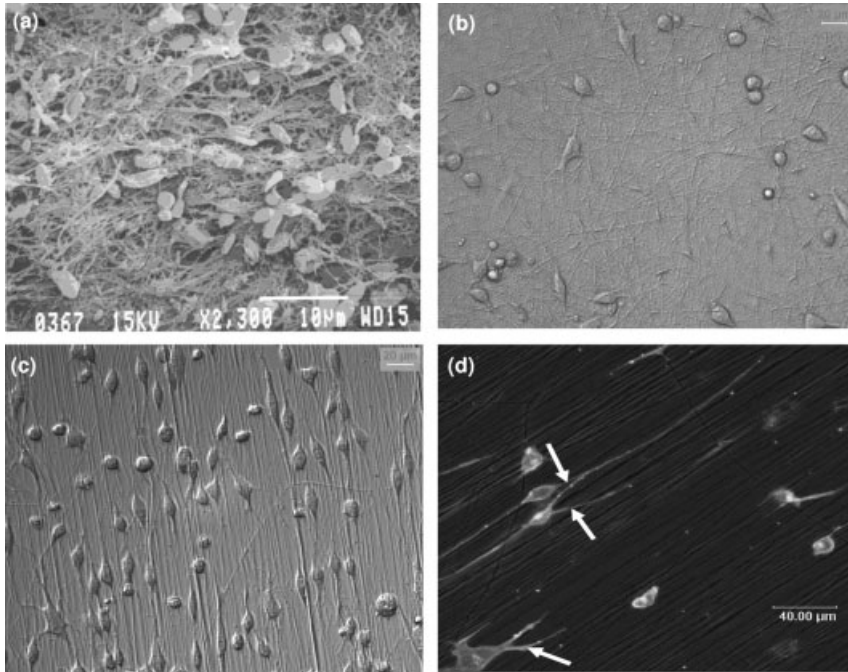


**Fig. 5.11.** SEM micrographs showing cell–matrix interactions within the electrospun nanofibrous scaffolds made of (a) collagen, (b) randomly-oriented poly(L-lactide) nanofibers. Phase contrast light microscopy (c) and LSCM

(d) images of well-aligned poly(L-lactide) nanofibers, evaluated in the authors’ laboratory. [Adopted with permission from Ref. [57] for part (a) and Ref. [58] for parts (b)–(d).]

emerged from the regions of the somas, parallel to aligned fibers and were symmetrically distributed around the soma. However, some exceptional cases were also noticed (indicated by arrows). Although neurites outgrowth was not affected by the fiber orientation during the initial period, they all turned through large angles to grow in the direction of fiber orientation, which implies the significance of fiber orientation in directing cell growth. The information thus obtained from the above experimental examples provides evidence for the enhanced performance of polymeric nanobiomaterials for tissue engineering applications.

## 5.7

### Concluding Remarks

Being the first inventor, nature sets high standards for researchers who design implants for tissue repair and regeneration. Tissue engineering is emerging as a potential alternative to traditional tissue transplantations, whereby tissue or organ failure is addressed by implanting tissue-engineered nanobiomaterials that holds

the ability to enhance the tissue growth with appropriate functions. Although preliminary investigations seem to support the impact of nanobiomaterials in tissue engineering, significant advancements are necessary to realize their full potential in clinical use. On the other hand, the nanobiomaterials are relatively less available than their microscale counterparts. Presently, there is a trend towards using nanobiomaterials due to their sophisticated surface functional properties, which are favorable for cell growth and host tissue interactions. This is an exciting time to be involved in nanobiomaterials in order to formulate them as a clinically ideal scaffolding system for tissue engineering, with great challenges and also great expectations ahead.

### Acknowledgments

Financial support of the National University of Singapore and the Singapore Millennium Foundation is gratefully acknowledged.

### Abbreviations

μm	Micrometer
3D	Three-dimensional
Ca/P	Calcium to phosphorous ratio
ECM	Extracellular matrix
HA	Hydroxyapatite
HSCs	Hematopoietic stem cells
LSCM	Laser scanning confocal microscopy
MSCs	Mesenchymal stem cells
nm	Nanometer
PA	Peptide-amphiphile
PCL	Poly(caprolactone)
PE	Polyethylene
PET	Poly(ethylene terephthalate)
PGA	Poly(glycolic acid)
PLA	Poly(lactic acid)
PLLA	Poly(L-lactide)
PLGA	Poly(lactide-co-glycolide)
PMMA	Poly(methyl methacrylate)
PTEF	Poly(tetrafluoroethylene)
PU	Polyurethane
rhBMP	Recombinant human bone morphogenetic protein
SEM	Scanning electron microscopy
TCP	Tricalcium phosphate
TGF-β	Transforming growth factor-β
Ti	Titanium

## Glossary

*Adult stem cell:* An undifferentiated cell found in a differentiated tissue that is able to self-renew and to differentiate into tissue-specific cell types from which it originated.

*Allograft:* Tissue or organ transplanted from one individual to another of the same species.

*Alloplast graft:* Any synthetic material substituted to repair or replace defective parts of the body.

*Artificial organ:* A medical device or implant intended to replace the body organs.

*Autograft:* Tissue or organ transplanted within the same body.

*Biactivity:* Ability of the implant, to play a vital role in the metabolic processes of living body.

*Bioceramics:* Inorganic and nonmetallic materials that are compatible with biological tissues.

*Biocompatibility:* Ability of the implant to perform with an appropriate host response in a specific application.

*Biodegradability:* Susceptibility of implant to be decomposed by a living organism.

*Bioinert:* No host response to the material.

*Biomaterial:* Any synthetic material that is biocompatible with the tissues and the body upon implantation. It can be metal, ceramic, polymer, and a composite of each.

*Biom mineralization:* A conversion process mediated by an organic matrix in which inorganic derivatives are produced by living organisms, especially microorganisms.

*Biopsy:* Removal of a small portion of tissue, usually for the purpose of making a diagnosis.

*Bone:* A rigid, yet dynamic connective tissue consisting of calcium phosphate based minerals embedded with collagen fibers in conjunction with osteogenic cellular elements.

*Bone marrow stromal cell:* A kind of stem cell found in bone marrow that has the ability to generate bone, cartilage, and other connective tissues.

*Cell:* Fundamental, structural, and functional unit of all living beings that is composed of an outer membrane enclosing protoplasm and nucleus.

*Collagen:* A fibrous structural protein that function to hold tissues together.

*Composite:* A heterogeneous combination of two or more materials.

*Corrosion:* A chemical or electrochemical degradation of metals due to surrounding environmental factors.

*Differentiation:* A process whereby an unspecialized cell acquires the features of a specialized cell.

*Electrospinning:* A fiber processing technique, which utilizes electrostatic forces to produce extremely fine fibers ranging from a few micrometers to nanometers in diameter.

*Embryonic stem cell:* An undifferentiated cell found in an embryo that is able to produce a spectrum of specialized cell/tissue types.

*Extracellular matrix:* The surrounding material of a cell, including ground substances and fibers.

*Fiber:* The individual strands of material that form a nonwoven construct.

*Graft:* A transplant.

*Growth factors:* A heterogeneous group of substances capable of enhancing tissue growth.

*Hard tissue:* The general term for calcified structures of the body (e.g., bone and tooth).

*Hematopoietic stem cells:* A stem cell from which all blood cells develop.

*Hydroxyapatite:* A calcium phosphate-based material, with chemical composition  $\text{Ca}_{10}(\text{PO}_4)_6(\text{OH})_2$ , that is abundant in bone minerals.

*Immunogenic:* Capable of stimulating an immune response.

*Implant:* Any medical device or prosthesis inserted or grafted in the human body.

*Implantation:* A surgical procedure by which medical device or prosthesis is placed in human body either temporarily or permanently.

*In vitro:* A biological study performed in the laboratory. In other words, outside the living body.

*In vivo:* A biological study performed inside the living body.

*Mesenchymal stem cell:* A cell derived from the immature embryonic connective tissue.

*Metabolism:* A general term used to designate all biochemical changes that occur to substances within the body by either anabolism or catabolism.

*Micro:* A unit prefix meaning one millionth (1/1 000 000).

*Modulus:* One of several measures of strain versus applied stress (e.g., Young's modulus).

*Monolithic:* Made from a single material.

*Multipotent:* Ability of a single stem cell to develop into a small number of cell types of the body that have a specific function.

*Nano:* A unit prefix meaning one billionth (1/1 000 000 000).

*Nanobiomaterials:* Biomaterials composed of particles or grains having nanometric tolerances; a nanometer is equal to  $10^{-9}$  m.

*Non-trauma:* Any injury or wound caused by disease.

*Organ:* A differentiated part of an organism adapted for a definite function.

*Osteoconduction:* An action associated with in-growth of capillaries and migration of bone-forming cells from the host into 3D matrix.

*Pathogen:* Any organism that is capable of producing disease.

*Phenotype:* Observable characteristics of an organism, resulting from the interaction of its genotype with the environment.

*Plasticity*: Ability of stem cells from one adult tissue to generate the differentiated cell type of another tissue.

*Pluripotent*: Ability of a single stem cell to develop into many different cell types of the body.

*Polymer*: Long-chain high molecular weight material consisting of repeated monomer units.

*Porosity*: A ratio of void volume to total volume expressed in terms of percentage.

*Proliferation*: Expansion of cell population by continuous division of a single cell into two identical daughter cells.

*Prosthesis*: A medical device that is capable of replacing the organs or tissues.

*Protein*: A large biomolecule composed of one or more chains of amino acids in a specific sequence.

*Resorption*: Dissolution of a substance.

*Scaffold*: A temporary structural construct or matrix used to support the cells for accommodation during tissue fabrication.

*Stem cell*: An undifferentiated cell that is capable of producing specialized types of cells.

*Stem cell-therapy*: A treatment in which stem cells are induced to differentiate into specific types of cells/tissues for the purpose of tissue repair.

*Surface area*: The total area of exposed surface of an object.

*Tissue*: A collection of similar cells and their surrounding intercellular substances.

*Tissue engineering*: Development of human tissues or organs in the laboratory from cells removed from the patient or other sources.

*Totipotent*: Ability of a single stem cell to develop into all types of cells/tissues of the body.

*Toughness*: The amount of energy absorbed by a material before breakage.

*Transplantation*: Surgical transfer of tissue or organ from one place to another.

*Trauma*: Any injury or wound caused by an external force.

*Vascular*: A medical term pertaining to blood vessel.

*Xenograft*: Tissue or organ transplanted from one species onto a different species.

## References

- MURUGAN, R., RAMAKRISHNA, S. Bioactive nanomaterials in bone grafting and tissue engineering. In: NALWA, H.S. (Ed.), *Handbook of Nanostructured Biomaterials and their Applications in Nanobiotechnology*, American Scientific Publishers, Stevenson Ranch, CA, 2005, pp. 141–168.
- NIKLASON, L.E., LANGER, R. Prospects for organ and tissue replacement., *J. Am. Med. Assoc.* 2001, 285, 573–576.
- MOTTEP® Facts and Figures, <http://www.nationalmottep.org/statistics.shtml>.
- STOCK, U.A., VACANTI, J.P. Tissue engineering: current state and prospects., *Ann. Rev. Med.* 2001, 52, 443–451.



- 5 WILLIAMS, D.F. Definitions in biomaterials. In: *Proceedings of a Consensus Conference of the European Society for Biomaterials*, Elsevier, Amsterdam, 1987.
- 6 KESEMO, B., LAUSMAA, J. Surface science aspects on inorganic biomaterials., *CRC Crit. Rev. Biocomp.* 1986, 2, 335–380.
- 7 LAURENCIN, C.T., AMBROSIO, A.M., BORDEN, M.D., COOPER, JR. Tissue engineering: Orthopedic applications., *Annu. Rev. Biomed. Eng.* 1999, 1, 19–46.
- 8 FRIEDENSTEIN, A.J., PETRAKOVA, K.V., KUROLESOVA, A.I. Heterotopic transplants of bone marrow. Analysis of precursor cells for osteogenic and haemopoietic tissues., *Transplantation* 1968, 6, 230–247.
- 9 PITTINGER, M.F., MACKAY, A.M., BECK, S.C., JAISWAL, R.K., DOUGLAS, R., MOSCA, J.D., MOORMAN, M.A., SIMONETTI, D.W., CRAIG, S., MARSHAK, D.R. Multilineage potential of adult human mesenchymal stem cells., *Science* 1999, 284, 143–147.
- 10 SESHU, B., KUMAR, S., SELLERS, D. Human bone marrow stromal cell: Co-expression of markers specific for multiple mesenchymal cell lineages., *Blood Cells Mol. Dis.* 2000, 26, 234–246.
- 11 CAPLAN, A.I., BRUDER, S.P. Mesenchymal stem cells: Building blocks for molecular medicine in the 21st century., *Trends Mol. Med.* 2001, 7, 259–264.
- 12 BRITTBURG, M., LINDAHL, A., NILSSON, A., OHLSSON, C., ISAKSSON, O., PETERSON, L. Treatment of deep cartilage defects in the knee with autologous chondrocyte transplantation., *New Engl. J. Med.* 1994, 331, 889–895.
- 13 PONDER, K.P., GUPTA, S., LELAND, F., DARLINGTON, G., FINEGOLD, M., DEMAYO, J., LEDLEY, F.D., CHOWDHURY, J.R., WOO, S.L. Mouse hepatocytes migrate to liver parenchyma and function indefinitely after intrasplenic transplantation. *Proc. Natl. Acad. Sci. U.S.A.* 1991, 88, 1217–1221.
- 14 BEHAVESH, E., MIKOS, A.G. Three-dimensional culture of differentiating marrow stromal osteoblasts in biomimetic poly(propylene fumarate-co-ethylene glycol)-based macroporous hydrogels., *J. Biomed. Mater. Res. A* 2003, 66, 698–706.
- 15 CINOTTI, G., PATTI, A.M., VULCANO, A., DELLA ROCCA, C., POLVERONI, G., GIANNICOLA, G., POSTACCHINI, F. Experimental posterolateral spinal fusion with porous ceramics and mesenchymal stem cells., *J. Bone Joint Surg. Br.* 2004, 86, 135–142.
- 16 PARK, D.J., CHOI, B.H., ZHU, S.J., HUH, J.Y., KIM, B.Y., LEE, S.H. Injectable bone using chitosan-alginate gel/mesenchymal stem cells/BMP-2 composites., *J. Cranio-Maxillofacial Surg.* 2005, 33, 50–54.
- 17 LI, W.J., TULI, R., OKAFOR, R., DERFOUL, A., DANIELSON, K.G., HALL, D.J., TUAN, R.S. A three-dimensional nanofibrous scaffold for cartilage tissue engineering using human mesenchymal stem cells., *Biomaterials* 2005, 26, 599–609.
- 18 YOSHIMOTO, H., SHIN, Y.M., TERAI, H., VACANTI, J.P. A biodegradable nanofiber scaffold by electrospinning and its potential for bone tissue engineering., *Biomaterials* 2003, 24, 2077–2082.
- 19 PATRICIA M. DEHMER. *The Scale of Things*, Office of Basic Energy Sciences, Office of Science, U.S. Department of Energy. [http://www.sc.doe.gov/production/bes/scale\\_of\\_things.html](http://www.sc.doe.gov/production/bes/scale_of_things.html).
- 20 MURUGAN, R., RAMAKRISHNA, S. Development of nanocomposites for bone grafting., *Comp. Sci. Technol.* 2005, 65, 2385–2406.
- 21 PARK, G.E., WEBSTER, T.J. A review of nanotechnology for the development of better orthopedic implants., *J. Biomed. Nanotechnol.* 2005, 1, 18–29.
- 22 THOMPSON, I., HENCH, L.L. Medical applications of composites. In: *Comprehensive Composite Materials*, Elsevier Science, Amsterdam, 2000, pp. 727–753.
- 23 BLACK, J., HASTINGS, G.W. *Handbook*

- of *Biomaterials Properties*, Chapman & Hall, London, 1998.
- 24 MURUGAN, R., RAMAKRISHNA, S. Nanostructured biomaterials. In: *Encyclopedia of Nanoscience and Nanotechnology*, NALWA, H.S. (Ed.), American Scientific Publishers, Stevenson Ranch, CA, 2004, pp. 595–613.
  - 25 DE GROOT, K. In: *Chemistry of Calcium Phosphates*, YAMMAMURO, T., HENCH, L.L. (Eds.), CRC Press, Boca Raton, FL, 1990.
  - 26 HENCH, L.L. Bioceramics., *J. Am. Ceram. Soc.* 1998, 81, 1705–1728.
  - 27 LeGEROS, R.Z., LeGEROS, J.P. In: *An Introduction to Bioceramics*, HENCH, L.L., WILSON, J. (Eds.), World Scientific, Singapore, 1993, pp. 139–180.
  - 28 KAY, M.I., YOUNG, R.A., POSNER, A.S. Crystal structure of hydroxyapatite., *Nature* 1964, 204, 1050–1052.
  - 29 MURUGAN, R., RAMAKRISHNA, S. Development of nanocomposites for bone grafting., *Composite Sci. Technol.* 2005, 65, 2385–2406.
  - 30 ROY, D.M., LINNEHAN, S.K. Hydroxyapatite formed from coral skeletal carbonate by hydrothermal exchange., *Nature* 1974, 247, 220–222.
  - 31 MURUGAN, R., RAO, K.P., KUMAR, T.S.S. Microwave synthesis of bioresorbable carbonated hydroxyapatite using goniopora., *Bioceramics* 2002, 15, 51–54.
  - 32 MURUGAN, R., RAMAKRISHNA, S. Coupling of therapeutic molecules onto surface modified coralline hydroxyapatite., *Biomaterials* 2004, 25, 3073–3080.
  - 33 MURUGAN, R., RAMAKRISHNA, S. Porous bovine hydroxyapatite for drug delivery., *J. Appl. Biomater. Biomech.* 2005, 3, 93–97.
  - 34 MURUGAN, R., KUMAR, T.S.S., RAO, K.P. Fluorinated bovine hydroxyapatite: Preparation and characterization., *Mater. Lett.* 2002, 57, 429–433.
  - 35 MURUGAN, R., RAMAKRISHNA, S. Crystallographic study of hydroxyapatite bioceramics derived from various sources., *Crystal Growth Design* 2005, 5, 111–112.
  - 36 SUCHANEK, W., YOSHIMURA, M. Processing and properties of hydroxyapatite-based biomaterials for use as hard tissue replacement implants., *J. Mater. Res.* 1998, 13, 94–117.
  - 37 MURUGAN, R., RAMAKRISHNA, S. Aqueous mediated synthesis of bioresorbable nanocrystalline hydroxyapatite., *J. Crystal Growth* 2005, 274, 209–213.
  - 38 MURUGAN, R., RAMAKRISHNA, S. Bioresorbable composite bone paste using polysaccharide based nano hydroxyapatite., *Biomaterials* 2004, 25, 3829–3835.
  - 39 WANG, F., LI, M.S., LU, Y.P., QI, Y.X., LIU, Y.X. Synthesis and microstructure of hydroxyapatite nanofibers synthesized at 37 °C., *Mater. Chem. Phys.* 2006, 95, 145–149.
  - 40 WEBSTER, T.J., ERGAN, C., DOREMUS, R.H., SIEGEL, R.W., BZIOS, R. Enhanced functions of osteoblasts on nanophase ceramics., *Biomaterials* 2000, 21, 1803–1810.
  - 41 OTA, Y., IWASHITA, T. Novel preparation method of hydroxyapatite fibers., *J. Am. Ceram. Soc.* 1998, 81, 1665–1668.
  - 42 HUANG, J., BEST, S.M., BONFIELD, W., BROOKS, R.A., RUSHTON, N., JAYASINGHE, S.N., EDIRISINGHE, M.J. In vitro assessment of the biological response to nano-sized hydroxyapatite., *J. Mater. Sci. Mater. Med.* 2004, 15, 441–445.
  - 43 MURUGAN, R., RAMAKRISHNA, S. Aqueous mediated synthesis of bioresorbable nanocrystalline hydroxyapatite., *J. Crystal Growth* 2005, 274, 209–213.
  - 44 ZHANG, S., CONSALVES, K.E. Preparation and characterization of thermally stable nanohydroxyapatite., *J. Mater. Sci. Mater. Med.* 1997, 8, 25–28.
  - 45 KOTHAPALLI, C.R., SHAW, M.T., WEI, M. Biodegradable HA-PLA 3-D porous scaffolds: Effect of nano-sized filler content on scaffold properties., *Acta Biomater.* 2005, 1, 653–662.
  - 46 NAKAMURA, S., TSOBE, T., SENNA, M. Hydroxyapatite nano sol prepared via

- a mechanochemical route., *J. Nanopart. Res.* **2001**, 3, 57–61.
- 47 KOUMOULIDIS, G.C., VAIMAKIS, T.C., SDOUKOS, A.T., BOUKOS, N.K., TRAPALIS, C.C. Preparation of hydroxyapatite lathlike particles using high-speed dispersing equipment., *J. Am. Ceram. Soc.* **2001**, 84, 1203–1208.
  - 48 SARIG, S., KAHANA, F. Rapid formation of nanocrystalline apatite., *J. Crystal Growth* **2002**, 237–239, 55–59.
  - 49 YANG, Y., ONG, J.L. Rapid sintering of hydroxyapatite by microwave processing., *J. Mater. Sci. Lett.* **2002**, 21, 67–69.
  - 50 YANG, F., MURUGAN, R., RAMAKRISHNA, S., WANG, X., MA, Y.-X., WANG, S. Fabrication of nano-structured porous PLLA scaffold intended for nerve tissue engineering., *Biomaterials* **2004**, 25, 1891–1900.
  - 51 YANG, F., MURUGAN, R., WANG, S., RAMAKRISHNA, S. Electrospinning of nano/micro scale poly(L-lactic acid) aligned fibers and their potential in neural tissue engineering., *Biomaterials* **2005**, 26, 2603–2610.
  - 52 MURUGAN, R., RAMAKRISHNA, S. Nano-featured scaffolds for tissue engineering: Spinning methodologies., *Tissue Eng.* **2006**, 12, 3, 435–447.
  - 53 BENIASH, E., HARTGERINK, J.D., STORRIE, H., STENDAHL, J.C., STUPP, S.I. Self-assembling peptide amphiphile nanofiber matrices for cell entrapment., *Acta Biomater.* **2005**, 1, 387–397.
  - 54 HARTGERINK, J.D., BENIASH, E., STUPP, S.I. Self-assembly and mineralization of peptide-amphiphile nanofibers., *Science* **2001**, 294, 1684–1688.
  - 55 YANG, F., MURUGAN, R., RAMAKRISHNA, S., WANG, X., MA, Y.-X., WANG, S. Fabrication of nano-structured porous PLLA scaffold intended for nerve tissue engineering., *Biomaterials* **2004**, 25, 1891–1900.
  - 56 CHEN, V.J., MA, P.X. Nano-fibrous Poly(L-lactic acid) scaffolds with interconnected spherical macropores., *Biomaterials* **2004**, 25, 2065–2073.
  - 57 MATTHEWS, J.A., WNEK, G.E., SIMPSON, D.G., BOWLIN, G.L. Electrospinning of collagen nanofibers., *Biomacromolecules* **2002**, 3, 232–238.
  - 58 YANG, F., MURUGAN, R., WANG, S., RAMAKRISHNA, S. Electrospinning of nano/micro scale poly(L-lactic acid) aligned fibers and their potential in neural tissue engineering., *Biomaterials* **2005**, 26, 2603–2610.
  - 59 ZELENY, J. The electrical discharge from liquid points and a hydrostatic method of measuring the electric intensity at their surfaces. *Phys. Rev.* **1914**, 3, 69–91.
  - 60 FORMHALS, A. Electrical spinning of fibers from solutions., *US Patent No. 2123992*, **1934**.
  - 61 FORMHALS, A. Apparatus for production and electric treatment of artificial fibers., *US Patent No. 2109333*, **1938**.
  - 62 FORMHALS, A. Artificial threads., *US Patent No. 2187306*, **1940**.
  - 63 FORMHALS, A. Apparatus for producing artificial fibers from fiber-forming liquids by an electrical spinning method., *US Patent No. 2323025*, **1943**.
  - 64 FORMHALS, A. Spinner for synthetic fibers., *US Patent No. 2349950*, **1944**.
  - 65 TAYLOR, G.I. Electrically driven jets., *Proc. R. Soc. London* **1969**, A313, 453–475.
  - 66 RAMAKRISHNA, S., FUJIHARA, K., TEO, W.E., LIM, T.C., MA, Z. *An Introduction to Electrospinning and Nanofibers*, World Scientific, Singapore, **2005**.
  - 67 RENEKER, D.H., CHUN, I. Nanometer diameter fibers of polymer produced by electrospinning., *Nanotechnology* **1996**, 7, 261–223.
  - 68 BOGNITZKI, M., CZADO, W., FRESE, T., SCHAPER, A.S., HELLWIG, M., STEINHART, M., GREINER, A., WENDROFF, J.H. Nanostructured fibers via electrospinning., *Adv. Mater.* **2001**, 13, 70–72.
  - 69 FRENOT, A., CHRONAKIS, I.S. Polymer nanofibers assembled by electrospinning., *Curr. Opin. Colloid Interface Sci.* **2003**, 8, 64–75.

- 70 HUANG, J., BEST, S.M., BONFIELD, W., BROOKS, R.A., RUSHTON, N., JAYASINGHE, S.N., EDIRISINGHE, M.J. In vitro assessment of the biological response to nano-sized hydroxyapatite., *J. Mater. Sci. Mater. Med.* **2004**, 15, 441–445.
- 71 MANSO, M., OGUETA, S., FERNANDEZ, P.H., VAZQUEZ, L., LANGLET, M., RUIZ, J.P.G. Biological evaluation of aerosol–gel-derived hydroxyapatite coatings with human mesenchymal stem cells., *Biomaterials* **2002**, 23, 3985–3990.
- 72 WEBSTER, T.J., ERGAN, C., DOREMUS, R.H., SIEGEL, R.W., BIZIOS, R. Enhanced functions of osteoblasts on nanophase ceramics., *Biomaterials* **2000**, 21, 1803–1810.
- 73 DU, C., CUI, F.Z., ZHU, X.D., DE GROOT, K. Three-dimensional nano-HAp/collagen matrix loading with osteogenic cells in organ culture., *J. Biomed. Mater. Res.* **1999**, 44, 407–415.
- 74 LIAO, S.S., CUI, F.Z., ZHANG, W., FENG, Q.L. Hierarchically biomimetic bone scaffold materials: Nano-HA/collagen/PLA composite., *J. Biomed. Mater. Res. Appl. Biomater.* **2004**, 69, 158–165.
- 75 LIAO, S.S., GUAN, K., CUI, F.Z., SHI, S.S., SUN, T.S. Lumbar spinal fusion with a mineralized collagen matrix and rhBMP-2 in a rabbit model., *Spine* **2003**, 28, 1954–1960.
- 76 LIAO, S.S., CUI, F.Z., ZHU, X.D. Osteoblasts adherence and migration through three-dimensional porous mineralized collagen based composite: nHAC/PLA., *J. Bioactive Compat. Polym.* **2004**, 19, 117–130.

## 6 Orthopedic Tissue Engineering Using Nanomaterials

*Michiko Sato and Thomas J. Webster*

### 6.1 Preface

Over the past nine decades of administering bioimplants to humans, most synthetic prostheses consist of material particles and/or grain sizes with conventional dimensions (on the order of 1 to  $10^4$   $\mu\text{m}$ ). But the lack of sufficient bonding of synthetic implants to surrounding body tissues has, in recent years, led to the investigation of novel material formulations. One such classification of materials, nanomaterials (or materials with constituent components less than 100 nm in at least one direction), can be used to synthesize implants with similar surface roughness to that of natural tissues. Natural tissues have numerous nanometer features available for cellular interactions since they are composed of many nanostructures (specifically, proteins).

Several nanophase biomedical implants are currently being investigated, and are likely to gain approvals for clinical use in the near future. The critical factor for this drive is the increasingly documented special, biologically-improved material properties of nanophase implants compared with conventional grain size formulations of the same material chemistry. In this manner, the present chapter highlights a novel property of nanophase materials that makes them attractive for use as implants: enhanced cyto-compatibility leading to increased tissue regeneration. Active works are focused in the domains of orthopedic, dental, bladder, neurological, vascular, cartilage, and cardiovascular applications. However, only orthopedic applications, which are the closest to clinical applications, will be emphasized here. In fact, the field of incorporating nanotechnology into orthopedics has matured enough to present exciting *in vivo* data. This entry will thus articulate the seeming revolutionary changes and the potential gains nanostructured materials can make for bone implant technology. This chapter will first cover problems with current orthopedic implants and then how nanotechnology is providing solutions as pertaining to the use of ceramics, metals, polymers, and composites thereof. Lastly, critical hurdles that need to be addressed before nanophase materials can be used in orthopedics are discussed. This chapter is different from other chapters on the use of nanotechnology towards orthopedic tissue engineering as it covers, for the first

time, *in vivo* studies that highlight increased bone growth on nanostructured compared with currently used materials.

## 6.2

### Introduction: Problems with Current Implants

Since 1990, the total number of hip replacements, which is the replacement of the femoral and hip bones, has been steadily increasing [1–7]. In fact, the 152 000 total hip replacements in 2000 is a 33% increase from the number performed in 1990 and a little over half of the projected number of total hip replacements (272 000) by the year 2030 in the United States alone [1–4]. However, in 1997, 12.8% of the total hip arthroplasties were simply due to revision surgeries of previously implanted failed hip replacements [1–4].

The fact that such a high percentage of hip replacements performed every year are revision surgeries is not surprising when you consider the life expectancy of the implant versus that of the patient receiving the implant. Consistently, over 30% of those requiring total hip replacements have been below the age of 65 and even those at 65 have a life expectancy of 17.9 years [5–7]. Females, which make up the majority of those receiving total hip replacements, have a life expectancy of 19.2 years at the age of 65. Since the longevity of implants ranges only from about 12–15 years, even most of those that receive bone implants at the age of 65 will require at least one revision surgery before the end of their lives [5–7].

For the dental community the story is not any better. Since dental implants may be necessary for the young and old alike, it is imperative that they are able to last for the duration of the patient's life. Recent studies have found that dental implants that have been used in over 300 000 cases in the United States have up to a 96% success rate (meaning that the implant was not mobile and was non-inflamed) after five years, 80% after ten, and less than 75% after 15 years [1–7].

The above strongly suggests that the longevity of the prostheses is a reoccurring problem for the orthopedic/dental community that has to be dealt with since current approaches clearly fail. Orthopedic implant failure can be due to numerous reasons, including poor initial bonding of the implant to juxtaposed bone, generation of wear debris that lodges between the implant and surrounding bone to cause bone cell death, and/or stress and strain imbalances between the implant and surrounding bone causing implant loosening and eventual failure [8]. Although there are many reasons why implants fail, a central one is the lack of sufficient bone regeneration around the implant immediately after insertion [8]. Shockingly, about a quarter of dental implant failures are attributed to incomplete healing of the implant to juxtaposed bone (for those that failed between three and six months) [1–7]. Importantly, this leads to eventual implant loosening and regions for possible wear debris to situate between the implant and surrounding bone further complicating bone loss [8–11].

To improve this performance and hence extend the lifetime of bone implants, it is essential to design biomaterial surface characteristics that interface optimally with select proteins and subsequently with pertinent bone cell types. That is, im-

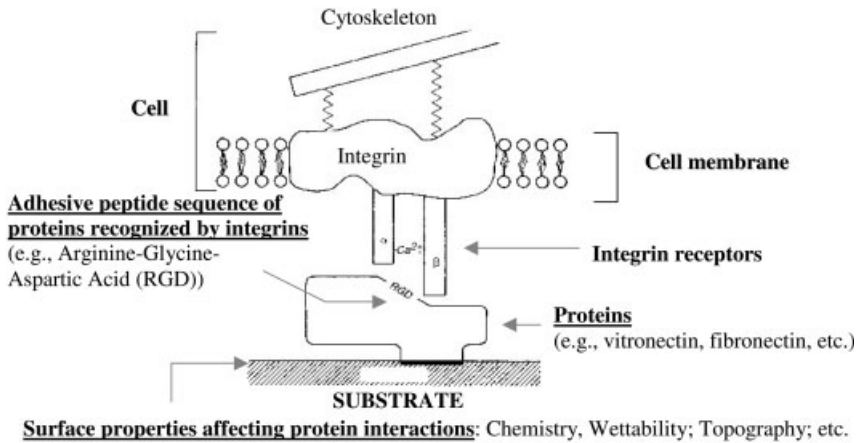


**Fig. 6.1.** Cell recognition of biomaterial surfaces controlled by initial protein interactions. Initial protein interactions can influence cell adhesion and, thus, the degree of bone tissue formation on biomaterials. Changing the material properties will alter the protein interactions and influence subsequent cell function. (Adapted and redrawn from Ref. [13], with permission.)

mediately after implantation, proteins will adsorb from plasma to biomaterial surfaces to control cell attachment and eventual tissue regeneration (Fig. 6.1) [12, 13]. Initial protein interactions that mediate cell function depend on many biomaterial properties, including chemistry, charge, wettability, and topography [12, 13]. Of significant influence for protein interactions is surface roughness [14–18], and this represents the promise of nanophase materials in bone implant applications.

### 6.3 A Potential Solution: Nanotechnology

Nanotechnology embraces a system whose core of materials is in the range of nanometers ( $10^{-9}$  m) [19–29]. The application of nanomaterials for medical diagnosis, treatment of failing organ systems or prevention and cure of human diseases can generally be referred to as nanomedicine [28, 29]. The branch of nanomedicine devoted to the development of biodegradable or non-biodegradable prostheses falls within the purview of nano-biomedical science and engineering [28, 29]. Although various definitions are attached to the word “nanomaterial” by different experts, the commonly accepted concept refers nanomaterials as that material with the basic structural unit in the range 1–100 nm (nanostructured), crystalline solids with grain sizes 1–100 nm (nanocrystals), individual layer or multilayer surface coatings in the range 1–100 nm (nanocoatings), extremely fine powders with an average particle size in the range 1–100 nm (nanopowders) and, fibers with a diameter in the range 1–100 nm (nanofibers) [19, 20].

Since nature itself exists in the nanometer regime, especially tissues in the hu-

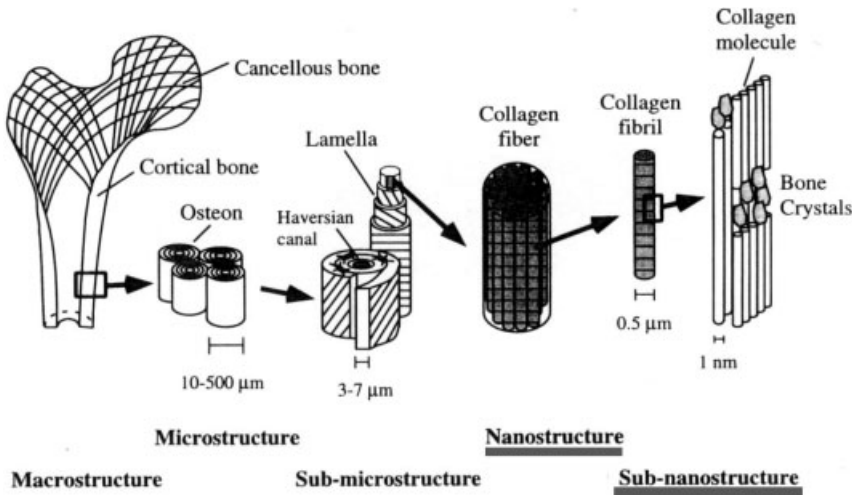


**Fig. 6.2.** Nanocomponents of bone provide a high degree of nanostructured surface roughness for bone cells. (Adapted and redrawn from Ref. [31], with permission.)

man body [30], clearly, nanotechnology can play an integral role in the biological milieu. Specifically, bone is composed of numerous nanostructures – like collagen and hydroxyapatite that, most importantly, provide a unique nanostructure for protein and bone cell interactions in the body (Fig. 6.2) [31]. Although mimicking constituent components of bone is novel in itself, there are additional reasons to consider nanomaterials for orthopedic applications: their special surface properties compared with conventional (or micron constituent component structured) materials [24–27]. For example, a nanomaterial has increased numbers of atoms at the surface, grain boundaries or material defects at the surface, surface area, and altered electron distributions compared with conventional materials (Fig. 6.3) [27]; in summary, nanophase material surfaces are more reactive than their conventional counterparts. In this light, clearly, proteins that influence cell interactions that lead to tissue regeneration will be quite different on a nanophase compared with conventional implant surfaces (Fig. 6.1).

Despite this, the evolution of orthopedic implants has centered on the use of materials with non-biologically inspired micron surface features [32, 33], mostly changing in chemistry or micron roughness but not degree of nanometer roughness (Fig. 6.4). In this manner, it should not be surprising why the optimal material to regenerate bone has not been found.

### 6.3.1

#### **Current Research Efforts to Improve Implant Performance Targeted at the Nanoscale**

Nanoscale materials currently being investigated for bone tissue engineering applications can be placed in the following categories: ceramics, metals, polymers, and



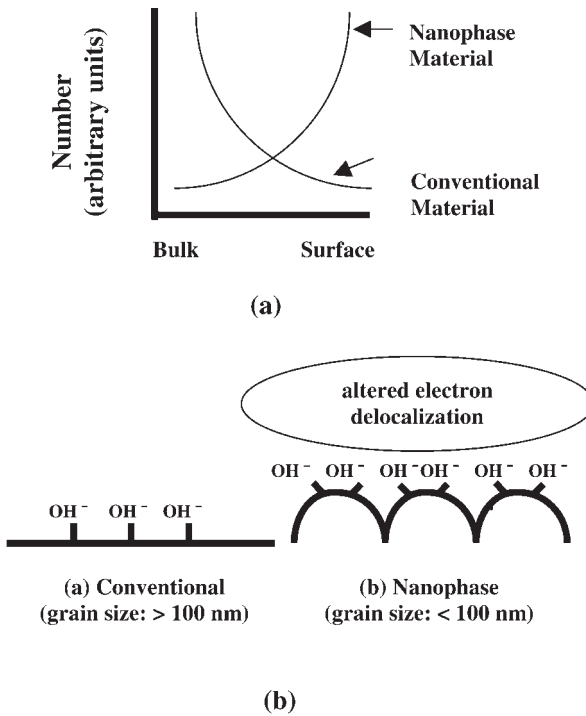


**Fig. 6.3.** Special surface properties of nanophase materials. (a) Higher number of atoms at the surface for nanophase compared with conventional materials. (b) Nanophase materials have higher surface areas, possess greater numbers of material defects at the

surface, and altered electron delocalization. Such special properties will influence protein interactions for controlling cell functions. (Adapted and redrawn from Ref. [25], with permission.)

composites thereof. Each type of material has distinct properties that can be advantageous for specific bone regrowth applications. For example, hydroxyapatite, a ceramic mineral present in bone (Fig. 6.2), can also be made synthetically. Ceramics, however, are not mechanically tough enough to be used in bulk for large-scale bone fractures; nonetheless, they have found applications for a long time as bioactive coatings due to their ionic bonding mechanisms, which are favorable for osteoblast (or bone-forming cells) function [34].

Unlike ceramic materials, metals are not found in the body. However, due to their mechanical strength and relative inactivity with biological substances, metals (specifically, Ti, Ti6Al4V, and CoCrMo) have been the materials of choice for large bone fractures [32, 33]. Polymers exhibit unique properties (such as viscosity, malleability, moldability) and possess mechanical strength that is comparable to many soft (not hard) tissues in the body [35]. To date, because of their excellent friction properties, polymers (like ultrahigh molecular weight polyethylene) have been primarily used as articulating components of orthopedic joint replacements [35].

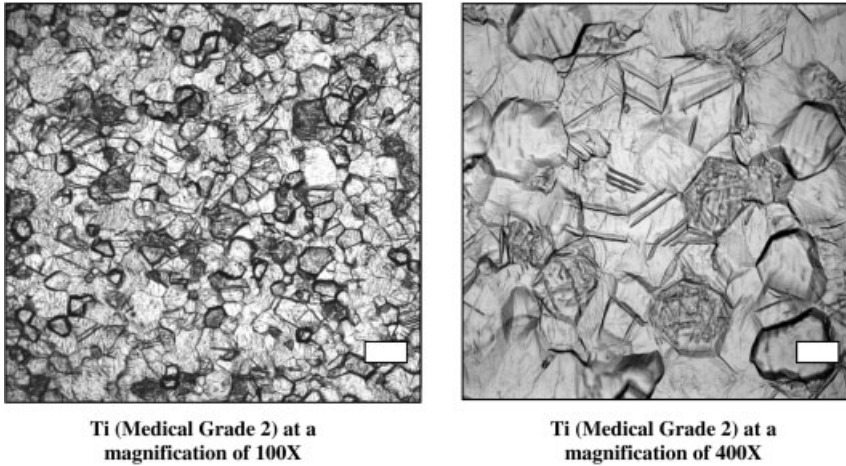


**Fig. 6.4.** Conventional grain size of currently used orthopedic implants. Bar = 10 and 2.5  $\mu\text{m}$  for the left and right micrograph, respectively.

Additionally, some polymers (particularly the polyester family) can be resorbed or degraded in the body, which opens the window for controllable repair of damaged bone that is actively being investigated in tissue engineering circles. Lastly, composites of any or all of the above can be synthesized to provide a wide range of material properties to increase bone implant performance [36]; such ability to tailor composite properties to specific orthopedic applications makes them attractive.

Due to the numerous materials currently being used and investigated in orthopedics, this review will cover selected efforts to create nanoscale surfaces in all of these categories: ceramics, metals, polymers, and composites. Several current and potential materials that have shown promise in nanotechnology for bone biomedical applications, as well as needed future directions, will be emphasized.

#### 6.3.1.1 Ceramic Nanomaterials

**Increased Osteoblast Functions** The first report correlating increased bone cell functions with decreased material grain or particulate size into the nanometer regime dates back to 1998 and involves ceramics [37]. Such reports described that *in vitro* osteoblast (bone-forming cell) adhesion, proliferation, differentiation (as measured by intracellular and extracellular matrix protein synthesis such as alkaline phosphatase), and calcium deposition was enhanced on ceramics with particulate or grain sizes less than 100 nm [37–46]. Specifically, this was first demonstrated for a wide range of ceramic chemistries, including titania (Fig. 6.5), alumina, and hydroxyapatite [39]. For example, four, three, and two times the amount of calcium-mineral deposition was observed when osteoblasts were cultured for up to 28 days on nanophase compared with conventional alumina, tita-

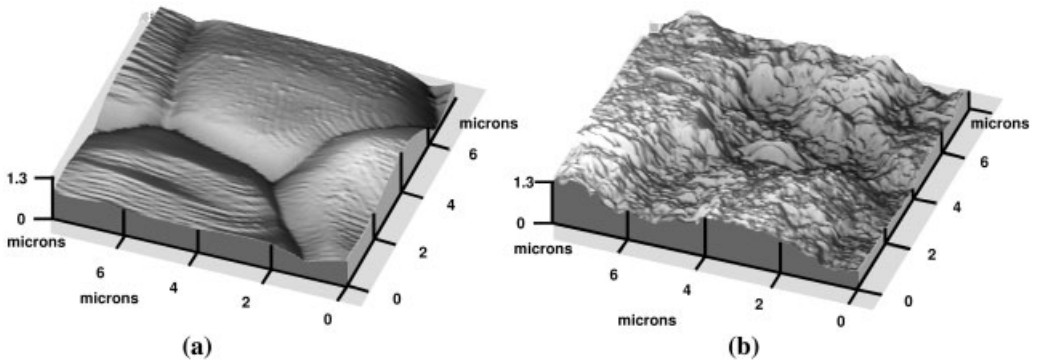


**Fig. 6.5.** (a) Conventional and (b) nanophase titania. One of the first studies correlating increased osteoblast function with decreasing ceramic grain size was carried out on titania as pictured here. (From Ref. [39], with permission.)

nia, and hydroxyapatite, respectively [41]. Notably, for each respective nanophase and conventional ceramic mentioned in these first reports, similar chemistry and material phase were studied [37–46]. That is to say, only the degree of nanometer surface features was altered between respective nanophase and conventional alumina, titania, and hydroxyapatite. This is important since as previously discussed, it is well known that alterations in surface chemistry will influence bone cell function [8, 32–36], but this was the first time changes in the degree of nanometer roughness alone were reported to enhance bone cell responses [37].

Although these studies provided preliminary evidence that osteoblast functions can be promoted on nanostructured compared with conventional materials regardless of ceramic chemistry, Elias et al. further described a study where the topography of compacted carbon nanometer fibers were transferred to poly(lactic-co-glycolic acid) (PLGA) using well-established silastic mold techniques [47]. The same was done for compacts composed of conventional carbon fibers. Figure 6.6 illustrates the successful transfer of nanometer compared with micron surface features from the carbon nanometer compared with conventional fiber compacts, respectively [47]. Importantly, osteoblast adhesion increased on PLGA molds made from nanometer compared with conventional carbon fibers [47]. Increased osteoblast functions were also observed on the starting materials of nanometer compared with conventional carbon fiber compacts [47]. In this manner, this study provided further evidence of the importance of nanometer surface features (and not chemistry) in promoting functions of bone-forming cells.

Equally as interesting, a step-function increase in osteoblast performance has been reported at distinct ceramic grain sizes: specifically, at alumina and titania spherical grain sizes below 60 nm [39]. This is intriguing since when creating alumina or titania ceramics with average grain sizes below 60 nm, a drastic increase in osteoblast function was observed compared with respective ceramics with grain sizes just 10 nm higher (i.e., those with average grain sizes of 70 nm) [39]. This

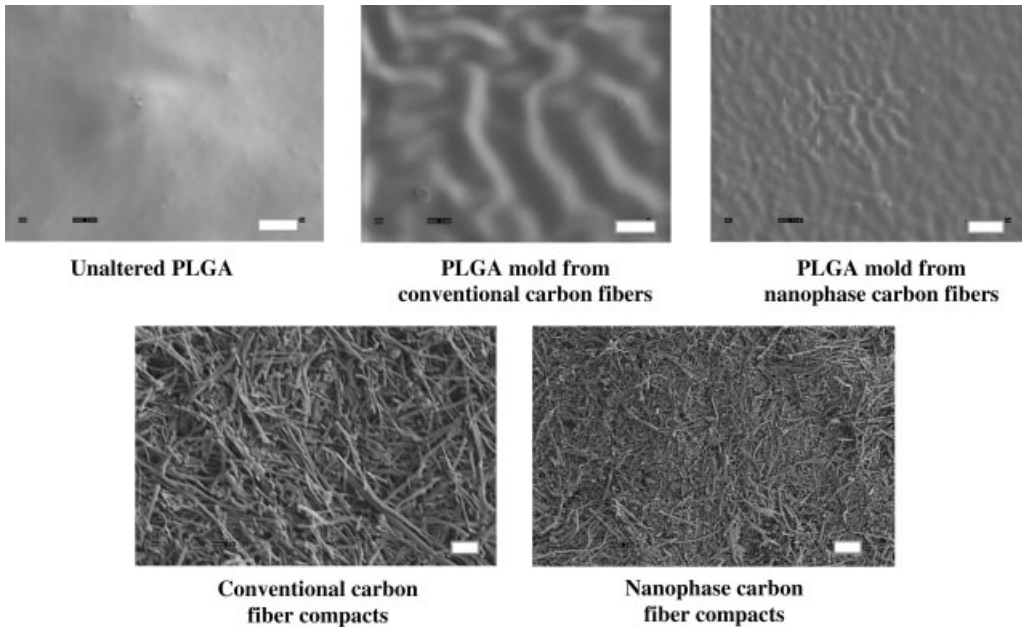


**Fig. 6.6.** Poly(lactic-co-glycolic acid) (PLGA) molds of conventional and nanophase carbon fiber compacts. To highlight the importance of nanometer surface roughness regardless of substrate chemistry, studies have shown increased functions of osteoblasts on PLGA molds of nanophase compared with conventional carbon compacts. In addition, increased functions of osteoblasts have been found on compacts composed of nanometer compared with conventional carbon fibers. Bar = 1  $\mu\text{m}$ . (From Ref. [47], with permission.)

critical grain size for improving osteoblast function is also of paramount importance since numerous other special properties (such as mechanical, electrical, catalytic, etc.) of materials have been reported when grain size is specifically reduced to below 100 nm [19–27]. With this information, evidence has been provided to show for the first time that the ability of nanophase ceramics to promote bone cell function is indeed limited to grain sizes (or subsequent surface features) below 100 nm, specifically those below 60 nm [39]. Thus, another novel size-dependent property of nanostructured ceramics has been elucidated by these pioneering studies.

Although an exact explanation as to why greater bone regeneration is observed on smaller grain size ceramics into the nanometer regime is not known, the importance of this specific grain size in improving osteoblast function is connected with interactions of vitronectin (a protein known to mediate osteoblast adhesion with linear dimensions remarkably similar to the critical grain size of 60 nm mentioned above) [40, 44]. Moreover, as previously mentioned, several studies have indicated that vitronectin and other proteins important for osteoblast adhesion are more well-spread and, thus, expose amino acid sequences to a greater extent when interacting with nanometer compared with conventional ceramics [40, 44]. Intriguingly, numerous investigators have confirmed that the minimum distance between

protein ligands (such as arginine-glycine-aspartic acid or RGD) necessary for cell attachment and spreading is in the nanometer regime (specifically, from 10 to 440 nm, depending on whether the study was completed with full proteins, protein fragments, or single RGD units) [48–53]. Therefore, an underlying substrate surface that mediates protein spreading (as opposed to protein folding) to expose such ligands coupled with a nanometer surface roughness, to further project such ligands to the cell, may promote cell adhesion due to this optimal ligand spacing.

**Increased Osteoclast Functions** In addition to studies highlighting enhanced osteoblast functions on nanophase ceramics, increased functions of osteoclasts (bone-resorbing cells) have been reported on nanospherical compared with larger grain size alumina, titania, and hydroxyapatite (HA) [45]. Specifically, osteoclast synthesis of tartrate-resistant acid phosphatase (TRAP) and subsequent formation of resorption pits was up to two-times greater on nanophase than on conventional ceramics such as hydroxyapatite. Coordinated functions of osteoblasts and osteoclasts are imperative for the formation and maintenance of healthy new bone juxtaposed to an orthopedic implant [8]. Frequently, newly formed bone juxtaposed to implants is not remodeled by osteoclasts and thus becomes unhealthy or necrotic [34]. At this time, the exact mechanism of greater functions of osteoclasts on nanophase ceramics is not known, but it may be tied to the well-documented increased solubility properties of nanophase compared with conventional materials [25]. In other words, due to larger numbers of grain boundaries at the surface of smaller grain size materials, increased diffusion of chemicals (such as TRAP) may be occurring to subsequently result in the formation of more resorption pits.

Collectively, results of promoted functions of osteoblasts coupled with greater functions of osteoclasts imply increased formation and maintenance of healthy bone juxtaposed to an implant surface composed of nanophase ceramics. In fact, although not compared with conventional grain size apatite coated metals, some studies have indeed demonstrated increased new bone formation on metals coated with nanophase apatite [54]. As shown in Fig. 6.7, bone formation can be clearly seen on the surface of metals coated with nano-apatite, whereas there is no indication of new bone formation on the underlying metal without the coating [54]. Incidentally, coating metals with nanophase HA has been problematic [55]. For example, due to their small grain size, techniques that use high temperatures (like plasma spray deposition) are not an option since they will result in HA grain growth into the micron regime [55]. To circumvent such difficulties, some investigators have allowed nanophase HA to precipitate on metal surfaces; this can be time consuming and not very controllable [54]. In contrast, others have developed novel techniques that use high-pressure based processes that do not significantly create elevated temperatures to coat nanophase ceramics on metals so as to retain their bioactive properties (Fig. 6.8) [56].

**Decreased Competitive Cell Functions** Importantly, it has also been shown that competitive cells do not respond in the same manner to nanophase materials as osteoblasts and osteoclasts do [40, 47, 57]. In fact, decreased functions of fibro-

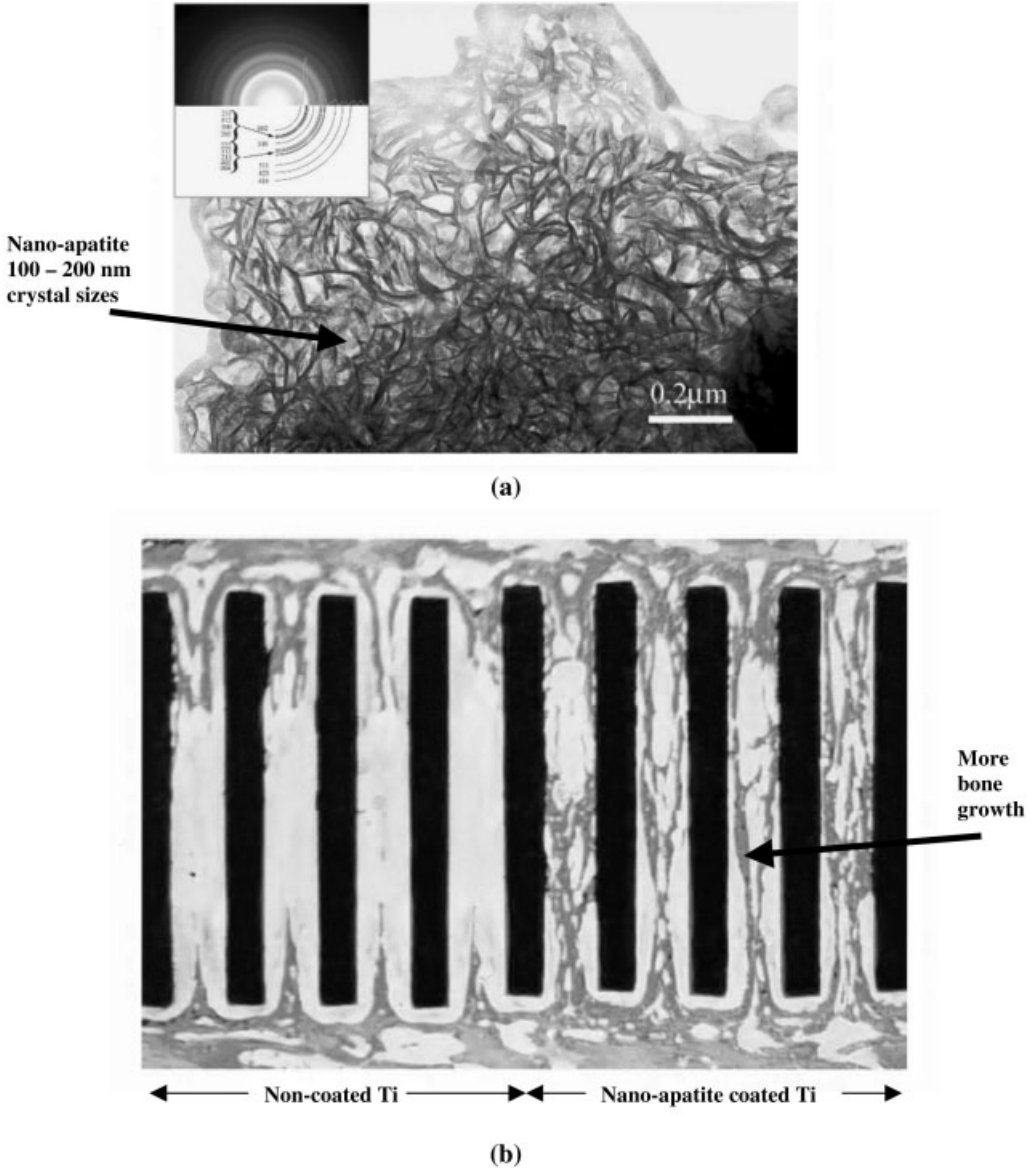
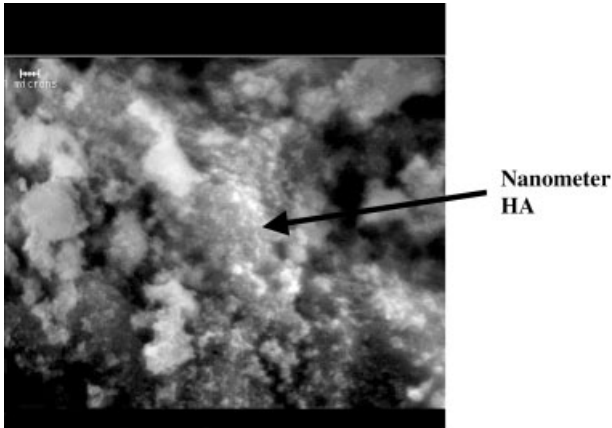


Fig. 6.7. Increased *in vivo* bone regeneration on titanium coated with nanophase apatite. Scanning electron micrograph of nanometer dimensioned apatite (100–200 nm) is depicted in (a). Increased bone regeneration in titanium cages when coated with nano-apatite is depicted in (b). (From Ref. [54], with permission.)



**Fig. 6.8.** Nanophase hydroxyapatite (HA) coated on titanium. Due to elevated temperatures, traditional coating techniques, such as plasma spray deposition, cannot be used to coat metals with nanophase ceramics.

This process, developed by Spire Biomedical (Bedford, MA), uses high pressure at low temperatures so as to not allow for grain growth. Bar = 1  $\mu\text{m}$  (upper left).

blasts (cells that contribute to fibrous encapsulation and callus formation events that may lead to implant loosening and failure [8]) and of endothelial cells (cells that line the vasculature of the body) have been observed on nanophase compared with conventional ceramics [40]. Indeed, the ratio of osteoblast to fibroblast adhesion increased from 1:1 on conventional alumina to 3:1 on nanophase alumina [40].

Previously, such selectively in bone cell function on materials has only been observed through delicate surface chemistry (such as through the immobilization of peptide sequences such as Lys-Arg-Ser-Arg or KRSR) [58]. It has been argued that immobilized delicate surface chemistries may be compromised once implanted due to macromolecular interactions that render such epitopes non-functional *in vivo*. For these reasons, notably, studies demonstrating selective enhanced osteoblast and osteoclast functions with decreased functions of competitive cells on nanophase compared with conventional materials have been conducted on surfaces that have not been chemically modified by the immobilization of proteins, amino acids, peptides, or other entities [40, 47, 57]. Rather it is the unmodified, raw material surface that is specifically promoting bone cell functions.

Fibroblast function was also investigated in the same study that was previously mentioned in which Elias et al. transferred the topography of compacted carbon nanometer compared with conventional fibers to PLGA using well-established silastic mold techniques (again please refer Fig. 6.6) [47]. Similar to the observed greater osteoblast adhesion already noted, decreased fibroblast adhesion was measured on PLGA molds synthesized from carbon nanometer compared with conventional fibers [47]. Again, this was the same trend observed on the starting material of carbon nanometer compared with conventional fiber compacts [47]. Thus, this

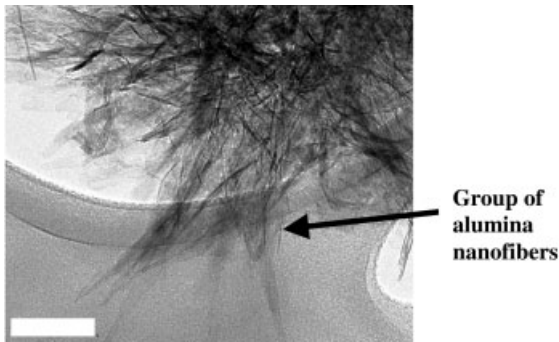


**Fig. 6.9.** Transmission electron microscope image of alumina nanofibers. Compared with spherical conventional alumina, increased functions of osteoblasts have been reported on nanophase fibrous alumina. Scale bar = 10 nm. (From Ref. [57], with permission.)

study demonstrated the importance of a nanometer surface roughness (and not chemical composition of the material) in decreasing functions of fibroblasts that may lead to undesirable fibrous encapsulation and callus formation events inhibiting osseointegration of orthopedic implants with surrounding bone.

**Increased Osteoblast Functions on Nanofibrous Materials** Recently, researchers have further modified nanophase ceramics to simulate not only the nanometer dimension but also the aspect ratio of proteins and hydroxyapatite crystals found in the extracellular matrix of bone [57]. For example, consolidated substrates formulated from nano-fibrous alumina (diameter: 2 nm, length > 50 nm; Fig. 6.9) increased osteoblast functions in comparison with similar alumina substrates formulated from the aforementioned nanospherical particles [57]. Specifically, Price et al. determined a two-fold increase in osteoblast cell adhesion density on nanofiber versus conventional nanospherical alumina substrates, following only a 2 h culture [57]. Greater subsequent functions leading to new bone synthesis has also been reported on nanofibrous compared with nano and conventional spherical alumina [57]. Thus, perhaps not only is the nanometer grain size of components of bone important to mimic in materials, but the aspect ratio may also be key to simulate in synthetic materials to optimize bone cell response.

Another classification of novel biologically-inspired nanofiber materials that has been investigated for orthopedic applications is self-assembled helical rosette nanotubes [59]. These organic compounds are composed of guanine and cytosine DNA pairs that self-assembled when added to water to form unique nanostructures (Fig. 6.10). These nanotubes have been reported to be 1.1 nm wide and up to several millimeters long [59]. Compared with currently used titanium, recent studies have indicated that osteoblast function is increased on titanium coated with helical rosette nanotubes (Fig. 6.10) [59]. Although in these studies it has not been possi-



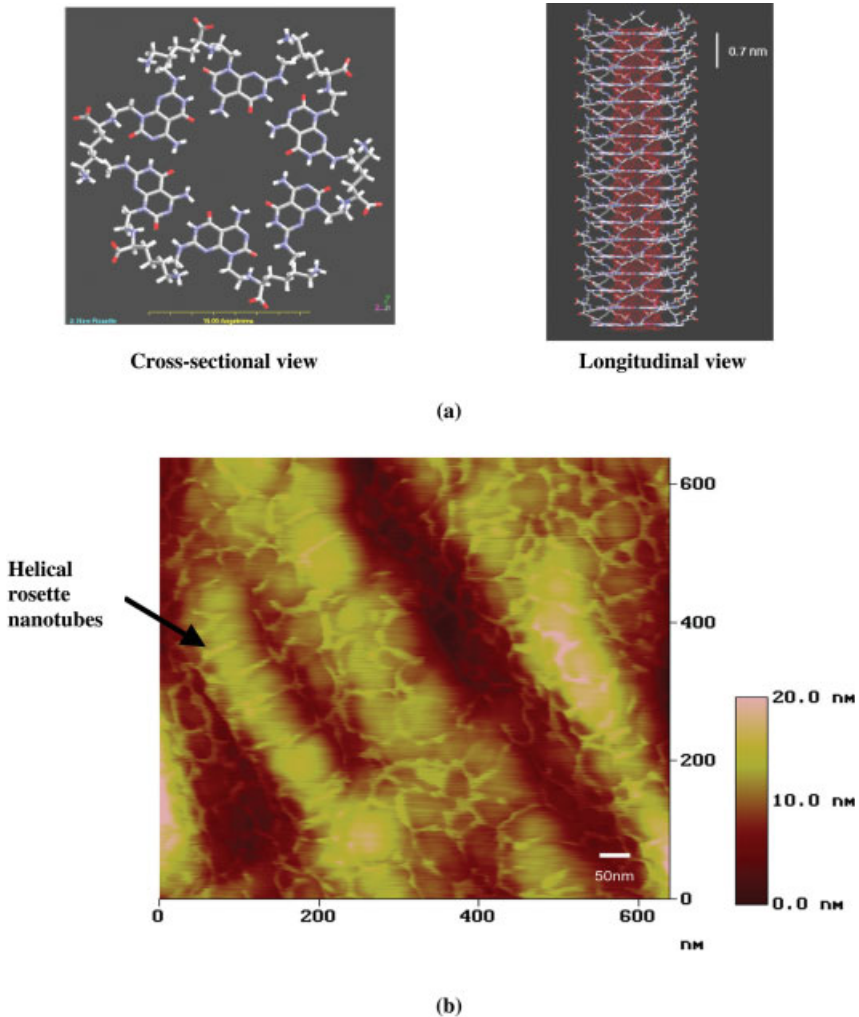


**Fig. 6.10.** Helical rosette nanotubes. (a) Drawings of the cross-sectional and longitudinal views of self-assembled helical rosette nanotubes. (b) Helical rosette nanotubes coated on titanium. Note the

nanophase dimension of these organic tubes. Increased osteoblast function has been observed on helical rosette nanotubes coated on Ti. (From Ref. [59], with permission.)

ble to separate the influence of nanometer dimensions from the effects of nanotube chemistry on cell functions, these nanotubes are clearly another category of novel nanostructured materials that can be used to promote bone formation. It is also intriguing to consider what role self-assembled nanofibers may play in orthopedics since bone itself is a self-assembled collection of nanofibers.

In this context, notably, only nanophase materials can mimic the unique aspect ratio of hydroxyapatite and proteins found in the extracellular matrix of bone; it is not possible for micron-sized materials to simulate the unique nanometer constituent components of bone. As previously mentioned, results concerning the importance of nanofibrous materials in promoting functions of osteoblasts have been reported for carbon and polymer molds of carbon nanofibers (Fig. 6.6) [47]. These findings consistently testify to the unprecedented ability to create nanomaterials to mimic the dimensions of components of physiological bone to promote new bone formation.

#### 6.3.1.2 Metal Nanomaterials

Although much more work has been conducted on nanophase ceramics to date, several recent studies have focused on the analysis of bone regeneration on nanophase metals. Metals investigated to date include titanium,  $Ti_6Al_4V$ , and CoCrMo [60]. While many have attempted to create nanostructured surface features using chemical etchants (such as  $HNO_3$ ) on titanium, results concerning increased bone synthesis have been mixed [35]. Moreover, through the use of chemical etchants it is unclear to what the cells may be responding – changes in chemistry or changes in topography. For this reason, as was done for the ceramics in this review, it is important to focus on studies that have attempted to minimize large differences in material chemistry and focus only on creating surfaces that alter in their degree of nanometer roughness.

One such study by Ejiofor et al. utilized traditional powder metallurgy techniques without the use of heat to avoid changes in chemistry to fabricate different particle size groups of Ti,  $Ti_6Al_4V$ , and CoCrMo (Fig. 6.11) [60]. Increased osteoblast adhesion, proliferation, synthesis of extracellular matrix proteins (like alkaline phosphatase and collagen), and deposition of calcium containing mineral was observed on respective nanophase compared conventional metals [60]. This was the first study to demonstrate that the novel enhancements in bone regeneration previously seen in ceramics by decreasing grain size can be achieved in metals.

Interestingly, when Ejiofor et al. examined spatial attachment of osteoblasts on the surfaces of nanophase metals, they observed directed osteoblast attachment at metal grain boundaries (Fig. 6.12) [60]. Because of this, the authors speculated that the increased osteoblast adhesion may be due to more grain boundaries at the surface of nanophase compared with conventional metals. As was the case with nanophase ceramics [40, 44], it is plausible that protein adsorption and conformation at nanophase metal grain boundaries may be greatly altered compared with non-grain boundary areas and/or conventional grain boundaries; in this manner, protein interactions at grain boundaries may be key for osteoblast adhesion.

#### 6.3.1.3 Polymeric Nanomaterials

For ceramics and metals, most studies conducted to date have created desirable nanometer surface features by decreasing the size of constituent components of the material, e.g., a grain, particle, or fiber. However, due to the versatility of poly-

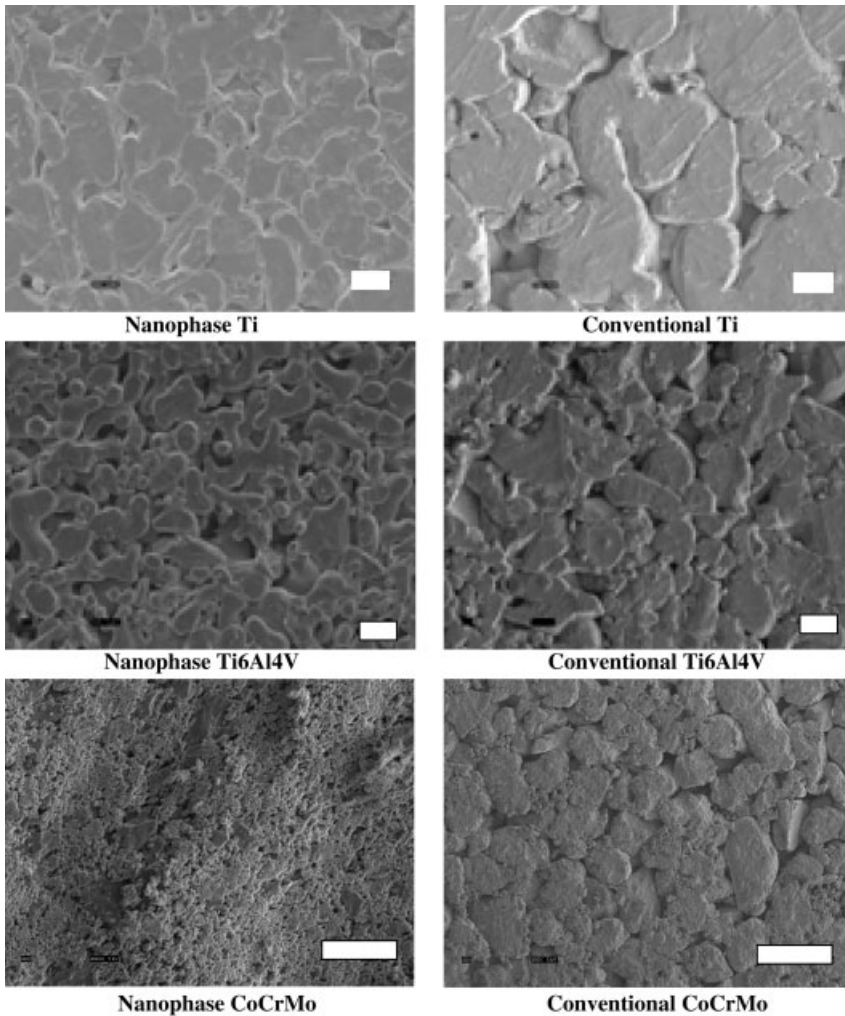


**Fig. 6.11.** Scanning electron micrographs of nanophase metals. Increased functions of osteoblasts have been observed on nanophase compared with conventional c.p. Ti, Ti6Al4V, and CoCrMo. Scale bar = 1  $\mu\text{m}$  for nanophase

Ti/Ti6Al4V and 10  $\mu\text{m}$  for conventional Ti/Ti6Al4V. Scale bar = 10  $\mu\text{m}$  for nanophase and conventional CoCrMo. (From Ref. [60], with permission.)

mers, many additional techniques exist to create nanometer surface roughness values. In addition, polymers contribute even further to rehabilitating damaged tissue by, possibly, providing a degradable scaffold that dissolves within a controllable time while the native tissue reforms. Techniques utilized to fabricate nanometer features on polymers include e-beam lithography, polymer demixing, chemical

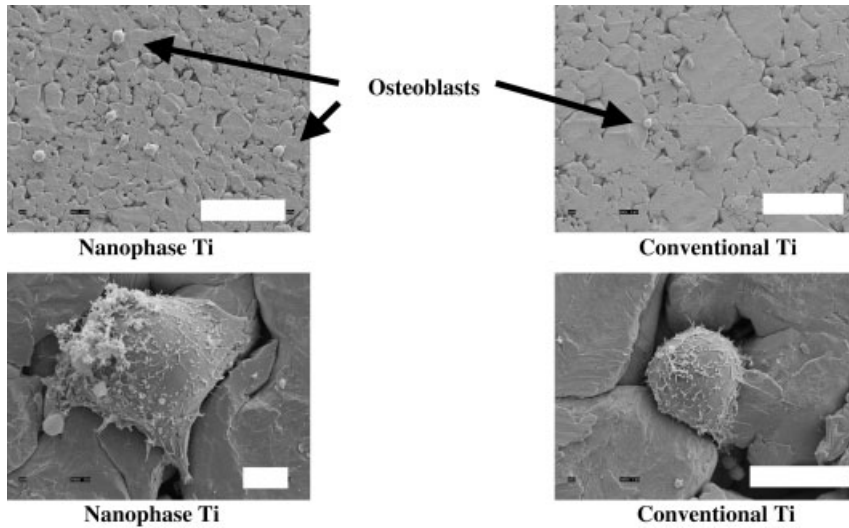


**Fig. 6.12.** Scanning electron micrographs of adherent osteoblasts on nanophase c.p. Ti. Directed osteoblast adhesion on nanophase metal grain boundaries has been reported. Scale bar = 100  $\mu\text{m}$  for top and 10  $\mu\text{m}$  for bottom; adhesion time = 30 min. (From Ref. [60], with permission.)

etching, cast-mold techniques, and the use of spin-casting [60–68]. For those that have been applied to orthopedics, chemical etching followed by mold casting and polymer demixing techniques have received the most attention [61, 62].

For chemical etching techniques, polymers investigated to date include poly(lactic-co-glycolic acid) (PLGA; Fig. 6.13), polyurethane, and polycaprolactone [62, 64–66]. The idea proposed by Kay et al. has been to treat acidic polymers with basic solutions (i.e., NaOH) and basic polymers with acidic solutions (i.e.,  $\text{HNO}_3$ ) to create nanosurface features [62]. While only on two-dimensional (2D) films, Kay et al. observed greater osteoblast adhesion on PLGA treated with increasing concentrations and exposure times of NaOH. As expected, data was also provided indicating larger degrees of nanometer surface roughness with increased concentrations and exposure time of NaOH on PLGA. Park et al. took this one step further and fabricated three-dimensional (3D) tissue engineering scaffolds by NaOH treatment of PLGA [64]. When comparing osteoblast functions on such scaffolds, even though similar porosity properties existed between non-treated and NaOH treated PLGA (since similar amounts and sizes of NaCl crystals were used to create the pores through salt-leaching techniques), greater numbers of osteoblasts were counted on and in NaOH treated PLGA [64]. Unfortunately, due to these fabrication techniques, it is unclear whether the altered PLGA chemistry or nano-etched surface promoted osteoblast adhesion; however, in light of the previous studies mentioned in this review, the authors of that study suggested the

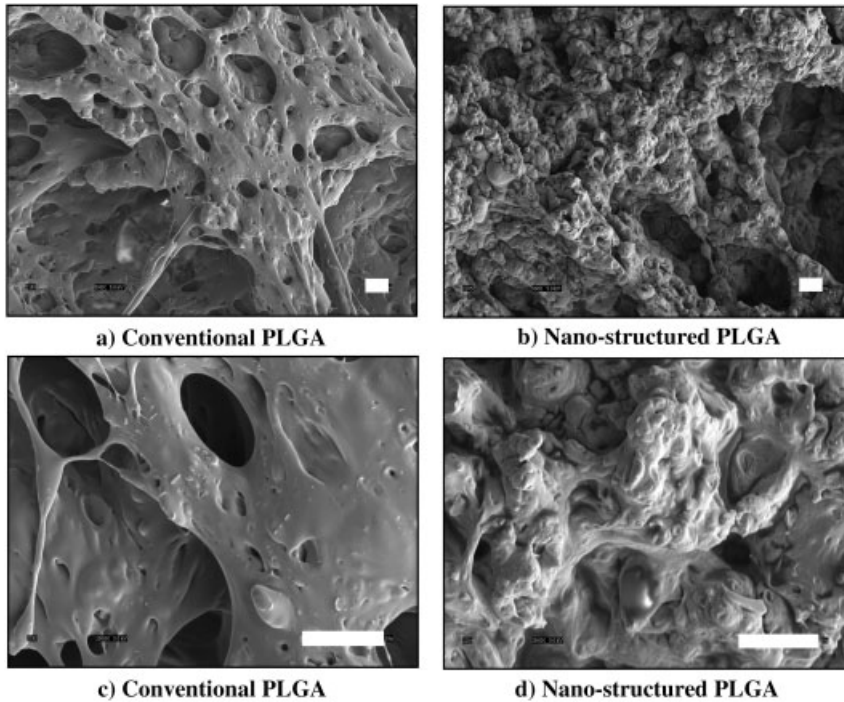


**Fig. 6.13.** Scanning electron micrographs of conventional and nanophase PLGA scaffolds. Increased osteoblast functions have been demonstrated on nanophase PLGA scaffolds. Scale bar = 10  $\mu\text{m}$ . (From Ref. [64], with permission.)

nanometer surface roughness of the NaOH-treated PLGA played an important role [64].

Studies have also been conducted on cell responses to polymers with changes in nanometer surface roughness without changes in chemistry. Specifically, Li et al. utilized polymer demixing techniques to create well-controlled nanometer islands of polystyrene and poly(bromo-styrene) [67]. Although osteoblast functions have not been tested on these constructs to date, fibroblast morphology was significantly influenced by incremental nanometer changes in polymer island dimensions (Fig. 6.14). Again, this study points to the unprecedented control that can be gained over cell functions by synthesizing materials to have nanometer surface features.

Although not related to orthopedic applications, vascular and bladder cell responses have also been promoted by altering the topography of polymeric materials in the nanometer regime [62, 64, 66, 68]. In these studies, chondrocytes [62], bladder [66], and vascular smooth muscle cell [65] adhesion and proliferation were greater on 2D nanometer surfaces of biodegradable polymers such as PLGA, polyurethane, and polycaprolactone; similar trends have recently been reported on 3D PLGA scaffolds [68].

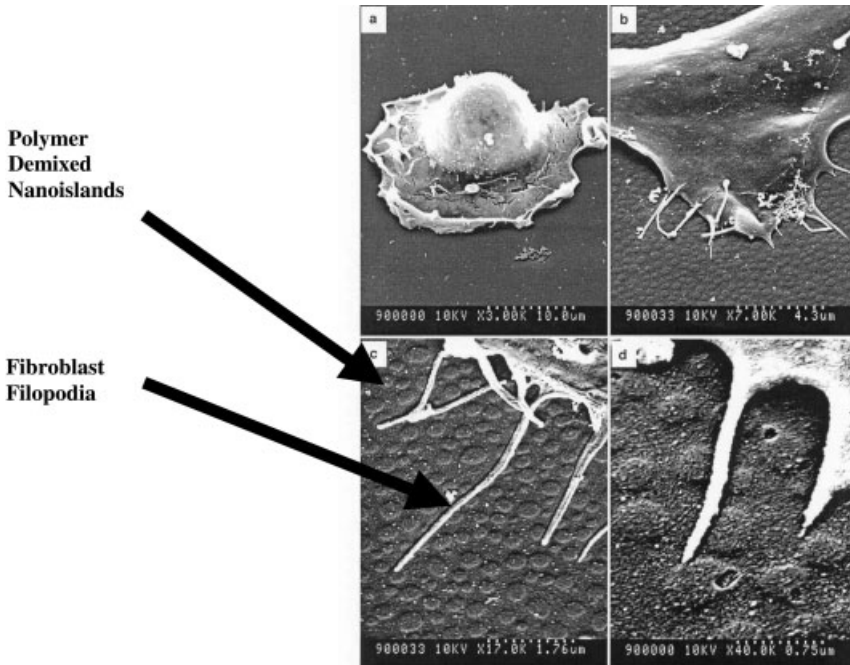


**Fig. 6.14.** Polymer nanoislands created by demixing polystyrene and poly(bromo-styrene). Altered cell functions have been observed on polymer nanoislands compared with conventional polymer topographies; (a)–(d) represent increased magnification. (From Ref. [67], with permission.)

#### 6.3.1.4 Composite Nanomaterials

Due to the previous information of increased osteoblast function on ceramics and polymers, investigators have also determined bone cell function on nanophase ceramic polymer composites (Fig. 6.15). Specifically, studies conducted to date show promoted osteoblast responses on composites of PLGA combined separately with nanophase alumina, titania, and hydroxyapatite (30:70 wt.% PLGA:ceramic) [62, 69]. For example, up to three times more osteoblasts adhered to PLGA when it contained nanophase compared with conventional titania particles [62]. Since similar porosity (both % and diameters) existed between PLGA with conventional compared with nanophase titania, another novel property of nanophase ceramic composites was elucidated in this study: increased osteoblast functions. This is in addition to numerous reports in the literature highlighting greater toughness of nanophase compared with conventional ceramic:polymer composites [21–23].

Moreover, promoted responses of osteoblasts have also been reported when carbon nanofibers were incorporated into polymer composites; specifically, three

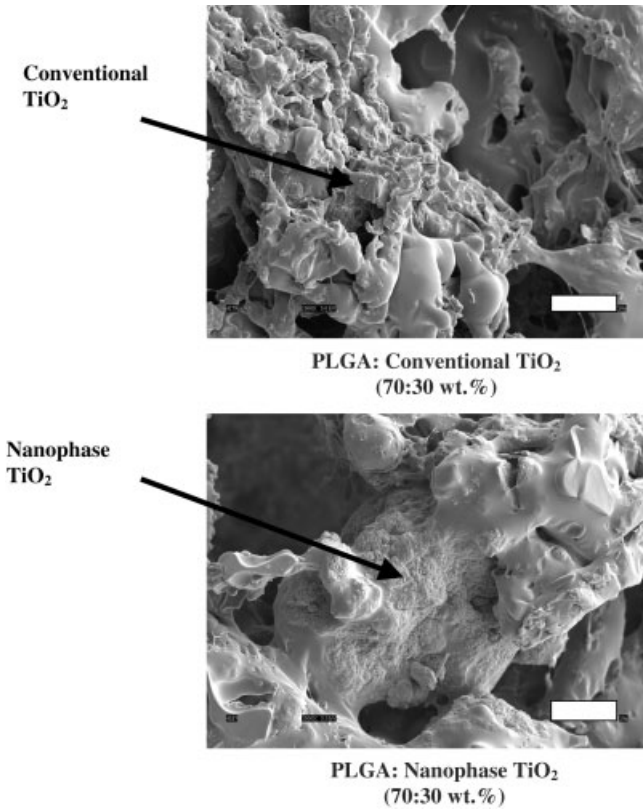


**Fig. 6.15.** Scanning electron micrographs of poly(lactic-*co*-glycolic acid) (PLGA):titania composites. Increased osteoblast function has been observed on polymer composites containing nanophase compared with conventional ceramics. Scale bar = 10  $\mu\text{m}$ . (From Ref. [69], with permission.)

times the number of osteoblasts adhered on polyurethane (PU) with increasing weight percentages of nanometer not conventional dimension carbon fibers (Fig. 6.16) [70]. As mentioned, reports in the literature have demonstrated higher osteoblast adhesion on carbon nanofibers in comparison with conventional carbon fibers (or titanium (ASTM F-67, Grade 2) [70]), but this study demonstrated greater osteoblast adhesion with only a 2 wt.% increase of carbon nanofibers (CN) in the PU matrix. Up to three and four times the number of osteoblasts that adhered on the 100:0 PU:CN wt.% adhered on the 90:10 and the 75:25 PU:CN wt.% composites, respectively [70]. This exemplifies the unprecedented ability of nanophase materials to increase functions of bone cells whether used alone or in polymer composite form.

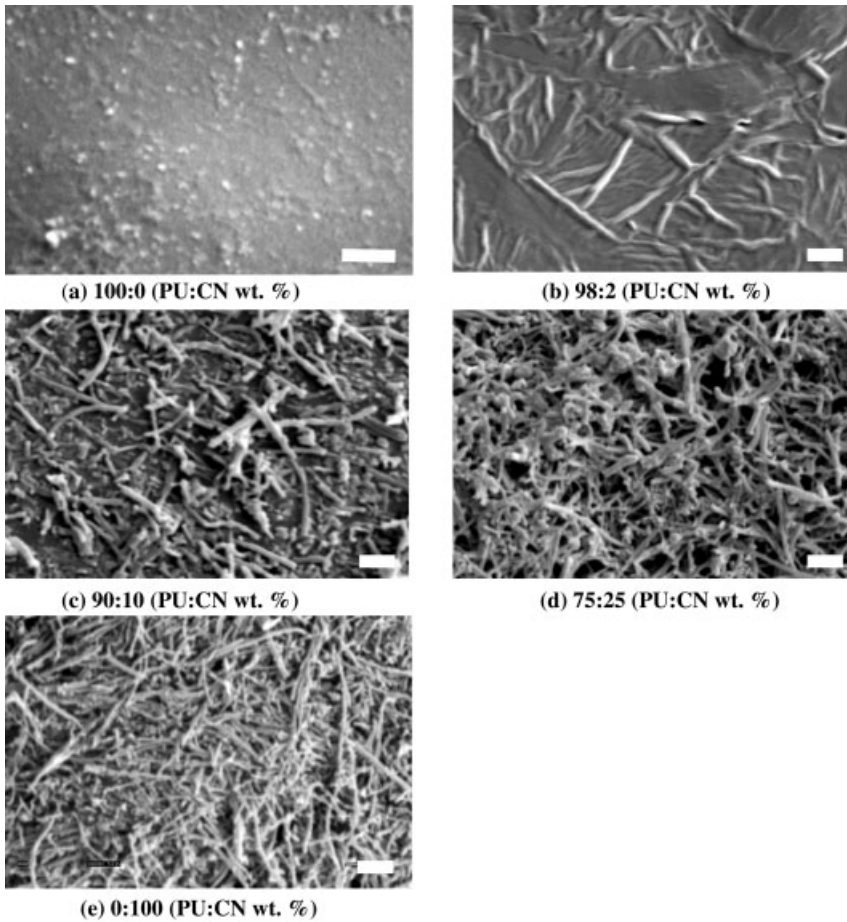


**Fig. 6.16.** Scanning electron micrographs of poly-ether-urethane (PU):carbon nanofibers (CN) (wt.%) composites. Increased functions of osteoblasts have been observed on polymer composites containing carbon nanofibers. Scale bar = 1  $\mu\text{m}$ . (From Ref. [70], with permission.)

### 6.3.2

#### ***In Vivo* Compared with *In Vitro* Studies**

Of course, in any new field of biomaterials, it is completely natural to conduct extensive *in vitro* analysis before conducting *in vivo* studies. The *in vitro* studies emphasized in the previous sections provided key preliminary promise for the use of these materials in orthopedics. Moreover, they provided an important mechanism as to why osteoblasts prefer nanophase over conventional materials. To date, though, there have been few *in vivo* studies that specifically address increased new



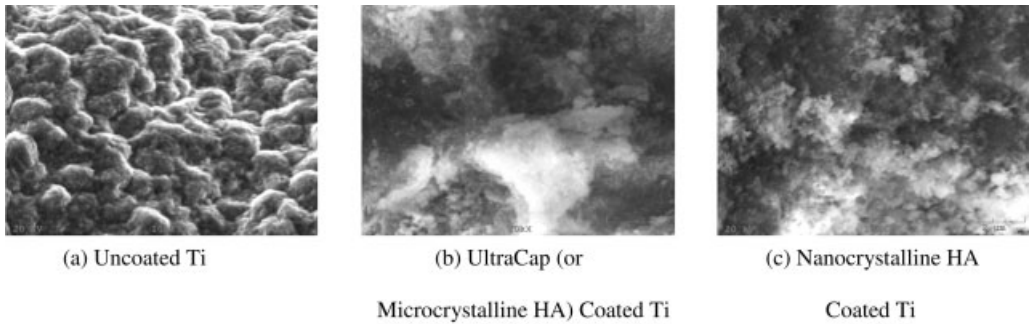


**Fig. 6.17.** SEM pictures of uncoated and coated porous titanium. Coating process maintained the nanoscale features of hydroxyapatite (HA) after coating on titanium.

bone growth on materials of the same chemistry but altering only in grain or particle size. That is, while some *in vivo* studies were presented in the early sections, they did not specifically evaluate the influence of grain size on *in vivo* new bone growth. However, one study exists that utilized a novel coating process developed at Spire Biomedical (call IonTite™) to deposit nanocrystalline particles of hydroxyapatite (HA) onto porous titanium scaffolds (Fig. 6.17). Importantly, when implanted into the calvaria of rats for 6 weeks, increased bone infiltration was seen only on titanium scaffolds coated with nanocrystalline HA (Fig. 6.18). That is, little to no bone ingrowth was measured on either uncoated titanium or titanium coated with conventional (or microcrystalline HA) after the same time period. This exciting *in vivo* data confirms the promising *in vitro* data of increased responses from osteoblasts on nano compared with micron HA. Furthermore, while much work is still needed (as outlined in the next section), this *in vivo* study may begin to pave the way for the widespread use of nanophase materials either in bulk or as coatings on traditionally used bone implant materials.

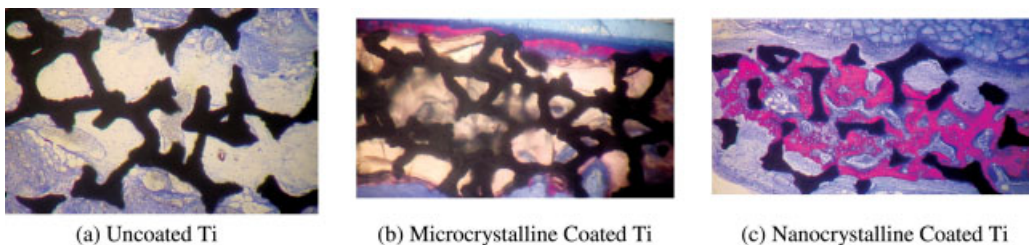


**Fig. 6.18.** Increased bone ingrowth for Ti coated with nanocrystalline HA by IonTite™. Implantation time = 6 weeks. Stain = Sanford (blue indicates bone and red indicates collagen).

#### 6.4

#### Considerations and Future Directions

Although preliminary attempts to incorporate nanophase materials into orthopedic implants seem promising, numerous urgent questions still remain about this new field. First and foremost, the safety of nanoparticles once in the human body remains largely unanswered both from a manufacturing point of view and when used in full or as a component of an implantable device. Since such particles are smaller than many pores of biological tissues, this information will, clearly, have to be obtained before further consideration of implantable nanomaterials is undertaken. Such nanoparticles can easily become dislodged from implants during surgical implantation or from fragmentation of articulating components of a joint prosthetic composed of nanophase materials. Although preliminary *in vitro* studies highlight a less adverse influence of nanometer compared with micron particulate wear debris on bone cell viability [71, 72], many more experiments are needed especially *in vivo* to evaluate their efficacy.

In addition, once exact optimal nanometer surface features are elucidated for increasing bone regeneration, inexpensive tools that can be used in industry will be required. In this context, if the only nanofabrication devices that can be used to synthesize desirable nanometer surface features for bone regeneration are e-beam lithography or other equally expensive techniques, industry may not participate in this boom of nanotechnology at the intersection of tissue engineering. Inexpensive, but effective, nanometer synthesis techniques must continually be a focus of many investigators.

Still, the direction of the nanotechnology should be and is geared towards dealing with these issues. For example, according to the U.S. government's research agenda, the current and future broad interests in nano biomedical activity can be categorized in three broad related fronts [28, 29]:

1. Development of pharmaceuticals for inside-the-body applications – such as drugs for anticancer and gene therapy.
2. Development of diagnostic sensors and lab-on-a-chip techniques for outside-the-body applications – such as biosensors to identify bacteriological infections in biowarfare.
3. Development of prostheses and implants for inside-the-body uses.

Whereas the European governments emphasize commercial applications in all three fronts above, according to Malsch [29], the U.S. government tends to gear towards fundamental research on biomedical implants and biodefense, leaving commercial applications to industry. Both classifications identify nanophase biomedical implants as of potential interest. The biological and biomimetic nanostructures to be used as an orthopedic implant involve some sort of an assembly in which smaller materials later on assume the shape of a body part, such as hipbone. These final biomimetic, bulk nanostructures can start with a predefined nanochemical (like an array of large reactive molecules attached to a surface) or nanophysical

(like a small crystal) structure. It is believed that by using these fundamental nanostructured building blocks as seed molecules or crystals, a larger bulk material will self-assemble or keep growing by itself.

In summary, significant evidence exists that highlights changes in cellular functions on materials with nanoscale surface features, particularly in the bone arena. Clearly, nanomaterials as mentioned here are at their infancy and require much more testing before their full potential can be realized. However, even if nanophase materials never make it to the marketplace due to safety concerns, we have already learned much about how cells interact with nanostructured surfaces through their application in the orthopedic environment.

### Acknowledgments

The authors (M.S. and T.W.) would like to thank the NSF and NIH for funding part of the research summarized here through the Bio-nanotechnology National Initiative.

### References

- 1 <http://www.aaos.org/wordhtml/press/arthropl.htm>
- 2 <http://www.azcentral.com/health/0617newhips17/html>
- 3 <http://www.aaos.org/wordhtml/press/joinrepl.htm>
- 4 [http://www.aaos.org/wordhtml/press/hip\\_knee.htm](http://www.aaos.org/wordhtml/press/hip_knee.htm)
- 5 MININO, A.M. and SMITH, B.L., Vital statistics, *National Vital Statistics Rep.*, **2001**, 49, 12.
- 6 <http://www.cdc.gov/nchs/fastats/lifexpec.htm>
- 7 DOWSON, D., New joints for the millennium: wear control in total hip replacement hip joints, *Proc. Institution Mechanical Eng. Part H – J. Eng. Med.*, **2001**, 215(4), 335.
- 8 KAPLAN, F.S., HAYES, W.C., KEAVENY, T.M., BOSKEY, A., EINHORN, T.A., IANOTTI, J.P., Bone in *Orthopedic Basic Science*, SIMON, S.P. (Ed.), American Academy of Orthopedic Surgeons, Columbus, OH, **1994**, pp. 127–185.
- 9 OPARAUGO, P.C., CLARKE, I.C., MALCHAU, H., HERBERTS, P., Correlation of wear debris-induced osteolysis and revision with volumetric wear-rate of polyethylene: A survey of 8 reports in literature, *Acta Orthopaed. Scand.*, **2001**, 72, 22.
- 10 URBAN, R.M., JACOBS, J.J., TOMILSON, M.J., GAVRILOVIC, J., BLACK, J., PEOC'H M., Dissemination of wear particles in the liver, spleen, and abdominal lymph nodes of patients with hip or knee replacement, *Am. J. Bone Joint Surg.*, **2000**, 82, 457.
- 11 LEROUGE, S., HUK, O., YAHIA, L.H., SEDEL, L., Characterization of in vitro wear debris from ceramic-ceramic total hip arthroplasties, *J. Biomed. Mater. Res.*, **1996**, 32, 627.
- 12 HORBETT, T.A., Proteins: Structure, properties, and adsorption to surfaces, in *Biomaterials Science: An Introduction to Materials in Medicine*, RATNER, B.D., HOFFMAN, A.S., SCHOEN, F.S., LEMMONS, J.E. (Eds.), Academic Press, New York, **1996**, p. 133.
- 13 SCHAKENRAAD, J.M., Cells: Their surfaces and interactions with materials, in *Biomaterials Science: An Introduction to Materials in Medicine*, RATNER, B.D., HOFFMAN, A.S., SCHOEN, F.S., LEMMONS, J.E. (Eds.), Academic Press, New York, **1996**, pp. 133–140.

- 14 BRUNETTE, D.M., The effects of implant surface topography on the behavior of cells, *Int. J. Oral Maxillofac Implants*, **1988**, 3, 231.
- 15 MARTIN, J.Y., SCHWARTZ, Z.Z., HUMMERT, T.W., SCHRAUB, D.M., SIMPSON, J., LANKFORD, J.J., DEAN, D.D., COCHRAN, D.L., BOYAN, B.D., Effect of titanium surface roughness on proliferation, differentiation, and protein synthesis of human osteoblast-like cells (MG63), *J. Biomed. Mater. Res.*, **1995**, 29, 389.
- 16 WEN, H.B., CUI, F.Z., ZHU, X.D., Microstructural features of non-union of human humeral shaft fracture, *J. Mater. Sci.: Mater. Med.*, **1998**, 9(3), 121.
- 17 LARSSON, C., THOMSEN, P., ARONSSON, B.O., RODAL, M., LAUSMAA, J., KASEMO, B., ERICSON, L.E., Bone response to surface modified titanium implants: Studies on electropolished implants with different oxide thickness and morphology, *Biomaterials*, **1994**, 15(13), 1325.
- 18 BORDJI, K., JOUZEAU, J.Y., MAINARD, D., PAYAN, E., WETTER, P., RIE, K.T., STUCKY, T., HAGE-ALI, M., Cytocompatibility of Ti6Al4V ad Ti5Al2.5Fe alloys according to three surface treatments using human fibroblasts and osteoblasts, *Biomaterials*, **1996**, 17(9), 929.
- 19 SIEGEL, R.W., FOUGERE, G.E., Mechanical properties of nanophase metals, in *Nanophase Materials: Synthesis-Properties Applications*, HADJIPANAYIS, G.C., SIEGEL, R.W. (Eds.), Kulwer, Dordrecht, **1994**, p. 233.
- 20 ROCO, M.S., WILLIAMS, R.S., ALVISATOS, P., Nano-technology research directions, *Nano-Technology Research Directions: IWGN Workshop Report*, **1999**.
- 21 SIEGEL, R.W., FOUGERE, G.E., Mechanical properties of nanophase metals, *Nanostruct. Mater.*, **1995**, 6, 205.
- 22 SIEGEL, R.W., Creating nanophase materials, *Sci. Am.*, **1996**, 275, 42.
- 23 SIEGEL, R.W., HU, E., ROCO, M.C., *Nano-Structure Science and Technology*, Kluwer Academic Press, Boston, **1999**.
- 24 BARATON, M.I., CHEN, X., GONSALVES, K.E., FTIR study of nanostructured alumina nitride powder surface: determination of the acidic/basic sites by CO, CO<sub>2</sub>, and acetic acid adsorptions, *Nanostruct. Mater.*, **1999**, 8, 435.
- 25 KLABUNDE, K.J., STRAK, J., KOPER, O., MOHS, C., PART, D., DECKER, S., JIANG, Y., LAGADIC, I., ZHANG, D., Nanocrystals as stiochiometric reagents with unique surface chemistry, *J. Phys. Chem.*, **1996**, 100, 12141.
- 26 WU, S.J., DEJONG, L.C., RAHAMAN, M.N., Sintering of nanophase  $\gamma$ -Al<sub>2</sub>O<sub>3</sub> powder, *J. Am. Ceram. Soc.*, **1996**, 79, 2207.
- 27 MARTYANOV, I.N., KLABUNDE, K.J., Photocatalytic oxidation of gaseous 2-chloroethyl ethyl sulfide over TiO<sub>2</sub>, *Environ. Sci. Technol.*, **2003**, 37, 3448.
- 28 MALSCH, I., Biomedical applications of nanotechnology, *The Industrial Physicist*, June/July, 15, **2002**.
- 29 MALSCH, I., The nano-bosy:sense and non-sense on biomedical applications of nanotechnology, Lecture for COST and NanoSTAG Conference, Leuven, Oct. 29, 2001.
- 30 AYAD, S., BOOT-HANDFORD, R., HUMPHRIES, M.J., KADLER, K.E., SHUTTLEWORTH, A., *The Extracellular Matrix Factsbook*, Academic Press, San Diego, **1994**, pp. 29–149.
- 31 COWIN, R., *Handbook of Bioengineering*, McGraw Hill, New York, **1987**.
- 32 BRUNETTE, D., The effect of surface topography on cell migration and adhesion, in *Titanium in Medicine*, BRUNETTE, D.M., TENGVALL, P., TEXTOR, M., THOMSEN, P. (Eds.), Springer-Verlag, New York, **2001**, pp. 486–512.
- 33 BUSER, D., NYDEGGER, T., OXLAND, T., COCHRAN, D.L., SCHENK, R.K., HIRT, H.P., SNETIVY, D., NOLTE, L.P., Interface shear strength of titanium implants with a sandblasted and acid-etched surface: A biomechanical study in the maxilla of miniature pigs, *J. Biomed. Mater. Res.*, **1999**, 45(2), 75.
- 34 HENCH, L.L., ETHRIDGE, E.C.,

- Histochemical responses at a biomaterial's interface. *J. Biomed. Mat. Res.*, **1974**, *8*, 49.
- 35 LITSY, A.S., SPECTOR, M., Biomaterials, in *Orthopedic Basic Science*, SIMON, S.P. (Ed.), American Academy of Orthopedic Surgeons, Columbus, **1994**, p. 482.
  - 36 NIKOLOVSKI, J., MOONEY, D.J., Smooth muscle cell adhesion to tissue engineering scaffolds, *Biomaterials*, **2000**, *21*, 2025.
  - 37 WEBSTER, T.J., SIEGEL, R.W., BIZIOS, R., An in vitro evaluation of nanophase alumina for orthopedic applications, in *Bioceramics 11: Proceedings of the 11<sup>th</sup> International Symposium on Ceramics in Medicine*, LEGEROS, R.Z., LEGEROS, J.P. (Eds.), World Scientific, New York, **1998**, pp. 273–276.
  - 38 WEBSTER, T.J., SIEGEL, R.W., BIZIOS, R., Design and evaluation of nanophase alumina for orthopaedic/dental applications, *Nanostruct. Mater.*, **1999**, *12*, 983.
  - 39 WEBSTER, T.J., SIEGEL, R.W., BIZIOS, R., Osteoblast adhesion on nanophase ceramics, *Biomaterials*, **1999**, *20*, 1221.
  - 40 WEBSTER, T.J., ERGUN, C., DOREMUS, R.H., SIEGEL, R.W., BIZIOS, R., Specific proteins mediate osteoblast adhesion on nanophase ceramics, *J. Biomed. Mat. Res.*, **2000**, *51*(3), 475.
  - 41 WEBSTER, T.J., SIEGEL, R.W., BIZIOS, R., Enhanced functions of osteoblasts on nanophase ceramics, *Biomaterials*, **2000**, *21*, 1803.
  - 42 WEBSTER, T.J., SIEGEL, R.W., BIZIOS, R., Enhanced surface and mechanical properties of nanophase ceramics for increased orthopaedic/dental implant efficacy, in *Bioceramics 13: Proceedings of the 13<sup>th</sup> International Symposium on Ceramics in Medicine*, GIANNINI S. and MORONI, A. (Eds.), World Scientific, New York, **2000**, p. 321.
  - 43 WEBSTER, T.J., The future orthopedic and dental implant materials, in *Advances in Chemical Engineering Vol. 27*, YING J.Y. (Ed.), Academic Press, New York, **2001**, pp. 125–166.
  - 44 WEBSTER, T.J., SCHADLER, L.S., SIEGEL, R.W., BIZIOS, R., Mechanisms of enhanced osteoblast adhesion on nanophase alumina involve vitronectin, *Tissue Eng.*, **2001**, *7*(3), 291–301.
  - 45 WEBSTER, T.J., ERGUN, C., DOREMUS, R.H., SIEGEL, R.W., BIZIOS, R., Enhanced functions of osteoclast-like cells on nanophase ceramics, *Biomaterials*, **2001**, *22*(11), 1327–1333.
  - 46 WEBSTER, T.J., SIEGEL, R.W., BIZIOS, R., Nanoceramics surface roughness enhances osteoblast and osteoclast functions for improved orthopaedic/dental implant efficacy, *Script. Mater.*, **2001**, *44*, 1639–1642.
  - 47 ELIAS, K.L., PRICE, R.L., WEBSTER, T.J., Enhanced functions of osteoblasts on nanometer diameter carbon fibers, *Biomaterials*, **2002**, *23*, 3279–3287.
  - 48 DANILOV, Y.N. and JULIANA, R.L., (Arg-Gly-Asp)<sub>n</sub>-albumin conjugates as a model substratum for integrin-mediated cell adhesion, *Exp. Cell Res.*, **1989**, *182*, 186.
  - 49 HUGHES, R.C., PENA, S.D.J., CLARK, J., DOURMASHKIN, R.R., Molecular requirements for adhesion and spreading of hamster fibroblasts, *Exp. Cell Res.*, **1979**, *121*, 307.
  - 50 HUMPHRIES, M.J., AKIYAMA, S.K., KOMORIYA, A., OLDEN, K., YAMADA, K.M., Identification of an alternatively spliced site in human plasma fibronectin that mediates cell type-specific adhesion, *J. Cell Biol.* **1986**, *103*, 2637.
  - 51 SINGER, I.I., KAWKA, D.W., SCOTT, S., MUMFORD, R.A., LARK, M.W., Cell surface distribution of fibronectin and vitronectin receptors depends on substrate composition and extracellular matrix accumulation, *J. Cell Biol.* **1987**, *104*, 573.
  - 52 UNDERWOOD, P.A. and BENNETT, F.A., A comparison of the biological activities of the cell-adhesive proteins: Vitronectin and fibronectin, *J. Cell Sci.*, **1989**, *93*, 641.
  - 53 MASSIA, S.P., HUBBELL, J.A., Human endothelial cell interactions with surface-coupled adhesion peptides on a nonadhesive glass substrate and two polymeric biomaterials, *J. Cell Biol.* **1991**, *14*(5), 1089.

- 54 LI, L., Biomimetic nano-apatite coating capable of promoting bone ingrowth, *J. Biomed. Mater. Res.* **2003**, *66*, 79–85.
- 55 THULL, R., GRANT, D., Titanium surface modification, in *Titanium in Medicine*, BRUNETTE, D.M., TENGVALL, P., TEXTOR, M., THOMSEN P. (Eds.), Springer-Verlag, New York, **2001**, pp. 284–302.
- 56 SATO, M., SLAMOVICH, E.B., WEBSTER, T.J., Novel nanophase hydroxyapatite coatings on titanium, 29<sup>th</sup> International Conference on Advanced Ceramics and Composites, Cocoa Beach, FL, 2005.
- 57 PRICE, R.L., GUTWEIN, L.G., KALEDIN, L., TEPPER, F., WEBSTER, T.J., Osteoblast functions on nanophase alumina: Influence of chemistry, phase, and topography, *J. Biomed. Mater. Res.*, **2003**, *67*(4), 1284–1293.
- 58 DEE, K.C., ANDERSEN, T.T., RUEGER, D.C., BIZIOS, R., Conditions with promote mineralization at the bone-implant interface: A model in vitro study, *Biomaterials*, **1996**, *17*, 209.
- 59 CHUN, A., MORALEZ, J., FENIRRI, H., WEBSTER, T.J., Helical rosette nanotubes: A more effective orthopaedic implant materials, *Nanotechnology*, **2004**, *15*, S234–S239.
- 60 EJIOR, J.U. and WEBSTER, T.J., Increased osteoblast functions on nanostructured metals, *ASM Conference*, Las Vegas, NV, **2004**.
- 61 DALBY, M.J., RIEHLE, M.D., JOHNSTONE, H., AFROSSMAN, S., CURTIS, A.S.G., In vitro reaction of endothelial cells to polymer demixed nanotopography, *Biomaterials*, **2002**, *23*, 2945–2954.
- 62 KAY, S., THAPA, A., HABERSTROH, K.M., WEBSTER, T.J., Nanostructured polymer:nanophase ceramics composites enhance osteoblast and chondrocyte adhesion, *Tissue Eng.*, **2002**, *8*, 753–761.
- 63 ZHANG, R. and MA, P.X., Porous poly(L-lactic acid)/apatite composites created by biomimetic process, *J. Biomed. Mater. Res.*, **1999**, *45*(4), 285–293.
- 64 PARK, G.E., PARK, K., WEBSTER, T.J., Accelerated chondrocyte functions on NaOH-treated PLGA scaffolds, *Biomaterials*, **2005**, *26*, 3075.
- 65 MILLER, D.C., THAPA, A., HABERSTROH, K.M., WEBSTER, T.J., Endothelial and vascular smooth muscle cell functions on poly(lactic-co-glycolic acid) with nanostructured surface features, *Biomaterials*, **2004**, *25*, 53–61.
- 66 THAPA, A., WEBSTER, T.J., HABERSTROH, K.M., Nano-structured polymers enhance bladder smooth muscle cell function, *J. Biomed. Mater. Res.*, **2003**, *67*, 1374–1383.
- 67 LI, W.-J., LAURENCIN, C., CATERSON, E.J., TUAN, R.S., KO, F.K., Electrospun nanofibrous structure: a novel scaffold for tissue engineering, *J. Biomed. Mater. Res.*, **2002**, *60*, 613–621.
- 68 PATTISON, M., WEBSTER, T.J., HABERSTROH, K.M., Three-dimensional nano-structured PLGA scaffolds for bladder tissue replacement applications, *Biomaterials*, **2005**, *26*, 3075–3082.
- 69 SMITH, T.A., WEBSTER, T.J., Improved osteoblast functions on polymer:nanophase ceramics composites, *J. Biomed. Mater. Res.*, **2005**, *74*, 677–686.
- 70 PRICE, R.L., WAID, M.C., HABERSTROH, K.M., WEBSTER, T.J., Select bone cell adhesion on formulations containing carbon nanofibers, *Biomaterials*, **2003**, *24*(11), 1877.
- 71 GUTWEIN, L.G., WEBSTER, T.J., Osteoblast and chondrocyte proliferation in the presence of alumina and titania nanoparticles, *J. Nanoparticle Res.*, **2002**, *4*, 231–238.
- 72 PRICE, R.L. and WEBSTER, T.J., Increased osteoblast viability in the presence of smaller nano-dimensional carbon fibers, *Nanotechnology*, **2004**, *15*(8), 892–900.

## 7

## Hydroxyapatite Nanocrystals as Bone Tissue Substitute

Norberto Roveri and Barbara Palazzo

## 7.1

### Overview

Nanoscience, where the properties of materials are exploited to innovative amazing applications, is involved in the size-dependent chemical and biological activity of bone substitute materials, which is indeed a fascinating field. The present chapter reviews the synthesis and chemical–physical characteristics of hydroxyapatite (HA) nano-crystals, which have excellent properties to represent an elective material covering a wide range of applications for bone substitution. We start from an examination of biogenic bone and tooth hydroxyapatite nanocrystals morphological and chemical–physical characteristics. The highlighted concepts have been used to review up-to date main new ideas on the preparation of synthetic apatitic bone substitutes mimicking the above biogenic properties, among which the nano-size is the basis of their self-assembly, self-mineralization and bone regeneration ability.

Hydroxyapatite (HA) nanocrystals with high bioreabsorbability containing foreign ions and mimicking bone HA chemical–physical and physiological behaviour have been described. We have pointed to their possible use in preparing scaffolds with a porosity simulating that of spongy bone and upon which cells can be seeded, thereby developing “*in vitro* autologous bone”. Biologically inspired HA nanocrystals/collagen composites have been reviewed, focusing on the role of a self-assembling strategy in conditioning the bone repairing activity of this biomaterial. Furthermore, considering that calcium phosphate/collagen composites are not limited to loading application, the possibility of preparing bio-inspired coating on the surface of metallic implants could be an advantageous approach.

Finally, surface functionalization of HA nano-crystals with bioactive molecules makes them able to transfer information and to act selectively on the biological environment and can be considered one of the main future challenges for innovative bone substitute materials.

## 7.2

### Introduction

Biomaterials represent one of the most interesting and interdisciplinary areas of science, where chemical, biological, engineering scientists are contributing to human health care and improving the quality of life. Skeletal deficiencies resulting from trauma, tumors or abnormal development are common, and are usually treated by surgical intervention. As a consequence, there is an increasing demand for materials that can potentially replace, repair or even regenerate injured or diseased bone tissue. Currently, autografts and allografts, or, alternatively, surface-treated metals, inorganic, polymeric and polymeric/inorganic hybrid materials, are applied for the reconstruction of skeletal defects [1]. Due to the limited supply of autografts, and the potential for pathogen transfer and possible stress shielding around the surrounding bones, none of the currently used biomaterials can provide completely the required properties. The enormous need for bone grafts and recent progress in biomaterial science have resulted in the newly evolving approach of “bone tissue engineering” [2–4]. This may be performed by using cell transplantation and culturing on biodegradable scaffolds for the development of hybrid constructs aiming at the regeneration of bone tissue [5].

Calcium phosphates are an interesting subject of research and development in the preparation of biomaterials for bone substitution. Calcium phosphates used as bone grafts can be classified either bioinert or bioactive. Bioinert phosphates have no influence in the surrounding living tissue; by contrast, bioactive materials exhibit the ability to bond with bone tissues. Initially, bioinert materials used in clinical applications were chosen because of their lack of chemical reactions with the environment, which could yield an undesirable outcome. The bioactivity of a bone substitute material can be evaluated through its chemical reactivity with the environment. This reactivity can be evaluated *in vitro* by means of an artificial solution simulating body fluids, and *in vivo* when the material is in contact with physiological fluids, towards the production of newly formed bone. The bioactivity of some reabsorbable calcium phosphate bioceramics is so high as to induce, in repairing a skeletal section, not only replacement of the damaged part but to substitute it, regenerating new bone.

This review focuses on nanosized hydroxyapatite, which is an elective biomaterial for bone substitution. Hydroxyapatite nano-crystals are similar to the mineral component of bone for composition and attempt to mimic the features, structure and morphology of natural bone crystals by their nanosize, blade-like shape, low degree of crystallinity and high surface reactivity.

## 7.3

### Biogenic Hydroxyapatite: Bone and Teeth

Bone and teeth of vertebrates are natural composite materials constituted of calcium phosphate in the form of hydroxyapatite (HA) and organic matter prevalently



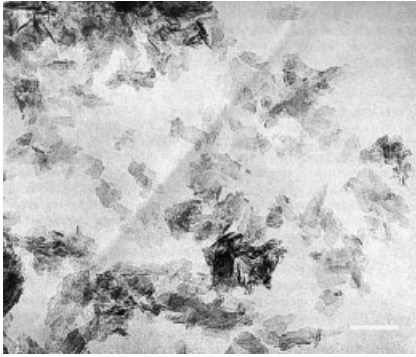


**Fig. 7.1.** Deproteinized bone hydroxyapatite nanocrystals observed by transmission electron microscopy. Scale bar = 100 nm. (Reproduced by permission from Ref. [10].)

formed of proteins and polysaccharides. Biological HA can only be represented ideally with the formula  $\text{Ca}_{10}(\text{PO}_4)_6(\text{OH})_2$ . It is not stoichiometric as many cations replace  $\text{Ca}^{2+}$ , such as  $\text{Mg}^{2+}$ ,  $\text{Sr}^{2+}$ ,  $\text{Na}^+$ ,  $\text{K}^+$ , and some anions replace  $\text{PO}_4^{3-}$  and  $\text{OH}^-$ , such as  $\text{CO}_3^{2-}$ ,  $\text{HPO}_4^{2-}$ ,  $\text{P}_2\text{O}_7^{4-}$ ,  $\text{SiO}_4^{4-}$ , and  $\text{CO}_3^{2-}$ ,  $\text{F}^-$ ,  $\text{Cl}^-$ ,  $\text{Br}^-$ . The carbonate content of bone hydroxyapatite is about 4–8 wt.% [6] and increases with the age of the individual [7, 8] with increasing  $\text{CO}_3^{2-}$  groups substituting  $\text{OH}^-$  sites (type A carbonate apatite). Conversely,  $\text{CO}_3^{2-}$  groups substituting  $\text{PO}_4^{3-}$  sites (type B carbonate apatite) is the prevalent type in young humans [9]. The nano-sized carbonate hydroxyapatite bone crystals have a blade shape approximately 25 nm wide, 2–5 nm thick and about 60 nm long, as can be appreciated in the Transmission Electron Microscopy (TEM) image shown in Fig. 7.1 [10].

Bone tissues can be defined as mineral–organic composite materials. The organic–mineral phase ratio can vary, depending on species, tissue location, age, diet and pathologies [11], [12].

In mammal long bone (cortical bone), the organic matrix represents 22 wt.%, mineral 69 wt.% and the rest (9 wt.%) is the water associated with the organic matrix or with the mineral. The organic matrix is mainly composed of type I collagen (90 wt.%) that would act as template upon which the first mineral crystals were formed [13]. The not yet completely elucidated mechanism of cell-mediated collagen mineralization may be considered a sequence of events requiring the interaction of many different promoting or inhibiting factors [14]. It is widely accepted that matrix vesicles are formed by release of budding from osteoblasts surfaces [15–18], inside which the amount of calcium and phosphate raise to a saturation level, favorable for deposition of amorphous calcium phosphate, octacalcium phosphate and/or brushite with later transformation into HA [19]. The apatite nuclei from matrix vesicles act as templates for new crystal proliferation, which spread into the adjacent collagenous matrix [18]. Type I collagen is produced by osteoblasts and then processed outside the cell, ending in the surrounding extracellular

space, where the fibrils self-assemble into mature collagen fibrils that undergo biomineralization. For this reason, bone is the typical example of an “organic matrix-mediated” mineralization process [10]. Each collagen I polypeptidic chain contains a helical domain with 338 contiguous repetitions of the sequence (Glycine-X-Y) where X and Y are often proline and hydroxyproline. Each individual chain coils in a triple-stranded helix, stabilized by interchain crosslinking. The triple-stranded helical filaments of uniform size (280 nm long, 1.5 nm wide) and a molecular mass of about 285 kDa present N and C non-helicoidal terminal domains [20]. Figure 7.2(a) reports the collagen fibril structure as a revised quarter-stagger model

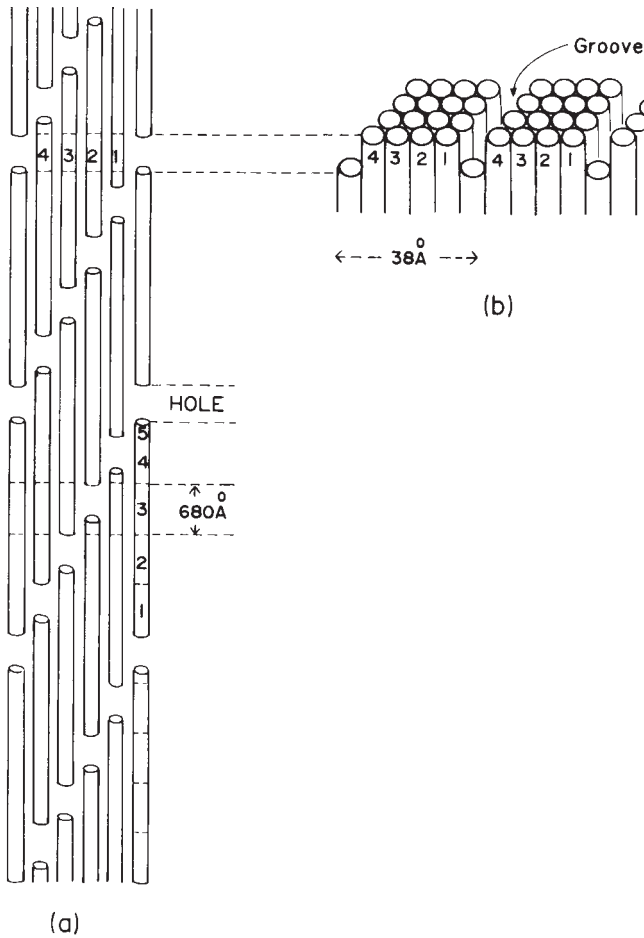


**Fig. 7.2.** Quarter stagger model of collagen fibers: (a) alignment of collagen gap regions to form grooves. In them HA crystals grow with crystallographic *c*- and *a*-axes preferentially aligned parallel to the collagen fiber axis and groove directions, respectively (b). (Reproduced by permission from Ref. [10].)

where molecules are lined up head-to-tail in rows that are staggered of 64 nm along their long axis. Each molecule is transposed by 64 nm with respect to the previous one, and is divided into five sectors, the first four are 64 nm long and the fifth is 25 nm long. This arrangement, stabilized by strong intermolecular crosslinks, produces a regular array of small gaps, 40 nm long and about 5 nm wide, referred to as “hole zones” which are considered to be the *loci* of the nucleation and growth of hydroxyapatite nanocrystals. Adjacent hole zones overlap to form grooves structured in parallel rows along the main axis of the three-dimensional (3D) fibril structure, allowing hydroxyapatite to grow into plate-shaped nano-crystals, oriented such that the crystallographic *c*-axis is preferentially aligned along the collagen fibril axis (Fig. 7.2b) [21]. Utilizing the coincidence, in orientation, between HA crystallographic *c*-axis and collagen fibrils main axis, X-ray diffraction patterns recorded using conventional and synchrotron radiation sources at both wide and low angles from single osteons and osteonic lamellae have allowed to determination of the orientation of hydroxyapatite crystallites and, consequently, collagen fibrils in bone [22–25]. The bone of vertebrates can be considered as a “living biomaterial” since inside it there are cells under permanent activity. The osteoblasts remain trapped inside the mineral phase, evolving towards osteocytes, which continuously maintain the bone formation activity.

In teeth, dentine, which resides within the central regions of the tooth, is similar in structure and composition to bone. Enamel on the outside of tooth, however, has a high inorganic content, close to 95 wt.%, which is constituted mainly of long thin ribbon-like crystals of carbonated hydroxyapatite. The “spaghetti-shaped” nano-crystals are arranged in bundles oriented in three different directions, associated with a matrix of proteins excluding collagen (Fig. 7.3). Amelogenins, present in relatively large amount in the early stages of enamel formation, are degraded and removed by up to 5 wt.% as the hydroxyapatite crystals grow [10]. Apatite nanocrystals grow with their *c*-axis preferentially oriented parallel to the long axes of the microribbons [26]. Dental enamel does not contain cells and as a conse-

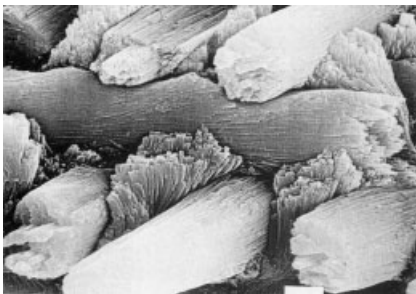


**Fig. 7.3.** Scanning electron micrograph of enamel carbonated hydroxyapatite “spaghetti shaped nanocrystals” arranged in bundles oriented along three different directions. Scale bar = 10  $\mu\text{m}$ . (Reproduced by permission from Ref. [10].)

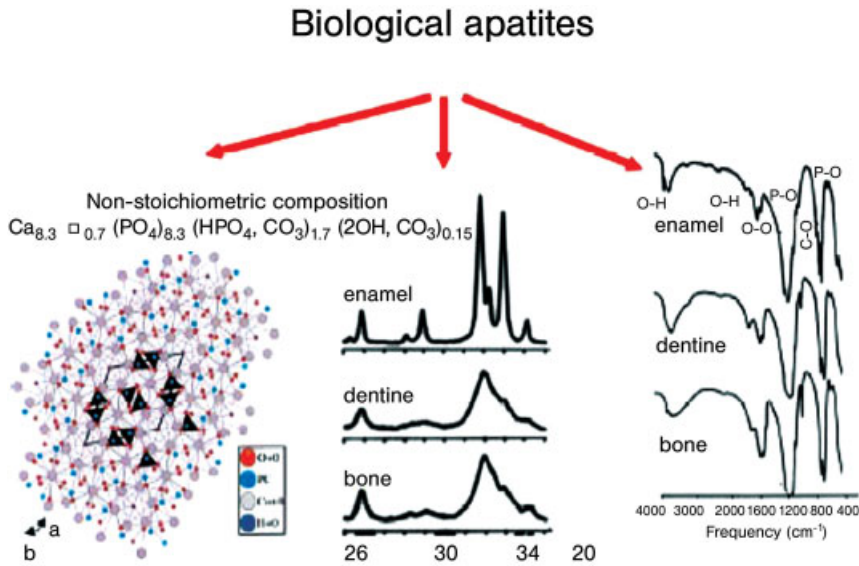


Fig. 7.4. Crystal structure of natural carbonate hydroxyapatite. Powder X-ray diffraction patterns and infrared spectra of enamel, dentine and bone are given. (Reproduced by permission of Ref. [27].)

quence of it any degradation or damage cannot be biologically repaired, evidencing the need for synthetic enamel biocompatible materials repairing tooth deterioration.

Biogenic hydroxyapatite exhibits special behavior due to its nano-size dimensions, low degree of crystallinity, non-stoichiometric composition, crystalline surface disorder and presence of carbonate ions in the crystal lattice. Figure 7.4 shows the crystal structure of biological hydroxyapatite, together with the X-ray diffraction patterns and infrared spectra of enamel, dentine and bone [27].

#### 7.4

##### **Biomimetic Hydroxyapatite: Porous and Substituted Apatites**

In the last decade advanced technology has been utilized to synthesize a new generation of inorganic alloplastic materials that mimic natural bone and can function as a scaffold upon which cells can be seeded, developing “*in vitro* autologous bone” [28–30].

The aim is to provide synthetic 3D scaffolds onto which cells are cultured and the artificial piece can be colonized both under *in vitro* and *in vivo* conditions. To control the interaction with biological entities much attention has been devoted to charactering the surface properties of the scaffolds. The use of nanosized hydroxyapatite to prepare apatitic bioceramics with tailored microstructure and porosity

opens up many possibilities. In fact poorly crystalline HA nanocrystals, in addition to the excellent biological properties of HA such as non-toxicity and lack of inflammatory and immunitary responses, have a high bioresorbability. This further property allows this kind of bioceramic to be completely replaced by neo-formed bone.

The bioresorbability of hydroxyapatite under physiological conditions can be modulated by modifying its degree of crystallinity which can be obtained by implementation of innovative synthesis with a nanodimensional control. Sol-gel, spray-drying, hydrothermal synthesis, recently reviewed [31], have been developed to obtain nanoparticles with high specific surface area, high bioresorbability and containing foreign ions, mimicking bone hydroxyapatite chemical-physical and physiological behavior [32–35].  $Mg^{2+}$  ions which cause acceleration of nucleation kinetics of hydroxyapatite and inhibit its crystalline growth [36], are present in high concentration in bone tissue during the initial phases of osteogenesis and tend to disappear when the bone is mature [37]. Similar behavior can be reproduced in synthetic  $Mg^{2+}$ -substituted hydroxyapatites characterized by a low degree of crystallinity and an high bioresorbability. Carbonate apatite containing different amounts of  $Mg^{2+}$  can be synthesized by dropping solutions of  $NaHCO_3$  and  $H_3PO_4$  simultaneously into a  $Ca^{2+}$  and  $Mg^{2+}$  basic suspension [38], or, under aqueous conditions, by employing a cyclic pH variation technique [36]. The replacement of magnesium for  $Ca^{2+}$  in the hydroxyapatite structure and its destabilizing effect on hydroxyapatite crystallization has been widely investigated [39–41]. The effect of magnesium in limiting the degree of hydroxyapatite crystallinity has been utilized to synthesize powders that form agglomerates of about 10–25  $\mu m$  from primary particles about 30–50 nm in size. The contemporary substitution of 0.25–0.30 of  $Mg^{2+}$  relative to  $Ca^{2+}$  and a carbonation fraction between 0.07 and 0.13 relative to  $PO_4^{3-}$  optimizes the most favorable and biomimetic stoichiometry, reflecting as much as possible the composition of bone tissue. An *in vivo* experiment performed filling defects in rabbit femur with granules of the carbonate Mg-HA showed that a period of one month is enough for this filler to be completely replaced by new bone tissue [42]. After preparing powders that preserve the composition of natural apatite, the next step is to use them to design implants having a biomimetic porosity. Porous HA with a morphology simulating that of spongy bone (Fig. 7.5) (porosity varying from a microporosity of  $>1 \mu m$  to a macroporosity ranging from 300 to 2000  $\mu m$ ) has been prepared using various technologies to control pores dimension, shape, distribution and interconnections. HA ceramics processed by high-temperature treatment [43] present a significant reduction of reactivity and growth kinetics of new bone. New formation methods at lower temperatures have been developed, allowing one to obtain porous bioceramics with a low degree of crystallinity. Colloidal processing [44], starch consolidation [45, 46], gel casting and foams out [47] have yielded excellent results, producing bioceramics with a bimodal distribution of the pores size that can be modified as a function of the sintering conditions.

Porous coralline HA can be synthesized by a hydrothermal method for HA formation directly from natural sea corals [48] and HA replaces aragonite whilst preserving its porous structure. The biaxial strength of coralline apatite could be

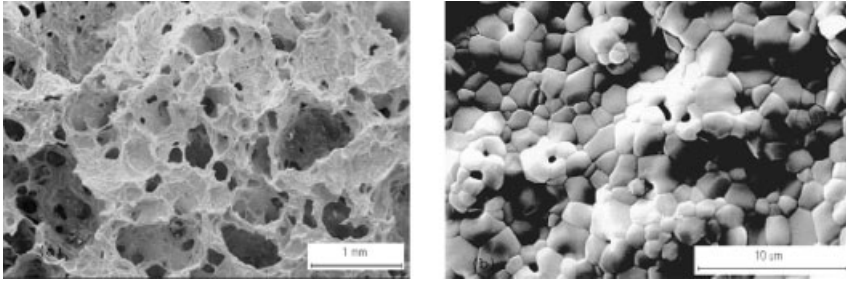


**Fig. 7.5.** SEM images of a porous apatitic bioceramic mimicking spongy bone porosity, having a macroporosity ranging from 300 to 2000  $\mu\text{m}$  (scale bar = 1 mm) (a) and microporosity of  $>1 \mu\text{m}$  (scale bar = 10  $\mu\text{m}$ ) (b).

improved due to a unique double treatment that includes a nano-coating layer to cover meso- and nanopores. In this two-stage process, the coral is fully converted into hydroxyapatite and then coated with a sol-gel-derived apatite (Fig. 7.6a–c). This new material can be applied to bone graft applications where high strength requirements and longevity are pertinent [49, 50].

The interconnected network of pores promotes bone in-growth, but also allows bioceramics to be utilized as drug delivery agents, by inserting different bioactive molecules. Many studies have demonstrated that hydroxyapatite ceramics can be used to deliver steroids, antibiotics, proteins, hormones, anticancer drugs. The aim has been to develop devices able to deliver the appropriate drug amount for a relatively long period of time, whilst minimizing the concentration of the drug in the bloodstream and other organs and the potential side effects produced by systemic administration. Porous ceramics closely mimicking spongy bone morphology have been synthesized by impregnation of cellulosic sponges with poorly crystalline HA water suspension [51]. These porous ceramics have been tested as controlled drug delivery bone grafts to evaluate the fundamental parameters that control release kinetics. A theoretical approach, based on the use of the Finite Element Method, was adopted to describe the Ibuprofen-lysine and Hydrocortisone Na-succinate release kinetics, comparing the numerical results with the experimental ones [52].

An alternative approach to tissue engineering, which uses cells seeded onto macropores of these HA scaffolds to promote bone ingrowth, is represented by filling the macro and micropores with gelatine, which can act as cell nutrient and/or delivery agent of bioactive molecules [53].

If bioceramics are used in powder form for bone filling applications, the HA powder is usually mixed with a polymeric carrier matrix to avoid migration out of the implant region. Both non-absorbable [poly(methyl methacrylate) [54], polyethylene [55] and polysulfone] and biodegradable (poly(lactic acid) [56], polyglycolic acid, collagen, cellulose and starch [57, 58]) polymeric matrices can be used, even

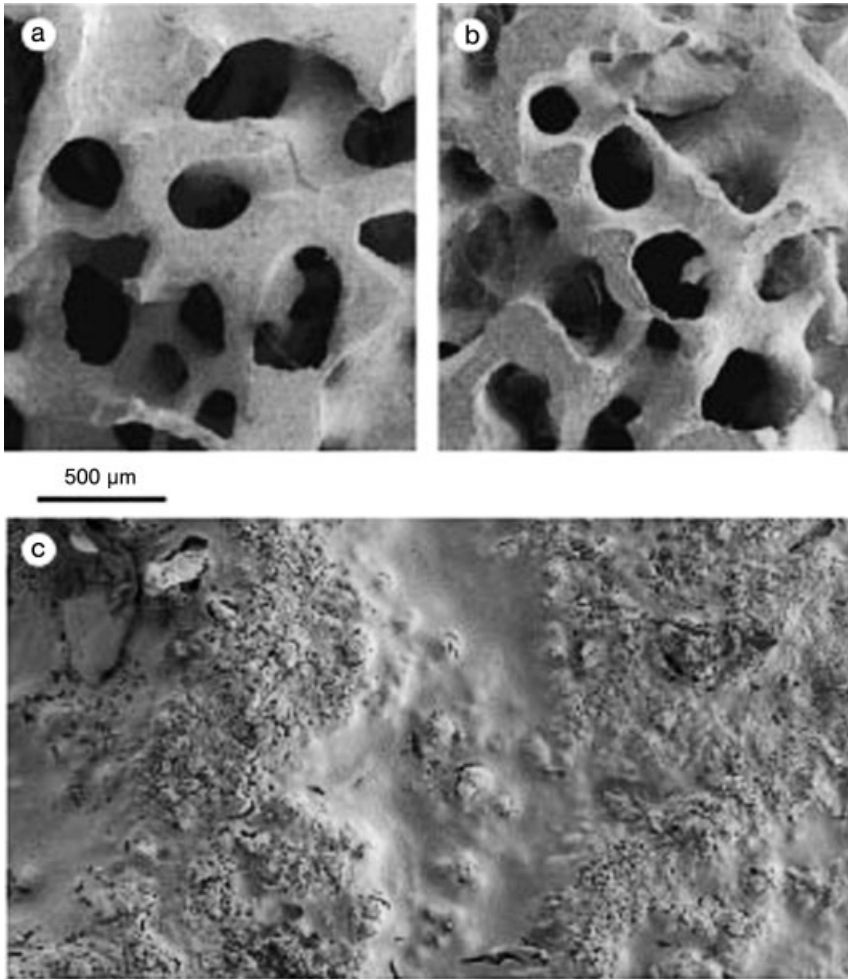


**Fig. 7.6.** SEM images of (a) *Goniopora* coral morphology, (b) *Goniopora* coral converted into pure HA, and (c) sol-gel derived nanocoated surface of previously converted *Goniopora* coral (scale bar = 500  $\mu\text{m}$ ). (Reproduced by permission of Ref. [49].)

if the non-biodegradability reduces drastically the bioactivity of the HA crystals. Biodegradable polymers are widely used in the medical field as scaffolds in tissue engineering. Among natural polymers, those from the vegetable kingdom are sometimes preferred to those of animal origin to avoid immunogenic reactions. Alginates, a family of unbranched binary copolymers are extracted from marine brown algae. They form insoluble hydrogels for binding with bivalent cations like

Ca<sup>2+</sup> and, as a consequence, of it calcium crosslinked alginate hydrogels have been utilized in many biomedical applications, including cell transplantation and drug delivery [59–61]. A biomimetic composite has been prepared by direct nucleation of HA on alginate copolymer, exploiting a self-assembly process and a typical egg-box structure can be obtained in samples with a 60/40 HA/Alg. wt ratio [62].

HA nucleation on alginate leads to the nucleation of HA nanocrystals – the polymer prevents further growth. In fact the X-ray diffraction pattern of the HA-alginate scaffold shows the characteristic diffraction maxima of poorly crystalline bone-like apatitic crystals, and TG analysis reveals that HA nanocrystals are 4 wt.%-carbonated [63]. An alginate-HA nanocrystals scaffold seeded with MG63 cells, cultured for 7 days and then subjected to morphological analysis has been shown to favor cell growth while maintaining their osteoblastic functionality [64]. An alginate-Mg carbonated HA nanocrystals bone filler has been patented for orthopedic and odontoiatric implantations [65].

## 7.5

### Biologically Inspired Hydroxyapatite: HA–Collagen Composites and Coatings

Biological organisms are the only true intelligent systems capable of acting as a real “functional material”. However, recently, synthetic biologically inspired materials have been prepared with the aim of reproducing, even if only partially, some specific functionalities of biological tissue. Presently, the induction of spontaneous self-assembling of molecules by building intelligent interfaces capable of interactive responses is a real possibility that resembles what occurs in living organisms. The driving forces governing the self-assembly are essentially hydrogen bonding, Van der Waals electrostatic forces and electron-transfer interactions [66, 67].

New methods of synthesis have been developed to utilize the capacity of biological systems to store and transfer information at a molecular level to obtain the spontaneous self-assembly of these entities into a superior architectural arrangement. These syntheses are denoted “biologically inspired” because they reproduce an ordered structure and an environment very close to the biological one. As the complex hierarchic structure of bone originates from the nano-sizes of the first apatite crystals inside the gap regions of collagen fibril structure, nanotechnology concepts and techniques are predominant in preparing biologically inspired bone grafts materials. The *in vitro* self-assembly of collagen molecules induced by thermal or pH variation, to form native fibrils, illustrates that collagen molecules themselves contain all of the structural information necessary for the assembly [68, 69]. Teloepitides-free type I collagen molecules have been utilized as a storehouse of information to nucleate carbonated hydroxyapatite nanocrystals inside the self-assembled collagen fibers (Fig. 7.7a and b) [70].

The two components hydroxyapatite nanocrystals and collagen fibrils, exhibit strong chemical and structural interactions that show a complete analogy of the synthesized composite with natural bone. The apatite crystals have nanometric dimensions, acicular-shaped morphology, and preferential orientation of their *c*-axis



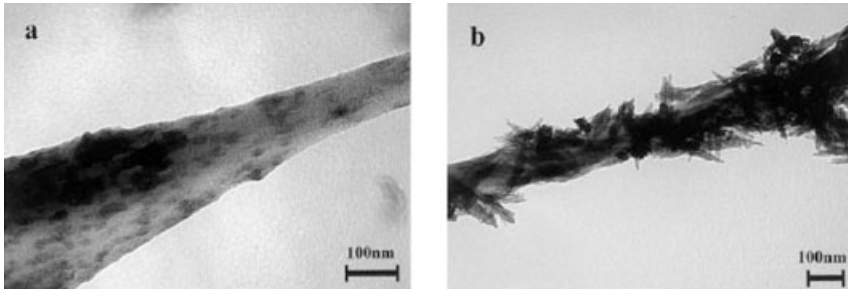


**Fig. 7.7.** TEM micrographs of synthetic biologically inspired self-assembled collagen fibers/HA nanocrystals composites showing HA nanocrystals nucleated inside the self-assembled collagen fibers (scale bar = 100

nm) (a) and acicular-shaped HA nanocrystals subsequently grown onto the collagen fibers surface (scale bar = 100 nm) (b). (Reproduced by permission of Ref. [71].)

parallel to the direction of orientation of collagen fibers [71]. X-ray diffraction analysis revealed not only the crystal preferential orientation, but also a poor degree of crystallinity very close to that of bone apatite reported in Fig. 7.4. Further evidence of the chemical interaction between collagen fibrils and inorganic crystals is furnished by FTIR analysis. In fact the  $\text{COO}^-$  groups of collagen are the sites for a possible interaction with HA, and in the FTIR spectra of synthetic HA–Collagen composite a shift of the  $\text{COO}^-$  antisymmetric stretching band from  $1340\text{ cm}^{-1}$  of pure collagen to  $1337\text{ cm}^{-1}$  can be appreciated, resembling what is observed for naturally calcified collagen [72]. The adsorption band at  $870\text{ cm}^{-1}$  present in the FTIR spectra of HA–collagen composite indicates that the nucleation of hydroxyapatite nanocrystals onto collagen implies carbonation of the apatite phase. Moreover, the carbonation can be assigned only to the B position, as confirmed by the absence of the band at  $880\text{ cm}^{-1}$  and by EDS analysis, which reveals that the increase in C content, due to  $\text{CO}_3^{2-}$  groups, corresponds to a decrease in P concentration, maintaining almost constant the stoichiometric ratio  $\text{Ca}/(\text{C}+\text{P})$ . The interaction of HA with collagen seems to prevent carbonation in the A position, probably by blocking access to  $\text{OH}^-$  groups [73]. Carbonation of synthetic hydroxyapatite nanocrystals reduces their crystalline degree increasing the similarity with bone inorganic phase and, especially, raising their bioactivity and biodegradability [74, 75]. Histological sections of implants in rabbit femur after two months showed, along with osteoblastomas, osteoclastic-like cells revealing that hydroxyapatite nanocrystals–collagen fibrils composite induces an active remodeling process, characterized by simultaneous osteoclastic phagocytosis and osteoblastic osteogenesis. The bone tissue reaction of hydroxyapatite nanocrystals–self-assembled collagen fibrils composite was examined in rat tibias to clarify the new bone formation mechanism [76]. This biologically inspired composite was implanted into tibias of rats, and observed at different days after implantation. Bone tissue reactions of the composite demonstrated osteoclastic resorption of the biomaterial, followed by new bone formation by osteoblasts. Alkaline phosphatase

activity has been observed in the neighborhood of the composite and new bone was actively formed around these sites in a way very similar to the reaction of a transplanted autogenous-bone. Detailed study on these bone reactions is currently progressing, and it has been assumed that the substitution process of the composites to new bone occurs as follows:

1. Formation of the composite debris via erosion by body fluid.
2. Phagocytosis of the debris and the composite surface by macrophages.
3. Induction of osteoclastic cells on the composite surface and resorption of the composite via a similar process to that of bone.
4. Induction of osteoblasts to the resorption lacunae created by osteoclastic cells and formation of new bone in the surroundings of the composite.

These reactions have not been reported on other HA/Collagen composite materials [77, 78] synthesized without using the self-organization process, which causes difference in cell reaction. In fact it is the bone-like nanostructure that can deceive the bone-related cells into starting the remodeling process. The hydroxyapatite nanocrystals–self-assembled collagen fibrils composite can be successfully utilized as an artificial bioinspired material in both the orthopedic and dental fields as an *in vivo* filler and an *in vitro* tissue regenerator.

Nevertheless, calcium phosphate/collagen composites exhibit weak mechanical behavior which can be improved by chemical crosslinking collagen, but at the expense of reducing their bioreabsorbability [79]. Calcium phosphate/collagen composites are limited to non-loading applications, but are particularly suitable to prepare bioactive coatings onto the surface of metallic implants with the aim of accelerating bone formation and implant fixation. Because of the presence of collagen fibers inside this kind of hybrid composite, a coating of it on metallic implants cannot be made by plasma spray or physical vapor deposition. Instead, electrolytic deposition appears to be the most promising technical procedure. Calcium phosphate coatings have been synthesized by electrochemical deposition from different  $\text{Ca}^{2+}$  and  $(\text{PO}_4)^{3-}$  solutions, in acid and in basic conditions [80–83], but also without conditioning pH by adding acid or basic reagents (Fig. 7.8a) [84]. Many technical difficulties have arisen in making a homogeneous and uniform collagen/calcium phosphate coating by electrolytic deposition on top of metallic supports. A collagen/calcium phosphate coating has been crystallized on an apposite electrode, but is not surface stable and is spontaneously chipped off forming a precipitate [85]. A bioactive multilayer collagen/calcium phosphate coating has been obtained by electrocrystallization of calcium phosphate on titanium electrode where the collagen was previously physically absorbed on the surface, but the thickness and the collagen/mineral composition ratio are strongly limited [86]. A double-layered collagen fibril/octacalcium phosphate composite coating on silicon substrates has been recently obtained by electrolytic deposition. The Si cathode surface is covered by a 100 nm thin layer of calcium phosphate coating on top of which a 100  $\mu\text{m}$  thick collagen fibril/octacalcium phosphate cluster composite layer is formed [87].

Electrolytic deposition of a biomimetic, bone-like self-assembled collagen fibrils/

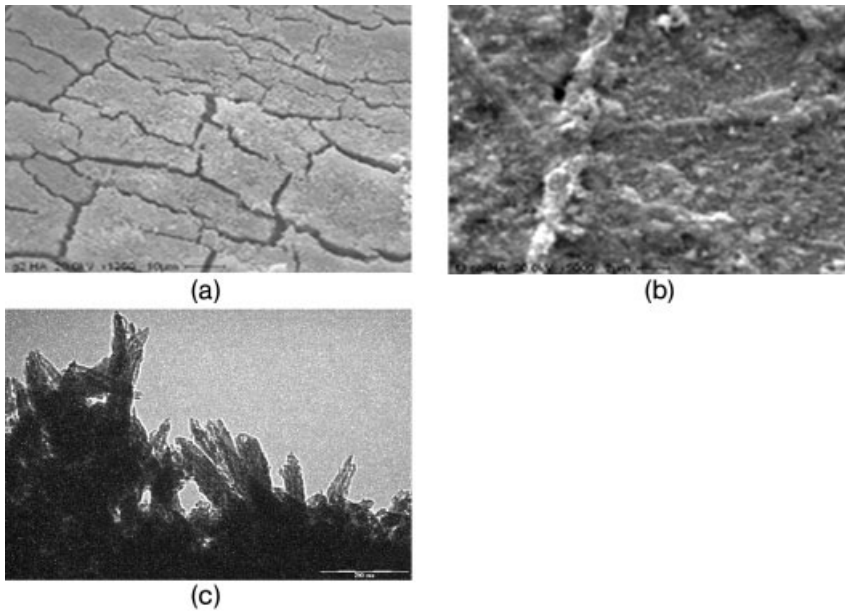


**Fig. 7.8.** SEM micrograph of coatings, electrolytically deposited on titanium plate, consisting of (a) apatite synthesized from  $\text{Ca}(\text{NO}_3)_2$  and  $\text{NH}_4\text{H}_2\text{PO}_4$  solutions (scale bar =  $10\ \mu\text{m}$ ) and (b) self-assembled collagen fibrils/HA nano-crystals composite, both obtained without conditioning solution pH by adding acid or basic reagents (scale bar =  $2\ \mu\text{m}$ ). (c) TEM image of the collagen/HA composite shown in (b) (scale bar =  $200\ \text{nm}$ ).

HA nano-crystals composite coating on titanium plates has been performed, using  $\text{Ca}(\text{NO}_3)_2$  and  $\text{NH}_4\text{H}_2\text{PO}_4$  solutions in a purely helical type I collagen molecule suspension. The use of dilute electrolytic solutions, low current density at the cathode and room temperature affords a coating composed of poorly crystalline carbonate hydroxyapatite nano-crystals that nucleate inside and around the reconstituted collagen fibrils distributed in a homogeneous network on Ti plate surface (Fig. 7.8b).

If the telopeptides-free collagen molecule assembling takes place during the crystallization of the apatite phase, the neo-forming collagen fibrils mineralize with a close structural relationship to the inorganic phase. FTIR analysis of this composite shows a shift of  $\text{COO}^-$  stretching of collagen resembling natural mineralized collagen fibers. This biomimetic feature of nanocrystals that nucleate and grow inside the fibrils is of interest only at the beginning of the calcification process, which continues with the massive growth of HA nanocrystals onto the collagen fibrils surface (Fig. 7.8c).

These two different kinds of collagen fibers mineralization resemble what has been observed in the self-assembled collagen fibers–hydroxyapatite nanocrystals in aqueous solutions [71]. The FTIR adsorption band at  $870\ \text{cm}^{-1}$  and the absence of that at  $880\ \text{cm}^{-1}$  observed for the composite coating allows assigning the car-

bonation of the hydroxyapatite only to the B position, closely resembling the carbonation of bone apatite.

These results [84, 88] suggest auspicious applications in the preparation of medical devices such as biomimetic bone-like composite-coated metallic implants with a loading capability deriving from the metal core and having, at the same time, a bioactive surface that accelerates bone formation and implant fixation.

## 7.6

### Functionalized Hydroxyapatite: HA Nanocrystals – Bioactive Molecules

An important question in biocompatibility is how the device or material communicates its structural make-up to direct or influence the response of proteins, cells, and the organism to it. For devices and materials that do not leach undesirable substances, this communication occurs through the surface structure; the body reads the surface structure and responds. The distribution of ions and molecules on the surface of all condensed matter has a special organization and reactivity and requires novel methods to be tailored above all because these ions and molecules may drive many of the biological reactions that occur in response to the biomaterial.

HA nanocrystals exhibit a high surface area (from 60–130 up to 180 m<sup>2</sup> g<sup>-1</sup> for natural ones) characterized by an elevated surface disorder in which the ions stoichiometry is not maintained. This property is considered responsible for the higher HA nanocrystals reactivity in respect to the larger ones and can be affected by the crystals shape. In fact the crystals expose different planes to the biological environment as a function of their shape (plate, acicular or needle shape) even if they exhibit the same surface area. Needle and plate shape (about 100 nm and 15 nm sized) synthetic HA nanocrystals TEM images are shown in Fig. 7.9(a) and (b) respectively. Only in recent years has high-resolution electron microscopy (HREM) been successfully applied to investigate hydroxyapatite structure to discern different calcium phosphate phases that often coexistent in the same crystalline granule. Among the rather few HREM studies on hydroxyapatite, some refer to the material itself [89], others to HA thin films [90]. This kind of analysis allows us to view the surface disorder at the boundaries of the crystallites constituting the single nanocrystals (Fig. 7.10a). Furthermore, HREM at high resolution allows us to observe the HA nanocrystals interplanar spacing (Fig. 7.10b), permitting discernment between HA and OCP, which are both elongated along the *c*-axis.

Surface functionalization of HA nanocrystals by bioactive molecules is an innovative approach not only to modulate but also to drive their reactivity. In this way HA nanocrystals will not only guarantee, for instance, either osteointegration or osteoinduction enhanced properties but they will also perform, by stimulating specific cellular responses, at the molecular level.

Only in recent years have scientists begun to use biomolecules for the synergistic coupling of crystals synthesis and functionalization. In fact, previous studies have limited the use of biomolecules as simple growth inhibitors of HA crystallization,

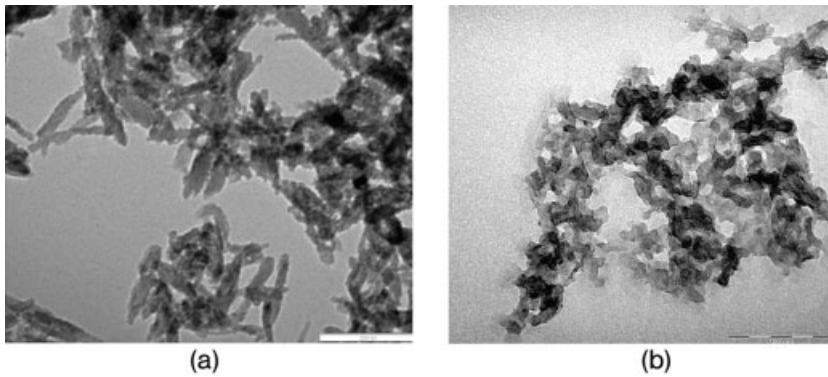


**Fig. 7.9.** TEM images of synthetic HA nanocrystals that are (a) needle shaped (approx 100 nm in size; scale bar = 200 nm) and (b) plate shaped (approx. 15 nm in size; scale bar 100 nm).

rather than considering their use as a strategy to fine-tune the bioactivity of the nanoparticles [91, 92]. Studies of the effect of biological molecules onto hydroxyapatite crystal growth have been related directly to physiological or pathological calcification processes. Particular interest has been dedicated to amino acids, which are compounds of major importance for living organisms, even because their con-

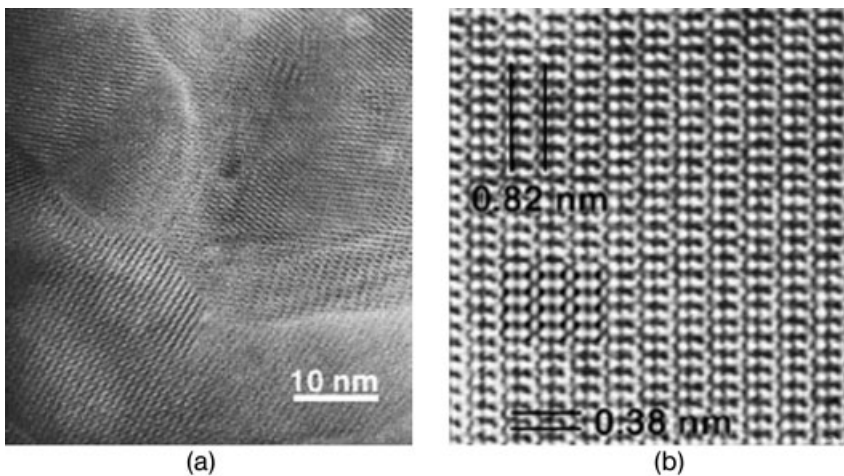


**Fig. 7.10.** HREM images of HA deposited by laser showing (a) the grain boundaries of crystallites with different orientation at low magnification and (b) in a single crystallite the interplanar spaces  $D_{hkl} = 0.82$  and  $0.38$  that are characteristic of HA. (Reproduced by permission of Ref. [90].)

centration is controlled by physiological mechanisms and they enter inside the cell environment by simple diffusion [93, 94]. The effects of 4-hydroxyproline, tyrosine and serine (amino acids with uncharged polar side groups), glycine, cysteine, cystine, and glutamine (amino acids with neutral polar side groups) and lysine, which is an amino acid with a basic side group, on HA crystallization have been studied by the “constant composition technique” [95–97]. Using this technique, the chemical potentials of the species in the working solution are kept constant during the crystallization process by the stoichiometric addition of reactants and therefore the crystal growth reaction is performed under pseudo-steady-state conditions. Diverse inhibiting activities were observed as a function of the different amino acid side group. These studies have shown that crystallization kinetics are affected by blockage of the active growth sites on the crystal surface.

Considering that the presence of proteins, (and hence amino acids) in biological materials is intrinsic to the bioactivity of HA, amino acids can be considered as agents that can increase the bioactivity of the synthetic HA. Concerning this, aqueous colloids of positively charged amino acid-functionalized HA nano-rods less than 80 nm long and ca. 5 nm wide have been synthesized by hydrothermal crystallization [98]. The colloidal stabilization and its positive zeta potential, together with FTIR spectroscopy data, were consistent with a general model in which the  $\alpha$ -carboxylate of the amino acid was preferentially bound to the crystal surfaces, inducing a crystal growth inhibition predominantly onto the Ca-rich surfaces during the initial stages of crystallization. To better define the surface  $\text{Ca}^{2+}$  role on amino acid linking, calcium deficient hydroxyapatite nanocrystals (CDHA) were synthesized in the presence of differently charged amino acids (alanine, cysteine, arginine, aspartic acid). The data obtained suggest a binding model in which the amino acid amino group is preferentially bound to the CDHA crystals, probably through a phosphorus amiditic linkage, such that the negatively charged carboxylate group exposed at the crystal/solvent interface determines the surface charge. In fact, zeta potential measurements showed that the CDHA/amino acids nanoparticles had an enhanced negative charge with respect to CDHA synthesized in the absence of amino acids [99]. The isoelectric point of the amino acid used as additive during the synthesis strongly affects the nanocrystals morphology and crystallites dimensions.

An innovative improvement of the functionalization process is represented by the synthesis of apatite nano-crystals surface loaded with bioactive molecules that promote a desirable cellular response if released with controlled kinetics. To reach this goal, it is a priority to investigate the chemical mechanisms of the binding and desorption of bioactive molecules by crystals surface. In fact, bioactive ceramics with drug delivery function, previously described, adsorb and release molecules through a mechanism dominated predominantly by physical parameters, such as carrier porosity and dimensions, bioactive molecule steric hindrance and environment diffusive conditions.

Slurries of hydroxyapatite have been successfully used to investigate the link and release processes of cisplatin, one of the most frequently prescribed drugs for the treatment of several solid tumors. Chemotherapeutic treatments applied locally to

osteosarcoma can result in tumor inhibition and much less-toxic systemic values of released drugs. Both the adsorption and release process of cisplatin were found to depend significantly on the ionic composition of the aqueous media used [100]. In fact, at a constant pH of 7.4, significantly more cisplatin is adsorbed by the hydroxyapatite crystals from a free buffer solution than from a buffered solution containing chloride ions. The amount of hydroxyapatite-bound cisplatin desorbed into solution was also progressively increased as a function of the increasing concentration of chloride in the equilibrating solution. These results suggest that it is the hydrated positively charged derivatives of cisplatin, whose hydrolysis is inhibited in chloride-rich solution, that are involved in the adsorption of cisplatin by the surface phosphate-rich hydroxyapatite crystals. Further work has demonstrated that subtle variations of the chemical–structural characteristics of the apatitic crystals affect both the adsorption and desorption of the drug cisplatin [101].

Adsorption isotherms obtained in ultrapure water and kinetic release in EPES buffer saline solution (containing chloride to favor release of the adsorbed platinum complex) indicate that cisplatin kinetics increase with decreasing crystallinity, the latter being associated with either smaller nanocrystals dimensions or greater surface area, which is strictly related to the amount of surface lattice defects which create active binding sites [102].

On the other hand, apatitic phase for bone specific delivery of geminal bisphosphonates (BPs) – a class of drugs that have been developed for use in various diseases of bone, tooth and calcium metabolism – are currently under investigation [103]. BPs are compounds characterized by two phosphonate groups attached to a single carbon atom, forming a “P-C-P” structure which is affine to  $\text{Ca}^{2+}$  ions. As a consequence, they strongly bind to calcium phosphate crystals and inhibit bone resorption by hindering their growth, aggregation and dissolution. However, BPs *in vivo* action mechanism involves cellular effects that are added to the surface physicochemical outcome of inhibiting HA crystal growth [104, 105]. Interestingly, while the affinity of BPs for bone mineral hydroxyapatite is the basis for their use as inhibitors of bone resorption, at the same time their coordinating abilities towards ions present on apatitic surfaces might be extended to design new delivery system for bone targeted drugs. In this context, calcium phosphate ceramics have been shown to be good biocompatible carriers for BPs, such as 1-hydroxy-2-(imidazol-1-yl-amino)-ethylidenebisphosphonic acid (Zoledronate) that is efficient for the treatment of post-menopausal osteoporosis and bone metastases [106]. A simple mathematical model was designed that correctly described the Zoledronate–calcium phosphate interaction at equilibrium, in simplified media such as ultrapure water or phosphate buffers [107]. However, the chemical link occurring between the BPs and calcium on the surface of HA nanocrystals is so strong that the BPs release kinetics appear affected by the bioresorbability of apatitic nanocrystals [108].

Because of the affinity of bisphosphonate groups to calcium, Keppler has proposed platinum compounds containing aminobisphosphonate ligands, which are expected to have a selective tropism for bone apatite and, at the same time, to present the well-known cytotoxic activity typical of platinum complexes [109]. Bis(ethy-

lenediamino)diplatinum medronate ( $[\text{Pt}_2(\text{C}_2\text{H}_8\text{N}_2)_2(\text{CH}_2\text{P}_2\text{O}_6)]$ ) has been linked to two different biomimetic synthetic hydroxyapatite nanocrystals having the same composition but different physicochemical properties such as crystal shape, crystallinity, domain size, and specific surface area. A detailed surface characterization of the drug-loaded HA nanocrystals, necessary to determine the surface stoichiometry, has been carried out on the Pt complex/HA conjugate by Attenuated Total Reflection (ATR) spectroscopy and XPS (X-ray Photoelectric Spectroscopy) analyses. Results have shown a Pt/N ratio very close to that of the not-linked bis(ethylenediamino)diplatinum medronate, confirming that it does not undergo degradation, as concerned the Pt–N bound, during absorption onto the apatite nanocrystals [102].

Finally, an innovative approach to fine-tune the cellular response to implanted apatite nanoparticles, without using the release of bioactive molecules can be ob-

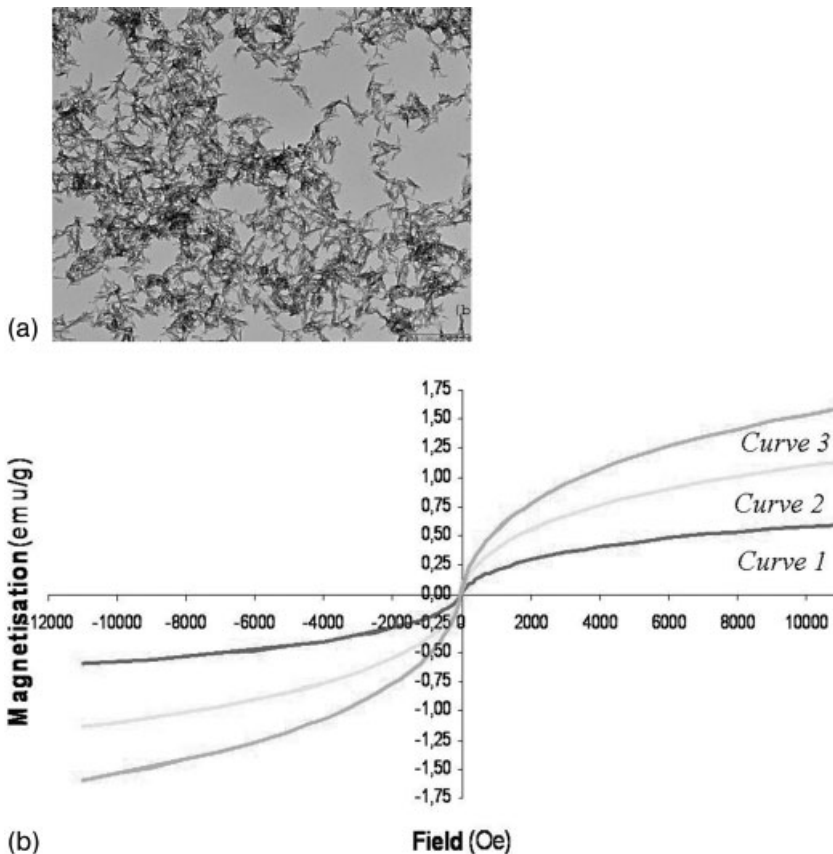


Fig. 7.11. (a) TEM image of needle-shaped magnetic HA nanocrystals (scale bar = 100 nm). (b) Magnetic susceptibility of apatite nanocrystals synthesized in the presence of

different amounts of the magnetite complex. Curves 2 and 3 are for samples that contain double and triple, respectively, the amount of complex in the sample for curve 1.



tained inducing a specific physical property onto apatite nanocrystals. With this aim a bone-like nanocrystalline apatite showing magnetic properties has been synthesized using a magnetite complex as a co-reagent (Fig. 7.11a) [110, 111]. The magnetic susceptibility of this material shows an increase in magnetization as a function of magnetite complex content (Fig. 7.11b). The well-known bioactive properties of the poorly crystalline apatite, along with the magnetic responsiveness of such HA nanocrystals, make this innovative material an attractive potential candidate for selective heating by external electromagnetic induction and then for bone anticancer hyperthermia treatment [112].

## 7.7

### Conclusion and Future Challenges

Synthesis of substituted, biomimetic, biologically inspired, functionalized hydroxyapatite nano-crystals has been described and their morphological, structural, chemical–physical, surface characterization has been evaluated to explain their high bioactivity and ability to induce bone regeneration and remodeling. The discussion should be enough to describe how size is a crucial factor in determining the HA bone substitutes chemistry in the nano-regime.

Even if spontaneous self-organization is a fascinating and inimitable essence of life material, the biomimetic chemical–physical characteristics of synthetic hydroxyapatite nanocrystals can render themselves *in vitro* and *in vivo* spontaneously mineralizable. The main guides for biomimetic approaches such as supramolecular organization, interfacial molecular recognition and multilevel processing, are strongly connected to the nano-sized dependent chemistry of apatite crystals. Pursuing the aim to mimic more and more the characteristics of bone tissue, the synthesis of biomineral-inspired hydroxyapatite nanocrystals is a reality that is becoming transferable into the preparation of technologically innovative biomedical devices. The synthesis of nanostructured biomimetic bone substitutes resembling the complex hierarchical structure of the biological tissue is an attractive field of research that is achieving the promised results. Moreover, the ability to functionalize the surfaces of apatite nano-crystals with bioactive molecules makes them able to transfer information and to act selectively on the biological environment. Furthermore, this approach offers a promising route to the construction of hierarchically ordered biomaterials based on the principle of controlled nanoparticle self-assembly, allowing us to consider inert mineral materials as templates for life.

### Acknowledgments

We thank MIUR (Cofin 2004-032118) and University of Bologna (funds for selected research topics) for financial support, and Bologna University Laboratory of

Environmental and Biological Structural Chemistry (LEBSC) research group and Bristol University Mann's research group for fruitful discussions.

## References

- 1 J. BLACK, G. HASTING, in *Handbook of Biomaterials Properties*, CHAPMAN and HALL (Ed.), American Society, Washington, DC, 1998.
- 2 R. LANGER, J. P. VACANTI, Tissue engineering, *Science* **1993**, 260, 920–926.
- 3 U. KNESER, D. J. SHAEFER, B. MUNDER, C. KLEMT, C. ANDREE, G. B. STARK, Tissue engineering of bone, *Minimally Invasive Therapy and Allied Technologies*, **2002**, 11, 107–116.
- 4 C. T. LAURENCIN, A. M. A. AMBROSIO, M. D. BORDEN, J. A. COOPER, Tissue engineering: Orthopedic application, *Annu. Rev. Biomed. Eng.* **1999**, 1, 19–46.
- 5 L. D. K. BUTTERY, J. M. POLAK, in *Learning from Nature: How to Design New Implantable Biomaterials*, R. L. REIS, S. WEINER (Eds.), NATO Science Series, Kluwer Academic Publisher, Dordrecht, **2004**, pp. 199–204.
- 6 F. M. C. DRIESSENS, Formation and stability of calcium phosphates in relation to the phase composition of the mineral in calcified tissues, in *Bioceramic Calcium Phosphate*, CRC Press, Boca Raton, FL, **1983**, pp. 1–32.
- 7 C. REY, V. RENUGOPALAKRISHNAN, B. COLLINS, M. GLIMCHER, Fourier transform infrared spectroscopic study of the carbonate ions in bone mineral during aging, *Calcif. Tissue Int.* **1991**, 49, 251–258.
- 8 J. M. BURNELL, E. J. TEUBNER, A. G. MILLER, Normal maturational changes in bone matrix, mineral, and crystal size in the rat. *Calcif. Tissue Int.* **1980**, 31, 13–19.
- 9 C. REY, B. COLLINS, T. GOEHL, I. R. DICKSON, M. GLIMCHER, The carbonate environment in bone mineral: A resolution-enhanced Fourier transform infrared spectroscopy study, *Calcif. Tissue Int.* **1989**, 45, 157–164.
- 10 H. A. LOWESTAN, S. WEINER, *On Biomineralization*, Oxford University Press, New York, **1989**.
- 11 R. LEGROS, N. BALMAIN, G. BONEL, Age-related changes in mineral of rat and bovine cortical bone, *Calcif. Tissue Int.*, **1987**, 41, 137–144.
- 12 R. G. HANDSCHIN, W. B. STERN, Crystallographic and chemical analysis of human bone apatite (Crista Iliaca), *Clin. Rheumatol.*, **1994**, 13, 75–90.
- 13 A. S. POSNER, Crystal chemistry of bone mineral, *Physiol. Rev.* **1969**, 49, 760–762.
- 14 V. L. SIKAVITSAS, J. S. TEMENOFF, A. G. MIKOS, Biomaterials and bone mechano-transduction, *Biomaterials* **2001**, 22, 2581–2593.
- 15 H. C. ANDERSON, Mineralization by matrix vesicles, *Scan. Electron Microsc.* **1984**, 953–964.
- 16 A. S. POSNER, The mineral of bone, *Clin. Orthop.* **1985**, 87–99.
- 17 G. A. RODAN, Introduction to bone biology, *Bone* **1992**, 13, 53–56.
- 18 H. C. ANDERSON, Molecular biology of matrix vesicles, *Clin. Orthop.* **1995**, 314, 266–280.
- 19 H. C. ANDERSON, Matrix vesicles and calcification, *Curr. Rheumatol. Rep.* **2003**, 5, 222–226.
- 20 *Collagen: Biochemistry, Biomechanics, Biotechnology*, M. E. NIMNI (Ed.), CRC Press, Boca Raton FL, **1988**.
- 21 S. WEINER, H. D. WAGNER, The material bone: Structure-mechanical function relations, *Ann. Rev. Mat. Sci.* **1998**, 28, 271–298.
- 22 A. ASCENZI, E. BONUCCI, A. RIPAMONTI, N. ROVERI, X-ray diffraction and electron microscope study of osteons during calcification, *Calcif. Tiss. Res.* **1978**, 25, 133–143.
- 23 A. ASCENZI, E. BONUCCI, P. GENERALI, A. RIPAMONTI, N. ROVERI, Orientation of apatite in single osteon samples as

- studied by pole figures, *Calcif. Tissue Int.* **1979**, *29*, 101–105.
- 24 A. ASCENZI, A. BIGI, A. RIPAMONTI, N. ROVERI, X-ray diffraction analysis of transversal osteonic lamellae, *Calcif. Tissue Int.* **1983**, *35*, 279–283.
  - 25 A. ASCENZI, A. BIGI, M. H. J. KOCH, A. RIPAMONTI, N. ROVERI, A low-angle X-ray diffraction analysis of osteonic inorganic phase using synchrotron radiation, *Calcif. Tissue Int.* **1985**, *37*, 659–664.
  - 26 C. DU, G. FALINI, S. FERMANI, C. ABBOTT, J. MORADIAN-OLDAK, Supramolecular assembly of amelogenin nanospheres into birefringent microribbons, *Science*, **2005**, *307*, 1450–1454.
  - 27 M. VALLET-REGI, J. M. GONZALES CALBET, Calcium phosphates as substitution of bone tissue, *Progr. Solid State Chem.* **2004** *32*(1–2), 1–31.
  - 28 K. SATO, Y. KUMAGAI, J. TANAKA, Apatite formation on organic monolayers in simulated body environment, *J. Biomed. Mater. Res.* **2000**, *50*(1), 16–20.
  - 29 A. L. BOSKEY, Will biomimetics provide new answers for old problems of calcified tissues?, *Calcified Tissue Int.* **1998**, *63*(3), 179–182.
  - 30 CHANG, MYUNG CHUL, T. IKOMA, M. KIKUCHI, J. TANAKA, Preparation of a porous hydroxyapatite/collagen nanocomposite using glutaraldehyde as a crosslinkage agent, *J. Mater. Sci. Lett.* **2001**, *20*(13), 1199–1201.
  - 31 M. P. FERRAZ, F. J. MONTEIRO, C. M. MANUEL, Hydroxyapatite nanoparticles: A review of preparation methodologies, *J. Appl. Biomater. Biomech.* **2004**, *2*, 74–80.
  - 32 E. BOUYER, F. GITZHOFFER, M. I. BOULOS, Morphological study of hydroxyapatite nanocrystal suspension, *J. Mater. Sci. Mater. Med.* **2000**, *11*, 523–531.
  - 33 L. YUBAO, K. DE GROOT, J. DE WIJN, C. P. A. T. KLEIN, S. V. D. MEER, Morphology and composition of nanograde calcium phosphate needle-like crystals formed by simple hydrothermal treatment, *J. Mater. Sci. Mater. Med.* **1994**, *5*, 326–331.
  - 34 G. BEZZI, G. CELOTTI, E. LANDI, T. M. G. LA TORRETTA, I. SOPYAN, A. TAMPIERI, A novel sol-gel technique for hydroxyapatite preparation, *Mater. Chem. Phys.* **2003**, *78*(3), 816–824.
  - 35 D. JANACKOVIC, I. PETROVIC-PRELEVIC, L. KOSTIC-GVOZDENOVIC, R. PETROVIC, V. JOKANOVIC, D. USKOKOVIC, Influence of synthesis parameters on the particle size of nano-structured calcium-hydroxyapatite, *Key Eng. Mater.* **2001**, *192-5*(*Bioceramics*), 203–206.
  - 36 A. BIGI, F. MARCHETTI, A. RIPAMONTI, N. ROVERI, Magnesium and strontium interaction with carbonate-containing hydroxyapatite in aqueous medium, *J. Inorg. Biochem.* **1981**, *15*, 317–327.
  - 37 A. BIGI, E. FORESTI, R. GREGORIANI, A. RIPAMONTI, N. ROVERI, J. S. SHAH, The role of magnesium on the structure of biological apatites, *Calcif. Tissue Int.* **1992**, *50*(5), 439–444.
  - 38 R. Z. LE GEROS, J. P. LE GEROS, in *Phosphate Minerals*, J. O. NRIAGU, P. B. MOORE (Eds.), Springer, New York, **1984**, pp. 351–385.
  - 39 S. BARAVELLI, A. BIGI, E. FORESTI, A. RIPAMONTI and N. ROVERI, Thermal behavior of bone and synthetic hydroxyapatites submitted to magnesium interaction in aqueous media, *J. Inorg. Biochem.* **1984** *20*, 1–12.
  - 40 A. BIGI, G. FALINI, E. FORESTI, M. GAZZANO, A. RIPAMONTI, N. ROVERI, Rietveld structure refinements of calcium hydroxylapatite containing magnesium, *Acta Crystallogr., Sect. B: Struct. Sci.* **1996**, *52*(1), 87–92.
  - 41 A. BIGI, G. FALINI, E. FORESTI, M. GAZZANO, A. RIPAMONTI, N. ROVERI, Magnesium influence on hydroxyapatite crystallization, *J. Inorg. Biochem.* **1993**, *49*(1), 69–78.
  - 42 A. TAMPIERI, G. CELOTTI, E. LANDI, From biomimetic apatite to biologically inspired composites, *Anal. Bioanal. Chem.* **2005**, *381*, 568–572.
  - 43 L. M. RODRIGUEZ-LORENZO, M. VALLET-REGI, J. M. F. FERREIRA, Fabrication of hydroxyapatite bodies by uniaxial pressing from a precipitated

- powder, *Biomaterials* **2001**, *22*(6), 583–588.
- 44 D. TADIC, F. BECKMANN, K. SCHWARZ, M. EPPLE, A novel method to produce hydroxyapatite objects with interconnecting porosity that avoids sintering. *Biomaterials* **2004**, *25*(16), 3335–3340.
  - 45 D. TADIC, F. BECKMANN, K. SCHWARZ, M. EPPLE, A novel method to produce hydroxyapatite objects with interconnecting porosity that avoids sintering. *Biomaterials* **2004**, *25*(16), 3335–3340.
  - 46 L. M. RODRIGUEZ-LORENZO, M. VALLET-REGI, J. M. F. FERREIRA, M. P. GINEBRA, C. APARICIO, J. A. PLANELL, Hydroxyapatite ceramic bodies with tailored mechanical properties for different applications. *J. Biomed. Mater. Res.* **2002**, *60*(1), 159–166.
  - 47 S. PADILLA, J. ROMAN, M. VALLET-REGI, Synthesis of porous hydroxyapatites by combination of gelcasting and foams burn out methods. *J. Mater. Sci.: Mater. Med.* **2002**, *13*(12), 1193–1197.
  - 48 D. M. ROY, S. K. LINNEHAN, Hydroxyapatite formed from coral skeletal carbonate by hydrothermal exchange, *Nature* **1974**, *247*(438), 220–222.
  - 49 B. BEN-NISSAN, Natural bioceramics: From coral to bone and beyond, *Curr. Opin. Solid State Mater. Sci.* **2003**, *7*(4–5), 283–288.
  - 50 B. BEN-NISSAN, A. MILEV, R. VAGO, Morphology of sol-gel derived nano-coated coralline hydroxyapatite, *Biomaterials* **2004**, *25*(20), 4971–4975.
  - 51 A. TAMPPIERI, G. CELOTTI, S. SPRIO, A. DELCOGLIANO, S. FRANZESE, Porosity-graded hydroxyapatite ceramics to replace natural bone. *Biomaterials* **2001**, *22*(11), 1365–1370.
  - 52 B. PALAZZO, M. C. SIDOTI, N. ROVERI, A. TAMPPIERI, M. SANDRI, L. BERTOLAZZI, F. GALBUSERA, G. DUBINI, P. VENA, R. CONTRO, Controlled drug delivery from porous hydroxyapatite grafts: An experimental and theoretical approach. *Mater. Sci. Eng., C: Biomimetic Supramol. Systems* **2005**, *C25*(2), 207–213.
  - 53 A. TAMPPIERI, G. CELOTTI, E. LANDI, M. MONTEVECCHI, N. ROVERI, A. BIGI, S. PANZAVOLTA, M. C. SIDOTI, Porous phosphate-gelatin composite as bone graft with drug delivery function, *J. Mater. Sci.: Mater. Med.* **2003**, *14*(7), 623–627.
  - 54 J. PENA, M. VALLET-REGI, J. SAN ROMAN, TiO<sub>2</sub>-polymer composites for biomedical applications, *J. Biomed. Mater. Res.* **1997**, *35*(1), 129–134.
  - 55 M. WANG, T. KOKUBO, W. BONFIELD, in *Bioceramics*, T. KOKUBO, T. NAKAMURA, F. MIYAJI (Eds.), Elsevier, Osaka, Japan **1996**, Vol. 9, p. 387.
  - 56 M. KIKUCHI, K. SATO, Y. SUETSUGU, J. TANAKA, in *Bioceramics*, R. Z. LE GEROS, J. P. LE GEROS (Eds.), World Scientific, New York, **1998**, Vol. 11, p. 153.
  - 57 D. BAKOS, M. SOLDAN, I. HERNANDEZ-FUENTES, Hydroxyapatite-collagen-hyaluronic acid composite, *Biomaterials* **1999**, *20*, 191–195.
  - 58 A. CHERNG, S. TAKAGI, L. C. CHOW, Effects of hydroxypropyl methyl cellulose and other gelling agents on the handling properties of calcium phosphate cement, *J. Biomed. Mater. Res.* **1997**, *35*(3), 273–277.
  - 59 P. EISELT, J. YEH, R. K. LATVALA, L. D. SHEA, D. J. MOONEY, Porous carriers for biomedical applications based on alginate hydrogels, *Biomaterials* **2000**, *21*(19), 1921–1927.
  - 60 B. AMSDEN, N. TURNER, Diffusion characteristics of calcium alginate gels, *Biotechnol. Bioeng.* **1999**, *65*(5), 605–610.
  - 61 K. H. BOUHADIR, K. Y. LEE, E. ALSBERG, K. L. DAMM, R. W. ANDERSON, D. J. MOONEY, Degradation of partially oxidized alginate and its potential application for tissue engineering, *Biotechnol. Progr.* **2001**, *17*(5), 945–950.
  - 62 S. C. N. CHANG, J. A. ROWLEY, G. TOBIAS, N. G. GENES, A. K. ROY, D. J. MOONEY, C. A. VACANTI, L. J. BONASSAR, Injection molding of chondrocyte/alginate constructs in the shape of facial implants, *J. Biomed. Mater. Res.* **2001**, *55*(4), 503–511.
  - 63 E. LANDI, A. TAMPPIERI, G. CELOTTI,

- L. VICHI, M. SANDRI, Influence of synthesis and sintering parameters on the characteristics of carbonate apatite, *Biomaterials* **2004**, *25*(10), 1763–1770.
- 64 S. YANG, K. F. LEONG, Z. DU, C. K. CHUA, The design of scaffolds for use in tissue engineering. Part I. Traditional factors, *Tissue Eng.* **2001**, *7*(6), 679–689.
- 65 A. TAMPIERI, M. SANDRI, E. LANDI, G. CELOTTI, N. ROVERI, M. MATTIOLI-BELMONTE, L. VIRGILI, F. GABBANELLI, G. BIAGINI, HA/alginate hybrid composites prepared through bio-inspired nucleation, *Acta Biomater.* **2005**, *1*, 343–351.
- 66 E. RUIZ-HITZKY, Functionalizing inorganic solids: Towards organic-inorganic nanostructured materials for intelligent and bioinspired systems, *Chem. Record* **2003**, *3*, 88–100.
- 67 B. DIETRICH, P. VIOUT, J. M. LEHN, in *Macrocyclic Chemistry: Aspects of Organic and Inorganic Supra Molecular Chemistry*, VCH, Weinheim, **1993**, pp. 384.
- 68 L. DONALD, A. VEIS, Collagen self-assembly in vitro, *J. Biol. Chem.* **1981**, *256*, 7118–7128.
- 69 G. FALINI, S. FERMANI, E. FORESTI, B. PARMA, K. RUBINI, M. C. SIDOTI, N. ROVERI, Films of self-assembled purely helical type I collagen molecules, *J. Mater. Chem.* **2004**, *14*, 2297–2302.
- 70 N. ROVERI, G. FALINI, M. C. SIDOTI, A. TAMPIERI, E. LANDI, M. SANDRI, B. PARMA, Biologically inspired growth of hydroxyapatite nanocrystals inside self-assembled collagen fibers, *Mater. Sci. Eng., C: Biomimetic Supramol. Systems* **2003**, *C23*, 441–446.
- 71 A. TAMPIERI, G. CELOTTI, E. LANDI, M. SANDRI, N. ROVERI, G. FALINI, Biologically inspired synthesis of bone-like composite: Self-assembled collagen fibers/hydroxyapatite nanocrystals, *J. Biomed. Mater. Res., A* **2003**, *67*, 618–625.
- 72 M. KIKUCHI, S. ITOH, S. ICHINOSE, K. SHINOMIYA, J. TANAKA, Self organization mechanism in a bone-like hydroxyapatite/collagen nanocomposite synthesized in vitro and its biological reaction in vivo, *Biomaterials* **2001**, *22*, 1705–1711.
- 73 A. TAMPIERI, G. CELOTTI, E. LANDI, N. ROVERI, *Eur. Patent 04001417.7*, **2004**.
- 74 S. A. REDEY, S. RAZZOUK, C. REY, D. BERNACHE-ASSOLANT, G. LEROY, M. NARDIN, G. COURNOT, Osteoclast adhesion and activity on synthetic hydroxyapatite, carbonated hydroxyapatite, and natural calcium carbonate: Relationship to surface energies, *J. Biomed. Mater. Res.* **1999**, *45*, 140–147.
- 75 G. GUILLEMIN, S. J. HUNTER, C. V. GAY, Resorption of natural calcium carbonate by avian osteoclasts in vitro, *Cells Mater.* **1995**, *5*(2), 157–165Y.
- 76 M. KIKUCHI, T. IKOMA, S. ITOH, H. N. MATSUMOTO, Y. KOYAMA, K. TAKAKUDA, K. SHINOMIYA, J. TANAKA, Biomimetic synthesis of bone-like nanocomposites using the self-organization mechanism of hydroxyapatite and collagen, *Composites Sci. Technol.* **2004**, *64*(6), 819–825.
- 77 MIYAMOTO, K. ISHIKAWA, M. TAKECHI, T. TOH, T. YUASA, M. NAGAYAMA et al., Basic properties of calcium phosphate cement containing atelocollagen in its liquid or powder phases, *Biomaterials* **1998**, *19*, 707–715.
- 78 C. DU, F. Z. CUI, X. D. ZHU, K. DE GROOT, Three-dimensional nano-HAp/collagen matrix loading with osteogenic cells in organ culture, *J. Biomed. Mater. Res.* **1999**, *44*, 407–415.
- 79 M. KIKUCHI, H. N. MATSUMOTO, T. YAMADA, Y. KOYAMA, K. TAKAKUDA, J. TANAKA, Glutaraldehyde cross-linked hydroxyapatite/collagen self-organized nanocomposites, *Biomaterials* **2004**, *25*, 63–69.
- 80 M. SHIRKHAZADEH, Direct formation of nanophase hydroxyapatite cathodically polarised electrodes, *J. Mater. Sci. Mater. Med.* **1998**, *9*, 67–72.
- 81 H. SCHLIEPHAKE, D. SCHARNWEBER, M. DA, S. ROSSELER, A. SEWING, C. HUTTMANN, Biological performance of biomimetic calcium phosphate coating of titanium implants in the dog

- mandible, *J. Biomed. Mater. Res.* **2003**, *64*, 225–234.
- 82 M. MANSO, C. JIMENEZ, C. MORANT, P. HERRERO, J. M. MARTINEZ DUART, Electrodeposition of hydroxyapatite coating in basic conditions, *Biomaterials* **2000**, *21*, 1755–1761.
- 83 K. DUAN, Y. W. FAN, R. WANG, Electrochemical deposition and patterning of calcium phosphate bioceramics coating, *Ceram. Trans.* **2003**, *147*, 53–61.
- 84 S. MANARA, F. PAOLUCCI, B. PALAZZO, M. MARCACCIO, E. FORESTI, N. PARMA, N. ROVERI, Electrochemical deposition of hydroxyapatite-collagen fibrils composites" Submitted to *Advanced Functional Materials*.
- 85 H. OKAMURA, M. YASUDA, M. OHTA, Synthesis of calcium-deficient hydroxyapatite-collagen composite, *Electrochemistry* **2000**, *68*, 486–488.
- 86 H. SCHLIEPHAKE, D. SCHARNWEBER, M. DARD, S. ROSSLER, A. SEWING, C. HUTTMANN, Biological performance of biomimetic calcium phosphate coating of titanium implants in the dog mandible. *J. Biomed. Mater. Res.* **2003**, *64*, 225–234.
- 87 Y. FAN, K. DUAN, R. WANG, A composite coating by electrolysis-induced collagen self-assembly and calcium phosphate mineralization, *Biomaterials* **2004**, *26*, 1623–1632.
- 88 G. FALINI, E. FORESTI, S. MANARA, B. PALAZZO, M. MARCACCIO, F. PAOLUCCI, N. ROVERI, Electrochemically co-deposition of hydroxyapatite-collagen composite on Ti surface, 19<sup>th</sup> *European Conference on Biomaterials*, Sorrento 11–15 September 2005.
- 89 E. I. SUVOROVA, P. A. BUFFAT, Electron diffraction from micro and nanoparticles of hydroxyapatite, *J. Microsc. (Oxford)* **1999**, *196(1)*, 46–58.
- 90 L. C. NISTOR, C. GHICA, V. S. TEODORESCU, S. V. NISTOR, M. DINESCU, D. MATEI, N. FRANGIS, N. VOUREUTZIS, C. LIUTAS, Deposition of hydroxyapatite thin films by Nd:YAG laser ablation: A micro structural study, *Mater. Res. Bull.* **2004**, *39*, 2089–2101.
- 91 L. ADDADI, S. WEINER, Stereochemical and structural relations between macromolecules and crystals in biomineralization, in *Biomineralization: Chemical and Biochemical Prospective*, S. MANN, J. WEBB, R. J. P. WILLIAMS (Eds.), VCH Verlagsgesellschaft, Weinheim, **1980**, pp. 132–156.
- 92 A. L. BOSKEY, Phospholipids and calcification: An overview, in *Cell Mediated Calcification and Matrix Vesicles*, S. Y. ALI (Ed.), Elsevier, Amsterdam, **1986**, pp. 175–179.
- 93 A. MEISTER, *Biochemistry of Amino Acids*, 2nd edn., Academic Press, New York, **1965**.
- 94 A. L. LEHNINGER, *Biochemistry*, 2nd edn., Worth Publishing, New York, **1975**.
- 95 S. KOUTSOPOULOS, E. DALAS, Hydroxyapatite crystallization in the presence of serine, tyrosine and hydroxyproline amino acids with polar side groups, *J. Crystal Growth*, **2000**, *216*, 443–449.
- 96 S. KOUTSOPOULOS, E. DALAS, Hydroxyapatite crystallization in the presence of amino acids with uncharged polar side groups: glycine, cysteine, cystine, and glutamine, *Langmuir* **2001**, *17*, 1074–1079.
- 97 S. KOUTSOPOULOS, E. DALAS, The crystallization of hydroxyapatite in the presence of lysine, *J. Colloid Interface Sci.* **2000**, *231*, 207–212.
- 98 R. GONZALEZ-MCQUIRE, J. Y. CHANE-CHING, JEAN-YVES, E. VIGNAUD, A. LEBUGLE, S. MANN, Synthesis and characterization of amino acid-functionalized hydroxyapatite nanorods, *J. Mater. Chem.* **2004**, *14(14)*, 2277–2281.
- 99 B. PALAZZO, S. MANN, D. WALSH, N. ROVERI, G. FALINI, E. FORESTI, G. NATILE, M. LAFORGIA, Apatite surface functionalization with aminoacids and platinum complexes, *IV Symposium on Pharmaco-Biometallics*, CIRCMSB (ed.), Tecnomack, Bari, Italy, p. 23.
- 100 A. BARROUG, J. M. GLIMCHER, Hydroxyapatite crystals as a local delivery system for cisplatin: Adsorption and release of cisplatin in vitro, *J. Orthopaedic Res.* **2002**, *20*, 274–280.
- 101 A. BARROUG, L. T. KUHN, L. C.

- GERSTENFELD, M. J. GLIMCHER, Interaction of cisplatinum with calcium phosphate nanoparticles: In vitro controlled adsorption and release, *J. Orthopaedic Res.* **2004**, *22*, 703–708.
- 102 B. PALAZZO, M. IAFISCO, M. LAFORGIA, N. MARGIOTTA, G. NATILE, C. L. BIANCHI, D. WALSH, N. ROVERI, “Biomimetic hydroxyapatite nanocrystals as bone substitute with anti-tumour drugs delivery function” Submitted to *Advanced Functional Materials*.
- 103 S. JOSSE, C. FAUCHEUX, A. SOUEIDAN, G. GRIMANDI, D. MASSIOT, B. ALONSO, P. JANVIER, S. LAIB, P. PILET, O. GAUTHIER, G. DACULSI, J. GUICHEUX, B. BUJOLI, J. M. BOULER, Novel biomaterials for bisphosphonate delivery, *Biomaterials* **2005**, *26(14)*, 2073–2080.
- 104 R. G. G. RUSSELL, M. J. ROGERS, Bisphosphonates: From the laboratory to the clinic and back again, *Bone (New York)* **1999**, *25(1)*, 97–106.
- 105 A. EZRA, G. GOLOMB, Administration routes and delivery systems of bisphosphonates for the treatment of bone resorption, *Adv. Drug Deliv. Rev.* **2000**, *42*, 175–195.
- 106 L. S. ROSEN, D. GORDON, M. KAMINSKI, A. HOWELL, A. BELCH, J. MACKAY, J. APFFELSTAEDT, M. HUSSEIN, R. E. COLEMAN, D. J. REITSMA, J. J. SEAMAN, B. L. CHEN, Y. AMBROS, Zoledronic acid versus pamidronate in the treatment of skeletal metastases in patients with breast cancer or osteolytic lesions of multiple myeloma: A phase III, double-blind, comparative trial, *Cancer J. (Sudbury, Mass.)*, **2001**, *7(5)*, 377–387.
- 107 H. ROUSSIERE, G. MONTAVON, S. LAIB, P. JANVIER, B. ALONSO, F. FAYON, M. PETIT, D. MASSIOT, J. M. BOULER, B. BUJOLI, Hybrid materials applied to biotechnologies: Coating of calcium phosphates for the design of implants active against bone resorption disorders, *J. Mater. Chem.* **2005**, *15(35–36)*, 3869–3875.
- 108 B. PALAZZO, M. IAFISCO, M. LAFORGIA, N. MARGIOTTA, G. NATILE, N. ROVERI, Hydroxyapatite nanocrystals as local anticancer platinum complexes delivery system. V *Symposium on Pharmaco-Biometallics*, 11–12 November 2005 Bertinoro (Bologna), Italy, CIRCMSB (ed.), Tecnomack, Bari, Italy.
- 109 T. KLENNER, P. VALENZUELA-PAZ, F. AMELUNG, H. MUNCH, H. ZAHN, B. K. KEPPLER, H. BLUM, in *Metal Complexes in Cancer Chemotherapy*, B. K. KEPPLER (Ed.), VCH, Weinheim, **1993**, pp. 85–127.
- 110 B. PALAZZO, D. WALSH, S. MANN, N. ROVERI, Magnetic nanoapatite for bone tissue cancer treatment by locally induced hyperthermia, V *Symposium on Pharmaco-Biometallics*, 11–12 November 2005, Bertinoro (Bologna), Italy, CIRCMSB (ed.), Tecnomack, Bari, Italy.
- 111 B. PALAZZO, D. WALSH, S. MANN, N. ROVERI, Magnetic hydroxyapatite nanocrystals for bone tissue cancer treatment by locally induced hyperthermia, submitted to *J. Mater. Chem.*
- 112 J. N. WEINSTEIN, R. L. MAGIN, M. B. YATVIN, D. S. ZAHARKO, Liposomes and local hyperthermia: Selective delivery of methotrexate to heated tumors, *Science*, **1979**, *204*, 188–191.

## 8

# Magnetic Nanoparticles for Tissue Engineering

*Akira Ito and Hiroyuki Honda*

### 8.1

#### Introduction

Magnetic nanoparticles, from nanometer to submicron size, have been developed for medical applications by many researchers [1, 2]. Since magnetic nanoparticles have unique magnetic features not present in other materials, they can be applied to special medical techniques. Magnetic particles are attracted to high magnetic flux density and this feature is used for drug targeting [3] and bioseparation [4–6], including cell sorting [7]. A comprehensive review on the use of magnetic particles in clinical applications was given by Häfeli et al. [8]. In these applications, magnetic particles are given various names, e.g. magnetic microspheres, magnetic nanospheres, and ferrofluids, among others. Here, we use the general term “magnetic nanoparticles”, and review and discuss their new applications in tissue engineering.

Magnetite ( $\text{Fe}_3\text{O}_4$ ) particles are being used in an increasing number of biological and medical applications, including cell sorting. To add an affinity and target ability to cells, we applied the concepts involved in drug delivery systems (DDSs) to magnetite nanoparticles and developed functionalized magnetite nanoparticles. We developed magnetite cationic liposomes (MCLs), which are cationic liposomes containing 10-nm magnetite nanoparticles, to improve accumulation of magnetite nanoparticles in target cells by taking advantage of the electrostatic interaction between MCLs (positively charged) and the cell membrane (negatively charged) [9–11]. Since MCLs are designed to interact with target cells via electrostatic interaction, there is the risk of non-specific interaction between MCLs and various non-target cell types. A promising technique is the use of antibodies raised against target cells to isolate them from the other cells. We developed antibody-conjugated magnetoliposomes (AMLs) for use in cancer-targeted therapy [12–14]. The AMLs were made from magnetoliposomes (MLs) consisting of neutral lipids, to reduce electrostatic interaction with target cells. Target cells can be magnetically labeled by the functionalized magnetite nanoparticles (MCLs or AMLs), via uptake of magnetite nanoparticle into the cells (Fig. 8.1).

The loss or failure of an organ or tissue is one of the most frequent, devastating,



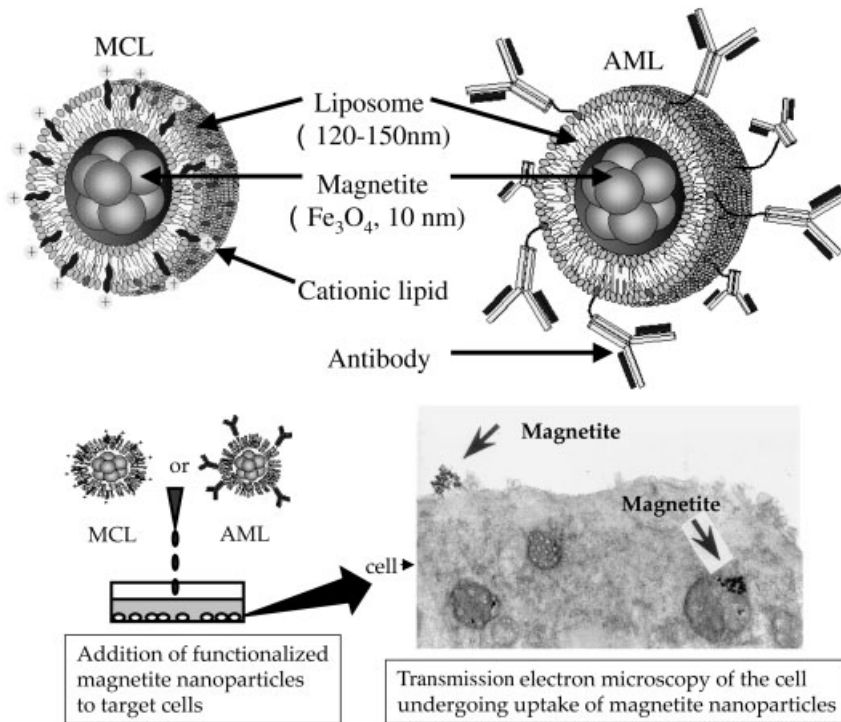


Fig. 8.1. Schematic of functionalized magnetic nanoparticles.

and costly problems in human health care. Tissue engineering applies the principles of biology and engineering to the development of functional substitutes for damaged tissue. Langer and Vacanti laid the foundations of this interdisciplinary field in 1993 [15], and worldwide interest in tissue engineering was initiated. The following decade saw growing enthusiasm for tissue engineering, and tissue engineering has been a promising technology for overcoming the organ transplantation crisis resulting from donor organ shortage. In general, tissue engineering consists of the following processes: (a) Target cells are isolated and expanded to the required cell number; (b) cells are harvested and reseeded into three-dimensional (3D) biodegradable scaffolds, allowing 3D cell culture; and (c) the cultured 3D constructs are implanted into patients.

Although an overall technology of these processes in tissue engineering has been established, there is still room for improvement in each process. From the point of view of bioprocess engineering, development of a methodology of “physical manipulation of target cells” is essential for tissue engineering in the next few decades. We selected magnetic force as a physical force, and manipulated target cells labeled with magnetite nanoparticles using DDS techniques. Thus, we have developed a novel cell-manipulating technology using functionalized magnetite nanoparticles and magnetic force, which we have designated “Mag-TE”. The pres-

ent chapter focuses on Mag-TE that has been applied to the processes in tissue engineering: (a) Magnetic isolation and expansion of mesenchymal stem cell (Section 8.2); (b) magnetic cell-seeding into 3D biodegradable scaffolds (Mag-seeding, Section 8.3); and (c) construction of 3D tissue-like structure by using magnetic force (Section 8.4).

## 8.2

### Mesenchymal Stem Cell Isolation and Expansion

Bone marrow-derived mesenchymal stem cells (MSCs) can differentiate into osteoblasts, chondrocytes, adipocytes, muscle cells or nerve cells *in vitro* and *in vivo* [16–19]. Since MSCs can easily be obtained by bone marrow aspiration, transplantation of bone marrow MSCs may provide a new treatment for regeneration of mesenchymal tissues [18]. However, marrow aspiration of too great a volume causes damage and pain to the donor. Thus, it is difficult to obtain the large number of MSCs required for regeneration of injured tissues. Expansion of MSCs *in vitro* is a necessary step in the clinical application of MSCs.

Despite the great interest in MSCs, there is still no well-defined protocol for isolation and expansion of MSCs in culture. Most experiments have been conducted using MSCs isolated primarily from bone marrow aspirates by their tight adherence to plastic dishes, as described by Friedenstein et al. [20]. However, this method for isolating cells does not help increase the number of MSCs, as there is only a small number of MSCs in bone marrow aspirate. Pittenger et al. reported that only a small percentage (0.0001–0.01%) of bone marrow aspirate cells that attached to the culture dishes were MSCs [16]. In addition, culture volume inevitably becomes large, since there are numerous nonadherent cells such as hematopoietic cells that must be diluted and removed by washing and changes in medium, resulting in low-density culture of MSCs. Under such low-density culture conditions, MSCs do not proliferate immediately, and require much time to develop into colonies as growth factors, including autocrine [21–24], paracrine [24], and juxtacrine [25] factors, play an important role in cell growth. Therefore, we developed a new method for producing high-density culture, using magnetic nanoparticles to promote expansion of MSCs.

#### 8.2.1

##### MSC Expansion using MCLs

We have developed MCLs that have been used as carriers to introduce DNA into cells [26], and as heat generating mediators for cancer therapy [27–31]. Here, in this study [32], magnetic forces were used to move MSCs labeled with MCLs, to hold them *in situ*, and to culture them at high density. First, we investigated the applicability of this combined methodological approach to the enrichment and proliferation of MSCs using MCLs. Figure 8.2 illustrates a schematic of MSC expansion using MCLs.

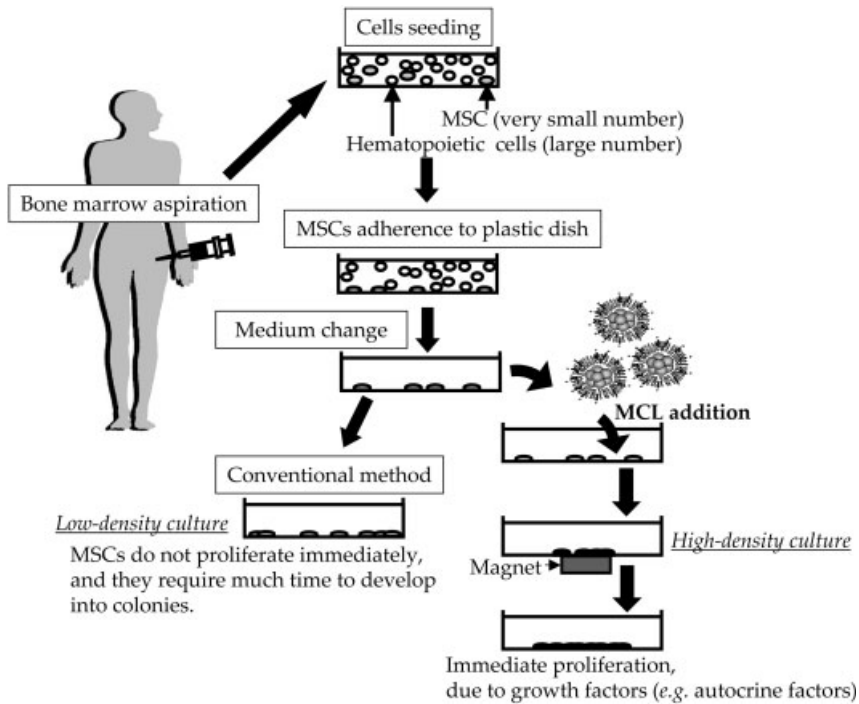
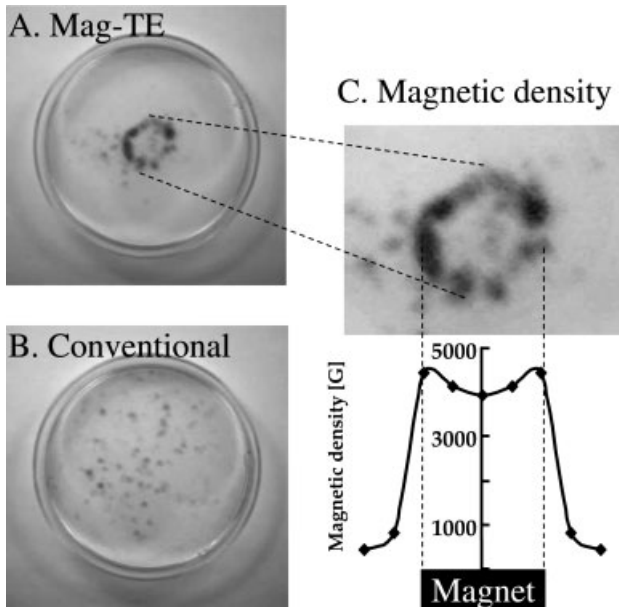


Fig. 8.2. Schematic of the expansion of MSCs using MCLs.

Expansion of MSCs using MCLs was investigated as follows. At 4 h after addition of the MCLs, 1000 human MSCs (a very small cell number corresponding to the MSCs in 1 mL of bone marrow aspirate) were seeded into a 100-mm cell culture dish with 10 mL of cell culture medium; a cylindrical neodymium magnet (diameter, 2.2 cm; height, 1 cm; 4000 Gauss) was then placed under the dish to provide magnetic force vertical to the dish.

When the MCLs were added to human MSCs at 100-pg magnetite per cell, uptake of magnetic nanoparticles began rapidly and maximum uptake ( $20 \text{ pg cell}^{-1}$ ) was achieved at 4 h after addition. Subsequently, the amount of magnetite per cell decreased due to dilution as a result of cell growth. Growth of MSCs in medium containing MCLs (MCL(+))MSCs) was compared with growth of MSCs in medium without MCLs (MCL(-))MSCs). MCLs did not inhibit nor stimulate growth of MSCs. Furthermore, no effects of MCL addition on MSC differentiation were observed. Osteogenic differentiation of MCL(+))MSCs transferred into osteogenic medium was attained 17 days after transfer. MSCs incubated in osteogenic medium changed shape from fibroblastic (undifferentiated MSC) to polygonal, and formed calcium nodules. Adipogenic induction of MCL(+))MSCs was attained after culturing in adipogenic medium, as indicated by accumulation of lipid-rich vacuoles within cells and the presence of Oil red-O-positive cells. Thus, we observed no tox-



**Fig. 8.3.** Cultures of MSCs produced by Mag-TE (A), compared with conventional means (B), have a high density (C).

icity against MSC proliferation or differentiation when the magnetite concentration was  $100 \text{ pg cell}^{-1}$ .

MCL(+)MSCs accumulated circumferentially along the edge of the magnet at the center of dish where the magnet was positioned (Fig. 8.3A), while MCL(-)MSCs formed scattered colonies throughout the dish (Fig. 8.3B). Since magnetic particles are attracted to high magnetic flux density, MCL(+)MSCs were attracted to where the magnetic density was highest (Fig. 8.3C). The growth area regulated by the magnetic force was approximately  $1 \text{ cm}^2$ , as indicated by image analysis. These results suggest that the MCL(+)MSCs were seeded at  $1000 \text{ cells cm}^{-2}$ , which was a much higher concentration than that of MCL(-)MSCs ( $18 \text{ cells cm}^{-2}$ ;  $1000 \text{ cells per } 55\text{-cm}^2 \text{ dish}$ ). A total of  $2.2 \times 10^4$  cells were counted on day 7, corresponding to the number of cells in  $1 \text{ cm}^2$  of confluent culture (approximately  $2 \times 10^4 \text{ cells cm}^{-2}$ ). This was five-fold greater than the number obtained for MCL(-)MSCs using the conventional method.

Methods for expansion of MSCs are in great demand for clinical applications. One approach to expansion of MSCs is identification of growth factors involved in self-renewal of MSCs. Tsutsumi et al. reported that fibroblast growth factor-2 (FGF-2) increases the growth rate of rabbit, canine and human bone marrow MSCs [33]. However, the mechanism by which FGF-2 maintains proliferation without differentiation is unknown, and clinical applications of cytokines should be pursued

with caution due to the unknown functions of cytokines. Alternatively, growth factors such as cytokines are produced by cells themselves and act as autocrine factors. Huss et al. reported that autocrine factors such as stem cell factor (SCF) and interleukin-6 (IL-6) are involved in proliferation and differentiation of a canine bone marrow-derived cell line, and that an increase in local cell concentration is associated with cell viability [34]. In addition, Gregory et al. reported that conditioned medium from cultures of human MSCs increases the rate of proliferation of freshly plated cultures of human MSCs; secretion of high levels of dickkopf-1 (Dkk-1), an inhibitor of the canonical Wnt signaling pathway, was involved in the reentry of MSCs into the cell cycle in lag phase because of low cell density [35]. These results prompted us to use magnetic force for MSC separation. As mentioned above, when MSCs were seeded at high density using MCLs, the number of cells obtained was five-fold greater than the number obtained from culture without MCLs. These results suggest that growth factors, including autocrine, paracrine, and juxtacrine factors, are involved in the proliferation of MSCs. “High-density culture” using magnetic nanoparticles provides a new methodology for expansion of MSCs.

### 8.2.2

#### MSC Isolation and Expansion using AMLs

As mentioned in Section 8.2.1, we used magnetic force to move MSCs labeled with MCLs and to culture them at high density, and demonstrated the feasibility of magnetic force-based high-density culture for proliferation of MSCs *in vitro*. Because MCLs were designed to interact with target cells via electrostatic interaction, there is the risk of non-specific interaction between MCLs and various non-target cell types. The MCLs were mixed with purified MSCs that had been isolated from bone marrow aspirates.

A promising technique is the use of antibodies raised against MSCs to isolate MSCs from bone marrow aspirates. We previously developed antibody-conjugated magnetoliposomes (AMLs) for use in cancer therapy [12–14]. The AMLs were made from magnetoliposomes (MLs) that consisted of neutral lipids, to reduce electrostatic interaction with target cells. Recently, many researchers have used antibodies to isolate or characterize MSCs [36–38]. Barry et al. reported that CD105 (endoglin), which is the TGF (transforming growth factor)- $\beta$  receptor I/III present on endothelial cells, macrophages, and connective tissue stromal cells, is a useful surface antigen for isolation of MSCs [36]. Therefore, we investigated whether magnetic force-based high-density culture of MSCs, using anti-CD105 antibody-conjugated magnetoliposomes, is an effective method for expansion of MSCs [39]. Figure 8.4 illustrates a strategy for MSCs expansion using AMLs.

Magnetic separation of human MSCs from bone marrow aspirates using anti-CD105 antibody-conjugated magnetoliposomes was performed as follows. After obtaining informed consent, an average of 10 mL of iliac and maxillofacial bone marrow was collected from donors. These bone marrow aspirates were mixed with 20 mL of cell growth medium, and 3 mL of that mixture was combined with 7 mL of

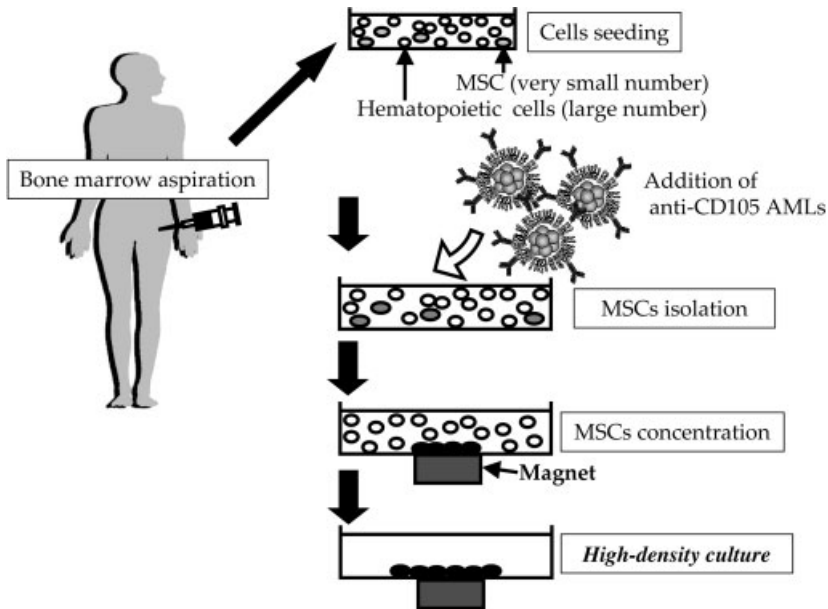


Fig. 8.4. Schematic of the separation and expansion of MSCs using AMLs.

medium containing AMLs, after which bone marrow aspirates with AMLs were placed in 100-mm tissue culture dishes. A disk-shaped neodymium magnet (diameter, 2.2 cm; 4000 Gauss) was then placed under the 100-mm dish to expose the aspirate to magnetic force vertical to the bottom of the dish. After every 3 to 4 days of culture, the nonadherent cells were removed and the medium was replaced.

The immobilization density and average particle size of  $\alpha$ CD105-AMLs were 47.7  $\mu$ g-antibody/mg-magnetite and 136.7 nm, respectively. As shown in Fig. 8.5, 85% of the human MSCs were magnetically separated using  $\alpha$ CD105-AMLs, which was a significantly higher percentage than the values obtained using magnetoliposomes not conjugated to antibody (MLs; 30%).

In the initial state of cell culture after the magnet was placed under the culture dish, the AMLs accumulated at the center of the dish along the edge of the magnet. At 1 day after the start of culture, when the medium was replaced, nonadherent cells and excess AMLs were removed, and very few cells with fibroblastic morphology were found to have adhered to the dish. In the control dishes, cultured using the conventional method, none or very few colonies were observed. In contrast, in the  $\alpha$ CD105-AML cultures, cells accumulated at the center of dish along the edge of the magnet, followed by development of those cells into variously sized colonies at the periphery of the magnet, resulting in high-density cell culture. On day 7, the number of viable cells was assayed (Fig. 8.6). In  $\alpha$ CD105-AML culture of iliac bone marrow aspirate, an average of 246 cells were detected per dish, which

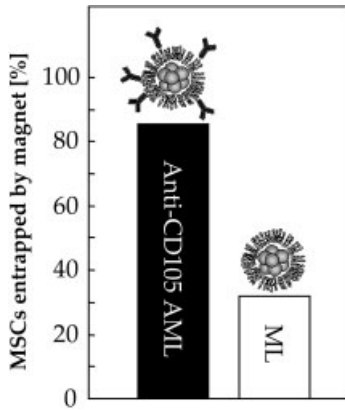


Fig. 8.5. Separation of MSCs using anti-CD105 AML or non-antibody-conjugated MLs.

was 24-fold greater than the numbers obtained with control cultures. No viable cells were detected in the control maxillofacial bone marrow culture. In contrast, an average of 138 cells per dish was detected in the  $\alpha$ CD105-AML maxillofacial bone marrow culture.

In this study, we used AMLs to create a “high-density MSC culture” from bone marrow aspirate. A net bone marrow aspirate of 1 mL was used as a model for expansion of MSCs from an extremely small number of cells. In this model, few or no cells were detected in cultures obtained from iliac and maxillofacial bone marrow aspirates using conventional methods based on the plastic-adherent tendencies of cells. In contrast, after 7 days of culture with  $\alpha$ CD105-AMLs, 246 cells were

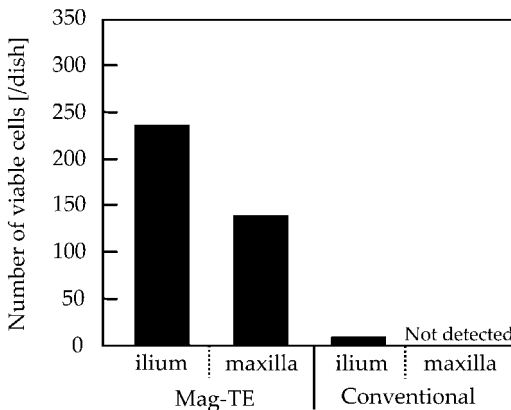


Fig. 8.6. MSC separation and expansion from bone marrow aspirates using anti-CD105 AMLs (Mag-TE) or without AMLs (a conventional method).

detected in iliac bone marrow culture and 138 cells were detected in maxillofacial bone marrow (Fig. 8.6). These results suggest that this method, which we have termed “Mag-TE”, is an effective method for expansion of MSCs from very small initial numbers of cells. Typically, only a small number of cells can be obtained from bone marrow aspirates; this is especially true for maxillofacial bone marrow. However, we achieved efficient expansion of MSCs from maxillofacial bone marrow using  $\alpha$ CD105-AMLs and a magnet.

### 8.3

#### Mag-seeding

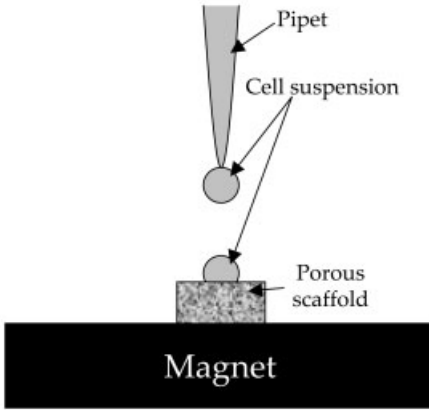
One approach to tissue engineering is to seed the cells in 3D porous biodegradable scaffolds that allow the cells to form a continuous structure via cell adhesion, proliferation, and deposition of ECM. Although cell-seeding into scaffolds at a high density is closely associated with enhancement of tissue formation in 3D constructs (e.g., cartilage [40], bone [41] and cardiac tissue [42]), effective and high-density cell seeding into 3D scaffolds is difficult to achieve. Technical difficulties in cell-seeding are caused by the complicated structure of the scaffold [43–46], and insufficient migration into the scaffolds due to their pore sizes and materials, which may cause crucial prolongation of the culture period due to a shortage of initially seeded cells. Therefore, numerous methodologies for effective cell-seeding into 3D scaffolds have been investigated [47], and novel methodologies have been also highly sought.

One conventional cell-seeding methodology (static-seeding) involves cell suspension being seeded onto small scaffolds using small volumes of highly concentrated cell suspension, as such a large number of cells cannot be obtained from Petri dish culture [47]. Here, the inevitable problem arises, namely that the cell suspension seeded onto the scaffold flows away along with medium flow, and only a small number of cells remains on the scaffolds. Mag-TE could help overcome this problem, as magnetic force would attract seeded cells that had been magnetically labeled to prevent them from flowing away, with the result that numerous cells could be seeded onto the scaffolds.

We applied a Mag-TE technique to a tissue engineering process in cell-seeding, (termed “Mag-seeding”), and investigated whether Mag-seeding enhances cell-seeding efficiency into 3D porous scaffolds for tissue engineering [48]. NIH/3T3 fibroblast cells (FBs) were used as the model, along with six kinds of scaffold: five were collagen sponges, each of a different pore size (50–600  $\mu$ m), while the other was a D,D-L,L-poly(lactic acid) (PLA) sponge. Mag-seeding was performed as follows: FBs were incubated with culture medium containing MCLs, while scaffolds were hydrated in culture medium and then placed in the well of tissue culture plates. A magnet was placed on the reverse side of the tissue culture plate to provide magnetic force vertical to the plate, and aliquots (100  $\mu$ L) of the magnetically labeled cell suspension then poured onto the top of the hydrated scaffolds. Figure 8.7(A) illustrates a schematic of Mag-seeding.



## A. Schematic of Mag-seeding



## B. Cell-seeding effect of Mag-seeding by pore size

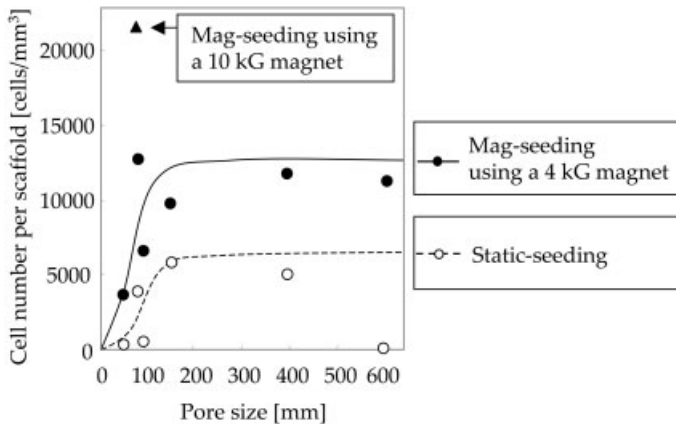


Fig. 8.7. Mag-seeding (A) and its cell-seeding efficacy (B).

The cell-seeding efficiency of Mag-seeding was compared with that of static-seeding. As shown in Fig. 8.7(B), the cell-seeding efficiency for all scaffolds was enhanced by Mag-seeding. Accompanying an increase in pore size, the number of cells in the scaffold increased, and then reached a plateau; approximately 5000 cells mm<sup>-3</sup> for static-seeding and 12 000 cells mm<sup>-3</sup> for Mag-seeding. Since the apparent size of the scaffold was particularly small in a collagen sponge with a pore size of 600  $\mu\text{m}$ , very few cells were detected when the cells were seeded by static-seeding. This is because the poured cell suspension onto the scaffold flowed away. Conversely, a substantial number of cells was detected when the cells were seeded by Mag-TE, suggesting that the magnetic force facilitated cell-seeding.

The effects of magnetic force intensity on cell-seeding efficiency were examined. Two kinds of magnet (magnetic field intensity; 4 and 10 kG) were used in this experiment. The seeding efficiency by Mag-seeding using the 10-kG magnet was significantly higher than the efficacy by static-seeding or by Mag-seeding using the 4-kG magnet (Fig. 8.7B).

In conclusion, we demonstrated that a large number of cells can be seeded into scaffolds by Mag-seeding. Magnetically labeled cells are attracted by magnetic force and consequently numerous cells remain in the scaffold across the medium flow. The cell-seeding efficiency depends on the pore size of the scaffolds. In static-seeding, cells seeded onto scaffolds may enter into the scaffold due to natural precipitation by gravity. For scaffolds with small pore size, most of the cells poured onto the scaffold cannot enter, and thus only a small number of cells are seeded within the scaffold. By Mag-seeding, a significantly larger number of cells enter the scaffold, regardless of pore size (50–600  $\mu\text{m}$  tested). Moreover, cell-seeding efficiency is enhanced by the use of a magnet with higher magnetic induction. These results indicate that Mag-seeding is an easy and reliable cell-seeding technique. In addition, since cells labeled with MCLs can be easily manipulated using magnetic force, automation of cell-seeding for tissue engineering is a distinct possibility, which could aid industrial engineered-tissue production.

## 8.4

### Construction of 3D Tissue-like Structure

Currently, tissue engineering is based on seeding cells onto 3D biodegradable scaffolds, which allows the cells to reform their original structure [15]. However, some problems remain with this approach, e.g., insufficient cell migration into the scaffolds and inflammatory reactions due to scaffold biodegradation, and thus novel approaches for achieving 3D tissue-like constructs are required. We applied Mag-TE to the construction of “scaffold-less” 3D tissue-like structures.

#### 8.4.1

##### Cell Sheet Engineering using RGD-MCLs

A major difficulty obstructing the fabrication of *in vivo*-like 3D constructs without the use of artificial 3D scaffolds is a lack of cell adherence in the vertical direction via cell–cell junctions. This non-adherence is caused by enzymatic digestion of adhesive proteins. To overcome this, Okano et al. employed a thermo-responsive culture surface grafted to poly (*N*-isopropylacrylamide) (PIPAAm) [49–51]. Cells adhered to and proliferated on the thermo-responsive surface, as well as on tissue culture polystyrene dishes. Furthermore, confluent cells on the PIPAAm dishes were expelled as intact contiguous sheets by decreasing the temperature to below the lower critical solution temperature (LCST) of PIPAAm. Kushida et al. recovered monolayer cell sheets from a surface grafted with PIPAAm and then deposited extracellular matrices (ECMs); digestive enzymes were not used and the ECMs

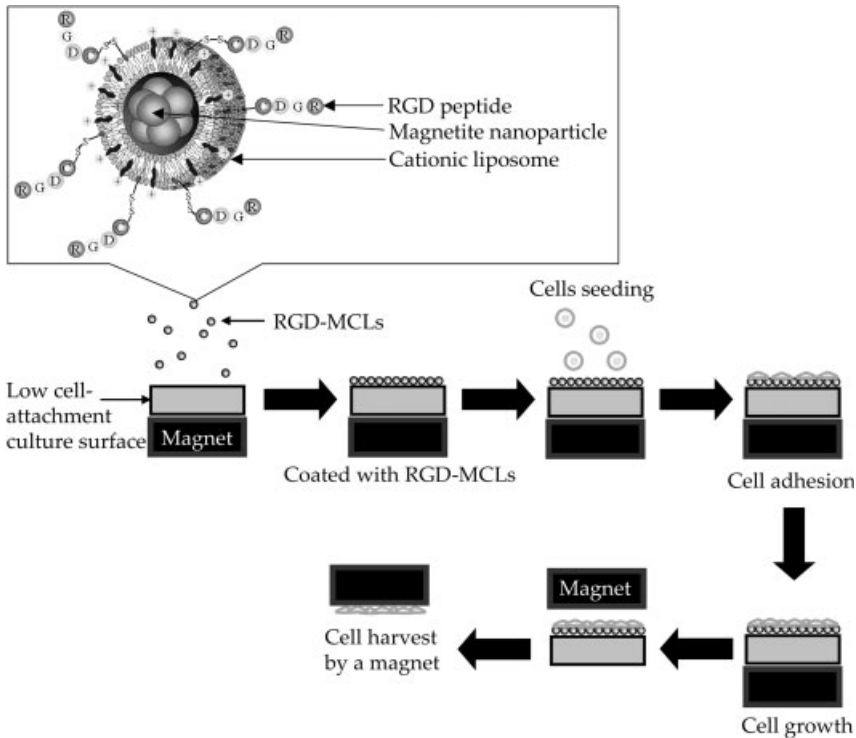


Fig. 8.8. Schematic for Mag-TE using RGD-MCLs.

remained to enhance cell–cell attachment [52]. These engineered cell sheets could be layered to construct multi-layered 3D cell sheets, and Okano et al. proposed the concept of “cell sheet engineering”.

We have developed a new biomaterial and methodology for Mag-TE. The RGD (Arg-Gly-Asp) sequence, an integrin recognition motif found in fibronectin [53, 54] and one of the most extensively studied cell adhesion peptides, was conjugated with magnetite cationic liposomes (RGD-MCLs) [55]. Figure 8.8 illustrates the RGD-MCLs.

RGD-MCLs, which contained magnetite nanoparticles that possessed a positively charged cationic lipid surface and were coupled covalently with the cell adhesion peptide RGD (Arg-Gly-Asp-Cys), were constructed according to the method of Gyongyossy-Issa et al. [56] with slight modifications. The average particle size of the RGD-MCLs was 243 nm. The density of the immobilized peptides in RGD-MCLs was 0.226 mg peptide/mg magnetite.

The new technique using RGD-MCLs consists of the following processes. RGD-MCLs are pre-seeded onto a low cell-attachment culture surface, consisting of a hydrophilic and neutrally charged covalently bound hydrogel layer, and a magnet is set on the underside of the well to attract the RGD-MCLs to the well surface. Target

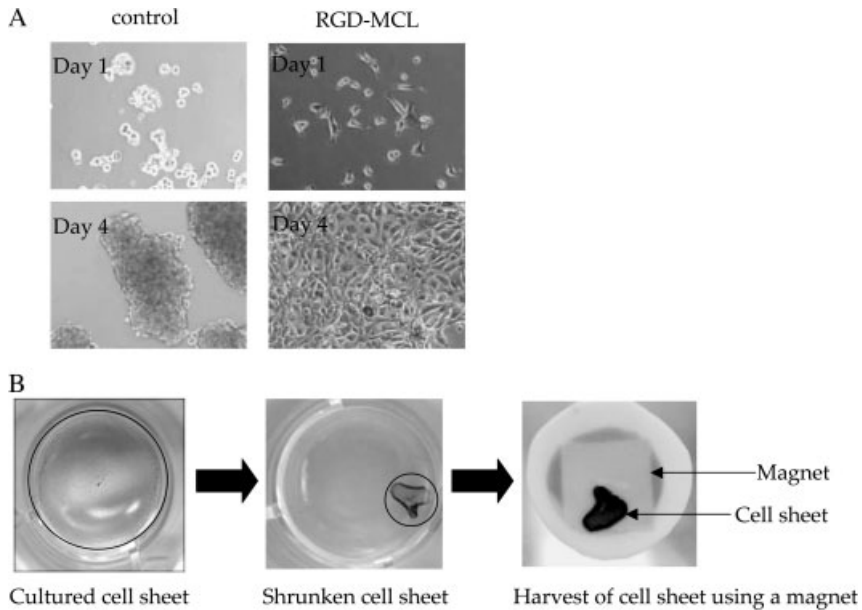


**Fig. 8.9.** (A and B) Formation of cell sheets by Mag-TE using RGD-MCLs.

cells are then seeded into the wells, which are coated with RGD-MCLs, and are then incubated until confluency. The magnet is removed to detach the cell sheets from the well, after which the cell sheets are harvested using a magnet inserted into the well. Figure 8.9 gives a schematic of Mag-TE using RGD-MCLs.

When NIH/3T3 cells, which are anchorage dependent, were cultured in low-attachment plates, the cell number did not change during the 4 day incubation period. For RGD-MCLs, apparent cell proliferation was observed and the cells proliferated to confluency during the 4 day incubation period. Figure 10.8(A) shows photomicrographs of NIH/3T3 cells cultured on the uncoated surface (Control), and that coated with RGD-MCLs for 1 day or 4 days. When the cells were cultured in low-attachment plates, the cells floated in the media and no cells were observed to be attached to the plate. Subsequently, the cells aggregated and formed spheroid constructs on day 4. Conversely, when the cells were cultured on the surface coated with RGD-MCLs, NIH/3T3 cells had adhered and spread by day 1, and had proliferated to confluency by day 4.

The NIH/3T3 cells grown to confluency on RGD-MCLs were subjected to a novel fabricating and harvesting method using a magnet. After 4 days of incubation on RGD-MCLs, the magnet placed on the underside of the low-attachment plate was removed. When the medium was gently pipetted to cause medium flow from the periphery of the cell sheets, the cell sheet detached from the bottom of the plate and shrank, thus resulting in the formation of a contiguous cell sheet-like construct. The cell sheets fabricated by Mag-TE were black-brown due to the magnetite

nanoparticles, and we investigated whether these cell sheets could be harvested using magnets. The cylindrical neodymium magnet positioned on the underside of the low-attachment plate was removed. A hydrophilically treated membrane was pasted to the head of a cylindrical alnico magnet, and the magnet moved into the well toward the surface of the culture medium. Due to the magnetic force, the cell sheets floated up to the surface of the culture medium and without disruption, stuck to the membrane (Fig. 8.9B).

In this study, cell integrin ligand RGD peptides were covalently coupled to cationic liposomes containing magnetite nanoparticles, and we used these RGD-MCLs as a novel biomaterial for tissue engineering. RGD-MCLs have two possible active effects on cell adherence; one is positive charge of the cationic liposomes, and the other is the RGD peptide on their surface. When cells were cultured on the surface of neutrally charged magnetoliposomes, the cells floated in the media and no cells were observed to be attached to the plate. Conversely, cells attached onto the culture surface coated with MCLs, thus suggesting that the positive charge due to cationic liposomes facilitated cell attachment to the culture surface. However, few NIH/3T3 cells spread and proliferated on MCLs. In contrast, when NIH/3T3 cells were cultured on a surface coated with RGD-MCLs, the cells adhered, spread, and proliferated, thus suggesting that RGD peptides strongly promote cell adhesion. These data encourage further development of tissue engineering techniques using magnetite cationic liposomes coupled with cell adhesion peptides, such as KQAGDV (Lys-Gln-Ala-Gly-Asp-Val) peptide for smooth muscle cells [57] and YIGSR (Tyr-Ile-Gly-Ser-Arg) peptide for neurons [58].

In cell sheet engineering, methodologies for handling cell sheets are needed because grafts fabricated by cell sheet engineering are easily damaged by handling. We proposed a novel methodology for handling cell sheets using RGD-MCLs and magnetic force; the Mag-TE method enabled us to handle cell sheet-engineered grafts. Because cell sheets constructed by Mag-TE contain magnetite nanoparticles, NIH/3T3 cell sheets can be recovered and handled using a magnet. This feature is not present in cell sheets produced using other methodologies, such as the use of a PIPAAm-grafted surface. These results also suggest the possibility of developing a “tissue-engineered graft delivery system” using Mag-TE, while Mag-TE could also be applied to industrial tissue engineering because magnetic force could greatly simplify the recovery step of cell sheet production. This recovery step could be automated by substituting the magnet used to harvest cell sheets with an electromagnet, which can immediately release the sheets from the surface of the magnet via electrical control. These findings indicate that RGD-MCLs are potent tools for industrial tissue engineering.

#### 8.4.2

##### **Construction of a Keratinocyte Sheet using MCLs**

The epidermis is one of only a few tissues for which it is possible to culture its principal cell (the keratinocyte) and to use these cultured cells to reconstitute stratified and differentiated human tissue [59, 60]. These skin equivalents have been

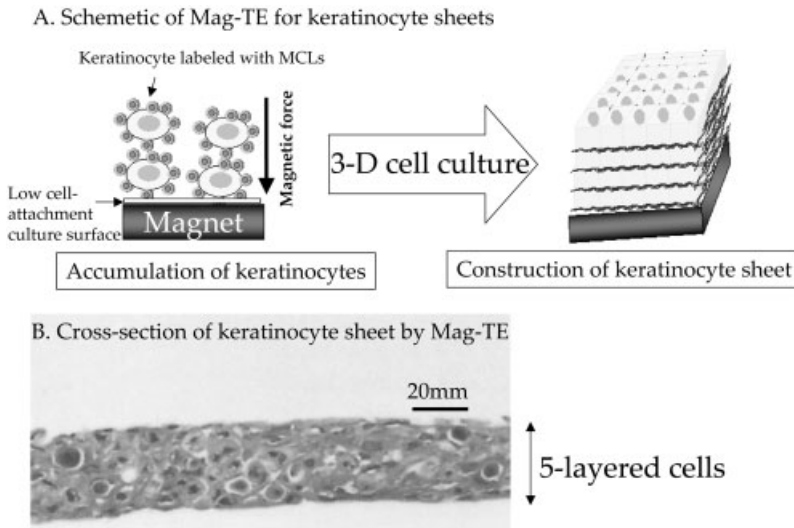


**Fig. 8.10.** (A) Scheme for the construction of a keratinocyte sheet by Mag-TE; (B) cross-section of a keratinocyte sheet so-produced.

used clinically to repair burns and wounds [61, 62]. In this study [63], MCLs were used to label human keratinocytes magnetically, and we investigated whether magnetically labeled keratinocytes could be accumulated using a magnet, and whether stratification is promoted by magnetic force to form a sheet-like 3D construct by Mag-TE (Fig. 8.10A).

In this case, MCLs were added to keratinocytes, to manipulate cells magnetically in a similar way to that described in Section 8.2.1. MCLs-labeled keratinocytes ( $2 \times 10^6$  cells, corresponding to five-fold confluency in 24-well plates) were seeded into 24-well low-attachment plates, to investigate whether five-layered keratinocyte sheets can be constructed by the accumulation of cells by magnetic force. A 30 mm neodymium magnet (4000 G) was placed under the plate. Keratinocytes without MCLs or with MCLs in the absence of a magnet did not attach to the plates. In contrast, keratinocytes labeled with MCLs at  $50 \text{ pg cell}^{-1}$  accumulated on the low-attachment plates in the presence of the magnet. Keratinocytes labeled with MCLs formed a sheet-like construct in the presence of the 30 mm magnet. Phase-contrast microscopy of the cross-sections of the sheets (Fig. 8.10B) revealed that keratinocytes labeled with MCLs formed five-layered sheets.

Notably, when keratinocytes were seeded onto monolayer keratinocytes cultured on tissue culture plates they did not form a sheet-like construct. Moreover, when keratinocytes were seeded onto the low-attachment plates, they did not attach to the surface of the plates and did not form sheets. When protease (trypsin) was used for preparation of keratinocyte suspension, the ECMs may have been digested. As a way to enhance layered cell–cell interactions, we took a physical

approach, using magnetic attraction. Keratinocytes magnetically labeled with MCLs evenly accumulated onto the low-attachment plates in the presence of a magnetic force. Keratinocytes magnetically labeled with  $50 \text{ pg cell}^{-1}$  MCLs formed 5-layered keratinocyte sheets. We speculate that the cell–cell adhesion was caused by the very close placement of cells by the magnetic force.

In our experience, if epithelial sheets fabricated by the method of Rheinwald and Green [64] have five or more cellular layers, they are sufficiently strong for recovery and transplantation [65]. Therefore, in this study, magnetically labeled keratinocytes of five-fold confluency against the culture area were seeded to construct five-layered keratinocytes. As a result, keratinocyte sheets with five layers were constructed. The sheets fabricated by Mag-TE consisted of undifferentiated keratinocytes, which apparently differs from the epidermal sheets fabricated by the method of Rheinwald and Green [64]. To the best of our knowledge, this is the first time that multilayered “undifferentiated” keratinocyte sheets have been constructed. Undifferentiated keratinocytes in keratinocyte sheets produced by Mag-TE may have greater effects on wound healing than cornified and anucleate keratinocytes fabricated by inducing terminal differentiation.

Yamato et al. have reported that thermo-responsive culture dishes grafted with PIPAAm allow the intact harvest of keratinocyte sheets without damage caused by protease (e.g. dispase) treatment [66]. Dispase, a neutral protease from *Bacillus polymyxa*, is widely used to harvest multilayered keratinocyte sheets from culture dishes [67]. In clinical use, extensive washing to remove dispase from keratinocyte sheets is required before they can be applied to wounds, because residual dispase is harmful to the wound site. In industrial production of keratinocyte sheets, this washing is laborious, and is a technological barrier to automation of the process. In our method, we used low-attachment plates, to harvest keratinocytes from the plate without enzymatic treatment after removing the magnet, because the keratinocytes did not adhere to the plate surface. Bioreactors automated for successive culture for epithelial sheet generation have been developed [68, 69]. Because Mag-TE does not require washing of the keratinocyte sheets, which is a laborious step, it allows automation of tissue engineering. Moreover, we used magnetic force to make the recovery step easier, which could aid industrial production of keratinocyte sheets. For automation of this recovery step, the magnet used to harvest keratinocyte sheets may be substituted with an electromagnet, which can release the sheets from the surface of the magnet when switched off. Together, these findings indicate that MCLs are potent tools for industrial engineered-tissue production.

#### 8.4.3

##### **Delivery of Mag-tissue Engineered RPE Sheet**

Age-related macular degeneration (AMD) is an eye disease and a major cause of blindness [70]. The most severe form of AMD is characterized by choroidal neovascularization (CNV), which causes rapid visual loss. When CNV is surgically excised from patients with AMD, the retinal pigment epithelium (RPE) is also removed along with CNV. Since RPE cells play a critical role in assisting photoreceptors in

vision, RPE cell transplantation into the sub-retinal space, from where these cells are surgically excised, is one possible approach [71]. RPE cells in suspension have been injected into the sub-retinal space of animal models and AMD patients. While some success has been achieved in animal models, with recovery of vision [72, 73], the results have been limited in humans [74, 75]. The poor outcomes are due to two major factors; limitations in obtaining autologous RPE cells and difficulty in RPE cell delivery.

Tissue engineering is a possible technology for solving the above-mentioned problems. Conventionally, tissue engineering has been based on two steps: expanding autologous cells *in vitro*, and seeding the cells onto 3D biodegradable scaffolds to reform their native structure [15]. First, a method for cultivating RPE cells from CNV specimens that have been surgically removed from patients with AMD has been developed [76]. The use of autologous RPE cells can overcome immune rejection, and the expansion of RPE cells may resolve donor shortage. Conversely, the use of biodegradable scaffolds poses problems, such as insufficient cell migration into the scaffolds and inflammatory reaction due to the biodegradation of the scaffolds. Particularly for tissue engineering of RPE, since RPE constructs desired for transplantation are of very small size (1–4 mm<sup>2</sup>) and also inflammation is a complicating factor in eye diseases, an autologous cell sheet-like structure without artificial scaffolds may be more suitable. However, since cell–cell interactions are difficult to manipulate, assembly of a 3D cell construct without scaffolds remains a challenge. Moreover, the difficulty faced constructing RPE cell sheets is in the handling of such small tissue-engineered grafts for transplantation. To the best of our knowledge, there are few reports on tissue-engineered graft delivery systems.

In one study [77] we investigated whether RPE cell sheets could be constructed using Mag-TE. Thus, MCLs were used to label RPE cells magnetically, and we investigated whether magnetically labeled RPE cells could be accumulated to form RPE cell sheets, instead of artificial scaffolds, using a magnet. Moreover, since the RPE cell sheets constructed by Mag-TE contained magnetite nanoparticles, we investigated whether these cell sheets could be handled with a magnet, and assessed the feasibility of using a tissue-engineered graft delivery system by Mag-TE *in vitro*.

ARPE-19 cells, used in this study, are a spontaneously arising human RPE cell line with normal karyology [78]. Figure 8.11 illustrates a schematic for the construction and transplantation of RPE cell sheets using MCLs and magnetic force (Mag-TE).

To produce small RPE cell sheets, less than 4 mm<sup>2</sup>, a cloning ring of 2.4 mm caliber (inner area, 4 mm<sup>2</sup>) was used. A cloning ring was placed at the center of a 24-well low-attachment plate and a 22 mm neodymium magnet was placed under the plate. Magnetically labeled ARPE-19 cells ( $8 \times 10^3$  cells mm<sup>-2</sup>, which corresponds to a 10-fold concentration of confluency) were seeded into the cloning ring to investigate whether multilayered RPE cell sheets less than 4 mm<sup>2</sup> can be constructed via accumulation of cells by magnetic force. ARPE-19 cells without MCLs or with MCLs in the absence of the magnet did not form cell sheets, and the cells were dispersed when the cloning ring was removed. In contrast, ARPE-19 cells labeled with MCLs formed an approximately 1 mm<sup>2</sup> sheet-like construct in the



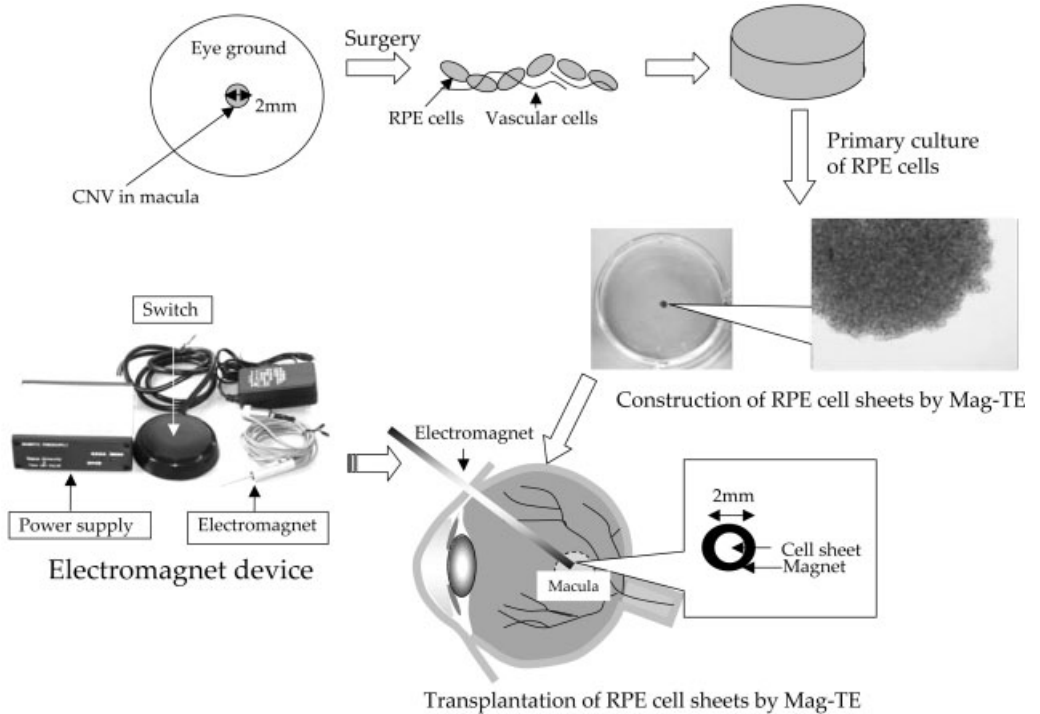


**Fig. 8.11.** Scheme for the construction and transplantation of RPE cell sheets by Mag-TE (the apparatus used is shown on the bottom left of the figure).

presence of a magnet. The cross-sections of the layers revealed that the ARPE-19 cells labeled with MCLs formed 15-layered sheets with a thickness of 60  $\mu\text{m}$  each.

Next, we investigated whether these magnetically labeled RPE cell sheets could be harvested and delivered using a magnet. When the cloning ring and the cylindrical neodymium magnet positioned on the reverse side of the 24-well low-attachment plate were removed, the RPE cell sheets detached from the bottom of the well. As a device for delivery of the magnetically labeled tissue, an iron wire was attached magnetically to the cylindrical neodymium magnet. The magnetic flux density at the tip of the iron wire was 1100 Gauss. The tip of the iron wire was then positioned at the surface of the culture medium. Due to the magnetic force, the RPE cell sheets floated up to the surface of the culture medium without disruption, and stuck to the tip of the iron wire. As a model for transplantation, we investigated whether the RPE cell sheets constructed by Mag-TE could be delivered onto the bottom of the tissue culture dish containing 10 mL of medium. When the magnet was removed from the iron wire and the wire was tapped gently, the cell sheet detached from the tip of wire and sank onto the tissue culture surface. After incubation for 1 day, the cell sheets had attached to the tissue culture dish. Subse-

quently, the cell sheets were further incubated. ARPE-19 cells growing from the cell sheets were observed after a 16 day incubation period, suggesting that the transplanted cells had retained their activity.

The Mag-TE method enabled us to handle the tissue-engineered grafts using magnetic force. We showed that the small RPE cell sheets constructed by Mag-TE could be recovered and delivered using magnetic force. Due to the magnetic force, the RPE cell sheets labeled with MCLs floated up to the surface of the culture medium and stuck to the tip of the iron wire on the magnet. To deliver the RPE cell sheet into the sub-retinal space of AMD patients, the cell sheet must be sufficiently strong so as not to break in the intraocular space, in which a balanced salt solution is added during surgery to adjust intraocular pressure. Furthermore, the cell sheets should not disperse into unintended spaces in the eye during transplantation. In our study, the RPE cell sheets were transplanted into the tissue culture dish containing 10 mL medium, as an *in vitro* model. In this experimental model, the RPE cell sheets were successfully transferred into another dish and released from the tip of iron wire by detaching the magnet and nullifying the magnetic effect of the iron wire. In the near future, we intend to study the feasibility of Mag-TE in animals and clinical trials. Presently, we have developed a tissue delivery device for Mag-TE, which is an electromagnet device that enables on-off control, to manipulate Mag-tissue engineered grafts (Fig. 8.11).

#### 8.4.4

#### **Construction of a Liver-like Structure using MCLs**

Tissues and organs *in vivo* often consist of several types of cell layers. Cell–cell interactions among these layers are important in maintaining the normal physiology of organ systems, such as the vasculature (smooth muscle and endothelial cells [79]), skeletal muscle (myocytes and peripheral nerves [80]), and liver (hepatocytes and sinusoidal endothelial cells [81]). However, cell–cell interactions are difficult to manipulate in co-culture systems with two or more cell types, even in 2D cultures. Moreover, the assembly of 3D tissues containing various cell types remains a challenge.

Heterotypic interactions play a fundamental role in liver function. Since the liver is formed from endodermal foregut and mesenchymal vascular structures, it may be functionally mediated by heterotypic interactions [82, 83]. Liver-specific functions in isolated hepatocytes that require nonparenchymal cells disappear in homotypic cultures [84]. Various 2D co-culture systems of hepatocytes and nonparenchymal cells have been investigated, including those using microfabrication [85] and 2D patterning [86]. However, novel technologies are required to reconstruct the liver to function as it does *in vivo*. This would require a 3D construct containing various types of cells that could thrive beyond the cell type limitations of co-culture. This study [87] uses magnetic force to precisely place magnetically labeled cells onto target cells and to promote heterotypic cell–cell adhesion to form a 3D construct. Here, we magnetically labeled human aortic endothelial cells (HAECs) using MCLs. We then investigated whether the labeled HAECs could be placed onto

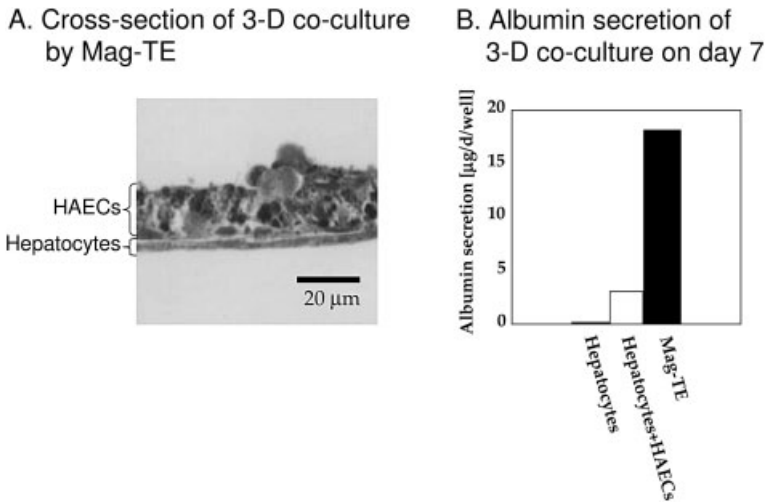


**Fig. 8.12.** (A and B) Construction of liver-like structure by Mag-TE.

a rat hepatocyte layer using magnetic force, and whether magnetic force promotes the adhesion of heterotypic cells.

We seeded  $1.2 \times 10^5$  HAECs (the number of cells required to reach confluence in 24-well cell culture plates) onto hepatocyte monolayers and manipulated a 22 mm magnet to form double cell layers throughout the wells. HAECs labeled or not with MCLs did not attach to hepatocytes in the absence of a magnet. Conversely, in the presence of the magnet, HAECs evenly attached to the hepatocyte layer throughout the wells. The hepatocyte layer expressed albumin under the HAEC monolayer that stained positively with Berlin blue, indicating the presence of MCLs (Fig. 8.12A). We measured hepatic albumin expression to determine cellular function in the layered co-culture system by Mag-TE (Fig. 8.12B). Albumin secretion in homotypic hepatocyte culture was undetectable on day 7. Hepatic albumin secretion was slightly enhanced in co-cultures of HAECs, even when the magnet was not present. Conversely, layered co-cultures in the presence of a magnetic force maintained a high level of albumin secretion on day 7.

Two major difficulties obstruct fabrication of an *in vivo*-like 3D construct for 3D tissue engineering including heterotypic cells. One is non-adherence to heterotypic cells caused by the cell type limitation of co-culture. Okano et al. have developed double layered co-cultures using a thermo-responsive surface of grafted PIPAAm to overcome this difficulty [49–51]. Harimoto et al. [88] reported that whereas trypsinized single endothelial cells do not attach to hepatocytes, endothelial cell sheets fabricated by cell sheet engineering would attach to hepatocyte monolayers. However, the assembly of heterotypic cells into complex tissues such as duct-like constructs also presents a challenging technological barrier, even for cell sheet engineering. Another difficulty is to spatially control the positioning of target cells. Mironov et al. [89] have developed a computer-aided jet-based cell printer that

could place cells at specific sites on thermo-responsive gels, and termed this “organ printing”. This technology seemed to overcome the difficulties with spatial control. However, printed cells can only form monolayers, which must be stratified layer-by-layer to assemble 3D organs. Here, we developed a new method using magnetite nanoparticles and magnetic force, which we refer to as Mag-TE, to overcome these difficulties.

Co-culture systems with nonparenchymal cells maintain hepatocyte functions for long periods [90–92]. To examine the feasibility of the layered co-culture system using magnetic force, we used the liver model of hepatocytes and endothelial cells. We seeded  $1.2 \times 10^5$  HAECs, which corresponds to the number at confluence in 24-well cell culture plates, onto hepatocyte monolayers and positioned a 22 mm magnet that could apply 4000 G uniformly throughout the plates. This caused an almost uniform upper layer of HAECs. Albumin secretion by hepatocytes was enhanced in this double-layered co-culture system. The precise mechanisms that regulate increases in liver-specific function in hepatocyte co-cultures have not been elucidated. Bhandari et al. [93] have reported that 3T3 fibroblast cells persist in co-cultures with hepatocytes, but 3T3 cell conditioned medium could not substitute for viable co-cultured 3T3 cells in preserving hepatocyte function, suggesting that cell–cell interaction is essential for modulating hepatocyte functions. Potential mediators of cell–cell interactions include soluble factors such as cytokines [94] and insoluble cell-associated factors such as ECMs [95]. We surmise that the tight and close interaction of overlaying HAECs and monolayer hepatocytes using magnetic force caused ECMs and cytokines to be deposited between the layers, thus powerfully enhancing liver function. In contrast, cellular interaction was very weak in co-cultures without the magnetic force and HAECs hardly attached to the hepatocytes. The mechanism by which close cell–cell distance enhances cell to cell interaction, such as gap junction formation, remains to be elucidated.

#### 8.4.5

#### **Construction of Tubular Structures using MCLs**

Tissues and organs *in vivo* have unique shapes, and are often composed of several types of cell layers required to maintain the normal physiology of organ systems. In one study [96] we investigated whether we could use Mag-TE to form tubular structures such as ureters (which consist of monotypic urothelial cell layers) and blood vessels (which consist of heterotypic layers of aortic endothelial cells, smooth muscle cells, and fibroblasts).

First of all, Mag-tissue engineered cell sheets were constructed. After incubation with MCLs, human aortic endothelial cells (ECs), human aortic smooth muscle cells (SMCs), mouse NIH/3T3 fibroblasts (FBs), or canine urothelial cells (UCs) were seeded into low-attachment plates. A cylindrical neodymium magnet (diameter, 30 mm; magnetic induction, 4000 G) was then placed on the reverse side of the low-attachment plates to provide magnetic force vertical to the plate, and the cells were cultured for 24 h. Figure 8.13(A) illustrates the procedure used to construct tubular structures. A cylindrical magnet with magnetic poles on its curved surface

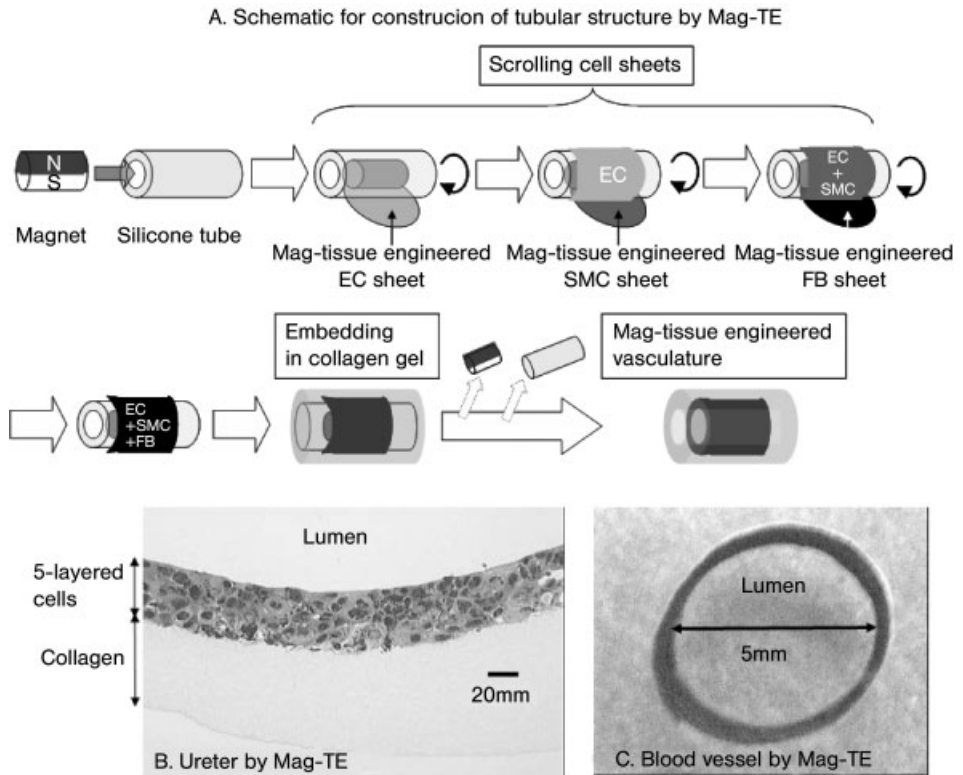


**Fig. 8.13.** (A) Scheme for the construction of tubular structures by Mag-TE. (B and C) Ureter and blood vessel, respectively, produced by Mag-TE.

was used (diameter, 3 mm; length, 10 mm; magnetic induction, 1300 G). The magnet was inserted into a silicone tube (outer diameter, 5 mm; inner diameter, 3 mm; length, 25 mm). The 5 mm outer diameter was chosen to construct small-diameter blood vessels (inner diameter, <6 mm). The cylindrical magnet in the silicone tube was then rolled over the magnetically labeled cell sheet. To construct a tissue-engineered ureter, a UC sheet only was used. To construct a blood vessel, an EC sheet was used first, followed by addition of an SMC sheet and an FB sheet. Collagen was injected and allowed to gelate around the cell sheets, to support the cell constructs.

When the cylindrical magnet in the silicone tube was rolled over the magnetically labeled UC sheet, UCs were attracted onto the silicone tube by magnetic force. UCs ultimately covered the entire surface of the silicone tube. The sheets formed from ECs, SMCs and FBs in the construction of blood vessels were thicker than the UC sheets. When the silicone tube and magnet were removed, we obtained tubular constructs of tissue engineered urothelial and vascular tissue. Histo-

logical observation revealed that the constructed urothelial and vascular tissues formed contiguous tubular structures with a lumen of 5 mm; Fig. 8.13(C) shows a macroscopic view of the vascular tissue. The urothelial structure consisted of five- to seven-layer monotypic urothelial tissue that formed on the collagen gel (Fig. 8.13B).

In this study, for the construction of magnetically labeled cell sheets using magnetic force, four types of cells (UCs, ECs, SMCs, FBs) were used. In general, it is difficult to fabricate 3D tissue constructs without using 3D scaffolds, due to the lack of cell adherence via cell–cell junctions, particularly in the vertical direction. We developed a novel methodology for fabrication of cell sheets, which we have termed “Mag-TE”.

For clinical applications, tubular constructs of urothelial and vascular tissue can be cultured for long periods in tubular tissue-oriented bioreactors, such as those that provide biomechanical stimuli similar to those that occur *in vivo* [97–99], to induce these cells to express differentiated phenotypes. For cultivation using bioreactors, because the tubular tissues constructed by Mag-TE contain a sufficient amount of suitably placed cells, culturing for cell proliferation may not be required. Consequently, only culturing for expression of differentiated phenotypes and deposition of ECMs (e.g., collagens and elastins of vascular tissues [100]) would be required. This suggests that use of tubular constructs created using Mag-TE can shorten the culture period required before treatment. In this study, collagen gel was used as a support to reinforce the mechanical strength of tubular tissue constructed by Mag-TE; there has been no quantitative analysis of the mechanical properties of such tissue constructs. Several groups are working to improve the mechanical properties of collagen-gel-based vascular grafts. Control of collagen gel fibril orientation has been investigated in an effort to maximize the mechanical strength of collagen-gel-based scaffolds [101, 102].

## 8.5

### Conclusion

In this chapter, we have only been able to highlight magnetic nanoparticles and Mag-TE as “metallic nanoparticles for tissue engineering”. These techniques for tissue engineering are based on biochemical engineering, cell biology, magnetism, nanotechnology, and many other scientific fields. Currently, magnetic techniques complement other methods presently used in medical applications, and this combination therapy should result in more effective medical treatment, including tissue engineering and regenerative medicine. Greater understanding of the properties of magnetic particles will increase their potential for medical application.

When considering the use of metallic nanoparticles, toxicity is an important issue in clinical applications. For magnetite nanoparticles, no toxic effects against proliferation of several cell types were observed within the range of magnetite concentrations tested (e.g., human keratinocytes, <50-pg magnetite/cell; human endothelial cells, human smooth muscle cells, mouse fibroblast cells, canine urothelial

cells, human mesenchymal stem cells [MSCs],  $<100 \text{ pg cell}^{-1}$ ), and no effect on the differentiation of MSCs was observed. Moreover, in a preliminary study [103], we investigated the toxicity of systemically administered MCLs (90 mg, i.p.) in mice; none of the 10 mice injected with MCLs died during the study. Transient accumulation of magnetite was observed in the liver and spleen of the mice, but the magnetite nanoparticles had been cleared from circulation by hepatic Kupffer cells and/or fixed macrophages in the spleen by the 10th day after administration [103]. However, further study is required to assess the toxicity of residual magnetic nanoparticles in grafts before Mag-TE can be used for clinical applications.

## References

- GUPTA, A.K., GUPTA, M. Synthesis and surface engineering of iron oxide nanoparticles for biomedical applications. *Biomaterials*, **2005**, *26*, 3995–4021.
- SHINKAI, M., ITO, A. Functional magnetic particles for medical application. *Adv. Biochem. Eng. Biotechnol.* **2004**, *91*, 191–220.
- LUBBE, A.S., ALEXIOU, C., BERGEMANN, C. Clinical applications of magnetic drug targeting. *J. Surg. Res.* **2001**, *95*, 200–206.
- DUNNILL, P., LILLY, M.D. Letter: Purification of enzymes using magnetic bio-affinity materials. *Biotechnol. Bioeng.* **1974**, *16*, 987–990.
- MOSBACH, K., ANDERSSON, L. Magnetic ferrofluids for preparation of magnetic polymers and their application in affinity chromatography. *Nature* **1977**, *270*, 259–261.
- SAFARIK, I., SAFARIKOVA, M. Magnetic techniques for the isolation and purification of proteins and peptides. *Biomagn. Res. Technol.* **2004**, *2*, 7.
- DAVID, R., GROEBNER, M., FRANZ, W.M. Magnetic cell sorting purification of differentiated embryonic stem cells stably expressing truncated human CD4 as surface marker. *Stem Cells* **2005**, *23*, 477–482.
- HÄFELI, U., SHÜTT, W., TELLER, J., ZBOROWSKI, M. *Scientific and Clinical Applications of Magnetic Carriers*, Plenum Publishing Corporation, New York, **1997**.
- SHINKAI, M., YANASE, M., HONDA, H., WAKABAYASHI, T., YOSHIDA, J., KOBAYASHI, T. Intracellular hyperthermia for cancer using magnetite cationic liposomes: in vitro study. *Jpn. J. Cancer Res.* **1996**, *87*, 1179–1183.
- YANASE, M., SHINKAI, M., HONDA, H., WAKABAYASHI, T., YOSHIDA, J., KOBAYASHI, T. Intracellular hyperthermia for cancer using magnetite cationic liposomes: An in vivo study. *Jpn. J. Cancer Res.* **1998**, *89*, 463–469.
- ITO, A., TANAKA, K., KONDO, K., SHINKAI, M., HONDA, H., MATSUMOTO, K., SAIDA, T., KOBAYASHI, T. Tumor regression by combined immunotherapy and hyperthermia using magnetic nanoparticles in an experimental subcutaneous murine melanoma. *Cancer Sci.* **2003**, *94*, 308–313.
- LE, B., SHINKAI, M., KITADE, T., HONDA, H., YOSHIDA, J., WAKABAYASHI, T., KOBAYASHI, T. Preparation of tumor-specific magnetoliposomes and their application for hyperthermia. *J. Chem. Eng. Jpn.* **2001**, *34*, 66–72.
- SHINKAI, M., LE, B., HONDA, H., YOSHIKAWA, K., SHIMIZU, K., SAGA, S., WAKABAYASHI, T., YOSHIDA, J., KOBAYASHI, T. Targeting hyperthermia for renal cell carcinoma using human MN antigen-specific magnetoliposomes. *Jpn. J. Cancer Res.* **2001**, *92*, 1138–1145.
- ITO, A., KUGA, Y., HONDA, H., KIKKAWA, H., HORIUCHI, A.,

- WATANABE, Y., KOBAYASHI, T. Magnetite nanoparticle-loaded anti-HER2 immunoliposomes for combination of antibody therapy with hyperthermia. *Cancer Lett.* **2004**, *212*, 167–175.
- 15 LANGER, R., VACANTI, J.P. Tissue engineering. *Science* **1993**, *260*, 920–926.
- 16 PITTENGER, M.F., MACKAY, A.M., BECK, S.C., JAISWAL, R.K., DOUGLAS, R., MOSCA, J.D., MOORMAN, M.A., SIMONETTI, D.W., CRAIG, S., MARSHAK, D.R. Multilineage potential of adult human mesenchymal stem cells. *Science* **1999**, *284*, 143–147.
- 17 MAKINO, S., FUKUDA, K., MIYOSHI, S., KONISHI, F., KODAMA, H., PAN, J., SANO, M., TAKAHASHI, T., HORI, S., ABE, H., HATA, J., UMEZAWA, A., OGAWA, S. Cardiomyocytes can be generated from marrow stromal cells in vitro. *J. Clin. Invest.* **1999**, *103*, 697–705.
- 18 DEANS, R.J., MOSELEY, A.B. Mesenchymal stem cells: biology and potential clinical uses. *Exp. Hematol.* **2000**, *28*, 875–884.
- 19 KOPEN, G.C., PROCKOP, D.J., PHINNEY, D.G. Marrow stromal cells migrate throughout forebrain and cerebellum, and they differentiate into astrocytes after injection into neonatal mouse brains. *Proc. Natl. Acad. Sci. U.S.A.* **1999**, *96*, 10711–10716.
- 20 FRIEDENSTEIN, A.J., GORSKAJA, J.F., KULAGINA, N.N. Fibroblast precursors in normal and irradiated mouse hematopoietic organs. *Exp. Hematol.* **1976**, *4*, 267–274.
- 21 MARUYAMA, Y., TOHDA, S., NAGATA, K., SUZUKI, T., MUROHASHI, I., NARA, N. Role of humoral and cellular factors on the growth of blast progenitors of acute myeloblastic leukemia in serum-free culture. *Hematol. Pathol.* **1990**, *4*, 115–123.
- 22 REILLY, I.A., KOZLOWSKI, R., RUSSELL, N.H. The role of cell contact and autostimulatory soluble factors in the proliferation of blast cells in acute myeloblastic leukemia. *Leukemia* **1989**, *3*, 145–150.
- 23 GLOECKNER, H., LEMKE, H.D. New miniaturized hollow-fiber bioreactor for in vivo like cell culture, cell expansion, and production of cell-derived products. *Biotechnol. Progr.* **2001**, *17*, 828–831.
- 24 KIMURA, A., KATO, O., HYODO, H., KUSUMI, S., KURAMOTO, A. Autocrine and/or paracrine mechanism operate during the growth of human bone marrow fibroblasts. *Br. J. Haematol.* **1991**, *78*, 469–473.
- 25 EHMANN, U.K., TERRIS, M.K. Juxtacrine stimulation of normal and malignant human bladder epithelial cell proliferation. *J. Urol.* **2002**, *167*, 735–741.
- 26 NAGATANI, N., SHINKAI, M., HONDA, H., KOBAYASHI, T. Development of a new transformation method using magnetite cationic liposomes and magnetic selection of transformed cells. *Biotechnol. Techniques* **1998**, *12*, 525–528.
- 27 TANAKA, K., ITO, A., KOBAYASHI, T., KAWAMURA, T., SHIMADA, S., MATSUMOTO, K., SAIDA, T., HONDA, H. Intratumoral injection of immature dendritic cells enhances antitumor effect of hyperthermia using magnetic nanoparticles. *Int. J. Cancer* **2005**, *116*, 624–633.
- 28 ITO, A., MATSUOKA, F., HONDA, H., KOBAYASHI, T. Heat shock protein 70 gene therapy combined with hyperthermia using magnetic nanoparticles. *Cancer Gene Ther.* **2003**, *10*, 918–925.
- 29 ITO, A., MATSUOKA, F., HONDA, H., KOBAYASHI, T. Antitumor effects of combined therapy of recombinant heat shock protein 70 and hyperthermia using magnetic nanoparticles in an experimental subcutaneous murine melanoma. *Cancer Immunol. Immunother.* **2004**, *53*, 26–32.
- 30 ITO, A., SHINKAI, M., HONDA, H., YOSHIKAWA, K., SAGA, S., WAKABAYASHI, T., YOSHIDA, J., KOBAYASHI, T. Heat shock protein 70 expression induces antitumor immunity during intracellular hyperthermia using magnetite nanoparticles. *Cancer Immunol. Immunother.* **2003**, *52*, 80–88.



- 31 ITO, A., SHINKAI, M., HONDA, H., KOBAYASHI, T. Heat-inducible TNF- $\alpha$  gene therapy combined with hyperthermia using magnetic nanoparticles as a novel tumor-targeted therapy. *Cancer Gene Ther.* **2001**, *8*, 649–654.
- 32 ITO, A., HIBINO, E., HONDA, H., HATA, K., KAGAMI, H., UEDA, M., KOBAYASHI, T. A new methodology of mesenchymal stem cell expansion using magnetic nanoparticles. *Biochem. Eng. J.* **2004**, *20*, 119–125.
- 33 TSUTSUMI, S., SHIMAZU, A., MIYAZAKI, K., PAN, H., KOIKE, C., YOSHIDA, E., TAKAGISHI, K., KATO, Y. Retention of multilineage differentiation potential of mesenchymal cells during proliferation in response to FGF. *Biochem. Biophys. Res. Commun.* **2001**, *288*, 413–419.
- 34 HUSS, R., HOY, C.A., DEEG, H.J. Contact- and growth factor-dependent survival in a canine marrow-derived stromal cell line. *Blood* **1995**, *85*, 2414–2421.
- 35 GREGORY, C.A., SINGH, H., PERRY, A.S., PROCKOP, D.J. The Wnt signaling inhibitor dickkopf-1 is required for reentry into the cell cycle of human adult stem cells from bone marrow. *J. Biol. Chem.* **2003**, *278*, 28 067–28 078.
- 36 BARRY, F.P., BOYNTON, R.E., HAYNESWORTH, S., MURPHY, J.M., ZAIA, J. The monoclonal antibody SH-2, raised against human mesenchymal stem cells, recognizes an epitope on endoglin (CD105). *Biochem. Biophys. Res. Commun.* **1999**, *265*, 134–139.
- 37 HAYNESWORTH, S.E., BABER, M.A., CAPLAN, A.I. Cell surface antigens on human marrow-derived mesenchymal cells are detected by monoclonal antibodies. *Bone* **1992**, *13*, 69–80.
- 38 QUIRICI, N., SOLIGO, D., BOSSOLASCO, P., SERVIDA, F., LUMINI, C., DELLIERS, G.L. Isolation of bone marrow mesenchymal stem cells by anti-nerve growth factor receptor antibodies. *Exp. Hematol.* **2002**, *30*, 783–791.
- 39 ITO, A., HIBINO, E., SHIMIZU, K., KOBAYASHI, T., YAMADA, Y., HIBI, H., UEDA, M., HONDA, H. Magnetic force-based mesenchymal stem cell expansion using antibody-conjugated magnetoliposomes. *J. Biomed. Mater. Res. B Appl. Biomater.* **2005**, *75*, 320–327.
- 40 FREED, L.E., LANGER, R., MARTIN, I., PELLIS, R.R., VUNJAK-NOVAKOVIC, G. Tissue engineering of cartilage in space. *Proc. Natl. Acad. Sci. U.S.A.* **1997**, *94*, 13 885–13 890.
- 41 HOLY, C.E., SHOICHET, M.S., DAVIES, J.E. Engineering three-dimensional bone tissue in vitro using biodegradable scaffolds: Investigating initial cell seeding density and culture period. *J. Biomed. Mater. Res.* **2000**, *51*, 376–382.
- 42 CARRIER, R.L., PAPADAKI, M., RUPNICK, M., SCHOEN, F.J., BURSAC, N., LANGER, R., FREED, L.E., VUNJAK-NOVAKOVIC, G. Cardiac tissue engineering: cell seeding, cultivation parameters, and tissue construct characterization. *Biotechnol. Bioeng.* **1999**, *64*, 580–589.
- 43 KIM, B.S., PUTNAM, A.J., KULIK, T.J., MOONEY, D.J. Optimizing seeding and culture methods to engineer smooth muscle tissue on biodegradable polymer matrices. *Biotechnol. Bioeng.* **1998**, *57*, 46–54.
- 44 BRUININK, A., SIRAGUSANO, D., ETEEL, G., BRANDSBERG, T., BRANDSBERG, F., PETITMERMET, M., MULLER, B., MAYER, J., WINTERMANTEL, E. The stiffness of bone marrow cell-knit composites is increased during mechanical load. *Biomaterials* **2001**, *22*, 3169–3178.
- 45 LI, Y., MA, T., KNISS, D.A., LASKY, L.C., YANG, S.T. Effects of filtration seeding on cell density, spatial distribution, and proliferation in nonwoven fibrous matrices. *Biotechnol. Progr.* **2001**, *17*, 935–944.
- 46 XIAO, Y.L., RIESLE, J., VAN BLITTERSWIJK, C.A. Static and dynamic fibroblast seeding and cultivation in porous PEO/PBT scaffolds. *J. Mater. Sci. Mater. Med.* **1999**, *10*, 773–777.
- 47 VUNJAK-NOVAKOVIC, G., RADISIC, M. Cell seeding of polymer scaffolds. *Methods Mol. Biol.* **2004**, *238*, 131–146.
- 48 SHIMIZU, K., ITO, A., HONDA, H.

- Enhancement of cell-seeding efficiency into 3D porous scaffolds by magnetic force for tissue engineering. *J. Biomed. Mater. Res. B Appl. Biomater.* **2006**, *77*, 265–272.
- 49 HIROSE, M., YAMATO, M., KWON, O.H., HARIMOTO, M., KUSHIDA, A., SHIMIZU, T., KIKUCHI, A., OKANO, T. Temperature-responsive surface for novel co-culture systems of hepatocytes with endothelial cells: 2-D patterned and double layered co-cultures. *Yonsei Med. J.* **2000**, *41*, 803–813.
- 50 SHIMIZU, T., YAMATO, M., ISOI, Y., AKUTSU, T., SETOMARU, T., ABE, K., KIKUCHI, A., UMEZU, M., OKANO, T. Fabrication of pulsatile cardiac tissue grafts using a novel 3-dimensional cell sheet manipulation technique and temperature-responsive cell culture surfaces. *Circ. Res.* **2002**, *90*, 40–48.
- 51 SHIMIZU, T., YAMATO, M., KIKUCHI, A., OKANO, T. Cell sheet engineering for myocardial tissue reconstruction. *Biomaterials* **2003**, *24*, 2309–2316.
- 52 KUSHIDA, A., YAMATO, M., KONNO, C., KIKUCHI, A., SAKURAI, Y., OKANO, T. Decrease in culture temperature releases monolayer endothelial cell sheets together with deposited fibronectin matrix from temperature-responsive culture surfaces. *J. Biomed. Mater. Res.* **1999**, *45*, 355–362.
- 53 RUOSLAHTI, E., PIERSCHBACHER, M.D. New perspectives in cell adhesion: RGD and integrins. *Science* **1987**, *238*, 491–497.
- 54 PIERSCHBACHER, M.D., RUOSLAHTI, E. Cell attachment activity of fibronectin can be duplicated by small synthetic fragments of the molecule. *Nature* **1984**, *309*, 30–33.
- 55 ITO, A., INO, K., KOBAYASHI, T., HONDA, H. The effect of RGD peptide-conjugated magnetite cationic liposomes on cell growth and cell sheet harvesting. *Biomaterials* **2005**, *26*, 6185–6193.
- 56 GYONGYOSSY-ISSA, M.I., MULLER, W., DEVINE, D.V. The covalent coupling of Arg-Gly-Asp-containing peptides to liposomes: purification and biochemical function of the lipopeptide. *Arch. Biochem. Biophys.* **1998**, *353*, 101–108.
- 57 MANN, B.K., WEST, J.L. Cell adhesion peptides alter smooth muscle cell adhesion, proliferation, migration, and matrix protein synthesis on modified surfaces and in polymer scaffolds. *J. Biomed. Mater. Res.* **2002**, *60*, 86–93.
- 58 SANEINEJAD, S., SHOICHET, M.S. Patterned glass surfaces direct cell adhesion and process outgrowth of primary neurons of the central nervous system. *J. Biomed. Mater. Res.* **1998**, *42*, 13–19.
- 59 YANNAS, I.V., BURKE, J.F., ORGILL, D.P., SKRABUT, E.M. Wound tissue can utilize a polymeric template to synthesize a functional extension of skin. *Science* **1982**, *215*, 174–176.
- 60 BELL, E., EHRLICH, H.P., BUTTLE, D.J., NAKATSUJI, T. Living tissue formed in vitro and accepted as skin-equivalent tissue of full thickness. *Science* **1981**, *211*, 1052–1054.
- 61 HANSBROUGH, J.F., BOYCE, S.T., COOPER, M.L., FOREMAN, T.J. Burn wound closure with cultured autologous keratinocytes and fibroblasts attached to a collagen-glycosaminoglycan substrate. *JAMA* **1989**, *262*, 2125–2130.
- 62 FALANGA, V., MARGOLIS, D., ALVAREZ, O., AUULETTA, M., MAGGIACOMO, F., ALTMAN, M., JENSEN, J., SABOLINSKI, M., HARDIN-YOUNG, J. Rapid healing of venous ulcers and lack of clinical rejection with an allogeneic cultured human skin equivalent. Human skin equivalent investigators group. *Arch. Dermatol.* **1998**, *134*, 293–300.
- 63 ITO, A., HAYASHIDA, M., HONDA, H., HATA, K., KAGAMI, H., UEDA, M., KOBAYASHI, T. Construction and harvest of multilayered keratinocyte sheets using magnetite nanoparticles and magnetic force. *Tissue Eng.* **2004**, *10*, 873–880.
- 64 RHEINWALD, J.G., GREEN, H. Serial cultivation of strains of human epidermal keratinocytes: The formation of keratinizing colonies from single cells. *Cell* **1975**, *6*, 331–343.

- 65 HATA, K., KAGAMI, H., UEDA, M., TORII, S., MATSUYAMA, M. The characteristics of cultured mucosal cell sheet as a material for grafting; comparison with cultured epidermal cell sheet. *Ann. Plast. Surg.* **1995**, *34*, 530–538.
- 66 YAMATO, M., UTSUMI, M., KUSHIDA, A., KONNO, C., KIKUCHI, A., OKANO, T. Thermo-responsive culture dishes allow the intact harvest of multi-layered keratinocyte sheets without disperse by reducing temperature. *Tissue Eng.* **2001**, *7*, 473–480.
- 67 GREEN, H., KEHINDE, O., THOMAS, J. Growth of cultured human epidermal cells into multiple epithelia suitable for grafting. *Proc. Natl. Acad. Sci. U.S.A.* **1979**, *76*, 5665–5668.
- 68 KINO-OKA, M., UMEGAKI, R., TAYA, M., TONE, S., PRENOSIL, J.E. Valuation of growth parameters in monolayer keratinocyte culture based on a two-dimensional cell placement model. *J. Biosci. Bioeng.* **2000**, *89*, 285–287.
- 69 UMEGAKI, R., MURAI, K., KINO-OKA, M., TAYA, M. Correlation of cellular life span with growth parameters observed in successive cultures of human keratinocytes. *J. Biosci. Bioeng.* **2002**, *94*, 231–236.
- 70 LEE, P., WANG, C.C., ADAMIS, A.P. Ocular neovascularization: An epidemiologic review. *Surv. Ophthalmol.* **1998**, *43*, 245–269.
- 71 BOULTON, M., ROANOWSKA, M., WESS, T. Ageing of the retinal pigment epithelium: Implications for transplantation. *Graefes Arch. Clin. Exp. Ophthalmol.* **2004**, *242*, 76–84.
- 72 GOURAS, P., KONG, J., TSANG, S.H. Retinal degeneration and RPE transplantation in Rpe65(–/–) mice. *Invest. Ophthalmol. Vis. Sci.* **2002**, *43*, 3307–3311.
- 73 LUND, R.D., ADAMSON, P., SAUVE, Y., KEEGAN, D.J., GIRMAN, S.V., WANG, S., WINTON, H., KANUGA, N., KWAN, A.S., BEAUCHENE, L., ZERBIB, A., HETHERINGTON, L., COURAUD, P.O., COFFEY, P., GREENWOOD, J. Subretinal transplantation of genetically modified human cell lines attenuates loss of visual function in dystrophic rats. *Proc. Natl. Acad. Sci. U.S.A.* **2001**, *98*, 9942–9947.
- 74 ALGVERE, P.V., GOURAS, P., DAFGARD KOPP, E. Long-term outcome of RPE allografts in non-immunosuppressed patients with AMD. *Eur. J. Ophthalmol.* **1999**, *9*, 217–230.
- 75 BINDER, S., STOLBA, U., KREBS, I., KELLNER, L., JAHN, C., FEICHTINGER, H., POVELKA, M., FROHNER, U., KRUGER, A., HILGERS, R.D., KRUGLUGER, W. Transplantation of autologous retinal pigment epithelium in eyes with foveal neovascularization resulting from age-related macular degeneration: a pilot study. *Am. J. Ophthalmol.* **2002**, *133*, 215–225.
- 76 SCHLUNCK, G., MARTIN, G., AGOSTINI, H.T., CAMATTA, G., HANSEN, L.L. Cultivation of retinal pigment epithelial cells from human choroidal neovascular membranes in age related macular degeneration. *Exp. Eye Res.* **2002**, *74*, 571–576.
- 77 ITO, A., HIBINO, E., KOBAYASHI, C., TERASAKI, H., KAGAMI, H., UEDA, M., KOBAYASHI, T., HONDA, H. Construction and delivery of tissue-engineered human retinal pigment epithelial cell sheets, using magnetic nanoparticles and magnetic force. *Tissue Eng.* **2005**, *11*, 489–496.
- 78 DUNN, K.C., AOTAKI-KEEN, A.E., PUTKEY, F.R., HJELMELAND, L.M. ARPE-19, a human retinal pigment epithelial cell line with differentiated properties. *Exp. Eye Res.* **1996**, *62*, 155–169.
- 79 FILLINGER, M.F., O'CONNOR, S.E., WAGNER, R.J., CRONENWETT, J.L. The effect of endothelial cell coculture on smooth muscle cell proliferation. *J. Vasc. Surg.* **1993**, *17*, 1058–1067.
- 80 STREIT, J. Mechanisms of pattern generation in co-cultures of embryonic spinal cord and skeletal muscle. *Int. J. Dev. Neurosci.* **1996**, *14*, 137–148.
- 81 GUGUEN-GUILLOUZO, C., CLEMENT, B., BAFFET, G., BEAUMONT, C., MOREL-CHANY, E., GLAISE, D., GUILLOUZO, A. Maintenance and reversibility of active albumin secretion by adult rat hepatocytes co-cultured with another

- liver epithelial cell type. *Exp. Cell Res.* **1983**, 143, 47–54.
- 82 HOUSSAINT, E. Differentiation of the mouse hepatic primordium. I. An analysis of tissue interactions in hepatocyte differentiation. *Cell Differ.* **1980**, 9, 269–279.
- 83 DOUARIN, N.M. An experimental analysis of liver development. *Med. Biol.* **1975**, 53, 427–455.
- 84 BHATIA, S.N., BALIS, U.J., YARMUSH, M.L., TONER, M. Effect of cell-cell interactions in preservation of cellular phenotype: Cocultivation of hepatocytes and nonparenchymal cells. *FASEB J.* **1999**, 13, 1883–1900.
- 85 BHATIA, S.N., YARMUSH, M.L., TONER, M. Controlling cell interactions by micropatterning in co-cultures: Hepatocytes and 3T3 fibroblasts. *J. Biomed. Mater. Res.* **1997**, 34, 189–199.
- 86 YAMATO, M., KWON, O.H., HIROSE, M., KIKUCHI, A., OKANO, T. Novel patterned cell coculture utilizing thermally responsive grafted polymer surfaces. *J. Biomed. Mater. Res.* **2001**, 55, 137–140.
- 87 ITO, A., TAKIZAWA, Y., HONDA, H., HATA, K., KAGAMI, H., UEDA, M., KOBAYASHI, T. Tissue engineering using magnetite nanoparticles and magnetic force: Heterotypic layers of cocultured hepatocytes and endothelial cells. *Tissue Eng.* **2004**, 10, 833–840.
- 88 HARIMOTO, M., YAMATO, M., HIROSE, M., TAKAHASHI, C., ISOI, Y., KIKUCHI, A., OKANO, T. Novel approach for achieving double-layered cell sheets co-culture: Overlaying endothelial cell sheets onto monolayer hepatocytes utilizing temperature-responsive culture dishes. *J. Biomed. Mater. Res.* **2002**, 62, 464–470.
- 89 MIRONOV, V., BOLAND, T., TRUSK, T., FORGACS, G., MARKWALD, R.R. Organ printing: Computer-aided jet-based 3D tissue engineering. *Trends Biotechnol.* **2003**, 21, 157–161.
- 90 GREGORY, P.G., CONNOLLY, C.K., GILLIS, B.E., SULLIVAN, S.J. The effect of coculture with nonparenchymal cells on porcine hepatocyte function. *Cell Transplant.* **2001**, 10, 731–738.
- 91 SHIMAOKA, S., NAKAMURA, T., ICHIHARA, A. Stimulation of growth of primary cultured adult rat hepatocytes without growth factors by coculture with nonparenchymal liver cells. *Exp. Cell Res.* **1987**, 172, 228–242.
- 92 VILLAFUERTE, B.C., KOOP, B.L., PAO, C.I., GU, L., BIRDSONG, G.G., PHILLIPS, L.S. Coculture of primary rat hepatocytes and nonparenchymal cells permits expression of insulin-like growth factor binding protein-3 in vitro. *Endocrinology* **1994**, 134, 2044–2050.
- 93 BHANDARI, R.N., RICCALTON, L.A., LEWIS, A.L., FRY, J.R., HAMMOND, A.H., TENDLER, S.J., SHAKESHEFF, K.M. Liver tissue engineering: A role for co-culture systems in modifying hepatocyte function and viability. *Tissue Eng.* **2001**, 7, 345–357.
- 94 MORIN, O., GOULET, F., NORMAND, G. Liver sinusoidal endothelial cells: Isolation, purification, characterization and interaction with hepatocytes. In: *Cell Biology Reviews*, MORIN, O., GOULET, F., NORMAND, G. (Eds.), Springer International, New York. **1988**, Vol. 15, pp. 1–73.
- 95 GOULET, F., NORMAND, C., MORIN, O. Cellular interactions promote tissue-specific function, biomatrix deposition and junctional communication of primary cultured hepatocytes. *Hepatology* **1988**, 8, 1010–1008.
- 96 ITO, A., INO, K., HAYASHIDA, M., KOBAYASHI, T., MATSUNUMA, H., KAGAMI, H., UEDA, M., HONDA, H. A novel methodology for fabrication of tissue-engineered tubular constructs using magnetite nanoparticles and magnetic force. *Tissue Eng.* **2005**, 11, 1553–1561.
- 97 NIKLASON, L.E., GAO, J., ABBOTT, W.M., HIRSCHI, K.K., HOUSER, S., MARINI, R., LANGER, R. Functional arteries grown in vitro. *Science* **1999**, 284, 489–493.
- 98 NARITA, Y., HATA, K., KAGAMI, H., USUI, A., UEDA, M., UEDA, Y. Novel pulse duplicating bioreactor system for tissue-engineered vascular construct. *Tissue Eng.* **2004**, 10, 1224–1233.
- 99 SODIAN, R., LEMKE, T., FRITSCH, C.,

- HOERSTRUP, S.P., FU, P., POTAPOV, E.V., HAUSMANN, H., HETZER, R. Tissue-engineering bioreactors: a new combined cell-seeding and perfusion system for vascular tissue engineering. *Tissue Eng.* **2002**, *8*, 863–870.
- 100 MITCHELL, S.L., NIKLASON, L.E. Requirements for growing tissue-engineered vascular grafts. *Cardiovasc. Pathol.* **2003**, *12*, 59–64.
- 101 TRANQUILLO, R.T., GIRTON, T.S., BROMBEREK, B.A., TRIEBES, T.G., MOORADIAN, D.L. Magnetically orientated tissue-equivalent tubes: application to a circumferentially orientated media-equivalent. *Biomaterials* **1996**, *17*, 349–357.
- 102 BAROCAS, V.H., GIRTON, T.S., TRANQUILLO, R.T. Engineered alignment in media equivalents: Magnetic prealignment and mandrel compaction. *J. Biomech. Eng.* **1998**, *120*, 660–666.
- 103 ITO, A., NAKAHARA, Y., TANAKA, K., KUGA, Y., HONDA, H., KOBAYASHI, T. Time course of biodistribution and heat generation of magnetite cationic liposomes in mouse model. *Jpn. J. Hyperthermic Oncol.* **2003**, *19*, 151–159.

## 9 Applications and Implications of Single-walled Carbon Nanotubes in Tissue Engineering

*Peter S. McFetridge and Matthias U. Nollert*

### 9.1 Introduction

The discovery of single-walled carbon nanotubes (SWNT) by Iijima in 1991 [1] initiated a surge of interest that continues to grow as our understanding of these unique materials evolves. The extraordinary mechanical [2, 3] and electrical properties [4] of SWNT have fueled continued interest as the spectrum of potential applications grows that can take advantage of these unique nano-scaled materials. Applications encompass a wide range of composite materials from electrically conducting polymers and biopolymers, and nanoelectronics, to biosensors and materials that interface directly with biological systems [5–7].

A rapidly growing discipline that may take advantage of SWNT unique properties is the area of regenerative medicine in the field of tissue engineering [8]. The broad concept, as the name implies, is the regeneration of diseased or damaged tissues such that complications of using transplant tissue can be avoided. Central to this theme is the use of 3D scaffolds that provide support for adhesion-dependent cells in a manner that guides tissue regeneration by the host, or other transplanted cells. The aim is that the preformed scaffold (in the shape of the end product) will guide cellular regeneration to result in the development of neo-tissue. Importantly, not only the physical parameters of the scaffold are critical to allow the correct structural and biochemical development, but also the environment in which the cells are cultured. It is the combination of these factors that are fundamentally important if fully functional tissue is to be developed.

Although the number of peer reviewed published articles on SWNT has been increasing dramatically (both in terms of material processing and its applications) as interest grows, there has been little published in the area of tissue engineering. In this chapter we will discuss general applications of SWNT in the field of tissue engineering, paying particular attention to the preparation of these nano-materials and how they interact with cells. We first review some of the history behind the electrical stimulation of cells and the reasoning behind the use of SWNT as a conductive material to support or promote organ regeneration. We then review

purification and preparation processes, and then take a closer look at cellular interactions, and how functionalizing or modifying SWNT surface chemistry can modulate cell function. The chapter concludes by reviewing specific applications of SWNT in tissue engineering and the current pertinent literature.

## 9.2

### Electromagnetic Fields for Tissue Regeneration

The particular attributes of carbon nanotubes that are of special interest to regenerative medicine are their mechanical and electrical properties. The importance of electrical properties in modulating biological processes has been recognized since the mid-1700s. In fact, by the end of the eighteenth century the injury potential, which is a direct current voltage gradient induced within an injured tissue space by current flowing into and around an injured nerve, had been recognized and measured. In recent times, these currents have been shown to be essential for regeneration [9, 10]. Within a hundred years of the early work of Galvani and Volta in describing and characterizing electric currents and fields, many others promoted bioelectricity for a wide variety of dubious medical applications [11], including insomnia, migraine and baldness among others. The dubious scientific work and downright charlatanism from this period tainted perceptions that last to this day regarding bioelectric phenomena.

There are now several systems that clearly demonstrate that electrical field modulation promotes tissue regeneration, for which the unique properties of carbon nanotubes may be exploited to develop improved therapeutic options. One such area is in nerve regeneration. The seminal work demonstrating the influence of electrical fields on nerve growth was by Borgens et al. [12]. They showed that injury currents carried by  $\text{Na}^+$  and  $\text{Ca}^{2+}$  ions were driven into the cut ends of severed lamprey spinal cord axons. Increased branching and faster regeneration of the axons was observed in the presence of a steady electric field of opposite polarity. This work has been extended to a guinea pig model in which the spinal cord was severed and significantly greater axonal growth was observed in the presence of an applied electrical field compared with the case where no electrical field was present [13]. In another study, improvements in nerve function were also observed with an applied electrical field [14].

Another area that has seen extensive work on the interaction between electrical fields and biomedical applications is in bone growth. Pulsed electromagnetic fields (PEMF) stimulation has been in clinical use for nearly 30 years on patients with delayed fracture healing and nonunion and has been demonstrated in a multitude of clinical case reports [15–17]. Double-blinded studies have confirmed the clinical effectiveness of pulsed electromagnetic fields stimulation on osteotomy healing [18, 19] and delayed union fractures [20]. Brighton et al. [21] conducted a multi-center study of the nonunion and reported an 84% clinical healing rate of nonunion with direct current treatment. Recently, Schaden et al. [22] reported 76% of

non-union or delayed union patients treated with one time extracorporeal shock wave therapy resulted in bony consolidation with a simultaneous decrease in symptoms.

Both of these applications have led investigators to develop electrically conducting materials that have favorable biocompatibility characteristics. The most widely studied conducting biomaterial is the polymer polypyrrole. The biocompatibility properties of this material were first studied by Wong et al. [23]. They showed that extracellular matrix proteins could adsorb on a thin film of polypyrrole and could support attachment and spreading of cells. In the presence of an electrical potential, cell growth and DNA synthesis were altered. A range of inherently conducting polymers has been developed and they have been reviewed [24]. Potential applications of polypyrrole based electrically conducting biomaterials include glucose biosensors [25, 26], neural prosthetics [27, 28], and bone tissue engineering [29–31]. Taken together, these studies demonstrate that there is great potential in developing novel biomaterials and biomedical devices with the capacity to be electrically conducting. Since carbon nanotubes can act as conductors, there is immense interest in exploring their potential in biomedical applications.

### 9.3

#### Tissue Engineering

As a discrete discipline, tissue engineering is little more than a decade old; however, growth of cells on synthetic materials as a means to improve the performance of implantable materials dates back to the 1970s [32–35]; in particular, in the development of small diameter vascular prosthetics where it became obvious that these materials need to be more than just immunologically inert, rather they need to functionally integrate with surrounding tissues to enhance performance. As such, there has been continuous development of these materials to understand and improve interactions with cell systems.

In addition to the many biological molecules that enhance cellular interactions, such as growth factors and adhesion peptides, magnetic and electrical stimulation (as described above) has a strong influence on cellular growth, cellular phenotype, and tissue regeneration [36–42]. As such, designer materials that allow modulation of mechanical, electrical and thermal properties may produce materials that can be fine-tuned to suit specific applications. For example, when a diseased and occluded blood vessel is to be excised and a prosthetic tube implanted, if the mechanical compliance between a patient's existing blood vessel and the new implant do not match, the chance of graft failure increases significantly [43]. By varying the concentration of SWNT within an appropriate polymer a wide range of compliance values can be obtained, then specifically matched to each patient. Although most polymer additives will allow control over the material's bulk mechanical properties, few materials offer the combined influence of mechanical and electrical modulation.

Incorporating conductive additives into a bulk material allows the gross conduc-



tive properties to be modulated such that electrical stimulation can be used to enhance tissue repair and/or regeneration [44]. One distinct advantage that SWNT have over other conductive additives is the dual capability of varying the material's conductivity *and* enhancing the material's mechanical properties. One biopolymer that has seen a wide range of clinical successes is the extracellular matrix (ECM) molecule collagen [45–49]. Typically collagen is hydrolyzed and stored in an acidic solution that is returned to a neutral pH to initiate polymerization. Unlike most synthetic polymers this method allows living cells to be added during the polymerization step, to produce preformed, homogenous, cell dense materials. This is particularly important as it reduces the time and cost of construct development. By starting with a cell dense material one can avoid having to wait several weeks for the cell populations to proliferate and fully populate the matrix. The earlier work of Weinberg and Bell, who developed the first collagen-based *de novo* blood vessel in 1986 [50], had shown the potential of these natural polymer scaffolds; however, the major draw back was poor mechanical strength and stability. Collagen in its natural form is composed of similarly repeating amino acids, where glycine is repeated every third amino acid, with many of the remaining amino acids being proline and hydroxyproline. As collagen is hydrolyzed, collagen bundles dissociate creating a mass of disorganized fibers that absorbs a significant amount of water to form what is called a hydrogel. Cells remodel the collagen and these disorganized fibers are realigned back into their original form as functional tissue is created. As the fibers realign, a significant amount of shrinkage occurs as the fibers condense and water is expelled.

The most common method used to enhance mechanical properties of collagen-based hydrogels is the addition of chemical crosslinks that bind, strengthen and minimize enzymatic digestion of the long-chain polymer [51–54]. Many crosslinkers, such as glutaraldehyde, are toxic and often leave residual toxins in the scaffold after processing. A further drawback of this approach is that it renders the material impervious to cellular infiltration. The barrage of ECM degrading and remodeling enzymes, secreted by cells, have little effect on many of these chemically induced crosslinks, and as such there is little cell penetration or remodeling of the scaffold. The result is stable, but inert, materials. From a tissue engineering perspective, cell migration into the scaffold and subsequent remodeling are fundamentally important if functional neo-tissue is to be formed. By using conductive additives, which also enhance the material's mechanical characteristics, the opportunity exists to develop off-the-shelf, high-performance materials that may improve repair and regeneration of diseased tissues.

However, with the current state of technology, single-walled carbon nanotubes (SWNT) cannot be used for medial applications straight from the production plant. In general the production of SWNT results in a high percentage of contaminants that must be removed prior to application. Purification technologies are diverse, and often change the surface chemistry of the SWNT, which in turn changes the way biological systems respond to the presence on SWNT. As often is the case with nano-scale materials, the particle's surface chemistry dominates the interactions between the nanotube and the surrounding environment. Changing func-

tional groups on the surface of SWNT can dramatically alter the way in which they interact with hydrophobic and hydrophilic materials; we can use this property to improve dispersion and function within various different polymers. In the next section we discuss the purification and dispersion of SWNT in relation to tissue engineering scaffolds for tissue regeneration.

#### 9.4

##### **SWNT Preparation: Purification and Functionalization**

As a potentially implantable material, not only will the SWNT be exposed to the body, but also any contaminants from the manufacturing process not removed through purification processes. If a SWNT composite is non-degradable with nanotubes bound within the material, any negative biological effects of the nanotubes will likely be minimized compared with materials that degrade over time. As in the case with degradable tissue engineering scaffolds, SWNT and contaminants would come into direct contact with host tissue at higher concentrations. Consequently, compatibility with cells and surrounding tissue is crucial, particularly if the SWNT are not eliminated through normal bodily function. For these new materials to be successful they must be biologically, mechanically, and chemically compatible with the host tissue, and, as such, a comprehensive understanding of how SWNT interact with living systems is required. This is important from not only a materials perspective, but also as an airborne contaminant, or any other interaction these nano-materials may have with biological systems.

Various different methods are used to produce SWNT, including chemical vapor deposition, laser pyrolysis, pulse laser vaporation, and carbon arc-discharge. Each of these methods results in differing qualities of nanotubes with yields containing different types and amounts of production contaminants. Different production methods will result in a different elemental composition, and as such the efficiency of purification techniques will have a strong bearing on biological interactions. By understanding these processes we can gain insight into what the dominant mode in which SWNT (or production contaminants) interfere with cell function. This may lead to determining the critical parameters of SWNT preparations that must be modulated to improve cell interactions and thus develop enhanced biomaterials.

To date, few investigations have assessed SWNT–cell interactions and those that have shown a toxic response by cells and tissues [55–59]. A study by Warheit et al. (2004) observed the formation of a series of multifocal granuloma in rats when SWNT were instilled intratracheally [59]. Interestingly these results were not dose-dependent as other studies have shown. Oberdörster et al. (2004) found that oxidative stress was induced when juvenile Largemouth Bass were exposed to C<sub>60</sub> fullerenes within brain tissue, with the fullerenes localizing in lipid-rich regions such as cell membranes [57]. Schuler et al. (2004) expressed concern that, due to the small dimensions of nanoparticles, they might penetrate the skin and possibly reach the brain by eluding the immune system [60]. Similarly, in a study by Shvedova et al. (2003), using unpurified SWNT produced by the HiPCO process with a

30% iron mass, (NASA-JSC, Houston TX), caused changes in cell ultrastructure and morphology, a loss of cell integrity and apoptosis, accelerated oxidative stress, an accumulation of peroxidative products, and depletion of antioxidants in immortalized human epidermal keratinocytes (HaCaT) [61].

Although the exact mechanism that causes these deleterious interactions with cell systems is unknown, a comprehensive understanding of how SWNT interact with living systems is, clearly, required. By understanding the mechanism(s) that causes these effects on cell function (such as production contaminants, mass transfer limitations, hydrophobic interactions etc.) it will be possible to modulate SWNT chemistry to improve SWNT–cell interactions, and as such develop improved materials.

A recent publication by Nimmagadda et al. (2006) describes how purification and SWNT surface chemistry variation effects the function and viability of 3T3 fibroblasts [62]. In these investigations SWNT were obtained from CarboLex Inc. (Lexington, KY), manufactured by a modified electric-arc technique. In this method a plasma discharge is induced at high temperatures onto a cathode containing graphite powder, metal catalysts, and adhesives. The deposit that forms contains the SWNT. This process results in 40–60% amorphous carbon, as well as non-carbon contaminants including, Ni, Y, Co, and others [63–65]. The study aimed to determine if SWNT themselves, or the production contaminants, were responsible for the toxic responses observed, and to assess if variation in SWNT surface hydrophobicity would improve cellular interactions. Three different preparations of SWNT were assessed, including “as purchased” nanotubes (AP-NT), nanotubes purified by acid washing to remove catalyst residue (PUR-NT), and purified nanotubes functionalized with the small hydrophilic carbohydrate, glucosamine (GA-NT). SWNT that were purified by nitric acid oxidation resulted in dissolution of much of the metal contaminants, but also functionalized the damaged (or defect) ends of the SWNT with carboxylic acid groups reducing the material’s hydrophobicity. With the additional functionalization step of added glucosamine, a small sugar molecule, to the SWNT, the overall hydrophobic nature of these NT is further reduced.

An assessment of the effects of these different SWNT preparations has shown a dose-dependent relationship between the viability of mouse 3T3 fibroblasts and concentration of SWNT, where increasing concentrations of SWNT resulted in decreased cell viability. The effects of “as-purchased” SWNT on 3T3 mouse fibroblasts are similar to other reported data, where cell viability was significantly diminished [55, 58, 66]. The observed effects are strongly influenced by contaminants in the preparation, as well as by soluble and non-soluble components. Improved cell viability occurs with PUR-NT and GA-NT over AP-NT preparations (at a given concentration), emphasizing that purity alone (and thus production method) plays an important role in biocompatibility of SWNT. These investigations have shown significant variation of 3T3 fibroblasts viability and metabolic function (after three days in culture) compared with control values. At the lowest concentration of AP-NT (0.001% w/v), cell viability was reduced to 55% of control values (Fig. 9.1a). In the same cell cultures 3T3 fibroblasts demonstrated dramatic changes in their met-

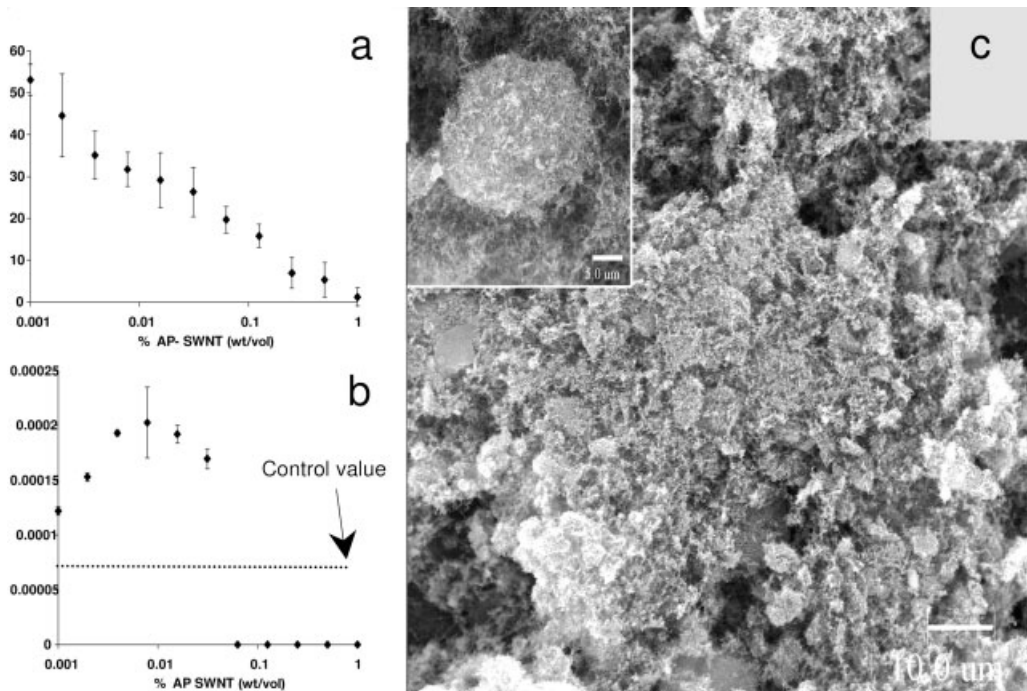


**Fig. 9.1.** (a) AP-NT/3T3 cultures demonstrated a negative dose-dependent relationship with increasing AP-NT concentration. At the lowest tested concentration of AP-NT (0.001%) only 55% of fibroblasts remained viable ( $p < 0.05$ ). (b) At lower concentrations, cells in AP-NT preparation reduced Alamar Blue dye as much as 200% more than the cells under control conditions ( $0.78 \times 10^{-4}$  fluorescence units). No metabolic activity was observed at and

above 0.0625% NT ( $n = 3$ ). (c) SEM displayed spherical bodies dispersed throughout AP-NT/3T3 cultures. These were hypothesized to be detached cells encased with nanotubes, where cells may have coalesced to form the larger spherical bodies. In this analysis 3T3 cells were cultured with an AP-NT concentration of 0.0625% NT (wt./vol.), with a cell viability of 19.65% compared with control values (100%) [62].

abolic activity (Fig. 9.1b), illustrating a nonlinear effect dependent on NT concentration. The variation observed in metabolic activity is consistent with results from a recent study by Cui et al. (2005) [55]. In their study, the ability of human HEK293 cells to adhere and proliferate when cultured in the presence of SWNT was also diminished. Cui et al. also assessed gene expression profiles for several specific genes and showed that variation in metabolic activity could in part be explained by the variation in gene expression profiles. Unfortunately, neither the elemental composition nor the purification process (if any) of the nanotubes purchased from Carbon Nanotechnologies, Inc. was described. As such the effect, or comparative effect, of residual contaminants was not assessed.

SEM analysis of 3T3 cells cultures in AP-NT, gives further insight into cellular interactions with NT, where spherical bodies ranging from 5 to 15  $\mu\text{m}$  in size

have been observed (Fig. 9.1c) [62]. These spherical bodies were hypothesized to be detached, or semi-detached, cells encased in nanotubes that may, in some cases, have coalesced to form the larger spherical structures.

Purification and functionalization of AP-NT reduces the negative effect on cell viability and metabolic activity, demonstrating that as-purchased NT contain impurities/contaminants that may be responsible for the variation in cell viability and function seen in Fig. 9.1. The effect of these components was assessed by acid washing and chemical surface modification of AP-NT. This suggests that the removal of production contaminants and SWNT hydrophobicity both play an important role in cell-SWNT interactions. The overall trend shows cells incubated in GA-NT preparations having a higher cell viability with less deviation in metabolic activity (from control values) compared with cell/PUR-NT cultures. This suggests the surface properties of SWNT may have a profound effect on cell function. However, the dose-dependant relationship still exists as increasing concentrations of both PUR-NT and GA-NT preparations still reduce cell viability (Fig. 9.2).

At the concentration of 0.0625% w/v 3T3 fibroblasts cultured in the presence of glucosamine functionalized SWNT (GA-NT) for 6 days were found to migrate to the upper surface of the GA-NT to form sheets of cells over the nanotube preparation. Figure 9.3(a) shows an enlargement of Fig. 9.2(c) (incubated for 3 days), compared with sheets of cells seen spreading over the surface of the nanotube preparation after 6 days in culture (Fig. 9.3b).

Because of the small size of these particles, the surface properties dominate the overall chemistry of the molecule and, as such, the addition of functional moieties can dramatically alter the manner in which these particles interact with the surrounding solution. The basic structure of SWNT is a graphene sheet of carbon atoms linked by non-polar covalent bonds. Since electrons are equally shared there is no charge separation and these molecules cannot enter into a charge interaction with water [67]. They are therefore hydrophobic, resulting in minimal solubility in aqueous media. In an investigation by Nimmagadda et al. all NT preparations aggregated to some degree, although the purified nanotubes with carboxylic acid groups and the SWNT functionalized with glucosamine displayed varying degrees of solubility [62]. SEM analysis of AP-NT (the most hydrophobic of the three NT preparations) cultured with 3T3 fibroblasts displayed spherical structures encased in NT-like particles. This led us to the hypothesis that the hydrophobic NT were penetrating, and aggregating within the hydrophobic cell membrane leading to cell rupture (Fig. 9.1c). These effects were not seen with NT functionalized with glucosamine where the hydrophobic nature of SWNT was reduced.

Evidence for the translocation of nanotubes through cell membranes has been confirmed by fluorescence imaging, with [68, 69] and without [70] functionalized markers or molecules. These studies clearly show the nanotubes entering cells, and the potential of nanotubes localizing in hydrophobic regions of the cell membranes. A study by Cherukuri et al. (2004) using a pluronic surfactant that disperses the nanotubes suggests an active mechanism of SWNT uptake. In this study, mouse peritoneal macrophage-like cells were used whose function is the active uptake of targeted particles. However, this may be a secondary uptake path-

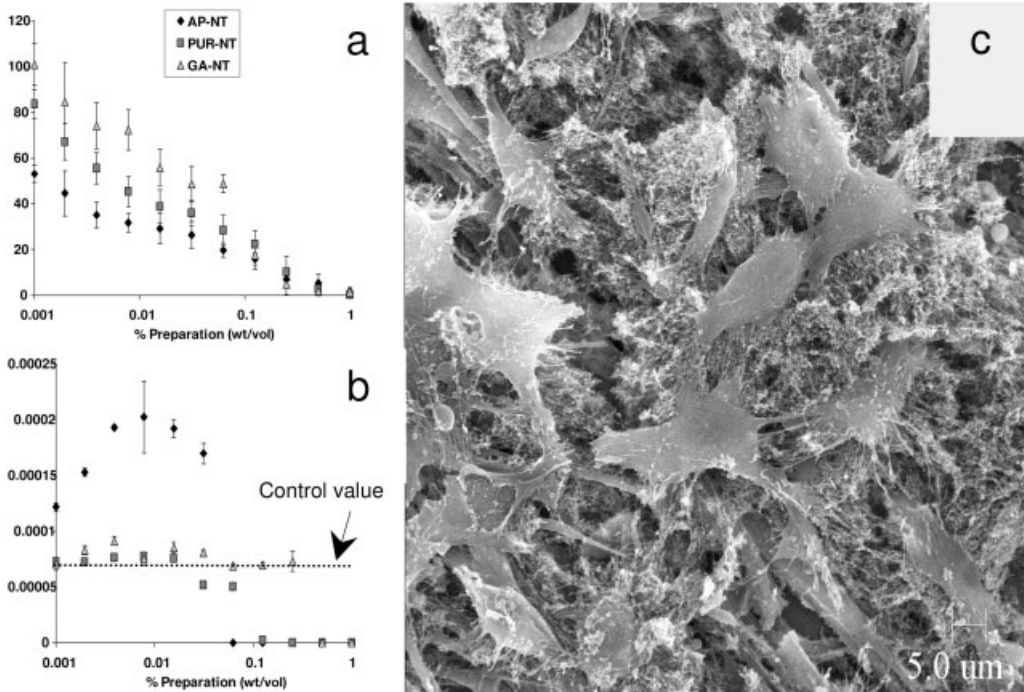


**Fig. 9.2.** (a) Cells incubated with GA-NT showed the highest viability followed by cells/PUR-NT cultures, and cell/AP-NT cultures have the lowest viability at SWNT concentrations below 0.125%. Preparations and concentrations below 0.125% NT (wt./vol.) show a statistically significant difference ( $p < 0.05$ ), with the exception of concentrations above 0.125%, where no significant difference between each preparation was

found ( $n = 3$ ). (b) 3T3's in GA-NT and PUR-NT preparations show metabolic activity similar to 3T3's in control cultures. There was no significant difference ( $p < 0.05$ ) between preparations or concentrations between 0.5 and 1.0% NT (wt./vol.). (c) SEM displays 3T3 cells dispersed throughout the 3D GA-NT matrix. No spherical bodies were observed as seen with 3T3 cells incubated with AP-NT [62].

way, whereas in normal stromal cells uptake may be passive translocation driven by hydrophobic/hydrophilic interactions. The results presented by Cherukuri et al. (2004) do not show any toxicity effects at SWNT concentrations of  $3.8 \mu\text{g mL}^{-1}$ , where they estimated an uptake rate of 1 nanotube per cell per second (total of 70 000 nanotubes ingested) over the incubation period of approximately 20 h [70]. By comparison, at the lowest SWNT concentrations assessed by Nimmagadda et al. [62], 0.000976 w/v, or  $9.76 \mu\text{g mL}^{-1}$ , fibroblast viability was reduced to  $50.08 \pm 3.74\%$  for “as purchased” nanotubes (AP-NT), with  $83.58 \pm 6.22\%$  viability with “purified” nanotubes (PUR-NT). Only glucosamine functionalized nanotubes (GA-NT) had no effect on cell viability at these concentrations (Fig. 9.2).

Cherukuri et al. have shown a 40% reduction of SWNT internalization when incubated at  $27^\circ\text{C}$  compared with  $37^\circ\text{C}$ , which is consistent with the temperature

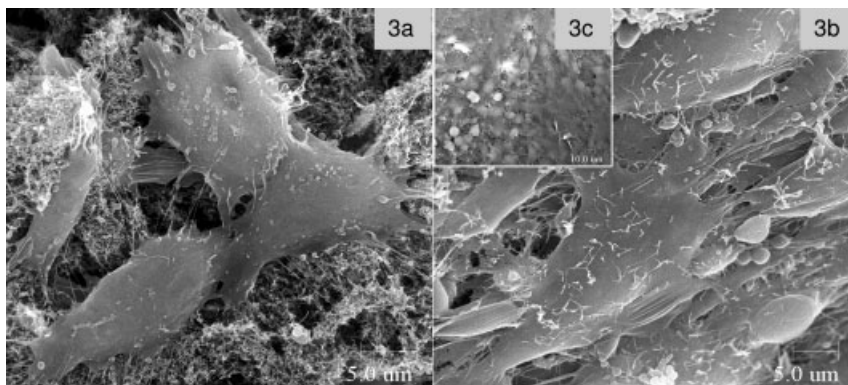


**Fig. 9.3.** (a) 3T3 fibroblasts cultured in the presence of GA-NT at 0.0625% (w/v) for 3 days, showing an enlargement over Fig. 9.2(c). (b) Similar magnification of 3T3 cells cultured under the same conditions for 6 days that have migrated to the upper surface of the GA-NT to form sheets, with (c) (inset) showing a lower magnification of cells covering the surface of the nanotube preparation [62].

dependence of phagocytosis [71]. By contrast, Pantarotto et al. (2004) used amino-modified SWNT functionalized with the fluorescent probe fluorescein isothiocyanate (FITC) and SWNT functionalized with a peptide responsible for G-protein function (also covalently bonded to FITC) to show that uptake by human 3T6 and murine 3T3 fibroblasts was not affected by temperature variation or the use of endocytosis inhibitors. They concluded that the method of translocation appeared similar to cell penetrating peptides, which is not associated with the endocytosis pathway, but the exact mechanism was unclear [72, 73]. Recently, Monteiro-Riviere et al. (2005) have shown that multi-walled carbon nanotubes (MWCNT) were present in cytoplasmic vacuoles of human epidermal keratinocytes [56]. Our investigations have shown that, depending on the hydrophobicity state of the SWNT, these nano-particles appear to aggregate on the surface of cell-like structures. Although several different mechanisms of SWNT translocation are likely, we hypothesize that due to the hydrophobic nature of these nano-particles they tend to aggregate within hydrophobic regions of the lipid bilayer to form focal points. As yet there is no clear evidence that hydrophobic nanotubes move from the lipid bilayer and back into the aqueous environment (either cytoplasmic or extracellular) and as such there is some question as to whether these nanotubes remain within hydrophobic lipid membranes or as postulated enter the cells aqueous environment. The fluidity of these lipid membranes, which interact with other cell membranes, may transport SWNT into the cell, though not necessarily out of the lipid membranes. From our observations, as concentrations increase, the likelihood of the small focal aggregations enlarging in size increases; it is therefore quite possible that, at sufficiently high concentrations, SWNT interfere with membrane integrity, resulting in rupture and cell death.

In our investigations SWNT within each preparation settled out of solution over

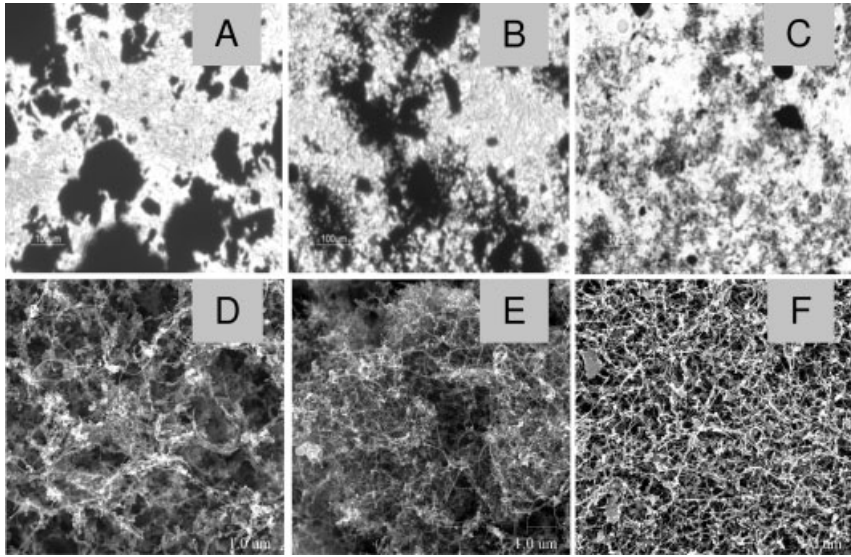


**Fig. 9.4.** Images (A–C light microscopy, D–F SEM) displaying SWNT preparations dispersed in aqueous cell culture media inoculated on 3T3 fibroblasts after 3 days incubation. (A) AP-NT displaying large aggregates of nanotubes, (B) SWNT aggregates are progressively dispersed through purification steps (PUR-NT), and (C) further reduced hydrophobic interactions of SWNT within the aqueous environment by functionalization with glucosamine. Lower SEM images show (D) AP-NT, (E) PUR-NT and (F) GA-NT surface topography as the SWNT become less hydrophobic, with improved dispersion.

the 3 day incubation period to form layers directly on the cell cultures. Light microscopy illustrates how the differentially treated nanotubes tend to aggregate as a function of hydrophobicity, GA-NT layers appeared more dispersed compared with AP-NT and PUR-NT preparations (Fig. 9.4a–c), with SEM images showing variable surface topography as NT dispersion increases (Fig. 9.4d–f). The presence of glucosamine molecules functionalized on the surface of SWNT improved SWNT interactions with the aqueous media, allowing SWNT bundles to disperse more uniformly with less aggregation [74].

It is unlikely that tissue engineered scaffolds would be made solely of SWNT, rather they will be formed as a composite material where the bulk polymer will be chosen for selected characteristics pertinent to its endpoint application. Materials designed for use in soft tissue repair applications will be vastly different from bone, or artificial limbs, and as such properties such as elasticity, biocompatibility, porosity, charge, etc. need to be considered.

From a materials perspective, carbon nanotubes used as an additive within a bulk polymer need to be dispersed uniformly, ideally as aligned, individual tubes rather than large random aggregates. Without uniform dispersion we will not be able to take full advantage of the unique properties of SWNT, and as such is a critical issue. Significant effort has focused on full-length SWNT and MWNT disper-



sion, with several approaches being taken to improve dispersion and alignment. Both chemical and mechanical dispersion methods have been used, including, but not limited to, sonication, surfactants, and functionalization with different moieties or macromolecules. Improving alignment of SWNT has been equally challenging and several methods have been investigated, including mechanical shear [75, 76], anisotropic flow [77], and magnetic fields [78, 79].

As discussed, the surface chemistry of these nano-particles dictates the manner in which SWNT are prepared to interface appropriately with the bulk polymer. Clearly, SWNT dispersion within aqueous hydrogels requires a different approach than dispersion in non-polar polymers. Sennett et al. (2003) mixed both SWNT and MWCT in molten polycarbonate (PC) using a twin-screw extruder to disperse the nanotubes, then used a melt-spinning technique to align the NT with the PC fibers. MWCT and SWNT displayed different dispersion characteristics, with larger individual MWCT dispersing uniformly; however, SWNT dispersion was limited to bundles of nanotubes rather than single tubes [76]. This effect will in part be due to the mixing characteristics of different sized particles but dispersion will again be dominated by the nano-particle's surface chemistry. MWCT and SWNT that are produced using different production methods will have different contaminants and will require different purification strategies, most of which can alter the surface charge/chemistry. As such the two materials will likely behave very differently under similar solution conditions.

Other methods of dispersion include functionalization of nanotubes to alter their surface chemistry and/or provide secondary chemical bonding sites. These functional moieties range in chemistry and function, and include (amongst others) biological polymers, including DNA and other large macromolecules. One of the more common methods to functionalize nanotubes is the formation of carboxylic acid groups as either a final process or as an intermediate in a process called defect functionalization using a strong oxidant such as nitric acid ( $\text{HNO}_3$ ) [80–83]. Fu et al. (2002) functionalized SWNT with oligomeric poly(ethylene glycol) to solubilize SWNT and MWNT in aqueous solutions. They then added serum albumin using surface-bound ester linkages, citing an ester to amide transformation as the mechanism of adsorption [83]. These preparations were shown to have a high solubility in water and suggested this method to conjugate fragile biological species. Of the biological polymers used, Zheng et al. (2003) have shown effective dispersion of SWNT in water when sonicated in the presence of single stranded DNA (ssDNA), suggesting binding through  $\pi$ -stacking of ssDNA wrapping in a helical fashion around the SWNT [84]. Baker et al. (2002) oxidized SWNT to form carboxylic acid groups then reacted with thionyl chloride and then ethylenediamine to generate a terminal amine group to which (after several intermediate steps) single-stranded DNA oligonucleotides were functionalized to the SWNT. These investigations have shown the ability of DNA to be covalently bound to SWNT, then for complementary DNA sequences to hybridize with minimal interaction from non-complementary sequences [81]. Bianco et al. (2005) have discussed several strategies for using, and functionalizing, nanotubes in biomedical applications. The paper focuses on nanotube functionalization for specific applications in drug, vac-

cine, and gene delivery and provides an excellent overview of different functionalization strategies [85].

As a material with potential biomedical applications the absorption pattern of these and other molecules to the surface of SWNT is important to further our understanding of how SWNT are likely to interact with not only the bulk polymer but with surrounding cells and tissues. The inherent hydrophobic nature of SWNT has been hypothesized to play a dominant role in the non-specific molecular binding of various molecules to the surfaces of SWNT [69, 72, 86–88]. In addition to these direct effects of SWNT on cells, it is also possible that SWNT aggregates may indirectly alter cell function by limiting mass transfer of substances either to or from the cell surface. We investigated this possibility by examining the interactions of differentially functionalized SWNT on glucose and protein transfer through SWNT membranes [62]. These investigations were designed to assess any mass transfer limitation that might occur as the SWNT settled onto the cell layer and potentially affected cell function. At sufficiently high concentrations, all SWNT preparations (AP-NT, PUR-NT and GA-NT) resulted in a reduced rate of glucose transfer, compared with controls. However, because the glucose mass transfer rate was still in excess of cellular demand it was concluded that there was no inhibition of cell function. Although no conclusions can be drawn regarding glucose adsorption from the data available, the three preparations clearly had a different topography and porosity (Fig. 9.4), which would be the likely cause of variation in mass transfer rate. Similarly, protein (balanced salts with 10% serum) transfer through the membrane displayed mass transfer variation, indicating inhibition. At lower concentrations of SWNT there was no significant variation in mass transfer across any of the three SWNT preparations. At higher SWNT concentrations (0.25% and 1%) a significant decrease in protein transfer was noted across the PUR-NT preparation compared with AP-NT and GA-NT preparations (Fig. 9.5b) [62].

The results of this study clearly demonstrate that chemical composition and nature of nanotube preparation is of fundamental importance for biological applications. Furthermore, choice of supplier, manufacturing method, and the effectiveness of NT purification will strongly influence the overall composition, including contaminants within the raw material. These impurities will have a range of effects on cellular viability and metabolism, depending on the contaminants involved and their concentration; however, the mechanism by which either the contaminants or the SWNT alter cell viability or metabolism is yet to be resolved. SWNT purification is therefore a critical step and it is important to note that these processes can alter the surface chemistry of the nanotubes and thus their interactions with cells and tissues. We have hypothesized that when SWNT remain strongly hydrophobic (AP-NT and PUR-NT preparations) these nanoparticles interfere with the lipid bilayer of the cell membrane by aggregating within these hydrophobic regions and disrupting cell membrane. Although other mechanisms presumably also occur, SEM evidence points strongly to these hydrophobic interactions as playing a dominant role in early cell failure.

The nanotubes used in the above investigations showed significant effects on *in vitro* cellular function that cannot be attributed to one factor alone, but are likely

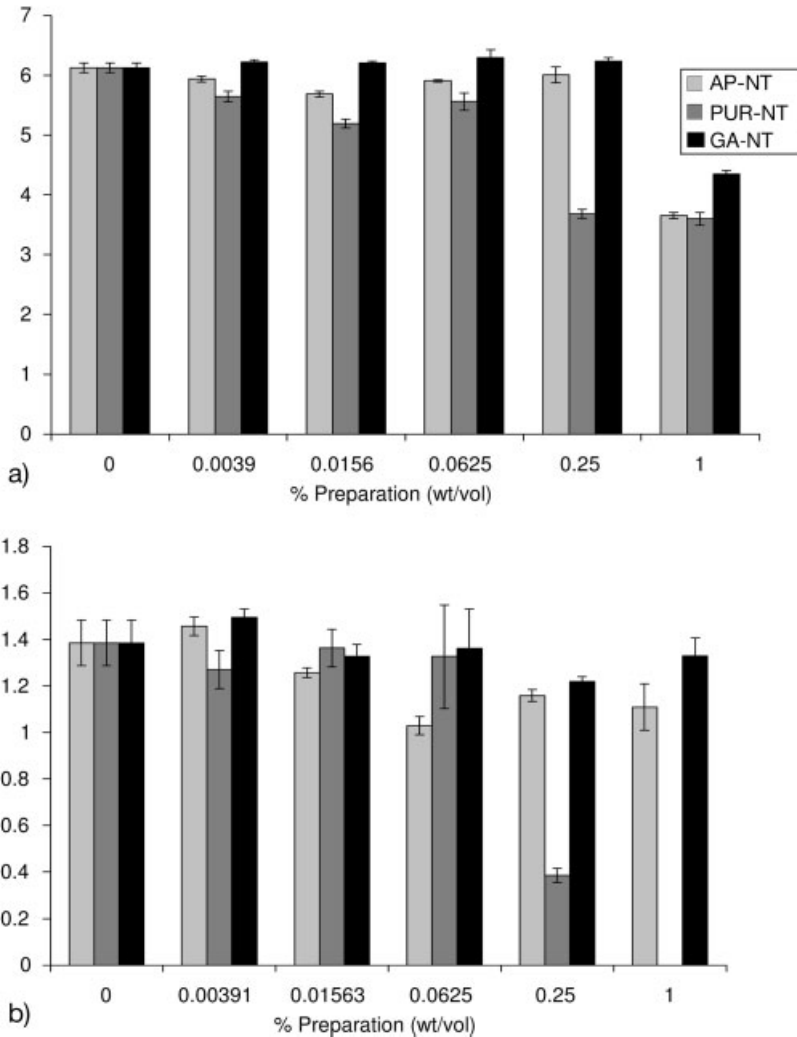


**Fig. 9.5.** (a) A decrease in glucose transfer rate was observed at higher concentrations of NT preparations (1%). From the transfer rates observed and the cell consumption rate ( $1.368 \times 10^{-6} \text{ mg dL}^{-1} \text{ h}^{-1} \text{ cell}^{-1}$ ), no apparent mass transfer limitation is likely to

have occurred. (b) Analysis of total protein (human plasma) transfer through NT layers showed no significant difference ( $p < 0.01$ ) between AP-NT, GA-NT and control values, whereas PUR-NT layers displayed a significant reduction at higher concentrations [62].

the result of several unfavorable interactions. These interactions were significantly reduced by comprehensive purification processes, and by modifying NT surface chemistry to reduce hydrophobicity and/or the introduction of functional groups. With high purity SWNT the end application will dominate the requirement to modify NT surface chemistry.

## 9.5

### Specific Applications of Carbon Nanotubes in Tissue Engineering

Carbon nanotubes offer a unique potential to develop smart materials that can be tailored to meet specific mechanical and electrical properties. These properties can be optimized to suit specific applications in areas such as bone development where materials must be rigid yet retain a degree of elasticity. The ability to alter the material's conductivity also provides the opportunity to modulate cell interactions/function by applying electrical fields. The same process can be used for most tissues, especially those that respond in a positive way to electrical stimulation. Some of the more obvious applications include bone, nerve, and cardiac tissue engineering; however, other areas, including skin wound healing, have been shown to respond to electrical fields and are thus candidates for SWNT scaffolds.

There are three primary drivers for the use of SWNT as additives in tissue engineering scaffolds: first is to fine tune scaffold mechanical properties (application specific); the second is to use the NT conductive properties to modulate the materials electrical properties so electrical fields can be used to stimulate the growth and development of tissue engineered constructs; and the third is to promote phenotype specific cellular regeneration by varying the scaffold's conductivity and modulating an applied electrical field. Clearly, a significant amount of basic research is required to verify these goals, but the potential is there given the current status of our knowledge.

In this last section we review several recent publications that focus directly on tissue applications using NT as a component of scaffold materials. Due to the relative infancy of this research area, publications are limited but they clearly show the direction and potential of these novel materials. In a series of investigations interfacing structural biological polymers with SWNT, MacDonald et al. (2005) have assessed the interactions between cell-loaded collagen hydrogels dispersed with varying concentrations of SWNT (0.2, 0.4, 0.8, and 2.0 wt.%) (Fig. 9.6). Figure 9.7 shows progressive enlargements of the composite scaffolds using SEM image analysis of the cartoon given in Fig. 9.6 [89].

The overall goal of these investigations is to enhance the mechanical and functional properties of these hydrogels for potential use in areas such as orthopedic, cardiac and neuronal tissue engineering. Collagen hydrogels have been used in a wide variety of medial implants with excellent results; however, from a purely structural perspective these gels lack the mechanical stability that more demanding applications such as blood vessels and bone replacement require.

The potential to improve the material's mechanical attributes while at the same time adding functionality to the matrix will undoubtedly prove to be a productive avenue of research for both hard and soft tissue replacement or repair. As one of the few investigations that use a degradable polymer with NT dispersed at concentrations as high as 2.0 wt.% it is promising that the authors show no loss in cell viability (rat aortic smooth muscle cells) over the 7 day culture period. Although there was a general reduction in cell number at day 3, by day 7 there was no statis-

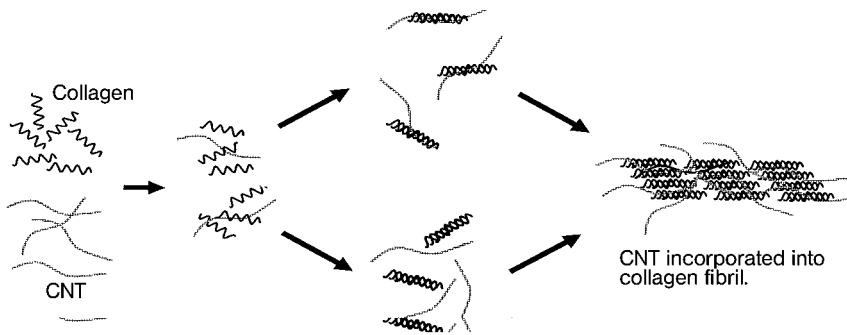


**Fig. 9.6.** Diagrammatic representation of the process by which CNT can be incorporated firstly into collagen fibrils then form a collagen–CNT composite material [89].

tical difference in total cell number between controls (hydrogels less NT), and NT treated constructs [89].

This data contrasts the reduced cell viability seen in our own investigations [62] where at 1.0 wt.% SWNT no cells were viable. In our investigations the SWNT were dispersed directly in the cell culture media, eventually coming out of suspension, and as such where in direct physical contact with cells. The increased cell viability in the studies by MacDonald et al. (2005) is likely due to the interaction between NT and collagen fibers, where collagen fibers may bind the NT, reducing the direct interactions/contact with cells seen in our investigations. This adds weight to our hypothesis that non-bound hydrophobic NT localize in hydrophobic regions of the cell membrane, resulting in mechanical disruption of the cell membrane (Fig. 9.1).

Not surprisingly, bone and neuronal engineering have been an early focus for several tissue engineering groups. In one of the earliest publications using NT in a tissue engineering application, Supronowicz et al. (2002) assessed cellular interactions with NT composite materials. In these investigations the interactions of

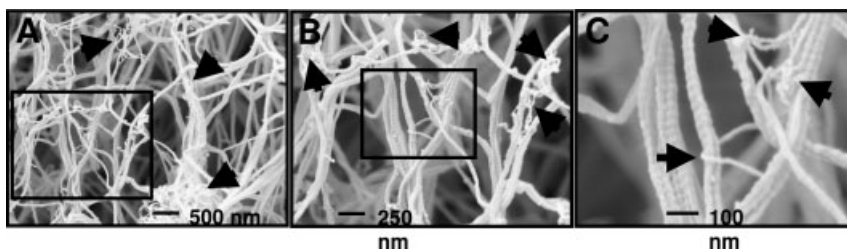


**Fig. 9.7.** Progressive enlargement of the same section of a composite scaffold (A–C), using scanning electron microscopy, showing examples of nanotubes and nanotube bundles incorporated into the collagen fibrils, identified by their typical banding pattern [89].

murine osteoblasts seeded onto poly(lactic acid) (PLA)/MWNT composites were assessed while stimulating cells with alternating current. PLA, normally an insulator, was made conductive with the addition of 20% (w/w) NT, resulting in a resistivity of 0.2 ohms ( $\Omega$ ). Osteoblasts seeded at a density of 7500 cells  $\text{cm}^{-2}$  were exposed to an alternating current of 10  $\mu\text{A}$  at a frequency of 10 Hz with a 50% duty cycle. Results show a significant increase in cellular proliferation, type I collagen deposition, and calcium content although no expression of alkaline phosphatase or bone sialoprotein was recorded. Using only the MWNT/PLA composite, samples were either subjected to the alternating current, or not. Unfortunately, there was no control using PLA alone (no MWNT additive), and as such we cannot determine whether the effects noted were the result of the applied current or the presence of MWNT [90]. The translation of this polymer composite to a tissue engineering scaffold requires a degree of porosity be built into the initial material; however, at such high MWNT concentrations (20% w/w) the structural properties may be negatively effected.

A different approach by Zhao et al. (2005) used differentially functional SWNT as a scaffold template aiming to mimic collagen fibrils at the nanoscale such that nucleation is initiated and crystallization of hydroxyapatite (HA) occurs to encourage bone formation. Various functional groups were explored to expose negatively charged surfaces that are believed to promote supersaturation of local ions leading to mineralization. Unlike carboxylic acid functionalized SWNT, the paper shows that sulfonate- and phosphonate-functionalized nanotubes lead to nucleation of HA on their surfaces [91]. This is a promising approach to a complex issue where the defined orientation of HA in natural mineralization processes may be mimicked using SWNT to enhance the regeneration capacity of newly formed bone.

The mechanical and rheological properties of poly(propylene fumarate) (PPF)/SWNT composites were investigated by Shi et al. (2005) as a potential injectable scaffold for bone repair. This work again draws attention to the importance of SWNT dispersion within any polymer matrix. Although the mechanical properties were enhanced at lower concentrations (0.02, 0.03, 0.05 wt.%), higher concentrations (0.1 and 0.2 wt.%) resulted in air bubble formation and SWNT aggregates within the polymer matrix [92]. Interestingly, functionalization of the NT or the addition of surfactants did not improve dispersion in PPF, underscoring our earlier observation that NT surface chemistry may need to be specifically tailored for improved dispersion in this particular polymer.

A second area of specific interest in SWNT composite materials is as a substrate for neuronal growth and development [93, 94]. Lovat et al. (2005) describe the use of MWNT neural signal transfer whilst supporting cell adhesion and dendrite elongation. These results show adhered hippocampal neuronal cells spontaneously fire action potentials with an increased frequency. The authors suggest that growing neuronal circuits on NT substrates promotes an increase in network operation [95]. Also using NT as substrates for neuronal growth, Hu et al. (2005) have prepared polyethyleneimine (PEI) functionalized SWNT films deposited on glass surfaces as a copolymer to assess hippocampal neuron function. These investigations assessed neurite outgrowth and branching as a comparative investigation to sub-

strates of PEI (a widely used substrate for neuronal culture) and as-purchased MWNT. Results show that neuronal cells cultured on SWNT-PEI substrates produce outgrowths and branching intermediate between PEI (alone) and as-purchased MWNT, suggesting that the ratio of NT to PEI could be titrated to produce neurons with specific characteristics [96]. In an earlier paper, Webster et al. (2004) showed the potential of carbon nanofiber reinforced polycarbonate urethane (PU) as a scaffold to promote adhesion and growth of cell-specific phenotypes compared with cells grown on glass or 100% PU substrates. Using different cell types on increasing concentrations of NT (NT with a diameter 60 nm), it was shown that the adhesion of astrocytes and fibroblasts generally decreased with increasing concentrations of NT (ratio of PU:NT wt.%); conversely, osteoblast adhesion increased under the same conditions [97]. The authors see the potential of either PU/NT coated or bulk materials being used that offer reduced fibroblast adhesion, and thus reduce the soft tissue formation on orthopedic implants, while at the same time increasing the opportunity for osteoblast adhesion leading to new bone growth. Correa-Duarte et al. (2004) have discussed the generation of thin films of MWNT to form 3D sieve architectures [98]. Using specific treatments and lengths of NT, SEM analysis shows NT forming in perpendicular alignments, pyramid-like formations, and also honeycomb structures. In addition to scaffold surface treatments to modulate cell function, this technology would also be useful in determining the effect of physical patterning and cell adhesion at the nanoscale with identical materials with different structures.

## 9.6

### Conclusions

Clearly, cell survival on a biomaterial is not adequate, in itself, for functional tissue regeneration. The use of NT offers several unique opportunities to develop nano-textured surfaces, variably conductive materials, and materials with adjustable mechanical properties that can be tailored to meet specific design considerations. As these investigations continue to test and further understand cell interactions at macro, micro, and nano-scales the promise of smart, functional materials will become a reality. Ultimately, it is likely to be a combination of multiple stimuli, including mechanical, chemical, and electrical factors that will enhance the development of new functional tissue engineered devices.

### References

- 1 IJIMA S. Helical microtubules of graphitic carbon. *Nature* **1991**, 354, 56–58.
- 2 WONG EW, PAUL E. SHEEHAN, CHARLES M. LIEBER. Nanobeam mechanics: Elasticity, strength, and toughness of nanorods and nanotubes. *Science* **1997**, 277, 1971–1975.
- 3 DRESSELHAUS MS, DRESSELHAUS G, CHARLIER JC, HERNANDEZ E. Electronic, thermal and mechanical properties of carbon nanotubes. *Philos.*

- Transact A Math. Phys. Eng. Sci.* **2004**, 362, 2065–2098.
- 4 SANDER TJ, DEVORET MH, DAI H, THESS A, SMALLEY RE, GEERLIGS LJ, DEKKER C. Individual single-wall carbon nanotubes as quantum wires. *Nature* **1997**, 386.
  - 5 LIN Y, SHELBY TAYLOR, HUAPING LI, SHIRAL FERNANDO KA, LIANGWEI QU, WEI WANG, LINGRONG GU, BING ZHOU, YA-PING SUN. Advances toward bioapplications of carbon nanotubes. *J. Mater. Chem.* **2004**, 14, 527–541.
  - 6 WEBSTER TJ, WAID MC, MCKENZIE JL, PRICE RL, EJIORF JU. Nanobiotechnology: Carbon nanofibres as improved neural and orthopaedic implants. *Nanotechnology* **2004**, 15, 48–54.
  - 7 CHEN RJ, BANGSARUNTIP S, DROUVALAKIS KA, WONG SHI KAM N, SHIM M, LI Y, KIM W, UTZ PJ, DAI H. Noncovalent functionalization of carbon nanotubes for highly specific electronic biosensors. *Proc. Acad. Natl. Sci. U.S.A.* **2003**, 100(9), 4984–4989.
  - 8 MATTON MP HR, RAO AM. Molecular functionalization of carbon nanotubes and use as substrates for neuronal growth. *J. Mol. Neurosci.* **2000**, 14(3), 175–182.
  - 9 ALTIZER AM, STEWART SG, ALBERTSON BK, BORGENS RB. Skin flaps inhibit both the current of injury at the amputation surface and regeneration of that limb in newts. *J. Exp. Zool.* **2002**, 293(5), 467–477.
  - 10 MCGINNIS ME, VANABLE JW, JR. Voltage gradients in newt limb stumps. *Prog. Clin. Biol. Res.* **1986**, 210, 231–238.
  - 11 VANABLE JW, JR. A history of bioelectricity in development and regeneration. In: *A History of Regeneration Research*, DINAMORE CE (Ed.), Cambridge University Press, Cambridge, **1991**, pp. 151–177.
  - 12 BORGENS RB, ROEDERER E, COHEN MJ. Enhanced spinal cord regeneration in lamprey by applied electric fields. *Science* **1981**, 213(4508), 611–617.
  - 13 BORGENS RB. Restoring function to the injured human spinal cord. *Adv. Anat. Embryol. Cell Biol.* **2003**, 171, III–IV, 1–155.
  - 14 BORGENS RB, BLIGHT AR, MCGINNIS ME. Functional recovery after spinal cord hemisection in guinea pigs: The effects of applied electric fields. *J. Comp. Neurol.* **1990**, 296(4), 634–653.
  - 15 BASSETT CA. Fundamental and practical aspects of therapeutic uses of pulsed electromagnetic fields (PEMFs). *Crit. Rev. Biomed. Eng.* **1989**, 17(5), 451–529.
  - 16 EYRES KS, SALEH M, KANIS JA. Effect of pulsed electromagnetic fields on bone formation and bone loss during limb lengthening. *Bone* **1996**, 18(6), 505–509.
  - 17 RYABY JT. Clinical effects of electromagnetic and electric fields on fracture healing. *Clin. Orthop. Relat. Res.* **1998**(355 Suppl), S205–215.
  - 18 BORSALINO G, BAGNACANI M, BETTATI E, FORNACIARI F, ROCCHI R, ULUHOGLAN S, CECCHERELLI G, CADOSSO R, TRAINA GC. Electrical stimulation of human femoral intertrochanteric osteotomies. Double-blind study. *Clin. Orthop. Relat. Res.* **1988**(237), 256–263.
  - 19 MAMMI GI, ROCCHI R, CADOSSO R, MASSARI L, TRAINA GC. The electrical stimulation of tibial osteotomies. Double-blind study. *Clin. Orthop. Relat. Res.* **1993**(288), 246–253.
  - 20 SHARRARD WJ. A double-blind trial of pulsed electromagnetic fields for delayed union of tibial fractures. *J. Bone Joint Surg. Br.* **1990**, 72(3), 347–355.
  - 21 BRIGHTON CT, BLACK J, FRIEDENBERG ZB, ESTERHAI JL, DAY LJ, CONNOLLY JF. A multicenter study of the treatment of non-union with constant direct current. *J. Bone Joint Surg. Am.* **1981**, 63(1), 2–13.
  - 22 SCHADEN W, FISCHER A, SAILLER A. Extracorporeal shock wave therapy of nonunion or delayed osseous union. *Clin. Orthop. Relat. Res.* **2001**(387), 90–94.
  - 23 WONG JY, LANGER R, INGBER DE. Electrically conducting polymers can noninvasively control the shape and growth of mammalian cells. *Proc.*



- Acad. Natl. Sci. U.S.A.* **1994**, 91(8), 3201–3204.
- 24 WALLACE GG, INNIS PC. Inherently conducting polymer nanostructures. *J. Nanosci. Nanotechnol.* **2002**, 2(5), 441–451.
  - 25 RUBIO RETAMA J, LOPEZ CABARCOS E, MECERREYES D, LOPEZ-RUIZ B. Design of an amperometric biosensor using polypyrrole-microgel composites containing glucose oxidase. *Biosens. Bioelectron.* **2004**, 20(6), 1111–1117.
  - 26 LIU X, NEOH KG, CEN L, KANG ET. Enzymatic activity of glucose oxidase covalently wired via viologen to electrically conductive polypyrrole films. *Biosens. Bioelectron.* **2004**, 19(8), 823–834.
  - 27 LAKARD S, HERLEM G, VALLES-VILLAREAL N, MICHEL G, PROPPER A, GHARBI T, FAHYS B. Culture of neural cells on polymers coated surfaces for biosensor applications. *Biosens. Bioelectron.* **2005**, 20(10), 1946–1954.
  - 28 KIM DH, ABIDIAN M, MARTIN DC. Conducting polymers grown in hydrogel scaffolds coated on neural prosthetic devices. *J. Biomed. Mater. Res. A* **2004**, 71(4), 577–585.
  - 29 CASTANO H, O'REAR EA, MCFETRIDGE PS, STKAVITSAS VI. Polypyrrole thin films formed by admicellar polymerization support the osteogenic differentiation of mesenchymal stem cells. *Macromol. Biosci.* **2004**, 4(8), 785–794.
  - 30 DE GIGLIO E, GUASCITO MR, SABBATIN L, ZAMBONIN G. Electropolymerization of pyrrole on titanium substrates for the future development of new biocompatible surfaces. *Biomaterials* **2001**, 22(19), 2609–2616.
  - 31 MATTIOLI-BELMONTE M, GIAVARESI G, BIAGINI G, VIRGILI L, GIACOMINI M, FINI M, GIANTOMASSI F, NATALI D, TORRICELLI P, GIARDINO R. Tailoring biomaterial compatibility: In vivo tissue response versus in vitro cell behavior. *Int. J. Artif. Organs* **2003**, 26(12), 1077–1085.
  - 32 HERRING M, GARDNER A, GLOVER J. Seeding endothelium on to canine arterial prostheses. *Arch. Surgery* **1979**, 114, 679–682.
  - 33 GRAHAM LM, VINTER DW, FORD JW, KAHN RH, BURKEL WE, STANLEY JC. Cultured autogenous endothelial cell seeding of prosthetic vascular grafts. *Surg. Forum* **1979**, 30, 204–206.
  - 34 ESKIN SG, TREVINO L, CHIMOSKEY JE. Endothelial cell culture on dacron fabrics of different configurations. *J. Biomed. Mater. Res.* **1978**, 12(4), 517–524.
  - 35 ESKIN SG, ARMENIADES CD, LIE JT, TREVINO L, KENNEDY JH. Growth of cultured calf aortic smooth muscle cells on cardiovascular prosthetic materials. *J. Biomed. Mater. Res.* **1976**, 10(1), 113–122.
  - 36 CHENG WL, LIN CC. The effects of different electrical stimulation protocols on nerve regeneration through silicone conduits. *J. Trauma* **2004**, 56(6), 1241–1246.
  - 37 KERNS JM, PAVKOVIC IM, FAKHOURI AJ, WICKERSHAM KL, FREEMAN JA. An experimental implant for applying a DC electrical field to peripheral nerve. *J. Neurosci. Methods* **1987**, 19(3), 217–223.
  - 38 KOTWAL A, SCHMIDT CE. Electrical stimulation alters protein adsorption and nerve cell interactions with electrically conducting biomaterials. *Biomaterials* **2001**, 22(10), 1055–1064.
  - 39 MCDEVITT L, FORTNER P, POMERANZ B. Application of weak electric field to the hindpaw enhances sciatic motor nerve regeneration in the adult rat. *Brain Res.* **1987**, 416(2), 308–314.
  - 40 SHEN N, ZHU J. Experimental study using a direct current electrical field to promote peripheral nerve regeneration. *J. Reconstr. Microsurg.* **1995**, 11(3), 189–193.
  - 41 SIDZHANOV Zh M, SHABANOV AM, PAMURZIN LG, ZHARMAGAMBEV S, SADYKOV RG. Use of an electrical current for accelerating bone healing. *Ortop. Travmatol. Protez.* **1976**(10), 64–66.
  - 42 WEIGERT M. Stimulation of bone formation using electrical current. *Hefte Unfallheilkd* **1973**, 115(Suppl 115) 1–10.

- 43 SEIFALIAN AM, GIUDICEANDREA A, SCHMITZ-RIXEN T, HAMILTON G. Non-compliance: The silent acceptance of a villain. In: *Tissue Engineering of Vascular Prosthetic Grafts*. ZILLA P, GREISLER HP (Eds.), R.G. Landers Company, Austin, 1999, p. 621.
- 44 ROBINSON KR. The response of cells to electrical field: A review. *J. Cell Biol.* 1985, 101, 2023–2027.
- 45 CRISPIN B, WEINBERG CB, BELL E. A blood vessel model constructed from collagen and cultured vascular cells. *Science* 1986, 231(4736), 397–400.
- 46 GUIDOIN R, MARCEAU D, COUTURE J, JIAN RAO T, MERHI Y, ROY PE, DE LA FAYE D. Collagen coatings as biological sealants for textile arterial prostheses. *Biomaterials* 1989, 10(April), 156–165.
- 47 KUNTZ E. Ethicon, Inc., assignee. Preparation of collagenous materials. *US Patent 3 152 976*, 1964.
- 48 LEE CH, SINGLA A, LEE Y. Biomedical applications of collagen. *Int. J. Pharm.* 2001, 221(1–2), 1–22.
- 49 RAMSHAW JAM, WERKMEISTER JA, GLATTAUER V. Collagen-based biomaterials. *Biotechnol. Genetic Eng. Rev.* 1995, 13, 335–382.
- 50 WEINBERG CB, BELL E. A blood vessel model constructed from collagen and cultured vascular cells. *Science* 1986, 231(4736), 397–400.
- 51 ELBJEIRAMI WM, YONTER EO, STARCHER BC, WEST JL. Enhancing mechanical properties of tissue-engineered constructs via lysyl oxidase crosslinking activity. *J. Biomed. Mater. Res. A* 2003, 66(3), 513–521.
- 52 MOU SS, MA AD, TU M, LI LH, ZHOU CR. Preparation and biocompatibility of tissue-engineered scaffold materials based on collagen. *Di Yi Jun Yi Da Xue Xue Bao* 2002, 22(10), 878–879.
- 53 ORBAN JM, WILSON LB, KOFROTH JA, EL-KURDI MS, MAUL TM, VORP DA. Crosslinking of collagen gels by transglutaminase. *J. Biomed. Mater. Res. A* 2004, 68(4), 756–762.
- 54 PIEPER JS, VAN DER KRAAN PM, HAFMANS T, KAMP J, BUMA P, VAN SUSANTE JL, VAN DEN BERG WB, VEERKAMP JH, VAN KUPPEVELT TH. Crosslinked type II collagen matrices: Preparation, characterization, and potential for cartilage engineering. *Biomaterials* 2002, 23(15), 3183–3192.
- 55 CUI D, TIAN F, OZKAN CS, WANG M, GAO H. Effect of single wall carbon nanotubes on human HEK293 cells. *Toxicol. Lett.* 2005, 155(1), 73–85.
- 56 MONTEIRO-RIVIERE NA, NEMANICH RJ, INMAN AO, WANG YY, RIVIERE JE. Multi-walled carbon nanotube interactions with human epidermal keratinocytes. *Toxicol. Lett.* 2005, 155(3), 377–384.
- 57 OBERDÖRSTER E. Manufactured nanomaterials (fullerenes, C<sub>60</sub>) induce oxidative stress in the brain of juvenile Largemouth Bass. *Environ. Health Perspectives* 2004, 112(10), 1058.
- 58 SHVEDOVA AA, CASTRANOVA V, KISIN ER, SCHWEGLER-BERRY D, MURRAY AR, GANDELSMAN VZ, MAYNARD A, BARON P. Exposure to carbon nanotube material: Assessment of nanotube cytotoxicity using human keratinocyte cells. *J. Toxicol. Environ. Health A* 2003, 66(20), 1909–1926.
- 59 WARHEIT DB, LAURENCE BR, REED KL, ROACH DH, REYNOLDS GA, WEBB TR. Comparative pulmonary toxicity assessment of single-wall carbon nanotubes in rats. *Toxicol. Sci.* 2004, 77(1), 117–125.
- 60 SCHULER E. Perception of risks and nanotechnology. In: *Discovering the Nanoscale*, BAIRD D, NORDMANN A, SCHUMMER J (eds.), IOS Press. 2004, 219.
- 61 SHVEDOVA AA. Exposure to carbon nanotube material: Assessment of nanotube cytotoxicity using human keratinocyte cells. *J. Toxicol. Environ. Health, Part A* 2003, 66, 1909–1926.
- 62 NIMMAGADDA A, THURSTON K, NOLLERT UM, McFETRIDGE PS. Chemical modification of SWNT alters in vitro cell-SWNT interactions. *J. Biomed. Mater. Res. Part A* 2006, 76A(3), 614–625.
- 63 BETHUNE DS, KLANG CH, DEVRIES MS, GORMAN G, SAVOY R, VAZQUEZ J, BEYERS R. Cobalt-catalysed growth of carbon nanotubes with single-atomic-layer wall. *Nature* 1993, 363, 605–607.

- 64 CHEN J, HAMON MA, HU H, CHEN Y, RAO AM, EKLUND PC, HADDON RC. Solution properties of single-walled carbon nanotubes. *Science* **1998**, *282*, 95–98.
- 65 IIJIMA S. Single shell carbon nanotubes of one nanometer diameter. *Nature* **1993**, *363*, 503–605.
- 66 MAYNARD AD, BARON PA, FOLEY M, SHVEDOVA AA, KISIN ER, CASTRANOVA V. Exposure to carbon nanotube material: Aerosol release during the handling of unrefined single-walled carbon nanotube material. *J. Toxicol. Environ. Health A* **2004**, *67*(1), 87–107.
- 67 DRESSELHAUS MS. Nanotechnology – New tricks with nanotubes. *Nature* **1998**, *391*, 19.
- 68 WU W, WIECKOWSKI S, PASTORIN G, BENINCASA M, KLUMPP C, BRIAND JP, GENNARO R, PRATO M, BIANCO A. Targeted delivery of amphotericin B to cells by using functionalized carbon nanotubes. *Angew. Chem. Int. Ed.* **2005**, *44*(39), 6358–6362.
- 69 WONG SHI KAM N, JESSOP TC, WENDER PA, DAI H. Nanotube molecular transporters: Internalization of carbon nanotube-protein conjugates into mammalian cells. *J. Am. Chem. Soc.* **2004**, *126*, 6850–6851.
- 70 CHERUKURI P, BACHILO SM, LITOVSKY SH, WEISMAN RB. Near-infrared fluorescence microscopy of single-walled carbon nanotubes in phagocytic cells. *J. Am. Chem. Soc.* **2004**, *126*(48), 15 638–15 639.
- 71 MATSUI H, ITO T, OHNISHI S. Phagocytosis by macrophages. III. Effects of heat-labile opsonin and poly(L-lysine). *J. Cell Sci.* **1983**, *59*, 133–143.
- 72 PANTAROTTO D, BRIAND JP, PRATO M, BIANCO A. Translocation of bioactive peptides across cell membranes by carbon nanotubes. *Chem Commun (Camb)* **2004**(1), 16–17.
- 73 PANTAROTTO D, SINGH R, MCCARTHY D, ERHARDT M, BRIAND JP, PRATO M, KOSTARELOS K, BIANCO A. Functionalized carbon nanotubes for plasmid DNA gene delivery. *Angew. Chem. Int. Ed.* **2004**, *43*(39), 5242–5246.
- 74 POMPEO F, RESASCO DE. Water solubilization of single-walled carbon nanotubes by functionalization with glucosamine. *Nano Lett.* **2002**, *2*(4), 369–373.
- 75 JIN YP, GUPTA D, DZIARSKI R. Endothelial and epithelial cells do not respond to complexes of peptidoglycan with soluble CD14 but are activated indirectly by peptidoglycan-induced tumor necrosis factor-alpha and interleukin-1 from monocytes. *J. Infectious Dis.* **1998**, *177*(6), 1629–1638.
- 76 SENNETT M, WELSH ER, WRIGHT JB, LI WZ, WEN JG, REN ZF. Dispersion and alignment of carbon nanotubes in polycarbonate. *Appl. Phys. A: Mater. Sci. Proc.* **2003**, *76*, 111–113.
- 77 HAGGENMUELLER R, GOMMANS HH, RINZLER AG, FISCHER JE, WINEY KI. Aligned single-wall carbon nanotubes in composites by melt processing methods. *Chem. Phys. Lett.* **2000**, *330*(3–4), 219–225.
- 78 FISCHER JE, ZHOU W, VAVRO J, LLAGUNO MC, GUTHY C, HAGGENMUELLER R, CASAVANT MJ, WALTERS DE, SMALLEY RE. Magnetically aligned single wall carbon nanotube films: Preferred orientation and anisotropic transport properties. *J. Appl. Phys.* **2003**, *94*(4), 2157–2163.
- 79 WALTERS DA, CASAVANT MJ, QIN XC, HUFFMAN CB, BOUL PJ, ERICSON LM, HAROZ EH, O'CONNELL MJ, SMITH K, COLBERT DT et al. In-plane-aligned membranes of carbon nanotubes. *Chem. Phys. Lett.* **2001**, *338*(1), 14–20.
- 80 POMPEO F, RESASCO D. Water solubilization of single-walled carbon nanotubes by functionalization with glucosamine. *Nano Lett.* **2002**, *2*(4), 369–373.
- 81 BAKER SE, CAI W, LASSETER TL, WEIDKAMP KP, HAMERS RJ. Covalently bonded adducts of deoxyribonucleic acid (DNA) oligonucleotides with single-wall carbon nanotubes: Synthesis and hybridization. *Nano Lett.* **2002**, *2*(12), 1413–1417.
- 82 CHEN J, RAO AM, LYUKSYUTOV S, ITKIS ME, HAMON MA, HU H, COHN RW, EKLUND PC, COLBERT DT,

- SMALLEY RE and others. Dissolution of full-length single-walled carbon nanotubes. *J. Phys. Chem. B* **2001**, 105(13), 2525–2528.
- 83 FU K, HUANG W, LIN Y, ZHANG D, HANKS TW, RAO AM, SUN YP. Functionalization of carbon nanotubes with bovine serum albumin in homogeneous aqueous solution. *J. Nanosci. Nanotechnol.* **2002**, 2(5), 457–461.
- 84 ZHENG M, JAGOTA A, SEMKE ED, DINER BA, MCLEAN RS, LUSTIG SR, RICHARDSON RE, TASSI NG. DNA-assisted dispersion and separation of carbon nanotubes. *Nat. Mater.* **2003**, 2(5), 338–342.
- 85 BIANCO A, KOSTARELOS K, PARTIDOS CD, PRATO M. Biomedical applications of functionalised carbon nanotubes. *Chem. Commun. (Camb)* **2005**(5), 571–577.
- 86 MING Z, JAGOTA A, SEMKE ED, DINER BA, MCLEAN RS, LUSTIG SR, RICHARDSON RE, TASSI NG. DNA-assisted dispersion and separation of carbon nanotubes. *Nat. Mater.* **2003**, 2, 338.
- 87 ERLANGER BF, BI-XING CHEN, MIN ZHU, LOUIS BRUS. Binding of an anti-fullerene IgG monoclonal antibody to single wall carbon nanotubes. *Nano Lett.* **2001**, 1(9), 465–467.
- 88 MATARREDONE O, HEATHER RHOADS, ZHONGRUI LI, JEFFREY H. Harwell, Leandro Balzano, Daniel E. Resasco. Dispersion of single-walled carbon nanotubes in aqueous solutions of the anionic surfactant NaDDBS. *J. Phys. Chem. B* **2003**, 107, 13 357–13 367.
- 89 MACDONALD RA, LAURENZI BF, VISWANATHAN G, AJAYAN PM, STEGEMANN JP. Collagen-carbon nanotube composite materials as scaffolds in tissue engineering. *J. Biomed. Mater. Res. A* **2005**, 74(3), 489–496.
- 90 SUPRONOWICZ PR, AJAYN PM, ULLMANN KR, ARULANADAM BP, METZGER DW, BIZIOS R. Novel current-conducting composite substrates for exposing osteoblasts to alternating current stimulation. *J. Biomed. Mater. Res.* **2002**, 59, 499–506.
- 91 ZHAO B, HU H, MANDAL SK, HADDON RC. A bone mimic based on the self-assembly of hydroxyapatite on chemically functionalized single-walled carbon nanotubes. *Chem. Mater.* **2005**, 17, 3235–3241.
- 92 SHI X, HUDSON JL, SPICER PP, TOUR JM, KRISHNAMOORTI K, MIKOS AG. Rheological behaviour and mechanical characterization of injectable poly(propylene fumarate)/single-walled carbon nanotube composites for bone tissue engineering. *Nanotechnology* **2005**, 16, S531–S538.
- 93 HU H, NI Y, MONTANA V, HADDON RC, PARPURA V. Chemically functionalized carbon nanotubes as substrates for neuronal growth. *Nano Lett.* **2004**, 4, 507–511.
- 94 MATTSON MP, HADDON RC, RAO AM. Molecular functionalization of carbon nanotubes and use as substrates for neuronal growth. *J. Mol. Neurosci.* **2000**, 14(3), 175–182.
- 95 LOVAT V, PANTAROTTO D, LAGOSTENA L, CACCIARI B, GRANDOLFO M, RIGHI M, SPALLUTO G, PRATO M, BALLERINI L. Carbon nanotube substrates boost neuronal electrical signaling. *Nano Lett.* **2005**, 5(6), 1107–1110.
- 96 HU H, NI Y, MANDAL SK, MONTANA V, ZHAO B, HADDON RC, PARPURA V. Polyethyleneimine functionalized single-walled carbon nanotubes as a substrate for neuronal growth. *J. Phys. Chem. B: Lett.* **2005**, 109, 4285–4289.
- 97 WEBSTER TJ, WAID MC, MCKENZIE JL, PRICE RL, EJIUFOR JU. Nanobiotechnology: Carbon nanofibres as improved neural and orthopaedic implants. *Nanotechnology* **2004**, 15(1), 48–54.
- 98 CORREA-DUARTE MA, WAGNER N, ROJAS-CHAPANA J, MORSCZECK C, THIE M, GIERSIG M. Fabrication and biocompatibility of carbon nanotube-based 3D networks as scaffolds for cell seeding and growth. *Nano Lett.* **2004**, 4(11), 2233–2236.

## 10

# Nanoparticles for Cell Engineering – A Radical Concept

*Beverly A. Rzigalinski, Igor Danelisen, Elizabeth T. Strawn,  
Courtney A. Cohen, and Chengya Liang*

### 10.1 Introduction and Overview

Nanotechnology holds great promise for the treatment of disease through cellular engineering. Engineering has made substantial advances in materials science and construction of nanoscale devices over the last decade. Movement of this emerging technology into the realm of cell biology and medicine involves applying these advances to biological systems, providing novel opportunities to intervene in the progression and pathology of disease. To accomplish this, scientists must develop the ability to work and reason in a manner that merges previously distinct disciplines; applying the principles of physics and engineering to cell biology and physiology. This chapter is directed towards achieving this goal.

It is of critical importance to address this merging of disciplines in our written discussions of nanotechnological inroads into the biomedical sciences. The present chapter discusses such a progression in an interdisciplinary manner for the first time, by examining the role of engineered nanoparticles as free radical scavengers at the cellular level and their potential use as pharmacological agents for free radical-mediated disorders.

We begin with a brief discussion of free radicals and their role in cellular function and dysfunction, followed by examination of the role of oxidative stress in aging and disease. The current pharmacology of oxidative stress will be addressed along with its limited efficacy. Comparisons will be made regarding free radical processes in biological vs. industrial and chemical processes. Next, we will examine an alternative, nanotechnological approach to oxidative stress at the cellular level and examine the emerging potential for the utilization of different nanoparticles in the treatment of disease.

## 10.2

### Free Radicals and Oxidative Stress

Free radicals are highly reactive compounds, lacking the full complement of electrons necessary for molecular stability. In biological organisms, unstable free radicals can strip electrons from cellular macromolecules, rendering them dysfunctional. Free radical species encountered within the cell include superoxide ( $O_2^-$ ), the hydroxyl radical ( $OH^\cdot$ ), nitric oxide (NO), peroxynitrite ( $ONOO^-$ ), lipid hydroperoxides, and others [1–5]. Importantly, many free radical reactions in the cell are self-propagating [6]. An example of this is the lipid peroxidation chain reaction, initiated by the hydroxyl radical ( $OH^\cdot$ ). The reaction is initiated by interaction of the hydroxyl radical with a membrane lipid (L):



In the second phase of the propagation process:

1.  $LH^\cdot + O_2 \rightarrow LHOO^\cdot$
2.  $LHOO^\cdot + LH_2 \rightarrow LHOOH + LH^\cdot$

Thus, the free radical species is regenerated to propagate the peroxidation reaction. In hydrophobic areas such as the plasma membrane, chain reactions of lipid peroxidation can damage membrane structure and induce cell death [6–8]. One of the end products of peroxidative damage to cellular lipids is the destructive aldehyde 4-hydroxy-2-nonenal (4HNE), a highly reactive electrophile that interacts with protein constituents such as cysteine, histidine, and lysine [9, 10]. 4-HNE has been implicated as a damaging factor in many human disease states, by virtue of disruption of protein function. Formation of prostaglandin-like compounds, termed isoprostanes, by free radical-mediated lipid peroxidation has also been implicated in numerous pathological conditions [11]. In addition to lipid peroxidation, cellular sugars and proteins can also undergo free radical mediated oxidation, which may induce loss of catalytic function, destruction of cellular architecture, increased degradation or accumulation of damaged cellular constituents, as occurs in many neurodegenerative, ischemic, diabetic, and other disorders (Table 10.1). Engineering and materials science readers should note that these biological free radical processes are similar to those encountered in industrial and materials science applications – the players are somewhat different but the game remains the same.

#### 10.2.1

##### Sources of Intracellular Free Radicals

Free radicals arise from many sources within the cell, as described in several good reviews [5, 12–16]. Mitochondria and the oxidative phosphorylation process are considered to be a primary site of free radical production, giving rise to superoxide

**Tab. 10.1.** Human disease states that generate oxidative stress or of which oxidative stress is a known component.

Organ system	Disease
Brain, CNS, PNS	Alzheimer's, Parkinson's, Huntington's, Multiple Sclerosis Trauma, Stroke, Ischemia, Other Neurodegenerative disorders
Circulatory	Atherosclerosis, Hyperlipidemia, Cardiovascular diseases Vascular disorders, Hypertension
Endocrine	Diabetes, Metabolic Syndrome
Musculoskeletal	Arthritis, Physical injury, Joint disorders
Immune	Allergic disorders, Autoimmune disorders, Inflammatory disorders
Respiratory	Asthma, emphysema, COPD, Bronchitis
Digestive	Inflammatory bowel disease, Crohn's disease

radicals during the passage of electrons through the electron transport chain [17–19]. Free radicals are also formed at sites of inflammation, released by neutrophils and macrophages to destroy invading bacteria [1, 18]. However, cells of the immune system also generate free radicals in inflammatory disorders such as Alzheimer's disease, arthritis, and cardiovascular disease, where they initiate or propagate tissue damage [5].

Free radical production is also a by-product of certain normal cellular enzymatic reactions. The cyclooxygenase enzyme produces free radicals during prostaglandin synthesis [20, 21]. NADPH oxidase and xanthine/xanthine oxidase are also intracellular enzyme systems associated with generation of free radicals during normal metabolic function [1, 6, 21]. NO is a free radical produced by nitric oxide synthase (NOS) and is commonly utilized in cell signaling in the nervous and cardiovascular systems [22]. However, overproduction of NO in inflammatory and disease states such as atherosclerosis can result in formation of the highly reactive peroxynitrite radical (ONOO<sup>•</sup>), which can subsequently induce nitrosylation of critical cellular proteins and damage their function.

In addition to endogenously generated free radicals, organisms are exposed to numerous exogenous sources of free radicals and free radical generating agents during a typical life span. These include environmental toxins such as pesticides, radiation, pharmacological agents, industrial pollutants, food additives, cigarette smoke, and many others. In summary, the typical cell is exposed to numerous free radicals from both endogenous and exogenous sources during a lifetime. Such free radical exposure, if unchecked or excessive, may induce considerable damage to cellular constituents necessary for survival and function.

## 10.2.2

**Oxidative Stress**

Healthy cells are able to counteract the damaging effects of free radicals via innate, natural, enzymatic or molecular mechanisms. Superoxide dismutase (SOD) catalyzes the conversion of the superoxide radical into  $\text{H}_2\text{O}_2 + \text{O}_2$ . Although  $\text{H}_2\text{O}_2$  is also damaging to biological systems, catalase and glutathione peroxidase enzymes convert  $\text{H}_2\text{O}_2$  into  $\text{O}_2 + 2\text{H}_2\text{O}$ . Other endogenous reductants that ameliorate cellular free radicals include *n*-acetyl cysteine, vitamin E, vitamin C, carotenes, melatonin, and lipoic acid derivatives, and are the subject of many recent reviews [1, 23–27].

Although excessive free radical production can be damaging, production of free radicals in low amounts is necessary for normal cell function and signaling. For example, the free radical NO is necessary for normal signal transduction pathways in the vasculature [28] and neurotransmission in the brain [23]. Phagocytic cells routinely utilize free radicals for destruction of invading bacteria or cells infected with viruses. Regulation of cell signaling pathways such as phosphatase activity, calcium signaling, and transcription factors have all been implicated in having regulatory links with free radical production within the cell [22, 29, 30]. Hence a low amount of free radicals appears to be important to normal cell function and the healthy cell achieves a biological balance between free radical production and degradation.

Cellular havoc arises when the production of free radicals exceeds the capacities of cellular defense mechanisms or when cell defense mechanisms are compromised by aging and other pathological states, disturbing the biological balance. In this case, production of free radicals far exceeds their normal signaling functions and damage to cellular macromolecules ensues. The burden of free radicals imposed upon a cell in such a situation is termed oxidative stress, and often arises as a prerequisite or result of aging or disease states. For an example of this, let us return to the subject of the NO free radical. NO is an important neurotransmitter in regulated, low, amounts. However, when produced in overabundance due to neuronal damage or in the presence of hydroxyl radicals, oxidative stress can be imposed upon the brain. The damaging ONOO<sup>-</sup> radical is formed under these conditions, which can induce lipid peroxidation and nitration of protein tyrosine residues [31]. Tyrosine nitration inhibits phosphorylation of tyrosine residues in proteins, an important signaling mechanism in cell regulation. Other free radicals may catalyze formation of carbonyl groups on proteins, which can interfere with tertiary conformation and inhibit or reduce their function [30, 32, 33]. The end result of such cumulative damage is cell dysfunction or demise.

Within the cell, there is a balance between the rate of free radical production and the capacity of cellular defense mechanisms to mitigate free radical damage. When cellular mitigating systems are compromised, high levels of oxidative stress can do extensive cell damage. Cellular pathologies associated with free radicals include lysosome and proteasome dysfunction leading to cell death [34–36], loss of signaling cascades mediated by phosphorylation [32, 37], oxidation of DNA bases [38, 39],



destruction of the membrane lipid environment [40, 41], loss of vascular tone and responsivity [32, 42], aberrant neurotransmission [16, 43, 44], mitochondrial dysfunction [1, 13, 14], and initiation of cell death pathways [12, 16, 45].

### 10.2.3

#### **Oxidative Stress and Disease**

A multitude of disease pathologies are caused or otherwise related to oxidative stress, including Alzheimer's disease, inflammatory disorders, Parkinson's disease, diabetes, atherosclerosis, hypertension, and mechanical injury, which are summarized in Table 10.1 and are the subject of numerous works [1, 18, 25, 43, 46–49]. As with Alzheimer's disease, free radical production is often not the ultimate causative factor, but is a byproduct of cellular malfunction initiated by amyloid beta peptide. Aberrant free radical production by damaged cells can lead to destruction of uninjured “bystander” tissue, thereby propagating the damage. In Alzheimer's disease, excessive free radical production in damaged neurons and inflammatory activation of microglia leads to free radical injury of healthy, neighboring neurons [37, 44, 50]. Similar pathologies have been associated with atherosclerosis, arthritis, and other inflammatory disorders that are prevalent in aging organisms [1, 6, 51–54].

Of particular interest to us all has been the role of free radicals in aging and age-associated disorders. As described by Harman [55], aging began with the origin of life, and represents the accumulation of diverse deleterious changes in cells and tissues that increase the risk of disease and death. Although there are several theories on aging, the “Free Radical Theory of Aging” appears to have the most biochemical support [23, 50, 55]. According to this theory, aging is associated with accumulation of macromolecular free radical damage to lipid membranes, mitochondria, protein, and DNA, promoting cell dysfunction and death. Numerous lines of evidence support this hypothesis and are the subject of several excellent reviews [1, 45, 49, 50]. Aging is accompanied by an increase in the level of oxidative damage such as carbonyl groups and tyrosine nitration of cellular proteins, a general index of free radical damage [32, 33, 56]. Late onset Alzheimer's is characterized by an accumulation of oxidatively modified proteins [32, 57]. The antioxidant spin trap *n*-*t*-butyl- $\alpha$ -phenylnitron improved spatial memory of aged rats relative to untreated controls, and also decreased the level of oxidative damage to cellular macromolecules in the brain [32]. Lipid peroxidation products have also been shown to increase with age [58], suggesting that membrane damage accumulates over the course of a lifespan.

Quality of life, not only life span, is important in the aging process. Once again, the free radical hypothesis maintains that free radical production is associated with cognitive deficits, neuronal dysfunction, atherosclerotic conditions, and inflammatory conditions associated with aging. Neural tissue has the highest ATP and oxygen utilization of all the organs in the body. It follows that neural tissue is therefore exposed to some of the highest levels of oxidative stress in neurodegenerative diseases and aging. Several reviews [59–61], suggest that free radical scavengers

may be useful therapeutic adjuncts in treatment and prevention of age-associated disorders, improving the quality of life.

Given the widespread involvement of free radicals in aging and disease, the use of free radical scavengers or antioxidants as pharmacological therapy has been reported in many disorders (reviewed in Refs. [25, 27, 52, 54, 59–61]). Free radical scavengers such as vitamin E, vitamin C, *n*-acetyl cysteine, melatonin, SOD mimetics, 21-aminosteroids, 2-methylaminochromans and nitrosone spin traps have been utilized to lessen the severity of disorders associated with free radical production. However, many of these free radical scavengers have met with only limited clinical success. For example, SOD and poly(ethylene glycol)-conjugated SOD showed promise in the treatment of traumatic head injury, where superoxide radical production contributes to disease pathology [59, 61, 62]. Yet clinical trials of these agents yielded far from promising results, likely due to lack of cell or tissue penetration. On the whole, pharmacological use of free radical scavengers has several problematic aspects. The first is lack of penetration to the site of radical production, as may be the case with exogenous SOD mimetics. Similarly, vitamin C is also a free radical scavenger, yet it is thought to function only in aqueous environments and has difficulty crossing the lipid membrane of the cell. Additionally, due to its chemical structure, high concentrations of vitamin C are also reported to act as free radical generators, so proper dose is critical to antioxidant function. The second problematic issue is the requirement for repeated dosage. Many of these scavengers require repetitive daily dosing to replace molecular species that were utilized in free radical reduction. In the case of vitamins C or E and other antioxidants, one molecule of antioxidant is utilized for each free radical detoxified, and regeneration is low or non-existent in the case of exogenous agents such as spin traps and 21-aminosteroids. In summary, although supplementation with free radical scavengers has shown to be beneficial in several disease states, the overall success has been limited at the clinical level.

### 10.3

#### A Nanotechnological Approach to Oxidative Stress

Up to this point, our discussion of free radicals and oxidative stress have focused on events from a biological standpoint. However, if we examine the basic chemistry of free radical mechanisms, the engineer will realize that the cellular processes underlying biological oxidative stress are encountered in many non-biological instances. Let us take, for example, the processes involved in three-way catalysis for improved combustion and removal of environmental contaminants from engine exhaust. These processes have much in common with the biological concept of redox reactions and antioxidants from a chemical and physical standpoint. Likewise, the role of coatings in reduction of metal oxidation involves chemical principles similar to those associated with prevention of oxidation of biomolecules, intracellularly. Nanoparticle formulations added to such industrial catalytic systems often serve the role of a catalysis promoter or a stabilizer, to improve the efficiency

of the catalyst. However, looking at this issue from a cross-disciplinary standpoint, the actions of enzymes and cofactors involved in biochemical reactions can be defined in a similar manner, in that they act at catalysis promoters that are unchanged by the reaction they catalyze. From an engineering standpoint, nanotechnology has provided dramatic improvement in industrial applications related to efficiency of redox reactions. Cross-disciplinary application of these processes to cellular redox reactions occurring on the nano-scale intracellularly may provide a new basis for pharmacological treatment of many diseases related to oxidative stress.

Three of the most-studied nanoparticle redox reagents, at the cellular level, are rare earth oxide nanoparticles (particularly cerium), fullerenes and their derivatives, and carbon nanotubes. In the following sections, we discuss the chemistry and biological properties of these nanoparticles and their potential use in preservation of cellular redox status and treatment of disease.

### 10.3.1

#### Rare Earth Oxide Nanoparticles – Cerium

Rare earth oxides of cerium, neodymium, praseodymium, and ruthenium have been utilized in three-way catalysts for enhancement of fuel combustion, removal of soot from engine exhaust, removal of environmental free radical contaminants such as NO and SO from fuel exhaust, removal of organics from wastewater, promoters of catalysis in environmental clean up, and in development of fuel cell technologies [75]. These applications are all related to the high redox capabilities of rare earth oxides; that being their ability to serve as free radical scavengers. Out of the lanthanide series of elements, oxides of cerium (ceria,  $\text{CeO}_2$ ) nanoparticles are reported to have several unique properties that make them highly efficient redox reagents (Fig. 10.1). To date, on the intracellular level, ceria has been the most-studied of this nanoparticle group.

As a rare earth element of the lanthanide series, cerium oxide has a characteristic fluorite lattice structure. Lanthanides exist in the earth's crust at about 100 ppm,

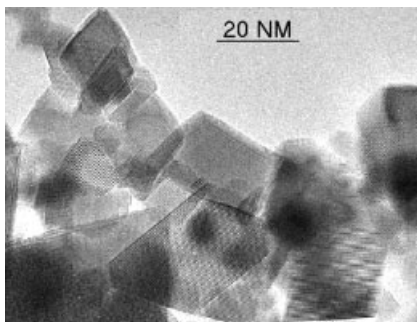


**Fig. 10.1.** Electron micrograph of cerium oxide nanoparticles. (Courtesy of Nanophase Inc., Romeoville, Illinois.)

with cerium making up approximately 24 ppm [63]. However, cerium has several unique properties among the rare earths, established by examining microcrystalline cerium oxide structures [65]. First, cerium has two partially filled subshells of electrons, 4f and 5d, with 14 excited sub-states of cerium predicted [66]. The cerium atom can exist in either the +3 (fully reduced) or +4 (fully oxidized) state, and may readily flip-flop between the two in a redox reaction [66–68]. Both the crystal lattice size and the bond length change when alterations in redox state occur. It is hypothesized that cerium oxides make excellent oxygen buffers with high oxygen storage capacities, because of their high redox capabilities [64]. In addition to alterations in cerium redox state, cerium oxide also exhibits oxygen vacancies, or defects, in the lattice structure, by loss of oxygen and/or its electrons [66, 67]. Formation of each defect removes a subgroup of ions from the lattice structure. Thus, creation and annihilation of oxygen vacancies occurs in the cerium oxide lattice during redox reactions [65]. Cerium and its oxides are also unique, among the rare earths, in that there is a high hydrogen absorbing capacity on the surface, providing for ease of reactions with  $H_2$ ,  $O_2$ , or  $H_2O$ , as compared with other rare earths.

The valence and defect structure of cerium oxide is dynamic and may change spontaneously or in response to physical parameters such as temperature, pH, presence of other ions, and oxygen partial pressure [67–69]. Several groups have examined the use of cerium oxide particles as metal coatings to reduce oxidation and as coatings for catalytic converters, to enhance oxidation of carbon monoxide and hydrocarbons, and reduce nitrogen oxide emissions [70, 71]. A primary role of cerium oxide under these conditions is to act as an oxygen storage and release component [69]. The chemical reactions of cerium oxide have been reviewed [68, 72–75] and include oxygen atom transfer and absorption, oxidation of unsaturated hydrocarbons, electron transfer to hydrocarbon radicals, high catalytic activity in redox reactions, and reduction of nitrogen oxide. One cannot avoid noting the similarities between these uses and the properties necessary for a good cellular antioxidant. Thus, the chemistry of cerium oxide further supports a potential role as either a biological free radical scavenger or antioxidant.

The atomic and molecular properties of materials at the nanometer scale change in ways we are just beginning to comprehend. The chemical behavior of cerium oxide nanoparticles may reflect the chemical properties of its macromolecular structure to some extent, but altered characteristics are likely at the nanoscale. For example, Raman spectra of cerium oxide nanoparticles are very different from microparticles [68]. Creation and annihilation of oxygen vacancies is reported to occur more rapidly in nano-ceria, making it a more efficient redox center in industrial applications. Guo and Waser have reported that the electrical conductivity of nanocrystalline  $CeO_2$  is several orders of magnitude higher than its microcrystalline form [76]. Several other groups report that nanocrystalline cerium oxide shows enhanced electrical conductivity as grain size decreases below 100 nm, due to a decrease in the enthalpy of oxygen defect formation [67–69]. Thus, oxygen vacancies are likely to form more readily at the nanoscale, increasing the number of sites available for free radical scavenging. Additionally, the surface area of cerium oxide

particles (grain boundary) is dramatically increased at the nanoscale, so greater oxygen exchange and redox reactions may occur over the increased surface area [71]. It is precisely these proposed alterations in cerium oxide nanoparticles that may impart cellular biological effects. Several reports indicate that ceria and its oxides are the only rare earth elements capable of undergoing redox transformations at ambient temperatures, such as those encountered in the intracellular environment [77, 78]. However, the chemical properties of cerium oxide nanoparticles under physiologically relevant parameters remain unknown, as most studies to date utilize temperatures and pressures well above the physiological range. Thus, there is a distinct need to further study the chemistry and physics of ceria nanoparticles at physiological temperatures and in medium with ionic composition similar to the intracellular and interstitial fluid environment.

#### 10.3.1.1 Biological Effects of Cerium

Biologically, cerium has been utilized most often in the form of nitrates or chlorides of cerium. In China, cerium chlorides and nitrates are used in fertilizers, to increase harvest [74]. Aged rice seed treated with cerium nitrate showed an enhanced respiratory rate and increased activities of superoxide dismutase, catalase, and peroxidase, enzymes associated with reduction of oxidative stress and free radicals [79].

Cerium has been found in humans and other animals, with amounts varying from several parts per billion to parts per million. In a feeding study conducted in pigs, feed containing rare earth elements (38% La, 52% Ce, 10% other) increased weight gain and feed conversion ratios [80], thereby enhancing biomass production. No negative health effects were observed. Serum cholesterol, triglycerides, total protein, albumin and ionic composition were normal and concentration of rare earths in the tissues was below 52  $\mu\text{g}$  per kg dry weight. Cerium nitrate has been used in treatment of burns, and improved the outcome of burn patients [81, 82]. Improved outcome was associated with a reduction in the systemic inflammatory response observed in burn victims and improved capacity for tissue repair. Rare earths in general have potent anti-atherosclerotic, anti-arthritis, and anti-inflammatory activity. Histologically, the chloride form of cerium has been used to identify subcellular sites of free radical (superoxide,  $\text{H}_2\text{O}_2$ ) production [83, 84]. It has also been used to study the location of xanthine/xanthine oxidase in rat liver cells, an enzyme associated with free radical production [22]. Although these studies involve the use of nitrates and chlorides of cerium, they support a distinct role for cerium in interaction with cellular free radicals.

From the few existing reports, cerium is relatively inert from the biological standpoint of toxicity – but reports are scarce and do not address oxides of cerium, much less nanoparticles. However, some negative biological effects have been reported, particularly at high concentrations. One report of inhalation pneumoconiosis was identified, occurring in a lens grinder exposed to prolonged high inhaled concentrations of rare earths [85]. Millimolar solutions have been shown to aggregate erythrocyte membranes *in vitro*, through disulfide bond crosslinks [86]. At high concentrations and non-physiological pH, cerium chloride served as a catalyst

for DNA and peptide hydrolysis [87]. Cerium chloride given to rats at 0.2–20 mg kg<sup>-1</sup> increased the oxygen affinity of hemoglobin by alteration of the secondary structure [87]. Based on its redox activities, it appears likely that cerium interacts with proteins such as hemoglobin and cytochrome P450, which contain heme-iron centers at the active site. However, once again, these reports represent the activity of cerium in the chloride or nitrate form, at millimolar concentrations. The biological properties of cerium oxide nanoparticles are likely to substantially differ.

#### 10.3.1.2 Biological Effects of Cerium Oxide Nanoparticles

The previous section describes the biological effects of cerium in general; however, cerium oxide nanoparticles, although having some similar properties, appear to be quite different on the whole. At the cellular level, cerium oxide nanoparticles have several potent properties, notably at extension of cellular longevity and as regenerative antioxidants.

In several studies, the Rzigalinski laboratory has demonstrated that nanoparticles of cerium oxide, of the size range of 6–20 nm, prolong the lifespan of mixed brain cell cultures, by 6–8-fold [88–90]. Ceria nanoparticles of greater than 20 nm were without effect at prolongation of life span, as were ruthenium, titanium, and neodymium oxide nanoparticles. In these experiments, cerium oxide nanoparticles were added directly to the tissue culture medium on day 10 *in vitro*, allowed to remain in the medium for 48 h, followed by replacement with fresh medium. Thus, a 48 h period was allowed for particle uptake. The optimal particle dose was 10 nM in the tissue culture medium. Figure 10.2 shows representative light micrographs of mixed brain cell cultures treated with cerium oxide. Importantly, neurons present in these aged cultures demonstrated signaling characteristics similar to their younger, untreated counterparts, demonstrating that normal neuronal function was also preserved in ceria nanoparticle-treated cultures [88–90].

Based on the industrial uses of ceria nanoparticles in redox reactions, it was hypothesized that the cellular effects of ceria nanoparticles were due to a free radical scavenging activity. To examine the mechanism of action further, cell cultures were exposed to free radical generating conditions of UV light,  $\gamma$ -radiation, H<sub>2</sub>O<sub>2</sub>, and trauma [88, 90–93]. Cultures treated with ceria nanoparticles showed dramatic resistance to these forms of oxidative stress, and survival exceeded that observed with the biological free radical scavengers vitamin E, melatonin, and *n*-acetyl cysteine.

Of critical importance is the dosing regime used in these studies. First, cultures were only treated once, on day 10 *in vitro*. At this time in culture, a confluent astrocyte monolayer covers the bottom of the tissue culture well, with neurons, microglia, and oligodendrocytes loosely attached to the astrocyte layer. Little cell division occurs at this time, and most of the cells in culture are terminally differentiated. A single dose of ceria nanoparticles was responsible for the dramatic extension of lifespan observed in these cultures. Further, a single dose on day 10 demonstrated enhanced protection against oxidative stressors through the extended lifespan of the cultures. This suggests that the antioxidant capacity of ceria nanoparticles in the cell may be, unlike many free radical scavengers, regenerative. The known

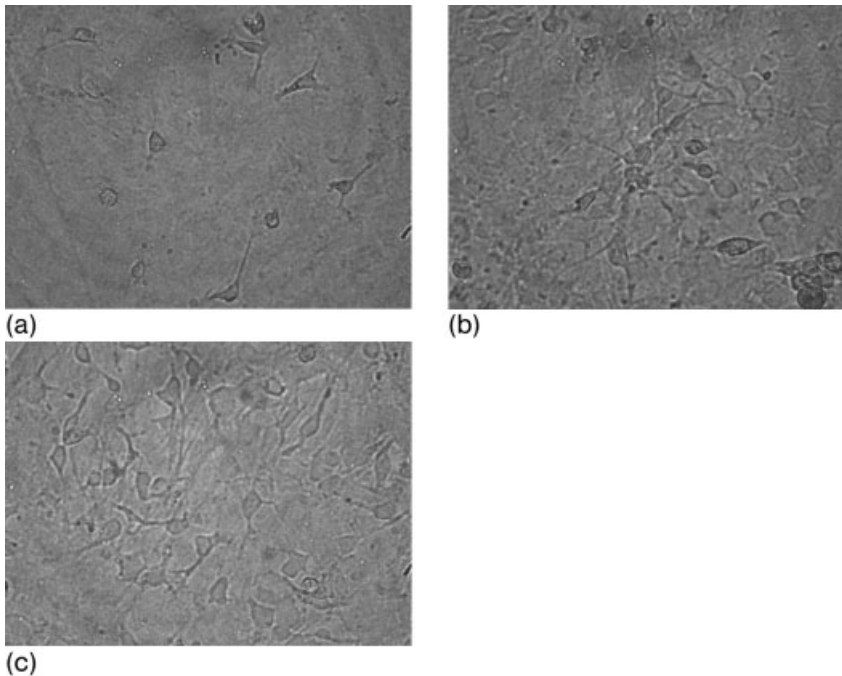


**Fig. 10.2.** Light micrograph of control and nanoparticle treated rat cortical mixed cell cultures. (A) 27-day-old organotypic culture near the end of its *in vitro* life span. Note the lack of confluent astrocyte monolayer in the background and low numbers of remaining, processed neurons. (B) 27-day-old culture

treated with 10 nm cerium oxide nanoparticles once, on day 10 *in vitro*. Note the healthy, confluent astrocyte monolayer and abundant neurons with robust processes. (C) 123-day-old culture treated with 10 nm cerium oxide nanoparticles on day 10 *in vitro*. Total magnification 800 $\times$ .

chemistry of ceria nanoparticles appears to support this hypothesis. Ceria undergoes rapid, reversible reduction and oxidation and can readily take up and release oxygen, alternating between  $\text{CeO}_2$  and  $\text{CeO}_{2-x}$  [64, 68, 94]. Therefore, it is a redox cycling agent that does not in itself generate free radicals in the process. Based on reports from the materials science field, we can only speculate on the actions of ceria nanoparticles in the physiological milieu. In aqueous medium, it appears likely that formation of adsorbed OH groups occurs on the surface of the ceria, with a concomitant reduction of the Ce atom from +4 to +3 (Fig. 10.3). This change in cerium valence alters the structure of the oxide lattice, creating oxygen vacancies and expansion of the lattice [95, 96]. This electron shuffling in the lattice, along with the oxygen vacancies generated, provide redox potential for free radical scavenging [76, 97]. After the scavenging event, the original lattice structure may be regenerated by  $\text{H}_2\text{O}$  and the cerium atom returned to the +4 state [98]. However, we would point out that the precise mechanisms responsible for lattice regeneration in the intracellular environment can only be speculated (Fig. 10.3). Thus,

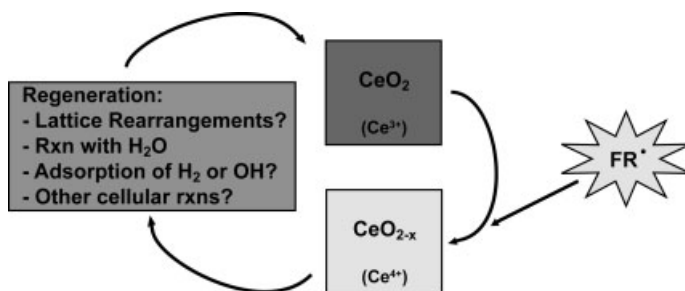


**Fig. 10.3.** Hypothesized intracellular mechanism(s) of action of ceria nanoparticles (see text for description).  $\text{FR}^\bullet$  = free radical.

the redox properties of ceria appear to make it possible for the nanoparticles to both oxidize and reduce molecules, depending on the conditions in the surrounding milieu and the level of oxidative stress.

Why then, are micro-sized ceria particles ineffective or weakly effective as biological free radical scavengers? First, and probably most obvious, micro-ceria is unlikely to enter the cell due to its size. As shown in Fig. 10.4, nano-ceria readily enter mixed brain cell cultures and other cells [99], and hence are able to carry out redox reactions. Figure 10.4 shows brain macrophage or microglia that has phagocytosed one nanoparticle, with possibly a second in the process of consumption. Figure 10.5 is an electron micrograph taken from mixed brain cell cultures, demonstrating the presence of nanoparticles in the cytoplasmic space. Second, nano-ceria has a dramatically increased surface area as compared with micro-sized particles, thereby increasing the available redox sites. Last, nano-ceria is capable of redox behavior at far lower temperatures than its micro-sized counterparts, and has more oxygen vacancies for scavenging electrons, which may allow for redox cycling in physiological environs [96, 98, 100].

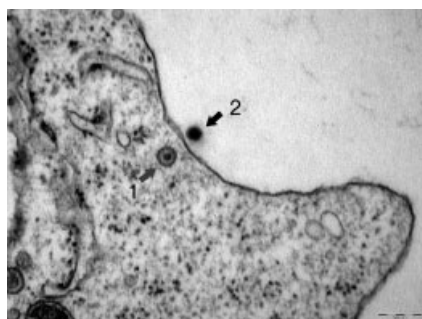


**Fig. 10.4.** Electron micrograph of intracellular cerium oxide. Note that one particle appears to already have entered the cell (first arrow), while a second may be in the early stages of phagocytosis (second arrow).



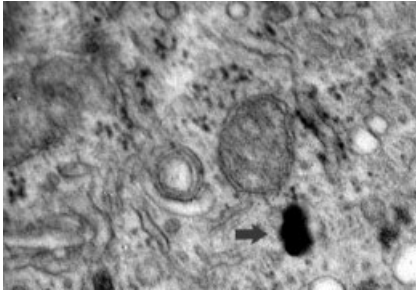


**Fig. 10.5.** Electron micrograph of mixed cortical cultures, showing intracellular accumulation of ceria nanoparticles (arrow).

#### 10.3.1.3 Other Oxide Nanoparticles

Materials science has utilized other oxides of the lanthanide series for redox reactions, including neodymium, ruthenium, praseodymium, lanthanum, and titanium. In many cases, ceria nanoparticles are doped with these compounds to enhance redox activity or stability. Although pure nano-oxides of these rare earths were without the life extension and radical scavenging abilities of ceria, mixtures of ceria-doped nanoparticles remain to be further examined for biological effects. The stability of ceria nanoparticles within the cell and the persistence during repetitive challenges of oxidative stress are presently unknown, and dopants may improve the intracellular half-life. Toxicities of these oxides have not been noted, with the exception of ruthenium, which can interfere with mitochondrial function [101]. However, there remains much work to be done regarding biological properties of ceria-doped nanoparticles.

Nanoparticles of zinc oxide and iron oxide have also received much attention at the biological level. Zinc oxide nanoparticles are routinely used as UV-absorbing agents in sunscreens. Their effects as intracellular antioxidants and lifespan extenders remain to be examined. Iron oxide nanoparticles have several emerging applications for drug delivery and biomedical imaging. However, problematic issues arise in that iron oxides may produce free radicals via the Fenton reaction, and hence may have damaging effects on cells. In this case, the addition of ceria nanoparticles to iron oxide nanoparticle preparations utilized in drug delivery may serve to abrogate deleterious effects of Fenton-reaction generated intracellular free radicals.

#### 10.3.1.4 Fullerene Derivatives and Carbon Nanotubes

Ceria nanoparticles are not the only nanoparticles that have future potential as free radical scavengers. Although experiments on cell lifespan are lacking, numerous reports suggest that fullerenes and carbon nanotubes may also act intracellularly as potent free radical scavengers. Corona-Morales et al. [102] have demonstrated that the water soluble carboxylic acid derivative of fullerene, carboxyfullerene, prolonged survival of adrenal chromaffin cells exposed to the free radical generating

neurotransmitter dopamine. In a series of papers, Dugan et al. [103–105] showed that carboxyfullerenes acted as free radical scavengers and dramatically reduced neuronal death induced by excitotoxic doses of NMDA, amyloid beta peptide, and  $H_2O_2$ , suggesting a role in neuroprotection. Carboxyfullerenes out-performed several other groups of free radical scavengers, including 21-aminosteroid compounds, vitamin E analogs, and spin trap agents. The extensive double bond system in fullerenols has led Krusic et al. to characterize them as a “free radical sponge” [106]. In rats, carrying the mutant SOD gene responsible for amyotrophic lateral sclerosis, carboxyfullerenes infusion delayed both functional deterioration and death [105]. Additionally, carboxyfullerene prevented the iron-induced oxidative injury in the nigrostriatal dopaminergic system of rats by acting as an antioxidant and suppressing free radical damage [107], suggesting potential use in Parkinson’s disease-like disorders. The mechanism of action of fullerenes has been hypothesized by Jain [108], in which a free radical forms a bond with fullerene creating a stable, non-reactive fullerene radical. Taken together, these reports suggest that like ceria nanoparticles, fullerene derivatives hold great potential in treating oxidative-stress related degenerative conditions, such as those associated with aging. Their role in aging, however, remains to be investigated.

The free radical scavenging and generating activities of carbon nanotubes have also been a subject of great debate. Unpurified single-walled carbon nanotubes (SWCNT) were shown to stimulate production of free radicals in human keratinocytes and bronchial epithelial cells [109, 110]. However, the free radical generating activities of SWCNT appeared to be due, in part, to metal contamination during particle synthesis. Muller et al. [111] reported that multi-walled carbon nanotubes (MWCNT) induced inflammatory and fibrotic reactions in rat lung after intratracheal instillation. They hypothesized that the mechanism of action was via free radical generation. In a recent subsequent study, Fenoglio et al. [112] directly examined the effect of MWCNT on free radical generation via electron spin resonance and found that MWCNT did not generate free radicals in physiological buffers. In contrast, they found that MWCNT were excellent scavengers of free radicals, including hydroxyl and superoxide radicals. In support of a role for CNT as free radical scavengers, one must consider that functionalization and polymer grafting onto CNT involves reactions similar to radical addition to the carbon framework [113, 114].

#### 10.4

##### **Nano-pharmacology**

Substantial evidence suggests that nanoparticles comprise a class of materials that may be potent antioxidants and intracellular redox reagents. However, treatment at the organismal level is confounded by the need for establishing the behavior of nanoparticles within the pharmacological parameters of ADME – absorption, distribution, metabolism, and excretion. Given the novelty of nanotechnology and the requirement for alternative ways of thinking about chemistry and physics in

the realm of the very small, traditional pharmacological parameters will no doubt require additional adjustments.

#### 10.4.1

##### Absorption

For a nanoparticle to be utilized in pharmacotherapy, absorption into the system is generally one of the first hurdles to be met. Several reviews address the study of nanoparticle-assisted drug delivery [115, 116] but much work remains in this realm, particularly for rare earth nanoparticles such as ceria and carbon derivatives such as CNT and fullerene compounds. It has been well established that various nanoparticles can enter an organism via skin absorption, digestive tract, and parenteral administration. Many even cross the blood–brain barrier. Our laboratory has conducted experiments injecting ceria nanoparticles into the tail vein of the mouse (Fig. 10.6). We found that injection of a 90 nmol total over 3 days via tail vein resulted in an increased accumulation of tissue cerium in brain, heart, and lung at 3 months post injection (Fig. 10.6). Interestingly, these three tissues are the most highly oxidative organs of the body. During the 3 month post injection period, no overt toxicological effects were noted in these experiments; however, histological assessments were not conducted (most of the tissue available was utilized to mea-

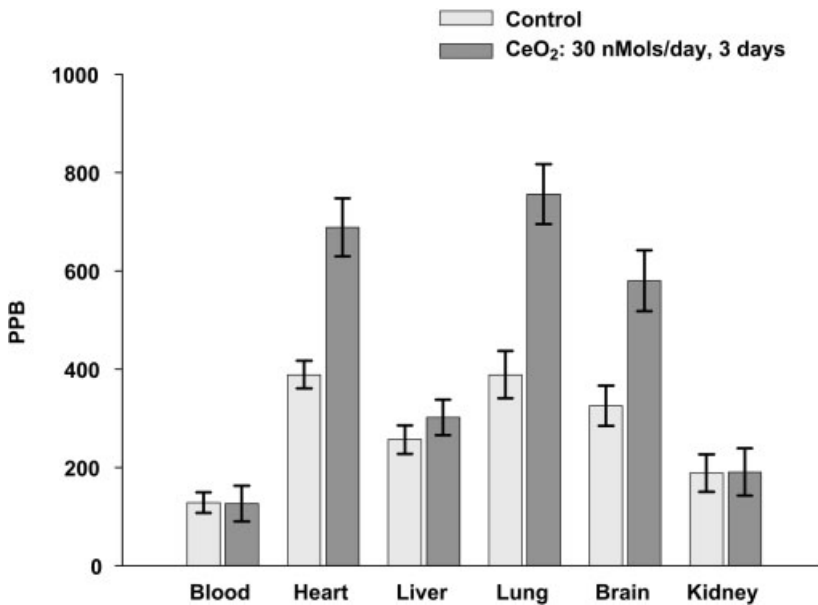


**Fig. 10.6.** Distribution of cerium in mouse tissues. Mice were injected with CeO<sub>2</sub> nanoparticles in saline via the tail vein (10  $\mu$ L, 3 mM stock), every other day for a total of

three injections. Mice were sacrificed 3 months post injection. Tissues were collected, ashed, and analyzed for cerium content by inductively coupled mass spectrometry.

sure tissue cerium levels). As measured by ashing followed by inductively coupled plasma mass spectrometry, tissue cerium levels were approximately doubled, but remained in the ppb range (Fig. 10.6). Six months post injection, tissue cerium levels were similar. These studies suggest that ceria nanoparticles are readily absorbed by tissues and tend to accumulate and persist in highly oxidative areas. One particular difficulty in administration was noted during intravenous injection in that injection of stock solutions higher than 3 mM appeared to agglomerate at the site of injection, blocking circulation and resulting in necrosis at the tail. Thus, agglomeration may be problematic in nanoparticle delivery. Additionally, notably, the long-term effects of accumulated ceria have not yet been examined and metabolic parameters such as excretion in urine and feces are unknown.

#### 10.4.1.1 Agglomeration

Agglomeration appears to be a primary issue in dosing, as mentioned above. Ceria, as well as other nanoparticles, have a high propensity for agglomeration, particularly in physiological medium. Agglomeration increases particle size and may block cellular or tissue uptake mechanisms. At the organismal level, systemic agglomeration of nanoparticles may block capillary circulation, lymphatic vessels, alveoli, or kidney perfusion. Thus, the use of dilute, well dispersed solutions of nanoparticles is critical. In our studies, care was taken to eliminate pre-administration agglomeration of nano-ceria by avoiding phosphate buffers and the use of rigorous sonication prior to delivery [88]. Poorly dispersed ceria solutions or solutions prepared in phosphate buffer, result in poor intracellular delivery of nanoparticles. However, as can be seen in Figs. 10.4 and 10.5, it appears likely that some agglomeration occurs in the cells themselves, since the particle size in electron micrographs appears to be somewhat larger than that in the stock solutions and intracellular particles shown in Fig. 10.5 appear to be associated. In lung cells, Stark et al. also found agglomerates of ceria [99], which appeared to be localized to vacuole-like structures.

In addition to agglomeration, contaminants from synthesis of nanoparticle preparations may also cause a range of effects and must be carefully controlled in cellular and animal studies. Metal contaminants from synthesis of carbon nanotubes may promote free radical generation and toxic effects. Likewise, tailing surfactant in nano-ceria preparations synthesized via micro-emulsion techniques have also proved damaging to the cell. Therefore, an assessment of preparation purity is a critical step that must be considered prior to biological use.

#### 10.4.1.2 Dose

Dose is also a parameter that needs to be addressed in a somewhat non-traditional pharmacological manner. Traditional pharmacology generally expresses dose in a molar or  $\text{mg kg}^{-1}$  manner. However, nanoparticles are engineered “mini-reactors”, and dose via mass or molar number may be an inappropriate descriptor, since each individual particle appears to be an entity unto itself. For example, in nano-ceria or fullerenes, the radical scavenging effect is primarily due to surface area reactions, which are enhanced at the nano-scale. Based on this premise, Oberdorster et al.

[117] propose that dose be described in terms of surface area, rather than mass. Other groups have utilized the descriptor of number of nanoparticles delivered per cell for *in vitro* experiments, which works well for nanoparticles of discrete size. Until further experimentation provides adequate guidelines, both these types of dose descriptors appear useful for experimental analysis and comparison. In the cases of carbon nanotubes, additional parameters of particle length and circumference need to be considered.

#### 10.4.2

#### **Distribution, Metabolism, and Excretion**

Distribution, metabolism, and excretion are parameters that also must be addressed as nanotechnology moves into the realm of conventional pharmacology. This area is one in which research is decidedly scarce. Studies with ultrafine particulates have shown that inhaled doses reach the systemic circulation and penetrate the blood–brain barrier, and this scenario is likely for many forms of nanoparticles [118, 119]. However, progress in this area has been hindered by our lack of ability to detect nanoparticle distribution and excretion. In the case of fullerenes, chemical detection in tissues is confounded by the fact that carbon is a ubiquitous backbone of all organic molecules. With cerium oxide and other rare earth nanoparticles, assessment of distribution is hindered by our ability to extract cerium oxide from tissues and the lack of chemical assessment of its presence. Of course, it is certainly possible to measure rare earths in tissue by inductively coupled mass spectrometry, but this only measures the rare earth element itself, and not the presence of oxides or other derivatives. Current research directed to the use of fluorescent tags may improve our ability to track the distribution of nanoparticles in living cells and tissues. Additionally, nanoparticles synthesized with heavy metal cores may permit localization via CT or MRI in the whole animal.

### 10.5

#### **Nanoparticle Antioxidants and Treatment of Disease**

Research to date suggests that nanoparticles may provide the field of medicine with effective, long lasting antioxidants for the treatment of diseases associated with free radical production (Table 10.1). Neurodegenerative disorders such as Alzheimer's disease, Parkinson's disease, multiple sclerosis, amyotrophic lateral sclerosis, and traumatic and ischemic brain injury all have free radical mediated components [1, 3, 5, 6, 120, 121]. Efficient nanoparticle free radical scavengers may hold great potential in abrogating the functional deficits associated with many of these neurological disorders. Using an *in vitro* model for traumatic brain injury [122–125], our group has shown that pre-treatment of brain cell cultures with ceria nanoparticles prior to injury, reduces cell death and neuronal dysfunction after injury [91, 92]. Importantly, ceria nanoparticles were effective at reducing neuronal death and dysfunction even when delivered up to 3 h post injury – an effect not

reproduced by other free radical scavengers. These effects were due, in part, to a reduction in the inflammatory reactions in brain microglia [92]. Other work also supports a role for fullerene derivatives in mediation of free radical damage in the nervous system [102–106].

Cardiovascular disorders are another realm in which nanoparticle free radical scavengers may hold great promise. Development of atherosclerotic lesions is promoted by free radical-mediated vascular damage and free radical generation to the vessel wall increases and promotes the subsequent inflammatory processes. Hence, effective administration of nanoparticle antioxidants may blunt this process, particularly in susceptible populations. Percutaneous transluminal angioplasty (PTCA) is a widely used procedure in treatment of acute and chronic ischemic heart disease. One of the most serious and reoccurring complications of PTCA is re-stenosis, leading to further blockage and occurrence of new ischemic events. The pathophysiology of re-stenosis is multifactorial and consists of inflammation, smooth muscle cell migration, proliferation, extracellular matrix remodeling, and free radical damage. Poly(ethylene glycol)-based core shell nanoparticles (NK911) loaded with the antineoplastic drug doxorubicin were able to prevent re-stenosis after balloon angioplasty in animal models [126]. It appears the core shell nanoparticles directed the doxorubicin to the damaged vascular epithelium. Incorporation of free radical scavenging nanoparticles into the core shell of such preparations may lead to further enhancement of endothelial function and reduction in future damage. Similarly, the use of coronary stents in treatment of chronic and acute coronary occlusion is also complicated by the occurrence of in-stent re-stenosis [127] and is a clinical problem treatable only by coronary artery by-pass. Stent re-stenosis is a result of continuing inflammatory reactions within the vascular walls, of which free radical production is an important component. Coating of vascular stents with ceria or other nanoparticles may aid in reducing inflammation around the site of stent insertion and decrease the incidence of re-stenosis.

Oxidative stress and free radical production are also a primary component of inflammatory disorders such as arthritis. Accumulation of activated inflammatory cells within the arthritic joint release high levels of free radicals that promote destruction of tissue within the joint. An as-yet unexplored possibility lies in the use of ceria and other antioxidant nanoparticles in reduction of damage to the arthritic joint, by direct delivery to the joint itself or via coating of implantable materials. In support of this potential usage, our laboratory has found that treatment of activated microglia and macrophages with ceria nanoparticles reduces release of free radicals from these cells and protects bystander cells from damage from activated immune cells [88, 92, 93]. Further, work by our collaborators, Drs. S. Olgun and C. Reilly, suggests that treatment of lupus mice with ceria nanoparticles decreases disease severity and inflammatory cell activation (Olgun, Reilly and Rzigalinski, unpublished results).

Of importance to us all is the association between oxidative stress and aging and age-related disorders. Can nanoparticles be the fountain of youth long sought by Ponce de Leon? Although promising, the utility of nanoparticles in retarding aging are far more complex than to venture an answer to such a question. Ceria nanopar-

ticles, and possibly others, certainly hold promise for extension of lifespan and abrogation of age related disorders. However, much work is necessary to move the current work in cellular studies, to the level of organism longevity. In preliminary studies in the fruit fly, we have found a 30% increase in lifespan in flies fed cerium oxide nanoparticles, dosed at 10–100 nM in the food. However, doses above 1 mM appeared to result in a decrease in lifespan. Hence, total cumulative dose to the organism is likely to be an important parameter. Also, the effect of dosing throughout the lifespan vs. dosing for a limited time period needs to be examined. Although excessive free radical production contributes to cell damage, free radicals, as discussed in Section 10.1, also have beneficial effects on survival – particularly in the vascular and nervous systems. Thus, blockade of free radical production may reach the level of “too much of a good thing”. For example, NO radicals are critical to maintenance of vascular tone and endothelial function. Satoh et al. [128] have shown that fullerene nanoparticles interfere with NO-mediated vasodilation and may have deleterious effects on the vasculature at high concentrations. For ceria nanoparticles, the vasoactive actions of NO may also be rendered non-functional at certain concentrations, resulting in disruption of the normal vascular response *in vivo*. Thus the question arises as to how much free radical scavenging is too much, and at which point these highly efficient nanoparticle scavengers interfere with normal cell function. Further engineering of nanoparticle structure may provide a solution to this problem. However, much work is needed to assess these parameters.

An additional paradox arises when one considers the increased incidence of neoplasia with age. If resistance to free radical damage is conferred to normal cells by nanoparticles, might not cancerous cells or dysfunctional cells destined for apoptosis also receive a degree of protection when nanoparticles are delivered? Such events might potentially counteract the tumor killing effects of radiation or chemotherapy, both of which may act through free-radical mediated cell death. Alternatively, if such nanoparticles could be delivered to healthy cells surrounding the site of a radiation dose, they may afford protection to healthy bystander cell injury associated with radiation therapy. Again, further engineering and targeting of nanoparticles may provide solutions to these issues. Nonetheless, such avenues remain to be explored before the full medicinal capabilities of nanoparticles can be put to use.

## 10.6 Toxicology

Despite the beneficial potential of antioxidant nanoparticles in the treatment of disease, there remains a major hurdle that must be surpassed before progress can be made in this area. Toxicological data is seriously lacking. Presently, there are only scant reports on the effects of nanoparticles in general on organism metabolism and function. As discussed in Section 10.3, some nanoparticles appear to have the potential to induce free radical formation and damage, which may be due to con-

taminants from synthesis procedures [109, 110, 119]. Several studies have reported that SWCNT and MWCNT induce granulomas and fibrosis in the lung during intratracheal or inhalation exposure [110, 129]. Oberdorster et al. [130] have reviewed the potential toxicological effects of fullerenes as free radical generating agents, particularly after exposure to light. Kamat et al. [131] also report significant lipid peroxidation due to photosensitized C60. Hussain et al. have reported that oxide nanoparticles of molybdenum, aluminum, iron, and titanium were toxic, albeit at high doses [132]. Ueng et al. [133] demonstrated that certain fullerene derivatives suppressed microsomal enzymes and mitochondrial oxidative phosphorylation *in vitro*, although the compounds were able to scavenge free radicals in brain tissue [134, 135]. Chen et al. report that SiO<sub>2</sub> nanoparticles were taken up into the cell nucleus, where they caused aberrant clustering of nuclear proteins and inhibited replication and transcription [136]. Thus, although highly promising, antioxidant nanoparticles are certainly not a magic bullet as yet and the road ahead is likely long – but equally likely one worth traveling.

## 10.7

### Summary

Free radicals and oxidative stress are associated with a broad spectrum of human diseases. Despite their prominence in pathological conditions, antioxidant therapy has met with only limited success. Nanoparticle technology encompassing rare earth oxides, fullerene derivatives, and carbon nanotubes show great promise in antioxidant therapy in a myriad of disease conditions. However, much work is needed to fully realize their capacity in nanomedicine.

### References

- 1 BECKMAN, K.B., AMES, B.N. The free radical theory of aging matures, **1998**, *Physiol. Rev.* 78, 547–581.
- 2 COMPORTI, M., SIGNORINI, C., BUONOCORE, G., CICCOLI, L. Iron release, oxidative stress, and erythrocyte aging, **2002**, *Free Rad. Biol. Med.* 32, 568–576.
- 3 DROGE, W. Free radicals in the physiological control of cell function, **2002**, *Physiol. Rev.* 82, 47–95.
- 4 SPITELLER, G. Are changes of the cell membrane structure causally involved in the aging process? **2002**, *Ann. New York Acad. Sci.* 959, 30–44.
- 5 MARKESBERY, W.R. Oxidative stress hypothesis in Alzheimer's Disease, **1997**, *Free Rad. Biol. Med.* 23, 134–147.
- 6 MASHIMA, R., WITTING, P.K., STOCKER, R. Oxidants and antioxidants in atherosclerosis, **2001**, *Curr. Opin. Lipidol.* 12, 411–418.
- 7 CARMODY, R.J., COTTER, T.G. Signalling apoptosis: A radical approach, **2001**, *Redox. Rep.* 6, 77–90.
- 8 PRATICO, D., LAWSON, J.A., ROKACH, J., FITZGERALD, G.A. The isoprostanes in biology & medicine, **2001**, *Trends Endocrinol. Metab.* 12, 243–247.
- 9 PETERSEN, D.R., DOORN, J.A. Reactions of 4-hydroxynonenal with proteins and cellular targets, **2004**, *Free Rad. Biol. Med.* 37, 937–945.
- 10 ESTERBAUER, H., SHAUR, R.J., ZOLLNER, H. Chemistry and



- biochemistry of 4-hydroxynonenal, malonaldehyde and related aldehydes, **1991**, *Free Rad. Biol. Med.* 11, 81–128.
- 11 MONTUSCHI, P., BARNES, P.J., ROBERTS, L.J. II. Isoprostanes: Markers and mediators of oxidative stress, **2004**, *FASEB J.* 18, 1791–1800.
  - 12 KIM, D., WON, S., GWAG, B. Analysis of mitochondrial free radical generation in animal models of neuronal disease, **2002**, *Free Rad. Biol. Med.* 33, 715–726.
  - 13 SOHAL, R.S., SOHAL, B.H. Hydrogen peroxide release by mitochondria increases during aging, **1991**, *Mech. Aging Develop.* 57, 187–202.
  - 14 FRIDOVICH, I. Fundamental aspects of reactive oxygen species, or what's the matter with oxygen?, **1999**, *Ann. New York Acad. Sci.* 893, 13–18.
  - 15 LENAZ, G., BOVINA, C., D'AURELIO, M., FATO, R., FORMIGGINI, G., GENOVA, M.L., GIULIANO, G., PICH, M.M., PAOLUCCI, U., CASTELLI, G.P., VENTURA, B. Role of mitochondria in oxidative stress and aging, **2001**, *Ann. New York Acad. Sci.* 959, 199–213.
  - 16 MATTSON, M.P. Modification of ion homeostasis by lipid peroxidation: Roles in neuronal degeneration and adaptive plasticity, **1998**, *Trends Neurosci.* 21, 53–57.
  - 17 AZBIL, R.D., MU, X., BRUCE-KELLER, A.J., MATTSON, M.P., SPRINGER, J.E. Impaired mitochondrial function, oxidative stress and altered antioxidant enzyme activities following traumatic spinal cord injury, **1997**, *Brain Res.* 765, 283–290.
  - 18 TORTORELLA, C., PIAZZOLLA, G., ANTONACI, S. Neutrophil oxidative metabolism in aged humans: A perspective, **2001**, *Immunopharmacol. Immunotoxicol.* 23, 565–572.
  - 19 BRAND, M.D., AFFOURTIT, C., ESTEVES, T.C., GREEN, K., LAMBERT, A.J., MIWA, S., PAKAY, J.L., PARKER, N. Mitochondrial superoxide: Production, biological effects, and activation of uncoupling proteins, **2004**, *Free Rad. Biol. Med.* 37, 755–767.
  - 20 SMITH, W.L. Prostanoid biosynthesis and mechanisms of action, **1991**, *Am. J. Physiol.* 263, F181–F191.
  - 21 FREDERIKS, W.M., VREELING-SINDELAROVA, H. Ultrastructural localization of xanthine oxidoreductase activity in isolated rat liver cells, **2002**, *Acta Histochem.* 104, 29–32.
  - 22 ESPLUGUES, J.V. NO as a signaling molecule in the nervous system, **2002**, *Br. J. Pharmacol.* 135, 1079–1095.
  - 23 HARMAN, D. Aging: Overview, **2001**, *Ann. New York Acad. Sci.* 928, 1–21.
  - 24 MARCHIOLI, R., SCHWEIGER, C., LEVANTESI, G., TAVAZZI, L., VALAGUSSA, F. Antioxidant vitamins and prevention of cardiovascular disease: Epidemiological and clinical trial data, **2001**, *Lipids* 36, S53–S63.
  - 25 KAUL, N., DEVARAJ, S., JIALAL, I. Alpha-tocopherol and atherosclerosis, **2001**, *Exp. Biol. Med.* 226, 5–12.
  - 26 MELDRUM, B.S. Implications for neuroprotective treatments, **2002**, *Prog. Brain Res.* 135, 487–495.
  - 27 MAXWELL, A.J. Mechanisms of dysfunction of the nitric oxide pathway in vascular diseases, **2002**, *Nitric Oxide* 6, 101–124.
  - 28 ABRAMSON, S.B., AMIN, R.A., CLANCY, R.M., ATTUR, M. The role of nitric oxide in tissue destruction, **2001**, *Best Pract. Res. Clin. Rheumatol.* 15, 831–845.
  - 29 TONKS, N.K. Redox redux: Revisiting PTP's and the control of cell signaling, **2005**, *Cell* 121, 667–670.
  - 30 SZWEDA, P.A., FRIGUET, B., SZWEDA, L.I. Proteolysis, free radicals, and aging, **2002**, *Free Rad. Biol. Med.* 33, 29–36.
  - 31 CARNEY, J.M., STARKE-REED, P.E., OLIVER, C.N., LANDUM, R.W., CHENG, M.S., WU, J.F., FLOYD, R.A. Reversal of age-related increase in brain protein oxidation, decrease in enzyme activity, and loss in temporal and spatial memory by chronic administration of the spin-trapping compound n-tert-butyl-alpha-phenylnitron, **1991**, *Proc. Natl. Acad. Sci. U.S.A.* 88, 3633–3636.
  - 32 SMITH, C.D., CARNEY, J.M., STARKE-REED, P.E., OLIVER, C.N., STADTMAN, E.R., FLOYD, R.A., MARKESBERY, W.R. Excess brain protein oxidation and enzyme dysfunction in normal aging and in Alzheimer's disease, **1991**,

- Proc. Natl. Acad. Sci. U.S.A.* 88, 10 540–10 543.
- 33 SOHAL, R.S. Role of oxidative stress and protein oxidation in the aging process, **2002**, *Free Rad. Biol. Med.* 33, 37–44.
  - 34 FRIGUET, B., BULTEAU, A.L., CHONDROGIANNI, N., CONCONI, M., PETROPOULOS, I. Protein degradation by the proteasome and its implications in aging, **2000**, *Ann. New York Acad. Sci.* 908, 143–154.
  - 35 KELLER, J.N., HUANG, F.F., ZHU, H., YU, J., HO, Y.S., KINDY, T.S. Oxidative stress-associated impairment of proteasome activity during ischemia-reperfusion injury, **2000**, *J. Cereb. Blood Flow Metab.* 20, 1467–1473.
  - 36 AKSENOV, M.Y., AKSENOVA, M.V., BUTTERFIELD, D.A., GEDDES, J.W., MARKESBERY, W.R. Protein oxidation in the brain in Alzheimer's disease, **2001**, *Neuroscience* 103, 373–383.
  - 37 GRUNE, T., DAVIES, K.J., Oxidative processes in aging. In: MASORO, E.J., AUSTAD, S.N. (Eds.), *Handbook of the Biology of Aging*, **2001**, San Diego, Academic Press, pp. 25–58.
  - 38 FLOYD, R.A. Oxidative damage to behavior during aging, **1991**, *Science* 254, 1597.
  - 39 PRATICO, D. Lipid peroxidation in mouse models of atherosclerosis, **2001**, *Trends Cardiovasc. Med.* 11, 112–116.
  - 40 CINI, M., MORETTI, A. Studies on lipid peroxidation and protein oxidation in the aging brain, **1995**, *Neurobiol. Aging* 16, 53–57.
  - 41 WEI, E.P., KONTOS, H.A., DIETRICH, W.D., POVLISSHOCK, J.T., ELLIS, E.F. Inhibition of free radical scavengers and by cyclooxygenase inhibitors of pial arteriolar abnormalities from concussive brain injury in cats, **1981**, *Circ. Res.* 48, 95–103.
  - 42 NAKAO, N., FRODL, E.M., WIDNER, H., CARLSON, E., EGGERTING, F.A., EPSTEIN, C.J., BRUNDIN, P. Overexpressing Cu/Zn superoxide dismutase enhances the survival of transplanted neurons in a rat model of Parkinson's disease, **1995**, *Nat. Med.* 1, 226–231.
  - 43 GREENLUND, L.J.S., DECKWERTH, T.L., JOHNSON, E.M. JR. Superoxide dismutase delays neuronal apoptosis: A role for reactive oxygen species in programmed neuronal death, **1995**, *Neuron* 14, 303–315.
  - 44 SKULACHEV, V.P. Why are mitochondria involved in apoptosis? Permeability transition proes and apoptosis as selective mechanisms to eliminate superoxide-producing mitochondria, **1996**, *FEBS Lett.* 397, 7–10.
  - 45 BUTTERFIELD, D.A., DRAKE, J., POCERNICH, C., CASTEGNA, A. Evidence of oxidative damage in Alzheimer's disease brain: Central role for amyloid beta-peptide, **2001**, *Trends Mol. Med.* 7, 548–554.
  - 46 UCHIDA, K. Cellular response to bioactive lipid peroxidation products. **2000**, *Free Rad. Res.* 33, 731–737.
  - 47 FORMAN, L.J., LIU, P., NAGELE, R.G., WONG, P.Y. Augmentation of nitric oxide, superoxide, and peroxynitrite production during cerebral ischemia and reperfusion in the rat, **1998**, *Neurochem. Res.* 23, 141–148.
  - 48 BONDY, S.C., LEBEL, C.P. The relationship between excitotoxicity and oxidative stress in the central nervous system, **1993**, *Free Rad. Biol. Med.* 14, 633–642.
  - 49 HALLIWELL, B. Role of free radicals in the neurodegenerative diseases: Therapeutic implications for antioxidant treatment, **2001**, *Drugs Aging* 18, 685–716.
  - 50 WICKENS, A.P. Aging and the free radical theory. **2001**, *Resp. Physiol.* 128, 379–391.
  - 51 SAYRE, L.M., SMITH, M.A., PERRY, G. Chemistry and biochemistry of oxidative stress in neurodegenerative disease, **2001**, *Curr. Med. Chem.* 8, 721–738.
  - 52 CONTESTABILE, A. Oxidative stress in neurodegeneration: Mechanisms and therapeutic perspectives. **2001**, *Curr. Top. Med. Chem.* 1, 553–568.
  - 53 SOHAL, R.S., WEINDRUCH, R. Oxidative stress, caloric restriction, and aging, **1996**, *Science* 273, 59–63.
  - 54 LAURER, H.L., MCINTOSH, T.K. Pharmacologic therapy in traumatic

- brain injury: Update on experimental treatment strategies, **2001**, *Curr. Pharm. Des.* 7, 1505–1516.
- 55** HARMAN, D. Aging: a theory based on free radical and radiation chemistry, **1956**, *J. Gerontol.* 11, 298–300.
- 56** MARKESBERY, W.R., LOVELL, M.A. 4-Hydroxynonenal, a product of lipid peroxidation, is increased in the brain in Alzheimer's disease, **1998**, *Neurobiol. Aging* 19, 33–36.
- 57** PAMPLONA, R., BARJA, G., PORTERO-OTIN, M. Membrane fatty acid unsaturation, protection against oxidative stress, and maximum life span, **2002**, *Ann. New York Acad. Sci.* 959, 475–490.
- 58** LEE, C.K., KLOPP, R.G., WEINDRUCH, R., PROLLA, T.A. Gene expression profile of aging and its retardation by caloric restriction, **1999**, *Science* 285, 1390–1393.
- 59** SALVEMINI, D., RIPLEY, D.P., CUZZOCREA, S. SOD mimetics are coming of age, **2002**, *Nat. Rev. Drug Discov.* 1, 367–374.
- 60** LEKER, R.R., SHOHAMI, E. Cerebral ischemia and trauma – different etiologies yet similar mechanisms: Neuroprotective opportunities, **2002**, *Brain Res. Rev.* 39, 55–73.
- 61** DOPPENBERG, E.M.R., CHOI, S.C., BULLOCK, R. Clinical trials in traumatic brain injury: What can we learn from previous studies?, **1997**, *Ann. New York Acad. Sci.* 825, 305–322.
- 62** KONTOS, H.A., WEI, E.P., DIETRICH, W.D., NAVARI, R.M., POVLISHOCK, J.T., GHATAK, N.R., ELLIS, E.F., PATTERSON, J.L. JR. Mechanism of cerebral arteriolar abnormalities after acute hypertension, **1981**, *Am. J. Physiol.* 240, H511–H527.
- 63** EVANS, C.H. *Biochemistry of the Lanthanides*, **1990**, Plenum Press, New York.
- 64** DAVIS, V.T. Measurement of the electron affinity of cerium, **2002**, *Phys. Rev. Lett.* 88, 1–4.
- 65** LAND, P.L. Defect equilibria for extended point defects, with application to nanstoichiometric ceria, **1973**, *J. Phys. Chem. Solids* 34, 1839–1845.
- 66** SUZUKI, K.T., KOSACKI, I., ANDERSON, H.U. Electrical conductivity and lattice defects in nanocrystalline cerium oxide thin films, **2001**, *J. Am. Ceram. Soc.* 84, 2007–2014.
- 67** HERMAN, G.S. Characterization of surface defects on epitaxial CeO<sub>2</sub> (001) films, **1999**, *Surf. Sci.* 437, 207–214.
- 68** CONESA, J.C. Computer modeling of surfaces and defects on cerium dioxide, **1995**, *Surf. Sci.* 339, 337–352.
- 69** MAMONTOV, E. and EGAMI, T. Lattice defects and oxygen storage capacity of nanocrystalline ceria and ceria-zirconia, **2000**, *J. Phys. Chem. B* 104, 11 110–11 116.
- 70** SEAL, S., SHUKLA, S. Sol-gel derived oxide and sulfide nanoparticles. In: BARATON, M., NALWA, H.S. (Eds.), **2002**, *Functionalization and Surface Treatment of Nanoparticles*, Academic Press, San Diego.
- 71** HEINEMANN, C., CORNEHL, H.H., SCHRODER, D., DOLG, M., SCHWARZ, H. The CeO<sub>2</sub>+ Cation: Gas-phase reactivity and electronic structure, **1996**, *Inorg. Chem.* 35, 2463–2475.
- 72** TSCHOPE, A., YING, J.Y., TULLER, H.L. Catalytic redox activity and electrical conductivity of nanocrystalline non-stoichiometric cerium oxide, **1996**, *Sensors Actuators, B* 31, 111–115.
- 73** DU, X., ZHANG, T., LI, R., WANG, K. Nature of cerium(III)- and lanthanum(III)-induced aggregation of human erythrocyte membrane proteins, **2001**, *J. Inorg. Biochem.* 84, 67–75.
- 74** FASHUI, H. Study on the mechanism of cerium nitrate effects on germination of aged rice seed, **2002**, *Biol. Trace Elem. Res.* 87, 191–200.
- 75** BERNAL, S., KASPAR, J., TROVARELLI, A. (Eds.), Recent progress in catalysis by ceria and related compounds, *Catal. Today*, **1999**, 50, 173–443.
- 76** GUO, X., WASER, R. Electrical properties of the grain boundaries of oxygen ion conductors: Acceptor doped zirconia and ceria, **2006**, *Progr. Mater. Sci.* 51, 151–210.
- 77** FRANKLIN, S.J. Lanthanide-mediated DNA hydrolysis, **2001**, *Curr. Opin. Chem. Biol.* 5, 201–208.

- 78 YULIATI, L., HAMAJMA, T., HATTORI, T., YOSHIDA, H. Highly dispersed Ce(III) species on silica and alumina as new photocatalysts for non-oxidative direct methane coupling, **2005**, *Chem. Commun. (Camb.)* 4824–4826.
- 79 HE, M.L., RANZ, D., RAMBECK, W.A. Study on the performance enhancing effect of rare earth elements in growing and fattening pigs, **2001**, *J. An. Phys. An. Nutr.* 85, 263–274.
- 80 DE GRACIA, C.G. An open study comparing topical silver sulfadiazine and topical silver sulfadiazine-cerium nitrate in the treatment of moderate and severe burns, **2001**, *Burns*, 27, 67–74.
- 81 ESKI, M., DEVECI, M., CELIKOZ, B., NISANCI, M., TUREGUN, M. Treatment with cerium nitrate bathing modulates systemic leukocyte activation following burn injuries: An experimental study in rat cremaster muscle flap, **2001**, *Burns* 27, 739–746.
- 82 GRABOWSKI, G.M., PAULASKIS, J.D., GODLESKI, J.J. Mediating phosphorylation events in the vanadium-induced respiratory burst of alveolar macrophages, **1999**, *Tox. Appl. Pharmacol.* 156, 170–178.
- 83 TELEK, G., SCOAZEC, J.-Y., CHARIOT, J., DUCROC, R., FELDMANN, G., ROZE, C. Cerium-based histochemical demonstration of oxidative stress in taurocholate-induced acute pancreatitis in rats: A confocal laser scanning microscopic study, **1999**, *J. Histochem. Cytochem.* 47, 1202–1212.
- 84 McDONALD, J.W., GHIO, A.J., SHEEHAN, C.E., BERNHARDT, P.F., ROGGLI, V.L. Rare earth (cerium oxide) pneumoconiosis: Analytical scanning electron microscopy and literature review, **1995**, *Modern Path.* 8, 859–865.
- 85 DU, X., ZHANG, T., LI, R., WANG, K. Nature of cerium (III)- and lanthanum (III)-induced aggregation of human erythrocyte membrane proteins, **2001**, *J. Inorg. Biochem.* 84, 67–75.
- 86 FRANKLIN, S.J. Lanthanide-mediated DNA hydrolysis, **2001**, *Curr. Opin. Chem. Biol.* 5, 201–208.
- 87 CHENG, Y., LI, Y., LI, R., LU, J., WANG, K. Orally administered cerium chloride induces the conformational changes of rat hemoglobin, the hydrolysis of 2,3-DPG and the oxidation of heme-Fe(II), leading to changes of oxygen affinity, **2000**, *Chem. Biol. Interac.* 125, 191–208.
- 88 RZIGALINSKI, BEVERLY, A. Nanoparticles & cell longevity, **2005**, *Tech. Cancer Res. Treat.* 4, 651–660.
- 89 BAILEY, D., CHOW, L., MERCHANT, S., KUIRY, S.C., PATIL, S., SEAL, S., RZIGALINSKI, B.A. Cerium oxide nanoparticles extend cell longevity and act as free radical scavengers, **2003**, *Nat. Biotechnol.* 14, 112.
- 90 CLARK, A., ELLISON, A., FRY, R., MERCHANT, S., KUIRY, S., PATIL, S., SEAL, S., RZIGALINSKI, B.A. Engineered oxide nanoparticles increase neuronal lifespan in culture and act as free radical scavengers, *Soc. for Neurosci.*, Abs. #878.2, **2003**, published online.
- 91 FRY, R., ELLISON, A., COLON, J., MERCHANT, S., KUIRY, S., PATIL, S., SEAL, S., RZIGALINSKI, B.A. Engineered oxide nanoparticles protect against neuronal damage associated with in vitro trauma, **2003**, *J. Neurotrauma* 20, 1054.
- 92 CALLAGHAN, P., COLON, J., MERCHANT, S., KUIRY, S., PATIL, S., SEAL, S., RZIGALINSKI, B.A. Deleterious effects of microglia activated by in vitro trauma are blocked by engineered oxide nanoparticles, **2003**, *J. Neurotrauma* 20, 1053.
- 93 CLARK, A., STRAWN, E., COHEN, C., RZIGALINSKI, B. Cerium oxide nanoparticles provide superior antioxidant activity and neuroprotection as compared with vitamin E, n-acetyl cysteine, and melatonin, *Soc. for Neuroscience*, Abs. #93.4, **2005**, published online.
- 94 EVANS, D.E., KU, B.K., RAMSEY, D., MAYNARD, A., KAGAN, V.E., CASTRANOVA, V., BARON, P. Unusual inflammatory and fibrogenic pulmonary responses to single-walled carbon nanotubes in mice, **2005**, *Am. J. Physiol. Lung Cell. Mol. Physiol.* 289, L698–L708.

- 95 ANEGGI, E., BOARO, M., DE LEITENBURG, C., DOLCETTI, G., TROVARELLI, A. Insights into the redox properties of ceria-based oxides and their implications in catalysis, **2006**, *J. Alloys Compds*, 408–412, 1096–1102.
- 96 TROVARELLI, A. *Catalysis by Ceria and Related Materials*, **2002**, Imperial College Press, London.
- 97 NOLAN, M., PARKER, S.C., WILSON, G.W. The electronic structure of oxygen vacancy defects at the low index surfaces of ceria, **2005**, *Surf. Sci.* 595, 223–232.
- 98 SATO, S., TAKAHASHI, R., SODESAWA, T., HONDA, N. Dehydration of diols catalyzed by CeO<sub>2</sub>, **2004**, *J. Mol. Catal. A* 221, 177–183.
- 99 LIMBACH, L.K., LI, Y., GRASS, R.N., BRUNNER, T.T., HINTERMANN, M.A., MULLER, M., GUNTHER, D., STARK, W.T. Oxide nanoparticle uptake in human lung fibroblasts: Effects of particle size, agglomeration, and diffusion at low concentrations, **2005**, *Environ. Sci. Technol.* 39, 9370–9376.
- 100 QIU, L., LIU, F., ZHAO, L., MA, Y., YAO, J. Comparative XPS study of surface reduction for nanocrystalline and microcrystalline ceria powder, **2006**, *Appl. Surf. Sci.* 252, 4931–4935.
- 101 VELASIO, I., TAPIA, D. Alteration of intracellular calcium homeostasis and mitochondrial function are involved in ruthenium red neurotoxicity in primary cortical cells, **2000**, *J. Neurosci. Res.* 60, 543–551.
- 102 CORONA-MORALES, A.A., CASTELL, A., ESCOBAR, A., DRUCKER-COLFIN, R. Fullerene C60 and ascorbic acid protect cultured chromaffin cells against levodopa toxicity, **2003**, *J. Neurosci. Res.* 71, 121–126.
- 103 DUGAN, L.L., LOVETT, E.G., QUICK, K.L., LOTHARIUS, J., LIN, T.T., O'MALLEY, K.L. Fullerene-based antioxidants and neurodegenerative disorders, **2001**, *Parkinsonism Rel. Disord.* 7, 243–246.
- 104 DUGAN, L.L., GABRIESEN, J.K., YU, S.P., LIN, T.S., CHOI, D.W. Buckminsterfullerenol free radical scavengers reduce excitotoxic and apoptotic death of cultured cortical neurons, **1996**, *Neurobiol. Dis.* 3, 129–135.
- 105 DUGAN, L.L., TURETSKY, D.M., DU, C., LOBNER, D., WHEELER, M., ALMLI, C.R., SHEN, C.K., LUH, T.Y., CHOI, D.W., LIN, T.S. Carboxyfullerenes as neuroprotective agents, **1997**, *Proc. Natl. Acad. Sci. U.S.A.* 94, 9434–9439.
- 106 KRUSIC, P.J., WASSERMAN, E., KEIZER, P.N., MORTON, J.R., PRESTON, K.F. Radical reactions of C60, **1991**, *Science* 254, 1183–1185.
- 107 LIN, A.M.Y., CHYI, B.Y., WANG, S.D., YU, H.-H., KANAKAMMA, P.P., LUH, T.-Y., CHOU, C.K., HO, L.T. Carboxyfullerene prevents iron-induced oxidative stress in rat brain, **1999**, *J. Neurochem.* 72, 1634–1640.
- 108 JAIN, K.K. The role of nanobiotechnology in drug discovery, **2005**, *Drug Disc. Today* 10, 1435–1442.
- 109 SHVEDOVA, A.A., KISIN, E.R., MERCER, R., MURRAY, A.R., JOHNSON, V.J., POTAPOVICH, A.I., TYURINA, Y.Y., GORELIK, O., AREPALLI, S., SCHWEGLER-BERRY, D., HUBBS, A.F., ANTONINI, J., SHVEDOVA, A.A., CASTRANOVA, V., KISIN, E.R., SCHWEGLER-BERRY, D., MURRAY, A.R., GANDELSMAN, V.Z., MAYNARD, A., BARON, P. Exposure to carbon nanotube material: Assessment of nanotube cytotoxicity using human keratinocyte cells, **2003**, *J. Toxicol. Environ. Health* 66, 1909–1926.
- 110 SHVEDOVA, A.A., KISIN, E.R., MURRAY, A.R., SCJWELER-BERRY, D., GANDELSMAN, V.Z., BARON, P., MAYNARD, A., GUNTHER, M.R., CASTRANOVA, V. Exposure of human bronchial epithelial cells to carbon nanotubes causes oxidative stress and cytotoxicity. In: **2004**, *Proceedings of the Society of Free Radical Research Meeting, European Section, June 26–29, 2003, Ioannina, Greece*, pp. 91–103.
- 111 MULLER, J., HUAUX, F., HEILIER, J.F., ARRAS, M., DELOS, M., NAGY, B.J., LISON, D. Respiratory toxicity of carbon nanotubes, **2004**, *Toxicol. Appl. Pharmacol.* 197, 305.

- 112 FENOGLIO, I., TOMATIS, M., LISON, D., MULLER, J., FONSECA, A., NAGY, J.B., FUBINI, B. Reactivity of carbon nanotubes: Free radical generation or scavenging activity?, 2005, *Free Rad. Biol. Med.*, in the press.
- 113 MYLVAGANAM, K., ZHANG, L.C. Nanotube functionalization and polymer grafting: An ab initio study, 2004, *J. Phys. Chem. B* 108, 15 009–15 012.
- 114 HOLZINGER, M., VOSTROWSKY, OI, HIRSCH, A., HENRICH, F., KAPPES, M., WEISS, R., JELLEN, F. Sidewall functionalization of carbon nanotubes, 2001, *Angew. Chem. Int. Ed.* 40, 4002–4005.
- 115 KALLINTERI, P., HIGGINS, S., HUTCHEON, G.A., ST. POURCAIN, C.B., GARNETT, M.C. Novel functionalized biodegradable polymers for nanoparticle drug delivery systems, 2005, *Biomacromolecules* 6, 1885–1894.
- 116 BIANCO, A., KOSTARELOS, K., PRATO, M. Applications of carbon nanotubes in drug delivery, 2005, *Curr. Opin. Chem. Biol.* 9, 674–679.
- 117 OBERDORSTER, G., OBERDORSTER, E., OBERDORSTER, A. Nanotoxicology: An emerging discipline evolving from studies of ultrafine particles, 2005, *Environ. Health Persp.* 113, 823–839.
- 118 REJMAN, J., OBERLE, V., ZUHORN, I.S., HOEKSTRA, D. Size-dependent internalization of particles via the pathways of clathrin- and caveolae-mediated endocytosis, 2004, *Biochem. J.* 377, 159–169.
- 119 DA ROS, T., PRATO, M. Medicinal chemistry with fullerenes and fullerene derivatives, 1999, *Chem. Commun.* 663–669.
- 120 HOFFMAN, S.W., RZIGALINSKI, B.A., WILLOUGHBY, K.A., ELLIS, E.F. Astrocytes generate isoprostanes in response to trauma or oxygen radicals, 2000, *J. Neurotrauma* 28, 844–849.
- 121 LAMB, R.G., HARPER, C.C., MCKINNEY, J.S., RZIGALINSKI, B.A., ELLIS, E.F. Alterations in phosphatidylcholine metabolism of stretch-injured cultured rat astrocytes, 1997, *J. Neurochem.* 68, 1904–1910.
- 122 WEBER, J.T., RZIGALINSKI, B.A., ELLIS, E.F. Traumatic injury of cortical neurons causes changes in intracellular free calcium stores and capacitative calcium influx, 2001, *J. Biol. Chem.* 276, 1800–1807.
- 123 AHMED, S.M., WEBER, J.T., LIANG, S., WILLOUGHBY, K.A., SITTERDING, H.A., RZIGALINSKI, B.A., ELLIS, E.F. NMDA receptor activation contributes to elevated intracellular calcium and decreased mitochondrial membrane potential in stretch-injured neurons, 2002, *J. Neurotrauma* 12, 619–629.
- 124 WEBER, J.T., RZIGALINSKI, B.A., ELLIS, E.F. Calcium responses to caffeine and muscarinic receptor agonists are altered in traumatically injured neurons, 2002, *J. Neurotrauma* 11, 1433–1443.
- 125 ZHANG, L., RZIGALINSKI, B.A., ELLIS, E.F., SATIN, L.S. Reduction of voltage-dependent Mg<sup>2+</sup> blockade of NMDA currents in mechanically injured cortical neurons, 1997, *Science* 274, 1921–1923.
- 126 UWATOKU, T., SHIMOKAWA, H., ABE, K., MATSUMOTO, Y., HATTORI, T., OI, K., MATSUDA, T., KATAOKA, K., TAKESHITA, A., Application of nanoparticle technology for the prevention of restenosis after balloon injury in rats. 2003, *Circ. Res.* 92(suppl), e62–e69.
- 127 SCHIELE, T.M. Current understanding of coronary in-stent restenosis. Pathophysiology, clinical presentation, diagnostic work-up, and management. 2005, *Z. Kardiol.* 94, 772–790.
- 128 SATOH, M., MATSUO, K., KIRIYA, H., MASHINO, T., NAGANO, T., HIROBE, M., TAKAYANAGI, I. Inhibitory effects of fullerene derivative dimalonic acid C60, on nitric oxide-induced relaxation of rabbit aorta, 1997, *Eur. J. Pharm.* 327, 175–181.
- 129 LAM, C.-W., JAMES, J.T., MCCLUSKEY, R., HUNTER, R.L. Pulmonary toxicity of single-wall carbon nanotubes in mice 7 and 90 days after intratracheal instillation, 2004, *Toxicol. Sci.* 77, 126–134.
- 130 OBERDORSTER, G., OBERDORSTER, E., OBERDORSTER, A. Nanotoxicology: An emerging discipline evolving from

- studies of ultrafine particles, **2005**, *Environ. Health Persp.* 113, 823–839.
- 131** KAMAT, J.P., DEVASAGAYAM, T.P.A., PRIYADARSINI, K.I., MOHAN, H., MITTAL, J.P. Oxidative damage induced by the fullerene C60 on photosensitization in rat liver microsomes, **1998**, *Chemico.-Biolog. Interact.* 114, 145–159.
- 132** HUSSAIN, S.M., HESS, K.L., GEARHART, J.M., GEISS, K.T., SCHLAGER, J.J. In vitro toxicity of nanoparticles in BRL 3A rat liver cells, **2005**, *Tox. In Vitro* 19, 975–983.
- 133** UENG, T.-H., KANG, J.-J., WANG, H.-W., CHENG, Y.-W., CHIANG, L.Y. Suppression of microsomal cytochrome P450-dependent monooxygenases and mitochondrial oxidative phosphorylation by fullereneol, a polyhydroxylated fullerene C60, **1997**, *Toxicol. Lett.* 93, 29–37.
- 134** CHIANG, L.Y., LU, F.-J., LIN, J.-T. Free radical scavenging activity of water-soluble fullerenols, **1995**, *J. Chem. Soc., Chem. Commun.* 1283–1284.
- 135** TSAI, M.C., CHEN, Y.H., CHIANG, L.Y. Polyhydroxylated C60 fullereneol, a novel free radical treapper, prevented the hydrogen peroxide and cumene hydroperoxide elicited changes in rat hippocampus in vitro, **1997**, *J. Pharm. Pharmacol.* 49, 438–445.
- 136** CHEN, M., VON MIKECZ, A. Formation of Nucleoplasmic Protein Aggregates Impairs Nuclear Function in Response to SiO<sub>2</sub> Nanoparticles, **2005**, *Exp. Cell. Res.* 305, 51–62.

## 11 Nanoparticles and Nanowires for Cellular Engineering

Jessica O. Winter

### 11.1 Introduction

The use of nanostructures (e.g., nanoparticles and nanowires) has increased dramatically in the last decade. Most applications have exploited the unique optical properties of mesoscale materials for imaging applications, both *in vivo* and *in vitro*. More recently, nanostructures have been investigated as components of actuating systems that can interact directly with the cellular environment. Because of the complementary size-scale of nanostructures and biological components, these systems provide the opportunity to precisely manipulate cells and proteins. This ability will produce greater insight into cellular function and pave the way for novel therapies.

This chapter discusses applications of nanostructures, including nanoparticles and nanowires, to cellular engineering. While several authors discuss specific aspects of nanomaterial interactions with cells (e.g., cell adhesion), this chapter is one of the first comprehensive investigations of the role of nanoparticles and nanowires in manipulating specific cellular components. Most of these approaches are in nascent stages, and therefore much of this chapter is focused on *potential* opportunities. Discussion is confined to semiconductor, metallic, silica, and magnetic materials, as carbon-based materials, polymeric nanostructures, and protein nanoparticles are discussed elsewhere. This chapter is divided into several subsections. Section 11.2 describes the motivation for using nanostructures to explore the biological milieu, their synthesis, and modifications required for biocompatibility. Section 11.3 examines nanostructures that interact with the cell exterior. Methods for modifying cell adhesion, migration and for manipulation of the cytoskeleton are discussed. Section 11.4 explores techniques for nanostructure delivery to the cell interior. Upon contact with cells, nanostructures enter the endocytosis pathway. Methods for eluding this fate are evaluated. Additionally, applications in intracellular tracking and sensing are considered. Section 11.5 describes nanostructure transport using the cytoskeletal system, including actin- and myosin-based approaches. Potential use for internal cytoskeletal manipulation and cargo delivery are evaluated. Section 11.6 considers the use of nanostructures for biomolecule



delivery, including drug delivery and gene therapy. As applications in the area of drug delivery are vast, nanotherapeutics for cancer therapy are presented as examples. Section 11.7 examines the potential of nanostructures to manipulate proteins, membrane bound receptors, and ion channels. Finally, concluding thoughts and a look to the future are presented in Section 11.8.

## 11.2

### Biological Opportunities at the Nanoscale

#### 11.2.1

##### Nanostructures and Cells

Nanoparticles and nanowires have captured the interest of researchers because of their small size and unique characteristics. Materials in this size regime (i.e., <100 nm diameter [1, 2]) display properties that differ from their bulk counterparts. These properties, resulting from quantum confinement, include electron transfer, strong dipole moments, and size-tunable absorbance and fluorescent emission [1, 3]. Applications of these materials have been widespread, particularly in the electronics field, where there is a constant impetus to uphold Moore's law [4] and produce ever smaller electrical components. Nanoparticles have been integrated into LEDs, solar cells, and lasers [5], whereas nanowires have been used primarily to create electronic and computational components, including p-n diodes, field effect transistors, and logic gates [6].

Although the applications have not been as obvious, nanostructures also show great potential in the biological sciences [7]. Many of life's most basic functions occur in the nanometer regime. For example, the diameter of DNA is ~2 nm, of a cell surface receptor is ~10 nm, and of a virus is ~50 nm [8] (Fig. 11.1). Because of their similar size scales, nanocomponents easily interface with biological molecules [9], a feature that has already been exploited to create new sensing technologies, diagnostics, and therapeutics. Nanoparticles have been utilized as fluorescent dyes for cell labeling [10, 11], biosensors [12, 13], cell sorting aides [14], and chemotherapy alternatives [15]. Nanowires have been used for biological separations, biosensing, and gene therapy [16]. Thus, the combination of similar size scales with unique optical properties has produced several passive applications for biosensing. Future developments will likely exploit biological machinery to manipulate cells directly.

Nanostructures hold particular promise in the fields of cell and tissue engineering. In addition to possessing favorable size scales to many biological components, nanoparticles and nanowires can be manipulated in external optical [17], electric [1], and magnetic fields [18]. Their high surface to volume ratios present favorable sites for chemical reaction, and their optical properties allow for *in situ* monitoring of local structures and biochemistry [19]. Because of these capabilities, nanostructures provide some of the first opportunities to actively manipulate subcellular components. Some of this work has already been realized *ex vivo*. For example,

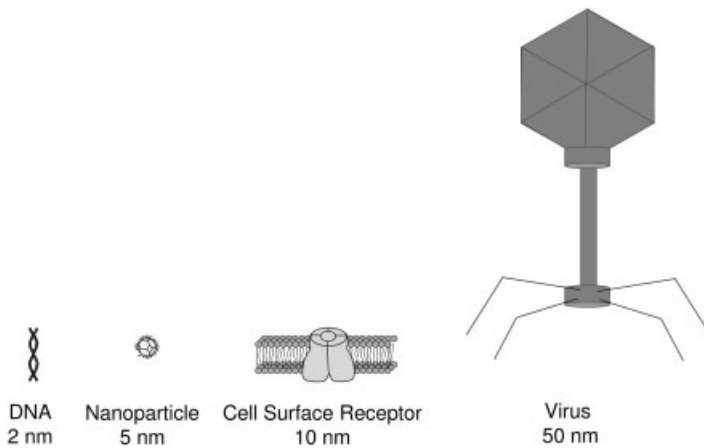


**Fig. 11.1.** Comparative diameters of a nanoparticle and selected biological molecules.

nanoparticles have been harnessed to kinesin and transported along microtubules [20]. However, most possibilities for nanostructures in cellular engineering have yet to be realized.

### 11.2.2

#### **Nanoparticle and Nanowire Synthesis for Biological Systems**

Nanostructures can be synthesized using various techniques, depending on the desired composition and properties. However, developing water-soluble, non-toxic nanostructures has been challenging. Most synthesis methods were originally designed for optical or electronic applications. Particles are commonly made under harsh conditions with high temperatures or organic solvents, incompatible with biological requirements. In fact, the nanomaterials themselves may be toxic (Section 11.2.5). Cadmium, a major component of semiconducting nanostructures, is known to interfere with DNA mismatch repair [21], can inhibit certain types of neuronal firing [22], and is a known carcinogen [23]. Carbon nanotubes and fullerenes can produce asbestos-like lesions in the lung [24]. Carbon [25–27], graphite [27], and iridium [28] particulates can damage tissues. The difficulties of making biological relevant, non-toxic nanostructures are great, yet several synthetic strategies have been developed.

##### 11.2.2.1 Nanoparticle Synthesis

Biologically active nanoparticles may be synthesized from semiconducting, metallic, or magnetic materials. Semiconducting particles, also known as quantum dots, are typically composed of CdX (where X is S, Se, or Te), and have been used primarily in optical applications, as a result of their high fluorescence quantum yields [19]. Metallic particles are usually made from gold. They have been used for bio-

sensing because they experience a color change with decreasing inter-particle proximity [13]. Additionally, they have formed the basis of several therapeutic treatments, as particles produce a temperature elevation with near-infrared excitation [15]. Magnetic particles are usually made from iron oxides [18]. Frequently, these particles are embedded in a micron-sized polymer matrix and used as MRI contrast enhancers and for cell and protein separation [18]. The variety of particles used has resulted in several synthetic techniques, each specific to the particle material employed.

**Semiconductor Nanoparticles** The most common method of semiconductor nanoparticle synthesis is high temperature precursor decomposition [29]. This procedure allows control of nanoparticle growth and nucleation, and thus size distribution. Depending on the reaction time and final temperature, particles synthesized using precursor decomposition can vary in size from 1 to 11 nm, with size distributions as narrow as 5% [29]. Regular size distributions are critically important for the creation of templated nanostructures, which form the basis of many cellular engineering applications (Section 11.3.2). These structures, created through the ordered self-assembly of nanoparticles, require uniform size distributions to develop patterns over large length scales.

Unfortunately, precursor decomposition utilizes organic solvents, presenting several difficulties to direct application in biology. Particles synthesized with the most common passivating ligands, tri-octyl phosphine (TOP) or tri-octyl phosphine oxide (TOPO), are soluble in chloroform and other organic solvents, but not in alcohols or aqueous solution [29]. Additionally, TOPO is a weakly bound ligand, which can disassociate from the particle over time, producing a cytotoxic product [30]. This loss of passivation exposes the particle core to oxidative attack, which can release toxic ions into the cellular environment [31], eventually resulting in particle dissolution. To protect the particle core from photooxidation and surface reactions, semiconductor particles are often modified with a shell of a wider band gap (i.e., more insulating) material. Most semiconductor particles employed in biological applications contain a shell, with the most common material used being zinc sulfide (ZnS) [32]. ZnS is an ideal shell material as it is substantially less toxic than cadmium, possesses a larger band gap than CdSe, and does not easily form alloys with CdSe [31, 33]. CdSe/ZnS capped particles are stable for months, even in the presence of oxygen and are less toxic than uncapped particles [31].

As an alternative to organic syntheses, nanocrystals have been produced in aqueous solvents through a process known as arrested precipitation. Bulk CdS is relatively insoluble in water ( $K_{sp} \sim 10^{-29}$ ) [34]. However, with the addition of aqueous thiols, nanometer-sized water-soluble colloids are produced. Briefly, upon thiol addition, complexes with cadmium ions are formed. Sulfur ions are added and crystal growth occurs, but it is hindered by the steric presence of the thiol compounds. Eventually, free sulfur anions cannot overcome these steric forces and particle growth is terminated. If the surface is well passivated, the crystals can remain suspended in water.

This process is controlled by many factors, including the reactant ratios, the thio-

lated ligand in question, and the pH of the reacting mixture; all of which contribute to nanoparticle size and uniformity [35, 36]. Aqueous syntheses are very flexible. Various materials can be used as reactants. The first CdS nanocrystals were produced using Cd(SO<sub>4</sub>) as a cadmium source [37], although Cd(ClO<sub>4</sub>)<sub>2</sub> [38] and CdCl<sub>2</sub> [35, 36] have also been used. Sulfur can be introduced through various mechanisms, and (NH<sub>4</sub>)<sub>2</sub>S [37], Na<sub>2</sub>S [38], and H<sub>2</sub>S [39] have all been investigated. Thiolated ligands can range widely, including mercaptoacetic acid, mercaptopropionic acid, mercaptoethylamine, and β-mercaptoethanol [35, 40, 41]. Although thiolated ligands are used most frequently, any ligand that binds to Cd<sup>2+</sup> ions and promotes water solubility of the particle may be employed.

Nanoparticles produced using aqueous syntheses offer many benefits for biological studies. For example, they can be manufactured using simple bench-top chemistry, requiring only a fume hood. Particle surfaces may be readily altered through the use of cysteine- or thiol-terminated biomolecules, or by performing post-synthetic conjugation chemistry on a ligand functional group. The main limitation of this procedure is the large particle size distribution, which can increase with time, developing a tail at larger sizes, indicating particle instability [42]. This is likely a result of Ostwald ripening, the growth of larger particles at the expense of the thermodynamically less stable smaller ones [41]. However, we have observed that only solutions of larger particles exhibit this behavior; solutions containing smaller particles (i.e., ~3 nm and less) can be stable in aqueous solution for months. Thus, the particles can exhibit remarkable stability, comparable only to silica-capped CdSe/ZnS [10, 43].

**Metallic Nanoparticles** Gold or silver nanoparticles, the most widely investigated, have a long history, originally being described by Michael Faraday in 1857 [44]. They are normally synthesized by the reduction of metal salts in citrate solution [45]. Similar to aqueous syntheses for semiconductor nanoparticles, various capping agents can be added to control particle surface properties and growth [46]. Gold nanoshells can also be created through the reduction of metal salts onto a pre-existing substrate [47]. Shell growth occurs by the formation of nanoparticles on a surface (i.e., gold [47] or silica [48]). As nanoparticle growth continues, particles coalesce to form a shell. These shells exhibit interesting plasmon resonance shifts, which can produce local heating in the presence of IR irradiation. As an alternative to aqueous routes, gold particles have also been produced in inverse micelle preparations [49]. In this synthesis technique, particle growth is limited by the size of the micelles formed. Unfortunately, most inverse micelle preparations utilize organic solutions, which may necessitate ligand exchange to create biologically stable particles.

Gold particles, in particular, have found application in the biomedical field because of their easily altered surface chemistry and optical properties. Gold readily binds thiol-containing molecules [50], offering a wide-range of surface chemistry options. Additionally, gold colloid solutions change color, from red to purple, upon particle aggregation [13], and particles can be deposited in self-assembled monolayers, facilitating integration into biosensors [51]. The presence of gold particles

can be detected using various methods, including optical and electron microscopy and Raman spectroscopy, and gold particles have been used in various diagnostic methods [46]. Finally, gold particles and nanoshells experience a temperature increase upon near-infrared irradiation that has been used for cancer therapy, e.g., hyperthermia (part of Section 11.6.2.2).

**Magnetic Nanoparticles** Most magnetic nanoparticles are composed of iron oxides. In general, particles are prepared by the addition of base to an aqueous solution of iron ions, forming iron oxide [18]. To prevent oxidation, particles are produced under nitrogen. For example, magnetite ( $\text{Fe}_3\text{O}_4$ ) may be prepared by Reaction (1) [18].



Crystal growth proceeds through nucleation of small complexes that grow as a result of Ostwald ripening. Particles formed range from 6–15 nm and consist of single magnetic domains. The strategy is very similar to aqueous syntheses for semiconductor and metallic nanoparticles described above. Reactions are controlled by passivating surface molecules, which take on an additional importance because particles are attracted to each other through their magnetic fields in addition to traditional electrostatic and van der Waals forces [18]. Passivating molecules can be added to the reactants, during reaction, which forms microemulsions, or after the reaction. A wide variety of natural and synthetic polymers, chemical stabilizers, and metallic coatings have been investigated. Typically, the passivating coating is not magnetic and can be as much as 20 nm thick, effectively doubling the diameter of the particle [52], which may prove problematic, depending on the application.

Magnetic nanoparticles are characterized by the nature of their magnetic properties. Nanoparticles may be ferromagnetic or superparamagnetic. In ferromagnetic materials, individual atomic dipole magnetic moments align to create permanent magnetization. This occurs because the internal thermal energy of the material is not sufficient to overcome the magnetic attraction of the individual dipoles. Particles in the micron-size range exhibit this behavior [18]. However, as particle size decreases, an interesting phenomenon is observed. Although the particle still possess insufficient thermal energy to overcome individual atomic magnetic attractions, the internal thermal energy of the particle is sufficient to alter the direction of all aligned dipoles. This produces a fluctuation of the magnetic dipole for the entire crystal, resulting in a net magnetic moment of zero. Particles below 15 nm exhibit this behavior [18], known as superparamagnetism. Although they are not “true” paramagnetic materials in that their atomic dipoles are aligned, the entire crystal exhibits paramagnetic behavior (e.g., temporary polarization).

#### 11.2.2.2 Nanowire Synthesis

Nanowires have been manufactured using various techniques, including templated synthesis, directed growth in solution, and vapor phase growth [3, 16]. Because of the range of methods employed, nanowires can be created from many substances, in-

cluding magnetic, semiconducting, and ceramic materials. In templated synthesis, nanowires or hollow nanotubes are grown inside a porous membrane using electrodeposition or sol-gel techniques. Using this method, magnetic [53], metallic [16], and ceramic [16] nanowires with aspect ratios of up to 250 have been manufactured. Templated synthesis has several advantages. Particles of varying composition can be created by changing the electric potential or electroplating solution. The presentation of nanowires may be varied. They can be constructed as supported arrays or, by dissolving the membrane, free-standing entities.

Solution phase synthesis proceeds through several mechanisms [3, 16]. In surfactant driven assembly, surfactants attach to a specific crystal face, limiting growth in those directions. Alternatively, chemical reaction may occur preferentially at a specific crystal face, and reduction at this surface produces nanowire growth and extension. Solution-phase synthesis has the advantage of being scalable (to gram quantities [3]) and occurring at modest temperatures, which are more amenable to biological components. The greatest limitation of this technique is that directed growth in solution is the not well understood and difficult to control.

Vapor-phase synthesis requires high temperatures to create gaseous reactants that are deposited on a substrate as nanowires or nanotubes. High temperature syntheses are primarily used to produce carbon nanotubes, but silicon and several other semiconductor nanowires have also been created using this approach [3, 6]. Nanowire formation is catalyzed by a metallic liquid droplet. As the temperature is increased, gaseous vapor of the desired component begins to form a eutectic mixture within the droplet, entering the liquid phase. Further increases in temperature raise the dissolved concentration, favoring formation of a pure solid composed of the desired component. The size of the droplet restricts crystal growth in a preferred direction and defines the diameter of the nanowires, with an average of 10 nm [6]. Nanowires produced are frequently contaminated by the seed crystal. Because many of the seed metals used (e.g., nickel) are toxic, the development of biocompatible nanowires may be hindered.

As with nanoparticles, surface functionalization is often required to produce biologically compatible, water-soluble nanowires. Many of the techniques employed are similar to those for nanoparticles, including the use of thiols, carboxylic acids, and siloxanes [16]. Because nanowires may be constructed of segments of alternating materials, several passivation strategies may be required. For example, metallic nanowires containing segments of nickel and gold can be labeled with distinct fluorescent agents using differences in surface chemistry (Fig. 11.2) [54]. Nanowires have also been functionalized with biological molecules including DNA and proteins [55, 56].

### 11.2.3

#### **Surface Passivation Strategies**

The main limitation of nanostructures produced in organic solutions is their lack of water solubility. Several techniques have been offered to correct this condition, all relying on modification of the nanostructure surface. This can be accomplished by altering the nature of the passivating ligands or augmenting the crystal with a

shell material that is biocompatible. These techniques have both been used to create nanoparticles employed for biological labeling [10, 11]. However, the process for transferring particles into water can be time-consuming and requires equipment outside the reach of most biological laboratories.

The most common method for rendering particles water-soluble includes an additional post-processing step known as ligand exchange. During ligand exchange, the existing chemical surface coating of the particle is replaced with one that can alter the solubility of the colloid [57]. There are several variations in the ligand exchange technique; however, the basic premise remains the same [29]. The particles are dried to remove unreacted ligand and the organic solvent, and are introduced into a solution containing a gross excess of the new ligand. After an incubation of several hours, exchange occurs. Exchange can be confirmed by altered solubility of the particles, or through analytical techniques like FTIR (Fourier-transform Infrared Spectroscopy) and XPS (X-ray Photoelectron Spectroscopy).

The most common ligand exchange used to produce biologically compatible quantum dots exchanges TOPO, bound to CdSe/ZnS core-shell particles, for mercaptoacetic acid (MAA = HS-CH<sub>2</sub>-COOH) [11, 57]. The binding of MAA occurs through the sulfur group at the molecule's terminus, which adheres to Zn atoms on the ZnS coating [57]. The carboxyl end of MAA provides water solubility. In addition to MAA, several other thiolated chemicals have been examined, including mercaptopropionic acid (MPA = HS-(CH<sub>2</sub>)<sub>2</sub>-COOH), mercaptoethylamine (MEA, HS-(CH<sub>2</sub>)<sub>2</sub>-NH<sub>2</sub>), and  $\beta$ -mercaptoethanol (MBE, HS-CH<sub>2</sub>-CHOH). In fact, any molecule that binds to the surface of the particle and is water-soluble can be used, thus allowing a range of surface chemistries to be explored. However, ligand exchange is a long, multi-step process spanning as many as three days. The particles are only stable in solution for 1–3 weeks [57], indicating possible loss of ligand coverage over time. If the ligands are toxic (e.g., MBE [58]) or bioactive (e.g., MEA [59]), desorption can have deleterious effects on cells exposed to particles.

Another method to create water-soluble nanoparticles alters the surface by applying a biocompatible shell material. An example of this technique, developed by Alivisatos et al. [10, 43], coats TOPO-capped CdSe/ZnS particles with silica. Particles were exposed to a gross excess of mercaptopropyltris(methoxy)silane (MPS), to which tetramethylammonium hydroxide (TMAH) had been added, producing a 2–5 nm silica shell [43]. This technique is versatile and could be applied to any TOPO-capped particle. Additionally, silica-coated particles meet several of the criteria for biological applications. Unlike particles that undergo ligand exchange, silica-coated nanocrystals exhibit stability for months [10, 43]. Also, biomolecules can be readily conjugated to silica using well-established techniques developed for chromatography. The only potential disadvantage of this technique is that silica is insulating and might alter the properties of the encapsulated particle.

#### 11.2.4

#### **Bioconjugation**

Once particles have been prepared for aqueous use, it may be desirable to attach biomolecules to their surface. The range of biomolecules that can be bound to

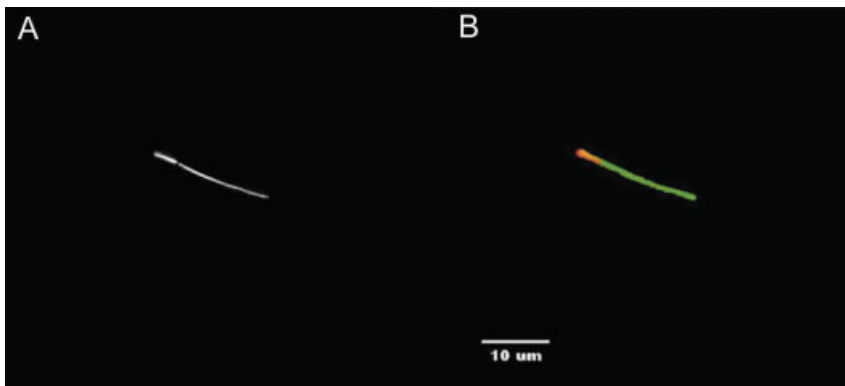


**Fig. 11.2.** Selective functionalization of multi-component nanowires can be achieved by taking advantage of the selective surface chemistry of the nanowire segments. (A) Reflection image of a two-segment nickel-gold nanowire. The brighter portion of the nanowire represents the more reflective gold surface. (B)

The corresponding fluorescence image shows a nanowire that was modified by coupling different fluorescent dyes to each segment, which allowed the Ni segment to emit green and the Au segment to emit red. (Photo courtesy of Gerald Meyer, Johns Hopkins University, Baltimore, MD.)

nanostructures is staggering, and this is one of the factors that have led to their broad appeal for biological applications (see Volume 1 of this series for more detail). There are several methods to link biomolecules to nanostructures [60], the simplest being physisorption on the nanostructure surface (e.g., Zhang et al. [61]). However, most nanostructures are charged, thus electrostatic attraction is more frequently used to mediate attachment. For example, DNA will bind to nanoparticles presenting trimethylammonium ligands [62], and layer-by-layer assembly has been used to create films of alternating-charged nanoparticles and biomolecules [63–65]. Additionally, binding affinities between materials have been exploited to link biomolecules to surfaces. Thiolated compounds bind strongly to Cd-based and gold nanostructures [50], and biomolecules containing cysteine can be attached to nanostructures in this way [66]. Nanostructures can also be functionalized with biomolecules through directed recognition. The avidin-biotin system has been well studied in this regard. Avidin and biotin display strong binding to each other. A molecule that has been modified with avidin can be linked to any biotin-labeled biomolecule. This technique has served as the basis for commercially available fluorescent quantum dot labels [10].

#### 11.2.4.1 Conjugation Strategies to Promote Non-specific Cellular Affinity

Once on a surface, biomolecule-conjugated nanostructures can be directed to a cell or tissue of interest. In some cases, this occurs on the basis of charge, resulting in non-specific adsorption. This recognition strategy is the most straightforward, requiring only adjustment of the surface charge, but has the least specificity. Particles cannot be directed to a specific part of a cell or a specific group of cells. This



method was first used by Alivisatos et al. [10], who investigated CdSe–CdS core–shell nanocrystals enclosed in a silica shell (Section 11.2.3) [43]. The shell conferred water-solubility on the particle, but also provided functional groups (e.g., aminosiloxanes) for bioconjugation. To demonstrate non-specific binding, the silica coating was modified with trimethoxysilylpropyl urea (urea =  $\text{NH}_2\text{-C-NH}_3^+$  at neutral pH), which binds negatively charged acetate groups ( $-\text{CH}_2\text{-COO}^-$  at neutral pH) in the cell nucleus. Nanocrystals introduced to cells were located in the nucleus, as evidenced through fluorescence microscopy measurements. Binding was suppressed with the addition of a negatively-charged reagent or sodium dodecyl sulfate (SDS), indicating that binding was primarily caused by non-specific electrostatic interactions.

#### 11.2.4.2 Biomolecular Recognition

Apart from electrostatic interactions, which are non-specific, particles can be directed to cells and tissue using biomolecular recognition, the strong and highly specific binding that exists between a receptor and its ligand target. This binding is not completely understood, but arises from a combination of electrostatic attractions, hydrogen bonding, and hydrophobic/hydrophilic interactions [67]. The cumulative interaction of these forces, which are individually weak, produces tight binding. Additionally, this affinity is unique to the ligand and its analogs, as only molecules with a certain conformation can access the binding site and form the appropriate bonds. Thus, the interfaces formed through biomolecular recognition are highly specific and controlled.

Several molecules have been identified as biorecognition elements, and can be used to connect small molecules to components of the cell. Typically, these fall into three classes: antibodies, proteins, and peptides [67]. Antibodies recognize components that are foreign to their host system, and can be produced for almost any cellular component. A wide range of antibodies are commercially available, and their large size and high number of functional groups allow for ready conjugation to many surfaces. Antibodies are by far the most commonly used biorecognition element in conjugate chemistry [68]. However, when antibodies cannot be applied, alternatives (e.g., proteins and peptides) may be employed. Because protein or peptide binding will produce a cellular response, these methods are often utilized to impose a specific cellular function (e.g., receptor-mediated endocytosis [11]) to the attached molecule. Proteins can be linked to these molecules through chemistry techniques, the success of which depends widely on the nature of the protein employed. For applications where an entire protein might be too large or expensive, protein fragments, known as peptides, can be employed. Peptides can be synthesized with additional amino acids to allow for conjugation to a chosen molecule.

#### 11.2.4.3 Conjugation Strategies for Antibody-mediated Recognition

Antibody binding is extremely useful for directing nanostructures to particular cell elements. A wide selection of antibodies is commercially available, and they may

be easily conjugated to nanostructure surfaces. Antibody–nanoparticle binding was first demonstrated by Nie et al. [11], using CdSe–ZnS core–shell particles. The particle surface was altered through mercaptoacetic acid ligand exchange, placing carboxyl groups on the surface. Using carbodiimide chemistry (i.e., EDC), carboxyl groups were conjugated to the reactive amines of IgG antibodies. Because aggregation is a side-effect of EDC chemistry, conjugates were examined with transmission electron microscopy and were found to be primarily single particles. Fluorescence optical microscopy confirmed that conjugated particles maintained their initial optical properties. To demonstrate biorecognition, IgG conjugates were shown to aggregate in the presence of a specific polyclonal antibody known to bind IgG fragments. Antibody recognition has also been demonstrated on live cells using aqueous CdS quantum dots conjugated to IgG secondary antibodies through EDC chemistry [66]. Primary antibodies recognized and attached to integrin receptors. Quantum dot–IgG conjugates were then able to bind and recognize the primary antibodies with no adverse cellular effects.

#### 11.2.4.4 Conjugation Strategies for Protein- and Peptide-mediated Recognition

Proteins and peptides (i.e., protein fragments) have also been conjugated to particles for cellular recognition. For example, phalloidin protein conjugated to silica-coated quantum dots was used to bind to actin filaments in fixed cells [10]. Phalloidin was attached to the nanoparticle surface using avidin–biotin chemistry. First, the silica coating of the nanocrystal was modified to include primary amines using 3-aminopropyltrimethoxysilane. Then, biotinamidocaproic acid 3-sulfo-*N*-hydroxysuccinimide ester was introduced. The NHS ester group of the activated biotin reacts quickly with primary amines to produce amide bonds, linking the nanocrystals to biotin molecules. The cells were exposed to a separate solution of biotinylated-phalloidin, which adhered to F-actin filaments in the cytoskeleton. Then, streptavidin was introduced, binding the biotin component of biotin–phalloidin. Finally, cells were incubated with the biotinylated-nanocrystals, which bound to the phalloidin–biotin–streptavidin complexes at avidin sites. Additionally, particles have been bound to transferrin, a surface protein that promotes uptake of iron molecules through receptor-mediated endocytosis [11]. EDC chemistry was used to mediate attachment to CdSe/ZnS particles. Transferrin-conjugated particles were incubated with living cells, and were found in intracellular vesicles, as would be expected following receptor-mediated endocytosis.

As an alternative to whole proteins, which can be bulky, a second approach utilizing peptides was developed. Peptides were attached to quantum dots as surface passivation molecules [66], providing a single-step technique for nanocrystal synthesis and bioconjugation. Aqueous CdS nanoparticles were attached to RGDS and YIGSR peptides, which bind to integrin receptors [69, 70] through thiolated ligand-binding using cysteine residues. Peptide–cell binding has several advantages to antibody- or protein-cell binding. The minimum peptide length for recognition depends on the protein selected, but can be as short as 3–5 amino acids (e.g., 1–1.5 nm) [69, 70]. Additionally, peptides can be manufactured to almost any length, with each amino acid roughly corresponding to 3 Å (0.3 nm) for a straight-

chain conformation [71]. Thus, the separation distance between the particle and the cell surface can be tuned through altering the length of the peptide. Their small size and tunable length make peptides ideal alternatives to large conjugation molecules. Given these factors, peptide bioconjugation presents a superior approach for forming close-range interfaces between semiconductor quantum dots and cellular receptors.

#### 11.2.5

##### **Toxicity (see also Volume 5 of this Series)**

Very few studies have examined the potential health risks of nanostructures. There is limited evidence that suggests risks are present, particularly through inhalation. A recently published report demonstrated that inhaled carbon nanotubes can produce asbestos-like lesions in the lung [24]. Among the highest dose group, the mortality rate was 55% ( $N = 9$ ) after only 7 days of exposure. Although these results were for pulmonary tissue, a separate set of studies examining carbon [25–27], graphite [27], and iridium [28] particulates established the ability of nanomaterials to damage other tissues, including the immune system [26] and brain [25, 27]. Particle effects on the brain included an increase in lipid peroxidation and damage to lipid-rich tissues [25]. The most troubling finding of these studies is that particle clearance proceeds slowly. A low level (i.e., 6% in lung) of particulates remained in tissue a full six months after exposure [28].

However, it is unclear if these results will apply to nanostructures used in biomedical applications. Most of these investigations examined toxicity through inhalation, but semiconducting, metallic, and magnetic particles are primarily produced in solution-phase. A more likely route of exposure is through ingestion or skin contact [72]. Additionally, the materials studied (i.e., carbon particulates and nanotubes) bear little similarity to the nanostructures reviewed here other than size. Several groups have employed semiconducting nanoparticles *in vitro* and *in vivo* without noticeable cell damage [73–78]; however, they did not specifically assess cell viability and function. To date, only a single study [31] has confirmed that semiconducting nanoparticles may be cytotoxic to cells when presented in aqueous solution. This was attributed to the release of free  $\text{Cd}^{2+}$  ions following oxidation of the particle core. Nanoparticles are susceptible to oxidation and photooxidation [1, 31, 79–82], particularly with UV exposure. Reaction of oxygen with group VI elements (e.g., S, Se, Te) produces oxides [1] that can disassociate from the particle surface. Free Cd atoms are left behind and may eventually enter solution. Elevated free cadmium levels have been reported for poorly-capped particles and particles exposed to prolonged UV excitation [31].

$\text{Cd}^{2+}$  ions have well-established health risks [83]. Cadmium is a known carcinogen, and has been linked to lung, testicular, adrenal, liver, and kidney cancer [23]. Although the exact mechanism of carcinogenicity is not understood, cadmium has been shown to interfere with DNA mismatch repair [21]. It also binds strongly to the sulfhydryl groups of mitochondrial proteins [84], and this is the believed source of toxicity observed for the primary hepatocytes studied previously [31]. Ad-

ditionally, cadmium is a commonly used blocking agent in patch-clamp studies that interferes with neuronal firing [22]. Given all of these factors, the stability of the nanoparticle core is of great concern. Modifying particles with a strongly-bound passivating ligand, an inorganic layer (e.g., ZnS), or a polymer coating can increase particle stability by preventing the entry of oxygen [31, 72]. Most recent reports on semiconducting quantum dot use for living systems utilize some coating of this nature [73–78].

Data for metallic nanoparticles and nanowires is even scarcer. Gold, in the bulk form, is fairly well-tolerated and has been used as an electrode coating in prosthetic implants for some time [85]. However, gold nanostructures have a dramatically higher surface area than bulk material. They are much more reactive and can potentially interfere with biochemical syntheses [86]. Reports on silver nanoparticles are conflicting. Although silver displays toxicity when employed in the nervous system, it has been widely used as a biomedical antimicrobial coating [87]. Silver nanoparticles employed in bone cement exhibited no overt cytotoxicity and a strong antibacterial effect at 1% loading [87]. However, mouse spermatogonia cells demonstrated a reduction in mitochondrial activity, increases in cell lysis and apoptosis, and changes in cell morphology when exposed to silver nanoparticles [88].

Uncapped iron oxide (i.e., magnetic) nanoparticles can also be cytotoxic, reducing cell viability by 20% at concentrations of only  $0.05 \text{ mg mL}^{-1}$  and 60% at higher concentrations (i.e.,  $2 \text{ mg mL}^{-1}$ ) [89]. Reduced viability may result from excessive particle internalization, producing apoptosis and limiting cell migration [90]. This behavior can be altered by the addition of a surface coating. For example, pullulan-conjugated nanoparticles showed no statistical difference in cell viability from control cells at  $2 \text{ mg mL}^{-1}$  concentrations [89].

Although the data on nanostructure toxicity is slim, it is apparent that coating the particles with a biocompatible shell (e.g., silica) or biomolecule (e.g., pullulan) reduces the risk of adverse reaction. This may result from isolation of a toxic core material, as in the case of Cd-containing particles, or from reduced protein adsorption, which limits particle endocytosis. The most effective coatings are likely those that reduce uptake through the endocytotic pathway [90], allowing the nanoparticle to remain in the extracellular environment as long as possible. As more research is performed, additional modifications to prevent toxicity will likely arise.

### 11.3

#### **Nanostructures to Modify Cell Adhesion and Migration**

An area of cellular engineering with great possibility for nanostructure use is the selective modification of cell adhesion. Cell adhesion is ideal for nanostructure-based evaluations because most of the salient events occur on the extracellular surface. Thus, nanostructure modifications for intracellular delivery (Section 11.4) are not required. Additionally, there is much to be gained from nanoscale investigations of cell adhesion and migration, as these processes are responsible for cancer metastasis [91], angiogenesis [91], tissue repair [92], and synapse formation [93].

Selective cell adhesion is also critical to the development of biocompatible implants and prostheses [94]. Integration with target cells is crucial to the function of the implant. However, in many cases this adhesion must occur while excluding undesirable cell types (e.g., immune cells, glia) that can interfere with device performance and tissue compatibility.

At the micron scale, cell responses to both chemical and physical cues are well established (for a review see Folch and Toner [95]). Surfaces with micron-sized pillars can influence cell adhesion and cytoskeletal protein distributions [96]. Cell extensions (e.g., neurites) are influenced by both the depth and width of surface grooves [97]. Chemical surfaces, containing adhesive islands, can confine cells to regions as small as 10  $\mu\text{m}$  [98]. As area decreases the number of adherent cells, degree of cell spreading, and even the signal for apoptosis (i.e., controlled cell death) can be controlled [99]. Physical and chemical patterns can produce a synergistic response. Neurons cultured on micropatterned substrates align their extensions with regions containing both cues (Fig. 11.3). These patterns have been incorporated into various applications. Physical patterns have been used in biosensors and implants to improve biocompatibility and tissue adherence [100]. Micropatterned adhesive regions can create ordered arrays of muscle cells [101, 102], and guide neurite extension for neural networks [103–106].

### 11.3.1

#### Cell Adhesion at the Nanoscale

Although the ability of cells to respond to micron-scale structures has been established, there has been doubt as to whether responses would extend into the nano-

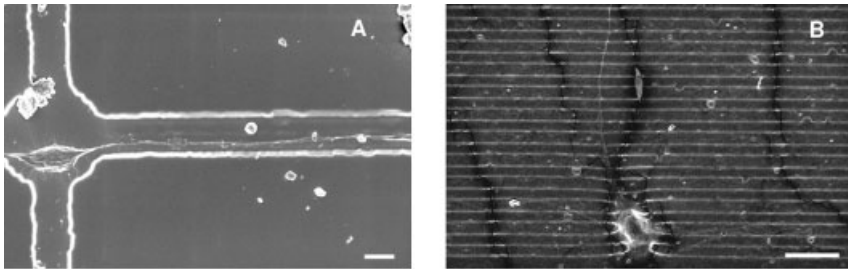


**Fig. 11.3.** (A) PC12 cell micropositioned on PDMS microfabricated structure. The cross-shaped pattern was fabricated as a geometry to analyze neuron responses to multiple extracellular cues localized on the arms. In this case, microchannels 2  $\mu\text{m}$  wide and 500 nm deep were patterned on the right arm for stimulating the cell via contact guidance, as evidenced by the extension of an aligned neurite. (B) Rat embryonic hippocampal cell (E18) cultured on a PDMS substrate with

microchannels and immobilized NGF. Microchannels 2  $\mu\text{m}$  wide and 1  $\mu\text{m}$  deep were patterned in PDMS using replica molding from silicon masters. NGF was immobilized using arylazido photolinkers. The substrate provides a combination of physical and biochemical cues to accelerate polarization of the cell (i.e., determination of an axon). (Photo courtesy of Christine Schmidt, Natalia Gomez University of Texas at Austin, Austin, TX.)

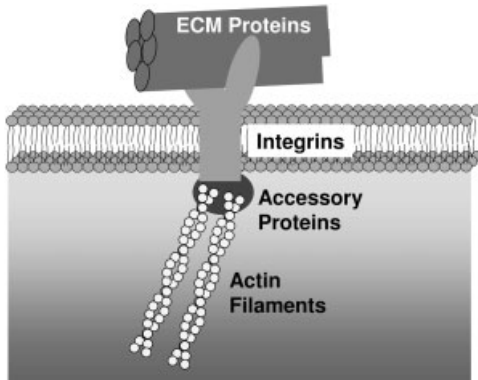


**Fig. 11.4.** Integrin binding to the ECM and cytoskeleton. Integrins embedded in the plasma membrane are used to form contacts with the extracellular matrix (e.g., collagen, laminin) and cytoskeleton (e.g., actin).

scale [2]. However, the environment surrounding cells is peppered with nanoscale cues. Cells are surrounded by a lipid bilayer  $\sim 5$  nm thick [8] (Fig. 11.4). Cell adhesion is mediated by 10 nm diameter integrins embedded in the bilayer [8]. These integrins cluster to create various nanoscale contacts (Table 11.1) [107, 108]. Integrins bind extracellular matrix (ECM) components, which are the primary elements of the basement membrane surrounding most tissues. Some of these components display heights of  $\sim 150$  nm and band widths of  $\sim 60$ – $80$  nm (Table 11.1) [2, 109], and fibrils and pores in ECM structures as small as 5 nm have been reported [109]. On the cell interior, integrins attach to nanometer-sized cytoskeletal elements, including microtubules, actin, and intermediate filaments (Table 11.1). These elements produce cell shape and structure, and may respond to external forces [110].

### 11.3.2

#### Cell Adhesion and Nanoscale Physical Topography

However, creating materials with dimensions that could explore these biomolecules has been challenging. Unlike microfabricated devices, patterning methods are just beginning to extend to the nanoscale. Using lithographic techniques, several features, including grooves, ridges, steps, pillars and pores, have been investigated (see Flemming et al. [109] for a review). Despite being several times smaller than a cell diameter (i.e.,  $\sim 10$   $\mu\text{m}$ ), cell responses were observed. Nanoscale physical features can create networks of aligned cells [111–113], induce macrophage spreading and phagocytotic activity [114], and guide neuronal growth cones [115].

For example, 350 nm wide nanogrooves have been used to evaluate smooth muscle cell (SMC) adhesion *in vitro* [113]. More than 90% of SMCs cultivated on this surface aligned to the grooves, and proliferation of the cells was significantly

**Tab. 11.1.** Cell–matrix contacts at the nanoscale. (Adapted from Ref. [107].)

Element	Dimensions	Description/purpose
Cell–matrix contacts [107, 198]		
Filopodium	20–200 $\mu\text{m}$ $\times$ 200–500 nm	Cell protrusion, actin bundle connected to syndecans (proteoglycans)
Focal contact	1.5 $\mu\text{m}$ $\times$ 250 nm	Cell contact, actin microfilaments connected to integrins, substrate adhesion
Hemidesmosome	150 $\times$ 40 nm	Cell contact, intermediate filaments connected to integrins
Podosomes	200–400 nm diameter	Cell contact, actin bundle connected to integrins
Microspike	2–10 $\mu\text{m}$ $\times$ 200–500 nm	Cell protrusion, actin bundle connected to integrins, NG2 (proteoglycans)
Cell exterior: extracellular matrix proteins [8]		
Collagen	1.5 nm triple helix, 10–300 nm fibers	Structural protein
Fibronectin	2–3 nm arms separated by 100 nm, fibrils 10–1000 nm	Adhesive protein
Laminin	30 $\times$ 100 nm	Adhesive protein
Cell interior: cytoskeletal elements [8]		
Actin	5–9 nm diameter	Muscle contraction, cell locomotion, vesicle transport
Microtubules	25 nm diameter	Organelle and protein transport, chromosomal separation, cell division, vesicular transport, primary components of cilia and flagella
Intermediate filaments	10 nm diameter	Mechanical strength, compose nuclear lamina

lower than those grown on control surfaces (Fig. 11.5). Additionally, in a wound healing assay, SMC microtubule organizing centers (MTOCs) were preferentially aligned with the cell axis for grooved surfaces, and the wound location for control surfaces. These studies demonstrate the importance of nanoscale features in guid-

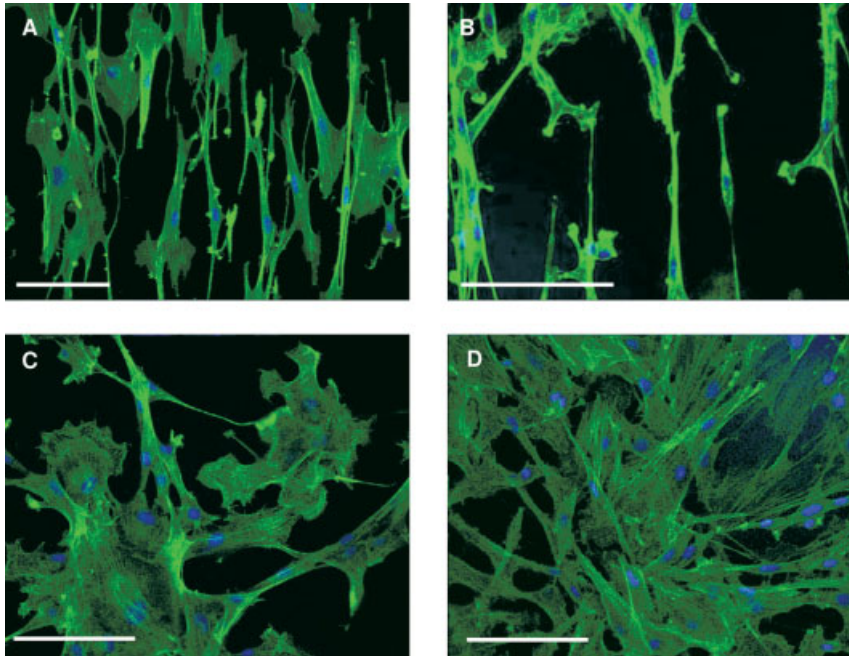


**Fig. 11.5.** Smooth muscle cell alignment on nanopatterned (A) PMMA and (B) PDMS. Muscle cells orient along the axis of the pattern, when compared with cells cultured on (C) unpatterned PMMA and (D) glass control surfaces. Scale bar = 100  $\mu\text{m}$ . (Photo courtesy of Christopher Chen, Evelyn Yim, University of Pennsylvania, Philadelphia, PA.)

ing cell extension and adhesion. Surfaces with smaller features have also been examined, most notably by direct application of nanoparticles. Silica nanoparticles with dimensions from 7 to 21 nm were deposited directly onto glass coverslips, producing amorphous nanoscale features [116]. Fibroblasts cultured on these surfaces formed clusters and were much less likely to adhere and spread when compared with plain glass controls.

Interest in the creation of nanoscale patterns has led to the development of a new technique, known as colloidal lithography, which uses arrays of ordered self-assembled nanoparticles as a resist (Fig. 11.6) [117]. Metal can be evaporated or sputtered through the colloidal resist, creating a pattern in the crevices between the particles. The shape and dimensions of this pattern can be varied by altering the size and packing of the nanoparticles in question. Particles used are commonly made of gold, silica, or polymers, with diameters on the order of 10–100 nm [118]. The structures formed can display order over length scales of several microns, with increasing order for assemblies of larger particles [51].

Colloidal lithography has been applied to cell adhesion only recently, with much of the work performed by the Sutherland and Curtis research groups (see Dalby et al. [119] for review). Using polystyrene beads roughly 100 nm, structures with



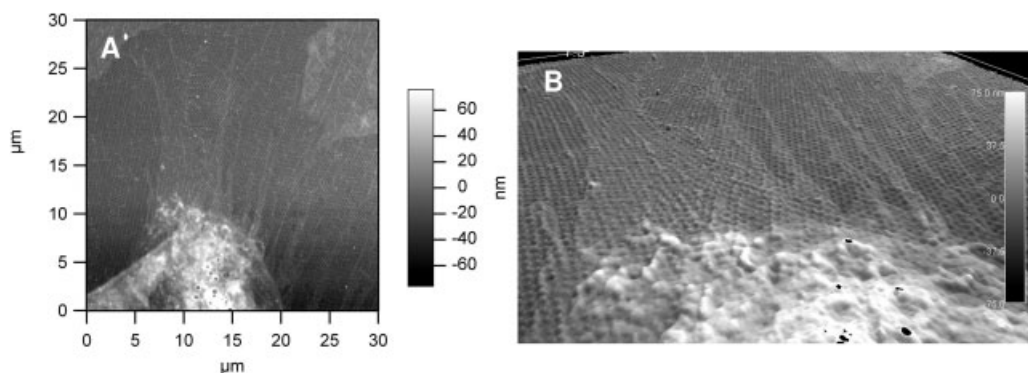


**Fig. 11.6.** (A) AFM image of colloidal lithography lattice. (B) Pseudo-3D view of same image. (Photo courtesy of Wolfgang Frey, University of Texas at Austin, Austin, TX.)

features ranging from  $\sim 50$  to 200 nm have been manufactured. Cellular responses to these patterns have been varied. Pancreatic epithelial cells [120] cultured on hemispherical titanium pillars of increasing width (i.e., from 60 to 170 nm) displayed less rounded morphologies and increased spreading with respect to flat control surfaces. However, fibroblasts on 160 nm high by 100 nm wide poly(methyl methacrylate) (PMMA) nanocolumns seemed to prefer smooth surfaces to nanostructures. Vinculin adhesions were smaller on nanocolumn surfaces than in the control group [121], and appeared similar to transient focal adhesion structures observed elsewhere in poor adhesive environments [122]. Cells cultured on nanocolumns contained fewer actin stress fibers [121] and displayed more filopodia per micron of cell perimeter [123] than the controls. These results suggest that the cells were unable to form solid attachments to nanocolumns and continued to explore the local environment (with filopodia) for suitable substrates.

The ability of titanium nanostructures to promote cell spreading, in contrast to PMMA, implies that cells respond not only to the dimensions but also the type of material used and is consistent with previous findings. In bulk conditions, endothelial cells adhere to bare titanium, whereas attachment to PMMA required preadsorption of ECM factors [124]. Adhesion to titanium also increases with surface roughness [125], consistent with the finding that cells preferred a rough nanopillared surface to the smooth control. Thus, in addition to physical properties, surface chemistry (e.g., metal vs. polymer) plays an important role in producing nanoscale cell adhesion.

### 11.3.3

#### Cell Adhesion and Nanoscale Chemical Patterns

Establishing nanoscale chemical patterns has proven more difficult than creating physical patterns. Many of the methods used at the micron-scale (i.e., microcontact printing) do not readily translate to nanometer dimensions [126]. Several inge-

nious techniques have been developed to overcome these obstacles. Clusters of adhesive peptide sequences, containing the RGD integrin binding fragment, have been attached to comb polymers with 2 nm monomer chain lengths. Cell adhesion increased with the number of RGD fragments per cluster and the overall density of the clusters [127]. Alternatively, arrays of protein-adsorbed spots have been created using dip-pen nanolithography [128]. An AFM-tip coated with thiolated proteins was exposed to a gold surface. Utilizing the strong attraction of thiols for gold surfaces, proteins are transferred to the gold substrate with tip contact. To examine cell adhesion, spots of the integrin binding protein retronectin 200 nm in diameter with 700 nm spacings were constructed against a non-adhesive background. Fibroblasts adhesion was demonstrated.

Nanoscale chemical patterning is just beginning to extend to nanoparticles. In a rather creative approach, polymer micelles containing gold precursors were used to create ordered arrays of gold nanodots. The micelles were deposited onto substrates and then exposed to oxygen plasma etch to remove the polymer. The remaining gold precursors formed nanodots *in situ*. Dots were then coated with cyclic RGD peptide fragments [108, 129]. RGD spots with diameters < 8 nm and spacings from 28–85 nm were created, with each dot theoretically large enough to accommodate only one integrin binding domain. Cell adhesion and focal contact formation was reduced for spacings > 73 nm, suggesting that integrin clusters separated by <70 nm are required for focal contact formation.

#### 11.3.4

#### Cytoskeletal Manipulation

Physical and chemical nanopatterns interact with cells passively. They are unable to directly probe specific cellular components. However, as a result of their unique optical, electrical, and magnetic properties, nanostructures *do* possess these capabilities. Most applications of direct cellular manipulation are still in the nascent stages. However, the use of magnetic particles for cell sorting and cytoskeletal manipulation has existed since the 1950s when it was pioneered by Crick (of DNA double helix fame) and Hughes [130]. Manipulation is accomplished using microspheres containing nanometer-sized magnetic colloids encapsulated in a polymer matrix, which are available from several commercial sources (e.g., Dynabeads, Dynal Corp., Brown Deer, WI) (Fig. 11.7).

The most common applications of this technology have been for cell sorting. Biomolecule-labeled magnetic microspheres can be used to isolate specific cells (for reviews see Chalmers et al. [14] and Zborowski et al. [131]), including rare cell lines [14, 132], which could be used for tissue engineering constructs or as a diagnostic tools. More recently, this technique has extended to magnetic nanowires. For example, magnetic nickel nanowires can be constructed using templated electrodeposition. Because of their large aspect ratios, the wires maintain residual magnetism (i.e., are ferromagnetic) in low magnetic field strengths. They can be used in sorting applications that traditional magnetite beads cannot, and in some cases, display superior performance [53, 133].

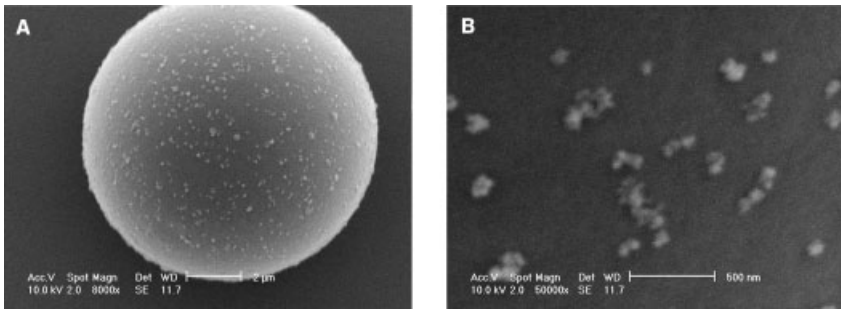


**Fig. 11.7.** Scanning electron microscopic image of a 10  $\mu\text{m}$  polystyrene particle labeled with Immunicon magnetic nanoparticles at magnifications of (A) 8000 $\times$  and (B) 50 000 $\times$ .

Note that the bound particles are on the order of 100 nm. (Photo courtesy of Jeffery Chalmers, Ohio State University, Columbus, OH.)

These cell sorting methods have been applied to tissue engineering. For example, magnetite ( $\text{Fe}_3\text{O}_4$ ) particles with an average diameter of 10 nm can be encapsulated into cationic liposomes [134]. These liposomes have been used to create tissue engineered cell sheets containing multiple cell types [135, 136]. Liposomes were exposed to cells, accumulating in the cytoplasm. Then, localized magnets were used to precisely position cells on a substrate. This technique has been used to create co-cultures of hepatocytes and endothelial cell [135], sheets of keratinocytes [137], and retinal pigment epithelium [138]. Similarly, nickel magnetic nanowires have also been used to control cell deposition on tissue engineered substrates [139]. Here, nanowires were coupled to cells through non-specific surface protein adsorption. Fibroblasts attached to the nanowires aligned with a magnetic field creating cell-cell chains.

Magnetic structures have also been used to investigate the effects of mechanical stress in cells. For example, the response of individual integrin receptors to external forces was examined using 5.5  $\mu\text{m}$  diameter magnetic spheres [140]. The spheres were coupled to RGD-peptide integrin binding motifs and incubated with cells to produce extracellular integrin binding. Then, spheres were exposed to magnetic fields, applying force to the cytoskeleton. Cytoskeletal stiffness was directly proportional to applied stress, demonstrating that integrins are mechanotransducers, modulating cell behavior in response to mechanical stress. This technique has also been expanded to allow manipulation of multiple cell culture dishes simultaneously, allowing for larger-scale biochemical analyses, including gene expression studies [141].

### 11.3.5

#### Future Applications of Nanostructures for Cell Adhesion and Migration

The potential for nanoparticles and nanowires to modulate cell adhesion is great, and many of the most exciting applications have not yet been realized. Most cur-

rent approaches manipulate whole cells rather than examining the effects of individual receptors and their ligands. Future methods may be able to compare cooperative and individual responses using micro- and nano-scale patterning techniques. Additionally, techniques will become increasingly active, directly manipulating cell receptors and proteins, as opposed to passive patterns on a substrate. These improvements will enhance understanding of the mechanisms for cell adhesion and migration, which may lead to new treatments for spinal cord injury, cancer, and vascular conditions. Increased knowledge of adhesion at the biomaterial–tissue interface will also provide improved prosthetic devices, implants, and tissue-engineered surfaces.

#### 11.3.5.1 Future Physical Nanostructures for Cell Adhesion

Most physical structures investigated to date have features  $>100$  nm. Although this is useful for investigating the cooperative action of cell surface proteins, it is not possible to explore individual receptors, with diameters of  $\sim 10$  nm, using these surfaces. Current technologies have been limited by the difficulty of creating regular, physical patterns that have structures on the order of 10 nm and repeat over several microns. Nanoparticle self-assembled monolayers offer several advantages to other physical patterning techniques at the  $<100$  nm length scale. Despite stacking faults, patterns display much more regularity than randomly oriented surfaces (e.g., Fig. 11.8), and at least short-scale order. Synthesis techniques to develop uniformly sized particles are well developed [51], and pattern roughness and dimensions can be easily changed by varying the particle diameter. Although more rigorous surfaces could be created using advanced lithography techniques (e.g., electron beam lithography), many of these techniques are expensive, difficult to reproduce, and inaccessible to the biologist, whereas many nanoparticles are now commercially available. Thus, in future applications, nanoparticle self-assembled monolayers will continue to be used in exploring cell adhesion either directly or as lithographic templates (Section 11.3.2). However, these techniques will probably emphasize directed self-assembly, allowing greater control of the pattern created.

For example, magnetic particles may be organized on a surface using magnetic fields to direct self-assembly [142]. This technique would allow much greater control of the resulting pattern than traditional self-assembly, which relies on thermodynamic forces to drive pattern formation [51]. When combined with techniques for specific cell placement (i.e., micropipette manipulation), magnetic assembly may allow for cells to be aligned with a specific pattern of interest. Extending these patterns to magnetic nanowires will bring further innovations. Because nanowires can be multifunctional, with domains of alternating materials, they offer a unique substrate for investigating cell adhesion. Nanowires produced using templated synthesis may have diameters from 10 nm to 1  $\mu\text{m}$  and lengths of up to 60  $\mu\text{m}$ . This compares favorably with receptor dimensions ( $\sim 10$  nm) and cell diameters ( $\sim 10$   $\mu\text{m}$ ) [53].

Other methods of directed assembly will also be explored. For example, Koo et al. [127] have demonstrated that star polymers can create structures with regularly-spaced adhesive peptides. The number of peptides bound and their spacing were

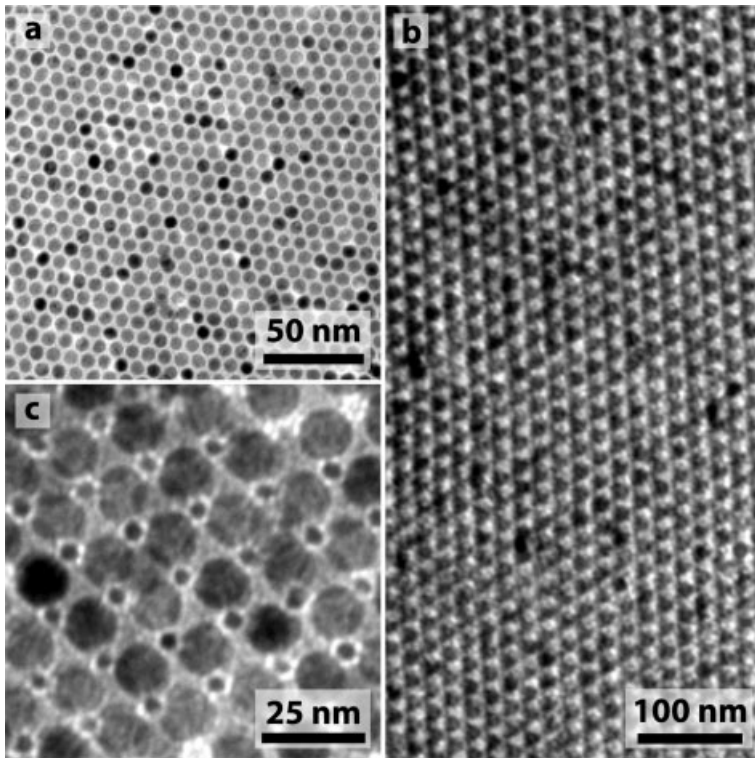


**Fig. 11.8.** Slow evaporation of an organic solvent containing monodisperse 11.5 nm iron nanocrystals results in the formation of extended regions of (a) monolayer or (b) multilayer superlattices. The superlattice structure can be tuned further through the co-assembly of two different sizes of nanocrystals, and provides a method to combine

nanocrystals with different functionality into ordered arrays. A binary nanocrystal lattice (c) with a rock salt (NaCl) structure is formed by evaporating a dispersion containing large iron nanocrystals (13.3 nm) and small gold nanocrystals (5.2 nm). (Photo courtesy of Brian Korgel, Aaron Saunders, University of Texas at Austin, Austin, TX.)

controlled by altering the number of monomers in the star and the monomer length. Similar techniques could be applied to nanostructures, and may employ new classes of polymers. For example, dendritic polymers are well-suited for attachment to spherical nanoparticles. Altering the length of the monomer could be used to control nanoparticle separation distance [143]. The use of various functional groups on the monomer exterior could also provide a method for directed assembly through electrostatic attractions or controlled crosslinking.

#### 11.3.5.2 Future Chemical Patterns for Cell Adhesion

**Applications in Cellular Engineering** The extension of the physical patterns discussed above to chemical patterning is straightforward. Colloidal lithography (Sec-

tion 11.3.2) could be used to produce patterned surfaces for chemical adsorption. Gold substrates, in particular, may be created through vacuum deposition and modified with thiolated chemicals and cysteine containing peptides. The dimensions of the pattern will be dependant on the size of the particles used and the method of their assembly. Alternatively, the nanoparticles themselves may be modified with biomolecules and assembled *in situ*. Nanoparticle arrays are an attractive substrate for cell adhesion studies because they provide the opportunity to investigate combined physical and chemical effects as the particles themselves provide shape, in addition to any chemical signatures.

One interesting possibility of nanoparticle arrays is the use of bimodal particle distributions. With a combination of small and large particles, ordered assemblies of alternating particle types can be created (Fig. 11.8) [144]. These assemblies would provide unique physical topography, but could also be used to create alternating adhesive and non-adhesive domains. For example, one particle size could be bound to RGD-containing peptide sequences, whereas another particle size could be passivated with cell resistant molecules (e.g., PEG [145]). Structures of this type would allow researchers to develop new understandings of the distribution requirements of adhesive sites. The greatest challenge in developing such assemblies will probably be controlling populations of particles that may be alternatively hydrophobic and hydrophilic. Micelles or lamellar sheets may be favored over monolayer particle structures. However, the use of amphiphilic peptides or particles of opposing charges may circumvent these difficulties.

**Applications in Tissue Engineering** Nanoparticles may also be incorporated into existing tissue engineering substrates to alter their chemical properties. Nanoparticles used in this context have the advantage of increasing the useful binding area without requiring a great deal of organic chemistry. One area where this would be of interest is the field of hydrogels. Some hydrogel materials possess good physical properties for tissue engineering, but are resistant to cell adhesion or migration [146, 147]. These substrates are modified through complicated bioconjugation strategies to contain adhesive binding sequences. The amount of biomolecule attached can be difficult to control and may be limited by the number of modifiable sites in the monomer. Scattered gold particles could be incorporated in the substrate to provide a thiol-mediated attachment point for biomolecules. Particles could be included directly in the uncured polymer mixture or could be deposited on the polymer surface and secured through annealing or covalent attachment. A similar approach has already been investigated using micron-sized particles [148]. Polymer templates composed of layer-by-layer assembled polyelectrolyte films were exposed to micron-sized, charged particles, which assembled on the pattern. These particles were then modified with RGD peptides and examined as substrates for cell adhesion.

Another exciting possibility is the incorporation of nanoparticles into smart-substrates. For example, gold nanoparticles have been used to create drug delivery substrates which expand upon exposure to radiation [17]. This technique could be adapted to produce active substrates for the evaluation of cell mechanics. For exam-

ple, a small number of fluorescent nanoparticles (e.g., CdSe) coupled to cellular integrin-binding domains could be introduced. Upon radiation (preferably in the IR to avoid cell damage), the substrate would expand. This expansion, and the cellular response, could be observed directly by monitoring the movement of the fluorescent particles. This approach has the advantage of potentially binding individual integrins. Expanding substrates might also aid researchers in constructing tissue engineering constructs for contractile tissue (e.g., muscle or heart) *ex vivo*.

#### 11.3.5.3 Active Investigation of the Cytoskeleton

To date, magnetic bead examinations of mechanical force in cells have primarily been confined to either the cell surface [140, 149] or to phagocytotic vesicles [150, 151]. However, as particles decrease in size and methods for intracellular delivery improve (Section 11.4.3), it may be possible to manipulate the cytoskeleton directly from the cytoplasm. This would greatly facilitate understanding of the role of the cytoskeleton in cell adhesion and cell mechanics. We already know that the cytoskeleton is a component of an elaborate mechanotransduction system and can influence cell differentiation, apoptosis, and polarity [110]. Many regulatory proteins are physically linked to the cytoskeleton, and changes in external force have been shown to influence local protein expression [110]. Several clinical ailments may have their basis in defective responses to mechanotransduction [110]. Intense study of the relationship between the cytoskeleton, external forces, and gene expression may lead to new treatments for these diseases.

A major challenge of this approach is the ability to develop sufficient magnetic force to manipulate objects. Microbeads encapsulate numerous nanometer-sized colloids that cumulatively generate enough force to produce changes in the cytoskeleton. It is unclear that single, nanometer-sized particles would produce measurable changes in cytoskeletal position, although there is some evidence that they will behave similarly to microparticles [152]. Additionally, cooperative action resulting from the attachment of multiple nanoparticles to the same structure can increase effective force. In some ways, nanoparticles may be particularly appropriate for investigation of the small structures of the cytoskeleton. Along with similar size scales, it is likely that smaller forces will be required to produce movement/tension as the size of the target structure declines (i.e., integrin vs. focal adhesion).

## 11.4

### Nanostructure Cellular Entry

Active cell manipulation requires methods to control nanostructure delivery and targeting. Whereas examination of the extracellular surface is straightforward, additional techniques are required to promote intracellular delivery. Nanostructures may be introduced to cells through endocytosis, but this is a passive technique. Most objects introduced into the endocytosis pathway are confined to lipid covered vesicles in the cell interior. Escape is difficult and materials are given little opportunity to interact with external proteins and biomolecules. Thus, direct delivery of

nanostructures is difficult. In this respect, the field of nanocomponent delivery shares many challenges with that of gene therapy, and many of the techniques introduced for the latter can be applied to nanostructures.

Controlled delivery is expected to have many applications. Fluorescent nanostructures could be used for real-time monitoring of intracellular features, which would greatly improve understanding of signal transduction, the endocytotic pathway, and intracellular transport. Magnetic and conducting nanoparticles could be used to control intracellular elements, potentially providing external control of cell adhesion, cell division, differentiation, gene expression, and apoptosis. Nanostructures could also be used as drug delivery agents for drugs, DNA, and proteins providing novel techniques for gene therapy, cancer treatments, and tissue engineering.

#### 11.4.1

##### **Biology of Molecular Delivery**

The cell plasma membrane is an effective method of excluding undesired components from the cell interior. This membrane is permeated with several transmembrane proteins, some of which serve as pores for small molecules to pass. However, despite their small size, nanostructures are still too large to enter the cell via this method (e.g., Rosenthal et al. [153]). Nanostructures are instead subject to endocytosis, a process through which objects are transferred from the local environment to the cell interior (Fig. 11.9). Endocytosis [8] is initiated by binding to the cell surface, followed by an invagination of the cell membrane. This membrane surrounds the foreign substance and pinches off from the bilayer, forming a vesicle in the cell interior, known as an endosome. After  $\sim 10$  min, the endosome migrates from the edge of the membrane to the Golgi apparatus. Endosomes are slightly acidic, with pH values near 6. Some proteins contain targeting sequences that are revealed in the acidic environment, allowing escape from the endosome. Other proteins, most notably membrane bound receptors, release their cargo and are returned to the surface by vesicle fusion. Yet other materials are delivered to lysosomes [8], which have an even lower pH (e.g., pH  $\sim 5$ ) and are filled with acid hydrolases. Lysosomes are the primary locations for digestion of proteins. Escape of foreign material from endosomes and lysosomes is exceedingly difficult. Endocytosis may be suppressed with temperature decreases (e.g.,  $4^\circ\text{C}$  [154]), but this affects other metabolic functions of the cell [155].

#### 11.4.2

##### **Nanostructure Endocytotic Delivery**

Internalization of foreign substances occurs through endocytosis, channel transport, or direct passage through the plasma membrane. However, channel transport is usually confined to ions [8], and, given current nanostructure surface treatments and size, it is unlikely that nanostructures could traverse the lipid bilayer unassisted. The endocytosis pathway, with an exclusion size of  $\sim 100$  nm [156], is the



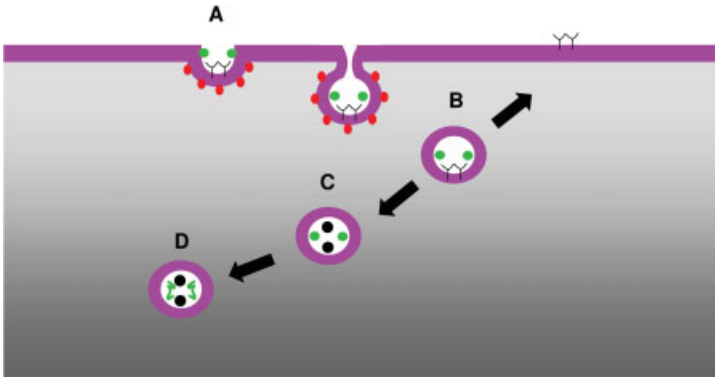


**Fig. 11.9.** Endocytotic pathway: (A) Following binding, the cell membrane invaginates to encompass membrane-bound substances. The formation of these indentations in the cell membrane is driven by the binding of clathrin protein (red) on the cytoplasmic side. The membrane continues to fold until a vesicle is pinched off from the membrane bilayer. With intracellular entry, the clathrin coat is lost. Vesicles in this stage are known as early endosomes (B) and have a pH of  $\sim 6$ . They are

responsible for sorting vesicle contents, e.g., returning membrane-bound receptors (Y-shaped structures) to the cell surface. (C) Next, vesicles migrate toward the Golgi apparatus, where they merge with digestive proteins (black) and become late endosomes (pH  $\sim 5.5$ ). Late endosomes attempt to digest internalized matter. To complete this process, late endosomes merge with lysosomes (D), which have a pH of  $\sim 5.2$ .

most likely mechanism for nanostructure uptake, and using sugar-coated quantum dot aggregates [156], uptake of particles as small as 5 nm has been demonstrated. Endocytosis can be non-specific, resulting from adsorption on the cell surface, or receptor-mediated, occurring as a consequence of biomolecular recognition binding events between specific receptors and their ligands.

Nanoparticle internalization has been observed for both the non-specific [74, 157] and receptor-mediated [11, 31, 77, 156] pathways. Using the non-specific pathway, particles have been internalized directly from cell culture medium [158], the cell culture substrate [74], and following non-specific binding to the cell surface [76, 159–161]. Internalization likely results from electrostatic attraction between the particle surface and the cell membrane [160]. Interestingly, binding can occur regardless of surface charge, as the plasma membrane exhibits both anion and cationic domains [18]. Receptor-mediated uptake has been observed using the RGD-peptide integrin binding motif [160], epidermal growth factor [31, 162] and transferrin [11, 163]. Remarkably, endocytosis of nanostructures attached to a solid support (e.g., polymeric nanocolumns) has also been observed [164]. In fibroblasts, columns were surrounded by cell membrane and were located near newly-formed intracellular vesicles and clathrin pits. Macrophage-like phagocytotic vesicles, which increased disruption of the cytoskeleton, were also observed.

Regardless of the mechanism, internalization occurs within 30 min, unless specific steps are taken to inhibit internalization pathways (e.g., low temperature [154]). In studies of sugar-coated nanoparticles, the rate of endocytosis was higher

with increasing particle size, up to 50 nm. Endocytosis was not observed for aggregates larger than 100 nm [156]. Others have shown that macrophage phagocytosis increases with increasing material size, up to 1.1  $\mu\text{m}$  [165]. Particle endocytosis rates can also be modulated by local biochemistry. For example, uptake of 35-nm dextran coated iron oxide particles was enhanced by high concentrations of interferon-gamma (IFN- $\gamma$ ) and interleukin-4 (IL-4), whereas the application of lovastatin decreased particle uptake [161].

When nanostructures enter the cell, they are found in clathrin-coated pits [162], as would be expected for endocytosis. Co-staining experiments have confirmed that particles are confined to endosomes or lysosomes [159, 162, 163]. Generally, particles remain sequestered in these compartments [18], and are unable to escape. For example, particles internalized by vero cells accumulated in large storage vesicles, similar to those found in macrophages [159]. Vesicles appeared to pass to select daughter cells through asymmetric mitosis. Accumulation of particles can be a significant problem, as aggregations can potentially disrupt the cytoskeleton and cell membrane [166]. It is even possible to overload cells with particles, resulting in apoptosis [18].

Particle endocytosis has been utilized in several applications, the largest area being cell labeling and tracking. Nanostructures, particularly quantum dots, have several advantages in this application. Their fluorescent signals are resistant to bleaching and oxidation over long time scales [11]. Additionally, endocytosed particles remain fluorescent for weeks and are passed to daughter cells [76]. Internalized nanoparticles have been used to investigate several systems that organic dyes could not, including division of HeLa cells [76], formation of aggregate centers in starved *D. discoideum* [76], phagokinetic tracks and metastatic potential [74], as endosomal markers [159], and retrograde transport in filopodia [162]. Particles have also been used to monitor macrophages in atherosclerotic plaques *in vivo* [161].

However, for targeted delivery to cytoplasmic elements, endocytosis is an undesired event, as most nanostructures remain sequestered in lysosomes or endosomes. Endocytosis can be prevented. For example, particles attached to insulin or lactoferrin surface molecules were not internalized as frequently as unmodified controls [157, 167]. Most likely this resulted from binding to “fixed” molecules on the cell surface that are endocytosed at low rates. Also, endocytosis does not occur when particle non-specific binding is low. Mercaptoacetic acid-bound and commercially available streptavidin-conjugated CdSe/ZnS particles with low cell binding potential are not internalized [11, 162] whereas silanized CdSe/ZnS nanocrystals that have shown high cell binding affinities are [10]. Thus, surface chemistry can be used to alter the endocytotic potential of nanostructures. Differences have even been seen for particles with the same surface passivation, but different synthesis techniques (compare, for example, Gomez et al. [160] and Nie et al. [11]). These differences indicate that the most important method of preventing endocytosis is ensuring that the nanocrystal passivation chemistries do not permit non-specific binding to the cell surface. However, notably, methods to prevent endocytosis also prevent *any* cellular entry. Clearly, additional technologies will be required for targeted delivery of nanostructures to the cytoplasm.

## 11.4.3

**Other Methods of Cellular Entry**

To circumvent the difficulties associated with endocytosis, several methods of particle entry have been devised. Most of these techniques have been extrapolated directly from the field of gene therapy, the most popular method being the use of translocation peptides. Although there is still much debate as to the exact mechanism of these peptides [168–170] it appears that cell entry begins normally, through the endocytotic pathway. However, the peptides are able to disrupt the endosomal membrane, releasing its contents to the cell interior. This technique has been used with various outcomes. The pep-1 sequence, which forms complexes with quantum dots through its hydrophobic domain, was used to deliver particles to CHO-K1 hamster epithelial cells [171]. However, quantum dots appeared to remain isolated in vesicles, indicating that endosomal escape most likely did not occur. Other peptides have demonstrated greater success. Adenoviral nuclear localization and receptor-mediated endocytosis sequences were used to introduce gold nanoparticles to the cytoplasm [172]. Delivery did not occur unless both sequences were present, with particles targeting the nucleus as expected. Similar results were reported for iron oxide nanoparticles conjugated to the HIV tat peptide [173, 174]. Particles were distributed throughout the cytoplasm with some increase near the nucleus. Quantum dots conjugated to trichosanthin protein [175] and R<sub>11</sub>KC peptides [176] displayed nuclear targeting with aggregation near the nucleolus [175]. Mitochondrial targeting has also been demonstrated using the Mito-8 peptide [176].

Apart from translocation peptides, other approaches have been examined, with a rather elegant analysis conducted by Derfus et al. [177]. The researchers compared intracellular delivery of quantum dots using translocation peptides, cationic liposomes, dendrimers, electroporation, and microinjection. Of the chemical approaches, cationic liposomes offered the greatest degree of quantum dot delivery, with over 90% of fluorescence distinct from that of separately labeled endocytotic vesicles. In contrast, translocation peptides (i.e., pep-1 as Chariot, Active Motif) displayed fluorescence signals slightly lower than that of the unconjugated control, possibly indicating fluorescence quenching as a result of aggregation, and were localized almost entirely in endosomal compartments. These results are similar to those of Tkachenko et al. [172] who found that pep-1 like peptides produce particle accumulation in lysosomes/endosomes. Additional translocation peptides (i.e., TAT or HA-TAT) were not investigated and may yield different results (e.g., Tkachenko et al. [178]). All three chemical techniques yielded particle aggregates that were on the order of a hundred nanometers in diameter. These aggregates can diminish nanoparticle fluorescence, and may interfere with intracellular manipulation and targeting.

As an alternative, Derfus et al. also investigated physical delivery methods, including electroporation and microinjection [177]. Electroporation produced significant intracellular delivery to the cytoplasm, but particles displayed aggregates with diameters as high as 500 nm. This effect was not related to a loss of surface passi-

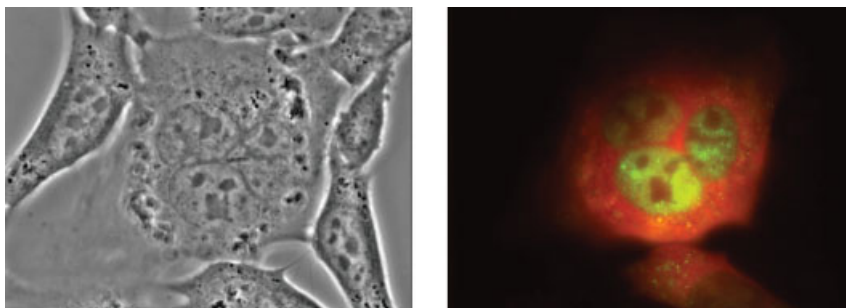


**Fig. 11.10.** Subcellular localization of quantum dots. A nuclear localization sequence (NLS) peptide was conjugated to the surface of PEGylated green quantum dots (emission maxima 550 nm). These particles were microinjected into the cytoplasm of 3T3 fibroblast cells, along with a 70 kDa rhodamine-dextran. After several hours, green emission from the quantum dots was observed in the nucleus of injected cells, while the red signal from high molecular weight dextran remained in the cytoplasm. (Photo courtesy of Sangeeta Bhatia and Austin Derfus, MIT, Boston, MA.)

vation, as highly crosslinked BSA coated particles exhibited similar results [177]. Similar aggregation has been reported with negatively-charged DNA plasmids [177], and may result from alterations of particle surface charge induced by the electric field. Alternatively, microinjection techniques delivered monodisperse particles that were not confined to endocytotic vesicles (Fig. 11.10) [177]. Previously, these particles were shown to pass to daughter cells during mitosis and retain fluorescence for up to 4 days [73]. The primary disadvantage of the microinjection technique is that it is difficult to scale-up to large populations, as injection is required for each cell.

#### 11.4.4

#### **Nanoparticle Intracellular Sensing**

A direct impact of intracellular delivery has been the ability to visualize internal components of a cell. Nanostructures have many optical properties that make them excellent candidates for intracellular labeling. For example, quantum dots display high quantum yields, narrow emission bandwidths, resist photobleaching, and can be readily modified with biomolecules to allow targeting [19]. Fluorescence persists for days [73] or weeks [76]. Additionally, magnetic nanostructures can be monitored with existing hospital equipment (e.g., MRI). Using nanostructures for sensing, it is possible that internal cell functions, including cell signaling and gene expression could be monitored in real time. This ability would represent a tremendous advance for diagnostics and treatment.

##### 11.4.4.1 **Semiconductor Quantum Dots**

Because of their unique optical properties, quantum dots have been widely used in sensing applications. Unfortunately, delivery of quantum dots to living cells has

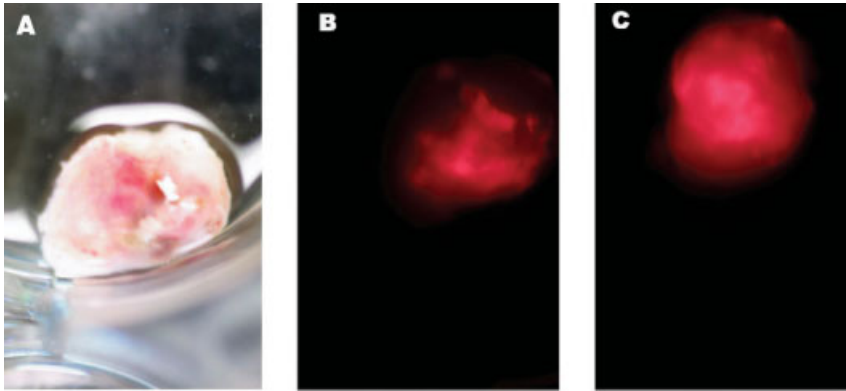


**Fig. 11.11.** (A) Transmission images of lung cancer (H1299) tumor. (B) Fluorescence image of same tumor incubated for 1 h with MPA-PEG-capped CdTe nanocrystals injected intratumorally and imaged at an excitation wavelength of 545 nm. (C) Fluorescence image of tumor, reverse angle. (Photo courtesy of Brian Korgel, Felice Shieh, University of Texas at Austin, Austin, TX.)

been challenging. Quantum dots can be introduced through endocytosis, and have been used to monitor cells during growth and development [76]. Particles introduced in this way remained in the cell for up to a week; however, targeting was non-specific, not directed to a particular intracellular component, and particles remained in endosomes. In another study, particles, introduced through microinjection, were used to follow development of *xenopus* embryos [73]. In this particular application, quantum dots were far superior to previous methods. Because quan-

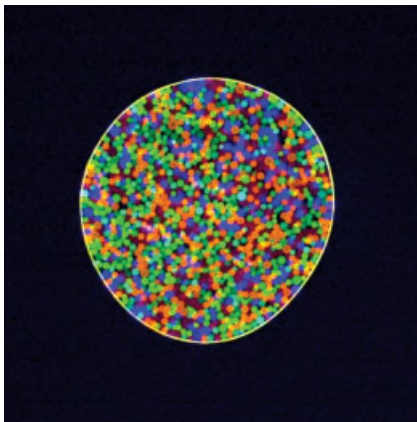


**Fig. 11.12.** True-color fluorescence images of mesoporous silica beads (5  $\mu\text{m}$  diameter) doped with single-color quantum dots emitting light at 488 (blue), 520 (green), 550 (yellow), 580 (orange), or 610 nm (red). A large population of the QD-beads is confined in a water droplet. (Photo courtesy of Xiaohu Gao, University of Washington, Seattle, WA.)

tum dots remained fluorescent in the daughter cell population for weeks, this technique allowed researchers to examine the fate of cells in the blastula, an achievement not possible using fluorescent dyes that photobleach in minutes. This technique was successful because only a few cells needed to be targeted for delivery; it would be difficult to use microinjection, a serial technique, in applications that require observation of multiple cells (e.g., organ labeling).

Both of these studies examined whole cells, and not specific targets. Most subcellular analyses have focused on extracellular targets, highlighting the difficulties of controlled intracellular delivery. For example, Dahan et al. [179] monitored the diffusion of glycine receptors in the synaptic cleft using semiconductor quantum dots. Quantum dots are particularly well-suited for this application because of their resistance to photobleaching. Traditional dyes only allow monitoring for short time periods, on the order of minutes, whereas quantum dots allowed receptor tracking for up to 20 min. Additionally, their small size allowed access to the synaptic cleft, a region that cannot be reached by microbeads (e.g., gold) that might be used in single particle studies. Alternatively, the diffusion of epidermal growth factor receptors (EGFR) was followed using quantum dots bound to EGF through avidin–biotin interactions [162]. Because of their resistance to photobleaching, receptor dynamics could be followed for long time periods, and a previously unreported mechanism of retrograde receptor transport was discovered. Quantum dots have also been conjugated to aptamers, DNA or RNA molecules that have been selected from populations for their specific binding affinities [180]. Aptamer-labeled particles were used to identify cancer cells *in vitro* and in lung cancer tumors (Fig. 11.11).

Applications for intracellular tracking are still in development. In particular, researchers are interested in creating tags that could be used for multiplexed intracellular measurements. Quantum dots are good candidates for these tags because they can exhibit a range of emission wavelengths under the same excitation, allowing for observation of multiple cues simultaneously (Fig. 11.12) [181]. These tags have great potential *ex vivo* as diagnostic tools and for high throughput screening. However, it may also be possible to observe the expression of several intracellular proteins concurrently through optical signals. In fixed cells, quantum dots conjugated to specific DNA sequences have been used to label the Y chromosome [182]. They have also been used to examine the intracellular expression of eNOS, a cardiovascular enzyme that converts nitrates into NO [183]. If successfully introduced into the cytoplasm, labeling of individual DNA strands or mRNAs may be possible. One limitation of quantum dots for intracellular tracking is the high blinking interval [184], which may prevent the tracking of intracellular components with a high diffusion rate. Nevertheless, with their persistent fluorescence and range of emission wavelengths, quantum dots will likely increase our understanding of intracellular signaling and could potentially revolutionize the field of diagnostics.

#### 11.4.4.2 Magnetic Nanoparticles

Magnetic nanoparticles have also been employed for whole cell labeling and intracellular tracking. Particles have been conjugated to the tat peptide, a nuclear local-

ization sequence, and utilized to determine the fate of stem cells [185]. With MRI, particles were visualized in blood and neuronal stem cells, allowing the location of those cells to be determined following injection in the rat tail vein. Alternatively, particles were coated with a combination of tat and Ha2 nuclear localization sequences and fluorescent dyes [174]. These particles responded to magnetic fields *in vivo* and were used to detect expression of the DEVD peptide, an apoptosis inhibitor. Particles have also been used for extracellular protein detection. For example, nanoparticles conjugated to transferrin have been used to monitor the expression of the transferrin receptor *in vitro* [186].

#### 11.4.5

#### Future Directions

##### 11.4.5.1 Nanostructure Intracellular Delivery

Existing methods of particle delivery have not yet yielded a technique for large-scale introduction of monodisperse particles. Biochemical methods can be used to evade endocytotic vesicles, but reports indicate [171, 172, 177] significant aggregation of particles. Alternatively, microinjection can produce disperse particle delivery, but is a serial technique, requiring cell-by-cell injections. Taking cues from research in gene therapy, researchers will continue to develop methods of particle delivery. Several new techniques are being explored as possible drug or DNA delivery methods, and could be extrapolated to nanoparticle delivery.

For example, polymersomes of PEG-polyester have been shown to foster endosome rupture and have been used to deliver two anti-cancer drugs [187, 188]. The low pH of endosomes encourages polymersome degradation. Soluble polymer components are then free to disrupt the lipid membrane, facilitating cargo escape into the cytoplasm. Similar polymersomes might be constructed to deliver nanoparticles to the cytoplasm. Likewise, fusogenic liposomes have been created to encapsulate polymeric nanoparticles [189]. Liposomes were created by encapsulating polymeric particles in traditional liposomes whose surface was modified by the addition of inactivated Sendai virus. The liposomes were able to deliver DNA to the cytoplasm, technology that could easily be adapted for delivery of magnetic or semiconducting nanoparticles.

Another potential delivery method uses carbon nanotubes to promote rupture of endocytotic vesicles [190] or directly penetrate the cell membrane [191, 192]. For example, nanotubes can be internalized through endocytosis, and then irradiated in the near-infrared to produce endosomal release. The primary limitation of this method is ensuring that heating levels remain low enough to prevent cell death. It is also possible that magnetic particles in a magnetic field could be used for this purpose (see, for example, Won et al. [174]), and a similar technique has been developed by Cai et al. using the Ni catalyst at a carbon nanotube tip for magnetic manipulation [192]. A rotating magnetic field allowed the nanotubes to penetrate the cell plasma membrane, where they remained. Soluble factors (i.e., DNA) bound to the surface were released from the nanotube surface through an unknown mechanism. Alternatively, carbon nanotubes functionalized with ammo-

nium permeate the cell membrane without the aid of magnetic fields [191]. The hydrophobic nanotubes can insert into the lipid bilayer of the plasma membrane, possibly transversing it. Any of these techniques might be adapted for nanostructure delivery; however, adjustment may be challenging as the surface chemistry and size of nanostructure cargos are significantly different from the DNA normally transported.

#### 11.4.5.2 Intracellular Sensing

An interesting possibility for sensing subcellular components is the use of fluorescence resonance energy transfer (FRET). This simple method for detection employs fluorescent molecules to produce an on or off signal upon binding. FRET occurs when an excited electron dissipates its energy by transferring it to a second molecule rather than through photon emission. This quenches the fluorescence of the first molecule. FRET is a distance dependant event. As the FRET donor and acceptor move away from each other, transfer no longer occurs and fluorescence in the donor is restored [193]. If a binding-induced conformational change separates two fluorescent molecules, e.g., attached to different portions of a protein, a fluorescent on/off signal can be produced.

This has been accomplished in several systems. A combination of gold quantum dots (which do not fluoresce) and organic fluorophores have been utilized to create DNA sensors [194]. Gold quantum dots were bound to single-stranded DNA sequences, which were terminated with fluorescent molecules, or fluorophores. The fluorophores formed an arched structure that interacted with the nanoparticle surface, quenching fluorescence (Fig. 11.13). However, when the complement DNA was introduced, binding occurred and the conformation changed. The fluorophore migrated away from the quantum dot surface and its fluorescence was restored. This technique is very accurate, the mismatch of a single base pair in a 30 amino acid DNA sequence could be detected [194].

A second, similar system utilized fluorescent CdSe/ZnS quantum dots to detect sugar binding [195]. The initial configuration contained cyclodextrin molecules

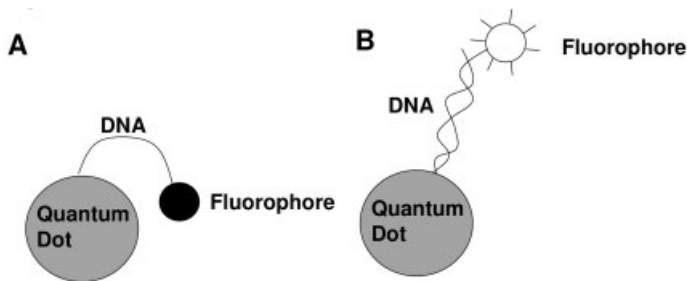


**Fig. 11.13.** Detection of DNA binding through FRET. (A) Fluorophore-conjugated single-stranded DNA is bound to a quantum dot, forming an arched structure with the nanoparticle surface. Fluorophore fluorescence is quenched through FRET with the nanoparticle. (B) When the complement DNA is added, the DNA structure changes, moving the fluorophore away from the nanoparticle and restoring fluorescence.



conjugated to a non-fluorescent FRET acceptor. The cyclodextrin adhered to maltose (i.e., sugar) binding protein, which was present on the quantum dot surface. FRET between the nanoparticle and the acceptor molecule quenched quantum dot fluorescence. However, when maltose was introduced, the cyclodextrin was displaced, restoring fluorescence to the quantum dot. Although maltose sensing was demonstrated, these sensors could eventually be adapted to detect glucose, a crucial molecule to monitor in the management of diabetes.

Finally, systems need not be hybrids, incorporating nanoparticles and fluorescent dyes; homogeneous systems have also been constructed [196, 197]. Two types of CdTe quantum dots were bound to model proteins. Red-emitting quantum dots were conjugated to bovine serum albumin (BSA), while green-emitting quantum dots were conjugated to an antibody that binds BSA (i.e., anti-BSA). When the two quantum dots were incubated together, the green fluorescence was quenched, as excited electrons transferred their energy to the red-emitting particles. Further, the red fluorescence was enhanced because energy transferred from the green-emitting quantum dots was dissipated through the red-emitting quantum dot. Similarly, the fluorescence of biotinylated-CdTe nanowires has been extinguished by the presence of streptavidin-coated gold nanoparticles (Fig. 11.14). Biotinylated-wires exposed to streptavidin alone displayed no change in fluorescence over time (Fig. 11.14A); however, upon addition of streptavidin-coated gold, fluorescence was increased in the CdTe acceptors (Fig. 11.14B).

FRET-based quantum dot sensing is elegant, and in theory can provide analyte detection of as few as 10 parts per trillion [196]. Additionally, the signal is easy to interpret: fluorescence indicates the presence of an analyte. FRET-based sensing can also provide quantitative information, as fluorescent intensity can be correlated to the number of molecule binding events. Although FRET systems could be constructed entirely from fluorescent dye molecules, quantum dots provide an excellent alternative. They display high quantum yield; and their acceptor energy and emission wavelengths can be tailored by changing the size of the particle.

## 11.5 Intracellular Transport of Nanostructures

Nanostructures that evade endocytosis have the potential to interact with intracellular structures, including components of the cytoskeleton. The cytoskeleton is responsible for the movement of proteins and vesicles through the cytoplasm, as well as cell mitosis, locomotion, and signaling. Nanostructures have been used to manipulate and interact with the cytoskeleton from the cell exterior (Section 11.3.4), but numerous additional possibilities exist for intracellular interactions. Perhaps the most intriguing potential application is the use of cytoskeletal elements to control intracellular nanostructure transport. This line of inquiry will not only improve biologists understanding of motion through the cell interior, but may aid in assembly of nanoscale structures *ex vivo*. To date, nanostructure-cytoskeleton research has focused on *ex vivo* applications, including sensing and molecular assembly.

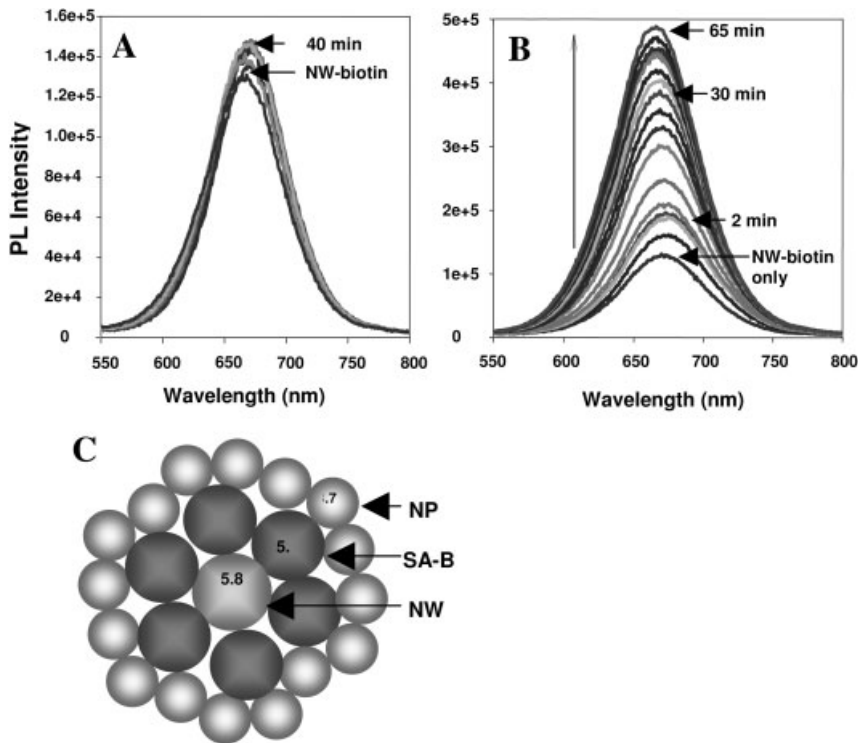


**Fig. 11.14.** (A, B) Transient luminescence spectra of bioconjugated nanowires in solution. (A) Nanowire-biotin with streptavidin (without Au) monitored for 40 min after mixing, (B) Nanowire-biotin with streptavidin-Au monitored for 65 min. Excitation

wavelength for both (A) and (B) is 420 nm. (C) Cross section of closely packed model arrangement of CdTe nanowires and Au nanoparticles in the bioconjugate. (Photo courtesy of Nicholas Kotov, University of Michigan, Ann Arbor, MI.)

The primary focus has been on kinesin-microtubule structures, but actin–myosin interactions have also been examined. Direct translation of these methods to the clinic is not expected. However, the techniques developed for *ex vivo* studies might be adapted to nanostructures in the cytoplasm. The ability to perform cytoskeletal manipulations would allow researchers to explore internal mechanotransduction and manipulate intracellular transport, providing new insight to gene regulation, protein expression, vesicular transport and mitosis.

### 11.5.1

#### Biology of Intracellular Transport

The cytoskeleton is composed of a network that includes actin filaments, intermediate filaments, and microtubules [8]. Intermediate filaments, which are about 10

nm in diameter, provide the cell with mechanical strength and form the nuclear lamina, whereas motion primarily occurs along 5–9 nm actin filaments or 25 nm microtubules. Actin filaments interact with myosin proteins and are responsible for muscle contraction, cell locomotion, and vesicle transport [198]. Myosins contain heavy and light chains, with the heavy chain mediating attachment to actin filaments and the cargo. Motion is driven by the hydrolysis of ATP (i.e., adenosine triphosphate), which initiates conformational changes in the myosin protein, producing a stepping motion along the actin filament. Microtubules interface with kinesins and dyneins and are responsible for organelle and protein transport, chromosomal separation, cell division, vesicular transport, and are the primary components of cilia and flagella [198]. Microtubules are directional, continuously growing at their plus ends and slowly dissociating at their minus ends. Kinesin contains two heavy chains that include microtubule binding sites, whereas the structure of dynein is not well understood, but includes heavy chains and intermediate chains. Both kinesin and dynein movement occur through ATP hydrolysis. However, kinesin moves from the minus to plus end of the protein in discrete 8 nm steps, whereas dynein moves from the plus to minus end of the track [198]. Dyneins are primarily associated with cilia and flagella, cellular elements which produce cell movement.

### 11.5.2

#### **Actin-based Nanostructure Transport**

Movement in actin networks is initiated by ATP-binding to myosin proteins. The myosin II form, which is responsible for muscle contraction, is the most common, but myosin V may be the best suited for hauling cargo because of its processive motion [198]. Several nanostructure cargos have been attached to myosin. For example, quantum dots have been conjugated to myosin V heads [199]. Fluorescence signals from the particles allowed direct visualization of the “hand-over-hand” mechanism of myosin movement down the actin filament. Also, rabbit muscle myosin was conjugated to magnetic nanoparticles obtained from bacteria [152]. Using magnetic force, it was possible to alter the velocity of a myosin molecule along the actin filament. It is envisioned that such a system could be used to analyze single molecule interactions between myosin and actin filaments.

Alternatively, actin has been conjugated directly to nanostructures. Biotinylated phalloidin (which binds actin strongly) was attached to quantum dot surfaces and used to link nanoparticles to actin [200]. Proposed applications of this system include the creation of *in vitro* networks of actin filaments or delivery of specific cargos. Actin has also been attached to the surface of gold nanoparticles, a system used as a template for gold nanowire formation [201]. Gold nanoparticles bound to actin monomers could be connected to form nanowires on either side of an exposed actin protein core. Additionally, when placed on a myosin substrate, actin–myosin interactions directed nanowire movement. This technology is primarily intended for the creation of nanoelectronic networks, but might be used to assemble or transport nanostructures in cells.

## 11.5.3

**Microtubule-based Nanostructure Transport**

In contrast to actin filaments, microtubules have been more extensively studied for nanostructure transport, probably because they move a wider variety of natural cargos *in vivo*. Again, much of the work to date has been performed *ex vivo*, with proposed applications in nanoassembly and nanoelectronics. For example, microtubules have been organized in microfabricated channels using electric fields [202, 203] and their motion has been directed by absorbed kinesins [204]. Although this method does not apply directly to cellular engineering, many of the tools to adapt these techniques *in vitro* are in place. Silica microbeads were attached to kinesin as early as 1990 [20]. *Ex vivo* binding or transport of microchips [205], 1–10  $\mu\text{m}$  glass, gold, and polystyrene microbeads [206], CdSe quantum dots [207], CdSe nanorods [208], and gold nanowires [202] have all been demonstrated using the kinesin-microtubule system. The wide variety of cargos transported suggests that various nanostructures can be moved with ease. Techniques to control cargo motion have been developed. Photo-caged ATP can be activated with the application of light, permitting control of kinesin movement [209]. Collectively, these advances should allow for intracellular manipulation of the cytoskeleton in the near future.

## 11.5.4

**Future Directions**

Future research will focus on adapting *ex vivo* techniques to cell studies. For example, motor proteins without nanostructure modification have already been used *ex vivo* to transport and manipulate DNA [210]. The addition of nanostructures to these systems could provide the ability to control (e.g., magnetic manipulation) and monitor (e.g., fluorescent signal) biomolecule interactions *in situ*. Development of these assays would allow researchers to directly measure the force, speed, and dynamics of protein–cytoskeleton interactions. Additionally, nanostructure transport could be used for controlled delivery of drugs, proteins, vesicles, or even organelles (Section 11.6). A limitation of previous attempts to use nanostructures for this purpose has been the inability to control cargo release. One possibility is the use of photocleavable linkages [211]; however, the use of photo-caged ATP may limit the wavelengths available for this chemistry. An alternative approach might be to use the heat generated by excited magnetic particles to promote release of an attached biomolecule.

In addition to intracellular transport, cytoskeletal systems in whole cells may be harnessed to transport and manipulate objects. For example, the flagella of close-packed bacteria grown on a solid surface can be used to manipulate beads suspended in fluid [212]. Flagellated algae (e.g., *Chlamydomonas reinhardtii*) were used to move polymer beads through solution [211]. Algae were directed to specific locations using phototaxis, and bead attachment did not appear to significantly impede algae movement. It is unlikely that flagella or cilia could be harnessed directly to

nanostructures, as they are significantly larger ( $\sim 1 \mu\text{m}$ ). However, these whole-cell systems could be used for controlled delivery of nanostructures amongst a population of cells. For example, it might be possible to deliver toxic nanostructures to cancer cells using “safe” bacteria to transport particles into a specific organ.

## 11.6

### Biomolecule Delivery Using Nanostructures

One of the most promising applications of nanostructures is their use to deliver biomolecules to specific cells and cellular locations. Nanostructures with diameters from 10 to 100 nm can be introduced intravenously, and remain in the blood for significant periods of time [18]. Their surfaces may be modified with drugs, biomolecule cargos, and sequences to promote recognition by certain cell types (Section 11.2.4), resulting in specific targeting. The magnetic and heat-generating properties of nanostructures may be used to control biomolecule release. Nanostructures with these features have been incorporated into traditional drug delivery constructs to produce “smart” drug delivery devices (e.g., Sershen et al. [17]). Although much work has focused on extracellular delivery, intracellular delivery is also possible (Section 11.4). Nanostructure–DNA binding has been well-established [13], and gene therapy is a logical extension of this work. With their small size and flexible surface chemistry, nanostructures are ideal candidates for biomolecule delivery to cells.

#### 11.6.1

##### Biology of Controlled Delivery

###### 11.6.1.1 Drug Delivery

Therapeutic drugs typically display half-lives on the order of minutes to hours [213]. To control release and prolong the effectiveness of these molecules, drug delivery systems have been developed. Drug delivery devices may target any component of the cell interior or exterior and have been investigated as treatments for various conditions, including cancer [214], diabetes [215], and neurological disorders [216, 217]. In many cases, the desired treatment requires controlled release of a biomolecule over time, possibly many years [215]. Several systems have been developed to fine tune release, including polymer coatings and degradable hydrogels [218].

Drug delivery systems must operate *in vivo*, where the environment can be harsh. Introducing drugs targeted to specific cell types without direct implantation of a drug delivery system is difficult. Drugs may be administered orally or through direct injection, but the primary method is through intravenous injection [219]. Once inside the body, these molecules must evade the natural defense mechanisms of the body, including the reticulo-endothelial system (RES). Components that are too large ( $>200 \text{ nm}$ ) will be isolated in the spleen, whereas molecules that are too small ( $<10 \text{ nm}$ ) are removed from blood vessels by diffusion to sur-

rounding tissues or the kidneys [18, 145]. Some drug delivery applications require release to a specific target (e.g., gene therapy, cancer treatment), and achieving this is challenging. For example, the endocytotic pathway (Section 11.4.1) presents a significant barrier to controlled intracellular delivery (e.g., for cancer treatment). With their readily functionalized surfaces and small size, nanocomponents provide a unique method to address these issues.

#### 11.6.1.2 Gene Therapy

In contrast to most drug delivery applications, gene therapy focuses primarily on nuclear delivery of DNA in a one-time application. The concept behind gene therapy is straightforward. Many diseases result from defective copies of a particular gene. Gene therapy attempts to incorporate functional copies of those genes into the genome of affected individuals. For this to take place, the defective genes must be identified in the individual. New, working copies of these genes must be synthesized, delivered to the nucleus, and incorporated into the existing genome. This is usually achieved with the aid of transcription agents, which may use viral or non-viral mechanisms (for review see Johnson-Saliba et al. [220]). Viral vectors have been the most successful, but can provoke an immune response. Additionally, viruses do not infect all cell types equally, and targeting specific cell types can be difficult [221]. Non-viral delivery has been plagued by the difficulties of traversing the plasma membrane and directed targeting to the nucleus. Transfection efficiencies have remained low (0.01–10% [220]). Some of the greatest barriers to clinical gene transfection have been the long times required to achieve transfection and the low concentrations of available transfection agents [222]. For gene therapy to become a viable clinical option, these barriers must be surmounted.

### 11.6.2

#### Drug Delivery

Applications for nanostructures in drug delivery are vast (see Volume 10 of this series for more detail). Although usage of metallic and semiconducting materials has been more recent, nanostructured ferrofluids have been investigated since the early 1970s [223, 224]. Drug delivery systems have been envisioned to treat diabetes [215], cardiovascular diseases [225], and cancer [214]. As a result, this section will focus on several of the challenges facing drug delivery systems, and how nanostructures are poised to meet them. This will be illustrated with a few examples of targeted drug delivery applications, primarily in the area of cancer treatment. These applications are not intended to be comprehensive, but represent general cases where nanostructures improve upon existing technology.

##### 11.6.2.1 Cell Targeting *In Vivo*

For optimal control, nanostructures for drug delivery usually display three separate functionalities: a core material, drug or therapeutic element, and a targeting element [213]. The core material provides physical stability, controls size, and provides a template for drug attachment/encapsulation. In some cases, the core mate-

rial may serve multiple purposes, incorporating an additional targeting or sensing function. For example, magnetic particles may be manipulated with a magnetic field [18]; gold particles can be detected using Raman spectroscopy [47]; and quantum dots can be seen using fluorescence microscopy [19]. The drug or therapeutic element may be attached directly to the nanostructure, or encapsulated in its interior. Targeting molecules (e.g., biorecognition elements, see Section 11.2.4.2) can be added to the nanostructure surface to direct interactions with the cell of interest.

Many systems also include a component to increase circulation time and reduce RES recognition. Early efforts to use micro- or nano-sized particulates for drug delivery were plagued by short circulation lifetimes. Attachment to a carrier molecule can prevent these difficulties. For example, a significant improvement in delivery occurred with the addition of poly(ethylene glycol) (PEG) to particle surfaces [213]. PEG prevents the adsorption of proteins, which might be recognized by the RES [145]. Additionally, small nanoparticles (<10 nm) coated with specific targeting peptides accumulate in the tissue of interest while evading the RES [75]. Thus, particle surface modification can facilitate drug targeting and prevent RES clearance.

Nanostructures offer several advantages to traditional drug delivery systems. Nanostructures may be loaded with vast quantities of drug through encapsulation or binding to the particle surface. They can be further modified with specific targeting molecules. For each binding event, an entire nanostructure payload may be delivered, in contrast to the single molecules delivered using direct drug-biomolecule conjugation schemes [213]. Additionally, nanostructures can reach some target sites that are not accessible by therapeutic agents administered via traditional routes. For example, they have demonstrated the ability to cross the blood-brain barrier [213]. Unlike traditional systems, nanostructures can also be targeted to specific elements through external manipulation (e.g., magnetic fields), and those same signals can be used to trigger controlled release.

#### 11.6.2.2 Drug Delivery for Cancer Treatment

The possibilities for nanostructures in cancer therapy are staggering (also Volumes 6 and 7 of this series for more detail). Nanostructures can provide imaging capabilities, allowing detection of cancer in early stages [213, 226]. Therapeutics may be administered using nanostructure carriers [213]. If these particles are combined with imaging modalities, drug distribution can be monitored in real time. Delivery vehicles could be coupled to biorecognition elements that target only cancerous, and not healthy, cells [213]. Most research to date has focused on magnetic therapies to deliver cytotoxic agents; however, new materials and new approaches are beginning to be investigated. In some cases, the nanomaterial itself becomes the cytotoxic agent, activated by a remote optical source. Because of the ease of surface modification, size selection, and tunable optical, electrical, and magnetic properties, these drug delivery systems will likely become powerful additions to current clinical cancer treatments.

**Molecular Approaches** For recovery, cancer treatment requires complete removal of the cancerous cells [227]. In many cases, tumors cannot be fully excised surgi-

cally and traditional chemotherapy is either not possible or undesirable. Targeted cytotoxic drug delivery to the tumor provides one alternative to these standard treatments, and it was for this purpose that therapeutic nanostructures were first investigated [223, 224]. The concept is straightforward. Magnetic particles are conjugated to cytotoxic drugs. External magnetic fields are then used to concentrate the particles near the tumor. Particles are internalized, and the drug payload is released by physiological change (e.g., temperature, pH, enzymatic activity) [228].

Magnetic targeting has been used in many environments. Magnetic microspheres have been utilized to deliver drugs to the brain, with concentrations 100–400× higher than those of mice exposed to drug solution alone [229]. In brain tumor-bearing rats, similar systems administered 41–48% of the dose directly to the tumor, in comparison to 23–31% of dose in the absence of the magnetic field [230]. Particle localization in the vasculature has been controlled with magnetic targeting in a swine model [231]. Starch-coated particles, administered to rabbits intra-arterially, were concentrated in invasive squamous cell carcinomas following applications of magnetic fields up to 1.7 T [232]. Magnetic liposomes were delivered to osteosarcomas, suppressing tumor growth [233].

Nanostructure magnetic therapies have also been applied in the clinic. Lübbe et al. [227, 234] investigated the efficacy of magnetic particle bound-epirubicin to advanced tumors. Tumors were less than 0.5 cm from the magnet source and were subjected to magnetic fields of 0.5–0.8 T. No adverse reactions to the magnetic particles were observed, although toxicity was seen at high epirubicin doses. Results were mixed, as particle accumulation in tumors was not successful in 50% of patients [227]. Physiological parameters played a great role in this variability and must be addressed in future attempts to develop successful therapies.

One difficulty in implementing magnetic therapies is that magnetic field strengths high enough to overcome natural body forces (e.g., blood vessel flow) are difficult to develop and maintain, particularly for deep tissue targets [227]. In addition, optimizing particle size to provide the highest level of particle concentration at a tumor site is difficult. Magnetic susceptibility is inversely related to particle size, but larger particles are more likely to be removed from circulation by the RES [227].

Magnetic fields can be used to produce particle accumulation in a chosen tissue, but specific targeting sequences are required to promote selective internalization by cancerous cells. These surface agents are designed to prevent macrophage endocytosis (i.e., immune reaction), while increasing endocytosis in target cancer cells. Several coatings have been investigated. Poly(ethylene glycol) increased uptake in breast cancer cells, while reducing internalization by macrophages [235]. Modification with folate also produced selective internalization by breast cancer cells, but not other cell types [235]. Amino-poly(vinyl alcohol) (PVA) coatings encouraged endocytosis of magnetic particles by melanoma cells, whereas PVA, carboxylate-PVA, and thiol-PVA did not [236].

Once inside the cell, the drug must be released, enter the cytoplasm, and diffuse to its target (in most cases the nucleus or mitotic spindle). Drug release must be precisely controlled. Once the drug payload has detached from the magnetic



particle it can no longer be manipulated by a magnetic field. Drug escape from endosomal/lysosomal compartments is possible. The release of drug payloads from nanoparticles in lysosomal environments has been documented and correlated to observed cytotoxicity in breast and cervical cancer cells [237]. Additionally, oleic acid/pluronic coated-particles containing doxorubicin were internalized by prostate and breast cancer cells, producing dose-dependent cytotoxicity [238].

Apart from magnetic materials, researchers have investigated other nanostructures as nanochemotherapeutics, including colloidal gold [239] and silica [240]. Colloidal gold has been used to deliver tumor necrosis factor (TNF) [239] in a mouse model. Native TNF has been used as an anti-cancer therapy before but, however, was found to be toxic at therapeutic doses [239]. Particles bound to TNF, and containing PEG modifications to reduce RES clearance, accumulated in MC-38 colon carcinoma tumors and produced 50–90% reduction in tumor volume. Additionally, toxicity was drastically reduced. None of the animals examined demonstrated adverse reactions, whereas 25–100% of animals exposed to native TNF died. Development of silica nanoparticle carriers, though, is still in early stages. Silica has been attached to cefradine, a broad spectrum antibiotic [240]. Silica particles demonstrate drug release profiles that are likely tunable with particle size, but have yet to be tested *in vitro* or *in vivo*.

**Hyperthermia** Apart from their use as drug delivery vehicles, nanostructures can also provide the toxic moiety, treating cancer directly. Because of their unique optical properties, certain types of nanomaterials can produce local temperature elevations. This process, known as hyperthermia, has been investigated by several groups. As a result, this discussion is limited in scope, for more detailed information the reader is directed to recent review articles (e.g., Moroz et al. [241], Ramachandran et al. [242]). Hyperthermia is a result of particle Néel relaxation [243] in an AC magnetic field [228] (e.g., 5–30 kA m<sup>-1</sup> at 100–500 kHz [242]), producing a temperature elevation. When the temperature is maintained at 42 °C or higher for 30 min, cell death, primarily through necrosis, will occur [228, 242]. The exact mechanisms of cell death are not completely understood, but the effects of heat on DNA repair and protein expression are well-documented [244].

The use of magnetic particles to locally heat tumor tissue was first proposed in 1957 by Gilchrist et al. [245]. In that study, 20–100 nm magnetite particles were directly injected into the intestines of dogs. Since that time, several alternatives to direct injection have been developed [241]. Arterial embolization employs the tumor vasculature to deliver particles to the tumor interior. Particles may be surgically implanted, although this technique tends to focus on macroscopic structures (~1 mm) [241]. Finally, particles can be conjugated to appropriate biomolecules and may enter the cell (intracellular delivery).

The most limiting features of magnetic hyperthermia have been poor AC field control, temperature control, and cell targeting. High AC fields are not tolerated well, as they can lead to muscle response (e.g., spasms). The advent of nanometer-sized magnetic particles [246, 247] has allowed for the use of lower, more compatible AC fields [242], which may alleviate this concern. However, a clear understand-

ing of the relationship between AC field strength and the resulting temperature profile has not yet been obtained. Temperature control is critical because if body tissues are heated above 56 °C undesired tissue ablation results [242]. Modeling is helpful to address these concerns, but extensive modeling of magnetic hyperthermia systems has not been performed [242]. Additionally, it is difficult to target nanometer-sized particles to tissues of interest using magnetic fields. In this size regime, Brownian motion becomes dominant [242] and substantial force is required to manipulate particles to regions of interest. For this reason, biomolecular targeting may be a superior approach for directing magnetic particles to particular cells. In addition to these factors, magnetic hyperthermia must compete with other better established, approaches, including whole-body hyperthermia and thermistors, to deliver heat [244].

More recently an exciting new material, gold nanoshells, has demonstrated the potential to produce local hyperthermia (Fig. 11.15) [248]. These nanoshells exhibit unique optical properties, which are tunable, based on their size. Nanoshells absorb light in the near-infrared (NIR), and convert this energy into heat, primarily through vibrations of the crystal lattice (i.e., plasmon-resonance) [249]. Nanoshells offer several advantages to magnetic hyperthermia because of the excellent tissue penetration in the NIR and the small number of particles needed to produce a temperature increase [248]. Small particle size allows facile penetration of tumors through the vasculature [249], which is known to be more permeable in cancerous than healthy tissue. Particles introduced in this way may accumulate in tumors

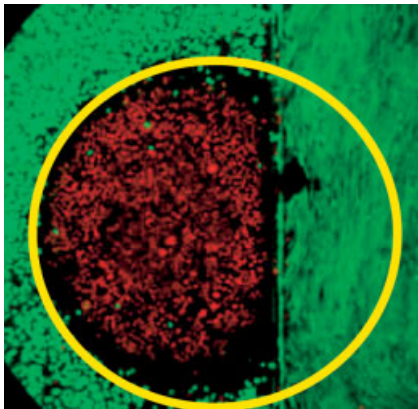


**Fig. 11.15.** Side-by-side co-culture of SKBR-3 breast carcinoma cells and hamster dermal fibroblasts. Anti-HER2 (a tumor marker overexpressed on the breast carcinoma cells) targeted nanoshells were incubated with the co-culture. After rinsing, the cells were exposed to a near-infrared laser (808 nm, 1 min), then stained for viability with calcein AM (green),

indicating live cells, and ethidium homodimer (red), indicating cell death. The laser spot is indicated by the yellow circle. The targeted breast carcinoma cells were ablated while the “normal” cells were unharmed. (Photo courtesy of Jennifer West, Rice University, Houston, TX.)

non-specifically, or through direct, antibody-mediated targeting [250]. This effect has been used to create selective, local tissue ablation targeted specifically to tumors [249]. Additionally, the presence of nanoshells can be confirmed using optical techniques (e.g., using optical coherence tomography), allowing *in situ* monitoring of nanoshell targeting and therapy [15].

**Photodynamic Therapy** Another interesting application of nanomaterials in cancer therapy is the generation of cytotoxic singlet oxygen. In this process, known as photodynamic therapy (PDT), photosensitizers (PS) are encapsulated in or conjugated to the surface of nanostructures. Additionally, nanostructures can be conjugated to targeting molecules that direct them to local tissues. Upon absorption of light, the photosensitizers excite molecular O<sub>2</sub> to the singlet state, causing cell damage, most notably through disruption of cellular membranes [251]. Singlet oxygen can also cause tissue damage through disruptions of the vasculature, resulting in tissue starvation [251]. Although application of nanomaterials to PDT is recent, several materials have been investigated, including silica, gold, and quantum dot nanoparticles.

Silica nanoparticles are easily modified to allow encapsulation of PS, which are largely hydrophobic. For example, native silica was modified with aminosilanes to promote encapsulation of meta-tetra(3-hydroxyphenyl)-chlorin PS [252, 253]. When excited, the PS-silica nanoparticles produced more singlet oxygen than free PS [253], possibly as a result of increased PS concentration. Silica nanoparticles have also been used to entrain 2-devinyl-2-(1-hexyloxyethyl) pyropheophorbide (HPPH) PS [252]. When exposed to cells, nanoparticles entered the cell interior, most likely through endocytosis. Upon excitation singlet oxygen was produced, resulting in cell death.

Similarly, gold nanoparticles have been prepared as carriers for PS; however, in this case the molecules are linked to the particle surface rather than entrained in particle pores. Using the strong binding affinity between gold and thiol groups, mercaptoalkyl-modified phthalocyanine PS were tethered to the surface of gold nanoparticles [254]. Singlet-oxygen generation was enhanced when compared with that of free phthalocyanine, possibly as a result of the phase transfer agent (i.e., tetraoctylammonium bromide) also tethered to the nanoparticle surface.

An interesting possibility for PDT is the use of semiconductor quantum dots [255]. CdSe quantum dot surfaces (~5 nm) conjugated to Pc4 PS produced excitation and singlet-oxygen generation through fluorescence resonance energy transfer (FRET) [256]. Additionally, unconjugated CdSe quantum dots produced singlet oxygen [256]. Although the efficiency of singlet oxygen generation through this mechanism was very low (5% quantum dots vs. 43% Pc4 PS), quantum dots are extremely resistant to photobleaching and could potentially produce singlet oxygen over longer time periods than traditional PS [255]. The greatest effects on cell viability appear to occur when quantum dots are combined with tethered traditional PS [e.g., trifluoperazine (TFPZ), sulfonated aluminum phthalocyanine (SALPC)] [257]. The exact mechanism for the loss of cell viability in the presence of quantum dots is unclear. It may be attributed to the generation of reactive species, including

singlet oxygen, but could also result from the liberation of Cd ions, which are cytotoxic [31, 257].

### 11.6.3

#### Gene Therapy

Gene therapy can be thought of as a specific subset of drug delivery. The agent delivered is DNA, instead of a pharmaceutical; and the release of the agent occurs one time rather than at a controlled rate. The ability of nanostructures to bind DNA is well known and was initially investigated for sensing and high throughput screening applications [13]. Recently, several investigators have expanded this research to examine potential applications in gene therapy. There are several potential advantages to nanostructure-based vectors. Like other non-viral systems, they can minimize adverse immune responses. Additionally, nanostructures can be readily modified with biomolecules to promote targeting and uptake. Some nanostructures can also be targeted using external fields and monitored optically.

Initially, nanoparticles were investigated as passive carriers. Silica nanoparticles and gold nanoparticles, in particular, have been examined because of the numerous surface modification strategies available. These systems use nanoparticles to increase presentation of DNA to the cell surface and to couple transfection agents with targeted recognition molecules. Conversely, magnetic nanoparticles have been used as active transfection agents, with magnetic fields directing cell targeting.

##### 11.6.3.1 Silica Nanocarriers

Silica nanocarriers are good candidates for DNA delivery because they are biocompatible, present concentrated DNA to the cell surface, and are easily synthesized. Normally, silica nanoparticles are negatively-charged and will not interact with DNA, which is also negatively-charged. However, their surfaces may be modified with aminosilanes to provide cationic surfaces, and zeta potentials of up to ~50 mV have been observed [258]. These surfaces bind up to 90% of available DNA, primarily through electrostatic attraction [259], and have produced transfection efficiencies 30% as high as those of polyethylenimine (PEI) (60 kDa), a standard cationic carrier. Successful transfection has also been demonstrated *in vivo* (e.g., in the brain), with transfection efficiencies equivalent to those of some viral vectors [260]. Additionally, silica nanocarriers demonstrate far less toxicity than cationic delivery systems [261] or viral vectors [260].

Apart from improvements in biocompatibility, it has been suggested that nanoparticles may enhance transfection efficiencies by concentrating DNA near the cell surface [222]. Traditional transfection systems rely on diffusion to initiate contact between the DNA carrier and cell membrane. Many transfection agents are toxic to cells, and contact time must be limited. Most of the DNA complexes in solution never reach the cell membrane. Because of their increased bulk, nanostructures can overcome these difficulties. In one study, dense silica nanoparticles, coupled to dendrimer transfection agents, sedimented on cell surfaces, increasing transfec-

tion efficiencies by almost eight-fold over traditional dendrimers [222]. In another study, the chain length of the dendrimer transfection agent used could be reduced when coupled to silica particles. This is advantageous because long chain (e.g.,  $G > 5$ ) dendritic polymers have been found to be effective gene transfection agents; however, they are difficult to synthesize and isolate [262]. When coupled to mesoporous silica, short-chain (i.e.,  $G_2$ ) poly-amidoamine (PAMAM) dendrimers were able to deliver gene with transfection efficiencies of 35% [262], comparable to unconjugated long-chain variants.

#### 11.6.3.2 Gold Nanocarriers

Like silica, gold nanocarrier surfaces can be readily modified, in this case using thiolated molecules. However, much smaller sizes can be obtained with gold than silica nanocarriers (e.g., 1–10 nm vs. ~30 nm). Smaller nanocarriers potentially increase complex internalization and DNA cargo release [263]. Transfection efficiencies of DNA bound-gold nanocarriers are dependant on the surface charge or hydrophobicity and the chain length of the surface coating. The most successful nanocarriers display efficiencies up to  $8\times$  that of PEI (60 kDa) [263].

Gold particles also enhance the efficacy of existing agents. For example, PEI (2 kDa)-bound gold displayed an eight-fold transfection increase over PEI alone [264]. When combined with chemically modified PEI treatments, transfection of up to 50% of cells was possible [264]. The mechanism for this enhancement is uncertain. Physical concentration of DNA molecules through increased sedimentation may play a role, as hypothesized for silica particles [222]. However, the efficiencies of gold nanocarriers are much greater than those of silica (30% of PEI vs. 800% of PEI) despite being almost an order of magnitude smaller. Thus, additional factors likely contribute to transfection enhancements. Studies of endocytosis have shown an increase in internalization for particles in the 50 nm region [156], and it is possible that the smaller size of DNA-gold complexes enhances their uptake.

#### 11.6.3.3 Magnetic Nanocarriers

By far the most widely studied non-polymeric nanocarriers have been magnetic particles. Magnetic particles can improve the effectiveness of traditional vectors by promoting specific targeting to the cell surface, and possibly the cell interior [265]. In a technique similar to that used for cell sorting, magnetic nanoparticles have been used to concentrate retroviral vectors, which were isolated in concentrations up to 4200 times that of the control [266]. Using a magnetic field, these particles were then directed to certain portions of a cell culture dish, producing extremely efficient, patterned *in vitro* transfection. In a more comprehensive study, cationic magnetic nanoparticles were examined with non-viral (i.e., PEI, AVET, lipofectamine, geneporter, and DOTAP-cholesterol) and viral (i.e., recombinant adenovirus and a retrovirus) transfection agents *in vitro* and *in vivo* [265]. Using magnetic fields, transfection could be confined to specific regions of a cell culture plate, in agreement with Hughes et al. [266].

The application of a magnetic field produces an extraordinary reduction in transfection times, from 2–4 h to as little as 10 min [265]. This is most likely explained

by an increase in vector concentration near the cell surface, resulting from direct magnetic targeting and increased sedimentation [221, 222]. As many vectors demonstrate chronic toxicity in cell culture, a reduction in required transfection time is an important innovation. Additionally, the required DNA dose declined, potentially allowing the use of retroviral transfer agents, which are difficult to isolate in high concentration. Further, targeting of magnetic nanocarriers is extremely specific. Few receptors for the transfection agents employed were required, allowing transfection of cell types that previously did not respond to the viral vectors investigated. A modest increase in transfection was evident for viral agents bound to magnetic particles, and transfection drastically increased (e.g., 20× that of control) the presence of a magnetic field.

Magnetotransfection also shows great promise *in vivo*. Magnetic particle-bound viral agents produced transfection in the gut and stomach, normally inhospitable environments for viral agents and DNA [265]. Transfection has been achieved in primary endothelial cells (i.e., human umbilical vein endothelial cells) that normally display remarkable resistance to DNA and might be used as stem cells [267]. Magnetic nanospheres conjugated to the vascular endothelial growth factor (VEGF) gene have been examined as a treatment for limb ischemia [268]. Using magnetotransfection, overexpression of VEGF was produced, resulting in an increase in capillary formation. This treatment method offers great improvements over either systemic delivery of VEGF or delocalized gene therapy. Systemic delivery has not been very successful because the VEGF half-life is very short, whereas traditional untargeted vector delivery does not target the limb in question and can produce unwanted angiogenesis in alternative locations. Although these studies used external magnets to guide particles, existing MRI technology may also be used for this purpose, reducing one barrier to clinical implementation.

#### 11.6.4

##### Future Directions

###### 11.6.4.1 Drug Delivery

Nanostructures offer several advantages that will encourage their future use in drug delivery. One benefit is the ability to encapsulate large amounts of drug in a small space. Recent work has highlighted the increased storage potential of magnetic nanotubes/wires in particular. Nanowires possess many of the size advantages of nanoparticles, while having an increased length along which diffusion can occur or drug can be encapsulated. Electrospun nanofibers containing magnetic particles have been manufactured, providing potential MRI targeting ability while increasing available drug storage area [269]. Alternatively, magnetic nanoparticles were deposited on the inner surface of silica nanotubes using templated synthesis, and the controlled release of ibuprofen, 5-FU, and 4-nitrophenol drugs was evaluated [270].

Another interesting system to increase storage is the use of hollow polymeric nanospheres. In a technique similar to colloidal lithography (Section 11.3.2), nanoparticles may be used as templates to self-assemble nanometer-sized degradable

polymer shells [271]. Known as layer-by-layer assembly, this technique systematically adds oppositely charged molecules [e.g., polyelectrolytes, including poly(sodium styrenesulfonate) and poly(allylamine hydrochloride)] to a surface through electrostatic attraction. Once the shell is assembled, the core material, usually a polymer nanoparticle (e.g., polystyrene latex [271] or poly(lactic acid)/poly(lactic acid-co-glycolic acid) [272]), can be dissolved. Permeability of the resulting shell is dependant on the polyelectrolytes selected and on the solution pH [272], allowing for specific drug release in pH-altered environments (e.g., endosomes, gut, and stomach). As well as drug, shells can also encapsulate nanostructures, including magnetic particles [273, 274], CdTe [275, 276], Cd<sub>x</sub>Hg<sub>1-x</sub>Te [276] and HgTe [276] semiconductor quantum dots, and gold-cobalt nanoparticles [277]. The shells provide a protective coating that may facilitate intracellular delivery of nanoparticles and their cargos.

Nanostructures also provide ideal drug delivery agents because their surfaces may be altered with multiple agents: drugs, targeting molecules, and chemicals to facilitate intracellular delivery. For example, one system, conceived by Ferrari [213], would use nanoparticles to treat large tumor masses. Traditionally, drugs must access the tumor from its periphery. However, in Ferrari's system, elaborate mechanisms are used to avoid these barriers. First, the nanoparticle encapsulates actin monomers and myosin-bound therapeutic agents. The nanoparticle surface would be bound to molecules that target appropriate cells (e.g., endothelial cells forming the neovascular tumor barrier). The nanoparticle would also be attached to molecules that enhance permeation of the endothelium, allowing nanoparticle access to the tumor interior. Once inside the tumor, the nanoparticle would release its actin cargo, forming filaments along which the myosin-bound drug payload can travel. The drug would then be delivered to tumor cells beyond the tumor periphery.

Nanostructures can also be used to create "smart" delivery vehicles, with triggered release produced by an environmental change. For example, the polymeric nanospheres described above can encapsulate nanoparticles that alter their permeability, actuating release. Au-coated cobalt nanoparticles were able to disrupt polymeric capsules in the presence of a magnetic field, releasing FITC molecules [277]. Another example of selectively triggered release is the use of CdS nanoparticles as capping agents for mesoporous silica storage spheres [278]. CdS nanoparticles were used to block surface pores of mesoporous silica. Upon addition of chemicals that disrupt disulfide bonds, the CdS particles were removed, allowing controlled release of the drug cargo. Alternatively, gold nanoshells have been encapsulated in thermoresponsive hydrogels [17]. When the nanoshells are exposed to infrared light, the temperature increased [Section 11.6.2.2 (Hyperthermia)], causing the polymer to collapse and release its drug cargo.

Future nanoscale drug delivery devices will likely incorporate many of these techniques. Nanocavities, as found in nanotubes or polymeric nanospheres, may provide space for increased drug storage. Nanostructure surfaces may be altered to target release to a specific location. Additional adaptations may allow for safe passage of molecules through tissue barriers and into the cell interior. Once in place, optical

or magnetic excitation may be used to actuate drug release. Ultimately, these systems will provide heretofore unseen control in drug delivery.

#### 11.6.4.2 Gene Therapy

**Multifunctional Systems** Similar to drug delivery, multifunctional systems will likely form the cornerstone of improved nanostructure–DNA delivery. Nanostructures can be attached to several types of biomolecules, creating modular DNA delivery systems that include DNA, cell membrane transporters, and endosomolytic agents. For example, researchers have combined hybrid viruses conjugated to nanoparticle surfaces with magnetic force to create novel gene delivery systems [279]. Previously, the envelope of the hemagglutinating virus of Japan (HVJ) was modified to transfer DNA through cell fusion; however, efficiency remained slow and untargeted. To improve transfection, the virus was coupled with magnetic particles modified with either protamine sulfate or heparin. Successful transfection was achieved using protamine sulfate *in vitro*, whereas heparin was needed to maximize transfection *in vivo*. It is unclear whether these factors enhance direction by promoting cell binding through specific receptors, or simply by altering the zeta potential of the particle surface. In another example of composite systems, researchers combined DNA-covered gold nanoparticles with electromigration and electroporation to enhance delivery. Up to 82× the amount of DNA was delivered when gold particles were subjected to electric fields, promoting electromigration and subsequent electroporation. Although not compared directly with electroporation of free DNA, it is probable that the addition of conductive gold particles enhanced delivery. Although much work is in the early stages, combination approaches can, clearly, merge two mediocre delivery systems to create powerful transfection systems.

**Nanorods** Polymeric microparticles are by far the most common nanostructures studied for gene therapy. However, nanorods offer some distinct advantages as combination transfection agents. Metallic nanorods can be constructed from alternating material segments (Section 11.2.2.2). Through specific surface chemistry interactions, these segments can be chosen to promote selective attachment of biomolecules to each element [280]. For example, rhodamine dye and DNA were attached to segments of Au–Ni nanorods, respectively. The rhodamine was used to locate nanorods, which were found in acidic organelles, probably cytoplasmic vesicles. Alternatively, DNA and transferrin were attached to nanorods, and transfection efficiencies improved by 2–3-fold [280]. This method represents an advantage to nanoparticle-based systems, which attach multiple elements to the same molecule. In single material systems, kinetic considerations may favor binding of one molecule over that of another.

Another advantage of nanotubes is their potential ability to penetrate the cell membrane directly, reducing dependence on the endocytotic pathway for vector delivery. There is some evidence that magnetic particles may be forced through the cell membrane under the influence of a magnetic field [221]. Also, carbon nano-



tubes with a magnetic cap can penetrate the cell in a magnetic field [192]. This system was examined as a method of gene delivery, with up to 85% of cells displaying the gene of interest. Transfection was not evidenced in the absence of the magnetic field, demonstrating that the mechanism of infection was active spearing, and not passive diffusion of vectors to the cell surface. However, both rotating and static fields were required for optimal gene delivery. Because of their surface modifiable segments and high aspect ratios favorable for cell penetration, nanotubes may prove to be superior materials for forming composite delivery systems.

**Frontiers of DNA Delivery** One of the greatest difficulties in assessing *in vivo* gene therapy success is ascertaining whether the intended target has been transfected. Magnetic particles have been used for some time as diagnostic agents in magnetic resonance imaging (MRI). The combination of magnetic particles as gene delivery agents and imaging modalities may allow researchers to monitor transfection *in vivo* [281, 282]. In addition, it may be possible to monitor gene *expression*. Genes that encode for ferritin formation have been used to synthesize metallic particles directly inside cells [283]. If linked to a transfected gene, ferritin molecules could serve as reporter molecules, indicating the transcription level of the gene of interest. Using existing MRI systems, these exciting developments could allow external observation of transfection and subsequent gene expression *in vivo*.

Also, the potential ability of nanostructures to deliver large quantities of DNA is creating new possibilities for therapeutic treatment. The initial focus of most gene therapy approaches has been delivery of a working copy of a deficient gene. However, in many cases the gene in question *overexpresses* a protein, and it would be desirable to “turn-off” the gene. It has been proposed that complimentary oligonucleotides may bind mRNA, preventing protein synthesis [284]. However, as opposed to the one-shot delivery of vectors, silencing genes will require large amounts of DNA to be delivered continuously. Initial reports indicate that transfection using magnetic particles may provide high levels of these oligonucleotides [285]. Ammonium-modified gold nanoparticles bound DNA, preventing RNA polymerase attachment and subsequent DNA transcription [62]. Reversible hybridization has also been demonstrated on a gold nanocrystal platform [286]. DNA conjugated to gold nanoparticles denatured in the presence of a radio-frequency magnetic field. When the magnetic field was removed, DNA appeared to return to the native configuration. Although the exact mechanism is uncertain, it is likely that heating effects produced by the presence of a magnetic field [Section 11.6.2.2 (Hyperthermia)] caused the loss of hybridization.

## 11.7

### Protein Manipulation

Another potential therapeutic use of nanostructures is the active manipulation of proteins. Enzymes and proteins can be directly conjugated to a nanostructure surface, and, in many cases, activated or deactivated through optical or magnetic ef-

fects. Alternatively, substrate molecules can be linked to nanostructures, and used to indirectly manipulate bound proteins, including cell surface receptors or ion channels. Although the applications of nanostructures in this field of cellular engineering are the least developed, they offer the ability to directly control cellular signaling pathways and responses. As techniques continue to advance, nanoscale protein manipulation will lead to new therapies, a greater understanding of cell function, and external systems for large-scale biochemical synthesis.

### 11.7.1

#### **Biology of Protein Manipulation**

Most cell functions, including signaling, replication, and metabolism, are dictated by proteins. Most proteins are globular structures containing positively- and negatively-charged hydrophobic and hydrophilic residues [8]. Upon folding, the hydrophobic residues are confined to the center of the protein, producing secondary structure. The secondary structure frequently contains an active site, a series of charged residues that recognize and bind substrates. Protein–substrate binding affinities result from a combination of electrostatic, hydrogen bonding, and van der Waals interactions [8]. Substrate binding often produces a conformational change in the protein, which activates a signaling pathway or catalyzes a chemical reaction [8].

Proteins may be free or bound to the cell membrane. Proteins embedded in the membrane usually contain several hydrophobic residues, arranged in alpha helices, which span the membrane [8]. These proteins contribute to intercellular signaling, cell motility and adhesion, and the flow of components into and out of the cell. Ion channels, in particular, represent one class of membrane-bound proteins that can respond to electrical, mechanical, or chemical signals [8], and therefore are an interesting target for nanostructure manipulation.

### 11.7.2

#### **Manipulation of Free Proteins: Enzymes**

Nanostructures can be bound to free proteins using many of the techniques discussed previously (Section 11.2.4). The most widely-studied nanostructure system for enzymatic manipulation consists of mesoporous silica containing enzymes immobilized in the particle matrix. This technique has been used to entrap butyrylcholinesterase, an enzyme that cleaves ester bonds, with retention of over 90% of activity [287]. Enzymes bound to silica were more resistant to temperature changes, preserving 100% of activity versus an 85% decrease for free enzyme in solution. Enhanced stability most likely resulted from enzyme interactions with the nanoparticle support, as others have found that enzyme–nanoparticle binding lowers kinetic barriers for conformational rearrangements that may prevent denaturation [288]. Enzymes have also been encapsulated in hollow silica nanoparticles; however, these systems were less successful. Enzyme activity was reduced when compared with free enzyme, most likely as a result of diffusion limitations [289].

Control of the amount of enzyme encapsulated has been obtained using layer-by-layer techniques. Films or shells containing alternative layers of electrolyte and silica nanoparticle or enzyme have been constructed [290, 291]. The amount of enzyme incorporated is controlled by adjusting the number of layers constructed. This technique can also prevent unanticipated enzyme desorption from the particle [292]. Although most of the envisioned applications of this technique are for biosensing or the development of large scale reactors [293], it is possible that layer-by-layer assemblies could be used to construct prosthetic elements that contain a missing or inactive enzyme in the patient.

In addition to silica particles, other materials have been investigated. Trypsin enzyme has been linked to dextran-modified gold through supramolecular interactions [294], and chymotrypsin has been bound to mixed-monolayer protected gold clusters through electrostatic interactions [295]. For chymotrypsin, binding was designed to occur at the active site, and inhibited the enzyme completely with a 1:5 nanoparticle to chymotrypsin ratio. Chymotrypsin has also been attached to CdSe quantum dots with varying surface functionalities. Capping ligands terminated with hydroxyl groups did not interact with enzyme, whereas carboxyl-terminated ligands inactivated enzyme [296]. Enzymes have been coupled to magnetic particles as well, which have the potential benefit of targeting using magnetic fields; however, these are most commonly used in bioreactors, not living systems [297].

Also, nanoparticles have been trapped in the pore of certain proteins, chaperonins, which are responsible for repairing defects in protein folding [298]. Normally, these proteins encompass misfolded proteins, providing a permissible environment for reconfiguration. After folding has been corrected, the protein is released in an ATP-driven process. CdS nanoparticles were complexed with chaperonin proteins with the aid of dimethylformamide. Particles displayed unusually long-lived fluorescence, indicating that chaperonins were able to shield nanoparticles from adverse reactions (e.g., oxidation) in much the same way that misfolded proteins are protected. Further, upon ATP addition, colloids were released and could be isolated through centrifugation.

### 11.7.3

#### **Manipulation of Bound Proteins: Receptors and Ion Channels**

Utilizing nanostructures to manipulate cell surface receptors and ion channels is in many ways easier than the manipulation of free biomolecules. The exterior of the cell is much more accessible than its interior, and introducing nanostructures to an extracellular *in vitro* or *in vivo* environment is straightforward. Although endocytosis may still be an issue, particularly if nanostructures are designed to remain on the cell surface for long periods, performing experiments at low temperatures can alleviate these concerns [154]. This section focuses primarily on nanostructure manipulation of cell surface receptors and ion channels, as nanostructure cytoskeletal manipulation was discussed previously (Section 11.3.4).

Nanoparticle binding to cell surface receptors can influence cell function, particularly the internalization of substances. Magnetic nanoparticles, conjugated to in-

sulin, prevented endocytosis and increased cell proliferation and viability [167]. Gold nanoparticles bound to certain glycoproteins, may inhibit cellular HIV virus transmission [299]. CdSe quantum dots attached to serotonin were used to inactivate serotonin transporters [153], a class of receptors that remove excess transmitter from the extracellular environment following a synaptic event. The particles inhibited serotonin in a dose-dependant manner, most likely because transporters became obstructed when attempting to internalize serotonin-bound nanoparticles.

Nanoparticles have also been employed to investigate ion channels, proteins responsible for signaling in nerve cells. Collagen- and laminin-coated magnetite particles were used to non-specifically coat cell surfaces. When exposed to a magnetic field, an increase in intracellular calcium was observed [300]. These increases result from activation of mechanosensitive ion channels, found often in cardiac tissue. Alternatively, nanoparticles were bound to neuron cell surface receptors, near ion channels of interest. CdS nanoparticles conjugated to integrin-binding peptides were used to explore the potential of electrically exciting ion channels with nanoparticle electrical fields [66, 301]. Ion channels have even been directly linked to nanoparticles. For example, ion channels entrained in silica nanoparticles displayed activity for over a month [302].

#### 11.7.4

##### **Future Directions**

The potential of nanostructures to manipulate biomolecules continues to emerge. For example, it is possible that nanostructures could be used to investigate prion proteins, which have recently been identified as potential sources of transmission for mad-cow disease. Defective prions propagate by converting normal prions into the abnormal structure, forming structures similar to amyloid complexes found in Alzheimer's and Parkinson's disease [303]. Gold nanoparticles have been linked to prions, which were used to create self-assembled arrays [304]. Although the main focus of this work was to create stable nanowires, it may be possible to use nanostructures (e.g., magnetite) to manipulate prions and prion propagation, forming a basis for therapeutic treatment. At the very least, manipulation of this new class of biomolecules could provide valuable insight into structure, folding, and prion-prion interactions.

Additionally, future nanostructure-protein systems will expand the ability to manipulate ion channels. For example, organic dyes have been linked to a mechanosensitive channel in such a way that the channels become activated with light [305]. Given their optical and magnetic properties, it is likely that a similar design could be constructed with nanostructures. Although this system was constructed *ex vivo*, it demonstrates the possibility of direct cell manipulation using optical and mechanical elements. Along these lines, gold nanotubes have been used to create artificial ion channels [306]. Nanotubes were embedded in an artificial plasma membrane, composed of polymers, and linked to a DNA molecule. The DNA molecule was used to provide rectification (e.g., on and off states), and was electrophoretically driven to block the mouth of the pore, preventing ion flow. It is

likely that nanostructures will continue to be used in this way, possibly being integrated into cells for control of ion flow, signaling, and protein binding.

## 11.8 Summary and Conclusions

### 11.8.1 Summary

Nanostructures present several advantages for biological research. They are of similar size to many biological materials. Nanostructure surface areas are high and easily altered through various surface chemistry techniques, allowing for easy biomolecule addition and presentation. Combined with the unique optical and electrical properties of nanostructures, these features have heightened interest in the use of nanostructures for biological investigation. Nanostructures may be composed of many different materials, including semiconductors, metals, and magnetic materials, and may be fashioned into particles, wires, tubes, and shells. Synthesis techniques vary depending on the material employed and the desired shape, but generally include solution-phase synthesis, templated electrodeposition, and deposition from the vapor phase. Once manufactured, nanocomponents can be modified with a range of biomolecules using physisorption, electrostatic attraction, material specific affinities, or biomolecular recognition. These bioconjugates can be used to attach nanostructures to specific components of cells. Although there is some evidence that nanostructures may be cytotoxic, these risks can be mitigated through the application of surface coatings, and nanostructures have already been employed successfully in several *in vivo* and *in vitro* applications.

Nanostructures can be used easily for external investigation of cells. For example, they are ideal for the exploration of cell adhesion, migration, and mechanics, primarily as a result of their small size, similar to that of many components that mediate cell attachment. Interactions with physical topography have chiefly been achieved using structures created through optical lithography. However, colloidal lithography offers a facile technique to create nanostructures much smaller than those produced previously. Additionally, nanoparticles themselves may be organized in self-assembled sheets to create roughened physical surfaces with nanoscale dimensions. Chemical patterns can be produced using many of these same methods. For example, gold-thiol binding affinity may be exploited to assemble proteins on nanoparticles or surfaces created through colloidal lithography. In addition to these passive investigations, magnetic nanostructures can be used to directly manipulate cells. These methods have been implemented for cell sorting and to construct tissue engineering substrates. Also, direct cytoskeletal manipulation is possible, and magnetic nanostructures have been utilized to study the role of integrins in mechanotransduction. Future work will likely focus on integrating physical and chemical cues into multifunctional devices, as well as the creation of active substrates to directly manipulate cells.

Whereas it is straightforward to interface nanomaterials with external structures that govern cell adhesion and migration, controlled intracellular delivery of nanostructures is difficult. Materials can be introduced easily through endocytosis, but remain sequestered in endosomes or lysosomes and are unable to interact with the intracellular environment. Several techniques have been developed to elude this fate, including the addition of translocation peptides, liposomes, dendrimers, electroporation, and microinjection. However, most of these techniques produced significant particle aggregation, which can reduce optical signals and impede interactions with subcellular components. Among these techniques, only microinjection has produced discrete intracellular delivery, but this is a serial technique, difficult to adapt to large numbers of cells or *in vivo* delivery. Despite the limited techniques, several researchers have successfully delivered nanostructures to the cell interior. The primary applications have been for cellular and subcellular tracking. Future research will likely concentrate on improving targeting and delivery of nanostructures, perhaps using biomimetic rather than natural methods.

If controlled delivery can be achieved, it presents the opportunity to directly manipulate internal cellular components, including the cytoskeleton. The cytoskeleton is responsible for cell division, signal regulation, transport, and mechanical properties. Movement along the cytoskeleton is mediated by transport proteins, which bind to specific components, including actin filaments and microtubules. It is possible to conjugate nanostructures to both cytoskeletal components and transport proteins, providing a method for nanostructure movement. These systems have been demonstrated *ex vivo*, primarily for self-assembly and electronics applications; however, it is possible that these techniques may also be explored *in vitro*. Future work will likely adapt *ex vivo* methods for *in vitro* studies. If successful, nanostructures could be used to manipulate the cytoskeleton, increasing understanding of mechanical stimuli in cell signaling and division. Additionally, nanostructures may be transported along cytoskeletal elements, providing a method for directing nanostructures to an organelle of interest, with potential applications in drug delivery and gene therapy.

Additionally, internalized nanostructures could be used for controlled cellular delivery of biomolecules, with applications in drug delivery and gene therapy. The half-lives of drugs are very short, and in many cases, sustained long-term delivery is required for optimal therapeutic effect. Several polymeric release systems have been designed, but these lack targeting ability to specific cells or cell components. Also, many delivery agents are quickly removed from the body through the reticulo-endothelial system. Because nanostructure surfaces can be modified easily, they can surmount these challenges. Biorecognition molecules can be added for selective cell targeting; stealth molecules, e.g., poly(ethylene glycol), can be added to increase particle circulation times.

The greatest immediate potential impact lies in the field of cancer therapy, where discrimination between healthy and diseased cells is essential for treatment. Nanostructures have been used for direct molecule delivery, primarily through magnetic targeting. However, they have also been used for triggered release, actuated by an external event or environmental change. For example, gold and magnetic nano-

structures experience temperature elevations in the presence of near-infrared irradiation. This effect, hyperthermia, can be used to produce local tissue damage. Alternatively, nanostructures have been linked to photosensitizers for photodynamic therapy. In response to optical excitation, these chemicals catalyze the reaction of nearby molecules to create cytotoxic substances.

Nanostructures have also been used for gene therapy, which is in effect a subset of the field of drug delivery. Nanocarriers for DNA delivery have been created using silica, gold, and magnetic particles. Even in passive systems, increases in transfection efficiency were seen. Improvements most likely resulted from the density of the nanostructures, which promoted sedimentation on the cell surface, concentrating DNA presentation. However, increases were also seen for smaller nanostructures, indicating that the small size of nanocarriers may enhance cellular uptake. The addition of active targeting (e.g., magnetic field) further enhanced DNA delivery.

Future systems for drug and DNA delivery will likely incorporate multiple functionalities. Carriers may contain the cargo, targeting molecules, agents to enhance permeation, and means for optical detection. Many carriers include an intrinsic targeting capability (e.g., magnet or electric field response) that can be incorporated to maximize release. The use of nanorods will likely be investigated, as their larger surface area increases available storage for cargo. Also, there is some evidence that magnetic nanorods can directly penetrate the cell membrane, evading the endocytotic pathway. These enhancements will provide delivery vehicles that can control the location and time of release.

Finally, internalized nanostructures may be used to directly manipulate proteins, an area of huge potential, still in initial stages of investigation. Free proteins, including enzymes, can be encapsulated in or attached to nanostructures, and these composite systems can be used to control enzymatic activity. Most of this work has focused on the creation of biochemical reactor devices, but may serve as the basis for the creation of prosthetic elements, which replace a missing enzymatic function. Additionally, nanostructures may be linked to substrates and used to manipulate membrane-bound proteins. These interactions can modulate the internalization of substances and ion channel activity. Future research will likely continue to examine new classes of proteins (e.g., prions) and expand research in ion channel manipulation.

### 11.8.2

#### **Conclusions**

Nanostructures provide scientists with exciting opportunities to manipulate cells directly. They possess similar sizes to many biological components, including DNA, proteins, peptides, and organelles. Nanostructures are easy to synthesize and can be composed of metallic, semiconducting, ceramic or magnetic materials (in addition to carbon, polymeric, and peptide materials discussed elsewhere). Their surfaces are readily modifiable with a range of biomolecules, which provide a direct means to interact with the cell and its environment. Although there is

some concern that certain nanostructures may be cytotoxic, they have nonetheless been employed in several *in vitro* and *in vivo* applications.

Because of their unique optical and electrical properties, nanostructures can be used to manipulate and visualize components of the cell exterior and interior. Most of these investigations have been passive. However, as technologies, particularly for controlled delivery, continue to advance, experiments will shift to more active manipulations of cells and their components. This ability will allow scientists to examine intracellular function with increased control. Additionally, these developments will likely lead to new diagnostic and therapeutic applications, particularly for gene therapy and cancer treatment.

## References

- 1 ALIVISATOS, A. P., Perspectives on the physical chemistry of semiconductor nanocrystals., *J. Phys. Chem.* **1996**, 100, 13 226–13 239.
- 2 CURTIS, A., WILKINSON, C., Nanotechniques and approaches in biotechnology., *Trends Biotechnol.* **2001**, 19, 97–101.
- 3 LAW, M., GOLDBERGER, J., YANG, P., Semiconductor nanowires and nanotubes., *Annu. Rev. Mater. Res.* **2004**, 34, 83–122.
- 4 MOORE, G. E., *Electronics* **1965**, 38.
- 5 BUKOWSKI, T. J., SIMMONS, J. H., Quantum dot research: Current state and future prospects., *Crit. Rev. Solid State Mater. Sci.* **2002**, 27, 119–142.
- 6 HUANG, Y., LIEBER, C. M., Integrated nanoscale electronics and optoelectronics: Exploring nanoscale science and technology through semiconductor nanowires., *Pure Appl. Chem.* **2004**, 12, 2051–2068.
- 7 MURPHY, C. J., COFFER, J. L., Quantum dots: A primer., *Appl. Spectrosc.* **2002**, 56, 16–27.
- 8 ALBERTS, B. A., BRAY, D., LEWIS, J., RAFF, M., ROBERTS, K., WATSON, J. D., *Molecular Biology of the Cell*, 3<sup>rd</sup> Ed., Garland Publishing, New York, **1994**, pp. 101, 111, 130–131, 195–198, 275, 477, 486–487, 523–524, 610–611, 618–626, 789, 979, 986, 990, 996–997.
- 9 MEDINTZ, I. L., UYEDA, H. T., GOLDMAN, E. R., MATTOUSSI, H., Quantum dot bioconjugates for imaging, labeling and sensing., *Nat. Mater.* **2005**, 4, 435–446.
- 10 BRUCHEZ, M., JR., MORONNE, M., GIN, P., WEISS, S., ALIVISATOS, A. P., Semiconductor nanocrystals as fluorescent biological labels., *Science* **1998**, 281, 2013–2016.
- 11 CHAN, W. C. W., NIE, S., Quantum dot bioconjugates for ultrasensitive nonisotopic detection., *Science* **1998**, 281, 2016–2018.
- 12 GAO, X., NIE, S., Molecular profiling of single cells and tissue specimens with quantum dots., *Trends Biotechnol.* **2003**, 21, 371–373.
- 13 ROSI, N. L., MIRKIN, C. A., Nanostructures in biodiagnostics., *Chem. Rev.* **2005**, 105, 1547–1562.
- 14 CHALMERS, J. J., ZBOROWSKI, M., SUN, L., MOORE, L., Flow through, immunomagnetic cell separation., *Biotech. Prog.* **1998**, 14, 141–148.
- 15 LOO, C., LIN, A., HIRSCH, L., LEE, M.-H., BARTON, J., HALAS, N., WEST, J., DREZEK, R., Nanoshell-enabled photonic-based imaging and therapy of cancer., *Technol. Cancer Res. Treat.* **2004**, 3, 33–40.
- 16 BAUER, L. A., BIRENBAUM, N. S., MEYER, G. J., Biological applications of high aspect ratio nanoparticles., *J. Mater. Chem.* **2004**, 14, 517–526.
- 17 SERSHEN, S. R., WESTCOTT, S. L., HALAS, N. J., WEST, J. L., Temperature-sensitive polymer-nanoshell composites for photothermally



- modulated drug delivery., *J. Biomed. Mater. Res.* **2000**, 51, 293–298.
- 18 GUPTA, A. K., GUPTA, M., Synthesis and surface engineering of iron oxide nanoparticles for biomedical applications., *Biomaterials* **2005**, 26, 3995–4021.
  - 19 GAO, X., YANG, L., PETROS, J. A., MARSHALL, F. F., SIMONS, J. W., NIE, S., In vivo molecular and cellular imaging with quantum dots., *Curr. Opin. Biotechnol.* **2005**, 16, 63–72.
  - 20 BLOCK, S. M., GOLDSTEIN, L. S. B., SCHNAPP, B. J., Bead movement by single kinesin molecules studied with optical tweezers., *Nature* **1990**, 348, 348–352.
  - 21 HARTWIG, A., SCHWEDTLE, T., Interactions by carcinogenic metal compounds with DNA repair processes: Toxicological implications. *Toxic. Lett.* **2002**, 127, 47–54.
  - 22 LANSMAN, J. B., HESS, P., TSIEN, R. W., Blockade of current through single calcium channels by  $\text{Cd}^{2+}$ ,  $\text{Mg}^{2+}$ , and  $\text{Ca}^{2+}$ ., *J. Gen. Physiol.* **1986**, 88, 321–347.
  - 23 WAALKES, M. P., Cadmium carcinogenesis., *Mut. Res.* **2003**, 533, 107–120.
  - 24 LAM, C.-W., JAMES, J. T., McCLUSKEY, R., HUNTER, R. L., Pulmonary toxicity of single-wall carbon nanotubes in mice 7 and 90 days after intratracheal instillation., *Toxic. Sci.* **2004**, 77, 126–134.
  - 25 OBERDÖRSTER, E., Manufactured nanomaterials (fullerenes, C60) induce oxidative stress in the brain of juvenile largemouth bass., *Environ. Health Persp.* **2004**, 112, 1058–1062.
  - 26 ELDER, A. C. P., GELEIN, R., AZADNIV, M., FRAMPTON, M., FINKELSTEIN, J., OBERDÖRSTER, G., Systematic effects of inhaled ultrafine particles in two compromised, aged rat strains., *Inhalation Toxic.* **2004**, 16, 461–471.
  - 27 OBERDÖRSTER, G., SHARP, Z., ATUDOREI, V., ELDER, A., GELEIN, R., KREYLING, W., COX, C., Translocation of inhaled ultrafine particles to the brain., *Inhalation Toxic.* **2004**, 16, 437–445.
  - 28 SEMMIER, M., SEITZ, J., ERBE, F., MAYER, P., HEYDER, J., OBERDÖRSTER, G., KREYLING, W. G., Long-term clearance kinetics of inhaled ultrafine insoluble iridium particles from the rat lung, including translocation into secondary organs., *Inhalation Toxic.* **2004**, 16, 453–459.
  - 29 MURRAY, C. B., NORRIS, D. J., BAWENDI, M. G., Synthesis and characterization of nearly monodisperse CdE (E = S, Se, Te) semiconductor nanocrystallites., *J. Am. Chem. Soc.* **1993**, 115, 8706–8715.
  - 30 Tri-octyl phosphine Oxide MSDS Product Number 223301, version 1.5, 6/28/2004, Sigma Aldrich.
  - 31 DERFUS, A. M., CHAN, W. C. W., BHATIA, S. N., Probing the cytotoxicity of semiconductor quantum dots., *Nano Lett.* **2004**, 4, 11–18.
  - 32 CHAN, W. C. W., MAXWELL, D. J., GAO, X., BAILEY, R. E., HAN, M., NIE, S., Luminescent quantum dots for multiplexed biological detection and imaging., *Curr. Opin. Biotechnol.* **2002**, 13, 40–46.
  - 33 HINES, M. A., GUYOT-SIONNEST, P., Synthesis and characterization of strongly luminescing ZnS-capped CdSe nanocrystals., *J. Phys. Chem.* **1996**, 100, 468–471.
  - 34 WEAST, R. C., ASTLE, M. J. (Eds.), *CRC Handbook of Chemistry and Physics*, 60th Ed., CRC Press, Boca Raton, FL, 1979, p. B-220.
  - 35 NOSAKA, Y., OHTA, N., FUKUYAMA, T., FUJII, N., Size control of ultrasmall CdS particles in aqueous solution by using various thiols., *J. Colloid Interface Sci.* **1993**, 155, 23–29.
  - 36 WINTER, J. O., GOMEZ, N., GATZERT, S., SCHMIDT, C. E., KORGEL, B. A., Variation of cadmium sulfide nanoparticle size and photoluminescence intensity with altered aqueous synthesis conditions, *Colloid Surf. A* **2005**, 254, 147–157.
  - 37 KALYANASUNDARAM, K., BORGARELLO, E., DUONGHONG, D., GRÄTZEL, M., Cleavage of water by visible-light irradiation of colloidal CdS solutions: Inhibition of photocorrosion by  $\text{RuO}_2$ ., *Angew. Chem. Int. Ed.* **1981**, 20, 987–988.
  - 38 HENGLEIN, A., Photo-degradation and

- fluorescence of colloidal cadmium sulfide in aqueous solution., *Ber. Bunsenges. Phys. Chem.* **1982**, *86*, 301–305.
- 39 EYCHMÜLLER, A., HÄSELBARTH, A., KATSIKAS, L., WELLER, H., Fluorescence mechanism of highly monodisperse Q-sized CdS colloids., *J. Luminescence* **1991**, *48–49*, 745–749.
- 40 NOSAKA, Y., YAMAGUCHI, K., MIYAMA, H., HAYASHI, H., Preparation of size-controlled CdS colloids in water and their optical properties., *Chem. Lett.* **1988**, *4*, 605–608.
- 41 KUNDU, K., KHOSRAVI, A. A., KULKARNI, S. K., SINGH, P., Synthesis and study of organically capped ultra small clusters of cadmium sulphide., *J. Mater. Sci.* **1997**, *32*, 245–258.
- 42 ROSSETTI, R., ELLISON, J. L., GIBSON, J. M., BRUS, L. E., Size effects in the excited electronic states of small colloidal CdS crystallites., *J. Phys. Chem.* **1984**, *80*, 4464–4469.
- 43 GERION, D., PINAUD, F., WILLIAMS, S. C., PARAK, W. J., ZANCHET, D., WEISS, S., ALIVISATOS, A. P., Synthesis and properties of biocompatible water-soluble silica-coated CdSe/ZnS semiconductor quantum dots., *J. Phys. Chem. B* **2001**, *105*, 8861–8871.
- 44 FARADAY, M., The Bakerian lecture. Experimental relations of gold (and other metals) to light., *Philos. Trans.* **1857**, *147*, 145–181.
- 45 TURKEVICH, J., STEVENSON, P. C., HILLIER, J., A study of the nucleation and growth processes in the synthesis of colloidal gold., *Disc. Faraday Soc.* **1951**, *11*, 55–75.
- 46 SCHMID, G., Large clusters and colloids. Metals in the embryonic state. *Chem. Rev.* **1992**, *92*, 1709–1727.
- 47 AVERITT, R. D., SARKAR, D., HALAS, N. J., Plasmon resonance shifts of Au-coated Au<sub>2</sub>S nanoshells: Insight into multicomponent nanoparticle growth., *Phys. Rev. Lett.* **1997**, *78*, 4217–4220.
- 48 WESTCOTT, S. L., OLDENBURG, S. J., LEE, T. R., HALAS, N. J., Formation and adsorption of clusters of gold nanoparticles onto functionalized silica nanoparticle surfaces., *Langmuir* **1998**, *14*, 5396–5401.
- 49 WILCOXON, J. P., WILLIAMSON, R. L., BAUGHMAN, R., Optical properties of gold colloids formed in inverse micelles., *J. Chem. Phys.*, **1992**, *12*, 9933–9950.
- 50 COLVIN, V. L., GOLDSTEIN, A. N., ALIVISATOS, A. P., Semiconductor nanocrystals covalently bound to metal-surfaces with self-assembled monolayers., *J. Am. Chem. Soc.* **1992**, *114*, 5221–5230.
- 51 MURRAY, C. B., KAGAN, C. R., BAWENDI, M. G., Synthesis and characterization of monodisperse nanocrystals and close-packed nanocrystal assemblies., *Ann. Rev. Mater. Sci.* **2000**, *30*, 545–610.
- 52 TOURINHO, F., FRANCK, R., MASSART, R., PERZYNSKI, R., Synthesis and magnetic properties of manganese and cobalt ferrofluids., *Prog. Col. Polym. Sci.* **1989**, *79*, 128–134.
- 53 REICH, D. H., TANASE, M., HULTGREN, A., BAUER, L., CHEN, C. S., MEYER, G. J., Biological applications of multifunctional magnetic nanowires., *J. Appl. Phys.* **2003**, *93*, 7275–7280.
- 54 BAUER, L. A., REICH, D. H., MEYER, G. J., Selective functionalization of two-component magnetic nanowires., *Langmuir* **2003**, *19*, 7043–7048.
- 55 NGUYEN, C. V., DELZEIT, L., CASSELL, A. M., LI, J., HAN, J., MEYYAPPAN, M., Preparation of nucleic acid functionalized carbon nanotube arrays., *Nano Lett.*, **2002**, *2*, 1079–1081.
- 56 BIRENBAUM, N. S., LAI, T. B., REICH, D. H., CHEN, C. S., MEYER, G. J., Selective noncovalent adsorption of protein to bifunctional metallic nanowire surfaces., *Langmuir* **2003**, *19*, 9580–9582.
- 57 CHAN, W. C. W., PRENDERGAST, T. L., JAIN, M., NIE, S., One-step conjugation of biomolecules to luminescent nanocrystals, in *Molecular Imaging: Reporters, Dyes, Markers, and Instrumentation*, BORNHOP, D. J., LICHA, K., Eds., Proceedings of SPIE., **2000**, vol. 3924, pp. 2–9.
- 58  $\beta$ -Mercaptoethanol MSDS Product Number M7522, version 1.12, 4/6/2004, Sigma Aldrich.

- 59 SCHNEIDER, J. A., KATZ, B., MELLES, R. B., Update on nephropathic cystinosis., *Pediat. Nephrol.* **1990**, *4*, 645–653.
- 60 KATZ, E., WILLNER, I., Integrated nanoparticle-biomolecule hybrid systems: Synthesis, properties, and applications., *Angew. Chem. Int. Ed.* **2004**, *43*, 6042–6108.
- 61 ZHANG, J., MATVEEVA, E., GRZYNSKI, I., LEONENKO, Z., LAKOWICZ, J. R., Metal-enhanced fluoroimmunoassay on a silver film by vapor deposition., *J. Phys. Chem. B* **2005**, *109*, 7969–7975.
- 62 MCINTOSH, C. M., ESPOSITO, III, E. A., BOAL, A. K., SIMARD, J. M., MARTIN, C. T., ROTELLO, V. M., Gold nanoparticles with biological activity: Disruption of transcription via electrostatic attraction., *J. Am. Chem. Soc.* **2001**, *123*, 7626–7629.
- 63 HUANG, H. Z., YANG, X. R., Chitosan mediated assembly of gold nanoparticles multilayers., *Colloid Surf. A* **2003**, *226*, 77–86.
- 64 LU, L. P., WANG, S. Q., LIN, X. Q., Fabrication of layer-by-layer deposited multilayer films containing DNA and gold nanoparticle for norepinephrine biosensor., *Anal. Chim. Acta* **2004**, *519*, 161–166.
- 65 HE, P. L., HU, N. F., RUSLING, J. F., Driving forces for layer-by-layer self-assembly of films of SiO<sub>2</sub> nanoparticles and heme proteins., *Langmuir* **2004**, *20*, 722–729.
- 66 WINTER, J. O., LIU, T. Y., KORGEL, B. A., SCHMIDT, C. E., Recognition molecule directed interfacing between semiconductor quantum dots and nerve cells., *Adv. Mater.* **2001**, *13*, 1673–1677.
- 67 McCAMMON, J. A., Theory of biomolecular recognition., *Curr. Opin. Struct. Biol.* **1998**, *8*, 245–249.
- 68 HERMANSON, G. T., *Bioconjugate Techniques*, Academic Press, San Diego, **1996**, pp. 456–460.
- 69 PIERSCHBACHER, M. D., RUOSLAHTI, E., Cell attachment activity of fibronectin can be duplicated by small synthetic fragments of the molecule., *Nature* **1984**, *309*, 30–33.
- 70 GRAF, J., OGLE, R. C., ROBEY, F. A., SASAKI, M., MARTIN, G. R., YAMADA, Y., KLEINMAN, H. K., A pentapeptide from the laminin B1 chain mediates cell adhesion and binds the 67,000 laminin receptor., *Biochemistry* **1987**, *26*, 6896–6900.
- 71 CREIGHTON, T. E., *Proteins: Structures and Molecular Principles*, W. H. FREEMAN and Co., New York, **1983**.
- 72 COLVIN, V. L., The potential environmental impact of engineered nanomaterials., *Nat. Biotechnol.* **2003**, *21*, 1166–1170.
- 73 DUBERTRET, B., SKOURIDES, P., NORRIS, D. J., NOIREAUX, V., BRIVANLOU, A. H., LIBCHABER, A., In vivo imaging of quantum dots encapsulated in phospholipid micelles., *Science* **2002**, *298*, 1759–1762.
- 74 PARAK, W. J., BOUDREAU, R., LE GROS, M., GERION, D., ZANCHET, D., MICHEEL, C. M., WILLIAMS, S. C., ALIVISATOS, A. P., LARABELL, C., Cell motility and metastatic potential studies based on quantum dot imaging of phagokinetic tracks., *Adv. Mater.* **2002**, *14*, 882–885.
- 75 ÅKERMAN, M. E., CHAN, W. C. W., LAKKONEN, P., BHATIA, S. N., RUOSLAHTI, E., Nanocrystal targeting in vivo., *Proc. Natl. Acad. Sci. U.S.A.* **2002**, *99*, 12617–12621.
- 76 JAISWAL, J. K., MATTOUSSI, H., MAURO, J. M., SIMON, S. M., Long-term multiple color imaging of live cells using quantum dot bioconjugates., *Nat. Biotechnol.* **2003**, *21*, 47–51.
- 77 WU, X., LIU, H., LIU, J., HALEY, K. N., TREADWAY, J. A., LARSON, J. P., GE, N., PEALE, F., BRUCHEZ, M. P., Immunofluorescent labeling of cancer marker her2 and other cellular targets with semiconductor quantum dots., *Nat. Biotechnol.* **2003**, *21*, 41–46.
- 78 LARSON, D. R., ZIPFEL, W. R., WILLIAMS, R. M., CLARK, S. W., BRUCHEZ, M. P., WISE, F. W., WEBB, W. W., Water-soluble quantum dots for multiphoton fluorescence imaging in vivo., *Science* **2003**, *300*, 1434–1436.
- 79 SPANHEL, L., HAASE, M., WELLER, H., HENGLEIN, A., Photochemistry of

- colloidal semiconductors. 20. Surface modification and stability of strong luminescing CdS particles., *J. Am. Chem. Soc.* **1987**, 109, 5649–5655.
- 80 BOWEN KATARI, J. E., COLVIN, V. L., ALIVISATOS, A. P., X-ray photoelectron spectroscopy of CdSe nanocrystals with applications to studies of the nanocrystal surface., *J. Phys. Chem.* **1994**, 98, 4109–4117.
- 81 DABBOUSI, B. O., RODRIGUEZ-VIEJO, J., MIKULEC, F. V., HEINE, J. R., MATTOUSSI, H., OBER, R., JENSEN, K. F., BAWENDI, M. G., CdSe(ZnS) core-shell quantum dots: Synthesis and characterization of a size series of highly luminescent nanocrystallites., *J. Phys. Chem. B* **1997**, 101, 9463–9475.
- 82 ALDANA, J., WANG, Y. A., PENG, X., Photochemical instability of CdSe nanocrystals coated with hydrophilic thiols., *J. Am. Chem. Soc.* **2001**, 123, 8844–8850.
- 83 PATRICK, L., Toxic metals and antioxidants: Part II. The role of antioxidants in arsenic and cadmium toxicity., *Alt. Med. Rev.* **2003**, 8, 106–128.
- 84 RIKANS, L. E., YAMANO, T., Mechanisms of cadmium-mediated acute hepatotoxicity., *J. Biochem. Mol. Toxic.* **2000**, 14, 110–117.
- 85 HAMBRECHT, F. T., Neural prostheses., *Ann. Rev. Biophys. Bioeng.* **1979**, 8, 239–267.
- 86 LEE, B. I., QI, L., COPELAND, T., Nanoparticles for materials design: Present and future., *J. Ceram. Proc. Res.* **2005**, 6, 31–40.
- 87 ALT, V., BECHERT, T., STEINRÜCKE, P., WAGENER, M., SEIDEL, P., DINGELDEIN, E., DOMANN, E., SCHNETTLET, R., An in vitro assessment of the antibacterial properties and cytotoxicity of nanoparticulate silver bone cement., *Biomaterials* **2004**, 25, 4383–4391.
- 88 BRAYDICH-STOLLE, L., HUSSAIN, S., SCHLAGER, J., HOFMANN, M.-C., In vitro cytotoxicity of nanoparticles in mammalian germ-line stem cells., *Toxic. Sci.* **2005**, 88, 412–419.
- 89 GUPTA, A. K., GUPTA, M., Cytotoxicity suppression and cellular uptake enhancement of surface modified magnetic nanoparticles., *Biomaterials* **2005**, 26, 1565–1573.
- 90 BERRY, C. C., WELLS, S., CHARLES, S., AITCHISON, G., CURTIS, A. S. G., Cell response to dextran-derivatised iron oxide nanoparticles post internalization., *Biomaterials* **2004**, 25, 5405–5413.
- 91 HARLOZINSKA, A., Progress in molecular mechanisms of tumor metastasis and angiogenesis., *Anticanc. Res.* **2005**, 25, 3327–3333.
- 92 KIRFEL, G., RIGORT, A., BORM, B., HERZOG, V., Cell migration: Mechanisms of rear detachment and the formation of migration tracks., *Eur. J. Cell Biol.* **2004**, 83, 717–724.
- 93 CLEGG, D. O., WINGERD, K. L., HIKITA, S. T., TOLHURST, E. C., Integrins in the development, function and dysfunction of the nervous system., *Front. Biosci.* **2003**, 8, d723–d750.
- 94 WILSON, C. J., CLEGG, R. E., LEAVESLEY, D. I., PEARCY, M. J., Mediation of biomaterial-cell interactions by adsorbed proteins: A review., *Tissue Eng.* **2005**, 11, 1–18.
- 95 FOLCH, A., TONER, M., Microengineering of cellular interactions., *Annu. Rev. Biomed. Eng.* **2000**, 2, 227–256.
- 96 TURNER, A. M. P., DOWELL, N., TURNER, S. W. P., KAM, L., ISAACSON, M., TURNER, J. N., CRAIGHEAD, H. G., SHAIN, W., Attachment of astroglial cells to microfabricated pillar arrays of different geometries., *J. Biomed. Mater. Res.* **2000**, 51, 430–441.
- 97 RAJNICEK, A., BRITLAND, S., McCAIG, C., Contact guidance of CNS neurites on grooved quartz influence of groove dimensions, neuronal age and cell type., *J. Cell Sci.* **1997**, 110, 2905–2913.
- 98 CHEN, C. S., MRKSICH, M., HUANG, S., WHITESIDES, G. M., INGBER, D. E., Geometric control of cell life and death., *Science* **1997**, 276, 1425–1428.
- 99 CHEN, C. S., JIANG, X., WHITESIDES, G. M., Microengineering the environment of mammalian cells in culture., *MRS Bull.* **2005**, 30, 194–201.

- 100 BRITLAND, S., PERRIDGE, C., DENYER, M., MORGAN, H., CURTIS, A., WILKINSON, C., Morphogenetic guidance cues can interact synergistically and hierarchically in steering nerve cell growth., *Exp. Biol. Online* **1997**, 1, 1–15.
- 101 CLARK, P., COLES, D., PECKHAM, M., Preferential adhesion to and survival on patterned laminin organizes myogenesis in vitro., *Exp. Cell Res.* **1997**, 230, 275–283.
- 102 GOESSL, A., BOWEN-POPE, D. F., HOFFMAN, A. S., Control of shape and size of vascular smooth muscle cells in vitro by plasma lithography., *J. Biomed. Mater. Res.* **2001**, 57, 15–24.
- 103 CLARK, P., BRITLAND, S., CONNOLLY, P., Growth cone guidance and neuron morphology on micropatterned laminin surfaces., *J. Cell Sci.* **1993**, 105, 203–212.
- 104 COREY, J. M., BRUNETTE, A. L., CHEN, M. S., WEYHENMEYER, J. A., BREWER, G. J., WHEELER, B. C., Differentiated B104 neuroblastoma cells are a high-resolution assay for micropatterned substrates., *J. Neurosci. Methods* **1997**, 75, 91–97.
- 105 TURCU, F., TRATSK-NITZ, K., THANOS, S., SCHUHMAN, W., HEIDUSCHKA, P., Ink-jet printing for micropattern generation of laminin for neuronal adhesion., *J. Neurosci. Methods* **2003**, 30, 141–148.
- 106 VOGT, A. K., BREWER, G. J., DECKER, T., BOCKER-MEFFERT, S., JACOBSEN, V., KREITER, M., KNOLL, W., OFFENHAUSSER, A., Independence of synaptic specificity from neuritic guidance., *Neuroscience* **2005**, 134, 783–790.
- 107 ADAMS, J. C., Cell-matrix contact structures., *Cell. Mol. Life. Sci.* **2001**, 58, 371–392.
- 108 ARNOLD, M., CAVALCANTI-ADAM, E. A., GLASS, R., BLÜMMEL, J., ECK, W., KANTLEHNER, M., KESSLER, H., SPATZ, J. P., Activation of integrin function by nanopatterned adhesive interfaces., *ChemPhysChem* **2004**, 5, 383–388.
- 109 FLEMMING, R. G., MURPHY, C. J., ABRAMS, G. A., GOODMAN, S. L., NEALEY, P. F., Effects of synthetic micro- and nano-structured surfaces on cell behavior., *Biomaterials* **1999**, 20, 573–588.
- 110 INGBER, D. E., Mechanobiology and diseases of mechanotransduction., *Ann. Med.* **2003**, 35, 1–14.
- 111 CLARK, P., CONNOLLY, P., CURTIS, A. S. G., DOW, J. A. T., WILKINSON, C. D. W., Cell guidance by ultrafine topography in vitro., *J. Cell Sci.* **1991**, 99, 73–77.
- 112 TEIXEIRA, A. I., ABRAMS, G. A., MURPHY, C. J., NEALEY, P. F., Cell behavior on lithographically defined nanostructured substrates., *J. Vac. Sci. Technol. B* **2003**, 21, 683–687.
- 113 YIM, E. K. F., REANO, R. M., PANG, S. W., YEE, A. F., CHEN, C. S., LEONG, K. W., Nanopattern-induced changes in morphology and motility of smooth muscle cells., *Biomaterials* **2005**, 26, 5405–5413.
- 114 WÓJCIAK-STOTHARD, A., CURTIS, A., MONAGHAN, W., MACDONALD, K., WILKINSON, C., Guidance and activation of murine macrophages by nanometric scale topography., *Exp. Cell Res.* **1996**, 223, 426–435.
- 115 RAJNICEK, A. M., MCCAIG, C. D., Guidance of CNS growth cones by substratum grooves and ridges: Effects of inhibitors of the cytoskeleton, calcium channels and signal transduction pathways., *J. Cell Sci.* **1997**, 110, 2915–2924.
- 116 COUSINS, B. G., DOHERTY, P. J., WILLIAMS, R. L., FINK, J., GARVEY, M. J., The effect of silica nanoparticulate coatings on cellular response., *J. Mater. Sci. Mater. Med.* **2004**, 15, 355–359.
- 117 FREY, W., WOODS, C. K., CHILKOTI, A., Ultraflat nanosphere lithography: A new method to fabricate flat nanostructures., *Adv. Mater.* **2000**, 12, 1515–1519.
- 118 STEIN, A., SCHRODEN, R. C., Colloidal crystal templating of three-dimensionally ordered macroporous solids: Materials for photonics and beyond., *Curr. Opin. Solid State Mater. Sci.* **2001**, 5, 553–564.
- 119 DALBY, M. J., RIEHLE, M. O., SUTHERLAND, D. S., AGHELI, H., CURTIS, A. S. G., Morphological and

- microarray analysis of human fibroblasts cultured on nanocolumns produced by colloidal lithography., *Eur. Cell Mater.* **2005**, 9, 1–8.
- 120 ANDERSSON, A.-S., BRINK, J., LIDBERG, U., SUTHERLAND, D. S., Influence of systematically varied nanoscale topography on the morphology of epithelial cells., *IEEE Trans. Nanobiosci.* **2003**, 2, 49–57.
- 121 DALBY, M. J., RIEHLE, M. O., SUTHERLAND, D. S., AGHELI, H., CURTIS, A. S. G., Fibroblast response to a controlled nanoenvironment produced by colloidal lithography., *J. Biomed. Mater. Res.* **2004**, 69A, 314–322.
- 122 BERSHADSKY, A. D., TINT, I. S., NEYFAKH, A. A., JR., VASILIEV, J. M., Focal contacts of normal and RSV-transformed quail cells. Hypothesis of the transformation-induced deficient maturation of focal contacts., *Exp. Cell Res.* **1985**, 158, 433–444.
- 123 DALBY, M. J., RIEHLE, M. O., SUTHERLAND, D. S., AGHELI, H., CURTIS, A. S. G., Changes in fibroblast morphology in response to nano-columns produced by colloidal lithography., *Biomaterials* **2004**, 25, 5415–5422.
- 124 VAN KOOTEN, T. G., KLEIN, C. L., KÖHLER, H., KIRKPATRICK, C. J., WILLIAMS, D. F., ELOY, R., From cytotoxicity to biocompatibility testing in vitro: Cell adhesion molecule expression defines a new set of parameters., *J. Mater. Sci. Mater. Med.* **1997**, 8, 835–841.
- 125 KELLER, J. C., STANFORD, C. M., WIGHTMAN, J. P., DRAUGHN, R. A., ZAHARIAS, R., Characterizations of titanium implant surfaces. III., *J. Biomed. Mater. Res.* **1994**, 28, 939–946.
- 126 MRKSICH, M., WHITESIDES, G. M., Using self-assembled monolayers to understand the interactions of man-made surfaces with proteins and cells. *Ann. Rev. Biophys. Biomol. Struct.* **1996**, 25, 55–78.
- 127 KOO, L. Y., IRVINE, D. J., MAYES, A. M., LAUFFENBURGER, D. A., GRIFFITH, L. G., Co-regulation of cell adhesion by nanoscale RGD organization and mechanical stimulus., *J. Cell Sci.* **2002**, 115, 1423–1433.
- 128 LEE, K.-B., PARK, S.-J., MIRKIN, C. A., SMITH, J. C., MRKSICH, M., Protein nanoarrays generated by dip-pen nanolithography., *Science* **2002**, 295, 1702–1705.
- 129 SPATZ, J. P., MÖSSMER, S., HARTMANN, C., MÖLLER, M., HERZOG, T., KRIEGER, M., BOYEN, H.-G., ZIEMANN, P., KABIUS, B., Ordered deposition of inorganic clusters from micellar block copolymer films., *Langmuir* **2000**, 16, 407–415.
- 130 CRICK, F., HUGHES, A., The physical properties of the cytoplasm. I. Experimental., *Exp. Cell Res.* **1950**, 1, 37–80.
- 131 ZBOROWSKI, M., CHALMERS, J. J., Magnetic cell sorting., *Methods Mol. Biol.* **2005**, 295, 291–300.
- 132 NAKAMURA, M., DECKER, K., CHOSY, J., COMELLA, K., MELNIK, K., MOORE, L., LASKY, L. C., ZBOROWSKI, M., CHALMERS, J. J., Separation of a breast cancer cell line from human blood using a quadrupole magnetic flow sorter., *Biotechnol. Prog.* **2001**, 17, 1145–1155.
- 133 HULTGREN, A., TANASE, M., FELTON, E. J., BHADRIRAJU, K., SALEM A. K., CHEN, C. S., REICH, D. H., Optimization of yield in magnetic cell separations using nickel nanowires of different lengths., *Biotechnol. Prog.* **2005**, 21, 509–515.
- 134 SHINKAI, M., YANASE, M., HONDA, H., WAKABAYASHI, T., YOSHIDA, J., KOBAYASHI, T., Intracellular hyperthermia for cancer using magnetite cationic liposomes: *in vitro* study., *Jpn. J. Canc. Res.* **1996**, 87, 1179–1183.
- 135 ITO, A., TAKIZAWA, Y., HONDA, H., HATA, K., KAGAMI, H., UEDA, M., KOBAYASHI, T., Tissue engineering using magnetite nanoparticles and magnetic force: Heterotypic layers of cocultured hepatocytes and endothelial cells., *Tissue Eng.* **2004**, 10, 833–840.
- 136 ITO, A., INO, K., KOBAYASHI, T., HONDA, H., The effect of RGD peptide-conjugated magnetite cationic

- liposomes on cell growth and cell sheet harvesting., *Biomaterials* **2005**, *26*, 6185–6193.
- 137 ITO, A., HAYASHIDA, M., HONDA, H., HATA, K., KAGAMI, H., UEDA, M., KOBAYASHI, T., Construction and harvest of multilayered keratinocyte sheets using magnetite nanoparticles and magnetic force., *Tissue Eng.* **2004**, *10*, 873–880.
- 138 ITO, A., HIBINO, E., KOBAYASHI, C., TERASAKI, H., KAGAMI, H., UEDA, M., KOBAYASHI, T., HONDA, H., Construction and delivery of tissue-engineered human retinal pigment epithelial cell sheets, using magnetite nanoparticles and magnetic force., *Tissue Eng.* **2005**, *11*, 489–496.
- 139 TANASE, M., FELTON, E. J., GRAY, D. S., HULTGREN, A., CHEN, C. S., REICH, D. H., Assembly of multicellular constructs and microarrays of cells using magnetic nanowires., *Lab Chip* **2005**, *5*, 598–605.
- 140 WANG, N., BUTLER, J. P., INGBER, D. E., Mechanotransduction across the cell surface and through the cytoskeleton., *Science* **1993**, *260*, 1124–1127.
- 141 CHEN, J., FABRY, B., SCHIFFRIN, E. L., WANG, N., Twisting integrin receptors increases endothelin-1 gene expression in endothelial cells., *Am. J. Physiol. Cell. Physiol.* **2001**, *280*, C1475–C1484.
- 142 TANASE, M., SILEVITCH, D. M., HULTGREN, A., BAUER, L. A., SEARSON, P. C., MEYER, G. J., REICH, D. H., Magnetic trapping and self-assembly of multicomponent nanowires., *J. Appl. Phys.* **2002**, *91*, 8549–8551.
- 143 BIELINSKA, A., EICHMAN, J. D., LEE, I., BAKER, J. R., BALOGH, L., Imaging {Au-0-PAMAM} gold-dendrimer nanocomposites in cells., *J. Nanopart. Res.* **2002**, *4*, 395–403.
- 144 SAUNDERS, A. E., KORGEL, B. A., Observation of an AB phase in bidisperse nanocrystal superlattices., *ChemPhysChem* **2005**, *6*, 61–65.
- 145 MOGHIMI, S. M., HUNTER, A. C., MURRAY, J. C., Nanomedicine: Current status and future prospects., *FASEB J.* **2005**, *19*, 311–330.
- 146 BELLAMKONDA, R., RANIERI, J. P., AEBISCHER, P., Laminin oligopeptide derivatized agarose gels allow three-dimensional neurite extension in vitro., *J. Neurosci. Res.* **1995**, *41*, 501–509.
- 147 HERN, D. L., HUBBELL, J. A., Incorporation of adhesion peptides into nonadhesive hydrogels useful for tissue resurfacing., *J. Biomed. Mater. Res.* **1998**, *39*, 266–276.
- 148 ZHENG, H., BERG, M. C., RUBNER, M. F., HAMMOND, P. T., Controlling cell attachment selectively onto biological polymer-colloid templates using polymer-on-polymer stamping., *Langmuir* **2004**, *20*, 7215–7222.
- 149 BAUSCH, A. R., ZIEMANN, F., BOULBITCH, A. A., JACOBSON, K., SACKMANN, E., Local measurements of viscoelastic parameters of adherent cell surfaces by magnetic bead microrheometry., *Biophys. J.* **1998**, *75*, 2038–2049.
- 150 VALBERG, P. A., ALBERTINI, D. F., Cytoplasmic motions, rheology, and structure probed by a novel magnetic particle method., *J. Cell Biol.* **1985**, *101*, 130–40.
- 151 BAUSCH, A. R., MOLLER, W., SACKMANN, E., Measurement of local viscoelasticity and forces in living cells by magnetic tweezers., *Biophys. J.* **1999**, *76*, 573–579.
- 152 TANAKA, T., YAMASAKI, H., TSUJIMURA, N., NAKAMURA, N., MATSUNAGA, T., Magnetic control of bacterial magnetite-myosin conjugate movement on actin cables., *Mater. Sci. Eng. C* **1997**, *5*, 121–124.
- 153 ROSENTHAL, S. J., TOMLINSON, I., ADKINS, E. M., SCHROETER, S., ADAMS, S., SWAFFORD, L., MCBRIDE, J., WANG, Y., DEFELICE, L. J., BLAKELY, R. D., Targeting cell surface receptors with ligand-conjugated nanocrystals., *J. Am. Chem. Soc.* **2002**, *124*, 4586–4594.
- 154 PASTAN, I., WILLINGHAM, M. C. (Eds.), *Endocytosis*, Plenum Press, New York, **1985**.
- 155 GAO, D., CRITSER, J. K., Mechanisms of cryoinjury in living cells. *ILAR J.* **2000**, *41*, 187–196.

- 156 OSAKI, F., KANAMORI, T., SANDO, S., SERA, T., AOYAMA, Y., A quantum dot conjugated sugar ball and its cellular uptake. On the size effects of endocytosis in the subviral region., *J. Am. Chem. Soc.* **2004**, 126, 6520–6521.
- 157 GUPTA, A. K., CURTIS, A. S. G., Lactoferrin and ceruloplasmin derivatized superparamagnetic iron oxide nanoparticles for targeting cell surface receptors., *Biomaterials* **2004**, 25, 3029–3040.
- 158 DAHAN, M., LAURENCE, T., PINAUD, F., CHEMLA, D. S., ALIVISATOS, A. P., SAUER, M., WEISS, S., Time-gated biological imaging by use of colloidal quantum dots., *Opt. Lett.* **2001**, 26, 825–827.
- 159 HANAOKI, K.-I., MOMO, A., TAISUKE, O., KOMOTO, A., MAENOSONO, S., YAMAGUCHI, Y., YAMAMOTO, K., Semiconductor quantum dot/albumin complex is a long-life and highly photostable endosome marker., *Biochem. Biophys. Res. Commun.* **2003**, 302, 496–501.
- 160 GOMEZ, N., WINTER, J. O., SHIEH, F., SAUNDERS, A. E., KORGEL, B. A., SCHMIDT, C. E., Challenges in quantum dot-neuron active interfacing., *Talanta*, **2005**, 67, 462–471.
- 161 ROGERS, W. J., BASU P., Factors regulating macrophage endocytosis of nanoparticles: Implications for targeted magnetic resonance plaque imaging., *Atherosclerosis* **2005**, 178, 67–73.
- 162 LIDKE, D. S., NAGY, P., HEINTZMANN, R., ARNDT-JOVIN, D. J., POST, J. N., GRECCO, H. E., JARES-ERIJMAN, E. A., JOVIN, T. M., Quantum dot ligands provide new insights into erbB/HER receptor-mediated signal transduction., *Nat. Biotechnol.* **2004**, 22, 198–203.
- 163 YANG, P.-H., SUN, X., CHIU, J.-F., SUN, H., HE, Q.-Y., Transferrin-mediated gold nanoparticle cellular uptake., *Bioconj. Chem.* **2005**, 16, 494–496.
- 164 DALBY, M. J., BERRY, C. C., RIEHLE, M. O., SUTHERLAND, D. S., AGHELI, H., CURTIS, A. S. G., Attempted endocytosis of nano-environment produced by colloidal lithography by human fibroblasts., *Exp. Cell Res.* **2004**, 295, 387–394.
- 165 PRATTEN, M. K., LLOYD, J. B., Pinocytosis and phagocytosis: The effect of size of a particle substrate on its mode of capture by rat peritoneal macrophages cultured in vitro., *Biochem. Biophys. Acta* **1986**, 881, 307–313.
- 166 GUPTA, A. K., CURTIS, A. S. G., Surface modified superparamagnetic nanoparticles for drug delivery: Interaction studies with human fibroblasts in culture., *J. Mater. Sci. Mater. Med.* **2004**, 15, 493–496.
- 167 GUPTA, A. K., BERRY, C., GUPTA, M., CURTIS, A., Receptor-mediated targeting of magnetic nanoparticles using insulin as a surface ligand to prevent endocytosis., *IEEE Trans. Nanobiosci.* **2003**, 2, 255–261.
- 168 MORRIS, M. C., DEPOLLIER, J., MERY, J., HEITZ, F., DIVITA, G., A peptide carrier for the delivery of biologically active proteins into mammalian cells., *Nat. Biotechnol.* **2001**, 19, 1173–1176.
- 169 VIVES, E., RICHARD, J. P., RISPAL, C., LEBLEU, B., TAT peptide internalization: Seeking the mechanism of entry., *Curr. Protein Pept. Sci.* **2003**, 4, 125–132.
- 170 NORI, A., KOPECEK, J., Intracellular targeting of polymer-bound drugs for cancer chemotherapy., *Adv. Drug Deliv. Rev.* **2005**, 57, 609–636.
- 171 MATTHEAKIS, L. C., DIAS, J. M., CHOI, Y.-J., GONG, J., BRUCHEZ, M. P., LIU, J., WANG, E., Optical coding of mammalian cells using semiconductor quantum dots., *Anal. Biochem.* **2004**, 327, 200–208.
- 172 TKACHENKO, A. G., XIE, H., COLEMAN, D., GLOMM, W., RYAN, J., ANDERSON, M. F., FRANZEN, S., FELDHEIM, D. L., Multifunctional gold nanoparticle-peptide complexes for nuclear targeting., *J. Am. Chem. Soc.* **2003**, 125, 4700–4701.
- 173 JOSEPHSON, L., TUNG, C.-H., MOORE, A., WEISSLEDER, R., High-efficiency intracellular magnetic labeling with novel superparamagnetic-Tat peptide



- conjugates., *Bioconj. Chem.* **1999**, *10*, 186–191.
- 174 WON, J., KIM, M., YI, Y.-W., KIM, Y. H., JUNG, N., KIM, T. K., A magnetic nanoprobe technology for detecting molecular interactions in live cells., *Science* **2005**, *309*, 121–125.
- 175 ZHANG, C., MA, H., NIE, S., DING, Y., JIN, L., CHEN, D., Quantum dot-labeled trichosanthin., *Analyst* **2000**, *125*, 1029–1031.
- 176 HOSHINO, A., FUJIOKA, K., OKU, T., NAKAMURA, S., SUGA, M., YAMAGUCHI, T., SUZUKI, K., YASUHARA, M., YAMAMOTO, K., Quantum dots targeted to the assigned organelle in living cells., *Microbiol. Immunol.* **2004**, *48*, 985–994.
- 177 DERFUS, A. M., CHAN, W. C. W., BHATIA, S. N., Intracellular delivery of quantum dots for live cell labeling and organelle tracking., *Adv. Mater.* **2004**, *16*, 961–966.
- 178 TKACHENKO, A. G., XIE, H., LIU, Y., COLEMAN, D., RYAN, J., GLOMM, W. R., SHIPTON, M. K., FRANZEN, S., FELDHEIM, D. L., Cellular trajectories of peptide-modified gold particle complexes: Comparison of nuclear localization signals and peptide transduction domains., *Bioconj. Chem.* **2004**, *15*, 482–490.
- 179 DAHAN, M., LÉVI, S., LUCCARDINI, C., ROSTAING, P., RIVEAU, B., TRILLER, A., Diffusion dynamics of glycine receptors revealed by single-quantum dot tracking., *Science* **2003**, *302*, 442–445.
- 180 CHU, T. C., SHIEH, F., LAVERY, L. A., LEVY, M., RICHARDS-KORTUM, R., KORGEL, B. A., ELLINGTON, A. D., Labeling tumor cells with fluorescent nanocrystal-aptamer bioconjugates., *Biosens. Bioelectron.* **2006**, *21*, 1859–1866.
- 181 GAO, X., NIE, S., Quantum dot-encoded beads., *Methods Mol. Biol.* **2005**, *303*, 61–71.
- 182 PATHAK, S., CHOI, S.-Y., ARNHEIM, N., THOMPSON, M., Hydroxylated quantum dots as luminescent probes for in situ hybridization., *J. Am. Chem. Soc.* **2001**, *123*, 4103–4104.
- 183 FERRARA, D. E., WEISS, D., CARNELL, P. H., VITO, R. P., VEGA, D., GAO, X., NIE, S., TAYLOR, W. R., Quantitative 3D fluorescence technique for the analysis of en face preparations of arterial walls using quantum dot nanocrystals and two-photon excitation laser scanning microscopy., *Am. J. Physiol. Regul. Integr. Comp. Physiol.* **2006**, *290*, R114–23.
- 184 JAISWAL, J. K., SIMON, S. M., Potentials and pitfalls of fluorescent quantum dots for biological applications., *Trends Cell Biol.* **2004**, *14*, 497–504.
- 185 LEWIN, M., CARLESSO, N., TUNG, C.-H., TANG, X.-W., CORY, D., SCADDEN, D. T., WEISSELEDER, R., Tat peptide-derivatized magnetic nanoparticles allow in vivo tracking and recovery of progenitor cells., *Nat. Biotechnol.* **2000**, *18*, 410–414.
- 186 MOORE, A., JOSEPHSON, L., BHORADE, R. M., BASILION, J. P., WEISSELEDER, R., Human transferrin receptor gene as a marker gene for MR imaging., *Radiology* **2001**, *221*, 244–250.
- 187 AHMED, F., DISCHER, D., Self-porating polymersomes of PEG-PLA and PEG-PCL: Hydrolysis-triggered controlled release vesicles., *J. Controlled Release* **2004**, *96*, 37–53.
- 188 AHMED, F., DISCHER, D., Breaking down endolysosomal barriers for drug delivery with degradable polymersomes., Proceedings of American Institute of Chemical Engineers Annual Meeting, October 29–November 5, **2005**, Cincinnati, OH, available online at <http://aiche.confex.com/aiche/2005/techprogram/P28864.htm>.
- 189 KUNISAWA, J., MASUDA, T., KATAYAMA, K., YOSHIKAWA, T., TSUTSUMI, Y., AKASHI, M., MAYUMI, T., NAKAGAWA, S., Fusogenic liposome delivers encapsulated nanoparticles for cytosolic controlled gene release., *J. Controlled Release* **2005**, *105*, 344–353.
- 190 KAM, N. W. S., O'CONNELL, M., WISDOM, J. A., DAI, H., Carbon nanotubes as multifunctional biological transporters and near-infrared agents for selective cancer cell destruction., *Proc. Natl. Acad. Sci. U.S.A.* **2005**, *102*, 11 600–11 605.

- 191 PANTAROTTO, D., SINGH, R., MCCARTHY, D., ERHARDT, M., BRIAND, J.-P., PRATO, M., KOSTARELOS, K., BIANCO, A., Functionalized carbon nanotubes for plasmid DNA gene delivery., *Angew. Chem. Int. Ed.* **2004**, 32, 5242–5246.
- 192 CAI, D., MATARAZA, J. M., QIN, Z.-H., HUANG, Z., HUANG, J., CHILES, T. C., CARNAHAN, D., KEMPA, K., REN, Z., Highly efficient molecular delivery into mammalian cells using carbon nanotube spearing., *Nat. Meth.* **2005**, 2, 449–454.
- 193 STRYER, L., HAUGLAND, R. P., Energy transfer: A spectroscopic ruler., *Proc. Natl. Acad. Sci. U.S.A.* **1967**, 58, 719–726.
- 194 MAXWELL, D. J., TAYLOR, J. R., NIE, S., Self-assembled nanoparticle probes for recognition and detection of biomolecules., *J. Am. Chem. Soc.* **2002**, 124, 9606–9612.
- 195 MEDINTZ, I. L., CLAPP, A. R., MAITTOUSSI, H., GOLDMAN, E. R., FISHER, B., MAURO, J. M., Self-assembled nano-scale biosensors based on quantum dot FRET donors., *Nat. Mater.* **2003**, 2, 630–638.
- 196 WANG, S., MAMEDOVA, N., KOTOV, N. A., CHEN, W., STUDER, J., Antigen/antibody immunocomplex from CdTe nanoparticle bioconjugates., *Nano Lett.* **2002**, 2, 817–822.
- 197 LEE, J., GOVOROV, A. O., KOTOV, N. A., Bioconjugated superstructures of CdTe nanowires and nanoparticles: Multistep cascade Förster resonance energy transfer and energy channeling., *Nano Lett.* **2005**, 5, 2063–2069.
- 198 KINBARA, K., AIDA, T., Toward intelligent molecular machines: Directed motions of biological and artificial molecules and assemblies., *Chem. Rev.* **2005**, 105, 1377–1400.
- 199 WARSHAW, D. M., KENNEDY, G. G., WORK, S. S., KREMENTSOVA, E. B., BECK, S., TRYBUS, K. M., Differential labeling of myosin V heads with quantum dots allows direct visualization of hand-over-hand processivity., *Biophys. J. Biophys. Lett.* **2005**, 88, L30–L32.
- 200 MÅNSSON, A., SUNDBERG, M., BALAZ, M., BUNK, R., NICHOLLS, I. A., OMLING, P., TÅGERUDA, S., MONTELIUS, L., In vitro sliding of actin filaments labeled with single quantum dots., *Biochem. Biophys. Res. Commun.* **2004**, 314, 529–534.
- 201 PATOLSKY, F., WIEZMANN, Y., WILLNER, I., Actin-based metallic nanowires as bio-nanotransporters., *Nat. Mater.* **2004**, 3, 692–695.
- 202 JIA, L., MOORJANI, S. G., JACKSON, T. N., HANCOCK, W. O., Microscale transport and sorting by kinesin molecular motors., *Biomed. Microdev.* **2004**, 6, 67–74.
- 203 VAN DEN HEUVEL, M. G. L., BUTCHER, C. L., LEMAY, S. G., DIEZ, S., DEKKER, C., Electrical docking of microtubules for kinesin-driven motility in nanostructures., *Nano Lett.* **2005**, 5, 235–241.
- 204 VAN DEN HEUVEL, M. G. L., BUTCHER, C. L., SMEETS, R. M. M., DIEZ, S., DEKKER, C., High rectifying efficiencies of microtubule motility on kinesin-coated gold nanostructures., *Nano Lett.* **2005**, 5, 1117–1122.
- 205 LIMBERIS, L., STEWART, R. J., Toward kinesin-powered microdevices., *Nanotechnology* **2000**, 11, 47–51.
- 206 BÖHM, K. J., STRACKE, R., MÜHLIG, P., UNGER, E., Motor protein-driven unidirectional transport of micrometer-sized cargoes across isopolar microtubule arrays., *Nanotechnology* **2001**, 12, 238–244.
- 207 BACHAND, G. D., RIVERA, S. B., BOAL, A. K., GAUDIOSO, J., LIU, J., BUNKER, B. C., Assembly and transport of nanocrystal CdSe quantum dot nanocomposites using microtubules and motor proteins., *Nano Lett.* **2004**, 4, 817–821.
- 208 RIEGLER, J., NICK, P., KIELMANN, U., NANN, T., Visualizing the self-assembly of tubulin with luminescent nanorods., *J. Nanosci. Nanotechnol.* **2003**, 3, 380–385.
- 209 HESS, H., CLEMMENS, J., QIN, D., HOWARD, J., VOGEL, V., Light-controlled molecular shuttles made from motor proteins carrying cargo on engineered surfaces., *Nano Lett.* **2001**, 1, 235–239.
- 210 DIEZ, S., REUTHER, C., DINU, C.,

- SEIDEL, R., MERTIG, M., POMPE, W., HOWARD, J., Stretching and transporting DNA molecules using motor proteins., *Nano Lett.* **2003**, *3*, 1251–1254.
- 211 WEIBEL, D. B., GARSETCKI, P., RYAN, D., DI LUZIO, W. R., MAYER, M., SETO, J. E., WHITESIDES, G. M., Microoxen: Microorganisms to move microscale loads., *Proc. Natl. Acad. Sci. U.S.A.* **2005**, *102*, 11 963–11 967.
- 212 DARNTON, N., TURNER, L., BREUER, K., BERG, H. C., Moving fluid with bacterial carpets., *Biophys. J.* **2004**, *86*, 1863–1870.
- 213 FERRARI, M., Cancer nanotechnology: Opportunities and challenges., *Nat. Rev. Canc.* **2005**, *5*, 161–171.
- 214 MOSES, M. A., BREM, H., LANGER, R., Advancing the field of drug delivery: Taking aim at cancer., *Cancer Cell.* **2003**, *4*, 337–341.
- 215 CAPALDI, B., Treatments and devices for future diabetes management., *Nurs. Times* **2005**, *101*, 30–32.
- 216 STAHL, S. M., Applications of new drug delivery technologies to Parkinson's disease and dopaminergic agents., *Neural Transm. Suppl.* **1988**, *27*, 123–132.
- 217 HARBAUGH, R. E., Novel CNS-directed drug delivery systems in Alzheimer's disease and other neurological disorders., *Neurobiol. Aging* **1989**, *10*, 623–629.
- 218 LANGER, R., PEPAS, N. A., Advances in biomaterials, drug delivery, and bionanotechnology., *AIChE J.* **2003**, *49*, 2990–3006.
- 219 MÜLLER, R. H., KECK, C. M., Drug delivery to the brain-realization by novel drug carriers., *J. Nanosci. Nanotechnol.* **2004**, *4*, 471–483.
- 220 JOHNSON-SALIBA, M., JANS, D. A., Gene therapy: Optimizing DNA delivery to the nucleus., *Curr. Drug Targ.* **2001**, *2*, 371–399.
- 221 PLANK, C., SCHILLINGER, U., SCHERER, F., BERGEMANN, C., RÉMY, J.-S., KRÖTZ, F., ANTON, M., LAUSIER, J., ROSENECKER, J., The magneto-transfection method: Using magnetic force to enhance gene delivery., *Biol. Chem.* **2003**, *384*, 737–747.
- 222 LUO, D., SALTZMANN, W. M., Enhancement of transfection by physical concentration of DNA at the cell surface., *Nat. Biotechnol.* **2000**, *18*, 893–895.
- 223 WIDDER, K. J., SENYEI, A. E., SCARPELLI, D. G., Magnetic microspheres: A model system for site specific drug delivery in vivo., *Proc. Soc. Exp. Biol. Med.* **1978**, *58*, 141–146.
- 224 WIDDER, K. J., MORRIS, R. M., POORE, G. A., HOWARD, D. P., SENYEI, A. E., Selective targeting of magnetic albumin microspheres containing low-dose doxorubicin: Total remission in Yoshida sarcoma-bearing rats., *Eur. J. Cancer Clin. Oncol.* **1983**, *19*, 135–139.
- 225 SWANSON, N., GERSHLICK, A. H., Drug eluting stents in interventional cardiology – current evidence and emerging uses., *Curr. Drug Targets Cardiovasc. Haematol. Disord.* **2005**, *5*, 313–321.
- 226 HUH, Y.-M., JUN, Y.-W., SONG, H.-T., KIM, S., CHOI, J.-S., LEE, J.-H., YOON, S., KIM, K.-S., SHIN, J.-S., SUH, J.-S., CHEON, J., In vivo magnetic resonance detection of cancer by using multifunctional magnetic nanocrystals., *J. Am. Chem. Soc.* **2005**, *127*, 12 387–12 391.
- 227 LÜBBE, A. S., ALEXIOU, C., BERGEMANN, C., Clinical applications of magnetic drug targeting., *J. Surg. Res.* **2000**, *95*, 200–206.
- 228 PANKHURST, Q. A., CONNOLLY, J., JONES, S. K., DOBSON, J., Applications of magnetic particles in biomedicine., *J. Phys. D, Appl. Phys.* **2003**, *36*, R167–R181.
- 229 GALLO, J. M., VARKONYI, P., HASSAN, E. E., GROOTHUIS, D. R., Targeting anti-cancer drugs to the brain: II. Physiological pharmacokinetic model of oxantazole following intraarterial administration to rat glioma-2 (RG-2) bearing rats., *J. Pharmacokin. Biopharm.* **1993**, *21*, 575–592.
- 230 PULFER, S. K., CICCOTTO, S. L., GALLO, J. M., Distribution of small magnetic particles in tumor-bearing rats., *J. Neurooncol.* **1999**, *41*, 99–105.
- 231 GOODWIN, S., PETERSON, C., HOH, C., BITTNER, C., Targeting and retention of magnetic targeted carriers

- enhancing intra-arterial chemotherapy., *J. Magn. Magn. Mater.* **1999**, *194*, 132–139.
- 232** ALEXIOU, C., ARNOLD, W., KLEIN, R. J., PARAK, F. G., HULIN, P., BERGEMANN, C., ERHARDT, W., WAGENPFEIL, S., LÜBBE, A. S., Locoregional cancer treatment with magnetic drug targeting., *Cancer Res.* **2000**, *60*, 6641–6648.
- 233** KUBO, T., SUGITA, T., SHIMOSE, S., NITTA, Y., MARAKAMI, T., Targeted systemic chemotherapy using magnetic liposomes with incorporated adriamycin for osteosarcoma in hamsters., *Int. J. Oncol.* **2001**, *18*, 121–125.
- 234** LÜBBE, A., BERGEMANN, C., RIESS, H., SCHRIEVER, F., REICHARDT, P., POSSINGER, K., MATTHIAS, M., DORKEN, B., HERRMANN, F., GÜRTLER, R., HOHENBERGER, P., HAAS, N., SOHR, R., SANDER, B., LEMKE, A. J., OHLENDORF, D., HUHNT, W., HUHNT, D., Clinical experiences with magnetic drug targeting: A phase I study with 4'-epidoxorubicin in 14 patients with advanced solid tumors., *Cancer Res.* **1996**, *15*, 4686–4693.
- 235** ZHANG, Y., KOHLER, N., ZHANG, M., Surface modification of superparamagnetic magnetite nanoparticles and their intracellular uptake., *Biomaterials* **2002**, *23*, 1553–1561.
- 236** PETRI-FINK, A., CHASTELLAIN, M., JUILLERAT-JEANNERET, L., FERRARI, A., HOFMANN, H., Development of functionalized superparamagnetic iron oxide nanoparticles for interaction with human cancer cells., *Biomaterials* **2005**, *26*, 2685–2694.
- 237** KOHLER, N., SUN, C., WANG, J., ZHANG, M., Methotrexate-modified superparamagnetic nanoparticles and their intracellular uptake into human cancer cells., *Langmuir* **2005**, *21*, 8858–8864.
- 238** JAIN, T. K., MORALES, M. A., SAHOO, S. K., LESLIE-PELECKY, D. L., LABHASETWAR, V., Iron oxide nanoparticles for sustained delivery of anticancer agents., *Mol. Pharmacol.* **2005**, *2*, 194–205.
- 239** PACIOTTI, G. F., MYER, L., WEINREICH, D., GOIA, D., PAVEL, N., McLAUGHLIN, R. E., TAMARKIN, L., Colloidal gold: A novel nanoparticle vector for tumor directed drug delivery. *Drug Deliv.* **2004**, *11*, 169–183.
- 240** CHEN, J.-F., DING, H.-M., WANG, J.-X., SHAO, L., Preparation and characterization of porous hollow silica nanoparticles for drug delivery applications., *Biomaterials* **2004**, *25*, 723–727.
- 241** MOROZ, P., JONES, S. K., BRAY, B. N., Magnetically mediated hyperthermia: Current status and future directions., *Int. J. Hypertherm.* **2002**, *18*, 267–284.
- 242** RAMACHANDRAN, N., MAZURUK, K., Magnetic microspheres and tissue model studies for therapeutic applications., *Ann. New York Acad. Sci.* **2004**, *1027*, 99–109.
- 243** HERGT, R., ANDRÄ, W., d'AMBLY, C. G., HILGER, I., KAISER, W. A., RICHTER, U., SCHMIDT, H.-G., Physical limits of hyperthermia using magnetite fine particles., *IEEE Trans. Magn.* **1998**, *34*, 3745–3754.
- 244** WUST, P., HILDEBRANDT, B., SREENIVASA, G., RAU, B., GELLERMAN, J., RIESS, H., FELIX, R., SCHLAG, P. M., Hyperthermia in combined treatment of cancer., *Lancet* **2002**, *3*, 487–497.
- 245** GILCHRIST, R. K., MEDAL, R., SHOREY, W. D., HANSELMAN, R. C., PARROTT, J. C., TAYLOR, C. B., Selective induction heating of lymph nodes., *Ann. Surg.* **1957**, *146*, 596–606.
- 246** CHAN, D. C. F., KIRPOTIN, D. B., BUNN, P. A., Synthesis and evaluation of colloidal magnetic iron oxides for the site-specific radiofrequency-induced hyperthermia of cancer., *J. Magn. Magn. Mater.* **1993**, *122*, 374–378.
- 247** JORDAN, A., WUST, P., SCHOLZ, R., TESCHE, B., FAHLING, H., MITROVICS, T., VOGL, T., CERVOS-NAVARRO, J., FELIX, R., Cellular uptake of magnetic fluid particles and their effects on human adenocarcinoma cells exposed to AC magnetic fields *in vitro.*, *Int. J. Hypertherm.* **1996**, *12*, 705–722.
- 248** HIRSCH, L. R., STAFFORD, R. J., BANKSON, J. A., SERSHEN, S. R., RIVERA, B., PRICE, R. E., HAZLE, J. D.,

- HALAS, N. J., WEST, J. L., Nanoshell-mediated near-infrared thermal therapy of tumors under magnetic resonance guidance., *Proc. Natl. Acad. Sci. U.S.A.* **2003**, 100, 13 549–13 554.
- 249 O'NEAL, D. P., HIRSCH, L. R., HALAS, N. J., PAYNE, J. D., WEST, J. L., Photothermal tumor ablation in mice using near infrared-absorbing nanoparticles., *Cancer Lett.* **2004**, 209, 171–176.
- 250 LOO, C., LOWERY, A., HALAS, N., WEST, J., DREZEK, R., Immunotargeted nanoshells for integrated cancer imaging and therapy., *Nano Lett.* **2005**, 5, 709–711.
- 251 WANG, S., GAO, R., ZHOU, F., SELKE, M., Nanomaterials and singlet oxygen photosensitizers: Potential applications in photodynamic therapy., *J. Mater. Chem.* **2004**, 14, 487–493.
- 252 ROY, I., OHULCHANSKY, T. Y., PUDAVAR, H. E., BERGEY, E. J., OSEROFF, A. R., MORGAN, J., DOUGHERTY, T. J., PRASAD, P. N., Ceramic-based nanoparticles entrapping water-insoluble photosensitizing anticancer drugs: A novel drug-carrier system for photodynamic therapy., *J. Am. Chem. Soc.* **2003**, 125, 7860–7865.
- 253 YAN, F., KOPELMAN, R., The embedding of meta-tetra(hydroxyphenyl)-chlorin into silica nanoparticle platforms for photodynamic therapy and their singlet oxygen production and pH-dependant optical properties., *Photochem. Photobiol.* **2003**, 78, 587–591.
- 254 HONE, D. C., WALKER, P. I., EVANS-GOWING, R., FITZGERALD, S., BEEBY, A., CHAMBRIER, I., COOK, M. J., RUSSELL, D. A., Generation of cytotoxic singlet oxygen via phthalocyanine-stabilized gold nanoparticles: A potential delivery vehicle for photodynamic therapy., *Langmuir* **2002**, 18, 2985–2987.
- 255 BAKALOVA, R., OHBA, H., ZHELEV, Z., ISHIKAWA, M., BABA, Y., Quantum dots as photosensitizers?, *Nat. Biotechnol.* **2004**, 22, 1360–1361.
- 256 SAMIA, A. C. S., CHEN, X., BURDA, C., Semiconductor quantum dots for photodynamic therapy., *J. Am. Chem. Soc.* **2003**, 125, 15 736–15 737.
- 257 BAKALOVA, R., OHBA, H., ZHELEV, Z., NAGASE, T., JOSE, R., ISHIKAWA, M., BABA, Y., Quantum dot anti-CD conjugates: Are they potential photosensitizers or potentiators of classical photosensitizing agents in photodynamic therapy of cancer?, *Nano Lett.* **2004**, 4, 1567–1573.
- 258 CSÖGÖR, ZS., NACKEN, M., SAMETI, M., LEHR, C.-M., SCHMIDT, H., Modified silica particles for gene delivery., *Mater. Sci. Eng. C* **2003**, 23, 93–97.
- 259 KNEUER, C., SAMETI, M., HALTNER, E. G., SCHIESTEL, T., SCHIRRA, H., SCHMIDT, H., LEHR, C. M., Silica nanoparticles modified with aminosilanes as carriers for plasmid DNA., *Int. J. Pharm.* **2000**, 196, 257–261.
- 260 BAHARALI, D. J., KLEJBOR, I., STACHOWIAK, E. K., DUTTA, P., ROY, I., KAUR, N., BERGEY, E. J., PRASAD, P. N., STACHOWIAK, M. K., Organically modified silica nanoparticles: A nonviral vector for in vivo gene delivery and expression in the brain., *Proc. Natl. Acad. Sci. U.S.A.* **2005**, 102, 11 539–11 544.
- 261 KNEUER, C., SAMETI, M., BAKOWSKY, U., SCHIESTEL, T., SCHIRRA, H., SCHMIDT, H., LEHR, C.-M., A nonviral DNA delivery system based on surface modified silica-nanoparticles can efficiently transfect cells in vitro., *Bioconj. Chem.* **2000**, 11, 926–932.
- 262 RADU, D. R., LAI, C.-Y., JEFTINIJA, K., ROWE, E. W., JEFTINIJA, S., LIN, V. S.-Y., A polyamidoamine dendrimer-capped mesoporous silica nanosphere based gene transfection reagent., *J. Am. Chem. Soc.* **2004**, 126, 13 216–13 217.
- 263 SANDHU, K. K., MCINTOSH, C. M., SIMARD, J. M., SMITH, S. W., ROTELLO, V. M., Gold nanoparticle-mediated transfection of mammalian cells., *Bioconj. Chem.* **2002**, 13, 3–6.
- 264 THOMAS, M., KLIBANOV, A. M., Conjugation to gold nanoparticles enhances polyethylenimine's transfer of plasmid DNA into mammalian cells., *Proc. Natl. Acad. Sci. U.S.A.* **2003**, 100, 9138–9143.
- 265 SCHERER, F., ANTON, M.,

- SCHILLINGER, U., HENKE, J., BERGEMANN, C., KRÜGER, A., GÄNSBACHER, B., PLANK, C., Magnetotransfection: Enhancing and targeting gene delivery by magnetic force in vitro and in vivo., *Gene Ther.* **2002**, 9, 102–109.
- 266 HUGHES, C., GALEA-LAURI, J., FARZANEH, F., DARLING, D., Streptavidin paramagnetic particles provide a choice of three affinity-based capture and magnetic concentration strategies for retroviral vectors., *Mol. Ther.* **2001**, 3, 623–630.
- 267 KRÖTZ, F., SOHN, H.-Y., GLOE, T., PLANK, C., POHL, U., Magnetotransfection potentiates gene delivery to cultured endothelial cells., *Vasc. Res.* **2003**, 40, 425–434.
- 268 JIANG, H., ZHANG, T., SUN, X., Vascular endothelial growth factor gene delivery by magnetic DNA nanospheres ameliorates limb ischemia in rabbits., *J. Surg. Res.* **2005**, 126, 48–54.
- 269 TAN, S. T., WENDORFF, J. H., PIETZONKA, C., JIA, Z. H., WANG, G. Q., Biocompatible and biodegradable polymer nanofibers displaying superparamagnetic properties., *ChemPhysChem* **2005**, 6, 1461–1465.
- 270 SON, S. J., REICHEL, J., HE, B., SCHUCHMAN, M., LEE, S. B., Magnetic nanotubes for magnetic-field-assisted bioseparation, biointeraction, and drug delivery. *J. Am. Chem. Soc.* **2005**, 127, 7316–7317.
- 271 DONATH, E., SUKHORUKOV, G. B., CARUSO, F., DAVIS, S. A., MÖHWALD, H., Novel hollow polymer shells by colloid-templated assembly of polyelectrolytes., *Angew. Chem. Int. Ed.* **1998**, 37, 2201–2205.
- 272 SHENOY, D. B., ANTIPOV, A. A., SUKHORUKOV, G. B., MÖHWALD, H., Layer-by-layer engineering of biocompatible, decomposable core-shell structures., *Biomacromolecules* **2003**, 4, 265–272.
- 273 VOIGT, A., BUSKE, N., SUKHORUKOV, G. B., ANTIPOV, A. A., LEPORATTI, S., LICHTENFELD, H., BÄUMLER, H., DONATH, E., MÖHWALD, H., Novel polyelectrolyte multilayer micro- and nanocapsules as magnetic carriers., *J. Magn. Magn. Mater.* **2001**, 225, 59–66.
- 274 SHCHUKIN, D. G., RADTCHENKO, I. L., SUKHORUKOV, G. B., Micron-scale hollow polyelectrolyte capsules with nanosized magnetic Fe<sub>3</sub>O<sub>4</sub> inside., *Mater. Lett.* **2003**, 57, 1743–1747.
- 275 GAPONIK, N., RADTCHENKO, I. L., SUKHORUKOV, G. B., WELLER, H., ROGACH, A. L., Toward encoding combinatorial libraries: Charge-driven microencapsulation of semiconductor nanocrystals luminescing in the visible and near IR., *Adv. Mater.* **2002**, 14, 879–882.
- 276 GAPONIK, N., RADTCHENKO, I. L., GERSTENBERGER, M. R., FEDUTIK, Y. A., SUKHORUKOV, G. B., ROGACH, A. L., Labeling of biocompatible polymer microcapsules with near-infrared emitting nanocrystals., *Nano Lett.* **2003**, 3, 369–372.
- 277 LU, Z., PROUTY, M. D., GUO, Z., GOLUB, V. O., KUMAR, C. S. S. R., Lvov, Y. M., Magnetic switch of permeability for polyelectrolyte microcapsules embedded with Co@Au nanoparticles., *Langmuir* **2005**, 21, 2042–2050.
- 278 LAI, C.-Y., TREWYN, B. G., JEFTINIJA, D. M., JEFTINIJA, K., XU, S., JEFTINIJA, S., LIN, V. S.-Y., A mesoporous silica nanosphere-based carrier system with chemically removable CdS nanoparticle caps for stimuli-responsive controlled release of neurotransmitters and drug molecules., *J. Am. Chem. Soc.* **2003**, 125, 4451–4459.
- 279 MORISHITA, N., NAKAGAMI, H., MORISHITA, R., TAKEDA, S.-I., MISHIMA, F., TERAZONO, B., NISHIJIMA, S., KANEDA, Y., TANAKA, N., Magnetic nanoparticles with surface modification enhanced gene delivery of HVJ-E vector., *Biochem. Biophys. Res. Commun.* **2005**, 334, 1121–1126.
- 280 SALEM, A. K., SEARSON, P. C., LEONG, K. W., Multifunctional nanorods for gene delivery., *Nat. Mater.* **2003**, 2, 668–671.
- 281 KUEHN, B. M., MRI reveals gene

- activity in vivo. *J. Am. Med. Assoc.* **2005**, *21*, 2584.
- 282** BHAKOO, K. K., BELL, J. D., COX, I. J., TAYLOR-ROBINSON, S. D., The application of magnetic resonance imaging and spectroscopy to gene therapy., *Meth. Enzymol.* **2004**, *386*, 303–313.
- 283** GENOVE, G., DEMARCO, U., XU, H., GOINS, W. F., AHRENS, E. T., A new transgene reporter for in vivo magnetic resonance imaging., *Nat. Med.* **2005**, *11*, 450–454.
- 284** ABOUL-FADL, T., Antisense oligonucleotides: The state of the art., *Curr. Med. Chem.* **2005**, *12*, 2193–2214.
- 285** KRÖTZ, F., DE WIT, C., SOHN, H.-Y., ZAHLER, S., GLOE, T., POHL, U., PLANK, C., Magnetotransfection – a highly efficient tool for antisense oligonucleotide delivery in vitro and in vivo., *Mol. Ther.* **2003**, *7*, 700–710.
- 286** HAMAD-SCHIFFERLI, K., SCHWARTZ, J. J., SANTOS, A. T., ZHANG, S., JACOBSON, J. M., Remote electronic control of DNA hybridization through inductive coupling to an attached metal nanocrystal antenna., *Nature* **2002**, *415*, 152–155.
- 287** LUCKARIFT, H. R., SPAIN, J. C., NAIK, R. R., STONE, M. O., Enzyme immobilization in a biomimetic silica support., *Nat. Biotechnol.* **2004**, *22*, 211–213.
- 288** LUNDQVIST, M., SETHSON, I., JONSSON, B.-H., Transient interaction with nanoparticles “freezes” a protein in an ensemble of metastable near-native conformations., *Biochemistry* **2005**, *44*, 10 093–10 099.
- 289** SHARMA, R. K., DAS, S., MAITRA, A., Enzymes in the cavity of hollow silica nanoparticles., *J. Colloid Interface Sci.* **2005**, *284*, 358–361.
- 290** LIU, H., RUSLING, J. F., HU, N., Electroactive core-shell nanocluster films of heme proteins, polyelectrolytes, and silica nanoparticles., *Langmuir* **2004**, *20*, 10 700–10 705.
- 291** JI, Q., KAMIYA, S., JUNG, J.-H., SHIMIZU, T., Self-assembly of glycolipids on silica nanotube templates yielding hybrid nanotubes with concentric organic and inorganic layers., *J. Mater. Chem.* **2005**, *15*, 743–748.
- 292** WANG, Y., CARUSO, F., Mesoporous silica spheres as supports for enzyme immobilization and encapsulation., *Chem. Mater.* **2005**, *17*, 953–961.
- 293** LVOV, Y., CARUSO, F., Biocolloids with ordered urease multilayer shells as enzymatic reactors., *Anal. Chem.* **2001**, *73*, 4212–4217.
- 294** VILLALONGA, R., FRAGOSO, A., CAO, R., ORTIZ, P. D., VILLALONGA, M. L., DAMIAO, A. E., Supramolecular-mediated immobilization of trypsin on cyclodextran-modified gold nanospheres., *Supramol. Chem.* **2005**, *17*, 387–391.
- 295** FISCHER, N. O., MCINTOSH, C. M., SIMARD, J. M., ROTELLO, V. M., Inhibition of chymotrypsin through surface binding using nanoparticle-based receptors., *Proc. Natl. Acad. Sci. U.S.A.* **2002**, *99*, 5018–5023.
- 296** HONG, R., FISCHER, N. O., VERMA, A., GOODMAN, C. M., EMRICK, T., ROTELLO, V. M., Control of protein structure and function through surface recognition by tailored nanoparticle scaffolds., *J. Am. Chem. Soc.* **2004**, *126*, 739–743.
- 297** WILLNER, I., KATZ, E., Magnetic control of electrocatalytic and bioelectrocatalytic processes., *Angew. Chem. Int. Ed.* **2003**, *42*, 4576–4588.
- 298** ISHII, D., KINBARA, K., ISHIDA, Y., ISHII, N., OKOCHI, M., YOHDA, M., AIDA, T., Chaperonin-mediated stabilization and ATP-triggered release of semiconductor nanoparticles., *Nature* **2003**, *423*, 628–632.
- 299** NOLTING, B., YU, J.-J., LIU, G.-Y., CHO, S.-J., KAUZLARICH, S., GERVAY-HAGUE, J., Synthesis of gold glyconanoparticles and biological evaluation of recombinant Gp120 interactions., *Langmuir* **2003**, *19*, 6465–6473.
- 300** NIGGEL, J., SIGURDSON, W., SACHS, F., Mechanically induced calcium movements in astrocytes, bovine aortic endothelial cells, and C6 glioma cells., *Membr. Biol.* **2000**, *174*, 121–134.
- 301** WINTER, J. O., GOMEZ, N., KORGEL,

- B. A., SCHMIDT, C. E., Quantum dots for electrical stimulation of neural cells., *Nanobiophotonics and Biomedical Applications II*, CARTWRIGHT, A. N., OSINSKI, M. (Eds.), Proceedings of SPIE, **2005**, Vol. 5705, pp. 235–246.
- 302** BESANGER, T. R., EASWARAMOORTHY, B., BRENNAN, J. D., Entrapment of highly active membrane-bound receptors in macroporous sol-gel derived silica., *Anal. Chem.* **2004**, 76, 6470–6475.
- 303** LEE, S., EISENBERG, D., Seeded conversion of recombinant prion protein to a disulfide-bonded oligomer by a reduction-oxidation process., *Nat. Struct. Biol.* **2003**, 10, 725–730.
- 304** SCHEIBEL, T., PARTHASARATHY, R., SAWICKI, G., LIN, X. M., JAEGER, H., LINDQUIST, S. L., Conducting nanowires built by controlled self-assembly of amyloid fibers and selective metal deposition., *Proc. Natl. Acad. Sci. U.S.A.* **2003**, 100, 4527–4532.
- 305** KOÇER, A., WALKO, M., MEIJBERG, W., FERINGA, B. L., A light-activated nanovalve derived from a channel protein., *Science* **2005**, 309, 755–758.
- 306** HARRELL, C. C., KOHLI, P., SIWY, Z., MARTIN, C. R., DNA-nanotube artificial ion channels., *J. Am. Chem. Soc.* **2004**, 126, 15 646–15 647.



## 12

# Nanoengineering of Biomaterial Surfaces

*Ashwath Jayagopal and Venkatram Prasad Shastri*

### 12.1

#### Introduction

Cells sample their environment through sensory elements that can discern minute changes in chemical composition and surrounding mechanical forces. These sensory elements are on the order of tens to hundreds of nanometers, and include lamellopodia that aid in cell locomotion, and receptor tyrosine kinases that can bind growth factors. Nanoscale interactions mediated by these elements lead to the activation of signaling pathways that influence cellular processes at different levels, ranging from mRNA synthesis and cell cycle progression to apoptosis. Therefore, it comes as no surprise that biomaterial surface characteristics, namely chemistry and topography, have a profound influence on the elicited cellular response of a tissue engineering construct. Early biomedical devices rarely incorporated nanoscale surface engineering as part of the design paradigm. However, this has changed in light of the growing biological evidence that has elucidated potential therapeutic avenues made possible by the nanoscale presentation of information. New approaches seek to reconstruct the natural tissue environment replete with biochemical and topological cues for the optimum restoration of function. In this chapter, we review the unique contributions and key examples of traditional and rapidly-emerging surface engineering techniques directed toward the progression of biomimetic tissue engineering. As various fundamentally different techniques are discussed, we have grouped biomaterial surface engineering strategies by their primary enabling features, from which some similarities can be drawn, such as the utilization of chemically-based or instrument-guided approaches. We discuss the amenability of these techniques for achieving micro- and nanoscale surface features, the applicability toward hard and soft materials and three-dimensional (3D) geometries, and the future implications of each technology concerning the development of clinically-relevant cellular and tissue engineering devices.

## 12.2

### Conventional Photolithography

The demand for miniaturization strategies in microelectronics long preceded the need for micro- and nanoscale features in tissue engineering devices prompted by the elucidation of extracellular matrix (ECM) proteins and signaling mechanisms, and thus many biomaterial surface engineering strategies are convenient adaptations of these well-established methods. An example is photolithography. The resolution limit of this technology is generally the wavelength of the light used for irradiation, so given the availability of UV excitation sources, photolithography has been frequently utilized to create organized cellular or biomolecular patterns upon nanoscale features engineered on planar surfaces. In the conventional scheme, a patterned photomask is used to control the light-induced decomposition of a spin-coated photoresist on the substrate, exposing defined regions of the substrate. These regions can be etched to create topographical features such as grooves, and can be chemisorbed with compounds such as organosilanes, which promote adhesion to proteins, as well as compounds that resist adsorption. The surface can then be utilized to site-specifically pattern cells and biomolecules. This photoresist-based photolithographic technique was employed for the micropatterned, cocultivation of hepatocytes and fibroblasts, and cell placement was spatially-controlled by the patterning of collagen to the glass surface [1]. The topographical features produced by photolithographic processes have generated potent cellular responses, such as cell alignment and parallel cytoskeletal filament orientation along grooved features, as well as several other responses, as reviewed by Fleming et al. [2].

Photolithography-based surface engineering techniques can be modified such that the biomolecule itself, not the surface, is the photoactivatable conduit for biopatterning. Variations of photolithography include the use of photoreactive chemicals conjugated to a biomolecule, such that irradiation directly mediates site-specific biomolecular immobilization to the surface. Commonly used strategies based on this principle include arylazide, diazirine, benzophenone, and nitrobenzyl photochemistries [3, 4]. In the first three methods, UV irradiation results in active groups that insert themselves within chemical bonds, enabling photoimmobilization of the species attached to the photolabile moiety. The first two chemistries have been successfully applied to the attachment of cell adhesion peptides (RGD-containing) [5, 6] and/or proteins, such as biotin and antibodies [6, 7]. Benzophenone chemistry was applied to covalently attach a laminin peptide fragment [4]. Thus, these photochemical surface engineering techniques can be employed to recreate ECM-like environments that are most supportive of natural cellular proliferation and migration patterns. Nitrobenzyl chemistries have been successfully applied towards the photobiotinylation of polymer surfaces [8].

Photolithographic and photochemical techniques can reproducibly produce nanoscale features that are critical for influencing cellular behavior. The technology is well characterized, and facilitates the surface engineering of chemistry, through adsorption of compounds containing functional groups or biomolecules, and also

provides a conduit for producing certain topographies. However, several elements of this technology are generally not satisfactory for tissue engineering applications. First, photolithography is not suitable for patterning nonplanar surfaces, and is associated with costly, specialized equipment, often using solvents not suitable for cell and protein patterning [9]. Thus, it is difficult to utilize photolithography for the ultimate goal of tissue engineering, which is the 3D biomimesis of the natural tissue environment. Furthermore, for photoreactive chemistries, extensive biomolecule conjugation to the photoactivatable adduct may be involved, UV irradiation must be used, which is damaging to biomolecules, and most processes cannot be carried out in aqueous media, all of which complicate tissue engineering device fabrication strategies that make use of this technology [10]. In addition, illumination is conventionally conducted through photomasks that do not alter the intensity of incoming light; thus, illumination is said to be “all-or-none”, making it difficult to produce features of non-uniform height. This is a primary limitation in adapting photolithographic techniques for producing 3D features.

To address shortcomings of photoresist-based photolithographic techniques, several modifications in techniques and materials have been reported that have reinforced the utility of these methods in modern tissue engineering, in which biomolecule and cellular sensitivity to the processing environment is of critical importance. One approach has been the development of biocompatible photoresists. To expand on the applicability of photoresist-based techniques for protein and cell patterning, a “bioresist” based on a copolymer of methyl methacrylate and vinyl pyrrolidone was applied for the alignment of fibroblasts, obviating the need for potentially-denaturing solvent development steps used to remove photoresist [11]. Another biocompatible photoresist, based on poly(*t*-butyl acrylate), was utilized to pattern a polystyrene tubular support with antibodies, with only mild resist removal steps (specifically, 60 °C and exposure to basic media) that were tolerated by the biomolecules. Features of this technique were comparable with the high resolution of photolithographic techniques, with the patterning of 0.13 μm lines with protein arrangements <10 μm [12–14]. The feature of non-denaturing conventional photolithography is an important step in the transition from established microelectronics processes to tissue engineering micro and nanofabrication procedures that do not necessitate the use of biologically-incompatible solvents in processing steps. To address the all-or-none limitation inherent in the photomask used, several strategies involving what is called gray-scale photolithography have been utilized. In this approach, the mask itself contains tunable features, mainly varying light transmission levels, which control the site-specific degree of photoresist irradiation. In one approach, dye-filled microfluidic channels within an elastomeric mask consisting of varying concentrations of dye were successful in producing 3D features in resist, using standard equipment, with resolution in the single micron range [15].

Recent developments in photochemistry have introduced the possibility of photoconjugating biomolecules, and perhaps cells without the use of UV irradiation and dry environments. Furthermore, complex bioconjugation techniques used to attach photoactivatable compounds such as caging compounds to the bioactive agent are

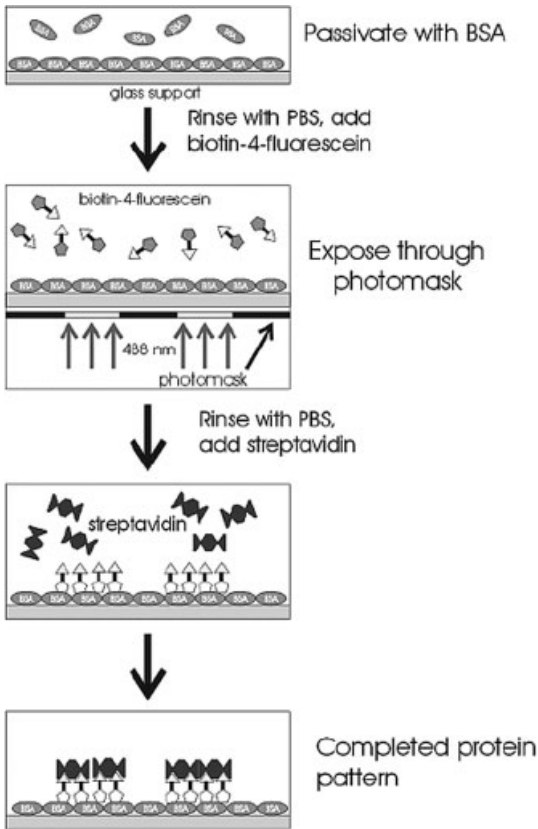


**Fig. 12.1.** Schematic for photoimmobilization of biotin-4-fluorescein to a bovine serum albumin (BSA)-coated glass surface using visible-light laser irradiation through a photomask. Photobleaching of the fluorescent dye initiates a singlet-oxygen-mediated binding reaction. (Reproduced with permission from Ref. [10].)

no longer the only option for utilizing light-guided patterning strategies. Holden et al. have reported a method for the fluorophore-mediated attachment of biomolecules such as enzymes to electron-rich surfaces in aqueous, neutral media, using visible light that is not harmful to proteins [10, 16] (Fig. 12.1). The technique uses the well-known fluorescein photobleaching reaction to immobilize biomolecules in patterns as arranged by photomasks and fluorescence illumination. Fluorescein and similar organic dyes used for patterning are commonly conjugated to proteins using simple, rapid laboratory techniques [17], thus making the technology accessible to most biological laboratories. One can envision the application of photochemical techniques such as this one for the patterning of biomolecules on complex geometries, simply by controlling the localization of laser irradiation in the  $x$ - $y$ - $z$  plane for site-specific radical-mediated immobilization, although this has not been explored to any significant degree. In another approach that obviates the need

for UV-activatable groups, Luebke et al. described a Trp-containing peptide or protein crosslinking system based on blue excitation light and a ruthenium complex for specific cell patterning on a poly(ethylene glycol) (PEG)-coated glass surface, with single-cell resolution enabled by the use of digital micromirrors [18, 19]. These methods, like the advancements in biocompatible photoresists, also facilitate the use of non-denaturing chemistries in the photolithographically-mediated controlled patterning of tissue engineering scaffolds and implants.

By judicious selection of biomaterials, surface engineering of 3D cellular matrices can be accomplished by photolithographic and photochemical techniques, thus potentially addressing, at least in part, the difficulties of nonplanar patterning with conventional approaches. As an example, PEG-diacrylate hydrogels, known to photopolymerize in the presence of an initiator, were conjugated to nonspecific and specific cell adhesion peptides and exposed through a transparency-based photomask to create 3D layered hydrogel patterns, upon which dermal fibroblasts were specifically attached in specific cell adhesion peptide-defined regions [20] (Fig. 12.2). The study demonstrated that photolithographic methods can be used for the surface engineering of complex 3D cell and biomolecule spatial arrangements, with minimum expense, as the mask was printed on a transparency sheet by laser printer. A photochemistry-based technique for the 3D surface engineering of agarose hydrogels was demonstrated by Luo and coworkers, who conjugated

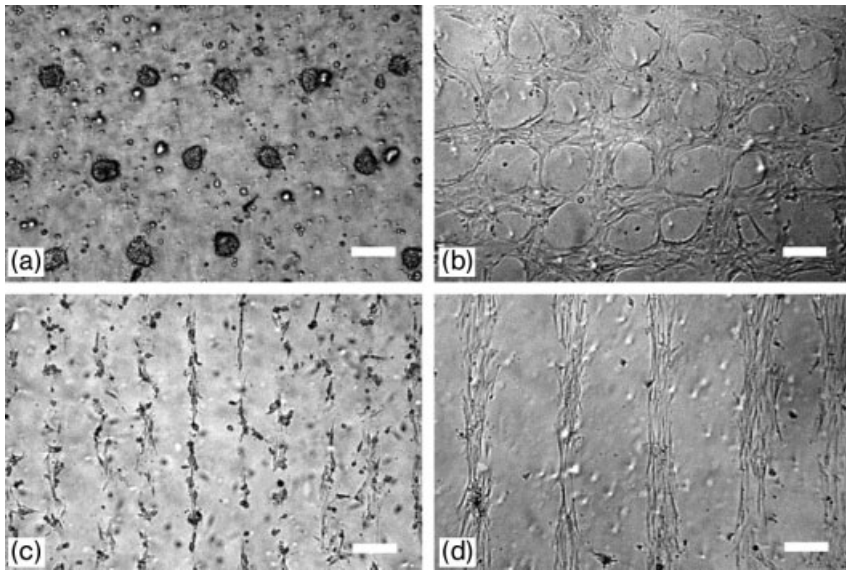


**Fig. 12.2.** Site-specific adhesion of human dermal fibroblasts to RGDS-immobilized PEG-diacrylate (PEGDA) hydrogels. (a)–(c) Hydrogel patterned with RGDS generic cell adhesion peptide. (d) Hydrogel patterned with

RGDS and REDV (nonspecific) peptide. In all images, HDF-binding is limited to RGDS-patterned regions only. Scale bar = 250  $\mu\text{m}$ . (Reproduced with permission from Ref. [20].)

photolabile nitrobenzyl-Cys groups to the hydrogel [21, 22]. Upon UV exposure, exposed sulfhydryl functional group channels were then exploited to site-specifically conjugate RGD-containing cell adhesion peptides, which were patterned to guide neurite outgrowth. In work by Revzin et al., 3D PEG hydrogels could be engineered to bear immobilized fluorescent proteins, supporting the possibility of incorporating ECM-signaling cues within hydrogel microstructures [23]. These findings demonstrate the potential of techniques based on conventional photolithographic and photochemical approaches to construct, with high-resolution and reliability, complex 3D environments based on tissue-like hydrogels to be potentially applied towards the controlled organization of functional tissue. Thus, photolithography and photochemistry, often suggested to be incompatible for tissue engineering applications, may actually be a potential route to the fabrication of 3D tissue constructs using a well-established technology.

### 12.3

#### Electron-beam Lithography

As previously discussed, we have found that nanoscale interactions are paramount to the optimization of a desired cellular response. To this end, nanofabrication techniques used in high-density storage media and electronics might be extended for purposes of patterning sub-10 nm features for tissue engineering applications, given the appropriate material and chemical conduits to enable such an approach. Electron beam lithography (EBL) is a technology capable of achieving such a high resolution, and initially has been shown to be potentially applicable to tissue engineering applications. In this technology, in a manner similar to photolithography, electron beams rather than light are used to irradiate polymer resists (e-beam resists), such as poly(methyl methacrylate) (PMMA). The resist can then be developed to produce several nanotopographies. The current resolution limits of this strategy are as low as 5 nm in the *X-Y* plane and 1 nm in the *Z* plane [24], thus warranting applications of EBL in tissue engineering device fabrication.

Given the advantage of high-resolution, biological applications of EBL have only recently emerged. While EBL is currently being utilized to first study in detail such nanoscale interactions between cells and their surrounding chemistry and topography [25–27], it seems plausible that such a technology could be also directed towards the precise fabrication of complex tissue engineering scaffolds. The potential of EBL to create high-resolution protein patterns on conventional substrates, such as silane-coated silicon wafers, has been demonstrated [28, 29]. In one example, EBL-patterned 1  $\mu\text{m}$  PMMA grooves were seeded with collagen to control lung fibroblast orientation and patterning [30]. Hippocampal neuron perpendicular alignment was influenced heavily by EBL-etched nanoscale grooves [31, 32]. In another application, an EBL method capable of producing 20 nm features surface engineered with poly(caprolactone) (PCL) [33], a biodegradable polymer used in biomedical implants, was used to study the filopodial extensions of fibroblasts in response to different nanotopographies [34] (Fig. 12.3). Thus, as we elucidate the

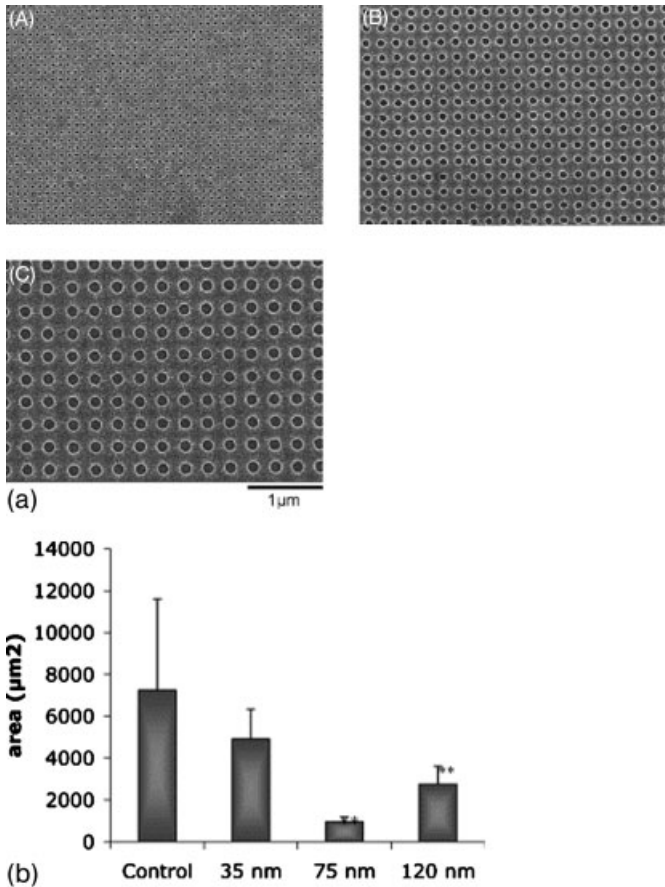


**Fig. 12.3.** (a) Scanning electron micrographs of nanopit topographies produced by electron-beam lithography, nickel die fabrication, and hot embossing. Diameters: (A) 35, (B) 40, (C) 120 nm. (b) Average number of filopodia per cell on planar and nanopit-containing surfaces. Results are mean  $\pm$  SD;  $P < 0.05^*$ ,  $P < 0.01^{**}$  (student's *t*-test). (Reproduced with permission from Ref. [34].)

specific geometries capable of optimizing tissue organization and function, EBL, at least on a limited amount of materials, is a candidate for creating such features. Three-dimensional surface engineering features, while not explored in depth with EBL, have been at least demonstrated to be achievable, using EBL-enabled amino-functionalization of a gold surface templated with a self-assembled monolayer (SAM), upon which proteins are sequentially layered [35]. These preliminary findings suggest the potential utility of EBL in the surface engineering of tissue engineering devices, provided the materials and biological agents are compatible with the process.

Given the biocompatibility of PCL and PMMA substrates (discussed above for EBL applications) in tissue engineering, EBL has initially been demonstrated to

be relevant to the surface engineering of biomaterials, and it is likely that, in conjunction with other fabrication techniques, EBL-based nanopatterns can be plated on other polymeric and metallic biomaterials as well. However, this has yet to be extensively investigated in a true cellular and protein surface engineering context, especially since most patterning for tissue engineering applications has been primarily explored on the microscale, where high-resolution EBL was not necessary. This might be addressed by investigating more biomaterials for their potential utility as e-beam resists. Furthermore, this highly-specialized technique can be both costly and time-consuming, with the serial drawing nature of the technology, and the extensive effort (computationally and physically) that is necessitated by patterns of increasing complexity. Similar to light-based techniques, EBL can require extensive optimization of process parameters, such as beam current, scan mode, and diameter, as well as resist properties [36]. Pattern reproducibility and resolution, as well as feature width, can be problems with this technology under various conditions. Nevertheless, the high resolution achievable by EBL warrants its further investigation concerning the surface engineering of biomaterials, and the method can still be utilized as an *in vitro* tool to study the fundamentals of cellular responses to varying topographies on the order of single nanometers, since that is the scale of cell plasma membrane features.

## 12.4

### Soft Lithography

The enhanced specialization of biomaterial surfaces required for realistic functional tissue arrays has necessitated the development of new surface engineering techniques. Photolithography and EBL technologies, for instance, in general are not suitable for patterning on nonplanar surfaces. As a result, the diversity of biomaterials available to accommodate specific tissue structures may not be suitable fabrication platforms using these technologies. Furthermore, these techniques are time-consuming, can involve denaturing solvents, and require costly equipment and clean-rooms not accessible to biological laboratories [9, 37, 38]. For biomaterial surface engineering to complement advances in our knowledge base of optimal cellular environments, a family of micro- and nanofabrication technologies known as soft lithography have been developed that are suitable for patterning cellular and biomolecular arrays, with resolutions comparable to those of photolithography [9, 39–41].

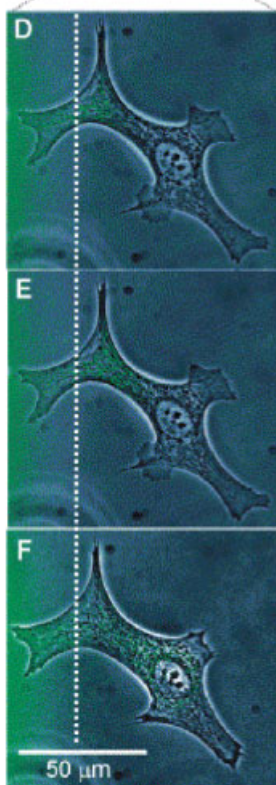
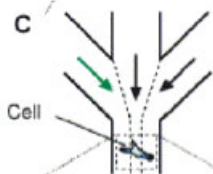
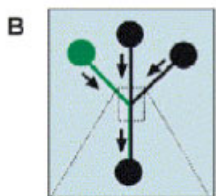
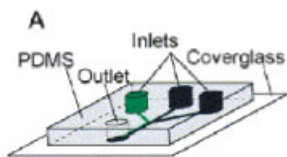
Soft lithographic approaches, such as microcontact printing (uCP), microfluidic patterning [micromolding in capillaries (MIMIC)], membrane-based patterning (MEMPAT), and laminar flow patterning [38, 39, 41, 42], are related by the use of elastomeric stamps or channels for patterning, typically based on the silicone rubber poly(dimethylsiloxane) (PDMS). The polymer is cast against a patterned master mold generated by conventional photolithography to create a stamp with various features. PDMS stamps have been used effectively in the patterning of biomolecules and cells through uCP, in which the patterned stamp is coated or “inked”



with a functional chemical substance, such as a self-assembled monolayer (SAM), normally consisting of alkanethiols, and transferred by brief contact to another surface, such as gold, glass, or polymeric materials [37]. Self-assembled films on the target surface can then be used to create patterns in the nanoscale regime [43–45]. MIMIC involves the use of elastomeric channels, a support (e.g., glass, gold, polymer, metal), and a liquid polymer of low viscosity, to form patterned layers by capillary action [42]. In MEMPAT and related techniques, a thin elastomeric lift-off membrane with circles and square-shaped features are used to constrain cell and protein seeding [39, 46, 47]. Laminar flow patterning takes advantage of the low Reynolds' number, parallel non-mixing fluid streams of molded capillary channels to selectively pattern cells and their biomolecular environment [48, 49]. Other novel techniques involve multilayering schemes for the development of 3D elastomeric devices such as microfluidic on/off valves [50]. The variety of soft lithographic techniques provides significant versatility in surface engineering applications.

Soft lithographic procedures incorporate versatile materials and procedures that are readily accessible to biologists [51]. The key component of these technologies, PDMS, is a biocompatible, inexpensive, oxygen-permeable material that can be utilized for cell culture [52], and, due to its elastomeric nature, it can readily assume the shape of nonplanar structures, and is a robust material that can be reused as a stamp for the same application, without leaving residual polymer on the targeting surface. Furthermore, while PDMS is hydrophobic and non-functional for bioconjugation, surface oxidation or polymer grafting procedures can be utilized to make the surface hydrophilic and surface functionalized [53–55]. A previous drawback in soft lithography was the photolithographic step used to generate the original stamp. However, this potentially time-consuming and costly step has been modified with the development of rapid prototyping (RP) steps that use less expensive materials and processing equipment, such as transparency-based photomasks [56] and inexpensive computer-aided design and printing tools [57]. Generally, soft lithography is a low-cost technique that does not necessitate specialized accommodations such as clean-rooms. Hence, the attractive features of soft lithography are versatility in the type of surface that can be patterned (including some 3D applications), low cost compared with other methods, micro- or nanoscale resolution appropriate for tissue engineering applications, and biocompatibility.

Soft lithography is a significant example of a technique that complements the need to fabricate complex cellular and biomolecular arrays for tissue engineering. The appeal of this technology for the engineering of surface chemistries and topologies on biomaterials can be illustrated through several examples. Nanoscale features of varying shape such as lines and circles can be achieved by uCP with certain modifications [58–60]. Alkanethiol SAMs terminated with fibronectin-adhesive and resistant groups were patterned by uCP on gold and silver surfaces to control endothelial cell adsorption on the microscale [61, 62]. uCP techniques have been used to pattern cells and proteins on gold, silver, glass and polymer substrates. Using SAMs with certain specificities toward a given biomolecule or cell, control is provided over cell–cell interactions, as well as cell confinement and



migration within a microscale area, which is critical to the goal of biomimesis. For example, by patterning biomolecules in a tight distribution on the nanoscale, subsequently a high density of protein-based information is created, which makes it possible to mimic the same density of information in living systems, such as integrin clustering. Findings that are a result of the patterning of cells using uCP techniques include the correlation of geometrical and biomolecular surface information with several biologically important events, such as cell growth and differentiation, cell cycle, cytoskeletal arrangement, and cell polarization [9, 37, 40]. For the fabrication of more complex structures, 3D channel networks can be harnessed by using MIMIC to fabricate multiple patterned arrays of protein gradients and cells, on a diverse pool of surfaces, such as biodegradable polymers (PLGA, PEG), glass, gold, and silicon [9, 37, 42]. Laminar flow patterning, due to its ability to deposit multiple cells or proteins in separate streams, adds significantly to this functionality, as streams containing distinct information (cells, growth factors, serum) can be rapidly patterned without the placement of physical implements to separate the streams. Furthermore, patterning directly over cell cultures, or even certain regions of cells, is possible with this technique, which is perhaps its major distinguishing feature. For example, Takayama et al. were able to demonstrate selective labeling of mitochondrial subpopulations, as well as the disruption of actin filaments in specific cell regions, using a technique known as partial treatment of cells using laminar flows (PARTCELL) [49, 63] (Fig. 12.4). Thus, soft lithographic patterning can be utilized to specifically influence cellular organization and function, with the added functionality of biochemical and physical manipulation on the single cell level, which could be useful for developing regions within a tissue construct, whereby different cells would require certain nutrients at distinct spatial and temporal intervals.

Biomaterial surface engineering techniques based on soft lithography have been shown to provide controlled cellular environments with various biochemical cues for optimum tissue function and organization. Fundamental information concerning the influence of such signals on cellular phenotype and function have been made possible by these methods, which can employ SAM and direct cellular and/or protein patterning strategies to present complex biochemical information with high resolution. To translate the past decade of patterning cells and biomolecules on mostly planar surfaces toward work to develop functional tissues and organs, increased attention is needed regarding the amenability of these approaches on other biocompatible substrates. The investigation of other elastomeric materials as

←

**Fig. 12.4.** (A)–(C) Schematic describing the partial treatment of cells using the laminar flow (PARTCELL) technique. A channel network molded in PDMS (A) is placed on a coverglass and consists of inlet and outlet ports. (B) The green inlet channel is injected with a mitochondrial staining probe (Mitotracker Green FM, Molecular Probes Invitrogen), while the other inlets are injected with cell media. (C) Illustration of non-mixing parallel streams. (D)–(F) Time-lapse fluorescence microscopy at 5, 11, and 35 min confirms the selective labeling of the mitochondria within the region of the cell exposed to the dye-injected port alone. (Reproduced with permission from Ref. [49].)

stamps with varying properties may enable new approaches. The most commonly used material currently, PDMS, is a hydrophobic polymer, and thus is susceptible to protein adsorption unless surface-modified, and can slowly recover hydrophobicity even in that case [64]. Also, in addition to the hydrophobic properties of the material, the ability to produce quality patterns on the stamp, as well as the quantity of different nanopatterns to be produced using the same stamp, are major factors affecting reproducibility of the pattern and the scope of application of the technique. In addition, the true nanoscale resolution limit of most of these technologies has not been ascertained. However, as there is no wavelength-imposed limit as in other technologies, it is likely this limit will be suitable for nanoscale feature patterning, if not already suitable. The usefulness of soft lithography for presenting topological information has not been explored for the most part, although PDMS is easy to mold and could be used in studies of cell–substrate interactions in such a context. In addition, soft lithography could potentially be combined with other nanofabrication techniques to produce desired features such as grooves if necessary. Even though some questions the technology may raise, this family of methods is still a low-cost method of producing quality patterns of cells and proteins at potentially nanoscale resolutions on nonplanar substrates. Furthermore, improvements have been demonstrated in extending the types of materials that can be used for pattern transfer. Patterned agarose hydrogel stamps have been used in inking/stamping procedures, such as in the method employed by Stevens et al. to transfer osteoblasts to hydroxyapatite scaffolds [65]. Thus, soft lithography pattern transfer can be accomplished with wet stamps which enhance cell viability, likely without sacrificing much control over patterns produced. Further work will likely improve the resolution provided by rapid prototyping methods, and continued efforts concerning multilayered, multifunctional surfaces that present structurally-favorable cellular microenvironments using these techniques, especially laminar flow patterning of biomolecules and cells using parallel nonmixing streams, are capable of facilitating the development of novel tissue engineering devices.

## 12.5

### Polymer-demixed Nanotopographies

As discussed previously, highly specialized EBL techniques provide for the reproducible topological patterning of biomaterial surfaces, with biologically-relevant features such as grooves. However, such methods are time-consuming and expensive, and candidate surfaces and materials for EBL are limited. Accessible techniques for the high-resolution nanopatterning of biomaterial topographies at low cost are thus necessary to facilitate the progression of surface engineering strategies in tissue engineering fabrication. Recently, methods in surface engineering have been developed that exploit the bulk interactions between polymeric domains to produce a desired surface feature upon a substrate. By manipulating these phenomena, it has been demonstrated that surface *topologies*, in addition to surface

chemistries, can be patterned upon a surface. Here we discuss a concept known as polymer demixing, whereby the inherent immiscibility of a binary polymer system, when cast upon a surface, results in phase separation-induced surface features [66]. Polymer demixing is a process tunable by polymer selection, relative polymer proportions and solubilities within the common solvent, and solvent selection, and can be utilized to produce nanoscale topographies such as pits and hills of tunable height and depth on the 10s of nanometers. Polymer blends initially explored with this strategy include poly(styrene) (PS) and poly(methyl methacrylate) (PMMA), PS and poly(4-bromostyrene) (PBrS), and poly(n-butyl methacrylate) (PnBMA) [66–69].

Surface engineering strategies of high tunability are highly desirable in the field for achieving specific, reproducible surface features. With polymer demixing, polymer fraction composition is a determinant of the type of topology produced, whereas polymer concentration in the solvent mixture is the parameter governing topology size. For example, by varying a 60/40 blend of PS/PBrS in total concentrations of 0.5–5% in toluene, nanoscale island features of heights from 13 to 95 nm were produced [67]. Interestingly, this study showed that positive-phenotyped human endothelial cells elicited nanoisland height-specific cytoskeletal and morphological responses, with the slightest grade (13 nm) eliciting the most rapid cellular spreading, relative to flat surfaces and higher features of the same polymer blend. Filopodia were observed to be in contact with the nanoislands, and cell shape was arcuate, in agreement with *in vivo* morphologies, suggesting that nanofeature-presenting surfaces may provide a more natural cell phenotype than flattened surfaces, such as the tissue culture polystyrene commonly employed. The 13 nm features produced by this method were also tested for fibroblast response, and again a greater cellular response was observed on the nanoisland-laden surface compared with the planar surface of the same composition. In addition, gene expression as assessed by microarrays was significantly enhanced for hundreds of signals in response to the nanoislands, with the timing of upregulation being consistent with focal adhesion formation upon the surface structures [69]. As an extension to tissue engineering approaches utilizing tubular constructs, polymer demixing was recently applied to the inner lining of nylon tubing to develop nanoislands of 40 and 90 nm, which had profound effects on cell spreading and cytoskeletal organization [70]. Thus, the application of polymer demixing could have implications for the development of neural growth cone elongation conduits and vascular grafts, for the control of cell adhesion and morphology, as well as gene expression. In these preliminary studies it is apparent that nanotopologies on the 10s of nanometers directly influence cell shape, proliferation, and signal transduction. Collectively, polymer demixing studies complement EBL studies on cell–biomaterial surface interactions in reinforcing the importance of nanoscale surface information on cellular response. Also, this work demonstrates that topography as the dominating feature, rather than chemistry as the primary mechanism, can be tuned to control cellular adhesion and signaling.

New strategies to present tunable nanoscale topological features will undoubtedly be useful in tissue engineering device fabrication as the knowledge base

concerning optimum cell growth and function conditions is expanded to include in-depth nanoscale interactions. However, as technologies such as EBL and, in this case, polymer demixing are rather in their infancy in terms of biological applications there is considerable uncertainty of the extent of application of these technologies. The utility of polymer demixing in tissue engineering applications will depend on the number of biocompatible polymeric blends that can be induced by phase separation to form the desired structural features at the necessary resolution. If the ribbon and hill nanopatterns cannot be generated upon well-characterized biomaterials, it is unlikely that polymer demixing techniques can be utilized for tissue engineering, other than for the detailed study of cell–surface interactions in tissue engineering-like 3D constructs. However, phase separation techniques based on some different principles, such as *temperature*-induced phase separation (TIPS) [71], have been reported for developing relevant biomaterial constructs, in this case porous biodegradable polymer architectures. Therefore, additional parameters other than polymer–polymer and polymer–solvent interactions should be investigated for families of polymers to identify more relevant phase separations. In addition, future studies than address the combination of surface chemistries with these nanotopographies would be helpful and likely provide new insight on detailed nanoscale biochemical interactions, and also enable added features to this platform. For instance, while tall features were shown to be relatively inhibitory to cell adhesion, the grafting of cell adhesion peptides to the same feature might evoke a drastically different response in terms of cell spreading and growth rate. Nevertheless, polymer-demixed surfaces provide an interesting platform towards the study of nanotopography and its influence on cellular responses. The capability of reproducing *in vivo*-like cell phenotypes on an *in vitro* platform, as suggested by the arcuate morphology and structural changes of endothelial cells and the molecular expression profiles of fibroblasts on nanofeatures produced by this technology, could establish this technique as a correlative study tool to predict, for example, post-implantation responses. Of significance in this technology is the data gathered from cellular growth patterns on structures of varying height, which has some relevance should the same cells be patterned on 3D arrays in tissue engineering applications.

## 12.6

### Star-shaped and other Novel Polymer Structures

In addition to phase separation strategies, novel properties resulting from alterations in the polymeric structural configurations themselves have been of significant benefit in surface engineering approaches. Since polymers can be tailored to present functional groups on their surface, the density of that information on a given surface can be of critical importance to the evoked tissue engineering response, in the form of cell adhesion or spreading, for example. Star polymers, for example, are such a structure. They consist of a central core from which multiple branches of varying physicochemical properties emanate. By incorporating star-

shaped polymers onto biomaterial surfaces, the multivalency of the polymer can be exploited to present multiple surface chemistries, with a tunable number of branches and branch length, while the central core can impart its characteristic properties upon the whole surface.

Star-shaped architectures have been investigated in studies appropriate to tissue engineering applications. A promising application can be found in PEG-star architectures within hydrogel constructs. Initial studies by the Peppas laboratory concerning the utility of PEG star polymer hydrogels, for example, indicated that swelling properties of the construct could be adjusted by branch length, as well as the incorporation of acrylate moieties within the structure [72, 73], thus suggesting the utility of this approach in developing controlled-release tissue engineering surfaces, perhaps for the timely release of growth factors to encourage functional tissue development prior to or following implantation. In another example, star PEG coatings on titanium were explored for their utility of resisting nonspecific adhesion while promoting site-specific attachment of cells through a branch-conjugated RGD sequence [74], which illustrates the benefit of this approach in conferring added functionality upon titanium-coated implants in enhancing interactions and tissue integration with the surrounding environment, and reducing the adsorptive capacity of titanium for proteins, while also taking advantage of its mechanical stability in bioimplants. In other work to highly-tune cell adhesion on bioimplant surfaces, Griffith and coworkers investigated the utility of a “comb” copolymer consisting of a PMMA backbone with PEO branches, conjugated with varying RGD peptide densities. Surface film clustering of comb-presenting films either modified or unmodified with the peptide was demonstrated to be tunable for controlling cell–surface interactions [75–77]. The multifunctionality of star and comb polymers allows for incorporation of adsorption-resistant and adhesive surfaces within the same construct, and parameters such as the number and length of branches, and backbone/branch polymer composition, can be tuned, albeit with some difficulty, depending on the desired configuration, to develop complex surface arrangements of optimum density and spacing.

The degree of tunability of star-shaped polymer configurations appears to be very extensive, and the approaches used to make such modifications are diverse. In one example, such modifications are used to reversibly change the surface properties of a self-assembled film. Using a heteroarm star block copolymer of poly(2-vinylpyridine) and polystyrene, a self-assembled “brush” developed that could be tuned by solvent and pH-induced environments to present core–shell micelles with one of the two polymers on the surface. In addition to unimicellar interactions, lateral phase segregation was also observed for the monolayer, creating “dimple” and “ripple” morphologies, thus illustrating the development of an intelligent polymer coating with tunable, switchable surface chemistries and morphologies [78]. In another application, an amphiphilic diblock copolymer consisting of polystyrene and poly(ethylene oxide) (PEO) was synthesized in various star-shaped configurations, resulting in relative spreading and compaction of each polymer along the surface that were different than the linear form of the copolymer [79]. An exciting tuning approach highly relevant to star-shaped and dendrimer-branching poly-

mers is the concept of molecular imprinting. In this process, the polymerization step is accompanied by a “templating” step, in which the polymer and template, such as a biomolecule or metabolite-binding probe, are crosslinked. Extraction of the template, for example by hydrolysis, creates highly-specific complementary binding sites for the templating structure. The presence of multiple surface functionality sites on star and other multibranched polymers thus facilitates this approach to developing highly-sensitive recognitive networks, and has been exploited in the specific imprinting of porphyrin and glucose-based recognition systems [80, 81]. These works are interesting precursors to the development of smart multifunctional biomaterial surface constructs that are responsive to the changing conditions of the microenvironment. While molecular imprinting is generally considered a technology for drug delivery and biosensor applications, it is conceivable that such imprinting technologies incorporated into hydrogels could serve as specific biomolecule-recruitment devices that sort out serum proteins to capture the proper growth factors for the cells that are entrapped within the construct. Alternatively, such a technique could be used to recruit specific endogenous stem cells within a construct to generate new tissue *in vivo*, although the technology is in its infancy. Nevertheless, the versatility of star and other hyperbranched, nonlinear polymers makes them promising candidates for several tissue engineering applications in which the presentation of surface chemistries on the nanoscale level is required. Manipulation of the biomaterial itself in this manner may avoid the time-consuming optimization of process parameters used in other methods to achieve desired surface chemistries within biomaterial constructs.

## 12.7

### Vapor Deposition

In tissue engineering scaffolds or cellular and protein arrays for biosensor applications, patterns have been generated using the aforementioned photolithographic and soft lithographic techniques. These approaches may have limitations in the equipment and procedures involved, and/or the range of biomaterials that can be patterned. For instance, photolithographic equipment can be expensive, and soft lithographic fabrication techniques have been carried out primarily on gold and silicon substrates. Furthermore, PDMS, a common building block of microfluidic devices, nonspecifically adsorbs proteins via hydrophobic interactions, and does not express native functional groups for bioconjugation techniques [54, 55]. Thus, techniques adapted from the semiconductor industry have evolved that permit the thin film deposition of a wide variety of materials. Chemical vapor deposition (CVD) and related strategies, for example, are essentially a family of techniques that involve the chemical transformation of volatile gaseous precursors into thin films upon a substrate. The highlights of CVD that are relevant to biomaterial surface engineering are the capability of this technique to deposit various coatings (including multiple surface functionalities) on several substrates of varying composition and geometry. The process can be performed without catalysts and poten-



tially-denaturing solvents at room temperature. These advantages have encouraged the exploration of CVD technologies in the patterning of defined chemistries on substrates of complex geometries that might be considered candidate tissue engineering constructs.

We now illustrate the versatility of CVD-based approaches for the patterning of surface chemistries on various biomaterial surfaces. Lahann and coworkers have employed CVD polymerization of poly(2-chloro-para-xylylene) to homogeneously coat metallic stents, which permitted subsequent plasma treatments to significantly reduce platelet adhesion [82]. In addition, polymer deposition enabled the immobilization of a thrombin inhibitor on the stent to further reduce thrombogenicity [83]. This process addressed several shortcomings with previous attempts to coat Nitinol-based stents with polymers, such as the use of solvent-based defects, and the difficulty of evenly coating thin films below the micron scale. Thus, CVD is a potentially powerful technique for the coating of potentially thrombogenic or non-biocompatible metal surfaces with stable, evenly distributed functional polymer coatings for improving the performance and expanding the scope of application of existing materials. In other work by Lahann, CVD polymerization of functionalized poly(xylylenes) was applied for the thin film coating of steel, glass, gold, silicon, Teflon, and polyethylene surfaces, and, in conjunction with uCP, layer by layer (LbL) self-assembly was permitted for the controlled deposition of endothelial cells [84]. Therefore, the synergy of CVD with other patterning techniques for the spatial patterning of surface information is particularly of interest, as the benefits of soft lithographic pattern transfer techniques can be combined with the ability of CVD to pattern chemical functionalities on various surfaces. As further support that soft lithography and CVD polymerization can complement each other in the development of novel tissue engineering constructs, PDMS-based microfluidic devices themselves were functionalized on the luminal surface with the same functionalized paracyclophanes [85]. Reactive or nonreactive polymeric coatings of sub-100 nm thickness were homogeneously-deposited within the luminal surface of both straight and curved PDMS microchannel geometries [86] (Fig. 12.5), suggesting the potential of this technique in the ultrathin patterning of biofunctional groups within complex tissue constructs.

In addition to the capability of CVD techniques to deposit a given material on various substrates, the properties of the materials and surface chemistries that can be patterned are diverse as well, and are highly-relevant to bioimplant and tissue engineering applications. As a first example, by the CVD-based deposition of a photoactivatable surface chemistry upon a microfluidic channel, a template was provided for the spatially-controlled functionalization of both hydrophilic (PEG) and protein coatings in discontinuous arrangements [87]. In a second example, CVD-based thin film formation of poly(2-hydroxyethyl methacrylate) (HEMA), a biocompatible polymer with extensive biomedical applications, was observed to be a swelling property-tunable process by adjusting the partial pressure of a cross-linking agent incorporated into the vapor phase [88]. As a result, the deposited film had tunable crosslinking properties and could function as a hydrogel. Recently, the utilization of CVD for the deposition of thin films with chemically-tunable top-

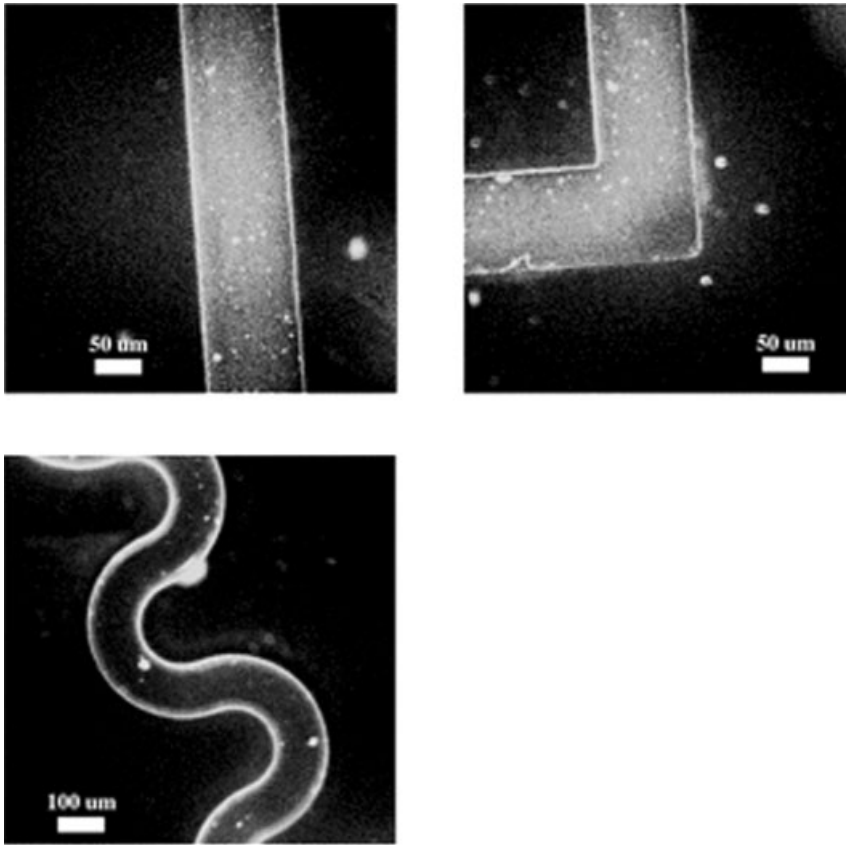


Fig. 12.5. Chemical vapor deposition (CVD) of straight and curved PDMS microchannel geometries of a hydrazide-reactive coating. The channels were exposed to biotin-hydrazide followed by TRITC-streptavidin. Channel depth is  $75\ \mu\text{m}$ , channel width is  $100\ \mu\text{m}$ . (Reproduced with permission from Ref. [86].)

ographies suitable for biological applications was demonstrated by the fabrication of aligned carbon nanotube arrays on a silicon substrate for the promotion of fibroblast growth [89]. This example suggests that CVD can serve as the patterning method for powerful, exciting nanotechnologies, to allow exploitation of their unique properties, and thus CVD can play an important role in the fabrication of complex 3D architectures for tissue engineering scaffolds.

CVD techniques provide a mechanism for the homogenous deposition of thin films presenting surface chemistries for the specific patterning of cells and biomolecules. While its application has primarily been directed towards *in vitro* diagnostic assays, the variety of compatible substrates and deposition candidate materials suggest the substantial applicability of CVD for biomaterial surface engineering for *in vivo* devices. While many of the polymer coatings investigated for CVD of stents

and cellular patterning surfaces have not been associated with apparent cytotoxicity, more extensive *in vivo* studies would be welcomed concerning the biocompatibility of deposited polymer coatings, particularly with metallic stents, given the better characterized nature of that application. Given the well-deserved appeal of hydrogels in tissue engineering applications, it would also be desirable to attempt to expand the list of candidate polymer films that can be tuned to behave as hydrogels using CVD processes with suitable co-polymerization agents. The versatility of CVD for the solvent/catalyst-free deposition of multiple coatings and surface chemistries on various materials and geometries make it an attractive option for surface engineering applications, either alone or in conjunction with other known techniques such as photopatterning and soft lithography.

## 12.8 Self-assembly

We have discussed the utility of soft lithography in the patterning of cells and proteins on complex geometries. A technology that has facilitated this application (as well as photolithographic approaches) is the use of self-assembled monolayers (SAMs), namely alkanethiols, for patterning on gold and silver surfaces. These SAMs are known to pack onto a gold surface with nearly crystalline density. Thus, the properties of the SAM itself are assumed by the new surface, allowing for chemical tuning of the biomaterial. For example, through organic synthesis modifications, alkanethiols can be modified to present bioconjugation sites, such as carboxylic acid, or protein-resistant sites, based on the hydrophilic PEG moiety. Using uCP, alkanethiols have been patterned with resolutions of 200 nm [90]. uCP techniques have been routinely used to create alternating patterns of ECM proteins and cells, with adsorption-resistant surfaces in between them conferred by PEG groups. The surface properties of SAM-adsorbed surfaces can be analyzed by a host of techniques, such as ellipsometry, X-ray photoelectron spectroscopy, electron microscopy, and quartz crystal microbalance, thus enabling many standard quality control procedures in the development of biosensors and cell/protein arrays. In addition to nanoscale resolution, when combined with the molding properties of PDMS stamps, SAMs can be utilized in conjunction with soft lithography and other standard techniques to produce complex features of varying chemistry and topology [61].

Despite the highly-useful features provided by SAMs on these substrates, the overall utility in tissue engineering applications is unclear. While chemisorption of alkanethiols on gold is useful in studying fundamental interactions of proteins and cells on the nanoscale, there is limited application in using SAMs to produce patterns on other surfaces that are not noble metals. Furthermore, organic synthesis techniques are complex, with each functional group requiring its own set of synthesis protocols. Other SAMs, such as alkylsilanes on hydroxyl-presenting surfaces have been applied, but their synthesis is especially complex and its use is far less than alkanethiols for biological surface engineering applications. However,

the biocompatible aspects of gold make it suitable in several tissue engineering applications, and should a host of biomaterials, such as titanium, be modified with gold surfaces where needed for SAM-assisted surface engineering, then SAM associated-strategies can conceivably be employed to create high-definition patterns for *in vivo* applications.

The nanoscale assembly of cells, proteins, and biomaterials such as polymers achieved by multiple nanofabrication processes has been also accomplished by the exploitation of alternating layers of materials containing opposing charges or hydrogen bond donor–acceptor pairs. Layer by layer (LbL) assembly techniques have emerged as low-cost nanopatterning strategies upon which various surface chemistries and topographies have been patterned. The method is simple, can be used to pattern stable films upon various hard and soft surfaces of varying geometries, and can bear biological information at varying heights within the film, without disturbing the overall assembly of the LbL network [91]. The use of electrostatically-complementary building blocks has also facilitated the use of other nanofabrication technologies, such as soft lithography, by enhancing pattern transfer from a stamped mold.

Several examples indicate the potential utility of LbL for the development of complex tissue engineering devices. In a co-culturing application, negatively-charged hyaluronic acid (HA), deposited by lithography, and the adhesive protein fibronectin were co-adsorbed to a glass substrate, followed by the specific attachment of cells to the fibronectin. A second adsorption medium consisted of positively-charged poly(L-lysine) (PLL), which bound electrostatically to the non-cell-coated HA layer to “switch” the originally non-adhesive chemistry to a cell-adhesive moiety that was permissive for the attachment of a secondary cell type, thus demonstrating the simplicity of LbL for patterned co-culture applications [92]. In another application, discrete, multiprotein regions were patterned within the same substrate using LbL in conjunction with photolithography, demonstrating the utility of LbL for facilitating hierarchical assemblies of distinct information [93]. Another LbL-based technology, colloidal lithography, has shown to be a promising, versatile application. In this technique, nanospheres are self-assembled on any number of surfaces, and can be the template for lithographic or vapor deposition processes, or themselves can contain functional groups for patterning. Since the nanoparticles are highly uniform and size-tunable, and can be tightly-packed if needed, they are highly-versatile materials for several surface engineering applications in a tissue engineering context. Additionally, the capability of this technology for the simultaneous presentation of surface texture and chemistry has been demonstrated. Shastri et al. investigated a functionalized nanoparticle-based system for simultaneously modifying surface chemistry and roughness (topology) without altering bulk substrate properties, on hard and soft materials such as titanium and polyurethane [94]. In another study involving microparticles electrostatically adsorbed on multilayer polyelectrolyte films, adjustments involving RGD peptide density on the microparticles and the packing density of the microparticles on the film surface, a function of the patterning area, were used to tune surface chemistries and roughness, with profound effects on cellular morphology [95].

LbL-based approaches obviate the need for substrate-specific bonding agents, such as SAMs based on alkanethiols and organosilanes [96]. The compatible materials, be it the thin film to be deposited or the substrate, are endless due to the availability of oppositely-charged polyelectrolytes, and with colloidal assemblies, both surface chemistry and surface texture can be presented to the cellular environment on microscale dimensions. This is a rare feature in biomaterial surface engineering techniques, which typically can present surface chemistry or surface topology, but not both simultaneously. The technique can be inexpensive compared with existing nanofabrication techniques, and/or can complement them. The size of nano/microparticles chosen for the application can be selected to modify thickness and surface area available for bioconjugation. Surface chemistries can be confined to different depths of a 3D multilayered construct, which enables the development of complex environments needed for tissue engineering applications as the library of matrix biology expands to define ever more complicated cell–ligand signaling processes.

The self-assembly phenomena observed for alkanethiols and polyelectrolytes on surfaces can also be observed for biomolecules. Here, the monomeric building blocks of the biomaterial surface chemistry and topology are peptides or proteins, which associate with each other through various non-covalent interactions. This has been very useful for biological surface engineering, since proteins do not have the same biocompatibility issues associated with polymers or other synthetic materials. Furthermore, protein structure and alignment is of great interest to the biological community, and the fact that this field has developed extensively will enable tissue engineering applications that take advantage of protein structural morphology to present high-resolution information to cells. Proteins themselves are the nanoscale messengers of information to cells, providing signals in the form of chemistry and topology, and thus techniques that directly apply this information to surfaces are desirable.

Nanoscale features from biomolecules can be created by hierarchical, irreversible systems, such as those based on avidin–biotin stacking systems, or interchangeable complexations. Such strategies have been used to develop beta-sheet monolayers [97, 98], as well as peptide-based nanotube architectures [99, 100]. Spontaneous formation of porous networks by a set of peptide families yielded filaments of 10–20 nm, with pores 50–100 nm in size, with complex geometries [101]. Thus, various nanoscale chemistries and topologies are achievable with this strategy. Self-assembling peptides can be patterned using uCP, to control cell–cell interactions by modulating the peptide sequence and surface density. The self-assembled peptides may be further conjugated to cell-signaling peptides, such as RGD for example, to allow for methods that are focused on presenting a surface topology and chemistry simultaneously. As an alternative to hydrogels based on synthetic polymers, Mi [102] and colleagues have developed RGD-incorporated hydrogels by the self-assembly of proteins with the included sequence, in a process dictated by temperature and pH. The RGD incorporation enabled the binding and spreading of fibroblasts on the surface. While this is a feat achievable by other approaches, this work illustrates that it is possible to encode biological signals within proteins

that naturally assemble into modules, each consisting of similar or varying information. One can envision the modular construction of natural self-assembled polymeric architectures on a host of biocompatible surfaces to direct multiple processes such as cell proliferation, migration, and cytokine secretion, at the same time. Further tuning is possible, such as the mechanical properties of the self-assembled species, and the degree of self-assembly. For example, a peptide-amphiphile complex on the order of 6 nm developed by Hartgerink and coworkers have provided for a pH-tunable (and reversible) self-assembly mechanism, with reversible crosslinking of the complex tunable by disulfide bridges [103]. These features enabled the mineralization of hydroxyapatite on the complex surface in an orientation that resembled the collagen–hydroxyapatite alignment in bone. thus illustrating the advantage of using biomimetic structures based on biomolecule-based monomers.

As the enabling technology in this mode of self-assembly are the peptides themselves, then there is no particular substrate specificity. Any surface that allows the desired nanoscale self-assembly is then a candidate substrate for this approach, which makes the scope of application potentially quite extensive in tissue engineering applications. The ease with which biologists can synthesize recombinant proteins and peptides with functional domains, all without an appreciable reduction in normal protein function, makes self-assembled biomolecule arrays an exciting prospect that is also readily accessible.

In general, nanoengineering of surfaces based on self-assembly can be a very convenient approach. Ambient temperatures, no need for organic solvents, and the use of well-characterized films or biofilms for predictable, reproducible results are all potential features of this technique. As the number of bioactive agents that influence cellular and tissue function are elucidated, the number of potential biomolecular self-assembling candidates will likely expand as well. Future studies that investigate the synergistic effect of bioactive agents and surface topology (as initially achieved with colloidal-based approaches above) are warranted, as is the transition from protein patterning to viable tissue engineering constructs by extensive *in vivo* studies.

## 12.9

### Particle Blasting

An important challenge of surface engineering strategies for biomaterials is the modification of a surface to achieve sufficient surface free energies that are required for adequate cell adhesion, motility, and proliferation. Surface engineering of implants, commonly in the orthopedic and dental implant arenas, often employ sandblasting technology for the attainment of certain tunable surface morphologies. By varying the physical properties of the blast material itself, and the pressure with which it is ejected, surface topographies can be achieved for modulating various biological responses similar to those observed for topographies produced by

other methods. These techniques are generally applicable to a wide variety of biomaterials, and are relatively inexpensive.

Sandblasting techniques, while simple, can be readily applied to several well-characterized biomaterials and biomedical applications to modulate their biological response. An example can be seen with the sandblasting of PMMA, a widely-used material in bone cements and ocular applications, with alumina microparticles [104]. Compared to smooth PMMA, vascular and corneal cell adhesion was higher on roughened PMMA surfaces. The simplicity of sandblasting can also be applied toward the deposition of films in addition to surface texturing. By loading a sandblaster with hydroxyapatite powder, Ishiwaka et al., produced a high-strength bond between the powder and the titanium surface that was higher than titanium coated by electrochemical and electrophoretic deposition processes [105].

These examples illustrate the principle that surface roughness alone, whether patterned by the previously-mentioned techniques, or randomly distributed by simple sandblasting techniques, has a profound influence on the affinity of cells for biomaterial surfaces. Furthermore, to generate such topology to evoke the desired cellular response in terms of adhesion and organization, it may not be necessary to employ expensive, time-consuming steps, if simple and rapid techniques such as sandblasting can achieve the same effect. However, this technology is generally not suitable for advanced tissue engineering applications that require precise control of biomolecule and cell placement, since it does not provide for surface chemistry modifications, is random in topography distribution, and has not thus far offered fine nanoscale resolution. Furthermore, blasting particles can be embedded within the target surface, which may complicate biological applications. Nevertheless, there is utility of sandblasting for creating microscale surface topography at room temperature, without the need for chemical modifications (although acid etching steps often accompany it), and surface chemistry can also be deposited onto a surface using this technology. While its main applicability is directed toward orthopedic and implant dentistry techniques, and has not been extensively performed on most biomaterial surfaces not relevant to those fields, it is conceivable that particle blasting could be utilized for a broad range of tissue engineering devices. For example, controlled-release microspheres could be used as the blast material for a deformable hard substrate, to serve as a cell-supportive nutrient reservoir during cell seeding on titanium or polymer-coated implants, thus potentially providing both surface roughness and chemistry in the form of released biomolecules or surface functionalities (e.g., RGD).

## 12.10

### **Ion Beam and Plasma-guided Surface Engineering**

These are surface engineering techniques that provide mechanical and chemical alteration of a biomaterial surface, without negatively affecting the overall bulk properties of the original material. For decades, ion beam-related technologies,

such as ion implantation, plasma immersion ion implantation, and ion beam-assisted deposition, have been highly reproducible techniques for the modification of surface properties due to the degree of control provided over the process. Furthermore, these techniques and variations on these techniques have been utilized to modify the properties of many biomaterials in many ways, including the overall response of the biomaterial to *in vivo* environments. A plasma is generally defined as a mixture of gas in a reactor containing one or more charged and uncharged species, which can be energized/accelerated with an applied electric field. Ion implantation involves the bombardment of a surface with accelerated ions from an excited plasma. Superficial layers of the target material (generally  $<1\ \mu\text{m}$ ) are disrupted by the ions, and a host of physicochemical modifications occur as a result, depending on process parameters and intrinsic material and ion properties. The modifications generally do not “strip” material off the surface as may chemical treatment-based approaches or reactive ion etching, which makes this technique useful for enhancing biomaterials selected for their intrinsic properties. The ion-polymer interactions can strengthen the resultant material properties by the formation of crosslinks. Similarly, for metallic biomaterials, ion implantation can strengthen the original material without bulk modifications by the formation of alloyed species, such as that produced by titanium modification by nitrogen.

A main application of ion implantation strategies has been directed toward the improvement of titanium implants for integration with bone, a major tissue engineering arena. Titanium has long been utilized as a biomaterial due to its rigidity and biocompatibility. Several techniques such as those discussed previously have been carried out to enhance the bone-Ti interaction, such as with hydroxyapatite deposition. These endpoints can also be achieved with ion implantation methods. For example, implantation into Ti with sodium ions resulted in a complex that enhanced hydroxyapatite precipitation from a pretreatment solution, which led to improved cell densities relative to untreated surfaces [106]. An alternative route to hydroxyapatite deposition has been realized with ion implantation for enhancing osteointegration. Implantation of carbon ( $\text{C}^+$ ) and carbon monoxide ( $\text{CO}^+$ ) ions into titanium dental implants significantly improves bone integration, with stronger contacts between bone and implant made possible by covalent bonds not observed in the standard titanium oxide-bone interface [107]. Ion implantation techniques are also suited to the enhancement of other biomaterial interactions. Vascular smooth muscle cells seeded on fluorine-treated polystyrene was observed to have improved adhesion and survival characteristics. Ion implantation has also improved the endothelialization properties of polyurethane, polystyrene, and poly(ethersulfones) for the construction of vascular grafts [108–110].

Other related technologies are useful for surface engineering of biomaterials, by other mechanisms. Ion beam-assisted deposition (IBAD) directs the acceleration of ions toward a simultaneously-generated, vapor-deposited thin film on the surface. The deposited film then reacts with the ions, resulting in modified properties such as film density, texture, interfacial properties, and stress. This technique has been utilized to deposit bacteriostatic silver films on catheters, as well as sealant and



electrode coatings on polymeric substrates [111]. In response to the “line-of-sight,” serial modification limitations imposed by conventional ion beam technologies, a technique called plasma immersion ion implantation (PIII) was developed in the 1980s. This method enables the rapid implantation of complex geometries, and has been used to enhance the hydrophobicity of various polymers such as poly(tetrafluoroethylene) (PTFE), PDMS, and polyurethane, and to improve material properties of various metals [112–117]. Another technology, reactive ion etching (RIE), utilizes both ions and chemically-reactive species, to impart a chemical component to the primarily physical process. When the reactive species formed by the chemical component and the substrate surface is created, the byproduct can be removed by various means, such as the physical ejection of atoms from the substrate. For surface patterning applications, inductively-coupled plasma reactive ion etching (ICP-RIE) was utilized to etch 3D features in PMMA blocks for protein patterning and modification of the surface to resist nonspecific binding, thus obviating a nonspecific adsorption blocking step [118]. This variation on RIE allows for independent control of ion density and ion energy, to address the tradeoff between substrate damage and etching efficiency. RIE allows for tuning of both chemical and physical components, which are generally isotropic and anisotropic, respectively, to influence the detail of the etching process. Other plasma-based techniques for the etching, sterilization, and surface property modification of biomaterials are extensively reviewed elsewhere [119]. Of note are tetrafluoromethane plasmas for hydrophobic treatment of a surface, and oxygen and nitrogen plasmas for enhancing surface hydrophilicity.

Plasma-based techniques are a versatile method for the modification of many biomaterials, and are suited for developing new surface properties without substantially changing those of the background material, due in general to the low penetration of the bombardment species. Processes can be performed in dry conditions without harsh chemicals to tailor to a specific tissue engineering application, and the engineer has multiple tunable process parameters that can be modified to achieve desired surface properties. The technique is applicable to metals, ceramics, and polymers that may be used as biomaterials; in general, plasma treatments can enhance the biomaterial surface in terms of biocompatibility, biochemistry, tissue function, and mechanical properties, and are thus a key technology. However, caution must be exercised in process parameter optimization, such that undesired stripping of the surface and underlying layers does not occur. This is especially the case with new technologies such as deep RIE, which have etch rates far beyond single microns. In addition, these processes can be both expensive and hazardous, due to the equipment needed and the plasma compositions (e.g.,  $\text{Cl}_2$ ), respectively. Furthermore, ion interactions with a surface create a chemically-different species that must be independently evaluated (from the original polymer) for typical features, such as biocompatibility, etc. Nevertheless, this technology, due to the myriad of tunable parameters and candidate substrates, makes plasma-based treatments important for the development of biomaterial surfaces with novel properties.

## 12.11

### Sol–Gel Technology

In addition to a biomaterial featuring certain metrics, such as satisfactory biocompatibility criteria and appropriate tissue interactions (cell adhesion, low thrombogenicity, etc.), in many cases the porosity of the structure within specific macroporous and mesoporous ranges are critical to the success of the bioimplant. Cells and tissues require specific porous architectures characteristic of their *in vivo* environment for tissue ingrowth and fully functional regeneration. For bone tissue regeneration, long a main focus of tissue engineering, specific porous architectures are essential for cellular migration and vascularization with a steady influx of nutrients and molecular cues to facilitate the process. Sol–gel technology has served as a promising route to achieving such structures for various tissue engineering applications. This processing technique can be utilized to enhance the biocompatibility of biomaterial surfaces, can readily coat a number of surfaces, and forms chemically-stable coatings in physiological environments. Of particular interest are the sol–gel derived bioactive glasses. Several incorporations of sol–gel processes are described elsewhere in detail, but they generally involve the gelation of a nanoparticulate suspension into a continuous network. Following an “aging” step, the gel is dried to produce a glassy solid. The process enables the synthesis of materials with various physical properties, made possible by allowing the mixture of organic and inorganic materials within the same process.

Several applications of bioactive glasses illustrate the importance of this technique in creating mechanically stable, highly-functional tissue engineering constructs. Scaffolds based on bioactive glasses were shown to have compressive strength similar to trabecular bone, with pore diameters within the microscale sufficient to allow vascularization of regenerated tissue, as well as cell migration [120]. Furthermore, it was determined that the sintering temperature of the process was a determinant of mesoscale pore size, which had profound effects on the dissolution rate and hydroxyapatite layer formation, as well as the compressive strength of the material. The tuning of surface area, and thus dissolution rates, in tissue engineering scaffolds for bone is highly powerful, as it allows for a mechanism of tuning the implant to the natural bone resorption rate in the body. In another example, sol–gel processing was utilized to develop bioactive foams presenting amine and mercaptan groups to allow for biomolecule incorporation with similar mesoscale and macroscale porosity as the previous application [121]. Thus, these networks supportive of natural tissue ingrowth and vascularization can also be biofunctionalized to allow for appropriate molecular signaling throughout the interconnected matrix. In other applications, sol–gel processing has provided a method of making conventional biomaterial surfaces more biocompatible. Titanium surfaces coated with hydroxyapatite sol–gel layers were shown to exhibit a higher activity of osteoblast-like cells compared with bare titanium, with tunable surface dissolution rates achievable by the incorporation of fluor-hydroxyapatite [122]. Other coatings, such as PLGA and titanium oxide, have also been patterned on titanium

substrates using sol-gel processes, with cell adhesion on the sol-gel coated hydroxyapatite layer being higher than the plasma-sprayed substrate [123].

The low cost, favorable mechanical properties, and tunable nano and macroporous architectures made possible by sol-gel technology using a wide blend of organic and inorganic materials make it a promising surface engineering technique. With the added advantage of introducing chemical functionalities within the sol-gel processing steps, bone tissue engineering devices that utilize bioactive glasses and other sol-gel derived materials will benefit from the advances in bone tissue biology, which are already elucidating key molecules such as bone morphogenic protein (BMP-2), which have spatial and temporal distribution profiles that could be tuned by an implant for optimum tissue regeneration [124]. However, tissue engineering applications utilizing sol-gel processes would be enhanced by more extensive studies of the effects of process parameters on porosity of manufactured architectures for various composites. Further studies should also investigate the type of chemical functionalities that can be incorporated within porous architectures produced by sol-gel processes.

## 12.12

### Nanolithography

A family of surface engineering technologies has been developed to produce high-contrast and high-resolution nanoscale patterns for the purpose of readily integrating this information within novel BioMEMS and tissue engineering applications. Collectively known as nanolithography, these strategies include soft lithography, which has been discussed previously, as well as dip-pen lithography (DPN) and nanoimprint, or nanoindentation lithography (NIL). In DPN, an atomic force microscope (AFM) scanning probe is “inked” analogous to a PDMS stamp with specific information, in the form of SAMs, peptides, oligonucleotides, or other biomolecules, and patterned upon a solid substrate by capillary transport, to produce features as low as 30 nm [125]. Substrates tested with DPN have primarily included silicon and gold, with multiple inks. The major advantage of DPN is not only its nanoscale resolution appropriate for biology, but also its direct-writing capability inherent in the probe-based technology, which allows for single cell and potentially single biomolecule manipulations.

DPN is not an old technology, and thus direct tissue engineering applications have not yet been reported at the time of this writing. Most studies are focused on determining the species that can be successfully patterned using DPN, and have been reviewed by Mirkin et al. [126]. Of particular interest is the development of SAMs that function as DPN-sensitive resists for forming features on solid substrates as low as 25 nm. Proteins have been successfully patterned with DPN, with features as small as 45 nm, and cells have specifically-adhered to patterned protein recognition sites [127, 128] (Fig. 12.6). To address the serial nature of the process inherent in other techniques, several studies are in place to develop mul-

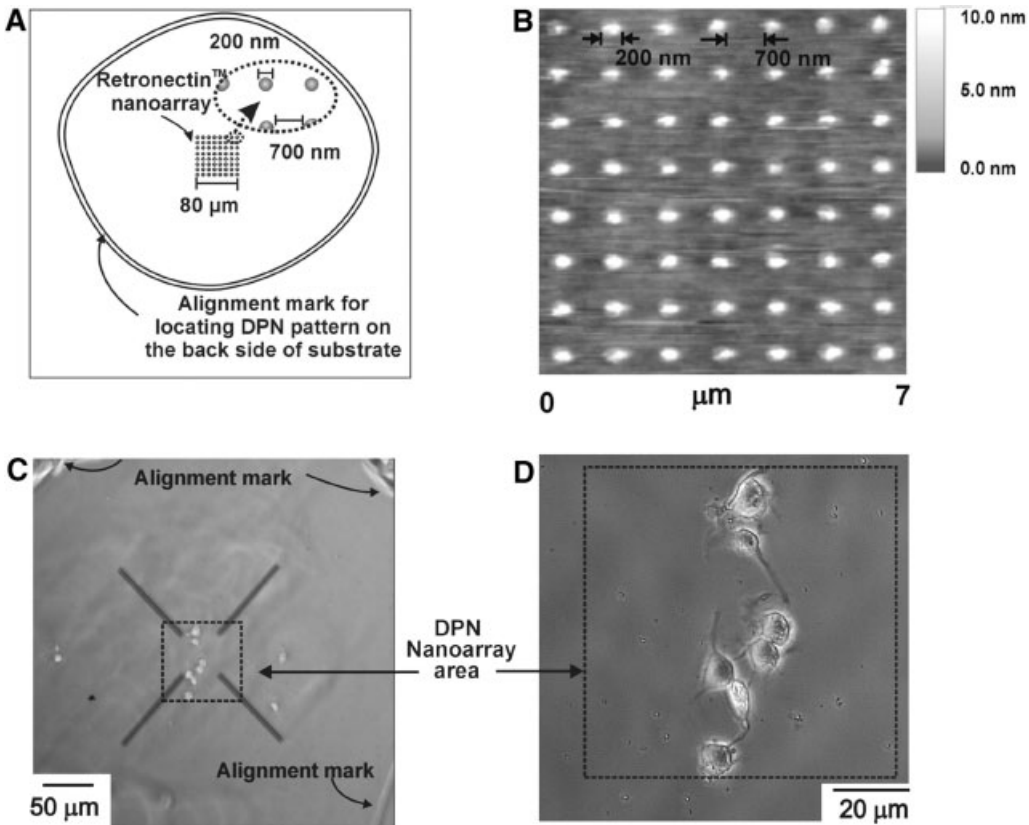


**Fig. 12.6.** Fibroblast adhesion to dip-pin lithography (DPN)-patterned retronectin (cell adhesion protein) arrays. (A) Fibroblasts were adsorbed onto a retronectin-patterned area of 6400  $\mu\text{m}^2$ . (B) Retronectin protein array. (C, D) Optical images of intact cells adsorbed on retronectin-patterned area. (Reproduced with permission from Lee et al. [126].)

tiprobe arrays for higher throughput DPN. While these developments are exciting for semiconductor and biosensor applications, the applicability of this technique for the surface engineering of biomaterials is not clear. However, gold-plated biomaterials, such as Au pits within titanium implants, can be readily manufactured using previously discussed techniques, thus enabling AFM probe access if an application is found. Also, it seems likely, based on the variety of inks that can coat an AFM tip, that DPN could conceivably be utilized to pattern living tissues or tissue scaffolds to construct cell–protein arrays with nanoscale precision. If such a feat was achieved, then single biomolecules and cells could be manipulated and oriented toward appropriate functional locations within a tissue engineering construct, not unlike that achieved with LGDW as discussed previously. Regardless of whether such a transition is made, further investigations concerning the dynamics of inking and ink transfer to a substrate are warranted to optimize the technol-

ogy. Various parameters govern this process, not limited to chemistry and geometry, which allow for some tunability in the process. However, the specialized equipment and conditions necessary to apply the technique will limit its accessibility to biological laboratories seeking patterning tools for hypothesis testing, although the embracing of DPN by industry carries with it the potential vision of developing high-throughput, accessible DPN methods for nanofabrication on order.

Similar to DPN technology, NIL is capable of resolutions down to 10 nm [129, 130]. In this technology, a silicon template generated by conventional patterning techniques serves as the template for a polymer (e.g., PMMA) elevated beyond its glass transition temperature, such that it is elastically deformable. Following a cooling step, the polymer assumes the pattern transferred by the mold. Several features make this technology very attractive over existing techniques, including DPN. The technology is not limited in resolution by beam parameters, requires no expensive equipment, and can be utilized in high-throughput processes for reproducible quality patterns. This was furthered by the development of air cushion press (ACP) technology to create more uniform pressures during mold imprinting (Nanonex Corp.). Furthermore, NIL is not as time-consuming as DPN and other beam-based serial technologies, and, like DPN, it is conceivable that single biomolecules could be manipulated with this technique. Thus, NIL is generally a user-friendly biocompatible technology that can be readily applied to surface engineering applications. Applications have included nanoscale protein patterning with preserved activity and high signal to noise ratios [131]. NIL has been combined with further processing steps such as self-assembly and RIE to create defined bioactive regions, thus demonstrating the synergy of NIL with various existing techniques [132]. Given the ultimate resolution of 10 nm for this technique, it could replace electron beam lithography for tissue engineering applications on a cost and biomaterial flexibility basis alone. However, not all materials can be manipulated by NIL, and until the full scope of candidate molding materials is investigated the true utility of the technique will not be fully realized. Furthermore, stamp fabrication can be a tedious process; in addition, the 10 nm resolution limit has not yet been realized for biological applications, and its suitability for most biomaterials has not been determined. Nevertheless, the NIL technique promises to be a flexible, low-cost, high-throughput technique for producing nanoscale features.

### 12.13

#### Laser-guided Strategies

The wide range of technologies discussed thus far have been associated with their own unique advantages and limitations, as there is no one size fits all approach in biomaterials surface engineering, in terms of patterning any surface with reproducible chemistries and topologies of perfect resolution for the application of interest. For example, EBL, plasma/ion beam, and photolithography are constrained by specialized equipment costs and lengthy procedures, whereas sandblasting techniques generally do not produce precisely repeatable features. We now discuss a

family of technologies based on lasers, which is a promising alternative to the above techniques for the tuning of various biomaterial surface properties. Potential advantages of this approach include high reproducibility, the potential for automated guidance systems, and various sources to choose from of different excitation wavelengths and power densities, which immediately suggests the potential of generating patterns of varying intensity in a manner not unlike a “maskless” grayscale photolithography. The wide availability and familiarity with lasers is also an enticing aspect in incorporating this technology in tissue engineering applications, as well as the potential to incorporate into existing methods, recalling the method of Holden et al. for laser patterning of multiple dye-labeled biomolecules using photomasks [10]. Lasers have been successfully applied to the surface texturing and patterning of polymers, biomolecules, and even cells, to a host of material surfaces.

The generation of surface topologies is possible with multiple laser types, due mainly to the material properties of the target surface. First, since many substances absorb strongly in the ultraviolet range of the spectrum, UV-emitting lasers can thus be used to successfully modify biomaterial surfaces without altering bulk properties, since the penetration depth is limited by the high surface absorption of energy. This feature enables two surface modification routes: (a) the etching of material through photoablation and (b) the nanopatterning of topologies, made possible by the low UV wavelengths of the lasers. Photomasks can be incorporated in patterning steps if necessary to facilitate the formation of certain surface features as described elsewhere. Technically, this process could be performed on any geometry, since the only requirements of this technology is that the laser beam is in contact with the surface to be patterned, and that the surface has chemical bonds that are photolabile at the illuminating wavelengths. Excimer lasers have been used for the photoablation of polymeric surfaces for over two decades [133, 134], and thus an extensive library is available concerning candidate materials and their responses to texturing. Other (higher-emitting) lasers for the patterning of either non-polymeric or low UV-absorbing materials have also been employed. An example is the Nd:YAG laser texturing of titanium surfaces [135]. In general photoablation does not require chemicals or specialized equipment other than the laser to achieve the basic task, although the technology seems capable of incorporating multiple added functionalities, such as computer guidance (discussed below), complex masks, and incorporation into device fabrication assembly lines for rapid, simultaneous patterning of multiple features. Despite the scope of applicability of photoablative techniques, recent studies have demonstrated that they do not possess the resolution necessary for BioMEMs applications when compared with dry etching methods [136], and thus, as with any technique, the geometrical features required of the application must be assessed for suitability with the method used to pattern them.

The same ablative nature of laser irradiation of surfaces has also been exploited to deposit polymer and other biomaterial films, using pulsed laser deposition (PLD) techniques. Laser light is directed inside a vacuum chamber, and several process parameters such as wavelength, power, and duration can be tuned to con-

control the vaporization of the surface material. Potential advantages of this technique are similar to those for texturing/etching using photoablation, such as the broad range of materials that can be ablated with laser irradiation. Furthermore, the tunability of process parameters and the high resolution (small spot size of irradiation) provides for an important control mechanism over the vaporization process. No chemicals or other catalysts (such as exogenous heating of substrate) are needed for PLD. This approach has been successfully applied to the layering of PTFE (Teflon) [137] and PMMA films [138, 139]. In addition, using protective detergent capsules, thin films of glucose oxidase were also formed by PLD, with preservation of activity [140]. While PLD provides for some biomaterial surface engineering applications, especially with polymer thin film deposition on complex geometries, it is difficult to extend its applications to keep up with the need for different scaffolds and bioimplants. Each PLD specimen requires optimized process parameters such that heating of the substance is not too substantial such that the polymer architecture is irreversibly damaged. Even more caution is required in the PLD-based manipulation of biomolecules and cells, and it is unlikely protective substances can safely encapsulate all such species while facilitating high-quality surface patterning. The lack of compatibility between biomolecules and UV irradiation is a limiting aspect. Nevertheless, the laser positioning outside of the vacuum chamber may provide for a favorable alternative to other film deposition techniques, in that the source orientation can be adjusted as needed, in addition to the other previously discussed process parameters that are user-tunable.

Recent approaches have been developed to circumvent some of the limitations of PLD. To improve laser-assisted film deposition methods, a technique called matrix-assisted pulsed laser evaporation (MAPLE) and its related direct-write counterpart (MAPLE DW) were devised, whereby the material to be deposited is dissolved in a judiciously-selected solvent and frozen; the complex is then irradiated to deposit the film of interest with removal of the solvent *in vacuo* [141]. With this system, exposure to laser irradiation is generally limited to the solvent capsule, which aids in preserving the integrity of the dissolved species. As an example, PEG films, which were damaged by direct UV irradiation, deposited using MAPLE were of favorable structural integrity for typical applications [142]. Interestingly, by encapsulating cells in a glycerol-based matrix, successful deposition with acceptable cell viability can be achieved with features  $<10\ \mu\text{m}$  [141]. In a fundamentally different approach to enhance the biocompatibility of laser-based processes with cells without the use of UV light, the exploitation of optical forces have been used to laser-guide cells to specific locations on substrates. Near-infrared light irradiation can exert tiny forces on the cells, the net effect of which is for cells to move toward the center of the beam and away from the light source. This technique, called laser-guided direct writing (LGDW) is capable of single-cell resolution patterning, and has been employed for the co-patterning of endothelial cells and hepatocytes within Matrigel constructs to create self-assembled 3D constructs with similar morphology to hepatic sinusoids [143] (Fig. 12.7). This technique has the advantage of “point and shoot” control of single cells to create multicellular arrays without a compromise in cell viability, as the irradiation source is not ultraviolet. Further-

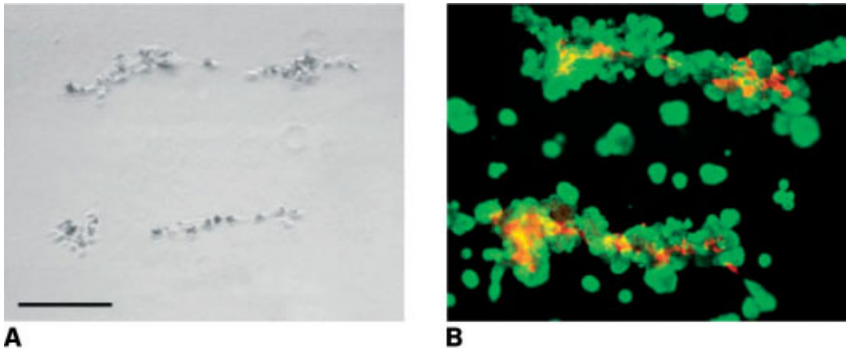


**Fig. 12.7.** Laser-guided direct writing (LGDW) of cell patterns approximating liver sinusoids *in vitro*. (A) HUVECs deposited by LGDW. Cell elongation along the pattern was observed. (B) 24 h post-deposition, added hepatocytes surrounded HUVECs to form sinusoid-like structures. (Green – albumin, red – CD31 staining; bar = 200  $\mu\text{m}$ .) (Reproduced with permission from Ref. [141].)

more, optical trapping could likely pattern cells on multiple surface types, provided there is an aqueous medium to support light guidance. Although the method is time-consuming, involving a cell-by-cell manipulation technique, theoretically, multiple laser arrays could be utilized for the guidance of multiple cells at once to form hierarchical organization of tissue. This method could be incorporated into advanced schemes that seek to optimize tissue structural and functional properties, for instance by the enhanced migration of a slow-moving cell type by added optical guidance.

Future applications of lasers in biomaterial surface engineering could potentially be in areas in which scale-up for mass production is necessary. Laser-based approaches could be exploited for the capability of modifying surface texture with one laser type, and performing film and biomolecule deposition with other wavelengths, in an assembly line-style fashion. This readily-accessible technology has already been successfully applied to the surface engineering of biomaterials with promising results in producing nanoscale and microscale features. However, a much more detailed investigation of the interface between lasers and biological materials/environments is necessary to expedite such a transition.

#### 12.14 Rapid Prototyping Techniques

The future of biomaterial surface engineering for tissue regeneration and bioimplant applications is highly dependent on the development of procedures for the nanofabrication of 3D cell-protein arrays that can be scaled-up for mass production. Early techniques that constituted the primary methods of scaffold fabrication, such as salt/porogen leaching, fiber bonding, and gas foaming, were not capable of



high-throughput, reproducible construction of multilayered, highly interconnected porous architectures of consistent structural and morphological characteristics [144, 145]. To this end, several rapid prototyping (RP) or solid freeform fabrication (SFF) techniques, some of which have already been described (such as MAPLE DW), have emerged to meet the need for high-throughput, reproducible construction of functional tissue architectures. Various RP approaches are related by the use of computational design and fabrication guidance, using CAD-based software. The 3D model of interest is designed on computer using CAD software, and linked instrumentation translates this data into a physical model on a layer-by-layer basis. The building blocks can be powders, liquids, or crystalline materials, depending on the instrumentation employed. RP, if proven to be (a) flexible in the candidate biomaterials that can be used, (b) reproducible in the patterns produced, and (c) capable of achieving tissue engineering-relevant features, will undoubtedly constitute one of the most significant milestones in the field, as it will enable the application of numerous designs and concepts gathered from decades of multi-disciplinary research into clinical practice using high-throughput, reliable manufacturing processes. Here, we discuss four interesting RP technologies that in initial stages have demonstrated utility in their potential to recreate useful tissue architectures: stereolithography (SLA), selective laser sintering (SLS), three-dimensional printing (3DP), and fused deposition molding (FDM).

Computer-guided manufacturing of tissue engineering devices has been explored for some time as the need to not simply design devices but to manufacture them was anticipated by many groups. One route to this goal has been achieved through laser-mediated technologies. For example, Mikos et al. have adapted commercial stereolithographic (SLA) technology for the 3DP of a scaffold using servomotor controlled, laser-based crosslinking of a polymer-photoinitiator composite layers upon a movable stage [146]. While the features produced were on the order of hundreds of microns, nevertheless the utility of CAD-CAM approaches for the manufacturing of clinically-useful biodegradable tissue scaffolds was demonstrated. SLA (and its improved-resolution derivative technology  $\mu$ SLA) has been applied with promising results in the manufacture of scaffolds incorporating polymers (e.g., PCL) [147] or ceramics [148] with improved microscale resolution, although the use of lasers presents potentially degradation problems as discussed below. Another laser-based commercial manufacturing technology applied to biomaterial surface modification is SLS. In this technology, a laser is directed upon a thin layer of powdered polymer. The heat generated at the surface, which is elevated beyond the polymer's glass transition, is capable of particle fusion, with some control over the pattern and microstructure generated. The 3D model within the CAD software contains slice-by-slice information that guides the laser rastering, scan speed, and intensity, while fresh powders are deposited above the fused layer for the formation of a new one. Early results concerning the use of SLS for polymeric scaffolds are mixed. SLS (as well as SLA) is a laser-based technique and, thus, the same issues concerning polymer degradation observed in laser applications discussed previously are equally applicable here. Degradative effects can include chain scission as well as photo-oxidation. Degradation was observed in the

application of SLS for the manufacturing of polyethylene (PE)-based implants [149]. However, SLS has yielded useful results in the fabrication of ceramic and hydroxyapatite-based devices [150]. For example, SLS process parameters such as laser scan speed and laser intensity were tuned to successfully fabricate polyetherketone (PEEK)–hydroxyapatite constructs for bone tissue engineering applications [151]. Thus, while the same precautions necessary in other laser-based nanoengineering strategies are applicable to SLA and SLS, the flexibility of the technique in accommodating a wide variety of materials and substrates is of particular significance, as well as the potential of the technique to be incorporated in computer-automated high-throughput and high-reliability manufacturing of tissue engineering scaffolds. For this technology to be successful in the surface engineering of biomaterials for clinical usage, work to study the influence of laser tuning parameters on the resulting morphology (e.g., porosity) and mechanical characteristics of the construct produced is necessary. The resolution of the technique will be limited by the wavelength of the laser used, and thus optimization of laser choice should be carried out to achieve the necessary spatial control during the production process. Additionally, the compatibility of these processes with existing methods to engineer surface chemistries is unclear, and should be addressed in future work. It seems feasible, however, to layer functionalized polymer microparticles as needed, or to possibly surface engineer functionalized moieties using other methods as each layer is constructed. The ability of the laser to not only crosslink polymers but to also initiate chemical reactions should be useful in developing SLS and SLA-based processes that incorporate biofunctionalization into scaffold construction. A potential advantage of this technique, which would allow such possibilities, is the amenability of this method for constructing tissues layer-by-layer, using local heating of the polymer in a room temperature environment, thus avoiding heating chambers, although “part bed” temperature is an adjustable parameter as needed [151]. Furthermore, organic solvents used in casting procedures are not necessary by this technique, which needs only a steady supply of deposited polymer microparticles as the starting material. The applicability of these techniques for manufacturing using the broad spectrum of biocompatible polymer-based biomaterials (i.e. those that can be synthesized in a powder form), followed by extensive *in vivo* investigations of scaffold performance, is certainly warranted given the promising results in preliminary work.

Another RP method that can be utilized in ambient temperatures is 3D printing (3DP), which uses essentially a specialized inkjet printer to deposit a binding solution layer-by-layer upon pre-deposited powder beds. Thus, any material that can be obtained in a powder form is a candidate for this technique if a compatible binder can be identified. Upon drying of the bed, unbound powder is removed. Key process control parameters in this technology are the size of the deposition nozzle and polymer microparticles (which dictate layer thickness), the type of binding solution utilized (biocompatibility, hydrophilicity), as well as the resolution step of the printer head. The binding material can be biocompatible, although several studies have used organic solvents as the binder [152]. Early work demonstrated the potential utility of 3DP for the manufacturing of biodegradable, functional polymeric

scaffolds for cell adhesion [153]. A multilayered osteochondral scaffold intended for tissue engineering of articular cartilage based on PLGA, PLA, and CaP was fabricated using 3DP with bone and cartilage-like regions of suitable porosity and layer mechanical characteristics within acceptable ranges for hard and soft tissues [154]. This study demonstrates the benefits of a high-throughput multilayering approach for building hierarchically-organized hybrid materials, with sections delegated to specific functions. A problem with 3DP that is especially relevant to the creation of porous scaffolds has been a difficulty with removing internally-embedded compounds, and due to incomplete fusion of polymer particles during the process, undesired micropores can develop that compromise the resulting integrity of the construct [152]. However, future investigations into optimal binders and polymers will likely overcome these issues. The success of 3DP technologies for the surface engineering of biomaterials will depend on work to study the capability of the technique to accommodate micro- and nanoscale features as needed for multiple applications, such as bone tissue engineering (for ingrowth, cell migration, and vascularization), as well as elucidation of polymers (and binder materials) that are compatible with this technique in a tissue engineering context. As with SLS, traditional surface chemistry modifications could be performed after the deposition of each layer to impart bioactivity or mechanical characteristics within the model, but efforts to incorporate such steps during 3DP would be welcomed. Also, as with SLS, the polymers must be supplied in powder-form to be compatible with the process. However, in contrast to SLS, because the whole process is performed without heat, it is possible that bioactive molecules or cells could be incorporated within the constructs, although this has not been extensively investigated. The capability of cell or protein co-deposition will depend on the use of biocompatible binders. This young technology has been licensed to several companies (<http://web.mit.edu/tdp>), and will certainly yield therapeutically useful constructs of sufficient mechanical and biochemical properties should the scope of compatible biomaterials be expanded.

Reproducible, porous scaffold architectures have also been generated by a related nozzle-based technique known as fused deposition molding (FDM). In this technology, a thermoplastic material is pumped through a heated nozzle to fabricate the device layer-by-layer. A z-axis stepper facilitates the process, and the nozzle diameter as well as the polymer melt thickness influences thickness (z-resolution). An advantage of this technique is the ability to deposit architectures that are porous in three dimensions by adjusting the horizontal distance between deposited filaments (fill gap). Initial studies are supportive of the utility of the approach. FDM was used for the fabrication of 3D interconnected porous and resorbable PCL scaffolds, with satisfactory biocompatibility and mechanical properties [155, 156]. Furthermore, tissue formation was demonstrated with osteoblast-like cells and fibroblasts within the construct, and the mechanical properties and porosity were controllable by process parameters. Similar positive results have been obtained with PCL/CaP and other polymer hybrid systems [157, 158]. However, the scope of FDM is limited by the amount of biomaterials that can be deposited in the manner described. Compatible materials must have the proper melt character-

istics that allow it to be extruded through the nozzle. Furthermore, FDM likely cannot be used to simultaneously deposit proteins or cells due to the melting process, as well potential viscosity modifications and nozzle clogging that would make the application very difficult. Z-resolution, as mentioned, is limited by the size of the extruded polymer filament. Nevertheless its application for PCL-based scaffolds warrants its further investigation, due to the favorable aspects of the polymer, such as its FDA-approved status and numerous tissue engineering applications that have already been investigated.

While each RP/SFF approach has its characteristic advantages and disadvantages, they each constitute major steps in the effort to rapidly and reliably produce functional tissue architectures. Given the wide variety of synthetic polymeric constructs that are compatible with these processes, the next step is to integrate these methods with natural polymers, such as ECM, which is underway in several laboratories. Furthermore, as many modifications such as surface chemistry are performed post-processing, the technology would greatly benefit from methods to incorporate such steps within the process itself when possible. Lastly, the further integration of SFF with established nanoengineering approaches discussed in this chapter will expand the capabilities of the constructs produced, especially if such nanoengineering can be performed following the deposition of each layer to develop highly-customized architectures. If these steps can be incorporated to some extent within these processes, the result will be a highly-tunable system for the development of “made to order” tissue engineering constructs that can be fabricated using CAD-based modeling that incorporates features specific to the patient’s needs.

## 12.15

### Conclusions

We have described both established and emerging biomaterial surface engineering technologies for the molecular-level presentation of information to cells. Each approach makes an overall contribution to the tissue engineering field by serving as a potential tool to tune the interfacial characteristics of a biomaterial for the optimal reconstruction of the tissue environment. The future will witness further advances in the effort to construct functional tissues with nanoscale precision through integrative strategies that control biochemical and topographical signaling, as nature-inspired developments in materials science continue to adapt to the criteria imposed by biology for recreating complex living systems.

### Acknowledgments

This chapter was made possible by funding from the Vanderbilt University Institute for Integrative Biosystems Research and Education (VIIBRE), and a graduate research fellowship to AL through the Vanderbilt Vision Research Center Training Grant (NE1 T32 EY07135).

## References

- 1 BHATIA, S. N., YARMUSH, M. L., TONER, M., Controlling cell interactions by micropatterning in co-cultures: Hepatocytes and 3T3 fibroblasts. *J. Biomed. Mater. Res.* **1997**, 34(2), 189–199.
- 2 FLEMMING, R. G., MURPHY, C. J., ABRAMS, G. A., GOODMAN, S. L., NEALEY, P. F., Effects of synthetic micro- and nano-structured surfaces on cell behavior. *Biomaterials* **1999**, 20(6), 573–588.
- 3 BLAWAS, A. S., REICHERT, W. M., Protein patterning. *Biomaterials* **1998**, 19(7–9), 595–609.
- 4 CLEMENCE, J. F., RANIERI, J. P., AEBISCHER, P., SIGRIST, H., Photoimmobilization of a bioactive laminin fragment and pattern-guided selective neuronal cell attachment. *Bioconj. Chem.* **1995**, 6(4), 411–417.
- 5 SUGAWARA, T., MATSUDA, T., Photochemical surface derivatization of a peptide-containing Arg-Gly-Asp (Rgd). *J. Biomed. Mater. Res.* **1995**, 29(9), 1047–1052.
- 6 SIGRIST, H., COLLILOUD, A., CLEMENCE, J. F., GAO, H., LUGINBUHL, R., SANGER, M., SUNDARABABU, G., Surface immobilization of biomolecules by light. *Opt. Eng.* **1995**, 34(8), 2339–2348.
- 7 PRITCHARD, D. J., MORGAN, H., COOPER, J. M., Patterning and regeneration of surfaces with antibodies. *Anal. Chem.* **1995**, 67(19), 3605–3607.
- 8 HENGSAKUL, M., CASS, A. E. G., Protein patterning with a photo-activatable derivative of biotin. *Bioconj. Chem.* **1996**, 7(2), 249–254.
- 9 KANE, R. S., TAKAYAMA, S., OSTUNI, E., INGBER, D. E., WHITESIDES, G. M., Patterning proteins and cells using soft lithography. *Biomaterials* **1999**, 20(23–24), 2363–2376.
- 10 HOLDEN, M. A., CREMER, P. S., Light activated patterning of dye-labeled molecules on surfaces. *J. Am. Chem. Soc.* **2003**, 125(27), 8074–8075.
- 11 HE, W., HALBERSTADT, C. R., GONSALVES, K. E., Lithography application of a novel photoresist for patterning of cells. *Biomaterials* **2004**, 25(11), 2055–2063.
- 12 DIAKOUMAKOS, C. D., DOUVAS, A., RAPTIS, I., KAKABAKOS, S., DIMOTIKALLI, D., TERZOUDI, G., ARGITIS, P., Dilute aqueous base developable resists for environmentally friendly and biocompatible processes. *Microelectron. Eng.* **2002**(61–62), 819–827.
- 13 DOUVAS, A., ARGITIS, P., MISIAKOS, K., DIMOTIKALI, D., PETROU, P. S., KAKABAKOS, S. E., Biocompatible photolithographic process for the patterning of biomolecules. *Biosens. Bioelectron.* **2002**, 17(4), 269–278.
- 14 DOUVAS, A., ARGITIS, P., DIAKOUMAKOS, C. D., MISIAKOS, K., DIMOTIKALI, D., KAKABAKOS, S. E., Photolithographic patterning of proteins with photoresists processable under biocompatible conditions. *J. Vacuum Sci. Technol. B* **2001**, 19(6), 2820–2824.
- 15 CHEN, C. C., HIRDES, D., FOLCH, A., Gray-scale photolithography using microfluidic photomasks. *Proc. Natl. Acad. Sci. U.S.A.* **2003**, 100(4), 1499–1504.
- 16 HOLDEN, M. A., JUNG, S. Y., CREMER, P. S., Patterning enzymes inside microfluidic channels via photo-attachment chemistry. *Anal. Chem.* **2004**, 76(7), 1838–1843.
- 17 HERMANSON, G. T., *Bioconjugate Techniques* Academic Press: San Diego, 1996, p. xxv, 785 pp.
- 18 LUEBKE, K. J., CARTER, D. E., GARNER, H. R., BROWN, K. C., Patterning adhesion of mammalian cells with visible light, tris(bipyridyl)ruthenium(II) chloride, and a digital micromirror array. *J. Biomed. Mater. Res. Part A* **2004**, 68A(4), 696–703.
- 19 SAMPSELL, J. B., Digital micromirror device and its application to projection displays. *J. Vacuum Sci. Technol. B* **1994**, 12(6), 3242–3246.
- 20 HAHN, M. S., TAITE, L. J., MOON, J. J., ROWLAND, M. C., RUFFINO, K. A.,

- WEST, J. L., Photolithographic patterning of polyethylene glycol hydrogels. *Biomaterials* **2005**.
- 21 LUO, Y., SHOICHEL, M. S., Light-activated immobilization of biomolecules to agarose hydrogels for controlled cellular response. *Biomacromolecules* **2004**, 5(6), 2315–2323.
- 22 LUO, Y., SHOICHEL, M. S., A photolabile hydrogel for guided three-dimensional cell growth and migration. *Nature Materials* **2004**, 3(4), 249–253.
- 23 REVZIN, A., RUSSELL, R. J., YADAVALLI, V. K., KOH, W. G., DEISTER, C., HILE, D. D., MELLOTT, M. B., PISHKO, M. V., Fabrication of poly(ethylene glycol) hydrogel microstructures using photolithography. *Langmuir* **2001**, 17(18), 5440–5447.
- 24 DALBY, M. J., RIEHLE, M. O., SUTHERLAND, D. S., AGHELI, H., CURTIS, A. S., Use of nanotopography to study mechanotransduction in fibroblasts – methods and perspectives. *Eur. J. Cell Biol.* **2004**, 83(4), 159–169.
- 25 CURTIS, A. S. G., WILKINSON, C. D., Reactions of cells to topography. *J. Biomater. Sci.-Polym. Ed.* **1998**, 9(12), 1313–1329.
- 26 WILKINSON, C. D. W., RIEHLE, M., WOOD, M., GALLAGHER, J., CURTIS, A. S. G., The use of materials patterned on a nano- and micro-metric scale in cellular engineering. *Mater. Sci. Eng. C-Biomimetic Supramol. Systems* **2002**, 19(1–2), 263–269.
- 27 CURTIS, A. S. G., GADEGAARD, N., DALBY, M. J., RIEHLE, M. O., WILKINSON, C. D. W., AITCHISON, G., Cells react to nanoscale order and symmetry in their surroundings. *IEEE Trans. Nanobiosci.* **2004**, 3(1), 61–65.
- 28 HARNETT, C. K., SATYALAKSHMI, K. M., COATES, G. W., CRAIGHEAD, H. G., Direct electron-beam patterning of surface coatings and sacrificial layers for micro-total analysis systems. *J. Photopolym. Sci. Technol.* **2002**, 15(3), 493–496.
- 29 HARNETT, C. K., SATYALAKSHMI, K. M., CRAIGHEAD, H. G., Low-energy electron-beam patterning of amine-functionalized self-assembled monolayers. *Appl. Phys. Lett.* **2000**, 76(17), 2466–2468.
- 30 DUPONT-GILLAIN, C. C., ALAERTS, J. A., DEWEZ, J. L., ROUXHET, P. G., Patterned layers of adsorbed extracellular matrix proteins: Influence on mammalian cell adhesion. *Bio-Med. Mater. Eng.* **2004**, 14(3), 281–291.
- 31 RAJNICEK, A. M., BRITLAND, S., McCAIG, C. D., Contact guidance of CNS neurites on grooved quartz: Influence of groove dimensions, neuronal age and cell type. *J. Cell Sci.* **1997**, 110, 2905–2913.
- 32 RAJNICEK, A. M., McCAIG, C. D., Guidance of CNS growth cones by substratum grooves and ridges: effects of inhibitors of the cytoskeleton, calcium channels and signal transduction pathways. *J. Cell Sci.* **1997**, 110, 2915–2924.
- 33 GADEGAARD, N., THOMS, S., MACINTYRE, D. S., MCGHEE, K., GALLAGHER, J., CASEY, B., WILKINSON, C. D. W., Arrays of nano-dots for cellular engineering. *Microelectron. Eng.* **2003**(67–68), 162–168.
- 34 DALBY, M. J., GADEGAARD, N., RIEHLE, M. O., WILKINSON, C. D. W., CURTIS, A. S. G., Investigating filopodia sensing using arrays of defined nanopits down to 35 nm diameter in size. *Int. J. Biochem. Cell Biol.* **2004**, 36(10), 2005–2015.
- 35 BIEBRICHER, A., PAUL, A., TINNEFELD, P., GOLZHAUSER, A., SAUER, M., Controlled three-dimensional immobilization of biomolecules on chemically patterned surfaces. *J. Biotechnol.* **2004**, 112(1–2), 97–107.
- 36 PETRONIS, S., GRETZER, C., KASEMO, B., GOLD, J., Model porous surfaces for systematic studies of material-cell interactions. *J. Biomed. Mater. Res. Part A* **2003**, 66A(3), 707–721.
- 37 SHIM, J., BERSANO-BEGEY, T. F., ZHU, X. Y., TKACZYK, A. H., LINDERMAN, J. J., TAKAYAMA, S., Micro- and nanotechnologies for studying cellular function. *Curr. Top. Med. Chem.* **2003**, 3(6), 687–703.
- 38 XIA, Y. N., WHITESIDES, G. M., Soft

- lithography. *Angew. Chem.-Int. Ed.* **1998**, 37(5), 551–575.
- 39 OSTUNI, E., KANE, R., CHEN, C. S., INGBER, D. E., WHITESIDES, G. M., Patterning mammalian cells using elastomeric membranes. *Langmuir* **2000**, 16(20), 7811–7819.
- 40 ZHAO, X. M., XIA, Y. N., WHITESIDES, G. M., Soft lithographic methods for nano-fabrication. *J. Mater. Chem.* **1997**, 7(7), 1069–1074.
- 41 WHITESIDES, G. M., OSTUNI, E., TAKAYAMA, S., JIANG, X. Y., INGBER, D. E., Soft lithography in biology and biochemistry. *Annu. Rev. Biomed. Eng.* **2001**, 3, 335–373.
- 42 KIM, E., XIA, Y. N., WHITESIDES, G. M., Polymer microstructures formed by molding in capillaries. *Nature* **1995**, 376(6541), 581–584.
- 43 ODOM, T. W., THALLADI, V. R., LOVE, J. C., WHITESIDES, G. M., Generation of 30–50 nm structures using easily fabricated, composite PDMS masks. *J. Am. Chem. Soc.* **2002**, 124(41), 12112–12113.
- 44 ODOM, T. W., LOVE, J. C., WOLFE, D. B., PAUL, K. E., WHITESIDES, G. M., Improved pattern transfer in soft lithography using composite stamps. *Langmuir* **2002**, 18(13), 5314–5320.
- 45 SCHMID, H., MICHEL, B., Siloxane polymers for high-resolution, high-accuracy soft lithography. *Macromolecules* **2000**, 33(8), 3042–3049.
- 46 FOLCH, A., TONER, M., Cellular micropatterns on biocompatible materials. *Biotechnol. Progr.* **1998**, 14(3), 388–392.
- 47 FOLCH, A., JO, B. H., HURTADO, O., BEEBE, D. J., TONER, M., Microfabricated elastomeric stencils for micropatterning cell cultures. *J. Biomed. Mater. Res.* **2000**, 52(2), 346–353.
- 48 TAKAYAMA, S., McDONALD, J. C., OSTUNI, E., LIANG, M. N., KENIS, P. J. A., ISMAGILOV, R. F., WHITESIDES, G. M., Patterning cells and their environments using multiple laminar fluid flows in capillary networks. *Proc. Natl. Acad. Sci. U.S.A.* **1999**, 96(10), 5545–5548.
- 49 TAKAYAMA, S., OSTUNI, E., LEDUC, P., NARUSE, K., INGBER, D. E., WHITESIDES, G. M., Selective chemical treatment of cellular microdomains using multiple laminar streams. *Chem. Biol.* **2003**, 10(2), 123–130.
- 50 UNGER, M. A., CHOU, H. P., THORSEN, T., SCHERER, A., QUAKE, S. R., Monolithic microfabricated valves and pumps by multilayer soft lithography. *Science* **2000**, 288(5463), 113–116.
- 51 McDONALD, J. C., DUFFY, D. C., ANDERSON, J. R., CHIU, D. T., WU, H. K., SCHUELLER, O. J. A., WHITESIDES, G. M., Fabrication of microfluidic systems in poly(dimethylsiloxane). *Electrophoresis* **2000**, 21(1), 27–40.
- 52 PINO, C. J., HASELTON, F. R., CHANG, M. S., Seeding of corneal wounds by epithelial cell transfer from micropatterned PDMS contact lenses. *Cell Transplant.* **2005**, 14(8), 565–571.
- 53 BOWDEN, N., HUCK, W. T. S., PAUL, K. E., WHITESIDES, G. M., The controlled formation of ordered, sinusoidal structures by plasma oxidation of an elastomeric polymer. *Appl. Phys. Lett.* **1999**, 75(17), 2557–2559.
- 54 HU, S. W., REN, X. Q., BACHMAN, M., SIMS, C. E., LI, G. P., ALLBRITTON, N., Surface modification of poly(dimethylsiloxane) microfluidic devices by ultraviolet polymer grafting. *Anal. Chem.* **2002**, 74(16), 4117–4123.
- 55 HU, S. W., REN, X. Q., BACHMAN, M., SIMS, C. E., LI, G. P., ALLBRITTON, N. L., Tailoring the surface properties of poly(dimethylsiloxane) microfluidic devices. *Langmuir* **2004**, 20(13), 5569–5574.
- 56 DUFFY, D. C., McDONALD, J. C., SCHUELLER, O. J. A., WHITESIDES, G. M., Rapid prototyping of microfluidic systems in poly(dimethylsiloxane). *Anal. Chem.* **1998**, 70(23), 4974–4984.
- 57 QIN, D., XIA, Y. N., WHITESIDES, G. M., Rapid prototyping of complex structures with feature sizes larger than 20  $\mu\text{m}$ . *Adv. Mater.* **1996**, 8(11), 917.
- 58 BURGIN, T., CHOONG, V. E., MARACAS,

- G., Large area submicrometer contact printing using a contact aligner. *Langmuir* **2000**, 16(12), 5371–5375.
- 59 ROGERS, J. A., PAUL, K. E., JACKMAN, R. J., WHITESIDES, G. M., Generating similar to 90 nanometer features using near-field contact-mode photolithography with an elastomeric phase mask. *J. Vacuum Sci. Technol. B* **1998**, 16(1), 59–68.
- 60 ROGERS, J. A., PAUL, K. E., WHITESIDES, G. M., Quantifying distortions in soft lithography. *J. Vacuum Sci. Technol. B* **1998**, 16(1), 88–97.
- 61 MRKSICH, M., CHEN, C. S., XIA, Y. N., DIKE, L. E., INGBER, D. E., WHITESIDES, G. M., Controlling cell attachment on contoured surfaces with self-assembled monolayers of alkanethiolates on gold. *Proc. Natl. Acad. Sci. U.S.A.* **1996**, 93(20), 10775–10778.
- 62 MRKSICH, M., DIKE, L. E., TIEN, J., INGBER, D. E., WHITESIDES, G. M., Using microcontact printing to pattern the attachment of mammalian cells to self-assembled monolayers of alkanethiolates on transparent films of gold and silver. *Exp. Cell Res.* **1997**, 235(2), 305–313.
- 63 TAKAYAMA, S., OSTUNI, E., LEDUC, P., NARUSE, K., INGBER, D. E., WHITESIDES, G. M., Laminar flows – Subcellular positioning of small molecules. *Nature* **2001**, 411(6841), 1016–1016.
- 64 LINDER, V., VERPOORTE, E., THORMANN, W., DE ROOIJ, N. F., SIGRIST, M., Surface biopassivation of replicated poly(dimethylsiloxane) microfluidic channels and application to heterogeneous immunoreaction with on-chip fluorescence detection. *Anal. Chem.* **2001**, 73(17), 4181–4189.
- 65 STEVENS, M. M., MAYER, M., ANDERSON, D. G., WEIBEL, D. B., WHITESIDES, G. M., LANGER, R., Direct patterning of mammalian cells onto porous tissue engineering substrates using agarose stamps. *Biomaterials* **2005**, 26(36), 7636–7641.
- 66 WALHEIM, S., BOLTAU, M., MLYNEK, J., KRAUSCH, G., STEINER, U., Structure formation via polymer demixing in spin-cast films. *Macromolecules* **1997**, 30(17), 4995–5003.
- 67 DALBY, M. J., RIEHLE, M. O., JOHNSTONE, H., AFFROSSMAN, S., CURTIS, A. S. G., In vitro reaction of endothelial cells to polymer demixed nanotopography. *Biomaterials* **2002**, 23(14), 2945–2954.
- 68 DALBY, M. J., RIEHLE, M. O., JOHNSTONE, H. J. H., AFFROSSMAN, S., CURTIS, A. S. G., Nonadhesive nanotopography: Fibroblast response to poly(n-butyl methacrylate)-poly(styrene) demixed surface features. *J. Biomed. Mater. Res. Part A* **2003**, 67A(3), 1025–1032.
- 69 DALBY, M. J., YARWOOD, S. J., RIEHLE, M. O., JOHNSTONE, H. J., AFFROSSMAN, S., CURTIS, A. S., Increasing fibroblast response to materials using nanotopography: Morphological and genetic measurements of cell response to 13-nm-high polymer demixed islands. *Exp. Cell Res.* **2002**, 276(1), 1–9.
- 70 BERRY, C. C., DALBY, M. J., MCCLOY, D., AFFROSSMAN, S., The fibroblast response to tubes exhibiting internal nanotopography. *Biomaterials* **2005**, 26(24), 4985–4992.
- 71 NAM, Y. S., PARK, T. G., Porous biodegradable polymeric scaffolds prepared by thermally induced phase separation. *J. Biomed. Mater. Res.* **1999**, 47(1), 8–17.
- 72 PEPPAS, N. A., KEYS, K. B., TORRES-LUGO, M., LOWMAN, A. M., Poly(ethylene glycol)-containing hydrogels in drug delivery. *J. Controlled Release* **1999**, 62(1–2), 81–87.
- 73 KEYS, K. B., ANDREPOULOS, F. M., PEPPAS, N. A., Poly(ethylene glycol) star polymer hydrogels. *Macromolecules* **1998**, 31(23), 8149–8156.
- 74 GROLL, J., FIEDLER, J., ENGELHARD, E., AMERINGER, T., TUGULU, S., KLOK, H. A., BRENNER, R. E., MOELLER, M., A novel star PEG-derived surface coating for specific cell adhesion. *J. Biomed. Mater. Res. Part A* **2005**, 74A(4), 607–617.
- 75 BANERJEE, P., IRVINE, D. J., MAYES, A. M., GRIFFITH, L. G., Polymer



- latexes for cell-resistant and cell-interactive surfaces. *J. Biomed. Mater. Res.* **2000**, 50(3), 331–339.
- 76 IRVINE, D. J., RUZETTE, A. V. G., MAYES, A. M., GRIFFITH, L. G., Nanoscale clustering of RGD peptides at surfaces using comb polymers. 2. Surface segregation of comb polymers in polylactide. *Biomacromolecules* **2001**, 2(2), 545–556.
- 77 IRVINE, D. J., MAYES, A. M., GRIFFITH, L. G., Nanoscale clustering of RGD peptides at surfaces using comb polymers. 1. Synthesis and characterization of comb thin films. *Biomacromolecules* **2001**, 2(1), 85–94.
- 78 LUPITSKY, R., ROITER, Y., TSITSILIANIS, C., MINKO, S., From smart polymer molecules to responsive nanostructured surfaces. *Langmuir* **2005**, 21(19), 8591–8593.
- 79 LOGAN, J., MASSE, P., SKOLNIK, A., FRANCIS, R., ANGOT, S., TATON, D., GNANOU, Y., DURAN, R. S., Novel dendrimer-like and star architectures of poly(ethylene oxide)-block-polystyrene copolymers as monolayers at the air/water interface. *Abstr. Papers Am. Chem. Soc.* **2003**, 225, U610–U610.
- 80 ZIMMERMAN, S. C., WENDLAND, M. S., RAKOW, N. A., ZHAROV, I., SUSLICK, K. S., Synthetic hosts by monomolecular imprinting inside dendrimers. *Nature* **2002**, 418(6896), 399–403.
- 81 ORAL, E., PEPPAS, N. A., Responsive and cognitive hydrogels using star polymers. *J. Biomed. Mater. Res. Part A* **2004**, 68A(3), 439–447.
- 82 LAHANN, J., KLEE, D., THELEN, H., BIENERT, H., VORWERK, D., HOCKER, H., Improvement of haemocompatibility of metallic stents by polymer coating. *J. Mater. Sci. Mater. Med.* **1999**, 10(7), 443–448.
- 83 LAHANN, J., KLEE, D., PLUESTER, W., HOECKER, H., Bioactive immobilization of r-hirudin on CVD-coated metallic implant devices. *Biomaterials* **2001**, 22(8), 817–826.
- 84 LAHANN, J., BALCELLS, M., RODON, T., LEE, J., CHOI, I. S., JENSEN, K. F., LANGER, R., Reactive polymer coatings: A platform for patterning proteins and mammalian cells onto a broad range of materials. *Langmuir* **2002**, 18(9), 3632–3638.
- 85 LAHANN, J., BALCELLS, M., LU, H., RODON, T., JENSEN, K. F., LANGER, R., Reactive polymer coatings: a first step toward surface engineering of microfluidic devices. *Anal. Chem.* **2003**, 75(9), 2117–2122.
- 86 CHEN, H. Y., ELKASABI, Y., LAHANN, J., Surface modification of confined microgeometries via vapor-deposited polymer coatings. *J. Am. Chem. Soc.* **2006**, 128(1), 374–380.
- 87 CHEN, H. Y., LAHANN, J., Fabrication of discontinuous surface patterns within microfluidic channels using photodefinable vapor-based polymer coatings. *Anal. Chem.* **2005**, 77(21), 6909–6914.
- 88 CHAN, K., GLEASON, K. K., Initiated chemical vapor deposition of linear and cross-linked poly(2-hydroxyethyl methacrylate) for use as thin-film hydrogels. *Langmuir* **2005**, 21(19), 8930–8939.
- 89 CORREA-DUARTE, M. A., WAGNER, N., ROJAS-CHAPANA, J., MORSCZECK, C., THIE, M., GIERSIG, M., Fabrication and biocompatibility of carbon nanotube-based 3D networks as scaffolds for cell seeding and growth. *Nano Lett.* **2004**, 4(11), 2233–2236.
- 90 WILBUR, J. L., KIM, E., XIN, Y. N., WHITESIDES, G. M., Lithographic molding – a convenient route to structures with submicrometer dimensions. *Adv. Mater.* **1995**, 7(7), 649–652.
- 91 HAMMOND, P. T., Form and function in multilayer assembly: New applications at the nanoscale. *Adv. Mater.* **2004**, 16(15), 1271–1293.
- 92 KHADEMOSSEINI, A., SUH, K. Y., YANG, J. M., ENG, G., YEH, J., LEVENBERG, S., LANGER, R., Layer-by-layer deposition of hyaluronic acid and poly-L-lysine for patterned cell co-cultures. *Biomaterials* **2004**, 25(17), 3583–3592.
- 93 MOHAMMED, J. S., DECOSTER, M. A., MCSHANE, M. J., Micropatterning of nanoengineered surfaces to study

- neuronal cell attachment in vitro. *Biomacromolecules* **2004**, 5(5), 1745–1755.
- 94 SHASTRI, V. P., LIPSKI, A. M., SY, J. C., ZNIDARSIĆ, W., CHOI, H., CHEN, I.-W., Functionalized Nanoparticles as Versatile Tools for the Introduction of Biomimetics on Surfaces in Nano-engineered Nanofibrous Materials, GUCERI, S. et al. (ed.), Kluwer Academic Publishers, **2004**, 257–264.
- 95 ZHENG, H. P., BERG, M. C., RUBNER, M. F., HAMMOND, P. T., Controlling cell attachment selectively onto biological polymer-colloid templates using polymer-on-polymer stamping. *Langmuir* **2004**, 20(17), 7215–7222.
- 96 JIANG, X. P., ZHENG, H. P., GOURDIN, S., HAMMOND, P. T., Polymer-on-polymer stamping: Universal approaches to chemically patterned surfaces. *Langmuir* **2002**, 18(7), 2607–2615.
- 97 SNEER, R., WEYGAND, M. J., KJAER, K., TIRRELL, D. A., RAPAPORT, H., Parallel beta-sheet assemblies at interfaces. *ChemPhysChem* **2004**, 5(5), 747–750.
- 98 RAPAPORT, H., MOLLER, G., KNOBLER, C. M., JENSEN, T. R., KJAER, K., LEISEROWITZ, L., TIRRELL, D. A., Assembly of triple-stranded beta-sheet peptides at interfaces. *J. Am. Chem. Soc.* **2002**, 124(32), 9342–9343.
- 99 RECHES, M., GAZIT, E., Casting metal nanowires within discrete self-assembled peptide nanotubes. *Science* **2003**, 300(5619), 625–627.
- 100 RANGANATHAN, D., SAMANT, M. P., KARLE, I. L., Self-assembling, cystine-derived, fused nanotubes based on spirane architecture: Design, synthesis, and crystal structure of cystinospiranes. *J. Am. Chem. Soc.* **2001**, 123(24), 5619–5624.
- 101 ZHANG, S. G., ALTMAN, M., Peptide self-assembly in functional polymer science and engineering. *Reactive Funct. Polym.* **1999**, 41(1–3), 91–102.
- 102 MI, L., FISCHER, S., CHUNG, B., SUNDELACRUZ, S., HARDEN, J. L., Self-assembling protein hydrogels with modular integrin binding domains, *Biomacromol* **2006**, 7, 38–47.
- 103 HARTGERINK, J. D., BENIASH, E., STUPP, S. I., Self-assembly and mineralization of peptide-amphiphile nanofibers. *Science* **2001**, 294(5547), 1684–1688.
- 104 LAMPIN, M., WAROCQUIER CLEROUT, R., LEGRIS, C., DEGRANGE, M., SIGOT LUIZARD, M. F., Correlation between substratum roughness and wettability, cell adhesion, and cell migration. *J. Biomed. Mater. Res.* **1997**, 36(1), 99–108.
- 105 ISHIKAWA, K., MIYAMOTO, Y., NAGAYAMA, M., ASAOKA, K., Blast coating method: New method of coating titanium surface with hydroxyapatite at room temperature. *J. Biomed. Mater. Res.* **1997**, 38(2), 129–134.
- 106 MAITZ, M. F., PHAM, M. T., MATZ, W., REUTHER, H., STEINER, G., RICHTER, E., Ion beam treatment of titanium surfaces for enhancing deposition of hydroxyapatite from solution. *Biomol. Eng.* **2002**, 19(2–6), 269–272.
- 107 DE MAEZTU, M. A., ALAVA, J. I., GAY-ESCODA, C., Ion implantation: Surface treatment for improving the bone integration of titanium and Ti6Al4V dental implants. *Clin. Oral Implants Res.* **2003**, 14(1), 57–62.
- 108 LEE, J. S., KAIBARA, M., IWAKI, M., SASABE, H., SUZUKI, Y., KUSAKABE, M., Selective adhesion and proliferation of cells on ion-implanted polymer domains. *Biomaterials* **1993**, 14(12), 958–960.
- 109 BACAKOVA, L., MARES, V., BOTTONE, M. G., PELLICCIARI, C., LISA, V., SVORCIK, V., Fluorine ion-implanted polystyrene improves growth and viability of vascular smooth muscle cells in culture. *J. Biomed. Mater. Res.* **2000**, 49(3), 369–379.
- 110 PIGNATARO, B., CONTE, E., SCANDURRA, A., MARLETTA, G., Improved cell adhesion to ion beam-irradiated polymer surfaces. *Biomaterials* **1997**, 18(22), 1461–1470.
- 111 SIOSHANSI, P., TOBIN, E. J., Surface treatment of biomaterials by ion beam processes. *Surf. Coatings Technol.* **1996**, 83(1–3), 175–182.
- 112 RANGEL, E. C., BENTO, W. C. A., KAYAMA, M. E., SCHREINER, W. H.,

- CRUZ, N. C., Enhancement of polymer hydrophobicity by SF6 plasma treatment and argon plasma immersion ion implantation. *Surf. Interface Anal.* **2003**, 35(2), 179–183.
- 113 THORWARTH, G., MANDL, S., RAUSCHENBACH, B., Plasma immersion ion implantation using titanium and oxygen ions. *Surf. Coatings Technol.* **2000**, 128, 116–120.
- 114 THORWARTH, G., MANDL, S., RAUSCHENBACH, B., Plasma immersion ion implantation of cold-work steel. *Surf. Coatings Technol.* **2000**, 125(1–3), 94–99.
- 115 MANOVA, D., HUBER, P., MANDL, S., RAUSCHENBACH, B., Surface modification of aluminium by plasma immersion ion implantation. *Surf. Coatings Technol.* **2000**, 128, 249–255.
- 116 MANDL, S., RAUSCHENBACH, B., Plasma immersion ion implantation. New technology for homogeneous modification of the surface of medical implants of complex shapes. *Biomedizinische Technik* **2000**, 45(7–8), 193–198.
- 117 MANDL, S., KRAUSE, D., THORWARTH, G., SADER, R., ZEILHOFER, F., HORCH, H. H., RAUSCHENBACH, B., Plasma immersion ion implantation treatment of medical implants. *Surf. Coatings Technol.* **2001**, 142, 1046–1050.
- 118 RÜCKER, V. C., HAVENSTRITE, K. L., SIMMONS, B. A., SICKAFOOSE, S. M., HERR, A. E., SHEDIAC, R., Functional antibody immobilization on 3-dimensional polymeric surfaces generated by reactive ion etching. *Langmuir* **2005**, 21(17), 7621–7625.
- 119 PONCIN-EPAILLARD, F., LEGEAY, G., Surface engineering of biomaterials with plasma techniques. *J. Biomater. Sci.-Polym. Ed.* **2003**, 14(10), 1005–1028.
- 120 JONES, J. R., EHRENFRIED, L. M., HENCH, L. L., Optimising bioactive glass scaffolds for bone tissue engineering. *Biomaterials* **2006**, 27(7), 964–973.
- 121 LENZA, R. F. S., VASCONCELOS, W. L., JONES, J. R., HENCH, L. L., Surface-modified 3D scaffolds for tissue engineering. *J. Mater. Sci.-Mater. Med.* **2002**, 13(9), 837–842.
- 122 KIM, H. W., KIM, H. E., KNOWLES, J. C., Fluor-hydroxyapatite sol-gel coating on titanium substrate for hard tissue implants. *Biomaterials* **2004**, 25(17), 3351–3358.
- 123 SATO, M., SLAMOVICH, E. B., WEBSTER, T. J., Enhanced osteoblast adhesion on hydrothermally treated hydroxyapatite/titania/poly(lactide-co-glycolide) sol-gel titanium coatings. *Biomaterials* **2005**, 26(12), 1349–1357.
- 124 DERNER, R., ANDERSON, A. C., The bone morphogenic protein. *Clin. Podiatr. Med. Surg. North Am.* **2005**, 22(4), 607–618, vii.
- 125 PINER, R. D., ZHU, J., XU, F., HONG, S. H., MIRKIN, C. A., “Dip-pen” nanolithography. *Science* **1999**, 283(5402), 661–663.
- 126 GINGER, D. S., ZHANG, H., MIRKIN, C. A., The evolution of dip-pen nanolithography. *Angew. Chem.-Int. Ed.* **2004**, 43(1), 30–45.
- 127 LEE, K. B., LIM, J. H., MIRKIN, C. A., Protein nanostructures formed via direct-write dip-pen nanolithography. *J. Am. Chem. Soc.* **2003**, 125(19), 5588–5589.
- 128 LEE, K. B., PARK, S. J., MIRKIN, C. A., SMITH, J. C., MRKSICH, M., Protein nanoarrays generated by dip-pen nanolithography. *Science* **2002**, 295(5560), 1702–1705.
- 129 CHOU, S. Y., KRAUSS, P. R., RENSTROM, P. J., Imprint of sub-25 nm vias and trenches in polymers. *Appl. Phys. Lett.* **1995**, 67(21), 3114–3116.
- 130 CHOU, S. Y., KRAUSS, P. R., RENSTROM, P. J., Nanoimprint lithography. *J. Vacuum Sci. Technol. B* **1996**, 14(6), 4129–4133.
- 131 HOFF, J. D., CHENG, L. J., MEYHOFER, E., GUO, L. J., HUNT, A. J., Nanoscale protein patterning by imprint lithography. *Nano Lett.* **2004**, 4(5), 853–857.
- 132 FALCONNET, D., PASQUI, D., PARK, S., ECKERT, R., SCHIFT, H., GOBRECHT, J., BARBUCCI, R., TEXTOR, M., A novel approach to produce protein nanopatterns by combining nanoimprint lithography and molecular self-assembly. *Nano Lett.* **2004**, 4(10), 1909–1914.

- 133 DYER, P. E., JENKINS, S. D., SIDHU, J., Novel method for measuring excimer laser ablation thresholds of polymers. *Appl. Phys. Lett.* **1988**, 52(22), 1880–1882.
- 134 DYER, P. E., SIDHU, J., Excimer laser ablation and thermal coupling efficiency to polymer-films. *J. Appl. Phys.* **1985**, 57(4), 1420–1422.
- 135 ROMANOS, G. E., EVERTS, H., NENTWIG, G. H., Effects of diode and Nd: YAG laser irradiation on titanium discs: A scanning electron microscope examination. *J. Periodontol.* **2000**, 71(5), 810–815.
- 136 MELLO, A. P., BARI, M. A., PRENDERGAST, P. J., A comparison of excimer laser etching and dry etching process for surface fabrication of biomaterials. *J. Mater. Processing Technol.* **2002**, 124(3), 284–292.
- 137 SMAUSZ, T., HOPP, B., KRESZ, N., Pulsed laser deposition of compact high adhesion polytetrafluoroethylene thin films. *J. Phys. D-Appl. Phys.* **2002**, 35(15), 1859–1863.
- 138 CRISTESCU, R., SOCOL, G., MIHAILESCU, I. N., POPESCU, M., SAVA, F., ION, E., MOROSANU, C. O., STAMATIN, I., New results in pulsed laser deposition of poly-methyl-methacrylate thin films. *Appl. Surf. Sci.* **2003**, 208, 645–650.
- 139 SAVA, F., CRISTESCU, R., SOCOL, G., RADVAN, R., SAVASTRU, R., SAVASTRU, D., Structure of bulk and thin films of poly-methyl-methacrylate (PMMA) polymer prepared by pulsed laser deposition. *J. Optoelectronics Adv. Mater.* **2002**, 4(4), 965–970.
- 140 PHADKE, R. S., AGARWAL, G., Laser-assisted deposition of preformed mesoscopic systems. *Mater. Sc. Eng. C-Biomim. Supramol. Systems* **1998**, 5(3–4), 237–241.
- 141 WU, P. K., RINGEISEN, B. R., CALLAHAN, J., BROOKS, M., BUBB, D. M., WU, H. D., PIQUE, A., SPARGO, B., MCGILL, R. A., CHRISEY, D. B., The deposition, structure, pattern deposition, and activity of biomaterial thin-films by matrix-assisted pulsed-laser evaporation (MAPLE) and MAPLE direct write. *Thin Solid Films* **2001**, 398, 607–614.
- 142 BUBB, D. M., RINGEISEN, B. R., CALLAHAN, J. H., GALICIA, M., VERTES, A., HORWITZ, J. S., MCGILL, R. A., HOUSER, E. J., WU, P. K., PIQUE, A., CHRISEY, D. B., Vapor deposition of intact polyethylene glycol thin films. *Appl. Phys. a-Mater. Sci. Processing* **2001**, 73(1), 121–123.
- 143 NAHMIAS, Y., SCHWARTZ, R. E., VERFAILLIE, C. M., ODDE, D. J., Laser-guided direct writing for three-dimensional tissue engineering. *Biotechnol. Bioeng.* **2005**, 92(2), 129–136.
- 144 CHEN, G. P., USHIDA, T., TATEISHI, T., Scaffold design for tissue engineering. *Macromol. Biosci.* **2002**, 2(2), 67–77.
- 145 TSANG, V. L., BHATIA, S. N., Three-dimensional tissue fabrication. *Adv. Drug Delivery Rev.* **2004**, 56(11), 1635–1647.
- 146 COOKE, M. N., FISHER, J. P., DEAN, D., RIMNAC, C., MIKOS, A. G., Use of stereolithography to manufacture critical-sized 3D biodegradable scaffolds for bone ingrowth. *J. Biomed. Mater. Res. Part B-Appl. Biomater.* **2003**, 64B(2), 65–69.
- 147 MATSUDA, T., MIZUTANI, M., Liquid acrylate-endcapped biodegradable poly(epsilon-caprolactone-co-trimethylene carbonate). II. Computer-aided stereolithographic microarchitectural surface photoconstructs. *J. Biomed. Mater. Res.* **2002**, 62(3), 395–403.
- 148 ZHANG, X., JIANG, X. N., SUN, C., Micro-stereolithography of polymeric and ceramic microstructures. *Sensors Actuators A-Phys.* **1999**, 77(2), 149–156.
- 149 RIMELL, J. T., MARQUIS, P. M., Selective laser sintering of ultra high molecular weight polyethylene for clinical applications. *J. Biomed. Mater. Res.* **2000**, 53(4), 414–420.
- 150 HUTMACHER, D. W., SITTINGER, M., RISBUD, M. V., Scaffold-based tissue engineering: Rationale for computer-aided design and solid free-form fabrication systems. *Trends Biotechnol.* **2004**, 22(7), 354–362.
- 151 TAN, K. H., CHUA, C. K., LEONG, K. F.,

- CHEAH, C. M., CHEANG, P., ABU BAKAR, M. S., CHA, S. W., Scaffold development using selective laser sintering of polyetheretherketone-hydroxyapatite biocomposite blends. *Biomaterials* **2003**, 24(18), 3115–3123.
- 152 LAM, C. X. F., MO, X. M., TEOH, S. H., HUTMACHER, D. W., Scaffold development using 3D printing with a starch-based polymer. *Mater. Sci. Eng. C-Biomimetic Supramol. Systems* **2002**, 20(1–2), 49–56.
- 153 PARK, A., WU, B., GRIFFITH, L. G., Integration of surface modification and 3D fabrication techniques to prepare patterned poly(L-lactide) substrates allowing regionally selective cell adhesion. *J. Biomater. Sci.-Polym. Ed.* **1998**, 9(2), 89–110.
- 154 SHERWOOD, J. K., RILEY, S. L., PALAZZOLO, R., BROWN, S. C., MONKHOUSE, D. C., COATES, M., GRIFFITH, L. G., LANDEEN, L. K., RATCLIFFE, A., A three-dimensional osteochondral composite scaffold for articular cartilage repair. *Biomaterials* **2002**, 23(24), 4739–4751.
- 155 HUTMACHER, D. W., SCHANTZ, T., ZEIN, I., NG, K. W., TEOH, S. H., TAN, K. C., Mechanical properties and cell cultural response of polycaprolactone scaffolds designed and fabricated via fused deposition modeling. *J. Biomed. Mater. Res.* **2001**, 55(2), 203–216.
- 156 ZEIN, I., HUTMACHER, D. W., TAN, K. C., TEOH, S. H., Fused deposition modeling of novel scaffold architectures for tissue engineering applications. *Biomaterials* **2002**, 23(4), 1169–1185.
- 157 ENDRES, M., HUTMACHER, D. W., SALGADO, A. J., KAPS, C., RINGE, J., REIS, R. L., SITTINGER, M., BRANDWOOD, A., SCHANTZ, J. T., Osteogenic induction of human bone marrow-derived mesenchymal progenitor cells in novel synthetic polymer-hydrogel matrices. *Tissue Eng.* **2003**, 9(4), 689–702.
- 158 RAI, B., TEOH, S. H., HO, K. H., HUTMACHER, D. W., CAO, T., CHEN, F., YACOB, K., The effect of rhBMP-2 on canine osteoblasts seeded onto 3D bioactive polycaprolactone scaffolds. *Biomaterials* **2004**, 25(24), 5499–5506.

## Index

- 3D cell organization 10
  - 3D cellular matrices 465
  - 3D matrix adhesion 150
  - 3D nanofibrous scaffolds 139
  - 3D porous biodegradable scaffolds 316
  - 3D printing 494
  - 3D structure
    - bone tissue engineering 102
    - construction 318
  - 3T3 fibroblasts 343–344, 347
  - 4HNE *see* 4-hydroxy-2-nonenal
- a**
- absorption, nano-pharmacology 375–377
  - absorption kinetics, nanofiber scaffolds 74–76
  - absorption patterns, carbon nanotubes 350
  - actin-based nanostructure transport 423
  - additives, carbon nanotubes 348
  - adhesion
    - electrospun scaffolds 150
    - human dermal fibroblasts 465
    - stem cells 43–47
  - adhesion proteins, tissue formation 202–203
  - adsorption
    - cell adhesion molecules 146–147
    - electrospun scaffolds 146
  - adult stem cells 110
    - *see also* stem cells
  - AFM *see* atomic force microscopy
  - age associated disorders, free radicals 365
  - age-related macular degeneration (AMD)
    - magnetic nanoparticles 323
    - nanofibers application 90
  - agglomeration, nano-pharmacology 376
  - alginate-HA nanocrystals scaffold 292
  - aligned nanofibrous scaffolds 144
  - aligned polymeric nanofiber matrices 47
  - alkanethiols, self-assembly 481
  - allografting
    - organ shortage 2
    - therapeutic problems 216
  - alumina nanofibers, orthopedic tissues 268
  - Alzheimer's disease, oxidative stress 365
  - AMD *see* age-related macular degeneration
  - AML *see* antibody-conjugated magnetoliposomes
    - magnetic nanoparticles 313–316
    - MSC expansion 313
  - amphiphile, structure 37
  - amphiphilic peptides (PA), self-assembly 34
  - antibody-conjugated magnetoliposomes (AML) 308
    - magnetic nanoparticles 313–316
    - MSC expansion 313
  - antibody-mediated recognition 397
  - antioxidants 366, 377–379
  - AP-NT *see* as purchased nanotubes
  - apatites, bone tissue 288–292
  - aprotic solvent, electrospinning 143
  - aqueous solvents, nanoparticle synthesis 391
  - arginine-glycine-aspartate (RGD) 137
  - arginine-glycine-aspartateserine (GRGDS) 18
  - as purchased nanotubes (AP-NT) 343
  - atomic force microscopy (AFM) 22
  - ATP-binding 423
  - autografting
    - organ shortage 2
    - therapeutic problems 216
- b**
- benzyl triethylammonium chloride (BTEAC) 143
  - bimodal particle distributions, chemical patterns 410
  - bioactive glasses, sol-gel technology 486
  - bioactive molecules
    - coated 168
    - functionalized hydroxyapatite 296–300
  - bioactive peptides, scaffolds 137

- bioactive scaffolds, tissue engineering 1
  - bioceramics, bone tissue 290
  - biochemical reactions, oxidative stress 367
  - biocompatibility
    - implants 82–87
    - synthetic polymers 69
  - biocompatible nanofibers, reverse transcription-polymerase chain reaction (RT-PCR) 86
  - biocompatible photoresist, photolithography 463
  - bioconjugated nanowires 422
  - bioconjugation 396–400
  - biodegradable polymers 76, 235
    - synthetic 236
  - biogenic hydroxyapatite 284–288
  - biological tissues, mechanical properties 229
  - biologically inspired hydroxyapatite 292–296
  - biomass production, cerium 369
  - biomaterials
    - clinical uses 218
    - electrospun scaffolds 151–168
    - mechanical properties 229
    - nanophase 216–256
    - self-assembly 481
    - surfaces 461–505
    - types 88
  - biomimesis 471
  - biomimetic hydroxyapatite 288–292
  - biomimetic nano-scaffold 115
  - biomimetic surface modification 18
  - biomolecular recognition, surface passivation 397
  - biomolecule delivery 425–437
  - biomolecule-labeled magnetic microspheres, cytoskeletal manipulation 406
  - biopatterning, photolithography 462
  - biopolymers 69
  - biopsy 219
  - bioreabsorbability, biomimetic hydroxyapatite 289
  - bioresist, photolithography 463
  - bioresorbable implant, neural tissue engineering 96
  - bioresorbable polymers 3
  - biotin-4-fluorescein, photoimmobilization 464
  - blood vessels
    - engineered tissues 170–171
    - scaffold 106
    - tissue engineering 49–54, 105–106
    - tissue formation 208–214
    - tubular structure 329
  - bone
    - biogenic hydroxyapatite 284–288
    - engineered tissues 172
    - graft substitute 86
    - hierarchical structure 225
    - nanocomponents 260
    - nanofibers application 102
  - bone hydroxyapatite, deproteinized 285
  - bone implants 258
  - bone ingrowth 277
  - bone marrow aspiration, magnetic nanoparticles 310
  - bone regeneration 104
    - increased 266
  - bone tissue engineering 54–55, 84–85, 206–207
    - 3D structure 102
    - carbon nanotubes 104
    - nanotexturing 103
  - bone tissue reaction, hydroxyapatite 293
  - bone tissue substitute 283–307
  - bovine serum albumin (BSA), intracellular sensing 421
  - BP *see* geminal bisphosphonate
  - BSA *see* bovine serum albumin
  - BTEAC *see* benzyl triethylammonium chloride
- c**
- C17-2
    - neural stem cell (NSC) 175
    - *see also* stem cells
  - CA *see* cellulose acetate
  - cadmium, toxicity 399
  - calcium phosphate/collagen composites, mechanical behavior 294
  - calcium phosphates, bone substitute 284
  - cancer therapy 442
    - drug delivery 427–432
  - carbodiimide chemistry, surface immobilization 19
  - carbon nanofibers (CN) 275
  - carbon nanotubes 338–360
    - bone tissue engineering 104
    - carboxylic acid groups 349
    - cellular viability 350
    - electromagnetic fields 339
    - free radicals 373–374
    - hydroxyapatite (HA) 354
    - polyethyleneimine (PEI) 354–355
    - purification 342–351
    - single stranded DNA (ssDNA) 349
    - specific applications 352
  - carboxyfullerenes, free radicals 374

- carboxylic acid groups, carbon nanotubes 349
- cardiac muscle, tissue formation 208
- cardiac tissue engineering 49–54
  - cardiomyocytes 52–53
- cardiomyocyte contraction, engineered tissues 174
- cardiomyocytes, cardiac tissue engineering 52–53
- cardiovascular disorders, nanoparticle antioxidants 378
- cardiovascular tissue, formation 208
- cartilage
  - engineered tissues 171
  - nanofibers application 102
  - tissue engineering 54–55
  - tissue formation 205–206
- cartilage associated genes, reverse transcription-polymerase chain reaction 171
- cartilage oligomeric matrix protein (COMP) 149
- $\alpha$ CD105-AMs 314
- cell-matrix contact types 17
- cell adhesion 400–411
  - colloidal lithography 404
  - cytoskeletal manipulation 406–407
  - extracellular matrix (ECM) 15, 402
  - future applications 407–411
  - human mesenchymal bone marrow 22
  - integrin-mediated 18
  - magnetic particles 408
  - PC12 micropositioning 401
  - peptides 321, 408
  - titanium 272, 405
- cell adhesion molecules, adsorption 146–147
- cell attachment, tissue formation 202
- cell behavior
  - ECM mechanisms 15
  - nano-based matrices 39–43
- cell-cell interactions, magnetic nanoparticles 326
- cell-ceramic scaffold interactions, scaffold processing 244–247
- cell culture techniques 4
- cell-ECM interaction, electrospun scaffolds 147–148
- cell engineering 361–387
- cell functions, competitive 265
- cell fusion 11
- cell isolation, magnetic nanoparticles 310
- cell-matrix contacts 403
- cell-matrix interactions, scaffold processing 244, 248
- cell orientation, ECM 15
- cell pellet (CP) culture, tissue engineering 56
- cell phenotype, electrospun scaffolds 148–149
- cell plasma membrane 412
- cell-polymer interactions, scaffold processing 247
- cell printing, synthetic scaffolds 10
- cell proliferation 40
- cell-seeding
  - magnetic nanoparticles 316
  - mag-seeding 317
- cell sheet engineering 318–321
- cell sheets, magnetic nanoparticles 328
- cell signaling pathway, electrospun scaffolds 150
- cell sorting, cytoskeletal manipulation 406
- cell surface receptors, ECM mechanisms 15
- cells, nanostructures 389–390
- cellular affinity 396
- cellular engineering 388–460
  - chemical patterns 409
- cellular entry 411
  - alternative routes 415
  - endocytosis 412
  - particle size 414
  - receptor-mediated uptake 413
- cellular havoc, free radicals 364
- cellular recognition 259
  - nanoparticle synthesis 398
- cellular response
  - functionalized hydroxyapatite 300
  - nanotopographies 473
- cellular scaffold 136
- cellular viability, carbon nanotubes 350
- cellulose acetate (CA) 167
- central nervous system (CNS) 94
- ceramic nanobiomaterials 227–234
- ceramic nanomaterials, orthopedic tissues 262
- cerium
  - biological effects 369
  - oxidative stress 367–374
  - redox capabilities 368
- cerium distribution, mouse tissue 375
- cerium oxide nanoparticles, biological effects 370–373
- charge density, electrospinning 143
- chemical patterns
  - cell adhesion 409
  - gold particles 410
  - nanoscale 405–406
- chemical tuned biomaterials, self-assembly 479



- chemical vapor deposition (CVD) 476  
chemoselective ligation, surface  
  immobilization 19  
chitin, electrospun natural scaffolds 161  
chitosan 84, 161, 236  
chondrocytes 147  
choroidal neovascularization (CNV) 323  
chymotrypsin, protein manipulation 439  
cisplatin desorption, functionalized  
  hydroxyapatite 299  
CN *see* carbon nanofibers  
CNS *see* central nervous system  
CNV *see* choroidal neovascularization  
coatings  
  – electrospun scaffolds 168  
  – HA-collagen 292–296  
collagen 84  
  – carbon nanotubes 341  
  – ECM ultratructure 13  
  – electrospun scaffolds 151, 168  
  – natural extracellular matrix 189  
  – neural tissue engineering 95  
  – ophthalmology 91  
  – wound dressing 100  
collagen-elastin nanofibrous mesh, vascular  
  grafts 108  
collagen fibers, quarter stagger model 286  
collagen fibers/HA composites, biologically  
  inspired 293  
collagen fibrils 12  
  – arrangement patterns 14  
  – carbon nanotubes 353  
collagen-GAG scaffolds 92  
collagen-glycosaminoglycan (GAG) 91  
collagen I polypeptidic chain 286  
collagen molecule assembling 295  
collector, electrospinning 191  
colloidal lithography  
  – cell adhesion 404  
  – lattice 405  
colloidal stabilization, functionalized  
  hydroxyapatite 298  
COMP *see* cartilage oligomeric matrix  
  protein  
competitive cell functions 265  
composite scaffolds 353  
  – polymeric nanofibrous 166–168  
composites  
  – HA-collagen 292–296  
  – nanofibrous scaffolds 198–201  
  – nanotube 354  
  – natural-natural 166  
  – natural-synthetic 167  
  – orthopedic tissues 274–277  
  – poly(lactic-co glycolic acid) (PLGA):titania  
    275  
  – poly-etherurethane:carbon nanofiber  
    276  
  – polymers 70, 166–168  
computer-assisted design  
  – scaffolds 76  
  – tissue engineering 7–8  
computer-guided manufacturing, tissue  
  engineering 493  
conductivity  
  – electrospinning 143  
  – nanofibers 81–82  
conjugation strategies, biomolecules 396  
connective tissue, tissue formation 205  
contact types, cell-matrix 17  
copolymers 70  
cornea disease 89  
covalent stabilization, self-assembled  
  nanofibers 38  
CP *see* cell pellet  
critical grain size, osteoblast performance  
  264  
current therapies 216–219  
CVD *see* chemical vapor deposition  
cyto-compatibility, enhanced 257  
cytoskeleton 411, 422  
  – cell adhesion 406–407
- d**  
DDS *see* drug delivery systems  
dental implants, current implants 258  
dickkopf-1 (Dkk-1) 313  
differentiation  
  – stem cells 43–47, 149–150  
  – tissue formation 203–204  
N,N-dimethylformamide (DMF) 143  
dip-pen nanolithography (DPN) 487  
disease  
  – oxidative stress 365–366  
  – treatment 377–379  
Dkk-1 *see* dickkopf-1  
DMF *see* N,N-dimethylformamide  
DNA binding, intracellular sensing 420  
DNA delivery, frontiers 437  
dose  
  – cerium oxide nanoparticles 370  
  – nano-pharmacology 376–377  
DPN *see* dip-pen nanolithography  
drug delivery  
  – electrospun polymers 114  
  – growth factors 113  
  – RES recognition 427  
  – smart delivery vehicles 435

- drug delivery systems (DDS) 425–432, 434
  - cancer therapy 427–432
  - magnetic nanoparticles 308
  - polymer nanofibers 112
- drug release, inorganic composites 201
- dyes, intracellular sensing 417
- dynamic collection grids, scaffold fabrication 192
- e**
- e-beam resists 466
- ear, tissue engineered 11
- EBL *see* electron-beam lithography
- ECM *see* extracellular matrix
- ECM / cell interactions 16
- elastin, electrospun natural scaffolds 160
- electric-arc technique, carbon nanotubes purification 343
- electrolytic deposition, hydroxyapatite 294
- electromagnetic fields, carbon nanotubes 339
- electron-beam lithography 466–467
- electrospinning 73–74, 135–187
  - apparatus 141
  - enzyme encapsulation 31
  - experimental system 240–241
  - fiber alignment 29–30
  - fiber collector types 242
  - fiber morphology 27–29
  - nanofibers 79–80
  - nanofibrous scaffolds 139
  - NPC differentiation 45
  - poly(ethylene oxide) (PEO) 26
  - polymeric nanofiber scaffolds 24
  - polymers 152–158
  - porosity 145–146
  - process 140–144
  - process parameters 25
  - scaffold fabrication 190–192
  - scaffold processing 240
  - working parameters 142–144
- electrospraying, polymeric nanofiber scaffolds 25
- electrospun fibers, orientation 192
- electrospun polymers, drug delivery 114
- electrospun scaffolds 151–168, 243
  - 3D matrix adhesion 150
  - adsorption 146
  - cartilage oligomeric matrix protein (COMP) 149
  - coatings 168
  - synthetic 167
- embryonic stem cells 109
- enamel carbonated hydroxyapatite 287
- endocytosis, cellular entry 412
- endocytotic delivery 412–414
- endocytotic pathway 413
- endosome rupture, intracellular delivery 419
- endothelial cells, growth on scaffolds 107
- endothelialization, blood vessel scaffold 106–107
- engineered tissues 169
  - blood vessels 170–171
  - bone 172
  - cardiomyocyte contraction 174
  - muscle 173
  - nerve 175
  - transforming growth factor- $\beta$  (TGF- $\beta$ ) 176
- enzymatic digestion, polymer additives 341
- enzyme actions, oxidative stress 367
- enzyme encapsulation 31
- enzymes, protein manipulation 438–439
- epithelial sheets fabrication 322
- epithelialization, skin 99
- excretion, nano-pharmacology 377
- extracellular matrix (ECM)
  - cell adhesion 402
  - cellular function 15
  - photolithography 462
  - scaffold 3–4
  - self-assembling molecules 34–35
  - tissue engineering 1
  - tissue repair
  - ultrastructure 13
- f**
- factor delivery scaffolds, inorganic composites 201
- FAK *see* focal adhesion kinase
- FDM *see* fused deposition model
- Fe<sub>3</sub>O<sub>4</sub> particles 308
- ferritin molecules, DNA delivery 437
- FGF-2 *see* fibroblast growth factor-2
- fiber alignment, electrospinning 29–30
- fiber collector types, electrospinning 242
- fiber morphology, electrospinning 27–29
- fiber orientation
  - cardiac tissue engineering 51
  - scaffold processing 247
- fiber strength 80
- fibrinogen, electrospun natural scaffolds 160
- fibroblast adhesion, nanolithography 488
- fibroblast cells, proliferation 79
- fibroblast function, orthopedic tissues 267
- fibroblast growth factor-2 (FGF-2) 312
- fibrosis, nanotubes 380
- fluorescence resonance energy transfer (FRET) 420
- fluorescent CdSe/ZnS quantum dots 420

- fluorite lattice structure, rare earth oxides 367
- focal adhesion kinase (FAK) 41  
– electrospun scaffolds 150
- free proteins, protein manipulation 438–439
- free radical hypothesis, aging 365
- free radical scavengers 366  
– engineered nanoparticles 361
- free radicals 362–366  
– carbon nanotubes 373–374  
– generation 363
- FRET *see* fluorescence resonance energy transfer
- fullerene derivatives, free radicals 373–374
- functional SWNT, scaffold template 354
- functionalized hydroxyapatite 296–300  
– magnetic susceptibility 301
- functionalized magnetic nanoparticles 309
- functionalized peptides, cardiac tissue engineering 52
- fused deposition model (FDM) 8
- g**
- GA *see* glycolic acid
- GA-NT *see* glucosamine functionalized nanotubes
- GAG *see* collagen-glycosaminoglycan
- gelatin 235  
– electrospun natural scaffolds 159
- geminal bisphosphonates (BPs), functionalized hydroxyapatite 299
- gene therapy 426–427, 432–437  
– future directions 436–437  
– magnetotransfection 434  
– tissue engineering 2
- glass substrate, nano-based matrices 40
- glucosamine functionalized nanotubes (GA-NT) 343
- glucose transfer rate, carbon nanotubes 351
- glycolic acid (GA) 7
- gold  
– gene therapy 433  
– hyperthermia 430  
– nanoparticle synthesis 392
- gold particles, chemical patterns 410
- gold-plated biomaterials, nanolithography 488
- gold quantum dots, intracellular sensing 420
- Goniopora coral morphology, biomimetic hydroxyapatite 291
- graft delivery system, cell sheet engineering 321
- graft rejection, therapeutic problems 217
- GRGDS *see* arginine-glycine-aspartateserine
- growth factors  
– drug delivery 113  
– ECM mechanisms 15
- guidance channels, neural tissue engineering 96
- guided bone regeneration membrane 104
- h**
- HA *see* hydroxyapatite, hyaluronic acid
- HAEC *see* labeled human aortic endothelial cells
- HAP *see* hydroxyapatite
- hard gelatin capsule, drug delivery 113
- HBMSC *see* human mesenchymal bone marrow stromal cell
- HCAEC *see* human coronary artery endothelial cells  
– viability 108
- heart grafts, nanofibers application 105–109
- helical rosette nanotubes, orthopedic tissues 269–270
- hematopoietic stem cells (HSC) 221
- hepatocytes  
– magnetic nanoparticles 327  
– nanofibers application 94  
– PCLEEP nanofibers 95
- heterotypic interactions, magnetic nanoparticles 326
- hip replacements, current implants 258
- HIV virus transmission, bound proteins 440
- HLF *see* human ligament fibroblasts
- human aortic valves, collagen fibrils 12
- human coronary artery endothelial cells (HCAEC) 50
- human dermal fibroblasts, adhesion 465
- human disease states, oxidative stress 363
- human ligament fibroblasts (HLF) 54–55
- human mesenchymal bone marrow stromal cell (HBMSC) adhesion 22
- human umbilical vein endothelial cells (HUVEC) 39
- HUVEC  
– adhesion potential *see* human umbilical vein endothelial cells  
– laser guided direct writing (LGDW) 492
- hyaluronan, electrospun natural scaffolds 161
- hyaluronic acid (HA), self-assembly 480
- 4-hydroxy-2-nonenal (4HNE) 362
- hydroxyapatite (HA) 199, 227  
– biogenic 284–288  
– biologically inspired 292–296  
– biomimetic 288–292  
– bone substitute 283–307

- hydroxyapatite (HA) (cont.)  
 – carbon nanotubes 354  
 – coating 277  
 – crystal structure 288  
 – enamel carbonated 287  
 – fabrication methods 231  
 – functionalized 296–300  
 – hydrothermal process 232  
 – nanocrystals 296–300  
 – orthopedic tissues 267, 277  
 – properties 230  
 – scaffold processing 244–245  
 – self-assembling molecules 36  
 – slurries 298  
 hydroxyapatite-collagen composites 292–296  
 $\alpha$ -hydroxyester 5  
 hyperthermia  
 – cancer treatment 429  
 – gold 430
- i**  
 IBAD *see* ion beam-assisted deposition  
 IgG conjugates, specific binding 397  
 IKVAV *see* isoleucine-lysine-valine-alanine-valine  
 immunicon magnetic nanoparticles 407  
 implant performance, improvement 260–271  
 implants, biocompatibility 82–87  
 inflammatory disorders, disease treatment 378  
 initial protein interactions 259  
 inorganic composites  
 – drug release 201  
 – scaffold fabrication 199–200  
 integrin binding, cell adhesion 402  
 integrin ligand RGD peptides, cell sheet engineering 321  
 integrins  
 – ECM mechanisms 15  
 – RGD binding 19  
 internal pore structure, PLLA matrix 198  
 internalized nanostructures 443  
 intracellular cerium oxide 372  
 intracellular free radicals, sources 362–363  
 intracellular mechanisms, cerium oxide nanoparticles 372  
 intracellular sensing 416–419  
 – bovine serum albumin (BSA) 421  
 – fluorescent CdSe/ZnS quantum dots 420  
 intracellular transport 421–425  
 ion beam-assisted deposition (IBAD), surface engineering 484  
 ion beam surface engineering 483–485  
 ion channels, protein manipulation 439–443  
 ion implantation strategies, surface engineering 484  
 ionic self-complementary peptide, self-assembling molecules 36  
 iron oxide, free radicals 373  
 ischemic heart disease, disease treatment 378  
 isoleucine-lysine-valine-alanine-valine (IKVAV) 44
- k**  
 keratinocyte sheet construction 321–323  
 keratoprosthesis, ophthalmology 89
- l**  
 LA *see* lactic acid  
 labeled human aortic endothelial cells (HAEC) 326  
 lactic acid (LA), synthetic scaffolds 7  
 lanthanides, rare earth oxides 367  
 laser guided direct writing (LGDW) 491  
 – HUVEC deposition 492  
 laser-guided strategies 489–492  
 laser scanning confocal microscopy (LSCM), scaffold processing 247  
 layer by layer (LbL), self-assembly 477, 480  
 layered cell-cell interactions 321  
 LbL *see* layer by layer  
 LCST *see* lower critical solution temperature  
 LGDW *see* laser guided direct writing  
 ligaments  
 – engineered tissues 175  
 – histological sections 206  
 – tissue engineering 54–55  
 – tissue formation 205  
 ligand exchange, nanowire synthesis 395  
 lipid peroxidation chain reaction, cell engineering 362  
 liquid-liquid phase separation, polymeric nanofibers 32  
 lithographic techniques, synthetic scaffolds 9  
 liver, nanofibers application 93  
 liver-like structure, construction 326–328  
 liver tissue, formation 208  
 lower critical solution temperature (LCST) 318  
 LSCM *see* laser scanning confocal microscopy  
 lung cancer, intracellular sensing 418
- m**  
 macropores, PLLA matrix 197  
 mag-seeding, magnetic nanoparticles 316–318

- Mag-TE technique
    - cell sheet engineering 319
    - keratinocyte sheet construction 323
    - magnetic nanoparticles 316
    - RPE sheet 323–325
  - magnetic flux density 325
  - magnetic force, MSC expansion 313
  - magnetic HA nanocrystals 301
  - magnetic nanocarriers, gene therapy 433–434
  - magnetic nanoparticles 308–337, 418–419
    - cell adhesion 408
    - cell isolation 310
    - cell-cell interactions 326
    - cell-seeding 316
    - choroidal neovascularization (CNV) 323
    - drug delivery systems (DDS) 308
    - magnetite cationic liposomes (MCL) 310–313
    - retinal pigment epithelium (RPE) 324
    - synthesis 393
  - magnetic susceptibility, functionalized hydroxyapatite 301
  - magnetic targeting, cancer treatment 428
  - magnetically labeled cell sheets 330
  - magnetite (Fe<sub>3</sub>O<sub>4</sub>) particles 308
  - magnetite cationic liposomes (MCL)
    - cell sheet engineering 319
    - liver-like structure 326–328
    - magnetic nanoparticles 308, 310–313
    - tubular structure construction 328
  - magnetotransfection, gene therapy 434
  - MAPLE *see* matrix assisted pulsed laser evaporation
  - mass transfer alteration, carbon nanotubes 350
  - matrices, nano-based 39–43
  - matrix assisted pulsed laser evaporation (MAPLE) 491
  - MCL *see* magnetite cationic liposomes
  - mechanical stress, cytoskeletal manipulation 407
  - mechanochemical route, hydroxyapatite 233
  - membrane-based patterning, soft lithography 468
  - mesenchymal stem cells (MSC) 45–47, 221, 310–316
    - histological analysis 172
    - *see also* stem cells
    - magnetic nanoparticles 313–316
  - mesengenic process, stem cells 222
  - mesoporous silica beads 418
  - metabolism, nano-pharmacology 377
  - metal coatings, cerium 368
  - metallic nanoparticles 390
    - synthesis 392
    - toxicity 400
  - metals
    - orthopedic tissues 261, 270
    - scanning electron micrographs 271
  - microcontact printing, soft lithography 468
  - microencapsulation, synthetic scaffolds 10
  - microfiber, polymer 77–78
  - microfluidic patterning, soft lithography 468
  - microtubule-based nanostructure transport 424–425
  - microtubule organizing centers (MTOC) 403
  - microwave processing, hydroxyapatite 233
  - migration 400–402
    - future applications 407–411
    - tissue formation 204
  - mineral-organic composite materials, bone tissue 285
  - mixed cortical cultures, oxide nanoparticles 373
  - molecular self-assembly
    - pore spaces 194
    - scaffold fabrication 193
  - morphogenesis, cell behavior 40
  - morphogenesis promotion, nano-based matrices 42
  - MSC *see* mesenchymal stem cells
  - MTOC *see* microtubule organizing centers
  - multicomponent nanowires, selective functionalization 395
  - multifunctional systems, gene therapy 436
  - multipotent stem cells 220
  - muscle, engineered tissues 173
  - myocardium, regeneration 174
- n**
- nano-based matrices
    - cell behavior 39–43
    - stem cells 43–47
  - nano-pharmacology 374–377
  - nano-structured implants, biocompatibility 82–87
  - nanobiomaterials 223–237
    - classification 228
  - nanofiber matrices, non-woven 31
  - nanofiber scaffolds 74–76
    - innovations 111
    - polymeric 23
  - nanofibers
    - advantages 83
    - classification 69–70
    - conductivity 81–82
    - electrospinning 79–80

- nanofibers (cont.)
    - fabrication 70
    - polymeric 66–134
    - self-assembled 38
  - nanofibrous scaffolds
    - biological effects 188–215
    - composites 198–201
    - electrospinning technology 135–187
    - fabrication methods 190–198
    - properties 144–151
    - self-assembly 138–140
  - nanoindentation lithography (NIL) 487
  - nanoislands
    - polymer 274
    - synthetic scaffolds 22
  - nanolithography 487–489
  - nanoparticle synthesis 390–391
    - cellular recognition 398
    - gold 392
    - protein-mediated recognition 398–400
  - nanoparticles 388–460
    - antioxidants 377–379
    - internalization 413
    - magnetic 308–337
  - nanophase biomaterials 216–256
  - nanorods, gene therapy 436
  - nanotechnology, scaffold development 21–39
  - nanotexturing, bone tissue engineering 103
  - nanotubes
    - quality 342
    - toxicology 380
  - nanowires 388–460
    - bioconjugated 422
    - synthesis 390–394
  - natural carbonate hydroxyapatite, crystal structure 288
  - natural extracellular matrix 12–22, 188
  - natural-natural composites, electrospun synthetic scaffolds 166
  - natural polymers, scaffolds 151–162
  - natural scales 224
  - natural-synthetic composites, electrospun synthetic scaffolds 167
  - naturally-derived biodegradable polymers 235
  - Nd:YAG laser, titanium surfaces 490
  - neodymium magnet, MSC expansion 314
  - nerve
    - engineered tissues 175
    - nanofibers application 93–99
  - nerve cable, regenerated 97
  - nerve regeneration 87, 96
    - carbon nanotubes 339
    - tissue engineering 48
  - neural progenitor cells (NPC), stem cells 44
  - neural stem cell (NSC) 98
    - engineered tissues 175
    - *see also* stem cells
  - neural tissue engineering (NTE) 47–49, 93
    - bioresorbable implant 96
  - neural tissues
    - formation 207–214
    - PLLA scaffolds 97–98
  - neuronal growth, carbon nanotubes 354
  - new generation biomaterial 223–237
  - NFM *see* PLLA-CL nanofiber mesh
  - NIH 3T3 fibroblasts 41
  - NIH/3T3 cells 320
  - NIL *see* nanoindentation lithography
  - NLS *see* nuclear localization sequence
  - NO free radicals 364
    - disease treatment 379
  - non-antibody-conjugated MLs 315
  - non-woven nanofiber matrices 31
  - non-woven nanofibrous membrane mats 101
  - non-woven nanofibrous scaffolds 144
  - normal rat kidney (NRK) cells, nano-based matrices 40
  - NPC *see* neural progenitor cells
  - NPC differentiation, stem cells 45
  - NRK *see* normal rat kidney
  - NSC-matrix interaction, tissue engineering 49
  - NT concentration effects, 3T3 fibroblasts 343–344
  - NTE *see* neural tissue engineering
  - nuclear localization sequence (NLS) peptide 416
- o**
- ophthalmology, nanofibers application 89–93
  - organ printing, magnetic nanoparticles 328
  - organ shortage, tissue engineering 2
  - organic solvent 409
  - organosilanes, self-assembly 481
  - orthopedic tissue engineering 257–282
  - osteoblasts
    - attachment 7
    - bone tissue engineering 102
    - engineered tissues 173
    - increased functions 269
    - orthopedic tissues 262–263
    - phenotype development 206
    - titanium adhesion 272
  - osteoclast functions, orthopedic tissues 265
  - oxidative stress 362–366
    - nanotechnological approach 366–374
  - oxide nanoparticles 373
  - oxygen vacancies, nanoscale cerium 368

- p**
- PA *see* amphiphilic peptides, *see* peptide-amphiphiles
- PAMAM *see* poly-amidoamine
- PARTCELL *see* partial treatment of cells using laminar flows
- partial treatment of cells using laminar flows (PARTCELL), soft lithography 471
- particle blasting 482–483
- particle size
- antibody-conjugated magnetoliposomes (AML) 314
  - cellular entry 414
- particulate leaching
- scaffolds 76
  - synthetic scaffolds 6
- passivating ligands, nanoparticle synthesis 391
- PC12 micropositioning, cell adhesion 401
- PCL *see* polycaprolactone
- PCLEEP nanofibers, hepatocytes 95
- PCLEEP scaffolds, liver 93
- PDGF *see* platelet derived growth factor
- PDMS *see* poly(dimethylsiloxane)
- PEDT *see* polyethylene dioxythiophene
- PEG, synthetic-synthetic composites 167
- PEG-polyester, intracellular delivery 419
- PEG star polymer hydrogels 475
- PEI *see* polyethyleneimine
- PEMF *see* pulsed electromagnetic fields
- PEO *see* poly(ethylene oxide)
- natural-synthetic composites 167
- peptide-amphiphiles (PA)
- scaffold fabrication 193
  - stability 38
- peptide-mediated recognition 398–400
- peptides
- cell adhesion 408
  - functionalized 52
  - self-assembly 34, 36
  - structure 37
- percutaneous transluminal angioplasty (PTCA) 378
- peripheral nervous system (PNS) 94
- PET *see* poly(ethylene terephthalate)
- PEVA *see* poly(ethylene-*co*-vinyl alcohol)
- PGA *see* poly(glycolic acid)
- pH shock wave method, hydroxyapatite 233
- phagocytotic vesicles, cytoskeleton investigation 411
- phase separation 72–73
- nanofibrous scaffolds 138
  - polymeric nanofibers 32
  - scaffold processing 194, 239–240
- PHBV *see* poly(3-hydroxybutyrate-*co*-3-hydroxyvalerate)
- PHEMA *see* poly(2-hydroxyethyl methacrylate)
- photodynamic therapy, cancer treatment 431
- photoimmobilization 464
- photolithography, conventional 462–466
- photosensitizers (PS), cancer treatment 431
- physical topography, nanoscale 402–405
- PIII *see* plasma immersion ion implantation
- PLA *see* poly(l-lactic acid)
- PLAGA *see* poly(lactide-*co*-glycolide)s
- plasma-guided surface engineering 483–485
- plasma immersion ion implantation (PIII) 485
- platelet derived growth factor (PDGF) 201
- platinum complexes 299
- PLD *see* pulsed laser deposition
- PLGA scaffolds
- electrospun synthetic 163
  - ophthalmology 90–91
- PLL-CL fiber matrices 39
- PLLA *see* poly(l-lactic acid), 69
- PLLA-CL nanofiber mesh (NFM), vascular grafts 107
- PLLA-CL nanofiber surface 50
- PLLA-CL nanofibers, aligned 31
- PLLA matrix
- internal pore structure 198
  - macropores 197
  - scaffold fabrication 195
- PLLA scaffolds
- bone tissue 104
  - morphology 148
  - neural tissue 97–98
- PLLA/nHAP composite scaffolds 199
- pluripotent stem cells 220
- *see also* stem cells
- PMMA *see* poly(methyl methacrylate)
- smooth muscle cell alignment 404
- PNS *see* peripheral nervous system
- poly(acrylamide-*co*-hydrazide) (PAH) 75
- poly(aldehyde guluronate) (PAG) hydrogel 75
- poly-amidoamine (PAMAM), gene therapy 433
- poly(*t*-butyl acrylate), photolithography 463
- polycaprolactone (PCL) 69, 86
- bone tissue 102
  - electrospun synthetic scaffolds 163
  - engineered tissues 169
  - stem cells 223
  - wound dressing 100–101

- poly(*ε*-caprolactone-*co*-ethyl ethylene phosphate) 70
- poly(*ε*-caprolactone) (PCL) 146
- poly(dimethylsiloxane) (PDMS) 69
- soft lithography 468
  - vapor deposition 478
- poly-etherurethane:carbon nanofiber composites 276
- polyethylene (PE)-based implants, rapid prototyping 494
- poly(ethylene-*[co*-vinyl alcohol) (PEVA) 112, 164
- polyethylene dioxythiophene (PEDT) 81
- poly(ethylene glycol) (PEG) 427
- poly(ethylene oxide) (PEO) 26, 143, 166
- novel polymer structures 475
- poly(ethylene terephthalate) (PET) 51, 165
- polyethyleneimine (PEI) 354–355
- poly(glycolic acid) (PGA) 69, 236
- poly( $\alpha$ -hydroxy esters) 162–164
- poly(3-hydroxybutyrate-*co*-3-hydroxyvalerate) (PHBV) 164
- poly(2-hydroxyethyl methacrylate) (PHEMA) 89
- poly(*N*-isopropylacrylamide) (PIPAAm) 318
- poly(L-lactic acid) (PLA) 33, 236, 239
- poly(L-lactic acid-*co*-caprolactone) copolymer 31
- poly(L-lactic acid) foams 6
- poly(lactic-*co*-glycolic acid) (PLGA) molds 264
- poly(lactic-*co* glycolic acid) (PLGA):titania composites 275
- poly(L-lactide-*co*-*ε*-caprolactone) 70
- Poly(lactide-*co*-glycolide)s (PLAGA) 6–7
- polymer additives, carbon nanotubes 340
- polymer-demixed nanotopographies 472–474
- polymer films, synthetic scaffolds 22
- polymer melt thickness, rapid prototyping 495
- polymeric nanofibers, drug delivery systems 112
- polymer poly(lactide-*co*-glycolide), electrospinning 26
- polymer powder, scaffolds 76
- polymer scaffolds, porous structure 8
- polymer solution, electrospinning 143
- polymeric biomaterials 151, 234–237
- RGD binding 20
  - topography 272
- polymeric blends, nanotopographies 474
- polymeric nanofibers 23, 66–134
- applications 87–115
  - electrospinning 24
  - phase separation 32
- polymeric nanomaterials, orthopedic tissues 270–274
- polymers 4
- biodegradable 235–236
  - composites 166–168
  - electrospinning 152–158
  - microfiber 77–78
  - nanoislands 274
  - natural 151–162
  - synthetic 69, 162–166
- poly(methyl methacrylate) (PMMA)
- electron-beam lithography 466
  - ophthalmology 89
- poly(*p*-dioxane) (PPDO) 86
- poly(propylene fumarate) (PPF) 9, 354
- poly(tetrafluoroethylene) (PTFE) 69, 485
- polyurethane (PU) 54, 165
- poly(vinyl chloride) (PVC) 69
- poly(xylylenes), vapor deposition 477
- pore size control 6
- pore spaces, molecular self-assembly 194
- pores
- interconnected network 290
  - scaffolds 7–8
- porosity, electrospinning 145–146
- porous apatites, bone tissue 288–292
- porous titanium, orthopedic tissues 277
- post-drawing, scaffold fabrication 192
- PPDO *see* poly(*p*-dioxane)
- PPF *see* poly(propylene fumarate)
- precursor decomposition, nanoparticle synthesis 391
- proliferation
- fibroblast cells 79
  - tissue formation 203
- prostheses, longevity 258
- protein manipulation 437–443
- protein-mediated recognition, nanoparticle synthesis 398–400
- PS *see* photosensitizers
- PTCA *see* percutaneous transluminal angioplasty
- PTFE *see* poly(tetrafluoroethylene)
- PTFE layering, laser-guided strategies 491
- PU *see* polyurethane
- PU/NT coated materials 355
- pulsed electromagnetic fields (PEMF) 339
- pulsed laser deposition (PLD) 490
- PuraMatrix 34
- PVC *see* poly(vinyl chloride)
- q**
- QD *see* quantum dots
- quantum dots (QD) 22



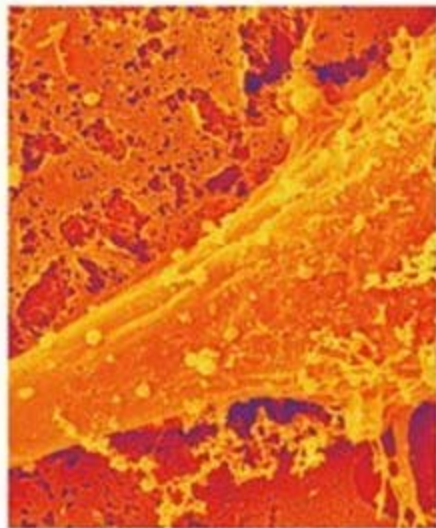
- cellular entry 415
  - intracellular sensing 417, 420
  - ligand exchange 395
  - nanoparticle synthesis 390
  - photodynamic therapy 431
  - semiconductor 416
- r**
- RAD12-II peptide scaffolds 208
  - rapid prototyping 492
    - polyethylene (PE)-based implants 494
    - scaffold fabrication 197
    - soft lithography 469
  - rare earth oxides, oxidative stress 367–374
  - reactive ion etching (RIE) 485
  - receptor-mediated uptake, cellular entry 413
  - receptors, protein manipulation 439–443
  - reconstructive surgery 67
  - redox capabilities, cerium 368
  - regenerative medicine, carbon nanotubes 338
  - RES recognition, drug delivery 427
  - retinal pigment epithelium (RPE) 90, 324
  - retinal pigment epithelium cell sheets
    - construction 325
    - magnetic nanoparticles 324
  - retinal progenitor cell (RPC) 90
  - retinitis pigmentosa (RP) 90
  - reverse transcription-polymerase chain reaction (RT-PCR) 171, 86
  - RGD
    - synthetic scaffolds 18–20
    - *see also* arginine-glycine-aspartate
  - RGD binding 19–20
  - RGD clustering 21
  - RGD-MCL 318–321
  - RIE *see* reactive ion etching
  - RP *see* rapid prototyping, *see* retinitis pigmentosa
  - RPC *see* retinal progenitor cell
  - RPE *see* retinal pigment epithelium
  - RT-PCR *see* reverse transcription-polymerase chain reaction
- s**
- sandblasting techniques 483
  - scaffold development 21–39
    - bottom-up approach 24–33
    - top-down approach 33
  - scaffold fabrication
    - dynamic collection grids 192
    - electrospinning 190–192
    - molecular self-assembly 193
    - PLLA matrix 195
    - rapid prototyping 197
    - thermally induced phase separation (TIPS) 195–196
  - scaffold processing
    - cell-ceramic scaffold interactions 244–247
    - electrospinning 240
    - methods 237
    - phase separation 194, 239–240
    - self-assembly 237–239
    - spinning mechanism 241
  - scaffolds 3–4
    - 3D structure 102
    - biomimetic surface modification 18
    - blood vessels 106
    - carbon nanotubes 352
    - cardiac tissue engineering 50
    - characteristics 225–227
    - comparison 74–82
    - composite 198–201
    - electrospinning technology 135–187
    - functional SWNT 354
    - history 68
    - ideal characteristics 136
    - IKVAV 44
    - magnetic nanoparticles 316
    - material types 227–237
    - MSC cultures 111
    - nanobiomaterials 223–237
    - nanofibrous 138–146
    - natural polymers 151–162
    - PGA nonwoven 76
    - PLAGA 6
    - polymeric 23
    - pores 7–8
    - rapid prototyping 495
    - stem cell tissue engineering 110–111
    - surface topography 97
    - tissue engineering 1
    - vascular grafts 106
  - scanning probe microscopic techniques (SPM) 22
  - scavenging activity
    - cerium oxide nanoparticles 370
    - single-walled carbon nanotubes 374
  - SCF *see* stem cell factor
  - self-assembled monolayers
    - cell adhesion 408
    - electron-beam lithography 467
  - self-assembled nanofibers 38
  - self-assembly 33, 73, 479–482
    - cell adhesion 408
    - nanofibrous scaffolds 138–140
    - peptides 34, 36

- self-assembly (cont.)
    - scaffold fabrication 193–194
    - scaffold processing 237–239
  - semiconductor nanoparticles, synthesis 391
  - semiconductor quantum dots 416
  - SFF *see* solid freeform fabrication
  - signal transduction pathways, free radicals 364
  - silica microbeads 424
  - silica nanocarriers, gene therapy 432
  - silica nanoparticles, photodynamic therapy 431
  - silk fibroin 160
  - silver, nanoparticle synthesis 392
  - single stranded DNA (ssDNA) 349
  - single-walled carbon nanotubes 338–360, 374
    - preparations 348
    - *see also* carbon nanotubes
  - sintered microsphere matrix, synthetic scaffolds 6
  - skin
    - engineered tissues 169–170
    - nanofibers application 99–101
  - smart delivery vehicles, drug delivery 435
  - smart materials, carbon nanotubes 352
  - smart substrates, chemical patterns 410
  - SMC *see* smooth muscle cells
  - smooth muscle cells (SMC) 108, 402
  - soft lithography 468–472
  - sol-gel derived nano HA 246
  - sol-gel technology 486–487
  - solid freeform fabrication (SFF) 493
  - solid-state reaction, hydroxyapatite 231
  - solution phase synthesis, nanowires 394
  - spinning mechanism, scaffold processing 241
  - SPM *see* scanning probe microscopic techniques
  - spongy bone porosity, biomimetic hydroxyapatite 290
  - ssDNA *see* single stranded DNA
  - star polymers, cell adhesion 408
  - star-shaped architectures 475
  - static-seeding, magnetic nanoparticles 316
  - stem cell factor (SCF), MSC expansion 313
  - stem cells
    - differentiation 149–150
    - essentials 220–223
    - nano-based matrices 43–47
    - nanofibers application 109
    - neural tissue engineering 98
  - stereolithographic techniques, synthetic scaffolds 9
  - substituted apatites 288–292
  - surface chemistries patterns, vapor deposition 477
  - surface chemistry, carbon nanotubes 349
  - surface engineering 473, 483–485
  - surface functionalization
    - hydroxyapatite 296
    - nanowires 394
  - surface immobilization, RGD sequence 19
  - surface modification, inorganic composites 200–201
  - surface passivation
    - biomolecular recognition 397
    - strategies 394
  - surface roughness
    - particle blasting 483
    - scaffold properties 138
  - SWNT *see* single-walled carbon nanotubes
  - SWNT-cell interactions 342
  - synergistic interactions, ECM mechanisms 15
  - synthetic biodegradable polymers 236
  - synthetic cornea replacement 89–90
  - synthetic polymer nanofibers, biocompatibility 85
  - synthetic polymers 69, 162–166
  - synthetic prostheses 257
  - synthetic scaffolds
    - bioresorbable porous 4
    - cell printing 10
    - glycolic acid (GA) 7
    - lithographic techniques 9
    - nanoislands 22
    - particulate leaching 6
    - RGD 18–20
  - synthetic-synthetic composites, electrospun synthetic scaffolds 167
  - systemic inflammatory response, Cerium 369
- t**
- T47D epithelial cells 42
  - tartrate-resistant acid phosphatase (TRAP) 265
  - TCPS *see* tissue culture polystyrene surface
  - teeth, biogenic hydroxyapatite 284–288
  - template synthesis 71–72
  - therapeutic drugs 426
  - thermally induced phase separation (TIPS) 195–196
  - thin film coating 477
  - TIPS *see* thermally induced phase separation
  - tissue culture polystyrene surface (TCPS) 107

- tissue engineered implants, biocompatibility 82–87
  - tissue engineering 1
    - $\alpha$ -hydroxyester 5
    - blood vessels 49–54
    - carbon nanotubes 340–342
    - cartilage 54–55
    - cell pellet (CP) culture 56
    - chemical patterns 410
    - computer-assisted design 7–8
    - computer-guided manufacturing 493
    - general concept 136
    - history 68
    - nerve regeneration 48
    - orthopedic 257–282
    - polymers 4
    - process scheme 3
  - tissue formation 205–214
    - cell attachment 202
    - differentiation 203–204
  - tissue reconstruction, cell types 219
  - tissue regeneration, carbon nanotubes 339–340
  - tissue repair, ECM 10
  - tissue substitute, bone 283–307
  - tissue transplantation, schematic view 217
  - titanium
    - apatite coatings 295
    - cell adhesion 272, 405
    - orthopedic tissues 263
    - porous 277
  - titanium-coated implants, novel polymer structures 475
  - titanium surfaces
    - cell growth 103
    - laser-guided strategies 490
  - TOPO, ligand exchange 395
  - topographies, electron-beam lithography 467
  - topological features, tunable 473
  - totipotent stem cells 220
    - *see also* stem cells
  - toxicity
    - metallic nanoparticles 400
    - nanomaterials 390
    - nanoparticle synthesis 399
  - toxicology 379–380
  - transforming growth factor- $\beta$  (TGF- $\beta$ )
    - engineered tissues 176
    - stem cells 223
  - translocation peptides, cellular entry 415
  - TRAP *see* tartrate-resistant acid phosphatase
  - trimethylene carbonate-*co- $\epsilon$* -caprolactone 96
  - tubular structure
    - blood vessels 329
    - construction 328
    - tumor tissue, local heating 429
  - tunable topological features 473
  - type I collagen 189
    - ECM ultrastructure 13
  - type II collagen 55
- U**
- ureter, tubular structure 329
  - urinary bladder wall, replacement 85
  - UV irradiation, photolithography 463
- V**
- vapor-phase synthesis, nanowires 394
  - vascular conduits, polymer based 106
  - vascular endothelial growth factor (VEGF) 434
  - vascular grafts 105–109
  - VEGF *see* vascular endothelial growth factor
- W**
- wet chemical method, hydroxyapatite 232
  - Wnt signaling pathway, MSC expansion 313
  - wound dressing 100
    - non-woven nanofibrous membrane mats 101
- X**
- xenograft, therapeutic problems 216
- Z**
- zinc oxide, free radicals 373
  - zirconia 227



# Nanomaterials for Medical Diagnosis and Therapy



## Contents

**Foreword** VII

**Preface** XXI

**List of Contributors** XXVII

<b>1</b>	<b>Nanotechnologies for Diagnosis – Present and Future</b>	<b>1</b>
	<i>Gareth A. Hughes</i>	
1.1	Introduction to Patient Diagnostics	1
1.2	Nanotechnology and Patient Diagnostics	2
1.3	Optical	9
1.3.1	Fluorescence	9
1.3.2	Quantum Dots	11
1.3.3	Surface Plasmon Resonance (SPR), Nanoparticles and Nanoshells	14
1.3.4	Fiber Optic Biosensors	19
1.4	Electrical	19
1.4.1	Nanomaterials for Enhanced Electron Transfer	20
1.4.2	Electrochemical Biosensors	24
1.5	Magnetic	28
1.6	Mechanical	30
1.7	Imaging Diagnostics	33
1.8	Nanotechnology-enhanced Tools	34
1.8.1	Analytical Tools	35
1.8.2	Raman Spectroscopy	35
1.8.3	Mass Spectrometry	36
1.8.4	Genetics	37
1.8.5	Immunoassays	39
1.9	Nanotechnology and the Future of Patient Diagnostics	40
1.9.1	Multifunctional Platforms	40
1.9.2	Real-time Monitoring	40
1.9.3	Multiplexed Diagnostic Assays	40
1.9.4	Point-of-care Diagnostics	41
1.9.5	Regulations, Risks and Ethics	42
	References	44

<b>2</b>	<b>Superparamagnetic Nanoparticles of Iron Oxides for Magnetic Resonance Imaging Applications</b>	<b>51</b>
	<i>Jean-Marc Idee, Marc Port, Isabelle Raynal, Michel Schaefer, Bruno Bonnemain, Philippe Prigent, Philippe Robert, Caroline Robic, and Claire Corot</i>	
2.1	Introduction	51
2.2	Physicochemical Characteristics	53
2.2.1	Physicochemical Properties of the Crystal	54
2.2.2	Hydrodynamic Particle Size and Charge	54
2.3	Pharmacology and Metabolism	56
2.3.1	Role of Physicochemical Parameters	57
2.3.2	Mechanism and Consequences of Interaction with Macrophages	58
2.3.3	Pharmacokinetics	59
2.3.4	Nanoparticle Vectorization	60
2.4	Current Clinical Uses and Future Developments	61
2.4.1	Gastrointestinal Tract Imaging	61
2.4.2	Liver and Spleen Diseases	63
2.4.3	Lymph Node Metastases	64
2.4.4	Blood Pool Characteristics	66
2.4.5	Characterization of the Atheromatous Plaque	67
2.4.6	Other Potential Uses	68
2.4.6.1	Stroke	68
2.4.6.2	Cerebral Tumor Characterization	68
2.4.6.3	Multiple Sclerosis	69
2.4.6.4	Arthritis	70
2.4.6.5	Infection	70
2.4.6.6	Kidney Imaging	71
2.4.6.7	Acute Cardiac Transplant Rejection	72
2.4.6.8	<i>In Vivo</i> Monitoring of Cell Therapy	72
2.4.6.9	T-staging of Uterine Neoplasms	73
2.4.6.10	MRI-detectable Embolotherapy	73
2.5	Conclusion	75
	References	76
<b>3</b>	<b>Carbon Nanotube-based Vectors for Delivering Immunotherapeutics and Drugs</b>	<b>85</b>
	<i>Alberto Bianco, Wei Wu, Giorgia Pastorin, Cédric Klumpp, Lara Lacerda, Charalambos D. Partidos, Kostas Kostarelos, and Maurizio Prato</i>	
3.1	Introduction	85
3.2	Chemical Functionalization of CNTs	86
3.2.1	Noncovalent Functionalization	86
3.2.1.1	$\pi$ - $\pi$ Stacking Interactions	86
3.2.1.2	Hydrophobic Interactions	88
3.2.2	Covalent Functionalization	89
3.2.2.1	Defect Functionalization	90
3.2.2.2	Sidewall Functionalization	91

3.3	CNTs in Diagnosis	96
3.3.1	CNTs in FETs	97
3.3.1.1	Fabrication	97
3.3.1.2	FET Biosensors	98
3.3.2	CNT-based Electrodes	100
3.3.2.1	Fabrication	101
3.3.2.2	Nanoelectrode Biosensors	102
3.4	CNT Cell Uptake	105
3.5	CNTs as Delivery Devices for Antigens and Adjuvants	107
3.5.1	Interaction of <i>f</i> -CNTs with CpG Motifs and Potentiation of their Immunostimulatory Activity	107
3.5.2	Presentation and Immunogenic Potential of Peptide Antigens Attached onto <i>f</i> -CNTs	109
3.6	CNTs for Drug Delivery	111
3.7	CNTs for Gene Transfer	115
3.7.1	Interaction with DNA and RNA	115
3.7.2	Delivery and Expression of Gene-encoding DNA and RNA	116
3.8	Health Impact of CNTs	118
3.8.1	Parameters of CNTs Related to Health Impact	119
3.8.1.1	Purity	119
3.8.1.2	Solvents	123
3.8.1.3	Surface of CNTs	123
3.8.1.4	Length	123
3.8.2	<i>In Vitro</i> Effect of CNTs	123
3.8.3	<i>In Vivo</i> Effects of CNTs	125
3.9	General Conclusions	127
	Acknowledgments	128
	References	128
<b>4</b>	<b>Core–Shell Nanoparticles for Drug Delivery and Molecular Imaging</b>	<b>143</b>
	<i>Sung Kyun Han, Ree Sun Kim, Jin Ho Lee, Giyoong Tae, Sun Hang Cho, and Soon Hong Yuk</i>	
4.1	Introduction	143
4.2	Core–shell Nanoparticles with a Lipid Core	145
4.3	Core–Shell Nanoparticles with a Polymeric Core	156
4.3.1	Hyaluronic Acid (HA)-functionalized PLGA Nanoparticles	157
4.3.2	Heparin-functionalized PLGA Nanoparticles	166
4.4	Core–shell Nanoparticles with a Metallic Core	174
4.5	Conclusions	181
	Acknowledgments	181
	References	182
<b>5</b>	<b>Nanotechnologies for Targeted Delivery of Drugs</b>	<b>189</b>
	<i>Pavel Brož and Patrick Hunziker</i>	
5.1	Introduction	189
5.2	Basic and Special Pharmacology	192



5.2.1	Outline	192
5.2.2	Basic Pharmacology	193
5.2.2.1	Absorption	193
5.2.2.2	Bioavailability	196
5.2.2.3	Distribution	197
5.2.2.4	Elimination	198
5.2.3	Special Pharmacology	201
5.2.3.1	Skin Epithelium	201
5.2.3.2	Mucosal Epithelium of the Respiratory Tract	202
5.2.3.3	Mucosal Epithelium of the Gastrointestinal Tract	202
5.2.3.4	Mononuclear Phagocyte System (MPS)	204
5.2.3.5	Endothelial Barrier	206
5.2.3.6	Cell Membrane	207
5.3	Strategies for Targeted Delivery – Observed in Nature	209
5.3.1	Outline	209
5.3.2	Bacteria	210
5.3.2.1	Host Invasion	210
5.3.2.2	Immune System Evasion	213
5.3.3	Viruses	215
5.3.3.1	Immune System Evasion	216
5.3.3.2	Host Cell Invasion	217
5.3.3.3	Viral Vectors for Therapeutic Applications	219
5.3.4	Prions	221
5.4	Strategies for Targeted Delivery – Designed by Man	223
5.4.1	Outline	223
5.4.2	Noninvasive Delivery Systems	223
5.4.2.1	Oral Delivery Systems	224
5.4.2.2	Transdermal Delivery Systems	224
5.4.2.3	Transmucosal Delivery Systems	225
5.4.3	Invasive Delivery Systems	225
5.4.4	Targeted Delivery to the Brain	226
5.4.5	Macrophage Targeting	228
5.4.6	Other Targets	230
5.5	Conclusion and Outlook	233
	References	234
<b>6</b>	<b>Nanoporous and Nanosize Materials for Drug Delivery Systems</b>	<b>255</b>
	<i>Yoshinobu Fukumori, Kanji Takada and Hirofumi Takeuchi</i>	
6.1	Introduction	255
6.2	Nanomaterials for Coating	256
6.2.1	Commercially Available Aqueous Polymeric Nanomaterials	257
6.2.2	Novel Terpolymer Nanoparticles for Coating	259
6.2.3	Core-shell Nanoparticles for Fine Particle Coating	260
6.2.4	Core-Shell Nanoparticles for Thermosensitively Drug-releasing Microcapsules	261

6.2.5	Chitosan Nanoparticles for Microparticle Coating	263
6.3	Materials for Nanoparticulate Therapy and Diagnosis	264
6.3.1	Inorganic Nanoparticles	265
6.3.2	Polymeric Nanoparticles	267
6.3.3	Other Case Studies	267
6.4	Nanoporous Materials as Drug Delivery System Carriers	270
6.4.1	Inorganic Calcium Compounds	270
6.4.2	Silastic Compounds	271
6.4.2.1	Nanoporous Silastic Materials for Solidifying Oily Drugs	271
6.4.2.2	Nanoporous Silastic Materials for Poorly Absorbable Drugs	275
6.4.2.3	Nanoporous Silica Materials for Controlled Release of Drugs	278
6.4.3	Carbon Nanotubes (CNTs)	280
6.4.3.1	CNTs for Oral Delivery of Protein Drug	280
6.4.3.2	CNTs for Intracellular Delivery of Protein	282
6.4.3.3	Toxicity of CNTs	284
6.4.3.4	Functionalized CNTs ( <i>f</i> -CNTs) for Drug Delivery	285
6.4.3.5	<i>f</i> -CNTs for Gene Delivery	286
6.4.4	CNHs for Drug Delivery	286
6.5	Physicochemical Aspects of Porous Silastic Materials for Drug Delivery	287
6.5.1	Solid Dispersion Particles with Porous Silica	288
6.5.2	Mesoporous Silica	295
	References	299
<b>7</b>	<b>NANOEGG® Technology for Drug Delivery</b>	<b>310</b>
	<i>Yoko Yamaguchi and Rie Igarashi</i>	
7.1	Introduction	310
7.2	New Nanoparticles with a Core–Shell Structure: The NANOEGG System	311
7.2.1	Physicochemical Properties and Action of ATRA	311
7.2.2	NANOEGG Preparation and Characterization	314
7.2.3	Improved Lability of ATRA in the NANOEGG System	317
7.3	NANOEGG for Dermatological Aspects	319
7.3.1	Improved Irritation of ATRA in the NANOEGG System	320
7.3.2	Pharmacological Effects of the NANOEGG System	323
7.3.3	Expression of mRNA Heparin-binding Epidermal Growth Factor-like Growth Factor (HB-EGF) on Mouse Skin	325
7.3.4	Proliferation and Differentiation of Keratinocytes	326
7.3.5	Production of Hyaluronic Acid (HA) in the Epidermal Layer	328
7.3.6	Hyperpigmentation and Fine Wrinkle Improvements by NANOEGG Treatment on Animal Skin	330
7.3.7	Clinical Trials of Fine Wrinkles and Brown Spots on the Human Face	331
7.4	Why does NANOEGG Show the High Performance on the Improvement of Brown Spot and Wrinkles?	334

7.5	NANOEGG for Other Indications	335
7.6	NANOEGG for Other Drugs	338
7.7	Conclusion	338
	References	339
<b>8</b>	<b>Polymeric Nanomaterials – Synthesis, Functionalization and Applications in Diagnosis and Therapy</b>	<b>342</b>
	<i>Jutta Rieger, Christine Jérôme, Robert Jérôme, and Rachel Auzély-Velty</i>	
8.1	Introduction	342
8.2	Polymer Materials Used for the Synthesis of Nanoparticles	345
8.2.1	Natural Polymers	346
8.2.2	Degradable Synthetic Polymers	349
8.2.3	Nondegradable Synthetic Polymers	352
8.2.4	PEO	352
8.3	Preparation of Polymeric Nanoparticles	354
8.3.1	Preparation of Nanospheres from Preformed Polymers	354
8.3.1.1	Emulsion-evaporation	354
8.3.1.2	Salting-out	355
8.3.1.3	Emulsification-diffusion	356
8.3.1.4	Nanoprecipitation	356
8.3.2	Synthesis of Nanospheres by <i>In Situ</i> Polymerization	357
8.3.3	Preparation of Nanocapsules	358
8.4	Surface Functionalization	359
8.4.1	Functionalization with Biological (Macro)molecules	359
8.4.2	Functionalization with Specific Ligands: Specific Interaction through Biological Recognition	360
8.4.2.1	Mono- or Oligosaccharides (Carbohydrates)	360
8.4.2.2	Folate Receptor	361
8.4.2.3	Antibodies	362
8.4.2.4	Biotin	362
8.4.3	Strategies for Surface Modification	363
8.4.3.1	Adsorption on Preformed Nanoparticles	364
8.4.3.2	Functional Surfactants as Stabilizers and Surface Modifiers	366
8.4.3.3	Emulsion, Miniemulsion or Dispersion Polymerization	369
8.4.3.4	Covalent Linking of Functional Molecules to Preformed Nanoparticles	370
8.4.4	Analytical Techniques for Surface Modification	375
8.4.4.1	Physicochemical Techniques	376
8.4.4.2	Biological Assays/Methods	377
8.5	Applications	380
8.5.1	Drug Delivery Systems	380
8.5.1.1	Routes of Administration	380
8.5.1.2	Therapeutic Applications of Nanoparticles	382
8.5.1.3	Triggered Release	384

8.5.2	Diagnosis	388
8.5.2.1	Fluorescence Labeling of Polymeric Nanoparticles	388
8.5.2.2	Contrast Agents for MRI	392
8.5.2.3	Magnetic Nanoparticles for <i>In Vitro</i> Assays	393
8.5.2.4	Electron Dense Agents for Transmission Electron Microscopy (TEM)	396
8.5.2.5	Radiolabeled Nanoparticles	396
8.6	Conclusion and Perspectives	396
	References	397

## **9 Polymeric Nanoparticles for Drug Delivery** 409

*Paraskevi Kallinteri and Martin C. Garnett*

9.1	Introduction: Application of Nanoparticles for Noncancer Applications	409
9.1.1	Physiological and Uptake of Particles	410
9.1.1.1	Routes of Tissue and Cellular Uptake of Particles	410
9.1.1.2	Uptake by Macrophages and Lymphoid Tissues	411
9.1.1.3	Mucosal-associated Lymphoid Tissues (MALT)	411
9.1.2	Routes of Delivery	412
9.1.2.1	Oral	412
9.1.2.2	Nasal	413
9.1.2.3	Pulmonary	413
9.1.2.4	Transdermal/Subcutaneous	414
9.2	Drug Delivery	415
9.2.1	Ocular Delivery	415
9.2.1.1	Anatomy of the Eye	415
9.2.1.2	Pathology	416
9.2.1.3	Drug Delivery	416
9.2.1.4	Tolerability	422
9.2.1.5	Future Prospects for Nanoparticles in Ocular Delivery	422
9.2.2	Macrophage-related Diseases	423
9.2.2.1	Leishmaniasis	423
9.2.2.2	Other Parasitic Infections	426
9.2.3	Antifungal	427
9.2.3.1	Treatment	427
9.2.3.2	Drug Delivery Systems	428
9.2.4	Tuberculosis	431
9.2.4.1	Physiology and Pathology	431
9.2.4.2	Treatment	431
9.2.4.3	Future Prospects	434
9.2.5	AIDS	434
9.2.5.1	Pathology	434
9.2.5.2	Treatment	434
9.2.5.3	Nanoparticle Delivery Systems	435
9.2.5.4	Vaccines and AIDS	439

9.2.6	Vaccines	441
9.2.6.1	Delivery Route	442
9.2.7	Diabetes	451
9.2.7.1	Treatment	451
9.2.7.2	Delivery Routes	452
9.3	Conclusions	460
	References	461
<b>10</b>	<b>Solid Lipid and Polymeric Nanoparticles for Drug Delivery</b>	<b>471</b>
	<i>José Luis Pedraz, Gorka Orive, Manoli Igartua, Alicia R. Gascón, Rosa M. Hernández, Maria Angeles Solinis, and Amaia Esquisabel</i>	
10.1	Introduction	471
10.2	SLNs	472
10.2.1	Introduction	472
10.2.2	Composition	473
10.2.3	Production Processes	474
10.2.3.1	Preparation Techniques	474
10.2.3.2	Scaling-up, Sterilization and Drying	475
10.2.4	Drug Incorporation, Loading, Incorporation Efficiency, Nanoparticle Recovery and Drug Release	476
10.2.4.1	Drug Incorporation	476
10.2.4.2	Drug Loading	477
10.2.4.3	Determination of Nanoparticle Recovery and Drug Incorporation Efficiency	477
10.2.4.4	Drug Release	478
10.2.5	Related Structures and Stability	478
10.2.6	Analytical Characterization of SLNs	480
10.2.6.1	Particle Size	480
10.2.6.2	The $\zeta$ Potential	481
10.2.6.3	Crystallinity and Polymorphism and Colloidal Structures	481
10.2.7	Applications	481
10.2.7.1	Gene Therapy	482
10.2.7.2	Peptide and Protein Delivery	486
10.2.7.3	Low-soluble Drugs	488
10.2.7.4	Topical and Transdermal Administration	490
10.2.7.5	Cosmetic Applications for SLNs	491
10.3	Polymeric Nanoparticles	491
10.3.1	Introduction	491
10.3.2	Nanoparticle Preparation Methods	492
10.3.2.1	Nanoparticles Prepared by <i>In Situ</i> Polymerization of Monomers	492
10.3.2.2	Nanoparticles Prepared from Preformed Polymers	493
10.3.3	Characterization of Polymeric Nanoparticles	494
10.3.4	Pharmaceutical Applications of Nanoparticles	495
10.3.4.1	Protein Delivery	495

10.3.4.2	Protein Delivery by Mucosal Routes	496
10.3.4.3	Vaccine Adjuvants	498
	References	499
<b>11</b>	<b>Intelligent Hydrogels in Nanoscale Sensing and Drug Delivery Applications</b>	<b>509</b>
	<i>J. Zach Hilt</i>	
11.1	Introduction	509
11.2	Intelligent Hydrogels	510
11.2.1	Ionic Hydrogels	510
11.2.2	Temperature-responsive Hydrogels	510
11.2.3	Biohybrid Hydrogels	510
11.2.4	Imprinted Hydrogels	511
11.3	Sensor Applications	511
11.3.1	Actuation Detection	511
11.3.2	Optical Detection	513
11.3.3	Electrical Detection	517
11.4	Drug Delivery Applications	519
11.4.1	Micro/nanoscale Devices	520
11.4.2	Nanoscale Macromolecular Structures	520
11.5	Conclusions	522
	References	522
<b>12</b>	<b>Nanoshells for Drug Delivery</b>	<b>527</b>
	<i>Melgardt M. De Villiers and Yuri Lvov</i>	
12.1	Introduction	527
12.2	Metallic Nanoshells	528
12.2.1	Synthesis of the Nanoshells	528
12.2.2	Application in Nanomedicine	530
12.3	Nanoshells Formed by Polyion E-LbL Self-assembly	532
12.3.1	Preparation of E-LbL Nanoshells	532
12.3.1.1	Proving the Nanoshells	535
12.3.1.2	Influence of the Core on Nanoshell Properties	538
12.3.1.3	Barrier Properties of E-LbL Assembled Nanoshells	539
12.3.2	Controlled Release of Active Pharmaceutical Ingredients Encapsulated by E-LbL Assembled Nanoshells	540
12.3.2.1	Nanoshell Permeability for Low-molecular-weight Compounds	542
12.3.2.2	Nanoshell Permeability for High-molecular-weight Compounds	543
12.3.3	E-LbL Assembled Nanoshells as Protective and Functional Barriers	545
12.3.4	Magnetic Nanoshells	548
12.3.5	Nano-organized Shells with Functions other than a Adjustable Diffusion Barrier	550
12.3.5.1	Colloidal Stabilization	550
12.3.5.2	Interpolyelectrolyte Complex Formation	550

12.3.5.3	Biomimetic Approach	551
12.4	Conclusion	552
	References	553
<b>13</b>	<b>Bionanoparticles and their Biomedical Applications</b>	<b>557</b>
	<i>L. Andrew Lee, Hannah N. Barnhill, and Qian Wang</i>	
13.1	Introduction	557
13.2	BNPs	558
13.3	Genetic and Chemical Alterations of BNPs	560
13.3.1	Chemical Modifications	560
13.3.1.1	Conventional Bioconjugation Methods for Selective Modifications	560
13.3.1.2	“Click Chemistry” for Bioconjugation of BNPs	567
13.3.1.3	New Developments in Tyrosine Modification	569
13.3.2	Genetic Alterations	570
13.3.2.1	Heterologous Peptide Insertions	571
13.3.2.2	NAA Substitutions	576
13.3.2.3	Protein Expression Systems	576
13.4	BNPs in Therapeutics	577
13.4.1	Cell Targeting	578
13.4.2	Gene Delivery	579
13.4.3	Bioimaging	580
13.4.4	Drug Encapsulation and Release	583
13.5	Immune Response	584
13.5.1	Vaccine Development	584
13.5.2	Immune Modulation	585
13.6	Future Directions	586
	Acknowledgments	587
	References	587
<b>14</b>	<b>Nanotechnology for Gene Therapy – HVJ-E Vector</b>	<b>597</b>
	<i>Hironori Nakagami, Yasuhiko Tabata, and Yasufumi Kaneda</i>	
14.1	Introduction	597
14.2	Biological Barriers to Gene Transfer	599
14.2.1	Reaching Target Cells	599
14.2.1.1	Recognition by Specific Target Tissues	599
14.2.1.2	Avoidance of Nonspecific Uptake	599
14.2.1.3	Resistance to Degradation in Systemic Circulation	600
14.2.2	Crossing the Cell Membrane	600
14.2.3	Nuclear Targeting	601
14.2.4	Regulation of Gene Expression	602
14.2.4.1	Stable Retention of Transgenes	602
14.2.4.2	Regulation of Transcription	603
14.3	HVJ-E Vector	604
14.3.1	Development of HVJ-E Vector	604
14.3.2	Approaches to Cancer Gene Therapy Utilizing HVJ-E Vector	609

- 14.3.2.1 Transfection of Dendritic Cells (DCs) with Melanoma-associated Antigen (MAA) using HVJ Envelope Vector for Immunotherapy of Melanoma 609
- 14.3.2.2 Fusion of DC Tumor Cells and Simultaneous Gene Transfer to the Hybrid Cells using HVJ-E for the Prevention and Treatment of Cancers 611
- 14.4 Biocompatible Polymer with HVJ-E 613
- 14.5 Magnetic Nanoparticles for Medicine 615
- 14.6 Conclusion 620
- References 620
  
- 15 Nanotoxicology of Synthetic Gene Transfer Vectors: Poly(ethyleneimine)- and Polyfectin-mediated Membrane Damage and Apoptosis in Human Cell Lines 629**  
*Seyed M. Moghimi*
- 15.1 Introduction 629
- 15.2 PEI as a Nonviral Vector 630
- 15.2.1 Structure and Properties of PEI and PEI–DNA Complexes 630
- 15.2.2 Cytotoxicity 630
- 15.3 PEI-mediated Cell Dysfunction and Apoptosis 631
- 15.3.1 PEI and PEI–DNA Complex Internalization 631
- 15.3.2 Plasma Membrane Damage and Apoptosis 632
- 15.3.3 Effect of PEI on the Function of Isolated Mitochondria 634
- 15.3.4 Other Plausible Apoptotic Routes 637
- 15.4 Cell Damage and Apoptosis with Related Polycations and Cationic Lipids 638
- 15.5 Conclusions and Future Outlook 639
- References 640
  
- 16 Nanoparticles for the Treatment of Alzheimer's Disease: Theoretical Rationale, Present Status and Future Perspectives 644**  
*Gang Liu, Ping Men, George Perry and Mark A. Smith*
- 16.1 Introduction 644
- 16.2 Rationales: The Ability of Nanoparticles to Cross the BBB – A Useful Tool to Deliver Drugs into the Brain 645
- 16.2.1 Physiological Functions of the BBB 645
- 16.2.2 Strategies for Drug BBB Penetration 646
- 16.2.3 Preparation of Polymeric Nanoparticulate Drug Delivery Systems 648
- 16.2.4 Possible Mechanisms by which Nanoparticles Cross the BBB 650
- 16.3 Status: Nanoparticle Targeting Transport of Therapeutic Agents for Potential Treatment of AD 652
- 16.3.1 Nanoparticle Targeting of A $\beta$  to Deliver Potentially Therapeutic Agents 652
- 16.3.2 Nanoparticulate Antioxidant Delivery to Increase Efficacy against A $\beta$ -mediated Oxidative Stress 653



16.3.3	Nanoparticle Delivery of Copper Chelator for Preventing and Reversing $A\beta$ Deposition	657
16.3.4	Nanoparticle Transport of Iron Chelators and Metal Chelator Complexes Into and Out of the Brain, Respectively	661
16.3.4.1	Increased Levels of Various Metals in the Brain of AD Patients	661
16.3.4.2	Problems with Iron Chelators for Simultaneous Removal of Multimetal Ions for Treatment of AD	662
16.3.4.3	Nanoparticle Transport Technology to Improve Chelation Therapy for AD	665
16.3.4.4	Experimental Descriptions	666
16.3.4.5	Results and Discussion	676
16.4	Perspectives	683
	Acknowledgments	685
	References	685

<b>Index</b>	<b>707</b>
--------------	------------

## Preface

From the time the human mind emerged, about fifty thousand years ago, our understanding of the human body and of ways and means to protect ourselves better from both natural degradation as well as diseases has been continuously growing. The human mind has been responsible for triggering creative technological breakthroughs at different intervals, significantly improving our quality of life at each of these stages. We are again standing on the threshold of yet another technological mastery with the ability to create nanomaterials akin to natural sub-micron biomolecules for the protection of our body and to prolong its life. The purpose of this book, *Nanomaterials for Medical Diagnosis and Therapy*, is to reveal for the first time how man-made nano-sized materials are being judiciously combined with biological molecules in order to find hitherto unimaginable, superior diagnostic tools and novel therapeutic approaches to alleviate human suffering. Most of what you will read here will provide you with a broader perspective to how nanotechnology is going to revolutionize medicine in the close future. You are unlikely to get such a perspective reading individual articles from the scientific journals. This is the final volume in the ten-volume series on *Nanotechnologies for the Life Sciences (NtLS)* and in a way reflects the ultimate goal of all life scientists, with the other nine volumes as guide posts, to improve our health and quality of living. The book has sixteen chapters, covering all aspects of medical diagnosis and therapy except cancer as this subject is covered in volumes six and seven. With over 700 pages, it is the largest of all the ten volumes. Before I go ahead with giving you details of individual chapters in this final volume, I would like to take this opportunity to provide you glimpses of the information contained in the first nine volumes, which many of you may have already read.

The first volume in the series *Biofunctionalization of Nanomaterials*, with eleven chapters, dealt with various approaches to attach biomolecules to nanomaterials for applications in the life sciences, and the second volume *Biological and Pharmaceutical Nanomaterials*, with twelve chapters, focused on natural nanomaterials that are relevant to the life sciences. The ability to characterize systems in nanoscale is pivotal to the success of nanotechnology, and the third volume *Nanosystem Characterization Tools for the Life Sciences*, with eleven chapters, is a useful source of information both for life scientists interested in nanoscale systems and for characterization specialists interested in applying their tools in biological systems. The

fourth volume of the series, *Nanodevices for the Life Sciences*, contains thirteen chapters and is a compendium of the exciting possibilities that exist in the world of tiny devices. The fifth volume, entitled *Nanomaterials – Toxicity, Health and Environmental Issues*, reviews some of the critical risk assessment issues, which are crucial in life sciences, that are currently being investigated by the health & environmental nano researchers, and has twelve chapters. The sixth and the seventh volumes, *Nanomaterials for Cancer Therapy* and *Nanomaterials for Cancer Diagnosis*, with a total of twenty-two chapters, captured nanotechnological approaches for the treatment of cancer and their utility in developing tools and materials for sensitive and early diagnosis of this serious affliction. While the eighth volume, *Nanomaterials for Biosensors*, containing thirteen chapters, touches upon biomolecular sensing using a variety of Nanomaterials, the ninth volume *Tissue, Cell and Organ Engineering* with its twelve chapters is an encyclopedia on nanotechnological approaches to the engineering of biologically functional matter capable of serving as tissue or organ replacement. The ten volume series on *Nanotechnologies for the Life Sciences* with 122 chapters contributed by about 150 researchers across the globe totaling some 4600 pages comes to conclusion with the publication of the tenth volume.

This tenth volume begins with the chapter entitled *Nanotechnologies for Diagnosis – Present and Future*, which is a contribution by Gareth A. Hughes of Zyvex Corporation in Richardson, Texas, USA. In this chapter, a general discussion on various aspects of diagnostics including *in vitro* diagnostics (IVDs), implantable sensors and imaging techniques is presented in addition to touching upon regulatory and ethical considerations. Moving to a more specific diagnostic tool, authors lead by Jean-Marc Idée from Guerbet, Aulnay-sous-Bois, France, brings out the importance of Superparamagnetic Iron Oxide Nanoparticles (SPIONs) as contrast agents in Magnetic resonance Imaging. The chapter, *Superparamagnetic Nanoparticles of Iron Oxides for Magnetic Resonance Imaging Applications*, is a comprehensive source of information on the unique capability of SPIONs as contrast agents for MRI of the gastrointestinal tract, liver & spleen, lymph node, blood pool, and atheromatous plaque.

The third chapter, *Carbon Nanotube-based Vectors for Delivering Immunotherapeutics and Drugs*, reviews the application of carbon nanotubes in drug delivery and biosensing. Alberto Bianco and co-workers from the Institute of Molecular and Cellular Biology in Strasbourg, France, have done a commendable job in delineating the pros and cons of utilizing the unique property of CNTs, the penetration ability with capacity for high loading, for innovative medical diagnosis and therapies. The team lead by Soon Hong Yuk from Hannam University in Taejeon, Korea, contributed the fourth chapter, entitled *Core-Shell Nanoparticles for Drug Delivery and Molecular Imaging*. In this chapter, the authors focus on core-shell nanoparticle architecture with a layer of polymeric materials surrounding an organic or inorganic nanoparticle core, and demonstrate that such architectures provide improved stability and a sustained release pattern of protein drug and decreased cytotoxicity. In the fifth chapter, *Nanotechnologies for Targeted Delivery of Drugs*, various aspects of targeted delivery utilizing different types of nanomaterials are highlighted. Authors Pavel Brož and Patrick Hunziker from the Medical Inten-

sive Care unit of Basel University Hospital in Switzerland present successful targeting strategies employed that use both 'natural nanostructures' (such as bacteria and viruses) and 'artificial nanostructures' (lipid-based ones such as liposomes and micelles, protein-based ones such as dendrimers, and polymer-based ones such as nanoparticles, nanospheres and nanocontainers) in areas other than cancer.

The sixth chapter, *Nanoporous and Nanosize Materials for Drug Delivery Systems*, written by Yoshinobu Fukumori, Kanji Takada and Hirofumi Takeuchi from Kyoto Pharmaceutical University, Japan, covers application of a number of inorganic, organic and natural nanoporous materials in general and nanoporous silica-based materials in particular for medical therapy. Continuing on the theme of core-shell nanoparticles as described in a general way in the fourth chapter, Yoko Yamaguchi and Rie Igarashi from the Institute of Medical Science of St Marianna University in Kanagawa, Japan, present their efforts in the seventh chapter towards the development of a specific non-spherical core-shell product, NanoEgg<sup>TM</sup>, for dermatological applications. The chapter, *NanoEgg<sup>TM</sup> Technology for Drug Delivery*, describes the commercialization of these particles for overcoming the limitations of classical ATRA (all-*trans* retinoic acid) treatment through controlled release.

Polymeric nanomaterials have been receiving a lot of attention as materials of choice for both drug delivery as well as diagnostic tools due to their unique physicochemical characteristics that allow for controlling the fate of a drug within the patient. Three chapters, 8, 9 and 10, have been dedicated to bring out comprehensively the information present in the literature on different facets and types of polymeric nanomaterials for application in medical diagnosis and therapy. The eighth chapter, *Polymeric Nanomaterials – Synthesis, Functionalization and Applications in Diagnosis and Therapy*, a contribution from the laboratories of Rachel Auzély-Velty from the Centre de Recherches sur les Macromolécules Végétales (CERMAV) in Grenoble, France, focuses on 'frozen', non-dynamic polymeric nanomaterials, where an exchange between individual polymer chains and polymer chains of the nanoobject cannot take place, unlike the dynamic systems such as micelles and liposomes. On the other hand, the ninth chapter, *Polymeric Nanoparticles for Drug Delivery*, authored by P. Kallinteri and M. C. Garnett from the School of Pharmacy of Nottingham University, UK, brings out the physiology and anatomy underlying the diseases which may be treatable using polymeric nanomaterials and the way these are handled by the body. In the tenth chapter, *Solid Lipid and Polymeric Nanoparticles for Drug Delivery*, the authors José Luis Pedraz and co-workers from the University of Basque Country in Vitoria, Spain, present a comparative analysis of solid lipid nanoparticles (SLNs) and polymeric nanoparticles with reference to their production processes, characterization, and a wide ranging therapeutic applications.

Chapter eleven by Zach Hilt from the University of Kentucky in Lexington, USA, explores the relatively underdeveloped field of hydrogels. In this chapter aptly titled as *Intelligent Hydrogels in Nanoscale Sensing and Drug Delivery Applications*, the author has done a great job in providing an up-to-date review on the application of intelligent hydrogels such as ionic and temperature-responsive, biohybrid and imprinted hydrogels in micro/nanoscale sensing and drug delivery. In the twelfth chapter, *Nanoshells for Drug Delivery*, a layer-by-layer self assembly approach to

nanoshell formation is described in addition to the utility of nanoshells in controlled release of pharmaceutical ingredients. Authors Melgardt M. De Villiers and Yuri Lvov from the University of Wisconsin and Louisiana Tech University respectively, compare in a systematic fashion two types of nanoshells – metallic nanoparticles composed of a dielectric core (e.g. silica) coated with an ultra thin metallic layer (e.g. gold) and nanoshells formed by electrostatic layer-by-layer molecular self-assembling (E-LbL) for drug delivery applications. L. Andrew Lee, Hannah N. Barnhill and Qian Wang from University of South Carolina provide an overview on the topic of the programming of the Bionanoparticles (BNPs) and current research on their biomedical applications in the thirteenth chapter entitled *Bionanoparticles and their Biomedical Applications*. This chapter is a must-read for all those interested in BNPs and how they can be exploited for generating novel biotemplates in the nanometer range for a myriad of biomedical applications.

As we reach the end of the book, the last three chapters assume special importance. While chapter fourteen contributed by Hironori Nakagami, Yasuhiko Tabata and Yasufumi Kaneda from Osaka University, Japan, reiterates the importance of nanotechnologies in gene therapy, the fifteenth chapter, written by S. M. Moghimi from the University of Brighton, UK, cautions about the possible toxic effects of a well-known gene transfer vector. The titles of the two chapters are *Nanotechnology for Gene Therapy – HVJ-E Vector* and *Nanotoxicology of Synthetic Gene Transfer Vectors: Poly (ethyleneimine) – and Polyfectin-mediated Membrane Damage and Apoptosis in Human Cell Lines*, respectively. The final chapter by Gang Liu and Ping Men from the University of Utah in Salt Lake City, USA, entitled *Nanoparticles for the Treatment of Alzheimer's Disease: The Theoretical Rationale, Present Status and Future Perspectives* indicates that nanotechnology has potential to treat Alzheimer's disease (AD), the most devastating neurodegenerative disorder with progressive and irreversible damage to thought, memory and language. I am very confident that the information that is presented in these sixteen chapters in this tenth volume will help in furthering the utility of nanotechnological approaches in medical diagnosis and therapy. I am, as always, very grateful to all the authors for their scholarly presentations of their topics, providing timely inputs and corrections in making the final volume in this series a reality.

As I conclude this ten-volume series, I would like to reinforce some of the comments that I made in my preface to the first volume. As I said, nanotechnology's greatest gift to mankind, in my view, is its ability to promote lateral thinking amongst not only scientists, but all those who are associated with this new approach, the so called 'nano thinking' to problem solving. On behalf of all the authors who have made contributions to this exciting series, it is my privilege to play the role of a catalyst in inculcating this new thinking by providing a multi-pronged base of knowledge in nanotechnologies for the life sciences. It is my hope that this book series will help in stretching the limits of thinking in all those who come in contact with it.

It is yet another opportunity for me to convey my thanks to each and every person (unfortunately due to lack of space I am unable to mention all the names) with whom I had the privilege of interacting and who have helped me directly or in-

directly during the course of the publication of the whole series. I would like to express my gratitude to the following people for their support and assistance. My employer and colleagues at the Center for Advanced Microstructures and Devices, graduate advisor Prof. N.R. Krishnaswamy who laid the foundation to my career, family and friends, and the Wiley-VCH publishing team, Martin Ottmar, Esther Döring, Nele Denzau and Eva Wille, with whom I had great pleasure in working.

Finally, my special thanks to you, the readers, for ensuring that the knowledge base provided in this book series will be a building block for further understanding of nanoscience. I do realize that there is a lot of scope for improvement and need to add new topics to this book series. I am hoping that I will be able to, with your comments and suggestions, take this series to a new level in the near future.

October 2006, Baton Rouge

*Challa S.S.R. Kumar*



# 1

## Nanotechnologies for Diagnosis – Present and Future

Gareth A. Hughes

### 1.1 Introduction to Patient Diagnostics

This chapter highlights the capabilities of nanoscale materials and devices for patient diagnostics. Current state-of-the-art diagnostic applications in development are reviewed with an extensive list of references provided for further investigation. The chapter is broken down into four major areas: *in vitro* and *in vivo* diagnostics (optical, electrical, magnetic, mechanical), imaging diagnostics, nanotechnology-enhanced analytical tools and techniques for diagnostics, and the future for patient diagnostics. In comparison to other published chapters on the subject of nanotechnology for diagnostics, this chapter covers the gamut of diagnostics including *in vitro* diagnostics (IVDs), implantable sensors and imaging techniques. Finally, in addition to covering a variety of diagnostic tools and methods where nanotechnology can be implemented, regulatory and ethical considerations are briefly discussed, providing a foundation on which to build scientifically responsible nanotechnology developments for life sciences.

Patient diagnostics involves more than analyzing the symptoms of disease. Diagnostic tools and assays are used to determine tissue type prior to organ transplantation, to determine blood type for patients requiring blood transfusions, and to monitor the progression of disease and the effects of therapy. Diagnosing a patient prior to onset of any symptoms would be ideal. Catching a disease early would allow the patient to take appropriate precautions to slow, halt or possibly reverse the progression of the ailment. The ability to combine diagnostic testing with patient profiling such as a genetic screen could open up the possibility of personalized therapy. Table 1.1 lists examples of applications for patient diagnostics.

A variety of techniques and testing protocols are available for performing patient diagnostics. Many times, a combination of techniques or tests are performed to provide accurate diagnosis. Current diagnostic techniques include immunoassays, genetic-based tests, cell-based assays, tissue or histological tests and medical imaging. Immunoassays are used for numerous diagnostic applications including monitoring levels of endocrine hormones such as estrogen, cortisol and prolactin, detecting biomarkers following myocardial infarction such as troponin and myoglobin, diagnosing hepatitis A–E, and searching for various biomarkers for cancer.



**Tab. 1.1.** List of diagnostic applications.

---

Diagnose disease susceptibility, risk assessment
Infectious disease assessment
Tissue typing for organ transplants
Screening for blood transfusions
Monitor therapy activity
Check disease progression
Personalized medicine
Genetic screening

---

Genetic-based diagnostics involve a variety of analytical techniques and gene expression profiling to determine susceptibility of disease. Cell-based assays involve high-throughput cell sorting along with intracellular imaging techniques. Two of the major focus areas for tissue-based testing are in cancer detection and in tissue typing for transplant patients. A variety of medical imaging tools exist ranging from magnetic resonance imaging to ultrasound. Imaging methods provide non-invasive means to diagnose disease.

There are also numerous specialized diagnostic techniques that are used when symptoms exist that warrant the use of a particular test. Specialized diagnostic techniques include electromyography (EMG) for monitoring nerve and muscle activity, electroencephalograph (EEG) to assess electrical activity of the brain, electrocardiography (ECG or EKG) to monitor electrical activity of the heart, tonometry for measuring internal eye pressure and spirometry to measure lung function. A summary of examples for testing protocols and techniques which are used in diagnostics are listed in Tab. 1.2. A comprehensive resource for diagnostics is the *Merck Manual of Diagnosis and Therapy* [1].

## 1.2 Nanotechnology and Patient Diagnostics

This chapter will summarize diagnostic applications of nanotechnology currently being development. Life science and medical applications of nanotechnology are numerous, ranging from tissue engineering, drug discovery to drug delivery and diagnostics [2, 3]. Nanotechnology is enabling a variety of diagnostic methods, including optical, electrical, magnetic, electrochemical and mechanical, and is enhancing established methods such as biomedical imaging techniques and spectroscopic methodology [4–22]. Handheld, wearable and implantable diagnostic tools for real-time patient monitoring can be manufactured when comprised of devices and materials precisely fabricated at the nanoscale [23].

Functionalized nanoparticles can enable multiplexed bioassays for simultaneous diagnostic screening of multiple diseases [24, 25]. High-capacity screening and combined molecular and immunological diagnostics will play a role in establishing

**Tab. 1.2.** Examples of techniques and testing protocols used in patient diagnostics.

Diagnostic type	Tool or technique used	Example applications
Immunoassay	enzyme-linked immunosorbent assay (ELISA)	cancer detection allergy tests, immunoglobulin (IgA, IgE, etc.) levels hormone levels C-reactive protein (CRP) infectious diseases autoimmune diseases diabetes assays prion disease diagnosis pancrease function tests
	bead-based assays	multiplexed assays cytokine levels cystic fibrosis testing blood typing metabolic disorders
	radioimmunoassay (RIA)	hormone levels liver function tests viral detection
	fluorescence polarization immunoassay (FPIA)	kidney function tests homocysteine levels
Genetic	single nucleotide polymorphism (SNP) analysis	sickle-cell cystic fibrosis testing p53 mutation detection metabolic disorders pharmacogenomics drug efficacy
	DNA chips and microarrays	multiplexed assays cancer detection tuberculosis drug efficacy
	polymerase chain reaction (PCR)	DNA amplification infectious diseases inheritable diseases
	Northern blot	mRNA detection gene regulation analysis
	Southern blot	DNA detection inheritable diseases restriction fragment length polymorphisms (RFLP) for prenatal diagnostics

Tab. 1.2 (continued)

Diagnostic type	Tool or technique used	Example applications
Cellular	flow cytometry	leukocyte analysis detection of cancer cells in urine and blood monitoring HIV therapies bone marrow transplants
	hematology analyzers	blood cell count
	immunocytochemistry	evaluating intracellular activity
	fluorescent <i>in situ</i> hybridization (FISH)	infectious diseases
Tissue	immunohistochemical stains (IHC)	cancer detection organ transplants bone marrow transplants
	laser capture microdissection	cancer detection
Imaging	dielectric property analysis	cancer detection
	magnetic resonance imaging (MRI)	brain disorders spinal cord disorders blood vessel diseases internal organ diseases
	computed tomography (CT)	stroke internal organ diseases soft tissue diagnostics
	X-ray	arthritis osteoporosis congestive heart failure respiratory diseases
	ultrasound	internal organ diseases blood flow analysis
	positron emission tomography (PET)	cancer detection monitoring of cancer therapy coronary heart disease myocardial infarction blood flow analysis memory disorders seizure disorders
	optical coherence tomography (OCT)	high-resolution tissue diagnostics retinal diseases glaucoma

Tab. 1.2 (continued)

Diagnostic type	Tool or technique used	Example applications
Specialty	optoacoustic tomography (OAT) or photoacoustic tomography (PAT)	cancer detection
	electromyography (EMG)	muscle activity nerve conduction
	electroencephalography (EEG)	brain electrical activity
	electrocardiography (ECG or EKG)	heart electrical activity
	tonometry	glaucoma
	spirometry	evaluate lung function

a broader range of testing capabilities that will allow diagnostics to be not disease-specific, but patient-specific and support the development of pharmacogenomics [26, 27]. Ultimately, smart nanostructures such as nanoparticles, nanotubes and dendrimers could be fabricated with both targeting capability and therapeutic moieties enabling site-specific delivery of therapy and personalized medicine [28]. Table 1.3 lists diagnostic techniques enhanced or enabled by nanotechnology which will be described in further detail in this chapter.

Nanoscale entities are abundant in biological systems. Viruses, proteins, small molecule drugs and fluorescent dyes are all less than 100 nm, as shown in Fig. 1.1. Through the manipulation of organic and inorganic materials at the atomic level, novel materials, structures and devices can be realized. Thermal, optical, electrical and mechanical properties of materials can be enhanced. Novel properties, not observed in the bulk form of materials, can be harnessed. Chemical activity of substances can be tailored to a desired end use such as improving biocompatibility of implantable materials and developing artificial receptors for targeted analyte binding. Surface properties of materials, such as adhesion, can be modified. Properties of materials at the nanoscale can be quite different than bulk material properties. Due to greater surface area per unit volume, nanomaterials can exhibit higher chemical reactivity, increased mechanical strength, and faster electrical and magnetic responses.

The field of nanotechnology brings about the necessary convergence of technical disciplines such as physics, chemistry, engineering and computer science with the biological disciplines of molecular and cell biology, genetics, neuroscience, biophysics, and biochemistry. Through the convergence of all these disciplines, the field of nanotechnology is poised to create many breakthroughs across all industries. Medical applications show particular promise, including building blocks of

Tab. 1.3. Diagnostic techniques enabled or enhanced by nanotechnology.

Technique	Applications
Optical	enhanced fluorescence quantum dots surface plasmon resonance (SPR) nanoparticles nanoshells bio-barcodes Probes encapsulated by biologically localized embedding (PEBBLEs) fiber optics
Electrical	amperometric conductimetric potentiometric enzymatic
Magnetic	immunoassays magnetofection magneto-resistive
Mechanical	nanocantilevers surface acoustic waves (SAWs) quartz crystal balance
Imaging	contrast agents multifunctional agents
Mass spectrometry	nanoparticle pre-concentrator
Raman spectroscopy	surface enhanced Raman spectroscopy (SERS) tip enhanced Raman spectroscopy (TERS)
Genetics	nanopore sequencing
Immunoassays	luminescent nanoparticles

nucleic acids as structural components as binding agents similar to antibodies rather than typical genetic maps, nanostructured biosensors for implantable patient monitoring and nanoparticles as imaging contrast agents.

Patient diagnostics can be broken down into three major modalities: assays, biosensors and imaging. Nanotechnology plays a role in improving these modalities and also creating novel diagnostic methods. *In vitro* assays are used extensively for diagnostics. Three commonly used assay formats are enzyme-linked immunosorbent assays (ELISAs), polymerase chain reaction (PCR)-based genetic assays, and staining assays such as Giemsa and Gram for viral and bacterial diagnostics. While many diseases and infections can be diagnosed with such assays, most of these assays require laboratory equipment. Point-of-care diagnostics are typically not possible using these assays. Samples are usually shipped to laboratories that

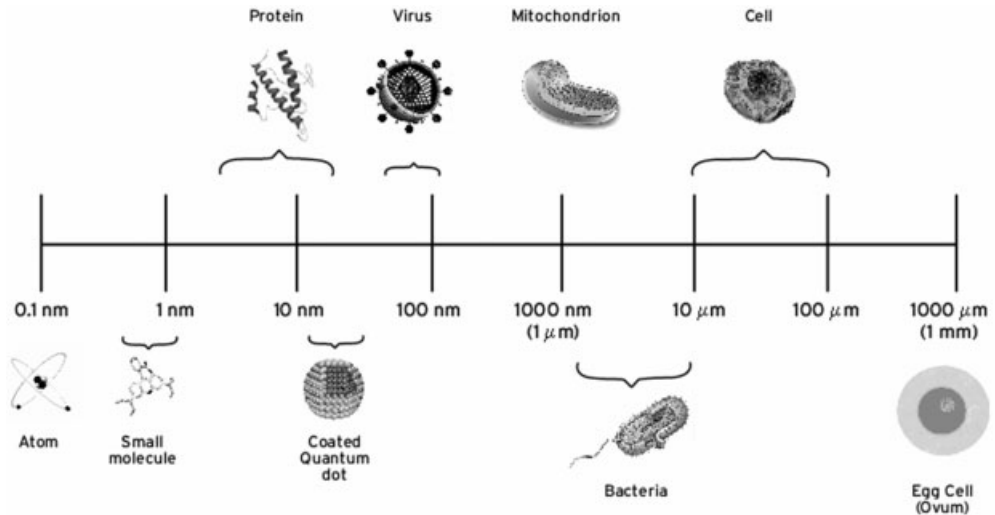


Figure 1.1. Scale of things, from atom to embryo.

specialize in performing these *in vitro* assays. Nanotechnology can improve these assays by increasing throughput for rapid diagnostics or by enhancing sensitivity which could enable catching a disease earlier.

Biosensors provide the ability to perform diagnostics at point-of-care and enable real-time diagnostics in the form of implantable devices. The general format of a biosensor, shown in Fig. 1.2, comprises of a biologically receptive site which binds specifically to the analyte in question and a transducer that translates the binding event into a measurable signal, which can be optical, electrical, magnetic or mechanical. Nanostructures can be used to enhance any of these transduction mechanisms. For example, nanoscale semiconductor materials (quantum dots) can be used in optical biosensors. In comparison to traditional organic fluorophores, quantum dots are much more photostable, have greater quantum efficiency and have much narrower emission. Such advantages could be used to develop highly sensitive optical biosensors and multiplexed assays. Due to high surface area, nanowires and nanotubes can greatly enhance charge transfer in biosensors based on electrical mechanisms. Functionalized magnetic nanoparticles can be targeted to desired analytes and detected with miniature magnetic sensors, creating portable diagnostics. Finally, nanocantilevers, modified with antibodies or other biological receptors, can be sensitive enough to detect a single biomolecule such as an individual viral particle.

Aptamers make up one particular class of biological receptor structures which show increasing potential for use in diagnostics. Aptamers are oligonucleotide sequences that are structured for high affinity and specificity towards a desired ligand, similar to antibodies, but formed from nucleic acids rather than amino acids. Since their discovery in the early 1990s [30] through the use of an *in vitro* technique named systematic evolution of ligands by exponential enrichment (SELEX),

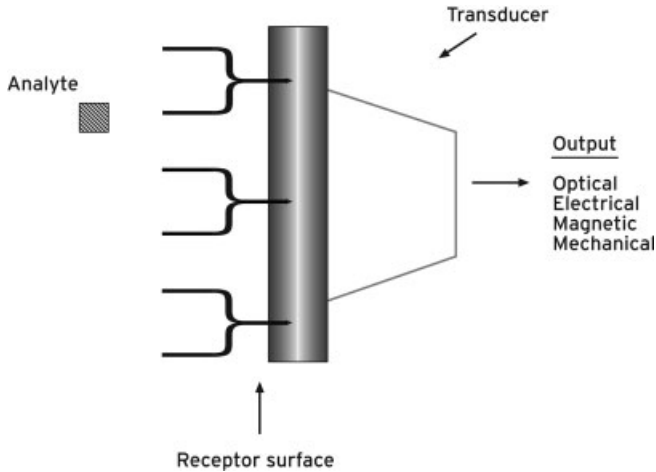


Figure 1.2. Major components of a biosensor.

many aptamers have been developed that bind various targets including thrombin, platelet-derived growth factor (PDGF) and keratinocyte growth factor (KGF). Recently, an anti-vascular endothelial growth factor (VEGF) aptamer was introduced as a new treatment for macular degeneration. Developing therapeutic applications for aptamers is an expanding area of research.

Aptamers have several advantages over monoclonal antibodies which have likewise generated much interest in therapeutics. Aptamers are fully processed *in vitro*. Antibodies require an animal model as a starting point. Therefore, tight process control and scale-up are much more achievable for aptamer production paving the way for lower cost therapeutics. Aptamers, especially DNA aptamers, are much

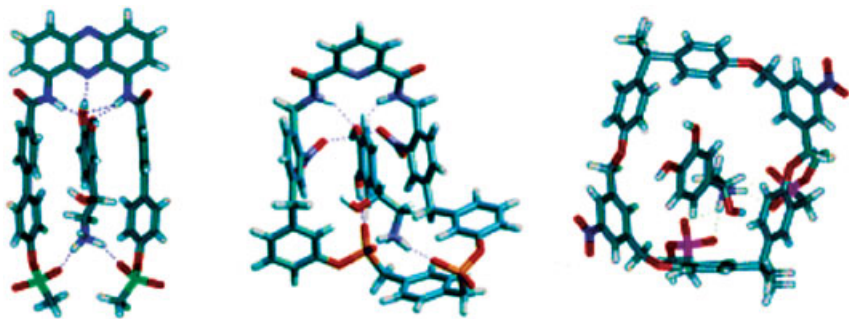


Figure 1.3. Synthetic noradrenaline receptors [42]. Reproduced with permission from J. Am. Chem. Soc., Vol. 127, S. Kolesheva et al., Selective detection of catecholamines by synthetic receptors embedded in chromatic polydiacetylene vesicles, p. 10000–10001. © (2005) American Chemical Society.

more stable than their antibody counterparts, which are large protein molecules that can readily degrade if appropriate storage conditions are not used. Even if the aptamer does denature, the structure can be easily regenerated. Furthermore, aptamers have not shown any appreciable evidence of toxicity or immunogenicity. These same properties show promise for aptamers in the field of diagnostics, both *in vitro* and *in vivo* [30–38].

One strength of aptamer-based diagnostic sensors over antibody- or enzyme-based techniques is the ability to denature and regenerate the aptamer. This ability could enable reusable biosensors that match the affinity and specificity of antibody and enzyme sensors [37, 38]. Combining aptamer recognition with nanoscale sensing capability such as optical, electrochemical or magnetic transduction methods will enable development of highly sensitive, portable and, eventually, implantable diagnostic tools [39–41].

Medical imaging for diagnostics comes in a variety of forms including X-ray imaging such as computed tomography (CT) scans, magnetic resonance imaging (MRI), positron emission tomography (PET) scans, ultrasound and more recent optical techniques such as optical coherence tomography (OCT). The advantage of imaging over assays and biosensors for diagnostics is the elimination of the need for a patient sample, such as blood or tissue. In the case of implantable biosensors, imaging has the advantage of being noninvasive. However, most medical imaging equipment is expensive and requires trained personnel to both operate and interpret. Furthermore, the low resolution of most of these techniques limits sensitivity. Nanoparticles as contrast agents can be used to increase sensitivity which may allow earlier diagnosis of diseases. If sensitivity is greatly increased using contrast agents, then less-powerful imaging components, such as magnets for MRI, may be used reducing size and cost.

## 1.3

### Optical

#### 1.3.1

##### Fluorescence

Fluorescent tags, such as fluorescein isothiocyanate (FITC) and rhodamine, have been used extensively as optical markers for a variety of biological assays. Traditional fluorophores have a broad user base and are available in many forms such as voltage-sensitivity dyes, membrane-specific chemistries and pH-sensitive structures. However, traditional fluorophores typically have broad emission spectra, exhibit short emission lifetimes and are susceptible to photobleaching. With the desire for greater sensitivity, multiplexed assays, single-molecule detection and *in vivo* diagnostics, enhancement of traditional fluorophores and the development of novel markers are transforming optical detection methods.

Fluorescent tags can be improved by conjugation with receptor molecules, with coatings for improved photostability, and by combining with metals for greater emission. Figure 1.3 shows three synthetic receptors for noradrenaline which



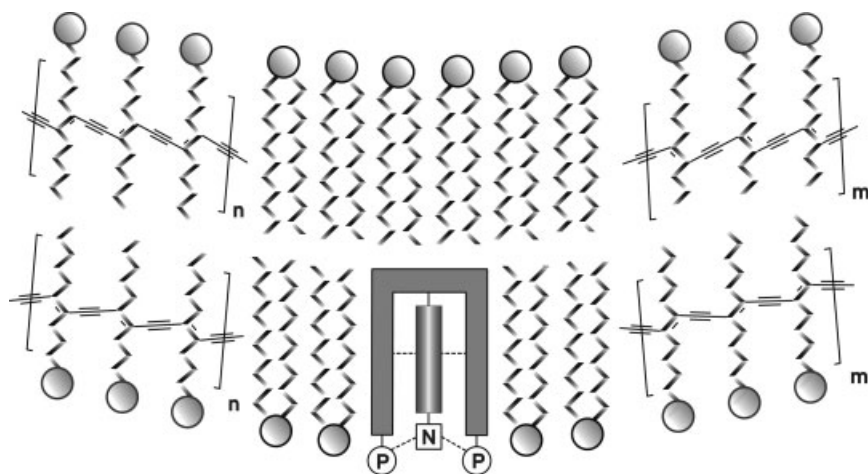


**Figure 1.4.** Synthetic receptor embedded within a phospholipid/polydiacetylene membrane [42]. Reproduced with permission from J. Am. Chem. Soc., Vol. 127, S. Kolusheva et al.,

Selective detection of catecholamines by synthetic receptors embedded in chromatic polydiacetylene vesicles, p. 10000–10001. © (2005) American Chemical Society.

provide sensitive fluorescent assays when embedded with phospholipid/polydiacetylene membrane assemblies [42]. By embedding the synthetic receptor within the phospholipid/polydiacetylene membrane (Fig. 1.4), single micromolar detection of catecholamines in urine samples was achieved producing a 1000-fold improvement over existing synthetic receptor-based catecholamine detection systems. Such a sensitive method could provide an earlier diagnostic for Parkinson's disease. Also see Fig. 1.5.

Nanoparticle platforms consisting of surface-functionalized, silica-coated nanospheres can be used for bioimaging applications [43, 44]. Silica coating enhances aqueous dispersion of nanoparticles, and allows surface functionalization of peptides and nucleic acids for specificity. Fluorescence emission can be tuned by controlling the size of the nanoparticle. A range of nanoparticle sizes can be used simultaneously for multiplexed assays due to each size of nanoparticle emitting a different color. Due to little to no autofluorescence, the signal-to-noise ratio can be quite high, enabling highly sensitive bioimaging techniques for early diagnostics.

Dendrimers are highly branched, monodisperse polymers that have well-defined size and chemical functionality. Voids and channels within the dendritic structure can be carriers for drug molecules. Size, composition and morphology of dendrimer composites can be precisely controlled by pH, temperature and concentration. In addition to drug molecules, metal ions can be entrapped within dendrimer voids creating novel fluorescent nanoparticles [45]. Silver/dendrimer composites absorb in the 300- to 400-nm range with emission from 400 to 500 nm. By using low concentrations of silver/dendrimer composite (below 1  $\mu\text{M}$ ) to minimize cytotoxicity, intracellular fluorescent assays can be performed due to cellular uptake of nanoscale dendrimer structures.

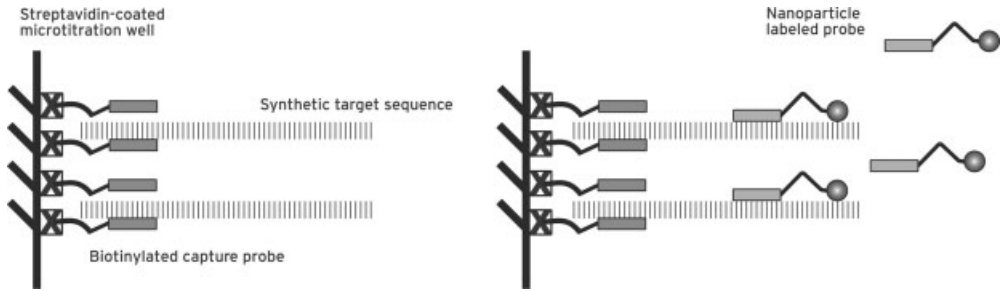


**Figure 1.5.** Example of assay using nanoparticle tags [48]. Reproduced from *Nanotechnology*, Vol. 15, P. Huhtinen et al., Europium (III) nanoparticle-label-based assay for the detection of nucleic acids, p. 1708–1715, © (2004), with permission from Institute of Physics and P. Huhtinen.

Fluorescence can also be enhanced using metallic nanostructures such as silver or gold nanorods and nanospheres [46, 47]. Such phenomenon is termed metal-enhanced fluorescence (MEF). When a fluorophore is exposed to a nearby metallic surface, quantum efficiencies can increase due to interactions of the excited-state fluorophore with free electrons in the metal. At short distances between fluorophore and metal (less than 5 nm), quenching can occur. Highly sensitive *in vitro* diagnostic assays may be realized using MEF. Other metals that exhibit enhanced fluorescence are the Lanthanide series of metals or the “rare earth” elements such as europium, samarium and terbium [48, 49].

### 1.3.2

#### Quantum Dots

Quantum dots are nanometer-size crystals in which electrons are confined in all three directions. Electron energies are quantized within the nanocrystalline quantum dot enabling an array of emission wavelengths to be produced depending upon the band gap of the crystalline material and quantum dot size as shown in Fig. 1.6. Common quantum dot materials include CdSe which emits blue, InP which emits green and InAs which emits red [50]. Typical quantum dot cores are 3–4 nm in diameter; however, due to water insolubility and possible toxicity of typical cores, polymeric or silica coatings are added to make them water-soluble and biocompatible [51, 52]. ZnS is also a commonly used coating for CdSe core quantum dots for protection against photooxidation [53].

Coatings can increase quantum dot diameter to greater than 30 nm in some cases, creating a tag much larger than standard fluorescent dyes which poses challenges for intracellular delivery and creates potential alterations of the very biological activity that one may be investigating [55]. In addition to water insolubility and large size, quantum dots exhibit thermoquenching where emission decreases as temperature increases. For isothermal bioanalytical applications, thermoquenching poses no problems. However, for *in vitro* assays and, possibly, *in vivo* imaging

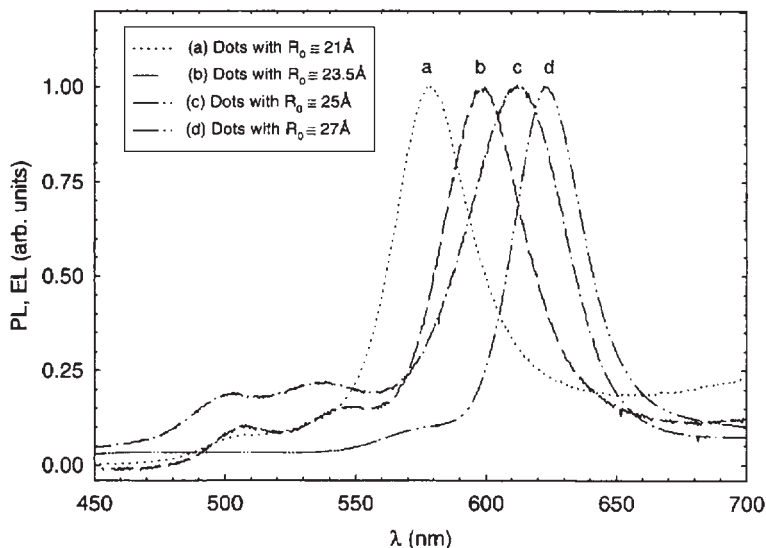


**Figure 1.6.** Emission wavelength as function of quantum dot size [54]. Reused with permission from H. Mattoussi, *J. Appl. Phys.*, 83, 7965 (1988). Copyright 1998, American Institute of Physics.

applications, where temperatures may fluctuate, thermoquenching effect must be taken into account.

Another limitation of quantum dots is their susceptibility to intermittent emission (“blinking”). Due to their high quantum efficiencies and the use of multiple quantum dots per typical assay, the effects of intermittent emission are negligible. However, where the “blinking” phenomenon becomes a limiting factor is with fluorescence intensity studies, single-molecule spectroscopy and flow cytometry where temporal data is necessary [53, 56, 57].

Despite the larger size, quantum dots are being used for multiplexed *in vitro* assays and *in vivo* imaging applications due to brighter and narrower emission, broader absorption spectra, and high photostability. Quantum dots have much narrower emission spectra (around 30 nm at half maximal emission) in comparison to organic dyes (50–100 nm), such as fluorescein and rhodamine. Due to their narrow emission and the capability of achieving emission over a broad excitation range, multiple quantum dots of different color can be imaged simultaneously using a single excitation source [58–60]. Typical organic dyes limit the ability to perform multiplexed assays because of their overlapping emission spectra and their limited absorption capability, requiring multiple excitation sources to be used when multiple fluorophores are desired.

Through surface functionalization by covalent, noncovalent and chemisorption modifications, quantum dots can be used in protein and DNA immunoassays. Biotinylated, streptavidin-conjugated and antibody-conjugated quantum dots are now readily available, enabling a variety of sandwich-based assays. It is the ability to functionalize quantum dots that make them attractive for diagnostic applications.

By encasing the core quantum dot nanocrystal with a biocompatible, hydrophilic, readily functionalized coating such as silica or polymer and modifying the coating with biologically specific entities such as antibodies, enzymes and nucleic acids, sensitive fluorimetric assays and biosensors can be realized. Assays and biosensors based on quantum dots are being developed for diagnosing breast and prostate cancer, for simultaneously detecting multiple toxins, and for sensing levels of acetylcholine [61].

For *in vivo* applications, it is desirable to have quantum dots that emit in near-infrared (NIR) range of 700–1550 nm, where such energy absorption in tissue is minimal. Example nanocrystalline materials for NIR quantum dots include CdTe, InP and InAs. CdTe-based quantum dots consist of a CdTe core with a CdSe shell which have lower quantum yields and weaker NIR absorption than InP and InAs quantum dots. InP quantum dots are larger (above 6 nm) than most other nanocrystalline structures which, after coating, limits their use for *in vivo* applications. InAs quantum dots are much smaller (below 2 nm), but have limited absorption capability in the NIR due to their small size [62]. Alloys and core–shell structures comprised of nanocrystalline materials improve NIR absorption capability while keeping the quantum dot to a functional size. Figure 1.7 shows the size distributions for InAsP, InP and ZnSe alloys, and core–shell quantum dot structures.

Figure 1.8 shows emission spectra for InP, InAs and InAsP alloy quantum dots. With increasing percentage of arsenic in the alloy, greater NIR luminescence is observed. Figure 1.9 shows the effect of the core–shell structure on emission. As the InAsP alloy core is coated with shell material, first with InP and finishing with ZnSe, the emission of the quantum dot is pushed further into the NIR range.

Another interesting phenomenon of quantum dots is the observation of fluorescent downshift (“blue” shift) when bound to bacterial surfaces [63]. By conjugating antibodies or aptamers to quantum dot surfaces, specific bacteria can be targeted. Upon binding of antibody- or aptamer-conjugated quantum dots to bacterial surfaces, shifts in fluorescent emission peaks ranging from 60 to 140 nm have been

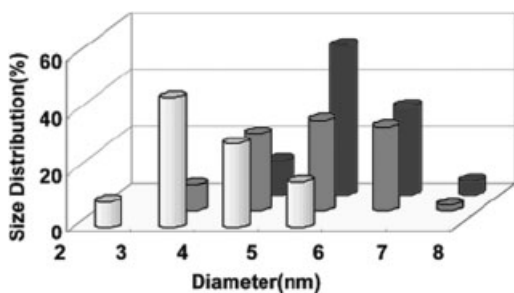


**Figure 1.7.** Size distribution for quantum dot core and core–shell combinations. InAs<sub>0.82</sub>P<sub>0.18</sub> (yellow), InAs<sub>0.82</sub>P<sub>0.18</sub> core and InP shell (red), and InAs<sub>0.82</sub>P<sub>0.18</sub> core, InP shell and ZnSe outer shell (blue) [62]. Reproduced with

permission from J. Am. Chem. Soc., Vol. 127, S.-W. Kim et al., Engineering InAs<sub>x</sub>P<sub>1-x</sub>/InP/ZnSe III–V alloyed core/shell quantum dots for the near-infrared, p. 10526–10532. Copyright (2005) American Chemical Society.

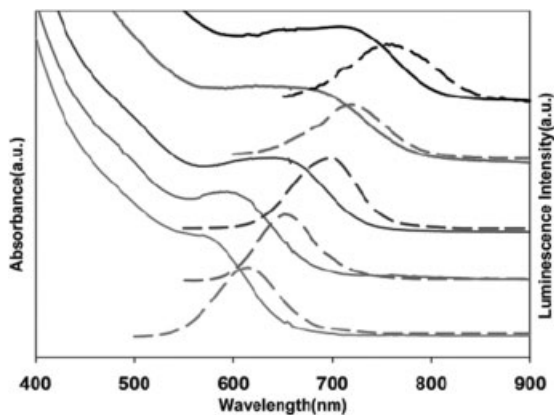


**Figure 1.8.** Emission of InP (614 nm), InAs<sub>0.33</sub>P<sub>0.66</sub> (652 nm), InAs<sub>0.66</sub>P<sub>0.33</sub> (699 nm), InAs<sub>0.82</sub>P<sub>0.18</sub> (738 nm) and InAs (755 nm) quantum dots. Absorbance shown as solid line [62]. Reproduced with permission from J. Am.

Chem. Soc., Vol. 127, S.-W. Kim et al., Engineering InAs<sub>x</sub>P<sub>1-x</sub>/InP/ZnSe III–V alloyed core/shell quantum dots for the near-infrared, p. 10526–10532. Copyright (2005) American Chemical Society.

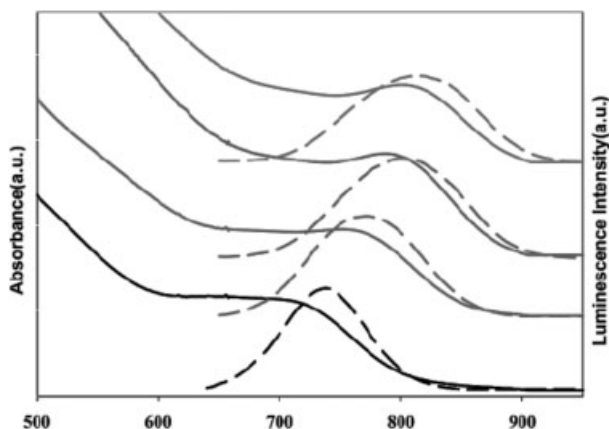


**Figure 1.9.** Emission of InAs<sub>0.82</sub>P<sub>0.18</sub> core (738 nm), with a shell of InP (765 nm), with a second shell of InP (801 nm) and with a final shell of ZnSe (815 nm). Absorbance shown as solid line [62]. Reproduced with permission

from J. Am. Chem. Soc., Vol. 127, S.-W. Kim et al., Engineering InAs<sub>x</sub>P<sub>1-x</sub>/InP/ZnSe III–V alloyed core/shell quantum dots for the near-infrared, p. 10526–10532. Copyright (2005) American Chemical Society.

observed which can be readily optically detected. This method could be used to determine the presence of bacteria in a sample.

### 1.3.3

#### Surface Plasmon Resonance (SPR), Nanoparticles and Nanoshells

Molecular-recognition molecules immobilized using self-assembled monolayers (SAMs) coupled with SPR sensing create sensitive, label-free biosensors [64–74].

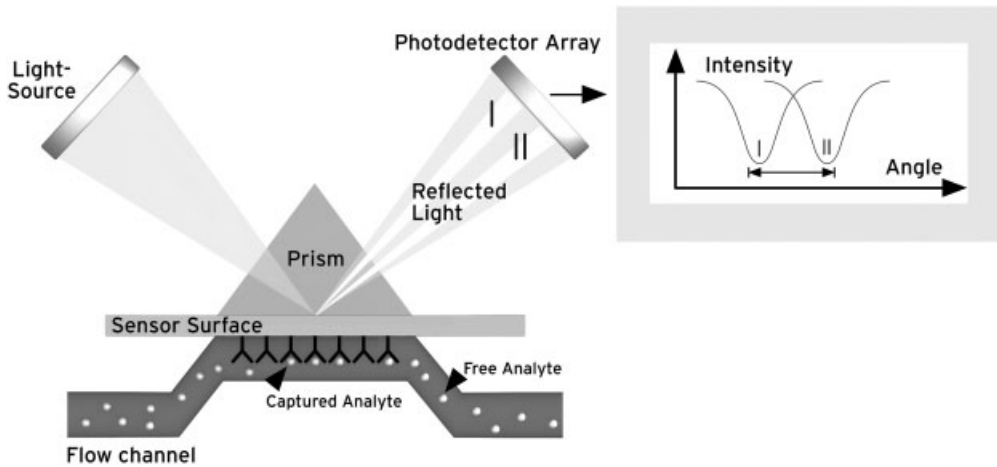


Figure 1.10. Typical set-up for SPR [68].

A typical SPR set-up is depicted in Fig. 1.10, with main components consisting of a sensor substrate (chip) coated with a thin metal film (typically gold or silver), a polarized light source and an optical detection unit. Polarized light is directed toward the sensor chip at an angle such that an evanescent wave is created on the surface of the metal film. Changes in the dielectric constant of the adjacent medium shift the intensity of the evanescent wave, resulting in a change in angle of reflection from the metal surface. The angular shift is detected with a photodetector [70].

By modifying the metal film for biological specificity, the SPR sensor can be tailored to respond to a desired analyte. Upon binding of the analyte to the molecular-recognition site of the modified metal film, the index of refraction changes at the sensor surface, which results in an angular shift of the reflected light. The metal surface is typically first modified with alkane thiol or alkyl siloxane chemistry. Subsequent modification defines the biological specificity of the SPR sensor and can consist of streptavidin for biotinylated analytes, biotin for streptavidin-conjugated analytes or sandwich assays using free streptavidin followed by biotinylated analyte, antibodies for antibody–antigen interactions and enzymes or aptamers for affinity assays.

Using metal nanoparticles and nanoshells with SPR phenomena creates localized SPR (LSPR) which enables field-portable, lower-cost SPR systems with improved capability to detect small molecules, all of which could pave the way for greater use of SPR in patient diagnostics [69, 71–74]. An example of a LSPR set-up using gold-coated silica nanoparticles and a fiber optic probe for excitation and detection is shown in Fig. 1.11.

Optical properties of nanoparticles depend highly on size, shape and local environment. When the nanoparticle diameter is much smaller than the wavelength of light, then the optical interaction of nanoparticles can be described by Mie theory

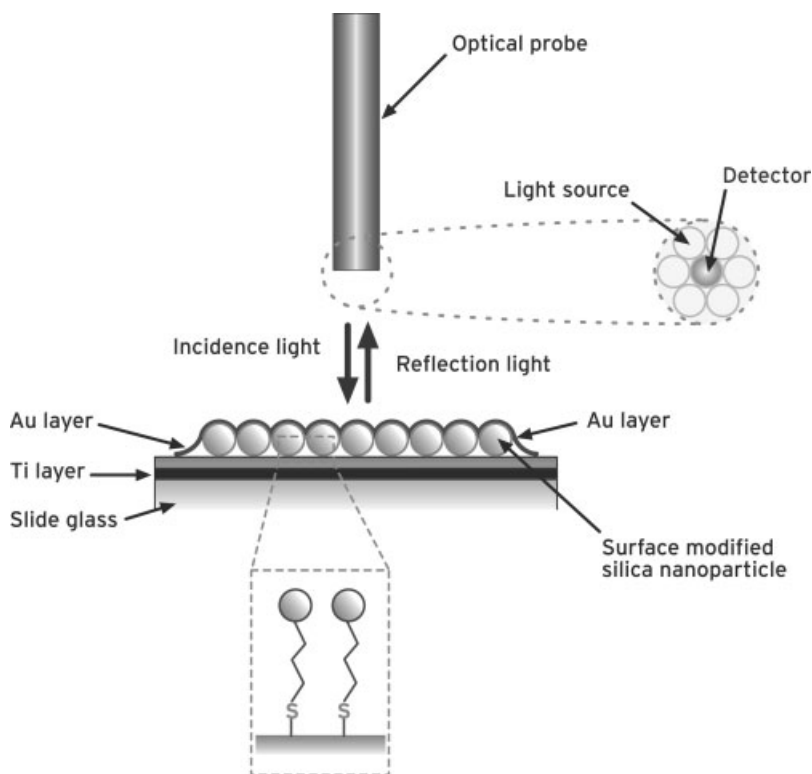


**Figure 1.11.** LSPR biosensor set-up [71]. Reproduced with permission from Analytical Chemistry, Vol. 77, T. Endo et al., Label-free detection of peptide nucleic acid-DNA

hybridization using localized surface plasmon resonance based optical biosensor, p. 6976–6984. Copyright (2005) American Chemical Society.

of electromagnetic radiation scattering stated in Eq. (1) [69, 75, 76]. SPR occurs when  $\epsilon_r = -\chi\epsilon_m$  and  $\epsilon_i$  is small:

$$E(\lambda) = \frac{24\pi N_A a^3 \epsilon_m^{3/2}}{\lambda \ln(10)} \left[ \frac{\epsilon_i}{(\epsilon_r + \chi\epsilon_m)^2 + \epsilon_i^2} \right], \quad (1)$$

where  $E(\lambda)$  is the optical extinction (sum of absorption and scattering),  $N_A$  is the areal density of nanoparticles,  $a$  is the radius of nanoparticles,  $\epsilon_m$  is the dielectric constant of the medium,  $\lambda$  is the wavelength of the absorbing radiation,  $\epsilon_i$  is the imaginary portion of the nanoparticle dielectric constant,  $\epsilon_r$  is the real portion of the nanoparticle dielectric constant and  $\chi$  is the aspect ratio of nanoparticles ( $\chi = 2$ , for a sphere).

Probes encapsulated by biologically localized embedding (PEBBLEs) are optical nanosensors which can be used to monitor intracellular conditions such as pH and



**Figure 1.12.** Diagram of PEBBLE nanosensor [79]. Reproduced with permission from Analytical Chemistry, Vol. 76, Y.-E. L. Koo et al., Copyright (2004) American Chemical Society. Real-time measurements of dissolved oxygen inside living cells by organically modified silicate fluorescent nanosensors, p. 2498–2505.

calcium ion levels [77–79]. Fluorescent molecules are entrapped within a permeable polymer gel creating PEBBLE nanoparticles typically ranging from 20 to 200 nm, as represented in Fig. 1.12. The polymer gel coating protects the internal fluorophore from nonspecific protein binding and reduces cytotoxicity. Due to the porosity of the polymer coating, small ions such as calcium, oxygen and hydrogen can penetrate the coating, and reach the entrapped fluorophore. Therefore, pH- and calcium-sensitive dyes can be encapsulated while maintaining their desired function.

Single base-pair mismatches in a sequence of DNA can be detected using colorimetric assays comprised of electrostatic absorption of DNA onto colloidal gold nanoparticles [80–83]. Such assays eliminate target labeling and do not require any covalent modifications of DNA or substrate surfaces. Furthermore, sensitivity is high enough to obviate the need for DNA amplification such as PCR. Color detected is dependent upon degree of aggregation of gold nanoparticles. Due to the ability to perform the assay in less than 10 min, RNA degradation is minimized and, therefore, RNA sequences can also be determined.

Another technique which results in high sensitivity without the need for target amplification is the Bio-Barcode Assay (Fig. 1.13), which can be used for both nucleic acid and protein analysis [84–89]. The Bio-Barcode Assay uses both gold nanoparticles and magnetic microparticles functionalized with the same antibody specific for the particular analyte to be detected. Antibody-functionalized gold nanoparticles are further modified with oligonucleotide strands of a known sequence, giving the gold nanoparticles a unique identity or barcode. When exposed to the target analyte, both gold nanoparticles and magnetic microparticles bind to the analyte creating complexes of gold nanoparticle–analyte–magnetic microparticle.



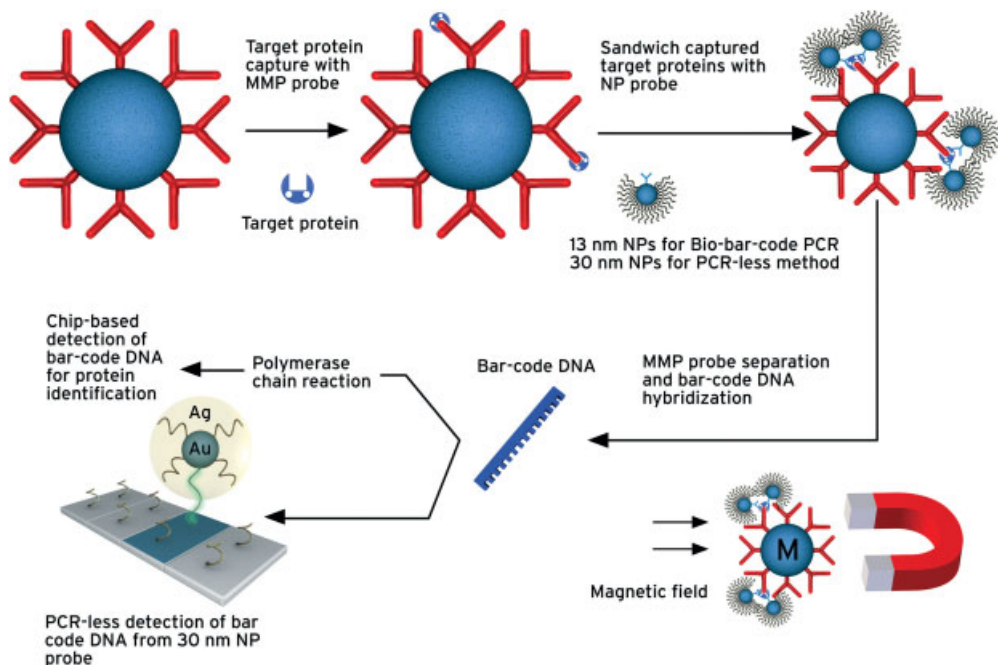


**Figure 1.13.** Bio-barcode assay [6]. Reproduced from *Clinical Chimica Acta*, Vol. 358, K. K. Jain, *Nanotechnology in clinical laboratory diagnostics*, p. 37–54, Copyright (2005), with permission from Elsevier.

After the complexes are magnetically separated and washed, the barcode DNA is dehybridized and released from the gold nanoparticles into solution. The single-stranded barcode DNA is then collected and bound to a microarray containing oligonucleotides complementary to half of the targeted barcode DNA. Gold nanoparticles functionalized with oligonucleotides complementary to the other half of targeted barcode DNA are then hybridized to the microarray-captured DNA. Finally, the gold nanoparticles are coated with silver for amplification and the microarray is read using light scattering intensity measurements. The Bio-Barcode Assay enables detection of molecules down to attomolar sensitivity.

Aptamer-conjugated gold nanoparticles can bind desired protein targets forming gold-tagged proteins for subsequent analysis [90]. The bound gold nanoparticles can be enlarged in catalytic solution of gold chloride resulting in higher absorbance at 540 and 650 nm as the size of gold nanoparticles increases. An example using thrombin as target protein is shown in Fig. 1.14. A greater concentration of protein binds more aptamer–gold nanoparticle conjugates, which provides a greater surface density for catalytic solution to deposit more gold. Observed absorbance then is a function of protein concentration. Sensitivity down to single nanomolar protein concentrations have been achieved with this method.

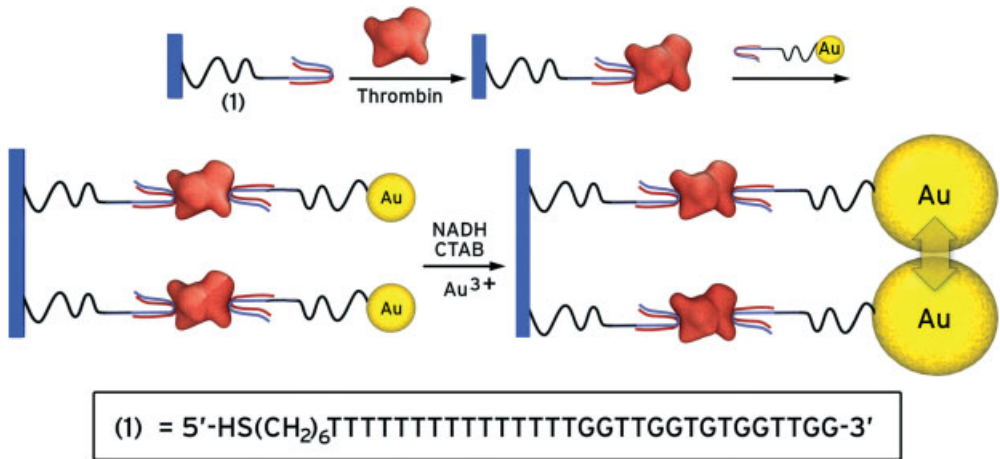


**Figure 1.14.** Aptamer-functionalized gold nanoparticles for binding assay amplification [90]. Reproduced with permission from J. Am. Chem. Soc., Vol. 126, V. Pavlov et al., Aptamer- functionalized Au nanoparticles for the amplified optical detection of thrombin, p. 11768–11769. Copyright (2004) American Chemical Society.

#### 1.3.4

#### Fiber Optic Biosensors

Fiber optic biosensors show potential use in intracellular assays and *in vivo* applications [91–95]. Modifying the distal tip of the optical fiber to create a biologically active surface allows for binding events or reactions at the distal tip surface to be monitored optically through fluorescent or spectroscopic (IR and Raman) methods. An example of a modified optical fiber tip is shown in Fig. 1.15. Due to containment of the reactive species to the fiber tip surface, localized detection of the desired analyte can be achieved. Furthermore, highly sensitive diagnostic devices could potentially be developed by combining fiber optic biosensors with nanoparticles or nanoshells for amplification of optical response (i.e. LSPR or surface-enhanced Raman spectroscopy).

### 1.4

#### Electrical

Electrical methods to measure analytes include amperometric, conductimetric and potentiometric techniques (Fig. 1.16) [96]. Amperometric techniques utilize a working electrode containing chemistry, typically an enzyme, specific to the analyte being monitored. A voltage potential is set up between the reference electrode and the working electrode. Products from the binding of the analyte to the surface chemistry of the working electrode become oxidized or reduced depending on the voltage potential between the electrodes. Electrical current is measured at the work-

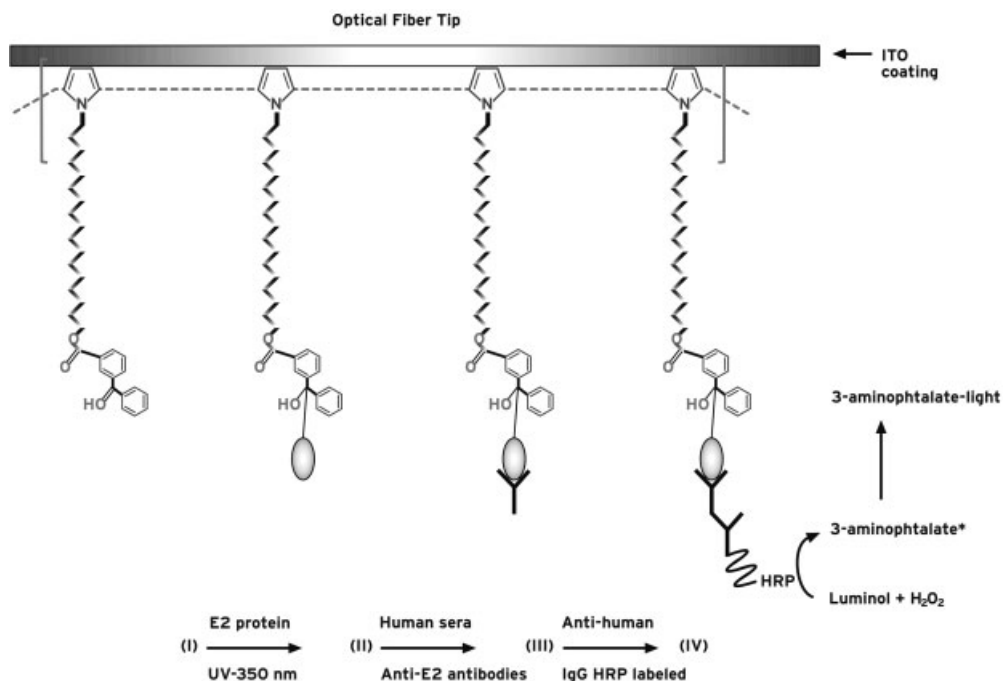


**Figure 1.15.** Surface modification of optical fiber distal tip [95]. Reproduced with permission from *Analytical Chemistry*, Vol. 77, T. Konry et al., Optical fiber immunosensor

based on a poly(pyrrolebenzophene) film for the detection of antibodies to viral antigen, p. 1771–1779. Copyright (2005) American Chemical Society.

ing electrode providing a method to determine the presence and concentration of the analyte. Conductimetric techniques measure the conductance of the analytical solution as a function of the analyte concentration. Measurement electrodes can be modified with biological receptors concentrating the analyte near the electrode surfaces. Potentiometric techniques are based on field effect transistor devices in which the current flowing between source and drain is affected by analyte concentration. Voltage is monitored as the current is affected providing a method to measure analyte concentration.

#### 1.4.1

#### Nanomaterials for Enhanced Electron Transfer

Nanomaterials, such as nanotubes and nanoparticles, can enhance electron transfer and can be readily modified for biological specificity [97, 98]. Integrating nanomaterials with microfabricated electrodes and circuits, enable portable, miniature instrumentation. Using electrical methods of detection eliminates the need for enzymatic amplification techniques typically used in optical detection assays. Due to the use of electronics, amplification and signal conditioning can be integrated within the assay substrate.

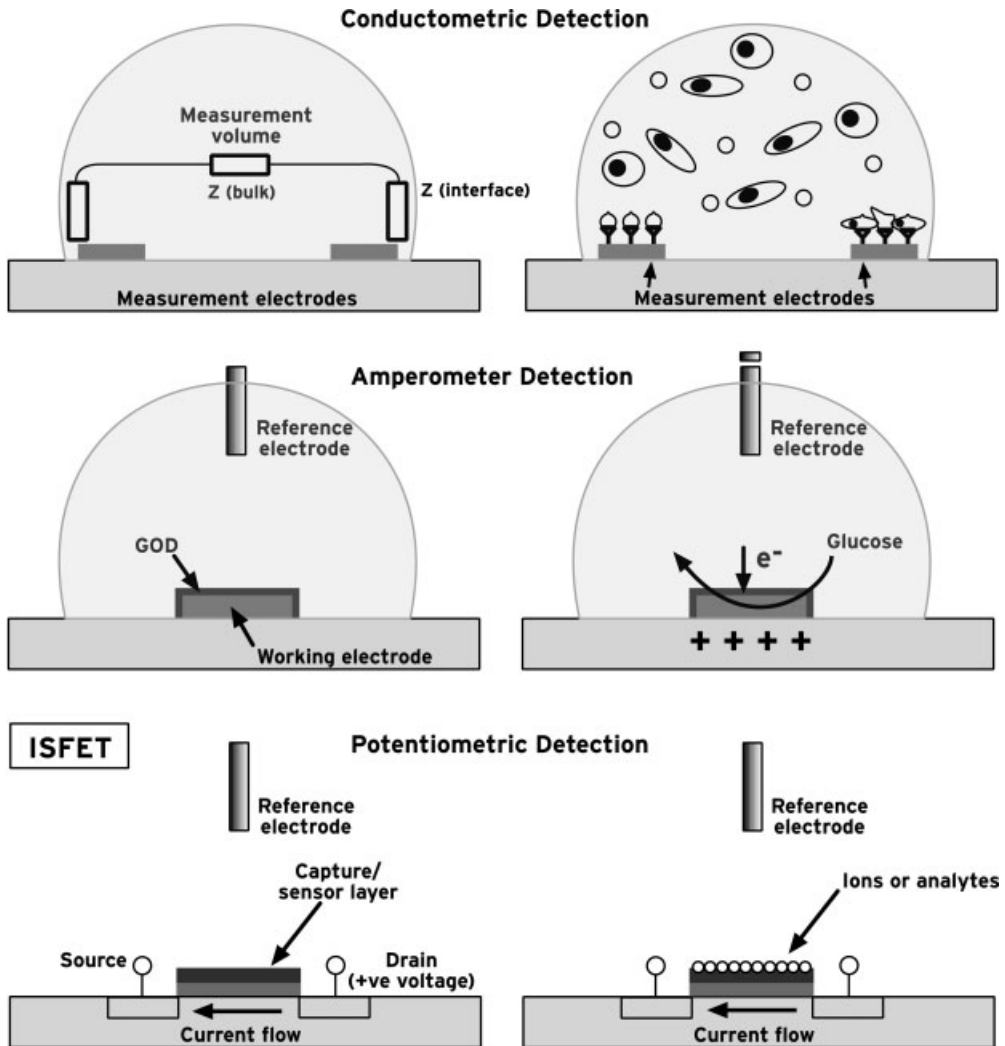


**Figure 1.16.** Electrical detection methods [96]. Reproduced from *Advanced Drug Delivery Reviews*, Vol. 56, R. Bashir, *BioMEMS: state-of-the-art in detection, opportunities and prospects*, p. 1565–1586, Copyright (2004) with permission from Elsevier.

Multiwalled carbon nanotubes (MWNTs) can be functionalized with single-stranded DNA. When exposed to the complementary DNA, after target hybridization, charge conductance through the carbon nanotube changes indicating binding of the cDNA [99]. MWNTs can be selectively grown on electrode surfaces coated with nickel catalyst. A conformal  $\text{SiO}_2$  layer passivates the exposed substrate between MWNTs. Ethylene glycol-modified siloxanes can be deposited onto the oxide surface to inhibit nonspecific binding. Finally, siloxanes can be selectively removed

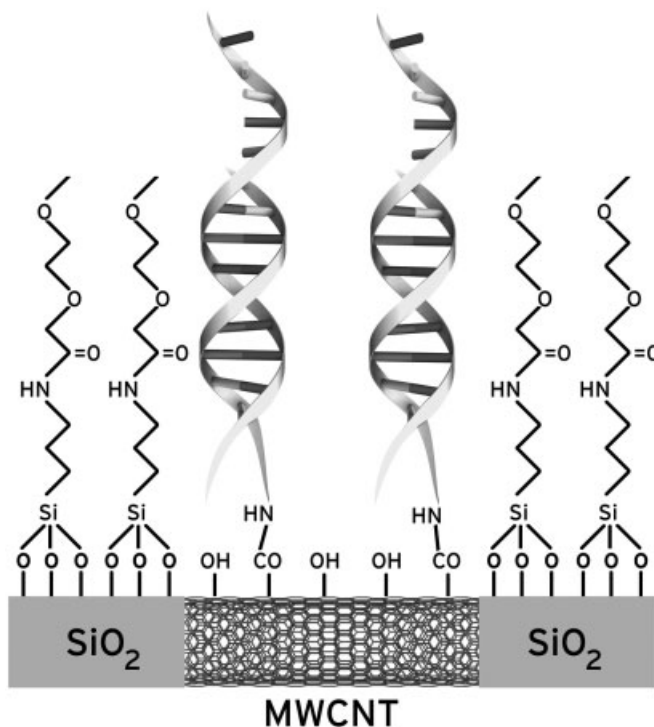


**Figure 1.17.** MWNT functionalized with DNA [99]. Reproduced from *Clinical Chemistry*, Vol. 50, J. E. Koehne et al., *Minutized multiplex label-free electronic chip for rapid nucleic*

*acid analysis based on carbon nanotube nanoelectrode arrays*, p. 1886–1893, Copyright (2004), with permission from American Association for Clinical Chemistry.

from the MWNTs through electrochemical etching, exposing the MWNT surface for subsequent functionalization with single-stranded DNA (Fig. 1.17). The cycle of siloxane removal from selected MWNTs followed by single-stranded DNA functionalization provides a method to produce dense arrays of different single-stranded DNA probes.

Target DNA, extended with additional guanine bases, is exposed to the MWNT array and allowed to hybridize. The additional guanine produces a small current when electrochemically oxidized. The current generated is transferred to the MWNTs, which transfer the charge to the underlying electronic circuit for eventual signal acquisition. Due to generation of a very small current, electrocatalytic amplification of guanine oxidation current can be achieved using polypyridyl complexes of ruthenium (Fig. 1.18) or osmium.

Nanowires fabricated from semiconducting single-wall carbon nanotubes (SWNTs), silicon and zinc oxide can be integrated into field effect transistors (FETs) [100], and functionalized for biological specificity enabling rapid, label-free, detection of small molecules [61, 65, 101, 102]. The ability of FET devices to sense

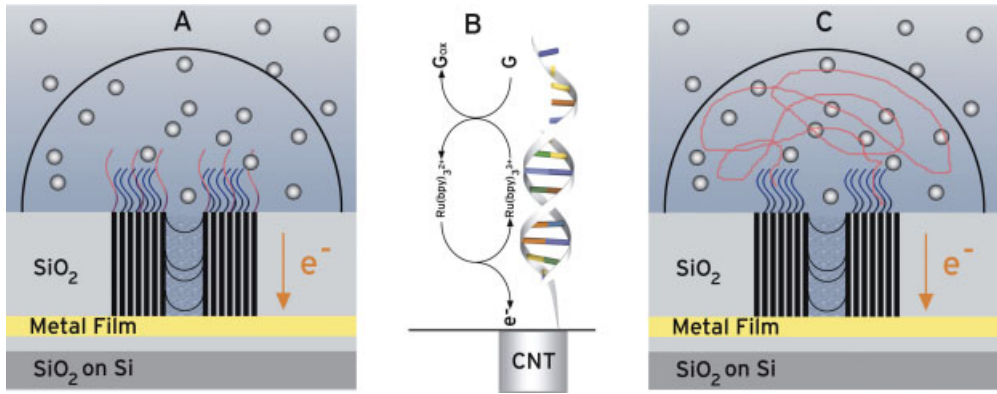


**Figure 1.18.** Electrochemical detection of nucleic acids with electrocatalytic amplification by ruthenium-polypyridyl complex [99]. Reproduced from *Clinical Chemistry*, Vol. 50, J. E. Koehne et al., Minutized multiplex label-

free electronic chip for rapid nucleic acid analysis based on carbon nanotube nanoelectrode arrays, p. 1886–1893, Copyright (2004), with permission from American Association for Clinical Chemistry.

small molecules is due to a change in surface charge upon adsorption onto the gate material of target molecules. Nanowire FETs consist of functionalized nanowires as the gate material deposited or placed between transistor source and drain (Fig. 1.19). Such a physical arrangement produces devices highly sensitive to electrical changes. Due to the high surface area to volume of nanowires, extremely minor surface charge changes may be monitored, possibly enabling detection of single molecules.

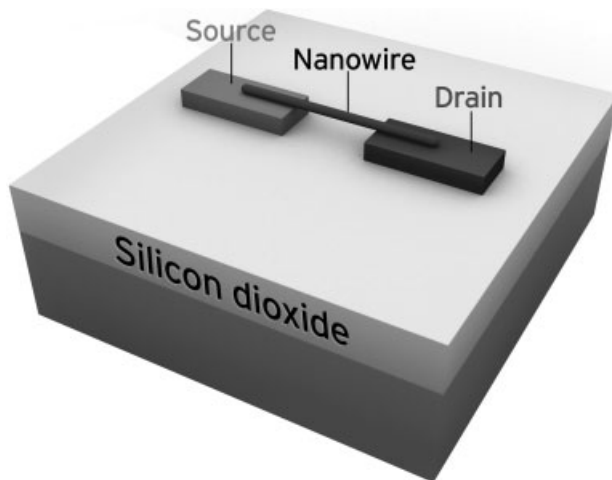


**Figure 1.19.** Nanowire FET sensor schematic.

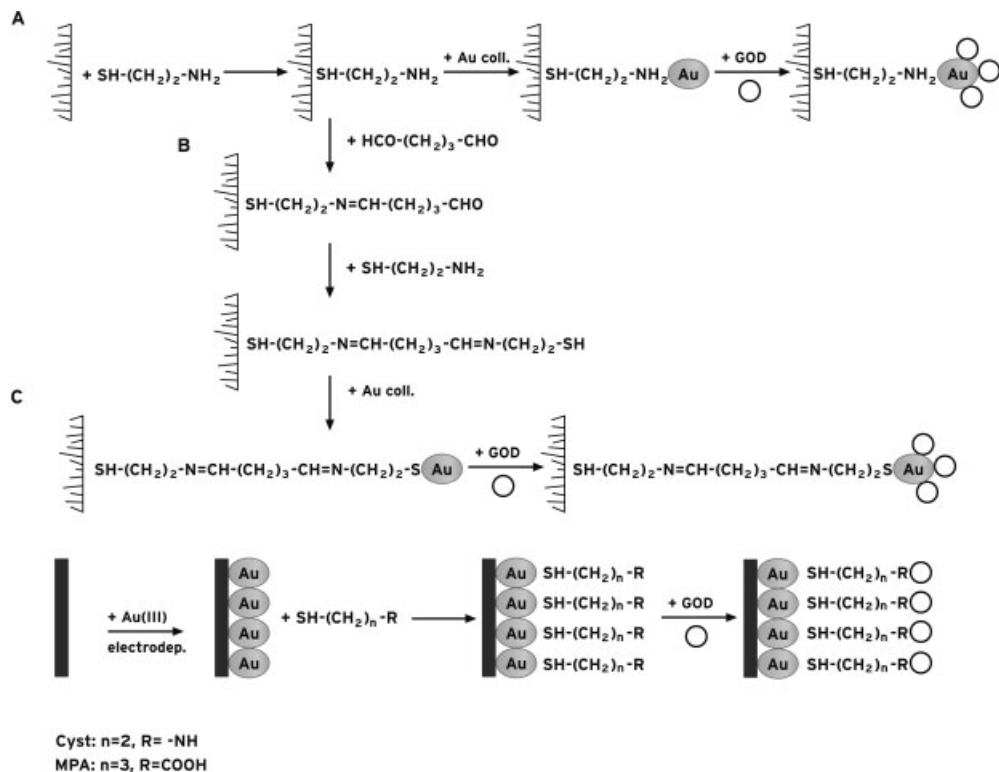


**Figure 1.20.** Methods to enhance enzyme assays using gold nanoparticles [109]. Reproduced with permission from Anal. Bioanal. Chem., Vol. 382 (2005), p. 884–886, Gold nanoparticle-based electrochemical

biosensors, P. Yanez-Sedeno and J. M. Pingarron, Fig. 1. © (2005) with kind permission of Springer Science and Business Media.

#### 1.4.2

##### Electrochemical Biosensors

Low-cost, portable, fast-response diagnostic systems can be realized with electrochemical biosensors [103]. Glucose biosensors based on glucose oxidase are one of the most common diagnostic tools currently available. Electrochemical DNA analysis has also been widely investigated [104]. Aptamers can also be immobilized onto electrode surfaces and be used in electrochemical sensing systems [105–107]. To enhance charge transfer and to improve immobilization of enzyme or target, nanostructures such as carbon nanotubes and metallic nanoparticles can be used in conjunction with immobilized enzymes to form high specificity and high sensitivity biosensors. Due to their large surface area, nanoparticles provide enhanced adsorption of DNA and enzymes over flat surfaces which are typically used in microarrays and immunoassays [108, 109]. Biosensors can be created by linking silica or gold nanoparticles carrying immobilized DNA or specific enzyme onto gold electrodes. Electrochemical impedance analysis can be used to monitor hybridiza-

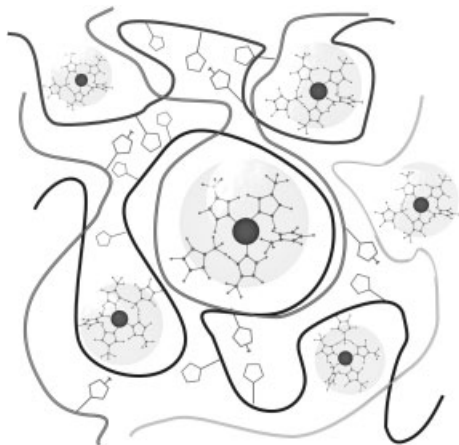


**Figure 1.21.** PMP complex [110]. Reproduced from *Current Applied Physics*, Vol. 5, T. Haruyama et al., *Bio-, nano-technology for cellular biosensing*, p. 108–111, Copyright (2005), with permission from Elsevier.

tion of cDNA or enzyme activity. Several methods for using gold nanoparticles to enhance enzyme-based diagnostic assays are shown in Fig. 1.20.

Through self-assembly of two or more different polymers with metal ions, thin films with nanoscale cavities can be formed (Fig. 1.21). These polymer–metal–polymer (PMP) complexes can be tailored for biochemical specificity and be used as amperometric transducers for electrochemical assays [110]. PMP complexes can be readily spin coated onto metal electrodes for biosensor formation. Another advantage of PMP films is their cellular compatibility. Cells can be cultured directly on the surface of PMP film allowing for cell-based diagnostics to be performed.

Electrochemical detection of DNA hybridization opens up the opportunity for low-cost gene mutation and single nucleotide polymorphism (SNP) analysis. The portability of such genetic sensors (genosensors) provides exciting possibilities for clinical use. Multifunctional gold nanoparticles is one platform that can be used in electrochemical genosensors [111]. First, target single-stranded DNA is immobilized onto the working electrode, such as a pencil graphite electrode (PGE), of the electrochemical cell. Thiol-terminated oligonucleotides, of the sequence to which the target DNA is to be compared, are then added to solution containing gold nanoparticles. The DNA-immobilized working electrode is immersed into the solution which now contains oligonucleotide-functionalized gold nanoparticles and gold oxidation is measured using differential pulse voltammetry which produces an electrical current depending on degree of hybridization (Fig. 1.22). A perfect match produces the highest current. A single point mutation is discernible due to lower current being generated. The absence of hybridization still produces some current, but much less than the single point mutation.

Many electrochemical reactions can be enhanced through electrocatalytic amplification using electron-transfer mediators. These mediators help transfer of



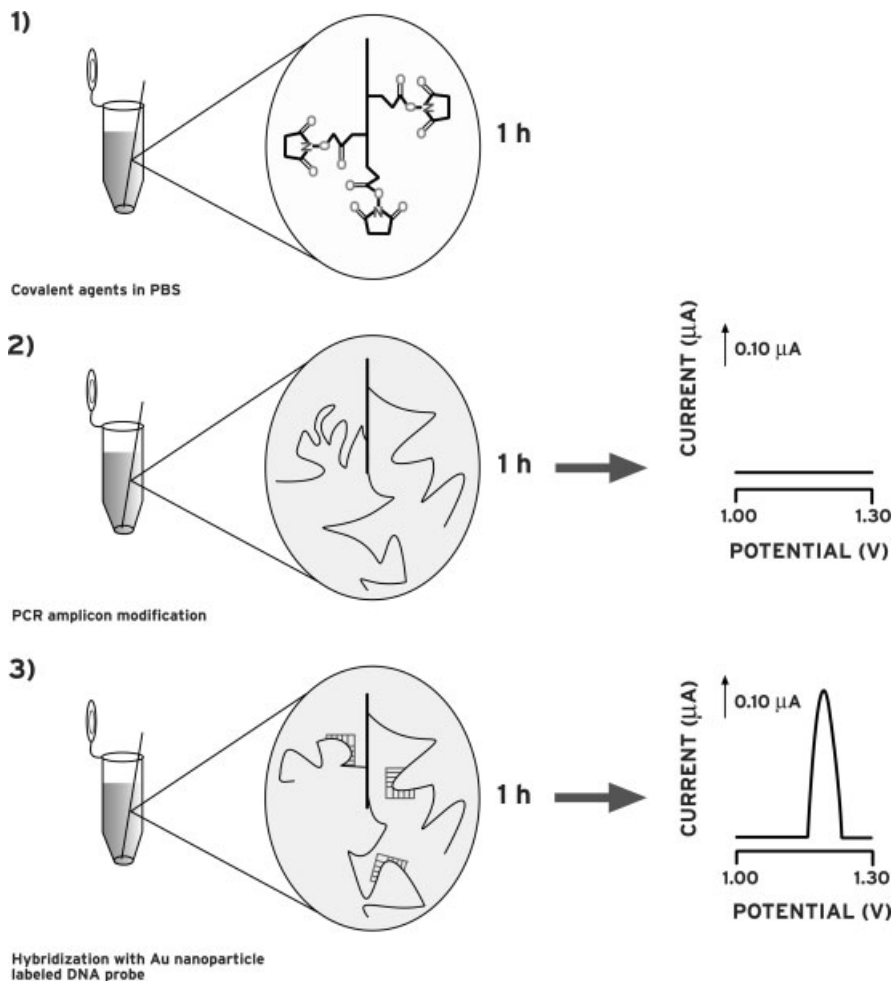


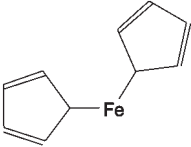
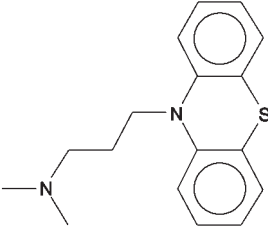
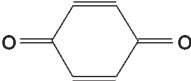
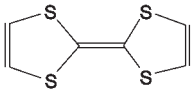
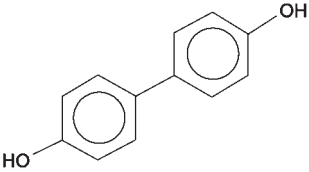
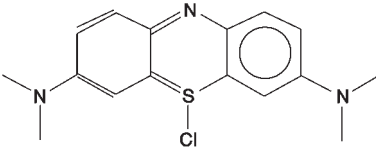
**Figure 1.22.** DNA hybridization detected electrochemically with gold nanoparticle probes [111]. Reproduced with permission from *Analytical Chemistry*, Vol. 75, M. Ozsoz et al., Electrochemical genosensor based on

colloidal gold nanoparticles for the detection of Factor V Leiden mutation using disposable pencil graphite electrodes, p. 2181–2187. Copyright (2003) American Chemical Society.

electrons between the working electrode and the enzymatic reactants, essentially creating a molecular conduit to shuttle electrons. Without electron-transfer mediators, many of the electrons produced by enzymatic activity may be lost due to diffusion. Methods utilizing electron-transfer mediators involve coimmobilizing them with the enzyme in a conductive polymer matrix, inorganic sol-gel or carbon paste [112–115]. Several frequently used electron-transfer mediators are listed in Tab. 1.4.

Precision assembly of materials is routinely achieved in biological systems through use of proteins. One particular nanostructure formed by bacteria is a monolayer of crystalline proteins called an S-layer. These crystalline proteins can

Tab. 1.4. Examples electron-transfer mediators.

Electron-transfer mediator	
Ferrocene	$C_{10}H_{10}Fe$ 
Promazine	$C_{17}H_{20}N_2S$ 
<i>p</i> -Benzoquinone	$C_6H_4O_2$ 
Tetrathiafulvalene	$C_6H_4S_4$ 
<i>p</i> -Dihydroxydiphenyl	$C_{12}H_{10}O_2$ 
Methylene blue	$C_{16}H_{18}ClN_3S$ 

be removed from the exterior of bacteria, resuspended in solution and allowed to self-assemble on solid support surfaces such as silicon, metal or polymer. The self-assembled S-layer monolayer can be modified with enzymes or antibodies for analyte specificity. Optical or electrical measurements can then be used to detect the presence of binding analyte. One such diagnostic tool is an S-layer dipstick shown in Fig. 1.23 [116–118].

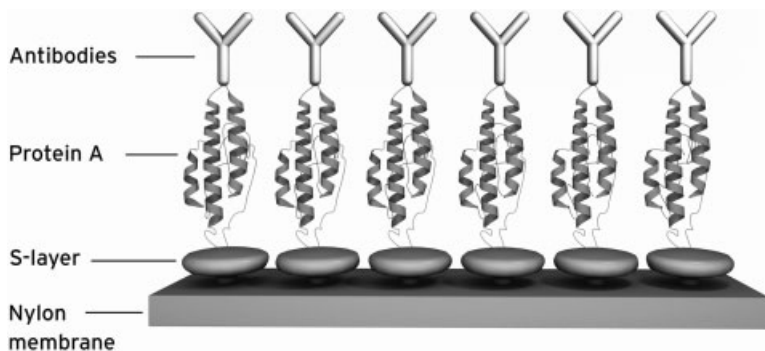


**Figure 1.23.** Filtration membrane modified with protein A immobilized on S-layer for antibody functionalization.

## 1.5 Magnetic

Ferrite nanoparticles can be coated with gold (Fig. 1.24) or silica which can then be functionalized with targeting molecules. Antibody-conjugated magnetic nanoparticles can be used to tag proteins for magnetic immunoassays [119]. Using magnetic methods to report binding could enable multiplexed assays to be performed on chip-based substrates.

Genomagnetic nanocaptors are silica-coated, magnetic nanoparticles functionalized to bind with RNA or DNA [121]. Molecular beacons, e.g. loop–stem structures of single-stranded oligonucleotides, can be bound to magnetic nanoparticles to enable capture of single-base mismatched DNA and target mRNAs for intracellular gene expression analysis (Fig. 1.25) [120, 122]. In comparison to linear single-stranded DNA typically used in hybridization assays, the loop–stem structure of molecular beacons provides greater discrimination between perfect match and single-base mismatched DNA [123].

Combining molecular beacons with magnetic nanoparticles, single-base mismatched DNA can be magnetically separated (Fig. 1.26). Genomagnetic nanocaptors (GMNCs) colabeled with molecular beacons perfectly complementary and single-base mismatched to target DNA can be dispersed within a mixture of sample DNA to be analyzed. Both perfectly complementary DNA and single-base mismatched DNA will bind to the molecular beacons on the surface of the GMNCs which can be magnetically separated from solution. Due to the differences in melting temperature for each of the DNA complexes, complementary DNA can be separated from single-base mismatched DNA.

For intracellular applications, magnetic nanoparticles can be coated with cell-penetrating peptides [124]. One class of protein which has been used for efficient cellular internalization is membrane translocating signal (MTS) protein which include HIV-1 tat protein and VP22 herpes virus protein. Other cell-penetrating peptides include penetratin and transportan. These cell-penetrating peptides and proteins show promise as effective carriers to transport impermeable nanoparticles

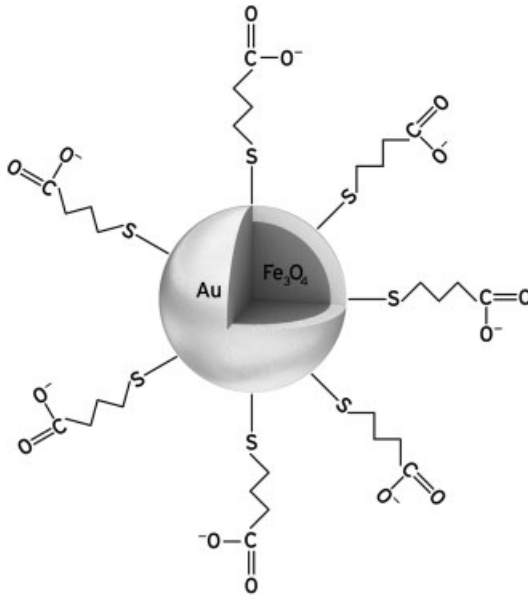


**Figure 1.24.** Iron oxide nanoparticle with gold coating for surface functionalization [120]. Reproduced from *Materials Today*, Vol. 7, P. Gould, *Nanoparticles probe biosystems*, p. 36–43, © (2004), with permission from Elsevier.

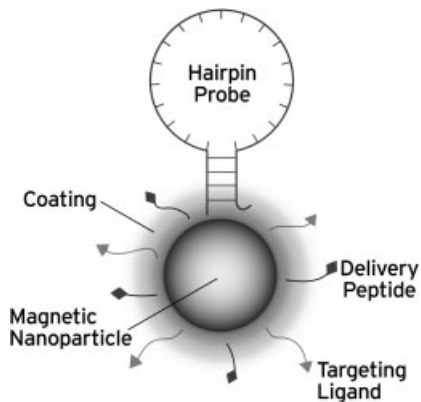


**Figure 1.25.** Magnetic nanoparticle tagged with molecular beacon oligonucleotide structure [120]. Reproduced from *Materials Today*, Vol. 7, P. Gould, *Nanoparticles probe biosystems*, p. 36–43, © (2004), with permission from Elsevier.

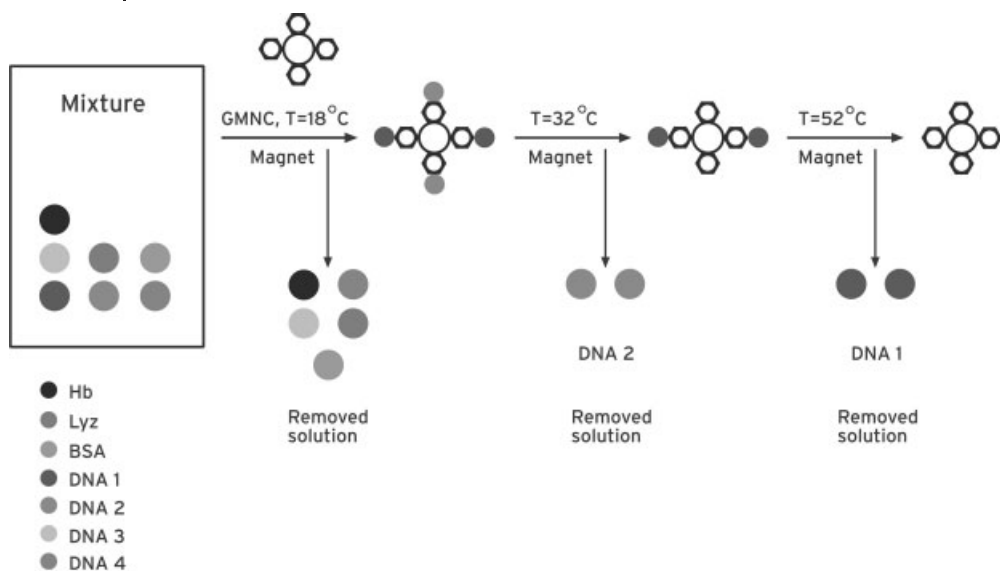


**Figure 1.26.** Genomagnetic capture separation [121]. Reproduced with permission from *Analytical Chemistry*, Vol. 75, X. Zhao et al., Collection of trace amounts of DNA/mRNA molecules using genomagnetic nanocaptors, p. 3476–3483. Copyright (2003) American Chemical Society.

across cell membranes. Functionalized magnetic nanoparticles may also be internalized through magnetofection – the application of external magnetic to attract magnetic nanoparticles into the cell (Fig. 1.27) [125–127].

Similar to chip-based electrical methods for biological analysis, sensors based on magnetic nanoparticles could also be used for benchtop and handheld diagnostics. For instance, arrays of DNA probes can be immobilized on surfaces as in DNA chips. Biotinylated complementary target DNA can then be hybridized with the DNA probes on the chip followed by washing of the substrate to remove unbound DNA. Streptavidin-functionalized magnetic nanoparticles can then be exposed to the chip, resulting in the capture of magnetic nanoparticles to target cDNA [120]. The capture sites can be detected with underlying magnetoresistive, spin valve or magnetic tunnel junction sensors which produce signals based on changes in the magnetic field [128]. The magnetic field above the sensor is perturbed due to the presence of bound magnetic nanoparticles. See Fig. 1.28.

## 1.6 Mechanical

Biosensors based on mechanical transduction methods include cantilevers [129–133], surface acoustic waves (SAWs) [38] and quartz crystal microbalances [134]. These mechanical structures can be mass-produced using combination of photoli-

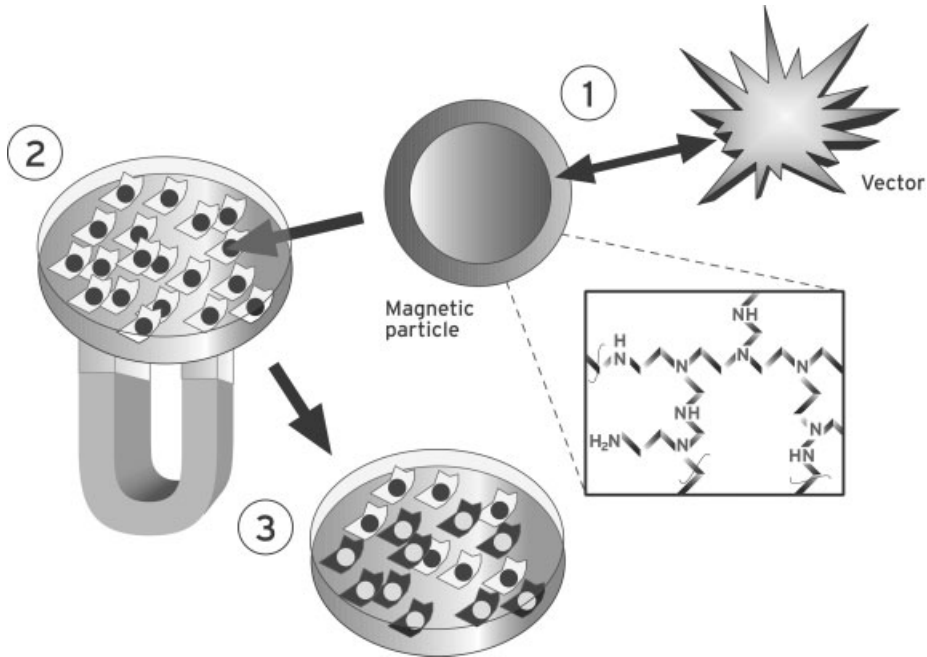


**Figure 1.27.** Magnetofection [126]. Reproduced from *Biological Chemistry*, Vol. 384, C. Plank et al., The magnetofection method: using magnetic force to enhance gene delivery, p. 737–747, Copyright (2003), with permission from Walter de Gruyter GmbH & Co. KG and C. Plank.

thographic, micromachining and thin film techniques. As the capabilities of these techniques continue to be improved, nanoscale mechanical structures, such as nanocantilevers, can be fabricated. The advantage of making mechanical structures with nanoscale dimensions is their resulting ability to respond to extremely small mechanical stimuli such as molecular binding. For example, nanocantilevers can be used to detect subfemtograms of material. A single viral particle on a nanocantilever produces a measurable response.

Biosensors based on nanocantilever structures can be fabricated by modifying the cantilever surface with biological receptors such as antibodies, aptamers and complementary DNA. Upon target binding, the cantilever will deflect if operating in static mode or its resonant frequency will shift if operating in dynamic mode. Deflection of the cantilever is typically monitored optically by focusing a laser onto the cantilever and measuring deflection with a photodetector (Fig. 1.29), similar to an atomic force microscope (AFM). Although static mode cantilevers perform better than the dynamic mode due to mechanical damping of the resonating cantilevers, as the cantilevers are reduced to the nanoscale measuring the deflection becomes challenging while resonant cantilevers become much more sensitive to mass loading. Therefore, most nanocantilever biosensors operate in dynamic mode.

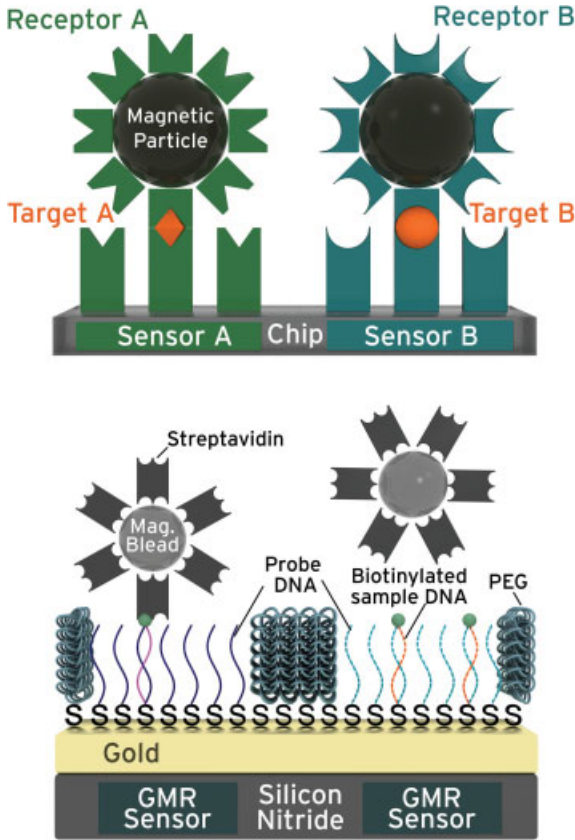


**Figure 1.28.** Biosensor based on magneto-resistive arrays [120]. Reproduced from *Materials Today*, Vol. 7, P. Gould, Nanoparticles probe biosystems, p. 36–43, Copyright (2004), with permission from Elsevier.

In dynamic mode, the resonant frequency of the nanocantilever can be monitored with optical methods as described above or with electrical methods such as capacitive or piezoelectric. The binding of additional mass results in a downshift of the resonant frequency as indicated by:

$$\frac{1}{f_1^2} - \frac{1}{f_0^2} = \frac{\Delta m}{4\pi^2 k}, \quad (2)$$

where  $f_0$  is the initial cantilever resonant frequency,  $f_1$  is the resulting cantilever resonant frequency after binding,  $\Delta m$  is the mass of analyte bound to the cantilever and  $k$  is the spring constant of the cantilever. The spring constant for a rectangular cantilever is expressed by:

$$k = \frac{Ewt^3}{4L^3}, \quad (3)$$



**Figure 1.29.** Typical optical measurement of cantilever deflection [130]. Reproduced with permission from Nickolay V. Lavrik, *Review of Scientific Instruments*, 75, 2229 (2004). Copyright 2004, American Institute of Physics.

where  $E$  is the Young's modulus of the cantilever,  $w$  is the cantilever width,  $t$  is the cantilever thickness and  $L$  is the cantilever length.

Using techniques based on semiconductor fabrication methods, nanocantilevers can be batch-fabricated in large volumes (hundreds to thousands per substrate) establishing potential for low-cost manufacturing. Nanocantilevers can be individually functionalized such that arrays can be formed providing multiplexing capability. With the use of electrical readout methods instead of optical methods, low-power portable cantilever-based diagnostic systems could be realized.

## 1.7 Imaging Diagnostics

Medical imaging diagnostics include MRI, PET, CT, OCT, optoacoustic or photoacoustic tomography (OAT or PAT) and NIR imaging. Nanoparticles containing hundreds of contrast agents can greatly enhance the sensitivity of these imaging methods [24, 122, 135, 136]. Examples of MRI contrast agents include gadolinium-diethylene-triamine-pentacetic acid (Gd-DTPA) and superparamagnetic iron oxide particles (SPIOs). Ultrasound contrast agents are designed to affect the propagation of sound waves in the surrounding sample area by altering the acoustic properties. Liquid perfluorocarbon nanoparticles and liposomes are examples of ultrasound contrast agents. Due to the small scale of nanoparticle contrast agents, the body does not quickly clear them, which prolongs the time that can be taken during imaging for a more thorough diagnosis.

Noninvasive detection at the single-cell level may be possible with nanocarriers loaded with contrast agent and functionalized with biological receptors specific to the desired cell. Such sensitivity could greatly improve early disease detection.



Nanocarriers could include liposomes, dendrimers or porous polymeric nanoparticles. Multifunctional nanocarriers combine biological specificity with the ability to use multiple imaging modalities. For instance, crosslinked iron oxide (CLIO) nanoparticles have branched structure which facilitates complexing with targeting entities such as enzymes or aptamers in addition to attachment of fluorophores or quantum dots [137]. Therefore, magnetic nanoparticles which function as MRI contrast agents can be modified to target a specific cell type and can be simultaneously monitored optically due to addition of optical tags.

An advantage of optical imaging methods over MRI, PET and CT is the potential of manufacturing lower cost imaging equipment. Lasers and optical (for OCT and NIR) or acoustic (for OAT/PAT) detectors are relatively inexpensive in comparison to large magnets and X-ray machines. One drawback of optical imaging is tissue absorption and reflection of photonic energy. Nanoparticle contrast agents that possess greater absorption than surrounding tissue or produce enhanced luminescence when irradiated can help alleviate tissue effects. Another advantage of using optics for imaging is the ability to guide the optical path with fiber optics, as in endoscopy, enabling internal imaging of vasculature, deep tissue and possibly the brain.

Optoacoustic or photacoustic tomography uses optical irradiation to induce localized thermal perturbations in the absorbing tissue [138]. Thermal vibrations produce acoustic waves which propagate from the underlying tissue to the skin surface. Acoustic detectors on the surface of the skin pick up the resulting acoustic waves. Optically absorbing gold nanoparticles can be used as contrast agents for optoacoustic imaging [139]. By controlling shape and structure, nanoparticles can be designed to optimally absorb at a desired wavelength. Simultaneously using optically absorbing nanoparticles of various designs that are each targeted to different cell or tissue types could provide a means for multiplexed bioimaging.

Gold nanoparticles as small as organic fluorophores can be irradiated with NIR and produce luminescence from lower excitation intensities than typical bioimaging fluorophores. Gold nanoparticles are also highly photostable (an advantage over organic fluorophores) and do not produce significant blinking (an advantage over semiconductor quantum dots). Furthermore, gold nanoparticles are easier to fabricate than quantum dots, can be readily modified for biological specificity and exhibit very low toxicity. All of these characteristics show promise for gold nanoparticles as an enabling technology to achieve single-molecule *in vivo* imaging for early diagnostics [140].

## 1.8 Nanotechnology-enhanced Tools

Although nanotechnology promises to develop novel diagnostic methods, current tools and methods can also benefit. Analytical instrumentation such as IR and mass spectrometers are widely used tools which are breaking into patient diagnostics. Enhancements of these instruments and techniques using nanotechnology should further this potential. Genetic-based techniques such as PCR, sequencing and gene chips are being made more affordable and more portable. Even standard

immunoassays can be improved upon using multivalent nanoparticles to improve the signal-to-noise ratio.

### 1.8.1

#### **Analytical Tools**

Analytical chemistry techniques such as IR and Raman spectroscopy and mass spectrometry are widely used in life sciences – from pharmaceutical process monitoring to drug discovery. Due to the versatility of these techniques, diagnostic applications are being developed. As discussed earlier, IR spectroscopy, especially in the near IR region, is being used in diagnostic imaging. Raman spectroscopy, with its ability to perform analysis in aqueous samples and less-stringent requirements on sample preparation, is especially promising for diagnostics with the potential for single-molecule detection using Raman enhancement techniques. Finally, mass spectrometry as the gold standard in analytical chemistry and proteomics is already being investigated for use in breath diagnostics and shows potential for diagnosis progression of disease based on protein profiles.

One drawback with using IR, Raman or mass spectroscopy for diagnosis is the need for specialized equipment and trained personnel to operate the equipment. Such equipment is typically situated in separate laboratories, requiring samples to be shipped for analysis. Lower-cost and easier to use equipment may open up the possibility of having analytical spectroscopic techniques at the patient bedside. One advantage of these techniques over biosensor or assay-based diagnostics is their nonspecialization. Biosensors and assays are typically formulated to detect a particular analyte of interest. Enzymes, antibodies, aptamers and complementary DNA strands are all used in biosensors and *in vitro* assays, making the sensors or substrates specific to the target in question. This specificity limits the ability of such diagnostics to detect a multitude of targets unless an array of sensors or substrates are prepared, each with their own specificity. Furthermore, one needs to have an idea of what to target for the biosensor or assay to be useful. Spectroscopic techniques are not target specific, but provide a fingerprint, or spectral signature, based on the chemical profile of the sample. The resulting fingerprint is compared to a database to find matches which delineate the chemicals that exist in the sample. This provides a powerful mechanism to analyze unknown samples and to simultaneously detect a multitude of analytes.

### 1.8.2

#### **Raman Spectroscopy**

One of the challenges using Raman spectroscopy is the weak Raman signal that is generated from the sample being interrogated. The use of more powerful lasers for excitation combined with sensitive detectors has helped Raman spectroscopy become more widespread. For diagnostic use, powerful lasers are not always practical, so another way to improve the Raman signal is to enhance the interaction between the optical excitation and the sample. Two techniques used to enhance

Raman signal are surface-enhanced Raman spectroscopy (SERS) and tip-enhanced Raman spectroscopy (TERS) [141–147].

For SERS, gold or silver nanoparticles are most commonly used to amplify the Raman signal. These nanoparticles can be used within living cells to amplify weak Raman signals from intracellular moieties, enabling the tracking of such entities without the need for fluorescent tags. Nanostructured tips, typically less than 50 nm in tip radius, are used in TERS. These tips can be AFM cantilever tips or scanning tunneling microscope (STM) tips coating with thin gold or silver film. SERS and TERS techniques amplify the Raman signal by establishing resonance between the applied optical field propagating through the sample and the surface plasmon waves propagating through the metallic nanostructures. The potential for single-molecule detection within living cells using SERS or TERS could open up the opportunity for early detection of disease.

### 1.8.3

#### **Mass Spectrometry**

Two of the challenges of using mass spectrometry for diagnostics are sample delivery and sensitivity. For mass spectrometer analysis, samples must be analyzed in an ionized, gaseous form. Therefore, biological samples must be prepared prior to delivery. Two methods are predominantly used for biological sample preparation and delivery with mass spectrometers. The first method involves spotting of the sample onto a substrate. A laser is used to desorb and ionize the sample which is then passed into the mass spectrometer. Matrix-assisted laser desorption and ionization (MALDI) and surface-enhanced laser desorption and ionization (SELDI) are the two commonly used substrate-based techniques. The second method involves use of a fine capillary to deliver the liquid sample towards electrodes situated near the tip of the capillary. The liquid sample aerosolizes upon emission from the capillary and a high field across the electrodes ionizes the aerosol, which travels into the vacuum chamber of the mass spectrometer and transforms to vapor phase.

Nanostructured materials and surfaces can help enhance MALDI and SELDI techniques. By enabling smaller spot sizes, dense arrays could be nanofabricated, helping increase the throughput of MALDI and SELDI systems [148]. Nanoscale surfaces functionalized with an array of biological receptors could be used to bind with desired targets within the protein population of the sample providing a pre-sorting mechanism prior to mass spectrometry analysis. Many proteins of clinical relevance are overshadowed by more abundant proteins and can be difficult to detect. Nanoparticles specific for these lower-abundant proteins could be used as harvesting agents in preparation for mass spectrometry analysis [149].

Finally, protein quantification and binding analysis can be performed in conjunction with fingerprinting and structural elucidation by combining binding-based assay with mass spectrometry. One technique amenable to coupling with mass spectrometry is SPR (Fig. 1.30) [150]. Using immobilized receptors on the SPR substrate, binding of targeted proteins can be detected. Once SPR detection is complete, the substrate can be coated with matrix and used for MALDI mass spectrometry or microfluidics could be used to draw the sample from the SPR sub-

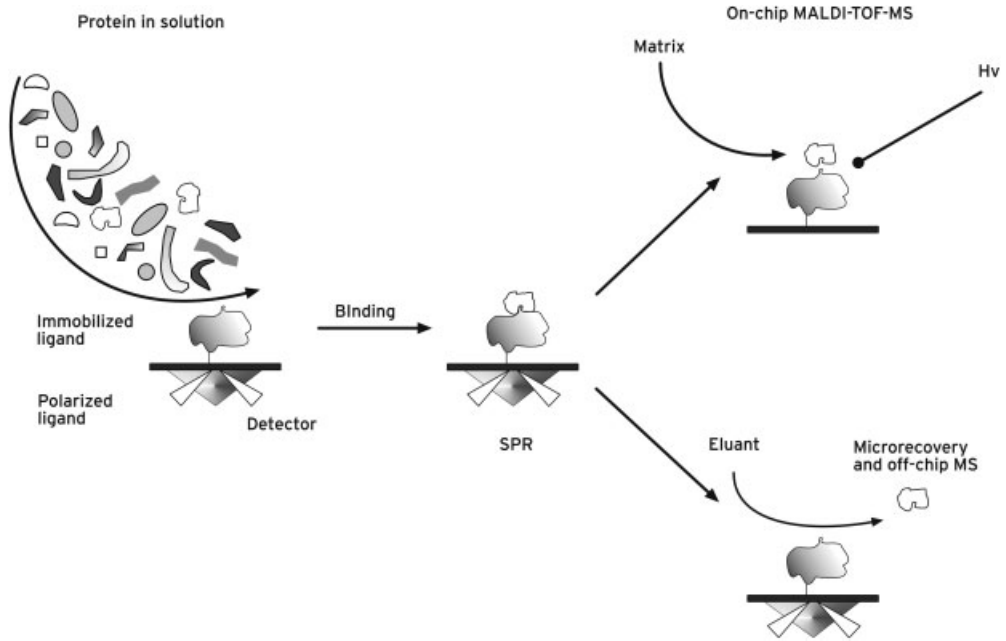


**Figure 1.30.** SPR mass spectrometry [150]. Reproduced from *Trends in Biotechnology*, D. Nedelkov and R. W. Nelson, Surface Plasmon resonance mass spectrometry: recent progress and outlooks, p. 301–305. Copyright (2003) with permission from Elsevier.

strate for electrospray ionization (ESI) mass spectrometry. An enhancement of this combination technique would be the use of nanoparticles establishing localized SPR to increase the sensitivity of quantifying low-abundance proteins prior to mass spectrometry.

#### 1.8.4

##### Genetics

Traditional bacterial diagnostics involve culturing followed by identification and often another confirming step which can take days to weeks for results to be achieved. ELISAs can provide faster results due to higher sensitivity so that fewer cells are required for analysis. However, immunoassays do not necessarily provide information on the particular strain of a pathogen. Here is where strain-specific tests are performed using genetic-based assays. Such assays typically involve amplification of the nucleic acids, such as PCR, to provide enough genetic material to perform the assay. Nanotechnology is enabling even quicker results by speeding up the PCR process or even by obviating the need for amplification altogether.

One nanostructure being investigated is the nanopore for DNA sequencing [151–154]. Nanopores fabricated from organic materials, such as proteins, or inor-

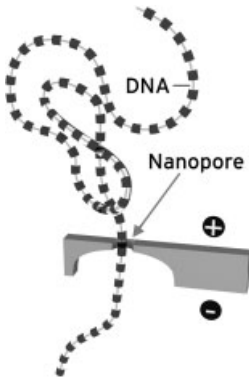


Figure 1.31. DNA nanopore.

ganic materials, such as semiconductors, could be designed to allow only single-stranded DNA to file through (Fig. 1.31). Electrical or optical methods could be used to detect each DNA base as it transcends through the pore, providing a direct readout method for sequencing without the need to amplify the DNA. The resulting sequence can then be analyzed to determine mutations for genetic screening or can be compared to pathogen sequences for diagnosing infections.

Nanopores can be machined within semiconductor materials using focused ion beam (FIB) milling [155]. With FIB milling, a high-energy ion beam is finely focused onto the sample to be machined. Arrays of nanopores can be machined by manipulating the sample stage and alternating the ion beam on and off. Isolated organic structures may also have the capability of nanopore sequencing. One particular biological structure that has an internal pore diameter of 1.5 nm, which will allow only single-stranded DNA to pass through, is the  $\alpha$ -hemolysin ion channel shown in Fig. 1.32.

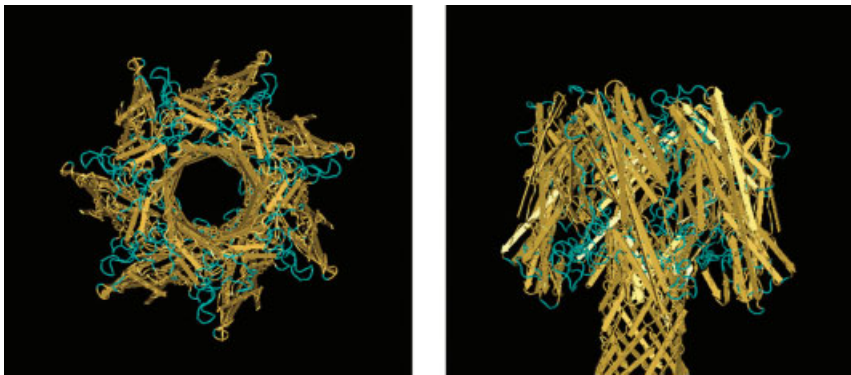
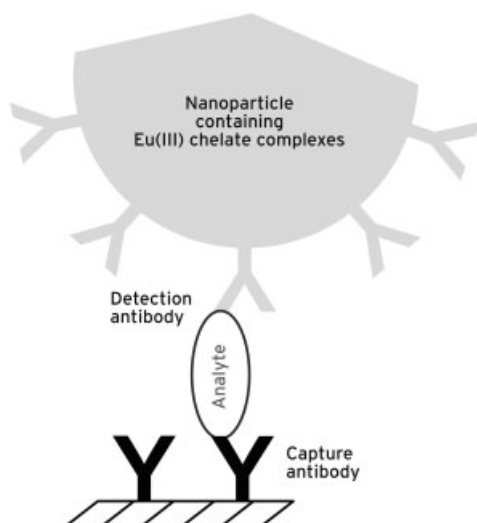


Figure 1.32.  $\alpha$ -Hemolysin ion channel, approximately 10 nm long with 1.5 nm internal pore diameter.

## 1.8.5

**Immunoassays**

Immunoassays are routinely used for diagnostics due to their high sensitivity and high selectivity. With the growing desire for smaller sample sizes and earlier disease capture, improvements in immunoassays would be welcome. One method to enhance sensitivity of immunoassays is through the use of antibody-conjugated nanoparticles [156]. For instance, lanthanide-based chelate complexes can be attached to antibody-conjugated nanoparticle carriers creating dense luminescent particles with biological specificity. Lanthanide ions, such as Eu(III) and Tb(III), exhibit narrow emission spectra in the visible wavelength range. Therefore, increasing the density of the chelate complexes by nanoparticle immobilization will produce greater emission to enhance sensitivity. A capture probe can be immobilized onto the substrate surface which targets the desired analyte. The detection antibodies conjugated to the nanoparticle carrying the Lanthanide complexes then bind to the captured analyte, if present. Luminescence is then measured to determine the presence of the analyte. Other small molecule dyes could also be used if nanoparticle immobilization of such dyes could be achieved. See Fig. 1.33.



**Figure 1.33.** Immunoassay enhanced with antibody-conjugated nanoparticle containing luminescent lanthanide complexes [156]. Reproduced with permission from *Anal. Bioanal. Chem.*, Vol. 380 (2004), p. 24–30,

Detection strategies for bioassays based on luminescent lanthanide complexes and signal amplification, T. Steinkamp and U. Karst, Fig. 10, Copyright (2004). With kind permission of Springer Science and Business Media.

## 1.9

### Nanotechnology and the Future of Patient Diagnostics

#### 1.9.1

##### Multifunctional Platforms

An area of future impact of nanotechnology for patient care is the development of *in vivo* modular, multifunctional platforms to target, detect and react [157–160]. Dendrimers, due to their highly branched structure, are potential multifunctional nanostructured platforms. Crosslinking to two or more different types of nanoparticles could also create a multifunctional platform. For targeting, biological receptors such as aptamers or antibodies could be immobilized onto the nanostructured platforms. Reporting moieties such as quantum dots or contrast agents could be attached to a separate branch within the dendrimer or attached to or embedded within the crosslinked, nontargeting nanoparticle. This will allow for tracking of the multifunctional platforms with noninvasive imaging methods. Therapeutics could be harbored within the dendrimer core or coated onto the nontargeting nanoparticle enabling targeted drug delivery in conjunction with imaging for combination diagnosis and therapy.

Figure 1.34 shows a multifunctional dendrimer carrying folic acid as a targeting agent, fluorescein as a reporter and methotrexate as the therapeutic. Folic acid, or folate, has a high affinity for folic acid receptors which many cancer cells overexpress. FITC is a widely used fluorophore. Methotrexate (MTX) is an effective anti-cancer drug, but with high toxicity. By adding targeting capability to drugs such as MTX, less amounts of drug should be necessary for therapy. Also, systemic side-effects should be minimized. The use of a multifunctional carrier platform not only enables transport of the drug to its desired destination, but also allows for tracking with the addition of reporter entities.

#### 1.9.2

##### Real-time Monitoring

Implantable sensor technologies that can be remotely monitored enable on-demand and real-time patient monitoring. *In vivo* nanoscale sensors may also provide feedback, based on physiological status, as part of replacement biological systems, such as an artificial kidney or pancreas [161]. Due to the ultraminiature form factor, identical sensors may be implanted for redundancy as a safeguard against sensor failure. Multiple sensors for different targets may also be implanted to simultaneously monitor patient condition.

#### 1.9.3

##### Multiplexed Diagnostic Assays

Nanoscale sensing platforms combined with microfluidic systems for sample delivery offer the potential to simultaneously perform large numbers of analyses and increase sample throughput [162–164]. Also, biomimetic molecular constructs,

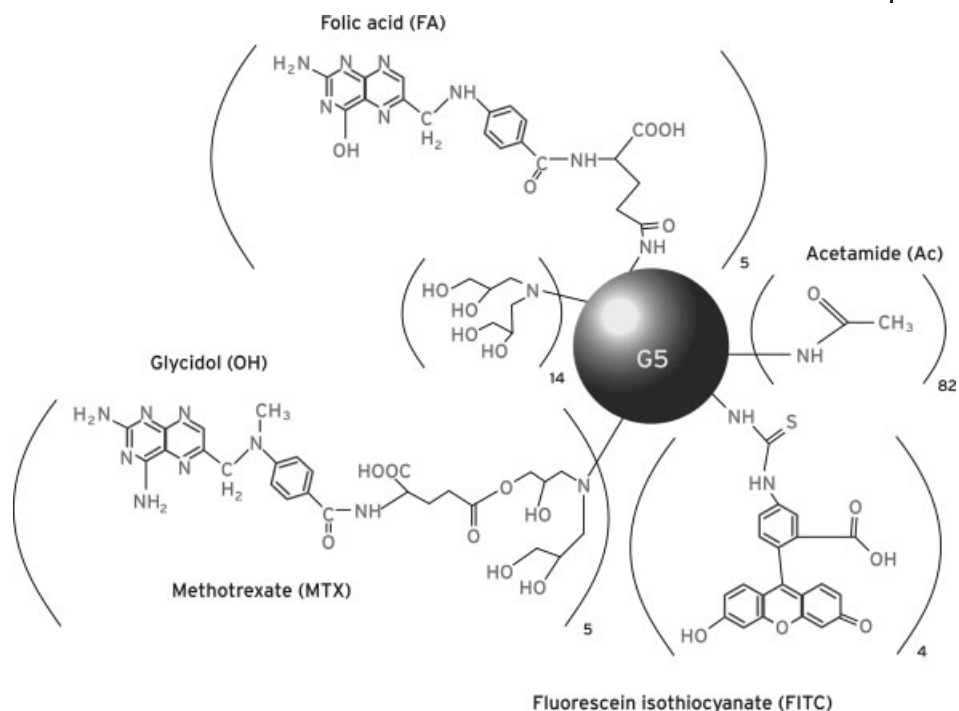


**Figure 1.34.** Fifth-generation dendrimer simultaneously functionalized with MTX, folic acid and FITC [157]. Reproduced with permission from Molecular Pharmaceutics, Vol. 2, X. Shi et al., Capillary electrophoresis of

(poly)amidoamine dendrimers: from simple derivatives to complex multifunctional nanodevices, p. 278–294. Copyright (2005) American Chemical Society.

such as peptide or aptamer structures, have the potential to be derived with high affinity for numerous analytes [165]. Being able to analyze a single sample for a number of disease biomarkers at one time could lower the cost of diagnosis and enable a more accurate assessment of the patient's condition.

#### 1.9.4

##### Point-of-care Diagnostics

Bringing the diagnostic tool to the patient, i.e. point-of-care, as opposed to sending samples to a laboratory has the potential to benefit everyone in the healthcare chain. The doctor or nurse will be able to perform quicker diagnoses. The healthcare institution may reduce operating costs due to less need to take and process patient samples. The insurance company or other third-party payer may reduce their costs due to fewer reimbursable events that are typically involved in diagnostic procedures, such as drawing patient samples, using laboratory time and purchasing diagnostic reagents. Finally, the patient should also benefit from faster, more accurate and less-costly diagnosis.



Sample handling is one technical hurdle that must be overcome for point-of-care diagnostics to truly reach the clinic. Micro/nanofluidics will likely play a major role in delivering the patient sample to the sensing portion of the diagnostic tool. However, sample delivery is only one of the challenges in getting a sample, such as blood, to the biologically sensitive area of the tool. For instance, in the case of blood analysis, the sample may need to be filtered and desired analytes separated out, all automatically within the portable diagnostic tool. Without filtering and separation, the sensor surface may quickly become saturated with nonspecific proteins.

### 1.9.5

#### **Regulations, Risks and Ethics**

Although a thorough discussion is beyond the scope of this chapter, the risks and benefits of nanotechnology for patient diagnostics must be carefully addressed. Nanotechnology enables the construction of materials and devices that can intimately interact with biological systems. Such interaction has its benefits, as exhibited by the various opportunities described in this chapter and from numerous other sources. However, we must proceed diligently to understand the effects of artificial nanostructures on biological systems. The benefits of nanotechnology must be understood along with the risks. Early and close interaction with regulatory agencies, such as the Food and Drug Administration (FDA) and the Environmental Protection Agency (EPA), should be part of the technology development process [166, 167].

Currently, additional or special regulatory handling of biomedical nanotechnology products is not being anticipated, although new toxicological testing and standards may need to be developed. For regulatory purposes, the FDA defines nanotechnology as “research and technology or development of products regulated by FDA that involve all of the following:

- (1) the existence of materials or products at the atomic, molecular or macromolecular levels, where at least one dimension that affects the functional behavior of the drug/device product is in the length scale range of approximately 1–100 nm;
- (2) the creation and use of structures, devices and systems that have novel properties and functions because of their small size; and,
- (3) the ability to control or manipulate the product on the atomic scale.”

With the potential of multifunctional capability, many biomedical nanotechnology products will likely not fall into a single FDA category, but may be handled as combination products [168]. Examples of existing combination products are listed in Tab. 1.5. To regulate combination products, the FDA established the Office of Combination Products (OCP) in 2002. As defined by the FDA in Section 3.2(e) of 21 CFR (Code of Federal Regulations) Part 3, a combination product includes:

- (1) A product comprised of two or more regulated components, i.e. drug/device, biologic/device, drug/biologic or drug/device/biologic, that are physically, chemically or otherwise combined or mixed and produced as a single entity.

**Tab. 1.5.** Examples of combination products.

---

Drug-eluting stents  
 Catheter with antimicrobial coating  
 Antibody combined with therapeutic  
 Transdermal drug delivery patches  
 Orthopedic implant with growth factors

---

- (2) Two or more separate products packaged together in a single package or as a unit and comprised of drug and device products, device and biological products, or biological and drug products.
- (3) A drug, device or biological product packaged separately that according to its investigational plan or proposed labeling is intended for use only with an approved individually specified drug, device or biological product where both are required to achieve the intended use, indication or effect and where upon approval of the proposed product the labeling of the approved product would need to be changed, e.g. to reflect a change in intended use, dosage form, strength, route of administration or significant change in dose.
- (4) Any investigational drug, device or biological product packaged separately that according to its proposed labeling is for use only with another individually specified investigational drug, device or biological product where both are required to achieve the intended use, indication or effect.

For nanotechnology diagnostic products used *in vitro*, the FDA Office of *In Vitro* Diagnostic Device Evaluation and Safety has regulatory control. As defined by the FDA in 21 CFR 809.3, an *in vitro* diagnostic product includes:

*In vitro* diagnostic products are those reagents, instruments and systems intended for use in diagnosis of disease or other conditions, including a determination of the state of health, in order to cure, mitigate, treat or prevent disease or its sequelae. Such products are intended for use in the collection, preparation and examination of specimens taken from the human body.

Scientists must not only weigh the health risks, but also the ethical risks. Scientists should be concerned with public perception and ethical issues of nanotechnology [169–175]. With the potential to perform highly sensitive, multiplexed and rapid diagnostics, guidelines and protocols should be established to aid clinicians and patients to make sense of all the data and proceed with the most appropriate course of action. A diagnostic test may be developed and used to which no counter treatment is available. If patients are willing to take such tests, then they should be made well aware of the possible quandaries.

Nanotechnology has the potential to revolutionize medicine as we know it today. Nanostructured materials and devices may make possible the ability for targeted drug delivery, real-time patient monitoring, high-resolution noninvasive imaging, high-throughput screening and multiplexed diagnostics. Such an arsenal of tools

and techniques could enable the ability to capture a disease at its earliest onset, specifically target the diseased site and rapidly treat the patient before any physiological damage is done and without any detrimental side-effects.

## References

- 1 BEERS, M. H., R. BERKOW (Eds.), *The Merck Manual of Diagnosis and Therapy*. 17th edn. Merck, West Point, PA, 1999.
- 2 WILKINSON, J. M., Nanotechnology applications in medicine. *Med. Device Technol.* **2003**, 14, 29–31.
- 3 SPRINTZ, M., C. BENEDETTI, M. FERRARI, Applied nanotechnology for the management of breakthrough cancer pain. *Minerva Anesthesiol.* **2005**, 71, 419–423.
- 4 HEATH, J. R., M. E. PHELPS, L. HOOD, NanoSystems biology. *Mol. Imaging Biol.* **2003**, 5, 312–325.
- 5 JAIN, K. K., Nanodiagnosics: application of nanotechnology in molecular diagnostics. *Expert Rev. Mol. Diagn.* **2003**, 3, 153–161.
- 6 JAIN, K. K., Nanotechnology in clinical laboratory diagnostics. *Clin. Chim. Acta* **2005**, 358, 37–54.
- 7 KUBIK, T., K. BOGUNIA-KUBIK, M. SUGISAKA, Nanotechnology on duty in medical applications. *Curr. Pharm. Biotechnol.* **2005**, 6, 17–33.
- 8 WALT, D. R., Chemistry. Miniature analytical methods for medical diagnostics. *Science* **2005**, 308, 217–219.
- 9 EMERICH, D. F., C. G. THANOS, Nanotechnology and medicine. *Expert Opin. Biol. Ther.* **2003**, 3, 655–663.
- 10 ROCO, M. C., Nanotechnology: convergence with modern biology and medicine. *Curr. Opin. Biotechnol.* **2003**, 14, 337–346.
- 11 JIANRONG, C., et al., Nanotechnology and biosensors. *Biotechnol. Adv.* **2004**, 22, 505–518.
- 12 EMERICH, D. F., Nanomedicine – prospective therapeutic and diagnostic applications. *Expert Opin. Biol. Ther.* **2005**, 5, 1–5.
- 13 McNEIL, S. E., Nanotechnology for the biologist. *J. Leukocyte Biol.* **2005**, 78, 585–594.
- 14 WILEY, C., Nanotechnology and molecular homeostasis. *J. Am. Geriatr. Soc.* **2005**, 53 (9 Suppl.), S295–S298.
- 15 GUETENS, G., et al., Nanotechnology in bio/clinical analysis. *J. Chromatogr.* **2000**, 739, 139–150.
- 16 FERRARI, M., Cancer nanotechnology: opportunities and challenges. *Nat. Rev.* **2005**, 5, 161–171.
- 17 SAHOO, S. K., V. LABHASETWAR, Nanotech approaches to drug delivery and imaging. *Drug Discov. Today* **2003**, 8, 1112–1120.
- 18 SILVA, G. A., Introduction to nanotechnology and its applications to medicine. *Surg. Neurol.* **2004**, 61, 216–220.
- 19 WEIS, R. P., et al., Calcified nanostructured silicon wafer surfaces for biosensing: effects of surface modification on bioactivity. *Dis. Markers* **2002**, 18, 159.
- 20 BOGUNIA-KUBIK, K., M. SUGISAKA, From molecular biology to nanotechnology and nanomedicine. *Biosystems* **2002**, 65, 123–38.
- 21 CSAKI, A., R. MOLLER, W. FRITZSCHE, Gold nanoparticles as novel label for DNA diagnostics. *Expert Rev. Mol. Diagn.* **2002**, 2, 187–93.
- 22 LEARY, S. P., et al., Toward the emergence of nanoneurosurgery: part I – progress in nanoscience, nanotechnology, and the comprehension of events in the mesoscale realm. *Neurosurgery* **2005**, 57, 606.
- 23 HOOD, E., Nanotechnology: looking as we leap. *Environ. Health Perspect.* **2004**, 112, A740–A749.
- 24 BUXTON, D. B., et al., Recommendations of the National Heart, Lung, and Blood Institute Nanotechnology Working Group. *Circulation* **2003**, 108, 2737–2742.
- 25 FORTINA, P., et al., Nanobiotechnology: the promise and reality of new approaches to molecular recognition. *Trends Biotechnol.* **2005**, 23, 168–173.

- 26 BARATHUR, R., et al., New disc-based technologies for diagnostic and research applications. *Psychiatr. Genet.* **2002**, *12*, 193–206.
- 27 CARELLA, M., S. VOLINIA, P. GASPARINI, Nanotechnologies and microchips in genetic diseases. *J. Nephrol.* **2003**, *16*, 597–602.
- 28 JAIN, K. K., Applications of biochips: from diagnostics to personalized medicine. *Curr. Opin. Drug Discov. Dev.* **2004**, *7*, 285–289.
- 29 WILKINSON, J. M., M. H. KUOK, G. ADAMSON, Biomedical applications of optical imaging. *Med. Device Technol.* **2004**, *15*, 22–24.
- 30 PROSKE, D., et al., Aptamers – basic research, drug development, and clinical applications. *Appl. Microbiol. Biotechnol.* **2006**, *69*, 367–374.
- 31 ACHENBACH, J. C., R. NUTTU, Y. LI, Structure-switching allosteric deoxyribozymes. *Anal. Chim. Acta* **2005**, *534*, 41–51.
- 32 LE, X. C., V. PAVSKI, H. WANG, W. A. E. MCBRYDE, Award Lecture – Affinity recognition, capillary electrophoresis, and laser-induced fluorescence polarization for ultrasensitive bioanalysis. *Can. J. Chem.* **2005**, *83*, 185–194.
- 33 SHAW, B. R., et al., Reading, writing, and modulating genetic information with boranophosphate mimics of nucleotides, DNA, and RNA. *Ann. NY Acad. Sci.* **2003**, *1002*, 12–29.
- 34 VAISH, N. K., et al., A Novel, modification-dependent ATP-binding aptamer selected from an RNA library incorporating a cationic functionality. *Biochemistry* **2003**, *42*, 8842.
- 35 BRODY, E. N., L. GOLD, Aptamers as therapeutic and diagnostic agents. *J. Biotechnol.* **2000**, *74*, 5–13.
- 36 BRODY, E. N., et al., The use of aptamers in large arrays for molecular diagnostics. *Mol. Diagn.* **1999**, *4*, 381–388.
- 37 JAYASENA, S. D., Aptamers: an emerging class of molecules that rival antibodies in diagnostics. *Clin. Chem.* **1999**, *45*, 1628–1650.
- 38 THOMPSON, M., A. K. DEISINGH, Biosensors for the detection of bacteria. *Can. J. Microbiol.* **2004**, *50*, 69–77.
- 39 DANKE, X., et al., Label-free electrochemical detection for aptamer-based array electrodes. *Anal. Chem.* **2005**, *77*, 5107–5113.
- 40 KAWDE, A.-N., et al., Label-free bioelectronic detection of aptamer-protein interactions. *Electrochem. Commun.* **2005**, *7*, 537–540.
- 41 RADİ, A.-E., et al., Reusable impedimetric aptasensor. *Anal. Chem.* **2005**, *77*, 6320–6323.
- 42 KOLUSHEVA, S., et al., Selective detection of catecholamines by synthetic receptors embedded in chromatic polydiacetylene vesicles. *J. Am. Chem. Soc.* **2005**, *127*, 10000–10001.
- 43 HOLM, B. A., et al., Nanotechnology in biomedical applications. *Mol. Crystals Liquid Crystals* **2002**, *374*, 589–598.
- 44 PRASAD, P., Emerging opportunities at the interface of photonics, nanotechnology and biotechnology. *Mol. Crystals Liquid Crystals* **2004**, *415*, 1–7.
- 45 LESNIAK, W., et al., Silver/dendrimer nanocomposites as biomarkers: fabrication, characterization, *in vitro* toxicity, and intracellular detection. *Nano Lett.* **2005**, *5*, 2123–2130.
- 46 ASLAN, K., J. R. LAKOWICZ, C. D. GEDDES, Metal-enhanced fluorescence using anisotropic silver nanostructures: critical progress to date. *Anal. Bioanal. Chem.* **2005**, *382*, 926–933.
- 47 ASLAN, K., et al., Metal-enhanced fluorescence: an emerging tool in biotechnology. *Curr. Opin. Biotechnol.* **2005**, *16*, 55–62.
- 48 HUHTINEN, P., et al., Europium(III) nanoparticle-label-based assay for the detection of nucleic acids. *Nanotechnology* **2004**, *15*, 1708–1715.
- 49 VALANNE, A., et al., A sensitive adenovirus immunoassay as a model for using nanoparticle label technology in virus diagnostics. *J. Clin. Virol.* **2005**, *33*, 217–223.
- 50 LAKHTAKIA, A., *Nanometer Structures: Theory, Modeling, and Simulation. The Handbook of Nanotechnology.* ASME Press, New York, **2004**.
- 51 ETHIRAJ, A. S., et al., Synthesis and investigation of ZnS nanoparticles adsorbed on functionalised silica particles. *Surf. Eng.* **2004**, *20*, 367–372.

- 52 OZKAN, M., Quantum dots and other nanoparticles: what can they offer to drug discovery? *Drug Discov. Today* **2004**, *9*, 1065–1071.
- 53 RIEGLER, JR., T. NANN, Application of luminescent nanocrystals as labels for biological molecules. *Anal. Bioanal. Chem.* **2004**, *379*, 913–919.
- 54 MATTOUSSI, H., et al., Electroluminescence from heterostructures of poly(phenylene vinylene) and inorganic CdSe. *J. Appl. Phys.* **1998**, *83*, 7965.
- 55 COTTINGHAM, K., Quantum dots leave the light on. *Anal. Chem.* **2005**, *77*, 354A–357A.
- 56 KUNO, M., et al., Nonexponential “blinking” kinetics of single CdSe quantum dots: a universal power law behavior. *J. Chem. Phys.* **2000**, *112*, 3117–3120.
- 57 KUNO, M., et al., “On”/“off” fluorescence intermittency of single semiconductor quantum dots. *J. Chem. Phys.* **2001**, *115*, 1028–1040.
- 58 GOLDMAN, E. R., et al., Multiplexed toxin analysis using four colors of quantum dot fluororeagents. *Anal. Chem.* **2004**, *76*, 684–688.
- 59 GAO, X., W. C. CHAN, S. NIE, Quantum-dot nanocrystals for ultrasensitive biological labeling and multicolor optical encoding. *J. Biomed. Opt.* **2002**, *7*, 532–7.
- 60 GAO, X., S. NIE, Quantum dot-encoded beads. *Methods Mol. Biol.* **2005**, *303*: p. 61–71.
- 61 WANG, Y., Z. TANG, N. A. KOTOV, Bioapplication of nanosemiconductors. *Mater. Today* **2005**, *8*, 20–31.
- 62 SANG-WOOK, K., et al., Engineering InAs<sub>x</sub>P<sub>1-x</sub>/InP/ZnSe III–V alloyed core/shell quantum dots for the near-infrared. *J. Am. Chem. Soc.* **2005**, *127*, 10526–10532.
- 63 DWARAKANATH, S., et al., Quantum dot–antibody and aptamer conjugates shift fluorescence upon binding bacteria. *Biochem. Biophys. Res. Commun.* **2004**, *325*, 739–743.
- 64 DISLEY, D. M., et al., Covalent coupling of immunoglobulin G to self-assembled monolayers as a method for immobilizing the interfacial-recognition layer of a surface plasmon resonance immunosensor. *Biosensors Bioelectron.* **1998**, *13*, 1213–1225.
- 65 JAIN, K. K., The role of nanobiotechnology in drug discovery. *Drug Discov. Today* **2005**, *10*, 1435–1442.
- 66 HAES, A. J., R. P. VAN DUYN, A unified view of propagating and localized surface plasmon resonance biosensors. *Anal. Bioanal. Chem.* **2004**, *379*, 920–930.
- 67 HAES, A. J., R. P. V. DUYN, Preliminary studies and potential applications of localized surface plasmon resonance spectroscopy in medical diagnostics. *Expert Rev. Mol. Diagn.* **2004**, *4*, 527–537.
- 68 COOPER, M. A., Label-free screening of bio-molecular interactions. *Anal. Bioanal. Chem.* **2003**, *377*, 834–842.
- 69 HAES, A. J., R. P. VAN DUYN, A unified view of propagating and localized surface plasmon resonance biosensors. *Anal. Bioanal. Chem.* **2004**, *379*, 920–930.
- 70 HOMOLA, J., Present and future of surface plasmon resonance biosensors. *Anal. Bioanal. Chem.* **2003**, *377*, 528–539.
- 71 ENDO, T., et al., Label-free detection of peptide nucleic acid–DNA hybridization using localized surface plasmon resonance based optical biosensor. *Anal. Chem.* **2005**, *77*, 6976–6984.
- 72 DAHLIN, A., et al., Localized surface plasmon resonance sensing of lipid-membrane-mediated biorecognition events. *J. Am. Chem. Soc.* **2005**, *127*, 5043–5048.
- 73 HAES, A. J., et al., Detection of a biomarker for Alzheimer’s disease from synthetic and clinical samples using a nanoscale optical biosensor. *J. Am. Chem. Soc.* **2005**, *127*, 2264–2271.
- 74 CHANDA RANJIT, Y., et al., A comparative analysis of localized and propagating surface plasmon resonance sensors: the binding of concanavalin A to a monosaccharide functionalized self-assembled monolayer. *J. Am. Chem. Soc.* **2004**, *126*, 12669–12676.
- 75 LINK, S., M. A. EL-SAYED, Optical properties and ultrafast dynamics of metallic nanocrystals. *Annu. Rev. Phys. Chem.* **2003**, *54*, 331.

- 76 LINK, S., M. A. EL-SAYED, Shape and size dependence of radiative, non-radiative and photothermal properties of gold nanocrystals. *Int. Rev. Phys. Chem.* **2000**, *19*, 409–453.
- 77 CLARK, H. A., M. HOYER, Optical nanosensors for chemical analysis inside single living cells. 1. Fabrication. *Anal. Chem.* **1999**, *71*, 4831.
- 78 CLARK, H. A., et al., Optical nanosensors for chemical analysis inside single living cells. 2. Sensors for pH and calcium and the intracellular application of PEBBLE sensors. *Anal. Chem.* **1999**, *71*, 4837–4843.
- 79 Koo, Y.-E. L., et al., Real-time measurements of dissolved oxygen inside live cells by organically modified silicate fluorescent nanosensors. *Anal. Chem.* **2004**, *76*, 2498–2505.
- 80 LI, H., L. ROTHBERG, Detection of specific sequences in RNA using differential adsorption of single-stranded oligonucleotides on gold nanoparticles. *Anal. Chem.* **2005**, *77*, 6229–6233.
- 81 LI, H., L. ROTHBERG, Colorimetric detection of DNA sequences based on electrostatic interactions with unmodified gold nanoparticles. *Proc. Natl Acad. Sci. USA* **2004**, *101*, 14036–14039.
- 82 LI, H., L. J. ROTHBERG, DNA sequence detection using selective fluorescence quenching of tagged oligonucleotide probes by gold nanoparticles. *Anal. Chem.* **2004**, *76*, 5414–5417.
- 83 LI, H., L. J. ROTHBERG, Label-free colorimetric detection of specific sequences in genomic DNA amplified by the polymerase chain reaction. *J. Am. Chem. Soc.* **2004**, *126*, 10958–10961.
- 84 NAM, J.-M., A. R. WISE, J. T. GROVES, colorimetric bio-barcode amplification assay for cytokines. *Anal. Chem.* **2005**, *77*, 6985–6988.
- 85 GEORGANOPOULOU, D. G., et al., Nanoparticle-based detection in cerebral spinal fluid of a soluble pathogenic biomarker for Alzheimer's disease. *Proc. Natl Acad. Sci. USA.* **2005**, *102*, 2273–2276.
- 86 NAM, J.-M., S.-J. PARK, C. A. MIRKIN, Bio-barcodes based on oligonucleotide-modified nanoparticles. *J. Am. Chem. Soc.* **2002**, *124*, 3820.
- 87 NAM, J.-M., C. S. THAXTON, C. A. MIRKIN, Nanoparticle-based bio-barcodes for the ultrasensitive detection of proteins. *Science* **2003**, *301*, 1884–1886.
- 88 THAXTON, C. S., D. G. GEORGANOPOULOU, C. A. MIRKIN, Gold nanoparticle probes for the detection of nucleic acid targets. *Clin. Chim. Acta* **2006**, *363*, 120–126.
- 89 LI, Y., Y. T. CU, D. LUO, Multiplexed detection of pathogen DNA with DNA-based fluorescence nanobarcodes. *Nat. Biotechnol.* **2005**, *23*, 885–889.
- 90 PAVLOV, V., et al., Aptamer-functionalized Au nanoparticles for the amplified optical detection of thrombin. *J. Am. Chem. Soc.* **2004**, *126*, 11768–11769.
- 91 MONK, D. J., D. R. WALT, Optical fiber-based biosensors. *Anal. Bioanal. Chem.* **2004**, *379*, 931–945.
- 92 VO-DINH, T., Nanobiosensors: probing the sanctuary of individual living cells. *J. Cell Biochem. Suppl.* **2002**, *39*, 154–161.
- 93 VO-DINH, T., Optical nanosensors for detecting proteins and biomarkers in individual living cells. *Methods Mol. Biol.* **2005**, *300*, 383–401.
- 94 VO-DINH, T., P. KASILI, Fiber-optic nanosensors for single-cell monitoring. *Anal. Bioanal. Chem.* **2005**, *382*, 918–25.
- 95 KONRY, T., et al., Optical fiber immunosensor based on a poly(pyrrrole-benzophenone) film for the detection of antibodies to viral antigen. *Anal. Chem.* **2005**, *77*, 1771–1779.
- 96 BASHIR, R., BioMEMS: state-of-the-art in detection, opportunities and prospects. *Adv. Drug Deliv. Rev.* **2004**, *56*, 1565–1586.
- 97 SOTIROPOULOU, S., N. A. CHANIO-TAKIS, Carbon nanotube array-based biosensor. *Anal. Bioanal. Chem.* **2003**, *375*, 103–105.
- 98 YEMINI, M., et al., Peptide nanotube-modified electrodes for enzyme-biosensor applications. *Anal. Chem.* **2005**, *77*, 5155–5159.

- 99 KOEHNE, J. E., et al., Miniaturized multiplex label-free electronic chip for rapid nucleic acid analysis based on carbon nanotube nanoelectrode arrays. *Clin. Chem.* **2004**, *50*, 1886–93.
- 100 HUANG, Y., C. M. LIEBER, Integrated nanoscale electronics and optoelectronics: exploring nanoscale science and technology through semiconductor nanowires. *Pure Appl. Chem.* **2004**, *76*, 2051–2068.
- 101 YUQING, M., G. JIANGUO, C. JIANRONG, Ion sensitive field effect transducer-based biosensors. *Biotechnol. Adv.* **2003**, *21*, 527–534.
- 102 FRIEDRICH, M. J., Nanoscale biosensors show promise. *J. Am. Med. Ass.* **2005**, *293*, 1965–1965.
- 103 CASTILLO, J., et al., Biosensors for life quality: design, development and applications. *Sensors Actuators B* **2004**, *102*, 179–194.
- 104 DRUMMOND, T. G., M. G. HILL, J. K. BARTON, Electrochemical DNA sensors. *Nat. Biotechnol.* **2003**, *21*, 1192–1199.
- 105 IKEBUKURO, K., C. KIYOHARA, K. SODE, Electrochemical detection of protein using a double aptamer sandwich. *Anal. Lett.* **2004**, *37*, 2901–2909.
- 106 IKEBUKURO, K., C. KIYOHARA, K. SODE, Novel electrochemical sensor system for protein using the aptamers in sandwich manner. *Biosensors Bioelectron.* **2005**, *20*, 2168–2172.
- 107 BANG, G. S., S. CHO, B.-G. KIM, A novel electrochemical detection method for aptamer biosensors. *Biosensors Bioelectron.* **2005**, *21*, 863–870.
- 108 ZHANG, D., et al., Silica-nanoparticle-based interface for the enhanced immobilization and sequence-specific detection of DNA. *Anal. Bioanal. Chem.* **2004**, *379*, 1025–1030.
- 109 YANEZ-SEDENO, P., J. M. PINGARRON, Gold nanoparticle-based electrochemical biosensors. *Anal. Bioanal. Chem.* **2005**, *382*, 884–886.
- 110 HARUYAMA, T., et al., Bio-, nano-technology for cellular biosensing. *Curr. Appl. Phys.* **2005**, *5*, 108–111.
- 111 OZSOZ, M., et al., Electrochemical genosensor based on colloidal gold nanoparticles for the detection of Factor V Leiden mutation using disposable pencil graphite electrodes. *Anal. Chem.* **2003**, *75*, 2181–2187.
- 112 SHINKAI, S., M. TAKEUCHI, A.-H. BAE, Rational design and creation of novel polymeric superstructures by oxidative polymerization utilizing anionic templates. *Supramol. Chem.* **2005**, *17*, 181–186.
- 113 COVINGTON, J. A., et al., Conductive polymer gate FET devices for vapour sensing. *IEE Proc. Circuits Devices Syst.* **2004**, *151*, 326–334.
- 114 GUANG-MING, Z., et al., Determination of trace chromium(VI) by an inhibition-based enzyme biosensor incorporating an electropolymerized aniline membrane and ferrocene as electron transfer mediator. *Int. J. Environ. Anal. Chem.* **2004**, *84*, 761–774.
- 115 JIN, L., et al., Amperometric biosensor with HRP immobilized on a sandwiched nano-Au/polymerized *m*-phenylenediamine film and ferrocene mediator. *Anal. Bioanal. Chem.* **2003**, *376*, 902–907.
- 116 VOLKEL, D., et al., Immunochemical detection of prion protein on dipsticks prepared with crystalline bacterial cell-surface layers. *Transfusion* **2003**, *43*, 1677–1682.
- 117 SLEYTR, U. B., et al., Applications of S-layers. *FEMS Microbiol. Rev.* **1997**, *20*, 151–175.
- 118 SLEYTR, U. B., M. SARA, Bacterial and archaeal S-layer proteins: structure–function relationships and their biotechnological applications. *Trends Biotechnol.* **1997**, *15*, 20–26.
- 119 JAIN, K. K., Current trends in molecular diagnostics. *Med. Device Technol.* **2002**, *13*, 14–8.
- 120 GOULD, P., Nanoparticles probe biosystems. *Mater. Today* **2004**, *7*, 36.
- 121 ZHAO, X., et al., Collection of trace amounts of DNA/mRNA molecules using genomagnetic nanocapturers. *Anal. Chem.* **2003**, *75*, 3476–3483.
- 122 LA CONTE, L., N. NITIN, G. BAO, Magnetic nanoparticle probes. *Mater. Today* **2005**, *8*, 32–38.
- 123 WANG, Y., et al., Polyacrylamide gel film immobilized molecular beacon array for single nucleotide mismatch

- detection. *J. Nanosci. Nanotechnol.* **2005**, *5*, 653–8.
- 124 JOSEPHSON, L., et al., High-efficiency intracellular magnetic labeling with novel superparamagnetic–Tat peptide conjugates. *Bioconjug. Chem.* **1999**, *10*, 186–191.
- 125 KROTZ, F., et al., Magnetofection potentiates gene delivery to cultured endothelial cells. *J. Vasc. Res.* **2003**, *40*, 425–434.
- 126 PLANK, C., et al., The magnetofection method: using magnetic force to enhance gene delivery. *Biol. Chem.* **2003**, *384*, 737–747.
- 127 SCHERER, F., et al., Magnetofection: enhancing and targeting gene delivery by magnetic force *in vitro* and *in vivo*. *Gene Therapy* **2002**, *9*, 102.
- 128 WANG, S. X., et al., Towards a magnetic microarray for sensitive diagnostics. *J. Magn. Mater.* **2005**, *293*, 731–736.
- 129 SEPANIAK, M., et al., Microcantilever transducers: a new approach in sensor technology. *Anal. Chem.* **2002**, *74*, 568.
- 130 LAVRIK, N. V., M. J. SEPANIAK, P. G. DATSKO, Cantilever transducers as a platform for chemical and biological sensors. *Rev. Sci. Instrum.* **2004**, *75*, 2229–2253.
- 131 ZIEGLER, C., Cantilever-based biosensors. *Anal. Bioanal. Chem.* **2004**, *379*, 946–959.
- 132 MAJUMDAR, A., Bioassays based on molecular nanomechanics. *Dis. Markers* **2002**, *18*, 167.
- 133 MYHRA, S., A review of enabling technologies based on scanning probe microscopy relevant to bioanalysis. *Biosensors Bioelectron.* **2004**, *19*, 1345.
- 134 HIANIK, T., et al., Detection of aptamer–protein interactions using QCM and electrochemical indicator methods. *Bioorg. Med. Chem. Lett.* **2005**, *15*, 291–295.
- 135 WICKLINE, S. A., G. M. LANZA, Nanotechnology for molecular imaging and targeted therapy. *Circulation* **2003**, *107*, 1092–1095.
- 136 MORAWSKI, A. M., G. A. LANZA, S. A. WICKLINE, Targeted contrast agents for magnetic resonance imaging and ultrasound. *Curr. Opin. Biotechnol.* **2005**, *16*, 89–92.
- 137 THRALL, J. H., Nanotechnology and medicine. *Radiology* **2004**, *230*, 315–318.
- 138 WANG, X., et al., Photoacoustic tomography of biological tissues with high cross-section resolution: reconstruction and experiment. *Med. Phys.* **2002**, *29*, 2799–2805.
- 139 COPLAND, J. A., et al., Bioconjugated gold nanoparticles as a molecular based contrast agent: implications for imaging of deep tumors using optoacoustic tomography. *Mol. Imaging Biol.* **2004**, *6*, 341–349.
- 140 FARRER, R. A., et al., Highly efficient multiphoton-absorption-induced luminescence from gold nanoparticles. *Nano Lett.* **2005**, *5*, 1139–1142.
- 141 ZHENJIA, W., et al., The structural basis for giant enhancement enabling single-molecule Raman scattering. *Proc. Natl Acad. Sci. USA* **2003**, *100*, 8638.
- 142 PETTINGER, B., et al., Nanoscale probing of adsorbed species by tip-enhanced Raman spectroscopy. *Phys. Rev. Lett.* **2004**, *92*, 096101–096101.
- 143 PETTINGER, B., et al., Surface-enhanced and STM tip-enhanced Raman spectroscopy of CN<sup>-</sup> ions at gold surfaces. *J. Electroanal. Chem.* **2003**, *554–555*, 293–299.
- 144 DOOTZ, R., et al., Raman and surface enhanced Raman microscopy of microstructured polyethylenimine/DNA multilayers. *Langmuir* **2006**, *22*, 1735–1741.
- 145 KNEIPP, J., et al., Optical probes for biological applications based on surface-enhanced Raman scattering from indocyanine green on gold nanoparticles. *Anal. Chem.* **2005**, *77*, 2381–2385.
- 146 KNEIPP, K., et al., Single molecule Raman detection of enkephalin on silver colloidal particles. *Spectroscopy* **2004**, *18*, 433–440.
- 147 KNEIPP, K., H. KNEIPP, Ultrasensitive chemical analysis by Raman spectroscopy. *Chem. Rev.* **1999**, *99*, 2957.
- 148 GEHO, D. H., et al., Opportunities for nanotechnology-based innovation in tissue proteomics. *Biomed. Microdevices* **2004**, *6*, 231–239.



- 149 PETRICOIN, E. F., et al., Toxicoproteomics: serum proteomic pattern diagnostics for early detection of drug induced cardiac toxicities and cardioprotection. *Toxicol. Pathol.* **2004**, *32* (s1), 122–130.
- 150 NEDELKOV, D., R. W. NELSON, Surface plasmon resonance mass spectrometry: recent progress and outlooks. *Trends Biotechnol.* **2003**, *21*, 301–305.
- 151 KASIANOWICZ, J. J., Nanometer-scale pores: potential applications for analyte detection and DNA characterization. *Dis. Markers* **2002**, *18*, 185.
- 152 LAVAN, D. A., D. M. LYNN, R. LANGER, Timeline: moving smaller in drug discovery and delivery. *Nat. Rev. Drug Discov.* **2002**, *1*, 77.
- 153 FOLOGEA, D., et al., Detecting single stranded DNA with a solid state nanopore. *Nano Lett.* **2005**, *5*, 1905–1909.
- 154 LI, J., et al., DNA molecules and configurations in a solid-state nanopore microscope. *Nat. Mater.* **2003**, *2*, 611–615.
- 155 TONG, et al., Silicon nitride nanosieve membrane. *Nano Lett.* **2004**, *4*, 283–287.
- 156 STEINKAMP, T., U. KARST, Detection strategies for bioassays based on luminescent lanthanide complexes and signal amplification. *Anal. Bioanal. Chem.* **2004**, *380*, 24–30.
- 157 SHI, X., I. J. MAJOROS, J. R. BAKER, JR., Capillary electrophoresis of poly(amidoamine) dendrimers: from simple derivatives to complex multifunctional medical nanodevices. *Mol. Pharmacol.* **2005**, *2*, 278–294.
- 158 CHOI, Y., et al., Synthesis and functional evaluation of DNA-assembled polyamidoamine dendrimer clusters for cancer cell-specific targeting. *Chem. Biol.* **2005**, *12*, 35–43.
- 159 FERRARI, M., G. DOWNING, Medical nanotechnology: shortening clinical trials and regulatory pathways? *BioDrugs* **2005**, *19*, 203–210.
- 160 TKACHENKO, A. G., et al., Multifunctional gold nanoparticle-peptide complexes for nuclear targeting. *J. Am. Chem. Soc.* **2003**, *125*, 4700–4701.
- 161 NISSENSON, A. R., et al., Continuously functioning artificial nephron system: the promise of nanotechnology. *Hemodial. Int.* **2005**, *9*, 210–217.
- 162 LEE, S. J., S. Y. LEE, Micro total analysis system (micro-TAS) in biotechnology. *Appl. Microbiol. Biotechnol.* **2004**, *64*, 289–99.
- 163 GULLIKSEN, A., et al., Real-time nucleic acid sequence-based amplification in nanoliter volumes. *Anal. Chem.* **2004**, *76*, 9–14.
- 164 WALTER, G., et al., High-throughput protein arrays: prospects for molecular diagnostics. *Trends Mol. Med.* **2002**, *8*, 250–253.
- 165 SARIKAYA, M., et al., Molecular biomimetics: nanotechnology through biology. *Nature materials.* **2003**, *2*, 577–585.
- 166 MILLER, J., Beyond biotechnology: FDA regulation of nanomedicine. *Columbia Sci. Technol. Law rev.* **2003**, *4*, E5–E5.
- 167 RADOS, C., Nanotechnology: the size of things to come. *FDA Consumer* **2005**, *39*, 40–42.
- 168 DONAWA, M. E., The New FDA Combination Products Programme. *Med. Device Technol.* **2002**, *13*, 25.
- 169 BRUCE, D., The question of ethics. *Mater. Today* **2006**, *1*, 6–7.
- 170 MILLS, K., C. FLEDDERMANN, Getting the best from nanotechnology: approaching social and ethical implications openly and proactively. *IEEE Technol. Soc. Mag.* **2005**, *24*, 18–26.
- 171 GORDIJN, B., Nanoethics: from utopian dreams and apocalyptic nightmares towards a more balanced view. *Sci. Eng. Ethics* **2005**, *11*, 521–533.
- 172 GRUNWALD, A., Nanotechnology – a new field of ethical inquiry? *Sci. Eng. Ethics* **2005**, *11*, 187–201.
- 173 BERNE, R. W., Towards the conscientious development of ethical nanotechnology. *Sci. Eng. Ethics* **2004**, *10*, 627–638.
- 174 EINSIEDEL, E. F., L. GOLDENBERG, Dwarfing the social? Nanotechnology lessons from the biotechnology front. *Bull. Sci. Technol. Soc.* **2004**, *24*, 28–33.
- 175 LOPEZ, J., Compiling the ethical, legal and social implications of nanotechnology. *Health Law Rev.* **2004**, *12*, 24–27.

## 2 Superparamagnetic Nanoparticles of Iron Oxides for Magnetic Resonance Imaging Applications

*Jean-Marc Idee, Marc Port, Isabelle Raynal, Michel Schaefer,  
Bruno Bonnemain, Philippe Prigent, Philippe Robert,  
Caroline Robic, and Claire Corot*

### 2.1 Introduction

Superparamagnetic nanoparticles of iron oxides have become a major tool for medical imaging with a wealth of applications. This chapter will first describe their physicochemical characteristics, which are of paramount importance for their interaction with macrophage-like cells and, more broadly, for their biodistribution. The general pharmacological properties of these nanoparticles (including their interaction with macrophages and pharmacokinetic behavior) will subsequently be reviewed. Nanoparticles of iron oxides are currently marketed or undergoing clinical trials for cancer imaging applications, which will be described, but also for indications related to their blood pool characteristics and their unique potential for interaction with inflammatory cells. Since inflammatory infiltrates are found in a vast number of diseases (from atheromatous plaques to degenerative diseases such as multiple sclerosis), it appeared of clinical interest to numerous researchers to investigate the relevance of nanoparticles in such indications. The results of these studies will be presented for each of these potential new indications. Last, the noninvasive tracking of stem cells with superparamagnetic nanoparticles, which has attracted much attention in both neurological and cardiologic research over recent years, will be detailed.

For nearly 20 years, research in the field of magnetic resonance imaging (MRI) contrast agents has been oriented towards the study and development of superparamagnetic nanoparticles. These are iron oxides – magnetite ( $\text{Fe}_3\text{O}_4$ ), maghemite ( $\gamma\text{-Fe}_2\text{O}_3$ ) or other ferrites that are insoluble in water. Unlike ferromagnetic substances and because of their size, superparamagnetic agents have no magnetic properties outside an external magnetic field [1]. These nanoparticles have in common their specific uptake by macrophages, explaining why, even if they are not entirely captured by the liver and spleen, they are widely evaluated as MRI markers for diagnosis of inflammatory and degenerative disorders associated with high macrophage phagocytic activity.

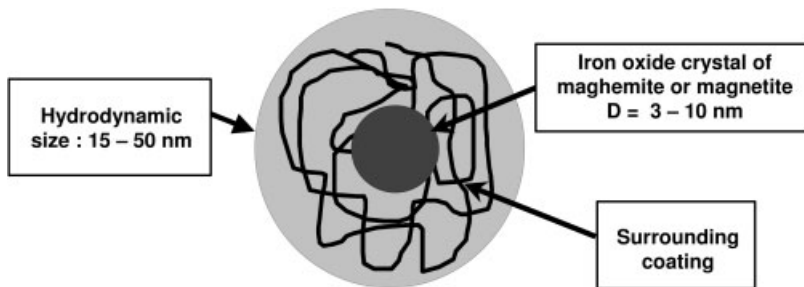


**Figure 2.1.** General structure of USPIO nanoparticles.

Superparamagnetic agents are highly effective in MRI as they are strong enhancers of proton relaxation.

Superparamagnetic nanoparticles are small coated crystals of iron oxides (Figs. 2.1 and 2.2), characterized by a large magnetic moment in the presence of a static external magnetic field. This large magnetic moment is caused by a crystal ordering (spinel) which induces a cooperativity between the individual paramagnetic ions constituting the crystal. Consequently, the magnetic moment of superparamagnetic particle is greater than the sum of each paramagnetic ions constituting the crystal. These small superparamagnetic crystals are smaller than a magnetic domain (approximately 30 nm) and, consequently, they do not show any magnetic

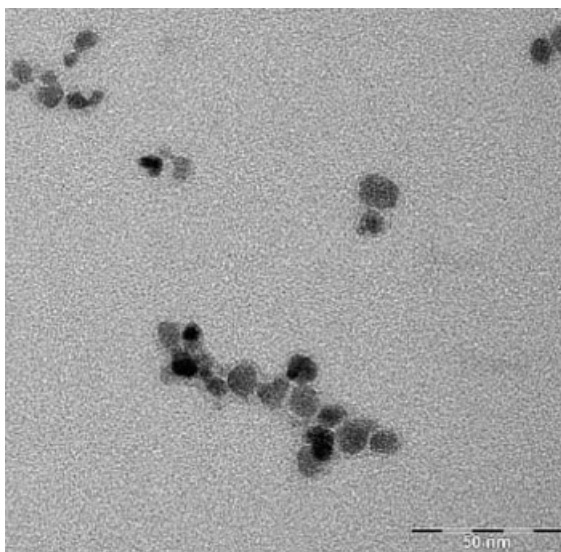


**Figure 2.2.** Transmission electron microscopy images of USPIOs (iron oxide crystals diameter: 5–7 nm) (Guerbet, unpublished data).

remanence (i.e. restoration of the induced magnetization to zero upon removal of the external magnetic field), unlike ferromagnetic materials. The interaction between surrounding protons of water molecules and the magnetic moment of superparamagnetic particles results in an increase in longitudinal  $r_1$  and transverse  $r_2$  relaxation rates.

The T1 relaxation of superparamagnetic particles has been explained by various models, and Roch and coworkers [2] have proposed a model introducing the anisotropy energy to explain the relaxivity at low magnetic fields while the relaxivity at high fields is mainly related to the outer-sphere Curie relaxation mechanism. The nuclear magnetic relaxation dispersion (NMRD) profile of contrast agents shows the relationship between their relaxivity and the proton Larmor frequency. The NMRD profile of these particles has been obtained, and shows that the magnetic field applied has a considerable and nonlinear influence on the signal [3]. These authors have proposed a new theory which takes account of the magnetic moment of the monodomains and the saturation of the macroscopic magnetization. This fact should be taken into consideration when analyzing the imaging data.

In most situations, it is the significant capacity of superparamagnetic nanoparticles to reduce the spin–spin T2 relaxation time and thus reduce the MRI signal that is used, and such molecules are mostly employed because of their negative enhancement effect on T2-weighted sequences. This drop in signal intensity is related to the field gradients produced by the magnetic particles that dephase nearby diffusing protons and shorten T2/T2\*. This effect is rationalized by outer-sphere relaxation (Ayant and Freed's theory).

This predominant effect on the T2 relaxation time does not prevent these agents' properties from being put to use on the T1 relaxation time if the imaging sequences are chosen appropriately [4]. This is why their use in increasing the signal in the myocardium tissue [5] and in magnetic resonance angiography has been proposed [6].

The multiple components which govern the efficacy of these agents require them to be characterized as accurately as possible by information such as the size of the iron oxide crystals, the charge, the nature of the coating, the hydrodynamic size of the coated particle, etc. These physicochemical characteristics not only affect the efficacy of the superparamagnetic particles in MRI, but also their stability, biodistribution, opsonization and metabolism as well as their clearance from the vascular system.

## 2.2

### Physicochemical Characteristics

The synthesis of superparamagnetic nanoparticles is a complex process because of their colloidal nature [7]. Consequently, a full set of analytical methods should be used in order to characterize the efficacy (in terms of magnetization and relaxivity) and purity of nanoparticles and the reproducibility of the synthesis process. Moreover, since the size, the geometry, the composition of the crystals as well as the

Tab. 2.1. Size of iron oxide nuclei (nm) [8].

	X-ray diffraction	Transmission electron microscopy
Ferumoxides	$4.96 \pm 0.14$	$4.8 \pm 1.9$
Ferumoxtran-10	$5.85 \pm 0.09$	$4.9 \pm 1.5$
Ferumoxsil	$8.3 \pm 1.03$	$8.4 \pm 2.5$
Ferumoxytol	$6.76 \pm 0.41$	–

charge of the particles and the nature of the coating strongly influence the physicochemical and biological behavior of the particles, an accurate description of the physicochemical properties of these nanoparticles is crucial in establishing any structure–activity relationship [8, 9].

### 2.2.1

#### Physicochemical Properties of the Crystal

The size of the crystals varies from agent to agent, but also depends on the measurement technique. The core size is generally between 4 and 10 nm (Tab. 2.1). The size of the crystal can be appreciated by transmission electronic microscopy (TEM) and needs to be measured on a statistically significant number of crystals. Moreover, the sample preparation can induce aggregation of the colloids and the TEM measurements may consequently not reflect the crystal size in solution. The size of the crystals can also be measured by X-ray diffraction (XRD) by analyzing the X-ray line broadening. Moreover, XRD can provide information concerning the crystal composition and structure. A detailed characterization by TEM and XRD analyses of new nonpolymeric-coated  $\text{Fe}_3\text{O}_4$  nanoparticles has been recently described by Cheng and coworkers [10].

Composition of the crystal can also be analyzed by Mössbauer spectroscopy. The magnetic properties of the nanoparticles can be studied by the behavior of the magnetization according to the applied magnetic field (magnetometry) which confirms the superparamagnetic property and gives the magnetization at saturation (MS). Of course, the magnetic properties can also be studied by recording the NMRD curve. According to the relaxivity theory developed by Roch and coworkers [2], the fitting of the NMRD curves can provide information on the relaxometric size and the magnetization at saturation.

### 2.2.2

#### Hydrodynamic Particle Size and Charge

The hydrodynamic size of the nanoparticles [i.e. the global size of the particle comprising one or several magnetic crystal(s) surrounded by the coating molecules] is

usually measured by photon correlation spectroscopy (PCS), which analyses the quasielastic light diffusion of nanoparticles when illuminated by a monochromatic laser beam. The intensity of the diffused light is modulated by the Brownian motion of the particles in solution. Different mathematical analyses of the PCS data can provide an estimation of the hydrodynamic size and the polydispersity of the nanoparticles. However, the values obtained by PCS dramatically depend on the mathematical models and weighting parameters used (unimodal or multimodal distribution, distribution in number, volume or intensity). Consequently, the hydrodynamic size measurements described in the literature for different nanoparticles are very difficult to compare, and any relationship between size and biodistribution should be made with caution.

The size of the particles themselves with their coating varies even more and the measurement method contributes significantly to this variability (Tab. 2.2).

It is currently agreed that two main categories of superparamagnetic agents must be distinguished [9]:

**Tab. 2.2.** Size and coating agent of the nanoparticles currently marketed or under clinical investigation.

Brand name or common name	Company	Other names	Coating agent	Size (laser light scattering) (nm)
Endorem <sup>®</sup> / Feridex <sup>®</sup>	Guerbet Advanced Magnetics	Ferumoxides AMI-25	dextran	120–180
Sinerem <sup>®</sup> / Combidex <sup>®</sup>	Guerbet Advanced Magnetics	Ferumoxtran-10 AMI-227 BMS-180549	dextran T-10	15–30
–	Advanced Magnetics	Ferumoxytol Code 7228	semisynthetic carbohydrate	30
Lumirem <sup>®</sup> / Gastromark <sup>®</sup>	Guerbet Advanced Magnetics	Ferumoxsil AMI-121	silicon	300
Resovist <sup>®</sup>	Schering	Ferucarbotran SHU-555A	carboxy-dextran	60
Clariscan <sup>®</sup>	GE-Healthcare	Feruglose NC100150	pegylated starch	20
Abdoscan <sup>®</sup>	GE-Healthcare	Ferristene	sulfonated styrene– divinylbenzene copolymer	3500
VSOP-C184	Ferropharm	–	citrate	7.0 ± 0.15

Tab. 2.3. Magnetization and relaxivity measurements [8, 13, 90].

	Magnetization (e.m.u. g Fe <sup>-1</sup> )		Relaxivity (mM s <sup>-1</sup> ) <sup>[a]</sup>	
	0.1 T	5.0 T	r <sub>1</sub>	r <sub>2</sub>
Ferumoxides	37.7 ± 0.6	93.6 ± 1.6	23.7 ± 1.2	107 ± 11
Ferumoxtran-10	53.6 ± 0.4	94.8 ± 0.7	22.7 ± 0.2	53.1 ± 3.3
Ferucarbotran	–	–	25	164
Ferumoxsil	49.4 ± 0.1	91.1 ± 0.2	3.2 ± 0.9	72 ± 12
VSOP	–	–	18.7	30.0
Ferumoxytol	–	–	38	83

<sup>a</sup>At 20 MHz (0.47 T).

- Superparamagnetic iron oxides (SPIOs), the hydrodynamic size of which including coating is greater than 50 nm.
- Ultrasmall superparamagnetic iron oxides (USPIOs) which are less than 50 nm in size.

This difference in size is reflected by significant differences in the ratio of relaxivity constants  $r_2/r_1$  (Tab. 2.3), but also by a significant difference in plasma half-life and biodistribution.

Another fundamental characteristic of these agents is the nature and charge of the particle coating. The charge on the surface of the nanoparticles is usually appreciated by the  $\zeta$  potential measurement deduced from the measurement of electrophoretic mobility. Unfortunately, the value of  $\zeta$  potential of superparamagnetic nanoparticles is rarely described in the literature. Although most superparamagnetic particles are covered by dextran or dextran derivatives (e.g. carboxy-dextran), they have occasionally been coated with other molecules such as starch, siloxane, arabinogalactose, amino-functionalized polyvinyl alcohol (PVA), citrate, etc.

Therefore, when referring to superparamagnetic agents, these must be properly characterized and their characteristics compared with the other agents by using the same measurement methods. The relationship between the structure, the composition and the charge of nanoparticles and their potential in terms of efficacy, biodistribution and safety is not yet well understood.

### 2.3 Pharmacology and Metabolism

Iron oxide nanoparticles are internalized into macrophages (Fig. 2.3) and other phagocytic cells following intravenous administration.

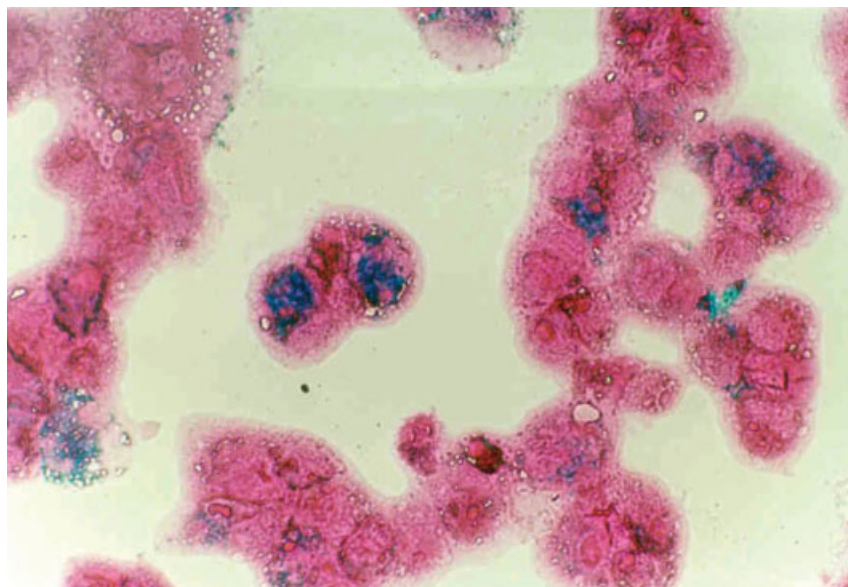


**Figure 2.3.** Intracellular localization of the USPIO ferumoxtran-10 ( $7.1 \text{ mmol L}^{-1}$ ) following a 24-h incubation with activated THP-1 human monocytes. Iron staining with Prussian blue and counter-staining with eosin (Guerbet, unpublished data).

### 2.3.1

#### Role of Physicochemical Parameters

The size and physicochemical surface properties of SPIOs and USPIOs strongly interfere with their capacity to be internalized into macrophages or other phagocytic cells following intravenous administration.

Ferumoxtran-10, which has a small hydrodynamic diameter (15–30 nm, see Tab. 2.2), shows a long blood residence time, which allows it to easily access macrophages located in deep and pathologic tissues (such as lymph nodes, kidney, brain, osteoarticular tissues, etc.). Indeed, these tissues are far less accessible than well-vascularized tissues such as the liver or spleen.

Other USPIOs such as ferucarbotran or very small superparamagnetic iron oxide particles (VSOPs) have a higher macrophage uptake. This is associated with a faster blood clearance and, consequently, a more limited access time to the deep compartments [11, 12]. For example, the elimination half-life of VSOP-C184 in healthy volunteers is only 0.5–1.5 h after bolus injection [13]. Conversely, feruglose (Clariscan<sup>®</sup>), because of the pegylation of the coating starch, can be regarded as “stealth nanoparticles” which are hardly recognized by the macrophage–monocytic system and probably not suitable for macrophage imaging [14].

It has recently been shown that superparamagnetic nanoparticles with an amino-functionalized PVA coating can interact with human melanoma cells with-



out any cytotoxicity. This interaction of the nanoparticles with melanoma cells was found to be active, energy-dependent and saturable [15]. It also depended on the amino-PVA:iron oxide ratio – the increased uptake in the presence of amino groups is consistent with the well-known uptake of cationic liposomes, mainly for transfection purposes.

A recent study compared anionic nanoparticles (AN) (coating: meso-2,3-dimercaptosuccinic acid, hydrodynamic diameter 24 nm) with ferumoxtran-10 [16]. *In vitro* uptake by the human prostatic adenocarcinoma cells PC3 was found to be superior with AN than with ferumoxtran-10. In mice grafted with PC3 cells, the iron concentration inside tumors reached two peaks: first one at 1 h (ferumoxtran-10 > AN) and second one at 12 h (ferumoxtran-10 = AN). Imaging studies showed tumor brightening on T1-weighted images with ferumoxtran-10 and darkening on T2-weighted images with both compounds. With ferumoxtran-10, an early peak at 1 h on T2 imaging and a second peak at 12 h on T1 imaging suggested an initial intravascular distribution and, possibly, a secondary extravasation in the interstitium (or, alternatively, some intracellular uptake) at 12 h [16].

### 2.3.2

#### Mechanism and Consequences of Interaction with Macrophages

According to their coating (negative charges and hydrophilicity), nanoparticles display different degrees of uptake by macrophage-like cells, as previously mentioned.

The macrophage is a specialized host defense cell with endocytic properties. Its involvement in the pathogenesis of numerous diseases is well known and makes it a very interesting pharmaceutical target.

It has been shown *in vitro* that ferumoxides endocytosis by mouse peritoneal macrophages was dose-dependently inhibited by polyinosinic acid and fucoidan, suggesting that a scavenger receptor SR-A mediated endocytosis is involved for this contrast agent [17].

On the human activated monocyte THP-1, ferumoxide was shown to undergo a higher macrophage uptake compared with ferumoxtran-10, probably because of its larger size [17]. This result was confirmed in another study [18] which also showed that, apart from particle size, the phagocytic uptake is dependent on the surface properties of the nanoparticles since, both for SPIO or USPIO categories, ionic carboxy-dextran coating leads to a higher uptake than nonionic dextran coating [18].

Another study also found a higher cellular uptake (on hematopoietic progenitor, mesenchymal fibroblast and epithelial HEP-G2 cell lines) with the SPIO ferucarbo-tran than with the USPIO SHU-555C (hydrodynamic diameter 30 nm) [19].

Rogers and Basu recently showed that the hydroxymethyl glutaryl coenzyme A (HMG-CoA) reductase inhibitor lovastatin dose-dependently reduced the uptake of the SPIO ferumoxides by a murine macrophage-like cell line (J774A) [20]. The mechanism of this effect is unclear, and may be explained by a downregulation of class A types I and II receptors, or, alternatively, by interference of lovastatin in macrophage–receptor binding, reduced receptor recycling or at the level of

scavenger receptor mRNA expression. The clinical relevance of such *in vitro* data for the detection and characterization of atheromatous plaques with USPIOs in patients treated with HMG-CoA reductase inhibitors remains unclear.

The same authors also demonstrated that the pro-inflammatory cytokine interferon (IFN)- $\gamma$ , but also the anti-inflammatory cytokine interleukin (IL)-4 increased SPIO uptake at relatively high concentrations [20].

Another study has investigated the biological consequences of the rat macrophage labeling with the citrate-coated nanoparticles VSOP [21]. Cell growth and viability were minimally affected. However, transient oxidative stress was evidenced by an acute increase in both malonyldialdehyde and protein carbonyls.

In addition to their phagocytic properties, macrophages also possess a high secretory capability leading to the release of growth factors and cytokines. Very low IL-1 release (comparable to negative control) was observed after incubation of macrophages with ferumoxides or ferumoxtran-10, even at a high concentration ( $500 \mu\text{g Fe mL}^{-1}$ ), thus suggesting a low pro-inflammatory potential for these nanoparticles [17].

### 2.3.3

#### Pharmacokinetics

Ferumoxtran-10 is completely degraded in the macrophage lysosomal compartment within 7 days [22]. The plasma elimination half-life is strongly species dependent. It is 2 h in rats (after intravenous injection of a 30 or  $45 \mu\text{mol kg}^{-1}$  dose), approximately 6 h in rabbits whereas it is around 24–36 h in humans following intravenous administration [11, 23]. In both rats and rabbits, increasing the dose caused a longer half-life because of the progressive saturation of uptake by liver and spleen.

Since the access of USPIOs to deep compartments is favored by prolonged blood residence time, animal imaging experiments are generally performed using high doses of USPIO ( $200\text{--}1000 \mu\text{mol kg}^{-1}$ ) compared to the human clinical dose of  $45 \mu\text{mol kg}^{-1}$  [11].

It has been shown that the age of rats significantly influences the half-lives of the signal intensities in vessels and in the liver following injection of VSOP-C43. In the younger animals, the intravascular signal decrease was about 50% of the value seen in older animals [24]. This suggests a higher macrophage uptake in younger animals. Since pharmacokinetic data are classically obtained during phase I clinical studies in young healthy volunteers, caution seems necessary when it comes to extrapolating imaging window to elderly patients.

The iron contained in SPIOs and USPIOs is bioavailable, and is incorporated into the normal body iron pools, such as hemoglobin [25]. This is consistent with the increase in ferritin levels reported in several articles with various USPIOs [13, 26]. Ferritin is the physiologic storage form of iron. Actually, it is believed that K upffer cells degrade dextran-coated iron oxide nanoparticles by incorporating most of the iron they contain into ferritin and/or hemosiderin (when the intracellular concentration of ferritin becomes relatively high) before exocytosis [27].

The USPIO ferumoxtran-10 (Sinerem<sup>®</sup>/Combidex<sup>®</sup>) is currently under clinical trial for the detection of nodal metastases (see Section 2.4.3). After intravenous infusion, USPIO nanoparticles are distributed to the lymph nodes by two distinct pathways: (i) direct transcapillary passage through venules into the medullary sinuses of the lymph node, followed by phagocytosis by macrophages, and (ii) non-selective, endothelial transcytosis into the interstitial space in the body, followed by uptake of the nanoparticles by draining lymphatic vessels and transport to the lymph nodes via afferent lymphatic channels [28, 29].

Several routes of administration have been suggested for SPIOs and USPIOs. The SPIO ferumoxides (Endorem<sup>®</sup>/Feridex<sup>®</sup>) is administered using slow intravenous infusion, ferucarbotran (Resovist<sup>®</sup>) is injected as a bolus. Clinical studies on ferumoxtran-10 have so far used slow intravenous infusion but preclinical studies have shown that this USPIO can also be directed to specific lymph nodes via subcutaneous injections at distinct sites [30]. In human volunteers, it was shown that interstitial administration of ferumoxtran-10 ( $0.28 \text{ mg Fe kg}^{-1}$ ) increases the number of lymph nodes that can be adequately detected with MRI.

The site of injection in the pelvis influenced the location of visualized lymph nodes, with the largest number of nodes visualized with periprostatic injection. This interstitial approach may also allow a reduction of the dose when compared with the intravenous route [31].

The optimal temporal window for imaging lymph nodes with ferumoxtran-10 is 24–36 h after intravenous infusion [29].

#### 2.3.4

#### Nanoparticle Vectorization

Although it has a good temporal and spatial resolution, MRI displays a relatively low sensitivity (about three to six orders of magnitude less than that of isotope techniques). It therefore requires amplification to enable its use in molecular imaging. Molecular imaging includes a large array of applications (study of tissular blood flow changes, spectroscopic quantification of metabolite concentrations, generation of pH maps, studies of vascular volume or permeability, pharmacokinetic studies of chemotherapeutic drugs, denoting of gene expression, specific imaging of molecules that are overexpressed in pathological states, etc.) [32]. A promising option for local signal amplification is vectorization of nanoparticles to enable them to reach their biological target [33]. Several strategies have been selected to vectorize nanoparticles. One example is the oxidative conjugation producing aldehydes on the dextran coating of the particles, at the expense of a substantial loss of the biological activity of the protein. To reduce this effect, the protein that binds the biological target has been linked to the iron oxide nanoparticles through a linker molecule [34].

Nonoxidative strategies have become an interesting alternative method: epichlorohydrin is first coupled to the hydroxyl groups of the dextran coating to provide a terminal halogen derivative which can subsequently be used to link any molecule containing an amine function (peptide, protein, antibodies, etc.) [35]. As an exam-

**Tab. 2.4.** Functionalized USPIOs: some examples.

Biological target	Type of functionalized USPIO	Experimental model	Reference
Acute inflammation	MION-IgG	rat model of myositis	38
Asialoglycoprotein receptors on hepatocytes	arabinogalactan (AG)-USPIO	blockade of AG-USPIO uptake by hepatocytes with D[+]-galactose	39
Transferrin receptor on tumor cells	dextran-stabilized USPIO covalently labeled with receptor-specific transferrin	SMT/2A tumor-bearing rats	40
$\alpha_{\text{IIB}}\beta_3$ integrin	USPIO functionalized with cyclic RGD peptide specific for the $\alpha_{\text{IIB}}\beta_3$ integrin	<i>ex vivo</i> : clot on a glass tube <i>in vivo</i> : clots induced in the jugular veins of domestic pigs	41
Phosphatidylserine	Annexin V-functionalized USPIO	apoptotic Jurkat cells	42
$\alpha_v\beta_3$ integrin	USPIO functionalized with RGD peptide	<i>in vitro</i> : PMA-activated Jurkat cells <i>in vivo</i> : ApoE <sup>-/-</sup> atherosclerotic mice	43

ple, vectorizing groups [such as the connecting segment-1 fragment of fibronectin, the peptide GRGD (Gly-Arg-Gly-Asp) or a nonpeptidic small-molecular-weight RGD mimetic] have been grafted with the dextran coating of USPIO previously coated with epichlorhydrin [36].

Another approach uses 2,3-dimercaptosuccinic acid (DMSA) and *N*-succinidyl 3-(2-pyridylthio)propionate (SPDP) [37]. Recent examples of functionalized USPIOs used for experimental molecular imaging are shown in Tab. 2.4 [38–43].

## 2.4

### Current Clinical Uses and Future Developments

#### 2.4.1

##### Gastrointestinal Tract Imaging

As in computed tomography (CT) scanning, it is clinically necessary to improve the differentiation between the gastrointestinal tract and surrounding organs. Para-

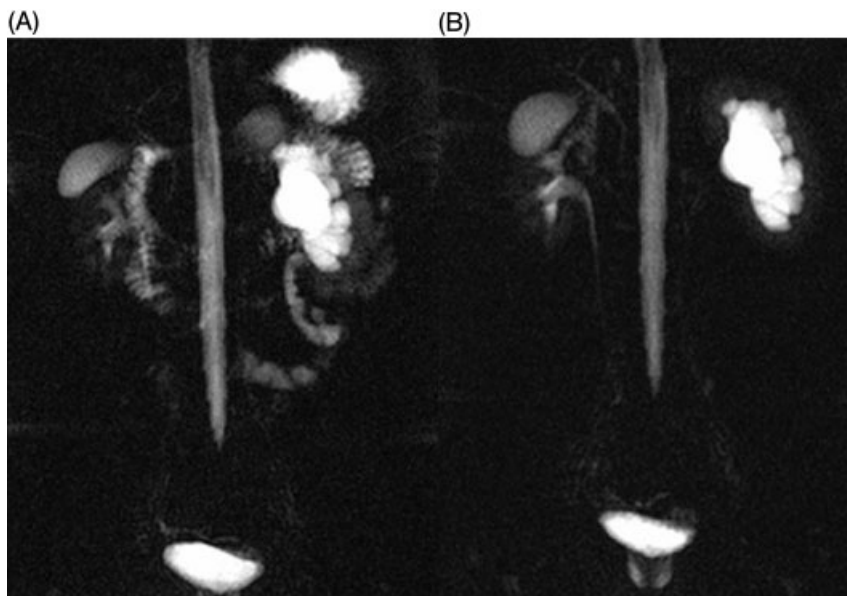


**Figure 2.4.** Signal suppression of the gastrointestinal structures in pyelography. MRI prior (A) and after (B) oral administration of 500 mL ferumoxsil (courtesy Dr A. Blandino, Policlinico G. Martino, Messina, Italy).

magnetic contrast agents, which increase the gastrointestinal tract signal, may also increase movement artifacts. Specific superparamagnetic contrast agents have been developed for this reason. A first agent, ferumoxsil (AMI-121), has been tested in clinical trials by oral administration at 600–900 mL [44–47] and is licensed in Europe as Lumirem® (or Gastromark® in the USA).

This product is composed of iron oxide particles coated in a layer of inert silicon and its diameter is 300 nm (Tabs. 2.1 and 2.2). After oral administration, it significantly improves the definition of organ boundaries such as the uterus and lymph nodes [47] (Fig. 2.4). Other agents have been developed for the same application: WIN-39996 [48], oral magnetic particles (OMPs), also referred as to ferristene (Abdoscan®) (polystyrene coated) [49–53].

Ferumoxsil has also been used as well in MR enteroclysis in 60 patients with Crohn's disease [54]. Aliquots of 600 mL of ferumoxsil associated with 2.5 L of tide water and methylcellulose were instilled through a transjejunal tube, in order to reduce the signal intensity of the lumen. Additional rectal instillation of water for positive contrast improved the distension and identification of large bowel and terminal ileum.

Similarly, an Italian team [55] used a double-contrast method for evaluating the inflammatory activity in patients with Crohn's disease, after darkening the lumen of the bowel with oral administration of Lumirem®, the gadolinium contrast agent was injected. Parameters such as wall thickness, wall T2-weighted signal, wall con-

trast enhancement, amount of fibroproliferation and T2-weighted signal of fibrofatty proliferation on fat-suppressed images were evaluated.

These negative contrast agents for gastrointestinal imaging are generally well tolerated, with mild side-effects such as nausea, vomiting (1–5% of patients) or flatulence [56]. Oral SPIO are generally administered over 30–60 min, with a volume of 900 mL for contrast enhancement of the whole abdomen and 400 mL for the upper abdomen [57].

#### 2.4.2

#### Liver and Spleen Diseases

The first clinical indication for iron oxide nanoparticles was hepatic imaging. Following intravenous injection, SPIOs are rapidly taken up by hepatic Kupffer cells and the spleen (marginal zone and red pulp) macrophages, resulting in a drop in magnetic resonance signal intensity, and therefore in hypointense images, mostly because of a susceptibility effect.

Since Kupffer cells are exclusively located in the healthy hepatic parenchyma [58], SPIOs increase the contrast between healthy and diseased tissue devoid of Kupffer cells. The first agent to be developed (and marketed in Europe more than 10 years ago under the name Endorem<sup>®</sup>) was ferumoxides (or AMI-25) (Feridex<sup>®</sup> in the US). These are T10-dextran coated particles and their hydrodynamic size is 120–180 nm (Tabs. 2.1 and 2.2). Many preclinical and clinical trials have demonstrated the efficacy of ferumoxides in the detection of the focal lesions of the liver as well as for their characterization [59–64] (Fig. 2.5).

The same product has been studied in terms of its capacity to detect lesions of the spleen [65, 66]. The most common side-effects reported with ferumoxides are

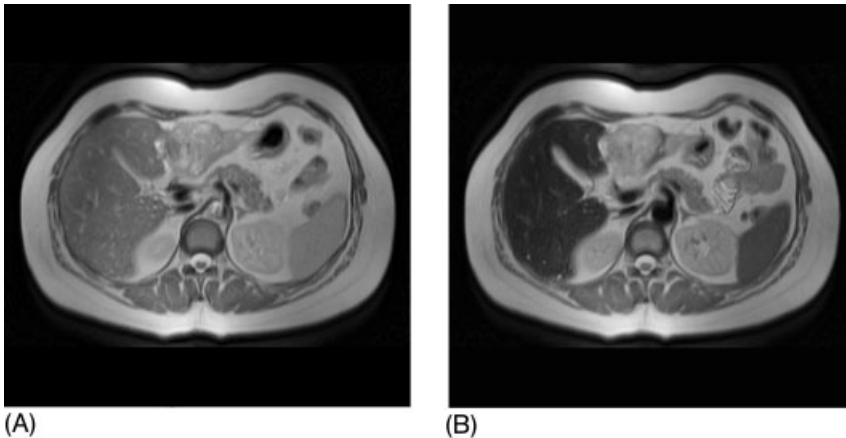


**Figure 2.5.** Liver imaging prior (A) and after (B) injection of ferumoxides (HASTE sequence) allowing a better depiction of a cholangiocarcinoma which does not uptake the nanoparticles and appears in isosignal

intensity pre/postinjection while the signal of the normal parenchyma becomes dark. (courtesy Dr C. Matos, Erasmus Hospital, Brussels, Belgium)

lower back pain (4%), flushing (2%) and various combined gastrointestinal complaints (5.6%) [67].

Another product was subsequently developed for this clinical application in MRI: ferucarbotran (SHU-555A) (Resovist®), the particles of which are coated with carboxy-dextran and are approximately 60 nm in diameter [19, 68]. Safety data obtained during phase I–III trials of this compound revealed a total of 162 side-effects in 1053 patients, of which 75 (7.1%) were possibly, probably or definitely drug related. The majority of events occurred within the first 3 h [69].

Chondroitin sulfate iron colloid (CSIC) has also been put forward [70] as well as MDL (liver-directed nanoparticles) [71], but these particles have not been marketed. Furthermore, other hepatocyte-specific agents were evaluated but not marketed either: asialofetuin-coated USPIO or arabinogalactan-coated USPIO, which are particularly well recognized by the asialoglycoprotein receptor (ASGPR) present on the surface of normal hepatocytes [72]. ASGPR is of interest for hepatocyte targeting in that it is prototypic of the class of receptors that constitutively enters cells and allows delivery of molecules to the intracellular compartments [73]. In addition to their ability to assess focal hepatic lesions, these agents can be used to assess hepatocyte function [57].

In addition to SPIOs, USPIOs such as ferumoxtran-10 can be located in several compartments of the liver (extracellular space, reticuloendothelial cells and possibly hepatocytes). In the rat, ferumoxtran-10 acts mainly as an extracellular agent for at least 1 h (increase in liver signal intensity on T1-weighted images) and is taken up by cells from the reticuloendothelial system at later time points [74]. A subsequent rat study showed that the USPIO feruglose induced an hepatic T2\* effect at late (up to 133 days after injection for 5 mg Fe kg<sup>-1</sup>) time-points when the concentrations of iron oxide nanoparticles in the liver were below method detection limits. This effect is probably a result of nanoparticle breakdown products [27].

In a clinical study comparing the SPIO ferumoxides with the USPIO ferumoxtran-10 in patients with focal hepatic diseases (hepatocellular carcinoma, metastases, hepatocellular adenoma and focal nodular hyperplasia), Mergo and coworkers observed that, although both compounds had similar T2 effects (comparable loss of hepatic signal intensity in their study conditions) and improved the lesion-to-liver contrast when compared with non-contrast-enhanced images, the USPIO allowed more in-depth characterization of the lesions, because of its additional blood pool effect [75].

Further studies are needed to better understand the potential utility of USPIOs for assessment of hepatic vascular structures and clinical benefit in the characterization of focal hepatic lesions, notably by optimizing the USPIO injected dose and the chronology of MRI.

### 2.4.3

#### Lymph Node Metastases

Nodal disease is an independent adverse prognostic factor in many types of cancer. The only widely accepted method for assessing nodal involvement by means of

imaging so far is measurement of the node size. This preoperative staging will influence the oncologist's decision to use neoadjuvant therapy or the surgeon's decision to perform nodal dissection [76]. Superparamagnetic agents which can be taken up by normal nodes following intravenous or subcutaneous injection have raised great interest. The first agent, and that on which most research has been carried out, is ferumoxtran-10 (or AMI-227). Its iron oxide core is surrounded by a 8- to 12-nm layer of T-10 dextran coating [23], leading to a final size of around 30 nm (Tabs. 2.1 and 2.2). It has similar physicochemical properties to the monocrystalline iron oxide nanocompounds (MION) which have a monocrystalline crystal core with an approximate diameter of 4 nm and a dextran coating resulting in a hydrodynamic diameter of 17 nm [77].

Numerous studies on ferumoxtran-10 have shown its efficacy in metastatic lymph node imaging [78–81] (Fig. 2.6). Schematically, as previously mentioned,

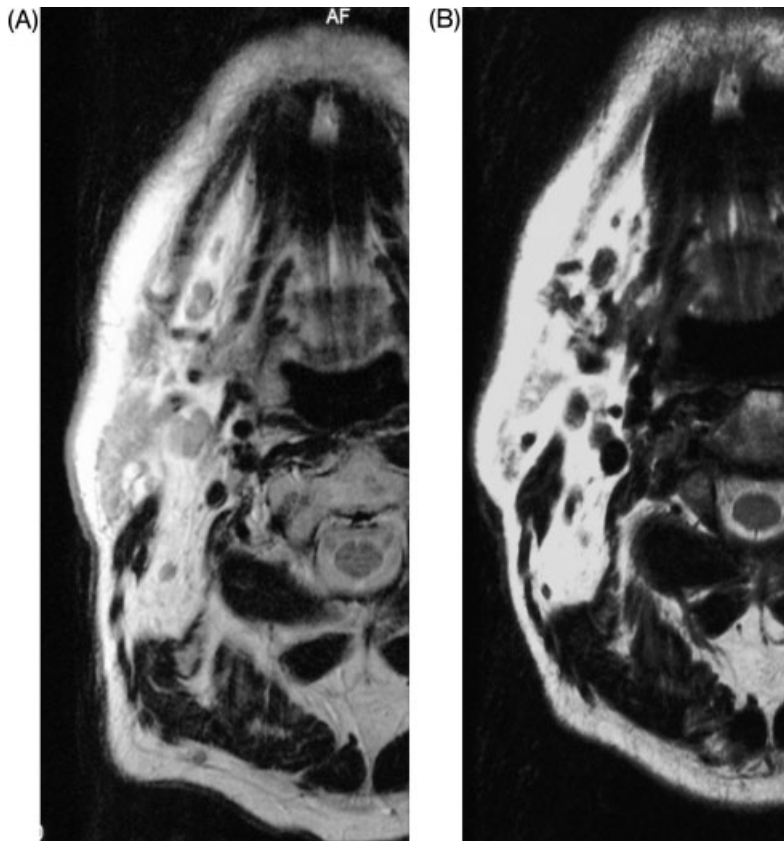


**Figure 2.6.** MRI (T2\* sequence) of lymph node metastases prior (A) and after (B) ferumoxtran-10 injection in a patient with head and neck cancer (courtesy Dr M. Mack, University Hospital, Frankfurt/Main, Germany).



USPIO slowly extravasate from the vessels into the interstitial space, from which they are transported into the lymph nodes through lymphatic vessels [28, 29, 82]. Upon USPIO administration, normal lymph nodes will appear dark on the MR images, while tumor metastases remain isointense with the precontrast image (i.e. before USPIO uptake by lymph node macrophages). In eighty patients with presurgical clinical stage T1, T2 or T3 prostate cancer who underwent lymph-node resection or biopsy, MRI was done before and 24 h after the intravenous injection of 2.6 mg kg<sup>-1</sup> of ferumoxtran-10. Sixty-three lymph nodes, from 33 patients, had histopathologically detected metastases. Of these, 45 (71.4%) did not fulfill the usual imaging criteria for malignancy. However, the ferumoxtran-10-enhanced MRI correctly identified all patients with nodal metastases. Nodal metastatic infiltration measuring 5–10 mm were identified [81].

Several phase III clinical trials using USPIO ferumoxtran-10 for the detection of lymph node metastases, especially in the head and neck and pelvis regions, are currently in their final stages. Promising results have also been published for rectal cancer [76].

#### 2.4.4

#### Blood Pool Characteristics

Uptake of ferumoxtran-10 and the MIONs or other USPIOs by the liver and the spleen is quite low because of their physicochemical characteristics. They consequently remain in the blood circulation for a very long time. With their long blood half-life and T1-shortening effect, these agents have been evaluated as blood pool agents for indications such as measurement of cerebral perfusion [83, 84], myocardial or renal perfusion [85], angiography [6], or detection of vascular hepatic lesions [86]. These compounds are classically referred to as slow-clearance blood pool agents. Whereas these agents are confined to the vascular compartment, their molecular volume only allows a slow “sieving” through the glomerular fenestrae. Their renal clearance is consequently much lower than the normal glomerular filtration rate.

These blood pool characteristics provide a much longer time window for data acquisition during radiological procedures, with little loss of intravascular signal intensity.

The potential clinical indications related to these properties are:

- *Cerebral imaging*: measurement of the cerebral blood volume [87] and functional imaging [88]. The MR evaluation of stroke and its functional consequences may benefit from the use of blood pool agents. Even if emergency treatment of cerebral vascular accidents is currently limited, there is reason to believe that a diagnostic aid which precisely defines the cerebral shadow zone would demonstrate the value of better managed care, as was the case in myocardial ischemia.
- *Cardiac imaging*: quantification of the hypoperfused zones and MR coronary angiography.

- *First-pass angiography* [89, 90].
- *Tumor imaging*: detection and characterization of the lesion-associated microvascular environment. These agents would enable prediction of the treatment efficacy by evaluating the endothelial permeability and size of neovessels (calculation of blood volume and vessel size index) [91, 92].
- *Optimization of hyperpolarized  $^3\text{He}$  gas MRI* [93].

#### 2.4.5

#### Characterization of the Atheromatous Plaque

The composition and stage of atherosclerotic plaque are clinically more relevant than the severity of stenosis for evaluation of the risk of acute ischemic events. Atherosclerosis is basically an inflammatory disease [94]. Monocytes adhere to the vascular endothelium and accumulate in lesion-prone arterial sites. This adherence is facilitated by the endothelial expression of adhesion molecules. Adherent monocytes are subsequently enticed into the arterial intima where they differentiate into macrophages [95]. Macrophage-rich areas are more frequently found in the atheromatous plaques of patients with unstable angina and non-Q-wave myocardial infarction [96]. This suggests that macrophages are a marker of unstable atherosclerotic plaques and that specific targeting of these cells may lead to the characterization of atheromatous plaques prone to rupture.

Animal studies have clearly shown that USPIO induce focal signal intensity decreases in the aortic wall of atheromatous rabbits [97, 98] or apolipoprotein E (ApoE) knockout mice [99].

Interestingly, the exposure period of atherosclerotic plaque to circulating USPIO seems to be critical for the uptake of nanoparticles: in a comparative study in hyperlipidemic rabbits, the *in vivo* MRI signal intensity was found to be significantly higher with the long half-life agent ferumoxtran-10 than with another USPIO of similar size, ferumoxytol ( $T_{1/2} \sim 6$  h), whereas *in vitro* macrophage phagocytosis was greater with the latter compound [100].

Preliminary clinical studies or case reports using ferumoxtran-10 have also shown USPIO-induced signal loss in aorta and pelvic arteries [101] or in carotid atheromatous plaques [102–104]. In one of these clinical trials [102], histological analysis showed USPIO in 27/36 (75%) of the ruptured or rupture-prone plaques and 1/14 (7%) of the stable atheromatous lesions. Postcontrast images should systematically be compared with corresponding precontrast images in order to exclude USPIO-induced signal reduction from other effects such as plaque calcification (which can also lead to strong susceptibility effects).

Given the heterogeneity of plaque formation and progression mechanisms, the macrophages which have endocytosed USPIO could be activated macrophages derived from activated blood-borne monocytes, activated macrophages derived from smooth muscle cells or foam cells which correspond to macrophages at a later stage [11]. Further studies are definitely required to better understand the precise mechanism of USPIO-uptake by atheromatous plaques. Obviously, such preliminary data open very interesting prospects for clinicians.

#### 2.4.6

#### Other Potential Uses

Given the wide spectrum of inflammatory diseases, it is evident that these nanoparticles have a huge clinical potential. Some clinical applications of high interest are discussed below.

##### 2.4.6.1 Stroke

Ischemic focal lesions are associated with a strong inflammatory local response that involves microglial cell activation as well as infiltration of hematogenous leukocytes, mostly monocytes [105, 106].

Ischemia-associated inflammation plays a major role in the pathogenesis of neurodegeneration associated with stroke. Activated macrophages produce numerous cytokines which exacerbate the ischemic tissue damage [107]. Consequently, non-invasive imaging of inflammation associated with subacute ischemic stroke lesions could be of predictive value and helpful for the development of cytoprotective drugs.

When injected in Fisher rats 5.5 h after permanent occlusion of the middle cerebral artery, the USPIO ferumoxtran-10 was shown to allow MR visualization of macrophage infiltration associated with focal ischemic lesions [108].

However, this technique did not allow determination of the specific contribution of microglia and blood-borne macrophages to USPIO accumulation. These results were confirmed by a subsequent study in rats where cerebral infarction was induced by photothrombosis of cortical microvessels. In this study, ferumoxtran-10 was injected 5 days after the induction of the cerebral ischemic lesions. Magnetic resonance imaging performed 24 h later displayed a rim-like signal loss around the lesion, which was in full spatial agreement with the histological data [109].

In a clinical phase II study, this USPIO was administered at the end of the first week after symptom onset in a series of 10 consecutive patients with ischemic stroke [110]. Two follow-up MR scans were performed 24–36 and 48–72 h after infusion. Vessel-associated changes were noticed (as signal loss on T2/T2\*-weighted images) and decreased from the first to second scan. This effect was most likely related to the blood-pool effect of the USPIO. In addition to this effect, a parenchymal enhancement was noticed, mostly on T1-weighted images. This effect increased over time and matched with the expected distribution of macrophages. Larger clinical studies are clearly needed to demonstrate the clinical benefit associated with the use of USPIOs as a MRI surrogate markers for brain inflammation.

##### 2.4.6.2 Cerebral Tumor Characterization

As mentioned above, according to their physicochemical properties, USPIOs can have a long blood half-life and therefore be found into the vascular compartment before being progressively endocytosed by tissue macrophages. Therefore, the nanoparticles can be used both for imaging tumor-associated microvessels during the early vascular equilibrium phase and, later, as a macrophage imaging agent for the characterization of the tumor-associated inflammatory lesion.

Preliminary clinical data [11, 111] have shown that there are distinct contrast enhancement mechanisms between early  $Gd^{3+}$  nonspecific contrast agent-based imaging, early USPIO injection, and late (24 h postinfusion) USPIO imaging. This could be of value for brain tumor characterization. USPIO nanoparticles do not cross the ruptured blood–brain barrier at early postinjection stages. This may prove helpful for the assessment of tumoral microvascular heterogeneity. Interestingly, in this preliminary study, the late USPIO-induced tumoral enhancement was found to be higher in high-grade than in low-grade glioblastomas [111].

In a preliminary study comparing the SPIO ferumoxides to the USPIO ferumoxtran-10 in 20 patients with primary and metastatic intracranial tumors, it was found that ferumoxtran-10, in contrast to ferumoxides, can be used as an intravenous contrast agent for MRI of intracranial tumors. Tumor enhancement was found to be comparable to but more variable than that observed with a nonspecific  $Gd^{3+}$  chelate. Histological examination showed similar distribution of the USPIO to be similar to that seen on MR images, i.e. primarily at the tumor margin, with less central localization. Most of the staining within the tumor was found in parenchymal cells with fine fibrillar processes, thus suggesting an astrocytic or microglial derivation [112].

#### 2.4.6.3 Multiple Sclerosis

Multiple sclerosis, an idiopathic inflammatory disease of the central nervous system, is characterized pathologically by demyelination and subsequent axonal degeneration. It is currently accepted that MRI with  $Gd^{3+}$  nonspecific contrast agent, especially during or following a first attack, can be helpful in providing evidence of lesions in other parts of the brain and spinal cord [113]. Edema formation is detected by T2-weighted MRI, and a second MR scan could be useful at least three months after the initial attack to identify new lesions and provide evidence of dissemination over time [113]. Furthermore, magnetization transfer imaging or T1-weighted imaging can also be used for investigation of the demyelination process.

However, these parameters can only provide information on the consequences of the inflammatory process, but not on inflammation itself.

Some USPIOs (ferumoxtran-10, MION-46L) have been shown to be useful for *in vivo* macrophage activity imaging on experimental autoimmune encephalomyelitis (EAE) – a commonly used animal model that mimics human multiple sclerosis in several aspects [114, 115]. Post-USPIO sensitivity was found to be better than either pre-USPIO or post-nonspecific  $Gd^{3+}$  chelate-enhanced images [114].

A phase II pilot study investigated inflammatory lesions in 10 patients with definite relapsing-remitting multiple sclerosis who were included during one relapse episode. MRI with T1-weighted,  $Gd^{3+}$ -enhanced, T2- and T2\*-weighted images was performed before and 24–48 h post-ferumoxtran-10 infusion. Nine out of the 10 patients studied showed multiple sclerosis lesion enhancement with USPIO. Some lesions enhanced up to 3 days after USPIO infusion. Seven patients showed multiple sclerosis lesion enhancement with the  $Gd^{3+}$  chelate.

Several patterns of enhancement were described when comparing USPIO- and  $Gd^{3+}$  chelate-induced enhancement: lesions enhancing with both contrast agents

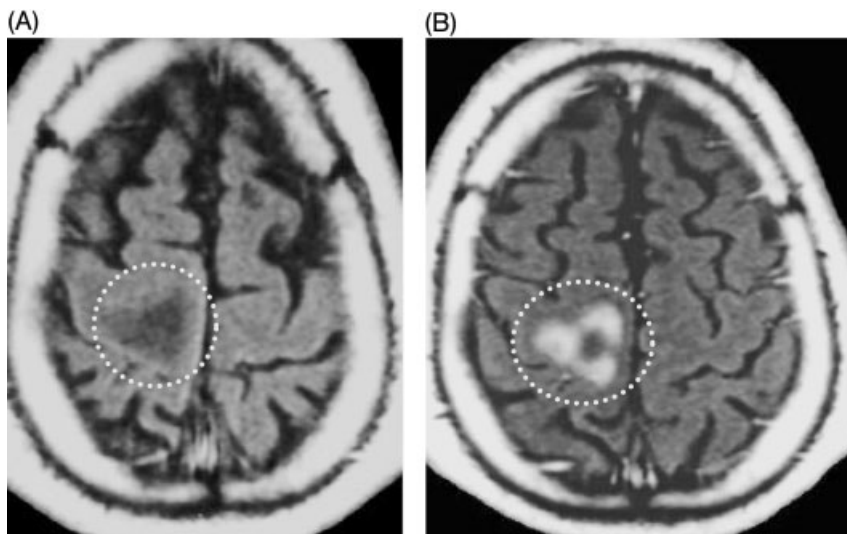


**Figure 2.7.** Multiple sclerosis: phase II clinical trial – ferumoxtran-10: (A) T1-weighted MRI images before injection and (B) T1-weighted MRI images 24 h postinjection of ferumoxtran-10. (courtesy Professor Vincent Dousset, Pellegrin Hospital, Bordeaux, France)

( $n = 31$  lesions), with  $Gd^{3+}$  chelate only ( $n = 24$ ) or with USPIO only ( $n = 2$ ). Interestingly, the enhancement with USPIO was not superimposed on that related to the  $Gd^{3+}$  chelate [11, 116]. One example of USPIO-enhanced plaque is shown on Fig. 2.7.

#### 2.4.6.4 Arthritis

Arthritis is characterized by infiltration of  $CD4^+$  T cells, B cells and macrophages that sometimes organize into discrete lymphoid aggregates with germinal centers [117]. In a rabbit model of unilateral arthritis, MRI at 1.5 T was performed before and 24 h after intravenous injection of the USPIO ferumoxytol. Significant T1 and more predominantly T2\* and T2 effects were evidenced in the synovium of all arthritic knees. Conversely, no significant changes in MR signal characteristics were found in the nonarthritic control knees. Histologic examination confirmed iron uptake in the macrophages within the hyperplastic synovium of the arthritic knees [118]. USPIO nanoparticles have also been found in macrophages located in synovial inflammatory infiltrates in a rat model of osteoarthritis (unpublished data) (Fig. 2.8).

#### 2.4.6.5 Infection

Macrophages are activated during infection and migrate to the site of microbiotic invasion, thus providing a theoretical rationale for testing USPIO in such an indi-

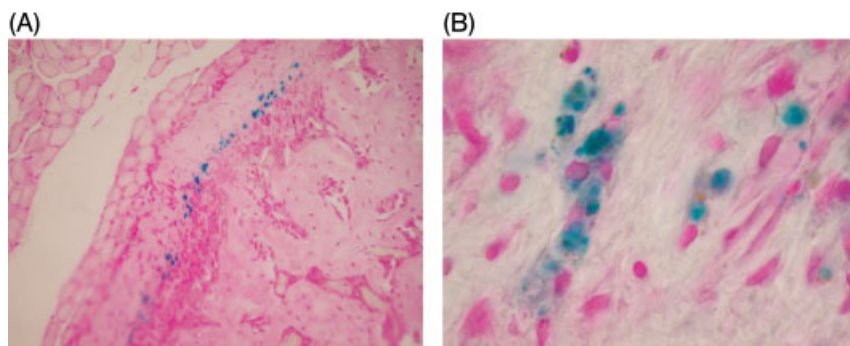


**Figure 2.8.** Representative photomicrographs of Perl's staining of iron oxide in macrophagic cells located in rat inflammatory synovium: (A) low- and (B) high-power magnification view (unpublished data).

cation. An experimental model of infection was developed in rats (unilateral deep calf muscle abscess following intramuscular injection of a *Staphylococcus aureus* suspension). Animals were imaged before and 3, 24, 48 and 72 h after intravenous injection of the USPIO ferumoxtran-10. Visualization was more sensitive with a T2\*-weighted gradient echo sequence. The T2\* effect was most prominent 3 h after ferumoxtran injection because of the high amount of intravascular USPIO at this time-point. A significant decrease in T2\* relative signal intensity was found at 24 h, reflecting the intracellular iron accumulation within macrophages. Only a slight decrease in T2\* signal intensity was found at 48 and 72 h. Local signal intensity changes were correlated with macrophagic uptake of the USPIO [119].

In fact, signal intensity characteristics of abscesses on T1- and T2\*-weighted sequences obtained 24 h following USPIO injection strongly depend upon the administered dose. At low dose ( $50 \mu\text{mol Fe kg}^{-1}$ ), T1 effects were stronger than T2\* effects [120].

#### 2.4.6.6 Kidney Imaging

Intravenous injection of puromycin amino-nucleoside (PAN) in the rat is a good model of nephrotic syndrome secondary to glomerular epithelial cell lesions associated with glomerular and tubulointerstitial infiltration by macrophages. In nephrotic rats, the USPIO ferumoxtran-10 injected intravenously ( $90 \mu\text{mol kg}^{-1}$ ) induced a significant decrease in signal intensity in all compartments of the kidney in the PAN group, whereas the signal from the control group did not vary 24 h postinjection. This effect was correlated with the presence of macrophages with iron oxide nanoparticles at histology [121]. Interestingly, the same USPIO was also found to decrease signal intensity in the cortex in a model of nephrotoxic nephropathy (by injection of sheep anti-rat glomerular basement membrane serum). In this model, equivalent to Goodpasture's syndrome in humans, inflammatory lesions were exclusively located at the level of glomeruli. Conversely, in a rat

model of obstructive nephropathy, which is known to induce diffuse interstitial lesions with macrophage infiltration in all kidney compartments, the USPIO induced a decrease in signal intensity in all compartments [122].

Renal allograft rejection is associated with a massive inflammatory infiltration [123]. In a rat renal allograft model, USPIO, when injected on the fourth day following transplantation, induced a decrease in MR signal intensity at 24 h in some rejecting allografts, whereas isografts and allografts with immunosuppressant treatment had no signal reduction [124]. Promising results were obtained in a preliminary clinical study performed in seven patients with suspected proliferative glomerulonephritis and five with suspected renal graft rejection imaged 72 h following injection of ferumoxtran-10. USPIO-enhanced MRI may allow acute tubular necrosis to be distinguished from other acute nephropathies in native and transplanted kidneys and may also allow active proliferative nephropathies to be differentiated from chronic ones [125]. Of course, such preliminary clinical data, obtained in a small number of patients, need to be confirmed by other studies. Dextran-coated USPIOs serving as blood pool agent were also used to evaluate renal perfusion in dynamic MRI in normal and transplanted rat kidneys.

A good agreement between renal graft perfusion and histopathological changes associated with graft rejection suggests that USPIO-enhanced dynamic MRI may be used to evaluate acute allograft rejection [126].

Iodinated contrast agents can be nephrotoxic in at-risk patients by inducing medullary hypoxia [127]. Intravenous injection of USPIO has been used in rat models of contrast nephropathy to assess renal lesions induced by the iodinated contrast agent [128] as well as their reversibility [129].

#### 2.4.6.7 Acute Cardiac Transplant Rejection

In addition to kidney graft evaluation, USPIO may be used to noninvasively detect inflammatory changes associated with cardiac graft rejection as elegantly shown in two studies involving intravenous administration of either dextran-coated USPIO (27 nm in diameter) [130] or feruglose (NC100150) [131] in rats with heterotopic heart transplantation. Feruglose was used for its blood pool properties in dynamic T1 MRI whereas the dextran-coated USPIO was used for its ability to be captured by macrophages. However, it is worth mentioning that macrophagic infiltration may be associated with other pathophysiological situations such as reperfusion injury or myocardial infection.

#### 2.4.6.8 *In Vivo* Monitoring of Cell Therapy

Recent progress in the field of stem and progenitor cells suggests that their use to correct or replace defective cell populations may soon become a clinical reality. Clinical applications are numerous and promising, both for the central nervous system-related diseases (spinal cord injury, Parkinson's disease, myelin disorders, Huntington's disease, etc) and regeneration of the myocardium. Renal and hepatic pathologies may also benefit from the progress of cell therapies. It is therefore crucial to track the location and *in vivo* distribution of these cells in a noninvasive manner [132].

For this purpose, stem cells must first be magnetically labeled *in vitro* before being administered to a living organism [132].

Several approaches have been described to optimize the internalization process [132], including linking the nanoparticles to the highly cationic HIV *tat* peptide [35] or the use of an anti-transferrin receptor monoclonal antibody covalently linked to nanoparticles (MION-46L) [133].

In fact, it is more convenient to use commercially available and registered nanoparticles. Several studies have shown that ferumoxides or MION-46L can be internalized after mixing with a transfection agent (such as dendrimers, high-molecular-weight poly-L-lysine, lipofectamine, protamine sulfate, etc.) [132, 134] or without such agents [135]. Actually, unmodified SPIOs or USPIOs have been successfully used, at high concentrations, to label cells (fluid phase mediated endocytosis) in the absence of transfection agents [12, 135]. However, it is worth mentioning that SPIO particles, with a diameter of about 100–150 nm were found to be more efficient for cell targeting than were USPIO nanoparticles, which have average hydrodynamic diameters of 20–40 nm [135]. This is probably related to the fact that phagocytic and endocytic uptake increases with increasing particle diameter (at equivalent coating thickness).

Uptake of the nanoparticles increases with time, but cell viability decreases with increasing incubation time. An incubation time of 2–4 h has been considered an acceptable compromise in the case of hematopoietic progenitor cells [135].

There is ample preclinical literature showing that MRI tracking of stem cells is feasible. Some recent examples are shown in Tab. 2.5 [136–139].

Due to the high anatomical spatial resolution of MRI, its potential for quantification, the low cytotoxicity of superparamagnetic nanoparticles and the promising studies currently available, MR monitoring of cell therapy seems to be a technique with a good future.

#### 2.4.6.9 T-staging of Uterine Neoplasms

USPIO ferumoxtran-10, evaluated for MR lymph node staging in uterine carcinoma, was serendipitously found to induce a significant decrease in signal intensity of both myometrium and cervical stroma, thus allowing improved delineation of uterine neoplasms.

A clinical study involving 17 patients subsequently confirmed that the contrast-to-noise ratio between tumor and myometrium and between tumor and cervical stroma was significantly higher on USPIO-enhanced images compared with unenhanced images [140].

#### 2.4.6.10 MRI-detectable Embolotherapy

Embolization is frequently used for the treatment of cancer, but it is so far difficult to locate the injected embolic material and to monitor changes in its structure over time.

SPIOs embedded in polyglucosamine (chitosan) (100–150  $\mu\text{m}$  in diameter) were detected by MRI after selective embolization of a renal artery in rabbits [141]. How-



Tab. 2.5. Animal models of cell tracking: some examples.

Animal model	Stem cells	Nanoparticle used	Result	Reference
Experimental myocardial infarction in pigs	swine mesenchymal stem cells	ferumoxides + poly-L-lysine; intramyocardial injection	successful imaging at 1.5 T and correlation with histology	136
<i>mdx</i> mice (murine model of Duchenne's muscular dystrophy)	multipotent, muscle-derived stem cells	ferumoxides + poly-L-lysine; intramuscular injection	Successful sequential imaging and correlation with histology	137
Healthy rats	mesenchymal stem cells from the bone marrow of a syngenic rat strain	ferumoxides + dendrimer transfection agent (Superfect®); intra-arterial injection into the kidney	Signal intensity loss in the cortex; detection for up to 7 days	138
CCl <sub>4</sub> -induced hepatocyte necrosis and inflammation in rats	mesenchymal stem cells from the bone marrow of a syngenic rat strain	ferumoxides + dendrimer transfection agent (Superfect®); intraportal injection	Irregular signal intensity loss, reflecting the lobular structure of the liver; detection for up to 12 days	138
C57Bl/6 mice injected with ovalbumin-transfected B16 melanoma cells (B16-OVA) and B16 F0 melanoma cells	CD8 <sup>+</sup> cytotoxic T lymphocytes	CLIO-HD (highly-derivatized crosslinked iron oxide) incubated with CD8 <sup>+</sup> T cells and injected intraperitoneally	<i>in vivo</i> detection of CLIO-HD-labeled CD8 <sup>+</sup> T cells with a threshold of around 3 cells voxel <sup>-1</sup>	139
Myelin-deficient <i>md</i> rats	rat oligodendrocyte progenitor cell line CG-4	MION-46-L targeted to the transferrin receptor Tf <sub>r</sub> and grafted into the spinal cord of neonate <i>md</i> rats	Successful <i>ex vivo</i> three-dimensional MRI of the migratory capacity of transplanted cells; correlation with histology	133

ever, although they are derived from nanoparticles, such objects can no longer be considered as being nanoparticles.

## 2.5

### Conclusion

The use of superparamagnetic nanoparticulate agents in MRI has been a major development in the range of tools available to clinicians. The efficacy of these agents has led to their being proposed in gastrointestinal tract and hepatic lesion imaging. The prospects for increased use in lymph node and functional imaging look very promising. These nanoparticles are also potential disease-specific agents. This potential depends on improved knowledge of the fundamental mechanisms of the interaction of the superparamagnetic agents with the MR signal and also on the control of the pharmacokinetic behavior of these molecules. In terms of effect on the MR signal, the use of the dose-dependent effect of the nanoparticles on the T1 relaxation time will undoubtedly be an increasingly widely studied research topic in the near future. The importance of the  $r_2/r_1$  ratio as a function of the magnetic field is also emphasized in studies establishing the most appropriate sequences for the molecules under clinical development. In terms of pharmacokinetics, research into preventing the iron oxide particles from being taken up by the liver and spleen reticuloendothelial system by appropriate selection of particle charge, size and coating is of major interest.

The chemical coating of these nanoparticles may also allow them to be linked to molecules (“pharmacophores”) capable of specifically targeting a specific area such as an organ, a disease or a particular biological system such as macrophages or stem cells. This opens major research avenues with important potential clinical consequences.

Nanoparticulate molecules can also behave as blood pool contrast agents for MR angiography at both first-pass and equilibrium. Here, again, clinical applications are numerous. Furthermore, the ability for such nanoparticles to target inflammatory lesions offers major and very exciting prospects for the characterization of numerous inflammatory and degenerative diseases.

Last, but not least, nanoparticles used for medical imaging purposes are also at the interface with targeted therapies and can be expected to have the potential to contribute to the follow-up of such treatments.

In addition to the intravenous route, local administration may also be envisaged (aerosol, interstitial, subcutaneous injection, etc). This opens up an important research field into more specific agents adapted to clinicians’ needs. Fundamental research is needed to better understand the toxicity issues potentially associated with nanoparticulate molecules in general and particularly their interaction with the immune system.

A bright future can be anticipated for nanoparticulate contrast agents provided their development is based on a rational design through a thorough understanding of their physicochemistry and biological environment.

## References

- 1 KLAVENESS J. Particulate agents. In *Enhanced MRI*, RUNGE VM (Ed.). Mosby, St Louis, MO, 1989, pp. 117–128.
- 2 ROCH A, MULLER RN, GILLIS P. Theory of proton relaxation induced by superparamagnetic particles. *J. Chem. Phys.* 1999, 110, 5403–5411.
- 3 ROCH A, MULLER RN. Longitudinal relaxation of water protons in colloidal suspensions of superparamagnetic crystals. In *11th Annual Scientific Meeting SMRM, Works in Progress*, Berlin, 1992, p. 1447.
- 4 CHAMBON C, CLÉMENT O, LE BLANCHE A, SCHOUMAN-CLAEYS E, FRIJA G. Superparamagnetic iron oxides as positive MR contrast agents: *in vitro* and *in vivo* evidence. *Magn. Reson. Imaging* 1993, 11, 509–519.
- 5 CANET E, REVEL D, FORRAT R, BALDY-PORCHER C, DE LORGERIL M, SEBBAG L, VALLÉE JP, DIDIER D, AMIEL M. Superparamagnetic iron oxide particles and positive enhancement for myocardial perfusion studies assessed by subsecond T1-weighted MRI. *Magn. Reson. Imaging* 1993, 11, 1139–1145.
- 6 FRANCK H, WEISSELEDER R, BRADY TJ. Enhancement of MR angiography with iron oxide: preliminary studies in whole-blood phantom and in animals. *Am. J. Roentgenol.* 1994, 162, 209–213.
- 7 BOMATÍ-MIGUEL O, MORALES MP, TARTAJ P, RUIZ-CABELLO J, BONVILLE P, SANTOS M, ZHAO X, VEINTEMILLAS-VERDAGUER S. Fe-based nanoparticulate metallic alloys as contrast agents for magnetic resonance imaging. *Biomaterials* 2005, 26, 5695–5703.
- 8 JUNG CW, JACOBS P. Physical and chemical properties of superparamagnetic iron oxide MR contrast agents: ferumoxides, ferumoxtran, ferumoxsil. *Magn. Reson. Imaging* 1995, 13, 661–674.
- 9 BENDERBOUS S, COROT C, JACOBS P, BONNEMAIN B. Superparamagnetic agents: physicochemical characteristics and preclinical imaging evaluation. *Acad Radiol.* 1996, 3 (Suppl. 2), S292–S294.
- 10 CHENG FY, SU CH, YANG YS, YEH CS, TSAI CY, WU CY, WU MT, SHIEH DB. Characterization of aqueous dispersions of Fe<sub>3</sub>O<sub>4</sub> nanoparticles and their biomedical applications. *Biomaterials* 2005, 26, 729–738.
- 11 COROT C, PETRY KG, TRIVEDI R, SALEH A, JONKMANN C, LE BAS JF, BLEZER E, RAUSCH M, BROCHET B, FOSTER-GAREAU P, BALÉRIAUX D, GAILLARD S, DOUSSET V. Macrophage imaging in central nervous system and in carotid atherosclerotic plaque imaging using ultrasmall superparamagnetic iron oxide in magnetic resonance imaging. *Invest. Radiol.* 2004, 39, 619–625.
- 12 FLEIGE G, SEEBERGER F, LAUX D, KRESSE M, TAUPITZ M, PILGRIMM H, ZIMMER C. *In vitro* characterization of two different ultrasmall iron oxide particles for magnetic resonance cell tracking. *Invest. Radiol.* 2002, 37, 482–488.
- 13 TAUPITZ M, WAGNER S, SCHNORR J, KRAVEC I, PILGRIMM H, BERGMANN-FRITSCH H, HAMM B. Phase I clinical evaluation of citrate-coated monocrystalline very small superparamagnetic iron oxide particles as a new contrast medium for magnetic resonance imaging. *Invest. Radiol.* 2004, 39, 394–405.
- 14 BJORNERUD A, JOHANSSON LO, AHLSTROM HK. Pre-clinical results with Clariscan (NC100150 Injection); experience from different disease models. *MAGMA* 2001, 12, 99–103.
- 15 PETRI-FINK A, CHASTELLAIN M, JUILLERAT-JEANNERET L, FERRARI A, HOFMANN H. Development of functionalized superparamagnetic iron oxide nanoparticles for interaction with human cancer cells. *Biomaterials* 2005, 26, 2685–2694.
- 16 BRILLET PY, GAZEAU F, LUCIANI A, BESSOUD B, CUÉNOD CA, SIAUVE N, PONS JN, POUAPON J, CLÉMENT O. Evaluation of tumoral enhancement by superparamagnetic iron oxide particles: comparative studies with ferumoxtran and anionic iron oxide

- nanoparticles. *Eur. Radiol.* **2005**, *15*, 1369–1377.
- 17 RAYNAL I, PRIGENT P, PEYRAMAURE S, NAJID A, REBUZZI C, COROT C. Macrophage endocytosis of superparamagnetic iron oxide nanoparticles. Mechanisms and comparison of ferumoxides and ferumoxtran-10. *Invest. Radiol.* **2004**, *39*, 56–63.
  - 18 METZ S, BONATERRA G, RUDELIUS M, SETTLES M, RUMMENY EJ, DALDRUP-LINK H. Capacity of human monocytes to phagocytose approved iron oxide MR contrast agents *in vitro*. *Eur. Radiol.* **2004**, *14*, 1851–1858.
  - 19 SUN R, DITTRICH J, LE-HUU M, MUELLER MM, BEDKE J, KARTENBECK J, LEHMANN WD, KRUEGER R, BOCK M, HUSS R, SELIGER C, GRÖNE HJ, MISSELWITZ B, SEMMLER W, KIESSLING F. Physical and biological characterization of superparamagnetic iron-oxide- and ultrasmall superparamagnetic iron oxide-labeled cells. A comparison. *Invest. Radiol.* **2005**, *40*, 504–513.
  - 20 ROGERS WJ, BASU P. Factors regulating macrophage endocytosis of nanoparticles: implications for targeted magnetic resonance plaque imaging. *Atherosclerosis* **2005**, *178*, 67–73
  - 21 STROH A, ZIMMER C, GUTZEIT C, JAKSTADT M, MARSCHINKE F, JUNG T, PILGRIMM H, GRUNE T. Iron oxide particles for molecular magnetic resonance imaging cause transient oxidative stress in rat macrophages. *Free Radic. Biol. Med.* **2004**, *36*, 976–984.
  - 22 SCHULZE E, FERRUCCI JT JR, POSS K, LAPOINTE L, BOGDANOVA A, WEISSELEDER R. Cellular uptake and trafficking of a prototypical magnetic iron oxide label *in vitro*. *Invest. Radiol.* **1995**, *30*, 604–610.
  - 23 LEENDERS W. Ferumoxtran-10. *Drugs* **2003**, *6*, 987–993.
  - 24 SCHNORR J, TAUPITZ M, WAGNER S, PILGRIMM H, HANSEL J, HAMM B. Age-related blood half-life of particulate contrast material: experimental results with a USPIO in rats. *J. Magn. Reson. Imaging.* **2000**, *12*, 740–744.
  - 25 WEISSELEDER R, STARK DD, ENGELSTAD BL, BACON BR, COMPTON CC, WHITE DL, JACOBS P, LEWIS J. Superparamagnetic iron oxide: pharmacokinetics and toxicity. *Am. J. Roentgenol.* **1989**, *152*, 167–173.
  - 26 TAYLOR AM, PANTING JR, KEEGAN J, GATEHOUSE PD, AMIN D, JHOOTI P, YANG GZ, MCGILL S, BURMAN ED, FRANCIS JM, FIRMIN DN, PENNELL DJ. Safety and preliminary findings with the intravascular contrast agent NC100150 injection for MR coronary angiography. *J. Magn. Reson. Imaging* **1999**, *9*, 220–227.
  - 27 BRILEY-SAEBO K, HUSTVEDT SO, HALDORSEN A, BJORNERUD A. Long-term imaging effects in rat liver after a single injection of an iron oxide nanoparticles based MR contrast agent. *J. Magn. Reson. Imaging* **2004**, *20*, 622–631.
  - 28 WEISSELEDER R, ELIZONDO G, WITTENBERG J, RABITO CA, BENGELE HH, JOSEPHSON L. Ultrasmall superparamagnetic iron oxide: characterization of a new class of contrast agents for MR imaging. *Radiology* **1990**, *175*, 489–493.
  - 29 BELLIN MF, BEIGELMAN C, PRECETTI-MOREL S. Iron oxide-enhanced MR lymphography: initial experience. *Eur. J. Radiol.* **2000**, *34*, 257–264.
  - 30 BENGELE HH, PALMACCI S, ROGERS J, JUNG CW, CRENSHAW J, JOSEPHSON L. Biodistribution of an ultrasmall superparamagnetic iron oxide colloid, BMS 180549, by different routes of administration. *Magn. Reson. Imaging* **1994**, *12*, 433–442.
  - 31 MCCAULEY TR, RIFKIN MD, LEDET CA. Pelvic lymph node visualization with MR imaging using local administration of ultra-small superparamagnetic iron oxide contrast. *J. Magn. Reson. Imaging* **2002**, *15*, 492–497.
  - 32 POMPER MG. Molecular imaging: a review. *Acad. Radiol.* **2001**, *8*, 1141–1153.
  - 33 MORAWSKI AM, LANZA GA, WICKLINE SA. Targeted contrast agents for magnetic resonance imaging and ultrasound. *Curr. Opin. Biotechnol.* **2005**, *16*, 89–92.

- 34 HÖGEMANN D, JOSEPHSON L, WEISSLEDER R, BASILION JP. Improvement of MRI probes to allow efficient detection of gene expression. *Bioconjug. Chem.* **2000**, *11*, 941–946.
- 35 JOSEPHSON L, TUNG CH, MOORE A, WEISSLEDER R. High efficiency intracellular magnetic labelling with novel superparamagnetic tat-peptide conjugates. *Bioconjug. Chem.* **1999**, *10*, 186–191.
- 36 BURTEA C, LAURENT S, ROCH A, VANDER ELST L, MULLER RN. C-MALISA (cellular magnetic-linked immunosorbent assay), a new application of cellular ELISA for MRI. *J. Inorg. Biochem.* **2005**, *99*, 1135–1144.
- 37 HALBREICH A, ROGER J, PONS JN, DE FATIMA DA SILVA M, HASMONAY E, ROUDIER M, BOYNARD M, SESTIER C, AMRI A, GELDWERTH D, FERTIL B, BACRI JC, SABOLOVIC D. Magnetic maghemite nanoparticles: their preparation, properties, and applications in cell sorting and characterization of cellular membrane *in vitro*. In *Scientific and Clinical Applications of Magnetic Carriers (Proceedings of the International Conference on Scientific and Clinical Applications of Magnetic Carriers)*, HAEFELI U (Ed.). Plenum Press, New York, **1997**, pp. 399–417.
- 38 WEISSLEDER R, LEE AS, FISCHMAN AJ, REIMER P, SHEN T, WILKINSON R, CALLAHAN RJ, BRADY TJ. Polyclonal human immunoglobulin G labeled with polymeric iron oxide: antibody MR imaging. *Radiology* **1991**, *181*, 245–249.
- 39 REIMER P, KWONG KK, WEISSKOFF R, COHEN MS, BRADY TJ, WEISSLEDER R. Dynamic signal intensity changes in liver with superparamagnetic MR contrast agent. *J. Magn. Reson. Imaging* **1992**, *2*, 177–181.
- 40 KRESSE M, WAGNER S, PFEFFERER D, LAWACZECK R, ELSTE V, SEMMLER W. Targeting of ultrasmall superparamagnetic iron oxide (USPIO) particles to tumor cells *in vivo* by using transferring receptor pathways. *Magn. Reson. Med.* **1998**, *40*, 236–242.
- 41 JOHANSSON LO, BJÖRNERUD A, AHLSTRÖM HK, LADD DL, FUJII DK. A targeted contrast agent for magnetic resonance imaging of thrombus: implications of spatial resolution. *J. Magn. Reson. Imaging* **2001**, *13*, 615–618.
- 42 VAN TILBORG GAF, STRIJKERS GJ, REUTELINSPERGER CPM, NICOLAY K. Annexin V-functionalized USPIO as a contrast agent for apoptotic Jurkat cells. In *Proceedings of the ESMRMB Meeting*, Copenhagen, **2004**, p. 223.
- 43 BURTEA C, CHAABANE L, LAURENT S, CANET-SOULAS E, VANDER ELST L, BRIGUET A, MULLER RN. Preclinical evaluation of a new  $\alpha_v\beta_3$ -targeted nonpeptidic RGD mimetic grafted to USPIO. Preliminary investigations on the molecular imaging of vulnerable atherosclerotic plaques. In *Proceedings of the ESMRMB Meeting*, Copenhagen, **2004**, p. 373.
- 44 BONNEMAIN B. Superparamagnetic agents in magnetic resonance imaging: physicochemical characteristics and clinical applications. A review. *J. Drug Target.* **1998**, *6*, 167–174.
- 45 HAHN PF, STARK DD, LEWIS J, SAINI S, ELIZONDO G, WEISSLEDER R, FRETZ CJ, FERRUCCI JT. First clinical trial of a new superparamagnetic iron oxide for use as an oral gastrointestinal contrast agent in MR imaging. *Radiology* **1990**, *175*, 695–700.
- 46 HALDEMANN-HEUSLER RC, WIGHT E, MARINCEK B. Oral superparamagnetic contrast agent (ferumoxsil): tolerance and efficacy in MR imaging of gynecologic diseases. *J. Magn. Reson. Imaging* **1995**, *4*, 385–391.
- 47 JOHNSON WK, STOUPIS C, TORRES GM, ROSENBERG EB, ROS PR. Superparamagnetic iron oxide (SPIO) as an oral contrast agent in gastrointestinal (GI) magnetic resonance imaging (MRI): comparison with state-of-the-art computed tomography (CT). *Magn. Reson. Imaging* **1996**, *14*, 43–49.
- 48 RUBIN DL, MULLER HH, YOUNG SW, HUNKE WA, GORMAN WG, LEE KC. Influence of viscosity of WIN 39996 as

- a contrast agent for gastrointestinal resonance magnetic imaging. *Invest. Radiol.* **1995**, *30*, 226–231.
- 49 MACVICAR D, JACOBSEN TF, GUY R, HUSBAND JE. Phase III trial of oral magnetic particles in MRI of abdomen and pelvis. *Clin. Radiol.* **1993**, *47*, 183–188.
  - 50 BACH-GANSMO T, DUPAS B, GAYET-DELACROIX M, LAMBRECHTS M. Abdominal MRI using a negative contrast agent. *Br. J. Radiol.* **1993**, *66*, 420–425.
  - 51 VLAHOS L, GOULIAMOS A, ATHANASOPOULOU G, KOTOULAS G, CLAUS W, HATZIOANNOU A, KALOVIDOURIS A, PAPAVALILOU C. A comparative study between Gd-DTPA and oral magnetic particles (OMP) as gastro-intestinal (GI) contrast agents for MRI of the abdomen. *Magn. Reson. Imaging* **1994**, *12*, 719–726.
  - 52 VLAHOS L, GOULIAMOS A, KALOVIDOURIS A, ATHANASOPOULOU A, KOTOULAS G, LYGIDAKIS N, LIAOU A, MATSAIDONIS D, PAPAVALILOU C. Oral magnetic particles as contrast agent for MR imaging of the abdomen. A phase III clinical trial. *Hepatogastroenterology* **1994**, *41*, 82–85.
  - 53 JACOBSEN TF, LANIADO M, VAN BEERS BE, DUPAS B, BOUDGHENE FP, RUMMENY E, FALK TH, RINCK PA, MACVICAR D, LUNDBY B. Oral magnetic particles (ferri-stene) as a contrast medium in abdominal magnetic resonance imaging. *Acad Radiol.* **1996**, *3*, 571–580.
  - 54 HERRMANN K, ZECH CJ, MICHAELY HJ, SEIDERER J, OCHSENKUEHN T, REISER MF, SCHOENBERG SO. Comprehensive magnetic resonance imaging of the small and large bowel using intraluminal dual contrast technique with iron oxide solution and water in magnetic resonance enteroclysis. *Invest. Radiol.* **2005**, *40*, 621–629.
  - 55 MACCIONI F, VISCIDO A, BROGLIA L, MARROLLO M, MASCIANGELO R, CAPRILLI R, ROSSI P. Evaluation of Crohn disease activity with magnetic resonance imaging. *Abdom. Imaging* **2000**, *25*, 219–228.
  - 56 LAGHI A, PAOLANTONIO P, IAFRATE F, ALTOMARI F, MIGLIO C, PASSARIELLO R. Oral contrast agents for magnetic resonance imaging of the bowel. *Top. Magn. Reson. Imaging* **2002**, *13*, 389–396.
  - 57 WANG YXJ, HUSSAIN SM, KRESTIN GP. Superparamagnetic iron oxide contrast agents: physicochemical characteristics and applications in MR imaging. *Eur. Radiol.* **2001**, *11*, 2319–2331.
  - 58 WAKE K, DECKER K, KIRN A, KNOOK DL, MCCUSKEY RS, BOUWENS L, WISSE E. Cell biology and kinetics of K upffer cells in the liver. *Int. Rev. Cytol.* **1989**, *118*, 173–229.
  - 59 SAINI S, STARK DD, HAHN PF, WITTENBERG J, BRADY TJ, FERRUCCI JT Jr. Ferrite particles: a superparamagnetic MR contrast agent for the reticuloendothelial system. *Radiology* **1987**, *162*, 211–216.
  - 60 BELLIN MF, ZAIM S, AUBERTON E, SARFATI G, DURON JJ, KHAYAT D, GRELLET J. Liver metastases: safety and efficacy of detection with superparamagnetic iron oxide in MR imaging. *Radiology* **1994**, *193*, 657–663.
  - 61 ROS PR, FREENY PC, HARMS SE, SELTZER SE, DAVIS PL, CHAN TW, STILLMAN AE, MUROFF LR, RUNGE VM, NISSENBAUM MA, JACOBS P. Hepatic MR imaging with ferumoxides: a multicenter clinical trial of the safety and efficacy in the detection of focal hepatic lesions. *Radiology* **1995**, *195*, 481–488.
  - 62 S ENETERRE E, TAUREL P, BOUVIER Y, PRADEL J, VAN BEERS B, DAURES JP, PRINGOT J, MATHIEU D, BRUEL JM. Detection of hepatic metastases: ferumoxides-enhanced MR imaging versus unenhanced MR imaging and CT during arterial portography. *Radiology* **1996**, *200*, 785–792.
  - 63 ABE Y, YAMASHITA Y, NAMIMOTO T, TANG Y, TAKAHASHI M. The value of fast and ultrafast T2-weighted MR imaging sequences in hepatic enhancement with ferumoxides: comparison with conventional spin-echo sequences. *Radiat. Med.* **2000**, *18*, 97–105.

- 64 KIM MJ, KIM JH, CHUNG JJ, PARK MS, LIM JS, OH YT. Focal hepatic lesions: detection and characterization with combination gadolinium- and superparamagnetic iron oxide-enhanced MR imaging. *Radiology* 2003, 228, 719–726.
- 65 WEISSELER R, HAHN PF, STARK DD, ELIZONDO G, SAINI S, TODD LE, WITTENBERG J, FERRUCCI J JR. Superparamagnetic iron oxide: enhanced detection of focal splenic tumors with MR imaging. *Radiology* 1988, 169, 399–403.
- 66 STORM BL, ABBITT PL, ALLEN DA, ROS PR. Splenosis: superparamagnetic iron oxide-enhanced MR imaging. *Am. J. Roentgenol.* 1992, 159, 333–335.
- 67 SCHULTZ JF, KUHN JA, MCCARTHY TM. Hepatic imaging with iron oxide magnetic resonance imaging. *Oncology* 2000, 14 (Suppl. 3), 29–36.
- 68 WEISHAUPT D, WILLMANN JK, LUTZ AM, MARINCEK B. Resovist for imaging of hepatocarcinoma in the cirrhotic liver. *Eur. Radiol.* 2004, 14 (Suppl. 1), C5–C6.
- 69 REIMER P, BALZER T. Ferucarbotran (Resovist): a new clinically-approved RES-specific contrast agent for contrast-enhanced MRI of the liver: properties, clinical development, and applications. *Eur. Radiol.* 2003, 16, 1266–1276.
- 70 SUTO Y, KATO T, MATSUO T, KAMBA M, SHIMATANI Y, OHUCHI Y, NAKAMURA K, OHTA Y. Chondroitin sulfate iron colloid as MR contrast agent in differentiation between hepatocellular carcinoma and adenomatous hyperplasia. *Acta Radiol.* 1993, 34, 226–229.
- 71 POULIQUEN D, LUCET I, CHOULY C, PERDRISOT R, LE JEUNE JJ, JALLET P. Liver-directed superparamagnetic iron oxide: quantitation of T2-relaxation effects. *Magn. Res. Imaging* 1993, 11, 219–228.
- 72 WISNER E, AMPARO E, VERA D, BROCK JM, BARLOW TW, GRIFFEY SM, DRAKE C, KATZBERG RW. Arabinogalactan-coated superparamagnetic iron oxide: effect of particle size in liver MRI. *J. Comput. Assist. Tomogr.* 1995, 19, 211–215.
- 73 STOCKERT RJ. The asialoglycoprotein receptor: relationship between structure, function and expression. *Physiol. Rev.* 1995, 75, 591–609.
- 74 VAN BEERS BE, SEMPoux C, MATERNE R, DELOS M, SMITH AM. Biodistribution of ultrasmall iron oxide particles in the rat liver. *J. Magn. Reson. Imaging* 2001, 13, 594–599.
- 75 MERGO PJ, ENGELKEN JD, HELMBERGER T, ROS PR. MRI in focal liver disease: a comparison of small and ultrasmall superparamagnetic iron oxide as hepatic contrast agents. *J. Magn. Reson. Imaging* 1998, 8, 1073–1078.
- 76 KOH DM, BROWN G, TEMPLE L, RAJA A, TOOMEY P, BETT N, NORMAN AR, HUSBAND JE. Rectal cancer: mesorectal lymph nodes at MR imaging with USPIO versus histopathologic findings. Initial observations. *Radiology* 2004, 231, 91–99.
- 77 WEISSELER R, HEAUTOT JF, SCHAFFER BK, NOSSIFF N, PAPISOV MI, BOGDANOV A JR, BRADY TJ. MR lymphography: study of a high-efficient lymphotropic agent. *Radiology* 1994, 191, 225–230.
- 78 ROGERS JM, LEWIS J, JOSEPHSON L. Visualization of superior mesenteric lymph nodes by the combined oral and intravenous administration of the ultrasmall superparamagnetic iron oxide, AMI-227. *Magn. Reson. Imaging* 1994, 12, 1161–1165.
- 79 ANZAI Y, MCLACHLAN S, MORRIS M, SAXTON R, LUFKIN RB. Dextran-coated superparamagnetic iron oxide, an MR contrast agent for assessing lymph nodes in the head and neck. *Am. J. Neuroradiol.* 1994, 15, 87–94.
- 80 BELLIN MF, ROY C, KINKEL K, THOMAS D, ZAIM S, VANEL D, TUCHMANN C, RICHARD F, JACQUIN D, DELCOURT A, CHALLIER E, LEBRET T, CLUZEL P. Lymph node metastases: safety and effectiveness of MR imaging with ultrasmall superparamagnetic iron oxide particles. Initial clinical experience. *Radiology* 1998, 207, 799–808.

- 81 HARISINGHANI MG, BARENTSZ J, HAHN PF, DESERNO WM, TABATABAEI S, HULSBERGEN VAN DE KAA C, DE LA ROSETTE J, WEISSLEDER R. Noninvasive detection of clinically occult lymph-node metastases in prostate cancer. *New Engl. J. Med.* **2003**, *348*, 2491–2499.
- 82 MOGHIMI SM, HUNTER AC, MUTTAY JC. Nanomedicine: current status and future prospects. *FASEB J.* **2005**, *19*, 311–330.
- 83 ZIMMER C, WEISSLEDER R, O'CONNOR D, LAPOINTE L, BRADY TJ, ENOCHS WS. Cerebral iron oxide distribution: *in vivo* mapping with MR imaging. *Radiology* **1995**, *196*, 521–527.
- 84 REITH W, FORSTING M, VOGLER H, HELLAND S, SARTOR K. Early MR detection of experimentally induced cerebral ischemia using magnetic susceptibility contrast agents: comparison between gadopentetate dimeglumine and iron oxide particles. *Am. J. Neuroradiol.* **1995**, *16*, 53–60.
- 85 TRILLAUD H, DEGRÈZE P, COMBE C, DEMINIÈRE C, PALUSSIÈRE J, BENDERBOUS S, GRENIER N. USPIO-enhanced MR Imaging of glycerol-induced acute renal failure in the rabbit. *Magn. Res. Imaging* **1995**, *13*, 233–240.
- 86 MERGO PJ, HELMBERGER T, NICOLAS AI, ROS PR. Ring enhancement in ultrasmall superparamagnetic iron oxide MR imaging: a potential new sign for characterization of liver tissues. *Am. J. Roentgenol.* **1996**, *166*, 379–384.
- 87 BERRY I, BENDERBOUS S, RANJEVA JP, GRACIA-MEAVILLA D, MANELFE C, LE BIHAN D. Contribution of Sinerem used as blood-pool contrast agent: detection of cerebral blood volume changes during apnea in the rabbit. *Magn. Reson. Med.* **1996**, *36*, 415–419.
- 88 VANDUFFEL W, FIZE D, MANDEVILLE JB, NELISSEN K, VAN HECKE P, TOOTELL RB, ORBAN GA. Visual motion processing investigated using contrast agent-enhanced fMRI in awake behaving monkeys. *Neuron* **2001**, *32*, 565–577.
- 89 SCHNORR J, WAGNER S, ABRAMJUK C, WOJNER I, SCHINK T, KROENCKE TJ, SCHELLENBERGER E, HAMM B, PILGRIMM H, TAUPITZ M. Comparison of the iron oxide-based contrast medium VSOP-C184 with gadopentetate dimeglumine for first-pass magnetic resonance angiography of the aorta and renal arteries in pigs. *Invest. Radiol.* **2004**, *39*, 546–553.
- 90 LI W, TUTTON S, VU AT, PIERCHALA L, LI BSY, LEWIS JM, PRASAD PV, EDELMAN RR. First-pass contrast-enhanced magnetic resonance angiography in humans using ferumoxytol, a novel ultrasmall superparamagnetic iron oxide (USPIO)-based blood pool agent. *J. Magn. Reson. Imaging* **2005**, *21*, 46–52.
- 91 TROPÈRES I, GRIMAUULT S, VAETH A, GRILLON E, JULIEN C, PAYEN JF, LAMALLE L, DÉCORPS M. Vessel size imaging. *Mag. Reson. Med.* **2001**, *45*, 397–408.
- 92 TROPÈRES I, LAMALLE L, PÉOC'H M, FARION R, USSON Y, DÉCORPS M, RÉMY C. *In vivo* imaging of tumoral angiogenesis. *Magn. Reson. Med.* **2004**, *51*, 533–541.
- 93 VIGNAUD A, MAÎTRE X, GUILLOT G, DURAND E, DE ROCHEFORT L, ROBERT P, VIVÈS V, SANTUS R, DARRASSE L. Magnetic susceptibility matching at the air-tissue interface in rat lung by using a superparamagnetic intravascular contrast agent: influence on transverse relaxation time of hyperpolarized helium-3. *Magn. Reson. Med.* **2005**, *54*, 28–33.
- 94 ROSS R. Atherosclerosis: an inflammatory disease. *N. Engl. J. Med.* **1999**, *340*, 115–126.
- 95 KEANEY JF JR, VITA JA. The value of inflammation for predicting unstable angina. *N. Engl. J. Med.* **2002**, *347*, 55–57.
- 96 MORENO PR, FALK E, PALACIOS IF, NEWELL JB, FUSTER V, FALON JT. Macrophage infiltration in acute coronary syndromes. Implications for plaque rupture. *Circulation* **1994**, *90*, 775–778.
- 97 SCHMITZ SA, COUPLAND SE, GUST R, WINTHERHALTER S, WAGNER S, KRESSE M, SEMMLER W, WOLF KJ. Superparamagnetic iron-oxide-



- enhanced MRI of atherosclerotic plaques in Watanabe hereditary hyperlipidemic rabbits. *Invest. Radiol.* **2000**, *35*, 460–471.
- 98 RUEHM SG, COROT C, VOGT P, KOLB S, DEBATIN JF. Magnetic resonance imaging of atherosclerotic plaque with ultrasmall superparamagnetic particles of iron oxide in hyperlipidemic rabbits. *Circulation* **2001**, *103*, 415–422.
- 99 LITOVSKY S, MADJID M, ZARRABI A, CASSCELLS SW, WILLERSON JT, NAGHAVI M. Superparamagnetic iron oxide-based method for quantifying recruitment of monocytes to mouse atherosclerotic lesions *in vivo*. Enhancement by tissue necrosis factor- $\alpha$ , interleukin-1- $\beta$ , and interferon- $\gamma$ . *Circulation* **2003**, *107*, 1545–1549.
- 100 YANCY AD, OLZINSKI AR, HU TCC, LENHARD SC, ARAVINDHAN K, GRUVER SM, JACOBS PM, WILLETTE RN, JUCKER BM. Differential uptake of ferumoxtran-10 and ferumoxytol, ultrasmall superparamagnetic iron oxide contrast agents in rabbits: critical determinants of atherosclerotic plaque labelling. *J. Magn. Reson. Imaging* **2005**, *21*, 432–442.
- 101 SCHMITZ SA, TAUPITZ M, WAGNER S, WOLF KJ, BEYERSDORFF D, HAMM B. Magnetic resonance imaging of atherosclerotic plaques using superparamagnetic iron oxide particles. *J. Magn. Reson. Imaging* **2001**, *14*, 355–361.
- 102 KOOI ME, CAPPENDIJK VC, CLEUTJENS KBJM, KESSELS AGH, KITSLAAR PJEHM, BORGERS M, FREDERIK PM, DAEMEN MJAP, VAN ENGELSHOVEN JMA. Accumulation of ultrasmall superparamagnetic particles of iron oxide in human atherosclerotic plaques can be detected *in vivo* magnetic resonance imaging. *Circulation* **2003**, *107*, 2453–2458.
- 103 TRIVEDI RA, U-KING-IM JM, GRAVES MJ, KIRKPATRICK PJ, GILLARD JH. Noninvasive imaging of carotid plaque inflammation. *Neurology* **2004**, *63*, 187–188.
- 104 TRIVEDI RA, U-KING-IM JM, GRAVES MJ, CROSS JJ, HORSLEY J, GODDARD MJ, SKEPPER JN, QUARTEY G, WARBURTON E, JOUBERT I, WANG L, KIRKPATRICK PJ, BROWN J, GILLARD JH. *In vivo* detection of macrophages in human carotid atheroma: temporal dependence of ultrasmall superparamagnetic particles of iron oxide-enhanced MRI. *Stroke* **2004**, *35*, 1631–1635.
- 105 ARVIN B, NEVILLE LF, BARONE FC, FEUERSTEIN GZ. The role of inflammation and cytokines in brain injury. *Neurosci. Biobehav. Rev.* **1996**, *20*, 445–452.
- 106 STOLL G, JANDER S, SCHROETER M. Inflammation and glial response in ischemic brain lesions. *Prog. Neurobiol.* **1998**, *56*, 149–171.
- 107 BANATI RB, GEHRMANN J, SCHUBERT P, KREUTZBERG GW. Cytotoxicity of microglia. *Glia* **1993**, *7*, 111–118.
- 108 RAUSCH M, SAUTER A, FRÖHLICH J, NEUBACHER U, RADÜ EW, RUDIN M. Dynamic patterns of USPIO enhancement can be observed in macrophages after ischemic brain damage. *Magn. Reson. Med.* **2001**, *46*, 1018–1022.
- 109 SALEH A, WIEDERMANN D, SCHROETER M, JONKMANN C, JANDER S, HOEHN M. Central nervous system inflammatory response after cerebral infarction as detected by magnetic resonance imaging. *NMR Biomed.* **2004**, *17*, 163–169.
- 110 SALEH A, SCHROETER M, JONKMANN C, HARTUNG HP, MÖDDER U, JANDER S. *In vivo* MRI of brain inflammation in human ischemic stroke. *Brain* **2004**, *127*, 1670–1677.
- 111 LAMALLE L, KREMER S, TROPÈS I, VSI and BV MRI of human brain. *Proc. Int. Soc. Mag. Reson. Med.* **2003**, *11*, 1271.
- 112 VARALLYAY P, NESBIT G, MULDOON LL, NIXON RR, DELASHAW J, COHEN JI, PETRILLO A, RINK D, NEUWELT EA. Comparison of two superparamagnetic viral-sized iron oxide particles ferumoxides and ferumoxtran-10 with a gadolinium chelate in imaging intracranial tumors. *Am. J. Neuroradiol.* **2002**, *23*, 510–519.
- 113 Calabresi PA. Diagnosis and management of multiple sclerosis.

- Am. Fam. Physician* **2004**, *70*, 1935–1944.
- 114 DOUSSET V, BALLARINO L, DELALANDE C, COUSSEMAGQ M, CANIONI P, PETRY KG, CAILLÉ JM. Comparison of ultrasmall particles of iron oxide (USPIO)-enhanced T2-weighted, conventional T2-weighted, and gadolinium-enhanced T1-weighted MR images in rats with experimental autoimmune encephalomyelitis. *Am. J. Neuroradiol.* **1999**, *20*, 223–227.
- 115 XU S, JORDAN E, BROCKE S, BULTE JW, QUIGLEY L, TRESSER N, OSTUNI JL, YANG Y, MCFARLAND HF, FRANK JA. Study of relapsing remitting experimental allergic encephalomyelitis SJL mouse model using MION-46L enhanced *in vivo* MRI: early histopathological correlation. *J. Neurosci. Res.* **1998**, *52*, 549–558.
- 116 DOUSSET V, BROCHET B, CAILLÉ JM, PETRY KG. Enhancement of multiple sclerosis lesions with ultrasmall particle iron oxide: phase II study. *Proc. Int. Soc. Magn. Reson. Med.* **2001**, *9*, 261.
- 117 FIRESTEIN GS. Evolving concept of rheumatoid arthritis. *Nature* **2003**, *423*, 356–361.
- 118 LUTZ AM, SEEMAYER C, COROT C, GAY RE, GOEPFERT K, MICHEL K, MARINCEK B, GAY S, WEISHAUP T. Detection of synovial macrophages in an experimental rabbit model of antigen-induced arthritis: ultrasmall superparamagnetic iron oxide-enhanced MR imaging. *Radiology* **2004**, *233*, 149–157.
- 119 KAIM AH, WISCHER T, O'REILLY T, JUNDT G, FRÖHLICH J, VON SCHULTHESS GK, ALLEGRINI PR. MR imaging with ultrasmall superparamagnetic iron oxide particles in experimental soft-tissue infection in rats. *Radiology* **2002**, *225*, 808–814.
- 120 LUTZ AM, WEISHAUP T, PERSOHN E, GOEPFERT K, FRÖHLICH J, SASSE B, GOTTSCHALK J, MARINCEK B, KAIM AH. Imaging of macrophages in soft-tissue infection in rats: relationship between ultrasmall superparamagnetic iron oxide dose and MR signal characteristics. *Radiology* **2005**, *234*, 765–775.
- 121 HAUGER O, DELALANDE C, TRILLAUD H, DEMINIÈRE C, QUESSON B, KAHN H, CAMBAR J, COMBE C, GRENIER N. MR imaging of intrarenal macrophage infiltration in an experimental model of nephrotic syndrome. *Magn. Reson. Med.* **1999**, *41*, 156–162.
- 122 HAUGER O, DELALANDE C, DEMINIÈRE C, FOUQUERAY B, OHAYON C, GARCIA S, TRILLAUD H, COMBE C, GRENIER N. Nephrotoxic nephritis and obstructive nephropathy: evaluation with MR imaging enhanced with ultrasmall superparamagnetic iron oxide. Preliminary findings in a rat model. *Radiology* **2000**, *217*, 819–826.
- 123 STROM TB, CARPENTER CB. Immunobiology of kidney transplantation. In *The Kidney*, 4th edn, BRENNER BM, RECTOR FC (Eds.). Saunders, Philadelphia, PA, **1991**, pp. 2336–2407.
- 124 ZHANG Y, DODD SJ, HENDRICH KS, WILLIAM M, HO C. Magnetic resonance imaging detection of rat renal transplant rejection by monitoring macrophage infiltration. *Kidney Int.* **2000**, *58*, 1300–1310.
- 125 HAUGER O, DELMAS Y, DEMINIÈRE C, MERVILLE P, COMBE C, GRENIER N. Late Sinerem-enhanced MR imaging of renal diseases: a pilot study. *Eur. Radiol.* **2004**, *14* (Suppl. 2), 202 (abstr. B-349).
- 126 YANG D, YE Q, WILLIAMS M, SUN Y, HU TCC, WILLIAMS DS, MOURA JMF, HO C. USPIO-enhanced dynamic MRI: evaluation of normal and transplanted rat kidneys. *Magn. Reson. Med.* **2001**, *46*, 1152–1163.
- 127 PERSSON PB, HANSELL P, LISS P. Pathophysiology of contrast medium-induced nephropathy. *Kidney Int.* **2005**, *68*, 14–22.
- 128 LAISSY JP, BENDERBOUS S, IDÉE JM, CHILLON S, BEAUFILS H, SCHOUMAN-CLAFYS E. MR assessment of iodinated contrast medium-induced nephropathy in rats using ultrasmall particles of iron oxide. *J. Magn. Reson. Imaging* **1996**, *7*, 164–170.
- 129 LAISSY JP, IDÉE JM, LOSHKAJIAN A, BENDERBOUS S, CHILLON S, BEAUFILS

- H, SCHOUMAN-CLAEYS E. Reversibility of experimental acute renal failure in rats: assessment with USPIO-enhanced MR imaging. *J. Magn. Reson. Imaging* **2000**, *12*, 278–288.
- 130 KANNO S, WU YJL, LEE PC, DODD SJ, WILLIAMS M, GRIFFITH BP, HO C. Macrophage accumulation associated with rat cardiac allograft rejection detected by magnetic resonance imaging with ultrasmall superparamagnetic iron oxides particles. *Circulation* **2001**, *104*, 934–938.
- 131 JOHANSSON L, JOHANSSON C, PENNO E, BJÖRNERUD A, AHLSTRÖM H. Acute cardiac transplant rejection: detection and grading with MR imaging with a blood pool contrast agent. Experimental study in the rat. *Radiology* **2002**, *225*, 97–103.
- 132 BULTE JWM, KRAITCHMAN DL. Monitoring cell therapy using iron oxide MR contrast agents. *Curr. Pharm. Biotechnol.* **2004**, *5*, 567–584.
- 133 BULTE JWM, ZHANG SC, VAN GELDEREN P, HERYNEK V, JORDAN EK, DUNCAN ID, FRANK JA. Neurotransplantation of magnetically-labeled oligodendrocyte progenitors: magnetic resonance tracking of cell migration and myelination. *Proc. Natl Acad. Sci. USA* **1999**, *96*, 15256–15261.
- 134 FRANK JA, MILLER BR, ARBAB AS, ZYWICKE HA, JORDAN EK, LEWIS BK, BRYANT LH, JR, BULTE JWM. Clinically applicable labelling of mammalian and stem cells by combining superparamagnetic iron oxides and transfection agents. *Radiology* **2003**, *228*, 480–487.
- 135 DALDRUP-LINK HE, RUDELIUS M, OOSTENDORP RAJ, SETTLES M, PIONTEK G, METZ S, ROSENBROCK H, KELLER U, HEINZMANN U, RUMMENY EJ, SCHLEGEL J, LINK TM. Targeting of hematopoietic progenitor cells with MR contrast agents. *Radiology* **2003**, *228*, 760–767.
- 136 KRAITCHMANN DL, HELDMAN AW, ATALAR E, AMADO LC, MARTIN BJ, PITTENGER MF, HARE JM, BULTE JWM. *In vivo* magnetic resonance imaging of mesenchymal stem cells in myocardial infarction. *Circulation* **2003**, *107*, 2290–2293.
- 137 CAHILL KS, GAIDOSH G, HUARD J, SILVER X, BYRNE BJ, WALTER GA. Noninvasive monitoring and tracking of muscle stem cell transplant. *Transplantation* **2004**, *78*, 1626–1633.
- 138 BOS C, DELMAS Y, DESMOULIÈRE A, SOLANILLA A, HAUGER O, GROSSET C, DUBUS I, IVANOVIC Z, ROSENBAUM J, CHARBORD P, COMBE C, BULTE JWM, MOONEN CTW, RIPOCHE J, GRENIER N. *In vivo* MR imaging of intravascularly injected magnetically labeled stem cells in rat kidney and liver. *Radiology* **2004**, *233*, 781–789.
- 139 KIRCHER MF, ALLPORT JR, GRAVES EE, LOVE V, JOSEPHSON L, LICHTMAN AH, WEISSLEDER R. *In vivo* high resolution three-dimensional imaging of antigen-specific cytotoxic T-lymphocyte trafficking to tumors. *Cancer Res.* **2003**, *63*, 6838–6846.
- 140 LAGHI A, PAOLANTONIO P, PANEBIANCO V, MIGLIO C, IAFRATE F, DI TONDO U, PASARIELLO R. Decrease of signal intensity of myometrium and cervical stroma after ultrasmall superparamagnetic iron oxide (USPIO) particles administration. *Invest. Radiol.* **2004**, *39*, 666–670.
- 141 LEE HS, KIM EH, SHAO H, KWAK BK. Synthesis of SPIO–chitosan microspheres for MRI-detectable embolotherapy. *J. Magn. Magn. Mater.* **2005**, *293*, 102–105.

### 3

## Carbon Nanotube-based Vectors for Delivering Immunotherapeutics and Drugs

*Alberto Bianco, Wei Wu, Giorgia Pastorin, Cédric Klumpp, Lara Lacerda, Charalambos D. Partidos, Kostas Kostarelos, and Maurizio Prato*

### 3.1

#### Introduction

Administration of drugs is very often limited by problems of insolubility, inefficient distribution, lack of selectivity and side-effects raising health concerns. Currently, most of these problems are the subject of very intense studies, aiming to improve efficiency, availability and toxicity profiles. In addition, cell membranes that act as barriers can pose a problem in drug delivery by selectively allowing only certain structures to pass based on hydrophilicity:hydrophobicity ratios. Among the currently available delivery systems, which include liposomes, emulsions, polymers and microparticles [1–3], carbon nanotubes (CNTs) have recently gained high popularity as potential drug carriers, therapeutic agents and for applications in diagnosis [4–10].

CNTs possess a unique and fascinating one-dimensional nanostructure, which imparts intriguing properties to the nanomaterial, such as tremendous strength [11], high thermal conductivity [12] and amazing electronic properties ranging from metallic to semiconducting [13–16]. These all-carbon hollow graphitic tubes with high aspect and nanoscale diameter [17] can be classified by their structure into two main types: single-walled CNTs (SWNTs), which consist of a single layer of graphene sheet seamlessly rolled into a cylindrical tube, and multiwalled CNTs (MWNTs), which comprise multiple layers of concentric cylinders with a space of about 0.34 nm between the adjacent layers (Fig. 3.1) [18].

Several techniques, e.g. arc-discharge [19], laser ablation [20], chemical vapor deposition (CVD) [21] or the gas-phase catalytic process (HiPCO) [22], have been used to synthesize CNTs. However, up to now, the CNTs prepared by all currently known methods are mixtures of different tubes with a broad distribution in diameter and chirality, and often contaminated by impurities (mainly including amorphous carbon and catalyst particles). Various methods have been developed to purify CNTs, such as oxidation of contaminants [23–28], microfiltration [29], chromatographic procedures [30, 31] and microwave irradiation [32–34].

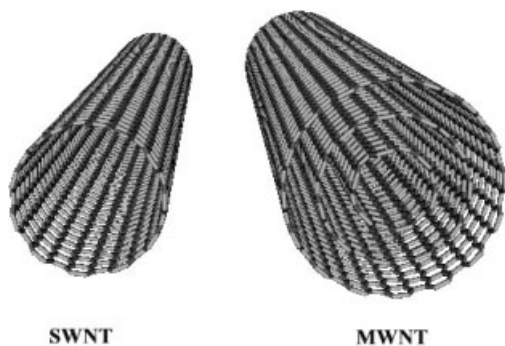


**Figure 3.1.** Molecular structures of defect-free SWNTs (left) and MWNTs (right) with open ends.

One important feature of CNTs is that this material is practically insoluble in both aqueous and polar/nonpolar organic solvents. Although this characteristic has hindered their chemical manipulation and potential applications in many fields, it has stimulated research in their chemical and physical functionalization.

A great effort has been invested in the search for new ways to chemically derivatize the CNTs. Although their tips are very reactive, similar to fullerenes, their sidewalls are much more inert toward chemical reagents. For this reason, there are not so many methods exhibiting general applicability.

Both covalent and noncovalent functionalization approaches are currently known that are very helpful in disentangling the CNT bundles, but which have different impacts on their electronic properties.

## 3.2 Chemical Functionalization of CNTs

### 3.2.1 Noncovalent Functionalization

The methods of functionalization of CNTs based on noncovalent interaction can be performed without destroying the intrinsic  $sp^2$ -hybridized structure of the nanotube sidewall, so that the original electronic structure and properties of CNTs can be preserved. Different kinds of noncovalent functionalization have been explored.

#### 3.2.1.1 $\pi$ - $\pi$ Stacking Interactions

The noncovalent functionalization of CNTs could be achieved by  $\pi$ - $\pi$  stacking interactions between conjugated molecules and the graphitic sidewall of CNTs. Compounds with the pyrene moiety, e.g. *N*-succinimidyl-1-pyrenebutanoate (Fig. 3.2), could be adsorbed irreversibly onto the surface of SWNTs through  $\pi$ - $\pi$  interaction [35]. Furthermore, via the succinimidyl ester group on this bifunctional anchor,

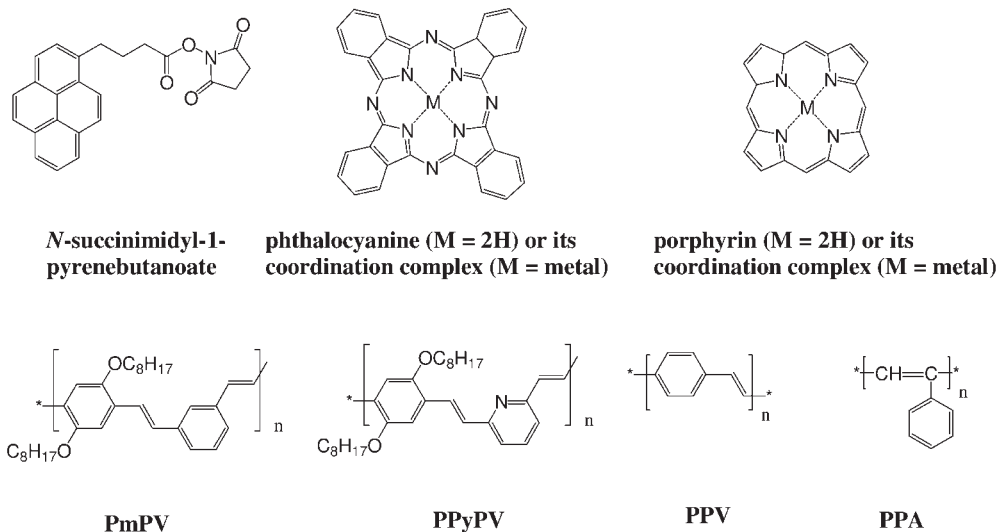


**Figure 3.2.** Typical molecules that can noncovalently modify CNTs via  $\pi$ - $\pi$  stacking interaction.

various molecules with primary or secondary amines [such as ferritin, streptavidin (SA) or biotin-polyethyleneoxide-amine] were covalently attached to the activated pyrene by nucleophilic attack of the amino group [35]. Using a similar strategy, some other biomolecules (e.g. protein and DNA) [36–38] and gold nanoparticles [39] were also coupled to CNTs.

Through the  $\pi$ - $\pi$  stacking interactions, other classes of molecules, including phthalocyanines [40–42], porphyrins [43–53] and their derivatives, have been immobilized onto the surface of CNTs (Fig. 3.2). It was demonstrated that this kind of composite could display photoinduced charge transfer from the dye molecules to CNTs [42, 45]. The selective interaction between the porphyrin derivative and CNTs was also discovered [46]. The use of Raman spectroscopy, near-infrared (NIR) absorption and buck conductivity has shown that porphyrin derivatives could be selectively adsorbed onto semiconducting nanotubes in a solubilized sample. This is a convenient method to separate the semiconductive CNTs from metallic CNTs.

Polymers with conjugated structures could also be coupled to CNTs by  $\pi$ - $\pi$  forces (Fig. 3.2) [54–75]. The strong interaction between the conjugated polymer and the nanotube remarkably increased CNT dispersibility [54, 61, 66–68]. Some conjugated polymers have been used to purify CNTs by efficient phase separation from the main impurity, consisting of amorphous graphitic shells [62, 64, 65]. In this way, amorphous carbon impurities tend to sediment out of solution, whereas the nanotubes stay in suspension. In addition, this kind of composite has potential applications in the optoelectronic field because of energy transfer from the excited conjugated polymer to the nanotubes [55–60, 63, 66, 69–75].

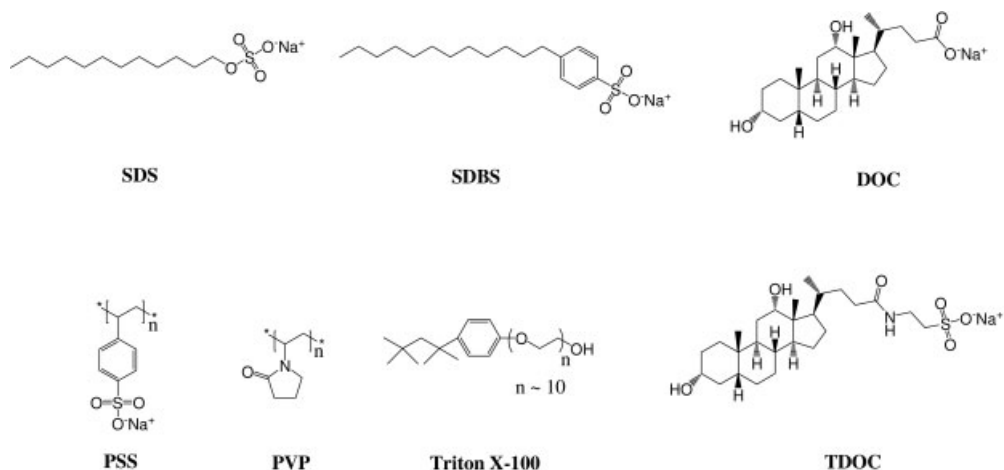


**Figure 3.3.** Typical molecules that can noncovalently modify CNTs via hydrophobic interactions.

### 3.2.1.2 Hydrophobic Interactions

Another method of noncovalent functionalization of CNTs involves association of CNTs with amphiphilic molecules through hydrophobic interactions in aqueous media. In this system, the amphiphilic molecules interact noncovalently with the aromatic surface of CNTs using their hydrophobic parts, while exposing the hydrophilic parts to the aqueous solution to minimize the hydrophobic interface between the nanotubes and their polar environment.

Through hydrophobic interactions, water-soluble polymers polyvinylpyrrolidone (PVP) and polystyrenesulfonate (PSS) (Fig. 3.3) wrapped helically around the surface of SWNTs helped to dissolve the nanotubes in water [76]. The association between the polymer and SWNTs, which is reversible by changing the solvent system, was very robust, independent of the presence of excess of polymer in solution and uniform along the surface of the nanotubes.

Surfactants were also conjugated to CNTs via hydrophobic interactions. So far, various anionic, nonionic and cationic surfactants have been used to suspend CNTs in aqueous medium (Fig. 3.3) [77–81]. Among them, bile salt surfactants such as deoxycholic acid (DOC) and taurodeoxycholic acid (TDOC) have been found to be very efficient in solubilizing SWNTs. This is because the aggregation was further prevented by the coulombic repulsion between surfactant-coated SWNTs [81]. In addition, if aromatic moieties in the hydrophobic part of the amphiphilic molecule were present, particularly strong interactions between the molecule and the CNTs could be established. This kind of aggregates forms additional  $\pi$ – $\pi$  stacking between the aromatic part of the molecule and the graphitic sidewalls of CNTs while exposing the hydrophilic groups to the aqueous solution. As an example, sodium dodecylbenzene sulfonate (SDBS) presented an increased ability in suspending CNTs in water [80]. Some of the surfactants including so-

dium dodecyl sulfate (SDS), SDBS, DOC or TDOC were found to be very effective in dispersing individually SWNTs [79–81]. This provided the possibility to study the properties of individual SWNTs and further manipulate single tubes [82–86].

Hydrophobic interactions were also used to couple biomolecules to CNTs. In particular, an amphiphilic peptide was wrapped around the SWNT surface. The peptide was able to adopt an  $\alpha$ -helical structure in aqueous solution, exposing the hydrophobic face of the helix to the nanotube surface [87, 88]. Atomic force microscopy (AFM), transmission electronic microscopy (TEM), and absorption and Raman spectroscopy proved that the SWNTs were debundled by the peptide. The peptide-coated nanotubes were assembled into macromolecular structure through charged peptide–peptide interactions between adjacent peptide-wrapped nanotubes. The size and morphology of the supermolecular structure can be regulated by controlling the factors that affect peptide–peptide interactions. It was also demonstrated that the ability to disperse individual SWNTs increased with increasing the amount of aromatic residues inside the peptide sequence [89]. In a similar manner, different proteins have also been adsorbed onto the surface of SWNTs and uptaken by mammalian cells (see Section 3.4) [90].

Another interesting approach involved the conjugation of single-stranded DNA with SWNTs resulting in helical wrapping around the surface of the tube exposing the hydrophilic sugar-phosphate backbone towards the exterior [91, 92]. Using this strategy, individually dispersed nanotubes in solution were obtained. CNT wrapping by single-stranded DNA was strongly dependent on the DNA sequence. Moreover, the dependence of the electrostatic properties of the DNA–CNT hybrid on the tube diameter and electronic properties enable nanotube separation by anion-exchange chromatography.

In addition to a direct interaction with CNTs, biomolecules have also been attached to SWNTs via amphiphilic molecules as a bifunctional linker. For instance, phospholipid molecules with phospholipid (PL)–poly(ethylene glycol) (PEG) chains and terminal amine (PL–PEG–NH<sub>2</sub>) were noncovalently conjugated to SWNTs. PL alkyl chains were adsorbed to the surface of SWNTs via hydrophobic interactions while the PEG chain extended into the aqueous phase for SWNTs dispersion. After incorporation of a heterobifunctional crosslinker sulfosuccinimidyl 6-(3'-[2-pyridyldithio]propionamido)hexanoate (sulfo-LC-SPDP), the functionalized SWNTs (*f*-SWNTs) were coupled with DNA and RNA via disulfide linkage. The complexes were subsequently delivered to cells (see Section 3.7) [93].

### 3.2.2

#### Covalent Functionalization

The characteristics of CNTs such as low curvature, low solubility and bundling tendency make these carbon nanomaterials relatively inert to chemical treatment. So far, a number of routes to covalent functionalization of CNTs have been developed. According to the location of the functional groups, the strategies to covalently functionalize CNTs can be classified into two main types: (i) defect functionalization,



and (ii) sidewall functionalization. The covalent functionalization of nanotubes is more robust and better controllable compared to functionalization based on non-covalent methods.

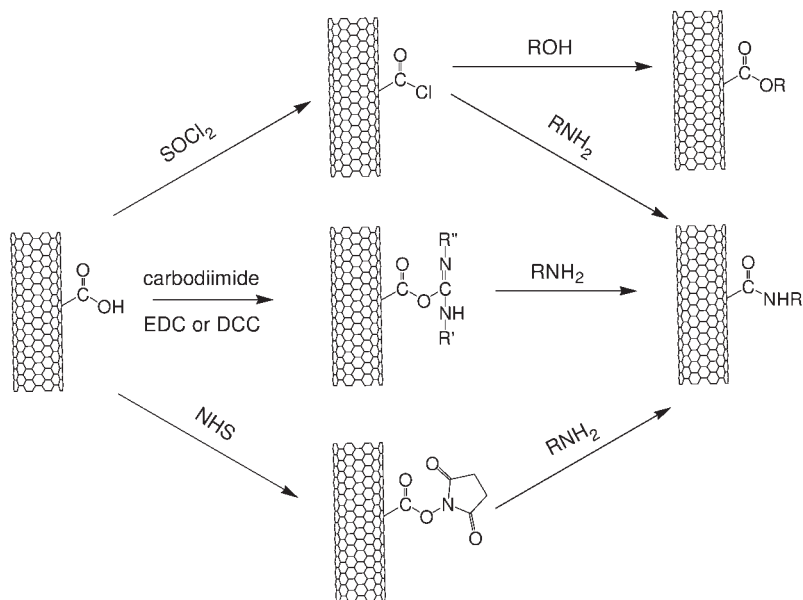
### 3.2.2.1 Defect Functionalization

CNTs synthesized by any available method are not free of defects. The intrinsic defects include five- or seven-membered rings called Stone–Wales defects,  $sp^3$ -hybridized defects and vacancies in the  $sp^2$ -hybridized six-membered ring carbon structure of the sidewall [94, 95]. A limited number of defects can be tolerated by CNTs without losing their macroscopic electronic and mechanical properties [96–98]. In addition, the tips of the tubes, forming a hemispherical fullerene, have stronger reactivity than the sidewalls because of their higher curvature [99, 100]. When treated with strong oxidizing agents such as nitric acid,  $KMnO_4/H_2SO_4$ ,  $O_2$ ,  $K_2Cr_2O_7/H_2SO_4$  or  $OsO_4$ , CNTs could be opened and cut into short tubes. In the meantime defects were introduced around the CNT surface [28, 95, 100, 101]. Moreover, oxygenated functional groups such as carboxylic acid, ketone, alcohol and ester groups were generated by the oxidization process to the ends and the defect sites of the nanotubes [102]. These functional groups were very important to further functionalize CNTs. Sonication could also produce defects on the sidewall of CNTs that were eager for further chemical reactions [103–106].

Using the nanotube-bound carboxylic acid groups introduced by oxidization treatment, further functionalization was performed via amidation, esterification or the zwitterionic  $COO^-NH_3^+$  formation. Before covalent modification, the carboxylic acids are often activated by thionyl chloride, carbodiimide [e.g. *N*-(3-dimethylaminopropyl)-*N'*-ethylcarbodiimide (EDC) or *N,N'*-dicyclohexylcarbodiimide (DCC)] or *N*-hydroxysuccinimide (NHS), to get highly reactive intermediate groups (Scheme 3.1). Esterification was achieved by the nucleophilic substitution reaction of nanotube carboxylate salt with alkyl halides [107]. The functionalization of CNTs via nanotube carboxylic acids, located at the ends or pre-existing defects of CNTs, preserved the essential features of the CNT electronic structure as well as the bulk properties of the material [102, 108].

The first shortened soluble SWNTs were obtained through carboxylic amidation using octadecylamine [102]. Since then, various lipophilic and hydrophilic dendrons have been attached to CNTs via amide or ester linkages, which significantly improved the solubility of CNTs in organic or aqueous solvents [109]. These groups could be subsequently removed under basic or acidic hydrolysis conditions [110]. In addition, following this functionalization process, CNT bundles were largely exfoliated into individual nanotubes [96]. This enabled further manipulation and investigation of the spectroscopic properties of individual SWNTs.

Via amidation or esterification, polymers like poly-propionyl-ethylenimine-co-ethylenimine (PPEI-EI), poly-*n*-vinylcarbazole (PVK-PS) and PEG were grafted to the surface of CNTs [111]. Another approach called “graft from” was developed to attach polymer to CNTs. The polymerization initiators were first covalently bound to CNTs and then the nanotube-based macroinitiators were exposed to monomers to accomplish the polymerization. In particular, polymer poly-*n*-butyl methacry-



**Scheme 3.1.** Typical CNT carboxylic acid derivatization routes.

late (PnBMA), poly-methyl methacrylate (PMMA) and copolymer PMMA-*b*-poly-hydroxyethyl methacrylate (PHEMA) have been coupled to CNTs via atom transfer radical polymerization (ATRP) [112, 113].

Defect functionalization was used to link biological molecules to CNTs via stable covalent bonds. For example, *f*-SWNTs and *f*-MWNTs with bovine serum albumin (BSA) were synthesized via diimide-activated amidation at ambient condition. It was found that the protein bound to nanotubes remained active [114]. SA (a protein with potential clinical applications in anticancer therapy) was complexed to SWNTs prefucionalized with biotin through EDC activated amidation [115]. Similarly, using the biotin–SA interaction, a biotinylated DNAzyme was covalently attached to MWNTs prefucionalized with SA via amide linkage. The nanotube-bound DNAzymes displayed highly active and classical enzymatic behavior [116].

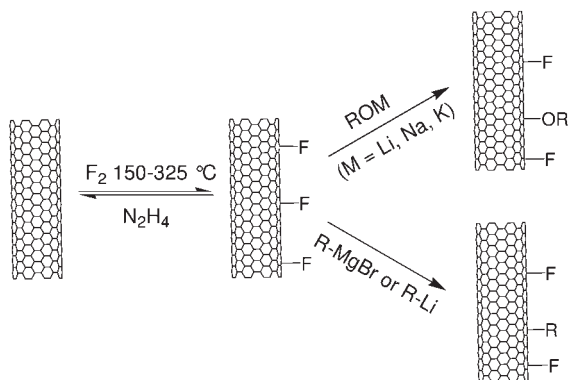
DNA was also bound to CNTs via amide linkage [117, 118]. DNA–CNT conjugates were hybridized with their complementary sequences and this hybridization was apparently reversible upon a denaturation process. The derived single-strand DNA–CNTs could be reused in a second-round of hybridization. In another case, DNA recognition was achieved by peptide nucleic acid (PNA) *f*-SWNTs, in which PNA was attached to SWNTs via NHS activated SWNTs [119].

### 3.2.2.2 Sidewall Functionalization

The sidewalls of CNTs have an aromatic, six-membered ring structure. So far, various kinds of reactions of the sidewall have been developed such as fluorina-

tion, radical addition, nucleophilic addition, electrophilic addition and cycloaddition [120]. There are two principal sources of molecular strain that affect the reactivity in nonplanar conjugated molecules: (i) pyramidalization of the conjugated carbon atom and (ii)  $\pi$ -orbital misalignment between adjacent pairs of conjugate carbon atoms. Unlike fullerene, in which the strain is primarily from pyramidalization,  $\pi$ -orbital misalignment is the main source of the strain for the sidewalls of CNTs. Since  $\pi$ -orbital misalignment, as well as pyramidalization, scales inversely with nanotube diameter, nanotubes with a smaller diameter display a higher chemical reactivity [99]. Differing from defect reactions, sidewall reactions disrupted the conjugated structure of CNTs, as monitored by Raman or absorption spectroscopy. In the Raman spectrum of pristine SWNTs, three main characteristic modes were disclosed: (i) the radial breathing ( $\omega_r$ ) below  $350\text{ cm}^{-1}$ , (ii) the tangential ( $\omega_t$ ) mode at  $1550\text{--}1600\text{ cm}^{-1}$  and (iii) the disorder ( $\text{sp}^3$ ) mode at  $1250\text{--}1450\text{ cm}^{-1}$ . The radial breathing mode was demonstrated to be in strong relationship with the diameter of the nanotube [121]. The relative intensity of the disorder mode was related to the amount of  $\text{sp}^3$ -hybridized carbon atoms in the SWNTs and thus provided direct information of the extent of sidewall functionalization, in which the carbons linked to functional groups were converted from  $\text{sp}^2$ -hybridized into  $\text{sp}^3$ -hybridized carbon [122]. The absorption spectrum reflected the sidewall covalent modification of SWNTs. The disruption of the conjugated structure caused by the reaction led to the loss of optical transitions between van Hove singularities in the electronic density of state (DOS) of CNTs, which was detected as the loss of the structure of the absorption spectrum [123].

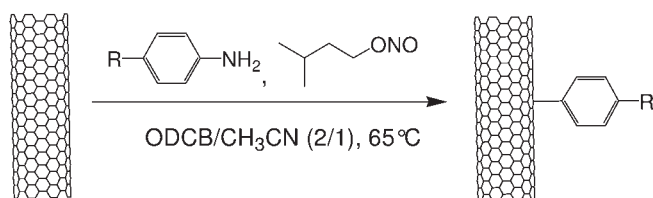
**3.2.2.2.1 Fluorination** The fluorination of SWNTs was accomplished through the reaction of SWNTs with elemental fluorine at temperatures ranging from  $150$  to  $600\text{ }^\circ\text{C}$  [124]. By controlling the reaction conditions such as temperature and time, the stoichiometry could be regulated. In some cases, a stoichiometry of  $\text{C}_2\text{F}$  was obtained (see Scheme 3.3). The investigation of absorption and Raman spectra indicated the electronic perturbation of fluorinated SWNTs. The fluorination allowed exfoliation of SWNTs bundles into individual nanotubes and remarkably improved the solubility of SWNTs in tetrahydrofuran (THF), dimethylformamide (DMF) and various alcohols [125]. The C–F bonds were very sensitive to the treatment with hydrazine, which allowed almost complete recovery of the conductivity and the spectroscopic properties of the pristine SWNTs [124]. It was demonstrated that the Fermi energy level of fluorinated SWNTs, as well as the conduction band energy, were significantly shifted to lower values compared to those of the pristine SWNTs. This revealed that fluorinated CNTs were better electron acceptors than pristine nanotubes, and thus displayed higher chemical reactivity to strong nucleophilic reagents like Grignard, alkyllithium reagents and metal alkoxides (Scheme 3.2). The same result was reached by exploiting the eclipsing strain effect that weakened the C–F bonds in fluorinated CNTs relative to the C–F bond in alkyl fluorides [126, 127]. It was proposed that the substitution of fluorine by nucleophilic reagents proceeds via a concerted allylic displacement [126].



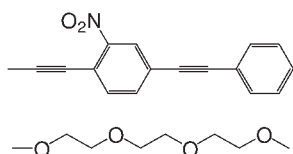
**Scheme 3.2.** Fluorination of CNTs and further modification routes.

**3.2.2.2.2 Radical Addition** The addition of radicals to SWNTs was carried out using different radical sources including perfluorinated alkyl radicals photoinduced from perfluoroalkyl iodide [128], aryl radicals generated by one-electron reduction of the diazonium salt [129–131], radicals produced by decomposition of benzoyl peroxide in the presence of alkyl iodides [132], or directly produced by decomposition of benzoyl or lauroyl peroxide [133].

The functionalization of SWNTs with diazonium reagents was achieved by three different methods: electrochemical reaction [119], thermochemical reaction in solvent [130] and using a solvent-free system [131] (Scheme 3.3). The resultant SWNTs displayed very high degree of functionalization. It was also demonstrated that metallic SWNTs showed higher reactivity in these types of reactions than semiconductive SWNTs, which would allow CNT separation [134].

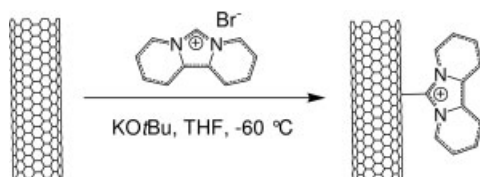


R = halogen,  $\text{CO}_2\text{CH}_3$ ,  $\text{NO}_2$ , *tert*-butyl,  $\text{COOH}$ ,



**Scheme 3.3.** Example of a strategy to functionalize SWNTs with diazonium compounds. ODCB = orthodichlorobenze.

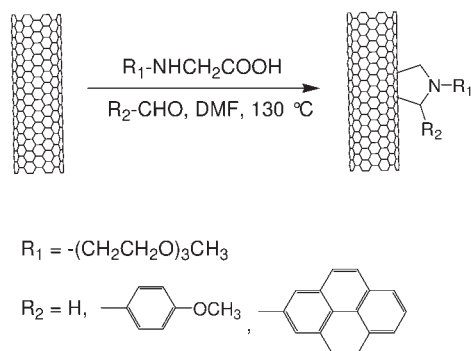
**3.2.2.2.3 Nucleophilic and Electrophilic Addition** Due to the high electron affinity imparted by the curvature of sidewall [135], CNTs were reacted with strong nucleophilic reagents such as nucleophilic carbene [128], *sec*-butyllithium [136], polymeric carbanions [137] and Birch reduction reagents (lithium/1,2-diaminoethane [108] or lithium/ammonia [138]) to form various *f*-CNTs (Scheme 3.4).



**Scheme 3.4.** Reaction of SWNTs with nucleophilic carbene.

In addition, the electrophilic addition was also achieved by the reaction of chloroform with the sidewall of CNTs in the presence of Lewis acid [139].

**3.2.2.2.4 Cycloaddition** Various cycloaddition reactions to CNTs have been developed, including [2 + 1] cycloaddition of dichlorocarbene [108], nitrenes [128] and bromomalonates under Bingel reaction conditions [140], [4 + 2] Diels–Alder cycloaddition of *o*-quinodimethane performed under microwave irradiation [141], [3 + 2] cycloaddition of azido groups under ultraviolet (UV) irradiation [142], and azomethine ylides [143]. The 1,3-dipolar addition of azomethine ylides is particularly versatile for the functionalization of CNTs [143–145]. This strategy is suitable for different types of CNTs (e.g. pristine and purified SWNTs or MWNTs), and involves the *in situ* generation of an azomethine ylide through the decarboxylation of an immonium salt derived from condensation of a  $\alpha$ -amino acid and an aldehyde in the presence of CNTs. This afforded functionalization of CNTs with the 2-substituted pyrrolidine (Scheme 3.5).



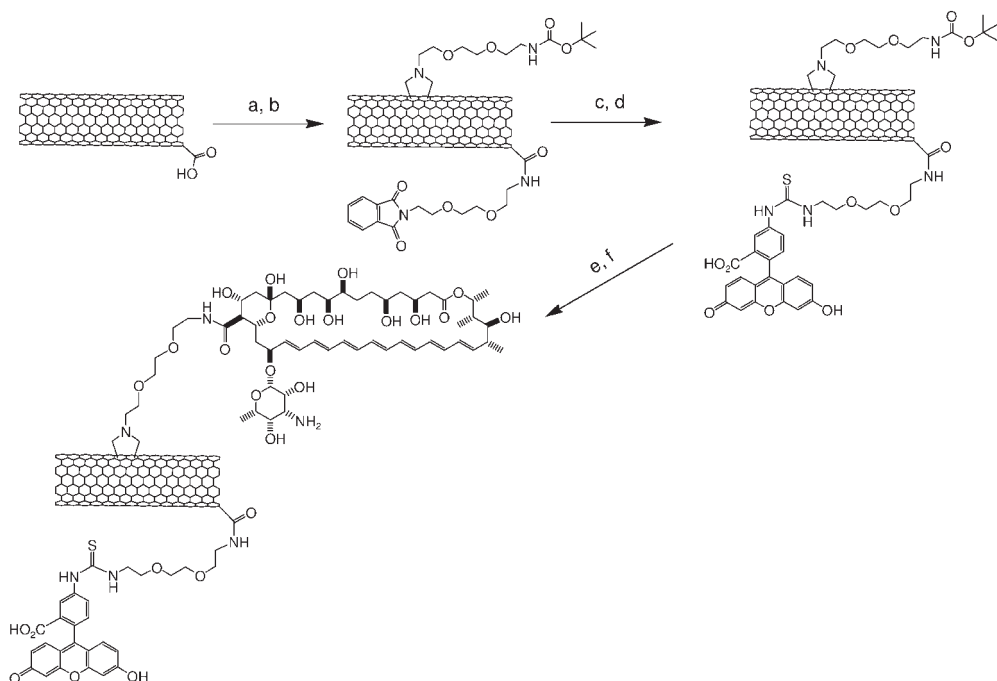
**Scheme 3.5.** 1,3-Dipolar cycloaddition reaction of azomethine ylides to SWNTs.

The CNTs modified by this method possessed a very high degree of functionalization and improved solubility in organic or aqueous solvents [143, 146]. The disruption of the aromatic structure of the sidewalls of the *f*-SWNTs was proven by absorption spectroscopy [143]. This functionalization technique was also used to purify CNTs [147]. Protected amino groups were introduced onto the surface of CNTs via 1,3-dipolar cycloaddition of azomethine ylides [143, 148]. For instance, *f*-CNTs with N-protected glycine were achieved using N-protected amino acid, which were subsequently used to link biomolecules (e.g. bioactive peptides) by fragment condensation or selective chemical ligation (see Section 3.5) [148, 149].

**3.2.2.2.5 Multifunctionalization of CNTs** The first multifunctionalization of CNTs was achieved using a vertically aligned MWNT membrane. One method involved the protection of the sidewalls of CNTs with polystyrene in the process of plasma oxidation that produced carboxylate derivatization. Under this process, aligned MWNT membranes functionalized with carboxylic acid groups at the terminal parts were obtained. Thereafter, bifunctional CNTs with thiol groups on one end and carboxylic groups on the other end were accomplished by floating on top of a 2-aminoethanethiol reaction solution one side of the oxidized CNTs membrane [150]. Another approach was carried out by floating directly one side of an aligned MWNTs membrane on 3'-azido-3'-deoxythymidine (AZT) solution in ethanol under UV irradiation and, after removal of absorbed AZT molecules by washing with ethanol, laying the unmodified side on the surface of a perfluorooctyl iodide solution in 1,1,2,2-tetrachloroethane (TEC) under UV irradiation. Thus, bifunctionalized MWNTs with AZT molecules and perfluorooctyl chains were obtained [151].

These two methods of CNT bifunctionalization are quite complicated and limited to aligned MWNTs. Using a different method, Wu and coworkers introduced an orthogonal protecting methodology into the chemical modification of nanotube to achieve the multifunctionalization of CNTs [152]. In particular, diaminotriethylene glycol chains mono-protected by phthalimide were linked to the carboxylic acids of oxidized MWNTs. In a second step, a suitable N-substituted glycine with a diaminotriethylene glycol chain mono-protected by *tert*-butyloxycarbonyl (Boc) was introduced via 1,3-dipolar cycloaddition (Scheme 3.6). Since the phthalimide is stable to harsh acidic conditions and orthogonal to the Boc, the selection and control of attachment of different molecules was possible [152]. In this case, CNTs containing both fluorescein and amphotericin B (AmB) were prepared, and bioactivity of the conjugates was studied (see Section 3.6) [152]. This method of bifunctionalization is general and suitable for different types of CNTs.

In summary, the functionalization and consequent applications of CNTs have been dramatically increased in the last few years. The chemical modification of CNTs cannot only endow these intriguing nanomaterials with various functions, but also extend their potential applications to different fields of research.



**Scheme 3.6.** One of the routes to the bifunctionalization of CNTs. (a) Neat  $(\text{COCl})_2$ ; Pht-N $(\text{CH}_2\text{CH}_2\text{O})_2\text{-CH}_2\text{CH}_2\text{-NH}_2$ , dry THF, reflux; (b) Boc-NH- $(\text{CH}_2\text{CH}_2\text{O})_2\text{-CH}_2\text{CH}_2\text{-NHCH}_2\text{COOH}/(\text{CH}_2\text{O})_n$ , DMF, 125 °C; (c) hydrated  $\text{NH}_2\text{-NH}_2$ , EtOH, reflux; (d) FITC, DMF; (e) HCl 4 M in dioxane;

(f) Fmoc-AmB, HOBt/EDC  $\times$  HCl/DIPEA, DMF; 25% piperidine in DMF. Boc = *tert*-butyloxycarbonyl; DIPEA = diisopropylethylamine; Fmoc = fluorenyl-methyloxycarbonyl; FITC = fluorescein isothiocyanate; HOBt = 1-hydroxybenzo-triazole; Pht = phthalimide.

### 3.3 CNTs in Diagnosis

A biosensor can be defined as the spatial combination of a biological recognition element and a transduction process into an electrical signal [153]. One of the most used recognition element, due to its high chemical specificity and inherent biocatalytic signal amplification, is an enzyme. Other elements like antibodies, nucleic acid and aptamers are also commonly incorporated into biosensing devices. An important issue in the elaboration of new sensors for application in living systems is to avoid invasive tools, which may cause trauma [154]. In this context, the development of electrical instrumentations has paved the way for miniaturization of noninvasive biosensors. This type of device requires an electronic conductor and a binding agent for recognition [155]. Due to their particular structure [156, 157], CNTs are very promising for the development of new alternative biosensors. The

aromatic carbon structure of CNTs is characterized by a  $(m, n)$  lattice vector in the graphene plane. The two indices determine the diameter and chirality of the nanotubes. When  $n = m$ , the rolling process leads to an armchair tube with a metallic behavior. When  $n - m = 3i$ , where  $i$  is an integer, the nanotubes adopt a zigzag conformation and behave as semimetallic species. Finally, when  $n - m \neq 3i$ , the resulting nanotubes are chiral and semiconductor. Semiconducting nanotubes represent about two-thirds of the SWNTs, whereas metallic tubes represent about one-third. These properties could be exploited for the fabrication of new electronic devices containing CNTs such as field-effect transistors (FETs), nanoelectrode arrays (NEAs), nanoelectrode ensembles (NEEs) or screen-printed electrodes (SPEs) [158–167]. FET devices need semiconductor-type nanotubes. Currently, no method of production permits us to obtain a specific type of nanotubes. Some studies were carried out on the separation or selection of semiconducting and metallic nanotubes [168–171].

This section will describe the utilization of CNTs in FETs and in modified electrodes (NEAs, NEEs and SPEs). Initially, the methods of preparation of the devices will be addressed and then their applications in the field of biosensing will be illustrated.

### 3.3.1

#### CNTs in FETs

The FET is a transistor that relies on an electric field to control the shape and hence the conductivity of a channel in a semiconductor material. Basically, two metal electrodes called the source and drain are connected by the channel, and a third component (the gate) is separated from the channel by a thin insulator film. The latter, usually made up of Si, is replaced by semiconducting SWNTs in CNT-based FETs [158, 164]. There are two types of FETs: (i) p-type and (ii) n-type. If a negative charge is placed on the gate and the applied voltage exceeds a certain threshold, then a hole current flows in a p-type system. For a n-type FET, the current flows when a positive charge is present on the gate and the voltage exceeds the threshold [166].

##### 3.3.1.1 Fabrication

As CNTs are still emerging in the field of electronic devices, the protocols for their preparation are not yet optimized. A CNT-based FET was built by positioning a semiconducting SWNT between two metal electrodes. Typically, as-prepared SWNTs were purified by acid treatment to remove metal particles, which can interfere with the electronic properties of the nanotubes. Other, more elaborate techniques to obtain highly pure nanotubes (up to 95% wt) consisted of heating as-grown HiPCO SWNTs in wet air in the presence of  $H_2O_2$ , followed by acid treatment, magnetic fractionation and vacuum annealing [168]. Subsequently, the nanotubes were dispersed in an organic (dichloromethane) or aqueous solution with a surfactant like sodium dodecyl benzene sulfonate [164, 168]. The suspension was then deposited on a substrate constituted of a degenerately doped, oxidized silicon



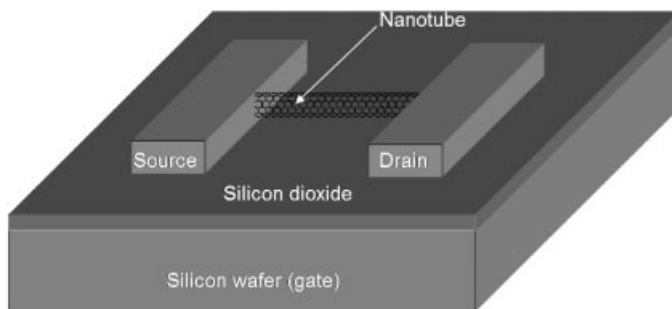


**Figure 3.4.** A typical CNT-based FET. The nanotube serves as a semiconductor between the source and the drain electrode. The silicon wafer in this case is used as a back gate.

wafer. An alternative technique consisted on the growth of SWNTs directly on the SiO<sub>2</sub>/Si wafer by chemical vapor deposition (CVD) [36, 172–176]. Once the SWNTs were deposited, the electrodes were fabricated with electron beam lithography, followed by thermal evaporation and lift-off. The degenerately doped silicon was used as back gate electrode. At this stage, the channel was composed of a simple SWNTs or a small bundle with properties ranging from semiconducting to metallic behavior (Fig. 3.4). To select only semiconducting SWNTs, a source-drain current  $I$  was applied at different bias voltage  $V_b$  and gate voltage  $V_g$ . Typically, the  $I$ – $V_g$  curve at low voltage bias shows a low source–drain resistance and almost no gate response for metallic nanotubes [168]. These types of CNT FET devices behave as p-type FETs with holes as dominant carriers. However, by using a network of SWNTs between the drain and the source, the network exhibited a semiconductor-like conductance as semiconducting SWNTs represented about two-thirds of the tubes [176]. Efforts have been made to improve them, thus now they can be built with a  $g_m$  transconductance of  $2300 \mu\text{S } \mu\text{m}^{-1}$  whereas a  $g_m$  of  $650 \mu\text{S } \mu\text{m}^{-1}$  was obtained for the same device based on silicon. Moreover, the parasitic contact resistance changed from more than 1 to 100 k $\Omega$  or above [166]. In addition, a method to select semiconducting SWNTs by current-induced electrical breakdown was developed. This technique permitted a direct current-induced oxidation only at the metallic SWNT component of the CNT bundle by previously depleting semiconducting SWNTs with the gate [177].

Even at this early stage of development, CNT-based FETs have been shown to outperform the corresponding Si-based devices. Their applications in sensing can therefore offer considerable improvements.

### 3.3.1.2 FET Biosensors

CNTs have already been successfully employed for sensing chemical species. In fact, molecules were adsorbed onto the surface of nanotubes. The fringing electric field radiating from the CNT surface polarized the molecules, increasing the capac-

ity of the system. Different chemical vapors including  $\text{NO}_2$  and  $\text{NH}_3$ , and a wide range of chemicals were detected [35, 160, 178–181]. A more sophisticated system based on a single-strand DNA-SWNT-FET was designed. The source–drain current was a function of the chemical environment and was modulated by the DNA sequence. In fact, depending on the DNA sequence covering the nanotube, the response for a same gas can be different in both sign and magnitude. Thus, the selection of a DNA sequence can enhance the detection of a specific gas and can serve for the design of “molecular noses” able to detect one molecule in a strong and variable background. The sensor had a rapid response and was also self-regenerating as it could undergo 50 gas exposure cycles [174].

In the field of biosensing, CNT-based FETs appeared as promising devices. Glucose biosensors are particularly requested. In industrialized countries, about 4% of the population is prone to diabetes. Thus, the selective determination of blood glucose is of crucial importance. *In vivo* monitoring requires a biosensor with long-term stability, selectivity and sensitivity in the millimolar range. Usually, the sensor for this type of application requires to couple the enzyme glucose oxidase to the electrochemical transducer. In the case of a CNT-based FET, it was possible to link noncovalently the enzyme via a pyrene moiety [35]. 1-Pyrenebutanoic acid succinimidyl ester was adsorbed onto the nanotube surface by strong van der Waals interactions. The enzyme was subsequently reacted with the active ester, thus forming a covalent linkage. The quantity of enzyme deposited on the CNT support was about one enzyme molecule every 12 nm of nanotube. Such FET allowed the detection of pH changes down to 0.1, by measuring the difference of conductance. Similarly, the CNT sensor could detect the activity of the enzyme in the presence of glucose down to 0.03 mM [36]. This technique was also applied to the recognition of proteins by using biomimetic sensors. One example concerned the sensing of thrombin via an aptamer [172]. An aptamer is an artificial oligonucleotide that can bind any kind of entity (e.g. metal ions, small organic molecules, proteins and/or cells). The affinity, selectivity and specificity are equal or superior to those of antibodies. Practically, the immobilization of thrombin aptamer was achieved by first covering the nanotube in the FET with carbodiimidazole (CDI)-Tween. Tween possess a hydrophobic part, which bound noncovalently to the tube, while the CDI moiety allowed covalent fixation of the aptamer. The measurement of the conductance permitted the detection of thrombin in the millimolar range. The selectivity appeared very high in comparison to elastase. Elastase is another serine protease with an isoelectric point ( $pI$ ) and molecular weight similar to thrombin. However, no changes in the conductance were observed in its presence. Although the specificity and selectivity could be very high, the mechanism of electrical conductance changes is still not well understood. Dai and coworkers fabricated three different types of devices to better comprehend this phenomenon [175]. The first device consisted of a system with unmodified CNTs and Pd/Au electrodes. The second had a methoxy(PEG)thiol covering the metal electrodes to block nonspecific protein adsorption. The third tool was modified at the electrode and the nanotube was coated with Tween 20. The conductance measurements were performed in the presence of different proteins including BSA, human serum albumin (HAS), human cho-

ronic gonadotropin (hCG),  $\alpha$ -hCG, human immunoglobulin G (hIgG) and avidin. Unspecific binding led to a decrease of conductance on the first device, a change was detected only for avidin on the second and any change at all was observed on the third. All the proteins used have a  $pI$  around 5–7, meaning that at physiological pH they are neutral or slightly charged. Avidin was an exception, because its  $pI$  is between 10 and 11, highlighting the importance of the positive charges. The advanced hypothesis for the mechanism of conductance modifications was that the variation originated from the metal–tube contact. These p-type devices always exhibit a decrease upon protein adsorption. This behavior was similar to a reduction of the work function of a metal. In the case of Pd electrodes, the Schottky barrier to the valence band of the nanotubes is mainly zero. The biomolecular adsorption increased this barrier. However, in the case of avidin, the charges on the CNT surface exerted gating effects or charge transfer causing variations in the electrical conductance.

The CNT-based FETs have also been used in an antibody-based sensor [175]. For example, the hCG– $\alpha$ -hCG antigen–antibody system is currently used for clinical pregnancy tests. The hCG protein could be adsorbed and detected onto the nanotube FET. A signal was observed upon the addition of  $\alpha$ -hCG. This biosensor was capable of detecting species in the nanomolar range. The same comparison was done by using antibody-specific binding onto the tubes [176]. CNTs were first covered by Tween. Then U1A RNA splicing factor was linked to the Tween after activation with 1,1-carbonyldiimidazole. U1A is a prominent autoantigen target in systemic lupus erythematosus. The measurements revealed the binding of the monoclonal antibody 10E3, which recognizes U1A specifically, at a concentration of 1 nM or below. CNT-based FETs were also functionalized with hemagglutinins (HAs) [173]. Instead of binding the proteins directly to the nanotubes, they were attached on the reverse side of the silicon wafer (Fig. 3.5). The silicon wafer was oxidized with  $H_2SO_4$  for the fixation of a dithiothreitol linker. Next, the introduction of a maleimide linker permitted the coupling of HA. The  $I-V_g$  curves measured in the presence of various concentrations of an antibody anti-HA showed a detection limit of approximately of  $5 \times 10^{-8}$  mg mL<sup>-1</sup>. Comparing these results to the same experiment with an enzyme-linked immunoadsorbent assay (ELISA), the FET increased the limit of detection by three orders of magnitude.

Therefore, the preliminary results on CNT-based FETs displayed an increase in the sensitivity as well as better detection limits. The great advantage of these new FETs stems from their small size, because miniaturization is an important parameter for the development of biosensors able to work at the single-cell level.

### 3.3.2

#### CNT-based Electrodes

The construction of nanoelectrodes is a great challenge to create miniaturized sensors. Reducing the size will enable us to detect species in microenvironments with high sensitivity. Thus, the utilization of nanomaterials is highly recommended. CNTs can be considered ideal candidates.

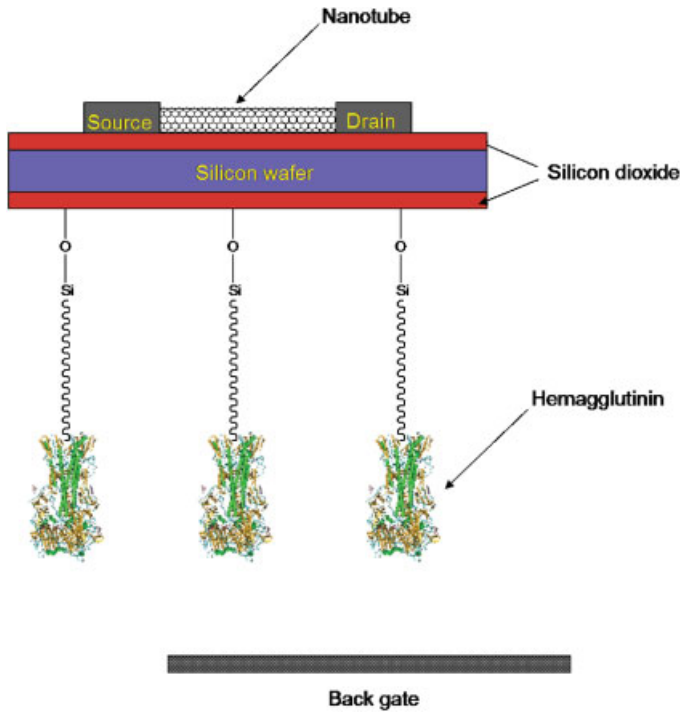


**Figure 3.5.** CNT-based FET functionalized on its reverse side. The silicon wafer is oxidized on the reverse side to allow the linkage with HA. The current is measured in air by applying a voltage to the back gate facing the reverse side.

### 3.3.2.1 Fabrication

Several techniques were used to prepare CNT-modified electrodes. One approach consisted on the covalent linkage of oxidized nanotubes to a metal electrode (usually Au) [182, 183]. The purification of nanotubes by acid treatment shortened the nanotubes leading to free carboxylic functions mainly at the tips. An Au electrode was functionalized with a mixture of cysteamine and 2-thioethanol. The CNT coupling reaction was performed in the presence of an activator of the carboxylic groups (EDC or DCC). 2-Thioethanol was used to avoid nonspecific adsorption of the nanotubes onto the electrode surface as well as to prevent accumulation of the nanotubes on it. The obtained CNT array was further functionalized with any biological species to finalize the elaboration of the electrode (Fig. 3.6).

Another technique was based on the deposition of a metal film (usually Pt or Cr) on a Si wafer to serve as an electrical contact for the nanotubes. Then, a Ni catalyst was deposited on the top of the metal film and the nanotubes were grown by CVD [165, 184]. The forest-like vertically aligned nanotube array was encapsulated by a dielectric film ( $\text{SiO}_2$  or Epon 828 epoxy-based polymer), dramatically increasing the mechanical strength of the nanotube array, so that a chemical mechanical polish-

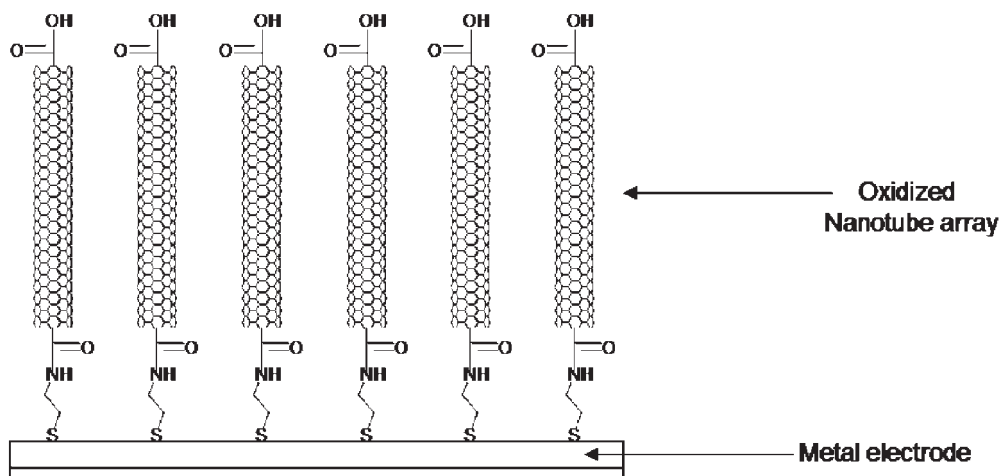


**Figure 3.6.** Nanoelectrode made of CNT arrays. The CNTs are disposed in a forest-like structure. The carboxylic groups on their tips are not hindered and can be easily functionalized.

ing process could be applied. This treatment oxidized the exposed end of the tubes and allowed control of the quantity of available nanotubes. Again, the nanotubes were ready to be further functionalized to create the nanoelectrode sensor (Fig. 3.7). A third approach to fabricate the electrodes was based on the utilization of the SPE technique [185, 186]. The working and the reference electrodes were made of carbon paste. Three masks were used to form: (i) sliver conducting lead wires, (ii) the carbon film for electrochemical reactions and (iii) the insulating film. In the reaction compartment, the carbon paste film was modified by CNTs. Oxidized CNTs were dropped with a solution of *N*-cyclohexyl-*N'*-( $\beta$ -[*N*-methylmorpholino]ethyl)carbodiimide *p*-toluenesulfonate (CMC) to afford a hydrophilic polymer layer after drying in hot air. Alternatively, oxidized CNTs were dispersed in DMF and then incubated with EDC and NHS to be activated for the coupling of the bioactive molecule.

### 3.3.2.2 Nanoelectrode Biosensors

As mentioned for CNT-based FETs, the environment around the tubes changes their conductance. The measurement of the current will give direct information of the medium. A modified glassy carbon electrode was constructed to detect hydrogen peroxide. Nanotubes were first suspended in Nafion, which possess ion-exchange, discriminative and biocompatibility properties [187]. The suspension was then simply deposited onto the electrode. In this case, cyclic voltammograms displayed oxidation and reduction currents, whereas in comparison no redox activity was observed for a simple glassy carbon electrode. Nevertheless, the preparation of biosensor required the immobilization of a biological entity. This can be done by linking the molecule to the free carboxylic groups of the nanotube tips. To control

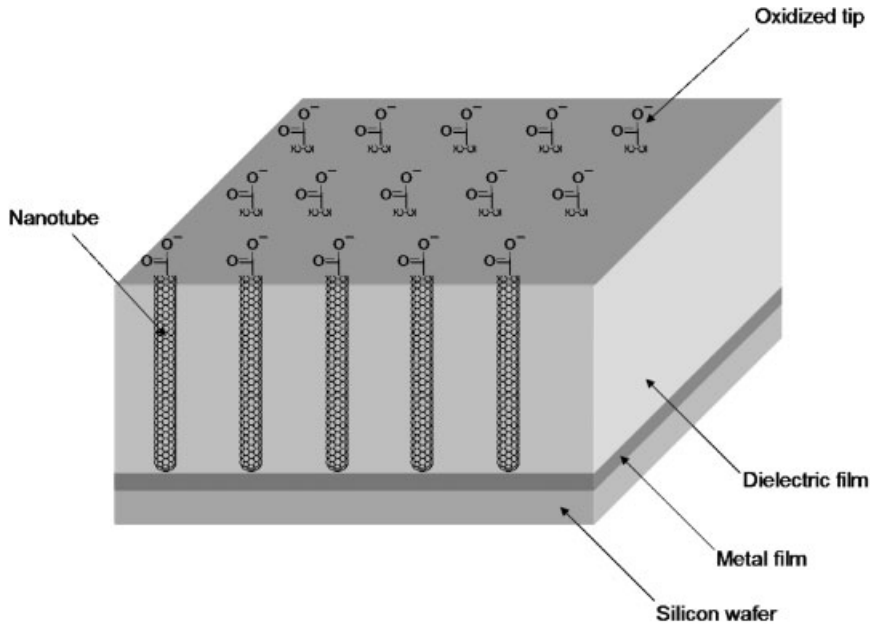


**Figure 3.7.** A nanoelectrode ensemble. The nanotubes are grown directly on the metal film via a catalyst (usually nickel). After deposition of the dielectric film, the number of nanotubes

tips present on the surface can be selected by polishing. A weak polishing lets only the longest tubes appear with a low-density nanoelectrode array.

the specificity of the binding location, it is crucial to avoid any nonspecific absorption. Some reports described the interaction of proteins with nanotubes [188, 189]. For example, SA strongly bound to nanotubes [188]. Hence, the protection of the sidewall of the tube can be performed by wrapping a polymer like Triton X co-adsorbed with PEG [189]. This provided an efficient barrier against protein adsorptions. As a consequence, specific immobilization of glucose oxidase at one tip of the nanotube was achieved via reconstitution of the apo-flavoenzyme glucose oxidase with the flavin adenine dinucleotide (FAD) cofactor [183]. The free amine of the FAD was coupled to the carboxylic end by activation with EDC. After addition of the apo-glucose oxidase, the glucose enzyme was reconstituted at the top of the tubes. The turnover rate of electrons transferred to the electrodes was 6-fold higher than for the active site of the glucose oxidase to its natural  $O_2$  electron acceptor. By controlling the length of the tubes in the array, the measurements of the current revealed that the electrons could be transported along distances greater than 150 nm. Evidently, a shorter length enhances the electrocatalytic current. Another method used the nanoelectrode ensembles where the carboxylic end-groups of the nanotubes were directly coupled to the glucose oxidase [184]. This glucose sensor showed high selectivity towards the substrate. Indeed, a negligible signal was observed for ascorbic, uric acid and acetaminophen. The nanoelectrode gave a linear

response up to 30 mM glucose. For practical use, the required linear response is 15 mM. The detection limit of the system was 0.08 mM. These types of sensors could be extended to other enzymes, like microperoxidase MP-11 [182].

The utilization of nanotubes also permitted the development of nucleic acid sensors [165, 185]. The free carboxylic functions on the carbon nanoelectrode were used to covalently link different 5'-amine modified oligonucleotides. In this manner, the oxidation of guanine bases could be monitored to detect DNA hybridization. Several ways were explored to construct this type of sensor. Initially, the sensors exploited the utilization of oligonucleotide probes in which guanines were replaced by nonelectroactive inosines to eliminate the redox background [165]. The complementary DNA sequence was instead modified with a 10-base polyguanine at the 3' position. However, the background noise remained high because of the low oxidative current resulting from the small number of guanines. To circumvent this problem, a  $\text{Ru}(\text{bpy})_2^{3+}$  mediator was introduced to transfer the electrons from the base to the electrode. Polymerase chain reaction (PCR) amplicons were then detected. An improvement of at least 30 times was obtained in comparison to the use of the same kind of technique with a silane-modified electrode. In a similar approach, hybridization was observed with the single-strand binding (SSB) protein, which plays an important role in DNA replication [185]. The SSB protein binds specifically to the single-strand DNA, while it has almost no affinity toward double-strand DNA. The protein sequence comprises four tyrosines and four tryptophans. The electrochemical oxidation of these residues was measured when the protein was immobilized onto the electrode. Then, specific detection of single-strand DNA in the medium was monitored by signal changes upon binding. At this stage of development, the performances of the biosensor remained constant for 1 week, but decreased 10-fold after 1 month and vanished after 2 months. A third technique of fabrication was applied to carbon nanoelectrodes for monitoring total cholesterol in blood [186]. Cholesterol oxidase, peroxidase, potassium ferrocyanide and threhalose dissolved in a buffer were deposited onto the reaction area of the electrode. Then, a hydrophilic polymer was applied to coat the rest of the electrode. Finally, cholesterol esterase, threhalose and Triton X in a phosphate buffer were deposited. The enzymatic cascade led to the formation of hydrogen peroxide, which was reduced by the ferrocyanide. The resulting current was recorded at various concentrations of cholesterol. While a nonlinear relationship was obtained between the cholesterol concentration and the current response for an unmodified electrode, an almost linear response was observed for a CNT-modified electrode. Moreover, the CNTs provided almost double the sensitivity, an acceptable repeatability over three consecutive assays, no interference effect from ascorbic and uric acids, and a stability at room temperature over 2 months.

In summary, CNTs are endowed with appropriate characteristics for the elaboration of biosensors. They possess high electronic conductivity and nanometric size. Miniaturization is an important parameter in the conception of more efficient sensors, which could be used to control biochemicals at the single-cell level. The current performance of nanotube-based biosensors has already overtaken the other sensors, but optimization still needs to be reached. Glucose biosensors are very

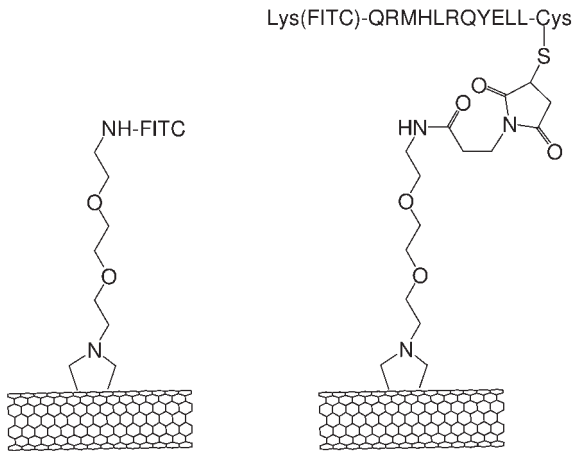


**Figure 3.8.** Molecular structure of FITC– (left) and fluorescent peptide–CNT (right) conjugates.

promising. However, numerous other oxidases exist and can be employed for the design of novel CNT-based biosensors. A bright future awaits these new sensors for pharmaceutical and clinical use.

### 3.4 CNT Cell Uptake

CNTs started to develop as new drug delivery systems because of their capacity to penetrate cell membranes and distribute into the cytoplasm and/or the nucleus.

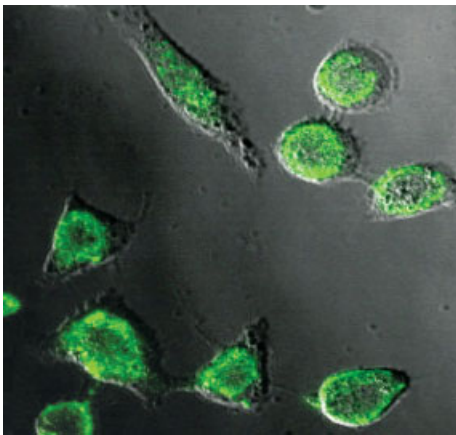


**Figure 3.9.** Confocal image of HeLa cells incubated with the fluorescent peptide–CNT conjugate.



This behavior was observed for the first time in 2004 by Pantarotto and coworkers [190]. The amino groups of *f*-CNTs were coupled either to fluorescein isothiocyanate (FITC) or to a peptide bearing FITC on the side-chain of a lysine (Fig. 3.8).

Subsequently, fibroblasts were incubated with the fluorescent nanotubes. It was found that these tubes were easily internalized by the cells and could be detected in the cytoplasm and the nucleus using epifluorescence and confocal microscopy [190]. This penetrating capacity was also observed in other types of cells (Fig. 3.9).

The mechanism of uptake of this type of *f*-CNTs was energy independent and nonendocytotic. Indeed, the incubation of the fluorescent tubes with different types of cells in the presence of sodium azide or 2,4-dinitrophenol, well-known endocytosis inhibitors, did not block the penetration capacity of the tubes. The reduction of the temperature of incubation from 37 to 4 °C again did not affect cell uptake to a significant extent.

When the CNTs were devoid of the fluorescent moiety, they could be detected in the cells using transmission electron microscopy (TEM) [191]. Ammonium *f*-CNTs were incubated with HeLa cells. After washing, staining and fixing, the cells were embedded into a polymer that was cut into thin slices of 90 nm thicknesses using a diamond microtome. Each slice was deposited on a TEM grid and observed under the microscope. Functionalized nanotubes were visible in the cytoplasm and the nucleus. The tubes were also identified at the level of the cellular membrane in the process of crossing this barrier [191]. The shape of the tube was elongated, suggesting a behavior as a nanoneedle, capable of piercing the lipid bilayer of the membrane without provoking cell death. This mechanism, which can be defined as nanopenetration, was observed by Cai and coworkers, who developed an efficient molecular delivery technique called nanotube spearing [192]. In this case, CNTs filled with magnetic particles were cultured with MCF-7 cells. Under the action of a magnetic field, the suspended tubes were put in rotation to spear the cells. A second static magnetic field was applied under the plate where the cells were grown to pull the tubes through the cell membrane into the cytoplasm. Scanning electron microscopy showed the nanotubes crossing the cell membrane like tiny needles.

NIR fluorescence microscopy could be also used to detect CNTs in the cells [193]. Macrophages were able to phagocytose pristine CNTs without apparent toxic effects. Subsequently, the tubes were tracked into the cells by irradiation at 1100 nm and recovery of a fluorescence signal. This technique seems very promising since it could be extended to the visualization of CNTs in the tissue and the organs. However, only non-*f*-CNTs were used in this study and concerns are emerging about their toxicity once injected into a body (see Section 3.8).

An alternative pathway of penetration of CNTs into the cells was reported by Dai and coworkers. Oxidized CNTs were initially functionalized with biotin and then complexed to a fluorescent SA [115]. The protein–nanotube conjugates were taken up in an endocytosis-mediated mechanism, as they were localized into the endosomes. This behavior was also confirmed by complexing different proteins or nucleic acids to the nanotubes via noncovalent interactions [90, 194]. HeLa and HL-60

cell lines were treated with fluorescent BSA or SA, and a fluorescent 15-mer oligonucleotide at low temperature and in a adenosine triphosphate (ATP)-depleted environment [194]. Preincubation of the cells with sodium azide or cell culture performed at 4 °C clearly influenced nanotube uptake. In addition, it has been demonstrated that the endocytosis was clathrin dependent. To assess the role of clathrin, experiments were carried out in the presence of sucrose and potassium-depleted medium to disrupt the clathrin-coated vesicles. Under these conditions, the level of nanotube cellular uptake was drastically reduced. In parallel, it has also been demonstrated that the nanotubes were not internalized through the caveolae or lipid-raft pathway. In this case the cells were treated with filipin and nystatin, known to perturb the cholesterol distribution on the cell membrane, which is implicated in the lipid-raft mechanism. The two drugs did not hamper the uptake of the CNTs. Therefore, it could be concluded that *f*-CNTs complexed to proteins and nucleic acids penetrate following a clathrin-dependent endocytotoxic process. Elucidation of the different mechanism of cellular entry is crucial for the development of CNTs as delivery system for therapeutic molecules.

### 3.5 CNTs as Delivery Devices for Antigens and Adjuvants

The development of new delivery systems for the successful and effective administration of vaccines and immunotherapeutics still remains a great challenge. The listing of “delivery” among the top 10 biotechnologies required for improving global health has recently reinforced this view [195]. Among the novel delivery options, CNTs have emerged as a promising option for biomedical applications. This is because CNTs can enter into the cells and can be functionalized (see Section 3.4) [148, 190]. The later property makes them soluble, nontoxic and permits modification of their surface [7]. Moreover, these molecules in the nanometer size range offer the control that modern drug delivery and targeting demands – control of the chemical nature of the carrier, control of the surface and, important in targeting, control of dimensions. CNTs can serve as vaccine delivery and adjuvant vehicles by virtue of their nanoparticulate nature. The hydrophobic nature of CNTs contributes to vaccine delivery capability by facilitating the interaction of CNTs with antigens or immunostimulatory molecules and uptake of the vaccine particles by immunocompetent cells.

#### 3.5.1 Interaction of *f*-CNTs with CpG Motifs and Potentiation of their Immunostimulatory Activity

Immune responses to vaccine antigens are normally enhanced by immunostimulants called adjuvants. Recently, synthetic oligodeoxynucleotides (ODN) containing immunostimulatory CpG motifs (ODN CpG) have been considered as candidate adjuvants for vaccines or immunomodulators for therapeutic applications against

tumors, allergy or to combat bioterrorist threats [196–199]. CpG motifs are unmethylated sequences that derive from bacterial DNA. The activation of the immune system by CpG motifs is a highly evolved defense mechanism, whose actual aim is to detect the microbial nucleic acid [200]. This can be achieved through the Toll-like receptor 9 [201], which belongs to the Toll family of pattern recognition receptors, conserved during the evolution in species from insects to humans [202]. CpG motifs induce B cell proliferation, antibody secretion and activate antigen-presenting cells (APCs) to express costimulatory molecules and secrete cytokines including, interleukin (IL)-12 and tumor necrosis factor (TNF)- $\alpha$  [200, 203]. In particular, the increased production of IL-12 promotes interferon (IFN)- $\gamma$  production by natural killer (NK) cells and T cells, and enhances the antigen-specific T cell proliferation and differentiation of naive T cells towards the T helper ( $T_h$ ) 1 phenotype [200, 203]. The triggering of the Toll-like receptor 9 by the ODN CpG is a critical event for the activation of innate immune system [203]. This requires the entry of ODN CpG into the cell for recognition by its receptor, which is expressed in endosomal compartments. Despite the potent immunostimulatory properties of ODN CpGs, their effect is short-lived because of their low uptake by the cells. In order to increase their biological properties, delivery of CpG using CNTs was explored. Therefore, ODN CpGs were first complexed with *f*-CNTs and their interaction analyzed [204], and then the immunostimulatory properties of the complexes were tested *in vitro* [204].

Cationic CNTs lend themselves as vectors for delivery because of their ability to form complexes with ODN CpG. Surface plasmon resonance (SPR) help in the understanding of the interaction that occurred between a *f*-CNT and ODN CpG to form complexes in real time, and gave an insight of how these molecules were bound [204]. Three types of *f*-CNTs were selected in the first series of experiments (Fig. 3.10).

Each *f*-CNT was attached onto the sensor chip by forming a stable amide bond between the amino groups on the tubes and the carboxylic functions on the chip's carboxylated dextran matrix, activated in turn with EDC and NHS. Following attachment, the increase in mass due to the interaction of *f*-CNTs with the ODN CpG 1668 present in the fluid phase was measured using the Biacore 3000 system.

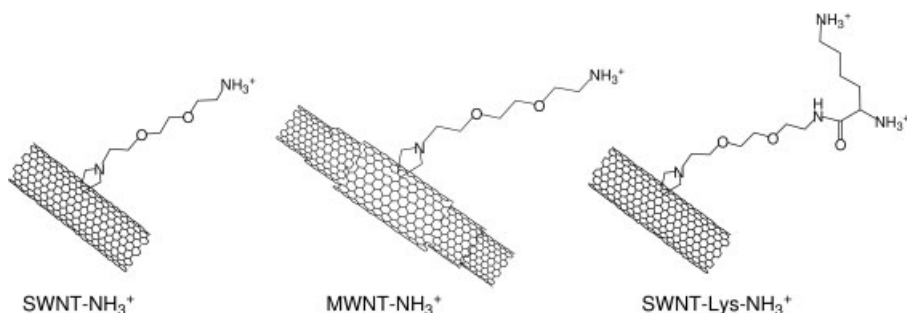


Figure 3.10. Molecular structures of ammonium *f*-CNTs for ODN CpG complexation.

Although there were no significant differences between the affinity of binding between the two SWNT preparations and the ODN CpG 1668, the ODN CpG 1668 bound to the MWNT-NH<sub>3</sub><sup>+</sup> formulation with much lower affinity. This difference was probably due to the relative dimensions and charge distributions of the two types of *f*-CNTs. Both SWNT-Lys-NH<sub>3</sub><sup>+</sup> and MWNT-NH<sub>3</sub><sup>+</sup> displayed the same amount of positive charges. However, there must be an avidity effect, resulting from a double electrostatic interaction per ODN CpG molecule after their binding to SWNT-Lys-NH<sub>3</sub><sup>+</sup> where the two ammonium groups on each lysine residue are in close proximity with respect to the single ammonium on the MWNT-NH<sub>3</sub><sup>+</sup>.

Following the demonstration of complexation of the ODN CpGs with *f*-CNTs, their immunopotentiating effect was tested [204]. SWNTs were the CNTs of choice since they bound to ODN CpG 1668 with higher affinity than the MWNTs. After incubating the SWNT-Lys-NH<sub>3</sub><sup>+</sup> at various excess ratios with a minimal immunostimulatory dose of the ODN CpG 1668, the complexes were added to a culture of naive mouse splenocytes. Complexes of SWNT-Lys-NH<sub>3</sub><sup>+</sup> at 18:1 and 9:1 ratios over the ODN CpG 1668 increased its immunostimulatory properties by 58 and 45%, respectively. There was no significant effect on immunostimulation when lower ratios of SWNT-Lys-NH<sub>3</sub><sup>+</sup>/ODN CpG were tested. Although the mechanism of this immunopotentiating effect is not quite clear, it could be argued that the high excess of SWNT-Lys-NH<sub>3</sub><sup>+</sup> over the ODN CpG 1668 had a neutralizing effect of its negative charge. As a consequence, the repulsion forces by the negatively charged cell membrane were presumably reduced and therefore, the cellular uptake of ODN CpG 1668 was increased.

These preliminary findings pave the way for future *in vivo* experiments using animal models of disease or vaccination protocols to test the therapeutic or adjuvant potential of such complexes. Moreover, further studies will need to address whether serum proteins can alter the surface potential of CNTs, their size, the stability of complexes and the formation of aggregates.

### 3.5.2

#### **Presentation and Immunogenic Potential of Peptide Antigens Attached onto *f*-CNTs**

Peptides representing selected regions from the amino acid sequence of a protein antigen (epitopes) can be used as immunogens to induce peptide- and pathogen-specific B cell and CD4<sup>+</sup> (T<sub>h</sub>) or cytotoxic CD8<sup>+</sup> [cytotoxic T lymphocyte (CTL)] T cell responses. Activated CD4<sup>+</sup> T cells help B cells to produce antibodies that neutralize viruses and bacterial toxins [205], enhance the magnitude of cytotoxic T cell responses to clear virus-infected cells [206], and regulate the immune responses to foreign antigens on the basis of the cytokine profile they secrete [207]. CD8<sup>+</sup> T cells are the main effector cells responsible for the clearance of viral infections [208]. The development of such peptide vaccines requires a basic knowledge of the role of the various antigens of the pathogen in infection and immunity, the use of a cocktail of epitopes able to induce a broad range of protective antibody and T cell responses, and a delivery system for presentation of these epitopes to immunocompetent cells.

B cell epitopes are mainly located on the surface of a protein antigen. Therefore, the native structure of the antigen is critical for recognition by antibodies. Immunization with flexible peptides normally induces a diverse set of antibody specificities that bind several different conformations of the peptide [209]. However, a subset of these antibodies can cross-react with the native protein, presumably because these peptides adopt a conformation similar to the native epitope [209]. Therefore, for a synthetic peptide vaccine to elicit a protective antibody response it is important the B cell epitope to be presented to the immune system at a conformation mimicking the native structure. The ability of *f*-CNTs to present a covalently linked synthetic peptide representing a neutralizing and protective B cell epitope from the foot-and-mouth disease virus (FMDV) corresponding to the 141–159 region of the VP1 viral envelope protein was tested [210]. SWNTs-NH<sub>3</sub><sup>+</sup> and SWNTs-Lys-NH<sub>3</sub><sup>+</sup> modified with a maleimido group were used. This functionality allowed linking the FMDV peptide bearing an additional cysteine at the N-terminus necessary for a selective chemical ligation (Fig. 3.11).

To elucidate the structural and functional relationship between *f*-CNTs-linked peptide and peptide-specific polyclonal and monoclonal antibodies, the ELISA test and SPR were used. Both methods demonstrated that the SWNTs-linked peptide retained the structural features required for recognition by anti-FMDV peptide monoclonal and polyclonal antibodies [148, 211].

Since the FMDV peptide was not immunogenic (i.e. not capable of eliciting an immune response) in BALB/c mice (T cell help is required) [212] an immunization protocol that has been previously shown to overcome the requirement of coupling nonimmunogenic peptides to carrier proteins or T<sub>h</sub> epitopes was employed [213]. To this end, the SWNT-linked FMDV peptide was coimmunized with a protein antigen that provided T cell help, like ovalbumin (OVA) in a Freund's emulsion. After two injections, strong antipeptide antibody responses were induced that had significantly higher virus neutralizing capacity than the antibodies elicited after coimmunizing the free peptide with OVA [211]. This finding highlights the potential of *f*-CNTs to act as a delivery system capable of presenting critical epitopes at an

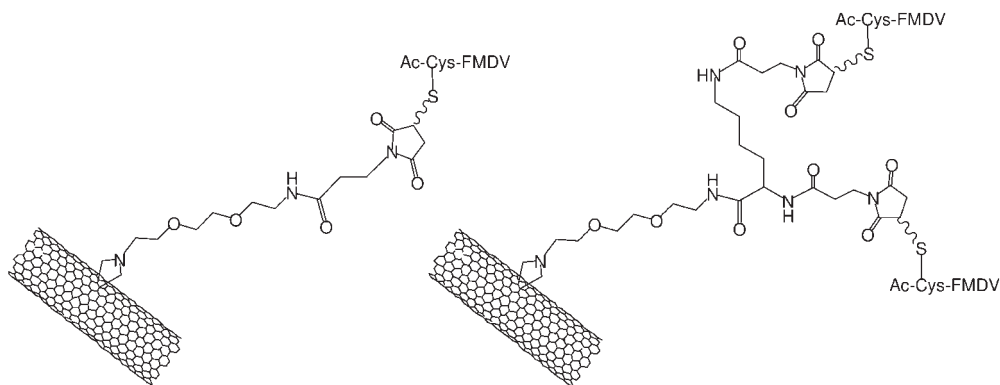


Figure 3.11. Molecular structures of FMDV peptide *f*-CNTs.

appropriate conformation to elicit antibodies with the right specificity. Moreover, no antibody responses were induced against the *f*-CNTs, which could potentially hamper the successful outcome of the immunization procedure, particularly when several administrations are required [214].

Although the application of CNTs in the field of vaccine delivery is in its infancy, CNTs offer several attractive features, including the control one has over the primary nature of the system. They provide a platform for the attachment of adjuvants and antigens. Their potential use as vaccine delivery and adjuvant vehicles is likely to have a significant impact on the route that vaccines will be administered in the future and the required dose, conferring a competitive advantage in the market place. Obviously, their immunogenicity, toxicity, biodegradability, stability, biocompatibility, cost and consistent GMP manufacturing with readily scalable production processes has to be studied for each system and each application. These challenging issues should not inhibit research in examining the potential of CNTs to deliver vaccines since the most interesting and valuable delivery systems are yet to come.

### 3.6

#### CNTs for Drug Delivery

Drug delivery systems are necessary to improve the pharmacological profile and the therapeutic properties of administered drugs [1]. Among the wide variety of available delivery systems, CNTs may represent a promising alternative [215]. The application of *f*-CNTs as new nanovectors for drug delivery became possible soon after the demonstration of cellular uptake of this new material. However, only a few examples of delivery of therapeutic agents using CNTs are currently reported in the literature. Dai and coworkers have shown the potential of CNTs to transport proteins into the cells [90]. Single-walled CNTs were shortened to a length between 20 and 100 nm using strong acid conditions. This treatment also allowed the generation of carboxylic groups at the terminal parts of the tubes and at their defect sites. The carboxylated tubes were complexed with different types of proteins including SA, protein A, BSA and cytochrome *c* (Fig. 3.12).

Mammalian cell lines were incubated with the complexes to study the capacity of CNTs to drive the adsorbed proteins into the cells. The complexes were localized in the endosomes and released into the cytoplasm by addition of chloroquine (a molecule able to destroy the endosomes). In the case of cytochrome *c*, it was verified that the protein exerted its biological function after liberation from the endosomal trap. Indeed, the cells entered into apoptosis. At the same time, it was shown that CNT-protein complexes were biocompatible by measuring cell proliferation.

In a different approach, Wu and coworkers used *f*-CNTs with AmB – one of the most effective antimycotic molecules for the treatment of chronic fungal infections (Fig. 3.13) [152].

MWNTs were treated with strong acid conditioned to reduce their length to about 180–940 nm. The carboxylic groups were coupled with a phthalimide

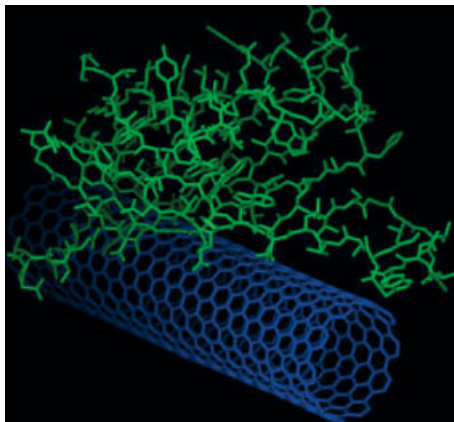


**Figure 3.12.** Molecular model of the complex between a shortened CNTs and SA.

mono-protected triethylene glycol diamine. Subsequently, the tubes underwent the 1,3-dipolar cycloaddition reaction to introduce a N-functionalized pyrrolidine ring on the external walls of the tubes. A second Boc-protected amino group was therefore introduced on the nanotubes. The two protecting groups are orthogonal and permitted to modify the tubes with a fluorescent probe to follow the cell internalization of the conjugate and the active drug AmB to exert its antifungal activity. It

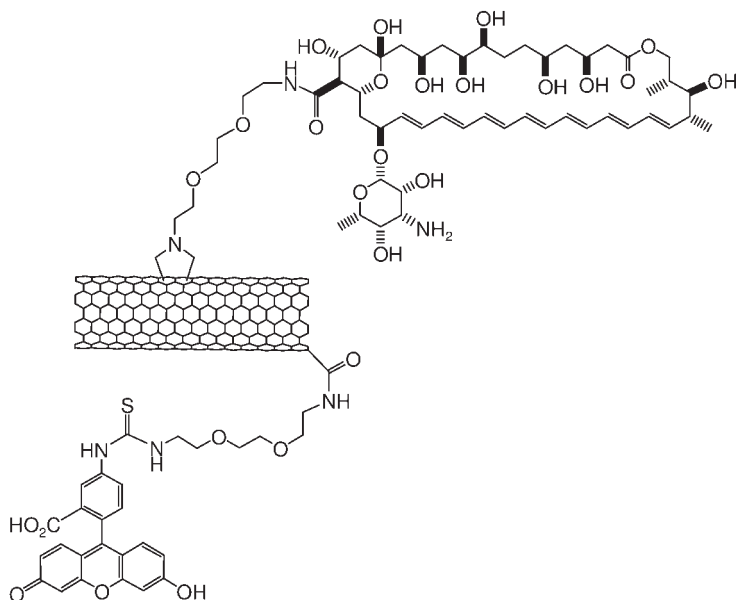


**Figure 3.13.** Molecular structure of CNTs functionalized with FITC and AmB.

has been shown that AmB–CNTs were rapidly internalized into Jurkat cells in a dose-dependent manner. The process was nonendocytotoxic since the incubation of the cells at 4 °C or in the presence of sodium azide did not completely block the uptake. The drug was internalized into mammalian cells with a remarkable reduction of toxicity. Indeed, AmB is widely used, but it suffers from high toxicity. At the highest dose, more than 40% of cells died by the effect of free AmB, while all cells remained alive following the treatment with AmB covalently conjugated to CNTs. Very interestingly, AmB preserved its high antifungal activity once linked to the nanotubes. Different types of pathogens including *Candida albicans*, *Candida parapsilosis* and *Cryptococcus neoformans* were treated with AmB–CNT conjugates, and the activity was in some cases higher than the drug alone. Although only some hypotheses on the action of the AmB linked to the tubes could be formulated (increase of the solubility of the drug, multipresentation of the drug by CNTs that favor interaction with the fungal membrane), the conjugation of AmB to the tubes modulated its therapeutic effect by decreasing mammalian toxicity and increasing the antifungal activity.

Using another strategy, Hosmane and coworkers prepared SWNTs with a carborane cage for boron neutron capture therapy (BNCT) [216]. CNTs were functionalized with a substituted  $C_2B_{10}$  carborane derivative via nitrene cycloaddition. Following treatment with sodium hydroxide, a water-soluble CNT conjugate was obtained (Fig. 3.14).

Then, the biodistribution study on different tissues showed that carborane nanotubes were concentrated more in tumor cells than in blood, liver, lung or spleen when administered intravenously. However, the mechanism for this it is not yet understood. The results are preliminary, although promising for future applications of CNTs on delivery of boron-based agents for effective BNCT treatment of cancer, provided that cytotoxicity and more complete biodistribution studies prove the biocompatibility of this system. Another application of CNTs in cancer therapy was shown by Kam and coworkers [217]. The property of CNTs to adsorb NIR irradiation was exploited to kill cancer cells. Pristine SWNTs were wrapped with PEG modified with a PL moiety on one side and folic acid (FA) on the other side. As

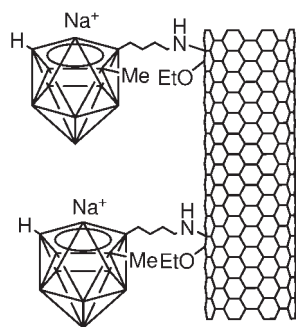
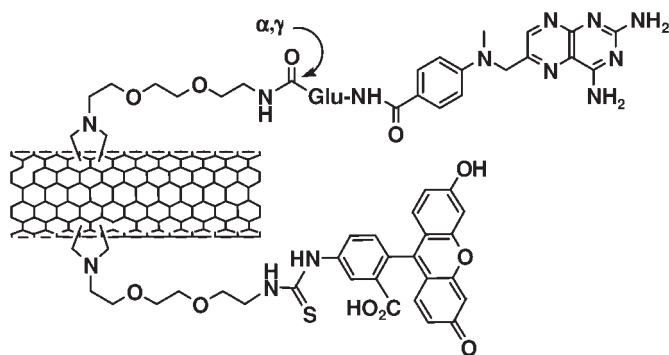


Figure 3.14. Molecular structure of CNTs functionalized with a carborane cage.





**Figure 3.15.** Molecular structure of CNTs functionalized with FITC and methotrexate.

tumor cells are known to overexpress folate receptors, the PL-PEG-FA/SWNT construct was mainly taken up by cancer cells, which were then destroyed by using a laser wavelength of 808 nm. Laser pulses induced local heating and consequently death only of those tumor cells that had internalized the CNTs.

Pastorin and coworkers have developed an alternative method to exploit CNTs in cancer [218]. CNTs were doubly functionalized using 1,3-dipolar cycloaddition reaction. Two orthogonally protected amino groups were introduced on the sidewalls and the tips of the tubes. After selective deprotection, an anticancer molecule [methotrexate (MTX)] and a fluorescent probe (FITC) were linked to the tubes (Fig. 3.15).

MTX is a drug widely used against cancer, but it displays a reduced cellular uptake. Therefore, the limited capacity of MTX to cross the cell membrane could be overcome by its conjugation to CNTs, which are able to enhance cell uptake of linked moieties. The presence of fluorescein provided the optical signal for imaging CNT-drug into the cells. Jurkat cells were incubated with different doses of MTX-CNT and the fluorescent tubes were localized around the nuclear membrane in a dose-dependent manner. Preliminary studies have shown that MTX conjugated to the CNTs had the same cytotoxic activity of the drug alone.

Another class of carbon nanomaterials very similar to CNTs called carbon nanohorns were found to be effective systems for delivery of anticancer agents. Single-walled carbon nanohorns (SWCHs) are spherical aggregates of graphitic tubes with dimensions in the nanorange scale. These nanostructures were loaded with dexamethasone [219]. Binding and release of the drug were subsequently evaluated using two types of nanohorns. It was found that oxidized nanohorns were able to adsorb more dexamethasone than as-grown horns. The analysis of activation of glucocorticoid response in mouse bone marrow cells and induction of alkaline phosphatase in mouse osteoblasts confirmed the biological activity of the drug released from the carbon support. Similarly, carbon nanohorns were used to encapsulate cisplatin (another anticancer agent) [220]. Again, the structure of the drug was preserved into the aggregates. Cisplatin was slowly liberated into water and it was effective in blocking the growth of human lung cancer cells. Unloaded oxi-

dized carbon nanohorns were instead not active. Therefore, this type of carbon material is potentially useful as a carrier of anticancer agents.

In view of the overall results, functionalized carbon nanostructures represent an emerging and new class of delivery tools for the transport, encapsulation and release of molecules into mammalian cells. However, it will be important in the near future to assess the metabolism, biodistribution and clearance from the body of nanotubes for further development and complete integration in living systems.

## 3.7

### CNTs for Gene Transfer

#### 3.7.1

##### Interaction with DNA and RNA

In the quest for a useful nonviral gene transfer system, the interaction between a cationic component (liposome, polymer, nanoparticle) and the negatively charged nucleic acids to be delivered is critical for the eventual effectiveness of the gene transfer construct. CNTs have very recently been explored for the first time as novel materials for the complexation and delivery of gene-encoding nucleic acids [191, 221]. However, the physicochemical interactions between CNTs and DNA have been studied under different contexts for much longer, particularly in attempts to disperse non-*f*-CNTs, and for the construction of sensors, nanocircuits, nanocomposites and gene delivery vectors.

Theoretical predictions of DNA interactions with CNTs by molecular dynamics simulations have shown that single-stranded DNA spontaneously inserts into non-*f*-CNTs through a combination of van der Waals and hydrophobic forces [222]. However, a recent molecular modeling simulation has demonstrated that double-stranded DNA can also wrap around non-*f*-CNTs or, in the case of positively charged CNTs in an aqueous environment, DNA molecules could electrostatically adhere onto the CNTs surface [223].

Experimentally, a range of different techniques has been used to understand the CNT–DNA interactions and the ensuing supramolecular structures between the two components. However, most studies agree that the nature and mechanism of such interactions will be highly dependent on the type of CNTs surface functionalization and the characteristics of the nucleic acids.

UV and IR spectroscopy have both been used to show that non-*f*-SWNTs and double-stranded DNA interact through hydrogen bonds [224, 225]. Changes in the electronic levels in the nucleotide bases of the DNA molecule were found in these studies and the DNA acquired a chaotic sphere conformation upon interaction with CNTs.  $\pi$ – $\pi$  interactions between the CNT sidewalls and the nucleic acid bases have been proposed as the mechanistic basis for this wrapping effect. Moreover, the ability of DNA to wrap around the CNT surface has been described for both double-stranded DNA [226, 227] and single-stranded DNA [91], and has been utilized to disperse CNTs in solvents of varying polarity.

As described earlier in this chapter, CNT surface characteristics can be altered through organic and defect functionalization. By strong oxidation, OH and C=O defects are introduced at the tips and sidewalls of CNTs. Several studies describe that these oxidized CNTs (CNT-ox) covalently bond DNA-NH<sub>2</sub> in a controllable assembling process [38, 118, 228, 229] or are helically wrapped ( $\pi$ - $\pi$  interactions) by double-stranded DNA and single-stranded DNA [230–232]. An alternative functionalization reaction described by Georgakilas and coworkers produces positively charged ammonium-*f*-CNTs (CNT-NH<sub>3</sub><sup>+</sup>) [146]. The interaction of CNT-NH<sub>3</sub><sup>+</sup> with plasmid DNA (pDNA) was studied in detail in our laboratories [221, 233]. We have found that these *f*-CNTs interact with pDNA to form complexes primarily through electrostatic forces and that the pDNA was condensed around the CNT-NH<sub>3</sub><sup>+</sup>. Moreover, these studies have indicated that the total available surface area and the surface charge density of CNTs were critical parameters in the interaction and complexation of pDNA.

With regard to interactions between RNA and CNTs, to our knowledge there has only been one published report describing the interaction between non-*f*-SWNTs and RNA polymer poly(rU) [234]. In this study the RNA polymer poly(rU) was observed in a blob-like conformation when bound at the surface of CNTs as imaged by scanning electron microscopy, resembling the condensation of pDNA strands. These authors suggested that the binding occurs through  $\pi$ -stacking and hydrophobic interactions; however, no detailed mechanistic study has been published so far describing how the CNT–RNA interactions occur.

### 3.7.2

#### Delivery and Expression of Gene-encoding DNA and RNA

The development of water-soluble CNTs automatically renders them compatible with the biological fluids and milieu. The complex formation between CNTs and nucleic acids in combination with the improved CNT biocompatibility recently achieved allowed for exploration of the hypothesis that CNTs can be used as gene-delivery systems. So far, the intracellular translocation and expression of gene-encoding nucleic acids (DNA and RNA) involving CNTs have been shown for mammalian cells to bacteria *in vitro*. The following is a comparative description of the different techniques used to deliver nucleic acids to cells through CNTs.

The first ever study to demonstrate CNT-mediated gene delivery and expression of marker gene-encoding nucleic acids was carried out in our laboratories. Pantarotto and coworkers reported that CNTs covalently functionalized with ammonium groups (CNT-NH<sub>3</sub><sup>+</sup>) were able to associate with pDNA through electrostatic interactions [191]. Transmission electron microscopy images of the supramolecular complexes showed the pDNA attaining a condensed globular conformation at the surface of the CNT-NH<sub>3</sub><sup>+</sup>. The delivery of pDNA and expression of  $\beta$ -galactosidase (a marker gene) in CHO cells was found to be approximately 10 times higher than naked pDNA. An endosome-independent penetration mechanism was proposed for the complex uptake based on evidence of spontaneous cellular uptake of the *f*-CNTs alone. Similar to other nonviral gene delivery systems based on the elec-

trostatic supramolecular complex formation between a cationic macromolecule or nanoparticle and nucleic acids, the charge ratio (+/−) CNT-NH<sub>3</sub><sup>+</sup>:pDNA was found to be a critically important factor determining the level of gene expression.

A similar approach was later followed by Liu and coworkers, which reported a noncovalent association of pDNA onto the surface of CNTs functionalized with polyethylenimine (PEI) – a polymer with high density of terminal amine groups [235]. The complexes were tested at different charge ratios in different cell lines (293, COS7 and HepG2 cells) and the level of gene (pCMV-Luc) expression was found to be much higher than those of DNA alone. This study suggested that the uptake mechanism of the CNT-PEI-pDNA conjugates was took place by endocytosis.

Kam and coworkers later used two distinct methods to deliver nucleic acids via CNTs into HeLa cells. In a first study [217], CNTs functionalized with Cy3-labeled single-stranded DNA through noncovalent adsorption were used. These CNTs were excited with NIR light. The release and nuclear translocation of the single-stranded DNA was reported by confocal microscopy only in the case of NIR treatment. In the absence of cell illumination by NIR, the Cy3-DNA was seen by Kam and coworkers to remain in the cytoplasm. This group also suggested an endosome-mediated cellular uptake.

In a subsequent study by the same group [93], CNTs were functionalized by non-covalent adsorption of PL molecules, which contained a PEG chain terminating in an amine (CNT-PL-PEG-NH<sub>2</sub>) or maleimide (CNT-PL-PEG-maleimide) group. Then a thiol-containing SH-DNA-Cy3 was covalently linked to the CNTs via a disulfide bond by a heterobifunctional cross-linker. In this way, a complicated CNT-PL-PEG-single-stranded DNA-Cy3 complex was formed, sensitive to enzymatic cleavage upon endocytosis and translocation to the lysosomal compartments. It was reported in that study that nuclear localization of Cy3-DNA was possible only in the presence of the disulfide linkage. However, in this study gene-encoding nucleic acids were not used therefore no gene expression was reported at all.

A very different strategy to introduce exogenous pDNA into mammalian cells was described recently by Cai and coworkers [192]. The pDNA was immobilized on the CNTs, which contained Ni particles (CNT-Ni) enclosed and suspended with the surfactant Nanospere AQ. Then, with a magnetic spearing technique (exposure to an external magnetic field followed by centrifugation) the complexes were added to Bal 17 cells, mouse splenic cells and a primary culture of mice cortical neurons. The expression of the enhanced green fluorescent protein (*EGFP*) gene was evaluated by fluorescence microscopy and flow cytometry. Gene delivery through CNT-Ni produced 80–100% fluorescent cells, while CNTs deprived of Ni particles did not produce any fluorescence signal. In this way, another illustration of the possibility to use CNTs to transport intracellularly gene expressing nucleic acids was seen. However, such techniques are only appropriate for *in vitro* or *ex vivo* gene transfer.

The delivery of exogenous genes by CNTs has been shown to be also possible in bacterial cultures. Rojas-Chapana and coworkers have demonstrated that oxidized, water-dispersible CNTs deliver pDNA into *Escherichia coli* through temporary nano-

channels across the cell envelope [236]. The pUC19-transformed bacteria were examined by optical microscopy, and an efficient transformation between 9 and 32 transformants was observed. The authors achieved that by an electroporation technique using microwave-activated CNTs, which apparently orient their tips in a conformation perpendicular to the bacterial cell membrane.

CNTs have also been shown to transport RNA into mammalian cells. Lu and coworkers have studied the cellular uptake of CNT–RNA polymer poly(rU) hybrids formed through nonspecific binding. MCF7 cells were examined by confocal microscopy after addition of the hybrids, and their translocation in cellular and nuclear membranes reported [237]. In agreement with these findings, Kam and coworkers, in more a recent report, used a complex CNT–small interfering RNA (siRNA) conjugate linked with disulfide bonds (as described above for single-stranded DNA) and have shown preliminary observations of siRNA-mediated gene silencing [93].

All of these studies have been initiated by our initial observations that it was indeed feasible to use *f*-CNTs to complex, deliver and express gene-encoding nucleic acids. The most recent study in this exploratory exercise has been very recently published using GFP-encoding pDNA condensed with *f*-CNTs carrying positive charges [238]. In this way our initial reports and observations were indeed substantiated and reproduced in an independent study. The development of CNTs as delivery systems for nucleic acids is still in its exploratory stage, and many more studies are needed to determine the advantages and limitations offered by these novel materials.

### 3.8

#### Health Impact of CNTs

Nanotechnology has been rapidly developing due to the possibility of engineering at nanometer scales. The resulting nanoproducts display physicochemical characteristics that confer electrochemical, mechanical and thermal properties that are very useful in the medical, scientific, commercial and environmental fields. However, it is too early to say whether the “nanostructures” will wean the world from dirty technologies or if they will definitely backfire, basically because the laws of chemistry or physics are different when particles get down to the nanoscale. Even substances that are normally innocuous can trigger intense chemical reactions and biological anomalies as nanospecies [239].

For this reason, there is a heated debate between the desire of introducing nanomaterials in everyday life and the moralistic tendency of blocking the nanotech factory until the risks will be better understood. Currently, available information concerning the relative environmental and health risks of manufactured nanoparticles or nanomaterials is severely absent and defective. In fact, most of nanomaterials (fullerenes, nanoparticles, nanofibers and nanotubes) are made of carbon atoms, with distinct geometries, different surface areas, and diverse physical and chemical

properties. The existence of such variables produced a lot of contrasting evidence. Doses, effects and cell viability of different carbon nanomaterials are summarized in Tab. 3.1. For example, Adelmann and coworkers have studied the *in vitro* effect of fullerenes on alveolar macrophages, prepared in an arc between two graphite electrodes [240]. A 60% reduction in macrophage viability and increased levels of some inflammatory cytokines were found, suggesting that such structures had similar toxicity to quartz particles. Moreover, it was discovered that stable solutions of C<sub>60</sub> nanoparticles (nano-C<sub>60</sub>) displayed a high toxicity against bacteria at a concentration of 0.4 μg mL<sup>-1</sup> [241]. Other highly water-soluble nanofullerenes (13–100 mg mL<sup>-1</sup>) showed also a remarkable cytotoxicity both in fibroblasts and in liver carcinoma cells at very low concentrations (50 μg mL<sup>-1</sup>) [242]. It could be deduced that such behavior conveys a common toxicity of all C<sub>60</sub> materials [243]. On the contrary, it was observed that the lethal doses varied by seven orders of magnitude, strongly depending on the functionalization of the fullerene surface [242]. Therefore, the further modification at the surface deeply influenced the toxicological profile of the nanomaterials [244].

In contrast, some *in vivo* studies on fullerene showed that intraperitoneal injections of amounts of C<sub>60</sub> up to 2.5 g kg<sup>-1</sup> in mice and rats had neither lethal effects nor acute toxicity [245, 246]. What was evident was only a hypertrophy of livers and spleens, which could be ascribed to the high amount of compound injected that had exceeded the absorption capacity of the animal. Similarly, mice subcutaneously implanted with Hat-stacked carbon nanofibers did not show severe inflammatory responses such as necrosis or degeneration after 4 weeks of incubation [247]. However, these encouraging results are not exhaustive in representing the reduced harmfulness of all the different nanomaterials.

### 3.8.1

#### Parameters of CNTs Related to Health Impact

The data reported above suggest that, in general, carbon nanoparticles can be considered as dangerous as quartz, only on the basis of the common “starting material”, i.e. carbon. In particular, CNTs represent a class of substances which are, at the same time, intriguing (for their characteristics) and doubtful. In fact, they revealed unusual toxicological properties, because their shapes can be both fibers and nanoparticles, and they are often characterized by the presence of metallic components even after their purification. CNTs, both single and multiwalled, are classified as “synthetic graphite” by the National Occupational Safety and Health Administration, on the basis of the same hexagonal/honeycomb pattern. However, such extrapolation might not be protective for exposure to CNTs, because they show physicochemical properties that are often influenced by several variables.

##### 3.8.1.1 Purity

CNTs generally show different levels of purity, which are strictly dependent on the methods employed for their production. The impurities are essentially made up of

Tab. 3.1. Doses, effects and cell viability of different carbon nanomaterials.

Type of nanomaterial	Amount/ concentration	Cell/animal target	Effect	Possible causes	Ref.
Fullerenes	not specified	alveolar macrophages	60% reduction on cell viability; inflammatory cytokines (IL-6, IL-8)	intrinsic toxicity	240
Nano C <sub>60</sub>	0.4 µg mL <sup>-1</sup>	bacteria	growth inhibition		241
Nano C <sub>60</sub>	50 µg mL <sup>-1</sup>	fibroblast; liver carcinoma cells	decreasing cytotoxicity with increasing functionalization and solubility	oxidative stress; surface effect	242
Functionalized gold nanoparticles	250 µM	leukemia cells	no remarkable cell death; rapid internalization		244
C <sub>60</sub>	2.5 g kg <sup>-1</sup>	mice and rats	no acute toxicity; hypertrophy	too high amount	245, 246
Hat-stacked carbon nanofibers (H-CNF)	not specified	rats	no toxicity		247
SWNTs, MWNTs, fullerenes	≥1.41 µg cm <sup>-2</sup>	alveolar macrophages	20% reduction on cell viability (SWNTs)	low purity	248
Pristine SWNTs	0.1–10 µg mL <sup>-1</sup>	HaCaT cells	increased cell death	oxidative stress or solvent (DMF)	249
<i>f</i> -SWNTs	3 µg mL <sup>-1</sup> – 30 mg mL <sup>-1</sup>	HDF	cell death 50% or below		252
MWNTs (220 and 825 nm)	50–500 ng mL <sup>-1</sup> ( <i>in vitro</i> )	leukemia cells THP-1	inflammation (especially with 825-nm samples)	length	253
	0.1 mg mL <sup>-1</sup> ( <i>in vivo</i> )	mice	granulomatous inflammation		253
HiPCO, CVD- SWNTs and CVD- double-walled CNTs	0.62–2.5 mg	red blood cells	complement activation	C1q activation	254
Arc-SWNTs and CVD-H-CNF	10 µg mL <sup>-1</sup>	leukemia cells THP-1; mouse spleen cells	immune response	Induction of TNF- $\alpha$	255

Tab. 3.1 (continued)

Type of nanomaterial	Amount/ concentration	Cell/animal target	Effect	Possible causes	Ref.
<i>f</i> -SWNTs	<5 $\mu\text{M}$	fibroblasts	no remarkable cell death (90%); rapid internalization		190
<i>f</i> -SWNTs and <i>f</i> -MWNTs + plasmid DNA	1 mg mL <sup>-1</sup>	HeLa cells	no remarkable cell death; efficient delivery		191
MWNT-PEI + DNA	<5 $\mu\text{g mL}^{-1}$	HEK293 cells	below 40% reduction on cell viability	increased PEI weight	235
SWNT-CpG ODN	5 ng-5 $\mu\text{g}$	mouse splenocytes	no remarkable cell death		204
SWNT-RNA	$\leq 1$ mg mL <sup>-1</sup>	breast cancer cells (MCF7)	efficient delivery		237
SWNTs	1-250 $\mu\text{g mL}^{-1}$	embryo kidney cells (HEK293 cells)	apoptosis; 20/30-kDa protein secretion	downregulation of genes for adhesion; upregulation of genes involved in apoptosis	256
Pristine MWNTs	0.1-0.4 mg mL <sup>-1</sup>	embryo kidney cells (HEK293)	inflammation	production of IL-8	257
Pristine and oxidized MWNTs	400 $\mu\text{g mL}^{-1}$	T lymphocytes	40% reduction on cell viability (pristine) 80% reduction on cell viability (oxidation)	better dispersion of oxidized tubes	258
MWNTs	0.5, 2 or 5 mg	rats	upregulation of pro-inflammatory and profibrotic mediators	biopersistence in the lung	259
Raw, HiPCO and arc-SWNTs	0.1 or 0.5 mg per mouse	mice	granulomas	intrinsic toxicity	260
Pristine SWNTs	1 or 5 mg kg <sup>-1</sup>	rats	pulmonary inflammation, with non-dose-dependent granulomas	blockage of upper airways	261



Tab. 3.1 (continued)

Type of nanomaterial	Amount/ concentration	Cell/animal target	Effect	Possible causes	Ref.
Fullerenes and CNTs	0.2 mL (not specified)	four albino rabbits and 40 human volunteers	no remarkable skin irritation or allergen risks		262 263
Carbon fiber particles	not specified	341 workers	contact dermatitis	exposure to organic solvents or to carbonaceous particles	264 265
Pristine HiPCO–SWNTs	0.06, 0.12 or 0.24 mg mL <sup>-1</sup>	HaCaT cells	alteration of cell morphology and surface integrity	transition metal catalysts	266
Pristine HiPCO or laser ablation SWNTs (aerosol)	15.5 mg	cotton gloves	deposition on individual gloves ranged from 217 to 6020 µg (aerosol below 53 µg m <sup>-3</sup> )	ultrafine powders	267

residual catalysts and amorphous carbon. Their high amount might enhance the toxicity. In this context, Jia and coworkers investigated the cytotoxicity caused by nanostructures such as SWNTs, MWNTs and fullerenes on alveolar macrophages (AM) [248]. The different carbon particles, all with a purity superior than 90%, were suspended in RPMI medium using a Dounce homogenizer and sonicated for 20 min. In this way, a stable suspension was obtained and immediately used to measure the phagocytic ability of AM after a 6-h exposure to carbon materials. The amount of materials used was expressed as µg cm<sup>-2</sup>, because CNTs are characterized by a wide length distribution. As expected, the tested samples exhibited different cytotoxicity to AM. At low doses (1.41 µg cm<sup>-2</sup>) SWNTs showed a high cytotoxic effect, corresponding to above 20% inhibition of cell growth with a dose-dependent trend. MWNTs and fullerene were instead much less toxic. One possible reason for such a major difference could be attributed to the purity level of SWNTs that was lower than the other samples. Indeed, residual amorphous carbon and trace amounts of metallic catalysts, such as Fe, Ni and Y, were present in SWNT samples. These impurities, even at a low level, can influence cell viability, so ultrapure material should be employed; in any case, human and environmental health evaluations of different carbon nanomaterials must be considered individually.

### 3.8.1.2 Solvents

Any kind of cell evaluation needs a medium to dissolve the sample. Physiological solutions, with the addition of nutritional elements, are the most appropriate, but sometimes the low solubility of the carbon material requires the use of polar, organic solvents. Manna and coworkers investigated the essential mechanism involved in the toxicity of SWNTs [249]. Human keratinocytes (HaCaT cells) were exposed to concentrations between 0.1 and 10  $\mu\text{g mL}^{-1}$  of nanotubes, displaying increased cell death. This observation was attributed to the excess of oxidative stress within the cells and to the associated activation of transcription factor NF- $\kappa$ B. However, DMF was used to dissolve the samples and might have induced some alterations of the results. In fact, DMF is a solvent known to be toxic and thus it should be avoided in cell manipulation.

### 3.8.1.3 Surface of CNTs

Until now, the size cut-off below which particles are surely toxic has not been demonstrated. However, there are at least two main reasons that render CNTs potentially harmful: (i) their large surface area and (ii) the reactivity or intrinsic toxicity of the surface [250, 251]. The smaller the particles, the more toxic they become. This is due to the fact that there is more surface area per mass unit. As a consequence, any intrinsic toxicity of the surface will deeply influence the toxicological profile of the samples. For example, Sayes and Ausman investigated the effect on human fibroblasts (HDF) of some water-dispersible SWNTs [252]. It was found that cytotoxicity of compounds decreased significantly with the increased degree of functionalization on the surface. In addition, although a dose–response relationship of toxicity in the considered range of concentrations (0.003–30  $\text{mg mL}^{-1}$ ) was observed, cell death did not exceed 50%, apart from in one case in which 1% surfactant was employed. This could be justified by the fact that surfactant was coated on the surface of the nanotubes in a noncovalent, reversible way, whereas the functional groups were covalently bound and were not removed in the conditions of the biological tests.

### 3.8.1.4 Length

Another parameter that was found to influence the toxicity profile of CNTs is their length. Sato and coworkers separated MWNTs of 220 and 825 nm using controlled strong acid conditions [253]. During a short incubation time, clusters of both samples were shown to be surrounded by macrophages as a consequence of the activation of innate immunity. The shorter tubes displayed a lower inflammatory response. In both cases, no severe effects, such as necrosis or degeneration, were observed around CNTs throughout the experimental period of 4 weeks.

## 3.8.2

### *In Vitro* Effect of CNTs

SWNTs were investigated to verify if they affected the immune system through the activation of complement [254]. For this purpose, SWNTs in concentrations be-

tween 0.62 and 2.5 mg were tested in rabbit red blood cells. They displayed a dose-dependent potency in complement activation comparable to that of the known, potent activator zymosan. In particular, it seemed that such activation followed the classical pathway, but with high selectivity. This was confirmed by the demonstration of a direct binding of CNTs to the main complement subunit C1q. On the contrary, chemical modifications at the surface of CNTs reduced or even eliminated the complement activation, but further investigations are necessary to confirm this observation.

In a parallel study, SWNTs were evaluated in terms of their capacity to activate mouse spleen cells [255]. Since different cell types (monocytic leukemia THP-1 and spleen cells) and incubation times were employed, it was difficult to compare the obtained results. It has been confirmed that SWNTs induced an immune response, although the stimulating activity resulted to be lower than that of microbial systems.

The effect of functionalized, water-soluble CNTs on cell viability was also analyzed by Pantarotto and coworkers during the study of translocation of bioactive peptides across the cell membrane [190]. 3T6 and 3T3 fibroblasts were treated with 1–10  $\mu\text{M}$  concentration of fluorescent SWNTs. The cytotoxicity was evaluated by flow cytometry, using the markers Annexin V and propidium iodide as indicators of apoptosis and necrosis, respectively. It was observed that below 5  $\mu\text{M}$  almost 90% of the cell population remained alive, indicating a nontoxic behavior of *f*-CNTs. Low toxicity was not only a characteristic of SWNTs functionalized with peptides. Both *f*-SWNTs and *f*-MWNTs, regardless of cell subtypes, are nontoxic on their own [90, 220]. HeLa cells, incubated for several hours with about 1 mg mL<sup>-1</sup> of CNTs mixed with plasmid DNA in different charge ratios, did not demonstrate signs of apoptosis [191]. In addition, *f*-CNTs complexed to different types of nucleic acids including plasmid DNA, RNA and oligodeoxynucleotides CpG sequences were not toxic for cells like breast cancer cells (MCF7) or splenocytes [204, 235, 237].

Apart from the investigation of the effect of CNTs on cells, it is also important to understand the mechanism involved in their interaction with biological systems. Cui and coworkers evaluated the activity of human embryo kidney cells (HEK293) during 5 days treatment with SWNTs in concentrations between 1 and 250  $\mu\text{g mL}^{-1}$  [256]. It was found that SWNTs were able to inhibit the proliferation of HEK293, and to induce apoptosis in a dose- and time-dependent way. The most interesting finding was that cells actively responded to SWNTs, secreting a series of 20- to 30-kDa proteins able to aggregate and wrap this unknown material, regardless of the uniformity of the starting samples. The possible mechanism for this phenomenon was attributed to a stimuli induced by SWNTs attached at the cell surface, followed by a downregulation of the genes responsible for adhesion. It was also envisaged that SWNTs could determine an upregulation of the genes associated with apoptosis and secretion of small proteins as protection for cells that were preserved from the contact with the tubes. This phenomenon presents a double advantage, since it allows us to investigate the rules at the basis of this interaction and, at the same

time, it offers the possibility to consider these secreted proteins as potential targets in future medical therapy.

The same type of cells was also used to verify if bigger material, like MWNTs, was able to cross the external membrane and to affect the cell functions. It was shown that unmodified MWNTs were able to enter HEK293 cells and to induce the release of the pro-inflammatory cytokine IL-8 [257]. In addition, it was demonstrated that they were less toxic towards T lymphocytes than chemically functionalized tubes [258]. This was attributed to the fact that oxidized MWNTs were better dispersed in aqueous solution, determining higher weight/volume concentrations and, thus, a deeper impact on toxicity. At the dose of  $400 \mu\text{g mL}^{-1}$ , oxidized tubes killed more than 80% of cells in 5 days, while pristine MWNTs decreased the cell viability of less than 40%. However, although it is obvious that CNTs toxicity does not depend only on concentration, the dose used in this study was very high and the same experiments with concentrations below  $40 \mu\text{g mL}^{-1}$  did not affect the function of T cells [258].

### 3.8.3

#### ***In Vivo* Effects of CNTs**

Apart from *in vitro* experiments, some CNTs were implanted at the subcutaneous level in rats to study their effects *in vivo*. Sato and coworkers demonstrated that coagulated MWNTs of 825 nm determined granulomas, since they were not easily phagocytosed by macrophages in comparison to MWNTs of 220 nm length [253].

MWNTs were also administrated intratracheally to rats to evaluate their respiratory toxicity due to their biopersistence in the lungs [259]. The results clearly showed that, once they reach the lung, MWNTs have the capacity to induce an overexpression of pro-inflammatory and profibrotic mediators. However, there might be some artifacts on the experimental strategy, since the method of administration presents several limitations, such as the formation of big aggregates that could remain entrapped in the airways. A different mode of administration (e.g. inhalation) and the real ability of these materials to translocate from the respiratory system to other organs would give more reliable data.

Other *in vivo* studies were conducted by Lam and coworkers [260] and Warheit and coworkers [261] to investigate the pulmonary toxicity of SWNTs in rodents. In particular, Lam and coworkers evaluated histopathological alterations in mice at 7 and 90 days after exposure to three differently manufactured SWNTs that contained varying amounts of residual catalytic metals: (i) raw nanotubes (RNT) and (ii) purified nanotubes (PNT), both iron-containing HiPCO products from Rice University, and (iii) CarboLex's Ni-containing electric-arc nanotubes (CNTs). Carbon black and quartz were employed as low and high pulmonary toxicity controls, respectively [260]. The experiments indicated that the three types of tubes induced dose-dependent lung lesions characterized by interstitial granulomas, regardless of the amount of metal impurities inside the samples. Even the product containing very low quantities (2% by weight) of iron produced granulomas, suggesting that

CNTs themselves are toxic. However, the methods employed for this study were somehow ambiguous, since the suspension was obtained by briefly shearing and short sonication to avoid any alteration of the nature of SWNTs, but the instillation was performed through a plastic catheter placed in the trachea. Thus, further studies would be needed to elucidate the cause of death. However, it was clear that mice treated with 0.5 mg of nanotubes showed the formation of granulomas, containing macrophages laden with black particles, few lymphocytes, neutrophils, eosinophils and other inflammatory cells. Interestingly, it was encouraging to observe that the lowest dose (0.1 mg per 30 kg) determined no evident clinical signs. The same (5 mg kg<sup>-1</sup>), or even a lower (1 mg kg<sup>-1</sup>), amount of SWNTs was employed in the study of Warheit and coworkers, in which histopathological evaluation of lung tissue was conducted after 24 h, 1 week and 3 months postinstillation [261]. In these experiments, SWNTs and graphite particles, together with the corresponding controls (carbonyl iron and quartz particles) were prepared in a volume of 1% Tween 80 surfactant and phosphate saline buffer subjected to polytron dispersion. Rats, intratracheally instilled with carbonyl iron or graphite, did not present adverse effects, while no dose-dependent multifocal granulomas were visible after exposure to SWNTs, even if they did not progress beyond 1 month. In 15% of the rats, the highest dose induced mortality, but the main reason for that was due to mechanical blockage of the upper airways and not to the inner toxicity of SWNTs particulate. The death index was somehow incorrect, because the nanotubes tended to form nanoropes instead of being individually dispersed. A proof was the observation that the surviving animals appeared normal through the whole 3 months. In addition, studies on chemotaxis concerning quartz treatment showed a reduced motility as a consequence of a deficiency in macrophages after 1 week. This phenomenon was not observed in the case of SWNTs, which differed from quartz also in the formation of granulomas in a non-dose-dependent manner.

Additional studies by Huczko and coworkers have contributed to understanding further the impact of nanomaterials on health. They tested the effect of fullerenes and CNTs on skin irritation and allergen risks [262, 263]. There is only some evidence of contact dermatitis caused by exposure to carbon fibers [264, 265]. The authors applied two protocols that are commonly employed for testing skin irritation, i.e. a patch and a Draize rabbit eye test. In the first case, 40 people showing predisposition to irritation and allergy were treated with a patch of Whatman filter paper saturated with a water suspension of CNTs, and then they were examined for 96 h. In the second method, four albino rabbits were administered with 0.2 mL of CNT aqueous suspension, and observed after 24, 48 and 72 h. The absence of adverse effects seemed not to be dependent on the time of exposure nor on the type of material used, since there were no differences in comparison with the reference material (which did not contain CNTs). On the whole, the encouraging results in all experiments on skin irritation suggested that no specific precautions should be adopted while handling such nanomaterial [262, 263].

In general, the manufacturing of carbon nanomaterial is based on the use of transition metal catalysts. Therefore, the eventual health hazards are potentially connected with carbon and metals. In fact, free iron or nickel and transition metal

complexes are known to produce reactive radicals, which could induce radical oxidation and enhance oxidative stress. In order to investigate this aspect, Shvedova and coworkers identified and quantified the reactive species that were produced during the manipulation and evaluated the effects of pristine SWNTs on human epidermal keratinocytes (HaCaT) [266]. SEM and TEM allowed us to verify that oxidative stress, caused by treatment with SWNTs, caused a change in the morphology of cells, besides altering surface integrity. These unwanted effects were reduced by the subsequent use of an iron chelator that displayed a protecting role towards HaCaT cells and, thus, confirmed that cytotoxicity of SWNTs was mainly correlated with iron catalytic effects.

A parallel study investigated the adverse effects recorded by aerosol release obtained through mechanical collisions of as-produced SWNTs with bronze beads [267]. The results were somehow ambiguous, since the production of ultrafine powders was not very efficient and it was not possible to discriminate if such particles were made up mainly of nanotubes or of catalyst. Moreover, although nanotubes tended to agglomerate into nanoropes, thus reducing the formation of an appreciable respirable aerosol, it was possible that such nanoparticles remained in the mouth and nasopharyngeal region, causing a potential health risk.

On the whole, CNTs have shown uncommon and interesting physicochemical properties, which increase their possible biomedical applications; however, at the same time, they might persist in biological systems and, consequently, be responsible for adverse health effects and environmental safety. It is imperative that a clear understanding of what really happens to nanoparticles months and years after their release is needed, since some encouraging evidence is not exhaustive in guaranteeing complete innocuous behavior. For all these very important reasons, further studies are required to investigate if CNTs can be widely used for their useful characteristics as well as if they safely represent a promising beginning of the so-called “next industrial revolution”.

### 3.9

#### General Conclusions

Although still debatable, the use of CNTs in drug delivery and biosensing is acquiring more and more substantiating evidence for efficient development. It is clear that many important issues have to be faced before CNTs can be proposed for clinical trials. However, CNTs show unusual carrier properties, with a very strong tendency to pass cell membranes and seem to perfectly fit into the new discipline of nanobiotechnology. Although the first toxicological reports on pristine CNTs were very discouraging, labeling CNTs as very dangerous species, it is becoming widely accepted that *f*-CNTs are by far less toxic than non-*f*-CNTs. Therefore, the combination of penetration ability with high loading achievable with CNTs makes these new carbon species promising candidates for innovative therapies. Another aspect that should not be disregarded is that other functions can be introduced on CNTs by using different functionalization methods.

In conclusion, we do hope that, in a few years, *f*-CNTs will be considered as valuable building blocks for pharmaceutical uses.

### Acknowledgments

The authors are deeply indebted to all their coworkers who have partly contributed to the development of the research described in this chapter and whose names are cited in the references. This work has been supported by the CNRS, MRNT (Gen-Homme 2003), University of Trieste and MIUR (PRIN 2004, prot. 2004035502). G. P. and W. W. are recipients of a fellowship from MNRT. C. K. is grateful to the Università Italo-Francese/Université Franco-Italienne (VINCI Programme 2003) for financing his international PhD.

### References

- ALLEN, T. M., CULLIS, P. R. Drug delivery systems: entering the mainstream, *Science* **2004**, *303*, 1818–1822.
- KOSTARELOS, K. Rational design and engineering of delivery systems for therapeutics: biomedical exercises in colloid and surface science, *Adv. Colloid Interface Sci.* **2003**, *106*, 147–168.
- MERDAN, T., KOPECEK, J., KISSEL, T. Prospects for cationic polymers in gene and oligonucleotide therapy against cancer, *Adv. Drug Deliv. Rev.* **2002**, *54*, 715–758.
- BIANCO, A., KOSTARELOS, K., PARTIDOS, C. D., PRATO, M. Biomedical applications of functionalised carbon nanotubes, *Chem. Commun.* **2005**, 571–577.
- LIN, Y., TAYLOR, S., LI, H., FERNANDO, K. A., QU, L., WANG, W., GU, L., ZHOU, B., SUN, Y. P. Advances toward bioapplications of carbon nanotubes, *J. Mater. Chem.* **2004**, *14*, 527–541.
- KOSTARELOS, K., LACERDA, L., PARTIDOS, C. D., PRATO, M., BIANCO, A. Carbon nanotube-mediated delivery of peptides and genes to cells: translating nanobiotechnology to therapeutics, *J. Drug Deliv. Sci. Technol.* **2005**, *15*, 41–47.
- BIANCO, A., HOEBEKE, J., KOSTARELOS, K., PRATO, M., PARTIDOS, C. D. Carbon nanotubes: on the road to deliver, *Curr. Drug Deliv.* **2005**, *2*, 253–259.
- PASTORIN, G., KOSTARELOS, K., PRATO, M., BIANCO, A. Functionalized carbon nanotubes: towards the delivery of therapeutic molecules, *J. Biomed. Nanotechnol.* **2005**, *1*, 133–142.
- KATZ, E., WILLNER, I. Biomolecule-functionalized carbon nanotubes: applications in nanobioelectronics, *ChemPhysChem* **2004**, *5*, 1084–1104.
- FORTINA, P., KRICKA, L. J., SURREY, S., GRODZINSKI, P. Nanobiotechnology: the promise and reality of new approaches to molecular recognition, *Trends Biotechnol.* **2005**, *23*, 168–173.
- YU, M.-F., FILES, B. S., AREPALLI, S., RUOFF, R. S. Tensile loading of ropes of single wall carbon nanotubes and their mechanical properties, *Phys. Rev. Lett.* **2000**, *84*, 5552–5555.
- SAITO, R., DRESSELHAUS, G., DRESSELHAUS, M. S. *Physical Properties of Carbon Nanotubes*. Imperial College Press, London, **1998**.
- SAITO, R., FUJITA, M., DRESSELHAUS, G., DRESSELHAUS, M. S. Electronic structure of chiral graphene tubules, *Appl. Phys. Lett.* **1992**, *60*, 2204–2206.
- SAITO, R., FUJITA, M., DRESSELHAUS, G., DRESSELHAUS, M. S. Electronic structure of graphene tubules based on C<sub>60</sub>, *Phys. Rev. B* **1992**, *46*, 1804–1811.

- 15 HAMADA, N., SAWADA, S., OSHIYAMA, A. New one-dimensional conductors: graphitic microtubules, *Phys. Rev. Lett.* **1992**, *68*, 1579–1581.
- 16 KAISER, A. B., DÜSBERG, G., ROTH, S. Heterogeneous model for conduction in carbon nanotubes, *Phys. Rev. B* **1998**, *57*, 1418–1421.
- 17 DRESSELHAUS, M. S., DRESSELHAUS, G., EKLUND, P. C. *Science of Fullerenes and Carbon Nanotubes*. Academic Press, New York, **1996**.
- 18 IJIMA, S. Carbon nanotubes: past, present, and future, *Physica B* **2002**, *323*, 1–5.
- 19 JOURNET, C., MASER, W. K., BERNIER, P., LOISEAU, A., LAMY DE LA CHAPELLE, M., LEFRANT, A., DENARD, P., LEE, R., FISCHER, J. E. Large-scale production of single-walled carbon nanotubes by the electric-arc technique, *Nature* **1997**, *388*, 756–758.
- 20 RINZLER, A. G., LIU, J., DAI, H., NIKOLAEV, P., HUFFMAN, C. B., RODRIGUEZ-MACIAS, F. J., BOUL, P. J., LU, A. H., HEYMANN, D., COLBERT, D. T., LEE, R. S., FISCHER, J. E., RAO, A. M., EKLUND, P. C., SMALLEY, R. E. Large-scale purification of single-wall carbon nanotubes: process, product, and characterization, *Appl. Phys. A* **1998**, *67*, 29–37.
- 21 ENDO, M., TAKEUCHI, K., KOBORI, K., TAKAHASHI, K., KROTO, H. W., SARKAR, A. Pyrolytic carbon nanotubes from vapor-grown carbon fibers, *Carbon* **1995**, *33*, 873–881.
- 22 NIKOLAEV, P., BRONIKOWSKI, M., BRADLEY, R. K., ROHMUND, F., COLBERT, D. T., SMITH, K., SMALLEY, R. E. Gas-phase catalytic growth of single-walled carbon nanotubes from carbon monoxide, *Chem. Phys. Lett.* **1999**, *313*, 91–97.
- 23 AJAYAN, P. M. Nanotubes from carbon, *Chem. Rev.* **1999**, *99*, 1787–1799.
- 24 XIE, S. S., CHANG, B. H., LI, W. Z., PAN, Z. W., SUN, L. F., MAO, J. M., CHEN, X. H., QIAN, L. X., ZHOU, W. Y. Synthesis and characterization of aligned carbon nanotube arrays, *Adv. Mater.* **1999**, *11*, 1135–1138.
- 25 DAI, L., MAU, A. W. H. Controlled synthesis and modification of carbon nanotubes and C<sub>60</sub>: carbon nanostructures for advanced polymeric composite materials, *Adv. Mater.* **2001**, *13*, 899–913.
- 26 RAO, C. N. R., SATISHKUMAR, B. C., GOVINDARAJ, A., NATH, M. Nanotubes, *ChemPhysChem* **2001**, *2*, 78–105.
- 27 BAHR, J. L., MICKELSON, E. T., BRONIKOWSKI, M. J., SMALLEY, R. E., TOUR, J. M. Dissolution of small diameter single-wall carbon nanotubes in organic solvents?, *Chem. Commun.* **2001**, 193–194.
- 28 LIU, J., RINZLER, A. G., DAI, H., HAFNER, J. H., BRADLEY, R. K., BOUL, P. J., LU, A., IVERSON, T., SHELIMOV, K., HUFFMAN, C. B., RODRIGUEZ-MACIAS, F., SHON, Y.-S., LEE, T. R., COLBERT, D. T., SMALLEY, R. E. Fullerene pipes, *Science* **1998**, *280*, 1253–1256.
- 29 BANDOW, S., RAO, A. M., WILLIAMS, K. A., THESS, A., SMALLEY, R. E., EKLUND, P. C. Purification of single-wall carbon nanotubes by microfiltration, *J. Phys. Chem. B* **1997**, *101*, 8839–8842.
- 30 DUESBERG, G. S., BURGHARD, M., MUSTER, J., PHILIPP, G., ROTH, S. Separation of carbon nanotubes by size exclusion chromatography, *Chem. Commun.* **1998**, 435–436.
- 31 HOLZINGER, M., HIRSCH, A., BERNIER, P., DUESBERG, G. S., BURGHARD, M. A new purification method for single-wall carbon nanotubes (SWNTs), *Appl. Phys. A* **2000**, *70*, 599–602.
- 32 MARTINEZ, M., CALLEJAS, M., BENITO, A. M., MASER, W. K., COCHET, M., ANDRES, J. M., SCHREIBER, J., CHAUVET, O., FIERRO, J. L. G. Microwave single walled carbon nanotubes purification, *Chem. Commun.* **2002**, 1000–1001.
- 33 VAZQUEZ, E., GEORGAKILAS, V., PRATO, M. Microwave-assisted purification of HIPCO carbon nanotubes, *Chem. Commun.* **2002**, 2308–2309.
- 34 HARUTYUNYAN, A. R., PRADHAN, B. K., CHANG, J., CHEN, G., EKLUND, P. C. Purification of single-wall carbon nanotubes by selective microwave



- heating of catalyst particles, *J. Phys. Chem. B* **2002**, *106*, 8671–8675.
- 35 CHEN, R. J., ZHANG, Y., WANG, D., DAI, H. Noncovalent sidewall functionalization of single-walled carbon nanotubes for protein immobilization, *J. Am. Chem. Soc.* **2001**, *123*, 3838–3839.
  - 36 BESTEMAN, K., LEE, J.-O., WIERTZ, F. G. M., HEERING, H. A., DEKKER, C. Enzyme-coated carbon nanotubes as single-molecule biosensors, *Nano Lett.* **2003**, *3*, 727–730.
  - 37 XIN, H., WOOLLEY, A. T. DNA-templated nanotube localization, *J. Am. Chem. Soc.* **2003**, *125*, 8710–8711.
  - 38 TAFT, B. J., LAZARECK, A. D., WITHEY, G. D., YIN, A., XU, J. M., KELLEY, S. O. Site-specific assembly of DNA and appended cargo on arrayed carbon nanotubes, *J. Am. Chem. Soc.* **2004**, *126*, 12750–12751.
  - 39 LIU, L., WANG, T., LI, J., GUO, Z., DAI, L., ZHANG, D., ZHU, D. Self-assembly of gold nanoparticles to carbon nanotubes using a thiol-terminated pyrene as interlinker, *Chem. Phys. Lett.* **2003**, *367*, 747–752.
  - 40 CAO, L., CHEN, H., WANG, M., SUN, J., ZHANG, X., KONG, F. Photoconductivity study of modified carbon nanotube/oxotitanium phthalocyanine composites, *J. Phys. Chem. B* **2002**, *106*, 8971–8975.
  - 41 WANG, X., LIU, Y., QIU, W., ZHU, D. Immobilization of tetra-*tert*-butylphthalocyanines on carbon nanotubes: a first step towards the development of new nanomaterials, *J. Mater. Chem.* **2002**, *12*, 1636–1639.
  - 42 CAO, L., CHEN, H.-Z., ZHOU, H.-B., ZHU, L., SUN, J.-Z., ZHANG, X.-B., XU, J.-M., WANG, M. Carbon-nanotube-templated assembly of rare-earth phthalocyanine nanowires, *Adv. Mater.* **2003**, *15*, 909–913.
  - 43 GULDI, D. M., RAHMAN, G. N. A., RAMEY, J., MARCACCIO, M., PAOLUCCI, D., PAOLUCCI, F., QIN, S., FORD, W. T., BALBINOT, D., JUX, N., TAGMATARCHIS, N., PRATO, M. Donor–acceptor nanoensembles of soluble carbon nanotubes, *Chem. Commun.* **2004**, 2034–2035.
  - 44 GULDI, D. M., RAHMAN, G. M. A., PRATO, M., JUX, N., QIN, S., FORD, W. Single-wall carbon nanotubes as integrative building blocks for solar-energy conversion, *Angew. Chem. Int. Ed.* **2005**, *44*, 2015–2018.
  - 45 MURAKAMI, H., NOMURA, T., NAKASHIMA, N. Noncovalent porphyrin-functionalized single-walled carbon nanotubes in solution and the formation of porphyrin–nanotube nanocomposites, *Chem. Phys. Lett.* **2003**, *378*, 481–485.
  - 46 LI, H., ZHOU, B., LIN, Y., GU, L., WANG, W., FERNANDO, K. A. S., KUMAR, S., ALLARD, L. F., SUN, Y.-P. Selective interactions of porphyrins with semiconducting single-walled carbon nanotubes, *J. Am. Chem. Soc.* **2004**, *126*, 1014–1015.
  - 47 CHEN, J., COLLIER, C. P. Noncovalent functionalization of single-walled carbon nanotubes with water-soluble porphyrins, *J. Phys. Chem. B* **2005**, *109*, 7605–7609.
  - 48 SATAKE, A., MIYAJIMA, Y., KOBUE, Y. Porphyrin–carbon nanotube composites formed by noncovalent polymer wrapping, *Chem. Mater.* **2005**, *17*, 716–724.
  - 49 GULDI, D. M., RAHMAN, G. M. A., JUX, N., TAGMATARCHIS, N., PRATO, M. Integrating single-wall carbon nanotubes into donor–acceptor nanohybrids, *Angew. Chem. Int. Ed.* **2004**, *43*, 5526–5530.
  - 50 GULDI, D. M., RAHMAN, G. M. A., JUX, N., BALBINOT, D., TAGMATARCHIS, N., PRATO, M. Multiwalled carbon nanotubes in donor–acceptor nanohybrids – towards long-lived electron transfer products, *Chem. Commun.* **2005**, 2038–2040.
  - 51 GULDI, D. M., TAIEB, H., RAHMAN, G. M. A., TAGMATARCHIS, N., PRATO, M. Novel photoactive single-walled carbon nanotube–porphyrin polymer wraps: efficient and long-lived intracomplex charge separation, *Adv. Mater.* **2005**, *17*, 871–875.
  - 52 GULDI, D. M., RAHMAN, G. M. A., JUX, N., BALBINOT, D., HARTNAGEL, U., TAGMATARCHIS, N., PRATO, M. Functional single-wall carbon

- nanotube nanohybrids-associating SWNTs with water-soluble enzyme model systems, *J. Am. Chem. Soc.* **2005**, *127*, 9830–9838.
- 53 CHICHAK, K. S., STAR, A., ALTOE, M. V. P., STODDART, J. F. Single-walled carbon nanotubes under the influence of dynamic coordination and supra-molecular chemistry, *Small* **2005**, *1*, 452–461.
- 54 TANG, B. Z., XU, H. Preparation, alignment, and optical properties of soluble poly(phenylacetylene)-wrapped carbon nanotubes, *Macromolecules* **1999**, *32*, 2569–2576.
- 55 ROMERO, D. B., CARRARD, M., DE HEER, W., ZUPPIROLI, L. A carbon nanotube/organic semiconducting polymer heterojunction, *Adv. Mater.* **1996**, *8*, 899–902.
- 56 AGO, H., PETRITSCH, K., SHAFFER, M. S. P., WINDLE, A. H., FRIEND, R. H. Composites of carbon nanotubes and conjugated polymers for photovoltaic devices, *Adv. Mater.* **1999**, *11*, 1281–1285.
- 57 AGO, H., SHAFFER, M. S. P., GINGER, D. S., WINDLE, A. H., FRIEND, R. H. Electronic interaction between photo-excited poly(*p*-phenylene vinylene) and carbon nanotubes, *Phys. Rev. B* **2000**, *61*, 2286–2290.
- 58 WERY, J., AARAB, H., LEFRANT, S., FAULQUES, E., MULAZZI, E., PEREGO, R. Photoexcitations in composites of poly(paraphenylene vinylene) and single-walled carbon nanotubes, *Phys. Rev. B* **2003**, *67*, 115202 (1–6).
- 59 FOURNET, P., COLEMAN, J. N., LAHR, B., DRURY, A., BLAU, W. J., O'BRIEN, D. F., HORHOLD, H. H. Enhanced brightness in organic light-emitting diodes using a carbon nanotube composite as an electron-transport layer, *J. Appl. Phys.* **2001**, *90*, 969–975.
- 60 FOURNET, P., O'BRIEN, D. F., COLEMAN, J. N., HORHOLD, H. H., BLAU, W. J. A carbon nanotube composite as an electron transport layer for M3EH-PPV based light-emitting diodes, *Synth. Met.* **2001**, *121*, 1683–1684.
- 61 DALTON, A. B., STEPHAN, C., COLEMAN, J. N., MCCARTHY, B., AJAYAN, P. M., LEFRANT, S., BERNIER, P., BLAU, W. J., BYRNE, H. J. Selective interaction of a semiconjugated organic polymer with single-wall nanotubes, *J. Phys. Chem. B* **2000**, *104*, 10012–10016.
- 62 COLEMAN, J. N., DALTON, A. B., CURRAN, S., RUBIO, A., DAVEY, A. P., DRURY, A., MCCARTHY, B., LAHR, B., AJAYAN, P. M., ROTH, S., BARKLIE, R. C., BLAU, W. J. Phase separation of carbon nanotubes and turbostratic graphite using a functional organic polymer, *Adv. Mater.* **2000**, *12*, 213–216.
- 63 STAR, A., LU, Y., BRADLEY, K., GRUNER, G. Nanotube optoelectronic memory devices, *Nano Lett.* **2004**, *4*, 1587–1591.
- 64 MURPHY, R., COLEMAN, J. N., CADEK, M., MCCARTHY, B., BENT, M., DRURY, A., BARKLIE, R. C., BLAU, W. J. High-yield, nondestructive purification and quantification method for multiwalled carbon nanotubes, *J. Phys. Chem. B.* **2002**, *106*, 3087–3091.
- 65 COLEMAN, J. N., O'BRIEN, D. F., DALTON, A. B., MCCARTHY, B., LAHR, B., BARKLIE, R. C., BLAU, W. J. Electron paramagnetic resonance as a quantitative tool for the study of multiwalled carbon nanotubes, *J. Chem. Phys.* **2000**, *113*, 9788–9793.
- 66 STAR, A., STODDART, J. F., STEUERMAN, D., DIEHL, M., BOUKAI, A., WONG, E. W., YANG, X., CHUNG, S. W., CHOI, H., HEATH, J. R. Preparation and properties of polymer-wrapped single-walled carbon nanotubes, *Angew. Chem. Int. Ed.* **2001**, *40*, 1721–1725.
- 67 STEUERMAN, D. W., STAR, A., NARIZZANO, R., CHOI, H., RIES, R. S., NICOLINI, C., STODDART, J. F., HEATH, J. R. Interactions between conjugated polymers and single-walled carbon nanotubes, *J. Phys. Chem. B* **2002**, *106*, 3124–3130.
- 68 STAR, A., STODDART, J. F. Dispersion and solubilization of single-walled carbon nanotubes with a hyper-branched polymer, *Macromolecules* **2002**, *35*, 7516–7520.
- 69 MUSA, I., BAXENDALE, M., AMARA-TUNGA, G. A. J., ECCLESTON, W.

- Properties of regioregular poly(3-octylthiophene)/multi-wall carbon nanotube composites, *Synth. Met.* **1999**, *102*, 1250.
- 70 ALEXANDROU, I., KYMAKIS, E., AMARATUNGA, G. A. J. Polymer-nanotube composites: burying nanotubes improves their field emission properties, *Appl. Phys. Lett.* **2002**, *80*, 1435–1437.
- 71 VALENTINI, L., ARMENTANO, I., BIAGIOTTI, J., FRULLONI, E., KENNY, J. M., SANTUCCI, S. Frequency dependent electrical transport between conjugated polymer and single-walled carbon nanotubes, *Diam. Rel. Mater.* **2003**, *12*, 1601–1609.
- 72 KYMAKIS, E., AMARATUNGA, G. A. J. Single-wall carbon nanotube/conjugated polymer photovoltaic devices, *Appl. Phys. Lett.* **2002**, *80*, 112–114.
- 73 KYMAKIS, E., ALEXANDROU, I., AMARATUNGA, G. A. J. High open-circuit voltage photovoltaic devices from carbon-nanotube-polymer composites, *J. Appl. Phys.* **2003**, *93*, 1764–1768.
- 74 BHATTACHARYYA, S., KYMAKIS, E., AMARATUNGA, G. A. J. Photovoltaic properties of dye functionalized single-wall carbon nanotube/conjugated polymer devices, *Chem. Mater.* **2004**, *16*, 4819–4823.
- 75 LANDI, B. J., RAFFAELLE, R. P., CASTRO, S. L., BAILEY, S. G. Single-wall carbon nanotube-polymer solar cells, *Prog. Photovolt. Res. Appl.* **2005**, *13*, 165–172.
- 76 O'CONNELL, M. J., BOUL, P., ERICSON, L. M., HUFFMAN, C., WANG, Y., HAROZ, E., KUPER, C., TOUR, J. M., AUSMAN, K. D., SMALLEY, R. E. Reversible water-solubilization of single-walled carbon nanotubes by polymer wrapping, *Chem. Phys. Lett.* **2001**, *342*, 265–271.
- 77 ISLAM, M. F., ROJAS, E., BERGEY, D. M., JOHNSON, A. T., YODH, A. G. High weight fraction surfactant solubilization of single-wall carbon nanotubes in water, *Nano Lett.* **2003**, *3*, 269–273.
- 78 RICHARD, C., BALAVOINE, F., SCHULTZ, P., EBBESEN, T. W., MIOSKOWSKI, C. Supramolecular self-assembly of lipid derivatives on carbon nanotubes, *Science* **2003**, *300*, 775–778.
- 79 O'CONNELL, M. J., BACHILO, S. M., HUFFMAN, C. B., MOORE, V. C., STRANO, M. S., HAROZ, E. H., RIALON, K. L., BOUL, P. J., NOON, W. H., KITTRELL, C., MA, J., HAUGE, R. H., WEISMAN, R. B., SMALLEY, R. E. Band gap fluorescence from individual single-walled carbon nanotubes, *Science* **2002**, *297*, 593–596.
- 80 MOORE, V. C., STRANO, M. S., HAROZ, E. H., HAUGE, R. H., SMALLEY, R. E. Individually suspended single-walled carbon nanotubes in various surfactants, *Nano Lett.* **2003**, *3*, 1379–1382.
- 81 WENSELEERS, W., VLASOV, I. I., GOOVAERTS, E., OBRAZTSOVA, E. D., LOBACH, A. S., BOUWEN, A. Efficient isolation and solubilization of pristine single-walled nanotubes in bile salt micelles, *Adv. Funct. Mater.* **2004**, *14*, 1105–1112.
- 82 BACHILO, S. M., STRANO, M. S., KITTRELL, C., HAUGE, R. H., SMALLEY, R. E., WEISMAN, R. B. Structure-assigned optical spectra of single-walled carbon nanotubes, *Science* **2002**, *298*, 2361–2366.
- 83 HAGEN, A., HERTEL, T. Quantitative analysis of optical spectra from individual single-wall carbon nanotubes, *Nano Lett.* **2003**, *3*, 383–388.
- 84 STRANO, M. S., DOORN, S. K., HAROZ, E. H., KITTRELL, C., HAUGE, R. H., SMALLEY, R. E. Assignment of (*n*, *m*) Raman and optical features of metallic single-walled carbon nanotubes, *Nano Lett.* **2003**, *3*, 1091–1096.
- 85 WEISMAN, R. B., BACHILO, S. M. Dependence of optical transition energies on structure for single-walled carbon nanotubes in aqueous suspension: an empirical Kataura plot, *Nano Lett.* **2003**, *3*, 1235–1238.
- 86 DYKE, C. A., TOUR, J. M. Unbundled and highly functionalized carbon nanotubes from aqueous reactions, *Nano Lett.* **2003**, *3*, 1215–1218.
- 87 DIECKMANN, G. R., DALTON, A. B., JOHNSON, P. A., RAZAL, J., CHEN, J., GIORDANO, G. M., MUÑOZ, E.,

- MUSSELMAN, I. H., BAUGHMAN, R. H., DRAPER, R. K. Controlled assembly of carbon nanotubes by designed amphiphilic peptide helices, *J. Am. Chem. Soc.* **2003**, *125*, 1770–1777.
- 88** ZORBAS, V., ORTIZ-ACEVEDO, A., DALTON, A. B., YOSHIDA, M. M., DIECKMANN, G. R., DRAPER, R. K., BAUGHMAN, R. H., JOSE-YACAMAN, M., MUSSELMAN, I. H. Preparation and characterization of individual peptide-wrapped single-walled carbon nanotubes, *J. Am. Chem. Soc.* **2004**, *126*, 7222–7227.
- 89** ZORBAS, V., SMITH, A. L., XIE, H., ORTIZ-ACEVEDO, A., DALTON, A. B., DIECKMANN, G. R., DRAPER, R. K., BAUGHMAN, R. H., MUSSELMAN, I. H. Importance of aromatic content for peptide/single-walled carbon nanotube interactions, *J. Am. Chem. Soc.* **2005**, *127*, 12323–12328.
- 90** KAM, N. W. S., DAI, H. Carbon nanotubes as intracellular protein transporters: generality and biological functionality, *J. Am. Chem. Soc.* **2005**, *127*, 6021–6026.
- 91** ZHENG, M., JAGOTA, A., SEMKE, E. D., DINER, B. A., MCLEAN, R. S., LUSTIG, S. R., RICHARDSON, R. E., TASSI, N. G. DNA-assisted dispersion and separation of carbon nanotubes, *Nat. Mater.* **2003**, *2*, 338–342.
- 92** ZHENG, M., JAGOTA, A., STRANO, M. S., SANTOS, A. P., BARONE, P., CHOU, S. G., DINER, B. A., DRESSELHAUS, M. S., MCLEAN, R. S., ONOA, G. B., SAMSONIDZE, G. G., SEMKE, E. D., USREY, M., WALLS, D. J. Structure-based carbon nanotube sorting by sequence-dependent DNA assembly, *Science* **2003**, *302*, 1545–1548.
- 93** KAM, N. W. S., LIU, Z., DAI, H. Functionalization of carbon nanotubes via cleavable disulfide bonds for efficient intracellular delivery of siRNA and potent gene silencing, *J. Am. Chem. Soc.* **2005**, *127*, 12492–12493.
- 94** HIRSCH, A. Functionalization of single-walled carbon nanotubes, *Angew. Chem. Int. Ed.* **2002**, *41*, 1853–1859.
- 95** BANERJEE, S., HEMRAJ-BENNY, T., WONG, S. S. Covalent surface chemistry of single-walled carbon nanotubes, *Adv. Mater.* **2005**, *17*, 17–29.
- 96** HAMON, M. A., CHEN, J., HU, H., CHEN, Y., ITKIS, M. E., RAO, A. M., EKLUND, P. C., HADDON, R. C. Dissolution of single-walled carbon nanotubes, *Adv. Mater.* **1999**, *11*, 834–840.
- 97** KUKOVECZ, A., KRAMBERGER, C., HOLZINGER, M., KUZMANY, H., SCHALKO, J., MANNSBERGER, M., HIRSCH, A. On the stacking behavior of functionalized single-wall carbon nanotubes, *J. Phys. Chem. B* **2002**, *106*, 6374–6380.
- 98** CHEN, J., RAO, A. M., LYUKSYUTOV, S., ITKIS, M. E., HAMON, M. A., HU, H., COHN, R. W., EKLUND, P. C., COLBERT, D. T., SMALLEY, R. E., HADDON, R. C. Dissolution of full-length single-walled carbon nanotubes, *J. Phys. Chem. B* **2001**, *105*, 2525–2528.
- 99** NIYOGI, S., HAMON, M. A., HU, H., ZHAO, B., BHOWMIK, P., SEN, R., ITKIS, M. E., HADDON, R. C. Chemistry of single-walled carbon nanotubes, *Acc. Chem. Res.* **2002**, *35*, 1105–1113.
- 100** HIURA, H., EBBESEN, T. W., TANIGAKI, K. Opening and purification of carbon nanotubes in high yields, *Adv. Mater.* **1995**, *7*, 275–276.
- 101** AJAYAN, P. M., EBBESEN, T. W., ICHIHASHI, T., IJIMA, S., TANIGAKI, K., HIURA, H. Capillarity-induced filling of carbon nanotubes, *Nature* **1993**, *361*, 333–334.
- 102** CHEN, J., HAMON, M. A., HU, H., CHEN, Y., RAO, A. M., EKLUND, P. C., HADDON, R. C. Solution properties of single-walled carbon nanotubes, *Science* **1998**, *282*, 95–98.
- 103** LAGO, R. M., TSANG, S. C., LU, K. L., CHEN, Y. K., GREEN, M. L. H. Filling carbon nanotubes with small palladium metal crystallites: the effect of surface acid groups, *Chem. Commun.* **1995**, 1355–1356.
- 104** LU, K. L., LAGO, R. M., CHEN, Y. K., GREEN, M. L. H., HARRIS, P. J. F., TSANG, S. C. Mechanical damage of carbon nanotubes by ultrasound, *Carbon* **1996**, *34*, 814–816.

- 105 MONTHIOUX, M., SMITH, B. W., BURTEAUX, B., CLAYE, A., FISCHER, J. E., LUZZI, D. E. Sensitivity of single-wall carbon nanotubes to chemical processing: an electron microscopy investigation, *Carbon* **2001**, *39*, 1251–1272.
- 106 KOSHIO, A., YUDASAKA, M., ZHANG, M., IJIMA, S. A simple way to chemically react single-wall carbon nanotubes with organic materials using ultrasonication, *Nano Lett.* **2001**, *1*, 361–363.
- 107 QIN, Y., SHI, J., WU, W., LI, X., GUO, Z., ZHU, D. Concise route to functionalized carbon nanotubes, *J. Phys. Chem. B* **2003**, *107*, 12899–12901.
- 108 CHEN, Y., HADDON, R. C., FANG, S., RAO, A. M., EKLUND, P. C., LEE, W. H., DICKEY, E. C., GRULKE, E. A., PENDERGRASS, J. C., CHAVAN, A., HALEY, B. E., SMALLEY, R. E. Chemical attachment of organic functional groups to single-walled carbon nanotube material, *J. Mater. Res.* **1998**, *13*, 2423–2431.
- 109 SUN, Y.-P., HUANG, W., LIN, Y., FU, K., KITAYGORODSKIY, A., RIDDLE, L. A., YU, Y. J., CARROLL, D. L. Soluble dendron-functionalized carbon nanotubes: preparation, characterization, and properties, *Chem. Mater.* **2001**, *13*, 2864–2869.
- 110 FU, K., HUANG, W., LIN, Y., RIDDLE, L. A., CARROLL, D. L., SUN, Y.-P. Defunctionalization of functionalized carbon nanotubes, *Nano Lett.* **2001**, *1*, 439–441.
- 111 SUN, Y.-P., FU, K., LIN, Y., HUANG, W. Functionalized carbon nanotubes: properties and applications, *Acc. Chem. Res.* **2002**, *35*, 1096–1104.
- 112 KONG, H., GAO, C., YAN, D. Controlled functionalization of multi-walled carbon nanotubes by in situ atom transfer radical polymerization, *J. Am. Chem. Soc.* **2004**, *126*, 412–413.
- 113 QIN, S., QIN, D., FORD, W. T., RESASCO, D. E., HERRERA, J. E. Polymer brushes on single-walled carbon nanotubes by atom transfer radical polymerization of *n*-butyl methacrylate, *J. Am. Chem. Soc.* **2004**, *126*, 170–176.
- 114 HUANG, W., TAYLOR, S., FU, K., LIN, Y., ZHANG, D., HANKS, T. W., RAO, A. M., SUN, Y.-P. Attaching proteins to carbon nanotubes via diimide-activated amidation, *Nano Lett.* **2002**, *2*, 311–314.
- 115 KAM, N. W. S., JESSOP, T. C., WENDER, P. A., DAI, H. Nanotube molecular transporters: internalization of carbon nanotube–protein conjugates into mammalian cells, *J. Am. Chem. Soc.* **2004**, *126*, 6850–6851.
- 116 YIM, T., LIU, J., LU, Y., KANE, R. S., DORDICK, J. S. Highly active and stable DNAzyme–carbon nanotube hybrids, *J. Am. Chem. Soc.* **2005**, *127*, 12200–12201.
- 117 BAKER, S. E., CAI, W., LASSETER, T. L., WEIDKAMP, K. P., HAMERS, R. J. Covalently bonded adducts of deoxyribonucleic acid (DNA) oligonucleotides with single-wall carbon nanotubes: synthesis and hybridization, *Nano Lett.* **2002**, *2*, 1413–1417.
- 118 HAZANI, M., NAAMAN, R., HENNRICH, F., KAPPES, M. M. Confocal fluorescence imaging of DNA–functionalized carbon nanotubes, *Nano Lett.* **2003**, *3*, 153–155.
- 119 WILLIAMS, K. A., VEENHUIZEN, P. T. M., DE LA TORRE, B. G., ERITJA, R., DEKKER, C. Nanotechnology: carbon nanotubes with DNA recognition, *Nature* **2002**, *420*, 761.
- 120 TASIS, D., TAGMATARCHIS, N., BIANCO, A., PRATO, M. Chemistry of carbon nanotubes, *Chem. Rev.* **2006**, *106*, 1105–1136.
- 121 JORIO, A., DRESSELHAUS, G., DRESSELHAUS, M. S., SOUZA, M., DANTAS, M. S. S., PIMENTA, M. A., RAO, A. M., SAITO, R., LIU, C., CHENG, H. M. Polarized Raman study of single-wall semiconducting carbon nanotubes, *Phys. Rev. Lett.* **2000**, *85*, 2617–2620.
- 122 HOLDEN, J. M., ZHOU, P., BI, X., EKLUND, P. C., BANDOW, S., JISHI, R. A., CHOWDHURY, K. D., DRESSELHAUS, G., DRESSELHAUS, M. S. Raman scattering from nanoscale carbons

- generated in a cobalt-catalyzed carbon plasma, *Chem. Phys. Lett.* **1994**, *220*, 186–191.
- 123** BAHR, J. L., TOUR, J. M. Covalent chemistry of single-wall carbon nanotubes, *J. Mater. Chem.* **2002**, *12*, 1952–1958.
- 124** MICKELSON, E. T., HUFFMAN, C. B., RINZLER, A. G., SMALLEY, R. E., HAUGE, R. H., MARGRAVE, J. L. Fluorination of single-wall carbon nanotubes, *Chem. Phys. Lett.* **1998**, *296*, 188–194.
- 125** MICKELSON, E. T., CHIANG, I. W., ZIMMERMAN, J. L., BOUL, P. J., LOZANO, J., LIU, J., SMALLEY, R. E., HAUGE, R. H., MARGRAVE, J. L. Solvation of fluorinated single-wall carbon nanotubes in alcohol solvents, *J. Phys. Chem. B* **1999**, *103*, 4318–4322.
- 126** BOUL, P. J., LIU, J., MICKELSON, E. T., HUFFMAN, C. B., ERICSON, L. M., CHIANG, I. W., SMITH, K. A., COLBERT, D. T., HAUGE, R. H., MARGRAVE, J. L., SMALLEY, R. E. Reversible sidewall functionalization of buckytubes, *Chem. Phys. Lett.* **1999**, *310*, 367–372.
- 127** KHABASHESKU, V. N., BILLUPS, W. E., MARGRAVE, J. L. Fluorination of single-wall carbon nanotubes and subsequent derivatization reactions, *Acc. Chem. Res.* **2002**, *35*, 1087–1095.
- 128** HOLZINGER, M., VOSTROWSKY, O., HIRSCH, A., HENNRICH, F., KAPPES, M., WEISS, R., JELLEN, F. Sidewall functionalization of carbon nanotubes, *Angew. Chem. Int. Ed. Engl.* **2001**, *40*, 4002–4005.
- 129** BAHR, J. L., YANG, J., KOSYNNIN, D. V., BRONISKOWSKI, M. J., SMALLEY, R. E., TOUR, J. M. Functionalization of carbon nanotubes by electrochemical reduction of aryl diazonium salts: a bucky paper electrode, *J. Am. Chem. Soc.* **2001**, *123*, 6536–6542.
- 130** BAHR, J. L., TOUR, J. M. Highly functionalized carbon nanotubes using in situ generated diazonium compounds, *Chem. Mater.* **2001**, *13*, 3823–3824.
- 131** DYKE, C. A., TOUR, J. M. Solvent-free functionalization of carbon nanotubes, *J. Am. Chem. Soc.* **2003**, *125*, 1156–1157.
- 132** YING, Y., SAINI, R. K., LIANG, F., SADANA, A. K., BILLUPS, W. E. Functionalization of carbon nanotubes by free radicals, *Org. Lett.* **2003**, *5*, 1471–1473.
- 133** PENG, H., REVERDY, P., KHABASHESKU, V. N., MARGRAVE, J. L. Sidewall functionalization of single-walled carbon nanotubes with organic peroxides, *Chem. Comm.* **2003**, 362–363.
- 134** STRANO, M. S., DYKE, C. A., USREY, M. L., BARONE, P. W., ALLEN, M. J., SHAN, H., KITTRELL, C., HAUGE, R. H., TOUR, J. M., SMALLEY, R. E. Electronic structure control of single-walled carbon nanotube functionalization, *Science* **2003**, *301*, 1519–1522.
- 135** HAMON, M. A., ITKIS, M. E., NIYOGI, S., ALVARAEZ, T., KUPER, C., MENON, M., HADDON, R. C. Effect of rehybridization on the electronic structure of single-walled carbon nanotubes, *J. Am. Chem. Soc.* **2001**, *123*, 11292–11293.
- 136** VISWANATHAN, G., CHAKRAPANI, N., YANG, H., WEI, B., CHUNG, H., CHO, K., RYU, C. Y., AJAYAN, P. M. Single-step *in situ* synthesis of polymer-grafted single-wall nanotube composites, *J. Am. Chem. Soc.* **2003**, *125*, 9258–9259.
- 137** WU, W., ZHANG, S., LI, Y., LI, J., LU, L., QIN, Y., GUO, Z., DAI, L., YE, C., ZHU, D. PVK-modified single-walled carbon nanotubes with effective photoinduced electron transfer, *Macromolecules* **2003**, *36*, 6286–6288.
- 138** PEKKER, S., SALVETAT, J.-P., JAKAB, E., BONARD, J.-M., FORRO, L. Hydrogenation of carbon nanotubes and graphite in liquid ammonia, *J. Phys. Chem. B* **2001**, *105*, 7938–7943.
- 139** TAGMATARCHIS, N., GEORGAKILAS, V., PRATO, M., SHINOHARA, H. Sidewall functionalization of single-walled carbon nanotubes through electrophilic addition, *Chem. Commun.* **2002**, 2010–2011.
- 140** COLEMAN, K. S., BAILEY, S. R., FOGDEN, S., GREEN, M. L. H. Functionalization of single-walled

- carbon nanotubes via the Bingel reaction, *J. Am. Chem. Soc.* **2003**, *125*, 8722–8723.
- 141 WORSLEY, K. A., MOONOOSAWMY, K. R., KRUSE, P. Long-range periodicity in carbon nanotube sidewall functionalization, *Nano Lett.* **2004**, *4*, 1541–1546.
- 142 MOGHADDAM, M. J., TAYLOR, S., GAO, M., HUANG, S., DAI, L., MCCALL, M. J. Highly efficient binding of DNA on the sidewalls and tips of carbon nanotubes using photochemistry, *Nano Lett.* **2004**, *4*, 89–93.
- 143 GEORGAKILAS, V., KORDATOS, K., PRATO, M., GULDI, D. M., HOLZINGER, M., HIRSCH, A. Organic functionalization of carbon nanotubes, *J. Am. Chem. Soc.* **2002**, *124*, 760–761.
- 144 LU, X., TIAN, F., XU, X., WANG, N., ZHANG, Q. Theoretical exploration of the 1,3-dipolar cycloadditions onto the sidewalls of (*n, n*) armchair single-wall carbon nanotubes, *J. Am. Chem. Soc.* **2003**, *125*, 10459–10464.
- 145 YAO, Z., BRAIDY, N., BOTTON, G. A., ADRONOV, A. Polymerization from the surface of single-walled carbon nanotubes – preparation and characterization of nanocomposites, *J. Am. Chem. Soc.* **2003**, *125*, 16015–16024.
- 146 GEORGAKILAS, V., TAGMATARCHIS, N., PANTAROTTO, D., BIANCO, A., BRIAND, J.-P., PRATO, M. Amino acid functionalization of water soluble carbon nanotubes, *Chem. Commun.* **2002**, 3050–3051.
- 147 GEORGAKILAS, V., VOULGARIS, D., VAZQUEZ, E., PRATO, M., GULDI, D. M., KUKOVECZ, A., KUZMANY, H. Purification of HiPCO carbon nanotubes via organic functionalization, *J. Am. Chem. Soc.* **2002**, *124*, 14318–14319.
- 148 PANTOROTTO, D., PARTIDOS, C. D., GRAFF, R., HOEBEKE, J., BRIAND, J.-P., PRATO, M., BIANCO, A. Synthesis, structural characterization, and immunological properties of carbon nanotubes functionalized with peptides, *J. Am. Chem. Soc.* **2003**, *125*, 6160–6164.
- 149 BIANCO, A., PRATO, M. Can carbon nanotubes be considered useful tools for biological applications?, *Adv. Mater.* **2003**, *15*, 1765–1768.
- 150 CHOPRA, N., MAJUMDER, M., HINDS, B. J. Bifunctional carbon nanotubes by sidewall protection, *Adv. Funct. Mater.* **2005**, *15*, 858–864.
- 151 LEE, K. M., LI, L., DAI, L. Asymmetric end-functionalization of multi-walled carbon nanotubes, *J. Am. Chem. Soc.* **2005**, *127*, 4122–4123.
- 152 WU, W., WIECKOWSKI, S., PASTORIN, G., BENINCASA, M., KLUMPP, C., BRIAND, J.-P., GENNARO, R., PRATO, M., BIANCO, A. Targeted delivery of amphotericin B to cells using functionalized carbon nanotubes, *Angew. Chem. Int. Ed.* **2005**, *44*, 6358–6362.
- 153 SCHELLER, F. W., WOLLENBERGER, U., WARSINKE, A., LISDAT, F. Research and development in biosensors, *Curr. Opin. Biotechnol.* **2001**, *12*, 35–40.
- 154 MEADOWS, D. Recent developments with biosensing technology and applications in the pharmaceutical industry, *Adv. Drug. Deliv. Rev.* **1996**, *21*, 179–189.
- 155 TESS, M. E., COX, J. A. Chemical and biochemical sensors based on advances in materials chemistry, *J. Pharm. Biomed. Anal.* **1999**, *19*, 55–68.
- 156 POPOV, V. N. Carbon nanotubes: properties and application, *Mater. Sci. Eng.* **2004**, *R43*, 61–102.
- 157 Special Issue on Carbon Nanotubes, *Acc. Chem. Res.* **2002**, *35*, 997–1113.
- 158 TANS, S. J., VERSCHUEREN, A. R. M., DEKKER, C. Room-temperature transistor based on a single carbon nanotube, *Nature* **1998**, *393*, 49–52.
- 159 DAVIS, J. J., GREEN, M. L. H., HILL, H. A. O., LEUNG, Y. C., SLOAN, J., SADLER, P. J., XAVIER, A. V., TSANG, S. C. The immobilisation of proteins in carbon nanotubes, *Inorg. Chim. Acta* **1998**, *272*, 261–266.
- 160 SNOW, E. S., PERKINS, F. K., HOUSER, E. J., BADESCU, S. C., REINECKE, T. L. Chemical detection with a single-walled carbon nanotube capacitor, *Science* **2005**, *307*, 1942–1945.
- 161 QIAN, K., YAN, B., LIN, Y., XU, D., CAI, B., CHEN, T., SUN, Z. Research

- on carbon nanotube array field emission pressure sensors, *Electron. Lett.* **2005**, *41*, 824–825.
- 162** POSTMA, H. W. C., TEEPEN, T., YAO, Z., GRIFONI, M., DEKKER, C. Carbon nanotube single-electron transistors at room temperature, *Science* **2001**, *293*, 76–79.
- 163** MERKOÇI, A., PUMERA, M., LLOPIS, X., PÉREZ, B., DEL VALLE, M., ALEGRET, S. New materials for electrochemical sensing VI: carbon nanotubes, *Trends Anal. Chem.* **2005**, *24*, 826–838.
- 164** MARTEL, R., SCHMIDT, T., SHEA, H. R., HERTEL, T., AVOURIS, P. Single- and multi-wall carbon nanotube field-effect transistors, *Appl. Phys. Lett.* **1998**, *73*, 2447–2449.
- 165** LI, J., KOEHNE, J. E., CASSELL, A. M., CHEN, H., NG, H. T., YE, Q., FAN, W., HAN, J., MEYAPPAN, M. Inlaid multi-walled carbon nanotube nanoelectrode arrays for electroanalysis, *Electroanalysis* **2005**, *17*, 15–27.
- 166** AVOURIS, P. Molecular electronics with carbon nanotubes, *Acc. Chem. Res.* **2002**, *35*, 1026–1034.
- 167** DAI, H. Carbon nanotubes: synthesis, integration, and properties, *Acc. Chem. Res.* **2002**, *35*, 1035–1044.
- 168** JOHNSTON, D. E., ISLAM, M. F., YODH, A. G., JOHNSON, A. T. Electronic devices based on purified carbon nanotubes grown by high-pressure decomposition of carbon monoxide, *Nat. Mater.* **2005**, *4*, 589–592.
- 169** NIYOGI, S., HU, H., HAMON, M. A., BHOWMIK, P., ZHAO, B., ROZENZHAK, S. M., CHEN, J., ITKIS, M. E., MEIER, M. S., HADDON, R. C. Chromatographic purification of soluble single-walled carbon nanotubes (s-SWNTs), *J. Am. Chem. Soc.* **2001**, *123*, 733–734.
- 170** ZHAO, B., HU, H., NIYOGI, S., ITKIS, M. E., HAMON, M. A., BHOWMIK, P., MEIER, M. S., HADDON, R. C. Chromatographic purification and properties of soluble single-walled carbon nanotubes, *J. Am. Chem. Soc.* **2001**, *123*, 11673–11677.
- 171** DYKE, C. A., STEWART, M. P., TOUR, J. M. Separation of single-walled carbon nanotubes on silica gel. Materials morphology and Raman excitation wavelength affect data interpretation, *J. Am. Chem. Soc.* **2005**, *127*, 4497–4509.
- 172** SO, H.-M., WON, K., KIM, Y. H., KIM, B.-K., RYU, B. H., NA, P. S., KIM, H., LEE, J.-O. Single-walled carbon nanotube biosensors using aptamers as molecular recognition elements, *J. Am. Chem. Soc.* **2005**, *127*, 11906–11907.
- 173** TAKEDA, S., SBAGYO, A., SAKODA, Y., ISHII, A., SAWAMURA, M., SUEOKA, K., KIDA, H., MUKASA, K., MATSUMOTO, K. Application of carbon nanotubes for detecting anti-hemagglutinins based on antigen–antibody interaction, *Biosensors Bioelectron.* **2005**, *21*, 201–205.
- 174** STALL, C., JOHNSON JR., A. T., CHEN, M., GELPERIN, A. DNA-decorated carbon nanotubes for chemical sensing, *Nano Lett.* **2005**, *5*, 1774–1778.
- 175** CHEN, R. J., CHOI, H. C., BANGSARUNTIP, S., YENILMEZ, E., TANG, X., WANG, Q., CHANG, Y.-L., DAI, H. An investigation of the mechanisms of electronic sensing of protein adsorption on carbon nanotube devices, *J. Am. Chem. Soc.* **2004**, *126*, 1563–1568.
- 176** CHEN, R. J., BANGSARUNTIP, S., DROVALAKIS, K. A., KAM, N. W. S., SHIM, M., LI, Y., KIM, W., UTZ, P. J., DAI, H. Noncovalent functionalization of carbon nanotubes for highly specific electronic biosensors, *Proc. Natl Acad. Sci. USA* **2003**, *100*, 4984–4989.
- 177** COLLINS, P. G., ARNOLD, M. S., AVOURIS, P. Engineering carbon nanotubes and nanotube circuits using electrical breakdown, *Science* **2001**, *292*, 706–709.
- 178** KONG, J., FRANKLIN, N. R., ZHOU, C., CHAPLINE, M. G., PENG, S., CHO, K., DAI, H. Nanotube molecular wires as chemical sensors, *Science* **2000**, *287*, 622–625.
- 179** FENG, X., IRLE, S., WITEK, H., MOROKUMA, K., VIDIC, R., BORGUET, E. Sensitivity of ammonia interaction with single-walled carbon nanotube bundles to the presence of defect sites



- and functionalities, *J. Am. Chem. Soc.* **2005**, *127*, 10533–10538.
- 180** LUCI, M., REGOLI, P., REALE, A., DI CARLO, A., ORLANDUCCI, S., TAMBURRI, E., TERRANOVA, M. L., LUGLI, P., DI NATALE, C., D'AMICO, A., PAOLESSE, R. Gas sensing using single wall carbon nanotubes ordered with dielectrophoresis, *Sensors Actuators B* **2005**, *111–112*, 181–186.
- 181** ZHANG, B., FU, R. W., ZHANG, M. Q., DONG, X. M., LAN, P. L., QIU, J. S. Preparation and characterization of gas-sensitive composites from multi-walled carbon nanotubes/polystyrene, *Sensors Actuators, B* **2005**, *109*, 323–328.
- 182** GOODING, J. J., WIBOWO, R., LIU, J., YANG, W., LOSIC, D., ORBONS, S., MEARN, F. J., SHAPTER, J. G., HIBBERT, D. B. Protein electrochemistry using aligned carbon nano-tube arrays, *J. Am. Chem. Soc.* **2003**, *125*, 9006–9007.
- 183** PATOLSKY, F., WEIZMANN, Y., WILLNER, I. Long-range electrical contacting of redox enzymes by SWCNT connectors, *Angew. Chem. Int. Ed.* **2004**, *43*, 2113–2117.
- 184** LIN, Y., LU, F., TU, Y., REN, Z. Glucose biosensors based on carbon nanotube nanoelectrode ensembles, *Nano Lett.* **2004**, *4*, 191–195.
- 185** KERMAN, K., MORITA, Y., TAKAMURA, Y., TAMIYA, E. *Escherichia coli* single-strand binding protein–DNA interactions on carbon nanotube-modified electrodes from a label-free electrochemical hybridization sensor, *Anal. Bioanal. Chem.* **2005**, *381*, 1114–1121.
- 186** LI, G., LIAO, J. M., HU, G. Q., MA, N. Z., WU, P. J. Study of carbon nanotube modified biosensor for monitoring total cholesterol in blood, *Biosensors Bioelectron.* **2005**, *20*, 2140–2144.
- 187** WANG, J., MUSAMEH, M., LIN, Y. Solubilization of carbon nanotubes by nafion toward the preparation of amperometric biosensors, *J. Am. Chem. Soc.* **2003**, *125*, 2408–2409.
- 188** BALAVOINE, F., SCHULTZ, P., RICHARD, C., MALLOUH, V., EBBESEN, T. W., MIOSKOWSKI, C. Helical crystallization of proteins on carbon nanotubes: a first step towards the development of new biosensors, *Angew. Chem. Int. Ed.* **1999**, *38*, 1912–1915.
- 189** SHIM, M., KAM, N. W. S., CHEN, R. J., LI, Y., DAI, H. Functionalization of carbon nanotubes for biocompatibility and biomolecular recognition, *Nano Lett.* **2002**, *2*, 285–288.
- 190** PANTAROTTO, D., BRIAND, J.-P., PRATO, M., BIANCO, A. Translocation of bioactive peptides across cell membranes by carbon nanotubes, *Chem. Commun.* **2004**, 16–17.
- 191** PANTAROTTO, D., SINGH, R., MCCARTHY, D., ERHARDT, M., BRIAND, J.-P., PRATO, M., KOSTARELOS, K., BIANCO, A. Functionalised carbon nanotubes for plasmid DNA gene delivery, *Angew. Chem. Int. Ed.* **2004**, *43*, 5242–5246.
- 192** CAI, D., MATARAZA, J. M., QIN, Z. H., HUANG, Z., HUANG, J., CHILES, T. C., CARNAHAN, D., KEMPA, K., REN, Z. Highly efficient molecular delivery into mammalian cells using carbon nanotube spearing, *Nat. Methods* **2005**, *2*, 449–454.
- 193** CHERUKURI, P., BACHILO, S. M., LITOVSKY, S. H., WEISMAN, R. B. Near-infrared fluorescence microscopy of single-walled carbon nanotubes in phagocytic cells, *J. Am. Chem. Soc.* **2005**, *127*, 15638–15639.
- 194** KAM, N. W. S., LIU, Z., DAI, H. Carbon nanotubes as intracellular transporters for proteins and DNA: an investigation of the uptake mechanism and pathway, *Angew. Chem. Int. Ed.* **2006**, *46*, 577–581.
- 195** ACHARYA, T., KENNEDY, R., DAAR, A. S., SINGER, P. A. Biotechnology to improve health in developing countries – a review, *Mem. Inst. Oswaldo Cruz* **2004**, *99*, 341–350.
- 196** MICONNET, I., KOENIG, S., SPEISER, D., KRIEG, A., GUILLAUME, P., CEROTTINI, J. C., ROMERO, P. CpG are efficient adjuvants for specific CTL induction against tumor antigen-derived peptide, *J. Immunol.* **2002**, *168*, 1212–1218.
- 197** KLINMAN, D. M., CURRIE, D., GURSEL, I., VERTHELYI, D. Use of CpG

- oligodeoxynucleotides as immune adjuvants, *Immunol. Rev.* **2004**, *199*, 201–216.
- 198 KLINMAN, D. M. Immunotherapeutic uses of CpG oligodeoxynucleotides, *Nat. Rev. Immunol.* **2004**, *4*, 249–258.
- 199 KLINMAN, D. M., VERTHELYI, D., TAKESHITA, F., ISHII, K. J. Immune recognition of foreign DNA: a cure for bioterrorism?, *Immunity* **1999**, *11*, 123–129.
- 200 KRIEG, A. M. CpG motifs in bacterial DNA and their immune effects, *Annu. Rev. Immunol.* **2002**, *20*, 709–760.
- 201 HEMMI, H., TAKEUCHI, O., KAWAI, T., KAISHO, T., SATO, S., SANJO, H., MATSUMOTO, M., HOSHINO, K., WAGNER, H., TAKEDA, K., AKIRA, S. A. A Toll-like receptor recognizes bacterial DNA, *Nature* **2000**, *408*, 740–745.
- 202 HOFFMANN, J. A., KAFATOS, F. C., JANEWAY, C. A., EZEKOWITZ, R. A. B. Phylogenetic perspectives in innate immunity, *Science* **1999**, *284*, 1313–1318.
- 203 KRIEG, A. M. The role of CpG motifs in innate immunity, *Curr. Opin. Immunol.* **2000**, *12*, 35–43.
- 204 BIANCO, A., HOEBEKE, J., GODEFROY, S., CHALOIN, O., PANTAROTTO, D., BRIAND, J.-P., MULLER, S., PRATO, M., PARTIDOS, C. D. Cationic carbon nanotubes bind to CpG oligodeoxynucleotides and enhance their immunostimulatory properties, *J. Am. Chem. Soc.* **2005**, *127*, 58–59.
- 205 LEIST, T. P., COBBOLD, S. P., WALDMANN, H., AGUET, M., ZINKERNAGEL, R. M. Functional analysis of T lymphocyte subsets in antiviral host defense, *J. Immunol.* **1987**, *138*, 2278–2281.
- 206 MATLOUBIAN, M., CONCEPCION, R. J., AHMED, R. CD4<sup>+</sup> T cells are required to sustain CD8<sup>+</sup> cytotoxic T-cell responses during chronic viral infection, *J. Virol.* **1994**, *68*, 8056–8063.
- 207 MOSMANN, T. R., COFFMAN, R. L. T<sub>H</sub>1 and T<sub>H</sub>2 cells: different patterns of lymphokine secretion lead to different functional properties, *Annu. Rev. Immunol.* **1989**, *7*, 145–173.
- 208 BARCHET, W., OEHEN, S., KLENERMAN, P., WODARZ, D., BOCHAROV, G., LLOYD, A. L., NOWAK, M. A., HENGARTNER, H., ZINKERNAGEL, R. M., EHL, S. Direct quantitation of rapid elimination of viral antigen-positive lymphocytes by antiviral CD8<sup>+</sup> T cells *in vivo*, *Eur. J. Immunol.* **2000**, *30*, 1356–1363.
- 209 PARTIDOS, C. D. Peptide mimotopes as candidate vaccines, *Curr. Opin. Mol. Ther.* **2000**, *2*, 74–79.
- 210 FRANCIS, M. J. Peptide vaccines for viral diseases, *Sci. Prog.* **1990**, *74*, 115–130.
- 211 PANTAROTTO, D., PARTIDOS, C. D., HOEBEKE, J., BROWN, F., KRAMER, E., BRIAND, J.-P., MULLER, S., PRATO, M., BIANCO, A. Immunization with peptide-functionalized carbon nanotubes enhances virus-specific neutralizing antibody responses, *Chem. Biol.* **2003**, *10*, 991–966.
- 212 FRANCIS, M. J., HASTINGS, G. Z., SYRED, A. D., MCGINN, B., BROWN, F., ROWLANDS, D. J. Non-responsiveness to a foot-and-mouth disease virus peptide overcome by addition of foreign helper T-cell determinants, *Nature* **1987**, *330*, 168–170.
- 213 PARTIDOS, C. D., OBEID, O. E., STEWARD, M. W. Antibody responses to non-immunogenic synthetic peptides induced by co-immunization with immunogenic peptides, *Immunology* **1992**, *77*, 262–266.
- 214 SCHUTZE, M. P., LECLERC, C., JOLIVET, M., AUDIBERT, F., CHEDID, L. Carrier-induced epitopic suppression, a major issue for future synthetic vaccines, *J. Immunol.* **1985**, *135*, 2319–2322.
- 215 POUTON, C. W., SEYMOUR, L. W. Key issues in non-viral gene delivery, *Adv. Drug. Deliv. Rev.* **2000**, *46*, 187–203.
- 216 YINGHUI, Z., PENG, A. T., CARPENTER, K., MAGUIRE, J. A., HOSMANE, N. S., TAKAGAKI, M. Substituted carborane-appended water-soluble single-wall carbon nanotubes: New approach to boron neutron capture therapy drug delivery, *J. Am. Chem. Soc.* **2005**, *127*, 9875–9880.
- 217 KAM, N. W. S., O'CONNELL, M., WISDOM, J. A., DAI, H. Carbon

- nanotubes as multifunctional biological transporters and near-infrared agents for selective cancer cell destruction, *Proc. Natl Acad. Sci. USA* **2005**, *102*, 11600–11605.
- 218 PASTORIN, G., WU, W., WIECKOWSKI, S., BRIAND, J.-P., KOSTARELOS, K., PRATO, M., BIANCO, A. Double functionalization of carbon nanotubes for multimodal drug delivery, *Chem. Commun.* **2006**, 1182–1184.
- 219 MURAKAMI, T., AJIMA, K., MIYAWAKI, J., YUDASAKA, M., IJIMA, S., SHIBE, K. Drug-loaded carbon nanohorns: adsorption and release of dexamethasone *in vitro*, *Mol. Pharm.* **2004**, *1*, 399–405.
- 220 AJIMA, K., YUDASAKA, M., MURAKAMI, T., MAIGNÉ, A., SHIBA, K., IJIMA, S. Carbon nanohorns as anticancer drug carriers, *Mol. Pharm.* **2005**, *2*, 475–480.
- 221 SINGH, R., PANTAROTTO, D., MCCARTHY, D., CHALOIN, O., HOEBEKE, J., PARTIDOS, C. D., BRIAND, J.-P., PRATO, M., BIANCO, A., KOSTARELOS, K. Binding and condensation of plasmid DNA onto functionalized carbon nanotubes: towards the construction of nanotube-based gene delivery vectors, *J. Am. Chem. Soc.* **2005**, *127*, 4388–4396.
- 222 GAO, H., KONG, Y., CUI, D. X., OZKAN, C. S. Spontaneous insertion of DNA oligonucleotides into carbon nanotubes, *Nano Lett.* **2003**, *3*, 471–473.
- 223 LU, G., MARAGAKIS, P., KAXIRAS, E. Carbon nanotube interaction with DNA, *Nano Lett.* **2005**, *5*, 897–900.
- 224 MATYSHEVSKA, O. P., KARLASH, A. Y., SHTOGUN, Y. V., BENILOV, A., KIRGIZOV, Y., GORCHINSKIY, K. O., BUZANEVA, E. V., PRYLUTSKIY, Y. I., SCHARFF, P. Self-organizing DNA/carbon nanotube molecular films, *Mater. Sci. Eng. C* **2001**, *15*, 249–252.
- 225 BUZANEVA, E., KARLASH, A., YAKOVKIN, K., SHTOGUN, Y., PUTSELYK, S., ZHEREBETSKIY, D., GORCHINSKIY, A., POPOVA, G., PRILUTSKIY, Y., LYTVYN, P., SCHARFF, P., EKLUND, P. C. DNA nanotechnology of carbon nanotube cells: physico-chemical models of self-organization and properties, *Mater. Sci. Eng. C* **2002**, *19*, 41–45.
- 226 DOVBESHKO, G. I., REPNYTSKA, O. P., OBRATSOVA, E. D., SHTOGUN, Y. V. DNA interaction with single-walled carbon nanotubes: a SEIRA study, *Chem. Phys. Lett.* **2003**, *372*, 432–437.
- 227 NEPAL, D., SOHN, J. I., AICHER, W. K., LEE, S., GECKELER, K. E. Supramolecular conjugates of carbon nanotubes and DNA by a solid-state reaction, *Biomacromolecules* **2005**, *6*, 2919–2922.
- 228 DWYER, C., GUTHOLD, M., FALVO, M., WASHBURN, S., SUPERFINE, R., ERIE, D. DNA-functionalized single-walled carbon nanotubes, *Nanotechnology* **2002**, *13*, 601–604.
- 229 GUO, M. L., CHEN, J. H., LIU, D. Y., NIE, L. H., YAO, S. Z. Electrochemical characteristics of the immobilization of calf thymus DNA molecules on multi-walled carbon nanotubes, *Bioelectrochemistry* **2004**, *62*, 29–35.
- 230 NAKASHIMA, N., OKUZONO, S., MURAKAMI, H., NAKAI, T., YOSHIKAWA, K. DNA dissolves single-walled carbon nanotubes in water, *Chem. Lett.* **2003**, *32*, 456–457.
- 231 RAJENDRA, J., BAXENDALE, M., DIT RAP, L. G., RODGER, A. Flow linear dichroism to probe binding of aromatic molecules and DNA to single-walled carbon nanotubes, *J. Am. Chem. Soc.* **2004**, *126*, 11182–11188.
- 232 RAJENDRA, J., RODGER, A. The binding of single-stranded DNA and PNA to single-walled carbon nanotubes probed by flow linear dichroism, *Chem. Eur. J.* **2005**, *11*, 4841–4847.
- 233 LACERDA, L., PASTORIN, G., WU, W., PRATO, M., BIANCO, A., KOSTARELOS, K. Luminescence of functionalized carbon nanotubes as a tool to monitor bundle formation and dissociation in water: the effect of plasmid-DNA complexation, *Adv. Funct. Mater.* **2006**, *16*, 1839–1846.
- 234 RAO, R., LU, Q., KESKAR, G., FREEDMAN, K. O., FLOYD, W. C., RAO, A. M., KE, P. C. Single-molecule

- fluorescence microscopy and Raman spectroscopy studies of RNA bound carbon nanotubes, *Appl. Phys. Lett.* **2004**, *85*, 4228–4230.
- 235 LIU, Y., WU, D. C., ZHANG, W. D., JIANG, X., HE, C. B., CHUNG, T. S., GOH, S. H., LEONG, K. W. Poly-ethylenimine-grafted multiwalled carbon nanotubes for secure noncovalent immobilization and efficient delivery of DNA, *Angew. Chem. Int. Ed.* **2005**, *44*, 4782–4785.
- 236 ROJAS-CHAPANA, J., TROSZCZYNSKA, J., FIRKOWSKA, I., MORSZCEK, C., GIERSIG, M. Multi-walled carbon nanotubes for plasmid delivery into *Escherichia coli* cells, *Lab on a Chip* **2005**, *5*, 536–539.
- 237 LU, Q., MOORE, J. M., HUANG, G., MOUNT, A. S., RAO, A. M., LARCOM, L. L., KE, P. C. RNA Polymer translocation with single-walled carbon nanotubes, *Nano Lett.* **2004**, *4*, 2473–2477.
- 238 GAO, L., NIE, L., WANG, T., QIN, Y., GUO, Z., YANG, D., YAN, X. Carbon nanotube delivery of the GFP gene into mammalian cells, *ChemBioChem.* **2006**, *7*, 239–242.
- 239 WEISS, R. Nanotech poses big unknowns, *Washington Post*, February **2004**, A01.
- 240 ADELMANN, P., BAIERL, T., DROSSELMAYER, E., POLITIS, C., POLZER, G., SEIDEL, A., SCHWEGLER-BERRY, D., STEINLEITNER, C. Effects of fullerenes on alveolar macrophages *in vitro*, in *Toxic and Carcinogenic Effects of Solid Particles in the Respiratory Tract*. U. MOHR, D. L. DUNGWORTH, J. MAUDERLY, G. OBERDOERSTER, (Eds.). ILSI Press, Washington, DC, **1994**, pp. 405–407.
- 241 FORTNER, J. D., LYON, D. Y., SAYES, C. M., BOYD, A. M., FALKNER, J. C., HOTZE, M., ALEMANY, L. B., TAO, Y. J., GUO, W., AUSMAN, K. D., COLVIN, V. L., HUGES, J. B. C<sub>60</sub> in water: nanocrystal formation and microbial response, *Environ. Sci. Technol.* **2005**, *39*, 4307–4316.
- 242 SAYES, C. M., FORTNER, J. D., GUO, W., LYO, D., BOYD, A. M., AUSMAN, K. D., TAO, Y. J., SITHARAMAN, B., WILSON, L. J., HUGES, J. B., WEST, J. L., COLVIN, V. L. The differential cytotoxicity of water-soluble fullerenes, *Nano Lett.* **2004**, *4*, 1881–1887.
- 243 COLVIN, V. L. The potential environmental impact of engineered nanomaterials, *Nat. Biotechnol.* **2003**, *21*, 1166–1170.
- 244 CONNOR, E. E., MWAMUKA, J., GOLE, A., MURPHY, C. J., WYATT, M. D. Gold nanoparticles are taken up by human cells but do not cause acute cytotoxicity, *Small* **2005**, *1*, 325–327.
- 245 MOUSSA, F., PRESSAC, M., HADCHOUEL, M., ARBEILLE, B., CHRÉTIEN, P., TRIVIN, F., CÉOLIN, R., SZWARC, H. C<sub>60</sub> fullerene toxicity: preliminary account of an *in vivo* study, *Electrochemical Soc. Proc.* **1997**, *5*, 332–336.
- 246 GHARBI, N., PRESSAC, M., HADCHOUEL, M., SZWARC, H., WILSON, S. R., MOUSSA, F. [60]Fullerene is a powerful antioxidant *in vivo* with no acute or subacute toxicity, *Nano Lett.* **2005**, *5*, 2578–2585.
- 247 YOKOYAMA, A., SATO, Y., NODASAKA, Y., YAMAMOTO, S., KAWASAKI, T., SHINDOH, M., KOHGO, T., AKASAKA, T., UO, M., WATARI, F., TOHJI, K. Biological behavior of hat-stacked carbon nanofibers in the subcutaneous tissue in rats, *Nano Lett.* **2005**, *5*, 157–161.
- 248 JIA, G., WANG, H., YAN, L., WANG, X., PEI, R., YAN, T., ZHAO, Y., GUO, X. Cytotoxicity of carbon nanomaterials: single-wall nanotube, multi-wall nanotube, and fullerene, *Environ. Sci. Technol.* **2005**, *39*, 1378–1383.
- 249 MANNA, S. K., SARKAR, S., BARR, J., WISE, K., BARRERA, E. V., JEJELOWO, O., RICE-FICHT, A. C., RAMESH, G. T. Single-walled carbon nanotube induces oxidative stress and activates nuclear transcription factor- $\kappa$ B in human keratinocytes, *Nano Lett.* **2005**, *5*, 1676–1684.
- 250 DONALDSON, K., STONE, V., TRAN, C. L., KREYLING, W., BORM, P. J. A. Nanotoxicology, *Occup. Environ. Med.* **2004**, *61*, 727–728.
- 251 TRAN, C. L., BUCHANAN, D., CULLEN, R. T., SEARL, A., JONES, A. D., DONALDSON, K. Inhalation of poorly

- soluble particles. II. Influence of particle surface area on inflammation and clearance, *Inhal. Toxicol.* **2000**, *12*, 113–126.
- 252 SAYES, C. M., LIANG, F., HUDSON, J. L., MENDEZ, J., GUO, W., BEACH, J. M., MOORE, V. C., DOYLE, C. D., WEST, J. L., BILLUPS, W. E., AUSMAN, K. D., COLVIN, V. L. Functionalization density dependence of single-walled carbon nanotubes cytotoxicity *in vitro*, *Toxicol. Lett.* **2006**, *161*, 135–142.
- 253 SATO, Y., YOKOYAMA, A., SHIBATA, K., AKIMOTO, Y., OGINO, S., NODASAKA, Y., KOHGO, T., TAMURA, K., AKASAKA, T., UO, M., MOTOMIYA, K., JEYADEVAN, B., ISHIGURO, M., HATAKEYAMA, R., WATARI, F., TOHJI, K. Influence of length on cytotoxicity of multi-walled carbon nanotubes against human acute monocytic leukemia cell line THP-1 *in vitro* and subcutaneous tissue of rats *in vivo*, *Mol. BioSyst.* **2005**, *1*, 176–182.
- 254 SALVADOR-MORALES, C., FLAHAUT, E., SIM, E., SLOAN, J., GREEN, M. L. H., SIM, R. B. Complement activation and protein adsorption by carbon nanotubes, *Mol. Immunol.* **2006**, *43*, 193–201.
- 255 KIURA, K., SATO, Y., YASUDA, M., FUGETSU, B., WATARI, F., TOHJI, K., SHIBATA, K. Activation of human monocytes and mouse splenocytes by single-walled carbon nanotubes, *J. Biomed. Nanotechnol.* **2005**, *1*, 359–364.
- 256 CUI, D., TIAN, F., OZKAN, S., WANG, M., GAO, H. Effect of single wall carbon nanotubes on human HEK293 cells, *Toxicol. Lett.* **2005**, *155*, 73–85.
- 257 MONTEIRO-RIVIERE, N. A., NEMANICH, R. J., INMAN, A. O., WANG, Y. Y., RIVIERE, J. E. Multi-walled carbon nanotube interactions with human epidermal keratinocytes, *Toxicol. Lett.* **2005**, *155*, 377–384.
- 258 BOTTINI, M., BRUCKNER, S., NIKA, K., BOTTINI, N., BELLUCCI, S., MAGRINI, A., BERGAMASCHI, A., MUSTELIN, T. Multi-walled carbon nanotubes induce T lymphocyte apoptosis, *Toxicol. Lett.* **2005**, *160*, 121–126.
- 259 MULLER, J., HUAUX, F., MOREAU, N., MISSON, P., HEILIER, J.-F., DELOS, M., ARRAS, M., FONSECA, A., NAGY, J. B., LISON, D. Respiratory toxicity of multi-wall carbon nanotubes, *Toxicol. Appl. Pharmacol.* **2005**, *207*, 221–231.
- 260 LAM, C. W., JAMES, J. T., MCCLUSKEY, R., HUNTER, R. L. Pulmonary toxicity of single-wall carbon nanotubes in mice 7 and 90 days after intratracheal instillation, *Toxicol. Sci.* **2004**, *77*, 126–134.
- 261 WARHEIT, D. B., LAURENCE, B. R., REED, K. L., ROACH, D. H., REYNOLDS, G. A. M., WEBB, T. R. Comparative pulmonary toxicity assessment of single-wall carbon nanotubes in rats, *Toxicol. Sci.* **2004**, *77*, 117–125.
- 262 HUCZKO, A., LANGE, H., CALKO, E. Fullerenes: experimental evidence for a null risk of skin irritation and allergy, *Fullerene Sci. Technol.* **1999**, *7*, 935–939.
- 263 HUCZKO, A., LANGE, H. Carbon nanotubes: experimental evidence for a null risk of skin irritation and allergy, *Fullerene Sci. Technol.* **2001**, *9*, 247–250.
- 264 EEDY, D. J. Carbon-fibre-induced airborne irritant contact dermatitis, *Contact Derm.* **1996**, *35*, 362–363.
- 265 KASPAROV, A. A., POPOVA, T. B., LEBEDEVA, N. V., GLADKOVA, E. V., GURVICH, E. B. Evaluation of the carcinogenic hazard in the manufacture of graphite articles, *Vopr. Onkol.* **1989**, *35*, 445–450.
- 266 SHVEDOVA, A. A., KISIN, E. R., MURRAY, A. R., GANDELSMAN, V. Z., MAYNARD, A. D., BARON, P. A., CASTRANOVA, V. Exposure to carbon nanotube material: Assessment of nanotube cytotoxicity using human keratinocytes cells, *J. Toxicol. Environ. Health A* **2003**, *66*, 1909–1926.
- 267 MAYNARD, A. D., BARON, P. A., FOLEY, M., SHVEDOVA, A. A., KISIN, E. R., CASTRANOVA, V. Exposure to carbon nanotube material: aerosol release during the handling of unrefined single-walled carbon nanotube material, *J. Toxicol. Environ. Health A* **2004**, *67*, 87–107.

## 4

## Core–Shell Nanoparticles for Drug Delivery and Molecular Imaging

*Sung Kyun Han, Ree Sun Kim, Jin Ho Lee, Giyoong Tae, Sun Hang Cho, and Soon Hong Yuk*

## 4.1

### Introduction

Core–shell nanoparticle structures, in which a layer of polymeric materials surrounds an organic or inorganic nanoparticle core, have been investigated both as a means to improve the stability of the core nanoparticle and as a way of accessing unique physical properties that are not possible from one nanomaterial alone. This chapter describes the preparation method and characterization of a novel protein delivery system and molecular imaging agent composed of core–shell nanoparticles with the variation of core materials such as lipid, polymeric or inorganic nanoparticles.

With rapid advancements in the field of biotechnology/genetic engineering, a growing number of protein drugs have been produced [1, 2]. Although they show potent and specific physiologic actions in small doses, most of them are difficult to administer clinically. Although a wide variety of delivery systems have been designed and characterized, the parenteral route has been most widely selected for the efficient delivery of protein [3–7]. However, the problems still remain in the parenteral delivery of protein because most proteins have a short half-life in the physiological condition. Loss of biological activity and change in immunogenicity as a result of protein aggregation or denaturation are the most important challenges faced in the delivery of protein drugs [8–10]. Hence, they cannot be utilized effectively in conventional dosage forms. For such active agents, new types of drug delivery systems must be developed to deliver the drug more effectively. Among the various approaches investigated, extensive research has been conducted on the ability of colloidal systems such as liposomes and polymeric nanoparticles as an optimal delivery system for protein drugs. A wide variety of drugs such as hydrophilic drugs, hydrophobic drugs, proteins, vaccines and biological macromolecules can be delivered using colloidal systems via a number of routes [11–15]. They can be formulated for targeted delivery to the lymphatic system, brain, arterial walls, lungs, liver or spleen, or made for long-term systemic circulation [16–18]. There-

fore, numerous protocols exist for colloidal systems based on the type of drug used and the desired delivery route.

A number of liposomal formulations have been reported as drug delivery vehicles for sustained release of protein drugs and some have been evaluated for clinical applications [19–21]. Most of the previous studies involved traditional liposomes (unilamellar [22, 23] or multilamellar vesicular systems [24, 25]) and multivesicular liposomes (DepoFoam) [26–29]. However, the liposomal system shows a mechanical instability under physiological conditions, which results in a total release of the internal aqueous content (burst effect). As each multivesicular liposome is composed of discontinuous internal aqueous chambers, bounded by a continuous, nonconcentric network of lipid membranes with a higher aqueous volume:lipid ratio, the multivesicular liposomes have exhibited an improved stability. This enables us to design the sustained release form of encapsulated protein drug since, unlike unilamellar vesicular systems, a single breach in the external membrane of a multivesicular liposome will not result in a total release of internal aqueous content containing protein drug. They have been evaluated with recombinant human insulin [30–32], leuprolide (a 9-amino-acid peptide analog of luteinizing hormone releasing hormone) [33–35], met-enkephalin (an endogenous opioid peptide of 5 amino acids) [36, 37] and octreotide (a cyclic octapeptide analog of somatostatin) [38, 39]. However, the sustained release formulation of protein drugs using multivesicular liposomes still remains a major challenge, achieving high drug loading with high drug recovery and controlling the release pattern over a prolonged period.

Recently, polymersome (polymer vesicle) has been prepared by the molecular assembly of an amphiphilic diblock copolymer composed of poly(ethylene glycol) (PEG) and polyesters or polycarbonates [40, 41]. Biodegradable diblock copolymers based on PEG and poly(lactide) have been used to prepare carriers such as micelles, nano/microparticles and gels for controlled or targeted delivery. However, the formation of polymersomes has been reported and suggests a promising application in drug delivery system for water-soluble drugs and protein drugs; similar advantages and disadvantages founded in the liposomal system are observed in the polymersome.

Polymeric nano/microparticles are the most suitable and preferred systems in the delivery of protein drugs by the parenteral or nonparenteral route. Due to the large amount of toxicological and chemical data available, biocompatibility/histocompatibility, predictable biodegradation kinetics, ease of fabrication, and variety in copolymer ratio and molecular weight, polyesters have been found the most widespread use as a major component of polymeric nano/microparticles and they have been approved in clinical applications [42, 43]. Despite many advantages, polyesters like poly(lactide-co-glycolide) (PLGA) also have some inherent shortcomings. Due to the hydrophobic nature of the polymer compared to most of the protein drugs to be encapsulated, the serious problems associated with protein activity were observed during storage or *in vivo* release. Since hydration and degradation of PLGA are prerequisites for the release of protein drugs during the bioerosion phase, this results in an acidic microenvironment due to the formation of lactic

acid and glycolic acid, which leads to denaturation (hydrolytic degradation and aggregation) of protein drugs. Although improvement of protein drug compatibility has been investigated by coencapsulating buffer salts and stabilizer for protein drugs and modification of polyesters, it still remains challenging.

With the significant progress in the treatment of diseases and diagnosis, the importance of molecular imaging as well as that of drug delivery has increased tremendously. The prerequisite for efficient molecular imaging is to prepare the magnetic nanoparticles with a narrow size distribution. Information technology which has been used in data storage devices now enables us to prepare magnetic (metal) nanoparticles with such a narrow size distribution. However, as such particles have a strong tendency to agglomerate due to their large specific surface area, various methods have been studied in order to stabilize the nanoparticles. For this purposes, many attempts have been made to establish the preparation method of magnetic nanoparticles coated with a biocompatible polymer (core-shell nanoparticles with metallic core) to improve the stability and biocompatibility under physiological conditions.

As described previously, there are number of studies on the protein delivery system and molecular imaging agent using a single nanomaterial system. However, these systems showed major drawbacks in terms of the stability, release pattern and cytotoxicity. Recently, a number of investigations have been devoted to understanding the formation of core-shell nanoparticles [44, 45] and much interest has been focused on developing core-shell nanoparticles as an effective means of delivering bioactive materials [46–50]. Due to their distinct geometry, numerous applications have evolved, and core-shell nanoparticles with a variation of core materials have been designed and characterized as drug delivery systems based on the type of drug used. In this chapter, a new type of protein delivery system and molecular imaging agent will be introduced using core-shell nanoparticles, which exhibit the improved stability, a sustained release pattern of protein drug and decreased cytotoxicity.

## 4.2

### Core-shell Nanoparticles with a Lipid Core

As an effective oil-soluble drug carrier, lipid and mixed micelles have been developed. However, lipid-based drug carriers composed of a single lipid phase have several inherent problems, including the burst effect and difficulty in achieving zero-order release. To overcome these difficulties, core-shell nanoparticles with drug-loaded lipid core were prepared (see Fig. 4.1). For the formation of the polymeric shell, drug-loaded lipid cores were usually freeze-dried in the aqueous solution containing polymers used for the shell material. Freeze-drying of vesicular structure and subsequent recovery of the very same structure on the microscale is simple and straightforward [51, 52]. However, with the vesicular structure on the nanoscale, the situation is more complex [51]. A solution to the problem that allows the recovery of vesicular structure on the nanoscale was found to be the inclu-



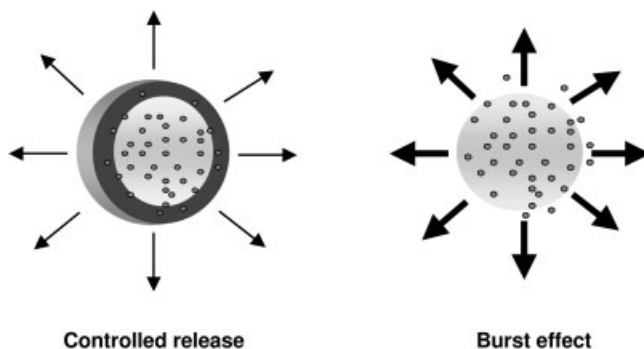


**Figure 4.1.** Schematic description of the advantages gained with the formation of core–shell nanoparticles.

sion of relatively high concentrations (around 30 wt%) of cryoprotectants such as trehalose, sucrose, mannose or glucose. The role attributed to these cryoprotectants is replacement of structure-stabilizing water-based hydrogen bonds at the liposomal surface, which are lost in the process of drying [53].

Another approach to cryoprotection, which does not require the inclusion of additives such as the sugars listed above, has been made by chemical modification of phospholipid with hydrophilic polymers, surfactants or block copolymers [54].

A novel method for the preparation of core–shell nanoparticles with a lipid core was designed and characterized (see Fig. 4.2). The lipid core is composed of lecithin, which forms a spherical supramolecular structure (multilamellar vesicles) in the concentrated state [55]. The polymeric shell is composed of pluronics [poly(ethylene oxide)–poly(propylene oxide)–poly(ethylene oxide) triblock copolymer, F-127]. In this study, a F-127/trehalose mixture was used to stabilize the drug-loaded lipid core in the form of core–shell nanoparticles. With the combina-

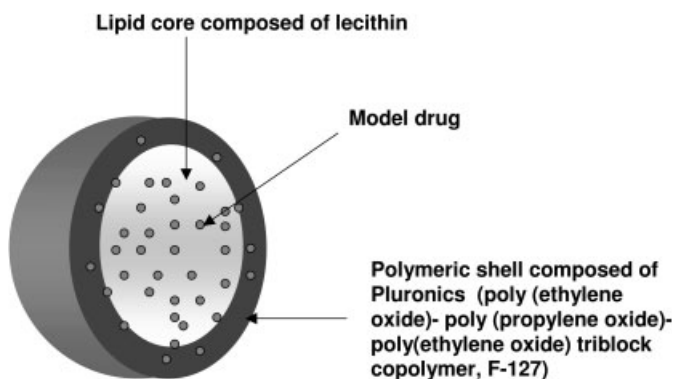


**Figure 4.2.** Schematic description of core–shell nanoparticles with drug-loaded lipid cores.

tion of F-127 and trehalose, the concentration of cryoprotectant can be reduced into approximately 5 wt% and chemical modification of lipid to improve the stability of vesicular structure on the nanoscale was not required.

First, the core-shell nanoparticles with a drug-loaded lipid core were prepared for a lipophilic drug. A drug suspension composed of 90/10 (w/w) [Tween 80/paclitaxel (model drug)] mixture was prepared in which the oil phase was subsequently dispersed. The oil phase was composed of 40 wt% aqueous solution of lecithin from soy bean oil. The obtained drug dispersion and oil phase were mixed in equal amounts, and were then subjected to sonication in an ice bath for 3 min to prepare the drug-loaded lipid core using a probe-type ultrasonic wave homogenizer (Branson Sonifier Model 185). The solution mixtures composed of 90/10 (w/w) (F-127 aqueous solution/drug-loaded lipid core) were prepared to induce the formation of the polymeric shell on the surface of the drug-loaded lipid core. F-127 aqueous solutions were prepared with or without trehalose to observe the preservation of integrity of the core-shell structure of nanoparticles during the freeze-drying.

Aqueous concentrated lecithin mixtures show typical lamellar liquid crystalline behavior and the individual lamellae tend to form a spherical supramolecular structure [55]. Figure 4.3 shows the particle size distribution of 5 wt% lecithin aqueous solution, which exhibits the formation of a spherical supramolecular structure with a diameter of 45.6 nm. The size, polydispersity and surface charge of nanoparticles were determined using an electrophoretic light-scattering spectrophotometer equipped with a 10 mW He-Ne laser (632.8 nm) (ELS-8000; Otsuka Electronics, Japan). Based on this, paclitaxel solubilized in Tween 80 was added to 40 wt% lecithin aqueous solution and subjected to sonication leading to the complete dissolution of paclitaxel. This is a universal principle for all drugs that are

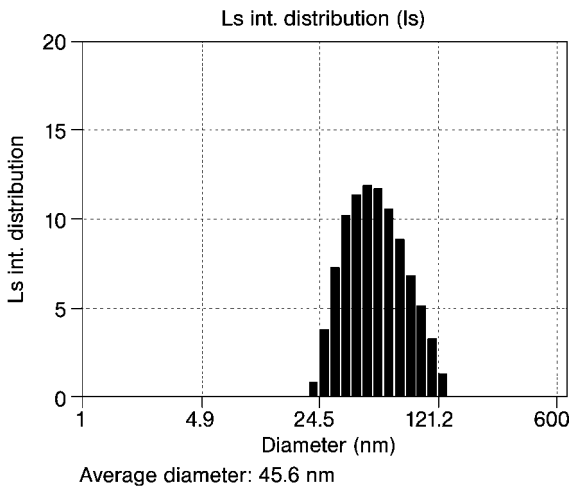


**Figure 4.3.** Size distribution of 5 wt% lecithin in aqueous medium with 5 wt% Tween 80. (From Ref. [48].)

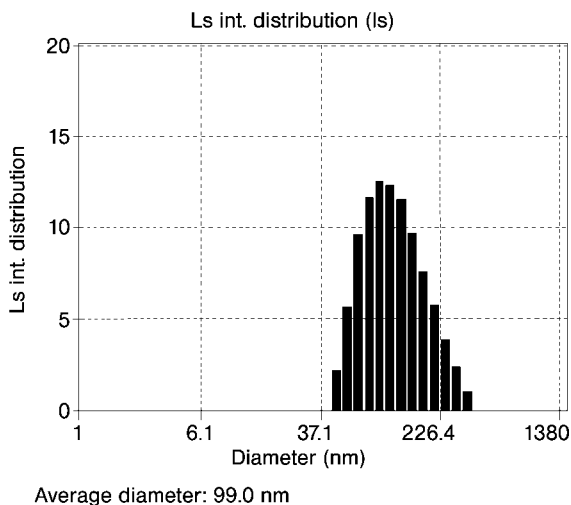


**Figure 4.4.** Size distribution of paclitaxel-loaded lipid cores in the aqueous medium. (From Ref. [48].)

poorly soluble in the water phase of emulsions and simultaneously in the oil phase, but possessing a suitable lipophilicity to interact with the lecithin molecules in the interfacial layer [56]. Of course, the incorporation capacity of an oil-in-water (o/w) emulsion is not unlimited. At a certain stage, the interfacial layer is saturated with paclitaxel, leading to the formation of nondissolved small drug crystals in the dispersion. As shown in Fig. 4.4, paclitaxel-loaded lipid cores dispersed in 10 wt% F-127 aqueous solution exhibit a stable emulsion with diameter of 99 nm.

Freeze-drying was performed for the formation of a polymeric shell composed of F-127. As shown in Fig. 4.5(A), significant aggregation was observed to show that the spherical supramolecular structure was disintegrated during the freeze-drying process. This phenomenon is usually found in the freeze-drying of protein solution. With freeze-drying, the protein activity is significantly decreased due to the disintegration of supramolecular structure. It has been reported that trehalose, a naturally occurring osmolyte, is known to be an efficient stabilizer of proteins and helps the activity of enzymes in solution as well as in the freeze-dried state [57]. This led us to use trehalose as a stabilizer of the spherical supramolecular structure of core–shell nanoparticles. Note that exposure of freshly collected oocytes to a concentration of trehalose between 0.5 and 1.0 M for up to 10 min had no significant effect, indicating that trehalose is not toxic [58]. With adding 5 wt% trehalose in F-127 aqueous solution, freeze-drying was performed to induce the formation of the polymeric shell. As shown in Fig. 4.5(B), nanoparticles with diameter of 267.4 nm were observed, indicating minimal disintegration of spherical supramolecular structure.

A cryogenic transmission electron microscopy (cryo-TEM) image was obtained for the verification of the formation of core–shell nanoparticles. For the measure-

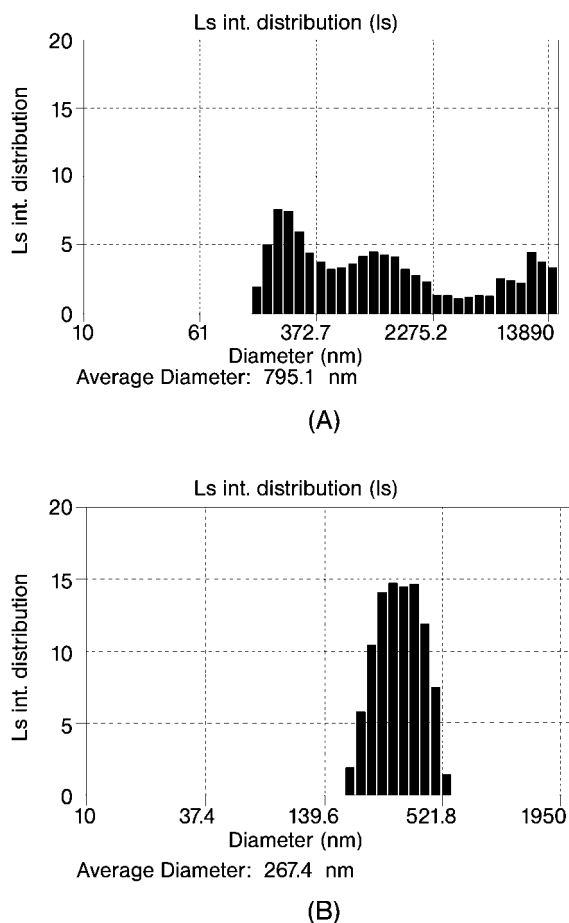


**Figure 4.5.** (A) Size distribution of nanoparticles formed from 10 wt% F-127 aqueous solution without trehalose. (B) Size distribution of nanoparticles formed from 10 wt% F-127 aqueous solution with 5 wt% trehalose. (From Ref. [48].)

ment, the samples were prepared as a thin liquid film (less than 0.25  $\mu\text{m}$  thick) supported on cryo-grid. These were quenched into liquid ethane at its freezing point and stored under liquid nitrogen. They were later transferred to a Tecnai 12 electron microscope (Philips, The Netherlands). Direct imaging was carried out at a temperature of approximately  $-170^\circ\text{C}$  and with a 120 kV acceleration voltage, using the images acquired with a Multiscan 600 W CCD camera (Gatan, USA). With the nanoparticles formed from 10 wt% F-127 aqueous solution, the formation of core-shell nanoparticles was observed as shown in Fig. 4.6.

In this study, lecithin was used as the main component for the preparation of nanoparticles (self-assembled aggregates). The addition of other substances, espe-

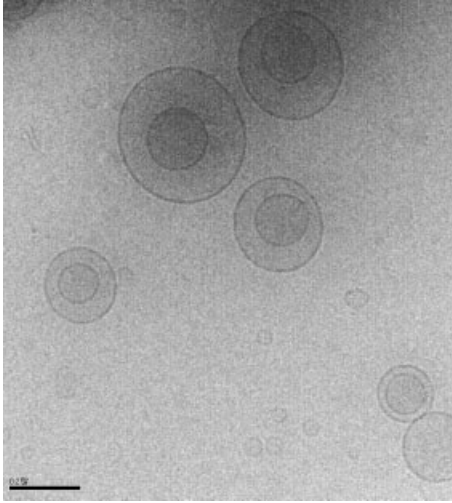


**Figure 4.6.** Cryo-TEM image of nanoparticles formed from 10 wt% F-127 aqueous solution with 5 wt% trehalose. (From Ref. [48].)

cially surfactants and drug, may result in the alteration of the original structures. Differential scanning calorimetry (DSC) was used to characterize the lipid core with addition of surfactant, F-127 and drug as shown in Fig. 4.7. Although a minimal peak was observed with 15 wt% F-127 aqueous solution, no characteristic peaks

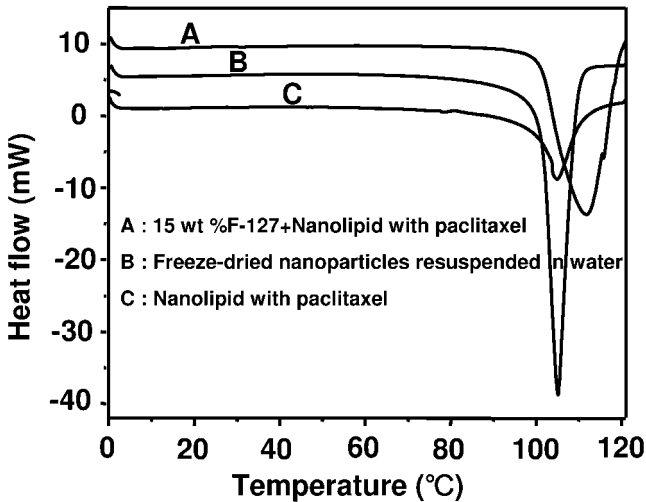


**Figure 4.7.** DSC thermograms of components used to prepare for the core-shell nanoparticles. (From Ref. [48].)

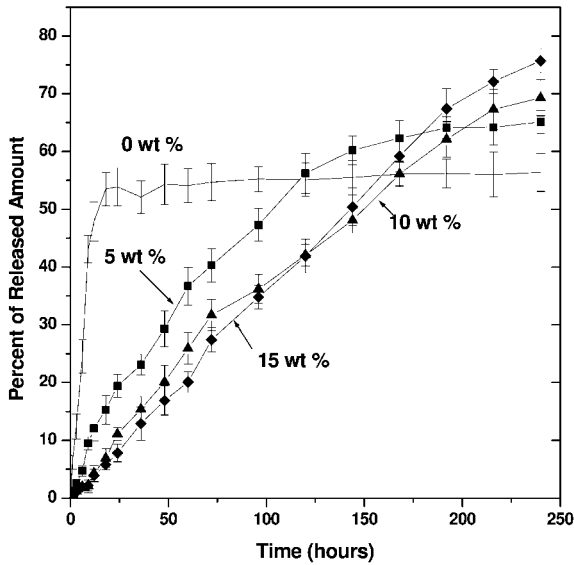


**Figure 4.8.** The release pattern of paclitaxel from nanoparticles formed as a function of the concentration of F-127 aqueous solution.  $N = 3$  experiments. (From Ref. [48].)

were observed with lecithin and Tween 80 mixed with paclitaxel. However, the characteristic peaks were observed at 105.5 and 111.9 °C with paclitaxel-loaded lipid cores (loading amount: 4 wt%) and with paclitaxel-loaded lipid cores in the presence of F-127 and trehalose, respectively. A similar peak was observed at 104.9 °C with the freeze-dried nanoparticles resuspended in water. This indicates that the original structure of the paclitaxel-loaded lipid core was maintained in the presence of F-127 and trehalose during the freeze-drying, resulting in the formation of core-shell nanoparticles with a drug-loaded lipid core.

For application as a drug delivery system for lipophilic drugs, core-shell nanoparticles with paclitaxel-loaded lipid core were prepared and the release behavior of paclitaxel was observed as shown in Fig. 4.8. Without the polymeric shell (0 wt% of F-127 aqueous solution), a significant burst effect was observed, resulting in the precipitation of paclitaxel into the release medium. This is due to the poorly solubilized paclitaxel in the lipid phase and its poor solubility in aqueous media. With the formation of the polymeric shell, released paclitaxel from the lipid phase diffused through the polymeric shell (F-127 phase), resulting in a significant decrease in the burst effect and an almost zero-order release pattern was observed with nanoparticles formed from 10 wt% F-127 aqueous solution.

Based on the formation of core-shell nanoparticles, the application has evolved in the area of protein delivery. Figure 4.9 shows the chemical structure of lecithin used as a core material. Due to its low isoelectric point (below 3.5), zwitterionic lecithin shows anionic characteristics under physiological pH as presented in Fig. 4.9.

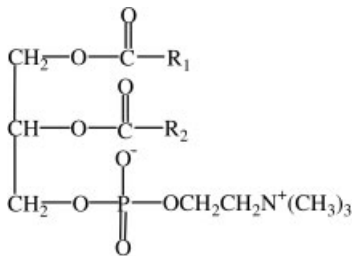


**Figure 4.9.** Chemical structure of lecithin used as a lipid core.

With a proper choice of protein drug with a higher isoelectric point (above 7.4), the ionic interaction between lecithin nanolipid and protein drug can be achieved as presented schematically in Fig. 4.10.

Vascular endothelial growth factor (VEGF) was used as a model protein drug. VEGF is a potent mitogen in embryonic and somatic angiogenesis with a unique specificity for vascular endothelial cells [59, 60]. VEGF has been considered as a potential treatment for stroke due to its angiogenic and direct neuroprotective action [61]. One potential mechanism for the treatment of stroke is the induction of angiogenesis with increasing oxygen availability. The extent of newly formed vessels is probably an important factor in determining the improvement in the blood flow, culminating in the recovery and repair of neurons, and a reduction in the ischemic damage.

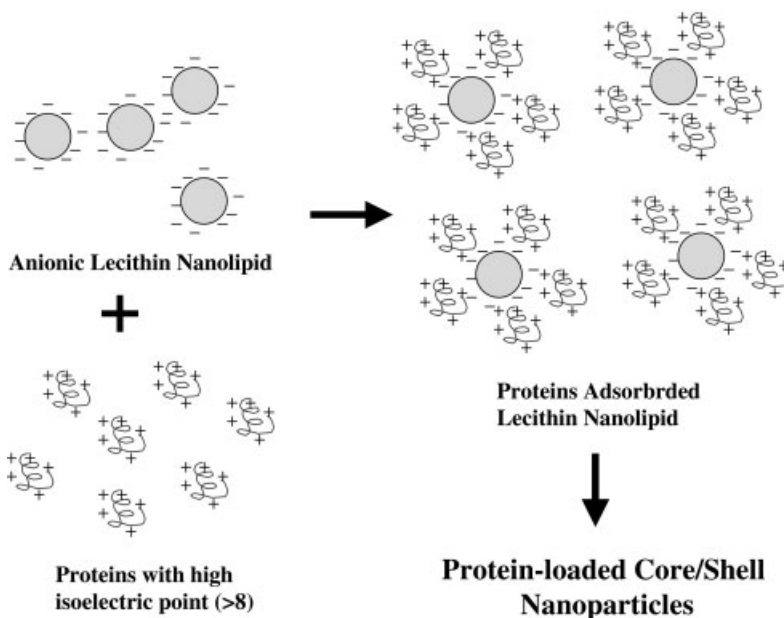


**Figure 4.10.** Schematic description of the formation of protein-loaded core-shell nanoparticles.

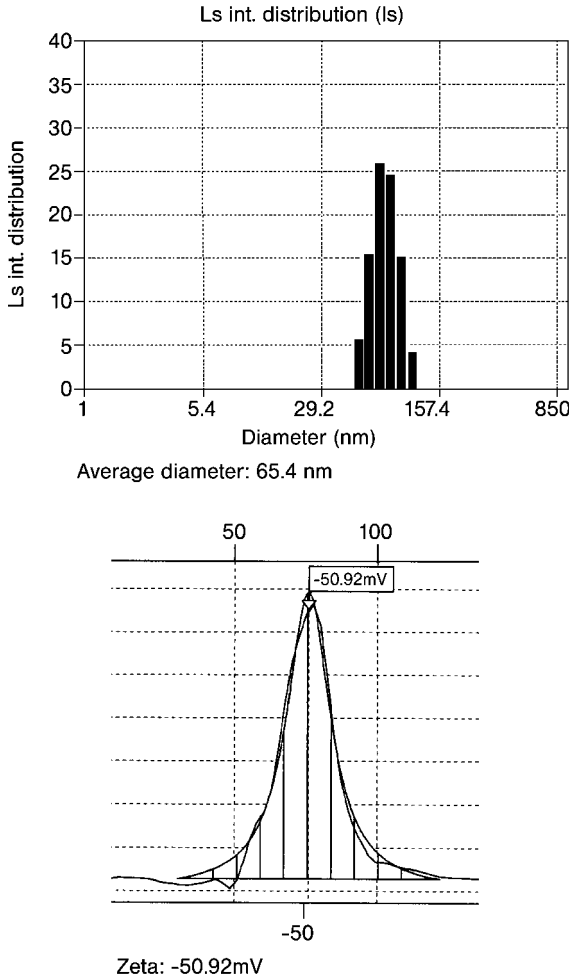


**Figure 4.11.** The size distribution and  $\zeta$  potential of lecithin nanoparticles.

The medical product related to VEGF is being developed for the treatment of coronary artery disease [62]. As a result of blocked arteries in the heart, patients with coronary artery disease typically experience severe, often immobilizing, pain from minimum physical activity such as walking. This product is intended to improve blood flow in the heart through the formation of new blood vessels, a process known as angiogenesis, with the delivery the angiogenic protein, VEGF-121. In this approach, the product is directly injected into the heart wall by an endocardial injection catheter and this enables the sustained, controlled production of VEGF-121 protein in the area of the heart with poor blood flow. It was reported that there were no VEGF-related serious adverse events or dose-limiting toxicities.



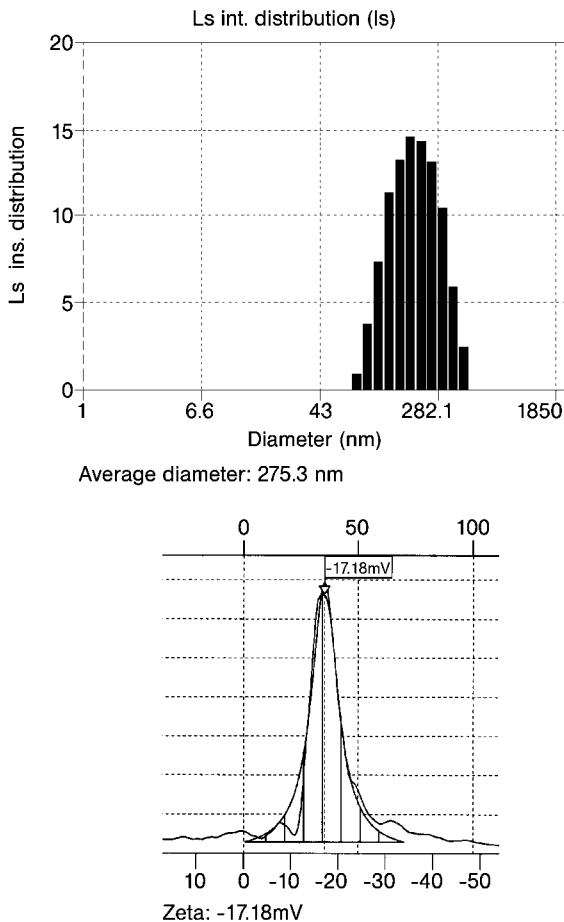


**Figure 4.12.** The size distribution and  $\zeta$  potential of core–shell nanoparticles with a VEGF-loaded lecithin core.

The core–shell nanoparticles are utilized as a delivery vehicle of VEGF with a sustained release pattern. For the preparation of the protein-loaded core–shell nanoparticles, a similar process to that described previously was employed. For efficient loading of protein drug, complex formation was induced between lecithin and VEGF, and this complex was mixed with F-127 aqueous solution containing 5 wt% trehalose. Freeze-drying was conducted to form the polymeric shell on the surface of the complex composed of lecithin and VEGF (see Fig. 4.10).

In the freeze-drying process, trehalose used as a cryoprotectant plays two roles. One is to preserve the core–shell structure of nanoparticles, which is very important for the accomplishment of the sustained release pattern of VEGF. The other is to preserve the activity of loaded VEGF. It has been reported that globular proteins invariably show higher melting (denaturation) temperatures in the presence

of sugars (in dilute solution) and concentrated sugar systems confer textural consistency that prevents microbial attack in foods. It is not clear, however, whether these two different types of stabilization have a common physicochemical origin; in particular, whether water-sugar interactions are the only basis of both phenomena. Among all the sugars, trehalose has received the greatest attention, both because of its wide role in nature and its potential use as a highly efficient natural preservative [63].

Figure 4.11 shows the  $\zeta$  potential and size distribution of lecithin nanolipid. The size of lecithin nanolipid was approximately 65.4 nm and a negative value of the  $\zeta$  potential was observed, indicating that anionic lecithin nanolipid is suitable for the immobilization of cationic VEGF. After freeze-drying of VEGF/lecithin nanolipid complex in the F-127 aqueous solution containing 5 wt% trehalose, the obtained powder was resuspended in water and characterized with a particle size analyzer. As shown in Fig. 4.12, the diameter was approximately 270 nm and the magnitude of the negative value of the  $\zeta$  potential was decreased. With the formation of the polymeric shell, the size of the nanoparticles was increased and the negative charge of the lecithin nanolipid was decreased. The cryo-TEM image clearly demonstrates the formation of core-shell nanoparticles as shown in Fig. 4.13.

The release of VEGF from the nanoparticles was measured as shown in Fig. 4.14. A VEGF-loaded nanoparticle suspension (0.2 mL) was subsequently put into a dialysis tube. The dialysis tube was placed into 15 mL PBS containing 2.0 mM sodium azide and 0.1% (w/v) bovine serum albumin (BSA), and kept in reciprocal shaking water bath (Sangwoo Scientific, Korea) at 37 °C and 35 r.p.m. At each time-point, the whole medium was taken and replaced with the fresh release medium.

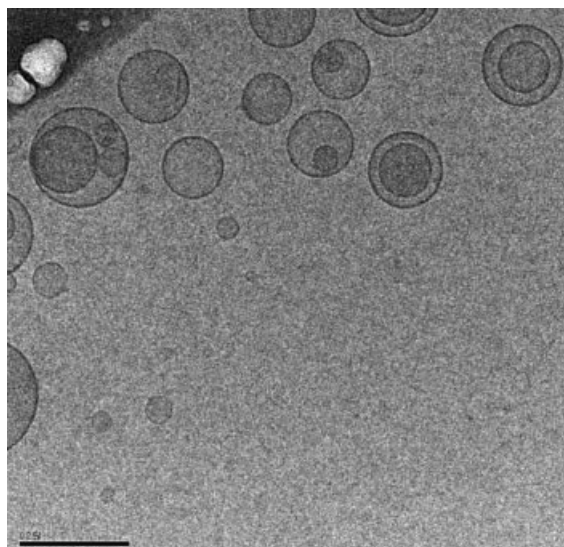


**Figure 4.13.** Cryo-TEM image of core-shell nanoparticles with a VEGF-loaded lecithin core.

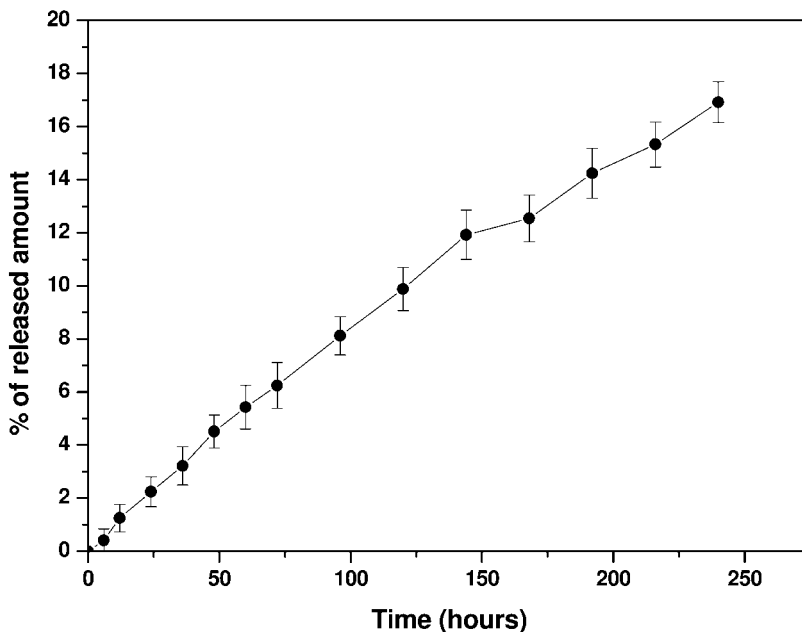


Figure 4.14. The release of VEGF from the core–shell nanoparticles.

The amount of released VEGF into the release medium was determined by ELISA analysis (Neogen, USA). The sustained release pattern was observed up to 10 days, releasing about 16% of the initial loading and this indicates that a 1-month period of VEGF release can be achieved with core–shell nanoparticles.

With the adsorption of F-127 on the surface of lipid core by freeze-drying, the stabilized core–shell nanoparticles were formed in the presence of trehalose. This indicates that trehalose, which is generally used as a protein stabilizer, preserves the integrity of the spherical supramolecular structure of the lecithin core during the freeze-drying. Due to the distinct geometry of core–shell nanoparticles with a lipid core, the lipophilic drug can be loaded in the lipid core and protein drugs can be loaded in the polymeric shell.

### 4.3

#### Core–Shell Nanoparticles with a Polymeric Core

PLGA micro/nanoparticles have been designed and characterized for the delivery of a couple of proteins. Biodegradable microspheres containing recombinant human erythropoietin (EPO) were prepared from ABA triblock copolymers, consisting of hydrophobic PLGA A blocks and poly(ethylene oxide) (PEO) B blocks [64]. Using excipients with known protein stabilizing properties, such as BSA, poly(L-histidine), poly(L-arginine) or a combination of poly(L-arginine) and dextran, the EPO aggregate content was significantly reduced to below 5% of the encapsulated

EPO. In particular, the microspheres composed of ABA triblock copolymer (35 mol% PEO; 30 kDa) in combination with 5% BSA yielded both an acceptable level of EPO aggregate and a continuous release profiles under *in vitro* conditions for up to 14 days. Pharmacokinetic characterization of VEGF controlled release microspheres composed of PLGA was performed using a rat model. The microspheres were administered subcutaneously to the rat and the pharmacokinetic parameters were compared with those of VEGF solution [65]. The subcutaneous administration of protein solution resulted in rapid clearance from the tissue, with high plasma concentrations as expressed by rapid absorption and elimination. However, the subcutaneous administration of VEGF microspheres produced low plasma concentrations and high subcutaneous concentrations over a period of 7 weeks.

However, because of the hydrophobic character of PLGA, the loading of protein into PLGA micro/nanoparticles with a minimal decrease of protein activity still remains challenging. In addition, nanoparticles have a further advantage over larger microparticles because they are better suited for intravenous delivery. The smallest capillaries in the body are 5–6  $\mu\text{m}$  in diameter. The size of particles being distributed into the blood stream must be significantly smaller than 5  $\mu\text{m}$ , without forming aggregates, to ensure that the particles do not form an embolism.

The rapid removal of intravenously administered colloidal drug carrier by the mononuclear phagocytic system, comprising mainly the Kupffer cells of the liver and the macrophages of the spleen, has been identified as the major obstacle to the efficient targeting of colloidal carriers to target sites such as the circulation itself, tumor, sites of inflammation and bone marrow. Various studies have been carried out for the successful avoidance of these difficulties. One of the related studies reported that the *in vitro* interaction with isolated macrophages and the biodistribution of model polystyrene nanospheres after modification of the particle surface using PEO/poly(propylene oxide) (PPO) block copolymers of the poloxamer (Pluronic) poloxamine series and the presence of PEO on the surface of nanospheres decrease the extent of phagocytosis [66]. It was also verified that poloxamer and poloxamine copolymers are bound to the nanosphere surface by hydrophobic interaction of the PPO chains, whereas the hydrophilic PEO chains protrude into the surrounding medium to create a steric barrier and this barrier prevents or decreases the adsorption of plasma proteins onto the particle surface, resulting in the decreased recognition by the liver and spleen macrophages [67–69]. Similar results have been reported with PLGA nanoparticles coated with Pluronic [70]. In particular, the size of nanoparticles and coating layer thickness were measured using photon correlation spectroscopy, indicating the presence of a hydrogel layer on the surface of nanoparticles. These results enable us to design PLGA nanoparticles with a hydrogel layer on the surface, which are utilized as cores in the formation of core–shell nanoparticles with a polymeric core.

#### 4.3.1

##### **Hyaluronic Acid (HA)-functionalized PLGA Nanoparticles**

A novel preparation method for core–shell nanoparticles with a hydrophilic polymeric shell was designed and characterized based on the preparation method of

hydrophilized PLGA nanoparticles with Pluronics described previously. The core is composed of PLGA and polymeric shell is composed of Pluronics (F-127) and HA. The role of the core is to provide the nucleus for the stable formation of the hydrophilic polymeric shell by physical adsorption and that of the polymeric shell is to provide the hydrophilic network for protein loading. Specifically, HA was used as one of the components for polymeric shell to induce the ionic interaction between protein and HA for the efficient loading and sustained release of ionized and hydrophilic protein. For the characterization of core-shell nanoparticles as a drug carrier, lysozyme, which was used as a model protein drug, was loaded into the nanoparticles, and the loading amount and release pattern was observed with the variation of the composition of the polymeric shell.

In the previous study, PLGA nanoparticles were prepared based on the temperature-induced phase transition in the F-127/PLGA mixture without solvent [71]. This method provides F-127-coated PLGA nanoparticles (hydrophilized nanoparticles) used as a core. Figure 4.15 describes the preparation method of nanoparticles used as a polymeric core schematically. F-127 is in a flaky state and PLGA is in a powdery state at room temperature. The mixtures were prepared individually by weighing 85 mg of polymers with 0.2 weight ratio of (PLGA/F-127) and 3 mg of Tween 80 into 20 mL vials, which were immediately put into a vacuum oven at 60 °C. Within 30 min, both polymers were liquidized completely to form a transparent polymer solution. The melted mixtures were transferred to vacuum oven at 25 °C to induce the phase transition (the solidification of liquidized polymer mixture). With the phase transition, PLGA formed the phase-separated domain with a spherical form and F-127 formed the continuous phase as shown in Fig. 4.16. Following the equilibration period for 3 h, the solidified mixture was withdrawn from the vacuum oven and immersed in distilled/deionized water for 3 days to solubi-

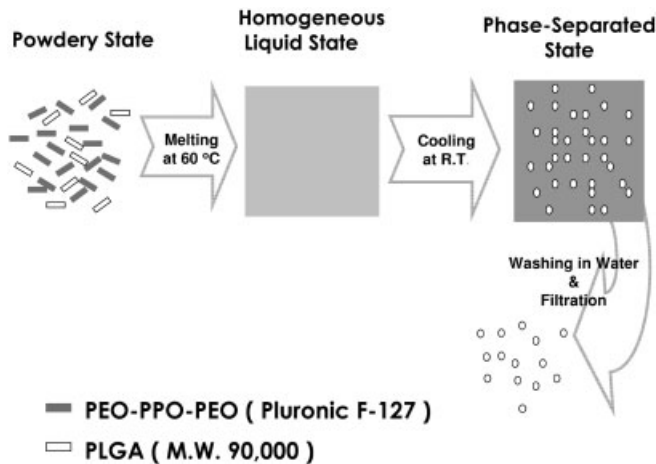


**Figure 4.15.** Schematic description of the method of preparation of PLGA nanospheres. (From Ref. [71].)

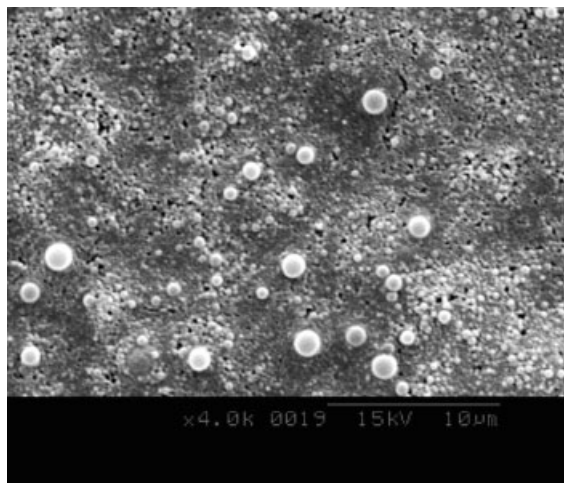


**Figure 4.16.** SEM image of phase-separated (8:2) (w/w) F-127/PLGA mixture. (From Ref. [71].)

lize F-127 using a dialysis bag (molecular weight cut-off range: 40–50 kDa; Fisher Scientific, USA), replacing the distilled/deionized water every hour. This aqueous solution containing PLGA nanoparticles was centrifuged for 20 min and filtered through the 0.45- $\mu\text{m}$  filter membrane. The obtained PLGA nanoparticles were freeze-dried. In the final stage for preparing PLGA nanoparticles, Pluronic was removed from the phase-separated aggregate. However, the complete removal of Pluronic was impossible due to the hydrophobic interaction between the PLGA and the PPO domain of F-127, resulting in the formation of Pluronic-adhered PLGA nanoparticles. Due to the presence of F-127 on the surface of PLGA nanoparticles, stability in aqueous medium was significantly improved as shown in Fig. 4.17.

For the preparation of core–shell nanoparticles with a hydrophilic polymeric shell, the formation of a gel layer was induced. First, PLGA nanoparticles prepared previously were suspended in HA/F-127 aqueous solution with a variation of the weight ratio of HA/F-127. Subsequently, this aqueous solution mixture was subjected to freeze-drying to induce the formation of the polymeric shell.

Figure 4.18 describes the formation of core–shell nanoparticles with a hydrophilic polymeric shell and the protein-loading process [49]. F-127 forms a spherical micelle at low concentration. In this low micellar concentration regime, micelles are well-separated and the solution is an isotropic fluid. At higher concentrations, the micelles approach close packing and ordered domains, consisting of cubic packing of spherical micelles, are induced resulting in the gelation. With the freeze-drying process in this study, the concentration of F-127 aqueous solution was increased with the evaporation of water and gelation was induced to form a polymeric shell. With the evaporation of water by freeze-drying, F-127 was adsorbed (gelled) into F-127-coated PLGA nanoparticles and HA might be adsorbed

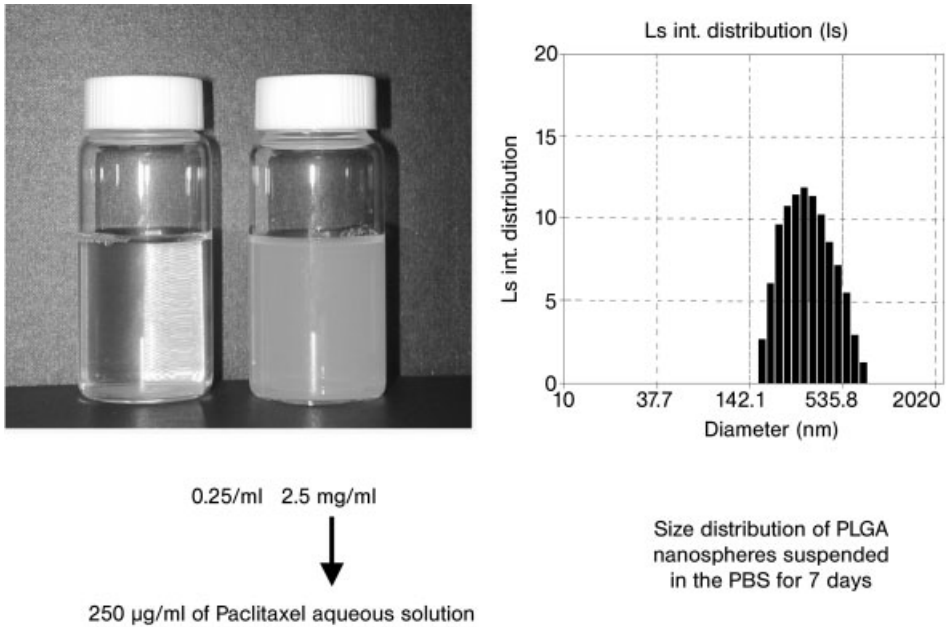


Figure 4.17. The enhanced stability of F-127-coated PLGA nanoparticles in aqueous media.

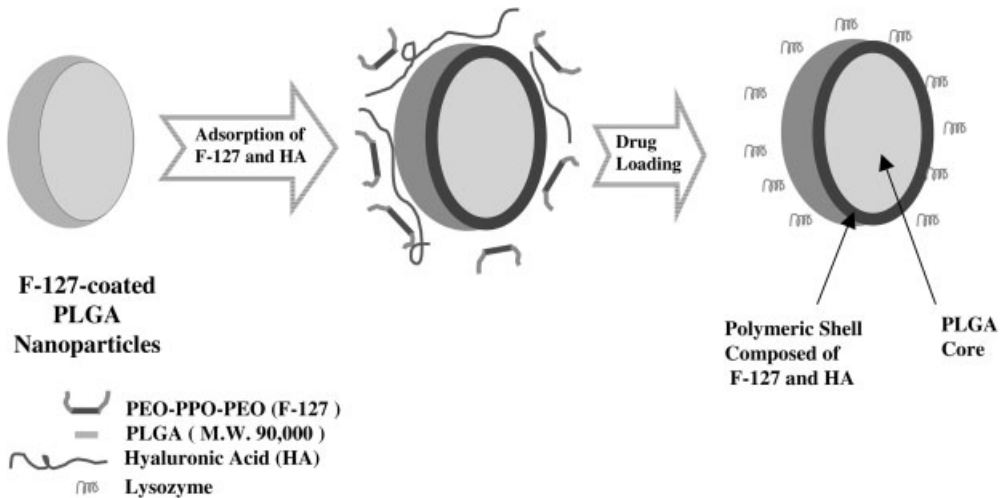
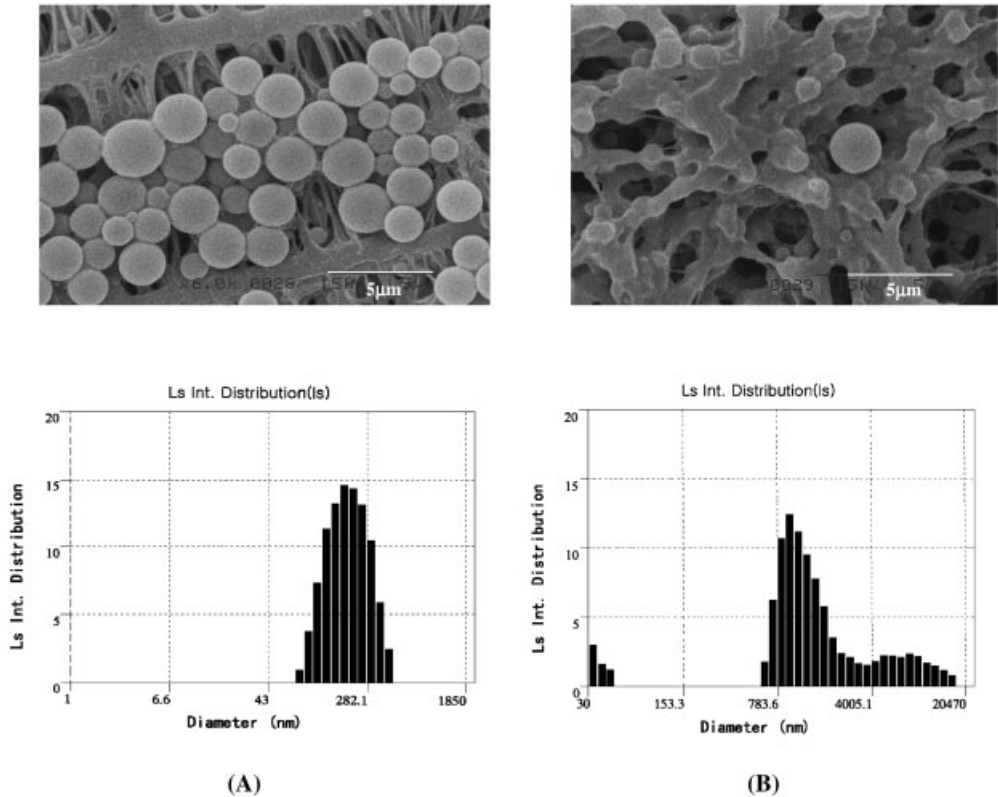


Figure 4.18. The formation of core-shell nanoparticles with a hydrophilic polymeric shell and the protein loading process. (From Ref. [49].)



**Figure 4.19.** (A) SEM image and size distribution of core–shell nanoparticles formed from 5 wt% F-127 aqueous solution. (B) SEM image and size distribution of core–shell nanoparticles formed from 10 wt% F-127 aqueous solution. (From Ref. [49].)

into F-127-coated PLGA nanoparticles with F-127, resulting in the formation of a polymeric shell composed of F-127/HA composite.

The shape of core–shell nanoparticles formed at different concentrations of F-127 in the absence of HA was examined by scanning electron microscopy (SEM) to observe the optimum concentration of F-127 for the stable formation of the polymeric shell. As shown in Fig. 4.19, the aggregation of nanoparticles was observed at core–shell nanoparticles formed as 10 wt% F-127 aqueous solution. This is due to the formation of a polymer network between free F-127 (which was not adsorbed on the surface of the PLGA nanoparticle). However, aggregation was not observed at the core–shell nanoparticles formed at 5 wt%, indicating that most F-127 in the aqueous media was adsorbed on the surface of PLGA nanoparticles. Therefore, the concentration of polymeric shell material was fixed at 5 wt% throughout the experiment. Note that the fibrous structure in the background of Figs. 4.19(A) and 4.20(A) is from the filter paper.



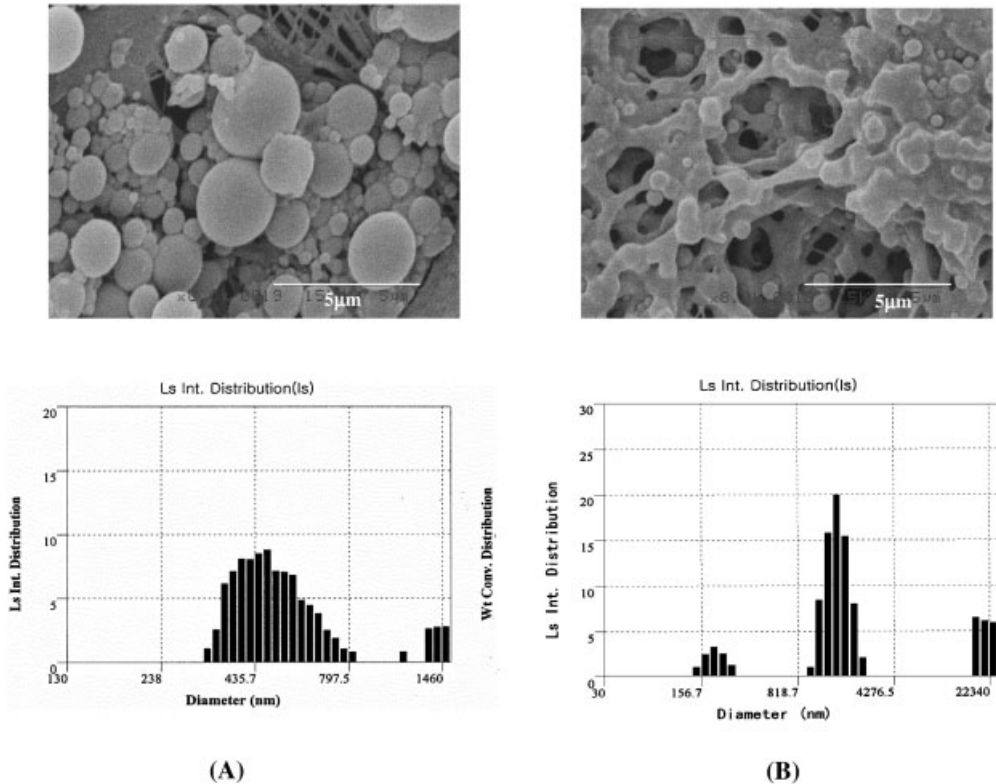


**Figure 4.20.** (A) SEM image and size distribution of core–shell nanoparticles with 0.2 weight ratio of HA/F-127. (B) SEM image and size distribution of core–shell nanoparticles with 0.4 weight ratio of HA/F-127. (From Ref. [49].)

For the efficient loading of cationic lysozyme (isoelectric point: 11.1) under physiological conditions, anionic HA was incorporated into the polymeric shell by co-adsorption with F-127. Core–shell nanoparticles were prepared with the variation of the HA/F-127 weight ratio. As shown in Fig. 4.20, the aggregation of nanoparticles was observed at 0.4 weight ratio of HA/F-127. This is due to the formation of a polymer network between free HA (which was not incorporated into the polymeric shell). In the adsorption of F-127 and HA on the surface of F-127-coated nanoparticles, the main driving force forming the polymeric shell is the hydrophobic interaction between F-127. As HA does not have intermolecular interactions with F-127 or PLGA nanoparticles, it is embedded physically in the F-127 network within the range of 0–0.3 weight ratio of HA/F-127. However, the formation of the HA/lysozyme complex without the PLGA core could be possible due to unstable embedding of HA in the polymeric shell. This property should be improved for

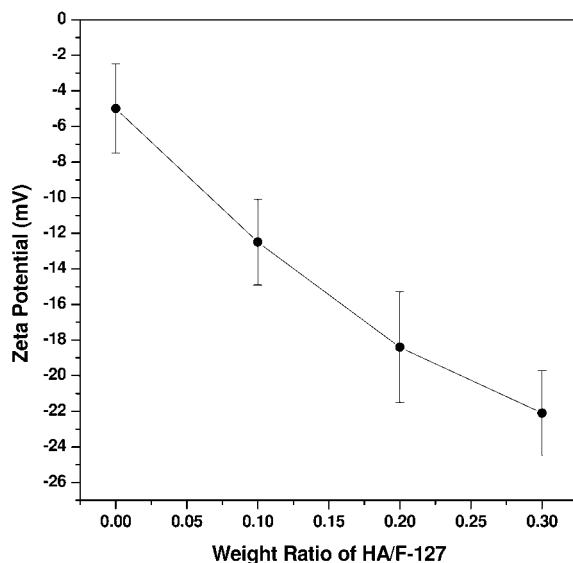


**Figure 4.21.** The variation of the  $\zeta$  potential of core–shell nanoparticles as a function of the weight ratio of HA/F-127. (From Ref. [49].)

the exact manipulation of loading lysozyme (or negatively charged proteins under physiological conditions).

Figure 4.21 shows the variation of the  $\zeta$  potential of core–shell nanoparticles with the variation of weight ratio of HA/F-127. The negative value was observed with the increase of weight ratio of HA/F-127, indicating that anionic HA is embedded in the polymeric shell and that the polymeric shell is suitable for the immobilization of cationic lysozyme.

Figure 4.22 shows the change of loading amount with the variation of weight ratio of HA/F-127. Lysozyme was loaded into core–shell nanoparticles by sorption method. Samples of 100 mg of dried core–shell nanoparticles were suspended in 100 mL of PBS containing 10 mg of lysozyme and stored at 25 °C to induce the ionic interaction between lysozyme and HA in the polymeric shell. After equilibrium for 12 h, this aqueous solution was centrifuged for 20 min and filtered through a 0.45- $\mu$ m filter membrane. The obtained lysozyme-loaded core–shell nanoparticles were freeze-dried. The amount of unloaded lysozyme in the aqueous media was analyzed by high-performance liquid chromatography (HPLC) to measure the amount of drug loaded. Lysozyme was determined by reversed-phase HPLC using a Shodex RSpak RP 18-415 column and trifluoroacetic acid/ acetonitrile (0.1/99.9, v/v%) mobile phase at a flow rate of 1 mL min<sup>-1</sup>. The elute was monitored by UV absorption at 220 nm. The amount of drug loading is defined as the ratio of the amount of drug in the nanoparticles/total weight of nano-

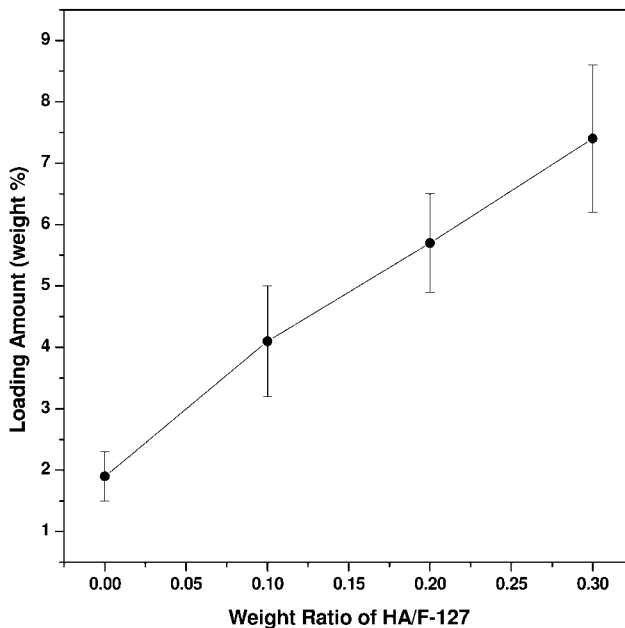


**Figure 4.22.** The variation of loading amount of core-shell nanoparticles as a function of the weight ratio of HA/F-127. (From Ref. [49].)

particles. The loading amount was increased up to 7 wt% with the increase of HA content in the polymeric shell. Due to the ionic interaction between cationic lysozyme and anionic HA in the PBS (pH 7.4), stable immobilization of lysozyme into the polymeric shell was induced and this led to the increase of the loading amount.

Figure 4.23 shows the release pattern of lysozyme from the core-shell nanoparticles formed as a function of weight ratio of HA/F-127. To measure the release pattern of lysozyme from the nanoparticles, 5 g of freeze-dried core-shell nanoparticles was put into 500 mL of PBS (pH 7.4). Temperature was maintained at 37 °C and stirring was maintained at 600 r.p.m. At given time intervals, 5-mL aliquots were withdrawn from release medium (PBS). HPLC analysis can then be performed as previously described. To maintain the sink condition in the release medium, 5 mL of fresh PBS was added to release medium after sampling. Without HA in the polymeric shell, a significant burst effect was observed. With the formation of the polymeric shell composed of F-127 and HA, the release rate was reduced significantly and an almost zero-order release pattern was observed at nanoparticles with 0.2 weight ratio of HA/F-127. Although HA is embedded in the F-127 network within the range of 0–0.3 weight ratio of HA/F-127 as shown in Fig. 4.21, it does not have intermolecular interactions with F-127 or PLGA nanoparticles and this leads to the release of HA from the polymeric shell. As lysozyme is ionically bound to HA, lysozyme and HA release together with the formation of

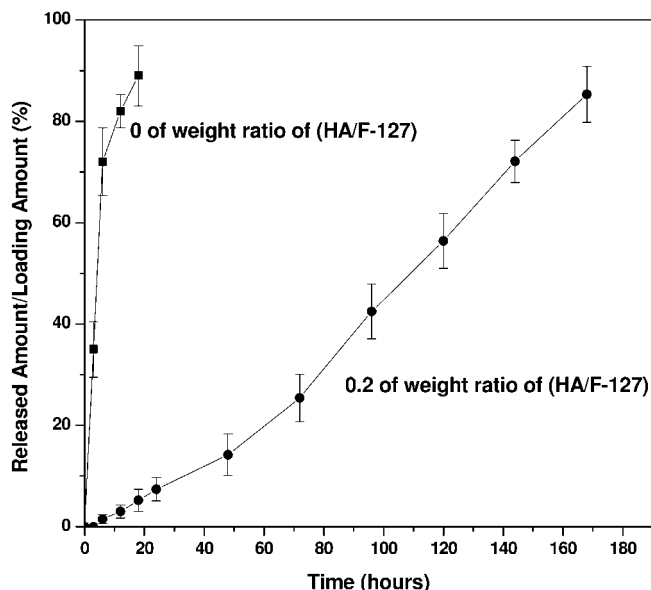


**Figure 4.23.** The release pattern of lysozyme from the core–shell nanoparticles. (From Ref. [49].)

an ion complex. To verify the release of HA from the polymeric shell, the variation of the  $\zeta$  potential was measured as a function of time for equilibrium in the release media. Figure 4.24 shows that the  $\zeta$  potential of core–shell nanoparticles with 0.2 weight ratio of HA/F-127 was increased with the increase of equilibrium time. This indicates that HA is released from the polymeric shell during the release of lysozyme and the sustained release of lysozyme is due to the release of the ionic complex composed of HA and lysozyme, which has a higher molecular weight compared with free lysozyme.

The specific enzyme activity of lysozyme in the release media after the 1-week release experiment was measured. For lysozyme activity assay, a suspension of  $0.1 \text{ mg mL}^{-1}$  *Micrococcus lysodeikticus* was prepared in PBS ( $37^\circ\text{C}$ ). To  $2.95 \text{ mL}$  *M. lysodeikticus* suspension,  $0.05 \text{ mL}$  lysozyme solution was added and mixed immediately. The turbidity of the suspension was measured at  $450 \text{ nm}$  by a Shimadzu UV-1601 spectrophotometer. One unit of activity corresponds to a decrease in turbidity of  $0.001 \text{ min}^{-1}$  at  $450 \text{ nm}$  [72]. In comparison to the activity of native lysozyme, 81.3% activity was preserved and this indicates that the activity of lysozyme was preserved during the freeze-drying process.

Core–shell nanoparticles with a composite polymeric shell composed of F-127 and HA have been prepared based on the hydrophobic interaction between PLGA and the PPO domain of F-127. Although HA does not have intermolecular interactions in the polymeric shell, the formation of the polymeric shell composed of F-127 and HA within the range of 0.3 weight ratio of HA/F-127 was observed.

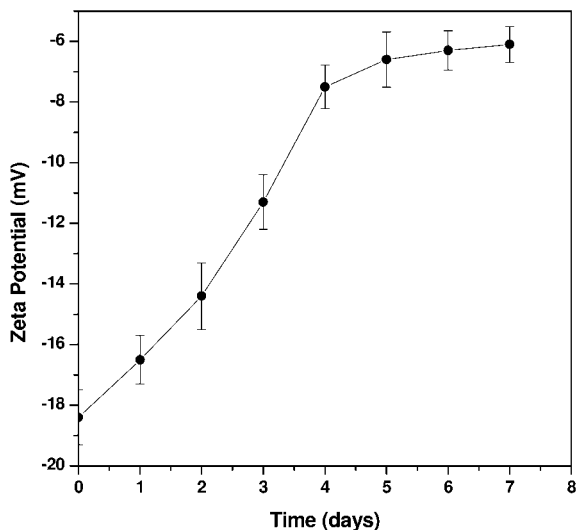


**Figure 4.24.** The variation of the  $\zeta$  potential of core-shell nanoparticles as a function of the time for equilibrium in PBS. (From Ref. [49].)

Due to the ionic interaction of cationic lysozyme and anionic HA under physiological conditions, the efficient loading and sustained release of lysozyme were accomplished. This enables us to prepare charged nanoparticles with a core-shell structure for the delivery of protein drug.

#### 4.3.2

#### Heparin-functionalized PLGA Nanoparticles

A new, facile method to prepare heparin-functionalized PLGA nanoparticles for the controlled release of growth factors has been developed [73]. This system is composed of PLGA as a hydrophobic core, F-127 as a hydrophilic surface layer (polymeric shell) and heparin as the functional moiety. Nanoparticles were prepared by a solvent-diffusion method without chemical modification of the components.

Heparin is a highly sulfated, anionic polysaccharide composed of repeating disaccharides of 1-4-linked glucosamine and uronic acid residues. Heparin is best known for its anticoagulant properties that are mediated through a pentasaccharide sequence that binds antithrombin III (AT-III) and subsequently complexes thrombin [74]. Heparin also interacts with a variety of proteins that have heparin-binding domains, including various growth factors, e.g. fibroblast growth factor (FGF) family [75], VEGF family [76], platelet-derived growth factor (PDGF) family [77], transforming growth factor (TGF)- $\beta$  family [78] and glial-derived neurotrophic factor (GDNF) [79]. This binding between growth factor and heparin or heparan

sulfate proteoglycans enables the growth factors to crosslink their receptors, and the association stabilizes the growth factor and protects it from proteolytic degradation [80, 81].

Based on the high specific binding of heparin for various growth factors, several heparin-containing systems have been developed for the controlled release of the growth factors. Edelman and coworkers encapsulated heparin-conjugated and basic FGF (bFGF)-loaded Sepharose beads in calcium alginate microspheres and demonstrated the controlled release of bFGF [82]. Sakiyama-Elbert and coworkers incorporated heparin-binding peptide 5 domains into a fibrin gel to bind heparin, which was then used to load and release bFGF [75] or  $\beta$ -nerve growth factor (NGF) [83]. Wissink and coworkers grafted collagen matrices with heparin and the sustained release of loaded bFGF was observed [84]. Tanihara and coworkers cross-linked alginate and heparin with diamine using carbodiimide activation to construct a hydrogel which showed sustained release of loaded bFGF [85]. Seal and coworkers covalently attached heparin-binding peptides to multi-arm PEGs, which were then physically crosslinked with heparin [86]. Among the heparin-binding growth factors, VEGF is of particular interest in tissue engineering due to its proangiogenic properties [87, 88]. So far, PLGA microspheres have been generally adapted for the particle-type sustained release system of growth factors [89, 90]. However, the encapsulation of proteins into hydrophobic PLGA cores has easily denatured proteins to aggregate and adsorb on the degrading PLGA surface [91–94], and also the presence of a water/organic solvent interface during protein loading has been identified as a major cause of protein denaturation and aggregation [95–97]. Alginate has also been used to encapsulate growth factors [98–100]. Even though there is no interfacial problem when proteins are encapsulated in alginate beads, rapid release and an initial burst of encapsulated proteins, as well as irreversible complexation with alginate were reported [100, 101]. Growth factor delivery by gelatin microspheres is very similar to the case of the alginate system [102, 103]. The main interaction between protein and gelatin is polyion complexation and the conformational change of the gelatin molecule is also followed. In addition, even though alginate and gelatin are natural polymers, growth factors do not have any binding domains on these polymers, thus limiting the binding events to the proteins with net positive charges [104]. Several heparin-based micelles or nanoparticles have also been developed as drug carriers [105–107]. However, all these systems employed chemical modifications of the functional group sequence of heparin to attach with either hydrophobic polymers or the low-molecular-weight hydrophobic moiety, thus reducing the bioactivity of the heparin, as represented by antithrombic activity [108].

The nanoparticles were prepared by a spontaneous emulsion solvent diffusion method as follows (Fig. 4.25). Samples of 40 mg of PLGA were dissolved in 2 mL DMSO at room temperature. The organic phase was then slowly added to 30 mL of deionized water containing 1.5 g of F-127 and a fixed amount of heparin with vigorous stirring. The amount of heparin was varied to control the entrapped heparin on the nanoparticles. The nanoparticles formed in the aqueous solution were col-

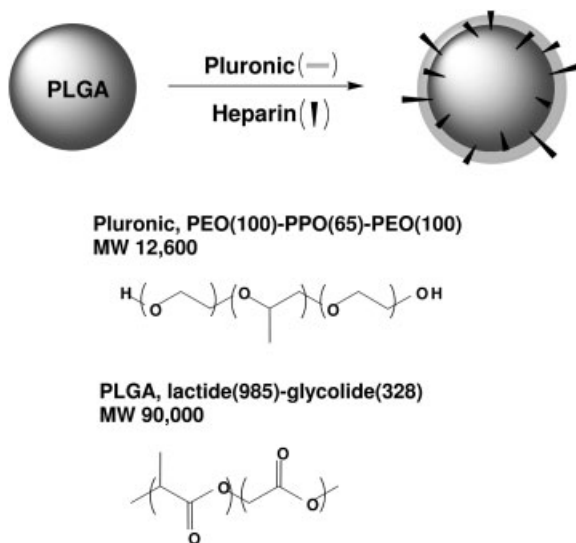
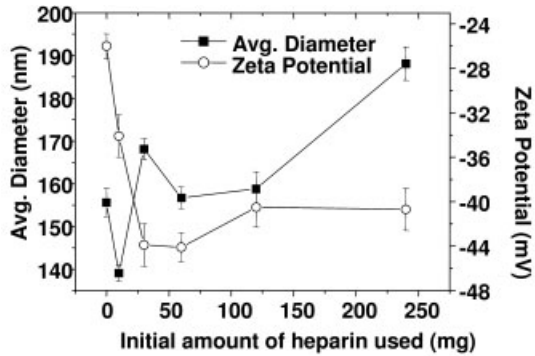


**Figure 4.25.** Schematic representation of heparin-functionalized PLGA nanoparticle preparation and chemical structures of the components. (From Ref. [73].)

lected by high-speed centrifugation (Hanil Science Industrial, Korea) at 12 000 r.p.m. for 1 h and resuspended in 0.5 mL of PBS solution containing 1.0% (w/v) Tween 80.

The size, polydispersity and surface charge of the nanoparticles were characterized by varying the amount of heparin in the aqueous phase. For the nanoparticles prepared from the aqueous solution containing no heparin, monodispersed nanoparticles with an average diameter of  $156 \pm 3$  nm and polydispersity of  $0.09 \pm 0.03$  were obtained. The surface charge from the  $\zeta$  potential measurement was  $-26.0 \pm 1.1$  mV (Fig. 4.26). By increasing the amount of heparin in the aqueous phase during the preparation of nanoparticles, the  $\zeta$  potential value decreased significantly, whereas the size and the polydispersity of nanoparticles varied little. However, when the amount of heparin in the aqueous phase was increased to 240 mg, both the size and the polydispersity of the nanoparticles increased noticeably to  $188 \pm 4$  and  $0.13 \pm 0.04$  nm. Thus, it can be concluded that heparin molecules were entrapped in the nanoparticles, maintaining their monodisperse distribution when the amount of heparin in the aqueous phase was less than 240 mg.

To obtain specific information about the amount and distribution of heparin in the nanoparticles, the anti-factor Xa (FXa) assay of the nanoparticles prepared at various conditions was carried out. Anti-FXa assay (Chromogenix Instrumentation Laboratory, Italy) on nanoparticles was carried out to calculate the amount of heparin in nanoparticles. The principle of this assay is that the amount of neutralized FXa binding with a heparin-antithrombin (AT) complex is proportional to the



(A)

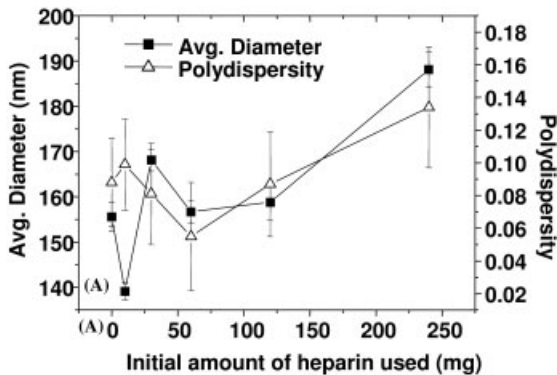


**Figure 4.26.** The size, surface charge and polydispersity of heparin-functionalized PLGA nanoparticles obtained by varying the amount of heparin in the aqueous phase during preparation.  $N = 6$  experiments. (From Ref. [73].)

amount of heparin. In order to measure the total amount of heparin in nanoparticles, the lyophilized nanoparticles were dissolved in methylene chloride to extract PLGA and F-127, and then the precipitated heparin was collected. On the other hand, the amount of heparin available on the nanoparticle surface was directly measured using the nanoparticle-AT complexation. In this assay, the activity of heparin distributed in the nanoparticle surface layer was measured using the diluted nanoparticle suspension and the heparin activity was increased by increasing the amount of heparin in the aqueous phase during the nanoparticle preparation. The activity of total heparin both in the nanoparticle core and surface layer, measured by extracting the entire heparin molecules entrapped in the nanoparticles, was a little higher than the heparin activity in the surface layer. The heparin activity was converted to the amount of heparin by using the anti-FXa activity of the heparin sodium used. The amount of heparin in the surface layer and the core of the nanoparticles, obtained by subtracting the amount in the surface layer from the



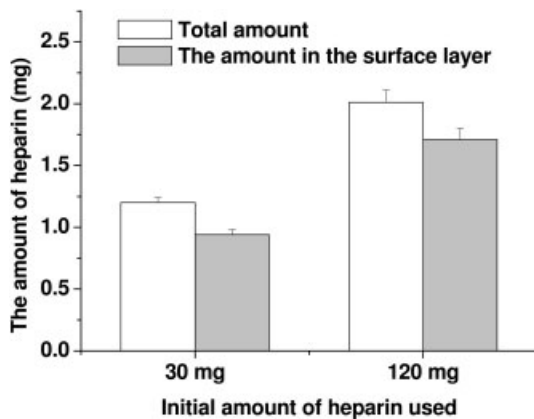


**Figure 4.27.** The amount of heparin in heparin-functionalized PLGA nanoparticles determined by the anti-FXa assay.  $N = 3$  experiments. (From Ref. [73].)

total amount, revealed that heparin molecules were mainly distributed in the nanoparticle surface layer and only a relatively small amount of heparin was in the nanoparticle core (Fig. 4.27).

$^1\text{H}$ -nuclear magnetic resonance (NMR) analysis of nanoparticles was performed to obtain the mole ratio between F-127 and PLGA in the nanoparticles. The  $^1\text{H}$ -NMR (JEOL JNM-LA300WB FT-NMR Spectrometer, Japan) analysis was performed to calculate the molar ratio between PLGA and F-127 in the nanoparticles. The suspension of nanoparticles was freeze-dried and then dissolved in  $\text{CDCl}_3$ . The molar ratio was calculated using the integral of separate peaks of CH (5.1 p.p.m.) of PLGA and  $\text{CH}_3$  (1.1 p.p.m.) of F-127 (Fig. 4.28).

The weight percentage of the heparin entrapped in the nanoparticles was 0.0, 2.4 and 4.7 for the nanoparticles prepared from an aqueous phase containing 0, 40 and 120 mg of heparin, respectively. Thus, the proposed method can manufacture the monodisperse nanoparticles containing heparin up to 4.7 wt% in total (4.0 wt% at the surface layer) and the amount of heparin can be controlled by adjusting the amount of heparin in the aqueous phase during preparation. The localization of F-127 molecules to the PLGA cores during particle formation is probably due to the hydrophobic interaction between the PPO block of F-127 and PLGA. The interaction between heparin and PEO blocks of F-127 may also contribute to localization of heparin on the nanoparticles, resulting in a high concentration of heparin in the nanoparticles. A similar observation has been reported between alginate and Pluronic F-127; the formation of crosslinks between the carboxyl group of alginate and PEO blocks of PF-127 leads to the formation of a three-dimensional network, resulting in improved shear stress.

Lysozyme was selected as a model protein for the *in vitro* release experiments using the heparin-functionalized PLGA nanoparticles. To load lysozyme into the nanoparticles, the resuspended nanoparticles were mixed with 0.1 mL PBS

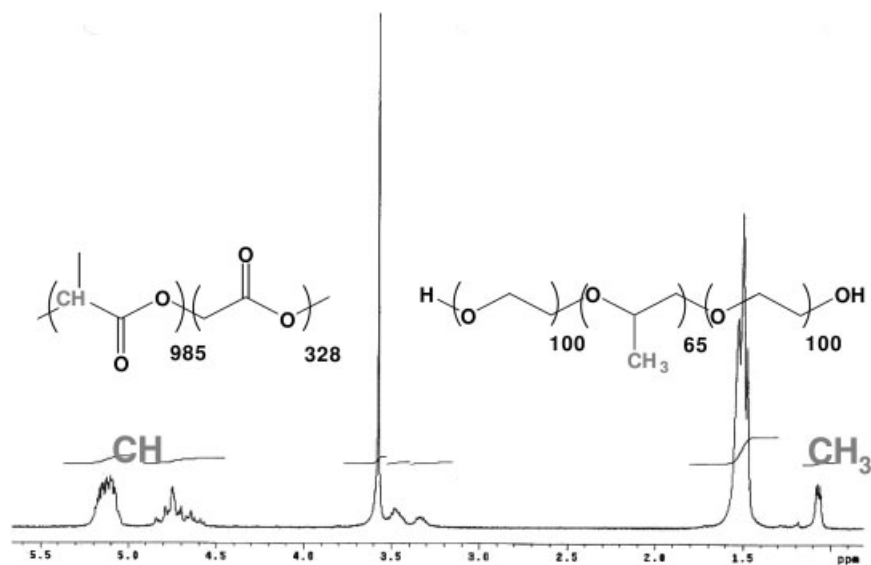


**Figure 4.28.**  $^1\text{H}$  NMR analysis to calculate the molar ratio between PLGA and F-127 constituting the heparin-functionalized PLGA nanoparticles by comparing  $^1\text{H}$  from CH of PLGA (5.1 p.p.m.) and  $^3\text{H}$  from  $\text{CH}_3$  of Pluronic F-127 (1.1 p.p.m.). (From Ref. [73].)

containing 1 mg of lysozyme and then incubated at 4 °C overnight with gentle rotation, which yields the loading of 1 mg of lysozyme into 43.3 mg of heparin-functionalized PLGA nanoparticles. Then, lysozyme-loaded nanoparticle suspension (0.6 mL) was subsequently put into a dialysis tube. The dialysis tube was placed in 100 mL PBS containing 2.0 mM sodium azide and kept under the same conditions as described previously.

Lysozyme can interact electrostatically with the heparin because lysozyme is net positively charged (the isoelectric point of lysozyme is pH 11.1). The average diameter and size distribution of nanoparticles after loading lysozyme were not changed after loading, and there was no aggregated complex among lysozyme-loaded nanoparticles. Figure 4.29 shows release profiles of lysozyme from three kinds of nanoparticles with different heparin contents of 0.0, 2.4 and 4.7%, respectively. In the case of the nanoparticles with no heparin, over two-thirds of the total lysozyme loaded was released within 3 days. In contrast, the nanoparticles with heparin contents of 2.4 and 4.7% showed linear and complete release profiles without any initial burst up to 10 and 19 days, respectively which shows net positively charged lysozyme was well bound in the negatively charged surface layer of the nanoparticles. To characterize the deactivation of lysozyme released from the heparin-functionalized nanoparticles, the concentration of the released lysozyme was analyzed based on the bioactivity of the released lysozyme on *M. lysodeikticus* cell walls using a lysozyme assay kit and compared with the concentration of the total

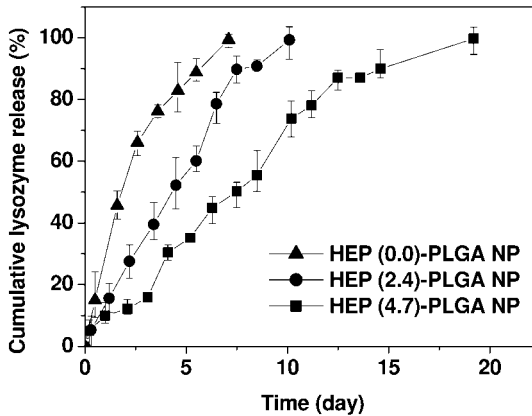


**Figure 4.29.** Cumulative lysozyme release from three kinds of heparin-functionalized PLGA nanoparticles with different heparin contents.  $N = 3$  experiments. (From Ref. [73].)

protein measured using the Micro BCA protein assay (Fig. 4.30). There were no differences between the total protein concentration and the bioactive lysozyme concentration at each time-point, showing that no denaturation of lysozyme occurred during loading into the nanoparticles and release from them.

Nanoparticles with a heparin content of 4.7% were selected as a VEGF release system, based on the result of the lysozyme release experiment. First, the release experiment was performed with loading 250 ng of VEGF into 14.4 mg of the nanoparticles. To load VEGF into the nanoparticles, both one-third and one-tenth of re-

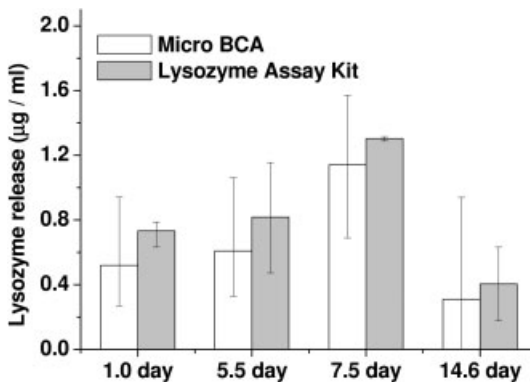


**Figure 4.30.** Comparison of the concentrations of lysozyme released from heparin-functionalized PLGA nanoparticles measured by the bioactivity on *M. lysodeikticus* cell walls using a lysozyme assay kit and the total protein concentration using a Micro BCA protein assay.  $N = 3$  experiments. (From Ref. [73].)

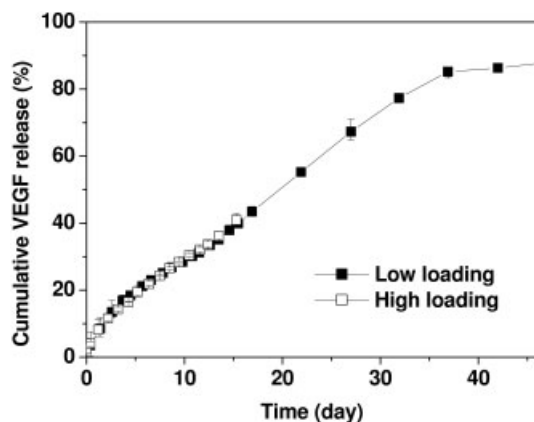


**Figure 4.31.** Cumulative VEGF release from heparin-functionalized PLGA nanoparticle with 4.7% w/w of heparin for two different loading amounts.  $N = 3$  experiments. (From Ref. [73].)

suspended nanoparticles were mixed with 25  $\mu\text{L}$  PBS containing 250 ng of VEGF and 75  $\mu\text{L}$  PBS containing 750 ng of VEGF, respectively, and then incubated at 4  $^{\circ}\text{C}$  overnight with gentle rotation, which yields loading of 250 ng of VEGF into 14.4 mg of nanoparticles and 750 ng of recombinant human VEGF into 4.3 mg of nanoparticles.

After loading, no aggregation among the protein-loaded nanoparticles was observed. The stability of VEGF in the release medium (PBS solution containing 0.1 wt% BSA) was conformed by comparing the concentration of VEGF in the release medium incubated at 37  $^{\circ}\text{C}$  for 24 h. The release of VEGF from the nanoparticles showed a linear profile without any initial burst up to day 37, releasing about 85% of the initial loading amount, and then the release rate was slowed down (Fig. 4.31). This release pattern was similar to the case of lysozyme; however, a much more prolonged release pattern was obtained. To elucidate whether the prolonged release was responsible from the decreased loading amount of the protein or the more specific interaction between VEGF and heparin than that between lysozyme and heparin, the loading amount of VEGF to the nanoparticles was increased 10-fold. The relative release rates (percent of the total amount) were almost same in both cases. Thus, the prolonged release pattern was mainly due to the more strong and specific interaction between VEGF and heparin than that between lysozyme and heparin.

Nanoparticles with heparin molecules on the surface were prepared by solvent diffusion without any chemical reaction. Monodispersed nanoparticles containing heparin up to 4.7 wt% in total (4.0 wt% at the surface layer) were manufactured and the amount of heparin was controlled by adjusting the amount of heparin in the aqueous phase during preparation. The release of lysozyme from the nanoparticles with 4.7 wt% heparin showed a linear and complete release profile with-

out any initial burst over 2 weeks, and the released lysozymes maintained their bioactivity. The release of VEGF from the nanoparticles showed a linear and more prolonged profile without any initial burst over 1 month, mainly due to the stronger and more specific interaction between VEGF and heparin than that between lysozyme and heparin. Thus, the heparin-functionalized PLGA nanoparticles can be employed a growth factor delivery component in tissue engineering scaffolds as well as a sustained release system for various heparin binding growth factors.

#### 4.4

#### Core–shell Nanoparticles with a Metallic Core

Core–shell nanoparticles with a metallic core have been studied intensively for application in the biomedical areas such as for magnetic resonance contrast agents [109], targeted drug delivery [110], and cancer diagnosis and treatment [111]. With the formation of core–shell nanoparticles with a metallic core (polymer-coated magnetic nanoparticles), a magnetic resonance contrast agent with enhanced stability and biocompatibility under physiological conditions can be achieved. Previously, iron oxide nanoparticles were stabilized with the formation of a polymeric layer on the surface of iron oxide nanoparticles using dextran, starch, albumin, silicones or PEG [112, 113]. The coprecipitation of iron salts in a polymeric coating solution by the microemulsion method [114] or and laser-induced pyrolysis [115] was used to prepare polymer-coated iron oxide nanoparticles. However, the wide size distribution remains still challenging with regard to the formation of a polymer shell on the surface of magnetic nanoparticles.

Recently, PVP-coated iron oxide nanoparticles with a narrow size distribution were prepared [109] based on the thermal decomposition presented previously [117–125]. First, 1 g of PVP was dissolved in 3 mL of DMF and this solution was purged with nitrogen to remove oxygen in a three-neck, round-bottom flask. The resulting mixture was heated to around 160 °C under vigorous mechanical stirring and  $\text{Fe}(\text{CO})_5$  was injected into the mixture. The reaction mixture was stirred for 2 h at 160 °C. During this process, the initial orange color of the solution gradually became a brownish black colloid solution. The colloid solution was cooled at room temperature and dialyzed for the removal of excess unreacted PVP at 37 °C for 2–3 days whilst being continuously stirred. For the characterization of PVP-coated nanoparticles, the dialyzed colloidal solution was freeze-dried.

Figure 4.32 shows the X-ray diffraction (XRD) data of pure PVP and PVP-coated iron oxide nanoparticles to confirm the crystallinity of the PVP-coated iron oxide nanoparticles. The characteristic patterns of the spinel phases  $\text{Fe}_2\text{O}_3$  and  $\text{Fe}_3\text{O}_4$  were observed, and this showed that iron oxide nanoparticles in PVP-coated iron oxide nanoparticles were mixtures of  $\text{Fe}_2\text{O}_3$  and  $\text{Fe}_3\text{O}_4$ .

The hysteresis loop of PVP-coated iron oxide at in room temperature is shown in Fig. 4.33. The magnetic properties of PVP-coated iron oxide nanoparticles were measured at room temperature with  $|H| \leq 20$  kOe using Quantum Design MPMS 5 superconducting quantum interface device (SQUID) magnetometer. The mass

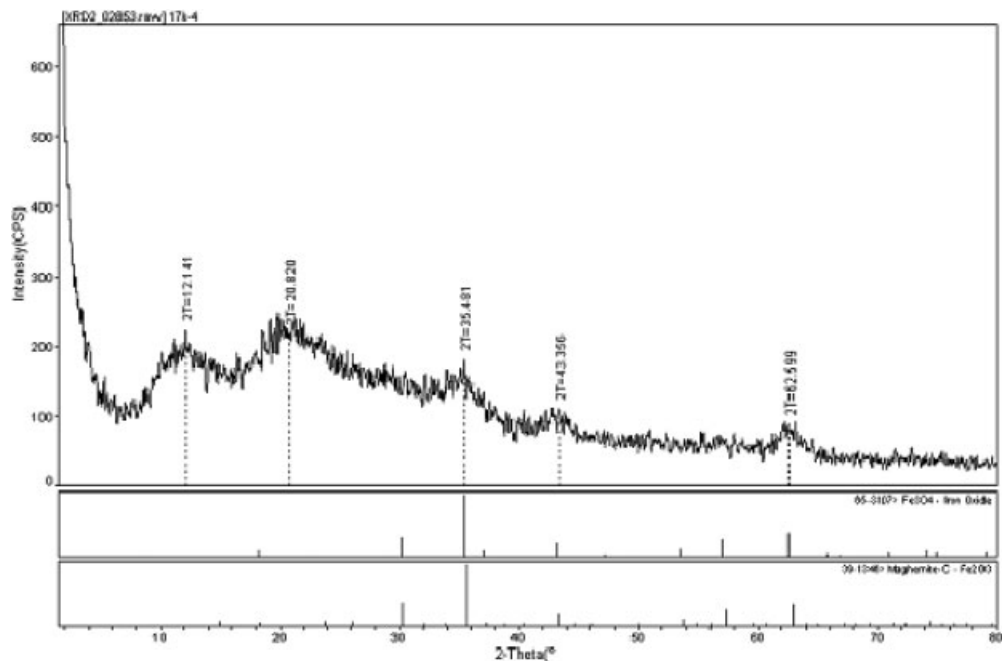
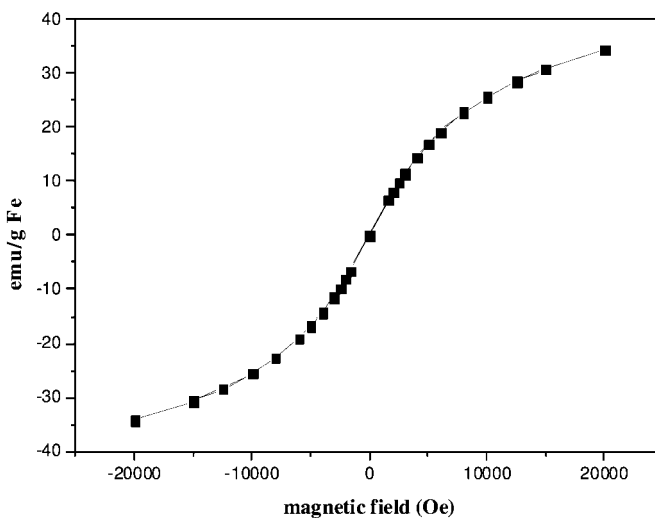


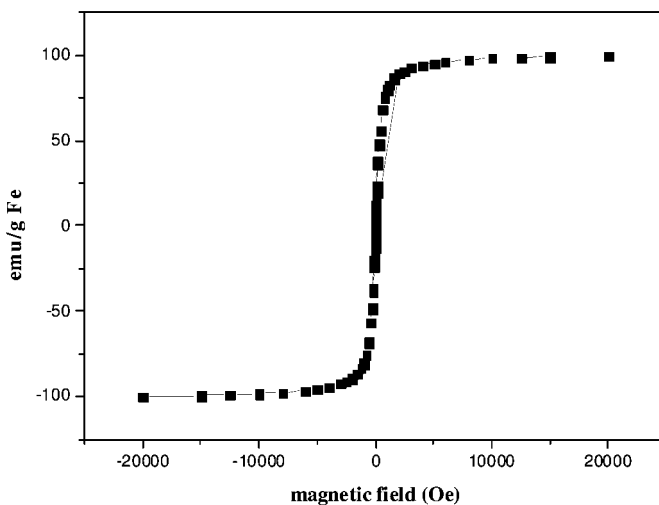
Figure 4.32. XRD pattern of PVP-coated iron oxide. (From Ref. [109].)

magnetization is defined as the magnetic moment per total mass of sample measured. The PVP-coated iron oxide nanoparticles produced were characterized by a high magnetic moment in a high magnetic field (generally, about 5–90 e.m.u.  $g^{-1}$  of metal oxide) and a negligible magnetic moment in the absence of an applied field. Such behavior is characteristic of superparamagnetic particles. From the results, 3- and 50- to 100-nm PVP-coated iron oxide nanoparticles exhibited superparamagnetic properties. The saturation magnetization of 3-nm particles was 34 e.m.u.  $g^{-1}$  Fe and the saturation magnetization of 50- to 100-nm nanoparticles was 90 e.m.u.  $g^{-1}$  Fe. These results showed that bigger iron oxide nanoparticles had larger mass magnetization.

Figure 4.34 shows a TEM image and particle size analysis of PVP-coated iron oxide nanoparticles prepared in DMF. The TEM image shows that the diameter of nanoparticles is 50–100 nm with a spherical shape. Following resuspension of nanoparticles into aqueous media, the size distribution analysis demonstrates that the colloid has the diameter of 200 nm. A similar process was applied to PVP-coated iron oxide nanoparticles prepared in Carbitol as shown in Fig. 4.35. Nanoparticles of 3 nm diameter were observed in the dried state and those of 100 nm diameter were observed in the aqueous media with a narrow size distribution. These size differences are due to the swelling of PVA on the surface of the iron oxide nanoparticles (metallic core); this indicates the formation of PVP-coated iron oxide nanoparticles.



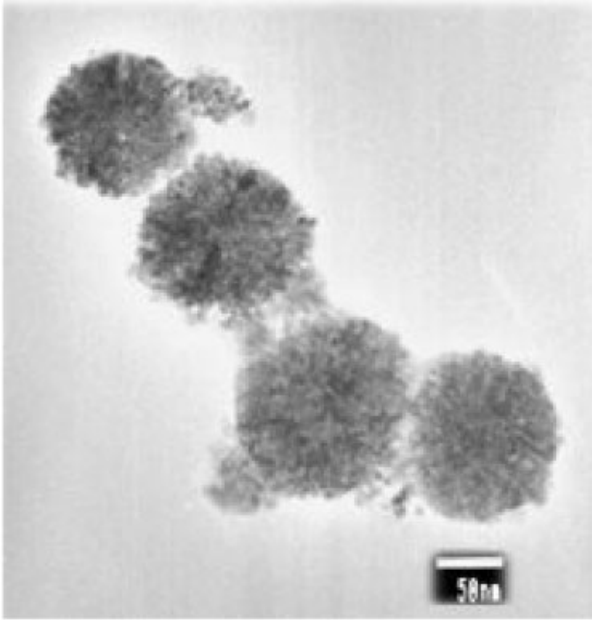
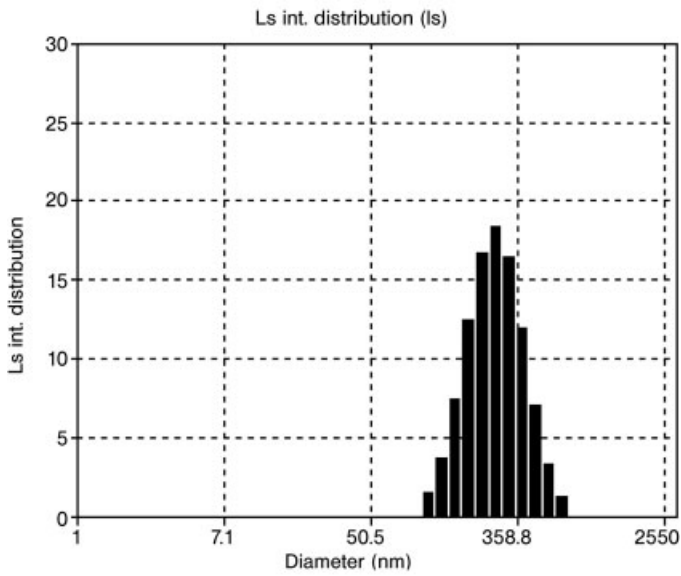
(A)



(B)

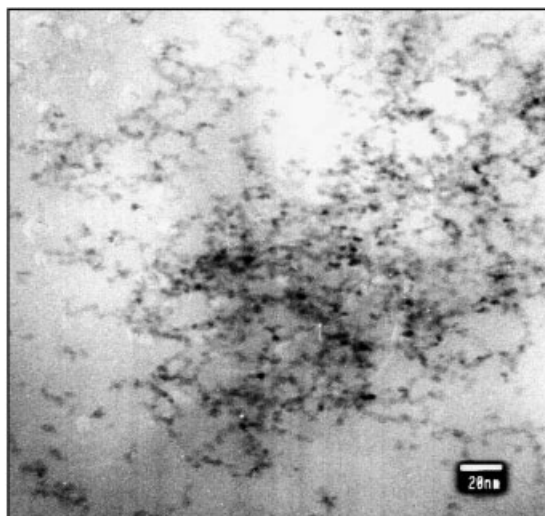
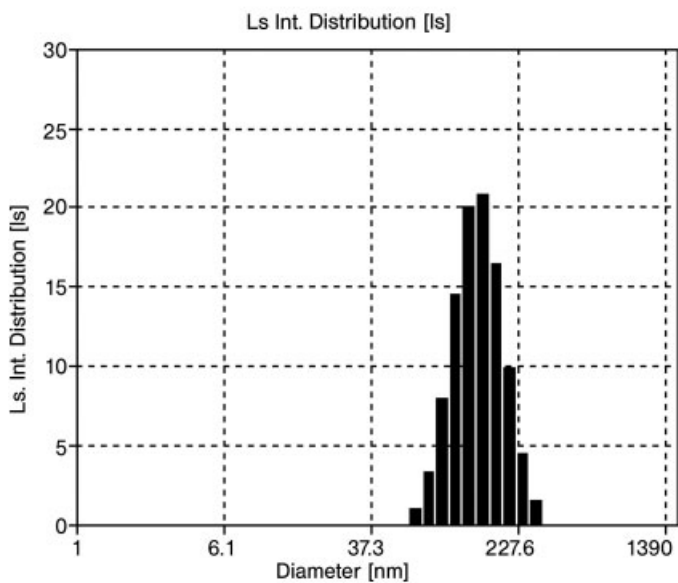
**Figure 4.33.** Magnetization curve of PVP-coated iron oxide nanoparticles of (A) 3 and (B) 50–100 nm at room temperature. (From Ref. [109].)

Fourier transform IR (FTIR) spectra of pure PVP and PVP-coated iron oxide nanoparticles are presented in Fig. 4.36. With the increase of PVP/ $\text{Fe}(\text{CO})_5$  molar ratios, the C=O absorption bands were shifted from 1670 to  $1653.56\text{ cm}^{-1}$ . The results showed that iron oxide was coordinated through the carbonyl group of PVP,

**(A)****(B)**

**Figure 4.34.** (A) TEM image and (B) size distribution of PVP-coated iron oxide nanoparticles prepared with DMF as solvent. (From Ref. [109].)



**(A)****(B)**

**Figure 4.35.** (A) TEM image and (B) size distribution of PVP-coated iron oxide nanoparticles prepared with Carbitol as solvent. (From Ref. [109].)

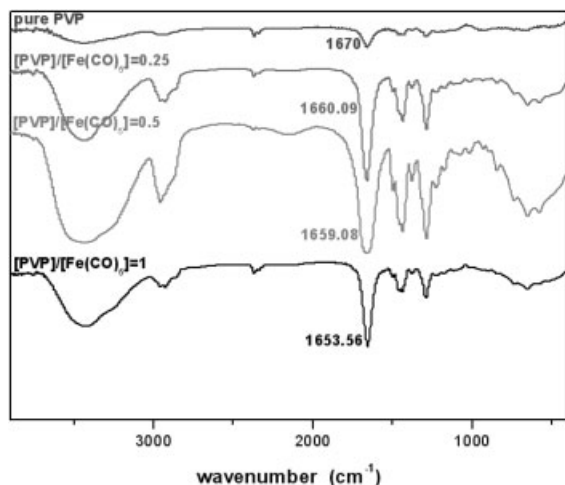


**Figure 4.36.** FTIR spectra of pure PVP and PVP-coated iron oxide nanoparticles. (From Ref. [109].)

and the interaction between PVP and iron oxide was increased with the increase of the particle size.

For further confirmation of coordination between iron oxide and the carbonyl group of PVP, X-ray photoelectric spectroscopy (XPS) spectra were observed as shown in Fig. 4.37. Correction of the energy shift due to the static charging of the samples was accomplished with the C 1s peak at 284.6 eV as a reference. The accuracy of the reported binding energies was  $\pm 0.1$  eV. The photoelectron peaks at 711.3 and 726 eV are the characteristic doublets of Fe 2p from iron oxide. The N

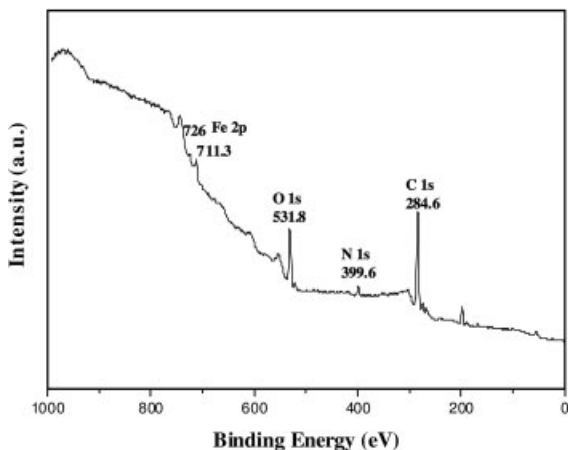


**Figure 4.37.** XPS spectra of PVP-coated iron oxide nanoparticles. (From Ref. [109].)

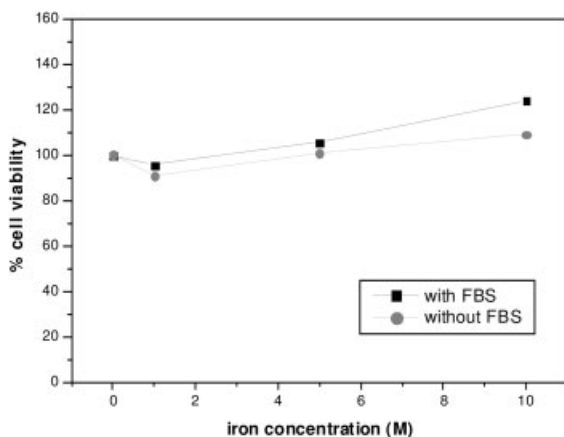


**Figure 4.38.** Viability of cells exposed to a solution containing PVP-coated iron oxide nanoparticles at various iron concentrations. (From Ref. [109].)

1s peak centered at 399.6 eV indicates that the nitrogen is influenced by the iron oxide. The O 1s peak at 531.8 eV is shifted toward to higher binding energy compared with pure PVP (530.3 eV), implying the decrease of electron density around O atoms in the carbonyl group of PVP, probably due to the interaction between iron oxide and O atoms in PVP [126].

Figure 4.38 shows the viability of cells exposed to the solution containing PVP-coated iron oxide nanoparticles at various iron concentrations for 4 h. To test whether the PVP-coated iron oxide nanoparticles had biocompatibility, a 5-dimethylthiazol-2-yl-2,5-diphenyl tetrazolium bromide (MTT) assay was performed. Cell viability is expressed as the mean  $\pm$  SE of percentage of absorbance of controls where 100% equals viability of untreated control cells. Although the iron concentration increased, cell viability did not decrease. Following the formation of the PVP layer on the surface of iron oxide nanoparticles, a significant increase in the biocompatibility was observed.

With the administration of 40  $\mu\text{mol}$  PVP-coated iron oxide intravenously into the rabbit, T2-weighted magnetic resonance imaging (MRI) images were observed as shown in Fig. 4.39. Samples 0.24 g of PVP-coated iron oxide nanoparticles were added to 1.4 mL distilled water and this solution was administered to rabbits weighing 4 kg. The concentration was equal to the concentration of commercially available Resovist (40  $\mu\text{mol Fe kg}^{-1}$ ). *In vitro* MRI test were performed with a 3.0 T MRI system (Philips, The Netherlands). The T2-weighted MRI images of prepared and commercial samples were observed. The sequence parameter was T2-weighted images; fast gradient echo with repetition time (TR) = 9.6 ms, echo time (TE) = 4.6 ms, flip angle = 8.0°, field of view = 10  $\times$  5 cm<sup>2</sup>. The images are T2-weighted MRI images before injection of contrast agent (left) and after injection

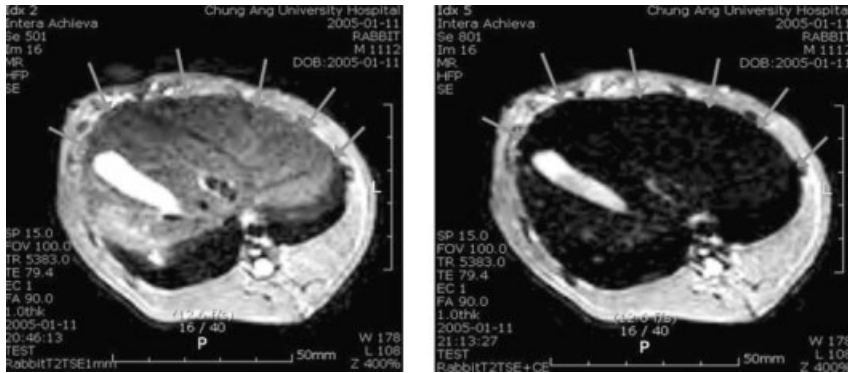


**Figure 4.39.** T2-weighted MRI images before injection of contrast agent (left) and after injection of PVP-coated iron oxide nanoparticles (right). (From Ref. [109].)

of PVP-coated iron oxide nanoparticles (right). This showed a profound negative enhancement of the liver after injection of PVP-coated iron oxide, indicating that the iron oxide contrast agent improved the detection of the liver lesions significantly.

#### 4.5

#### Conclusions

With the variation of core materials, various types of core-shell nanoparticles are being introduced. Although numerous studies and applications have been made using single-phased nanoparticles mainly composed of lipid, polymer or metal, there remain a number of problems to be solved. With the formation of nanoparticles with a core-shell structure, a significant improvement has been accomplished in the stability of nanoparticles, and the activity and release profile of loaded model drugs. The core-shell nanoparticles discussed in this chapter may be one of the leading examples of biocompatible polymer systems for drug delivery and molecular imaging purposes. Associated considerations may include the characterization in the *in vivo* models and retaining more appropriate physicochemical properties for practical applications in pharmaceuticals.

#### Acknowledgments

This work was financially supported by the Ministry of Science and Technology (M10414030001-05N1403-00130) in Korea.

## References

- 1 SAD, W., Protein drugs: a revolution in therapy?, *Pharm. Res.* **1986**, *3*, 3–6.
- 2 LEE, V. H., Peptide and protein drug delivery: opportunities and challenges, *Pharm. Int.* **1986**, *7*, 208–212.
- 3 PITT, C. G., The controlled parenteral delivery of peptides and protein. *Int. J. Pharm.* **1990**, *59*, 173–196.
- 4 LEUNG, S. H. S., ROBINSON, J. R., LEE, V. H., Parenteral products. In *Controlled Drug Delivery*, ROBINSON, J. R., LEE, V. H. (Eds.). Marcel Dekker, New York, **1987**, pp. 433–480.
- 5 TICE, T. R., MASON, D. W., GILLEY, R. M., Clinical use and future of parenteral microsphere systems. In *Novel Drug Delivery and its Therapeutic Application*, PRESCOTT, F. and NIMMO, W. S. (Eds.). Wiley, Chichester, **1989**, pp. 223–235.
- 6 OGAWA, Y., OKADA, H., YAMAMOTO, Y., SHIMAMOTO, T., A new technique to efficiently entrap leuporelide acetate into microcapsules of poly(lactic acid) or copoly(lactic/glycolic) acid, *Chem. Pharm. Bull.* **1988**, *36*, 1095–1108.
- 7 BODMER, D., KISSEL, T., TRAECHSLIN, E., Factors influencing the release of peptides and proteins from biodegradable parenteral depot systems, *J. Control. Release* **1992**, *21*, 129–138.
- 8 MANNING, M. C., PATEL, K., BORCHARDT, R. T., Stability of protein pharmaceuticals, *Pharm. Res.* **1989**, *6*, 903–918.
- 9 LIPKA, E., CRISON, J., AMIDON, G. L., Transmembrane transport of peptide type compounds: prospects for oral delivery, *J. Control. Release* **1996**, *39*, 121–129.
- 10 CLELAND, J. L., POWELL, S. J., SHIRE, S. J., The development of stable protein formulation: a close look at protein aggregation, deamidation, and oxidation, *Crit. Rev. Ther. Drug. Carrier Syst.* **1993**, *10*, 307–377.
- 11 COWSAR, D. R., TICE, T. R., GILEY, R. M., ENGLISH, J. P., Poly(lactide-co-glycolide) microcapsules for controlled release of steroids, *Methods Enzymol.* **1985**, *112*, 101–116.
- 12 MOORE, A., MCGUIRK, P., ADAMS, S., JONES, W. C., MCGEE, J. P., O'HAGON, D. T., MILLS, K. H., Immunization with a soluble recombinant HIV protein entrapped in biodegradable microparticles induces HIV-specific CD8<sup>+</sup> cytotoxic T lymphocytes and CD4<sup>+</sup> T<sub>H</sub>1 cells, *Vaccine* **1995**, *13*, 1741–1749.
- 13 BITTNER, B., MORLOCK, M., KOLL, H., WINTER, G., KISSEL, T., Recombinant human erythropoietin (rHEPO) loaded poly(lactide-co-glycolide) microspheres: influence of the en capsulation technique and polymer purity on microspheres characteristics, *Eur. J. Pharm. Biopharm.* **1998**, *45*, 295–305.
- 14 ANDO, S., PUTNAM, D., PACK, D. W., LANGER, R., PLGA microspheres containing plasmid DNA: preservation of super coiled DNA via cryopreparation and carbohydrate stabilization, *J. Pharm. Sci.* **1999**, *88*, 126–130.
- 15 WANG, D., ROBINSON, D. R., KOWN, G. S., SAMUEL, J., Encapsulation of plasmid DNA in biodegradable poly(D,L-lactic-co-acid) microspheres as a novel approach for immunogene delivery, *J. Control. Release* **1999**, *57*, 9–18.
- 16 LEWIS, K. J., IRWIN, W. J., AKHTAR, S., Development of a sustained release biodegradable polymer delivery system for site-specific delivery of oligonucleotides: characterization of P(LA-GA) copolymer microspheres *in vitro*, *J. Drug Target.* **1998**, *5*, 291–302.
- 17 YAMAMOTO, Y., NAGASAKI, Y., KATO, Y., SUGIYAMA, Y., KATAOKA, K., Long-circulating poly(ethylene glycol)-poly(D,L-lactide) block copolymer micelles with modulated surface charge, *J. Control. Release* **2001**, *77*, 27–38.
- 18 ILLUM, L., DAVIS, S. S., Effect of the nonionic surfactant poloxamer 338 on the fate and deposition of polystyrene microspheres following intravenous administration, *J. Pharm. Sci.* **1983**, *72*, 1086–1089.
- 19 LASIC, D. D., *Liposomes: From Physics To Applications*. Elsevier, Amsterdam, **1993**.

- 20 ANDERSON, P. M., HANSON, D. C., HASZ, D. E., HALET, M. R., BLAZAR, B. R., OCHOA, A. C., Cytokines in liposomes: preliminary studies with IL-1, IL-2, IL-6, GM-CSF and interferon-gamma, *Cytokine* **1994**, *6*, 92–101.
- 21 YE, Q., ASHERMAN, J., STEVENSON, M., BROWNSON, E., KATRE, N. V., DepoForm™ technology: a vehicle for controlled delivery of protein and peptide drugs, *J. Control. Release* **2000**, *64*, 155–166.
- 22 MAYER, L. D., HOPE, M. J., CULLIS, P. R., Vesicles of variable sizes produced by a rapid extrusion procedure, *Biochim. Biophys. Acta* **1986**, *858*, 161–168.
- 23 CULLIS, P. R., HOPE, M. J., BALLY, M. B., MADDEN, T. D., MAYER, L. D., FENSKE, D. B., Influence of pH gradients on the transbilayer transport of drugs, lipids, peptides and metal ions into large unilamellar vesicles, *Biochim. Biophys. Acta* **1997**, *1331*, 187–211.
- 24 HUANG, C., Studies on phosphatidylcholine vesicles. Formation and physical characteristics, *Biochemistry* **1969**, *8*, 344–352.
- 25 BANGHAM, A. D., STANDISH, N. M., WATKINS, J. C., Diffusion of univalent ions across the lamellae of swollen phospholipids, *J. Mol. Biol.* **1965**, *13*, 238–252.
- 26 KIM, S., TURKER, M. S., CHI, E. Y., SELA, S., MARTIN, G. M., Preparation of multivesicular liposomes, *Biochim. Biophys. Acta* **1983**, *728*, 339–348.
- 27 KIM, S., DepoFoam-mediated drug delivery into cerebrospinal fluid, *Methods Neurosci.* **1994**, *21*, 118–131.
- 28 KIM, T., MURDANDE, S., GRUBER, A., KIM, S., Sustained-release morphine for epidural analgesia in rats, *Anesthesiology* **1996**, *85*, 331–338.
- 29 KATRE, N. V., ASHERMAN, J., SCHAEFER, H., HORA, M., Multivesicular liposome (DepoFoamE) technology for the sustained delivery of insulin-like growth factor-I (IGF-I), *J. Pharm. Sci.* **1998**, *87*, 1341–1346.
- 30 HEINEMANN, L., RICHTER, B., Clinical pharmacology of human insulin, *Diabetes Care* **1993**, *16*, 90–100.
- 31 HOFFMAN, A., ZIV, F., Pharmacokinetic considerations of new insulin formulations and routes of administration, *Clin. Pharmacokinet.* **1997**, *33*, 285–301.
- 32 SPANGLER, R. S., Insulin administration via liposomes, *Diabetes Care* **1990**, *13*, 911–922.
- 33 OKADA, H., HEYA, T., OGAWA, Y., SHIMAMOTO, T., One-month release injectable microcapsules of a luteinizing hormone-releasing hormone agonist (leuprolide acetate) for treating experimental endometriosis in rats, *J. Pharmacol. Exp. Ther.* **1988**, *244*, 744–750.
- 34 DLUGI, A. M., MILLER, J. D., KNITTLE, J., Lupron depot (leuprolide acetate for depot suspension) in the treatment of endometriosis: a randomized, placebo-controlled, double-blind study, *Fertil. Steril.* **1990**, *54*, 419–427.
- 35 OKADA, H., DOKEN, Y., OGAWA, Y., TOGUCHI, H., Preparation of three-month depot injectable microspheres of leuprorelin acetate using biodegradable polymers, *Pharm. Res.* **1994**, *2*, 1143–1147.
- 36 HUGHES, J., KOSTERLITZ, H. W., SMITH, T. W., The distribution of methionine-enkephalin and leucine-enkephalin in the brain and peripheral tissues, *Br. J. Pharmacol.* **1997**, *120*, 428–436.
- 37 KURAISHI, Y., HIROTA, N., SATOH, M., TAKAGI, H., Antinociceptive effects of intrathecal opioids, noradrenaline and serotonin in rats: mechanical and thermal algesic tests, *Brain Res.* **1985**, *326*, 168–171.
- 38 LAMBERTS, S. W., Acromegaly and its treatment, *J. Endocrinol.* **1997**, *155*, S49–S51.
- 39 POLLAK, M. N., SCHALLY, A. V., Mechanisms of antineoplastic action of somatostatin analogs, *Proc. Soc. Exp. Biol. Med.* **1998**, *217*, 143–152.
- 40 MENG, F., HIEMSTRA, C., ENGBERS, G. H. M., FEIJEN, J., Biodegradable polymersomes, *Macromolecules* **2003**, *36*, 3004–3006.
- 41 KUKULA, H., SCHLAAD, H., ANTONIETTI, M., FORSTER, S., The formation of polymer vesicles or

- “peptosomes” by polybutadiene-*block*-poly(L-glutamate)s in dilute aqueous solution, *J. Am. Chem. Soc.* **2002**, *124*, 1658–1663.
- 42 LEWIS, D. H., Controlled release of bioactive agents from lactide/glycolide polymers. In *Biodegradable Polymers as Drug Delivery Systems, Drugs and Pharmaceutical Sciences*, CHASIN, M., LANGER, R. (Eds.). Marcel Dekker, New York, **1990**, pp. 9–41.
  - 43 JEYANTHI, R., MEHTA, R. C., THANOO, B. C., DELUCA, P. P., Effect of processing parameters on the properties of peptide-containing PLGA microspheres, *J. Microencapsul.* **1997**, *14*, 163–174.
  - 44 VAN ZYL, A. J. P., SANDERSON, R. D., WET-ROOS, D., KLUMPERMAN, B., Core/shell particles containing liquid cores: morphology prediction, synthesis, and characterization, *Macromolecules* **2003**, *36*, 8621–8629.
  - 45 PEKAREK, K. J., DYRUD, M. J., FERRER, K., JONG, Y. S., MATHIOWITZ, E., In vitro and in vivo degradation of double-walled polymer microsphere, *J. Control. Release* **1996**, *40*, 169–178.
  - 46 DAVIS, S. S., ILLUM, L., Polymeric microspheres as drug carriers, *Biomaterials* **1988**, *9*, 111–115.
  - 47 PEKAREK, K. J., DYRUD, M. J., FERRER, K., JONG, Y. S., MATHIOWITZ, E., In vitro and in vivo degradation of double-walled polymer microspheres *J. Control. Release* **1996**, *40*, 169–178.
  - 48 OH, K. S., LEE, K. E., HAN, S. S., CHO, S. H., KIM, D., YUK, S. H., Formation of core/shell nanoparticles with a lipid core and their application as a drug delivery system, *Biomacromolecules* **2005**, *6*, 1062–1067.
  - 49 HAN, S. K., LEE, J. H., KIM, D., CHO, S. H., YUK, S. H., Hydrophilized poly(lactide-*co*-glycolide) nanoparticles with core/shell structure for protein delivery, *Sci. Technol. Adv. Mater.* **2005**, *6*, 468–474.
  - 50 KIM, B. K., KIM, D., CHO, S. H., YUK, S. H., Hydrophilized poly(lactide-*co*-glycolide) nanospheres with poly(ethylene oxide)–poly(propylene oxide)–poly(ethylene oxide) triblock copolymer, *J. Microencapsul.* **2004**, *21*, 697–707.
  - 51 LIU, S., O'BRIEN, D. F., Stable polymeric nanoballoons: lyophilization and rehydration of cross-linked liposomes, *J. Am. Chem. Soc.* **2002**, *124*, 6037–6042.
  - 52 HINCHA, D. K., ZUTHER, E., HELLWEGE, E. M., HEYER, A. G., Specific effects of fructo- and gluco-oligosaccharides in the preservation of liposomes during drying, *Glycobiology* **2002**, *12*, 103–110.
  - 53 ANCHORDOGUY, T., CARPENTER, J. F., LOOMIS, S. H., CROWE, J. H., Mechanisms of interaction of amino acids with phospholipid bilayers during freezing, *Biochim. Biophys. Acta* **1988**, *946*, 299–306.
  - 54 PEER, D., FLORENTIN, A., MARGALIT, R., Hyaluronan is a key component in cryoprotection and formulation of targeted unilamellar liposome, *Biochim. Biophys. Acta* **2003**, *1612*, 76–82.
  - 55 ROBERTSON, D., HELLWEG, T., TIESCH, B., KOEITZ, J., Polymer-induced structural changes in lecithin/sodium dodecyl sulfate-based multilamellar vesicles, *J. Colloid Interface Sci.* **2004**, *270*, 187–194.
  - 56 FENG, S. S., GONG, K., CHEW, J., Molecular interaction between a lipid and an antineoplastic drug paclitaxel (Taxol) within the lipid monolayer at the air/water interface, *Langmuir* **2002**, *18*, 4061–4070.
  - 57 KAUSHIK, J. K., BHAT, R., Why is trehalose an exceptional protein stabilizer? *J. Biol. Chem.* **2003**, *278*, 26458–26465.
  - 58 KALESHOVA, L. L., MACFARLANE, D. R., TROUNSON, A. O., SHAW, J. M., Sugar exert a major influences on the vitrification properties of ethylene glycol-based solutions and have low toxicity to embryos and oocytes, *Cryobiology* **1999**, *38*, 119–130.
  - 59 MULLER, Y. A., LI, B., CHRISTINGER, H. W., WELLS, J. A., CUNNINGHAM, B. C., DE VOS, A. M., Vascular endothelial growth factor: crystal structure and functional mapping of kinase domain receptor binding site,

- Proc. Natl Acad. Sci. USA* **1997**, *94*, 7192–7197.
- 60 COUPER, L. L., SHANE, R. B., ELDRUP-JORGENSEN, J., BREDEBERG, C. E., LINDER, V., Vascular endothelial growth factor increase the mitogenic response to fibroblast growth factor-2 in vascular smooth muscle cells *in vivo* via expression of fms-like tyrosine kinase-1, *Circ. Res.* **1997**, *82*, 932–939.
- 61 HAN, M. K., KIM, M., BAE, S. Y., KANG, L., HAN, S. Y., LEE, Y. S., RHA, J. H., KIM, S. U., ROH, J. K., VEGF protects human cerebral hybrid neurons from *in vitro* ischemia, *Neurochemistry* **2004**, *15*, 847–850.
- 62 GenVec, A randomized, double-blind, placebo-controlled, multicenter, pilot study of the safety and feasibility of Biobypass® (Ad GVVEGF121.10) via an intramyocardial injection catheter in patients with advanced coronary artery disease. Presented at *American College of Cardiology 52nd Annual Scientific Conference* Chicago, IL, **2003**.
- 63 SUSSICH, F., SKOPEC, C., BRADY, J., CESARO, A., Reversible dehydration of trehalose and anhydrobiosis: from solution state to an exotic crystal, *Carbohydrate Res.* **2001**, *334*, 165–176.
- 64 MORLOCK, M., KISSEL, T., LI, Y. X., KOLL, H., WINTER, G., Erythropoietin loaded microspheres prepared from biodegradable LPLG–PEP–LPLG triblock copolymers: protein stabilization and *in-vitro* release properties, *J. Control. Release* **1998**, *56*, 105–115.
- 65 KIM, T. K., BURGESS, D. J., Pharmacokinetic characterization of <sup>14</sup>C-vascular endothelial growth factor controlled release microspheres using a rat model, *J. Pharm. Pharmacol.* **2002**, *54*, 897–905.
- 66 KRISTER, E., FREDRICK, T., Equilibrium and kinetics properties of triblock copolymers at hydrophobic surface, *Macromolecules* **1997**, *30*, 6323–6332.
- 67 STOLNIK, S., DAUDALI, B., ARIEN, A., WHETSTONE, J., HEALD, C. R., GARNETT, M. C., DAVIS, S. S., ILLUM, L., The effect of surface coverage and conformation of poly(ethylene oxide) (PEO) chains of poloxamer 407 on the biological fate of model colloidal drug carriers, *Biochim. Biophys. Acta* **2001**, *1514*, 261–279.
- 68 PRUD'HOMME, R. K., WU, G., SCHNEIDER, D. K., Structure and rheology studies of poly(oxyethylene–oxypropylene–oxyethylene) aqueous solution, *Langmuir* **1996**, *12*, 4651–4659.
- 69 COOMBES, A. G., SCHOLES, P. D., DAVIS, M. C., ILLUM, L. and DAVIS, S. S., Resorbable polymeric microspheres for drug delivery – production and simultaneous surface modification using PEO–PPO surfactant, *Biomaterials* **1994**, *15*, 673–680.
- 70 DUNN, S. E., COOMBES, A. G. A., GARNETT, M. C., DAVIS, S. S., DAVIES, M. C., ILLUM, L. *In vitro* cell interaction and *in vivo* biodistribution of poly(lactide-co-glycolide) nanospheres surface modified by poloxamer and poloxamine copolymers. *J. Control. Release* **1997**, *44*, 65–76.
- 71 LEE, K. E., KIM, B. K., YUK, S. H., Biodegradable polymeric nanospheres formed by temperature-induced phase transition in a mixture of poly(lactide-co-glycolide) and poly(ethylene oxide)–poly(propylene oxide)–poly(ethylene oxide) triblock copolymer, *Biomacromolecules* **2002**, *3*, 1115–1119.
- 72 PENG, Z. G., HIDAJAT, K., UDDIN, M. S., Adsorption and desorption of lysozyme on nano-sized magnetic particles and its conformational changes, *Colloids Surf. B* **2004**, *35*, 169–174.
- 73 CHUNG, Y. I., TAE, G. Y., YUK, S. H., A facile method to prepare heparin-functionalized nanoparticles for controlled release of growth factors, *Biomaterials*, **2006**, *27*, 2621–2626.
- 74 SUNDARAM, M., QI, Y., SHRIVER, Z., LIU, D., ZHAO, G., VENKATARAMAN, G., LANGER, R., SASISEKHARAN, R., Rational design of low-molecular weight heparins with improved *in vivo* activity, *Proc. Natl Acad. Sci. USA* **2003**, *100*, 625–656.
- 75 SAKIYAMA-ELBERT, S. E., HUBBELL, J. A., Development of fibrin derivatives for controlled release of heparin-



- binding growth factors, *J. Control. Release* **2000**, *65*, 389–402.
- 76 TESSLER, S., ROCKWELL, P., HICKLIN, D., COHEN, T., LEVI, B. Z., WITTE, L., LEMISCHKA, I. R., NEUFELD, G., Heparin modulates the interaction of VEGF165 with soluble and cell associated flk-1 receptors, *J. Biol. Chem.* **1994**, *269*, 12456–12461.
- 77 FEYZI, E., LUSTIG, F., FAGER, G., SPILLMANN, D., LINDAHL, U., SALMIVIRTA, M., Characterization of heparin and heparan sulfate domains binding to the long splice variant of platelet-derived growth factor A chain, *J. Biol. Chem.* **1997**, *272*, 5518–5524.
- 78 LYON, M., RUSHTON, G. and GALLAGHER, J., The interaction of the transforming growth factor- $\beta$ s with heparin/heparan sulfate is isoform specific, *J. Biol. Chem.* **1997**, *272*, 18000–18006.
- 79 HAMILTON, J. F., MORRISON, P. F., CHEN, M. Y., HARVEY-WHITE, J., PERNAUTE, R. S., PHILLIPS, H., OLDFIELD, E., BANKIEWICZ, K. S., Heparin coinfusion during convection enhanced delivery (CED) increases the distribution of the glial-derived neurotrophic factor (GDNF) ligand family in rat striatum and enhances the pharmacological activity of neurturin, *Exp. Neurol.* **2001**, *168*, 155–161.
- 80 SAKSELA, O., MOSCATELLI, D., SOMMER, A., RIFKIN, D. B., Endothelial cell-derived heparan sulfate binds basic fibroblast growth factor and protects it from proteolytic degradation, *J. Cell Biol.* **1988**, *107*, 743–751.
- 81 SOMMER, A., RIFKIN, D. B., Interaction of heparin with human basic fibroblast growth factor: protection of the angiogenic protein from proteolytic degradation by a glycosaminoglycan, *J. Cell. Physiol.* **1989**, *138*, 215–220.
- 82 EDELMAN, E. R., MATHIOWITZ, E., LANGER, R., KLAGSBRUN, M., Controlled and modulated release of basic fibroblast growth factor, *Biomaterials* **1991**, *12*, 619–626.
- 83 SAKIYAMA-ELBERT, S. E., HUBBELL, J. A., Controlled release of nerve growth factor from a heparin-containing fibrin-based cell in growth matrix, *J. Control. Release* **2000**, *69*, 149–158.
- 84 WISSINK, M. J. B., BEERNINK, R., PIEPER, J. S., POOT, A. A., ENGBERS, G. H. M., BEUGELING, T., VAN AKEN, W. G., FEIJEN, J., Binding and release of basic fibroblast growth factor from heparinized collagen matrices, *Biomaterials* **2001**, *22*, 2291–2299.
- 85 TANIHARA, M., SUZUKI, Y., YAMAMOTO, E., NOGUCHI, A., MIZUSHIMA, Y., Sustained release of basic fibroblast growth factor and angiogenesis in a novel covalently crosslinked gel of heparin and alginate, *J. Biomed. Mater. Res.* **2001**, *56*, 216–221.
- 86 SEAL, B. L., PANITCH, A., Physical polymer matrices based on affinity interactions between peptides and polysaccharides, *Biomacromolecules* **2003**, *4*, 1572–1582.
- 87 YANCOPOULOS, G. D., DAVIS, S., GALE, N. W., RUDGE, J. S., WIEGAND, S. J., HOLASH, J., Vascular-specific growth factors and blood vessel formation, *Nature* **2000**, *407*, 242–248.
- 88 PETERS, M. C., ISENBERG, B. C., ROWLEY, J. A. and MOONEY, D. J., Release from alginate enhances the biological activity of vascular endothelial growth factors, *J. Biomater. Sci. Polymer Edn* **1998**, *9*, 1267–1278.
- 89 MURRAY, J. B., BROWN, L., LANGER, R., KLAGSBRUN, M., A micro-sustained release system for epidermal growth factor. *In Vitro* **1983**, *10*, 743–748.
- 90 MOONEY, D. J., KAUFMANN, P. M., SANO, K., SCHWENDEMAN, S. P., MAJAHOD, K., SCHLOO, B., VACANTI, J. P., LANGER, R., Localized delivery of epidermal growth factor improves the survival of transplanted hepatocytes, *Biotechnol. Bioeng.* **1996**, *50*, 422–429.
- 91 ZHU, G., MALLERY, S. R., SCHWENDEMAN, S. P., Stabilization of proteins encapsulated in injectable poly(lactide-co-glycolide), *Nat. Biotechnol.* **2000**, *18*, 52–57.
- 92 LI, X., ZHANG, Y., YAN, R., JIA, W., YUAN, M., DENG, X., HUANG, Z., Influence of process parameters on the protein stability encapsulated in poly-DL-lactide poly(ethylene glycol) microspheres, *J. Control. Release* **2000**, *68*, 41–52.

- 93 LU, W., PARK, T. G., Protein release from poly(lactic-co-glycolic acid) microspheres: protein stability problems, *J. Pharm. Sci. Technol.* **1995**, *49*, 13–19.
- 94 CROTTIS, G., PARK, T. G., Stability and release of bovine serum albumin encapsulated within poly(D,L-lactide-co-glycolide) microparticles, *J. Control. Release* **1997**, *44*, 123–134.
- 95 CLELAND, J. L., JONES, A. J. S., Stable formulations of recombinant human growth hormone and interferon- $\gamma$  for microencapsulation in biodegradable microspheres, *Pharm. Res.* **1996**, *13*, 1464–1475.
- 96 ZAMBAUX, M. F., BONNEAUX, F., GREF, R., DELLACHERIE, E., VIGNERON, C., Preparation and characterization of protein C-loaded PLA nanoparticles, *J. Control. Release* **1999**, *60*, 179–188.
- 97 SAH, H., Protein behavior at the water/methylene chloride interface, *J. Pharm. Sci.* **1999**, *88*, 1320–1325.
- 98 LEE, K. Y., PETERS, M. C., MOONEY, D. J., Comparison of vascular endothelial growth factor and basic fibroblast growth factor on angiogenesis in SCID mice, *J. Control. Release* **2003**, *87*, 49–56.
- 99 ELCIN, Y. M., DIXIT, V., GITNICK, G., Extensive *in vivo* angiogenesis following controlled release of human vascular endothelial cell growth factor: implications for tissue engineering and wound healing, *Artif. Organs* **2001**, *25*, 558–565.
- 100 MUMPER, R. J., HOFFMAN, A. S., PUOLAKKAINEN, P., BOUCHARD, L. S., GOMBOITZ, W. R., Calcium-alginate beads for the oral delivery of transforming growth factor- $\beta$ 1 (TGF- $\beta$ 1): stabilization of TGF- $\beta$ 1 by the addition of polyacrylic acid within acid-treated beads, *J. Control. Release* **1994**, *30*, 241–251.
- 101 LEE, K. W., YOON, J. J., LEE, J. H., KIM, S. Y., JUNG, H. J., KIM, S. J., JOH, J. W., LEE, H. H., LEE, D. S., LEE, S. K., Sustained release of vascular endothelial growth factor from calcium-induced alginate hydrogels reinforced by heparin and chitosan, *Transplant. Proc.* **2004**, *36*, 2464–2465.
- 102 NAKAOKA, R., TABATA, Y., IKADA, Y., Potentiality of gelatin microsphere as immunological adjuvant, *Vaccine* **1995**, *13*, 653–661.
- 103 MLADENOVSKA, K., KUMBARADZI, E. F., DODOV, G. M., MAKRADULI, L., GORACINOVA, K., Biodegradation and drug release studies of BSA loaded gelatin microspheres. *Int. J. Pharm.* **2002**, *242*, 247–249.
- 104 TABATA, Y., IKADA, Y., Protein release from gelatin matrices, *Adv. Drug Delivery Rev.* **1998**, *31*, 287–301.
- 105 PASSIRANI, C., BARRATT, G., DEVISSAGUET, J. P., LABARRE, D., Long-circulating nanoparticles bearing heparin or dextran covalently bound to poly(methyl methacrylate), *Pharm. Res.* **1998**, *15*, 1046–1050.
- 106 CHAUVIERRE, C., MARDEN, M. C., VAUTHIER, C., LABARRE, D., COUVREUR, P., LECLERC, L., Heparin coated poly(alkylcyanoacrylate) nanoparticles coupled to hemoglobin: a new oxygen carrier, *Biomaterials* **2004**, *25*, 3081–3086.
- 107 PARK, K., KIM, K., KWON, I. C., KIM, S. K., LEE, S., LEE, D. Y., BYUN, Y., Preparation and characterization of self-assembled nanoparticles of heparin–deoxycholic acid conjugates, *Langmuir* **2004**, *20*, 11726–11731.
- 108 LIN, H.-R., SUNG, K. C., VONG, W.-J., *In situ* gelling of alginate/pluronic solutions for ophthalmic delivery of pilocarpine, *Biomacromolecules* **2004**, *5*, 2358–2365.
- 109 LEE, H. Y., LIM, N. H., SEO, J. A., YUK, S. H., KWAK, B. K., KHANG, G., LEE, H. B., CHO, S. H., Preparation and magnetic resonance imaging (MRI) effect of polyvinylpyrrolidone (PVP)-coated iron oxide nanoparticles, *J. Biomed. Res. Part B: Appl. Biomater.* **2006**, *79B*, 142–150.
- 110 LI, Z., CHEN, H., BAO, H., GAO, M., One-pot reaction to synthesize water-soluble magnetite nanocrystals, *Chem. Mater.* **2004**, *16*, 1391–1393.
- 111 GUPTA, P. K., HUNG, C. T., LAM, F. C., PERRIER, D. G., Albumin microspheres. III. Synthesis and characterization of microspheres containing adriamycin and magnetite, *J. Pharm.* **1988**, *43*, 167–177.

- 112 JORDAN, A., SCHOLZ, R., MAIER-HAUFF, K., JOHANNSEN, M., WUST, P., NADOBNY, J., SCHIRRA, H., SCHMIDT, H., DEGER, S., LOENING, S., LANKSCH, W., FELIX, R., Presentation of a new magnetic field therapy system for the treatment of human solid tumors with magnetic fluid hyperthermia, *J. Magn. Magn. Mater.* **2001**, *225*, 118–126.
- 113 BERRY, C. C., WELLS, S., CHARLES, S., CURTIS, A. S. G., Dextran and albumin derivatised iron oxide nanoparticles: influence on fibroblasts *in vitro*, *Biomaterials* **2003**, *24*, 4551–4557.
- 114 HARRIS, L. A., GOFF, J. D., CARMICHAEL, A. Y., RIFFLE, J. S., HARBURN, J. J., ST PIERRE, T. G., SAUNDERS, M., Magnetite nanoparticle dispersions stabilized with triblock copolymers. *Chem. Mater.* **2003**, *15*, 1367–1377.
- 115 LIU, Z. L., DING, Z. H., YAO, K. L., TAO, J., DU, G. H., LU, Q. H., WANG, X., GONG, F. L., CHEN, X., Preparation and characterization of polymer-coated core-shell structured magnetic microbeads. *J. Magn. Magn. Mater.* **2003**, *265*, 98–105.
- 116 VEINTEMILLAS-VERDAGUER, S., BOMATÍ-MIGUEL, O., MORALES, M. P., Effect of the process conditions on the structural and magnetic properties of  $\gamma$ -Fe<sub>2</sub>O<sub>3</sub> nanoparticles produced by laser pyrolysis. *Scr. Mater.* **2002**, *47*, 589–593.
- 117 KING, S., HYUNH, K., TANNENBAUM, R., Kinetics of nucleation, growth, and stabilization of cobalt oxide nanoclusters, *J. Phys. Chem. B* **2003**, *107*, 12097–12104.
- 118 TANNENBAUM, R., REICH, S., FLENNIKEN, C. L., GOLDBERG, E. P., Shape control of iron oxide nanoclusters in polymeric media. *Adv. Mater.* **2002**, *14*, 1402–1405.
- 119 TANNENBAUM, R., FLENNIKEN, C. L., GOLDBERG, E. P., The solid-state decomposition and oxidation of dicobaltoctacarbonyl in a polymer matrix. *J. Polym. Sci. Polym. Phys.* **1987**, *25*, 1341–1358.
- 120 TANNENBAUM, R., FLENNIKEN, C. L., GOLDBERG, E. P., Magnetic metal-polymer composites: Thermal and oxidative decomposition of Fe(CO)<sub>5</sub> and CO<sub>2</sub>(CO)<sub>8</sub> in a poly(vinylidene fluoride) matrix. *J. Polym. Sci. Polym. Phys.* **1990**, *28*, 2421–2433.
- 121 TANNENBAUM, R., Polymer matrix influence on the kinetics of some fundamental inorganic colloidal reactions, *Langmuir* **1997**, *13*, 5056–5060.
- 122 HE, R., QIAN, X., YIN, J., XI, H., BIAN, L., ZHU, Z., Formation of monodispersed PVP-capped ZnS and CdS nanocrystals under microwave irradiation. *Colloid Surf. A* **2003**, *220*, 151–157.
- 123 YAO, H., TAKADA, Y., KITAMURA, N., Electrolyte effects on CdS nanocrystal formation in chelate polymer particles: optical and distribution properties, *Langmuir* **1998**, *14*, 595–601.
- 124 GARREC, D. L., GORI, S., LUO, L., LESSARD, D., SMITH, D. C., YESSINE, M. A., RANGER, M., LEROUX, J. C., Poly(*N*-vinylpyrrolidone)-block-poly(*D,L*-lactide) as a new polymeric solubilizer for hydrophobic anticancer drugs: *in vitro* and *in vivo* evaluation. *J. Control. Release* **2004**, *99*, 83–101.
- 125 CHENG, F.-Y., SU, C.-H., YANG, Y.-S., YEH, C.-S., TSAI, C.-Y., WU, C.-L., WU, M.-T., SHIEH, D.-B., Characterization of aqueous dispersions of Fe<sub>3</sub>O<sub>4</sub> nanoparticles and their biomedical applications. *Biomaterials* **2005**, *26*, 729–738.
- 126 JIANG, P., LI, S.-Y., XIE, S.-S., GAO, Y., SONG, L., Machinable long PVP-stabilized silver nanowires, *Chem. Eur. J.* **2004**, *10*, 4817–4821.

## 5 Nanotechnologies for Targeted Delivery of Drugs

*Pavel Brož and Patrick Hunziker*

### 5.1 Introduction

Targeting specific tissues, cell types or specific cellular targets such as membrane proteins and intracellular organelles in the body is desirable in modern medicine for improved diagnosis and treatment. Usual therapeutic concepts in somatic medicine involve either targeted mechanical changes of pathological tissues, cells or processes (e.g. cancer surgery, interventional cardiology and orthopedics), or the untargeted application of therapeutic agents (drugs) with an automated function. Both methods have their own limits, which we will highlight to create a common background of understanding that is essential for this chapter.

While modern, minimally invasive (e.g. endoscopic interventions) surgery has increased therapeutic precision and decreased the quantity of negative side-effects to healthy tissues, there still are natural limits to the morphological scale, which direct “human-controlled” (in contrast to automated or self-controlled processes) action can reach. Due to the natural limits of senses, it is most unlikely that we will be able to perform surgical operations at cellular or even subcellular dimensions without the help of nanometer-sized tools with an automated functionality.

On the other hand, medicine knows a huge stockpile of different pharmaceutical agents such as cardiovascular drugs, antibiotics and steroids, which are usually administered on an oral or intravenous route and find their desired therapeutic target (such as cancer cells, bacteria or pathologically altered tissue) on their own or with the help of cellular transport systems. This method allows reaching even subcellular targets such as specific receptors inside or outside the cell for a therapeutic purpose; however, this strategy obviously bears specific problems. Since most of the drugs are transported with the blood flow or bound to plasma proteins, they reach every part of the human body and targets other than just the desired ones. As a result, negative side-effects such as loss of hair, vomiting, diarrhea and destruction of fast growing cells in the bone marrow occur when using cytotoxic anticancer drugs. Some drugs can even lead to fatal complications during the therapeutic process. For further information about adverse drug effects [1], refer to Figs. 5.1 and 5.2.

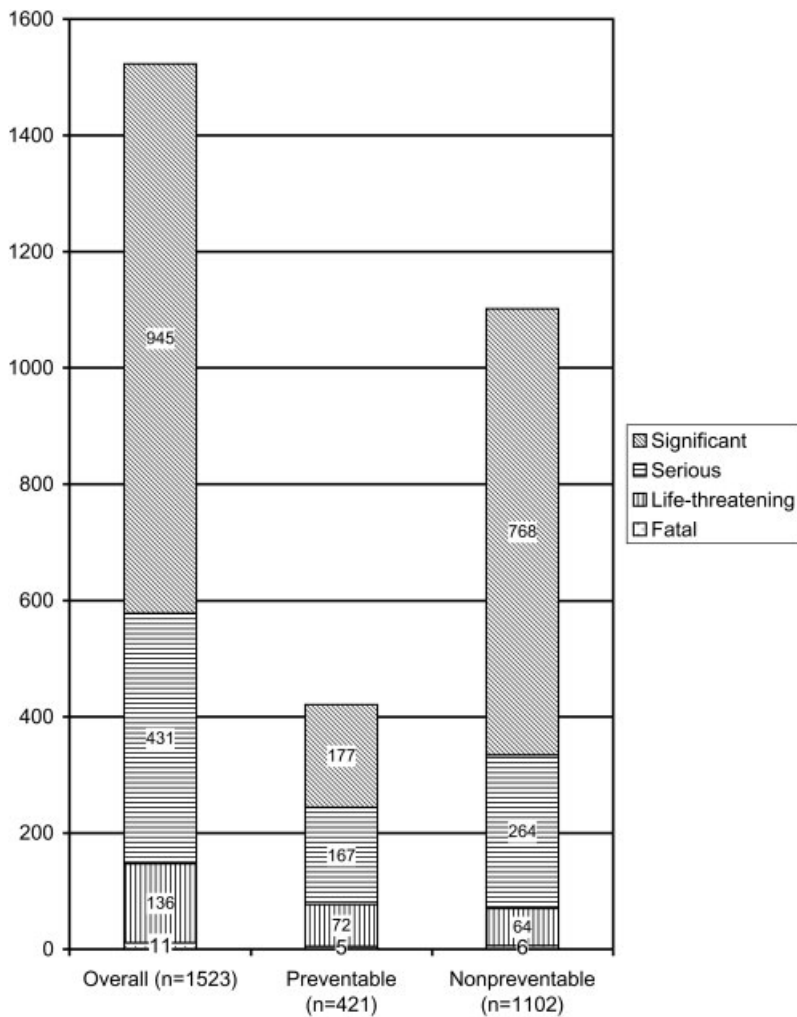


**Figure 5.1.** Incidence of adverse drug events (data from Ref. [1]). More than 30 000 elderly patients (mean age 74.7 years, 58.7% female, mean prescription drug dispensing over 12 months 21.1!) treated at a Medicare institution were monitored for adverse drug events over a period of 12 months. Observed drug events were rated from significant to fatal. The results show the high impact of adverse drug events

on healthcare systems and on patients taking multiple drugs. Even though about one-third of the events may have been prevented by the physician, two-thirds of all adverse drug events are not preventable and have to be explained by unselective drug targeting, which influences physiologic processes other than the expected target process in a negative way.

Modern highly active drugs with strong therapeutic potency that were introduced to medicine in recent years try to overcome these problems of side-effects and unwanted interactions by reaching higher target specificity than older drugs. Examples are therapeutic monoclonal antibodies (e.g. rituximab for non-Hodgkin's

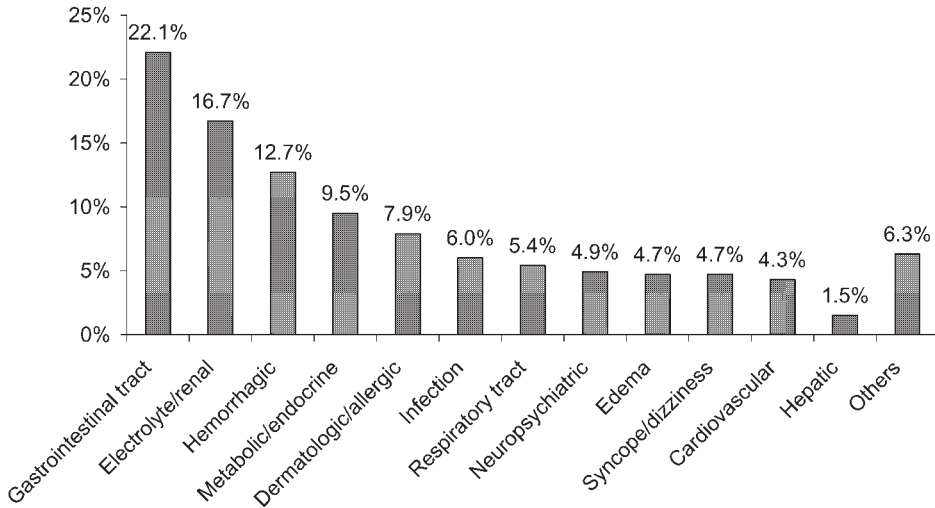


**Figure 5.2.** Frequency of types of adverse drug events (data from Ref. [1]). In the same study as in Fig. 5.1, adverse drug events were differentiated according to the type of event (organ, physiologic function). One adverse drug event may manifest itself as more than one type; the value gives the probability for an

adverse drug event to influence the mentioned organ/physiologic function. Most common events are nausea, vomiting, diarrhea, constipation, electrolyte disorders, renal malfunctioning, bleeding and allergic manifestations.

lymphoma, trastuzumab for breast cancer), which can even bear certain functionality such as (i) a radioactive isotope (e.g. tositumomab, an antibody linked with  $^{131}\text{I}$  used for treatment of non-Hodgkin's lymphoma), (ii) monoclonal antibodies for active cancer vaccination (e.g. mitumomab for small cell lung cancer) or (iii) artificially designed agents that can block certain types of intracellular proteins such as kinases (e.g. imatinib inhibits a pathological tyrosine kinase in chronic myeloid leukemia). However, even though these drugs create a much higher therapeutic potency, there are still the known problems with side-effects, even though they tend to be milder than the side-effects of standard anticancer therapy (surgery, chemotherapy and radiotherapy).

Another important area of medicine that will be changed by nanometer-sized tools is diagnostics. Diagnostics can be defined as every method that allows the doctor to assess a certain characteristic or development inside or on the surface of the human body that they cannot assess with their own sensory. This vast area ranges from common techniques such as X-ray imaging, blood cell counting, plasma analysis, drug level measurement, anatomic imagining of certain parts of the body by computed tomography (CT) or magnetic resonance imaging (MRI) and histological inspection of tissue samples to more specialized techniques such as protein assays, gene expression assays and receptor expression studies.

Common to all of these new methods is the trend to miniaturization, small sample measuring, and diagnostics at cellular and subcellular dimensions. Tools such

as microchip assays, target-specific contrast agents for imaging and small-sample diagnostics are some of the now commonly used techniques.

Clearly, nanotechnology will be able to introduce even more ground-breaking diagnostic and therapeutic methods to medicine in the years to come, which will contribute to a better detection of pathological processes and to better therapeutic options for sick people. A central problem which nanotechnology has to overcome is the difficulty of targeted delivery as described above. The idea is to increase the diagnostic signal or the therapeutic impact on the desired target with a small range of negative side-effects.

This chapter will highlight some basic problems for targeted delivery of nanometer-sized structures and will present successful targeting strategies employed by both “natural nanostructures” (such as bacteria and viruses) and “artificial nanostructures” (lipid-based such as liposomes and micelles, protein-based such as dendrimers, and polymer-based such as nanoparticles, nanospheres and nanocontainers) in areas other than cancer. The main goal of this chapter is to present different facets of the enormous field of targeted delivery, to present the main literature dealing with targeted delivery and to show the high level of interdisciplinarity. Only by combining parts of scientific disciplines such as pharmacology, microbiology, immunology, chemistry, physics and medicine will it be possible to build nanotechnological devices for targeted delivery.

The chapter is mainly suitable for physicists and chemists working in this research area and showing interest in the biomedical and pharmacological part of targeted delivery to the human body. Nonetheless, it is also written for people with a general interest in “nanomedicine” [2, 3] that share the belief that it will be possible to compose nanostructures with a complex and automated functionality for the benefit of humanity.

Section 2 describes some pharmacological basics and special pharmacological problems concerning targeted delivery of macromolecules and chemically complex carriers. In Section 3, we will discuss strategies for targeted delivery used by microorganisms such as bacteria and viruses, and by the “natural nanoparticle” prion. In Section 4, we will review targeting strategies for site-specific delivery of artificial nanotechnological carriers. In Section 5, we will sum up the main messages of the chapter and try to give an outlook into the future of targeted delivery. The reader is referred to the given references for a deeper insight into a certain topic.

## 5.2

### Basic and Special Pharmacology

#### 5.2.1

##### Outline

Pharmacology is the scientific discipline that describes and examines the effect of chemical substances on biological systems such as the human body and their use as therapeutic agents. The subspecialty of drug delivery concentrates on the development of new therapeutic systems with high target specificity, low side-effects

and controlled release of active substances with complex functionality. The toolbox of nanotechnology has revived this research area and is trying to develop new therapeutic concepts.

In this section, we will first discuss some basic characteristics of drug input and disposition that are essential for a deeper understanding of targeting strategies. In the second part of this section, we will point up specific hurdles for targeted delivery.

For more details about this topic, see Refs. [4–6].

## 5.2.2

### Basic Pharmacology

When giving a drug to the body there exist several steps the chemical substance has to go through before it can unfold its specific effect and other steps before it can be removed from the body. The most important ones are absorption, bioavailability, distribution and elimination. We will discuss these four steps to create a common basis of knowledge. Apart from this, it is obvious that the same physiological pathways and rules apply to both standard drugs and nanotechnological drug formulas, nanospheres, nanocontainers, nanoparticles, “nanobots”, etc., making it necessary for all involved researchers to understand these physiological pathways.

#### 5.2.2.1 Absorption

Absorption is the movement the drug has to perform from the administration site direct to the therapeutic site or to the systemic circulation. Absorption is determined by both physicochemical properties of the chemical substance or macromolecule and the biological construction of the administration site. Drugs are administered as solutions, tablets, capsules, aerosols or transdermal permeation systems. Usually the drug builds a complex with other ingredients (e.g. binders, surfactants, dispersants and diluents) that control the stability of the drug and its dissolution speed, and can control the release of the active ingredient. For instance, it is possible to lengthen the absorption time by creating special matrix tablets or tablets with encased granules with substance-specific release characteristics.

The drug complex can be administered by various routes such as oral, intravenous, intra-arterial, intramuscular, sublingual, inhalational, topical (eyes, skin), rectal or vaginal. Administration routes are divided into direct parenteral routes (intravenous, intra-arterial) where the drug does not have to permeate cellular barriers before reaching the circulation (the needle does the permeation) and indirect routes where the drug has to permeate through barriers in organs such as the intestine, the lung or the skin before it can reach the circulation. These barriers are mainly biologic semipermeable cell membranes (triblock hydrophilic–hydrophobic–hydrophilic with a central lipid block containing phospholipids and cholesterol) that selectively block the passage of smaller electrically charged molecules and all macromolecules. Various transmembrane proteins, receptors and transport systems are embedded into this triblock membrane, and are responsible for substance-specific uptake and cellular control. The drug or carrier of com-



plex functionality can cross this cell membrane by passive diffusion, facilitated passive diffusion, active transport or endocytosis according to its physicochemical properties.

Most drugs cross the cell membranes by simple passive diffusion according to the concentration gradient, which is directed from a site with high substance concentration to a site with low substance concentration (e.g. from the intestine to the epithelial cells or the blood vessel near the epithelial cells). Once the drug reaches the systemic circulation, it is washed away and the concentration stays low, thus ensuring a constant substance uptake. Apart from the concentration gradient and the size of the absorption surface, the transmembrane diffusion rate depends on the polarity (the unionized form has a faster permeation rate than the ionized), lipid solubility, drug size and pH of the drug molecule. Small, lipid-soluble substances have the fastest absorption rate.

For facilitated passive diffusion, the molecule (e.g. glucose) binds to substance-specific transmembrane carrier proteins on the cell surface, which speed up the diffusion by building a substance-carrier complex with a higher diffusion rate through the cell membrane without energy consumption. This method relies on a concentration gradient and is characterized by saturability because of the limited amount of carrier complexes.

On the other hand, there exist similar transmembrane proteins responsible for an active, energy-consuming transport. This method is characterized by high specificity (e.g. vitamins, amino acids), saturability and works against a concentration gradient.

Passive diffusion and active transport are limited to small molecules (the size of ions, glucose and amino acids); larger molecules, macromolecules, and micro/nanostructures such as viruses and bacteria can only reach the cell by endocytosis. To perform the endocytosis, the cell (mostly specialized cell types of the immune system such as granulocytes and macrophages) has to engulf the structure, enclose it into a cell membrane-derived vesicle and transport it into the cell interior. There the vesicle is transformed into a so-called lysosome. A major problem of this transport method is the intracellular degradation of the vesicle content by low pH (down to 2–3) and cellular enzymes such as phosphatases, lipases, esterases, proteases, etc., which the cell delivers into the endocytosis vesicle. This method is energy consuming, saturable and needs a ligand-receptor interaction.

Most drugs are administered orally and reach the circulation by crossing the diverse epithelial cell barriers found in the gastrointestinal system, mainly using passive diffusion and scarcely active transport (e.g. L-DOPA – a dopamine-derived drug for Parkinson's disease). Small and lipophilic molecules can use the short contact time inside the mouth to cross the epithelial cells of the buccal or sublingual area and enter the circulation rapidly. An example is nitroglycerin – a drug that dilates the coronary arteries in the case of a myocardial infarction.

Even though the next station in the way of the drug, the stomach, has a larger epithelial surface, almost no drugs enter the circulation here. Reasons are the thick mucous layer protecting the stomach from self-digestion and the usually fast passage time in the stomach. Apart from this, the stomach creates some important

problems to drug therapy because of the acidic (pH 1–2) environment and the digestive enzyme pepsin (a protease produced in the stomach wall). Some drugs can be degraded in such an environment (e.g. penicillin), especially when fatty foods or slow stomach emptying slow down the passage time. It is possible to overcome this problem by building gastric acid-resistant capsules and drug formulas when giving an instable drug orally.

Most orally applied drugs are absorbed in the small intestine (especially duodenum and proximal jejunum) over less than 6 h under normal circumstances. Special controlled-release formulations show a slower absorption kinetic and may reach the large intestine, where they can also be absorbed or may be subject to microbial degradation.

When giving a drug in a parenteral way, the substance is directly placed into the circulation (intravenous, intra-arterial) or injected into soft tissues such as the skin or muscles without having to cross the epithelial barriers. These methods are especially suitable for larger and complex molecules such as proteins, and for complex chemical structures such as liposomes or nanoparticles, because here they do not face any problems with degradation and inactivation compared with the intestine. Injections into the fat of the skin (subcutaneous) or into the muscle (intramuscular) are especially suitable for everyday applications of drugs such as insulin for diabetes or low-molecular-weight heparin for perioperative anticoagulation. The patient can perform these injections without facing serious complications such as blood infections and thrombosis when injecting substances into blood vessels. Due to passive diffusion into the porous small capillaries of these soft tissues, proteins up to a molecular weight of 20 kDa face fast and constant absorption, mostly depending on the quantity of capillaries and the perfusion speed. Larger molecules show unstable absorption, since their absorption occurs by the lymphatic system, where they also face contact with degrading enzymes and cells of the immune system such as macrophages that take up all macromolecules and produce an immune reaction (inflammation, allergic reaction) against this substance. On the other hand, parenteral injection of large molecules or rather insoluble drug formulas can be used for controlled release over a large-scale period (e.g. penicillin G benzathine or insulin in crystalline suspensions).

Drugs with a short circulation half-time have to be administered in a controlled-release form to guarantee a stable plasma concentration and persistent therapeutic effect. The best way to achieve this is to apply an intravenous catheter and to infuse the drug constantly. For long-term applications, it is necessary to change the strategy because of complications such as catheter infections, thrombosis and reduced convenience. For oral administration, the drug particles can be coated with wax or other water-soluble material such as biodegradable polymers, or can be embedded into a slow-release matrix. Another administration method is transdermal controlled-release systems consisting of drug-impregnated polymer materials with permeable membranes bonded to an adhesive bandage. These systems provide constant drug release into the skin for 12–24 h, but are restricted to smaller lipophilic molecules that can permeate the skin barrier (e.g. nitroglycerin, opiates).

### 5.2.2.2 Bioavailability

Bioavailability is the extent and the rate at which the active drug enters the systemic circulation, and is mostly determined by its physicochemical properties and the dosage form (as seen above). Different drug formulations result in different bioavailability and can have clinical significance in the terms of therapeutic effect and toxicity. The bioavailability is also determined by physiologic characteristics of the patient, mainly the gut perfusion rate and the metabolic liver function, or on a smaller scale by sex, genetic phenotype, stress, disease or previous gastrointestinal surgery.

When giving a drug parentally, the bioavailability is, by definition, 1 since all the active formula reaches the systemic circulation. On the other hand, the bioavailability of orally administered drugs is never 1, because the drug has to move down the gastrointestinal tract, has to cross the epithelial barriers of the intestine and has to pass through the metabolically active liver before it can reach the systemic circulation. This primary metabolic degradation and inactivation of the drug is called first-pass metabolism or the first-pass effect. A high first-pass effect results in a low or even zero oral bioavailability (e.g. most protein-based drugs such as insulin and complex molecules such as heparin or testosterone). Some drugs have a high oral bioavailability even though they undergo an extensive chemical change resulting in therapeutically active metabolites – this is called metabolic activation of therapeutically inactive prodrugs (e.g. the antihypertensive drug enalapril, the antiviral drug valaciclovir or heroin).

Physicochemical properties resulting in a low bioavailability are poor water solubility, slow or incomplete absorption during the passage through the gastrointestinal tract (total 1–2 days, but only 2–4 h in the small intestine) and molecule-specific chemical reactivity. Examples for molecule-specific chemical reactivity are (i) complex formation (e.g. the antibiotic tetracycline and polyvalent metal ions), (ii) conjugation in the intestinal epithelium (e.g. sulfoconjugation of the bronchodilative drug isoproterenol), (iii) hydrolysis by gastric acid (e.g. penicillin), (iv) adsorption to other drugs (e.g. the heart drug digoxin and the bile acid binder cholestyramine) or (v) metabolism by luminal bacterial microflora (normally only in the large intestine, under pathological circumstances even in the small intestine).

To assess the overall bioavailability, one has to take repetitive blood samples, and measure the time (called peak time) and the amount of the peak drug concentration in the plasma (here the drug absorption rate equals the elimination rate), and the so-called area under the plasma concentration–time curve (AUC). A higher absorption rate results in an earlier peak time and higher peak concentration; a slower absorption results in a later peak time. Parentally administered drugs have an early peak time, because the whole dose reaches the systemic circulation in a short time. The AUC is direct proportional to the total amount of drug that reaches the systemic circulation and usually allows the most reliable characterization of the bioavailability.

To increase the overall plasma concentration of the drug, it is possible to give multiple doses of the drug formulation before the entire previous dose is eliminated from the circulation. With fixed-dosing intervals, the drug concentration in-

creases for four to five plasma elimination half-lives (see the following sections for details) before reaching the steady state, where absorption and elimination are equal. Depending on the half-lives of the drug, the dosing interval can vary from some hours to some days.

### 5.2.2.3 Distribution

After entering the systemic circulation, a drug is delivered to all parts of the body through the bloodstream. Nonetheless the distribution is uneven because of differences in (i) blood flow (e.g. the eye or the kidney have much higher mean perfusion per volume than muscles or the connective tissue), (ii) tissue binding (e.g. lipophilic drugs bind to fatty tissue), (iii) regional pH and (iv) permeability of endothelial membranes of the blood vessels (e.g. very low permeability in the brain and high permeability in liver, spleen and kidney). All of these factors define the organ-specific distribution equilibrium, defined as the time-point when entry rates to the tissue and exit rates from the tissue are the same, and drug concentrations outside and inside the blood vessels are the same (plasma concentration = effective tissue concentration). Richly vascularized areas with high vessel permeability for a specific drug reach the equilibrium more rapidly than poorly vascularized areas with a low permeability, thus making it complex to assess the organ-specific concentrations when researching the borders for therapeutic and toxic effects.

To describe the distribution characteristics of a certain drug, one can use the idea of the apparent volume of distribution, defined as the fluid volume needed to contain the drug in the body at the same concentration as in the plasma. Clearly, a certain quantity of a drug with a high apparent volume of distribution (e.g. the anti-arrhythmic drug amiodarone) results in a much lower overall plasma concentration than a drug with a low apparent volume of distribution (e.g. heparin), since the same amount of drug molecules reach a higher fluid volume (e.g. the blood covers roughly 3–4 L and the whole extracellular fluid covers about 17 L). Apart from the fluid volume, other factors such as fat tissue binding, protein binding and pH of the drug influence the apparent volume of distribution, resulting in volumes up to 500 L for fat binding, mostly basic drugs such as digoxin or amiodarone. Acidic drugs such as salicylic acid and warfarin have smaller volumes of distribution than basic drugs such as amphetamine because of their preferential protein binding (the body has much more fat than free proteins for binding).

In the bloodstream, common drugs are transported either or both as unbound, free drug or bound to different blood components such as plasma proteins (mostly albumin for acidic drugs and different glyco/lipoproteins for basic drugs) and blood cells (mostly red blood cells). Differences in blood component concentrations and compositions result in unstable plasma concentrations of the given drugs, possibly decreasing the therapeutic effect or increasing toxicity.

To reach the desired “place of action”, the drug has to leave the systemic circulation (similar mechanisms to transcellular passage as described in Section 5.2.2.1) and for most drugs this is only possible for the unbound, free fraction. To assess the possible speed of vessel permeation, it is necessary to know the fraction unbound (defined as the ratio of unbound to total concentration) apart from

physicochemical properties of the drug (size, polarity, pH, hydration, chemical functionality) and the endothelial layer of the blood vessel (permeability, transport mechanisms). The fraction unbound usually has a better correlation to the effective pharmacological activity than the overall plasma concentration (both free and bound fraction). At low drug concentrations, not all the available plasma proteins or cells are bound to the drugs; increasing the drug concentration (higher single dose or shorter dosing interval) leaves the fraction unbound unchanged up to a certain upper limit where all the possible binding sites are saturated. By increasing the drug concentration above the saturation limit, the fraction unbound can be raised, thus increasing both possible therapeutic effect in the tissues and possible toxicity and interaction opportunity (e.g. with other drugs or physiological substances in the bloodstream, possibly creating unexpected side-effects).

An important idea when considering the drug effect is the drug reservoir. Clearly, tissues with a fast distribution equilibrium and high drug binding capacity (e.g. bone marrow, fat tissue) can accumulate high amounts of drug molecules before the desired drug target reaches a sufficient drug concentration for the therapeutic effect. Since the plasma and the tissue concentration are at equilibrium, the drug reservoir releases the drug when the plasma concentration decreases because of elimination mechanisms. Therefore, the drug reservoir is both responsible for lower peak concentration and slower concentration decrease, resulting in the same AUC than without a drug reservoir.

Some drugs such as antimalarial drugs, some antibiotics and cytotoxic drugs accumulate inside specific cell types because of substance-specific transport mechanisms, and binding to intracellular components such as proteins, phospholipids or nucleic acids. Thus, the drug concentration is much higher inside the cells (mostly white blood cells such as macrophages, granulocytes and liver cells, but also bacteria) than in the surrounding tissue and in the plasma. Similar to drug reservoirs in the tissue, the intracellular drug is in equilibrium with the plasma and leaves the cell, unless it binds to a certain target or performs a certain chemical reaction.

#### 5.2.2.4 Elimination

Elimination is the sum of processes of drug loss from the body, mainly metabolism (chemical alteration) and excretion (elimination without further chemical change).

Metabolism is mostly performed in the hepatocytes (main liver cell type) of the liver – different reaction pathways result in pharmacologically inactive or active metabolites. Drug metabolism pathways usually occur in two apparent phases: phase I and phase II. Phase I reactions involve forming a new or changed functional group or a cleavage (oxidation, reduction, hydrolysis) to ensure a higher rate of reactivity. Phase II reactions involve conjugation with an endogenous compound such as glucuronic acid, glycine or sulfate to ensure higher water solubility. The metabolites of these processes have a higher polarity and are excreted through the kidneys (urine) or the liver (bile) at a much higher rate than the original drug molecule.

The most important enzyme system of phase I metabolism is a microsomal family of isoenzymes called cytochrome P450, which can transfer electrons supplied by certain flavoproteins (NADPH-cytochrome P450 reductase) to catalyze drug oxidation. The cytochrome P450 superfamily is grouped into 14 families with gene sequence identity and 17 subfamilies. The isoenzymes are named by a root symbol CYP, followed by a number/letter combination. The most important CYP isoenzymes for drug metabolism are CYP1A2, CYP2C9, CYP2C19, CYP2D6 and CYP3A4. Every one of these isoenzymes is specific for different drugs and can be upregulated by repetitive drug application of so-called CYP-inductive drugs (e.g. glucocorticoids, rifampicin, carbamazepine, barbiturates, St John's wort, efavirenz, etc.) and downregulated by so-called CYP-inhibiting drugs (e.g. amiodarone, paroxetine, fluconazole, ketoconazole, ciprofloxacin, clarithromycin, ritonavir, grapefruit juice, etc.).

The most important phase II reaction is glucuronidation (conjugation to glucuronic acid), which occurs in the liver microsomal enzyme system (microsomes are intracellular organelles) and results in hydrophilic metabolites suitable for renal or biliary excretion (e.g. morphine, fluoroquinolone or chloramphenicol). Other important reactions are (i) amino acid conjugations with glutamine or glycine (e.g. salicylic acid), (ii) acetylation (e.g. sulfonamides, hydralazine), (iii) methylation (e.g. catecholamines, thiouracil, niacinamide), or (iv) sulfoconjugation of phenolic or alcoholic groups with inorganic sulfate gained from sulfur-containing amino acids such as cysteine (e.g. methyl dopa, thyroxine, acetaminophen, estradiol).

All metabolic pathways show different activities according to (i) the genetic background (most important are genetic variations in the CYP2C9 cytochrome P450, resulting in different metabolic activities for certain drugs), (ii) age (newborns and elderly patients show low metabolic activity), (iii) sex, (iv) history of liver diseases, (v) capacity of the enzyme (mostly upper limit of capacity) and (vi) up- or down-regulating endogenous or exogenous substances. Due to these individual variations in drug metabolism, it is difficult to predict the therapeutic effect of a given dose of a drug, especially when the patient is taking other drugs, drinking alcohol or smoking.

The excretion of the now hydrophilic drug metabolite or the original hydrophilic, unmetabolized drug mostly takes place in the kidneys; a smaller degree of the incorporated drug can be excreted through the biliary system (bile is produced in the liver and flows into the small intestine), saliva, sweat, breast milk and lungs (volatile substances such as anesthetics).

Kidney excretion is a complex process that can be separated into glomerular filtration, tubular reabsorption and tubular secretion. The central unit of the kidney is the so-called nephron consisting of a well-perfused capillary conglomerate called glomerulus and the tubular system that follows the glomerulus. In the glomerulus, plasma is filtered through pores in the glomerular endothelium according to (i) the pressure in the afferent and efferent arterioles, (ii) the perfusion speed, (iii) the filter permeability, (iv) the size and ionization of the molecule (maximum filterable size is 10–15 nm [7]; cationic molecules have higher permeability than anionic molecules because of the anionic charge of the glomerulus), and (v) the pressure

in the tubular system. Only unbound drugs up to certain size and ionization can be filtered through the glomerular endothelium, protein-bound drugs cannot be filtered. Most of the filtered ions (such as sodium, chloride, potassium, magnesium, calcium and bicarbonate), all glucose, amino acids, urea and other important substances are reabsorbed by specialized and substance-specific transport systems (active transport systems for glucose, amino acids and some ions; passive diffusion for most ions and water). Filtered drugs can also be reabsorbed if they show molecular closeness with endogenous physiologic substances (e.g. the antidepressant lithium is analogous to sodium). Unionized forms of nonpolar weak acids and weak bases are reabsorbed readily from the tubular filtrate, so acidification of urine increases the reabsorption of filtrated acidic drugs and decreases the reabsorption of basic drugs and *vice versa*.

Another excretion mechanism is the active, energy-dependent tubular secretion process in the proximal part of the tubule, typically used to remove drugs such as penicillin, salicylic acid, procainamide, dopamine, phenylbutazone and trimethoprim. It is possible to distinguish two separate transport mechanisms for anions and cations with a characteristic maximum of secretion. The anion secretory system is more important for drug elimination and transports metabolites conjugated with glycine, sulfate or glucuronic acid (conjugation done by phase II metabolism in the liver) into the tubular system. Due to the saturability of every active transport mechanism, anionic compounds compete with one another for secretion resulting in slower elimination times (e.g. penicillin elimination can be decreased by the therapeutically inactive molecule probenecid to increase therapeutic plasma concentrations of penicillin).

Some drugs can be removed by active biliary excretion (done by hepatocytes) across the biliary epithelium in the liver. This excretion mechanism is especially suitable for larger, lipophilic drugs conjugated with glucuronic acid. Once the excreted drug reaches the small intestine, it is treated in the same way as a drug coming from the stomach, resulting in an absorption by the intestinal epithelium, especially after enzymatic degradation of the “new” functional group (glucuronic acid). This is the enterohepatic cycle.

When assessing the overall rate of elimination, it is necessary to measure the concentrations of both unchanged drugs and possible metabolites in the main excretion routes (urine, bile, milk, saliva, sweat) over a certain time, and to compare these concentrations to the plasma concentrations. The parameter relating total elimination rate to plasma concentration is called total clearance (renal plus extrarenal clearance). The fraction of excreted unchanged drug helps to find out the impact of renal and extrarenal (mainly hepatic) elimination, since the unchanged drug can only be found in the urine and hepatic elimination is only possible for metabolites. A low fraction of unchanged drug shows that hepatic elimination is strongest and that hepatic disease may therefore affect drug elimination. The same applies to drugs with a high fraction of unchanged drug and renal diseases.

Another important assessment value is half-life elimination, defined as the time needed for the plasma drug concentration or the amount of drug in the body to

decrease by 50%. This time is usually independent of plasma drug concentration, characterizes both distribution and elimination of the drug, and determines the dosing intervals and time to reach steady state.

### 5.2.3

#### **Special Pharmacology**

Here, we will discuss the key factors found in nature that protect the internal environment from external “macroelements” (bacteria, viruses, proteins, DNA, nanovectors such as liposomes, nanoparticles, nanospheres and nanocontainers). It is important to understand the concept of these defense mechanisms when trying to overcome the challenges and develop a targeting system for site-specific delivery of drugs or diagnostic agents with a minimal negative impact on physiologic pathways. Successful strategies to overcome the defensive obstacles performed by both pathogenic organisms such as bacteria and viruses and therapeutic systems will be presented. For a deeper insight into the immune system and other defense mechanisms, refer to the specialized literature listed in the reference section.

##### **5.2.3.1 Skin Epithelium**

The outermost layer of our body consists of multiple layers of squamous epithelial cells, together building the stratum corneum of the epidermis [8]. The stratum corneum can be considered as a two-compartment system consisting of the epithelial cells themselves and the surrounding extracellular matrix. The cells produce and secrete various proteins (e.g. linking proteins for cell–cell adhesion), lipids (e.g. phospholipids, cholesterol, ceramides, sphingomyelin) and enzymes (e.g. lipases, proteases and antiproteases). This two-compartment system of lipid-depleted squamous cells and lipid-enriched, extracellular matrix ensures both physical and chemical protection, preferably against ultraviolet light, chemicals, physical force, temperature, bacteria and viruses, but also against the permeation of macrostructures such as nanovectors.

Nonetheless, the skin can be useful for therapeutic purposes, as transdermal permeation systems for morphine, nitroglycerin or female steroid hormones prove. Factors such as site of application, thickness and integrity of the stratum corneum, size, polarity and pH of the molecule, skin hydration, drug metabolism by bacterial skin flora, and change of blood flow in the skin by additives and body temperature influence the rate of transdermal drug absorption [9, 10].

Small, lipo- or amphiphilic molecules can permeate the complex skin barrier. Permeation is also possible for lipid-based nanostructures such as liposomes up to a diameter of 500 nm [10, 11]; permeation of polymer-based nanostructures is more difficult because of their hydrophilic surface. Once the drug has permeated across the epidermis, it reaches a well-perfused subepidermal layer where it can enter blood vessels through pores in the vessel wall. An intact skin barrier protects the organism from pathogenic microstructures such as bacteria and most viruses; the same applies to nanoparticles bigger than the mentioned 500 nm.



### 5.2.3.2 Mucosal Epithelium of the Respiratory Tract

The airways can be divided into the upper respiratory tract (nose, mouth, throat and larynx) and the lower respiratory tract (trachea, bronchi and terminal respiratory alveoli). Multilayered squamous epithelium consisting of epithelial cells and special cell types producing mucus and immunoglobulins covers the upper respiratory tract. The physicochemical characteristics of this squamous epithelium are comparable to the skin. Nonetheless, the permeability is much higher because of the absence of a stratum corneum and a strong perfusion with well-permeable blood vessels, making it possible to absorb small, mostly lipophilic drugs such as nitroglycerin, cocaine and steroids at a high rate.

The lower respiratory tract has to be subdivided into the trachea and bronchi with their respiratory epithelium, and the alveoli with their single-layered alveolar epithelium. The respiratory epithelium consists of ciliated epithelial cells and mucus-producing cells, together building a single-layered barrier connected by tight cell-cell adhesion complexes called tight junctions or zonulae occludentes [12].

Drug application to the lower respiratory tract [9] is possible by inhalation of vaporized, nebulized, powdered or aerosolized drugs (e.g.  $\beta_2$ -agonists, corticosteroids, and anticholinergics for asthma and chronic obstructive pulmonary disease therapy, or antibiotics for to treat children with cystic fibrosis). Access to distal airways depends on the particle size, because particles bigger than 4  $\mu\text{m}$  diameter deposit on the epithelium of the upper respiratory tract, and particles smaller than 500 nm diameter fail to deposit on the epithelium and are exhaled. Only particles with a diameter between 0.5 and 4  $\mu\text{m}$  can reach the distal airways and deposit on the epithelium of the bronchi. Once the drug molecule or drug carrier is deposited, it can permeate across the respiratory epithelium (lipophilic drugs better than hydrophilic) and can reach the systemic circulation.

### 5.2.3.3 Mucosal Epithelium of the Gastrointestinal Tract

The gastrointestinal tract consists of the esophagus, stomach, small intestine and large intestine. Because of the short passage time and the impermeable epithelial barrier in the esophagus and especially in the stomach (low pH, dense mucus layer, and strong intercellular bonds between the epithelial cells), the upper parts of the gastrointestinal tract play no role in absorbing macromolecules and microstructures such as bacteria, viruses or nanoparticles.

The small intestine is the longest section of the gastrointestinal tract, lies between the stomach and the large intestine, and has an overall length of 6 m. The small intestine with its large mucosal surface (250  $\text{m}^2$  because of mucosal folds, mucosal extensions called villi and epithelial cell membrane extensions called microvilli) and epithelial cell (also called enterocytes) lining is responsible for the enzymatic digestion and absorption of small nutritives such as monosaccharides, oligonucleotides, amino acids, fatty acids, vitamins and lipids, and macromolecules such as epidermal growth factor. Dense tight junctions join the enterocytes [13] and build a continuous layer with other cell types that are responsible for other tasks. (i) Enteroendocrine cells sense the luminal environment and can secrete peptide hormones [14] into the blood that influence the digestive process. (ii) Gob-

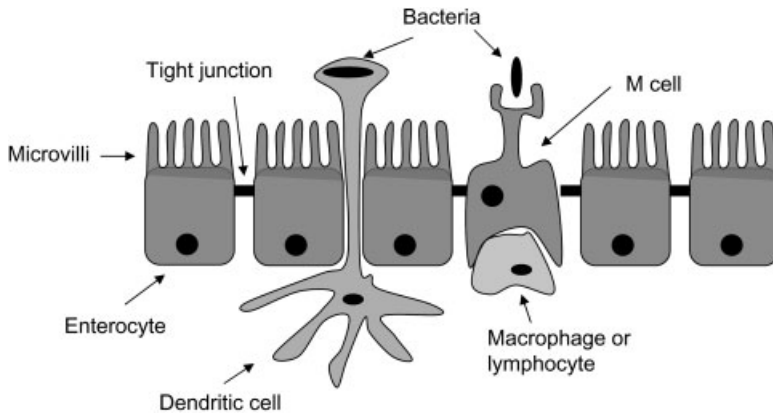


**Figure 5.3.** Schematic drawing of small intestine epithelium (for details refer to main text).

let cells produce peptides needed for epithelial growth and repair, and lubricating mucus consisting of glycoproteins that covers the mucosal surface, reduces the diffusion of macromolecules, and binds proteins and microorganisms. (iii) Paneth cells secrete antimicrobial digestive enzymes such as cryptidins or defensins. (iv) Finally, the M cells are phagocytic cells that control the luminal microbial environment and can trigger an immune response in the presence of harmful pathogens (see Fig. 5.3).

The epithelium is exposed to a wide variety of potentially harmful bacteria, viruses and other microorganisms that should not be able to permeate the epithelial layer [15]. It is obvious the epithelial cells had to develop sophisticated and specific receptors, transport systems and strong defense systems [16, 17] to cover all necessary functions such as digestion and absorption of all essential nutritives, endocrine functions, and immunologic and mechanical barrier for microorganisms and potentially harmful macromolecules.

The apical surface of the enterocytes is covered by closely placed microvilli (diameter 100 nm, intervillous space is variable and can decrease down to 25 nm) with a filamentous brush border glycocalyx (500 nm thick) consisting of negatively charged mucin-like glycoproteins and enzymes, responsible for terminal digestion of polysaccharides and polypeptides. Apart from this, the glycocalyx is another diffusion barrier that prevents macromolecular particles, bacteria and viruses from direct contact with the enterocyte cell membrane. Microstructures that want to enter the enterocytes have to move into the space between the microvilli or have to produce toxins or inflammatory agents that disrupt the microvilli continuity, thus allowing direct contact with the uncovered enterocytes surface.

Enterocytes take up luminal molecules by different methods. Small nutrient molecules such as glucose, amino acids and ions reach the cell through substance-specific epithelial transporters; larger molecules reach the cell by the receptor-mediated [18, 19], energy-dependent process of pinocytosis (for details,

see Section 5.2.3.6). Once the molecules have entered the enterocytes, they can enter different pathways. The first pathway leads to enzymatic degradation in lysosomes, the second pathway leads to transcytotic transport of the intact vesicle content and active release into the subepithelial space, where the molecules can reach the systemic circulation or the lymphatic vessels.

Another pathway for epithelium crossing is the paracellular transport that is only possible under pathological conditions, because normally the intercellular tight junctions block the permeation of large molecules and micro- and nanometer sized structures. Physiologically, the tight junctions can dilate up to a pore radius of 5 nm on activation of certain cellular  $\text{Na}^+$ -coupled transport systems, enabling a transjunctional osmotic flow for nutrients. Pathological insults such as inflammatory cytokines [e.g. interferon (IFN)- $\gamma$ , tumor necrosis factor (TNF)- $\alpha$ , interleukin (IL)-1 $\beta$ , IL-4 and IL-13], mechanical damage, infection, bacterial toxins (e.g. cholera toxin) and cell death can open these pores enough to allow the passage of macromolecules or nano/microstructures [15, 20, 21].

#### 5.2.3.4 Mononuclear Phagocyte System (MPS)

Once the drug molecule or drug complex reaches the systemic circulation – be it direct by intravenous or intra-arterial injection or indirect by other application ways – it comes in contact with various metabolic pathways and defensive systems. When discussing the possibility of targeted delivery of nanometer-sized structures (lipid-based such as liposomes and micelles, protein-based such as dendrimers, and polymer-based such as nanospheres, nanoparticles and nanocontainers), the most important hurdle is the MPS [22, 23] [also known as reticuloendothelial system (RES)] – a part of the innate immune system. The MPS consists of bone marrow (pro-) monoblasts, peripheral monocytes and monocyte-derived tissue macrophages in liver (called Kupffer cells), lungs, spleen, lymph nodes, thymus, gut, bone marrow and brain (called microglia). The MPS plays a major role in host defense, and is responsible for clearing unwanted and possibly pathogenic organisms (bacteria, fungi, protozoa, parasites, viruses) and macromolecules such as lipoproteins, polysaccharides, polynucleotides and nanoparticles. Macrophages can also be attracted to an infected focus by various chemotactic substances (bacterial endotoxins, immune complexes, complements factors, collagen fragments), where they phagocytose infectious agents. Apart from this, the cells of the MPS play an important role in the development of pathological conditions such as cancer, atherosclerosis, autoimmune diseases (rheumatoid arthritis, Crohn's disease, systemic lupus erythematosus, multiple sclerosis), diseases of the central nervous system and some infectious diseases (HIV, tuberculosis, leishmaniasis, salmonellosis, schistosomiasis).

When injecting macromolecular formulas such as liposomes, immunoliposomes, polymeric micro/nanospheres and nanoparticles into the circulation, the MPS clears the substances rapidly from the bloodstream, mainly in the well-perfused, macrophage-rich organs liver and spleen. For phagocytosis, the macrophages contact the particles with receptor-equipped pseudopods, attach the particle to the cell membrane and engulf them with lamellipods. After entering the macro-

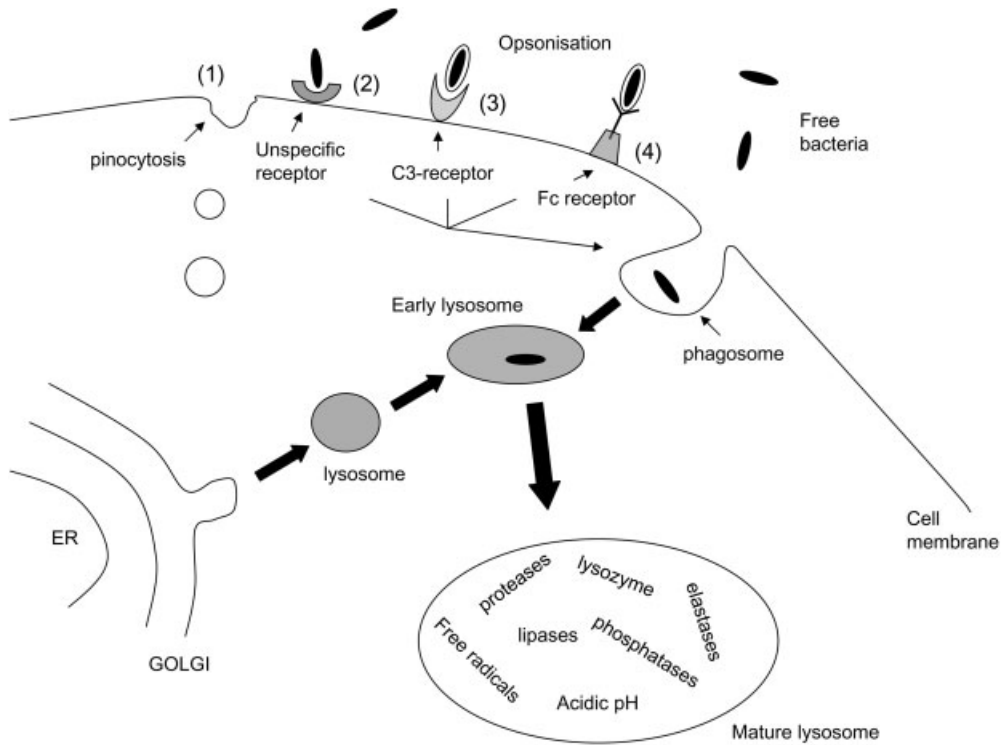


**Figure 5.4.** Schematic drawing showing the principles of receptor-mediated endocytosis: (1) shows the process of pinocytosis as described in the main text; (2)–(4) show the different pathways that lead to the receptor-mediated endocytosis of various ligands, in this case bacteria. (2) The binding of native, unchanged bacteria to “unspecific” receptors (e.g. scavenger receptors, mannose receptors, TLRs) found on phagocytic cell types (macrophages, dendritic cells). (3) The binding

of complement factor-labeled bacteria to the C3 receptor, which binds the activated complement factor 3. (4) The binding of antibody-labeled bacteria to the Fc receptor, which binds a subunit of immunoglobulins. The final steps in the case of receptor-mediated endocytosis consist of the development of the early and mature lysosome with various degrading systems as described in the main text.

phage by membrane–membrane fusion or receptor-mediated endocytosis, the microstructures are subject to aggressive enzymatic (proteases, esterases, glucuronidases, phosphatases, nucleases, lipases, etc.) and nonenzymatic (free radicals, acid) degradation inside specialized, low pH (down to pH 1–2) intracellular vesicles called lysosomes (Fig. 5.4). Most of the macrostructure material gets degraded down to its chemical constituents, but some remaining protein fragments can be used by the cells to create immunogenic antigen fragments for lymphocyte presentation on class I or II major histocompatibility complex (MHC) molecules. (The MHC is a transmembrane multiprotein construct for antigen-presentation to cells of the immune system such as T lymphocytes, which are able to create a spe-

cific, antibody-mediated immune response against the presented antigen.) The range of such an immune response reaches from a fast elimination of newly injected micro/nanostructures up to a possibly fatal anaphylactic (allergic) shock. Apart from the obvious loss of material and targeting efficiency, the possible immune response is the main reason why nanostructures for targeted delivery have to be protected from fast uptake into the MPS.

The most important condition for rapid uptake into the MPS [23] is the process of opsonization, defined as the deposition of blood opsonic factors (e.g. fibronectin, immunoglobulins and complement proteins) on the surface of bacteria, viruses, and nanostructures such as liposomes, micelles, nanoparticles, nanocontainers and dendrimers. Once the structures have been labeled by opsonization, the macrophages recognize them with their specialized surface receptors (scavenger receptors, Toll-like receptors (TLRs), Fc receptors, complement receptors, mannose receptors, fibronectin receptors, etc.) and take them up by receptor-mediated endocytosis. Size and surface characteristics of the nanostructures define the opsonization efficiency, the macrostructure–macrophage interaction and thus the clearance kinetics. For instance, smaller polymer-based nanoparticles (below 200 nm diameter) show longer circulation lifetimes than larger ones, but smaller lipid-based nanoparticles show shorter circulation lifetimes than bigger particles [24]. Particles with many available functional groups and stronger polarity also show shorter circulation lifetimes. Lipid-based nanostructures such as liposomes show much shorter circulation life-times than polymer-based nanostructures because of (i) lower physicochemical stability (higher leakage rates in bloodstream turbulences), (ii) better opsonization efficiency, (iii) opsonization-independent receptor interaction of liposome compositions containing phosphatidylserine, phosphatidylglycerol or phosphatidylcholine (all ligands for certain types of macrophage receptors) and (iv) easier uptake into the macrophages because of chemical likeness with the cellular membrane (also based on phospholipids). This allows the macrophages to take up the liposomes by direct membrane-membrane fusion instead of receptor-mediated endocytosis.

Special low-protein absorbing polymeric surfaces such as poly(ethylene glycol) (PEG), poly[*N*-(2-hydroxypropyl)methacrylamide], distearyl phosphotidyl ethanolamine (DSPE) or poly(2-methyl-oxazoline) (PMOXA) can prolong the circulation lifetime of both liposomes and polymer-based nanoparticles by decreasing the grade of opsonization, making it possible to reach the desired therapeutic target before being removed from the circulation. Nanoparticles with these specialized surfaces are referred to as “stealth” particles [24], since they “hide” themselves from the MPS [25].

#### 5.2.3.5 Endothelial Barrier

The endothelial cells cover the interior surface of all blood vessels, and build an important barrier between the blood components and the tissues. The endothelium actively controls the exchange between these two compartments and shows a high grade of impermeability in most tissues. Only a limited number of small molecules such as oxygen, carbon dioxide and water, and small lipophilic molecules

diffuse passively across or along the endothelial membrane according to the concentration gradient. For some macromolecules such as glucose and amino acids, the endothelial cells have active transport mechanisms to ensure a sufficient flow of supplies for the underlying organs. Macromolecules can only leave the circulation through so-called endothelial fenestrations, principally holes between the endothelial cells, and across endothelial clefts at the cell–cell junctions. Organs such as the liver, lymph nodes or the spleen show a well-developed endothelial fenestration with an easily permeable endothelial layer. On the other hand, organs such as the testis, the brain or the spinal cord have a dense endothelial barrier with a small permeability for most drugs and all hydrophilic substances. The specialized endothelium of the brain is called the blood–brain barrier and has no fenestrations.

An important characteristic of the endothelial layer is the increase of permeability under certain pathological conditions, known as vascular leakage [26, 27]. For instance, vascular leakage is a complication that can worsen a systemic inflammatory reaction in the case of a severe bacterial infection, and leads to excessive plasma extravasation into the lung, the skin and the abdomen when plasma proteins can leave the blood vessels through enlarged endothelial fenestrations. On the other hand, it allows the white blood cells to leave the circulation in much higher numbers than under physiological conditions, and increases the oxygen and nutrients supply for the tissue. Vascular leakage is also an early step in the development of atherosclerosis, where lipoproteins leave the circulation and gather inside the inner layers of the blood vessels. Some tumors have leaky vessels, making it easier for the tumor cells to reach the systemic circulation.

On the topic of site-specific drug delivery with nanotechnological delivery systems, it is important to consider the physicochemical properties of the endothelial barrier in different tissues and under different states according to the target, size, surface and functionalization of the carrier. For instance, it is almost impossible for “normal” nanoparticles to permeate through the intact blood–brain barrier; on the other hand, the vessels of aggressive brain tumors are leaky, making it possible to reach the tumor cells with nanoparticles. Another interesting target for delivery of nanoparticles is the so-called vulnerable plaque, defined as an inflamed atherosclerotic lesion of the blood vessel wall with a thin fibrous cap covering an amorphous mass of cell detritus, cholesterol, lipoproteins and collagen. A breakup of this instable system [28, 29] leads to the formation of blood clots and may stop the blood flow in the diseased vessel, resulting in potentially fatal diseases such as myocardial infarction, stroke, skin ulcers, etc. The endothelial layer on the vulnerable plaques is known to be leaky, making it possible for nanoparticles to reach the inflamed fibrous cap and influence the diseased state.

#### 5.2.3.6 Cell Membrane

The passage across the cell membrane is the last and possibly the most difficult hurdle for targeted delivery of macromolecules because of the complex nature of the membrane, and the variety of different receptors, channel proteins, cell surface functionalizations and transport systems [30, 31]. The membrane consists mainly of phospholipids, cholesterol and proteins building a hydrophilic–hydrophobic–

hydrophilic triblock bilayer membrane stabilized by structure proteins and intercellular connections. Integrated into the bilayer membrane are different transmembrane and nontransmembrane proteins with functions such as ion channels, glucose and amino acid transporters, receptors for ligands, cell communication receptors, cell–cell adhesion, etc.

Small, nonpolar molecules such as oxygen, carbon dioxide or nitrogen dissolve in the lipid bilayer and diffuse passively into the cell according to the concentration gradient. The same applies to small, noncharged molecules such as water or ethanol. Bigger molecules (e.g. glucose, amino acids or urea) and all charged molecules (e.g. sodium, potassium, chlorine or magnesium) have only a limited possibility of passive transmembrane diffusion, making it necessary for the cell to set up transport systems for essential molecules (as described in previous subsections).

When discussing the delivery of macromolecules such as nanoparticles into the cells, one has to be aware that most cells are not intended to take up macromolecules and the nanoparticles have to use transport systems with a different purpose than “nanovehicle transport”.

The first step in the transmembrane transport of macromolecules is the binding of a ligand to a specific cell surface receptor. Some receptors answer the ligand binding with a complex process called endocytosis that can be divided into phagocytosis and pinocytosis (Fig. 5.4). Phagocytosis means the uptake of micrometer-sized structures such as bacteria and fungi, which can only be done by specialized phagocytic cell types of the innate immune system such as macrophages, granulocytes, and dendritic cells. These cell types have special cell surface receptors such as (i) Fc receptors (for immunoglobulins bound to bacteria), (ii) complement receptors (for proteins of the complement system, which plays a major role in inflammation, immune defense and tumor cell killing), (iii) scavenger receptors [32–36] (for polyanionic molecules such as lipoproteins, polysaccharides and polynucleotides) and (iv) mannose receptors [37] (for mannosylated/*N*-acetylglucosamine-terminal and fucosylated glycoproteins) that stimulate phagocytosis of the mentioned macromolecules. Pinocytosis is possible for all other cell types and is restricted to nanometer-sized structures such as viruses, proteins, lipoproteins, transferrin, cholesterol, etc.

On a molecular level, pinocytosis occurs on different, energy-consuming pathways, e.g. clathrin-mediated, caveolin-mediated, or clathrin- and caveolin-independent. Clathrin-mediated endocytosis is the most important entry pathway for macromolecules in cell types other than phagocytes and is triggered by ligand–receptor binding. It starts with the binding of the protein clathrin to the intracellular part of the transmembrane receptor, followed by the creation of small cell membrane pits. Then the cell membrane pits with the ligand–receptor complexes are dragged into the cell by the cytoskeleton and form enclosed, clathrin-coated vesicles that finally lose the contact with the cell membrane. Once the vesicle is created, it starts to “uncoat” the clathrin coating, allowing the fusion with other intracellular compartments such as lysosomes for degradation and receptor recycling (Fig. 5.5).

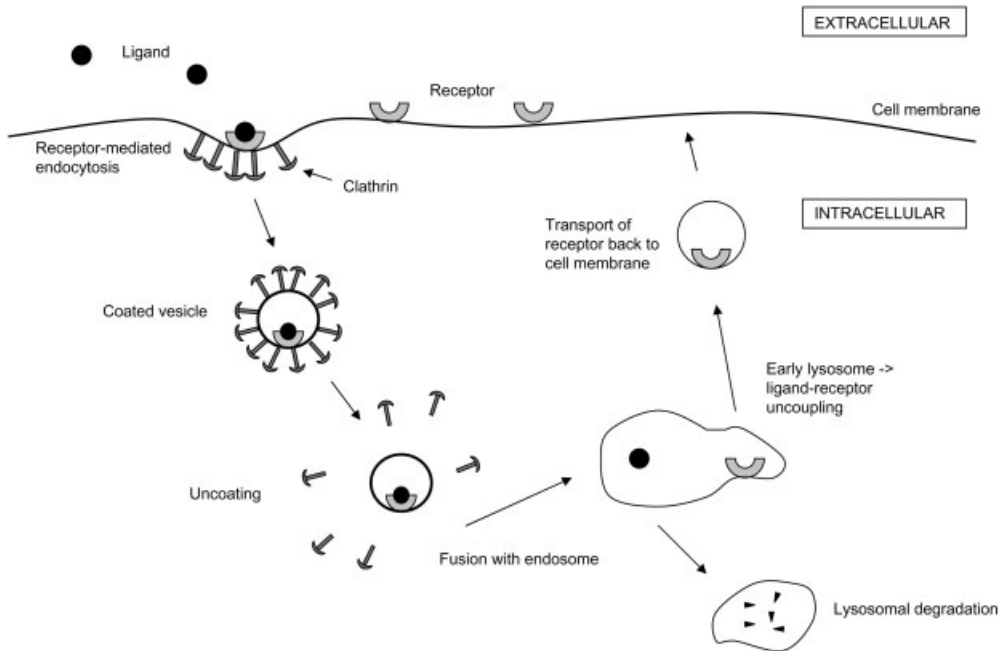


**Figure 5.5.** Schematic drawing of clathrin-mediated endocytosis (for details refer to main text).

During the process of phagocytosis, the phagocytic cell launches a signaling cascade that results in the formation of cell membrane protrusions that surround the pathogen and engulf it into so-called phagosomes, comparable to giant intracellular vesicles. The content of the phagosomes (bacteria, viruses, nanoparticles) is then attacked by lysosomal enzymes, free acids, and radicals, resulting in a degradation and inactivation of the macrostructure.

For targeted delivery of nanostructures, one has to overcome the inactivating lysosomal pathway when trying to cause a therapeutic impact on intracellular targets in the cytoplasm or nucleus.

### 5.3 Strategies for Targeted Delivery – Observed in Nature

#### 5.3.1 Outline

When discussing the use of nanotechnologies for targeted delivery, it is essential not to forget the enormous range of “natural micro/nanostructures”. Bacteria, viruses, fungi, parasites, prions, etc., have evolved over a long period and have spe-



cialized in targeted delivery to targets inside macroorganisms against strong defense mechanisms. To avoid the various defense systems, the microstructures had to develop specialized strategies for adherence, barrier invasion, immune system evasion, targeting and growth.

Obviously, understanding these microorganism strategies is important when trying to develop “artificial micro/nanostructures” for targeted delivery, because it is easier copying an existing targeting strategy than developing a new one. Further, there is no reason why well-tested strategies evolved during the long evolutionary fight between macro- and microorganisms should not work in a similar context like nanostructure delivery. It is also important to show that targeted nano/microstructure delivery is possible through other pathways than parenteral injection. To realize the different possibilities to reach a target inside the body by oral or transbronchial application might perhaps help to break the paradigm that says that nanoparticles can only be delivered by parenteral injection. Apart from this, it allows understanding the defense strategies of the human body from a different perspective and displays the need for a deeper understanding of the complex molecular pathways.

Here, we will discuss major strategies for barrier permeation, immune system evasion, and targeted delivery of bacteria, viruses, and prions. It is not the idea create an outline over all existing pathogenic strategies, but to highlight some of these strategies. Refer to the references section for a deeper insight into certain topics of interest.

### 5.3.2

#### **Bacteria**

To set up an infection of a macroorganism, bacteria have devised a vast range of strategies, also called virulence factors [38, 39]. Here, we will concentrate on two features of bacterial strategies that might become helpful for the design of artificial complex nanostructures for targeted delivery: host invasion and immune system evasion.

##### 5.3.2.1 **Host Invasion**

The first defense mechanism pathogenic bacteria meet when they try to invade a macroorganism is the native bacterial flora of the skin or the gastrointestinal tract, which consists of normally harmless bacteria that prevent the newly gained pathogenic bacterium from growth and invasion. By successfully erasing or suppressing this protective flora, the bacterium sets up its own nutritive environment on the skin or inside the gut. Iatrogenic (physician-made) elimination of the native flora of the gut by antibiotics also allows the spread of pathogenic bacteria such as *Clostridium difficile*.

The next step of the bacterial attack is bacterial adherence on outer body surfaces such as skin and mucosal epithelium of the respiratory and gastrointestinal tract. As we have discussed above, the outer layer of the body is build of impermeable epithelial barriers that protect the body from the entry of potentially harmful

macromolecules and structures of complex functionality. Most bacteria cannot cross the intact epithelial barrier, and can only reach the interior of the body and blood vessels through small mechanical lesions in the epithelial barrier. In particular, the skin is a reliable barrier for bacteria invasion because of the two-compartment, multilayered organization. Permeation across the single-layered epithelium of the mucosa of both the respiratory and gastrointestinal tract is much easier, and can be achieved by specialized bacteria even under physiologic conditions (no mechanical damage to the epithelium). These bacteria have special surface structures for adherence to the epithelial layers, called pili (also called fimbriae) and nonfimbrial adhesins [40]. Pili are rod-shaped protein structures on the cell walls of the bacteria consisting of long cylindrical protein subunits in a helical array. The continuously produced subunits are added from the pili interior and extend the pilus outward. The tip of the pilus adheres and binds to host cell molecules on the surface of the epithelial cells such as glycoproteins and glycolipids. Nonfimbrial adhesins are similar cell-contact structures like pili. The cell adherence structures are specific for certain host cell surface molecules and are one explanation for the tissue tropism of most bacteria (e.g. *Streptococcus mutans* colonizes teeth, but not the epithelium of the tongue). Once the bacteria has fixed the contact with the epithelial cell, it can perform a tighter binding to the cell by other bacterial proteins that can bind to surface structures such as different host cell receptors for cell–cell contact or signal transduction.

The next step is the passage across the intact epithelial layer or the invasion into the epithelial cells. Possible pathways for transepithelial passage without invasion or destruction of the epithelial cells involve paracellular entry, translocation through the M cells and luminal capture by dendritic cells [41].

The easiest method is to profit from temporary disruptions of the dense and normally impermeable cell–cell bonds caused by the paracellular transmigration of polymorphonuclear leucocytes (white blood cells) from the subepithelial tissue into the gut following an inflammatory signal. Leucocytes have the ability to weaken the intercellular connections by enzymatic degradation and cross the epithelial layer actively. Some bacteria such as *Shigella* can use these temporarily created intercellular holes to permeate across the epithelial layer without harming the cells.

The M cells, specialized phagocytic cells, are part of the mucosa-associated immune system and are placed inside the epithelial layer where they constantly take samples of the luminal flora for immunologic controlling. Some bacteria families such as *Shigella*, *Salmonella*, *Yersinia* and *Listeria* have different methods to evade the lysosomal destruction inside the M cells and can leave the M cells without loss of function. While *Listeria* have the ability to escape into the cytoplasm with their pore-forming protein listeriolysin O [42] and *Salmonella* can remodel their phagosomes for intracellular growth with the protein Spi2, *Yersinia* have an antiphagocytic strategy that inactivates the actin cytoskeleton by intracellular injection of the proteins YopE, YopH and YopT. Finally, *Shigella* can synthesize intracellular factors that cause the apoptosis (controlled cell death) of M cells, macrophages and monocytes, leading to the release of the unharmed *Shigella* bacterium after phagocytosis. *Shigella* is even able to synthesize cytokines (substances for cell–cell communica-

tion) such as IL-1 $\beta$  and IL-18 that disrupt epithelial impermeability and simplify further bacterial invasion on a paracellular pathway. All of these mechanisms allow the bacteria to cross the epithelial layer without having to kill the epithelial cells [41].

The last pathway for transepithelial passage without epithelial cell invasion is the luminal capture by dendritic cells. Dendritic cells are phagocytic cells of the innate immune system comparable to macrophages. They are not a constant part of the mucosa like the M cells, but have the ability to crawl between two epithelial cells or to send cell extensions called pseudopods through the intercellular compartment into the gut lumen. The pseudopods capture luminal bacteria and phagocyte them for degradation and detection. The bacteria mentioned above have strategies for phagocytosis evasion and can reach the systemic circulation once they leave the dendritic cells. Some bacteria such as the *Salmonella* family can even travel inside the dendritic cells as “blind passengers”.

Another method for transepithelial migration is the direct and active (not by phagocytosis [43]) invasion into the epithelial cells; these cell-invasion strategies [41] are more complicated than the methods we have met until now and require sophisticated molecular mechanisms. Bacteria such as *Yersinia pseudotuberculosis* or *Listeria monocytogenes* [44] express proteins such as invasins, internalins or InlB that can bind to surface receptors (mostly receptors for cell-matrix or cell–cell adhesion such as integrin, E-cadherin or Met) of the host cell, leading to a clustering of the bound receptors and a forming of vacuoles that engulf the bacterium through a so-called “zipper” mechanism. The ligand–receptor binding starts a cascade of signals (e.g. protein phosphorylation, recruitment of adaptors and effectors), resulting in an activation of actin cytoskeleton units and finally bacterial internalization through developing membrane extensions that enclose the bacterium.

Other bacteria such as *Shigella* or *Salmonella* can bypass the step of adherence to the host cell and interact directly with the intracellular actin cytoskeleton by injecting effectors through a secretory system that triggers the formation of macropinocytotic pits for bacterial entry. A key constituent of this “trigger mechanism” is the type III secretory system [45–48] – a complex multiprotein structure comparable to an injection needle of a syringe. The tip of the secretory system recognizes the surface of the host cell and triggers the insertion of an IpaB/C or SipB/C [49, 50] translocation pore into the cell membrane. This translocation pore allows permeation of the proteins IpaC and SipC that force the cell to form the mentioned macropinocytotic pockets by actin cytoskeleton nucleations, and of a protein called VirA that stimulates local destabilization and depolymerization of microtubules, another part of the cytoskeleton. In a next step, more proteins such as SopB/SigD, SopE or IpgD are injected through the type III secretory system and stimulate actin rearrangements and bacterial entry. In the last step, the macropinocytotic pocket closes, triggered by the injected proteins SptP and IpaA.

One major effect of these complex mechanisms is the direct invasion into intracellular vesicles or even into the cytoplasm without having to survive the direct contact with the lysosomal compartment. The bacteria can now persist inside the

epithelial cell and usually start intracytoplasmic reproduction, finally resulting in host cell killing. The newly created bacteria now can reach the well-perfused subepithelial tissue, where they can enter the blood vessels through the endothelial fenestrations.

Once the bacterium reaches the interior of the body, it has to evade the host defense if it wants to survive. In the tissue or inside the blood vessels, the bacterium meets the cellular and noncellular parts of both unspecific (innate) and specific (adaptive) immune system.

### 5.3.2.2 Immune System Evasion

One essential requirement for “targeted delivery” of complex structures such as bacteria is the ability to survive in the tissue and in the bloodstream by evading, suppressing or tricking the immune system of the host organism. The immune system [51, 52] consists mainly of the unspecific, innate immune system and the specific, adaptive immune system. The unspecific immune system organizes a first defensive barrier against microorganisms such as bacteria, fungi and parasites. It consists of noncellular (humoral) elements such as the complement system, the acute-phase proteins, the interferons and bactericidal substances such as lysozyme. Then cellular elements such as the epithelial layers, the native microbial flora and the white blood cell granulocytes (neutrophilic, basophilic and eosinophilic), mast cells, monocytes, macrophages, natural killer (NK) cells and dendritic cells. The specific immune system consists of the humoral element antibodies, and the cellular elements B lymphocytes, T lymphocytes and plasma cells. It is responsible for targeted defense against bacteria, viruses, allogeneous cells and tumor cells with molecule-specific antibodies and target-specific killer cells.

Bacteria have mainly specialized in manipulating the innate, unspecific immune system with several different strategies [53, 54]. We will discuss some of them to show successful strategies for innate immune system evasion that might be helpful for targeted delivery of artificial micro/nanostructures.

Recognizing microbial molecules by germline-encoded receptors such as the transmembrane TLRs [55, 56] of macrophages and dendritic cells, an important receptor family for the innate recognition of various microorganism, activates the innate immune system. One of the best-characterized of the TLRs is TLR4, which can bind lipopolysaccharides, an essential part of the cell wall of Gram-negative bacteria (e.g. *Escherichia coli*, *Salmonella*). Binding of a bacterium is a condition for uptake into the phagocyte and for the inflammatory cytokine response. On the other hand, many bacteria have manipulative systems that alter the function of the TLR4 system and enable an infection of the host organism. The *Shigella* bacterium, for instance, synthesizes a surplus of free lipopolysaccharides (also called endotoxins) that bind and block TLR4 of macrophages and stimulate an inflammatory response. As we have seen above, this inflammation can lead to a higher permeability of the intestinal epithelium and to a higher grade of bacterial invasion [57].

Bacteria such as *Yersinia pestis*, *Helicobacter pylori* and *Chlamydia trachomatis*, on the other hand, synthesize a slightly changed version of the free lipopolysaccharide that also blocks all TLR4, but that does suppress the inflammatory response in-

stead of stimulating it. Thus, the bacterium decreases the efficiency of the immune response and increases its own chance of surviving.

Some pathogenic members of the *Yersinia* family such as *Yersinia enterocolitica* and *Y. pseudotuberculosis* can be considered as specialists for immune system suppression. Not only do they block the TLR4 system with modified free lipopolysaccharides, they can also suppress phagocytosis (see above) and inflammatory response by injecting proteins such as YopM, and by the synthesis and secretion of the immune-suppressive V antigen [47]. The V antigen binds to another TLR, the TLR2, and activates IL-10- and CD14-dependent pathways that lead to immunity downregulation.

The bacterium *L. monocytogenes* produces a membrane-perforating protein to escape the lysosomes as we have seen in the last subsection. Once it reaches the cytoplasm of the macrophages, it can persist there and multiply by forcing the macrophage to produce the cytokine IFN- $\beta$  that suppresses the ability of the macrophage to fight the infection of its own cytoplasm [42, 58, 59].

Another specialist for innate immune system evasion is the bacterium *Mycobacterium tuberculosis*, responsible for the tuberculosis infection. Similar to *L. monocytogenes*, *M. tuberculosis* has various potent strategies [60] that allow the bacterium to survive and multiply inside macrophages [61]. For instance, it can suppress the response of the innate immune system by (i) downregulating the expression of the cytokine IL-12 [62], (ii) by blocking the response of the macrophage to the cytokine IFN- $\gamma$  that normally increases the ability and efficiency of the phagocytosis process [63], and (iii) by surrounding its own cell wall with stable and impermeable complex lipids, peptidoglycans and waxes [60] that protect the bacterium from the lysosomal enzymes.

Instead of surviving inside the macrophages or dendritic cells, some bacteria such as Enteropathogenic *E. coli*, *Pseudomonas aeruginosa* and *Yersinia* have strategies that prevent them from being subject to phagocytosis. As we have learned above, these bacteria can inject “antiphagocytic” substances (e.g. ExoS, ExoT, YopH, YopE and YopT) [64–68] into the phagocytic cells with their type III secretion system before the macrophage can bind the bacterium.

Other intracellular bacteria, *Legionella pneumophila* [69] and *Brucella* [70], use a type IV secretion system [71–73] to degrade the function of host lysosomes by intercepting intracellular vesicles from the endoplasmic reticulum that contain the lysosomal enzymes and to stop the presentation of bacterial antigens on class II MHC molecules [74, 75]. *C. trachomatis* [76] and *Chlamydia pneumoniae* [77], also obligate intracellular bacteria, have sophisticated strategies that can block the transition from innate to the adaptive immune system, thus making it hard for the immune system to remove the infected phagocytes. The *Chlamydia* bacteria secrete a proteolytic enzyme called chlamydial protease-like activity factor (CPAF) that degrades the host cell molecules RFX5 and USF-1 – transcription factors essential for activation of class I and class II MHC molecules that would present some *Chlamydia* antigens to lymphocytes for adaptive immune system activation.

The last bacterium we want to discuss here is *Streptococcus pyogenes*, which has evolved complex strategies to evade the inactivation by cells of the innate immune

system, in this case by the granulocytes (also called polymorphonuclear leukocytes) [78]. Normally granulocytes can kill invading bacteria and fungi by both phagocytosis and different microbicidal systems such as superoxide, reactive oxygen species, hydrogen peroxide and hypochlorous acid. *S. pyogenes* has the ability to inhibit the recruitment of new granulocytes to the site of infection by producing a serine endoprotease (C5a peptidase) that degrades and inactivates a potent host-derived chemotactic factor of the complement system, C5a [79].

Perhaps the most important defense strategy for our purpose is the ability of *S. pyogenes* to evade the opsonization by plasma proteins that would result in an efficient and fast clearance by phagocytes. To achieve this antiopsonic strategy, the bacterium has a dimeric coiled-coil surface protein called M protein that binds certain nonopsonic factors of the complement system such as C4b-binding protein, factor H, factor H-like protein and the plasma protein fibrinogen. In that way, it impedes the binding of the potent opsonic factor C3b to the bacterial surface [80]. Further, the bacterium produces a protein (Streptococcal inhibitor of complement, Sic) that inhibits the formation of the so-called membrane attack complex (MAC) [81, 82], the final cytotoxic formation of the complement factors C5b–C7 that would eventually perforate the bacterial wall (see below). Streptococcal pyrogenic exotoxin B (SpeB), another secretion product of the bacterium, inhibits opsonization and phagocytosis by cleaving opsonic factors such as fibronectin and vitronectin. Further, it blocks the granulocyte function by activating a metalloprotease and the pro-inflammatory and granulocyte-toxic cytokine IL-1 $\beta$  [83]. Finally, *S. pyogenes* produces the enzyme endoglycosidase (EndoS) that inactivates humoral antibodies directed against the bacterial surface for opsonization purposes, thus decreasing the possibilities for antibody-mediated phagocytosis [84].

*S. pyogenes* has also some interesting physical barriers that protect the bacterium against phagocytosis. A hyaluronic acid capsule composed of *N*-acetylglucosamine and glucuronic acid repeats offering a certain grade of phagocytosis protection covers the cell wall and inhibits the direct interaction of opsonins on the bacterial surface with granulocytes [85]. To increase the physical protection, *S. pyogenes* can cover itself with a matrix of fibronectin and collagen [86], and can even build aggregates with other bacteria, which as a result are difficult to remove for the immune system.

### 5.3.3

#### Viruses

When discussing the impact of nanotechnology for targeted delivery in biological systems, viruses are the best example found in nature and can be readily compared to artificial nanometer-sized structures such as nanocontainers. Viruses are nanometer-sized (15–300 nm diameter) complexes with a simple composition of a facultative lipid bilayer envelope with glycoproteins (viruses can be distinguished into viruses with an envelope and viruses without an envelope), a few enzymes such as reverse transcriptase, RNA polymerase or kinases, and a central nucleo-

protein complex called a capsid containing the viral DNA or RNA. Viruses themselves have no means of independent locomotion or growth and depend on host cell metabolism. Once they enter the host organism, they have to penetrate the different defense barriers such as mucus layer, epithelial layer, immune system, endothelial layer and finally the cell membrane of their target cell. Here, we will discuss some important virulence factors of different viral species and we will show their enormous ability for target-specific delivery of their content in biological systems. We will also briefly discuss the current state of viral gene therapy and the impact of nanotechnology in gene therapy.

#### 5.3.3.1 Immune System Evasion

Due to the much smaller size compared with bacteria and because of the intracellular reproduction, fighting viral infections is much more difficult for the immune system [87, 88]. To be able to recognize and inactivate the free virus, the immune system has to label the viral surface with opsonins such as unspecific complement factors or specific antibodies. As complement system activation is an important condition for an effective innate and adaptive immune response, most viruses have strategies to evade or manipulate the complement system [89, 90].

The complement system is a defensive method of the humoral innate immune system and consists of an interacting set of plasma enzymes (called C1–C9) synthesized in the liver, and in different cell lines such as monocytes, fibroblasts, endothelial cells and neurons (nerve cell). The complement system can be activated to perform a cascade of reactions leading (i) to the recruitment of antibodies, more complement factors and phagocytic leucocytes to the site of infection by producing potent anaphylatoxins (C3a–C5a), (ii) to the opsonization of viruses and virus-infected cells, and (iii) to the destruction of microorganisms and cells by the final ring-shaped, membrane-perforating MAC (consisting of activated C5–C9) [51]. The complement system activation can be achieved by three different pathways. (i) Classically by binding of the factor C1q to antibody–antigen complexes or certain viruses or virus-infected cells [91–94]. (ii) Lectin-mediated by binding of the mannan-binding lectin protein to oligosaccharides with unprotected repetitive carbohydrates such as mannose on certain viruses or virus-infected cells [95–97]. (iii) Alternatively by spontaneous and indiscriminate breakdown of the factor C3 in the serum or on surfaces of cells or particles when lacking sufficient levels of endogenous complement-regulating proteins such as C1 inhibitor factor 1 (C1-Inh), complement receptor 1 (CR1), decay-accelerating factor (DAF), protectin and Factor H [98–100]. Normally these factors inhibit the complement activation. All three pathways result in the terminal activation of a C3 convertase enzyme that activates C3 by cleavage. Active C3 activates C5, which launches the creation of the MAC. Viruses have a wide variety of complement-evading strategies; we will discuss some of them.

By forcing the virus-infected cell to shed or internalize antibody–antigen complexes on their surface, viruses from the families Herpes and Corona can obstruct the classical complement activation [101]. Further, Herpes and Pox viruses can produce and express proteins such as vaccinia virus complement control protein

(VCP) [102], glycoprotein C1 (gC1) [103, 104], glycoprotein C2 (gC2) [105] and complement control protein homolog (CCPH) [106], with functional likenesses [89] to the complement-regulating proteins that suppress the complement activation (see above). Some viruses of the families Pox [107], Herpes [108], Retro [109–112] and Toga [113] that cannot produce these proteins themselves are able to incorporate some of the complement-regulating proteins produced by the host organism into their envelope or to force the virus-infected cell to synthesize and secrete these proteins.

Another interesting strategy found in some Herpes [114, 115] and Corona [116] viruses enables these viruses to express Fc receptors (receptors for antibody binding) on the viral envelope or on the infected host cell. The Fc receptor binds non-immune immunoglobulin G (IgG) and protects the virus or the virus-infected cell by sterically blocking the binding of virus-specific IgG [117], and by decreasing the efficiency of an antibody-mediated immune response [118].

### 5.3.3.2 Host Cell Invasion

If a virus wants to multiply, it has to invade a potential host cell [119, 120], has to deliver its capsid and the content of the capsid into the cell, and has to force the infected cell to create new viruses by adding its own genetic information of DNA or RNA to the synthetic machinery of the host cell. One important point is the attachment to the host cell membrane and the invasion into the cell without damaging the cell and without creating an immune response that would finally kill the infected cell.

The first step of cell invasion is the attachment to cell surface proteins, carbohydrates, or lipids that can serve as pure anchors for the virus or can mediate its uptake. The most important cellular receptors for viral attachment are intercellular adhesion molecule (ICAM)-1, integrins, CD4,  $\alpha$ -dystroglycan, MHC-I, CXCR4, CCR5, CD46, DAF, CAR, LDLR, PVR, aminopeptidase-N, heparan sulfate glycosaminoglycan, and sialic acids [120].

One well-studied virus, HIV, even binds to multiple attachment factors such as C-type lectin receptors, the ICAM-3-grabbing nonintegrin (DC-SIGN) found on dendritic cells, and the ICAM-3-grabbing nonintegrin (L-SIGN) [121, 122] found in liver and lymph node tissue. Once HIV attaches to its target cell (macrophage, T lymphocyte, dendritic cell), its envelope-bound glycoprotein 120 binds to a surface receptor of the host cell, CD4, and changes its conformation – a condition for the final binding of glycoprotein 120 to the host cell co-receptors CXCR4 or CCR5 [123]. Only by cobinding to both CD4 and CXCR4 or CCR5 can the virus switch its envelope to the fusion-competent conformation [124, 125].

Attachment and binding factors used by other viruses are (i) heparan sulfate proteoglycans (binding site for glycoprotein C of alphaherpes viruses, for Dengue virus, for papilloma virus), (ii) sialic acid groups (for hemagglutinin of influenza virus, for myxo- and paramyxoviruses) [126], (iii) Herpes entry mediator A HVEA (for glycoprotein D of herpes simplex virus 1) [127], (iv) gangliosides GM<sub>1</sub>, GD<sub>1a</sub> and GT<sub>1b</sub> (for VP1 of polyoma virus) [128, 129], and (v) human lymphocyte antigen (HLA)-DR (for gp43 of Epstein–Barr virus) [130].



For viruses without an envelope, the next step is the endocytosis (clathrin-mediated, caveolin-mediated or clathrin- and caveolin-independent [131]) of the bound capsid that allows the virus to cross the barrier of the cortical cytoskeleton, and to reach deep intracellular structures such as the lysosomes, the endoplasmic reticulum and the Golgi complex [132, 133]. For some viruses the decrease in pH in the endo-lysosome acts as a molecular trigger for membrane penetration mechanisms [134–136]. For most viruses the activation starts at pH 6–6.5, matching early endosomes [137, 138]. Endosome escape is possible by different mechanisms. Adenoviruses become membrane-lytic at low pH and leave the ruptures endosomes intact [139, 140]. Reoviruses can expose a hydrophobic capsid peptide that makes the capsid membrane lytic [141]. Picorna viruses have the ability to sink into the bilayer and to form a protein-lined channel for the viral RNA in the endosomal membrane by exposing a myristic acid end group of the protein VP1 [142].

These methods allow the virus or its genetic information to leave the lysosomal pathway before the enzymatic environment reaches its full degrading power that would inactivate the virus. Further, the lysosomal escape prevents the virus from being subject to an adaptive, MHC-mediated immune response, because the cell does not have any viral antigens to present to lymphocytes on the MHC complex. After leaving the lysosomal compartment, the viral capsid can use the cytoskeleton or intracellular transport motor proteins [143, 144] to reach the cell nucleus or specific cytoplasmic membranes.

Viruses with a protective envelope around the capsid cannot only reach the cell interior by endocytosis as the nonprotected viruses, they can also perform a “simple” membrane fusion to reach the cell. As the protective envelope is a lipid bilayer, membrane fusion is theoretically easy and comparable to the fusion of liposomes and target cells. More complicated is the mechanism that protects the enveloped viruses from fusion with every available cell and allows the membrane fusion only with the desired target cell, thus ensuring a targeted delivery. Membrane fusion is triggered by events such as binding to specific cell surface receptor or a decrease in pH [142, 145], on which the viral envelope changes its conformation and allows the fusion with both host cell membrane and lysosomal membrane.

Viruses have two different fusion factors that can induce the mentioned conformation changes of the lipid bilayer. Type I factors found in the influenza virus consist of homotrimeric spike glycoproteins with coiled-coil subunits and can insert exposed hydrophobic fusion sequences of a lower energy conformation into the target membrane on activation. The released free energy forces both viral and target membranes closer together, resulting in a membrane fusion [124, 126, 146]. Type II factors found in flaviviruses and alpha viruses [147] build a heterodimer with another viral membrane protein and can change their quaternary protein structure after a pH decrease. The fusion subunits of these two proteins dissociate and build a new active homotrimer [148, 149] that forces the membrane fusion. One major advantage of the membrane fusion strategy is the possibility to reach the cytoplasm direct without the complicated way through the receptor-mediated endo-lysosomal system.

To be able to reach the cellular reproduction machinery, the virus capsid has to cross the membrane of the cell nucleus [150–152], mainly through nuclear pore complexes [153–155] that allow the passage of particles up to a diameter of 39 nm [156]. To activate this transport system, the virus has to bind to cytoplasmic import receptors. For example, HIV and adenovirus bind to importin  $\beta$ , and papilloma viruses, hepatitis B virus and influenza virus bind to importin  $\alpha$  and  $\beta$  [157–161].

Larger viruses and capsids have to deform or disassemble to allow the DNA or RNA to reach the nucleus. Adenovirus disassembles its capsid after binding to a subunit of the nuclear pore and releases its DNA for transmembrane passage [162]. The large capsid (diameter 120 nm) of herpes simplex virus 1 also binds to the nuclear pore and releases its DNA direct into the pore without disassembly of the capsid [163, 164], leaving the empty capsid bound to the nuclear pore.

### 5.3.3.3 Viral Vectors for Therapeutic Applications

Genetically modified viruses have been used in a wide range of experiments in gene therapy [165, 166] of both hereditary diseases and acquired illnesses such as cancer. The promising idea is to use the sophisticated viral targeting strategies without having to create new lipid-, protein- or polymer-based nanoparticulate carriers for targeted delivery of missing or defective genes to the diseased cells. After replacing the viral DNA with the necessary human sequence vector, the modified virus is applied to the patient and consequently targets its natural host cell according to its surface properties. The genetically modified virus enters the host cell and delivers its genetic content to the cell nucleus, where it can be integrated into the host cell genome.

After first successful results with retrovirus-based gene therapy of patients with different forms of severe combined immune deficiency [167–169] (mostly fatal disorders of the immune system in young children), the field of virus-mediated gene therapy suffered some setbacks such as a lethal complication in a trial of adenovirus-based gene therapy of a metabolic disease and the induction of leukemia in a retrovirus-based gene therapy trial [170–172]. It also became obvious that successful and efficient gene therapy is much more difficult than originally thought because of (i) low *in vivo* targeting efficiency of the used viral vectors, (ii) inadequate targeting specificity resulting in an unwanted gene expression in healthy tissues, (iii) inappropriate integration of the gene vector into the host genome resulting in a long-term decrease in targeted gene expression and (iv) safety problems with insufficiently replication-deficient viral vectors [165]. We will present some widely used targeting systems based on viruses in areas other than cancer therapy.

One well-established virus for gene therapy is the adeno-associated virus [173, 174], popular because of its efficient gene delivery and long-term expression. Disadvantages are its low target specificity with more or less randomized gene delivery, its low gene packing capacity (less than 4000 bases), problems with activation of endogenous genes and problems with pre-existing antibodies in many patients, which lead to inactivation of the viral vector before it can reach the

target cell. Adeno-associated virus-based gene therapy has been tried for patients with type IX hemophilia [175] (bleeding disorder), cystic fibrosis [176],  $\alpha_1$ -antitrypsin-deficiency [177], peripheral arterial occlusive disease [166] and spinal cord injury [178].

Another popular gene therapy vector is the adenovirus [179–181], known to produce high-titer virus stocks and efficient long-term gene expression. Disadvantages are the strong immunogenicity (especially insufficiently inactivated viral vectors [182]), pre-existing antibodies in most patients (adenovirus is a common virus and makes airway infections) and limited packing capacity of less than 7500 bases. Adenoviral gene vectors have been used for the treatment of brain cancers [183], pulmonary diseases [177] and neurological diseases [184].

The next interesting virus is the herpes simplex virus, popular because of its high packing capacity (above 30 000 bases), good long-term expression, high target specificity for neuronal cell lines, and low toxicity when using gene-deleted non-toxic vectors [185, 186]. Application fields for the use of herpes simplex virus-based gene therapy are various neurological disorders [187] and muscular dystrophy [188].

The last group is the family retrovirus [189], commonly characterized by the enzyme reverse transcriptase that allows the virus to integrate its genetic information precisely into the host genome without the aid of host cells enzymes. Members of the retrovirus family used for gene therapy are HIV [190] and the murine leukemia virus [169] – the pioneer virus for gene therapy. Advantages of the retroviruses are the efficient long-term gene expression, the precise genome integration and the good packing capacity of about 8000 bases. The major disadvantage is the risk of oncogenesis because of an activation of oncogenes after integrating the therapeutic gene into the host genome [166]. Retroviruses are usually restricted to dividing cells; only by modifying the viral envelope (e.g. fusion with other viruses [191]) can the vector also transfect nondividing cells. Retroviruses have been used for gene therapy of hematopoietic disorders [192], immune system deficiencies [167], central nervous system diseases [193] and chronic granulomatous disease [194].

In past years, nanotechnology has enriched the field of virus-based gene delivery with new materials and new ideas, which might help to overcome some of the short- and long-term problems of potentially infectious viruses. In a new approach with adenoviruses, the viral envelope was covered with poly[N-(2-hydroxypropyl) methacrylamide] to protect the virus from inactivating antibodies [195]. Further, fibroblast growth factor (FGF) and vascular endothelial growth factor (VEGF) were incorporated into the polymer to enable a higher grade of target specificity to FGF or VEGF receptor-positive cell lines such as endothelial cells [195].

Other research groups went further and built a chimerical gene carrier consisting of a plasmid DNA encapsulated in liposomes, which themselves were covered with a viral envelope with viral targeting proteins [196] (Fig. 5.6). The construct is called a virosome, and was used for gene delivery to vascular smooth muscle cells [197] and hepatocytes [198]. Disadvantages of the virosome-based delivery system

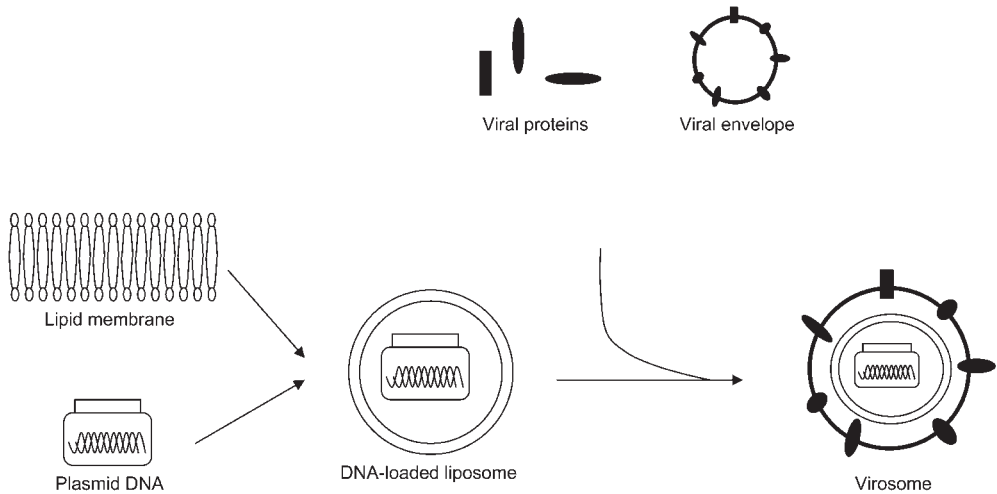


**Figure 5.6.** Schematic drawing of virosome synthesis. In a first step, a viral-derived and usually genetically modified plasmid DNA in a viral capsid is covered with a liposomal bilayer membrane. In the next step, viral proteins are

added to the liposome for targeted delivery or the whole liposomal complex is again covered with a viral envelope, resulting in the formation of the artificial “virosome”.

are the antigenicity of the viral proteins [196] and the high uptake into the MPS because of the liposomal constituents.

#### 5.3.4

##### Prions

Prion is the abbreviation for proteinaceous infectious particle [199–201] and describes the main characteristics of this fascinating infectious agent simply consisting of a badly conformed peptide of 27–30 kDa called prion protein (PrP). It is most surprising that a small peptide with almost no virulence factors, no genetic information, and no protecting envelope, membrane or hull can persist for years or even decades in the host organism and can cause fatal neurodegenerative (spongiform vacuolation and loss of neuronal cells) diseases such as the transmissible spongiform encephalopathies (e.g. bovine spongiform encephalopathy in cows and scrapie in sheep) and Creutzfeldt–Jakob disease in humans [202–204]. Here, we will discuss some important strategies that enable the prion to invade the host organism, to evade the immune system defense, to persist in cells of the innate and adaptive immune system, and to reach its target cells in the central nervous system [205]. It is important to bear in mind that these principles might become helpful for the targeted delivery of artificial protein-based nanoparticles. On the other hand, the prion pathogenesis is a warning example that illustrates the various paths

nanoparticles can take in a complex organism, and the huge damage even small particles can cause even after years and decades.

Prions reach the host orally and enter the organism mainly in the small intestine [206, 207] by both M cell-mediated [208] and dendritic cell-mediated luminal capture (as described above for bacteria). After binding or taking up the prions, the infected dendritic cells localized in specialized lymphatic tissue in the gut wall called Peyer's patches can infect other dendritic cells or lymphocytes [209–211]. On the surface or inside the dendritic cells and the lymphocytes, the prions can persist with the help of yet unknown mechanisms and can even “multiply” by passing on their pathological conformation onto normal cellular host-encoded prion protein (PrP<sup>c</sup>) [212–214]. Further, B-type lymphocytes [215] and complex cytokine functions [203] have been discovered as the main mechanisms responsible for prion spread and for neuroinvasion. One of the few facts is that the prions can spread to various lymphoid organs with a high concentration in the spleen [216].

The next step in the prion pathogenesis is the path from the widely infected lymphoid tissue to the nervous system. It is believed that dendritic cells of spleen and especially Peyer's patches [217, 218] play a major role by setting up a close contact with nervous endings of peripheral nerves. The prions cross the space between the dendritic cell and the nervous ending by passive diffusion or with the help of “mobile elements” such as exosomes (free micellar membrane components with prions) [219], endogenous viruses, B lymphocytes [215, 220] or even special dendritic cells [221, 222]. Once inside the peripheral nerves, the prions enter the neuroretrograde transport system of the nerve that leads to the transport of the prion to structures of the central nervous system, where the destruction of the nervous cells takes place.

One important characteristic of prion pathogenesis important for us is the ability to evade the innate immune system and even use the complement system for simplification of target cell infection. The central role is occupied by the dendritic cells that settle the first contact with the prion in the Peyer's patches and that can store the prions on the surface for lymphocyte presentation. Further, the dendritic cells (and other phagocytes such as macrophages) can also bind complement- or antibody-labeled prions with their Fc and complement receptors [223, 224], usually followed by receptor-mediated endocytosis. Unfortunately, an unknown conformational characteristic allows the prion to “survive” the enzymatic degradation by proteases, making it impossible for the immune system to create an efficient antibody-mediated adaptive immune response by MHC-mediated antigen presentation.

Obviously, an inadequate degradation of the prions in cells of the MPS only leads to widespread spread of the infectious agent when it binds complement factors, because the uptake of complement-labeled prions is much more efficient than the uptake of unlabeled prions to dendritic cells, macrophages and lymphocytes.

Applied to our topic, i.e. targeted delivery of nanostructures, it can be said that unselective uptake of artificial nanometer-sized structures – be it protein-based or polymer-based – can create grave side-effects if the cells of the MPS are not capable of degrading the structure efficiently.

## 5.4

### Strategies for Targeted Delivery – Designed by Man

#### 5.4.1

##### Outline

In this section, we will discuss strategies for targeted delivery of chemically complex, nanometer-sized structures to a well-defined target site developed by researchers in recent years [225, 226]. We will concentrate on the desired targets and on the targeting strategies and moieties, independent of the nature of the carrier and its content. The section will be divided into the most important targeting pathways and sites other than cancer therapy, i.e. noninvasive and invasive delivery systems, and targeting to the brain, to atherosclerotic plaques and other targets.

#### 5.4.2

##### Noninvasive Delivery Systems

When discussing the possibilities for targeted drug delivery for pathological conditions other than cancer, we have to be aware that we are dealing with chronic illnesses such as atherosclerosis, arterial hypertension, dyslipidemia, brain disorders (e.g. Parkinson's disease, Alzheimer's disease, psychiatric disorders), chronic inflammatory diseases, diabetes, etc. These diseases normally need a long-term medication. To ensure a good adherence to the therapeutic plan and to limit the possible side-effects, drugs for these chronic disorders have to be ideal from the pharmacological side. Important issues are easy application (oral, inhalatory, transdermal), once-a-day dosage, stable plasma concentrations and no serious adverse side-effects. In particular, the application method is important for the patient's comfort and adherence to the therapeutic procedure.

For diabetes, we have to administer the protein insulin to the systemic circulation, which is right now only possible with parenteral injections (subcutaneous or intravenously). Further, the patient has to inject the insulin up to 5–6 times a day to uphold an acceptable glucose concentration and risks a potentially fatal hypoglycemia when injecting an overdose of insulin. Obviously, such a therapeutic rule decreases the patient's quality of life and is only acceptable if the therapeutic benefit outweighs the negative side-effects to a high degree.

The design of noninvasive (in contrast to invasive methods such as injectable or implantable systems) drug delivery systems for oral, transdermal and transepithelial application and controlled passage of smaller and bigger molecules is therefore an important research area, and has been enriched by nanotechnological tools in recent years [225]. All noninvasive systems we will discuss in this section are a result of a so-called “top-down” manufacturing process, where the final tool is built from larger parts (in contrast to the “bottom-up” process, where atoms and/or molecules come together to build a superstructure). For the details about pharmacology and biology of the barriers, refer to the previous sections of this chapter.

#### 5.4.2.1 Oral Delivery Systems

The most attractive delivery route is oral application – it is convenient, noninvasive and effective because of the large intestinal epithelial surface in the small intestine. In recent years, manufacturers have developed new complex drug formulas for controlled release based on nanotechnology, to ensure a continuous drug release into the systemic circulation over a longer period without toxic initial peak levels [227]. The most important controlled release drug formulation method for tablets is the osmotic oral delivery system (also called osmotic pump technology). It is based on an inner drug reservoir or drug core, a semipermeable membrane with nanometer-sized pores around the drug reservoir and a polymeric push compartment, which triggers the diffusion of the drug through the membrane on activation (e.g. hydration). This method is now commonly used for drugs such as nifedipine (Procardia XL<sup>®</sup>, Pfizer), oxybutynin chloride (Ditropan XL<sup>®</sup>, Ortho-McNeil) and methylphenidate (Concerta<sup>®</sup>, ALZA).

Another important modern drug formulation method is the multilayer matrix tablet, based on a core drug reservoir and one or more surrounding barrier layers such as hydroxypropylmethylcellulose (HPMC) [228, 229]. Various additional ingredients trigger the controlled diffusion process by swelling, gelling or erosion of the barrier layers. This method is being used for drugs such as diltiazem (Dilacor XR<sup>®</sup>, Watson Labs), paroxetine (Paxil CR<sup>®</sup>, GlaxoSmithKline) and diclofenac (Voltaren XR<sup>®</sup>, Novartis).

The last controlled release technology is called spheroidal oral drug absorption system (SODAS), and is based on spherical beads (diameter 1–2 mm) containing drugs and excipients that are coated by controlled-release polymers [225, 230, 231]. In fluids, the polymers start to dissolve at a time-dependent rate and allows the fluid to dissolve the drug core, resulting in an immediate release, a sustained release or a pulsatile delivery. This method is being used for drugs such as diltiazem (Cardizem LA<sup>®</sup>, Bioavail), methylphenidate (Ritalin LA<sup>®</sup>, Novartis) and morphine sulfate (Avinza<sup>®</sup>, Ligand).

#### 5.4.2.2 Transdermal Delivery Systems

Transdermal application of drugs is another elegant method to ensure stable plasma drug concentrations, low maximum–minimum peak concentration differences, low first-pass effect and controlled release of potent, lipophilic drugs.

The most important technology for transdermal drug application is the transdermal delivery patch for drugs such as fentanyl, morphine, nicotine, nitroglycerin and steroid hormones we have already discussed above. Recently, new technologies have been introduced to expand the possibilities for transdermal drug delivery.

First, it is possible to use the so-called iontophoretic delivery by applying an electrical current to the skin, after which the drug molecules move actively through the epidermis according to the polarity of the electrical field (similar to electrophoresis) [232].

Second, new microtechnological devices called Macroflux<sup>®</sup> (ALZA) and Microstructured Transdermal System<sup>®</sup> (3M Drug Delivery) based on microprojection technology [233] allow the skin permeation of macromolecules such as proteins

and peptides. The device consists of an array (1–2 cm<sup>2</sup>) of drug-coated titanium microprojections (200 μm each) fixed to an adhesive patch backing. The device has to be applied to the skin by using a special applicator, on which the small microprojections pierce the protective stratum corneum of the epidermis mechanically, allowing the coated drug to dissolve and to permeate into the blood vessels of the subepidermal tissue [234].

#### 5.4.2.3 Transmucosal Delivery Systems

Drug application to sites such as the buccal, nasal, rectal, intrauterine, vaginal and ocular mucosa is another interesting alternative to intravenous injection and oral application, especially for special patient groups such as children, elderly or sick people, where the conventional application pathways may be problematic. Further, the absorption is fast in the well-perfused mucosa if the drug molecule is able to cross the epithelial barrier.

Special transmucosal drug delivery systems consist of bioadhesive polymers or hydrogels that increase the contact time and contact intensity to the epithelial layer [235]. For instance, polymers such as polyanhydrides stick physically to the intestinal epithelium and lectins stimulate a ligand–receptor interaction with receptors on the small intestine villi [236], making it possible to couple drug molecules or drug carriers to the lectin molecule [237] for better adhesion and permeation. A similar strategy with drug–polymer conjugates was tested for an oral administration formula for insulin [238].

The drugs in the polymer matrix or hydrogel can be free or attached to special controlled release devices such as microspheres and rings [239, 240], reservoirs [241], or nanoparticles [242].

Further, it is possible to improve the absorption rate across the endothelial layers by disturbing the epithelial barrier with special absorption enhancers [235] such as chitosan, cyclodextrin, poly-L-arginine and various lipids [243]. Formulas enriched with chitosan [244] powder have already been used for nasal administration of insulin and morphine [245].

#### 5.4.3

#### Invasive Delivery Systems

In this section, we will discuss controlled, “top-down” micro/nanotechnological devices for drug delivery that have to be injected or implanted [246]. The variety of uncontrolled, “bottom-up” liposomes, nanoparticles and other nanometer-sized superstructures will be discussed in the next sections.

One important example of invasive delivery systems are controllable microfabricated devices (based on silicon chips, “off-wafer” techniques or microfluidic devices) with a drug reservoir that can be triggered or programmed to release a certain volume of drugs to the tissue or to the circulation [247]. Older concepts relied on the surgical implantation of the microfabricated device under the skin or into other tissues. Currently, new micro/nanofabrication techniques are being developed that allow the top-down construction of devices down to a size of 10–100 μm. These



techniques make it possible to inject the devices into the target tissue with only slight damage or to inhale the macrostructure into the bronchi, where the drug could be released permanently over a certain time. By integrating microfluidic networks with multiple reservoirs, valves and pumps [248], it is possible to program the microfabricated to perform chemical reactions and release several reaction products [249].

One essential requirement for microfabricated device is the possibility for real-time control of the drug release according to changes in chemical and physiological parameters. One approach is the activation of molecular interactions using light radiation, radiofrequency or ultrasound energy. Ferromagnetic seeds [250], rods [251], microparticles [252] or superparamagnetic nanoparticles [253] can be injected or transported to a desired target, where they can be heated using localized radiofrequency or ultrasound for thermal treatment or release activation. Further, it had been shown that high-frequency radiofrequency changes the conformation of nucleic acid conjugates or proteins coupled to nanoparticles.

Another strategy for controlled drug release in microfabricated devices is based on hydrogels, three-dimensional, hydrophilic polymer (e.g. collagen, gelatin, dextrans, chitosans, poly-*N*-vinylpyrrolidone, polyphosphazenes, PLA/polyethylene oxide/PLA copolymers, PEGT–PBT copolymers [254]) networks that swell and change their diffusion properties reversibly when exposed to water. Thus, it is possible to control the drug diffusion out of a drug reservoir or a matrix with a hydrogel covering according to the swelling properties of the hydrogel. Special hydrogels are even sensitive to specific antigens [255], to an enzyme [256], to pH changes (methacrylates) or to an applied charge and change their swelling properties [257].

Finally, special polymer-based surfaces sensitive to light [258, 259], pH, charge [260] and heat offer further possibilities for triggered controlled release of the content.

Similar to the microfabricated devices are noncontrollable diffusion chambers [261] or diffusion tubes with a central chamber filled with one or more drugs and semipermeable membrane that controls the release rate. Diffusion chambers or tubes have to be implanted into a certain tissue, and have been tested for diseases such as diabetes [262, 263], epilepsy [264] and spinal cord damage [265], and for birth control implants [266]. Diffusion chambers can also be filled with living cells [267] to enable the production of proteins, hormones and other molecules (e.g. erythropoietin [268], insulin [269, 270] or IFN- $\alpha$  [271]), but we are not going to discuss this vast area further in this chapter.

#### 5.4.4

#### **Targeted Delivery to the Brain**

The brain is well protected against the diffusion of hydrophilic molecules and macromolecules by the blood–brain barrier, consisting of the dense, unfenestrated endothelial cell layer, the subendothelial space and specialized protecting cells of the brain – the astrocytes. The blood–brain barrier makes it difficult for micro-

organisms, toxic substances and macromolecules to reach the neurons of the brain, but also complicates therapeutic applications targeting cerebral pathologies such as Parkinson's disease, Alzheimer's disease, multiple sclerosis, meningitis or encephalitis. Only small lipophilic substances are able to cross the blood–brain barrier passively by diffusion; larger or hydrophilic substances need active transport system or a functional disruption of the blood–brain barrier to reach the neurons. Due to these limits, targeted delivery to the brain is one of the most active research areas using nanotechnological devices and researchers have developed a wide range of macromolecular targeting carriers. In recent years, new nanotechnological drug formulas have been tested for transport of bigger molecules such as peptides, proteins, and genes across the blood–brain barrier, both liposomal formulations [272] and polymer-based formulations [273].

Currently used liposomes are typically sterically stabilized for prolonged circulation lifetimes by a protective coating of PEG or other “antiopsonization agents” [24]; some liposomes are further functionalized with targeting moieties such as antibodies (immunoliposomes) [274], proteins, peptides or others [275, 276] for preferred target deposition. For details on the synthesis of nanotechnological carriers, refer to the specialized sections and references.

Well-studied targeting agents for trans-blood–brain barrier delivery are monoclonal antibodies such as OX26 [277] or 8D3 [278] directed against the ubiquitous (especially liver, muscles and brain) transferrin (iron-binding protein in plasma) receptors. The murine antibodies are typically conjugated to PEGylated liposomes that have to be injected intravenously and have shown a certain affectivity to the endothelial cells of the blood–brain barrier [279]. After binding to the transferrin receptor, the antibody with the liposome is transported across the blood–brain barrier by receptor-mediated endocytosis and transcellular transport [280, 281]. The antibody–liposome complex can now diffuse freely and spread into the brain tissue, which shows a clear liposome accumulation compared with native PEGylated liposomes [282].

Other targeting moieties for targeted brain delivery of liposomes are monoclonal antibodies directed against the human insulin receptor such as 83-14 [283], which can be found on endothelial cells and neurons in a high concentration. The functionalized liposomes bind to the cell surface receptor and can be internalized by receptor-mediated endocytosis. To increase the rate of *trans*-blood–brain barrier passage, it is also possible to functionalize the liposomes further with anti-transferrin receptor antibodies [284]. In this case, the antitransferrin receptor antibody ensures the passage across the blood–brain barrier, while the anti-insulin receptor ensures the uptake into the neurons.

Due to the well-known limits when using liposomes such as low physicochemical stability, leakage, difficult preparation procedures, low possibility for controlled release, low loading efficiency and short *in vitro* lifetimes, many researchers have turned to polymer-based formulas [273, 285] to overcome these problems.

The first nanoparticles for targeted brain delivery were made using poly(alkylcyanoacrylates) such as polybutylcyanoacrylate (PBCA) [286] coated with the nonionic surfactant polysorbate 80 [287–289], and later using nanoparticles consisting

of polylactide homopolymers (PLA) and poly(lactide-co-glycolide) heteropolymers (PLGA) coated with PEG [290] to protect the nanoparticles from opsonization and to ensure longer circulation lifetimes [291, 292].

The targeting moiety of PBCA nanoparticles is the polysorbate coating, which ensures a certain nanoparticle accumulation in the brain tissue, probably by a polysorbate-mediated disruption and permeabilization of the blood–brain barrier [293, 294] or by endocytosis by the brain capillary endothelial cells [285]. It has been hypothesized that the endogenous plasma protein apolipoprotein E (ApoE) absorbs to the polysorbate coating and triggers the receptor-mediated endocytosis [285]. On the other hand, a protein-binding nanoparticle surface obviously enables opsonization and leads to a fast uptake into the MPS [288, 295, 296], making it impossible to use these nanoparticles for target-specific delivery. Further, blood–brain barrier permeabilization is a serious adverse drug event [273] that might lead to neuronal damage by exogenous or endogenous toxic substances or microorganisms.

Nanoparticles made of polymers based on glycolic acid and D,L-lactic acid enantiomers have a proven record of good biocompatibility and resorbability [297, 298], and have been used for some years in building biodegradable devices and microspheres [299]. Further, PLA and PLGA are easily degraded by spontaneous hydrolysis of the ester bonds [300] into oligomers and monomers, which are further metabolized and degraded into CO<sub>2</sub> and H<sub>2</sub>O [273]. For nanoparticle targeting applications, the PLA/PLGA polymers have to be covered with PEG moieties to ensure a prolonged circulation lifetime [301] of some hours compared with some minutes for native PLA/PLGA nanoparticles [302–306].

Possible targeting moieties for brain-specific delivery of nanoparticles based on PLA/PLGA are the monoclonal antibodies (OX26 and 8D3) against the transferrin or insulin receptors we have already met. The targeting antibodies are bound to the tips of specially functionalized PEG strands (biotinylated [307], amine reactive [308] or thiol reactive [309, 310]) and enable the endocytosis of nanoparticles with a diameter of around 100 nm to the endothelial cells of the brain capillaries and the passage across the blood–brain barrier.

#### 5.4.5

#### Macrophage Targeting

Macrophages, the main cell type of the innate immune system, play a major role in a wide range of disease states, including infections (e.g. *Leishmania*, *M. tuberculosis*, *L. monocytogenes*), autoimmune diseases (e.g. rheumatoid arthritis, sarcoidosis, type I diabetes), cancer and atherosclerosis [311–318]. Therefore, the macrophage is an interesting pharmaceutical target, despite the fact there exist only a few therapeutic choices until now.

Targeting to macrophages is theoretically easy, because the macrophages of the MPS are the primary target for all nonstealth lipid- or polymer-based nanometer-sized vehicles. Nonetheless, the macrophages of the MPS in liver and spleen are only rarely the desired target when trying to achieve a therapeutic effect; the “de-

sired” macrophages are those found in vulnerable plaques of the blood vessels, in the peritoneum, the lung and other sites of disease. In contrast to the macrophages in liver (called Kupffer cells) and spleen, the macrophages in these tissues are normally protected from the nanovehicles by a dense endothelial layer (endothelium in liver and spleen has wide fenestrations). To be able to target the “desired” macrophages, a nanovehicle has to (i) evade the phagocytic cells of liver and spleen, (ii) uphold long circulation lifetimes, (iii) find a way to leave the circulation intact at a desired therapeutic target, (iv) reach the target cells specifically (v) and enter the macrophages (vi) avoiding the destruction in the endo-lysosomal compartment. All this makes targeting to the “desired” macrophages a serious task and calls for innovative solutions based on nanotechnological tools.

Early examples of macrophage-directed drugs are nonstealth liposomes containing the antimicrobial drug amphotericin B (AmBisome®, Gilead Sciences) for the therapy of the intracellular parasite *Leishmania* (which stays in macrophages) and various fungal infections [319–321]. Similar approaches with liposomes and nanoparticles were also used for improved targeting of antimicrobial agents such as  $\beta$ -lactam antibiotics, aminoglycosids and fluoroquinolones to intracellularly infected macrophages (e.g. *Salmonella*, *L. monocytogenes*, *M. tuberculosis*, *Mycobacterium avium*, *Mycobacterium intracellulare*, *Brucella abortus* and *L. pneumophila*) [322]. The liposomal formulas allow reducing the quantity of applied drug molecules and decrease the severity of adverse side-effects [323], because most of the encapsulated drug is rapidly transported to the phagocytic macrophages or the fungi and not to other healthy tissues. Targeting can be further improved using targeting moieties such as tuftsin, a natural macrophage activator tetrapeptide (threonine–lysine–proline–arginine) based on a part of the IgG heavy chain [324].

One interesting application area for nanoparticulate formulations targeting macrophages is the development of new nanotechnological vaccines. The required protein or peptide antigen is coupled physically or covalently to a polymer- or lipid-based nanocarrier adjuvant, which promotes the preferred uptake of the coupled antigen to macrophages of the innate immune system. The antigen is then processed by the endo-lysosomal compartment and presented to T lymphocytes using the MHC class I and especially class II molecules on the surface of antigen-presenting cells (APC), increasing the immunogenic potency of the used vaccination antigen [325–327]. Similar approaches have been tried for new DNA vaccines [328, 329]. Targeting can be further improved using targeting moieties such as various mannose receptor ligands [330].

Much progress has been achieved in the use of nanotechnology-based contrast agents for diagnostic applications. Detection of activated macrophages might help the doctors to find and define a diseased tissue, especially an inflamed tissue such as the vulnerable plaque or autoaggressive immunologic process. In recent years, paramagnetic iron oxide nanoparticles (4–5 nm diameter, usually coated with PEG or dextran) have been used for detecting macrophages using the readily available technique of MRI. Macrophages or other target cells take up the nanoparticles that can be detected by MRI (negative signal in T2), because the iron oxide shortens the spin relaxation compared with surrounding tissues. Paramagnetic

iron oxide nanoparticles have been used for detecting lymph nodes metastases [331, 332], arthritis [333], fibrin molecules [334], angiogenesis in atherosclerotic plaques [335] and other constituents of atherosclerotic plaques [253, 336, 337].

The detection of actively inflamed atherosclerotic plaques that are in danger of rupture (leading to heart infarction, stroke and other organ ischemia), called vulnerable plaques [28, 318], is an active and promising research area that has been enriched by nanometer-sized vehicles for targeted delivery [3]. Several characteristics of vulnerable plaques simplify the targeted delivery, i.e. the functional and morphological disruption of the endothelial layer that covers the atherosclerotic plaque and enables the extravasation of larger molecules and superstructures such as lipoproteins, polynucleotides, polypeptides, complex lipids and advanced glycation end-products (AGE). These macromolecules initiate and support the pathological process of atherosclerosis. In the vulnerable plaque, active macrophages take up the plasma proteins and lipids and transform into so-called foam cells, instable macrophages filled with lipids that produce various cytokines and other pro-inflammatory and proliferation-stimulating chemical substances. These substances attract more white blood cells to the plaque, trigger the growth of the plaque and finally cause the breakup of the fibrous cap [338].

Intelligently designed nanovehicles such as polymer nanocontainers [32] have several properties that might enable them to reach the vulnerable plaque and block the central cell type of the pathological process – the macrophage. Covered with the inert antiopsonization polymer PMOXA, the nanocontainers (diameter 100–200 nm) have long circulation lifetimes, allowing them to leave the circulation in sites with a disrupted endothelial layer such as the vulnerable plaque. Functionalized with the polynucleotide tracking ligand polyguanylic acid [339] by multi-functional biotin–avidin–biotin bonds [32], the nanocontainers bind specifically to a highly upregulated receptor subtype of active macrophages called scavenger receptor A1 [340]. It was shown that these innovative, functionalized nanocontainers reach specifically active macrophages that express the scavenger receptor A1 and do not reach macrophage precursor cells and tissue macrophages with a low grade of upregulation [32] (Figs. 5.7–5.9).

#### 5.4.6

##### **Other Targets**

PEGylated liposomes coated with plasminogen were designed for fibrin clot targeting. The plasminogen serves as a targeting moiety, because it binds to the fibrin in clots that block the blood flow in a case of heart infarction, lung embolism or stroke. The liposomes were filled with the fibrinolytic substance plasminogen activator, which triggers the degradation of fibrin in the clot and allows the reperfusion of the infarcted area [341].

PEGylated liposomes labeled with the targeting moiety RGD peptide (containing the arginine–glycine–aspartic acid sequence) were designed for targeted delivery to  $\alpha_v$  integrin receptors on endothelial cells [342, 343]. The liposomes can be filled with different drugs such as angiogenesis inhibitors, which block this important

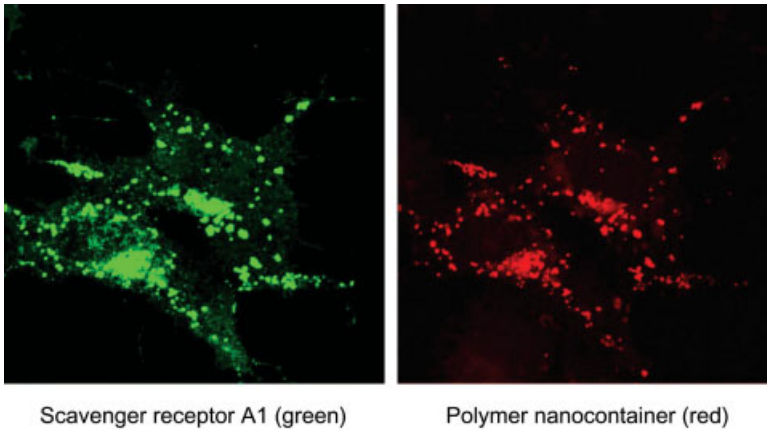


**Figure 5.7.** Scavenger receptor A1-mediated uptake of polyguanylic acid-functionalized polymer nanocontainers into intracellular vesicles (for details refer to Ref. [32]). PMOXA–PDMS–PMOXA triblock copolymer nanocontainers (diameter 100–200 nm) were functionalized with the oligonucleotide tracking ligand polyguanylic acid for macrophage scavenger receptor A1 targeting via biotin–avidin–biotin bonds. In cell cultures expressing the enhanced green fluorescent protein

(EGFP)-labeled scavenger receptor A1, rapid binding to the target receptor was detected by fluorescent microscopy. The nanocontainers were filled with the hydrophilic red fluorescent dye sulforhodamine B and can be detected both on the cell surface and in intracellular vesicles, most probably lysosomes. The colocalization of receptor (green, left) and nanocontainer (red, right) proves the receptor-specific targeting.

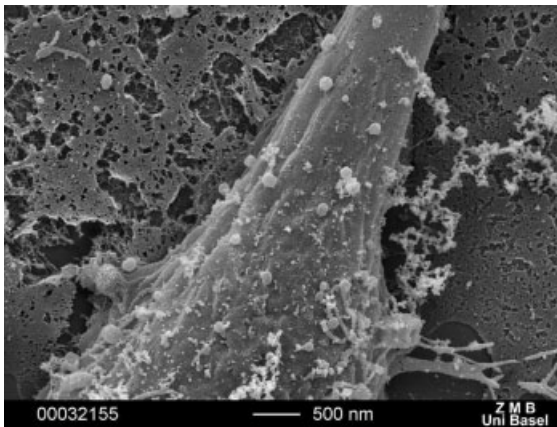


**Figure 5.8.** Functionalized polymer nanocontainers bound to macrophages (for details refer to Ref. [32]). The same functionalized nanocontainers as in Fig. 5.7 were targeted to endocytosis-inhibited macrophages in culture. Precise analysis of the experimental macrophages by scanning

electron microscopy discovered the presence of vesicular formations (diameter 100–200 nm) on the macrophage cell membrane, most probably the intact nanocontainers. Unfunctionalized nanocontainers lacking the tracking ligand polyguanylic acid did not bind to the activated macrophages.

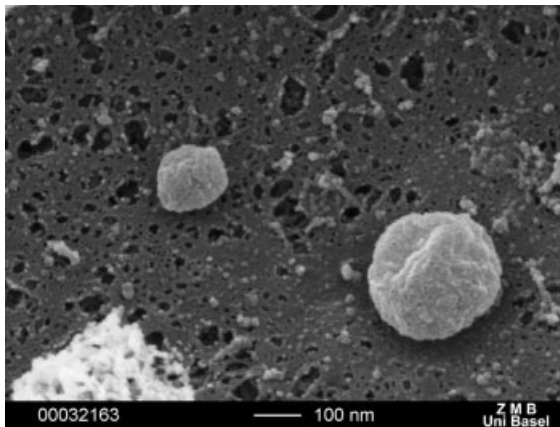


**Figure 5.9.** Functionalized polymer nanocontainers bound to macrophages – detail (for details refer to Ref. [32]). Same set-up as in Fig. 5.8; the scanning electron micro-

scopy image offers a unique insight into the morphology of polymer nanocontainers bound to the macrophage surface.

step in the development of disease conditions such as atherosclerosis and especially cancer.

Asialoglycoprotein receptor (ASGP-R) ligands such as asialofetuin and galactosylated cholesterol, glycolipids or polymers coupled to PEGylated liposomes or other carriers were used for hepatocyte targeting of both drugs and gene sequences for gene therapy [344–347]. Other strategies for hepatocyte targeting of lipid emulsions involve the use of the lipoprotein protein ApoE as a tracking ligand [348].

The last topic we want to discuss is the field of cell-penetrating peptides, which enable the invasion of nanovehicles into the cytoplasm of the target cell [31]. Cell-penetrating peptides are naturally occurring in viruses such as HIV, herpes virus and hepatitis B virus, and in macroorganisms such as *Drosophila*. They can be divided into two classes: the lysine-rich amphipathic helical peptides (e.g. transportan [349] and model amphipathic peptide [350]) and the arginine-rich peptides (e.g. TAT [351, 352], Antp [353], VP22 [354] and penetratin) [355–359]. We will discuss the principles and applications of the most important cell-penetrating peptide, the TAT (transactivating transcriptional activator) peptide, which is a central protein of HIV [31].

After binding to cell surface receptors such as  $\alpha_v\beta_5$  integrin [360], TAT is internalized rapidly and is transported to the nucleus, where it transactivates the HIV promoter [352]. The uptake of TAT peptide and TAT-coupled small molecules is thought to be triggered by strong electrostatic binding of the peptide to the cell membrane, upon which the peptide enters an energy-independent nonlysosomal endocytic pathway [361–363]. On the other hand, TAT-functionalized nanovehicles are taken up by the cell by an energy-dependent macropinocytosis, followed by a facilitated endosome escape into the cytoplasm [356, 364].

TAT-coupling was tested for intracellular and intranuclear delivery of various proteins and peptides [365–368], genes [369–371], oligonucleotides [372], antibodies [373, 374], imaging contrast agents for scintigraphy and MRI [375–377], and finally of various macrostructures. It was shown that TAT-coupling improved the fast and nondegrading internalization of dextran-coated superparamagnetic iron oxide nanoparticles (mean diameter 41 nm) into white blood cells [378, 379], of gold nanoparticles into cell cultures [380] and of various PEGylated liposomes [381–383].

## 5.5

### Conclusion and Outlook

In this chapter, we have defined the major obstacles and barriers that have to be overcome for a targeted delivery of diagnostic or therapeutic agents to a desired cellular or subcellular target. We have discussed microbial targeting and immune system evasion strategies, and tried to give an insight into the vast field of nanotechnology-based delivery tools. We are aware that we rather had to concentrate on general principles than on a precise summary of all available targeted delivery nanovehicles. We apologize to all groups that were not mentioned and we encourage them to send us material about their research activities for future publications from our side. Please refer to other chapters of this book and to the mentioned references for details on some special topics that were not fully covered in this chapter.

As we have seen, the field of targeted delivery using nanotechnological tools is an active and promising research area, and creates new ideas at a very fast pace. Clearly, nanotechnological targeted delivery will split into specialized subtopics in the future according to the desired target. Many medical disciplines such as neurology, cardiology, gastroenterology and surgery will profit from the toolbox of nanoscience that will revolutionize current diagnostic and therapeutic applications, and that will offer possibilities for new concepts.

The final goal of nanomedicine will be to create nanometer-sized, nontoxic and easily built carriers of complex functionality such as (i) undamaging epithelial barrier passage, (ii) long circulation lifetime, (iii) immune system evasion, (iv) controlled bloodstream extravasation, (v) target-specific deposition, (vi) undisruptive target cell invasion, and (vii) precise and (viii) automated diagnostic or therapeutic intervention (Fig. 5.10). Some these criteria have already been developed for certain nanovehicles, others will be developed in future years. Combining all of them will create an exciting and complex nanostructure – some will call it nanorobot or nanobot, others will call it an artificial virus, which is perhaps the best definition.

Obviously, such a nanorobot will create fear and concerns in the public, comparable to the concern we face nowadays with scientific topics such as biotechnology, stem cell research and bioterrorism. Miniaturized defense mechanisms penetrating and probably self-replicating artificial nanorobots that invade our body and have the ability to reach every organ and tissue are much more powerful than cur-



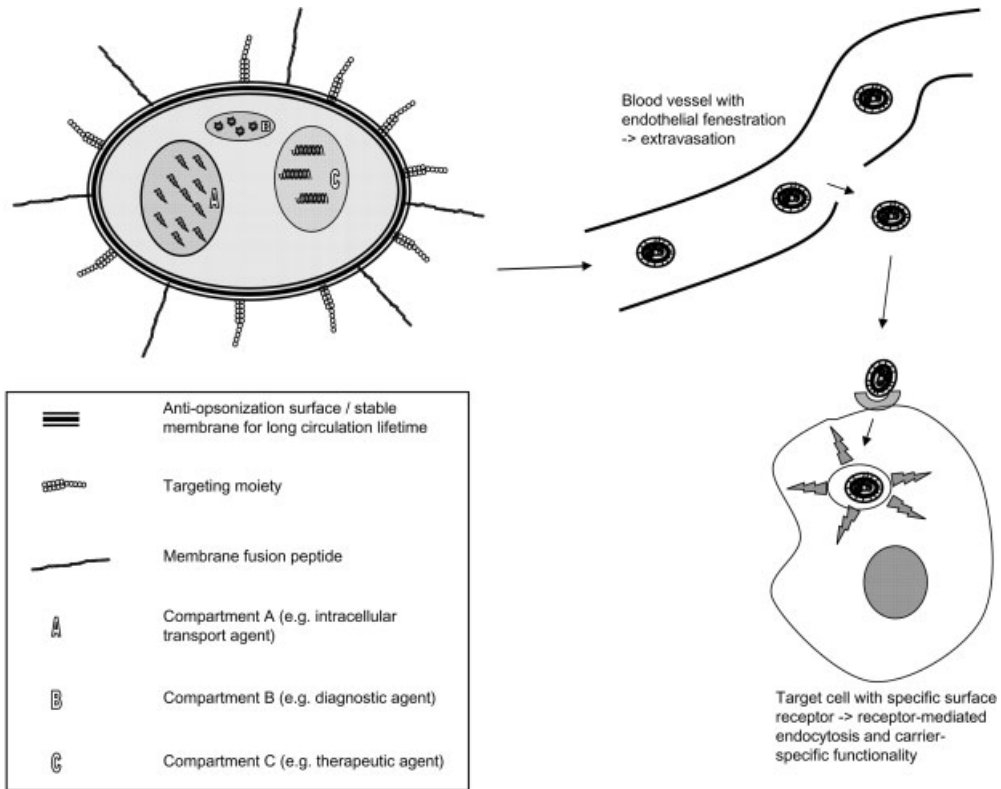


**Figure 5.10.** Theoretical construction of a long-circulating, receptor-specific nanocarrier with a highly complex functionality (such as cell invasion, intracellular transport, diagnostic and therapeutic agents).

rent scientific tools when it comes to creating worst-case scenarios. Therefore, it is fundamental that nanotechnology researchers understand this problem, and engage themselves actively and without legislative or media pressure in discussions about “nanotoxicity” [384–386] and “nanoethics” [387, 388], which were not covered in this chapter.

Only with careful considerations on the advantages and disadvantages of new technologies will it be possible to create nanoscaled tools that will help us to overcome severe and until now incurable diseases.

## References

- GURWITZ, J. H., FIELD, T. S., HARROLD, L. R., ROTHSCHILD, J., DEBELLIS, K., SEGER, A. C. et al. Incidence and preventability of adverse drug events among older persons in the ambulatory setting.

- J. Am. Med. Ass.* **2003**, *289*, 1107–1116.
- 2 MOGHIMI, S. M., HUNTER, A. C., MURRAY, J. C. Nanomedicine: current status and future prospects. *FASEB J.* **2005**, *19*, 311–330.
  - 3 WICKLINE, S. A., LANZA, G. M. Nanotechnology for molecular imaging and targeted therapy. *Circulation* **2003**, *107*, 1092–1095.
  - 4 *The Merck Manual of Diagnosis and Therapy*. 17th edn. Merck, West Point, PA, **1999**.
  - 5 *Pharmacology*. Edinburgh: Churchill Livingstone, **2003**.
  - 6 *Goodman & Gilman's: The Pharmacological Basis of Therapeutics*. McGraw-Hill, New York, **2001**.
  - 7 TENCER, J., FRICK, I.-M., OQUIST, B. W., ALM, P., RIPPE, B. Size-selectivity of the glomerular barrier to high molecular weight proteins: upper size limitations of shunt pathways. *Kidney Int.* **1998**, *53*, 709–715.
  - 8 ELIAS, P. M. Stratum corneum defensive functions: an integrated view. *J. Invest. Dermatol.* **2005**, *125*, 183–200.
  - 9 Committee on Drugs. Alternative routes of drug administration – advantages and disadvantages (subject review). *Pediatrics* **1997**, *100*, 143–152.
  - 10 SAUNDERS, J., DAVIS, H., COETZEE, L., BOTHA, S., KRUGER, A., GROBLER, A. A novel skin penetration enhancer: evaluation by membrane diffusion and confocal microscopy. *J. Pharm. Pharm. Sci.* **1999**, *2*, 99–107.
  - 11 PIERRE, M., TEDESCO, A., MARCHETTI, J., BENTLEY, M. V. Stratum corneum lipids liposomes for the topical delivery of 5-aminolevulinic acid in photodynamic therapy of skin cancer: preparation and *in vitro* permeation study. *BMC Dermatology* **2001**, *1*, 5.
  - 12 MORITA, K., MIYACHI, Y. Tight junctions in the skin. *J. Dermatol. Sci.* **2003**, *31*, 81–89.
  - 13 CHENG, H., LEBLOND, C. P. Origin, differentiation and renewal of the four main epithelial cell types in the mouse small intestine. I. Columnar cell. *Am. J. Anat.* **1974**, *141*, 461–479.
  - 14 ROTH, K. A., HERTZ, J. M., GORDON, J. I. Mapping enteroendocrine cell populations in transgenic mice reveals an unexpected degree of complexity in cellular differentiation within the gastrointestinal tract. *J. Cell Biol.* **1990**, *110*, 1791–1801.
  - 15 FASANO, A., SHEA-DONOHUE, T. Mechanisms of disease: the role of intestinal barrier function in the pathogenesis of gastrointestinal autoimmune diseases. *Nat. Clin. Pract. Gastroenterol. Hepatol.* **2005**, *2*, 416–422.
  - 16 SNOECK, V., GODDEERIS, B., COX, E. The role of enterocytes in the intestinal barrier function and antigen uptake. *Microb. Infect.* **2005**, *7*, 997–1004.
  - 17 MACDONALD, T. T., MONTELEONE, G. Immunity, inflammation, and allergy in the gut. *Science* **2005**, *307*, 1920–1925.
  - 18 STERN, M., WALKER, W. A. Food proteins and gut mucosal barrier I. Binding and uptake of cow's milk proteins by adult rat jejunum *in vitro*. *Am. J. Physiol.* **1984**, *246*, G556–G562.
  - 19 CHU, S. H., WALKER, W. A. Development of the gastrointestinal mucosal barrier: changes in phospholipid head groups and fatty acid composition of intestinal microvillus membranes from newborn and adult rats. *Pediatr. Res.* **1988**, *23*, 439–442.
  - 20 MCKAY, D. M., BAIRD, A. W. Cytokine regulation of epithelial permeability and ion transport. *Gut* **1999**, *44*, 283–289.
  - 21 BERIN, M. C., YANG, P. C., CIOK, L., WASERMAN, S., PERDUE, M. H. Role for IL-4 in macromolecular transport across human intestinal epithelium. *Am. J. Physiol.* **1999**, *276*, C1046–C1052.
  - 22 BRANNON-PEPPAS, L., BLANCHETTE, J. O. Nanoparticle and targeted systems for cancer therapy. *Adv. Drug Deliv. Rev.* **2004**, *56*, 1649–1659.
  - 23 AHSAN, F., RIVAS, I. P., KHAN, M. A., TORRES SUAREZ, A. I. Targeting to macrophages: role of physicochemical properties of particulate carriers – liposomes and microspheres – on the

- phagocytosis by macrophages. *J. Control. Release* **2002**, *79*, 29–40.
- 24 MOGHIMI, S. M., SZEKENI, J. Stealth liposomes and long circulating nanoparticles: critical issues in pharmacokinetics, opsonization and protein-binding properties. *Prog. Lipid Res.* **2003**, *42*, 463–478.
  - 25 MOGHIMI, S. M., HUNTER, A. C., MURRAY, J. C. Long-circulating and target-specific nanoparticles: theory to practice. *Pharmacol. Rev.* **2001**, *53*, 283–318.
  - 26 VAN NIEUW AMERONGEN, G. P., VAN HINSBERGH, V. W. M. Targets for pharmacological intervention of endothelial hyperpermeability and barrier function. *Vasc. Pharmacol.* **2002**, *39*, 257–272.
  - 27 MULLIN, J. M., AGOSTINO, N., RENDON-HUERTA, E., THORNTON, J. J. Keynote review: Epithelial and endothelial barriers in human disease. *Drug Discov. Today* **2005**, *10*, 395–408.
  - 28 BOYLE, J. J. Macrophage activation in atherosclerosis: pathogenesis and pharmacology of plaque rupture. *Curr. Vasc. Pharmacol.* **2005**, *3*, 63–68.
  - 29 OHASHI, R., MU, H., YAO, Q., CHEN, C. Atherosclerosis: immunopathogenesis and immunotherapy. *Med. Sci. Monit.* **2004**, *10*, RA255–260.
  - 30 BELTING, M., SANDGREN, S., WITTRUP, A. Nuclear delivery of macromolecules: barriers and carriers. *Adv. Drug Deliv. Rev.* **2005**, *57*, 505–527.
  - 31 GUPTA, B., LEVCHENKO, T. S., TORCHILIN, V. P. Intracellular delivery of large molecules and small particles by cell-penetrating proteins and peptides. *Adv. Drug Deliv. Rev.* **2005**, *57*, 637–651.
  - 32 BROŽ, P., BENITO, S. M., SAW, C., BURGER, P., HEIDER, H., PFISTERER, M. et al. Cell targeting by a generic receptor-targeted polymer nanocontainer platform. *J. Control. Release* **2005**, *102*, 475–488.
  - 33 WITZTUM, J. L. You are right too! *J. Clin. Invest.* **2005**, *115*, 2072–2075.
  - 34 WILLEKENS, F. L., WERRE, J. M., KRUIJT, J. K., ROERDINKHOLDER-STOELWINDER, B., GROENEN-DOPP, Y. A., VAN DEN BOS, A. G. et al. Liver Kupffer cells rapidly remove red blood cell-derived vesicles from the circulation by scavenger receptors. *Blood* **2005**, *105*, 2141–2145.
  - 35 VAN ECK, M., BOS, I. S., HILDEBRAND, R. B., VAN RIJ, B. T., VAN BERKEL, T. J. Dual role for scavenger receptor class B, type I on bone marrow-derived cells in atherosclerotic lesion development. *Am. J. Pathol.* **2004**, *165*, 785–794.
  - 36 KRIEGER, M. Scavenger receptor class B type I is a multiligand HDL receptor that influences diverse physiologic systems. *J. Clin. Invest.* **2001**, *108*, 793–797.
  - 37 LINEHAN, S. A., MARTINEZ-POMARES, L., STAHL, P. D., GORDON, S. Mannose receptor and its putative ligands in normal murine lymphoid and non-lymphoid organs: in situ expression of mannose receptor by selected macrophages, endothelial cells, perivascular microglia, and mesangial cells, but not dendritic cells. *J. Exp. Med.* **1999**, *189*, 1961–1972.
  - 38 DOMINGUE, G. J., WOODY, H. B. Bacterial persistence and expression of disease. *Clin. Microbiol. Rev.* **1997**, *10*, 320–344.
  - 39 FINLAY, B. B., FALKOW, S. Common themes in microbial pathogenicity revisited. *Microbiol. Mol. Biol. Rev.* **1997**, *16*, 136–169.
  - 40 SAUER, F. G., MULVEY, M. A., SCHILLING, J. D., MARTINEZ, J. J., HULTGREN, S. J. Bacterial pili: molecular mechanisms of pathogenesis. *Curr. Opin. Microbiol.* **2000**, *3*, 65–72.
  - 41 COSSART, P., SANSONETTI, P. J. Bacterial invasion: the paradigms of enteroinvasive pathogens. *Science* **2004**, *304*, 242–248.
  - 42 CARRERO, J. A., CALDERON, B., UNANUE, E. R. Type I interferon sensitizes lymphocytes to apoptosis and reduces resistance to *Listeria* infection. *J. Exp. Med.* **2004**, *200*, 535–540.
  - 43 FINLAY, B. B., COSSART, P. Exploitation of mammalian host cell functions by bacterial pathogens. *Science* **1997**, *276*, 718–725.

- 44 COSSART, P., PIZARRO-CERDA, J., LECUIT, M. Invasion of mammalian cells by *Listeria monocytogenes*: functional mimicry to subvert cellular functions. *Trends Cell Biol.* **2003**, *13*, 23–31.
- 45 GHOSH, P. Process of protein transport by the type III secretion system. *microbiol. Mol. Biol. Rev.* **2004**, *68*, 771–795.
- 46 HE, S. Y., NOMURA, K., WHITTAM, T. S. Type III protein secretion mechanism in mammalian and plant pathogens. *Biochim. Biophys. Acta Mol. Cell Res.* **2004**, *1694*, 181–206.
- 47 MUELLER, C. A., BROŽ, P., MULLER, S. A., RINGLER, P., ERNE-BRAND, F., SORG, I. et al. The V-antigen of *Yersinia* forms a distinct structure at the tip of injectisome needles. *Science* **2005**, *310*, 674–676.
- 48 GOURE, J., BROŽ, P., ATTREE, O., CORNELIS, G. R., ATTREE, I. Protective anti-V antibodies inhibit and *Yersinia* translocon assembly within host membranes. *J. Infect. Dis.* **2005**, *192*, 218–225.
- 49 GALAN, J. E. *Salmonella* interactions with host cells: type III secretion at work. *Annu. Rev. Cell Dev. Biol.* **2001**, *17*, 53–86.
- 50 SANSONETTI, P. J. Rupture, invasion and inflammatory destruction of the intestinal barrier by *Shigella*, making sense of prokaryote-eukaryote cross-talks. *FEMS Microbiol. Rev.* **2001**, *25*, 3–14.
- 51 *Immunobiology – The Immune System in Health and Disease*, 5th edn. Garland, New York, **2001**.
- 52 *Cellular and Molecular Immunology*, 4th edn. Saunders, New York, **2000**.
- 53 COOMBES, B. K., VALDEZ, Y., FINLAY, B. B. Evasive maneuvers by secreted bacterial proteins to avoid innate immune responses. *Curr. Biol.* **2004**, *14*, R856–R867.
- 54 PORTNOY, D. A. Manipulation of innate immunity by bacterial pathogens. *Curr. Opin. Immunol.* **2005**, *17*, 25–28.
- 55 TAKEDA, K., KAISHO, T., AKIRA, S. Toll-like receptors. *Annu. Rev. Immunol.* **2003**, *21*, 335–376.
- 56 AKIRA, S. Toll-like receptors and innate immunity. *Adv. Immunol.* **2001**, *78*, 1–56.
- 57 D’HAUTEVILLE, H., KHAN, S., MASKELL, D. J., KUSSAK, A., WEINTRAUB, A., MATHISON, J. et al. Two *msbB* genes encoding maximal acylation of lipid A are required for invasive *Shigella flexneri* to mediate inflammatory rupture and destruction of the intestinal epithelium. *J. Immunol.* **2002**, *168*, 5240–5251.
- 58 AUERBUCH, V., BROCKSTEDT, D. G., MEYER-MORSE, N., O’RIORDAN, M., PORTNOY, D. A. Mice lacking the type I interferon receptor are resistant to *Listeria monocytogenes*. *J. Exp. Med.* **2004**, *200*, 527–533.
- 59 O’CONNELL, R. M., SAHA, S. K., VAIDYA, S. A., BRUHN, K. W., MIRANDA, G. A., ZARNEGAR, B. et al. Type I Interferon production enhances susceptibility to *Listeria monocytogenes* infection. *J. Exp. Med.* **2004**, *200*, 437–445.
- 60 NGUYEN, L., PIETERS, J. The Trojan horse: survival tactics of pathogenic mycobacteria in macrophages. *Trends Cell Biol.* **2005**, *15*, 269–276.
- 61 SINAI, A. P., JOINER, K. A. Safe haven: the cell biology of nonfusogenic pathogen vacuoles. *Annu. Rev. Microbiol.* **1997**, *51*, 415–462.
- 62 NAU, G. J., RICHMOND, J. F. L., SCHLESINGER, A., JENNINGS, E. G., LANDER, E. S., YOUNG, R. A. Human macrophage activation programs induced by bacterial pathogens. *Proc. Natl Acad. Sci. USA* **2002**, *99*, 1503–1508.
- 63 FORTUNE, S. M., SOLACHE, A., JAEGER, A., HILL, P. J., BELISLE, J. T., BLOOM, B. R. et al. *Mycobacterium tuberculosis* inhibits macrophage responses to IFN-gamma through myeloid differentiation factor 88-dependent and -independent mechanisms. *J. Immunol.* **2004**, *172*, 6272–6280.
- 64 GOEHRING, U.-M., SCHMIDT, G., PEDERSON, K. J., AKTORIES, K., BARBIERI, J. T. The N-terminal domain of *Pseudomonas aeruginosa* exoenzyme S is a GTPase-activating

- protein for Rho GTPases. *J. Biol. Chem.* **1999**, *274*, 36369–36372.
- 65 COWELL, B. A., CHEN, D. Y., FRANK, D. W., VALLIS, A. J., FLEISZIG, S. M. ExoT of cytotoxic prevents uptake by corneal epithelial cells. *Infect. Immun.* **2000**, *68*, 403–406.
- 66 GARRITY-RYAN, L., KAZMIERCZAK, B., KOWAL, R., COMOLLI, J., HAUSER, A., ENGEL, J. N. The arginine finger domain of ExoT contributes to actin cytoskeleton disruption and inhibition of internalization of by epithelial cells and macrophages. *Infect. Immun.* **2000**, *68*, 7100–7113.
- 67 HAMID, N., GUSTAVSSON, A., ANDERSSON, K., MCGEE, K., PERSSON, C., RUDD, C. E. et al. YopH dephosphorylates Cas and Fyn-binding protein in macrophages. *Microbial Pathogenesis* **1999**, *27*, 231–242.
- 68 SHAO, F., MERRITT, P. M., BAO, Z., INNES, R. W., DIXON, J. E. A *Yersinia* effector and a avirulence protein define a family of cysteine proteases functioning in bacterial pathogenesis. *Cell* **2002**, *109*, 575–588.
- 69 LAMMERTYN, E., ANNE, J. Protein secretion in *Legionella pneumophila* and its relation to virulence. *FEMS Microbiol. Lett.* **2004**, *238*, 273–279.
- 70 CELLI, J., GORVEL, J.-P. Organelle robbery: *Brucella* interactions with the endoplasmic reticulum. *Curr. Opin. Microbiol.* **2004**, *7*, 93–97.
- 71 MA, Q., ZHAI, Y., SCHNEIDER, J. C., RAMSEIER, T. M., SAIER, J., MILTON, H. Protein secretion systems of *Pseudomonas aeruginosa* and *P. fluorescens*. *Biochim. Biophys. Acta Biomembranes* **2003**, *1611*, 223–233.
- 72 YEO, H.-J., WAKSMAN, G. Unveiling molecular scaffolds of the type IV Secretion system. *J. Bacteriol.* **2004**, *186*, 1919–1926.
- 73 SCHRÖDER, G., DEHIO, C. Virulence-associated type IV secretion systems of Bartonella. *Trends Microbiol.* **2005**, *13*, 336–342.
- 74 KAGAN, J. C., ROY, C. R. Legionella phagosomes intercept vesicular traffic from endoplasmic reticulum exit sites. *Nat. Cell Biol.* **2002**, *4*, 945–954.
- 75 CELLI, J., DE CHASTELLIER, C., FRANCHINI, D.-M., PIZARRO-CERDA, J., MORENO, E., GORVEL, J.-P. *Brucella* evades macrophage killing via VirB-dependent sustained interactions with the endoplasmic reticulum. *J. Exp. Med.* **2003**, *198*, 545–556.
- 76 FAN, P., DONG, F., HUANG, Y., ZHONG, G. *Chlamydia pneumoniae* secretion of a protease-like activity factor for degrading host cell transcription factors required for [correction of factors is required for] major histocompatibility complex antigen expression. *Infect. Immun.* **2002**, *70*, 345–349.
- 77 ZHONG, G., LIU, L., FAN, T., FAN, P., JI, H. Degradation of transcription factor RFX5 during the inhibition of both constitutive and interferon gamma-inducible major histocompatibility complex class I expression in chlamydia-infected cells. *J. Exp. Med.* **2000**, *191*, 1525–1534.
- 78 VOYICH, J. M., MUSSER, J. M., DELEO, F. R. *Streptococcus pyogenes* and human neutrophils: a paradigm for evasion of innate host defense by bacterial pathogens. *Microbes Infect.* **2004**, *6*, 1117–1123.
- 79 JI, Y., MCLANDSBOROUGH, L., KONDAGUNTA, A., CLEARY, P. P. C5a peptidase alters clearance and trafficking of group A streptococci by infected mice. *Infect. Immun.* **1996**, *64*, 503–510.
- 80 BISNO, A., BRITO, M., COLLINS, C. Molecular basis of group A streptococcal virulence. *Lancet Infect. Dis.* **2003**, *3*, 191–200.
- 81 RUS, H. G., NICULESCU, F. I., SHIN, M. L. Role of the C5b-9 complement complex in cell cycle and apoptosis. *Immunol. Rev.* **2001**, *180*, 49–55.
- 82 NICHOLSON-WELLER, A., HALPERIN, J. A. Membrane signaling by complement C5b-9, the membrane attack complex. *Immunol. Res.* **1993**, *12*, 244–257.
- 83 KAPUR, V., MAJESKY, M. W., LI, L. L., BLACK, R. A., MUSSER, J. M. Cleavage of interleukin 1 beta (IL-1 beta) precursor to produce active IL-1 beta by a conserved extracellular cysteine

- protease from *Streptococcus pyogenes*. *Proc. Natl Acad. Sci. USA* **1993**, *90*, 7676–7680.
- 84 COLLIN, M., SVENSSON, M. D., SJOHOLM, A. G., JENSENIUS, J. C., SJOBRING, U., OLSEN, A. EndoS and SpeB from *Streptococcus pyogenes* inhibit immunoglobulin-mediated opsonophagocytosis. *Infect. Immun.* **2002**, *70*, 6646–6651.
- 85 DALE, J. B., WASHBURN, R. G., MARQUES, M. B., WESSELS, M. R. Hyaluronate capsule and surface M protein in resistance to opsonization of group A streptococci. *Infect. Immun.* **1996**, *64*, 1495–1501.
- 86 DINKLA, K., ROHDE, M., JANSEN, W. T. M., CARAPETIS, J. R., CHHATWAL, G. S., TALAY, S. R. *Streptococcus pyogenes* recruits collagen via surface-bound fibronectin: a novel colonization and immune evasion mechanism. *Mol. Microbiol.* **2003**, *47*, 861–869.
- 87 VOSSEN, M., WESTERHOUT, E., SÖDERBERG-NAUCLÉR, C., WIERTZ, E. Viral immune evasion: a masterpiece of evolution. *Immunogenetics* **2002**, *54*, 527–542.
- 88 DAVIS, L. A., ROUSE, B. T. A skeptical look at viral immune evasion. *Front. Biosci.* **1997**, *2*, 596–605.
- 89 FAVOREEL, H. W., VAN DE WALLE, G. R., NAUWYNCK, H. J., PENSART, M. B. Virus complement evasion strategies. *J. Gen. Virol.* **2003**, *84*, 1–15.
- 90 LEE, S.-H., JUNG, J. U., MEANS, R. E. Viral infection: mechanisms for evading innate immunity. *Trends Microbiol.* **2003**, *11*, 449–452.
- 91 COOPER, N., JENSEN, F., WELSH, R., JR., OLDSTONE, M. Lysis of RNA tumor viruses by human serum: direct antibody-independent triggering of the classical complement pathway. *J. Exp. Med.* **1976**, *144*, 970–984.
- 92 EBENBICHLER, C., THIELENS, N., VORNHAGEN, R., MARSCHANG, P., ARLAUD, G., DIERICH, M. Human immunodeficiency virus type 1 activates the classical pathway of complement by direct C1 binding through specific sites in the trans-membrane glycoprotein gp41. *J. Exp. Med.* **1991**, *174*, 1417–1424.
- 93 IKEDA, F., HARAGUCHI, Y., JINNO, A., INO, Y., MORISHITA, Y., SHIRAKI, H. et al. Human complement component C1q Inhibits the Infectivity of Cell-Free HTLV-I. *J. Immunol.* **1998**, *161*, 5712–5719.
- 94 SPILLER, O. B., MORGAN, B. P. Antibody-independent activation of the classical complement pathway by cytomegalovirus-infected fibroblasts. *J. Infect. Dis.* **1998**, *178*, 1597–1603.
- 95 READING, P., MOREY, L., CROUCH, E., ANDERS, E. Collectin-mediated antiviral host defense of the lung: evidence from influenza virus infection of mice. *J. Virol.* **1997**, *71*, 8204–8212.
- 96 SASAKI, K., TSUTSUMI, A., WAKAMIYA, N., OHTANI, K., SUZUKI, Y., WATANABE, Y. et al. Mannose-binding lectin polymorphisms in patients with hepatitis C virus infection. *Scand. J. Gastroenterol.* **2000**, *35*, 960–965.
- 97 HAKOZAKI, Y., YOSHIBA, M., SEKIYAMA, K., SEIKE, E., IWAMOTO, J., MITANI, K. et al. Mannose-binding lectin and the prognosis of fulminant hepatic failure caused by HBV infection. *Liver* **2002**, *22*, 29–34.
- 98 MERI, S., PANGBURN, M. Discrimination between activators and nonactivators of the alternative pathway of complement: regulation via a sialic acid/polyanion binding site on factor H. *Proc. Natl Acad. Sci. USA* **1990**, *87*, 3982–3986.
- 99 VAN DEN BERG, C., MORGAN, B. Complement-inhibiting activities of human CD59 and analogues from rat, sheep, and pig are not homologously restricted. *J. Immunol.* **1994**, *152*, 4095–4101.
- 100 RUSHMERE, N. K., TOMLINSON, S., MORGAN, B. P. Expression of rat CD59: functional analysis confirms lack of species selectivity and reveals that glycosylation is not required for function. *Immunology* **1997**, *90*, 640–646.
- 101 FAVOREEL, H., NAUWYNCK, H., VAN OOSTVELDT, P., METTENLEITER, T., PENSART, M. Antibody-induced and

- cytoskeleton-mediated redistribution and shedding of viral glycoproteins, expressed on pseudorabies virus-infected cells. *J. Virol.* **1997**, *71*, 8254–8261.
- 102 KOTWAL, G. J., MILLER, C. G., JUSTUS, D. E. The inflammation modulatory protein (IMP) of cowpox virus drastically diminishes the tissue damage by down-regulating cellular infiltration resulting from complement activation. *Mol. Cell. Biochem.* **1998**, *185*, 39–46.
- 103 HUNG, S., SRINIVASAN, S., FRIEDMAN, H., EISENBERG, R., COHEN, G. Structural basis of C3b binding by glycoprotein C of herpes simplex virus. *J. Virol.* **1992**, *66*, 4013–4027.
- 104 FRIEDMAN, H. M., COHEN, G. H., EISENBERG, R. J., SEIDEL, C. A., CINES, D. B. Glycoprotein C of herpes simplex virus 1 acts as a receptor for the C3b complement component on infected cells. *Nature* **1984**, *309*, 633–635.
- 105 RUX, A. H., LOU, H., LAMBRIS, J. D., FRIEDMAN, H. M., EISENBERG, R. J., COHEN, G. H. Kinetic analysis of glycoprotein C of herpes simplex virus types 1 and 2 binding to heparin, heparan sulfate, and complement component C3b. *Virology* **2002**, *294*, 324–332.
- 106 ALBRECHT, J., FLECKENSTEIN, B. New member of the multigene family of complement control proteins in herpesvirus saimiri. *J. Virol.* **1992**, *66*, 3937–3940.
- 107 VANDERPLASSCHEN, A., MATHEW, E., HOLLINSHEAD, M., SIM, R. B., SMITH, G. L. Extracellular enveloped vaccinia virus is resistant to complement because of incorporation of host complement control proteins into its envelope. *Proc. Natl Acad. Sci. USA* **1998**, *95*, 7544–7549.
- 108 BETTS, R. F., SCHMIDT, S. G. Cytolytic IgM antibody to cytomegalovirus in primary cytomegalovirus infection in humans. *J. Infect. Dis.* **1981**, *143*, 821–826.
- 109 STOIBER, H., KACANI, L., SPETH, C., WURZNER, R., DIERICH, M. P. The supportive role of complement in HIV pathogenesis. *Immunol. Rev.* **2001**, *180*, 168–176.
- 110 NGUYEN, D. H., HILDRETH, J. E. K. Evidence for budding of human immunodeficiency virus type 1 selectively from glycolipid-enriched membrane lipid rafts. *J. Virol.* **2000**, *74*, 3264–3272.
- 111 SAIFUDDIN, M., PARKER, C., PEEPLES, M., GORNY, M., ZOLLA-PAZNER, S., GHASSEMI, M. et al. Role of virion-associated glycosylphosphatidylinositol-linked proteins CD55 and CD59 in complement resistance of cell line-derived and primary isolates of HIV-1. *J. Exp. Med.* **1995**, *182*, 501–509.
- 112 SAIFUDDIN, M., HEDAYATI, T., ATKINSON, J., HOLGUIN, M., PARKER, C., SPEAR, G. Human immunodeficiency virus type 1 incorporates both glycosyl phosphatidylinositol-anchored CD55 and CD59 and integral membrane CD46 at levels that protect from complement-mediated destruction. *J. Gen. Virol.* **1997**, *78*, 1907–1911.
- 113 HIRSCH, R. L., GRIFFIN, D. E., WINKELSTEIN, J. A. Natural immunity to sindbis virus is influenced by host tissue sialic acid content. *Proc. Natl Acad. Sci. USA* **1983**, *80*, 548–550.
- 114 WATKINS, J. F. Adsorption of sensitized sheep erythrocytes to HeLa cells infected with herpes simplex virus. *Nature* **1964**, *202*, 1364–1365.
- 115 WESTMORELAND, D., WATKINS, J. F. The IgG receptor induced by herpes simplex virus: studies using radioiodinated IgG. *J. Gen. Virol.* **1974**, *24*, 167–178.
- 116 OLESZAK, E. L., PERLMAN, S., PARR, R., COLLISSON, E. W., LEIBOWITZ, J. L. Molecular mimicry between S peplomer proteins of coronaviruses (MHV, BCV, TGEV and IBV) and Fc receptor. *Adv. Exp. Med. Biol.* **1993**, *342*, 183–188.
- 117 DOWLER, K. W., VELTRI, R. W. *In vitro* neutralization of HSV-2: inhibition by binding of normal IgG and purified Fc to virion Fc receptor (FcR). *J. Med. Virol.* **1984**, *13*, 251–259.
- 118 FRANK, I., FRIEDMAN, H. M. A novel function of the herpes simplex virus

- type 1 Fc receptor: participation in bipolar bridging of antiviral immunoglobulin G. *J. Virol.* **1989**, *63*, 4479–4488.
- 119 SMITH, A. E., HELENIUS, A. How viruses enter animal cells. *Science* **2004**, *304*, 237–242.
- 120 BARANOWSKI, E., RUIZ-JARABO, C. M., DOMINGO, E. Evolution of cell recognition by viruses. *Science* **2001**, *292*, 1102–1105.
- 121 BASHIROVA, A. A., GEIJTENBEEK, T. B. H., VAN DUINHoven, G. C. F., VAN VLIET, S. J., EILERING, J. B. G., MARTIN, M. P. et al. A Dendritic cell-specific intercellular adhesion molecule 3-grabbing nonintegrin (DC-SIGN)-related protein is highly expressed on human liver sinusoidal endothelial cells and promotes HIV-1 infection. *J. Exp. Med.* **2001**, *193*, 671–678.
- 122 POHLMANN, S., BARIBAUD, F., DOMS, R. W. DC-SIGN and DC-SIGNR: helping hands for HIV. *Trends Immunol.* **2001**, *22*, 643–646.
- 123 FENG, Y., BRODER, C. C., KENNEDY, P. E., BERGER, E. A. HIV-1 entry cofactor: functional cDNA cloning of a seven-transmembrane, G protein-coupled receptor. *Science* **1996**, *272*, 872–877.
- 124 GALLO, S. A., FINNEGAN, C. M., VIARD, M., RAVIV, Y., DIMITROV, A., RAWAT, S. S. et al. The HIV Env-mediated fusion reaction. *Biochim. Biophys. Acta Biomembranes* **2003**, *1614*, 36–50.
- 125 CARR, C. M., KIM, P. S. A spring-loaded mechanism for the conformational change of influenza hemagglutinin. *Cell* **1993**, *73*, 823–832.
- 126 SKEHEL, J. J., WILEY, D. C. Receptor binding and membrane fusion in virus entry: the influenza hemagglutinin. *Annu. Rev. Biochem.* **2000**, *69*, 531–569.
- 127 CARFI, A., WILLIS, S. H., WHITBECK, J. C., KRUMMENACHER, C., COHEN, G. H., EISENBERG, R. J. et al. Herpes simplex virus glycoprotein D bound to the human receptor HveA. *Mol. Cell* **2001**, *8*, 169–179.
- 128 TSAI, B., GILBERT, J. M., STEHLE, T., LENCER, W., BENJAMIN, T. L., RAPOPORT, T. A. Gangliosides are receptors for murine polyoma virus and SV40. *EMBO J.* **2003**, *22*, 4346–4355.
- 129 SMITH, A. E., LILIE, H., HELENIUS, A. Ganglioside-dependent cell attachment and endocytosis of murine polyomavirus-like particles. *FEBS Lett.* **2003**, *555*, 199–203.
- 130 MULLEN, M. M., HAAN, K. M., LONGNECKER, R., JARDETZKY, T. S. Structure of the Epstein–Barr virus gp42 protein bound to the MHC class II receptor HLA-DR1. *Mol. Cell* **2002**, *9*, 375–385.
- 131 CONNER, S. D., SCHMID, S. L. Regulated portals of entry into the cell. *Nature* **2003**, *422*, 37–44.
- 132 BANTEL-SCHAAL, U., HUB, B., KARTENBECK, J. Endocytosis of adeno-associated virus type 5 leads to accumulation of virus particles in the Golgi compartment. *J. Virol.* **2002**, *76*, 2340–2349.
- 133 DALES, S. Early events in cell-animal virus interactions. *Bacteriol. Rev.* **1973**, *37*, 103–135.
- 134 MARSH, M., HELENIUS, A. Virus entry into animal cells. *Adv. Virus Res.* **1989**, *36*, 107–151.
- 135 HELENIUS, A., KARTENBECK, J., SIMONS, K., FRIES, E. On the entry of Semliki forest virus into BHK-21 cells. *J. Cell Biol.* **1980**, *84*, 404–420.
- 136 MARTIN, K., HELENIUS, A. Nuclear transport of influenza virus ribonucleoproteins: the viral matrix protein (M1) promotes export and inhibits import. *Cell* **1991**, *67*, 117–130.
- 137 KIELIAN, M., HELENIUS, A. pH-induced alterations in the fusogenic spike protein of Semliki Forest virus. *J. Cell Biol.* **1985**, *101*, 2284–2291.
- 138 SCHMID, S., FUCHS, R., KIELIAN, M., HELENIUS, A., MELLMAN, I. Acidification of endosome subpopulations in wild-type Chinese hamster ovary cells and temperature-sensitive acidification-defective mutants. *J. Cell Biol.* **1989**, *108*, 1291–1300.
- 139 BLUMENTHAL, R., SETH, P., WILLINGHAM, M. C., PASTAN, I. pH-dependent



- lysis of liposomes by adenovirus. *Biochemistry* **1986**, *25*, 2231–2237.
- 140 FITZGERALD, D. J., PADMANABHAN, R., PASTAN, I., WILLINGHAM, M. C. Adenovirus-induced release of epidermal growth factor and pseudomonas toxin into the cytosol of KB cells during receptor-mediated endocytosis. *Cell* **1983**, *32*, 607–617.
  - 141 CHANDRAN, K., FARSETTA, D. L., NIBERT, M. L. Strategy for non-enveloped virus entry: a hydrophobic conformer of the reovirus membrane penetration protein  $\mu 1$  mediates membrane disruption. *J. Virol.* **2002**, *76*, 9920–9933.
  - 142 HOGLE, J. M. Poliovirus cell entry: common structural themes in viral cell entry pathways. *Annu. Rev. Microbiol.* **2002**, *56*, 677–702.
  - 143 SODEIK, B. Mechanisms of viral transport in the cytoplasm. *Trends Microbiol.* **2000**, *8*, 465–472.
  - 144 MARSH, M., BRON, R. SFV infection in CHO cells: cell-type specific restrictions to productive virus entry at the cell surface. *J. Cell Sci.* **1997**, *110*, 95–103.
  - 145 PORANEN, M. M., DAUGELAVICIUS, R., BAMFORD, D. H. Common principles in viral entry. *Annu. Rev. Microbiol.* **2002**, *56*, 521–538.
  - 146 COLMAN, P. M., LAWRENCE, M. C. The structural biology of type I viral membrane fusion. *Nat. Rev. Mol. Cell Biol.* **2003**, *4*, 309–319.
  - 147 GIBBONS, D. L., ERK, I., REILLY, B., NAVAZA, J., KIELIAN, M., REY, F. A. et al. Visualization of the target-membrane-inserted fusion protein of semliki forest virus by combined electron microscopy and crystallography. *Cell* **2003**, *114*, 573–583.
  - 148 MODIS, Y., OGATA, S., CLEMENTS, D., HARRISON, S. C. Structure of the dengue virus envelope protein after membrane fusion. *Nature* **2004**, *427*, 313–319.
  - 149 GIBBONS, D. L., VANEY, M.-C., ROUSSEL, A., VIGOUROUX, A., REILLY, B., LEPAULT, J. et al. Conformational change and protein–protein interactions of the fusion protein of Semliki Forest virus. *Nature* **2004**, *427*, 320–325.
  - 150 KASAMATSU, H., NAKANISHI, A. How do animal DNA viruses get to the nucleus? *Annu. Rev. Microbiol.* **1998**, *52*, 627–686.
  - 151 WHITTAKER, G. R., KANN, M., HELENIUS, A. Viral entry into the nucleus. *Annu. Rev. Cell Dev. Biol.* **2000**, *16*, 627–651.
  - 152 WHITTAKER, G. R. Virus nuclear import. *Adv. Drug Deliv. Rev.* **2003**, *55*, 733–747.
  - 153 NORKIN, L. C. Caveolae in the uptake and targeting of infectious agents and secreted toxins. *Adv. Drug Deliv. Rev.* **2001**, *49*, 301–315.
  - 154 PARTON, R. G., RICHARDS, A. A. Lipid rafts and caveolae as portals for endocytosis: new insights and common mechanisms. *Traffic* **2003**, *4*, 724–738.
  - 155 PELKMANS, L., HELENIUS, A. Insider information: what viruses tell us about endocytosis. *Curr. Opin. Cell Biol.* **2003**, *15*, 414–422.
  - 156 PANTE, N., KANN, M. Nuclear pore complex is able to transport macromolecules with diameters of  $\sim 39$  nm. *Mol. Biol. Cell* **2002**, *13*, 425–434.
  - 157 MERLE, E., ROSE, R. C., LEROUX, L., MOROIANU, J. Nuclear import of HPV11 L1 capsid protein is mediated by karyopherin  $\alpha 2\beta 1$  heterodimers. *J. Cell. Biochem.* **1999**, *74*, 628–637.
  - 158 NELSON, L. M., ROSE, R. C., LEROUX, L., LANE, C., BRUYA, K., MOROIANU, J. Nuclear import and DNA binding of human papillomavirus type 45 L1 capsid protein. *J. Cell. Biochem.* **2000**, *79*, 225–238.
  - 159 KANN, M., SODEIK, B., VLACHOU, A., GERLICH, W. H., HELENIUS, A. Phosphorylation-dependent binding of hepatitis B virus core particles to the nuclear pore complex. *J. Cell Biol.* **1999**, *145*, 45–55.
  - 160 O'NEILL, R. E., JASKUNAS, R., BLOBEL, G., PALESE, P., MOROIANU, J. Nuclear import of influenza virus RNA can be mediated by viral nucleoprotein and transport factors required for protein import. *J. Biol. Chem.* **1995**, *270*, 22701–22704.
  - 161 TROTMAN, L. C., MOSBERGER, N., FORNEROD, M., STIDWILL, R. P.,

- GREBER, U. F. Import of adenovirus DNA involves the nuclear pore complex receptor CAN/Nup214 and histone H1. *Nat. Cell Biol.* **2001**, *3*, 1092–1100.
- 162 GREBER, U. F., FASSATI, A. Nuclear import of viral DNA genomes. *Traffic* **2003**, *4*, 136–143.
- 163 OJALA, P. M., SODEIK, B., EBERSOLD, M. W., KUTAY, U., HELENIUS, A. Herpes simplex virus type 1 entry into host cells: reconstitution of capsid binding and uncoating at the nuclear pore complex *in vitro*. *Mol. Cell. Biol.* **2000**, *20*, 4922–4931.
- 164 NEWCOMB, W. W., JUHAS, R. M., THOMSEN, D. R., HOMA, F. L., BURCH, A. D., WELLER, S. K. et al. The UL6 gene product forms the portal for entry of DNA into the herpes simplex virus capsid. *J. Virol.* **2001**, *75*, 10923–10932.
- 165 LUNDSTROM, K. Latest development in viral vectors for gene therapy. *Trends Biotechnol.* **2003**, *21*, 117–122.
- 166 RELPH, K., HARRINGTON, K., PANDHA, H. Recent developments and current status of gene therapy using viral vectors in the United Kingdom. *Br. Med. J.* **2004**, *329*, 839–842.
- 167 CAVAZZANA-CALVO, M., HACEIN-BEY, S., BASILE, G. e. v. d. S., GROSS, F., YVON, E., NUSBAUM, P. et al. Gene therapy of human severe combined immunodeficiency (SCID)-X1 disease. *Science* **2000**, *288*, 669–672.
- 168 HACEIN-BEY-ABINA, S., FISCHER, A., CAVAZZANA-CALVO, M. Gene therapy of X-linked severe combined immunodeficiency. *Int. J. Hematol.* **2002**, *76*, 295–298.
- 169 BLAESE, R. M., CULVER, K. W., MILLER, A. D., CARTER, C. S., FLEISHER, T., CLERICI, M. et al. T lymphocyte-directed gene therapy for ADA SCID: initial trial results after 4 years. *Science* **1995**, *270*, 475–480.
- 170 RAPER, S. E., YUDKOFF, M., CHIRMULE, N., GAO, G.-P., NUNES, F., HASKAL, Z. J. et al. A pilot study of *in vivo* liver-directed gene transfer with an adenoviral vector in partial ornithine transcarbamylase deficiency. *Hum. Gene Ther.* **2002**, *13*, 163–175.
- 171 KIMMELMAN, J. Recent developments in gene transfer: risk and ethics. *Br. Med. J.* **2005**, *330*, 79–82.
- 172 RAPER, S. E. Gene therapy: the good, the bad, and the ugly. *Surgery* **2005**, *137*, 487–492.
- 173 RABINOWITZ, J. E., SAMULSKI, J. Adeno-associated virus expression systems for gene transfer. *Curr. Opin. Biotechnol.* **1998**, *9*, 470–475.
- 174 DAVIDSON, B. L., STEIN, C. S., HETH, J. A., MARTINS, I., KOTIN, R. M., DERKSEN, T. A. et al. From the cover: recombinant adeno-associated virus type 2, 4, and 5 vectors: transduction of variant cell types and regions in the mammalian central nervous system. *Proc. Natl Acad. Sci. USA* **2000**, *97*, 3428–3432.
- 175 RUSSELL, D. W., KAY, M. A. Adeno-associated virus vectors and hematology. *Blood* **1999**, *94*, 864–874.
- 176 FLOTTE, T. R., LAUBE, B. L. Gene therapy in cystic fibrosis. *Chest* **2001**, *120*, 124S–131.
- 177 WEST, J., RODMAN, D. M. Gene therapy for pulmonary diseases. *Chest* **2001**, *119*, 613–617.
- 178 HIDAKA, C., KHAN, S. N., FARMER, J. C., SANDHU, H. S. Gene therapy for spinal applications. *Orthop. Clin. North Am.* **2002**, *33*, 439–446.
- 179 STECHER, H., SHAYAKHMETOV, D. M., STAMATOYANNOPOULOS, G., LIEBER, A. A capsid-modified adenovirus vector devoid of all viral genes: assessment of transduction and toxicity in human hematopoietic cells. *Mol. Ther.* **2001**, *4*, 36–44.
- 180 HAVIV, Y. S., BLACKWELL, J. L., KANERVA, A., NAGI, P., KRASNKYH, V., DMITRIEV, I. et al. Adenoviral gene therapy for renal cancer requires retargeting to alternative cellular receptors. *Cancer Res.* **2002**, *62*, 4273–4281.
- 181 YOUNG, L. S., MAUTNER, V. The promise and potential hazards of adenovirus gene therapy. *Gut* **2001**, *48*, 733–736.
- 182 SCHIEDNER, G., MORRAL, N., PARKS, R. J., WU, Y., KOOPMANS, S. C., LANGSTON, C. et al. Genomic DNA transfer with a high-capacity adeno-

- virus vector results in improved *in vivo* gene expression and decreased toxicity. *Nat. Genet.* **1998**, *18*, 180–183.
- 183** GOMEZ-MANZANO, C., YUNG, W. K. A., ALEMANY, R., FUEYO, J. Genetically modified adenoviruses against gliomas: from bench to bedside. *Neurology* **2004**, *63*, 418–426.
- 184** SMITH, G. M. Adenovirus-mediated gene transfer to treat neurologic disease. *Arch. Neurol.* **1998**, *55*, 1061–1064.
- 185** SAMANIEGO, L. A., NEIDERHISER, L., DELUCA, N. A. Persistence and expression of the herpes simplex virus genome in the absence of immediate-early proteins. *J. Virology* **1998**, *72*, 3307–3320.
- 186** KRISKY, D. M., WOLFE, D., GOINS, W. F., MARCONI, P. C., RAMAKRISHNAN, R., MATA, M. et al. Deletion of multiple immediate-early genes from herpes simplex virus reduces cytotoxicity and permits long-term gene expression in neurons. *Gene Ther.* **1998**, *5*, 1593–1603.
- 187** KENNEDY, P. Potential use of herpes simplex virus (HSV) vectors for gene therapy of neurological disorders. *Brain* **1997**, *120*, 1245–1259.
- 188** AKKARAJU, G. R., HUARD, J., HOFFMAN, E. P., GOINS, W. F., PRUCHNIC, R., WATKINS, S. C., COHEN, J. B., GIORIOSO, J. C. Herpes simplex virus vector-mediated dystrophin gene transfer and expression in MDX mouse skeletal muscle. *J. Gene Med.* **1999**, *1*, 280–289.
- 189** BUCHSCHACHER, G. L., JR., WONG-STAAAL, F. Development of lentiviral vectors for gene therapy for human diseases. *Blood* **2000**, *95*, 2499–2504.
- 190** ELISA VIGNA, L. N. Lentiviral vectors: excellent tools for experimental gene transfer and promising candidates for gene therapy. *J. Gene Med.* **2000**, *2*, 308–316.
- 191** BURNS, J. C., FRIEDMANN, T., DRIEVER, W., BURRASCANO, M., YEE, J. K. Vesicular stomatitis virus G glycoprotein pseudotyped retroviral vectors: concentration to very high titer and efficient gene transfer into mammalian and nonmammalian cells. *Proc. Natl Acad. Sci. USA* **1993**, *90*, 8033–8037.
- 192** BAUM, C., DULLMANN, J., LI, Z., FEHSE, B., MEYER, J., WILLIAMS, D. A. et al. Side-effects of retroviral gene transfer into hematopoietic stem cells. *Blood* **2003**, *101*, 2099–2113.
- 193** SUHR, S. T., GAGE, F. H. Gene therapy in the central nervous system: the use of recombinant retroviruses. *Arch. Neurol.* **1999**, *56*, 287–292.
- 194** MALECH, H. L., CHOI, U., BRENNER, S. Progress toward effective gene therapy for chronic granulomatous disease. *Jpn. J. Infect. Dis.* **2004**, *57*, S27–28.
- 195** FISHER, K. D., STALLWOOD, Y., GREEN, N. K., ULBRICH, K., MAUTNER, V., SEYMOUR, L. W. Polymer-coated adenovirus permits efficient retargeting and evades neutralising antibodies. *Gene Ther.* **2001**, *8*, 341–348.
- 196** KANEDA, Y. Virosomes: evolution of the liposome as a targeted drug delivery system. *Adv. Drug Deliv. Rev.* **2000**, *43*, 197–205.
- 197** MORISHITA, R., GIBBONS, G. H., KANEDA, Y., OGIHARA, T., DZAU, V. J. Pharmacokinetics of antisense oligodeoxyribonucleotides (cyclin B1 and CDC 2 kinase) in the vessel wall *in vivo*: enhanced therapeutic utility for restenosis by HVJ-liposome delivery. *Gene* **1994**, *149*, 13–19.
- 198** RAMANI, K., BORA, R. S., KUMAR, M., TYAGI, S. K., SARKAR, D. P. Novel gene delivery to liver cells using engineered virosomes. *FEBS Lett.* **1997**, *404*, 164–168.
- 199** CHATIGNY, M. A., PRUSINER, S. B. Biohazards of investigations on the transmissible spongiform encephalopathies. *Rev. Infect. Dis.* **1980**, *2*, 713–724.
- 200** PRUSINER, S. B. Prions: novel infectious pathogens. *Adv. Virus Res.* **1984**, *29*, 1–56.
- 201** PRUSINER, S. B., KINGSBURY, D. T. Prions – infectious pathogens causing the spongiform encephalopathies. *CRC Crit. Rev. Clin. Neurobiol.* **1985**, *1*, 181–200.

- 202 MABBOTT, N. A. The complement system in prion diseases. *Curr. Opin. Immunol.* **2004**, *16*, 587–593.
- 203 AGUZZI, A., HEIKENWALDER, M. Prions, Cytokines, and chemokines: a meeting in lymphoid organs. *Immunity* **2005**, *22*, 145–154.
- 204 JOHNSON, R. T. Prion diseases. *Lancet Neurol.* **2005**, *4*, 635–642.
- 205 AGUZZI, A. Prions and the immune system: a journey through gut, spleen, and nerves. *Adv. Immunol.* **2003**, *81*, 123–171.
- 206 SIGURDSON, C. J., BARILLAS-MURY, C., MILLER, M. W., OESCH, B., VAN KEULEN, L. J. M., LANGEVELD, J. P. M. et al. PrP<sup>CWD</sup> lymphoid cell targets in early and advanced chronic wasting disease of mule deer. *J. Gen. Virology* **2002**, *83*, 2617–2628.
- 207 HEGGEBO, R., PRESS, C. M., GUNNES, G., ULVUND, M. J., TRANULIS, M. A., LSVERK, T. Detection of PrP<sup>Sc</sup> in lymphoid tissues of lambs experimentally exposed to the scrapie agent. *J. Comp. Pathol.* **2003**, *128*, 172–181.
- 208 NEUTRA, M. R., FREY, A., KRAEHENBUHL, J.-P. Epithelial M cells: gateways for mucosal infection and immunization. *Cell* **1996**, *86*, 345–348.
- 209 AGUZZI, A., HEIKENWALDER, M. Prion diseases: cannibals and garbage piles. *Nature* **2003**, *423*, 127–129.
- 210 MABBOTT, N. A., YOUNG, J., MCCONNELL, I., BRUCE, M. E. Follicular dendritic cell dedifferentiation by treatment with an inhibitor of the lymphotoxin pathway dramatically reduces scrapie susceptibility. *J. Virol.* **2003**, *77*, 6845–6854.
- 211 PRINZ, M., HEIKENWALDER, M., JUNGT, T., SCHWARZ, P., GLATZEL, M., HEPPNER, F. L. et al. Positioning of follicular dendritic cells within the spleen controls prion neuroinvasion. *Nature* **2003**, *425*, 957–962.
- 212 BRANDNER, S., ISENMANN, S., RAEBER, A., FISCHER, M., SAILER, A., KOBAYASHI, Y. et al. Normal host prion protein necessary for scrapie-induced neurotoxicity. *Nature* **1996**, *379*, 339–343.
- 213 BUELER, H., AGUZZI, A., SAILER, A., GREINER, R. A., AUTENRIED, P., AGUET, M. et al. Mice devoid of PrP are resistant to scrapie. *Cell* **1993**, *73*, 1339–1347.
- 214 MALLUCCI, G., DICKINSON, A., LINEHAN, J., KLOHN, P.-C., BRANDNER, S., COLLINGE, J. Depleting neuronal PrP in prion infection prevents disease and reverses spongiosis. *Science* **2003**, *302*, 871–874.
- 215 KLEIN, M. A., FRIGG, R., FLECHSIG, E., RAEBER, A. J., KALINKE, U., BLUETHMANN, H. et al. A crucial role for B cells in neuroinvasive scrapie. *Nature* **1997**, *390*, 687–690.
- 216 KAESER, P. S., KLEIN, M. A., SCHWARZ, P., AGUZZI, A. Efficient lymphoreticular prion propagation requires PrP<sup>C</sup> in stromal and hematopoietic cells. *J. Virol.* **2001**, *75*, 7097–7106.
- 217 BEEKES, M., MCBRIDE, P. A. Early accumulation of pathological PrP in the enteric nervous system and gut-associated lymphoid tissue of hamsters orally infected with scrapie. *Neurosci. Lett.* **2000**, *278*, 181–184.
- 218 MABBOTT, N. A., BRUCE, M. E. Prion disease: bridging the spleen–nerve gap. *Nat. Med.* **2003**, *9*, 1463–1464.
- 219 FEVRIER, B., VILETTE, D., ARCHER, F., LOEW, D., FAIGLE, W., VIDAL, M. et al. Cells release prions in association with exosomes. *Proc. Natl Acad. Sci. USA* **2004**, *101*, 9683–9688.
- 220 RAEBER, A. J., KLEIN, M. A., FRIGG, R., FLECHSIG, E., AGUZZI, A., WEISSMANN, C. PrP-dependent association of prions with splenic but not circulating lymphocytes of scrapie-infected mice. *EMBO J.* **1999**, *18*, 2702–2706.
- 221 HUANG, F.-P., FARQUHAR, C. F., MABBOTT, N. A., BRUCE, M. E., MACPHERSON, G. G. Migrating intestinal dendritic cells transport PrP<sup>Sc</sup> from the gut. *J. Gen. Virology* **2002**, *83*, 267–271.
- 222 AUCOUTURIER, P., GEISSMANN, F., DAMOTTE, D., SABORIO, G. P., MEEKER, H. C., KASCSAK, R. et al. Infected splenic dendritic cells are sufficient for prion transmission to the CNS in mouse scrapie. *J. Clin. Invest.* **2001**, *108*, 703–708.

- 223 YOSHIDA, K., VAN DEN BERG, T. K., DIJKSTRA, C. D. Two different mechanisms of immune-complex trapping in the mouse spleen during immune responses. *Adv. Exp. Med. Biol.* **1993**, 329, 377–382.
- 224 KLEIN, M. A., KAESER, P. S., SCHWARZ, P., WEYD, H., XENARIOS, I., ZINKER-NAGEL, R. M. et al. Complement facilitates early prion pathogenesis. *Nat. Med.* **2001**, 7, 488–492.
- 225 ROSEN, H., ABRIBAT, T. The rise and rise of drug delivery. *Nat. Rev. Drug Discov.* **2005**, 4, 381–385.
- 226 DUNCAN, R. The dawning era of polymer therapeutics. *Nat. Rev. Drug Discov.* **2003**, 2, 347–360.
- 227 THEEUWES, F., SWANSON, D., WONG, P., BONSEN, P., PLACE, V., HEIMLICH, K. et al. Elementary osmotic pump for indomethacin. *J. Pharm. Sci.* **1983**, 72, 253–258.
- 228 COLOMBO, P., CONTE, U., GAZZANIGA, A., MAGGI, L., SANGALLI, M. E., PEPPAS, N. A. et al. Drug release modulation by physical restrictions of matrix swelling. *Int. J. Pharm.* **1990**, 63, 43–48.
- 229 CONTE, U., MAGGI, L., COLOMBO, P., LA MANNA, A. Multi-layered hydrophilic matrices as constant release devices (Geomatrix™ Systems). *J. Control. Release* **1993**, 26, 39–47.
- 230 VERSI, E., APPELL, R., MOBLEY, D., PATTON, W., SALTZSTEIN, D. Dry mouth with conventional and controlled-release oxybutynin in urinary incontinence. *Obstet. Gynecol.* **2000**, 95, 718–721.
- 231 ANDERSON, R. U., MOBLEY, D., BLANK, B., SALTZSTEIN, D., SUSSET, J., BROWN, J. S. Once daily controlled versus immediate release oxybutynin chloride for urge urinary incontinence. OROS Oxybutynin Study Group. *J. Urol.* **1999**, 161, 1809–1812.
- 232 VISCUSI, E. R., REYNOLDS, L., CHUNG, F., ATKINSON, L. E., KHANNA, S. Patient-controlled transdermal fentanyl hydrochloride vs intravenous morphine pump for postoperative pain: a randomized controlled Trial. *J. Am. Med. Ass.* **2004**, 291, 1333–1341.
- 233 SEBASTIEN HENRY, D. V. M., MARK G. ALLEN, MARK R. PRAUSNITZ. Microfabricated microneedles: a novel approach to transdermal drug delivery. *J. Pharmaceutical Sciences* **1998**, 87, 922–925.
- 234 BARRY, B. W. Novel mechanisms and devices to enable successful transdermal drug delivery. *Eur. J. Pharm. Sci.* **2001**, 14, 101–114.
- 235 ORIVE, G., HERNANDEZ, R. M., GASCON, A. R., DOMINGUEZ-GIL, A., PEDRAZ, J. L. Drug delivery in biotechnology: present and future. *Curr. Opin. Biotechnol.* **2003**, 14, 659–664.
- 236 KILPATRICK, D. C., PUSZTAI, A., GRANT, G., GRAHAM, C., EWEN, S. W. B. Tomato lectin resists digestion in the mammalian alimentary canal and binds to intestinal villi without deleterious effects. *FEBS Lett.* **1985**, 185, 299–305.
- 237 CARRENO-GOMEZ, B., WOODLEY, J. F., FLORENCE, A. T. Studies on the uptake of tomato lectin nanoparticles in everted gut sacs. *Int. J. Pharm.* **1999**, 183, 7–11.
- 238 VERONESE, F. M., HARRIS, J. M. Introduction and overview of peptide and protein pegylation. *Adv. Drug Deliv. Rev.* **2002**, 54, 453–456.
- 239 FORAN, T. M. New contraceptive choices across reproductive life. *Med. J. Aust.* **2003**, 178, 616–620.
- 240 JAIN, S. K., CHOURASIA, M. K., JAIN, A. K., JAIN, R. K., SHRIVASTAVA, A. K. Development and characterization of mucoadhesive microspheres bearing salbutamol for nasal delivery. *Drug Deliv.* **2004**, 11, 113–122.
- 241 LUUKKAINEN, T., PAKARINEN, P., TOIVONEN, J. Progesterin-releasing intrauterine systems. *Semin. Reprod. Med.* **2001**, 19, 355–363.
- 242 ELEY, J. G., PUJARI, V. D., MCLANE, J. Poly (lactide-co-glycolide) nanoparticles containing coumarin-6 for suppository delivery: *in vitro* release profile and *in vivo* tissue distribution. *Drug Deliv.* **2004**, 11, 255–261.
- 243 MERKUS, F. W. H. M., VERHOEF, J. C., MARTIN, E., ROMELJN, S. G., VAN DER KUY, P. H. M., HERMENS, W. A. J. J.,

- et al. Cyclodextrins in nasal drug delivery. *Adv. Drug Deliv. Rev.* **1999**, *36*, 41–57.
- 244 DODANE, V., AMIN KHAN, M., MERWIN, J. R. Effect of chitosan on epithelial permeability and structure. *Int. J. Pharm.* **1999**, *182*, 21–32.
- 245 ILLUM, L., JABBAL-GILL, I., HINCHCLIFFE, M., FISHER, A. N., DAVIS, S. S. Chitosan as a novel nasal delivery system for vaccines. *Adv. Drug Deliv. Rev.* **2001**, *51*, 81–96.
- 246 LAVAN, D. A., MCGUIRE, T., LANGER, R. Small-scale systems for *in vivo* drug delivery. *Nat. Biotechnol.* **2003**, *21*, 1184–1191.
- 247 SANTINI, J. T., JR., CIMA, M. J., LANGER, R. A controlled-release microchip. *Nature* **1999**, *397*, 335–338.
- 248 UNGER, M. A., CHOU, H.-P., THORSEN, T., SCHERER, A., QUAKE, S. R. Monolithic microfabricated valves and pumps by multilayer soft lithography. *Science* **2000**, *288*, 113–116.
- 249 HANSEN, C. L., SKORDALAKES, E., BERGER, J. M., QUAKE, S. R. A robust and scalable microfluidic metering method that allows protein crystal growth by free interface diffusion. *Proc. Natl Acad. Sci. USA* **2002**, *99*, 16531–16536.
- 250 LILLY, M. B., BREZOVICH, I. A., ATKINSON, W. J. Hyperthermia induction with thermally self-regulated ferromagnetic implants. *Radiology* **1985**, *154*, 243–244.
- 251 TUCKER, R. D., HUIDOBRO, C., LARSON, T., PLATZ, C. E. Use of permanent interstitial temperature self-regulating rods for ablation of prostate cancer. *J. Endourol.* **2000**, *14*, 511–517.
- 252 ROTARIU, O., IACOB, G., STRACHAN, N. J. C., CHIRIAC, H. Simulating the embolization of blood vessels using magnetic microparticles and acupuncture needle in a magnetic field. *Biotechnol. Prog.* **2004**, *20*, 299–305.
- 253 LANZA, G. M., WINTER, P., CARUTHERS, S., SCHMEIDER, A., CROWDER, K., MORAWSKI, A. et al. Novel paramagnetic contrast agents for molecular imaging and targeted drug delivery. *Curr. Pharm. Biotechnol.* **2004**, *5*, 495–507.
- 254 BOS, G. W., CROMMELIN, D. J. A., HENNINK, W. E., VERRIJK, R., FRANSSSEN, O., BEZEMER, J. M. Hydrogels for the controlled release of pharmaceutical proteins. *Pharm. Technol. Eur.* **2001**, *13*, 64+67–68+70+72+74.
- 255 MIYATA, T., ASAMI, N., URAGAMI, T. A reversibly antigen-responsive hydrogel. *Nature* **1999**, *399*, 766–769.
- 256 HELLER, J., TRESCONY, P. V. Controlled drug release by polymer dissolution. II: Enzyme-mediated delivery device. *J. Pharm. Sci.* **1979**, *68*, 919–921.
- 257 KWON, I. C., BAE, Y. H., KIM, S. W. Electrically credible polymer gel for controlled release of drugs. *Nature* **1991**, *354*, 291–293.
- 258 ICHIMURA, K., OH, S.-K., NAKAGAWA, M. Light-driven motion of liquids on a photoresponsive surface. *Science* **2000**, *288*, 1624–1626.
- 259 ABBOTT, S., RALSTON, J., REYNOLDS, G., HAYES, R. Reversible wettability of photoresponsive pyrimidine-coated surfaces. *Langmuir* **1999**, *15*, 8923–8928.
- 260 LAHANN, J., MITRAGOTRI, S., TRAN, T.-N., KAIDO, H., SUNDARAM, J., CHOI, I. S. et al. A reversibly switching surface. *Science* **2003**, *299*, 371–374.
- 261 DESAI, T. A., CHU, W. H., TU, J. K., BEATTIE, G. M., HAYEK, A., FERRARI, M. Microfabricated immunisolating biocapsules. *Biotechnol. Bioeng.* **1998**, *57*, 118–120.
- 262 SEFTON, M. V., HORVATH, V., ZINGG, W. Insulin delivery by a diffusion-controlled micropump in pancreatized dogs: phase 1. *J. Control. Release* **1990**, *12*, 1–12.
- 263 HANAS, R. Selection for and initiation of continuous subcutaneous insulin infusion. *Hormone Res.* **2002**, *57*, 101–104.
- 264 FISHER, R. S., HO, J. Potential new methods for antiepileptic drug delivery. *CNS Drugs* **2002**, *16*, 579–593.
- 265 GARDNER, B., JAMOUS, A., TEDDY, P., BERGSTROM, E., WANG, D.,

- RAVICHANDRAN, G. et al. Intrathecal baclofen – a multicentre clinical comparison of the Medtronic Programmable, Cordis Secor and Constant Infusion Infusaid drug delivery systems. *Paraplegia* **1995**, *33*, 551–554.
- 266 DIAZ, S., PAVEZ, M., MIRANDA, P., ROBERTSON, D. N., SIVIN, I., CROXATTO, H. B. A five-year clinical trial of levonorgestrel silastic implants (Norplant™). *Contraception* **1982**, *25*, 447–456.
- 267 CHANG, T. M. S. Therapeutic applications of polymeric artificial cells. *Nat. Rev. Drug Discov.* **2005**, *4*, 221–235.
- 268 REGULIER, E., SCHNEIDER, B. L., DEGLON, N., BEUZARD, Y., AEBISCHER, P. Continuous delivery of human and mouse erythropoietin in mice by genetically engineered polymer encapsulated myoblasts. *Gene Ther.* **1998**, *5*, 1014–1022.
- 269 JOLLEY, W. B., HINSHAW, D. B., CALL, T. W., ALVORD, L. S. Xenogeneic pancreatic islet transplantation in proteolytic enzyme-bonded diffusion chambers in diabetic rats. *Transplant. Proc.* **1977**, *9*, 363–365.
- 270 DESAI, T., CHU, W., RASI, G., SINIBALDI-VALLEBONA, P., GUARINO, E., FERRARI, M. Microfabricated biocapsules provide short-term immunoisolation of insulinoma xenografts. *Biomed. Microdevices* **1998**, *1*, 131–138.
- 271 OGURA, H., TANI, K., OZAWA, K., NAGATA, S., ASANO, S., TAKAKU, F. Implantation of genetically manipulated fibroblasts into mice as antitumor alpha-interferon therapy. *Cancer Res.* **1990**, *50*, 5102–5106.
- 272 SCHNYDER, A., HUWYLER, J. Drug transport to brain with targeted liposomes. *NeuroRx* **2005**, *2*, 99–107.
- 273 OLIVIER, J. C. Drug transport to brain with targeted nanoparticles. *NeuroRx* **2005**, *2*, 108–119.
- 274 TORCHILIN, V. P. Immunoliposomes and PEGylated immunoliposomes: possible use for targeted delivery of imaging agents. *Immunomethods* **1994**, *4*, 244–258.
- 275 LEE, R., LOW, P. Delivery of liposomes into cultured KB cells via folate receptor-mediated endocytosis. *J. Biol. Chem.* **1994**, *269*, 3198–3204.
- 276 WU, D., YANG, J., PARDRIDGE, W. M. Drug targeting of a peptide radiopharmaceutical through the primate blood–brain barrier *in vivo* with a monoclonal antibody to the human insulin receptor. *J. Clin. Invest.* **1997**, *100*, 1804–1812.
- 277 HUWYLER, J., WU, D., PARDRIDGE, W. M. Brain drug delivery of small molecules using immunoliposomes. *Proc. Natl Acad. Sci. USA* **1996**, *93*, 14164–14169.
- 278 SHI, N., ZHANG, Y., ZHU, C., BOADO, R. J., PARDRIDGE, W. M. Brain-specific expression of an exogenous gene after i.v. administration. *Proc. Natl Acad. Sci. USA* **2001**, *98*, 12754–12759.
- 279 BITCKEL, U., YOSHIKAWA, T., PARDRIDGE, W. M. Delivery of peptides and proteins through the blood–brain barrier. *Adv Drug Deliv. Rev.* **2001**, *46*, 247–279.
- 280 FRIDEN, P. M., WALUS, L. R., MUSSO, G. F., TAYLOR, M. A., MALFROY, B., STARZYK, R. M. Anti-transferrin receptor antibody and antibody-drug conjugates cross the blood–brain barrier. *Proc. Natl Acad. Sci. USA* **1991**, *88*, 4771–4775.
- 281 PARDRIDGE, W. M., BUCIAK, J. L., FRIDEN, P. M. Selective transport of an anti-transferrin receptor antibody through the blood–brain barrier *in vivo*. *J. Pharmacol. Exp. Ther.* **1991**, *259*, 66–70.
- 282 HUWYLER, J., YANG, J., PARDRIDGE, W. M. Receptor mediated delivery of daunomycin using immunoliposomes: pharmacokinetics and tissue distribution in the rat. *J. Pharmacol. Exp. Ther.* **1997**, *282*, 1541–1546.
- 283 ZHANG, Y., ZHANG, Y.-f., BRYANT, J., CHARLES, A., BOADO, R. J., PARDRIDGE, W. M. Intravenous RNA interference gene therapy targeting the human epidermal growth factor receptor prolongs survival in intracranial brain cancer. *Clin. Cancer Res.* **2004**, *10*, 3667–3677.

- 284 ZHANG, Y., ZHU, C., PARDRIDGE, W. M. Antisense gene therapy of brain cancer with an artificial virus gene delivery system. *Mol. Ther.* **2002**, *6*, 67–72.
- 285 KREUTER, J. Nanoparticulate systems for brain delivery of drugs. *Adv. Drug Deliv. Rev.* **2001**, *47*, 65–81.
- 286 COUVREUR, P., TULKENS, P., ROLAND, M., TROUET, A., SPEISER, P. Nanocapsules: a new type of lysosomotropic carrier. *FEBS Lett.* **1977**, *84*, 323–326.
- 287 KREUTER, J., ALYAUTDIN, R. N., KHARKEVICH, D. A., IVANOV, A. A. Passage of peptides through the blood–brain barrier with colloidal polymer particles (nanoparticles). *Brain Res.* **1995**, *674*, 171–174.
- 288 GULYAEV, A. E., GELPERINA, S. E., SKIDAN, I. N., ANTROPOV, A. S., KIVMAN, G. Y., KREUTER, J. Significant transport of doxorubicin into the brain with polysorbate 80-coated nanoparticles. *Pharm. Res.* **1999**, *16*, 1564–1569.
- 289 ALYAUTDIN, R. N., PETROV, V. E., LANGER, K., BERTHOLD, A., KHARKEVICH, D. A., KREUTER, J. Delivery of loperamide across the blood–brain barrier with polysorbate 80-coated polybutylcyanoacrylate nanoparticles. *Pharm. Res.* **1997**, *14*, 325–328.
- 290 GREF, R., MINAMITAKE, Y., PERACCHIA, M. T., DOMB, A., TRUBETSKOY, V., TORCHILIN, V. et al. Poly(ethylene glycol)-coated nanospheres: potential carriers for intravenous drug administration. *Pharm. Biotechnol.* **1997**, *10*, 167–198.
- 291 DOUGLAS, S. J., DAVIS, S. S., ILLUM, L. Nanoparticles in drug delivery. *Crit. Rev. Ther. Drug Carrier Syst.* **1987**, *3*, 233–261.
- 292 PERACCHIA, M. T., FAITAL, E., DESMAELE, D., BESNARD, M., NOEL, J. P., GOMIS, J. M. et al. Stealth® PEGylated polycyanoacrylate nanoparticles for intravenous administration and splenic targeting. *J. Control. Release* **1999**, *60*, 121–128.
- 293 CALVO, P., GOURITIN, B., CHACUN, H. L. N., DESMAELE, D., D'ANGELO, J., NOEL, J.-P. et al. Long-circulating PEGylated polycyanoacrylate nanoparticles as new drug carrier for brain delivery. *Pharm. Res.* **2001**, *18*, 1157–1166.
- 294 AZMIN, M. N., STUART, J. F., FLORENCE, A. T. The distribution and elimination of methotrexate in mouse blood and brain after concurrent administration of polysorbate 80. *Cancer Chemother. Pharmacol.* **1985**, *14*, 238–242.
- 295 LODE, J., FICHTNER, I., KREUTER, J., BERNDT, A., DIEDERICHS, J. E., RESZKA, R. Influence of surface-modifying surfactants on the pharmacokinetic behavior of <sup>14</sup>C-poly(methylmethacrylate) nanoparticles in experimental tumor models. *Pharm. Res.* **2001**, *18*, 1613–1619.
- 296 DARIUS, J., MEYER, F. P., SABEL, B. A., SCHROEDER, U. Influence of nanoparticles on the brain-to-serum distribution and the metabolism of valproic acid in mice. *J. Pharm. Pharmacol.* **2000**, *52*, 1043–1047.
- 297 ANDERSON, J. M., SHIVE, M. S. Biodegradation and biocompatibility of PLA and PLGA microspheres. *Adv. Drug Deliv. Rev.* **1997**, *28*, 5–24.
- 298 VERT, M., SCHWACH, G., ENGEL, R., COUDANE, J. Something new in the field of PLA/GA bioresorbable polymers? *J. Control. Release* **1998**, *53*, 85–92.
- 299 UEDA, H., TABATA, Y. Polyhydroxyalkanoate derivatives in current clinical applications and trials. *Adv. Drug Deliv. Rev.* **2003**, *55*, 501–518.
- 300 SUMING LI. Hydrolytic degradation characteristics of aliphatic polyesters derived from lactic and glycolic acids. *J. Biomed. Mater. Res.* **1999**, *48*, 342–353.
- 301 RILEY, T., STOLNIK, S., HEALD, C. R., XIONG, C. D., GARNETT, M. C., ILLUM, L. et al. Physicochemical evaluation of nanoparticles assembled from poly(lactic acid)–poly(ethylene glycol) (PLA–PEG) block copolymers as drug delivery vehicles. *Langmuir* **2001**, *17*, 3168–3174.



- 302 STOLNIK, S., DUNN, S. E., GARNETT, M. C., DAVIES, M. C., COOMBS, A. G. A., TAYLOR, D. C. et al. Surface modification of poly(lactide-co-glycolide) nanospheres by biodegradable poly(lactide)-poly(ethylene glycol) copolymers. *Pharm. Res.* **1994**, *11*, 1800–1808.
- 303 LI, Y.-P., PEI, Y.-Y., ZHANG, X.-Y., GU, Z.-H., ZHOU, Z.-H., YUAN, W.-F. et al. PEGylated PLGA nanoparticles as protein carriers: synthesis, preparation and biodistribution in rats. *J. Control. Release* **2001**, *71*, 203–211.
- 304 ZAMBAUX, M.-F., FAIVRE-FIORINA, B., BONNEAUX, F., MARCHAL, S., MERLIN, J.-L., DELACHERIE, E. et al. Involvement of neutrophilic granulocytes in the uptake of biodegradable non-stealth and stealth nanoparticles in guinea pig. *Biomaterials* **2000**, *21*, 975–980.
- 305 VERRECCHIA, T., SPENLEHAUER, G., BAZILE, D. V., MURRY-BRELIER, A., ARCHIMBAUD, Y., VELLARD, M. Non-stealth (poly(lactic acid/albumin)) and stealth (poly(lactic acid-polyethylene glycol)) nanoparticles as injectable drug carriers. *J. Control. Release* **1995**, *36*, 49–61.
- 306 LE RAY, A. M., VERT, M., GAUTIER, J. C., BENOIT, J. P. Fate of [<sup>14</sup>C]poly(lactide-co-glycolide)nanoparticles after intravenous and oral administration to mice. *Int. J. Pharm.* **1994**, *106*, 201–211.
- 307 SALEM, A. K., CANNIZZARO, S. M., DAVIES, M. C., TENDLER, S. J. B., ROBERTS, C. J., WILLIAMS, P. M. et al. Synthesis and characterisation of a degradable poly(lactic acid)-poly(ethylene glycol) copolymer with biotinylated end groups. *Biomacromolecules* **2001**, *2*, 575–580.
- 308 TESSMAR, J. K., MIKOS, A. G., GOPFERICH, A. Amine-reactive biodegradable diblock copolymers. *Biomacromolecules* **2002**, *3*, 194–200.
- 309 TESSMAR, J., MIKOS, A., GOPFERICH, A. The use of poly(ethylene glycol)-block-poly(lactic acid) derived copolymers for the rapid creation of biomimetic surfaces. *Biomaterials* **2003**, *24*, 4475–4486.
- 310 OLIVIER, J.-C., HUERTAS, R., LEE, H. J., CALON, F., PARDRIDGE, W. M. Synthesis of pegylated immunonanoparticles. *Pharm. Res.* **2002**, *19*, 1137–1143.
- 311 MUNN, D. H., MELLOR, A. L. Macrophages and the regulation of self-reactive T cells. *Curr. Pharm. Des.* **2003**, *9*, 257–264.
- 312 TAKAHASHI, K., TAKEYA, M., SAKASHITA, N. Multifunctional roles of macrophages in the development and progression of atherosclerosis in humans and experimental animals. *Med. Electron Microsc.* **2002**, *35*, 179–203.
- 313 KAMRADT, T., MITCHISON, N. A. Tolerance and autoimmunity. *N. Engl. J. Med.* **2001**, *344*, 655–664.
- 314 TETLEY, T. D. Macrophages and the pathogenesis of COPD. *Chest* **2002**, *121* (5 Suppl.), 156–159.
- 315 BARNES, P. J. Chronic obstructive pulmonary disease. *N. Engl. J. Med.* **2000**, *343*, 269–280.
- 316 DAVIDSON, A., DIAMOND, B. Auto-immune diseases. *N. Engl. J. Med.* **2001**, *345*, 340–350.
- 317 GESKE, F. J., MONKS, J., LEHMAN, L., FADOK, V. A. The role of the macrophage in apoptosis: hunter, gatherer, and regulator. *Int. J. Hematol.* **2002**, *76*, 16–26.
- 318 LIBBY, P., RIDKER, P. M., MASERI, A. Inflammation and atherosclerosis. *Circulation* **2002**, *105*, 1135–1143.
- 319 VEERAREDDY, P. R., VOBALBOINA, V. Lipid-based formulations of amphotericin B. *Drugs Today* **2004**, *40*, 133–145.
- 320 LAVASANIFAR, A., SAMUEL, J., SATTARI, S., KWON, G. S. Block Copolymer micelles for the encapsulation and delivery of amphotericin B. *Pharm. Res.* **2002**, *19*, 418–422.
- 321 MILLER, C. B., WALLER, E. K., KLINGEMANN, H. G., DIGNANI, M. C., ANAISSIE, E. J., CAGNONI, P. J. et al. Lipid formulations of amphotericin B preserve and stabilize renal function in HSCT recipients. *Bone Marrow Transplant.* **2004**, *33*, 543–548.
- 322 PINTO-ALPHANDARY, H., ANDREMONT, A., COUVREUR, P. Targeted delivery of

- antibiotics using liposomes and nanoparticles: research and applications. *Int. J. Antimicrob. Agents* **2000**, *13*, 155–168.
- 323 SHADKCHAN, Y., KEISARI, Y., SEGAL, E. Cytokines in mice treated with amphotericin B-intralipid. *Med. Mycol.* **2004**, *42*, 123–128.
- 324 AGRAWAL, A. K., GUPTA, C. M. Tuftsin-bearing liposomes in treatment of macrophage-based infections. *Adv. Drug Deliv. Rev.* **2000**, *41*, 135–146.
- 325 SINGH, M., O'HAGAN, D. Advances in vaccine adjuvants. *Nature Biotechnology* **1999**, *17*, 1075–1081.
- 326 DILEO, J., BANERJEE, R., WHITMORE, M., NAYAK, J. V., FALO, J., LOUIS, D., HUANG, L. Lipid-protamine-DNA-mediated antigen delivery to antigen-presenting cells results in enhanced anti-tumor immune responses. *Mol. Ther.* **2003**, *7*, 640–648.
- 327 MISCHLER, R., METCALFE, I. C. Inflflexal®V a trivalent virosome subunit influenza vaccine: production. *Vaccine* **2002**, *20*, B17–B23.
- 328 SALEM, A. K., SEARSON, P. C., LEONG, K. W. Multifunctional nanorods for gene delivery. *Nat. Mater.* **2003**, *2*, 668–671.
- 329 CUI, Z., MUMPER, R. J. Microparticles and nanoparticles as delivery systems for DNA vaccines. *Crit. Rev. Ther. Drug Carrier Syst.* **2003**, *20*, 103–137.
- 330 TAYLOR, P. R., ZAMZE, S., STILLION, R. J., WONG, S. Y. C., GORDON, S., MARTINEZ-POMARES, L. Development of a specific system for targeting protein to metallophilic macrophages. *Proc. Natl Acad. Sci. USA* **2004**, *101*, 1963–1968.
- 331 HARISINGHANI, M. G., BARENTSZ, J., HAHN, P. F., DESERNO, W. M., TABATABAEI, S., VAN DE KAA, C. H. et al. Noninvasive detection of clinically occult lymph-node metastases in prostate cancer. *N. Engl. J. Med.* **2003**, *348*, 2491–2499.
- 332 MOGHIMI, S. M., BONNEMAIN, B. Subcutaneous and intravenous delivery of diagnostic agents to the lymphatic system: applications in lymphoscintigraphy and indirect lymphography. *Adv. Drug Deliv. Rev.* **1999**, *37*, 295–312.
- 333 DARDZINSKI, B. J., SCHMITHORST, V. J., HOLLAND, S. K., BOIVIN, G. P., IMAGAWA, T., WATANABE, S. et al. MR imaging of murine arthritis using ultrasmall superparamagnetic iron oxide particles. *Magn. Reson. Imaging* **2001**, *19*, 1209–1216.
- 334 FLACKE, S., FISCHER, S., SCOTT, M. J., FUHRHOP, R. J., ALLEN, J. S., MCLEAN, M. et al. Novel MRI contrast agent for molecular imaging of fibrin: implications for detecting vulnerable plaques. *Circulation* **2001**, *104*, 1280–1285.
- 335 WINTER, P. M., MORAWSKI, A. M., CARUTHERS, S. D., FUHRHOP, R. W., ZHANG, H., WILLIAMS, T. A. et al. Molecular imaging of angiogenesis in early-stage atherosclerosis with  $\alpha_v\beta_3$ -integrin-targeted nanoparticles. *Circulation* **2003**, *108*, 2270–2274.
- 336 RUEHM, S. G., COROT, C., VOGT, P., KOLB, S., DEBATIN, J. F. Magnetic resonance imaging of atherosclerotic plaque with ultrasmall superparamagnetic particles of iron oxide in hyperlipidemic rabbits. *Circulation* **2001**, *103*, 415–422.
- 337 KOOL, M. E., CAPPENDIJK, V. C., CLEUTJENS, K. B. J. M., KESSELS, A. G. H., KITSLAAR, P. J. E. H. M., BORGERS, M. et al. Accumulation of ultrasmall superparamagnetic particles of iron oxide in human atherosclerotic plaques can be detected by *in vivo* magnetic resonance imaging. *Circulation* **2003**, *107*, 2453–2458.
- 338 LUTGENS, E., VAN SUYLEN, R. J., FABER, B. C., GIJBELS, M. J., EURLINGS, P. M., BIJNENS, A. P. et al. Atherosclerotic plaque rupture: local or systemic process? *Arterioscler. Thromb. Vasc. Biol.* **2003**, *23*, 2123–2130.
- 339 PEARSON, A. M., RICH, M., M., K. Polynucleotide binding to macrophage scavenger receptors depends on the formation of base-quartet-stabilized four-stranded helices. *J. Biol. Chem.* **1993**, *268*, 3546–3554.
- 340 MATSUMOTO, A., NAITO, M., ITAKURA, H., IKEMOTO, S., ASAOKA, H.,

- HAYAKAWA, I. et al. Human macrophage scavenger receptors: primary structure, expression, and localization in atherosclerotic lesions. *Proc. Natl Acad. Sci. USA* **1990**, *87*, 9133–9137.
- 341 LEACH, J. K., PATTERSON, E., O'REAR, E. A. Improving thrombolysis with encapsulated plasminogen activators and clinical relevance to myocardial infarction and stroke. *Clin. Hemorheol. Microcirc.* **2004**, *30*, 225–228.
- 342 HOLIG, P., BACH, M., VOLKEL, T., NAHDE, T., HOFFMANN, S., MULLER, R. et al. Novel RGD lipopeptides for the targeting of liposomes to integrin-expressing endothelial and melanoma cells. *Protein Eng. Des. Select.* **2004**, *17*, 433–441.
- 343 KUMAR, C. C. Integrin alpha v beta 3 as a therapeutic target for blocking tumor-induced angiogenesis. *Curr. Drug Targets* **2003**, *4*, 123–131.
- 344 WU, J., NANTZ, M. H., ZERN, M. A. Targeting hepatocytes for drug and gene delivery: emerging novel approaches and applications. *Front. Biosci.* **2002**, *7*, d717–725.
- 345 WU, G. Y., WU, C. H. Receptor-mediated gene delivery and expression *in vivo*. *J. Biol. Chem.* **1988**, *263*, 14621–14624.
- 346 HASHIDA, M., KAWAKAMI, S., YAMASHITA, F. Lipid carrier systems for targeted drug and gene delivery. *Chem. Pharm. Bull. (Tokyo)* **2005**, *53*, 871–880.
- 347 NISHIKAWA, M. Development of cell-specific targeting systems for drugs and genes. *Biol. Pharm. Bull.* **2005**, *28*, 195–200.
- 348 RENSEN, P. C., HERIJGERS, N., NETSCHER, M. H., MESKERS, S. C., VAN ECK, M., VAN BERKEL, T. J. Particle size determines the specificity of apolipoprotein E-containing triglyceride-rich emulsions for the LDL receptor versus hepatic remnant receptor *in vivo*. *J. Lipid Res.* **1997**, *38*, 1070–1084.
- 349 POOGA, M., HALLBRINK, M., ZORKO, M., LANGE, U. Cell penetration by transportan. *FASEB J.* **1998**, *12*, 67–77.
- 350 OEHLKE, J., SCHELLER, A., WIESNER, B., KRAUSE, E., BEYERMANN, M., KLAUSCHENZ, E. et al. Cellular uptake of an  $\alpha$ -helical amphipathic model peptide with the potential to deliver polar compounds into the cell interior non-endocytically. *Biochim. Biophys. Acta Biomembranes* **1998**, *1414*, 127–139.
- 351 GREEN, M., LOEWENSTEIN, P. M. Autonomous functional domains of chemically synthesized human immunodeficiency virus tat *trans*-activator protein. *Cell* **1988**, *55*, 1179–1188.
- 352 FRANKEL, A. D., PABO, C. O. Cellular uptake of the tat protein from human immunodeficiency virus. *Cell* **1988**, *55*, 1189–1193.
- 353 JOLIOT, A., PERNELLE, C., DEAGOSTINI-BAZIN, H., PROCHIANTZ, A. Antennapedia homeobox peptide regulates neural morphogenesis. *Proc. Natl Acad. Sci. USA* **1991**, *88*, 1864–1868.
- 354 ELLIOTT, G., O'HARE, P. Intercellular trafficking and protein delivery by a herpesvirus structural protein. *Cell* **1997**, *88*, 223–233.
- 355 LUNDBERG, M., JOHANSSON, M. Positively charged DNA-binding proteins cause apparent cell membrane translocation. *Biochem. Biophys. Res. Commun.* **2002**, *291*, 367–371.
- 356 SNYDER, E., DOWDY, S. Cell penetrating peptides in drug delivery. *Pharm. Res.* **2004**, *21*, 389–393.
- 357 FAWELL, S., SEERY, J., DAIKH, Y., MOORE, C., CHEN, L. L., PEPINSKY, B. et al. Tat-mediated delivery of heterologous proteins into cells. *Proc. Natl Acad. Sci. USA* **1994**, *91*, 664–668.
- 358 KIM, D. T., MITCHELL, D. J., BROCKSTEDT, D. G., FONG, L., NOLAN, G. P., FATHMAN, C. G. et al. Introduction of soluble proteins into the MHC class I pathway by conjugation to an HIV tat peptide. *J. Immunol.* **1997**, *159*, 1666–1668.
- 359 SCHWARZE, S. R., HO, A., VOCERO-AKBANI, A., DOWDY, S. F. *In vivo* protein transduction: delivery of a

- biologically active protein into the mouse. *Science* **1999**, *285*, 1569–1572.
- 360 VOGEL, B., LEE, S., HILDEBRAND, A., CRAIG, W., PIERSCHBACHER, M., WONG-STAAI, F. et al. A novel integrin specificity exemplified by binding of the alpha v beta 5 integrin to the basic domain of the HIV Tat protein and vitronectin. *J. Cell Biol.* **1993**, *121*, 461–468.
- 361 CARON, N. J., QUENNEVILLE, S. P., TREMBLAY, J. P. Endosome disruption enhances the functional nuclear delivery of Tat-fusion proteins. *Biochem. Biophys. Res. Commun.* **2004**, *319*, 12–20.
- 362 ROTHBARD, J. B., JESSOP, T. C., LEWIS, R. S., MURRAY, B. A., WENDER, P. A. Role of membrane potential and hydrogen bonding in the mechanism of translocation of guanidinium-rich peptides into cells. *J. Am. Chem. Soc.* **2004**, *126*, 9506–9507.
- 363 SHEN, H., MAI, J. C., QIU, L., CAO, S., ROBBINS, P. D., CHENG, T. Evaluation of peptide-mediated transduction in human CD34<sup>+</sup> cells. *Hum. Gene Ther.* **2004**, *15*, 415–419.
- 364 WADIA, J. S., STAN, R. V., DOWDY, S. F. Transducible TAT–HA fusogenic peptide enhances escape of TAT-fusion proteins after lipid raft macropinocytosis. *Nature Medicine* **2004**, *10*, 310–315.
- 365 BECKER-HAPAK, M., MCALLISTER, S. S., DOWDY, S. F. TAT-mediated protein transduction into mammalian cells. *Methods* **2001**, *24*, 247–256.
- 366 EMBURY, J., KLEIN, D., PILEGGI, A., RIBEIRO, M., JAYARAMAN, S., MOLANO, R. D. et al. Proteins linked to a protein transduction domain efficiently transduce pancreatic islets. *Diabetes* **2001**, *50*, 1706–1713.
- 367 NAGAHARA, H., VOCERO-AKBANI, A. M., SNYDER, E. L., HO, A., LATHAM, D. G., LISSY, N. A. et al. Transduction of full-length TAT fusion proteins into mammalian cells: TAT-p27Kip1 induces cell migration. *Nature Medicine* **1998**, *4*, 1449–1452.
- 368 DOLGILEVICH, S., ZAIDI, N., SONG, J., ABE, E., MOONGA, B. S., SUN, L. Transduction of TAT fusion proteins into osteoclasts and osteoblasts. *Biochem. Biophys. Res. Commun.* **2002**, *299*, 505–509.
- 369 EGUCHI, A., AKUTA, T., OKUYAMA, H., SENDA, T., YOKOI, H., INOKUCHI, H. et al. Protein transduction domain of HIV-1 Tat protein promotes efficient delivery of DNA into mammalian cells. *J. Biol. Chem.* **2001**, *276*, 26204–26210.
- 370 RUDOLPH, C., PLANK, C., LAUSIER, J., SCHILLINGER, U., MULLER, R. H., ROSENECKER, J. Oligomers of the arginine-rich motif of the HIV-1 TAT protein are capable of transferring plasmid DNA into cells. *J. Biol. Chem.* **2003**, *278*, 11411–11418.
- 371 JIN, L. H., BAHN, J. H., EUM, W. S., KWON, H. Y., JANG, S. H., HAN, K. H. et al. Transduction of human catalase mediated by an HIV-1 TAT protein basic domain and arginine-rich peptides into mammalian cells. *Free Radic. Biol. Med.* **2001**, *31*, 1509–1519.
- 372 ASTRIAB-FISHER, A., SERGUEEV, D., FISHER, M., SHAW, B. R., JULIANO, R. L. Conjugates of antisense oligonucleotides with the tat and antennapedia cell-penetrating peptides: effects on cellular uptake, binding to target sequences, and biologic actions. *Pharm. Res.* **2002**, *19*, 744–754.
- 373 STEIN, S., WEISS, A., ADERMANN, K., LAZAROVICI, P., HOCHMAN, J., WELLHONER, H. A disulfide conjugate between anti-tetanus antibodies and HIV (37–72)Tat neutralizes tetanus toxin inside chromaffin cells. *FEBS Lett.* **1999**, *458*, 383–386.
- 374 MIE, M., TAKAHASHI, F., FUNABASHI, H., YANAGIDA, Y., AIZAWA, M., KOBATAKE, E. Intracellular delivery of antibodies using TAT fusion protein A. *Biochem. Biophys. Res. Commun.* **2003**, *310*, 730–734.
- 375 POLYAKOV, V., SHARMA, V., DAHLHEIMER, J. L., PICA, C. M., LUKER, G. D., PIWNICA-WORMS, D. Novel Tat–peptide chelates for direct transduction of technetium-99m and rhenium into human cells for imaging and radiotherapy. *Bioconjug. Chem.* **2000**, *11*, 762–771.

- 376 BHORADE, R., WEISSLEDER, R., NAKAKOSHI, T., MOORE, A., TUNG, C. H. Macrocyclic chelators with paramagnetic cations are internalized into mammalian cells via a HIV-tat derived membrane translocation peptide. *Bioconjug. Chem.* **11**, 301–305.
- 377 KAUFMAN, C. L., WILLIAMS, M., RYLE, L. M., SMITH, T. L., TANNER, M., HO, C. Superparamagnetic iron oxide particles transactivator protein–fluorescein isothiocyanate particle labeling for *in vivo* magnetic resonance imaging detection of cell migration: uptake and durability. *Transplantation* **2003**, *76*, 1043–1046.
- 378 JOSEPHSON, L., TUNG, C. H., MOORE, A., WEISSLEDER, R. High-efficiency intracellular magnetic labeling with novel superparamagnetic–Tat peptide conjugates. *Bioconjug. Chem.* **10**, 186–191.
- 379 DODD, C. H., HSU, H.-C., CHU, W.-J., YANG, P., ZHANG, H.-G., MOUNTZ, J., JOHN, D. et al. Normal T-cell response and *in vivo* magnetic resonance imaging of T cells loaded with HIV transactivator-peptide-derived superparamagnetic nanoparticles. *J. Immunol. Methods* **2001**, *256*, 89–105.
- 380 TKACHENKO, A. G., XIE, H., LIU, Y., COLEMAN, D., RYAN, J., GLOMM, W. R. et al. Cellular trajectories of peptide-modified gold particle complexes: comparison of nuclear localization signals and peptide transduction domains. *Bioconjug. Chem.* **15**, 482–490.
- 381 TORCHILIN, V. P., RAMMOHAN, R., WEISSIG, V., LEVCHENKO, T. S. Tat peptide on the surface of liposomes affords their efficient intracellular delivery even at low temperature and in the presence of metabolic inhibitors. *Proc. Natl Acad. Sci. USA* **2001**, *98*, 8786–8791.
- 382 LEVCHENKO, T. S., RAMMOHAN, R., VOLODINA, N., TORCHILIN, V. P. Tat peptide-mediated intracellular delivery of liposomes. *Methods Enzymol.* **2003**, *372*, 339–349.
- 383 TORCHILIN, V. P., LEVCHENKO, T. S., RAMMOHAN, R., VOLODINA, N., PAPAHDJOPOULOS-STERNBERG, B., D'SOUZA, G. G. M. Cell transfection *in vitro* and *in vivo* with nontoxic Tat peptide–liposome–DNA complexes. *Proc. Natl Acad. Sci. USA* **2003**, *100*, 1972–1977.
- 384 OBERDORSTER, G., OBERDORSTER, E., OBERDORSTER, J. Nanotoxicology: an emerging discipline evolving from studies of ultrafine particles. *Environ. Health Perspect.* **2005**, *113*, 823–839.
- 385 SEATON, A., DONALDSON, K. Nanoscience, nanotoxicology, and the need to think small. *Lancet* **365**, 923–924.
- 386 HAMPTON, T. Researchers size up nanotechnology risks. *J. Am. Med. Ass.* **2005**, *294*, 1881–1883.
- 387 GORDIJN, B. Nanoethics: from utopian dreams and apocalyptic nightmares towards a more balanced view. *Sci. Eng. Ethics* **2005**, *11*, 521–533.
- 388 JOACHIM, C. To be nano or not to be nano? *Nat. Mater.* **2005**, *4*, 107–109.

## 6 Nanoporous and Nanosize Materials for Drug Delivery Systems

*Yoshinobu Fukumori, Kanji Takada and Hirofumi Takeuchi*

### 6.1 Introduction

Nanomaterials have attracted much attention recently in the pharmaceutical field as structural components of pharmaceutical dosage forms. Such an application for nanomaterials has been found in coating materials in aqueous latex systems. Their use for granules and tablets has led to the successful development of many types of controlled release dosage forms. These have provided many excellent examples of nanostructure construction in micro- and macro-devices in the field of nanotechnology. In Section 6.2, nanomaterials for particle coating that are still useful and are expected to achieve further developments in pharmaceutical manufacturing, including commercially available polymeric nanoparticles, novel terpolymer nanoparticles, core-shell nanoparticles and biodegradable chitosan nanoparticles, are described.

Further, the recent development of biotechnology and its application to therapy and diagnosis requires nanoparticulate delivery of a variety of agents. The nanomaterials prepared for various purposes are simply analyzed according to their structural characteristics in Section 6.3.

In addition, the development of nanotechnology has produced many compounds that are specially structured to be nanoporous, and the obtained compounds are applied to many fields such electronics, microfabrication technology and biotechnology, including drug delivery systems. Section 6.4 deals with this hot and attractive topic. The purpose of drug delivery systems is to deliver drug molecules to their target sites for a desired period with a desired concentration. To accomplish this, several functions including sensing, targeting and controlled release are required. Nanoporous compounds are generally used to facilitate the controlled release function to drug delivery systems. Many nanoporous materials, mostly organic and some inorganic, have been studied for drug delivery system usage. Among them, calcium compounds like calcium carbonate ( $\text{CaCO}_3$ ), calcium phosphate [ $\text{Ca}(\text{H}_2\text{PO}_4)_2$ ], tricalcium phosphate [ $\text{Ca}_3(\text{PO}_4)_2$ ] hydroxyapatite [ $\text{Ca}_{10}(\text{PO}_4)_6(\text{OH})_2$ ] and silastic compounds are well-known drug delivery system carriers. In addition, nanofabrication technology has recently prepared new nano-

porous materials like carbon nanotubes (CNTs), fullerene and single-wall carbon nanohorns (SWNHs). These novel nanomaterials have also been used to clarify the possible biocompatibility, potential utilities and applications in biological settings, i.e. a drug delivery system carrier.

Section 6.5 will focus on the pharmaceutical application of porous silica, which includes both conventional and newly developed uses. One of the topics involves a solid dispersion system to improve the dissolution property of poorly water-soluble drugs. It is demonstrated that the well-ordered porous structure of silica particles can control the crystalline form of drugs in the solid dispersion system, which leads to a much improved dissolution rate. Mesoporous silica, having a highly controlled pore size and structure, is an attractive material. Some experimental data shown encourage us to use this novel material as a carrier of peptide drugs as well as poorly water-soluble drugs.

Thus, this chapter is the first challenge to describe the role of nanomaterials in pharmaceuticals in an integrated manner.

## 6.2 Nanomaterials for Coating

The pharmaceutical application of nanomaterials can be found in latex systems that have been used as coating materials for the last 40 years. Several types of latex are commercially used worldwide. Their application in granules and tablets has led to many controlled release dosage forms on the market. Therein, spray-coating processes such as fluidized bed, spouted bed and tumbling fluidized bed processes can easily provide multilayered particle structures with each layer being monolithic, a random multiphase nanostructure or ordered multiphase nanostructure, etc., as shown in Fig. 6.1. In general, the combination of different monolithic

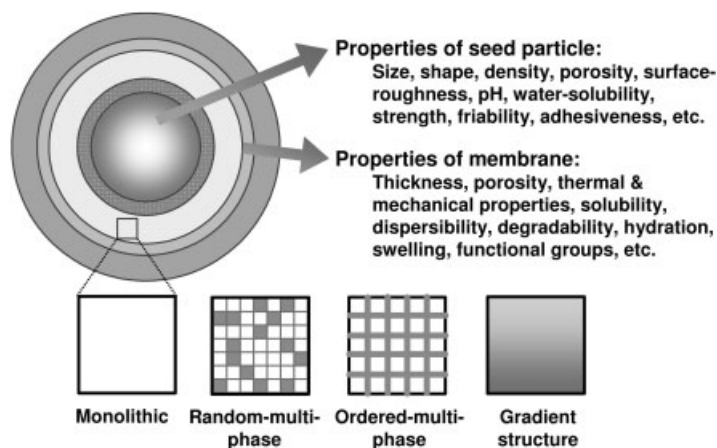


Figure 6.1. Construction of microparticles with nanomaterials.

nanomaterials and, especially, nanostructured nanomaterials can produce an almost infinite array of functional microparticulate products. However, commercially available latexes are formed as monolithic structures from random co- or terpolymerers that are designed to be used chiefly for coating such coarse particles as granules and tablets. For further and broader application of this technique, Fukumori and coworkers [1, 2] have been proposing the novel terpolymer and core-shell latexes through their development of fine particle-coating technology and highly functional microcapsules, such as thermosensitive drug-releasing microcapsules using sophisticated latexes with temperature-dependent swelling properties.

### 6.2.1

#### Commercially Available Aqueous Polymeric Nanomaterials

Table 6.1 lists commercially available nanomaterials for particle coating [1, 3, 4–16]. They are classified into two types based on the preparation methods [17]: (i) latexes synthesized by emulsion polymerization, and (ii) pseudolatexes prepared by emulsion processes such as emulsion-solvent evaporation, phase inversion and solvent change. Cellulose derivatives cannot be synthesized directly in latexes;

**Tab. 6.1.** Typical nanomaterials for coating

Brand	Supplier	Solubility	Main component	References
Aquacoat ECD	FMC	insoluble	ethylcellulose pseudolatex	4, 11, 13
Aquacoat CPD	FMC	enteric	cellulose acetate phthalate pseudolatex	
Surelease	Colorcon	insoluble	ethylcellulose pseudolatex	9
Eudragit RS30D	Röhm	insoluble	1:2:0.1 poly(EA–MMA–TAMC1) pseudolatex	7, 10–13, 16
Eudragit RL30D	Röhm	insoluble	1:2:0.2 poly(EA–MMA–TAMC1) pseudolatex	7, 16
Eudragit NE30D	Röhm	insoluble	2:1 poly(EA–MMA) latex	5, 6, 8, 11
Eudragit L30D	Röhm	enteric	1:1 poly(EA–MAA) latex	8, 12, 14
Eudragit FS30D	Röhm	enteric	7:3:1 poly(MA–MMA–MAA) latex	14–16
Kollocoat MAE30D/DP	BASF	enteric	1:1 poly(EA–MAA) latex	4
Kollocoat EMM30D	BASF	insoluble	2:1 poly(EA–MMA) latex	4
Kollocoat SR30D	BASF	insoluble	polyvinyl acetate latex	4



therefore, they are prepared as pseudolatexes (Aquacoat ECD [18], Aquacoat CPD and Surelease [19] in Tab. 6.1).

Eudragit™ L30D and NE30D are acrylic copolymer latexes synthesized by emulsion polymerization [20]. The particle sizes of these latexes are in the submicron order. L30D is a copolymer of ethyl acrylate (EA) as an ester component with methacrylic acid (MAA) (MAA:EA 1:1). It is used for enteric coating because of the presence of carboxyl groups in the copolymer. NE30D is a copolymer of ester components only, EA and MMA (2:1). The films formed from NE30D have a very low softening temperature ( $T_s$ ), and hence are flexible and expandable even under normal room conditions.

Eudragit RS and RL are terpolymers of EA and MMA as ester components with trimethylaminoethyl methacrylate chloride (TAMC1) as hydrophilic quaternary ammonium groups; RS and RL are 1:2:0.1 and 1:2:0.2 terpoly(EA–MMA–TAMC1), respectively. As Eudragit RS and RL contain MMA-rich ester components (EA:MMA 1:2), they have  $T_s$ s higher than those of NE30D (EA:MMA 2:1) and form hard films under room conditions. Eudragit RS and RL powders are easily transformed into pseudolatexes by emulsifying their powders in hot water without additives [20].

The film formation process from aqueous dispersion is shown schematically in Fig. 6.2. The mechanisms of film formation from aqueous polymeric dispersions have been discussed for a long time and many theories have been proposed. The

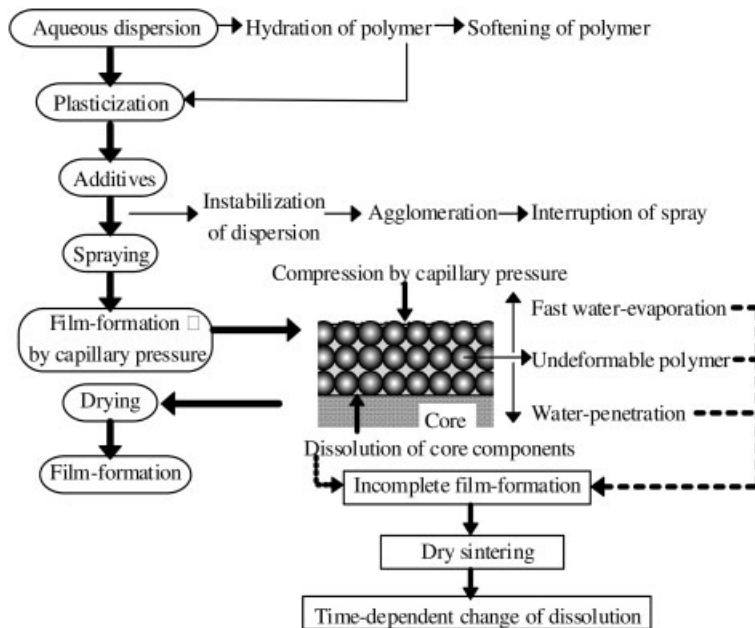


Figure 6.2. Film formation from aqueous dispersions of polymeric nanoparticles.

mechanisms were reviewed by Muroi [21]. Film formation in pharmaceutical applications was discussed by Steuernagel [18], Lehmann [20] and Fukumori [17]. Fusion and film formation of polymeric particles during the coating process can be explained by the wet sintering theory for particles suspended in water, the capillary pressure theory for particle layers containing water in various degrees of saturation and the dry sintering theory for dry particle layers. In all cases, as the particle size becomes smaller, film formation is further enhanced. This is the reason why nanomaterials have been used for aqueous suspension coating.

### 6.2.2

#### Novel Terpolymer Nanoparticles for Coating

The most serious problem encountered in fine particle coating using a wet-spraying process is agglomeration. Agglomeration takes place when coating materials supplied among seed particles possess a binding strength stronger than the separation force exerted on core particles. In water- or organic solvent-based solution systems, 10% of 53- to 63- $\mu\text{m}$  lactose particles was unavoidably agglomerated, although various additives to hydroxypropylcellulose (HPC) or ethylcellulose (EC) were sought to reduce the binding strength of sprayed materials [22–25]. In contrast, when aqueous lattices were sprayed, there were some cases where only a minor degree of agglomeration was observed, even for 32- to 44- $\mu\text{m}$  lactose particles [26].

In order to investigate latex as a candidate for spray liquid in fine particle coating, aqueous latexes of terpoly[EA–MMA–2-hydroxyethyl methacrylate (HEMA)] were newly synthesized [27, 28] (Fig. 6.3). When the molar ratio of the monomers used in polymerization was changed, the increase in MMA content raised the  $T_g$  of the cast film; HEMA affected  $T_g$  far less than MMA, but remarkably enhanced film formation and the release of a water-soluble substance (lactose) in aqueous medium. Further, when  $T_g$  was higher than the inlet air temperature, the terpolymer latexes exhibited a very low degree of agglomeration in the coating, due to their poor film-formability and, consequently, their low binding strength. This means

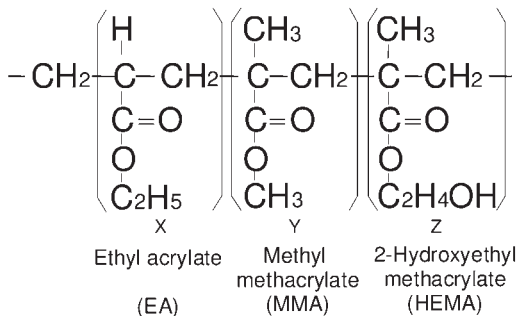


Figure 6.3. Chemical structure of poly(EA–MMA–HEMA).

that the drying/layering of latex particles has to be separated from the film-forming process to avoid agglomeration in fine particle coating; when both occur simultaneously, as in the solution systems; agglomeration of particles smaller than  $50\ \mu\text{m}$  cannot be avoided. This consequently led to a poor fixing efficiency of cosuspended solid particles, but the coating efficiency of the polymer dispersed as nanoparticles remained high [26]. This low tendency towards agglomeration was confirmed even in the coating of particles as fine as  $32\text{--}44\ \mu\text{m}$ .

### 6.2.3

#### Core-shell Nanoparticles for Fine Particle Coating

An aqueous latex exhibiting a low degree of agglomeration, low membrane permeation and high coating efficiency was developed using poly(EA-MMA-HEMA), whose monomer molar ratio was 6:12:8 or 12:6:4 [29]. Differing from blend latexes, the composite latexes (Fig. 6.4) composed of the low-permeable 12:6:4 polymer core and the nonadhesive 6:12:8 polymer shell with a 6:4 core-shell weight ratio formed a low-permeable membrane by curing. Thus, the 40% coated microcapsules of 53- to  $63\text{-}\mu\text{m}$  lactose released only 10% of the lactose at 3 h. Moreover, the composite latexes exhibited a very low degree of agglomeration, with the polymer yield remaining very high, and they did not induce any adhesive behavior during the coating operation. These properties were still effective even in the coating of cornstarch as fine as  $12\ \mu\text{m}$ : at a 50% level of coating, the mass median diameter of the product was  $16\ \mu\text{m}$  and it contained only 3% agglomerates. These results showed that by using the composite latex, particles of the order of  $10\ \mu\text{m}$  could be discretely coated as single-core microcapsules in the spouted bed process assisted with a draft tube.

However, there still remained five serious problems with the coating process of  $12\text{-}\mu\text{m}$  particles; (i) particle circulation and fluidization was too unsteady, (ii) the process was too time consuming, (ii) drug loading by spraying was not accom-

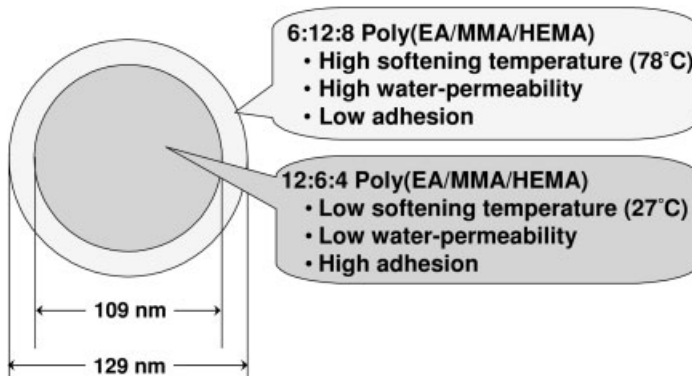
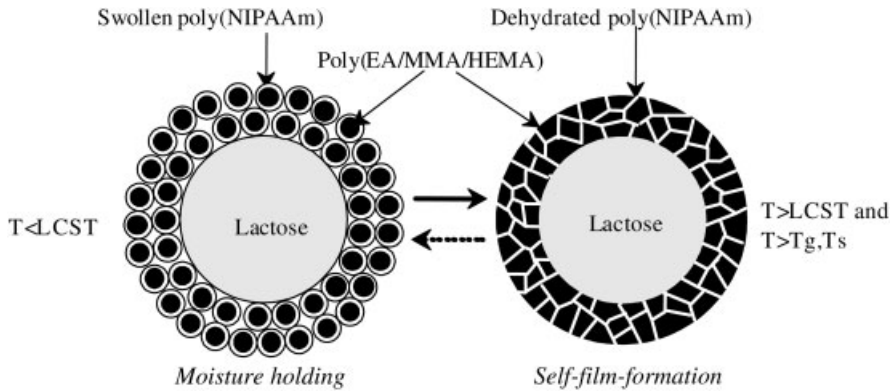


Figure 6.4. Composite nanoparticle with a core-shell structure for fine particle coating.



**Figure 6.5.** Microcapsules coated with composite nanoparticles with a poly(EA–MMA–HEMA) core and a poly(NIPAAm) shell.

plished because the corn starch particles were too small to avoid agglomeration, (iv) surfaces of the coated corn starch were too rough and porous to be cured by heating, and (v) to avoid agglomeration of core particles, spray liquid flow had to be adjusted to a low rate, leading to particle adhesion to the chamber wall due to electrostatic charge. Thus, in order to overcome the last two problems, aqueous composite latex that suppressed the particle adhesion in the coating process and had a self-film-formability in water was developed as a coating material [30]. This composite latex consisted of a poly(EA–MMA–HEMA) core and a thermosensitive poly(*N*-isopropylacrylamide) (NIPAAm) shell (Fig. 6.5). When compared to homogeneous latexes with no poly(NIPAAm) shell, the composite latexes reduced the production of poorly coated particles and the particle size dependence of polymer yield when the coating operation was done at a temperature where poly(NIPAAm) shells were able to swell, i.e. below the lower critical solution temperature (LCST: 32 °C) of poly(NIPAAm). Further, the microcapsules coated with the composite latexes also exhibited a self-film-formability in water at 37 °C, resulting from shrinkage of the poly(NIPAAm) shells in the membrane at temperatures above the LCST.

#### 6.2.4

#### Core–Shell Nanoparticles for Thermosensitively Drug-releasing Microcapsules

Recently, much attention has been focused on thermosensitive controlled-release systems developed from polymer networks with specific temperature-dependent swelling behaviors [31, 32]. In these systems, temperature variation triggers alteration of polymer configurations, leading to a thermally responsive change in the release rate of therapeutic agents to the systems.

One of the important issues in current thermosensitive release systems is how to facilitate the swelling/shrinking rate of hydrogels involving thermosensitivity. Improving swelling kinetics is an important subject for controlled drug release,

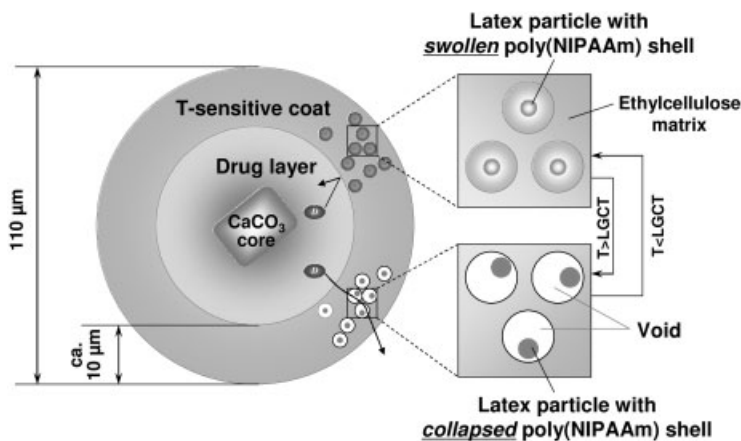


Figure 6.6. Microcapsules exhibiting positive thermosensitive drug release.

particularly pulsatile release with a thermal “on-off” switching response. The gel swelling/shrinking rate can be increased by an appropriate molecular and structural design of the polymer network. These include hydrogels with macroporous [33] and comb-type structures [34]. Incorporating thermosensitive hydrogels into fine particulate systems may be an alternative approach to make systems respond more rapidly to an external temperature change. Additionally, their small dimensions simultaneously offer considerable advantages over disk- or film-shaped macrogels hitherto developed in terms of a wide variety of biomedical applications.

The composite latexes composed of a hydrophobic poly(EA–MMA) core and a thermosensitive poly(NIPAAm) shell (Fig. 6.6) [35] were synthesized by a semicontinuous two-stage emulsion polymerization technique. The poly(NIPAAm) shell was crosslinked with methylene bisacrylamide. The microcapsules with thermosensitive coats were prepared using a Grow Max (140) spouted bed coater assisted with a draft tube and bottom spray (Fuji Paudal, Japan), known as the Wurster process. The microcapsules were cured by heating at 80 °C for 12 h and their dissolution properties were tested by a column method.

The key structure of the microcapsule designed here is its composite coat, consisting of nanosized thermosensitive hydrogels dispersed in a thermo-insensitive polymeric matrix. Ethyl cellulose pseudo latex, Aquacoat ECD (Tab. 6.1), was chosen as the polymeric matrix. As the nanosized thermosensitive hydrogels, a newly synthesized composite latex with a poly(NIPAAm)-rich shell was used. It is well known that poly(NIPAAm) has a phase transition temperature (LCST) of around 32 °C in water. The crosslinked network (hydrogel) constituted from this polymer shows an inverse temperature dependence of swelling: the hydrogel swells by imbibing water below a lower gel collapse temperature (LGCT; temperature for complete deswelling), while it shrinks at temperatures above the LGCT. At high temperatures, therefore, the poly(NIPAAm)-gel domains in the microcapsule membranes shrink, probably leading to the creation of many voids in the mem-

branes. Consequently, the water permeability increases as if a molecular valve has been opened. Due to the voids thus formed, the drug release rate at high temperatures is expected to become higher than that at low temperatures.

In order to confirm the reversibility of thermosensitive changes causing swelling, hydrodynamic size changes of the composite lattices in response to a stepwise shift in temperature were measured by photon correlation. As the temperature was elevated, particle size gradually decreased up to approximately 35 °C, near the volume transition temperature of crosslinked poly(NIPAAm) in water. Above 35 °C, particle size did not remarkably decrease any further. On the other hand, particle size became large again upon cooling. There was no significant difference between the traces of the particle size changes upon heating and cooling, indicating thermally reversible changes in the swelling/shrinking of the poly(NIPAAm) shells on the latex particles. Such a reversible change is a prerequisite to facilitate an “on-off” pulsatile drug release from the microcapsules.

No significant thermosensitivity was found in the release rate of the microcapsules with only Aquacoat film. In contrast, the microcapsules with the composite latex-dispersing coat in an 85:15 blending ratio of Aquacoat and the composite latex exhibited pulsatile thermosensitive release rate changes. Additionally, these microcapsules demonstrated a positive thermosensitivity of drug release, i.e. high release rates at high temperature (50 °C) and low release rates at low temperature (30 °C), except for a less pronounced burst effect in the initial period at 30 °C. It is noteworthy that the sharp release rate changes from the “on” state to the “off” state, and *vice versa*, occurred within a few minutes. Fabrication of composite latex having nanosized thickness poly(NIPAAm) shells and thin microcapsule coats in the order of 10 μm would be responsible for the resulting fast response.

### 6.2.5

#### **Chitosan Nanoparticles for Microparticle Coating**

As is well-known, chitosan (poly[ $\beta$ -(1-4)-2-amino-2-deoxy-D-glucopyranose]) is a hydrophilic and cationic polysaccharide derived from chitin deacetylation, which is the second most abundant polysaccharide in the world after cellulose and a promising resource originating from crustaceans shells and insects [36]. Chitosan has some interesting properties such as acting as a bioadhesive (cationic), with biocompatible (nontoxic) and biodegradable (bioerodible) capabilities. Therefore, it has been investigated in depth, and used in various industrial and medical applications. Furthermore, these interesting properties make it one of the most promising biopolymers for drug delivery [37–46]. Indeed, chitosan has been studied as a drug carrier in various forms, such as tablets, beads, granules, microparticles and nanoparticles. In particular, micro/nanoparticles are the most widely studied as drug carriers for protein, peptide, vaccine and DNA delivery.

A wide variety of preparation methods of chitosan particles such as solvent evaporation techniques, multiple emulsion methods, spray-drying methods, electrostatic complex formation with anionic materials (ionotropic gelation) and block copolymerization have been investigated. These methods often require a crosslinking

agent, such as glutaraldehyde. While the use of the crosslinking agent produces hardened particles as well as a drug-release rate possibly controllable in response to the degree of crosslinking, the toxicity of the crosslinking agent would become a major concern. In addition, it leads to a low loading of anionic drugs because amino groups in chitosan responsible for electrostatic interactions with anionic drugs become unavailable due to the crosslinking reaction between the amino groups in chitosan and aldehyde groups in crosslinking agents.

Masui and coworkers [47] reported a study aimed at preparing noncovalently crosslinked chitosan nanoparticles (CNSs) without the use of any organic solvents and additives. For this purpose, an aqueous neutralization–precipitation technique was newly developed. They prepared chitosan nanoparticles in the range of 150–300 nm. Furthermore, spouted-bed spray-coating of protein-layered particles with the noncovalently crosslinked chitosan nanoparticles was carried out and their excellent performance as a biodegradable coating agent was then demonstrated.

### 6.3

#### Materials for Nanoparticulate Therapy and Diagnosis

In general, nanoparticles for drug delivery, such as in cancer therapy and diagnosis, are simply constructed, and have a core, shell and surface (Fig. 6.7) [48]. The core determines the particle size and generally consists of an inactive matrix, the active agent itself or an active agent-containing matrix. The shell chemically or physically bound to the core acts as a base to which surface molecules, that sometimes include active agents, are anchored or bound with or without intermediate spacers; in some cases, it acts as an active agent-dispersed matrix. The surface

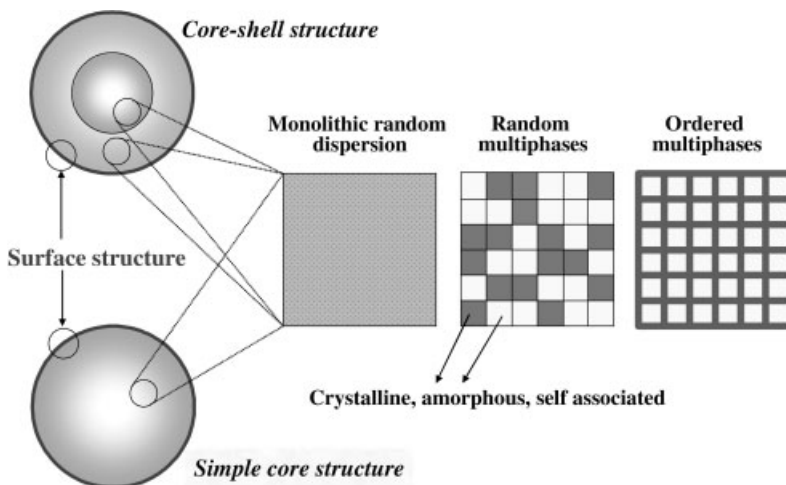


Figure 6.7. Typical structures of composite nanoparticles.

molecules strongly affect the biodistribution of the nanoparticles that usually consist of site-, tissue-, cell- and/or receptor-specific molecules (targeting agents). The poly(ethylene glycol) (PEG) molecules that possibly induce a bound water layer on the particle surface are attached to the shell or surface molecules by physical adsorption or covalent bonding with or without intermediate spacers. The mode of bonding used in particle construction is important from the viewpoint that the rate and timing of release or degradation of the components from the particles have to be controlled in order to achieve their biodistribution and active agent delivery in cancer treatment and diagnosis. The nanoparticles have to be degraded in the body and finally eliminated by globular filtration as molecules with a molecular weight of less than 30 000 or as particles with a size smaller than a few nanometers.

The structures of nanoparticles for cancer therapy and diagnosis are simple, as described above. Tables 6.2 and 6.3 show typical examples of the structures and components of nanoparticles.

### 6.3.1

#### **Inorganic Nanoparticles**

Recently, inorganic nanoparticles that interact with biological systems have attracted widespread interest in biology and medicine (Tab. 6.2). Such nanoparticles are thought to have potential as novel intravascular probes for both diagnostic (e.g. imaging) and therapeutic purposes (e.g. drug delivery). Critical issues for successful nanoparticle delivery include the ability to target specific tissues and cell types, and escape from the biological particulate filter – the reticuloendothelial system (RES).

Among inorganic materials, magnetite has been investigated most widely for cancer therapy and diagnosis [49–56]. Magnetite nanoparticles are used directly or dispersed in the polymeric matrix as cores. They have been used chiefly in hyperthermia treatment of cancer [49, 55] and, in some cases, for magnetic field-assisted targeting of nanoparticles [55]. For diagnostic purposes, they are used in magnetic resonance imaging (MRI) as contrast-enhancing agents for cancer diagnosis [49], hyperfusion region visualization [50], cell labeling in T cell-based therapy [51–53], and for detection of angiogenesis [50], apoptosis [54] and gene expression [56]. PEG [55] or oxidized starch [50] as a hydrophilic surface modifier, antibodies [49], fluorescein isothiocyanate (FITC)-labeled TAT peptide [51–53] or the Annexin V protein [54] as a specific targeting agent, and folic acid [55] or transferrin [56] as a ligand of the receptors overexpressed in tumor cells have been used as surface molecules.

Akerman and coworkers [57] (Tab. 6.2) explored the feasibility of *in vivo* targeting using semiconductor quantum dots. Quantum dots are small (less than 10 nm) inorganic nanocrystals that possess unique luminescent properties; their fluorescence emission is stable and is tuned by varying the particle size or composition. Akerman and coworkers showed that ZnS-capped CdSe quantum dots coated with a lung-targeting peptide accumulated in the lungs of mice after intravenous



Tab. 6.2. Typical examples of inorganic materials for nanoparticulate drug delivery

No.	Therapeutic purpose	Particle size (nm) [structure]	Characterization	Delivery agent	Core-shell component (additive)	Surface component	References
1	Hyperthermia, cancer diagnosis	[agglomerate-liposome]	biodistribution, anti-cancer effect, diagnosis	magnetite	magnetite	phospholipid bilayer, antibody	49
2	MRI, hyperfusion region visualization, angiogenesis		kidney perfusion, tumor capillary leakage	clariscan (superparamagnetite)	magnetite	oxidized starch	50
3	Cell-based therapy, cell labeling		T cell delivery to tumor, MRI	dextran-coated CLIO	CLIO	Tat peptide-FITC	51–53
4	MRI of apoptosis (phosphatidylserine recognition)		MRI imaging	CLIO	CLIO	Annexin V (protein)	54
5	MRI, hyperthermia, magnetic field-assisted radionuclide therapy	10	tumor and macrophage cell uptake	magnetite	magnetite	PEG, folate	55
6	MRI, detection of gene expression		conjugation number, cell binding, cell uptake, transferrin receptor expression	dextran-coated CLIO, MION	CLIO, MION	transferrin (TF-S-CLIO)	56
7	Disease sensing, drug delivery	<10 (uncoated); 3.5, 5.5 [core-shell]	cell binding, <i>in vivo</i> targeting, RES uptake		CdSe (core)–ZnS (shell)	peptide/PEG	57
8	Intracellular diagnostics, therapeutic delivery	20 (gold), 25 (whole) [core-shell]	nuclear targeting		gold (core)–BSA (shell)	five peptides (nuclear localization signal, etc.)	58

CLIO: crosslinked ion oxide; MION: monocrySTALLINE ion oxide nanoparticle.

injection, whereas two other peptides specifically directed quantum dots to blood vessels or lymphatic vessels in tumors. They also showed that adding PEG to the quantum dot coating prevented quantum dots from nonselective accumulation in reticuloendothelial tissues.

Tkachenko and coworkers [58] (Tab. 6.2) explored the ability of peptide-modified gold nanoparticles to target the nucleus of HepG2 cells. Five peptide/nanoparticle complexes were investigated to modify particles. They used gold nanoparticles because they are easy to identify using video-enhanced color differential interference contrast microscopy. Their studies highlight the challenges associated with nuclear targeting and the potential advantages of designing multifunctional nanostructured materials as tools for intracellular diagnostics and therapeutic delivery.

### 6.3.2

#### **Polymeric Nanoparticles**

The active agents are mostly incorporated in the cores to control or suppress their release. Polymers have been widely used as matrix materials. Table 6.3 shows examples of polymeric nanoparticles [59–78] that have recently been investigated for delivery; as an anticancer drug, doxorubicin, whose liposomes are on the market as Doxil™ (Alza) has often been used [62]. In these nanoparticles, biodegradable polymers, such as poly(lactic acid) (PLA) [59, 62], poly(lactic-co-glycolic acid), poly( $\epsilon$ -caprolactone) (PCL) [60, 61], chitosan [64, 69–72], poly(acrylcianoacrylate) (PACA), poly(lysine) [62] and poly(aspartic acid) [62], are used as the core matrix. Lipid [65, 78] and wax matrixes [63, 73–77] have also been used in nanoparticles, as shown in Tab. 6.2. The particles used in gene therapy are often cationic to enhance association with anionic cell surfaces and/or DNAs [63–66].

Kataoka and coworkers [62] developed block copolymer micelles for drug and gene delivery. They reported the utility of polymeric micelles formed through the multimolecular assembly of block copolymers as novel core–shell-type nanoparticles for drug and gene targeting. The segregated core embedded in the hydrophilic palisade was shown to function as a reservoir for genes, enzymes and a variety of drugs with diverse characteristics. Functionalization of the outer surface of the polymeric micelle to modify its physicochemical and biological properties was carried out for long circulation and receptor-mediated drug delivery.

### 6.3.3

#### **Other Case Studies**

A variety of methodologies of treatment and strategies of delivery have been applied to cancer therapy and diagnosis. In order to achieve an efficient outcome, nanoparticles have been designed using materials that are thought to be optimal for their respective applications. The following typical applications of nanoparticles have been reported: targeting lectin present on the intestinal epithelial cell surface by wheat germ agglutinin on a PCL matrix [67], antileishmania treatment by PCL matrix nanoparticles [68], gadolinium neutron capture therapy (GdNCT) by intra-

Tab. 6.3. Typical examples of organic materials for nanoparticulate drug delivery

No.	Therapeutic purpose	Particle size (nm) [structure]	Characterization	Delivery agent	Core-shell component (additive)	Surface component	References
1	Passive drug targeting	118 [polymeric matrix]	drug content, antitumor effect, plasma concentration	irinotecan	PLA, PEG-PPG-PEG	PEG-PPG-PEG	59
2	Passive and estrogen receptor targeting	250–300 [polymeric matrix]	cell uptake, intracellular distribution, localization	tamoxifen	PCL (MW: 14.8)	Pluronic F-68	60, 61
3	Passive and active targeting	50–100/32 [polymeric matrix]	biodistribution, transfection	doxorubicin, DNA	PEG-poly(aspartic acid)/PEG-PLA/PEG-Poly(lysine)	PEG	62
4	Gene therapy	100–160 [wax matrix]	DNA stability, transfection, biodistribution	plasmid DNA lipophilized with cationic lipid	Wax, Brij 78, Tween 20, Tween 80	Chol-pullulan	63
5	Gene therapy	309 [polymeric matrix]	<i>in vitro</i> proliferation, degradation	<i>Mycobacterium phlei</i> DNA	Chitosan (MW: 500 000, 84% deacetylated [TPP])		64
6	Anti-angiogenic gene therapy	40 (core) [lipid matrix]	tumor cell apoptosis, tumor regression	plasmid DNA (APTmu-Raf)	polymerized cationic lipid	Integrin $\alpha\beta_3$	65

7	Gene therapy	100–150 [polymeric matrix]	<i>in vitro</i> transfection	nucleic acid	cyclodextrin polycation	transferrin-PEG-adamantane	66
8	Neutron capture therapy	300–500 [polymeric matrix]	tumor retention, growth suppression	gadopentatete dimeglumine	chitosan		69–72
9	Neutron capture therapy	50–80 [wax matrix]	cell uptake, biodistribution, tumor retention	gadolinium hexan edione	wax [Brij 78/Brij 72/Tween 80]	folate/thiamine-PEG-DSPE, PEG-DSPE	73–77
10	Photodynamic therapy	120 [lipid matrix]	cytotoxicity, receptor binding	hematoporphyrin	triolein [egg PC, Tween 80]	folate, PEG spacer	78

Chol-pullulan: {N-[2-(cholesteryl(carboxyamino)ethyl)]carbamoylethyl]-pullulan; DSPE: distearylphosphatidylethanolamine.

tumorally injectable chitosan nanoparticles [69–72] (Tab. 6.2) and wax matrix nanoparticles surface-modified with folic acid or thiamine whose uptake is enhanced in tumor cells [73–77] (Tab. 6.2), photodynamic therapy by solid lipid nanoparticles (SLNs) [78] (Tab. 6.2) or silicate matrix nanoparticles [79], application of dendrimer [80], antiangiogenesis radiotherapy by  $^{90}\text{Y}$  chelated on the liposome surfaces using an integrin antagonist [81], drug delivery to the brain by PACA matrix nanoparticles [82] and detection of antigen by immunolabeled europium-holding poly(styrene)nanoparticles [83].

## 6.4

### Nanoporous Materials as Drug Delivery System Carriers

#### 6.4.1

##### Inorganic Calcium Compounds

Nanoporous materials have been used as a drug delivery system carrier [84–86]. Among them, Higuchi and coworkers used hydroxyapatite as a carrier for delivering drugs to skeletal tissue at high enough local concentrations for desirable therapeutic effects [87]. Using a self-setting hydroxyapatite cement with cephalexin, norfloxacin and indomethacin (IMC), the cement was transformed into hydroxyapatite with affinity for hard bone tissue. Continuous *in vitro* drug release profiles from loaded cement pellets in phosphate buffer, pH 7.4, were obtained. As the cements have good biocompatibility in both periodontal and periapical environments, self-setting cement skeletal drug delivery systems are thought to provide temporary replacement therapy for bone [88].

Porous  $\text{CaCO}_3$  particles were reported to be useful as an intranasal carrier of insulin and hydrophilic compounds, because of their easy production and slow biodegradability [89–91]. However, the binding of adsorbed drugs to  $\text{CaCO}_3$  was weak, i.e. drugs and proteins were adsorbed on the surface of solid particles or porous  $\text{CaCO}_3$  material. Therefore, sufficient sustained release was not obtained. Mizushima and coworkers devised a simple method to incorporate hydrophilic drugs and proteins into nano- $\text{CaCO}_3$  and regulate the size of the particles. The mean particle size of the  $\text{CaCO}_3$  was 44.8–140.7 nm depending on the mixing speed of both particles and the drug. Sustained-release of erythropoietin (EPO), granulocyte colony-stimulating factor (G-CSF) and bethamethasone phosphate (BP) was observed for 1 week both in *in vitro* and *in vivo* experiments [92].

On the other hand, Ogawa and coworkers used porous hydroxyapatite particles, of which the mean inside diameter was 100 nm, as a drug delivery system carrier for long-term sustained release peptide/protein preparation for injection [93]. After protein drug is entrapped into the hydroxyapatite particles, the obtained particles are coated with a biodegradable polymer which has a hydrophilic part, as shown in Fig. 6.8.

Human growth hormone (hGH) was at first entrapped into nanoporous hydroxyapatite particles where an inorganic metal compound was added to prevent the initial release of hGH, i.e. burst phenomenon. The obtained particles were coated

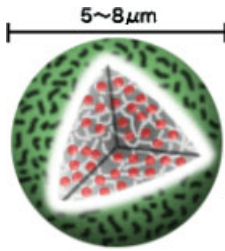


**Figure 6.8.** Basic concept of a hydroxyapatite drug delivery system for sustained-release protein [10].

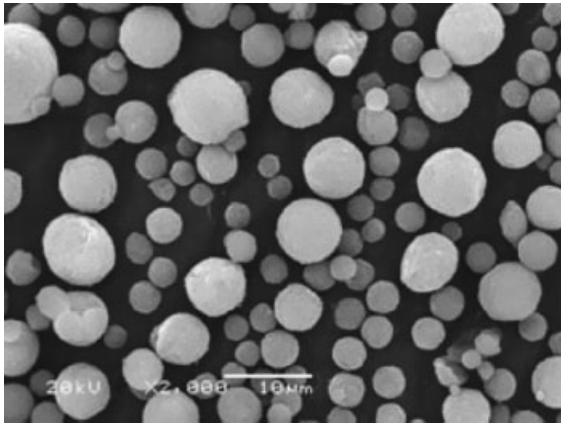


**Figure 6.9.** SEM images of a hydroxyapatite drug delivery system containing hGH [10].

with a hydrophilic biodegradable polymer like PEG–PLA. The mean particle size of the system is 5–8  $\mu\text{m}$ , as shown in Fig. 6.9. The hGH content of this system is around 15 wt%. About 80 mg of the preparation was injected to patients with dwarfism every 2 weeks with 27 G syringe needle. To evaluate the system, they injected the preparation into rats who received immunosuppressive therapy and it was confirmed that serum hGH levels were maintained over 2 weeks. In addition, the injected particles were not detected at the end of the experiment. They also performed a pharmacodynamic study using hypophysectomized rats. In the sustained-release hGH preparation group, the rat body weights gradually increased over 3 weeks. However, body weights did not increase in the control group rats [94].

#### 6.4.2

#### Silastic Compounds

##### 6.4.2.1 Nanoporous Silastic Materials for Solidifying Oily Drugs

Porous calcium silicate, Florite™ RE (FLR; Eisai, Japan) has the structure of assembled petal-like flakes, presenting a lot of pores in its surface. Pores show a par-

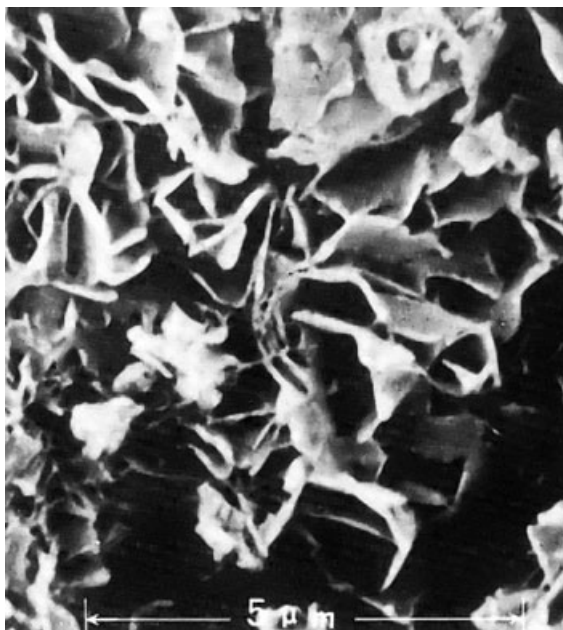


**Figure 6.10.** SEM image of FLR ([www.eisai-fc.co.jp/](http://www.eisai-fc.co.jp/)).

ticular size distribution with two peaks at 12 and 0.15  $\mu\text{m}$ , which are attributed to interparticle and intraparticle pores, respectively. The mean inside diameter is 150 nm. FLR has a porous structure, as shown in Fig. 6.10, and has an excellent liquid-holding ability, about 5.0  $\text{mL g}^{-1}$ , through its numerous pores. Both FLR and colloidal silica (Aerosil™ 200, AER; Nippon Aerosil, Japan) have greater adsorption efficiency than other adsorbents, i.e. microcrystalline cellulose, cornstarch and lactose dibasic calcium phosphate. Although AER does not have interparticle pores, FLR has both interparticle and intraparticle pores. AER absorbs liquid into interparticle pores by forming liquid bridges among the particles. On the other hand, FLR adsorbs liquid into the interparticle pores by a capillary phenomenon.

As oily drugs do not dissolve in water, they are usually developed as a soft capsule preparation. As the size of the oily capsule preparation is large, pediatric and elder patients often have trouble swallowing them. In particular, when the oily capsule is taken with a small amount of water, the possibility of capsule adhesion onto the esophageal mucosa increases. In the worst case, esophageal ulcer occurs. To solve these problems, Takeuchi and coworkers formulated vitamin E acetate into a drug emulsion system with colloidal silica [95].

On the other hand, Hanawa and coworkers reported the solidification of ethenzamide (EZA) by a “melt-adsorption” method [96]. When EZA crystals were heated with FLR in a sealed glass ampoule without any solvent, EZA melted and adsorbed on FLR in an amorphous state. The dissolution rate of EZA from the preparation was greatly enhanced as compared with crystal EZA. To enable large-scale manu-

facturing, Kinoshita and coworkers used a twin-screw extruder, in which both temperature and kneading force can be controlled simultaneously [97]. The extruder allows EZA to melt and adsorb onto FLR. Therefore, the process is also called the “melt-adsorption” method. They prepared melt-adsorbed products of TAS-301 [3-bis(4-methoxyphenyl)methylene-2-indolinone] which were adsorbed on FLR using a twin-screw extruder. TAS-301 is an antirestenosis drug for use after percutaneous transluminal coronary angioplasty (PTCA). The crystallinity, solubility and oral bio-availability (BA) of TAS-301 in the melt-adsorbed products were examined. The particle size distributions of FLR, physical mixture [TAS-301:FLR (1:2)] and the melt-adsorbed product [TAS-301: FLR(1:2)] made by both methods were approximately consistent. The specific surface area decreased in the following order: FLR > physical mixture > melt-adsorbed product > TAS-301 crystal. The specific surface area decreased by mixing due to partial adsorption of TAS-301 on FLR and further decreased by heating due to its penetration into FLR pores. TAS-301 was amorphized by heating with an adsorbent above its melting point. In addition, the decreased crystallinity of TAS-301 was suggested by the endothermic X-ray diffraction (XRD) peaks. Therefore, both the amorphization and decreased crystallinity of TAS-301 might be associated with hydrogen bonding between the C=O group of TAS-301 and the syanol group of FLR. Although the solubility of the TAS-301 crystal and physical mixture was similar, the melt-adsorbed products prepared by both methods showed temporary super-saturation in water and their initial solubility was approximately 20-fold greater than that of the TAS-301 crystal. The dissolution rates of TAS-301 from the melt-adsorbed products prepared by the two methods were markedly faster than those from the physical mixture and the drug crystal. Figure 6.11 shows the results on the absorption of TAS-30 from the system

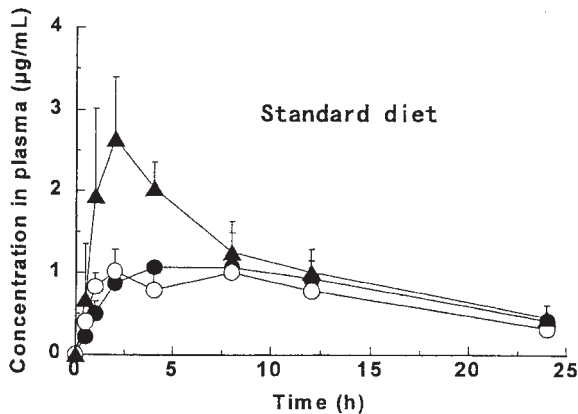


**Figure 6.11.** Plasma concentration of TAS-301 versus time profiles after oral administration of test preparations at a dose of 300 mg per dog.  $\blacktriangle$  = Melt-adsorbed product (capsule).  $\bullet$  = TAS-301 crystal (aqueous suspension).  $\circ$  = TAS-301 crystal (capsule). Each point represents the mean  $\pm$  SD ( $n = 3-6$ ).



after oral administration of three preparations to dogs being fed a standard diet. The AUC (area under the plasma drug concentration–time curve) values of the three test preparations were  $1.12 \pm 0.03$  (crystal suspension),  $1.18 \pm 0.43$  (crystal) and  $2.75 \pm 0.53 \mu\text{g h mL}^{-1}$  (melt-adsorbed products), respectively. Thus, melt-adsorption on a porous calcium silicate, FLR, is useful for improving the solubility and BA of hydrophobic drugs like TAS-301.

Yuasa and coworkers applied FLR to granulate a representative oily drug, *D,L*-tocopheryl nicotinate (TN), by adsorbing TN [98]. They also showed the possibility of tableting TN with FLR as an adsorbent and studied the possibility of the reduction of tablet coloration by TN exudation at compression, because TN was expected to be excluded from TN powder to the surface of the tablet by compression. With mixing, ethanol solution containing TN, 10–60 wt%, was added to FLR. After the adsorbents were dried, TN powder was obtained. In addition, TN powder was used to form granules. When the TN powder in which TN is adsorbed to FLR is compressed, the degree of tablet coloration caused by TN exudation from TN powder becomes larger with a higher TN content and compression pressure. It was clarified that the reduction of tablet coloration at tableting of TN is possible by compressing TN powder added with FLR or AER, both of which have a high liquid holding ability. In particular, when FLR is added at compression, a shorter disintegration time and a higher release property of TN were obtained when AER was added due to the difference of the liquid adsorbing and holding mechanism of FLR and AER. They proposed the models of the existent state of TN in the tablet at compression, which are shown in Fig. 6.12. When TN powder with hydroxypropylstarch (HPS) as a disintegrator is compressed, as shown in Fig. 6.12(A), TN is extruded by compression and reabsorbed by forming liquid bridges to the particles of TN powder and HPS. It was considered that the interparticle space decreased as these liquid bridges were formed, with the result that the penetration rate of water into the TN tablet decreased, and therefore the disintegration time was longer and the release rate of TN was slower. When TN powder with FLR and HPS is compressed, as shown in Fig. 6.12(B), TN is extruded by compression and reabsorbed to the pores in newly added FLR, with the result that a lot of interparticle spaces without TN are formed. In addition, they confirmed, by determining the pore size distributions in the tablets produced from FLR or AER alone, that the mean interparticle pore diameters among FLR or AER particles in the tablets were about 250 and 150+, respectively. It was considered that, since the interparticle space in the TNF tablet, i.e. the mean pore diameter, was larger than that in the TNA tablet, water easily penetrated into the TNF tablet. As a result, the disintegration time was shorter and the release property of TN was improved in comparison with TN and TN tablets with AER. When TN powder with AER and HPS is compressed, as shown in Fig. 6.12(C), TN is extruded by compression and reabsorbed by forming liquid bridges to the particles of TN powder, AER and HPS. When the formulated amount of AER increased, the disintegration time became shorter because the interparticle space without TN bridges increased. Furthermore, because the mean pore diameter of the TN tablet with AER is smaller and the amount of TN forming bridges to the particles in the TN tablet with AER is larger, it may be difficult to

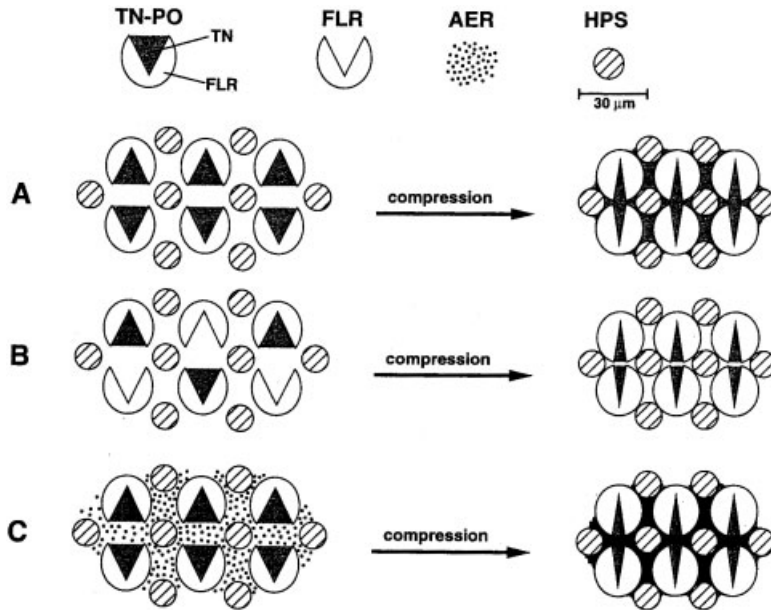


**Figure 6.12.** Model of the existent state of TN at compression of (A) TN powder, (B) TN tablets with FLR and (C) TN tablets with AER where HPS was used as a disintegrator of tablets.

penetrate into the TN tablet with AER. As a result, the rate of TN from the TN tablet with AER was slower than that from the TN tablet with FLR.

Hwang and coworkers prepared silica particles containing retinal with a fabrication method using an oil/water/oil (o/w/o) emulsion and the sol-gel method [99]. By controlling the formulated amount of surfactants, Span 80 and Tween 20, sustained-release characteristics of retinal were obtained for 100 h.

#### 6.4.2.2 Nanoporous Silastic Materials for Poorly Absorbable Drugs

The BA of hydrophobic drugs after oral administration is very low due to their poor solubility in the gastrointestinal tract. Solid dispersion and microemulsion have been applied to improve the solubility of poorly soluble drugs [100]. These drug delivery system technologies are often used to improve the oral BA of insoluble drugs, e.g. cyclosporin A (microemulsion, Neoral<sup>TM</sup>) and tacrolimus (solid dispersion) [101, 102]. However, solid dispersion technology has limited applicability in improving the oral BA of drugs having both low solubility and low membrane permeability. The principles of the intestinal absorption mechanism of drugs are classified into the following categories: (i) passive diffusion, (ii) facilitated diffusion (endocytosis) and (iii) carrier-mediated active transport [103]. Active transport takes part in the absorption process of a limited number of drugs like vitamin B<sub>12</sub>, 5-fluorouracil, etc. [104]. Most of the clinically applied drugs are absorbed from the

gastrointestinal tract by a passive diffusion mechanism. In this case, the concentration gradient of drug molecules between the intestinal luminal side and the enterocytes is the rate-limiting process for the overall absorption process. In addition, absorption-enhancing technologies have been developed for poorly absorbable drugs, i.e. macromolecular drugs such as protein/peptide drugs, e.g. insulin, low-molecular-weight heparin (LMWH), etc. [105–107]. Emisphere developed nonacylated non- $\alpha$ -amino acid, sodium *N*-[8-(2-hydroxybenzoyl) amino] caprylate (SNAC) as an absorption enhancer for LMWH [108]. After oral administration of LMWH, 30 mg kg<sup>-1</sup> (4971 IU mL<sup>-1</sup>), in accordance with SNAC, 150 mg kg<sup>-1</sup>, the peak plasma LMWH level measured as an anti-Xa activity level of 1.2 IU mL<sup>-1</sup> was obtained. SNAC thus effectively enhanced the oral absorption of LMWH. However, after the oral administration of LMWH with SNAC, both LMWH and SNAC are diluted in the small intestine. Therefore, the absorption enhancing effect of SNAC is insufficient. Takada and coworkers used nanoporous silastic materials as oral drug carriers [109]. In their system, both the drug and absorption enhancer are held in the carrier at high concentrations. As the result of the high concentration gradients of the drug and absorption enhancer between inside the system and the enterocytes, the formulated drug can be efficiently absorbed. This drug delivery system technology is termed a “liquid formulation holding microparticulate system (LFMPS)”, as shown in Fig. 6.13. In the LFMPS system, a hydrophobic drug is solubilized in either an oil or water phase with the help of surfactant(s). Thus, the obtained particles can be formulated either as a capsule or tablet. After the

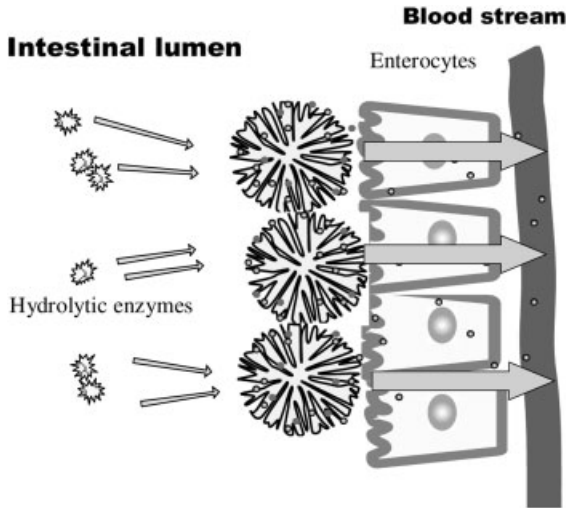


**Figure 6.13.** Concept of LFMPS. After oral administration of microparticles and adsorbent, holding both absorption enhancer and macromolecular drug-like protein drug in enteric capsules, the microparticles are

delivered to the enterocytes where high concentration gradients of enhancer and drug are formed. Consequently, high absorption efficiency of drug is obtained.

oral administration of LFMPs in an enteric capsule, the microparticles are exposed to the enterocytes, and form a high drug concentration gradient between the system and the enterocytes. In addition, when an absorption enhancer is formulated with the drug, good BA can be obtained. LFMPs can be also applied to highly soluble and poorly absorbable drugs that have a high molecular weight (e.g. gentamicin) [110] or high surface charge (e.g. LMWH) [111], resulting in poor membrane permeability. These drugs require the use of an absorption enhancer (e.g. surfactant) to improve their oral BA. The drug and absorption enhancer can be dissolved in water and, thus, the obtained mixture is introduced into the nanoporous material. Takada and coworkers first studied the effect of nanoporous materials on the BA of lansoprazole (LPZ) [109]. LPZ is a representative proton pump inhibitor, and has been clinically used in gastric and duodenal ulcerative disease therapy. LPZ is sparingly soluble in water and is unstable in the stomach, i.e. in gastric acid. According to the classification of drugs with low BA proposed by Amidon and coworkers [112], LPZ is a class II compound (low solubility and high membrane permeability) in the biopharmaceutical classification system (BCS). Clinically, gelatin capsules containing enteric-coated LPZ granules are supplied. Even if LPZ is protected from hydrolysis in the stomach, there is a possibility that LPZ does not dissolve well in the small intestine because of there being less water. Therefore, the oral BA of LPZ is low and shows wide intersubject variation. To solve these problems, nonionic surfactants were used to accelerate dissolution and improve the BA of LPZ. However, a liquid formulation is not as preferable as an oral formulation because no capsule can retain a liquid formulation without dissolution or degradation. LFMPs is composed of a surfactant, nanoporous adsorbent and LPZ. Its function is to improve the dissolution and absorption of LPZ. The BA of LPZ was measured in rats. As surfactants, Tween 80, polyoxyethylated, 60 mol, castor oil derivative (HCO-60<sup>TM</sup>) and PEG-8 caprylic/capric glycerides (Labrasol<sup>TM</sup>) were used. As adsorbents, porous silicon dioxide (Sylysia<sup>TM</sup> 550, 320), magnesium aluminosilicate (Neusilin<sup>TM</sup> S<sub>2</sub>, NS<sub>2</sub>N, US<sub>2</sub>) and porous calcium silicate (FLR) were used. Among the used surfactants, HCO-60 showed the highest absorption enhancing effect after the intra-small intestinal administration of LPZ solution. To solidify the LPZ solution with HCO-60, adsorbents were used and the obtained solid preparations were first used in an *in vitro* release experiment. Sylysia 320, Neusilin S<sub>2</sub> and Neusilin NS<sub>2</sub> showed a  $T_{50\%}$ , the time when half of the formulated amount of drug is released from the test preparation, of about 1 h. To evaluate the BA of LPZ from these solid preparations, an absorption study was performed in rats. The Sylysia 550 system showed a higher AUC than other systems, showing a BA of 28.1%. The Sylysia 550 system was placed in an enteric capsule and orally administered to dogs, and the BA was compared with an enteric tablet. The Sylysia 550 system had a BA of 71.7%, which was significantly greater than the enteric tablet. Thus, the solid system composed of LPZ, surfactant and nanoporous adsorbent, Sylysia 550, was shown to be a good system to improve the BA of LPZ.

Takada and coworkers also applied this system to gentamicin (GM), of which an oral preparation is not available because of a poor BA from the gastrointestinal tract [110]. As GM is a polar water-soluble compound, it is commonly recognized

that the intestinal membrane permeability of GM is poor. GM is a class III compound (high solubility and low membrane permeability) of BCS. They previously showed that the BA of GM was greatly increased by formulating GM in a self-microemulsifying drug delivery system (SMEDDS) using PEG-8 caprylic/capric glycerides (Labrasol™) as an absorption enhancer. Labrasol contains saturated polyglycolysed C<sub>6</sub>–C<sub>14</sub> glycerides, where C<sub>8</sub> is 58.1% and C<sub>10</sub> is 39.8%. Labrasol is a safe pharmaceutical additive, showing a high tolerance and low toxicity in animals; the LD<sub>50</sub> is 22.0 g kg<sup>-1</sup> for rats and is a surfactant listed in the European Pharmacopoeia. A SMEDDS is expected to self-emulsify rapidly in the aqueous environment of the small intestine, thereby presenting the drug in solution in small droplets of oil. The gentle agitation required for emulsification is provided by the digestive motility of the small intestine. By formulating GM in a Labrasol SMEDDS, a high BA value of GM, approximately 55%, was obtained after administration to the rat small intestine [113]. The dosage form that results from a SMEDDS is usually either a liquid or liquid-filled soft gelatin capsules. However, from the standpoint of pharmaceuticals, the solid dosage form is preferable to the liquid preparation in terms of cost-performance and the convenience of the manufacturing process. After GM was dissolved with Labrasol, the mixture was solidified with several kinds of adsorbents. The adsorbents were microporous calcium silicate (FLR), magnesium aluminometasilicate (Neusilin US<sub>2</sub>) and silicon dioxide (Sylsilia 320). An *in vitro* release study showed no significant difference between the three adsorbents. The *in vivo* rat absorption study showed that the preparation containing 10 mg of FLR had the highest C<sub>max</sub>, 2.14 ± 0.67 μg mL<sup>-1</sup> of GM. Other preparations had a C<sub>max</sub> of 0.69 ± 0.10 μg mL<sup>-1</sup> for FLR 20 mg, 1.07 ± 0.31 μg mL<sup>-1</sup> for Neusilin US<sub>2</sub> and 0.99 ± 0.21 μg mL<sup>-1</sup> for Sylsilia 320, respectively. The BA of GM from the FLR 10 mg system was 14.1%. The system was also evaluated in dogs after oral administration in an enteric capsule made of Eudragit S100. High plasma GM levels with a C<sub>max</sub> of 1.26 ± 0.20 μg mL<sup>-1</sup> were obtained. These results suggest that the FLR system is useful as an oral solid delivery system of poorly absorbable drugs such as GM [110]. LFMPs can also be applied to highly soluble and poorly absorbable drugs that have a high surface charge (e.g. LMWH) resulting in poor membrane permeability. Thus, LFMPs is a useful system for solving the low BA problem of both hydrophilic and hydrophobic drugs.

#### 6.4.2.3 Nanoporous Silica Materials for Controlled Release of Drugs

Calcium silicate was used as a porous carrier for repaglinide, an oral hypoglycemic agent, to prepare microspheres, and a gastroretentive floating drug delivery systems was challenged, as shown in Fig. 6.14 [114]. An *in vitro* release study showed the sustained-release characteristics of repaglinide for 8 h.

On the other hand, porous particle technology was applied to obtain an immediately dissolving intravenous preparation. Straub and coworkers prepared drug powder particles of paclitaxel, a water-insoluble hydrophobic anticancer drug. Ethanol solution containing paclitaxel, Tween 80 and polyvinylpyrrolidone (PVP) C15 was mixed with an aqueous solution containing the pore-forming agent, ammonium bicarbonate and mannitol. The mixture was spray-dried and porous dry

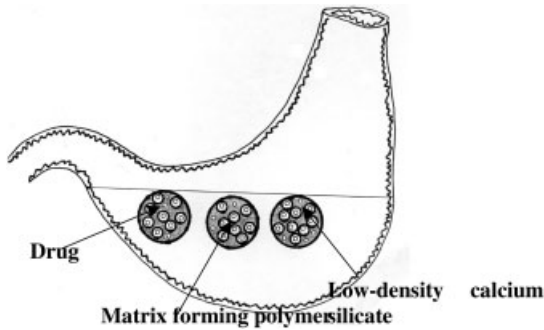


**Figure 6.14.** Gastroretentive floating drug delivery system made of calcium silicate-based microspheres.

powder particles (shown in Fig. 6.15) were obtained. The mean particle size was about 1  $\mu\text{m}$  and nanosize pores were formed. An *in vitro* dissolution experiment showed that more than 90% of paclitaxel was dissolved from the dry powder within 10 min, although about 80% of the authentic paclitaxel bulk was dissolved at 2 h after the start of the dissolution experiment [115].

Foraker and coworkers applied porous silicon (pSi) as a platform technology for a new generation of drug delivery systems. Macropores (above 50 nm), mesopores (2–50 nm) and nanopores (below 2 nm), occupying 1–95% of the Si volume, were used as a scaffold suitable for loading of drugs. As a model hydrophilic macromolecular drug, insulin was loaded into pSi particles by freeze drying, where sodium laurate was used as an absorption enhancer. Using an *in vitro* permeation system using Caco-2 monolayer, a 10- to 50-fold increase in insulin transport efficiency was obtained by the pSi particle system [116].

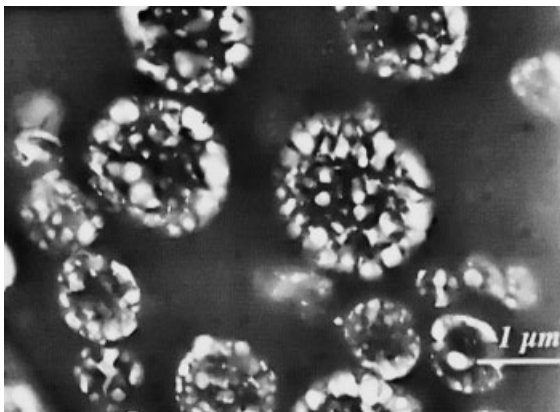


**Figure 6.15.** TEM image of a cross-section of paclitaxel porous particles.

## 6.4.3

**Carbon Nanotubes (CNTs)****6.4.3.1 CNTs for Oral Delivery of Protein Drug**

CNTs are produced by deposition of carbon atoms vaporized from graphite by an electric arc or by a laser onto metal particles. Recently, CNTs have been produced by the chemical vapor deposition (CVD) method. The obtained CNTs often aggregate into bundles or ropes. An individual CNT molecule is about 1 nm in diameter and several microns long [117]. The specific gravity of CNTs is very light because of their large outer and inner surface areas. The adsorption efficiency of CNTs is larger than the conventional adsorbents like silastic compounds. Takada and co-workers used CNTs as an adsorbent of both the absorption enhancer and drug, and the resulting system was evaluated as an oral drug delivery system for poorly-absorbable drugs like peptide/protein drugs [118]. Surfactants such as a saturated polyglycolysed C<sub>8</sub>-C<sub>18</sub> glyceride (Gelucire™ 44/14), Labrasol and HCO-60 were used as absorption enhancers at 50 mg kg<sup>-1</sup> and EPO was used as a model protein drug. As adsorbents, solid particles such as Sylysia 550, CNTs, carbon nanohorns (CNHs), fullerene, charcoal and bamboo charcoal were used. After either surfactant was loaded into the adsorbent by mixing well, disintegrator (Explotab™) was added and mixed thoroughly. Finally, EPO solution was added to this mixture and mixed well. The test preparations were directly administered into the rat small intestine at the EPO dose level of 100 IU kg<sup>-1</sup> and EPO absorption was studied by measuring serum EPO levels by ELISA. Labrasol showed the highest absorption

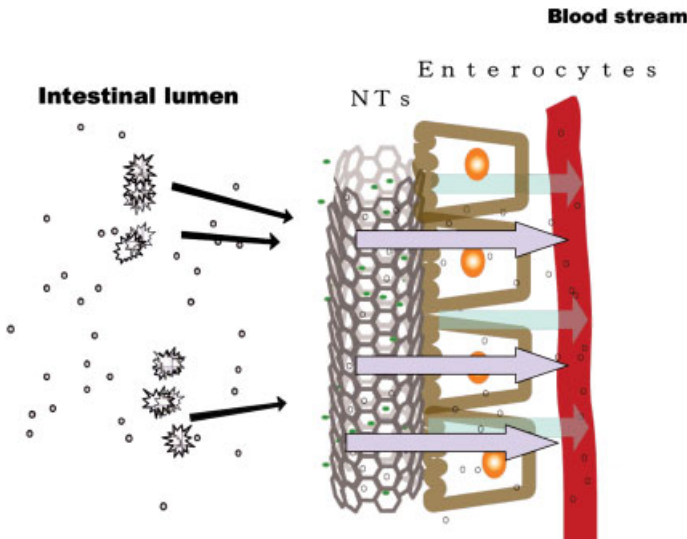


**Figure 6.16.** CNTs as carriers for oral delivery of macromolecular drug. After the oral administration of CNTs holding both absorption enhancer (Labrasol) and EPO in

enteric capsules, CNTs are delivered to the enterocytes where high concentration gradients of Labrasol and EPO are formed. Consequently, high absorption efficiency of EPO is obtained.

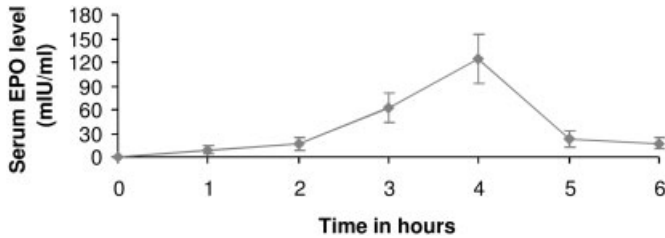


**Figure 6.17.** Serum EPO concentration versus time curve after small intestinal administration of CNTs holding both absorption enhancer (Labrasol) and EPO ( $100 \text{ IU kg}^{-1}$ ).

enhancing effect after intra-jejunum administration than Gelucire 44/14 and HCO-60. Therefore, Labrasol was used as an absorption enhancer for EPO and the systems were evaluated by an *in vivo* absorption model using rats. As in the case of LFMPS, CNTs can deliver both absorption enhancer and EPO by holding onto the enterocytes, and a high concentration gradient between the intestinal mucosal site and enterocytes is formed (Fig. 6.16). Scanning electron microscopy (SEM) image of CNTs used in this system is shown in Fig. 6.18. As a result, a high peak serum EPO level ( $C_{\max}$ ),  $62.7 \pm 11.6 \text{ mIU mL}^{-1}$ , was obtained. Other adsorbents showed lower  $C_{\max}$ s,  $25.9 \pm 3.7 \text{ mIU mL}^{-1}$  for Sylsya 550,  $18.7 \pm 5.3 \text{ mIU mL}^{-1}$  for CNH,  $50.0 \pm 11.4 \text{ mIU mL}^{-1}$  for fullerene,  $40.4 \pm 13.1 \text{ mIU mL}^{-1}$  for charcoal and  $34.1 \pm 7.5 \text{ mIU mL}^{-1}$  for bamboo charcoal, respectively. The other BA parameter, AUC, also showed the same absorption enhancing order. Among the used adsorbents, the BA values were in the order of CNT > fullerene > Sylsya 550 > CNH > bamboo charcoal > charcoal, where the BA of EPO from the CNT system was 6.7%. By formulating an enzyme inhibitor, casein, into the adsorbent system, the BA of EPO was increased, as shown in Fig. 6.17, where

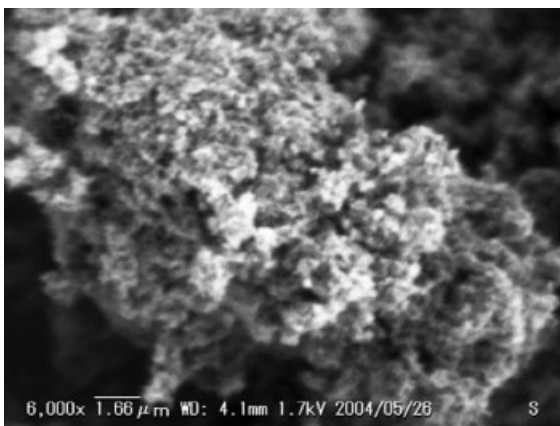


**Figure 6.18.** TEM image of CNTs used for the oral delivery of EPO.



$C_{\max}$  was  $143.1 \pm 15.2$  mIU mL<sup>-1</sup>, resulting in the highest BA of EPO, i.e. 11.5%. Labrasol also showed good absorption enhancing effects on other poorly absorbable drugs like insulin, vancomycin and gentamicin [119, 120]. CNT is a good adsorbent of Labrasol for the oral delivery of these poorly absorbable drugs.

#### 6.4.3.2 CNTs for Intracellular Delivery of Protein

CNTs were applied to the intracellular delivery of drugs, genes and proteins. Kam and coworkers suggested the ability of single-walled CNTs (SWNTs) to penetrate mammalian cells and deliver various drugs i.e. peptides, the protein streptavidin (SA) and nucleic acids inside living cells, as shown in Fig. 6.19 [121]. The investi-

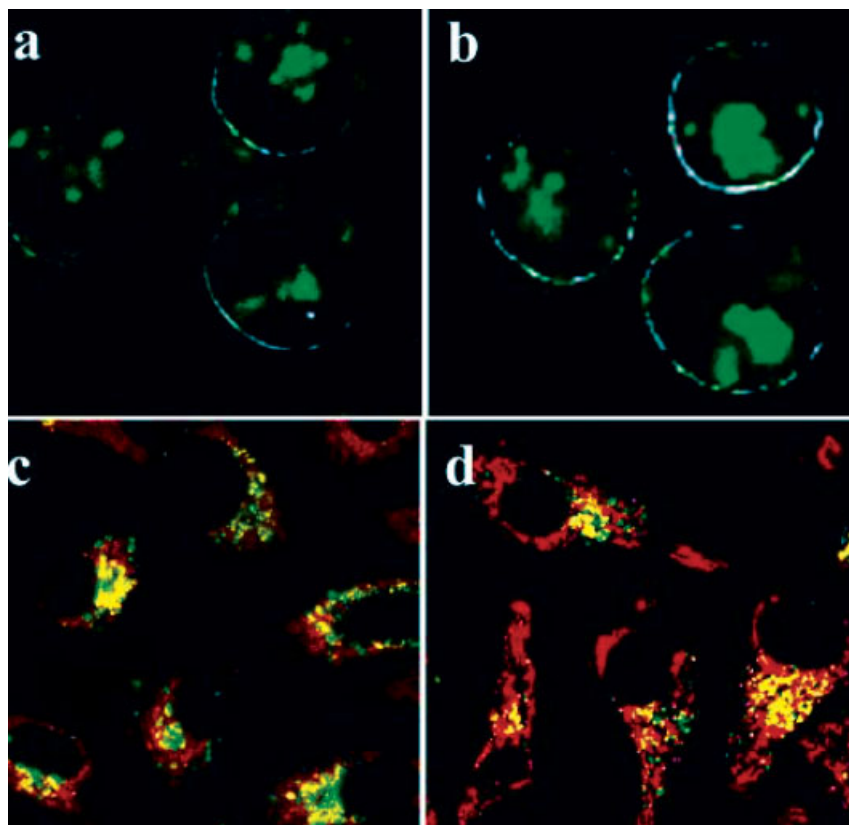


**Figure 6.19.** Confocal microscopy of cells after incubation in protein–SWNT (proteins labeled to be green fluorescent) solutions for 2 h.

(a) HL60 cells after incubation in SA–SWNTs. (b) HL60 cells after incubation in BSA–SWNTs. (c) HeLa cells after incubation in SA–SWNTs in the presence of the FM 4-64, a red membrane

and endocytotoxic vesicle marker. Yellow color in the image is due to colocalization of fluorescently labeled green proteins and red FM 4-64. (d) HeLa cells after incubation in cytochrome *c*–SWNTs in the presence of FM 4-64.

gated proteins were SA, protein A (SpA), bovine serum albumin (BSA) and cytochrome *c*. Intracellular protein transport and uptake by SWNT were also generic for various adherent and nonadherent mammalian cell lines, including HeLa, NIH-3T3 fibroblasts, HL60 and Jurkat cells. Energy-dependent endocytosis was confirmed to be the internalization mechanism. Furthermore, with cytochrome *c* as the cargo protein, they explored the fate of internalized protein–SWNT conjugates, attempted to release the conjugates from the endosome vesicles into the cell cytoplasm using chloroquine and investigated the biological functions of the released proteins. Once released into the cytoplasm of cells, the proteins can perform biological functions, i.e. apoptosis, or programmed cell death, induced by cytochrome *c* transported inside cells by SWNTs after their release from the endosomes. On the other hand, Pantarotto and coworkers and Bianco and coworkers showed that SWNTs were generic intracellular transporters for various types of proteins (below 80 kDa) noncovalently and nonspecifically [122, 123]. The SWNT uptake mechanism was suggested to be via insertion and diffusion through the lipid bilayer of the cell membrane. Therefore, a precise study must be performed to clarify the uptake mechanism of SWNTs. Thus, SWNTs may constitute a new class of molecular transporters for various *in vitro* and *in vivo* delivery applications.

Electroporation has been used to transfer molecules, like DNA or drugs, into living cells, where pulsed electric fields of several  $\text{kV cm}^{-1}$  in amplitude and submicrosecond duration are required. Thereby, membrane pores are formed temporarily and DNA or drugs penetrate. However, existing electroporation technology has limitations, i.e. a low efficiency. In addition, high electric field pulses lead to cell lysis. Chapana and coworkers applied CNTs to increase the efficiency of electroporation [124]. Their technology reduces to the nanoscale the large-scale process of electroporation by the use of CNTs as physical “electroporation vectors”. Their technique differs fundamentally from other methods used today, because electrodes are not needed. Water dispersible CNTs have an anionic surface charge attached to the surface of Gram-negative bacteria. This arises mainly due to an electrostatic interaction between the CNTs and the likewise charged bacterial surface. On the other hand, the effect of a microwave electromagnetic field pulse on the interaction of CNTs with the cells leads to electropermeabilization through individual CNTs. At first, they prepared water dispersible CNTs by treating them with acid solution for 1 h in a nitric:sulfuric (1:3) acid solution, which generates carboxylic groups at the ends as well as in the defects on the sidewalls of the CNTs. After purification, they obtained a stable CNT suspension with no precipitation after several months. Transmission electron microscopy (TEM) examination of the sample shows the presence of individual CNTs approximately 40 nm in diameter and less than 0.6  $\mu\text{m}$  in length. Plasmid DNA pUC19 was successfully introduced into *Escherichia coli* cells. TEM examination showed that the electroporation process proceeded through the intact cell wall of the suspended cells without inducing changes in their morphology. They could isolate pUC19 DNA from cultures made from blue colonies, because  $\beta$ -galactosidase activity was visualized by feeding the transformed cells a lactose analog called X-Gal that turns blue when hydrolyzed by  $\beta$ -galactosidase. Therefore, the transformation of *E. coli* was successfully facili-

tated by CNTs. CNTs having hollow structures were used to fulfill both requirements, i.e. electroporation and injection (nanopipette). If CNTs recognizing cell surfaces can be designed, it will be possible to deliver DNA molecules and colloidal particles confined in their interstitial channels to a particular cell type through the cell envelope and into compartments. These applications are new challenges in cell biology and biomedicine.

#### 6.4.3.3 Toxicity of CNTs

In the study of Takada and coworkers, CNTs were used as carriers of oral drug delivery systems. However, no toxicity information about CNTs after oral or systemic administration is available. On the other hand, when fine particles of CNTs are aspirated by humans, a health risk occurs. The Occupational Safety and Health Administration (OSHA) set the permissible inhalation exposure limit (PEL) for synthetic graphite at  $15 \text{ mg m}^{-3}$  of total dust and  $5 \text{ mg m}^{-3}$  for the respirable fraction [125]. Lam and coworkers performed a pulmonary toxicity study on SWNTs in mice 7 and 90 days after intratracheal instillation [126]. Three CNT products made by different methods and containing different types or amounts of residual metals, i.e. raw CNTs (RNTs) and purified CNTs (PNTs), iron-containing HiPco products of Rice and CarboLex's nickel-containing electric-arc product (CNT), were used for the toxicity study. For their study, mice were intratracheally administered 0, 0.1 or 0.5 mg of CNTs, a carbon black negative control or a quartz positive control and euthanized 7 days or 90 days after treatment for histopathological study of the lungs. All CNT products induced dose-dependent epithelioid granulomas and, in some cases, interstitial inflammation in the animals of the 7-day groups. The lesions persisted and were more pronounced in the 90-day groups; the lungs of some animals were also revealed to have peribronchial inflammation and necrosis that had extended into the alveolar septa. The lungs of mice treated with carbon black were normal, whereas those treated with high-dose quartz had mild to moderate inflammation. Their results showed that if CNTs reach the lungs, they are more toxic than carbon black and can be more toxic than quartz, which was considered a serious occupational health hazard in chronic exposures. Lung toxicity of intratracheally instilled SWNT was also studied in rats [127]. The lungs of rats were instilled either with 1 or  $5 \text{ mg kg}^{-1}$  of the following control or particle types: (i) SWNT, (ii) quartz particles (positive control), (iii) carbonyl iron particles (negative control), (iv) phosphate buffered saline (PBS) + 1% Tween 80 or (v) graphite particles. Exposures to high-dose ( $5 \text{ mg kg}^{-1}$ ) SWNT resulted in about 15% mortality in the SWNT-instilled rats within 24 h postinstillation. This mortality resulted from mechanical blockage of the upper airways by the instillation and was not due to inherent pulmonary toxicity of the instilled SWNT particulate. Exposures to quartz particles produced significant increases versus controls in pulmonary inflammation, cytotoxicity and lung cell parenchymal cell proliferation indices. Exposures to SWNT produced transient inflammatory and cell injury effects. Histopathological study indicated that pulmonary exposures to SWNT in rats produced a non-dose-dependent series of multifocal granulomas, which were evidence of a foreign tis-

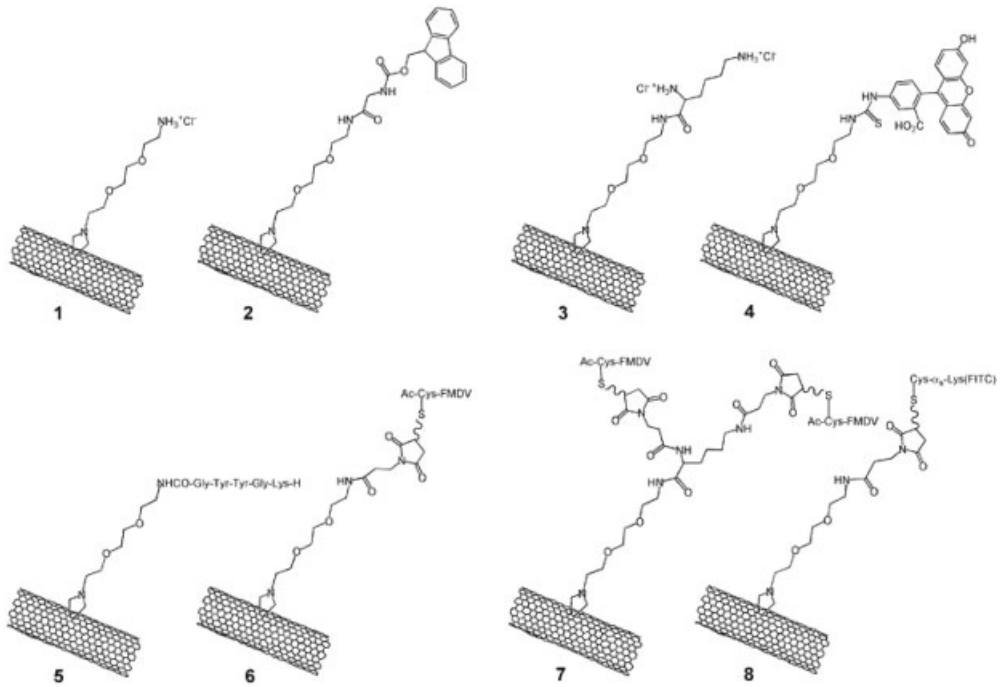


Figure 6.20. Structure of *f*-CNTs.

sue body reaction and were nonuniform in distribution and not progressive beyond 1-month postexposure.

#### 6.4.3.4 Functionalized CNTs (*f*-CNTs) for Drug Delivery

As shown in Fig. 6.20, Bianco and coworkers synthesized several hydrophilic CNT derivatives called *f*-CNTs), *f*-CNT 1–8 [128]. The aqueous solubility and cationic surface character of *f*-CNTs 1 render them potentially novel delivery vehicles. They initially showed the efficiency of *f*-CNTs to transport across the plasma membrane and penetrate into the cytoplasm of cells. To obtain the proof of the concept experiment, they prepared two different FITC-labeled *f*-CNTs, by introducing either FITC directly to the amino functions of the soluble CNTs or a fluorescent peptide. Their molecular structures are shown as conjugate 4 and 8 in Fig. 6.20. This peptide mimics the effect of  $G_s$ -protein by increasing the agonist affinity for the P-adrenergic receptor. The free peptide did not penetrate the cell membrane. To evaluate the ability of the *f*-CNTs to penetrate HeLa cells, both conjugates were incubated with the cells and analyzed. The intracellular distribution of the fluorescence was studied by fluorescence microscopy. While *f*-CNT conjugate 4 with the FITC alone mainly distributed into the cytoplasm, slowly moving towards the nucleus, peptide–CNTs 8 rapidly translocated into the cell nucleus. The same results

were obtained using other types of cells including human and murine fibroblasts and keratinocytes.

#### 6.4.3.5 *f*-CNTs for Gene Delivery

*f*-CNTs were also used for gene delivery. Gene therapy is one of the possible methods for cancer and genetic disorder therapy. For gene targeting, viral and nonviral vector systems must be developed. However, these vectors have several pitfalls, i.e. induction of undesirable immune responses, inflammations and oncogenic side-effects. Therefore, nonviral vectors have been studied because of their higher level of safety. However, they have several limitations: (i) poor membrane permeability of the administered oligonucleotide and plasmid DNA conjugates, and (ii) low levels of gene expression. As a vector system, Bianco and coworkers also examined the potential of *f*-CNTs [128]. The observation of the ensuing supramolecular assemblies using TEM indicated that nanotube–DNA complexes were formed. In addition, they obtained a clear effect using the DNA complexes with *f*-CNTs 1 to carry the P-gal gene inside the cells, by monitoring the expression of P-galactosidase. Improved levels of gene expression were also obtained for the *f*-CNT 1–DNA complex in the range of positive:negative charge ratios between 2:1 to 6:1. Gene expression offered by the complexes between plasmid DNA with *f*-CNTs was 5–10 times higher than that of DNA alone. These promising results suggest the possibility of exploiting *f*-CNTs in gene therapy and genetic vaccination.

#### 6.4.4

#### CNHs for Drug Delivery

Single-wall CNHs (SWNHs) are aggregates of graphitic tubes that have closed ends with cone-shaped caps (horns). Each tube has a diameter of 2–3 nm, which is larger than the 1.4 nm of typical SWNTs, while the aggregates are 80–100 nm in diameter and have “dahlia-like” or “bud-like” spherical structures [129]. SWNHs have extensive surface areas and multitudes of horn interstices, which enable large amounts of guest molecules to be adsorbed on SWNHs [130]. Moreover, the surface area can be further enlarged by oxidization, which causes the formation of nanowindows in the SWNH walls [131]. Through these nanowindows, a variety of small molecules [e.g. N<sub>2</sub>, Ar and fullerene (C<sub>60</sub>)] infiltrate into their inner space and quadruple the adsorptive surface areas. In addition, the sizes of the pores can be controlled by changing the oxidization conditions. Murakami and coworkers prepared a series of oxidized SWNHs (oxSWNHs) having distinct molecular sieving effects and their utility as a drug delivery system carrier was studied using dexamethasone (DEX), an anti-inflammatory drug, as a model drug [132]. DEX was adsorbed on oxSWNHs. oxSWNHs (100 μg mL<sup>-1</sup>) were dispersed by sonication in 0.1–20 mL of a 1:1 mixture of ethanol and water and was filtrated with a 0.22-μm filter, after which DEX (1000 μg mL<sup>-1</sup>) in ethanol:H<sub>2</sub>O (1:1) solution was added at a volume ratio of 1:1. The resultant mixture was incubated at room temperature overnight and then centrifuged at 18 000 g for 5 min to collect DEX–oxSWNH

complexes, which were then dried in the vacuum overnight for experiments. At first, they studied the release characteristics of DEX from the DEX–oxSWNHs complex. In the case of *in vitro* release experiments in PBS (pH 7.4) at 37 °C, the amount of DEX released was nearly proportional to the incubation time, i.e. 7–10% per day during the first few days. The release rate then gradually declined and about 50% of the total bound DEX was released from the complex within a period of 2 weeks. When cell culture medium was used instead of PBS, distinctly different release profiles were obtained. Almost half of the DEX was released within the first 8 h, after which the release rates sharply declined, so that by 24 h about 50% of the total bound DEX had been released into the RPMI 1640 medium. As mentioned above, only about 10% was released into PBS during the same time period. One possible explanation for this difference in the release profiles is that hydrophobic organic compounds present in the culture medium are competitively absorbed onto the surface of oxSWNHs or they may increase the apparent solubility of DEX in medium. They also performed the biological assay of the DEX–oxSWNH complex and showed that the DEX released from DEX–oxSWNHs had biological activity.

Murakami and coworkers also applied oxSWNHs for the delivery of the anti-cancer drug, doxorubicin (DXR) [133]. At first, they prepared the complex, PEG–DXR, of PEG and DXR by introducing PEG into the amino groups of DXR. With PEG–DXR, oxSWNHs were well dispersed in water and the mean diameter was about 200 nm. The obtained PEG–DXR–oxSWNH had a strong antitumor activity in the *in vitro* assay system.

## 6.5

### Physicochemical Aspects of Porous Silastic Materials for Drug Delivery

In the pharmaceutical field, several porous materials, such as silica, calcium silicate [97, 98], controlled pore glass [134, 135] and porous cellulose [136], are used to formulate solid dosage forms. Among them, silica particles are characteristic in having many silanol groups on their surfaces, which may be able to form hydrogen bonds with drug molecules [137]. There are several grades of silica particles with different properties, such as particle size, degree of hydrophilicity and pore structure. Recently, a new grade of porous silica, mesoporous silica, has also been developed. It has been pointed out that the porous structure itself confers special characteristics, such as a decrease of melting point and a decrease in the crystallinity of drugs entrapped in the pores [134–136, 138]. Using these characteristics of porous silica particles, several applications have been reported in the field of pharmaceutical preparations.

In this section, two different types of applications with porous silastic materials, i.e. improvement in the drug dissolution properties and entrapment of peptide drugs for their sustained release, will be introduced.

## 6.5.1

**Solid Dispersion Particles with Porous Silica**

Improvement of the dissolution property of pharmaceuticals is extremely important, especially since the percentage of drugs with poor water solubility has increased in recent years. According to the Noyes–Whitney equation [139], the dissolution rate of a drug depends on its surface area and solubility. It is easier to increase the surface area by reducing the particle size of drug crystals than to increase the drug solubility. The particle size may be easily reduced by simple grinding. However, the ground crystals tend to agglomerate, thereby creating a surface with higher energy than that of the original crystals and reducing the effective surface area for dissolution.

To improve the dissolution properties of drugs, several methods have been studied as pharmaceutical engineering techniques such as grinding with additive [140], formation of salt [141] and preparation of an inclusion compound with cyclodextrin [142], as well as simple grinding [143]. Solid dispersion is a useful method to disperse drugs in the molecular state in a carrier matrix [144, 145]. The interaction between the drug molecule and carrier is responsible for drug dispersion, and may depress the crystallization of the drug in the prepared system. The most popular carrier materials are water-soluble polymers such as PEG [146] or PVP [147]. However, it is often reported that drugs prepared by solid dispersion with a water-soluble polymer carrier tend to be sticky or tacky. This property leads to a decrease in the recovery of solid dispersion in the preparation and also a difficulty in handling in the subsequent processes. Milling or mixing with other excipients is required before preparing the final dosage forms by plugging into capsules or tableting. These processes sometimes facilitate crystallization of the drug in an amorphous state in the solid dispersion. The change in the crystalline forms of the drug in the dosage form affects its BA after administration.

Takeuchi and coworkers [148] demonstrated that solid dispersion particles of a poorly water soluble drug, tolbutamide (TBM), could be prepared by spray-drying the diluted ammonium solution of the drug with nonporous silica, AER 200. The spray-drying technique is a useful method to obtain spherical particles with a small size and narrow distribution. This method also has the advantage that granulation and drying are completed in one step. It was also confirmed that the drug was molecularly dispersed in the matrix formed with silica particles. The resultant solid dispersion particles were free-flowing and remarkably improved the dissolution property of the drug.

In preparing the solid dispersion particles of TBM using porous silica (Sylysia 350; Fuji Silisia, Japan) as a carrier from ethanol solution, the metastable crystalline form (type II) was observed in the resultant particles [149]. It is well known that the drug crystalline form can be controlled by controlling the crystallization conditions, such as the type of solvent and crystallization rate. In the case of TBM, four types of crystalline forms including the stable form of type I and three types of metastable crystalline forms (types II, III and IV) were characterized based

on their physicochemical properties, and the dissolution, BA and stability of these polymorphs have been investigated [150–152].

To confirm the factors controlling the crystalline forms of drug in the silica solid dispersion particles, solid dispersion particles of TBM were prepared by formulating various types of silica such as nonporous [AER 200 (hydrophilic), AER R972 (hydrophobic)] or porous [Sylysia 350 (hydrophilic), Sylophobic 200 (hydrophobic)] silica as carriers and applying the spray-drying or evaporation method. In the solid dispersion particles prepared by the spray-drying method, TBM existed in a metastable form (form II) irrespective of the type of silica. On the other hand, when the evaporation method was used, various crystalline forms of TBM were observed in the solid dispersion particles depending on the type of silica. Polymorphs of forms III and IV were prepared with AER 200 and AER R972, respectively, while crystalline form II was obtained when either of the forms of porous silica, Sylysia 350 or Sylophobic 200, was formulated [149].

There may be two main factors affecting the final crystalline form of the drug in this process – the removal rate of solvent from the drug solution and the type of carrier formulated with the solid dispersion. The rapid solvent evaporation from the drug solution in the spray-drying method facilitated formation of the metastable form II of TBM in the resultant particles irrespective of the type of silica. Formation of this crystalline form was also observed for evaporation solid dispersion with porous silica (Sylysia 350 or Sylophobic 200), although the solvent evaporation speed was not rapid. In this case, formation of the metastable crystalline form (form II) may have been due to restriction of the crystallization of drug molecules in the pores of carrier particles during evaporation.

To examine the pore size effect on the resultant crystalline form of TBM in evaporation solid dispersion particles, several types of porous silica with different average pore sizes (Tab. 6.4) were used. The solid dispersion with Sylysia 740, having an extremely small pore size, showed metastable form III, while form II was detected in other types of silica solid dispersion. This result suggested that pores of this type of silica were not effectively utilized in this solid dispersion formulation. In the case of other porous materials, a similar tendency was observed. Porous cel-

Tab. 6.4. Properties of porous silica and other materials

Commercial name	Average particle size ( $\mu\text{m}$ )	Specific surface area ( $\text{m}^2 \text{g}^{-1}$ )	Pore size (nm)	Pore volume ( $\text{mL g}^{-1}$ )
Sylysia 350	3.9	300	21.0	1.60
Sylysia 470	14.1	300	17.0	1.25
Sylysia 440	6.2	300	17.0	1.25
Sylysia 740	5.0	700	2.5	0.44
FLR	26.1	120	no data	150.0



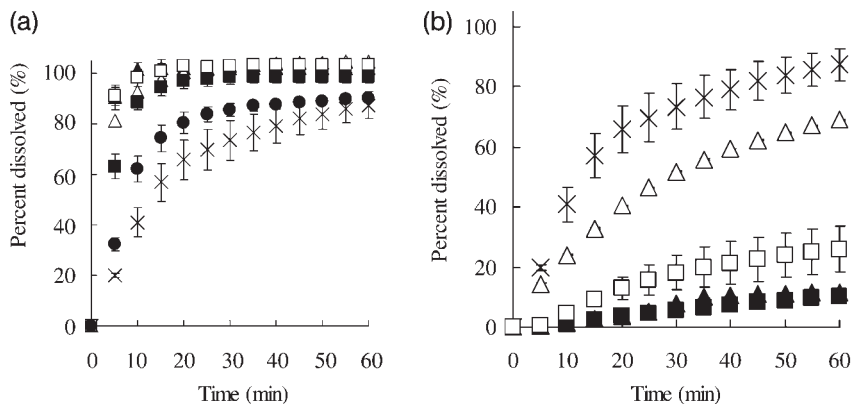


**Figure 6.21.** (a) Dissolution profile of TBM from solid dispersion particles with AER 200 or Sylysia 350 prepared by the spray-drying or evaporation method. × = Original TBM crystals; ● = spray-dried TBM; ▲ = spray-drying solid dispersion with AER 200; ■ = spray-drying solid dispersion with Sylysia 350; □ = evaporation solid dispersion with AER 200; ○ = evaporation solid dispersion with Sylysia 350. (b) Dissolution profile of TBM

from solid dispersion particles with AER R972 or Sylophobic 200 prepared by the spray-drying or evaporation method. × = Original TBM crystals; ▲ = spray-drying solid dispersion with AER R972; ■ = spray-drying solid dispersion with Sylophobic 200; □ = evaporation solid dispersion with AER R972; ○ = evaporation solid dispersion with Sylophobic 200.

lulose, having a small pore size of 4.0 nm, formed a mixture of forms II and IV in the resultant solid dispersion. The larger pore volume of porous cellulose than Sylysia 740 may be responsible for the formation of form II, although the average pore size of Sylysia 740 is as small as 2.5 nm. Another type of silastic particle, FLR, which has extremely larger pore volume, showed form II in the resultant solid dispersion. We should pay attention to the critical pore size and pore volume in using the porous silica as the drug carrier of solid dispersion [153].

The dissolution property of TBM was dramatically improved in the spray-drying solid dispersion system with hydrophilic silica (Sylysia 350 and AER 200), as shown in Fig. 6.21(a) [149]. Both the metastable crystalline form of the drug and the increased hydrophilicity of the solid dispersion particle may have contributed to this improvement. The latter effect was confirmed by measuring the drug dissolution of solid dispersions with the hydrophobic silica, Sylophobic 200 or AER R972. The spray-drying solid dispersion with the hydrophobic silica containing crystalline form II showed an extremely decreased dissolution rate (Fig. 6.21b). TBM of evaporation solid dispersion with Sylysia 350 and AER 200 showed a similar improved dissolution pattern to that of the corresponding spray-drying solid dispersion, as shown in Fig. 6.21.

The drug:carrier ratio is an important factor in designing an optimum solid dispersion system. In powder XRD analysis, the solid dispersion particles loading excess amount of drug, which was prepared in the formulation of TBM:silica =

5:1, showed much larger peaks than that prepared with the formulation of TBM:silica = 1:1. The resultant drug dissolution rate was decreased. When the spray-drying method was used, the results were almost the same [153].

From the practical point of view, the stability of metastable crystalline forms of drugs in the solid dispersion particles is an important factor in designing the final dosage forms. The metastable form of TBM in the solid dispersion particles was stable for at least 4 weeks when stored at 60 °C and 0% relative humidity (RH), while the spray-dried TBM without silica (form II) gradually changed to the stable form (form I) under the same storage conditions. Under humid storage conditions (60 °C, 75% RH), the spray-dried TBM without silica (form II) immediately converted into the stable form (form I) within 1 day, while TBM (form II) in the solid dispersions in a matrix of silica was stable for at least 1 week. In comparing their stability with respect to the type of carrier particles formulated in the solid dispersion, porous Sylysia 350 was more effective than nonporous AER 200. The same tendency was observed for the evaporation solid dispersion. As shown in Tab. 6.5, metastable form II in evaporation solid dispersion with Sylysia 350 was unchanged for up to 14 days, while metastable form III in AER 200 was converted to stable form I within the same storage period [149].

The effectiveness of porous silica as a solid dispersion carrier was confirmed using another model drug, IMC [154, 155]. IMC, whose solubility in water is 5  $\mu\text{g mL}^{-1}$  [156], has a tendency to form an amorphous state. This amorphous state property of IMC was examined extensively by many workers [157, 158]. Zografi

**Tab. 6.5.** Stability of the crystalline form of TBM in solid dispersion particles prepared by different methods stored at 0% or 75% RH and 60 °C

RH	Solid dispersion			Evaporation	
	No	AER 200	Sylysia 350	AER 200	Sylysia 350
0% 60 °C	II	II	II	III	II
	I+II	II	II	III	II
	I+II	II	II	III	II
	I+II	II	II	I+III	II
	I+II	II	II	I+III	II
	I	II	II	I+III	II
75%	II	II	II	III	II
	I	II	II	III	II
	I	II	II	I+III	II
	I	I+II	II	I	II
	I	I+II	hallo pattern	I	hallo pattern
	I	I+II	hallo pattern	I	hallo pattern
	I	I+II	hallo pattern	I	hallo pattern

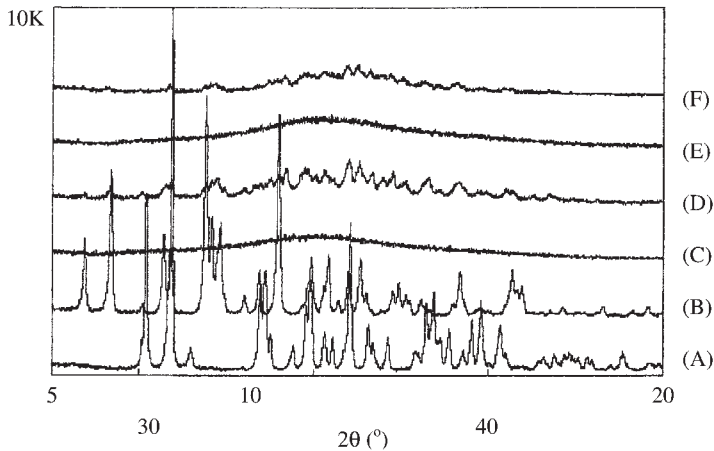


**Figure 6.22.** Powder XRD patterns of various types of IMC and solid dispersion particles (A) Original IMC crystals ( $\gamma$ -form). (B) Metastable IMC crystals ( $\alpha$ -form). (C) Amorphous IMC. (D) Spray-dried IMC. (E) Solid dispersion particles with AER1 200. (F) Solid dispersion particles with Sylysia 350.

and coworkers [159, 160] reported the interaction of IMC and PVP at the molecular level and the effect of PVP on the inhibition of crystallization of amorphous IMC in the solid dispersion system. Yoshioka and coworkers also reported the crystallization of IMC from the amorphous state above and below its glass transition temperature [161].

The solid dispersion particles of IMC were prepared with nonporous (AER 200) or porous silica (Sylysia 350) in a similar way as for TBM solid dispersion [155]. The powder XRD charts shown in Fig. 6.22 show the decreased crystallinity of IMC for spray-dried IMC and the solid dispersion particles. IMC in solid dispersion particles is almost amorphous irrespective of the type of silica formulated. In characterizing them based on the trace size of the peaks in the powder XRD charts, the crystalline form of the spray-dried IMC was a mixture of the metastable form ( $\alpha$ -form) and stable form ( $\gamma$ -form), while the original IMC crystals were the stable form ( $\gamma$ -form). Differential scanning calorimetry (DSC) patterns of various types of IMC and IMC in solid dispersion particles are shown in Fig. 6.23. The profile of spray-dried IMC showed transformation of the amorphous part of IMC into the metastable crystalline form by heating. On the other hand, the solid dispersion particles containing amorphous IMC showed a trace endothermic peak at the lower temperature compared to the melting endothermic peak for the stable or metastable IMC crystals, which confirmed that the carrier prevented the crystallization of amorphous IMC. Comparing the small endothermic peak for the two types of solid dispersion particles with different types of silica, the area of melting peak of IMC in solid dispersion with Sylysia 350 is smaller and the position of the peak is at a lower temperature than that with AER 200. In general, the melting point of drug molecules in the pore is lower than that in the bulk state [162, 163]. Nakai and

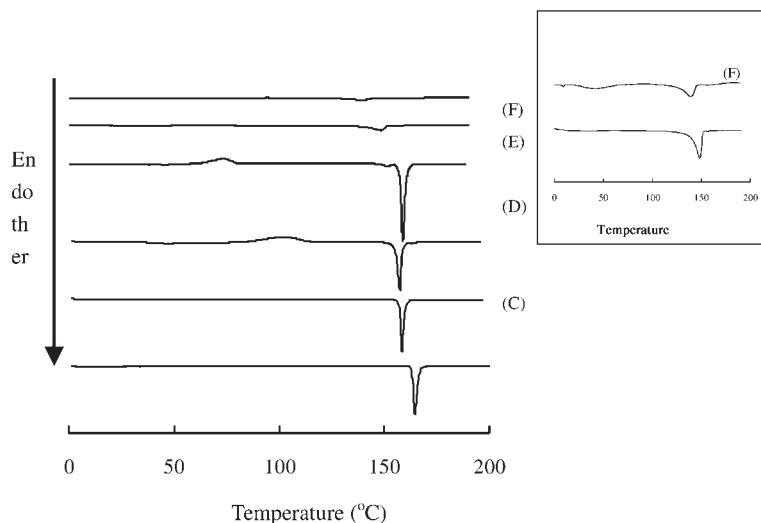


**Figure 6.23.** DSC patterns of various types of IMC and solid dispersion particles with AER 200 or Sylysia 350. (A) Original IMC crystals ( $\gamma$ -form). (B) Metastable IMC crystals ( $\alpha$ -form). (C) Amorphous IMC. (D) Spray-dried IMC. (E) Solid dispersion particles with AER1 200. (F) Solid dispersion particles with Sylysia 350.

coworkers reported this phenomenon with porous silica or porous cellulose as the carrier in the mixing system of drug crystals and the porous materials [97, 136, 138].

Figure 6.24 shows the dissolution profile of IMC from the solid dispersion particles with AER 200 or Sylysia 350 [155]. The dissolution rate of spray-dried IMC

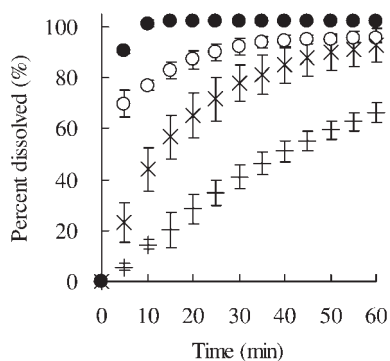


**Figure 6.24.** Dissolution profiles of IMC from solid dispersion particles with AER 200 or Sylysia 350. + = Original IMC crystals ( $\gamma$ -form).  $\times$  = Spray-dried IMC.  $\circ$  = Solid dispersion particles with AER 200.  $\bullet$  = Solid dispersion particles with Sylysia 350.

particles was faster than that of original IMC crystals because of the decrease in particle size, crystallinity and change in the crystalline form. However, 100% of spray-dried IMC could not dissolve within 60 min. On the other hand, the dissolution profile of IMC in the solid dispersions particles was remarkably improved irrespective of the type of silica formulated. This might be due to the improvement in wettability and dispersibility in the medium as well as the decrease in crystallinity of IMC in the particles, as mentioned above for the TBM solid dispersion with silica. Comparing the dissolution profiles of solid dispersion particles with AER 200 and Sylysia 350, the dissolution rate of IMC from solid dispersion particles with Sylysia 350 was faster than that with AER 200. As the drug crystallinity of the solid dispersion particles is almost the same, the difference in wettability may be responsible for the difference in the drug dissolution rate of the two different types of solid dispersion particles.

The effect of wettability on the dissolution property was clearly demonstrated with the solid dispersion particle with Sylysia 740, whose average pore size is 2.5 nm (Tab. 6.4). The dissolution rate of IMC solid dispersion with Sylysia 740 was much decreased compared with that of Sylysia 350, although Sylysia 740 was also hydrophilic silica and the drug to silica formulating ratio was the same at 1:1 [154]. The measured specific surface areas of the solid dispersion particle with Sylysia 740 and Sylysia 350 were 7.4 and 99.5 m<sup>2</sup> g<sup>-1</sup>, while those of Sylysia 740 and Sylysia 350 were 700 and 300 m<sup>2</sup> g<sup>-1</sup>, respectively. The greatly decreased specific surface area of Sylysia 740 solid dispersion implied the stuffing of pores with silica, which may lead to the reduced dispersion of the drug molecule in the pore of the carrier and covering of the silica particles with the hydrophobic drug molecule, as illustrated in Fig. 6.25. Thus, the resultant drug dissolution was decreased due to the hydrophobic property of the solid dispersion. These results may show that the pore size of silica is an important factor in obtaining the improved dissolution profile of the solid dispersion system.

The stabilizing effect of porous silica on the amorphous state of drugs was the same as observed in the case of the metastable form of TBM. In a stability test,

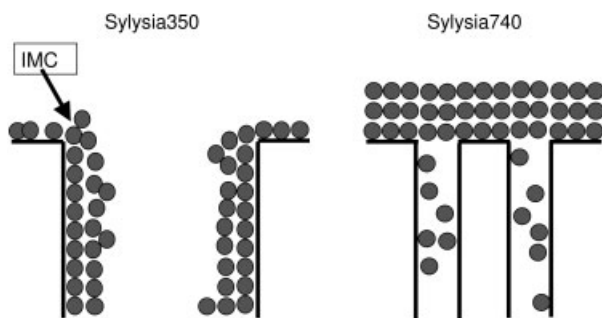


**Figure 6.25.** Schematic drawing of the state of IMC molecules in the pore of solid dispersions with Sylysia 350 or Sylysia 740.

amorphous IMC in the solid dispersion particles with each of the silica particles did not crystallize under storing at severe storage conditions (40 °C, 75% RH) for 2 months, while amorphous IMC without silica easily crystallized under the same conditions.

Through these two examples mentioned above, we can conclude that the porous silica particle effectively forms solid dispersion particles of poorly water-soluble drugs. Although nonporous colloidal silica has a similar carrier property to form an amorphous state of the drug in the particles, porous silica is sometimes superior to nonporous silica from the point of the resultant drug dissolution property or stability of the amorphous or metastable state of the drug.

Watanabe and coworkers [137] have reported that controlled release of IMC with nonporous silica leads to an improvement in its BA in an *in vivo* experiment. For this experiment, IMC was compounded with silica (AER 200) by cogrinding or melt-quenching. The initial dissolution rate of the coground compound was lower than the melt-quenched one, although both of them showed higher dissolution rates than a simple physical mixture of crystalline IMC and silica. The lower dissolution rate of coground IMC was explained by a stronger chemical interaction between IMC and the mechanically induced siloxane dangling bonds on the surface of silica. The resultant AUC values of coground and melt-quenched compounds were 1711 and 1519  $\mu\text{g h mL}^{-1}$ , respectively, while that of the physical mixture was 751  $\mu\text{g h mL}^{-1}$ . These results suggested that the initial controlled release of the drug leads to a higher BA.

### 6.5.2

#### Mesoporous Silica

Mesoporous silica is a porous silica with tightly size-controlled pores of 2–50 nm. Two types of mesoporous silica, i.e. FSM16 [164] and MCM-41 [165], have been developed by two different groups separately [166]. Both of them have the same hexagonal pore structure, although the proposed structure formation mechanism is different. FSM16 can be synthesized from a layered silicate, kanemaitite, and a folding sheet mechanism was proposed. The process including the resultant structure of FSM16 is illustrated in Fig. 6.26 [166]. The pore size and specific surface area of FSM16 are 3.0 nm and around 1000  $\text{m}^2 \text{g}^{-1}$ , respectively. Although there are several reports on mesoporous silica dealing with the preparation process and application in catalysis, few papers are available in the field of pharmaceutical engineering [166].

We have examined the usefulness of this porous particle as a carrier of the macromolecular drug insulin, because its pore size is comparable to that of the macromolecules. The simple adsorption profile of insulin on FSM16 is shown in Fig. 6.27 [167]. By assuming Langmuir-type adsorption, the maximum adsorption amount was estimated as 137  $\mu\text{g mg}^{-1}$  of FSM16. The adsorption amount of insulin to Sylysia 350 or Sylysia 740 was low, although their surface area is comparable to that of FSM16 and the pore size of Sylysia 740 (2.5 nm) is similar to that of FSM16.

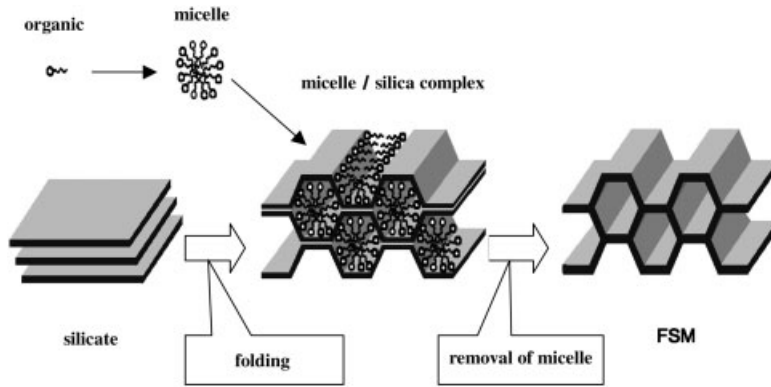


Figure 6.26. Formation and pore structure of FSM.

To increase the entrapment efficiency of insulin into the porous material, we devised a freeze–thawing method. Although the freeze–thawing method has been reported as a drug encapsulation method into liposomes, the concept of this freeze–thawing method for mesoporous silica is completely different. In this method, we used nonfrozen water formed in the pores of particles. In general, porous material has special properties such as a decreased melting point and forms nonfrozen water in the pores [162, 163]. It has also been reported that silica gel forms nonfrozen water on its surface and that nonfrozen water can be formed in the porous materials [168–170]. Morishige and coworkers [170] have observed that free water in the pores of MCM with a pore diameter of 4.2 nm was frozen abruptly around 232 K to give rise to cubic ice, while the water confined in the pores with a pore diameter of

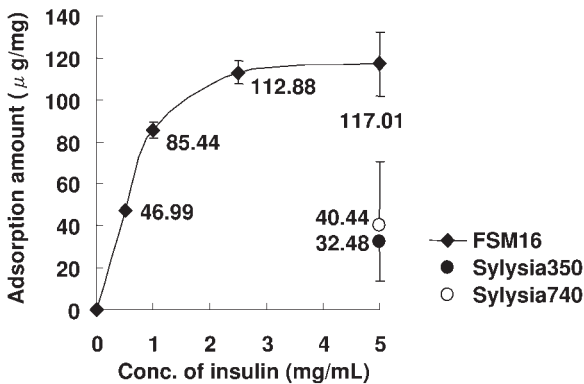


Figure 6.27. Adsorption amount of insulin on FSM16, Sylysia 350 and Sylysia 740 at various concentration of insulin solution. Adsorption conditions: temperature = 5 °C; shaking time = 24 h.

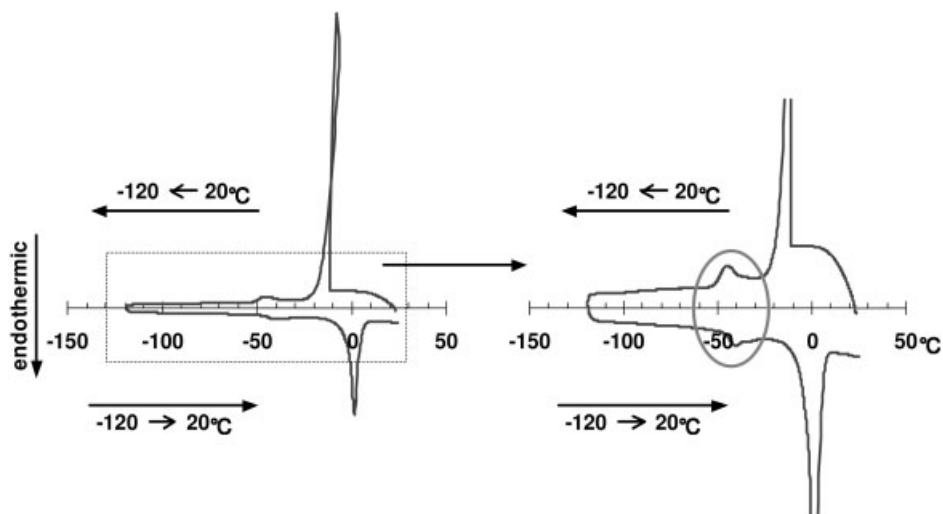


Figure 6.28. DSC profiles of FSM16 containing water.

2.4 nm was frozen very gradually at lower temperature. To confirm the formation of nonfrozen water in FSM16, we measured DSC patterns of FSM16 containing water. As shown in the DSC chart (Fig. 6.28), two clear exothermic peaks in the freezing process and two endothermic peaks in the melting process were observed [167]. The peaks observed at the lower temperature may be attributed to the freezing and melting of water in the pores. In the case of Sylysia 350, such peaks were not observed, because the pore size was much larger than FSM16. In the case of Sylysia 740, similar peaks were detected because its average pore size is as small as FSM16. However, the peaks were very small compared with that of FSM16. This may be attributed to its large pore size distribution, as observed for normal silica.

In freezing the FSM16 suspension in drug solution, the drug solution may be concentrated in the pores when the bulk water is frozen and then the freezing is stopped just before freezing of the pore water. Based on the DSC analysis which showed the pore water was frozen at around  $-40^{\circ}\text{C}$ , the freezing temperature in the freeze–thawing method was set at  $-30^{\circ}\text{C}$ . Figure 6.29 shows the increased entrapment of insulin into FSM16 using this freeze–thawing method. The entrapment amount increased by increasing the number of freezing–thawing cycles. When the freezing temperature was set at  $-100$  instead of  $-30^{\circ}\text{C}$ , the efficiency was much reduced. This result confirmed our assumption stated above for the mechanism of drug entrapment in the freeze–thawing method. In both cases of Sylysia 350 and Sylysia 740, the entrapment amount of insulin was in the range of  $50\text{--}100\ \mu\text{g mg}^{-1}$ , even by applying this freeze–thawing method (10 times) [167].

The drug release from the insulin-loaded FSM16 was measured *in vitro*. The result showed that half of the entrapped insulin was released within 1 h (burst re-



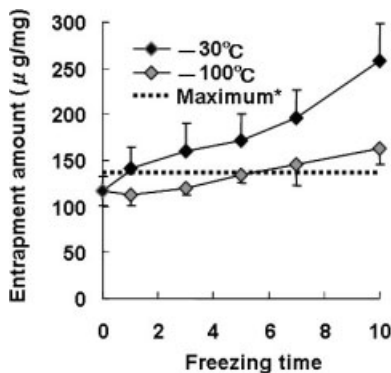


**Figure 6.29.** Entrapment of insulin into FSM16 with the freeze–thawing method. Initial adsorption conditions: temperature = 5 °C; shaking time = 24 h. \*Maximum adsorption amount of insulin on FSM16 calculated with the Langmuir adsorption isotherm (137.0  $\mu\text{g mg}^{-1}$ ).

lease) followed by a very slow and sustained release (1.3  $\mu\text{g mg}^{-1}$  of FSM16  $\text{day}^{-1}$ ). To utilize mesoporous silica as a drug carrier, it may be important to control the burst release. This might be achieved by modifying the entrance of the pores of FSM with some hydrophobic molecules.

To check the effectiveness of the freeze–thawing method in the encapsulation of macromolecules, three types of FITC–dextran with different molecular weights (4400, 9500 and 21 200) were selected as a model drugs [171]. When the adsorption amount of these FITC–dextran was compared under the same conditions, where 10 mg of FSM16 was dispersed in 1  $\text{mg mL}^{-1}$  of drug solution at 5 °C, the adsorption amount of FITC–dextran depended on their molecular weight, in the order of FITC–dex4400 > FITC–dex9500 > FITC–dex21200. In applying the freeze–thawing method to the entrapment of these FITC–dextrans, the entrapment amount was increased, as shown in Fig. 6.30. As the adsorbed amount of FITC–dex9500 and FITC–dex21200 was very small in the simple adsorption process, their adsorption amounts to FSM16 with the freeze–thawing method were 6.1 and 20.7 times higher compared with a simple adsorption procedure, respectively.

FSM16 is also an excellent carrier for poorly water-soluble drugs with low molecular weight as well as usual porous silica (as discussed in the previous section). We prepared a solid dispersion of beclomethasone propionate using FSM16 as a carrier in the same manner as for the Sylysia solid dispersion [172]. The simple adsorption amount of drug to FSM16 in the dichloromethane solution was large and the maximum adsorption amount was estimated as 333.3  $\mu\text{g mg}^{-1}$  of FSM16. In the case of Sylysia 350, the estimated maximum adsorption amount was 156.3  $\mu\text{g mg}^{-1}$  FSM16. In the dissolution test, FSM16 solid dispersion showed a supersaturated concentration of the drug, which was 3 times higher than the saturated concentration, while Sylysia 350 solid dispersion showed almost the same drug concentration as the crystalline drug. The different drug dissolution phenomenon

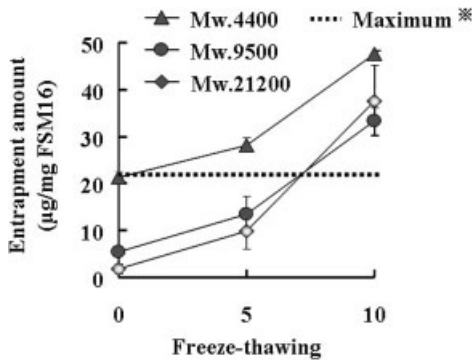


**Figure 6.30.** Entrapment of FITC–dextran with different molecular weights (4400, 9500 and 21 200) into FSM16 with the freeze–thawing method. Conditions of entrapment test: FITC–dex.sol., 1 mg mL<sup>-1</sup>, 1 mL solvent (Mcllvaine buffer, pH4.0); silica; FSM16 (10 mg); freezing temperature = –30 °C. \*Maximum adsorption amount of FITC–dex4400 on FSM16 calculated with the Langmuir adsorption isotherm (22.57 µg mg<sup>-1</sup>).

for FSM16 and Slysia 350 solid dispersions suggested different adsorption modes or forces between the surface of the silica and the drug molecule.

Tozuka and coworkers [173] recently investigated the adsorption and entrapment of salicylamide molecules into FSM16. They confirmed crystalline salicylamide converted into an amorphous state on heating at 120 °C for 3 h. By measuring a shift in the fluorescence emission peak of salicylamide in the carrier, they suggested dispersion of the drug molecule into the hexagonal channels during the heating process. It was also demonstrated that the dissolution rate of the solid dispersion was higher than the crystalline one.

As mesoporous silica such as FSM16 is quite a new product, for which large-scale production processes are still being developed, the number of reports in the pharmaceutical field is small. However, data shown in this section may indicate its unique characteristics due to its extremely high surface area and tightly controlled pore size. A lot of interesting data should follow in the near future.

## References

- 1 FUKUMORI, Y., ICHIKAWA, H. 2005. Design of controlled release pharmaceuticals in nanoparticle coating process. *J. Soc. Powder Technol., Japan* 42, 673–581.
- 2 JONO, K., ICHIKAWA, H., MIYAMOTO, M., FUKUMORI, Y. 2000. A review of particulate design for pharmaceutical powders and their production by spouted bed coating. *Powder Technol.* 113, 269–277.
- 3 FUKUMORI, Y., ICHIKAWA, H. 2003. Fluid bed processes for forming functional particles. In *Encyclopedia of Pharmaceutical Technology*. Edited by PARIKH, D. M., Marcel Dekker, New York, pp. 1–7.
- 4 DASHEVSKY, A., KOLTER, K., BODMEIER, R. 2004. Compression of pellets coated with various aqueous polymer dispersions. *Int. J. Pharmac.* 279, 19–26.

- 5 LIN, A. Y., MUHAMMAD, N. A., POPE, D., AUGSBURGER, L. L. **2003**. A study of the effects of curing and storage conditions on controlled release diphenhydramine HCl pellets coated with Eudragit NE30D. *Pharmac. Dev. Technol.* 8, 277–287.
- 6 LIN, A. Y., MUHAMMAD, N. A., POPE, D., AUGSBURGER, L. L. **2001**. Study of crystallization of endogenous surfactant in Eudragit NE30D-free films and its influence on drug-release properties of controlled-release diphenhydramine HCl pellets coated with Eudragit NE30D. *AAPS Pharmac. Sci.* 3, E14.
- 7 ALKHATIB, H. S., SAKR, A. **2003**. Optimization of methacrylic acid ester copolymers blends as controlled release coatings using response surface methodology. *Pharmac. Dev. Technol.* 8, 87–96.
- 8 LIU, Y., SCHWARTZ, J. B., SCHNAARE, R. L. **2003**. A multimechanistic drug release approach in a bead dosage form and *in vitro* predictions. *Pharmac. Dev. Technol.* 8, 163–173.
- 9 SADEGHI, F., FORD, J. L., RUBINSTEIN, M. H., RAJABI-SIAHBOOMI, A. R. **2000**. Comparative study of drug release from pellets coated with HPMC or Surelease. *Drug Dev. Ind. Pharm.* 26, 651–660.
- 10 LIPPOLD, B. C., MONELLS PAGES, R. **2001**. Control and stability of drug release from diffusion pellets coated with the aqueous quaternary polymethacrylate dispersion Eudragit RS30D. *Pharmazie* 56, 477–483.
- 11 LARSEN, C. C., SONNERGAARD, J. M., BERTELSEN, P., HOLM, P. **2003**. A new process control strategy for aqueous film coating of pellets in fluidized bed. *Eur. J. Pharmac. Sci.* 20, 273–283.
- 12 ICHIKAWA, H., FUKUMORI, Y., ADEYEYE, C. M. **1997**. Design of prolonged-release microcapsules containing diclofenac sodium for oral suspensions and their preparation by the Wurster process. *Int. J. Pharmac.* 156, 39.
- 13 ICHIKAWA, H., FUJIOKA, K., ADEYEYE, C. M., FUKUMORI, Y. **2001**. Use of ion-exchange resins to prepare 100  $\mu\text{m}$ -sized microcapsules with prolonged drug-release by the Wurster process. *Int. J. Pharmac.* 216, 67–76.
- 14 COLE, E. T., SCOTT, R. A., CORROR, A. L., WILDING, I. R., PETEREIT, H., SCHMINKE, C., BECKERT, T., CADE, D. **2002**. Enteric coated HPMC capsules designed to achieve intestinal targeting. *Int. J. Pharmac.* 231, 83–95.
- 15 RUDOLPH, M. W., KLEIN, S., BECKERT, T. E., PETEREIT, H., DRESSMAN, J. B. **2001**. A new 5-aminosalicylic acid multi-unit dosage form for the therapy of ulcerative colitis. *Eur. J. Pharmac. Biopharmac.* 51, 183–190.
- 16 GUPTA, V. K., BECKERT, T. E., DEUSCH, N. J., HARIHARAN, M., PRICE, J. C. **2002**. Investigation of potential ionic interactions between anionic and cationic polymethacrylates of multiple coatings of novel colonic delivery system. *Drug Dev. Ind. Pharm.* 28, 207–215.
- 17 FUKUMORI, Y. **1994**. Coating of multiparticulates using polymeric dispersions. Formulation and process consideration. In *Multiparticulate Oral Drug Delivery*, GHEBRE-SELLASSIE, I. (Ed.). Marcel Dekker, New York, pp. 79–111.
- 18 STEUERNAGEL, C. R. **1989**. Latex emulsions for controlled drug delivery. In *Aqueous Polymeric Coatings for Pharmaceutical Dosage Forms*, MCGENITY, J. W. (Ed.). Marcel Dekker, New York, pp. 1–62.
- 19 MOORE, K. L. **1989**. Physical properties of Opadry, Coateric, and Surelease. In *Aqueous Polymeric Coatings for Pharmaceutical Dosage Forms*, MCGENITY, J. W. (Ed.). Marcel Dekker, New York, pp. 303–316.
- 20 LEHMANN, K. O. R. **1989**. Chemistry and application properties of polymethacrylate coating. In *Aqueous Polymeric Coatings for Pharmaceutical Dosage Forms*, MCGENITY, J. W. (Ed.). Marcel Dekker, New York, pp. 153–246.
- 21 MUROI, S. **1984**. *High Polymer Latex Adhesives*. Kobunshi-Kankokai, Kyoto, Japan.
- 22 FUKUMORI, Y., ICHIKAWA, H., YAMAOKA, Y., AKAHO, E., TAKEUCHI, Y., FUKUDA, T., KANAMORI, R., OSAKO,

- Y. 1991. Effect of additives on physical properties of fine ethyl cellulose microcapsules prepared by the Wurster process. *Chem. Pharmac. Bull.* 39, 164–169.
- 23 FUKUMORI, Y., ICHIKAWA, H., YAMAOKA, Y., AKAHO, E., TAKEUCHI, Y., FUKUDA, T., KANAMORI, R., OSAKO, Y. 1991. Microgranulation and encapsulation of pulverized pharmaceutical powders with ethyl cellulose by the Wurster process. *Chem. Pharmac. Bull.* 39, 1806–1812.
- 24 FUKUMORI, Y., ICHIKAWA, H., JONO, K., TAKEUCHI, Y., FUKUDA, T. 1992. Computer simulation of agglomeration in the Wurster process. *Chem. Pharmac. Bull.* 40, 2159–2163.
- 25 FUKUMORI, Y., ICHIKAWA, H., JONO, K., TAKEUCHI, Y., FUKUDA, T., OSAKO, Y. 1993. Effect of additives on agglomeration in aqueous coating with hydroxypropyl cellulose. *Chem. Pharmac. Bull.* 41, 725–730.
- 26 ICHIKAWA, H., JONO, K., TOKUMITSU, H., FUKUDA, T., FUKUMORI, Y. 1993. Coating of pharmaceutical powders by fluidized bed process. V. Agglomeration and efficiency in the coating with aqueous latices of copoly(EA–MMA–HEMA). *Chem. Pharmac. Bull.* 41, 1132–1136.
- 27 FUKUMORI, Y., YAMAOKA, Y., ICHIKAWA, H., TAKEUCHI, Y., FUKUDA, T., OSAKO, Y. 1988. Coating of pharmaceutical powders by fluidized bed process. III. Aqueous coating with ethyl acrylate–methyl methacrylate–2-hydroxyethyl methacrylate copolymer and the dissolution properties of the products. *Chem. Pharmac. Bull.* 36, 3070–3078.
- 28 FUKUMORI, Y., YAMAOKA, Y., ICHIKAWA, H., TAKEUCHI, Y., FUKUDA, T., OSAKO, Y. 1988. Coating of pharmaceutical powders by fluidized bed process. IV. Softening temperature of acrylic copolymers and its relation to film-formation in aqueous coating. *Chem. Pharmac. Bull.* 36, 4927–4932.
- 29 ICHIKAWA, H., TOKUMITSU, H., JONO, K., OSAKO, Y., FUKUMORI, Y. 1994. Coating of pharmaceutical powders by fluidized bed process. VI. Microencapsulation using blend and composite latices of copoly(EA–MMA–HEMA). *Chem. Pharmac. Bull.* 42, 1308–1314.
- 30 ICHIKAWA, H., KANEKO, S., FUKUMORI, Y. 1996. Coating performance of aqueous composite latices with *N*-isopropylacrylamide shell and thermosensitive permeation properties of their microcapsule membranes. *Chem. Pharmac. Bull.* 44, 383–391.
- 31 KANEKO, Y., SAKAI, K., OKANO, T. 1998. *Biorelated Polymers and Gels*. Academic Press, Boston, MA, pp. 26–69.
- 32 ICHIKAWA, H., FUKUMORI, Y. 1997. New applications of acrylic polymers for thermosensitive drug release. *STP Pharma Sci.* 7, 529–545.
- 33 WU, X. S., HOFFMAN, A. S., YAGER, P. 1992. Synthesis and characterization of thermally reversible macroporous poly(*N*-isopropylacrylamide) hydrogels. *J. Polym. Sci. A Polym. Chem.* 30, 2121–2129.
- 34 KANEKO, Y., NAKAMURA, S., SAKAI, K., KIKUCHI, A., AOYAGI, T., SAKURAI, Y., OKANO, T. 1998. Deswelling mechanism for comb-type grafted poly(*N*-isopropylacrylamide) hydrogels with rapid temperature responses. *Polym. Gels. Netw.* 6, 333–345.
- 35 ICHIKAWA, H., FUKUMORI, Y. 2000. A novel positively thermosensitive controlled-release microcapsules with membrane of nano-sized poly(*N*-isopropylacrylamide) gel dispersed in ethyl cellulose matrix. *J. Control. Release* 63, 107–119.
- 36 KAS, H. S. 1997. Chitosan: properties, preparations and application to microparticulate systems. *J. Microencapsul.* 14, 689–711.
- 37 REGE, P. R., SHUKLA, D. J., BLOCK, L. H. 1999. Chitosans as tableting excipients for modified release delivery systems. *Int. J. Pharmac.* 181, 49–60.
- 38 SHU, X. Z., ZHU, K. J. 2000. A novel approach to prepare tripolyphosphate/chitosan complex beads for controlled release drug delivery. *Int. J. Pharmac.* 201, 51–58.

- 39 KAWASHIMA, Y., HANDA, T., KASAI, A., TAKENAKA, H., LIN, S. Y., ANDO, Y. 1985. Novel method for the preparation of controlled-release theophylline granules coated with a polyelectrolyte complex of sodium polyphosphate–chitosan. *J. Pharm. Sci.* 74, 264–268.
- 40 MI, F. L., SYU, S. S., CHEN, C. T., SCHOUNG, J. Y. 1999. Porous chitosan microsphere for controlling the antigen release of Newcastle disease vaccine: preparation of antigen-adsorbed microsphere and *in vitro* release. *Biomaterials* 20, 1603–1612.
- 41 ILLUM, L., FARRAJ, N., DAVIS, S. S. 1994. Chitosan as a novel nasal delivery system for peptide drugs. *Pharmac. Res.* 11, 1186–1189.
- 42 CALVO, P., REMUÑÁN-LÓPEZ, C., VILA-IATO, J. L., ALONSO, M. J. 1997. Chitosan and chitosan/ethylene oxide–propylene oxide block copolymer nanoparticles as novel carriers for proteins and vaccines. *Pharmac. Res.* 14, 1431–1436.
- 43 ERBACHER, P., ZOU, S., BETTINGER, T., STEFFAN, A. M., REMY, J. S. 1998. Chitosan-based vector/DNA complexes for gene delivery: biophysical characteristics and transfection ability. *Pharmac. Res.* 15, 1332–1339.
- 44 HASSAN, E. E., PARISH, R. C., GALLO, J. M. 1992. Optimized formulation of magnetic chitosan microspheres containing the anticancer agent, oxantazole. *Pharmac. Res.* 9, 390–397.
- 45 PAVANETTO, F., PERUGINI, P., CONTI, B., MODENA, T., GENTA, I. 1996. Evaluation of process parameters involved in chitosan microsphere preparation by the o/w/o multiple emulsion method. *J. Microencapsul.* 13, 679–688.
- 46 GANZA-GONZÁLEZ, A., ANGUIANO-IGEA, S., OTEO-ESPINAR, F. J., MÉNDEZ, J. B. 1999. Chitosan and chondroitin microspheres for oral-administration controlled release of metoclopramide. *Eur. J. Pharmac. Biopharmac.* 48, 149–155.
- 47 MASUI, S., ICHIKAWA, H., FUKUMORI, Y. 2005. Development of non-covalently cross-linked chitosan nanoparticles and their coating performance in spouted bed spray-coating process. In *Proceedings of 8th international Symposium on Agglomeration*, Bangkok, pp. 321–325.
- 48 FUKUMORI, Y., ICHIKAWA, H. 2006. Nanoparticles for cancer therapy and diagnosis. *Adv. Powder Technol.* 17, 1–28.
- 49 ITO, A., HONDA, H., KOBAYASHI, T. 2003. Cancer diagnosis and therapy using magnetite nanoparticles. *Chem. Eng., Japan* 67, 692–695.
- 50 BJORNERUD, A., JOHANSSON, L. O., AHLSTROM, H. K. 2001. Pre-clinical results with clariscan (NC100150 injection); experience from different disease models. *MAGMA* 12, 99–103.
- 51 KIRCHER, M. F., ALLPORT, J. R., GRAVES, E. E., LOVE, V., JOSEPHSON, L., LICHTMAN, A. H., WEISSLEDER, R. 2003. *In vivo* high resolution three-dimensional imaging of antigen-specific cytotoxic T-lymphocyte trafficking to tumors. *Cancer Res.* 63, 6838–6346.
- 52 JOSEPHSON, L., TUNG, C. H., MOORE, A., WEISSLEDER, R. 1999. High-efficiency Intracellular magnetic labeling with novel superparamagnetic–tat peptide conjugate. *Bioconjug. Chem.* 19, 186–191.
- 53 ZHAO, M., KIRCHER, M. F., JOSEPHSON, L., WEISSLEDER, R. 2002. Differential conjugation of tat peptide to superparamagnetic nanoparticles and its effect on cellular uptake. *Bioconjug. Chem.* 13, 840–844.
- 54 SCHELLENBERGER, E. A., BOGDANOV, JR., A., HOGEMANN, D., TAIT, J., WEISSLEDER, R., JOSEPHSON, L. 2002. Annexin V–CLIO: a nanoparticle for detecting apoptosis by MRI. *Mol. Imaging* 1, 102–107.
- 55 ZHANG, Y., KOHLER, N., ZHANG, M. 2002. Surface modification of superparamagnetic magnetite nanoparticles and their intracellular uptake. *Biomaterials* 23, 1553–1561.
- 56 HOGEMANN, D., JOSEPHSON, L., WEISSLEDER, R., BASILION, J. P. 2000. Improvement of MRI probes to allow efficient detection of gene expression. *Bioconjug. Chem.* 11, 941–946.

- 57 AKERMAN, M. E., CHAN, W. C., LAAKKONEN, P., BHATIA, S. N., RUOSLAHTI, E. 2002. Nanocrystal targeting *in vivo*. *Proc. Natl Acad. Sci. USA* 99, 12617–12621.
- 58 TKACHENKO, A. G., XIE, H., COLEMAN, D., GLOMM, W., RYAN, J., ANDERSON, M. F., FRANZEN, S., FELDHEIM, D. L. 2003. Multifunctional gold nanoparticle–peptide complexes for nuclear targeting, *J. Am. Chem. Soc.* 125, 4700–4701.
- 59 ONISHI, H., MACHIDA, Y., MACHIDA, Y. 2003. Antitumor properties of irinotecan-containing nanoparticles prepared using poly(DL-lactic acid) and poly(ethylene glycol)-block-poly(propylene glycol)-block-poly(ethylene glycol). *Biol. Pharmac. Bull.* 26, 116–119.
- 60 CHAWLA, J. S., AMIJI, M. M. 2003. Cellular uptake and concentrations of tamoxifen upon administration in poly(epsilon-caprolactone) nanoparticles. *AAPS Pharmac. Sci.* 5, E3.
- 61 CHAWLA, J. S., AMIJI, M. M. 2002. Biodegradable poly(epsilon-caprolactone) nanoparticles for tumor-targeted delivery of tamoxifen. *Int. J. Pharmac.* 24, 127–138.
- 62 KATAOKA, K., HARADA, A., NAGASAKI, Y. 2001. Block copolymer micelles for drug delivery: design, characterization and biological significance. *Adv. Drug Deliv. Rev.* 47, 113–131.
- 63 CUI, Z., MUMPER, R. J. 2002. Plasmid DNA-entrapped nanoparticles engineered from microemulsion precursors: *in vitro* and *in vivo* evaluation. *Bioconjug. Chem.* 13, 1319–1327.
- 64 KABBAJ, M., PHILLIPS, N. C. 2001. Anticancer activity of mycobacterial DNA: effect of formulation as chitosan nanoparticles. *J. Drug Target.* 9, 317–328.
- 65 HOOD, J. D., BEDNARSKI, M., FRAUSTO, R., GUCCIONE, S., REISFELD, R. A., XIANG, R., CHERESH, D. A. 2002. Tumor regression by targeted gene delivery to the neovasculature. *Science*, 296 5577, 2404–2407.
- 66 BELLOCQ, N. C., PUN, S. H., JENSEN, G. S., DAVIS, M. E. 2003. Transferrin-containing, cyclodextrin polymer-based particles for tumor-targeted gene delivery. *Bioconjug. Chem.* 14, 1122–1132.
- 67 GREF, R., COUVREUR, P., BARRATT, G., MYSIKINE, E. 2003. Surface-engineered nanoparticles for multiple ligand coupling. *Biomaterials* 24, 4529–4537.
- 68 ESPUELAS, M. S., LEGRAND, P., LOISEAU, P. M., BORIES, C., BARRATT, G., IRACHE, J. M. 2002. *In vitro* antileishmanial activity of amphotericin B loaded in poly(epsilon-caprolactone) nanospheres. *J. Drug Target.* 10, 593–599.
- 69 TOKUMITSU, H., ICHIKAWA, H., FUKUMORI, Y., BLOCK, L. H. 1999. Preparation of gadopentetic acid-loaded chitosan microparticles for gadolinium neutron-capture therapy of cancer by a novel emulsion-droplet coalescence technique. *Chem. Pharmac. Bull.* 47, 838–842.
- 70 TOKUMITSU, H., ICHIKAWA, H., FUKUMORI, Y. 1999. Chitosan-gadopentetic acid complex nanoparticles for gadolinium neutron-capture therapy of cancer: preparation by novel emulsion-droplet coalescence technique and characterization. *Pharmac. Res.* 16, 1830–1835.
- 71 TOKUMITSU, H., HIRATSUKA, J., SAKURAI, Y., KOBAYASHI, T., ICHIKAWA, H., FUKUMORI, Y. 2000. Gadolinium neutron-capture therapy using novel gadopentetic acid–chitosan complex nanoparticles: *in vivo* growth suppression of experimental melanoma solid tumor. *Cancer Lett.* 150, 177–182.
- 72 SHIKATA, F., TOKUMITSU, H., ICHIKAWA, H., FUKUMORI, Y. 2002. *In vitro* cellular accumulation of gadolinium incorporated into chitosan nanoparticles designed for neutron-capture therapy of cancer. *Eur. J. Pharmac. Biopharmac.* 53, 57–63.
- 73 OYEWUMI, M. O., YOKEL, R. A., JAY, M., COAKLEY, T., MUMPER, R. J. 2004. Comparison of cell uptake, biodistribution and tumor retention of folate-coated and PEG-coated gadolinium nanoparticles in tumor-

- bearing mice. *J. Control. Release* 95, 613–626.
- 74 OYEWUMI, M. O., LIU, S., MOSCOW, J. A., MUMPER, R. J. 2003. Specific association of thiamine-coated gadolinium nanoparticles with human breast cancer cells expressing thiamine transporters. *Bioconjug. Chem.* 14, 404–411.
- 75 OYEWUMI, M. O., MUMPER, R. J. 2003. Influence of formulation parameters on gadolinium entrapment and tumor cell uptake using folate-coated nanoparticles. *Int. J. Pharmac.* 251, 85–97.
- 76 OYEWUMI, M. O., MUMPER, R. J. 2002. Engineering tumor-targeted gadolinium hexanedione nanoparticles for potential application in neutron capture therapy. *Bioconjug. Chem.* 13, 1328–1335.
- 77 OYEWUMI, M. O., MUMPER, R. J. 2002. Gadolinium-loaded nanoparticles engineered from microemulsion templates. *Drug Dev. Ind. Pharm.* 28, 317–328.
- 78 STEVENS, P. J., SEKIDO, M., LEE, R. J. 2004. Synthesis and evaluation of a hematoporphyrin derivative in a folate receptor-targeted solid-lipid nanoparticle formulation. *Anticancer Res.* 24, 161–165.
- 79 ROY, I., OHULCHANSKY, T. Y., PUDAVAR, H. E., BERGEY, E. J., OSEROFF, A. R., MORGAN, J., DOUGHERTY, T. J., PRASAD, P. N. 2003. Ceramic-based nanoparticles entrapping water-insoluble photosensitizing anticancer drugs: a novel drug-carrier system for photodynamic therapy. *J. Am. Chem. Soc.* 125, 7860–7865.
- 80 NIGAVEKAR, S. S., SUNG, L., LIANES, Y. M., EL-JAWAHRI, A., LAWRENCE, T. S., BECKER, C. W., BALOGH, L., KHAN, M. K. 2004. <sup>3</sup>H dendrimer nanoparticle organ/tumor distribution. *Pharmac. Res.* 21, 4764–4683.
- 81 LI, L., WARTCHOW, C. A., DANTHI, S. N., SHEN, Z., DECHENE, N., PEASE, J., CHOI, H. S., DOEDE, T., CHU, P., NING, S., LEE, D. Y., BEDNARSKI, M. D., KNOX, S. J. 2004. A novel antiangiogenesis therapy using an integrin antagonist or anti-Flk-1 antibody coated <sup>90</sup>Y-labeled nanoparticles. *Int. J. Radiat. Oncol. Biol. Phys.* 58, 1215–1227.
- 82 KREUTER, J. 2001. Nanoparticulate systems for brain delivery of drugs. *Adv. Drug Deliv. Rev.* 47, 65–81.
- 83 VAISANEN, V., HARMA, H., LILJA, H., BJARTELL, A. 2000. Time-resolved fluorescence imaging for quantitative histochemistry using lanthanide chelates in nanoparticles and conjugated to monoclonal antibodies. *Luminescence* 15, 89–397.
- 84 MAJETI, N. V., KUMAR, R. 2000. Nano and microparticles as controlled drug delivery devices. *J. Pharm. Pharmac. Sci.* 3, 234–258.
- 85 AKERMAN, M. E., CHAN, W. C. W., LAAKKONEN, P., BHATIA, S. N., RUOSLAHTI, E. 2002. Nanocrystal targeting *in vivo*. *Natl Acad. Sci. USA* 99, 12617–12621.
- 86 PAUL, W., SHARMA, C. P. 2003. Ceramic drug delivery: a perspective. *J. Biomater. Applic.* 17, 253–264.
- 87 OTSUKA, M., MATSUDA, Y., DUNCAN, Y. U., WONG, J., FOX, J. L., HIGUCHI, W. I. 1990. A novel skeletal drug delivery system for anti-bacterial drugs using self-setting hydroxyapatite cement. *Chem. Pharmac. Bull.* 38, 3500–3502.
- 88 OTSUKA, M., MATSUDA, Y., SUWA, Y., FOX, J. L., HIGUCHI, W. I. 1994. A novel skeletal drug delivery system using self-setting calcium phosphate cement. 2. Physicochemical properties and drug release rate of the cement-containing indomethacin. *J. Pharmac. Sci.* 83 5, 611–615.
- 89 HARUTA, S., HANAFUSA, T., FUKASE, H., MIYAJIMA, H., OKI, T. 2003. An effective absorption behavior of insulin for diabetic treatment following intranasal delivery using porous spherical calcium carbonate in monkeys and healthy human volunteers. *Diabetes Technol. Ther.* 5, 1–9.
- 90 ISHIKAWA, F., MURANO, M., HIRAISHI, M., YAMAGUCHI, T., TAMAI, I., TSUJI, A. 2002. Insoluble powder formulation as an effective nasal drug delivery system. *Pharmac. Res.* 19, 1097–1104.

- 91 YANAGAWA, A., KUDO, T., MIZUSHIMA, Y. 1995. A novel particle carrier for transnasal peptide absorption. *Jpn. J. Clin. Pharmacol. Ther.* 26, 127–128.
- 92 UENO, Y., FUTAGAWA, H., TAKAGI, Y., UENO, A., MIZUSHIMA, Y. 2005. Drug-incorporating calcium carbonate nanoparticles for a new delivery system. *J. Control. Release* 103, 93–98. <http://www.galenisearch.com>.
- 94 OGAWA, Y. 2005. Novel sustained-release system for protein drugs: optimization for the application to human growth hormone and evaluation of the function. *Drug Deliv. Syst.* 20, 288.
- 95 TAKEUCHI, H., SASAKI, H., NIWA, T., HINO, T., KAWASHIMA, Y., UESUGI, K., OZAWA, H. 1991. Redispersible dry emulsion system as novel oral dosage form of oily drugs: *in vivo* studies in beagle dogs. *Chem. Pharmac. Bull.* 39, 3362–3364.
- 96 HANAWA, T., IKOMA, R., WATANABE, A., HIDAKA, M., SUGIHARA, M. 1996. Preparation and characterization of sealed heated mixture of ethenzamide and porous calcium silicate. *Chem. Pharmac. Bull.* 44, 1367–1371.
- 97 KINOSHITA, M., BABA, K., NAGAYASU, A., YAMABE, K., SHIMOOKA, T., TAKEICHI, Y., AZUMA, M., HOUCHE, H., MINAKUCHI, K. 2002. Improvement of solubility and oral bioavailability of a poorly water-soluble drug, TAS-301, by its melt-adsorption on a porous calcium silicate. *J. Pharmac. Sci.* 91, 362–370.
- 98 TAKASHIMA, Y., YUASA, H., KANAYA, Y., NOMURA, I., SHINOZAWA, K. 1999. Reduction of tablet coloration at tableting for oily medicine (tocopheryl nicotinate). *Int. J. Pharmac.* 187, 125–135.
- 99 HWANG, Y.-J., OH, C., OH, S.-G. 2005. Controlled release of retinal from silica particles prepared in O/W/O emulsion: The effects of surfactants and polymers. *J. Control. Release* 106, 339–349.
- 100 TENJARLA, S. 1999. Microemulsions: an overview and pharmaceutical applications. *Ther. Drug Carrier Syst.* 16, 461–521.
- 101 GURSOY, R. N., BENITA, S. 2004. Self-emulsifying drug delivery systems (SEDDS) for improved oral delivery of lipophilic drugs. *Biomed. Pharmacother.* 58, 173–182.
- 102 CHARMAN, W. N. 2000. Lipids, lipophilic drugs, and oral drug delivery – some emerging concepts. *J. Pharmac. Sci.* 89, 967–978.
- 103 BARTHE, L., WOODLEY, J., HOUIN, G. 1999. Gastrointestinal absorption of drugs: methods and studies. *Fund. Clin. Pharmacol.* 13, 154–168.
- 104 RINAKI, E., VALSAMI, G., MACHERAS, P. 2003. Quantitative biopharmaceutics classification system: the central role of dose/solubility ratio. *Pharmac. Res.* 20, 1917–25.
- 105 MICHAEL, S., THOLE, M., DILLMANN, R., FAHR, A., DREWE, J., FRICKER, G. 2000. Improvement of intestinal peptide absorption by a synthetic bile acid derivative, cholylsarcosine. *Eur. J. Pharmac. Sci.* 10, 133–140.
- 106 CHAO, A. C., NGUYEN, J. V., BROUGHALL, M., GRIFFIN, A., FIX, J. A., DADDONA, P. E. 1999. *In vitro* and *in vivo* evaluation of effects of sodium caprate on enteral peptide absorption and on mucosal morphology. *Int. J. Pharmac.* 191, 15–24.
- 107 MESIHA, M., PLAKOGIANNIS, F., VEJOSOTH, S. 1994. Enhanced oral absorption of insulin from desolvated fatty acid–sodium glycocholate emulsions. *Int. J. Pharmac.* 111, 213–216.
- 108 RIVERA, T. M., LEONE-BAY, A., PATON, D. R., LEIPOD, H. R., BAUGHMAN, R. A. 1997. Oral delivery of heparin in combination with sodium N-[8-(2-hydroxybenzoyl) amino] caprylate: pharmacological considerations. *Pharmac. Res.* 14, 1830–1834.
- 109 ITO, Y., ARAI, H., UCHINO, K., IWASAKI, K., SHIBATA, N., TAKADA, K. 2005. Effect of adsorbents on the absorption of lansoprazole with surfactant. *Int. J. Pharmac.* 289, 69–77.
- 110 ITO, Y., KUSAWAKE, T., ISHIDA, M., TAWA, R., SHIBATA, N., TAKADA, K. 2005. Oral solid gentamicin preparation using emulsifier and adsorbent. *J. Control. Release* 105, 23–31.



- 111 RAMA PRASAD, Y. V., MINAMIMOTO, T., YOSHIKAWA, Y., SHIBATA, N., MORI, S., MATSUURA, A., TAKADA, K. 2004. *In situ* intestinal absorption studies on low molecular weight heparin in rats using Labrasol as absorption enhancer. *Int. J. Pharmac.* 271, 225–232.
- 112 AMIDON, G. L., LENNERNÄS, H., SHAH, V. P., CRISON, J. R. 1995. A theoretical basis for a biopharmaceutical drug classification: the correlation of *in vitro* drug product dissolution and *in vivo* bioavailability. *Pharmac. Res.* 12, 413–420.
- 113 HU, Z., TAWA, R., KONISHI, T., SHIBATA, N., TAKADA, K. 2001. A novel emulsifier, Labrasol, enhances gastrointestinal absorption of gentamicin. *Life Sci.* 69, 2899–2910.
- 114 JAIN, S. K., AWASTHI, A. M., JAIN, N. K., AGRAWAL, G. P. 2005. Calcium silicate based microspheres of repaglinide for gastroretentive floating drug delivery: Preparation and *in vitro* characterization. *J. Control. Release* 107, 300–309.
- 115 STRAUB, J. A., CHICKERING, D. E., LOVELY, J. C., ZHANG, H., SHAH, B., WAUD, W. R., BERNSTEIN, H. 2005. Intravenous hydrophobic drug delivery: a porous particle formulation of paclitaxel (AI-850). *Pharmac. Res.* 22, 347–355.
- 116 FORAKER, A. B., WALCZAK, R. J., COHEN, M. H., BOIARSKI, T. A., GROVE, C. F., SWAAN, P. W. 2003. Microfabricated porous silicon particles enhance paracellular delivery of insulin across intestinal Caco-2 cell monolayers. *Pharmac. Res.* 20, 110–116.
- 117 AJAYAN, P. M., EBBESEN, T. W. 1997. Nanometre-size tubes of carbon. *Rep. Prog. Phys.* 60, 1025–1062.
- 118 VENKATESAN, N., YOSHIMITSU, J., ITO, Y., SHIBATA, N., TAKADA, K. 2005. Liquid filled nanoparticles as a drug delivery tool for protein therapeutics. *Biomaterials* 26, 7154–7163.
- 119 EAIMTRAKARN, S., RAMA PRASAD, Y. V., OHNO, T., KONISHI, T., YOSHIKAWA, Y., SHIBATA, N., TAKADA, K. 2002. Absorption enhancing effect of Labrasol on the intestinal absorption of insulin in rats. *J. Drug Target.* 10, 255–260.
- 120 RAMA PRASAD, Y. V., PUTHLI, S. P., EAIMTRAKARN, S., ISHIDA, I., YOSHIKAWA, Y., SHIBATA, N., TAKADA, K. 2003. Enhanced intestinal absorption of vancomycin with Labrasol and D- $\alpha$ -tocopheryl PEF 1000 succinate in rats. *Int. J. Pharmac.* 250, 181–190.
- 121 WONG, N., KAM, S., DAI, H. 2005. Carbon nanotubes as intracellular protein transporters: generality and biological functionality. *J. Am. Chem. Soc.* 127, 6021–6026.
- 122 PANTAROTTO, D., BRIAND, J. P., PRATO, M., BIANCO, A. 2004. Translocation of bioactive peptides across cell membranes by carbon nanotubes. *Chem. Commun.* 16–17.
- 123 BIANCO, A., HOEBEKE, J., GODEFROY, S., CHALOIN, O., PANTAROTTO, D., BRIAND, J. P., MULLER, S., PRATO, M., PARTIDOS, C. D. 2005. Cationic carbon nanotubes bind to CpG oligodeoxynucleotides and enhance their immunostimulatory properties. *J. Am. Chem. Soc.* 127, 58–59.
- 124 CHAPANA, J. R., TROSZCZYNSKA, J., FIRKOWSKA, I., MORSZCZEK, C., GIERSIG, M. 2005. Multi-walled carbon nanotubes for plasmid delivery into *Escherichia coli* cells. *Lab on a Chip* 5, 536–539.
- 125 NIOSH/OSHA 1988. Synthetic graphite. National Institute for Occupational Safety and Health. <http://www.cdc.gov/niosh/pel88/npelname.html> and <http://www.cdc.gov/niosh/pel88/SYNGRAPH.html>.
- 126 LAM, C. W., JAMES, J. T., MCCLUSKEY, R., HUNTER, R. L. 2004. Pulmonary toxicity of single-wall carbon nanotubes in mice 7 and 90 days after intratracheal instillation. *Toxicol. Sci.* 77, 126–134.
- 127 WARHEIT, D. B., LAURENCE, B. R., REED, K. L., ROACH, D. H., REYNOLDS, G. A. M., WEBB, T. R. 2004. Comparative pulmonary toxicity assessment of single-wall carbon nanotubes in rats. *Toxicol. Sci.* 77, 117–125.

- 128 BIANCO, A., KOSTARELOS, K., PARTIDOS, C. D., PRATO, M. 2005. Biomedical applications of fictionalized carbon nanotubes. *Chem. Commun.* 571–577.
- 129 KASUYA, D., YUDASAKA, M., TAKAHASHI, K., KOKAI, F., IIJIMA, S. 2002. Selective production of single-wall carbon nanohorn aggregates and their formation mechanism. *J. Phys. Chem. B* 106, 4947–4951.
- 130 MURATA, K., KANEKO, K., KANO, H., KASUYA, D., TAKAHASHI, K., KOKAI, F., YUDASAKA, M., IIJIMA, S. 2002. Adsorption mechanism of supercritical hydrogen in internal and interstitial nanospaces of single-wall carbon nanohorn assembly. *J. Phys. Chem. B* 106, 11132–11138.
- 131 MURATA, K., HIRAHARA, K., YUDASAKA, M., IIJIMA, S., KASUYA, D., KANEKO, K. 2002. Nanowindow-induced molecular sieving effect in a single-wall carbon nanohorn. *J. Phys. Chem. B* 106, 12668–12669.
- 132 MURAKAMI, T., AJIMA, K., MIYAWAKI, J., YUDASAKA, M., IIJIMA, S., SHIBATA, K. 2004. Drug-loaded carbon nanohorns: adsorption and release of dexamethasone *in vitro*. *Mol. Pharmacol.* 1, 399–405.
- 133 MURAKAMI, T., FAN, J., YUDASAKA, M., IIJIMA, S., SHIBA, K. 2006. Solubilization of single-wall carbon-nanohorns using a PEG–doxorubicin conjugate. *Mol. Pharm.* 3, 407–414.
- 134 NAKAI, Y., YAMAMOTO, K., TERADA, K., ICHIKAWA, J. 1984. Interaction of medicinals and porous powder. I. Anomalous thermal behavior of porous glass mixtures. *Chem. Pharmac. Bull.* 32, 4566–4571.
- 135 YONEMOCHI, E., MATSUMOTO, M., OGUCHI, T., YAMAMOTO, K., NAKAI, Y. 1991. Stability of aspirin in controlled pore glass solid dispersions. *Chem. Pharmac. Bull.* 39, 1027–1031.
- 136 MATSUMOTO, K., NAKAI, Y., YONEMOCHI, E., OGUCHI, T., YAMAMOTO, K. 1998. Effect of pore size on the gaseous adsorption on ethenzamide on porous crystalline cellulose and the physicochemical stability of ethenzamide after storage. *Chem. Pharmac. Bull.* 46, 314–318.
- 137 WATANABE, T., OHNO, I., WAKIYAMA, N., KUSAI, A., SENNA, M. 2002. Controlled dissolution properties of indomethacin by compounding with silica. *STP Pharmac. Sci.* 12, 363–367.
- 138 MATSUMOTO, K., NAKAI, Y., YONEMOCHI, E., OGUCHI, T., YAMAMOTO, K. 1994. Physicochemical characteristics of porous crystalline cellulose and formation of an amorphous state of ethenzamide by mixing. *Int. J. Pharmacol.* 108, 167–172.
- 139 NOYES, A. A., WHITNEY, W. R. 1897. The rate of solution of solid substances in their own solutions. *J. Am. Chem. Soc.* 19, 930–934.
- 140 YAMAMOTO, K., NAKANO, M., TAKAICHI, A., NAKAI, Y. 1974. Dissolution rate and bioavailability of griseofulvin from a ground mixture with microcrystalline cellulose. *Eur. J. Pharmac. Biopharmac.* 2, 487–493.
- 141 BERGE, M. S., BIGHLEY, D. L., MONKHOUSE, S. D. 1977. Pharmaceutical salts. *J. Pharmac. Sci.* 66, 1–19.
- 142 KIMURA, K., HIRAYAMA, F., ARIMA, H., UEKAMA, K. 2000. Effect of aging on crystallization, dissolution and adsorption characteristics of amorphous tolbutamide-2-hydroxypropyl- $\beta$ -cyclodextrin complex. *Chem. Pharmac. Bull.* 48, 646–650.
- 143 KANENIWA, N., IKEKAWA, A., HASHIMOTO, K. 1973. Influence of operational variables on ball-milling of sulfadimethoxine and white alundum. *Chem. Pharmac. Bull.* 21, 676–681.
- 144 SERAJUDDIN, A. T. 1999. Solid dispersion of poorly water-soluble drugs: early promises, subsequent problems, and recent breakthroughs. *J. Pharmac. Sci.* 88, 1058–1065.
- 145 CHIOU, W. L. 1971. Pharmaceutical applications of solid dispersion system. *J. Pharmac. Sci.* 60, 1281–1302.
- 146 CHIOU, W. L., RIEGELMAN, S. 1969. Preparation and dissolution characteristic of several fast-release solid dispersions of Griseofulvin. *J. Pharmac. Sci.* 58, 1505–1509.
- 147 SIMONELLI, A. P., METHA, S. C., HIGUCHI, W. I. 1969. Dissolution

- rates of high energy polyvinylpyrrolidone (PVP)–sulfathiazole coprecipitates. *J. Pharm. Sci.* 58, 538–549.
- 148 TAKEUCHI, H., HANDA, T., KAWASHIMA, Y. 1987. Spherical solid dispersion containing amorphous tolbutamide embedded in enteric coating polymers or colloidal silica prepared by spray-drying technique. *Chem. Pharmac. Bull.* 35, 3800–3806.
- 149 TAKEUCHI, H., NAGIRA, S., HIROMITSU, Y., KAWASHIMA, Y. 2004. Solid dispersion particles of tolbutamide prepared with fine silica particles by the spray-drying method. *Powder Technol.* 141, 187–195.
- 150 BURGER, A. 1975. Zur polymorphie oraler antidiabetika. 2. Mitteilung: Tolbutamide. *Sci. Pharm.* 43, 161–168.
- 151 KIMURA, K., HIRAYAMA, F., ARIMA, H., UEKAMA, K. 1999. Characterization of tolbutamide polymorphs (Burger's form II and IV) and polymorphic transition behavior. *J. Pharm. Sci.* 88, 385–390.
- 152 KIMURA, K., HIRAYAMA, F., ARIMA, H., UEKAMA, K. 2000. Effect of aging on crystallization, dissolution and adsorption characteristics of amorphous tolbutamide-2-hydroxypropyl- $\beta$ -cyclodextrin complex. *Chem. Pharmac. Bull.* 48, 646–650.
- 153 NAGIRA, S. 2005. *PhD Thesis*. Gifu Pharmaceutical University.
- 154 TAKEUCHI, H., NAGIRA, S., HIROMITSU, Y., KAWASHIMA, Y. 2003. Design of solid dispersion particles of drug with fine porous carriers. *J. Soc. Powder Technol., Japan* 40, 157–162.
- 155 TAKEUCHI, H., NAGIRA, S., YAMAMOTO, H., KAWASHIMA, Y. 2005. Solid dispersion particles of amorphous indomethacin with fine porous silica particles by using spray-drying method. *Int. J. Pharm.* 288, 177–183.
- 156 HANCOCK, B.C., PARKS, M. 2000. What is the true solubility advantage for amorphous pharmaceuticals? *Pharmac. Res.* 74, 397–404.
- 157 IMAIZUMI, H., NAMBU, N., NAGAI, T. 1979. Stability and several physical properties of amorphous and crystalline forms of indomethacin. *Chem. Pharmac. Bull.* 28, 2565–2569.
- 158 FUKUOKA, E., MAKITA, M., YAMAMURA, S. 1986. Some physical properties of glassy indomethacin. *Chem. Pharmac. Bull.* 34, 4314–4321.
- 159 TAYLOR, L. S., ZOGRAFI, G. 1997. Spectroscopic characterization of interactions between PVP and indomethacin in amorphous molecular dispersions. *Pharmac. Res.* 14, 1691–1698.
- 160 MATSUMOTO, T., ZOGRAFI, G. 1999. Physical properties of solid molecular dispersions of indomethacin with poly(vinylpyrrolidone) and poly(vinylpyrrolidone-co-vinyl-acetate) in relation to indomethacin crystallization. *Pharmac. Res.* 16, 1722–1728.
- 161 YOSHIOKA, M., HANCOCK, B. C., ZOGRAFI, G. 1994. Crystallization of indomethacin from amorphous state below and above its glass transition temperature. *Pharmac. Res.* 83, 1700–1705.
- 162 ENÜSTÜN, B. V., SENTÜRK, H. S., YURDAKUL, O. 1978. Capillary freezing and melting. *J. Colloid Interface Sci.* 65, 509–516.
- 163 ETZLER, F. M., WHITE, P. J. 1987. The heat capacity of water in silica pores. *J. Colloid Interface Sci.* 120, 94–99.
- 164 INAGAKI, S., FUKUSHIMA, Y., KURODA, K. 1993. Synthesis of highly ordered mesoporous material from a layered polysilicate. *Chem. Commun.* 680–682.
- 165 KERSGE, C. T., LEONOWICZ, M. E., ROTH, W.J. 1992. Ordered mesoporous molecular sieves synthesized by a liquid-crystal template mechanism. *Nature* 710, 359.
- 166 INAGAKI, S. 1998. *PhD Thesis*. Nagoya University.
- 167 MORIMOTO, Y., YAMAMOTO, H., TAKEUCHI, H., KAWASHIMA, Y., TAKAHASHI, H. 2001. Entrapment of insulin into mesoporous material by using freeze-thawing method and its release property. In *Proceedings of the Autumn Research Meeting of the Society of Powder Technology of Japan*, pp. 18–19.
- 168 ISHIKIRIYAMA, K., TODOKI, M. 1995. Evaluation of water in silica pores

- using differential scanning calorimetry. *Thermo Chim. Acta* 256, 2213–2226.
- 169 ISHIKIRIYAMA, K., TODOKI, M., MOTOMURA, K. 1995. Pore size distribution (PSD) measurements of silica gels by means of differential scanning calorimetry: I. Optimization for determination of PSD. *J. Colloid Interface Sci.* 171, 92–102.
- 170 MORISHIGE, K., NOBUOKA, K. 1997. X-ray diffraction studies of freezing and melting of water confined in a mesoporous adsorbent (MCM-41). *J. Chem. Phys.* 107, 6965–6969.
- 171 MATSUOKA, M., TAKEUCHI, H. Unpublished data.
- 172 MATSUOKA, M., YAMAMOTO, H., TAKEUCHI, H., KAWASHIMA, Y., TAKAHASHI, H. 2003. Entrapment and release of drugs into mesoporous silica FSM. In *Proceedings of the 20th Symposium on Particulate Preparations and Designs*, 143–146.
- 173 TOZUKA, Y., OGUCHI, T., YAMAMOTO, K. 2002. Adsorption and entrapment of salicylamide molecules into the mesoporous structure of folded sheets mesoporous material (FSM-16). *Pharmac. Res.* 20, 926–930.

## 7

**NANOEGG<sup>®</sup> Technology for Drug Delivery**

*Yoko Yamaguchi and Rie Igarashi*

## 7.1

**Introduction**

Retinoids, the natural and synthetic metabolites and analogs of vitamin A (retinol), are important regulators of epidermal proliferation and differentiation [1–6]. All-*trans* retinoic acid (ATRA, vitamin A acid) is the major naturally occurring biologically active form among retinoids. In various epithelia that normally keratinize, ATRA inhibits keratinization and induces mucous metaplasia [7, 8]. Nevertheless, ATRA has been a focus of research into topical treatments for aged skin for more than 15 years. In 1986, Klingman and coworkers [9, 10] reported that ATRA could produce smoother, less wrinkled and less pigmented skin after a few months of treatment. Melanin loss and less-wrinkled skin are, however, frequently accompanied by excess skin irritation after ATRA treatment [11]. Clinical responses predominantly comprised severe irritant dermatitis in the early stages of application (around 3 or 4 days). Such damage with a high magnitude of inflammatory events after ATRA treatment can induce chronic skin pigmentation on the area being treated, potentially resulting in imperfect repair of skin displaying a pigmented appearance. Inflammation can occur through at least two mechanisms: the acidic function (-COOH) of the terminal domain is in principle an inducer, and the presence and long-term adhesion of ATRA molecules on the stratum corneum epidermidis would presumably act as a strong irritant. Preventing undesirable adverse effects would be expected to allow ATRA therapy to overcome the limitations of classical ATRA therapy.

In this chapter, we describe the development of a novel drug delivery system using nanotechnology with a core-shell structure using a boundary-organized nanoscale reaction. This reaction is based on the biological control of mineralization which refers to the general biochemical activity of the cells [12]. In the enclosed environments, the cells have several important functions, including spatial delineation, ion accumulation, mineral nucleation and transportation. Phospholipid and polypeptide vesicles, cellular assemblies, and macromolecular frameworks can be assembled into enclosed permeable structures that provide diffusion-limited spaces for biomineralization processes. The study of biomineralization offered valuable

insights into the scope of materials chemistry at the organic–inorganic interface. Mann [13] began some examples that involved biomineral-inspired approaches for the synthesis of inorganic nanoparticles using boundary-organized nanoscale reaction droplets. Reverse micelles, microemulsions, vesicles and lipid bilayer films are templates for the nucleation of minerals. The synthesis of nanoparticles with a core–shell (minerals) structure requires the supramolecular assembly of structures that contain chemical reactions or phase transformations.

The conceptual framework in this study is that the preparation of ATRA nanoparticles with a core–shell structure (NANOEGG) plays a crucial role in solving the low permeation of ATRA into spaces in the stratum corneum epidermidis and the strong symptoms of irritation. Preparation of NANOEGG particles was achieved using boundary-organized nanoscale reaction droplets [13]. The strategy in which micelles are utilized as a drug carrier is already well known in the drug delivery system field. Although the normal micelles are thermodynamically stable, for human application there remains the problem of stability of micelles in blood after the injection. As a result, drugs included in micelles would be immediately released. Thus, a micelle system is occasionally not enough to control the long-term drug-release kinetics. The novel NANOEGG system is not in the equilibrium state because ATRA molecules cannot migrate from the micelle self-assembly to the continuous aqueous phase due to an inorganic coating on the surface of the micelle. It can be expected that NANOEGG will improve the potential of micelles in the drug delivery system field. This chapter provides a novel drug delivery system technology such that NANOEGG may not only prevent adverse effects, but also markedly enhance its main effect. Indeed, this technology would become an evolution of classical ATRA therapy and may enhance the potential utility in the topical drug delivery field.

In Section 7.2, the discussion focuses on the equilibrium and kinetic parameters that govern the behavior of ATRA within aqueous phase, and how the core–shell structure of NANOEGG is prepared, and the shelf stability of ATRA molecule, which is one of the improved points of NANOEGG structure, is explained. The possible implications of NANOEGG for the pharmacological mechanisms underlying the dermatological aspects of ATRA biology are then considered. In final section, as well as other aspects and drugs of NANOEGG, attention is placed on the role of NANOEGG in regeneration medicine, especially diabetes therapy medicine.

## 7.2

### New Nanoparticles with a Core–Shell Structure: The NANOEGG System

#### 7.2.1

##### Physicochemical Properties and Action of ATRA

Retinoids, the natural and synthetic metabolites and analogs of vitamin A (retinol), are important regulators of epidermal proliferation and differentiation. In recent years, discovery of the *in vitro* and *in vivo* differentiation of acute promyelocytic

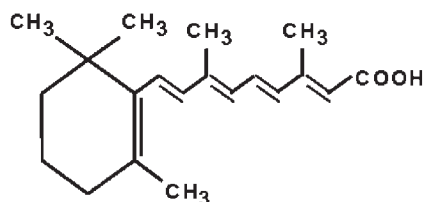


Figure 7.1. Structure of ATRA (molecular weight: 300.44).

leukemia (APL) blasts by ATRA has modified the therapeutic approach of APL, but has also led to important advances in the biology of APL and opened up new perspectives for differentiation therapy in cancer.

As a consequence of the presence of a large hydrophobic moiety in ATRA (Fig. 7.1), this compound is poorly soluble in water. This compound is comprised of three distinct structural domains: a  $\beta$ -ionone ring, a polyunsaturated chain and a polar end-group. The polar end-group of ATRA exists in a higher oxidation state than retinol and/or retinal. Quantitative data on the aqueous solubility of ATRA is scarce. One study used a spectrophotometric method relying on the differential absorption spectra of ATRA in water versus ethanol to measure the aqueous solubility of ATRA and found that the solubility limit of ATRA in water is 210 nM [14]. It should be noted, however, that interpretation of the data concerning ATRA may be complicated because whilst the absorption spectrum of ATRA is indeed sensitive to the polarity of the solvent, the spectrum also changes dramatically in response to variations in pH and in the ionization state of ATRA.

Self-aggregation of ATRA can have significant implications for the biological functions of this compound. For example, a reasonable explanation for the observation that the solubility of ATRA in water is higher than predicted [15] is that the observed solubility reflects self-association into micelles rather than the monomeric ATRA solubility. Thus, micelle formation may allow higher than expected aqueous concentrations of ATRA to be maintained and this concentration may be high enough to support diffusional fluxes of free ATRA sufficient for short-distance transport in cells or to allow metabolism of free ATRA. Another action of ATRA that may be affected by its self-association properties relates to the often-raised notion that at least some of the toxic effects of vitamin A are due to surface-active, “membranolytic”, properties. Consideration of the chemical structure of ATRA suggests that its amphipathic nature results in “detergent-like” characteristics, and several studies have shown that the presence of ATRA affects various aspects of membrane structure and function [16, 17]. As with other detergents, ATRA may disrupt membranes both by intercalating into the lipids, thereby changing the characteristics of the bilayer, and by drawing lipids out of the bilayers into ATRA–lipid mixed micelles, leading to dissolution of the membranes. Few studies have addressed the self-association properties of ATRA. The ATRA molecules may carry an actual net charge. This feature may result in a stronger detergent-like characteristic of the ATRA and perhaps provide an explanation for the reported differences

between the effects of ATRA versus other retinoids on membranes [17]. This consideration raises the question of whether the carboxyl group of ATRA is protonated or negatively charged at physiological pH and whether the self-association characteristics of ATRA affect the compound's ionization state.

The physicochemical properties of ATRA and the characteristics of its interactions with the various environments in which it is distributed *in vivo* affect its biological functions. As a consequence of the presence of a large hydrophobic moiety in ATRA, it is poorly soluble in water. However, self-aggregation of ATRA can have significant implications for the biological function of this compound. It has been reported that while the  $pK$  of monomeric ATRA in an aqueous medium is lower than 6.1, the transition from a monomeric to a micellar state results in an increase in  $pK$  to 8.5, i.e. micelle formation stabilizes the protonated form of ATRA [18]. Thus, at physiological pH and at concentrations of ATRA that are higher than the critical micellar concentration (CMC), a large fraction of ATRA is protonated; at concentrations of ATRA that are lower than the CMC, a predominant fraction of ATRA is ionized. As the aqueous solubility of the anionic ATRA is significantly higher than the solubility of the protonated form, these observations suggest that the concentrations of free ATRA molecules in aqueous spaces *in vivo* are indeed of the order of 20–50  $\mu\text{M}$ .

In the presence of alkaline or physiological pH, ATRA molecules self-associate and formed micelles in aqueous solution [19]. In an alkaline environment, hydrophobic ATRA molecules abruptly change to amphiphilic molecules and when a specific concentration of ATRA is exceeded, micelles spontaneously form in water as an oriented colloidal aggregate. The CMC of ATRA was detected by the specific electron conductivity method (Fig. 7.2). Phillips defined CMC as the concentration corresponding to the maximum change in the gradient in the solution property versus concentration ( $\phi-C_t$ ) curve [20]:

$$\left(\frac{d^3\phi}{dC_t^3}\right)_{C_t=\text{CMC}} = 0, \quad (1)$$

where:

$$\phi = \alpha[S] + \beta[M], \quad (2)$$

where  $\alpha$  and  $\beta$  are proportionality constants,  $C_t$  is the concentration of surfactant, and  $[S]$  and  $[M]$  are the concentrations of monomeric surfactant and micelle, respectively. Figure 7.2 shows the determination of CMC with surfactant in the case that the solution property  $\phi$  is the electrical conductivity change. In an ionic surfactant system, higher concentrations are necessary to overcome the electrostatic repulsion between ionic head-groups of ionic surfactants during aggregation. As a result, the repulsive interaction between the head-groups in an ionic micelle is moderated by the strong counterion binding to the surface in the process of micelle formation. This idea is easy to understand from the fact that the slope before formation of a micelle is larger than that above the CMC in the conductivity measurements.



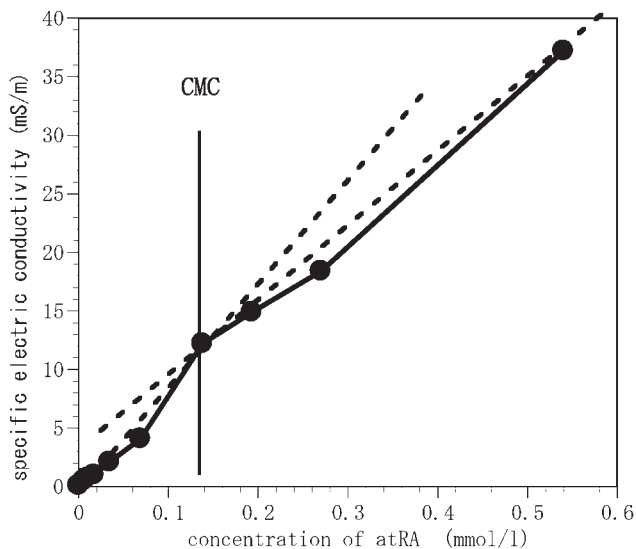


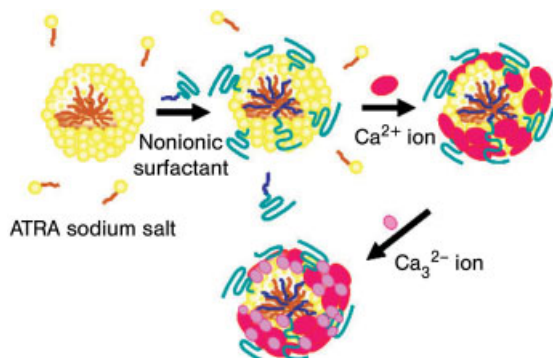
**Figure 7.2.** CMC of ATRA molecules in the presence of NaOH aqueous medium using the specific electric conductivity measurement. The measurement was carried out 25 °C under stirring. The dashed line corresponds to the CMC.

The CMC of ATRA is lower than 1 mM [19], but more than three orders of magnitude lower than reported CMC values for bile acids [21] and 10-fold lower than the CMC of the long-chain fatty acid palmitate [22]. This observation indicates that ATRA self-associate into micelles at substantially lower concentrations than other small amphiphatic compounds.

### 7.2.2

#### NANOEGG Preparation and Characterization

Above the CMC, we synthesized inorganic-coated nanoparticles using boundary-organized nanoscale reaction droplets. In turn, the interfacial properties of organic architectures, in ATRA micelles, were used to template the nucleation and growth of inorganic minerals ( $\text{CaCO}_3$ ). Since the surface of ATRA micelles displays numerous negative charges, oppositely charged ions (such as  $\text{Ca}^{2+}$  divalent ions) can easily thermodynamically adsorb on the surface. The interfacial properties of the ATRA micelle can thus be used to template the formation of a  $\text{CaCO}_3$  shell. This procedure is shown in Scheme 7.1. The surfaces of ATRA micelles containing nonionic surfactant were coated by inorganic  $\text{CaCO}_3$  with an amorphous structure. First, the mixed micelle of ATRA molecules and nonionic surfactant with polyoxyethylene function was prepared to prevent micelle sedimentation after the adsorption of divalent ions. The adsorption of divalent  $\text{Ca}^{2+}$  ions and the dissociation of surface charge of the micelle should be strongly suppressed. Finally, the micelle



**Scheme 7.1.** Schematic preparation process of NANOEGG particles with a core–shell ( $\text{CaCO}_3$ ) structure. The aqueous solution containing ATRA molecules is seen to be transparent in each step without any sedimentation.

would sediment. The presence of polyoxyethylene function on the micelle surface can maintain the hydrophilic character even if divalent ions are bound on ATRA micelle.

The solution properties of a binary surfactant mixture fall either between or outside the solution properties of the two single-surfactant solutions. Most CMCs of binary surfactant mixtures fall between the CMCs of the two components. Many of the theories concerning the CMC of binary surfactant mixtures have assumed the ideal of each component in the micellar phase [23]. An approach using a non-homologous surfactant mixture can elucidate binary mixtures quite well by using the single adjustable parameter developed by Rubingh [24]. At the CMC ( $C$ ) of the binary system, the following relationships are satisfied from the mass balances for components 1 and 2:

$$\alpha C = C_1 \quad \text{and} \quad (1 - \alpha)C = C_2, \quad (3)$$

where  $\alpha$  is the net mole fraction of component 1,  $C_1$  is the concentration of component 1 and  $C_2$  is the concentration of component 2. Then:

$$\begin{aligned} \alpha C &= \gamma_1 x C_1^0 \\ (1 - \alpha)C &= \gamma_2 (1 - x) C_2^0, \end{aligned} \quad (4)$$

where  $x$  is the mole fraction of component 1 in the binary surfactant phase,  $C_1^0$  and  $C_2^0$  are the CMCs of each single component, and  $\gamma$  is the activity coefficient due to nonideal mixing. If the values of  $C_1^0$ ,  $C_2^0$ ,  $\gamma_1$  and  $\gamma_2$  are available,  $x$ ,  $C_1$  and  $C_2$  may be determined by calculation. The values of  $C_1^0$  and  $C_2^0$  are obtained from the CMC values of the single-surfactant solutions, but the activity coefficients are given by the regular solution theory as:

$$\begin{aligned}\gamma_1 &= \exp[\beta(1-x)^2] \\ \gamma_2 &= \exp[\beta x^2].\end{aligned}\quad (5)$$

At the same time,  $\beta$  can be evaluated by substituting Eq. (4) into (5):

$$\beta = \ln(\alpha C/xC_1^0)/(1-x)^2. \quad (6)$$

In general, a single parameter value of  $\beta$  is determined by averaging the  $\beta$  values against each  $\alpha$  value over the entire composition range. The  $\beta$  value is an index of interaction between two surfactants. The sign of  $\beta$  corresponds to positive or negative deviation from ideal, and moderate interaction between anionic and nonionic surfactants was shown for many binary surfactant systems. Thus, our micellar system between ATRA as anionic surfactant and nonionic surfactant maybe forms homogenous mixed micelles, and could not form ATRA and nonionic surfactant micelles, respectively. In the dynamic light scattering (DLS) measurement, two different diffusion coefficients of each micelle are usually detected when the different micelles are present in the system. At this case the correlation function will decay double exponentially as a function of delay time. DLS measurement was carried out on the binary ATRA and nonionic surfactant system (Fig. 7.3). The correlation function almost decayed mono-exponentially (solid line in Fig. 7.3). This is evidence for the presence of only mixed micelles being formed under our conditions.

As  $\text{CaCO}_3$  is formed on the high curvature  $1/R$ , where  $R$  is the radius of the micelle, its structure is rather difficult in crystal state. Wide-angle X-ray scattering shows the broad scattering curve between  $5^\circ$  and  $10^\circ$  angles (data is not shown).

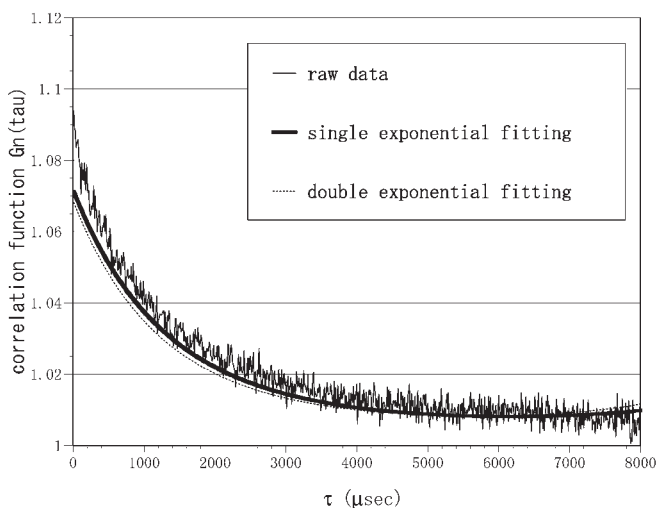


**Figure 7.3.** DLS measurements of ATRA sodium salt and nonionic surfactant in aqueous solution. The correlation function of ATRA sodium salt and nonionic surfactant mixed solution ( $45 \text{ mg L}^{-1}$  of ATRA and  $330$

$\text{mg L}^{-1}$  of nonionic surfactant) was measured at  $25^\circ \text{C}$  as a function of decay time. The curve fittings were carried out by two methods, i.e. single- and double-exponential decays.

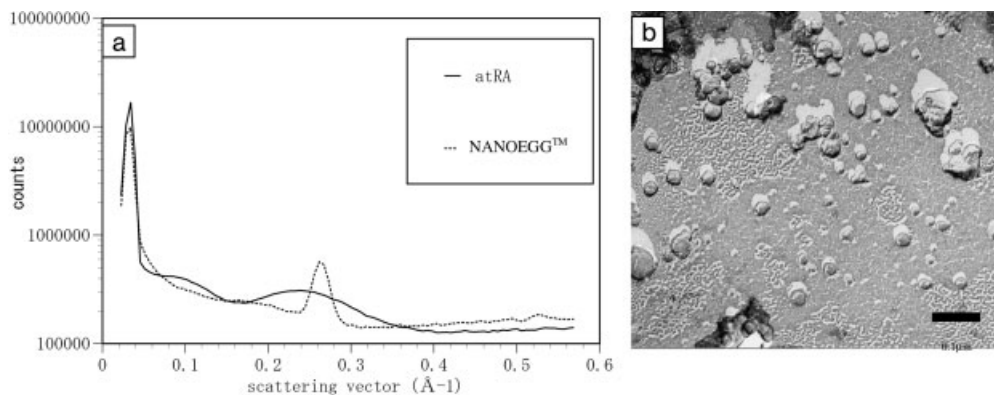


**Figure 7.4.** Physicochemical properties of NANOEGG in aqueous media. (a) SAXS patterns as a function of scattering vector. Solid line: ATRA micelle (1.0 wt%); dotted line: NANOEGG particles (1.0 wt% as ATRA). (b) Freeze-fracture TEM of NANOEGG aqueous solution. Bar = 0.1  $\mu\text{m}$ .

High biocompatibility of the  $\text{CaCO}_3$  structure is thus expected due to the amorphous coating on micelle. Thus, calcium storage in the epidermal and/or dermal region cannot take place after the external treatment.

Analysis by small-angle X-ray scattering (SAXS) reveals the presence of spherical micelles of ATRA molecules with a diameter of around 10 nm (Fig. 7.4a). This size corresponds well with the normal ionic surfactant system [13]. The SAXS profile reveals an eggshell-like structure with different electron densities in the inner structure. Discontinuous electron distribution in the inner structure is detected as a peak with a specific scattering-angle region (Fig. 7.4a). The presence of this sharp peak corresponds to a discrete thin layer of  $\text{CaCO}_3$  on the surface of the ATRA micelle. This micelle displaying a core–shell (ATRA– $\text{CaCO}_3$ ) structure represents the NANOEGG particles. In addition, since the diameter of NANOEGG is estimated to be 13–16 nm using the scattering curve in Fig. 7.4(a), the thickness of the  $\text{CaCO}_3$  layer is probably 1.5–3 nm. The presence of an egg-like core–shell structure was also confirmed using freeze-fracture transmission electron microscopy (Fig. 7.4b).

The schematic structure of the NANOEGG system is shown in Fig. 7.5. In fact, the shell-like structure of 1–2 nm width was observed outside of the spherical ATRA particles.

### 7.2.3

#### Improved Lability of ATRA in the NANOEGG System

The conjugated double bonds of the isoprenoid chain render ATRA susceptible to photodegradation, isomerization and oxidation. Consequently, naturally occurring ATRA is extremely labile. Actually, the structural integrity of ATRA must be maintained *in vivo*. The answer lies in part with the observation that most retinoids *in vivo* are associated with retinoid-binding proteins. Many of these proteins bind

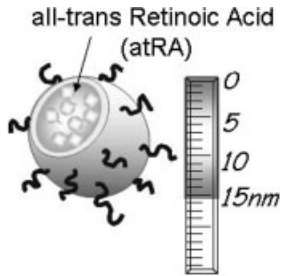


**Figure 7.5.** Schematic representation of a NANOEGG particle. The worm-like ribbon in the representation corresponds to the PEG function. The inside domain corresponds to ATRA molecules.

their ligands in hydrophobic pockets, thereby effectively shielding them from the aqueous environment. Binding to proteins is thus expected to protect ATRA from nonspecific oxidation and may also stabilize its isomerization state. In the same way, micelle formation of ATRA molecules can be expected to protect ATRA from the aqueous environment. The life-times of free ATRA in cytosol and in extracellular spaces, and the mechanisms by which the integrity of ATRA in these pools is maintained, are unknown. However, it has been reported that both degradation and isomerization of ATRA in water can be prevented by addition of biological antioxidants such as tocopherol [25, 26], suggesting the possibility that under at least some physiological conditions free ATRA can remain stable in cytosol. Even with the use of an antioxidant, the stability of ATRA micelles cannot be maintained over 95% of its activity for 3 years at room temperature and/or 6 months at 50 °C. Unfortunately, such a stability level of ATRA cannot be employed by pharmaceutical companies.

Figure 7.6 shows the high potential of NANOEGG for improved stability. As ATRA has a specific maximum absorbance at 340–345 nm, born of the decrease

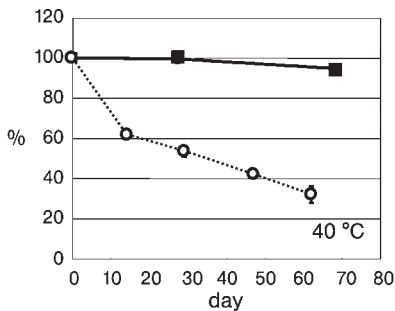


**Figure 7.6.** Stability of ATRA (circles) and NANOEGG (squares) at 40 °C. The ATRA was solubilized in ethanol as a negative control. Each sample was packed in the sunscreen tube.

of peak height and isomeric another peak detection in HPLC measurement are available concerning to the loss of activity. It can be seen that the peak height of NANOEGG scarcely changed for approximately 70 days in the accelerated environment at 40 °C, even without any antioxidant. It can be seen, thus, that the lability of the ATRA molecule was rather improved against temperature, as can be expected. As a result, long-term storage of ATRA ointment became possible.

### 7.3

#### NANOEGG for Dermatological Aspects

Within the epidermis, the processes of proliferation and differentiation are tightly controlled, resulting in a tissue at steady-state in which the cells that are desquamated and lost are equal to those that are produced in the germinative basal layer. Cells within the basal layer are highly proliferative and display an undifferentiated phenotype characterized by the coexpression of cytokeratin 5/14 (K5/K14) [27]. Mitosis is restricted to the basal layer and, as keratinocytes migrate into the suprabasal layers, they undergo a well-defined program of thermal differentiation, characterized by the coordinated induction of specific proteins. The initial change is the loss of K5/K14 expression and the synthesis of the K1/K10 keratins [28]. With subsequent movement into more suprabasal layers, cornified envelope substrate proteins are synthesized, including lorocrin [29], filaggrin and involucrin, together with type 1 transglutaminase – the calcium-dependent enzyme responsible for the crosslinking of the proteins. During the final stages of the differentiation process, the substrate protein crosslinking forms the resistant cornified envelopes, resulting in the cutaneous permeability barrier.

The dramatic effects of ATRA upon the skin have been known for many years. Hyperkeratinization is the result of ATRA deficiency in animals, with many epithelial sites becoming satisfied and keratinized. The historical data has been supported somewhat by more recent *in vitro* data. When keratinocytes are treated *in vitro*, ATRA inhibits terminal differentiation, suppressing the expression of K1/K10, profilaggrin, lorocrin, involucrin, transglutaminase and cornified envelope formation. The topical application of ATRA promotes keratinocyte proliferation, resulting in epidermal hyperplasia. Specifically, the thickness of the granular layer is increased and the stratum corneum is compacted, indicating effects upon differentiation in addition to proliferation. ATRA treatment not only leads to a decrease in stratum corneum thickness, but also to cell loosening and fragility, changes in lipid levels, and a subsequent decrease in the permeability barrier. As outlined, *in vivo* ATRA treatment upregulates differentiation markers.

Hyperpigmentation on the face is a anxiety-producing symptom. Photoaging refers to premature skin aging caused by repeated exposure to ultraviolet (UV) radiation from the sun for many years. Fine and coarse wrinkles, hyperpigmented macules, sallow color, dry texture, and loss of tone in habitually sun-exposed skin characterize the photoaged phenotype. Our understanding of photoaging has been greatly aided by the discovery that ATRA can repair photoaged skin, coupled with

tremendous advances in the field of molecular biology, especially in the areas of how retinoic acid receptors function and how intracellular signaling is initiated by UV irradiation. For several years, ATRA and other synthetic retinoids have been widely used in the treatment of a variety of skin diseases associated with hyperproliferative processes. Retinoids induce a characteristic series of biochemical and histological modifications when applied to skin. Their effects on keratinocytes are still incompletely understood in spite of the recent discovery of nuclear ATRA receptors, which are highly expressed in human adult skin [30].

In 1986, Klingman and coworkers [9, 10] reported in the first suspicion that ATRA molecules could produce smoother, less-wrinkled and less-pigmented skin after a few months of treatment, and this has been one focus of research into topical treatments for a potent inhibitor of new melanin production [31, 7, 8]. Since the 1990s, many dermatologists have recommended the use of ATRA for a variety of nonsurgical treatments of photodamaged skin, because of a certain physiological regulation and high induction of epithelial differentiation [2–6]. The substance has been approved by the Food and Drug Administration in the US, and has been marketed as RENOVA™ and Retin-A™. Clinical responses predominantly comprised severe irritant dermatitis in the early stages of application of RENOVA and Retin-A (around 3 or 4 days) [11, 7, 8]. Such damage with a high magnitude of inflammatory events after ATRA treatment can induce chronic skin pigmentation on the area being treated, potentially resulting in imperfect repair of skin displaying a pigmented appearance.

### 7.3.1

#### Improved Irritation of ATRA in the NANOEGG System

In addition to keratinocytes and melanocytes, the epidermis also contains Langerhans cells, dendritic cells and innervating peripheral neuron cells. This means that the skin is an organ capable of responding to signals from both outside and from within the body. A predominant feature during the pathogenesis of many skin disorders is chronic inflammation, characterized by the infiltration of activated T lymphocytes. Among the factors that are critical for controlling those processes, transcription factors (such as AP-1, NF- $\kappa$ B, etc.) appear to be essential. Interestingly, the members of the nuclear hormone receptor superfamily are known to interact with many of these transcription factors, suggesting that ligands for these nuclear receptors may be an effective means of modulating inflammation as well as the immune response in general.

As already mentioned, ATRA causes a variable amount of irritation, more properly a heightening of cutaneous reactivity termed ATRA dermatitis, early in therapy. In the first few weeks approximately 80% of patients experience stinging, hyperesthesia or pruritus, fine scaling, dryness and mild erythema (Fig. 7.7a).

The conceptual framework in this section is that NANOEGG plays a crucial role in solving of the symptoms of irritation. After daily treatment with NANOEGG at different ATRA concentrations on the dorsal area of Wistar rats (5 weeks old, male), the induction of inflammation was visually observed. Inflammation tests are his-

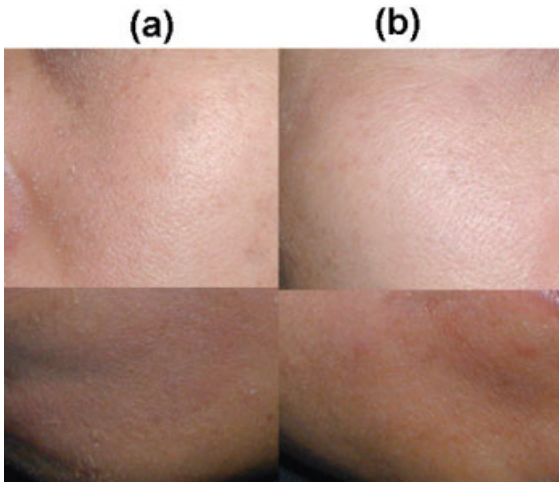


**Figure 7.7.** Facial features at 1 week following one time daily applications of (a) RENOVA ATRA 0.05% and (b) NANOEGG 0.05%. Note mild erythema and scaling along the jaw line and around the eye area in RENOVA treatment, while side-effects were rare in NANOEGG treatment.

torically carried out on the dorsal area of rats in cosmetic and medical companies as a standard method. It is known that this method will almost link to the degree of inflammation in the case of human skin. Hence, we also followed a rat system for the evaluation of NANOEGG. Only this experiment was carried out in a rat system. This stimulation degrees are normally numbered as three groups; 0–2: no change–fair, 2–4: stimulation, 4–6: high stimulation, which are based on visual observations. Figure 7.8 obviously shows the improvement of inflammation induced by the ATRA treatment in the case of NANOEGG.

Commercially, both Retin-A, a 0.1% ATRA cream, and RENOVA, a 0.05% ATRA cream, are marketed by Johnson & Johnson in the US. An *in vivo* experiment on the porcine dorsal area was performed for comparison with these commercial products. In the case of NANOEGG, the irritation against the porcine skin, which is known to be similar to human skin, showed the lowest level compared with other commercial products. One distinguishing feature of the human skin response to ATRA is the generation of clinical erythema. Since the erythema response of human skin to ATRA is normally dose-dependent [32], the reduced erythemogenic potential of NANOEGG should expect the reduction of irritation (Fig. 7.7b) with decreasing dose of ATRA, compared to the normal ATRA therapy.

The inflammation induced by topical ATRA treatment on skin should be caused by the elevation of AP-1 and NF- $\kappa$ B, and translated forms of inflammation cytokines, interleukin (IL)-1 $\alpha$  and tumor necrosis factor (TNF)- $\alpha$ . Thus, the inflammation cytokines IL- $\alpha$  and TNF- $\alpha$  mRNA were measured on the skin domain treated with NANOEGG ointment (Fig. 7.9).



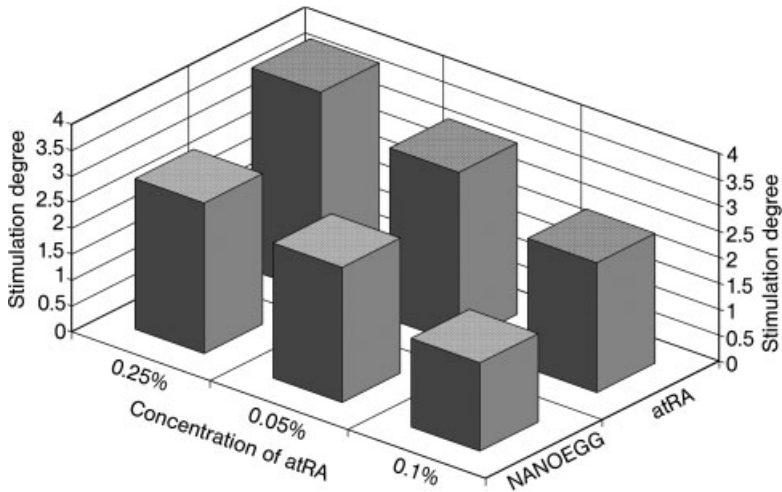


**Figure 7.8.** Stimulation degrees for the external administration on the dorsal area of ddY mouse of ATRA and NANOEGG in Vaseline media. Different concentrations (0.01, 0.05 and 0.25% of ATRA) were carried out as

daily treatment (30 mg,  $2 \times 2 \text{ cm}^2$  on the dorsal area of Wistar rats, 5 weeks old, male) for 2 weeks. Stimulation degree was determined by visual observation.

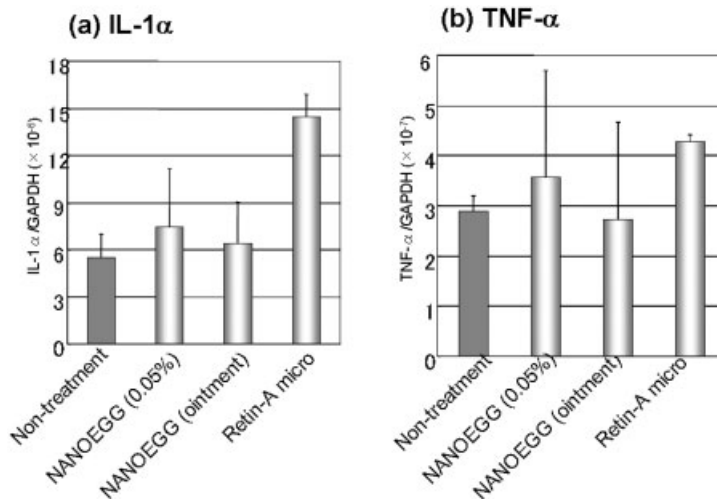


**Figure 7.9.** Expression of inflammation cytokines IL-1 $\alpha$  and TNF- $\alpha$  mRNA on mouse skin. Each compound (NANOEGG, its base and Retin-A-Micro) was administered as 30 mg on  $2 \times 2 \text{ cm}^2$  for 15 days. The tissues were sacrificed 4 days after the topical administration.

## 7.3.2

**Pharmacological Effects of the NANOEGG System**

Histological improvements in the appearance of photodamaged skin following ATRA usage are associated with thickening of the epidermis and a relative reduction in melanin content [7, 8]. A study was undertaken to specifically evaluate the efficacy of NANOEGG in treating hyperpigmented lesions. Histological evaluation of ddY mouse epidermis after daily application of NANOEGG Vaseline cream for 4 days revealed more than double the increase in epidermal thickness than when using ATRA Vaseline cream (Fig. 7.10a–d). In general, a period of at least a few months is required for clinical effectiveness in treating mottled pigmentation using ATRA. Given the major increase in thickness of the epidermis in our prelim-

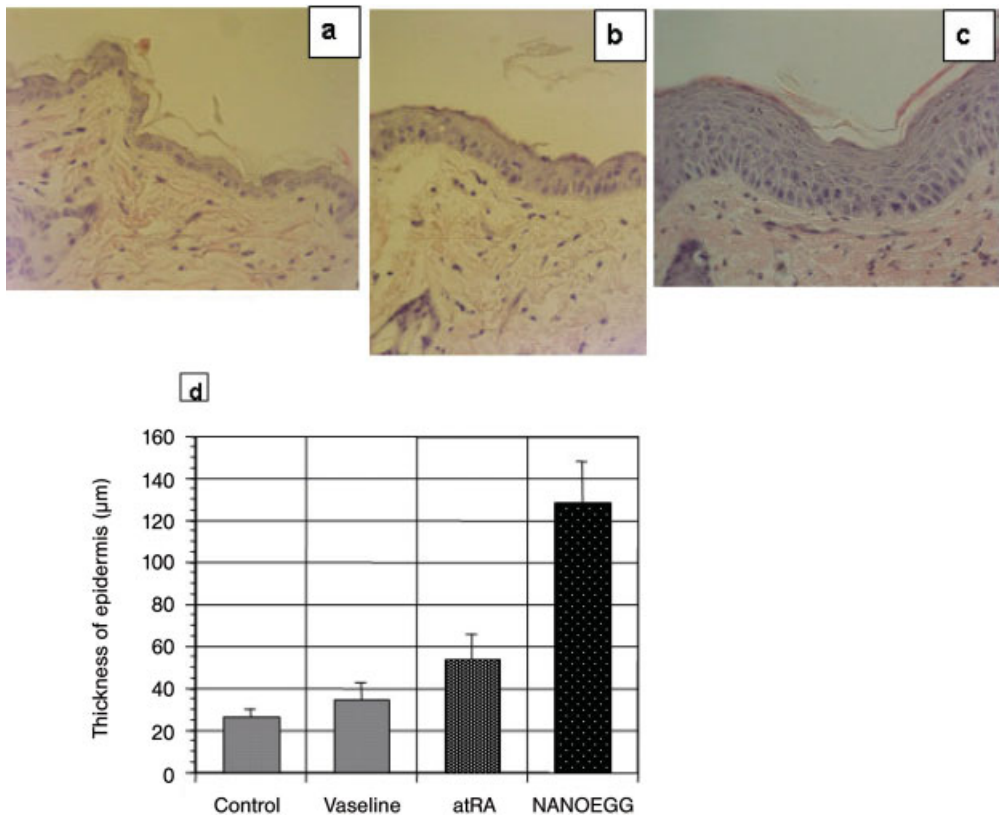


**Figure 7.10.** Histological and tissue analysis of the epidermis after a 4-day treatment. (a) Vehicle (Vaseline) treatment, (b) 0.1% ATRA treatment, (c) 0.1% NANOEGG treatment and (d) estimated epidermis thickness for each specimen ( $n = 10$ ).

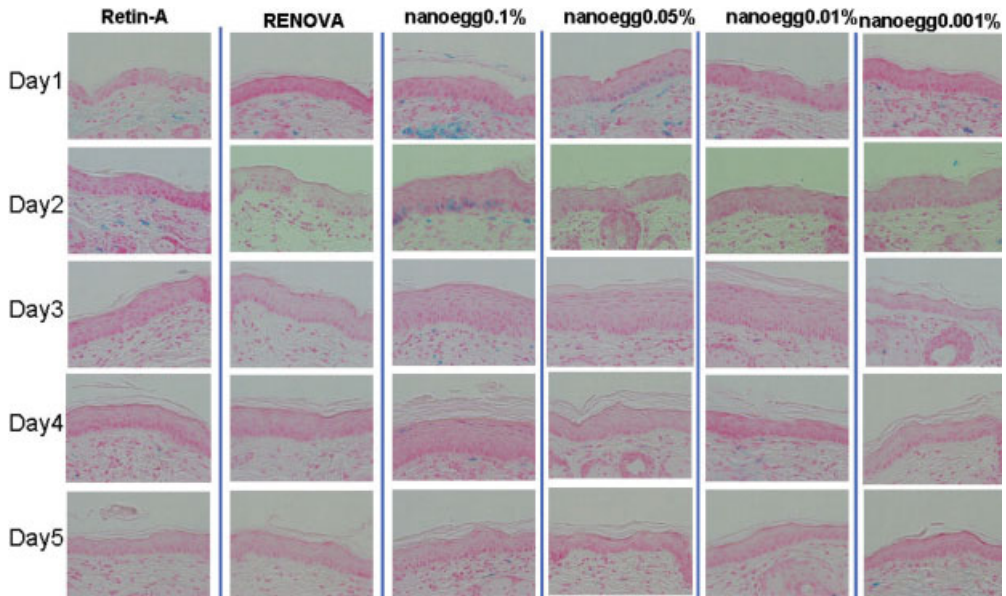


**Figure 7.11.** Histological evaluation of commercial products and NANOEGG 0.1, 0.05, 0.01 and 0.001% at each day after topical administration until day 5. All tissues were stained using the colloidal iron stain method to detect HA. Blue domains correspond to the presence of HA and red domains correspond

to nuclear staining. The external treatments were carried out once and the tissues were sacrificed at each day until day 5. The amount of 30 mg of compound was administered in a 1-cm<sup>2</sup> of dorsal area of hairless mice (HR-1, male, 5 weeks old).

inary trials, reduction of melanin should rapidly be produced by NANOEGG treatment in humans.

NANOEGG-treated hairless mice underwent more progressive epidermal hyperplasia than with the commercial products at the same dose (Fig. 7.11). Even at a lower dose of ATRA (0.001%), histological evaluations suggested the effective skin regeneration of mice. Significant increases in epidermal thickness for NANOEGG treatment at all doses was revealed compared with treatment using commercial product creams. The hyperplasia of epidermis in Fig. 7.11 shows the thickened epidermal layer in all tested groups, but the NANOEGG-treated groups at each concentration of ATRA were dominant to other commercial products. The thickness of the epidermis layer in NANOEGG 0.01% treatment corresponds to that in the Retin-A (ATRA 0.1%)-treated group, thus the efficacy of NANOEGG can be supposed to be approximately 10 times that of the Retin-A commercial product. Likewise, NANOEGG may show sustained release of ATRA molecules until at least 5 days because of the observed continued hyperplasia of epidermis.

## 7.3.3

**Expression of mRNA Heparin-binding Epidermal Growth Factor-like Growth Factor (HB-EGF) on Mouse Skin**

Stoll and coworkers reported that mRNA expression of HB-EGF is induced by ATRA in human keratinocytes and skin [33]. Recently, production of HB-EGF has been shown to be one of the hallmarks of the turnover of keratinocytes [33]. Figure 7.12 shows HB-EGF mRNA expression in mouse ears in ATRA- and NANOEGG-treated groups. Daily application was performed for 4 days. Excess expression of HB-EGF in the NANOEGG-treated group was apparent compared with ATRA. This correlates well with the increased epidermal thickening for NANOEGG treatment (Fig. 7.10). Even at 4 days after the external administration, it seems that NANOEGG would gradually release tretinoin molecules from its egg-like capsule. It was confirmed whether NANOEGG possesses the controlled release ability as a drug delivery system or pulsatile release. Figure 7.13 shows the result of the expression of HB-EGF mRNA each day after a single treatment of NANOEGG on the mouse dorsal area. The small figure in Fig. 7.13 shows the concentration dependence of the expression of HB-EGF mRNA on tretinoin. With increasing concentration of NANOEGG, the production of HB-EGF mRNA was enhanced from ker-

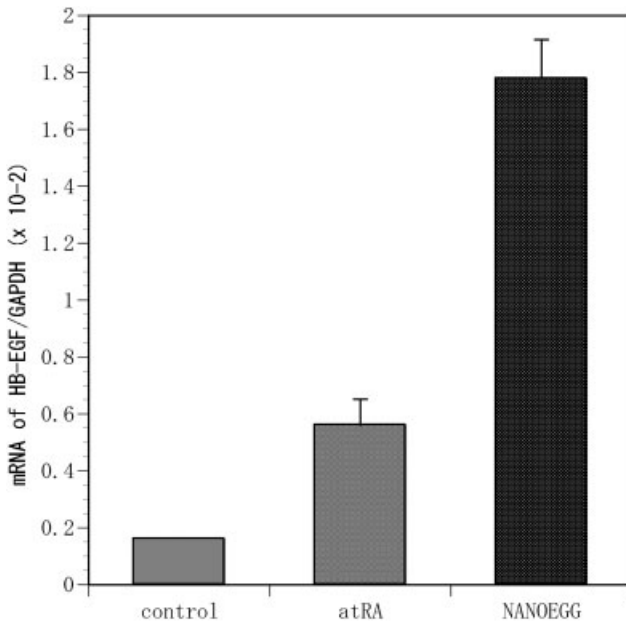


**Figure 7.12.** Expression of HB-EGF mRNA in mouse ears after continuous daily treatments for 4 days with ATRA or NANOEGG (0.1%) in Vaseline cream.

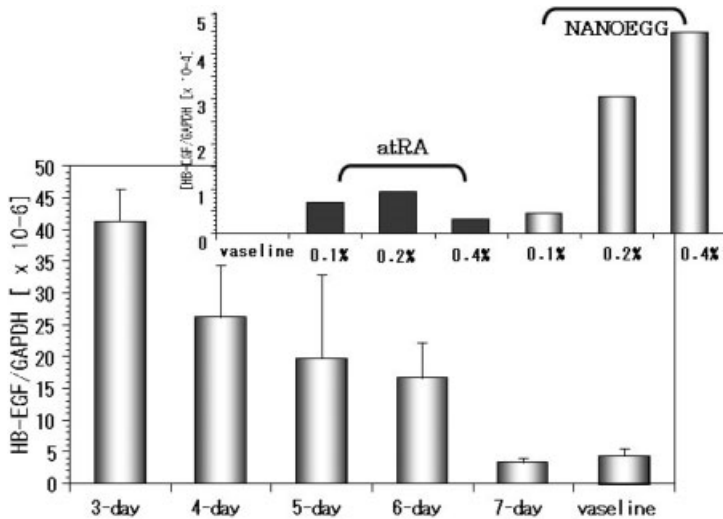


**Figure 7.13.** Expression of HB-EGF mRNA in mice dorsal areas at each day after 1-day treatment with NANOEGG. The large figure shows the continuous expression of HB-EGF mRNA by NANOEGG as tretinoin concentration 0.2%. The small figure shows the concentration dependence of

atinocytes, while this was different from the case with the single treatment of tretinoin. As is obvious in Fig. 7.13, NANOEGG treatment as 0.2% tretinoin concentration could achieve expression of HB-EGF mRNA for 1 week. It is suggested that, at least here, tretinoin would gradually release from NANOEGG and as a result long-term release for around 1 week was successfully achieved by NANOEGG technology.

Also, Fig. 7.14 shows HB-EGF mRNA expression in hairless mouse dorsal tissues in Retin-A-, RENOVA- and NANOEGG-treated groups. One-day application was performed, and tissue was sacrificed and frozen in liquid nitrogen daily until day 5. Especially on the first day, excess expression of HB-EGF mRNA in the NANOEGG-treated group was apparent compared with the commercial products, RENOVA and Retin-A. Furthermore, even at the most dilute ATRA dose, the elevated expression of HB-EGF mRNA at day 1 was observed that will be expected to accelerate proliferation and differentiation of keratinocytes. The hyperplasia of the epidermis in Fig. 7.11 almost corresponds to the expression of HB-EGF mRNA in Fig. 7.14, but it would seem that a 1- or 2-day period is needed due to the thickened epidermal layer after the production of HB-EGF.

#### 7.3.4

#### Proliferation and Differentiation of Keratinocytes

The mammalian epidermis is made up of multilayered epithelium consisting mainly of proliferating and differentiated, postmitotic keratinocytes. The differenti-

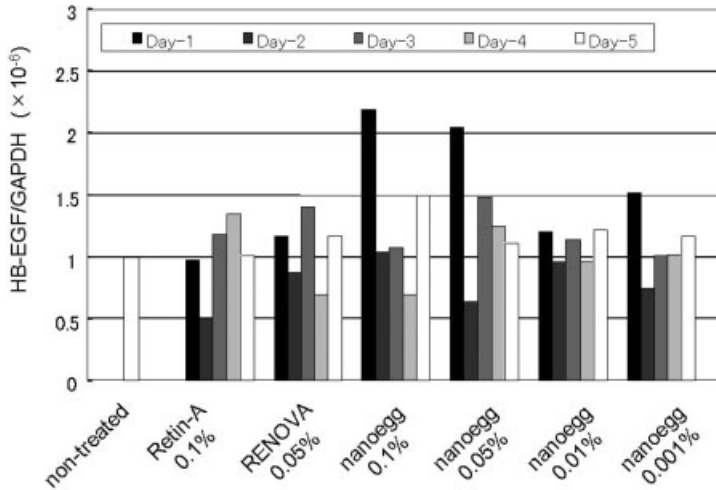


**Figure 7.14.** Expression of HB-EGF mRNA in hairless mice (HR-1, male, 5 weeks old) dorsal areas after 1-day treatment at day 5 with no treatment, NANOEGG (0.1, 0.05, 0.01 and 0.001%, respectively), RENOVA Retin-A. The tissues of dorsal areas were frozen using liquid nitrogen and extracted was RNA by the Isogen method.

ation is continuously replaced and recruited via transit-amplifying cells originating from stem cells, which represent a restricted number of basal keratinocytes. The continued renewal of cells in conjunction with mechanical strain poses a particular challenge to the cytoskeleton. It comes as no great surprise that epidermal keratinocytes have evolved a complex program of keratin expression along with mechanisms to alter the shape of the cytoskeleton during terminal differentiation.

As overexpression of HB-EGF mRNA was observed in NANOEGG treatment, we examined the expression of molecular markers in skin from the treated mice (5 weeks old, male) by immunofluorescence (Fig. 7.15). Cytokeratin 1 (K1) and larrikin (lord), markers of terminal differentiation in the normal epidermis layer, and cytokeratin 5 (K5), a maker of basal keratinocytes, were detected in the tissue after the treatment of atRA and NANOEGG 0.1% ointment. Expression of K5 (Fig. 7.15b and c) and larrikin (Fig. 7.15h and i) were rather enhanced in comparison with the control (wild-type mice, Fig. 7.15a), but the big difference between atRA and NANOEGG treatments was not observed, whereas the strongest expression of K1 was detected in the NANOEGG treatment (Fig. 7.15f). Excess expression of K1 might be associated with the enhanced thickening of the epidermis (Fig. 7.11b and Fig 11c). Thus, hyperplasia in the treatment of NANOEGG would mainly be due to the overexpression of HB-EGF, which could induce differentiation of keratinocytes. As a result, the differentiation of suprabasal and granule cells, which are related to the differentiation marker K1, seemed to be accelerated.

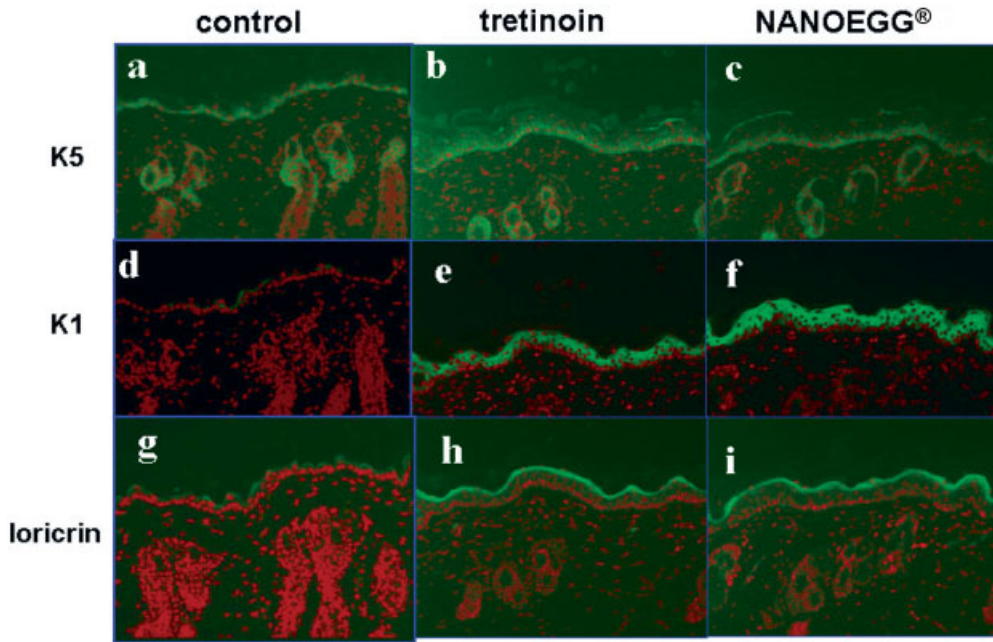


**Figure 7.15.** Expression of molecular markers in the epidermal layer of ddY mice. Green corresponds to antibody staining and red corresponds to nuclear staining. Dorsal skin sections from ddY mice at 4 days after the external treatment were stained with antibody against K1, K5 and loricrin (lor). The treatments were carried out by ATRA and

NANOEGG 0.1% as ATRA, respectively. The dorsal sections ( $1.0 \times 1.0 \text{ cm}^2$ ) were administrated 30 mg ointment (base is Vaseline). K1 is a marker from the suprabasal layer to the stratum corneum; K5 is a marker from the basal cell; and loricrin is a marker from the granular layer to stratum corneum.

### 7.3.5

#### Production of Hyaluronic Acid (HA) in the Epidermal Layer

Another change was noteworthy – the intercellular spaces were wider and more prominent. This probably accounts for the intensified result with colloidal iron staining. Interestingly, wrinkling and skin texture may also be influenced by other epidermal factors as well as HB-EGF expression. Another histological finding of NANOEGG efficacy was obtained in this study. The influence of ATRA on epidermal differentiation is associated with the metabolism of HA by keratinocytes [36]. Tammi and coworkers reported tentative results in 1989 that HA was produced between ATRA-exposed keratinocytes [34]. The ATRA molecule leads to an accumulation of HA in the superficial layers of the epidermis by stimulating HA synthesis in keratinocytes. Deposition of HA coincides with cell proliferation and migration in several developing tissues and organs [35, 36], whereas onset of differentiation is often accompanied by reduced HA synthesis [37]. In order to evalu-

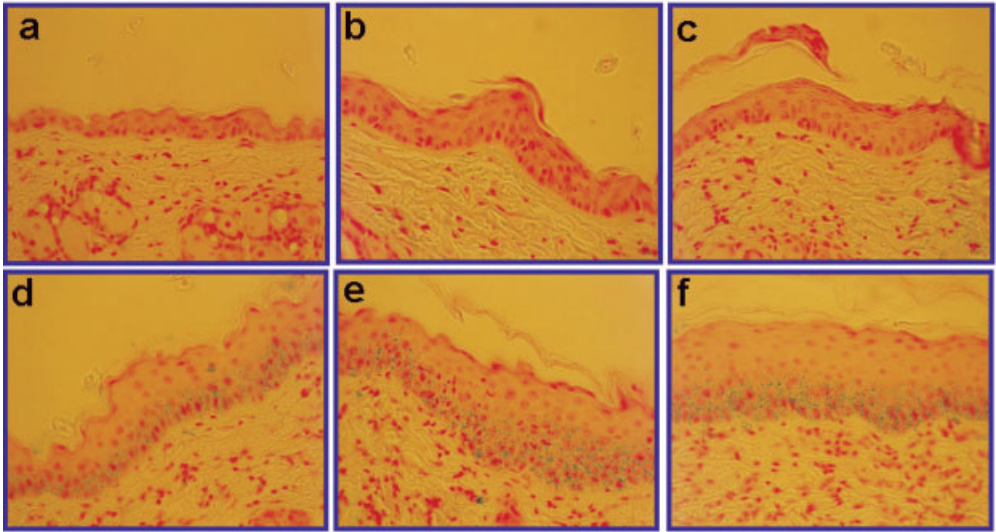


**Figure 7.16.** Expression of HA among keratinocytes after treatment by ATRA and NANOEGG. The dorsal tissues (ddY mouse, 5 weeks old, male) were stained using the colloidal iron stain method. The treatment of ATRA and NANOEGG was carried out once and the corresponding tissues were sacrificed

3 days after the treatment. Blue spots in the pictures correspond to HA, and they disappeared completely following the treatment with hyaluronidase (data not shown). ATRA (a) 0.1%, (b) 0.2% and (c) 0.4%; NANOEGG (d) 0.1%, (e) 0.2% and (f) 0.4%.

ate the efficacy of NANOEGG on HA production, empirical histology of the epidermis was investigated. Skin specimens treated daily for 4 days were taken from the mouse dorsal area. Specimens were prepared using colloidal iron staining to retain HA. In ATRA- and NANOEGG-treated groups, the intercellular spaces of the epidermal basal and spinous cells displayed negative and abundant presence of HA, respectively (dark blue spots correspond to accumulation of HA; Fig. 7.16a–c for ATRA treatment and Fig. 7.16d–f for NANOEGG treatment). Within the experimental period (4 days of treatment), it seems to be difficult to produce HA by ATRA treatment, at even with increasing the ATRA concentration to 0.4% (Fig. 7.16c).

Furthermore, intercellular spaces between both basal and suprabasal cells were extended wider with NANOEGG (Fig. 7.16d–f) than those with ATRA treatment (Fig. 7.16a–c). This may account for the reduced cohesion between cells compared to ATRA treatment, as HA displays a lubricating effect. Basal and suprabasal cells would therefore proliferate and migrate to the upper stratum corneum more easily. Finally, promotion of epidermal thickening accompanying melanin migration could occur with continuous application of NANOEGG on skin. In the NANOEGG system, rapid regulation of HA in the epidermis might effectively help keratinocyte growth. Production of hyaluronate in the epidermis would accelerate turnover of the epidermis, as the lubricant among cells eventually contributes to a reduction



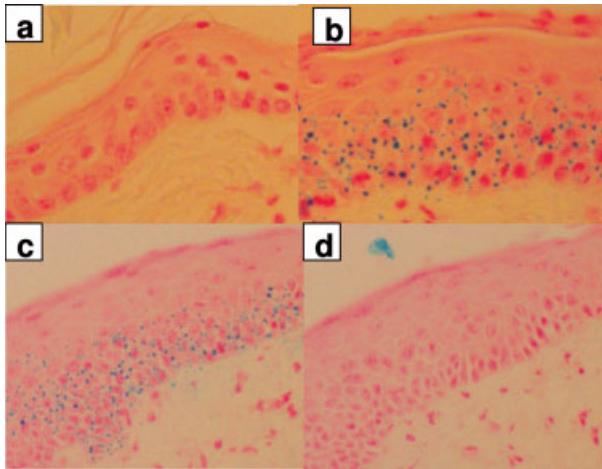


**Figure 7.17.** HA stain by colloidal iron. Dark-blue color domains correspond to the presence of HA. Each treatment was carried out for 4 days. (a) 0.1% ATRA in Vaseline, (b) 0.1% nano-ATRA in Vaseline, (c) same specimen as (b) but at a different area, (d) specimen (c)

after treatment by hyaluronidase for 16 h and (e) change of fine wrinkles on the neck area of an aged hairless mouse (18 weeks old, male). The treatment was carried out for 4 days, with 30 mg of ATRA and NANOEGG (0.1%) in Vaseline creams.

in macular hyperpigmentation and less apparent fine wrinkles [19]. Since hyaluronidase treatment on NANOEGG-treated specimens resulted in a complete disappearance of the stained domain, this histological evaluation identified production of HA (Fig. 7.17c and d).

### 7.3.6

#### **Hyperpigmentation and Fine Wrinkle Improvements by NANOEGG Treatment on Animal Skin**

Photoaging involves the adverse effects of chronic UV radiation (UVR) on the skin, superimposed on the intrinsic aging process. The later sections review evidence gathered from animal and human studies regarding the ability of topical NANOEGG application to reverse many aspects of the photoaging process.

By definition, photoaging involves UVR exposure – mainly from the sun, but also from therapeutic sources of UVR. UVC (200–290 nm) is the most biologically damaging portion of the UVR spectrum, but is almost entirely absorbed by the ozone layer of the Earth's atmosphere. The strongest UV light to reach the Earth's surface is UVB (290–320 nm). UVA (320–400 nm) has the greater penetration into the skin, but is much weaker than UVB. Clinical features of photoaging include fine and coarse wrinkles, skin roughness, sallowness, mottled hyper/hypopigmentation, lentigines, telangiectasias, and skin laxity.

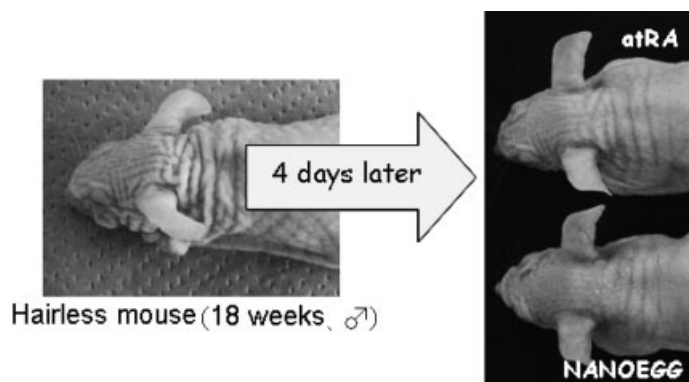


**Figure 7.18.** Change of fine wrinkles on the neck area of an aged hairless mouse (18-week, male). The treatment was carried out for 4 days, with 30 mg of ATRA and NANOEGG (0.1%, respectively) in Vaseline creams.

A systematic study of the photoaging process is difficult or impossible using human subjects. Animal models in which the process is accelerated are therefore desirable models. There is no naturally occurring animal model of photodamage, as diurnal animals are covered with fur, feathers or scales that protect them from UVR. The normally laboratory generated hairless mouse (HR-1) and guinea pig have been widely utilized because the animals wrinkle and produce brown spots in response to UVR within their relatively short life expectancies. To establishment fine wrinkles, first, the aged hairless mouse (HR-1, 18 weeks old) was utilized for the topical treatment of NANOEGG (Fig. 7.18). Guinea pigs (Weiser maple, 5 weeks old ) were irradiated with UVA and UVB using an established protocol for 10 days to induce photodamage, and topical NANOEGG was applied at a concentration 0.05% for an additional 5 days (Fig. 7.19).

### 7.3.7

#### Clinical Trials of Fine Wrinkles and Brown Spots on the Human Face

In general, a period of at least a few months is required for clinical effectiveness in treating mottled pigmentation using ATRA cream. Given the major increase in thickness of the epidermis in our animal trials (Figs. 7.11 and 7.12), a reduction of melanin pigments should be rapidly produced by NANOEGG 0.05% treatment in humans. As a preliminary clinical trial for *in vivo* treatment of wrinkles and pigmental spots, NANOEGG therapy was performed for 1 month on human faces. The Institutional Review Board of St Marianna University permitted the clinical trial of NANOEGG ointment in human faces over 40 years old. The trial was carried out for 1 month in 30 wrinkles and 30 brown spots induced by aging and/or

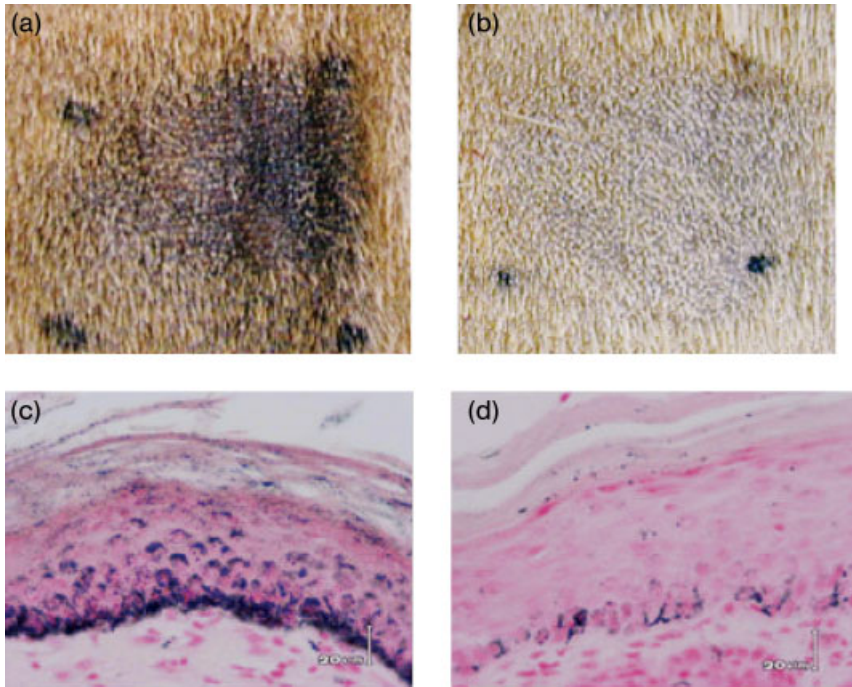


**Figure 7.19.** Improvement in hyperpigmentation of guinea pig dorsal skin with the topical application of NANOEGG. The establishment of brown spots was carried out by 10 days of total UVA and UVB irradiation.

(a) Before treatment, (b) after the treatment of NANOEGG 0.05%, and (c) and (d) histological research corresponding to (a) and (b). The tissue was stained by melanin staining. Black granules correspond to melanin.

UV irradiation. The brown spots were also fairly decreased (Fig. 7.20). Otherwise, coarse wrinkling at the side of the eyes was consistently diminished after NANOEGG 0.05% treatment without strong irritation and inflammation (Fig. 7.20). This would certainly be due to the abundant HA accumulation in the epidermal layer at an early stage. Commercial ointment treatment could not usually achieved the decrease of hyperpigmentation after only 1 month, while the NANOEGG system could reduce the hyperpigmentation without serious irritation, as is obvious in Fig. 7.20. Actually, after treatment of NANOEGG for several days weak inflammation took place for several people. Compared with commercial products, these levels were rather weak. Accordingly, we believe that the risks due to the continuous treatment of ATRA such as erythema and irritation can prevent exactly by NANOEGG technology. Because the pharmacological effect would be gotten by the short-term treatment with the NANOEGG system. Simultaneously, the amount of water in stratum corneum also showed a statistically increase for 1 month treatment of NANOEGG (Fig. 7.21).

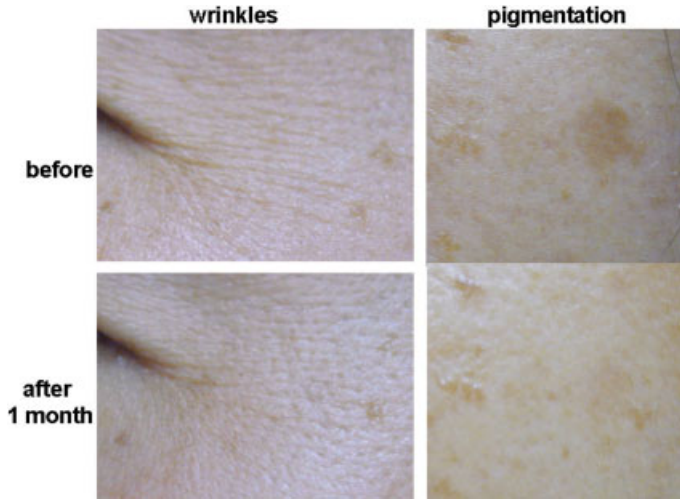


Figure 7.20. Pictures of wrinkles and photoaged hyperpigmentation on human faces (female, 48 years old). Before treatment with NANOEGG 0.05%, and after treatment for 1 month. The external daily administration was carried out one time at night, continuously.

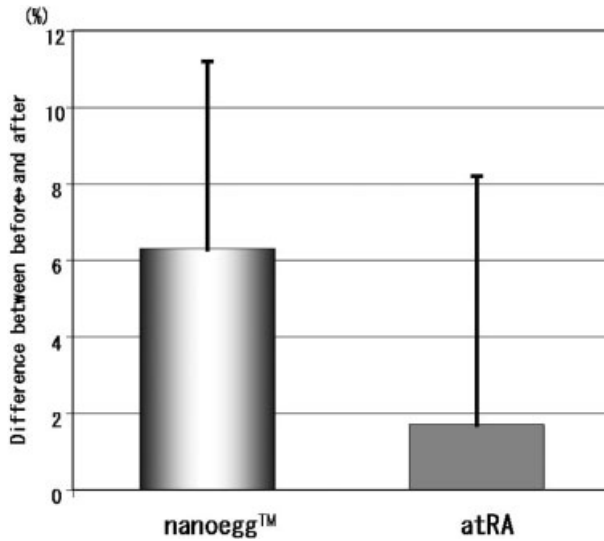


Figure 7.21. Change of amount of water in the stratum corneum of human skin. The measurements were carried out on people over 40 years old before and after treatments with NANOEGG and ATRA.

#### 7.4

### Why does NANOEGG Show the High Performance on the Improvement of Brown Spot and Wrinkles?

The superb results *in vivo* and histological evaluations obtained for NANOEGG are attributable to effective permeation into the skin. The stratum corneum is covered with lipids, natural moisturizing factors and ceramides as a barrier. In the presence of water, ceramide and other natural compounds spontaneously promote the formation of lyotropic lamella liquid crystals. When materials diffuse in such a lyotropic phase, the hydrophile–lipophile balance (HLB) of a molecule plays a significant role in the effective permeation into skin. In practice, hydrophobic ATRA would theoretically show minimal permeation through the stratum corneum epidermis. As a result, almost all of the ATRA would remain on the surface of the stratum corneum, eventually inducing irritation and inflammation. The surface of NANOEGG displays an amphiphilic character due to the coexistence of a hydrophobic domain ( $\text{CaCO}_3$ ) and a hydrophilic PEG domain. As our NANOEGG is therefore easily dispersed in both aqueous and nonpolar media (Fig. 7.22), its permeability through the stratum corneum was substantially enhanced. Fortunately, permeability of NANOEGG can be indirectly evaluated in terms of histological staining of  $\text{Ca}^{2+}$  ions (Fig. 7.23). After treatment, red-smear domains of biopsy specimens extended over time to the entire epidermis (Fig. 7.23b and c), while  $\text{CaCO}_3$ -treated subjects displayed no permeation to the inner dorsal skin (Fig. 7.23a).

Surprisingly, it is obvious that even in a quite short time (10 min, Fig. 7.23b) NANOEGG can already permeate into the skin. Not only the high permeation of NANOEGG, but also the stability of the capsule showed drastic performance in the epidermis. Since after 24 h the epidermal layer was more stained than the dermis, it indicates that NANOEGG capsules may be trapped in epidermis.

The skin is the outermost organ of the body. It is a complex membrane comprising of three major layers – epidermis, dermis and hypodermis. The epidermis is an avascular stratifying layer of epithelial cells that overlies the connective tissue layer – the dermis. The outermost layer of epidermis, i.e. the stratum corneum, is pri-

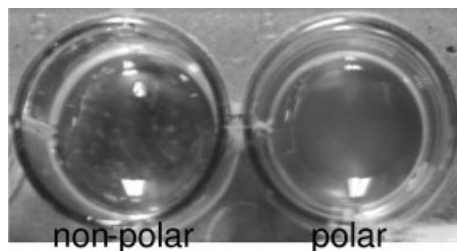


**Figure 7.22.** Solubility of NANOEGG 0.1% in polar (water) and nonpolar (corn oil) solvents. Both solutions showed a quite transparent appearance because of the amphiphilic property on the surface of NANOEGG.

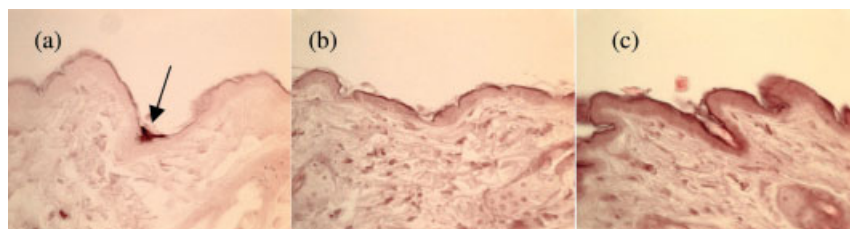


**Figure 7.23.** Dahl's calcium staining, which selectively traps the presence of Ca. Red smeared domains correspond to Ca distribution, particularly  $\text{CaCO}_3$  [indicated by arrow as positive control (a)]. Permeation potential of NANOEGG through mouse skin as a function of time after external administration. The tissues of ddY mice were utilized for staining. Calcium was regarded as a permeation maker from the stratum corneum epidermis to the dermis region. As the NANOEGG particle is at the nanoscale, the stain in the specimen would be detected as smeared domains. Treatment with 0.1% NANOEGG Vaseline cream after (b) 10 min and (c) 24 h.

marily responsible for the barrier properties of the skin. The underlying viable epidermis is different from the stratum corneum in being physiologically more akin to other living cellular tissues, but also plays the role as second barrier, especially for ions. Following passive application, the unionized form of any compound is better absorbed than its ionized counterpart [38]. However, the penetration rates of drug molecules across skin or other epithelial surfaces are usually low due to their excellent barrier properties.

For the reasons discussed above, it can be suggested here that NANOEGG capsules could successfully permeate into skin due to passive diffusion.

## 7.5 NANOEGG for Other Indications

In multicellular organisms, a balance between differentiation, proliferation and cell death maintains tissue homeostasis in adult tissues and directs normal development during embryonic morphogenesis. Retinoic acid is one of the critical factors regulating the molecular events involved in these processes. The requirement for ATRA for normal development and tissue homeostasis has been known since Wolbach and Howe first reported the defects that occurred in vitamin A-deficient animals in 1926. A large literature base has since appeared describing the role of retinoids in promoting proliferation, differentiation or apoptosis *in vivo*, in a variety of cell culture systems and more recently through studies using retinoid receptor knockout strategies. In addition, these investigations have provided the mechanisms by which retinoids induce teratogenic effects and inhibit neoplastic development, particularly in cancer. Significant progress has been made in understanding the molecular mechanism by which retinoids modulate the action of negative and positive growth factors including EGF, the transforming growth factor (TGF) family, insulin, IL-1 $\alpha$ , IL-6, IFN- $\gamma$ , estrogen and vitamin D $_3$ . Regulation by

retinoids can occur at the level of expression of growth factors and cytokines, and their respective receptors/binding proteins in the signaling pathway.

Many of the biological effects and changes in gene expression induced by ATRA are mediated by six known retinoic acid receptors (RAR $\alpha$ , RAR $\beta$  and RAR $\gamma$ ) and/or retinoid X receptors (RXR $\alpha$ , RXR $\beta$  and RXR $\gamma$ ) [39–41]. It is known that each of the RAR subtypes has a specific tissue distribution pattern [42]. For example, RAR $\gamma$  is the most abundant retinoid receptor in the skin [43, 44], whereas RAR $\beta$  is found primarily in the heart, lung and spleen. RAR $\alpha$  is expressed at low levels in many tissue types. It follows that retinoids that activate a particular receptor subtype may elicit biological responses in specific tissues. Thus, it can be expected that retinoids would greatly improve therapeutic indices in the treatment of retinoid-responsive diseases because of receptor expression on many tissues. The full therapeutic potential of ATRA may only be realized if new technologies with vastly improved therapeutic indices can be developed.

We have been investigated the radical therapy of diabetes mellitus induced by NANOEGG. Since the ATRA molecule is soluble in water, it is impossible to inject, whereas NANOEGG is easily soluble in aqueous media. Injection of NANOEGG may systematically induce the proliferation of pancreatic  $\beta$  cells and differentiation of anaplastic cells in Langerhans islands and/or pancreatic ducts, resulting in the regeneration of  $\beta$  cells. Recent studies showed that differentiation of in different cells on pancreatic ducts could be induced by HB-EGF and, as a result, glucose tolerance was improved [45]. As already shown, the topical treatment of NANOEGG could produce abundant HB-EGF. The pancreas must also express retinoic acid receptors. HB-EGF induced by NANOEGG, thus, will be expected to regenerate pancreatic  $\beta$  cells in diabetic animal models. Figure 7.24 shows the change of body weight of type I diabetic rats induced by streptozotocin in the case of subcutaneous administration of NANOEGG. Obviously the loss of weight was stopped

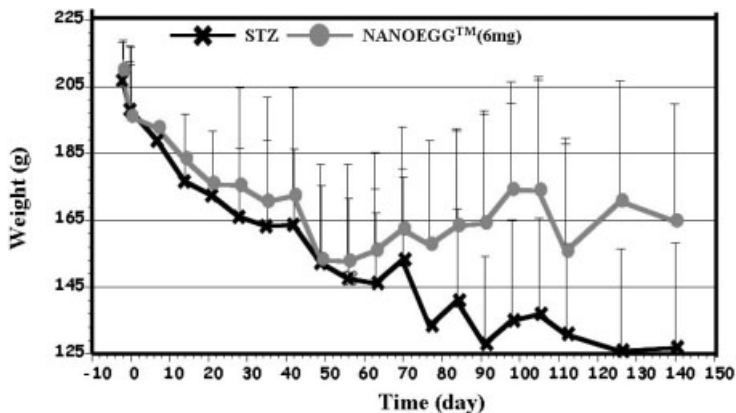
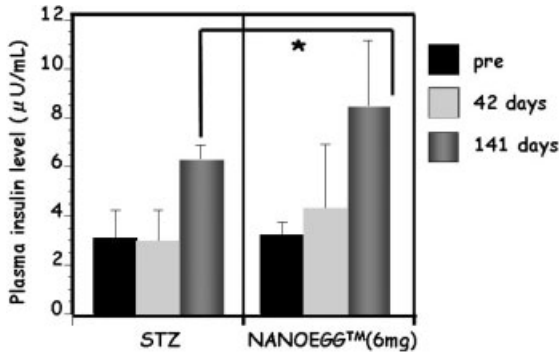
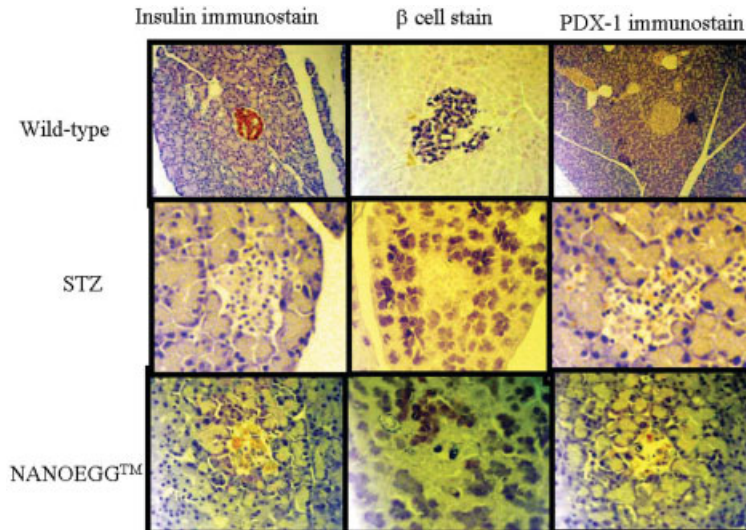


Figure 7.24. Change of body weight of Wistar rats (male) in subcutaneously administered NANOEGG (6 mg as ATRA, once a week). Model animals were induced with type I diabetes by STZ administration.



**Figure 7.25.** Change of insulin level in plasma after the administration of NANOEGG (6 mg as ATRA, once a week). Model animals were induced with type I diabetes by STZ administration.

in the NANOEGG-injected group around 60 days. In this case, the concentration of insulin in plasma also increased compared to the nontreated group (Fig. 7.25). Expression of transcription factor of pancreas PDX-1 in Langerhans islands relates to the differentiation of somatic stem cells to  $\beta$  cells [46, 47]. Figure 7.26



The newly developed DDS technology described

**Figure 7.26.** Immunostaining of insulin and transcription factor PDX-1, and  $\beta$  cells in Langerhans islands of rat pancreas. Model animals were prepared by the administration of STZ. Over 99% of  $\beta$  cells could not be observed in Langerhans islands in the case of STZ groups.



shows slight expression of PDX-1 in Langerhans islands in the group administered NANOEGG.

The administration of NANOEGG cannot only be used for the regeneration of skin, but also can be expected to be used for the regeneration therapy of  $\beta$  cells. New nanoshell technology NANOEGG may also be useful for other retinoid response diseases. Major advances with ATRA and/or its nanocapsule NANOEGG would be continuously in progress in clinical applications.

## 7.6

### NANOEGG for Other Drugs

The self-assembly property in aqueous media is absolutely necessary to prepare NANOEGG. The physicochemical amphiphilic balance of the molecular structure leads to molecular association in water. ATRA can spontaneously form micelles in water with a small amount of alkaline. If drugs can form self-assemblies like micelles and their surfaces have ionic charges, the NANOEGG structure should be prepared. Even if drugs have a high molecular weight, it is possible to form the core-shell structure of the NANOEGG system. Prostaglandin and its derivatives may be able to form micelle-like structures. It would expect that NANOEGG technology will be also indicated in other drugs.

## 7.7

### Conclusion

Up to now, clinical responses predominantly comprised severe irritant dermatitis in the early stages of application (around 3 or 4 days) of ATRA. This problem is generally managed by modifications to the dosage and schedule. Such damage with a high magnitude of inflammatory events after ATRA treatment can induce chronic skin pigmentation in the area being treated, potentially resulting in imperfect repair of skin displaying a pigmented appearance. Preventing undesirable adverse effects would be expected to allow ATRA therapy to overcome the limitations of classical ATRA therapy. Herein, we describe the development of a novel drug delivery system using nanotechnology. The conceptual framework in this study is that NANOEGG plays a crucial role in solving the low permeation of ATRA into spaces in the stratum corneum epidermis and the also the symptoms of irritation.

The newly developed drug delivery system technology described herein could help with nonsurgical treatment of photodamaged skin for which use of ATRA has been recommended. Detailed studies concerning the efficacy of NANOEGG have already been reported [19, 48, 49], suggesting not only improved permeability to the stratum corneum, but also simultaneous enhanced keratinization due to  $\text{CaCO}_3$ . Drastically increased epidermal thickness could be expected to result in a relative decrease in melanin content and excess expression of HA aids induction of hyperplasia, resulting in less-wrinkled skin. Moreover, the high permeability and

controlled release of ATRA induces accelerated epidermal turnover. Promotion of keratinocyte proliferation and acceleration of keratinocyte differentiation are most likely the result of ATRA in regimentering treatments. Melanin granules may be washed out of the epidermis by a rapid and stronger stream of keratinocytes in the epidermis compared to topical ATRA treatment. This study clearly shows that our newly developed novel drug delivery system technology for NANOEGG offers great potential for new ATRA therapy. Histological and ultrastructural findings for empirical evaluation of NANOEGG indicate that ATRA therapy causes more than esthetic improvement, inducing histological changes in the epidermis, in all likelihood without regard to changes induced by time or sunlight.

The new nanoshell technology NANOEGG can be useful for other clinical approaches and other drugs. It would expect that drastic advances in the treatment of intractable diseases will be achieved by the NANOEGG drug delivery system.

## References

- 1 SPORN M. B., ROBERTS A. B., Role of retinoids in differentiation and carcinogenesis. *Cancer Res.* **1983**, *43*, 3034–3040.
- 2 MANGELSDORF D. J., EVANS R. M., The RXR heterodimers and orphan receptors. *Cell* **1995**, *83*, 841–850.
- 3 WOLBACH S. B., HOWE P. R., Tissue changes following deprivation and fat-soluble A vitamin. *J. Exp. Med.* **1925**, *42*, 753–777.
- 4 FRAZIER C. N., HU C. K., Cutaneous lesions associated with a deficiency in vitamin A in man. *Arch. Intern. Med.* **1931**, *48*, 507–514.
- 5 LIVREA M. A., *Vitamin A and Retinoids: An Update of Biological Aspects and Clinical Applications*. Birkhäuser Verlag, Basel, **2000**.
- 6 FISHER G. J., VOORHEES J. J., Molecular mechanisms of retinoid actions in skin. *FASEB J.* **1996**, *10*, 1002–1013.
- 7 AYDELOTTE M. B., The effects of vitamin A and citral on epithelial differentiation. 1. The chick oesophageal and corneal epithelia and epidermis. *J. Embryol. Exp. Morphol.* **1963**, *11*, 621–635.
- 8 BELLOWS C. G., HARDY M. H., Histochemical evidence of mucosubstances in the metaplastic epidermis and hair follicles produced *in vitro* in the presence of excess vitamin A. *Anat. Rec.* **1977**, *187*, 257–271.
- 9 KLINGMAN L. H., DUO C. H., KLINGMAN A. M., Topical retinoic acid enhances the repair of ultraviolet damaged dermal connective tissue. *Connect. Tissue Res.* **1984**, *12*, 139–142.
- 10 KLINGMAN A. M., GROVE G. L., HIROSE R., LEYDEN J. J., Topical tretinoin for photoaged skin. *J. Am. Acad. Dermatol.* **1986**, *15*, 836–839.
- 11 OLSEN E. A., KATZ H. I., LEVINE N., SHUPACK J., BILLYS M. M., PRAWER S., GOLD J., STILLER M., LUFRAÑO L., THORNE E. G., Tretinoin emollient cream: a new therapy for photo-damaged skin. *J. Am. Acad. Dermatol.* **1992**, *26*, 215–224.
- 12 MIZUGUCHI K., TSUDA T., *Medical Technology, New Stain Method*. Ishiyaku, Shuppan, Japan, **1999**, pp. 122–123.
- 13 MOROI Y., *Micelles: Theoretical and Applied Aspects*. Plenum Press, New York, **1992**, pp. 66–73.
- 14 SZUTS E. Z., HAROSI I. H., Solubility of retinoids in water. *Arch. Biochem. Biophys.* **1991**, *287*, 297–304.
- 15 LI C. Y., ZIMMERMAN C. L., WIEDMANN T. S., Solubilization of retinoids by bile saltphospholipid aggregates. *Pharm. Res.* **1996**, *13*, 907–913.

- 16 DEBOECK H., ZIDOVETZKI R., NMR study of the interactions of retinoids with phospholipid bilayers. *Biochim. Biophys. Acta* **1988**, *946*, 244–252.
- 17 WASSALL S. R., PHELPS T. M., ALBRECHT M. R., LANGSFORD C. A., STILLWELL W., ESR study of the interactions of retinoids with a phospholipids model membrane. *Biochim. Biophys. Acta* **1988**, *939*, 393–402.
- 18 NOY N., The ionization behavior of retinoic acid in aqueous environments and bound to serum albumin. *Biochim. Biophys. Acta* **1992**, *1106*, 151–158.
- 19 YAMAGUCHI Y., NAGASAWA T., NAKAMURA N., TAKENAGA M., MIZOGUCHI M., KAWAI S., MIZUSHIMA Y., IGARASHI R., Successful treatment of photo-damaged skin of nano-scale ATRA particles using a novel transdermal delivery. *J. Control. Release* **2005**, *104*, 29–40.
- 20 BRECHT M., MAYER U., SCHLOSSER E., PREHM P., Increased hyaluronate synthesis is required for fibroblast detachment and mitosis. *Biochem. J.* **1986**, *239*, 445–450.
- 21 SMALL D. M., Micellar properties of sodium fusidate, a steroid antibiotic structurally resembling the bile salts. In *The Bile Acids*, NAIR P. P., KRITCHEVSKY S. (Eds.). Plenum, New York, **1971**, Vol. 1, pp. 249–355.
- 22 CISTRA D. P., HAMILTON J. A., JACKSON D., SMALL D. A., Ionization and phase behaviour of fatty acids in water application of the Gibbs phase rule. *Biochemistry* **1988**, *27*, 1881–1888.
- 23 MOROI Y., Micelles, theoretical and applied aspects. *J. Phys. Chem.* **1980**, *84*, 2186–2191.
- 24 HEITMANN P., Reactivity of sulfhydryl groups in micelles. A model for protein. *Eur. J. Biochem.* **1968**, *5*, 305–310.
- 25 JONES G. J., CROUCH R. K., WIGGERT B., CORNWALL M. C., CHADER G. J., Retinoid requirements for recovery of sensitivity after visual pigment bleaching in isolated photoreceptors. *Proc. Natl Acad. Sci. USA* **1989**, *86*, 9606–9610.
- 26 CROUCH R. K., HAZARD E. S., LIND T., WIGGERT B., CHADER G., CORSON D. W., Interphotoreceptor retinoid-binding protein and  $\alpha$ -tocopherol preserve the isomeric and oxidation state of retinol. *Photochem. Photobiol.* **1992**, *56*, 251–255.
- 27 FUCKS E., Epidermal differentiation: the bare essentials. *J. Cell Biol.* **1990**, *111*, 2807–2814.
- 28 FUCKS E., Keratins as biochemical markers of epithelial differentiation. *Trends Genet.* **1988**, *4*, 277–281.
- 29 MEHREL T., HOHL D., ROTHNAGEL J. A., LANGLEY M. A., BUNDMAN D., CHENGE C., LICHTI U., BISHER M. E., STEVEN A. C., STEINART P. M., YUSPA S. H., ROOP D. R., Identification of a major keratinocyte cell envelope protein, lorocrin. *Cell* **1990**, *61*, 1103–1112.
- 30 KURST A., KASTNER P., PETKOVITCH M., ZELENT A., CHAMBON P., A third human retinoic acid receptor, hRAR-gamma. *Proc. Natl Acad. Sci. USA* **1989**, *86*, 5310–5314.
- 31 SPORN M. B., ROBERTS A. B., Role of retinoids in differentiation and carcinogenesis. *Cancer Res.* **1983**, *43*, 3034–3040.
- 32 GRIFFITHS C. E. M., FINKEL L. J., TRANFAGLIA M. G., HAMILTON T. A., VOORTHEES J. J., An *in vivo* experimental model for effects of topical retinoic acid in human skin. *Br. J. Dermatol.* **1993**, *129*, 389–394.
- 33 STOLL S. W., ELDER J. T., Retinoid regulation of heparin-binding EGF-like growth factor gene expression in human keratinocytes and skin. *Exp. Dermatol.* **1998**, *7*, 391–397.
- 34 TAMMI R., RIPELLINO J. A., MARGOLIS R. U., MAIBACH H. I., TAMMI M., Hyaluronate accumulation in human epidermis treated with retinoic acid skin organ culture. *J. Invest. Dermatol.* **1989**, *92*, 326–332.
- 35 BRECHT M., MAYER U., SCHLOSSER E., PREHM P., Increased hyaluronate synthesis is required for fibroblast detachment and mitosis. *Biochem. J.* **1986**, *239*, 445–450.

- 36 CHEN W. Y., GRANT M. E., SCHOR A. M., SCHOR S. L., Differences between adult and foetal fibroblasts in the regulation of hyaluronate synthesis: correlation with migratory activity. *J. Cell Sci.* **1989**, *94*, 577–584.
- 37 TOOLE B. P., TRELSTAD R. L., Hyaluronate production and removal during corneal development in the chick. *Dev. Biol.* **1971**, *126*, 28–35.
- 38 SWARBRICK J., LEE G., BROM J., GENSMANTEL P., Drug permeation through skin. II. Permeability of ionized compounds. *J. Pharm. Sci.* **1984**, *73*, 1352–1354.
- 39 MANGELSDORF D. J., UMESONO K., EVANS R. M., The retinoid receptors. In *The Retinoids*. SPORN M. B., ROBERTS A. B., GOODMAN D. S. (Eds.). Raven, New York, **1994**, pp. 319–350.
- 40 GIGUÈRE V., RA receptors and cellular retinoid binding proteins: complex inter-play on retinoid signaling. *Endocr. Rev.* **1994**, *15*, 61–79.
- 41 CHAMBON P., A decade of molecular biology of retinoic acid receptors. *FASEB J.* **1996**, *10*, 940–954.
- 42 REES J., The molecular biology of retinoic acid receptors: orphan from good family seeks home. *Br. J. Dermatol.* **1992**, *126*, 97–104.
- 43 ELDER J. T., FISHER G. J., ZHANG Q.-Y., EISEN D., KRUST A., KASTNER P., CHAMBON P., VOORHEES J. J., Retinoic acid receptor gene expression in human skin. *J. Invest. Dermatol.* **1991**, *96*, 425–433.
- 44 RECZEK P. R., OSTOWSKI J., YU K.-L., CHEN S., HAMMER L., ROALSVIG T., STARRETT JR., J. E., DRISCOLL, G., WHITING J. P., SPINAZZE P. G., TRAMPOSCH K. M., MANSURI M. M., Role of retinoic acid receptor gamma in the rhino mouse and rabbit irritation models of retinoid activity. *Skin Pharmacol.* **1996**, *8*, 292–299.
- 45 KOZAWA J., TOKUI Y., MORIKAWA M., OHMOTO H. L., YUAN M., ZHANG J., IWAHASHI H., IMAGAWA A., YAMAGATA K., TOCHINO Y., SHIMOMURA I., HIGASHIYAMA S., MIYAGAWA J., Regenerative and therapeutic effects of heparin-binding epidermal growth factor-like growth factor on diabetes by gene transduction through retrograde pancreatic duct injection of adenovirus vector. *Pancreas* **2005**, *31*, 32–42.
- 46 MIYAZAKI S., YAMATO E., MIYAZAKI J., Regulated expression of pdx-1 promotes *in vitro* differentiation of insulin-producing cells from embryonic stem cells. *Diabetes* **2004**, *53*, 1030–1037.
- 47 TANIGUCHI H., YAMATO E., TASHIRO F., IKEGAMI H., OGIHARA T., MIYAZAKI J.,  $\beta$  cell neogenesis induced by adenovirus-mediated gene delivery of transcription factor pdx-1 into mouse pancreas. *Gene Ther.* **2003**, *10*, 15–23.
- 48 YAMAGUCHI Y., NAGASAWA T., NAKAMURA N., KITAGAWA A., MATSUMOTO K., TAKENAGA M., MIZOGUCHI M., IGARASHI R., Optical treatment new tretinoin nanoparticles with inorganic-coating. *J. Dermatol.* **2006**, in press.
- 49 YAMAGUCHI Y., NAKAMURA N., NAGASAWA T., KITAGAWA A., MATSUMOTO K., SOMA Y., MATSUDA T., MIZOGUCHI M., IGARASHI R., Enhanced skin regeneration of all-trans retinoic acid by nanoegg<sup>TM</sup> formulation, *Die Pharmazie* **2006**, *61*, 117–121.

## 8

# Polymeric Nanomaterials – Synthesis, Functionalization and Applications in Diagnosis and Therapy

*Jutta Rieger, Christine Jérôme, Robert Jérôme, and Rachel Auzély-Velty*

### 8.1 Introduction

In the last decade, polymeric nanoparticles have received increasing interest both for drug delivery purposes and as diagnostic tools. The interest in nanoparticles as drug carriers relies on the difficulties met in drug delivery. In fact, after extravascular administration of a drug, its fate is determined by the combination of several processes, i.e. absorption, distribution, metabolism and elimination (ADME). In contrast, intravenous routes circumvent the absorption process as the drug is directly available in the blood circulation. Regardless of the administration route, each of these processes depends mainly on the physicochemical properties of the drug. Therefore, drug carrier systems have been developed that allow for controlling the fate of a drug within the patient. These “drug delivery systems” cannot only influence the absorption of a drug from the gastrointestinal tract, but they also permit governing of the drug distribution within the organism. In particular, nanoparticles have received increasing interest because of their ability to deliver a wide range of drugs (or diagnostic agents) to various organs or tissues for sustained periods of time. In this chapter, two applications of nanosized polymeric colloidal carrier systems are discussed together: their use as drug delivery systems and as diagnostic tools. Indeed, for both applications most of the required features and preparation techniques are similar, if not identical.

As a remark, polymer nanoparticles are considered here as submicron carriers in the nanometer range (diameter below 1  $\mu\text{m}$ ) mainly prepared from natural or synthetic polymers. This definition does not take into account the morphological and structural organization of the polymer. The term “nanosphere” is used to describe nanoparticles that are constituted by a solid “homogeneous” polymeric matrix. The delivery of the therapeutics proceeds either by the diffusion through the polymer matrix or, in the case of biodegradable particles, by the degradation of the latter, or by both processes. In contrast, “nanocapsules” are nanoparticles where a polymeric membrane surrounds a cavity filled by an oily or an aqueous content. They are therefore considered as a “reservoir” system, where the diffusion of the hydro-

philic or hydrophobic drug is controlled by the nature of the polymeric membrane. In this chapter, we focus on “frozen”, not dynamic systems, i.e. systems where an exchange between individual polymer chains and polymer chains of the nano-object cannot take place. Consequently, dynamic systems such as micelles as well as liposomes are barely considered in this review. However, in Section 8.4.3.4.1, several approaches based on so-called shell crosslinked knedel-like (SCK) nanoparticles are quoted. Such SCK nanoparticles are micelles, whose outer shell is crosslinked. They can be prepared in two steps, starting from the self-assembly of amphiphilic block copolymers to form micelles, of which the shell formed by the outer block is frozen by crosslinking in a second step [1].

Polymeric nanoparticles have now been the subject of numerous studies for more than 20 years and have progressed since then. Three generations of nanoparticles may be considered.

(i) *First-generation nanoparticles.* Nanoparticles with no specific surface properties have been called “nanoparticles of the first generation”. Indeed, whenever such kinds of nanoparticles are introduced in the human body, they are rapidly recognized as foreign bodies and, as a consequence, removed from the blood circulation. Once nanoparticles are introduced in a biological system, numerous plasma proteins adsorb at their surface, leading to the activation of the complement system. As a consequence, the colloidal drug carriers are rapidly recognized by macrophages of the mononuclear phagocyte system (MPS) and removed within seconds from the blood stream. Organs with high phagocytic activity are the liver, spleen and bone marrow. These organs possess a discontinuous, i.e. more permeable, endothelium, where the blood is directly in contact with the immune active macrophages. Therefore, nanoparticles of the first generation accumulate in and passively target the liver, spleen and bone marrow. This natural tendency to be captured by the MPS has therefore found application in the treatment of liver cancer and other liver-related diseases.

The protein adsorption on the nanoparticle surface, i.e. the key step to induce a cascade of biological processes leading to their elimination, is based on various interactions, but especially on interactions of hydrophobic domains of the proteins with hydrophobic domains present at the nanoparticle surface.

(ii) *Second-generation nanoparticles.* In order to target other organs than tissues with high phagocyte activity, further developments strove for avoiding the rapid adsorption of blood proteins, i.e. the activation of the complement system. This has been achieved by modifying the surface of the nanoparticles, especially by hydrophilic materials, in order to inhibit hydrophobic protein–particle interactions. The coating of the particle surface by hydrophilic chains leads to repulsion of proteins and consequently a prolonged residence time of the particles in the blood stream. These surface-modified nanoparticles are also called carriers of the “second generation”, or “Stealth™” nanoparticles, as they are designed to successfully avoid MPS sequestration. The hydrophilic polymers that have been used for the surface coating of nanoparticles are synthetic polymers, particularly poly(ethylene oxide) (PEO) [2, 3], but also polysaccharides, such as heparin [4, 5] and dextran [6].

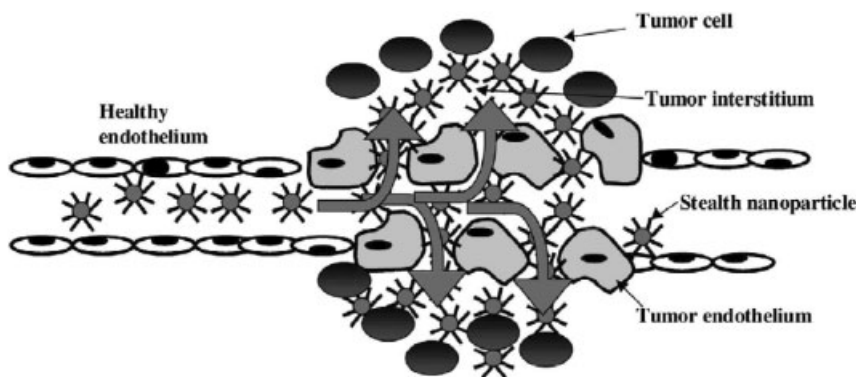


**Figure 8.1.** Extravasation of long-circulating (Stealth) nanoparticles in the tumor interstitium by passive diffusion or convection across the altered and hyperpermeable neoplastic endothelium.

These long-circulating colloidal systems have received much interest in the field of cancer diagnosis and treatment. Indeed, cancerous tissues are characterized by an “enhanced permeability and retention” effect [7] (Fig. 8.1). The phenomenon, that long-circulating colloidal systems are preferentially accumulated in cancerous tissues, is called “passive targeting”, and is used in numerous studies both for drug delivery purposes and diagnosis [8].

(iii) *Third-generation nanoparticles – active targeting.* It is possible to give carriers affinity to specific tissue by decorating their surface with targeting ligands. This kind of carrier delivers a drug specifically to its pharmacological site in the organism, and thus allows us to decrease the administered quantity of drugs and to minimize side-effects. Indeed, the latter are generally the result of the presence of the drug at other tissues than at the desired one.

Targeting ligands can be monoclonal antibodies, sugars, hormones, peptides (e.g. the tripeptide, arginine–glycine–aspartic acid (RGD) [9]), vitamins (e.g. biotin [10]) or other small organic molecules (e.g. folic acid [11]). Colloidal carriers, of which the surface is decorated with targeting moieties, are also called “nanoparticles of the third generation” and today most studies tend to design such nano-objects. Quite a lot of systems have already been patented. Targeting demands optimal interaction between a targeted site and its ligand. Therefore, targeting molecules have been fixed at the end of linker molecules, such as flexible PEO chains [10].

The surface functionalization of polymeric nanoparticles is thus the key point for both targeted drug delivery and diagnosis. Indeed, this chapter focuses mainly on nanoparticles of the third generation, i.e. surface-modified nanoparticles, designed for drug delivery and diagnosis. The objective of this chapter is to discuss (i) the different ways to obtain surface-modified nanoparticles, (ii) the biological molecules used for surface modification, and (iii) the current and future applications of such polymeric nanoparticles in the field of drug delivery and diagnosis. In line

with our subjects of research, we mainly report on nanospheres, rather than nanocapsules, and restrict the cited examples to approaches interesting for biomedical applications. Because of their importance for diagnosis purposes, we also report on nanoparticle composites composed of both polymer and inorganic materials (that serve as label/marker). However, metallic nanoparticles coated by polymer chains are not the subject of this chapter.

The chapter is divided into five main sections. Section 8.2 deals with polymeric materials used for the preparation of nano-sized carrier systems. In Section 8.3, the different techniques to obtain such systems are discussed. Section 8.4 describes how the surface of nanoparticles can be modified and briefly summarizes the most common techniques to characterize nanoparticle surfaces. Section 8.5 describes their application as drug delivery systems and diagnostics.

## 8.2

### Polymer Materials Used for the Synthesis of Nanoparticles

Depending on the route of administration (oral or parenteral) and the application of polymeric nanoparticles (drug carriers or diagnostic systems), the materials used to produce the colloidal systems meet different physiological and biological requirements. Among these requirements, biocompatibility and safety are of crucial importance.

Additionally, it must be considered whether bioerosion and/or biodegradation is desired or not. Although there is no universally accepted definition for the terms bioerosion and biodegradation, bioerosion refers to solubilization of an initially water-insoluble material with or without changes in the chemical structure, while biodegradation refers to solubilization that occurs as a consequence of cleavage of main-chain bonds. The prefix “bio” is used because the erosion or degradation takes place in a biological environment, either by biocatalytic processes (fungi, enzymes, etc.) or by chemical/radical processes (hydrolysis, oxidation, UV irradiation). Degradable synthetic polymers have great potential for drug delivery purposes. They are typically degraded by chemical hydrolysis, whereas the degradation of natural polymers (i.e. polymers derived from animal or plant sources) generally requires enzymes to catalyze the hydrolysis. On the other hand, polymers used for diagnosis purposes, especially in the case of *ex vivo* (*in vitro*) tests, should not be biodegradable; therefore, nondegradable, i.e. long-term stable polymers, which are often more easy to synthesize, are used. In that way, recycling and repeated use of the device are possible. Concerning synthetic biodegradable polymers, it must be noted that not only the polymer itself used for the formulation, but also the degradation products (metabolites) must be nontoxic, biocompatible and chemically inert. The practical consequence of that is that only a limited number of nontoxic, monomeric starting materials can be really applied for the development of biodegradable nanoparticles.

In the following, the main polymers used for the preparation of nanocarriers will be described. We distinguish three groups of polymers, i.e. (i) natural poly-



mers (“biopolymers”), (ii) synthetic polymers which are “degradable” by biological or chemical processes in the human body and (iii) “nondegradable” synthetic polymers.

### 8.2.1

#### Natural Polymers

Polysaccharides represent – besides polypeptides – the most important group of natural polymers [12]. We have chosen to focus here only on polysaccharides that display very interesting physicochemical properties, in terms of gelation characteristics, chelating properties and biological activity. Many polysaccharides show biocompatibility and biodegradability, which are the basic characteristics for using polymers as biomaterials, as reviewed by Dumitriu and coworkers [13]. Moreover, their physicochemical properties as well as their interactions with living medium can be altered by chemical modifications.

Several biocompatible polysaccharides such as chitosan, dextran, heparin and hyaluronic acid have been shown to be interesting candidates for the modification of nanoparticle surfaces. This allows, for instance, reducing nanoparticle uptake by the MPS and also, in some cases, conferring specific biological functions [14].

In addition, due to its polycationic nature, chitosan could be advantageously used as a constitutive core material of nanoparticles. This biopolymer is obtained by partial *N*-deacetylation of chitin – a natural polysaccharide found in crustacean shells. Chitosan consists of a linear chain of (1–4)-linked 2-amino-2-deoxy- $\beta$ -D-glucopyranose and 2-acetamido-2-deoxy- $\beta$ -D-glucopyranose units (Fig. 8.2). It is water-soluble in acidic conditions ( $\text{pH} < 6$ ) due to the existence of amino groups making it thus possible to prepare derivatives with optimized properties under homogeneous conditions. Its hydrophilicity allows covering the domain of applications in solution and in gel (after crosslinking by chemical or physical bonds). Due to its mucoadhesive properties, chitosan has been largely investigated for coating colloidal carriers administered to the gastrointestinal tract [15], or by nasal, ocular, buccal and vaginal routes. The strong mucoadhesion of chitosan can be explained by ionic interactions between this polycationic molecule and anionic substructures such as sialic moieties of the mucus gel layer on mucosa. Apart from its muco-

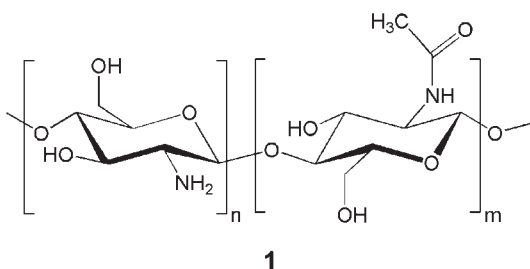


Figure 8.2. Chemical structure of chitosan.

adhesive properties, chitosan displays low toxicity, degradability by enzymes such as chitinase and lysozyme [13], anticoagulant properties, and antibacterial and antifungal action. It has also been demonstrated to be a promoter of wound healing in the field of surgery.

As mentioned above, taking advantage of the polycationic nature of chitosan, Alonso and coworkers [12, 16] developed chitosan nanoparticles based on ionic gelation of chitosan with sodium tripolyphosphate. The size, surface characteristics and *in vitro* release properties of these nanoparticles can be modulated by the preparation conditions and in particular by incorporation of an additional polymer such as a diblock copolymer of ethylene oxide and propylene oxide (PEO-*b*-PPO). The authors demonstrated that these nanoparticles have a great protein-loading capacity (protein loading up to 50%, i.e. 50 mg of protein per 100 mg of nanoparticles). Such drug-loaded chitosan-based nanocarriers have been mostly administered by mucosal routes (i.e. oral, nasal, ocular). Alonso and coworkers also investigated the nasal absorption of such chitosan nanoparticles loaded with insulin (via the glucose blood concentration) and, furthermore, studied the *in vitro* release profiles of hydrophilic drugs, such as anthracycline and doxorubicin [12], as well as of hydrophobic peptides such as cyclosporine A.

Furthermore, the polycationic character of chitosan makes it an interesting material for nonviral gene delivery. It forms polyelectrolyte complexes with the negatively charged DNA, condenses the DNA, which protects it from degradation by DNase [12, 17]. Nevertheless, the transfection rate of such chitosan-DNA complexes is very low. Therefore, more sophisticated DNA-loaded chitosan-based nanoparticles have been developed and shown to be promising gene delivery systems exhibiting better transfection rates [12].

Finally, the properties of chitosan have been modified by chemical modifications such as deacetylation, *N*-sulfation or modification by organic molecules (e.g. sugars etc.), which give rise to other applications. Very recently, polyelectrolyte complex nanoparticles have been prepared from self-complexation of amphoteric *N*-sulfated chitosan [18].

In contrast to topical (locally applied) application of chitosan-based formulations, the safety/toxicity of positively charged polysaccharides for systemic applications (e.g. intravenous administration) is currently controversial. Indeed, it has been reported that chitosan induces the opening of tight junctions between epithelial cells, enhancing their permeability [19, 20].

Exhaustive reviews on recent advances on chitosan-based micro/nanoparticles are given by several authors [21, 22].

Dextran is an  $\alpha$ -D-1,6-glucose-linked glucan with side-chains 1–3 or 1–4 linked to the backbone units (Fig. 8.3). The branches are mostly one or two glucose units long. This biopolymer can be obtained from fermentation of sucrose-containing media by *Leuconostoc mesenteroides* bacteria. The clinical use of dextran over the past 50 years provides impressive proof of its safety and quality. Dextran may be ingested orally and is well tolerated. Due to its biocompatibility and hydrophilicity, it is often utilized as a coating material for nanoparticles. Indeed, it has been demonstrated to display protein-repulsive properties and to decrease the uptake by the

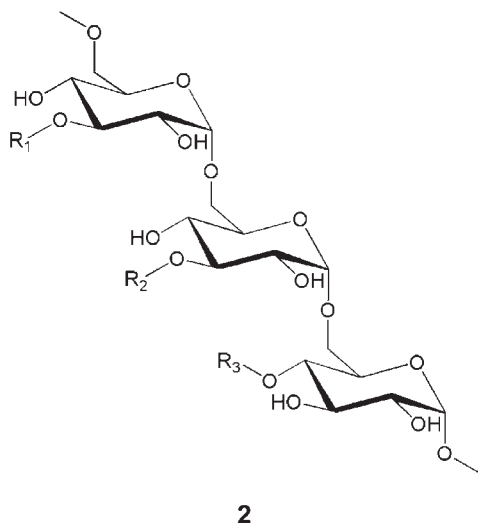


**Figure 8.3.** Chemical structure of dextran. R<sub>1</sub>, R<sub>2</sub> and R<sub>3</sub> are positions of branching.

MPS. Moreover, the dextran macromolecule presents a large number of reactive hydroxyl groups for chemical attachment of functional molecules. Many reactions characteristic for alcohol can be used; however, due to the presence of three hydroxyl groups per glucose residue in the backbone, such reactions are not selective.

Hyaluronic acid (HA) is a linear polysaccharide composed of a repeating disaccharide unit of *N*-acetyl-*D*-glucosamine and *D*-glucuronic acid, belonging to the glycosaminoglycan family (Fig. 8.4). It is a component of the synovial fluid, cartilage, vitreous humor and extracellular matrices [13, 23]. Protein interactions with HA play crucial roles in cell adhesion, cell mobility, inflammation, wound healing and cancer metastasis. Its carboxyl groups are mostly deprotonated at physiological pH, thus conferring a polyanionic character to the polymer. Similar to chitosan, the advantage of using HA as a surface modifier in the field of drug delivery/nanoparticles relies on its bioadhesive properties, which have been particularly ex-

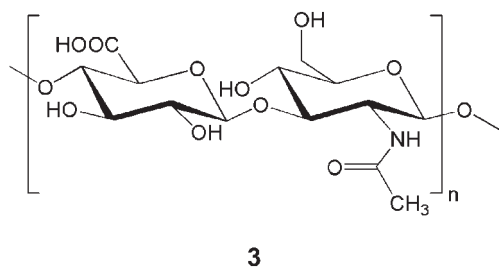


**Figure 8.4.** Repeating disaccharide units of HA.

ploited for ophthalmic applications. Indeed, as for other anionic polymers [e.g. poly(acrylic acid) (PAA)], it has been found that carboxylic groups are responsible for their adhesion to the mucus gel layer. Carboxylic acid moieties are supposed to form hydrogen bonds with hydroxyl groups of the oligosaccharide side-chains of mucus glycoproteins. It should also be emphasized, that the biological activity of HA depends on the molecular weight [24].

Chemically modified natural polymers have received increasing interest, and especially hybrid materials combining synthetic and natural polymers open up new possibilities and applications, combining the unique features of the different materials. As an example, poly( $\epsilon$ -caprolactone) (PCL)-grafted dextran copolymers (glycopolymers) have demonstrated amphiphilic properties, and have been used as emulsifiers and for the preparation of nanoparticles (by an emulsion-evaporation technique) [25].

### 8.2.2

#### Degradable Synthetic Polymers

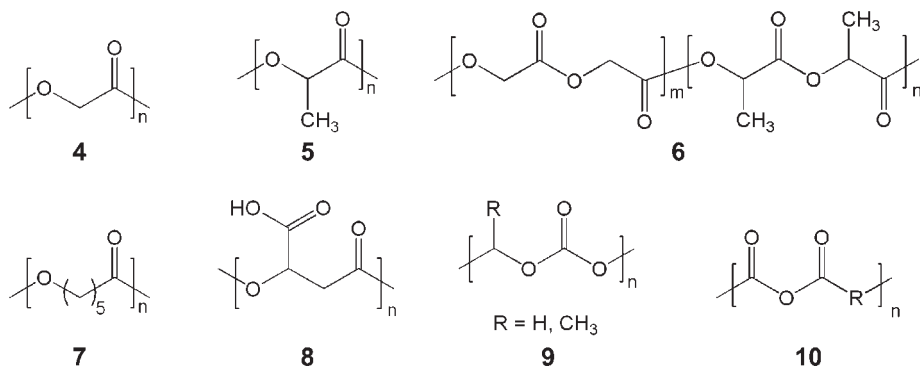
In contrast to natural polymers, of which the molecular weight and distribution depend on the fabrication and extraction procedure, synthetic polymers can be tailor-made. Their physical and chemical properties can be varied over a wide range, particularly by copolymerization with appropriate (functional) comonomers. Additionally, using controlled polymerization techniques, the macromolecular characteristics can be adjusted and narrow molecular weight distribution (PDI) can be reached, in contrast to most of the natural polymers. Furthermore, some synthetic polymers can be obtained in oil-in-water (o/w) emulsions, which makes the *in situ* synthesis of nanoparticles by emulsion-polymerization possible.

Fig. 8.5 presents the chemical structure of the main synthetic polymers used for the preparation of nanoparticles.

Domb and coworkers have given a complete review on “biodegradable polymers as drug carrier systems” [26]. The first and probably most important and frequently used groups of biodegradable polymers are linear polyesters. (Co)polyesters based on poly(lactic acid) [or poly(lactide) (PLA)], poly(glycolic acid) (PGA) and poly(lactide-*co*-glycolide) (PLGA) have been used for more than three decades for a variety of medical applications [26], and are considered as the best biomaterials with regard to design and performance. Indeed, they meet the biological requirements of safety and are biodegradable to nontoxic metabolites, and are approved by the Food and Drug Administration (FDA).

Since lactic acid contains an asymmetric  $\alpha$ -carbon atom, two different optical isomers exist, D- and L-lactic acid, that give rise to morphologically distinct polymers. The polymers derived from the optically active monomers, i.e. poly(D-lactide) [(P(D-LA))] and poly(L-lactide) [(P(L-LA))] are semicrystalline materials and exhibit identical physicochemical properties, whereas the racemic P(D,L-LA) is purely amorphous and has striking different properties. Furthermore, these racemic and semicrystalline polymers exhibit different degradation rates, as the (bio)degradation is dependent on the polymer crystallinity [27].

## (a) “Degradable” synthetic polymers



## (b) “Non degradable” synthetic polymers

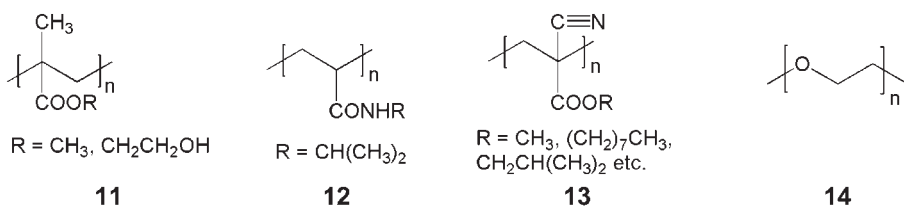


**Figure 8.5.** Chemical structure of (a) the main biodegradable synthetic polymers: (4) poly(glycolic acid), (5) poly(lactic acid), (6) poly(lactide-co-glycolide), (7) poly( $\epsilon$ -caprolactone), (8) poly(malic acid), (9) poly(ethylene carbonate) ( $R = \text{H}$ )/ poly(propylene carbonate) ( $R = \text{CH}_3$ ) and (10) poly(anhydride), and (b) the main

nondegradable synthetic polymers: (11) poly(methyl methacrylate) ( $R = \text{CH}_3$ )/ poly(hydroxyethyl methacrylate) ( $R = \text{CH}_2\text{CH}_2\text{OH}$ ), (12) poly(*N*-isopropylacrylamide), (13) poly(alkylcyanoacrylate) and (14) poly(ethylene oxide) used as core material for the preparation of polymeric nanoparticles.

However, apart from the morphological state of the macromolecule, the biodegradation of polymeric devices is affected by many other important factors such as the chemical stability of the hydrolytically sensitive groups in the polymer backbone, the hydrophilic/hydrophobic character of the repeating units, the initial molecular weight and the molecular weight distribution. The fabrication process, size, geometry (specifically the surface area to volume ratio) and porosity of the device also have a tremendous impact on the degradation rate as well as the environmental conditions [27]. Since the hydrolytic degradation is caused by the reaction of water with labile bonds, typically ester bonds in the polymer chain, the reaction rate is intimately connected with the ability of the polymer to absorb water. Thus, devices made of PGA erode faster than identical devices made of the more hydrophobic PLA, although the ester bonds have almost the same chemical reactivity toward water in both polymers. Furthermore, as mentioned above, although P(L-LA)

and P(<sub>D,L</sub>-LA) have chemically identical backbone structures and an identical degree of hydrophobicity, devices made of P(L-LA) tend to degrade much more slowly than identical devices made of P(<sub>D,L</sub>-LA). The slower rate of erosion of P(L-LA) is related to its semicrystalline morphology.

Vert and coworkers [28] demonstrated the complexity of PLA, PGA and PLGA degradation, and emphasized that the hydrolytic process depends on the size and morphology of the biomedical device. Although at first sight astonishing, it has been demonstrated that PLA microparticles degrade faster than PLA nanoparticles, and that this phenomenon relies on a diffusion mechanism [29]. Indeed, due to the large nanoparticle surface in relation to the volume, the acid (produced during the degradation) can easily diffuse out of the nanoparticle. On the contrary, within microparticles, the produced acid accumulates inside the particle as the diffusion is slower. This local decrease of the pH has an autocatalytic effect on the degradation process. Indeed, after the water uptake the polymer chains degrade in the core of the nanoparticles (corresponding to a decrease of the molecular weight), and only afterwards appears weight loss of the material due to the diffusion of the degraded polymer chains out of the bulky material.

Another example of a polyester is PCL, which is widely used in the field in biomaterials. This polymer is semicrystalline, more hydrophobic than PLA and PLGA, and hence is characterized by a slower (bio)degradation.

Furthermore, other biodegradable polyesters derived from naturally occurring, multifunctional hydroxy acids and amino acids, such as malic acid and aspartic acid, have been investigated by Lenz and Guerin [30]. Poly(malic acid) is biocompatible and degradable, and water-soluble in contrast to PLA and PCL. Biocompatibility tests indicated that poly( $\beta$ -malic acid) is nontoxic and nonimmunogenic [31].

Due to the fact that most of these polyesters lack functional groups, efforts have been made to prepare biodegradable aliphatic polyesters bearing functional groups available for further modification. Such copolymers can be reached by copolymerization of novel functional monomers with conventional ones [32–36]. Their features are affected by the comonomer compositions, the polymer architecture, and the molecular weight. Copolymers have thus been synthesized in order to adjust degradation rates as well as mechanical properties. For instance, PEO-*b*-PLA block copolymers have been synthesized and used to prepare nanoparticles showing a faster degradation with respect to plain PLA nanoparticles. Indeed, the introduction of a hydrophilic polymer (PEO) favors hydration of the polyester nanoparticles, which is the key requirement for the hydrolytic degradation to take place as explained above. For the same reason, the ester functions next to the PEO segment degrade first and the PEO chains are lost rapidly.

In addition, polycarbonates, such as poly(ethylene carbonate) and poly(propylene carbonate) have been explored in the design of new polyester-related structures for the preparation of nanoparticles for drug delivery. For instance, they have been tested as biodegradable carriers for the delivery of 5-fluorouracil [37] and were found to be degraded enzymatically [38].

In addition to natural proteins, synthetic (co)poly(amides), such as poly(lysine) and poly(glutamic acids), have also been studied as drug carriers [39].

As well as the described groups of biodegradable polymers, there are a lot of other classes of biodegradable polymers used for biomaterials, such as poly(anhydrides), poly(phosphate esters), poly(phosphazenes) and poly(orthoesters). An exhaustive overview on their properties, synthesis, degradation characteristics, biocompatibility and toxicity is beyond the scope of this work, and may be found in the literature [26].

### 8.2.3

#### Nondegradable Synthetic Polymers

Polymers made of acrylic or vinylic monomers constitute an important group of nondegradable materials used for the preparation of “biostable” polymeric nanoparticles. The interest of these materials relies mainly on the ease of preparation and the availability of functional groups.

Poly(alkylcyanoacrylate) (PACA) represents an intermediate class between the synthetic biodegradable and nonbiodegradable polymers [40]; indeed, it has been shown that PACA particles are degraded by a surface erosion process [41], through enzymatic hydrolysis of the ester side-chains of the polymer. The polymer chains are therefore degraded to hydrophilic compounds and the rate of elimination is dependent of the length of the nondegradable alkyl chain [42]. It was demonstrated that materials based on PACA are well tolerated *in vivo*.

Finally, we would like to emphasize, that stimuli responsive polymers, such as poly(*N*-isopropylacrylamide) (PNIPAAm), are promising materials for the preparation of stimuli responsive colloidal carrier systems. Despite the importance of this group of materials, we are not able to discuss the materials used for nanoparticles in this chapter. There are a lot of reviews on this subject [43, 44] (see also Sections 8.5.1.3 and 8.5.2.3).

### 8.2.4

#### PEO

This section is dedicated to PEO because of its importance and frequency of use for biomaterials and, especially, nanoparticles. PEO is a hydrophilic, neutral, very flexible polymer, which is widely used for the surface modification of nanoparticles. It is FDA approved and quite an important number of PEO–drug conjugates are on the market for intravenous administration. PEO is nonbiodegradable but, due to its hydrophilicity, bioeliminable whenever its molecular weight is less than 20 000 g mol<sup>-1</sup> [45].

The mechanisms of PEO–protein interactions are reported in the review by Vermette and coworkers [46]. Briefly, the protein repellence of PEO coatings has been associated to “steric repulsion” and/or “hydration”/“water structuring” of the chains. The flexibility of these PEO chains, which is particularly high in comparison to other hydrophilic polymers, is one explanation for its protein-repulsive, antifouling properties. Indeed, the reason for its flexibility must be found in the

easy rotation of the ether bonds and in the absence of any bulky substituent on the PEO skeleton. The rapid and transitory change of the conformation of PEO chains is probably responsible for the poor interaction of the PEO chain with proteins. In addition, whenever a protein or another surface approaches with sufficient kinetic energy, PEO chains forming a dense brush at a surface will be compressed by the collision. This will increase the local concentration of polymer segments (corresponding to a loss of entropy of the PEO chains), enhancing the free energy and inducing the repulsion of the protein from the surface [46]. The interaction energy is thus repulsive.

A lot of works tried to understand the influence of the density and length of PEO chains at surfaces on its protein-repulsive properties. The conformation of the PEO chains changes when the distance  $D$  that separates two neighboring PEO chains tethered at the surface becomes close to or smaller than the radius of gyration of the polymer ( $R_g$ ) (Fig. 8.6). In good solvents for PEO such as water, the polymer chains form “mushroom”-like structures at long distances ( $D \gg R_g$ ), as illustrated in Fig. 8.6(A) and (B), in poor solvents flat “pancake”-like structures are expected. With decreasing distance ( $D \sim R_g$ ), the chains start to interact with each other and approach the mushroom to brush transition (Fig. 8.6(C) and (D)). For  $D < R_g$ , the polymer chains strongly interact and in order to minimize the contact between them they stretch away from the surface, forming the so-called “brush” conformation [46]. It is thus clear that one of the most important parameters in determining the protein adsorption onto PEO layers is the grafting density of the PEO chains. It

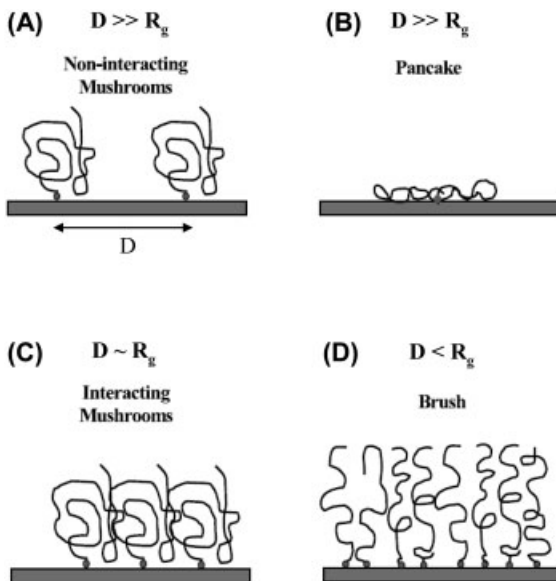


Figure 8.6. Schematic representation of polymer (PEO) structures at the interface.



has been reported that a distance  $d$  of 1.5 nm between two terminally attached PEO chains at the nanoparticle surface was found ideal for reducing protein adsorption. In addition, it has been demonstrated that rather long PEO chains (a molecular weight of 2000–5000 g mol<sup>-1</sup> has been proposed as ideal molecular weight earlier [47–49]) are not necessarily a prerequisite for low protein adsorption [46].

These are the reasons why PEO is the polymer of choice for the design of nanoparticles of the second generation and third generation.

### 8.3

#### Preparation of Polymeric Nanoparticles

In the last decades, several techniques have been developed to prepare colloidal carrier systems from polymeric materials. These can be obtained either (i) by association of preformed polymers (natural, modified natural or synthetic polymers, see Section 8.2) using techniques, such as emulsion-evaporation, emulsion-diffusion and salting-out, or (ii) by (mini)emulsion or micellar polymerization of polymerizable monomers dispersed in an aqueous phase. The preparation technique must be suitable for the material with regard to solubility and stability of the polymer. In the case of emulsion polymerization, the availability of monomers polymerizable in o/w emulsion is the limiting factor.

#### 8.3.1

##### Preparation of Nanospheres from Preformed Polymers

The use of preformed polymers for the preparation of nanospheres has several advantages, such as the availability of a large variety of materials with controlled and optimized macromolecular characteristics (molecular weight and polydispersity), as well as suitable physicochemical and biological properties. Indeed, in order to favor reproducibility, colloidal carriers must be synthesized from well-defined macromolecular materials. A large number of reviews are available describing in detail the different techniques to obtain colloidal carriers (e.g. Ref. [50]). In the following, we briefly discuss the most popular methods to obtain nanospheres from preformed polymers, i.e. emulsion-evaporation, emulsion-diffusion, salting-out and nanoprecipitation.

Polymers that are insoluble in water are generally used for the formation of dispersed colloidal systems in aqueous media. Thus, organic solvents are often required to dissolve the polymers – the first step to nanoparticle formation. Depending on the preparation procedure described in the following sections, the organic solvents used are either miscible or immiscible with water.

##### 8.3.1.1 Emulsion-evaporation

Organic volatile solvents, such as chloroform and dichloromethane that are poorly miscible or immiscible with water, are suitable for the emulsion-evaporation tech-

nique, patented by Vanderhoff and coworkers [51]. First, the polymer is dissolved in the organic solvent and tiny solvent droplets are formed by emulsification in an aqueous phase containing an emulsifier [e.g. poly(vinyl alcohol) (PVA) or albumin]. Then, the crude o/w emulsion is exposed to a high-energy source, such as ultrasonic devices or homogenizers, etc. [50], and, finally, stable solid nanoparticles are formed from the emulsion droplets by slight evaporation of the organic solvent (under reduced pressure). During the evaporation process, the organic solvent diffuses from the inner core of the droplets to the external phase, maintaining a saturation of the water phase by the organic solvent. The progressive elimination of the solvents induces the precipitation of the polymer and the nanoparticles formation. The size of the droplets and also the nanoparticles can be adjusted by the nature and quantity of emulsifier, the viscosity of the dispersing phase, and stirring rate. Unfortunately, this method requires the use of large quantities of surfactants (e.g. ranging from 0.5 to 8 wt% for PVA [50]) and high energy to form stable homogeneous emulsions. When ultrasonication is used instead of high-speed homogenizers, only very polydisperse nanosuspensions could be obtained. Only hydrophobic drugs can be efficiently encapsulated, by this o/w process. As far as hydrophilic drugs are concerned, a double-emulsion (w/o/w) technique has been developed in order to obtain nanospheres of hydrophobic polymer (such as PLGA) loaded by hydrophilic biomolecules, such as proteins [52]. Therefore, an inverse w/o emulsion is first prepared from an aqueous phase, containing the hydrophilic drug, and the organic phase, containing the matrix building polymer. Then this emulsion is emulsified in a second surfactant-containing aqueous phase to form the w/o/w emulsion. Finally, the organic solvent is removed by evaporation at reduced pressure.

#### 8.3.1.2 Salting-out

Solvent immiscibility and polymer precipitation can be induced through changes in temperature, pH or the addition of alcohol, but also by the addition of large quantities of salt ("salting-out"). The principle of the salting-out method [53] is to saturate the aqueous phase by electrolytes in order to reduce drastically the miscibility of the organic solvent (normally water miscible) with the aqueous phase. First, an o/w emulsion is formed between the organic phase and the surfactant [e.g. PVA, hydroxyethylcellulose or poly(vinyl pyrrolidone) (PVP)]-containing aqueous phase, which was previously saturated by the salt. Then, distilled water is added in such an amount that the total quantity of the organic solvent becomes miscible with the aqueous phase. As a result, the organic solvent diffuses into the aqueous phase, leading to the precipitation of the polymer as nanospheres. Several factors, such as stirring rate and polymer concentration, have been reported to influence the mean size of the nanoparticles. The salt is generally removed by cross-flow ultrafiltration/dialysis. This methodology allows using organic solvents of low toxicity (generally acetone) and which can be easily removed at the end of the preparation process by ultrafiltration or evaporation. However, the use of large amount of surfactants and electrolytes is necessary.

### 8.3.1.3 Emulsification-diffusion

The emulsification-diffusion method can be considered as a modification of the salting-out procedure, avoiding the use of salts and hence intensive purification steps [54]. Before dissolution of the polymer, the partially water-miscible organic solvent (ethyl acetate, propylene carbonate, benzyl alcohol) is saturated in water to ensure the thermodynamic equilibrium of both liquids. Then, the polymer solution is emulsified (o/w emulsion) under vigorous stirring in an aqueous solution containing a stabilizer (e.g. PVA or poloxamers, i.e. a series of copolymers composed of two PEO blocks separated by a PPO block). The subsequent addition of water to the system causes the diffusion of the organic solvent to the external aqueous phase, resulting in the formation of nanoparticles. Finally, the organic solvent is removed, depending on its boiling point, either by evaporation or crossflow ultrafiltration. The size of the nanoparticles depends on numerous factors, such as the concentration of the stabilizer (emulsifier), as well as the nature of the polymer and the stirring rate [55].

This method is only efficient for the encapsulation of lipophilic drugs. In addition, it requires the removal of large volumes of water due to the dilution-induced diffusion process. However, the advantages of this approach rely on its good reproducibility and high loading efficiencies.

### 8.3.1.4 Nanoprecipitation

Fessi and coworkers [56] described and patented a simple technique to obtain polymeric nanoparticles which does not require the preliminary formation of an emulsion. It relies on the use of organic solvents that are perfectly miscible with water, such as acetone, ethanol or dimethyl sulfoxide (DMSO). Furthermore, the polymer must be insoluble in the aqueous phase, but also in the mixture of both phases. This method is called the “nanoprecipitation” or “solvent displacement” technique.

Thus, the organic polymer solution is added drop-by-drop into a large volume of an aqueous phase, typically containing a surfactant (e.g. PVA, Poloxamer®). Under these conditions, the nanoparticles are formed instantaneously by the precipitation of the polymer induced by the diffusion of the organic solvent in the aqueous phase. Depending on its boiling point, the organic solvent is then eliminated by evaporation or dialysis. This technique has been modified and adjusted by various research groups [57, 58]. Polymer precipitation has also been induced by gentle progressive diffusion of water to an organic polymer solution placed in a tube of dialysis membranes [59]. The size of the nanoparticles obtained by nanoprecipitation processes is typically about 200 nm depending on the nature, miscibility and viscosity of the solvent, the polymer and its concentration in the organic solvent, and the preparation conditions.

This technique is especially interesting because of its low energy consumption and very simple handling.

As described above, most of these techniques require the use of surfactant in the aqueous phase, i.e. amphiphilic polymers such as PVA or triblock copolymers of

PEO and PPO (PEO-*b*-PPO-*b*-PEO, known as poloxamers) that exhibit interfacial activity, to guarantee the stability of the colloidal dispersions.

### 8.3.2

#### Synthesis of Nanospheres by *In Situ* Polymerization

In contrast to the techniques described above, where preformed polymers are used, nanoparticles can also be synthesized by polymerization of suitable monomers in (mini)emulsion [60, 61] or dispersion. Emulsion polymerizations employ water-insoluble monomers that are emulsified as micron-sized oil droplets (1–10  $\mu\text{m}$ ) in an aqueous phase stabilized by a surfactant. The initiators used in emulsion polymerizations are generally water-soluble and dissolved in the aqueous phase. Most emulsion polymerizations use a radical polymerization method. The drawback of such (macro)emulsion polymerizations is that the size of the latex particle does not correspond to the primary emulsion droplets, but rather depends on polymerization kinetic parameters. Miniemulsion polymerizations (Fig. 8.7) are a special class of emulsion polymerizations. They have many similarities, but the particle nucleation and reagent transport phenomena are different. In fact, miniemulsions consist of two immiscible liquids, a surfactant and a special cosurfactant (additive) that is only soluble in the dispersed phase. They are prepared by high-shear treatment of these mixtures, either by ultrasound or by a high-pressure microfluidizer and contain stable nanodroplets with a diameter of 30–300 nm.

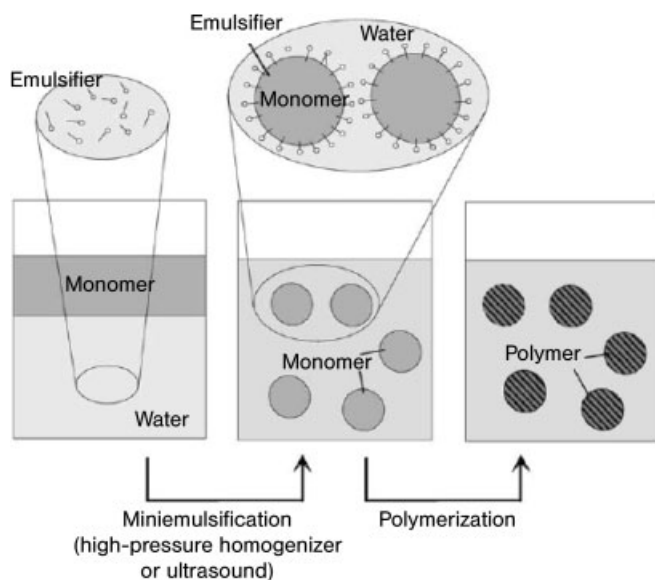


Figure 8.7. The principle of miniemulsion polymerization.

The combination of the two surfactants makes the droplets extremely stable, inhibiting the diffusion of monomers out of the miniemulsion droplets and preventing their coalescence [60]. The size of the polymer nanoparticles corresponds thus to that of the initially formed nanodroplets, which is controlled by the shear and the stabilizer system, and not [as for the (macro)emulsion] by the polymerization parameters. The active compound (drug) is generally incorporated in the dispersed phase, and therefore encapsulated in the nanoparticles during the polymerization process. More seldom, it is adsorbed onto the surface of preformed nanoparticles (after the polymerization).

Nanoparticles made of PNIPAAm, poly(*N*-vinylacetamide) (PNVA), poly(vinylamine) (PVAm) and poly(methacrylic acid) (PMAA) have been prepared according to this methodology. The corresponding vinylic and (meth)acrylic monomers are generally polymerized under free radical conditions using, for instance 2,2'-azobisisobutyronitrile (AIBN) as an initiator [62].

New processes based on the miniemulsion concept use amphiphilic polymers both as emulsifiers and surface modifiers of the final nanoparticles. For instance, the radical polymerization of styrene has been carried out in miniemulsions stabilized by amphiphilic derivatives of dextran [63]. The size of the polysaccharide-coated polystyrene particles was directly correlated to that of the initial nanodroplet and depended on the monomer concentration. The use of functional emulsifiers as surface modifiers is discussed in detail in Section 8.4.3.3.

Furthermore, other polymerization systems have also been used to prepare polymeric particles, such as dispersion or suspension polymerization. In the suspension polymerization process, the initiator is soluble in the monomer and larger particles (above 1  $\mu\text{m}$ ) are obtained.

In addition, dispersion polymerizations have been rediscovered in recent years for the preparation of (sub)micron-size polymer particles with narrow size distributions. This process differs notably from emulsion and suspension polymerization as it starts with a homogeneous solution of monomer(s), stabilizer(s) and initiator in a mostly organic solvent. The polymer precipitates as a colloidal dispersion during the polymerization process. As an interesting example, polystyrene core glycopolymer corona nanospheres have been obtained by free radical copolymerization of hydrophilic macromonomers and styrene (as hydrophobic comonomer) in dispersion in a polar solvent (e.g. ethanol/water mixture) [64–66] (details see Section 8.4.3.3).

One of the advantages of emulsion polymerization for the preparation of polymeric nanoparticles is its reproducibility regarding size and drug-loading rate, even at a semi-industrial level. On the other hand, the disadvantages of this approach are the possibility of residual emulsifiers, monomers, but also oligomers, and the risk of drug interaction (with the reactives) during polymerization and thus inactivation.

### 8.3.3

#### Preparation of Nanocapsules

As mentioned in the Introduction (Section 8.1), nanocapsules are built of an oily or sometimes aqueous core, surrounded by a thin polymeric wall. Similar to nano-

spheres, nanocapsules can be obtained from either preformed polymers or by (interfacial) polymerization of monomers at the oil–water interface. The main techniques for the synthesis of nanocapsules rely on the use of a water-miscible organic solvent, solubilizing the polymer or monomer, and the insolubility of them in both the oil and the aqueous phase. The miscibility of the organic solvent is thus the driving force for the diffusion of the polymer (or monomer) to the water–oil interface [67, 68].

In general, the polymer or monomer is first dissolved in the organic phase (consisting of the oil and a water-miscible organic solvent). Then, upon addition of the organic phase to the aqueous phase (containing a hydrosoluble surfactant), the polymer/monomer diffuses with the water-miscible organic solvent and is stranded at the interface between oil and water. As an example for interfacial polymerization, the polymerization of alkylcyanoacrylate has been initiated at the oil–water interface by hydroxyl ions present in the aqueous phase, leading to the formation of nanocapsules [69].

It should be mentioned that colloidal capsules can also be prepared by the layer-by-layer approach. This technique is based on the self-assembly of two oppositely charged species by electrostatic interactions [70, 71]. In general, the capsule wall is formed by alternating deposition of a two oppositely charged polyelectrolytes on a template core, which can be removed at the end of the process e.g. by dissolution. However, the size of the as-prepared capsules is generally in the micrometer-scale (1–5  $\mu\text{m}$ ) rather than in the nanoscale [72, 73].

One of the advantages of nanocapsules over nanospheres is their low polymer content and a high loading capacity for lipophilic drugs. The percentage of encapsulation is generally related to the solubility of the drug in the core phase [74].

## 8.4

### Surface Functionalization

The surface characteristics of nanoparticles are of fundamental importance for their interaction with the environment, i.e. with living medium. In the last decade, numerous surface-modified carrier systems have thus been developed allowing the targeting of specific tissues. Polymeric materials functionalized with targeting moieties, such as sugars [75], peptides [76], folic acid [77] and antibodies [78], have received considerable interest as means to generate intelligent delivery vehicles capable of (polyvalent) specific binding interactions.

#### 8.4.1

##### Functionalization with Biological (Macro)molecules

The first group of bioactive molecules considered here interacts nonspecifically with tissues. Among them, polysaccharides are of great interest, especially to confer to nanoparticles bioadhesive or mucoadhesive properties (*cf.* Section 8.2). Therefore, nanoparticles have been surface-coated by polysaccharides, such as chi-

tosan [19] and HA [14]. It could be demonstrated that nanoparticles coated by such bioadhesive polymers, especially HA, significantly increased the ocular drug availability [79].

To overcome the fast capture of nanoparticles by the MPS, nanoparticles have been coated with dextran and heparin. Such nanoparticles circulate for an enhanced period of time in the blood stream. The polysaccharide shell probably avoided complement activation and opsonization of the nanoparticles by preventing protein adsorption [80, 81]. Aside from being long circulating, heparin-coated nanoparticles showed antithrombic activity [81].

In the 1980s, a tripeptide, RGD, was identified to promote cell attachment [9]. Consequently, RGD peptides have been attached on the surface of polystyrene nanoparticles. These nanoparticles have been shown to induce a 50-fold increase in transport across the human intestine epithelial cells compared to blank polystyrene nanoparticles [82, 83]. It has also been demonstrated that a number of RGD peptides and peptidomimetics bind preferentially to a particular integrin  $\alpha_v\beta_3$ , which is often overexpressed on endothelial cells in tumor neovasculature [84]. A cyclic peptide with the RGD sequence has thus been covalently attached to the surface of doxorubicin-loaded nanoparticles and it was shown that they were preferentially internalized in tumoral tissues compared to other organs, such as the liver or the spleen [85].

#### 8.4.2

#### **Functionalization with Specific Ligands: Specific Interaction through Biological Recognition**

One of the greatest challenges is to find the optimal vector molecules or ligand to transport nanoparticles specifically to the targeted tissue. The strategy relies on the ability of the targeting agents or ligands to bind specifically to cell surface receptors triggering receptor endocytosis. The following will describe some examples of these ligands identified and used up to now for the functionalization of nanoparticles.

##### 8.4.2.1 Mono- or Oligosaccharides (Carbohydrates)

As well documented in the literature [86–88], cell surface carbohydrates from glycoproteins and glycolipids play an essential role as recognition sites between cells or cells and microorganisms. These recognition mechanisms are essentially based on specific interactions between the oligosaccharide chains and soluble or membrane proteins called lectins. The communication network based on carbohydrate–protein interactions is crucial in a large variety of important biological phenomena such as cell growth, inflammation, cancer, viral and bacterial infections.

Taking advantage of these specific carbohydrate–lectin interactions, numerous glycomimetics have been developed for analytical, diagnostic and therapeutic purposes. In particular, sugar-mediated drug delivery allows targeting cells that possess glycoreceptors on their plasma membrane. Such a mode of drug delivery is considered as one of the most promising routes in cell-specific targeting. Indeed,

membrane lectins of some cell types are able to internalize their ligands and hence the glycoconjugates that are specifically recognized by these lectins can be used as efficient carriers of drugs [89]. In particular dendritic cells of the human blood express cell surface mannose-specific lectins, i.e. specific receptors for mannose (mannose receptors) [90, 91]. In fact, these cells capture, process and present antigens to native T cells, inducing the cellular immune response [92, 93]. The possibility to target specifically dendritic cells thus makes mannose-coated nanoparticles attractive delivery systems for vaccines (see Section 8.5.1.2). Apart from this potential application, mannose-coated nanoparticles have been designed to target specifically Gram-negative bacteria, exposing mannose receptors at their surface. They could be used as carriers for antibacterial drugs [94].

In contrast to mannose, galactose interacts with hepatic cells via a Gal/GalNAc-binding mammalian lectin. Galactose conjugates have thus been synthesized, which have been used to carry antiparasitic [95] and antiviral drugs [96] specifically to liver cells. For the same purpose, polymeric nanoparticles decorated with galactose [97, 98], have been synthesized for hepatocyte-specific targeting.

It should be noted that the binding of a particular sugar to its glycoreceptor occurs in a regioselective manner [87] and thus the introduction of saccharidic ligands on polymers is generally performed by 1-*O* substitution of the sugar. Furthermore, it has been emphasized that sugar–lectin interactions depend on the “density” of the partners at a surface. Indeed, their affinity can be enhanced by multiple interactions between the binding proteins and the carbohydrate ligands, which is known as the glycoside cluster effect [99].

#### 8.4.2.2 Folate Receptor

All cells require folic acid as a vitamin for essential functions. They are thus equipped with several pathways for folate internalization. Folate conjugates were shown to enter cells only via the “alternative route”, i.e. via the folate receptor. This cell surface receptor is only expressed in measurable quantities on activated macrophages and at the apical surface of some polarized epithelia. In addition, the folate receptor is significantly overexpressed on the surface of many cancer cells because they require more extensive folic acid to enable their rapid proliferation. The folate receptor is thus a possible target for a number of types of cancer. Their localization on activated macrophages, but not on their quiescent or resting counterparts, makes folate conjugates promising in targeting inflammatory and autoimmune diseases because those specific macrophages cause or contribute to these diseases.

It has been shown that folate-targeted delivery cannot only enhance the drug uptake in the targeted pathologic cells, but can also reduce the drug deposition into nonpathologic cells, thereby diminishing collateral toxicity to normal tissues. This is due to the high specificity of folate for its receptors combined with the high stability of the folate-receptor complex ( $K_d \sim 10^{-10}$ ). Consequently, such conjugates can be administered at very low (nontoxic) concentrations and still achieve a clinical response [100].

Similar to the uptake of the free vitamin, folate conjugates are taken up into cells



via folate receptor-mediated endocytosis and released into the cytosol. Since folic acid is taken into cells to favor their proliferation, they are thus not delivered to lysosomes for destruction. In contrast to that, other ligands are destroyed in the latter in order to prevent continuous signalization of the cells. This feature is important when macromolecular or hydrolytically sensitive drugs have to be delivered, since most of them are inactivated by the lytic enzymes that are concentrated in lysosomes. A lot of studies on targeted drug delivery are thus based on the functionalization of nanoparticles by folic acid [11, 101–103].

#### 8.4.2.3 Antibodies

Apart from ligand–receptor interactions, antigen–antibody interactions are highly specific molecular recognition processes and thus promising tools for specific targeted delivery. In fact, with the advent of monoclonal antibody technology, the utilization of antibodies increased dramatically. Monoclonal immunoglobulin G antibodies represent today a promising groups of vector molecules to transport a colloidal carrier system very specifically to the target tissue. In particular, in the field of cancer, monoclonal antibodies have been shown to be able to bind to specific tumor antigens. The ideal antigen should be expressed on all tumor cells, but not expressed on critical host cells. To date, a remarkable number of antibodies that are specific to a certain cancer type have been identified and approved by the FDA.

Unlike folic acid, which is chemically very stable (e.g. to organic solvents, acids and bases), antibodies are sensitive biomolecules and thus their introduction on the surface of nanoparticles requires the use of mild chemical ligation reactions. Apart from the interest for targeted drug delivery, antibody-decorated nanoparticles are useful tools for clinical analysis by immunoassays and medical diagnostics [104].

#### 8.4.2.4 Biotin

Finally, biotin (vitamin H), a small organic biomolecule, is widely used as a versatile linker molecule to which a large variety of functional moieties can be bound via a biotin–avidin complex. Actually, biotin is known to form very stable complexes with its tetravalent ligand, avidin. The avidin–biotin complex is known as one of the strongest noncovalent biological interactions (association constant  $K_a = 10^{15} \text{ M}^{-1}$ ). In addition, a large variety of biotinylated targeting ligands are commercially available and they can be attached to the surface of biotin-coated nanoparticles via biotin–avidin–biotin complexes (Fig. 8.8) [10].

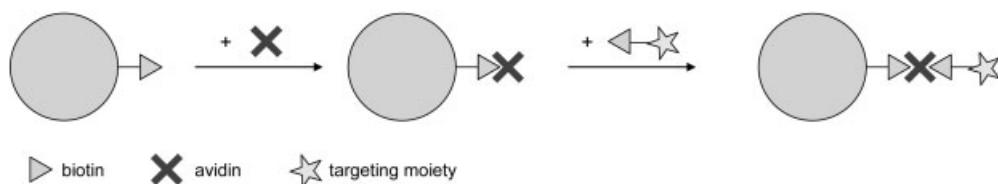
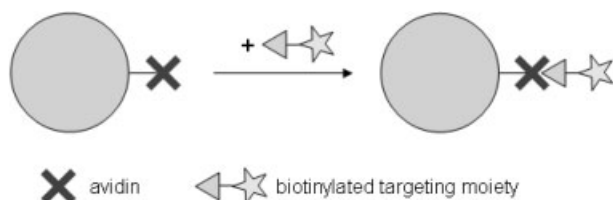


Figure 8.8. Surface functionalization via biotin–avidin–biotin complex formation.



**Figure 8.9.** Surface functionalization of avidin-bearing nanoparticles with biotinylated molecules.

Indeed, after complex formation with one of the sites of avidin, the residual three binding sites of avidin are still available for the binding of biotin conjugates. A very versatile tool for surface modification was thus made available. It is, however, questionable whether the stability of colloidal dispersions of such nanoparticles may be maintained after the addition of avidin, as interparticular cross-linking via free avidin binding sites might take place.

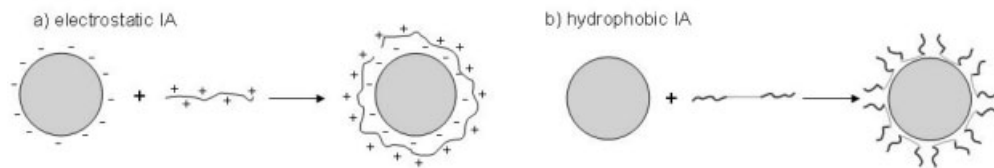
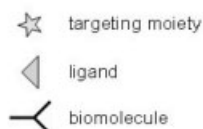
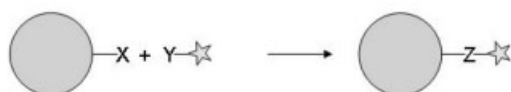
To avoid this problem, it might be advantageously to attach avidin (NeutrAvidin) directly in a covalent manner to the surface of nanoparticles (Fig. 8.9). This has been developed in the work of Balthasar and coworkers (see Section 8.4.3.4.2) who prepared antibody-decorated crosslinked gelatin nanoparticles as drug carriers for the specific targeting of T lymphocytes (using biotinylated anti-CD3 antibodies).

### 8.4.3

#### Strategies for Surface Modification

Surface functionalization of nanoparticles can be achieved by various approaches. In general, the posterior attachment of bioactive molecules on the surface of preformed nanoparticles may be achieved by (i) noncovalent interaction, (ii) specific complex formation and (iii) covalent linking of the targeting moieties to the nanoparticles by chemical reactions (Fig. 8.10).

These different strategies are closely connected with each other and often combined. As mentioned above, complexing molecules such as avidin have first been covalently coupled to the nanoparticle surface before the desired biotinylated targeting moiety could be attached to the surface by avidin–biotin complex formation [102]. Figure 8.10 makes it clear that the crucial condition for successful attaching targeting moieties at the nanoparticle surface is the presence of “reactive sites”, such as (i) charges, (ii) biomolecules and (iii) reactive groups, at surface of the nanoparticles. They can be introduced by different ways: by adsorption of reactive molecules on the surface of preformed nanoparticles, by preparing nanospheres from preformed polymers in the presence of “functional surfactants”, or by *in situ* emulsion polymerization using functional surfactants/emulsifiers or functional monomers or functional initiators. It should be noted that these techniques can also be used to directly modify the surface by bioactive targeting probes. Therefore, the synthesis of hybrid materials, i.e. materials containing both the biologically

**(i) Unspecific non-covalent interactions (IA)****(ii) Complex formation****(iii) Chemical reactions**

**Figure 8.10.** Different strategies for the conjugation of targeting moieties to nanoparticles. (i) Unspecific noncovalent interactions, adsorption of functional molecules by (a) electrostatic and (b) hydrophobic interactions. (ii) Complex formation. (iii) Covalent linking by chemical reactions.

active molecules and synthetic (polymeric) components, is often required. In this context, a major problem is maintaining the biomolecule–nanoparticle conjugates bioactive and to ensure the bioavailability of the bioactive entity. For this purpose, hydrophilic spacer molecules, such as PEO chains [10], have often been introduced between the surface and the biological ligand, thereby allowing the accessibility of the biomolecule and its interaction. Furthermore, the conjugation reactions must be carried out under mild, nondegrading reaction conditions.

The different strategies to achieve surface modifications of nanoparticles as well as the chemistry used to reach biomolecule–nanoparticle conjugates are detailed in the following sections. Finally, “molecular imprinting” of the surface of nanoparticles using template molecules is also discussed as a promising approach to modify the surface of nanoparticles.

#### 8.4.3.1 Adsorption on Preformed Nanoparticles

Polymer adsorption on solid–liquid interfaces is a widely studied phenomenon connected with many important processes such as colloidal stabilization, flocculation, adhesion and coating [105]. Based on this concept, several works report on the adsorption of functional molecules on preformed nanoparticles [106]. The driving force for physisorption to happen is the affinity of at least part of the molecule to the nanoparticle surface.

Two kinds of adsorption should be distinguished: (i) the adsorption of polyelectrolytes or charged molecules onto oppositely charged nanoparticles and (ii) the adsorption of hydrophobic or hydrophobically modified (macro)molecules onto preformed hydrophobic polymeric nanoparticles [107].

Quite a lot of studies used electrostatic interactions to coat nanoparticles. For instance, positively charged chitosan nanoparticles loaded with proteins have been coated with sodium alginate in order to avoid a burst release, and to enhance their mechanical and thermal stability [14]. Furthermore, chitosan has been adsorbed on negatively charged PLA nanoparticles to prepare fully bioresorbable mucoadhesive nanoparticles [108].

Very recently, potential targeting probes have been adsorbed onto polymer nanoparticles by electrostatic interactions: cationized antigens [Tat(1–72)] were adsorbed on negatively charged nanoparticles [109].

On the other hand, hydrophobic nanoparticles has been surface-functionalized by using amphiphilic or hydrophobically modified macromolecules, the hydrophobic part of the macromolecule ensuring their durable adsorption and physical anchorage. Based on this approach, numerous studies have used amphiphilic block copolymers, such as Pluronic® (block copolymers based on PEO and PPO, e.g. PEO-*b*-PPO-*b*-PEO triblock copolymer also called poloxamers) as surface modifiers of hydrophobic nanoparticles [110]. The hydrophobic PPO block is the driving element for the adsorption onto the surface of nanoparticle, while the hydrophilic PEO chains expand in the aqueous environment forming a steric barrier that stabilizes the nanoparticles, prevents their aggregation and makes them stealthy to the MPS. Similarly, polystyrene nanoparticles have been surface-modified by Pluronic F-108 (PEO<sub>129</sub>-*b*-PPO<sub>56</sub>-*b*-PEO<sub>129</sub>) end-capped by polypeptides containing the RGD sequence. Exposing cell adhesive peptides at their surface, these nanoparticles are promising devices for diagnostic purposes [83].

Apart from amphiphilic block copolymers, randomly hydrophobically modified polymers have also been used. Polystyrene-divinylbenzene (PS-DVB) particles have been coated with dextran partially substituted by phenoxy groups. Adsorption was achieved by simple incubation of the particles in the polymer solution (20 h) and the adsorbed polymer layer was then chemically crosslinked in order to avoid polymer desorption (using epichlorhydrin or butanediol diglycidyl ether). The dextran layer was shown to greatly reduce the nonspecific adsorption of bovine serum albumin (BSA) [105].

Furthermore, dextran-bearing hydrophobic phenoxy groups and comb-like copolymers of dextran-bearing pendant phenoxy groups and PEO chains (DexP-*g*-PEO) were synthesized [111]. They were adsorbed on polystyrene nanoparticles and the effects of the polymer composition and architecture on the protein adsorption were studied (Fig. 8.11).

It was found that the most important parameter in preventing the adsorption of BSA was the extent of the contact points between dextran and the surface, rather than the grafting density of PEO chains, in the case of DexP-*g*-PEO [111].

On the other hand, the naturally occurring adsorption of proteins, which is generally not desired, has also been exploited, e.g. in the case of protein delivery [109].

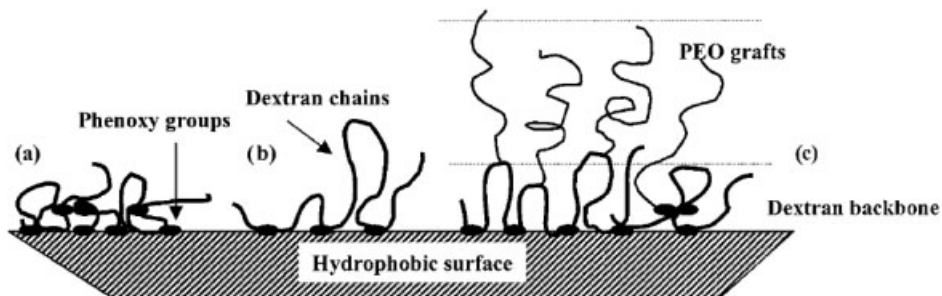
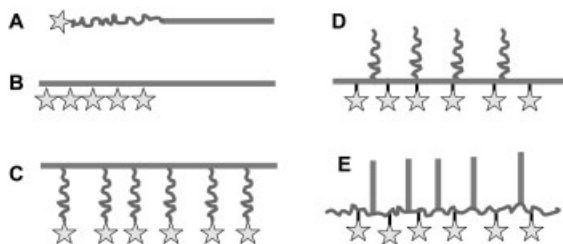


**Figure 8.11.** Adsorption of amphiphilic dextran (DexP) with (a) high and (b) low amounts of grafted phenoxy groups and (c) of graft DexP-g-PEO copolymer at the hydrophobic surface [111].

The advantage of surface modification via adsorption relies on the complete localization of the adsorbed molecules at the surface. However, it must be considered that the post-modification of the surface of preformed nanoparticles can alter their stability and induce their aggregation. In fact, the stability of colloidal systems relies on steric or electrostatic repulsion of the particles, so that the adsorption of material on the nanoparticle surface might diminish the interparticular repulsion and would thus induce their aggregation. Finally, the risk of desorption upon dilution and introduction into complex biological media must be considered. Therefore, most of the recent approaches rely on the covalent linking of the functional (macro)molecules to the nanoparticle's constitutive polymer (Section 8.4.3.2) or directly to the nanoparticle surface (Section 8.4.3.4).

#### 8.4.3.2 Functional Surfactants as Stabilizers and Surface Modifiers

As explained in Section 8.3, methods for the preparation of polymeric nanoparticles generally use surfactants, which play the role of emulsifier and stabilizer. It was demonstrated that in the case of hydrophobic nanoparticles, the amphiphilic surfactant is located at the surface of the particle, i.e. at the water–hydrophobic solid interface [14, 49]. Amphiphilic copolymers conjugated with bioactive molecules may thus serve as both emulsifiers and surface modifiers. Such copolymers may be synthesized with various architectures, e.g. block [diblock (Scheme 8.1A



**Scheme 8.1.** Amphiphilic copolymers: red = hydrophobic, blue = hydrophilic, star = functional (bio)molecule.

and B) or triblock] or comb-like structures (Scheme 8.1C–E), employing controlled polymerization techniques. The functional biomolecule is rather attached on the hydrophilic part of the copolymers, in order to optimize its availability for interaction in aqueous environment. PEO has preferentially been used because of its hydrophilicity and flexibility properties (see Section 8.2.4).

**8.4.3.2.1 Functional Amphiphilic Block Copolymers** A first group of copolymers used for surface functionalization typically consists of amphiphilic block copolymers as schematically presented in Scheme 8.1A. In general, such copolymers can be obtained through four different strategies: (i) by post-polymerization functionalization, where the functional moiety is grafted to the hydrophilic end of the amphiphilic block copolymer bearing a reactive group [112], (ii) by linking the bioactive group at one end of an  $\alpha,\omega$ -bifunctional hydrophilic homopolymer, followed by the initiation of the polymerization of the second block from the other chain end, (iii) by using biologically active molecules as initiators for the sequential polymerization of the diblock copolymer (hydrophilic block being polymerized first) or (iv) by using polymerizable hydrophilic biomolecules.

The first approach (i) has mainly been applied for the functionalization of diblock copolymers by sugars and peptides. For instance, the hydrophilic end of amphiphilic PEO-*b*-P(D,L-LA) diblock copolymers has been end-capped by mannose [112], lactose [113] or peptides [114] using a reductive amination reaction. For this purpose, aldehyde (CHO)-capped copolymers and amino or aminophenyl derivatives of the biomolecule were synthesized. Then, the conjugation of both compounds was carried out in the presence of reducing agents [NaBH(OAc)<sub>3</sub> or NaBH<sub>3</sub>CN] [112–114].

On the other hand, biotin [115] or protected monosaccharides [86] have been used to initiate the polymerization of the hydrophilic block (approach iii). For instance, Qi and coworkers [115] prepared nanoparticles coated by biotin from biotin-terminated PAA-*b*-poly(methyl acrylate) diblock copolymers (biotin–PAA-*b*-PMA). These functional copolymers were prepared using a biotinylated initiator for the sequential atom transfer radical polymerization (ATRP) of acrylic acid and methyl acrylate (Fig. 8.12).

Not only radical polymerizations, but also ring-opening polymerizations (ROPs) have been successfully initiated by suitably protected molecules. Yasugi and co-

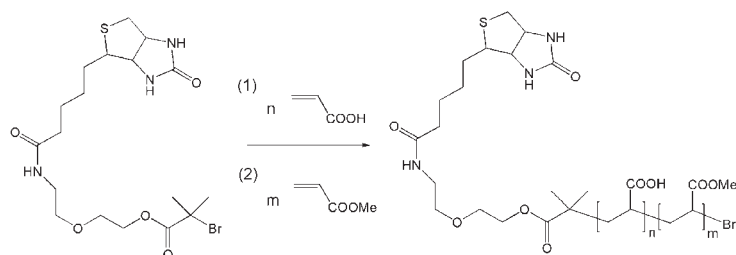


**Figure 8.12.** Synthesis of biotin end-capped PAA-*b*-PMA by ATRP.

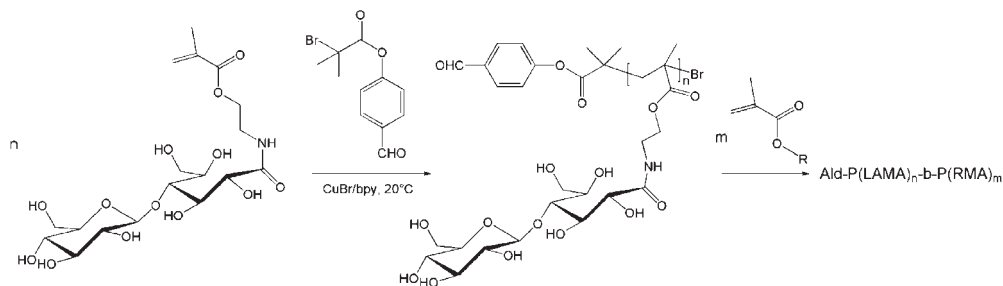


**Figure 8.13.** Sequential polymerization of 2-lactobionamidoethyl methacrylate (LAMA) with methacrylic monomers (R-MA) by ATRP at 20 °C.

workers [86] synthesized amphiphilic biodegradable PEO-*b*-PLA diblock copolymers that were end-functionalized by galactose. Therefore, they initiated the anionic polymerization of ethylene oxide by a metal alkoxide of a regioselectively protected galactose, followed by ROP of lactic acid.

Finally, amphiphilic functional copolymers were prepared using polymerizable carbohydrates as monomers. Armes and coworkers synthesized new sugar-modified methacrylic monomers (2-gluconamidoethyl methacrylate and 2-lactobionamidoethyl methacrylate) suitable for the preparation of sugar-modified methacrylate-based diblock (see Fig. 8.13) and triblock copolymers by ATRP starting from different (macro)initiators [116].

**8.4.3.2.2 Functional Random (Comb-like) Copolymers** The most popular pathway to amphiphilic random (comb-like) copolymers (Scheme 8.1C–E) functionalized by biomolecules relies on the synthesis of copolymers bearing groups that are prone to further chemical modification. Then, in a second step, reactive biomolecule derivatives can be grafted onto the (hydrophobic or hydrophilic) polymer backbone (called “grafting onto” approach).

For example, the pendant carboxylic acid groups of poly(methyl methacrylate-*co*-methacrylic acid) copolymers have been successfully used as reactive sites for the covalent linking of biotin molecules [117]. These random amphiphilic copolymers were efficient stabilizers and surface modifiers of PLA nanoparticles [117].

With the purpose to obtain fully biodegradable nanoparticles, biodegradable amphiphilic copolymers bearing reactive sites have been synthesized. For instance,  $\epsilon$ -caprolactone has been randomly copolymerized with  $\gamma$ -substituted functional  $\epsilon$ -caprolactone (comonomers) (bromo-, hydroxyl-, carboxylic acid-substituted), allowing the posterior reaction with biologically active compounds. Fully biodegradable surface-modified nanoparticles could be obtained by coprecipitation of PLA with these functional amphiphilic copolymers and the presence of the latter at the nanoparticle’s surface was demonstrated [118].

Maruyama and coworkers also prepared biodegradable nanoparticles based on poly(D,L-LA) and poly(L-lysine)-*g*-polysaccharide (dextran, maltose or amylose) co-

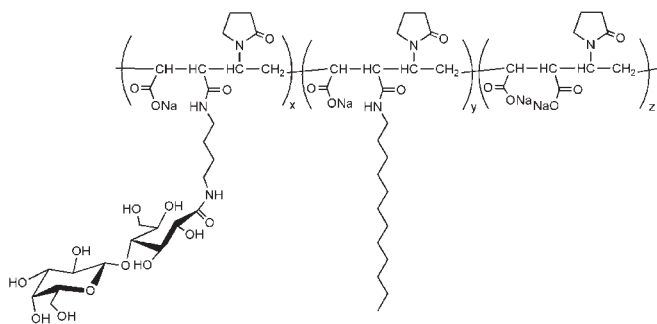


**Figure 8.14.** Structure of amphiphilic galactosylated copolymers Gal<sub>x</sub>-Dody<sub>y</sub>.

polymers either by a solvent evaporation process or a diafiltration method. These copolymers were easily prepared by a reductive amination reaction between the pendant amine function of the polypeptide and the reductive extremity of the polysaccharide. Aggregation assays using specific lectins revealed the presence of carbohydrate moieties at the nanoparticle surface. Furthermore, due to the polycationic nature of poly(lysine), the nanoparticles are positively charged. Consequently, they appear as promising candidates for the transfection of DNA (gene delivery) [119].

The efficient synthesis of amphiphilic maleic anhydride copolymers grafted by galactose units and dodecyl chains has been recently reported. (Fig. 8.14) In fact, reactive anhydride functions were introduced through copolymerization of maleic anhydride and *N*-vinylpyrrolidone in a copolymer backbone. They have then been used as reactive sites for further functionalization with *N*-(4-aminobutyl)-*O*- $\beta$ -D-galactopyranosyl-(1-4)-D-gluconamide (an amine-functionalized galactose derivative) and dodecylamine. As illustrated in Scheme 8.1(E), amphiphilic maleic anhydride copolymers bearing pendant hydrophilic galactose moieties, as biological targeting units, and hydrophobic alkyl chains (for the interfacial activity) could be obtained [120]. These copolymers were successfully used as stabilizers and surface modifiers to produce stable nanoparticles coated with galactoses as targetable moieties on their surface, using the emulsification-diffusion technique. The presence and bioavailability of the galactose moieties at the nanoparticle surface were clearly demonstrated by lectin-sugar interactions [98].

#### 8.4.3.3 Emulsion, Miniemulsion or Dispersion Polymerization

As mentioned in Section 8.3.2, polymeric nanoparticles can be prepared using emulsion, miniemulsion or dispersion polymerization. In order to modify the surface of nanoparticles, several approaches have been proposed. One relies on the miniemulsion polymerization of monomers in the presence of amphiphilic biopolymers as emulsifiers. A second approach is based on the dispersion copolymerization of a hydrophilic functional macromonomer with a hydrophobic comonomer.



According to the first strategy, the polycation chitosan [121] has been used as stabilizer to prepare chitosan-coated latexes by (mini)emulsion polymerization. While the use of chitosan alone resulted in rather large droplets and a major amount of coagulate, addition of a low-molecular-weight surfactant or a flexible polymeric costabilizer significantly improved the stabilization of the nanodroplets during the polymerization. This efficient stabilization allowed the production of well-defined chitosan-coated nanoparticles in the range of 100–300 nm.

Later, Dellacherie and coworkers coated polystyrene nanoparticles by dextran in a miniemulsion process which did not require the addition of any costabilizers and led to monodisperse nanoparticles. For this purpose, they hydrophobically modified dextran chains by randomly grafted phenoxy groups. This amphiphilic dextran showed strong interfacial activity, and could be successfully used as an emulsion stabilizer and surface modifier in miniemulsion processes to prepare polystyrene particles carrying dextran at the surface [63].

In contrast to this approach, the macromonomer method allows covalently linking biomolecules, such as monosaccharide moieties, to the surface of nanoparticles. A direct pathway to carbohydrate-functionalized nanoparticles has thus been proposed [66]. For this purpose, a hydrophilic macromonomer bearing glucose moieties has been synthesized by radical polymerization of 2-(glucosyloxy)ethyl methacrylate (GEMA) in the presence of 2-mercaptoethylamine as a chain transfer agent, followed by a peptide-like coupling reaction with 4-vinylbenzoic acid (VBA) (Fig. 8.15). Nanospheres with a polystyrene core and a GEMA oligomer corona were then obtained by free radical copolymerization of the GEMA macromonomer with styrene in an ethanol/water mixture. As mentioned in Section 8.4.2.1, such glucose-decorated nanoparticles were expected to increase the interaction with a glucose specific lectin [concanavalin A (Con A)] due to the cluster effect. Hence, investigation of the glucose-lectin interaction by the enzyme-linked lectin assay (ELLA) demonstrated that the binding activity of the carbohydrate decorated nanoparticles was less than that of the free GEMA macromonomer. It decreased even with increasing amount of glucose at the nanospheres. Steric hindrance was proposed as a possible explanation for the low bioavailability [66] (Fig. 8.16).

The choice of technique for the surface modification by biomolecules is thus crucial. Biological recognition assays are necessary to test the bioavailability of the biomolecules.

#### 8.4.3.4 Covalent Linking of Functional Molecules to Preformed Nanoparticles

The surface functionalization of nanoparticles by covalent grafting of functional molecules on preformed polymeric nanoparticles is challenging (see Fig. 8.10, iii).

Such reactions require (i) the availability of functional reactive groups at the nanoparticle surface, (ii) the synthesis of biomolecules bearing reactive groups, and (iii) the use of coupling reactions that are selective and efficient. Above all, they must be smooth, not causing neither denaturation of the biomolecules nor degradation of the polymer material. These challenges led to the development of “chemical ligation”, i.e. the selective covalent coupling of mutually and uniquely functional groups under mild and aqueous conditions [122]. Hitherto, only a few

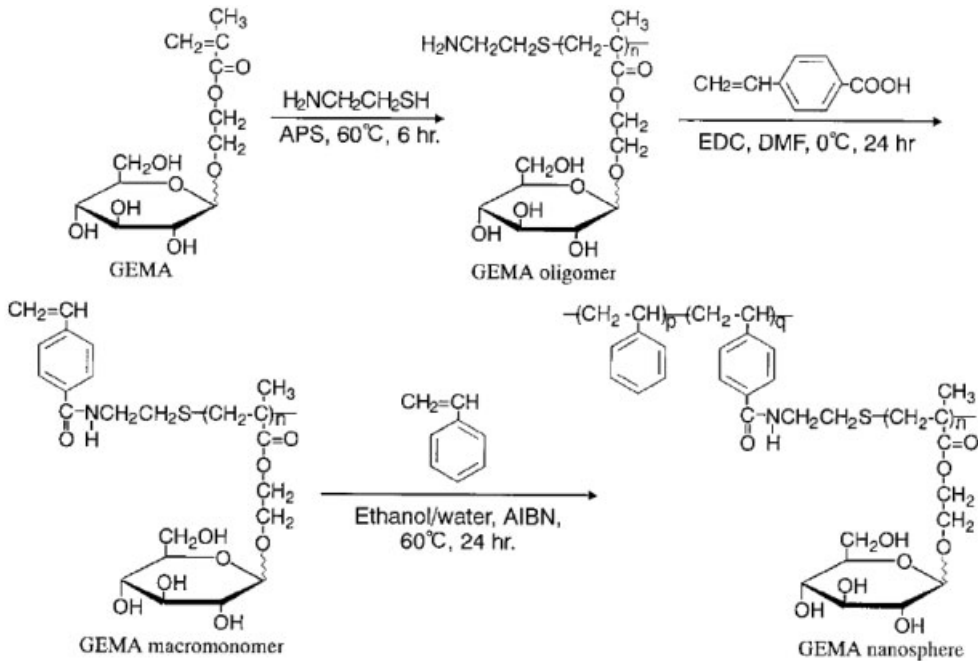


Figure 8.15. Synthesis and copolymerization of a glucose-capped macromonomer (GEMA macromonomer).

of these methods have been applied to the chemical coupling of biomolecules onto preformed nanoparticles.

In the following, we report on the universally applied amine–acid coupling and on another very selective and smooth coupling reaction, relying on the reaction of thiol groups with maleimides.

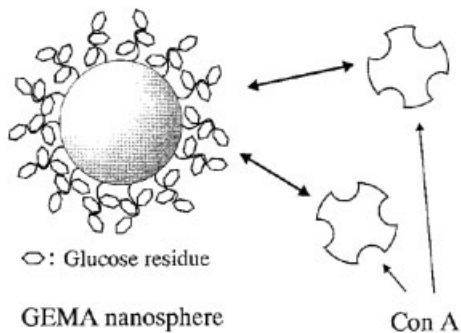


Figure 8.16. Schematic representation of a GEMA nanosphere and its interaction with Con A [66].

**8.4.3.4.1 Amine–Acid Coupling** The amine–acid coupling is one of the most universally applied and efficient coupling reactions. As an example, biomolecules bearing carboxylic acid groups have been conjugated onto  $\text{NH}_2$ -coated nanoparticles. Such nanoparticles have been prepared using amine-functionalized comonomers, either in an *in situ* copolymerization process (Section 8.3.2) [101], or by using amphiphilic copolymers that serve as surfactants and surface modifiers, e.g. in a nanoprecipitation technique (Section 8.3.1) [102]. Folic acid was then successfully conjugated to the surface using 1,3-dicyclohexylcarbodiimide (DCC).

Based on the same conjugation reaction, biomolecules bearing an amine function have been conjugated to nanoparticles exposing carboxylic acid groups. Woolley and coworkers prepared SCKs from micelles formed by poly( $\epsilon$ -caprolactone-*b*-acrylic acid) diblock copolymers (PCL-*b*-PAA) [123] followed by crosslinking of the PAA shell (consumption of approximately 50% of the acrylic acid groups) (Fig. 8.17, step 1). The remaining acrylic acid groups were then used for the conjugation to the amino group of a fluorescent dye [fluorescein-5-thiosemicarbazide (FTSC)] (Fig. 8.17, step 2) and a biologically active peptide sequence, respectively. The latter was prepared by standard solid-phase peptide synthesis (SPPS) and extended with a flexible linker. (Fig. 8.17, step 3). The following conjugation of the peptide to the SCK nanoparticle was performed on a solid support. This technique allows attaching the peptide selectively to the surface of the SCKs, as the reaction can only take place at the interface of the SCK and the peptide-bearing resin. Moreover, by performing the SCK–peptide coupling on a solid support, any nonconjugated nanoparticles were removed by washing of the resin support. Finally, by degradation of the PCL core, fluorescent peptide-exposing nanocapsules (nanocages) could be obtained, which demonstrated good binding interactions with cells and transduction into cells [124] (Fig. 8.17, step 4).

**8.4.3.4.2 Thiol–Maleimide Coupling** The introduction of thiol groups at the surface of nanoparticles opens up a lot of new possibilities in ligand conjugation (ligation). In particular, conjugation reactions between thiols and maleimides have received increasing interest due to their specificity and reactivity. Such reactions have been found to be quantitative under physiological conditions [125]. Antibody or protein conjugation is commonly performed using bifunctional crosslinkers such as *m*-maleimidobenzoyl-*N*-hydroxysuccinimide ester (MBS) that offers two binding sites – one for primary amino groups (present in antibodies, drugs, specific peptides) and one for thiol functions (Fig. 8.18) [126].

Thus, thiolated polymer nanoparticles have been synthesized. For instance, Langer and coworkers introduced free sulfhydryl groups onto the surface of gelatin (protein) nanoparticles by the reaction of primary amino groups with 2-iminothiolane [127]. Furthermore, Nobs and coworkers developed a suitable method for the introduction of thiol functions on the surface of PLA nanoparticles. The modification of the surface involved the activation of the carboxylic acid end-groups of PLA followed by the nucleophilic attack by cysteine or cystamine in a carbodiimide reaction (providing thiol functions via an amide bond) [128].

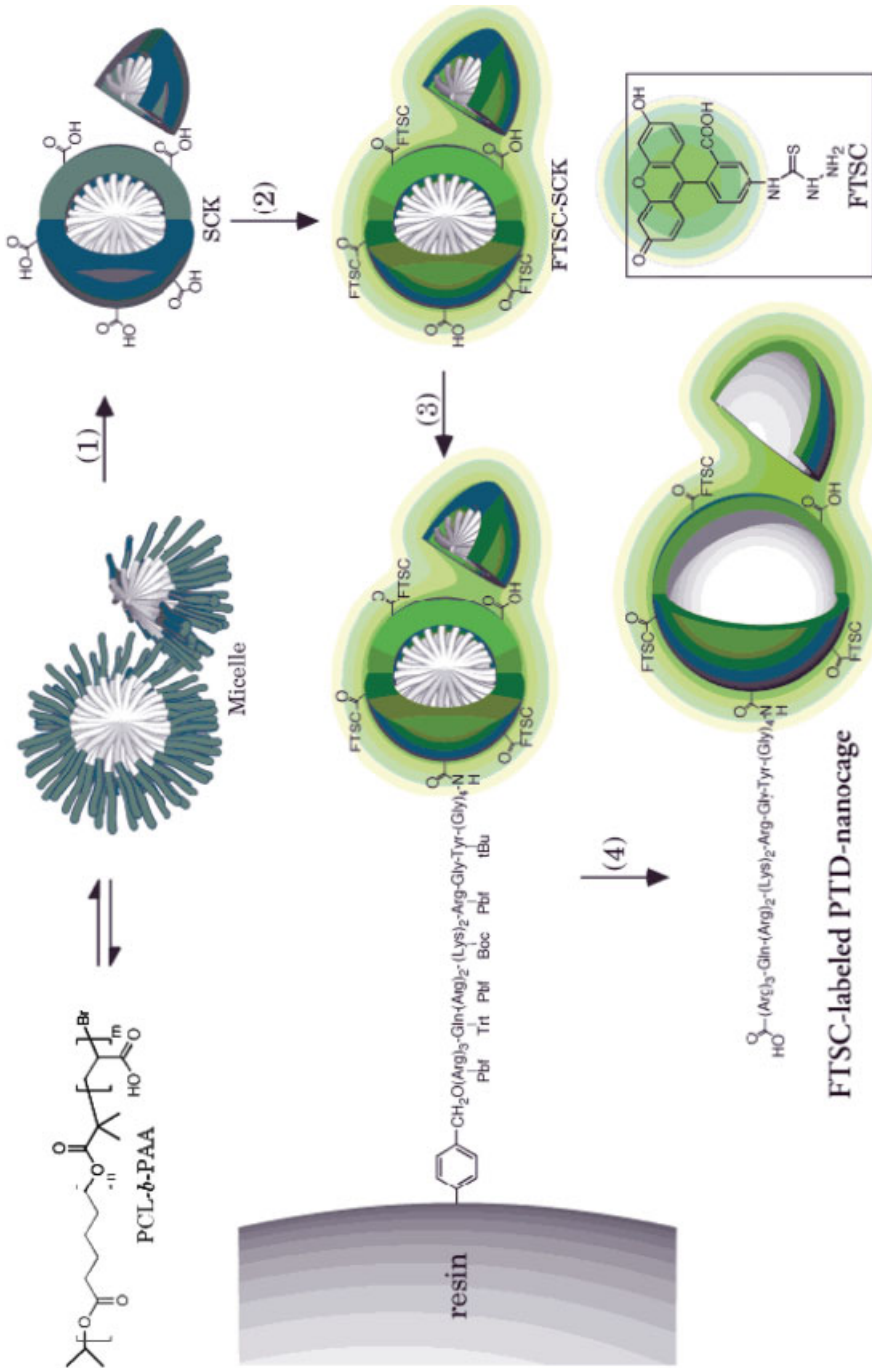


**Figure 8.17.** Solid-phase synthesis strategy involved coupling of the protein transduction domain (PTD) with fluorescein-labeled SCK nanoparticles, followed by cleavage from the support and excavation of the nanoparticle core domain to yield FTSC-labeled PTD nanocage bioconjugates.

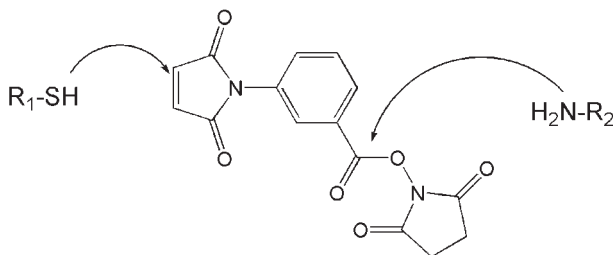


**Figure 8.18.** Coupling agent: bifunctional MBS.

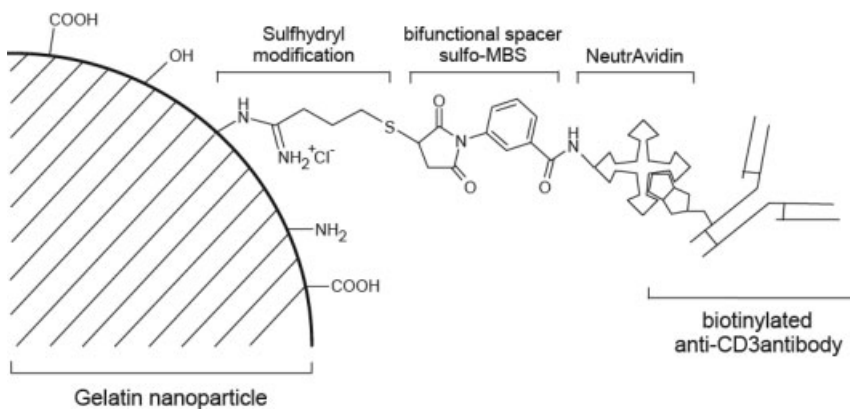


**Figure 8.19.** Schematic representation of antibody-loaded NeutrAvidin-modified gelatin nanoparticles. Sulfhydryl groups were introduced onto the particle surface by 2-iminothiolane followed by a conjugation

reaction with NeutrAvidin using the heterobifunctional crosslinker MBS. A biotinylated anti-CD3 antibody was then attached to the particle surface by avidin–biotin complex formation.

In both cases (gelatin and PLA nanoparticles), thiol-functionalized nanoparticles were thus made available. Then, avidin (NeutrAvidin), as a model protein and linker molecule (see Section 8.4.2.4), could be successfully conjugated to the nanoparticles via MBS, as illustrated in Fig. 8.19 [129]. Balthasar and coworkers have further attached biotinylated antibodies at the surface via avidin–biotin complex formation and their bioavailability could be shown using indirect methods, such as immunoblotting or fluorimetry [130].

**8.4.3.4.3 Molecular Imprinting** In the last decade, so called molecular-imprinted polymeric materials (MIP) have gained increasing interest for biomimetic molecular recognition elements [131]. The three-dimensional arrangement of the binding functional groups on the MIP is obtained by linking the functional monomers covalently or noncovalently to the template during polymerization (Fig. 8.20).

Removal of the template from the formed polymer then generates a structure that is complementary to the template structure. Very recently, based on this prin-

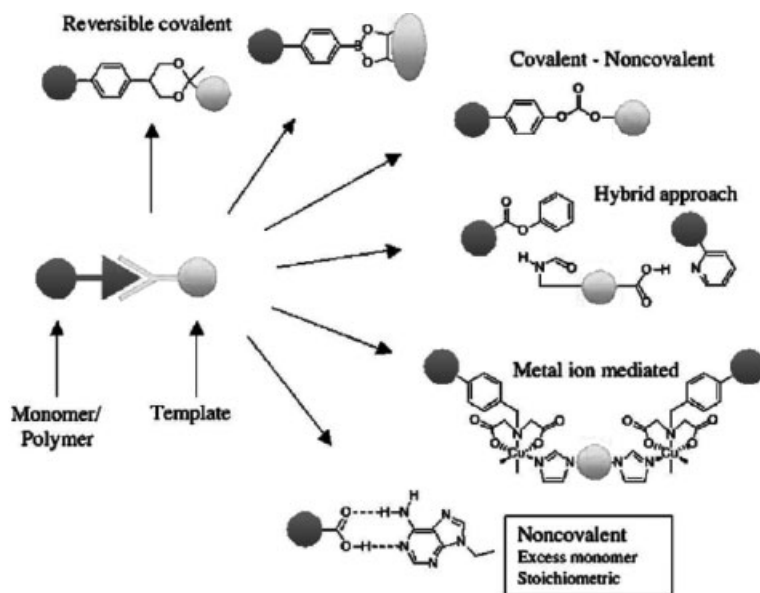


**Figure 8.20.** Strategies used to place binding or catalytic functional groups at defined positions in imprinted sites of network polymers.

Multiple interfacial imprinting techniques have been developed to reach surface-imprinted (colloidal systems). This approach has been used for the synthesis of surface-imprinted polymeric nanoparticles. Therefore, using emulsion or precipitation polymerization techniques monomers bearing bonds to a “template molecule” have been polymerized in the presence of bioactive molecules as templates [132]. Removal of the latter leaves a polymer nanoparticle containing a memory of its shape and functionality on its surface. They are therefore synthetic analogs of biological recognition systems.

First attempts have been undertaken, and Carter and coworkers synthesized nanoparticles bearing imprints of caffeine or theophylline at their surface that show a high affinity to the template molecule (caffeine or theophylline). Such particles possessed a core-shell structure [133]. The core was prepared first by emulsion polymerization of styrene and divinyl benzene monomers (1:1). The resulting particles were then coated, in a second polymerization stage, with the imprinting monomer mixture consisting of ethylene glycol dimethacrylate and oleyl phenyl hydrogen phosphate, and caffeine (or theophylline) as noncovalent template.

#### 8.4.4

#### Analytical Techniques for Surface Modification

The efficiency of the surface functionalization of nanoparticles with biomolecules, but also their bioavailability for recognition interactions, depends on many factors.

These include the architecture and composition of the polymers, the conformation of the polymer chains, and also the conditions employed for the nanoparticle formation. Therefore, numerous (indirect and direct) techniques have been developed and used to characterize the surface of nanoparticles [134]. Some of the most frequently used physicochemical techniques (Section 8.4.4.1) and biological assays (Section 8.4.4.2) are highlighted next.

#### 8.4.4.1 Physicochemical Techniques

Physicochemical techniques can supply information both on the chemical composition of the surface and also on its physical properties, such as hydrophilicity or surface charge. In addition, the biological properties of a surface can be investigated. Thus, specific interaction reactions between biomolecules fixed on the nanoparticles and their ligands fixed on the analytical device can be revealed by physicochemical means.

**8.4.4.1.1 The  $\zeta$  Potential** The  $\zeta$  potential measurement of aqueous suspensions of nanoparticles is one of the most common techniques to determine surface charges and therefore surface modification. The  $\zeta$  potential reflects the electrical surface potential of particles, which is influenced by the different materials located at the interface with the dispersing medium. Thus, the mobility of charged particles is monitored by applying an electrical potential. High  $\zeta$  potential values, above 30 mV (positive or negative value), lead generally to stable colloidal suspensions, because electrostatic repulsion between particles prevents their aggregation.

**8.4.4.1.2 X-ray Photoelectron Spectroscopy (XPS)** Another commonly used technique is XPS, also known as electron spectroscopy for chemical analysis (ESCA), which provides information about the chemical (atomic) composition of the top layer of nanoparticles. Here, under ultra-high vacuum, the dried sample is bombarded with X-rays. When the photon is of suitable energy, it is absorbed by an atom causing ionization and the emission of a core electron (inner shell electron). Since binding energies of core electrons are characteristic for elements in a certain chemical environment, the spectrum gives information on the elemental composition of the shallow surface region. From small shifts in the binding energies, additional chemical information can be derived (e.g. the oxidation state of the element). Since photons possess a limited penetration energy, only those electrons pertaining to atoms at or near the surface (up to 10 nm) escape and can be counted. This quantitative technique gives the average composition over about 10 nm depth inside the nanoparticles. XPS at various angles allows for the determination of the composition on different depth of the sample.

**8.4.4.1.3 Time-of-Flight Secondary Ion Mass Spectroscopy (TOF-SIMS)** SIMS is a physicochemical technique of the outmost surface (10 Å). TOF-SIMS uses a pulsed primary ion beam to desorb and ionize species from a sample surface. The resulting secondary ions are accelerated into a mass spectrometer, where they are mass

analyzed by measuring their TOF from the sample surface to the detector. The mass spectrum and the secondary ion images are then used to determine the composition and distribution of the sample's surface constituents. TOF-SIMS provides spectroscopy for the characterization of the surface's chemical composition, imaging for determining the distribution of the chemical species, and depth profiling for thin-film characterization. This technique thus allows to prove the chemical linkage of biomolecules to a surface via the analysis of the fragments.

**8.4.4.1.4 Electron Paramagnetic Resonance (EPR)** EPR, or electron spin resonance (ESR), is a spectroscopic technique that detects species that possess unpaired electrons. The basic physical concepts of the technique are analogous to those of nuclear magnetic resonance (NMR); however, instead of the spins of the atom's nuclei, electron spins are excited. Due to the difference in mass between nuclei and electrons, weaker magnetic fields and higher frequencies are used compared to NMR. For electrons in a magnetic field of 0.3 T, spin resonance occurs at around 10 GHz. EPR is helpful for nanoparticle characterization by using nanoparticles tagged with biological spin probes. EPR of free radicals conjugated to polymer chains has been used to discriminate between highly mobile (liquid-like) and slowly mobile (solid-like) spin labels on the basis of their magnetic relaxation times. EPR can thus provide useful information at the molecular level on the structure, mobility and organization of polymers at interfaces [135, 136].

**8.4.4.1.5 Surface Plasmon Resonance (SPR) [137]** SPR is a biophysical technique allowing us to measure biomolecular interactions in a quantitative, real-time manner. A ligand ("target") is immobilized on a special chip (SPR crystal) and a solution of the analyte ("binding partner") flows across the chip. The progress of binding is then measured by optical instruments.

This technique was applied to measure the interaction of nanoparticle–biomolecule conjugates with surfaces that had been modified by the corresponding ligand (generally a protein). As an example, for the measurement of interactions of folic acid-coated nanoparticles with the folate-binding protein, the latter was immobilized on the sensor surface [102]. It could be demonstrated that the folate nanoparticle conjugates were able to bind specifically to immobilized protein, whereas nanoparticles without folic acid-targeting moieties showed a much lower interaction (Fig. 8.21).

#### 8.4.4.2 Biological Assays/Methods

**8.4.4.2.1 Nonspecific Interactions with Proteins** The adsorption of proteins has often been used to indirectly demonstrate the presence of a protein-repulsive coating. For this purpose, the amount of adsorbed model proteins, such as bovine- or human serum albumin (BSA or HSA), has been determined by quantification of the nonadsorbed proteins in the supernatant after centrifugation and precipitation of the nanoparticles. In a recent study the repellent properties of dextran and PEO could be demonstrated. Indeed, PCL–dextran nanoparticles adsorbed



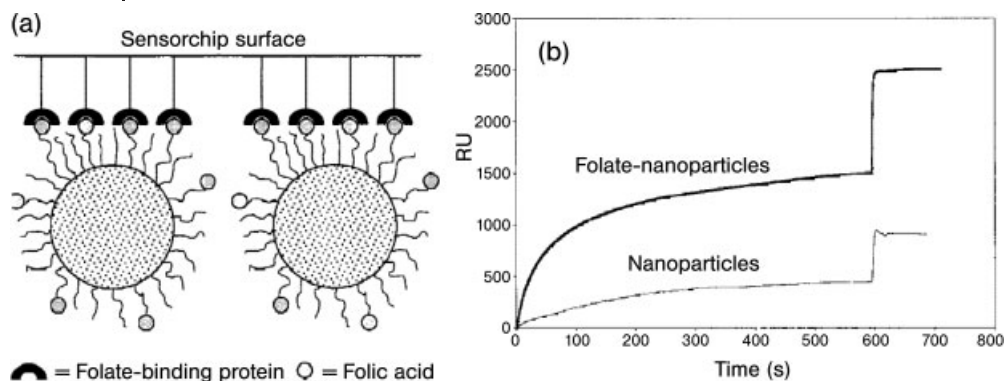


Figure 8.21. SPR on folate-coated nanoparticles.

only  $0.2 \text{ mg m}^{-2}$  BSA, which is comparable with the amount detected on the corresponding PEGylated nanoparticles taken as control [138, 139].

Other approaches tend to identify the proteins that are adsorbed most when incubating the nanoparticles with mixtures of proteins. Two-dimensional poly-(acrylamide) gel electrophoresis, (2-D PAGE) has thus been used to reveal adsorption and to identify proteins and fragments.

Finally, Passirani and coworkers [5] and Chauvierre and coworkers [81] evaluated the activation of the complement system by nanoparticles, which leads to their rapid elimination from the blood circulation through the uptake by macrophages of the MPS. In fact, the key step of complement activation to take place is the adsorption of serum proteins on the surface of the nanoparticles. Thus, nanoparticles coated by different polysaccharides were incubated in normal human serum (NHS) and the activation of the complement systems determined by quantification of a key protein – complement component C3.

**8.4.4.2.2 Specific Interactions (Carbohydrates–Lectins, etc.)** Apart from physico-chemical techniques, numerous biological methods have been used for the investigation of specific interactions between surface-functionalized nanoparticles and their targets, such as protein–ligand interactions.

Based on such lectin–carbohydrate interactions, the surface modification of nanoparticles by galactose could be demonstrated. Therefore, pyrene-labeled galactose-coated micelles (galactose–PEO-*b*-PLA) have been passed on a column packed with *Ricinus communis* lectin (RCA-1 lectin) immobilized beads. By fluorescence spectroscopy, they were shown to be specifically retained at the column, in comparison to non- and glucose-functionalized micelles [86].

Furthermore, numerous biological assays (based on specific biomolecular interactions) such as enzyme-linked immunosorbent assay (ELISA), ELLA and aggregation assays have been used to demonstrate the presence of biomolecules at the surface of nanoparticles.

ELISA is a biochemical test that quantifies by colorimetry a biological substance (e.g. proteins, sugars) in a biological liquid using the reaction of an antibody to its antigen. This method is based on the fixation of a first antibody to a solid device. Once the antibody is fixed and nonfixed residual free molecules are eliminated, the sample (to be quantified) is incubated, using conditions that favor antibody–protein interaction. Then, after a washing step, the complex formed is revealed by reaction with a second, detecting antibody, which is specific to another site of the protein. This antibody is typically linked to an enzyme, which serves for the quantification of the initial protein–antibody complex by reaction with a substrate and coloration of the medium by the formed product.

ELLA is a descendant of ELISA employing the lectin–carbohydrate interaction. It allows to quantify the capacity of a ligand X (e.g. sugar moieties at the surface of a nanoparticles) to inhibit the adhesion of a lectin on a reference ligand Y deposited on a solid device. Using this method, the surface functionalization of polymer nanoparticles with monosaccharides could be demonstrated via biotin–avidin sandwiching using streptavidin–horseradish peroxidase (HRP) as a detection system [98] (Fig. 8.22).

Finally, aggregation assays, based on the aggregation of carbohydrate-decorated nanoparticles by multivalent lectins, have been used to indirectly show the presence of poly- or monosaccharides at the surface of nanoparticles [119, 140] (see also Section 8.5.2.1.2). Similarly, hemagglutination inhibition assays have been developed, which are based on the inhibition of the agglutination of erythrocytes by lectins. In fact, erythrocytes are naturally decorated by saccharidic moieties. Carbohydrate-bearing polymeric particles can therefore act as inhibiting agents, as they compete with erythrocytes for the interaction with lectins [94].

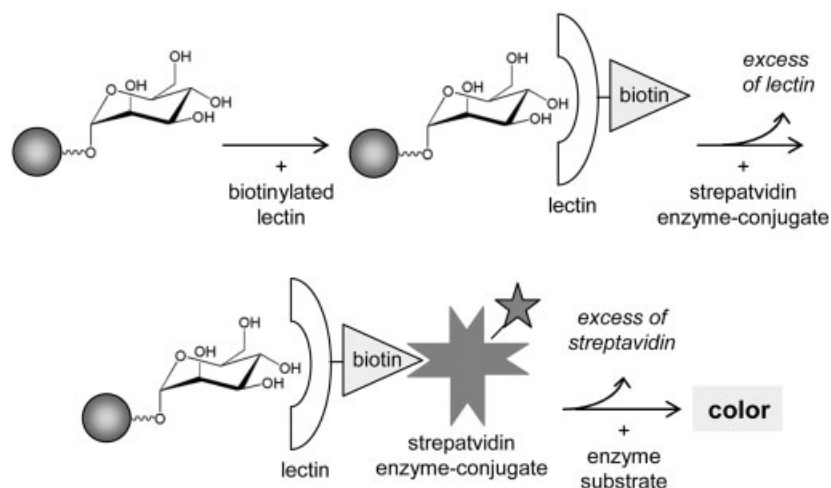


**Figure 8.22.** Scheme for the multistep titration of particle-fixed mannose by biotin-labeled biotin.

## 8.5 Applications

### 8.5.1 Drug Delivery Systems [141]

As already mentioned, colloidal drug delivery systems are designed to modify the pharmacokinetics and biodistribution of their associated drugs, and/or to serve as drug reservoirs (i.e. as sustained release systems). Indeed, one of the main problems of drug delivery is the poor solubility of hydrophobic drugs in aqueous media. Drug delivery systems that provide hydrophobic domains can be advantageously used to help “solubilization” of the drug. By the careful choice of the drug delivery system and the polymer material, the release profile of the drugs from the device and thus their blood concentration with time (pharmacokinetics) can be substantially controlled. Additionally, sensitive drugs can be protected from premature (enzymatic/metabolic) degradation by encapsulating them in a protecting polymer matrix.

Furthermore, colloidal drug carrier systems change the biodistribution of drugs. Due to their “large” size, colloidal drug delivery systems accumulate in diseased tissues such as tumors, which are characterized by an enhanced permeability and retention (“passive targeting”). On the other hand, the surface functionalization of particulate carriers by specific ligands should allow the specific targeting of tissues. The gain in selectivity thus leads to the concentration of the drugs at the targeted tissues, which permits to reduce the amounts of administered drug and consequently avoids side-effects resulting from the presence of the drug at undesired sites (“active targeting”).

#### 8.5.1.1 Routes of Administration

Nanoparticles can be administered via multiple routes, such as intravenous, oral, pulmonary, nasal and ocular routes, as a solid or suspension. It should be noted that most of the current systems are designed for intravenous and oral administration.

Oral administration is the most convenient route for drug delivery, improving the compliance and quality of life of the patients compared to therapy by injection or infusion. However, the oral absorption of many therapeutic agents, such as peptides [142] (e.g. insulin), proteins, oligodesoxynucleotides (ODN) and also cancer drugs, is one of the greatest challenges in the pharmaceutical field. Indeed, their bioavailability is low because of instability in the gastrointestinal tract and low permeability through the intestinal epithelium. Nanoparticles are promising carriers for such bioactive molecules, because they may protect them against enzymatic/hydrolytic degradation (e.g. by gastric or intestinal juices, which are rich in proteases such as trypsin and chymotrypsin) and they may enhance their bioavailability. Polymeric particles have been shown to cross the intestine barrier. The size of the particles as well as the nature of the polymer are critical parameters for the particle uptake by the gastrointestinal tract. Bioadhesion of nanoparticles to the

mucous membrane in the gastrointestinal tract can be a tool to prolong the residence time of the drug carriers at the absorption sites and thus enhance the drug absorption. In fact, the coating of nanoparticle surfaces with hydrophilic mucoadhesive polymeric chains, such as PMAA [143] and chitosan [15, 19, 22], was shown to increase the absorption of the nanoparticles from the gastrointestinal tract.

Whenever drugs or drug delivery systems are degraded or not sufficiently absorbed after oral administration, parenteral administration, i.e. administration other than via the digestive system, is the route of choice.

Nowadays, alternative routes of administration via mucosal membranes, such as pulmonary and nasal mucosae, that circumvent the passage by the gastrointestinal tract and the liver presystemic metabolism (known as the “first-pass effect” – the first metabolic process with cytochrome P450 in the liver) are receiving a great deal of attention. Pulmonary delivery for both local and systemic treatments via aerosol inhalation has many advantages over other delivery pathways. Indeed, the lungs are characterized by a large surface area (43–102 m<sup>2</sup>), slow mucociliary clearance and low enzymatic activity. Compared to other nasal administration, they possess a thinner, more permeable absorption barrier. Recently, various high-molecular-weight drugs have been successfully absorbed through alveolar region of the lungs, e.g. heparin, growth factors (e.g. granulocyte colony stimulating factor), peptides and proteins such as insulin [144, 145]. Micro/nanoparticles are interesting drug delivery systems for pulmonary administration as they [146] increase the systemic availability of substances by offering protection as well as exhibiting controlled release properties. The pulmonary route of application is challenging, requiring the optimal size of the drug formulation, in order to ensure the “atomization” of the drug formulation for inhalation and deposition of the aerosol particles in the alveolar region, where the drugs are absorbed best. It was found that microdrug particles (below 5 µm) were rapidly eliminated from the lung by ciliary movement and phagocytosis with macrophages [147]. Recently, polymeric nanoparticles for administration in the respiratory tract have been coated by mucoadhesive copolymers. Similar to the results of earlier studies on the intestine mucosa, chitosan-coated nanoparticles were proposed to open the tight junctions of the lung epithelium [20], enhance mucoadhesion and enable pulmonary systemic delivery [19]. Apart from the pulmonary route, nasal administration of drugs and especially of vaccines has found increasing interest. Similar to the lungs, the nasal mucosa is thin, highly permeable and incorporates a dense vascular network, and possesses a surface of “only” 50 cm<sup>2</sup>. As an example, chitosan-coated PLGA nanoparticles have been found to enhanced the nasal transport of encapsulated tetanus toxoid [148, 149].

Numerous colloidal carrier systems have also been designed for the intravenous route of administration, especially in the case of the delivery of proteins and oligonucleotides. However, severe requirements concerning the size, size distribution and surface properties of nanoparticles are imposed. In fact, the smallest capillaries in the body are only 5–6 µm in diameter. Consequently, particles being distributed in the blood stream must be significantly smaller than 5 µm in diameter

and ought not show aggregate formation in order to avoid clog formation and embolism. As mentioned in Section 8.1, the surface properties of the colloidal systems must be adapted in order to tune their biodistribution, pharmacokinetics and residence time in the vascular system before elimination by the MPS.

Compared to the intravenous route, subcutaneous/intramuscular administration imposes fewer requirements concerning particle size and size distribution. The subcutaneous route has proved to be promising in different therapeutic applications; subcutaneous injection of PLGA nanoparticles containing antitubercular drugs in mice resulted in sustained therapeutic drug levels in the plasma for 32 days and in lung/spleen for 36 days. In the field of tumor therapy, it has been demonstrated very recently that subcutaneous injection near the tumor site is the preferential route for facilitating high tumor uptake and retention, compared to intravenous or intraperitoneal injection [150]. Additionally, it should be emphasized that subcutaneous injection of nanoparticles proved to be very promising for vaccine delivery. Indeed, colloidal formulations of vaccines administered subcutaneously have been found to have strong “adjuvant activity” (defined in Section 8.5.1.2), which is usually required to cause a sufficient immune response [151, 152].

Polymeric nanoparticles have also demonstrated great potential for ophthalmic formulations. Probably the most severe disadvantage of eye-drop formulations is their rapid elimination of the instilled drug solution from the precorneal site [153]. In fact, only 1–2% of the applied dose reaches intraocular tissues. Consequently, colloidal suspensions were designed to combine ophthalmic sustained action with the ease of application of eye-drop solutions. Upon topical instillation, these particles are expected to be retained in the “cul-de-sac” and the drug to be slowly released from the particles through diffusion, chemical reaction or polymer degradation, or by an ion-exchange mechanism. Concerning the size of particles for ophthalmic purposes, Sieg and Triplett demonstrated that an upper size limit (below 10  $\mu\text{m}$ ) should be considered to avoid discomfort of the patients and that the retention time before washout diminishes with decreasing particle diameter. Apart from the size, the surface properties of nanoparticles have been changed in order to prevent their premature elimination. HA was found to be the polysaccharide of choice to coat polymeric nanoparticles and has been proved to enhance the ocular bioavailability of drugs, probably due to its mucoadhesive properties [79].

Finally, nanoparticles are also used for topical applications. In particular, polysaccharide-coated nanoparticles, such as chitosan-coated particles, are promising drug delivery systems for their enhanced wound-healing properties [154].

#### 8.5.1.2 Therapeutic Applications of Nanoparticles

Nanoparticles cannot only change the distribution of drugs at the organ or tissue level, but also at the cellular level, by increasing uptake or modifying the intracellular localization of the drug. This opens up the route for a large variety of therapeutic applications. In this section we report examples of three important groups of therapeutics that can be delivered by colloidal systems, i.e. chemotherapeutics (anticancer drugs), ODNs or genes, and proteins for cancer treatment, gene therapy and vaccination.

Anticancer drugs are often poorly bioavailable and barely compatible with oral delivery, due to their poor solubility, stability and permeability across biological membranes. After intravenous administration, they are distributed throughout the body as a function of the physicochemical properties of the molecule and do not necessarily accumulate in the targeted tissues. Due to the strong toxicity of cytostatic drugs, the specific targeting of the tumor cells is extremely interesting, allowing for effective therapy by reducing side-effects. Another major problem in cancer chemotherapy is the ability of tumor cells to develop simultaneous resistance to multiple lipophilic therapeutics. This resistance has been attributed to an active drug efflux from resistant cells linked to the presence of transmembrane P-glycoprotein (P-gp), which forms transmembrane channels and pumps the drugs out of the cell. The use of nanoparticulate carriers seems a promising solution to address these problems.

In fact, as already reported in Section 8.1, cancerous tissues possess a defective vascular architecture (due to the rapid vascularization, which is necessary to serve fast-growing cancers) coupled with poor lymphatic drainage. This phenomenon is known as an “enhanced permeation and retention” effect and allows long-circulating nanoparticles (due to their large size in comparison to free drugs) to passively target cancerous tissues [7]. The coating of nanoparticles by hydrophilic polymers avoids their rapid uptake in the liver and spleen, and favors their prolonged circulation time in the blood stream allowing the nanoparticles to accumulate in tumor tissues. It has actually been shown that anticancer drugs encapsulated in such surface-modified nanoparticles accumulate preferentially in cancer cells [8, 11]. To further enhance the targeting specificity, probes that are specific to tumor cells have been conjugated to the surface of nanoparticles. One of the greatest challenges is thus defining the optimal targeting agent to selectively and successfully transport nanoparticles systems (nanoparticles) to cancerous tissue. These strategies also rely on the ability of the targeting agents or ligands to bind to the tumor cells’ surface in an appropriate manner then triggering receptor endocytosis (receptor-mediated cell internalization). The therapeutic agent will hereby be delivered to the interior of the cancer cell. The folate receptor, which is over-expressed on malignant human cells, has been found to be a promising target. The folate-conjugated nanoparticles not only selectively target cancer cells, but they also improve the internalization of the encapsulated drugs within the targeted cancer cells [8]. On the other hand, monoclonal antibodies that specifically bind to the tumor antigens of a specific cancer type have been identified, and are currently used and approved by the FDA for targeted cancer treatment [11]. Thus, antibodies specific to breast cancer, etc. seem promising ligands for the covalent conjugation to nanoparticles [155].

Another challenging application of nanoparticles is their use as carriers for (anti-sense) nucleotides and plasmid DNA in the field of gene therapy. The ultimate goal of gene therapy is to cure both inherited and acquired disorders in a straightforward manner by removing their cause, i.e. by adding, correcting or replacing genes [156]. However, the administration of genes poses a challenge to pharmaceutical technology because of their susceptibility to enzymatic degradation (by nucleases) and their poor penetration across biological membranes (poor bioavailabil-

ity). The first potential gene delivery vectors were viruses. In the last decade, however, nanoparticles, similar to liposomes, have received growing interest as condensing nonviral gene carrier systems. These synthetic colloidal carrier systems are expected to be safer, but must be optimized in terms of keeping a comparable transfection rate. Such ODN-carrying nanoparticles are generally prepared on the basis of the electrostatic interactions (ion pairing); indeed, due to the phosphodiester group, ODN are negatively charged and can therefore be adsorbed at the surface of positively charged nanoparticles (such as chitosan nanoparticles [12]) or encapsulated in the core of nanoparticles.

Nanoparticles have also been designed as delivery vehicles for proteins. Similar to oligonucleotides and genes, proteins and peptides are very sensitive compounds that need to be protected from degradation in the biological environment. Moreover, their efficiency is highly limited by their inability to cross biological barriers and to reach the target site. As such, appropriate colloidal carriers for the successful delivery of proteins in the body have been designed, either incorporating the protein into the nanocarrier [157] or else adsorbing it on the surface of the nanocarrier [109].

Nowadays, both proteins and genes are the agents of choice for vaccination. Nanoparticles are very promising carriers for subcutaneous or mucosal vaccination [149, 151]. In fact, it has been reported that due to their size, nanoparticles have general “adjuvant” properties, i.e. act in a nonspecific manner to increase the specific immunity to an antigen (as compared to that introduced by the vaccine or the antigen alone) [158].

Concerning mucosal vaccination, the use of nanoparticles coated by mucoadhesive polymers is particularly interesting, because they exhibit prolonged residence time at the mucosae and avoid a premature clearance (see Section 8.5.1.1). As an example, chitosan nanoparticles have been found successful as a nasal vaccine in some animal studies, producing significant IgG serum responses when using influenza, pertussis and diphtheria vaccines [149].

Another approach to enhance the immune response after subcutaneous injection relies on the specific targeting of dendritic cells that are involved in the immune response and have been identified as target cells for the particle-mediated immune response [93]. It has been reported that dendritic cells expose specific receptors to mannose (mannose receptor) [91]. Therefore, the functionalization of vaccine-loaded particles by mannose seems a promising approach to specifically target dendritic cells [91, 93].

In contrast to other drug delivery systems, such as drug–polymer conjugates and liposome-based formulations, nanoparticles are in clinical trials, but have not yet reached the market [159].

### 8.5.1.3 Triggered Release

Recently, stimuli-responsive nanoparticles have been proposed as exciting delivery systems. Such delivery systems enable the release in response to an appropriate stimulus at the target site and/or at the right moment [160]. This stimulus can be environmental, chemical or physical, such as a change in pH [161, 162], tempera-

ture [101, 163, 164], ionic strength, application of laser light [165, 166] or magnetic field [167], and/or physiological, such as a change in enzyme concentration [168]. Up to date, only few works have been dedicated to the design of stimuli-responsive nanoparticles. Due to the importance of this application, some recent promising approaches to particulate-responsive systems are highlighted here.

It is known that in some tissues/physiological fluids of the human body, the pH may be different from most of the other physiological fluids. The pH is therefore an interesting stimulus. Apart from the drop in pH in the stomach, two other sites of low pH have been reported. So, the pH in endosomes is lower than that of the cytosol by 1–2 pH units [169]. It is known that endosomes are one of the principle transporters for drugs or drug delivery systems to enter a cell (by endocytosis). Once introduced in the cytosol, the release of the drug from the drug delivery systems may thus be induced by the drop in endosomal pH as triggering mechanism [169].

Furthermore, most solid tumors can be distinguished from normal surrounding tissues by a decrease in extracellular pH due to the higher aerobic and anaerobic glycolysis in cancer cells. Drug delivery systems have thus been designed that release anticancer drugs in response to a drop in pH [170].

For instance, Soppimath and coworkers prepared pH-triggered thermally responsive polymer core-shell nanoparticles for the delivery of chemotherapeutics (doxorubicin) to tumor cells [161]. They synthesized core-shell nanoparticles self-assembled from the amphiphilic tercopolymer poly(*N*-isopropylacrylamide-*co*-*N,N*-dimethylacrylamide-*co*-10-undecenoic acid), P(NIPAAm-*co*-DMAAm-*co*-UA) (Fig. 8.23). The UA was used as the core building hydrophobic and pH-sensitive segment, whereas the PNIPAAm segment exhibits a low critical solution temperature (LCST) in aqueous solution (about 32 °C) and is thus thermosensitive. DMAAm was employed to adjust the LCST of the polymer. The stability of nanoparticles prepared from the tercopolymer with optimized ratios of the different monomers at 37 °C depended on the environmental pH. Indeed, at physiological pH (pH 7.4) the LCST was 38.6 °C, meaning that the nanoparticles remained in their initial shape. However, in slightly acidic environments (pH < 6.6), the LCST of the terpolymer was decreased to 35.5 °C, i.e. a temperature lower than the normal body temperature. At this pH, the release of a model anticancer drug (doxorubicin) from

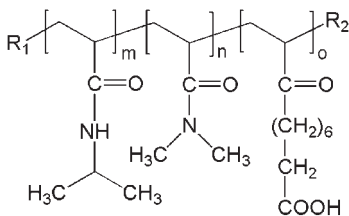
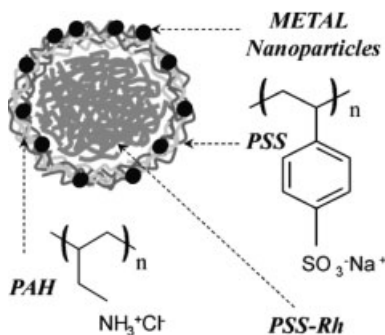


Figure 8.23. Molecular structure of P(NIPAAm-*co*-DMAAm-*co*-UA).



such nanoparticles was found to be significantly enhanced compared to the release at pH 7.4, probably due to the deformation and precipitation of the nanoparticles in acidic environment triggering the release of the entrapped anticancer drug (doxorubicin).

Recent efforts have focused on the development of optically addressable delivery systems, since irradiation with light promises to be an effective mean of releasing bioactive materials. The method relies on making the wall of polymer capsules sensitive to light by doping them with metal nanoparticles or organic dyes [171, 172]. Then, upon pulsed (below 10 ns) laser illumination, they absorb laser energy and disrupt the local environment due to a temperature increase, thus increasing the permeability of the capsule wall [166]. Such polyelectrolyte microcapsules were obtained using a layer-by-layer technique (see Section 8.3.3). This permitted for the tailoring of the composition of the wall, and the incorporation of metal nanoparticles (Fig. 8.24). In biological systems, it is desirable to trigger drug release in the near-infrared (NIR), around 800–1200 nm, as most tissues show negligible absorption in this region. Indeed, the absorption of gold nanoparticles incorporated in a polymeric capsule wall is red-shifted to the NIR (700–1500 nm) compared to the absorption of individual gold nanoparticles (around 500 nm). Such gold nanoparticles should thus absorb under *in vivo* conditions [171]. It has further been shown that fluorescein isocyanate (FITC)-labeled dextran [165] and rhodamine-labeled polystyrenesulfate (PSS-Rh) [166], convenient models for high-molecular-weight biomolecules, can be loaded into the capsules by exploiting the pH dependence of the shell permeability and then released on demand from the capsules by irradiation with 10-ns pulses of laser light at 1064 nm. These systems are thus promising vehicles for triggered topical or endoscopic drug delivery. Recently, the surface of such light-responsive polyelectrolyte/gold nanocapsules has been functionalized



**Figure 8.24.** Schematic representation of a polyelectrolyte multilayer capsule incorporating PSS-Rh. The polyelectrolyte multilayer walls consist of PSS and PAH polymers and metal nanoparticles.

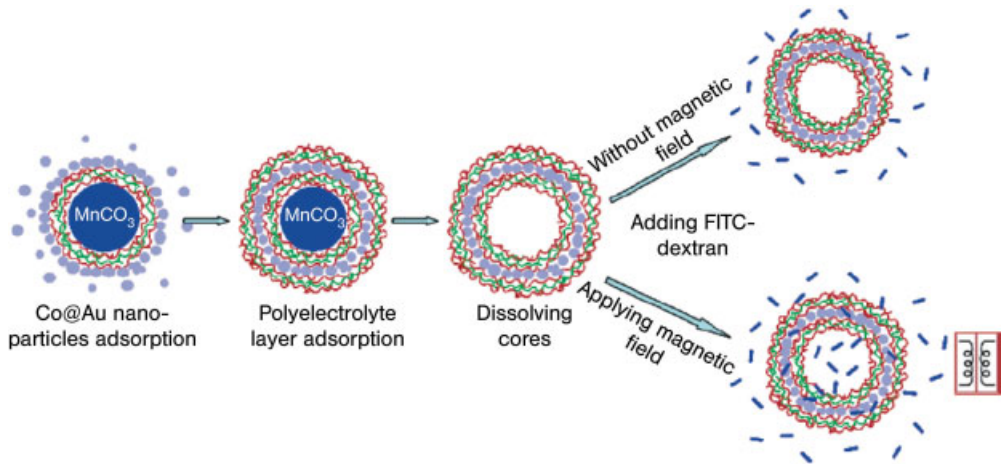


**Figure 8.25.** Scheme of the assembly and permeability test for microcapsules embedded with Co@Au nanoparticles under an oscillating magnetic field.

by model ligands (monoclonal immunoglobulin G antibodies), which opens new possibilities to targeted light-responsive drug delivery [165].

Similar to this work, magnetic fields has been used to trigger release from polyelectrolyte microcapsules. These capsules were designed to be more or less permeable to macromolecules depending on the application of a magnetic field. Indeed, ferromagnetic gold-coated cobalt nanoparticles (3 nm) (“Co@Au”) were embedded inside the capsule wall made of bilayers of poly(sodium styrene sulfonate)/poly(allylamine hydrochloride) (PSS/PAH). It could be shown that upon application of an external alternating magnetic field, the permeability of the capsules for hydrophilic macromolecules increased significantly due to the rapid movement of the embedded Co@Au nanoparticles. Figure 8.25 illustrates the synthesis of such particles by a layer-by-layer technique and shows how dextran can be encapsulated in such particles upon application of an oscillating magnetic field inducing an enhanced permeability of the capsule wall. This process was found to be reversible and the triggered release of dextran could be demonstrated [167].

Finally, magnetites of a suitable size and magnetic properties have also been used for magnetic heating [173]. The phenomenon of magnetic hyperthermia may be exploited for colloidal drug carrier systems that are composed of magnetites embedded in a thermoresponsive polymer matrix (exhibiting LCST). In fact, the application of a magnetic field leads to the heating of the colloidal system and may induce the phase transition of the thermosensitive polymers. Consequently, the release or entrapment of a drug may be triggered. Indeed biocompatible polymer drug carriers, which released drugs in response to the application of a high-frequency magnetic field, have been reported [174].

## 8.5.2

**Diagnosis**

Polymeric nanoparticles have found great interest not only as drug delivery systems, but they have also been used as carrier systems of molecules/labels that allow for their detection *in vivo* and *in vitro*. Labeling nanoparticles allows for their (optical) imaging, and thus provides a valuable tool to follow the delivery vehicle on its journey through the body, to elucidate the real-time cellular localization of nanoparticles and to determine their *in vivo* distribution after administration. It is a powerful means to ascertain whether successful delivery to the desired organ or tissue structure can take place.

As an example, the monitoring of optically labeled drug delivery devices in the field of tumor targeting is one of the many applications in which the imaging process has been implanted successfully. Indeed, many of the same techniques used to reach delivery of drugs to cancerous tissues may also be used to target imaging agents. In fact, as targeted delivery systems approach the stage where they can be used clinically, primary assessment of the utility of a particular colloidal formulation in a particular patient may be made with imaging agents to verify that the delivery system goes rapidly to the cancerous tissues before any drug regimen is begun.

Apart from that labeled polymeric nanocarrier have found rising interest as diagnostics, i.e. in the field of medical imaging [magnetic resonance imaging (MRI), etc.] to detect morbid tissues and diseases. The interest of using polymeric nanoparticles as diagnostic tools (by encapsulating the diagnostic label) relies in (i) its size, (ii) the possibility of using biocompatible materials and (iii) the possibility of modifying the surface of the colloidal vehicle to achieve targeting devices. As explained in Section 8.1, the nanoparticles' size allows for the passive targeting of organs such as the liver or spleen, whereas the use of coating materials (e.g. PEO) permits the passive targeting of cancerous tissues (due to the enhanced permeability of blood vessels), together with an enhanced residence time (half-life time) in the blood. In addition, the surface functionalization of nanoparticles by specific probes/molecules allows the active targeting of specific cellular districts.

The following gives a nonexhaustive overview on the different types of diagnostic systems based on polymeric nanoparticles. It is structured with regard to the different labels (fluorescent dyes, contrast agents for MRI, quantum dots, gold nanoparticles, radiolabeled nanoparticles, nanoparticles for ultrasound imaging). Furthermore, their utility for *in vitro* (immunoassays, biosensors, etc.) and *in vivo* tests (MRI, etc.) is mentioned.

**8.5.2.1 Fluorescence Labeling of Polymeric Nanoparticles**

**8.5.2.1.1 Organic Fluorescent Dyes** Fluorescent labeling is a widely used and convenient tool in biology and biological imaging. In the field of drug delivery, it has been used to (i) simulate drug release (establishment of release profiles) or (ii) to

localize nanoparticles and understand their fate after administration. The fluorescent label has to be chosen depending on the purpose and the physicochemical properties of the nanoparticles. In the first case (i), the fluorescent dye is used as a model drug and should therefore have similar physicochemical properties as the drug. For instance, commercially available FITC-labeled dextran (“FD-4”) and tetramethylrhodamine-labeled dextran have often been used as a model for hydrophilic macromolecular “drugs” (such as proteins) to study their release profile from nanospheres [143] and nanocapsules [165].

For diagnostic applications (case ii), however, a durable encapsulation of the dye is desired, requiring good affinity of the dye for the nanoparticles material. For instance, small organic hydrophobic fluorescent molecules (rhodamine [175], fluorescein [176], etc.) are suitable for nanoparticles made of hydrophobic polymers or nanocapsules with an oily core [146]. In the case of PLGA nanoparticles labeled by lipophilic 3-(2-benzothiazolyl)-7-(diethylamino)coumarin (“coumarin 6”) [177], it has been demonstrated that the nanoparticles’ physical properties, such as particle size and  $\zeta$  potential, were not significantly different from those of unloaded nanoparticles. As to the preparation, the small organic fluorescent molecule is generally dissolved together with the core-forming polymer during the nanoparticle preparation. These fluorescent nanoparticles thus allow the calculation of the amount of fluorescent carriers taken up by cells (*in vivo* or *in vitro*) by fluorimetry.

However, particles labeled by “free” fluorescein rapidly released this fluorescent probe in the medium used for the biological investigation [176], as a consequence of diffusion. Thus, recent developments tend to focus on covalently conjugate/link fluorescent dyes to (co)polymers in order to avoid diffusion of the dyes from the polymer matrix of nanoparticles to the surrounding medium, e.g. fluorescein has been conjugated to PLGA end-capped by a carboxylic group using carbodiimide chemistry in order to diminish the diffusion from the fluorescent dye from PLGA nanoparticles [178].

**8.5.2.1.2 Quantum Dots** Semiconductor nanocrystals (also known as quantum dots) are emerging as a new class of fluorescent probes for *in vitro* and *in vivo* biomolecular and cellular imaging [179, 180]. In comparison with organic dyes and fluorescent proteins, quantum dots, whose size ranges from 1 to 10 nm in radius, have unique optical and electronic properties, including sharp emission spectra (with full width at half maximum as narrow as 25 nm) improved signal brightness and photostability [181], resistance against photobleaching (long fluorescent lifetime), and tunable size dependent emission peaks. Due to their broad excitation profiles and narrow/symmetric emission spectra, high-quality quantum dots are also well-suited for multicolor optical coding for biological assays, by combining different color quantum dots with different intensity levels. Quantum dots are mostly synthesized in nonpolar organic solvents, such as tri-*n*-octylphosphine oxide, which coordinate on the surface of quantum dots to prevent the formation of bulk semiconductors. As a result, the nanoparticles are capped with a monolayer of organic ligands and are soluble only in nonpolar organic solvents. However, for biological imaging, quantum dots must be water-soluble. To address this, different

strategies have been devised including ligand exchange with thiol-functionalized molecules, and encapsulation by a layer of diblock or triblock copolymers or else in silica shells, phospholipid micelles or polymer beads. Further developments in biological applications of quantum dots aimed to functionalize the surface of quantum dots by bioaffinity ligands, such as monoclonal antibodies, peptides, oligonucleotides or carbohydrates. Thus, hydrophilic  $\alpha$ -mannopyranosyl moieties have been linked to a phosphine oxide, which could then be used as ligand in the surface-functionalized hydrophilic quantum dots [182]. Furthermore attachment of PEG could lead to improved biocompatibility and reduced nonspecific interactions [183]. Such bioconjugated quantum dots thus have raised new possibilities for ultrasensitive and multiplexed imaging of molecular targets in living cells, animal models and, possibly, in humans.

Recent works have focused on the encapsulation of the nanocrystals in natural or synthetic polymeric materials to form “bigger” quantum dot–polymer composites in the range of some hundreds of nanometers. Such systems were expected to reduce the toxicity of quantum dots and to be suitable for further conjugation with biomolecules, while maintaining the high emission quantum yield of the quantum dots. It should be emphasized that the use of a polymeric matrix also opens up the possibility of incorporating several probes (quantum dots of different size), allowing in particular multiplexed optical coding. In the following, we will focus on quantum dot–polymer composites.

Several strategies to embed quantum dots in polymer matrices have been envisaged. Quantum dots have been incorporated either by noncovalent interactions, such as electrostatic and hydrophobic interactions, or by copolymerization of monomers with quantum dots surrounded by polymerizable ligands.

In 2003, Chen and coworkers developed an interesting method to assemble negatively charged CdSe–ZnS quantum dots into glyconanospheres through electrostatic interactions with carboxymethyl dextran and poly(lysine). To enhance the long-term stability of these glyconanosphere composites built by the layer-by-layer procedure, quantum dots were cross-linked with the polysaccharide matrix by covalent amide bonds. Spherical luminescent glyconanospheres of an average diameter of 190 nm were thus obtained. The presence of glucose residues at the surface of the nanoparticles was evidenced by fluorescent imaging microscopy; indeed, upon addition of a carbohydrate-binding protein, Con A, the glyconanoparticles aggregated (Fig. 8.26(A)). As shown in Fig. 8.26(B), this aggregation was, however, prevented when free  $\alpha$ -D-glucose was added, since glucose effectively competes with the glyconanospheres on the binding sites of Con A. These quantum dot–polysaccharide composites are thus promising tools for real-time monitoring of carbohydrate–protein (lectin) interactions that are critical steps in bacterial and viral infection [140].

On the basis of hydrophobic interactions, polymeric microbeads loaded with quantum dots could be prepared, allowing multiplexed/multicolor optical probing for biological assays. Several groups have successfully incorporated quantum dots into polymeric nanoparticles via polymerization in dispersed media [184–187]. Hydrophobic quantum dots (ZnS-capped CdSe nanocrystals) with different sizes were

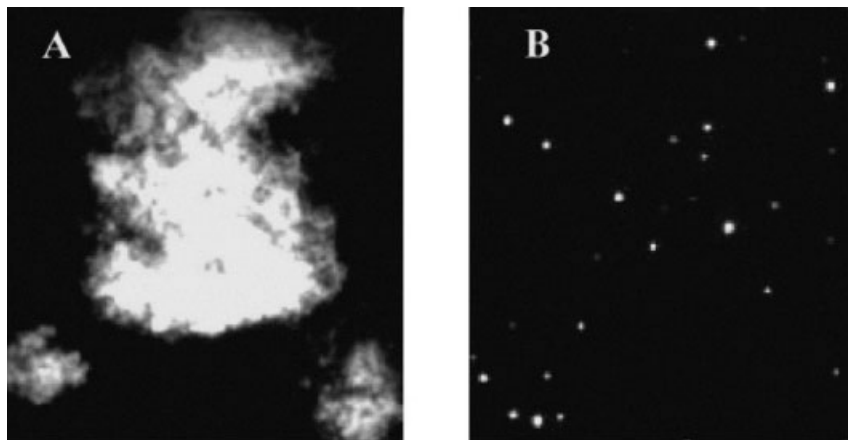


**Figure 8.26.** Lectin (Con A) initiated aggregation of CdSe–ZnS quantum dot luminescent glyconanospheres. (A) Luminescence image of aggregated glyconanospheres in the presence of Con A.

(B) Luminescence image of the glyconanospheres in the presence of Con A and free  $\alpha$ -D-glucose molecules. The latter compete with the glyconanospheres for the Con A binding sites and prevent nanoparticle aggregation.

thus embedded at precisely controlled ratios in the outer layer of swollen polystyrene polymer beads, previously prepared by miniemulsion polymerization of styrene, divinylstyrene and acrylic acid (98:1:1). The quantum dot-loaded particles were sealed by a silica layer, then, streptavidin molecules were covalently coupled to the surface via the carboxylic acid groups of acrylic acid [184]. Biomolecular probes, such as oligonucleotides or antibodies, were then conjugated to the silica surface via streptavidin–biotin complex formation. The fluorescence spectra of the quantum dot-tagged beads (1.2  $\mu\text{m}$ ) were narrow (even narrower than those of free quantum dots) and the emission maxima remained unchanged, which indicates that the beads were highly uniform and reproducible, and that the beads were spatially separated by the beads structure. Thanks to the identification code embedded in the interior of the beads, bead identification accuracies as high as 99.9% could be reached. This approach allows combining molecular recognition and optical “barcoding” by polymeric beads, which is expected to open new opportunities in gene expression studies, high-throughput screening and medical diagnostics [184]. In comparison with bigger (150  $\mu\text{m} \times 150 \mu\text{m} \times 150 \mu\text{m}$ ) planar DNA chips, encoded-bead technology is expected to be more flexible regarding target selection (e.g. adding new genes or single-nucleotide mutations), to show faster binding kinetics (similar to that in homogenous solution) and to be less expensive to produce.

In contrast to these approaches based on the noncovalent immobilization of quantum dots in polymeric materials, O’Brien and coworkers adapted an approach previously reported by Emrick and coworkers [188] and covalently incorporated

quantum dots into a polymer matrix using suspension polymerization. Thus, they prepared quantum dots surrounded by polymerizable ligands and copolymerized them with styrene using DVB as crosslinking agent. This facile procedure seems very promising for the commercialization of many bead-types with diameters ranging from 100 nm to 500  $\mu\text{m}$ , where the CdS quantum dots are evenly distributed throughout the polystyrene spheres. These quantum dot–polymer composites may be used for optical biological probing/assays or combinatorial chemistry applications (in solid phase organic chemistry), benefiting from quantum dots encoding [189, 190]. Employing miniemulsion polymerization, Elaissairi and coworkers synthesized quite monodisperse (100–350 nm) quantum dot-tagged colloids by copolymerization of styrene with vinyl-functionalized quantum dots [191]. Very recently, another promising approach to covalently incorporate quantum dots in latexes was proposed by Esteves and coworkers [192]. Indeed, they applied radical polymerization to miniemulsion using ATRP and initiated the miniemulsion polymerization of butyl acrylate by quantum dots functionalized by an ATRP initiator.

In conclusion, the use of fluorescent nanocrystal–polymer composites opens up new possibilities for designing luminescent surface-modified nanoparticles to deliver quantum dots specifically to the targeted tissue or cells. These luminescent quantum dots are ideal fluorophores for biological labeling because their fluorescence emission wavelength can be continuously tuned by changing the particle size and a single wavelength can be used for simultaneous excitation of different sized quantum dots. The unique properties of luminescent quantum dots thus allow multicolor experiments in cellular imaging and diagnosis, offering substantial advantages over organic dyes in multiplexed target detection.

#### 8.5.2.2 Contrast Agents for MRI

MRI is based on the NMR signal of hydrogen present in body tissues (water, membrane lipids, proteins, etc.). It is currently the most important available diagnostic method and as a noninvasive technique routinely clinically used for diagnostic imaging. However, the intrinsic sensitivity and selectivity of conventional MRI techniques is very low. It has been clearly shown that the use of contrast agents, which alter the relaxivity of water, can greatly improve the sensitivity and thus the diagnostic value of MRI.

The first generation of contrast agents consists of high-spin paramagnetic ions ( $\text{Gd}^{3+}$  chelates) that are at present routinely used as MRI contrast agents. More recently, magnetic nanoparticles, with a size generally between 3 and 10 nm, have been used as contrast agents for MRI. Due to their size, these superparamagnetic nanoparticles accumulate in MPS organs (passive targeting). Third-generation magnetic nanoparticles are surface-modified by specific ligands, such as antibodies, allowing the specific targeting of cells/tissues.

Recent works tend to incorporate magnetic nanoparticles in larger polymeric nanoparticles. Such relatively “big” polymer nanoparticles are expected to passively target tumors. In addition, targeting moieties may be attached at the surface of the latter (active targeting). For this purpose, polymeric nanoparticles decorated

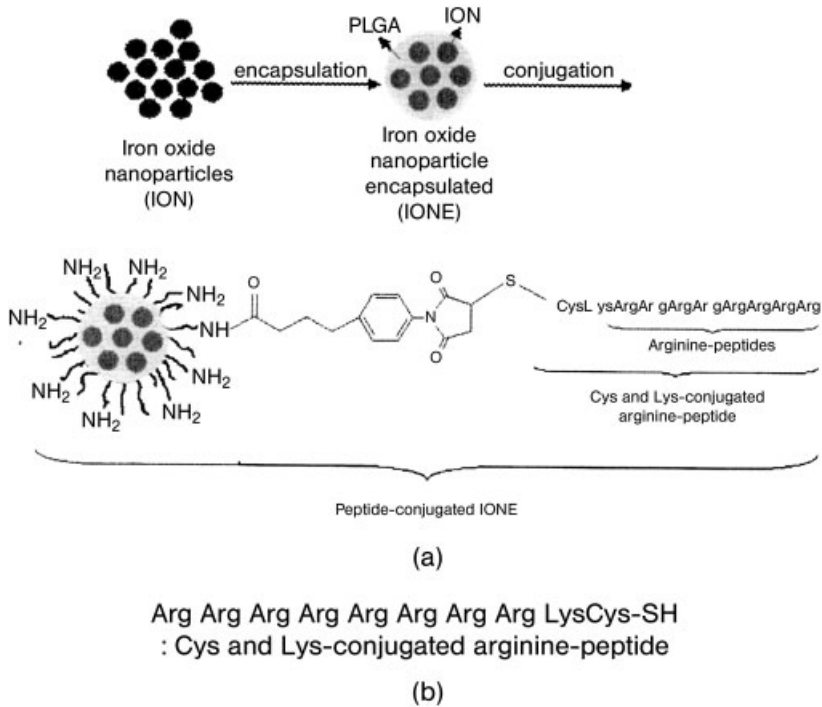


**Figure 8.27.** (a) Schematic diagram for preparing the  $\gamma\text{-Fe}_2\text{O}_3$ -PLGA-Arg-FITC nanoparticles. (b) Sequence of arginine peptide.

by targeting molecules and labeled by contrast agents have been designed. One interesting work published recently reports on the synthesis of a novel intracellular polymeric carrier as a MR molecular image diagnostic agent. Here, superparamagnetic iron oxide nanoparticles were encapsulated with peptide-conjugated PLGA using an emulsification-diffusion method. In addition, these polymer nanoparticles were labeled twice: first, by encapsulation of metallic nanoparticles for MRI and, second, by a fluorescent dye for detection by fluorescence microscopy; actually, a FITC-conjugated arginine peptide, a “cell penetration peptide”, was conjugated via its thiol group to maleimide-derivatized PLGA. Thus, nanoparticles of 110 nm diameter have been synthesized allowing for combined targeting and multiple/versatile detection [193] (Fig. 8.27).

Aside from their use in MRI, there are multiple other applications of magnetic particles encapsulated in polymer beads which are illustrated in the following.

### 8.5.2.3 Magnetic Nanoparticles for *In Vitro* Assays

Increasing interest has been focused on the preparation of surface-modified latexes, and their use as solid supports of biomolecules in biomedical diagnostics



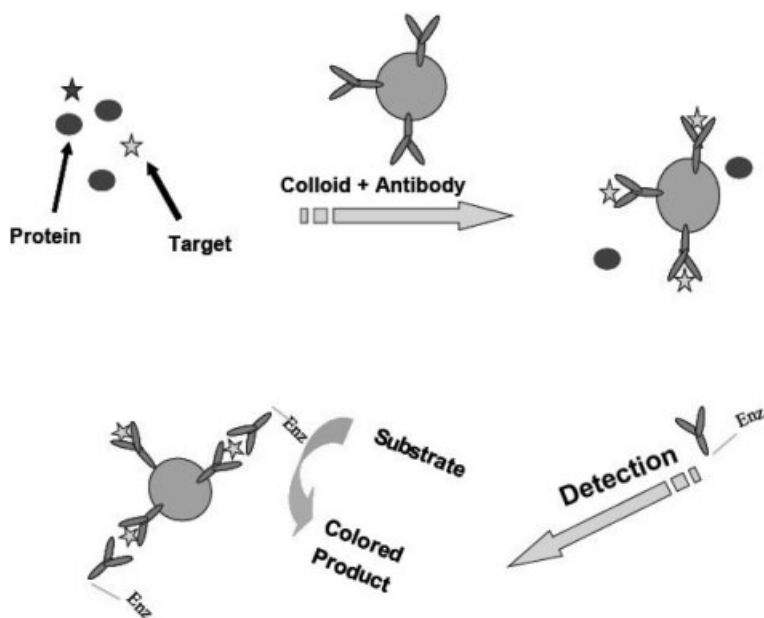


**Figure 8.28.** Schematic representation of the specific capture and detection of the targeted antigen (ELISA).

and purification of biological materials. The particular interest in using such colloidal systems for biomedical diagnostic systems relies on their high specific surface. Due to their size, surface-modified latex beads have been used for the capture of biological materials, their purification and concentration, and more specifically in immunoassays. In fact, the size of the nanoparticles allows their separation from the biological medium by centrifugation. Recent studies tend towards the use of magnetic latex particles. Magnetism is used here as an easy tool to separate the nanoparticles, replacing the centrifugation step applied in the case of classical non-magnetic particles. Similar to the latter, magnetic latex nanoparticles are principally used as a solid support for biomolecules involved in the specific capture of targeted biomolecules, such as antigens for immunoassays [i.e. ELISA, Fig. 8.28, and nucleic acid detection in “enzyme-linked oligosorbent assay” (ELOS), Fig. 8.29]. For that purpose, magnetic latex particles bearing either immobilized antibodies or ODNs, complementary to the single stranded DNA of interest, are used.

Furthermore, such nanoparticles can be used for the nonspecific capture of biomolecules or viruses [194] in order to concentrate or to purify samples. In fact, this process is based on the well-controlled adsorption of biomolecules on the colloidal particles, followed by the concentration of the nanoparticles and, finally, the desorption of the adsorbed biomolecules. Thus, for the capture of nucleic acids, cationic magnetic colloids are used in order to favor attractive electrostatic interactions. Adsorption and desorption are controlled by monitoring the pH and the salinity of

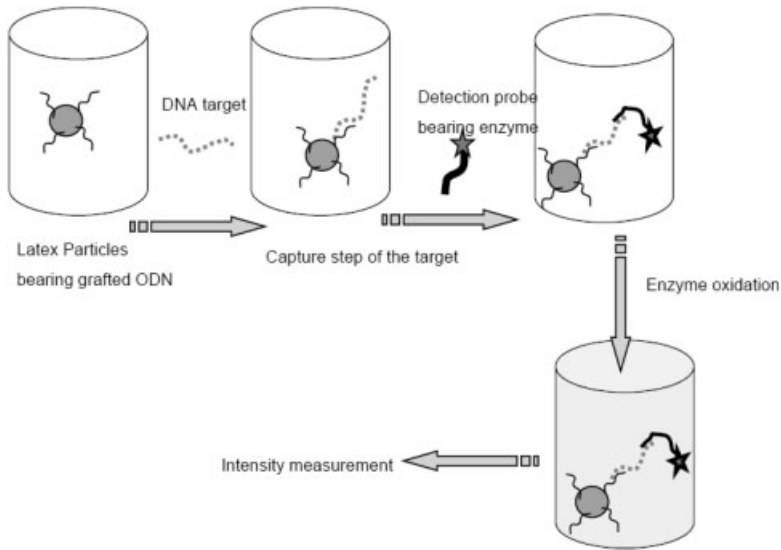


**Figure 8.29.** Schematic representation of the specific capture and detection of targeted DNA or RNA (ELOS).

the medium [195]. Similarly, magnetic latex particles with a hydrophobic surface have been successfully used for the extraction, purification and concentration of proteins. Indeed, as mentioned in Section 8.1, unspecific adsorption of proteins on surfaces is mainly governed by hydrophobic attractive forces, such as van der Waals forces [196].

The synthesis of “smart” magnetic colloids has also been reported. Thus, thermosensitive magnetic latex particles have been synthesized, allowing the controlled adsorption, concentration and desorption of proteins [197]. At temperatures above the LCST, thermosensitive polymers undergo a phase transition from a hydrophilic to a hydrophobic state. Thus, nanoparticles with a thermosensitive PNIPAAm shell showed a volume phase transition temperature ( $T_{VPT}$ ), below which protein adsorption was low (due to the hydrophilic character of the particle surface) and above which the adsorption was considerably high [198].

Recently, an interesting approach for the synthesis of fluorescent magnetic nanoparticles that possess reactive carboxylic acid groups at their surface was reported. First, fluorescent polystyrene nanodots (25 nm) were adsorbed onto magnetic emulsions (250 nm) via electrostatic interactions. The surface of these “hybrid” particles was then sealed by adsorbing film-forming polymer nanobeads (40 nm) on their surface and heating above the glass transition temperature ( $T_g$ ) [199].

A representative review about magnetic colloids, their preparation and their use in biomedical diagnostics was given by Elaissari [200]. The incorporation of magnetic nanoparticles in polymer beads is thus a promising tool in the field of diagnosis and triggered drug delivery, but they can also serve as therapeutic systems. In

fact, magnetic nanoparticles have potential therapeutic applications as they can locally induce hyperthermia by application of an alternating magnetic field. This magnetically induced hyperthermia remains promising for cancer therapy aside from conventional methods, such as surgery, chemotherapy and radiotherapy [173]. Depending on the temperature, hyperthermia can be used either for immune stimulation (41–46 °C) or tumor destruction (46–56 °C).

As illustrated in Section 8.1, encapsulating magnetic nanoparticles in a sub-micron polymeric vehicle allows for the size-controlled “passive targeting” to tumoral tissue. Besides, they are suitable for surface functionalization by targeting biomolecules. In fact, the combination of magnetic particles in a drug-containing polymeric matrix that is sensitive to temperature is a very comprising approach. As developed in Section 8.5.1.3, the release of drugs embedded in a stimuli-responsive polymer can be induced by various stimuli, such as pH or temperature. Intracellular drug release from polymeric nanoparticles could thus be triggered by the temperature increase during the hyperthermia sequence under MRI monitoring. Instead of using thermosensitive polymers (e.g. PNIPAAm), such a mechanism could also use thermolabile bonds [174].

#### 8.5.2.4 Electron Dense Agents for Transmission Electron Microscopy (TEM)

Organic fluorescent labels allow studying intracellular nanoparticle uptake and distribution using confocal fluorescence microscopy. More precise TEM observation requires the labeling of the nanoparticles by an electron-dense agent. For that purpose, e.g. PLGA nanoparticles have been successfully loaded with osmium tetroxide – a widely used staining agent for TEM observation [177].

Another approach relies on the labeling by gold nanoparticles. For this purpose, the surface of gold nanoparticles must be modified in order to enhance/optimize their affinity to the nanoparticles’ core-forming polymer. Indeed, Qiu and co-workers successfully encapsulated gold nanoparticles surface-modified by PLA chains in PLA nanospheres [58].

#### 8.5.2.5 Radiolabeled Nanoparticles

For a long time, radiolabeled (e.g.  $^3\text{H}$ ,  $^{14}\text{C}$ ) polymers have been synthesized for nanoparticles, and then the radioactivity could be quantified in order to elucidate their uptake and distribution [10, 201]. However, this method necessitates not only the synthesis of radiolabeled polymers, which require special laboratories, but also expensive equipment for the quantification.

## 8.6

### Conclusion and Perspectives

Polymeric nanoparticles are of particular interest due to their size, the wide range of polymeric materials available, and the possibility to tailor-make both the constituting elements and the nanoparticles. Furthermore, recent developments in (polymer) chemistry, biology, biotechnology and physics have drastically enlarged

the use and importance of polymeric nanoparticles. For drug delivery purposes, polymeric nanoparticles no longer possess only a protecting role, while releasing drugs in a controlled way. They are rather “Trojan” horses that allow drug delivery to a selected target, such as cancerous cells, organs or even viruses. Further trends go towards smart colloidal drug delivery systems that release drugs in response to an external trigger, such as light or a magnetic field, or even in response to an physiological internal trigger, such as pH, glucose concentration, etc.

Nanoparticles possessing targeting moieties on their surface have also found applications in diagnosis. In fact, the surface functionalization of fluorescent and magnetic colloids allows the selective detection of, for example, a tumor expressing specific antibodies at its surface. The latest developments in quantum dots technology allowing multiplexed sensing have been a revolution in the field of diagnostics.

Nowadays, the developments in polymeric nanoparticles tend towards multifunctional nanoparticles, which allow simultaneous targeting, imaging and treatment by one single system. Monitoring of the localization of the drug in a living system and the release of the drug as response to an external trigger is no longer a dream. First attempts of such combined drug delivery systems have been already proposed as “nanoclinics” [202], i.e. complex surface-functionalized polymeric nanoparticles that contain various probes for diagnostics and drugs for targeted delivery in one single unit.

## References

- 1 THURMOND, K. B., KOWALEWSKI, T., WOOLEY, K. L., Water-soluble knedel-like structures: the preparation of shell-cross-linked small particles. *J. Am. Chem. Soc.* **1996**, *118*, 7239–7240.
- 2 TORCHILIN, V. P., Long circulating microparticulate systems. *J. Microencapsul.* **1998**, *15*, 1–19.
- 3 GREF, R., MINAMITAKE, Y., PERACCHIA, M. T., TRUBETSKOY, V., TORCHILIN, V., LANGER, R., Biodegradable long-circulating polymeric nanospheres. *Science* **1994**, *263*, 1600–1603.
- 4 LABARRE, D., VAUTHIER, C., CHAUVIERRE, C., PETRI, B., MÜLLER, R., CHEHIMI, M. M., Interactions of blood proteins with poly(isobutylcyanoacrylate) nanoparticles decorated with a polysaccharidic brush. *Biomaterials* **2005**, *26*, 5075–5084.
- 5 PASSIRANI, C., BARRATT, G., DEVISSAGUET, J.-P., LABARRE, D., Interactions of nanoparticles bearing heparin or dextran covalently bound to poly(methyl methacrylate) with the complement system. *Life Science* **1998**, *62*, 775–785.
- 6 ÖSTERBERG, E., BERGSTROM, K., HOLMBERG, K., SCHUMAN, T. P., RIGGS, J. A., BURNS, N. L., VAN ALSTINE, J. M., HARRIS, J. M., Protein-rejecting ability of surface-bound dextran in end-on and side-on configurations: comparison with PEO. *J. Biomed. Mater. Res.* **1995**, *29*, 741–747.
- 7 MAEDA, H., WU, J., SAWA, T., MATSUMARA, Y., HORI, K., Tumor vascular permeability and the EPR effect in macromolecular therapeutics: a review. *J. Control. Release* **2000**, *65*, 271–284.
- 8 BRIGGER, I., DUBERNET, C., COUVREUR, P., Nanoparticles in cancer therapy and diagnosis. *Adv. Drug Deliv. Rev.* **2002**, *54*, 631–651.
- 9 RUOSLAHTI, E., PIERSCHBACHER, M. D., New perspectives in cell adhesion:

- RGD and integrins. *Science* **1987**, *238*, 491–497.
- 10 GREF, R., COUVREUR, P., BARRATT, G., MYSLAKINE, E., Surface-engineered nanoparticles for multiple ligand coupling. *Biomaterials* **2003**, *24*, 4529–4537.
  - 11 BRANNON-PEPPAS, L., BLANCHETTE, J. O., Nanoparticle and targeted systems for cancer therapy. *Adv. Drug Deliv. Rev.* **2004**, *56*, 1649–1659.
  - 12 JANES, K. A., CALVO, P., ALONSO, M. J., Polysaccharide colloidal particles as delivery systems for macromolecules. *Adv. Drug Deliv. Rev.* **2001**, *47*, 83–97.
  - 13 DUMITRIU, S., Polysaccharides as biomaterials. In *Polymeric Biomaterials*, 2nd edn, DUMITRIU, S. (Ed.). Marcel Dekker, New York, **2002**, pp. 1–61.
  - 14 LEMARCHAND, C., GREF, R., COUVREUR, P., Polysaccharide-decorated nanoparticles. *Eur. J. Pharm. Biopharm.* **2004**, *58*, 327–341.
  - 15 KAWASHIMA, Y., YAMAMOTO, H., TAKEUCHI, H., KUNO, Y., Mucoadhesive DL-lactide/glycolide copolymer nanospheres coated with chitosan to improve oral delivery of elcatonin. *Pharm. Dev. Technol.* **2000**, *5*, 77–85.
  - 16 ALONSO, M. J., CALVO, P., REMUÑAN, C., VILA, A., JATO, J. L., Application of nanoparticles based on hydrophilic polymers as pharmaceutical forms. *EU 0 860 166 A1*.
  - 17 HENDRICKS, S. K., KWOK, C., SHEN, M., HORBETT, B. D., RATNER, B. D., BRYERS, J. D., Plasma-deposited membranes for controlled release of antibiotic to prevent bacterial adhesion and biofilm formation. *J. Biomed. Mater. Res.* **2000**, *50*, 160–170.
  - 18 SCHATZ, C., BIONAZ, A., LUCAS, J.-M., PICHOT, C., VITON, C., DOMARD, A., DELAIR, T., Formation of polyelectrolyte complex particles from self-complexation of *N*-sulfated chitosan. *Biomacromolecules* **2005**, *6*, 1642–1647.
  - 19 YAMAMOTO, H., KUNO, Y., SUGIMOTO, S., TAKEUCHI, H., KAWASHIMA, Y., Surface-modified PLGA nanosphere with chitosan improved pulmonary delivery of calcitonin by mucoadhesion and opening of the intercellular tight junctions. *J. Control. Release* **2005**, *102*, 373–381.
  - 20 BORCHARD, G., LUESSEN, H. L., DE BOER, A. G., VERHOEF, J. C., LEHR, C. M., JUNGINGER, H. E., The potential of mucoadhesive polymers in enhancing intestinal peptide drug absorption. 3. Effects of chitosan-glutamate and carbomer on epithelial tight junctions *in vitro*. *J. Control. Release* **1996**, *39*, 131–138.
  - 21 AGNIHOTRI, S. A., MALLIKARJUNA, N. N., AMINABHAVI, T. M., Recent advances on chitosan-based micro- and nanoparticles in drug delivery. *J. Control. Release*, **2004**, *100*, 5–28.
  - 22 TAKEUCHI, H., YAMAMOTO, H., KAWASHIMA, Y., Mucoadhesive nanoparticulate systems for peptide drug delivery. *Adv. Drug Deliv. Rev.* **2001**, *47*, 39–54.
  - 23 FELT, O., EINMAHL, S., GURNY, R., FURRER, F., BAEYENS, V., Polymeric systems for ophthalmic drug delivery. In *Polymeric Biomaterials*, 2nd edn, DUMITRIU, S. (Ed.). Marcel Dekker, New York, **2002**, pp. 377–421.
  - 24 BALAZS, E. A., Why hyaluronan has so many biological activities? In *New Frontiers in Medical Sciences: Redefining Hyaluronan*, ABATANGELO, G., WEIGEL, P. H. (Eds.). Elsevier Science, Amsterdam, **2000**, pp. 3–10.
  - 25 LEMARCHAND, C., COUVREUR, P., BESNARD, M., COSTANTINI, D., GREF, R., Novel polyester-polysaccharide nanoparticles. *Pharm Res* **2003**, *20*, 1284–1292.
  - 26 DOMB, A. J., KUMAR, N., SHESKIN, T., BENTOLILA, A., SLAGER, J., TEOMIM, D., Biodegradable polymers as drug carrier systems. In *Polymeric Biomaterials*, 2nd edn, DUMITRIU, S. (Ed.). Marcel Dekker, New York, **2002**, pp. 91–121.
  - 27 VERT, M., MAUDUIT, L., SUMING, L., Biodegradation of PLA/GA polymers: increasing complexity. *Biomaterials* **1994**, *15*, 1209–1213.
  - 28 GRIZZI, I., GARREAU, H., LI, S., VERT, M., Hydrolytic degradation of devices based on poly(DL-lactic acid) size-dependence. *Biomaterials* **1995**, *15*, 305–311.

- 29 PARK, T. G., Degradation of poly-(lactic-co-glycolic acid) microspheres: effect of copolymer composition. *Biomaterials* **1995**, *16*, 1123–1130.
- 30 LENZ, R. W., GUERIN, P., Functional polyesters and polyamides for medical application of biodegradable polymers. In *Polymers in Medicine: Functional Polyesters and Polyamides for Medical Applications of Biodegradable Polymers*, CHIELLINI, E., GIUSTI, P. (Eds.). Plenum Press, New York, **1983**, pp. 219–230.
- 31 LEE, B.-S., VERT, M., HOLLER, E., Water-soluble aliphatic polyesters: poly(malic acid)s. In *Biopolymers*, DOI, Y., STEINBÜCHEL, A. (Eds.). Wiley-VCH, Weinheim, **2002**, Vol. 3a, pp. 75–103.
- 32 TIAN, D., DUBOIS, P., JÉRÔME, R., Macromolecular engineering of polylactones and polylactides. 22. Copolymerization of epsilon-caprolactone and 1,4,8-trioxaspiro[4.6]-9-undecanone initiated by aluminum isopropoxide. *Macromolecules* **1997**, *30*, 2575–2581.
- 33 DETREMBLEUR, C., MAZZA, M., HALLEUX, O., LECOMTE, P., MECERREYES, D., HEDRICK, J. L., JÉRÔME, R., Ring-opening polymerization of gamma-bromo-epsilon-caprolactone: a novel route to functionalized aliphatic polyesters. *Macromolecules* **2000**, *33*, 14–18.
- 34 LATERE, J.-P., LECOMTE, P., DUBOIS, P., JÉRÔME, R., 2-oxepane-1,5-dione: a precursor of a novel class of versatile semicrystalline biodegradable (co)polyesters. *Macromolecules* **2002**, *35*, 7857–7859.
- 35 RIVA, R., SCHMEITS, S., STOFFELBACH, F., JÉRÔME, C., JÉRÔME, R., LECOMTE, P., Combination of ring-opening polymerization and “click” chemistry towards functionalization of aliphatic polyesters. *Chem. Commun.* **2005**, *42*, 5334–5336.
- 36 RIEGER, J., BERNAERTS, K. V., DU PREZ, F. E., JÉRÔME, R., JÉRÔME, C., Lactone end-capped poly(ethylene oxide) as a new building block for biomaterials. *Macromolecules* **2004**, *37*, 9738–9745.
- 37 KAWAGUCHI, T., NAKANO, M., JUNI, K., INOUE, S., YOSHIDA, Y., Release profiles of 5-fluorouracil and its derivatives from polycarbonate *in vitro*. *Chem. Pharm. Bull.* **1982**, *30*, 1517–1520.
- 38 KAWAGUCHI, T., NAKANO, M., JUNI, K., INOUE, S., YOSHIDA, Y., Examination of biodegradability of poly(ethylene carbonate) and poly(propylene carbonate) in the peritoneal cavity in rats. *Chem. Pharm. Bull.* **1983**, *31*, 1400–1403.
- 39 ANDERSON, J. M., SPILIZEWSKI, K. L., HILTNER, A., Poly  $\alpha$ -amino acids as biomedical polymers. In *Biocompatibility of Tissue Analogs*, WILLIAMS, D. F. (Ed.). CRC Press, Boca Raton, FL, **1985**, Vol. 1, pp. 67–88.
- 40 WEBSTER, I., WEST, P. J., Adhesives for medical applications. In *Polymeric Biomaterials*, 2nd edn, DUMITRIU, S. (Ed.). Marcel Dekker, New York, pp. 717–737.
- 41 MÜLLER, R., LHERM, C., HERBORT, P., COUVREUR, P., In vitro model for the degradation of alkylcyanoacrylate nanoparticles. *Biomaterials* **1990**, *11*, 590–595.
- 42 LEONARD, F., KULKARNI, R. K., BRANDES, G., NELSON, J., MAMERON, J. J., Synthesis and degradation of poly(alkylcyanoacrylates). *J. Applied Polym. Sci.* **1966**, *10*, 259–272.
- 43 GIL, E. S., HUDSON, S. M., Stimuli-responsive polymers and their bioconjugates. *Prog. Polym. Sci.* **2004**, *29*, 1173–1222.
- 44 DE LAS HERAS ALARCÓN, C., PENNADAM, S., ALEXANDER, C., Stimuli-responsive polymers for biomedical applications. *Chem. Soc. Rev.* **2005**, *34*, 276–285.
- 45 LEE, J. H., LEE, H. B., ANDRADE, J. D., Blood Compatibility of poly(ethylene oxide) surfaces. *Prog. Polym. Sci.* **1995**, *20*, 1043–1079.
- 46 VERMETTE, P., MEAGHER, L., Interactions of phospholipid- and poly(ethylene glycol)-modified surfaces with biological systems: relation to physico-chemical properties and mechanism. *Coll. Surf. B Biointerfaces* **2003**, *28*, 153–198.

- 47 PERACCHIA, M. T., Stealth nanoparticles for intravenous administration. *STP Pharma. Sci.* **2003**, *13*, 155–161.
- 48 OTSUKA, H., NAGASAKI, Y., KATAOKA, K., PEGylated nanoparticles for biological and pharmaceutical applications. *Adv. Drug Deliv. Rev.* **2003**, *55*, 403–419.
- 49 GREF, R., LÜCK, M., QUELLEC, P., MARCHAND, M., DELLACHERIE, E., HARNISCH, S., BLUNK, T., MÜLLER, R. H., “Stealth” corona–core nanoparticles surface modified by polyethylene glycol (PEG): influences of the corona (PEG chain length and surface density) and of the core composition on phagocytic uptake and plasma protein adsorption. *Coll. Surf. B Biointerfaces* **2000**, *18*, 301–313.
- 50 QUINTANAR-GUERRERO, D., ALLÉMANN, E., FESSI, H., DOELKER, E., Preparation techniques and mechanisms of formulation of biodegradable nanoparticles from preformed polymers. *Drug Dev. Ind. Pharm.* **1998**, *24*, 1113–1128.
- 51 VANDERHOFF, J. W., EL-AASSER, M. S., UGELSTAD, J., Polymer emulsification process. *US Patent 4 177 177*, **1979**.
- 52 BLANCO, M. D., ALONSO, M. J., *Eur. J. Pharm. Biopharm.* **1997**, *43*, 287–294.
- 53 ALLÉMANN, E., GURNY, R., DOELKER, E., Development and characterization of protein-loaded poly(lactide-co-glycolide) nanospheres. *Int. J. Pharm.* **1992**, *87*, 247–253.
- 54 FESSI, H., PUISIEUX, F., DEVISSAGUET, J. P., AMMOURY, N., BENITA, S., Nanocapsule formation by interfacial polymer deposition following solvent displacement. *Int. J. Pharm.* **1989**, *55*, R1–R4.
- 55 QUINTANAR-GUERRERO, D., FESSI, H., ALLÉMANN, E., Influence of stabilizing agents and preparative variables on the formation of poly(D,L-lactic acid) nanoparticles by an emulsion-diffusion technique. *Int. J. Pharm.* **1996**, *143*, 133–141.
- 56 FESSI, H., PUISIEUX, F., DEVISSAGUET, J. P., Process for preparing a colloidal and disperse system in the shape of nanocapsules. *Eur. Patent 274 961*, **1986**.
- 57 BILATI, U., ALLÉMANN, DOELKER, E., Development of a nanoprecipitation method intended for the entrapment of hydrophilic drugs into nanoparticles. *Eur. J. Pharm. Sci.* **2005**, *24*, 67–75.
- 58 QIU, H., RIEGER, J., GILBERT, B., JÉRÔME, R., JÉRÔME, C., PLA-Coated gold nanoparticles for the labeling of PLA biocarriers. *Chem. Mater.* **2004**, *16*, 850–856.
- 59 VANGEYTE, P., GAUTIER, S., JÉRÔME, R., About the methods of preparation of poly(ethylene oxide)-*b*-poly( $\epsilon$ -caprolactone) nanoparticles in water analysis by dynamic light scattering. *Colloid Surf. A Physicochem. Eng. Asp.* **2004**, *242*, 203–211.
- 60 ANTONIETTI, M., LANDFESTER, K., Single molecule chemistry with polymers and colloids: a way to handle complex reactions and physical processes. *Chem. Phys. Chem.* **2001**, *2*, 207–210.
- 61 LANDFESTER, K., Polyreactions in miniemulsions. *Macromol. Rapid Commun.* **2001**, *22*, 896–936.
- 62 KISHIDA, K., AKASHI, A., SAKUMA, M., SUZUKI, S., KIKUCHI, N., HIWATARI, H., ARIKAWA, K., Oral Peptide delivery using nanoparticles composed of novel graft copolymers having hydrophobic backbone and hydrophilic branches. *Int. J. Pharm.* **1997**, *149*, 93–106.
- 63 DURAND, A., MARIE, E., ROTUREAU, E., LEONARD, M., DELLACHERIE, E., Amphiphilic polysaccharides: useful tools for the preparation of nanoparticles with controlled surface characteristics. *Langmuir* **2004**, *20*, 6956–6963.
- 64 UCHIDA, T., SERIWAZA, T., AKASHI, M., Graft copolymers having hydrophobic backbone and hydrophilic branches XXI. Preparation of galactose surface-accumulated polystyrene nanospheres and their interaction with lectin. *Polymer J.* **1999**, *31*, 970–973.
- 65 UCHIDA, T., SERIZAWA, T., ISE, H., AKAIKE, T., AKASHI, M., Graft copolymer having hydrophobic backbone and hydrophilic branches. 33. Interaction of hepatocytes and polystyrene nanospheres having lactose-immobilized hydrophilic

- polymers on their surface. *Biomacromolecules* **2001**, *2*, 1343–1346.
- 66 SERIZAWA, T., YASUNAGA, S., AKASHI, M., Synthesis and lectin recognition of polystyrene core-glycopolymer corona nanospheres. *Biomacromolecules* **2001**, *2*, 469–475.
- 67 GALLARDO, M. M., COUARRAZE, G., DENIZOT, B., TREUPEL, L., COUVREUR, P., PUISIEUX, F., Study of the mechanisms of formation of nanoparticles and nanocapsules of polyisobutyl-2-cyanoacrylate. *Int. J. Pharm.* **1993**, *100*, 55–64.
- 68 QUINTANAR-GUERRERO, D., ALLEMANN, E., DOELKER, H., FESSI, H., Preparation and characterization of nanocapsules from preformed polymers by a new process based on emulsification-diffusion technique. *Pharm. Res.* **1998**, *15*, 1056–1062.
- 69 AL KHOURI, N., FESSI, H., ROBOT-TREUPEL, J. P., DEVISSAGUET, F., PUISIEUX, F., An Original Procedure for preparing nanocapsules of polyalkylcyanoacrylates for interfacial polymerization. *Pharm. Acta* **1986**, *61*, 274–281.
- 70 KHOPADE, A. J., CARUSO, F., Two-component, ultrathin microcapsules prepared by a core-mediated layer-by-layer approach. *Chem. Mater.* **2004**, *16*, 2107–2112.
- 71 DECHER, G., Fuzzy nanoassemblies: toward layered polymeric multicomposites. *Science* **1997**, *277*, 1232–1237.
- 72 KHOPADE, A. J., CARUSO, F., Stepwise self-assembled poly(amidoamine) dendrimer and poly(styrenesulfate) microcapsules as sustained delivery vehicles. *Biomacromolecules* **2002**, *3*, 1154–1162.
- 73 SCHÜLLER, C., CARUSO, F., Decomposable hollow biopolymer-based capsules. *Biomacromolecules* **2001**, *2*, 921–926.
- 74 FRESTA, M., CAVALLARO, G., GIAMMONA, G., WEHRLI, E., PUGLISI, G., Preparation and characterization of polyethyl-2-cyanoacrylate nanocapsules containing antiepileptic drugs. *Biomaterials* **1996**, *17*, 751–758.
- 75 SEYMOUR, L. W., DUNCAN, R., KOPECKOVA, P., KOPECEK, J., Potential of sugar residues attached to *N*-(2-hydroxypropyl)methacrylamide copolymers as targeting groups for the selective delivery of drugs. *J. Bioact. Compat. Polym.* **1987**, *2*, 97–119.
- 76 ARAP, W., PASQUALINI, R., RUOSLAHTI, E., Cancer treatment by targeted drug delivery to tumor vasculature in a mouse model. *Science* **1998**, *279*, 377–388.
- 77 KONO, K., LIU, M., FRÉCHET, J. M., Design of dendritic macromolecules containing folate or methotrexate residues. *J. Bioconjug. Chem.* **1999**, *10*, 1115–1121.
- 78 SEYMOUR, L. W., FLANAGAN, P. A., AL-SHAMKHANI, A., SUBR, V., ULBRICH, K., CASSIDY, J., DUNCAN, R., Synthetic polymers conjugated to monoclonal antibodies: vehicles for tumor-targeted drug delivery. *Sel. Cancer Ther.* **1991**, *7*, 59–73.
- 79 LANGER, K., MUTSCHLER, E., LAMBRECHT, G., MAYER, D., TROSCHAU, G., STIENEKER, F., KREUTER, J., Methylmethacrylate sulfopropylmethacrylate copolymer nanoparticles for drug delivery part III: evaluation as drug delivery system for ophthalmic applications. *Int. J. Pharm.* **1997**, *158*, 219–231.
- 80 PASSIRANI, C., BARRATT, G., DESSAGUET, J.-P., LABARRE, D., Long-circulating nanoparticles bearing heparin or dextran covalently bound to poly(methyl methacrylate). *Pharm. Res.* **1998**, *15*, 1046–1050.
- 81 CHAUVIERRE, C., LABARRE, D., COUVREUR, P., VAUTHIER, C., Novel polysaccharide-decorated poly(isobutyl cyanoacrylate) nanoparticles. *Pharm. Res.* **2003**, *20*, 1786–1793.
- 82 GULLBERG, E., Particle transcytosis across the human intestinal epithelium. Model development and target identification for improved drug delivery. *Thesis*. Univeristatis Upsaliensis, **2005**.
- 83 ANDERSSON, M., FROMELL, K., GULLBERG, E., ARTURSSON, P., CALDWELL, K. D., Characterization of surface-modified nanoparticles for *in vivo* biointeraction. A sedimentation filed flow fraction study. *Anal. Chem.* **2005**, *77*, 5488–5493.



- 84 PASQUALINI, R., KOIVUNEN, E., RUOSLAHTI, E., Alpha v integrins as receptors for tumor targeting by circulating ligands. *Nat. Biotechnol.* **1997**, *15*, 542–546.
- 85 BIBBY, D. C., TALMADGE, J. E., DALAL, M. K., KURZ, S. G., CHYTIL, K. M., BARRY, S. E., SHAND, D. G., STEIERT, M., Pharmacokinetics and biodistribution of RGD-targeted doxorubicin-loaded nanoparticles in tumor-bearing mice. *Int. J. Pharmaceutics* **2005**, *293*, 281–290.
- 86 YASUGI, K., NAKAMURA, T., NAGASAKI, Y., KATO, M., KATAOKA, K., Sugar-installed polymer micelles: synthesis and micellization of poly(ethylene glycol)-poly(D,L-lactide) block copolymers having sugar groups at the PEG chain end. *Macromolecules* **1999**, *32*, 8024–8032.
- 87 VARKI, A., Biological roles of oligosaccharides: all of the theories are correct. *Glycobiology* **1993**, *3*, 97–130.
- 88 DWEK, R. A., Glycobiology: toward understanding the function of sugars. *Chem. Rev.* **1996**, *96*, 683–720.
- 89 SMART, J. D., NICHOLLS, T. J., GREEN, K. L., ROGERS, D. L., COOK, J. D., Lectins in drug delivery: a study of the acute local irritancy of the lectins from *Solanum tuberosum* and *Helix pomatia*. *Eur. J. Pharm. Sci.* **2000**, *9*, 93–99.
- 90 WAECKERLE-MEN, Y., GROETTRUPA, M., PLGA microspheres for improved antigen delivery to dendritic cells as cellular vaccines. *Adv. Drug. Deliv. Rev.* **2005**, *57*, 475–482.
- 91 FOGED, C., ARIGITA, C., SUNDBLAD, A., JISKOOT, W., STORM, G., FROKJAER, S., Interaction of dendritic cells with antigen-containing liposomes: effect of bilayer composition. *Vaccine* **2004**, *22*, 1903–1913.
- 92 MCGREAL, E. P., MILLER, J. L., GORDON, S., Ligand recognition by antigen-presenting cell C-type lectin. *Curr. Opin. Immunol.* **2005**, *17*, 18–24.
- 93 JILEK, S., MERKLE, H. P., WALTER, E., DNA-loaded biodegradable microparticles as vaccine delivery systems and their interaction with dendritic cells. *Adv. Drug Deliv. Rev.* **2005**, *57*, 377–390.
- 94 JORALEMON, M. J., SHANMUGANANDA, M., REMSEN, E. E., BECKER, M. L., WOOLEY, K. L., Synthesis, characterization, and bioavailability of mannose-sylated shell cross-linked nanoparticles. *Biomacromolecules* **2004**, *5*, 903–913.
- 95 TROUET, A., MASQUELIER, M., BAURAIN, R., DEPREZ-DE CAMPENEERE, D., A covalent linkage between daunorubicin and proteins that is stable in serum and reversible by lysosomal hydrolases, as required for a lysosomotropic drug-carrier conjugate. *Proc. Natl Acad. Sci. USA* **1982**, *79*, 626–629.
- 96 FIUME, L., BASSI, B., BUSI, C., MATTIOLI, A., SPINOSA, G., Conjugates of 9-beta-D-arabinofuranosyladenine 5-monophosphate (ARA-AMP) with lactosaminated albumin – characterization of the drug-carrier bonds. *Biochem. Pharmacol.* **1986**, *35*, 967–972.
- 97 CHO, C. S., CHO, K. Y., PARK, I. K., KIM, S. H., SASAGAWA, T., UCHIYAMA, M., AKAIKE, T., Receptor-mediated delivery of all *trans*-retinoic acid to hepatocyte using poly(L-lactic acid) nanoparticles coated with galactose-carrying polystyrene. *J. Control. Release* **2001**, *77*, 7–15.
- 98 CADE, D., RAMUS, E., RINAUDO, M., AUZÉLY-VELTY, R., DELAIR, T., HAMAIDE, T., Tailoring of bioresorbable polymers for elaboration of sugar-functionalized nanoparticles. *Biomacromolecules* **2004**, *5*, 922–927.
- 99 WOLLER, E. K., CLONINGER, M. J., The lectin-binding properties of six generations of mannose-functionalized dendrimers. *Organic Lett.* **2002**, *4*, 7–10.
- 100 ANTONY, A. C., Folate receptor-targeted drugs for cancer and inflammatory diseases. *Adv. Drug Deliv. Rev.* **2004**, *56*, 1055–1058.
- 101 NAYAK, S., LEE, H., CHMIELELEWSKI, J., LYON, L. A., Folate-mediated cell targeting and cytotoxicity using thermoresponsive microgels. *J. Am. Chem. Soc.* **2004**, *126*, 10258–10259.
- 102 STELLA, B., ARPICCO, S., PERACCHIA, M. T., DESMAËLE, D., HOEBEKE, J.,

- RENOIR, M., D'ANGELO, J., CATTEL, L., COUVREUR, P., Design of folic acid-conjugated nanoparticles for drug delivery. *J. Pharm. Sci.* **2000**, *89*, 1452–1464.
- 103 PARK, E., LEE, S. B., LEE, Y. M., Preparation and characterization of methoxy poly(ethylene glycol)/poly( $\epsilon$ -caprolactone) amphiphilic block copolymeric nanospheres for tumor-specific folate-mediated targeting of anticancer drugs. *Biomaterials* **2005**, *26*, 1053–1061.
- 104 PARK, J., KUROSAWA, S., WATANABE, J., ISHIHARA, K., Evaluation of 2-methacryloyloxyethyl phosphorylcholine polymeric nanoparticle for immunoassay of C-reactive protein detection. *Anal. Chem.* **2004**, *76*, 2649–2655.
- 105 FOURNIER, C., LEONARD, M., LE COQ-LEONARD, I., DELLACHERIE, E., Coating polystyrene particles by adsorption of hydrophobically modified dextran. *Langmuir* **1995**, *11*, 2344–2347.
- 106 ILLUM, L., JONES, P. D. E., BALDWIN, R. W., DAVIS, S. S., Tissue distribution of poly(hexyl 2-cyanoacrylate) nanoparticles coated with monoclonal antibodies in mice bearing human tumor xenografts. *J. Pharmacol. Exp. Ther.* **1984**, *230*, 733–736.
- 107 BORGES, O., BORCHARD, G., VERHOEF, J. C., DE SOUSA, A., JUNINGER, H. E., Preparation of coated nanoparticles for a new mucosal vaccine delivery system. *Int. J. Pharm.* **2005**, *299*, 155–166.
- 108 MESSAI, I., DELAIR, T., Adsorption of chitosan onto poly(D,L-lactic acid) particles: a physico-chemical investigation. *Macromol. Chem. Phys.* **2005**, *206*, 1665–1674.
- 109 CUI, Z., PATEL, J., TUZOVA, M., RAY, P., PHILLIPS, R., WOODWARD, J. G., NATH, A., MUMPER, R. J., Strong T cell type-1 immune response to HIV-1 Tat (1–72) protein coated nanoparticles. *Vaccine* **2004**, *22*, 2631–2640.
- 110 REDHEAD, H. M., DAVIS, S. S., ILLUM, L., Drug delivery in poly(lactide-co-glycolide) nanoparticles surface modified with poloxamer 407 and poloxamine 908: *in vitro* characterization and *in vivo* evaluation. *J. Control. Release* **2001**, *70*, 353–363.
- 111 DE SOUSA DELGADO, A., LÉONARD, M., DELLACHERIE, E., Surface properties of polystyrene nanoparticles coated with dextrans and dextran–PEO copolymers. Effect of polymer architecture on protein adsorption. *Langmuir* **2001**, *17*, 4386–4391.
- 112 STUDER, P., LIMAL, D., BRETON, P., RIESS, G., Synthesis and characterization of poly(ethylene oxide)-block-poly(methylidene malonate 2.1.2) block copolymers bearing a mannose group at the PEO chain end. *Bioconjug. Chem.* **2005**, *16*, 223–229.
- 113 JULE, E., NAGASAKI, Y., KATAOKA, K., Surface plasmon resonance study on the interaction between lactose-installed poly(ethylene glycol)–poly(D,L-lactide) block copolymer micelles and lectins immobilized on a gold surface. *Langmuir* **2002**, *18*, 10334–10339.
- 114 YAMAMOTO, Y., NAGASAKI, Y., KATO, M., KATAOKA, K., Surface charge modulation of poly(ethyleneglycol)-poly(D,L-lactide) copolymer micelles: conjugation of charged Peptides. *Colloid Surf. B Biointerfaces* **1999**, *16*, 135–146.
- 115 QI, K., MA, Q., REMSON, E. E., CLARK, C. G. JR., Determination of the bioavailability of biotin conjugated onto shell cross-linked (SCK) nanoparticles. *J. Am. Chem. Soc.* **2004**, *126*, 6599–6607.
- 116 NARAIN, R., ARMES, S. P., Synthesis and aqueous solution of novel sugar methacrylate-based homopolymers and block copolymers. *Biomacromolecules* **2003**, *4*, 1746–1758.
- 117 GAUTIER, S., GRUDZIELSKI, N., GOFFINET, G., HENRY DE HASSONVILLE, S., DELATTRE, L., JÉRÔME, R., Preparation of poly(D,L-lactide) nanoparticles assisted by amphiphilic poly(methyl methacrylate-co-methacrylic acid) copolymers. *J. Biomater. Sci. Polym. Edn.* **2001**, *12*, 429–450.
- 118 GAUTIER, S., D'ALOIA, V., HALLEUX, O., MAZZA, M., LECOMTE, Ph., JÉRÔME, R., Amphiphilic copolymers of

- $\epsilon$ -caprolactone and  $\gamma$ -substituted  $\epsilon$ -caprolactone. Synthesis and functionalization of poly(D,L-lactide) nanoparticles. *J. Biomater. Sci. Polym. Edn.* **2003**, *14*, 63–85.
- 119 MARUYAMA, A., ISHIHARA, T., KIM, J.-S., KIM, S. W., AKAIKE, T., Nanoparticle DNA carrier with poly(L-lysine) grafted polysaccharide copolymer and poly(D,L-lactic acid). *Bioconjug. Chem.* **1997**, *8*, 735–742.
- 120 AUZÉLY-VELTY, R., CRISTEA, M., RINAUDO, M., Galactosylated N-vinylpyrrolidone-maleic acid copolymers: synthesis, characterization, and interaction with lectins. *Biomacromolecules* **2002**, *3*, 998–1005.
- 121 MARIE, E., LANDFESTER, K., ANTONIETTI, M., Synthesis of chitosan-stabilized polymer dispersions, capsules, and chitosan grafting products via miniemulsion. *Biomacromolecules* **2002**, *3*, 475–481.
- 122 LEMIEUX, G. A., BERTOZZI, C. R., Chemoselective ligation reactions with proteins, oligosaccharides and cells. *Trends Biotechnol.* **1998**, *16*, 506–513.
- 123 ZHANG, Q., REMSEN, E. E., WOOLEY, K. L., Shell cross-linked nanoparticles containing hydrolytically degradable, crystalline core domains. *J. Am. Chem. Soc.* **2000**, *122*, 3642–3651.
- 124 LIU, J., ZHANG, Q., REMSEN, E. E., WOOLEY, K. L., Nanostructured materials designed for cell binding and transduction. *Biomacromolecules* **2001**, *2*, 362–368.
- 125 DUFRESNE, M. H., GAUTHIER, M. A., LEROUX, J.-C., Thiol-functionalized polymeric micelles: from molecular recognition to improved mucoadhesion. *Bioconjug. Chem.* **2005**, *16*, 1027–1033.
- 126 JIANG, F. N., JIANG, S., LIU, D., RICHTER, A., LEVY, J. G., Development of technology for linking photosensitizers to a model monoclonal antibody. *J. Immunol. Methods* **1990**, *134*, 139–149.
- 127 LANGER, K., COESTER, C., WEBER, C., VON BRIESEN, H., KREUTER, J., Preparation of avidin-labeled protein nanoparticles as carriers for biotinylated peptide nucleic acid. *Eur. J. Pharm. Biopharm.* **2000**, *49*, 303–307.
- 128 NOBS, L., BUCHEGGER, F., GURNY, R., ALLÉMANN, E., Surface modification of poly(lactic acid) nanoparticles by covalent attachment of thiol groups by means of three methods. *Int. J. Pharm.* **2003**, *250*, 327–337.
- 129 NOBS, L., BUCHEGGER, F., GURNY, R., ALLÉMANN, E., Poly(lactid acid) nanoparticles labeled with biologically active Neutravidin™ for active targeting. *Eur. J. Pharm. Biopharm.* **2004**, *58*, 483–490.
- 130 BALTHASAR, S., MICHAELIS, K., DINAUER, N., VON BRIESEN, H., KREUTER, J., LANGER, K., Preparation and characterization of antibody modified gelatin nanoparticles as drug carrier systems for uptake in lymphocytes. *Biomaterials* **2005**, *26*, 2723–2732.
- 131 HILT, J. Z., BYRNE, M. E., Configurational biomimesis in drug delivery: molecular imprinting of biologically significant molecules. *Adv. Drug Deliv. Rev.* **2004**, 1599–1620.
- 132 SILVESTRI, D., BORRELLI, C., GUISTI, P., CRISTALLINI, C., CIARDELLI, G., Polymeric devices containing imprinted nanospheres: a novel approach to improve recognition in water for clinical uses. *Anal. Chim. Acta* **2005**, *542*, 3–13.
- 133 CARTER, S. R., RIMMER, S., Molecular recognition of caffeine by shell molecular imprinted core-shell polymer particles in aqueous media. *Adv. Mater.* **2002**, *14*, 667–670.
- 134 SOPPIMATH, K., AMINABHAVI, T. M., KULKARNI, A. R., RUDZINSKI, W. E., Biodegradable polymeric nanoparticles as drug delivery devices. *J. Control. Release* **2001**, *70*, 1–20.
- 135 FOURNIER, C., LEONARD, M., DELLACHERIE, M., CHIKIHI, M., HOMMEL, H., LEGRAND, A. P., EPR spectroscopy analysis of hydrophobically modified dextran-coated polystyrene. *J. Colloid Interface Sci.* **1998**, *198*, 27–33.
- 136 CHAUVIERRE, C., VAUTHIER, C., LABARRE, D., HOMMEL, H., Evaluation of the surface properties of dextran-

- coated poly(isobutylcyanoacrylate) nanoparticles by spin-labeling coupled with electron resonance spectroscopy. *Colloid Polym. Sci.* **2004**, *282*, 1016–1025.
- 137 LIEDBERG, B., NYLANDER, C., LUNDSTRÖM, I., Biosensing with surface plasmon resonance – how it all started. *Biosensors Bioelectron.* **1995**, *10*, RI–RIX.
- 138 LEMARCHAND, C., COUVREUR, P., BESNARD, M., COSTANTINI, D., GREF, R., Novel polyester-polysaccharide nanoparticles. *Pharm. Res.* **2003**, *20*, 1284–1292.
- 139 QUELLEC, P., GREF, R., PERRIN, L., DELLACHERIE, E., SOMMER, F., VERBAVATZ, J. M., ALONSO, M. J., Protein encapsulation within polyethylene glycol-coated nanospheres. I. Physicochemical characterization. *J. Biomed. Mater. Res.* **1998**, *42*, 45–54.
- 140 CHEN, Y., JI, T., ROSENZWEIG, Z., Synthesis of glyconanospheres containing luminescent CdSe–ZnS quantum dots. *Nano Lett.* **2003**, *3*, 581–584.
- 141 BARRATT, G., COUARRAZE, G., COUVREUR, P., DUBERNET, C., FATTAL, E., GREF, R., LABARRE, D., LEGRAND, P., PONCHEL, G., VAUTHIER, C., Biodegradable polymers as drug carrier systems. In *Polymeric Biomaterials*, 2nd edn, DUMITRIU, S. (Ed.). Marcel Dekker, New York, pp. 753–781.
- 142 SAKUMA, S., HAYASHI, M., AKASHI, M., Design of nanoparticles composed of graft copolymers for oral peptide delivery. *Adv. Drug Del. Rev.* **2001**, *47*, 21–37.
- 143 SAKUMA, A., SUDO, R., SUZUKI, N., KIKUCHI, H., AKASHI, M., ISHIDA, Y., HAYASHI, M., Behavior of mucoadhesive nanoparticles having hydrophilic polymeric chains in the intestine. *J. Control. Release* **2002**, *81*, 281–290.
- 144 KOHLER, D., Aerosole for systemic treatment. *Lung* **1990**, *168 (Suppl.)*, 677–684.
- 145 GARCIA-CONTRERAS, L., MORCOL, T., BELL, S. J. D., HICKEY, A. J., Evaluation of novel particles as pulmonary delivery systems for insulin in rats. *AAPS Pharm. Sci.* **2003**, *5*, E9.
- 146 DAILEY, L. A., SCHMEHL, T., GESSLER, T., WITTMAR, M., GRIMMINGER, F., SEEGER, W., KISSEL, T., Nebulization of biodegradable nanoparticles: impact of nebulizer technology and nanoparticle characteristics on aerosol features. *J. Control. Release* **2003**, *86*, 131–144.
- 147 SHARMA, R., SAXENA, D., DWIVEDI, A. K., MISRA, A., Inhalable microparticles containing drug combinations to target alveolar macrophages for treatment of pulmonary tuberculosis. *Pharm. Res.* **2001**, 1405–1410.
- 148 VILA, A., SANCHEZ, A., TOBIO, M., CALVO, P., ALONSO, M. J., Design of biodegradable particles for protein delivery. *J. Control. Release* **2002**, *78*, 15–24.
- 149 ILLUM, L., JABBAL-GILL, M., HINCHCLIFFE, M., FISHER, A. N., DAVIS, S. S., Chitosan as a novel nasal delivery system for vaccines. *Adv. Drug. Del. Rev.* **2001**, *51*, 81–96.
- 150 REDDY, L. H., SHARMA, R. K., CHUTTANI, K., MISRA, A. K., MURTHY, R. S. R., Influence of administration route on tumor uptake and biodistribution of etoposide loaded solid lipid nanoparticles in Dalton's lymphoma tumor bearing mice. *J. Control. Release* **2005**, *105*, 185–198.
- 151 UCHIDA, T., GOTO, S., FOSTER, T. P., Size studies for subcutaneous delivery of poly(lactide-co-glycolide) microspheres containing ovalbumin as vaccine formulation. *J. Pharm. Pharmacol.* **1995**, *47*, 556–560.
- 152 PEYRE, M., FLECK, R., HOCKLEY, D., GANDER, B., SESARDIC, D., *In vivo* uptake of an experimental microencapsulated diphtheria vaccine following sub-cutaneous immunization. *Vaccine* **2004**, *22*, 2430–2437.
- 153 ZIMMER, A., KREUTER, J., Micro-particles and nanoparticles used in ocular delivery systems. *Adv. Drug Deliv. Rev.* **1995**, *16*, 61–73.
- 154 CONTI, B., GIUNCHEDI, P., GENTA, I., CONTE, U., The preparation and *in vivo* evaluation of the wound-healing

- properties of chitosan microspheres. *STP Pharma Sci.* **2001**, *10*, 101–104.
- 155 NIELSEN, U. B., KIRPOTIN, D. B., PICKERING, E. M., HONG, K., PARK, J. W., SHABABY, M. R., SHAO, Y., BENZ, J. D., MARKS, J. D., Therapeutic efficacy of anti-ErbB2 immunoliposomes targeted by a phage antibody selected for cellular endocytosis. *Biochim. Biophys. Acta* **2002**, *1591*, 109–118.
- 156 DALGLEISH, A. G., Why: gene therapy? *Gene Ther.* **1997**, *4*, 629–630.
- 157 RODRIGUES, J. S., SANTOS-MAGALHAES, N. S., COELHO, L. C. B. B., COUVREUR, P., PONCHEL, G., GREF, R., Novel core (polyester)–shell (polysaccharide) nanoparticles: protein loading and surface modification with lectins. *J. Control. Release* **2003**, *92*, 103–112.
- 158 WARREN, H. S., LECLERC, C., Adjuvants. In *Encyclopedia in Immunology*, 2nd edn, DELVES, P. J., ROITT, I. M. (Eds.). Academic press, San Diego, CA, **1998**, Vol. 1, pp. 36–39.
- 159 ALLEN, T. M., CULLIS, P. R., Drug delivery systems: entering the mainstream. *Science* **2004**, *303*, 1818–1822.
- 160 THOMPSON, D. H., Preface – triggering in drug delivery systems. *Adv. Drug Del. Rev.* **2001**, *53*, 245–245.
- 161 SOPPIMATH, K. S., TAN, D. C.-W., YANG, Y. Y., pH-triggered thermally responsive polymer core–shell nanoparticles for drug delivery. *Adv. Mater.* **2005**, *17*, 318–323.
- 162 SALVAGE, J. O., ROSE, S. F., PHILLIPS, G. J., HANLON, G. W., LLOYD, A. W., MA, I. Y., ARMES, S. P., BILLINGHAM, N. C., LEWIS, A. L., Novel biocompatible phosphorylcholine-based self-assembled nanoparticles for drug delivery. *J. Control. Release* **2005**, *104*, 259–270.
- 163 ICHIKAWA, H., FUKUMORI, Y., A novel positively thermosensitive controlled-release microcapsule with membrane of nano-sized poly(*N*-isopropylacrylamide) gel dispersed in ethylcellulose matrix. *J. Control. Release* **1999**, *63*, 107–119.
- 164 NERADOVIC, D., SOGA, O., VAN NOSTRUM, C. F., HENNINK, W. E., The effect of the processing and formulation parameters on the size of nanoparticles based on block copolymers of poly(ethylene glycol) and poly(*N*-isopropylacrylamide) with and without hydrolytically sensitive groups. *Biomaterials* **2004**, *25*, 2409–2418.
- 165 ANGELATOS, A. S., RADT, B., CARUSO, F., Light-responsive polyelectrolyte/gold nanoparticle microcapsules. *J. Phys. Chem. B* **2005**, *109*, 3071–3076.
- 166 SKIRTACH, A. G., DEJUGNAT, C., BRAUN, D., SUSHI, A. S., ROGACH, A. L., PARAK, W. J., MÖHWALD, H., SUKHORUKOV, G. B., The role of metal nanoparticles in remote release of encapsulated materials. *Nano Lett.* **2005**, *5*, 1371–1377.
- 167 LU, Z. H., PROUTY, M. D., GUO, Z., GOLUB, V. O., KUMAR, C. S. S. R., LVOV, Y. M., Magnetic switch of permeability for polyelectrolyte microcapsules embedded with Co@Au nanoparticles. *Langmuir* **2005**, *21*, 2042–2050.
- 168 QIU, Y., PARK, K., Environment-sensitive hydrogels for drug delivery. *Adv. Drug Del. Rev.* **2001**, *53*, 321–339.
- 169 LACKY, C. A., PRESS, O. W., HOFFMAN, A. S., STAYTON, P. S., A biomimetic pH-responsive polymer directs endosomal release and intracellular delivery of an endocytosed antibody complex. *Bioconjug. Chem.* **2002**, *13*, 996–1001.
- 170 STUBBS, M., MCSHEEHY, P. M. J., GRIFFITHS, J. R., BASHFORD, C. L., Causes and consequences of tumor acidity and implications for treatment. *Mol. Med. Today* **2000**, *6*, 15–19.
- 171 RADT, B., SMITH, T. A., CARUSO, F., Optically addressable nanostructured capsules. *Adv. Mater.* **2004**, *16*, 2184–2189.
- 172 SKIRTACH, A. G., ANTIPOV, A. A., SHCHUKIN, D. G., SUKHORUKOV, G. B., Remote activation of capsules containing Ag nanoparticles and IR dye by laser light. *Langmuir* **2004**, *20*, 6988–6992.
- 173 MORNET, S., VASSEUR, S., GRASSET, F., DUGUET, E., Magnetic nanoparticle

- design for medical diagnosis and therapy. *J. Mater. Chem.* **2004**, *14*, 2161–2175.
- 174 MUELLER-SCHULTE, D., Thermosensitive, biocompatible polymer carriers with a variable physical structure for treatment, diagnosis and analysis. *WO 2005042142*, **2005**.
- 175 GARCIA-FUENTES, M., PREGO, C., TORRES, D., ALONSO, M. J., A comparative study of the potential of solid triglyceride nanostructures coated with chitosan or poly(ethylene glycol) as carrier for oral calcitonin delivery. *Eur. J. Pharm. Sci.* **2005**, *25*, 133–143.
- 176 McLEAN, S., PROSSER, E., MEEHAN, E., O'MALLEY, D., CLARKE, N., RAMTOOLA, Z., BRAYDEN, D., Binding and uptake of biodegradable poly-DL-lactide micro- and nanoparticles in intestinal epithelia. *Eur. J. Pharm. Sci.* **1998**, *6*, 153–163.
- 177 PANYAM, J., SAHOO, S. K., PRABHA, S., BARGAR, T., LABHASETWAR, V., Fluorescence and electron microscopy probes for cellular and tissue uptake of poly(D,L-lactide-co-glycolide) nanoparticles. *Int. J. Pharm.* **2003**, *262*, 1–11.
- 178 TOSI, G., RIVASI, F., GANDOLFI, F., COSTANTINO, L., VANDELLI, M. A., FORNI, F., Conjugated poly(D,L-lactide-co-glycolide) for the preparation of *in vivo* detectable nanoparticles. *Biomaterials* **2005**, *26*, 4189–4195.
- 179 ALIVISATOS, A. P., Semiconductor clusters, nanocrystals, and quantum dots. *Science* **1996**, *271*, 933–937.
- 180 BRUCHEZ, M. JR., MORONNE, M., GIN, P., WEISS, S., ALIVISATOS, A. P., Semiconductor nanocrystals as fluorescent biological labels. *Science* **1998**, *281*, 2016–2018.
- 181 CHAN, W. C.-W., MAXWELL, D. J., GAO, X. H., BAILEY, R. E., HAN, M. Y., NIE, S. M., Luminescent quantum dots for multiplexed biological detection and imaging. *Curr. Opin. Biotechnol.* **2002**, *13*, 40–46.
- 182 TAMURA, J., FUKUDA, M., TANAKA, J., KAWA, M., Synthesis of hydrophilic ultrafine nanoparticles coordinated with carbohydrate cluster. *J. Carbohydrate Chem.* **2002**, *21*, 445–449.
- 183 BALLOU, B., LAGERHOLM, C., ERNST, L. A., BRUCHEZ, M. P., WAGGONER, A. S., Noninvasive imaging of quantum dots in mice. *Bioconjug. Chem.* **2004**, *15*, 79–86.
- 184 HAN, M., XIAOHU, G., SU, J. Z., NIE, S., Quantum-dot-tagged microbeads for multiplexed optical coding of biomolecules. *Nat. Biotechnol.* **2001**, *19*, 631–635.
- 185 YANG, X., ZHANG, Y., Encapsulation of quantum nanodots in polystyrene and silica micro-/nanoparticles. *Langmuir* **2004**, *20*, 6071–6073.
- 186 FLEISCHHAKER, F., ZENTEL, R., Photonic crystals from core-shell colloids with incorporated highly fluorescent quantum dots. *Chem. Mater.* **2005**, *17*, 1346–1351.
- 187 ESTEVES, A. C. C., BARROS-TIMMONS, A., MONTEIRO, T., TRINDADE, T., Optical properties of the synthetic nanocomposites SiO<sub>2</sub>/CdS/poly(styrene-co-maleic anhydride) and SiO<sub>2</sub>/CdS/poly(styrene-co-maleimide). *J. Nanosci. Nanotechnol.* **2005**, *5*, 766–771.
- 188 SKAFF, H., ILLKER, M. F., COUGHLIN, E. B., EMRICK, T., Preparation of cadmium selenide-polyolefin composites from functional phosphine oxides and ruthenium-based metathesis. *J. Am. Chem. Soc.* **2002**, *124*, 5729–5733.
- 189 O'BRIEN, P., CUMMINS, S. S., DARCY, D., DEARDEN, A., MASALA, O., PICKETT, N. L., RYLEY, S., SUTHERLAND, A. J., Quantum dot-labeled polymer beads by suspension polymerization. *Chem. Commun.* **2003**, 2532–2533.
- 190 LI, Y., LIU, E. C. Y., PRICKETT, N., SKABARA, P. J., CUMMINS, S. S., RYLEY, S., SUTHERLAND, A. J., O'BRIEN, P., Synthesis and characterization of CdS quantum dots in polystyrene microbeads. *J. Mater. Chem.* **2005**, *15*, 1238–1243.
- 191 JOUMAA, N., LANSALOT, M., THÉRETZ, A., ELAISSARI, A., Synthesis of quantum dot-tagged submicrometer polystyrene particles by miniemulsion

- polymerization. *Langmuir* **2006**, *22*, 1810–1816.
- 192 ESTEVES, A. C. C., BOMBALSKI, L., CUSICK, B., BARROS-TIMMONS, A., MATYJASZEWSKI, K., TRINDADE, T., AGET ATRP in miniemulsions from functionalized CdE (E = S, Se) q-dot's surfaces. *Polym. Prepr.* **2005**, *46*, 134–135.
- 193 LEE, S.-J., JEONG, J.-R., SHIN, S.-C., HUH, Y.-M., SONG, H.-T., SUH, J.-S., CHANG, Y.-H., JEON, B.-S., KIM, J.-D., Intracellular translocation of superparamagnetic iron oxide nanoparticles encapsulated with peptide-conjugated poly(D,L lactide-co-glycolide). *J. Appl. Phys.* **2005**, *97*, 10Q913.
- 194 VEYRET, R., ELAISSARI, A., MARIANNEAU, P., SALL, A. A., DELAIR, T., Magnetic colloids for generic capture of viruses. *Anal. Biochem.* **2005**, *346*, 59–68.
- 195 ELAISSARI, A., RODRIGUE, M., MEUNIER, F., HERVE, C., Hydrophilic magnetic latex for nucleic acid extraction, purification and concentration. *J. Magn. Magn. Mater.* **2001**, *225*, 127–133.
- 196 ANDRADE, J. D., *Protein Adsorption. Surface and Interfacial Aspect of Biomedical Polymers*. Plenum Press, New York, **1985**.
- 197 ELAISSARI, A., BOURREL, V., Thermosensitive magnetic latex particles for controlling protein adsorption and desorption. *J. Magn. Magn. Mater.* **2001**, *225*, 151–155.
- 198 DURACHER, D., ELAISSARI, A., MALLET, F., PICHOT, C., Adsorption of modified HIV-1 capsid p24 protein onto thermosensitive and cationic core-shell poly(styrene)-poly(*N*-isopropylacrylamide) nanoparticles. *Langmuir* **2000**, *16*, 9002–9008.
- 199 LANSALOT, M., SABOR, M., ELAISSARI, A., PICHOT, C., Elaboration of fluorescent and highly magnetic submicronic polymer particles via a stepwise heterocoagulation process. *Colloid Surf. Sci.* **2005**, 1267–1277.
- 200 ELAISSARI, A., Magnetic colloids: preparation and biomedical applications. *e-Polymers* **2005**, No 028.
- 201 LE RAY, A. M., VERT, M., GAUTIER, J. C., BENOIT, J. P., End-chain labeling and *in vitro* stability studies of radiolabeled poly(hydroxy acid) NP. *Pharm. Res.* **1994**, *83*, 845–851.
- 202 LEVY, L., SAHOO, Y., KIM, K.-S., BERGEY, E. J., PRASAD, P. N., Nanochemistry: synthesis and characterization of multifunctional nanoclinics for biological applications. *Chem. Mater.* **2002**, *14*, 3715–3721.

## 9

# Polymeric Nanoparticles for Drug Delivery

*Paraskevi Kallinteri and Martin C. Garnett*

### 9.1

#### Introduction: Application of Nanoparticles for Noncancer Applications

The scientific literature contains many reviews on the therapeutic uses of nanoparticles, from formulation through to *in vitro* and *in vivo* assessment of activity, and for various routes of delivery, including oral, lung, mucosal and parenteral. Therapeutic development of nanoparticulate delivery systems has been dominated by applications for cancer because of the potential advantages in localization in cancer tissues and hence in targeting advantages to drugs which lack specificity. However, there are a variety of more subtle reasons why nanoparticle therapeutics should be useful for other delivery routes and diseases. These include protection of the drug, enhancing circulation half-life, acting as a slow release system and compartmentalization of the delivery system either by preventing the drug reaching certain tissues or by enhancing uptake into particular cells/tissues. These potential advantages have led to work on nanoparticles in a number of other areas including delivery to local sites such as the eye and lung, the delivery of peptides and proteins via a number of alternative routes, including oral, nasal and pulmonary routes, and for treatments where cells of the immune system can be readily targeted by nanoparticles e.g. vaccine delivery, AIDS, antifungal treatment and tuberculosis. However, we have been unable to find any recent reviews covering the noncancer applications as a group, the distinctive reasons why these should be useful targets for polymeric nanoparticles or why nanoparticles may produce more effective delivery systems.

In this chapter, we have attempted to bring together a number of different areas. First, to understand the physiology and anatomy underlying the diseases which may be treatable using nanoparticulates and the way that nanoparticles are handled by the body. The effect of the route of application has also been considered here. Second, to review the main work that has been carried out with polymeric nanoparticle formulations for this range of applications and assess their future potential. This second area of work has been arranged into individual diseases or groups of diseases which would benefit from similar formulations or similar



principles of delivery for the nanoparticles. Finally, we draw some brief overall conclusions.

One of the first areas to consider in assessing the potential of nanoparticles as delivery systems are the potential physiological barriers to transport of nanoparticles and how physiological factors can be best exploited to maximize the advantages of nanoparticulates.

### 9.1.1

#### **Physiological and Uptake of Particles**

In general, nanoparticles cannot simply partition across membranes, or cells, so uptake is limited to specific transport pathways through cells and the paracellular route passing between cells. The paracellular route poses a problem for the passage of nanoparticles through epithelia and endothelia because of the presence of tight junctions in most of these tissues. The tight junctions typically restrict the gap between cells to about 4–6 nm in endothelia and 2 nm in epithelia, and would therefore be expected to prevent the passage of macromolecules and nanoparticles past these barriers [1]. In addition the presence of a basement membrane underlying these tissues, with a fibrous mesh thought to be around 15 nm between strands, would also be expected to restrict passage of nanoparticles [2].

##### **9.1.1.1 Routes of Tissue and Cellular Uptake of Particles**

Although unable to partition through membranes and gain direct access into cells, there are a variety of endocytic mechanisms for the uptake of macromolecules and small particles into cells. These include phagocytosis of large particles by specialized cells such as macrophages and neutrophils [3], and uptake of macromolecules and smaller particles by a variety of mechanisms, which probably include a non-specific pinocytosis as well as receptor-mediated uptake involving clathrin [4] or uptake via caveolae [5]. Endocytosis may offer two major drug delivery advantages: (i) a preferential uptake to macrophages and other cells associated with the immune system, and (ii) access to the endosomal/lysosomal compartments of cells where the acidic and degradative environment offers a useful drug release mechanism.

More recently, evidence is beginning to accumulate that the endothelium may be less of a barrier to nanoparticle delivery systems than once believed. It was proposed some years ago that the extravasation of macromolecules into lymphatic tissues was mediated by a process of transcytosis in which macromolecules were endocytosed on one side of the cell and exocytosed on the other through a vesicular system [6]. Recent evidence suggests that this process may be mediated by caveolae and involves some specific transport [7]. Some nanoparticles have been reported able to exploit this transcytosis process to pass across endothelia for the brain [8], lymph nodes [9] and bone marrow [10], although it is not yet clear how many tissues can be accessed by this route nor how selective it is for particular tissues. Too little work has been done in this area for this to be reflected in the development of drug delivery systems for specific applications, except as directed towards therapy

of brain tumors [8]. However, it offers prospects to widen the range of diseases, which may be accessible to nanotherapeutics.

#### 9.1.1.2 Uptake by Macrophages and Lymphoid Tissues

Delivery to macrophages and other cells of the immune system could allow access to a range of conditions. A number of parasites and diseases are known to inhabit the endosomal compartment of macrophages, e.g. malaria and tuberculosis [11]. In addition, both macrophages and other cells of the immune system are involved in antigen processing, so serve as a port of entry for vaccine antigens.

The macrophages are the main component of the mononuclear phagocytic system (MPS). Due to the preferential uptake of particulates by macrophages, particles tend to accumulate in the main tissues of the MPS such as liver, spleen and lymph nodes. For nanoparticles less than 250 nm, the spleen tends to be less important as a site for uptake [12]. This uptake is potentiated by opsonization [13] – the coating of particulates by blood proteins occurring either specifically through antigen recognition or nonspecifically mainly through hydrophobic interactions. The surface properties of nanoparticles are therefore very important and hydrophilic coatings by polymers such as polysaccharides or poly(ethylene glycol) (PEG) reduce both opsonization and uptake by the MPS. These coatings are usually achieved either by coating with PEG containing surfactants which adsorb to the surface of particles or by the use of PEG copolymers incorporated into the nanoparticles. The hydrophilic coatings also stabilize the particles against aggregation [14]. A further property of the coatings in reducing protein adsorption is that certain blood components can adsorb preferentially to the coated surfaces and this can result in adsorption of a protein, mediating transcytosis to specific organs such as the brain [8].

A further consequence of the MPS uptake of particulates is that, eventually, most particulate preparations do end up in the liver for detoxification and this has the potential to cause liver toxicity. This is particularly important because there is no opportunity for elimination of drug through the kidney until drug has been released from the particle, either by slow release from the particle or by metabolism at its target site or the liver. However, once more this offers a possible drug delivery opportunity by providing a generalized slow release system for drugs mediated by liver metabolism.

#### 9.1.1.3 Mucosal-associated Lymphoid Tissues (MALT)

The mucosae have an important role as an interface between the outside world and the body. They are thus a key element of the defense of the body, both from the point of view of acting as a barrier to the outside world, while at the same time being uniquely placed to sample the environment. Lymphatic tissue is found at a variety of mucosal sites including the bronchi (BALT), nose (NALT) and gut (GALT) [15]. These lymphoid tissues constitute an efficient way of inducing protective immune responses, both humoral and cellular. Moreover, the stimulation of one mucosal site can result in dissemination of response to other mucosal sites. MALT constitutes 80% of immunocytes and functions independently from the systemic

system. The lymphoid tissues contain a number of specialized cells, which include fixed macrophages, and also cells like dendritic cells, which act as mobile scouts sampling the environment. These lymphoid tissues, as will be seen below, also seem to act as conduits by which particles may pass through to other tissues.

### 9.1.2

#### **Routes of Delivery**

##### 9.1.2.1 **Oral**

The gut at first sight appears an unpromising route for nanoparticle delivery systems. The presence of a very acid environment in the stomach, high concentrations of degradative enzymes and a thick layer of mucus above an epithelial layer are all significant physiological barriers. Also, it is well known that macromolecules are poorly absorbed in the gut. However, reports of orally administered particles being present in the lymphatics and circulation have been documented for many years. There have been a number of recent and comprehensive reviews collating the evidence supporting this route of particle uptake. These include specific consideration of the physical barriers and their relevance to oral absorption [16], how particles are taken up across the epithelium and into the lymphatics [17], specific mechanisms and routes of transcytosis [18], and the role of polymers comprising the nanoparticles in influencing uptake [19]. Consequently, only a brief summary of these aspects of oral particulate delivery will be presented here.

Mucus does appear to operate as a barrier to uptake, particularly for larger particles (above 300 nm). Penetration of mucus by nanoparticles is also affected by surface characteristics, with hydrophilic particles penetrating more easily. There are several potential routes of nanoparticle uptake in the gut. Paracellular transport is not expected to be significant as there are tight junctions in the gut as in most other epithelial tissues. However, there have been reports of particles up to 50–100 nm penetrating by this route in the presence of modifiers such as chitosan or calcium ions. Polyacrylate and starch have also been reported to enhance paracellular transport. The process of persorption has also been described in the gut, where the tips of villi become denuded of epithelial cells allowing larger particles access to the underlying mucosa. However, it is not thought that this route of uptake is particularly prominent.

There has been intensive study of the lymphoid tissue within gut as a possible portal of entry for particles. Peyer's patches consisting of multiple lymphoid follicles are the most widely discussed, but are not the sole lymphoid tissue within the gut. A significant number of isolated lymphoid follicles and lymphocyte-filled villi also exist. However, the degree to which these various lymphoid tissues contribute to particle uptake is widely debated. Similarly, it is unclear the extent to which nonlymphoid epithelium is involved in nanoparticle uptake. The principal route of uptake is often assumed to be the M cells in Peyer's patches, but it may be that only a small proportion of M cells are involved.

Uptake of particles involves both transcytosis across the epithelial layer and translocation to other tissues. Peyer's patches, as well as containing M cells also have a

more porous basement membrane and are closely associated with efferent lymphatics. These characteristics would account for the reported route of translocation of nanoparticles via the mesenteric lymph ducts. It is also possible that particles may be shuttled to distant mucosal sites following uptake by immune cells.

The uptake of particles by Peyer's patches has, like passage through mucus, been found to be dependent on size. Uptake and translocation to mesenteries and liver seems to be greatest for particle of 50 nm. However, immune responses are most effectively stimulated by particles of 4  $\mu\text{m}$ , which correlates with the observation that larger particles tend to be found in dendritic cells. The surface characteristics of particles have also been reported to be important for both uptake and translocation.

Overall, studies show that there are clearly routes of nanoparticle uptake, but the extent of uptake is under debate due to the wide range of uptake rates reported. It is thought that in general uptake rates are lower than for typical small drug molecule administration. Consequently it is likely that nanoparticle delivery systems will be most appropriate for immune delivery, delivery to intestinal lymph and drugs which are poor for oral delivery because of poor solubility or permeability characteristics, e.g. potent and labile biological macromolecules.

#### 9.1.2.2 Nasal

The nasal epithelium has been investigated as a delivery route for conventional drugs, peptides and proteins, and vaccines. A useful description of the anatomy of the nose relevant to drug delivery can be found in reviews by Illum [20] and Jones [21]. The nasal epithelium has a relatively large surface area because of the presence of microvilli and has the advantage that it avoids first-pass metabolism to the liver. However, the nasal mucosa has a significant level of degradative enzymes. Like the gut, nasal mucosa is covered by a layer of mucus, which poses a barrier to delivery mainly because of the rate of clearance into the nasopharynx and gut. The epithelium is well vascularized.

In humans, there is a limited amount of macroscopically visible nasal lymphoid tissue, which is confined to the nasopharynx and tonsils. However, antigen-presenting cells (APCs), and B and T lymphocytes are present within the mucosa.

#### 9.1.2.3 Pulmonary

Delivery to the lung is an attractive route because of the easy access and administration of formulations, and the large surface area of the lung provided by the alveoli, estimated to be about 140  $\text{m}^2$  of internal surface area.

The lung structure is that of a multibranching tree with the airways dividing further at each branch. The airways divide repeatedly into primary bronchi, lobar, segmental bronchi and bronchioles until reaching the terminal bronchiole leading to 15–20 alveoli. The walls of the entire respiratory tract are covered by a mucus blanket about 5  $\mu\text{m}$  thick. The mucus is a mucopolysaccharide which can trap particles for subsequent removal by the ciliated cells of the bronchi. This happens by a continual upwards movement of mucus known as the mucociliary escalator.

The alveoli mainly consist of thin squamous cells about 5  $\mu\text{m}$  thick (type I cells). There are also a few thicker type II cells responsible for secreting the surfactant coating the surface of the lungs. The capillaries are closely associated with the alveolar cells and partly form the wall of the alveoli. The alveolar wall therefore consists of alveolar cells, basement membrane and capillary endothelial cells held together by connective tissue. The alveolar membrane is covered by a thin (15 nm) layer of surfactant. Due to the tight junctions joining the alveolar epithelia and the capillary endothelium, penetration of macromolecules from the alveolar space into the capillary circulation is limited, so it would be expected that penetration of nanoparticles would be even more limited. However, it is clear that there is transport of materials across lung endothelium and epithelium by caveolae [22], so this may also be a route for transport of small nanoparticles as well.

Alveolar macrophages may be found either fixed within the connective tissue of the alveoli or free within the mucus layer. They can leave the lung either via the mucus through the mucociliary escalator and out through the sputum or, alternatively, leave via the lymphatics within the lung. This may therefore be another route of transfer of materials from within the airways of the lung into the tissues.

Delivery of particles to the lung is dependent on a number of physical processes, which are diameter dependent. Particles larger than 5  $\mu\text{m}$  are deposited by inertial impaction on the trachea walls following a change in direction of air flow. Settling is proportional to the square of the particle diameter and is less important for small particles. Particles less than about 500 nm in diameter are deposited largely by Brownian diffusion. So, overall, particles in the size range 5  $\mu\text{m}$  down to 500 nm largely avoid impaction on the airways and are large enough to deposit by sedimentation, while those below 500 nm can only deposit by Brownian motion. In general, optimum pulmonary penetration is found with monodisperse aerosols of 2–3  $\mu\text{m}$  diameter. Extremely small aerosols (below 100 nm diameter) also appear to deposit very efficiently through Brownian diffusion, but such fine aerosols are very difficult to produce. Only particles that contact the mucus layer can be deposited and thus be available for either drug release into the mucus or uptake into the macrophages, or possibly the epithelial cells. There may therefore be some possibility of exploiting these various transport mechanisms for drug delivery systems.

A more complete description of pulmonary structure and its effects on drug delivery can be found in Washington and coworkers [23].

#### 9.1.2.4 Transdermal/Subcutaneous

One of the main functions of the skin is to act as a barrier to the entry of macromolecules and particles. The stratum corneum, consisting of eight to 16 layers of flattened, stratified and keratinized dead cells is largely responsible for the barrier function of the cell. Due to the barrier function of the skin, there is also a complex relationship with the immune system. Langerhans or dendritic cells are specialized APCs, which constantly monitor the environment by taking up antigens and processing them. They are an integral part of the immune system, and are involved in migration from the epidermis to the regional lymph nodes, resulting in the induction and maintenance of cutaneous immunity sensitization or stimulation of the

immune system [24]. These cells could therefore take up and transport particles to the lymph nodes and lymphatics.

In addition to topical application of particulates, the intradermal or subcutaneous route of injection delivers particles to the extracellular space, where they can be taken up by the lymphatics. This route therefore gives a potential route for delivery to the lymphatics, and in particular to the lymph nodes [25].

In summary, therefore, there are a number of routes with potential for delivery of nanoparticles for a variety of therapeutic applications. Work carried out on these applications is detailed below.

## 9.2 Drug Delivery

### 9.2.1

#### Ocular Delivery

##### 9.2.1.1 Anatomy of the Eye

Current ocular drug delivery is by administration of eye-drops, suspensions, ointments, gels, subconjunctival and intraocular injections, and, more recently, implants. There are, however, physiological and anatomical features of the eye that prevent effective therapy. Looking in detail at the eye (Fig. 9.1), there are anterior and posterior sections.

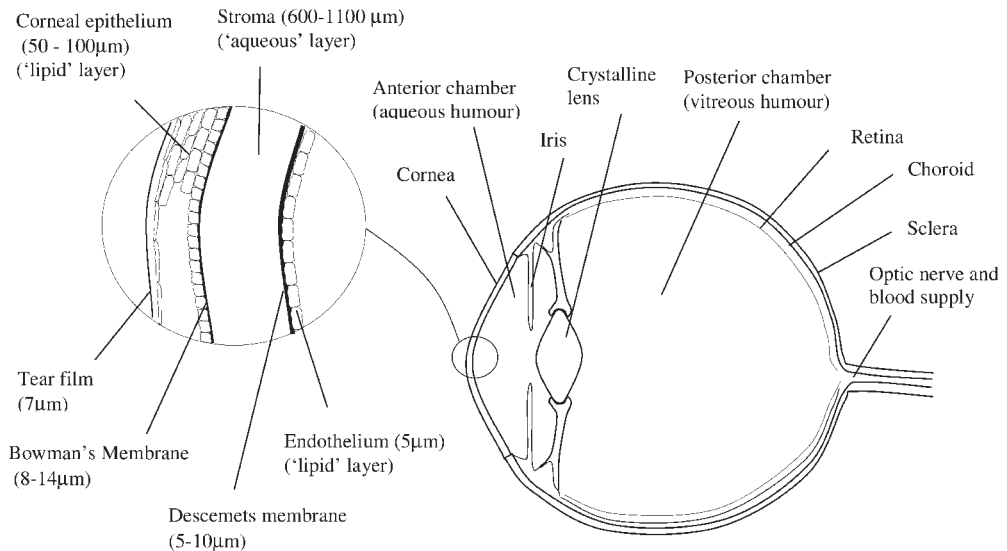


**Figure 9.1.** Anatomy of the eye. The general anatomy of the eye is shown on the right, with an inset on the left showing the detailed structure of the cornea.

The anterior section includes the lens and the cornea. The posterior segment consists of three layers, i.e. the sclera, choroid and retina, surrounding the vitreous cavity, which is filled by the vitreous humor [26].

The first barrier to drug uptake is the cornea comprising three parts. The outer part is the epithelium, consisting of five to six layers of tightly packed cells restricting the passage of hydrophilic and ionized compounds, with little penetration via the paracellular route. The middle part is the hydrophilic stroma restricting passage of lipophilic compounds. Due to a relatively open structure, drugs with a molecular size up to 50 000 can diffuse in normal stroma. The third part is a monolayer of endothelial cells. Effective drugs therefore need to combine both hydrophilic and hydrophobic properties to be able to pass through the cornea. Formulation pH adjustment can improve the trans-corneal drug accumulation.

It has been reported that less than 5% of the applied eye-drop reaches the intraocular tissues [26–28]. The percentage dose of the drug absorbed through the cornea depends very much upon the time that the instilled drop remains on the corneal surface, which is mainly dependent on the lachrymal system of the eye. The lachrymal glands secrete tears, which are distributed over the eyes by the blinking reflex of the eyelids and collected in the lower conjunctival sac. From there, the tears are drained into the lachrymal sac through the puncta and the lachrymal duct. Eventually, the fluid reaches the nasopharynx and, finally, the gastrointestinal tract. Consequently, blinking and tear secretion stimulated after the eye-drop instillation are responsible for the fast washout of the drug from the precorneal area, while nasolacrimal drainage can lead to serious side-effects through uptake into the blood circulation. A good example is the  $\beta$ -blocker, timolol, which is used for the treatment of the wide-angle glaucoma and can cause side-effects to the heart if transported to the systemic circulation via nasolacrimal drainage.

The conjunctiva, a thin vascularized mucus membrane, which lines the inner surface of the eyelids and covers the anterior part of the sclera up to the cornea is also responsible for a large amount drug uptake. This uptake route adds to the systemic side-effects [28].

In the posterior section, the sclera maintains the shape of the eyeball and the choroid is a vascular layer that provides the blood supply that supports the retinal cells. The retina is separated from the choroid by Bruch's membrane.

#### 9.2.1.2 Pathology

Ocular formulations aim to treat either inflammatory external eye infections (i.e. conjunctivitis, blepharitis, keratitis sicca) or intraocular diseases like glaucoma, uveitis, etc. The latter can be classified to anterior (iritis, iridocyclitis), intermediate (behind the iris and lens in the region of ciliary body and pars plana), posterior (retinitis, choroiditis, optic neuritis) and diffuse (all parts of the eye).

#### 9.2.1.3 Drug Delivery

Ocular delivery has a low efficiency due to the cornea's low permeability to drugs, rapid tear turnover and nasolacrimal drainage. Diseases of the posterior segment

are treated by intravitreal or subconjunctival injections, which are quite invasive and are able to cause inflammatory reactions.

There is a need for production of new formulations able to ensure increased stability of the drug and longer elimination half-life through sustained release. Nanoparticles and nanospheres are attractive as alternative delivery systems for the treatment of eye disorders because they are characterized by increased stability and longer elimination half-life in the tear fluid (20 min) in comparison to conventional drugs applied topically to the eye (1–3 min).

Ideally, particles need to be biodegradable, biocompatible, nontoxic, sterile, have a sustained release at a desirable rate, easy manufacturing procedure and be smaller than 10  $\mu\text{m}$  so as to avoid any scratching or discomfort to the patient. Other important factors influencing the efficiency of such carriers are the charge, the drug lipophilicity and/or the carrier.

A number of polymers can be used to prepare particles (nanoparticles or nanospheres), which can be classified mainly into two categories: acrylate derivatives like poly(butyl cyanoacrylate) (PBCA) [29], PEG–polyethyl-2-cyanoacrylate (PECA) [30], poly[methoxy poly(ethylene glycol)cyanoacrylate-co-hexadecyl cyanoacrylate] (PEG–PHDCA) [31], copolymers of poly(ethylacrylate, methyl methacrylate and chlorotrimethyl-ammonioethyl methacrylate) [Eudragit®] [32–34] and the positively charged chitosan [35–37]. Poly(lactic acid) (PLA) [38], poly(D,L-lactic-co-glycolic) acid (PLGA) [39] and poly( $\epsilon$ -caprolactone) (PCL) [40] have been tested, too. Particles have been made using the mucoadhesive poly(acrylic acid) (PAA) and poly(itaconic acid) (PIA) [41], while hyaluronic acid (HA) [40] has been treated as a coating material for nanospheres made out of PCL (Fig. 9.2). Enhanced polymer–cornea affinity is the main aim to increase the particle residence time in the eye.

The mechanism of action is different for each of these polymers. PBCA, PAA, PIA and HA are characterized as mucoadhesive because they attach to the precor-

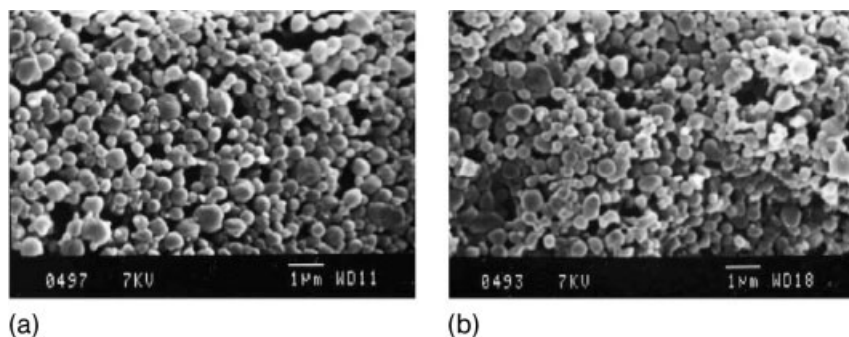


**Figure 9.2.** Scanning electron microscopy photographs of PCL nanospheres positively charged by stearylamine (SA) (a) or BKC (b) and coated with HA 0.025% (PCL/SA/HA ads

and PCL/BKC/HA ads) Bar = 1  $\mu\text{m}$ ; original magnification  $\times 10\,000$ . (Reprinted from Ref. [40], © 2002, with permission from Elsevier.)



neal mucin layer via noncovalent bonds [40]. PEG molecules interact via hydrogen bonds with the mucin macromolecules present on the ophthalmic surface and may induce reversible opening of the tight junctions of the conjunctival tissue (allowing paracellular transport of drug molecules across ophthalmic tissues) [30]. Positively charged Eudragit™ and chitosan interact strongly with the negatively charged sialic acid residues in mucus. PLA and PLGA are generic materials for particle preparation, with FDA approval.

The physicochemical and surface characteristics are important in efficient drug accumulation into the eye. Other important factors are the preparation method and the presence of surfactants. Most of the particles produced using the materials mentioned above have a size range between 35 [Eudragit RL100, poly(acrylic acid) (PAA)] and 280 nm [PBCA, chitosan, PCL–benzalkonium chloride (BKC)] with an average size around 100 nm. The particle size mainly depends on the preparation method. According to de Campos and coworkers [35], the production of chitosan nanoparticles is dependent upon the chitosan concentration (decreased concentration leads to decreased size) and the acetonitrile/water volume (increasing the ratio leads to size decrease). Ibuprofen-loaded Eudragit RL100 and RS100 nanoparticles are prepared by the quasi-emulsion solvent diffusion method. Thus, the particle size is reduced as the polymer concentration or the volume of ethanol decreases [32]. Giannavola and coworkers [38] studied the incorporation of acyclovir into PLA nanoparticles using the nanoprecipitation method using various nonionic surfactants (Triton X-100, Tween 80, Brij 96, Pluronic F68). The particle size decreased as the polymer molecular weight increased while Tween 80 was the most efficient in decreasing the size and maintaining particle stability. Fresta and coworkers [30] produced similar PECA nanospheres by micellar polymerization using Pluronic F68.

Nanoparticles are preferred to microparticles because Giordano and coworkers [42] reported that the latter can cause a localized reaction confined to the inferior retina involving macrophages and multinucleated giant cells. Also, there was a nonuniform drug distribution within the vitreous cavity due to the accumulation of the particulate systems at the inferior retina [43]. Calvo and coworkers [44] reported that the *in vivo* corneal uptake of indomethacin-loaded PCL colloidal particles was higher than microparticles after topical instillation into the albino rabbit eye. Qaddumi and coworkers [39] drew the same conclusion studying the uptake of PLGA nanoparticles of 100 nm, 800 nm and 10  $\mu\text{m}$  on primary cultured rabbit conjunctival epithelial cells (RCECs) The smaller (100 nm) particles exhibited the highest uptake.

The surface charge of the particles is important for particle adhesion to cornea. Positively charged colloids are able to deliver drugs to the eye due to their interaction with the negatively charged cornea. Positively charged chitosan nanoparticles or microspheres are much more effective than negatively charged particles due to the strong electrostatic interaction of the former with the negatively charged sialic acid residues in mucus [45]. The particulate nature is also important in increasing the intraocular penetration of drugs and decreasing the systemic absorption [46]. The importance of the cationic surface was shown by studying indomethacin con-

taining nanocapsules coated with either poly(L-lysine) (PLL) or chitosan, resulting in completely different drug kinetics profiles [47]. Chitosan-coated nanocapsules significantly increased the indomethacin concentration in the cornea and aqueous humor 30 min and 1 h after the instillation to the eye in comparison to the uncoated and PLL-coated nanocapsules. The bioavailability [area under the concentration–time curve (AUC)] of indomethacin from chitosan-coated nanocapsules was 7- to 8-fold higher in the cornea and aqueous humor respectively, while the values for PLL-coated capsules were almost 4-fold higher than the Idocollyre® in both cornea and aqueous humor.

Drug incorporation and drug release are the main limiting factors for these systems. The drug–polymer affinity, the drug hydrophilic/lipophilic balance and solubility are some of the main obstacles and challenges to efficient ocular nanoparticle formulations. A great example is cyclosporin A (CyA) – an endcapeptide used in a variety of immune-mediated ocular surface phenomena like vernal conjunctivitis, dry eye syndrome, prevention of corneal allograft rejection [36]. Its high lipophilicity reduces corneal uptake and many formulations (e.g. oil solutions, complexation with cyclodextrins, micelles, etc.) were unsuitable for a variety of reasons. However, Calvo and coworkers [48] achieved a 50% incorporation of CyA in the oily phase of Mygliol nanocapsules surrounded by PCL where the final drug concentration was 10 mg mL<sup>-1</sup>. These nanocapsules were taken up by corneal epithelial cells, so the drug level at the cornea was increased 5 times more than that obtained using the conventional 10 mg mL<sup>-1</sup> CyA oily solution. Even here, drug retention at the ocular mucosa was poor, so it was considered useful only for the treatment of extra-ocular diseases. Chitosan particles were more promising carriers since the drug loading was approximately 9%, but they were characterized by rapid drug release (62% in 15 min in sink conditions). Even so 2- to 6-fold increase of CyA was found in cornea and conjunctiva after topical instillation of these carriers. It was also noteworthy that the CyA amount found in cornea was higher than that in conjunctiva because drug-loaded carriers are cleared faster from the conjunctiva either due to the uptake by macrophages or to the passage to the blood circulation [35].

The antivirals, aciclovir and ganciclovir, have been in the focus of research since they are used for the treatment of herpes simplex infections and their ocular administration faces some problems. Aciclovir is used for Herpes simplex keratitis with the spread of the virus, at the most severe cases, in to the stromal cells, thus damaging them. However, the topical administration of the drug is difficult due to the low corneal penetration, and its poor water and lipid bilayer solubility [38].

The incorporation of aciclovir into PLA and PEG–PLA nanospheres was attempted in the presence of Tween 80 (0.5% w/v). The loading capacity was 2–5.9% in the former and 7.7% in the latter. The drug loading increased as the polymer molecular weight decreased for the PLA spheres, while it exhibited a further increase after the PEG insertion. This probably happened because the drug interacted with the PEG moiety, which retained the drug close to the particle surface. The drug release showed a burst effect and biphasic kinetics. Drug release reduced as the polymer molecular weight increased, while the presence of PEG did not offer any advantage in the release rate. In fact, the drug release was faster than the

uncoated particles, which indicated a different drug distribution in the polymeric matrix.

Fresta and coworkers [30] studied the drug loading in PECA or PEG–PECA nanospheres in the presence of Pluronic F68, and showed that the drug entrapment was not affected by the presence of either PEG or cyclodextrins, or the concentration of surfactant used. PEG-coated spheres released aciclovir slower than uncoated PECA nanospheres, while the presence of cyclodextrin did not improve the release rate. The aciclovir release showed the same profile as that observed using the PLA nanospheres.

Ocular bioavailability tests showed that using PLA nanospheres, the effective levels of aciclovir in the aqueous humor at 6 h were ( $1 \mu\text{g}$  of aciclovir  $\text{mL}^{-1}$  aqueous humor) in comparison to the free drug formulations (no drug was detected 6 h later). PEG-coated PLA nanospheres were more effective than the uncoated PLA nanospheres and the free drug formulation, with 1.8- and 12.6-fold increase, respectively [38]. Similar results were reported after the instillation of aciclovir-loaded PEG–PECA nanospheres to the eye, which showed a 25-fold increase in comparison to free drug suspensions. Both research groups attributed the higher degree of success to mucoadhesive properties because of the polyoxyethylene presence on the nanosphere surface.

Ganciclovir is used for the treatment of more acute viral infections like the human cytomegalovirus (HCMV) retinitis, which is the major cause of visual loss in AIDS patients. Intravitreal administration of the drug is quite effective with a half-life of about 13 h, so frequent injections are needed to maintain the therapeutic efficacy. On top of that, the administration route imposes a high risk of cataract development, retinal detachment and endophthalmitis [49–50].

Another Food and Drug Administration (FDA)-approved antiviral drug is fomivirsen, which exhibits a 55-h half-life after intravitreal administration [51]. Despite its resistance to the nucleases, the administration of this drug is problematic due to its poor penetration through cell membranes because it is a polyanion. Albumin nanoparticles have been investigated for the entrapment of those drugs and the study of the intraocular disposition after their intravitreal injection to rats. Ganciclovir-loaded albumin nanoparticles were prepared by either adding drug after the particle preparation or during the preparation procedure. Drug loading and release was  $15 \mu\text{g}$  ganciclovir  $\text{mg}^{-1}$  nanoparticles and 60% in 24 h for the first preparation, while it was  $27 \mu\text{g}$  ganciclovir  $\text{mg}^{-1}$  nanoparticles and 40% in 24 h for the latter. The first formulation was more active and inhibited the expression of the HCMV early antigens at a lower concentration than the conventional drug solution after their incubation on a cell line.

Formivirsen was entrapped into albumin nanoparticles made in the same way as the ganciclovir, and resulted in  $3.35$  and  $5.24 \mu\text{g}$   $\text{mg}^{-1}$  nanoparticles, respectively. The oligonucleotide release was 100% after 8 h, while the latter formulation exhibited sustained release for up to 5 days. The release of both drugs show the same biphasic release profile with burst release as described earlier. According to the literature [51, 52], the albumin molecules have fusogenic properties enabling the transfer of the oligonucleotides to the nucleus of the cells. The intraocular disposi-

tion of biotin-labeled albumin nanoparticles was studied by intravitreal injection of 900  $\mu\text{g}$  of particles per 5  $\mu\text{l}$ . Two weeks later it was shown that the carriers diffused through the vitreous space, with most of them located in a thin layer overlying the retina as well as in adjacent sites to the blood aqueous barrier and the ciliary body. There was no evidence of nanoparticles in the inner retinal layers like the visual cells and the neuronal interplay area.

Tamoxifen (nonsteroidal estrogen receptor modulator) for the treatment of uveoretinitis [31] has been formulated into PEG-coated PHDCA nanoparticles. The drug loading and release were not reported but it was found that the intraocular injection of 0.25  $\mu\text{g}$  of tamoxifen/10  $\mu\text{l}$  incorporated in PEG–PHDCA particles was efficient in reducing the uveoretinitis induced to rats while the free tamoxifen had no effect on the inflammation. According to the reported results in the rats carrying uveoretinitis, the nanoparticles were dispersed through the anterior and posterior segments of the eye 8 h after intravitreal injection. After 24 h, the particles passed through the edematous retina, and accumulated in the subretinal space and within the retinal pigment epithelium. Particles were not found in the choroid, but a high amount was detected in the anterior chamber of the eye. The particles were still detected in the retinal pigment epithelium 3–9 days after the injection.

The nonsteroidal anti-inflammatory drugs, ibuprofen and flurbiprofen, were formulated into RS100 and RL100 acrylate nanosuspensions to treat miosis induced by surgical manipulation, e.g. cataract extraction [32, 34]. Approximately 92% of flurbiprofen incorporation into both types of nanoparticles was achieved. Drug release from RS100 particles was slower than that from RL100 particles because the latter contain a higher amount of quaternary ammonium group which makes the nanoparticle matrix more permeable. Drug release studies showed no burst release. The flurbiprofen-loaded RS100 formulation was found in the aqueous humor and antagonized successfully the miosis caused because of a surgical trauma.

Ibuprofen incorporation was as high as flurbiprofen in RS100 particles (approximately 90%). Most of the drug was released after 24 h, but even though the drug concentration in the aqueous humor was higher than that of the free drug solution, the reduction of miosis was not significant [33].

Brimonidine ( $\alpha_2$ -adrenoreceptor antagonist) has been incorporated into PAA and polyitaconic acid (PIA) [41] nanoparticles with a loading capacity of 3.6 and 2.7 mg per 10 mg of nanoparticles respectively at pH 6.5. This corresponds to 80–85 and 70–75% loading efficiency in these systems, and 98% of the drug was retained for a period of 5 weeks at room temperature.

An alternative way to increase the residence time of the drug in the eye is the loading of nanocapsules into disposable soft contact lenses [53]. Nanocapsules were made with octadecyltrimethoxysilane (OTMS) in presence of Brij 97 (final size 13 nm) and loaded with lidocaine. OTMS creates a silica shell around the particles. The capsules were added to the polymerization medium, for lens formation of 1 mm thickness from poly(2-hydroxyethyl methacrylate) (pHEMA). The final particle content in the gel was 25%. When the gels were soaked in water, the drug was released almost completely after 7–8 days with burst release.

The mechanism of action is described herein. The drug diffuses from the particles through the lens matrix. A tear film is trapped between the cornea and lens; therefore, drug molecules will remain longer (30 min) in the post-lens tear film than in the case of eye-drops (2–5 min). This will enhance the influx of the drug through the cornea and reduce the systemic escape of the drug. Even so, there is still a fraction of the drug that will be lost due to tear drainage and absorption through the conjunctiva. According to these researchers, loading the lens with 0.024 mg of timolol will be enough to release therapeutic levels of the drug for 4 days.

The mechanism of interaction of various particles was studied either using primary cell lines or *in vivo*. Qaddoumi and coworkers [39] investigated the uptake mechanism of PLGA nanoparticles (100 nm) by primary cultured RCECs. After using a series of inhibitors for different specific uptake mechanisms located on the cell membrane, the group concluded that particle endocytosis takes place independently of both clathrin heavy chain and caveolin-1, although PLGA uptake may in part occur via clathrin-mediated processes. However, some endocytic process must be occurring because the conjunctival epithelium is a very strict barrier [54] and the paracellular pore radius is only 5 nm [55].

Chitosan nanoparticles are taken up by conjunctival epithelial cells more effectively than corneal epithelial cells because the conjunctival epithelium covers a larger surface area, and the concentration of mucin is higher there [56]. Chitosan nanoparticles can be transported by both paracellular and transcellular pathways because they are able to open the tight junctions between the epithelial cells due to the interactions between the positively charged groups of the polymer and the negative sites of the cell membrane and tight junctions. However, in conjunctiva, chitosan nanoparticles are located mostly in the cells rather than in the intercellular spaces. This happens because the conjunctival epithelium is more heterogeneous than that of cornea and contains goblet cells and APCs as well as epithelial cells. Thus, the particles could be transported to the APCs (Langerhans cells and macrophages) or even a specific cell receptor might be involved in the transport to some epithelial cells [45].

#### 9.2.1.4 Tolerability

As potential candidates for ocular drug delivery, most of the systems described above were well tolerated without any sign of irritation or inflammation to the animal model tested, apart from the PIA nanoparticles, which were proved highly cytotoxic. Approximately 90% loss of corneal epithelial cells viability was observed 30 min after the incubation of the PIA nanoparticles with the cells.

#### 9.2.1.5 Future Prospects for Nanoparticles in Ocular Delivery

Polymeric nanoparticles seem promising carriers for drug delivery to the eye. Some particles have shown adequate drug loading, prolonged site residence and good tolerability, but there are many more challenges to be faced yet. Drug loading, sustained release, storage stability and shelf-life are the main problems for many formulations. From a manufacturing point of view, the difficulty of producing sterile

dispersions is also problematic. No nanoparticulate systems have yet solved all these problems and reached the market.

## 9.2.2

### Macrophage-related Diseases

#### 9.2.2.1 Leishmaniasis

Leishmaniasis is a disease occurring mostly in tropical and subtropical countries. Leishmanial promastigotes invade macrophages and survive in the phagolysosomal compartments of the host cells [57]. Primaquine, an antimalarial drug, has demonstrated some activity against visceral leishmaniasis, but it is highly toxic against red blood cells. PACA nanoparticles without drug showed some activity against *Leishmania donovani* infection in rats [58]. Primaquine-loaded poly(isohexyl cyanoacrylate) (PIHCA) nanoparticles were tested for their anti-infection activity *in vitro* using the macrophage-like J774G8 cell line. PIHCA nanoparticles can be phagocytosed by Kupffer cells and spleen macrophages; hence, they can be potentially used against visceral leishmaniasis [59]. The nanoparticles were not toxic to the J774G8 cells at concentrations up to  $48 \mu\text{g mL}^{-1}$  for 48 h of incubation. Primaquine-loaded PIHCA nanoparticles showed a 21-fold increase of antileishmanial activity, while the two components, i.e. primaquine and nanoparticles, acted synergistically compared to the mixture of free drug and nanoparticles at equivalent concentrations.

Primaquine was also incorporated in poly(D,L-lactide) nanoparticles and was administered intravenously to healthy and infected BALB/c mice with the aim to evaluate tolerance [60]. The particles were formed in presence of phospholipids and Poloxamer (1%) and the final drug-loaded carriers were 150–200 nm, while the  $\zeta$  potential was  $-14.6 \text{ mV}$ . The efficiency of primaquine was 85–94% using an initial drug concentration  $0.5 \text{ mg mL}^{-1}$ .

The acute lethal toxicity of primaquine after intravenous administration to healthy mice was reduced after incorporation of the drug in the particles. For example,  $\text{LD}_{50}$  of free primaquine was  $17.5 \text{ mg kg}^{-1}$ , while for drug-loaded particles it was  $26.9 \text{ mg kg}^{-1}$ , corresponding to  $536 \text{ mg PLA kg}^{-1}$ . The lower toxicity is attributed to the rapid clearance of the particles to the MPS system so that the drug showed activity in the infected macrophages.

Neither free drug nor primaquine-loaded particles showed any lethal toxicity after injection of  $10 \text{ mg kg}^{-1}$  3 times in a 5-day period to infected BALB/c mice. As reported previously, the primaquine-loaded nanoparticles were 3.3 times more effective than the free drug in the suppression of the amastigotes of *L. donovani* in the liver of BALB/c mice [61].

Another drug used for the treatment against *Leishmania* is pentamidine, which is not fully effective and it has toxic side-effects [62]. Pentamidine has been incorporated onto the surface of methacrylate nanoparticles based on the ionic interactions with the free carboxyl groups of the polymer. Complete binding of pentamidine was obtained after mixing the drug ( $7 \mu\text{g mL}^{-1}$  nanoparticle suspension). The particle size was approximately 330 nm. Methylglucamine antimoniate was used as

the reference antileishmanial drug. The drug-loaded carriers suppressed the parasite burden by 77%, which was close to that achieved administering the reference drug (86%). The mean suppression by free drug was 35% while unloaded particles had no effect.

The pentamidine-loaded methacrylate particles were found to be effective against *Leishmania infantum* infection of BALB/c mice [63]. Parasite suppression of 50% was obtained after 1.06 mg of free drug  $\text{kg}^{-1}$  and 0.17 mg of pentamidine-loaded particles  $\text{kg}^{-1}$ . The latter  $\text{ED}_{50}$  was comparable to that achieved using liposomal amphotericin B (0.256 mg  $\text{kg}^{-1}$ ).

Paul and coworkers [64] studied the physicochemical properties of pentamidine-loaded methacrylate nanoparticles and shown that the optimum stabilization of the drug on the particle surface was pH 7.5, where both drug and polymer are highly ionized. They found out that at the lysosomal pH of 5, 50% of the drug is released. Following the fate of the drug-loaded vesicles in the liver Kupffer cells of infected BALB/c mice, the authors found that phagocytotic vacuoles containing nanoparticles were fused with primary lysosomes to form secondary lysosomes. Half of the pentamidine was released in the lysosome due to its acidic pH. However, the drug is still ionized, so it cannot pass through the lysosomal membrane. The parasitophorous vacuole (pH 4.7–5.2) is fused with the secondary lysosome and the drug is still retained in the vacuole. Despite the fact that nanoparticles cannot be internalized by the parasites, the released pentamidine resulted in parasite growth suppression.

Another group incorporated amphotericin B in PLGA nanoparticles (size 166 nm), and evaluated the leishmanicidal potency of those particles on macrophages *in vitro* as well as the effect of trehalose on the multiplication of promastigotes and the macrophage activation [65]. Amphotericin B is sometimes used for the treatment of visceral leishmaniasis when the usual antimonial drugs are noneffective [66]. Liposomal amphotericin is used to reduce the toxicity and increase the drug efficacy. However, the amphotericin-loaded nanoparticles did not exhibit any advantage over the free amphotericin B in treating the infected macrophages, probably because the majority of the particles were washed away so there was only a limited amount endocytosed by the macrophages. Moreover, trehalose reduced promastigote multiplication. It has been shown previously that *L. donovani* promastigotes interact with the mannose/fucose receptors on human monocyte-derived macrophages in order to invade the host cells [67]. The presence of trehalose was shown to be toxic to the macrophages in a concentration higher than 50%. The sugar was tolerated in a concentration of 1 mg  $\text{mL}^{-1}$  by both infected and noninfected macrophages, but infected macrophages showed higher tolerance than the noninfected ones. This happened because lower amounts of specific receptors were available on the infected macrophages rather than the noninfected ones. Also, both infected and noninfected macrophages were activated by the presence of trehalose, while a greater effect was obtained for the infected ones. Thus, the sugar can alter the fate of *L. donovani* in the cells.

There is still a need for the development of new molecules with antileishmanial activity due to the toxic effects of the current drugs or due to their lack of

efficiency [68]. Based on a previous report that the chalcones are quite effective against *L. donovani* [69], a group of researchers incorporated 2',6'-dihydroxy-4'-methoxychalcone (DMC) extracted from *Piper aduncum* in PLA nanoparticles [70]. Pluronic F68 (1%) was used as surfactant to facilitate the particle formulation. The size of empty and loaded-nanoparticles was 130 and 168 nm, respectively, and the encapsulation efficiency was approximately 92%. BALB/c mice infected with *L. amazonensis* promastigotes were injected intraperitoneally with either empty particles (1 mg), DMC-PLA particles (200 µg DMC mg<sup>-1</sup> PLA), glucantime (200 µg) or phosphate-buffered saline alone on days 42 and 48 after infection. It was shown that DMC-PLA particles were as effective as glucantime (first choice drug for the treatment of leishmaniasis) in reducing the number of parasites into the cells, making the drug-loaded particles promising agents for antileishmanial treatment.

Many other attempts to develop new antileishmanial agents have been reported [71–73]. One of these is quercetin, which belongs to the flavonoid family and is metabolized in the colon – it exhibits mostly antioxidant, anti-inflammatory, anti-hepatotoxic and antiulcer properties [71]. It has been formulated in different carriers, like liposomes, niosomes, microspheres and nanocapsules (PLA). It has been shown that quercetin inhibits the growth of *L. donovani* promastigotes and intracellular amastigotes both *in vitro* and *in vivo*, while it leads *L. donovani* promastigotes to apoptosis through inhibition of DNA topoisomerase II inhibition [74]. Quercetin EC<sub>50</sub> was 3 mg kg<sup>-1</sup> body weight; therefore, the different formulations were administered subcutaneously to hamsters after 30 days of their infection at a dose of 300 µg per 0.5 ml of vesicles suspension every 3 days for a total of 6 doses in 15 days. The final administered dose was equivalent to the EC<sub>50</sub> of quercetin. The highest efficiency was obtained after the quercetin-loaded nanocapsules, which demonstrated 87% reduction of spleen parasite burden compared to the 25% achieved with the free drug. As for the rest of the formulations tested, the efficacy was 68, 51 and 44% for drug loaded-niosomes, liposomes and microspheres, respectively.

The same set of experiments was carried out with the carriers mentioned above using another potential antileishmanial agent named harmine (7-methoxy 1-methyl β-carboline), previously shown to be effective at Parkinson's disease and related neurological/psychiatric diseases [72]. Harmine has also exhibited activity against *Trypanosome cruzi*, while it can be effective against AIDS and tumors. It is believed that harmine condenses chromatin [75] and inhibits DNA topoisomerase I [76]. The effective dose of harmine was found to be 25 µg kg<sup>-1</sup> body weight in 24 h after incubation of *L. donovani* *in vitro*. After the subcutaneous injection of the harmine-loaded particles, the reduction of the spleen parasite load was by 44% for the free drug, and 61, 67 and 79% for liposomes, niosomes and nanocapsules, respectively. One reason for the highest efficacy of the nanocapsules was the fact that they were the smallest formulation and their composition enabled them to circulate in the blood stream longer in comparison to the other type of vesicles, probably due to the presence of Tween 80 as a capsule component.

The same group carried out a similar piece of work on arjunglucoside, a pentacyclic triterpene glycoside of the saponin group, in nanogels of 90 nm or PLA



nanoparticles (250 nm) for similar reasons [73]. The nanogel consisted of *N*-isopropyl-acrylamide (NIPAAm) and *N*-vinyl-pyrrolidone (VP). The drug incorporation efficiency was 80 and 60% for nanogel and PLA nanoparticle, respectively. After the subcutaneous injection of the two formulations in infected hamsters, they both exhibited a similar reduction in the spleen parasite load, which was recorded to be 75 and 79% for the nanogel and the nanoparticles, respectively. The effective dose of the drug was 4 mg kg<sup>-1</sup> body weight. *In vitro* release of drug from nanogels was accompanied with an initial burst release of 50% and a total release of 75% after 25 h, while the drug release from PLA nanoparticles was 40% initially and it remained mostly constant up to 25 h.

Particles with neoglycoproteins having either glucose, mannose or fucose moieties grafted on the vesicle surface would enable more effective macrophage targeting according to comparative studies between liposomes, niosomes, microspheres and nanoparticles as presented by Basu and coworkers [77].

#### 9.2.2.2 Other Parasitic Infections

Unloaded poly(isobutyl cyanoacrylate) (PIBCA) nanoparticles demonstrated anti-trypanosomal activity after their *in vitro* and *in vivo* tests on *Trypanosoma brucei* [78]. More specifically, after *in vitro* treatment of *T. brucei* with different concentrations of PIBCA, the parasitic mobility disappeared in the presence of 1.2 μg mL<sup>-1</sup>. Mice pretreated with 1.2 μg mL<sup>-1</sup> and infected with trypanosomes survived until 30 days later, but they were not completely cured. The above nanoparticles were not effective against *Trypanosoma vaginalis* or *Entamoeba histolytica*.

Schistosomiasis is another serious public health problem in tropical countries. Praziquantel is the drug of choice, but the poor water solubility and the fast metabolism make long-lasting therapy hard to achieve. PLGA polymer was used to prepare nanoparticles with the emulsion-solvent evaporation method and a variety of factors were considered in order to prepare a formulation with optimum physicochemical properties [79] (Fig. 9.3). Those factors were PLGA and surfactant content in the formulation, time of sonication, ratio of the volume of aqueous to organic phase, and praziquantel content. Sonication (20 min) led to a particle size of 255 nm with polydispersity index of 0.22 and a monomodal distribution.

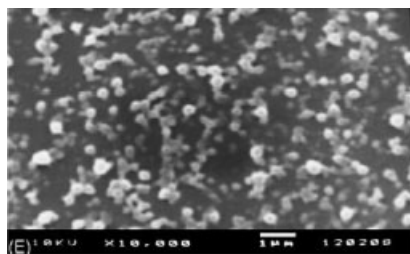


**Figure 9.3.** PLGA nanoparticles prepared with 20% of praziquantel. (Reprinted from Ref. [79], © 2005, with permission from Elsevier.)

Using 12.5 mg of PLGA polymer, the particles were of spherical shape without agglomeration.

As the polymer concentration (12.5, 25 and 50 mg) increased, the particle size increased and the particle shape deviated from the spherical pattern. As the surfactant content increased, the particle size reduced and the best formulation was obtained using 0.7% of surfactant. Also, the rate of evaporation of the organic solvent should be as slow as possible, so as the volume of the organic phase is reduced and the viscosity increases, the droplet size equilibrium will not change instantaneously and the particles will have the time to be formed in a good spherical shape of small size without agglomeration.

Praziquantel encapsulation efficiency was constant (approximately 75%) over the range of initial amount of the drug used from 10 to 30%. As the drug content increased, the size of the particles increased due to the increase of the dispersion viscosity. *In vitro* release of praziquantel was studied using particles prepared in the presence of 10 and 30% theoretical loadings; 100% of the drug was found in the dispersion medium in 2 h. As for the drug-loaded particles, 6 and 20% of drug was released from nanoparticles after 24 h from 10 and 30% drug-loaded particles. It is concluded that highest drug release is obtained with the highest drug loading.

An Antimalarial nanoparticle formulation has been reported by Legrand and coworkers [80]. Nanocapsules were prepared using PLA-PEG copolymers (PLA:PEG molecular weight ratios of 45:5 and 45:20) and Miglyol 810 to encapsulate halofantrine – a very hydrophobic antimalarial drug. Drug incorporation was better than 99.5% with 25% drug by weight of nanocapsules. Their particles were stable for more than 10 months at 4 °C and had a size of 175–220 nm.

Drug release was slow in the presence of Tween 80 (used to allow solubility of drug in water), but rapid in the present of serum proteins. The nanocapsules were long circulating and when administered to mice infected with *Plasmodium berghei* showed a reduction in parasite infection within a short period, which was maintained for several days. The nanocapsule treatment was much more rapid in onset than with the free drug. The toxicity of the encapsulated drug was also much reduced in comparison to free drug.

### 9.2.3

#### Antifungal

##### 9.2.3.1 Treatment

Drugs used in fungal infections are polyene antifungals (amphotericin, nystatin), imidazole antifungals (ketoconazole, miconazole), triazole antifungals (fluconazole, itraconazole), and others like griseofulvin, caspofungin, flucytosine and terbinafine [66]. Some of those drugs exhibit limitations either of absorption via the oral route or high toxicity. For example, polyene antifungals are not absorbed when given orally. They are used for oral, oropharyngeal and perioral infections by local application in the mouth. Amphotericin is highly toxic and mostly nephrotoxic, but lipid formulations (Abelcet<sup>®</sup>, AmBisome<sup>®</sup> and Amphocil<sup>®</sup>) have been produced reducing its toxicity.

Also, ketoconazole is characterized as highly hepatotoxic, but it is absorbed well when it is given orally. Itraconazole is another drug associated with liver damage.

### 9.2.3.2 Drug Delivery Systems

Only a few attempts have been reported using nanoparticles to improve the therapeutic prospects of the above mentioned drug molecules by reducing their limitations. Amphotericin B (used against infections by *Candida albicans*) was launched in the market as lipid formulations that are expensive. Thus, Tiyaboonchai and coworkers [81] have incorporated the antifungal drug in polyethylenimine (PEI)–dextran sulfate (DS) nanoparticles produced with the complex coacervation method (Fig. 9.4).

This method has the advantage of being simple and low cost without the need for organic solvents. It is based on the electrostatic interaction of the two oppositely charged molecules. Due to the poor water solubility of amphotericin B and low absorption from the gastrointestinal tract, the drug is administered parenterally. Particle size and size distribution are crucial parameters for parenteral formulations. The pH of PEI solutions, the charge and mass ratio of the two polymers as well as the zinc concentration influenced the particle size. The optimal conditions for am-

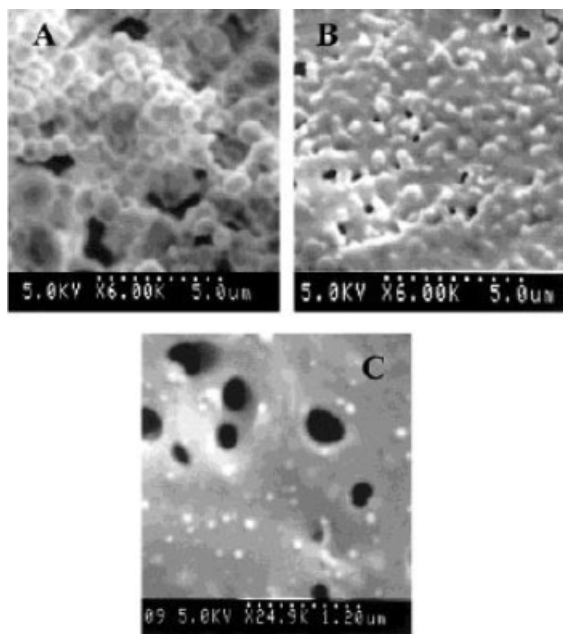


**Figure 9.4.** Scanning electron microscopy micrographs of unloaded nanoparticles formed with pH 7 PEI solution and a PEI:DS mass ratio of 1:1, and washed in (A) water and (B) 5% w/v mannitol. (C) Scanning electron

microscopy micrograph of amphotericin B particles formed with pH 8 PEI solution and a PEI:DS mass ratio of 2:1, and washed in 5% mannitol. (Reprinted from Ref. [81], © 2001, with permission from Wiley.)

photericin B nanoparticle formation was the use of a PEI solution of pH 8, PEI:DS polymer ratio 2:1 and 25  $\mu\text{m}$  zinc sulfate. Entrapment efficiency was about 85%. The particles produced had an average size of approximately 260 nm with a range of 100–600 nm. Mannitol was used as a cryoprotectant during the lyophilization procedure making the particles easily redispersable, which was not the case when mannitol was not present.

*In vitro* dissolution studies showed a rapid release of the drug, which, according to the authors, would be clinically useful due to the poor drug solubility and thus, the sustained release effect.

After incubating the drug-loaded nanoparticles with human cells, amphotericin B-loaded vesicles exhibited 100-fold lower toxicity compared to a reduction in the antifungal activity of the molecule of only 2-fold.

A different approach was to prevent the adhesion of *C. albicans* so to prevent the start of the infection [82]. This was based on using poly(propyl cyanoacrylate) nanoparticles in the presence of anionic, cationic or nonionic surfactants to promote adsorption onto the blastospore surface and, hence, reduce blastospore adherence to buccal epithelial cells. The adherence of blastospores that had been treated with nanoparticles produced in presence of docusate sodium was 73% lower than that of untreated blastospores. This phenomenon was reported to be due to the steric hindrance that the particles cause after their adherence on the spore's surface.

Molina and coworkers [83] improved the therapeutic efficacy of a sterol biosynthesis inhibitor, DO870, by incorporating it into PEG–PLA nanoparticles. This inhibitor was used successfully against the Y and CL strains of *Trypanosoma cruzi* in Chagas' disease, but its development has been discontinued [84]. Also, ketoconazole- and itraconazole-loaded particles were used for comparison. Particle sizes in the range 100–200 nm were achieved and entrapment efficiencies were 90, 87 and 92% for DO870, itraconazole and ketoconazole, respectively. The drug-loaded nanoparticles were administered to infected mice either orally or intravenously and were well tolerated by the mice for the treatment period of 93 days. In contrast, for the group of mice treated with free DO870, 100% death was observed at the day 93, postinfection period.

After administration of DO870-loaded particles via the intravenous route (1.5–3.0  $\text{mg kg}^{-1} \text{day}^{-1}$ ) or the oral route (5  $\text{mg kg}^{-1} \text{day}^{-1}$ ) no reappearance of parasites in the blood was observed. The cure rate for those formulations was approximately 80% in mice infected with the CL strain of *T. cruzi*. For the Y strain, infected mice received an intravenous administration of 3  $\text{mg kg}^{-1} \text{day}^{-1}$ . The cure rate of DO870-loaded particles was 60%, while there was no positive influence of the ketoconazole or itraconazole-loaded spheres.

Nisin is a bacteriosin produced by *Lactococcus lactis* and is used as a food preservative, but it is unstable and so it was incorporated into nanoparticles [85]. Those particles were made using PLA with the method of supercritical fluids. Using supercritical or compressed gas techniques to make nanoparticles is very attractive due to the omission of surfactants or stabilizers that may cause protein denaturation or toxic effects, the process flexibility, the high product yield and, possibly,

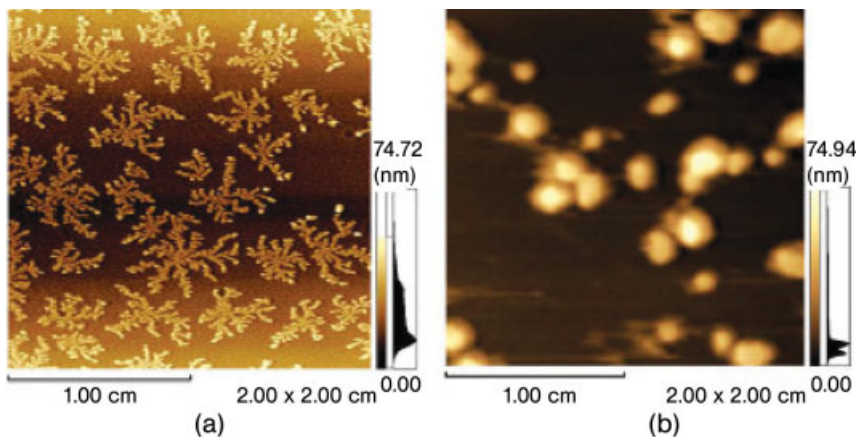


**Figure 9.5.** Atomic force micrographs of chitosan nanoparticles at pH 5.0: chitosan nanoparticles (A) and copper-loaded nanoparticles (B). (Reprinted from Ref. [86], © 2004, with permission from Elsevier.)

efficient protein encapsulation. The optimal ratios for particle preparation were: dimethylsulfoxide:dichloromethane 50:50 where the nisin solubility was  $60 \text{ mg mL}^{-1}$ , and a PLA solution of  $10 \text{ mg mL}^{-1}$  containing  $0.5$  or  $2 \text{ mg mL}^{-1}$  nisin. The optimal preparation conditions were:  $1 \text{ mL min}^{-1}$  organic solution injection into the precipitation vessel,  $288 \text{ K}$  and  $15 \text{ MPa}$ ,  $1500 \text{ NL (normal liters) h}^{-1}$   $\text{CO}_2$  flow rate and  $1 \text{ h}$   $\text{CO}_2$  washing after the particle preparation. The process yield was approximately 80% and the remaining DMSO and DCM were less than 300 and 15 p.p.m., respectively. Biological studies showed that nisin was entrapped in the particles in its active form so the efficacy of the preparation procedure was demonstrated. However, the nisin-loaded particles had a weaker antibacterial activity attributed to the delay of protein release from the spheres.

Finally, we should mention the recently reported antibacterial activity of chitosan nanoparticles and copper-loaded chitosan nanoparticles [86] (Fig. 9.5). The particle preparation took place in presence of tripolyphosphate (TPP) with anionic gelation at room temperature. Absorption of copper ions on the particle surface affected the physicochemical properties of the particles. The particle sizes were 4 and 275 nm and the  $\zeta$  potentials were 51 and 96 mV for the chitosan and copper-loaded chitosan nanoparticles, respectively.

Bacteria can adhere on the chitosan surface either in the particle or the molecular form in 30 min. According to the literature, chitosan possess antimicrobial activity against a number of Gram-negative and Gram-positive bacteria [87–88]. Chitosan nanoparticles and copper-loaded chitosan nanoparticles showed stronger antibacterial activity than chitosan alone or doxycycline. Chitosan nanoparticles surround the bacteria after 30 min. This leads to the cell degradation in 60 min and finally the cells begin to fragment after 3 h. A possible mechanism of action is that either it chelates with nutrients and so inhibits the bacteria growth or chito-

san interacts with the anionic groups of the cell surface and forms polyelectrolyte complexes with bacterial surface compounds. Hence, they form an impermeable layer around the cell, which prevents the transport of essential solutes in the bacterial cell. Also, it was shown that the nanoparticle nature of chitosan was responsible for the higher antimicrobial activity.

In the case of copper-loaded nanoparticles, copper was adsorbed on the chitosan particles and passes through the pores of the vesicles towards the inner surface of the particles, where it is chelated. The antimicrobial mechanism of action of copper is that copper is reduced from  $\text{Cu}^{2+}$  to  $\text{Cu}^{1+}$  in the bacteria. The  $\text{O}_2^-$  and  $\text{H}_2\text{O}_2$  produced by such redox reactions cause cytotoxicity by inhibition of DNA synthesis and thus reduction of cell viability.

## 9.2.4

### Tuberculosis

#### 9.2.4.1 Physiology and Pathology

*Mycobacterium tuberculosis* is the causative organism of tuberculosis, which occurs mainly in the lungs, although it can be disseminated to other organs. Bacteria reach the deep lung and are phagocytosed by alveolar macrophages. There, the bacteria will be either destroyed, replicate within the macrophages or remain latent indefinitely. If replication is not prevented the bacilli will multiply and eventually cause the macrophage to rupture.

Tuberculosis is transmissible between people and is most prevalent in places where poor hygienic conditions are found, e.g. during war, famine, homelessness, people lacking adequate medical care, etc. It continues to be found worldwide and causes about 2 million deaths per year. Treatment is long and inadequate or incomplete treatment promotes the development of resistant strains of tuberculosis.

#### 9.2.4.2 Treatment

Tuberculosis is treated in two phases. (i) An initial phase of 2 months, which comprises daily administration of a combination of at least three of the drugs rifampicin (RIF), isoniazid (INH), pyrazinamide (PZA) or ethambutol according to the patient tolerance or bacterial strain resistance. (ii) A continuation phase of 4 months using two drugs, mainly INH and RIF. The treatment is usually oral, but sometimes treatment is parenteral. INH, RIF and PZA are associated with liver toxicity, so hepatic function and renal function should be checked before the treatment commences. Visual acuity should be tested before induction of ethambutol to the therapeutic scheme. Patient noncompliance due to daily multidrug dosing is a significant drawback in tuberculosis therapy.

The main aim of microparticles or nanoparticles for antituberculosis therapy is to reduce the drug systemic toxicity and dosage whether by oral or pulmonary delivery. According to Pandey and coworkers [89], using nanoparticles is preferable to microspheres because of “the high drug loading minimizing the consumption of polymers, their ability to pass through various barriers due to their small size eliciting better therapeutic response”.

**9.2.4.2.1 Oral** Polymeric nanoparticles for oral delivery have been prepared using PLGA polymer [90–92]. The three drugs, RIF, INH and PZA were coencapsulated and exhibited a high drug encapsulation efficiency of 56.9, 66.3 and 68%, respectively with a particle size range of 186–290 nm. After a single oral administration (therapeutic dose of RIF: 12 mg kg<sup>-1</sup> + INH 10 mg kg<sup>-1</sup> + PZA 25 mg kg<sup>-1</sup>) of these particles to mice with experimental tuberculosis, therapeutic levels in plasma were maintained for 4 days in the case of RIF, and for up to 9 days for INH and PZA. Therapeutic concentrations in the tissues higher than the mean inhibitory concentration (MIC) were found for up to 11 days for INH. The free drugs or mixture of free drugs with empty PLGA nanoparticles, administered as a one single oral dose, were cleared rapidly since no drug was detected in the plasma after 12–24 h. According to Pandey and coworkers [90], PLGA polymers are adhesive to the intestinal mucosa so the nanoparticles can be adsorbed directly by intracellular or paracellular routes. More specifically, the nanoparticles can be taken up either by transcytosis via M cells, or intracellular uptake and transport via the epithelial cells lining the intestinal mucosa or uptake via Peyer's patches [93]. Increased lung accumulation was not observed with multiple dosing (five doses at 10 day intervals), but no tubercle bacilli could be detected in the tissues. It was also shown that reducing the oral administration of the previously mentioned formulation by one-third, RIF remained in the circulation for 5 days while INH and PZA remained for 12 days. The drug tissue levels were higher than the MIC up to 14 days in guinea pigs [91]. Even with two-thirds of the therapeutic dose of PLGA-NP, bacilli could not be detected after five doses of treatment.

In order to increase the therapeutic efficacy of the PLGA nanoparticles, the lectin, wheat germ agglutinin (WGA), was incorporated onto the particle surface [92] to interact with specific receptors on intestinal and alveolar epithelium. This lectin has very low immunogenicity, thus making these particles potential candidates for oral and aerosol drug delivery. After a single oral administration of drug-loaded WGA–PLG nanoparticles to guinea pigs with tuberculosis, RIF was still found in the blood circulation 7 days later, and INH and PZA after 13 days. The therapeutic levels in the tissues were maintained higher than the MIC for 15 days and nanoparticle formulations did not show any hepatotoxicity.

**9.2.4.2.2 Pulmonary** During oral administration, only a fraction of the total dose of drugs reaches the lungs and even this fraction is cleared quickly so that frequent doses of antitubercular drugs are necessary [89]. Bearing in mind those problems as well as the fact that the pulmonary route leads the drug directly to the most affected organ, the lungs, nanoparticle administration has also been attempted via nebulization or aerosolization. Pulmonary administration is particularly attractive because of the direct targeting of alveolar macrophages, which are used by mycobacteria as a site for their prolonged survival. Lung delivery will also reduce drug systemic toxicity, therefore improving patient compliance. The lungs offer an enormous surface area for absorption, a favorable environment for proteins, avoidance of first-pass metabolism and better patient acceptability than an injection [94].

PLGA nanoparticles loaded with RIF, INH and PZA with a mass median aerodynamic diameter (MMAD) of  $1.88 \pm 0.01 \mu\text{m}$  were used for inhalation as a single dose every 10 days in guinea pigs [95, 96]. The drug plasma concentration was detected from 6 h onwards until 6 days for RIF, and until 8 days for INH and PZA. The tissue drug concentration at levels higher than MIC was seen for up to 11 days. When the WGA lectin was incorporated on the surface of those nanoparticles [4] (MMDA  $2.8 \pm 1.4 \mu\text{m}$ ), the formulation showed improved potency. After one dose to guinea pigs the INH and PZA plasma levels were retained up to 13 and 14 days, respectively, whereas the RIF levels were detected for up to 6 days. The tissue drug levels higher than MIC were estimated up to 15 days and no hepatotoxicity was observed.

PLGA polymer has limitations as a carrier for lung delivery because of the degradation products of the polymer which can be accumulated in the lung tissue. The polymer induced a mild inflammation lasting for 2–3 weeks [97], but with no obvious consequence on lung function. Bulk PLGA degradation creates an acidic environment, which can damage pH-sensitive drugs such as peptides and proteins [94].

New biomaterials have also been used for drug delivery via aerosolization. Fu and coworkers [94] synthesized the polyether anhydride, sebacic acid (SA)–PEG copolymer, consisting of FDA-approved materials. The PEG content of this polymer leads to the decrease of aerodynamic diameter as well as to increased degradation times. These characteristics give the flexibility of producing particles of different properties for different parts of the lung.

Dailey and coworkers [98] prepared nanoparticles with the branched polyester, diethylaminopropylamine–poly(vinyl alcohol)-*g*-poly(lactide-*co*-glycolide) (DEAPA–PVAL-*g*-PLGA). The nanoparticles included some polyions [carboxymethylcellulose (CMC), dextran sulfate, DNA] in order to modify the physicochemical properties and to study the formulation with the best stability. The greatest advantage of these polymers was that they could be assembled into particles in the absence of surfactant, to reduce possible effects on lung function. It was shown that the positively charged particles interacted efficiently with lung cells, unfortunately only the anionic particles, which did not show any interaction with cells, could be nebulized efficiently.

Alginate, a biodegradable FDA-approved natural polymer, has also been investigated. Nanoparticles made after cation-induced controlled gelification of alginate were of approximately 235.5 nm diameter and the drug encapsulation efficiency was 80–90% for RIF, and 70–90% for INH and PZA. After aerosolization the MMAD was  $1.1 \pm 0.4 \mu\text{m}$  [99]. A single dose of particles loaded with RIF, INH and PZA was administered to guinea pigs. The drugs were detected in the plasma from 3 h onwards. RIF was found in the plasma up to 10 days, and INH and PZA for 14 days. The drug tissue levels were higher than MIC up to 15 days. Thus, overall, alginate particles appeared earlier in the plasma, and RIF was present in the serum for longer than WGA–PLGA nanoparticles with similar retention of tissue drug levels. Again, hepatotoxicity was not observed using the alginate nanopar-



ticles. All these formulations were capable of eliminating the mycobacteria after administration of five doses once every 10 days.

**9.2.4.2.3 Subcutaneous Administration** PLGA nanoparticles loaded with RIF, INH and PZA, and administered via subcutaneous injection to mice, showed sustained release maintaining therapeutic drug levels for up to 36 days in the lungs and the spleen and up to 32 days in the plasma [100]. This resulted in undetectable colony-forming units, while the subcutaneous injection of the free drugs did not reduce the bacterial presence in the organs of infected mice.

#### 9.2.4.3 Future Prospects

From the results reported so far, it seems that the formulation of the three main antitubercular drugs into nanoparticles is very promising for the effective treatment of the disease using either the oral or the pulmonary pathway. The drug loading was high and inhalable formulations were produced from polymer nanoparticles. The use of ligand-bearing particles or particles made with natural polymers promoting cell binding and uptake showed prolonged therapeutic efficacy. A significant reduction in dosage from 45 administrations to five was achieved without compromising performance. The reduction of the dosing scheme is very encouraging because it contributes to patient convenience. The problems that still have to be tackled are mainly the improvement of inhalable formulations, and the cost for the large-scale production of those particles and final products, which will have to exhibit long shelf-life.

### 9.2.5

#### AIDS

##### 9.2.5.1 Pathology

HIV is a retrovirus with two primary types: HIV-1 and HIV-2. There are many strains of both types and all mutate rapidly, which has made it particularly difficult for researchers to find an effective vaccine or treatment for the virus. HIV infection is often mostly or entirely asymptomatic (without symptoms) and the most common signs, which include fever, fatigue, rash and lymphadenopathy (swollen lymph nodes), are often mistaken for mononucleosis, flu or similar, comparatively harmless diseases. Eventually, full-blown AIDS develops in the vast majority of cases.

##### 9.2.5.2 Treatment

The infection caused by the HIV cannot be cured, but drugs are used to slow down the progression of the disease [66]. Drugs for HIV are toxic and expensive, but they increase life expectancy considerably. The aim of the treatment is to reduce the plasma viral load as much as possible and as long as possible before the immune system is irreversibly damaged. The treatment scheme should be chosen taking into account the drug toxicity, patient convenience and tolerance. Using a combina-

tion of drugs can halt the drug resistance. This drug combination should have a synergistic therapeutic effect, but not an additive toxic effect. The suggested treatment is the combination of two nucleoside reverse transcriptase inhibitors with either a non-nucleoside reverse transcriptase inhibitor or one or two protease inhibitors.

Nucleoside analogs or nucleoside reverse transcriptase inhibitors were the first substances used for the HIV treatment. They are DNA chain terminators or competitive inhibitors of the virus-associated reverse transcriptase. Such nucleoside analogues are zidovudine [azidothymidine (AZT)], abacavir, didanosine, lamivudine, stavudine, tenofovir and zalcitabine.

The second group of molecules used for HIV treatment are protease inhibitors, and include amprenavir, indinavir, lopinavir, nelfinavir, ritonavir and saquinavir. They can block the replication of HIV in chronically infected cells. They are metabolized by P450 enzyme systems, and are associated with lipodystrophy and metabolic effects.

The third category of anti-HIV drugs is made up of the non-nucleoside reverse transcriptase inhibitors efavirenz and nevirapine.

### 9.2.5.3 Nanoparticle Delivery Systems

Due to the high dosage scheme in order to achieve antiviral activity and the high toxicity of anti-HIV drugs, there have been attempts to entrap some of these drugs into polymeric nanoparticles to make the treatment more tolerable for the patient and to effectively reduce the drug dosage.

At first, the potential of the antiviral activity of zalcitabine or saquinavir loaded into nanoparticles was studied by incubating HIV-infected primary human macrophages *in vitro* and comparison with the free drug activity on the same cells [101]. The problem with zalcitabine is the rapid viral resistance, while saquinavir is a poorly soluble drug with low bioavailability. Poly(hexyl cyanoacrylate) (PHCA) was used as the polymer of choice to make nanoparticles, which entrapped 15–20% of zalcitabine and 50–60% of saquinavir, respectively. The particle size was approximately 200 and 475 nm, respectively. After the incubation of the drug-loaded nanoparticles with the macrophages, the antiviral activity of zalcitabine did not show any advantage by incorporating the drug into the polymeric carriers, while the activity of saquinavir showed 10-fold improvement. This can be explained on the basis that the zalcitabine molecule itself enters the cell through diffusion and through some transport mechanisms. The activity of this drug is depended on its intracellular conversion to the corresponding 5' mono-, di- and triphosphate derivatives [102].

Later, AZT bound to hexylcyanoacrylate nanoparticles was administered intravenously to rats to estimate the targeting feasibility of these nanoparticles to macrophages [103]. Polysorbate 80 (1%)-coated nanoparticles loaded with AZT were used as well to study the influence of the surfactant on the uptake by the brain with the aim of treating the dissemination of the virus to the brain (microglia). Indeed, 8 h postinjection, 60% of AZT was found in the reticuloendothelial system (RES) or-

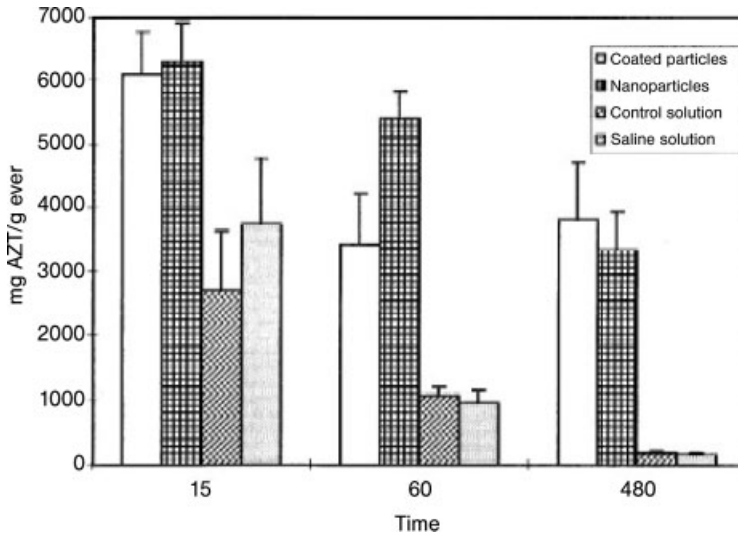


**Figure 9.6.** Liver concentrations of AZT (mg of AZT  $\text{g}^{-1}$  liver) after intravenous injection of Polysorbate-80-coated AZT nanoparticles, AZT nanoparticles, an AZT control solution (with emulsifier) and a saline AZT solution (without emulsifier). (Reprinted from Ref. [103], © 1998, with permission from Elsevier.)

gans, while only 12% of the drug injected in its free form was found in the same organs (Fig. 9.6). No trend was obtained in the other organs mainly due to the large fluctuations observed.

Polysorbate-80-coated nanoparticles showed a significant decrease in the liver accumulation, prolonged half-life and significant increase in the brain 1 h after intravenous injection. The increase of the surfactant coated nanoparticles was 35% higher compared to the uncoated particles and 45% compared to the unbound AZT, so there is the possibility of reducing the AZT dose to reduce the AZT side effects.

The same drug was formulated in nanospheres made by PIHCA aiming to concentrate AZT in the intestinal epithelium and associated immunocompetent cells which are known to be one of the major reservoirs of HIV [104]. PIHCA was used due to the controlled release properties in the gastrointestinal tract and its tendency to interact with the intestinal mucosa. The nanospheres were administered by intragastric intubation to rats. The carrier size was approximately 250 nm and the  $\zeta$  potential  $-23$  mV. The release of AZT was estimated in different media; a burst release of 35% of AZT was observed in water or USP XIII-simulated gastric medium containing pepsin. In the presence of pancreatin, 80% of AZT was released 8 h later, probably due to the presence of esterases.

AZT accumulation was 4.4 and 5.9 times higher in intestinal mucosa 30 and 90 min later, respectively, in comparison to the control systems. Similarly, 67% and 64% of the initial dose of AZT was found in the gastrointestinal tract, while only

15 and 11% of the drug was found, respectively, after the administration of drug solution.

The drug accumulation from the particles was 4- and 28-fold higher in stomach 30 and 90 min postadministration, respectively and around 5.5-fold higher in intestine. AZT concentration was maintained constant in the intestine, while it was very low in cecum and colon. Additionally, nanoparticles resulted in higher AZT concentrations in the mucus when compared to the solution (59 and 60.5 nmol AZT g<sup>-1</sup> organ for the nanoparticles at 30 and 90 min, respectively, compared to 8.1 and 10.6 nmol g<sup>-1</sup> organ for the solution). Moreover, 4-fold AZT increase was achieved in Peyer's patches while a very low concentration was found in the lymphatics.

HIV protease inhibitors are characterized by poor pharmacokinetic characteristics and bioavailability problems, which were addressed by the use of nanoparticles. Thus, the HIV protease inhibitor, CGP-57813, was incorporated into pH-sensitive nanoparticles made by Eudragit S100 or L100-55 (approximately 14% drug loading, 250 nm size) [105]. The difference between the two types of polymers lay in the part of the gastrointestinal tract where they were soluble. Also, the influence of the presence of food in the gastrointestinal tract in the effective delivery of the HIV protease inhibitor was studied after the oral administration (25 mg CGP 57813 mL<sup>-1</sup>) of the particles to dogs. According to these studies, Eudragit L100-55 particles did not show any improvement in bioavailability in fasted dogs and only a small increase was obtained in fed dogs, probably because of the rapid dissolution of the polymer in the intestinal pH, which led to the precipitation of the compound.

The presence of food had a more pronounced effect on CGP 57813 bioavailability, while no detectable plasma levels were reported in fasted dogs. The same series of experiments were carried out in mice with opposite results. Eudragit L100-55-loaded particles were more favorable in increasing the bioavailability of the protease inhibitor, indicating that the optimal formulation depends strongly on the animal species [106].

Eudragit L100-55 was studied for improvement of the solubility and bioavailability of HIV-1 protease inhibitor CGP 70726 after oral administration to dogs in the presence or absence of food [107]. Not only nanoparticles, but microspheres were studied here to investigate the influence of the size. The latter did not seem to make any significant difference in the performance of those pH-sensitive systems, but the presence of food reduced the bioavailability especially in the case of nanoparticles. This is probably due to the pH alterations in the gastrointestinal tract in presence of food, which resulted in fast release and precipitation of the drug in the stomach.

Saquinavir is a HIV-1 and HIV-2 protease inhibitor, which is well tolerated, but suffers from low oral bioavailability [108]. This is because it undergoes hepatic metabolism, it exhibits poor water solubility and thus a very low absorption, and it is unable to cross the intestinal barrier due to the multidrug resistance transporter, P-glycoprotein. Therefore, saquinavir was complexed with hydroxypropyl- $\beta$ -cyclodextrin (HP $\beta$ CD) and incorporated in nanoparticles made by either PIBCA or PIHCA polymers. Only 2.4 and 2.9  $\mu$ g of saquinavir mg<sup>-1</sup> of polymer, respectively,

were incorporated in to the nanoparticles mentioned earlier. However, in the presence of 10% HP $\beta$ CD, the entrapped saquinavir was 45 and 50  $\mu\text{g mg}^{-1}$  of particles for PIBCA and PIHCA, respectively. The drug loading reached a plateau when the HP $\beta$ CD-saquinavir complex attained 5 and 7.5  $\text{mg mL}^{-1}$  for PIBCA and PIHCA, respectively, which corresponds to a 20-fold increase. The  $\zeta$  potentials of unloaded nanoparticles were  $-36.9$  and  $-37.1$  mV for PIBCA and PIHCA, respectively. These values became more positive as the cyclodextrin concentration increased. Apparently, PIHCA exhibited higher drug loading because it was more hydrophobic. This study showed that these nanoparticles could potentially reduce the dose of saquinavir for the treatment of HIV patients.

Berton and coworkers [109] tried to protect a cytotoxic phosphorothioate oligonucleotide, GEM91 in polymeric nanoparticles consisting of PLA. Antisense oligonucleotides (AS-ODNs) are used to block different replication phases of the virus life cycle and phosphorothioate analogs are less sensitive to nucleases than phosphodiesteres. Another serious obstacle for the successful antiviral activity of these oligonucleotides is their uptake into appropriate cellular compartments. The results indicated that the PLA formulation facilitated the delivery of the incorporated oligonucleotides to both HeLa P $_{4-2}$ CD $_4^+$  and CEM (human lymphoid T cells) cell lines at nanomolar concentrations. [The P $_{4-2}$  indicators cells are HIV-1-susceptible HeLa CD $_4^+$  cells carrying the bacterial *lacZ* gene driven by the HIV-1 long terminal repeat (LTR).  $\beta$ -Galactosidase expression is induced by the LTR transactivation by the viral Tat protein produced during infection.]

Models used to test the antiviral activity were: (i) cells containing the Tat activation region (TAR) of the HIV-1-LTR, which controls the transcription of the  $\beta$ -galactosidase reporter gene. Incubation of cells with the oligonucleotide-loaded nanoparticles at the time of virus infection resulted in a reduction in  $\beta$ -galactosidase production 48 h later. This indicates that these antisense carrier systems have the ability to inhibit the early events of the viral cycle life. (ii) Acutely infected CEM cells were treated with the oligonucleotide carriers and it was showed that the HIV-1 reverse transcriptase activity was reduced significantly and kept at low levels for the duration of the experiment. GEM91 alone (100 nm) did not have any impact on the HIV-infected cells, while it caused 90% inhibition after incorporation into the particles.

Another way to enable the delivery of AS-ODNs into cells is by complex formation with protamine, which was studied using primary human macrophages and CD $_4^+$  T cells [110]. Protamine complexation shields the negative charge of the ODN and protects it from degradation. The mean particle size was 150–180 nm and the  $\zeta$  potential was positive for protamine:AS-ODN ratios above 1.5 and negative for protamine:AS-ODN ratios below 0.5. Complete complexation occurred when protamine:AS-ODN ratio was above 1.25. High internalization rates were obtained after the treatment of primary human macrophages and T cells with protamine/AS-ODN nanoparticles with no any sign of cytotoxicity up to 5  $\mu\text{M}$  concentration.

By tracking both components of the complex by fluorescent labeling and incubating them with primary human macrophages, it was shown that the AS-ODN

was released in the cell 24 h after cellular uptake. Complexes comprised of phosphorothioate (PTO) and protamine treated in the same way as the protamine/AS-ODN mentioned earlier, showed that the particles were stable even after 48 or 72 h following their cellular uptake. The specific inhibitory effect of protamine/anti-Tat AS-ODN nanoparticles was about 30% at a concentration of 2  $\mu\text{M}$ , in contrast to protamine/PTO complexes, which did not show any significant inhibition. The latter happened due to the very slow release of the PTO from its carriers indicating that the dissociation of the antisense compound from the complex was an essential process for antisense activity.

#### 9.2.5.4 Vaccines and AIDS

Apart from the improvement in delivery of anti-AIDS drugs incorporated into nanoparticles, research has been focused on development of anti-HIV vaccines. AIDS is characterized by immunosuppression due to the overproduction of immunosuppressive cytokine interferon (IFN)- $\alpha$  and the regulating HIV-1 Tat protein released in the extracellular compartment of acutely infected lymphoid tissue [111]. Tat reduces the immune reactivity of still uninfected T cells and further induces overproduction of IFN- $\alpha$  by APCs. Tat toxoid is the version of Tat that is detoxified, but still immunogenic. This is the antigen used to produce anti-Tat antibodies. Anti-Tat vaccination is aimed at mucosal immunity since the virus entry to the body is through the mucosal membranes, which constitutes the 70% of lymphoid tissues of an organism. Therefore, the induction of mucosal immunity was attempted towards Tat protein in mice by either intranasal or oral route using either an oily adjuvant, chitosan nanoparticles or PLGA microparticles. None of these formulations was found to be more advantageous over the other and it seems that all of them were effective enough to cause the production of anti-Tat IgA antibodies. It was shown that cell-mediated immunity was caused as the stimulation indices obtained after the treatment of splenocytes of anti-Tat-immunized mice with Tat protein or Tat toxoid were higher than those of nonimmunized mice.

Using Tat toxoid may not be the optimum antigen because some important epitopes could have been damaged due to the preparation procedure [112]. In more detail, Tat protein is a small protein consisting of 86–101 amino acids and encoded by two exons. There are five domains, but the three most important are the amino-terminal domain (1–21 amino acids), the cysteine rich domain (22–37 amino acids), which is the trans-activation domain, and the basic domain (49–72 amino acids), which contains the nuclear localization signals. That basic domain is responsible for the transactivation of HIV to the other cells and of cellular processes altering the intracellular signaling of various cell types [113, 114]. The biologically active Tat (1–72) protein, which was confirmed to be immunogenic and non-immunosuppressive, was adsorbed on the surface of anionic nanoparticles. The latter were made by the emulsification of wax (oil phase) and sodium dodecyl sulfate (SDS, anionic surfactant) dissolved in water. Tat was adsorbed on the particles (100 nm) produced by its basic domain and the final formulation was administered subcutaneously to mice on days 0 and 14. Immune responses recorded from mice immunized with the particle formulation were compared to those obtained from

mice immunized either with alum Tat ( $T_H2$  control) with alum adjuvant and Tat ( $T_H1$  control) with lipid A as adjuvant. There were strong antibody responses (IgG and IgM) and the IgG titer from the Tat-immunized mice was approximately 3-fold higher than that in “naive” mice, even after 10 000 dilution of the particle formulation. The Tat-coated nanoparticles caused the production of IFN- $\gamma$  to the same level as the Tat with lipid A as adjuvant, which indicates that the specific formulation induces an enhancement of  $T_H1$  immune response and, thus, is considered as a promising vaccine product.

Another novel nontoxic polyelectrolyte formulation is composed of polylysine modified with imidazole side-chains condensing HIV-2 *env* DNA into nanoparticles [115]. The size of the resulting nanoparticles was approximately 150 nm and it was considered ideal for targeting clathrin-coated pit uptake into the cell. The complexation with cationic polymer prevents DNA degradation in the lysosomal compartment and the imidazole side-chains optimize the escape to the cytoplasm of the target cell. The polyelectrolyte complexes induced higher levels of IgA, IgM and IgG antibodies by the intradermal route to BALB/c mice (Fig. 9.7).

Kawamura and coworkers [116] used concanavalin A-polystyrene nanospheres (Con A-NS) to capture HIV-1 envelope antigen gp120 due to the high affinity that the lectin exhibits for the HIV-1 antigen. In this study, dendritic cells were the targets for the immune response since they are unique major APCs capable of stimulating “naive” T cells in the primary immune response and more potent APCs

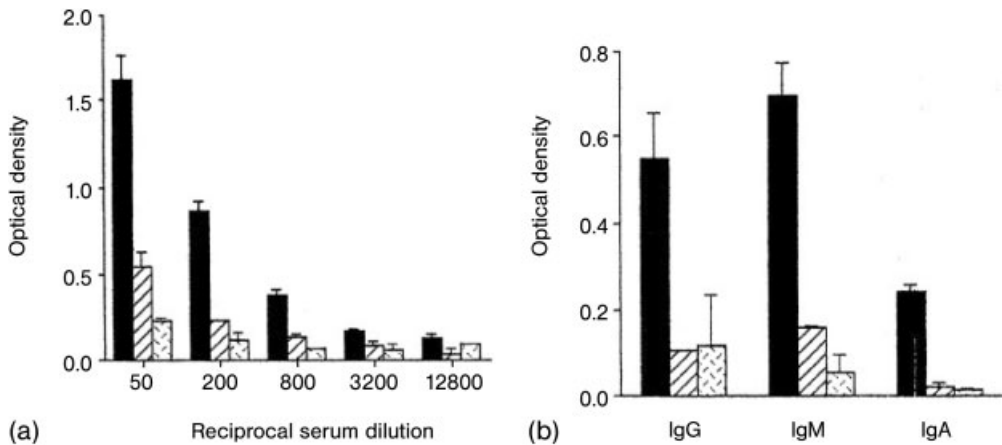


**Figure 9.7.** Comparison of HIV-2 gp120-specific antibodies in mice immunized with a polylysine nanoparticle formulation. Serum from mice was evaluated using samples taken 28 days after the third DNA immunization by the intradermal route. IgG subclasses (A) and antibody isotypes (B) were evaluated in mouse serum samples. ELISA results are shown using

serum from mice immunized with polylysine nanoparticles containing DNA encoding HIV-2 gp140 (solid bars), naked DNA encoding gp140 (diagonal lines) and plasmid vector DNA formulated with polylysine nanoparticles (stippled bars). (Reprinted from Ref. [115], © 2003, with permission from Elsevier.)

than monocytes/macrophages or B cells. This is due to the high level of expression of major histocompatibility complex (MHC) and costimulatory molecules such as CD40, CD80 and CD86. They cause the secretion of  $T_H1$  cytokines (interleukin-12, IFN- $\alpha$ ). BALB/c mice were immunized intranasally with either gp120, or p24 or HIV-NS suspension on days 0, 7, 14 and 42. After that, a low level of gp120-specific IgA was detected in the vaginal samples of the HIV-NS immunized mice. Con A-NS were taken by pulmonary dendritic cells 24 h after intranasal administration. Phagocytosis was partially responsible for the uptake of Con A-NS and gp120-NS. Thus, approximately a 100-fold increase of the gp120-NS uptake was observed in comparison to gp120 alone. T cells from mice immunized with gp120-NS produced much more IFN- $\gamma$  than those immunized with gp120, which indicates that the gp120-NS are more advantageous in inducing  $T_H1$  responses.

However, according to Miyake and coworkers [117], the mouse is not a representative model for developing a HIV-1 vaccine. That group tested inactivated simian/human immunodeficiency virus KU-2-capturing nanospheres (SHIV-NS) in macaques, while Con A-NS were used as control. Two groups of three macaques in each group were given a series of six immunizations in a week with either Con A-NS or SHIV-NS intranasally. Vaginal anti-HIV-gp120 IgA and IgG antibodies were detected in all SHIV-NS-immunized macaques, but not in the Con A-NS-immunized macaques. After intravaginal challenge with the virus SHIV-KU2, one of the three macaques of each group was infected. The population of  $CD4^+$  T cells was less in the Con A-NS and “naive” macaques, while it remained constant in the SHIV-NS-immunized mammals. The two uninfected macaques were rechallenged with the intravenous injection of SHIV-KU2, which led to infection of all macaques. A significant decrease of RNA viral loads was observed in SHIV-NS-immunized macaques 3 and 8 weeks after their rechallenge with the virus. The peripheral  $CD4^+$  T cell population decreased at the beginning of the infection and recovered to about 30–50% of the preinfected levels. Also, the intravenously infected SHIV-NS macaques showed a rapid antibody response and the highest levels of anti-gp120 antibodies, which means that gp120 specific memory cells were acquired.

### 9.2.6

#### Vaccines

Vaccines are a form of active immunity because they cause the production of antibodies and cellular responses in the patient [66]. Vaccines can be:

- Live attenuated form of a virus or bacteria.
- Inactivated preparations of the virus or bacteria.
- Extracts of or detoxified exotoxins produced by a microorganism.

The immunization after administration of live attenuated vaccines is generally achieved with a single dose and lasts for long time, but not as long as if it was produced from the natural infection. Inactivated vaccines need more than one dose for



adequate immunity to be achieved. The duration of immunity varies from months to years. Extracts of or detoxified exotoxins are more immunogenic if adsorbed onto an adjuvant (i.e. aluminum hydroxide). They require a series of injections followed by booster doses.

#### 9.2.6.1 Delivery Route

The most common way of administering vaccines is by injecting them intramuscularly or subcutaneously. Of course this is not a pleasant way, especially for children. Therefore, the formulation of vaccines to exploit other available routes (i.e. oral, intranasal) is under investigation. Also, many vaccines in the form of peptides are difficult to administer due to low immunogenic response or the toxicity of the adjuvants used. Nanoparticles have been tested as potential carriers to increase the immune response or for alternative routes of administration.

**9.2.6.1.1 Systemic** Again as reported in previous sections, chitosan and PLGA are the main polymers of choice for nanoparticle formulation. A number of parameters like polymer hydrophobicity, particle size and the use of adjuvants were evaluated for the best immunization responses. Raghuvanshi and coworkers [118] used a mixture of nanoparticles and microparticles prepared with either PLA or PLGA using the water/oil/water (w/o/w) emulsification technique to entrap tetanus toxoid (TT) in the particles. The mean size of nanoparticles and microparticles were 630 nm and 4  $\mu\text{m}$ , respectively. TT was released from the particles with a burst release (20%).

The immunization responses were recorded after intramuscular injection of a mixture of either, PLA (45 kDa) nanoparticles and microparticles (1/1) or PLGA (50:50) nanoparticles and microparticles (1:1) to rats. Immune responses from polymer-entrapped TT particles were higher than those obtained with saline TT and lasted for 5 months. However, a single injection of the particles, either one type or the physical mixture of particles, resulted in immune responses lower than those achieved after two doses of alum-adsorbed TT.

Low-molecular-weight PLGA particles elicited higher and faster immune responses in comparison to high-molecular-weight PLGA due to the lower  $T_g$  of the polymer. Thus, the polymeric matrix was softening and released the entrapped TT near the periphery of the particle matrix more rapidly, so the antigens were presented quickly to the APCs. Immunization with PLA particles elicited significantly higher anti-TT antibody titers than PLGA particles (antibody titers were 2-fold higher from PLA than PLGA particles). This is believed to be because the PLA polymer is more hydrophobic than the PLGA and so the APCs are attracted more to the PLA particles.

Coadministration of alum (adjuvant) at the same time as the particles improved serum immune responses still further. High antibody titers were detected 15 days postimmunization using PLGA and alum, which was faster than that obtained with the particles alone. PLA microparticles administered with alum proved almost as effective as a two-dose immunization with alum-adsorbed TT only. The antibody titers were not only high, but were also maintained for almost 150 days. This in-

creased effect is probably due to the adsorption of the TT by the alum, enabling the antigen to be presented to the APCs, resulting in high antibody response. Also, it was shown that  $Al^{3+}$  cations neutralize the negatively charged protein and make it more hydrophobic facilitating the attraction to APCs [119].

The desirable physicochemical properties that particles should possess to develop an optimum vaccine delivery system able to permeate the skin were investigated by other groups. Kohli's group [120] used latex nanoparticles of various sizes (50, 100, 200 and 500 nm) and surface charge (positively charged, neutral and negatively charged particles). Only negatively charged particles of size 50 and 500 nm permeated through the skin. The authors assumed that the contradictory phenomenon of the permeability of negative particles through the skin is due to repulsive forces between negatively charged lipids within the skin and particles at the surface. These forces might result in a temporary initiation of channels in the skin, allowing for particle permeation. On this basis, it was suggested that there might be a threshold charge, which must be reached to allow adequate repulsion of lipids to permit permeation of species through the skin, although this mechanism has not been confirmed yet.

According to Newman and coworkers [121], PLGA nanoparticles are taken up preferably by dendritic cells after intradermal administration of the particles in mice. Based on this finding, the same group studied the *in vitro* optimization of PLGA particle delivery for activation of T cells using murine bone marrow-derived dendritic cells [122]. Also, the influence of the coadministration of an immunomodulator [monophosphoryl-lipid A (MPLA)] was evaluated. The PLGA nanoparticles contained a human MUC1 lipopeptide, BLP25 prepared with the double-emulsion technique (mean size: 287 nm, peptide loading: 1% w/w). Particle uptake was found to depend on the incubation time and particle concentration. The optimum incubation conditions used were 2 mg of nanoparticles with  $1 \times 10^7$  dendritic cells (day 7 culture) in 20 ml medium for 24 h in a Petri dish. Finally, it was shown that after incubation of dendritic cells with PLGA particles, dendritic cells exhibited an increase in the expression of MHC class II and CD86 compared to untreated cells. This phenomenon was increased further after the coincubation of PLGA particles and the immunomodulator, MPLA. Particle size is an important parameter for the maturation of dendritic cells according to results reported after the incubation of PLGA microparticles (approximately 10  $\mu$ m) with dendritic cells, which did not increase the expression of MHC class II and CD86 [123].

PLGA nanoparticles were then used to incorporate either the hepatitis B core antigen (HBcAg) only or HBcAg plus the immunomodulator, MPLA, in order to examine their influence on the  $T_H1$  immune responses [124]. PLGA particles were prepared with the emulsification method, and the loading efficiency of HBcAg was 50.8 and 51.0% in the absence and presence of MPLA, respectively. When MPLA was incorporated in the particles, the loading efficiency was approximately 45%. The average size of all formulations was approximately 265–270 nm. Particles (10 mg) containing 1  $\mu$ g of HBcAg and 20  $\mu$ g of MPLA were injected subcutaneously to mice. It was shown that the mice immunized with HBcAg + MPLA nanoparticles exhibited the strongest HbcAg-specific T cell proliferation. The incorporation

of MPLA in the HBcAg nanoparticles increased the stimulation index almost 4 times compared to the unencapsulated HBcAg. Also, the high level of IFN- $\gamma$  production from the primed T cells due to the immunization with HBcAg + MPLA nanoparticles indicated a predominant T<sub>h</sub>1 immune induction.

Again, the particle size importance was emphasized by those authors because particles of size smaller than 500 nm induced higher immune responses than particles of mean size greater than 2  $\mu$ m [125].

Due to the fact that dendritic cells are the most important APCs involved in antigen uptake and presentation to antigen-specific T cells, the state of maturity of dendritic cells was evaluated as to the nanosphere uptake and the dendritic cell responses [126]. However, both immature and mature dendritic cells exhibited the same ability to take up polystyrene nanospheres or antigen-loaded nanospheres in a dose- and time-dependent manner. Phagocytosis was the suggested mechanism of nanosphere uptake. The particulate nature of the antigen-loaded nanoparticles was responsible for the enhanced immune responses by dendritic cells in comparison to soluble antigens. Thus, when low amounts of ovalbumin (OVA) were adsorbed on the nanosphere surface, strong antigen-primed T cell proliferation and production of IFN- $\gamma$  were induced *in vitro*. The antigen adsorption/loading on the particle surface means that lower amounts of antigens will be needed to induce immunity in the future.

Nanoparticles have also been used for DNA vaccine formulations. Cui and co-workers [127] have tried to develop chitosan-based nanoparticles containing plasmid DNA (pDNA) as a potential approach to genetic immunization by topical application. The pDNA was either added during the preparation procedure or added on preformed cationic chitosan/CMC nanoparticles. Different ratios of chitosan:CMC and chitosan oligomers (lower molecular weight than that of chitosan: 102 kDa) were used. The particle size range was between 90 and 270 nm for almost all of the ratios tested. A chitosan:CMC ratio of 1:1 (w/w) was chosen for pDNA coating studies because of the relatively small size (179 nm) and positive  $\zeta$  potential (+44 mV) of the particles produced. Chitosan oligomer:CMC ratios of 3:1 and 4:1 were chosen for pDNA coating studies due to the particle small size (121 and 93 nm, respectively) and positive  $\zeta$  potential (+24 and +25 mV respectively). The incorporation efficiency of pDNA on the chitosan oligomer/CMC complexes was almost 100%, which was expected using positively charged nanoparticles.

The final pDNA-coated chitosan/CMC or chitosan oligomers/CMC complexes selected for the genetic immunization by topical application were negatively charged. The latter is based on previous results reported by the same group [128], suggesting that the positively charged particles or complexes produce lower immune responses and gene expression in comparison to negatively charged ones. A number of particle specifications were tested. Also, "naked" DNA was administered topically as control. Only pDNA (300  $\mu$ g mL<sup>-1</sup>) coated on chitosan oligomer/CMC nanoparticles (300/100 w/w,  $\mu$ g mL<sup>-1</sup>) caused a 32-fold increase of the IgG titer in mice as compared to that obtained after immunization using "naked" pDNA alone applied topically. None of the other formulations tested demonstrate any influence in comparison to the administration of the "naked" pDNA alone.

The same group carried out further work using pDNA-coated nanoparticles to induce immune responses after topical application to the skin [129]. The difference in this study was the type of the nanoparticles. They were not made with chitosan but with a mixture of emulsifying wax/Polysorbate 60 in a ratio 20/1 with hexadecyltrimethyl-ammonium bromide (CTAB) as a surfactant (cationic) (mean size 100 nm,  $\zeta$  potential about 25 mV). No allergic, inflammatory or toxic effects have been observed with these systems in mice after their delivery via the intramuscular, subcutaneous and topical route. Also, dioleoyl phosphatidylethanolamine (DOPE) and cholesterol were part of the nanoparticle composition as endosomolytic agents. DOPE causes disruption of the endosomal membrane because it changes to the hexagonal conformation in the acidic environment of the endosome. *In vitro* studies showed a 7-fold increase of the transfection efficiency compared to nanoparticles without DOPE, but the effect of the cholesterol incorporation was not statistically significant. Also, pDNA remained functional after coating onto the preformed engineered cationic nanoparticles. Mannan cholesterol was also incorporated into the nanoparticles because human and mice dendritic cells have mannose receptors, which stimulated robust  $T_h1$  and cytotoxic T lymphocyte responses [130–132]. Negatively charged nanoparticles were also used for these formulations (Fig. 9.8).

It was shown that pDNA-coated nanoparticles and pDNA-coated particles with DOPE and the mannan ligand caused 6- and 16-fold enhancement of IgG titer, respectively, compared to that of “naked” DNA. *In vitro* and *in vivo* studies proved that the incorporation of DOPE in the nanoparticles improved both the transfec-

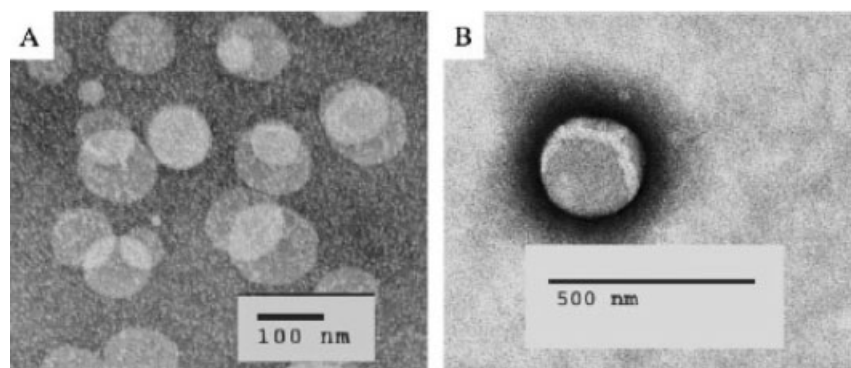


**Figure 9.8.** Transmission electron micrographs. (A) Mannan-coated cationic nanoparticles and (B) pDNA-coated nanoparticles. Spherical and homogeneous cationic nanoparticles were engineered directly from the oil droplets of a clear microemulsion composed of emulsifying wax (2 mg), DOPE (100  $\mu$ g) and CTAB (15 mM) in 1 mL water at 55 °C, cooling to room temperature during

gentle stirring. Chol-mannan was added. Mannan-coated nanoparticles were purified by gel permeation chromatography, prior to the addition of pDNA. pDNA (CMV- $\beta$ -galactosidase) was coated on the surface of the cationic nanoparticles (1 mL) to obtain a final pDNA concentration of 50  $\mu$ g mL<sup>-1</sup>. (Reprinted from Ref. [133], © 2003, with permission from Elsevier.)

tion efficiency and the overall immune response. Surprisingly, the mannan-coated nanoparticles showed only a modest effect on enhancing the immune response. This was subsequently shown to be due to the reduced binding of mannan caused by the presence of pDNA on the particle surface. Thus, maybe the topical route is not the most efficient to target the dendritic cells using the mannan ligand. In these studies, pDNA doses as low as 4–5  $\mu\text{g}$  applied topically to chemically untreated skin resulted in significant and measurable humoral and proliferative immune responses.

The route of injection has also been investigated. The same type of nanoparticles was administered either (i) via topical immunization with application of the formulation over the skin without applying pressure, (ii) via subcutaneous injection or (iii) via jet injection [133]. It was shown that the intradermal jet injection of pDNA-coated nanoparticles led to the highest antibody titer of all groups. The titer obtained with pDNA-coated nanoparticles delivered by jet injection was over 20 and 65 times higher than that obtained after subcutaneous or the topical route, respectively. After the administration of the “naked” DNA via the routes mentioned above, the IgG titers after jet injection and subcutaneous injection were almost the same, and both titers were significantly greater than after topical application of the “naked” DNA only. Also after the subcutaneous injection of pDNA-coated nanoparticles, the IgG titer in sera was 10-fold higher in comparison to DNA only. Intradermal injection of the same particles increased the IgG titer in sera 200-fold compared to DNA alone.

Various adjuvants have been investigated for promotion of DNA vaccine effectiveness. When the pDNA was coadministered with cholera toxin (CT) (10 or 100  $\mu\text{g}$ ) via the topical route, the IgG titer increased 4- and 20-fold, respectively, compared to pDNA alone. The IgG titer demonstrated a more than 300-fold increase after the topical administration of pDNA-coated nanoparticles with 100  $\mu\text{g}$  of CT compared to “naked” DNA alone. Another known adjuvant, lipid A, was coadministered subcutaneously in mice with either pDNA or pDNA-coated nanoparticles [134]. A 16-fold increase of the IgG titer was achieved after immunization with “naked” pDNA in presence of lipid A (50  $\mu\text{g}$ ) compared to pDNA alone. In the case of delivery of pDNA-coated nanoparticles with lipid A (50  $\mu\text{g}$ ), the IgG titer showed a 16- and 250-fold increase compared to pDNA nanoparticles without lipid A or pDNA alone in absence of lipid A, respectively. Therefore, lipid A (subcutaneous) and CT (topical route) are potential adjuvants to further improve immune responses using the novel cationic nanoparticle-based DNA vaccine delivery system described.

**9.2.6.1.2 Oral** The main reason to develop oral vaccines is that the mucosal surfaces are the entry point for many pathogens to the body [135]. However, purified antigens given orally are not effective due to their degradation in the gut and because the antigens give only short-lived low-titer immune responses. A major obstacle to mucosal vaccination is the absence of nontoxic but potent adjuvants, which are able to enhance the poor immunogenicity of antigens delivered via mucosal routes. In order to protect the antigens and change their immune potency,

nanoparticles have been formulated loaded with the mucosal antigens and help them to reach the desirable sites of action – the M cells in the Peyer's patches.

PLGA nanoparticles were made with the double-emulsification method incorporating *Helicobacter pylori* lysates with a loading efficiency of 67% and a mean particle size of 320 nm [135]. Oral immunization of mice took place in three doses at weeks 0, 1 and 2, and another booster dose was given at week 8. The adjuvant, CT, was given in a mixture with either the *H. pylori* lysates or the *H. pylori* lysate-loaded PLGA nanoparticles. *H. pylori* lysate-loaded PLGA nanoparticles induced high immune responses at week 9, after the booster dose at week 8. A mixture of *H. pylori* with 10 µg of CT induced high immune responses at week 4 and was enhanced significantly after the booster at week 8. A mixture of *H. pylori* with CT enhanced the immune response significantly higher than the *H. pylori*-loaded PLGA particles. Apart from IgA, the major IgG subclasses produced were IgG1, IgG2b and lower levels of IgG2a. The synthesis of those antibodies was supported by T<sub>H</sub>2 cell-secreted cytokines induced by CT. This means that the *H. pylori* loaded nanoparticles resembled the action of CT since both a mixture of *H. pylori* with CT and the *H. pylori*-loaded PLGA particles induced the production of the same antibodies after oral immunization.

The low entrapment efficiency of peptides/proteins in PLGA nanoparticles, the unavoidable use of organic solvents and the emulsification preparative technique are obstacles that demand alternative solutions. Therefore, Jung and coworkers [136] evaluated the adsorption of TT on particles made with the branched polymer poly(sulfobutyl-polyvinyl alcohol)-*g*-(lactide-*co*-glycolide) (SB-PVAL-*g*-PLGA) using a solvent displacement technique. The particle size was in the range from 100 to 200 nm and different degrees of sulfobutylation produced particles with different  $\zeta$  potentials ranging from -3.2 to -22 mV (for a degree of substitution of 43%). The amount of TT adsorbed on the particle surface started from 6.5 µg mg<sup>-1</sup> polymer in the case of PVAL-*g*-PLGA up to 56.8 µg mg<sup>-1</sup> for the 43% substituted polymer. Increasing surface hydrophilicity and/or surface charge density resulted in a higher TT adsorption onto the particle surface. The adsorption is a result of the electrostatic interactions between the negatively charged particle surface and positively charged protein residues. According to adsorption isotherm data, a monolayer adsorption model describes the interaction of TT with the particle surface. The antigenicity of the TT was influenced only slightly making the delivery system a potent one for mucosal immunization.

In another attempt to improve the formulation characteristics and preparation procedure, mucoadhesive cationic and anionic materials like alginate, carrageenans and pectin [137] were used. Also a different method was tried in order to omit the harmful organic solvent during the preparation procedure and to create a friendlier environment in the interior/core of the nanoparticles. According to this, the anionic solution (core) was introduced in the form of a mist into the cationic solution (corona), which resulted in instantaneous particle formation [138]. The antigen is part of the core and the shell according to the nature of the protein/peptide entrapped and the particle composition. The  $\zeta$  potential was positive and the entrapment efficiency varied (it could reach even almost 50%). By using

polydextran aldehyde, crosslinking could occur and, thus, the particles were stabilized even more. The 100% crosslinked particles released only about 20% OVA after 24 h incubation in presence of 3% NaCl as dissolution medium, while approximately 40% was released after 5 days incubation from the same particles in a medium of pH 1.83. Also, the crosslinked nanoparticles provoked high immune responses while the noncrosslinked ones did not cause any response after oral immunization. This was the case for particles having either OVA or TT incorporated. The OVA-loaded nanoparticles show a dramatic difference in the immune response compared to that obtained with OVA in solution and OVA in a mixture with empty nanoparticles. Concluding, this system seems to offer a higher versatility in developing protein-loaded carriers for oral vaccination.

The hydrophilic polymer chitosan, due to its mucoadhesive properties, is very popular in the field of vaccine development. The cationic nature of the polymer ensures electrostatic interactions with negatively charged proteins (i.e. BSA, TT, CT) according to the pH of the preparation solutions during the nanoparticle formation and the *pI* of each protein [139]. The loading efficiency was estimated as almost 90, 50 and 50% for BSA, TT and CT, respectively, when the proteins were dissolved in the TPP solution (pH 8.3) and the particle formation took place with a chitosan solution of pH 5.0. Poly(ethylene oxide-co-propylene oxide) (PEO-PPO) polymer was introduced to the nanoparticles during the preparation procedure in order to modify the particle size and  $\zeta$  potential. Thus, lower entrapment efficiency of BSA was obtained due to the lower amount of chitosan available when PEO-PPO was present. BSA release from 25% CS nanoparticles or 20% CS/PEO-PPO nanoparticles was slow and prolonged without a burst release. A burst release was exhibited by 40% BSA-loaded particles, probably due to adsorbed BSA molecules on the carrier surface. TT release from 14% TT-loaded CS particles at pH 5 was approximately 20% after 18 days and the toxoid was still antigenically active.

From a formulation point of view, coating of OVA-adsorbed chitosan nanoparticles with sodium alginate increased both the stability of protein adsorbed on the particle surface and the particle stability in simulated intestinal fluid at 37 °C [140] (Fig. 9.9).

The loading capacity with OVA on the chitosan nanoparticles ranged from 30 to 50%, but significant desorption of OVA occurred during the coating procedure, especially if the latter took place at pH 5.5. Thus, the coating procedure was carried out at pH 7.4 due to compromised results between loading capacity and coating efficiency. Another drawback of the preparation procedure was the high polydispersity of the particle population produced, with a mean average size of approximately 650 nm. Despite those disadvantages, the alginate coating offered protection against the degradation of chitosan and OVA in the simulated intestinal fluid as it showed a 60% release of OVA after 7 h of particle incubation at 37 °C.

The introduction of lectins on the particle surface was also shown to enhance the uptake of antigen-loaded nanoparticles by M cells or other epithelial cells of the intestinal wall [141, 142].

DNA vaccines have also been incorporated into nanoparticle formulations for oral delivery. *Toxoplasma gondii* GRA1-pDNA was incorporated into chitosan nano-

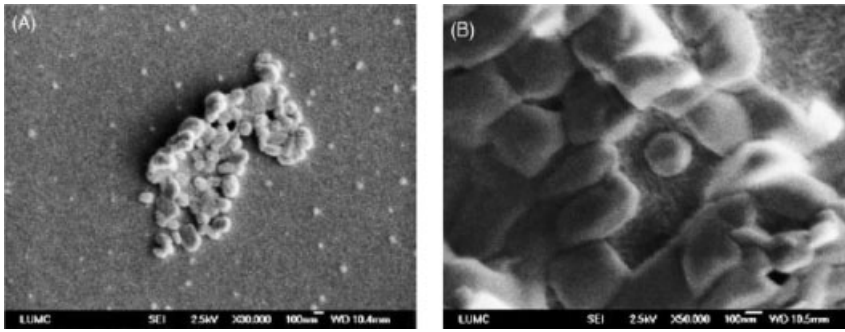


**Figure 9.9.** Scanning electron micrographs of chitosan nanoparticles. (A) After freeze-drying and resuspending in water. (B) After the coating procedure with sodium alginate. (Reprinted from Ref. [140], © 2005, with permission from Elsevier.)

particles of mean size of 400 nm and  $\zeta$  potential of 27 mV [143]. The incorporation into the polymeric carriers (more than 98%) protected the plasmid from the degradation of DNase I. The interaction of pDNA with the chitosan molecules in the formulation was strong enough so DNA did not escape into the dissolution medium 8 days after the carrier incubation in pH 7.3 at 25 °C. However, the plasmid-loaded nanoparticles did not induce any significant response 1 month postintra-gastric administration of the formulation in mice. Therefore, mice were boosted with intra-gastric administration of chitosan nanoparticles and, indeed, a higher response was obtained from mice immunized with either GRA1 microparticles or GRA1-pDNA-loaded nanoparticles. The latter response was enhanced more after a second round of immunization with intramuscular administration of pDNA, although, GRA1-loaded microparticles demonstrated the highest immune responses compared to GRA1-pDNA-loaded nanoparticles. The difference between the two types of formulations is that the GRA1-microparticles raised/caused a mixed  $T_H1/T_H2$  response, while the GRA1-pDNA-loaded nanoparticles induced the secretion of IgG1, which is associated with  $T_H2$ -type responses. The latter is unusual as  $T_H1$  immune responses were expected to be obtained as reported previously by the same and other research groups.

In another study it was shown that the pDNA of a house dust mite allergen, Der p1, was incorporated in chitosan nanoparticles efficiently enough to be able to cause immune responses (IgG2a production) to Der p1 and the Der p1-derived peptides after oral administration in mice [144]. The intramuscular administration of those particles could not raise such responses. However, the orally induced immune responses could be boosted about 13 weeks postfeeding by intramuscular injection of “naked” DNA.

**9.2.6.1.3 Intranasal** The advantages of drug delivery through the nasal cavity have already been highlighted, but the most important feature is that the drug



delivery system bypasses the liver. The required qualities for a drug delivery system appropriate for intranasal delivery, such as particle hydrophobicity, size and  $\zeta$  potential, were investigated more thoroughly by Tobio and coworkers [145]. TT-loaded PLA and PLA-PEG nanoparticles were prepared with the double-emulsification method and the final size was less than 200 nm. The  $\zeta$  potential of PLA and PLA-PEG particles was  $-50$  and  $-30$  mV, respectively. The encapsulation efficiency was about 35% regardless of the particle composition. PLA-PEG particles showed a prolonged TT release in comparison to the more hydrophobic PLA particles. At 24 and 48 h postintrasal administration of the toxoid-loaded PLA-PEG nanoparticles in rats, TT was found in a 10-fold higher concentration in blood and lymph nodes compared to TT levels obtained after PLA intranasal particle administration. The accumulation of TT in the lymph nodes after administration of PLA-PEG vesicles was almost 2-fold higher than that recorded in blood 24 and 48 h after intranasal administration. Also, the TT accumulation in the lymph nodes was significantly higher than that in organs like the liver, spleen, lungs and small bowel 24 and 48 h postadministration. Therefore, the suggested hypothesis was that a part of PLA-PEG nanoparticles was taken up by the M cells of the NALT and another part passed to the submucosal layer and then to the lymphatics and the blood. Also, some of the particles could have been taken up by the BALT and GALT. This hypothesis can be supported by the fact that the free toxoid was cleared from the blood rapidly and absorption by the organs was very much lower compared to the particles.

Another study demonstrated the potential of using PLGA as a carrier for the entrapment of bovine parainfluenza type 3 virus (BPI-3) for vaccination of young calves [146]. However, preliminary experiments were carried out by intranasal inoculation in mice using two particle types: PLGA, where BPI-3 was incorporated in the particle matrix, and poly(methyl methacrylate) (PMMA), where the antigen was adsorbed on the particle surface. The latter formulation was not successful in inducing any immune response in contrast to BPI-3-loaded PLGA particles.

The use of particles made from high-molecular-weight chitosan have already been described. Vila and coworkers [147] investigated the feasibility of using lower molecular weight chitosan (23 and 38 kDa molecular weight) to formulate nanoparticulate vaccine carriers incorporating TT. The nanoparticles had a size of approximately 350 nm and  $\zeta$  potential of  $+40$  mV, while the TT loading efficiency was 50–60%. Burst release occurred, but the release profile was prolonged and the TT was antigenically active. Indeed, it was shown that the TT-loaded nanoparticles significantly enhanced either the humoral (IgG) or mucosal (IgA) immune responses compared to those achieved by the soluble vaccine. Also, the immune responses were not affected significantly by the dose of the antigen-loaded low-molecular-weight chitosan nanoparticles for the range used between 70 and 200  $\mu$ g.

An alternative to the previous chitosan formulations was the development of chitosan-coated emulsions where OVA and CT were adsorbed on the emulsion surface [148]. Chitosan nanoparticles were prepared for comparison, and the two types of formulations were administered intranasally and intraperitoneally in rats. The particle sizes achieved for the nanoparticles and the chitosan-coated emulsions

were in the range of 0.4–3 and 0.4–0.7  $\mu\text{m}$ , respectively. The  $\zeta$  potential was positive due to the chitosan presence, and it was approximately 35 and 15 mV, respectively. The adsorbed OVA was very high in both formulations (85 and 100%, respectively) and there was no release of OVA detected after 3 h of incubation in phosphate-buffered saline (pH 7.2) at 37 °C. Nanoparticles induced significantly higher IgG response in comparison to control (OVA only, or nanoparticles only) administered either intraperitoneally or intranasally regardless of the particle size. Nanoparticles of 0.4 and 1  $\mu\text{m}$  exhibited significantly higher IgA response than those of 3  $\mu\text{m}$ .

Chitosan-coated emulsions did not elicit IgG production of any significance compared to control after intraperitoneal administration irrespective of the particle size, while the IgA levels were similar to those obtained with the nanoparticles after intraperitoneal administration. However, chitosan-coated emulsions showed a significant increase of both IgG and IgA levels compared to control after intranasal administration regardless of the particle size. Thus, the chitosan-coated emulsions are considered as another approach for vaccine formulation for intranasal delivery.

Some work has also been carried out on DNA vaccines for intranasal delivery. Cui and coworkers [149] worked on cationic emulsions made of the emulsifying wax CTAB and/or Brij 78 where pDNA was adsorbed on the surface of the final products. The positive  $\zeta$  potential of the particles is attributed to CTAB presence. Due to its potential toxicity, the amount used is being reduced and partly replaced by Brij 78. IgG responses caused by pDNA on the Brij 78 and CTAB nanoparticles were 18- and 28-fold higher than those recorded with pDNA alone. Also, the IgA levels increased 25- and 30-fold more than pDNA alone. It is worth noting that the amount used for the intranasal immunization in this study was 1.25  $\mu\text{g}$  compared to 50  $\mu\text{g}$  used by another group [150]. This system would probably enable immunization with significantly lower doses of pDNA.

### 9.2.7

#### Diabetes

Diabetes is classified as insulin- and noninsulin-dependent diabetes type I or II, respectively [66]. Type I diabetes is also known as diabetes mellitus (IDDM) and it is caused because of a deficiency of insulin following autoimmune destruction of pancreatic  $\beta$  cells. Patients with type I diabetes require administration of insulin. Type II diabetes (NIDDM) is due to insufficient secretion of insulin or to peripheral resistance to the action of insulin. Type II diabetes can be controlled by diet alone, but oral antidiabetic drugs or insulin can be used if needed.

##### 9.2.7.1 Treatment

Insulin is a polypeptide hormone of complex structure and is the required treatment for IDDM and ketoacidosis. Insulin used for therapeutic purposes can be extracted from pig pancreas, or, alternatively, human sequence insulin can be produced either semisynthetically by enzymatic modification of porcine insulin or biosynthetically by recombinant DNA technology from bacteria or yeast.

It is inactivated by gastrointestinal enzymes and has to be administered by subcutaneous injection. Fat hypertrophy can occur due to subcutaneous injections, but can be minimized by rotating the injection sites. Soluble insulin is administered for urgent treatment, for fine control in serious illness and in the perioperative period.

Drug administration via injections is not the most convenient or desirable route for the patient; therefore, alternative routes of insulin administration, mainly oral or intranasal, have been investigated. These have utilized complexation of insulin with polymeric materials into self-assembled nanoparticles. A brief overview of the current research towards these objectives follows.

### 9.2.7.2 Delivery Routes

**9.2.7.2.1 Oral** PIBCA and chitosan have been the polymers of choice for insulin formulation into nanoparticles. PIBCA was shown by Damgè and coworkers [151–152] to be able to deliver a sufficient amount of active insulin after oral administration of insulin-loaded PIBCA nanocapsules to fasted, streptozotocin-induced diabetic rats and they decreased the blood glucose level from 300 to the normal 125 mg dL<sup>-1</sup>. Indeed, PIBCA nanocapsules were found to protect insulin in the gastric environment both *in vitro* in reconstituted gastric and intestinal medium compared to phosphate-buffered saline as control, and *in vivo* (intragastric administration to rats; insulin dose: 57 and 2.8 IU kg<sup>-1</sup>) [153]. In the intestine, 75% of insulin was released, although most of the capsules were degraded after 30 min according to results deduced from the *in vitro* release of insulin in reconstituted intestinal medium. The remaining intact nanocapsules were localized on the intestinal mucosa and passed through the submucosal layers.

In another study, the same polymer was used to prepare nanoparticles and not nanocapsules, incorporating the insulin at the very beginning of the polymerization procedure and using a pluronic surfactant as stabilizer [154]. The desired particle size was less than 100 nm and was achieved by using an appropriate concentration of pluronic acid (2.0%) in contrast to nanocapsules of 265 nm used in the previously mentioned study. Insulin-loaded nanoparticles were administered subcutaneously or orally to streptozotocin-induced diabetic rats. A prolonged hypoglycemic effect of the hormone was observed up to 72 h postinjection. A similar pattern was observed after oral delivery of insulin-loaded nanoparticles with the hypoglycemic effect starting 2 h postadministration, while a less prominent effect was shown by the same dose of insulin-loaded nanocapsules as reported by Damgè and coworkers [151]. The enhanced effect in the case of nanoparticles could be due to the smaller particle size, leading to faster intestinal absorption.

Chitosan is used to enhance the absorption of insulin by the intestinal mucosa due to its mucoadhesive properties and transient opening of the tight junctions between the epithelial cells. Pan and coworkers [155] made insulin-loaded chitosan nanoparticles by ionotropic gelation of chitosan with tripolyphosphate anions. Insulin association was found up to be approximately 80%, and the electrostatic interactions between the acidic groups of insulin and the amino groups of chitosan

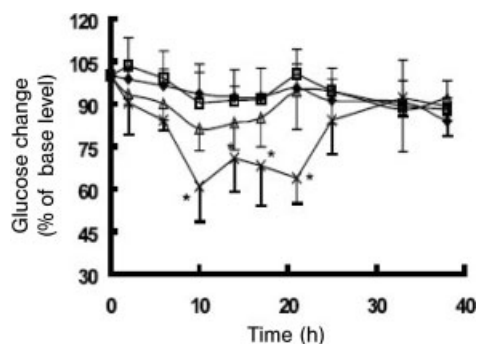


**Figure 9.10.** Hypoglycaemic effect of oral administration of: control (drinking saline without oral administrating anything, ♦); insulin-chitosan solution (Δ); insulin solution (◻); 14 IU kg<sup>-1</sup> insulin-loaded chitosan

nanoparticles suspended in pH 5.5 saline (×). Data represents the mean ± SD,  $n = 8$  per group. Statistically significant difference from control ( $*P < 0.01$ ). (Reprinted from Ref. [155], © 2002, with permission from Elsevier.)

were highly contributory to this. Insulin was rapidly released from nanoparticles in pH 7.4 and 4.0, but it was slower at pH 5.8, probably due to lower insulin solubility at this pH. After oral administration of insulin-loaded chitosan nanoparticles at a dosage of 14 IU kg<sup>-1</sup>, there was no significant blood glucose decrease observed for the first 6 h, but the hypoglycaemic effect was very prominent 10 h later (post-administration) in comparison to the insulin control solution and lasted for 10 h from the onset of the hypoglycemia (Fig. 9.10). Increasing the insulin-loaded nanoparticle dosage to 21 IU kg<sup>-1</sup>, the blood glucose dropped to normal levels for more than 8 h. These results show that the chitosan nanoparticles facilitated the intestinal absorption of insulin.

The presence of Poloxamer 188 in the nanoparticle formulation could have affected the *in vivo* behavior of insulin-loaded nanoparticles because it can reduce the intestinal peristalsis and so prolong the retention of nanoparticles in the intestinal tract. Also, the surfactant can reduce the opsonization and thus the particle clearance from the RES due to the hydrophilic groups on the particle surface.

The successful incorporation of insulin in the nanoparticles depends strongly on the formulation conditions and pH is a very important parameter of the procedure. Optimization of the formulation process will lead to highly efficient nanoparticles in delivering insulin after oral administration [156]. Thus, insulin was premixed with either pentasodium TPP anions or the chitosan solution prior to nanoparticle formulation and the particles produced were designated as TPP-np or CS-np, respectively [155] (Fig. 9.11). The particle preparation was carried out in a pH range of 2.3–6.3. Up to that maximum of pH 6.3, the particle size was not affected significantly by the pH changes, but beyond that value, particle agglomeration was observed.

When the initial insulin concentration was 0.88 mg mL<sup>-1</sup>, the association efficiency of insulin was pH-dependent. Maximum association efficiency was 62.99

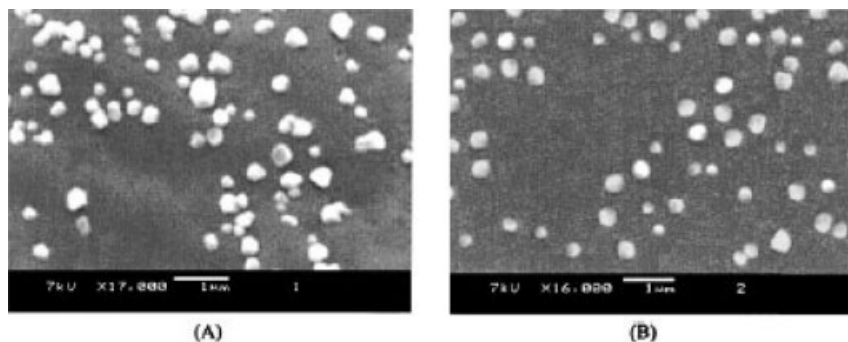


**Figure 9.11.** Scanning electron microscopy micrographs of (A) TPP-np and (B) CS-np prepared at pH 5.3 with an insulin-loading concentration of  $4.28 \text{ U mL}^{-1}$ . Nanoparticles were prepared by ionotropic gelation of chitosan with TPP anions; TPP-np were

obtained by premixing insulin with TPP solution, and CS-np by premixing insulin with chitosan solution, prior to nanoparticle formation. (Reprinted from Ref. [156], © 2002, with permission from Wiley.)

and 57.67 at pH 6.1 for the TPP-np and CS-np nanoparticles, respectively. Small changes around pH 6 led to big variations of association efficiency in both types of formulations. This is not the case for more acidic environments. The association efficiency of insulin was improved significantly by increasing insulin-loading concentrations. Regardless of the insulin concentration, the maximum association efficiency was achieved at pH 6.1. Insulin-loading concentration did not affect the mean particle size. The loading efficiency (amount of insulin incorporated per milligram of nanoparticle) was not affected by the pH of the formulation process.

Although, insulin was released rapidly (100%) from the particles made at pH 6.1 even if the association efficiency was approximately 80%, it was very much slower (10–20%) from particles made at pH 5.3 (association efficiency approximately 50%). At pH 5.3, the association of insulin to chitosan occurs via stronger electrostatic interactions and it is pH dependent, while at higher pH seems that the association is of a hydrophobic nature.

Lim's group also evaluated the uptake of chitosan molecules and chitosan nanoparticles by Caco-2 cells, and their ability to enhance the insulin transport into these cells [157]. They show that nanoparticle uptake was dependent on time, temperature and loading concentration. It was a saturable event and more likely to be taken up by clathrin-mediated adsorptive endocytosis.

In contrast, chitosan polymer molecules were taken up by endocytosis through caveolae. The chitosan polymer was more effective at disrupting the intercellular tight junctions than chitosan nanoparticles, so the former facilitated the insulin transport via the paracellular pathway, being more effective than the particles. Their results agree with those reported by Dyer and coworkers [158], where the insulin-loaded nanoparticles given intranasally showed a lower hypoglycemic effect in comparison to chitosan solutions in sheep and rats.

After particle optimization for different pH range and insulin-loading concentrations, *in vivo* evaluation of two chosen formulations [made at pH 5.3 (f5.3) and 6.1 (f6.1)] followed in streptozotocin-induced diabetic rats [159]. Particles were administered orally at two insulin doses: 50 or 100 IU kg<sup>-1</sup>. It was shown that the 100 IU kg<sup>-1</sup> insulin of f5.3 demonstrated a higher hypoglycemic effect lasting up to 11 h. The f6.1 nanoparticles were less efficient even if the hypoglycemic action started 2 h postadministration in comparison to f5.3 particles where blood glucose dropped only after 10 h.

**9.2.7.2.2 Nasal** The intranasal administration of insulin has been attempted using chitosan nanoparticles or more recently nanocomplexes with branched polyesters. Chitosan is by far the most used polymer in research in the delivery of small or larger molecules via the oral, nasal or pulmonary route due to the previously mentioned properties of mucoadhesion and transient opening of the tight junctions of the epithelial cells. Urrusuno and coworkers [160] studied the potential of chitosan nanoparticles as a formulation to increase the availability of insulin after nasal instillation to rabbits. The particles were made with the ionotropic gelation method using two types of chitosan (0.1% CS-210Cl and 0.2% CS-110Cl) with TPP in a ratio chitosan:TPP 6:1. The particle size was 300–400 nm and the  $\zeta$  potential varied from 25 to 54 mV. Insulin association efficiency was greater than 87% and loading efficiency was approximately 55%. After nanoparticle instillation to rabbits, the blood glucose level dropped to 60% of basal levels at 1 h postadministration of insulin-loaded CS-210Cl nanoparticles. This formulation demonstrated the strongest hypoglycemic effect. The same activity was obtained using the insulin-loaded CS-110Cl nanoparticles (two types of chitosan were used in the form of HCl salt, CS-110Cl and CS-210Cl, and their differences were molecular weight, below 50 and 130 respectively, deacetylation degree, 87 and below 70% respectively, and intrinsic viscosity, 10 and 20–200, respectively) (Fig. 9.12). In contrast, the administration of 5 IU kg<sup>-1</sup> insulin control solution (pH 4.3) resulted in a decrease of blood glucose levels of less than 15% at 30 min postinstillation. This is an indication that insulin was released from the nanoparticles in its active form, which meant that the formulation preparation did not affect the peptide. Moreover, these authors showed that chitosan in nanoparticle form decreased blood glucose more significantly than the chitosan solution, a finding that is different to that reported by other groups [157].

The pH of chitosan solutions plays an important role in their ability to act as absorption enhancers. The *in vivo* effect was investigated by comparing insulin-loaded nanoparticles with insulin solutions following nasal instillation at pH 6.4 and 4.3. The hypoglycemic effect of insulin solution at pH 6.4 was negligible due to slow solubility and formation of high-molecular-weight aggregates. When insulin-loaded chitosan nanoparticles were administered intranasally at the same pH, a reduction of blood glucose levels was recorded for 1.5 h. Even if the hypoglycemic effect of insulin from the nanoparticles was lower at pH 6.4 than 4.3, the increase in the response to the hormone-loaded nanoparticles and the insulin/chitosan solutions was the same: 18.6% at pH 6.4 and 17.4% at pH 4.3.

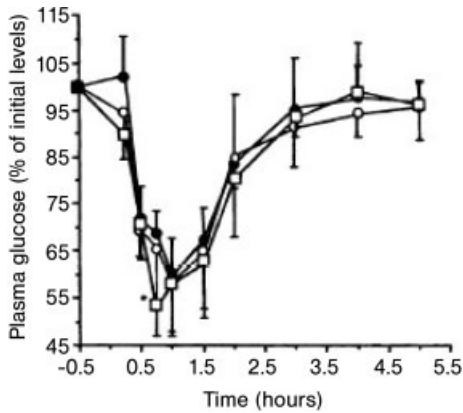


**Figure 9.12.** Plasma glucose levels achieved in rabbits following nasal administration (at pH 4.3) of: insulin-loaded chitosan 210 Cl nanoparticles suspended in acetate buffer, 0.16 mg kg<sup>-1</sup> chitosan (●) and 0.35 mg kg<sup>-1</sup> chitosan (◻), and insulin-loaded chitosan 110 Cl nanoparticles suspended in acetate buffer (◊) ( $n = 6$ ). (Mean  $\pm$  SD  $n = 6$ .) \*Statistically

significant differences from insulin-loaded chitosan 210 Cl nanoparticles suspended in acetate buffer, 0.16 mg kg<sup>-1</sup> chitosan ( $P < 0.05$ ). (Reprinted from Ref. [160], © Plenum Publishing Corporation with permission of Springer Science and Business Media.)

Insulin/chitosan solutions and insulin-loaded chitosan nanoparticles were studied for their ability to improve the bioavailability of insulin in two animal models [157]. Again particles were made by the same gelation method used by Urusuno and coworkers [159]. In this study, insulin-loaded chitosan nanoparticles were used as well as postloaded insulin/chitosan nanoparticles. The empty (non-loaded) nanoparticles had a mean particle size around 250 nm and a  $\zeta$  potential of about 29 mV. All nanoparticles exhibited a size less than 1  $\mu$ m. The result was that in the rat model the chitosan nanoparticles were not advantageous in comparison to the chitosan solutions in the overall hypoglycemic effect.

Regarding the response in the sheep model, the insulin/chitosan solution was more effective than the insulin-loaded and postloaded insulin chitosan nanoparticles. However, the best acting formulation was the insulin/chitosan powder, which is assumed to remain longer (115 min) in the nasal cavity of the sheep than the chitosan solution (45 min).

Another promising approach to develop a carrier system for insulin delivery exploiting the intranasal or the oral route was one based on the complexation between polymer/peptide according to the hydrophobic and electrostatic interactions of the two parts [161]. Therefore, a hydrophilic charged-modified poly(vinyl alcohol) backbone was produced with covalently bound diethylamine groups.  $\alpha$ -Lactide groups were grafted onto the backbone imparting a hydrophobic character to the previously hydrophilic molecule. The nanocomplexes produced were of a range of sizes between 200 and 500 nm according to the backbone composition and number of grafted lactic acid groups. Increasing the amount of lactic acid groups, the

complexes tend to be smaller and more compact. The  $\zeta$  potential ranged from +3 mV at a low substitution to +35 mV at the highest substitution. The insulin complexation was higher with high degrees of amine substitution or by a combination of medium charge density and a higher lactic acid content. When the initial insulin concentration was  $1.25 \text{ mg mL}^{-1}$ , approximately 98% of insulin was found in the complexes.

**9.2.7.2.3 Pulmonary** Drug delivery via the pulmonary route is, of course, preferable to injections because it is noninvasive and systemic absorption is expected to be at higher rates since the lung provides a large surface area and enzymic degradation is relatively low. PBCA nanoparticles were used to compare the pharmacological potential between pulmonary and subcutaneous delivery of insulin-loaded particles [162]. The mean size of the particles was 255 nm and the insulin association efficiency was 79%. Burst release phenomena accompanied the release profile of insulin at pH 7 in saline at  $37^\circ\text{C}$ . The particles were administered intratracheally to normal rats and an increase in the reduction of blood glucose level was observed as the insulin dose increased from 5 to  $20 \text{ IU kg}^{-1}$ , while the minimum glucose level was reached in 4, 4 and 8 h for 5, 10 and  $20 \text{ IU kg}^{-1}$ , respectively. The hypoglycemic effect of insulin-loaded nanoparticles at doses 10 and  $20 \text{ IU kg}^{-1}$  was prolonged compared to that obtained with the insulin solutions (Fig. 9.13). However, the hypoglycemic effect achieved after subcutaneous administration of  $5 \text{ IU kg}^{-1}$  insulin-loaded nanoparticles was much higher than that obtained after intratracheal delivery of the same nanoparticles. According to these authors, this phenomenon is attributed to the ability of normal rats to adjust the blood glucose level.

An idea for pulmonary delivery of insulin-loaded chitosan nanoparticles was the microencapsulation of those particles into microspheres made by lactose or mannitol by spray-drying [163]. Indeed, it was shown that the microspheres produced were mostly spherical with the appropriate aerodynamic properties for good deliv-

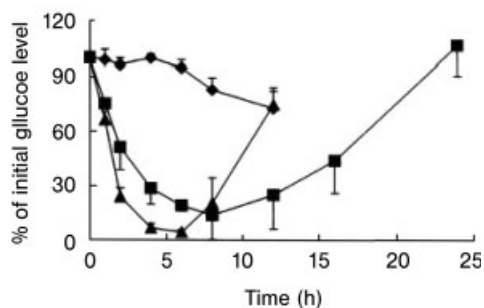


**Figure 9.13.** Hypoglycaemic effect of a single intratracheal administration of insulin-loaded nanoparticles of  $20 \text{ IU kg}^{-1}$  (■) and insulin solution of  $20 \text{ IU kg}^{-1}$  (▲) to normal rats fasted overnight. The glucose concentration at

time zero served as the basis for comparison (%). Results are means for five or six animals. The control (◆) is phosphate buffer solution (pH 7). (Reprinted from Ref. [162], © 2001, with permission from Elsevier.)



ery, but their morphology was strongly influenced by the nanoparticle content. The microspheres with the best properties were those made with mannitol:nanoparticles 80:20 and the nanoparticles were made with chitosan:TPP: 6:1. The insulin-loaded chitosan/TPP nanoparticles were of approximately 350 nm size, and had a  $\zeta$  potential of +40 mV and a protein loading capacity 65–80%. After 15 min incubation in phosphate-buffered saline (pH 7.4) at 37 °C, 75–80% of insulin was released from either nanoparticles or nanoparticles encapsulated into microspheres. Also, the nanoparticles could be recovered from microspheres after their contact with water with no significant changes in their physicochemical properties. Therefore, the microspheres containing nanoparticles would be able to be delivered to the deep lung and thereafter the aqueous environment would release the nanoparticles and subsequently the entrapped insulin.

**9.2.7.2.4 Parenteral Delivery (Subcutaneous, Intravenous, Intraperitoneal)** In addition to the high instability and degradation of insulin in the gastrointestinal tract, it also exhibits a short half-life when administered by subcutaneous injections. Its incorporation in to nanoparticles was therefore also investigated to sustain the hypoglycemic effect. Barichello and coworkers [164] evaluated the use of Pluronic gels (20% and 30% Pluronic concentration used), PLGA nanoparticles and their combination for parenteral delivery of peptides and proteins having short half-lives, using insulin as a model molecule. The important characteristic in using Pluronic gels is the enhanced protein stability into the gel matrix with complete recovery of full insulin activity when the gel is dissolved in excess buffer. The drawback is the loss of gelation ability in the presence of inorganic salts used to control the pH in such gels. Insulin was released more slowly from gels with higher concentration of Pluronic (20 and 30% Pluronic concentrations in the gels were used) while the possible mechanism is erosion and probably some diffusion due to zero-order release kinetics.

PLGA nanoparticles were produced with an insulin content around 60% and particle size 128 nm. After subcutaneous injection of insulin-loaded PLGA nanoparticles, a constant hypoglycemic effect was observed with a slow recovery of the serum glucose levels during the 2 h postadministration period. Subcutaneous injection of insulin solution only demonstrated an acute hypoglycemic effect of insulin with a peak 1 h later; however, when insulin loaded in the Pluronic gel was injected, the impact of the hormone was more prolonged. The same profile was obtained after nanoparticle-gel injection with an effect up to 6 h later. The bioavailability of the peptide from the nanoparticle-gel formulation increased almost 3-fold to that estimated after the subcutaneous injection of insulin solution only.

A sustained hypoglycemic effect up to 4 h after subcutaneous injection to diabetic rats was achieved using nanoparticles made with the oppositely charged PEI and DS stabilized by crosslinking with zinc [165]. PEI solution of pH 9 was mixed with DS in a ratio of approximately 2:1 with 25  $\mu$ M of zinc as a stabilizer in the presence of insulin in the polymer mixture. Ninety percent of insulin was entrapped in to particles of size 250 nm and of  $\zeta$  potential +30 mV. However, 70% of particle-bound insulin was dissociated from the particles in 10 mM phosphate

buffer in 5 min, which suggests that insulin was adsorbed on the particle surface through apolar interactions. The interaction of insulin with PEI caused conformational changes to insulin at low pH, but not at pH 9. Moreover, a hypoglycemic effect was induced in diabetic rats regardless of polymer ratio, indicating preservation of insulin biological activity.

Simple mixing of cholesterol-bearing pullulan with insulin resulted in complex formation (size of 20–30 nm) that did not demonstrate any particular advantage to the blood glucose reduction in comparison to free insulin solution after intravenous injection to normal fasting rats [166]. Insulin was stabilized in those complexes, but it was replaced with BSA after nanoparticle incubation in the presence of the latter protein (50 mg mL<sup>-1</sup>) for 1 h at 37 °C.

**9.2.7.2.5 Other Formulations** A very promising technique for enhancement of insulin incorporation into nanoparticles is the use of gas antisolvent techniques or supercritical fluids [167]. This method is considered advantageous for labile pharmaceutical molecules and polymers due to mild operation conditions and a reduction in the amount of organic solvent used. The remaining organic solvents in the final preparation are much reduced and the ability of drug entrapment higher as entrapment is not dependent on the drug partitioning between the liquid phases. Supercritical carbon dioxide precipitation was applied to a mixture of PLA (molecular weight 102 000)/insulin or PLA/PEG/insulin organic solutions (DMSO:dichloromethane 50:50) resulting in polymeric nanoparticles with a mean size of 400–600 nm. The residual dichloromethane was only 8 p.p.m., less than that of 400 and 600 p.p.m. reported by the US and European Pharmacopoeia, respectively. The residual DMSO was 300 p.p.m.

Insulin loading was 90% and it was affected by the presence of PEG in the nanoparticle composition. By increasing the PEG content or the PEG molecular weight, a decrease of insulin loading was observed. High insulin loading was achieved using PEG molecules of less than 1900 molecular weight. The content and molecular weight of PEG used influenced the insulin release from those particles. Using PEGs of higher molecular weight of 1900 or a high concentration of PEG, insulin was released with a burst release phenomenon, which is not the case with PEGs smaller than 1900. Less than 3% of insulin was released from particles with PEG of molecular weight 350, 750 or 1900. Additionally, 80% of the peptide activity was retained, as an induced-hypoglycaemic effect was caused in mice by the insulin extracted from the nanoparticles.

A self-regulating insulin delivery system was developed by Zhang and coworkers based on insulin release from membranes embedded with insulin-loaded nanoparticles. A decrease in the pH of the microenvironment is caused when the system senses an increase in glucose concentration [168]. When the pH of the microenvironment decreases, the particle size in the matrix decreases and insulin is released. Glucose oxidase (GOD) embedded in the membrane was used as a glucose sensor. GOD converts glucose to gluconic acid causing the pH to decrease. Due to the low amount of oxygen available for the amount of glucose to be oxidized and because of toxic hydrogen peroxide formation as a side-product, catalase is coentrapped in/

on to the membrane breaking down the hydrogen peroxide into oxygen and water. The GOD incorporated in to the membrane retained 80% of its activity in comparison to free enzyme and the addition of catalase favored the oxidation rate of glucose.

The nanoparticles were made with the pH sensitive polymer poly(NIPAAm-co-methacrylic acid) and the insulin was released after 5–15 min from the onset of hyperglycemia. The responsiveness of the system to glucose levels was evaluated by increasing the amount of glucose in the surrounding medium. It was found that the insulin permeability increased 3-fold as the glucose concentration increased from 50 to 200 mg mL<sup>-1</sup>. In general, it was shown that the glucose concentration fluctuations stimulated the insulin release in a rapid and reversible way.

### 9.3

#### Conclusions

This chapter has presented most of the ongoing research using polymeric nanoparticles for noncancer applications. The most important diseases have been discussed in some detail, but nanoparticles have been evaluated on a few other noncancer diseases as well, such as arthritis, osteoporosis, problems with arteries, etc. Most of the applications reported in this chapter have displayed very promising therapeutic results with only a few exceptions, and the advantages and limitations of using polymeric nanoparticles have been reported in each case examined.

The most obvious advantages of incorporating drugs into nanoparticles are the reduced toxicity of highly toxic drugs, the protection against environmental conditions, the reduction of the drug dose to give the prospect of better patient compliance and versatility in delivery route. The latter advantage arises because the characteristics of the final formulation, which can favor the use of alternative delivery routes over conventional ones (e.g. pulmonary or nasal delivery instead of subcutaneous injection).

PLGA polymer and chitosan have been the most used polymers. In general, chitosan seems to be more favorable than PLGA, especially when the particles are destined to interact with mucosal surfaces (pulmonary, nasal, ocular, oral/gastrointestinal tract interaction), because it seems to enable the paracellular transport of the nanoparticles. Also, chitosan particles can be made into nanoparticles using methods that do not need the use of organic solvents (important because solvents remain in the particles at low levels and can be irritant or toxic in some cases). In addition, PLGA can be disadvantageous because its degradation products can create an acidic environment, damaging pH-sensitive proteins or peptides.

The drug release profile is one factor that requires further development. With some drugs and applications, the rapid rate of drug release can be a limiting factor (e.g. PLGA almost always shows a significant initial burst release). Thus, there is a need for polymer development to produce particles with sustained drug release and which retain the essential properties of polymer delivery systems, such as biodegradability and biocompatibility.

Finally, in order to reach the clinic and the market, these polymeric formulations will need to be produced in a large scale, have to exhibit a long shelf-life, and to be characterized by reasonable manufacturing cost and formulation stability. There is still a problem of producing sterile dispersions for ocular delivery, too. However, with the promise already shown in the formulations discussed above, it seems likely that the necessary resources will be found to resolve these remaining issues.

## References

- DIAMOND, J. M. The epithelial junction: bridge gate and fence, *Physiologist* **1977**, *20*, 10–18.
- INOUE, S. Ultrastructure of basement membranes, *Int. Rev. Cytol.* **1989**, *117*, 57–98.
- VAN OSS, C. J. Phagocytosis: an overview, *Methods Enzymol.* **1986**, *132*, 3–15.
- VAN DEURS, B., PETERSON, O. W., OLSNES, S., SANDVIG, K. The ways of endocytosis, *Int. Rev. Cytol.* **1989**, *117*, 131–177.
- ANDERSON, R. G., KAMEN, B. A., ROTHBERG, K. G., LACEY, W. W. Potocytosis: sequestration and transport of small molecules by caveolae, *Science* **1992**, *255*, 410–411.
- GHITESCU, L., FIXMAN, A., SIMIONESCU, M. and SIMIONESCU, N. Specific binding sites for albumin restricted to plasmalemmal vesicles of continuous capillary endothelium: receptor mediated transcytosis, *J. Cell Biol.* **1986**, *102*, 1304–1311.
- SCHNITZER, J. E. Caveolae: from basic trafficking mechanisms to targeting transcytosis for tissue specific drug and gene delivery *in vivo*, *Adv. Drug Deliv. Rev.* **2001**, *49*, 265–280.
- KREUTER, J. Nanoparticulate systems for brain delivery of drugs, *Adv. Drug Deliv. Rev.* **2001**, *47*, 65–81.
- LIND, K., KRESSE, M., DEBUS, N. P., MÜLLER, R. H. A novel formulation for superparamagnetic iron oxide (SPIO) particle enhancing MR lymphography: comparison of physicochemical properties and the *in vivo* behaviour, *J. Drug Target.* **2002**, *10*, 221–230.
- GIBAUD, S., DEMOY, M., ANDREUX, J. P., WEINGARTEN, C., GOURITIN, B., COUVREUR, P. Cells involved in the capture of nanoparticles in hematopoietic organs, *J. Pharm. Sci.* **1996**, *85*, 944–950.
- AGRAWAL, A. K., GUPTA, C. M. Tuftsin bearing liposomes in treatment of macrophage based infections, *Adv. Drug Deliv. Rev.* **2000**, *41*, 135–146.
- MOGHIMI, S. M., PORTER, C. J. H., MUIR, I. S., ILLUM, L., DAVIS, S. S. Non-phagocytic uptake of intravenously injected microspheres in rat spleen: influence of particle size and hydrophilic coating, *Biochem. Biophys Res. Commun.* **1991**, *177*, 861–866.
- ABSOLOM, D. R. Opsonins & dysopsonins: an overview, *Methods Enzymol.* **1986**, *132*, 281–318.
- STOLNIK, S., ILLUM, L., DAVIS, S. S. Long circulating microparticulate drug carriers, *Adv. Drug Deliv. Rev.* **1995**, *16*, 195–214.
- HOLMGREN, J., CAPRON, P. B. P. A., FRANCOIS, M., KILIAN, M., KRAEHEBUHL, J. P., LEHNER, T., SELJELID, R. European Commission COST/STD Initiative, Report of the expert panel VI. Concerted efforts in the field of mucosal immunology, *Vaccine* **1996**, *14*, 644–664.
- NORRIS, D. A., PURI, N., SINKO, P. The effect of physical barriers and properties on the oral absorption of particulates, *Adv. Drug Deliv. Rev.* **1998**, *34*, 135–154.
- HUSSAIN, N., JAITLEY, V., FLORENCE, A. T. Recent advances in the understanding of uptake of microparticulates across the gastrointestinal

- lymphatics, *Adv. Drug Deliv. Rev.* **2001**, *50*, 107–142.
- 18 FLORENCE, A. T., HUSSAIN, N. Transcytosis of nanoparticle and dendrimer delivery systems: evolving vistas, *Adv. Drug Deliv. Rev.* **2001**, *50*, S69–S89.
  - 19 JUNG, T., KAMM, W., BREITENBACH, A., KAISERLING, E., XIAO, J. X., KISSEL, T. Biodegradable nanoparticles for oral delivery of peptides: is there a role for polymer to affect mucosal uptake, *Eur J. Pharm. Biopharm.* **2000**, *50*, 147–160.
  - 20 ILLUM, L. Nasal delivery. The use of animal models to predict performance in man, *J. Drug Target.* **1996**, *3*, 427–442.
  - 21 JONES, N. The nose and paranasal sinuses physiology and anatomy, *Adv. Drug Deliv. Rev.* **2001**, *51*, 5–19.
  - 22 GUMBLETON, M. J. Caveolae as potential macromolecule trafficking compartments within alveolar epithelium, *Adv. Drug Deliv. Rev.* **2001**, *49*, 281–300.
  - 23 WASHINGTON, N., WASHINGTON, C., WILSON, C. G. *Physiological Pharmacotics: Barriers to Drug Absorption*, 2nd edn. Taylor & Francis, London, **2001**.
  - 24 JAKOB, T., RING, J., UDEY, M. C. Multistep navigation of Langerhans/dendritic cells in and out of the skin, *J. Allergy Clin. Immunol.* **2001**, *108*, 688–696.
  - 25 HAWLEY, A. E., DAVIS, S. S., ILLUM, L. Targeting of colloids to lymph nodes: influence of lymphatic physiology and colloidal characteristics, *Adv. Drug Deliv. Rev.* **1995**, *17*, 129–148.
  - 26 MAINARDES, R. M., URBAN, M. C. C., CINTO, P. O., KHALIL, M. N., CHAUD, M. V., EVANGELISTA, R. C., GREMIAO, M. P. D. Colloidal carriers for ophthalmic drug delivery, *Curr. Drug Targets* **2005**, *6*, 363–371.
  - 27 LANG, J. C. Ocular drug delivery conventional ocular formulations, *Adv. Drug Deliv. Rev.* **1995**, *16*, 3943.
  - 28 ALONSO, M. J., SANCHEZ, A. The potential of chitosan in ocular drug delivery, *J. Pharm. Pharmacol.* **2003**, *55*, 1451–1463.
  - 29 SALGUEIRO, A., EGEE, M. A., ESPINA, M., VALLS, O., GARCIA, M. L. Stability and ocular tolerance of cyclophosphamide-loaded nanospheres, *J. Microencapsul.* **2004**, *21*, 213–223.
  - 30 FRESTA, M., FONTANA, G., BUCOLO, C., CAVALLARO, G., GIAMMONA, G., PUGLISI, G. Ocular tolerability and *in vivo* bioavailability of poly(ethylene glycol) (PEG)-coated polyethyl-2-cyanoacrylate nanosphere-encapsulate acyclovir, *J. Pharm. Sci.* **2001**, *90*, 288–297.
  - 31 DE KOZAK, Y., ANDRIEUX, K., VILLARROYA, H., KLEIN, C., THILLAYE-GOLDENBERG, B., NAUD, M. C., GARCIA, E., COUVREUR, P. Intraocular injection of tamoxifen-loaded nanoparticles: a new treatment of experimental autoimmune uveoretinitis, *Eur. J. Immunol.* **2004**, *34*, 3702–3712.
  - 32 PIGNATELLO, R., BUCOLO, C., SPEDALIERI, G., MALTESE, A., PUGLISI, G. Flurbiprofen-loaded acrylate polymer nanosuspensions for ophthalmic application, *Biomaterials* **2002**, *23*, 3247–3255.
  - 33 PIGNATELLO, R., BUCOLO, C., FERRARA, P., MALTESE, A., PULEO, A., PUGLISI, G. Eudragit RS100 nanosuspensions for the ophthalmic control delivery of ibuprofen, *Eur. J. Pharm. Sci.* **2002**, *16*, 53–61.
  - 34 PIGNATELLO, R., BUCOLO, C., PUGLISI, G. Ocular tolerability of Eudragit RS100 and RL100 nanosuspensions as carriers for ophthalmic controlled drug delivery, *J. Pharm. Sci.* **2002**, *91*, 2636–2641.
  - 35 DE CAMPOS, A. M., SANCHEZ, A., ALONSO, M. J. Chitosan nanoparticles: a new vehicle for the improvement of the delivery of drugs to the ocular surface. Application to cyclosporin A, *Int. J. Pharm.* **2001**, *224*, 159–168.
  - 36 LALLEMAND, F., FELT-BAEYENS, O., BESSEGHIR, K., BEHAR-COHEN, F., GURNY, R. Cyclosporine A delivery to the eye: a pharmaceutical challenge, *Eur. J. Pharm. Biopharm.* **2003**, *56*, 307–318.
  - 37 RABINOVICH-GUILATT, L., COUVREUR, P., LAMBERT, G., DUBERNET, C. Cationic vectors in ocular drug

- delivery, *J. Drug Target.* **2004**, *12*, 623–633.
- 38 GIANNAVOLA, C., BUCCO, C., MALTESE, A., PAOLINO, D., VANDELLI, M. A., PUGLISI, G., LEE, V. H. L., FRESTA, M. Influence of preparation conditions on acyclovir-loaded Poly-D,L-lactic acid nanospheres and effect of PEG coating on ocular drug bioavailability, *Pharm. Res.* **2003**, *20*, 584–590.
- 39 QADDOUMI, M. G., HOVHANNES, G. J., DAVDA, J., LABHASETWAR, V., KIM, K. J., LEE, V. H. L. Clathrin and caveolin-1 expression in primary pigmented rabbit conjunctival epithelial cells: role in PLGA nanoparticle endocytosis, *Mol. Vision* **2003**, *9*, 559–68.
- 40 BARBAULT-FOUCHER, S., GREFF, R., RUSSO, P., GUECHOT, J., BOCHOT, A. Design of poly-ε-caprolactone nanospheres coated with bioadhesive hyaluronic acid for ocular delivery, *J. Control. Release* **2002**, *83*, 365–375.
- 41 DE, T. K., BERGEY, E. J., CHUNG, S. J., RODMAN, D. J., BHARALI, D. J., PRASAD, P. N. Polycarboxylic acid nanoparticles for ophthalmic drug delivery: an *ex vivo* evaluation in human cornea, *J. Microencapsul.* **2004**, *21*, 841–855.
- 42 GIORDANO, G. G., REFOJO, M. F., ARROYO, M. H. Sustained delivery of retinoic acid from microspheres of biodegradable polymer in PVR, *Invest. Ophthalmol. Vis. Sci.* **1993**, *34*, 2743–2751.
- 43 COLTHURST, M. J., WILLIAMS, R. L., HISCOTT, P. S., GRIERSON, I. Biomaterials used in the posterior segment of the eye, *Biomaterials* **2000**, *2*, 649–665.
- 44 CALVO, P., ALONSO, M. J., VILA-JATO, J. L., ROBINSON, J. R. Improved ocular bioavailability of indomethacin by novel ocular drug carriers, *J. Pharm. Pharmacol.* **1996**, *48*, 1147–1152.
- 45 DE CAMPOS, A. M., DIEBOLD, Y., CARVALHO, E. L. S., SANCHEZ, A., ALONSO, M. J. Chitosan nanoparticles as new ocular drug delivery systems: *in vitro* stability, *in vivo* fate and cellular toxicity, *Pharm. Res.* **2004**, *21*, 803–810.
- 46 CALVO, P., VILA-JATO, J. L., ALONSO, M. J., Comparative *in vitro* evaluation of several colloidal systems, nanoparticles, nanocapsules, and nanoemulsions, as ocular drug carriers, *J. Pharm. Sci.* **1996**, *85*, 530–536.
- 47 CALVO, P., VILA-JATO, J. L., ALONSO, M. J. Evaluation of cationic polymer-coated nanocapsules as ocular drug carriers, *Int. J. Pharm.* **1997**, *153*, 41–50.
- 48 CALVO, P., SANCHEZ, A., MARTINEZ, J., LOPEZ, M. I., CALONGE, M., PASTOR, J. C., ALONSO, M. J. Polyester nanocapsules as new topical ocular delivery systems for cyclosporin A, *Pharm. Res.* **1996**, *13*, 311–315.
- 49 HEINEMANN, M. H. *Am. J. Ophthalmol.* **1989**, *107*, 643–644.
- 50 COCHEREAU-MASSIN, I., LEHOANG, P., LAUTIER-FRAU, M., ZERDOUN, E., ZAZOUN, L., ROBINET, M., MARCEL, P., LEPORT, C. Ocular toxoplasmosis in human immunodeficiency virus-infected patients. *Ophthalmology* **1991**, *98*, 1348–1355.
- 51 IRACHE, J. M., MERODIO, M., ARNEDO, A., CAMAPANERO, M. A., MIRSHAHI, M., ESPUELAS, S. Albumin nanoparticles for the intravitreal delivery of anticytomegaloviral drugs, *Mini-Rev. Med. Chem.* **2005**, *5*, 293–305.
- 52 SIMOES, S., SLEPUSHKIN, V., PIRES, P., GASPAS, R., PEDROSO DE LIMA, M. C., DUZGUNES, N. *Biochim. Biophys. Acta* **2000**, *1463*, 459–469.
- 53 GULSEN, D., CHAUBAN, A. Ophthalmic drug delivery through contact lenses, *IOVS* **2004**, *45*, 2342–2347.
- 54 SAHA, P., KIM, K. J., LEE, V. H. A primary culture model of rabbit conjunctival epithelial cells exhibiting tight barrier properties, *Curr. Eye Res.* **1996**, *15*, 1163–1169.
- 55 HORIBE, Y., HOSOYA, K., KIM, K. J., OGISO, T., LEE, V. H. Polar solute transport across the pigmented rabbit conjunctiva: size dependence and the influence of 8-bromo cyclic adenosine monophosphate, *Pharm. Res.* **1997**, *14*, 1246–1251.
- 56 NICHOLS, B. A., CHIAPPINO, M. L., DAWSON, C. R. Demonstration of the mucous layer of the tear film by elec-

- tron microscopy, *Invest. Ophthalmol. Vis. Sci.* **1985**, *24*, 464–473.
- 57 GASPAR, R., OPPERDOES, F. R., PREAT, V., ROLAND, M. Drug targeting with polyalkylcyanoacrylate nanoparticles: *in vitro* activity of primaquine-loaded nanoparticles against intracellular *Leishmania donovani*, *Ann. Trop. Med. Parasit.* **1992**, *86*, 41–49.
- 58 FOUARGE, M., OSUNA, A., COUVREUR, P., ROLAND, M., VRANCKX, H. Development of dehydroemetine nanoparticles for the treatment of visceral leishmaniasis, *J. Microencapsul.* **1989**, *6*, 29–34.
- 59 LENAERTS, V., NAGELKERKE, J. F., VAN BERKEL, T. J. C., COUVREUR, P., GRISLAIN, L., ROLAND, M., SPEISER, P. *In vivo* uptake of polyisobutylcyanoacrylate nanoparticles by rat liver, Kupffer, endothelial and parenchymal cells, *J. Pharm. Sci.* **1984**, *73*, 980–982.
- 60 RODRIGUES, JR., J. M., FESSI, H., BORIES, C., PUISIEUX, F., DEVISSAGUET, J.-Ph. Primaquine-loaded poly(lactide) nanoparticles: physicochemical study and acute tolerance in mice, *Int. J. Pharm.* **1995**, *126*, 253–260.
- 61 RODRIGUES, JR., J. M., CROFT, S. L., FESSI, H., BORIES, C., DEVISSAGUET, J. Ph. The activity and ultrastructural localization of primaquine-loaded poly(D,L-lactide) nanoparticles in *Leishmania donovani* infected mice, *Trop. Med. Parasitol.* **1994**, *45*, 223–228.
- 62 FUSAI, T., DENIAU, M., DURAND, R., BORIES, C., PAUL, M., RIVOLLET, D., ASTIER, A., HOUIN, R. Action of pentamidine-bound nanoparticles against *Leishmania* on an *in vivo* model, *Parasite* **1994**, *1*, 319–324.
- 63 DURAND, R., PAUL, M., RIVOLLET, D., HOUIN, R., ASTIER, A., DENIAU, M. Activity of Pentamidine-loaded Methacrylate nanoparticles against *Leishmania infantum* in a mouse model, *Int. J. Parasitol.* **1997**, *27*, 1361–1367.
- 64 PAUL, M., DURAND, R., BOULARD, Y., FUSAI, T., FERNANDEZ, C., RIVOLLET, D., DENIAU, M., ASTIER, A. Physicochemical characteristics of pentamidine-loaded polymethacrylate nanoparticles: implication in the intracellular drug release in *Leishmania major* infected mice, *J. Drug Target.* **1998**, *5*, 481–490.
- 65 VENIER-JULIENNE, M. C., VOULDOUKIS, I., MONJOUR, L., BENOIT, J. P. *In vitro* study of the antileishmanial activity of biodegradable nanoparticles, *J. Drug Target.* **1995**, *3*, 23–29.
- 66 *British National Formulary 43*, **2003**.
- 67 OFEK, I., SHARON, N. Lectinophagocytosis: a molecular mechanism of recognition between cell surface sugars and lectins in the phagocytosis bacteria, *Infect. Immun.* **1988**, *56*, 539–547.
- 68 DESJEUX, P. Leishmaniasis: public health aspects and control, *Clin. Dermatol.* **1996**, *14*, 417–423.
- 69 CHEN, M., CHRISTENSEN, S. B., THEANDER, T. G., KHARAZMI, A. Antileishmanial activity of licochalcone A in mice infected with *Leishmania major* and in hamsters infected with *Leishmania donovani*, *Antimicrob. Agents Chemother.* **1994**, *38*, 1339–1344.
- 70 TORRES-SANTOS, E. C., RODRIGUES, J. M., JR., MOREIRA, D. L., AUXILIADORA, M., KAPLAN, C., ROSSIBERGMANN, B. Improvement of *in vitro* and *in vivo* antileishmanial activities of 2',6'-dihydroxy-4'-methoxychalcone by entrapment in poly(D,L-lactide) nanoparticles, *Antimicrob. Agents Chemother.* **1999**, *43*, 1776–1778.
- 71 SARKAR, S., MANDAL, S., SINHA, J., MUKHOPADHYAY, S., DAS, N., BASU, M. K. Quercetin: critical evaluation as an antileishmanial agent *in vivo* in hamsters using different vesicular delivery modes, *J. Drug Target.* **2002**, *10*, 573–578.
- 72 LALA, S., PRAMANICK, S., MUKHOPADHYAY, S., BANDYOPADHYAY, S., BASU, M. K. Harmine: evaluation of its antileishmanial properties in various vesicular delivery systems, *J. Drug Target.* **2004**, *12*, 165–175.
- 73 TYAGI, R., LALA, S., VERMA, A. K., NANDY, A. K., MAHATO, S. B., MAITRA, A., BASU, M. K. Targeted delivery of

- arjunglucoside I using surface hydrophilic and hydrophobic nanocarriers to combat experimental leishmaniasis, *J. Drug Target.* **2005**, *13*, 161–171.
- 74 MITTRA, B., SAHA, A., CHOWDHURY, R., PAL, A., MANDAL, C., MUKHOPADHYAY, S., BANDYOPADHYAY, S., MAJUMBER, H. K. Luteolin – an abundant dietary component is a potent antileishmanial agent that acts by inducing topoisomerase-II mediated kinetoplast DNA cleavage leading to apoptosis, *Mol. Med.* **2000**, *6*, 527–541.
- 75 MOLERO, M. L., HAZEN, M. J., PEREZ-GORRANO, A. I., STOCKERT, J. C. Simple beta-carboline alkaloids as nucleic acid fluorochromes, *Acta Histochem.* **1995**, *97*, 165–173.
- 76 SOBHANI, A. M., EBRAHIM, S. A., MOHMOUDIAN, M. An *in vitro* evaluation of human DNA topoisomerase I inhibition by *Peganum harmala* L. seeds extract and its beta-carboline alkaloids, *J. Pharm. Pharm. Sci.* **2002**, *5*, 19–23.
- 77 BASU, M. K., LALA, S. Macrophage specific drug delivery in experimental leishmaniasis, *Curr. Mol. Med.* **2004**, *4*, 681–689.
- 78 LHERM, C., COUVREUR, P., LOISEAU, P., BORIEST, C., GAYRAL, P. Unloaded polyisobutylcyanoacrylate nanoparticles: efficiency against bloodstream trypanosomes, *J. Pharm. Pharmacol.* **1987**, *39*, 650–652.
- 79 MAINARDES, R. M., EVANGELISTA, R. C. PLGA nanoparticles containing praziquantel: effect of formulation variables on size distribution, *Int. J. Pharm.*, **2005**, *290*, 137–144.
- 80 LEGRAND, P., MOSQUEIRA, V., LOISEAU, P., BORIEST, C., BARRATT, G. Les nanocapsules à temps de circulation prolongé: intérêt dans le traitement du paludisme sévère par l'halofantrine, *Ann Pharm Fr.* **2003**, *61*, 196–202.
- 81 TIYANBOONCHAI, W., WOISZWILLO, J., MIDDGAUGH, C. R. Formulation and characterization of Amphotericin-B–polyethylenimine–dextran sulfate nanoparticles, *J. Pharm. Sci.* **2001**, *90*, 902–914.
- 82 MCCARRON, P. A., DONNELLY, R. F., CANNING, P. E., MCGOVERN, J. G., JONES, D. S. Bioadhesive, non-drug-loaded nanoparticles as modulators of candidal adherence to buccal epithelial cells: a potentially novel prophylaxis for candidosis, *Biomaterials* **2004**, *25*, 2399–2407.
- 83 MOLINA, J., URBINA, J., GREF, R., BRENER, Z., JÚNIOR, J. M. R. Cure of experimental Chagas' disease by the bis-triazole DO870 incorporated into "stealth" polyethyleneglycol–polylactide nanospheres, *J. Antimicrob. Chemother.* **2001**, *47*, 101–104.
- 84 URBINA, J. A. Chemotherapy of Chagas' disease: the how and the why, *J. Mol. Med.* **1999**, *77*, 332–338.
- 85 SALMASO, S., EIVASSORE, N., BERTUCCO, A., LANTE, A., CALICETTI, P. Nisin-loaded poly-L-lactide nanoparticles produced by CO<sub>2</sub> anti-solvent precipitation for sustained antimicrobial activity, *Int. J. Pharm.* **2004**, *287*, 163–173.
- 86 QI, L., XU, Z., JIANG, X., HU, C., ZOU, X. Preparation and antibacterial activity of chitosan nanoparticles, *Carbohydr. Res.* **2004**, *339*, 2693–2700.
- 87 UENO, K., YAMAGUCHI, T., SAKAIRI, N., NISHI, N., TOKURA, S. *Adv. Chitin Sci.* **1997**, *2*, 156–161.
- 88 JEON, Y. J., PARK, P. J., KIM, S. K. Antimicrobial effect of chitooligosaccharides produced by bioreactor, *Carbohydr. Polym.* **2001**, *44*, 71–76.
- 89 PANDEY, R., KHULLER, G. K. Antitubercular inhaled therapy: opportunities, progress and challenges, *J. Antimicrob. Chemother.* **2005**, *55*, 430–435.
- 90 PANDEY, R., ZAHOR, A., SHARMA, S., KHULLER, G. K. Nanoparticle encapsulated antitubercular drugs as a potential oral drug delivery system against murine tuberculosis, *Tuberculosis* **2003**, *83*, 373–378.
- 91 SHARMA, A., PANDEY, R., SHARMA, S., KHULLER, G. K. Chemotherapeutic efficacy of poly (DL-lactide-co-glycolide) nanoparticle encapsulated antitubercular drugs at sub-therapeutic dose against experimental tuberculosis, *Int.*



- J. Antimicrob. Agents* **2004**, *24*, 599–604.
- 92 SHARMA, A., SHARMA, S., KHULLER, G. K. Lectin-functionalized poly(lactide-co-glycolide) nanoparticles as oral/aerosolised antitubercular drug carriers for treatment of tuberculosis, *J. Antimicrob. Chemother.* **2004**, *54*, 761–766.
- 93 GELPERINA, S., KISICH, K., ISEMAN, M. D., HEIFETS, L. The potential advantages of nanoparticle drug delivery systems in chemotherapy of tuberculosis, *Am. J. Respir. Crit. Care Med.* **2005**, *17*, 1487–1490.
- 94 FU, J., FIEGEL, J., KRAULAND, E., HANES, J. New polymeric carriers for controlled drug delivery following inhalation or injection, *Biomaterials* **2002**, *23*, 4425–4433.
- 95 LIPWORTH, B. J. Targets for inhaled treatment. *Respir. Med.* **2000**, *94* (Suppl. D), S13–S16.
- 96 PANDEY, R., SHARMA, A., ZAHOR, A., SHARMA, S., KHULLER, G. K., PRASAD, B. Poly (DL-lactide-co-glycolide) nanoparticle-based inhalable sustained drug delivery system for experimental tuberculosis, *J. Antimicrob. Chemother.* **2003**, *52*, 9881–986.
- 97 GRAYSON, A. C., VOSKERICIAN, G., LYNN, A. Differential degradation rates *in vivo* and *in vitro* of biocompatible poly(lactic acid) and poly(glycolic acid) homo- and co-polymers for a polymeric drug-delivery microchip, *J. Biomater. Sci. Polym. Ed.* **2004**, *15*, 1281–304.
- 98 DAILEY, L. A., KLEEMANN, E., WITTMAR, M., GESSLER, T., SCHMEHL, T., ROBERTS, C., SEEGER, W., KISSEL, T. Surfactant-free, biodegradable nanoparticles for aerosol therapy based on the branched polyesters, DEAPA–PVAL-g-PLGA, *Pharm. Res.* **2003**, *20*, 2011–2019.
- 99 ZAHOR, A., SHARMA, S., KHULLER, G. K. Inhalable alginate nanoparticles as antitubercular drug carriers against experimental tuberculosis, *Int. J. Antimicrob. Agents* **2005**, *26*, 298–303.
- 100 PANDEY, R., KHULLER, G. K. Subcutaneous nanoparticle-based antitubercular chemotherapy in an experimental model, *J. Antimicrob. Chemother.* **2004**, *54*, 266–268.
- 101 BENDER, A. R., BRIESEN, H., KREUTER, J., DUNCAN, I. B., RUBSAMEN-WAIGMANN, H. Efficiency of nanoparticles as a carrier system for antiviral agents in human immunodeficiency virus-infected human monocytes/macrophages *in vitro*, *Antimicrob. Agents Chemother.* **1996**, *40*, 1467–1471.
- 102 HAO, Z., COONEY, D. A., HARTMAN, N. R., PERNO, C. F., FRIDLAND, A., DEVICO, A. L., SARGADHARAN, M. G., BRODER, S., JOHN, D. G. Factors determining the activity of 2',3'-dideoxynucleosides in suppressing human immunodeficiency virus *in vitro*, *Mol. Pharmacol.* **1988**, *34*, 431–435.
- 103 LÖBENBERG, R., ARAUJO, L., VON BRIESEN, H., RODGERS, E., KREUTER, J. Body distribution of azidothymidine bound to hexyl-cyanoacrylate nanoparticles after *i v.* injection to rats, *J. Control. Release* **1998**, *50*, 21–30.
- 104 DEMBRI, A., MONTISCI, M. J., GANTIER, J. C., CHACUN, H., PONCHEL, G. Targeting of 3'-azido-3'-deoxythymidine (AZT)-loaded poly(isohexylcyanoacrylate) nanospheres to the gastrointestinal mucosa and associated lymphoid tissues, *Pharm. Res.* **2001**, *18*, 467–473.
- 105 LEROUX, J. C., COZENS, R. M., ROESEL, J. L., GALLI, B., DOELKER, E., GURNY, R. pH-sensitive nanoparticles: an effective means to improve the oral delivery of HIV-1 protease inhibitors in dogs, *Pharm. Res.* **1996**, *13*, 485–487.
- 106 LEROUX, J. C., COZENS, R., ROESEL, J. L., GALLI, B., KUBEL, F., DOELKER, E., GURNY, R. Pharmacokinetics of a novel HIV-1 protease inhibitor incorporated into biodegradable or enteric nanoparticles following intravenous and oral administration to mice, *J. Pharm. Sci.* **1995**, *84*, 1387–1391.
- 107 DE JAEGHERE, F., ALLEMANN, E., KUBEL, F., GALLI, B., COZENS, R., DOELKER, E., GURNY, R. Oral bio-availability of a poorly water soluble

- HIV-1 protease inhibitor incorporated into pH-sensitive particles: effect of the particle size and nutritional state, *J. Control. Release* **2000**, *68*, 291–298.
- 108 BOUDAD, H., LEGRAND, P., LEBAS, G., CHERON, M., DUCHÊNE, D., PONCHEL, G. Combined hydroxypropyl- $\beta$ -cyclodextrin and poly(alkylcyanoacrylate) nanoparticles intended for oral administration of saquinavir, *Int. J. Pharm.* **2001**, *218*, 113–124.
- 109 BERTON, M., TURELLI, P., TRONO, D., STEIN, Cy. A., ALLÉMAN, E., GURNY, R. Inhibition of HIV-1 in cell culture by oligonucleotide-loaded nanoparticles, *Pharm. Res.* **2001**, *18*, 1096–1101.
- 110 DINAUER, N., LOCHMANN, D., DEMIRHAN, I., BOUAZZAOU, A., ZIMMER, A., CHANDRA, A., KREUTER, J., VON BRIESEN, H. Intracellular tracking of protamine/antisense oligonucleotide nanoparticles and their inhibitory effect on HIV-1 transactivation, *J. Control. Release* **2004**, *96*, 497–507.
- 111 LE BUANEC, H., VETU, C., LACHGAR, A., BENOIT, M. A., GILLARD, J., PATURANCE, S., AUCOUTURIER, J., GANE, V., ZAGURY, D., BIZZINI, B. Induction in mice of anti-Tat mucosal immunity by the intranasal and oral routes, *Biomed. Pharmacother.* **2001**, *55*, 316–320.
- 112 CUI, Z., PATEL, J., TUZOVA, M., RAY, P., PHILLIPS, R., WOODWARD, J. G., NATH, A., MUMPER, R. J. Strong T cell type-1 immune responses to HIV-1 Tat (1–72) protein-coated nanoparticles, *Vaccine* **2004**, *22*, 2631–2640.
- 113 FRANKEL, A. D., PABO, C. O. Cellular uptake of the Tat protein from human immunodeficiency virus, *Cell* **1988**, *55*, 1189–1193.
- 114 LI, C. J., UEDA, Y., SHI, B., BORODYANSKY, L., HUANG, L., LI, Y. Z. Tat protein induces self-perpetuating permissivity for productive HIV-1 infection, *Proc. Natl. Acad. Sci. USA* **1997**, *94*, 8116–8120.
- 115 LOCHER, C. P., PUTNAM, D., LANGER, R., WITT, S. A., ASHLOCK, B. M., LEVY, J. A. Enhancement of a human immunodeficiency virus *env* DNA vaccine using a novel polycationic nanoparticle formulation, *Immunol. Lett.* **2003**, *90*, 67–70.
- 116 KAWAMURA, M., WANG, X., TOMOFUMI, U., SATO, K., UENO, M., AKAGI, T., HIRAIISHI, K., MATSUYAMA, T., AKASHI, M., BABA, M. Induction of dendritic cell-mediated immune responses against HIV-1 by antigen-capturing nanospheres in mice, *J. Med. Virol.* **2005**, *76*, 7–15.
- 117 MIYAKE, A., AKAGI, T., ENOSE, Y., UENO, M., KAWAMURA, M., HORIUCHI, R., HIRAIISHI, K., ADACHI, M., SERIZAWA, T., NARAYAN, O., AKASHI, M., BABA, M., HAYAMI, M. Induction of HIV-specific antibody response and protection against vaginal SHIV transmission by intranasal immunization with inactivated SHIV-capturing nanospheres in macaques, *J. Med. Virol.* **2004**, *73*, 368–377.
- 118 RAGHUVANSHI, R. S., KATARE, Y. K., LALWANI, K., ALI, M. M., SINGH, O., PANDA, A. K. Improved immune response from biodegradable polymer particles entrapping tetanus toxoid by use of different immunization protocol and adjuvants, *Int. J. Pharm.* **2002**, *245*, 109–121.
- 119 NAIM, J. O., VAN OSS, C. J., WU, W., GIESE, R. F., NICKERSON, P. A. Mechanism of adjuvancy: I – metal oxide as adjuvants, *Vaccine* **1997**, *11*, 1183–1193.
- 120 KOHLI, A. K., ALPAR, H. O. Potential use of nanoparticles for transcutaneous vaccine delivery: effect of particle size and charge, *Int. J. Pharm.* **2004**, *275*, 13–17.
- 121 NEWMAN, K. D., ELAMANCHILI, P., KWON, G. S., SAMUEL, J. Uptake of poly(D,L-lactic-co-glycolic acid) microspheres by antigen-presenting cells *in vivo*, *J. Biomed. Mater. Res.* **2002**, *60*, 480–486.
- 122 ELAMANCHILI, P., DIWAN, M., CAO, M., SAMUEL, J. Characterization of poly(D,L-lactic-co-glycolic acid) based nanoparticulate system for enhanced delivery of antigens to dendritic cells, *Vaccine* **2004**, *22*, 2406–2412.
- 123 SUN, H., POLLOCK, K. G., BREWER, J. M. Analysis of the role of vaccine adjuvants in modulating dendritic cell

- activation and antigen presentation *in vitro*, *Vaccine* **2003**, *21*, 849–55.
- 124 CHONG, C. S. W., CAO, M., WONG, W. W., FISCHER, K. P., ADDISON, W. R., KWON, G. S., TYRELL, D. L., SAMUEL, J. Enhancement of T helper type 1 immune responses against hepatitis B virus core antigen by PLGA nanoparticle vaccine delivery, *J. Control. Release* **2005**, *102*, 85–99.
- 125 NIXON, D. F., HIOE, C., CHEN, P. D., BIAN, Z., KUEBLER, P., LI, M. L., QIU, H., LI, X. M., SINGH, M., RICHARDSON, A., MCGEE, P., ZAMB, T., KOFF, W., WANG, C. Y., O'HAGAN, D. Synthetic peptides entrapped in microparticles can elicit cytotoxic T cell activity, *Vaccine* **1996**, *14*, 1523–1530.
- 126 WANG, X., UTO, T., SATO, K., IDE, K., AKAGI, T., OKAMOTO, M., KANEKO, T., AKASHI, M., BABA, M. Potent activation of antigen-specific T cells by antigen-loaded nanospheres, *Immunol. Lett.* **2005**, *98*, 123–130.
- 127 CUI, Z., MUMPER, R. J. Chitosan-based nanoparticles for topical genetic immunization, *J. Control. Release* **2001**, *75*, 409–419.
- 128 CUI, Z., MUMPER, R. J. Dendritic cell-targeted genetic vaccines engineered from novel microemulsion precursors, *Mol. Ther.* **2001**, *3*, S352.
- 129 CUI, Z., MUMPER, R. J. Topical immunization using nanoengineered genetic vaccines, *J. Control. Release* **2002**, *81*, 173–184.
- 130 TODA, S., ISHII, N., OKADA, E., KUSAKABE, K. I., ARAI, H., HAMAJIMA, K., GORAI, I., NISHIOKA, K., OKUDA, K. HIV-1-specific cell-mediated immune responses induced by DNA vaccination were enhanced by mannan-coated liposomes and inhibited by anti-interferon- $\gamma$  antibody, *Immunology* **1997**, *92*, 111–117.
- 131 GU, X. G., SCHMITT, M., HIASA, A., NAGATA, Y., IKEDA, H., SASAKI, Y., AKIYOSHI, K., SUNAMOTO, J., NAKAMURA, H., KURIBAYASHI, K., SKIKU, H. A novel hydrophobized polysaccharide/oncoprotein complex vaccine induces *in vitro* and *in vivo* cellular and humoral immune responses against HER2-expressing murine sarcomas, *Cancer Res.* **1998**, *58*, 3385–3390.
- 132 TAN, M. C., MOMMAAS, A. M., DRIJFHOUT, J. W., JORDENS, R., ONDERWATER, J. J., VERWOERD, D., MULDER, A. A., VAN DER HEIDEN, A. N., SCHEIDEGGER, D., OOMEN, L. C., OTTENHOFF, T. H., TULP, A., NEEFJES, J. J., KONING, F. Mannose receptor-mediated uptake of antigens strongly enhances HLA antigens class II-restricted antigen presentation by cultured dendritic cells, *Eur. J. Immunol.* **1997**, *27*, 2426–2435.
- 133 MUMPER, R. J., CUI, Z. Genetic immunization by jet injection of targeted pDNA-coated nanoparticles, *Methods* **2003**, *31*, 255–262.
- 134 CUI, Z., MUMPER, R. J. The effect of co-administration of adjuvants with a nanoparticle-based genetic vaccine delivery system on the resulting immune responses, *Eur. J. Pharm. Biopharm.* **2003**, *55*, 11–18.
- 135 KIM, S. Y., DOH, H. J., JANG, M. H., HA, Y. J., CHUNG, S., PARK, H. J. Oral immunization with *Helicobacter pylori*-loaded poly(D,L-lactide-co-glycolide) nanoparticles, *Helicobacter* **1999**, *4*, 33–39.
- 136 JUNG, T., KAMM, W., BREITENBACH, A., KLEBE, G., KISSEL, T. Loading of tetanus toxoid to biodegradable nanoparticles from branched poly(sulfobutyl-polyvinyl alcohol)-g-(lactide-co-glycolide) nanoparticles by protein absorption: a mechanistic study, *Pharm. Res.* **2002**, *19*, 1105–1113.
- 137 PROKOP, A., KOZLOV, E., NEWMAN, G. W., NEWMAN, M. J. Water-based nanoparticulate polymeric system for protein delivery: permeability control and vaccine application, *Biotechnol. Bioeng.* **2002**, *78*, 459–466.
- 138 PROKOP, A. Micro-particulate and nano-particulate polymeric delivery system. Vanderbilt University, US patent pending, **1997**, also PCT application WO9918934A1.
- 139 CALVO, P., REMUÑAN-LÓPEZ, C., VILA-JATO, J. L., ALONSO, M. J. Chitosan and chitosan/ethylene oxide–

- propylene oxide block copolymer nanoparticles as novel carriers for proteins and vaccines, *Pharm. Res.* **1997**, *14*, 1431–1436.
- 140 BORGES, O., BORCHARD, G., VERHOEF, J. C., DE SOUSA, A., JUNGINGER, H. E. Preparation of coated nanoparticles for a new mucosal vaccine delivery system, *Int. J. Pharm.* **2005**, *299*, 155–166.
- 141 RUSSELL-JONES, G. J. Oral vaccine delivery, *J. Control. Release* **2000**, *65*, 49–54.
- 142 RUSSELL-JONES, G. J., VEITCH, H., ARTHUR, L. Lectin-mediated transport of nanoparticles across Caco-2 and OK cells, *Int. J. Pharm.* **1999**, *90*, 165–174.
- 143 BIVAS-BENITA, M., LALOUP, M., VERSTEYHE, S., DEWIT, J., BRAEKELLER, J. D., JONGERT, E., BORCHARD, G. Generation of *Toxoplasma gondii* GRA1 protein and DNA vaccine loaded chitosan particles: preparation, characterization and preliminary *in vivo* studies, *Int. J. Pharm.* **2003**, *266*, 17–27.
- 144 CHEW, J. L., WOLFOWICZ, C. B., MAO, H. Q., LEONG, K. W., CHUA, K. Y. Chitosan nanoparticles containing plasmid DNA encoding house dust mite allergen, Der p 1 for oral vaccination in mice, *Vaccine* **2003**, *21*, 2720–2729.
- 145 TOBIO, M., GREF, R., SÁNCHEZ, A., LANGER, R., ALONSO, M. J. Stealth PLA–PEG nanoparticles as protein carriers for nasal administration, *Pharm. Res.* **1998**, *15*, 270–275.
- 146 SHEPHARD, M. J., TODD, D., ADAIR, B. M., PO, A. L. W., MACKIE, D. P., SCOTT, E. M. Immunogenicity of bovine parainfluenza type 3 virus proteins encapsulated in nanoparticle vaccines, following intranasal administration to mice, *Res. Vet. Science* **2003**, *74*, 187–190.
- 147 VILA, A., SÁNCHEZ, A., JANES, K., BEHRENS, I., KISSEL, T., VILA-JATO, J. L., ALONSO, J. M. Low molecular weight chitosan nanoparticles as new carriers for nasal vaccine delivery in mice, *Eur. J. Pharm. Biopharm.* **2004**, *57*, 123–131.
- 148 NAGAMOTO, T., HATTORI, Y., TAKAYAMA, K., MAITANI, Y. Novel chitosan particles and chitosan-coated emulsions inducing immune response via intranasal vaccine delivery, *Pharm. Res.* **2004**, *21*, 671–674.
- 149 CUI, Z., MUMPER, R. J. Intranasal administration of plasmid DNA-coated nanoparticles results in enhanced immune responses, *Pharm. Pharmacol.* **2002**, *54*, 1195–1203.
- 150 KLAVINSKIS, L., BARNFIELD, C., GAO, L., PARKER, S. Intranasal immunization with plasmid DNA–lipid complexes elicits mucosal immunity in the female genital and rectal tracts, *J. Immunol.* **1999**, *162*, 254–262.
- 151 DAMGÈ, C., MICHEL, C., APRAHAMIAN, M., COUVREUR, P. New approaches for oral administration of insulin with polyalkyl-cyanoacrylate nanocapsules as a drug carrier, *Diabetes* **1988**, *37*, 246–251.
- 152 DAMGÈ, C., MICHEL, C., APRAHAMIAN, M., COUVREUR, P., DEVISSAGUET, J. P. Nanocapsules as carriers for oral peptide delivery, *J. Control. Release* **1990**, *13*, 233–239.
- 153 ABOUBAKAR, M., COUVREUR, P., PINTO-ALPHANDARY, H., GOURITIN, B., LACOUR, B., FARINOTTI, R., PUISIEUX, F., VAUTHIER, C. Insulin-loaded nanocapsules for oral administration: *in vitro* and *in vivo* investigation, *Drug Dev. Res.* **2000**, *49*, 109–117.
- 154 MESIHA, M. S., SIDHOM, M. B., FASIPE, B. Oral and subcutaneous absorption of insulin poly(isobutyl-cyanoacrylate) nanoparticles, *Int. J. Pharm.* **2005**, *288*, 289–293.
- 155 PAN, Y., LI, Y. J., ZHAO, H. Y., ZHENG, J. M., XU, H., WEI, G., HAO, J. S., CUI, F. D. Bioadhesive polysaccharide in protein delivery system: chitosan nanoparticles improve the intestinal absorption of insulin *in vivo*, *Int. J. Pharm.* **2002**, *249*, 139–147.
- 156 MA, Z., YEOH, H. H., LIM, L. Y. Formulation pH modulates the interaction of insulin with chitosan nanoparticles, *J. Pharm. Sci.* **2002**, *91*, 1396–1404.

- 157 MA, Z. and LIM, L. Y. Uptake of chitosan and associated insulin in Caco-2 Cell monolayers: a comparison between chitosan molecules and chitosan nanoparticles, *Pharm. Res.* **2003**, *20*, 1812–1819.
- 158 DYER, M. A., HINCHCLIFFE, M., WATTS, P., CASTILE, J., JABBAL-GILL, I., NANKERVIS, R., SMITH, A., ILLUM, L. Nasal delivery of insulin using novel chitosan based formulations: a comparative study in two animal models between simple chitosan formulations and chitosan nanoparticles, *Pharm. Res.* **2002**, *19*, 998–1008.
- 159 MA, Z., LIM, T. M., LIM, L. Y. Pharmacological activity of peroral chitosan-insulin nanoparticles in diabetic rats, *Int. J. Pharm.* **2005**, *293*, 271–180.
- 160 FERNÁNDEZ-URRUSUNO, R., CALVO, P., REMUÑÁN-LOPEZ, C., VILA-JATO, J. L., ALONSO, M. J. Enhancement of nasal absorption of insulin using chitosan nanoparticles, *Pharm. Res.* **1999**, *16*, 1576–1581.
- 161 SIMON, M., WITTMAR, M., BAKOWSKY, U., KISSEL, T. Self-assembling nanocomplexes from insulin and water-soluble branched polyesters, poly[(vinyl-3-(diethylamino)-propylcarbamate-co-(vinyl acetate)-co-(vinyl alcohol)]-graft-poly(L-lactic acid): a novel carrier for transmucosal delivery of peptides, *Bioconjug. Chem.* **2004**, *15*, 841–849.
- 162 ZHANG, Q., SHEN, Z., NAGAI, T. Prolonged hypoglycemic effect of insulin-loaded polybutylcyanoacrylate nanoparticles after pulmonary administration to normal rats, *Int. J. Pharm.* **2001**, *218*, 75–80.
- 163 GRENHA, A., SEIJO, B., REMUÑÁN-LOPEZ, C. Microencapsulated chitosan nanoparticles for lung protein delivery, *Eur. J. Pharm. Sci.* **2005**, *25*, 427–437.
- 164 BARICHELLO, J. M., MORISHITA, M., TAKAYAMA, K., NAGAI, T. Absorption of insulin from Pluronic F-127 gels following subcutaneous administration in rats, *Int. J. Pharm.* **1999**, *1884*, 189–198.
- 165 TIYABOONCHAI, W., WOISZWILLO, J., SIMS, R. C., MIDDGAUGH, C. R. Insulin containing polyethylenimine–dextran sulfate nanoparticles, *Int. J. Pharm.* **2003**, *255*, 139–151.
- 166 AKIYOSHI, K., KOBAYASHI, S., SHICHIBE, S., MIX, D., BAUDYS, M., KIM, S. W., SUNAMOTO, J. Self-assembled hydrogel nanoparticle of cholesterol-bearing pullulan as a carrier of protein drugs: complexation and stabilization of insulin, *J. Control. Release* **1998**, *54*, 313–320.
- 167 ELVASSORE, N., BERTUCCO, A., CALICETI, P. Production of insulin-loaded poly(ethylene glycol)/poly(L-lactide) (PEG/PLA) nanoparticles by gas antisolvent techniques, *J. Pharm. Sci.* **2001**, *90*, 1628–1636.
- 168 ZHANG, K., WU, X. Y. Modulated insulin permeation across a glucose-sensitive polymeric composite membrane, *J. Control. Release* **2002**, *80*, 169–178.

## 10

# Solid Lipid and Polymeric Nanoparticles for Drug Delivery

*José Luis Pedraz, Gorka Orive, Manoli Igartua, Alicia R. Gascón,  
Rosa M. Hernández, Maria Angeles Solinis,  
and Amaia Esquisabel*

### 10.1 Introduction

Over the past few years, significant effort has been devoted to design and develop nanoparticles and nanosystems for drug delivery. Scientists have understood that apart from the synthesis of the drug molecule, the efficient release of the latter from the drug delivery system is essential if a suitable therapeutic efficacy is to be achieved. Therefore, the development of effective drug delivery systems which could transport and deliver the drug at the right time, in a safe and reproducible way, and only to the target where it is needed is becoming the “holy grail” of pharmaceutical researchers [1, 2].

The idea that nanotechnology could be used as a tool for efficient drug delivery has recently emerged since nanoparticles can be designed with different structures and compositions favoring a wide range of therapeutic applications [3]. Nanoparticles do not only differ in their relative size, but also in their biopharmaceutical properties and therapeutic applications. In general, the therapeutic product [drug, peptide, protein, DNA, small interfering RNA (siRNA), etc.] is either entrapped, adsorbed, attached, dissolved or encapsulated into the particle, allowing the precise control over drug release profiles [4]. Nanoparticles are less than 1000 nm in size and they present higher intracellular uptake compared with microparticles, which makes nanoparticles excellent candidates for targeted drug delivery to specific intracellular compartments.

One focus of research is the technological design and development of the nanoparticles assuming that the latter can present very different compositions and biological properties. However, a more interesting and effective way to design these nanosystems would be to rationally fabricate them based on a full understanding of the pathobiological characteristics of the disease under study and the biological microenvironment where the nanoparticles are to suppose to work. For example, if the intracellular release of the drug is required, a deep knowledge of the mecha-

nisms that regulate the uptake of the particles, intracellular trafficking, retention and sorting pathways will be necessary [5]. Furthermore, the biopharmaceutical and technological properties of the nano drug delivery systems are also major issues to be considered. In fact, the therapeutic dose to be administered and the duration of drug delivery required at the target site are key factors in the pharmaceutical design of the nanoparticles in order to obtain an efficient treatment.

The present chapter describes two different types of nanoparticles suitable for continuous drug delivery. The selection of these nanoparticles is based on their extensive application for drug delivery purposes. The basic principles of solid lipid nanoparticles (SLNs) and polymeric nanoparticles will be presented in detail. The aim of this chapter is to describe the production processes and the main parameters related to their characterization. Furthermore, a wide range of therapeutic applications of both types of nanoparticles will be discussed in detail.

## 10.2 SLNs

### 10.2.1

#### Introduction

SLNs are colloidal carrier systems made from solid lipids with an average diameter in the nanometer range, introduced at the beginning of the 1990s as a drug delivery system alternative to existing colloidal carriers. Incorporation of a drug into a carrier system can protect it against degradation, the release can be controlled and it also offers possibilities of targeting. There is, however, a need for further, improved particulate carrier systems, which should fulfill as much as possible the following main requirements [6]:

- Easy to produce.
- Applicable to as many drugs as possible.
- Physically stable.
- Being composed of well-tolerated excipients that are accepted by the regulatory authorities.
- Feasibility of large-scale production.
- Production lines should be able to be qualified and acceptable by regulatory authorities.

The SLN is a particulate drug carrier system developed with the aim of combining the advantages of other innovative carrier systems such as lipid emulsions, liposomes and polymeric micro/nanoparticles, minimizing the associated problems. Excellent tolerability and the possibility of qualified industrial large-scale production are clear advantages of SLNs. Main disadvantages are the coexistence of alternative colloidal structures and, in general, low drug-loading capacity.

## 10.2.2

**Composition**

SLNs are particles made from solid lipids (usually lipids in solid state at room temperature and also at body temperature), water and stabilized by surfactant(s); for certain preparation methods a cosolvent, which is generally removed, is also used.

In general, physiological lipids such as triglycerides (e.g. tristearin), partial glycerides (e.g. Imwitor), fatty acids (e.g. stearic acid), steroids (e.g. cholesterol) and waxes (e.g. cetyl palmitate) are used. This physiological lipid matrix is more biocompatible, thus decreasing the danger of acute and chronic toxicity, and increasing their toxicological safety. There are a few exceptions and some authors have prepared SLNs with different types of molecules, such as amphiphilic cyclodextrins [7] and calixarenes [8, 9].

Most of the lipids used represent a mixture of several chemical compounds. The general lipid composition will have different crystallinities and capacities for accommodating foreign molecules. The composition might therefore vary from different suppliers and even for different batches. However, small differences in the lipid composition (e.g. impurities) might have a considerable impact on the quality of SLN dispersion [10] (e.g. by changing the  $\zeta$  potential, retarding crystallization processes, etc.).

In addition to the lipid composition, the influence of lipid content on particle size has been studied, showing that increasing the lipid content over 5–10% in most cases results in larger particles (including microparticles) and broader particle size distributions [11]. The other main SLN ingredient is the stabilizing agent; a large variety of ionic and nonionic emulsifiers of different molecular weight have been used to stabilize the lipid dispersions and to prevent particle agglomeration. The most frequently used compounds include different kinds of poloxamer, polysorbates, lecithin and bile salts. The choice of the emulsifier depends on the administration route and is more limited for parenteral administrations [10]. The emulsifiers selected and their concentration have a great impact on the quality and stability of the SLNs dispersion [12–14]. It has been found that the combination of emulsifiers might prevent particle agglomeration more efficiently than the use of a single surfactant. Another important point to consider is the influence of the emulsifier on drug incorporation; stabilizing agents are not localized exclusively on the lipid surface, but also in the aqueous phase in different forms, which might serve as an alternative location to accommodate the drug molecules [10].

As it has been reported [6, 10, 15, 16], the status of excipients for SLNs has to be discussed as a function of the administration routes. SLNs can be produced with regulatory accepted excipients or at least with material able to be degraded in the body to physiological compounds or to products used for parenteral nutrition. Therefore, they are not problematic at all for topical and oral administration. The full range of surfactants and lipids used in dermal products, tablets and capsules can be exploited. Even such “nasty” surfactants with regard to parenteral administration such as sodium dodecyl sulfate can be applied to stabilize the suspension. They possess excellent dispersing properties and are accepted up to a certain con-



centration in oral products. The situation is slightly different for parenteral administration – to our knowledge, no solid lipids have been administered parenterally; therefore, they would require a toxicity study before their use. However, the glycerides used for nanostructured lipid carrier (NLC) production can be selected with this purpose, since they are composed of fatty acids already present in the oils of emulsions for parenteral nutrition [6].

### 10.2.3

#### Production Processes

The four main procedures existing for the preparation of lipid nanoparticles dispersions are briefly described in this section. Later, scaling-up feasibility and secondary production steps such as drying and sterilization will be reviewed.

##### 10.2.3.1 Preparation Techniques

**10.2.3.1.1 High-shear Homogenization and Ultrasound** High-shear homogenization and ultrasound are dispersing techniques which were initially used for the production of solid lipid nanodispersions [17, 18]. Both methods are widespread and easy to handle. The disadvantages of these techniques are due to the presence of microparticles and the fact that metal contamination has to be considered when ultrasound is used.

**10.2.3.1.2 High-pressure Homogenization (HPH)** HPH has emerged as a reliable and powerful technique for the preparation of SLNs. Homogenizers of different sizes are commercially available from several manufacturers at reasonable prices. The two basic production methods for SLNs are the hot homogenization technique and the cold homogenization technique. In both cases the drug is incorporated in the lipid melt. The hot homogenization technique is carried out at temperatures above the melting point of the lipid. The drug-containing melt is dispersed under stirring in a hot aqueous surfactant solution to the same temperature. Then the obtained pre-emulsion is homogenized. The primary product is a hot oil/water (o/w) nanoemulsion that is cooled down to room temperature, leading to solid lipid nanoparticles.

Cold homogenization has been developed to overcome the following three problems of the hot homogenization technique: temperature-induced drug degradation, drug distribution into the aqueous phase during homogenization and complexity of the crystallization step of the nanoemulsion. This technique minimizes thermal exposure of the sample. The drug-containing lipid melt is rapidly cooled and the solid lipid ground to lipid microparticles which are dispersed in a cold surfactant solution yielding a presuspension. Then this presuspension is homogenized at or below room temperature leading to solid lipid nanoparticles.

**10.2.3.1.3 Microemulsion** Microemulsion-based SLNs preparation techniques have been developed by Gasco [19]. Emulsions are made by stirring the melted

lipid and a mixture of water, cosurfactant(s) and the surfactant heated to the same temperature as the lipid. A transparent, thermodynamically stable system is formed when the compounds are mixed in the correct ratio. Finally, this microemulsion is dispersed in a cold aqueous medium (2–3 °C) under stirring, thus resulting in the formation of SLNs.

**10.2.3.1.4 Solvent Emulsification/Evaporation** Sjöström and Bergenståhl described in 1992 a production method to prepare nanoparticles in o/w emulsions [20]. The lipophilic material is dissolved in a water-immiscible organic solvent that is emulsified in an aqueous phase to give an o/w emulsion. Upon evaporation of the solvent a nanoparticle dispersion is formed by precipitation of the lipid in the aqueous medium. An important advantage of this method is the avoidance of heat during the preparation, which makes it suitable for the incorporation of highly thermolabile drugs. However, problems might arise due to solvent residues in the final dispersion.

### 10.2.3.2 Scaling-up, Sterilization and Drying

**10.2.3.2.1 Scaling-up** The possibility of qualified industrial large-scale production must be provided for the introduction of a product to the market. HPH production for SLNs and scaling-up feasibilities have been widely investigated [21–24]. Moreover, production lines for HPH already exist in the pharmaceutical industry and have been even used for the production of parenteral products. The HPH lines used for parenteral nutrition can be qualified and accepted by the regulatory authorities. Based on this premise, no regulatory hurdles are expected in the use them for SLNs carriers systems [6]. A system has been developed and scale-up feasibility has been investigated for the production via microemulsions [25].

**10.2.3.2.2 Sterilization** SLN dispersions can be sterilized or prepared aseptically using already established techniques in the pharmaceutical industry. Aseptic production, filtration,  $\gamma$ -irradiation and heating are normally used in order to achieve sterility. Filtration sterilization of dispersed systems requires high pressure and is not applicable to particles larger than 0.2  $\mu\text{m}$ . SLN dispersions can be sterilized by filtration similar to emulsions for parenteral nutrition. It is very important to filter them in liquid state, since this allows particles with a size larger than the pores in the filter to be filtered [10, 15, 25].

**10.2.3.2.3 Drying** It is expected that the solid state of SLNs will present a better chemical and physical stability than aqueous lipid dispersions. Transformation into a solid form will prevent crystal growth by Ostwald ripening and avoid hydrolysis reactions.

Lyophilization is a widely used process in the pharmaceutical field to remove water from samples. This technique involves two necessary and additional transformations that may be the source of additional stability problems – freezing of the sample and evaporation of water under vacuum. The addition of cryoprotectants

to the sample will be necessary in order to decrease SLN aggregation and to obtain a better redispersion of the dry product. Typical cryoprotective agents are sorbitol, mannose, trehalose, glucose and polyvinylpyrrolidone. The lyophilization process has been optimized with regard to the operating conditions, lipid concentration, type and concentration of cryoprotectant, and redispersing conditions [26–28].

Spray-drying might be an alternative procedure to lyophilization. The influence of lipid type and concentration, carbohydrate type and concentration, redispersion medium, and spraying medium has been investigated by Freitas and coworkers [29]. An evaporative drying process with a nitrogen stream at low temperatures has been evaluated and compared to lyophilization by Marengo and coworkers [30]. The advantages of this process are the avoidance of freezing and the energy efficiency resulting from the higher vapor pressure of water.

#### 10.2.4

### Drug Incorporation, Loading, Incorporation Efficiency, Nanoparticle Recovery and Drug Release

#### 10.2.4.1 Drug Incorporation

In different studies, which were later reviewed by Müller [15], Menhert proposed that there are basically three different models for the incorporation of active ingredients into SLNs (Fig. 10.1):

- *Homogeneous matrix model*: consisting of a homogeneous matrix with molecularly dispersed drug or drug being present in amorphous clusters.
- *Drug-enriched shell model*: an outer shell enriched with active compound.
- *Drug-enriched core model*: a core enriched with active compound. This leads to a membrane controlled release governed by the Fick law of diffusion.

The structure obtained is a function of the formulation composition (lipid, active compound, surfactant) and of the production conditions (hot versus cold homogenization). A large number of drugs with a great variety of lipophilicity and different structures have been studied with regard to their incorporation into SLNs. However, few data exist on the localization site and the physical state of the drug mole-

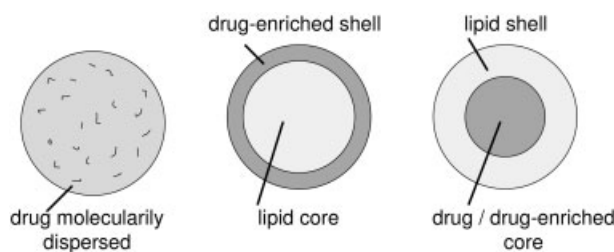


**Figure 10.1.** Three drug incorporation models. (Adapted from Ref. [15], with permission from Elsevier.)

cule. Drug incorporation implies the localization of the drug in the solid lipid matrix. Micelle-forming surfactant molecules will be present in different forms, and may lead to colloidal species such as micelles, mixed micelles and liposomes, that are known to solubilize drugs and are, therefore, alternative drug incorporation sites [10].

#### 10.2.4.2 Drug Loading

SLNs were first developed for the administration of lipophilic drugs, although they have been also applied for the encapsulation of hydrophilic drugs. One of the main drawbacks of particulate drug carriers is drug-loading capacity, which is limited to approximately 25% with regard to the lipid matrix. The drug-loading capacity of SLNs is limited by the solubility of drug in the lipid melt, miscibility of the melted drug and lipid, chemical and physical structure of the matrix, and the polymorphic state of the lipid matrix [15]. The prerequisite to obtain a sufficient loading capacity is a sufficiently high solubility of the drug in the lipid melt. To enhance the solubility in the lipid melt one can add solubilizers, especially in the case of hydrophilic drugs.

The structure of the lipid is important because if the lipid matrix consists of especially similar molecules (i.e. tristearin or tripalmitin), a perfect crystal with few imperfections is formed and cannot accommodate large amounts of drug. Therefore, the use of more complex lipids (mono-, di- and triglycerides with different chain lengths) is more sensible for higher drug loading.

Crystalline structure – related to the chemical nature of the lipid – is a key factor to determine whether a drug will be expelled or firmly incorporated. The transition to highly ordered lipid particles is also the reason for drug expulsion. Directly after production, lipids crystallize; if the crystallinity index increases during the storage, then the drug will be expelled from the lipid matrix and it can then neither be protected from degradation nor released in a controlled way [31]. Consequently, intensive characterization of the physical state of the lipid particles is highly essential in order to get a controlled optimization of drug incorporation and loading.

#### 10.2.4.3 Determination of Nanoparticle Recovery and Drug Incorporation Efficiency

These are general characterization parameters that can be applied to any type of nanoparticle, including SLNs.

The nanoparticle (NP) recovery, which is also referred to as nanoparticle yield in the literature, can be calculated using:

$$\text{nanoparticle recovery (\%)} = \frac{\text{mass of nanoparticle recovered} \times 100}{\text{mass of drug and excipients}}. \quad (1)$$

An additional important *in vitro* characterization parameter is the determination of the drug incorporation efficiency in nanoparticle formulations. Drug incorporation efficiency is expressed both as drug content (% w/w), also referred to as drug loading in the literature, and drug entrapment efficiency (%); represented by:

$$\text{drug loading (\% w/w)} = \frac{\text{mass of drug in nanoparticle}}{\text{mass of nanoparticle recovered}} \times 100 \quad (2)$$

$$\text{drug entrapment efficiency (\%)} = \frac{\text{mass of drug in nanoparticle}}{\text{mass of drug used in formulation}} \times 100. \quad (3)$$

Two different methods have been suggested for the determination of drug loading and entrapment efficiency. The first involves the solubilization of nanoparticles by dispersing a measured amount of them in a suitable medium under agitation. The second method is based on the estimation of the differences between the total amount of the drug added to the formulation and the untrapped amount detected in the supernatant of the nanoparticle dispersion. The amount of drug is analyzed by an appropriate analytical technique.

#### 10.2.4.4 Drug Release

The effect of formulation parameters and production conditions on the release profile from SLNs was intensively investigated by Mehnert and zur Mühlen [32, 33] by the study of the model drugs tetracaine, etomidate and prednisolone. A burst drug release was obtained with tetracaine and etomidate SLNs; in contrast, prednisolone SLNs showed a prolonged release. This demonstrated the principle suitability of the SLNs system for prolonged drug release. More interestingly, they showed that it was possible to modify the release profiles as a function of lipid matrix, surfactant concentration and production parameters (e.g. temperature).

Müller and coworkers [34] reviewed in detail the release of active compounds from SLNs and summarized that the higher the solubility in the water phase during production, the more pronounced is the burst effect. The solubility increases with increasing production temperature and increasing surfactant concentration (the latter only when the surfactant solubilizes the active compound). Consequently, little or no burst will be obtained when SLNs are produced at low temperatures, low surfactant concentration or in surfactant-free medium.

#### 10.2.5

##### Related Structures and Stability

Potential problems associated with SLNs such as limited drug-loading capacity, adjustment of drug release profile and potential drug expulsion during storage are avoided or minimized by the new generation of lipid nanoparticles, the NLCs, although the term SLNs is sometimes used to describe different types of lipidic matricial structures [such as NLCs and lipid–drug conjugates (LDCs)] regardless of their composition and arrangement. Using spatially incompatible lipids leads to special structures of the lipid matrix and, thus, three types of NLCs [35] (see Fig. 10.2):

- (i) *The imperfect type.* A potential problem in SLNs is the formation of a perfect crystal. Using spatially different lipids leads to imperfections in the crystal to accommodate the drug.

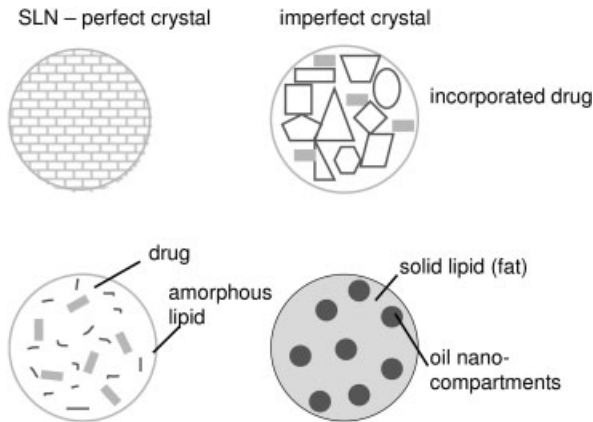


**Figure 10.2.** The three types of NLCs compared to the relatively ordered matrix of SLNs (upper left); NLCs types: imperfect type (upper right), amorphous type (lower left) and multiple type (lower right). (Adapted from Ref. [34], with permission from Elsevier.)

- (ii) *The amorphous (structureless) type.* Drug expulsion is caused by an ongoing crystallization process of the solid lipid towards a perfect crystal. The particles are solid, but crystallization upon cooling is avoided by mixing special lipids.
- (iii) *The multiple type.* System comparable to w/o/w emulsions since it is an oil-in-solid lipid-in-water dispersion. The solid lipid matrix contains tiny liquid oil nanocompartments. Many drugs show a higher solubility in oils than in solid lipids so that they can be dissolved in the oil and still be protected from degradation by the surrounding solid lipids.

Recent studies concluded that neither SLNs nor NLCs lipid nanoparticles showed any advantage with respect to the incorporation rate or retarded accessibility to the drug compared with conventional nanoemulsions. It has been shown that the liquid lipid forms a half drop on the solid platelet [36–38]. SLNs are useful for the incorporation of lipophilic (soluble) drugs. Aiming to increase the drug-loading capacity of hydrophilic drugs, the structure of LDCs has been recently suggested as more adequate [16].

LDC nanoparticles present drug-loading capacities of up to 33% [39, 40]. Here, an insoluble drug–lipid conjugate bulk is prepared either by salt formation (e.g. with a fatty acid) or by covalent linking (e.g. to esters or ethers). In the salt formation process, the free drug base and fatty acid are dissolved in a suitable solvent. The solvent is then consequently evaporated under reduced pressure. For the covalent linking, the drug (salt) and a fatty alcohol react in the presence of a catalyst, and the LDC bulk is then purified by recrystallization. The obtained LDC bulk is then processed with an aqueous surfactant solution to a nanoparticle formulation using HPH.

The physical stability of SLN dispersions has been investigated intensively, e.g. by measurements of particle size [photon correlation spectroscopy (PCS), laser diffraction (LD)], charge ( $\zeta$  potential) and thermal analysis [differential scanning calorimetry (DSC)], as reviewed later in this chapter. In addition, as noted above, transformation of SLNs into a solid form by drying will have a better chemical and physical stability than aqueous lipid dispersions.

#### 10.2.6

##### **Analytical Characterization of SLNs**

An adequate characterization of SLNs is a prerequisite for the control of the quality of the product. Several parameters have to be considered in the characterization of lipid nanoparticle formulations which have direct impact on the stability and release kinetics [10, 15]:

- (i) Particle size and  $\zeta$  potential.
- (ii) Degree of crystallinity and lipid modification.
- (iii) Coexistence of additional colloidal structures (micelles, liposomes, super-cooled melts, drug nanoparticles) and dynamic phenomena.

##### **10.2.6.1 Particle Size**

Particle size is predominantly used to evaluate the colloidal size range. This parameter is crucial in the development and optimization of preparation processes as well as in the evaluation of dispersion stability.

The most widely used method to characterize the size of SLNs is PCS. This method measures the fluctuation of the intensity of the scattered light which is caused by Brownian motion. PCS is a good tool to characterize nanoparticles, but it is not available for the detection of larger microparticles. They can be visualized by means of LD measurements. This method is based on the dependency of the diffraction angle on the particle radius (Fraunhofer spectra). Smaller particles cause more intense scattering at high angles compared with the larger ones. Difficulties may arise both in PCS and LD measurements for samples which contain several populations of different size. Therefore, additional techniques might be useful. The Coulter counter method and light microscopy may be considered to detect trace amounts of microparticles in SLN dispersions. Electron microscopy, in contrast to PCS and LD, provides direct information on the particle shape and structure. However, possible artifacts may be caused by the sample preparation.

Atomic force microscopy (AFM) has also been applied to image the morphological structure of SLNs [41, 42]. Advantages of AFM are the simplicity of sample preparation as no vacuum is needed during operation and that the sample does not need to be conductive. Therefore, it has the potential for the direct analysis of the originally hydrated, solvent-containing samples. A disadvantage of this method is the required fixation of the particles (by removal of water), which changes the status of emulsifier and might also cause polymorphic transitions of the lipid.

Particle sizing by field-flow fractionation (FFF) is based on the different effect of a perpendicular applied field on particles in a laminar flow. The separation principle corresponds to the nature of the perpendicular field and may, for example, be based on different mass (sedimentation FFF), size (cross-flow FFF) or charge (electric-field FFF). Mäder and coworkers have been applied recently cross-flow FFF to investigate nanoemulsions, SLNs and nanostructure lipid carriers [38].

#### 10.2.6.2 The $\zeta$ Potential

The surface charges and the strength and extension of the electrical field around the particles play an important role in the mutual repulsion of nanoparticles, and thus in their stability against aggregation. Therefore, the measurement of the  $\zeta$  potential allows for predictions about the storage stability of colloidal dispersion. In general, particle aggregation is less likely to occur for charged particles (high  $\zeta$  potential) due to electric repulsion. However, this rule cannot strictly be applied for systems which contain steric stabilizers, because the adsorption of steric stabilizers will decrease the  $\zeta$  potential due to the shift in the shear plane of the particle [10].

#### 10.2.6.3 Crystallinity and Polymorphism and Colloidal Structures

Particle size measurements alone are not sufficient for the characterization of SLN dispersions. The degree of crystallinity and lipid modifications are strongly correlated with drug incorporation and release rates. DSC and X-ray techniques are the most widely used for the characterization of crystallinity and polymorphism of solid lipid particles. DSC uses the fact that different lipid modifications possess different melting points and melting enthalpies. By means of X-ray scattering it is possible to assess the length of the long and short spacing of the lipid lattice [15]. The coexistence of additional colloidal structures (micelles, liposomes, mixed micelles, supercooled melts, drug nanoparticles) has to be taken into account for all SLN dispersions. Nuclear magnetic resonance (NMR) and electron spin resonance (ESR) are powerful tools for investigating dynamic phenomena and the characteristics of nanocompartments in colloidal lipid dispersions. Both methods are sensitive to the simultaneous detection of different colloidal species, do not require preparatory steps and, due to the noninvasiveness, repeated measurements of the same sample are possible. Similar results to the ERS experiments can be obtained with fluorescence measurements [36]. Rheometry has been used for the characterization of the viscoelastic properties of SLN formulations [43].

#### 10.2.7

##### Applications

Since the development of lipid microparticles by Speiser and coworkers at the beginning of the 1980s [44] and the later evolution in the 1990s towards SLNs, these lipidic particulate systems have been applied to encapsulate different drugs aiming to get sustained release of the entrapped drug, to improve drug stability by protecting the drug from degradation or to improve the bioavailability of poorly soluble drugs. SLNs can be administered by different routes: parenteral, oral, ocular, pulmonary, rectal, etc., as recently reviewed by Wissing and coworkers [16]. SLNs ap-



pear to be a promising sustained release for orally administered lipophilic drugs [45, 46], showing increased bioavailability and prolonged plasma peaks. In addition, these nanoparticles could be directly administered (as an aqueous dispersion) or formulated in different dosage forms, such as tablets or capsules. Regarding topical application, SLNs are considered as a good alternative to liposomes, possessing similar film-forming properties after application onto the skin [15]. These can be presented either in creams, gels or ointments, or topically applied as highly concentrated lipid dispersions [10]. Moreover, SLNs have been found to target drugs to particular skin layers and to sustain drug release into the skin.

When thinking about SLN administration one should bear in mind the *in vivo* fate after their administration. As widely reported in the literature, nanoparticles with a hydrophobic surface administered by different routes that will reach the blood stream will be rapidly taken up by the mononuclear phagocytic system (MPS). As a result, several approaches have been developed in order to increase the circulation time of the nanoparticles, and their targeting to organs and tissues other than the liver, lung and spleen [47]. In order to increase nanoparticle circulation time it has been stated that these particles should be 100 nm or less and have a hydrophilic surface. The approaches used to avoid unwanted uptake by macrophages include adsorption of surfactants to the nanoparticle surface, formation or inclusion with block copolymers with hydrophilic and hydrophobic domains (poloxamers and poloxamines) or grafting of a hydrophilic polymer such as poly(ethylene glycol) (PEG) [48].

In a recent study, Göppert and Müller [49] have investigated the surface modification of SLNs by the use of different poloxamers and poloxamines, and the influence of such surface modification on the adsorption of different proteins to SLNs assessed by two-dimensional polyacrylamide gel electrophoresis. They were looking for the type of poloxamer/poloxamine which would render the surface more hydrophilic, thus allowing the adsorption of albumin or apolipoproteins, giving rise to stealth SLNs and a more prolonged blood circulation time. They found that SLNs stabilized with low-molecular-weight Poloxamer 184 and Poloxamer 235 showed interestingly high adsorption of apolipoprotein E (ApoE), which mediates the uptake through the blood–brain barrier and, thus, the delivery to the brain. Interestingly, they have also reported that nanoparticles surface modified with high-molecular-weight Poloxamine 908 are able to circulate longer in the blood despite the high adsorption protein patterns found in this study, concluding that in order to avoid uptake by the MPS it is important to characterize the type of proteins that are adsorbed onto SLNs surface; if dysopsonins (such as albumin and apolipoproteins) are adsorbed and the absence of immunoglobulins and complement-activating proteins on the surface is avoided, a long circulation time of the nanoparticles might be expected.

Table 10.1 summarizes some of the main applications described for SLNs.

#### 10.2.7.1 Gene Therapy

Gene therapy is a rapidly advancing field with great potential for the treatment of genetic and acquired systemic diseases. Present delivery systems can be divided

**Tab. 10.1.** Some examples of drugs and genes encapsulated into SLNs.

Application	Drug/gene	Administration route	Reference
Gene therapy	$\beta$ -galactosidase expression plasmid	–	50
	dimeric HIV-1 Tat peptide (TAT2)	lung (inhalation)	51
	green fluorescent protein (GFP) plasmid	–	52
Peptides and proteins	gonadorelin	oral–parenteral	53
	calcitonin	oral	54
	insulin	oral	55
	[D-Trp-6]LHRH	parenteral	56
	thymopentin	parenteral	57
	lysozyme	oral, nasal, parenteral (immunization)	58
	cyclosporin A	oral	46, 59
	sodium cromoglycate	–	60
Low soluble drugs	tobramycin	ocular	61
	ketoconazole	topical	62
	clobetasol propionate	–	63
	clotrimazole	topical	64
	THP-adriamycin	parenteral	65
	ibuprofen	oral	66
	all- <i>trans</i> retinoic acid (anticancer drugs)	parenteral	67
	paclitaxel	parenteral	68
	progesterone	–	60
	doxorubicin	parenteral	69
	bupivacaine	parenteral	70
	5-fluoro-2'-deoxyuridine (FUdR) derivative	parenteral	71
	AZT and derivatives	parenteral	72, 73
	etoposide	parenteral	74
	acyclovir	–	75
	camptothecin	oral	45
ascorbyl palmitate	topical	76	
piribedil	oral	77	
Topical/cosmetics	vitamin A	topical	78
	coenzyme Q10	topical	79
	vitamin E	topical	80
	sunscreens: <i>n</i> -dodecyl-ferulate	topical	81
	perfumes	topical	82
	$\alpha$ -lipoic acid	topical	83

into virus-based, plasmid-based, and composites of both virus-based and plasmid-based systems. Plasmid-based delivery systems for so-called nonviral gene therapy are being developed as an alternative to virus-based systems. The isolated plasmid by itself can be administered locally, yielding expression in the injected tissue. Formulating the plasmid with synthetic gene delivery systems can increase the transfection efficiency.

In recent years, SLNs have been developed as potential carriers for a number of drugs, but there are only a few reports of the use of SLN delivery of genes [51, 84, 85]. However, there are a large number of publications about cationic liposomes for gene therapy; in spite of that, no marketed products have been developed. SLNs and liposomes formulated from the same cationic lipids showed equipotent *in vitro* transfection efficiencies. It is not the colloidal structure in which the cationic lipids are arranged, but the cationic lipid composition that seems to govern gene transfer efficiency. As SLNs can be produced in large scale and under favorable technological parameters, they may become a valuable addition to the well-established repertoire of nonviral transfection agents led by cationic liposomes [85].

Olbrich and coworkers [50] showed that cationic SLNs were able to transfect mammalian cells (COS-1) *in vitro*.

For over a decade, cationic lipids have been used for gene transfer both in cell culture and in animals [86, 87]. A cationic lipid is a positively charged amphiphile with a hydrophilic head and a hydrophobic tail that self-associates in aqueous solution to form either micelles or bilayer liposomes. This results in particles which can interact with the negative charges on a polynucleotide, such as DNA. The goal of cationic lipid-mediated gene transfer is to deliver a plasmid of DNA to a cell such that it becomes transcribed and translated into a desired protein/peptide [88]. The sequence of events involved in cationic lipid-mediated gene transfer include, but are not exclusive to: (i) the formation of the cationic lipid into a nanoparticle or liposome, providing a multivalent surface charge that is (ii) attached via electrostatics to the negative charges on the DNA phosphate backbone. This mixture forms a small particle. If these particles have an excess of positive charge they will (iii) bind to the negative charges on the surface of cells. The complexes become (iv) internalized through a vesicular pathway, followed by (v) the release of DNA from the particle into the cell cytoplasm. The release of DNA is thought to occur concomitantly with the release from the cationic lipid. Then some fraction of the released DNA is (vi) successfully trafficked by, as yet, an unknown mechanism to the nucleus where it is transcribed and later translated to protein. These cellular barriers to gene transfer are reviewed in depth by Meyer and coworkers [89].

SLNs must incorporate cationic lipids in order to facilitate DNA binding. When SLNs are produced with cationic lipids, a matrix lipid and, in most cases, additional surfactants are required. The resulting particles consist of a lipid core that presents cationic lipids on its surface. The cationic components are likely to be organized in raft-like monolayers that allow interaction between the modified SLN surface and DNA. Recent studies revealed the relation between transfection activity and SLN composition [85]. A large number of cationic lipids with low

toxicity and exhibiting different abilities to mediate gene transfer have been synthesized and studied for gene delivery [90–96]. In addition to *N*-[1-(2,3-dioleoyloxy)propyl]-*N,N,N*-trimethyl ammonium chloride (DOTMA) and 1,2-dioleoyloxy-3-(trimethylammonio)propane (DOTAP) (two of the most used cationic lipids), which are both two-chained amphiphiles whose acyl chains are linked to the propyl ammonium group (through ether and ester bonds, respectively), numerous new lipids have become commercially available for transfection purposes. Although a direct correlation between the nature of the cationic lipids and their ability to mediate transfection and to develop toxicity has been established, the nature of this dependency has not yet been completely clarified [97].

The incorporation into nanoparticles of colipids such as DOPE and others improves the ability to transfect cells. This fact has been attributed to the ability of dioleoyl-1- $\alpha$ -phosphatidylethanolamine (DOPE) to facilitate the formation of the complexes in conjunction with cationic lipids and to its tendency to undergo a transition from a bilayer to a hexagonal configuration under acidic pH, which facilitates fusion with or destabilization to target membranes. More recently, it was suggested that DOPE can also play a role in facilitating the disassembling of the lipid-based DNA formulations after internalization and escape of DNA from endocytotic vesicles. Cholesterol has also been employed as a colipid to prepare cationic liposomes, resulting in the formation of more stable but less efficient complexes than those containing DOPE [97].

Another approach to circumvent the problem of low efficiency of transfection is to incorporate peptides that are capable of penetrating the plasma membrane. Such peptides are called protein transduction domains (PTDs) or cell-penetrating peptides (CPPs). The most well-known CPPs are penetratin, corresponding to the third helix of the Antennapedia homeodomain, Tat(48–60), derived from HIV-1 Tat protein and oligoarginines [98]. Thorén and coworkers [98] have studied the interaction of different CPPs with phospholipids vesicles in order to better understand the mechanism of cellular uptake. Nonendocytotic uptake was only observed for the arginine-rich peptides TatP59W and R7W. Studies of the leakage from dye-loaded vesicles indicate that none of the assayed peptides (penetratin, R7W, TatP59W and TatLysP59W) forms membrane pores and that vesicles fusion is not accompanied by leakage of the aqueous content of the vesicles. The authors suggest that the discovered variations in propensity to destabilize phospholipid bilayers between the peptides investigated, in some cases to induce fusion, may be related to their different cellular uptake properties. Hyndman and coworkers [99] have demonstrated that the incorporation a protein transduction domain of the HIV-1 into gene delivery lipoplexes improves gene transfer, suggesting that the endocytosis uptake pathway is involved. The mechanism for the CPP-facilitated cellular uptake is unknown [100, 101]. Zieger and coworkers [102] have shown that membrane-associated heparan sulfate is involved in the uptake of HIV-1 protein.

The attachment of ligands to target the particles for cell-specific uptake via highly internalizing receptor can be a very useful strategy for the treatment of some diseases. Pedersen and coworkers [103] prepared SLNs with Compritol ATO 888 with a size of approximately 100 nm and a  $\zeta$  potential of +15 mV which

were able to condense DNA, they are very stable under physiological conditions and they display low cytotoxicity in cell culture. In addition to binding to DNA, the SLNs could simultaneously bind substantial amounts of streptavidin directly via electrostatic interactions. The SLN:DNA:streptavidin complexes are stable and are capable of binding biotinylated ligands, which can interact with surface receptors.

#### 10.2.7.2 Peptide and Protein Delivery

Over the last few years, and thanks to the development of the biotech industry, a great number of bioactive molecules and vaccines based on peptides, proteins and oligonucleotides have been discovered, showing great promise as therapeutic agents. However, the administration of these molecules is often limited because of their poor stability, low oral bioavailability, short *in vivo* half-lives and limited ability to cross cell membranes. In order to overcome such disadvantages, a suitable design of sustained release carrier systems is needed to enter the therapeutic market [104]. Peptide and protein nanoparticles can be administered by different routes, depending on the application intended. If they are to be administered by the oral route, formulation of peptides and proteins into a suitable drug carrier is a relevant task, especially due to epithelial barriers of the gastrointestinal tract, and gastrointestinal degradation by the acidic pH of the stomach and digestive enzymes [105].

The most commonly used particulate drug carriers for the administration of peptide and protein drugs have traditionally been poly(lactic acid) (PLA), poly(glycolic acid) (PGA) and their copolymers, poly(lactide-*co*-glycolide) (PLGA). However, there are only a few of products on the market based on PLGA microparticles and, to the best of our knowledge, no nanoparticulate product based on this kind of polymers has reached the market, probably because of the cytotoxicity of polymers and the difficulties for the scaling-up of the nanoencapsulation processes [15].

Among the different particulate drug carriers proposed as alternative materials, lipids appear to be suitable matrix materials for sustained release formulations of peptide and proteins, presenting good biocompatibility properties and being able to form different colloidal drug carriers, as microemulsions, SLNs, lipospheres, NLCs or microparticles.

In fact, one of the advantages of SLNs compared to PLGA nanoparticles is their better tolerability. Müller and coworkers [106] compared the *in vitro* toxicity of PLA, PLGA and SLN nanoparticles in order to determine the toxicological acceptance as an intravenous formulation. They found that the effective dose to reduce viability of the cells to 50% was around 0.30% for PLA polymers, 0.15% for PLGA and above 10% for SLNs, proving that SLNs are the least cytotoxic preparation.

Schöler and coworkers [107] have recently studied the cytotoxic properties of SLNs intended for parenteral administration, analyzing the viability and activation of macrophages [production of interleukin (IL)-6, IL-12 and tumor necrosis factor (TNF)- $\alpha$  as a function of the lipid type used and SLN particle size]. No activation of peritoneal was observed when triglycerides, cetylpalmitate or paraffin were used for the lipid matrices, although a concentration-dependent cytotoxicity was found for

SLNs. This is the reason why it is essential to select properly the lipid matrices of SLNs to be used for parenteral administration. As previously summarized in Tab. 10.1, SLNs have been applied to the encapsulation of different peptide and proteins aiming a controlled release of the entrapped protein, to overcome the gastrointestinal barriers for the oral administration of the peptide or even an adjuvant capacity of the particulate carrier system.

Olbrich and coworkers [108] have described the adjuvant capacity of antigens adsorbed or entrapped in SLNs, inducing an immune response comparable to that of Freund's incomplete adjuvant. However, this adjuvant capacity was found to be strongly dependent on the SLN size: SLNs bigger than 100 nm exhibited a strong adjuvant capacity, whereas for SLNs smaller than 100 nm this adjuvant capacity was quite low or even negligible. In addition, SLNs may offer a sustained release of the antigen, which can be continuously presented to the immune system contributing to an optimized immune response and making these systems appropriate for the administration of vaccines.

Morel and coworkers [56] first adapted the techniques they were using for the preparation of microemulsions for the encapsulation of the peptidic drug [D-Trp-6]LHRH. They obtained lipospheres by a warm multiple water/oil/water (w/o/w) microemulsion using stearic acid as lipid matrix. The encapsulation efficiency was about 90% and the drug was sustained release following a pseudo-zero-order kinetic. Later, the same research group [57] applied the same encapsulation method (w/o/w microemulsion) and the o/w microemulsion for the formulation of thymopentin. In order to increase the incorporation of hydrophilic drugs into lipospheres, lipophilic ion-pairs of the drug with hexadecylphosphate were prepared in this warm o/w microemulsion technique. As expected, this later technique allowed the incorporation of a much higher amount of the drug than the w/o/w multiple microemulsion technique (5.2 versus 1.7%). Moreover, the percentage of the drug released from lipospheres prepared by both methods was practically identical (10% in 6 h).

One of the most interesting studies on the feasibility of the encapsulation of peptide drugs into SLNs was published in 1997, when Almeida and coworkers [58] studied the influence of production parameters of peptide SLNs using lysozyme as model protein. These researchers applied the cold HPH technique for the encapsulation of this model peptide, studying different parameters that could affect the formation of these SLNs: the type of lipid used, the time of exposure to different temperatures, pressure and number of homogenization cycles. They showed that lysozyme was able to withstand the formulation conditions needed to prepare SLNs, without losing its activity and integrity. The entrapment efficiency of hydrophilic drugs of these SLNs is usually low (they obtained encapsulation efficiencies between 43.2 and 59.2%), and depends on the lipid mixture employed and the homogenization conditions. However, every protein may behave differently, and its encapsulation must be studied in depth and optimized accordingly.

As commented above, some of the peptidic drugs that have been successfully introduced to the market in particulate drug carrier form are luteinizing hormone-releasing hormone (LHRH) analogs. In order to improve the formulation by

means of improving drug stability during polymer degradation, Hu and coworkers [53] prepared SLNs to encapsulate gonadorelin. In this case, SLNs were obtained by a novel solvent diffusion method in an aqueous system. Using this technique, encapsulation efficiency increased up to 69.4%. In addition, gonadorelin showed a slow release profile after a burst release period of 6 h in which 24% of the drug was released, after that burst release almost 4% of gonadorelin was sustained-released every day during the 14 days of the study.

Another procedure that has been applied for the preparation of SLNs containing peptides is the w/o/w multiple emulsion technique. The group of Alonso [54, 55, 109] have modified this technique to develop surface-modified lipid nanoparticles for the encapsulation of different peptidic model drugs. As previously reviewed in this chapter, different polymers can be used to modify the surface properties of lipid nanoparticles. In the first study, poloxamer and PEG–stearate were used to form a coating on the surface, and thus protect orally administered nanoparticles from the effect of gastrointestinal fluids. They established that coating lipid nanoparticles with PEG–stearate prevents them from aggregation and reduced pancreatin-induced degradation, making them suitable for oral administration. In a later study, Prego and coworkers [109] coated lipid nanoparticles with chitosan, reporting that this type of coating can switch their  $\zeta$  potential from negative to positive, and confers on them the capacity of enhancing the *in vitro* intestinal absorption of calcitonin, assayed in Caco-2 cells – results that were corroborated after the oral administration of calcitonin in rats. Next, this group [54] studied the release profiles of these PEG–stearate- and chitosan-coated nanoparticles. Both types of nanoparticles exhibited an initial burst release (lower for chitosan-coated nanoparticles) followed by a more prolonged slow release in which 40% of calcitonin was released during the 6 h of the study, for both PEG–stearate- and chitosan-coated nanoparticles. Moreover, and as was the case for PEG–stearate nanoparticles, coating with chitosan also protected lipid nanoparticles from the acidic and intestinal environment. Recently, they have determined the interaction of these surface-modified nanoparticles (PEG–stearate and chitosan) with Caco-2 cells, concluding that PEG–stearate did not affect the permeability of Caco-2 cells monolayers unlike chitosan nanoparticles.

Cyclosporin is another of the peptidic drugs that has been successfully incorporated into SLNs [59, 46]. It is an undecapeptidic hydrophobic drug, insoluble in water and widely used for the prevention of xenograft rejection following organ transplantation. Cyclosporin was encapsulated into SLNs aiming to improve oral bioavailability and thus reducing toxic side-effects, maintaining at the same time good, sustained plasma levels.

### 10.2.7.3 Low-soluble Drugs

Despite having good therapeutic effects, many drugs fail in clinical situations due to their poor water solubility. Although many techniques have been employed to improve the oral absorption of poorly soluble drugs, little information is available in the literature on the improvement in the oral bioavailability of poorly soluble drugs by incorporation into SLNs. Like other formulations, such as microemul-

sions or submicron emulsions, reduction in the particle size is a key factor for improving the peroral performance of poorly soluble drugs. Due to their small particle size, SLNs may exhibit bioadhesion to the gastrointestinal tract wall or enter the intervillar spaces, thus increasing their residence time in the gastrointestinal tract. Another advantage of SLN formulations is the lipid protection of the drug from chemical and degradation, thereby delaying the *in vivo* metabolism. Good physical stability also plays an important key in the oral absorption of the incorporated drugs [110].

Incorporation of drugs into SLNs opens the perspective of enhanced and/or less-variable bioavailability and prolonged plasma levels [77, 111], which is postulated due to a controlled, optimized release in combination with general adhesive properties of small particles [112]. Zimmermann and Müller [113] evaluated the influence of artificial gastrointestinal media on the physical stability of SLN formulations consisting of different lipids and various surfactants/stabilizers with respect to ionic strength and pH. They showed that it is possible to produce SLNs stable in the gastrointestinal tract by optimizing the surfactant/mixture for each lipid *in vitro*. The stabilizing properties obviously depend on the specific interaction of the lipid matrix with the emulsifier, e.g. anchoring of the stabilizer on the lipid surface and density on the surface.

On the other hand, knowledge about enzymatic degradation velocity of SLNs is essential. Olbrich and Müller [114] studied the effects of different surfactants on the degradation velocity. These authors showed that the degradation velocity is substantially affected by the stabilizer used for the preparation of the SLNs. Some stabilizers such as cholic acid sodium salt have degradation accelerating effects, other such as Poloxamer 407 distinctly slow down the degradation velocity. Degradation velocity can be thus modulated by changing the surfactant ratio. Müller and coworkers [115] had previously showed that the degradation velocity of SLNs in solutions of pancreatic lipase/colipase depends on the composition on the lipid matrix. In general, degradation velocity increased with decreasing length of the fatty acid chain length when using glycerides as lipid matrix [116]. In addition, the degradation of SLNs based on waxes (e.g. cetylpalmitate) was found to be slower compared to glyceride matrices.

El-Gibaly and coworkers [117] encapsulated allopurinol into sustained-release solid lipospheres elaborated by melting wax components and hexaconasol, a new hydrophobic wax modifier. The drug was dispersed in the respective molten wax under continuous stirring using a magnetic stirrer. In this study, SLNs were intended for use in a suspension formulation and other oral dosage forms. A significant decrease of plasma uric acid levels and hepatic impairment in male rats was observed after oral administration of SLS suspension of one of their formulations, compared to suspensions of pure allopurinol.

All-*trans* retinoic acid (ATRA) has been limited in clinical use due to its poor aqueous solubility. ATRA has been formulated into SLNs [110] elaborated by HPH with Compritol 888 ATO and soy lecithin/Pluronic F 68 or soy lecithin/Tween 80 as emulsifiers in order to increase its oral bioavailability. After oral administration to male rats, SLNs produced a significant improvement in the bio-



availability of ATRA compared with ATRA solution. Compared with the ATRA emulsion, which also produced an improvement in oral absorption, SLNs exhibit a high physical stability.

#### 10.2.7.4 Topical and Transdermal Administration

SLNs are being investigated as drug carrier system for topical application. These carriers are composed of physiological and biodegradable lipids of low systemic toxicity and also low cytotoxicity [118]. SLNs for topical application to the skin are made up from lipids such as glyceryl behenate (Compritol 888 ATO), glyceryl monostearate (Inwitor 900), glyceryl palmitostearate (Precirol ATO 5), triglycerides (trimyristin, tripalmitin, tristearin) or the wax cetyl palmitate [119].

The generally low lipid content and the poor viscosity of lipid nanodispersions render these preparations, as they are, less suitable for dermal drug application. The handling of the preparation by the patient is improved by SLN incorporation into ointments, creams and gels. Alternatively, ready-to-use preparations may be obtained by one-step production, increasing the lipid phase to at least 30%. However, increasing the lipid frequently results in an unwanted increase in particle size. Surprisingly, it has been found that very concentrated (30–40%) semisolid cetyl palmitate formulations preserve the colloidal particle size [34]. If SLNs are incorporated into vehicles, interactions with the vehicle constituents may induce physical instabilities such as dissolution or aggregation of lipid particles. It is important to follow the particle size and the solid character of the particles during storage.

Particle size of the SLNs influences drug penetration, as has been shown for nanoemulsions, in such a manner that when decreasing particle size, drug penetration and systemic activity of drug increase [120]. Similar effects for particle size reduction on penetration into the skin were found for polymeric particles [121].

Occlusion properties which can enhance the penetration of drugs through the stratum corneum by increased hydration have been reported [120, 122]. Occlusion properties are due to the formation of a film on the skin which enhances the penetration of drugs through the stratum corneum.

SLNs can provide a sustained drug release due to the solid matrix of the particles [78]. Sustained drug release becomes important in dermal application concerning drugs that are irritating at high concentrations. Furthermore, it provides the possibility to supply an active agent over a prolonged period of time and can reduce systemic absorption. Controlled triggered release of drugs is feasible due to polymorphic transitions of the lipids induced by water evaporation from the dosage form after application to the skin. Furthermore, electrolytes present in the upper skin surface can initiate polymorphic transitions accompanied by drug expulsion due to the formation of a stable polymorph [123].

Common disadvantages of SLNs are their particle growth, their unpredictable gelatin tendency, their unexpected dynamic of polymorphic transitions and their inherent low incorporation rate because of the crystalline structure of the solid lipid [10, 124, 125]. It has been claimed that this last drawback can be overcome by oil-loaded solid nanolipids (also described as NLCs) [34, 35, 123]. Liquid lipids

solubilize the drug to a much higher extent than solid lipids. In a preferred scenario, the liquid lipids form inner droplets in the solid nanoparticles. In this model, the NLC nanoparticles would provide a high incorporation rate (because of the liquid lipid) and a controlled release (because of the outer solid lipid).

Souto and coworkers [62, 64] have prepared SLNs and NLCs for topical delivery of clotrimazole and ketoconazole. The authors show that these lipid nanoparticles are useful as modified release formulations for lipophilic drugs over a prolonged period of time.

#### 10.2.7.5 Cosmetic Applications for SLNs

SLNs are also considered a promising carrier system for cosmetic active ingredients due to their numerous advantages. These kind of delivery systems (i) provide protection to labile compounds against chemical degradation, as is the case of retinol and tocopherol, (ii) can provide sustained release of the active ingredients, (iii) act as occlusives, e.g. they can be used in order to increase the water content of the skin and (iv) show a ultraviolet (UV)-blocking potential, i.e. they act as physical sunscreens on their own and can be combined with molecular sunscreens in order to achieve improved photoprotection [126].

SLNs have been shown that they act as active carriers for sunscreens [127]. Song and Liu [128] prepared SLNs as carriers for 3,4,5-trimethoxybenzoylchitin, a new UV-absorbing macromolecule and vitamin E; the nanoparticles act both as physical sunscreens themselves and as carriers in order to enhance the effect of UVB protection. The incorporation of vitamin E appears to have a better effect on UVB absorption.

### 10.3

#### Polymeric Nanoparticles

##### 10.3.1

##### Introduction

Polymeric nanoparticles are small colloidal particles ranging in size from 10 to 1000 nm, which are made of nonbiodegradable or biodegradable polymers. Depending on the method used for their preparation, two different types of nanoparticles can be obtained: nanospheres and nanocapsules. Nanospheres have a matrix-type structure, where active compounds can be absorbed at their surface, entrapped or dissolved in the matrix. Nanocapsules, which are reservoir systems, have a polymeric shell and an inner core. In this case, the active substances are usually dissolved in the core, but may also be adsorbed at their surface. Among the polymeric nanoparticles currently under investigation for controlled drug delivery and drug-targeting applications, those receiving most attention are probably the nanoparticles based on synthetic polymers such as PLA, PGA and PLGA. These polymers are known for both their biocompatibility and resorbability through natural pathways. Additionally, the degradation rate and accordingly the drug release

rate can be manipulated by varying the ratio of PLA (increased hydrophobicity) to PGA (increased hydrophilicity).

### 10.3.2

#### Nanoparticle Preparation Methods

Nanoparticles can be prepared by a number of methods, which are classified into two main categories depending on whether the polymer is formed by *in situ* polymerization of monomers or by dispersion of the preformed polymers.

##### 10.3.2.1 Nanoparticles Prepared by *In Situ* Polymerization of Monomers

The polymerization methods can be classified into two groups based on whether nanospheres or nanocapsules are formed. Nanospheres are mostly prepared by emulsion polymerization, whereas nanocapsules are obtained by interfacial polymerization performed in emulsions or microemulsions.

**10.3.2.1.1 Emulsion Polymerization** The polymerization is usually initiated by the reaction of an initiator with the monomer molecules that are dissolved in the continuous phase of an o/w or w/o emulsion. Couvreur and coworkers [129, 130] reported the production of biodegradable poly(alkyl cyanoacrylate) (PACA) nanospheres (40–250 nm diameter) by a simple emulsification polymerization procedure. The nanospheres were obtained by mechanically emulsifying alkylcyanoacrylate monomers in an aqueous acidic medium in the presence of a non ionic surfactant (e.g. Polysorbate 20, Poloxamer 188) and stabilizers like Dextran 70. The polymerization is spontaneously initiated by the hydroxide ions present in water, under vigorous mechanical stirring at ambient temperature. The NP suspension is then purified by ultracentrifugation or by resuspending the particles in an isotonic surfactant-free medium. The drug is dissolved in the polymerization medium either before the addition of the monomer or at the end of the polymerization reaction, so that it can be either incorporated into the matrix or adsorbed at the surface of the nanospheres. A wide variety of drugs have been efficiently incorporated into PACA nanospheres including cytostatic agents, a peptide growth hormone and several antibiotics [131–133].

Methylidene malonates are other monomers that give biodegradable polymers and polymerize according to a mechanism similar to that of alkylcyanoacrylates [134]. Other polymers proposed for the production of nanospheres by emulsion polymerization include polyglutaraldehyde, poly(vinyl pyridine) and polystyrene; however, their lack of biodegradability compromises their clinical use [135, 136].

**10.3.2.1.2 Interfacial Polymerization** In this procedure an ethanolic phase containing an oil or a nonmiscible organic solvent, the monomers and the drug to be encapsulated is dispersed in an aqueous external phase containing a surfactant. The ethanol rapidly diffuses out of the organic phase giving tiny oil droplets. Due to their interfacial properties, the monomer molecules spontaneously locate at the surface of the oil nanodroplets at the water/oil interface, leading to the formation

of nanocapsules [137]. This method has been used for the encapsulation of oily soluble products into PACA nanocapsules. In order to entrap water-soluble molecules, the process was adapted by addition of the monomer to the oily phase of a previously prepared microemulsion [138, 139].

### 10.3.2.2 Nanoparticles Prepared from Preformed Polymers

The nanoparticles prepared by *in situ* polymerization suffer from two main drawbacks: (i) the presence of toxic residues (unreacted monomers, initiators and surfactant molecules) whose elimination is time-consuming and not always efficient, and (ii) the possible interaction of monomer molecules with the active substance during the polymerization process, leading to the denaturation and inactivation of the drug. Therefore, new encapsulation techniques involving the dispersion of already polymerized materials have been developed to avoid these problems. A major advantage of these methods over the previously described techniques is that the polymers are well characterized and the nanoparticle preparation conditions will not determine their physicochemical characteristics.

**10.3.2.2.1 Emulsification/Solvent Evaporation–Extraction Method** In this method, the polymer is dissolved in a volatile organic solvent like dichloromethane, chloroform or ethyl acetate. The drug is dissolved or dispersed into the polymer solution, and this mixture is further emulsified by high-speed homogenization or sonication into an aqueous solution containing a suitable emulsifier like poly(vinyl alcohol) (PVA), polysorbate, poloxamer, etc. After the formation of a stable o/w emulsion, the organic solvent is either extracted by the continuous phase (solvent extraction), diffuses into the same and evaporates by increasing the temperature/under pressure or by continuous stirring (solvent evaporation) or is removed by a combination of both, leading to the formation of nanoparticles. At the end of the procedure, the solidified particles are usually collected by centrifugation, washed and dried.

The emulsification/solvent evaporation–extraction method has been used for the production of nanospheres with a wide range of polymers including PLGA, poly( $\epsilon$ -caprolactone) (PCL) and poly(hydroxybutyrate) (PHB). Although this method was proposed for the encapsulation of lipophilic compounds [140, 141], a modification of this technique has been used for encapsulating a model protein, bovine serum albumin (BSA), achieving encapsulation efficiencies up to 70% [142]. An aqueous solution of BSA was emulsified in a PLGA solution in dichloromethane by sonication. This w/o emulsion was then added to an aqueous PVA solution resulting in a w/o/w emulsion which is sonicated again. Polymer hardening and nanoparticle formation is induced by solvent evaporation–extraction upon addition of an aqueous isopropanolic solution.

More recently, Freitas and coworkers [143] have developed a novel ultrasonic flow-through cell for the production of PLA or PLGA nanoparticles with a mean diameter of 500 nm. The equipment consisted of a glass tube for the conduction of the sonicated fluid, which was installed in a steel jacket excited by a transducer and filled with pressurized water for the transmission of sound waves. This novel

technology can avoid the contamination of the fluid from the environment and is well suited for aseptic continuous nanoparticle production.

**10.3.2.2.2 Emulsification/Solvent Diffusion Method** This method uses partially water-soluble solvents like benzyl alcohol or propylene carbonate instead of chlorinated solvents that could degrade certain drugs and proteins. The polymer and active compound are dissolved in the solvent and emulsified in the aqueous phase containing the stabilizer. Water is added to the emulsion to allow the diffusion of the solvent into the water and leading to the formation of the nanoparticles. Once the nanoparticles are formed, they can be collected by centrifugation or the solvent can be removed by dialysis [144].

**10.3.2.2.3 Salting-out Method** The salting-out method was first reported by Bindschadler and coworkers in 1988 [145]. In this case, an o/w emulsion is formed by addition of an aqueous phase saturated with electrolytes, and containing PVA as stabilizing agent to an acetone solution of polymer and the active compound. The miscibility of both phases is prevented by the saturation of the aqueous phase with electrolytes according to a salting-out phenomenon. Subsequently, water is added until the volume is sufficient to disrupt the equilibrium between the two phases and to allow diffusion of the acetone into the water, which results in polymer precipitation and the formation of nanoparticles. Finally, this suspension is purified by cross-flow filtration and lyophilization. One disadvantage of this procedure is the use of salts that are incompatible with many bioactive compounds.

**10.3.2.2.4 Direct Precipitation-based Method** The nanoprecipitation method developed by Fessi and coworkers [146] represents an easy and reproducible technique that allows us to obtain nanoparticles without a previous emulsification step. The process is based on the drop-wise addition of the polymer dissolved in water-miscible solvents such as acetone, ethanol or methanol to an aqueous medium under stirring. The polymer precipitation gives rise to nanoparticle formation. The solvent is then removed by evaporation under reduced pressure. This technique is mostly suitable for the encapsulation of hydrophobic compounds due to the rapid migration and therefore loss of water-soluble drugs into the aqueous phase. Molpeceres and coworkers [147] encapsulated cyclosporin A into PCL nanoparticles based on this method. The polymer and drug were dissolved in acetone and this organic phase was injected through a needle into an aqueous medium containing Poloxamer 188. Nanoparticle formation could be visualized by the Tyndall effect.

### 10.3.3

#### **Characterization of Polymeric Nanoparticles**

Nanoparticles are usually characterized in terms of size, morphology, charge, constituent properties, drug content and *in vitro* drug release. The techniques used are similar to those described for SLNs in Sections 10.2.4 and 10.2.6.

## 10.3.4

**Pharmaceutical Applications of Nanoparticles**

Polymeric nanoparticles are promising candidates for the delivery of a broad number of peptide and protein drugs for diagnostic and therapeutic applications, since they are advantageous in a number of ways. On the one hand, the solid matrix of particulate carriers protects the incorporated drugs against enzymatic and hydrolytic degradation. On the other hand, they present tissue-targeting capacities, thereby increasing the bioavailability of drugs at the site of action and simultaneously reducing both the total dose and the side effects associated with the drug. Furthermore, they can be used to modulate the immune responses against encapsulated antigens due to their ability to efficiently target professional antigen-presenting cells (APCs), and to facilitate appropriate processing and presenting antigens to T cells. One additional advantage of particulate carriers is that their surface properties can be modified in order to evade the macrophages of the reticuloendothelial system (RES) or in such a way as to improve the uptake and transport across mucosal barriers.

**10.3.4.1 Protein Delivery**

Advances in biotechnology and biochemistry had led to the discovery of numerous bioactive molecules, some of which are peptides and proteins. These macromolecules are characterized by poor solubility, limited chemical stability *in vitro* and *in vivo* after administration, and poor bioavailability. Indeed, they are usually administered by the parenteral route and frequent, high-dose injections are required to circumvent their extremely rapid clearance in the body. One approach for improving the therapeutic index of these macromolecules could be the development of nanoparticulate carriers able to maintain appropriate drug blood levels for long periods of time. Csaba and coworkers [148] have developed a new nanoparticulate system consisting on a blend nanomatrix of PLGA and a poly(ethylene oxide) (PEO) derivative for the encapsulation of insulin providing a more stable environment to the encapsulated macromolecules. These new nanoparticles release the insulin in a constant rate over a time period of 2 weeks with a negligible burst effect typically observed for proteins encapsulated in PLGA micro/nanoparticles. In another study reported by Barrichelo and coworkers [149], different bioactive agents and insulin were encapsulated into PLGA nanoparticles using the nanoprecipitation method. Insulin was preferentially bound to the surface of PLGA nanoparticles. Nevertheless, a strong hypoglycemic effect of the insulin was observed after administration of the nanoparticles suspension to the ileum loop of male Wistar rats, indicating that insulin was absorbed.

More recently nanoparticles are being investigated as drug carriers for proangiogenic growth factors proposed as a novel approach for the therapy of various ischemia-related pathophysiological conditions. Proangiogenic growth factors have shown promising results in preclinical studies using protein- and gene-based therapies. However, their success in clinical trials is hindered by the lack of an optimal delivery strategy that would provide sustained and localized levels of the

growth factors in the diseased tissue [150]. Davda and coworkers [151] evaluated the efficacy of sustained release biodegradable nanoparticles, formulated with PLGA, for the delivery of vascular endothelial growth factor protein (VEGF), a potent proangiogenic agent. Nanoparticles encapsulating VEGF, which were formulated using a double-emulsion solvent evaporation technique, demonstrated sustained release of the growth factor in bioactive form. Furthermore, the growth factor encapsulated in nanoparticles demonstrated greater and more sustained effect compared with a solution on endothelial cell proliferation, migration and morphogenesis, which are key elements of blood vessel outgrowth. The greater efficacy of encapsulated VEGF was due to the ability of nanoparticles to maintain the growth factor level in culture for a sustained period of time. The data thus suggest that nanoparticles can be used as an effective delivery system for growth factors to induce therapeutic angiogenesis.

A new method to prepare heparin-functionalized PLGA nanoparticles for the controlled release of growth factors has been recently reported by Chung and coworkers [152]. The system is composed of PLGA as a hydrophobic core, Pluronic F-127 as a hydrophilic surface layer and heparin as the functionalized moiety. The incorporation of heparin is based on its high specific binding for various growth factors, which enables them to crosslink their receptors and to be protected from proteolytic degradation. The release of VEGF from the nanoparticles (below 200 nm) showed a linear profile without initial burst over 1 month. The authors proposed that these nanoparticles can be used as a growth factor delivery system in tissue engineering scaffolds as well as sustained release systems of various heparin-binding growth factors.

Interferon (IFN)- $\alpha$  is another macromolecule that has been encapsulated in order to simplify its administration and improve its therapeutic effects. The currently approved therapies require the injection of repeated high nonphysiological doses due to the short half-life of the free macromolecule [153]. Nevertheless, the potential of IFN formulated in these controlled release systems has been limited by the reduction of its biological activity during the encapsulation and/or release process [154]. Sanchez and coworkers [155] have used Poloxamer 188 as a stabilizing agent for the encapsulation of IFN- $\alpha$  into biodegradable micro/nanoparticles. PLGA/poloxamer blend microspheres were able to provide significant amounts of active IFN- $\alpha$  for up to 96 days. These new delivery systems might improve the effectiveness of IFN- $\alpha$  and the quality of life of patients.

#### 10.3.4.2 Protein Delivery by Mucosal Routes

In recent years, considerable research has been done using nanoparticles for the delivery of protein and peptide drugs by mucosal routes. After oral administration the drug carriers are expected to remain in the gastrointestinal tract while protecting the entrapped peptide drugs from enzymatic degradation until they are absorbed. Carino and coworkers [156] developed an oral nanosphere formulation to protect insulin from degradation and facilitate systemic uptake by the oral route. This formulation was shown to have 11.4% of the efficacy of intraperitoneally de-

livered zinc insulin and was able to control plasma glucose levels when faced with a simultaneous administered glucose challenge.

The same concept could be also applied to the pulmonary route, which has been considered as a promising way to improve delivery of insulin with particulate systems. The nebulized PLGA nanospheres significantly reduced the blood glucose levels of fasted guinea pigs and the hypoglycemia was prolonged over 48 h compared to the nebulized aqueous insulin solution as a reference (6 h). This result could be attributed to the sustained release of insulin from the nanospheres deposited widely on to the whole lung [157]. When developing polymeric nanoparticles, controversy still exists on physicochemical factors governing nanoparticle uptake and transport across mucosal barriers, including size, size distribution, hydrophobicity and surface properties. Many studies on size effects have demonstrate that size is an important parameter controlling the internalization of nanoparticles into the epithelia of the gastrointestinal tract and, as a rule of thumb, sizes smaller than 500 nm are required [105]. Apart from particle size, surface properties seem to influence the uptake by intestinal epithelia. Summarizing numerous absorption studies of polymeric nanoparticles in intestinal tissues, it can be concluded that a combination of both nanoparticles surface charges and increased hydrophobicity of the matrix material seem to affect gastrointestinal uptake in a positive sense [158–160]. In addition, different research groups have demonstrated that increased nanoparticle internalization can be achieved by conferring mucoadhesive properties to them by coating their surface with mucoadhesive polymers such as chitosan and carbopol. Takeuchi and coworkers [161] reported the preparation of elcatonin-loaded PLGA nanospheres coated with chitosan. They found that, following the oral or pulmonary administration in rats and guinea pig, the reduction in calcium concentration obtained with mucoadhesive nanoparticles was more effective and prolonged in comparison with that obtained with noncoated systems. These results indicate that chitosan nanospheres adhere to the mucus layer in the gastrointestinal tract and lung tissues, due to the mucoadhesive properties of chitosan, and release the drug over a longer period of time. In another study by Vila and coworkers [162], it was demonstrated that the coating of tetanus toxoid-containing PLA nanoparticles with PEG or chitosan improved their stability in physiological fluids, and enhanced the transport across the intestinal and nasal mucosae, thereby confirming the usefulness of mucoadhesive nanoparticulate systems for the delivery of peptide drugs.

Nanoparticles have also been used in the induction of oral tolerance, since successive and extended exposure of the immune system to the antigen in the intestine is indispensable for inducing peripheral immune tolerance. Kim and coworkers reported that a single administration of PLGA nanoparticles entrapping type II collagen could induce oral tolerance more efficiently than repeated administration of intact protein [163]. In a subsequent study, they prepared PLGA nanoparticles entrapping PEG-conjugated immunodominant peptides of type II collagen for oral tolerance induction in collagen-induced arthritis. The single intragastric administration of these nanoparticles induced the production of IL-4 and



IL-10 in CD4<sup>+</sup> T cells of Peyer's patches, which was comparable to that in mice fed 6 times with peptide solution. Taking into account that IL-4 and IL-10 play a critical role in arthritis suppression, they conclude that oral administration of nanoparticles might block arthritis progression through this mechanism [164].

#### 10.3.4.3 Vaccine Adjuvants

Nanoparticles containing entrapped or adsorbed antigens have been intensively investigated as vaccine adjuvants alternatives to the currently used aluminum salts [165, 166]. A major drawback with current vaccination regimes lies in the method of administration, which generally employs the parenteral route, which might lead to noncompliance. Thus, alternative routes of vaccine administration have been tested: nasal, oral, intradermal and vaginal. Carcaboso and coworkers [167] have demonstrated the adjuvant properties of PLGA nanoparticles containing encapsulated Spf66 antigen. The systemic immune response obtained following nasal administration with nanoparticles was superior to that induced by the same dose of peptide solution; however, in this study, the best responses were obtained with 1- $\mu$ m particles. This latter formulation greatly improves and maintains higher antibody levels compared to conventional alum adjuvant and to the administration of the particles by others routes (subcutaneous, oral).

In recent studies, Coolí and coworkers [168] have investigated the effect of size and charge on the permeation of nanoparticles through the skin as the first step in designing a transdermal vaccine delivery system. The results showed that only 50- and 500-nm fluorescent particles that were negatively charged were able to permeate the pig skin. This provides evidence of the potential of nanoparticles as delivery vectors for antigens and DNA for the purpose of transdermal vaccination protocols.

In general, vaccination against major diseases requires a humoral immune response; however, in the case of intracellular viral, bacterial and parasitic infections a cellular response is needed [169]. It is known that aluminum hydroxide can preferentially induce T<sub>h</sub>2 immune responses [170, 171] and deposits the antigen only for 2–3 weeks [172]. Although aluminum hydroxide can induce the production of antibodies, it has little effect on eliciting CD4<sup>+</sup> T<sub>h</sub>1 cells (defined by their production of IL-2 and IFN- $\gamma$  cytokines, that induce cell-mediated immune responses) or CD8<sup>+</sup> T cell response. Polymeric nanoparticle delivery systems play an interesting role in the design of new vaccines since it have been demonstrated that they can elicit a T<sub>h</sub>1/T<sub>h</sub>2 combined response. According to the results reported by Schöll and coworkers [173], the subcutaneous administration of the major allergen of birch pollen loaded into PLGA nanoparticles modulated an ongoing T<sub>h</sub>2 response in the BALB/c mouse model. This response was demonstrated by downregulation of IgG1, and production of IFN- $\gamma$  and IL-10, suggesting that PLGA nanoparticles can be used for formulations of allergen extracts or derivatives for the “few-shot” treatment of type 1 allergy.

Furthermore, it has been suggested that PLGA nanoparticles are suitable for simultaneous targeting of immunoadjuvants and antigens to APCs, and can reduce the effective adjuvant dose significantly [174]. Chong and coworkers [175] investigated the immune-enhancing effects of codelivery hepatitis B core antigen

(HBcAg) and monophospholipid A (MPLA) in a murine model. In this study, a single subcutaneous immunization with a vaccine formulation containing MPLA and HBcAg coencapsulated in PLGA nanoparticles promoted a stronger T<sub>H</sub>1 cellular immune response with IFN- $\gamma$  production than those induced by the antigen alone, mixed with MPLA or HBcAg-loaded nanoparticles. Such response is critical for the control of viral replication and the elimination of chronic hepatitis B, indicating that the simultaneous delivery of antigens and immune modulators in a single particulate formulation may be an interesting strategy for the development of effective hepatitis B virus therapeutic vaccines.

## References

- 1 P. BASU. Technologies that deliver. *Nat. Med.* **2003**, *9*, 1100–1101.
- 2 G. ORIVE, A. R. GASCÓN, R. M. HERNÁNDEZ, A. DOMÍNGUEZ-GIL, J. L. PEDRAZ. Drug delivery in biotechnology: present and future. *Curr. Opin. Biotechnol.* **2003**, *14*, 659–664.
- 3 V. LABHASETWAR. Nanotechnology for drug and gene therapy: the importance of understanding molecular mechanisms of delivery. *Curr. Opin. Biotechnol.* **2005**, *16*, 674–680.
- 4 G. ORIVE, A. R. GASCÓN, R. M. HERNÁNDEZ, A. DOMÍNGUEZ-GIL, J. L. PEDRAZ. New approaches in the delivery of pharmaceuticals. *Trends Pharmacol. Sci.* **2003**, *24*, 207–210.
- 5 A. T. JONES, M. GUMBLETON, R. DUNCAN. Understanding endocytic pathways and intracellular trafficking: a prerequisite for effective design of advanced drug delivery systems. *Adv. Drug Deliv. Rev.* **2003**, *55*, 1353–1357.
- 6 R. H. MÜLLER, C. M. KECK. Challenges and solutions for the delivery of biotech drugs – a review of drug nanocrystal technology and lipid nanoparticles. *J. Biotechnol.* **2004**, *113*, 151–170.
- 7 A. DUBES, H. PARROT-LOPEZ, W. ABDELWAHED, G. DEGOBERT, H. FESSI, P. SHAHGALDIAN, A. W. COLEMAN. Scanning electron microscopy and atomic force microscopy imaging of solid lipid nanoparticles derived from amphiphilic cyclodextrins. *Eur. J. Pharm. Biopharm.* **2003**, *55*, 279–282.
- 8 J. GUALBERT, P. SHAHGALDIAN, A. W. COLEMAN. Interactions of amphiphilic calix[4]arene-based solid lipid nanoparticles with bovine serum albumin. *Int. J. Pharm.* **2003**, *257*, 69–73.
- 9 P. SHAHGALDIAN, E. DA SILVA, A. W. COLEMAN, B. RATHER, M. J. ZAWOROTKO. Para-acyl-calix-arene based solid lipid nanoparticles (SLNs): a detailed study of preparation and stability parameters. *Int. J. Pharm.* **2003**, *253*, 23–38.
- 10 W. MEHNERT, K. MÄDER. Solid lipid nanoparticles: production, characterization and applications. *Adv. Drug Deliv. Rev.* **2001**, *47*, 165–196.
- 11 B. SIEKMANN, K. WESTESEN. Melt-homogenized solid lipid nanoparticles stabilized by the nonionic surfactant tyloxapol. *Pharm. Pharmacol. Lett.* **1994**, *3*, 194–197.
- 12 R. CAVALLI, O. CAPUTO, E. MARENGO, F. PATTARINO, M. R. GASCO. The effect of the components of microemulsions on both size and crystalline structure of solid lipid nanoparticles (SLN) containing a series of model molecules. *Pharmazie* **1998**, *53*, 392–396.
- 13 R. H. MÜLLER, W. MEHNERT, J. S. LUCKS, C. SCHWARZ, A. ZUR MÜHLEN, H. WEYHERS, C. FREITAS, D. RÜHL. An alternative colloidal carrier system for controlled drug delivery. *Eur. J. Pharm. Biopharm.* **1995**, *41*, 62–69.
- 14 M. UNER, S. A. WISSING, G. YENER, R. H. MULLER. Influence of surfac-

- tants on the physical stability of solid lipid nanoparticle (SLN) formulations. *Pharmazie* **2004**, *59*, 331–332.
- 15 R. H. MÜLLER, K. MÄDER, S. GOHLA. Solid lipid nanoparticles (SLN) for controlled drug delivery – a review of the state of the art. *Eur. J. Pharm. Biopharm.* **2000**, *50*, 161–177.
  - 16 S. A. WISSING, O. KAYSER, R. H. MÜLLER. Solid lipid nanoparticles for parenteral drug delivery. *Adv. Drug Deliv. Rev.* **2004**, *56*, 1257–1272.
  - 17 P. SPEISER. Lipidnanopellets als Trägersystem für Arzneimittel zur peroralen Anwendung. *European Patent EP 0167825*, **1990**.
  - 18 A. J. DOMB. Lipospheres for controlled delivery of substances. *US Patent, USS 5,188,837*, **1993**.
  - 19 M. R. GASCO. Method for producing solid lipid microspheres having a narrow size distribution. *US Patents 5,250,236*, **1993**.
  - 20 B. SJÖSTRÖM, B. BERGENSTÄHL. Preparation of submicron drug particles in lecithin-stabilized o/w emulsions I. Model studies of the precipitation of cholesteryl acetate. *Int. J. Pharm.* **1992**, *88*, 53–62.
  - 21 A. DINGLER, S. GOHLA. Production of solid lipid nanoparticles (SLN): scaling up feasibilities. *J. Microencapsul.* **2002**, *19*, 11–16.
  - 22 S. H. GOHLA, A. DINGLER. Scaling up feasibility of the production of solid lipid nanoparticles (SLN). *Pharmazie* **2001**, *56*, 61–63.
  - 23 V. JENNING, A. LIPPACHER, S. H. GOHLA. Medium scale production of solid lipid nanoparticles (SLN) by high pressure homogenization. *J. Microencapsul.* **2002**, *19*, 1–10.
  - 24 R. H. MÜLLER, A. DINGLER, T. SCHNEPPE, S. GOHLA. Large scale production of solid lipid nanoparticles (SLN) and nanosuspensions (DissoCubes). In *Handbook of Pharmaceutical Controlled Release Technology*, WISE, D. (Ed.). Marcel Dekker, New York, **2000**, pp. 359–376.
  - 25 E. MARENGO, R. CAVALLI, O. CAPUTO, L. RODRIGUEZ, M. R. GASCO. Scale-up of the preparation process of solid lipid nanospheres. Part I. *Int. J. Pharm.* **2000**, *205*, 3–13.
  - 26 C. DULIEU, D. BAZILE. Influence of lipid nanocapsules composition on their aptness to freeze-drying. *Pharm. Res.* **2005**, *22*, 285–292.
  - 27 H. HEIATI, R. TAWASHI, N. C. PHILLIPS. Drug retention and stability of solid lipid nanoparticles containing azidothymidine palmitate after autoclaving, storage and lyophilization. *J. Microencapsul.* **1998**, *15*, 173–184.
  - 28 E. ZIMMERMANN, R. H. MÜLLER, K. MÄDER. Influence of different parameters on reconstitution of lyophilized SLN. *Int. J. Pharm.* **2000**, *196*, 211–213.
  - 29 C. FREITAS, R. H. MÜLLER. Spray-drying of solid lipid nanoparticles (SLN<sup>TM</sup>). *Eur. J. Pharm. Biopharm.* **1998**, *46*, 145–151.
  - 30 E. MARENGO, R. CAVALLI, G. ROVERO, M. R. GASCO. Scale-up and optimization of an evaporative drying process applied to aqueous dispersions of solid lipid nanoparticles. *Pharm. Dev. Technol.* **2003**, *8*, 299–309.
  - 31 C. FREITAS, R. H. MÜLLER. Correlation between long-term stability of solid lipid nanoparticles (SLN<sup>TM</sup>) and crystallinity of the lipid phase. *Eur. J. Pharm. Biopharm.* **1999**, *47*, 125–132.
  - 32 A. ZUR MÜHLEN, C. SCHWARZ, W. MEHNERT. Solid lipid nanoparticles (SLN) for controlled drug delivery – drug release and release mechanism. *Eur. J. Pharm. Biopharm.* **1998**, *45*, 149–155.
  - 33 A. ZUR MÜHLEN, W. MEHNERT. Drug release and release mechanism of prednisolone loaded solid lipid nanoparticles. *Pharmazie* **1998**, *53*, 552–555.
  - 34 R. H. MÜLLER, M. RADTKE, S. A. WISSING. Solid lipid nanoparticles (SLN) and nanostructured lipid carriers (NLC) in cosmetic and dermatological preparations. *Adv. Drug Deliv. Rev.* **2002**, *54*, S131–S155.
  - 35 R. H. MÜLLER, M. RADTKE, S. A. WISSING. Nanostructured lipid matrices for improved microencapsulation of drugs. *Int. J. Pharm.* **2002**, *242*, 121–128.

- 36 K. JORES, W. MEHNERT, K. MÄDER. Physicochemical investigations on solid lipid nanoparticles and on oil-loaded solid lipid nanoparticles: a nuclear magnetic resonance and electron spin resonance study. *Pharm. Res.* **2003**, *20*, 1274–1283.
- 37 K. JORES, A. HABERLAND, S. WARTEWIG, K. MADER, W. MEHNERT. Solid lipid nanoparticles (SLN) and oil-loaded SLN studied by spectrofluorometry and raman spectroscopy. *Pharm. Res.* **2005**, *22*, 1887–1897.
- 38 K. JORES, W. MEHNERT, M. DRECHSLER, H. BUNJES, C. JOHANN, K. MÄDER. Investigations on the structure of solid lipid nanoparticles (SLN) and oil-loaded solid lipid nanoparticles by photon correlation spectroscopy, field-flow fractionation and transmission electron microscopy. *J. Control. Release* **2004**, *95*, 217–227.
- 39 C. OLBRICH, A. GESSNER, O. KAYSER, R. H. MÜLLER. Lipid–drug-conjugate (LDC) nanoparticles as novel carrier system for the hydrophilic antitrypanosomal drug diminazene-diaceturate. *J. Drug Target.* **2002**, *10*, 387–396.
- 40 C. OLBRICH, A. GESSNER, O. KAYSER, R. H. MÜLLER. Lipid–drug conjugate (LDC) nanoparticles as an alternative carrier system with high drug content. *Proc. Int. Symp. Control. Release Bioact. Mater.* **2000**, 295–296.
- 41 M. IGARTUA, P. SAULNIER, B. HEURTAULT, B. PECH, J. E. PROUST, J. L. PEDRAZ, J. P. BENOIT. Development and characterization of solid lipid nanoparticles loaded with magnetite. *Int. J. Pharm.* **2002**, *233*, 149–157.
- 42 A. ZUR MÜHLEN, E. ZUR MÜHLEN, H. NIEHUS, W. MEHNERT. Atomic force microscopy studies of solid lipid nanoparticles. *Pharm. Res.* **1996**, *13*, 1411–1416.
- 43 E. B. SOUTO, S. A. WISSING, C. M. BARBOSA, R. H. MÜLLER. Comparative study between the viscoelastic behaviors of different lipid nanoparticle formulations. *J. Cosmet. Sci.* **2004**, *55*, 463–471.
- 44 T. ELDEM, P. SPEISER, A. HINCAL. Optimization of spray-dried and -congealed lipid micropellets and characterization of their surface morphology by scanning electron microscopy. *Pharm. Res.* **1991**, *8*, 47–54.
- 45 S. C. YANG, J. B. ZHU, Y. LU, B. W. LIANG, C. Z. YANG. Body distribution of camptothecin solid lipid nanoparticles after oral administration. *Pharm. Res.* **1999**, *16*, 751–757.
- 46 T. BEKERMAN, J. GOLENSER, A. DOMB. Cyclosporin nanoparticulate lipospheres for oral administration. *J. Pharm. Sci.* **2004**, *93*, 1264–1270.
- 47 L. BRANNON-PEPPAS, J. O. BLANCHETTE. Nanoparticle and targeted systems for cancer therapy. *Adv. Drug Deliv. Rev.* **2004**, *56*, 1649–1659.
- 48 G. STORM, S. O. BELLIOU, T. DAEMEN, D. D. LASIC. Surface modification of nanoparticles to oppose uptake by the mononuclear phagocyte system. *Adv. Drug Deliv. Rev.* **1995**, *17*, 31–48.
- 49 T. M. GOPPERT, R. H. MÜLLER. Protein adsorption patterns on poloxamer- and poloxamine-stabilized solid lipid nanoparticles (SLN). *Eur. J. Pharm. Biopharm.* **2005**, *60*, 361–372.
- 50 C. OLBRICH, U. BAKOWSKY, C. M. LEHR, R. H. MÜLLER, C. KNEUER. Cationic solid-lipid nanoparticles can efficiently bind and transfect plasmid DNA. *J. Control. Release* **2001**, *77*, 345–355.
- 51 C. RUDOLPH, U. SCHILLINGER, A. ORTIZ, K. TABATT, C. PLANK, R. H. MÜLLER, J. ROSENECKER. Application of novel solid lipid nanoparticle (SLN)-gene vector formulations based on a dimeric HIV-1 TAT-peptide *in vitro* and *in vivo*. *Pharm. Res.* **2004**, *21*, 1662–1669.
- 52 C. ERNI, C. SUARD, S. FREITAS, D. DREHER, H. P. MERKLE, E. WALTER. Evaluation of cationic solid lipid microparticles as synthetic carriers for the targeted delivery of macromolecules to phagocytic antigen-presenting cells. *Biomaterials* **2002**, *23*, 4667–4676.
- 53 F. Q. HU, Y. HONG, H. YUAN. Preparation and characterization of solid lipid nanoparticles containing peptide. *Int. J. Pharm.* **2004**, *273*, 29–35.

- 54 M. GARCIA-FUENTES, D. TORRES, M. J. ALONSO. New surface-modified lipid nanoparticles as delivery vehicles for salmon calcitonin. *Int. J. Pharm.* **2005**, *296*, 122–132.
- 55 M. GARCIA-FUENTES, D. TORRES, M. J. ALONSO. Design of lipid nanoparticles for the oral delivery of hydrophilic macromolecules. *Colloids Surf. B Biointerfaces* **2002**, *27*, 159–168.
- 56 S. MOREL, M. R. GASCO, R. CAVALLI. Incorporation in lipospheres of [D-Trp-6]LHRH. *Int. J. Pharm.* **1994**, *105*, R1–R3.
- 57 S. MOREL, E. UGAZIO, R. CAVALLI, M. R. GASCO. Thymopentin in solid lipid nanoparticles. *Int. J. Pharm.* **1996**, *132*, 259–261.
- 58 A. J. ALMEIDA, S. RUNGE, R. H. MÜLLER. Peptide-loaded solid lipid nanoparticles (SLN): influence of production parameters. *Int. J. Pharm.* **1997**, *149*, 255–265.
- 59 E. UGAZIO, R. CAVALLI, M. R. GASCO. Incorporation of cyclosporin A in solid lipid nanoparticles (SLN). *Int. J. Pharm.* **2002**, *241*, 341–344.
- 60 R. CORTESI, E. ESPOSITO, G. LUCA, C. NASTRUZZI. Production of lipospheres as carriers for bioactive compounds. *Biomaterials* **2002**, *23*, 2283–2294.
- 61 R. CAVALLI, M. R. GASCO, P. CHETONI, S. BURGALASSI, M. F. SAETTONI. Solid lipid nanoparticles (SLN) as ocular delivery system for tobramycin. *Int. J. Pharm.* **2002**, *238*, 241–245.
- 62 E. B. SOUTO, R. H. MÜLLER. SLN and NLC for topical delivery of ketoconazole. *J. Microencapsul.* **2005**, *22*, 501–510.
- 63 F. Q. HU, H. YUAN, H. H. ZHANG, M. FANG. Preparation of solid lipid nanoparticles with clobetasol propionate by a novel solvent diffusion method in aqueous system and physicochemical characterization. *Int. J. Pharm.* **2002**, *239*, 121–128.
- 64 E. B. SOUTO, S. A. WISSING, C. M. BARBOSA, R. H. MÜLLER. Development of a controlled release formulation based on SLN and NLC for topical clotrimazole delivery. *Int. J. Pharm.* **2004**, *278*, 71–77.
- 65 N. HODOSHIMA, C. UDAGAWA, T. ANDO, H. FUKUYASU, H. WATANABE, S. NAKABAYASHI. Lipid nanoparticles for delivering antitumor drugs. *Int. J. Pharm.* **1997**, *146*, 81–92.
- 66 A. LAMPRECHT, J. L. SAUMET, J. ROUX, J. P. BENOIT. Lipid nanocarriers as drug delivery system for ibuprofen in pain treatment. *Int. J. Pharm.* **2004**, *278*, 407–414.
- 67 S. J. LIM, C. K. KIM. Formulation parameters determining the physicochemical characteristics of solid lipid nanoparticles loaded with all-*trans* retinoic acid. *Int. J. Pharm.* **2002**, *243*, 135–146.
- 68 R. CAVALLI, O. CAPUTO, M. R. GASCO. Preparation and characterization of solid lipid nanospheres containing paclitaxel. *Eur. J. Pharm. Sci.* **2000**, *10*, 305–309.
- 69 A. FUNDARO, R. CAVALLI, A. BARGONI, D. VIGHETTO, G. P. ZARA, M. R. GASCO. Non-stealth and stealth solid lipid nanoparticles (SLN) carrying doxorubicin: pharmacokinetics and tissue distribution after i.v. administration to rats. *Pharmacol. Res.* **2000**, *42*, 337–343.
- 70 S. TOONGSUWAN, L. C. LI, B. K. ERICKSON, H. C. CHANG. Formulation and characterization of bupivacaine lipospheres. *Int. J. Pharm.* **2004**, *280*, 57–65.
- 71 J. X. WANG, X. SUN, Z. R. ZHANG. Enhanced brain targeting by synthesis of 3',5'-dioctanoyl-5-fluoro-2'-deoxyuridine and incorporation into solid lipid nanoparticles. *Eur. J. Pharm. Biopharm.* **2002**, *54*, 285–290.
- 72 H. HEIATI, R. TAWASHI, N. C. PHILLIPS. Solid lipid nanoparticles as drug carriers: II. Plasma stability and biodistribution of solid lipid nanoparticles containing the lipophilic prodrug 3'-azido-3'-deoxythymidine palmitate in mice. *Int. J. Pharm.* **1998**, *174*, 71–80.
- 73 R. LÖBENBERG, L. ARAUJO, H. VON BRIESEN, E. RODGERS, J. KREUTER. Body distribution of azidothymidine bound to hexyl-cyanoacrylate nanoparticles after i.v. injection to rats. *J. Control. Release* **1998**, *50*, 21–30.

- 74 L. HARIVARDHAN REDDY, R. K. SHARMA, K. CHUTTANI, A. K. MISHRA, R. S. R. MURTHY. Influence of administration route on tumor uptake and biodistribution of etoposide loaded solid lipid nanoparticles in Dalton's lymphoma tumor bearing mice. *J. Control. Release* **2005**, *105*, 185–198.
- 75 G. LUKOWSKI, P. PFLEGEL. Electron diffraction of solid lipid nanoparticles loaded with aciclovir. *Pharmazie* **1997**, *52*, 642–643.
- 76 J. KRISTL, B. VOLK, M. GASPERLIN, M. SENTJURC, P. JURKOVIC. Effect of colloidal carriers on ascorbyl palmitate stability. *Eur. J. Pharm. Sci.* **2003**, *19*, 181–189.
- 77 M. DEMIREL, Y. YAZAN, R. H. MÜLLER, F. KILIC, B. BOZAN. Formulation and *in vitro*–*in vivo* evaluation of piribedil solid lipid micro- and nanoparticles. *J. Microencapsul.* **2001**, *18*, 359–371.
- 78 V. JENNING, M. SCHÄFER-KORTING, S. GOHLA. Vitamin A-loaded solid lipid nanoparticles for topical use: drug release properties. *J. Control. Release* **2000**, *66*, 115–126.
- 79 H. BUNJES, M. DRECHSLER, M. H. J. KOCH, K. WESTESEN. Incorporation of the model drug ubidecarenone into solid lipid nanoparticles. *Pharm. Res.* **2001**, *18*, 287–293.
- 80 A. DINGLER, R. P. BLUM, H. NIEHUS, R. H. MÜLLER, S. GOHLA. Solid lipid nanoparticles (SLN<sup>TM</sup>/Lipopearls<sup>TM</sup>) – a pharmaceutical and cosmetic carrier for the application of vitamin E in dermal products. *J. Microencapsul.* **1999**, *16*, 751–767.
- 81 E. B. SOUTO, C. ANSELMINI, M. CENTINI, R. H. MÜLLER. Preparation and characterization of *n*-dodecyl-ferulate-loaded solid lipid nanoparticles (SLN<sup>®</sup>). *Int. J. Pharm.* **2005**, *295*, 261–268.
- 82 S. A. WISSING, K. MÄDER, R. H. MÜLLER. Solid lipid nanoparticles (SLN<sup>TM</sup>) as a novel carrier system offering prolonged release of the perfume Allure. *Proc. Int. Symp. Control. Release Bioact. Mater.* **2000**, 311–312.
- 83 E. B. SOUTO, R. H. MÜLLER, S. GOHLA. A novel approach based on lipid nanoparticles (SLN<sup>®</sup>) for topical delivery of alpha-lipoic acid. *J. Microencapsul.* **2005**, *22*, 581–592.
- 84 K. TABATT, M. SAMETTI, C. OLBRICH, R. H. MÜLLER, C. M. LEHR. Effect of cationic lipid and matrix lipid composition on solid lipid nanoparticle-mediated gene transfer. *Eur. J. Pharm. Biopharm.* **2004**, *57*, 155–162.
- 85 K. TABATT, C. KNEUER, M. SAMETTI, C. OLBRICH, R. H. MÜLLER, C. M. LEHR, U. BAKOWSKY. Transfection with different colloidal systems: comparison of solid lipid nanoparticles and liposomes. *J. Control. Release* **2004**, *97*, 321–332.
- 86 K. L. BRIGHAM, B. MEYRICK, B. CHRISTMAN, M. MAGNUSON, G. KING, L. C. BERRY, JR. *In vivo* transfection of murine lungs with a functioning prokaryotic gene using a liposome vehicle. *Am. J. Med. Sci.* **1989**, *298*, 278–281.
- 87 P. L. FELGNER, T. R. GADEK, M. HOLM, R. ROMAN, H. W. CHAN, M. WENZ, J. P. NORTHROP, G. M. RINGOLD, M. DANIELSEN. Lipofection: a highly efficient, lipid-mediated DNA-transfection procedure. *Proc. Natl. Acad. Sci. USA* **1987**, *84*, 7413–7417.
- 88 L. S. UYECHI-O'BRIEN, F. C. SZOKA. Mechanisms for cationic lipids in gene transfer. In *Pharmaceutical Gene Delivery Systems*, ROLLAND, A., SULLIVAN, S. M. (Eds.), Marcel Dekker, New York, **2003**, pp. 79–108.
- 89 K. E. B. MEYER, L. S. UYECHI, F. C. SZOKA. Manipulating the intracellular trafficking of nucleic acids. In *Gene Therapy for Diseases of the Lung*, BRIGHAM, K. L. (Ed.), Marcel Dekker, New York, **1997**, pp. 135–180.
- 90 J. H. FELGNER, R. KUMAR, C. N. SRIDHAR, C. J. WHEELER, Y. J. TSAI, R. BORDER, P. RAMSEY, M. MARTIN, P. L. FELGNER. Enhanced gene delivery and mechanism studies with a novel series of cationic lipid formulations. *J. Biol. Chem.* **1994**, *269*, 2550–2561.
- 91 C. M. GORMAN, M. AIKAWA, B. FOX, E. FOX, C. LAPUZ, B. MICHAUD, H.

- NGUYEN, E. ROCHE, T. SAWA, J. P. WIENERKRONISH. Efficient *in vivo* delivery of DNA to pulmonary cells using the novel lipid EDMPC. *Gene Ther.* **1997**, *4*, 983–992.
- 92 E. R. LEE, J. MARSHALL, C. S. SIEGEL, C. W. JIANG, N. S. YEW, M. R. NICHOLS, J. B. NIETUPSKI, R. J. ZIEGLER, M. B. LANE, K. X. WANG, N. C. WAN, R. K. SCHEULE, D. J. HARRIS, A. E. SMITH, S. H. CHENG. Detailed analysis of structures and formulations of cationic lipids for efficient gene transfer to the lung. *Hum. Gene Ther.* **1996**, *7*, 1701–1717.
- 93 T. PAUKKU, S. LAURAEUS, I. HUHTANIEMI, P. K. KINNUNEN. Novel cationic liposomes for DNA-transfection with high efficiency and low toxicity. *Chem. Phys. Lipids* **1997**, *87*, 23–29.
- 94 I. SOLODIN, C. S. BROWN, M. S. BRUNO, C. Y. CHOW, E. H. JANG, R. J. DEBS, T. D. HEATH. A novel series of amphiphilic imidazolium compounds for *in-vitro* and *in-vivo* gene delivery. *Biochemistry* **1995**, *34*, 13537–13544.
- 95 J. WANG, X. GUO, Y. XU, L. BARRON, F. C. SZOKA, JR. Synthesis and characterization of long chain alkyl acyl carnitine esters. Potentially biodegradable cationic lipids for use in gene delivery. *J. Med. Chem.* **1998**, *41*, 2207–2215.
- 96 C. J. WHEELER, P. L. FELGNER, Y. J. TSAI, J. MARSHALL, L. SUKHU, S. G. DOH, J. HARTIKKA, J. NIETUPSKI, M. MANTHORPE, M. NICHOLS, M. PLEWE, X. W. LIANG, J. NORMAN, A. SMITH, S. H. CHENG. A novel cationic lipid greatly enhances plasmid DNA delivery and expression in mouse lung. *Proc. Natl Acad. Sci. USA* **1996**, *93*, 11454–11459.
- 97 M. C. PEDROSO DE LIMA, S. SIMOES, P. PIRES, H. FANCA, N. DUZGUNES. Cationic lipid–DNA complexes in gene delivery: from biophysics to biological applications. *Adv. Drug Deliv. Rev.* **2001**, *47*, 277–294.
- 98 P. E. THORÉN, D. PERSSON, P. LINCOLN, B. NORDÉN. Membrane destabilizing properties of cell-penetrating peptides. *Biophys. Chem.* **2005**, *114*, 169–179.
- 99 L. HYNEMAN, J. L. LEMOINE, L. HUANG, D. J. PORTEOUS, A. C. BOYD, X. NAN. HIV-1 Tat protein transduction domain peptide facilitates gene transfer in combination with cationic liposomes. *J. Control. Release* **2004**, *99*, 435–444.
- 100 M. SILHOL, M. TYAGI, M. GIACCA, B. LEBLEU, E. VIVES. Different mechanisms for cellular internalization of the HIV-1 Tat-derived cell penetrating peptide and recombinant proteins fused to Tat. *Eur. J. Biochem.* **2002**, *269*, 494–501.
- 101 S. R. SCHWARZE, K. A. HRUSKA, S. F. DOWDY. Protein transduction: unrestricted delivery into all cells? *Trends Cell Biol.* **2000**, *10*, 290–295.
- 102 A. ZIEGLER, P. NERVI, M. DURRENBERGER, J. SEELIG. The cationic cell-penetrating peptide Cpp(TAT) derived from the HIV-1 protein TAT is rapidly transported into living fibroblasts: optical, biophysical, and metabolic evidence. *Biochemistry* **2005**, *44*, 138–148.
- 103 N. PEDERSEN, S. HANSEN, A. V. HEYDENREICH, H. G. KRISTENSEN, H. S. POULSEN. Solid lipid nanoparticles can effectively bind DNA, streptavidin and biotinylated ligands. *Eur. J. Pharm. Biopharm.* **2006**, *62*, 155–162.
- 104 S. KÖNNINGS, A. GÖPFERICH. Lipospheres as delivery systems for peptides and proteins. In *Lipospheres in Drug Targets and Delivery. Approaches, Methods and Applications*, NASTRUZZI, C. (Ed.). CRC Press, Boca Raton, FL, **2005**, pp. 67–86.
- 105 T. JUNG, W. KAMM, A. BREITENBACH, E. KAISERLING, J. X. XIAO, T. KISSEL. Biodegradable nanoparticles for oral delivery of peptides: is there a role for polymers to affect mucosal uptake? *Eur. J. Pharm. Biopharm.* **2000**, *50*, 147–160.
- 106 R. H. MÜLLER, S. MAASEN, H. WEYHERS, F. SPECHT, J. S. LUCKS. Cytotoxicity of magnetite-loaded polylactide, poly(lactide)/glycolide

- particles and solid lipid nanoparticles. *Int. J. Pharm.* **1996**, *138*, 85–94.
- 107 N. SCHÖLER, H. HAHN, R. H. MÜLLER, O. LIESENFELD. Effect of lipid matrix and size of solid lipid nanoparticles (SLN) on the viability and cytokine production of macrophages. *Int. J. Pharm.* **2002**, *231*, 167–176.
- 108 C. OLBRICH, R. H. MÜLLER, K. TABATT, O. KAYSER, C. SCHULZE, R. SCHADE. Stable biocompatible adjuvants – a new type of adjuvant based on solid lipid nanoparticles: a study on cytotoxicity, compatibility and efficacy in chicken. *Altern. Lab. Anim.* **2002**, *30*, 443–458.
- 109 C. PREGO, M. GARCIA, D. TORRES, M. J. ALONSO. Transmucosal macromolecular drug delivery. *J. Control. Release* **2005**, *101*, 151–162.
- 110 L. D. HU, X. TANG, F. D. CUI. Solid lipid nanoparticles (SLNs) to improve oral bioavailability of poorly soluble drugs. *J. Pharm. Pharmacol.* **2004**, *56*, 1527–1535.
- 111 L. PENKLER, R. H. MÜLLER, S. RUNGE, V. RAVELLI. Pharmaceutical cyclosporine formulation with improved biopharmaceutical properties, improved physical quality and greater stability, and method for producing said formulation. WO 99/56733, **1999**.
- 112 G. PONCHEL, M. J. MONTISCI, A. DEMBRI, C. DURRER, D. CUCHENE. Mucoadhesion of colloidal particulate systems in the gastro-intestinal tract. *Eur. J. Pharm. Biopharm.* **1997**, *44*, 25–31.
- 113 E. ZIMMERMANN, R. H. MÜLLER. Electrolyte- and pH-stabilities of aqueous solid lipid nanoparticle (SLN<sup>TM</sup>) dispersions in artificial gastrointestinal media. *Eur. J. Pharm. Biopharm.* **2001**, *52*, 203–210.
- 114 C. OLBRICH, R. H. MÜLLER. Enzymatic degradation of SLN – effect of surfactant and surfactant mixtures. *Int. J. Pharm.* **1999**, *180*, 31–39.
- 115 R. H. MÜLLER, D. RÜHL, S. A. RUNGE. Biodegradation of solid lipid nanoparticles as a function of lipase incubation time. *Int. J. Pharm.* **1996**, *144*, 115–121.
- 116 C. OLBRICH, W. MEHNERT, R. H. MÜLLER. Development of an *in vitro* degradation assay for solid lipid nanoparticles. *Proc. 2nd World Meeting APGI/APV*, **1998**, 627–628.
- 117 I. EL-GIBALY, S. K. BDEL-GHAFFAR. Effect of hexacosanol on the characteristics of novel sustained-release allopurinol solid lipospheres (SLS): factorial design application and product evaluation. *Int. J. Pharm.* **2005**, *294*, 33–51.
- 118 R. H. MÜLLER, D. RÜHL, S. RUNGE, K. SCHULZE-FORSTER, W. MEHNERT. Cytotoxicity of solid lipid nanoparticles as a function of the lipid matrix and the surfactant. *Pharm. Res.* **1997**, *14*, 458–462.
- 119 M. SCHÄFER-KORTING, W. MEHNERT. Delivery of lipophilic compounds with lipid nanoparticles. Applications in dermatics and for transdermal therapy. In *Lipospheres in Drug Targets and Delivery. Approaches, Methods and Applications*, NASTRUZZI, C. (Ed.). CRC Press, Boca Raton, FL, **2005** pp. 127–142.
- 120 T. DE VRINGER, H. A. DE RONDE. Preparation and structure of a water-in-oil cream containing lipid nanoparticles. *J. Pharm. Sci.* **1995**, *84*, 466–472.
- 121 A. ROLLAND, N. WAGNER, A. CHATELUS, B. SHROOT, H. SCHAEFER. Site-specific drug delivery to pilosebaceous structures using polymeric microspheres. *Pharm. Res.* **1993**, *10*, 1738–1744.
- 122 V. JENNING, G. E. HILDEBRAND, A. GYSLER, R. H. MÜLLER, M. SCHÄFER-KORTING, S. GOHLA. Solid lipid nanoparticles (SLN<sup>TM</sup>) for topical application: occlusive properties. *Proc. Int. Symp. Control. Release Bioact. Mater.* **1999**, 405–406.
- 123 V. JENNING, A. F. THUNEMANN, S. H. GOHLA. Characterisation of a novel solid lipid nanoparticle carrier system based on binary mixtures of liquid and solid lipids. *Int. J. Pharm.* **2000**, *199*, 167–177.
- 124 K. WESTESEN, H. BUNJES, M. H. J. KOCH. Physicochemical characterization of lipid nanoparticles and evaluation



- tion of their drug loading capacity and sustained release potential. *J. Control. Release* **1997**, *48*, 223–236.
- 125 K. WESTESEN, B. SIEKMANN. Investigation of the gel formation of phospholipid-stabilized solid lipid nanoparticles. *Int. J. Pharm.* **1997**, *151*, 35–45.
- 126 S. A. WISSING, R. H. MÜLLER. Cosmetic applications for solid lipid nanoparticles (SLN). *Int. J. Pharm.* **2003**, *254*, 65–68.
- 127 S. A. WISSING, R. H. MÜLLER. A novel sunscreen system based on tocopherol acetate incorporated into solid lipid nanoparticles. *Int. J. Cosmet. Sci.* **2001**, *23*, 233–243.
- 128 C. SONG, S. LIU. A new healthy sunscreen system for human: solid lipid nanoparticles as carrier for 3,4,5-trimethoxybenzoylchitin and the improvement by adding Vitamin E. *Int. J. Biol. Macromol.* **2005**, *36*, 116–119.
- 129 P. COUVREUR, B. KANTE, M. ROLAND, P. GOIT, P. BAUDUIN, P. SPEISER. Polycyanoacrylate nanocapsules as potential lysosomotropic carriers: preparation, morphology and sorptive properties. *J. Pharm. Pharmacol.* **1979**, *31*, 331–332.
- 130 P. COUVREUR, M. ROLAND, P. SPEISER. Biodegradable submicroscopic particles containing a biologically active substance. *US patent 4,329,332*, **1982**.
- 131 C. CHAVANY, T. LE DOAN, P. COUVREUR, F. PUISIEUX, C. HELENE. Polyalkylcyanoacrylate nanoparticles as polymeric carriers for antisense oligonucleotides. *Pharm. Res.* **1992**, *9*, 441–449.
- 132 C. E. SOMA, C. DUBERNET, D. BENTOLILA, S. BENITA, P. COUVREUR. Reversion of multidrug resistance by co-encapsulation of doxorubicin and cyclosporin A in polyalkylcyanoacrylate nanoparticles. *Biomaterials* **2000**, *21*, 1–7.
- 133 K. KRAUEL, T. PITAKSUTEEPONG, N. M. DAVIES, T. RADES. Entrapment of bioactive molecules in poly(alkylcyanoacrylate) nanoparticles. *Am. J. Drug Del.* **2004**, *2*, 251–259.
- 134 F. LESCURE, C. SEGUIN, P. BRETON, P. BOURRINET, D. ROY, P. COUVREUR. Preparation and characterization of novel poly(methylidene malonate 2.1.2.)-made nanoparticles. *Pharm. Res.* **1994**, *11*, 1270–1277.
- 135 J. KREUTER. *Colloidal Drug Delivery Systems*. Marcel Dekker, New York, **1994**.
- 136 C. VAUTHIER-HOLTZSCHERER, S. BENABBOU, G. SPENLEHAUER, M. VEILLARD, P. COUVREUR. Methodology for the preparation of ultra-dispersed polymer systems. *STP Pharm. Sci.* **1991**, *1*, 109–16.
- 137 M. GALLARDO, G. COUARRAZE, B. DENIZOT, L. TREUPEL, P. COUVREUR, F. PUISIEUX. Study of the mechanisms of formation of nanoparticles and nanocapsules of polyisobutyl-2-cyanoacrylate. *Int. J. Pharm.* **1993**, *100*, 55–64.
- 138 S. WATNASIRICHAIKUL, T. RADES, I. G. TUCKER, N. M. DAVIES. Effects of formulation variables on characteristics of poly(ethylcyanoacrylate) nanocapsules prepared from w/o microemulsions. *Int. J. Pharm.* **1–2**, **2002**, *235*, 237–246.
- 139 T. PITAKSUTEEPONG, N. M. DAVIES, I. G. TUCKER, T. RADES. Factors influencing the entrapment of hydrophilic compounds in nanocapsules prepared by interfacial polymerisation of water-in-oil microemulsions. *Eur. J. Pharm. Biopharm.* **2002**, *53*, 335–342.
- 140 L. MU, S. FENG. Vitamin E TPGS used as emulsifier in the solvent evaporation/extraction technique for fabrication of polymeric nanospheres for controlled release of paclitaxel (Taxol®). *J. Control. Release* **2002**, *80*, 129–144.
- 141 R. GREF, P. QUELLEC, A. SANCHEZ, P. CALVO, E. DELLACHERIE, M. J. ALONSO. Development and characterization of CyA-loaded poly(lactic acid)–poly(ethylene glycol) PEG micro- and nanoparticles. Comparison with conventional PLA particulate carriers. *Eur. J. Pharm. Biopharm.* **2001**, *51*, 111–118.
- 142 I. GUTIERRO, R. M. HERNÁNDEZ, M. IGARTUA, A. R. GASCÓN, J. L. PEDRAZ. Size dependent immune response after subcutaneous, oral and intranasal

- administration of BSA loaded nanospheres. *Vaccine* **2002**, *21*, 67–77.
- 143 S. FREITAS, G. HIELSCHER, H. P. MERKLE, B. GANDER. Continuous contact- and contamination-free ultrasonic emulsification – a useful toll for pharmaceutical development and production. *Ultrason. Sonochem.* **2006**, *13*, 76–85.
- 144 J. C. LEROUX, E. ALLÉMAN, E. DOELKER, R. GURNY. New approach for the preparation of nanoparticles by an emulsification-diffusion method. *Eur. J. Pharm. Biopharm.* **1995**, *41*, 14–18.
- 145 C. BRINDSCHAEDLER, R. GURNY, A. W. DOELKER. Process for preparing a powder of water-insoluble polymer which can be redispersed in a liquid phase, the resulting powder and utilization thereof. *Patent WO 88/08011*, **1988**.
- 146 H. FESSI, J. P. DEVISSAGUET, F. PUISIEUX, C. THIES. Procédé de préparation de systèmes colloïdaux dispersibles d'une substance sous forme de nanoparticules. *French Patent 2,608,988*, **1986**.
- 147 J. MOLPECERES, M. GUZMAN, M. R. ABERTURAS, M. CHACON, L. BERGES. Application of central composite designs to the preparation of polycaprolactone nanocapsules. *J. Pharm. Sci.* **1996**, *85*, 206–213.
- 148 N. CSABA, L. GONZÁLEZ, A. SÁNCHEZ, M. J. ALONSO. Design and characterization of new nanoparticulate polymer blends for drug delivery. *J. Biomater. Sci. Polym. Ed.* **2004**, *15*, 1137–1151.
- 149 J. M. BARRICHELLO, M. MORISHITA, K. TAKAYAMA, T. NAGAI. Encapsulation of hydrophilic and lipophilic drugs in PLGA nanoparticles by the nano-precipitation method. *Drug Dev. Ind. Pharm.* **1999**, *25*, 471–476.
- 150 J. DAVDA, V. LABHASETWAR. An update on angiogenesis therapy. *Crit. Rev. Eukaryot. Gene Expr.* **2001**, *11*, 1–21.
- 151 J. DAVDA, V. LABHASETWAR. Sustained proangiogenic activity of vascular endothelial growth factor following encapsulation in nanoparticles. *J. Biomed. Nanotech.* **2005**, *1*, 74–82.
- 152 Y. CHUNG, G. TAE, S. H. YUK. A facile method to prepare heparin-functionalized nanoparticles for controlled release of growth factors. *Biomaterials* **2006**, in press.
- 153 A. KOZŁOWSKI, J. M. HARRIS. Improvements in protein PEGylation: pegylated interferons for treatment of hepatitis C. *J. Control. Release* **2001**, *72*, 217–224.
- 154 J. L. CLELAND, A. J. S. JONES. Stable formulations of recombinant human growth hormone and interferon-gamma for microencapsulation in biodegradable microspheres. *Pharm. Res.* **1996**, *13*, 1464–1475.
- 155 A. SÁNCHEZ, M. TOBÍO, L. GONZÁLEZ, A. FABRA, M. J. ALONSO. Biodegradable micro- and nanoparticles as long-term delivery vehicles for interferon-alpha. *Eur. J. Pharm. Sci.* **2003**, *18*, 221–229.
- 156 G. P. CARINO, J. S. JACOB, E. MATHIOWITZ. Nanosphere based oral insulin delivery. *J. Control. Release* **2000**, *65*, 261–269.
- 157 Y. KAWASHIMA, H. YAMAMOTO, H. TAKEUCHI, S. FUJIOKA, T. HINO. Pulmonary delivery of insulin with nebulized DL-lactide/glycolide copolymer (PLGA) nanospheres to prolong hypoglycemic effect. *J. Control. Release* **1999**, *62*, 279–287.
- 158 D. A. NORRIS, P. J. SINKO. Effect of size, surface charge and hydrophobicity on the translocation of polystyrene microspheres through gastrointestinal mucin. *J. Appl. Polym. Sci.* **1997**, *63*, 1481–1492.
- 159 A. M. HILLERY, A. T. FLORENCE. The effect of adsorbed poloxamer 188 and 407 surfactants on the intestinal uptake of 60-nm polystyrene particles after oral administration in the rat. *Int. J. Pharm.* **1996**, *132*, 123–154.
- 160 S. K. SAHOO, J. PANYAM, S. PRABHA, V. LABHASETWAR. Residual polyvinyl alcohol associated with poly(D,L-lactide-co-glycolide) nanoparticles affects their physical properties and cellular uptake. *J. Control. Release* **2002**, *82*, 105–114.
- 161 H. TAKEUCHI, H. YAMAMOTO, Y. KAWASHIMA. Mucoadhesive nano-

- particulate systems for peptide drug delivery. *Adv. Drug Deliv. Rev.* **2001**, *47*, 39–54.
- 162 A. VILA, M. SANCHEZ, M. TOBÍO, P. CALVO, M. J. ALONSO. Design of biodegradable particles for protein delivery. *J. Control. Release* **2002**, *78*, 15–24.
- 163 W. U. KIM, W. K. LEE, J. W. RYOO, S. H. KIM, J. KIM, J. YOUN, S. Y. MIN, E. Y. BAE, S. Y. HWANG, S. H. PARK, C. S. CHO, J. S. PARK, H. Y. KIM. Suppression of collagen-induced arthritis by single administration of poly(lactic-co-glycolic acid) nanoparticles entrapping type II collagen: a novel strategy for induction of oral tolerance. *Arthritis Rheum.* **2002**, *46*, 1109–1120.
- 164 W. LEE, J. PARK, S. JUNG, Ch. YANG, W. KIM, H. KIM, J. PARK, J. PARK. Preparation and characterization of biodegradable nanoparticles entrapping immunodominant peptide conjugated with PEG for oral tolerance induction. *J. Control. Release* **2005**, *105*, 77–88.
- 165 P. ELAMANCHILI, M. DIWAN, M. CAO, J. SAMUEL. Characterization of poly(D,L-lactic-co-glycolic acid) based nanoparticulate system for enhanced delivery of antigens to dendritic cells. *Vaccine* **2004**, *22*, 2406–2412.
- 166 M. J. SHEPHARD, D. TODD, B. M. ADAIR, A. L. W. PO, D. P. MACKIE, E. M. SCOTT. Immunogenicity of bovine parainfluenza type 3 virus proteins encapsulated in nanoparticle vaccines, following intranasal administration to mice. *Res. Vet. Sci.* **2003**, *74*, 187–190.
- 167 A. M. CARCABOSO, R. M. HERNÁNDEZ, M. IGARTUA, J. E. ROSAS, M. E. PATARRROYO, J. L. PEDRAZ. Potent, long lasting systemic antibody levels and mixed T<sub>H</sub>1/T<sub>H</sub>2 immune response after nasal immunization with malaria antigen loaded PLGA microparticles. *Vaccine* **2004**, *22*, 1423–1432.
- 168 A. K. COOLÍ, H. O. ALPAR. Potential use of nanoparticles for transcutaneous vaccine delivery: effect of particle size and charge. *Int. J. Pharm.* **2004**, *275*, 13–17.
- 169 N. L. LETVIN, B. R. BLOOM, S. L. HOFFMAN. Prospects for vaccines to protect against AIDS, tuberculosis and malaria. *J. Am. Med. Ass.* **2001**, *285*, 606–611.
- 170 J. M. BREWER, M. CONACHER, C. A. HUNTER, M. MOHR, F. BROMBACHER, J. ALEXANDER. Aluminum hydroxide adjuvant initiates strong antigen-specific T<sub>H</sub>2 responses in the absence of IL-4- or IL-13-mediated signaling. *J. Immunol.* **1999**, *163*, 6448–54.
- 171 T. R. MOSMANN, R. L. COFFMAN. T<sub>H</sub>1 and T<sub>H</sub>2 cells: different patterns of lymphokine secretion lead to different functional properties. *Annu. Rev. Immunol.* **1989**, *7*, 145–73.
- 172 R. K. GUPTA, E. H. RELYVELD, E. B. LINDBLAD, B. BIZZINI, S. BEN-EFRAIM, C. K. GUPTA. Adjuvants – a balance between toxicity and adjuvanticity. *Vaccine* **1993**, *11*, 293–306.
- 173 I. SCHÖLL, A. WEISSENBÖCK, E. FÖRSTER-WALDI, E. UNTERSMAJR, F. WALTER, M. WILLHEIM, G. BOLTZ-NITULESCU, O. SCHEINER, F. GABORW, E. JENSEN-JAROLIM. Allergen-loaded biodegradable poly(D,L-lactic-co-glycolic) acid nanoparticles down-regulate an ongoing T<sub>H</sub>2 response in the BALB/c mouse model. *Clin. Exp. Allergy* **2004**, *34*, 315–321.
- 174 M. DIWAN, M. TAFAGHODI, J. SAMUEL. Enhancement of immune responses by co-delivery of a CpG oligodeoxynucleotide and tetanus toxoid in biodegradable nanospheres. *J. Control. Release* **2002**, *85*, 247–262.
- 175 C. S. W. CHONG, M. CAO, W. W. WONG, K. P. FISCHER, W. R. ADDISON, G. S. KWON, D. L. TYRELL, J. SAMUEL. Enhancement of T helper type 1 immune responses against hepatitis B virus core antigen by PLGA nanoparticle vaccine delivery. *J. Control. Release* **2005**, *102*, 85–99.

## 11 Intelligent Hydrogels in Nanoscale Sensing and Drug Delivery Applications

*J. Zach Hilt*

### 11.1

#### Introduction

This chapter highlights recent activities in the field of intelligent hydrogels, specifically in sensing and drug delivery micro/nanotechnologies. This is a relatively undeveloped field, but there is high promise and interest in the area, which has led to rapid growth. Here, some selected examples of the cutting-edge research being conducted are presented and, where appropriate, the reader is directed to key reviews within the field. In the past, numerous research groups have utilized hydrogels as functional components in biomedical applications, such as in biomaterials and biosensors, but only recently have hydrogels begun to be applied at the micro/nanoscale.

Example applications of hydrogels at the small scale include work by Ito and collaborators [1–3] patterning pH-sensitive and thermosensitive hydrogels for potential use in various microdevices. In other studies by Matsuda and coworkers [4–8], hydrogels have been micropatterned using a surface polymerization technique to create regions with different physicochemical properties to control the direction of cell adhesion and cellular behavior. In addition, Peppas and coworkers micropatterned poly(ethylene glycol) (PEG)-based hydrogels for application in biomedical devices [9]. Several other groups have focused on developing microdevices utilizing the mechanical response of environmentally sensitive hydrogels for microactuation. Beebe and coworkers [10, 11] have micropatterned pH-responsive hydrogels inside microfluidic channels to create flow controls that could respond to the ambient environmental conditions.

The application of intelligent hydrogels in micro/nanoscale sensing and drug delivery applications are highlighted within this chapter. First, in Section 11.2, the field of intelligent hydrogels is introduced and several example systems are highlighted, including ionic, temperature responsive, biohybrid and imprinted hydrogels. Section 11.3 focuses on sensor applications of intelligent hydrogels. Section 11.4 introduces drug delivery applications of intelligent hydrogels, such as in microfabricated devices and nanoscale structures.

## 11.2

### Intelligent Hydrogels

The molecular structure of polymer networks can be designed to result in preprogrammed and intelligent interactions with their environment. Of particular interest, environmentally responsive hydrogels have been synthesized that are capable of sensing and responding to changes to external stimuli such as changes to the pH, specific analytes and temperature, and recent reviews have highlighted the extensive research focused on developing new and applying current environmentally sensitive hydrogels [12–15]. The response mechanism of these hydrogel systems results from the chemical structure of the polymer network, such as the functionality of side-chain groups, branches and crosslinks.

#### 11.2.1

##### Ionic Hydrogels

In ionic hydrogels containing weakly acidic or basic pendent groups, differentials in water sorption can result from ionization of these pendent groups depending on the solution pH and ionic composition. In the ionized state, these hydrogels act as semipermeable membranes to the counterions influencing the osmotic balance between the hydrogel and the external solution through ion exchange, depending on ion–ion interactions. For ionic gels containing weakly acidic pendent groups, the equilibrium degree of swelling increases as the pH of the external solution increases, while the degree of swelling increases as the pH decreases for gels containing weakly basic pendent groups.

#### 11.2.2

##### Temperature-responsive Hydrogels

Temperature-responsive hydrogels are some of the most widely studied responsive hydrogel systems, with most systems based on poly(*N*-isopropyl acrylamide) (PNIPAAm) and its derivatives. The response to changes in temperature is due to a reversible volume-phase transition with a change in the temperature and these systems have been studied for a variety of applications, including in drug delivery and tissue engineering [13, 16]. This type of behavior is related to polymer phase separation as the temperature is raised above a critical value known as the lower critical solution temperature (LCST), e.g. PNIPAAm exhibits a LCST around 33 °C. Networks showing lower critical miscibility temperature are in a collapsed state above the LCST and the networks swell upon lowering the temperature below the LCST.

#### 11.2.3

##### Biohybrid Hydrogels

Biohybrid hydrogels can be created by integrating biological entities with synthetic hydrogels, and these systems have the potential to synergistically combine the well-

evolved biological mechanisms (e.g. high affinity and specificity of binding) and the tailorable hydrogel properties (e.g. mechanical stability and environmentally responsive nature). For example, research groups have immobilized enzymes within the network structure of hydrogels. Activated glucose oxidase has been incorporated into pH-sensitive cationic hydrogels. The glucose oxidase converts glucose into gluconic acid, lowering the pH of the local environment and causing the hydrogel network to swell in the case of a cationic gel [17]. In other work, Miyata and coworkers [18] prepared biohybrid hydrogels containing grafted antigen and corresponding antibody within the hydrogel network and demonstrated these systems to be responsive to a specific antigen. Furthermore, Wang and coworkers [19] have prepared hybrid hydrogels containing hydrophilic monomers and coiled-coil protein domains, which were demonstrated to exhibit a temperature-dependent swelling response based on the change in protein structure.

#### 11.2.4

#### **Imprinted Hydrogels**

Another class of intelligent hydrogels is based on molecularly imprinted polymers (MIPs), which are prepared using template-mediated polymerization techniques that create recognition domains able to specifically bind template molecules with high affinity. Although MIPs have been studied for more than three decades, imprinted hydrogel systems have only recently gained attention [20–23]. These systems are designed and synthesized to create chemical functionality and structure that is organized in a precise three-dimensional configuration, and these have potential application where controlled recognition properties to various biological analytes and physiological processes are required.

### 11.3

#### **Sensor Applications**

By tailoring the response properties of hydrogel systems, they can be optimized for application in sensor devices. In particular, environmentally responsive hydrogels have been applied as sensing elements for development of novel sensor platforms. For example, hydrogels have been utilized as actuation elements where the mechanical response of the network was applied to actuate various transduction elements. In other examples, hydrogel matrices have been used for optical sensing platforms and electrical sensing platforms. In the following, selected examples are highlighted.

#### 11.3.1

#### **Actuation Detection**

The mechanical response of hydrogels resulting from network swelling with changes in ambient environmental conditions can be used to actuate a transduc-

ing element to create a sensor platform. For example, Grimes and coworkers [24, 25] demonstrated wireless pH sensors utilizing the actuation response of pH-responsive hydrogels integrated with magnetoelastic thick films. The sensor device functioned by monitoring the change in resonance frequency due to applied mass load of the magnetoelastic sensor device. In other research, Han and coworkers [26] demonstrated a constant-volume hydrogel osmometer as a novel sensor platform. The concept was illustrated with a device where a pH-responsive hydrogel was confined between a rigid semipermeable membrane and the diaphragm of a miniature pressure sensor, where changes in the osmotic swelling pressure of the hydrogel resulting from changes pH were accurately measured via the pressure sensor. Although the device was of macroscale in dimensions, the design can be easily miniaturized for microscale or even nanoscale sensor development.

Recently, microelectromechanical system (MEMS) sensor platforms have been applied in a wide variety of applications. Gerlach and coworkers [27] developed piezoresistive sensors which measured the swelling of hydrogel systems by monitoring the deflection of the silicon membrane within the sensor chip (Fig. 11.1). Specifically, two systems, i.e. a network based on a poly(vinyl alcohol) (PVA) and poly(acrylic acid) (PAA) blend and a network based on PNIPAAm, were applied in

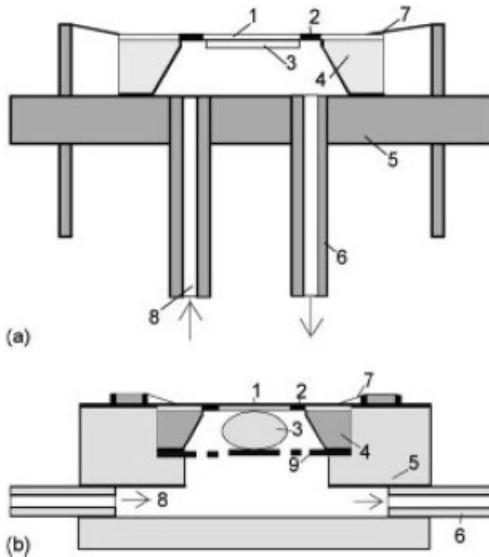


**Figure 11.1.** Operational principle of hydrogel-based sensors: (a) with PVA/PAA hydrogel layer, deposited onto the bending plate and (b) with PNIPAAm foil piece in a cavity. (1) Bending plate; (2) mechano-electrical transducer (piezoresistive bridge); (3) swellable hydrogel; (4) Si chip; (5) socket; (6) tube; (7) interconnect; (8) solution; (9) grate [27].

this sensor platform to develop pH and organic solvent concentration sensors, respectively. In other work, a MEMS sensor based on a capacitive pressure sensing technique and an uncrosslinked poly(2-hydroxyethyl methacrylate) (PHEMA) hydrophilic polymer was demonstrated [28]. An inductor–capacitor (LC) LC circuit was utilized to enable wireless detection of the sensor response.

MEMS sensor platforms based on micro/nanocantilevers have also been of high interest, as a result of their ultrahigh sensitivity. For example, environmentally responsive hydrogels have been integrated with silicon microcantilevers to develop an ultrasensitive bioMEMS sensor platform (Fig. 11.2). Specifically, a pH microsensor was demonstrated based on a methacrylic acid based pH-responsive hydrogel [29, 30] and this was the first demonstration of a microscale MEMS sensor device where actuation is controlled by an intelligent polymer network. In similar work, Thundat and coworkers [31] have demonstrated a variation on this sensor platform by integrating hydrogels responsive to  $\text{CrO}_4^{2-}$  with commercial silicon microcantilevers to create  $\text{CrO}_4^{2-}$  sensors. More recently, another variation has been demonstrated where hydrogels containing benzo-18-crown-6 coated on microcantilevers to create  $\text{Pb}^{2+}$  sensors [32].

In other research, Richter and collaborators [33] investigated the suitability of a quartz crystal microbalance as a transducer element for hydrogel-based liquid sensors. A blend of PAA and PVA was polymerized onto the sensor surface, and the system was demonstrated to have response time of 500 ms for a pH change from 1.8 to 3.1. Ionic hydrogels, microparticles [34] and thin films [35, 36] have also been applied for the detection of  $\text{CO}_2$  gas by measuring the pH decrease that occurs when  $\text{CO}_2$  diffuses through a gas-permeable membrane and into an electrolyte solution. A commercially available pressure sensor was used for the transduction of the swelling event and a schematic of the device is included in Fig. 11.3.

### 11.3.2

#### Optical Detection

There have been various optical-based detection schemes applied to hydrogel-based systems, and a few of these are highlighted in the following. For example, researchers have demonstrated a multianalyte hydrogel biosensor array platform which consists of analyte specific features that are indexed by shape [37]. The platform was based on lithographically patterned PEG diacrylates that contained biomolecules for oligonucleotide and cell-based sensing applications.

In other research, McShane and coworkers have developed a novel hydrogel microsphere sensor platform based on polyelectrolyte-coated calcium alginate microspheres (Fig. 11.4) [38, 39]. In particular, glucose oxidase was encapsulated with an oxygen-quenched ruthenium compound, allowing for the detection of glucose concentrations. The polyelectrolyte multilayer films were nanoscale in thickness (around 10–100 nm), and were used to stabilize enzyme entrapment and control of substrate diffusion.



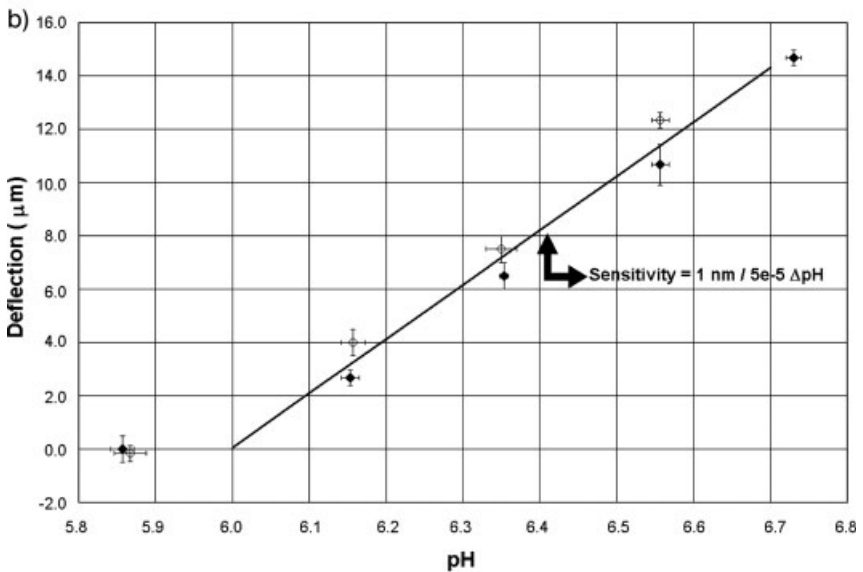
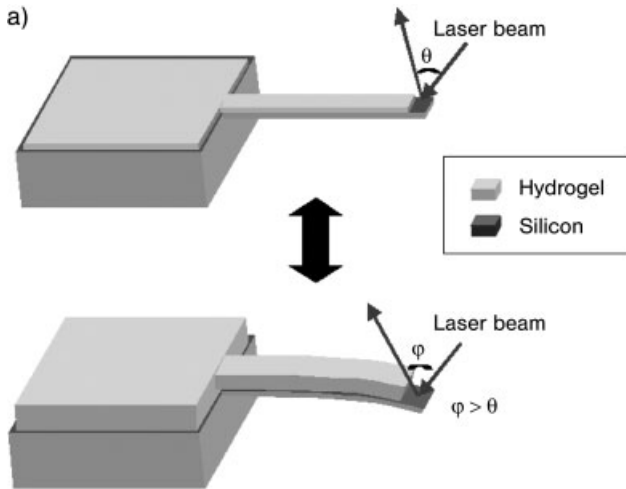


**Figure 11.2.** Hydrogel as a sensing element in a bioMEMS sensor platform. (a) A schematic of the bioMEMS sensor platform based on a microcantilever patterned with an environ-

tally responsive hydrogel. (b) A detailed examination of the equilibrium bending response versus pH (constant ionic strength of 0.5 M) is shown [30].

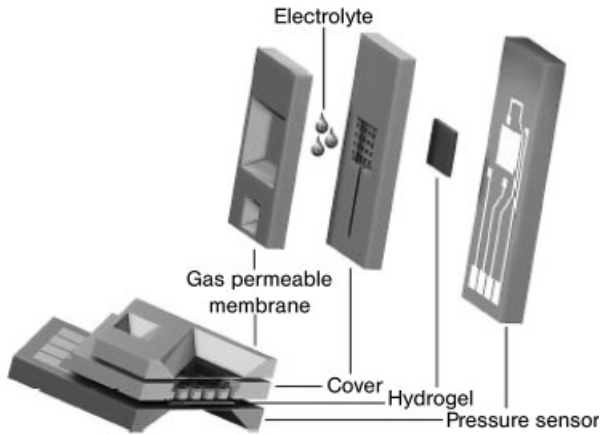


**Figure 11.3.** Cross-section and exploded view of the hydrogel-based CO<sub>2</sub> sensor [35] (permission pending).

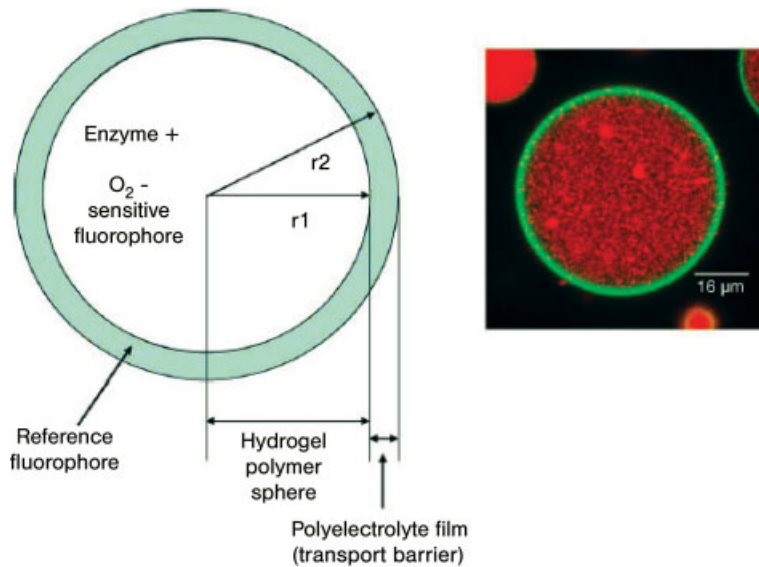


**Figure 11.4.** Illustration of nanoengineered microspheres optical glucose sensors. (a) A functional schematic of the microsphere sensor. (b) Confocal laser scanning micrograph of an actual prototype glucose sensor (red fluorescence = O<sub>2</sub> indicator in alginate microsphere, green fluorescence = reference fluorescence in polyelectrolyte film) [39].

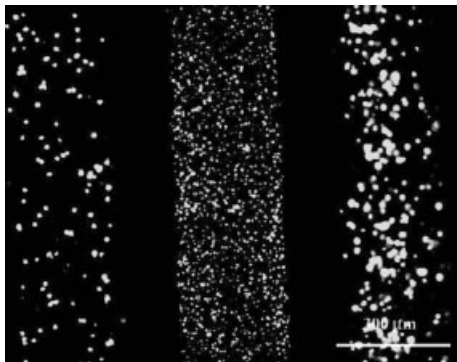


**Figure 11.5.** A multiphenotypic microdevice containing (left to right) hepatocytes, macrophages and endothelial cells stained with calcein AM [41].

Other researchers have applied hydrogel microstructures as three-dimensional scaffolds for the encapsulation of living cells [40–42], and these structures have potential advantages in the development of cell-based sensors for detecting chemical and biological toxins, and for assaying cellular responses to target compounds (e.g. drug screening). For example, a multiphenotypic whole-cell microsensor platform (Fig. 11.5) was demonstrated that could monitor cell viability via optical methods [41]. This platform enabled the comparison of the toxic effect of concanavalin A on macrophages and hepatocytes relative to the relatively unaffected endothelial cells.

By incorporating enzymes within hydrogel networks, biosensing elements can be fabricated. These biohybrid structures can be advantageous by allowing the precise control over the micro/nanoenvironment of the enzymes. In addition, these biohybrid structures can be patterned at the micro/nanoscale, allowing for their integration into sensor devices [43–45]. Pishko and coworkers [43, 44] have applied photolithography techniques to pattern hydrogel arrays containing immobilized enzymes, such as alkaline phosphatase, acetylcholinesterase and urease. The enzymes were conjugated to pH-sensitive fluorophores, allowing for optical detection of the changes in microenvironment pH due to the enzyme-catalyzed reactions. In addition, Crooks and coworkers [45] have demonstrated a microfluidic biosensor based on arrays of hydrogel-entrapped enzymes (micropatches). This platform was applied to simultaneously detect different concentrations of the same analyte (e.g. glucose) and multiple analytes in real time (Fig. 11.6).

Nanoscale probes encapsulated by biologically localized embedding (PEBBLEs) have been developed by Kopelmann and collaborators [46], and these sensing and imaging probes range from 20 to 600 nm in diameter, and are often constructed of hydrogel networks (e.g. polyacrylamide). For information on recent activities in this area, the reader is referred to a recent review of the topic [46].

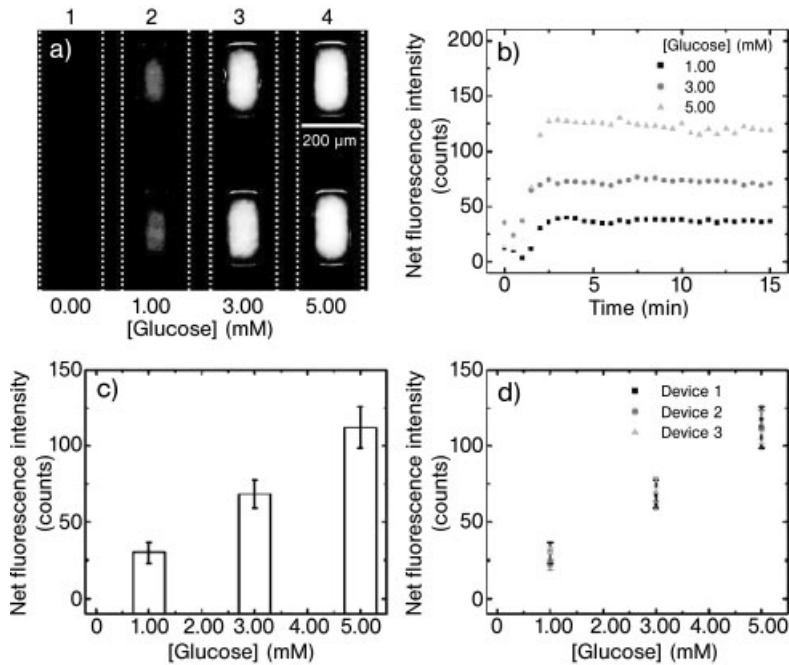


**Figure 11.6.** Biosensor based on hydrogel-containing microchannels. (a) Fluorescence micrograph obtained 15 min after solutions containing 0.10 mM Amplex Red plus different concentrations of glucose (shown at the bottom of each channel) were introduced into each of the four channels. The flow rate was  $1.0 \mu\text{L min}^{-1}$ . Each micropatch contained both glucose oxidase and hydrogen peroxidase. The fluorescence emission was integrated for 0.7 s. The dashed white lines indicate the positions of channel walls. (b) Time-dependent net fluorescence intensity profiles collected from the hydrogel micropatches shown in the top row of (a). The net fluorescence intensity was obtained by subtracting the intensity of the

micropatch in channel 1 (no glucose present) from the fluorescence intensities arising from the micropatches in channels 2–4. (c) Graph showing the average net fluorescence intensity as a function of the glucose concentration for the three micropatches present in each channel of the device shown in (a). The error bars represent  $1\sigma$  for the three micropatches. (d) Plot of net fluorescence intensity as a function of glucose concentration for three independently prepared microfluidic devices. The error bars represent  $1\sigma$  for the three micropatches in each channel of each device. Fluorescence micrographs were obtained with a Photometrics 16-bit gray scale CCD camera [45].

### 11.3.3

#### Electrical Detection

Several research groups have patterned biohybrid hydrogels containing immobilized oxidoreductase enzymes, such as glucose oxidase, lactate oxidase and alcohol oxidase, onto electrodes to create biosensors for monitoring various analyte levels [47–50]. For example, Jimenez and coworkers [50] fabricated enzymatic microsensors that employed polyacrylamide as a entrapment matrix for immobilization of enzyme recognition elements, including glucose oxidase and urease, that was pat-

terned onto a pH-sensitive ion selective field-effect transistor (FET). In other work, Sheppard and coworkers developed miniature conductimetric pH sensors based on the measurement of the conductivity of pH-responsive hydrogels that were photolithographically patterned onto planar interdigitated electrode arrays [51–53]. The sensor monitored the changes in the electrical conductivity of the hydrogel membrane that resulted with its swelling/collapsing. In related work, Guiseppe-Elie and coworkers [54] demonstrated chemical and biological sensors that applied conducting electroactive hydrogel composites as recognition elements and utilized electrochemical detection.

In the above sensor applications, the majority of patterning applications of hydrogels have relied on UV photolithography and, thus, have been limited to microscale applications. For the application of hydrogels in nanoscale sensing applications, it is critical that nanopatterning techniques are developed, and this is a new area receiving much research attention. For example, Libera and coworkers [55] have applied electron-beam crosslinking methods to pattern amine-terminated PEG thin films on silicon substrates with lateral dimensions of order of 200 nm (Fig. 11.7). It was demonstrated that the amine groups remained functional after electron-beam exposure, enabling the covalent attachment of proteins of interest.

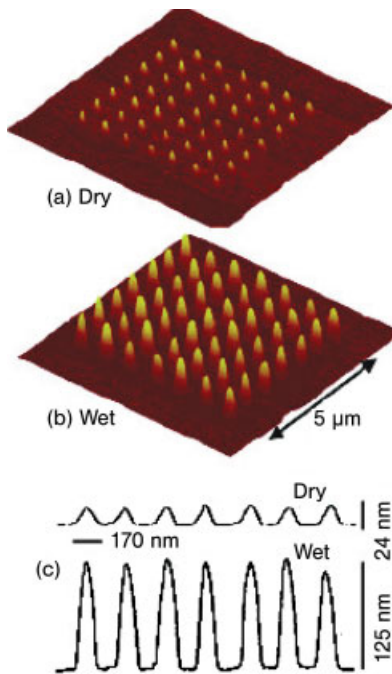


**Figure 11.7.** AFM images of a  $5\ \mu\text{m} \times 5\ \mu\text{m}$  array of amine-terminated PEG hydrogels with an inter-gel spacing of 715 nm. (A) Dry, (B) hydrated and (C) height profiles of a row of nanogels which swell by a factor exceeding 5 times [55].

## 11.4 Drug Delivery Applications

For the application of hydrogels as intelligent carriers in controlled drug delivery, researchers have optimized their properties by engineering their physical and chemical properties at the molecular level, such as permeability for sustained release applications, environmentally responsive nature for pulsatile release applications, surface functionality for targeted or stealth release (PEG coatings) and biodegradability for bioresorbable applications [12, 15, 56, 57]. In particular, environmentally responsive hydrogels have been applied in a wide variety of controlled drug delivery applications, since they allow for release that is controlled by the conditions of the environment. For example, temperature-responsive hydrogels have been widely used to create drug delivery systems exhibiting a pulsatile release profile in response to temperature changes [13, 16]. In addition, pH-responsive hydrogels have been applied in numerous controlled release applications, such as

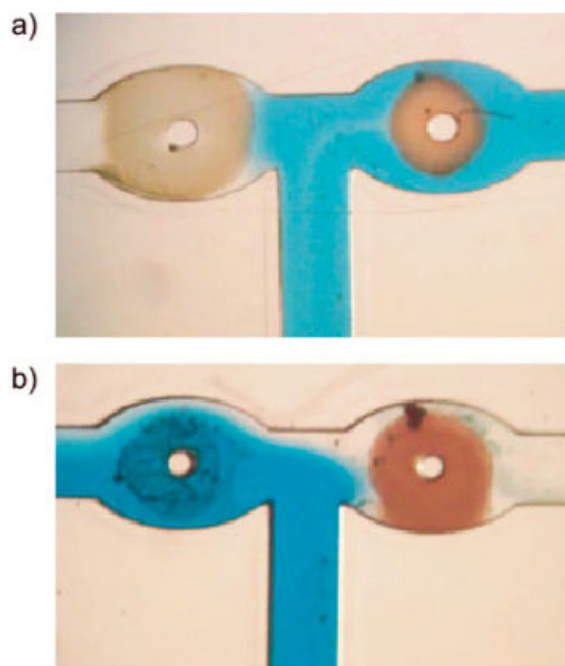


**Figure 11.8.** Two valves formed at a T-junction in a microfluidics device, one made of a gold–colloid nanocomposite hydrogel and the other a gold–nanoshell nanocomposite hydrogel. The channels are 100  $\mu\text{m}$  wide. (a) When the entire device was illuminated with green light (532 nm, 1.6  $\text{W cm}^{-2}$ ), the gold colloid valves

opened while the nanoshell valve remained closed. (b) However, when the device was illuminated with near infrared light (832 nm, 2.7  $\text{W cm}^{-2}$ ), the opposite response was observed. In both cases, the valves opened within 5 s [65].

PEG-containing ionic networks that have been applied for the oral delivery of proteins, including insulin [58, 59] and calcitonin [60, 61].

In therapeutic applications, polymeric micro/nanotechnologies have found widespread application in the form of implantable devices, functional particles and tissue engineering constructs. The reader is directed to Ref. [62] for detailed information on the application of hydrogel nanoparticles. In the following, the application of hydrogels as functional components of devices is highlighted, and there is also a brief mention of nanoshell hydrogel structures.

#### 11.4.1

##### **Micro/nanoscale Devices**

In a recent review, polymeric systems for implantable drug delivery systems have been highlighted [63]. In recent years, several controlled drug delivery devices where a target release is controlled by hydrogel valves have been proposed [64–67]. Optomechanically responsive nanocomposite hydrogels have been developed based on poly(*N*-isopropylacrylamide-*co*-acrylamide) and particles with distinct and strong optical-absorption profiles (gold colloids and nanoshells) [64, 65]. These nanocomposite hydrogels were photopatterned as valves in a microfluidics device and their wavelength dependent actuation was demonstrated (Fig. 11.8). Recently, Daunert and collaborators [66] developed novel biohybrid hydrogel systems that exhibited stimuli responsive swelling due to  $\text{Ca}^{2+}$  and applied these as valves in a microdevice (Fig. 11.9). Madou and coworkers [67] developed electro-active polymers for application as microvalves potentially for controlled drug delivery.

#### 11.4.2

##### **Nanoscale Macromolecular Structures**

In recent years, there has been increased interest in the practical application of organic chemistry, and its molecular-level control, for the preparation of nanostructured macromolecular structures with tailored properties and functions [68]. A prime example has been the work of Wooley and coworkers [69–72], where well-defined nanostructured materials have been created by organizing polymers into micellar assemblies followed by stabilization through intramolecular crosslinking of the chain segments that compose the polymer micelle shell [shell crosslinked knedel-like (SCK)]. In Fig. 11.10, a schematic of the synthetic approach for preparing SCK polymer assemblies is provided. These SCK nanostructures have great potential as nanoscale intelligent drug delivery carriers, such as their ability to be tailored to be entirely hydrophilic and responsive to environmental conditions [70], be functionalized for targeted drug delivery applications (e.g. cancer cell targeting) [71], and be mineralized on their surface to further control dissolution and permeability properties for controlled drug delivery applications [72].

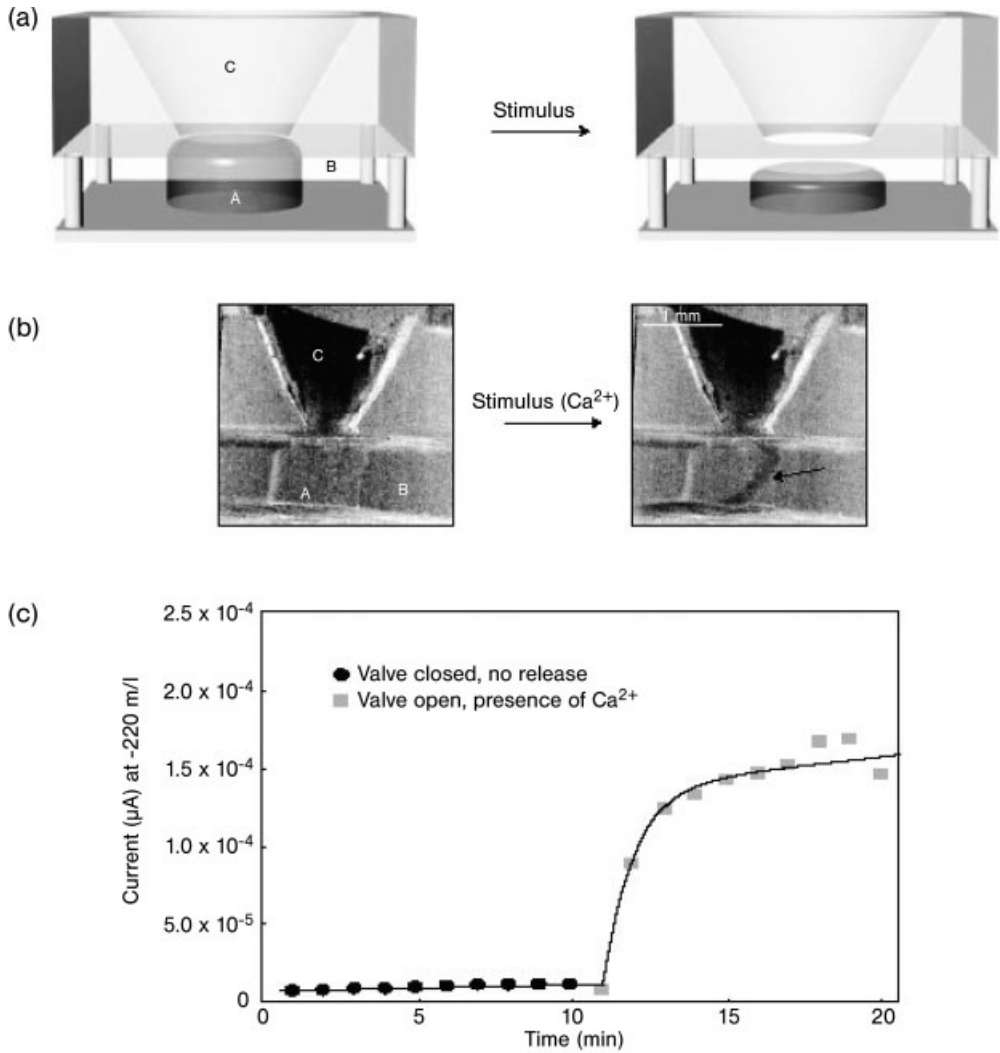


**Figure 11.9.** Incorporation of hydrogels in microfluidic systems. (a) Schematic of microactuator ‘plunger’ configuration. The stimuli-responsive hydrogel (A) shrinks in the presence of a stimulus in the bulk solution (B) allowing release from a reservoir (C). (b) The

release of a solution containing blue dextran and an electrochemical probe [hexamine ruthenium chloride(III)] in the presence of a stimulus ( $\text{Ca}^{2+}$ ). Arrow denotes release plume. (c) Electrochemical response of probe during the release event [66].



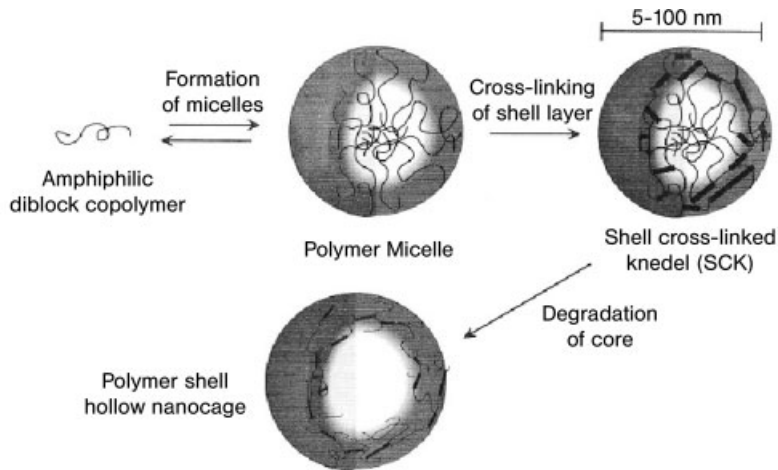


**Figure 11.10.** The general synthetic approach for the preparation of SCK polymer assemblies involves a combination of self-assembly and covalent stabilization, providing robust nanostructured materials from supramolecular, dynamic precursors [69].

## 11.5

### Conclusions

This chapter has highlighted the recent activities in the field of intelligent hydrogels, with a focus on the applications in sensing and drug delivery micro/nanotechnologies. The field of intelligent hydrogels was introduced and several example systems (e.g. ionic, temperature-responsive, biohybrid and imprinted hydrogels) were highlighted. Selected sensor and drug delivery applications of intelligent hydrogels were introduced and briefly discussed. Although this is a new field, the potential is clear with many expected applications where intelligent hydrogel systems will positively impact the fields of sensing and drug delivery.

### References

- 1 ITO, Y., Photolithographic synthesis of intelligent microgels. *J. Intell. Mater. Syst. Struct.* **1999**, *10*, 541–547.
- 2 CHEN, G., IMANISHI, Y., ITO, Y., Photolithographic synthesis of hydrogels. *Macromolecules* **1998**, *31*, 4379–4381.
- 3 CHEN, G., ITO, Y., IMANISHI, Y., Micropattern immobilization of a pH-sensitive polymer. *Macromolecules* **1997**, *30*, 7001–7003.
- 4 NAKAYAMA, Y., ANDERSON, J., MATSUDA, T., Laboratory-scale mass production of a multi-micropatterned grafted surface with different polymer regions. *J. Biomed. Mater. Res. (Appl. Biomater.)* **2000**, *53*, 584–591.
- 5 DEFIFE, K., COLTON, E., NAKAYAMA, Y., MATSUDA, T., ANDERSON, J., Spatial regulation and surface chemistry control of monocyte/macrophage adhesion and foreign body giant cell

- formation by photochemically micropatterned surfaces. *J. Biomed. Mater. Res.* **1999**, *45*, 148–154.
- 6 HIGASHI, J., NAKAYAMA, Y., MARCHANT, R., MATSUDA, T., High-spatioresolved microarchitectural surface prepared by photograft copolymerization using dithiocarbamate: surface preparation and cellular responses. *Langmuir* **1999**, *15*, 2080–2088.
  - 7 NAKAYAMA, Y., NAKAMATA, K., HIRANO, Y., GOTO, K., MATSUDA, T., Surface hydrogelation of thiolated water-soluble copolymers on gold. *Langmuir* **1998**, *14*, 3909–3915.
  - 8 NAKAYAMA, Y., MATSUDA, T., Surface macromolecular architectural designs using photo-graft copolymerization based on photochemistry of benzyl *N,N*-diethyldithiocarbamate. *Macromolecules* **1996**, *29*, 8622–8630.
  - 9 WARD, J., BASHIR, R., PEPPAS, N. A., Micropatterning of biomedical polymer surfaces by novel UV polymerization techniques. *J. Biomed. Mater. Res.* **2001**, *56*, 351–360.
  - 10 BEEBE, D. J., MOORE, J. S., BAUER, J. M., YU, Q., LIU, R. H., DEVADOSS, C., JO, B., Functional hydrogel structures for autonomous flow control inside microfluidic channels. *Nature* **2000**, *404*, 588–590.
  - 11 BEEBE, D. J., MOORE, J. S., YU, Q., LIU, R. H., KRAFT, M. L., JO, B., DEVADOSS, C., Microfluidic tectonics: a comprehensive construction platform for microfluidic systems. *Proc. Natl Acad. Sci. USA* **2000**, *97*, 13488–13493.
  - 12 PEPPAS, N. A., BURES, P., LEOBANDUNG, W., ICHIKAWA, H., Hydrogels in pharmaceutical formulations. *Eur. J. Pharm. Biopharm.* **2000**, *50*, 27–46.
  - 13 JEONG, B., KIM, S., BAE, Y., Thermo-sensitive sol-gel reversible hydrogels. *Adv. Drug Deliver. Rev.* **2002**, *54*, 37–51.
  - 14 MIYATA, T., URAGAMI, T., NAKAMAE, K., Biomolecule-sensitive hydrogels. *Adv. Drug Deliver. Rev.* **2002**, *54*, 79–98.
  - 15 VAN DER LINDEN, H., HERBER, S., OLTHUIS, W., BERGVELD, P., Stimulus-sensitive hydrogels and their applications in chemical (micro)analysis. *Analyst* **2003**, *128*, 325–331.
  - 16 SERSHEN, S., WEST, J., Implantable, polymeric systems for modulated drug delivery. *Adv. Drug Deliver. Rev.* **2002**, *54*, 1225–1235.
  - 17 PODUAL, K., DOYLE, F. J., PEPPAS, N. A., Glucose-sensitivity of glucose oxidase-containing cationic copolymer hydrogels having poly(ethylene glycol) grafts. *J. Control. Release* **2000**, *67*, 9–17.
  - 18 MIYATA, T., ASAMI, N., URAGAMI, T., A reversibly antigen-responsive hydrogel. *Nature* **1999**, *399*, 766–769.
  - 19 WANG, C., STEWART, R. J., KOPECEK, J., Hybrid hydrogels assembled from synthetic polymers and coiled-coil protein domains. *Nature* **1999**, *397*, 417–420.
  - 20 BYRNE, M. E., ORAL, E., HILT, J. Z., PEPPAS, N. A., Networks for recognition of biomolecules: Molecular imprinting and micropatterning poly(ethylene glycol)-containing films. *Polym. Adv. Technol.* **2002**, *13*, 798–816.
  - 21 PEPPAS, N. A., HUANG, Y., Polymers and gels as molecular recognition agents. *Pharm. Res.* **2002**, *19*, 578–587.
  - 22 BYRNE, M. E., PARK, K., PEPPAS, N. A., Molecular imprinting within hydrogels. *Adv. Drug Deliver. Rev.* **2002**, *54*, 149–161.
  - 23 HILT, J. Z., BYRNE, M. E., Configurational biomimesis in drug delivery: molecular imprinting of biologically significant molecules. *Adv. Drug Deliver. Rev.* **2004**, *56*, 1599–1620.
  - 24 RUAN, C., ONG, K. G., MUNGLE, C., PAULOSE, M., NICKL, N. J., GRIMES, C. A., A wireless pH sensor based on the use of salt-independent micro-scale polymer spheres. *Sensors Actuators B* **2003**, *96*, 61–69.
  - 25 RUAN, C., ZENG, K., GRIMES, C. A., A mass-sensitive pH sensor based on a stimuli-responsive polymer. *Anal. Chim. Acta* **2003**, *497*, 123–131.
  - 26 HAN, I., HAN, M., KIM, J., LEW, S., LEE, Y. J., HORKAY, F., MAGDA, J. J., Constant-volume hydrogel osmometer: a new device concept for miniature

- biosensors. *Biomacromolecules* **2002**, *3*, 1271–1275.
- 27 GERLACH, G., GUENTHER, M., SORBER, J., SUCHANECK, G., ARNDT, K., and RICHTER, A., Chemical and pH sensors based on the swelling behavior of hydrogels. *Sensors Actuators B* **2005**, *111–112*, 555–561.
- 28 STRONG, S., WANG, A., MCCONAGHY, C., Hydrogel-actuated capacitive transducer for wireless biosensors. *Biomed. Microdev.* **2002**, *4*, 97–103.
- 29 BASHIR, R., HILT, J. Z., GUPTA, A., ELIBOL, O., PEPPAS, N. A., Micro-mechanical cantilever as an ultrasensitive pH microsensor. *Appl. Phys. Lett.* **2002**, *81*, 3091–3093.
- 30 HILT, J. Z., GUPTA, A. K., BASHIR, R., PEPPAS, N. A., Ultrasensitive bioMEMS sensors based on micro-cantilevers patterned with environmentally responsive hydrogels. *Biomed. Microdev.* **2003**, *5*, 177–184.
- 31 ZHANG, Y., JI, H., BROWN, G. M., THUNDAT, T., Detection of  $\text{CrO}_4^{2-}$  using a hydrogel swelling micro-cantilever sensor. *Anal. Chem.* **2003**, *75*, 4773–4777.
- 32 LIU, K., JI, H., Detection of  $\text{Pb}^{2+}$  using a hydrogel swelling microcantilever sensor. *Anal. Sci.* **2004**, *20*, 9–11.
- 33 RICHTER, A., BUND, A., KELLER, M., ARNDT, K., Characterization of a microgravimetric sensor based on pH sensitive hydrogels. *Sensors Actuators B* **2004**, *99*, 579–585.
- 34 HERBER, S., OLTHUIS, W., BERGVELD, P., A swelling hydrogel-based  $\text{P}_{\text{CO}_2}$  sensor. *Sensors Actuators. B* **2003**, *91*, 378–382.
- 35 HERBER, S., BOMER, J., OLTHUIS, W., BERGVELD, P., VAN DEN BERG, A., A miniaturized carbon dioxide gas sensor based on sensing of pH-sensitive hydrogel swelling with a pressure sensor. *Biomed. Microdev.* **2005**, *7*, 197–204.
- 36 HERBER, S., EIJKEL, J., OLTHUIS, W., BERGVELD, P., VAN DEN BERG, A., Study of chemically induced pressure generation of hydrogels under isochoric conditions using a micro-fabricated device. *J. Chem. Phys.* **2004**, *121*, 2746–2751.
- 37 MEIRING, J., SCHMID, M., GRAYSON, S., RATHSACK, B., JOHNSON, D., KIRBY, R., KANNAPPAN, R., MANTHIRAM, K., HSIA, B., HOGAN, Z., ELLINGTON, A., PISHKO, M., WILLSON, C., Hydrogel biosensor array platform indexed by shape. *Chem. Mater.* **2004**, *16*, 5574–5580.
- 38 BROWN, J., SRIVASTAVA, R., MCSHANE, M., Encapsulation of glucose oxidase and an oxygen-quenched fluorophore in polyelectrolyte-coated calcium aginate microspheres as optical glucose sensor systems. *Biosensors Bioelectron.* **2005**, *21*, 212–216.
- 39 BROWN, J., MCSHANE, M., Modeling of spherical fluorescent glucose microsensor systems: design of enzymatic smart tattoos. *Biosensors Bioelectron.* **2006**, *21*, 1760–1769.
- 40 ZGURIS, J., ITLE, L., KOH, W., PISHKO, M., A novel single-step fabrication technique to create heterogeneous poly(ethylene glycol) hydrogel microstructures containing multiple phenotypes of mammalian cells. *Langmuir* **2005**, *21*, 4168–4174.
- 41 ITLE, L., PISHKO, M., Multiphenotypic whole-cell sensor for viability screening. *Anal. Chem.* **2005**, *77*, 7887–7893.
- 42 LIU, V., BHATIA, S., Three-dimensional photopatterning of hydrogels containing living cells. *Biomed. Microdev.* **2002**, *4*, 257–266.
- 43 YADAVALLI, V., KOH, W., LAZUR, G., PISHKO, M., Microfabricated protein-containing poly(ethylene glycol) hydrogel arrays for biosensing. *Sensors Actuators B* **2004**, *97*, 290–297.
- 44 KOH, W., PISHKO, M., Immobilization of multi-enzyme microreactors inside microfluidic devices. *Sensors Actuators B* **2005**, *106*, 335–342.
- 45 HEO, J., CROOKS, R., Microfluidic biosensor based on an array of hydrogel-entrapped enzymes. *Anal. Chem.* **2005**, *77*, 6843–6851.
- 46 BUCK, S., XU, H., BRASUEL, M., PHILBERT, M., KOPELMAN, R., Nanoscale probes encapsulated by biologically localized embedding (PEBBLEs) for ion sensing and imaging in live cells. *Talanta* **2004**, *63*, 41–59.

- 47 SIRKAR, K., PISHKO, M. V., Amperometric biosensors based on oxidoreductases immobilized in photopolymerized poly(ethylene glycol) redox polymer hydrogels. *Anal. Chem.* **1998**, *70*, 2888–2894.
- 48 MUNOZ, A., MAS, R., GALAN-VIDAL, C. A., DOMINIGUEZ, C., GARCIA-RAURICH, J., ALEGRET, S., Thin-film microelectrodes for biosensing. *Quim. Anal.* **1999**, *18*, 155–157.
- 49 JOBST, G., MOSER, I., VARAHAM, M., SVASEK, P., ASCHAUER, E., TRAJANSKI, Z., WACH, P., KOTANKO, P., SKRABAL, F., URBAN, G., Thin-film microbiosensors for glucose–lactate monitoring. *Anal. Chem.* **1996**, *68*, 3173–3179.
- 50 JIMENEZ, C., BARTROL, J., DE ROOIJ, N. F., KOUDELKA, M., Use of photopolymerizable membranes based on polyacrylamide hydrogels for enzymatic microsensor construction. *Anal. Chim. Acta* **1997**, *351*, 169–176.
- 51 SHEPPARD, JR., N. F., LESHO, M. J., McNALLY, P., FRANCOMACARO, A. S., Microfabricated conductimetric pH sensor. *Sensors Actuators B* **1995**, *28*, 95–102.
- 52 LESHO, M. J., SHEPPARD, JR., N. F., Adhesion of polymer films to oxidized silicon and its effect on performance of a conductometric pH sensor. *Sensors Actuators B* **1996**, *37*, 61–66.
- 53 SHEPPARD, JR., N. F., TUCKER, R. C., SALEHI-HAD, S., Design of a conductimetric pH microsensor based on reversibly swelling hydrogels. *Sensors Actuators B* **1993**, *10*, 73–77.
- 54 BRAHIM, S., WILSON, A. M., NARINESINGH, D., IWUOHA, E., GUISEPPI-ELIE, A., Chemical and biological sensors based on electrochemical detection using conducting electroactive polymers. *Microchim. Acta* **2003**, *143*, 123–137.
- 55 HONG, Y., KRASKO, P., LIBERA, M., Protein surface patterning using nanoscale PEG hydrogels. *Langmuir* **2004**, *20*, 11123–11126.
- 56 PEPPAS, N. A., Hydrogels and drug delivery. *Curr. Opin. Colloid* **1997**, *2*, 531–537.
- 57 PEPPAS, N. A., WOOD, K. M., BLANCHETTE, J. O., Hydrogels for oral delivery of therapeutic proteins. *Expert Opin. Biol. Ther.* **2004**, *4*, 881–887.
- 58 LOWMAN, A. M., MORISHITA, M., KAJITA, M., NAGAI, T., PEPPAS, N. A., Oral delivery of insulin using pH-responsive complexation gels. *J. Pharm. Sci.* **1999**, *88*, 933–937.
- 59 MORISHITA, M., LOWMAN, A. M., TAKAYAMA, K., NAGAI, T., PEPPAS, N. A., Elucidation of the mechanism of incorporation of insulin in controlled release systems based on complexation polymers. *J. Control. Release* **2002**, *81*, 25–32.
- 60 TORRES-LUGO, M., GARCIA, M., RECORD, R., PEPPAS, N. A., Physicochemical behavior and cytotoxic effects of p(methacrylic acid-g-ethylene glycol) nanospheres for oral delivery of proteins. *J. Control. Release* **2002**, *80*, 197–205.
- 61 TORRES-LUGO, M., GARCIA, M., RECORD, R., PEPPAS, N. A., pH-sensitive hydrogels as gastrointestinal tract absorption enhancers: transport mechanisms of salmon calcitonin and other model molecules using the Caco-2 cell model. *Biotechnol. Prog.* **2002**, *18*, 612–616.
- 62 NAYAK, S., LYON, L., Soft nanotechnology with soft nanoparticles. *Angew. Chem. Int. Ed.* **2005**, *44*, 7686–7708.
- 63 SERSHEN, S., WEST, J., Implantable, polymeric systems for modulated drug delivery. *Adv. Drug Deliv. Rev.* **2002**, *54*, 1225–1235.
- 64 SERSHEN, S., WESTCOTT, S., HALAS, N., WEST, J., Temperature-sensitive polymer–nanoshell composites for photothermally modulated drug delivery. *J. Biomed. Mater. Res.* **2000**, *51*, 293–298.
- 65 SERSHEN, S., MENSING, G., NG, M., HALAS, N., BEEBE, D., WEST, J., Independent optical control of microfluidic valves formed from optomechanically responsive nanocomposite hydrogels. *Adv. Mater.* **2005**, *17*, 1366–1368.
- 66 EHRICK, J., DEO, S., BROWNING, T., BACHAS, L., MADOU, M., DAUNERT, S., Genetically engineered protein in

- hydrogels tailors stimuli-responsive characteristics. *Nat. Mater.* **2005**, *4*, 298–302.
- 67 LOW, L., SEETHARAMAN, S., HE, K., MADOU, M., Microactuators toward microvalves for responsive controlled drug delivery. *Sensors Actuators B* **2000**, *67*, 149–160.
- 68 HAWKER, C., WOOLEY, K., The convergence of synthetic organic and polymer chemistries. *Science* **2005**, *309*, 1200–1205.
- 69 WOOLEY, K., Shell crosslinked polymer assemblies: nanoscale constructs inspired from biological systems. *J. Polym. Sci. A Polym. Chem.* **2000**, *38*, 1397–1407.
- 70 MA, Q., REMSEN, E., KOWALEWSKI, T., SCHAEFER, J., WOOLEY, K., Environmentally-responsive, entirely hydrophilic, shell cross-linked (SCK) nanoparticles. *Nano Lett.* **2001**, *1*, 651–655.
- 71 PAN, D., TURNER, J., WOOLEY, K., Folic acid-conjugated nanostructured materials designed for cancer cell targeting. *Chem. Commun.* **2003**, 2400–2401.
- 72 PERKIN, K., TURNER, J., WOOLEY, K., MANN, S., Fabrication of hybrid nanocapsules by calcium phosphate mineralization of shell cross-linked polymer micelles and nanocages. *Nano Lett.* **2005**, *5*, 1457–1461.

## 12

### Nanoshells for Drug Delivery

Melgardt M. De Villiers and Yuri M. Lvov

#### 12.1

##### Introduction

Nanomedicine, especially the field of nanopharmaceuticals (drugs and drug delivery systems), describes the preparation of nanoscale assemblies, which can be relatively simple nanoemulsions, nanoparticles or polymer conjugates (of proteins or drugs), or complex multicomponent systems containing drugs, proteins or genes, arrays of targeting ligands and/or signal systems to enable *in vitro* or *in vivo* detection. Therefore, nanopharmaceuticals is defined as the science and technology of nanometer-sized complex drug delivery systems, consisting of at least two components, one of which is the active ingredient. In this field the concept of “nanoscale” is seen to range from 1 to 1000 nm. Currently just one nanoparticle product – Abraxane® (an albumin nanoparticle containing paclitaxel) – has been approved, but many more are being developed and are in phase I, II or III of the drug development process. This means that this class of drug delivery systems is rapidly growing, and is moving from the development of individual building blocks to multifunctional, often biomimetic and bioresponsive systems [1, 2].

These more complex nanosized drug delivery systems are either self-assembling or involve covalent conjugation of multicomponent systems, e.g. drug, protein and polymer. The bioresponsive and/or biomimetic materials used to create such drug delivery systems typically include synthetic or semisynthetic polymers, and/or natural materials such as lipids, polymers and proteins. One nanosystem that is being proposed as a drug carrier is nanoshells or nanocapsules because these novel “nanoparticles” can address the three principal goals of drug delivery research today, i.e. more specific drug delivery and targeting, greater safety and biocompatibility, and faster development of new, safe medicines. Current research in nanoshell drug delivery could lead to, amongst others, vectors that will overcome the biological barriers for effective gene delivery, cancer targeting, brain delivery and the combination of the potential of antibody targeting with nanoparticle technology. This would improve drug targeting to the whole body or cellular and subcellular localization of drugs, proteins and genes [2].

The nanoshells most studied as potential nanopharmaceuticals are metallic nanoparticles composed of a dielectric (e.g. silica) core coated with an ultrathin metallic (e.g. gold) layer and nanoshells formed by electrostatic layer-by-layer molecular self-assembling (E-LbL). Here, the two types of nanoshells are compared and their application in drug delivery illuminated. Although several reviews and chapters have appeared describing the properties of these nanoshells separately, this chapter focuses on the differences between the two types of nanoshells as it applies to drug delivery. As, to date, metallic nanoshells have found limited application in drug delivery the bulk of the chapter describes the assembly, characterization and properties of E-LbL self-assembled polymeric or polymeric/nanoparticulate nanoshell drug delivery systems.

## 12.2

### Metallic Nanoshells

In the past few years, silica–gold nanoshells have emerged as powerful building blocks for devices in which electromagnetic waves can be controlled at the nanometer length scale [1]. Due to this unique property, Halas and West demonstrated in a series of clever experiments how silica–gold nanoshells are uniquely suitable for use in whole-blood immunoassays, optically triggered drug delivery and targeted photothermal destruction of cancer cells [2]. The use of metallic nanoparticles dates back to the Renaissance when artists handcrafted vibrantly colored church windows and glass vases by dissolving minute amounts of noble metal impurities in a glass melt to induce precipitation of nanometer-size metallic clusters [3]. Gustav Mie provided the theory explaining this phenomenon [4]. This theory predicts that metallic nanoclusters strongly absorb visible light at a well-defined plasmon resonance frequency that depends on the particle size and shape, the presence of other particles, and the dielectric environment [5]. Due to this phenomenon the silica–gold nanoshells offer enormous flexibility to tune the resonance frequency by varying the relative dimensions of the silica core and gold shell [6, 7]. In contrast to solid-core metallic nanoparticles, the resonance of a silica–gold nanoshell particle can easily be positioned in the near-infrared (NIR) region between 800 and 1300 nm, where absorption by biomatter is low. Together with the high degree of biocompatibility of these nanoshells, low bioabsorption opens the door to a wide variety of biological applications.

#### 12.2.1

##### Synthesis of the Nanoshells

Numerous methods have been reported for preparing metallic nanoshells. For example gold nanoshells with a gold sulfide core and a gold shell are formed by combining specific volumes of 2 mM  $\text{HAuCl}_4$  and 1 mM  $\text{Na}_2\text{S}$ . The progress of the reaction is monitored using an ultraviolet (UV)/visible spectrophotometer to observe the extinction spectrum of the solution from 400 to 1050 nm [8, 9]. As

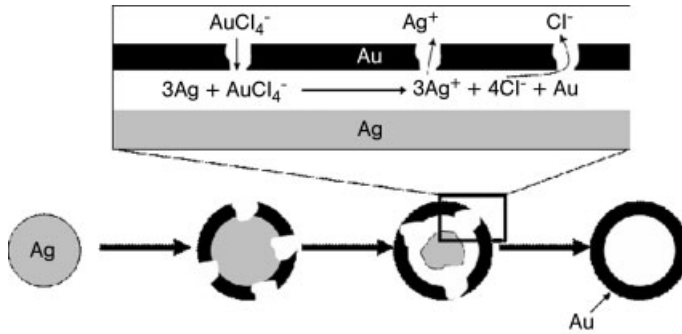


**Figure 12.1.** Schematic representation of the production of gold nanoshells by templating against silver nanoparticles [adapted from Ref. 10].

the nanoshells formed, the extinction spectra exhibit a peak that red-shifts into the IR, then halts and begin to blue-shift into the visible spectrum. The peak narrows and increase in magnitude as this occurs. Mercaptopropionic acid is added to halt this shift by halting the growth of the gold shell when the extinction peak is centered around 1050 nm. The solution then is adjusted to pH 10.5 with 1 M NaOH, centrifuged at 3000 r.p.m. for  $4 \times 20$  min and stored at 4 °C. The size and polydispersity of the resulting nanoshells are determined by evaporating a drop of the nanoshell solution onto a carbon film on a copper grid and viewing the nanoshells via transmission electron microscopy (TEM).

Sun and coworkers demonstrated a procedure based on replacement reactions for generating highly crystalline nanoshells from various metals [10]. The major steps involved are shown in Fig. 12.1 with gold/silver combination as an example. Since the standard reduction potential of the  $\text{AuCl}_4^-/\text{Au}$  redox pair is higher than that of the  $\text{Ag}^+/\text{Ag}$  redox pair silver nanoparticles are immediately oxidized to silver ions when mixed with an aqueous  $\text{HAuCl}_4$  solution. Elemental gold is thus confined in the vicinity of the template surface where it will nucleate and grow into small clusters and eventually will evolve into a shell around the silver template. The reaction initiates at facets with the highest surface free energy. As a result the thin shell formed initially is incomplete, and therefore both the  $\text{HAuCl}_4$  and  $\text{AgCl}$  will diffuse across the layer until the silver template is completely dissolved. The wall of each gold nanoshell can then be reconstructed into a highly crystalline structure via processes such as Ostwald ripening. Since stoichiometrically one gold atom is generated when three silver atoms are oxidized the thickness of the gold nanoshell is only one-ninth of the lateral dimension of the silver template.

In an alternative preparation method, Caruso and coworkers employed the LbL adsorption of polyelectrolytes and charged gold colloids to build shell-like structures around colloidal template particles whose surfaces have been derivatized with appropriately charged groups [11]. However, the gold nanoparticles prepared by all these methods are characterized by relatively low yields, problems with sur-



face roughness, polycrystallinity, nonuniformity in shell thickness, poorly defined composition and difficulty in removing colloidal templates without breaking the shells [12].

### 12.2.2

#### **Application in Nanomedicine**

In one study, Halas and West showed how NIR resonant nanoshells could be used to enable fast whole-blood immunoassays [13]. For conventional blood immunoassays, optical tests are performed at visible wavelengths. As a purification step needs to be performed to separate out a variety of unwanted biomaterials that absorb visible light, the whole procedure can take several hours or days. In the proposed immunoassay procedure nanoshells are conjugated with antibodies that act as recognition sites for a specific analyte. The analyte causes the formation of dimmers, which modify the plasmon-related absorption feature in a known way. The presence of analyte can then be determined by a fast absorption measurement in the water window, circumventing the time-intensive purification step.

Gold nanoshells can also be incorporated into temperature-sensitive hydrogels to synthesize a new type of composite material that collapses on laser irradiation [2]. Upon irradiation plasmon excitations are quickly damped and the electron kinetic energy is converted into heat through electron–phonon interactions. This fast damping is usually undesirable, but here the efficient light-to-heat conversion in metallic nanoshells is used to shrink the volume of the hydrogel from a remote location. The absorption cross-section of a nanoshell is about a million times larger than that of a typical molecular chromophore and hydrogel collapse thus occurs at relatively low pump-power densities. By incorporating nanoshells with different resonance frequencies, one can selectively collapse specific hydrogel volumes. Such remotely addressable hydrogels may find application in drug delivery and microfluidic valves or pumps.

For example, composites of thermally sensitive hydrogels and optically active nanoparticles have been developed for the purpose of photothermally modulated drug delivery [2]. Copolymers of *N*-isopropylacrylamide (NIPAAm) and acrylamide (AAm) exhibit a lower critical solution temperature (LCST) that is slightly above body temperature. When the temperature of the copolymer exceeds the LCST, the hydrogel collapses, causing a burst release of any soluble material held within the hydrogel matrix. When gold–gold sulfide nanoshells, a new class of nanoparticles designed to strongly absorb NIR light, were incorporated into poly(NIPAAm-*co*-AAm) hydrogels temperature changes in the hydrogel could be induced with light. Light at wavelengths between 800 and 1200 nm, which is transmitted through tissue with relatively little attenuation, was absorbed by the nanoparticles and converted to heat. Using this system, significantly enhanced drug release from composite hydrogels was achieved in response to irradiation by light at 1064 nm as shown in Fig. 12.2. This system controlled the release of methylene blue and proteins of varying molecular weight.

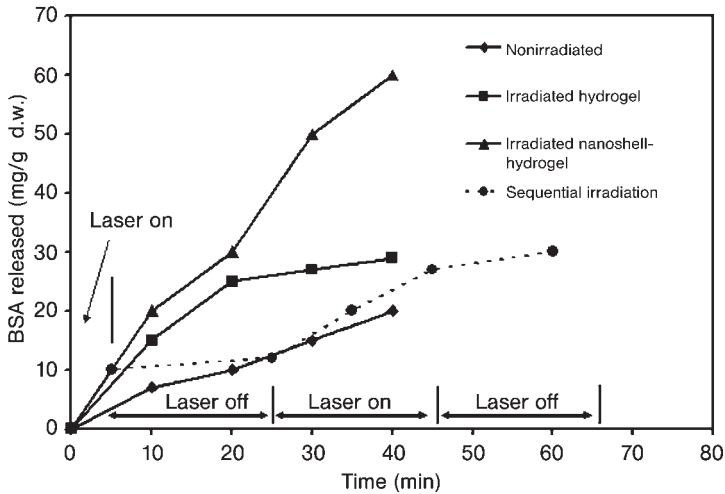


**Figure 12.2.** Release of BSA from nonirradiated and irradiated hydrogel with and without nanoshells. Irradiation was at 1064 nm at  $164 \text{ mJ pulse}^{-1}$ , 7 ns pulse length and 10 Hz repetition rate. (Adapted from Ref. [2].)

The nanoshell composite hydrogels can also release multiple bursts of protein in response to repeated NIR irradiation [2]. If the entire drug load is not released during the initial irradiation sequence, additional bursts of release of the drug can be elicited by subsequent irradiation. Once the laser irradiation is stopped, the driving force for the convective transport of material out of the hydrogel matrix is removed. During this time, the drug release is driven by diffusion and the amount released is much less than that generated by irradiation. The hydrogel will begin to swell as soon as the laser is turned off, returning to its equilibrium state. A second irradiation sequence delivered at this time will cause the hydrogel to collapse again, resulting in another burst of release of the “drug” molecule. Such a release pattern for bovine serum albumin is shown in Fig. 12.2. This type of release profile may be useful in insulin therapy as well as in other applications where controlled pulsatile release of a drug is necessary.

Additionally, it has been speculated that metallic nanoshells could play a role in future cancer treatments. These particles are small enough to find their way through the human circulatory system on injection. Bioactive molecules can be attached to the nanoshell surface to cause selective binding or accumulation of these particles within a tumor. Using a NIR laser, carcinoma tissue can then be destroyed by local thermal heating around the nanoshells. For example by tuning the nanoshells to strongly absorb light in the NIR, where optical transmission through tissue is optimal, a distribution of nanoshells at depth in tissue can be used to deliver a therapeutic dose of heat by using moderately low exposures of extracorporeally applied NIR light [14]. In this study, human breast carcinoma cells

incubated with nanoshells *in vitro* were found to have undergone photothermally induced morbidity on exposure to NIR light (820 nm,  $35 \text{ W cm}^{-2}$ ), as determined by using a fluorescent viability stain. Cells without nanoshells displayed no loss in viability after the same periods and conditions of NIR illumination. Likewise, *in vivo* studies under magnetic resonance guidance revealed that exposure to low doses of NIR light (820 nm,  $4 \text{ W cm}^{-2}$ ) in solid tumors treated with metal nanoshells reached average maximum temperatures capable of inducing irreversible tissue damage ( $\Delta T \sim 38 \text{ }^\circ\text{C}$ ) within 5 min. Controls treated without nanoshells demonstrated significantly lower average temperatures on exposure to NIR light ( $\Delta T < 10 \text{ }^\circ\text{C}$ ). These findings demonstrated good correlation with histological findings. Tissues heated above the thermal damage threshold displayed coagulation, cell shrinkage, and loss of nuclear staining, which are indicators of irreversible thermal damage. Control tissues appeared undamaged.

Due to all these positive developments, the design and fabrication of new types of plasmonic metallic nanostructures have seen a flurry of activity. In particular, the unique properties of nanoshells seem to promise a golden future for metallic nanostructures in drug delivery and it will be fascinating to see what other applications arise in the near future [12–14].

### 12.3

#### Nanoshells Formed by Polyion E-LbL Self-assembly

This nanoencapsulation method involves the formation of an outer nanothick shell around a core that is stable, permeable, compatible and allows the release of the core material through the shell. In the last decade, E-LbL self-assembly has been developed as a practical and versatile nanoencapsulation method to form nanoshells. The core templates may be “passive” (such as 50–300 nm latex or silica), which later will be dissolved, or “active” and functional (such as drug micro/nanocrystals). Tailoring of the different components of individual particles becomes important in order to develop these functionalized colloids, i.e. to combine several properties in one core–shell structure. Due to these advantages E-LbL assembly has the capacity to employ a great variety of substances as shell constituents as well as core material. Only general aspects of the method had been elaborated to demonstrate its potential, and it still has to be further developed and better understood [15–20].

#### 12.3.1

##### Preparation of E-LbL Nanoshells

The sequential adsorption of oppositely charged colloids was reported in a seminal paper in 1966 by Iler [21]. The technique of E-LbL self-assembly of thin films by means of alternate adsorption of oppositely charged linear polyions was then further developed in earnest starting in the early 1990s [22–25]. The basis of the

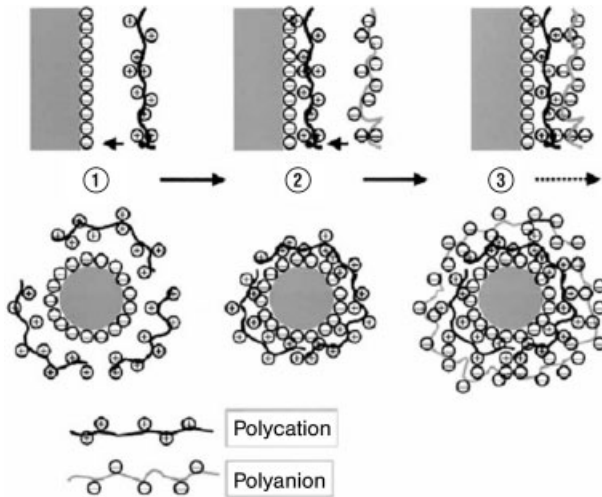


**Figure 12.3.** The procedure of E-LbL self-assembly on two-dimensional substrates and three-dimensional micro/nanotemplates. Particles with negative surface charge is coated with a layer of polycation (step 1). This

reverses the surface charge, which is then coated with an anionic polyelectrolyte (step 2). The original surface charge change is restored and the surface is ready for further assembly (step 3). (Adapted from Refs. [20, 22].)

method involves resaturation of polyion adsorption, resulting in the reversal of the terminal surface charge of the film after deposition of each layer (Fig. 12.3) [20, 22].

As a standard approach for film preparation on a solid support, the following steps are employed [22, 24, 26]:

- (i) Take aqueous solutions of polyion, nanoparticles or protein at a concentration of  $0.1\text{--}1\text{ mg mL}^{-1}$  and adjust the pH in such a way that the components are oppositely charged.
- (ii) Take a substrate carrying a surface charge [e.g. plates or polymer films covered by a layer of cationic poly(ethylenimine) (PEI) which may be readily attached to many surfaces].
- (iii) Carry out alternate immersion of the substrate in the component's solutions for 10 min with 1 min of intermediate water rinsing. To rinse a sample use a solution with pH that keeps the polyions ionized.
- (iv) Dry the sample using a stream of nitrogen (note that drying may hinder the assembly process and it is not necessary for the procedure).

The method provides the possibility of designing ultrathin multilayer films with a precision better than 1 nm of defined molecular composition. To date, this method has been used with more than 50 different charged macromolecules. The polyions predominately used in the assembly are:

- Polycations: PEI, poly(dimethyldiallylammonium chloride) (PDDA), poly(allylamine) (PAH), polylysine, chitosan.
- Polyanions: poly(styrene sulfonate) (PSS), poly(vinylsulfate), poly(acrylic acid) (PAA), dextran sulfate, sodium alginate, gelatin, chondroitin, heparin, DNA.

These charged materials can be combined with enzymes, antibodies, viruses and inorganic nanoparticles to produce multifunctional shells in both two- and three-dimensional nanoassembly processes. The architecture of these shells can be designed with nanometer precision (in cross-section) to meet different requirements such as thickness, biocompatibility, controlled permeability, targeting and optical or magnetic properties.

The only crucial factor for successful deposition is the surface charge reversal upon deposition of layers, which can be achieved by choice of proper deposition conditions. Since then various polyelectrolyte species could be adsorbed onto the surface of solid or liquid materials by means of electrostatic adsorption, forming layered structures with unique properties. It has been established that films can contain more than 1000 polyelectrolyte multilayers [27]. The universal character of the method does not impose any restriction on the type of polyelectrolyte. The multilayers can also produce diverse shapes when various materials beside polyelectrolytes, such as organic, inorganic nanoparticles and crystals, biomolecules, lipids and viruses, are used in the coating process. Such a coating produces complicated laminated structures. The use of polymers as the coating component is often advantageous in comparison with employment of their low-molecular-weight analogs. Mechanical strength, elasticity, electrical, optical and other properties make them unique building blocks for the creation of composite materials. In addition, the incorporation of proteins and nucleic acids in multilayer films may lead to the application as biosensors and in biotechnology [28–30].

The latter may even provide the base for development of ultrathin multistep chemical catalysts or photosynthesis systems mimicking plants. Applications can also be found in the fabrication of optical devices [31] and gas separation membranes [32]. The efficient use of this unique multilayer coating is interlinked with investigations of their properties. Although the methods for studying multilayer properties are straightforward, they are very often not applicable or are time consuming because of the low amount of material studied and the possible influence of the surface used as a support for layer growth. To eliminate the first factor, one should drastically increase the total surface of the multilayers, which can be done by using colloidal particles as templates [33]. Dissolution of the colloidal core could avoid the second objection. The derived hollow capsules allow the study of polyelectrolyte multilayers at the liquid–liquid interface, which seems to be very difficult while working on the solid support [23, 34].

These developments show that after the first publications on nanoshell formation in 1992–1999 [15–17], the structure of nanoshells has been characterized and the procedures to increase the functionality of the nanoshells have been elaborated through the efforts of several research groups [18, 22, 30]. For example, pore openings in these polyion multilayers were first discovered by Mendelsohn and co-

workers [35], and then later applied for enzyme loading into nanoshells by Lvov and Caruso [18]. This growth in our knowledge regarding E-LbL nanoshell fabrication, structure and properties has led to noteworthy achievements that have many advantages. However, many practical clinical applications in nanomedicine remain to be developed.

#### 12.3.1.1 Proving the Nanoshells

For the time-dependent monitoring of the assembly *in situ*, a quartz crystal microbalance (QCM) is most often used because of its proven suitability [22, 36, 37]. First of all, the kinetics of the adsorption process can be delineated by the QCM technique, which is indispensable for establishing proper assembly conditions (e.g. saturation adsorption time). Multilayer assembly is generally characterized by means of the QCM technique in two ways: (i) after drying a sample in a nitrogen stream we measure the resonance frequency shift and calculated an adsorbed mass by the Sauerbrey equation or (ii) by monitoring of the resonator frequency during the adsorption process onto one side of the resonator which is in permanent contact with the polyion solutions. Frequency shifts of about 800 Hz are seen for every adsorption cycle in solution QCM, which is more than that detected, for example, for a dried film of PSS/PAH. This difference is ascribed to the strong hydration of the layer that had just been adsorbed. The bound water is included in the film and is removed after drying. This means that most polyion films swell by 40–60% before drying and that only 5–10% of the water remains in polyion films after drying.

It is assumed that polyion adsorption occurs in two stages: quick anchoring to a surface and slow relaxation. To reach a surface charge reversion during linear polyion adsorption one needs a concentration greater than  $10^{-5}$  M [36]. However, the dependence of polyion layer thickness on concentration is not great because in the concentration range of 0.1–5 mg mL<sup>-1</sup> the PSS/PAH pair yielded a similar bilayer thickness. A further decrease in polyion concentration (using 0.01 mg mL<sup>-1</sup>) decreased the layer thickness of the adsorbed polyion. Other the other hand, an increase in the component concentrations to 20–30 mg mL<sup>-1</sup> may result in the nonlinear (exponential) enlargement of the growth rate with adsorption steps, especially if an intermediate sample rinsing is not long enough [38].

In addition, at the beginning of the alternate assembly process one often sees nonlinear film growth [36, 39]. As shown in Fig. 12.4, in the first two to three layers, smaller amounts of polyion are adsorbed as compared with further assembly, when the film mass and thickness increase linearly with the number of adsorption cycles. Tsukruk and coworkers [40] explained this as an island-type adsorption of the first polyion layer on a weakly charged solid support. In the following two to three adsorption cycles these islands spread and cover the entire surface, and further multilayer growth occurs linearly. If a substrate is well charged then a linear growth with repeatable steps begins earlier.

In addition to measuring weight changes with a QCM, following changes in the UV spectra is another simple method to control LbL assembly on glass or quartz slides. After every other layer one can measure the sample UV spectra and use Beer's law (absorbance is proportional to the material mass) to judge the amount

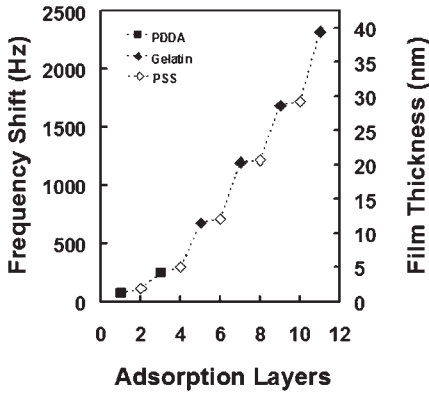


**Figure 12.4.** Frequency shift and film thickness of each assembly layer for PDDA + (PSS/PDDA)<sub>2</sub> + (PSS/gelatin)<sub>4</sub> adsorption on QCM electrodes. The first four-layer precursor is about 4 nm thick. The averaged frequency shift of every gelatin layer is 483 Hz, corresponding to a thickness of 8 nm.

of adsorbed polymer and whether the assembly process linear with number of adsorbed layers. Figure 12.5 shows the UV spectra for three, five, seven and nine bilayers of PSS/PAH deposited on quartz slide. There is a linear increase of absorbency with an increase in the number of layers; therefore, the mass of the film was increasing linearly too. The absorbance maximum at 225 nm corresponds to the absorbency of benzyl rings of PSS.

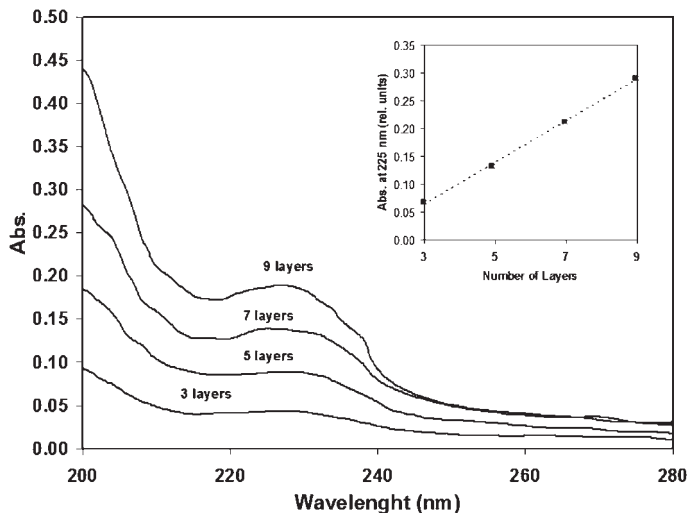


**Figure 12.5.** The increase in absorbance with an increase in the number of PSS/PAH layers deposited on a glass slide. The insert show the linear increase in layer mass.

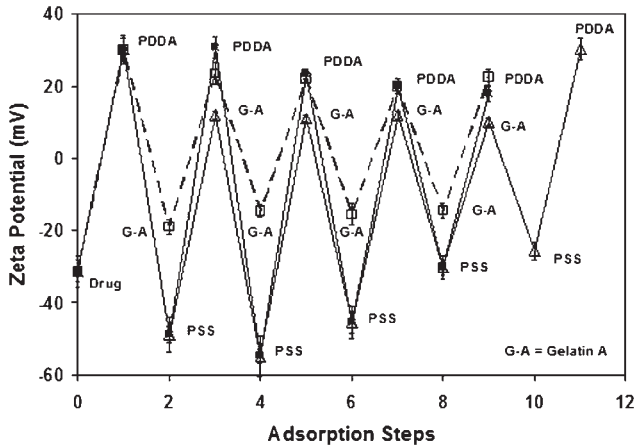


**Figure 12.6.** Changes in the  $\zeta$  potential of the coated dexamethasone particles as a function of the number of adsorption steps for capsule composition of dexamethasone core/(PDDA/gelatin A)<sub>4</sub>/PDDA (broken line and open squares) and dexamethasone core/PDDA/(PSS/gelatin A)<sub>4</sub>/(PSS/PDDA)<sub>1</sub> (solid line and open triangles). dexamethasone core/(PDDA/PSS)<sub>4</sub>/PDDA (solid line and solid squares),

Another method to monitor the assembly process is to ensure the reversal of charge after each polyion coating as shown in Fig. 12.6 [41]. For this the  $\zeta$  potential of the suspended nanoshells is measured after each layer has been applied. If the solid support (e.g. drug crystal) with negative surface charge is, for example, incubated in a solution containing a cationic polyelectrolyte, a layer of polycation is adsorbed. As the adsorption is carried out at a relatively high concentration of polyelectrolytes, a number of ionic groups remain exposed at the interface with the solution and thus the surface charge is effectively reversed. The reversed surface charge prevents further polyion adsorption. Solid supports or microtemplates are then rinsed with pure water or washed by centrifugation, respectively, to remove excess free polyions. The surface is then immersed in a solution of anionic polyelectrolytes. Again, a layer is adsorbed, but now the original surface charge (negative) is restored and the surface is ready for further assembly. These two steps are repeated alternately until a layer of the desired thickness is obtained. More than two components can be used in the assembly as long as one condition, i.e. a proper alternation of positive and negative charge, is observed [20, 22, 41].

More detail structural information can be obtained from X-ray and neutron reflectivity data. X-ray or neutron reflectivity measurements of polyion films show patterns with profound intensity oscillations, the so-called Kiessig fringes, due to the interference of radiation beams reflected from solid support/film and air/film interfaces [42]. From the periodicity of these oscillations one can calculate the film thickness (with the help of the Bragg-like equation and taking into account refraction phenomena which are essential at small-angles). Growth steps for a bilayer of 1.1–2.0 nm are typical for alternate linear polyion assembly and a thickness of one



layer often equals half of this value [43]. These values correspond to a polyion cross-section and show that in one cycle of excessive adsorption we have approximately one monolayer coverage of the substrate. The nanoparticle/polyion bilayer thickness is determined by the diameter of the particle. Model fitting of X-ray data gives a surface roughness of the polyion film of order 1 nm, while atomic force microscopy (AFM) and scanning electron microscopy (SEM) data revealed a surface roughness of 1–2 nm [42]. Polyion films are insoluble in water and in many organic solvents and are stable to 250–280 °C [44].

The polycation/polyanion bilayer thickness depends on the charge density of the polyions. It was shown that more than 10% of polyion side-groups have to be ionized for a stable reproducible multilayer assembly via alternate electrostatic adsorption [45]. High ionization of polyions results in a smaller step of film growth (1–2 nm) and lower ionization gives a larger growth step (3–6 nm). It can be reached either by adding salt to a polyion solution (as discussed above for strong polyelectrolytes, such as PDDA and PSS) or by varying the pH for weak polyelectrolytes [46].

#### 12.3.1.2 Influence of the Core on Nanoshell Properties

So far it has been shown that the procedure of E-LbL nanoshell formation is a multistep process. Although the further properties of capsules depend strongly on the choice of polyelectrolytes employed and adsorption conditions, such as ionic strength, temperature, solvent composition, number of layers, etc., an extremely important step in determining the success of the experiment is the proper choice of the cores type [27]. This is especially important when fabricating intact capsules consisting only of the material used during the coating – the process of core dissolution should result in 100% elimination of the core without affecting the polyelectrolyte multilayers. In fact, the molecular weight of core components is typically 100 times more than that of the polymers forming the shell and the task of complete core removal seems to be complicated from a chemical point of view. At present, cores that have been exploited to template hollow capsules can be classified into three groups differing by dissolution properties and chemical interaction with polyelectrolyte components of the shell [27].

The first class is made up of organic cores made of water-insoluble oligomers including the widely studied melamine formaldehyde (MF) cores dissolvable at low pH and in some organic solvents, polystyrene (PS) cores soluble in tetrahydrofuran (THF) and biofriendly poly(lactic acid)/poly(lactic-co-glycolic acid) (PLA/PLGA) soluble in acetone/*N*-methyl-2-pyrrolidinone mixture. The second class is made up cores that dissolves into small molecules and ions. These can be either ionic or molecular crystals soluble in acidic or basic conditions or in an organic solvent. At present, different carbonate particles ( $\text{CaCO}_3$ ,  $\text{CdCO}_3$  and  $\text{MnCO}_3$ ) [47] and  $\text{SiO}_2$  particles [48] have been used for polyelectrolyte multilayer templating. The main advantage of exploiting such inorganic particles is the absence of osmotic stress upon dissolution and complete elimination of the core. The third class of cores is made up of those subjected to strong oxidation. A biological cell is a typical example of this kind of cores. For example, the assembly of polyelectrolyte multi-

layers can be performed using fixed erythrocyte cells as templates [49, 50]. The removal of the cell cores can be achieved by oxidation with sodium hypochlorite solution. The main effect of changing the core is that the employment of a different core material will result in different permeability properties of the shell.

### 12.3.1.3 Barrier Properties of E-LbL Assembled Nanoshells

The barrier properties of nanoshells formed by E-LbL depend on film thickness, ionic strength and charge of the permeating molecule, temperature annealing, re-sealing by additional layers, and chemical modification. If the permeability of the polyelectrolyte multilayer is provided by diffusion through the entangled polymer network, it should scale with the inverse of the layer thickness. However, most studies show that the permeability decreases with increasing layer number much faster than expected for a straightforward thickness increase. Only from approximately eight layers onwards does the permeability multiplied by the shell thickness become constant, indicating that the permeability is now controlled by the thickness increase and the diffusion-limiting region relates to the properties of the polyelectrolyte layer [51]. Normally, the deeper layers are denser, resulting in a 5-fold reduction of the estimated diffusion coefficient, while the loose structure of the interfacial layers leads to a very slow increase in the dissolution time. This means that only the presence of the internal dense layers can slow down the dissolution time. For thinner walls, the drastic dependence on shell thickness may be explained either by the existence of pores that are successively closed by further layer deposition or by a thickness-dependent diffusion coefficient. Diffusion dependent on layer depth was indeed observed when the diffusion of polar labels in planar polyelectrolyte films was studied [51].

Another parameter that can influence the multilayers structure is the ionic strength [27]. It has been shown that the multilayer structure is affected if the salt concentration is changed once the film is built up. Polyelectrolyte multilayer vesicles can be subjected to temperature treatment that significantly influences their properties. For example, at temperatures up to 95 °C the polyelectrolyte capsules keep their integrity, but undergo irreversible structural changes [52]. The resulting structure is characterized by decreasing capsule diameter with simultaneously increasing shell thickness as revealed by scanning force microscopy (SFM). From thermodynamic point of view this effect can be explained by approaching the equilibrium state of polyelectrolyte complexes. In another example hollow capsules were fabricated by LbL deposition of oppositely charged diblock copolymers each containing a PNIPAAm block and a charged negative or positive block (20 mol%) [53]. PNIPAAm is known to undergo a phase transition at a temperature of 32 °C (the so-called LCST), after which it is not soluble. This transition is rather sharp and completely reversible upon cooling. The obtained capsules exhibit changes in morphology and permeability at elevated temperatures. However, this process is only partially reversible in the multilayers. Relaxation requires more than 1 month, which limits their thermosensitivity to one heating circle.

Chemical modification can be another way to induce the excessive charge into the polyelectrolyte multilayers and change other characteristics of the film. One

method proposed is using PAA, partially modified by Fisher esterification with different alcohols, as a multilayer constituent [54]. Depending on the nature of the derivatizing alcohol, the hydrophobicity of the film could be tuned. The hydrophobicity of ester groups was shown to result in advancing water contact angles to more than  $100^\circ$ . Crosslinking of these hydrophobic films via heat-induced amidation stabilized coatings over a wide pH range, but did not significantly influence their permeability. It has been proposed that crosslinking of the reactive groups in the multilayers is sometimes the only possibility of making films composed of weak polyelectrolytes stable at a wide range of pH and ionic strength. One example is PAA/PAH multilayers, which readily decompose upon a shift of pH or ionic strength, that can be crosslinked in order to gain stability [55]. In contrast, nanoshells composed of PSS/PAH multilayers have semipermeable properties [26]. They are permeable for small molecules, such as dyes and ions, while under most conditions high-molecular-weight compounds are excluded. One of the explanations for this is the much smaller size of the pores in the multilayer film in comparison with the hydrodynamic radius of the permeating molecule.

Filled capsules can also serve as microreactors [56]. This is advantageous because for macromolecules there is an advantage in encapsulating enzymes and proteins in general because their inaccessibility for inhibitors, proteases (which are polymers and cannot permeate the capsule wall) and, of course, for bacteria. This means the activity of enzymes encapsulated is higher as compared with typical values of chemically immobilized enzymes. In addition, the native conformation of proteins such as hemoglobin does not change upon encapsulation due to contact with the nanoshell because there was no change registered in the position of a so-called Soret band, which is very sensitive to the changes in the heme conformation. All these studies showed that the possibility exists to control and reversibly change the capsule permeability for both low- and high-molecular-weight molecules as shown in Fig. 12.7. This can be desirable for many applications, including drug delivery. This means that the exploration of the permeability properties of capsules and multilayers must be further developed because it promises many possibilities as drug carriers, biosensors, micro-reactors and catalysts, construction materials, etc. [56].

### 12.3.2

#### **Controlled Release of Active Pharmaceutical Ingredients Encapsulated by E-LBL Assembled Nanoshells**

A major challenge in the development of carrier systems of submicron dimensions lies in the field of advanced drug formulations, especially when it comprises the elaboration of delivery systems capable of providing sustained release of bioactive materials [27]. Mainly, these bioactive compounds are small molecules with different solubility and diffusion coefficients. If we consider only physical entrapment without any covalent binding in order to develop a delivery system, one has to encapsulate the active molecules within the shell proving certain release character-

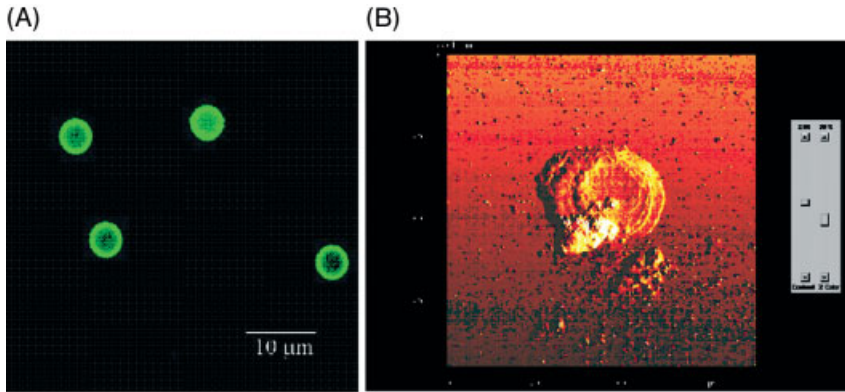


**Figure 12.7.** (A) Polyelectrolyte microcapsules with (PSS/PAH)<sub>5</sub> wall composition loaded with FITC-labeled glucose oxidase (confocal image). (B) AFM tapping mode image of the same broken dry capsule on mica; release of the encapsulated material is visible. (Adapted from Ref. [56].)

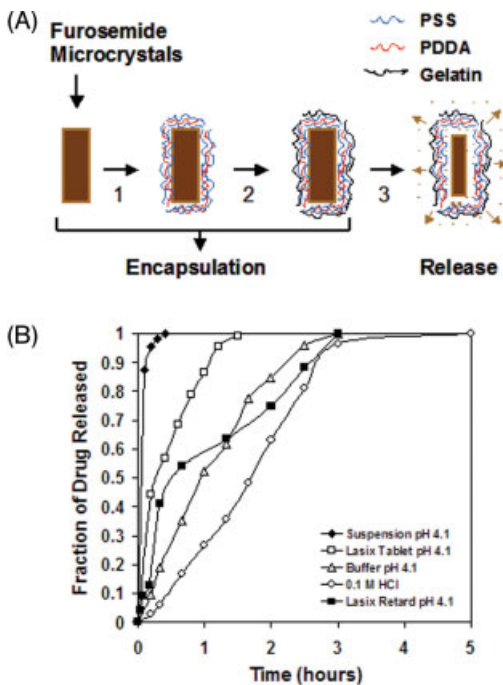


**Figure 12.8.** (A) Illustration of furosemide microcrystal encapsulation and release study. In step 1, precursor layers of (PSS/PDDA)<sub>2</sub> are assembled onto positively charged furosemide microcrystals. In step 2, (PSS/gelatin)<sub>2-6</sub> layers are added. In step 3, drug release in aqueous solution was monitored at different pH values.

(B) Dissolution profiles of (PSS/PDDA)<sub>2</sub> + (PSS/gelatin)<sub>4</sub>-coated furosemide micro-particles compared to uncoated particles and a commercially available tablet in physiologically relevant media using the dissolution test described in the USP 24. (Adapted from Ref. [22].)

istics. The potential use of polyelectrolyte capsules with drug entrapped in the nanoshell for controlled drug delivery currently requires more study and is not well established. In contrast, microencapsulation of drug microparticles is a well-established technique for prolonging release. When microcapsules are coated with appropriate antigens, they can also be targeted to specific regions in the body. This can lead to lowered overall dosage requirements, increased drug concentrations in the necessary regions and reduced side-effects. Polymer- and liposome-based systems have been used for drug encapsulation, mostly as unordered drug-polymer conjugates [57–60].

The E-LbL self-assembly technique based on alternate adsorption of oppositely charged components was developed to add nanometer-thick films to surfaces [15, 17, 35, 61, 62], offering the opportunity to design controlled release systems by encapsulating micron-scale cores with a very thin outer shell. The core must be insoluble under some conditions, such as low pH, and soluble under the conditions at which controlled release is to take place. The release rate generally depends on the thickness of the encapsulating shell and the material used in the coating. Thicker shells lead longer release times.

#### 12.3.2.1 Nanoshell Permeability for Low-molecular-weight Compounds

In the first report on controlled release, fluorescent dye microcrystals were used as a model system for controlled release studies [24]. PSS and PAH were used to form a polyelectrolyte shell on the fluorescein core. Increasing the number of layers decreased the shell permeability and resulted in prolonged dye-core dissolution. Encapsulation of ibuprofen also resulted in prolonged release at different pH values [63]. The ibuprofen dissolution time from capsules with walls built from 15 bilayers of chitosan-dextran was 40 s at pH 7.4, compared to 10 s with no coating. Therefore, prolongation of the release was minimal.

To determine whether encapsulation by E-LbL assembly can substantially increase drug release time, the technique was used to assemble polypeptides and polyions on microcrystals of 5-(aminosulfonyl)-4-chloro-2-[(furanylmethyl)amino] benzoic acid, commonly known as furosemide [22]. Furosemide is a diuretic and antihypertension drug that is practically insoluble in water. Although the therapeutic effect is fast and intense after oral administration of furosemide, the oral bioavailability of the drug from an immediate release dosage form is poor and highly variable [64]. These problems can potentially be overcome by developing a modified release dosage form. Ai and coworkers encapsulated furosemide microcrystals with polyions and gelatin to control the release of the drug in aqueous solutions (Fig. 12.8) [22]. In step 1, precursor layers of (PSS/PDDA)<sub>2</sub> are assembled onto positively charged furosemide microcrystals. In step 2, (PSS/gelatin)<sub>2–6</sub> layers are added. In step 3, drug release in aqueous solution was monitored at different pH values. Charged linear polyions and gelatin were alternatively deposited on 5- $\mu\text{m}$  drug microcrystals through E-LbL self-assembly. Sequential layers of PDDA and PSS were followed by adsorption of two to six gelatin/PSS bilayers with corresponding capsule wall thicknesses ranging from 45 to 115 nm. They

then determined furosemide release from the E-LbL encapsulated crystals under two physiological pH conditions, i.e. pH 1.4 (stomach) and pH 7.4 (blood). At both pH values, the release rate of furosemide from the encapsulated particles was reduced by 50–300 times (for capsules coated with two to six bilayers) compared to uncoated furosemide. The results provide a method of achieving prolonged drug release through self-assembly of polymeric nanoshells on drug microcrystals.

In a study that further expanded the application of core–shell structures fabricated by E-LbL self-assembling for drug delivery, Pargaonkar and coworkers reported the controlled release of dexamethasone from microcrystals encapsulated with a polyelectrolyte shell [41]. The E-LbL self-assembly process was used to produce dexamethasone particles layered with  $\text{PDDA}^+$ ,  $(\text{PDDA}/\text{PSS})_4/\text{PDDA}$ ,  $(\text{PDDA}/\text{gelatin A})_4/\text{PDDA}$ , dexamethasone core/ $(\text{PDDA}/\text{gelatin B})_4/\text{PDDA}$  or dexamethasone core/ $\text{PDDA}/(\text{PSS}/\text{gelatin A})_4/(\text{PSS}/\text{PDDA})_1$ . The nanothin shells were characterized by QCM measurements, microelectrophoresis, microcalorimetry, confocal microscopy and SEM. The *in vitro* release of dexamethasone from the microcapsules suspended in water or carboxymethylcellulose (CMC) gels, measured using vertical Franz-type diffusion cells, showed that the assembly of multiple polyelectrolyte layers around these monodispersed cores produced a polyelectrolyte multilayer shell around the drug microcrystals which allowed for controlled release depending on the composition and the number of layers.

Ye and coworkers showed that indomethacin microcrystals can be directly encapsulated with polysaccharides sodium alginate and chitosan multilayers through LbL self-assembly [65]. The retention of the drug microcrystal was found to gradually decrease due to its partial dissolution in the deposition solution. It was very significant that increasing the deposition temperature from 20 to 60 °C reduced the release rate efficiently, due to the increase in multilayer thickness and formation of a more perfect multilayer film. This finding provides a new and simple method to control the permeability of the LbL assembled multilayer films.

#### 12.3.2.2 Nanoshell Permeability for High-molecular-weight Compounds

DNA and polynucleotides (polyuridylic and polyadenylic acids) can be readily assembled in alternation with polycations (PEI, PAH, polylysine) [66]. Alternate adsorption of 0.1 mg mL<sup>-1</sup> DNA at pH 5.2 with polycations gave multilayers with a DNA/PEI bilayer thickness of 4.4 nm and DNA/PAH bilayer thickness of 3.6 nm. Fourier-transform IR spectra confirmed the native double-stranded DNA conformation in DNA/PEI and DNA/PAH multilayers. Coating DNA/polyion films on medical implants may have applications in local gene therapy. In other studies, proteins including lysozyme, horseradish peroxidase, albumin, bacteriorhodopsin, immunoglobulins, glucoamylase, glucose oxidase (GOx), catalase, glucose isomerase and diaphorase were used at concentrations of 0.1–2 mg mL<sup>-1</sup> for LbL assembly [20]. As the surface structure of the solid support can affect the stability of proteins, precursor films of alternate PEI/PSS are normally used as standard surfaces.

Proteins immobilized in multilayers with strong polyions, such as PSS, PEI and PDDA, are insoluble in buffers in a pH range between 3 and 10. Protein multilayers with weak polyions are partially soluble in solutions with a pH close to the isoelectric point of one of the components, but such multilayers can be stabilized with crosslinking agents. Assembled proteins are in most cases not denatured [67, 68].

Nano-organized encapsulation of protein microcores such as insulin nanoparticles in the presence of high concentration of neutral polymers (PEG) was also elaborated with a LbL assembly. Uncoated insulin PROMAXX microparticles formed by controlled phase separation from hydrophilic compounds undergo to a fast dissolution if the PEG concentration is decreased [69]. Insulin release from PROMAXX was extended with LbL encapsulation. After the complex of insulin in the core and the first layer of oppositely charged polymer is formed, the microparticle is stabilized and adding new polyelectrolyte layers can be continued. Balancing strong interaction of the first polyelectrolyte layer with protein microcore and easing this interaction by depositing the second oppositely charge polyelectrolyte (polyanion/polycation for positive cores at pH 5.8 and polycation/polyanion for negative cores at pH 7.0) allowed us to control complexation of the encapsulated proteins and to reach a sustained insulin release. Fine tuning of the release profile was reached by using the third and fourth polyelectrolyte layer addition.

Therefore, the general idea of controllable complex formation is as follows. Adsorption of the first polyelectrolyte layer results in strong complex formation and very slow release. An addition of the second, oppositely charged polyelectrolyte layer results in relaxed complex and quicker release. The third oppositely charged layer again gives slower release, etc. Just growing thickness of the capsule walls within five to 10 bilayers (30–60 nm) did not slow insulin release from the microparticles. With this, the concept formulated in a Max Planck Institute research group [23, 24, 28] defining LbL multilayer as a tight diffusion barrier with adjustable thickness in the range of five to 12 bilayers was converted to a new approach where the main role in the controlled release from protein microaggregates is given to adjustable interpolyelectrolyte complex formation controlled by alternate polycation/polyanion coating of two to three monolayers.

E-LbL can also increase the stability of macromolecules as demonstrated for membrane-disrupting peptide that are easily degraded *in vivo* [70]. The peptides are important because when conjugated to peptide hormones they have been shown to specifically destroy primary tumors and metastases in mouse models. Consequently, the encapsulation and sustained systemic release of these peptides could further improve treatment efficacy by protecting the peptides from degradation. When silica nanoshells are coated by E-LbL with polyelectrolyte layers of gelatin B or CMC carrying the peptide drug, Phor21- $\beta$ CG(ala), the release kinetics of the embedded peptide drug, can be controlled and its potency to destroy breast cancer cells can be enhanced *in vitro*. The silica-peptide nanoshells produced by this process had a diameter of 450 nm, and the adsorption efficacy was 20% and was linear with an increasing numbers of layers. Up to 34% of the embedded Phor21- $\beta$ CG(ala) was released in a linear fashion from the CMC multilayers over

a period of 20 h. The release kinetics was dependent on the pH. *In vitro* toxicity to human breast cancer cells using gelatin B and CMC silica-peptide nanoshells showed that Phor21- $\beta$ CG(ala) was released from the multilayers, and the peptide retained its potency in destroying human breast cancer cells and did not cause aggregation of the peptide drug. This showed that E-LbL assembled silica-peptide nanoshells may be used not only for sustained release of a peptide cancer drug to treat primary tumors and metastases, but also to increase the stability of the active ingredient.

Taken together, all these studies demonstrate the successful controlled delivery of large biomolecules not only from a core encapsulated with a nanoshell, but also from the nanoshell where the active molecule was used in the construction of the nanoshell via the E-LbL process.

### 12.3.3

#### **E-LbL Assembled Nanoshells as Protective and Functional Barriers**

Nanoshells prepared by E-LbL self-assembly can be used as a new type of protective microcontainer, capable of preventing oxidation of encapsulated compounds by low-molecular-weight oxidizing agents [29, 30, 34]. These researchers developed protective polyelectrolyte microcapsules that effectively prevents the oxidation of encapsulated bovine serum albumin by a low-molecular-weight agent,  $H_2O_2$  (Fig. 12.9). Two approaches for designing protective capsule microcontainers were demonstrated. First, the “passive armor” approach is composed of a sacrificial reducing agent as a shell constituent, while the “active armor” approach includes the catalyst for  $H_2O_2$  decomposition deposited onto the shell as the outer layer. In the latter case, the protective material is not consumed during the  $H_2O_2$  treatment, thus prolonging the protection activity of the microcapsule. The designed microcontainers combine the protective function with the controlled release of the encapsulated substance and, moreover, can possess magnetic activity to perform magnetically adjusted delivery of the encapsulated material in aggressive media. Protective polyelectrolyte capsules can find applications as delivery and depot systems in medicine, drug industry and biotechnology. These results demonstrated the possibility of using developed microcontainers for preserving the bioactivity of different encapsulated enzymes such as urease, chymotrypsin, etc.

Another novel use of E-LbL nanoassembly is using biocompatible nanoparticulate  $TiO_2$  multilayers to coat photosensitive materials to increase their photostability. The added benefit of this process is that due to surface modification, an increase the dissolution rate and possibly the bioavailability of a poorly water-soluble drug can be achieved. The photostability of nifedipine microcrystals (35  $\mu$ m) coated with a nanoshell composed of multiple bilayers of positively charged PDDA and negatively charged nanosized  $TiO_2$  particles (20–25 nm) was increased because even with one  $TiO_2$  layer the shelf-life of nifedipine was increased by 30 h independent of the intensity of the light exposure, as shown in Fig. 12.10. With an increase in the number of  $TiO_2$  layers, the photostability of the drug was enhanced even more. In addition, a  $TiO_2$  monolayer decreased the contact angle by 20° for water



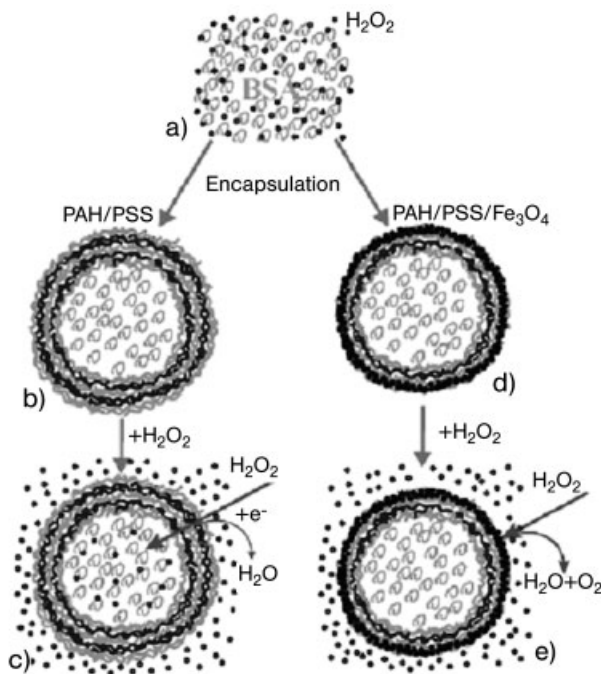


**Figure 12.9.** Schematic overview of the “passive” and “active” protection approaches for nanoengineered polyelectrolyte capsules. For “passive” shells (b and c), part of the  $H_2O_2$  is reduced by the PAH/PSS shell material. “Active” ones (d and e) combine

catalytic and redox mechanisms to provide a more efficient protection barrier. The magnetic activity of polyelectrolyte capsules doped with  $Fe_3O_4$  is also preserved after (and during)  $H_2O_2$  treatment. (Adapted from Ref. [33].)

and  $33^\circ$  for the dissolution medium as compared with uncoated nifedipine surfaces. This increase in wettability due to a decrease in contact angle increased the dissolution rate of nifedipine microcrystals coated with one PDDA/ $TiO_2$  bilayer 13-fold after 10 min, 5-fold after 1 h and 2-fold after 12 h when compared to uncoated microcrystals. It is assumed that  $TiO_2$  increased the photostability because the nanoparticulate multilayers act as a potential filter protecting the drug from damaging light rays reaching the drug crystals. The dissolution rate was increased because the hydrophilic  $TiO_2$  nanoparticles increased the aqueous wettability of the drug crystals, thereby preventing aggregation in the dissolution medium. This ensured that the maximum drug surface area was exposed to the dissolution medium.

The increased dissolution observed for  $TiO_2$ -coated drug particles showed that in addition to protecting the drug load, E-LbL nanoshells can also assist in changing the physicochemical properties of drug cores. This was also illustrated for dexamethasone where sonication during the layering process helped to reduce the particle size of the drug, thereby increasing the dissolution rate of this practically water-

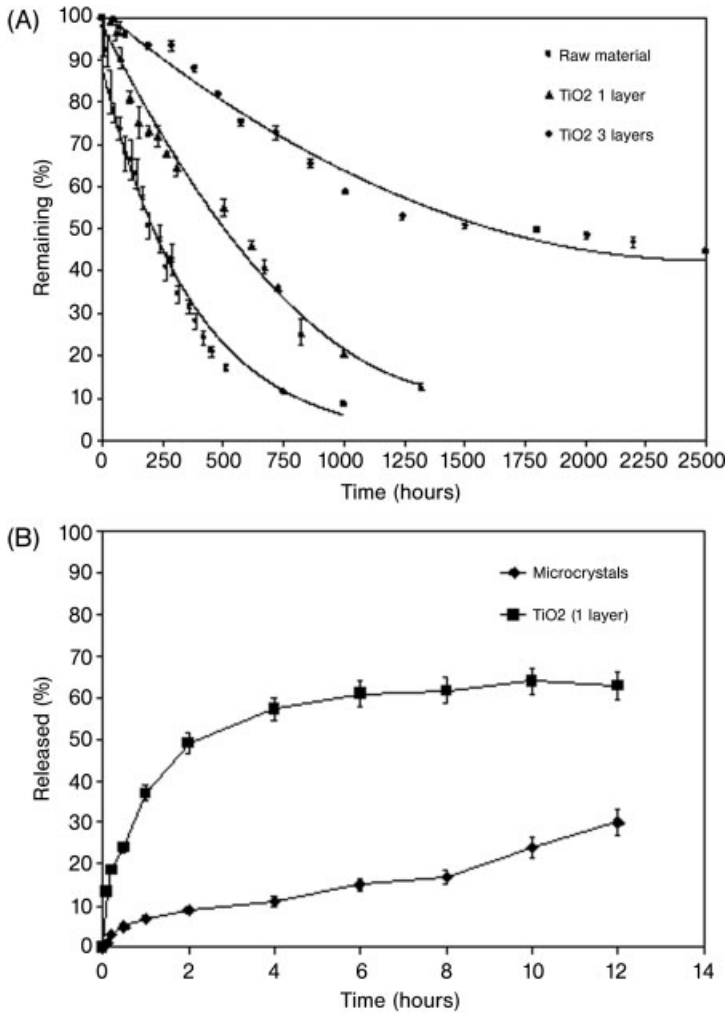


**Figure 12.10.** (A) Decrease in the photostability of nifedipine microcrystals when LbL coated with nanosized  $\text{TiO}_2$  particles where exposed to an illuminance of  $12 \text{ W m}^{-2}$  corre-

sponding to a light dose of 30 klux. (B) *In vitro* release profiles for nifedipine showing the increase in the dissolution rate of the drug when coated with one layer of  $\text{TiO}_2$  nanoparticles.

insoluble drug, while also increasing the suspension stability [41]. For negatively charged micronized dexamethasone particles the effective adsorption of a first layer of PDPA during sonication as evidenced by microelectrophoresis measurement of the reversal in charge caused enhanced dispersability of the dexamethasone particles because of the colloidal stabilization produced by the positively charged PDPA coating combined with a significant reduction particles size to below  $2 \mu\text{m}$ . Stabilizing of the practically monodispersed particles also reduced the

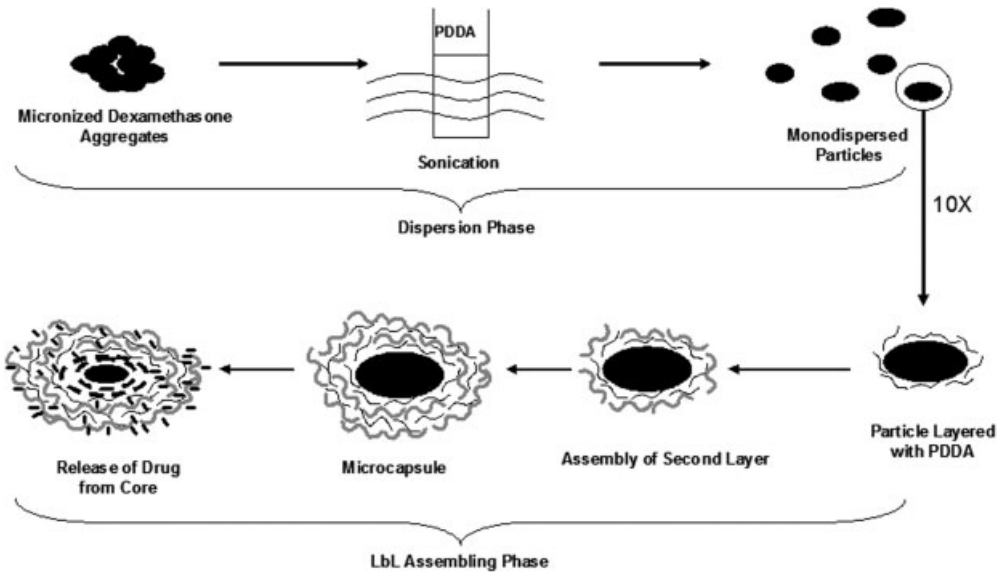


**Figure 12.11.** Illustration of the monodispersion of micronized dexamethasone drug particles by E-LbL encapsulation followed by the subsequent controlled release of the drug through the insoluble porous shell.

Ostwald maturation of the colloidal particles of the scarcely soluble dexamethasone, thereby preserving the reduction in particles size and the integrity and the shape of the original crystals. A schematic of this process is shown in Fig. 12.11.

#### 12.3.4

#### Magnetic Nanoshells

By using the E-LbL assembly it is also possible to include magnetic nanoparticles (such as magnetite or cobalt) into the shell, thereby making the entire capsule magnetic. The example in Fig. 12.12 shows a 400-nm diameter capsule composed of a glucose oxidase core covered with a shell composed of two bilayers of 12-nm diameter magnetite alternating with cationic PEI. Deposition of magnetite nanoparticles provided a magnetic momentum that allowed the nano/bioreactors to be self-stirred and even be separated by the application of an external magnetic field [71].

In a further development based on this work, ferromagnetic cobalt nanoparticles coated with gold (Co@Au) were included in the capsule shell. With these particles, the application of a low-frequency rotating magnetic field rotated these particles, eventually providing shell distortion and release of the capsule content (Fig. 12.13) [72]. While looking at these functional capsules it is important to underline that the effect is not due to hypothermal heating because this effect works at much

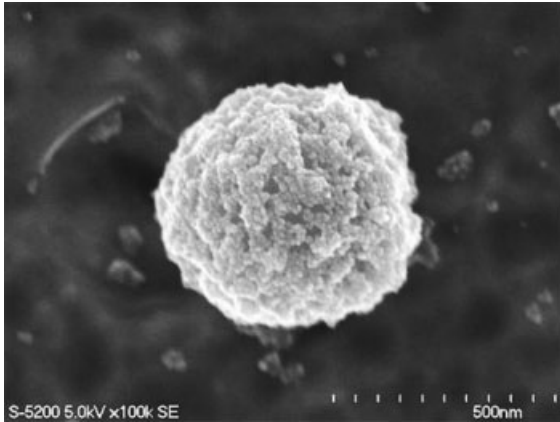


**Figure 12.12.** A 400-nm diameter GOx core coated with (PSS/PEI)<sub>2</sub> + (magnetite/PEI)<sub>2</sub> shells. The 12-nm diameter magnetite nanoparticles are visible on the surface.

higher frequencies of the magnetic field. However, a magnetic field to modulate the permeability of polyelectrolyte microcapsules prepared by LbL self-assembly was also explored. For this purpose 5-nm diameter ferromagnetic Co@Au nanoparticles were embedded inside capsule walls. The final 5- $\mu\text{m}$  diameter microcapsules had wall structures consisting of four bilayers of PSS/PAH, one layer of Co@Au and five bilayers of PSS/PAH. Applying an external alternating magnetic field of 100–300 Hz and 1200 Oe rotated the embedded Co@Au nanoparticles. This rotation subsequently disturbed and distorted the capsule wall, and drastically increased its permeability for macromolecules like fluorescein isothiocyanate (FITC)-labeled dextran. The capsule permeability change was estimated by taking the capsule interior and exterior fluorescent intensity ratio using confocal laser scanning microscopy. Capsules with one layer of Co@Au nanoparticles and 10

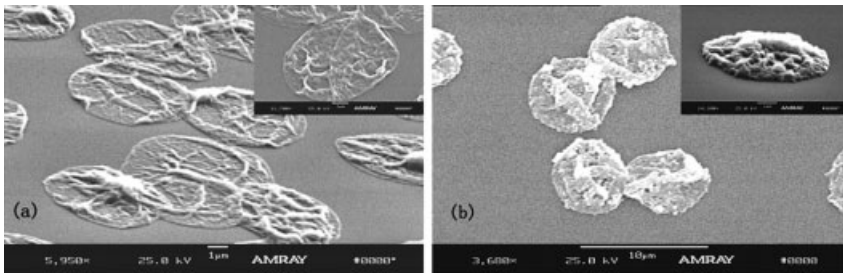


**Figure 12.13.** SEM images of (a) hollow capsules with (PSS/PAH)<sub>11</sub> and (b) magnetic capsules with one layer of embedded Co@Au [(PSS/PAH)<sub>4</sub>(PSS/Co@Au)<sub>1</sub>(PSS/PAH)<sub>6</sub>] (both in the dry and collapsed state).

polyelectrolyte bilayers were optimal for magnetically controlling permeability. In this study the authors provided a theoretical explanation for the permeability control mechanisms. What is important to realize is that “switching on” of these microcapsules using a magnetic field makes this method a good candidate for controlled drug delivery in biomedical applications.

### 12.3.5

#### **Nano-organized Shells with Functions other than a Adjustable Diffusion Barrier**

##### **12.3.5.1 Colloidal Stabilization**

The above discussions have focused on the concept of nanoshell assembly based on the possibility to design multilayer walls with controllable diffusion which may include active defense of the capsule interior. One of the advantages of this approach is using in mild cooperative electrostatic interaction not involving covalent bonding that may disturb drug molecules structure (especially for enzymatic drugs). One of disadvantages of this technology is the necessity of a multistep deposition process which often may be reached only after 10–16 sequential adsorption steps. During development of this technique, we found that not only slow drug release is in demand, but colloidal stabilization and faster release for poorly soluble drugs are also important. In such an application, one does not need many adsorption steps that produce a thick nanoshell and we can convert submicron insoluble drug particles to stable colloids with controllable fast release only with two to three deposition steps as shown in Fig. 12.11.

##### **12.3.5.2 Interpolyelectrolyte Complex Formation**

Working with soft protein microcores (such as insulin), the crucial importance of interpolyelectrolyte complexation between the shell polyelectrolyte layers and the protein core was shown [69]. In this case, the shell grows “roots” into the core and for controlled release the optimization of this complex formation is more important than just increasing of number of polymer layers in the shell wall [69]. To illustrate this, nano-organized encapsulation of protein microcores in the presence of high concentrations of a neutral polymer (PEG) was elaborated using the E-LbL process. This is important because it was found that uncoated insulin microparticles formed by controlled phase separation from hydrophilic compounds undergo fast dissolution if the PEG concentration is decreased. For the same insulin, when E-LbL encapsulation was used, the microparticle was stabilized after complexation of the insulin core with the first layer of oppositely charged polymer. This meant that the addition of new polyelectrolyte layers was easier. However, balancing the strong interaction of the first polyelectrolyte layer with the protein microcore was crucial, and the controlled release depended on the second and subsequent layers because this interaction was decreased by depositing the second oppositely charge polyelectrolyte. This allows for the control of complexation of the encapsulated proteins with the first polyelectrolyte layer until sustained release of the insulin is achieved. The general idea of controllable complex formation can be summarized as follows. First, adsorption of the first polyelectrolyte layer results in strong com-

plex formation and very slow release. Addition of the second, oppositely charged polyelectrolyte layer results in a relaxed complex and quicker release. The third oppositely charged layer again gives slower release, etc. Therefore just increasing the thickness of the capsule walls within five to 10 bilayers (30–60 nm) did not slow insulin release from the microparticles. With this, the concept formulated earlier [69] where the LbL multilayer was considered as a tight diffusion barrier with adjustable thickness is now converted to a new approach where the main role in the controlled release from protein microaggregates is governed by adjustable interpolyelectrolyte complex formation controlled by alternate polycation/polyanion coating of as few as two to three monolayers.

### 12.3.5.3 Biomimetic Approach

The concept of using E-LbL shells to act as a nonbiological (engineered) replica allows the reproduction of the shape and maybe even some organization features of biological cells and viruses. Ai and coworkers [73] demonstrated the E-LbL nano-coating of blood platelets. This nanocoating included an antigen outermost layer for targeting these cells to antibody-coated regions in a capillary that simulated a blood vessel. Using this approach, other small biological cores may also be reproduced through shell formation. For example, the nonbiological replication of the shape and dimensions of a virus with E-LbL nanoassembly is a feasible goal to develop, for example, a viral-like drug delivery vehicle. Figure 12.14 gives preliminary results for the design of a nanoparticulate shell replica of bacteriophage Sd that has an average diameter of 78 nm. As can be seen for the transmission electron microscopy (TEM) images, the nanocapsule E-LbL assembly may be a good instrument for designing artificial virus systems to serve as intercellular drug carriers. In addition, with this nano-architecture, the E-LbL method can be used to reproduce some features of the virus structure, such as certain protein or lipid layers, in the replica shell, making this drug nanocarrier very similar to the virus. This means that treatment with such replicas will follow the same biological path as the viral infection.

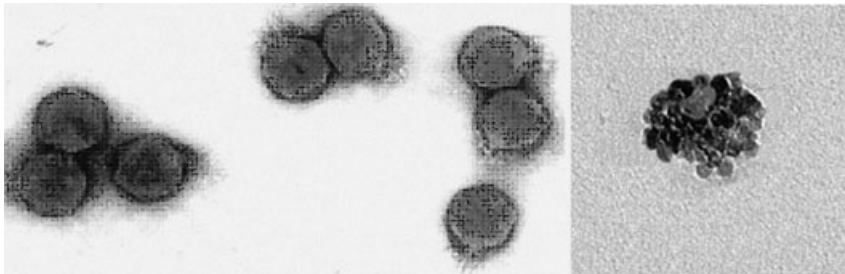


**Figure 12.14.** TEM images of bacteriophage Sd used as a template for the formation of a 8-nm silica nanoparticle shell (right image with the icosahedra shape), overall diameter  $D = 78$  nm, clearly showing the small tail or “basal plate”. The DNA core diameter is 68 nm and protein shell thickness is about 5 nm.

## 12.4

### Conclusion

Nanoshells present a unique class of nano/microparticles with a wide range of potential application in nanomedicine. The most exciting include the possibility of engineering very small and/or very thin structures that through experimentation can be developed into reproducible and reliable platforms that integrate micro/nanotechnologies for the advanced delivery and targeting of drugs. In addition they can be used to immobilize and copy cells or viruses, and to trap, embed and protect small and macromolecules on surfaces. Although this field is still in its infancy, many ongoing developments (and the products produced) offer some unique opportunities for possible clinical applications that still need to be explored. Concurrently exploring of these technologies can also lead to the development of very sensitive *in vivo* testing methods and targeted *in vivo* diagnostic systems. The ultimate goal is to combine delivery, sensing and targeting into a single multifunctional nanoshell.

These novel possibilities should ensure that the future for nanoshell technologies remains bright. As we learn more about the construction and permeability properties of these nanothick shells, their applications as drug carriers, biosensing devices, microreactors, etc., are becoming clearer. This is especially true if one looks at recent research results that have uncovered the effect of and the controlled use of variables such as pH, ionic strength and temperature to modulate not only the fabrication of nanoshells, but also to control the permeability of these shells. Progress in the understanding of these principles of multilayer construction, interaction of charges within the shell and competition of various interactions within the crowded environment of polyelectrolyte layers is vital for the future progress in the area of responsive metallic and polyelectrolyte nanoshells.

In addition, answering the fundamental questions of the effect of self-assembly conditions and the strength of intermolecular adhesion within nanoshells and their effect on the rate of macromolecular rearrangements in responsive films and the permeation rate of solute molecules within or from nanoshells may enable the rational design of nanoshells with specific response characteristics. Hopefully, unraveling these fundamental properties may lead to new strategies in the construction of responsive coatings, e.g. those that respond to multiple stimuli and deliver multiple active molecules in a controlled way, thus producing novel drug delivery systems.

Last, but not least, we speculate that nanoshells could play a role in the future treatment of specific diseases such as cancers. These particles can be designed in such a way that they are small enough to find their way through the human circulatory system after injection. Bioactive molecules can be attached to the nanoshell surface, trapped within the shell or covered by the shell to cause selective binding or accumulation of these particles within a tumor. Using external sources such as magnetic fields or heating with a NIR laser, carcinoma tissue can then be destroyed by local effects such as thermal heating around the nanoshells.

To conclude, nanotechnology as represented by nanoshells can provide numerous advances for medicine. It might revolutionize methods used in medical science, enabling future medicine to become even more successful in its objective to save lives. We believe that the examples mentioned here represent a small fraction of the future advances that will come from nanoshells. We also believe that although the two methods to prepare nanoshells have the same foundation, there is no evidence that the future developments obtained using the two methods will be equivalent. The presence of some trends and research data leads us to believe that the versatility of polyelectrolyte LbL nanoencapsulation currently makes its wide application in drug delivery perhaps more promising. However, it will be fascinating to see what new applications arise in the future for both these systems.

## References

- 1 S. A. MAIER, P. G. KIK, H. A. ATWATER, S. MELTZER, E. HAREL, B. E. KOEL, A. R. G. Local detection of electromagnetic energy transport below the diffraction limit in metal nanoparticle plasmon waveguides, *Nat. Mater.* **2003**, *2*, 229–232.
- 2 S. R. SERSHEN, S. L. WESTCOTT, N. J. HALAS, J. L. WEST. Temperature-sensitive polymer–nanoshell composites for photothermally modulated delivery, *J. Biomed. Mater. Res.* **2000**, *51*, 293–298.
- 3 K. NASSAU. *The Physics and Chemistry of Color*. Wiley, New York, **2001**.
- 4 G. MIE. Contributions to the optics of turbid media, especially colloidal metal solutions, *Ann. Phys. (Leipzig)* **1908**, *25*, 377–445.
- 5 U. KREIBIG, M. VOLLMER. *Optical Properties of Metal Clusters*. Springer, Berlin, **1995**.
- 6 S. J. OLDENBURG, R. D. AVERITT, S. L. WESTCOTT, N. J. HALAS. Nano-engineering of optical resonances, *Chem. Phys. Lett.* **1998**, *288*, 243–247.
- 7 E. PRODAN, A. LEE, P. NORDLANDER. The effect of a dielectric core and embedding medium on the polarizability of metallic nanoshells, *Chem. Phys. Lett.* **2002**, *360*, 325–332.
- 8 R. D. AVERITT, S. L. WESTCOTT, N. J. HALAS. Ultrafast optical properties of gold nanoshells, *J. Opt. Soc. Am. B* **1999**, *16*, 1824–1832.
- 9 R. D. AVERITT, D. SARKAR, N. J. HALAS. Plasmon resonance shifts of Au-coated Au<sub>2</sub>S nanoshells: insight into multicomponent nanoparticle growth, *Phys. Rev. Lett.* **1997**, *78*, 4217–4220.
- 10 Y. SUN, B. T. MAYERS, Y. XIA. Template-engaged replacement reaction: a one-step approach to the large-scale synthesis of metal nanostructures with hollow interiors, *Nano Lett.* **2002**, *2*, 481–485.
- 11 F. CARUSO, M. SPASOVA, V. SALGUIRINO-MACEIRA, L. M. LIZ-MARZAN. Multilayer assemblies of silica-encapsulated gold nanoparticles on decomposable colloid templates, *Adv. Mater.* **2001**, *13*, 1090–1094.
- 12 Y. SUN, B. MAYERS, Y. XIA. Metal nanostructure with hollow interiors, *Adv. Mater.* **2003**, *15*, 641–646.
- 13 L. R. HIRSCH, A. JACKSON, A. LEE, N. J. HALAS, J. L. WEST. A whole blood immunoassay using gold nanoshells, *Anal. Chem.* **2003**, *75*, 2377–2381.
- 14 L. R. HIRSCH, R. J. STAFFORD, J. A. BANKSON, S. R. SERSHEN, B. RIVERA, R. E. PRICE, J. D. HAZLE, N. J. HALAS, J. L. WEST. Nanoshell-mediated near-infrared thermal therapy of tumors under magnetic resonance guidance, *Proc. Natl Acad. Sci. USA* **2003**, *100*, 13549–13554.
- 15 Y. M. LVOV, G. DECHER, H. MÖHWALD. Assembly, structural characterization



- and thermal behavior of layer-by-layer deposited ultrathin films of polyvinyl-sulfate and polyallylamine, *Langmuir* **1993**, *9*, 481–486.
- 16 Y. M. Lvov, K. Ariga, I. Ichinose, K. Kunitake. Assembly of multicomponent protein films by means of electrostatic layer-by-layer adsorption, *J. Am. Chem. Soc.* **1995**, *117*, 6117–6123.
  - 17 G. Decher. Fuzzy nanoassemblies: toward layered polymeric multicomposites, *Science* **1997**, *227*, 1232–1237.
  - 18 Y. M. Lvov, F. Caruso. Biocolloids with ordered urease multilayer shells as enzymatic reactors, *Anal. Chem.* **2001**, *73*, 4212–4217.
  - 19 J. B. Tieke, F. van Ackern, L. Krasemann, A. Toutianoush. Ultrathin self-assembled polyelectrolyte multilayer membranes, *Eur. Phys. J* **2001**, *5*, 29–39.
  - 20 H. Ai, S. A. Jones, Y. M. Lvov. Biomedical applications of electrostatic layer-by-layer nano-assembly of polymers, enzymes and nanoparticles, *Cell Biochem. Biophys.* **2003**, *39*, 23–43.
  - 21 R. K. Iler. Multilayers of colloidal particles, *J. Colloid Interface Sci.* **1966**, *21*, 569–594.
  - 22 H. Ai, S. A. Jones, M. M. de Villiers, Y. M. Lvov. Nano-encapsulation of furosemide microcrystals for controlled drug release, *J. Control. Release* **2003**, *86*, 59–68.
  - 23 G. B. Sukhorukov, E. Donath, S. Davis, H. Lichtenfeld, F. Caruso, V. I. Popov, H. Möhwald. Step-wise polyelectrolyte assembly on particle surfaces—a novel approach to colloid design, *Polym. Adv. Technol.* **1998**, *9*, 759–767.
  - 24 A. A. Antipov, G. B. Sukhorukov, E. Danoth, H. Möhwald. Sustained release properties of polyelectrolyte multilayer capsules, *J. Phys. Chem. B* **2001**, *105*, 2281–2284.
  - 25 I. Suzuki, T. Ishizaki, H. Ihoue, J. Anzai. Modification of polyelectrolyte layered assembly using an active ester of azobenzene carboxylate, *Macromolecules* **2002**, *35*, 6470–6474.
  - 26 G. B. Sukhorukov, E. Danoth, E. Moysa, S. Sussha, A. Voigt, A. Hartmann, H. Möhwald. Micro-encapsulation by means of step-wise adsorption of polyelectrolytes, *J. Microencapsul.* **2000**, *17*, 177–185.
  - 27 A. A. Antipov, G. B. Sukhorukov. Polyelectrolyte multilayer capsules with tunable permeability, *Adv. Colloid Interface Sci.* **2004**, *111*, 46–61.
  - 28 A. Voigt, N. Buske, G. B. Sukhorukov, A. A. Antipov, S. Leporatti, H. Lichtenfeld, H. Baumlér, E. Donath, H. Möhwald. Novel polyelectrolyte multilayer micro- and nanocapsules as magnetic carriers, *J. Magn. Magn. Mater.* **2001**, *225*, 59–66.
  - 29 R. Ghan, T. Shutava, A. Patel, V. John, Y. M. Lvov. Enzyme-catalyzed polymerization of phenols within polyelectrolyte microcapsules, *Macromolecules* **2004**, *37*, 4519–4524.
  - 30 T. Shutava, Z. Zheng, V. John, Y. M. Lvov. Microcapsule modification with peroxidase-catalyzed phenol polymerization, *Biomacromolecules* **2004**, *5*, 914–921.
  - 31 M. Gao, C. Lesser, S. Kirstein, H. Möhwald, A. L. Rogach, H. Weller. Electroluminescence of different colors from polycation/CdTe nanocrystal self-assembled films, *J. Appl. Phys.* **2000**, *87*, 2297–2302.
  - 32 P. Stroeve, V. Vasquez, M. A. Coelho, J. F. Rabolt. Gas transfer in supported films made by molecular self-assembly of ionic polymers, *Thin Solid Films* **1996**, *284–285*, 708–712.
  - 33 D. G. Shchukin, T. Shutava, E. Shchukina, G. B. Sukhorukov, Y. M. Lvov. Modified polyelectrolyte microcapsules as smart defense systems, *Chem. Mater.* **2004**, *16*, 3446–3451.
  - 34 T. Shutava, M. Prouty, D. Kommireddy, Y. M. Lvov. pH responsive decomposable layer-by-layer nanofilms and capsules on the basis of tannic acid, *Macromolecules* **2005**, *38*, 2850–2858.
  - 35 J. Mendelsohn, C. Barrett, V. Chan, A. Pal, A. Mayes, M. Rubner. Fabrication of microporous thin films from polyelectrolyte multilayers, *Langmuir* **2000**, *16*, 5017–5023.

- 36 M. SANO, Y. M. LVOV, T. KUNITAKE. Formation of ultrathin polymer layers on solid substrates by means of polymerization-induced epitaxy and alternate adsorption, *Annu. Rev. Mater. Sci.* **1996**, *26*, 153–187.
- 37 Y. M. LVOV, K. ARIGA, T. KUNITAKE. Layer-by-layer assembly of alternate protein/polyion ultrathin films, *Chem. Lett.* **1994**, 2323–2326.
- 38 D. ELBERT, C. HERBERT, J. HUBBELL. Thin polymer layers formed by polyelectrolyte multilayer techniques on biological surfaces, *Langmuir* **1999**, *15*, 5355–5362.
- 39 G. DECHER, Y. M. LVOV, J. SCHMITT. Proof of multilayer structural organization of polycation/polyanion self-assembled films, *Thin Solid Films* **1994**, *244*, 772–777.
- 40 V. TSUKRUK, F. RINDERSPACHER, V. BLIZNYUK. Self-assembled multilayer films from dendrimers, *Langmuir* **1997**, *13*, 2171–2176.
- 41 N. PARGAONKAR, Y. M. LVOV, N. LI, J. H. STEENEKAMP, M. M. DE VILLIERS. Controlled release of dexamethasone from microcapsules produced by polyelectrolyte layer-by-layer nanoassembly, *Pharm. Res.* **2005**, *22*, 826–835.
- 42 Y. M. LVOV, R. R. PRICE, J. V. SELINGER, A. SINGH, M. S. SPECTOR, J. M. SCHNUR. Imaging nanoscale patterns on biologically derived microstructures, *Langmuir* **2000**, *16*, 5932–5935.
- 43 Y. M. LVOV, K. ARIGA, M. ONDA, I. ICHINOSE, T. KUNITAKE. A careful examination of the adsorption step in the alternate layer-by-layer assembly of linear polyanion and polycation, *Colloids Surf. A* **1999**, *146*, 337–346.
- 44 M. ONDA, Y. M. LVOV, K. ARIGA, T. KUNITAKE. Sequential reaction and product separation on molecular films of glucoamylase and glucose oxidase assembled on an ultrafilter, *J. Ferment. Bioeng.* **1996**, *82*, 502–506.
- 45 N. G. HOOGVEEN, M. A. C. STUART, G. J. FLEER, M. R. BOEHMER. Formation and stability of multilayers of polyelectrolytes, *Langmuir* **1996**, *12*, 3675–3681.
- 46 D. YOO, S. S. SHIRATORI, M. F. RUBNER. Controlling bilayer composition and surface wettability of sequentially adsorbed multilayers of weak polyelectrolytes, *Macromolecules* **1998**, *31*, 4309–4318.
- 47 A. A. ANTIPOV, D. SHCHUKIN, Y. FEDUTIK, A. I. PETROV, G. B. SUKHORUKOV, H. MOHWALD. Carbonate microparticles for hollow polyelectrolyte capsules fabrication, *Colloids Surf. A Physicochem. Eng. Asp.* **2002**, *224*, 535–541.
- 48 G. IBARZ, L. DAHNE, E. DONATH, H. MOHWALD. Controlled permeability of polyelectrolyte capsules via defined annealing, *Chem. Mater.* **2002**, *14*, 4059–4062.
- 49 B. NEU, A. VOIGT, R. MITLOHNER, S. LEPORATTI, I. L. RADCHENKO, E. DONATH, H. MOHWALD. Biological cells as templates for hollow microcapsules, *J. Microencapsul.* **2001**, *18*, 385–395.
- 50 S. MOYA, L. DAHNE, A. VOIGT, S. LEPORATTI, E. DONATH, H. MOHWALD. Polyelectrolyte multilayer capsules templated on biological cells: core oxidation influences layer chemistry, *Colloids Surf. A Physicochem. Eng. Asp.* **2001**, 183–185, 27–40.
- 51 R. VONKLITZING, H. MOHWALD. A realistic diffusion model for ultrathin polyelectrolyte films, *Macromolecules* **1996**, *29*, 6901–6906.
- 52 S. LEPORATTI, C. GAO, A. VOIGT, E. DONATH, H. MOHWALD. Shrinking of ultrathin polyelectrolyte multilayer capsules upon annealing: a confocal laser scanning microscopy and scanning force microscopy study, *Eur. Phys. J. E Soft Matter* **2001**, *5*, 13–20.
- 53 K. GLINEL, G. B. SUKHORUKOV, H. MOHWALD, V. KHRENOV, K. TAUER. Thermosensitive hollow capsules based on thermoresponsive polyelectrolytes, *Macromol. Chem. Phys.* **2003**, *204*, 1784–1790.
- 54 J. DAI, A. W. JENSEN, D. K. MOHANTY, J. ERNDT, M. L. BRUENING. Controlling the permeability of multilayered polyelectrolyte films through derivatization, cross-linking, and hydrolysis, *Langmuir* **2001**, *17*, 931–937.

- 55 A. I. PETROV, A. A. ANTIPOV, G. B. SUKHORUKOV. Base–acid equilibria in polyelectrolyte systems: from weak polyelectrolytes to interpolyelectrolyte complexes and multilayered polyelectrolyte shells, *Macromolecules* **2003**, *36*, 10079–10086.
- 56 Y. LVOV, A. ANTIPOV, A. MAMEDOV, H. MOHWALD, G. SUKHORUKOV. Urease encapsulation in nanoorganized microshells, *Nano Lett.* **2001**, *1*, 125–128.
- 57 K. LEONG, B. BROTT, R. LANGER. Bioerodible polyanhydrides as drug-carrier matrices. I: characterization, degradation, and release characteristics, *J. Biomed. Mater. Res.* **1985**, *9*, 941–955.
- 58 B. JEONG, Y. BAE, D. LEE, S. KIM. Biodegradable block copolymers as injectable drug-delivery systems, *Nature* **1997**, *388*, 860–862.
- 59 L. MOUNKES, W. ZHONG, G. CIPRES-PALACIN, T. HEATH, R. DEBS. Proteoglycans mediate cationic liposome–DNA complex-based gene delivery *in vitro* and *in vivo*, *J. Biol. Chem.* **1998**, *273*, 26164–26170.
- 60 V. JUNYAPRASERT, A. MITREVEJ, N. SINCHAIPANID, P. BOONME, D. WURSTER. Effect of process variables on the microencapsulation of vitamin a palmitate by gelatin-acacia coacervation, *Drug. Dev. Ind. Pharm.* **2001**, *27*, 561–566.
- 61 S. KELLER, H.-N. KIM, T. MALLOUK. Layer-by-layer assembly of intercalation compounds and superlattices on surfaces: towards molecular “beaker” epitaxy, *J. Am. Chem. Soc.* **1994**, *116*, 8817–8821.
- 62 J. SCHLENOFF. Redox-active polyelectrolyte multilayers, *Adv. Mater.* **1998**, *10*, 347–351.
- 63 X. QIU, S. LEPORATTI, E. DONATH, H. MOHWALD. Studies on the drug release properties of polysaccharide multilayers encapsulated ibuprofen microparticles, *Langmuir* **2001**, *17*, 5375–5380.
- 64 H. BEYERS, S. MALAN, J. VAN DER WATT, M. M. DE VILLIERS. Structure–solubility relationship and thermal decomposition of furosemide, *Drug. Dev. Ind. Pharm.* **2000**, *26*, 1077–1083.
- 65 S. YE, C. WANG, X. LIU, Z. TONG. Deposition temperature effect on release rate of indomethacin microcrystals from microcapsules of layer-by-layer assembled chitosan and alginate multilayer films, *J. Control. Release* **2005**, *106*, 319–328.
- 66 G. B. SUKHORUKOV, H. MOHWALD, G. DECHER, Y. M. LVOV. Assembly of polyelectrolyte multilayer films by consecutively alternating adsorption of polynucleotides and polycations, *Thin Solid Films* **1996**, *284*, 220–223.
- 67 J. KONG, Z. LU, Y. M. LVOV, R. DESAMERO, H. FRANK, J. Direct electrochemistry of cofactor redox sites in bacterial photosynthetic reaction center protein, *J. Am. Chem. Soc.* **1999**, *120*, 7371–7372.
- 68 F. CARUSO, K. NIKURA, N. FURLONG, Y. OKAHATA. Assembly of alternating polyelectrolyte and protein multilayer films for immunosensing, *Langmuir* **1997**, *13*, 3427–3433.
- 69 J. RASHBA-STEP, R. DARVARI, Q. LIN, J. KELLY, T. SHUTAVA, Y. LVOV, T. SCOTT. Surface modification of PROMAXX microparticles. In *Proceedings 33rd Annual Controlled Release Society Meeting*, Vienna, **2006**, pp. 126–129.
- 70 C. LEUSCHNER, W. HANSEL. Membrane disrupting lytic peptides for cancer treatments, *Curr. Pharm. Des.* **2004**, *10*, 2299–2310.
- 71 M. FANG, P. GRANT, M. MCSHANE, G. SUKHORUKOV, V. GOLUB, Y. M. LVOV. Magnetic bio/nanoreactor with multilayer shells of glucose oxidase and inorganic nanoparticles, *Langmuir* **2002**, *18*, 6338–6344.
- 72 Z. LU, M. PROUTY, Z. GUO, V. GOLUB, C. KUMAR, Y. M. LVOV. Magnetic switch of permeability for polyelectrolyte microcapsules embedded with Co@Au nanoparticles, *Langmuir* **2005**, *21*, 2042–2050.
- 73 H. AL, M. FANG, S. JONES, Y. LVOV. Electrostatic layer-by-layer nano-assembly on biological microtemplates: platelets, *Biomacromolecules* **2002**, *3*, 560–564.

## 13

# Bionanoparticles and their Biomedical Applications

*L. Andrew Lee, Hannah N. Barnhill, and Qian Wang*

### 13.1

#### Introduction

Bionanotechnology is a newly emerging field in which novel nanomaterials are developed from biological building blocks. Primary building materials, DNA and peptides (or peptidomimetics), have been extensively studied as starting materials for nanomaterial synthesis [1–4]. Other basic elements derived from Nature's own designs include the virus and virus-like particles, ferritins, and other self-assembled protein cages such as heat shock protein (Hsp) cages [5] and some enzyme complexes [6]. These biogenic systems self-assemble based on multiple noncovalent interactions to become highly organized scaffolds with robust physical properties. These bionanoparticles (BNPs), in particular, offer fascinating structural features and sophisticated chemistries, yet are under the control of malleable genetic information. These qualities are exploited to tailor the BNPs at the atomic and molecular scales with specific functionalities (i.e. biomedical applications, supramolecular chemistry, etc.). Moreover, Hsp cages and ferritin average 12 nm in diameter, and the different viral cages span from 15 [7] to 160 nm [8], offering an extensive array of sizes.

Distinctive features of BNPs, in comparison to synthetic nanoparticles, make these biomaterials attractive for the following reasons:

- Monodispersed particles with uniform size distributions.
- Three-dimensional structures characterized at atomic or near-atomic levels.
- Genetic control over the composition and surface properties.
- High stability and organization of self-assembled architecture in nanometer ranges.
- Economic large-scale production in gram and kilogram quantities.

The aim of this chapter is to provide an overview in BNP programming and its current research in biomedical applications. There is a growing interest in BNPs as new biomaterials for directing cellular processes, such as cell growth and differentiation. Multiple ligands and peptides can be anchored to the biomaterials with

predetermined nanometer spacing to act as homing signals for tissue-specific targeting, and these precise adornments on the nanosystems can even be transferred to more complex schemes for host immune evasion or activation. Notable nanosystems already in clinical uses as vaccines are the recombinant chimeric hepatitis B virus (HBV) particles [9] and the virus-like particles of human papillomavirus [10, 11]. The highly ordered and repetitive structures of BNPs facilitate pattern recognition by the immune systems and, consequently, are of a great benefit in protective immunity induction [12, 13]. Additionally, both genetic and chemical tools can be used to mold the scaffolds, which ultimately allows the precise control over the spatial layout of functional groups at the molecular level.

The different methods involved in manipulating the viruses and ferritins without affecting the self-assembly process is covered in section 13.2. In the following section, there is particular emphasis on controlling the orientation and density of ligands decorated on the surface of biomolecular shells via chemical and genetic methods. Then the following sections in this chapter have been divided and devoted to the various programmed functionalities of the protein-based nanoparticles: cell targeting, gene/drug delivery, bioimaging, vaccine development, immune response modulation and, lastly, the future directions of BNP research.

### 13.2 BNPs

Viruses provide a wide array of shapes such as rods and spheres, and a variety of sizes spanning from tens to hundreds of nanometers. These protein structures are evolutionary tested, multifaceted systems with highly ordered spatial arrangements, and natural cell-targeting and genetic information-storing capabilities. The years of dissecting the details of virus infection, replication and assembly pathways have imparted a wealth of information on the stabilities and functionalities of these materials. The structural information provided by X-ray crystallography, nuclear magnetic resonance and previous mutagenesis studies lay the firm, primary foundation for viral vector redesign. Intricately fashioned, multifunctional BNPs for various biomedical applications have spun off from viral vector-based gene therapy and vaccine development founded on the polyvalent antigen display on virus coat proteins. Virus-based assemblies are, and continue to be, a major point in the nexus of bionanotechnology.

Ferritin, another primary building block in bionanoscience, is a highly conserved protein complex that spans approximately 12–13 nm in diameter as a tetracosameric protein shell. The interior shell measures approximately 7–8 nm in diameter and encapsulates the mineralized iron core. This protein shell is endowed with astounding thermal and pH stabilities, along with tremendous resistance to denaturation in high ion concentrations to act as protein templates for inorganic material synthesis. The biomineralization with a variety of other metal atoms in apoferritin,

the hollow protein shell without the iron core, exemplifies this concept of using such a biological template for inorganic nanoparticle synthesis [14–16].

Although research on viruses and ferritin outweighs the other protein cages, new systems such as chaperones [5, 17] and carboxysomes [18] have sprung up as possible alternative protein cages for bionanosciences. The characterizations of these systems are in much earlier phases compared to the preceding nanosystems of viruses and ferritin, but each individual system is a potential novel nanomaterial for future chemistries and genetic reprogramming. These platforms, derived from protein-based systems like viruses and ferritin, offer a high degree of spatial organization with well-characterized self-assembly motifs – a quality that can be of major advantage in BNPs for controlling functional group density and orientation. Many of these protein shells permit biological modifications by genetic insertions of foreign peptide sequences and orthogonal chemistries to alter the native protein to incorporate multiple functionalities.

Viruses and other BNPs have been previously employed as vaccine carriers and gene therapy vectors [19–23], but the potential applications of viruses and BNPs for chemical reactions and material synthesis have not been systematically explored until recently. Current research topics in BNP chemistry can be broadly classified as host–guest chemistry (including biomineralization and phage display), controlled self-assembly and bioconjugate chemistry.

BNP-based inorganic materials development has advanced greatly over the past few years, pioneered by S. Mann, T. Douglas (together with M. Young) and A. M. Belcher. Mann and coworkers have prepared magnetic nanoparticles with apoferritin as nanoreactors by biomimetic syntheses [14]. Douglas, Young and coworkers have made important contributions in the syntheses of inorganic nanoparticles with cowpea chlorotic mottle virus (CCMV) and other protein cages as templates [15, 24–28] or catalysts [16]. Belcher and coworkers' work on using filamentous bacteriophage M13 to bind and align nanocrystals in an ordered array is another example of harnessing the logic of biological synthesis for nanomaterial development [6, 29, 30]. Genetically modified M13 have been used as templates to align inorganic, organic and biological nanosized materials into nanowires [31, 32], nanorings [33], nanofibers [34], films [35, 36] and other nanostructures [29, 37–39].

In addition to the organic reactions of ferritin and adenovirus [40–44], there have been many recent developments in the chemoselective organic modifications of BNPs. Finn and coworkers have extensively quantified the organic chemical reactions of viruses as molecular entities [45–48]. Cowpea mosaic virus (CPMV) has been demonstrated to be a robust platform for conjugation with a variety of molecules, including fluorescent dyes [45–48], poly(ethylene glycol) (PEG) chains [49], stilbene derivatives [45], biotin [47, 48], DNA, peptides [50], antibodies [45] and carbohydrates [51]. This strategy permits the covalent installation of functional groups in multiples of 60 at well-defined locations. Following CPMV, the chemical reactivities of many other viruses have been studied, including CCMV [52], *Nu-daurelia capensis*  $\omega$  virus (N $\omega$ V) [53], tobacco mosaic virus (TMV) [54], small Hsp

[5], turnip yellow mosaic virus (TYMV) [55, 56] and bacteriophage MS2 [57]. In short, BNPs provide chemists and material scientists with conveniently accessible scaffolds whose structure and functionality can be genetically programmed and manipulated.

These protein shells are treated as complex chemical compounds that can be utilized as vehicles for drug/gene delivery [58–60], two-dimensional ordered arrays [35], nanowire synthesis [31], depositions on films or polymers or even biocomposite material synthesis [29, 32, 34, 37–39]. The precise manipulation of these platforms relies heavily on the multidisciplinary integration of organic synthesis, molecular, structural and cell biology, and bio-organic chemistry to devise, functionalize and analyze these complex macromolecular structures. These disciplines are unified under a unique theme of re-engineering the self-organizing biological systems in the nanometer range with molecular specificity for a strategic purpose – gene or drug delivery, eliciting an immune response or *in vivo* bioimaging.

### 13.3

#### Genetic and Chemical Alterations of BNPs

##### 13.3.1

##### Chemical Modifications

Although a few organic reactions of ferritin and adenovirus have been reported [40–44], it was not until recently that the chemoselective organic modification of BNPs has been studied systematically. In all the cases, the accessibility is the key to the reactivity of a functional residue on BNPs. In other words, if a functional side-chain is exposed on the surface (either interior or exterior) or is accessible to the reactant, it generally can be modified.

##### 13.3.1.1 Conventional Bioconjugation Methods for Selective Modifications

The conventional way to modify the BNP relies on the protein chemistry, particularly the reactivity of the functional groups of the side-chains. The amino group of lysine residues (Lys), the thiol group of cysteine residues (Cys), the carboxylic groups of glutamic acid (Glu) and aspartic acid (Asp), and the phenol groups of tyrosines (Tyr) are among the best for chemical modification (Fig. 13.1) [61]. If accessible Lys, Cys, Glu/Asp and Tyr can be found or created, they should be able to be derivatized. In addition, orthogonal reaction conditions are generally required to modify a group of residues selectively without interference with the other functional groups.

CPMV, as a prototype of icosahedral viruses for organic reactions, is now well understood from the studies of Finn and Johnson groups over the past 5 years [45–48, 51, 62, 63]. The particle has been found to be highly rigid in the X-ray crystal structure, such that residues are shown to be hindered and remain inaccessible to chemical reagents in solution.





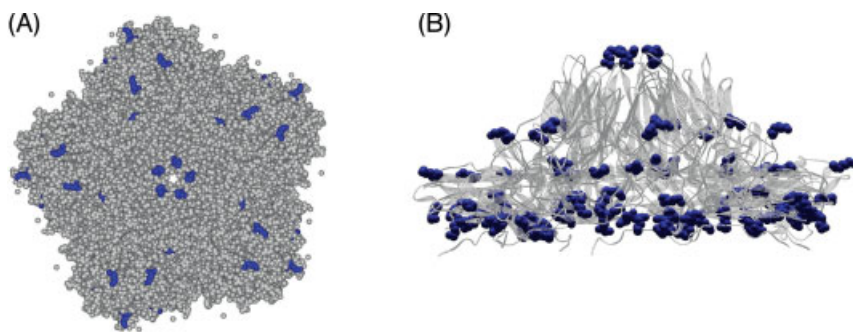
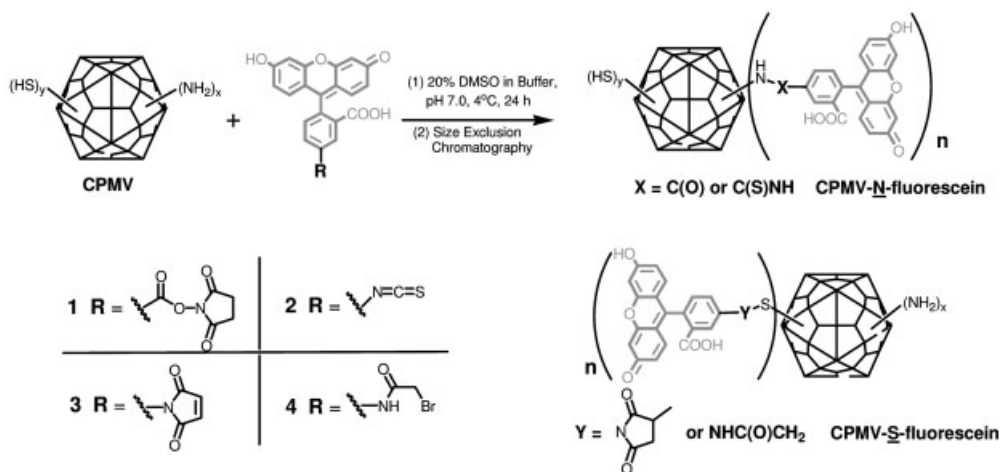


**Figure 13.2.** Structure of the pentameric units of CPMV coat protein with lysines marked in blue. (A) Top view of the space-filling model showing the exterior surface-exposed lysines. (B) Side view of the ribbon diagram of the pentamer with all lysines highlighted. Most of the lysines locate at the interior surface of the protein cell to bind to the RNA inside.

**13.3.1.1.1 Lysine Reactivity** Figure 13.2 shows the space-filling and ribbon diagrams of the outside surface of the CPMV pentameric unit. Only five lysine residues appear to be exposed to the solvent on the exterior, whereas at least 10 are found on the interior surface, presumably involved in electrostatic interactions with the packaged RNA genome and therefore unreactive with external reagents. In initial studies, fluorescent dyes were employed as probes to monitor the reactivities of CPMV. The exposed lysines of wild-type CPMV were reacted with fluorescein *N*-hydroxysuccinimide (NHS) ester **1** and isothiocyanate **2**, which are reagents selective for reactions with available lysine residues (Scheme 13.1) [48].



**Scheme 13.1.** Chemical modification of CPMV at reactive lysines and cysteines (virus shown in a schematic manner).

The particles were very stable, which can withstand the organic reagents and the conditions. The integrity of the modified viral particles was confirmed by sucrose gradient sedimentation, transmission electron microscopy (TEM) and fast protein liquid chromatography (FPLC) analysis. Covalently modified virions were separated from excess dye reagents by multiple passages through size-exclusion columns until dye was undetectable in the wash solution and the relevant absorbance ratios for the virus samples were constant. Nonspecific dye adsorption to the virus had not been observed. The stoichiometries were determined by absorption measurements on solutions of labeled particles by comparison of the intensities of dyes (495 nm for fluorescein) to viruses (260 nm), each having nonoverlapping bands with well-established molar absorptions.

At neutral pH, wild-type CPMV was found to be readily labeled by NHS esters at room temperature, up to a ratio of between 60 and 70 dye molecules per virion, in a dose-dependent fashion through a reagent ratio (dye:viral protein) of 200:1 (Fig. 13.3B). Pushing the reaction with greater amounts of 1 (up to

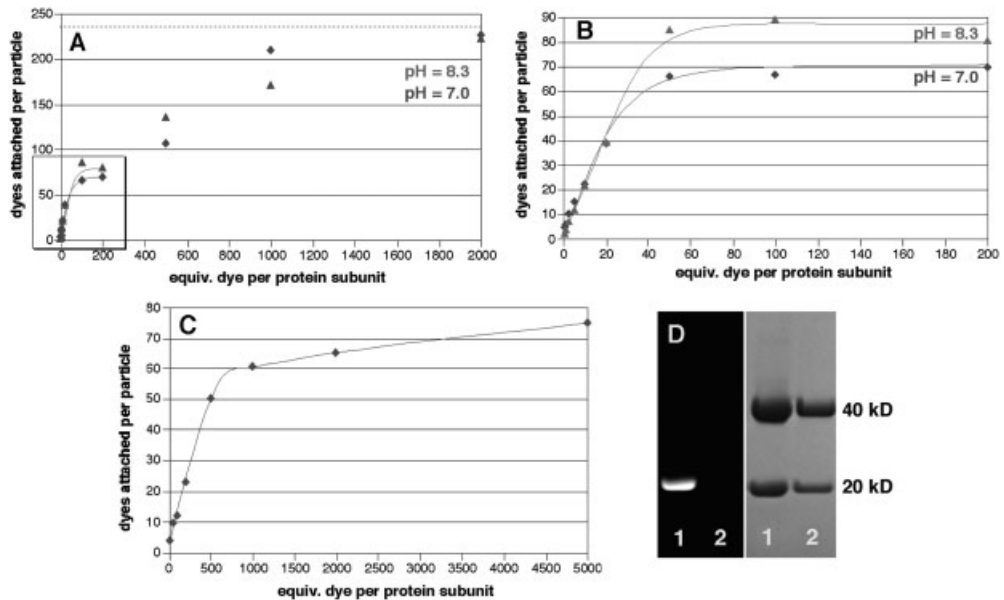


**Figure 13.3.** Relationship of the ratio of reactants (Scheme 13.1) to the number of attached dyes per CPMV particle. (A) Results of reactions using fluorescein NHS ester 1, showing the full range of ratios of the reactants used. (B) Expansion of the boxed area in (A). (C) Results of reactions using fluorescein isothiocyanate (FITC) 2. (D) Sodium dodecyl sulfate–polyacrylamide gel electrophoresis (SDS–PAGE): lanes 1, CPMV-

*N*-fluorescein prepared using reagent 2, containing approximately 50 dyes per particle; lanes 2, underivatized wild-type CPMV. Left (black background), visualized directly under UV illumination showing the attachment of fluorescein to the small subunit; right (lighter background), stained with Coomassie blue to reveal both subunits. (Reprinted from Ref. [48], © 2002, with permission from Elsevier.)

dye:protein = 4000:1) gave a maximum loading at both pH 7.0 and 8.3 of about 240 dyes per virion, indicating that four lysine residues per asymmetric unit are accessible under forcing conditions (Fig. 13.3A). The isothiocyanate reagent proved to be less reactive and thus more selective, requiring approximately 1000 equivalents to get a loading of 60 dyes per virus particle (Fig. 13.3C). Further increasing the amount of isothiocyanate dye by a factor of 5 resulted in only a modest increase in the number of dye molecules attached per virion. Electrophoresis of the resulting particles under denaturing conditions showed predominant lysine reactivity at lower loading (50 dyes per particle using isothiocyanate 2) to be associated with the small subunit (Fig. 13.3D).

NHS esters and isothiocyanates are very efficient reagents to modify accessible lysines on BNP. For example, fluorescent dye 1 has also been applied to derivatize the lysines of CCMV [52] and the small Hsp (MjHsp) cage from *Methanococcus jannaschii* [5]. The latter has been used in selective attachment and release of chemotherapeutic agents [64]. A similar strategy has been applied to study the differentiated reactivities of lysine residues of  $N\omega$ V virus-like particles (VLPs) during a pH-induced conformational change [53].  $N\omega$ V is a single-stranded RNA icosahedral insect virus, whose capsid is composed of 240 copies of the 70-kDa subunit protein. The VLPs of  $N\omega$ V are readily produced using a recombinant baculovirus system. At pH 7.6 the coat protein assembled into a stable (“procapsid”) particle, which is 480 Å in diameter and quite porous. Upon lowering the pH to 5.0, a concerted reorganization into a 410-Å diameter mature capsid structure occurs. The

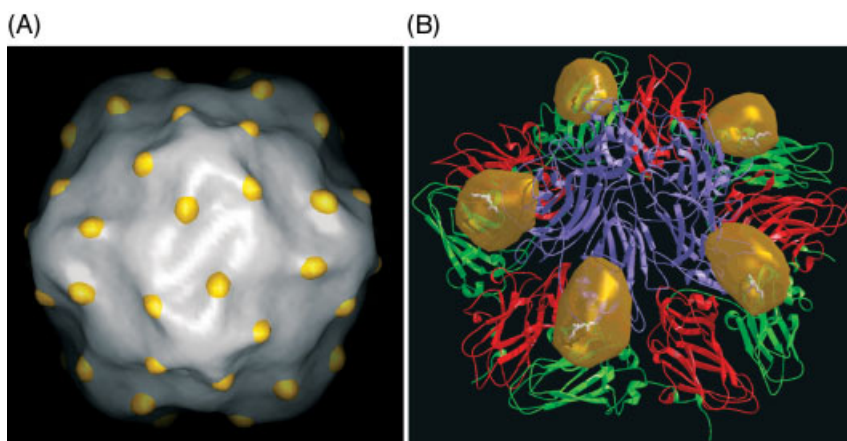


**Figure 13.4.** (A) Cryo-electron microscopy analysis results of Nanogold-modified CPMV with the density of gold labeled with a golden color. The electron densities of gold clusters were generated by subtracting density computed with the native CPMV X-ray structure from the density of Nanogold-

derivatized CPMV cysteine mutants. (B) A pentameric section of the gold densities superimposed on the atomic model of CPMV showing that the gold is attached at the site of designed cysteine mutation. (Reprinted from Ref. [46], © 2002, with permission from Wiley-VCH.)

pH-induced contraction of N $\omega$ V is one of the largest relative changes known to occur in virus particles. Since both the procapsid and capsid forms of N $\omega$ V VLPs are stable at pH 7.6, this system offers a rare opportunity to study the chemical reactivities of such large assemblies in two dramatically different states. With fluorescein derivatives **1** and **2**, approximately 240 dye units can be attached per VLP in the mature capsid form. As expected, procapsid VLPs were significantly more reactive than their capsid counterparts under identical conditions [53]. This result clearly demonstrated the importance of accessibility of a functional group to its reactivity.

**13.3.1.1.2 Cysteine Reactivity** The reactivity of cysteines of CPMV has also been carefully studied. The crystal structure of CPMV displays no free cysteine residue exposed on the exterior surface of the capsid. When wild-type CPMV was treated with thiol-selective reagents such as *N*-bromoacetamide **3** and maleimide **4** (Scheme 13.1), the reactions were very slow and give alkylation of thiol residues located exclusively on the *interior* surface of the protein capsid. There were no obvious reactions after 6 h of incubation with **3** and **4** [46, 51]. Additional amino acids can be inserted into a few solvent-exposed sites without interfering the ability of the resulting mutant virus to propagate in the host plant [20, 65–67]. Taking advantage of the biological nature of the virus, addressable cysteine residues were genetically introduced on the exterior surface of CPMV, using standard cloning techniques. These sites, the  $\beta$ B– $\beta$ C and  $\beta$ C'– $\beta$ C'' loops of the small subunit and the  $\beta$ E– $\beta$ F loop of the large subunit, are color-marked in Fig. 13.5. Each of the virus mutants contain a cysteine residue inserted as part of an added small loop or as a point mutation, and thus each particle contains 60 such insertions arrayed in icosahedral symmetry on the 30-nm diameter capsid. The altered sequences are genetically stable through multiple rounds of infection, harvesting, and reinoculation. The average purification yield of the mutant viruses is comparable to wild-type, but the presence of  $\beta$ -mercaptoethanol (BME) or tris(2-carboxyethyl)phosphine (TCEP) was necessary throughout the isolation procedure to avoid crosslinking of particles when they were pelleted by ultracentrifugation or stored after purification.

The thiol groups of the introduced cysteine residues of the mutant viruses are more exposed to the surface than the native cysteines of CPMV. Compared with the wild-type virus, the new inserted cysteines demonstrated much higher reactivity. All the thiol groups could be derivatized with very low concentration of the maleimide or bromoacetamide electrophiles at neutral pH within 6 h at 4 °C (Scheme 13.1). More importantly, the different sites of attachment could be programmed by genetic mutagenesis based on the structure information. For example, when mutant virus was reacted with monomaleimido-Nanogold<sup>®</sup>, derivatized particles were flash frozen and examined by cryo-electron microscopy and a three-dimensional image reconstruction was computed. In Fig. 13.4, the electron densities of the gold clusters are clearly visible at the positions of the inserted cysteine residues [46]. This provided an example of the engineering of chemically reactive functional groups at designated positions on the icosahedral protein template by genetic methods.

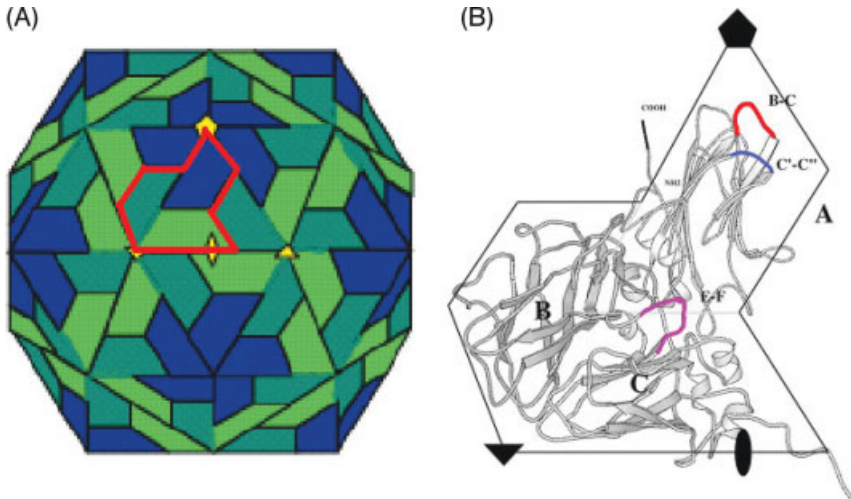


**Figure 13.5.** CPMV structure. (A) A diagrammatic representation of CPMV showing the distribution of the two subunits that comprise the “asymmetric unit”, 60 copies of which form the icosahedral particle. The trapezoids in red and green represent the two domains of the large subunit clustered around the 3-fold symmetry axes and the blue trapezoid

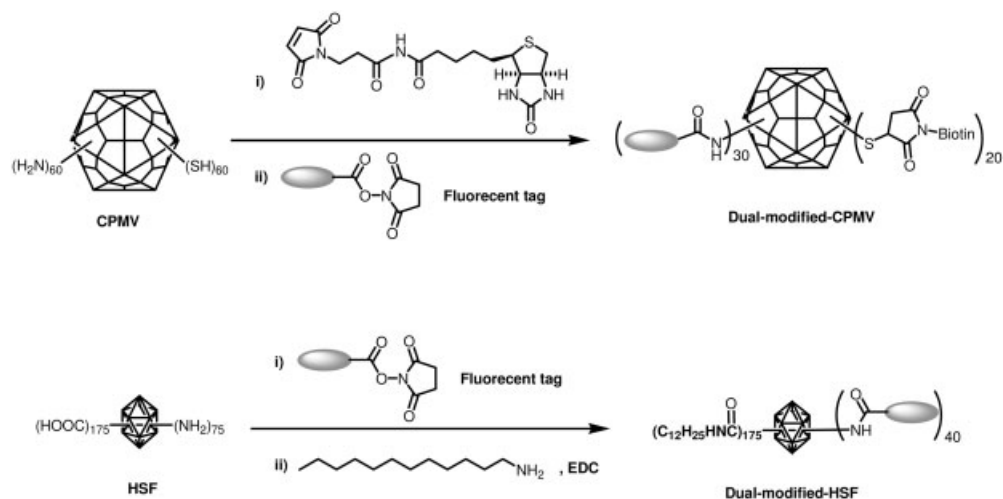
represents the small subunit clustered about the 5-fold symmetry axes. (B) Ribbon diagram of the two subunits of the CPMV coat protein, with the sites of mutational insertion highlighted in red ( $\beta$ B– $\beta$ C loop) and purple ( $\beta$ E– $\beta$ F loop). (Reprinted from Ref. [48], © 2002, with permission from Elsevier).

It is an interesting observation that in general there is no cysteine exposed to the exterior environment for any native virus or other BNPs. While that may be a result of evolution to avoid nonspecific aggregation, it offers a unique opportunity to selectively modify the BNPs. Genetic introduction of accessible cysteine very often brings in a unique reactive site, which can be derivatized chemoselectively and regioselectively. In addition to CPMV, such a technique has also been applied to CCMV [52, 68] and MjHsp [5].

**13.3.1.1.3 Reactivity on Carboxylic Groups (Glutamate And Aspartate)** At neutral pH and mild conditions, amines can be used to derivatize surface-exposed carboxylic groups upon activation. A cocatalyzed system, 1-ethyl-3-(3-dimethylaminopropyl)carbodiimide (EDC) and NHS, is commonly used in the modification of the carboxylic groups of BNPs. For example, horse spleen ferritin (HSF) has been modified with long-chain aliphatic amine activated by EDC/NHS. The resulted particles can be dissolved in nonaqueous solutions [41, 69]. Similarly, CCMV [52], TMV [54] and TYMV [55] can also be addressed on the exterior surface.

**13.3.1.1.4 Orthogonal Modification of BNPs** Based on conventional bioconjugation methods, it is possible to attach multiple, distinct functionalities on BNPs

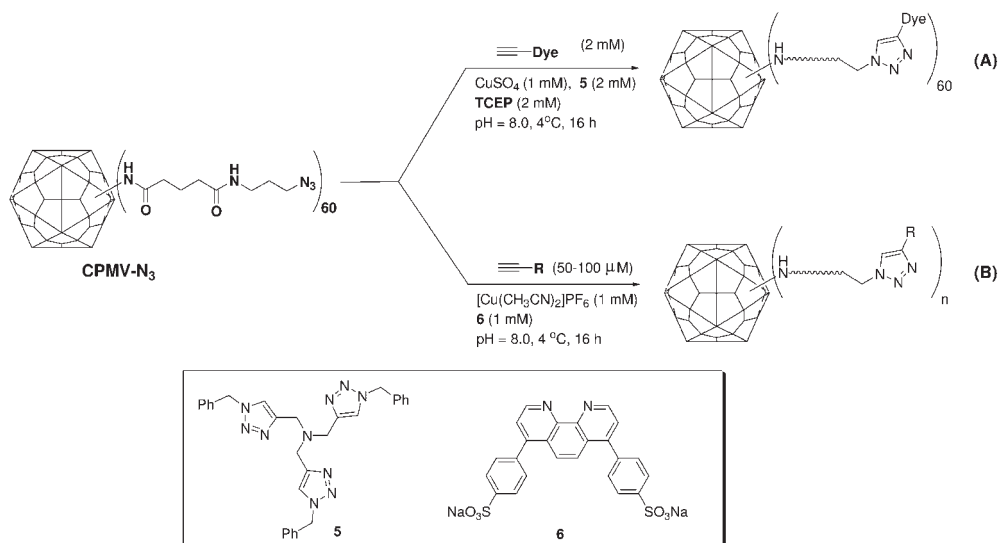
with orthogonal reactions. For example, the cysteine-inserted CPMV particles maintain the native reactive lysines. Therefore, one can selectively modify the lysines with NHS ester (or isothiocyanate) and the cysteines with maleimides. With this method, blue fluorescent antibody and PEG have been attached to CPMV cysteine mutants [45]. Scheme 13.2 shows two other examples of dual modification of BNPs [70, 71].



**Scheme 13.2.** Dual modification of CPMV and HSF with orthogonal reactive lysines and cysteines.

### 13.3.1.2 “Click Chemistry” for Bioconjugation of BNPs

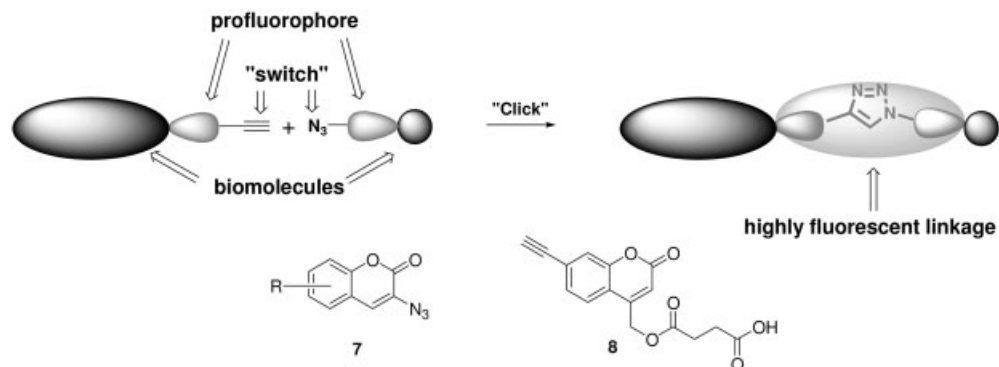
The copper-catalyzed azide–alkyne cycloaddition (CuAAC) reaction, discovered in 2002 [72, 73], has emerged as an excellent method for connecting diverse building blocks in organic synthesis. It is a classic example of “click chemistry” coined by Sharpless and his coworkers [73, 74]. As the azide and alkyne groups are each almost entirely unreactive with proteins, nucleic acids, acids, bases and water, the reaction is well suited to the formation of covalent bonds to biological molecules with no side-reactions. In particular, shortly after the discovery of the CuAAC reaction, many other new catalytic systems were reported [72, 75–77], which further promoted the application of this reaction in bioconjugation process. Finn and coworkers pioneered in using this reaction for the bioconjugation of plant virus [78]. CPMV was successfully labeled at all 60 identical protein asymmetric units of the capsid (Scheme 13.3A). Tris(carboxylethyl)phosphine (TCEP), a water-soluble reducing agent, was used to reduce Cu(II) to Cu(I) at 4 °C. Addition of ligand 5 drastically enhanced the reaction rate and an almost quantitative amount of modified proteins could be recovered after the reaction. The azide moiety could be attached to lysine, cysteine or tyrosine residues [62, 78]. Different fluorescent compounds



**Scheme 13.3.** Bioconjugation by azide–alkyne cycloaddition to derivatized CPMV particles through the Cu(I)-catalyzed azide–alkyne coupling reaction under different catalytic conditions [77, 78].

contained acetylene groups were anchored on viral surfaces with this reaction, while only millimolar concentrations of dye reactants were required [78, 79]. Using a new catalyst **6** [77], the reactivity of the reaction has been improved significantly so that micromolar protein can be connected to mid-micromolar concentrations of small molecules, polymers and proteins, all in high yield and with excellent purity (Fig. 13.3B) [80].

The ligation strategy developed by Finn and coworkers was confirmed to be remarkably reliable and suitable for most of bio-platforms and has been followed by other groups for different purposes. For example, Tirrell and coworkers incorporated non-natural azido-amino acids into the *Escherichia coli* cell membrane protein OmpC, which were successfully modified with biotin-alkyne via a Cu(I)-mediated 1,3-dipolar cycloaddition [75, 81]. Schultz and coworkers introduced azido-amino acids or alkyne-amino acids into proteins in yeast [82, 83] and the pIII protein of M13 filamentous phage [84]. These were sequentially reacted with fluorescent dyes or polyethylene glycols via the CuAAC reaction. Recently, two useful fluorogenic click reactions have been reported independently by the groups of Fahrni and Wang (Scheme 13.4) [85, 86]. Wang and coworkers synthesized 3-azidocoumarins (**7**), which show no or very weak fluorescence due to the quenching effect from the 3-azido groups. Upon coupling with arylalkynes, most of the triazole products strongly fluoresce [86]. The mild reaction conditions allowed the combinatorial screening of the best azidocoumarin–alkyne pairs on the basis of fluorescent emis-



**Scheme 13.4.** Schematic illustration of the fluorogenic "click" reactions.

sion. Similarly, the fluorescence of **8**, synthesized by the Fahrni group, can be greatly enhanced by the triazole formation [85].

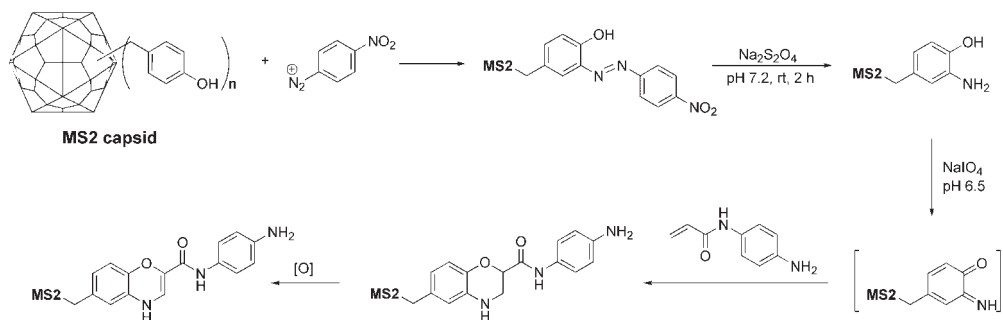
As this reaction tolerates most of functional groups and the azidocoumarin will only attack the acetylenes [62, 78], the location of the acetylene groups can be predetermined by detailed proteomic study. Then, the CuAAC reaction with azidocoumarins can anchor different kinds of functionalities on predefined positions of BNPs and the fluorescent signals from the product can be used to monitor the reaction efficiency.

### 13.3.1.3 New Developments in Tyrosine Modification

The electron donating effect of the hydroxyl group makes the phenol group of tyrosine a good nucleophile towards electrophilic attack at the *ortho* position of the OH group. Using diazonium salts ( $Ar-N\equiv N^+$ ), tyrosine can be selectively derivatized under mild conditions [61]. This reaction has been applied to modified TMV on surface tyrosines [54]. However, the reactivity of the reaction is reduced when the diazonium reagents without electron-withdrawing group on the aromatic rings are used. To solve this shortcoming, Francis and coworkers further improved the reaction with sequential derivations to render the tyrosine residue more susceptible to sophisticated modifications [57]. As shown in Scheme 13.5, the nitro-substituted diazonium salts afforded excellent tyrosine modification with MS2 bacteriophage. The resulting particles were reduced with sodium dithionite and reoxidized to *o*-iminoquinone. A further Diels–Alder reaction with acrylamides was completed in 2 h at room temperature with conversion levels exceeding 90% [57]. This modified protocol affords a versatile orthogonal pathway for bionanoparticle modification at tyrosines.

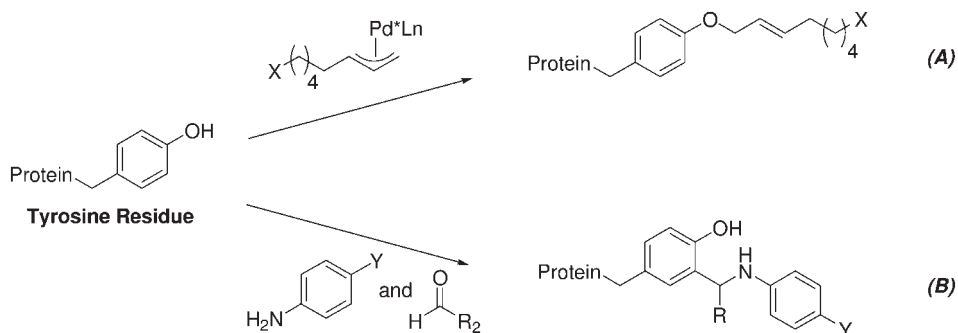
The unique structural feature of tyrosine can support multifaceted reactions other than simple nucleophilic or electrophilic substitution reactions with amino, thiol or carboxylic groups. Many new bioconjugation pathways have been revealed or re-elaborated recently, which opened new venues toward the selective modifica-





**Scheme 13.5.** Sequential functionalization of bacteriophage MS2.

tion of BNPs. For example, selective alkylation of protein tyrosines can be achieved by  $\pi$ -allylpalladium complexes (Scheme 13.6A) [87] and the *ortho* position of the hydroxyl group of tyrosine can be addressed with Mannich-type coupling reactions (Scheme 13.6B) [88].



**Scheme 13.6.** New reactions in the selective modification of protein tyrosine residues.

### 13.3.2

#### Genetic Alterations

Many of the viruses in isolated forms are complex macromolecular assemblies of metabolically inert molecules, which can be chemically modified. Alternatively, the virus can be genetically reprogrammed in its hosts with foreign peptides to express an antigen [89, 90] or to alter the affinity of the recombinant viral particle for different cell surface receptor [59, 91]. Furthermore, single-amino-acid substitution mutagenesis allows the site-specific incorporation of reactive amino acids, such as lysines or cysteines, or non-natural amino acids (NAAs) [92] on the virus coat protein for regioselective chemical modifications. Using such methods, Schultz and his group have incorporated PEG [83], alkyne-modified amino acids [93] and pho-

toisomerizable amino acids into the proteins [94]. *In vivo* and *in vitro* protein expression systems derived from cell lysates have also been used to drive viral protein synthesis with the NAAs [93, 95]. To that end, molecular cloning techniques are well integrated into the generation of hybrid BNPs with novel biological, chemical and physical properties.

#### 13.3.2.1 Heterologous Peptide Insertions

The structural information provided by X-ray crystallography and NMR studies can be hallmarks for discovering strategic locations when designing a recombinant virus particle. Many of the BNPs have their structures resolved at near-atomic resolution, facilitating the generation of the recombinant nanoparticles. Often the outer surface exposed loops between major secondary structures ( $\beta$ -sheets and  $\alpha$ -helices) or amino/carboxy-termini of the coat protein can be prime candidate sites for insertional mutagenesis. These alterations have ranged from single-amino-acid substitutions [47] to entire protein domain incorporations [96, 97].

The biological, physical, and structural properties of CPMV have been well characterized [98, 99]. The virus resists temperatures of up to 60 °C and is stable at extremely low pH levels for extended periods [65], providing the system with an extended shelf-life. The structure of the nonenveloped plant virus has been determined at 2.8-Å resolution [100], indicating that the virus displays a picorna-like  $T = 1$  ( $P = 3$ ) protein shell (termed a “capsid”). Each capsid is composed of 60 copies of the asymmetric units and each unit contains three jelly-roll  $\beta$ -sandwich folds formed by two polypeptides (identified as “small” subunit, A domain and “large” subunit, B + C domains in Fig. 13.5).

The asymmetric units are assembled in an icosahedral surface lattice around the single-stranded viral genomic RNA to form the virus particle of approximately 30 nm in diameter. The two different RNA molecules are required for infection, which are packaged by identical capsid structures, giving virions of differing densities and molecular weights ( $5.16 \times 10^6$  and  $5.98 \times 10^6$  Da, correspondingly). The viral genes have been cloned to a robust vector driven by CMV 35S promoter [101], which eases the transfection process by allowing direct infection with the cDNA clone rather than with RNA transcripts. Thus, the virus can be easily and inexpensively isolated from in yields of 1–2 g of virus per kilogram of infected leaves by using a simple and convenient procedure [102].

A series of peptide insertions on different positions of the virus revealed that the coat protein accommodates inserts of up to 30 amino acids with little effect on virus host range [103]. Moreover, among all the recombinant vectors synthesized, increases in viral coat protein isoelectric point had an adverse effect on the ability of the virus to spread systemically [103]. In vaccine development studies, short peptide inserts on the virus with a variety of foreign antigenic sequences have been successfully engineered on the surface of the virus with gp41 of HIV type 1 [67, 104] and VP2 protein of mink enteritis virus (MEV) [105]. These chimeric viral particles properly displayed the epitopes to elicit neutralizing antibodies against the viruses and confer protective immunity in mink against a lethal challenge of MEV. In particular, the large subunit contains a highly exposed  $\beta$ B– $\beta$ C loop on

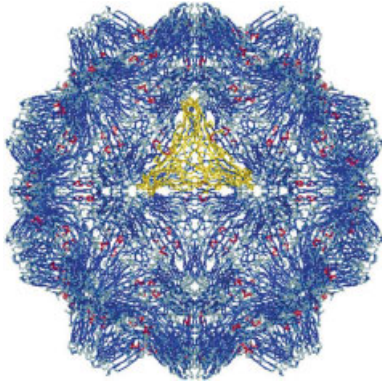


**Figure 13.6.** TYMV particle and its asymmetric unit highlighted in yellow.

the surface (Fig. 13.5), which appears to be uninvolved in intersubunit assembly and exhibits high variability in viruses within the comoviridae family [106]. A chimeric CPMV particle incorporating a 12-mer insert from the CD46 receptor on the exposed  $\beta$ B– $\beta$ C loop was shown to inhibit measles virus entry into neurons in the brains of treated mice and prevented a brain infection when the mice were pre-treated with the chimeric particles [107].

Similar protein structures within a family of viruses can be compared to reveal permissible mutational sites and identify critical residues for gene encapsidation or supramolecular assembly. TYMV (Fig. 13.6) is an RNA plant virus within the family of tymoviridae, which contains at least 20 different known species, among which three have been determined at near-atomic resolution. Selective replacements on TYMV with the homologous regions of another tymovirus, belladonna mottle virus (BeMV), had not affected the infectivity in Chinese cabbages [108]. Six of 10 such recombinants were fully viable and gave symptoms in the plants. According to this study, the amino-terminus region was particularly amendable to short peptide substitutions. The first 9 amino acids were successfully replaced with 9 amino acids from E-71 major merozoite surface antigen of *Plasmodium falciparum* to generate chimeric TYMV particles [108]. However, the study indicated that these residues reacted poorly to the antibodies raised against the E-71 epitope and the antigenic inserts were weakly immunogenic [108], suggesting that these inserts were less accessible to the surface.

In the structural comparison of the three related viruses, TYMV, physalis mottle virus (PhyMV) and desmodium yellow mottle virus (DYMov) (Fig. 13.7), the residues His68 and His/Ser180 have been identified in the crystal structures to adopt similar configurations [109]. Bink and coworkers suggest that these two residues are involved in the RNA encapsidation or decapsidation by the virus, as mutations of the two histidines to alanines showed an absence of systemic symptoms in plants, but had not affected capsid assembly when virus coat proteins were over-expressed in *E. coli* cells [109]. The comparative analysis also revealed conserved

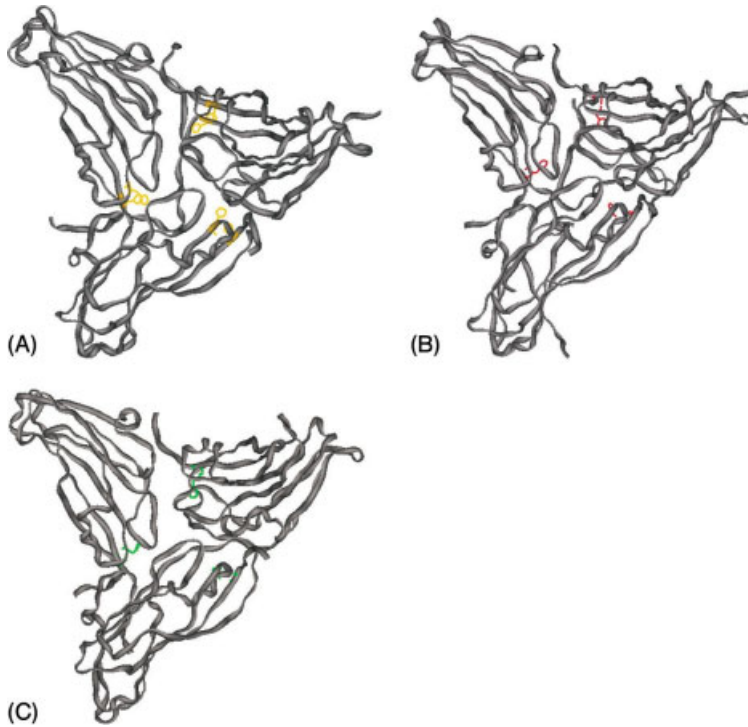


**Figure 13.7.** Asymmetric unit (a) TYMV with H68, I180 in yellow (b) DYMoV with H68 and S180 in red, and (c) PhyMV with H69 and S181 in green.

regions throughout the coat protein gene and highly variable loops on the viral coat protein. A systematic peptide insert study on TYMV, similar to studies in CPMV, may provide valuable information on potential permutation sites.

An exceptional behavior of TYMV is its ability to release its genomic contents without completely losing its entire capsid structure. The empty vesicles can be generated via high pressures [110] or deep-freeze/thaw methods [111] and these unique structures have been visualized by cryo-electron microscopy as intact particles in solution after decapsidation. The particles offer the unique opportunity to decorate the interior cavity of about 18 nm in diameter.

TMV is a rod shaped plant virus measuring 300 nm in length and 18 nm in diameter, and assembles in a highly ordered fashion with both amino- and carboxy-termini exposed to the surface of the particle (Fig. 13.8).

The virus is highly immunogenic in mammalian hosts, which is ideal for adapting TMV-based vectors for antigen display. An initial study by Haynes and co-workers demonstrated the feasibility of incorporating immunogenic peptides as fusion proteins on the plant virus capsids [112]. Short peptide fragments of up to 21 residues had been repeatedly fused to the carboxyl-terminus of TMV using



**Figure 13.8.** Ribbon diagram of TMV CP. Amino- and carboxy-terminal residues are marked in blue and red, respectively. Residues Ser154 and Gly155 marked as green spheres.

a leaky “UAG” stop codon without losing viral replication or assembly [113, 114]. By exploiting the suppressible amber stop codon, a mixed pool of fused coat proteins and native coat proteins are synthesized, which can then assemble together to form the rod-like structures [113, 114]. In other studies, a variety of short inserts were made between Ser154 and Gly155 (see Fig. 13.3) using polymerase chain reaction (PCR)-based site-directed mutagenesis [115, 116]. Similar to CPMV chimeras, the isoelectric points of the TMV chimeric particles influenced the virus infectivity and systemic spreading of the recombinant virus through the plants [115]. Longer peptide sequences of up to 25 amino acids had also been fused to the carboxy-terminus by deleting 4–6 amino acids at the carboxyl end [117].

*In lieu* of crystallography data, other studies can provide the necessary structural information for designing a fusion peptide on the virus. Potato virus X (PVX), which has no crystallographic data, has structural [118] and serological [119] evidence suggesting that the amino-terminal domain is displayed on the surface of the virus. Based on this evidence, one team utilized PVX as foreign peptide display vector by fusing a 27-kDa green fluorescent protein (GFP) to the viral coat protein [96]. The strategy involved incorporating a 16-residue peptide derived from foot and mouth disease virus peptide 2A (FDMV 2A) at the GFP carboxy-terminus, followed by the amino-terminus of the viral coat protein gene. The linker peptide sequence, FDMV 2A, mediates a processing event that signals the cleavage of the peptides at the carboxy-terminal glycine residue [120]. This strategy allowed the generation of a heterogeneous pool of fused and free forms of viral coat proteins, which had been necessary to form virus-like rod structures in PVX, as well as in TMV [113]. Subsequently, a similar study showed the plant vector assembled as rod-like structures with a single-chain antibody fused to the viral coat protein using a mixture of native coat proteins with modified coat proteins [121]. Apparently, the fusion of larger peptides on the viral coat protein is limited by the steric constraints and the chimeric particles fails to assemble to rod-like structures without the presence of the native viral coat proteins [121]. PVX vector also facilitated the expres-

sion of an unstable peptide derived from the sequence of microbicidal yeast killer toxin (KT) by direct attachment to the viral coat protein [122]. The purified recombinant virus fused with the 10 amino acids from the yeast KT had shown enhanced antimicrobial activity against a variety of plant and human pathogens [122]. The authors suggest that the higher efficacy observed in virus-fused peptides may be due to the increased stability of the fused KP in solution when compared to the chemically synthesized KP [122].

Ferritins serve as an iron storage particle, ubiquitously found as highly ordered protein cages in higher eukaryotes [123]. The bioparticles have been demonstrated to accommodate polypeptides and proteins fused to the amino- and carboxy-termini to display the polypeptides in the interior and exterior of the protein shell, respectively [124]. A silver nucleating polypeptide fused to the carboxy-terminus had been used to sequester silver metals within the confines of the protein cage, demonstrating the potential of the ferritin cages to template inorganic materials [124].

Both site-directed and random mutagenesis are practical means of generating chimeric BNPs. However, the rate at which chimeric particles are generated in site-directed mutagenesis cannot rival the rate of chimeric particles generated by random mutagenesis. One common system, the phage display library, utilizes the natural ability of the biological system to express random polypeptides fused to the viral protein. The polypeptide is then isolated through a series of selections based on functionality or binding affinity [125]. The directed evolution of the phage system has been investigated thoroughly over the years [126] and utilized as a display platform for a variety of polypeptides (antibodies [127] and peptide ligands [125] with altered functionalities). Belcher's group exploited this feature of M13 phage to synthesize ordered nanostructures, directing the growth and assembly of the nanoparticles into one-dimensional arrays [31, 32, 36, 128]. A series of polypeptides were screened on the phage template to yield nucleating peptides for semiconductors and ferromagnetic alloys [31]. The study demonstrates that in biological systems, substrate-specific peptides can be achieved through the modification of templates.

Similar to phage display systems, a BNP can be subjected to random mutagenesis to generate variants, which can then be selected based on functionality. This combinatorial approach would be an untapped, powerful advantage in BNPs, which would require overcoming two major issues. First, the mutations of polypeptide inserts must be in the context of the BNPs as a supramolecular unit. The screening of the mutants is based on functionality and its capacity to self-assemble, which is problematic in the frame of phage display. An example is the peptide screening system designed directly on adeno-associated virus (AAV) that resulted in altered vector tropism, redirecting the selected AAV vector to primary human coronary artery endothelial cells [129]. Multiple mutation sites on the exterior of the virus coat protein had been identified and with the use of a helper virus, a series of mutant AAVs were produced. In addition, many BNPs are incompatible with bacterial expressions for rapid protein synthesis and screening. Advances in

inducible protein expression and cell-free protein synthesis systems have been integrated in this field to generate many of the plant viruses.

#### 13.3.2.2 NAA Substitutions

The advantage of generating proteins with novel functional groups encoded by the genetic template is the production of a homogenous protein unit with novel physical, chemical, and biological functionalities. Exogenous chemical agents can attach to nonspecific residues of the protein, leading to a heterogenous particle, whereas the NAA incorporation takes advantage of the natural biosynthetic translation machinery to yield a modified protein. Currently, two major methodologies exist in the production of proteins with NAAs. One method incorporates NAAs directly into the proteins *in vivo* by introducing a new tRNA–tRNA synthetase pair [82, 84, 92, 93]. The tRNA synthetase specifically aminoacylates the tRNA with the NAA, after which the charged tRNA is used in the translation process to precisely decode the RNA template. The method was used in conjunction with phage display to generate proteins with an alkyne functional group attached to the surface which was then conjugated to a variety of chemical compounds via “click chemistry” [84]. The other method involves an *in vitro* biosynthetic pathway with bacterial cell lysates and mammalian cell lysates. Over the years, Sisido and coworkers have optimized the system with a versatile tRNA aminoacylation technique [95, 130–133] to incorporate a blue-laser-excitable fluorescent amino acid [134] and multiple NAAs on a single protein using a four codon/anticodon tRNA [133].

#### 13.3.2.3 Protein Expression Systems

Ultimately, the display of polypeptides on viruses for epitope presentation has its limitations. In some cases, foreign sequence insertions in the viral coat protein can result in loss of infectivity, replication or protein folding. Two major themes have evolved to address this limitation in virus systems. The heterologous peptide sequence can be chemically conjugated to the virus scaffold by using a bifunctional linker [80] or an alternative expression system can be explored.

Since the loss of infectivity or replication in a virus is not always correlated with the assembly pathway, recombinant virions can be produced from a variety of other protein expression systems, such as the *E. coli* expression system, *Arabidopsis thaliana* protoplast, baculovirus expression and wheat germ embryo cell extract. The generation of these reactive mutants utilizes many of the protein expression technologies developed over the years to greatly expand the repertoire of programming a protein with novel functionalities. The primary route of expression still relies on the original host cell for virus expression. However, the mutations leading to the loss of infectivity eliminates the possibility of propagation and production of the virus. The bacterial expression system is another possible option or better-suited production of some viral protein shells. Recently, the bacterial expression system has been modified to incorporate NAAs with high sequence specificity. These unnatural amino acids, such as propargylglycine, consist of an alkyne group that reacts with azide with a Cu(I) catalyst to form a triazole ring complex [78, 84, 93].

However, in other viruses, the proteins synthesized from the prokaryotes fail to assemble correctly without the proper post-translational modifications made in eukaryotic systems, ultimately requiring an economic eukaryotic protein strategy.

Plant protoplasts can also be used to directly transfect with viral RNA for the production of many types of plant viruses without the necessity of retaining the natural infection pathway. The cell-free wheat germ embryo extracts have become another possible peptide synthesis factory with several advantages over the previous protein expression systems, particularly in terms of the production of cytotoxic peptides and maintaining correct eukaryotic post-translation modifications. However, until the cost and production efficiency of the cell-free system can rival or even closely match the preceding systems, it is likely to remain as the last resort to synthesize viral coat proteins.

### 13.4

#### BNPs in Therapeutics

As described in previous sections, BNPs have several advantages over synthetic platforms, such as their ease of isolation, uniform size and defined structures. The large surface area and well-defined reactivities allow regioselective expression of polyvalent targeting units, which is extremely important for cell binding or recognition. In particular, the polyvalent display of cell-binding ligands can enhance the binding affinity and specificity dramatically. For example, Manchester and coworkers have used mutant CPMV in antiviral applications [107]. A well-characterized interaction between measles virus (MV) and its cellular receptor, CD46, were chosen for the anti-MV study. Since a specific region of CD46 has been previously identified to mediate the interaction with MV and the infection could be blocked by competition with short peptides from CD46 corresponding to the MV-interacting domains [135, 136], CPMV chimeras displaying the inhibitory peptide had been generated, which efficiently inhibited MV infection of HeLa cells *in vitro*, while wild-type CPMV did not. Furthermore, CPMV CD46 protected mice from mortality induced by an intracranial challenge with MV. The CD46 peptide presented in the context of CPMV was also up to 100-fold more effective than the solution CD46 peptide at inhibiting MV infection *in vitro* [107]. These results highlighted the polyvalent effect with BNPs as display scaffolds. In addition, the benefits of BNPs include:

- (i) They represent very stable self-assembled architectures at the nanometer level with many size ranges, which are otherwise difficult to produce by standard synthetic methods in the laboratory.
- (ii) They are inexpensive to isolate in large quantities. Both CPMV and TYMV can be grown in plants and purified in gram quantities with a half-day procedure.
- (iii) Their structures have been characterized at near-atomic resolution.
- (iv) The infectious cDNA clones of viruses are available as high-yield expression



vectors. Thus, their composition and surface properties can be precisely controlled using molecular biology techniques.

- (v) In-capsid cavity can be used to encapsulate fluorescent dyes or drugs to avoid the nonspecific binding being observed with other systems.
- (vi) The large surface area and well-defined reactivity allow regioselective expression of polyvalent targeting units, which is extremely important for the requirement of weak-binding ligands (e.g. boronic acid and carbohydrates) or the demand of special geometrical arrangement.
- (vii) Orthogonal cell-targeting mechanisms can be engineered simultaneously on one BNP platform. Similarly, multiple detection functionalities (e.g. optical, magnetic resonance imaging, etc.) can be programmed.

#### 13.4.1

##### Cell Targeting

Targeting the specific diseased cell types would localize the therapeutic agent, reducing potential side-effects and increasing the therapeutic efficacy. A few strategies have evolved over the years in arming cell-targeting moieties on various systems, including BNPs. One involves taking advantage of the natural affinity of the BNPs to target the cells. In other cases, genetic modifications on the BNPs with short peptide fragments redirect the system towards different cell surface receptors. Short peptide sequences from ligands can be genetically engineered on the BNPs. Portions of antibodies can be chemically conjugated to the protein cages to confer novel cell-targeting capability. Finally, small molecules are attached to the particles to modulate the affinity of the nanosystems for different cell types [137].

One strategy is to use the pre-existent cell-targeting motifs on the noninfectious replicas for therapeutic purposes, such as gene delivery or bioimaging. Many viruses of Polyomaviridae family generate intact VLPs, solely constructed of the major coat protein, VP1, without the two minor coat proteins (VP2 and VP3) [138]. VP1, when expressed in insect cells [139–142], yeast [143] and *E. coli* [144, 145], self-assembles as protein cages, and naturally targets a cell surface glycoprotein with a terminal  $\alpha$ 2,3-linked *N*-acetyl neuraminic acid [138, 146], and is internalized by the cells via  $\alpha_4\beta_1$  integrin receptors [147, 148]. Human JC polyomavirus, which in its native form infects human oligodendrocytes in the brain [149], was engineered as VLPs to deliver therapeutic genes to human fetal glial cells [150]. HBV, a human liver-specific virus, contains three overlapping envelope genes in a single open reading frame, encoding for small, medium and large proteins in its 3.2-kb genome [91]. The large protein subunit of HBV can be isolated as an aggregate form of a phospholipoprotein vesicle with an average size of 80 nm, with a targeting motif for human hepatocytes specified by the sequence located in the amino-terminus of the large subunit [151]. These hybrid vesicles have been demonstrated as safe vehicles for delivery of genes with high *ex vivo* and *in vivo* transfection efficiencies, and high targeting specificity to human hepatocyte-derived cells [91, 151].

A cell-targeting system based primarily on natural binding motifs would severely limit its potential therapeutic applications. Redirecting the protein shells to other cell types by inserting peptide ligands or portions of ligands have been shown to be effective in programming altered affinities. In one study, urokinase plasminogen activator (uPA) sequences had been genetically inserted into VP1 proteins of polyomaviruses to direct the recombinant particles to uPA receptor (uPAR) expressing cells [139]. In HBV nanoparticles, its native biorecognition motif was replaced with the epidermal growth factor (EGF) moiety to direct the particles to EGF receptor overexpressing cells [152]. Similarly, when an integrin receptor-targeting sequence had been fused to a small Hsp, the protein cage exhibited cell-binding capability *in vitro* [153].

Another docking concept involves attaching an antibody on the surface of BNP to change its tropism. The murine polyomavirus-like particles were engineered with eight glutamic acid residues and one cysteine residue in one of the exterior loops to attach a portion of the anti-tumor antibody B3 [154]. The antibody fragment was modified at the carboxy-terminus with peptide sequences (Arg<sub>8</sub>CysPro), which associates with the mutant VLP via electrostatic interactions, and the complex is further stabilized by the formation of a disulfide linkage. This coupling reaction yielded polyoma VLPs with 30–40 antibody fragments bound to the surface, allowing the modified VLPs to bind to the breast carcinoma cells with high efficiencies [154]. Alternatively a bifunctional crosslinker had been used to conjugate the antibodies, which can effectively target specific cells within a mixed population [153].

The conjugation of antibodies on the BNPs can be difficult and costly to manufacture. Facile chemical modifications with small molecules can be designed to modify the surface of BNPs for cell-specific targeting. CPMV, TYMV, TMV and many other viral platforms have demonstrated robust chemical modifications directed via conventional bioconjugation techniques and alternative methods (see Section 13.3.1).

#### 13.4.2

##### **Gene Delivery**

Gene therapy is still a promising frontier in medicine with unparalleled potential to combat genetic diseases, cancer or viral infections. Many of the retroviruses efficiently package, deliver and integrate into the host chromosomal DNA, but the wide range of cell infectivity provides little cell specificity. In addition, the labor-intensive design and high production costs in obtaining tropism-modified recombinant retroviral vectors have diverted attention to safer and more economic gene delivery systems with VLPs, which are innocuous counterparts of the original virus. The noninfectious particles in many ways mimic the functions of the original virus, but lack the essential components of the viral genome to self-propagate in the host, reducing its potential safety hazards. HBV nanoparticles and polyoma VLPs are capable of packaging a therapeutic gene and efficiently delivering it to the

target cells and organs *in vitro* and *in vivo* [152, 155–157]. These particles consist of proteins produced in bacterial or yeast expression systems, which are also easily programmable by genetic and chemical methods to adapt various cell-targeting ligands, receptors or carbohydrates.

Since the initial proposal in 1970 to develop polyomavirus as a potential gene delivery vector by Osterman and coworkers [158], various methods have been established to introduce genes into a variety murine, monkey and human tissues [159–161]. Circular DNA sequences of up to 17.7 kb can be encapsulated *in vitro* by polyomavirus VP1 [159], and have been used to deliver exogenous DNA to human brain cells and fetal kidney epithelial cells [155]. Atomic force microscopy images indicated that polyoma VLPs aggregated around the heterologous DNA to form loosely associated structures and DNA transfer was mediated by cell surface sialic acid residues [60]. The polyoma VLPs were also adapted to deliver plasmids expressing short hairpin RNAs and synthetic small interfering RNAs to human lymphoblastoid cells and HeLa cells to downregulate gene expression [162].

Regardless of the vehicle, all effective gene delivery agents deal with complicated issues of targeting appropriate cells or tissue, efficient packaging, transferring, precisely integrating the therapeutic gene in the host genome, and properly expressing the therapeutic gene in the host genome with economic production and safety considerations [152].

#### 13.4.3

#### Bioimaging

For *in vivo* or *in vitro* imaging (such as diffusion fluorescent tomography), it is important to have high local concentrations with no quenching of fluorescence to enhance the imaging contrast. Since BNPs can be genetically or chemically modified in a chemoselective manner, high-loading fluorescent dyes can be loaded with a precisely designed geometrical distribution on the surface of BNPs and inside the cage of BNPs. The rigid and highly ordered structures of the protein structures of BNPs “fix” the attached imaging agents at designed positions on the surface. Therefore, the attached dye molecules have no mobility to interact or aggregate to each other, which often quench the fluorescence. The observation that no fluorescence quenching of the virus–dye conjugates occurred even at a high local concentration of the dyes has been evidently demonstrated [55, 56].

Fluorescent probes are the most common imaging reagent used in BNP labeling. For example, using fluorescent dye-modified CPMV, Manchester and her coworkers have studied the systemic trafficking of CPMV in mice via the oral route [163]. The pattern of localization of CPMV particles to mouse tissues following oral or intravenous dosing was then determined by confocal fluorescent microscopy and viral RNA detection. For several days following oral or intravenous inoculation, CPMV was found in a wide variety of tissues throughout the body, including the spleen, kidney, liver, lung, stomach, small intestine, lymph nodes, brain and bone marrow. CPMV particles were detected after cardiac perfusion, suggesting that the particles entered the tissues [163]. Fluorescent dye-labeled CPMV has also been

employed for intravital vascular imaging [164]. The CPMV can be labeled with high densities of Alexa Fluor or fluorescein dyes, showing no measurable quenching. The resulting exceptionally bright particles were used to visualize the vasculature and blood flow in living mouse and chick embryos to a depth of up to 500  $\mu\text{m}$ . Therefore, the intravital visualization of human fibrosarcoma-mediated tumor angiogenesis using fluorescent CPMV provides a means to identify arterial and venous vessels, and to monitor the neovascularization of the tumor microenvironment [164]. In another study, the lateral mobility of fluorescent labeled murine polyoma virus-like particles bound to living cells and artificial lipid bilayers was studied by single fluorescent particle tracking using total internal reflection fluorescence microscopy [165].

To minimize the background and enhance the deep-tissue penetration ability, near-infrared (NIR) fluorescent dyes are often used for *in vivo* imaging. Significant efforts have been placed on the development of efficient bioconjugation methods for the attachment of NIR fluorescent agents to BNPs. As shown in Fig. 13.9, cyanine NIR-782 dye was attached to CPMV with over 40 dye molecules per viral particle, making a local concentration of around 1.8 mM. The purified viral–dye hybrid has been employed as a probe for NIR fluorescence imaging. Using tissue-like phantoms, fluorescent tomographic data have been obtained through a multi-channel frequency domain system. The spatial maps of fluorescence quantum yield were detected with a finite element-based reconstruction algorithm [166]. In addition, a new class of carbocyanine dyes has been synthesized and conjugated to CPMV by the “click” reaction of azides and alkynes [79].

Magnetic imaging complexes or other probes can also be used to decorate BNPs. For example, luminescent semiconductor nanocrystals (quantum dots) were employed to modify CPMV [167]. Using CPMV mutants expressing available 6-histidine sequences inserted at loops on the viral coat protein [168], it was shown that CPMV particles were specifically immobilized on NeutrAvidin functionalized substrates in a controlled fashion via metal-affinity coordination. Two linking chemistries were employed to decorate CPMV with CdSe–ZnS core–shell quantum dots to target the histidine or lysine residues on the exterior virus surface and utilize biotin–avidin interactions. In the first case, quantum dots are immobilized on the surface-tethered CPMV via electrostatic attachment to avidin previously bound to the virus particle. In the second case, chemical modification of the surface lysine residues with biotin groups and the biotinylated CPMV is discretely immobilized onto the substrate via NeutrAvidin–biotin interactions. The biotin units on the upper exposed surface of the immobilized CPMV then serve as capture sites for avidin-derivatized quantum dots [167]. Similar conjugation chemistry has been used to produce virus–carbon nanotube [169] and virus–metal nanoparticle complexes [170], which have potential as biological sensors. For example, networks of gold nanoparticles and bacteriophage have recently been engineered to preserve the cell-targeting and internalization properties mediated by the specific peptide display [171]. In addition, the gold nanoparticles acted as signal reporters for fluorescence and dark-field microscopy and NIR surface-enhanced Raman scattering (SERS) spectroscopy [171]. In all these cases, BNPs

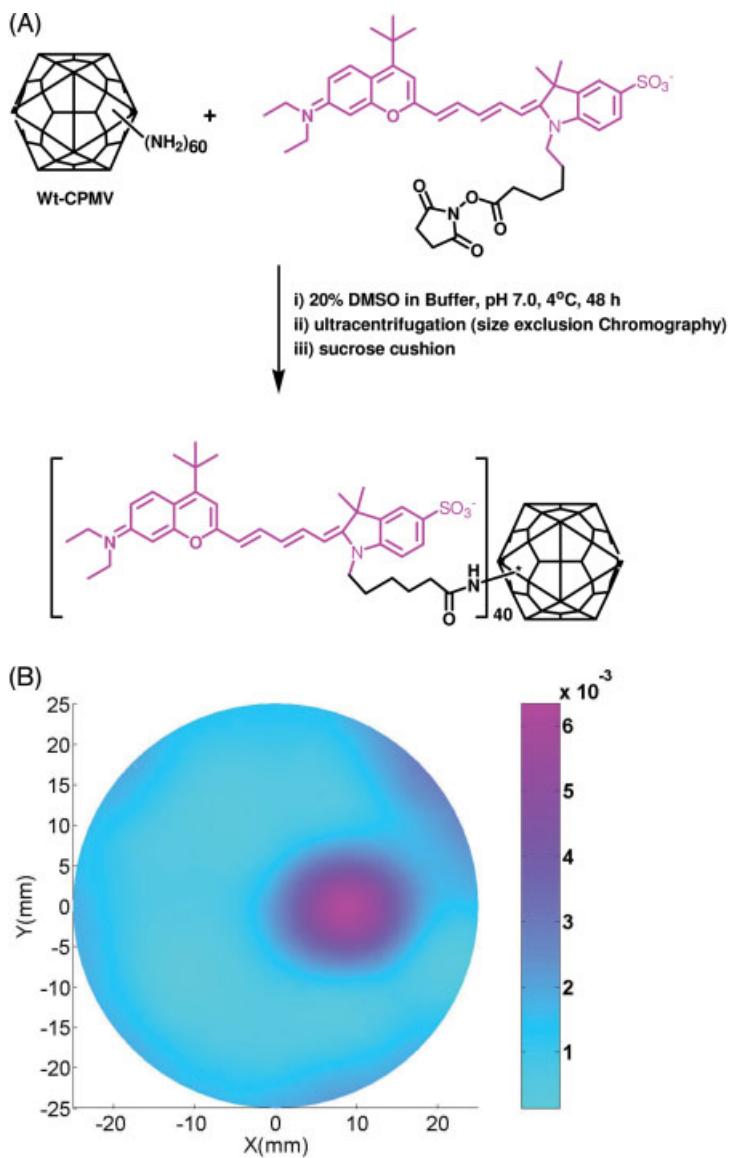


**Figure 13.9.** (A) Attachment of NIRF-782 to CPMV. (B) Reconstruction image of fluorescent quantum yield of dye-modified CPMV. The left and bottom axes illustrate the spatial scale in millimeters, which the color scale records the value of the quantum yield.

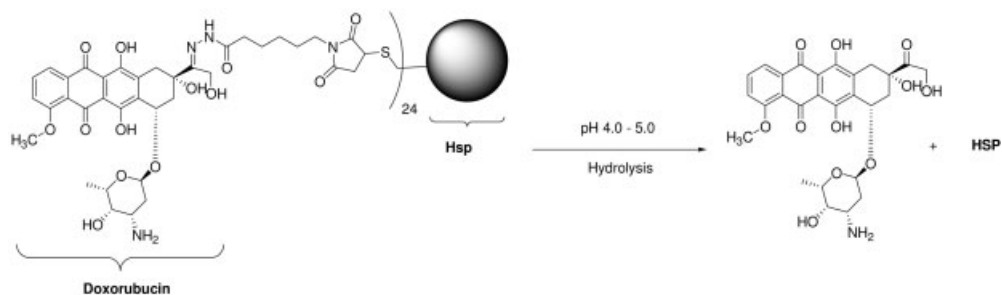
served as an excellent scaffold to modulate the organization of reporters for bio-sensing or bioimaging.

#### 13.4.4

#### Drug Encapsulation and Release

The interior cavities of BNPs are hollow spaces that can encapsulate other elements for drug delivery by genetic and chemical modifications. Covalently attached small molecules are tethered to the BNPs, preventing leakage from the interior, and circumventing drug degradation and avoiding nonspecific binding, until a signal or low endosomal pH within the cell releases the drug from the carrier. Recent studies with polyoma VLPs and Hsp demonstrated the feasibility of packaging chemical compounds within the protein cage. In the case with polyoma VLPs, Schmidt and coworkers inserted the first WW domain of mouse formin binding protein 11 (FBP 11) to the amino-terminus of VP1 to attach proline-rich ligands (bearing the consensus sequence PPLP) to the inner surface of the VLPs [172]. In a similar study with polyoma VLPs, a stretch of 49 amino acids of the inner core protein from polyomavirus VP2 protein had been fused to GFP or covalently attached to methotrexate (MTX) [173]. The amino acids specifically anchored GFP and MTX to VP1, resulting in VLPs with GFP or MTX enclosed by VP1 coat proteins [173]. The encapsulated MTX retained similar cytotoxicity in the cells, and destroyed MTX-resistant cell by circumventing MTX transport.

Flenniken and coworkers covalently modified the Hsp cage interior with anti-tumor drugs by genetically introducing cysteine residues at the inner surface and selectively attaching the chemical compound to the reactive cysteines with a pH-sensitive linker [64]. This Hsp assembles into a 24-subunit spherical structure with an octahedral symmetry, which is 12 nm in diameter and has a porous protein shell that allows free small-molecular exchange between the interior and bulk solution [5]. The (6-maleimidocaprol) hydrazone derivative of doxorubicin was linked to the interior surface of this Hsp via coupling of maleimide and cysteine (Scheme 13.7) [64]. The quantitative analysis by absorbance spectroscopy indicated



**Scheme 13.7.** Controlled release of doxorubicin from the interior of a small Hsp cage [64].

that 24 doxorubicin moieties were encapsulated and, under acidic conditions, doxorubicin was selectively released through the hydrolysis of hydrazone linkage (Scheme 13.7). This study demonstrates that a therapeutic agent could be housed within the interior of a BNP cage to realize its controlled release. Therefore, a BNP system has the potential to serve as a versatile drug delivery system.

## 13.5

### Immune Response

#### 13.5.1

##### Vaccine Development

The virus surface consists of highly organized repeating motifs that are ideally suited for eliciting an immune response. Although this is problematic for gene therapy or drug delivery, the polyvalent display on the BNPs can be extremely advantageous for vaccine development. In particular, plant viruses show great potential for production of pharmaceuticals in plants. The small size of plant viral genomes, the ease with which they can be manipulated and the simplicity of the infection process make the plant viral vectors an attractive alternative as transgenic systems for the displaying antigenic proteins. CPMV, TMV, PVX and alfalfa mosaic virus (ALMV) have all demonstrated enormous potential to incorporate recombinant peptide sequences to confer protective immunity and to combat against viral and bacterial infections [65, 174].

The immunological analysis of plant virus-based chimeras has been one of the most thoroughly documented among all of the BNP systems. An important demonstration of CPMV-based vaccines and its potential to stimulate protective immunity was reported by Dalsgaard and coworkers [105] using the chimeric plant virus inserted with a short linear epitope derived from the amino-terminal region of VP2 of MEV. A single, subcutaneous injection of 1 mg of chimeric particles protected mink against challenge with MEV. In a following study, dogs immunized with ultraviolet (UV)-irradiated chimera elicited high titers of neutralizing antibodies and conferred resistance to canine parvovirus [175].

PVX, another plant-based antigen display vector, showed similar results in mice with the highly conserved ELDKWA epitope from HIV-1 gp41 expressed on the viral coat proteins [176]. The mice inoculated with the PVX-derived chimeric particles were able to elicit high levels of HIV-1 epitope-specific antibodies without adjuvants. Furthermore, the human immune response to chimeric viral particles was studied with severe combined immunodeficient mice reconstituted with human peripheral blood lymphocytes (hu-PBL-SCID). hu-PBL-SCID mice immunized with chimeric viral particle-pulsed autologous dendritic cells were able to mount a specific human primary antibody response against the gp41-derived epitope [176]. Remarkably, anti-HIV-1-neutralizing activity was present in the sera from both normal and hu-PBL-SCID mice. Similar vaccine studies with ALMV have also demonstrated that peptides containing antigenic determinants of rabies virus

glycoprotein and nucleoprotein fused to the viral coat protein conferred immunity in mice against lethal challenge [177].

Chimeric TMV particles containing 10 or 15 amino acids from the spike protein of murine hepatitis virus (MHV) gave rise to intact chimeric viral particles with the MHV peptides displayed on the surface [116]. The study indicated that mucosal and parenteral immunization with the chimeric TMV particles protected the treated mice against lethal doses of MHV. However, displaying larger protein structures as genetic fusions to the capsid protein has not been possible on TMV. To address this issue, a reactive lysine was introduced near the amino-terminus of TMV CP, which was further modified with biotin [178]. The biotinylated end was then tagged with GFP–streptavidin or L2 protein of canine oral papillomavirus, resulting in TMV particles with GFP or L2 protein, respectively, decorated on the exterior. The L2 protein-coupled biotinylated-TMV was found to be more immunogenic in mice than uncoupled L2 protein fragments.

Chimeras expressing epitopes of a bacterial origin have also been shown to confer protective immunity. For example, a chimeric CPMV particle expressing amino acid sequences containing two epitopes from the outer membrane protein F (ompF) of *Pseudomonas aeruginosa* protected mice against challenge with *P. aeruginosa* in a model of chronic pulmonary infection [179, 180]. Likewise, a chimera plant virus expressing the D2 domain of the fibronectin-binding protein (FnBP) from *Staphylococcus aureus* has been shown to be able to protect rats against endocarditis [181]. Thus, plant virus-based chimeras carrying neutralizing epitopes can offer novel avenues for producing effective vaccines against various infectious viruses and, more generally, for the design of new vaccination strategies in humans. (See Refs. [20, 174] for more detailed reviews on plant virus-based vaccine development.)

### 13.5.2

#### Immune Modulation

In addition to the peptide displays, the BNPs can also be adapted to present multiple sugar residues on the exterior surface. The polyvalent scaffolds decorated with various carbohydrates have shown increased binding affinity and biological responses when compared with their monomeric constituents [182–184]. Similar to previous studies with polymers and other supports, the virus has been shown to accommodate multiple mannose residues via chemical coupling [80] and inhibit cell agglutination [51]. The virus–carbohydrate conjugate can further be designed to supplement immune responses or other biological processes.

The repetitive patterns on BNPs, while beneficial for antigen display in vaccine display, can become a major problem in adapting the BNPs for diagnostic and therapeutic applications. One modality has been to modify the particle surface with PEG polymers and other polymers to reduce the immunogenic response towards the particles [185]. In adenovirus, its bioavailability and pharmacokinetics have been investigated extensively with the intention of improving adenovirus-delivered gene therapeutics [44, 186]. To facilitate the use of other protein-based systems,



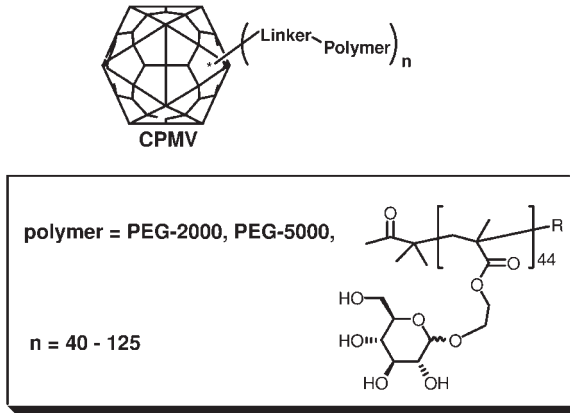


**Figure 13.10.** Schematic drawing of viral particle-modified polymer.

such as BNPs, Finn and his group studied the immune response towards viral particles modified with PEG and other polymers (Fig. 13.10) [49, 80]. The preliminary study was to assess the immunogenic response in mice towards PEG-modified CPMV. The levels of CPMV-specific antibodies in the mice treated with PEGylated CPMV were comparably similar to the levels in mice treated with unmodified CPMV, but the serum antibody level had drastically declined over the following 2 months in mice treated with modified CPMV compared with unmodified CPMV [49].

### 13.6

#### Future Directions

The major features of BNPs that were exploited for generating novel biotemplates in the nanometer range have been iterated throughout the chapter. In general, these protein structures naturally self-assemble to highly organized structures and many of the systems, either virus- or ferritin-based, demonstrate robust physical properties that can be exploited for variety purposes. The systems can be genetically engineered and chemically addressed to alter functionalities for future therapeutic applications. As platforms, the viruses provide a wide array of shapes such as rods and spheres, and vast ranges of sizes spanning from tens to hundreds of nanometers. Hsps and ferritin arrange as nanometer-sized materials with well-characterized hierarchical motifs as templates for mineralization. Several studies have demonstrated the feasibility of using various nanoparticles (BNPs, liposomal carriers, inorganic materials, etc.) tailored with ligands and small molecules to target different cell types for drug/gene delivery and cell imaging [56, 137, 151, 152, 164]. The nanosized probes can further be modified with chemical compounds, such as bioimaging agents (NIR fluorescent dyes, magnetic resonance imaging contrast agents) and drugs at high local concentrations to increase detection sensi-

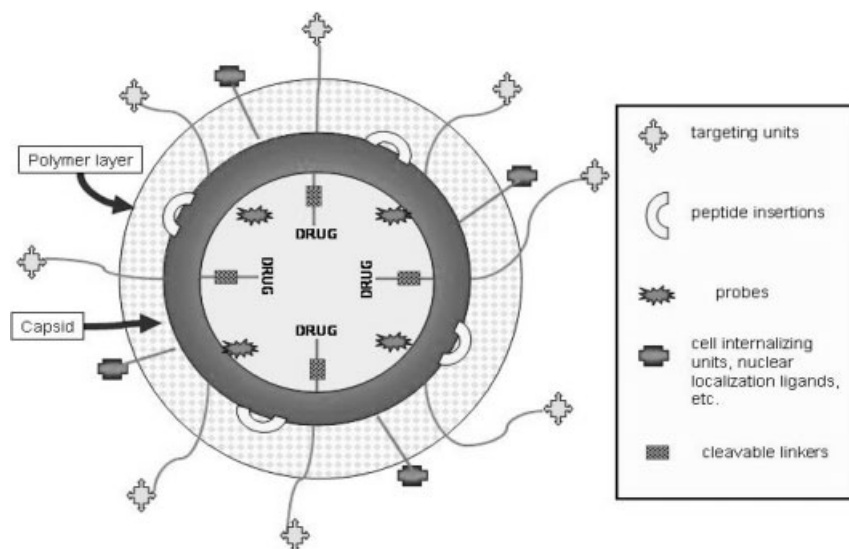


Figure 13.11. Multifunctional BNP hybrid.

tivity and efficacy for therapeutic applications [166, 187, 188]. Furthermore, the BNPs can be modified with polymers to boost the half-life of the biological system either by shielding the protein structures from enzymatic degradation or immune response. Ultimately, the combination of these multiple derivatizations on the nanoparticles could yield versatile units with specific cell targeting for drug/gene delivery, with simultaneous *in vivo* imaging for biomedical purposes (Fig. 13.11).

### Acknowledgments

The authors are grateful of the Nanocenter of University of South Carolina, the USA Army–MURI program, DOD-DURIP, the W. M. Keck Foundation and the NSF-NER program.

### References

- 1 C. M. NIEMEYER, Nanoparticles, protein, and nucleic acids: biotechnology meets materials science. *Angew. Chem. Int. Ed.* **2001**, *40*, 4128–4158.
- 2 E. DUJARDIN, S. MANN, Bio-inspired materials chemistry. *Adv. Eng. Mater.* **2002**, *4*, 461–474.
- 3 N. C. SEEMAN, At the crossroads of chemistry, biology, and materials: structural dna nanotechnology. *Chem. Biol.* **2003**, *10*, 1151–1159.
- 4 W. M. SHIH, J. D. QUISPE, G. F. JOYCE, A 1.7-kilobase single-stranded DNA that folds into a nanoscale octahedron. *Nature* **2004**, *427*, 618–621.
- 5 M. L. FLENNIKEN, D. A. WILLITS, S. BRUMFIELD, et al., The small heat

- shock protein cage from *Methanococcus Jannaschii* is a versatile nanoscale platform for genetic and chemical modification. *Nano Lett.* **2003**, *3*, 1573–1576.
- 6 K. S. RAJA, Q. WANG, Bionanoparticles and nanotechnology. *Encycl. Nanosci. Nanotechnol.* **2004**, *B*, 321–330.
  - 7 N. BAN, A. MCPHERSON, The structure of satellite panicum mosaic virus at 1.9 Å resolution. *Nat. Struct. Biol.* **1995**, *2*, 882–890.
  - 8 N. NANDHAGOPAL, A. A. SIMPSON, J. R. GURNON, et al., The structure and evolution of the major capsid protein of a large, lipid-containing DNA virus. *Proc. Natl Acad. Sci. USA* **2002**, *99*, 14758–14763.
  - 9 W. J. McALEER, E. B. BUYNAC, R. Z. MAIGETTER, et al., Human hepatitis B vaccine from recombinant yeast. *1984. Biotechnology* **1992**, *24*, 500–502.
  - 10 D. M. HARPER, E. L. FRANCO, C. WHEELER, et al., Efficacy of a bivalent L1 virus-like particle vaccine in prevention of infection with human papillomavirus types 16 and 18 in young women: a randomised controlled trial. *Lancet* **2004**, *364*, 1757–1765.
  - 11 L. L. VILLA, R. L. COSTA, C. A. PETTA, et al., Prophylactic quadrivalent human papillomavirus (types 6, 11, 16, and 18) L1 virus-like particle vaccine in young women: a randomised double-blind placebo-controlled multicentre phase II efficacy trial. *Lancet Oncol* **2005**, *6*, 271–278.
  - 12 M. F. BACHMANN, U. H. RÖHRER, T. M. KUNDIG, et al., The influence of antigen organization on B cell responsiveness. *Science* **1993**, *262*, 1448–1451.
  - 13 M. F. BACHMANN, R. M. ZINKERNAGEL, A. OXENIUS, Immune responses in the absence of costimulation: viruses know the trick. *J. Immunol.* **1998**, *161*, 5791–5794.
  - 14 K. K. W. WONG, T. DOUGLAS, S. GIDER, et al., Biomimetic synthesis and characterization of magnetic proteins (magnetoferritin). *Chem. Mater.* **1998**, *10*, 279–285.
  - 15 T. DOUGLAS, V. T. STARK, Nanophase cobalt oxyhydroxide mineral synthesized within the protein cage of ferritin. *Inorg. Chem.* **2000**, *39*, 1828–1830.
  - 16 D. ENSIGN, M. YOUNG, T. DOUGLAS, Photocatalytic synthesis of copper colloids from Cu(II) by the ferrihydrite core of ferritin. *Inorg. Chem.* **2004**, *43*, 3441–3446.
  - 17 C. PAAVOLA, S. CHAN, K. MAZZARELLA, et al., A versatile platform for nanotechnology based on circular permutation of a chaperonin protein. *Nanotechnology* **2006**, *17*, 1171–1176.
  - 18 C. A. KERFELD, M. R. SAWAYA, S. TANAKA, et al., Protein structures forming the shell of primitive bacterial organelles. *Science* **2005**, *309*, 936–938.
  - 19 G. P. LOMONOSOFF, J. E. JOHNSON, Use of macromolecular assemblies as expression systems for peptides and synthetic vaccines. *Curr. Opin. Struct. Biol.* **1996**, *6*, 176–182.
  - 20 G. P. LOMONOSOFF, W. D. O. HAMILTON, Cowpea mosaic virus-based vaccines. *Curr. Top. Microbiol. Immunol.* **1999**, *240*, 177–189.
  - 21 L. NIEBA, M. F. BACHMANN, A new generation of vaccines. *Mod. Asp. Immunobiol.* **2000**, *1*, 36–39.
  - 22 K. K. HUNT, S. A. VORBURGER, Tech.Sight. Gene therapy. hurdles and hopes for cancer treatment. *Science* **2002**, *297*, 415–416.
  - 23 D. FERBER, Gene therapy. Safer and virus-free? *Science* **2001**, *294*, 1638–1642.
  - 24 T. DOUGLAS, M. YOUNG, Virus particles as templates for materials synthesis. *Adv. Mater.* **1999**, *11*, 679–681.
  - 25 T. DOUGLAS, M. YOUNG, Host-guest encapsulation of materials by assembled virus protein cages. *Nature* **1998**, *393*, 152–155.
  - 26 T. DOUGLAS, E. STRABLE, D. WILLITS, et al., Protein engineering of a viral cage for constrained nanomaterials synthesis. *Adv. Mater.* **2002**, *14*, 405–418.
  - 27 M. ALLEN, D. WILLITS, M. YOUNG, et al., Constrained synthesis of cobalt

- oxide nanomaterials in the 12-subunit protein cage from *Listeria innocua*. *Inorg. Chem.* **2003**, *42*, 6300–6305.
- 28 M. ALLEN, D. WILLITS, J. MOSOLF, et al., Protein cage constrained synthesis of ferrimagnetic iron oxide nanoparticles. *Adv. Mater.* **2002**, *14*, 1562–1565.
- 29 C. E. FLYNN, S.-W. LEE, B. R. PEELE, et al., Viruses as vehicles for growth, organization and assembly of materials. *Acta Mater.* **2003**, *51*, 5867–5880.
- 30 N. C. SEEMAN, A. M. BELCHER, Emulating biology: building nanostructures from the bottom up. *Proc. Natl Acad. Sci. USA* **2002**, *99*, 6451–6455.
- 31 C. MAO, D. J. SOLIS, B. D. REISS, et al., Virus-based toolkit for the directed synthesis of magnetic and semiconducting Nanowires. *Science* **2004**, *303*, 213–217.
- 32 C. MAO, C. E. FLYNN, A. HAYHURST, et al., Viral assembly of oriented quantum dot nanowires. *Proc. Natl Acad. Sci. USA* **2003**, *100*, 6946–6951.
- 33 K. T. NAM, B. R. PEELE, S.-W. LEE, et al., Genetically driven assembly of nanorings based on the M13 virus. *Nano Lett.* **2004**, *4*, 23–27.
- 34 S.-W. LEE, A. M. BELCHER, Virus-based fabrication of micro- and nanofibers using electrospinning. *Nano Lett.* **2004**, *4*, 387–390.
- 35 S.-W. LEE, B. M. WOOD, A. M. BELCHER, Chiral smectic C structures of virus-based films. *Langmuir* **2003**, *19*, 1592–1598.
- 36 S. W. LEE, C. MAO, C. E. FLYNN, et al., Ordering of quantum dots using genetically engineered viruses. *Science* **2002**, *296*, 892–895.
- 37 S.-W. LEE, S. K. LEE, A. M. BELCHER, Virus-based alignment of inorganic, organic, and biological nanosized materials. *Adv. Mater.* **2003**, *15*, 689–692.
- 38 C. E. FLYNN, C. MAO, A. HAYHURST, et al., Synthesis and organization of nanoscale II–VI semiconductor materials using evolved peptide specificity and viral capsid assembly. *J. Mater. Chem.* **2003**, *13*, 2414–2421.
- 39 B. D. REISS, C. MAO, D. J. SOLIS, et al., Biological routes to metal alloy ferromagnetic nanostructures. *Nano Lett.* **2004**, *4*, 1127–1132.
- 40 K. WETZ, R. R. CRICHTON, Chemical modification as a probe of the topography and reactivity of horse-spleen apoferritin. *Eur. J. Biochem.* **1976**, *61*, 545–550.
- 41 K. K. W. WONG, H. COLFEN, N. T. WHILTON, et al., Synthesis and characterization of hydrophobic ferritin proteins. *J. Inorg. Biochem.* **1999**, *76*, 187–195.
- 42 M. LI, K. K. W. WONG, S. MANN, Organization of inorganic nanoparticles using biotin-streptavidin connectors. *Chem. Mater.* **1999**, *11*, 23–26.
- 43 H. ROMANCZUK, C. E. GALER, J. ZABNER, et al., Modification of an adenoviral vector with biologically selected peptides: a novel strategy for gene delivery to cells of choice. *Hum. Gene Ther.* **1999**, *10*, 2615–2626.
- 44 M. A. CROYLE, N. CHIRMULE, Y. ZHANG, et al., Pegylation of E1-deleted adenovirus vectors allows significant gene expression on readministration to liver. *Hum. Gene Ther.* **2002**, *13*, 1887–1900.
- 45 Q. WANG, K. S. RAJA, K. D. JANDA, et al., Blue fluorescent antibodies as reporters of steric accessibility in virus conjugates. *Bioconjug. Chem.* **2003**, *14*, 38–43.
- 46 Q. WANG, T. LIN, L. TANG, et al., Icosahedral virus particles as addressable nanoscale building blocks. *Angew. Chem. Int. Ed.* **2002**, *41*, 459–462.
- 47 Q. WANG, T. LIN, J. E. JOHNSON, et al., Natural supramolecular building blocks: cysteine-added mutants of cowpea mosaic virus. *Chem. Biol.* **2002**, *9*, 813–819.
- 48 Q. WANG, E. KALTGRAD, T. LIN, et al., Natural supramolecular building blocks: wild-type cowpea mosaic virus. *Chem. Biol.* **2002**, *9*, 805–811.
- 49 K. S. RAJA, Q. WANG, M. J. GONZALEZ, et al., Hybrid virus–polymer materials. 1. Synthesis and properties of peg-decorated cowpea mosaic virus. *Biomacromolecules* **2003**, *4*, 472–476.

- 50 A. CHATTERJI, L. L. BURNS, S. S. TAYLOR, et al., Cowpea mosaic virus: from the presentation of antigenic peptides to the display of active biomaterials. *Intervirology* **2002**, *45*, 362–370.
- 51 K. S. RAJA, Q. WANG, M. G. FINN, Icosahedral virus particles as polyvalent carbohydrate display platforms. *ChemBioChem* **2003**, *4*, 1348–1351.
- 52 E. GILLITZER, D. WILLITS, M. YOUNG, et al., Chemical modification of a viral cage for multivalent presentation. *Chem. Commun.* **2002**, 2390–2391.
- 53 D. TAYLOR, Q. WANG, B. BOTHNER, et al., Correlation of chemical reactivity of nudaurelia capensis omega virus with a pH-induced conformational change. *Chem. Commun.* **2003**, 2770–2771.
- 54 T. L. SCHLICK, Z. DING, E. W. KOVACS, et al., Dual-surface modification of the tobacco mosaic virus. *J. Am. Chem. Soc.* **2005**, *127*, 3718–3723.
- 55 H. N. BARNHILL, V. S. KOTAKADI, R. ZIESSEL, et al., Dual modification of turnip yellow mosaic virus: synthesis of a biotinylated luminescent nanoparticle. *ACS Meet. PMSE* **2006**, preprints.
- 56 H. N. BARNHILL, W. ZHAN, H. TIAN, et al., Display of image contrast agents on bionanoparticles and their potential applications for *in vivo* imaging. *ACS Meet. PMSE* **2005**, *92*, 398.
- 57 J. M. HOOKER, E. W. KOVACS, M. B. FRANCIS, Interior surface modification of bacteriophage MS2. *J. Am. Chem. Soc.* **2004**, *126*, 3718–3719.
- 58 N. MAHESHRI, J. T. KOERBER, B. K. KASPAR, et al., Directed evolution of adeno-associated virus yields enhanced gene delivery vectors. *Nat. Biotechnol.* **2006**, *24*, 198–204.
- 59 N. MUZYCZKA, K. H. WARRINGTON, JR., Custom adeno-associated virus capsids: the next generation of recombinant vectors with novel tropism. *Hum. Gene Ther.* **2005**, *16*, 408–416.
- 60 N. KRAUZEWICZ, J. STOKROVA, C. JENKINS, et al., Virus-like gene transfer into cells mediated by polyoma virus pseudocapsids. *Gene Ther.* **2000**, *7*, 2122–2131.
- 61 G. T. HERMANSON, *Bioconjugate Techniques*. Academic Press, San Diego, **1996**.
- 62 S. MEUNIER, E. STRABLE, M. G. FINN, Crosslinking of and coupling to viral capsid proteins by tyrosine oxidation. *Chem. Biol.* **2004**, *11*, 319–326.
- 63 S. SEN GUPTA, K. S. RAJA, E. KALTGRAD, et al., Virus–glycopolymer conjugates by copper(I) catalysis of atom transfer radical polymerization and azide–alkyne cycloaddition. *Chem. Commun.* **2005**, 4315–4317.
- 64 M. L. FLENNIKEN, L. O. LIEPOLD, B. E. CROWLEY, et al., Selective attachment and release of a chemotherapeutic agent from the interior of a protein cage architecture. *Chem. Commun.* **2005**, 447–449.
- 65 C. PORTA, V. E. SPALL, T. LIN, et al., The development of cowpea mosaic virus as a potential source of novel vaccines. *Intervirology* **1996**, *39*, 79–84.
- 66 K. M. TAYLOR, T. LIN, C. PORTA, et al., Influence of three-dimensional structure on the immunogenicity of a peptide expressed on the surface of a plant virus. *J. Mol. Recog.* **2000**, *13*, 71–82.
- 67 L. MCLAIN, Z. DURRANI, N. J. DIMMOCK, et al., A plant virus-HIV-1 chimera stimulates antibody that neutralizes HIV-1. *Vaccines* **1996**, *14*, 311–316.
- 68 M. T. KLEM, D. WILLITS, M. YOUNG, et al., 2-D Array formation of genetically engineered viral cages on Au surfaces and imaging by atomic force microscopy. *J. Am. Chem. Soc.* **2003**, *125*, 10806–10807.
- 69 K. K. W. WONG, N. T. WHILTON, T. DOUGLAS, et al., Hydrophobic proteins: synthesis and characterization of organic-soluble alkylated ferritins. *Chem. Commun.* **1998**, 1621–1622.
- 70 J. T. RUSSELL, Y. LIN, A. BÖKER, et al., Self-assembly and cross-linking of bionanoparticles at liquid–liquid interfaces. *Angew. Chem. Int. Ed.* **2005**, *44*, 2420–2426.

- 71 Y. LIN, A. BOKER, J. HE, et al., Self-directed self-assembly of nanoparticle/copolymer mixtures. *Nature* **2005**, *434*, 55–59.
- 72 C. W. TORNOE, C. CHRISTENSEN, M. MELDAL, Peptidotriazoles on solid phase: [1,2,3]-triazoles by regioselective copper(I)-catalyzed 1,3-dipolar cycloadditions of terminal alkynes to azides. *J. Org. Chem.* **2002**, *67*, 3057–3064.
- 73 V. V. ROSTOVTSSEV, L. G. GREEN, V. V. FOKIN, et al., A stepwise Huisgen cycloaddition process: copper(I)-catalyzed regioselective “ligation” of azides and terminal alkynes. *Angew. Chem. Int. Ed.* **2002**, *41*, 2596–2599.
- 74 H. C. KOLB, M. G. FINN, K. B. SHARPLESS, Click chemistry: diverse chemical function from a few good reactions. *Angew. Chem. Int. Ed.* **2001**, *40*, 2004–2021.
- 75 A. J. LINK, M. K. S. VINK, D. A. TIRRELL, Presentation and detection of azide functionality in bacterial cell surface proteins. *J. Am. Chem. Soc.* **2004**, *126*, 10598–10602.
- 76 F. PEREZ-BALDERAS, M. ORTEGA-MUNOZ, J. MORALES-SANFRUTOS, et al., Multivalent neoglycoconjugates by regioselective cycloaddition of alkynes and azides using organic-soluble copper catalysts. *Org. Lett.* **2003**, *5*, 1951–1954.
- 77 W. G. LEWIS, F. G. MAGALLON, V. V. FOKIN, et al., Discovery and characterization of catalysts for azide-alkyne cycloaddition by fluorescence quenching. *J. Am. Chem. Soc.* **2004**, *126*, 9152–9153.
- 78 Q. WANG, T. R. CHAN, R. HILGRAF, et al., Bioconjugation by copper(I)-catalyzed azide-alkyne 3 + 2 cycloaddition. *J. Am. Chem. Soc.* **2003**, *125*, 3192–3193.
- 79 W. H. ZHAN, H. N. BARNHILL, K. SIVAKUMAR, et al., Facile synthesis of new cyanine dyes for bioconjugation of bionanoparticles with “click” chemistry. *Tetrahedron Lett.* **2005**, *46*, 1691–1695.
- 80 S. SEN GUPTA, J. KUZELKA, P. SINGH, et al., Accelerated bioorthogonal conjugation: a practical method for the ligation of diverse functional molecules to a polyvalent virus scaffold. *Bioconjug. Chem.* **2005**, *16*, 1572–1579.
- 81 A. J. LINK, D. A. TIRRELL, Cell surface labeling of *Escherichia coli* via copper(I)-catalyzed 3 + 2 cycloaddition. *J. Am. Chem. Soc.* **2003**, *125*, 11164–11165.
- 82 A. DEITERS, T. A. CROPP, M. MUKHERJI, et al., Adding amino acids with novel reactivity to the genetic code of *Saccharomyces cerevisiae*. *J. Am. Chem. Soc.* **2003**, *125*, 11782–11783.
- 83 A. DEITERS, T. A. CROPP, D. SUMMERER, et al., Site-specific pegylation of proteins containing unnatural amino acids. *Bioorg. Med. Chem. Lett.* **2004**, *14*, 5743–5745.
- 84 F. TIAN, M. L. TSAO, P. G. SCHULTZ, A phage display system with unnatural amino acids. *J. Am. Chem. Soc.* **2004**, *126*, 15962–15963.
- 85 Z. ZHOU, C. J. FAHRNI, A fluorogenic probe for the copper(I)-catalyzed azide-alkyne ligation reaction: modulation of the fluorescence emission via (3)(N,Pi\*)-(1)(Pi,Pi\*) inversion. *J. Am. Chem. Soc.* **2004**, *126*, 8862–8863.
- 86 K. SIVAKUMAR, F. XIE, B. CASH, et al., A fluorogenic 1,3-dipolar cycloaddition reaction of 3-azidocoumarins and acetylenes. *Org. Lett.* **2004**, *6*, 4603–4606.
- 87 S. D. TILLEY, M. B. FRANCIS, Tyrosine-selective protein alkylation using pi-allylpalladium complexes. *J. Am. Chem. Soc.* **2006**, *128*, 1080–1081.
- 88 N. S. JOSHI, L. R. WHITAKER, M. B. FRANCIS, A three-component Mannich-type reaction for selective tyrosine bioconjugation. *J. Am. Chem. Soc.* **2004**, *126*, 15942–15943.
- 89 K. UHDE, R. FISCHER, U. COMMANDEUR, Expression of multiple foreign epitopes presented as synthetic antigens on the surface of potato virus X particles. *Arch. Virol.* **2005**, *150*, 327–340.
- 90 L. LIU, M. C. CANIZARES, W. MONGER, et al., Cowpea mosaic virus-based systems for the production of antigens

- and antibodies in plants. *Vaccine* **2005**, *23*, 1788–1792.
- 91 T. YAMADA, M. UEDA, M. SENO, et al., Novel tissue and cell type-specific gene/drug delivery system using surface engineered hepatitis B virus nano-particles. *Curr. Drug Targets Infect. Disord.* **2004**, *4*, 163–167.
  - 92 J. XIE, P. G. SCHULTZ, Adding amino acids to the genetic repertoire. *Curr. Opin. Chem. Biol.* **2005**, *9*, 548–554.
  - 93 A. DEITERS, P. G. SCHULTZ, *In vivo* incorporation of an alkyne into proteins in *Escherichia coli*. *Bioorg. Med. Chem. Lett.* **2005**, *15*, 1521–1524.
  - 94 M. BOSE, D. GROFF, J. XIE, et al., The Incorporation of a photoisomerizable amino acid into proteins in *E. coli*. *J. Am. Chem. Soc.* **2006**, *128*, 388–389.
  - 95 T. HOHSAKA, Y. ASHIZUKA, H. TAIRA, et al., Incorporation of nonnatural amino acids into proteins by using various four-base codons in an *Escherichia coli in-vitro* translation system. *Biochemistry* **2001**, *40*, 11060–11064.
  - 96 S. S. CRUZ, S. CHAPMAN, A. G. ROBERTS, et al., Assembly and movement of a plant virus carrying a green fluorescent protein overcoat. *Proc. Natl Acad. Sci. USA* **1996**, *93*, 6286–6290.
  - 97 R. L. TOTH, S. CHAPMAN, F. CARR, et al., A novel strategy for the expression of foreign genes from plant virus vectors. *FEBS Lett.* **2001**, *489*, 215–219.
  - 98 G. P. LOMONOSOFF, M. SHANKS, C. L. HOLNESS, et al., Comovirus capsid proteins: synthesis, structure, and evolutionary implications. *Proc. Phytochem. Soc. Eur.* **1991**, *32*, 76–91.
  - 99 G. P. LOMONOSOFF, J. E. JOHNSON, The synthesis and structure of comovirus capsids. *Prog. Biophys. Mol. Biol.* **1991**, *55*, 107–137.
  - 100 T. LIN, Z. CHEN, R. USHA, et al., The refined crystal structure of cowpea mosaic virus at 2.8 Å resolution. *Virology* **1999**, *265*, 20–34.
  - 101 L. LIU, G. LOMONOSOFF, Agro-infection as a rapid method for propagating cowpea mosaic virus-based constructs. *J. Virol. Methods* **2002**, *105*, 343–348.
  - 102 D. J. SILER, J. BABCOCK, G. BRUENING, Electrophoretic mobility and enhanced infectivity of a mutant of cowpea mosaic virus. *Virology* **1976**, *71*, 560–567.
  - 103 C. PORTA, V. E. SPALL, K. C. FINDLAY, et al., Cowpea mosaic virus-based chimaeras. Effects of inserted peptides on the phenotype, host range, and transmissibility of the modified viruses. *Virology* **2003**, *310*, 50–63.
  - 104 L. MCLAIN, C. PORTA, G. P. LOMONOSOFF, et al., Human immunodeficiency virus type 1-neutralizing antibodies raised to a glycoprotein 41 peptide expressed on the surface of a plant virus. *AIDS Res. Hum. Retroviruses* **1995**, *11*, 327–334.
  - 105 K. DALSGAARD, A. UTTENTHAL, T. D. JONES, et al., plant-derived vaccine protects target animals against a viral disease. *Nat. Biotechnol.* **1997**, *15*, 248–252.
  - 106 C. PORTA, G. WANG, H. CHENG, et al., Direct imaging of interactions between an icosahedral virus and conjugate F(ab) fragments by cryoelectron microscopy and X-ray crystallography. *Virology* **1994**, *204*, 777–788.
  - 107 I. W. KHOR, T. LIN, J. P. LANGEDIJK, et al., Novel strategy for inhibiting viral entry by use of a cellular receptor–plant virus chimera. *J. Virol.* **2002**, *76*, 4412–4419.
  - 108 C. M. HAYDEN, A. M. MACKENZIE, M. L. SKOTNICKI, et al., Turnip yellow mosaic virus isolates with experimentally produced recombinant virion proteins. *J. Gen. Virol.* **1998**, *79*, 395–403.
  - 109 H. H. BINK, S. K. ROEPAN, C. W. PLEIJ, Two histidines of the coat protein of turnip yellow mosaic virus at the capsid interior are crucial for viability. *Proteins* **2004**, *55*, 236–244.
  - 110 M. LEIMKUEHLER, A. GOLDBECK, M. D. LECHNER, et al., The Formation of empty shells upon pressure induced decapsulation of turnip yellow mosaic virus. *Arch. Virol.* **2001**, *146*, 653–667.
  - 111 M. ADRIAN, P. A. TIMMINS, J. WITZ, *In vitro* decapsulation of turnip yellow mosaic virus investigated by cryo-

- electron microscopy: a model for the decapsidation of a small isometric virus. *J. Gen. Virol.* **1992**, *73*, 2079–2083.
- 112 J. HAYNES, J. CUNNINGHAM, A. VON SEEFRIED, et al., Development of a genetically-engineered, candidate polio vaccine employing the self-assembling properties of tobacco mosaic virus coat protein. *Biotechnology* **1986**, *4*, 637–641.
- 113 Y. SUGIYAMA, H. HAMAMOTO, S. TAKEMOTO, et al., Systemic production of foreign peptides on the particle surface of tobacco mosaic virus. *FEBS Lett.* **1995**, *359*, 247–250.
- 114 H. HAMAMOTO, Y. SUGIYAMA, N. NAKAGAWA, et al., A new tobacco mosaic vector and its use for the systemic production of angiotensin-I-converting enzyme inhibitor in transgenic tobacco and tomato. *Biotechnology* **1993**, *11*, 930–932.
- 115 M. BENDAHDANE, M. KOO, E. KARRER, et al., Display of epitopes on the surface of tobacco mosaic virus: impact of charge and isoelectric point of the epitope on virus–host interactions. *J. Mol. Biol.* **1999**, *290*, 9–20.
- 116 M. KOO, M. BENDAHDANE, G. A. LETTIERI, et al., Protective immunity against murine hepatitis virus (MHV) induced by intranasal or subcutaneous administration of hybrids of tobacco mosaic virus that carries an MHV epitope. *Proc. Natl Acad. Sci. USA* **1999**, *96*, 7774–7779.
- 117 L. JIANG, Q. LI, M. LI, et al., A modified TMV-based vector facilitates the expression of longer foreign epitopes in tobacco. *Vaccine* **2006**, *24*, 109–115.
- 118 L. A. BARATOVA, N. I. GREBENSHCHIKOV, E. N. DOBROV, et al., The organization of potato virus X coat proteins in virus particles studied by tritium planigraphy and model building. *Virology* **1992**, *188*, 175–180.
- 119 R. KOENIG, L. TORRANCE, Antigenic analysis of potato virus X by means of monoclonal antibodies. *J. Gen. Virol.* **1986**, *67*, 2145–2151.
- 120 M. D. RYAN, A. M. KING, G. P. THOMAS, Cleavage of foot-and-mouth disease virus polyprotein is mediated by residues located within a 19 amino acid sequence. *J. Gen. Virol.* **1991**, *72*, 2727–2732.
- 121 L. SMOLENSKA, I. M. ROBERTS, D. LEARMONTH, et al., Production of a functional single chain antibody attached to the surface of a plant virus. *FEBS Lett.* **1998**, *441*, 379–382.
- 122 M. DONINI, C. LICO, S. BASCHIERI, et al., Production of an engineered killer peptide in *Nicotiana benthamiana* by using a potato virus X expression system. *Appl. Environ. Microbiol.* **2005**, *71*, 6360–6367.
- 123 N. D. CHASTEEN, P. M. HARRISON, Mineralization in ferritin: an efficient means of iron storage. *J. Struct. Biol.* **1999**, *126*, 182–194.
- 124 R. M. KRAMER, C. LI, D. C. CARTER, et al., Engineered protein cages for nanomaterial synthesis. *J. Am. Chem. Soc.* **2004**, *126*, 13282–13286.
- 125 F. UCHIYAMA, Y. TANAKA, Y. MINARI, et al., Designing scaffolds of peptides for phage display libraries. *J. Biosci. Bioeng.* **2005**, *99*, 448–456.
- 126 J. W. KEHOE, B. K. KAY, Filamentous phage display in the new millennium. *Chem. Rev.* **2005**, *105*, 4056–4072.
- 127 C. GAO, S. MAO, C. H. LO, et al., Making artificial antibodies: a format for phage display of combinatorial heterodimeric arrays. *Proc. Natl Acad. Sci. USA* **1999**, *96*, 6025–6030.
- 128 A. B. SANGHVI, K. P. MILLER, A. M. BELCHER, et al., Biomaterials functionalization using a novel peptide that selectively binds to a conducting polymer. *Nat. Mater.* **2005**, *4*, 496–502.
- 129 O. J. MULLER, F. KAUL, M. D. WEITZMAN, et al., Random peptide libraries displayed on adeno-associated virus to select for targeted gene therapy vectors. *Nat. Biotechnol.* **2003**, *21*, 1040–1046.
- 130 K. NINOMIYA, T. MINOHATA, M. NISHIMURA, et al., In situ chemical aminoacylation with amino acid thioesters linked to a peptide nucleic acid. *J. Am. Chem. Soc.* **2004**, *126*, 15984–15989.



- 131 M. SISIDO, K. NINOMIYA, T. OHTSUKI, et al., Four-base codon/anticodon strategy and non-enzymatic aminoacylation for protein engineering with non-natural amino acids. *Methods* **2005**, *36*, 270–278.
- 132 T. HOHSAKA, M. FUKUSHIMA, M. SISIDO, Nonnatural mutagenesis in *E. coli* and rabbit reticulocyte lysates by using four-base codons. *Nucleic Acids Res. Suppl* **2002**, 201–202.
- 133 N. MURANAKA, T. HOHSAKA, M. SISIDO, Four-base codon mediated mRNA display to construct peptide libraries that contain multiple nonnatural amino acids. *Nucleic Acids Res.* **2006**, *34*, e4.
- 134 H. HAMADA, N. KAMESHIMA, A. SZYMANSKA, et al., Position-specific incorporation of a highly photodurable and blue-laser excitable fluorescent amino acid into proteins for fluorescence sensing. *Bioorg. Med. Chem.* **2005**, *13*, 3379–3384.
- 135 M. MANCHESTER, J. E. GAIRIN, J. B. PATTERSON, et al., Measles virus recognizes its receptor, CD46, via two distinct binding domains within Scr1-2. *Virology* **1997**, *233*, 174–184.
- 136 M. MANCHESTER, M. K. LISZEWSKI, J. P. ATKINSON, et al., Multiple isoforms of CD46 (membrane cofactor protein) serve as receptors for measles virus. *Proc. Natl Acad. Sci. USA* **1994**, *91*, 2161–2165.
- 137 R. WEISSELEDER, K. KELLY, E. SUN, et al., Cell-specific targeting of nanoparticles by multivalent attachment of small molecules. *Nat. Biotechnol.* **2005**, *23*, 1418–1423.
- 138 A. E. SMITH, H. LILLIE, A. HELENIUS, Ganglioside-dependent cell attachment and endocytosis of murine polyomavirus-like particles. *FEBS Lett.* **2003**, *555*, 199–203.
- 139 Y. C. SHIN, W. R. FOLK, Formation of polyomavirus-like particles with different Vp1 molecules that bind the urokinase plasminogen activator receptor. *J. Virol.* **2003**, *77*, 11491–11498.
- 140 Z. SANDALON, A. OPPENHEIM, Self-assembly and protein–protein interactions between the SV40 capsid proteins produced in insect cells. *Virology* **1997**, *237*, 414–421.
- 141 D. CHANG, C. Y. FUNG, W. C. OU, et al., Self-assembly of the JC virus major capsid protein, VP1, expressed in insect cells. *J. Gen. Virol.* **1997**, *78*, 1435–1439.
- 142 E. T. GILLOCK, S. ROTTINGHAUS, D. CHANG, et al., Polyomavirus major capsid protein VP1 is capable of packaging cellular DNA when expressed in the baculovirus system. *J. Virol.* **1997**, *71*, 2857–2865.
- 143 K. SASNAUSKAS, O. BUZAITE, F. VOGEL, et al., Yeast cells allow high-level expression and formation of polyomavirus-like particles. *Biol. Chem.* **1999**, *380*, 381–386.
- 144 U. SCHMIDT, J. KENKLIES, R. RUDOLPH, et al., Site-specific fluorescence labeling of recombinant polyomavirus-like particles. *Biol. Chem.* **1999**, *380*, 397–401.
- 145 W. C. OU, M. WANG, C. Y. FUNG, et al., The major capsid protein, VP1, of human JC virus expressed in *Escherichia coli* is able to self-assemble into a capsid-like particle and deliver exogenous DNA into human kidney cells. *J. Gen. Virol.* **1999**, *80*, 39–46.
- 146 B. TSAI, J. M. GILBERT, T. STEHLE, et al., Gangliosides are receptors for murine polyoma virus and SV40. *EMBO J.* **2003**, *22*, 4346–4355.
- 147 M. CARUSO, L. BELLONI, O. STHANDIER, et al., Alpha4beta1 integrin acts as a cell receptor for murine polyomavirus at the post-attachment level. *J. Virol.* **2003**, *77*, 3913–3921.
- 148 M. CARUSO, M. CAVALDESI, M. GENTILE, et al., Role of sialic acid-containing molecules and the alpha4beta1 integrin receptor in the early steps of polyomavirus infection. *J. Gen. Virol.* **2003**, *84*, 2927–2936.
- 149 B. F. SABATH, E. O. MAJOR, Traffic of JC virus from sites of initial infection to the brain: the path to progressive multifocal leukoencephalopathy. *J. Infect. Dis.* **2002**, *186*, S180–186.
- 150 M. WANG, T. H. TSOU, L. S. CHEN, et al., Inhibition of simian virus 40 large tumor antigen expression in

- human fetal glial cells by an antisense oligodeoxynucleotide delivered by the JC virus-like particle. *Hum. Gene Ther.* **2004**, *15*, 1077–1090.
- 151 D. YU, C. AMANO, T. FUKUDA, et al., The specific delivery of proteins to human liver cells by engineered bio-nanocapsules. *FEBS J.* **2005**, *272*, 3651–3660.
- 152 T. YAMADA, Y. IWASAKI, H. TADA, et al., Nanoparticles for the delivery of genes and drugs to human hepatocytes. *Nat. Biotechnol.* **2003**, *21*, 885–890.
- 153 M. L. FLENNIKEN, D. A. WILLITS, A. L. HARMSEN, et al., Melanoma and lymphocyte cell-specific targeting incorporated into a heat shock protein cage architecture. *Chem. Biol.* **2006**, *13*, 161–170.
- 154 S. GLEITER, H. LILIE, Coupling of antibodies via protein Z on modified polyoma virus-like particles. *Protein Sci.* **2001**, *10*, 434–444.
- 155 N. KRAUZEWICZ, C. COX, E. SOEDA, et al., Sustained *ex vivo* and *in vivo* transfer of a reporter gene using polyoma virus pseudocapsids. *Gene Ther.* **2000**, *7*, 1094–1102.
- 156 A. TOUZE, L. BOUSARGHIN, C. STER, et al., Gene transfer using human polyomavirus BK virus-like particles expressed in insect cells. *J. Gen. Virol.* **2001**, *82*, 3005–3009.
- 157 S. GLEITER, H. LILIE, Cell-type specific targeting and gene expression using a variant of polyoma VP1 virus-like particles. *Biol. Chem.* **2003**, *384*, 247–255.
- 158 J. V. OSTERMAN, A. WADDELL, H. V. APOSHIAN, DNA and gene therapy: uncoating of polyoma pseudovirus in mouse embryo cells. *Proc. Natl Acad. Sci. USA* **1970**, *67*, 37–40.
- 159 C. KIMCHI-SARFATY, M. M. GOTTESMAN, SV40 pseudovirions as highly efficient vectors for gene transfer and their potential application in cancer therapy. *Curr. Pharm. Biotechnol.* **2004**, *5*, 451–458.
- 160 C. KIMCHI-SARFATY, O. BEN-NUN-SHAUL, D. RUND, et al., *In vitro*-packaged SV40 pseudovirions as highly efficient vectors for gene transfer. *Hum. Gene Ther.* **2002**, *13*, 299–310.
- 161 C. KIMCHI-SARFATY, M. ARORA, Z. SANDALON, et al., High cloning capacity of *in vitro* packaged SV40 vectors with no SV40 virus sequences. *Hum. Gene Ther.* **2003**, *14*, 167–177.
- 162 C. KIMCHI-SARFATY, S. BRITAIN, S. GARFIELD, et al., Efficient delivery of RNA interference effectors via *in vitro*-packaged SV40 pseudovirions. *Hum. Gene Ther.* **2005**.
- 163 C. S. RAE, I. W. KHOR, Q. WANG, et al., Systemic trafficking of plant virus nanoparticles in mice via the oral route. *Virology* **2005**, *343*, 224–235.
- 164 J. D. LEWIS, G. DESTITO, A. ZIJLSTRA, et al., Viral nanoparticles as tools for intravital vascular imaging. *Nat. Med.* **2006**, *12*, 354–360.
- 165 H. EWERS, A. E. SMITH, I. F. SBALZARINI, et al., Single-particle tracking of murine polyoma virus-like particles on live cells and artificial membranes. *Proc. Natl Acad. Sci. USA* **2005**, *102*, 15110–15115.
- 166 C. WU, H. BARNHILL, X. LIANG, et al., A new probe using hybrid virus-dye nanoparticles for near-infrared fluorescence tomography. *Optics Commun.* **2005**, *255*, 366–374.
- 167 I. L. MEDINTZ, K. E. SAPSFORD, J. H. KONNERT, et al., Decoration of discretely immobilized cowpea mosaic virus with luminescent quantum dots. *Langmuir* **2005**, *21*, 5501–5510.
- 168 A. CHATTERJI, W. F. OCHOA, T. UENO, et al., A virus-based nanoblock with tunable electrostatic properties. *Nano Lett.* **2005**, *5*, 597–602.
- 169 N. G. PORTNEY, K. SINGH, S. CHAUDHARY, et al., Organic and inorganic nanoparticle hybrids. *Langmuir* **2005**, *21*, 2098–2103.
- 170 A. S. BLUM, C. M. SOTO, C. D. WILSON, et al., An engineered virus as a scaffold for three-dimensional self-assembly on the nanoscale. *Small* **2005**, *1*, 702–706.
- 171 G. R. SOUZA, D. R. CHRISTIANSON, F. I. STAQUICINI, et al., Networks of gold nanoparticles and bacteriophage as biological sensors and cell-targeting agents. *Proc. Natl Acad. Sci. USA* **2006**, *103*, 1215–1220.

- 172 U. SCHMIDT, C. GUNTHER, R. RUDOLPH, et al., Protein and peptide delivery via engineered polyomavirus-like particles. *FASEB J.* **2001**, *15*, 1646–1648.
- 173 A. ABBING, U. K. BLASCHKE, S. GREIN, et al., Efficient intracellular delivery of a protein and a low molecular weight substance via recombinant polyomavirus-like particles. *J. Biol. Chem.* **2004**, *279*, 27410–27421.
- 174 J. JOHNSON, T. LIN, G. LOMONOSOFF, Presentation of heterologous peptides on plant viruses: genetics, structure, and function. *Annu. Rev. Phytopathol.* **1997**, *35*, 67–86.
- 175 J. P. LANGEVELD, F. R. BRENNAN, J. L. MARTINEZ-TORRECUADRADA, et al., Inactivated recombinant plant virus protects dogs from a lethal challenge with canine parvovirus. *Vaccine* **2001**, *19*, 3661–3670.
- 176 C. MARUSIC, P. RIZZA, L. LATTANZI, et al., Chimeric plant virus particles as immunogens for inducing murine and human immune responses against human immunodeficiency virus type 1. *J. Virol.* **2001**, *75*, 8434–8439.
- 177 V. YUSIBOV, D. C. HOOPER, S. V. SPITSIN, et al., Expression in plants and immunogenicity of plant virus-based experimental rabies vaccine. *Vaccine* **2002**, *20*, 3155–3164.
- 178 M. L. SMITH, J. A. LINDBO, S. DILLARD-TELM, et al., Modified tobacco mosaic virus particles as scaffolds for display of protein antigens for vaccine applications. *Virology* **2006**.
- 179 F. R. BRENNAN, L. B. GILLELAND, J. STACZEK, et al., A chimaeric plant virus vaccine protects mice against a bacterial infection. *Microbiology* **1999**, *145*, 2061–2067.
- 180 F. R. BRENNAN, T. D. JONES, L. B. GILLELAND, et al., *Pseudomonas aeruginosa* outer-membrane protein F epitopes are highly immunogenic in mice when expressed on a plant virus. *Microbiology* **1999**, *145*, 211–220.
- 181 A. RENNERMALM, Y. H. LI, L. BOHAUFS, et al., Antibodies against a truncated *Staphylococcus aureus* fibronectin-binding protein protect against dissemination of infection in the Rat. *Vaccine* **2001**, *19*, 3376–3383.
- 182 J. J. LUNDQUIST, E. J. TOONE, The cluster glycoside effect. *Chem. Rev.* **2002**, *102*, 555–578.
- 183 J. J. LUNDQUIST, S. D. DEBENHAM, E. J. TOONE, Multivalency effects in protein–carbohydrate interaction: the binding of the Shiga-like toxin 1 binding subunit to multivalent C-linked glycopeptides. *J. Org. Chem.* **2000**, *65*, 8245–8250.
- 184 J. E. GESTWICKI, C. W. CAIRO, L. E. STRONG, et al., Influencing receptor–ligand binding mechanisms with multivalent ligand architecture. *J. Am. Chem. Soc.* **2002**, *124*, 14922–14933.
- 185 J. A. HARDING, C. M. ENGBERS, M. S. NEWMAN, et al., Immunogenicity and pharmacokinetic attributes of poly(ethylene glycol)-grafted immunoliposomes. *Biochim. Biophys. Acta* **1997**, *1327*, 181–192.
- 186 Z. L. XU, H. MIZUGUCHI, F. SAKURAI, et al., Approaches to improving the kinetics of adenovirus-delivered genes and gene products. *Adv. Drug Deliv. Rev.* **2005**, *57*, 781–802.
- 187 A. DIRKSEN, S. LANGEREIS, B. F. DE WAAL, et al., A supramolecular approach to multivalent target-specific MRI contrast agents for angiogenesis. *Chem. Commun.* **2005**, 2811–2813.
- 188 H. KOBAYASHI, M. W. BRECHBIEL, Nano-sized MRI contrast agents with dendrimer cores. *Adv. Drug Deliv. Rev.* **2005**, *57*, 2271–2286.

## 14 Nanotechnology for Gene Therapy – HVJ-E Vector

*Hironori Nakagami, Yasuhiko Tabata, and Yasufumi Kaneda*

### 14.1 Introduction

Currently, more than 400 clinical protocols have been approved for human gene therapy. In 1995, the Orkin–Motulsky report indicated the importance of vector development in human gene therapy. Numerous vectors have been developed to date. In general, viral vectors are more effective for gene transfer; however, safety remains an issue [1]. In 1999, a young patient died following infusion of an adenoviral vector via the hepatic artery [2] and, in 2002, two patients with X-linked severe combined immunodeficiency treated with retroviral vector gene therapy developed leukemia-like symptoms, likely to have been induced by insertional mutagenesis of the retroviral DNA [3]. Hemophilia B gene therapy using the adeno-associated virus (AAV) vector looks promising [4], but several potential risks, such as germline transmission, remain. On the other hand, the safety of a nonviral vector has been evaluated, but inefficient gene transfection is a limitation of this vector system [5]. Therefore, the current consensus on vector development is that highly efficient and minimally invasive vectors are the most appropriate for human gene therapy. Before developing vector systems, we should analyze the biological barriers to gene transfer and create methods to overcome such difficulties.

All the current vector systems have their advantages and limitations [6]. Currently, there are several approaches to correct the limitations of each vector system. In adenovirus vector systems, one crucial improvement is reduced vector antigenicity and a helper-dependent or “gutless” vector in which most of the adenovirus genome is deleted has been developed [7]. However, the production of this “gutless” vector was much lower than that of the classical adenovirus vector. Another approach is to overcome the limitations of one vector system by drawing upon the strengths of another. Examples of chimeric vectors include the pseudo-type retrovirus vector in which the envelope component of the classical retrovirus vector is replaced with the vesicular stomatitis virus (VSV) G protein [8] and a new lentivirus vector containing human immunodeficiency virus (HIV) proteins with the pseudo-type retrovirus envelope-containing VSV G protein [9]. However, combinations of

viral vector systems are thought to be of limited utility, because the components necessary for viral replication and packaging cannot be eliminated, and the constituent viruses may interfere with each other during vector production.

Limitations of vector systems are inevitable, and the introduction of foreign genes into cells is abnormal and is directed to disturb cellular function. Current gene therapy strategies mimic viral infection and cells are designed to resist the gene transfer. Cells have biological barriers that protect against invasion by foreign genes and inhibit expression of foreign gene products [5]. Protocols for *in vivo* gene transfection consist of several steps. The first step entails the approach of the vector to the target cell from the outside environment. The second is the introduction of the transgene into the cytoplasm. Third, the transgene must migrate to the nucleus. Finally, the transgene must be retained and stably expressed. Each of these steps has barriers. For example, serum proteins and immune cells can attack gene transfer vectors before they reach target cells, the cell membrane can prevent transfer of foreign genes to the cytoplasm, the nuclear envelope can restrict nuclear targeting of molecules, and expression of the transgene can be inhibited by degradation of the DNA or by transcriptional silencing. In a narrow sense, “gene transfer” means the introduction of a transgene into the cytoplasm, and it encompasses the first and second steps described above. However, it is pointless to only refer to the introduction of a transgene into the cell without considering the final step of gene expression. Thus, Section 14.2 highlights biological barriers from the first step (approach to the target cell) to the fourth step (effective expression of the transgene) and discusses potential solutions for each barrier with respect to future possibilities for gene transfer systems.

We have developed a unique vector, “HVJ-E (Hemagglutinating Virus of Japan-envelope)”, that can rapidly transfer plasmid DNA, oligonucleotides and protein into cells by cell fusion. A detailed description is given in Section 14.3. However, this modality of targeting is still insufficient for rapid and specific accumulation of active vectors in target tissues. One solution is to engineer the surface proteins of viral vectors or to couple targeting ligands to viral as well as nonviral vectors, which might further improve tissue selectivity. Section 14.4 describes other candidates for nonviral vectors, such as cationized gelatin (CG) and magnetic nanoparticles. Finally, Section 14.5 discusses modification of the membrane surface of HVJ to achieve improvement as a future prospect. We modified HVJ-E conjugated with protamine sulfate (PS) and/or CG, which enhanced the transfection efficiency *in vitro* or *in vivo*. Moreover, we recently developed magnetic nanoparticle-conjugated HVJ-E. Importantly, the size and surface chemistry of magnetic particles could be tailored to meet specific demands of physical and biological characteristics. For example, coating with PS could be suitable for *in vitro*, but not *in vivo*, culture, whereas heparin sulfate was suitable for *in vivo* gene expression. Overall, CG or magnetic nanoparticles can enhance HVJ-E-based gene transfer by modification of the size or charge, which could potentially help to overcome fundamental limitations to gene therapy *in vivo*.

## 14.2

### Biological Barriers to Gene Transfer

#### 14.2.1

##### Reaching Target Cells

To achieve tissue-specific targeting, vector system development should be approached from at least three aspects: recognition by specific target tissues, avoidance of nonspecific uptake and resistance to degradation in the systemic circulation.

##### 14.2.1.1 Recognition by Specific Target Tissues

Targeting vectors to specific tissues has been considered an ideal method for gene delivery. Ligand-specific delivery systems have been developed for tissue-specific targeting. In one experiment, asialoglycoprotein was conjugated with DNA–polylysine complexes [10]. Since asialoglycoprotein binds to receptors on hepatocytes, DNA can be delivered specifically to hepatocytes by receptor-mediated endocytosis using this complex [11]. Transferrin has also been used for receptor-mediated delivery of DNA to cancer cells, because cancer cells express high levels of the transferrin receptor [12]. These complexes worked well in cultured cells, but the efficiency of *in vivo* gene delivery was so good. Some viruses do, however, target specific tissues [13]. Epstein–Barr virus (EBV) primarily infects B lymphocytes, hepatitis virus B attacks hepatocytes, and HIV targets lymphocytes and macrophages. Currently, adenovirus-based gene delivery vectors are being used for many gene therapy applications because of the broad range of hosts [14]. Cellular tropism of the adenovirus vector in tissues is regulated by fiber proteins and, based on the tissue tropism of these viruses, targeting viral vectors can be developed [15–17].

##### 14.2.1.2 Avoidance of Nonspecific Uptake

Colloidal particles with a diameter of more than 300 nm are trapped by reticulo-endothelial system (RES) cells in the liver, spleen and lung [18]. HVJ-liposomes containing both hemagglutinin/neuraminidase (HN) protein and fusion (F) proteins target the liver, spleen and lung when the vector is injected into the saphenous vein of monkeys [19], probably because the phosphatidylserine residues [20] present on the envelope are recognized by the RES and the particle size is 470 nm in diameter. Some phospholipids such as phosphatidylserine are also recognized by the RES. The liposome–PS–plasmid DNA (LPD) vector targets the lung, kidney, heart, liver and spleen, with the highest level of gene expression in the lung [21, 22]. To avoid such nonspecific uptake, stealth liposomes have also been developed [23]. By selecting lipid components, the liposomes are retained in the systemic circulation much longer than other liposomes. Such stealth liposomes are used for drug delivery to tumor tissues [24]. In particular, liposomes conjugated with poly(ethylene glycol) (PEG) are also of the “stealth” type [25, 26]. Cationic lipid–

DNA complexes accumulate mostly into the lung, while “PEGylated” lipid–DNA complexes exhibit lower lung accumulation. The folate receptor is abundant in tumor tissues. When folate is conjugated with PEGylated lipid–DNA complexes, pulmonary accumulation of DNA is reduced and tumor-targeted DNA increases [27]. PEGylation of various types of vectors may regulate tissue-targeting when tissue-specific molecules are conjugated with the complex.

#### 14.2.1.3 Resistance to Degradation in Systemic Circulation

In the human body, protective mechanisms against viral invasion exist. Anti-galactose antibodies present in human serum bind to retrovirus envelope proteins to induce complement-mediated lysis [28]. To avoid such lysis, a complement-resistant retrovirus has been developed [29]. Adenovirus is highly immunogenic and is attacked by the host immune system after repeated transfection [30]. As described above, to reduce immunogenicity, a “gutless” adenovirus vector has also been developed [7].

Another barrier to gene transfer is the penetration and distribution of vectors in tissues. To extravasate from blood vessels to the target tissues and cells, vectors must penetrate endothelial cells. To induce gene expression in a large area of tissue, vectors must be spread diffusely throughout the entire area. Many viral vectors including adenovirus vector and AAV vector cannot penetrate endothelial cells when administered systemically [31]. Among the nonviral gene delivery systems, cationic liposomes are the most frequently used for gene transfer. When injected into the mouse tail vein, gene expression is detected primarily in the lung [32]. However, cationic liposomes cannot penetrate past the endothelial cells when injected into the vasculature [33]. In contrast, anionic liposomes are able to penetrate endothelial cells [34]. Moreover, anionic liposomes can distribute to broader areas in the target tissues than cationic liposomes. The mean size of liposomes is also important, because tissues are more permeable to smaller liposomes.

#### 14.2.2

##### Crossing the Cell Membrane

After reaching the target cells, transgene DNA must cross the cell membrane, which is a very effective barrier that excludes foreign substances from cells. There are several ways to overcome this barrier. Although one is to facilitate DNA transfer by utilizing endocytosis or phagocytosis, in this process the foreign DNA must penetrate the membrane of the endosome or phagosome rapidly. Otherwise, the DNA will be degraded. Adenovirus can escape from the endosome by disrupting the endosomal membrane with penton fibers [35, 36]. This ability has been utilized to enhance the efficiency of gene transfer by transferrin/poly-L-lysine/DNA complexes [12]. Other viruses can fuse with the cell membrane to introduce their genomes into the cytoplasm. There are two different mechanisms of virus–cell fusion: pH-dependent and pH-independent. Influenza virus [37], Semliki forest virus (SFV) [38] and VSV [39] exhibit pH-dependent fusion, whereas HVJ (Sendai virus) [40] and retroviruses [41, 42] can fuse with the cell membrane at both acidic and

neutral pH. Viral fusion proteins have been identified and synthetic vectors that express these viral fusion proteins can transfer foreign genes efficiently into the cytoplasm [43].

### 14.2.3

#### **Nuclear Targeting**

Transport of the foreign gene to the nucleus is required for gene expression in gene therapy. In nondividing cells especially, DNA is not transported efficiently to the nucleus where transcription occurs. However, it should be noted that naked plasmid DNA can be transported to the nucleus without breakdown of the nuclear envelope. The efficiency is generally 1–2% of the DNA in the cytoplasm [44]. Therefore, nuclear targeting increases gene expression, especially in tissues. Some viruses such as adenovirus, SV40, HIV and herpes virus are known to induce rapid migration of their genomes to the nucleus even in nondividing cells [43]. In SV40, viral capsid proteins contain nuclear localization sequences (NLSs) that trigger translocation of the virion to the nucleus and disassembly of the virion within the nucleus [44]. Although rapid nuclear transport also occurs with adenovirus, disassembly of the viral capsid occurs in the cytoplasm and the DNA-NLS-containing proteins are then sorted in the nucleus [45, 46]. In HIV, an integrase is required for nuclear migration of the viral genome [44]. However, the DNA–integrase complex, or preintegration complex, of oncoretroviruses such as Moloney leukemia virus cannot pass through the nuclear pores and, thus, transport of the transgene to the nucleus does not occur in nondividing cells in these retroviral systems [1]. In nonviral vector systems, nuclear transport of plasmid DNA occurs, but the efficiency is very low [5]. Enhancing nuclear migration of plasmid DNA is an important issue for increasing transgene expression. Complexes of plasmid DNA and nuclear proteins have been constructed to improve nuclear migration of DNA [47, 48]. It was recently reported that conjugation of the NLS peptide derived from SV40 with a luciferase gene fragment enhanced luciferase gene expression approximately 1000-fold compared with the luciferase gene without the NLS peptide [49]. The NLS peptide at either the 5' or 3' end of the DNA enhanced luciferase gene expression, but incorporation of the NLS at both ends was not effective. It is thought that positioning of the NLS at one end of the gene stimulates nuclear migration of the luciferase gene, whereas incorporation of the NLS at both ends ensnares the DNA at the nuclear envelope. However, it remains unknown whether NLS conjugation improves the nuclear migration of larger DNA molecules and if NLS conjugation improves the efficiency of translocation *in vivo*. This raises the question, does only a small fraction of all the plasmid DNA go to the nucleus? Recently, several papers have suggested that nuclear migration of plasmid DNA may be sequence dependent [50]. The SV40 enhancer sequence appears to facilitate nuclear migration of DNA by binding transcription factors [51] which are transported to the nucleus by the Ran/importin system.

RNA-based vectors have also been developed. Alphaviruses such as SFV and Sindbis virus are converted into gene expression recombinant RNA vectors [52,



53], which do not require the transport of DNA into the nucleus. In general, RNA vectors produce large amounts of proteins and this production inhibits host protein synthesis, inducing cell death (apoptosis) [54]. Thus, tight regulation of protein synthesis will be required for the use of gene therapy using RNA vector systems.

#### 14.2.4

#### **Regulation of Gene Expression**

Effective expression of a transgene is also a major issue in gene therapy. We should view this step from at least two aspects. One is the stable retention of a transgene and the other is the regulation of transcription. The export of mRNA, translation and post-translational modification of polypeptides generally affect gene expression, but they are not specific for expression of a transgene. Therefore, this section focuses on the events occurring before mRNA production.

##### 14.2.4.1 **Stable Retention of Transgenes**

There are two distinct approaches to this issue. One is the integration of the transgene into the host genome. Retroviruses can integrate into random sites of the host chromosomes, but integration occurs only in dividing cells [1]. HIV inserts its genome into the host chromosomes even in nondividing cells. A lentivirus vector system containing the recombinant HIV genome along with a therapeutic gene and the vesicular stomatitis virus G protein (VSVG) gene was used to generate long-term gene expression in mouse neurons [9]. The mechanism of insertion of the viral genome into host chromosomes has been investigated. However, reconstitution of the viral machinery that confers the ability of genome insertion to non-viral gene delivery systems has not yet been successful. In 1997, *sleeping beauty*, a fish transposon/transposase system, was developed [55]. This system inserts the neomycin-resistance gene into the HeLa cell genome with very high efficiency. Application of this system to gene transfer is currently under investigation. However, insertion of the transgene into the host genome occurs at random. Although AAV integrates specifically into the AAVS1 site of human chromosome 19 [56], the recombinant AAV vector is unable to do so because it does not express Rep 65 protein [57].

Another approach is the stable retention of an episomal piece of DNA. EBV has been analyzed thoroughly in terms of latent infection. The *cis*-acting oriP (the latent viral DNA replication origin) sequence and the *trans*-acting EBV nuclear antigen-1 (EBNA-1) gene are required for latent EBV infection, which is characterized by autonomous replication and nuclear retention of the EBV genome in host cells [58–60]. It has been reported that stable retention of the EBV genome is mediated by binding of the oriP sequence with the nuclear matrix. The EBV vector can transfer genes primarily to B lymphocytes, with minimal transfer to other somatic cells. To improve long-term transgene expression, an EBV replicon-based plasmid that contains oriP and EBNA-1 was constructed and transferred to various animal

tissues using HVJ-liposomes. With the EBV replicon vector system, gene expression was sustained and enhanced both *in vitro* and *in vivo*, in several cell lines and mouse liver, respectively [61]. Without EBNA-1, transgene expression of an oriP-containing plasmid was diminished in mouse liver. However, by re-introducing EBNA-1 to the mouse liver, transgene expression was reactivated [62]. This indicates that EBNA-1 can restore gene expression of an episomal plasmid containing an oriP sequence within the nucleus. When the luciferase gene was introduced into a mouse melanoma cell line, with or without the EBV replicon components (oriP and EBNA-1), effective long-term gene expression was obtained in the plasmid containing the EBV replicon components. However, Southern blot analysis revealed that the copy number of the plasmid without the EBV components was much higher than that with the EBV replicon plasmid. This result suggests that effective gene expression by the EBV replicon plasmid results from transcriptional activation, and not from stable retention of the plasmid DNA. The regulation of transcription is further discussed below.

#### 14.2.4.2 Regulation of Transcription

Silencing of transgene expression occurs in host cells, despite insertion of transgenes into the host genome [63]. Similar silencing has also been reported in certain viral infections. For example, retroviral gene expression was inhibited after retrovirus infection of mouse embryos [64, 65]. Although low or silenced transgene expression after transfection has been a major problem in human gene therapy [66], the mechanism(s) by which transgene expression is regulated have not yet been elucidated. Since it will be essential to control transgene expression in human gene therapy, basic research on transgene expression in human gene therapy should be pursued further.

Although transcription factors have been investigated extensively [67, 68], previous studies have not fully clarified the mechanism(s) of regulation of transcription in higher eukaryotes. Recent studies have shown that chromatin remodeling factors such as the switch/sucrose nonfermenting (SWI/SNF) family and the imitation switch (ISWI) family [69] are involved in regulation of transcription. It is thought that histone acetylase and deacetylase also regulate transcription by modifying chromatin [70, 71]. Acetylation and deacetylation of histones and other proteins associated with DNA have been shown to be important in the epigenetics of regulating gene expression [70–72]. Recently, amplification of transgene expression in animals treated with a novel histone deacetylase inhibitor was reported [73]. This amplification was more effective for transgene expression than for endogenous gene expression. These data suggest that transgene expression can be regulated by chromatin modifications, such as histone acetylation/deacetylation. Methylated DNA-binding protein MeCP2 is a component of the complex that contains histone deacetylase [74]. This suggests that DNA methylation status may dictate the state of histone acetylation/deacetylation in chromatin. To overcome the silencing of transgene expression and to sustain transgene expression, *cis*-elements such as “insulators” [75–77] that are not affected by chromatin modification may be applied for transgene expression in gene therapy.

Many significant barriers to gene transfer have been elucidated. If omnipotent vector systems are eventually developed, however, gene transfer may harm patients – this is far from therapeutic. An all-encompassing vector system may not be feasible and each vector system must be evaluated with respect to the target disease. In some diseases such as arteriosclerosis obliterans, transient gene expression would be sufficient to cure the disease and sustained gene expression would be detrimental. In other diseases such as SCID-X1 and hemophilia B, it may be necessary to induce transformation of only a small population of cells. Cancer gene therapy comprises more than 60% of current human gene therapy approaches and no remarkable successes have been reported in this area to date. When we consider why gene therapy is necessary for cancer treatment, the answer is that it should be used to inhibit tumor metastasis and suppress the recurrence of cancers. For these purposes, investigations on basic cancer cell biology and technological developments should be promoted much more than at present. The issues described in this chapter present a road map for future technological developments in cancer gene therapy. Thus, technology for gene therapy should be developed on the basis of analysis of the target tissues, target cells, cellular components and relevant molecules.

### 14.3

#### **HVJ-E Vector**

##### 14.3.1

#### **Development of HVJ-E Vector**

HVJ is a mouse parainfluenza virus and is not a human pathogen. As molecules that enter the cell by phagocytosis or endocytosis often become degraded before reaching the cytoplasm, fusion-mediated delivery systems have been developed. A fusigenic viral liposome with a fusion proteins derived from HVJ was constructed [78]. HVJ fuses with the cell membrane at a neutral pH, and the HN protein and F protein of the virus contribute to cell fusion [79]. For fusion-mediated gene transfer, DNA-loaded liposomes were fused with ultraviolet (UV)-inactivated HVJ to form the fusigenic viral-liposome called the HVJ-liposome (Fig. 14.1).

Fusion-mediated delivery protected the molecules in the endosomes and lysosomes from degradation [80]. When fluorescein isothiocyanate (FITC)-tagged oligodeoxynucleotide (ODN) was introduced into vascular smooth muscle cells using HVJ-liposomes, fluorescence was detected in the nuclei 5 min after transfer and fluorescence was stable in the nucleus for at least 72 h. In contrast, fluorescence was observed in cellular components (most likely endosomes) and not in the nucleus when FITC-ODN was transferred directly in the absence of HVJ-liposomes and no fluorescence was detected 24 h after transfer. Using a fluorescence resonance energy transfer system, we demonstrated that more than 80% of oligonucleotides labeled with two different fluorescent dyes at the 5' and 3' ends were

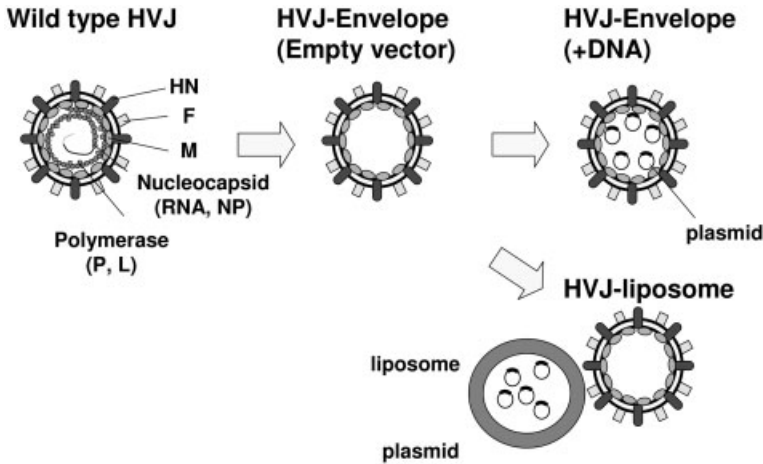


**Figure 14.1.** HVJ-E vector system. For constructing HVJ-E vector, plasmid DNA is mixed with inactivated HVJ particles, and the mixture is treated with mild detergent and centrifugation to incorporate DNA inside the

particle. For constructing HVJ-liposome vector, plasmid DNA is incorporated in liposome and mixed with inactivated HVJ particles. HVJ can fuse with the cell membrane to directly transfer DNA into cells.

intact in the nucleus, while less than 30% of the oligonucleotides were intact when Lipofectin was used [81].

Another advantage of HVJ-liposomes is the ability to perform repeated injections. Gene transfer to rat liver cells was not inhibited by repeated injections. After repeated injections, the anti-HVJ antibodies generated in the rat were not sufficient to neutralize HVJ-liposomes. Cytotoxic T cells recognizing HVJ determinants were not detected in the rats transfected repeatedly with HVJ-liposomes [82].

A similar approach has been used to enhance the gene transfer efficiency of a receptor-mediated gene delivery system by combining fusion peptide derived from influenza virus hemagglutinin (HA) [83]. A tissue-specific gene delivery system has been developed by binding tissue-specific molecules to a poly-L-lysine/DNA complex [84]. Binding asialoglycoprotein and transferrin to a poly-L-lysine/DNA complex successfully targets DNA to hepatocytes and cancer cells, respectively [84, 85]. However, the limitation of this system is the degradation of the DNA in the lysosomes. To avoid such degradation, a fusion-mediated gene delivery system has been investigated using influenza fusion proteins. Influenza virus fuses with cell membranes at an acidic pH, and HA protein on the viral envelope is involved in the fusion between viral envelope and endosomal membrane. It has also been elucidated that a mutant N-terminal peptide of influenza HA subunit, HA-2, can fuse with cell membranes at neutral pH. The transferrin/poly-L-lysine/DNA complex bound with the HA-2 peptide increases gene transfer efficiency in cultured cancer cells more than 1000-fold compared with that in the absence of the peptide [83].

Reconstituted particles containing fusion proteins of HVJ have also been developed to promote fusion-mediated gene delivery [86, 87]. HVJ virion was completely lysed with detergent and the lysates were mixed with DNA solution. In some cases, several lipids were added to the mixture. By removing the detergent with dialysis or a column procedure, reconstituted HVJ particles containing DNA were constructed. Instead of the whole virion of HVJ, fusion proteins (F and HN) isolated from the virion were mixed with the lipid/DNA mixture in the presence or absence of detergent. Since F protein is recognized by the asialoglycoprotein receptor on hepatocytes, reconstituted HVJ particles containing only F protein have been constructed to specifically target hepatocytes *in vivo* [88]. However, DNA trapping efficiency of the reconstituted particles was not so high. To improve the limitation, another approach was that liposomes containing fusion proteins of HVJ and DNA-loaded liposomes were prepared separately, and then both liposomes were fused together [89]. These reconstituted fusion liposomes were as effective as conventional HVJ-liposomes, which contain the fully intact HVJ virion, in terms of the delivery of FITC-ODN and the luciferase gene to cultured cells. The *LacZ* gene was also transferred directly to mouse skeletal muscle *in vivo* using these reconstituted fusion particles.

A more direct and practical approach is the conversion of a fusigenic virion to a nonviral gene delivery particle. Numerous viruses such as influenza, VSV and HVJ induce cell fusion. HVJ is the most abundantly produced in chick eggs. Therefore, we tried to construct an HVJ-E vector system by incorporating plasmid DNA into inactivated HVJ particle [90]. Our approach has been to use inactivated viral envelope in which the viral genome has been destroyed to develop highly efficient and minimally invasive vectors.

There are some drawbacks to HVJ-liposomes, although they have been widely used for gene transfer both *in vitro* and *in vivo*. One disadvantage of HVJ-liposomes is the complicated procedure used to isolate and produce both inactivated HVJ and DNA-loaded liposomes. Additionally, the fusion activity of the HVJ-liposomes decreases to approximately 2% of that of native HVJ because of the reduced density of fusion proteins on the surface of HVJ-liposomes. To simplify the vector system and to develop a more effective gene delivery system, we attempted to incorporate plasmid DNA into inactivated HVJ particles without using liposomes.

HVJ is a mouse parainfluenza virus and is not a human pathogen [79]. HVJ can fuse with cell membranes in both neutral and acidic conditions. Two distinct glycoproteins, HN and F, are required for cell fusion [79, 91]. HN is required for the binding of HVJ to cell surface sialic acid receptors and the subsequent degradation of the receptors by its sialidase activity. Then, F associates with lipids, such as cholesterol, in the cell membrane to induce cell fusion. The F glycoprotein is first synthesized as inactive F0 in cells infected with HVJ. F0 is then cleaved by host protease into the active F1 and F2 forms. F1 contains hydrophobic peptides with approximately 25 amino acids that induce cell fusion [91, 92]. F protein produced in chick eggs is converted to the active F1 form by the protease in chorioallantoic fluid, while the virus produced from cultured cells contains inactive F0 that needs

to be cleaved by a protease to form active F1. Cells in the rodent airway contain enzymes to convert inactive F0 to active F1. Therefore, HVJ induces severe pneumonia in rodents but not in humans. Large amounts of viral proteins are produced in infected cells. Viral nucleocapsid protein induces cytotoxic T lymphocytes (CTLs) against infected cells [93]. However, nucleocapsid protein is indispensable for virus production. Therefore, to develop highly efficient and minimally invasive vectors based on HVJ, our approach has been to use inactivated viral envelope in which the viral genome has been destroyed.

For this purpose, we have converted HVJ to a nonviral vector containing therapeutic genes instead of the viral genome [90]. HVJ amplified in the chorioallantoic fluid of 10- to 14-day-old chick eggs was inactivated with  $\beta$ -propiolactone (0.0075–0.001%) [94] followed by UV irradiation ( $99 \text{ mJ cm}^{-2}$ ) [95]. Then, inactivated HVJ-E was purified by ion-exchange column chromatography and gel filtration (Nakajima and coworkers, unpublished method). With this inactivation procedure, virus replication was completely destroyed, but hemagglutinating activity was not affected. HVJ particles in the chorioallantoic fluid were very heterogeneous with a diameter ranging from 150 to 600 nm. More homogeneous HVJ-E was isolated with the improved purification method using the column procedure. The diameter of HVJ-E obtained from the column procedure was 280 nm and the  $\zeta$  potential was approximately  $-5 \text{ mV}$ .

Aliquots of the inactivated virus ( $3 \times 10^{10}$  particles per 1.5-ml tube) were centrifuged (10 000 g, 5 min) and the viral pellet was mixed with exogenous plasmid DNA. Exogenous plasmid DNA was incorporated into inactivated HVJ by treatment with mild detergent and centrifugation. First, inactivated HVJ ( $3 \times 10^{10}$ ) particles were mixed with 0.24–0.80% Triton X-100 in the presence of plasmid DNA (200  $\mu\text{g}$ ) in less than 100  $\mu\text{l}$  of Tris–EDTA buffer for 5 min on ice and the mixture was centrifuged at 10 000 g for 5 min to move the DNA into the HVJ particle. The DNA trapping efficiency of HVJ-E vector was approximately 15–20%. Without centrifugation, the DNA trapping efficiency was approximately 3%. Different detergents were available for the preparation of HVJ-E vector including NP-40, CHAPS, octylglucoside, sodium cholate and dodecyl maltoside, although the optimal concentration of detergent for preparation of HVJ-E vector is different. Without detergent treatment, DNA does not become incorporated into the viral particle. Electron microscopy confirms that DNA became incorporated into all of the particles of inactivated HVJ. The largest plasmid tested was 14 kb and its trapping efficiency was 18%.

The HVJ-E vector differs from the reconstituted HVJ particles that are prepared by reassembling lipids and fusion proteins after solubilization of the virus particle. To prepare HVJ-E vector, plasmid DNA is incorporated into inactivated HVJ particles by treatment with mild detergent. The virion is not destroyed, and not subjected to the dialysis, purification and addition of lipids or proteins that occurs during the preparation of reconstituted HVJ particles [86, 87, 89]. Protein analysis of HVJ-E vector using sodium dodecyl sulfate–polyacrylamide gel electrophoresis indicates that the composition of HVJ-E vector is very similar to that of native HVJ [90]. Most native HVJ proteins are retained in HVJ-E vector. Fusion proteins HN

and F1 are retained, and the molar ratio of these proteins in HVJ-E vector was approximately 2:2.3, which is the same as the ratio in native HVJ [79]. This ratio of F and HN is very important for fusion activity. Therefore, the fusion activity of HVJ-E vector is as robust as wild-type HVJ. Electron microscopic observation confirmed that the fusion between HVJ-E vector and cell membrane occurs only 3–5 s after the attachment of the plasmid-containing HVJ-E vector to a cell surface.

In contrast to recombinant HVJ viral vector [96], the HVJ-E is a nonviral vector system that consists of an envelope derived from wild-type HVJ virus by inactivation and purification. Since the viral genome is inactivated in HVJ-E vector, the virus does not replicate and viral genes are not expressed in the cells that are transfected with HVJ-E vector. However, cells infected with recombinant HVJ viral vector produce viral proteins. The recombinant HVJ vector produces a large amount of therapeutic products, but it may cause cellular toxicity and be highly immunogenic, which make it less desirable for repeated administration.

For *in vitro* transfection, HVJ-E vector containing luciferase expression plasmid was mixed with PS and this mixture was added to culture cells. Protamine sulfate enhanced luciferase gene expression 10- to 50-fold in several cell lines and the optimum conditions for *in vitro* gene transfer have been previously summarized [90]. Small interfering RNA (siRNA) is an attractive and effective tool for suppressing target protein by specifically digesting its mRNA [97, 98]. siRNA is superior to antisense oligonucleotides and ribozyme in terms of efficiency and specificity [99, 100], but finding a suitable delivery system for siRNA has been problematic [101]. Drugs, synthetic oligonucleotides, proteins and peptides as well as siRNA can be incorporated into HVJ-E vector, and delivered into cells. The HVJ-E-mediated delivery efficiency of siRNA in cultured cells was 100%. Other researchers have also demonstrated that HVJ-E vector efficiently delivers siRNA to islet cell lines [102] and Jurkat cells [103].

HVJ-E vector system can be used for *in vivo* gene transfer. The HVJ-E vector has mediated gene transfer to a variety of tissues (lung, liver, uterus, eye, skin, muscle, brain and heart) in animals including mice, rats, rabbits and monkeys. In mouse liver, HVJ-E vector-mediated luciferase gene expression was 2 times higher than the expression mediated by HVJ-liposomes prepared from inactivated HVJ. In mouse skeletal muscle, consecutive injection of DNA-loaded HVJ-E vector did not inhibit gene transfection. In this experiment, empty HVJ-E vector was injected into mouse muscle tissue twice with a 2-week interval in one experimental group, while another group received saline injections. Two weeks later, HVJ-E vector-containing luciferase gene was intramuscularly injected in all mice. In the two groups, similar luciferase gene expression was observed. Thus, HVJ-E vector appears to be less immunogenic than other viral vector.

We reported the successful gene transfection into uterus and brains by HVJ-E vector [104, 105]. For the transfection into uterus, HVJ-E vector containing plasmid DNA was slowly injected into the uterine cavity and the cervix was clamped for 10 min. For the transfection into brain tissue, we intrathecally injected HVJ-E vector containing the *LacZ* gene into the cerebrospinal fluid (CSF). HVJ-envelope vector containing plasmid DNA was infused at the rate of 50  $\mu\text{L min}^{-1}$  after removing

100  $\mu$ l of CSF. Then, the animals were placed head-down for 30 min. No behavioral changes, such as convulsions or abnormal movements, were observed. Cells that expressed  $\beta$ -galactosidase were present in the spiral ganglion cells (SGCs), cerebral cortex and medulla.

We also examined the transfection efficiency in the intravenous injection of HVJ-E vector. Luciferase gene-loaded HVJ-E vector ( $6 \times 10^9$  particles) was injected into the mouse tail vein and luciferase activity in several organs was measured 24 h after injection. Luciferase expression was detected in the spleen for at least 1 week. When HVJ-E vector containing FITC-ODNs was systemically injected, FITC-ODNs were observed in the marginal zone of the spleen. However, by intravenous injection of HVJ-E vector, coagulation functions in the mouse blood is transiently suppressed, but the functions are recovered at 24 h after the injection. It is probable that the hemagglutinating activity of HN protein will be necessary for systemic injection of HVJ-E vector to ensure the safety in gene therapy.

#### 14.3.2

### Approaches to Cancer Gene Therapy Utilizing HVJ-E Vector

#### 14.3.2.1 Transfection of Dendritic Cells (DCs) with Melanoma-associated Antigen (MAA) using HVJ Envelope Vector for Immunotherapy of Melanoma

Our first approach for developing cancer gene therapy was to construct cancer vaccines using the HVJ-E vector system. Polyvalent tumor antigen vaccines have been evaluated to increase the repertoire of antitumor T cells [106]. In this study, we chose MAA genes, glycoprotein 100 (gp100) and tyrosine-related protein 2 (TRP2), and transfected DCs with these two genes to evaluate *ex vivo* vaccination for prophylactic and therapeutic melanoma treatment.

DCs are the most potent antigen-presenting cells. DCs are capable of highly effective presentation of antigens to naive T cells and they can initiate immune responses [107]. Several clinical studies have now been conducted in cancer patients with tumor-associated antigen (TAA)-loaded DCs [108, 109]. In several of these clinical studies the DCs were loaded by pulsing with protein antigens or with peptides derived from TAAs. Studies have demonstrated that *ex vivo* transfected DCs and adoptive therapy can be very effective in inducing antigen-specific immune responses. This type of strategy has been demonstrated in animals and pilot clinical studies for a variety of cancers [110, 111].

Transfected DCs with vectors expressing TAA genes have shown promising results. Studies have demonstrated that xenogeneic TAAs are very strong immunogens capable of cross-priming to host syngeneic TAAs. Human TRP2 and gp100 proteins have a high amino acid sequence homology to their mouse counterparts. We used xenogeneic TAAs for several reasons: to break self-antigen tolerance in the host, to induce strong antitumor immunity and to enhance individual TAA immunogenicity. The approach provides a large expression of TAAs and activates DC presentation. Therefore, highly efficient transfection system is absolutely necessary for efficient induction of tumor immunity. In recent studies, adenoviral vector was the original vector of choice for efficiently transfecting DCs [112, 113]. However, ad-



enovirus has serious disadvantages as a vector for engineering DCs because of its high toxicity. Some studies have demonstrated that plasmid DNA in liposomes [114], vaccinia virus [115, 116] and retroviruses [117, 118] could be used to infect or transfect human DCs to present a variety of antigens. However, a highly efficient and minimally invasive vector system has not yet been achieved for transfection of DCs. To develop more efficient gene transfer to DCs that cause only minimal damage, we tested the potential of HVJ-E vector for transfection of DCs with two different TAA genes.

We used the luciferase gene to determine the optimal conditions for transfection of DCs. As previously reported, the optimum ratio of HVJ-E vector to cultured cells is  $6 \times 10^3$  to  $1.2 \times 10^4$  [90]. We identified  $1.2 \times 10^4$  as the optimal ratio and determined the most effective transfection conditions. When DCs were incubated with HVJ-E vector containing the luciferase gene, luciferase gene expression was not significant. We attempted to increase the luciferase gene expression by centrifuging the mixture of DCs and HVJ-E vector. Centrifugation at 9000 g was much more effective for gene transfection than 3000 and 13 000 g. The viability of DCs after transfection was approximately 70%. The centrifugation time required for the most effective gene expression was 90 min. The highest luciferase gene expression was obtained in DCs that were centrifuged for 90 min at 9000 g and 37 °C. Six days after DCs were isolated was the best time to transfect the DCs for optimal luciferase gene expression. Thus, the optimal conditions for the most effective transfection of DCs were at 9000 g for 90 min at 37 °C in DCs cultured for 6 days after isolation from bone marrow. Under these optimal conditions, we assessed the expression of yellow fluorescent protein (YFP) expression to determine the transfected DCs population. Almost all DCs that were recognized with phycoerythrin (PE)-conjugated CD11c antibody expressed YFP, as determined by fluorescence microscopy. Flow cytometry analysis revealed that approximately 99% of DCs expressed YFP.

Surface markers of mature DCs were studied by flow cytometry analysis to confirm that differentiation was not inhibited by gene transfection using HVJ-E vector. The lipopolysaccharide (LPS)-induced expression of CD40, CD80, CD86 and HLA-DR was equivalent on nontransfected DCs and transfected DCs. The nonspecific phagocytotic activity of DCs (evaluated by uptake of FITC-labeled dextran) was suppressed in transfected DCs as well as in nontransfected DCs. Thus, gene transfer with HVJ-E vector did not inhibit LPS-induced maturation of DCs.

Next, we used HVJ-E vector to transfect the gp100 and TRP2 genes into DCs. The expression of each transfected antigen was detected by flow cytometry analysis of cells stained with antigen-specific antibody. On day 1, gp100 and TRP2 were detected in 36 and 63% of DCs, respectively. Approximately 80% of DCs expressed both antigens on day 7.

DCs transfected with either the gp100 or TRP2 gene or both genes after one day were injected intradermally into C57BL/6 mice. The delayed-type hypersensitivity (DTH) response was assessed in mice immunized with MAA-transfected DCs at 24, 48, and 72 h after TAA protein challenge. Significant cutaneous DTH was detected in mice immunized with MAA gene-transfected DCs compared to the con-

trol mice that were injected with DCs without MAA. The DTH response to gp100 was significant in the groups immunized with gp100-transfected DCs or gp100/TRP2-transfected DCs. The level of response was equivalent in the two groups. A similar response to TRP2 was obtained in the groups immunized with TRP2-transfected DCs or gp100/TRP2-transfected DCs.

We examined CTLs against BL6 tumor cells on day 7 after DC administration. TAA-specific CTLs were generated with variable response rates. Mice immunized with DCs expressing gp100 and TRP-2 had the highest level of CTL activity against  $^{51}\text{Cr}$  – labeled BL6 target cells. Mice immunized with single TAA-transfected DCs generated significant CTL activity against BL6 cells when compared to the control groups that received HVJ-E vector containing pcDNA-3.1. However, these responses were lower than those generated by the cotransfer of gp100 and TRP2. Vaccination of DCs transfected with TAA genes induced TAA-specific cellular immunity consisting of CTL activity and DTH helper cell activity against melanoma cells.

We tested the effect of vaccination with MAA-transfected DCs on the inhibition of tumor growth in mice. No tumor growth was observed in mice immunized with gp100/TRP2 transfected DCs, although significant tumor masses were palpable in all control mice injected with DCs without TAA. Immunization with DCs transfected with single TAA gene was not effective, as small tumor masses were detected. However, the tumor growth rate was slower than that of the control group. In this prophylactic study, vaccination with DCs transfected with both gp100 and TRP2 was much more effective for inhibition of tumor growth than vaccination with DCs transfected with TRP2 alone.

To investigate the therapeutic effect of vaccination with TAA-transfected DCs, we vaccinated the mice with various DC vaccines 24 h after intravenous inoculation with  $10^4$  BL6 cells. All control mice injected with PBS-treated DCs and pcDNA3.1-transfected DCs died of lung metastasis in 45 and 62 days after inoculation, respectively. Vaccination with DCs that were transfected with a single TAA gene improved the survival. Vaccination with TRP2-transfected DCs was more effective than vaccination with gp100-transfected DCs. Vaccination with gp100/TRP2-transfected DCs significantly prolonged the survival rate. Eight of nine mice vaccinated with gp100/TRP2-transfected DCs survived more than 80 days after tumor inoculation. Vaccination with immature DCs that were not treated with LPS was not effective for improving survival and all of these mice died in 60 days (including the mice that received gp100/TRP2-transfected DCs).

#### 14.3.2.2 Fusion of DC Tumor Cells and Simultaneous Gene Transfer to the Hybrid Cells using HVJ-E for the Prevention and Treatment of Cancers

TAAAs have been identified in some cancers such as melanoma [119, 120]. However, TAAAs in many cancers have not been identified. The identification of TAAAs is required for the development of TAA-loaded DC vaccines.

To solve the problem, hybrid cell vaccines have been developed by fusing DCs with tumor cells [121, 122]. There is evidence that these DC–tumor fused cells possess the properties of both tumor cells containing known and unknown TAAAs and

DCs with high levels of MHC class I and II molecules and costimulatory molecules for priming and activating naive CD4<sup>+</sup> and CD8<sup>+</sup> T cells. Therefore, even though tumor cells lose MHC class I molecules, TAAs can be presented on the surface of the fused cells by DC-derived MHC class I molecules. PEG and electroporation have been used to induce tumor cell–DC fusion. HVJ has been identified as a powerful fusogen. We stained mouse DCs with red fluorescent reagent. Mouse melanoma cells were stained green and irradiated with  $\gamma$ -rays. Both cells were mixed with inactivated HVJ. After 30 min, the fusion of DCs and tumor cells occurred with approximately 50% efficiency.

We used HVJ-E to generate powerful tumor–DC vaccines, because HVJ-E can induce tumor cell–DC fusion and simultaneously transfer DNA or proteins to activate the immune response. To confirm simultaneous fusion and gene transfer mediated by HVJ-E, DCs and tumor cells were mixed with HVJ-E containing the green fluorescent protein (GFP) gene. Fusion between DCs and irradiated-tumor cells was observed, and YFP expression was detected in fused cells as well as in DCs.

Using this system, we attempted to generate anti-tumor immunity using HVJ-E with or without the interleukin (IL)-12 gene. Ten days after the second immunization, spleen cells were isolated to assess cytolytic activity. The cytolytic activity of the effector cells obtained from the mice immunized with fused cells was significantly higher than that obtained from other vaccination protocols such as PBS, IL-12, “Mix” (mixture of DCs and tumor cells without fusion) and “Mix” plus IL-12. Higher cytolytic activity was observed in the mice that received fused cells plus IL-12 as compared with that in the mice that received fused cells alone.

First, we examined the effect of this hybrid cell vaccine on the prevention of tumor generation. After two vaccinations, melanoma cells or renal cancer cells were intradermally injected. The mice vaccinated with fused cells plus IL-12 had significantly increased survival; all of these mice were alive 60 days after tumor challenge in the B16BL6 tumor model. The survival rate was 20% in the mice vaccinated with fused cells without IL-12. All mice in the other groups died. The effect of fused cells and IL-12 on the enhancement of tumor-specific immunity in mice was also observed against renal cancer. Therefore, these findings indicate that immunization with fused cells plus IL-12 strongly induces T<sub>h</sub>1 cytokines and activates tumor-specific CTLs, resulting in significant protection from melanoma, which has known TAAs or renal cancers which has unknown TAAs.

Next, we treated solid tumors by *in vivo* fusion and gene expression using HVJ-E vector. Mouse DCs and HVJ-E vector were injected into solid tumors. The effect of the transfer of a therapeutic gene by HVJ-E vector was also evaluated. To detect *in vivo* fusion of DCs with tumor cells, red-stained DCs were injected into melanoma masses expressing YFP with inactivated HVJ. Megakaryocytes, which indicate tumor cell–tumor cell fusion, were detected, as well as large orange-stained cells indicate DC–tumor cell fusion. However, the fusion efficiency *in vivo* was much less than that of *in vitro* cell fusion.

For therapeutic experiments, melanoma cells were intradermally injected. When the tumor diameter was greater than 5 mm, an injection of DCs and HVJ-E vector

was administered. Spleen cells were isolated and assayed for antimelanoma CTL activity. No therapeutic genes were incorporated into HVJ-E vector. The coinjection of DCs and empty HVJ-E vector resulted in significant antimelanoma CTL activity. DCs or HVJ-E vector alone did not induce CTL activity. When tumor growth was observed, the coinjection of DCs and empty HVJ-E vector inhibited tumor growth, but the tumor volume still gradually increased. When DCs were coinjected with HVJ-E vector that contained the IL-12 gene, a greater inhibitory effect was obtained. The coinjection of DCs and HVJ-E vector effectively prolonged mouse survival. The most effective therapeutic effect was obtained when HVJ-E vector that contained IL-12 gene was coinjected with DCs into the tumor mass; approximately 60% of these mice survived 35 days after treatment.

Thus, we developed a novel cancer vaccine using HVJ-E-mediated DC–tumor cell fusion. The DC–tumor cell fusion was induced by HVJ-E vector at a high efficiency. Both known and unknown TAAs were presented on fused cells by MHC class I molecules from DCs. Furthermore, IL-12 gene transfer was achieved in the fused cells. The expression of IL-12 stimulates the maturation of naive T cells and promotes a  $T_{h1}$  response [123]. It is believed that the presentation of TAAs and the promotion of a  $T_{h1}$  response together induce an efficient antitumor CTL response.

The HVJ-E vector holds great promise for human gene therapy. We are improving the HVJ-E vector system so that it can be used in clinical trials. So far, the virus has been produced in chick eggs, but egg-derived HVJ is difficult to use for clinical trials. It has been very difficult to produce large amounts of the virus in cultured cells and the production in cultured cells are less than 2% of that in chick eggs. We recently developed the system in producing HVJ in human cells. We cloned HEK-293 cells that produce a high titer of HVJ after infection and determined the growth conditions for these cells in an animal product-free medium using a bioreactor. We are able to culture these cells in 10 L of serum-free medium at a density of more than  $10^6$  cells  $\text{mL}^{-1}$  and we can obtain HVJ at the efficiency of more than  $3 \times 10^9$  particles  $\text{mL}^{-1}$ . The production in a 10-L culture is comparable to that in 500 chick eggs. A pilot plant to commercially produce clinical grade HVJ-E vector was established in a venture company named Genemidea (Japan; <http://www.anges-mg.com/news/030324.htm>). Genemidea created a working cell bank, master cell bank and master virus bank for producing clinical-grade HVJ for phase I and IIa trials. They also set up an apparatus to purify inactivated HVJ using two different column systems. The human cell-derived HVJ-E vector was more effective for gene transfection than the egg-derived HVJ-E vector. Human cell-derived HVJ-E vector is also available for drug delivery both *in vitro* and *in vivo*. This vector will be available for human gene therapy soon.

#### 14.4

##### Biocompatible Polymer with HVJ-E

Recent advances in biotechnology have made it possible to produce various clinically useful DNA and proteins. While this technology has brought about the dis-

covery and mass production of these bioactive macromolecules, several challenges need to be addressed with regard to their sustained delivery in a convenient, controlled manner and targeting formulations. It has been demonstrated that complexation with positively charged polymers enabled negatively charged DNA to have an enhanced stability and transfection efficiency to cells [124–126]. Recently, the use of biodegradable gelatin as a nonviral vector augmented adrenomedulin expression and thereby enhanced the therapeutic effects of adrenomedulin gene transfer which potentially induces angiogenesis [127]. They demonstrated that rhodamine isothiocyanate-labeled adrenomedulin DNA was incorporated into positively charged gelatin. In addition, intramuscular administration of adrenomedulin DNA–gelatin complexes strongly enhanced adrenomedulin production compared with that of naked adrenomedulin DNA. These results suggest that biodegradable gelatin may serve as a vector for gene transfer. In fact, adrenomedulin DNA–gelatin complexes induced more potent angiogenic effects in a rabbit model of hind limb ischemia than naked adrenomedulin DNA, as evidenced by significant increases in histological capillary density, calf blood pressure ratio, laser Doppler flow and muscle weight ratio, and a decrease in necrosis of lower hind limb and thigh muscles. These results suggest that the use of biodegradable gelatin as a nonviral vector augments adrenomedulin expression and enhances adrenomedulin-induced angiogenic effects. Adrenomedulin DNA–gelatin complexes were distributed mainly in connective tissues. They have recently demonstrated that gelatin–DNA complex is readily phagocytosed by macrophages, monocytes, endothelial progenitor cells, etc., resulting in gene expression within these phagocytes [128, 129]. These findings raise the possibility that adrenomedulin secreted from these cells acts on muscles in a paracrine fashion. Unlike adrenomedulin production in the naked adrenomedulin group, adrenomedulin overexpression in the adrenomedulin–gelatin group lasted for longer than 2 weeks. Thus, it is interesting to speculate that delaying gene degradation by gelatin may be responsible for the highly efficient gene transfer.

We succeeded in enhancing the transfection efficiency of HVJ-E by combining it with cationic polymers [130]. For cultured cells *in vitro*, the most efficient transfection was obtained by combining HVJ-E with both CG and PS. However, for *in vivo* transfection, CG–HVJ-E without PS resulted in the highest gene expression. These findings are consistent with our previous report indicating that the particle size of cationic liposomes may affect gene transfection efficiency [131]. By adding both PS and CG to HVJ-E, the size and charge of the resulting complex may have been the most suitable for *in vitro* transfection. PS and CG affected gene transfection efficiency in a variety of cell lines as well as in primary cells, although the efficiency was varied among cell types. The ratio of PS and CG used for these experiments was determined by gene transfection experiments with CT26 cells. Thus, gene expression in the other cell types may be enhanced when the conditions are optimized for each cell type.

We determined that cell fusion is the mechanism responsible for a PS–CG–HVJ-E-mediated gene transfer system. Although endocytosis appeared to be involved in gene transfection based on the wortmannin experiments, transfection

was completely inhibited by antibody against the fusion protein of HVJ. Since the fusion activity of HVJ is pH independent, HVJ can fuse with the cell membrane both on the cell surface and in endocytotic vesicles. Even for the HVJ-E complex with PS and CG, the F protein of HVJ appeared to associate with the cell membrane, and fusion activity appeared to be necessary for gene transfection.

HVJ-E complexed with CG targeted the liver. With PS, gene expression in the liver after intravenous injection was lower than with CG–HVJ-E. We speculate that larger particles with positive charge are less mobile when intravenously administered. Comparison with PS–HVJ-E and PS–CG–HVJ-E suggests that CG–HVJ-E may have the appropriate size and potential for targeting the liver after intravenous injection. Our results suggest that the CG–HVJ-E vector may be effective and practical for the treatment of liver diseases, such as liver cirrhosis and hepatitis, when therapeutic genes encoding secreted proteins, such as human growth factor, soluble transforming growth factor- $\beta$  receptor and decorin, are employed. An adverse effect of this treatment is that coagulation function is transiently decreased by CG–HVJ-E in mice, although it recovered in 1 day. This adverse effect is probably caused by HVJ hemagglutinating protein, which is necessary for binding with sialic acid, a virus receptor. When HVJ-E is complexed with CG, CG may perform the function of hemagglutinating protein and enhance the association with cell membranes. If HVJ-E without hemagglutinating protein is combined with CG, the complex may reduce adverse effects to a much lower level.

An additional advantage of CG is that it protects HVJ-E from degradation in fresh mouse serum. Although the *in vitro* transfection efficiency of HVJ-E was not inhibited by culture medium containing 10% FBS, the activity of HVJ-E was rapidly lost in the presence of fresh mouse serum. However, CG–HVJ-E was significantly stable in 50% fresh mouse serum. The high transfection activity of CG–HVJ-E after intravenous injection appears to be mediated by the stability of the vector in fresh serum. Liposomes composed of hydrogenated egg phosphatidylcholine and cholesterol activate the complement system in rats by interacting with IgG and IgM. Although it is unproven that HVJ is degraded by complement lysis in mouse serum, the interaction of serum proteins with HVJ-E may be involved in the loss of transfection activity of HVJ-E. Conjugation to CG appears to protect the surface molecules of HVJ-E from the detrimental effects of serum proteins.

The results of this study suggest that low-molecular-weight CG may be appropriate for complex formation with various envelope viruses, such as retrovirus, herpes virus and HIV, and that the CG-envelope virus vector may enhance transfection efficiency both *in vitro* and *in vivo*. This technology may lead to the achievement of an ideal vector system with high efficiency and minimal toxicity.

## 14.5 Magnetic Nanoparticles for Medicine

A novel transfection method, so called magnetofection, which comprises the association of vectors with superparamagnetic iron oxide nanoparticles and gene deliv-

ery under the application of a magnetic field, has been developed [132]. Using the method of magnetofection the efficiency of synthetic gene carriers has been enhanced up to several-hundred-fold. In particular, the duration of the transfection procedure has been reduced to minutes [132]. For magnetofection, gene carriers such as poly(ethylenimine) (PEI), which are associated with superparamagnetic iron oxide nanoparticles, are complexed with plasmid DNA (these complexes are called magnetofectins) and gene delivery is targeted by the application of a magnetic field. For an unrestricted use of magnetofection and its benefits it would be advantageous to gain more insights into the cellular uptake mechanism of the magnetofectins. For polyplexes an endocytic uptake mechanism, probably mediated by heparan sulfate proteoglycan receptors via endosomes, has been shown [133]. Due to its high buffering capacity, PEI is able to destabilize the endosomal membrane leading to the so-called endosomolysis. PEI apparently induces a massive proton accumulation in the endosomes followed by passive chloride influx leading to osmotic swelling of the endosomes and, finally, to its burst releasing the gene vectors into the cytoplasm as a prerequisite for the transport of DNA towards the nucleus. This effect is called the “proton sponge effect” [134–136]. In this context the question arises whether the PEI-based magnetofectins function in the same way as PEI gene vectors. In particular, we asked if the applied magnetic force result only in an increased accumulation of magnetofectins on the cell surface or if it is even able to pull them directly into the cells, circumventing endocytosis and leading to a different gene transfer mechanism as for PEI gene vectors.

Endocytosis is involved in various cellular processes like the transmission of neuronal, metabolic and proliferative signals, the uptake of many essential nutrients, and the ability of defense against invading microorganisms [137]. It is characterized by the formation of membrane vesicles at the plasma membrane. One distinguishes between clathrin-dependent and clathrin-independent endocytosis. The clathrin-dependent endocytosis is the best described so far. Here the vesicles (diameter of approximately 100 nm) are coated with clathrin [137, 138]. After internalization, the clathrin coat gets recycled and the vesicle fuses with an endosome where the sorting, mediated by microtubules, and the dissociation of potential receptors take place. This step is followed by degradation in lysosomes and further transport to the final destination [138]. Well-known examples for the clathrin-dependent uptake mechanism of receptor-bound ligands are transferrin and the low-density lipoprotein (LDL) [137]. The clathrin-independent pathways include phagocytosis, macropinocytosis, constitutive nonclathrin uptake and caveolae-mediated uptake [137]. Phagocytosis is generally restricted to macrophages, whereby macropinocytosis refers to the formation of large, irregular primary endocytic vesicles [138]. Clathrin-independent endocytosis in the absence of caveolae and caveolin is found and designated as constitutive nonclathrin uptake. The caveolae-mediated uptake is characterized by caveolae, which are omega-shaped, noncoated membrane invaginations (diameter 50–100 nm) present in many cell types, but especially abundant in endothelial cells [138]. Their structure is maintained by a family of cholesterol-binding proteins called caveolin. Besides caveolin, caveolae

are enriched in cholesterol, sphingomyelin and glycosphingolipids [138]. There is some evidence for a potential role of caveolae in the internalization and intracellular delivery of gene-based therapeutics, as used for somatic gene transfer or single-stranded oligonucleotide technology [139].

We focused on magnetic nanoparticles, such as magnetite and maghemite, with an average size of from 20 to 50 nm, which can be positionally regulated by a magnetic force. Magnetic nanoparticles basically consist of oxidized iron, which is commonly used as a supplement for the treatment of anemia. We hypothesized that the association of magnetite and HVJ-E technology could allow the rapid attachment of HVJ-E and cells by application of a magnetic force, leading to enhanced transfection efficiency. Moreover, magnetic nanoparticles can be modified with several chemical compounds to allow modification of the charge, size and affinity. In addition, there is increasing interest in using magnetic resonance imaging (MRI) to monitor the *in vivo* behavior of proteins labeled with magnetic nanoparticles [140, 141]. Indeed, magnetic nanoparticles were recently used for gene transfection, because magnetic targeting exploits paramagnetic particles as drug carriers, guiding their accumulation in target tissues with strong local magnetic fields [142, 143].

To evaluate the HVJ-E vector system mixed with maghemite, we mixed several doses of maghemite with HVJ-E vector infusing luciferase plasmid. However, unexpectedly, we did not find any improvement in transfection efficiency. From these results, we speculated that there might be a close association, such as electrostatic interaction, between HVJ-E and maghemite. Since we have previously reported that PS, a low-molecular-weight naturally polycationic peptide (around 4000 Da), enhanced the transfection efficiency based on HVJ-E vector in an *in vitro* culture system, we coated the surface of maghemite with PS. After modification with PS, the  $\zeta$  potential of maghemite was changed to  $23.8 \pm 1.8$  from  $17.5 \pm 1.6$  mV, which suggests that surface coating of maghemite enhanced its cationic charge. Interestingly, a mixture of PS-coated maghemite with HVJ-E vector significantly enhanced the transfection efficiency in a dose-dependent manner. Using the same system, high transfection efficiency into BHK cells was also achieved using the enhanced GFP (EGFP) gene or FITC-ODN. To confirm the interaction of magnetite and HVJ-E vector, we performed electron microscopy. PS-coated maghemite and HVJ-E vector co-existed even though a number of maghemite particles were aggregated around HVJ-E vector (Fig. 14.2).

To explore transfection *in vivo*, we further evaluated the maghemite-attached HVJ-E vector by direct injection into mouse liver. Unexpectedly, a mixture of maghemite surface-coated with PS did not enhance the transfection efficiency in the analysis of luciferase activity, differing from the *in vitro* system. Since cotreatment with heparin has been reported to enhance the transfection efficiency of HVJ-E vector in brain tissue, we next coated the surface of maghemite with heparin, which might antagonize the function of PS. The  $\zeta$  potential of maghemite was changed to  $-10.1 \pm 2.3$  from  $17.5 \pm 1.6$  mV, which suggests that the surface coating of maghemite was changed to a fairly negative net charge. A mixture of



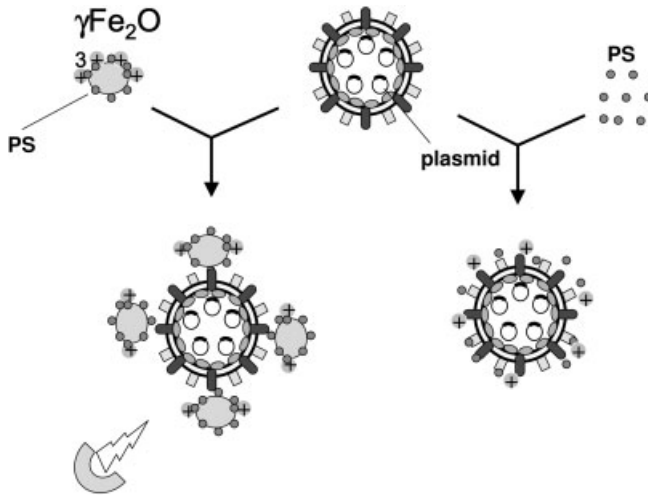


**Figure 14.2.** Modified HVJ-E vector. PS enhanced the transfection efficiency based on HVJ-E vector in an *in vitro* culture system. In addition, we coated the surface of magnetic nanoparticles with PS and further enhanced the transfection efficiency based on HVJ-E vector.

heparin-coated maghemite with HVJ-E vector significantly enhanced the transfection efficiency in the liver. These data suggest that suitable modifications for gene transfection differ between *in vitro* and *in vivo*. Analysis of EGFP expression in the liver by immunostaining, also confirmed marked expression obtained with heparin-coated maghemite with HVJ-E vector containing the EGFP gene as compared to PS-coated maghemite. For safety evaluation, the serum levels of alanine aminotransferase (ALT) and aspartate aminotransferase (AST) were not further elevated in the heparin-coated maghemite group compared to the control group. Furthermore, we tried to enhance the transfection efficiency under the influence of a magnetic field by placing a magnet on the surface of the liver. However, no obvious improvement in luciferase activity in the liver was observed. Probably, a stronger magnetic field or more accurate control of magnetite might be necessary to enhance it.

In the system of magnetofection, the gene carrier itself represents a hybrid system characterized by an iron oxide inner core and a coat consisting of the cationic PEI which might also assist the endosomal escape of a gene after transfection into cells. In contrast, in our system, transfection was mediated by a cell fusion process of HVJ-E vector, which did not require endosomal escape, are not by endocytosis. Thus, we selected PS as the coating material of maghemite in combination with the HVJ-E system, as PS is a low-molecular-weight polycationic peptide that has Food and Drug Administration approval as an antidote to heparin anticoagulation

[144, 145]. Since both the surface of HVJ-E and the cell membrane have a negative net charge, cationic charged PS-coated maghemite can be speculated to enhance the association of HVJ-E with the cell membrane. Thus, PS-coated maghemite would actively carry HVJ-E to cultured cells under a magnetic force.

However, in an *in vivo* system, heparin, but not PS, was suitable as the coating material in combination with HVJ-E vector, consistent with a previous *in vivo* report. Of special interest regarding this result was a previous report showing that coinjection of trophic factors and heparin into the rat brain significantly enhanced the volume of distribution. Thus, we speculate that the distribution of these vectors may be a key to explaining this discrepancy between *in vitro* and *in vivo* gene transfer. In addition, no immunohistochemical data has been presented on potential toxic effects of heparin. The size and surface chemistry of magnetic particles could be tailored accordingly to meet specific demands of physical and biological characteristics.

Magnetically targeted drug delivery by particulate carriers to a localized disease site may be efficient as drugs and a very high concentrations of chemotherapeutic or radiological agent can be achieved near the target site, such as a tumor, without any toxic effects on normal surrounding tissue or the whole body. Magnetic carriers receive their magnetic responsiveness to a magnetic field from incorporated materials such as magnetite, iron, nickel, cobalt, neodymium–iron–boron or samarium–cobalt. As for biomedical applications, magnetic carriers must be water-based, biocompatible, nontoxic and nonimmunogenic. The first medical application directly applied magnetite or iron powder. The first clinical cancer therapy trial was performed in Germany for the treatment of advanced solid cancer in 14 patients using magnetic microspheres that were about 100 nm in diameter and filled with 4'-epidoxorubicin [146]. The phase I study clearly showed low toxicity of the method and accumulation of MMS in the target area. However, MRI measurements indicated that more than 50% of MMS ended up in the liver [147]. Conceptually, magnetic targeting is a very promising approach. However, there are a number of physical, magnetism-related properties which require careful attention. (i) More responsive magnetic materials with defined and homogenous material properties in a stable and defined oxidation state need to be synthesized. (ii) The size must be small enough that they do not clog the blood vessels through which they are guided to the target organ. (iii) Altering the surface of magnetite with appropriate molecules should be considered, to either increase or decrease the interaction of magnetite with tissues or organs. (iv) The magnetite size must be uniform enough to provide an equal probability of magnetic capture for each magnetite particle. (v) The fate of the particles in the body is an important consideration both for local and systemic short- and long-term toxicity. Thus, further improvements of this hybrid vector were required in future studies.

Overall, we have developed a novel hybrid vector of HVJ-E and magnetic nanoparticles with different surface modifications in an *in vitro* culture system as well as *in vivo*. Further modification of this system with MRI might provide new therapeutic potential to achieve tissue targeting.

## 14.6

## Conclusion

If omnipotent vector systems are eventually developed, gene transfer may harm patients – this is far from therapeutic. An all-encompassing vector system may not be feasible and each vector system must be evaluated with respect to the target disease. In some diseases such as arteriosclerosis obliterans, transient gene expression would be sufficient to cure the disease and sustained gene expression would be detrimental. In other diseases, such as SCID-X1 and hemophilia B, it may be necessary to induce the transformation of only a small population of cells. Cancer gene therapy occupies more than 60% of current human gene therapy approaches and no remarkable successes have been reported in this area to date. When we consider why gene therapy is necessary for cancer treatment, the answer is that gene therapy should be used to inhibit tumor metastasis and suppress the recurrence of cancers. For these purposes, investigations in basic cancer cell biology and technological developments should be promoted much more than at present. The issues in this chapter present a road map for the future technological developments for gene therapy. Thus, technologies in gene therapy should be developed on the basis of analysis of the target tissues, target cells, cellular components and molecules which are relevant to the biology.

## References

- MULLIGAN, R. C., The basic science of gene therapy. *Science* **1993**, *260*, 926–932.
- MARSHALL, E., Gene therapy death prompts review of adenovirus vector. *Science* **1999**, *286*, 2244–2245.
- KAISER, J., Gene therapy. Seeking the cause of induced leukemias in X-SCID trial. *Science* **2003**, *299*, 495.
- RAGNI, M. V., Safe passage: a plea for safety in hemophilia gene therapy. *Mol. Ther.* **2002**, *6*, 436–440.
- LEDLEY, F. D., Nonviral gene therapy: the promise of genes as pharmaceutical products. *Hum. Gene Ther.* **1995**, *6*, 1129–1144.
- KANEDA, Y., Gene therapy: a battle against biological barriers. *Curr. Mol. Med* **2001**, *1*, 493–499.
- MORRAL, N., O'NEAL, W., RICE, K., LELAND, M., KAPLAN, J., PIEDRA, P. A., ZHOU, H., PARKS, R. J., VELJI, R., AGUILAR-CORDOVA, E., WADSWORTH, S., GRAHAM, F. L., KOCHANEK, S., CAREY, K. D., BEAUDET, A. L., Administration of helper-dependent adenoviral vectors and sequential delivery of different vector serotype for long-term liver-directed gene transfer in baboons. *Proc. Natl Acad. Sci. USA* **1999**, *96*, 12816–12821.
- BURNS, J. C., FRIEDMANN, T., DRIEVER, W., BURRASCANO, M., YEE, J. K., Vesicular stomatitis virus G glycoprotein pseudotyped retroviral vectors: concentration to very high titer and efficient gene transfer into mammalian and nonmammalian cells. *Proc. Natl Acad. Sci. USA* **1993**, *90*, 8033–8037.
- NALDINI, L., BLOMER, U., GALLAY, P., ORY, D., MULLIGAN, R., GAGE, F. H., VERMA, I. M., TRONO, D., *In vivo* gene delivery and stable transduction of nondividing cells by a lentiviral vector. *Science* **1996**, *272*, 263–267.
- WU, G. Y., WU, C. H., Receptor-mediated *in vitro* gene transformation by a soluble DNA carrier system. *J. Biol. Chem.* **1987**, *262*, 4429–4432.

- 11 WU, G. Y., WU, C. H., Receptor-mediated gene delivery and expression *in vivo*. *J. Biol. Chem.* **1988**, *263*, 14621–14624.
- 12 WAGNER, E., ZATLOUKAL, K., COTTEN, M., KIRIAPPOS, H., MECHTLER, K., CURIEL, D. T., BIRNSTIEL, M. L., Coupling of adenovirus to transferrin–polylysine/DNA complexes greatly enhances receptor-mediated gene delivery and expression of transfected genes. *Proc. Natl Acad. Sci. USA* **1992**, *89*, 6099–6103.
- 13 FLINT, S. J., ENQUIST, L. W., KRUG, R. M., RACANIELLO, V. R., SKALK, A. M. (Eds.). *Principles of Virology*. ASM Press, Washington, DC, **2000**.
- 14 GALL, J., KASS-EISLER, A., LEINWAND, L., FALCK-PEDERSEN, E., Adenovirus type 5 and 7 capsid chimera: fiber replacement alters receptor tropism without affecting primary immune neutralization epitopes. *J. Virol.* **1996**, *70*, 2116–2123.
- 15 KRASNYYKH, V. N., MIKHEEVA, G. V., DOUGLAS, J. T., CURIEL, D. T., Generation of recombinant adenovirus vectors with modified fibers for altering viral tropism. *J. Virol.* **1996**, *70*, 6839–6846.
- 16 ZABNER, J., CHILLON, M., GRUNST, T., MONINGER, T. O., DAVIDSON, B. L., GREGORY, R., ARMENTANO, D., A chimeric type 2 adenovirus vector with a type 17 fiber enhances gene transfer to human airway epithelia. *J. Virol.* **1999**, *73*, 8689–8695.
- 17 VON SEGGERN, D. J., HUANG, S., FLECK, S. K., STEVENSON, S. C., NEMEROW, G. R., Adenovirus vector pseudotyping in fiber-expressing cell lines: improved transduction of Epstein–Barr virus-transformed B cells. *J. Virol.* **2000**, *74*, 354–362.
- 18 IKOMI, F., HANNA, G. K., SCHMID-SCHONBEIN, G. W., Mechanism of colloidal particle uptake into the lymphatic system: basic study with percutaneous lymphography. *Radiology* **1995**, *196*, 107–113.
- 19 TSUBONIWA, N., MORISHITA, R., HIRANO, T., FUJIMOTO, J., FURUKAWA, S., KIKUMORI, M., OKUYAMA, A., KANEDA, Y., Safety evaluation of Hemagglutinating Virus of Japan-artificial viral envelope liposomes in nonhuman primates. *Hum. Gene Ther.* **2001**, *12*, 469–487.
- 20 ALLEN, T. M., WILLIAMSON, P., SCHLEGEL, R. A., Phosphatidylserine as a determinant of reticuloendothelial recognition of liposome models of the erythrocyte surface. *Proc. Natl Acad. Sci. USA* **1988**, *85*, 8067–8071.
- 21 LI, S., HUANG, L., *In vivo* gene transfer via intravenous administration of cationic lipid–protamine–DNA (LPD) complexes. *Gene Ther.* **1997**, *4*, 891–900.
- 22 LI, S., RIZZO, M. A., BHATTACHARYA, S., HUANG, L., Characterization of cationic lipid–protamine–DNA (LPD) complexes for intravenous gene delivery. *Gene Ther.* **1998**, *5*, 930–937.
- 23 HUANG, S. K., LEE, K. D., HONG, K., FRIEND, D. S., PAPAHAJIOPOULOS, D., Microscopic localization of sterically stabilized liposomes in colon carcinoma-bearing mice. *Cancer Res.* **1992**, *52*, 5135–5143.
- 24 LITZINGER, D. C., BUITING, A. M., VAN ROOIJEN, N., HUANG, L., Effect of liposome size on the circulation time and intraorgan distribution of amphipathic poly(ethylene glycol)-containing liposomes. *Biochim. Biophys. Acta* **1994**, *1190*, 99–107.
- 25 BLESSING, T., KURSA, M., HOLZHAUSER, R., KIRCHEIS, R., WAGNER, E., Different strategies for formation of pegylated EGF-conjugated PEI/DNA complexes for targeted gene delivery. *Bioconjug. Chem.* **2001**, *12*, 529–537.
- 26 CHOI, Y. H., LIU, F., CHOI, J. S., KIM, S. W., PARK, J. S., Characterization of a targeted gene carrier, lactose-polyethylene glycol-grafted poly-L-lysine and its complex with plasmid DNA. *Hum. Gene Ther.* **1999**, *10*, 2657–2665.
- 27 REDDY, J. A., ABBURI, C., HOFLAND, H., HOWARD, S. J., VLAHOV, I., WILS, P., LEAMON, C. P., Folate-targeted, cationic liposome-mediated gene transfer into disseminated peritoneal tumors. *Gene Ther.* **2002**, *9*, 1542–1550.

- 28 PENSIERO, M. N., WYSOCKI, C. A., NADER, K., KIKUCHI, G. E., Development of amphotropic murine retrovirus vectors resistant to inactivation by human serum. *Hum. Gene Ther.* **1996**, *7*, 1095–1101.
- 29 OROSZIAN, S., NOWINSKI, R. C., Lysis of retroviruses with monoclonal antibodies against viral envelope proteins. *Virology* **1980**, *101*, 296–299.
- 30 DICKSON, G., *Molecular and Cell Biology of Human Gene Therapeutics*. Chapman & Hall, London, **1995**.
- 31 ESLAMI, M. H., GANGADHARAN, S. P., SUI, X., RHYNHART, K. K., SNYDER, R. O., CONTE, M. S., Gene delivery to *in situ* veins: differential effects of adenovirus and adeno-associated viral vectors. *J. Vasc. Surg.* **2000**, *31*, 1149–1159.
- 32 WHEELER, C. J., FELGNER, P. L., TSAI, Y. J., MARSHALL, J., SUKHU, L., DOH, S. G., HARTIKKA, J., NIETUPSKI, J., MANTHORPE, M., NICHOLS, M., PLEWE, M., LIANG, X., NORMAN, J., SMITH, A., CHENG, S. H., A novel cationic lipid greatly enhances plasmid DNA delivery and expression in mouse lung. *Proc. Natl Acad. Sci. USA* **1996**, *93*, 11454–11459.
- 33 SAWA, Y., SUZUKI, K., BAI, H. Z., SHIRAKURA, R., MORISHITA, R., KANEDA, Y., MATSUDA, H., Efficiency of *in vivo* gene transfection into transplanted rat heart by coronary infusion of HVJ liposome. *Circulation* **1995**, *92*, 479–482.
- 34 YONEMITSU, Y., KANEDA, Y., MORISHITA, R., NAKAGAWA, K., NAKASHIMA, Y., SUEISHI, K., Characterization of *in vivo* gene transfer into the arterial wall mediated by the Sendai virus (hemagglutinating virus of Japan) liposomes: an effective tool for the *in vivo* study of arterial diseases. *Lab. Invest.* **1996**, *75*, 313–323.
- 35 SETH, P., Mechanism of adenovirus-mediated endosome lysis: role of the intact adenovirus capsid structure. *Biochem. Biophys. Res. Commun.* **1994**, *205*, 1318–1324.
- 36 GREBER, U. F., WEBSTER, P., WEBER, J., HELENIUS, A., The role of the adenovirus protease on virus entry into cells. *EMBO J.* **1996**, *15*, 1766–1777.
- 37 MAEDA, T., OHNISHI, S., Activation of influenza virus by acidic media causes hemolysis and fusion of erythrocytes. *FEBS Lett.* **1980**, *122*, 283–287.
- 38 MARSH, M., BOLZAU, E., HELENIUS, A., Penetration of Semliki Forest virus from acidic prelysosomal vacuoles. *Cell* **1983**, *32*, 931–940.
- 39 BLUMENTHAL, R., BALI-PURI, A., WALTER, A., COVELL, D., EIDELMAN, O., pH-dependent fusion of vesicular stomatitis virus with Vero cells. Measurement by dequenching of octadecyl rhodamine fluorescence. *J. Biol. Chem.* **1987**, *262*, 13614–13619.
- 40 OKADA, Y., Sendai virus-induced cell fusion. *Methods Enzymol.* **1993**, *221*, 18–41.
- 41 MCCLURE, M. O., SOMMERFELT, M. A., MARSH, M., WEISS, R. A., The pH independence of mammalian retrovirus infection. *J. Gen. Virol.* **1990**, *71*, 767–773.
- 42 MCCLURE, M. O., MARSH, M., WEISS, R. A., Human immunodeficiency virus infection of CD4-bearing cells occurs by a pH-independent mechanism. *EMBO J.* **1988**, *7*, 513–518.
- 43 WAGNER, E., PLANK, C., ZATLOUKAL, K., COTTEN, M., BIRNSTIEL, M. L., Influenza virus hemagglutinin HA-2 N-terminal fusogenic peptides augment gene transfer by transferrin-polylysine-DNA complexes: toward a synthetic virus-like gene-transfer vehicle. *Proc. Natl Acad. Sci. USA* **1992**, *89*, 7934–7938.
- 44 IZAURRALDE, E., KANN, M., PANTE, N., SODEIK, B., HOHN, T., Viruses, microorganisms and scientists meet the nuclear pore. Leysin, VD, Switzerland, February 26–March 1, 1998. *EMBO J.* **1999**, *18*, 289–296.
- 45 GREBER, U. F., KASAMATSU, H., Nuclear targeting of SV40 and adenovirus. *Trends Cell Biol.* **1996**, *6*, 189–195.
- 46 GREBER, U. F., SUOMALAINEN, M., STIDWILL, R. P., BOUCKE, K., EBERSOLD, M. W., HELENIUS, A., The

- role of the nuclear pore complex in adenovirus DNA entry. *EMBO J.* **1997**, *16*, 5998–6007.
- 47 FRITZ, J. D., HERWEIJER, H., ZHANG, G., WOLFF, J. A., Gene transfer into mammalian cells using histone-condensed plasmid DNA. *Hum. Gene Ther.* **1996**, *7*, 1395–1404.
- 48 SEBESTYEN, M. G., LUDTKE, J. J., BASSIK, M. C., ZHANG, G., BUDKER, V., LUKHTANOV, E. A., HAGSTROM, J. E., WOLFF, J. A., DNA vector chemistry: the covalent attachment of signal peptides to plasmid DNA. *Nat. Biotechnol.* **1998**, *16*, 80–85.
- 49 ZANTA, M. A., BELGUISE-VALLADIER, P., BEHR, J. P., Gene delivery: a single nuclear localization signal peptide is sufficient to carry DNA to the cell nucleus. *Proc. Natl Acad. Sci. USA* **1999**, *96*, 91–96.
- 50 DEAN, D. A., Import of plasmid DNA into the nucleus is sequence specific. *Exp. Cell Res.* **1997**, *230*, 293–302.
- 51 WILSON, G. L., DEAN, B. S., WANG, G., DEAN, D. A., Nuclear import of plasmid DNA in digitonin-permeabilized cells requires both cytoplasmic factors and specific DNA sequences. *J. Biol. Chem.* **1999**, *274*, 22025–22032.
- 52 SMERDOU, C., LILJESTROM, P., Alphavirus vectors: from protein production to gene therapy. *Gene Ther. Reg.* **2000**, *1*, 33–64.
- 53 BREDENBEEK, P. J., FROLOV, I., RICE, C. M., SCHLESINGER, S., Sindbis virus expression vectors: packaging of RNA replicons by using defective helper RNAs. *J. Virol.* **1993**, *67*, 6439–6446.
- 54 LILJESTRÖM, P., GAROFF, H., A new generation of animal cell expression vectors based on the Semliki Forest virus replicon. *Biotechnology* **1991**, *9*, 1356–1361.
- 55 IVICS, Z., HACKETT, P. B., PLASTERK, R. H., IZSVAK, Z., Molecular reconstruction of Sleeping Beauty, a Tc1-like transposon from fish, and its transposition in human cells. *Cell* **1997**, *91*, 501–510.
- 56 SUMMERFORD, C., BARTLETT, J. S., SAMULSKI, R. J., Adeno-associated viral vectors and successful gene therapy, the gap is closing. *Gene Ther. Reg.* **2000**, *1*, 9–32.
- 57 RUTLEDGE, E. A., RUSSELL, D. W., Adeno-associated virus vector integration junctions. *J. Virol.* **1997**, *71*, 8429–8436.
- 58 LUPTON, S., LEVINE, A. J., Mapping genetic elements of Epstein–Barr virus that facilitate extrachromosomal persistence of Epstein–Barr virus-derived plasmids in human cells. *Mol. Cell. Biol.* **1985**, *5*, 2533–2542.
- 59 YATES, J. L., WARREN, N., SUGDEN, B., Stable replication of plasmids derived from Epstein–Barr virus in various mammalian cells. *Nature* **1985**, *313*, 812–815.
- 60 JANKELEVICH, S., KOLMAN, J. L., BODNAR, J. W., MILLER, G., A nuclear matrix attachment region organizes the Epstein–Barr viral plasmid in Raji cells into a single DNA domain. *EMBO J.* **1992**, *11*, 1165–1176.
- 61 SAEKI, Y., WATAYA-KANEDA, M., TANAKA, K., KANEDA, Y., Sustained transgene expression *in vitro* and *in vivo* using an Epstein–Barr virus replicon vector system combined with HVJ liposomes. *Gene Ther.* **1998**, *5*, 1031–1037.
- 62 KANEDA, Y., SAEKI, Y., NAKABAYASHI, M., ZHOU, W. Z., KANEDA, M. W., MORISHITA, R., Enhancement of transgene expression by cotransfection of oriP plasmid with EBNA-1 expression vector. *Hum. Gene Ther.* **2000**, *11*, 471–479.
- 63 PALMER, T. D., ROSMAN, G. J., OSBORNE, W. R., MILLER, A. D., Genetically modified skin fibroblasts persist long after transplantation but gradually inactivate introduced genes. *Proc. Natl Acad. Sci. USA* **1991**, *88*, 1330–1334.
- 64 HARBERS, K., JAHNER, D., JAENISCH, R., Microinjection of cloned retroviral genomes into mouse zygotes: integration and expression in the animal. *Nature* **1981**, *293*, 540–542.
- 65 JAHNER, D., STUHLMANN, H., STEWART, C. L., HARBERS, K., LOHLER, J., SIMON, I., JAENISCH, R., *De novo* methylation and expression of retroviral genomes during mouse

- embryogenesis. *Nature* **1982**, *298*, 623–628.
- 66 GROSSMAN, M., RAPER, S. E., KOZARSKY, K., STEIN, E. A., ENGELHARDT, J. F., MULLER, D., LUPIEN, P. J., WILSON, J. M., Successful *ex vivo* gene therapy directed to liver in a patient with familial hypercholesterolaemia. *Nat. Genet* **1994**, *6*, 335–341.
  - 67 ROEDER, R. G., The role of general initiation factors in transcription by RNA polymerase II. *Trends Biochem. Sci.* **1996**, *21*, 327–335.
  - 68 TYLER, J. K., KADONAGA, J. T., The “dark side” of chromatin remodeling: repressive effects on transcription. *Cell* **1999**, *99*, 443–446.
  - 69 LUO, R. X., DEAN, D. C., Chromatin remodeling and transcriptional regulation. *J. Natl. Cancer Inst.* **1999**, *91*, 1288–1294.
  - 70 KUO, M. H., ALLIS, C. D., Roles of histone acetyltransferases and deacetylases in gene regulation. *BioEssays* **1998**, *20*, 615–626.
  - 71 CHEN, W. Y., BAILEY, E. C., McCUNE, S. L., DONG, J. Y., TOWNES, T. M., Reactivation of silenced, virally transduced genes by inhibitors of histone deacetylase. *Proc. Natl Acad. Sci. USA* **1997**, *94*, 5798–5803.
  - 72 DION, L. D., GOLDSMITH, K. T., TANG, D. C., ENGLER, J. A., YOSHIDA, M., GARVER, R. I., JR., Amplification of recombinant adenoviral transgene products occurs by inhibition of histone deacetylase. *Virology* **1997**, *231*, 201–209.
  - 73 YAMANO, T., URA, K., MORISHITA, R., NAKAJIMA, H., MONDEN, M., KANEDA, Y., Amplification of transgene expression *in vitro* and *in vivo* using a novel inhibitor of histone deacetylase. *Mol. Ther.* **2000**, *1*, 574–580.
  - 74 NAN, X., NG, H. H., JOHNSON, C. A., LAHERTY, C. D., TURNER, B. M., EISENMAN, R. N., BIRD, A., Transcriptional repression by the methyl-CpG-binding protein MeCP2 involves a histone deacetylase complex. *Nature* **1998**, *393*, 386–389.
  - 75 WOLFFE, A. P., Transcriptional control: imprinting insulation. *Curr. Biol* **2000**, *10*, R463–465.
  - 76 STEINWAERDER, D. S., LIEBER, A., Insulation from viral transcriptional regulatory elements improves inducible transgene expression from adenovirus vectors *in vitro* and *in vivo*. *Gene Ther.* **2000**, *7*, 556–567.
  - 77 MULLER, J., Transcriptional control: The benefits of selective insulation. *Curr. Biol* **2000**, *10*, R241–244.
  - 78 KANEDA, Y., SAEKI, Y., and MORISHITA, R., Gene therapy using HVJ-liposomes: the best of both worlds? *Mol. Med. Today* **1999**, *5*, 298–303.
  - 79 DZAV, V., MANN, M. J., MORISHITA, R., KANEDA, Y., Fusigenic viral liposome for gene therapy in cardiovascular diseases. *Proc. Natl. Acad. Sci. USA* **1996**, *93*, 11421–11425.
  - 80 NAKAMURA, N., HART, D. A., FRANK, C. B., MARCHUK, L. L., SHRIVE, N. G., OTA, N., TAIRA, T., YOSHIKAWA, H., KANEDA, Y., Efficient transfer of intact pligonucleotides into the nucleus of ligament scar fibroblasts by HVJ-cationic liposomes is correlated with effective antisense gene inhibition. *J. Biochem.* **2001**, *129*, 755–759.
  - 81 HIRANO, T., FUJIMOTO, J., UEKI, T., YAMAMOTO, H., IWASAKI, T., MORISHITA, R., KANEDA, Y., TAKAHASHI, H., OKAMOTO, E., Persistent gene expression in rat liver *in-vivo* by repetitive transfections using HVJ-liposome. *Gene Ther.* **1998**, *5*, 459–464.
  - 82 ZENKE, M., STEINLEIN, P., WAGNER, E., COTTON, M., BEUG, H., BIRNSTIEL, M. L., Receptor-mediated endocytosis of transferrin–polycation conjugates: an efficient way to introduce DNA into hematopoietic cells. *Proc. Natl Acad. Sci. USA* **1990**, *87*, 3655–3659.
  - 83 BAGAI, S., SARKER, D. P., Targeted delivery of hygromycin B using reconstituted Sendai viral envelopes lacking hemagglutinin–neuraminidase. *FEBS Lett.* **1993**, *326*, 183–188.
  - 84 RAMANI, K., BORA, R. S., KUMAR, M., TYAGI, S. K., SARKAR, D. P., Novel gene delivery to liver cells using engineered virosomes. *FEBS Lett.* **1997**, *404*, 164–168.

- 85 RAMANI, K., HASSAN, O., VENKAIAH, B., HASNAIN, S. E., SARKAR, D. P., Site-specific gene delivery *in vivo* through engineered Sendai virus envelopes. *Proc. Natl Acad. Sci. USA* **1998**, *95*, 11886–11890.
- 86 SUZUKI, K., NAKASHIMA, H., SAWA, Y., MORISHITA, R., MATSUDA, H., KANEDA, Y., Reconstituted fusion liposomes for gene transfer *in vitro* and *in vivo*. *Gene Ther. Reg.* **2000**, *1*, 65–77.
- 87 KANEDA, Y., NAKAJIMA, T., NISHIKAWA, T., YAMAMOTO, S., IKEGAMI, H., SUZUKI, N., NAKAMURA, H., MORISHIRA, R., KOTANI, H., Hemagglutinating virus of Japan (HVJ) envelope vector as a versatile gene delivery system. *Mol. Ther.* **2002**, *6*, 219–226.
- 88 YEAGLE, P. L., The fusion of Sendai virus. In *Viral Fusion Mechanisms*, BENTY, J. (Ed.), CRC Press, London, **1993**, pp. 313–334.
- 89 GHOSH, J. K., PEISAJOVICH, S. G., SHAI, Y., Sendai virus internal fusion peptide: structural and functional characterization and a plausible mode of viral entry inhibition. *Biochemistry* **2000**, *39*, 1581–92.
- 90 CHEN, Y., WEBSTER, R. G., WOODLAND, D. L., Induction of CD8<sup>+</sup> T cell responses to dominant and subdominant epitopes and protective immunity to Sendai virus infection by DNA vaccination. *J. Immunol.* **1998**, *160*, 2425–2432.
- 91 RACE, E., STEIN, C. A., WIGG, M. D., BAKSH, A., ADDAWE, M., FREZZA, P., OXFORD, J. S., A multistep procedure for the chemical inactivation of human immunodeficiency virus for use as an experimental vaccine. *Vaccine* **1995**, *13*, 1567–1575.
- 92 KANEDA, Y., In *Gene Therapy Protocol*, 2nd edn. (MORGAN, J. R. (Ed.)), Humana Press, Totowa, NJ, **2002**, pp. 63–72.
- 93 YONEMITSU, Y., KITSON, C., FERRARI, S., FARLEY, R., GRIESENBACH, U., JUDA, D., STEEL, R., SCHEID, P., ZHU, J., JEFFERY, P., ALTON, E. F. W., Efficient gene transfer to airway epithelium using recombinant Sendai virus. *Nat. Biotechnol.* **2000**, *18*, 970–973.
- 94 DORSETT, Y., TUSCHL, T., siRNAs: applications in functional genomics and potential as therapeutics. *Nat. Rev. Drug Discov.* **2004**, *3*, 318–329.
- 95 TIJSTERMAN, M., PLASTERK, R. H., Dicers at RISC; the mechanism of RNAi. *Cell* **2004**, *117*, 1–3.
- 96 MIYAGISHI, M., HAYASHI, M., TAIRA, K., Comparison of the suppressive effects of antisense oligonucleotides and siRNAs directed against the same targets in mammalian cells. *Antisense Nucleic Acid Drug Dev.* **2003**, *13*, 1–7.
- 97 YOKOTA, T., MIYAGISHI, M., HINO, T., MATSUMURA, R., TASINATO, A., URUSHITANI, M., RAO, R. V., TAKAHASHI, R., BREDESEN, D. E., TAIRA, K., MIZUSAWA, H., siRNA-based inhibition specific for mutant SOD1 with single nucleotide alternation in familial ALS, compared with ribozyme and DNA enzyme. *Biochem. Biophys. Res. Commun.* **2004**, *314*, 283–291.
- 98 SLOUD, M., Ribozyme- and siRNA-mediated mRNA degradation: a general introduction. *Methods Mol. Biol.* **2004**, *252*, 1–8.
- 99 ITOH, Y., KAWAMATA, Y., HARADA, M., KOBAYASHI, M., FUJII, R., FUKUSUMI, S., OGI, K., HOSOYA, M., TANAKA, Y., UEJIMA, H., TANAKA, H., MARUYAMA, M., SATOH, R., OKUBO, S., KIZAWA, H., KOMATSU, H., MATSUMURA, F., NOGUCHI, Y., SHINOHARA, T., HINUMA, S., FUJISAWA, Y., FUJINO, M., Free fatty acids regulate insulin secretion from pancreatic beta cells through GPR40. *Nature* **2003**, *422*, 173–176.
- 100 ISHII, T., OHNUMA, K., MURAKAMI, A., TAKASAWA, N., YAMOCHI, T., IWATA, S., UCHIYAMA, M., DANG, N. H., TANAKA, H., MORIMOTO, C., SS-A/Ro52, an autoantigen involved in CD28-mediated IL-2 production. *J. Immunol.* **2003**, *170*, 3653–3661.
- 101 NAKAMURA, H., KIMURA, T., IKEGAMI, H., OGITA, K., KOHYAMA, S., SHIMOYA, K., TSUJIE, T., KOYAMA, M., KANEDA, Y., MURATA, Y., Highly-efficient and minimally invasive *in vivo* gene transfer to the mouse uterus by Hemagglutinating Virus of Japan



- (HVJ) envelope vector. *Mol. Hum. Reprod.* **2003**, *9*, 603–609.
- 102** SHIMAMURA, M., MORISHITA, R., ENDOH, M., OSHIMA, K., AOKI, M., KURINAMI, H., WAGURI, S., UCHIYAMA, Y., OGIHARA, T., KANEDA, Y., MORISHITA, R., HVJ-envelope vector for gene transfer into central nervous system. *Biochem. Biophys. Res. Commun.* **2003**, *300*, 464–471.
- 103** VILELLA, R., BENITEZ, D., MILA, J., VIALTA, A., RULL, R., CUELLAR, F., CONILL, C., VIDAL-SICART, S., COSTA, J., YACHI, E., PALOU, J., MALVEHY, J., LUIG, S., MARTI, R., MELLADO, B., CASTEL, T., Treatment of patients with progressive unresectable metastatic melanoma with a heterologous polyvalent melanoma whole cell vaccine. *Int. J. Cancer* **2003**, *106*, 626–631.
- 104** FIGDOR, C. G., DE VRIES, I. J., LESTERHUIS, W. J., MELIEF, C. J., Dendritic cell immunotherapy: mapping the way. *Nat. Med.* **2004**, *10*, 475–480.
- 105** NESTLE, F. O., ALIJAGIC, S., GILLIET, M., SUN, Y., GRABBE, S., DUMMER, R., BURG, G., SCHADENDORF, D., Vaccination of melanoma patients with peptide- or tumor lysate-pulsed dendritic cells. *Nat. Med.* **1998**, *4*, 328–332.
- 106** THURNER, B., HAENDLE, I., RODER, C., DIECKMANN, D., KEIKAVOUSSI, P., JONULEIT, H., BENDER, A., MACZEK, C., SCHREINER, D., VON DEN DRIESCH, P., BROCKER, E. B., STEINMAN, R. M., ENK, A., KAMPGEN, E., SCHULER, G., Vaccination with mage-3A1 peptide-pulsed mature, monocyte-derived dendritic cells expands specific cytotoxic T cells and induces regression of some metastases in advanced stage IV melanoma. *J. Exp. Med.* **1999**, *190*, 1669–1678.
- 107** GILBOA, E., NATR, S. K., LYERLY, H. K., Immunotherapy of cancer with dendritic-cell-based vaccines. *Cancer Immunol. Immunother.* **1998**, *46*, 82–87.
- 108** ENGLEMAN, E. G., Dendritic cells: potential role in cancer therapy. *Cytotechnology* **1997**, *25*, 1–8.
- 109** ARTHUR, J. F., BUTTERFIELD, L. H., ROTH, M. D., BUI, L. A., KIERTSCHER, S. M., LAU, R., DUBINETT, S., GLASPY, J., MCBRIDE, W. H., ECONOMOUS, J. S., A comparison of gene transfer methods in human dendritic cells. *Cancer Gene Ther.* **1997**, *4*, 17–25.
- 110** KAPLAN, J. M., YU, Q., PIRAINO, S. T., PENNINGTON, S. E., SHANKARA, S., WOODWORTH, L. A., ROBERTS, B. L., Induction of antitumor immunity with dendritic cells transduced with adenovirus vector-encoding endogenous tumor-associated antigens. *J. Immunol.* **1999**, *163*, 699–707.
- 111** PECHER, G., SPAHN, G., SCHIRRMANN, T., KULBE, H., ZIEGNER, M., SCHENK, J. A., SANDIG, V., Mucin gene (MUC1) transfer into human dendritic cells by cationic liposomes and recombinant adenovirus. *Anticancer Res.* **2001**, *21*, 2591–2596.
- 112** YANG, S., KITTLESEN, D., SLINGLUFF, JR., C. L., VERVAERT, C. E., SEIGLER, H. F., DARROW, T. L., Dendritic cells infected with a vaccinia vector carrying the human gp100 gene simultaneously present multiple specificities and elicit high-affinity T cells reactive to multiple epitopes and restricted by HLA-A2 and -A3. *J. Immunol.* **2000**, *164*, 4204–4211.
- 113** PRABAKARAN, I., MENON, C., XU, S., GOMEZ-YAFAL, A., CZERNIECKI, B. J., FRAKER, D. L., Mature CD83<sup>+</sup> dendritic cells infected with recombinant gp100 vaccinia virus stimulate potent antimelanoma T cells. *Ann. Surg. Oncol.* **2002**, *9*, 411–418.
- 114** AKIYAMA, Y., MARUYAMA, K., WATANABE, M., YAMAUCHI, K., Retroviral-mediated IL-12 gene transduction into human CD34<sup>+</sup> cell-derived dendritic cells. *Int. J. Oncol.* **2002**, *21*, 509–514.
- 115** BELLO-FERNANDEZ, C., MATYASH, M., STROBL, H., PICKL, W. F., MAJDIC, O., LYMAN, S. D., KNAPP, W., Efficient retrovirus-mediated gene transfer of dendritic cells generated from CD34<sup>+</sup> cord blood cells under serum-free conditions. *Hum. Gene Ther.* **1997**, *8*, 1651–1658.

- 116 BOON, T., CEROTTINI, J. C., VAN DEN EYNDE, B., VAN DER BRUGGEN, P., VAN PEL, A., Tumor antigens recognized by T lymphocytes. *Annu. Rev. Immunol.* **1994**, *12*, 337–365.
- 117 KAWAKAMI, Y., ROSENBERG, S. A., Human tumor antigens recognized by T-cells. *Immunol. Res.* **1997**, *16*, 313–339.
- 118 GONG, J., CHEN, D., KASHIWABA, M., KUFFE, D., Induction of antitumor activity by immunization with fusions of dendritic and carcinoma cells. *Nat. Med.* **1997**, *3*, 558–561.
- 119 WANG, J., SAFFOLD, S., CAO, X., KRAUSS, J., CHEN, W., Eliciting T cell immunity against poorly immunogenic tumors by immunization with dendritic cell–tumor fusion vaccines. *J. Immunol.* **1998**, *161*, 5516–5524.
- 120 XU, S., KOSKI, G. K., FARIES, M., BEDROSIAN, I., MICK, R., MAEURER, M., CHEEVER, M. A., COHEN, P. A., CZERNIECKI, B. J., Rapid high efficiency sensitization of CD8<sup>+</sup> T cells to tumor antigens by dendritic cells leads to enhanced functional avidity and direct tumor recognition through an IL-12-dependent mechanism. *J. Immunol.* **2003**, *171*, 2251–2261.
- 121 KABANOV, A. V., KABANOV, V. A., DNA complexes with polycations for the delivery of genetic material into cells. *Bioconjug. Chem.* **1995**, *6*, 7–20.
- 122 LEDLEY, F. D., Nonviral gene therapy: the promise of genes as pharmaceutical products. *Hum. Gene Ther.* **1995**, *6*, 1129–1144.
- 123 TOMLINSON, E., ROLLAND, A. P., Controllable gene therapy. Pharmaceuticals of non-viral gene delivery systems. *J. Control. Release* **1996**, *39*, 357–372.
- 124 TOKUNAGA, N., NAGAYA, N., SHIRAI, M., TANAKA, E., ISHIBASHI-UEDA, H., HARADA-SHIBA, M., KANDA, M., ITO, T., SHIMIZU, W., TABATA, Y., UEMATSU, M., NISHIGAMI, K., SANO, S., KANGAWA, K., MORI, H., Adrenomedullin gene transfer induces therapeutic angiogenesis in a rabbit model of chronic hind limb ischemia: benefits of a novel nonviral vector, gelatin. *Circulation.* **2004**, *109*, 526–531.
- 125 TABATA, Y., IKADA, Y., Macrophage activation through phagocytosis of muramyl dipeptide encapsulated in gelatin microspheres. *J. Pharm. Pharmacol.* **1987**, *39*, 698–704.
- 126 NAGAYA, N., KANGAWA, K., KANDA, M., UEMATSU, M., HORIO, T., FUKUYAMA, N., HINO, J., HARADA-SHIBA, M., OKUMURA, H., TABATA, Y., MOCHIZUKI, N., CHIBA, Y., NISHIOKA, K., MIYATAKE, K., ASAHARA, T., HARA, H., MORI, H., Hybrid cell-gene therapy for pulmonary hypertension based on phagocytosing action of endothelial progenitor cells. *Circulation.* **2003**, *108*, 889–895.
- 127 MIMA, H., TOMOSHIGE, R., KANAMORI, T., TABATA, Y., YAMAMOTO, S., ITO, S., TAMAI, K., KANEDA, Y., Biocompatible polymer enhances the *in vitro* and *in vivo* transfection efficiency of HVJ envelope vector. *J. Gene Med.* **2005**, *7*, 888–897.
- 128 SAEKI, Y., MATSUMOTO, N., NAKANO, Y., MORI, M., AWAI, K., KANEDA, Y., Development and characterization of cationic liposomes conjugated with HVJ (Sendai virus): reciprocal effect of cationic lipid for *in vitro* and *in vivo* gene transfer. *Hum. Gene Ther.* **1997**, *8*, 2133–2141.
- 129 SCHERER, F., ANTON, M., SCHILLINGER, U., HENKE, J., BERGEMANN, C., KRÜGER, A., GÄNSBACHER, B., PLANK, C., Magnetofection: enhancing and targeting gene delivery by magnetic force *in vitro* and *in vivo*. *Gene Ther.* **2002**, *9*, 102–109.
- 130 MISLICK, K. A., BALDESCHWIELER, J. D., Evidence for the role of proteoglycans in cation-mediated gene transfer. *Proc. Natl Acad. Sci. USA* **1996**, *93*, 12349–12354.
- 131 BOUSSIF, O., LEZOUALC'H, F., ZANTA, M. A., MERGNY, M. D., SCHERMAN, D., DEMENEIX, B., BEHR, J. P., A versatile vector for gene and oligonucleotide transfer into cells in culture and *in vivo*: polyethylenimine. *Proc. Natl Acad. Sci. USA* **1995**, *92*, 7297–7301.

- 132 BIEBER, T., MEISSNER, W., KOSTIN, S., NIEMANN, A., ELSASSER, H. P., Intracellular route and transcriptional competence of polyethylenimine–DNA complexes. *J. Control. Release* **2002**, *82*, 441–454.
- 133 MERDAN, T., KUNATH, K., FISCHER, D., KOPECEK, J., KISSEL, T., Intracellular processing of poly(ethylene imine)/ribozyme complexes can be observed in living cells by using confocal laser scanning microscopy and inhibitor experiments. *Pharm. Res.* **2002**, *19*, 140–146.
- 134 MELLMAN, I., Endocytosis and molecular sorting. *Annu. Rev. Cell Dev. Biol.* **1996**, *12*, 575–625.
- 135 NICHOLS, B. J., LIPPINCOTT-SCHWARTZ, J., Endocytosis without clathrin coats. *Trends Cell Biol.* **2001**, *11*, 406–412.
- 136 GUMBLETON, M., ABULROB, A. G., CAMPBELL, L., Caveolae: an alternative membrane transport compartment. *Pharm. Res.* **2000**, *17*, 1035–1048.
- 137 ARBAB, A. S., YOCUM, G. T., KALISH, H., JORDAN, E. K., ANDERSON, S. A., KHAKOO, A. Y., READ, E. J., FRANK, J. A., Efficient magnetic cell labeling with protamine sulfate complexed to ferumoxides for cellular MRL. *Blood* **2004**, *104*, 1217–1223.
- 138 BULTE, J. W., DOUGLAS, T., WITWER, B., ZHANG, S. C., STRABLE, E., LEWIS, B. K., ZYWICKE, H., MILLER, B., VAN GELDEREN, P., MOSKOWITZ, B. M., DUNCAN, I. D., FRANK, J. A., Magnetodendrimers allow endosomal magnetic labeling and *in vivo* tracking of stem cells. *Nat. Biotechnol.* **2001**, *19*, 1141–1147.
- 139 SCHERER, F., ANTON, M., SCHILLINGER, U., HENKE, J., BERGEMANN, C., KRUGER, A., GANSBACHER, B., PLANK, C., Magnetofection: enhancing and targeting gene delivery by magnet force *in vitro* and *in vivo*. *Gene Ther.* **2002**, *9*, 102–109.
- 140 HUTH, S., LAUSIER, J., GERSTING, S. W., RUDOLPH, C., PLANK, C., WELSCH, U., ROSENECKER, J., Insights into the mechanism of magnetofection using PEI-based magnetofections for gene transfer. *J. Gene Med.* **2004**, *6*, 923–936.
- 141 BULL, B. S., HUSE, W. M., BRAUER, F. S., KORPMAN, R. A., Heparin therapy during extracorporeal circulation. II. The use of a dose–response curve to individualize heparin and protamine dosage. *J. Thorac. Cardiovasc. Surg.* **1975**, *69*, 685–659.
- 142 GERVIN, A. S., Complications of heparin therapy. *Surg. Gynecol. Obstet.* **1975**, *140*, 789–796.
- 143 LUBBE, A. S., BERGEMANN, C., RIESS, H., SCHRIEVER, F., REICHARDT, P., POSSINGER, K., MATTHIAS, M., DORKEN, B., HERRMANN, F., GURTNER, R., HOHENBERGER, P., HAAS, N., SOHR, R., SANDER, B., LEMKE, A. J., OHLENDORF, D., HUHN, W., HUHN, D., Clinical experiences with magnetic drug targeting: a phase I study with 4'-epidoxorubicin in 14 patients with advanced solid tumors. *Cancer Res.* **1996**, *56*, 4686–4693.
- 144 LUBBE, A. S., BERGEMANN, C., HUHN, W., FRICKE, T., RIESS, H., BROCK, J. W., HUHN, D., Pre-clinical experiences with magnetic drug targeting: tolerance and efficacy. *Cancer Res.* **1996**, *56*, 4694–4701.

## 15

# Nanotoxicology of Synthetic Gene Transfer Vectors: Poly(ethyleneimine)- and Polyfectin-mediated Membrane Damage and Apoptosis in Human Cell Lines

*Seyed M. Moghimi*

### 15.1

#### Introduction

Viral vectors are extremely efficient in transfecting cells; however, they can induce severe immunotoxicity and inflammatory responses, which restrain repeated administration [1]. The death of Jesse Gelsinger in September 1999 during an experimental adenoviral gene therapy trial conducted at the University of Pennsylvania is a grim reminder of these adverse effects. The autopsy findings confirmed that the adenoviral vector initiated an unusual and deadly immune system response that led to multiple organ failure and adult respiratory distress syndrome, and ultimately brain death. Another potential complication is insertional mutagenesis, which could pose additional risks in gene therapy programmes involving retroviruses, as evident from stem cell gene therapy trials for treatment of X-linked severe combined immunodeficiency disease at Necker Hospital, Paris, France [1–3]. Of 17 patients who participated in this programme, virtually all showed major improvement. However, three developed leukemia-like conditions; of these, one subsequently died. These issues, together with the limited loading capacity and difficulties in large-scale production of viral vectors, have generated a surge in design and engineering of synthetic cationic nonviral gene transfer systems. Examples include a plethora of cationic lipids (lipofectins) and polycations (polyfectins) such as poly(L-lysine) and poly(ethyleneimine) (PEI) in linear, branched and dendrimeric form, and variations thereof [poly(ethylene glycol)- and ligand-tagged] [4–6]. These materials can condense genetic materials into nanostructures readily amenable for transfection. PEIs have received considerable attention in gene transfer protocols as a result of excellent transfection efficiencies [4–6].

This chapter briefly reviews the structure and properties of PEI-based transfectants. PEI is also cytotoxic, but the molecular basis of its cytotoxicity is poorly understood and therefore not discussed in detail in previous reviews. The major part of this chapter critically examines recent breakthroughs in understanding of the molecular mechanisms of PEI-mediated cytotoxicity.

## 15.2

### PEI as a Nonviral Vector

#### 15.2.1

##### Structure and Properties of PEI and PEI–DNA Complexes

PEI exists in both linear and branched form and is available in a broad range of molecular weights (from a few hundred Daltons to 1500 kDa). Ring-opening polymerization of 2-substituted 2-oxazoline leads to formation of poly(*N*-formalethylenimine), which is then hydrolyzed to yield linear PEI. In contrast, the branched form of PEI is produced by acid-catalyzed polymerization of aziridine.

PEI is capable of condensing DNA and RNA into stable toroidal and globular nanostructures mainly via electrostatic interactions, as supported by a range of biophysical characterization studies [7–10]. The physicochemical nature and stability of the PEI–DNA complex (polyplex) is dependent on a number of factors, including PEI type, molecular weight, charge density, ionic strength of the media, the tertiary structure of nucleic acids (e.g. linear versus supercoiled DNA), polymer:DNA ratio and even the sequence of component addition, and these are reviewed recently in detail by Neu and coworkers [6]. For example, low-molecular-weight PEIs (2 kDa and smaller) form larger polyplexes (greater than 500 nm) than their high-molecular-weight counterparts (less than 200 nm). Also, linear PEI possesses lower DNA condensation capacity when compared to a branched counterpart, which is attributed to its lower content in primary amines [6].

Polyplex formation not only protects DNA and RNA from degradation by nucleases, but also is a necessary prerequisite for the efficient delivery of nucleic acids into cells via endocytosis and macropinocytosis [10]. Following internalization, PEI can rapidly destabilize endosomal membrane following protonation. Indeed, every third atom of PEI is a nitrogen capable of protonation. PEI exhibits a very high buffering capacity above pH 7, which is attributed to the secondary amines in the structure, but additionally shows buffering capacity in the range of endosomal pH (pH 4–6). Thus, following internalization, PEI-based polyfectins act as proton sponges, buffering the low endosomal pH and inducing membrane rupture [11–14]. This releases PEI and PEI–DNA complexes into the cytoplasm.

#### 15.2.2

##### Cytotoxicity

Various reports have indicated that PEI can induce cytotoxicity, often defined by assessing the *in vitro* metabolic activity of cells (e.g. MTT assay), but the mechanism(s) remain unclear [6, 15–17]. High-molecular-weight PEIs are more cytotoxic than their smaller counterparts and increasing the degree of branching induces more cytotoxic effects [15, 17]. The issue of PEI-induced cytotoxicity is particularly important in protocols that attempt to restore gene function, e.g. in metabolic disorders. PEI-induced cytotoxicity in normal and nontarget cells, particularly the type

of cells that the cationic vectors will encounter when first administered to the patient, must also be considered. One of the most striking features of PEI polyplexes is the large amount of PEI that remains in the free form, which may induce cell dysfunction and explain the observed cytotoxicity [18]. However, the presence of free PEI is essential for modification and permeabilization of the endosomal membrane structure, thus affording polyplexes a mode of access into the cytoplasm [6, 18]. Indeed, partially purified PEI complexes were recently shown to induce less cytotoxicity, but this also led to a decrease in transfection efficiency [19]. The removal of excess PEI may also affect the stability of polyplexes, since complex formation is an equilibrium process [18].

In light of these observations and with the view that the intracellular levels of endogenous polyamines (e.g. spermine and spermidine) are tightly regulated by means of several homeostatic mechanisms, whereas their excessive cytoplasmic accumulation (e.g. resulting from insults to anionic cellular structures) transduces a death signal to mitochondria by an oxygen-independent mechanism [20, 21], we sought to investigate the effect of PEI and related polyfectins on human cell dysfunction and apoptosis. For the first time, we have identified PEI as an apoptotic agent [22, 23]. Our observations and findings may provide a likely explanation for previously reported transient gene expression associated with polyfectin vectors. A brief overview of our findings as well as recent breakthroughs in polycation-induced cytotoxicity mechanisms is therefore discussed.

### 15.3 PEI-mediated Cell Dysfunction and Apoptosis

#### 15.3.1 PEI and PEI–DNA Complex Internalization

PEI and PEI–DNA complexes enter most cells presumably via binding to transmembrane heparan sulfate/chondroitin sulfate proteoglycans that belong to the syndecan family (e.g. syndecan-1 and -4) [24–27]. Cells, like fibroblasts, express glycosylphosphatidylinositol-anchored heparan sulfate proteoglycans (glypican) instead, which may also serve as a receptor for polyamine uptake [28].

Earlier, fluorescence-labeled studies have demonstrated that within 3 h of incubation with human cell lines, a significant fraction of PEI and PEI–DNA complexes appears in endosomes and endolysosomes [11]. Subsequent attempts with double fluorescence-labeled PEI–DNA complexes have shown disruption of some endosomes, beginning at 4 h postincubation, with evidence of some separation of DNA from PEI in cytosol [11]. Nuclear localization of PEI or PEI–DNA was relatively common by 3.5–4.5 h postincubation and the earliest localization of complexes within nuclei preceded the earliest observed transgene expression by 1 h [11]. The molecular basis of PEI–DNA complex localization to the nucleus still remains unclear, but such complexes may attract a lipophilic coating within cytosol,

thus promoting fusion with the nuclear membrane. However, PEIs in the range of 5–25 kDa are most efficient in transfection experiments because of their small size (less than 200 nm) and relatively faster cytosolic movements [6].

### 15.3.2

#### Plasma Membrane Damage and Apoptosis

We have shown that exposure of three different primary human cell lines (hepatocytes, endothelial cells and lymphocytes) to branched (B)-PEI (25 kDa) or linear PEI (750 kDa) in both free form (10 and 30  $\mu\text{g mL}^{-1}$ ) as well as complexed with a mammalian DNA (regardless of PEI:DNA) causes considerable release of lactate dehydrogenase (LDH) within 1 h, followed by a time-dependent gradual rise in LDH release, thus confirming plasma membrane damage (Fig. 15.1A) [22]. Parallel to rapid LDH release, we also reported rapid (30–60 min) redistribution of phosphatidylserine (PS) from the inner plasma membrane to the outer cell surface with PEI concentrations of 20  $\mu\text{g mL}^{-1}$  and above (Fig. 15.1B) [22]. PS redistribution was increased gradually with time. However, at lower PEI concentrations (e.g. 10  $\mu\text{g mL}^{-1}$ ) PS externalization was significant only after prolonged incubation periods (e.g. 24 h). PS translocation is a hallmark of apoptosis; caspase-3 in active form impairs the activity of aminophospholipid translocase, which leads to PS externalization [29, 30]. Early PS expression, however, was not inhibited in the pre-

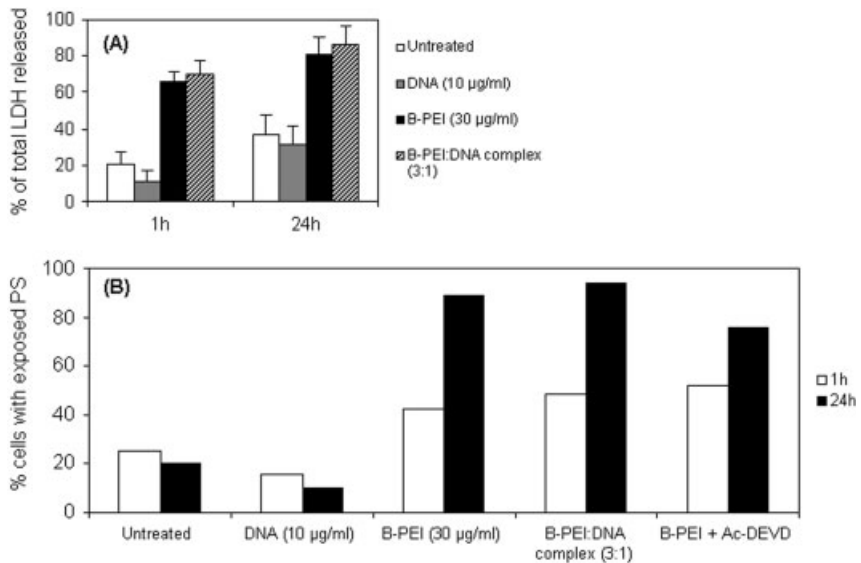


**Figure 15.1.** The effect of B-PEI in free form and DNA-complexed on Jurkat T cell plasma membrane integrity. The release of the cytoplasmic LDH from cells is shown in (A),

whereas (B) demonstrates the extent of PS externalization from the inner to the outer cell surface. Detailed experimental procedures are outlined in reference [22].

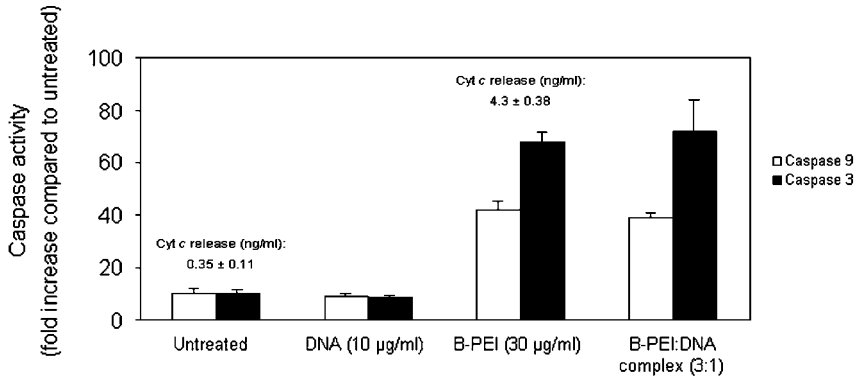


**Figure 15.2.** The effect of B-PEI in free form and DNA-complexed on caspase activation and cytochrome *c* release in Jurkat T cells.

sence of Ac-DEVD (a broad-spectrum caspase inhibitor) and therefore occurs independent of procaspase-3 cleavage. A substantial delay between PS exposure and activation of the executioner caspase-3 was also observed [22]. The activity of this protease was profound particularly at 24 h post-B-PEI/B-PEI–DNA treatment (Fig. 15.2) and could be inhibited by Ac-DEVD. Also, caspase-3 activation was detectable at 24 h post-treatment with lower concentrations of PEI and PEI–DNA complexes; this was in accord with PS expression in tandem with propidium iodide staining. Hence, both PEI types induce apoptosis, but early exposure of PS is presumably the result of plasma membrane destabilization during internalization processes, where PEI may crosslink syndecan molecules and/or induce syndecan clustering. Subsequently, syndecan/glypican clustering may mediate actin stress fiber formation and activate associated signaling pathways such as those of Src family of kinases, contractin, tubulin, microfilament-regulated processes and phosphatidylinositol 4,5-bisphosphate-dependent processes [27, 28, 31]. In certain cells these processes may initiate apoptosis via activation of protein kinases, depending on polycation type and architecture (discussed later). Dissociation of PEI–DNA complexes is also known to occur in the presence of negatively charged macromolecules [32]. It is likely that PEI may interact with actin and alter membrane integrity.

However, through which of the two primary caspase activation pathways, mitochondrially mediated and death receptor-mediated, do PEIs and PEI–DNA complexes induce apoptosis? Here, studies were restricted to PEI–DNA complexes that expressed positive  $\zeta$  potential (PEI:DNA of 3:1), thus mimicking the established transfection protocols [6]. Stress-induced stimuli triggers mitochondrial permeabilization and causes the release of proapoptotic proteins such as cytochrome *c*, apoptosis-inducing factor (AIF), and Smac/DIABLO from mitochondrial intermembrane space [33, 35]. For example, cytochrome *c* release initiates apoptosis via the Apaf-1-containing apoptosome complex assembly. This results in subse-



quent cleavage of caspase-9, which, in turn, activates the executioner caspase-3 [33, 35]. On the other hand AIF, a 50-kDa protease, is capable of inducing DNA fragmentation and chromatin condensation directly [35]. PEI and PEI–DNA treatment in human cell lines was associated with substantial activation of both caspase-3 and -9; significant accumulation of cytochrome *c* in cytosol was also observed (Fig. 15.2) [22]. Since nuclear accumulation of PEI–DNA complexes was reported to occur within a few hours of transfection [11], PEI may also induce genotoxic stress via caspase-2 activation [36, 37]. Indeed, activated caspase-2 can directly permeabilize the outer mitochondrial membrane and stimulate the release of death-promoting proteins without the involvement of mitochondrial permeability transition [36, 37]. However, no evidence for caspase-2 activation even after prolonged periods following PEI and PEI–DNA complex treatment was reported [22, 38]. Also, the absence of caspase-8 activity further suggested that plasma membrane manipulation by PEI and PEI–DNA complexes has no effect on death receptor signaling, which could lead to activation of caspase-3 and -7 directly or indirectly via subsequent cleavage of the amino portion of cytosolic Bid. This would have generated truncated Bid, which, in turn, could activate proapoptotic Bax or Bak proteins to release cytochrome *c* from mitochondrial intermembrane space [35].

The loss of mitochondrial membrane potential (MMP) is also an early event in several types of apoptosis [39, 40]. In our hands, MMP in human cell lines was dramatically dropped in a time-dependent manner [22, 23] and was consistent with caspase activation (with peak activity at 24 h). MMP was determined by a specific cationic fluorescent probe, JC-1, which fluoresces differently in healthy and apoptotic cells (Fig. 15.3). JC-1 forms aggregates in healthy mitochondria with a high orange/red fluorescence, indicating a normal MMP, but following MMP loss these aggregates dissipate into the cytoplasm in the monomeric state, which is detectable with a concurrent gain in green fluorescence [22]. Therefore, these observations confirm that PEI and PEI–DNA complexes induce apoptosis via the mitochondrial pathway.

### 15.3.3

#### **Effect of PEI on the Function of Isolated Mitochondria**

To further understand the molecular basis of PEI-induced mitochondrially mediated apoptosis, attention was focused on studies with isolated mitochondria [22]. Here, PEI was able to release cytochrome *c* from the mitochondrial intermembrane space in a concentration-dependent manner. Indeed, cytochrome *c* release was detectable following treatment with both PEI types even at levels as low as 0.1  $\mu\text{g mL}^{-1}$ . Interestingly, cytochrome *c* release was not associated with changes in mitochondrial volume (Fig. 15.4). This observation may indicate a minor role for permeability transition in the release of apoptogenic proteins from mitochondria. However, it should be emphasized that permeability transition is reversible; permeability transition may cause an individual mitochondrion to swell, releasing apoptogenic proteins, and then reverse and regenerate membrane potential [41]. Therefore, this route may still operate in intact cells.

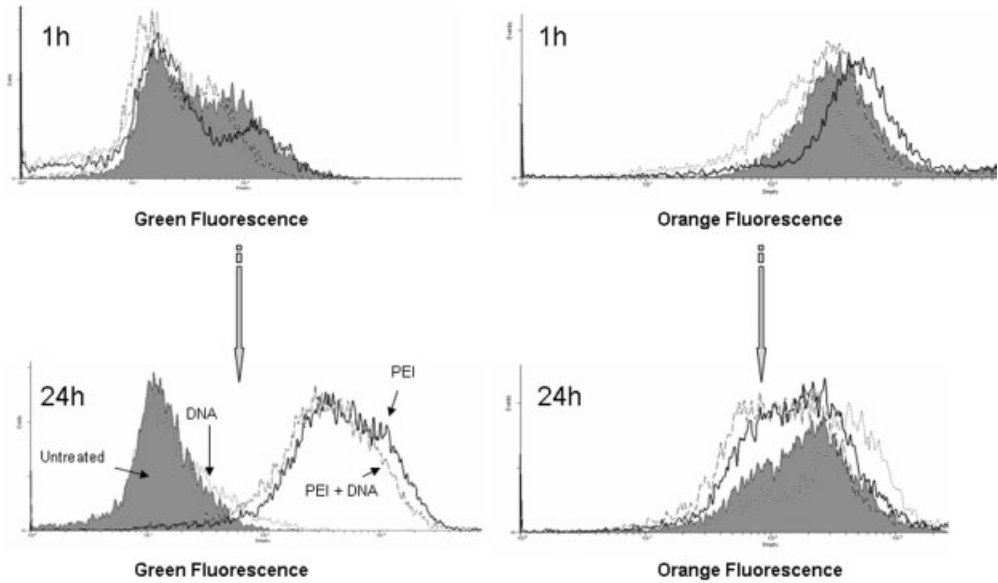


**Figure 15.3.** Time-dependent changes in MMP in Jurkat T cells by free ( $30 \mu\text{g mL}^{-1}$ ) and DNA-complexed (PEI:DNA, weight ratio 3:1) branched PEI, as determined by specific MMP fluorescent probe JC-1. Detailed experimental procedures are outlined in Ref. [22].

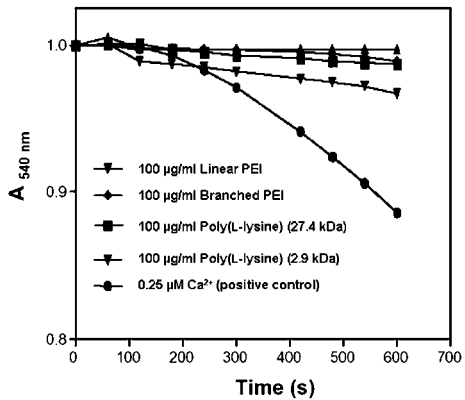


**Figure 15.4.** The effect of polycations on continuous swelling of isolated rat liver mitochondria, monitored as changes in  $A_{540}$  at room temperature. Detailed experimental procedures are outlined in Refs. [22, 50].

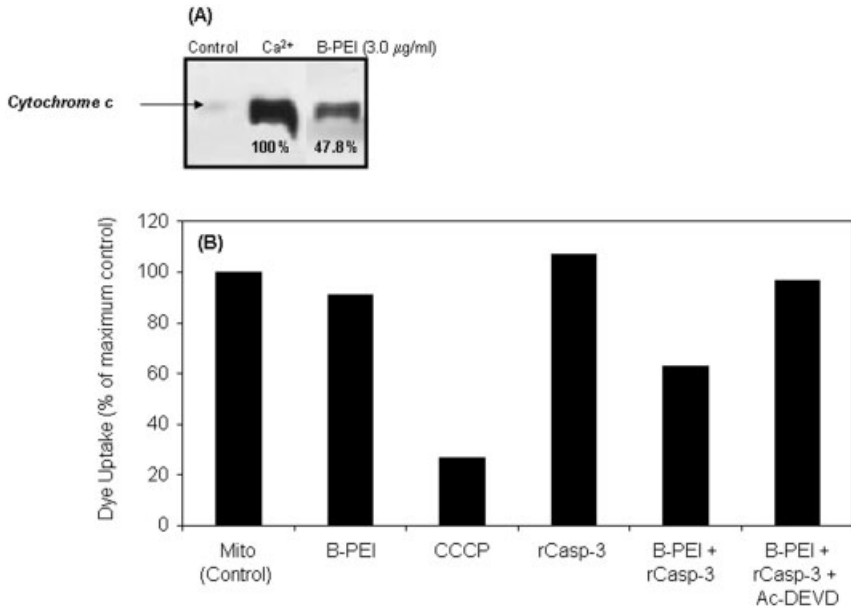


**Figure 15.5.** The effect of branched PEI on function of isolated rat liver mitochondria. (A) The effect of PEI on cytochrome *c* release (Western blot analysis). (B) The extent of DiOC<sub>6</sub>(3) uptake by isolated mitochondria at different treatment protocols. Following incubation with PEI and rCasp-3 (15 min),

DiOC<sub>6</sub>(3) was added and the sample was incubated for a further 10 min at 22 °C. Samples were then diluted in the buffer, filtered and incubated for a further 10 min before flow cytometric analysis content of individual mitochondria.

Changes in the membrane potential of isolated mitochondria can be followed by measuring the uptake of the cationic lipophilic fluor DiOC<sub>6</sub>(3) (Fig. 15.5). This membrane potential-sensitive dye electrophoretically accumulates in the negatively charged matrix of healthy mitochondria. When mitochondrial depolarization occurs, accumulation of DiOC<sub>6</sub>(3) is reduced and can be followed by flow cytometry as a decrease in mitochondrial-associated green fluorescence. Interestingly, dye uptake remained unaltered in the presence of PEI (i.e. after cytochrome *c* release) when compared to healthy intact mitochondria (where no cytochrome *c* release is detectable) (Fig. 15.5). As a control experiment DiOC<sub>6</sub>(3) responded to acute changes in mitochondrial membrane potential induced by the protonophore carbonyl cyanide *p*-chlorophenylhydrazone (CCCP). Thus, cytochrome *c* release is independent of mitochondrial depolarization [22], but in intact cells PEI was capable of altering MMP. This discrepancy may indicate a role for activated caspases in altering MMP. Remarkably, the addition of an active recombinant human caspase 3 (rCasp-3) exerted no effect on dye accumulation in intact mitochondria, whereas in the presence of PEI dye uptake was reduced dramatically unless Ac-DEVD was present (Fig. 15.5). These experiments strongly support that PEI is capable of forming channels in the outer membrane large enough to allow the release of cy-

tochrome *c*, presumably in a manner similar to proapoptotic peptides and oligomeric Bax [42, 43], without altering MMP. Thus, these observations are also in accord with the loss of MMP in intact cells following PEI or PEI–DNA uptake, which is believed to occur after cytochrome *c* release and presumably is mediated by activated caspases. Indeed, recently it was demonstrated that following cytochrome *c* release, activated caspases gain access to the intermembrane space of mitochondrion where they cleave the 75-kDa subunit of respiratory complex I, resulting in disruption of complex I activity, loss of MMP and production of reactive oxygen species [44].

#### 15.3.4

#### Other Plausible Apoptotic Routes

Recently, a spatial and functional connection between Bax and the mitochondrial fission process was suggested [45, 46]. In normal interphase cells the mitochondria exists as a tubular network. During apoptosis, the mitochondrial network becomes fragmented and Bax colocalized with the fission- and fusion-related proteins (Drp1,

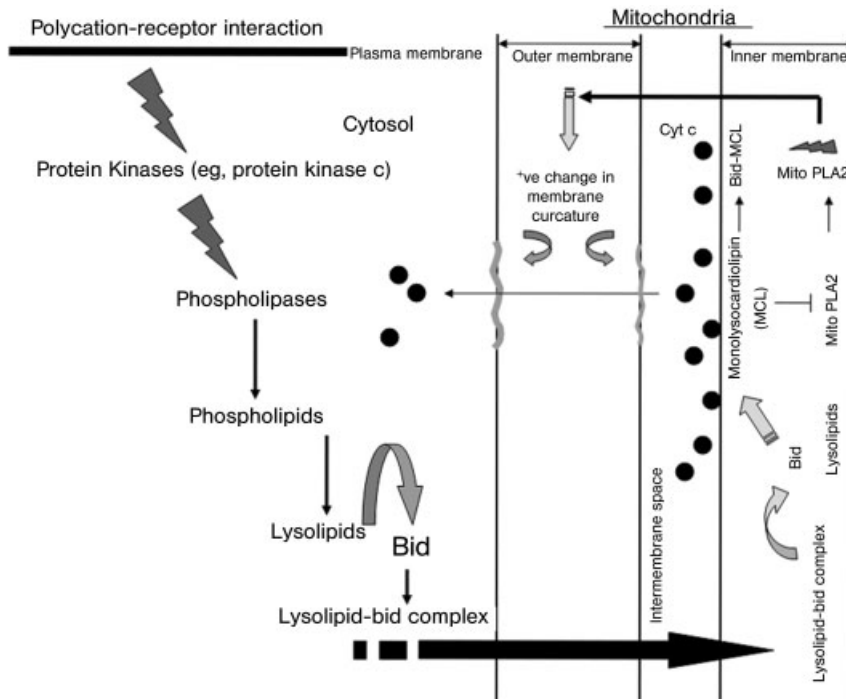


**Figure 15.6.** Schematic representation of possible polycation effect on protein kinase and phospholipase activation, and the role of full-length Bid in initiation of mitochondrially mediated apoptosis.

Mfn2) at fission sites in the outer mitochondrial membrane. Due to their polycationic nature and molecular architecture, PEI molecules could hypothetically promote mitochondrial fission, which may lead to destabilization of the outer mitochondrial membrane.

It can also be speculated that following binding to plasma membrane proteoglycans, such as syndecan or glypican, PEI and related polycations may initiate apoptosis via signaling and activation of protein kinases (Fig. 15.6). For example, poly(L-lysine)s and poly(arginine)s are known to stimulate a number of cellular kinases and protein phosphatases, particularly phospholipases, even at suboptimal cytotoxic concentrations [47]. For instance, poly(L-lysine) is capable of inducing phospholipase D activation in bovine pulmonary artery endothelial cells through the involvement of protein kinase C [47]. Phospholipase activation may lead towards insertion of lysolipids into the outer mitochondrial membrane via the recently identified lipid transfer capacity of full-length Bid [48]. Once bound to lysolipid, full-length Bid is suggested to transfer lysolipid to intracellular membranes rich in cardiolipin and monolysocardiolipin, towards which the protein has a “static” selectivity of binding, thereby altering cardiolipin homeostasis [48]. Indeed, monolysocardiolipin is an inhibitor of mitochondrial phospholipase A2 [49] and thus tight binding of full-length Bid to monolysocardiolipin may lead to activation of this phospholipase. These modifications may induce a positive change in the outer mitochondrial membrane curvature leading to the release of apoptogenic factors, either directly or through other mediators.

#### 15.4

##### Cell Damage and Apoptosis with Related Polycations and Cationic Lipids

Poly(L-lysine) are also used widely in DNA compaction and gene transfer protocols [4]. Recent observations from this laboratory have shown that poly(L-lysine)s are also capable of inducing mitochondrially mediated apoptosis in a wide range of human cell lines [50]. However, low- and high-molecular weight poly(L-lysine)s/poly(L-lysine)–DNA complexes had different effect on mitochondrial functions and initiated mitochondrially mediated apoptosis differently. For example, high-molecular-weight poly(L-lysine)s were not only capable of inducing cytochrome *c* release from isolated mitochondria, but were also able to dramatically alter mitochondrial respiration and membrane potential without swelling [50]. Interestingly, in intact cells inhibition of Bax channel-forming activity was shown to reduce the extent of cytochrome *c* release from mitochondria by half. In the case of low-molecular weight poly(L-lysine)s neither cytochrome *c* release nor changes in the function of isolated mitochondria was noticed, whereas in intact cells such treatments resulted in significant accumulation of cytochrome *c* in cytosol within 24 h with a concurrent MMP drop, and caspase-3 and -9 activation [50]. These observations may indicate a possible role for protein kinases and phospholipases in initiation of apoptosis by low-molecular weight poly(L-lysine)s, as discussed above (Fig. 15.6).

Poly[2-(dimethylamino)ethyl methacrylate] is another example of a cationic polymer that facilitates cell transfection. This polymer is also cytotoxic, but the mechanisms of its cytotoxicity is primarily due to necrotic cell death [51]. Nanoparticles made from poly(D,L-lactide-co-glycolide) have also been suggested for transfection studies; these particles can escape the endolysosomal compartment within minutes of internalization in intact form and reach the cytoplasm [52]. The mechanism of rapid escape is by selective reversal of the surface charge of nanoparticles from the anionic to the cationic state in endolysosomes, thus resulting in a local particle-membrane interaction with subsequent cytoplasmic release. However, degradation products arising from poly(L-lactic acid) particles also show cytotoxicity, and can induce apoptotic and necrotic cell death [53].

We have also proposed an apoptotic role for cationic surfactants and related structures (micelles), thus limiting the applicability of cationic drug carriers for intracellular drug release [54]. Cationic lipids have also been employed in gene transfer/therapy protocols [4], but recent studies have indicated that cationic lipids are also capable of inducing apoptosis [55]. For example, apoptosis in macrophage-like cell line RAW264.7 following treatment with stearylamine-incorporated liposomes was mediated by mitogen-activated protein kinase p38 and c-jun N-terminal kinase, and a caspase 8-dependent Bid cleavage pathway [55].

Furthermore, cDNA microarray expression profiling studies are beginning to reveal that the cationic delivery vehicle can adversely influence the desired effects of the delivered genetic agents [56], which is in agreement with the observation that polycations such as PEI and poly(L-lysine) in both free form and complexed with DNA can localize to the nucleus. Gene expression changes in a wide range of gene ontologies were recently demonstrated with PEI in both *in vitro* and *in vivo* studies [56]. Remarkably, both PEI concentration and architecture had a dramatic effect on non-target gene expression.

## 15.5

### Conclusions and Future Outlook

Polycations such as PEI and poly(L-lysine) induce rapid perturbation of the plasma membrane (within 30–120 min of exposure) with characteristics resembling early necrotic-like changes, which is followed by activation of a “mitochondrially mediated” apoptotic programme at later stages (24 h), at least in human endothelial, lymphocyte and hepatic cell lines [22, 38, 50]. These findings are of relevance to transient gene expression following polycation-mediated DNA compaction and transfection both *in vitro* and *in vivo*. There are numerous developments with respect to the design and synthesis of “less cytotoxic” polycations [6, 57–59]. Cytotoxicity, however, is often assessed by the MTT assay, which is not indicative of apoptosis. Future cytotoxicity studies with newly designed cationic macromolecules and polyfectins should address and consider the time-dependent apoptotic processes, as apoptosis may compromise transcription and translation processes, and limit protein expression. Additionally, the process of apoptosis in intact cells is stochas-

tic, with different cells entering apoptosis at different times. Furthermore, different cationic polymers may interact differently with mitochondria or the endoplasmic reticulum (leading to perturbation of intracellular calcium) and initiate apoptosis differently. The inherent heterogeneity of mitochondria that make up any particular population of these organelles should also be taken into the account.

Attempts in polycation-mediated gene transfer, however, could benefit through recent advances in high-throughput approaches to polymer design and screening [60]. Such approaches may enhance our understanding of the molecular basis of interaction between cationic polymers and intracellular membranes. An understanding of such events may eventually help to design novel and safer materials, particularly those that can provide duration period-specific gene expression in clinical scenarios.

### References

- 1 CAVAZZANO-CALVO, M., THRASHER, A., MAVILIO, F. The future of gene therapy, *Nature* **2004**, *427*, 779–781.
- 2 GORE, M. Gene therapy can cause leukemia: no shock, mild horror but a probe, *Gene Ther.* **2003**, *10*, 4–4.
- 3 GANSBACHER, B. Report of a second serious adverse event in a clinical trial of gene therapy for X-linked severe combined immunodeficiency (X-SCID). Position of the European Society of Gene Therapy (ESGT), *J. Gene Med.* **2003**, *5*, 261–262.
- 4 SCHMIDT-WOLF, G. D., SCHMIDT-WOLF, I. G. H. Non-viral and hybrid vectors in human gene therapy: an update, *Trend. Mol. Med.* **2003**, *9*, 67–72.
- 5 KICHLER, A. Gene transfer with modified polyethylenimine, *J. Gene Med.* **2004**, *6*, S3–S10.
- 6 NEU, M., FISCHER, D., KISSEL, T. Recent advances in rational gene transfer vector design based on poly(ethyleneimine) and its derivatives, *J. Gene Med.* **2005**, *7*, 992–1009.
- 7 TANG, M. X., SZOKA, F. C. The influence of polymer structure on the interaction of cationic polymers with DNA and morphology of the resulting complexes, *Gene Ther.* **1997**, *4*, 823–832.
- 8 BLOOMFIELD, V. A., DNA condensation, *Curr. Opin. Struct. Biol.* **1996**, *6*, 334–341.
- 9 BRONICH, T., KABANOV, A., MARKY, L. A thermodynamic characterization of the interaction of a cationic copolymer with DNA, *J. Phys. Chem. B* **2001**, *105*, 6041–5050.
- 10 OH, Y. K., SUH, D., KIM, J. M., CHOI, H. G., SHIN, K., KO, J. J. Polyethylenimine-mediated cellular uptake, nucleus trafficking and expression of cytokine plasmid DNA, *Gene Ther.* **2002**, *9*, 1627–1632.
- 11 GODBEY, W. T., WU, K. K., MIKOS, A. G. Tracking the intracellular path of poly(ethyleneimine)/DNA complexes for gene delivery, *Proc. Natl Acad. Sci. USA* **1999**, *96*, 5177–5181.
- 12 BOUSSIF, O., LEZOUALC'H, F., ZANTA, M. A., MERGNY, M. D., SCHERMAN, D., DEMENEIX, B., BEHR, J.-P. A versatile vector for gene and oligonucleotide transfer into cells in culture and *in vivo*: polyethylenimine, *Proc. Natl Acad. Sci. USA* **1995**, *92*, 7297–7301.
- 13 CLAMME, J. P., KRISHNAMOORTHY, G., MÉLY, Y. Intracellular dynamics of the gene delivery vehicle polyethylenimine during transfection: investigation by two-photon fluorescence correlation spectroscopy, *Biochim. Biophys. Acta Biomembr.* **2003**, *1617*, 52–61.

- 14 FORREST, M. L., PACK, D. W. On the kinetics of polyplex endocytic trafficking: Implications for gene delivery vector design, *Mol. Ther.* **2002**, *6*, 57–66.
- 15 FISCHER, D., BIEBER, T., LI, Y., ELASSASSER, H. P., KISSEL, T. A novel non-viral vector for DNA delivery based on low molecular weight, branched polyethylenimine: effect of molecular weight on transfection efficiency and cytotoxicity, *Pharm. Res.* **1999**, *16*, 1273–1279.
- 16 FLOREA, B. I., MEANEY, C., JUNGINGER, H. E., BORCHARD, G. Transfection efficiency and toxicity of polyethylenimine in differentiated Calu-3 and nondifferentiated Cos-1 cell cultures, *AAPS PharmSci.* **2002**, *4*, article 12.
- 17 FISCHER, D., VON HARPE, A., KUNATH, K., PETERSEN, H., LI, Y. X., KISSEL, T. Copolymers of ethyleneimine and *N*-(2-hydroxyethyl)ethyleneimine as tools to study effects of polymer structure on physicochemical and biological properties of DNA complexes, *Bioconjug. Chem.* **2002**, *13*, 1124–1133.
- 18 CLAMME, J. P., AZOULAY, J., MÉLY, Y. Monitoring of the formation and dissociation of polyethylenimine/DNA complexes by two photon fluorescence spectroscopy, *Biophys. J.* **2003**, *84*, 1960–1968.
- 19 BOECKLE, S., VON GERSDORFF, K., VAN DER PIEPEN, S., CULMSEE, C., WANGNER, E., OGRIS, M. Purification of polyethylenimine polyplexes highlights the role of free polycations in gene transfer, *J. Gene Med.* **2004**, *6*, 1102–1110.
- 20 STEFANELLI, C., BONAVITA, F., STANIC, I., PIGNATTI, C., FLAMIGNI, F., GUARNIERI, C., CALDARERA, C. M. Spermine triggers the activation of caspase-3 in a cell-free model of apoptosis, *FEBS Lett.* **1999**, *451*, 95–98.
- 21 STEFANELLI, C., STANIC, I., ZINI, M., BONAVITA, F., FLAMIGNI, F., ZAMBONIN, L., LANDI, L., PIGNATTI, C., GUARNIERI, C., CALDARERA, C. M. Polyamines directly induce release of cytochrome c from heart mitochondria, *Biochem. J.* **2000**, *347*, 875–880.
- 22 MOGHIMI, S. M., SYMONDS, P., MURRAY, J. C., HUNTER, A. C., DEBSKA, G., SZEWCZYK, A. A two-stage poly(ethylenimine)-mediated cytotoxicity: implications for gene transfer/therapy, *Mol. Ther.* **2005**, *11*, 990–995.
- 23 MOGHIMI, S. M., HUNTER, A. C., MURRAY, J. C. Nanomedicine: current status and future prospects, *FASEB J.* **2005**, *19*, 311–330.
- 24 MISLICK, K. A., BALDESCHWIELER, J. D. Evidence for the role of proteoglycans in cation-mediated gene transfer. *Proc. Natl Acad. Sci. USA* **1996**, *93*, 12349–12354.
- 25 MOUNKES, L. C., ZHONG, W., CIPRESPALACIN, HEATH, T. D., DEBS, R. J. Proteoglycans mediate cationic liposome–DNA complex-based gene delivery *in vitro* and *in vivo*, *J. Biol. Chem.* **1998**, *273*, 26164–26170.
- 26 KOPATZ, I., REMY, J. S., BEHR, J.-P. A model for non-viral gene delivery: through syndecan adhesion molecules and powered by actin, *J. Gene Med.* **2004**, *6*, 769–776.
- 27 DULL, R. O., DINAVAHI, R., SCHWARTZ, L., HUMPHRIES, D. E., BERRY, D., SASISEKHARAN, R., GARCIA, J. G. N. Lung endothelial heparan sulfate mediate cationic peptide-induced barrier dysfunction: a new role for the glycocalyx, *Am. J. Physiol. (Lung Cell. Mol. Physiol.)* **2003**, *285*, L986–L995.
- 28 BELTING, M., PERSSON, S., FRANSSON, L.-A. Proteoglycan involvement in polyamine uptake, *Biochem. J.* **1999**, *338*, 317–323.
- 29 MARTIN, S. J., FINUCANE, D. M., AMARANTEMENDES, G. P., O'BRIEN, G. A., GREEN, D. A. Phosphatidylserine externalization during CD95-induced apoptosis of cells and cytoplasts requires ICE/Ced-3 protease activity, *J. Biol. Chem.* **1996**, *271*, 28753–28756.
- 30 MANDAL, D., MOITRA, P. K., SAHA, S., BASU, J. Caspase 3 regulates phosphatidylserine externalization and phagocytosis of oxidatively stressed erythrocytes, *FEBS Lett.* **2002**, *513*, 184–188.



- 31 SAONCELLA, S., ECHTERMAYER, F., DENHAZ, F., NOWLEN, J. K., MOSHER, D. F., ROBINSON, S. D., HYNES, R., GOETINCK, P. F. Syndecan-4 signals cooperatively with integrins in a Rho-dependent manner in the assembly of focal adhesions and actin stress fibers, *Proc. Natl Acad. Sci. USA* **1999**, *96*, 2805–2810.
- 32 WONG, G. C. L., TANG, J. X., LIN, A., LI, Y., JANMEY, P. A., SAFINYA, C. R. Hierarchical self-assembly of F-actin and cationic lipid complexes: stacked three-layer tubule networks, *Science* **2000**, *288*, 2035–2039.
- 33 NEWMAYER, D. D., FERGUSON-MILLER, S. Mitochondria: releasing power for life and unleashing the machineries of death, *Cell* **2003**, *112*, 481–490.
- 34 KLUCK, R. M., BOSSY-WETZEL, E., GREEN, D. R., NEWMAYER, D. D. The release of cytochrome *c* from mitochondria: a primary site for Bcl-2 regulation of apoptosis, *Science* **1997**, *275*, 1132–1136.
- 35 HENGARTNER, M. O. The biochemistry of apoptosis, *Nature* **2000**, *407*, 770–776.
- 36 ROBERTSON, J. D., GOGVADEZ, V., KROPOTOV, A., VAKIFAHMETOGLU, H., ZHIVOTOVSKY, B., ORRENIUS, S. Processed caspase-2 can induce mitochondria-mediated apoptosis independently of its enzymatic activity, *EMBO Rep.* **2004**, *5*, 643–648.
- 37 ENOKSSON, M., ROBERTSON, J. D., GOGVADEZ, V., BU, P., KROPOTOV, A., ZHIVOTOVSKY, B. and ORRENIUS, S. Caspase-2 permeabilizes the outer mitochondrial membrane and disrupts the binding of cytochrome *c* to anionic phospholipids, *J. Biol. Chem.* **2004**, *279*, 49575–49578.
- 38 MOGHIMI, S. M., SYMONDS, P., HUNTER, A. C., MURRAY, J. C. The molecular basis of immediate and delayed polycation/polyamine-induced cytotoxicity in gene transfer, *Toxicology* **2006**, *219*, 234–235.
- 39 BORTNER, C. D., CIDLOWSKI, J. A. Caspase independent/dependent regulation of K<sup>+</sup>, cell shrinkage, and mitochondrial membrane potential during lymphocyte apoptosis, *J. Biol. Chem.* **1999**, *274*, 21953–21962.
- 40 DINSDALE, D., ZHUANG, J., COHEN, G. M. Redistribution of cytochrome *c* precedes the caspase-dependent formation of ultra-condensed mitochondria, with a reduced inner membrane potential, in apoptotic monocytes, *Am. J. Pathol.* **1999**, *155*, 607–618.
- 41 SCARLETT, J. L., MURPHY, M. P. Release of apoptogenic proteins from the mitochondrial intermembrane space during the mitochondrial permeability transition, *FEBS Lett.* **1997**, *418*, 282–286.
- 42 GOGVADEZ, V., ROBERTSON, J. D., ZHIVOTOVSKY, B., ORRENIUS, S. Cytochrome *c* release occurs via Ca<sup>2+</sup>-dependent and Ca<sup>2+</sup>-independent mechanisms that are regulated by Bax, *J. Biol. Chem.* **2001**, *276*, 19066–19071.
- 43 LETAI, A., BASSIK, M. C., WALENSKY, L. D., SORCINELLI, M. D., WEILER, S., KORSMEYER, S. J. Distinct BH3 domains either sensitize or activate mitochondrial apoptosis, serving as prototype cancer therapeutics, *Cancer Cell* **2002**, *2*, 183–192.
- 44 RICCI, J. E., MUNOZ-PINEDO, C., FITZGERALD, P., BAILLY-MAITRE, B., PERKINS, G. A., YADAVA, N., SCHEFFLER, I. E., ELLISMAN, M. H., GREEN, D. R. Disruption of mitochondrial function during apoptosis is mediated by caspase cleavage of the p75 subunit of complex I of the electron transport chain, *Cell* **2004**, *117*, 773–786.
- 45 FRANK, S., GAUME, B., BERGMANN-LEITNER, E. S., LEITNER, W. W., ROBERT, E. G., CATEZ, F., SMITH, C. L., YOULE, R. J. The role of dynamin-related protein 1, a mediator of mitochondrial fission, in apoptosis, *Dev. Cell* **2001**, *1*, 515–525.
- 46 KARBOWSKI, M., LEE, Y.-J., GAUME, B., JEONG, S.-Y., FRANK, S., NECHUSHTAN, A., SANTEL, A., FULLER, M., SMITH, C. L., YOULE, R. J. Spatial and temporal association of Bax with mitochondrial fission sites, Drp1, and Mfn2 during

- apoptosis, *J. Biol. Chem.* **2002**, *159*, 931–938.
- 47 VEPA, S., SCRIBNER, W. M., NATARAJAN, V. Activation of endothelial cell phospholipase D by polycations, *Am. J. Physiol. (Lung Cell. Mol. Physiol.)* **1997**, *272*, L608–L613.
- 48 GOONESINGHE, A., MUNDY, E. S., SMITH, M., KHOSRAVI-FAR, R., MARTINOU, J. C., ESPOTI, M. D. Pro-apoptotic Bid induces membrane perturbation by inserting selected lysolipids into the bilayer, *Biochem. J.* **2005**, *387*, 109–118.
- 49 REERS, M., PFEIFFER, D. R. Inhibition of mitochondrial phospholipase A2 by mono- and diacylcardiolipin, *Biochemistry* **1987**, *26*, 8038–8041.
- 50 SYMONDS, P., MURRAY, J. C., HUNTER, A. C., DEBSKA, G., SZEWCZYK, A., MOGHIMI, S. M. Low and high molecular weight poly(L-lysine)s/poly(L-lysine)–DNA complexes initiate mitochondrial-mediated apoptosis differently, *FEBS Lett.* **2005**, *579*, 6191–6198.
- 51 JONES, R. A., PONIRIS, M. H., WILSON, M. R. pDMAEMA is internalised by endocytosis but does not physically disrupt endosomes, *J. Control. Release* **2004**, *96*, 379–391.
- 52 PANYAM, J., ZHOU, W. Z., PRABHA, S., SAHOO, S. K., LABHASETWAR, V. Rapid endo-lysosomal escape of poly(D,L-lactide-co-glycolide) nanoparticles: implications for drug and gene delivery, *FASEB J.* **2002**, *16*, 1217–1226.
- 53 LAM, K. H., SCHAKENRAAD, J. M., ESSELBRÜGGE, H., FEIJEN, J., NIEUWENHUIS, P. The effect of phagocytosis of poly(L-lactic acid) fragments on cellular morphology and viability, *J. Biomed. Mat. Res.* **1993**, *27*, 1569–1577.
- 54 MOGHIMI, S. M., HUNTER, A. C., MURRAY, J. C., SZEWCZYK, A. Cellular distribution of nonionic micelles, *Science* **2004**, *303*, 626–627.
- 55 IWAOKA, S., NAKAMURA, T., TAKANO, S., TSUCHIYA, S., ARAMAKI, Y. Cationic liposomes induce apoptosis through p38 MAP kinase–caspase-8–bid pathway in macrophage-like RAW264.7 cells, *J. Leukoc. Biol.* **2006**, *79*, 184–191.
- 56 HOLLINS, J., OMIDI, Y., AKHTAR, S. Drug delivery system induced gene expression changes in cells *in vitro* and *in vivo*, *J. Pharm. Pharmacol. (Suppl.)* **2005**, *57*, S85.
- 57 FORREST, M. L., KOERBER, J. T., PACK, D. W. A degradable polyethylenimine derivative with low toxicity for highly efficient gene delivery, *Bioconjug. Chem.* **2003**, *14*, 934–940.
- 58 THOMAS, M., LU, J. J., GE, Q., ZHANG, C., CHEN, J., KLIBANOV, A. M. Full deacylation of polyethylenimine dramatically boosts its gene delivery efficiency and specificity to mouse lung, *Proc. Natl Acad. Sci. USA* **2005**, *102*, 5679–5684.
- 59 YAMASHITA, A., CHOI, H. S., OOYA, T., YUI, N., AKITA, H., KOGURE, K., HARASHIMA, H. Improved cell viability of linear polyethylenimine through  $\gamma$ -cyclodextrin inclusion for effective gene delivery, *ChemBioChem* **2006**, *7*, 297–302.
- 60 ANDERSON, D. G., AKINC, A., HOSSAIN, N. and LANGER, R. Structure/property studies of polymeric gene delivery using a library of poly(beta-amino esters), *Mol. Ther.* **2005**, *11*, 426–434.

## 16

# Nanoparticles for the Treatment of Alzheimer's Disease: Theoretical Rationale, Present Status and Future Perspectives

*Gang Liu, Ping Men, George Perry and Mark A. Smith*

### 16.1

#### Introduction

Alzheimer's disease (AD) is the most common form of dementia among people over the age of 65 years, progressing slowly from mild forgetfulness to the need for total care [1]. This disease is a devastating neurodegenerative disorder with progressive and irreversible damage to thought, memory and language. In America alone, 360 000 new AD cases were identified in 2000, bringing the total to 4.5 million, and the affected population will continue to increase as the population ages [2, 3]. It is expected that the number of people with AD in the US and worldwide will be 14 and over 100 million, respectively, by 2050 if no effective prevention and treatment become available [4, 5]. As such, the disease poses a heavy economic and societal burden, with associated annual costs of care over US\$100 billion [1]. In addition, AD places an incalculable emotional and physical drain on families and caretakers. The ravaging effects of the disease call for efforts to prevent, forestall and reverse the disease. Unfortunately, despite much interest, an explicative etiology or a viable cure is not available. The current Food and Drug Administration (FDA)-approved drugs, targeted towards managing cognitive symptoms such as changes in memory and perception, provide only partial benefit to select patients and fall tremendously short as adequate means of therapeutic management. In addition to donepezil (Aricept®), tacrine (Cognex®), rivastigmine (Exelon®) and galantamine (Reminyl®), memantine (Namenda®) has recently won FDA approval for the treatment of AD. Unlike the acetylcholinesterase inhibitors (Aricept, Exelon and Reminyl) and the cholinesterase inhibitor (Cognex), memantine blocks excess amounts of glutamate that can damage or kill nerve cells. This new drug is becoming the first-line choice for advanced stages of AD [6, 7]. In contrast, the earlier approved drugs mentioned above work in the early stages of AD by delaying the breakdown of acetylcholine, vital for nerve cell communication [8, 9]. Although treatment with these drugs provides symptomatic improvements or delays in the progression of cognitive, behavioral and functional deficits, this treatment does not stop or reverse the progression of AD.

There are many medications used to treat AD, including anti-inflammatory drugs [10–14], antioxidants and vitamins [15–24], hormones [25–30], calcium

channel blockers [31, 32], angiotensin-converting enzyme (ACE) inhibitors [33], cholesterol-lowering statins [34–39], ethylenediaminetetraacetic acid (EDTA) and clioquinol [40–44], gabapentin, lamotrigine, prazosin and risperidone [15, 45–47], vaccines against amyloid- $\beta$  ( $A\beta$ ) [48–52], and even a drug (rosiglitazone) to treat insulin resistance [53, 54]. Antihypertensive medications or regular exercise are also suggested to reduce risk for AD and dementia among people aged 65 years and older [55–57]. Other medications and substances being investigated at the present time include cannabinoids, physostigmine, nerve growth factor,  $\beta$ -sheet breakers, valproate, huperzine and nicotine [58–65]. New studies on the regulation of  $A\beta$  protein precursor translation by Phenserine [66, 67], the regulation of  $A\beta$  by neprilysin [68], inhibition of the activity of amyloid precursor protein (APP) secretases [69–74] and CD45 [75] show promising progress toward the identification of new therapeutic agents. Other studies, such as targeting glycosaminoglycans or metalloprotein attenuating compounds, new chelation agents, tau phosphorylation inhibitors, NF- $\kappa$ B blocker, gene delivery and human embryonic stem cells are under investigation [51, 59, 76–95]. Unfortunately, none of the treatments or drugs currently available can prevent or cure AD. Indeed, it is likely that more than one type of drug will be required to control AD. A recent study shows that Aricept and Namenda work in tandem to ameliorate symptoms of AD [96]. These studies reveal the complexity of the disease, and indicate a great need for a better understanding of AD pathophysiology and for more effective therapeutic agents.

In addition to the complex mechanisms of AD development, another obstacle to a deeper understanding and better treatment of AD is the presence of the blood–brain barrier (BBB). Many drugs of interest cannot gain access to the brain by crossing the BBB. Its presence may also negatively affect drug efficacy and tolerance because a large dosage of drugs must be applied to achieve therapeutic effectiveness. Nanoparticulate drug delivery offers an opportunity to overcome this impediment. Accumulating studies provide evidence that this delivery method can improve drug targeting of the central nervous system and drug penetration of the BBB, thus reducing drug toxicity and improving therapeutic efficacy [97–105]. Although there are many promising studies regarding nanoparticle delivery of drugs across the BBB to treat central nervous system diseases, only a few address treatment of AD [106–110]. In this chapter, the rationale for nanoparticulate drug delivery in the treatment of AD is presented, the current studies of using this delivery systems for AD treatment are reviewed and brief perspectives on this new approach are outlined.

## 16.2

### Rationales: The Ability of Nanoparticles to Cross the BBB – A Useful Tool to Deliver Drugs into the Brain

#### 16.2.1

##### Physiological Functions of the BBB

The BBB, constituted by endothelial cells of the cerebral vasculature together with perivascular elements such as astrocytes, pericytes and basement membrane,

strictly limits and specifically controls the passage of substances between the blood and the cerebral extracellular space [111, 112]. Brain blood vessel endothelial cells characteristically have tight continuous circumferential junctions between them, thus abolishing any aqueous paracellular pathways between the cells [113]. Due to the presence of the tight junctions and the lack of aqueous pathways between cells, polar solutes and lipid-insoluble substances are greatly restricted in movement across the cerebral endothelium [114]; however, noncharged, small, lipophilic molecules may cross the BBB through the endothelial membrane by passive diffusion. This pathway is closely checked by efflux pump systems, which include the multiple organic anion transporter (MOAT), P-glycoprotein (P-gp) and multidrug resistance-associated protein (MDR) [114]. As a result, even molecules with a favorable lipophilicity, which should enable them to cross the endothelial cells, may be rapidly pumped back to the blood stream. These efflux pump systems can also effectively prevent anions, amphipathic organic cations or neutral compounds from entering the central nervous system [114, 115]. As the BBB contains biochemical systems consisting of enzymes, many drugs and blood-borne substances are specifically metabolized before entering the brain [116]. In order to allow essential substances to enter the brain and metabolic waste to leave, the BBB provides specific routes such as receptor and transporter systems to accomplish this transport [114, 117, 118]. Substances that can be absorbed or eliminated by the brain using these carrier-mediated transporter systems include amino acids, hexoses, monocarbonic substances, lipoproteins, insulin and purine compounds [99, 100]. Nanoparticulate drug delivery systems may utilize the low-density lipoprotein (LDL) receptor and the transferrin transcytosis systems to transport drugs into the brain [117, 118]. These transport pathways at the BBB are depicted in Fig. 16.1 [119].

### 16.2.2

#### **Strategies for Drug BBB Penetration**

Although the BBB's existence is absolutely necessary to isolate the central nervous system, with broad consequences for physiology, biology, pharmacology and pathology (most of which remain to be fully elucidated), the BBB represents an insurmountable difficulty for brain uptake of many therapeutic agents. These agents include some antibiotics, antineoplastic drugs and central nervous system-active therapeutics, especially neuropeptides [99, 100]. To overcome this obstacle, various strategies have been developed, which include osmotic opening of the brain endothelial cell tight junctions [120], prodrug preparation [121, 122], and utilization of carrier-mediated transporter systems such as antibodies [123–125], carbohydrate conjugation [126–129], viral and nonviral gene delivery vectors [130–132], peptide vectors [133, 134], liposomes [135–137], micelles [138, 139], and nanoparticles [100, 102, 103, 140–142]. While these studies have shown promise, most of these methods have been of limited use [133, 140]. For example, use of osmotic pressure to open tight junctions is a very invasive procedure and the opened junctions enable the passage of unwanted molecules. Prodrugs designed with higher lipophilicity and/or the ability to circumvent the efflux pump systems may enable them

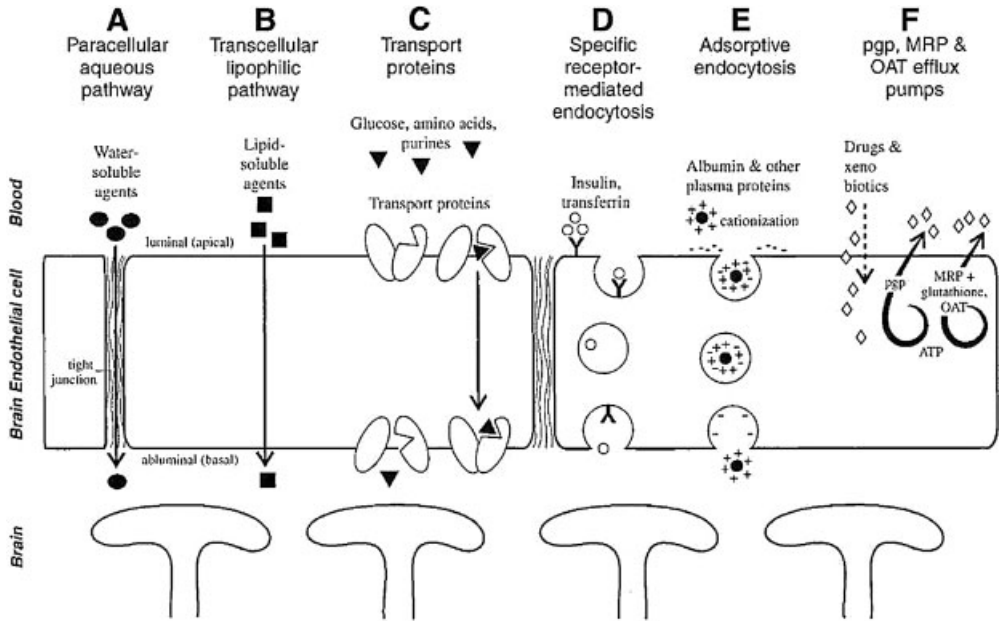


**Figure 16.1.** Physiological functions of the BBB (with permission after Ref. [119], see original article for full details).

more effectively to penetrate the BBB and transport into the brain, but this approach is not often possible [99]. It is common to use viral vectors for transfecting the expression of specific protein, but this drug delivery method shows certain disadvantages such as safety of both vector and expressed transgene, and stability and regulation of transgene expression [130]. Drugs conjugated to a natural protein molecule as carrier, so called vector-mediated drug delivery utilizing chimerical peptide technology, have shown effectiveness in brain delivery; however, the amount of transported drugs is limited because the maximal ratio of drug to carrier protein is usually about 1:1 [142]. Carbohydrate drug delivery, using sugar-mediated transporters in the BBB, may only work for drugs with small molecular sizes. On the other hand, colloidal drug delivery systems including liposomes, micelles and polymeric nanoparticles have become an important tool to transport drugs into the brain [100, 102, 103, 105, 124, 140]. Compared with other colloidal systems, the polymeric nanoparticle delivery system in particular has the advantage of easier preparation and higher stability in biological fluids [141, 143]. Controlled and sustained drug release is an added virtue of the nanoparticulate drug delivery systems [104, 141]. However, passive targeting of nanoparticles, which refers to the natural distribution of a drug delivery system in organs containing sessile actively phagocytosing cells such as liver and spleen, has to be solved, especially with parenteral administration [143–147]. This passive uptake represents a major problem for nanoparticle targeting to other parts of the body including the

brain. Fortunately, studies have demonstrated that, by modification of the properties of nanoparticulate drug delivery systems, they can actively target specific organs or cells [141]. These modifications can be approached through various means that include (i) surfactant or macromolecule coating to alter system surface properties, (ii) conjugating specific antibodies to the system surface, (iii) changing the particle size and/or electric charge on the surface, and (iv) incorporating magnetite particles into the system and using a magnetic field for targeting. These techniques open the door for nanoparticulate drug targeting development and provide many possibilities to optimize particle-targeting delivery.

### 16.2.3

#### Preparation of Polymeric Nanoparticulate Drug Delivery Systems

Drugs delivered by polymeric nanoparticles can be dissolved, entrapped or encapsulated in the nanoparticles, forming a solid solution or dispersion. Also, the drugs can be adsorbed onto the particle surface or chemically attached (Fig. 16.2) [99, 100, 104]. Nanoparticles of 10–1000 nm, composed of either natural or synthetic macromolecules as therapeutic adjuvants and/or drug carriers, have potential for pharmaceutical and medical uses [99, 100, 141]. With respect to drug delivery to the brain, nanoparticles that are too small in size may result in reduced brain uptake due to rapid dissolution in the blood [101, 141]. Also, at smaller sizes it becomes difficult to obtain a monodispersed particle population [104]. On the other hand, larger size particles may suffer an increase in uptake by the mononuclear phagocytic system before reaching the brain, and increase the risk of blood capillary blockade and embolism, especially with intravenous administration [101, 148–150]. Nanoparticles in the region of 200 nm have, with surface modification, the ability to deliver drugs such as central nervous system-active substances and anticancer agents across the BBB, as shown by therapeutic efficacy [98, 100, 102, 141, 142, 151, 152].

Nanospheres (Fig. 16.2A), generally defined as a dense polymeric matrix in which drugs are dispersed, can be prepared via an emulsion and/or dispersion po-

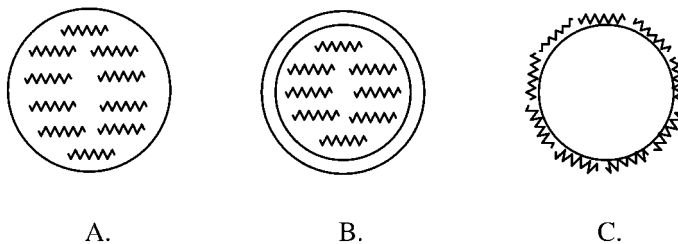


**Figure 16.2.** Different types of nanoparticulate drug delivery systems such as: (A) nanosphere with drug incorporated in polymeric matrix, (B) nanocapsule with drug surrounded by a thin polymeric envelope and (C) drug adsorbed or chemically attached on the polymeric nanoparticle surface.

lymerization of monomers, depending on the nature of the polymers used [103, 110, 153] or by preformed polymers [103]. For example, poly(alkylcyanoacrylate) nanospheres, which are rapidly biodegradable and widely used for *in vivo* studies of drug delivery to the brain, are obtained by the emulsion polymerization process. In this method, droplets of water-insoluble monomers are emulsified in aqueous solution and stabilized by surfactants. The anionic polymerization reaction is initiated by the water itself and started in micelles after diffusion of monomers through the aqueous phase. Polymeric chains continue growing until prohibited by free-radical termination, then aggregate into fine particles. To incorporate them into nanospheres, drugs can be dissolved in the polymerization medium either before the monomer introduction or after its polymerization [104]. Using the solution-emulsification technique, nanosphere drug delivery systems can be obtained from preformed, well-defined macromolecules. This approach can avoid some potential problems associated with polymerization of monomers such as residual monomer and drug interaction and inactivation [104]. An example of this method is briefly described here. Polyester is dissolved in chloroform and this solution is mixed with an aqueous phase to form a uniform oil/water emulsion [154, 155]. Continuous emulsification under mixing is necessary to prevent organic droplet coalescence and to allow spontaneous solvent evaporation and particle formation [104]. To obtain particles with sizes less than 1  $\mu\text{m}$ , ultrafine emulsification must be performed and microfluidization was recently used for this purpose [156]. An improved method based on desolvation has been developed, in which macromolecules can be precipitated from solution following the introduction of a third component or a nonsolvent miscible with the solution. Many nanoparticulate drug delivery systems are prepared using this technique or its modifications, as reviewed in [104].

Nanocapsules (Fig. 16.2B) are characterized by the presence of a liquid core surrounded by a thin polymeric shell. Interfacial deposition and emulsification diffusion are the two main approaches for nanocapsule preparation. The interfacial deposition procedure involves mixing a water-miscible organic phase containing oil (with or without lipophilic surfactant) with an aqueous solution containing hydrophilic surfactants. This approach can also use either preformed polymers or monomers that polymerize at the oil/water interface [104, 157, 158]; preformed macromolecules should first be dissolved in the organic phase (or in a phase that can dissolve them). After mixing the organic and aqueous phases, the macromolecules diffuse with the organic solvent and are stranded at the oil/water interface. If monomers are used, e.g. alkylcyanoacrylates, they are dissolved in ethanol and oil, then dispersed in water containing surfactants. Polymerization in the oil phase is initiated at the interface, resulting in the formation of nanocapsules [104]. The emulsification diffusion technique provides a simple approach to produce nanocapsules. It also has several advantages including a large choice, small solvent quantities, and controlled size and shell thickness [104]. Using this method, nanocapsules with an inner aqueous core can be prepared [159]. Emulsification diffusion is based on the initial formation of an oil/water emulsion, which contains a polymer, a drug and oil in the organic solvent, in an aqueous solution of a stabiliz-



ing agent. Then, displacement of the organic solvent into the external phase is conducted by adding excess water [104, 160]. It is worth noting that nanocapsules have higher drug-loading capacity and lower polymeric content than nanospheres.

Drugs can also be adsorbed onto the surface of preformed nanoparticles (Fig. 16.2C) by mixing the particles with the drugs in solutions. The absorptive capacity is dependent on several factors such as the polymer, the drug and the medium pH [141, 161]. In some cases, chemical binding of drugs to nanoparticle surface (Fig. 16.2C) may be necessary as described later in our studies. The covalent bonds can be formed through chemical reactions between functional groups present in the drugs and the particles [141, 162]. Apart from polymeric nanoparticulate drug delivery, drug nanocrystals (nanosuspensions), lipid–drug conjugate nanoparticles and lipid nanoparticles are also widely used and take advantage of high drug-loading capacity. Their features, including preparation and medical application, are reviewed in Refs. [101, 102].

The nanoparticle sizes and their distribution can be evaluated by elastic light scattering. This can also be done using scanning or transmission electron microscopy (SEM, TEM), which may provide information about nanoparticle structure [103, 104, 141]. Measurement of the  $\zeta$  potential is often made to characterize the nanoparticle surface properties such as electrical surface potential, drug location and particle stability [103, 104, 141]. Some more commonly performed characterizations such as drug loading and releasing capacities are summarized in Refs. [103, 141].

#### 16.2.4

#### **Possible Mechanisms by which Nanoparticles Cross the BBB**

There is a little doubt that nanoparticles conjugated with antibody against transferrin receptor (TfR) or ligands such as thiamine are transported across the BBB by utilizing TfR or thiamine-mediated transport systems, respectively [123, 142, 148, 163]. However, the mechanisms by which nonantibody or non-ligand-coated nanoparticles deliver drugs into the brain are not fully understood. Surface coating of nanoparticles, e.g. using poly(ethylene glycol) (PEG) [164–166] and some poloxamers [100, 167, 168], and especially with polysorbates [151, 152, 169, 170] and apolipoprotein E and/or B (ApoE and/or B) [100, 167, 171], plays a critical role in nanoparticle-mediated drug transport across the BBB. The coating with these materials apparently alters the natural blood opsonization process of the nanoparticles, thus reducing macrophage recognition in the liver and spleen. This effect consequently increases the nanoparticle blood half-life and extravasation to non-reticuloendothelial systems including the brain [142].

To further elucidate the role of coating, patterns of human plasma protein absorption on the nanoparticle surface have been examined after incubation of nanoparticles in the plasma. Analyses were performed by separating the nanoparticles and releasing the absorbed plasma proteins followed by two-dimensional polyacrylamide gel electrophoresis (2-D PAGE). These analyses showed that polysorbate-coated nanoparticles preferentially absorb ApoE on their surface. In contrast, no

such adsorption was found after incubation of noncoated nanoparticles or nanoparticles coated with many other surfactants [100, 167, 168]. Moreover, in *in vivo* studies on central nervous diseases, only drugs delivered via polysorbate or ApoE (and/or B) coated nanoparticles have therapeutic effectiveness and ApoE-deficient animals exhibit a reduced therapeutic response compared to controls [172]. These findings strongly indicate the involvement of ApoE and B in nanoparticle-mediated drug transport across the BBB and the surfactant on the particle surface may serve as an anchor for ApoE [171]. It is well known that ApoE plays a key role in the transport of LDLs into the brain, and the LDL receptor exists on the BBB [118, 173–177]. Also, lipoprotein particles containing ApoE and ApoA-I are found in human cerebrospinal fluid [178]. After the polysorbate coated nanoparticles absorb ApoE from blood plasma, it is very possible that nanoparticles mimic LDL particles and interact with the LDL receptor. Thus, brain capillary endothelial cells take up the nanoparticles by receptor-mediated endocytic processes [99]. Endocytosis of nanoparticles coated with polysorbate has been demonstrated in both *in vitro* and *in vivo* studies [169, 171, 172, 179, 180]. Significant and rapid uptake of polysorbate-coated nanoparticles by endothelial cells is found at an incubation temperature of 37 °C, whereas only minimal uptake is observed for noncoated nanoparticles [169, 172]. Further evidence shows that uptake is inhibited at lower temperatures (4 °C) or by cytochalasin B (a potent phagocytic uptake inhibitor) pretreatment [169, 172].

After nanoparticle endocytotic uptake, the nanoparticles may be transcytosed through the brain blood vessel endothelial cells since LDL transcytosis across the BBB has been demonstrated [118]. It is also possible that the drug is released from the nanoparticle in the endothelial cells and diffuses into the brain [99]. Several other mechanisms involved in nanoparticle-mediated drug transport across the BBB have been suggested [99]. For example, opening of the tight junctions between the brain endothelial cells by nanoparticles could occur, and the drug could then penetrate through the opened junctions either with the particles and/or in free form. Studies show that inulin spaces, an indicator of the tight junction opening, are increased only by 10 and 99% after 10 and 45 min, respectively, in rats treated with polysorbate-coated nanoparticles. In contrast, the increase of these spaces is 1000–2000% by osmotic methods [180–184]. These studies indicate that the coated nanoparticles increase the volume available to the intravascular inulin; however, they do not disrupt the BBB significantly. The slight opening of the tight junctions caused by the particles may result from folding-up of the cell membrane accompanied by endocytotic events or from an increase in fluid-phase endocytosis of inulin associated with the internalization of the nanoparticles [99]. It is known that some surfactants such as polysorbate show the ability to inhibit P-gp present in the brain endothelial cells and responsible for the multidrug resistance [185–187]. This inhibition of the efflux pump by surfactant could be responsible for nanoparticle-mediated drug delivery into the brain [99]. It may be significant that nanoparticle brain penetration increases when brain pathologies such as cancer [188, 189] and allergic encephalomyelitis [164] occur. The potential toxicity of the polysorbate-coated nanoparticle to the brain endothelial cell has also been sug-

gested to facilitate particulate drug delivery across the BBB [170]. In fact, many studies show that there are no significant signs of toxicity associated with this process [99, 190, 191]. However, it should be mentioned that nanoparticle surface charges may affect BBB function and studies show that cationic nanoparticles pose a toxic effect on the BBB, while the neutral or anionic nanoparticles at low concentrations do not disrupt BBB integrity [192]. Lipid coating may prevent the toxic effect of the ionically charged particles to the endothelial cell and enable the particles to cross the endothelial cell layer via transcytosis with no or little degradation [99, 193].

The preparation of the drug–nanoparticle system is relatively easy and in general the system is very stable. It is also important that there is a large variety of ways to improve the bioavailability and specific targeting of the particulate drug delivery systems and to minimize the toxicity of the systems. Based on the nanoparticle-mediated transport technology, a novel approach was recently developed in our laboratories [109]. This approach allows the nanoparticles not only to deliver metal chelation agents into the brain for the treatment of AD and other metal-mediated neurodegenerative diseases, but also to bring the toxic metals out of the brain, thus increasing therapeutic efficacy and limiting metal-chelate toxicity. This principle may be useful for other biomedical applications in the delivery of drugs to disease targets and/or depletion of toxicants using nanoparticle transport technology.

### 16.3

#### **Status: Nanoparticle Targeting Transport of Therapeutic Agents for Potential Treatment of AD**

The technology of nanoparticulate drug delivery has been developed for many years, and has been demonstrated not only to improve drug safety and efficacy, but also to lead to new therapeutic agents. However, its application in the treatment of AD has only appeared recently in very limited studies, due perhaps to the complexity of the disease pathogenesis and to an incomplete understanding of the mechanisms by which nanoparticles deliver drugs across the BBB. A lack of collaboration between scientists in differing, but relevant, disciplines may also impede application. In order to understand how to advance nanoparticle application, a review of recent developments in nanoparticulate drug delivery for AD treatment is now presented.

#### 16.3.1

##### **Nanoparticle Targeting of A $\beta$ to Deliver Potentially Therapeutic Agents**

Senile plaques in the brain, composed mainly of insoluble deposits of A $\beta$  peptide with 39–43 amino acids, are a major hallmark of AD [69]. Studies, albeit controversial studies, show that the accumulation of A $\beta$  derived from APP by proteolytic cleavage are neurotoxic and believed to be responsible for the neurodegeneration observed in AD [194, 195]. Therefore, preventing and reversing the A $\beta$  accumulation is an important pharmacological target in AD treatment and several potential

therapeutics such as  $\beta$ -sheet breakers [196, 197], regulators of APP translation [66, 198–200], inhibitors of APP secretases [69–74], vaccines against  $A\beta$  [48] and metal chelators [42, 76–78] have been developed and tested. As many potential drugs are electrically charged hydrophilic and/or large size molecules, a lack of ability to enter the brain may hamper their treatment efficacy. Although nanoparticles serving as a vehicle can provide a valuable approach to carry many otherwise impermeable drugs across the BBB, the tissue distribution of nanoparticles and drug release are not fully elucidated. However, a recent study showed that the nanoparticles as well as delivered drugs are present predominantly in microglia and also in neurons [106], where the  $A\beta$  accumulation may occur and cause neurotoxicity [69, 194, 195, 201].

In this study, core-shell latex particles containing Thioflavin-(TfT) as a marker for fibrillar  $A\beta$  were synthesized by aqueous polymerization of butylcyanoacrylate and seeded onto polystyrene cores filled with TfT, then collected by ultrafiltration. The cores were prepared using emulsion polymerization of styrene in aqueous ethanol solution containing TfT and purified by dialysis against deionized water [202]. The formed core-shell nanoparticles are reported to be sphere-shaped with a diameter of about 90 nm, as demonstrated by SEM and TEM (Fig. 16.3A and B). The nanoparticles were injected into the hippocampus (AP = -1.7 mm, L = 1 mm and DV = 2 mm, relative to bregma) of C57B6 mice after anesthesia. Three days postinjection, the animals were transcardially perfused with 4% paraformaldehyde and 0.5% glutaraldehyde in 0.1 M phosphate buffer (pH 7.4). The brains were then fixed in 4% paraformaldehyde overnight and coronal vibratome 50- $\mu$ m sections of the dentate gyrus were cut. Using the oxygen-enriched photoconversion method [203], the TfT was photoconverted into an electron-dense material to localize the TfT-containing nanoparticles in the brain. After washing, osmication and dehydration, the brain tissue blocks were embedded in Ducurpan and semithin or ultrathin sections were prepared. Aggregated nanoparticles were detected in dentate granule cells and vacuolated cytoplasm in the vicinity of nanoparticle aggregates using light microscopy (Fig. 16.3C). Using TEM, this study also found clustered nanoparticles in microglia (Fig. 16.3D) and in neurons (Fig. 16.3E and F). Moreover, vacuolated inclusions and amorphous structures with moderated electron density were found in both cell types. The core-shell structure of the nanoparticles and the TfT delivered from the nanoparticles were further confirmed by TEM at higher power (Fig. 16.3F).

This study indicates that nanoparticles and the nanoparticle-delivered drugs may target  $A\beta$  in the brain, and provides strong evidence to further support the possibility of nanoparticle drug delivery for AD treatment with increased efficacy and lowered toxicity.

### 16.3.2

#### **Nanoparticulate Antioxidant Delivery to Increase Efficacy against $A\beta$ -mediated Oxidative Stress**

One of the neurotoxic effects of  $A\beta$  is to induce lipid peroxidation [204–207] that can lead to the formation of cytosolic free radicals and reactive oxygen species

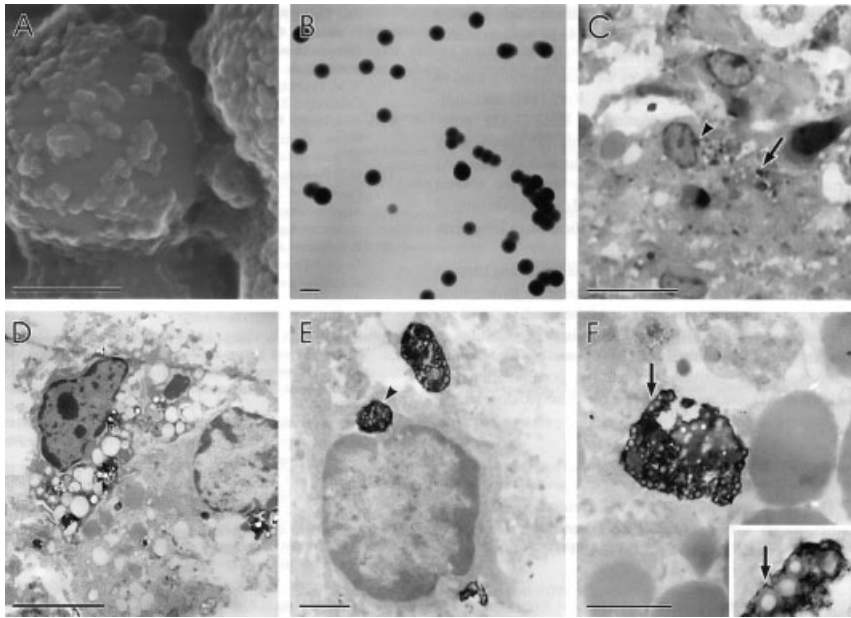


**Figure 16.3.** (A) The Tft-containing latex nanoparticles with a diameter of about 90 nm (SEM analysis). (B) Image of the nanoparticles on a Pioloform-coated slot grid (TEM analysis). (C) Light microscopic analysis of a section from fixed and plastic-embedded mouse dentate gyrus after 3-day intrahippocampal injection of nanoparticles and following photoconversion of Tft. Arrows and arrowheads indicate representative adducts of photoconversion. (D–F) TEM analyses of cells in the dentate gyrus after 3-day Tft particle injection and photoconversion. (D) Analyses show clusters of aggregated particles

incorporated in microglia (left) and in a granular cell (right). The vacuolar inclusions and amorphous structures with moderate electron density are found in both cells. (E) Photoconverted, aggregated lattices are located in the cytoplasm of a granule cell and an arrowhead marks the same cluster in (C). (F) High magnification of intraneuronal particle clusters. Photoconverted electron-dense materials surround the most core–shell-type microspheres (arrows), indicating Tft delivered by the nanoparticles. Scale bar: 1  $\mu\text{m}$  for A, E and F; 0.1  $\mu\text{m}$  for B; 20  $\mu\text{m}$  for C; 5  $\mu\text{m}$  for D. (With permission after Ref. [106].)

(ROS) [208]. Free radicals and ROS are highly active and can cause oxidative damage to all classes of biomolecules found *in vivo*, which include cellular lipids, nucleic acids, proteins and carbohydrates [209, 210]. This is believed to be a key factor in AD development [211, 212]. With aging, the endogenous antioxidant systems may gradually lose their ability to provide adequate neuroprotection and fail to compensate for the increased ROS formation [213]. Thus, antioxidant intake may provide protective effects against oxidative neurodegeneration [214, 215]; however, as discussed before, one impediment to the success of AD antioxidant therapy is the BBB that may limit appropriate antioxidant concentrations within the brain, thus diminishing its efficacy. Reduced efficacy may also result from the inability

of antioxidants to reach specific targets. It is known that vitamin E, a lipophilic antioxidant, shows mixed results in the treatment of AD [19, 216–218]. Furthermore, although vitamin E is capable of preventing  $A\beta$ -induced ROS in cultured cells, the cells have to be treated with vitamin E before  $A\beta$  exposure, or treated simultaneously with vitamin E and  $A\beta$ . In contrast, antioxidants that can enter the cytosolic compartment of these cells give neuroprotection even if applied after  $A\beta$  exposure [219–221]. This limitation is suggested to be a consequence of the lipophilic nature of vitamin E. The lipophilicity of vitamin E reduces its access to the hydrophilic cytosolic compartment, thus minimizing its ability to quench cytosolic ROS, as well as ROS produced from antecedent membrane oxidative damage [208]. It is possible that nanoparticle-mediated drug delivery cannot only send antioxidants into the brain more effectively, but also facilitate targeting specific locations, hence increasing their antioxidative effects.

A recent study [108] showed that vitamin E encapsulated in nanoparticles possesses an improved ability to quench  $A\beta$ -induced ROS even if applied about 1 h after  $A\beta$  exposure; in contrast, nonencapsulated vitamin E does not have such a capability. This study indicates that although vitamin E can protect against  $A\beta$ -mediated ROS, it lacks the ability to access the secondary ROS, which radiates into the cytosolic compartment following prior  $A\beta$  exposure, due to the lipophilicity of vitamin E [205–208, 213, 221].

In this study, nanoparticles containing vitamin E were prepared by mixing PEG 1500 decanyl polymer and vitamin E in chloroform solution. After removal of the solution, the mixture of PEG polymer and vitamin E was redissolved into water to induce self-assembly by vortexing. Resultant vitamin E-containing nanoparticles were purified by dialysis against water to remove unencapsulated vitamin E [222]. To examine the antioxidative efficacy of vitamin E encapsulated in PEG polymer nanoparticles, SH-SY-5Y human neuroblastoma cells were used. The cells were cultured in DMEM with 10% fetal calf serum and differentiated for 7 days with 10  $\mu$ M retinoic acid. Cell cultures were exposed to  $A\beta$  (25–35) for 2 h. Vitamin E and vitamin E encapsulated in nanoparticles were added to additional cultures either simultaneously with, or 1 h following, the addition of  $A\beta$ . To monitor the intracellular peroxide concentrations as an index of ROS, 2',7'-dichlorofluorescein diacetate was added to cultures for 20 min and then cultures visualized under fluorescein UV optics. The results indicate that vitamin E prevents an increase in ROS induced in differentiated neuroblastoma cells following  $A\beta$  treatment only if applied prior to or simultaneously with  $A\beta$  (Fig. 16.4). In contrast, vitamin E encapsulated in nanoparticles can prevent ROS even 1 h after  $A\beta$  exposure. The protective effectiveness was same as application of an equivalent concentration of non-encapsulated vitamin E simultaneously with  $A\beta$  exposure (Fig. 16.4). Nanoparticles without encapsulated vitamin E do not have neuroprotective ability. This result that the nanoparticles can deliver vitamin E into cytosol, thus increasing vitamin E antioxidative capability to quench cytosolic ROS, indicates that nanoparticle-mediated delivery may serve as a valuable tool for targeted transportation of antioxidants or other therapeutic agents for the treatment of AD. However, this result needs to be confirmed using normal neuro-cells and *in vivo* studies.

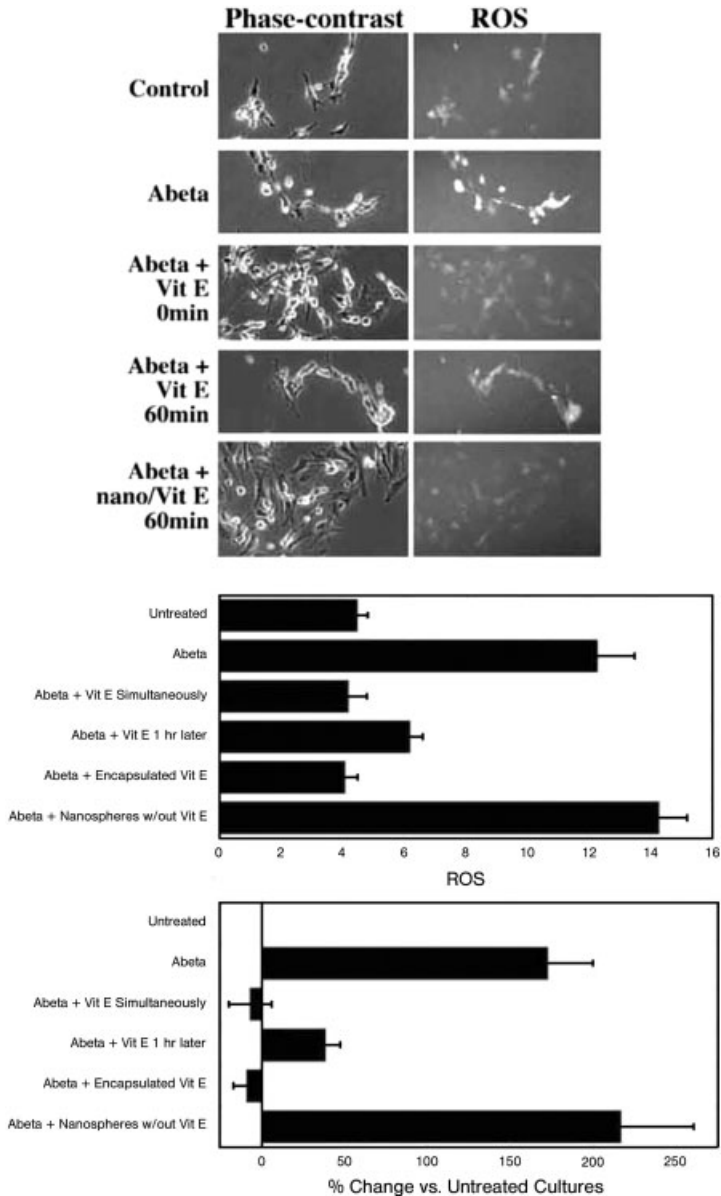


**Figure 16.4.** Nanoparticle drug delivery improves the efficacy of delayed application of vitamin E against  $A\beta$ -induced ROS. Panels present phase-contrast and fluorescent images of SH-SY-5Y neuroblastoma cells examined for ROS before (control) or 1 h following addition of  $A\beta$  with or without vitamin E or nanoparticulated vitamin E at the indicated intervals. Note the increase in ROS following addition of  $A\beta$ . Note that this increase is prevented by simultaneous, but not delayed,

addition of vitamin E, yet is prevented by delayed addition of nanoparticulated vitamin E. The accompanying graphs present the mean 2',7'-dichlorofluorescein diacetate (DCF-DA) fluorescent intensity  $\pm$  standard deviation of at least 50 cells. Values are also presented in the percent change in fluorescent intensity for each condition versus untreated controls (the mean intensity for controls are defined as 1). (With permission after Ref. [108].)

## 16.3.3

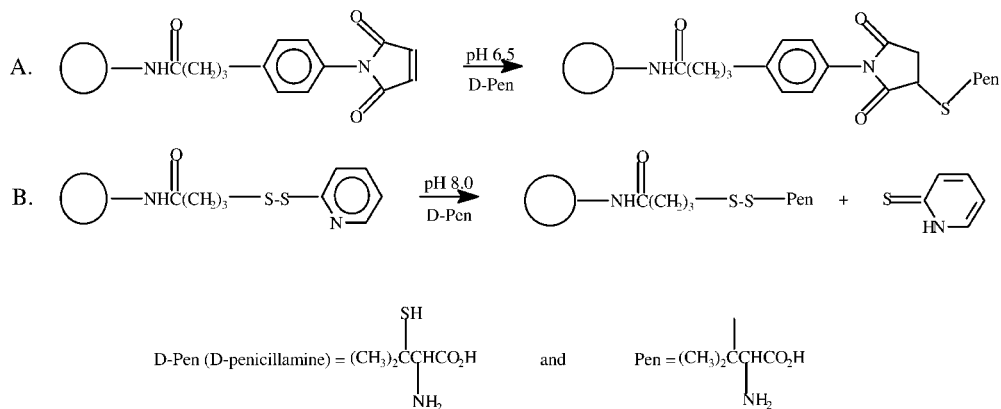
**Nanoparticle Delivery of Copper Chelator for Preventing and Reversing A $\beta$  Deposition**

Copper and zinc are essential in the body, but their excess is toxic. Accumulation of these metals in the central nervous system is believed to contribute to the oxidative stress and inflammation associated with AD [223–225]. Studies reveal that A $\beta$  has the ability to bind copper and zinc with high affinity, and that these metals may, in turn, mediate the A $\beta$  deposition in AD [226–233]. The evidence showing the association of these metals with A $\beta$  deposition is that simple coinubation of A $\beta$  from postmortem AD brain tissue with copper and/or zinc chelators results in resolvable aqueous A $\beta$  [234]. This association is also demonstrated by other findings from both animal experimental studies and human clinical trials [42, 43, 77, 80, 235]. Severe changes in some metal distributions are found in the brain of AD patients compared with healthy controls [225]. Concentrations of copper and zinc are significantly elevated in amyloid plaques and neuropil regions in the brains of AD patients (about 400  $\mu$ M for copper and 1 mM for zinc) compared to the healthy brains (70  $\mu$ M for copper and 350  $\mu$ M for zinc) [226, 236]. Treatment of APP transgenic mice (an AD mouse model) with the copper and zinc chelator, clioquinol, was shown to reverse A $\beta$  deposition [237], leading to a near halving of A $\beta$  deposition in the animal brain, compared with sham-treated controls [77]. The reduction of A $\beta$  deposition was accompanied by a significant improvement in behavior and general health parameters. Clinical studies also demonstrate that AD patients treated with clioquinol show significantly slowed cognitive deterioration and lowered plasma A $\beta$  levels [42, 43]. There were no indications of toxicity associated with chelation treatment for either experimental or clinical studies. These results suggest a potential approach that can prevent and treat AD by targeting the interaction of copper and zinc with A $\beta$  using chelation agents. However, an implication of clioquinol toxicity in an epidemic of subacute myelo-optic neuropathy in Japan has forced withdrawal of the drug from the market. For neuro-chelation therapy, the BBB represents a major hurdle for most available chelation therapeutics [109, 238]. To gain a deeper understanding of the roles of metals in AD development and to make progress in AD chelation therapy, there is a great need to develop more effective and safer chelation agents. Nanoparticle-mediated drug transport as an alternative means of drug delivery to the brain may provide an opportunity for such development [109, 110].

A recent study showed that D-penicillamine, a specific copper chelator for Wilson's disease (copper overload), can be successfully conjugated to nanoparticles through covalent bonding [107]. The nanoparticles have a long circulating ability in the blood and have been shown to be taken up by the brain *in situ* and *in vivo* without significant changes in BBB integrity or permeability [107, 147, 239, 240]. The nanoparticles containing 1,2-dioleoyl-*sn*-glycero-3-phosphoethanolamine-N-[4-(*p*-maleimidophenyl)butyramide] (MPB-PE) or 1,2-dioleoyl-*sn*-glycero-3-phosphoethanolamine-N-[3-(2-pyridyldithio)propionate] (PDP-PE) were synthesized by warming microemulsion precursors composed of emulsifying wax and surfactants such as Brij 78 or Tween 80 [107, 241]. These core components of the nanopar-



ticles are considered nontoxic and nonirritant materials [107, 241]. This study shows that the stability of these nanoparticles is greatly affected by the final concentration of surfactants, and the use of 4–6 mM of Brij and 2 mg mL<sup>-1</sup> of emulsifying wax can form the most-stable particles. A further increase in Brij concentration leads to the formation of less-stable nanoparticles. This study provides a simple preparation method for stable nanoparticles that can anchor chelation agents with them. In the preparation procedure, emulsifying wax was first melted and then stirred at 50–55 °C after adding deionized and filtered water in order to form a homogenous milky slurry. The surfactant was then added with continuously stirring. After microemulsions were formed, the mixture was cooled to room temperature to produce nanoparticles. The formed particles were characterized using a Coulter N4 Plus Sub-micron Particle Sizer. To provide functional sites on the nanoparticles for covalent conjugation with the sulfhydryl group in D-penicillamine, various amounts of MPB-PE or PDP-PE were incorporated into the particles by adding different concentrations of MPB-PE or PDP-PE in chloroform. The solvent was removed by evaporation before adding the emulsifying wax. The diameter of the formed nanoparticles was less than 100 nm with a narrow size range. Size is influenced by the MPB-PE or PDP-PE concentration, although not significantly [107]; however, if the concentration of MPB-PE or PDP-PE reaches 15% w/w, the microemulsion cannot be formed and the size of the resulting particles is relatively large. This study suggests that the hydrophilic heads of MPB or PDP are exposed on the nanoparticle surface while the lipophilic dioleoyl groups in both MPB-PE and PDP-PE insert into the lipophilic core of nanoparticles [107, 241, 242]. This molecular orientation, leaving the functional groups on the nanoparticle surface, is favorable for chelator conjugation. D-Penicillamine contains a sulfhydryl group and can either react with MPB-PE or PDP-PE to form thioether or disulfide bonds, respectively, which link the chelator and nanoparticles [243–245] (Scheme 16.1). The reactions were conducted at room temperature in approximately neutral aqueous solution (pH 6.5 for MPB-PE containing particles; pH 8.0 for PDP-PE containing particles). Nitrogen gas was used to prevent atmospheric oxygen from disturbing the conjugation reaction. The chelator-conjugated nanoparticles were purified by gel permeation chromatography using a Sephadex G75 column. The short-term stability of the chelator-nanoparticles containing PDP-PE was tested by particle size measured at intervals. The stability of the particles to salt or serum was also examined: D-penicillamine-conjugated nanoparticles are stable at 37 °C for 30 min in several different biologically compatible media such as saline, 10 mM phosphate-buffered saline solution (PBS), 10% lactose and 10% fetal bovine serum in saline. The linkage of disulfide bonds between D-penicillamine and PDP-PE incorporated into particles is also quite stable in PBS at pH 6, 7 and 8. Both D-penicillamine conjugated PDP-PE nanoparticles and MPB-PE nanoparticles are stable when treated with simulated serum, thus being suitable for chelator delivery *in vivo*. D-penicillamine conjugated MPB-PE nanoparticles are more stable than D-penicillamine–PDP-PE conjugated ones because of the formation of a more stable thioether linkage of D-penicillamine–MPB compared to the less stable disulfide link between D-penicillamine and PDP [245].



**Scheme 16.1.** Conjugation reactions of D-penicillamine to (A) MPB- and (B) PDP-nanoparticles. (Minor modification from Ref. [107].)

It should be mentioned that linkages using the sulfhydryl group of D-penicillamine totally deprive its copper binding activity. This, however, may provide a targeting chelation approach by which D-penicillamine can chelate copper within the brain only if it is released from nanoparticles, thus minimizing chelator toxicity in other places. To restore the chelation activity of D-penicillamine, it was proposed that the release could take place when the D-penicillamine conjugated nanoparticles react with reducing agents such as glutathione under normal physiological conditions. In cells, glutathione is the most concentrated nonprotein thiol and its concentration is about 1–6 mM [107, 246]. In order to test this hypothesis, a reducing agent, dithiothreitol (DTT) was used to incubate with the D-penicillamine-conjugated nanoparticles. After a 1-h incubation at 37 °C in water at pH 6.7, D-penicillamine was partially released from PDP-PE-containing particles by DTT, indicating cleavage of the disulfide bond between D-penicillamine and PDP. Although this result indicates the possibility of D-penicillamine release from nanoparticles by reducing agents, further studies are warranted such as increasing the releasing efficacy in both *in vitro* and *in vivo* investigations. As A $\beta$  is known to bind metals with high affinity and its aggregates are associated with copper, the ability of D-penicillamine, D-penicillamine-nanoparticles and D-penicillamine released from nanoparticles to reverse copper-mediated A $\beta$  aggregates were evaluated in this study. The A $\beta$  deposition is obtained from incubation of A $\beta$ (1–42) with cupric chloride in Tris buffer (pH 7.4) for 1 h at 37 °C and then incubated with those chelation agents for a further 1 h at 37 °C. To determine the redissolved copper A $\beta$  aggregates in the soluble fraction, the samples were centrifuged (10 000 g for 20 min) and the supernatants were analyzed for protein concentrations using the Pierce method [107]. In order to release D-penicillamine from nanoparticles, the chelator-conjugated PDP-PE-containing particles were incubated in basic aqueous solution (0.1 M, sodium hydroxide) at 45 °C for 1 h. Under these conditions, the

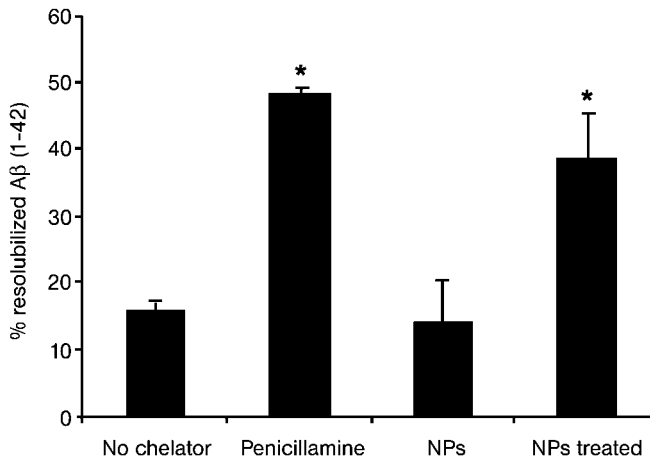


**Figure 16.5.** Experiments of Cu-A $\beta$ (1-42) aggregate resolubilization. The treatments are control (no chelator), D-penicillamine, D-penicillamine conjugated to PDP-NPs (NPs) and D-penicillamine conjugated to PDP-NPs (NPs) after being treated in 0.1 N NaOH at 45

°C for 1 h (NPs treated). An asterisk indicates that the values for D-penicillamine and treated NPs are not different from each other, but are significantly higher than that of no chelator and NPs. (With permission after Ref. [107].)

disulfide bond of D-penicillamine-particle linkage is more labile [243, 247]. Results show that the D-penicillamine conjugated to nanoparticles can no longer resolubilize the insoluble A $\beta$  aggregates mediated by copper while the free D-penicillamine does. D-Penicillamine released from nanoparticles restores its ability to effectively resolubilize the copper-A $\beta$  aggregates (Fig. 16.5).

This study provides a method to prepare D-penicillamine-conjugated nanoparticles that may have the ability to cross the BBB without adverse effects on cerebral perfusion, BBB integrity and permeability [107, 239, 240]. This study also shows that the nanoparticle-delivered chelator may be released after targeting and resolubilize metal-mediated A $\beta$  deposition, thus being able to prevent and treat AD. D-Penicillamine is used to treat Wilson's disease, wherein copper is accumulated initially in the liver and eventually in other organs including the brain [248]. D-Penicillamine can conveniently be administered orally and its effect on urinary copper excretion is dramatic [249]. However, development of D-penicillamine intolerance is frequently seen among patients and the ability of D-penicillamine to cross the BBB is not clear [107, 250, 251]. Thus, nanoparticle D-penicillamine delivery may increase the brain targeting of D-penicillamine and reduce its intolerance. Although more *in vivo* studies are needed and this chelation may be imperfect due to the possible accumulation of the chelator-metal complexes in the brain, this study provides evidence to support nanoparticle drug delivery as a potential approach for AD management.

## 16.3.4

**Nanoparticle Transport of Iron Chelators and Metal Chelator Complexes Into and Out of the Brain, Respectively****16.3.4.1 Increased Levels of Various Metals in the Brain of AD Patients**

It is already known from the above that copper and zinc play an important role in the accumulation of  $A\beta$  deposits, which in the form of preamyloid lesions and neuritic plaques, are one of the key neuropathological features of AD [107, 195]. Other metal ions are also known to be toxic and may be potential risk factors for AD. For example, excess iron in the body is extremely dangerous even though it is an essential nutrient for virtually all mammalian cells. Studies demonstrate that in individuals with primary or secondary iron overload disease, extreme iron accumulation in organs is recognized as a contributor to the manifestation of other diseases, including cardiac, hepatic, endocrine and bone disorders as well as cancer [252–254]. Even moderate elevations of iron in the body, which may be associated with age, is believed to play a significant role in causing diseases such as atherosclerosis, cancer, diabetes, dementia and osteoporosis [210, 255–260]. The toxic effects of excess iron and copper result largely from their ability to catalyze free radical generation through the Fenton reaction or Haber–Weiss reaction [209]. Iron also plays a key role in the regulation of cellular functions such as respiration, oxygen transport, DNA synthesis, nitric oxide formation and other redox reactions [209]. Therefore, iron levels in particular biological compartments have a close association with various disease processes. Although the etiology of AD is not well understood, accumulating evidence supports the hypothesis that oxidative stress generated by various mechanisms may be among the major risk factors that initiate and promote neurodegeneration [16, 211, 261–263]. Compared with other tissues, the central nervous system may be particularly susceptible to oxidative damage [264, 265]. Since iron and copper catalyze oxidation reactions, the likelihood that an oxidation reaction will take place is probably increased by regional concentrations of these metals [209, 223]. Substantial studies show that the metabolism of iron is involved in AD and that the concentration of iron, like copper, in the brain of AD patients is elevated [224, 266–270]. The iron levels in neuropil of human brain are  $39 \mu\text{g g}^{-1}$  for AD patients and  $19 \mu\text{g g}^{-1}$  for controls determined by microparticle-induced X-ray emission [236, 271–273]. Studies also demonstrate that iron can induce  $A\beta$  aggregation at acidic pH [232], a pathological value found in inflammatory disorders. Another metal ion, aluminum, has also received attention in AD [274], although its role in AD development has not yet been convincingly demonstrated. Nonetheless, aluminum is found in high concentrations in both senile plaques and intra-neuronal fibrillar tangles in the brains of subjects with AD, which suggests that this metal may be involved in the etiopathology of AD [224, 269, 275, 276]. Aluminum, unlike iron and copper, is unable to participate in redox cycles of electron transfer reactions due to a fixed oxidation state of  $3+$  in biological systems, but growing evidence suggests that it can act synergistically with iron to increase free radical damage [264, 277]. A recent study shows that accumulated alu-

minimum in the central nervous system modulates  $A\beta$  formation and deposition [278]. As mentioned early, evidence already shows that copper [211, 236, 279–283] and zinc [229, 236, 269, 284, 285] are implicated in the development of AD. In the AD brain, the concentration of copper is elevated in the rim of senile plaques and the concentration of zinc is significantly elevated in senile plaques. Taken together, these studies indicate that the environmental conditions in AD, exacerbated by imbalances in several metals, have the potential of catalyzing and stimulating free radical formation [109], and of facilitating  $A\beta$  aggregation and deposition [286], thus enhancing neurodegeneration.

Simultaneously elevated levels of multiple metals promoting oxidative damage to the brain present a complex system of pathophysiology that is not yet fully understood. Despite this complexity, metal dysregulation may in fact be the Achilles' heel of AD, opening a door for chelation therapy. A chelator, regardless of synthetic or natural origin, may have high affinity for one metal ion, but it can also undesirably chelate other metals in the body leading to serious side-effects. The affinity for multiple metals such as aluminum, copper, iron and zinc may pose useful rather than detrimental effects since various metals are implicated as oxidative instigators. Perhaps this is why desferrioxamine (DFO), a specific iron chelator also with high affinities for aluminum, copper and zinc, has demonstrated some therapeutic benefits for patients with AD. Thus, simultaneous chelation of several excess metals in the AD brain may provide a novel approach for safe and effective treatment of AD.

#### 16.3.4.2 Problems with Iron Chelators for Simultaneous Removal of Multimetal Ions for Treatment of AD

Iron chelation therapy shows potential as an alternative treatment for AD by simultaneously chelating multiple excess metals. However, this promising approach is hindered by chelator toxicity and/or poor bioavailability, especially BBB impenetrability. A few clinically available iron chelators also negatively affect the development of iron chelation therapy for this disease.

DFO and deferasirox (ICL670, Exjade<sup>®</sup>) are the only iron chelation drugs approved by the FDA for iron overload disease (Fig. 16.6). Their therapy can promote iron excretion, and has led to great improvements in the quality and duration of life of patients who suffer from  $\beta$ -thalassemia and other refractory anemias [287,

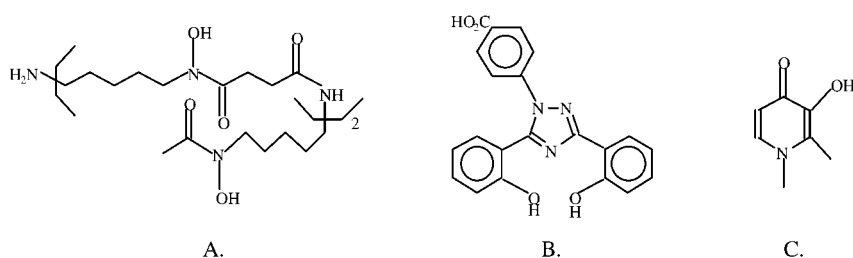


**Figure 16.6.** Chemical structures of (A) DFO, (B) ICL670 and (C) L1.

288]. Although there are no reports yet on deferasirox for potential treatment of AD, DFO is found to significantly slow the progression of AD in one clinical trial [289]. In this study, only the chelation of aluminum was examined, but it is possible that the therapeutic effect may also have been due to removal of iron since DFO preferably chelates iron forming 1:1 complex (DFO, a hexadentate chelator) [290, 291]. DFO also has an appreciable affinity for copper and zinc [290, 292]. The affinity constants of DFO for Fe(III), Al(III), Cu(II), and Zn(II) are 30.6, 22.0, 14.1 and 11.1 ( $\log K$ ), respectively [293]. In this particular clinical study, copper and zinc were not monitored. Thus, it is unclear if the DFO treatment simultaneously removes these metals and/or whether such a removal plays a role in slowing the clinical progression of AD. However, 2 years after the initial publication, a verbal report at the International Conference on Alzheimer's Disease (Padua, Italy, 1992) provides evidence that iron and zinc concentrations are decreased in a post-mortem analysis for DFO-treated patients [271, 290]. This clinical study, in addition to the follow-up report, provides strong evidence that multiple metal accumulations in the brain may be key contributors to AD development and simultaneous removal of them mitigates disease progression. Aside from effective chelation of several metals, DFO also inhibits nigrostriatal degeneration induced by 6-hydroxydopamine [294]. Unfortunately, DFO has serious side-effects including neurotoxicity and neurological changes [223, 274, 295–300]. Furthermore, DFO is poorly absorbed by the gastrointestinal tract and rapidly degrades after administration [301]. Therefore, it requires long subcutaneous administration to yield significant iron excretion [287, 291, 302]. Moreover, some studies show DFO does not easily penetrate the BBB due to its hydrophilic nature [303], although this point remains open to debate [304]. Indeed, some penetration may occur due to a compromised BBB via lesion sites [303]. Nonetheless, the neurotoxicity and difficulty of administration and delivery present serious hindrances to the use of DFO for AD treatment.

Another iron chelator, L1 (deferiprone or 1,2-dimethyl-3-hydroxyl-4-pyridinone), is a bidentate chelator and approved in Europe, but not in the US, for iron or aluminum overload diseases [305–307] (Fig. 16.6). It chelates iron and aluminum with very high stability constants of  $\log \beta = 37$  and 32, respectively. Since it can also chelate copper and zinc with appreciable efficiencies ( $\log \beta = 19.6$  for copper and 13.5 for zinc), L1 is capable of simultaneously chelating these metal ions. L1 virtually lacks affinity for calcium or magnesium; therefore, unlike many other chelators, L1 has no toxic effects due to chelation of these essential metals [307]. L1 also has high oral activity and BBB penetration because of its lipophilicity and relatively small molecular size. However, its use is limited because of serious side-effects [308, 309]. Moreover, studies show that L1 lacks the ability to remove iron from the brain [304] probably due to strong hydrophilicity of the iron–L1 complex. Additionally, there is no carrier-mediated transport system available to remove the complex from the brain. Other L1 derivatives with higher lipophilicity also have the ability to cross the BBB and complex iron in the brain, but they also possess considerable neurotoxicity [295, 298, 308]. Deferasirox is a tridentate iron chelator with oral bioavailability, which is currently approved by FDA for treatment of transfu-

sional iron overload in thalassemia. However, its long-term profiles are not yet available [288]. Furthermore, its lipophilic nature like L1 may raise questions concerning potential toxicity in AD treatment.

Thus, the use of the currently available iron chelators to simultaneously remove several excess metals in the brain of AD is limited because of their toxicity and/or poor transference across the BBB. Most bi- or tridentate iron chelators with small molecular weight and high lipophilicity have the ability to penetrate the BBB, but show toxicity [310]. On the other hand, hexadentate iron chelators are considered better candidates for chelation therapy than bi- and tridentate ones because of their lower toxicity before and after chelation [310], but they have difficulty penetrating the BBB [122, 304, 310] due to their hydrophilicity and relative high molecular weight. One strategy to increase the BBB penetration is by enhancing the lipophilicity and lowering the molecular weight of the iron chelators, but this is believed to increase toxicity [311]. In addition, the increase in lipophilicity of iron chelators will decrease the solubility in aqueous solution with probable a decrease in bioavailability [309]. Also, it is possible that some lipophilic chelators which normally should cross the brain endothelial cells are rapidly pumped back into the blood stream by extremely effective efflux pumps, as mentioned before [99]. Many promising attempts have been made to develop iron chelators with oral activity (membrane penetration) and low toxicity for the treatment of iron overload disease [312–347]. This leads to the hope, that if successful, some iron chelators may also be suitable for simultaneous chelation of several excess metal ions for AD treatment.

Some existing USP drugs such as clioquinol (iodochlorohydroxyquin) that possess chelation properties and BBB penetration ability have shown therapeutic benefits in AD [42, 43]. Clioquinol is an antibiotic agent and chelator with high affinity for zinc and copper, and less for calcium and manganese [77]. As mentioned before, oral administration of clioquinol in APP transgenic mice with advanced  $A\beta$  deposition leads to a significant reduction of  $A\beta$  deposition in the mouse brain compared to nontreated animals. This reduction of  $A\beta$  deposition is reported to be associated with copper and zinc chelation by clioquinol [77]. In clinical studies with clioquinol, the clinical rate of cognitive decline is slowed in a subset of AD patients compared with controls [42, 43]. Interestingly, the zinc concentration in plasma of AD patients treated with clioquinol was significantly higher than that of controls although no parallel change in plasma copper concentration has been indicated [43]. However, further investigation with this new approach is hindered by clioquinol toxicity. It should also be mentioned that this type of chelator generally may have a low affinity for iron and would be toxic at doses needed for sufficient iron removal [293]. EDTA has also shown some clinical improvements in the patients with dementia, including AD, in a small clinical trial and a large retrospective study [40, 41].

Currently, chelators with a hydroxyquinoline backbone or with high lipophilicity show BBB permeability and neuroprotective potential in experimental studies [78–80]. However, the toxicity of these chelators related to their lipophilicity has not been studied. Other therapeutic approaches are being explored to overcome the impediment of the BBB. For example, a prochelator has been designed for the pur-

pose of easily entering the BBB. The functional groups of the prochelator are then activated by enzymatic or nonenzymatic reactions after they have entered the target organ [121]. Another example is to use simple inorganic silicate that can form very stable complexes with many metals and probably has the ability to enter the BBB [348]. A newly developed copper chelator (tetrathiomolybdate) for Wilson's disease is also suggested as a potential treatment for AD [85, 349]. Iron chelators designed with near-optimal lipophilic/hydrophilic balance of the free chelator and iron complex for the purpose of passage into and out of the cell have been synthesized and studied [309]. However, no clear-cut clinical evidence for a beneficial effect of these chelators in AD has been demonstrated and new approaches are necessary.

#### 16.3.4.3 Nanoparticle Transport Technology to Improve Chelation Therapy for AD

The use of nanoparticles to transfer chelators represents an exciting therapeutic option that may prove safer and more effective for chelation therapy. There are four advantages to this particle chelator delivery approach: (i) the chelators need not be lipophilic to cross the BBB, (ii) the lipophilic character of the chelators no longer contributes to potential toxicity and (iii) hydrophilic hexadentate iron chelators with large molecular weights may be used, as previously demonstrated with nanoparticle technology [152, 350, 351]. Finally, the most important advantage is that the chelator conjugated to nanoparticles has the potential to leave the brain after complexing metals, thus further improving chelation safety and efficacy.

For metal chelation to be effective, the chelators must be capable of leaving the brain with the corresponding complexed metal ions. Many chelators are unable to prevent iron from catalyzing free radical formation via Fenton or Haber–Weiss reaction even though the chelators can complex iron tightly [352]. Thus, the metal–chelator complexes in the brain may still catalyze free radical formation, with possible new adverse effects on the brain. In fact, there is no systematic solution for this problem and finding the solution remains a big challenge in chelation therapy for AD as well as other neurodegenerative diseases associated with metal toxicity. If the nanoparticles are not biodegradable within the brain and can mimic lipoprotein particles by preferentially absorbing ApoA-I, known to facilitate the removal of particles from the brain [99, 353], the same carrier mediated transport systems of LDL will be able to carry the metal–complex nanoparticles out of the brain. This is in contrast to lipophilic chelators that can enter the brain, but when complexed with metals, are unable to cross the BBB due to a change in their lipophilicity. For example, the distribution coefficient (DC) of free L1 determined in *n*-octanol/Tris–HCl buffer system is 0.24, but when complexed with iron is down to about 0.001 [354]. Therefore, although L1 can reportedly penetrate the BBB, it fails to remove iron from the brain [304]. Obviously, the use of nanoparticles may provide a novel approach to transport of metal–chelator complexes out of the brain. The use of nanoparticles conjugated with chelators to mimic lipoprotein particles and transfer iron chelators into and out of the brain through selected apolipoprotein absorption not only provides a useful means of improving the efficacy and minimizing the toxicity of chelation therapy, but also provides insights into the mechanisms of AD development. This novel approach can also open a new area for nanoparticle technology to clean unwanted substances from diseased sites.



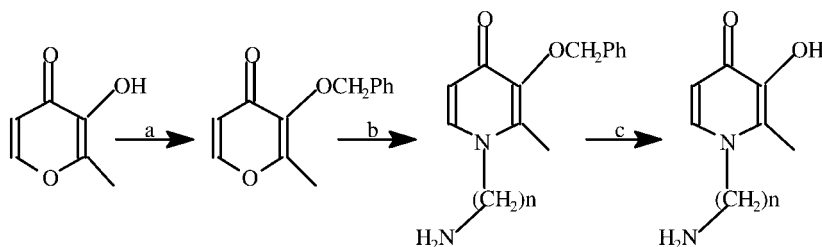
#### 16.3.4.4 Experimental Descriptions

To conjugate nanoparticles covalently, iron chelators must have a functional group to react with an active moiety on the particle surface. The functional group introduced into the iron chelators should not possess adverse effects on the chelator–metal binding. Synthetic methods to produce a series of iron chelators with such functional side-chains have been developed [126, 127, 355]. The metal binding properties of these chelators and some biological properties such as the *in vitro* ability to remove iron from tissue sections of AD brains and from ferritin (an important protein for iron storage) have been examined [126, 355]. Some of these chelators can remove iron from ferritin and are capable of depleting iron from tissue sections of the AD brain more effectively than DFO. Methods for conjugation of various iron chelators to nanoparticles have also been developed. The particles can be made of biocompatible synthetic or natural macromolecules [99, 100, 356] with functional groups such as amino and carboxyl groups on their surface for covalent bonding with chelators [162, 243]. After conjugation, the amounts of chelator that conjugate to the particles and the ability of the chelator–particle systems to bind iron are determined. Interestingly, some bidentate iron chelators converted to hexadentate chelators after conjugation to particles because the particles provided backbone linkages. This phenomenon greatly improved the metal binding stability and lowered toxicity associated with metal–chelator complexes. The human plasma protein absorption patterns on iron chelator particle systems are examined using 2-D PAGE technology [99, 357]. These studies show that the protein absorption pattern on the iron chelator particle systems is totally different from that of the human plasma proteins. Through changing the system surface properties, such as chelators and surfactants, the chelator–particle systems can preferentially absorb ApoE. With the same kind of changes, it is also found that the chelator–particle systems after binding metals can preferentially absorb ApoA-I. Such preferential absorptions allow the systems to mimic the ApoE or ApoA-I nanoparticles and to cross the BBB through LDL transport mechanisms [350, 353]. Uniform coating of the systems with ApoE, B or A-I can also be achieved by overcoating of these apolipoproteins, which may enable the systems to cross the BBB with high efficiency [171]. These studies indicate that iron chelator–nanoparticle systems have the potential to enter the brain and bring excess metals out of the brain, thus effectively preventing metal-associated oxidative damage. The results also show the potential to obtain chelator–nanoparticle systems with optimal surface properties via changing chelators, linkages, coating materials and nanoparticles with different surfaces. These findings are promising and suggest that this novel method of chelation may prove useful in the treatment of AD. More studies are warranted to demonstrate the chelation efficacy of the chelator–nanoparticle systems, to evaluate the system toxicity and to optimize their capability to cross the BBB. Some experiments are briefly described as follows.

**16.3.4.4.1 Synthesis of Iron Chelators with Functional Groups for Nanoparticle Conjugation** Iron chelators containing active functional groups have been synthesized. The preparation procedures are simple and product yields are good. The synthetic chelators have been characterized using standard methods such as

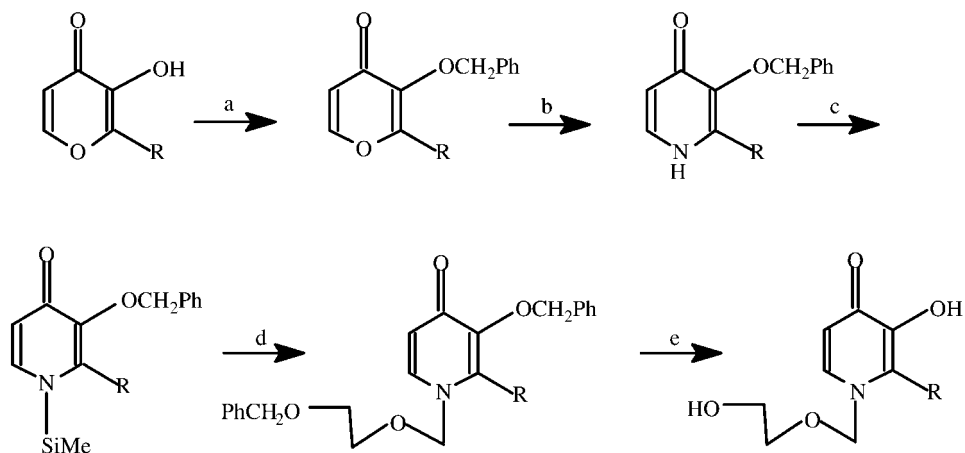
$^1\text{H}$ -nuclear magnetic resonance (NMR), mass spectrometry (MS), ultraviolet (UV)-vis and elemental analysis. Their preparations are briefly given below.

**2-Methyl-*N*-(2'-aminoethyl or 3'-aminopropyl)-3-hydroxyl-4-pyridinone (MAEHP and MAPHP)** The chelators were synthesized using a modified procedure as previously described (Scheme 16.2) [358, 359]. In brief, 3-hydroxyl-2-methyl-4-pyranone and benzyl chloride were mixed in a solution of water and methanol in the presence of NaOH. The mixture was refluxed for several hours with magnetic stirring. After removing methanol under vacuum, water was added and the 3-benzyloxy-2-methyl-4-pyranone was extracted with methylene chloride. The methylene chloride solution was then washed with 5% NaOH aqueous solution followed by water and dried over  $\text{MgSO}_4$ . The product was obtained after evaporation of the solvent under vacuum and then reacted with 1,2-diaminoethane or 1,3-diaminopropane in aqueous ethanol solution at room temperature. After 1 week, solvents and residual diamines were evaporated under vacuum and the residue was dissolved in chloroform, washed with water and dried with  $\text{Na}_2\text{SO}_4$ . After removing solvent, methanol was added and the pH is adjusted to 1 with HCl. 1-(2'-Aminoethyl)-3-benzyloxy-2-methyl-4-pyridinone or 1-(3'-aminopropyl)-3-benzyloxy-2-methyl-4-pyridinone was precipitated as dihydrochloride salt and collected by filtration. The pure products were obtained by recrystallization from methanol and ether, and further reacted with  $\text{BBr}_3$  (1.0 M  $\text{CH}_2\text{Cl}_2$  solution) in  $\text{CH}_2\text{Cl}_2$ . The mixture was stirred overnight at room temperature under a nitrogen atmosphere. Water was added and stirring was continued for an additional 4 h. The aqueous phase containing the MAEHP or MAPHP was separated and evaporated under vacuum. The crude MAEHP or MAPHP was purified through recrystallization from an ethanol/ether solution.



**Scheme 16.2.** (a) Benzylchloride/NaOH. (b)  $\text{NH}_2(\text{CH}_2)_n\text{NH}_2$ ,  $n = 2, 3$ . (c)  $\text{BBr}_3$  in  $\text{CH}_2\text{Cl}_2$  at  $4^\circ\text{C}$  or hydrogenation with  $\text{H}_2/\text{Pt}$  on active carbon. (With permission after [359].)

**2-Methyl (or ethyl)-*N*-(2'-hydroxyethoxy)methyl-3-hydroxyl-4-pyridinone (MHEHP or EHEHP)** The chelators were synthesized using established methods (Scheme 16.3) [355, 360]. Briefly, 3-benzyloxy-2-alkyl-4-pyridinone was synthesized as reported in reference [358] with a minor modification. First, to protect the 3-hydroxyl group, 2-alkyl-3-hydroxyl-4-pyranone with benzyl chloride was refluxed under alka-



**Scheme 16.3.** R = Me and Et. (a) PhCH<sub>2</sub>Cl/NaOH/refluxing/6 h. (b) NH<sub>4</sub>OH/room temperature/48 h. (c) Hexamethyldisilazane, chlorotri-methylsilane. (d) Benzyloxyethoxy-methylchloride, trimethylsilyl trifluoromethanesulfonate in 1,2-dichloroethane. (e) H<sub>2</sub>, Pd/C, AcOH in 95% EtOH. (With permission after [355].)

line conditions, as described above. Then, the ring oxygen of 3-benzyloxy-2-alkyl-4-pyranone was replaced by a nitrogen atom via a substitution reaction with aqueous ammonia at room temperature for 48 h. The 3-benzyloxy-2-alkyl-4-pyridinone was silylated in hexamethyldisilazane under refluxing and nitrogen gas for 2 h. After evaporation of the solvent under vacuum, the residue was redissolved in 1,2-dichloroethane and then benzyloxyethoxymethylchloride that could be replaced by (2-acetoxyethoxy)methyl bromide [361] was added in the presence of a catalytic amount of trimethylsilyl trifluoromethanesulfonate (SnCl<sub>4</sub> could also be used as catalyst in the alkylation reaction, but might result in separation difficulties and low yields) [362]. The resulting mixture was stirred at room temperature for 4 h and then treated with an aqueous solution saturated with sodium bicarbonate. After removing the aqueous phase, the organic phase was dried with sodium sulfate and the solvent evaporated under vacuum. Both of the protection groups were removed simultaneously by hydrogenation with H<sub>2</sub>/Pt on activated carbon in acidic aqueous ethanol at room temperature for 24 h or by BBr<sub>3</sub> in CH<sub>2</sub>Cl<sub>2</sub> at 4 °C [306, 363, 364]. The chelators were obtained in pure form after recrystallization from a 1:1 solution of CH<sub>3</sub>Cl:MeOH. To evaluate whether the linked (2'-hydroxyethoxy)methyl moiety affected the geometry of the iron binding site in the chelators, molecular and crystal structures of EHEMHP were determined by X-ray crystallographic analysis. A piece of colorless crystal (0.33 mm × 0.33 mm × 0.11 mm) formed in methanol/ethyl acetate solution was used for X-ray measurement with an Enraf-Nonius CAD-4 diffractometer equipped with a graphite monochromator of MoK<sub>α</sub> (0.71073 Å) [355]. An Oak Ridge Thermal Ellipsoid Plot (ORTEP) stereoview of the EHEMHP molecular structure is depicted in Fig. 16.7.

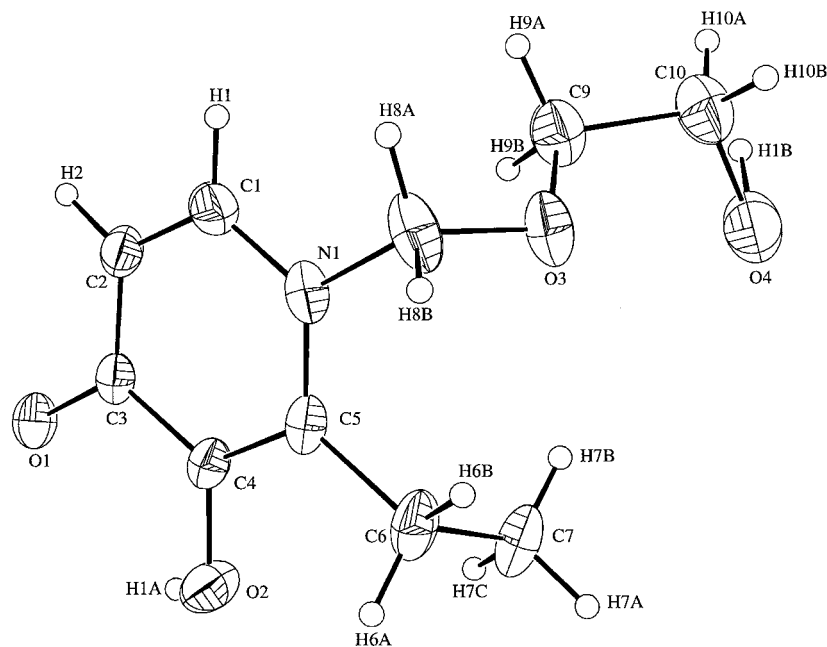
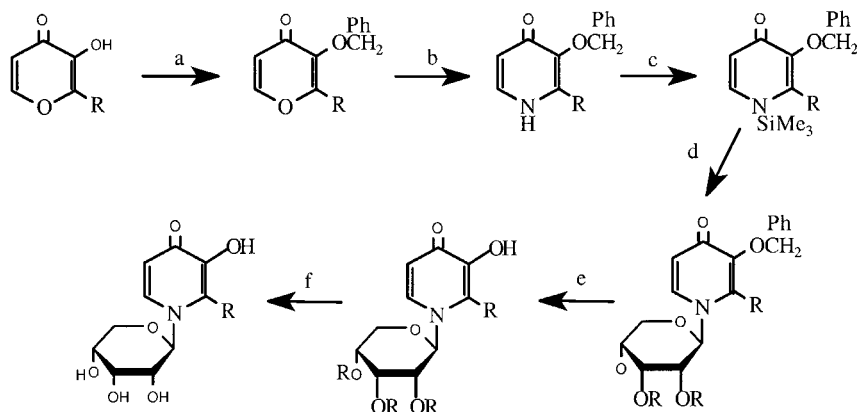


Figure 16.7. ORTEP stereoview of chelator EHEMHP. (With permission after Ref. [355].)

**2-Methyl-3-hydroxy-1-( $\beta$ -D-ribofuranosyl or ribopyranosyl)-4-pyridinone (MHRFP or MHRPP)** The synthesis of these chelators was similar to that of MHEMHP and EHEMHP above using a modified Hilbert–Johnson reaction (Scheme 16.4) [127, 360, 365]. In brief, after silylation the silylated 3-benzyloxyl-2-methyl-4-pyridinone



**Scheme 16.4.** R = Me. (a)  $\text{PhCH}_2\text{Cl}/\text{NaOH}/$  refluxing/6 h. (b)  $\text{NH}_4\text{OH}/$  room temperature/24 h. (c)  $\text{Me}_3\text{SiCl}/\text{Me}_3\text{SiNHSiMe}_3$ . (d) A prototype, 1,2,3,4-tetra-O-acetyl- $\beta$ -D-

ribofuranose/trimethylsilyltrifluoromethanesulfonate. (e)  $\text{H}_2$ , Pd/C in aqueous methanol with acetic acid. (f)  $\text{NH}_3$ -MeOH solution. (With permission after [127].)

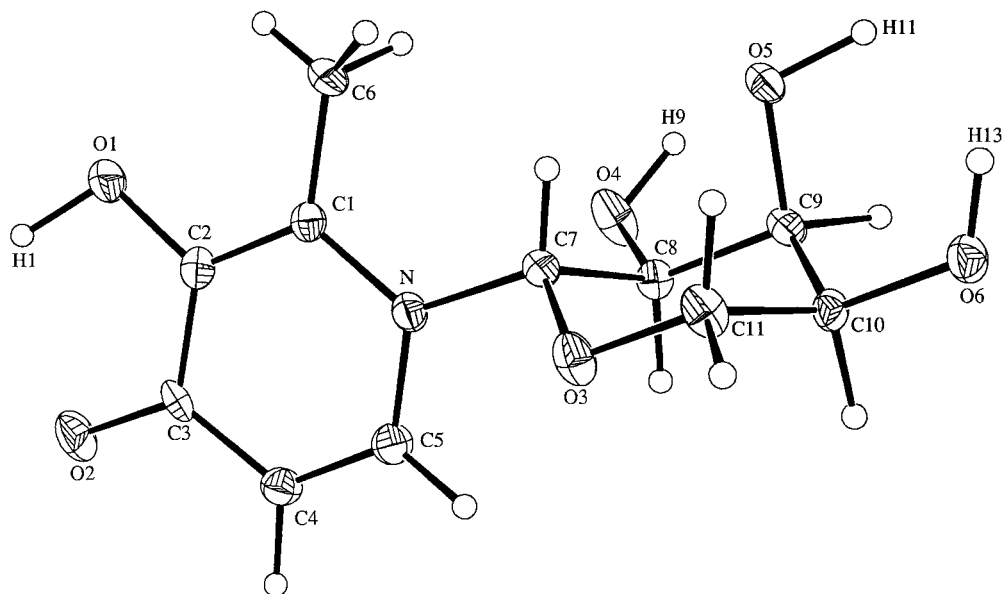


**Figure 16.8.** The molecular structure of chelator MHRPP. (With permission after Ref. [126].)

was alkylated by  $\beta$ -D-ribofuranosyl or ribopyranosyl groups. The benzyl protection group on the pyridinone was first removed by hydrogenation under  $H_2/Pt$  on activated carbon in acidic aqueous methanol [306, 363, 364]. Then, the hydroxyl groups of the sugar moiety were deprotected by basic hydrolysis in an  $NH_3$ /methanol medium overnight at room temperature. The chelators were obtained in pure form after recrystallization from a 1:1 solution of  $CH_3Cl:MeOH$ . Molecular and crystal structures of MHRPP were determined using X-ray crystallographic analysis to further evaluate the effects of the linked sugar moiety on the iron binding geometry in the chelators. An ORTEP stereoview of the molecular structure of MHRPP is depicted in Fig. 16.8.

#### 16.3.4.4.2 Ability of the Chelators to Complex Iron

**Reaction of Chelators with Iron Ions in Buffer Solution** The reaction between iron and chelators was indicated by a color change of buffer solutions (Tris buffer, 25 mM, pH 7.5, 22 °C) containing chelators following ferric iron  $[Fe(NO_3)_3]$  addition to the solution. The chelators and iron formed purple complexes with the chelator:iron stoichiometry of 3:1 [126, 355]. The typical visible absorption  $\lambda_{max}$  for free chelators and chelator–iron complexes was about 280 and over 450 nm, respectively (shown in Fig. 16.9). The stoichiometry was determined spectrophotometrically by titration of chelators in Tris buffer with freshly prepared iron solution

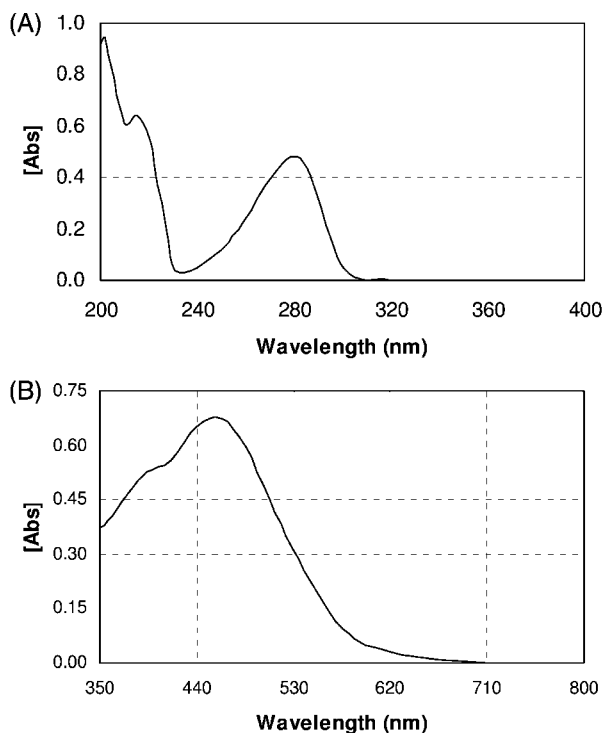


**Figure 16.9.** A. The UV-vis absorption of free MAPHP ( $\lambda_{\max} = 281 \text{ nm}$ ,  $\epsilon = 1.43 \times 10^4 \text{ Mcm}^{-1}$ ) and B. The absorption of iron-MAPHP complexes ( $\lambda_{\max} = 455 \text{ nm}$ ,  $\epsilon = 3.02 \times 10^3 \text{ Mcm}^{-1}$ ).

at room temperature. The iron solution was added gradually and the change in absorbance of the chelator-iron complexes was monitored by UV-vis spectrophotometry after the chelation reaction reaches equilibrium. Typical titration curves using MHEMHP and EHEMHP are presented in Fig. 16.10 and the endpoints of the titration indicate the formation of chelator:iron (3:1) complexes [355].

**Iron Mobilization by Chelators from Ferritin** The removal of iron from ferritin was studied by incubation of horse spleen ferritin with chelators in Tris buffer (25 mM, pH 7.5). Each chelator was mixed with the ferritin and incubated at 37 °C. The changes in absorbance of the iron-chelator complexes were measured spectrophotometrically at different time intervals. The concentrations of iron-chelator complexes were estimated from  $\epsilon_{\max}$  values at the wavelength of  $\lambda_{\max}$  of the complexes [126, 355]. The kinetics of the iron release was investigated for periods up to 72 h. Figure 16.11 shows the iron removal from ferritin by MHEMHP and EHEMHP as a prototype compared with DFO.

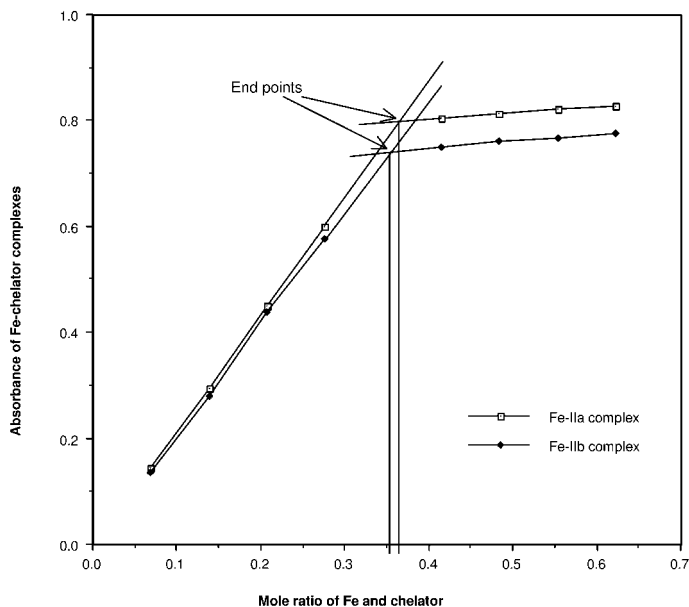


**Figure 16.10.** Titration of MHEMHP (IIa) and EHEMHP (IIb) with iron. (With permission after [355].)

**Iron Mobilization by Chelators from AD Brain Sections *In Vitro*** The ability of chelators to remove iron from brain sections was examined using a histochemical method [366]. Briefly, hippocampal tissues were collected from Alzheimer's disease patients, then fixed in methacarn (methanol:chloroform:acetic acid 6:3:1) overnight at 4 °C. After fixation, the tissues were placed in 50% ethanol, dehydrated in ascending concentrations of ethanol and embedded in paraffin. Six 6- $\mu\text{m}$  sections of the tissues were cut and then mounted on silane-coated slides (Sigma). The sections were deparaffinized with two changes of xylene (10 min each) and rehydrated through graded ethanol/TBS (50 mM Tris, 150 mM NaCl, pH 7.6). Then, 40  $\mu\text{L}$  of each chelator in PBS at various concentrations were applied to each section and incubated over night at 37 °C. The sections were rinsed thoroughly with TBS. After a 2-h incubation at 37 °C in 7% potassium ferrocyanide in aqueous hydrochloric acid (3%), the sections were rinsed with Tris buffer and subsequently incubated in 0.75  $\text{mg mL}^{-1}$  3,3'-diaminobenzidine and 0.015%  $\text{H}_2\text{O}_2$  for 5–10 min. Finally, sections were dehydrated through graded ethanol and cover slip.

**16.3.4.4.3 Conjugation of MAPHF and DFO with Nanosphere or Microsphere Particles** A variety of covalent bonds such as amido, amino, ether and thioether can easily be formed for conjugation of chelators and particles, depending on the existing functional groups located on chelator side-chains and on the surface of

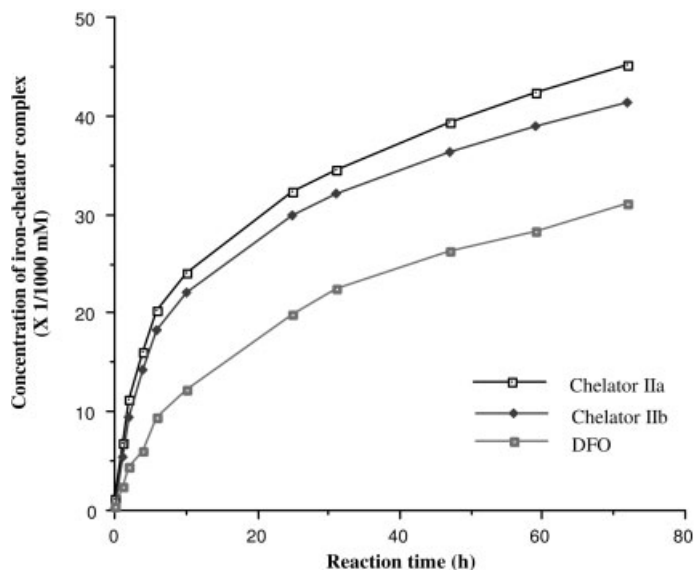
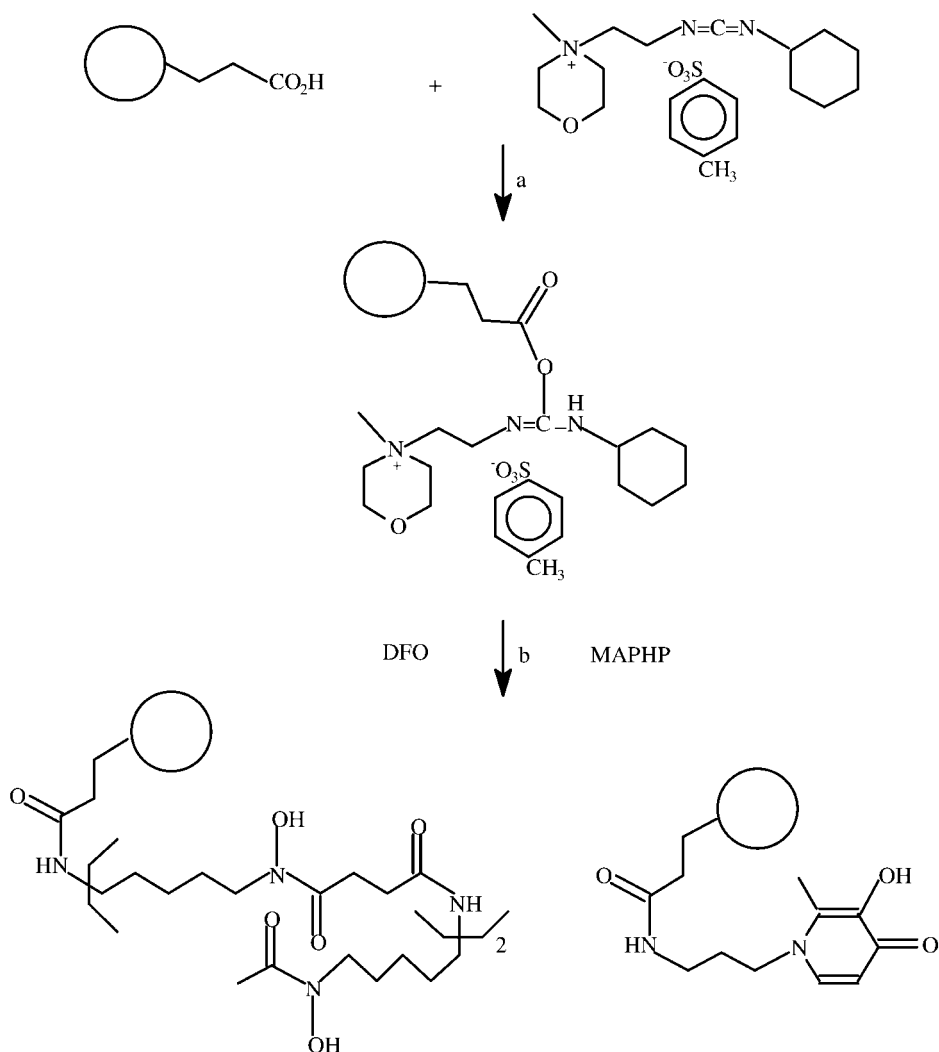


**Figure 16.11.** Removal of iron from ferritin by the chelators of MHEMHP (IIa), EHEMHP (IIb) and DFO. (With permission after [355].)

particles [162, 243]. Here, a simple method of particle–chelator conjugation by forming an amido bond is presented as a prototype. Monodispersed polystyrene particles with carboxyl groups on the surface were used to conjugate MAPHHP or DFO, each of which contained a free primary amino group available for the conjugation. The preparation of the chelator–particle conjugates is presented in Scheme 16.5. The carboxylic acid functional groups on the particle surface were preactivated by *N*-cyclohexyl-*N'*-(2-morpholinoethyl)carbodiimide methyl-*p*-toluenesulfonate (CMC) and conjugated with MAPHHP or DFO as described in Refs. [162, 243, 367]. The carboxylated particles were resuspended through pipetting and vortexing, and then the particles were immediately transferred into a microcentrifuge tube and the supernatant removed by centrifugation. The particles were suspended in 0.01 M NaOH solution, mixed well and the process was repeated. The particles were washed twice with 0.1 M of 2-(*N*-morpholino)ethane sulfonic acid (MES) buffer (pH 5.0) and once with cold Milli-Q water. Carboxyl groups on the particles were activated by adding cold Milli-Q water containing CMC (0.01 M) and incubating for 10 min at 4 °C with slow tilt rotation. After removal of the supernatant, CMC solution was added again along with MES buffer (0.3 M, pH 5.0). The mixture was vortexed and incubated as described above for 30 min. The particles with activated carboxyl groups were washed twice with cold 0.1 M MES as quickly as possible and resuspended in MES buffer (0.1 M, pH 5.0) containing excess MAPHHP or DFO (0.01 M). The mixture was vortexed, followed by incubation





**Scheme 16.5.** Conjugation of MAPHP and DFO to particles. (a) Reaction of CMC with carboxylic acid on particle surface in MES at room temperature for 30 min and (b) reactions of the activated carboxyl groups with excess chelators in MES for 30 min at room temperature.

for 30 min at room temperature with tilt rotation. The particles conjugated with chelators were washed with 0.1 M MES buffer twice and PBS (pH 7.4) twice and stored in PBS at 4 °C. The yield of conjugation was determined by measurements of the free chelator concentrations in the solutions before and after conjugation

using high-performance liquid chromatography (HPLC) or UV-vis spectrometry at the wavelength of maximum absorption [162]. The concentration and size distribution of the chelator–particle systems could be determined using a Beckman Coulter Multisizer II in a counting cuvette containing Isoton II diluent or using a Coulter N4 Plus Sub-micron Particle Sizer.

**16.3.4.4.4 Reaction of MAPHP– or DFO–Particle Systems with Ferric Iron** An aliquot of freshly prepared ferric iron solution [ $\text{Fe}(\text{NO}_3)_3$ , 0.002 M] in MES buffer (0.01 M, pH 5.0) was added to MES (0.01 M, pH 5.0) solution containing suspended MAPHP–particles or plain particles as a control. The mixture was rotated at room temperature for 4 h. The iron–chelator–particle systems and supernatant were separated by centrifugation. The systems were thoroughly washed with MES buffer 5 times to remove noncomplexed iron ions. After combining the supernatants, excess MAPHP in MES buffer (0.01 M) was added to complex the iron ions that did not react with the chelator–particle systems. The visible absorbance of the iron–MAPHP complex was measured using UV-vis spectrophotometry at a maximum wavelength of 455 nm ( $\epsilon = 3.02 \times 10^3$ ) after the chelating reaction reached equilibrium. A standard curve for iron concentration was obtained by measuring several solutions of iron–MAPHP complex with known iron concentrations. The identical procedure was applied in the investigation of the reaction of DFO–particle systems with ferric iron.

**16.3.4.4.5 Protein Absorption Patterns of Chelator–Particle Systems and Chelator–Particle Systems with Iron** The protein absorption patterns of chelator–particle systems and chelator–particle systems with iron, which were obtained by reaction of ferric iron with chelator–particle systems, were evaluated using 2-D PAGE analyses. In brief, the chelator–particle systems, overcoated with Polysorbate 80 at room temperature, and the chelator–particle system with iron (100  $\mu\text{L}$  of each system, 2.5% w/v in PBS buffer) were incubated separately in 1 mL of citrated human plasma (Sigma) for 5 min at 37 °C [357]. After separation by centrifugation and washing 4 times with Milli-Q water, the adsorbed proteins were eluted from the particle surface with a protein-solubilizing solution [5% sodium dodecyl sulfate (SDS), 5% dithioerythritol, 10% glycerol and 60 mM Tris, pH 6.8] [357] and analyzed by 2-D PAGE. In the first dimension, isoelectric focusing (IEF), the proteins were separated only according to their isoelectric points ( $pI$ ). The IEF was carried out in glass tubes of inner diameter 2.0 mm using 2.0% pH 3.5–10 ampholines for 9600 Vh. In the second dimension, SDS–polyacrylamide gel electrophoresis (PAGE), the separation was based on molecular weight. Each tube was equilibrated for 10 min in buffer (2.3% SDS, 50 mM dithioerythritol, 10% glycerol and 62.5 mM Tris, pH 6.8) and sealed to the top of a stacking gel that was on top of a 10% acrylamide slab gel (145 mm  $\times$  145 mm  $\times$  0.75 mm). SDS slab gel electrophoresis was performed for about 4 h at 12.5 mA per gel. After SDS–PAGE, the gels were dried between sheets of cellophane and silver-stained [357].

### 16.3.4.5 Results and Discussion

**16.3.4.5.1 Preparation of Iron Chelators with Functional Groups for Particle Conjugation** In order for chelators to conjugate with nanoparticles, the chelators must have a functional group to allow formation of a covalent bond between the two. As described above, several methods have been successfully developed to modify L1 by adding various side-chains that contain functional groups. The synthetic approaches are simple and the reaction yields in general are very high. In L1 (Fig. 16.6), the methyl group on the nitrogen atom at position 1 can be very easily replaced through various reactions, which provide many possibilities to obtain new chelators with functional groups. Also, the replacement has little effect on the geometry of metal-binding sites. Therefore, it is expected that the high binding affinity of L1 to iron as well as aluminum, copper and zinc will remain after its modification, enabling the new chelators to simultaneously complex multiple metals. The geometry of the metal-binding site in the modified chelators has been examined by X-ray crystallographic analysis. The analysis shows that the C3–O2, C2–O1 and C2–C3 bond distances of the metal binding site in MHRPP are 1.269(6), 1.361 and 1.428(7) Å, respectively (Fig. 16.8) [126]. These data compare well with the corresponding bond lengths of 1.271, 1.364 and 1.438 Å in L1 (Fig. 16.6) [368]. The unchanged geometry of the metal-binding site indicates that the affinity for iron as well as other metals is not affected [126, 355, 368, 369]. In EHEMHP, the C3–O1, C4–O2 and C3–C4 bond distances of iron binding site are 1.302(3), 1.350(3) and 1.418(4) Å, respectively (Fig. 16.7). The bond lengths of C4–O2 and C3–C4 are similar to that of L1, but the C3–O1 carbonyl bond distance is about 0.031 Å longer. These phenomena are explained by the increased electron donor effect of the ethyl group in EHEMHP compared with that of the methyl group in L1 on the 2 position of the pyridinone ring. Since the carbonyl group on the pyridinone ring is an electron draw group, the greater the electron density on the pyridinone ring donated by alkyl groups (ethyl > methyl), the longer the carbonyl bond length should be. Interestingly, the carbonyl bond distance of EHEMHP is close to that of the iron–L1 complex [370]. In the complex, the corresponding carbonyl bond length is 1.299(8) Å. The C4–O2 and C3–C4 bond lengths in EHEMHP also compare very well with the corresponding bond lengths of 1.342(7) and 1.408(7) Å in iron–L1 complex [370]. These observations indicate that the replacement of the 2-hydroxyethoxymethyl group has no negative effect on iron binding and that the iron-binding site of EHEMHP may be more favorable for iron chelation than L1 because of the preorganized effect [371].

**16.3.4.5.2 Examination of Modified Chelators Complexing to Iron** The ability of the modified chelators to complex metals was examined by titration of the chelators with iron in Tris buffer solution. The chelators react with iron forming purple complexes which have the chelator:iron stoichiometry of 3:1. The titration result also reveals that the functional groups in the side-chains are not involved in iron complexation under physiological conditions. This is important, because it ensures that

the use of the functional groups in chelator side-chains for conjugation with nanoparticles will not affect the chelator–metal binding ability.

To further examine the ability of the chelators to complex metals, the reaction of chelators with ferritin was evaluated. This protein is important for iron storage and in brain tissue most of nonheme iron is in the form of ferritin [266, 372]. Evidence shows that iron metabolism is altered in the brain of AD patients, with alterations including chelatable iron, ferritin and transferrin [267, 268, 275, 373]. The *in vitro* extraction of iron from the ferritin core by chelators is a convenient measurement of the potential efficacy of *in vivo* removal of iron from iron-overloaded organs [374]. All of the modified chelators can mobilize iron from ferritin in a slow reaction, which is monitored by the increase in absorbance of the iron–chelator complexes using a spectrophotometric method [126, 355, 374]. The formation of iron–chelator complexes in all the reactions indicated a common kinetic mobilization pattern that is characterized by initial rapid iron removal, followed by a slower iron removal rate. The end of the reaction as judged from stable absorbance. The modified chelators were more effective than DFO in mobilizing iron from ferritin at physiological pH. The initial rate of removal was faster with the modified chelators than with DFO, while the rate after 24 h was about the same, which can be seen in Fig. 16.11.

*In vitro* tests of iron removal from AD brain sections with various iron chelators were also performed and examinations of the sections using differential interference microscopy demonstrated that iron chelators have the ability to strip iron from the brain tissues. Results showed that the iron removal efficacy depends on the chelator chemical structures and concentrations used. For example, both MAEHP and MHEMHP had better ability to remove iron from AD brain sections, compared with DFO and MHRPP, at concentrations of 0.01 M (Tab. 16.1). The histochemical evaluation of iron in an AD brain section treated with MAEHP is presented in Fig. 16.12, showing remarkably less staining for iron compared with an untreated control. Importantly, this finding provides further support for the possible mechanism of metal-associated oxidative damage in AD development, by show-

**Tab. 16.1.** Iron evaluation by histochemical staining in AD brain sections after being treated with various iron chelators.

	0.1 M	0.01 M
Untreated	positive	positive
DFO	negative	very positive
MHRPP	few positive blood vessels	very positive
MHEMHP	negative	weakly positive
MAEHP	negative	weakly positive

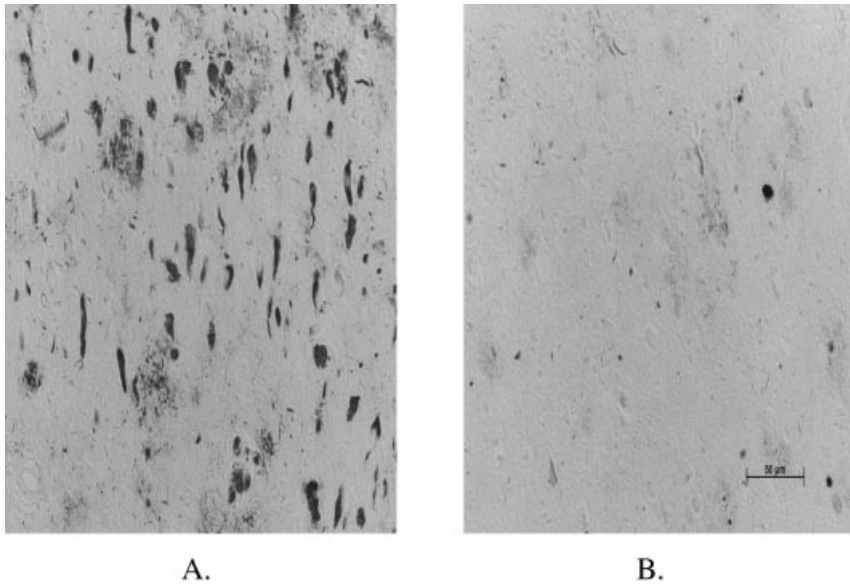


**Figure 16.12.** Lesion-associated chelatable iron in AD brain sections was depleted with iron chelator, which was evaluated by histochemistry. (A) Control and (B) MAEHP-treated section (with permission after [375]).

ing the existence of chelatable iron in the AD brain. The chelatable iron is believed to be one of the culprits that catalyze free radical formation, causing oxidative damage to all types of biomolecules [209]. Furthermore, this result indicates the potential of chelation therapy of AD by depletion of excess metals, hence preventing metal-mediated neuro-oxidative damage. These results are consistent with early reports that chelation treatment can affect iron accumulations that are closely associated with the places of senile plaques and neurofibrillary tangles in cases of AD [366]. This iron specifically localized to the lesions of AD could participate in *in situ* oxidation and catalyze an  $H_2O_2$ -dependent oxidation [366]. Our current study also identifies a useful tool to screen potential chelators which have suitable ability to mobilize iron from the AD brain *in vitro*. This method provides important information for selecting optimal chelators to use for conjugation with nanoparticles in our studies.

As discussed previously, currently available iron chelators used in chelation therapy are problematic due to both toxicity and/or poor bioavailability. It is difficult to develop iron chelators with an optimal balance of bioavailability and low toxicity by adjusting chelator size and lipophilicity. Therefore, other strategies have been explored in order to develop therapeutic iron chelators with suitable bioavailability as well as tolerable levels of toxicity. Relevant to particulate drug delivery, attempts to improve the pharmacological properties of current clinical iron chelators include covalently conjugating DFO to dextran and hydroxyethyl-starch [376–378] or conju-

gating DFO to large agarosepolyacrolein microsphere beads [379]. Results from these studies are consistent with our studies that the conjugation does not appear to affect the normal high iron-binding affinity of DFO. Also, improved bioavailability and/or stability of DFO as well as decreased toxicity are observed. Formulations of DFO with *n*-decanesulfonate or poly(fumaric anhydride-*co*-sebacic anhydride) produced particles with increased efficiency in chelation treatment by slowing down the release of DFO from the particles [380, 381]. In addition, microencapsulated formulations of L1 with Eudragit RS, RL and L90, and cellulose acetate phthalate have been developed to further improve its bioavailability [382]. Despite all of these improvements, there still is a tremendous need to develop iron chelators with specific organ-targeting ability. Optimal organ-targeting may in itself further improve bioavailability of chelators and limit toxicity. In addition to the primary purpose of correcting primary and secondary iron overload, this particular approach may also make it possible for chelation therapy to prevent and treat other diseases especially neurodegenerative disorders associated with excess metals.

**16.3.4.5.3 Chelator–Particle Conjugation, Metal Complexation and Potential BBB Penetration** Nanoparticulate drug delivery provides an opportunity for drugs to penetrate the BBB. The nanoparticle drug system also possesses the advantage of easy preparation and high stability. To explore the possibility of nanoparticle–chelator transport for AD treatment, practical methods for chelator conjugation with nanoparticles were investigated. Here, the reaction of MAPHP or DFO, each containing one primary amino group, with polystyrene nano/microparticles with a surface carboxylic acid moiety is presented as a prototypic conjugation. As mentioned before, it also is possible to synthesize iron chelators containing different functional groups that readily react to the nanoparticle surface active sites without any adverse effects on the chelator metal binding.

Carboxylic acid functional groups on the surface of the particles used here allowed the particles to conjugate with chelators by forming covalent amido bonds. Prior to conjugation, the carboxylic acid groups were activated using carbodiimide in MES buffer at an acidic pH value to form an active intermediate ester. To remove excess carbodiimide, the particles were rapidly washed with cool Mill-Q water since the ester is unstable and undergoes hydrolysis. An alternative method, such as adding a water-soluble *N*-hydroxyl compound like sulfo-*N*-hydroxysuccinimide (NHS), could increase the coupling yield since NHS is known to form a more stable intermediate ester by replacing the oacylisourea intermediate formed by carbodiimide. The NHS-formed ester is less susceptible to hydrolysis but still highly reactive toward amino groups [383, 384]. The primary amino group in the chelators reacts with active ester intermediates derived from carboxyl groups on the particle surface, consequently forming covalent amido bond linkages in good quality yields (over 70%). Coupling yields were determined by (i) measuring the free chelator concentration in solution before and after conjugation, using HPLC or UV-vis spectrophotometry readings, and (ii) calculating the difference between the two concentrations to indicate the amounts of the chelators conjugated to particles. After the conjugation reaction, the particle size distribution was

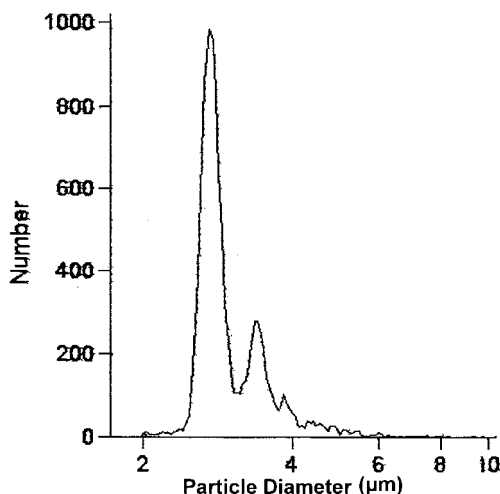


**Figure 16.13.** Particle size distributions measured by Multizer analyzer II. There is no distribution change between particles conjugated with MAPHp and particles without conjugation.

measured and compared with the distribution prior to conjugation. A distribution change was not observed, which indicated that there was no particle clumping (Fig. 16.13). A useful protocol for particle conjugation with various molecules can be found in Ref. [162].

With rapid development of nanoparticle technology in biomedical applications, most processes for preparing various nanoparticles with different sizes and properties have become routine and standard, and many of these nanoparticles are even commercially available. The technologies to make the nanoparticles virtually monodispersed, with a narrow diameter deviation, spherical shape and constant surface area, has really advanced the development of nanoparticulate drug delivery. Also, it has become easier to obtain suitable nanoparticles with various functional groups on their surface for the purpose of covalent bond conjugation by utilizing simple chemical reactions, as demonstrated by our studies.

To test whether chelators retain their ability to complex metals after conjugation with nanoparticles, the chelator–nanoparticle systems were incubated with a  $\text{Fe}(\text{NO}_3)_3$  solution. After the reaction was complete, the  $\text{Fe}(\text{NO}_3)_3$  solution was removed and noncomplexed iron was determined by adding MAPHp and measuring the iron–MAPHP complexes using UV-vis spectroscopy. Results indicated that about two MAPHp molecules conjugated to particles complexed with every iron atom. As each MAPHp can provide only two oxygen donors to chelate iron, two more iron-binding sites are needed to form a highly stable iron complex with an octahedral coordination sphere. According to our earlier studies [385], the oxygen atoms in amido groups may be involved in chelating iron; thus, two oxygen donors

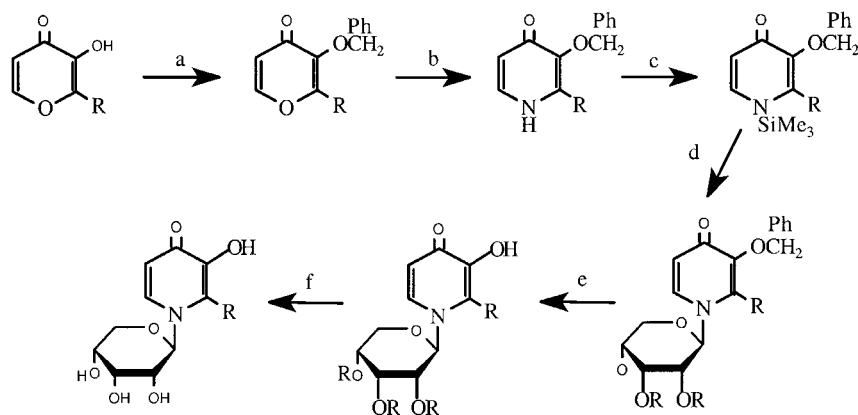


**Figure 16.14.** Four oxygen donors from two MAPHPs and two oxygen donors from amido groups constructing a hexadentate chelator through particle surface as the backbone.

from two amido groups and four oxygen donors from two MAPHPs may assemble into a hexadentate chelator, using particle surface linkages as the backbone (Fig. 16.14). This is significant, as hexadentate iron chelators possess many advantages including kinetic stability, concentration independence of iron affinity and low toxicity [310]. In addition, attempts to convert bi- or tridentate iron chelators into hexadentate chelators with various backbones suffer mainly from decreased bioavailability and the risk of potential toxicity. By contrast, the use of nano/microparticles to convert bi- or tridentate chelators to hexadentate chelators may circumvent these problems due to the particle targeting ability. In this manner, many bidentate or tridentate iron chelators, even with intolerable toxicity, can be modified by conjugation with nano/microparticles, since the toxic character of the free chelators may be diminished after particle conjugation. Our results also revealed that DFO still retains the 1:1 complex ratio with iron – an indication that conjugation with particles does not affect its iron binding ability. It is also worth mentioning that the bioavailability of some hexadentate iron chelators with high molecular weights and hydrophilicity can be improved after forming the chelator–particle delivery systems [386].

In order to demonstrate the possibility that chelator–nanoparticle systems enter the brain and that the chelator–nanoparticle systems leave the brain after chelation with metals, the protein absorption patterns of MAPHP–particle system and iron–MAPHP–particle system were evaluated; 2-D PAGE analyses were used to conduct this evaluation after incubation of the systems with human plasma. The 2-D PAGE images are presented in Fig. 16.15 and show that the protein patterns on the systems are totally different from that of the human plasma protein (Fig. 16.15a).



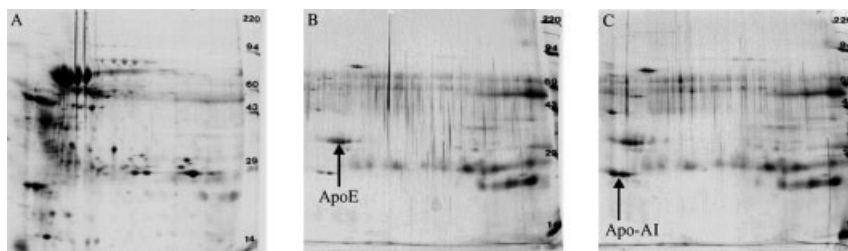


**Figure 16.15.** Images of plasma protein patterns examined by 2-D PAGE. (A) Plasma, (B) nanoparticle–chelator systems coated with Polysorbate 80 and (C) nanoparticle–chelator systems complexed with iron (with permission after [375]).

Through changing the surface properties of MAPH–particle system by coating surfactants such as Polysorbate 80, the system preferentially absorbed ApoE (Fig. 16.15b). On the other hand, after complexing of MAPH–particle system with iron, the iron–MAPHP–particle system possessed the absorption preference for ApoA-I (Fig. 16.15c). Such preferential protein absorptions may allow the MAPH–particle system and iron–MAPHP–particle system to mimic the ApoE and A-I nanoparticle, respectively, and therefore to enter brain without metal chelation and leave the brain with complexed metals via LDL transport mechanisms.

Simultaneous chelation of iron and other metals such as aluminum, copper and zinc may provide a useful therapeutic option for AD treatment. The use of nanoparticles to transport iron chelators into and out of the brain could lead to a safer and more effective chelation therapy for AD by means of decreasing the multiple metal load in neuro-tissue, and thereby staving off the harmful effects of oxidative damage and its sequelae. Iron chelators with functional groups can be synthesized and the functional groups can be used for conjugation with nanoparticles. The conjugation of such chelators to nanoparticles does not alter the chelator metal-binding ability and, in some cases, the conjugation even improves the chelation coordination property. The nanoparticles can be made of biocompatible synthetic or natural macromolecules with functional groups on their surface for conjugation with chelators. The macromolecules can be non- or controlled biodegradable for specific purposes. Changing nanoparticle surface properties can optimize the preferential protein absorption, thus improving the ability of the particle to cross the BBB. Many approaches to adjust particle surface properties can be used, such as coating with different surfactants or proteins, conjugating with different chelators or with various linkers and using antibodies to increase lipoprotein preferential absorption. Further studies with the chelator–nanoparticle system may provide more insights into the mechanisms of AD pathophysiology, and may show the possibility of prevention and treatment for other iron-mediated neurodegenerative diseases such as Friedrich ataxia, Huntington's disease, Parkinson's disease and Hallervorden–Spatz Syndrome. More studies are needed to demonstrate the protective efficacy of the chelator–nanoparticle systems, to evaluate their toxicity and

to optimize their capability to cross the BBB. Our studies may also open the door for the use of a nanoparticle-mediated transport to facilitate extraction of toxins from defective places in the body for disease prevention and treatment.

## 16.4

### Perspectives

Nanoparticulate drug delivery for AD prevention and treatment shows great potential; however, it is still at a very early stage of development. In order to advance this technology for AD application, knowledge is urgently needed in several basic research areas. For example, there is no study on the *in vivo* treatment of AD using nanoparticulate drug delivery technology. With the AD animal models available, the efficacy of nanoparticulate agents delivered to the brain that may offer therapeutic effects on AD based on a current understanding of AD pathogenesis should be evaluated. This will not only provide insights into the mechanisms of AD development, but also lead to more effective and safer therapeutics for the disease. It also is necessary to fully study whether the nanoparticulate drug systems possess adverse effects on the BBB and brain as well as other parts of the body, at tissue, cell and molecular levels. Additionally, the pharmacology and pharmacokinetics of the systems need to be examined, which will ensure the further development of the nanoparticulate drug systems for clinical use. Furthermore, it is suggested that the nanoparticle surface, and perhaps also the particle components, can be used to manipulate particle uptake into the brain via the LDL receptor, because nanoparticles preferentially absorb ApoE and/or B in blood, and thereby mimic these protein particles. However, the exact mechanisms are not fully understood, and thorough studies could provide valuable information that will help improve the ability of nanoparticulate drug systems to cross the BBB. Moreover, studies on improving drug-loading capacity in nanoparticulate drug systems, which should not affect the ability of these systems to enter the brain, must be carried out in order to reach sufficient drug level in the AD brain. In this regard, drug nanosuspensions have the advantage that no polymeric materials are required as carriers. Lipid nanoparticulate drug systems also show promise; both need to be investigated. Finally, because of the highly interdisciplinary nature of developing the technology of nanoparticulate drug delivery for AD treatment, it is necessary to bring together chemists, bioengineers and life scientists in order to accomplish this task.

Specifically, it would be useful to focus on nanoparticle chelation agents as a possible drug for AD treatment, because metal-mediated toxicity is believed to be an important contributor to AD development and chelation therapy shows some benefits to AD patients. In addition to nanoparticle delivery of drugs into the brain, which has been achieved in some cases, the ability of nanoparticles to bring chelator-metal complexes out of the AD brain needs to be demonstrated *in vivo*. Effects of the nanoparticulate chelator system on metal biokinetics and excretion should be studied, which will provide important information about chelation efficacy and toxicity.

Further studies should utilize the nanoparticulate drug delivery systems, one of the few valuable tools to deliver drugs into the brain, to transport available therapeutics to prevent or treat AD in clinical studies. This approach may significantly improve the efficacy of these therapeutic agents and minimize systemic side-effects or make it possible for some potential therapeutics such as nerve growth factors, non-brain-distributing ACE inhibitors and hydrophilic chelators with large molecular size to enter the brain for AD treatment. The use of this technology will also facilitate the development of other promising treatments such as antibody, gene and stem cell therapies. Simultaneous multidrug delivery can also be achieved through nanoparticle technology, which may provide better therapeutic efficacy. Biocompatible or biodegradable polymers to serve as carriers in nanoparticulate drug systems are now being developed, as are potential AD therapeutics. Coupling these studies may result in more rapid identification of more effective and safer drugs for the treatment of AD. As many nanoparticulate drug delivery systems are designed for intravenous administration, the possibility of oral administration as well as transdermal, ocular, nasal and inhalation routes should be investigated. The development of these patient-administrable nanoparticulate drug delivery systems would greatly facilitate the care of AD patients and benefit patients over extended time periods of therapy.

It is worth noting that an outstanding feature of nanoparticulate drug delivery technology is its simplicity of preparation, optimization and application. For example, the nanoparticles used for chelator transport can be made of synthetic or natural macromolecules with functional groups such as amino and carboxyl moieties on their surface for covalently bonding with chelators. Changing the chelators, linkages, surfactants and the nanoparticle surface can result in nanoparticulate chelator systems with desirable surface properties, which enable the systems to cross the BBB. Also, directly coating the chelator–nanoparticle with apolipoproteins or their antibodies may facilitate high-efficiency penetration of the BBB. In addition to nanoparticle delivery of drugs, nanoparticle conjugation with drugs or prodrugs can also offer the possibility of developing new therapeutics that not only possess specific organ targeting, but also have improved therapeutic efficacy and minimized toxicity for AD treatment. It is also possible that nanoparticles can serve as vehicles to bring toxic materials out of the brain, which will be a huge advance in nanoparticle technology for disease prevention and treatment.

The fundamentals of nanoparticulate drug delivery into the brain indicate the possibility of transporting therapeutic agents across the BBB for treatment of AD. Current investigations provide evidence to support this possibility and show promise. Further studies are needed to demonstrate therapeutic efficacy and tolerance. Enthusiasm for nanoparticle transport of drugs for AD treatment is high because this approach will not only provide more insights into the mechanisms of AD development, but also will lead to safer and more effective therapies for the disease. This approach can also be used for prevention and treatment other neurological diseases as well as for disease diagnosis.

## Acknowledgments

We are grateful for the financial support by the National Institutes of Health. We would also like to thank Drs. Mark Smith and Peggy Harris of the Case Western Reserve University for their histochemical analysis of AD brain tissues. Finally, we would want to thank all the various publishers for their kind permission to reproduce figures and schemes used in this chapter.

## References

- 1 SMITH MA. Alzheimer disease. *Int. Rev. Neurobiol.* 42, 1998, 1–54.
- 2 BROOKMEYER R, GRAY S, KAWAS C. Projections of Alzheimer's disease in the United States and the public health impact of delaying disease onset. *Am. J. Public Health* 88, 1998, 1337–42.
- 3 HEBERT LE, SCHERR PA, BIENIAS JL, BENNETT DA, EVANS DA. Alzheimer's disease in the US population: prevalence estimates using the 2000 census. *Arch. Neurol.* 60, 2003, 1119–22.
- 4 HEBERT LE, BECKETT LA, SCHERR PA, EVANS DA. Annual incidence of Alzheimer's disease in the United States projected to the years 2000 through 2050. *Alzheimer Dis. Assoc. Disord.* 15, 2001, 169–73.
- 5 SCORER CA. Preclinical and clinical challenges in the development of disease-modifying therapies for Alzheimer's disease. *Drug Discov. Today* 6, 2001, 1207–19.
- 6 MARDER K. Memantine approved to treat moderate to severe Alzheimer's disease. *Curr. Neurol. Neurosci. Rep.* 4, 2004, 349–50.
- 7 SONKUSARE SK, RAMARAO CLKP. Dementia of Alzheimer's disease and other neurodegenerative disorder – memantine, a new hope. *Pharmac. Res.* 51, 2005, 1–17.
- 8 COYLE J, KERSHAW P. GALANTAMINE. A cholinesterase inhibitor that allosterically modulates nicotinic receptors: effects on the course of Alzheimer's disease. *Biol. Psychiatry* 49, 2001, 289–99.
- 9 FARLOW MR. Pharmacokinetic profiles of current therapies for Alzheimer's disease: implications for switching to galantamine. *Clin. Ther.* 23 (Suppl. A), 2001, A13–24.
- 10 SZEKELY CA, THORNE JE, ZANDI PP, EK M, MESSIAS E, BREITNER JC, GOODMAN SN. Nonsteroidal anti-inflammatory drugs for the prevention of Alzheimer's disease: a systematic review. *Neuroepidemiology* 23, 2004, 159–69.
- 11 WEGGEN S, ERIKSEN JL, DAS P, SAGI SA, WANG R, PIETRZIK CU, FINDLAY KA, SMITH TE, MURPHY MP, BULTER T, KANG DE, MARQUEZ-STERLING N, GOLDE TE, KOO EH. A subset of NSAIDs lower amyloidogenic Abeta42 independently of cyclooxygenase activity. *Nature* 414, 2001, 212–6.
- 12 MCADAM BF, CATELLA-LAWSON F, MARDINI IA, KAPOOR S, LAWSON JA, FITZGERALD GA. Systemic biosynthesis of prostacyclin by cyclooxygenase (COX)-2: the human pharmacology of a selective inhibitor of COX-2. *Proc. Natl Acad. Sci. USA* 96, 1999, 272–7.
- 13 MONTINE TJ, SIDELL KR, CREWS BC, MARKESBERY WR, MARNETT LJ, ROBERTS LJ. 2nd, MORROW JD. Elevated CSF prostaglandin E<sub>2</sub> levels in patients with probable AD. *Neurology* 53, 1999, 1495–8.
- 14 ZANDI PP, ANTHONY JC, HAYDEN KM, MEHTA K, MAYER L, BREITNER JC. Cache County Study Investigators. Reduced incidence of AD with NSAID but not H2 receptor antagonists: the

- Cache County Study. *Neurology* 59, 2002, 880–6.
- 15 Prevention of Alzheimer's Disease by Vitamin E and Selenium (PREADVISE). <http://www.nia.nih.gov/HealthInformation/ClinicalTrials.htm>.
  - 16 PRASAD KN, HOVLAND AR, COLE WC, PRASAD KC, NAHREINI P, EDWARDS-PRASAD J, ANDREATTA CP. Multiple antioxidants in the prevention and treatment of Alzheimer disease: analysis of biologic rationale. *Clin. Neuropharmacol.* 23, 2000, 2–13.
  - 17 CASADESUS G, ZHU X, ATWOOD CS, WEBBER KM, PERRY G, BOWEN RL, SMITH MA. Beyond estrogen: targeting gonadotropin hormones in the treatment of Alzheimer's disease. *Curr. Drugs. Targets CNS Neurol. Disord.* 3, 2004, 281–5.
  - 18 WEBBER KM, BOWEN R, CASADESUS G, PERRY G, ATWOOD CS, SMITH MA. Gonadotropins and Alzheimer's disease: the link between estrogen replacement therapy and neuroprotection. *Acta Neurobiol. Exp. (Wars)* 64, 2004, 113–8.
  - 19 ZANDI PP, ANTHONY JC, KHACHATURIAN AS, STONE SV, GUSTAFSON D, TSCHANZ JT, NORTON MC, WELSH-BOHMER KA, BREITNER JC; Cache County Study Group. Reduced risk of Alzheimer disease in users of antioxidant vitamin supplements: the Cache County Study. *Arch. Neurol.* 61, 2004, 82–8.
  - 20 SUH YH, CHECLER F. Amyloid precursor protein, presenilins, and alpha-synuclein: molecular pathogenesis and pharmacological applications in Alzheimer's disease. *Pharmacol. Rev.* 54, 2002, 469–525.
  - 21 CORRADA M, KAWAS CH, HALLFRISCH J, MULLER D, BROOKMEYER R. Reduced risk of Alzheimer's disease with high folate intake: The Baltimore Longitudinal Study of Aging. *Alzheimer's & Dementia* 1, 2005, 11–8.
  - 22 SANO M, ERNESTO C, THOMAS RG, KLAUBER MR, SCHAFER K, GRUNDMAN M, WOODBURY P, GROWDON J, COTMAN CW, PFEIFFER E, SCHNEIDER LS, THAL LJ. A controlled trial of selegiline, alpha-tocopherol, or both as treatment for Alzheimer's disease. The Alzheimer's Disease Cooperative Study. *N. Engl. J. Med.* 336, 1997, 1216–22.
  - 23 MORRIS MC, EVANS DA, BIENIAS JL, TANGNEY CC, BENNETT DA, WILSON RS, AGGARWAL N, SCHNEIDER J. Consumption of fish and  $n - 3$  fatty acids and risk of incident Alzheimer disease. *Arch. Neurol.* 60, 2003, 940–6.
  - 24 MORRIS MC, EVANS DA, BIENIAS JL, TANGNEY CC, HEBERT LE, SCHERR PA, SCHNEIDER JA. Dietary folate and vitamin B12 intake and cognitive decline among community-dwelling older persons. *Arch. Neurol.* 62, 2005, 641–5.
  - 25 CHOLERTON B, GLEASON CE, BAKER LD, ASTHANA S. Estrogen and Alzheimer's disease: the story so far. *Drugs Aging* 19, 2002, 405–27.
  - 26 SHERWIN BB. Estrogen and cognitive aging in women. *Trends Pharmacol. Sci.* 23, 2002, 527–34.
  - 27 MULNARD RA, CORRADA MM, KAWAS CH. Estrogen replacement therapy, Alzheimer's disease, and mild cognitive impairment. *Curr. Neurol. Neurosci. Rep.* 4, 2004, 368–73.
  - 28 ROSIN RA, RASKIND MA. Gonadotrophin-releasing hormone agonist treatment of aggression in Alzheimer's disease: a case report. *Int. Psychogeriatr.* 17, 2005, 313–8.
  - 29 RASGON NL, SMALL GW, SIDDARTH P, MILLER K, ERCOLI LM, BOOKHEIMER SY, LAVRETSKY H, HUANG SC, BARRIO JR, PHELPS ME. Estrogen use and brain metabolic change in older adults. A preliminary report. *Psychiatry Res.* 107, 2001, 11–8.
  - 30 DUNKIN J, RASGON N, WAGNER-STEH K, DAVID S, ALTSHULER L, RAPKIN A. Reproductive events modify the effects of estrogen replacement therapy on cognition in healthy postmenopausal women. *Psychoneuroendocrinology* 30, 2005, 284–96.
  - 31 YASAR S, CORRADA M, BROOKMEYER R, KAWAS C. Calcium channel blockers and risk of AD: the Baltimore Longitudinal Study of Aging. *Neurobiol. Aging* 26, 2005, 157–63.

- 32 OHRUI T, MATSUI T, YAMAYA M, TOMITA N, SATO-NAKAGAWA T, MARUYAMA M, NIWA K, ARAI H, SASAKI H. ACE inhibitors and incidence of Alzheimer disease in Japan. *J. Am. Geriatr. Soc.* 52, 2004, 649–50.
- 33 OHRUI T, TOMITA N, SATO-NAKAGAWA T, MATSUI T, MARUYAMA M, NIWA K, ARAI H, SASAKI H. Effects of brain-penetrating ACE inhibitors on Alzheimer disease progression. *Neurology* 63, 2004, 1324–5.
- 34 ZAMRINI E, MCGWIN G, ROSEMAN JM. Association between statin use and Alzheimer's disease. *Neuroepidemiology* 23, 2004, 94–8.
- 35 KOJRO E, GIMPL G, LAMMICH S, MARZ W, FAHRENHOLZ F. Low cholesterol stimulates the non-amyloidogenic pathway by its effect on alpha-secretase ADAM 10. *Proc. Natl Acad. Sci. USA* 98, 2001, 5815–20.
- 36 SIMONS M, KELLER P, DE STROOPER B, BEYREUTHER K, DOTTI CG, SIMONS K. Cholesterol depletion inhibits the generation of beta-amyloid in hippocampal neurons. *Proc. Natl Acad. Sci. USA* 95, 1998, 6460–4.
- 37 SIMONS M, SCHWARZLER F, LUTJOHANN D, VON BERGMANN K, BEYREUTHER K, DICHGANS J, WORMSTALL H, HARTMANN T, SCHULZ JB. Treatment with simvastatin in normocholesterolemic patients with Alzheimer's disease: A 26-week randomized, placebo-controlled, double-blind trial. *Ann. Neurol.* 52, 2002, 346–50.
- 38 FASSBENDER K, SIMONS M, BERGMANN C, STROICK M, LUTJOHANN D, KELLER P, RUNZ H, KUHL S, BERTSCH T, VON BERGMANN K, HENNERICI M, BEYREUTHER K, HARTMANN T. Simvastatin strongly reduces levels of Alzheimer's disease beta-amyloid peptides Abeta 42 and Abeta 40 *in vitro* and *in vivo*. *Proc. Natl Acad. Sci. USA* 98, 2001, 5856–61.
- 39 KWAK B, MULHAUPT F, MYIT S, MACH F. Statin as a newly recognized type of immunomodulator. *Nat. Med.* 6, 2000, 1399–402.
- 40 CASDORPH HR. EDTA chelation therapy: efficacy in brain disorders. In *A Textbook on DETA Chelation Therapy*, 2nd edn, CRANTON EM (Ed.). Hampton Roads Publishing, Charlottesville, VA, 2001, pp. 142–63.
- 41 OLSZEWER E, CARTER JP. EDTA chelation therapy: a retrospective study of 2870 patients. In *A Textbook on DETA Chelation Therapy*, 2nd edn, CRANTON EM (Ed.). Hampton Roads Publishing, Charlottesville, VA, 2001, pp. 210–24.
- 42 REGLAND B, LEHMANN W, ABEDINI I, BLENNOW K, JONSSON M, KARLSSON I, SJOGREN M, WALLIN A, XILINAS M, GOTTFRIES CG. Treatment of Alzheimer's disease with clioquinol. *Dement. Geriatr. Cogn. Disord.* 12, 2001, 408–14.
- 43 RITCHIE CW, BUSH AI, MACKINNON A, MACFARLANE S, MASTWYK M, MACGREGOR L, KIERS L, CHERNY R, LI QX, TAMMER A, CARRINGTON D, MAVROS C, VOLITAKIS I, XILINAS M, AMES D, DAVIS S, BEYREUTHER K, TANZI RE, MASTERS CL. Metal–protein attenuation with iodochlorhydroxyquin (clioquinol) targeting Abeta amyloid deposition and toxicity in Alzheimer disease: a pilot phase 2 clinical trial. *Arch. Neurol.* 60, 2003, 1685–91.
- 44 IBACH B, HAEN E, MARIENHAGEN J, HAJAK G. Clioquinol treatment in familiar early onset of Alzheimer's disease: a case report. *Pharmacopsychiatry* 38, 2005, 178–9.
- 45 RAUDINO F, MASCALZI MG, ZAGAMI A. Gabapentin and behavioral disorders in severe Alzheimer disease. *J. Clin. Psychopharmacol.* 24, 2004, 459–60.
- 46 DE LEON OA. Treatment of psychotic symptoms with lamotrigine in Alzheimer disease. *J. Clin. Psychopharmacol.* 24, 2004, 232–3.
- 47 MINTZER J, GREENSPAN A, CAERS I, VAN HOVE I, KUSHNER S, WEINER M, GHARABAWI G, SCHNEIDER LS. Risperidone in the treatment of psychosis of Alzheimer disease: results from a prospective clinical trial. *Am. J. Geriatr. Psychiatry* 14, 2006, 280–91.

- 48 NASH JM. Alzheimer's disease. New insights into its cause lead to new drug strategies. *Time* 157, 2001, 80–1, 85.
- 49 DOMINGUEZ DI, DE STROOPER B. Novel therapeutic strategies provide the real test for the amyloid hypothesis of Alzheimer's disease. *Trends Pharmacol. Sci.* 23, 2002, 324–30.
- 50 SCHENK D. Amyloid-beta immunotherapy for Alzheimer's disease: the end of the beginning. *Nat. Rev. Neurosci.* 3, 2002, 824–8.
- 51 HIRSCHFELD GM, HAWKINS PN. Amyloidosis: new strategies for treatment. *Int. J. Biochem. Cell Biol.* 35, 2003, 1608–13.
- 52 MCGEER PL, MCGEER E. Is there a future for vaccination as a treatment for Alzheimer's disease? *Neurobiol. Aging* 24, 2003, 391–5.
- 53 SCHMITT B, BERNHARDT T, MOELLER HJ, HEUSER I, FROLICH L. Combination therapy in Alzheimer's disease: a review of current evidence. *CNS Drugs* 18, 2004, 827–44.
- 54 RISNER ME, SAUNDERS AM, ALTMAN JF, ORMANDY GC, CRAFT S, FOLEY IM, ZVARTAU-HIND ME, HOSFORD DA, ROSES AD. Efficacy of rosiglitazone in a genetically defined population with mild-to-moderate Alzheimer's disease. *Pharmacogenomics J* 6, 2006, 246–54.
- 55 LARSON EB, WANG L, BOWEN JD, McCORMICK WC, TERI L, CRANE P, KUKULL W. Exercise is associated with reduced risk for incident dementia among persons 65 years of age and older. *Ann. Intern. Med.* 144, 2006, 73–81.
- 56 KHACHATURIAN AS, ZANDI PP, LYKETSOS CG, HAYDEN KM, SKOOG I, NORTON MC, TSCHANZ JT, MAYER LS, WELSH-BOHMER KA, BREITNER JCS; for the Cache County Study Group. Antihypertensive medication use and incident Alzheimer disease: The Cache County Study. *Arch. Neurol.* 63, 2006, 686–92.
- 57 HENDRIE HC, ALBERT MS, BUTTERS MA, GAO S, KNOPMAN DS, LAUNER LJ, YAFFE K, CUTHBERT BN, EDWARDS E, WAGSTER MV. The NIH cognitive and emotional health project: Report of the critical evaluation study committee. *Alzheimer's & Dementia* 2, 2006, 12–32.
- 58 RAMIREZ BG, BLAZQUEZ C, GOMEZ DEL PULGAR T, GUZMAN M, DE CEBALLOS ML. Prevention of Alzheimer's disease pathology by cannabinoids: neuroprotection mediated by blockade of microglial activation. *J. Neurosci.* 25, 2005, 1904–13.
- 59 National Institute on Aging/National Institutes of Health, Progress Report on Alzheimer's Disease, 2000. <http://www.alzheimers.org/prog00.htm>.
- 60 SMITH DE, ROBERTS J, GAGE FH, TUSZYNSKI MH. Age-associated neuronal atrophy occurs in the primate brain and is reversible by growth factor gene therapy. *Proc. Natl Acad. Sci. USA* 96, 1999, 10893–8.
- 61 KORDOWER JH, ISACSON O, EMERICH DF. Cellular delivery of trophic factors for the treatment of Huntington's disease: is neuroprotection possible? *Exp. Neurol.* 159, 1999, 4–20.
- 62 BACHURIN SO. Medicinal chemistry approaches for the treatment and prevention of Alzheimer's disease. *Med. Res. Rev.* 23, 2003, 48–88.
- 63 TARIOT PN, LOY R, RYAN JM, PORSTEINSSON A, ISMAIL S. Mood stabilizers in Alzheimer's disease: symptomatic and neuroprotective rationales. *Adv. Drug Deliv. Rev.* 54, 2002, 1567–77.
- 64 BAI DL, TANG XC, HE XC, HUPERZINE A, a potential therapeutic agent for treatment of Alzheimer's disease. *Curr. Med. Chem.* 7, 2000, 355–74.
- 65 NEWHOUSE PA, POTTER A, SINGH A. Effects of nicotinic stimulation on cognitive performance. *Curr. Opin. Pharmacol.* 4, 2004, 36–46.
- 66 SHAW KZ, UTSUKI T, ROGERS J, YU QS, SAMBAMURTI K, BROSSI A, GE YW, LAHIRI DK, GREIG NH. Phenserine regulates translation of beta-amyloid precursor protein mRNA by a putative interleukin-1 responsive element, a target for drug development. *Proc. Natl Acad. Sci. USA* 98, 2001, 7605–10.

- 67 WITT A, MACDONALD N, KIRKPATRICK P. Memantine hydrochloride. *Nat. Rev. Drug Discov.* 3, 2004, 109–10.
- 68 IWATA N, TSUBUKI S, TAKAKI Y, SHIROTANI K, LU B, GERARD NP, GERARD C, HAMA E, LEE HJ, SAIDO TC. Metabolic regulation of brain Abeta by neprilysin. *Science* 292, 2001, 1550–2.
- 69 SELKOE DJ. Alzheimer's disease: genes, proteins and therapy. *Phys. Rev.* 81, 2001, 741–66.
- 70 CAI H, WANG Y, MCCARTHY D, WEN H, BORCHELT DR, PRICE DL, WONG PC. BACE1 is the major beta-secretase for generation of Abeta peptides by neurons. *Nat. Neurosci.* 4, 2001, 233–4.
- 71 DOERFLER P, SHEARMAN MS, PERLMUTTER RM. Presenilin-dependent gamma-secretase activity modulates thymocyte development. *Proc. Natl Acad. Sci. USA* 98, 2001, 9312–7.
- 72 CUMMING JN, ISERLOH U, KENNEDY ME. Design and development of BACE-1 inhibitors. *Curr. Opin. Drug Discov. Dev.* 7, 2004, 536–56.
- 73 THOMPSON LA, BRONSON JJ, ZUSI FC. Progress in the discovery of BACE inhibitors. *Curr. Pharm. Des.* 11, 2005, 3383–404.
- 74 STEINER H. Uncovering gamma-secretase. *Curr. Alzheimer Res.* 1, 2004, 175–81.
- 75 PENNINGER JM, IRIE-SASAKI J, SASAKI T, OLIVEIRA-DOS-SANTOS AJ. CD45: new jobs for an old acquaintance. *Nat. Immunol.* 2, 2001, 389–96.
- 76 TREIBER C, SIMONS A, STRAUSS M, HAFNER M, CAPPAI R, BAYER R, MULTHAUP G. Clioquinol mediates copper uptake and counteracts copper efflux activities of the amyloid precursor protein of Alzheimer's disease. *J. Biol. Chem.* 279, 2004, 51958–64.
- 77 CHERNY RA, ATWOOD CS, XILINAS ME, GRAY DN, JONES WD, MCLEAN CA, BARNHAM KJ, VOLITAKIS I, FRASER FW, KIM Y, HUANG X, GOLDSTEIN LE, MOIR RD, LIM JT, BEYREUTHER K, ZHENG H, TANZI RE, MASTERS CL, BUSH AI. Treatment with a copper–zinc chelator markedly and rapidly inhibits beta-amyloid accumulation in Alzheimer's disease transgenic mice. *Neuron* 30, 2001, 665–76.
- 78 SHACHAR DB, KAHANA N, KAMPEL V, WARSHAWSKY A, YODIM MB. Neuroprotection by a novel brain permeable iron chelator, VK-28, against 6-hydroxydopamine lesion in rats. *Neuropharmacology* 46, 2004, 254–63.
- 79 YODIM MBH, STEPHENSON G, SHACHAR DB. Ironing iron out in Parkinson's disease and other neurodegenerative disease with iron chelators. A lesson from 6-hydroxydopamine and iron chelators, desferal and VK-28. *Ann. NY Acad. Sci.* 1012, 2004, 306–25.
- 80 LEE JY, FRIEDMAN JE, ANGEL I, KOZAK A, KOH JY. The lipophilic metal chelator DP-109 reduces amyloid pathology in brains of human beta-amyloid precursor protein transgenic mice. *Neurobiol. Aging* 25, 2004, 1315–21.
- 81 REZNICHENKO L, AMIT T, ZHENG H, AVRAMOVICH-TIROSH Y, YODIM MB, WEINREB O, MANDEL S. Reduction of iron-regulated amyloid precursor protein and beta-amyloid peptide by (–)-epigallocatechin-3-gallate in cell cultures: implications for iron chelation in Alzheimer's disease. *J. Neurochem.* 97, 2006, 527–36.
- 82 ZHENG H, WEINER LM, BAR-AM. O, EPSZTEJN S, CABANTCHIK ZI, WARSHAWSKY A, YODIM MB, FRIDKIN M. Design, synthesis, and evaluation of novel bifunctional iron-chelators as potential agents for neuroprotection in Alzheimer's, Parkinson's, and other neurodegenerative diseases. *Bioorg. Med. Chem.* 13, 2005, 773–83.
- 83 RICHARDSON DR. Novel chelators for central nervous system disorders that involve alterations in the metabolism of iron and other metal ions. *Ann. NY Acad. Sci.* 1012, 2004, 326–41.
- 84 SHIN RW, KRUCK TP, MURAYAMA H, KITAMOTO T. A novel trivalent cation chelator Feralex dissociates binding



- of aluminum and iron associated with hyperphosphorylated tau of Alzheimer's disease. *Brain Res.* 961, 2003, 139–46.
- 85 VENTI A, GIORDANO T, EDER P, BUSH AI, LAHIRI DK, GREIG NH, ROGERS JT. The integrated role of desferrioxamine and phenserine targeted to an iron-responsive element in the APP-mRNA 5'-untranslated region. *Ann. NY Acad. Sci.* 1035, 2004, 34–48.
- 86 WOLOZIN B, BROWN III J, THEISLER C, SILBERMAN S. The cellular biochemistry of cholesterol and statins: insights into the pathophysiology and therapy of Alzheimer's disease. *CNS Drug Rev.* 10, 2004, 127–46.
- 87 BARTZOKIS G, TISHLER TA, SHIN IS, LU PH, CUMMINGS JL. Brain ferritin iron as a risk factor for age at onset in neurodegenerative diseases. *Ann. NY Acad. Sci.* 1012, 2004, 224–36.
- 88 BROWN M. Gene therapy success for Alzheimer's? *Drug Discov. Today* 8, 2003, 474–5.
- 89 CLAUSEN T, BULLOCK R. Medical treatment and neuroprotection in traumatic brain injury. *Curr. Pharm. Des.* 7, 2001, 1517–32.
- 90 HELMUTH L. New therapies. New Alzheimer's treatments that may ease the mind. *Science* 297, 2002, 1260–2.
- 91 SCARPINI E, SCHELTENS P, FELDMAN H. Treatment of Alzheimer's disease: current status and new perspectives. *Lancet Neurol.* 2, 2003, 539–47.
- 92 MANDELKOW E. Alzheimer's disease The tangled tale of tau. *Nature* 402, 1999, 588–9.
- 93 AHN JS, RADHAKRISHNAN ML, MAPLLI M, CHOI S, TIDOR B, CUNY GD, MUSACCHIO A, YRH L-A, KOSIK KS. Defining Cdk5 ligand chemical space with small molecule inhibitors of tau phosphorylation. *Chem. Biol.* 12, 2005, 811–23.
- 94 SUNG S, YANG H, URYU K, LEE EB, ZHAO L, SHINENMAN D, TROJANOWSKI JQ, LEE VM, PRATICO D. Modulation of nuclear factor-kappa B activity by indomethacin influences A beta levels but not A beta precursor protein metabolism in a model of Alzheimer's disease. *Am. J. Pathol.* 165, 2004, 2197–206.
- 95 HONG CS, GOINS WF, GOSS JR, BURTON EA, GLORIOSO JC. Herpes simplex virus RNAi and neprilysin gene transfer vectors reduce accumulation of Alzheimer's disease-related amyloid-beta peptide *in vivo*. *Gene Ther.* 13, 2006, 1068–79.
- 96 TARIOT PN, FARLOW MR, GROSSBERG GT, GRAHAM SM, McDONALD S, GERGEL I. Memantine treatment in patients with moderate to severe Alzheimer disease already receiving donepezil: a randomized controlled trial. *J. Am. Med. Ass.* 291, 2004, 317–24.
- 97 RAVI KUMAR MN. Nano and microparticles as controlled drug delivery devices. *J. Pharm. Pharm. Sci.* 3, 2000, 234–58.
- 98 GUTMAN R, PEACOCK G, LU D. Targeted drug delivery for brain cancer treatment. *J. Control. Release* 65, 2000, 31–41.
- 99 KREUTER J. Nanoparticulate systems for brain delivery of drugs. *Adv. Drug Deliv. Rev.* 47, 2001, 65–81.
- 100 KREUTER J. Influence of the surface properties on nanoparticle-mediated transport of drugs to the brain. *J. Nanosci. Nanotechnol.* 4, 2004, 484–8.
- 101 MULLER RH, JACOBS C, KAYSER O. Nanosuspensions as particulate drug formulations in therapy. Rationale for development and what we can expect for the future. *Adv. Drug Deliv. Rev.* 47, 2001, 3–19.
- 102 MULLER RH, KECK CM. Drug delivery to the brain-realization by novel drug carriers. *J. Nanosci. Nanotechnol.* 4, 2004, 471–83.
- 103 COUVREUR P, COUARRAZE G, DEVISSAGUET JP, PUISIEUX F. Nanoparticles: preparation and characterization. In *Microencapsulation: Methods and Industrial Applications*, BENITA S (Ed.). Marcel Dekker, New York, 1996, pp. 183–211.
- 104 BARRATT G, COUARRAZE G, COUVREUR P, DUBERNET C, FATTAL E, GREFF R, LABARRE D, LEGRAND P, PONCHEL G, VAUTHIER C. Polymeric Micro- and nanoparticles as drug carriers. In

- Polymeric Biomaterials*, 2nd edn, DUMITRIU S (Ed.). Marcel Dekker, New York, 2002, pp. 753–81.
- 105 MULDOON LL, TRATNYEK PG, JACOBS PM, DOOLITTLE ND, CHRISTOFORIDIS GA, FRANK JA, LINDAU M, LOCKMAN PR, MANNINGER SP, QIANG Y, SPENCE AM, STUPP SI, ZHANG M, NEUWELT EA. Imaging and nanomedicine for diagnosis and therapy in the central nervous system: report of the eleventh annual blood–brain barrier disruption consortium meeting. *Am. J. Neuroradiol.* 27, 2006, 715–21.
- 106 HARTIG W, PAULKE BR, VARGA C, SEEGER J, HARKANY T, KACZA J. Electron microscopic analysis of nanoparticles delivering thioflavin-T after intrahippocampal injection in mouse: implications for targeting beta-amyloid in Alzheimer’s disease. *Neurosci. Lett.* 338, 2003, 174–6.
- 107 CUI Z, LOCKMAN PR, ATWOOD CS, HSU CH, GUPTA A, ALLEN DD, MUMPER RJ. Novel D-penicillamine carrying nanoparticles for metal chelation therapy in Alzheimer’s and other CNS diseases. *Eur. J. Pharm. Biopharm.* 59, 2005, 263–72.
- 108 SHEA TB, ORTIZ D, NICOLOSI RJ, KUMAR R, WATTERSON AC. Nanosphere-mediated delivery of vitamin E increases its efficacy against oxidative stress resulting from exposure to amyloid beta. *J. Alzheimer’s Dis.* 7, 2005, 297–301.
- 109 LIU G, GARRETT MR, MEN P, ZHU X, PERRY G, SMITH MA. Nanoparticle and other metal chelation therapeutics in Alzheimer disease. *Biochem. Biophys. Acta* 1741, 2005, 246–52.
- 110 RONEY C, KULKARNI P, ARORA V, ANTICH P, BONTE F, WU A, MALLIKARJUANA NN, MANOHAR S, LIANG HF, KULKARNI AR, SUNG HW, SAIRAM M, AMINABHAVI TM. Targeted nanoparticles for drug delivery through the blood–brain barrier for Alzheimer’s disease. *J. Control. Release* 108, 2005, 193–214.
- 111 COURAUD PO, SCHERMAN D. Preface. In *Biology and Physiology of the Blood–Brain Barrier. Transport, Cellular Interactions, and Brain Pathologies*, COURAUD PO, SCHERMAN D (Eds.). Plenum Press, New York, 1996, p. vii.
- 112 BALLABH P, BRAUN A, NEDERGAARD M. An overview, structure, regulation and clinical implication. *Neurobiol. Dis.* 16, 2004, 1–13.
- 113 BRIGHTMAN M. Ultrastructure of the brain endothelium. In *Physiology and pharmacology Of The Blood–Brain Barrier. Handbook of Experimental Pharmacology*, BRADBURY MWB (Ed.). Springer, Berlin, 1992, vol. 103, pp. 1–22.
- 114 BEGLEY D. The blood–brain barrier: principles for targeting peptides and drugs to the central nervous system. *J. Pharm. Pharmacol.* 48, 1996, 136–46.
- 115 HABGOOD MD, LIU ZD, DEHKORDI LS, KHODR HH, ABBOTT J, HIDER RC. Investigation into the correlation between the structure of hydroxy-pyridinones and blood–brain barrier permeability. *Biochem. Pharmacol.* 57, 1999, 1305–10.
- 116 MINN A, EL-BACHA RDS, BAYOL-DENIZOT C, LAGRANGE P, SULEMAN FG. Drug metabolism in the brain: benefits and risks. In *The Blood–Brain Barrier and Drug Delivery to the CNS*, BEGLEY DJ, BRADBURY MW, KREUTER J (Eds). Marcel Dekker, New York, 2000, pp. 145–70.
- 117 RAPOPORT SI. Modulation of the blood–brain barrier perability. *J. Drug Target.* 3, 1996, 417–25.
- 118 DEHOUCQ B, FENART L, DEHOUCQ M-P, PIERCE A, TORPIER G, CECHELLI R. A new function for the LDL receptor: transcytosis of LDL across the blood–brain barrier. *J. Cell Biol.* 138, 1997, 877–89.
- 119 NEUWELT EA. Mechanisms of disease: the blood-brain barrier. *Neurosurgery.* 54, 2004, 131–40.
- 120 GUMMERLOCH MK, NEUWALT EA. Drug entry into the brain and its pharmacologic manipulation. In *Physiology and pharmacology Of The Blood–Brain Barrier. Handbook of Experimental Pharmacology*, BRADBURY MWB (Ed.). Springer, Berlin, 1992, vol. 103, pp. 525–42.

- 121 GALEY JB, DUMATS J, BECK I, FERNANDEZ B, HOCQUAUX M. *N,N'*-bis-dibenzyl ethylenediaminediacetic acid (DBED): a site-specific hydroxyl radical scavenger acting as an "oxidative stress activatable" iron chelator *in vitro*. *Free Radic. Res.* 22, 1995, 67–86.
- 122 GASSEN M, YOUDIM MB. The potential role of iron chelators in the treatment of Parkinson's disease and related neurological disorders. *Pharmacol. Toxicol.* 80, 1997, 159–66.
- 123 PARDRIDGE WM, BUCIAK JL, FRIDEN PM. Selective transport of an anti-transferrin receptor antibody through the blood–brain barrier *in vivo*. *J. Pharmacol. Exp. Ther.* 259, 1991, 66–70.
- 124 PARDRIDGE WM. *Brain Drug Targeting*. Cambridge University Press, Cambridge, 2001.
- 125 PARDRIDGE WM. Drug and gene targeting to the brain with molecular Trojan horses. *Nat. Rev. Drug Discov.* 1, 2002, 131–9.
- 126 LIU G, BRUENGER FW, MILLER SC, ARIF AM. Molecular structure and biological and pharmacological properties of 3-hydroxy-2-methyl-1-( $\beta$ -D-ribofuranosyl or pyranosyl)-4-pyridinone: potential iron overload drugs for oral administration. *Bioorg. Med. Chem. Lett.* 8, 1998, 3077–80.
- 127 LIU G, BRUENGER FW, BARRIOS AM, MILLER SC. Synthesis of 2-alkyl-3-hydroxy-4-pyridinone-ribonucleosides. Potential oral iron chelators. *Nucleosides Nucleotides* 14, 1995, 1091–104.
- 128 FOKT I, CONRAD CA, MADDEN T, YUNG AW, LANG FF, THAPAR N, PRIEBE W. The discovery and development of blood–brain barrier (BBB) penetrating anthracyclines for the treatment of brain tumors. Presented at AACR–NCI–EORTC International Conference on Molecular Targets and Cancer Therapeutics: Discovery, Biology, and Clinical Application. Philadelphia, PA, 2005, meeting abstract A199.
- 129 FOKT I, GRYNKIEWICZ G, SKIBICKI P, PRZEWŁOKA T, PRIEBE W. New strategies towards synthesis of doxorubicin analogs. *Polish J. Chem.* 79, 2005, 349–59.
- 130 CRISTIANO RJ, XU B, NGUYEN D, SCHUMACHER G, KATAOKA M, SPITZ FR, ROTH JA. Viral and nonviral gene delivery vectors for cancer gene therapy. *Cancer Detect. Prev.* 22, 1998, 445–54.
- 131 ISACSON O, BREAKEFIELD XO. Benefits and risks of hosting animal cells in the human brain. *Nat. Med.* 3, 1997, 964–9.
- 132 SCHUMACHER JM, ISACSON O. Neuronal xenotransplantation in Parkinson's disease. *Nat. Med.* 3, 1997, 474–5.
- 133 TEMSAMANI J, ROUSSELLE C, REES AR, SCHERRMANN JM. Vector-mediated drug delivery to the brain. *Expert Opin. Biol. Ther.* 1, 2001, 773–82.
- 134 TEMSAMANI J, BONNAFOUS C, ROUSSELLE C, FRAISSE Y, CLAIR P, GRANIER LA, REES AR, KACZOREK M, SCHERRMANN JM. Improved brain uptake and pharmacological activity profile of morphine-6-glucuronide using a peptide vector-mediated strategy. *J. Pharmacol. Exp. Ther.* 313, 2005, 712–9.
- 135 ZHOU X, HUANG L. Targeted delivery of DANN by liposomes and polymers. *J. Control. Release* 19, 1992, 269–74.
- 136 CHEN D, LEE KH. Biodistribution of calcitonin encapsulated in liposomes in mice with particular reference to the central nervous system. *Biochem. Biophys. Acta*, 1158, 1993, 244–50.
- 137 HUWYLER J, WU D, PARDRIDGE WM. Brain drug delivery of small molecules using immunoliposomes. *Proc. Natl Acad. Sci. USA* 93, 1996, 14164–9.
- 138 KATAOKA K, HARADA A, NAGASAKI Y. Block copolymer micelles for drug delivery: design, characterization and biological significant. *Adv. Drug Deliv. Rev.* 47, 2001, 113–31.
- 139 ALLEN C, MAYSINGER D, EISENBERG A. Nano-engineering block copolymer aggregates for drug delivery. *Colloids Surf. B* 16, 1999, 3–27.
- 140 MAYSINGER D, SAVIC R, TAM J, ALLEN C, EISENBERG A. Recent Developments in drug to the nervous system.

- In *Polymeric Biomaterials*, 2nd edn, DUMITRIU S (Ed.). Marcel Dekker, New York, 2002, pp 1083–99.
- 141 KREUTER J. Nanoparticles. In *Encyclopedia of Pharmaceutical Technology*, SWARBRICK J, BOYLAN JC (Eds.). Dekker, New York, 1994, vol. 10, pp. 165–90.
- 142 AKTAS Y, YEMISCI M, ANDRIEUX K, GURSOY RN, ALONSO MJ, FERNANDEZ-MEGIA E, NOVOA-CARBALLAL R, QUINOVA E, RIGUERA R, SARGON MF, CELIK HH, DEMIR AS, HINCAL AA, DALKARA T, CAPAN Y, COUVREUR P. Development and brain delivery of chitosan-PEG nanoparticles functionalized with the monoclonal antibody OX26. *Bioconjug. Chem.* 16, 2005, 1503–11.
- 143 TROESTER SD, MUELLER U, KREUTER J. Modification of the body distribution of poly(methylmethacrylate) nanoparticles in rats by coating with surfactants. *Int. J. Pharm.* 61, 1990, 85–100.
- 144 JUHLIN L. Retention of particles by the reticuloendothelial system. *Acta Physiol. Scand.* 48, 1960, 78–87.
- 145 KREUTER J, TAEUBER U, ILLI V. Distribution and elimination of poly(methyl-2-<sup>14</sup>C-methacrylate) nanoparticle radioactivity after injection in rats and mice. *J. Pharm. Sci.* 68, 1979, 1443–7.
- 146 LENAERTS V, NAGELKERKE JF, VAN BERKEL TJC, COUVREUR P, GRISLAIN L, ROLAND M, SPEISER P. *In vivo* uptake and cellular distribution of biodegradable polymeric nanoparticles. In *Sinusoidal Liver Cells*, KNOOK DL, WISSE E (Eds.). Elsevier, Amsterdam, 1982, pp. 343–52.
- 147 RESZKA R, BECK P, FICHTNER I, HENTSCHEL M, RICHTER J, KREUTER J. Body distribution of free, liposomal and nanoparticle-associated mitoxantrone in B16-melanoma-bearing mice. *J. Pharmacol. Exp. Ther.* 280, 1997, 232–7.
- 148 LOCKMAN PR, OYEWUMI MO, KOZIARA J, RODER KE, MUMPER RJ, ALLEN DD. Brain uptake of thiamine-coated nanoparticles. *J. Control. Release* 93, 2003, 271–82.
- 149 CRAFT TKS, MAHONEY JH, COURTNEY DEVRIES A, SARTER M. Microsphere embolism-induced cortical cholinergic deafferentation and impairments in attentional performance. *Eur. J. Neurosci.* 21, 2005, 3117–32.
- 150 SEKIGUCHI M, TAKAGI K, TAKAGI N, DATE I, TAKEO S, TANAKA O, YAMATO I, KOBASHIKAWA S, TORIGOE K, NOWAKOWSKI RS. Time course and sequence of pathological changes in the cerebellum of microsphere-embolized rats. *Exp. Neurol.* 191, 2005, 266–75.
- 151 GULYAEV AE, GELPERINA SE, SKIDAN IN, ANTROPOV AS, KIVMAN GY, KREUTER J. Significant transport of doxorubicin into the brain with polysorbate 80-coated nanoparticles. *Pharm. Res.* 16, 1999, 1564–9.
- 152 SCHROEDER U, SOMMERFELD P, ULRICH S, SABEL BA. Nanoparticle technology for delivery of drugs across the blood–brain barrier. *J. Pharm. Sci.* 87, 1998, 1305–7.
- 153 GUBHA S, MANDAL B. Dispersion polymerization of acrylamide. *J. Colloid Interface Sci.* 271, 2004, 55–9.
- 154 GURNY R, PEPPAS N, HARRINGTON DD, BANKS GS. Development of biodegradable and injectable lattices for controlled release of potent drugs. *Drug Dev. Ind. Pharm.* 7, 1981, 1–25.
- 155 KRAUSE HJ, SCHWARTZ A, ROHDEWALD P. Polylactic acid nanoparticles, a colloidal drug delivery system for lipophilic drugs. *Int. J. Pharm.* 27, 1985, 145–55.
- 156 VERRACCHIA T, SPENLEHAUER G, BAZILE DV, MURRY-BRELIER A, ARCHIMBAUD Y, VEILLARD M. Non-stealth (poly(lactic acid/albumin) and stealth (poly(lactic acid–poly-ethylene glycol)) nanoparticles as injectable drug carriers. *J. Control. Release* 36, 1995, 49–61.
- 157 FESSI H, PUISIEUX F, DEVISSAGUET JP, AMMOURY N, BENITA S. Nanocapsule formation by interfacial deposition following solvent displacement. *Int. J. Pharm.* 55, 1989, R1–4.
- 158 AL KHOURI N, FESSI H, ROBLOT-TREUPEL L, DEVISSAGUET JP, PUISIEUX F. An original procedure for pre-

- paring nanocapsules of polyalkylcyanoacrylates for interfacial polymerization. *Pharm. Acta Helv.* 61, 1986, 274–81.
- 159 VRANCKX H, DE MOUTIER M, DE LEERS M. Pharmaceutical compositions containing nanocapsules. *US Patent 5,500,224*, 1996.
- 160 RAVI KUMAR MN, BAKOWSKY U, LEHR CM. Preparation and characterization of cationic PLGA nanospheres as DNA carriers. *Biomaterials* 25, 2004, 1771–7.
- 161 ILLUM L, KHAN MA, MAK E, DAVIS SS. Evaluation of carrier capacity and release characteristics for poly (butyl 2-cyanoacrylate)nanoparticles. *Int. J. Pharm.* 30, 1986, 17–28.
- 162 Bangs Laboratories. *TechNote 201: Working with Microspheres*. Bangs Laboratories, Fishers, IN, 1999.
- 163 JEFFERIES WA, BRANDON MR, HUNT SV, WILLIAMS AF, GATTER KC, MASON DY. Transferrin receptor on endothelium of brain capillaries. *Nature* 312, 1984, 162–3.
- 164 CALVO P, GOURITIN B, VILLARROYA H, ECLANCHER F, GIANNAVOLO C, KLEIN C, ANDREUX JP, COUVREUR P. Quantification and localization of PEGylated polycyanoacrylate nanoparticles in brain and spinal cord during experimental allergic encephalomyelitis in the rat. *Eur. J. Neurosci.* 15, 2002, 1317–26.
- 165 CALVO P, GOURITIN B, CHACUN H, DESMAELE D, D'ANGELO J, NOEL JP, GEORGIN D, FATTAL E, ANDREUX JP, COUVREUR P. Long-circulating PEGylated polycyanoacrylate nanoparticles as new drug carrier for brain delivery. *Pharm. Res.* 18, 2001, 1157–66.
- 166 PERACCHIA MT, VAUTHIER C, DESMAELE D, GULIK A, DEDIEU JC, DEMOY M, D'ANGELO J, COUVREUR P. Pegylated nanoparticles from a novel methoxypolyethylene glycol cyanoacrylate–hexadecyl cyanoacrylate amphiphilic copolymer. *Pharm. Res.* 15, 1998, 550–6.
- 167 LUECK M. Plasmaproteinadsorption und moeglicher Schluesselfaktor fuer eine kontrollierte Arzneistoffapplikation mit partikulaeren Traegern. *PhD Thesis*. Freie Universitaet, Berlin, 1997, pp. 14–24 and 137–54.
- 168 KREUTER J, PETROV VE, KHARKEVICH DA, ALYAUTDIN RN. Influence of the type of surfactant on the analgesic effects induced by the peptide dalargin after its delivery across the blood-brain barrier using surfactant-coated nanoparticles. *J. Control. Release* 49, 1997, 81–7.
- 169 RAMGE P, UNGER RE, OLTROGGE JB, ZENKER D, BEGLEY D, KREUTER J, VON BRIESEN H. Polysorbate-80 coating enhances uptake of polybutylcyanoacrylate (PBCA)-nanoparticles by human and bovine primary brain capillary endothelial cells. *Eur. J. Neurosci.* 12, 2000, 1931–40.
- 170 OLIVIER JC, FENART L, CHAUVET R, PARIAT C, CECHELLI R, COUET W. Indirect evidence that drug brain targeting using polysorbate 80-coated polybutylcyanoacrylate nanoparticles is related to toxicity. *Pharm. Res.* 16, 1999, 1836–42.
- 171 KREUTER J, SHAMENKOV D, PETROV V, RAMGE P, CYCHUTEK K, KOCH-BRANDT C, ALYAUTDIN R. Apolipoprotein-mediated transport of nanoparticle-bound drugs across the blood–brain barrier. *J. Drug Target.* 10, 2002, 317–25.
- 172 RAMGE P. *Untersuchungen zur Ueberwindung der Blut-Hirn-Schranke mit Hilfe von Nanopartikeln*. Shaker Verlag, Aachen, 1998, pp. 99–110 and 123–39.
- 173 MERESSE S, DELBART C, FRUCHART JC, CECHELLI R. Low-density lipoprotein receptor on endothelium of brain capillaries. *J. Neurochem.* 53, 1989, 340–5.
- 174 DE VRIES HE, KUIPER J, DE BOER AG, VAN BERKEL TJ, BREIMER DD. Characterization of the scavenger receptor on bovine cerebral endothelial cells *in vitro*. *J. Neurochem.* 61, 1993, 1813–21.
- 175 DEHOUCK B, DEHOUCK MP, FRUCHART JC, CECHELLI R. Upregulation of the low density lipoprotein receptor at the blood–brain barrier: intercommunications between

- brain capillary endothelial cells and astrocytes. *J. Cell Biol.* 126, 1994, 465–73.
- 176 LUCARELLI M, GENNARELLI M, CARDELLI P, NOVELLI G, SCARPA S, DALLAPICCOLA B, STROM R. Expression of receptors for native and chemically modified low-density lipoproteins in brain microvessels. *FEBS Lett.* 401, 1997, 53–8.
- 177 CECHELLI R, FENART L, DECAMPS L, TORPIER G, DEHOUCQ MP. Receptor-mediated transcytosis of blood-borne molecules through blood–brain barrier endothelial cells: drug targeting by endogenous transport routes. *Proc Int. Symp. Control. Release Bioact. Mater.* 24, 1997, 221–2.
- 178 PITAS RE, BOYLES JK, LEE DH, FOSS D, MALEY RW. Astrocytes synthesize apolipoprotein E and metabolize apolipoprotein E-containing lipoproteins. *Biochem. Biophys. Acta* 917, 1987, 148–61.
- 179 KREUTER J, ALYAUDIN RN, KHARKEVICH DA, IVANOV AA. Passage of peptides through the blood–brain barrier with colloidal polymer particles (nanoparticles). *Brain Res.* 674, 1995, 171–4.
- 180 ALYAUDIN RN, REICHEL A, LOBENBERG R, RAMGE P, KREUTER J, BEGLEY DJ. Interaction of poly-(butylcyanoacrylate) nanoparticles with the blood–brain barrier *in vivo* and *in vitro*. *J. Drug Target.* 9, 2001, 209–21.
- 181 FENSTERMACHER JD, PATLAK CS. The exchange of materials between cerebrospinal fluid and brain. In *Fluid Environment of the Brain*, CSERR HF, FENSTERMACHER JD, FENCL V (Eds.). Academic Press, New York, 1975, pp. 201–14.
- 182 KESSLER JA, FENSTERMACHER JD, OWENS ES. Spinal subarachnoid perfusion of rhesus monkeys. *Am. J. Physiol.* 230, 1976, 614–8.
- 183 CREMER JE, SEVILLE MP. Regional blood flow, blood volume, and haematocrit values the adult rat. *J. Cereb. Blood Flow Metab.* 3, 1983, 254–6.
- 184 FENSTERMACHER JD, GROSS P, SPOSITO N, ACUFF V, PETTERSEN S, GRUBER K. Structural and functional variations in capillary systems within the brain. *Ann. NY Acad. Sci.* 529, 1988, 21–30.
- 185 WOODCOCK DM, LINSINMEYER ME, CHOJNOWSKI G, KRIEGLER AB, NINK V, WEBSTER LK, SAWYER WH. Reversal of multidrug resistance by surfactants. *Br. J. Cancer* 66, 1992, 62–8.
- 186 NERURKAR MM, BURTON PS, BORCHARDT RT. The use of surfactants to enhance the permeability of peptides through Caco-2 cells by inhibition of an apically polarized efflux system. *Pharm. Res.* 13, 1996, 528–34.
- 187 CORDON-CARDO C, O'BRIEN JP, CASALS D, RITTMAN-GRAUER L, BIEDLER JL, MELAMED MR, BERTINO JR. Multidrug-resistance gene (P-glycoprotein) is expressed by endothelial cells at blood–brain barrier sites. *Proc. Natl Acad. Sci. USA* 86, 1989, 695–8.
- 188 BRIGGER I, MORIZET J, AUBERT G, CHACUN H, TERRIER-LACOMBE MJ, COUVREUR P, VASSAL G., Poly(ethylene glycol)-coated hexadecylcyanoacrylate nanospheres display a combined effect for brain tumor targeting. *J. Pharmacol. Exp. Ther.* 303, 2002, 928–36.
- 189 PULFER SK, GALLO JM. Enhanced brain tumor selectivity of cationic magnetic polysaccharide microspheres. *J. Drug Target.* 6, 1998, 215–27.
- 190 KREUTER J, RAMGE P, PETROV V, HAMM S, GELPERINA SE, ENGELHARDT B, ALYAUDIN R, VON BRIESEN H, BEGLEY DJ. Direct evidence that polysorbate-80-coated poly(butylcyanoacrylate) nanoparticles deliver drugs to the CNS via specific mechanisms requiring prior binding of drug to the nanoparticles. *Pharm. Res.* 20, 2003, 409–16.
- 191 GELPERINA SE, KHALANSKY AS, SKIDAN IN, SMIRNOVA ZS, BOBRUSKIN AI, SEVERIN SE, TUROWSKI B, ZANELLA FE, KREUTER J. Toxicological studies of doxorubicin bound to polysorbate 80-coated poly(butyl cyanoacrylate) nanoparticles in healthy rats and rats with

- intracranial glioblastoma. *Toxicol. Lett.* 126, 2002, 131–41.
- 192 LOCKMAN PR, KOZIARA JM, MUMPER RJ, ALLEN DD. Nanoparticle surface charges alter blood–brain barrier integrity and permeability. *J. Drug Target.* 12, 2004, 635–41.
- 193 FENART L, CASANOVA A, DEHOUCQ B, DUHEM C, SLUPEK S, CECHELLI R, BETBEDER D. Evaluation of effect of charge and lipid coating on ability of 60-nm nanoparticles to cross an *in vitro* model of the blood–brain barrier. *J. Pharmacol. Exp. Ther.* 291, 1999, 1017–22.
- 194 KLEIN WI, KRAFFT GA, FINCH CE. Targeting small Ab oligomers: the solution to an Alzheimer's disease conundrum? *Trends Neurosci.* 24, 2001, 219–24.
- 195 GHISO J, FRANGIONE B. Amyloidosis and Alzheimer's disease. *Adv. Drug Deliv. Rev.* 54, 2002, 1539–51.
- 196 PERMANNE B, ADESSI C, FRAGA S, FROSSARD MJ, SABORIO GP, SOTO C. Are beta-sheet breaker peptides dissolving the therapeutic problem of Alzheimer's disease? *J. Neural. Transm. Suppl.* 62, 2002, 293–301.
- 197 PERMANNE B, ADESSI C, SABORIO GP, FRAGA S, FROSSARD MJ, VAN DORPE J, DEWACHTER I, BANKS WA, VAN LEUVEN F, SOTO C. Reduction of amyloid load and cerebral damage in a transgenic mouse model of Alzheimer's disease by treatment with a beta-sheet breaker peptide. *FASEB J.* 16, 2002, 860–2.
- 198 LLEO A, BEREZOVSKA O, GROWDON JH, HYMAN BT. Clinical, pathological, and biochemical spectrum of Alzheimer disease associated with PS-1 mutations. *Am. J. Geriatr. Psychiatry* 12, 2004, 146–56.
- 199 ROGERS JT, RANDALL JD, EDER PS, HUANG X, BUSH AI, TANZI RE, VENTI A, PAYTON SM, GIORDANO T, NAGANO S, CAHILL CM, MOIR R, LAHIRI DK, GREIG N, SARANG SS, GULLANS SR. Alzheimer's disease drug discovery targeted to the APP mRNA 5'-untranslated region. *J. Mol. Neurosci.* 19, 2002, 77–82.
- 200 ROGERS JT, RANDALL JD, CAHILL CM, EDER PS, HUANG X, GUNSHIN H, LEITER L, MCPHEE J, SARANG SS, UTSUKI T, GREIG NH, LAHIRI DK, TANZI RE, BUSH AI, GIORDANO T, GULLANS SR. An iron-responsive element type II in the 5'-untranslated region of the Alzheimer's amyloid precursor protein transcript. *J. Biol. Chem.* 277, 2002, 45518–28.
- 201 MARCHESI VT. An alternative interpretation of the amyloid Abeta hypothesis with regard to the pathogenesis of Alzheimer's disease. *Proc. Natl Acad. Sci. USA* 102, 2005, 9093–8.
- 202 PAULKE B-R, MOEGLICH P-M, KNIPPEL E, BUDE A, NITZSCHE R, MUELLER RH. Electrophoretic 3D-mobility profiles of latex particles with different surface groups. *Langmuir* 11, 1995, 70–4.
- 203 KACZA J, HARTIG W, SEEGER J. Oxygen-enriched photoconversion of fluorescent dyes by means of a closed conversion chamber. *J. Neurosci. Methods* 71, 1997, 225–32.
- 204 KOPPAL T, DRAKE J, BUTTERFIELD DA. *In vivo* modulation of rodent glutathione and its role in peroxynitrite-induced neocortical synaptosomal membrane protein damage. *Biochim. Biophys. Acta* 1453, 1999, 407–11.
- 205 BUTTERFIELD DA, KOPPAL T, SUBRAMANIAM R, YATIN S. Vitamin E as an antioxidant/free radical scavenger against amyloid beta-peptide-induced oxidative stress in neocortical synaptosomal membranes and hippocampal neurons in culture: insights into Alzheimer's disease. *Rev. Neurosci.* 10, 1999, 141–9.
- 206 BUTTERFIELD DA, HOWARD B, YATIN S, KOPPAL T, DRAKE J, HENSLEY K, AKSENOV M, AKSENOVA M, SUBRAMANIAM R, VARADARAJAN S, HARRIS-WHITE ME, PEDIGO NW JR, CARNEY JM. Elevated oxidative stress in models of normal brain aging and Alzheimer's disease. *Life Sci.* 65, 1999, 1883–92.
- 207 BUTTERFIELD DA, YATIN SM, VARADARAJAN S, KOPPAL T. Amyloid beta-peptide-associated free radical oxidative stress, neurotoxicity, and

- Alzheimer's disease. *Methods Enzymol.* 309, 1999, 746–68.
- 208 SUBRAMANIAM R, KOPPAL T, GREEN M, YATIN S, JORDAN B, DRAKE J, BUTTERFIELD DA. The free radical antioxidant vitamin E protects cortical synaptosomal membranes from amyloid beta-peptide(25–35) toxicity but not from hydroxynonenal toxicity: relevance to the free radical hypothesis of Alzheimer's disease. *Neurochem. Res.* 23, 1998, 1403–10.
- 209 HALLIWELL B, GUTTERIDGE JMC. *Free Radicals in Biology and Medicine*, 3rd edn. Oxford University Press, New York, 1999.
- 210 LIU G, MEN P, KENNER GH, MILLER SC. Age-associated iron accumulation in bone: Implications for post-menopausal osteoporosis and a new target for prevention and treatment by chelation. *BioMetals* 19, 2006, 245–51.
- 211 MARKESBERY WR, CARNEY JM. Oxidative alternations in Alzheimer's disease. *Brain Pathol.* 9, 1999, 133–46.
- 212 ZHU X, RAINA AK, LEE HG, CASADESUS G, SMITH MA, PERRY G. Oxidative stress signaling in Alzheimer's disease. *Brain Res.* 1000, 2004, 32–9.
- 213 ROTTKAMP CA, NUNOMURA A, RAINA AK, SAYRE LM, PERRY G, SMITH MA. Oxidative stress, antioxidants, and Alzheimer disease. *Alzheimer Dis. Assoc. Disord.* 14, 2000, S62–66.
- 214 POLIDORI MC, MATTIOLI P, ALDRED S, CECCHETTI R, STAHL W, GRIFFITHS H, SENIN U, SIES H, MECOCCI P. Plasma antioxidant status, immunoglobulin G oxidation and lipid peroxidation in demented patients: relevance to Alzheimer disease and vascular dementia. *Dement. Geriatr. Cogn. Disord.* 18, 2004, 265–70.
- 215 ANLASKI T, SIES H, GRIFFITHS HR, MECOCCI P, STAHL W, POLIDORI MC. Dietary habits are major determinants of the plasma antioxidant status in healthy elderly subjects. *Br. J. Nutr.* 94, 2005, 639–42.
- 216 BERMAN K, BRODATY H. Tocopherol (vitamin E) in Alzheimer's disease and other neurodegenerative disorders. *CNS Drugs* 18, 2004, 807–25.
- 217 GROWDON JH. Incorporating biomarkers into clinical drug trials in Alzheimer's disease. *J. Alzheimer's Dis.* 3, 2001, 287–92.
- 218 VINA J, LLORET A, ORTI R, ALONSO D. Molecular bases of the treatment of Alzheimer's disease with antioxidants: prevention of oxidative stress. *Mol. Aspects Med.* 25, 2004, 117–23.
- 219 DHITAVAT S, RIVERA ER, ROGERS E, SHEA TB. Differential efficacy of lipophilic and cytosolic antioxidants on generation of reactive oxygen species by amyloid-beta. *J. Alzheimer's Dis.* 3, 2001, 525–9.
- 220 EKINCI FJ, LINSLEY MD, SHEA TB. Beta-amyloid-induced calcium influx induces apoptosis in culture by oxidative stress rather than tau phosphorylation. *Brain Res. Mol. Brain Res.* 76, 2000, 389–95.
- 221 EKINCI FJ, MALIK KU, SHEA TB. Activation of the L voltage-sensitive calcium channel by mitogen-activated protein (MAP) kinase following exposure of neuronal cells to beta-amyloid. MAP kinase mediates beta-amyloid-induced neurodegeneration. *J. Biol. Chem.* 274, 1999, 30322–7.
- 222 KUMAR R, CHEN MH, PARMAR VS, SAMUELSON LA, KUMAR J, NICOLOSI R, YOGANATHAN S, WATTERSON AC. Supramolecular assemblies based on copolymers of PEG600 and functionalized aromatic diesters for drug delivery applications. *J. Am. Chem. Soc.* 126, 2004, 10640–4.
- 223 OLANOW CW. An introduction to the free radical hypothesis in Parkinson's disease. *Ann. Neurol.* 32, 1992, S2–9.
- 224 MARKESBERY WR, EHMANN WD. Oxidative stress in Alzheimer disease. In *Alzheimer Disease*, TERRY RD, KATZMAN R, BICK KL, SISODIA SS (Eds.). Lippincott Williams & Wilkins, Philadelphia, PA, 1999, pp. 401–14.
- 225 EHMANN WD, MARKESBERG WR, ALAUDDIN M, HOSSAIN TI, BRUBAKER EH. Brain trace elements in Alzheimer's disease. *Neurotoxicology* 7, 1986, 195–206.
- 226 HUANG X, ATWOOD CS, MOIR RD, HARTSHORN MA, VONSATTEL JP,



- TANZI RE, BUSH AI. Zinc-induced Alzheimer's A $\beta$ 1–40 aggregation is mediated by conformational factors. *J. Biol. Chem.* 272, 1997, 26464–70.
- 227 ATWOOD CS, PERRY G, ZENG H, KATO Y, JONES WD, LING KQ, HUANG X, MOIR RD, WANG D, SAYRE LM, SMITH MA, CHEN SG, BUSH AI. Copper mediates dityrosine cross-linking of Alzheimer's amyloid- $\beta$ . *Biochemistry* 43, 2004, 560–8.
- 228 ATWOOD CS, SCARPA RC, HUANG X, MOIR RD, JONES WD, FAIRLIE DP, TANZI RE, BUSH AI. Characterization of copper interactions with Alzheimer amyloid  $\beta$  peptides: identification of an attomolar-affinity copper binding site on amyloid  $\beta$ 1–42. *J. Neurochem.* 75, 2000, 1219–33.
- 229 BUSH AI, PETTINGELL WH, MULTHAUP G, D PARADIS M, VONSAITTEL JP, GUSELLA JF, BEYREUTHER K, MASTERS CL, TANZI RE. Rapid induction of Alzheimer A  $\beta$  amyloid formation by zinc. *Science* 265, 1994, 1464–7.
- 230 BUSH AI, MASTERS CL, TANZI RE. Copper,  $\beta$ -amyloid, and Alzheimer's disease: tapping a sensitive connection. *Proc. Natl Acad. Sci. USA* 100, 2003, 11193–4.
- 231 JOBLING MF, HUANG X, STEWART LR, BARNHAM KJ, CURTAIN C, VOLITAKIS I, PERUGINI M, WHITE AR, CHERNY RA, MASTERS CL, BARROW CJ, COLLINS SJ, BUSH AI, CAPPAI R. Copper and zinc binding modulates the aggregation and neurotoxic properties of the prion peptide PrP106–126. *Biochemistry* 40, 2001, 8073–84.
- 232 CHERNY RA, LEGG JT, MCLEAN CA, FAIRLIE DP, HUANG X, ATWOOD CS, BEYREUTHER K, TANZI RE, MASTERS CL, BUSH AI. Aqueous dissolution of Alzheimer's disease A $\beta$  amyloid deposits by biometal depletion. *J. Biol. Chem.* 274, 1999, 23223–8.
- 233 LOSKE C, GERDEMANN A, SCHEPL W, WYCISLO M, SCHINZEL R, PALM D, RIEDERER P, MUNCH G. Transition metal-mediated glycooxidation accelerates cross-linking of  $\beta$ -amyloid peptide. *Eur. J. Biochem.* 267, 2000, 4171–8.
- 234 CHERNY RA, BARNHAM KJ, LYNCH T, VOLITAKIS I, LI QX, MCLEAN CA, MULTHAUP G, BEYREUTHER K, TANZI RE, MASTERS CL, BUSH AI. Chelation and intercalation: complementary properties in a compound for the treatment of Alzheimer's disease. *J. Struct. Biol.* 130, 2000, 209–16.
- 235 LYNCH T, CHERNY RA, BUSH AI. Oxidative processes in Alzheimer's disease: the role of  $\beta$ -metal interactions. *Exp. Gerontol.* 35, 2000, 445–51.
- 236 LOVELL MA, ROBERTSON JD, TEESDALE WJ, CAMPBELL JL, MARKESBERY WR. Copper, iron and zinc in Alzheimer's disease senile plaques. *J. Neurol. Sci.* 158, 1998, 47–52.
- 237 PADMANABHAN G, BECUE I, SMITH JA. Clioquinol. In *Analytical Profiles of Drug Substances*, FLOREY K (Ed.). Academic Press, New York, 1989, pp 57–90.
- 238 ANDERSEN O. Chemical and biological considerations in the treatment of metal intoxications by chelating agents. *Mini-Rev. Med. Chem.* 4, 2004, 11–21.
- 239 LOCKMAN PR, KOZIARA J, RODER KE, PAULSON J, ABBRUSCATO TJ, MUMPER RJ, ALLEN DD. *In-vivo* and *in-vitro* assessment of baseline blood–brain barrier parameters in the presence of novel nanoparticle. *Pharm. Res.* 20, 2003, 705–13.
- 240 KOZIARA JM, LOCKMAN PR, ALLEN DD, MUMPER RJ. *In-situ* blood–brain barrier of nanoparticles. *Pharm. Res.* 20, 2003, 1772–8.
- 241 CUI Z, MUMPER RJ. Plasmid DNA-entrapped nanoparticles engineered from microemulsion precursors: *in-vitro* and *in-vivo* evaluation. *Bioconjug. Chem.* 13, 2002, 1319–27.
- 242 OYEWUMI MO, MUMPER RJ. Influence of formulation parameters on gadolinium entrapment and tumor cell uptake using folate-coated nanoparticles. *Int. J. Pharm.* 251, 2003, 85–97.
- 243 WONG SS. *Chemistry of Protein Conjugation and Cross-Linking*. CRC Press, Bioca Raton, FL, 1991.
- 244 MARTIN FJ, PAPAHDJOPULOS D. Irreversible coupling of immuno-

- globulin fragments to preformed vesicles. *J. Biol. Chem.* 257, 1982, 286–8.
- 245 MARTIN FJ, HUBBELL WL, PAPAHAJDOPOULOS D. Immunospecific targeting of liposomes to cells: a novel and efficient method for covalent attachment of Fab' fragments via disulfide bonds. *Biochemistry* 20, 1981, 4229–38.
- 246 KATO N, NAKAMURA M, UCHIYAMA T. <sup>1</sup>H NMR studies of the reactions of copper(I) and copper(II) with D-penicillamine and glutathione. *J. Inorg. Biochem.* 75, 1999, 117–21.
- 247 DANEHY JP, HUNTER WE. The alkaline decomposition of organic disulfides. II. Alternative pathways as determined by structure. *J. Org. Chem.* 32, 1967, 2047–53.
- 248 SUBRAMANIAN ZF, VANEK ZF. Diagnosis and treatment of Wilson's disease. *Curr. Neurol. Neurosci. Rep.* 2, 2002, 317–23.
- 249 WALSHE JM. Penicillamine, a new oral therapy for Wilson's disease. *Am. J. Med.* 21, 1956, 487–95.
- 250 WALSHE JM. Copper chelation in patients with Wilson's disease. A comparison of penicillamine and triethylene tetramine dihydrochloride. *Q. J. Med.* 42, 1973, 441–52.
- 251 WALSHE JM. Treatment of Wilson's disease with trientine (triethylene tetramine) dihydrochloride. *Lancet* i, 1982, 643–7.
- 252 POWELL LW, JAZWINSKA E, HALLIDAY JW. Primary iron overload. In *Iron Metabolism in Health and Disease*, BROCK JH, HALLIDAY JW, PIPPARD MJ, POWELL LW (Eds.). Saunders, London, 1994, pp. 227–270.
- 253 PIPPARD MJ. Secondary iron overload. In *Iron Metabolism in Health and Disease*, BROCK JH, HALLIDAY JW, PIPPARD MJ, POWELL LW (Eds.). Saunders, London, 1994, pp. 271–309.
- 254 CRICHTON RR. *Inorganic Biochemistry of Iron Metabolism from Molecular Mechanisms to Clinical Consequences*, 2nd edn. Wiley, Chichester, 2001.
- 255 SULLIVAN JL. Iron and the sex difference in heart disease risk. *Lancet* 1, 1981, 1293–4.
- 256 STADLER N, LINDNER RA, DAVIES MJ. Direct detection and quantification of transition metal ions in human atherosclerotic plaques: evidence for the presence of elevated levels of iron and copper. *Arterioscler. Thromb. Vasc. Biol.* 24, 2004, 949–54.
- 257 STEVENS RG, JONES DY, MICOZZI MS, TAYLOR PR. Body iron stores and the risk of cancer. *N. Engl. J. Med.* 319, 1988, 1047–52.
- 258 WOO J, MAK YT, LAW LK, SWAMINATHAN R. Plasma ferritin in an elderly population living in the community. *J. Med.* 20, 1989, 123–34.
- 259 MOIRAND R, MORTAJI AM, LOREAL O, PAILLARD F, BRISSOT P, DEUGNIER Y. A new syndrome of liver iron overload with normal transferrin saturation. *Lancet* 349, 1997, 95–7.
- 260 ROUAULT TA. Iron on the brain. *Nat. Genet.* 28, 2001, 299–300.
- 261 LOVELL MA, EHMANN WD, BUTLER SM, MARKESBERY WR. Elevated thiobarbituric acid-reactive substances and antioxidant enzyme activity in the brain in Alzheimer's disease. *Neurology* 45, 1995, 1594–601.
- 262 PERRY G, CASTELLANI RJ, HIRAI K, SMITH MA. Reactive oxygen species mediate cellular damage in Alzheimer disease. *J. Alzheimer's Dis.* 1, 1998, 45–55.
- 263 CASADESUS G, SMITH MA, ZHU X, ALIEV G, CASH AD, HONDA K, PETERSEN RB, PERRY G. Alzheimer disease: evidence for a central pathogenic role of iron-mediated reactive oxygen species. *J. Alzheimer's Dis.* 6, 2004, 165–9.
- 264 GUTTERIDGE JM. Hydroxyl radicals, iron, oxidative stress, and neurodegeneration. *Ann. NY Acad. Sci.* 738, 1994, 201–13.
- 265 EVANS PH. Free radicals in brain metabolism and pathology. *Br. Med. Bull.* 49, 1993, 577–87.
- 266 CONNOR JR, MENZIES SL, ST MARTIN SM, MUFSON EJ. Cellular distribution of transferrin, ferritin, and iron in normal and aged human brains. *J. Neurosci. Res.* 27, 1990, 595–611.
- 267 CONNOR JR, SNYDER BS, BEARD JL, FINE RE, MUFSON EJ. Regional

- distribution of iron and iron-regulatory proteins in the brain in aging and Alzheimer's disease. *J. Neurosci. Res.* 31, 1992, 327–35.
- 268 CONNOR JR, MENZIES SL, ST MARTIN SM, MUFSON EJ. A histochemical study of iron, transferrin, and ferritin in Alzheimer's diseased brains. *J. Neurosci. Res.* 31, 1992, 75–83.
- 269 CHRISTEN Y. Oxidative stress and Alzheimer disease. *Am. J. Clin. Nutr.* 71, 2000, 621S–9S.
- 270 COLLINGWOOD JF, MIKHAYLOVA A, DAVIDSON M, BATICH C, STREIT WJ, TERRY J, DOBSON J. In situ characterization and mapping of iron compounds in Alzheimer's disease tissue. *J. Alzheimer's Dis.* 7, 2005, 267–72.
- 271 FINEFROCK AE, BUSH AI, DORAISWAMY PM. Current status of metals as therapeutic targets in Alzheimer's disease. *J. Am. Geriatr. Soc.* 51, 2003, 1143–8.
- 272 SUH SW, JENSEN KB, JENSEN MS, SILVA DS, KESSLAK PJ, DANSCHER G, FREDERICKSON CJ. Histochemically-reactive zinc in amyloid plaques, angiopathy, and degenerating neurons of Alzheimer's diseased brains. *Brain Res.* 852, 2000, 274–8.
- 273 LEE JY, MOOK-JUNG I, KOH JY. Histochemically reactive zinc in plaques of the Swedish mutant B-amyloid precursor protein transgenic mice. *J. Neurosci.* 19, 1999, RC10.1–5.
- 274 McLACHLAN DR, KRUCK TP, LUKIW WJ, KRISHNAN SS. Would decreased aluminum ingestion reduce the incidence of Alzheimer's disease? *Can. Med. Ass. J.* 145, 1991, 793–804.
- 275 GOOD PF, PERL DP, BIERER LM, SCHMEIDLER J. Selective accumulation of aluminum and iron in the neurofibrillary tangles of Alzheimer's disease: a laser microprobe (LAMMA) study. *Ann. Neurol.* 31, 1992, 286–92.
- 276 KONG S, LIOCHEV S, FRIDOVICH I. Aluminum(III) facilitates the oxidation of NADH by the superoxide anion. *Free Radic. Biol. Med.* 13, 1992, 79–81.
- 277 BONDY SC, GUO-ROSS SX, TRUONG AT. Promotion of transition metal-induced reactive oxygen species formation by beta-amyloid. *Brain Res.* 799, 1998, 91–6.
- 278 PRATICO D, CLARK CM, LIU F, ROKACH J, LEE VY, TROJANOWSKI JQ. Increase of brain oxidative stress in mild cognitive impairment: a possible predictor of Alzheimer disease. *Arch. Neurol.* 59, 2002, 972–976.
- 279 KENNARD ML, FELDMAN H, YAMADA T, JEFFERIES WA. Serum levels of the iron binding protein p97 are elevated in Alzheimer's disease. *Nat. Med.* 2, 1996, 1230–5.
- 280 JEFFERIES WA, FOOD MR, GABATHULER R, ROTHENBERGER S, YAMADA T, YASUHARA O, MCGEER PL. Reactive microglia specifically associated with amyloid plaques in Alzheimer's disease brain tissue express melanotransferrin. *Brain Res.* 712, 1996, 122–6.
- 281 MULTHAUP G, SCHLICKSUPP A, HESSE L, BEHER D, RUPPERT T, MASTERS CL, BEYREUTHER K. The amyloid precursor protein of Alzheimer's disease in the reduction of copper(II) to copper(I). *Science* 271, 1996, 1406–9.
- 282 SAYRE LM, PERRY G, SMITH MA. Redox metals and neurodegenerative disease. *Curr. Opin. Chem. Biol.* 3, 1999, 220–5.
- 283 LINDER MC, HAZEGH-AZAM M. Copper biochemistry and molecular biology. *Am. J. Clin. Nutr.* 63, 1996, 797S–811S.
- 284 HENSLEY K, CARNEY JM, MATTSON MP, AKSENOVA M, HARRIS M, WU JF, FLOYD RA, BUTTERFIELD DA. A model for beta-amyloid aggregation and neurotoxicity based on free radical generation by the peptide: relevance to Alzheimer disease. *Proc. Natl Acad. Sci. USA* 91, 1994, 3270–4.
- 285 BUTTERFIELD DA. beta-Amyloid-associated free radical oxidative stress and neurotoxicity: implications for Alzheimer's disease. *Chem. Res. Toxicol.* 10, 1997, 495–506.
- 286 HOUSE E, COLLINGWOOD J, KHAN A, KORCHAZKINA O, BERTHON G, EXLEY C. Aluminium, iron, zinc and copper influence the *in vitro* formation of amyloid fibrils of Abeta42 in a manner which may have consequences

- for metal chelation therapy in Alzheimer's disease. *J. Alzheimer's Dis.* 6, 2004, 291–301.
- 287 HERSHKO C. Iron chelators for thalassaemia. *Br. J. Haematol.* 101, 1998, 399–406.
- 288 NEUFELD EJ. Oral chelators deferasirox and deferiprone for transfusional iron overload in Thalassemia major: new data, new questions. *Blood* 107, 2006, 3436–41.
- 289 McLACHLAN DR, DALTON AJ, KRUCK TP, BELL MY, SMITH WL, KALOW W, ANDREWS DF. Intramuscular desferrioxamine in patients with Alzheimer's disease. *Lancet*, 337, 1991, 1304–8.
- 290 CUAJUNGO MP, FAGET KY, HUANG X, TANZI RE, BUSH AI. Metal chelation as a potential therapy for Alzheimer's disease. *Ann. NY Acad. Sci.* 920, 2000, 292–304.
- 291 RICHARDSON DR, PONKA P. Development of iron chelators to treat iron overload disease and their use as experimental tools to probe intracellular iron metabolism. *Am. J. Hematol.* 58, 1998, 299–305.
- 292 KEBERLE H. The biochemistry of desferrioxamine and its relation to iron metabolism. *Ann. NY Acad. Sci.* 119, 1964, 758–68.
- 293 HIDER RC, HALL AD. Clinically useful chelators of tripositive elements. *Prog. Med. Chem.* 28, 1991, 41–173.
- 294 BEN-SHACHAR D, RIEDERER P, YODIM MB. Iron–melanin interaction and lipid peroxidation: implications for Parkinson's disease. *J. Neurochem.* 57, 1991, 1609–14.
- 295 FLOOR E. Iron as a vulnerability factor in nigrostriatal degeneration in aging and Parkinson's disease. *Cell Mol. Biol.* 46, 2000, 709–20.
- 296 BLAKE DR, WINYARD P, LUNEC J, WILLIAMS A, GOOD PA, CREWES SJ, GUTTERIDGE JM, ROWLEY D, HALLIWELL B, CORNISH A, HIDER RC. Cerebral and ocular toxicity induced by desferrioxamine. *Q. J. Med.* 56, 1985, 345–55.
- 297 KRUCK TP, FISHER EA, McLACHLAN DR. A predictor for side-effects in patients with Alzheimer's disease treated with deferoxamine mesylate. *Clin. Pharmacol. Ther.* 53, 1993, 30–7.
- 298 STRUCK M, WALDMEIER P, BERDOUKAS V. The treatment of iron overload – psychiatric implication. In *Iron in Central Nervous System Disorders*, RIEDERER P, YODIM MBH (Eds.). Springer Verlag, Wien, 1993, pp. 189–96.
- 299 KLAASEN CD. Heavy metals and heavy-metal antagonists. In *Goodman and Gilman's The Pharmacological Basis of Therapeutics*, HARDMAN JG, LIMBIRD LE, MOLINOFF PB, RUDDON RW, GILMAN AG (Eds.). McGraw-Hill, New York, 1996, pp. 1649–71.
- 300 JENNER P, OLANOW CW. Understanding cell death in Parkinson's disease. *Ann. Neurol.* 44, 1998, S72–S84.
- 301 MAY PM, BULMAN RA. The present status of chelating agents in medicine. *Prog. Med. Chem.* 20, 1983, 225–336.
- 302 OLIVIERI NF, BRITTENHAM GM. Iron-chelating therapy and the treatment of thalassemia. *Blood* 89, 1997, 739–61.
- 303 LYNCH SG, FONSECA T, LEVINE SM. A multiple course trial of desferrioxamine in chronic progressive multiple sclerosis. *Cell Mol. Biol.* 46, 2000, 865–9.
- 304 CROWE A, MORGAN EH. Effects of chelators on iron uptake and release by the brain in the rat. *Neurochem. Res.* 19, 1994, 71–6.
- 305 KONTOGHIOGHES GJ. New concepts of iron and aluminium chelation therapy with oral L1 (deferiprone) and other chelators. A review. *Analyst* 120, 1995, 845–51.
- 306 NELSON WO, TIMOTHY B, KARPISHIN TB, RETTING SJ, ORVIG C. Aluminum and gallium compounds of 3-hydroxy-4-pyridinones: synthesis, characterization, and crystallography of biologically active complexes with unusual hydrogen bonding. *Inorg. Chem.* 27, 1988, 1045–51.
- 307 HOFFBRAND AV. Oral iron chelation. *Semin. Hematol.* 33, 1996, 1–8.
- 308 WARD RJ, DEXTER D, FLORENCE A, AOUAD F, HIDER R, JENNER P, CRICHTON RR. Brain iron in the ferrocene-loaded rat: its chelation and

- influence on dopamine metabolism. *Biochem. Pharmacol.* **49**, **1995**, 1821–6.
- 309 RICHARDSON DR. The therapeutic potential of iron chelators. *Expert Opin. Invest. Drugs* **8**, **1999**, 2141–58.
- 310 HIDER RC, PORTER JB, SINGH S. The design of therapeutically useful iron chelators. In *The Development of Iron Chelators for Clinical Use*. BERGERON RJ, BRITTENHAM GM (Eds.). CRC, Boca Raton, FL, **1994**, pp. 353–71.
- 311 PORTER JB, MORGAN J, HOYES KP, BURKE LC, HUEHNS ER, HIDER RC. Relative oral efficacy and acute toxicity of hydroxypyridin-4-one iron chelators in mice. *Blood* **76**, **1990**, 2389–96.
- 312 RAYMOND KN, XU J. Siderophore-based hydroxypyridonate sequestering agents. In *The Development of Iron Chelators for Clinical Use*, BERGERON RJ, BRITTENHAM GM (Eds.). CRC Press, Boca Raton, FL, **1994**, pp. 354–71.
- 313 ZHOU T, LIU ZD, NEUBERT H, KONG XL, MA YM, HIDER RC. High affinity iron(III) scavenging by a novel hexadentate 3-hydroxypyridin-4-one-based dendrimer: synthesis and characterization. *Bioorg. Med. Chem. Lett.* **15**, **2005**, 5007–11.
- 314 HIDER RC, CHOUDHURY R, RAI BL, DEHKORDI LS, SINGH S. Design of orally active iron chelators. *Acta Haematol.* **95**, **1996**, 6–12.
- 315 MARTELL AE, MOTEKAITIS RJ, SUN Y, MA R, WELCH MJ, PAJEAU T. New chelating-agents suitable for the treatment of iron overload. *Inorg. Chim. Acta* **291**, **1999**, 238–46.
- 316 CARAVAN P, ORVIG C. Tripodal aminophenolate ligand complexes of aluminum(III), gallium(III), and indium(III) in water. *Inorg. Chem.* **36**, **1997**, 237–48.
- 317 FALLER B, SPANKA C, SERGEJEV T, TSCHINKE V. Improving the oral bioavailability of the iron chelator HBED by breaking the symmetry of the intramolecular H-bond network. *J. Med. Chem.* **43**, **2000**, 1467–75.
- 318 RICHARDSON DR, PONKA P. Pyridoxal isonicotinoyl hydrazone and its analogs: potential orally effective iron-chelating agents for the treatment of iron overload disease. *J. Lab. Clin. Med.* **131**, **1998**, 306–15.
- 319 RICHARDSON DR. Friedreich's ataxia: iron chelators that target the mitochondrion as a therapeutic strategy? *Expert Opin. Invest. Drugs* **12**, **2003**, 235–45.
- 320 GALANELLO R, PIGA A, ALBERTI D, ROUAN MC, BIGLER H, SECHAUD R. Safety, tolerability, and pharmacokinetics of ICL670, a new orally active iron-chelating agent in patients with transfusion-dependent iron overload due to beta-thalassemia. *J. Clin. Pharmacol.* **43**, **2003**, 565–572.
- 321 DONOVAN JM, PLONE M, DAGHER R, BREE M, MARQUIS J. Preclinical and clinical development of deferitron, a novel, orally available iron chelator. *Ann. NY Acad. Sci.* **1054**, **2005**, 492–4.
- 322 STERBA M, SIMUNEK T, MAZUROVA Y, ADAMCOVA M, POPELOVA O, KAPLANOVA J, PONKA P, GERSL V. Safety and tolerability of repeated administration of pyridoxal 2-chlorobenzoyl hydrazone in rabbits. *Hum. Exp. Toxicol.* **24**, **2005**, 581–9.
- 323 LOVEJOY DB, KALINOWSKI D, BERNHARDT PV, RICHARDSON DR. PCTH: a novel orally active chelator for the treatment of iron overload disease. *Hemoglobin* **30**, **2006**, 93–104.
- 324 KONTOGHIORGHES GJ, ERACLEOUS E, ECONOMIDES C, KOLNAGOU A. Advances in iron overload therapies. prospects for effective use of deferiprone (L1), deferoxamine, the new experimental chelators ICL670, GT56-252, LINA11 and their combinations. *Curr. Med. Chem.* **12**, **2005**, 2663–81.
- 325 BERGERON RJ, BHARTI N, WIEGAND J, McMANIS JS, YAO H, PROKAI L. Polyamine-vectored iron chelators: the role of charge. *J. Med. Chem.* **48**, **2005**, 4120–37.
- 326 FISHER AE, NAUGHTON DP. Metal ion chelating peptides with superoxide dismutase activity. *Biomed. Pharmacother.* **59**, **2005**, 158–62.
- 327 APOSTOL M, BARET P, SERRATRICE G, DESBRIERES J, PUTAUX JL, STEBE MJ, EXPERT D, PIERRE JL. Self-assembly of an amphiphilic iron(III) chelator:

- mimicking iron acquisition in marine bacteria. *Angew. Chem. Int. Ed.* **44**, **2005**, 2580–2.
- 328** NOVAKOVIC J, TESORO A, THIESSEN JJ, SPINO M. Metabolic and pharmacokinetic evaluation of a novel 3-hydroxypyridinone iron chelator, CP502, in the rat. *Eur. J. Drug Metab. Pharmacokinet.* **29**, **2004**, 221–4.
- 329** HOCHHAUSER E, BEN-ARI Z, PAPPO O, CHEPURKO Y, VIDNE BA. TPEN attenuates hepatic apoptotic ischemia/reperfusion injury and remote early cardiac dysfunction. *Apoptosis* **10**, **2005**, 53–62.
- 330** LEBEDEV AV, IVANOVA MV, LEVITSKY DO. Echinochrome, a naturally occurring iron chelator and free radical scavenger in artificial and natural membrane systems. *Life Sci.* **76**, **2005**, 863–75.
- 331** CHONG HS, TORTI SV, MA R, TORTI FM, BRECHBIEL MW. Synthesis and potent antitumor activities of novel 1,3,5-*cis,cis*-triaminocyclohexane *N*-pyridyl derivatives. *J. Med. Chem.* **47**, **2004**, 5230–4.
- 332** HODGES YK, ANTHOLINE WE, HORWITZ LD. Effect on ribonucleotide reductase of novel lipophilic iron chelators: the desferri-exochelins. *Biochem. Biophys. Res. Commun.* **315**, **2004**, 595–8.
- 333** LEWIS JA, PUERTA DT, COHEN SM. Metal complexes of the *trans*-influencing ligand thiomaltol. *Inorg. Chem.* **42**, **2003**, 7455–9.
- 334** HALPER SR, COHEN SM. Synthesis, structure, and spectroscopy of phenylacetylenylene rods incorporating meso-substituted dipyrin ligands. *Chemistry* **9**, **2003**, 4661–9.
- 335** BRANDON MS, PASZCZYNSKI AJ, KORUS R, CRAWFORD RL. The determination of the stability constant for the iron(II) complex of the biochelator pyridine-2,6-bis(monothiocarboxylic acid). *Biodegradation* **14**, **2003**, 73–82.
- 336** LADEN K, ZAKIAD H, SIMMON ED, KLEIN JY, CYJON RL, WINCHELL HS. *N,N',N''*-tris(dihydroxyphosphorylmethyl)-1,4,7-triazacyclononane (Deofix) – a high-affinity, high-specificity chelator for first transition series metal cations with significant deodorant, anti-microbial, and antioxidant activity. *J. Cosmet. Sci.* **54**, **2003**, 251–61.
- 337** PERSSON HL, YU Z, TIROSH O, EATON JW, BRUNK UT. Prevention of oxidant-induced cell death by lysosomotropic iron chelators. *Free Radic. Biol. Med.* **34**, **2003**, 1295–305.
- 338** DHUNGANA S, HEGGEMANN S, GEBHARDT P, MOLLMANN U, CRUMBLISS AL. Fe(III) coordination properties of a new saccharide-based exocyclic trihydroxamate analogue of ferrichrome. *Inorg. Chem.* **42**, **2003**, 42–50.
- 339** FERRALI M, BAMBAGIONI S, CECCANTI A, DONATI D, GIORGI G, FONTANI M, LASCHI F, ZANELLO P, CASOLARO M, PIETRANGELO A. Design, synthesis, and physicochemical and biological characterization of a new iron chelator of the family of hydroxochromenes. *J. Med. Chem.* **45**, **2002**, 5776–85.
- 340** KICIC A, CHUA AC, BAKER E. The desferri-thiocin (DFT) class of iron chelators: potential as antineoplastic agents. *Anticancer Drug Des.* **16**, **2001**, 195–207.
- 341** ROYT PW, HONEYCHUCK RV, RAVICH V, PONNALURI P, PANNELL LK, BUYER JS, CHANDHOKE V, STALICK WM, DESESSO LC, DONOHUE S, GHEI R, RELYEA JD, RUIZ R. 4-hydroxy-2-nonylquinoline: a novel iron chelator isolated from a bacterial cell membrane. *Bioorg. Chem.* **29**, **2001**, 387–97.
- 342** DHUNGANA S, HEGGEMANN S, HEINISCH L, MOLLMANN U, BOUKHALFA H, CRUMBLISS AL. Fe(III) coordination properties of two new saccharide-based enterobactin analogues: methyl 2,3,4-tris-*O*-[*N*-[2,3-di(hydroxy)benzoyl-glycyl]-aminopropyl]- $\alpha$ -D-glucopyranoside and methyl 2,3,4-tris-*O*-[*N*-[2,3-di(hydroxy)-benzoyl]-aminopropyl]- $\alpha$ -D-glucopyranoside. *Inorg. Chem.* **40**, **2001**, 7079–86.
- 343** SAMUNI AM, KRISHNA MC, DEGRAFF W, RUSSO A, PLANALP RP, BRECHBIEL MW, MITCHELL JB. Mechanisms underlying the cytotoxic effects of Tachpyr – a novel metal chelator.

- Biochim. Biophys. Acta* 1571, 2002, 211–8.
- 344 FERRALI M, DONATI D, BAMBAGIONI S, FONTANI M, GIORGI G, PIETRANGELO A. 3-Hydroxy-(4H)-benzopyran-4-ones as potential iron chelating agents *in vivo*. *Bioorg. Med. Chem.* 9, 2001, 3041–7.
- 345 NAUGHTON DP, GROOTVELD M. EDTA bis-(ethyl phenylalaninate): a novel transition metal-ion chelating hydroxyl radical scavenger with a potential anti-inflammatory role. *Bioorg. Med. Chem. Lett.* 11, 2001, 2573–5.
- 346 BORSARI M, GABBI C, GHELFI F, GRANDI R, SALADINI M, SEVERI S, BORELLA F. Silybin, a new iron-chelating agent. *J. Inorg. Biochem.* 85, 2001, 123–9.
- 347 GALEY JB, DESTREE O, DUMATS J, GENARD S, TACHON P. Protection against oxidative damage by iron chelators: effect of lipophilic analogues and prodrugs of *N,N'*-bis(3,4,5-trimethoxybenzyl)ethylenediamine-*N,N'*-diacetic acid (OR10141). *J. Med. Chem.* 43, 2000, 1418–21.
- 348 FASMAN GD, MOORE CD. The solubilization of model Alzheimer tangles: reversing the beta-sheet conformation induced by aluminum with silicates. *Proc. Natl Acad. Sci. USA* 91, 1994, 11232–5.
- 349 BREWER GJ. Neurologically presenting Wilson's disease: epidemiology, pathophysiology and treatment. *CNS Drugs* 19, 2005, 185–92.
- 350 ALYAUTDIN RN, TEZIKOV EB, RAMGE P, KHARKEVICH DA, BEGLEY DJ, KREUTER J. Significant entry of tubocurarine into the brain of rats by adsorption to polysorbate 80-coated polybutylcyanoacrylate nanoparticles: an *in situ* brain perfusion study. *J. Microencapsul.* 15, 1998, 67–74.
- 351 ALYAUTDIN RN, PETROV VE, LANGER K, BERTHOLD A, KHARKEVICH DA, KREUTER J. Delivery of loperamide across the blood–brain barrier with polysorbate 80-coated polybutylcyanoacrylate nanoparticles. *Pharm. Res.* 14, 1997, 325–8.
- 352 LUO Y, HAN Z, CHIN SM, LINN S. Three chemically distinct types of oxidants formed by iron-mediated Fenton reactions in the presence of DNA. *Proc. Natl Acad. Sci. USA* 91, 1994, 12438–42.
- 353 DAVSON H, SEGAL MB. *Physiology of the CSF and Blood–Brain Barriers*. CRC Press, Boca Raton, FL, 1996.
- 354 PORTER JB, GYPARAKI M, BURKE LC, HUEHNS ER, SARPONG P, SAEZ V, HIDER RC. Iron mobilization from hepatocyte monolayer cultures by chelators: the importance of membrane permeability and the iron-binding constant. *Blood* 72, 1988, 1497–503.
- 355 LIU G, MEN P, KENNER GH, MILLER SC, BRUENGER FW. Acyclonucleoside iron chelators of 1-(2-hydroxyethoxy)-methyl-2-alkyl-3-hydroxy-4-pyridinones: potential oral iron chelation therapeutics. *Nucleosides Nucleotides Nucleic Acids* 23, 2004, 599–611.
- 356 BREM H, WALTER KA, TAMARGO RJ, OLIVI A, LANGER R. Drug delivery to the brain. In *Polymeric Site-Specific Pharmacotherapy*, DOMB AJ (Ed.). Wiley, New York, 1994, pp. 117–39.
- 357 BLUNK T, HOCHSTRASSER DF, SANCHEZ JC, MULLER BW, MULLER RH. Colloidal carriers for intravenous drug targeting: plasma protein adsorption patterns on surface-modified latex particles evaluated by two-dimensional polyacrylamide gel electrophoresis. *Electrophoresis* 14, 1993, 1382–7.
- 358 DOBBIN PS, HIDER RC, HALL AD, TAYLOR PD, SARPONG P, PORTER JB, XIAO G, VAN DER HELM D. Synthesis, physicochemical properties, and biological evaluation of *N*-substituted 2-alkyl-3-hydroxy-4(1H)-pyridinones: orally active iron chelators with clinical potential. *J. Med. Chem.* 36, 1993, 2448–58.
- 359 LIU G, MILLER SC, BRUENGER FW. Synthesis of lipophilic 3-hydroxy-2-methyl-4-pyridinone derivatives. *Synth. Commun.* 25, 1995, 3247–53.
- 360 LIU G, MILLER SC, BRUENGER FW. Efficient synthesis of *N*-[2-hydroxyethoxy)methyl]-2-alkyl-3-hydroxy-4-pyridinone by a modified

- Hilbert–Johnson reaction. *Synthetic Commun.* 26, **1996**, 2681–6.
- 361** ROBINS MJ, HATFIELD PW. Nucleic acid related compounds. 37. Convenient and high-yield synthesis of *N*-[(2-hydroxyethoxy)methyl] heterocycles as “acyclic nucleoside” analogues. *Can J. Chem.* 60, **1982**, 547–53.
- 362** SCHAEFFER HJ, GURWARA S, VINCE R, BITTNER S. Novel substrate of adenosine deaminase. *J. Med. Chem.* 14, **1971**, 367–9.
- 363** STREATER M, TAYLOR PD, HIDER RC, PORTER J. Novel 3-hydroxy-2(1*H*)-pyridinones. Synthesis, iron(III)-chelating properties, and biological activity. *J. Med. Chem.* 33, **1990**, 1749–55.
- 364** HARRIS RLN. Potential wool growth inhibitors. Improved synthesis of mimosine and related 4(1*H*)-pyridones. *Aust. J. Chem.* 29, **1976**, 1329–34.
- 365** NIEDBALLA U, VORBRUEGGEN H. A general synthesis of pyrimidine nucleosides. *Angew Chem. Int. Ed.* 9, **1970**, 461–2.
- 366** SMITH MA, HARRIS PL, SAYRE LM, PERRY G. Iron accumulation in Alzheimer’s disease is a source of redox-generated free radicals. *Proc. Natl Acad. Sci. USA* 94, **1997**, 9866–8.
- 367** ARANO Y, MATSUSHIMA H, TAGAWA M, KOIZUMI M, ENDO K, KONISHI J, YOKOYAMA A. A novel bifunctional metabolizable linker for the conjugation of antibodies with radionuclides. *Bioconjug. Chem.* 2, **1991**, 71–6.
- 368** HIDER RC, TAYLOR PD, WALKINSHAW M, WANG JL, VAN DER HELM D. Crystal structure of 3-hydroxy-1,2-dimethyl-pyridin-4(1*H*)-one: an iron (III) chelator study. *J. Chem. Res. Synop.* 10, **1990**, 316–7.
- 369** NELSON WO, KARPISHIN TB, RETTING SJ, ORVIG C. Physical and structural studies of *N*-substituted-3-hydroxy-2-methyl-4(1*H*)-pyridinones. *Can. J. Chem.* 66, **1988**, 123–31.
- 370** CHARALAMBOUS J, DODD A, MCPARTLIN M, MATONDO SOC, PATHIRANA ND, POWELL HR. Synthesis and X-ray crystal structure of tris(1,2-dimethyl-3-hydroxypyrid-4-onato)iron(III). *Polyhedron* 7, **1988**, 2235–7.
- 371** XIAO GY, VAN DER HELM D, HIDER RC, RAI BL. Molecular modeling studies of a ferric hexadentate 3-hydroxy-2(1*H*)-pyridinone complex and an analogue by molecular mechanics, molecular dynamics, and free energy perturbation simulations. *J. Phys. Chem.* 100, **1996**, 2345–52.
- 372** KANEKO Y, KITAMATO T, TATEISHI J, YAMAGUCHI K. Ferritin immunohistochemistry as a marker for microglia. *Acta Neuropathol.* 79, **1989**, 129–36.
- 373** THOMPSON CM, MARKESBERY WR, EHMANN WD, MAO YX, VANCE DE. Regional brain trace-element studies in Alzheimer’s disease. *Neurotoxicology* 9, **1988**, 1–7.
- 374** KONGOHIORGHES GJ. Iron mobilization from ferritin using  $\alpha$ -oxohydroxy heteroaromatic chelators. *Biochem. J.* 233, **1986**, 299–302.
- 375** LIU G, MEN P, HARRIS PL, ROLSTON RK, PERRY G, SMITH MA. Nanoparticle iron chelators: a new therapeutic approach in Alzheimer disease and other neurologic disorders associated with trace metal imbalance. *Neurosci Lett.* 406, **2006**, 189–93.
- 376** HALLAWAY PE, EATON JW, PANTER SS, HEDLUND BE. Modulation of deferoxamine toxicity and clearance by covalent attachment to biocompatible polymers. *Proc. Natl Acad. Sci. USA* 86, **1989**, 108–12.
- 377** PANTER SS, BRAUGHLER JM, HALL ED. Dextran-coupled deferoxamine improves outcome in a murine model of head injury. *J. Neurotrauma* 9, **1992**, 47–53.
- 378** DRUGAS GT, PAIDAS CN, YAHANDA AM, FERGUSON D, CLEMENS MG. Conjugated desferoxamine attenuates hepatic microvascular injury following ischemia/reperfusion. *Circ. Shock* 34, **1991**, 278–83.
- 379** HOROWITZ D, MARGEL S, SHIMONI T. Iron detoxification by haemoperfusion through deferoxamine-conjugated agarose-polyacrolein microsphere beads. *Biomaterials* 6, **1985**, 9–16.



- 380 GOLENSER J, DOMB A, TEOMIM D, TSAFACK A, NISIM O, PONKA P, ELING W, CABANTCHIK ZI. The treatment of animal models of malaria with iron chelators by use of a novel polymeric device for slow drug release. *J. Pharmacol. Exp. Ther.* 281, 1997, 1127–35.
- 381 LOWTHER N, SPARKS K, NICKLIN J, JIN Y. A novel depot preparation of desferrioxamine-B: development of formulation principles. *Drug Dev. Ind. Pharm.* 25, 1999, 1157–66.
- 382 VENKATARAM S, KHOHLOKWANE M. Microencapsulation of an iron chelator for sustained release and crystal habit modification. *J. Microencapsul.* 13, 1996, 519–25.
- 383 ANJANEYULU PS, STAROS JV. Reactions of *N*-hydroxysulfosuccinimide active esters. *Int. J. Pept. Protein Res.* 30, 1987, 117–24.
- 384 STAROS JV, WRIGHT RW, SWINGLE DM. Enhancement by *N*-hydroxysulfosuccinimide of water-soluble carbodiimide-mediated coupling reactions. *Anal. Biochem.* 156, 1986, 220–2.
- 385 SHI Y, EYRING EM, VAN ELDIK R, LIU G, BRUENGER FW, MILLER SC. Kinetics and mechanisms of Fe(III) complexation by lipophilic 3-hydroxy-2methyl-1( $\gamma$ -stearoamidopropyl)-4-pyridinone (HMSP). *J. Bioinorg. Chem.* 2, 1997, 728–43.
- 386 MICHAELIS M, LANGER K, ARNOLD S, DOERR HW, KREUTER J, CINATL JR J. Pharmacological activity of DTPA linked to protein-based drug carrier systems. *Biochem. Biophys. Res. Commun.* 323, 2004, 1236–40.

## Index

### a

- $A\beta$  *see* amyloid- $\beta$
- absorption
  - drug delivery 193
  - targeted drug delivery 193–195
- active agents, polymeric nanoparticles 267
- active cancer vaccination, drug delivery 191
- active pharmaceutical ingredients, drug delivery applications 540
- active targeting 344
- active transport, drug delivery 194
- actuation detection, sensors 511–512
- acute cardiac transplant rejection, iron oxide nanoparticles MRI 72
- AD *see* Alzheimer's disease
- AD brain sections
  - iron evaluation 677–678
  - iron mobilization 672–673
- adeno-associated virus, gene therapy 219
- adjustable diffusion barrier, drug delivery applications 550
- adjuvants delivery, CNTs 107–110
- adsorption, surface functionalization 364–365
- adverse drug events 190–191
- aerosol release, CNT 127
- agents, TEM 396
- aggregation, core–shell nanoparticles 161
- AIDS
  - drug delivery 434
  - vaccines 439–440
- airways, special pharmacology 202
- all-*trans* retinoic acid (ATRA)
  - chemical structure 312
  - NANOEGG<sup>TM</sup> technology 311–313, 320–322
  - self-aggregation 312
- alveolar macrophages (AM), CNT 122
- alveolar membrane, delivery routes 414
- Alzheimer's disease (AD)
  - chelation therapy 665
  - metal levels 661
  - multimetal ions 662–664
  - perspectives 683
  - potential treatment 652–682
  - treatment 644–683
- AM *see* alveolar macrophages
- amidation, CNT functionalization 90
- 3O-aminopropyl-3-hydroxyl-4-pyridinone 666
- ammonium *f*-CNTs, molecular structure 108
- amperometric techniques 21
- amphiphilic
  - copolymers 366
  - dextran 366
  - molecules 88
- amyloid- $\beta$ 
  - $A\beta$ -mediated oxidative stress 653–656
  - deposition 657–660
  - drug delivery 652
- AN *see* anionic nanoparticles
- analytical characterization, SLNs 480–491
- analytical nanotechnology-enhanced tools, diagnostics 35
- analytical techniques, surface modification 375
- animal skin, NANOEGG treatment 330
- anionic nanoparticles (AN) 58
- anti-factor Xa (FXa) 168
- antibodies, surface functionalization 362
- antibody-loaded gelatin nanoparticles 374
- antibody recognition, CNT 109
- anticoagulant, Heparin 166
- antifungal, drug delivery 427
- antigen delivery, CNTs 107–110
- antigens
  - gene therapy 609–610
  - peptide 109–110

- antileishmanial agents 425
  - antioxidant delivery, oxidative stress 653–656
  - apoptosis 638
    - membrane damage 629–643
    - nonviral vector 632–633
    - PEI-mediated 631–637
    - routes 637
  - aptamers
    - biosensors 19
    - CNT 99
    - diagnostics 8
  - aqueous polymeric nanomaterials, drug delivery materials 257–258
  - area under the plasma concentration–time curve (AUC), drug delivery 196
  - arthritis, iron oxide nanoparticles MRI 70
  - ASGP-R *see* asialoglycoprotein receptor
  - asialoglycoprotein receptor (ASGP-R) ligands 232
  - assays
    - bio-barcode 16
    - biological 377–379
    - diagnostic 40
    - ELISA 3
    - enzyme assay enhancement 24
    - FPIA 3
    - *in vitro* 393–395
    - multiplexed diagnostic 40
    - RIA 3
    - *see also* immunoassay
  - atheromatous plaque, characterization 67
  - atherosclerotic plaques, macrophage targeting 230
  - ATRA *see* all-*trans* retinoic acid
  - AUC *see* area under the plasma concentration–time curve
  - azide–alkyne cycloaddition, CPMV 568
  - azomethine, cycloaddition 94
  - AZT (3'-azido-3'-deoxythymidine)
    - CNT functionalization 95
    - liver concentration 436
- b**
- bacteria, natural strategies 210
  - barrier
    - diffusion 550
    - E-LbL assembled nanoshells 545–547
    - endothelial 206
    - gene therapy 599–603
  - barrier crossing, nanoparticles 645–651
  - barrier penetration, targeted drug delivery 210
  - barrier properties, nanoshells 539
  - BBB *see* blood brain barrier
  - BBB penetration 679
  - bifunctionalization, CNTs 96
  - bio-barcode assay 16
  - bioadhesive polymers, transmucosal drug delivery systems 225
  - bioavailability
    - iron chelators 678
    - targeted drug delivery 196
  - biocompatible polymer, gene therapy 613–614
  - bioconjugation
    - BNPs 567–568
    - CPMV 568
    - methods 560–566
  - biodegradable polymer 349
    - calcium compounds 271
  - biodistribution, CNT 113
  - bioerosion, polymer materials 345
  - biohybrid hydrogels, drug delivery applications 510–511
  - bioimaging, BNPs 580–582
  - biological assays/methods, surface modification 377–379
  - biological barriers, gene therapy 599–603
  - biological (macro)molecules, surface functionalization 359
  - biological recognition, surface functionalization 360
  - biomedical applications, BNPs 557–596
  - bioMEMS sensor platform 514
  - biomimetic approach, drug delivery applications 551
  - bionanoparticles (BNP) 557–596
    - alterations 560–576
    - bioconjugation 567–568
    - hybrid 587
    - multiple functional groups 561
  - biosensing elements 516
  - biosensors
    - cantilevers 30
    - CNT 96
    - diagnostics 7
    - electrochemical 24–27
    - FET 98–99
    - fiber optic 18–19
    - major components 8
    - nanoelectrode 102–104
  - biotin, surface functionalization 362
  - biotin–avidin–biotin complex formation 362
  - blood–brain barrier (BBB)
    - crossing 645–651
    - physiological functions 645–647
    - targeted delivery 226

- blood pool characteristics, iron oxide nanoparticles MRI 66
- BNPs *see* bionanoparticles
- Boc *see tert*-butyloxycarbonyl
- boron neutron capture therapy (BNCT), CNT 113
- bovine spongiform encephalopathy, prions 221
- brain
  - AD 661
  - complex transport 661
  - drug delivery 645–651
  - *see also* blood–brain barrier
- brown spots, NANOEGG™ treatment 331–334
- c**
- calcium compounds, inorganic 270
- calcium silicate-based microspheres, drug delivery 279
- cancer
  - liver 63
  - lymph node 65
  - *see also* tumor
- cancer gene therapy 611–612
  - HVJ-E 609
- cancer vaccination, drug delivery 191
- cantilevers
  - biosensors 30
  - optical measurement 33
- capsids, viruses 218–219
- capsule preparation, silastic compounds 272
- carbohydrates, surface functionalization 360
- carbon electrode, biosensor 102
- carbon nanohorn (CNH), drug delivery 286
- carbon nanotube (CNT) arrays 102
- carbon nanotube (CNT)-based electrodes, diagnostics 100
- carbon nanotube (CNT)-based FET 98
  - backside functionalization 101
- carbon nanotube (CNT)-RNA polymer, cellular uptake 118
- carbon nanotubes (CNTs)
  - cell uptake 105–107
  - chemical functionalization 86–95
  - CNT-based vectors 85–142
  - delivery of antigens and adjuvants 107–110
  - diagnosis 96–104
  - drug delivery 111–114
  - drug delivery carriers 280–283
  - FET 97
  - functionalized 285
  - gene transfer 115–117
  - health impact 118–126
  - *in vitro* effects 123–124
  - *in vivo* effects 125–126
  - interaction with DNA and RNA 115
  - length 123
  - modification 88
  - purity 119–122
  - solvents 123
  - surface 123
  - toxicity 284
- carborane cage, functionalization 113
- carboxylic acid
  - CNT functionalization 90
  - derivatization routes 91
- cardiac imaging 66
- cardiac transplant rejection, iron oxide nanoparticles MRI 72
- carriers, drug delivery 270–286
- case studies, drug delivery materials 267–269
- cationic lipids
  - cell damage 638
  - gene transfer vectors 629
- cationic lysozyme, core–shell nanoparticles 162
- cell damage 638
- cell dysfunction, PEI-mediated 631–637
- cell invasion, viruses 217–218
- cell lines, human 629–643
- cell membrane 207–208
  - gene therapy 600
- cell targeting, BNPs 578
- cell therapy, *in vivo* monitoring 72
- cell tracking, animal models 74
- cell uptake, CNTs 105–107
- cell viability
  - CNT 120–122
  - core–shell nanoparticles 180
- cellular uptake
  - CNT–RNA polymer 118
  - drug delivery 410
- cerebral imaging 66
- cerebral tumor, characterization 68
- charge, SPIOs 54–55
- chelatable iron, lesion-associated 678
- chelation therapy, AD 665
- chelator, drug delivery 657–660
- chelator–particle conjugation 679
- chelator–particle systems, protein absorption patterns 675
- chemical alterations, BNPs 560–576
- chemical functionalization, CNTs 86–95
- chemical modifications, BNPs 560

- chitosan
    - chemical structure 346
    - nanoparticles 430
    - natural polymers 347
    - oral delivery 448
  - Chlamydia trachomatis* 213
  - cholangiocarcinoma 63
  - chronic inflammatory diseases
    - NANOEGG™ 320
    - noninvasive delivery systems 223
  - circulation, systemic 600
  - clathrin-mediated endocytosis 209
  - “click chemistry”, BNPs 567–568
  - clinical trials, NANOEGG™ treatment 331–333
  - clinical uses, iron oxide nanoparticles MRI 61–74
  - Clostridium difficile* 210
  - CNH *see* carbon nanohorn
  - CNT(s) *see* carbon nanotube(s)
  - CO<sub>2</sub> sensor, hydrogel based 515
  - coating
    - chitosan nanoparticles 263
    - CNT 89
    - core–shell nanoparticles 174
    - drug delivery materials 256–263
    - nanomaterials 257
    - polysaccharides 263
    - quantum dots 11
    - terpolymer 259
  - coating agents, SPIOs 55
  - cold homogenization 474
  - colloidal drug delivery systems 380
  - colloidal stabilization 550
  - colloidal structures 481
  - complexes
    - formation 550
    - metal chelator 661
    - PEI-DNA 630
    - ruthenium–polypyridyl 23
  - composite latexes, thermosensitive drug-releasing 262
  - composition, SLNs 473
  - computed tomography (CT) 4
  - contrast agents
    - MRI 392
    - paramagnetic 62
    - SPIOs 51
  - controlled release
    - drug delivery 278–279
    - pharmaceutical ingredients 540
  - conventional bioconjugation methods, BNPs 560–566
  - copper chelator, drug delivery 657–660
  - core, nanoshell properties 538
  - core–shell nanoparticles 311–318
    - drug delivery 143–188
    - drug delivery materials 260
    - liquid core 145–155
    - metallic core 174–180
    - molecular imaging 143–188
    - polymeric core 156–173
    - scheme 146
  - cornea, delivery routes 415
  - coronary artery disease, core–shell nanoparticles 153
  - cosmetic applications, SLNs 491
  - covalent functionalization, CNTs 89
  - covalent linking 370–374
    - surface modification 363
  - cowpea mosaic virus (CPMV)
    - chemical modification 562
    - coat protein 562
    - dye-modified 582
    - nanogold-modified 563
    - structure 564
  - CpG (Cytosin-phosphatidyl-Guanosin) motifs, interaction with *f*-CNTs 107–109
  - CPMV *see* cowpea mosaic virus
  - Creutzfeldt–Jakob disease, prions 221
  - Crohn’s disease 62
  - cryoprotection, drug delivery 146
  - crystal size, SPIOs 54
  - crystalline forms, solid dispersion particles 289
  - crystallinity, SLNs 481
  - crystals
    - MRI 54
    - SPIOs 52
  - CT *see* computed tomography
  - cycloaddition, azomethine 94
  - cysteines 567
    - reactives 562
  - cytochrome P450, drug delivery 199
  - Cytosin-phosphatidyl-Guanosin *see* CpG
  - cytotoxicity 630
    - CNT 122
    - water-soluble CNT 124
- d**
- Dahl’s calcium staining, NANOEGG™ 335
  - DC *see* dendritic cells
  - defect-free SWNTs, molecular structure 86
  - defect functionalization, CNTs 90
  - deferasirox *see* ICL670
  - degradable synthetic polymers, nanomaterials 349–351
  - degradation, gene therapy 600

- delivery routes
  - diabetes 452–459
  - vaccines 442–2450
- delivery systems
  - invasive 225
  - noninvasive 223
  - oral 224
  - transdermal 224
  - transmucosal 225
- dendrimers 11
  - patient diagnostics 40
  - surface modification 41
- dendritic cells (DCs) 444
  - gene therapy 609–612
  - transfection 610
- dense agents, TEM 396
- dermatology, NANOEGG™ technology 319–333
- desferrioxamine (DFO)
  - bioavailability 678
  - chemical structure 662
  - conjugation with nanosphere or microsphere particles 672–675
  - reaction with ferric iron 675
- desoxyribonucleic acid *see* DNA
- dextran, chemical structure 348
- DFO *see* desferrioxamine
- diabetes
  - drug delivery 451
  - NANOEGG™ 336
  - noninvasive delivery systems 223
- diagnosis 388
  - drug delivery materials 264–269
  - polymeric nanomaterials 342–408
- diagnostic assays, multiplexed 40
- diagnostical nanotechnology, overview 1–50
- diagnostics
  - biosensors 7
  - CNTs 96–104
  - electrical 19–28
  - future developments 40–43
  - imaging 33–34
  - magnetic 28–30
  - mechanical 30–33
  - nanotechnology-enhanced tools 34–39
  - optical 9–19
  - patient 1
  - point-of-care 41–42
- diazonium compounds, SWNT
  - functionalization 93
- diazonium reagents, CNT 93
- differential scanning calorimetry (DSC), core–shell nanoparticles 150
- differentiation, keratinocytes 326–327
- diffusion barrier, adjustable 550
- diffusion coefficients, NANOEGG™ 316
- 2,3-dimercaptosuccinic acid (DMSA) 61
- dioleoyl-L- $\alpha$ -phosphatidylethanolamine (DOPE) 485
  - 1,2-dioleoyl-*sn*-glycero-3-phosphoethanolamine-N-[3-(2-pyridyldithio)propionate] (PDP-PE) 657–659
  - 1,2-dioleoyl-*sn*-glycero-3-phosphoethanolamine-N-[4-(*p*-maleimidophenyl)butyramide] (MPB-PE) 657–659
- diseases
  - Alzheimer's *see* Alzheimer's disease
  - liver 63
  - macrophage-related 423–426
  - spleen 63
- dispersion particles, drug delivery 288–294
- dispersion polymerization, surface functionalization 369
- dissolution 288
- distribution, targeted drug delivery 197
- DMSA *see* 2,3-dimercaptosuccinic acid
- DNA (desoxyribonucleic acid)
  - delivery and expression 116–117
  - nanopore 38
- DNA hybridization
  - biosensors 26
  - electrochemical detection 25
- DOPE *see* dioleoyl-L- $\alpha$ -phosphatidylethanolamine
- doxorubicin, controlled release 583
- drug carrier 145
- drug delivery 415–459
  - absorption 193
  - AIDS 434
  - antioxidant 653–656
  - applications 519–522
  - BBB 645–651
  - brain 226–227
  - carbon nanohorn (CNH) 286
  - CNTs 111–114
  - controlled release 278–279
  - copper chelator 657–660
  - core–shell nanoparticles 143–188
  - diabetes 451
  - *f*-CNTs 285
  - macrophage targeting 228–229
  - materials 255–309
  - mucosal routes 496–497
  - NANOEGG™ technology 310–341
  - nanoshells 527–556
  - nasal 413

- drug delivery (*cont.*)
    - ocular 416–421
    - oral 412
    - polymeric nanoparticles 409–470
    - porous silastic materials 287–309
    - potentially therapeutic agents 652
    - proteins 495
    - pulmonary 413
    - routes 412
    - solid lipid nanoparticles 471–508
    - targeted *see* targeted drug delivery
    - transdermal/subcutaneous 414
    - vaccine adjuvants 498–499
    - with CNT-based vectors 85–142
  - drug delivery systems 380
    - AIDS 435–438
    - antifungal 428–430
    - BBB 648–649
    - carriers 270–286
    - gastroretentive 279
    - invasive 225
    - noninvasive 223
    - oral 224
    - transdermal 224
    - transmucosal 225
  - drug distribution 197
  - drug encapsulation, BNPs 583
  - drug incorporation
    - efficiency 477
    - models 476
    - SLNs 476
  - drug-loaded lipid core 146
  - drug loading, SLNs 477
  - drug release
    - BNPs 583
    - SLNs 476
  - drug-releasing microcapsules, thermosensitive 261–262
  - drug reservoir 198
  - drug:carrier ratio, solid dispersion particles 290
  - drugs
    - controlled release 278–279
    - low-soluble 488–489
    - poorly absorbable 275–277
    - uptake 410
  - drying, SLNs 475
  - DSC *see* differential scanning calorimetry
  - dye-modified CPMV 582
    - self-assembly 532–533
  - E-LbL assembled nanoshells 540
    - barrier properties 539
    - barriers 545–547
  - EA *see* ethyl acrylate
  - ECG *see* electrocardiography
  - EEG *see* electroencephalography
  - efficacy increase, oxidative stress 653–656
  - EHEMHP *see* ethyl-N-(20-hydroxyethoxy)methyl-3-hydroxyl-4-pyridinone
  - electrical detection, sensors 517–518
  - electrical diagnostics
    - electrochemical biosensors 24–27
    - nanomaterials for enhanced electron transfer 20–24
  - electrocardiography (ECG), patient diagnostics 5
  - electrocatalytic amplification, biosensors 23
  - electrochemical biosensors, electrical diagnostics 24–27
  - electrochemical detection, DNA hybridization 25
  - electrodes, CNT-based 100
  - electroencephalography (EEG), patient diagnostics 5
  - electromyography (EMG), patient diagnostics 5
  - electron dense agents, TEM 396
  - electron transfer, enhanced 20–24
  - electron-transfer mediator 27
  - electroporation, carbon nanotubes 283
  - elimination, targeted drug delivery 198–200
  - ELISA *see* enzyme-linked immunosorbent assay
  - embolotherapy, MRI-detectable 73–74
  - EMG *see* electromyography
  - emulsification-diffusion, polymeric nanomaterials 356
  - emulsion, surface functionalization 369
  - emulsion-evaporation, polymeric nanomaterials 354
  - encapsulation, controlled release 540
  - endocytosis
    - clathrin-mediated 209
    - HVJ-E Vector 616
    - receptor-mediated 205
  - endothelial barrier 206
  - enhanced electron transfer, nanomaterials 20–24
  - enhanced permeation and retention effect, therapeutic applications 383
  - Entamoeba histolytica*, parasitic infections 426
  - enterocytes, special pharmacology 203
- e**
- E-LbL
    - assembly 542
    - preparation 532–534

- entrapment efficiency, mesoporous silica 295  
 enzyme assay enhancement, biosensors 24  
 enzyme-linked immunosorbent assay (ELISA)  
   3  
   – surface modification 379  
 epidermal growth factor, dermatology 325  
 epidermal layer, HA production 328–329  
 epidermis  
   – NANOEGG™ 326, 318  
   – tissue analysis 323  
 epithelioid granulomas, CNT toxicity 284  
 epithelium  
   – gastrointestinal tract 202–203  
   – respiratory tract 202  
   – skin 201  
 erythropoietin (EPO)  
   – concentration 281  
   – core–shell nanoparticles 156  
*Escherichia coli* 213  
 esterification, CNT functionalization 90  
 ethics, patient diagnostics 42–43  
 ethyl acrylate (EA), nanoporous materials  
   259  
 ethyl-N-(20-hydroxyethoxy)methyl-3-hydroxyl-  
   4-pyridinone 666–669  
 evasion  
   – immune system 213–214  
 experimental descriptions, metal chelator  
   complexes 666–675  
 expression, gene-encoding DNA and RNA  
   116–117  
 external eye infections, inflammatory 416  
 extravasation 344  
 eye  
   – anatomy 415  
   – infections 416
- f**
- F-127 *see* Pluronics  
*f*-CNTs *see* functionalized carbon nanotubes  
*f*-SWNTs *see* functionalized SWNTs  
 fabrication  
   – CNT-based electrodes 101  
   – CNT-FETs 97  
   – face, NANOEGG™ treatment 331–333  
 FAD *see* flavin adenine dinucleotide  
 ferric iron, reaction with MAPHP and DFO  
   675  
 ferritin  
   – BNP 558  
   – iron mobilization 671–672  
 ferucarbotran, liver diseases 64  
 ferumoxides, liver diseases 63  
 ferumoxides endocytosis, SPIOs 58  
 ferumoxsil  
   – contrast agents 62  
   – gastrointestinal tract imaging 62  
 ferumoxtran, blood pool 66  
 ferumoxtran-10 57–60  
 FET *see* field effect transistor  
 fiber optic biosensors, optical diagnostics  
   18–19  
 fibroblast growth factor (FGF), gene therapy  
   220  
 field effect transistor (FET)  
   – biosensors 98–99  
   – CNT 97  
   – diagnostics 97  
 film formation, polymeric nanoparticles 258  
 film preparation 533  
 film thickness, QCM electrodes 536  
 films, biosensor 102  
 fine particle coating 260  
   – drug delivery materials 260  
   – nanoporous materials 259  
 fine wrinkles  
   – mouse tissue 331  
   – NANOEGG™ treatment 330–333  
 first-generation nanoparticles 343  
 FISH *see* fluorescent in situ hybridization  
 FITC *see* fluorescein isothiocyanate  
 flavin adenine dinucleotide (FAD), biosensor  
   103  
 flora, native 210  
 flow cytometry, patient diagnostics 4  
 fluidization, fine particle coating 260  
 fluorescein isothiocyanate (FITC)  
   – diagnostics 9  
   – molecular structure 105  
 fluorescence 11  
   – diagnostics 9–10  
   – labeling 388–391  
 fluorescence polarization immunoassay (FPIA)  
   3  
 fluorescent  
   – *in situ* hybridization (FISH) 4  
   – nanotubes 106  
   – peptide–CNT conjugate 105  
   – probes 580  
   – quantum yield 582  
 fluorination, CNTs 93  
 FMDV peptide *f*-CNTs, molecular structure  
   110  
 folate-coated nanoparticles 378  
 folate receptor, surface functionalization 361  
 folded-sheet mesoporous silica *see* FSM  
 Fourier transform IR (FTIR)-spectra, core–  
   shell nanoparticles 176



- FPIA *see* fluorescence polarization immunoassay
- freeze-thawing method, mesoporous silica 295–298
- FSM (folded-sheet mesoporous silica), pore structure 296
- FTIR *see* Fourier transform IR
- fullerenes, health impact 119
- functional barriers 545–547
- functional groups 375
- iron chelators 676
- functional molecules 370–374
- functional surfactants 366–368
- functionalization
- biological (macro)molecules 359
  - chemical 86–95
  - ligands 360
  - nano-organized shells 550
  - polymeric nanomaterials 342–408
- functionalized carbon nanotube (*f*-CNT)-attached peptide antigens, presentation and immunogenic potential 109–110
- functionalized carbon nanotubes (*f*-CNTs) 285
- cell uptake 106
  - gene delivery 286
  - interaction with CpG 107–109
- functionalized SWNTs (*f*-SWNTs), CNT 89
- fusigenic virion, HVJ-E Vector 606
- fusion, cancer 611–612
- Fxa *see* anti-factor Xa
- g**
- galactose, recognition mechanisms 361
- gastrointestinal tract
- imaging 61–62
  - mucosal epithelium 202–203
- gastroretentive floating drug delivery system 279
- gel layer, core-shell nanoparticles 159
- GEMA macromonomer 371
- gene delivery
- BNPs 579
  - *f*-CNTs 286
- gene-encoding DNA and RNA, delivery and expression 116–117
- gene expression, regulation 602
- gene therapy 597–628
- antigens 609–610
  - cancer 611–612
  - HVJ-E 609
  - retrovirus-based 219
  - SLNs 482–485
- gene transfer
- biological barriers 599–603
  - CNTs 115–117
  - simultaneous 611–612
  - synthetic vectors 629–643
- genetic alterations, BNPs 560–576
- genetics, nanotechnology-enhanced diagnostic tools 37–38
- genomagnetic capture separation 30
- genomagnetic nanocaptors 28
- glucose levels 456
- glucose sensors 515
- glucuronidation, drug delivery 199
- glyconanospheres, luminescent 391
- gold coating, surface modification 29
- gold nanoparticles, aptamer-functionalized 19
- gold nanoshells 530
- production 529
- granulocytes, bacteria 215
- growth factors
- dermatology 325
  - Heparin 167
- h**
- HA *see* hemagglutinins; *see also* hyaluronic acid
- HaCaT *see* human epidermal keratinocytes
- handheld diagnostics, magnetic nanoparticles 30
- HB-EGF *see* heparin-binding epidermal growth factor
- HB-EGF mRNA expression, mouse tissue 325
- HDF *see* human fibroblasts
- health impact, CNTs 118–126
- Helicobacter pylori* 213
- oral delivery 447
- Hemagglutinating Virus of Japan-Envelope vector *see* HVJ-E
- hemagglutinins (HA)
- biosensor 100
  - chemical structure 348
- $\alpha$ -Hemolysin ion channel, biosensors 38
- heparin-binding epidermal growth factor (HB-EGF), NANOEGG™ technology 325
- heparin functionalized PLGA 168
- heparin-functionalized PLGA nanoparticles 166–173
- hepatic imaging, liver diseases 63
- herpes simplex virus, gene therapy 220
- heterologous peptide insertions, BNPs 571–575
- high-molecular-weight compounds, drug delivery applications 543–544

- HIV (human immunodeficiency virus)
    - protease inhibitors 437
  - HMG-CoA *see* hydroxymethyl glutaryl coenzyme A
  - host cell invasion, viruses 217–218
  - host invasion, natural strategies 210–212
  - human cell lines, membrane damage
    - 629–643
  - human epidermal keratinocytes (HaCaT), CNT
    - 127
  - human face, NANOEGG™ treatment
    - 331–333
  - human fibroblasts (HDF), CNT surface
    - 123
  - human immunodeficiency virus *see* HIV
  - human immunoglobulin G, biosensor 100
  - human melanoma, SPIOs 57
  - HVJ-E (Hemagglutinating Virus of Japan envelope) vector 598
    - biocompatible polymer 613–614
    - cancer gene therapy 609
    - development 604–608
    - gene therapy 604–612
    - melanoma-associated antigen (MAA) 609–610
    - PS modified 618
    - system 605
    - tumor cells 611–612
  - hyaluronic acid (HA)
    - dermatology 328–329
    - natural polymers 348
  - hyaluronic acid (HA)-functionalized PLGA nanoparticles 157–165
  - hybrid cells, gene therapy 611–612
  - hydrodynamic particle size, SPIOs 54–55
  - hydrogel based sensors 512
  - hydrogels
    - biohybrid 510–511
    - biosensors 518
    - imprinted 511
    - intelligent 509–526
    - invasive delivery systems 226
    - ionic 510
    - temperature-responsive 510
  - hydrophilic polymeric shell, core–shell nanoparticles 160
  - hydrophobic interaction
    - CNT 89
    - CNTs 88
  - hydroxyapatite cement, calcium compounds
    - 270
  - hydroxyapatite drug delivery system 271
  - hydroxymethyl glutaryl coenzyme A (HMG-CoA) 58
  - hyperkeratinization, NANOEGG™ 319
  - hyperpigmentation 330
    - guinea pig 332
    - human faces 333
    - NANOEGG™ 319
  - hysteresis loop, iron-oxide 174
- i**
- ICL670, chemical structure 662
  - IHC *see* immunohistochemical stains
  - illnesses, chronic 223
  - imaging, molecular 143–188
  - imaging diagnostics 33–34
  - immune modulation, BNPs 585
  - immune response, BNPs 584–585
  - immune system activation, bacteria 214
  - immune system evasion
    - bacteria 213–214
    - viruses 216
  - immunoassay 39
    - nanotechnology-enhanced diagnostic tools 39
    - patient diagnostics 3
  - immunogenic potential, *f*-CNT-attached peptide antigens 109–110
  - immunoglobulin G
    - antibodies 362
    - viruses 217
  - immunohistochemical stains (IHC), patient diagnostics 4
  - immunopotentiating effect, CNT 108
  - Immunostaining, NANOEGG™ 337
  - immunostimulatory activity, CpG motifs 107–109
  - immunotherapeutics delivery, with CNT-based vectors 85–142
  - immunotherapy, gene therapy 609–610
  - imprinted hydrogels, drug delivery applications 511
  - improved lability, ATRA 317–318
  - in situ* polymerization
    - nanospheres 357
    - polymeric nanoparticles 492
  - in vitro* assays, magnetic nanoparticles 393–395
  - in vitro* effects, CNTs 123–124
  - in vivo* effects, CNTs 125–126
  - in vivo* monitoring, cell therapy 72
  - incorporation efficiency
    - determination 477
    - drug delivery 476
  - infections
    - iron oxide nanoparticles MRI 70
    - parasitic 426

inflammation  
 – cytokines expression 322  
 – multiple sclerosis 69  
 – NANOEGG™ 321  
 – stroke 68  
 – USPIO 61  
 inflammatory external eye infections, drug delivery 416  
 inorganic calcium compounds, drug delivery 270  
 inorganic minerals, NANOEGG™ 314  
 inorganic nanoparticles, drug delivery materials 265–266  
 Insulin 459  
 – FSM adsorption 296  
 – FSM entrapment 298  
 – oral delivery 454  
 insulin level change, NANOEGG™ 337  
 intelligent hydrogels, drug delivery applications 509–510  
 interactions,  $\pi$ - $\pi$  stacking 86–87  
 interferon (IFN)- $\alpha$  496  
 interferon (IFN)- $\gamma$  59  
 interleukin (IL)-4 59  
 internalization, nonviral vector 631–637  
 interpolyelectrolyte complex formation 550  
 intestine  
 – drug delivery 195  
 – special pharmacology 202  
 intracellular delivery, protein 282–283  
 introduction 51–52  
 invasion, host cell 217–218  
 invasive delivery systems 225  
 ionic hydrogels, drug delivery applications 510  
 iron chelators  
 – AD 662–664  
 – bioavailability 678  
 – functional groups 676  
 – transport 661  
 iron evaluation, AD brain sections 677–678  
 iron ions, reaction with chelators 670–671  
 iron oxide nanoparticles  
 – metabolism 56–60  
 – MRI applications 51–84  
 – pharmacology 56–60  
 – physicochemical characteristics 53–55  
 iron removal 673  
 iron–MAPHP complexes 680–682  
 irritation, ATRA 320–322  
 ischemia-associated inflammation, stroke 68  
 isolated mitochondria, PEI effect 634–636

**j**

Jurkat T cells 632–633

**k**

keratinocytes, dermatology 326–327  
 kidney imaging, iron oxide nanoparticles MRI 71  
 Kupffer cells  
 – liver diseases 63  
 – mononuclear phagocyte system 204

**l**

L1, chemical structure 662  
 labeling, polymeric nanoparticles 388–391  
 lability, ATRA 317–318  
 latex  
 – fine particle coating 260  
 – thermosensitive drug-releasing 262  
 lecithin  
 – core–shell nanoparticles 149  
 – lipid core 152  
*Legionella pneumophila* 214  
*Leishmania donovani* 423  
*Leishmania infantum* 424  
 leishmaniasis, macrophage-related diseases 423–425  
 length, CNTs 123  
 lesion-associated chelatable iron 678  
 LFMPs *see* liquid formulation holding microparticulate system  
 ligand–receptor binding, bacteria 212  
 ligands, surface functionalization 360  
 linking, covalent 370–374  
 lipid core, core–shell nanoparticles 146–147  
 lipid nanoparticles, drug delivery 471–508  
 lipids, cell damage 638  
 lipofectins, gene transfer vectors 629  
 liposomal system, drug delivery 144  
 liposomes, macrophage targeting 229  
 liquid core, core–shell nanoparticles 145–155  
 liquid formulation holding microparticulate system (LFMPs) 276  
*Listeria* 211  
 liver diseases, iron oxide nanoparticles MRI 63  
 liver imaging 63  
 LMWH *see* low molecular-weight heparin  
 loading, drug delivery 476  
 localised SPR biosensor 16  
 low-molecular-weight compounds, drug delivery applications 541–542  
 low molecular-weight heparin (LMWH), silastic compounds 276  
 low-soluble drugs 488–489  
 luciferase gene, HVJ-E Vector 610  
 luminescent glyconanospheres, quantum dots 391

- luminescent lanthanide complexes,  
immunoassay 39
- lymph node metastases 65
- iron oxide nanoparticles MRI 64–65
- lymphoid tissues, drug delivery 411
- lysines 567
- reactives 562
- lysozyme
- core-shell nanoparticles 163–165
  - release pattern 165
- m**
- M cells, targeted drug delivery 211
- macromolecular structures, drug delivery applications 520–522
- macromolecules, biological 359
- macrophage-related diseases, drug delivery 423–426
- macrophages
- drug delivery 228–229
  - interaction with SPIOs 58
  - SPIOs 56
- MAEHP *see* 2-methyl-N-(2'-aminoethyl)-3-hydroxyl-4-pyridinone
- magnetic diagnostics 28–30
- magnetic fields, therapeutic applications 387
- magnetic nanoparticles 393–395
- gene therapy 615–619
- magnetic nanoshells, drug delivery applications 548–549
- magnetic resonance imaging (MRI)
- acute cardiac transplant rejection 72
  - arthritis 70
  - clinical uses 61–74
  - contrast agents 392
  - embolotherapy 73–74
  - infections 70
  - iron oxide nanoparticles mri 51–84
  - kidney imaging 71
  - liver diseases 63
  - lymph node metastases 64–65
  - multiple sclerosis 69
  - nanoparticle vectorization 60
  - patient diagnostics 4
  - spleen diseases 63
  - stroke 68
- magnetization at saturation (MS), SPIOs 54
- magnetofection 31
- HVJ-E Vector 618
- magneto-resistive arrays, biosensors 32
- main biodegradable synthetic polymers, chemical structure 350
- MALDI *see* matrix-assisted laser desorption and ionization
- maleic anhydride, surface modification 369
- MALT *see* mucosal-associated lymphoid tissues
- mannose, recognition mechanisms 361
- MAPHP *see* 3O-aminopropyl-3-hydroxyl-4-pyridinone
- conjugation with nanosphere or microsphere particles 672–675
  - iron complexes 680–682
  - reaction with ferric iron 675
- mass spectroscopy
- nanotechnology-enhanced diagnostic tools 36–37
  - surface plasmon resonance 37
- material assembly, proteins 26
- materials, drug delivery 255–309
- matrix-assisted laser desorption and ionization (MALDI), enhancement tools 36
- mechanical diagnostics 30–33
- melanoma, gene therapy 609–610
- melanoma-associated antigen (MAA), gene therapy 609–610
- melt-adsorption method, silastic compounds 273
- membrane, cell 207–208
- membrane damage 629–643
- nonviral vector 632–633
- membrane transport, functionalized CNTs 285
- MEMS *see* microelectromechanical system
- metabolism, SPIOs 56–60
- metal chelator complexes, transport 661
- metal complexation 679
- metal film deposition, biosensor 101
- metal levels, AD 661
- metallic core, core-shell nanoparticles 174–180
- metallic nanoshells, drug delivery applications 528–531
- metallic SWNTs 93
- metastable crystalline forms, stability 291
- metastases, lymph node 64–65
- methotrexate (MTX), CNT 114
- 2-methyl-3-hydroxy-1-( $\beta$ -D-ribofuranosyl)-4-pyridinone 669–670
- 2-methyl-N-(2'-aminoethyl)-3-hydroxyl-4-pyridinone 666
- 2-methyl-N-(2O-hydroxyethoxy)methyl-3-hydroxyl-4-pyridinone 666–669
- MHEMHP *see* 2-methyl-N-(2O-hydroxyethoxy)methyl-3-hydroxyl-4-pyridinone
- MHRFP *see* 2-methyl-3-hydroxy-1-( $\beta$ -D-ribofuranosyl)-4-pyridinone

- MHRPP *see* 2-methyl-3-hydroxy-1-( $\beta$ -D-ribofuranosyl)-4-pyridinone  
 – chemical structure 670
- micro/nanoscale devices, drug delivery applications 520
- microactuator, biosensors 521
- microcapsules  
 – coating 261  
 – drug delivery 261–262  
 – permeability test 387
- microchannels, biosensors 517
- microcrystal encapsulation, drug delivery 542
- microelectromechanical system (MEMS) sensor platforms, actuation detection 512
- microfluidics device, valves 519
- micronized dexamethasone drug particles, monodispersion 548
- microorganism strategies, barrier penetration 210
- microparticle coating, drug delivery materials 263
- microsphere particles, conjugation with MAPHP and DFO 672–675
- microspheres  
 – calcium silicate-based 279  
 – optical glucose sensors 515
- Mie theory, quantum dots 15
- miniemulsion  
 – polymerization 357  
 – surface functionalization 369
- mitochondria, isolated 634–636
- mitochondrially mediated apoptosis 637
- modified chelators, complexing to iron 676
- molecular imaging, core–shell nanoparticles 143–188
- molecular markers expression, mouse tissue 328
- monitoring  
 – *in vivo* 72  
 – real-time 40
- monoclonal antibodies  
 – invasive delivery systems 227  
 – surface modification 28
- monodispersion, drug delivery 548
- monomers, *in situ* polymerization 492
- mononuclear phagocytic system (MPS) 204–205  
 – macrophages 411
- monosaccharides, surface functionalization 360
- mortality, CNT 126
- motifs, CpG 107–109
- mouse skin, growth factor expression 325
- mouse tissue, NANOEGG™ treatment 325–331
- MPB-PE *see* 1,2-dioleoyl-*sn*-glycero-3-phosphoethanolamine-N-[4-(*p*-maleimidophenyl)butyramide]
- MPS *see* mononuclear phagocyte system
- MRI *see* magnetic resonance imaging
- MRI-detectable embolotherapy 73–74
- mRNA, expression 325
- MS *see* magnetization at saturation
- MTX *see* methotrexate
- mucosal-associated lymphoid tissues (MALT) 411
- mucosal epithelium  
 – gastrointestinal tract 202–203  
 – respiratory tract 202
- mucosal routes, drug delivery 496–497
- mucus, delivery routes 412
- multifunctional BNP hybrid 587
- multifunctional dendrimer, patient diagnostics 40
- multimetal ions, AD 662–664
- multiple functional groups 561
- multiple sclerosis 70  
 – iron oxide nanoparticles MRI 69
- multiplexed diagnostic assays, patient diagnostics 40
- multistep titration 379
- multiwalled carbon nanotubes (MWNT) 21
- Mycobacterium tuberculosis* 214  
 – tuberculosis 431
- n**
- NAA *see* non-natural amino acids
- nano-organized shells, drug delivery applications 550
- nanocantilever, biosensors 31
- nanocapsules, synthesis 358
- NANOEGG™ 334  
 – chronic inflammatory diseases 320  
 – drugs 338  
 – epidermis 318  
 – hyperpigmentation 319  
 – indications 335–337  
 – pharmacological effects 323–324  
 – preparation 314–316  
 – solubility 334
- NANOEGG™ technology 310–341  
 – all-*trans* retinoic acid (ATRA) 317–318
- NANOEGG™ treatment  
 – animal skin 330  
 – human skin 321
- nanoelectrode, CNTs 102
- nanoelectrode arrays (NEA), CNT 97

- nanoelectrode biosensors, diagnostics 102–104
- nanoelectrode ensemble (NEE) 103
- CNT 97
- nanomaterials for enhanced electron transfer, electrical diagnostics 20–24
- nanomedicine 530–531
- nanoparticles
- barrier crossing 645–651
- chitosan 263
- core–shell 143–188
- delivery 657–660
- drug delivery systems 648–649
- inorganic 265–266
- MRI applications 51–84
- optical diagnostics 14–17
- PLGA 157–173
- recovery 476–477
- targeting 652–682
- transport technology 665
- vectorization 60
- nanopore, DNA 38
- nanoporous materials
- drug delivery 270–286
- silastic 271–277
- silica 278–279
- nanoprecipitation, polymeric nanomaterials 356
- nanoscale devices, drug delivery applications 520
- nanoscale sensing 509–526
- nanoshells
- barrier properties 539
- drug delivery 527–556
- E-LbL assembled 540
- magnetic 548–549
- optical diagnostics 14–17
- synthesis 528–529
- nanosphere particles, conjugation with MAPHP and DFO 672–675
- nanospheres, synthesis 354
- nanotechnology
- electrical diagnostics 19–28
- future of patient diagnostics 40–43
- imaging diagnostics 33–34
- magnetic diagnostics 28–30
- nanotechnology-enhanced diagnostic tools 34–39
- optical diagnostics 9–19
- patient diagnostics 2–8
- targeted drug delivery 189–254
- nanotoxicology 629–643
- nanowindows, CNH 286
- nasal, drug delivery 413
- native bacterial flora, targeted drug delivery 210
- natural polymers, nanomaterials 346–348
- NEA *see* nanoelectrode arrays
- NEE *see* nanoelectrode ensembles
- neoplasm, uterine 73
- NMRD *see* nuclear magnetic relaxation dispersion
- non-natural amino acids (NAA) substitutions 576
- noncancer applications, drug delivery 409–414
- noncovalent functionalization, CNTs 86
- noncovalent interaction, surface modification 363
- nondegradable synthetic polymers, nanomaterials 352
- noninvasive delivery systems 223
- nonplanar conjugated molecules, CNT functionalization 92
- nonspecific uptake, gene therapy 599
- nonstealth liposomes, macrophage targeting 229
- nonsteroidal anti-inflammatory drugs, delivery routes 421
- nonviral vector, PEI 630
- noradrenaline receptors, synthetic 9
- nuclear magnetic relaxation dispersion (NMRD) 53
- nuclear targeting, gene therapy 601
- nucleic acid sensors, CNT 104
- nucleic acids
- amplification 37
- electrochemical detection 23
- nucleophilic carbene, SWNT functionalization 94
- nucleoside reverse transcriptase inhibitors, HIV treatment 435
- nylon membrane, surface modification 28
- o**
- OAT *see* optoacoustic tomography
- OCT *see* optical coherence tomography
- ocular bioavailability, delivery routes 420
- ocular delivery 415–423
- future prospects 422
- ODN CpG complexation 108
- oily drugs, solidifying 271–274
- oligodeoxynucleotides (ODN), CNT 107
- oligosaccharides, surface functionalization 360
- OMP *see* oral magnetic particles
- ophthalmic formulations, polymeric nanoparticles 382

- optical coherence tomography (OCT), patient diagnostics 4
- optical detection, sensors 513–516
- optical diagnostics
- fiber optic biosensors 18–19
  - fluorescence 9–10
  - nanoparticles/-shells 14–17
  - quantum dots 11–13
  - SPR 14–17
- optical fiber distal tip, surface modification 20
- optical glucose sensors 515
- optically addressable delivery systems, therapeutic applications 386
- optoacoustic tomography (OAT), patient diagnostics 5
- oral administration, hypoglycaemic effect 453
- oral delivery 412
- carbon nanotubes 280
  - chitosan 448
  - CNTs 280
  - noninvasive systems 224
  - osmotic 224
  - protein drug 280–281
- oral magnetic particles (OMP) 62
- oxidative stress, drug delivery 653–656
- p**
- $\pi$ - $\pi$  stacking interactions, CNTs 86–87
- PACA *see* poly(alkylcyanoacrylate)
- paclitaxel, release pattern 151
- paclitaxel-loaded lipid core, core-shell nanoparticles 148–150
- paclitaxel porous particles 279
- parasitic infections, drug delivery 426
- particle conjugation, iron chelators 676
- particle size
- distributions 680
  - hydrodynamic 54–55
  - SLNs 480
- particles, solid dispersion 288–294
- passive diffusion, drug delivery 194
- PAT *see* photoacoustic tomography
- pathogenesis, prions 222
- pathology
- AIDS 434
  - tuberculosis 431
- patient diagnostics 3
- future developments 40–43
  - introduction 1
  - nanotechnology 2–8
- pattern recognition receptors, CNT 108
- PCL nanospheres, charged 427
- PCR *see* polymerase chain reaction
- pDNA *see* plasmid DNA
- PDP-PE *see* 1,2-dioleoyl-*sn*-glycero-3-phosphoethanolamine-*N*-[3-(2-pyridylidithio)propionate]
- peak time, drug delivery 196
- PEBBLE nanosensor, biosensors 17
- PEBBLEs *see* probes encapsulated by biologically localized embedding
- PEG *see* poly(ethylene glycol)
- PEI *see* poly(ethyleneimine)
- D-penicillamine, conjugation reactions 657
- PEO *see* poly(ethylene oxide)
- peptide antigens, *f*-CNT-attached 109–110
- peptide coating, CNT 89
- peptide delivery 486–487
- peptide insertions, heterologous 571–575
- peptide nucleic acid (PNA), CNT functionalization 91
- permeability
- high-molecular-weight compounds 543–544
  - low-molecular-weight compounds 541–542
- PET *see* positron emission tomography
- Peyer's patches, delivery routes 412
- pharmaceutical ingredients, controlled release 540
- pharmacokinetics, SPIOs 59
- pharmacology
- SPIOs 56–60
  - targeted drug delivery 192–208
- PHEMA *see* PMMA-*b*-polyhydroxyethyl methacrylate
- phospholipid (PL), CNT 89
- phospholipid/polydiacetylene membrane, synthetic receptors 10
- photoacoustic tomography (PAT), patient diagnostics 5
- photoaging, NANOEGG™ 331
- physicochemical characteristics, SPIOs 53–55
- physicochemical techniques, surface modification 376
- PIHCA *see* poly(isohexyl cyanoacrylate)
- PL *see* phospholipid
- plant-based antigen 584
- plaque, atheromatous 67
- plasma glucose levels 456
- plasma membrane damage, nonviral vector 632–633
- plasmid DNA (pDNA), gene therapy 116
- plasminogen, targeting 230
- platforms, multifunctional 40
- PLGA (poly(lactic-*co*-glycolic acid)) nanoparticles

- HA-functionalized 157–165
- heparin-functionalized 166–173
- preparation 158
- Pluronic (F-127), core–shell nanoparticles 158
- PMMA *see* poly-methyl methacrylate
- PMMA-b-polyhydroxyethyl methacrylate (PHEMA), CNT functionalization 91
- PMP complex, biosensors 25
- PNA *see* peptide nucleic acid
- PnBEMA *see* poly-n-butyl methacrylate
- point-of-care diagnostics 41–42
- poly-methyl methacrylate (PMMA), CNT functionalization 91
- poly-n-butyl methacrylate (PnBMA), CNT functionalization 91
- poly(alkylcyanoacrylate) (PACA), synthetic polymers 352
- polyanions, E-LbL nanoshells 534
- polycations
  - cell damage 638
  - cytotoxicity 639
  - E-LbL nanoshells 534
  - mitochondrially mediated apoptosis 637
- poly(EA–MMA–HEMA), chemical structure 259
- polyelectrolyte microcapsules, drug delivery 541
- polyelectrolyte multilayer capsule 386
- poly(ethylene glycol) (PEG), CNT 89
- polyethylene oxide (PEO)
  - core–shell nanoparticles 156
  - nanomaterials 352–353
- poly(ethyleneimine) (PEI)
  - cell dysfunction 631–637
  - DNA complexes 630–631
  - gene therapy 117
  - isolated mitochondria 634–636
  - membrane damage 629–643
  - nonviral vector 630
- polyfectins
  - gene transfer vectors 629
  - membrane damage 629–643
- polyguanylic acid-functionalized polymer nanocontainers 231
- polyion E-LbL self-assembly 532–551
- polyion films 538
- poly(isohexyl cyanoacrylate) (PIHCA), Leishmaniasis 423
- poly(lactic-co-glycolic acid) *see* PLGA
- polymer conjugation, CNT 87
- polymer materials 345–353
- polymer nanocontainers, functionalized 231
- polymerase chain reaction (PCR)
  - CNT 104
  - patient diagnostics 3
- polymeric core, core–shell nanoparticles 156–173
- polymeric micelles 267
- polymeric nanomaterials 342–408
  - aqueous 257–258
  - surface functionalization 359–379
- polymeric nanoparticles 409–470
  - characterization 494
  - drug delivery 471–508, 648–649
  - drug delivery materials 267
  - film formation 258
  - fluorescence labeling 388–391
  - pharmaceutical applications 495
  - preparation 354–358
- polymeric shell composition, drug delivery 148
- polymerization, *in situ* 357
- polymers
  - biocompatible 613–614
  - degradable 349–351
  - natural 346–348
  - nondegradable 352
  - preformed 354
  - viral particle-modified 586
- polymorphism, SLNs 481
- poly(propylene oxide) (PPO), core–shell nanoparticles 157
- polysaccharides
  - coating 263
  - natural polymers 346
- polysorbate-80-coated AZT nanoparticles 436
- polystyrene core, surface modification 370
- poorly absorbable drugs, drug delivery 275–277
- pore size effect, solid dispersion particles 289
- porous silastic materials, drug delivery 287–309
- porous silica, drug delivery 288–294
- porous silicon (pSi), drug delivery 279
- positron emission tomography (PET), patient diagnostics 4
- potential, immunogenic 109–110
- potentially therapeutic agents, drug delivery 652
- potentiation, CpG immunostimulatory activity 107–109
- PPO *see* poly(propylene oxide)
- praziquantel encapsulation efficiency, parasitic infections 427
- preformed nanoparticles
  - covalent linking 370–374
  - surface functionalization 364–365



- preformed polymers 354
- preparation techniques
  - polymeric nanoparticles 492
  - SLNs 474
- presentation, *f*-CNT-attached peptide antigens 109–110
- prevention, cancer 611–612
- prions, natural strategies 221–222
- pro-inflammatory cytokine IL-8, cytotoxicity 125
- proangiogenic growth factors, protein delivery 495
- probes encapsulated by biologically localized embedding (PEBBLEs), patient diagnostics 6
- production processes, SLNs 474
- proliferation, keratinocytes 326–327
- protective barriers, E-LbL assembled nanoshells 545–547
- protective envelope, viruses 218
- protein, intracellular delivery 282–283
- protein absorption patterns, chelator–particle systems 675
- protein delivery 486–487
  - mucosal routes 496–497
  - polymeric nanoparticles 495
- protein drug, delivery 280–281
- protein expression systems 576
- protein-loaded core–shell nanoparticles, formation 152
- protein loading process, core–shell nanoparticles 160
- protein transduction domain (PTD) 373
- proteinaceous infectious particle, prions 221
- proving, nanoshells 535–537
- pSi *see* porous silicon
- PTD *see* protein transduction domain
- pulmonary, drug delivery 413
- pulmonary toxicity, SWCNT 125
- purity, CNTs 119–122
- PVP-coated iron oxide 175–180
- pyelography 62
  
- q**
- QCM electrodes 536
- quantum dot core, size distribution 13
- quantum dots, optical diagnostics 11–13
- quantum yield, fluorescent 582
  
- r**
- radioimmunoassay (RIA), patient diagnostics 3
- radiolabeled nanoparticles 396
- Raman spectroscopy, nanotechnology-enhanced diagnostic tools 35–36
- rat liver mitochondria, polycation effect 635–636
- reaching target cells, gene therapy 599
- reaction enhancement 25
- reactive oxygen species (ROS) 653–656
- real-time monitoring, patient diagnostics 40
- receptor-mediated endocytosis 205
- receptor-specific nanocarrier, construction 234
- receptors, synthetic 10
- recognition
  - gene therapy 599
  - mechanisms 360
- rejection, cardiac transplant 72
- related structures, SLNs 478–479
- relaxation rates, SPIOs 53
- relaxivity measurements, SPIOs 56
- release, triggered 384–387
- removal, multimetal ions 662–664
- repaglinide, silica materials 278
- RES *see* reticuloendothelial system
- resistance, gene therapy 600
- respiratory tract, mucosal epithelium 202
- retention, gene therapy 602
- reticuloendothelial system (RES)
  - inorganic nanoparticles 265
  - special pharmacology 204
- retrovirus-based gene therapy 219
- reverse transcriptase, gene therapy 220
- RIA *see* radioimmunoassay
- risks, patient diagnostics 42–43
- RNA (ribonucleic acid), delivery and expression 116–117
- ROS *see* reactive oxygen species (ROS)
- routes of administration 380–381
- routes of tissue, drug delivery 410
- ruthenium–polypyridyl complex, biosensors 23
  
- s**
- S. pyogenes* 215
- Salmonella* 211
- salting-out, polymeric nanomaterials 355
- SAW *see* surface acoustic waves
- SAXS *see* small-angle X-ray scattering
- scaling-up, SLNs 475
- scavenger receptor a1, drug delivery 231
- SCK polymer assemblies, biosensors 522
- second-generation nanoparticles 343
- SELDI *see* surface-enhanced laser desorption and ionization
- selective modifications, BNPs 560–566

- self-aggregation, ATRA 312
- self-assembly, E-LbL 532–551
- semiconducting nanotubes 97
- sensing, nanoscale 509–526
- sensors
  - drug delivery applications 511–518
  - hydrogel based 512
- SERS *see* surface-enhanced Raman spectroscopy
- shells, nano-organized 550
- Shigella* 211
- sidewall functionalization, CNTs 91–95
- signal suppression 62
- silastic compounds, drug delivery 271
- silastic materials, drug delivery 271–274
- silica, drug delivery 295–309
- silica materials, drug delivery 278–279
- simultaneous gene transfer, cancer 611–612
- single nucleotide polymorphism (SNP)
  - analysis, patient diagnostics 3
- single-strand binding (SSB) protein, CNT 104
- single walled carbon nanohorns (SWCH), drug delivery 114
- skin, NANOEGG™ treatment 330
- skin epithelium, targeted drug delivery 201
- SLN *see* solid lipid nanoparticles
- small-angle X-ray scattering (SAXS), NANOEGG™ 317
- small intestine epithelium 203
- SNP *see* single nucleotide polymorphism
- SODAS *see* spheroidal oral drug absorption system
- solid dispersion particles, drug delivery 288–294
- solid lipid nanoparticles (SLN) 472–490
  - analytical characterization 480–491
  - drug delivery 471–508
- solidifying oily drugs, drug delivery 271–274
- solvents, CNTs 123
- source–drain current, biosensor 99
- specific complex formation, surface modification 363
- specific target tissues, gene therapy 599
- spectroscopy
  - mass 36–37
  - Raman 35–36
- spheroidal oral drug absorption system (SODAS), oral delivery 224
- spinel, SPIOs 52
- SPIOs *see* superparamagnetic iron oxides
- spirometry, patient diagnostics 5
- spleen diseases, iron oxide nanoparticles MRI 63
- spongiform encephalopathies, prions 221
- spots, NANOEGG™ treatment 331–333
- SPR *see* surface plasmon resonance
- SSB *see* single-strand binding
- stability, SLNs 478–479
- stabilization, diffusion barrier 550
- stabilizers, surface functionalization 366–368
- stable retention, gene therapy 602
- stealth nanoparticles 57
- stem cells, cell therapy monitoring 72–73
- sterilization, SLNs 475
- stratum corneum, special pharmacology 201
- Streptococcus mutans* 211
- stress, oxidative 653–656
- stroke, iron oxide nanoparticles MRI 68
- structures, colloidal 481
- subcutaneous, drug delivery 414
- sulfo-*N*-hydroxysuccinimide 679
- superparamagnetic iron oxide nanoparticles (SPIOs) 56
  - clinical uses 61–74
  - interaction with macrophages 58
  - metabolism 56–60
  - MRI applications 51–84
  - nanoparticle vectorization 60
  - pharmacokinetics 59
  - pharmacology 56–60
  - physicochemical characteristics 53–55
- surface, CNTs 123
- surface acoustic waves (SAWs), patient diagnostics 6
- surface-enhanced laser desorption and ionization (SELDI), enhancement tools 36
- surface-enhanced Raman spectroscopy (SERS) 36
  - patient diagnostics 6
- surface functionalization
  - formation of complexes 362
  - polymeric nanomaterials 359–379
- surface modification
  - analytical techniques 375
  - covalent linking 363
  - strategies 363
- surface modifiers 366–368
- surface plasmon resonance (SPR), optical diagnostics 14–17
- surfactants
  - CNT 88
  - surface functionalization 366–368
- SWCH *see* single walled carbon nanohorns
- SWNT functionalization, diazonium compounds 93
- synthesis
  - nanoshells 528–529
  - polymeric nanomaterials 345–353

- synthetic gene transfer vectors, nanotoxicology 629–643
  - synthetic polymers
    - chemical structure 350
    - degradable 349–351
    - nondegradable 352
  - systemic circulation, gene therapy 600
- t**
- T-staging, uterine neoplasms 73
  - target cells, gene therapy 599
  - target specificity, drug delivery 190
  - target tissues, gene therapy 599
  - targeted drug delivery 189–254
    - absorption 193–195
    - artificial strategies 223–232
    - bioavailability 196
    - brain 226–227
    - distribution 197
    - elimination 198–200
    - macrophage targeting 228–229
    - pharmacology 192–208
    - strategies observed in nature 209–222
  - targeting transport, AD 652–682
  - TAT *see* transactivating transcriptional activator peptide
  - TAT toxoid, HIV treatment 439
  - TEM *see* transmission electron microscopy
  - temperature-responsive hydrogels, drug delivery applications 510
  - terpolymer nanoparticles, drug delivery materials 259
  - TERS *see* tip-enhanced Raman spectroscopy
  - tert*-butyloxycarbonyl (Boc), CNT functionalization 95
  - therapeutic agents, targeting transport 652–682
  - therapeutic applications, drug delivery systems 382–383
  - therapy
    - BNPs 577–583
    - drug delivery materials 264–269
    - genetic 597–628
    - polymeric nanomaterials 342–408
  - thermosensitive drug-releasing microcapsules 261–262
  - thin film, core–shell nanoparticles 149
  - thioflavin-(TfT) 653–654
  - tip-enhanced Raman spectroscopy (TERS) 36
    - patient diagnostics 6
  - tissue, drug delivery 410
  - TMV CP, ribbon diagram 574
  - tolerability, ocular delivery 422
  - Toll-like receptors (TLR), mononuclear phagocyte system 205
  - tonometry, patient diagnostics 5
  - tools, nanotechnology-enhanced 34–39
  - topical administration, SLNs 490
  - toxicity, CNTs 284
  - transactivating transcriptional activator peptide (TAT), targeting 232
  - transcription, gene therapy 603
  - transcription factors 603
  - transdermal administration, SLNs 490
  - transdermal delivery systems, noninvasive 224
  - transdermal drug delivery 414
  - transepithelial passage, targeted drug delivery 212
  - transfection
    - DCs 609–610
    - HVJ-E Vector 610
  - transgenes, stable retention 602
  - transmembrane transport 208
  - transmission electron microscopy (TEM) 396
  - transmucosal delivery systems, noninvasive 225
  - transplant rejection, cardiac 72
  - transport, therapeutic agents 652–682
  - treatment
    - AD 644–683
    - AIDS 434
    - antifungal 427
    - cancer 611–612
    - diabetes 451
    - tuberculosis 431–433
  - triggered release, drug delivery systems 384–387
  - Trypanosoma vaginalis*, parasitic infections 426
  - Trypanosome cruzi* 425
  - tuberculosis, drug delivery 431
  - tubular secretion, drug delivery 200
  - tumor
    - cerebral 68
    - imaging 67
    - *see also* cancer
  - tumor cells, gene therapy 611–612
  - tyrosine modification, BNPs 569
- u**
- ultrasmall superparamagnetic iron oxides (USPIOs) 56
    - atheromatous plaque 67
    - clinical uses 68–71
    - functionalized 61

- intracellular localization 57
- unloaded nanoparticles 428
- unspecific immune system, bacteria 213
- uptake
  - drug delivery 410–411
  - nonspecific 599
- USPIOs *see* ultrasmall superparamagnetic iron oxides
- uterine neoplasm, T-staging 73
- UV radiation, NANOEGG™ 330

**v**

- vaccines
  - adjuvants 498–499
  - AIDS 439–440
  - antigens 107
  - carriers 559
  - development 584
  - drug delivery 441
- valves, microfluidics device 519
- vascular endothelial growth factor (VEGF), core-shell nanoparticles 152
- vascular leakage, endothelial cells 206
- vectorization, nanoparticle 60
- vectors
  - CNT-based 85–142
  - HVJ-E 609–614
  - nonviral 630
  - synthetic gene transfer 629–643
  - viral 219–220

- very small superparamagnetic iron oxide particles (VSOP) 57
- viral surface 216
- viral vectors, therapeutic applications 219–220
- virosome synthesis 221
- viruses, natural strategies 215
- vitamin E, efficacy improvement 656

**w**

- water-soluble CNT, cytotoxicity 124
- wettability, solid dispersion particles 294
- wrinkle improvements, NANOEGG™ treatment 330
- wrinkles, NANOEGG™ treatment 331–334

**x**

- X-ray diffraction (XRD), SPIOs 53
- X-ray photoelectric spectroscopy (XPS), core-shell nanoparticles 179

**y**

- Yersinia* 211–212

**z**

- ζ potential
  - core-shell nanoparticles 154
  - SLNs 481
- ζ potential changes, drug delivery 537
- zalcitabine, HIV treatment 435

